

Maintenance, Safety, Risk, Management and Life-Cycle Performance of Bridges

Editors

Nigel Powers, Dan M. Frangopol, Riadh Al-Mahaidi & Colin Caprani

International Association for Bridge Maintenance and Safety

CRC Press
Taylor & Francis Group
A BALKEMA BOOK

MAINTENANCE, SAFETY, RISK, MANAGEMENT
AND LIFE-CYCLE PERFORMANCE OF BRIDGES



Taylor & Francis
Taylor & Francis Group
http://taylorandfrancis.com

PROCEEDINGS OF THE NINTH INTERNATIONAL CONFERENCE ON BRIDGE MAINTENANCE, SAFETY AND MANAGEMENT (IABMAS 2018), MELBOURNE, AUSTRALIA, 9–13 JULY 2018

Maintenance, Safety, Risk, Management and Life-Cycle Performance of Bridges

Editors

Nigel Powers
VicRoads, Melbourne, Australia

Dan M. Frangopol
Department of Civil and Environmental Engineering, ATLSS Engineering Research Center, Lehigh University, Bethlehem, PA, USA

Riadh Al-Mahaidi
Swinburne University of Technology, Melbourne, Australia

Colin Caprani
Monash University, Melbourne, Australia

CRC Press
Taylor & Francis Group
Boca Raton London New York Leiden

CRC Press is an imprint of the
Taylor & Francis Group, an **informa** business

A BALKEMA BOOK

CRC Press/Balkema is an imprint of the Taylor & Francis Group, an informa business

© 2018 Taylor & Francis Group, London, UK

Typeset by MPS Limited, Chennai, India
Printed and bound in Great Britain by CPI Group (UK) Ltd, Croydon, CR0 4YY

All rights reserved. No part of this publication or the information contained herein may be reproduced, stored in a retrieval system, or transmitted in any form or by any means, electronic, mechanical, by photocopying, recording or otherwise, without written prior permission from the publishers.

Although all care is taken to ensure integrity and the quality of this publication and the information herein, no responsibility is assumed by the publishers nor the author for any damage to the property or persons as a result of operation or use of this publication and/or the information contained herein.

Published by: CRC Press/Balkema
Schipholweg 107C, 2316 XC Leiden, The Netherlands
e-mail: Pub.NL@taylorandfrancis.com
www.crcpress.com – www.taylorandfrancis.com

ISBN: 978-1-138-73045-8 (hardback + USB)
ISBN: 978-1-315-18939-0 (eBook PDF)

Maintenance, Safety, Risk, Management and Life-Cycle Performance of Bridges – Powers, Frangopol, Al-Mahaidi & Caprani (Eds)
© 2018 Taylor & Francis Group, London, ISBN 978-1-138-73045-8

Table of contents

Preface XXVII
Sponsors XXIX
Acknowledgements XXXI
IABMAS Executive Board XXXIII
Conference organization XXXV

T.Y. LIN LECTURE

Bridge maintenance, renovation and management – Research and development of governmental program in Japan 2
Y. Fujino

KEYNOTE LECTURES

Life-cycle reliability of bridges under independent and interacting hazards 16
M. Akiyama & D.M. Frangopol

Assessment of the dynamic behaviour of railway bridges for high-speed traffic 36
R. Calçada

A vision for vision-based technologies for bridge health monitoring 54
N. Catbas, C.Z. Dong, O. Celik & T. Khuc

The engineering and management of major steel box girder bridges; lessons from West Gate Bridge 63
I. Firth

Managing existing bridges – On the brink of an exciting future 70
R. Hajdin

Timber bridges in Australia, where to from here? 88
J.A. Hilton

Innovative and sustainable operation and maintenance of bridges 100
J.S. Jensen

Long term bridge performance program status and preliminary results 112
B.V. Johnson, J.E. Purdy & D.H. Liu

Value of monitoring data for long-span bridge operation – Aerodynamic point of view 130
H.K. Kim, S.J. Kim, S. Kim & W.H. Jung

Design concept of the Twin River Bridges in Chongqing 141
M.C. Tang

MINI-SYMPOSIA

MS01: Innovations and world leading research and practice in bridge management systems

Organizers: N. Powers & S. Joshi

Experience of management of bridges prior to and post evaluation of BMS on NH network of India 149
S. Joshi, N. Naga & U. Rajesh

BIM related workflow for an image-based deformation monitoring of bridges 157
N. Hallermann, J. Taraben & G. Morgenthal

Utilizing BMS to develop programs and reports for PEI transportation 165
D.J. Evans & R.M. Ellis

Creating the basis for implementing BIMS in existing infrastructure components 172
J.S. Jensen & F.R. Gottfredsen

Creation of "live data" for existing infrastructure 179
F.R. Gottfredsen & H. Pedersen

A simulated maintenance costing using a Markov deterioration model for bridge components 187
H.D. Tran, S. Setunge, Y.C. Koay & H. Luczak

Maintenance cost evaluation based on bridge performance degradation model 194
S.H. Kim, W.H. Heo, J.G. Choi & M. Gombosuren

An integrated model-based bridge management system 198
S.T. Hou, G. Wu & H.L. Li

Indian Bridge Management System – Overview and way forward 205
S. Joshi & S.S. Raju

Bridge management implemented by the South African National Roads Agency 206
E.J. Kruger & A.A. Nyokana

The optimal maintenance strategy of bridge using Bayesian approach 214
J.H. Lee, K.Y. Lee, S.M. Ahn & J.S. Kong

Development and implementation of digital bridge management systems in the Gulf region 219
D.E. Moore & S. Naelini

Research on bridge management system based on BIM technology 226
Y.D. Qin & R.C. Xiao

Bridge maintenance strategies – A brief comparison among different countries around the world 231
M.C. Scutaru, C.C. Comisu, G. Boacă & N. Ţăranu

The development of a modern bridge asset management system 239
A. Sonnenberg

Risk assessment for bridge management systems 246
P.D. Thompson

What are the attributes of a superior bridge management system? 254
H.D. Tran, S. Setunge, Y.C. Koay & H. Luczak

Using Petri-Net modelling for a data-driven approach to bridge management and safety 262
P.C. Yianni, L.C. Neves, D. Rama, J.D. Andrews & R. Dean

Network importance of Melbourne's metropolitan bridges – Development of a strategic bridge prioritisation framework 270
S. Di Cicco

MS02: Innovative methods in strengthening of concrete bridges

Organizers: R. Kalfat, R. Al-Mahaidi & B. Pham

Experimental investigation into the fatigue life of patch anchors used to anchor FRP laminates bonded to concrete 279
A. Al-Saoudi, R. Al-Mahaidi & R. Kalfat

Mathematical analysis of an innovative method for strengthening concrete beams using pre-stressed FRP laminates 285
S.R. Atashipour, J. Yang, R. Haghani & M. Al-Emrani

Bond performance of FRP-strengthened reinforced concrete in aggressive environmental conditions 294
R.J. Gravina, J. Li, H. Aydin, S. Setunge, P. Visintin, S.T. Smith & R. Al-Mahaidi

Developments in external post tensioning strengthening – An update of latest innovations and applications 302
D. Cecan & P.Y. Souesme

S-N curves for RC beams strengthened with FRP 310
L.C. Meneghetti, M.R. Garcez & R.M. Teixeira

UHPFRC technology to enhance the performance of existing concrete bridges 318
E. Brühwiler

Strengthening of concrete bridges girders using FRP and patch anchors 325
R. Jumaah, R. Kalfat & R. Al-Mahaidi

FRP strengthening of concrete structures using AS5100-2017 332
H.B. Pham

Flexural FRP strengthening of concrete bridges using an innovative concept 339
J. Yang, R. Haghani & M. Al-Emrani

CFRP strengthening of ASR affected concrete piers of railway bridges 346
M. Lima, R. Salamy & D. Miller

Feasibility of reinforcement in Brazilian concrete highway bridges using carbon fiber-reinforced polymer 354
A. Medeiros, W. Mazer, C.E. Rossigali & T.N. Bittencourt

Influence of arch bridge skewness 358
A. Outtier, E. Van Puymbroeck & H. De Backer

Ensuring safety and assessment of life-cycle costs using SHM for concrete bridges 365
J. Creighton, S.N. Kazi & K. Islami

MS03: Developments and trends in composite steel-concrete structures

Organizers: S.H. Kim, K.F. Chung & G. Ranzi

Push-out test on shear behavior of joint structure between corrugated steel web and concrete lower slab 374
S. Wang, Y. Liu, J. He & C. Li

Effect of rebar strength in Y-type perfobond rib shear connectors 381
S.H. Kim, O. Han, K.S. Kim, S.J. Kim & J.Y. Shin

Energy dissipating characteristics of Y-type perfobond rib shear connectors 386
S.H. Kim, K.S. Kim, O. Han & J.G. Choi

Strengthening of steel girder flanges with concrete-filled ribs 390
S.H. Kim, J. Shin, O. Han, K. Hwang & K.B. Rho

Redundancy evaluation of composite twin I-girder bridges in fractured condition 393
H. Lam, W. Lin, T. Yoda & K. Ono

Group effect of Y-type perfobond rib shear connectors 401
O. Altanzagas, E. Ganzorig, S.H. Kim, O. Han & T.S. Kim

Evaluation of the ultimate response of post-tensioned composite slabs 408
G. Ranzi

Service behaviour of composite steel-concrete slabs with a simplified approach and a hygro-thermo-chemical-mechanical model for the non-uniform shrinkage evaluation 412
M. Bocciarelli & G. Ranzi

Behavior of an innovative demountable steel-concrete connector under static loading 416
F. Yang & Y. Liu

A new era of steel bridge service life 424
F. Piccoli, R. Pavan & E. Siviero

Designing long integral bridges for environmental loading in South Africa 430
S.A. Skorpen, E.P. Kearsley & E.J. Kruger

Seismic performance and retrofit evaluation of hollow-core composite bridge columns 437
M.M. Abdulazeez, A. Gheni, N. Colbert & M.A. ElGawady

MS04: Strengthening, monitoring and life-cycle assessment of steel bridges

Organizers: E. Ghafoori, R. Al-Mahaidi, X.L. Zhao, M. Motavalli & M. Dawood

Fatigue improvement of welded bridge details in stainless steel using high-frequency mechanical impact treatment 446
M. Al-Emrani, P. Shams-Hakimi, C. Schneider, Z. Barsoum & H. Groth

The effect of the CFRP properties on the fatigue strengthening of steel plates in multiaxial loading 452
N.J. Aljabar, X.L. Zhao, R. Al-Mahaidi, E. Ghafoori, M. Motavalli & Y.C. Koay

Improving the fatigue design of orthotropic steel decks 458
H. De Backer, W. Nagy & A. Outtier

Flat Prestressed Unbonded Reinforcement (FPUR) system for strengthening of steel I-beams 465
A. Hosseini, E. Ghafoori, M. Motavalli, A. Nussbaumer, X.L. Zhao & R. Al-Mahaidi

Prestressed FRP-strengthening and wireless monitoring of a metallic bridge in Australia 472
E. Ghafoori, A. Hosseini, R. Al-Mahaidi, X.L. Zhao, M. Motavalli & Y.C. Koay

The peak stress method for fatigue analysis of welded details 481
G. Meneghetti, A. Campagnolo & B. Atzori

Prolonging the service life of steel truss bridges 489
A. Pipinato, R. Pavan, P. Collin, R. Hallmark, S. Ivanov, R. Geier & M. van der Burg

Steel bridge retrofit solution for movable cases 497
R. Pavan & A. Ruzzante

Steel box-girder bridge diseases identification based on computer vision system 504
D. Wang, Y. Pan & B. Peng

Bond behaviour of CFRP-steel double-lap shear joints exposed to marine atmosphere 512
Q.Q. Yu, R.X. Gao, X.L. Gu & X.L. Zhao

Drilling-hole shape for retarding the fatigue crack propagation 517
Z.Y. YuanZhou, B.H. Ji & Z.Q. Fu

Study on crack stop holes in weld of orthotropic steel bridge decks 521
Z.Q. Fu, G.Y. Sun, Y. Yao & B.H. Ji

Fatigue performance of hammer-peened diaphragm-to-rib welds in orthotropic steel decks 528
Q.D. Wang, B.H. Ji & Z.Q. Fu

Fatigue stress analysis of diaphragm-U-rib welding joints and local optimization 534
Y. Zhi, Y.X. Wang, H.B. Sun & B.H. Ji

Grouting compactness monitoring of concrete-filled steel tube arch bridge using electro-mechanical impedance technique 541
Q. Feng, Y.B. Liang & T.H. Yi

Study on soil-steel bridge response during backfilling 547
T. Maleska & D. Beben

Experimental investigation of retrofitted web-gap regions in steel bridge girders 555
M. Motaleb, M. Rahman, R. Hindi, W. Lindquist & A. Ibrahim

Investigation of live load deflection limit for steel cable stayed and suspension bridges 559
E.S. Hwang, D.Y. Kim & K.J. Park

MS05: Advancements in performance assessment, monitoring, and management of bridges under fatigue deterioration

Organizers: M. Soliman & D.M. Frangopol

Large-scale strain sensing approach for detecting fatigue cracks in steel bridges 567
X. Kong, J. Li, C. Bennett, W. Collins, S. Laflamme & H. Jo

Fatigue assessment of concrete girder bridges based on traffic information 576
P.J. Zhang, C.S. Wang, Q. Wang & L. Duan

Historical load effects on fatigue of metallic railway bridges 584
B. Imam & P.A. Salter

Multi-objective optimum service life bridge management based on fatigue damage detection 592
S. Kim & D.M. Frangopol

Probabilistic fatigue life prediction employing an advanced crack propagation model 598
Y.-J. Lee, J.H. Lee & S. Lee

Development of calibration factor for fatigue assessment 605
J.Y. Park, H.K. Kim & Y.C. Park

Fatigue assessment of deteriorated steel bridge members considering corrosion 609
Y.C. Park, L.S. An & H.K. Kim

Reliability analysis of steel bridges under propagating fatigue cracks 614
H. Ali & M. Soliman

A non-concurrent multiscale simulation of fatigue crack on orthotropic steel decks 620
B. Wang, H. De Backer & A. Chen

Numerical fracture mechanics analysis of distortion-induced fatigue in steel bridges 626
C.S. Wang, B. Cui, N.X. Ma, L. Duan & Y.Z. Wang

Fatigue life assessment of reinforced concrete bridges from monitoring data 634
P. Junges, R.C.A. Pinto & L.F. Fadel Miguel

Measurement of time-dependent corrosion of steel bridge from corrosion monitoring 642
S.-H. Jeon, J.M. You, J.-H. Ahn, K.-I. Cho & Y.S. Jeong

Structural monitoring of Eltham Rail Trestle Bridge using advanced non-destructive testing techniques 650
M. Maizuar, L. Zhang, S. Miramini & P. Mendis

Fatigue life assessment of damaged steel strands 654
Y.C. Park, S.M. Yoo, C.Y. Kim & M.S. Park

MS06: Footbridges: Advances in vibration serviceability assessment

Organizers: C. Caprani, F. Tubino, K. Van Nimmen & F. Venuti

Dynamic analysis of scissors-type of deployable pedestrian bridge under earthquake 659
Y. Chikahiro, S. Zenzai, S. Shigeru & I. Ario

A dynamic system identification of the Ha'penny footbridge 660
R. Donnelly, M. Nogal, P. Gorman & A.J. O'Connor

Parameter identification of a biodynamic walking model for human-structure interaction 668
A. Firus, J. Schneider, H. Berthold, M. Albinger & A. Seyfarth

Robust vibration serviceability assessment of footbridges for crowd walking excitation 675
K. Lievens, P. Van den Broeck, G. De Roeck & G. Lombaert

Model updating of a GFRP footbridge using Tchebichef moment descriptors 683
J.W. Ngan, C. Caprani & Y. Bai

Vibration serviceability assessment of a multi-span footbridge 691
J.W. Ngan, C. Caprani & A. de Lacy

A study of pedestrian evacuation on bridge sidewalk by simulation method 699
Z.R. Jin, X. Ruan & Y. Li

Uncertainty propagation in serviceability assessment of footbridges 706
F. Tubino, L. Pagnini & G. Piccardo

Vision-based methodology for characterizing the flow of a high-density crowd 713
J. Van Hauwermeiren, P. Van den Broeck, K. Van Nimmen & M. Vergauwen

Using full-scale observations to estimate the parameters governing human-structure interaction 721
K. Van Nimmen, P. Van den Broeck & G. Lombaert

Comparison between structure- and crowd-based mitigation strategies on vibrating footbridges 728
F. Venuti & A. Reggio

Dynamic study of Yangtze River Bridge at Chongqing-Lichuan railway 736
K.J. Chen, Y.P. Zeng & S.X. Chen

FIR and IIR filtering and data driven stochastic subspace identification for the continuous dynamic modal parameter identification of cable stayed bridge 741
I. Khan, K. Malik, S. Ali & D. Shan

MS07: Recent advances in bridge design and construction

Organizers: U. Attanayake & H. Aktan

Deployable mobile bridge created from *Origami* 751
I. Ario, S. Ono, I. Tanikura, Y. Chikahiro, M. Nakazawa, P. Pawlowski, C. Graczykowski & J. Holnicki-Szulc

Rational decision-support system for selecting bridge construction alternatives 759
U.B. Attanayake & H.M. Aktan

Standardizing lateral bridge slide design 767
U.B. Attanayake & H.M. Aktan

Accelerated construction of robust bridges through material and detailing innovations 775
B. Graybeal, Z. Haber, I. De la Varga & R. Spragg

Bearing friction values for slide-in bridge construction 783
K.R. Johnson, S. Dorafshan, M.W. Halling, M. Maguire, P.J. Barr & M.P. Culmo

Dynamic effects caused by SPMT bridge transport 791
S. Dorafshan, M. Maguire, M.W. Halling, P. Barr & M.P. Culmo

Development of precast slab using ultra high strength fiber reinforced concrete for replacement on highway bridge 797
T. Kitamura, W. Zhao, I. Iwasaki, M. Kishida, Y. Ishihara & I. Iwaki

An advanced technique for the analysis of box girder bridge superstructures 805
K. Kashefi & A.H. Sheikh

Construction simulation of cable-stayed bridges 813
J.A. Lozano-Galant, D. Xu & J. Turmo

Design of pergola structures for high speed rail bridges 820
A.P. Ranasinghe & E.G. Honarvar

How new performance based contracts add value in maintenance contracts 825
J.D. van der Walt & E. Scheepbouwer

Design method for scissors-type bridges 832
Y. Hama, I. Ario & K. Adachi

MS08: Submerged floating tunnels and underwater tunnel: Design, safety and maintenance issues

Organizers: L. Martinelli, Y. Xiang & B. Faggiano

Dynamic interaction with travelling vehicles in a submerged floating tunnel 838
M.G. Mulas, L. Martinelli & G. Palamà

Maximum stresses in mooring lines during parametric excitation 845
D. Cantero & A. Rønnquist

Overview on the structural features of Submerged Floating Tunnels 851
B. Jiang, B. Liang, B. Faggiano, G. Iovane & F.M. Mazzolani

Research on the finite element analysis method of the bucket foundation of submerged floating tunnel 859
J. Xiang, X. Feng, S. Feng & J. Mao

Feasibility study on a submerged floating tunnel for the Qiongzhou Strait in China 865
B. Jiang, B. Liang, B. Faggiano, G. Iovane & F.M. Mazzolani

Research on simulation of traffic loads in submerged floating tunnel 872
B. Jiang, S. Wu, B. Liang & L. Chen

Submerged floating tunnels under seismic and seaquake loadings 877
L. Martinelli

SFTs under dynamic loads: New design issues and numerical simulation 885
F. Perotti, F. Foti, L. Martinelli & M. Tomasin

An experimental study on bending behavior of composite hollow RC in Submerged Floating Tunnel (SFT) 893
J.H. Seo, D.H. Won & W.S. Park

A novel life-cycle based management system for disaster mitigation of bridges 901
Y.C. Sung, K.C. Chang, C.C. Chen, C.C. Hsu, K.W. Chou & H.H. Hung

MS09: Vibration-based structural health monitoring of bridges: Research and applications

Organizers: M.P. Limongelli, J.R. Casas & A. Cunha

Monitoring footbridges using wireless mesh networks 909
M. Domaneschi, C. Apostoliti, G.P. Cimellaro, B. Glisic & K. Kliewer

Effectiveness damage characterization for different sensor settings: Full scale case 917
J. Grandón & F. Cerda

Ambient vibration monitoring of a railway bridge for scour detection 923
C.W. Kim, D. Kawabe & M. Kondo

System identification of a bridge by a sparse-like system matrix 929
T. Mimasu, Y. Goi & C.W. Kim

Obtaining full-field response for optimal sensor placement 937
J. Kullaa

Potential of drive-by inspection for railway bridges 945
A.H. Eslami-Khouzani & C. Caprani

The interpolation method for vibration based damage localization: Influence of feature uncertainties 953
M.P. Limongelli & A. Fathi

Uncertainties reduction on modal parameters estimation in existing bridges using ambient and free-vibration test 961
N. De Conto, F. Lorenzoni, F. da Porto & C. Modena

Monitoring of the Chillon viaduct after strengthening with UHPFRC 968
H. Martín-Sanz, V. Dertimanis, L.D. Avendaño-Valencia, E. Chatzi & E. Brühwiler

Development of vibration-based parameters as damage sensitive features for bridge structures 976
J.J. Moughty & J.R. Casas

A bespoke signal processing algorithm for operational modal testing of post-tensioned steel and concrete beams 984
D. Noble, M. Nogal, A.J. O'Connor & V. Pakrashi

The effect of local scour of a single pier on the vibration parameters of a multi-span bridge under seismic excitation 992
A. Anžlin, L.J. Prendergast, K. Gavin & M.P. Limongelli

MS10: Corrosion and safety of existing concrete bridges

Organizers: M. Akiyama, D.M. Frangopol & H. Matsuzaki

Effect of different steel weight loss distributions on the life-cycle reliability of PC girders 1001
N. Nishiya, H. Fukushima, A. Sakurai, M. Akiyama, P. Bocchini & D.M. Frangopol

Optimum strengthening strategy for deteriorating reinforced concrete bridges 1007
H. Baji & C.Q. Li

Strengthening of reinforced concrete bridges by external prestressing 1015
L.H.B. Pinheiro, L.M. Trautwein & L.C. Almeida

Inhibiting corrosion of prestressed cables using an ultrasonic impregnation process 1020
X. Hallopeau, P.M. Dubois & D. Michaux

Effects of current density on the spatial variability associated with steel corrosion and flexural behavior of corroded RC beams 1024
S. Lim, H. Song, M. Akiyama & D.M. Frangopol

Seismic failure mode evaluation of bridges with deteriorated isolators 1029
H. Matsuzaki, Y. Kubo, T. Tsumura & S. Unjoh

Durability of reinforced concrete bridges in marine environments 1036
R.E. Melchers & I.A. Chaves

Damage accumulation in aging highway bridges considering multiple earthquake events 1044
B. Panchireddi, U. Yadav & J. Ghosh

Optimum lifetime inspection and maintenance planning for bridges considering utility 1052
S. Sabatino & D.M. Frangopol

FEM approach to appraise bridges affected by Alkali-Silica Reaction (ASR) 1058
R.V. Gorga, L.F.M. Sanchez, B. Martín-Pérez & M. Noël

Techniques to rehabilitate bridge columns affected by Alkali-Silica Reaction (ASR) 1066
L.F.M. Sanchez, M. Noël & V.A.A. Santos

Influence of tendon breaks on structural behavior of concrete beams 1074
H. Kaneko, K. Suzuki, K. Amaya, K. Hamaoka, M. Hara, M. Fukuda, E. Sasaki, P. Tuttipongsawat, T. Kuroda, K. Takase & Y. Ikawa

MS11: Special elements in bridge construction and practice

Organizer: M. Nasser Darwish

Bridges approach slabs with fibre reinforced polymers 1083
M. Nasser Darwish

Guidance on defects in hidden bridge components 1091
T.M. Pape, P. Burnton, J. Collins, D. Ashurst, P. Sparkes, J. Webb & C. Christodoulou

Captain Cook Bridge bearing replacement 1099
W. Mengel, P. Adams, W. Hansford & J. Spathonis

Reliability assessment of reinforced concrete pylons subjected to biaxial bending 1107
J. Hyeon Kim & H. Sung Lee

Experimental research on shear behavior of rubber-ring perfobond connector 1115
Y.Q. Liu, Y. Liu & F. Wang

Effect of hinge-type connections on the lateral cyclic behavior of a prestressed high-strength concrete pile 1123
B. Lim, J.W. Kang, Y.J. Kim & H. Yoon

Seismic vulnerability analysis of typical bearings for simply supported railway bridges 1131
G. Yang, J. Dong & D.S. Shan

Hanger replacement effect: Experimental and numerical investigation on the Bosphorus Bridge 1139
S. Bas, N.M. Apaydin, A. Ilki & N. Catbas

Investigation of limit temperature span of continuous bridges considering track-bridge interaction 1145
Y.H. Yan, D.J. Wu & Q. Li

MS12: Bridge safety evaluation and risk assessment: Code requirements vs. practical considerations

Organizers: M. Liu & H. Nassif

Code development for existing structures: Influence of concrete strength statistics 1153
B.L. Badimuena & S.M.C. Diniz

Risk-based performance evaluation for concrete bridge deck repair 1161
H. Huang & M. Liu

The bridge assessment maze 1169
C. Jager, T.M. Pape, P. Shaw & R. Heywood

Bridge risk management: Credibility gaps 1177
P.S. McCarten

Codes and standard issues in assessing existing bridges 1185
R. Pavan & E. Siviero

Horizontal interface shear requirements for precast prestressed concrete bridge beams with slender webs in beam and slab bridge constructions 1192
M. Slevin & A.J. O'Connor

Bridge safety assessment for strength II limit state in AASHTO LRFD specifications 1200
H. Nassif, P. Lou & P. Truban

Large skewed bridge for high speed trains. Northwest of Spain 1204
C. Jurado

Repair and retrofitting of bridges – present and future 1208
H. Singh

Displacement coefficient method for bridge subjected to pulse-like ground motions 1216
K.Y. Liu, S.T. Wang, C.C. Hwang & C.H. Kuo

The condition of Padang's bridges after 2009 earthquake disaster 1224
Masrilayanti, R. Kurniawan, Nidiasari & Nurhamidah

MS13: Advanced computational and experimental techniques for extreme load performance of bridges

Organizers: J. Hashemi, R. Al-Mahaidi & D.M. Frangopol

Advanced nonlinear finite element modelling of reinforced concrete bridge piers 1231
E.P.G. Bruun, A. Kuan, G.T. Proestos, E.C. Bentz & M.P. Collins

Seismic analysis of a stone masonry arch railway bridge 1239
C. Costa, A. Arêde & R. Silva

Numerical assessment of composite bridges subjected to Wildland Urban Interface (WUI) fires 1247
A.P. Dissanayake, S. Setunge, S. Venkatesan, K.A.M. Moinuddin & D. Sutherland

Joint irregularity in the seismic behavior of highway bridges 1256
M.C. Gómez-Soberón, A.E. Gómez-Benítez & R.J. Aguirre-Eligio

Linking seismic resilience into sustainability assessment of limited-ductility RC bridges 1264
A.Y. Al-Attraqchi, M.J. Hashemi, R. Al-Mahaidi & P. Rajeev

Study on impact behavior of piers subjected to vehicle collisions 1272
R.W. Li & D.Y. Zhou

Fragility analysis of non-ductile RC bridges subjected to extreme hydrodynamic forces 1279
I.M.I. Qeshta, M.J. Hashemi, R.J. Gravina & S. Setunge

Dynamic response of an isolated bridge under basic pulse-type ground motions 1286
M.H. Tsai & Z.Y. Jiang

Research on seismic performance of self-compacting concrete bridge columns 1294
Z. Wang, H. Duan, H. Wei, J. Yang & X. Sun

Seismic fragility of high-speed railway bridge with high pier 1299
J. Dong, D.S. Shan, G.J. Yang & Y.P. Zeng

Research on the influence law of central buckle on long-span suspension bridge's dynamic and seismic performance 1306
L.P. Liu, Y. Liu & Y. Li

MS14: Steel bridge rehabilitation

Organizer: M. Sakano

Ayala bridge, retrofitting of an historic steel bridge in Manilla (Philippines) 1314
V. Buchin-Roulie, N. Kaczkowski, A. Gros & F. Tesson

Orthotropic steel bridge deck study with UHPFRC cold composite overlay 1319
L. Duan, T.O.N. Houankpo, C.S. Wang & E. Brühwiler

Effect of diaphragms on the exterior girders during bridge construction 1327
F. Hraib, L. Hui & R. Hindi

Inspection of Bingo Bridge by using high-sensitivity magnetic nondestructive testing 1333
T. Ishikawa, Y. Kuramitsu, H. Furuta & K. Tsukada

Theoretical analysis of CFRP bonding repair method using low-elasticity adhesive at the plate end 1337
K. Komon, T. Ishikawa, H. Suzuki, Y. Fujii & H. Namaki

Fatigue strength and improvement effect of the center stay rod 1343
S. Kawano, S. Ogo, A. Okumura, Y. Mizokami & M. Sakano

Repair of corroded steel plate girders with ultra-high performance concrete 1350
K.F. McMullen, A.E. Zaghi & M.P. Culmo

Retrofitting method against fatigue cracking of web gap plates 1359
C. Sakamoto, M. Sakano, H. Konishi & M. Koyama

Adhesive and bolting reinforcement for distortion-induced fatigue of steel bridges 1367
Y.Z. Wang, B. Cui, Q. Wang, L. Duan & C.S. Wang

Vibration study of train passing bridge with small radius and reverse curve 1375
Y.M. Song, D.J. Wu & J. Zhang

Repairing a sinking bridge over Guadalquivir river 1384
C. Jurado

MS15: Bridge loading – measurement and modelling

Organizers: C. Caprani, A. Nowak, E.J. O'Brien & X. Ruan

Traffic load patterning on long span bridges 1389
D. Guo & C. Caprani

Traffic and wind simulation for extreme loads on long-span bridges 1397
A.A. Hayrapetova, A.J. O'Connor, J.D. Sørensen & H.S. Toft

Developing a new bridge live load model for South Africa 1405
P.F. van der Spuy & R. Lenner

Using images to estimate traffic loading on long-span bridges 1411
F. Daize, E.A. Micu, E.J. O'Brien & A. Malekjafarian

Long span bridges – current age & design life – a global survey 1417
J. De Maria, C. Caprani & D. Guo

A new method to understanding loading and traffic characteristics of traffic flow 1427
X.J. Wang & X. Ruan

Bridge live load models in U.S. and Europe 1434
A. Ramesh Babu, A.S. Nowak & E.J. O'Brien

Bridge network planning for heavy vehicles in Queensland 1442
T.M. Pape, P.A. Shaw, C. Doherty, G. Danicic, A. Robertson & D. Wilson

Strength evaluation of prestressed concrete bridges by dynamic load testing 1450
E.S. Hernandez & J.J. Myers

Limiting exterior girder rotation during construction for non-skewed bridges 1456
L. Hui, F. Hraib & R. Hindi

Impacts of specialized hauling vehicles on the Texas bridge network 1462
J. Weissmann & A.J. Weissmann

Impact of quantity of weigh-in-motion data on load effects on bridges 1467
A. Žnidarič, M. Kreslin, J. Kalin & G. Turk

MS16: Bridge monitoring: Techniques and results regarding bridge condition and loading

Organizers: E.O.L. Lantsoght & D.A. Hordijk

Structural health monitoring and serviceability assessment of bridges in Romania 1476
C.C. Comisu, M.C. Scutaru, N. Ţăranu & G. Boacă

Deformation monitoring of a simply supported railway bridge under varying dynamic loads 1484
K. Faulkner, F. Huseynov, J. Brownjohn & Y. Xu

DIC-monitoring of full-scale concrete bridge using high-resolution wide-angle lens camera 1492
P.S. Halding, J.W. Schmidt & C.O. Christensen

Monitoring crack width and strain during proof load testing 1500
E.O.L. Lantsoght, C. van der Veen & D.A. Hordijk

Twenty years monitoring of a high strength concrete cantilever bridge 1507
E.O.L. Lantsoght, C. van der Veen, H. van der Ham & A. de Boer

Estimating climate effects on bridge decks deterioration 1515
S. Liu, H. Zhu, L. Yang & M. Habib

Railway bridge monitoring system using inertial sensors 1522
P. Olaszek, D. Sala, M. Kokot & M. Piątek

Non-destructive testing of bridges – Health assessment & monitoring 1530
C.R. Raikar

Rating of masonry arch bridges in USA 1536
A.P. Ranasinghe, N.Y. Khadbai & A.K. Ranasinghe

Monitoring design for long-span bridges 1540
K. Suzuki, C. Miki, E. Sasaki & A. Tanabe

Testing of bridge structures using laser scanning method 1548
W. Anigacz, D. Beben & J. Kwiatkowski

SPECIAL SESSIONS

SS01: Perturbations on SHM results due to environmental changes

Organizers: M. Baessler, F. Hille, W.H. Hu & G. Morgenthal

A study on diverse strategies for discriminating environmental from damage based variations in monitoring data 1557
M. Baeßler & F. Hille

Automated operational modal analysis of a lively footbridge for tracking long term dynamic behaviour 1565
D.H. Tang, W.H. Hu, J. Teng, E.S. Caetano & Á. Cunha

Damage detection under environmental variability using Bayesian virtual sensing 1569
J. Kullaa

Assessment of MEMS-based sensors for inclination measurements 1577
S. Rau & G. Morgenthal

Fine temperature effect analysis based time-varying dynamic properties evaluation of long-span suspension bridges in natural environments 1585
J.S. Zhu & Q.L. Meng

Inverse analysis using compatible displacements 1590
J. Lei, D. Xu & J. Turmo

SS02: Continuous bridge monitoring and damage detection

Organizers: A. Miyamoto, E. Brühwiler, R. Kiviluoma & P. Hradil

Combined structural and traffic monitoring of steel suspension bridge 1597
P. Hradil & K. Koski

"Pocket-monitoring" for the fatigue safety verification of bridge members in steel and reinforced concrete 1605
E. Brühwiler

Structural risk assessment and management through the capture of dynamic movement 1613
M. Kudrenko

Continuous structural health monitoring for short and medium span bridges 1618
A. Miyamoto

A strain sensor based monitoring and damage detection system for a two-span beam bridge 1627
P. Waibel, O. Schneider, H.B. Keller, J. Müller, O. Schneider & S. Keller

Automatic data collection system for structural health monitoring 1635
A. Yabe, T. Iye & A. Miyamoto

SS03: Bridge safety, maintenance and management under hazards and changing climate

Organizers: Y. Dong, M. Soliman & D.M. Frangopol

Vulnerability of bridges exposed to coastal hazards and climate change 1643
G.P. Balomenos, S. Kameshwar, B. Bass, J.E. Padgett & P. Bedient

Probabilistic multi-hazard assessment of seismic and scour effects on bridge structures 1650
Z. Chen & X. Guo

Reliability based corrosion damage assessment for concrete bridge decks under a changing climate 1658
L.I. Peng & M.G. Stewart

Risk-informed assessment of climate change by considering deterioration and hazards 1666
Y.H. Li & Y. Dong

Climate change and potential impact on the seismic vulnerability of highway bridge structures 1672
M. Mortagi & J. Ghosh

SS04: Structural health monitoring for infrastructure asset management

Organizers: J. Li, X.-W. Ye, T.-H. Yi & H.P. Chen

Traffic load modelling for urban highway bridges using weigh-in-motion data 1681
T.L. Huang, J.J. Liao, J. Zhong, J.W. Zhong & H.P. Chen

Acceleration response analysis of a long-span steel arch bridge subjected to high-speed trains integrating SHM data 1689
H.L. Li, Y.L. Ding, H.W. Zhao & S.T. Hou

Optimal weight problem for response sensitivity-based damage identification 1696
J. Zhou, L. Wang & Z.-R. Lu

A mesoscopic analysis of chloride diffusion with adaptive mesh refinement 1703
Z. Pan, D. Wang, R. Ma & A. Chen

Bridge displacement monitoring using acceleration measurement for efficient bridge management 1710
Y. Umekawa & H. Suganuma

Guide for a successful monitoring project from Finland 1718
J. Wuorenjuuri

Bending-shear fatigue behavior of concrete girder bridges 1725
M. Yuan, D. Yan & Y. Liu

SS05: Self-sensing and connected infrastructures for a smart transport future

Organizer: F. Giustozzi

Global instrumentation, vehicle, track and bridge on operation railway of MRS logistic railway 1731
R. Montoya & L. Fernando Martha

Pervasive fibre-optic sensor networks in bridges: A UK case study 1738
L.J. Butler, M.Z.E.B. Elshafie & C.R. Middleton

Shear force-based method for detecting vehicle speed and axle spacing 1746
L. Deng, W. He, Y. Yu & C.S. Cai

Virtual design of adaptive road-bridge-types in a comprehensive 5D-BIM assessment 1754
M. Nöldgen, J.B.P. Lim & S. Giebat

TRUSS-ITN methods for detecting bridge damage from response to traffic 1761
A. González, D. Martínez, E.J. O'Brien, M. Casero, J.J. Moughty, J.R. Casas, M. Vagnoli, R. Remenyte-Prescott, J.D. Andrews, F. Huseynov & J. Brownjohn

SS06: Advances in corrosion modelling of steel bridges

Organizer: M. Mahmoodian

Structural reliability analysis of corroding steel bridges using random-field representation 1770
V. Aryai, M. Mahmoodian, N.V. Ferdowsi & F. Ariai

Corrosion risks: Assessment of enclosed spaces, monitoring real bridges 1776
M.W.K. Bowers

Effect of corrosion on mechanical properties of steel bridge elements 1783
L. Li, M. Mahmoodian & C.Q. Li

3D cellular automata based numerical simulation of atmospheric corrosion process on weathering steel 1791
J.S. Zhu, X.Y. Guo & J.F. Kang

Structural performance of bridges under deterioration processes: Bicentenario bridge 1798
J.D. González & F.A. Cerda

Predictive modelling of the deterioration of Australian state bridge network 1806
H.D. Tran, S. Setunge, Y.C. Koay & H. Luczak

SS07: European standardization of quality specifications for roadway bridges

Organizers: J.R. Casas & J.C. Matos

Quality specifications for roadway bridges in Europe 1814
J.R. Casas & J.C. Matos

Quality specifications and performance indicators for road bridges in Europe 1822
A. Strauss, S. Fernandes, J.R. Casas, L. Mold & J.C. Matos

Quality control plan for RC bridges exposed to flooding events 1832
N. Tanasic & R. Hajdin

Monitoring in management of roadway bridges 1839
J. Bień, T. Kamiński & M. Kużawa

Bridge management in Australia and New Zealand: Current approaches and future needs 1845
M.M. Melhem, C. Caprani & A. Ng

Repair and retrofitting of bridges under IBMS protocol 1852
S.S. Raju & T. Kiran Kumar

SS08: Construction management issues in bridge engineering and construction

Organizer: M. Nasser Darwish

The construction of the new Tappan Zee Bridge 1860
R.D. Csogi

A case study of early cracks of a concrete pylon 1867
J. Song & X.F. Shi

A case study of using a support vector machine on bridge inspection data 1873
Arong, S. Murakami & Yiliguoqi

Evaluation of slab lifting strategies for maintenance of middle slabs in double-deck tunnels 1881
S.M. Kim, Y.K. Cho & B.K. Park

Research and application of maintenance for a combined highway-railway bridge 1887
J. Fu, T. Zhang, Z. Li, Q. Ding & J. Huang

SS09: CIM: Community Information Modeling – The new frontier of civil engineering

Organizers: G.P. Cimellaro, M. Domaneschi & S. Mahin

Fuzzy based tool to measure the resilience of communities 1895
O. Kammouh, A. Zamani Noori, M. Domaneschi & G.P. Cimellaro

Resilience assessment of city-scale transportation networks using Monte Carlo simulation 1902
O. Kammouh, A. Cardoni, S. Marasco, G.P. Cimellaro & S. Mahin

Seismic resilience of electric power networks in urban areas 1911
S. Sordo, M. Domaneschi, G.P. Cimellaro & S. Mahin

Seismic resilience of bridges in transportation networks 1920
M. Domaneschi, G. Scutiero, G.P. Cimellaro, A.A. Khalil, C. Pellecchia & E.M. Ricciardi

Resilience framework for seaport infrastructure: Theory and application 1928
A. Balbi, M.P. Repetto, O. Kammouh & G.P. Cimellaro

Seismic damage assessment of a virtual large-scale city model 1936
M. Domaneschi, S. Marasco, G. Scutiero, A. Zamani Noori, O. Kammouh, V. Taurino & G.P. Cimellaro

SS10: Assessment and evaluation of deteriorated bridges

Organizers: H.K. Kim & J.R. Casas

Seismic retrofit of truss bridge for highway and railway 1944
T. Hanai, T. Tamura & Y. Hirayama

Safety assessment of bridges for transportation of power plant generator 1951
I.Y. Paik, K.H. Jeong, M.K. Jun, J.H. Jeong, S.-H. Hong, H. Koo & R.C. Lee

Evaluation of adhered sea-salt particle amount to bridge, anti-adhesion countermeasures 1958
A. Toktorbai uulu, H. Katsuchi & H. Yamada

Influence of collision on structural performance of steel girder 1966
E. Yamaguchi, Y. Tanaka & H. Tsuji

Sectional analysis of corroded wires in chloride-contaminated tendon 1972
C.H. Yoo, S.H. Bong, H.K. Kim & Y.C. Park

GA-based model updating for existing bridges 1976
J.C. Kim, J. Yoon & S. Shin

SS11: Life-cycle structural redundancy, robustness and resilience of bridges under multiple hazards

Organizers: F. Biondini & D.M. Frangopol

Survey on life-cycle structural performance indicators for bridges 1983
F. Biondini & D.M. Frangopol

Seismic resilience of road bridges: Lessons learned from the 14 November 2016 Kaikōura earthquake 1988
A.I. Sarkis, A. Palermo, O. Kammouh & G.P. Cimellaro

Renewal-theory-based life-cycle risk assessment of bridge deck unseating under hurricanes 1996
D.Y. Yang & D.M. Frangopol

Life-cycle seismic resilience of aging bridges and road networks considering bridge capacity correlation 2004
L. Capacci & F. Biondini

Time-dependent probability of exceeding restoration levels in resilience analysis 2012
F. Nocera, P. Gardoni & G.P. Cimellaro

Computational investigation on the piers of a U-slab bridge under raising flood intensity 2020
M. Nasim, S. Setunge, H. Mohseni & S.W. Zhou

SS12: Centenary bridges – An insight into construction and technology history

Organizers: P. Cruz & P.G. Malerba

The dream of building bridges over the Tagus River mouth in Lisbon 2029
P.J.S. Cruz

Articulated and continuous cantilever bridges after a century of experience 2037
P.G. Malerba

Whipple's 1841 Bowstring Truss – World's first scientifically designed Truss bridge 2045
I.A. Nitschke & F.E. Griggs Jr.

The use of machine learning techniques to assess damage in critical infrastructure 2053
M.A. Terra, R.A. Pereira Junior, L.F.M. Sanchez, M. Noël & W.R. Junior

Shear capacity of an existing RC bridge deck slab: FE analysis using continuum elements 2061
J. Shu

Rehabilitation of timber bridge piles using a wrapping system 2069
R. Borzou & W. Lokuge

Investigating snipe depth in girders and corbels in timber bridges 2075
J. Cohen, W. Lokuge & N. Herath

SS13: Value of information of SHM for life-cycle management of bridges

Organizers: S. Thöns, M. Stewart, D.G. Lu & A.J. O'Connor

Sensitivity analysis of value of information framework 2081
M.S. Khan, S. Ghosh, J. Ghosh & C. Caprani

Health monitoring data modeling and reliability prediction of an actual bridge based on ARMA model 2089
D.G. Lu, W.H. Zhang & Z. Zhao

Assessment of terrorism risk mitigation measures for iconic bridges 2097
S. Thöns & M.G. Stewart

Evaluation of fatigue crack propagation considering the modal superposition technique 2105
C.S. Horas, G. Alencar, R. Calçada & A. Jesus

Inspection and assessment of one of Australia's earliest masonry bridges 2113
D. McDonnell, D. Ashurst & I. Berger

SS14: Resilience of bridges to climate change, natural & man-made hazards

Organizers: A.J. O'Connor & M. Nogal

Seismic performance of bridges with rocking piers in Hanshin Expressway 2122
K. Azumi, K. Sugioka & N. Mitsukawa

Resilience assessment of highway bridges using SMA-based isolation bearings 2128
Y. Dong, Y. Zheng & Y.H. Li

Resilience evaluation of a cable-stayed bridge 2133
H. Gil, K. Han, S. Seo & J. Park

Seismic fragility of highway bridges considering improved bearing deterioration modeling 2138
S. Shekhar & J. Ghosh

Structural behavior of a steel-concrete composite beam under fire condition 2146
M.S. Kang, H. Pak, J.W. Kang, S.H. Kee & B.J. Choi

The performance estimation of pile-protective structures using simplified collision model 2154
G.H. Lee

Effect of slenderness-ratio parameter on seismic performance of steel piers 2160
H. Takezawa, K. Ono, S. Okada & K. Azumi

SS15: Latest developments on jointless bridges

Organizers: B. Briseghella, W.P. Yen & B.C. Chen

Trial design study on integral abutment bridge supported on UHPC-RC segmental pile 2166
G.D. Chen, B.C. Chen, F.Y. Huang, Y.Z. Zhuang & H. Tabatabai

Parametric studies on seismic behavior of integral abutment steel bridges considering SSI 2173
Q. Zhao, S. Dong, Z. Qi & B.C. Chen

Research on SSI simulation method of integral abutment bridge under earthquake 2181
Q. Zhao, J. Qiu, Z. An & Z. Qi

Seismic behavior and cyclic tests on integral abutment–pile joints 2189
Q. Zhao, Y. Li, Z. Qi & B.C. Chen

Design and construction challenges of jointless bridges in seismic regions 2197
B. Khaleghi & W.P. Yen

Fatigue strength improvement of welded joints using SBHS700 by applying ICR treatment 2205
Y. Ono & K. Kinoshita

Three bridges with the same name "Kömürhan Bridge" 2213
N. Apaydin & O. Yaldiz

SS16: Revised fatigue detail categories for bridges (in European standards)
Organizer: U. Kuhlmann

Assessment of fatigue tests to review detail categories of EC3 2220
H. Bartsch & M. Feldmann

Recommended fatigue strengths of thick-walled circular K-joints and influence of weld root irregularities 2228
S. Bove, M. Euler & U. Kuhlmann

Considering high frequency mechanical impact treatments in design 2236
S. Breunig & U. Kuhlmann

Statistical analysis of fatigue test data according to Eurocode 3 2244
K. Drebenstedt & M. Euler

Quantifying uncertainty in visual inspection data 2252
J. Bennetts, G. Webb, S. Denton, P.J. Vardanega & N. Loudon

BrIM bridge inspections in the context of industry 4.0 trends 2260
M. Salamak & M. Januszka

SS17: Smart bridge components: Monitoring and optimization of EJs, bearings and dampers
Organizer: K. Islami

"Smart" bridge expansion joints enabling optimized decision-making at different life-cycle stages 2269
P. Savioz, K. Islami & V.V. Ghodke

Advances in materials and further improvements in bridge pot bearings 2277
S.N. Kazi, V.V. Ghodke & C. Sarmiento

Breaking the Asphalt code – Polyurethane flexible plug expansion joint 2285
C. Sarmiento, G. Pope & S.N. Kazi

Critical factors in minimizing total life cycle costs of bridge expansion joints 2294
G. Pope, J. Creighton & V.V. Ghodke

Smart bridge components (expansion joints, bearings, seismic devices) for intelligent infrastructure 2302
K. Islami, N. Meng & C. O'Suilleabhain

SS18: Challenges for bridge technology implementation and management in developing countries
Organizers: T.N. Bittencourt, M.A. Valenzuela, F.C. Carrizo & M. Márquez

Maintenance plan proposal on cable-stayed bridge: Application to Yelcho Bridge 2311
M. Márquez, J. Campusano, F. Hernández, J. Errazuriz & M.A. Valenzuela

Management systems for inspection and maintenance of Chilean road bridges 2319
M. Márquez, M.A. Valenzuela, G. Arias, M. Pertierra & C. Sepulveda

Dynamic analysis of a steel-concrete composite railway bridge considering vehicle-bridge interaction 2327
L.R. Ticona Melo, T.N. Bittencourt, D. Ribeiro & R. Calçada

Management system for natural risk disaster on infrastructure: A regional approach 2335
M.A. Valenzuela, N. Valenzuela, A. Peña-Fritz & R. Romo

Strengthened Chilean bridges using carbon fiber: State of knowledge 2343
M. Márquez, M.A. Valenzuela & H. Pinto

UAV: First Chilean proposal of use on road bridge inspections 2350
M.A. Valenzuela, N. Valenzuela, A. Peña-Fritz, D. Torres & M. Márquez

SS19: Bridge deterioration modeling and probabilistic bridge maintenance needs forecasting
Organizers: R. Goyal, M. Whelan & T.L. Cavalline

Predictive fidelity of bridge deterioration models: Probabilistic vs deterministic 2359
R. Goyal, M. Whelan & T.L. Cavalline

Life cycle assessment for civil engineering structures of railway bridges 2367
G. Lener, J. Schmid & A. Strauss

National-scale bridge element deterioration model for the USA 2373
P.D. Thompson

Damage location in experimental/numerical models by acceleration amplitude change 2380
R.L. Silva, L.M. Trautwein, L.C. Almeida, G.H. Siqueira & C.S. Barbosa

Early detection of reinforcing-bar corrosion with linearized inverse scattering method 2385
T. Tsunoda & K. Suzuki

Fragility curves for concrete girder bridges under flood hazard 2393
F. Kalendher, S. Setunge, D. Robert & H. Mohseni

SS20: Monitoring and assessment of bridges using novel techniques
Organizers: A. Strauss, K. Bergmeister & D.M. Frangopol

Performance analysis of distributed optical fiber bonding adhesives to concrete 2401
A. Barrias, J.R. Casas & S. Villalba

Structural performance assessment using digital image correlation systems 2409
A. Strauss, R. Wendner, M. Marcon, B. Krug, P. Castillo & D.M. Frangopol

Development of response-based load and resistance factor rating (RB-LRFR) methodology 2416
M. Ghosn, B. Sivakumar & E. Senturk

Monitoring-based quantification of input parameters for chloride ion ingress models 2424
M. Šomodíková, B. Teplý, A. Strauss & I. Zambon

In-service stress and strain behavior of Missouri bridge A7957 2432
H.H. Alghazali & J.J. Myers

GENERAL SESSIONS

Numerical assessment of the load-carrying capacity of a masonry bridge 2439
R. Silva, C. Costa & A. Arêde

Fatigue performance of diaphragm cutouts in steel box girder 2446
C.X. Li, L. Ke, Z.Y. Chen, Y.M. Xiong & Z. Hu

Assessment of shear lag in pultruded GFRP bridge decks 2453
S. Zhang & C. Caprani

Dynamic response analysis of widening bridge due to moving vehicles 2461
Y. Li, T. Yang, Z. Li & L. Liu

A preventive strengthening strategy for aged steel columns 2470
W. Lin, N. Taniguchi, T. Yoda & S. Satake

Generalized Pareto distribution for reliability of bridges exposed to fatigue 2477
M. Nesterova, F. Schmidt, E. Brühwiler & C. Soize

Numerical model updating of cable-stayed bridge based on experimental data 2485
I.C. Santos, J.L.V. Brito & E.S. Caetano

Rotational stiffness between vertical and horizontal members of system supports 2493
J.H. Won, H.D. Lee, A.R. Oh & N.K. Jang

Research on transverse mechanical property of widened box girder bridge 2499
W.Q. Wu, H. Zhang & Z.X. Tang

Sensitivity and reliability analysis of long span cable stayed bridge 2507
X. Wang, W. Wu, J. Zhang & Y. Cai

The development of the reinforcement method for U-shaped rib on orthotropic steel decks to improve the fatigue durability from the lower side 2515
H. Yatsumoto, A. Tabata, H. Kobayashi, S. Inokuchi & H. Matsushita

Effect of the shear deformation in the structural system identification methods 2522
J.A. Lozano-Galant, D. Tomás, G. Ramos & J. Turmo

Optimizing rehabilitation strategies for bridge decks under performance-based contracting setting 2529
M. Alsharqawi, T. Zayed & S. Abu Dabous

Impacts of dynamic loads on the soil-steel bridges 2537
D. Beben

Automated steel bridge coating inspection using neural network trained image processing 2545
A. Elbeheri & T. Zayed

Inspection, structural health monitoring and maintenance of a cable-stayed bridge in Vienna, Austria 2552
P. Furtner

Determination of stay cable forces using highly mobile vibration measurement devices 2558
G. Morgenthal, S. Rau, J. Taraben, T. Abbas & N. Hallermann

Estimation of bridge frequencies from a passing vehicle 2566
N. Jin, T.S. Paraskeva & E.G. Dimitrakopoulos

Study on compressive strength of steel plates with a partial loss of cross-sectional area 2573
K. Saito & K. Nozaka

Use of stochastic optimization in the analysis of weigh-in-motion data 2581
F. El Hajj Chehade, R. Younes, H. Mroueh & F. Hage Chehade

Parametric analysis of rib distortion in orthotropic steel decks 2587
H. Fang & H. De Backer

Rehabilitation of the swing bridge from 1905, North of Spain 2594
F. Collazos-Arias, D. Garcia-Sánchez, M.L. Ruiz-Bedia, O.-R. Ramos-Gutiérrez & M.-A. Delgado-Nuñez

Management of risk disasters: Application in Aysen and Valparaiso, Chile 2599
M.A. Valenzuela, N. Valenzuela, P. Moraga, F. Pineda, M. Márquez & R. Romo

Fatigue behavior of full-penetration inclined cruciform welded-joints with artificial pit corrosion 2606
X. Wei & Z.Y. Jie

Stress-concentration effects due to weld root imperfections in orthotropic steel decks 2613
H. De Backer, W. Nagy & A. Outtier

AS5100.2: 2017 changes to traffic-barrier loadings – a Victorian perspective 2621
B.E. Gibbens

Displacement-based seismic design to AS5100.2: 2017 – simplified 2629
B.E. Gibbens

How did the future work out? The tale of E.J. Whitten Bridge 2637
R.A. Percy & P.J. Robinson

How strong is your bridge? Optimising New Zealand's longest road bridge 2643
J. Waldin, B. McHaffie & V. Wong

Performance of prestressed concrete girder in ultimate bending for AS5100:2004 and AS5100:2017 2651
M.M. Melhem, C. Caprani & M.G. Stewart

Coupling finite elements to model steel to concrete bond 2658
R.J. Gravina, L.A.G. Bitencourt Jr. & L.C. Meneghetti

Shear and torsion design review – Australian and international standards 2664
T. Hossain, S. Mikhael, A. Chaudry & S. Mohanakumar

Intermodal research to increase the reliability of transport infrastructures 2672
R. Holst

Traffic safety and passenger comfort for steel railway bridges 2679
E.S. Hwang & D.-Y. Kim

The ultimate limit state vs. limit analysis of masonry arch bridges 2687
T. Kamiński

Importance of simulation in the design of experimental tests 2695
M. Karalar & M. Dicleli

Experimental investigation on the low cycle fatigue life of piles 2703
M. Karalar & M. Dicleli

Investigation on the closed longitudinal U-ribs corrosion of cable stayed bridge with steel plate deck 2709
K.Y. Lee, S.H. Jin, D.S. Oh, H.S. Joo & D.K. Kim

Experimental and analytical investigation of bridge deck under restrained shrinkage 2717
M. Rahman, Y. Chen, R. Hindi, A. Ibrahim & W. Lindquist

Methods for fast and reliable determination of damping and tension force of stay cables 2724
T. Mack & R. Geier

Noise radiation from steel bridge structure – Old Årsta bridge Stockholm 2732
A. Olsen, R.S. Lützen & S. Holmes

Damping performance identification for large-scale dampers of a cable-stayed bridge 2740
X.H. Hu & C.X. Ge

Use of comparative vacuum monitoring sensors for automated, wireless health monitoring of bridges and infrastructure 2747
D. Roach

Considerations for identification of moisture in building materials using Bluetooth® 2752
R. Helmerich, L. Moldenhaue, G. Voigt, F. Adao & E. Köppe

Quantifying increases in maintenance costs of Prestressed Reinforced Concrete (PRC) bridges due to increasing fatigue from heavier traffic loads 2760
M. Frizzarin, L. Mancassola & P. Franchetti

Assessment of concrete pylon of cable stayed bridge with floating crane collision 2767
J.H. Lee, S.-C. Lee, H.-Y. Kim & S.K. Park

Parametric analysis of dissipative rocking superstructures 2771
Z. Chegini & A. Palermo

Mechanical properties of alkali activated concrete based class C fly ash 2780
E. Gomaa, S. Sargon, A. Gheni & M.A. ElGawady

Bayesian integration of NDT with corrosion model for service-life predictions 2786
S.A. Faroz & S. Ghosh

Brunei Temburong Link – Temburong Viaduct 2793
N. Hussain, S. Yip & J. Cain

Effect of cracks on air-tightness of vacuum tube bridge structures 2799
P. Devkota, J. Park & E. Choi

Moving substrate in an ephemeral stream revisited: A continuing case study 2805
G.R. Herrmann & T.G. Cleveland

Experimental study on the fatigue resistance of prestressing strands at low temperature 2813
F. Bomholt, H. Alawieh & M. Knobloch

Multi-scale finite element model updating of highway bridge based on long-gauge strain response 2820
S. Chen, G. Wu & H. Li

Limit analysis of an old and damaged R.C. grillage deck 2827
E. Conti, P.G. Malerba, M. Quagliaroli & A. Maffei

Nonlinear analysis of a R.C. grillage deck exposed to corrosion 2835
E. Conti, P.G. Malerba, M. Quagliaroli & D. Scaperrotta

Determining vehicle weight limit based on the cumulative fatigue damage on bridges 2843
L. Deng & W. Yan

Vortex-induced vibration prediction of bridges based on data fusion theory 2849
S. Xu, D. Wang, R. Ma, A. Chen & H. Tian

Development of phased array ultrasonic test system for detection of fatigue crack of rib-to-deck weld of orthotropic steel deck system 2857
H. Shirahata

Inspection of steel bridges by modal hammer from bridge deck only 2865
B.T. Svendsen, G.T. Frøseth & A. Rønnquist

Assessment of lateral thermal diffusion of impulse thermography method in measuring size of non-planar defects 2873
H.Q. Tran, J. Huh, C. Kang, K. Kwak & J. Ahn

Corrosion segmentation and quantitative analysis based on deep neural networks 2881
D. Wang, B. Peng & Y. Pan

Effect of small steel-piece size on Charpy absorbed energy 2889
D. Kitazume, K. Ono, K. Anami & T. Iida

A two-stage static structural system identification by observability method 2894
J. Lei, M. Nogal, J.A. Lozano-Galant, D. Xu & J. Turmo

Author index 2901



Taylor & Francis
Taylor & Francis Group
http://taylorandfrancis.com

Maintenance, Safety, Risk, Management and Life-Cycle Performance of Bridges – Powers, Frangopol, Al-Mahaidi & Caprani (Eds)
© 2018 Taylor & Francis Group, London, ISBN 978-1-138-73045-8

Preface

One of the biggest challenges facing bridge asset managers globally is to effectively, efficiently and safely manage aging and deteriorating bridges while also accommodating ever increasing loading. The budgets available are often constrained which adds to the challenge considering the cost of maintenance, operation and construction steadily increasing. In this context, academics and practitioners are rising to the challenge with research and practice focusing on innovative approaches to understand the problem and develop and implement solutions. IABMAS conferences bring together academic and technological developments in the fields of bridge maintenance, safety, risk, management, life-cycle performance, resilience, sustainability, among others. The most recent developments in the field are expected to be discussed at the 9th International Conference on Bridge Maintenance, Safety and Management (IABMAS'18), held in Melbourne, Victoria, Australia, July 9–13, 2018 (www.iabmas2018.org).

The First (IABMAS'02), Second (IABMAS'04), Third (IABMAS'06), Fourth (IABMAS'08), Fifth (IABMAS'10), Sixth (IABMAS'12), Seventh (IABMAS'14) and Eighth (IABMAS'16) International Conferences on Bridge Maintenance, Safety and Management were held in Barcelona, Spain, July 14–17, 2002, Kyoto, Japan, October 18–22, 2004, Porto, Portugal, July 16–19, 2006, Seoul, Korea, July 13–17, 2008, Philadelphia, USA, July 11–15, 2010, Stresa, Lake Maggiore, Italy, July 8–12, 2012, Shanghai, China, July 7–11, 2014, and Foz do Iguaçu, Brazil, June 26–30, 2016, respectively.

IABMAS 2018 is organized on behalf of the International Association for Bridge Maintenance and Safety (IABMAS) under the auspices of VicRoads, Australia with the organizational support of Monash University, Swinburne University of Technology, RMIT University and the Australian IABMAS Group. IABMAS encompasses all aspects of bridge maintenance, safety and management. Specifically, it deals with: bridge repair and rehabilitation issues; bridge management systems; needs of bridge owners, financial planning, whole life costing and investment of the future; bridge-related safety and risk issues and economic and other implications. The objective of the Association is to promote international cooperation in the fields of bridge maintenance, safety and management for the purpose of enhancing the welfare of society (www.iabmas.org). The interest of the international bridge community in the fields covered by IABMAS has been confirmed by the large response to IABMAS 2018 call for papers. The Conference Secretariat received over 660 abstracts, 385 of which were selected for final publication as full papers and presentation at the Conference within mini-symposia, special sessions, and general sessions.

Contributions presented at IABMAS 2018 deal with the state of the art as well as emerging concepts and innovative applications related to the main aspects of bridge maintenance, safety, risk, management and life-cycle performance. Major topics include: new design methods, bridge codes, heavy vehicle and load models, bridge management systems, prediction of the future traffic models, service life prediction, residual service life, sustainability and life-cycle assessments, maintenance strategies, bridge diagnostics, health monitoring, non-destructive testing, field testing, safety and serviceability, assessment and evaluation, damage identification, deterioration modelling, repair and retrofitting strategies, bridge reliability, fatigue and corrosion, extreme loads, advanced experimental simulations, and advanced computer simulations, among others.

Maintenance, Safety, Risk, Management and Life-Cycle Performance of Bridges contains 393 contributions, comprising the T.Y. Lin Lecture and 10 Keynote Lectures, and 382 technical papers from all around the world. This volume provides both an up-to-date overview of the field of bridge engineering and significant contributions to the process of making more rational decisions on bridge maintenance, safety, risk, management and life-cycle performance of bridges for the purpose of enhancing the welfare of society. The Editors hope that these Proceedings will serve as a valuable reference to all concerned with bridge structure and infrastructure systems, including students, researchers and engineers from all areas of bridge engineering.

Nigel Powers, Dan M. Frangopol, Riadh Al-Mahaidi and Colin Caprani
Editors of IABMAS 2018



Taylor & Francis
Taylor & Francis Group
http://taylorandfrancis.com

Maintenance, Safety, Risk, Management and Life-Cycle Performance of Bridges – Powers, Frangopol, Al-Mahaidi & Caprani (Eds)
© 2018 Taylor & Francis Group, London, ISBN 978-1-138-73045-8

Sponsors

HOST ORGANISATIONS

VicRoads

Monash University

Swinburne University of Technology

RMIT University

ORGANIZING ASSOCIATIONS

IABMAS, International Association for Bridge Maintenance and Safety

IABMAS Australia, International Association for Bridge Maintenance and Safety – Australia

SUPPORTING ORGANISATIONS

IALCCE, International Association for Life-Cycle Civil Engineering

ATLSS Engineering Research Center, Lehigh University, Bethlehem, PA, USA

RCEAS, P.C. Rossin College of Engineering and Applied Science, Lehigh University, Bethlehem, PA, USA

TRB, Transportation Research Board, Washington, DC, USA

IABMAS Brazil Group

IABMAS Chile Group

IABMAS China Group

IABMAS Italy Group

IABMAS Japan Group

IABMAS Portugal Group (ASCP)

INTERNATIONAL MEDIA PARTNER

Bridge design & engineering magazine

EXHIBITORS

MOOG GmbH Under-Bridge Access Solutions

NVMS Solutions

Board of Professional Engineers of Queensland

Simpson Strong-Tie

Maintenance, Safety, Risk, Management and Life-Cycle Performance of Bridges –
Powers, Frangopol, Al-Mahaidi & Caprani (Eds)
© 2018 Taylor & Francis Group, London, ISBN 978-1-138-73045-8

Acknowledgements

The Editors are extremely grateful to all the people who contributed to the scientific program and organization of the IABMAS 2018 Conference. The Editors would like to express their sincere thanks to all authors for their contributions, to the members of the International Scientific Committee for their role in ensuring the highest scientific level of the Conference, and to the members of the Local Organizing Committee for their time and efforts dedicated to making IABMAS 2018 a successful event.

Moreover, the Editors wish to thank all organizations, institutions, and authorities that offered their sponsorship. A special acknowledgement has to be given to VicRoads for being the lead host and organizer of the conference and to Monash University, RMIT University and Swinburne University of Technology for being co-hosts and organizers. Also, a special thank you to the International Association for Bridge Maintenance and Safety (IABMAS) and IABMAS Australia for endorsing and supporting the conference organization.

IABMAS 2018 was conceived in 2011 with the support of the Melbourne Convention Bureau which was invaluable to support the conference in the early stages and obtaining hosting rights. The conference has been planned and developed in close consultation and cooperation with several individuals, in particular Frieder Seible, Honorary Chair of the Conference. Thank you for your invaluable support for the conference and its organization.

The Editors are also extremely thankful to Tulio N. Bittencourt, Joan Ramon Casas, Airong Chen, Hitoshi Futura, Michel Ghosn, Pier Giorgio Malerba and Richard Sause, co-chairs of the International Scientific Committee and Geoff Taplin, co-chair of the Local Organizing Committee.

Finally, the Editors wish to express their sincerest appreciation to Diana Cavasinni, Kate Stevens and all the team at ICMS Australasia, who professionally managed the Organizing Secretariat with outstanding expertise, patience, energy and commitment which have been very important for the successful organization of this Conference.



Taylor & Francis
Taylor & Francis Group
http://taylorandfrancis.com

Maintenance, Safety, Risk, Management and Life-Cycle Performance of Bridges –
Powers, Frangopol, Al-Mahaidi & Caprani (Eds)
© 2018 Taylor & Francis Group, London, ISBN 978-1-138-73045-8

IABMAS Executive Board

President of IABMAS:
D.M. Frangopol, USA

Vice-Presidents of IABMAS:
P.G. Malerba, Italy
E. Watanabe, Japan

Members:
M. Akiyama, Japan
A.H.-S. Ang, USA
F. Biondini, Italy
T.N. Bittencourt, Brazil
E. Brühwiler, Switzerland
A. Chen, China
Y. Fujino, Japan
H. Furuta, Japan
J. Jensen, Denmark
H.-M. Koh, Korea
A.S. Nowak, USA
V. Popa, Romania
M.-C. Tang, USA

Secretary General of IABMAS:
J.R. Casas, Spain

Secretary of Executive Committee of IABMAS:
P.J.S. Cruz, Portugal



Taylor & Francis
Taylor & Francis Group
http://taylorandfrancis.com

Maintenance, Safety, Risk, Management and Life-Cycle Performance of Bridges – Powers, Frangopol, Al-Mahaidi & Caprani (Eds)
© 2018 Taylor & Francis Group, London, ISBN 978-1-138-73045-8

Conference organization

CONFERENCE CHAIRS

Nigel Powers	*VicRoads, Melbourne, Australia*
Dan M. Frangopol	*Lehigh University, Bethlehem, PA, USA*

CONFERENCE HONORARY CHAIR

Frieder Seible	*Monash Unversity, Melbourne, Australia*

INTERNATIONAL SCIENTIFIC COMMITTEE

Co-Chairs

Riadh Al-Mahaidi	*Swinburne University of Technology, Melbourne, Australia*
Tulio Nogueira Bittencourt	*University of São Paulo, São Paulo, SP, Brazil*
Joan R. Casas	*Technical University of Catalonia, Barcelona, Spain*
Airong Chen	*Tongji University, Shanghai, China*
Hitoshi Furuta	*Kansai University, Osaka, Japan*
Michel Ghosn	*The City College of New York, New York, USA*
Pier Giorgio Malerba	*Politecnico di Milano, Milan, Italy*
Richard Sause	*Lehigh University, Bethlehem, PA, USA*

Secretary

Colin Caprani	*Monash University, Melbourne, Australia*

Members

Mitsuyoshi Akiyama	*Waseda University, Tokyo, Japan*
Haluk Aktan	*Western Michigan University, Kalamazoo, MI, USA*
Sreenivas Alampalli	*New York State Department of Transportation, Albany, NY, USA*
Alfredo H.S. Ang	*University of California, Irvine, CA, USA*
Nurdan M. Apaydin	*Ankara, Turkey*
André Beck	*University of São Paulo, São Carlos, Brazil*
Jan Bien Wroclaw	*University of Science and Technology, Wroclaw, Poland*
Fabio Biondini	*Politecnico di Milano, Milan, Italy*
Franco Bontempi	*Sapienza University of Rome, Rome, Italy*
Fernando Branco	*Technical University of Lisbon, Lisbon, Portugal*
James Brownjohn	*The University of Sheffield, Sheffield, UK*
Eugen Brühwiler	*EPFL, Lausanne, Switzerland*
Rui Calçada	*University of Porto, Porto, Portugal*
Alp Caner	*Middle East Technical University, Ankara, Turkey*
Necati Catbas	*University of Central Florida, Orlando, FL, USA*
Baochun Chen	*Fuzhou University, Fuzhou, China*
Paulo Cruz	*University of Minho, Guimaraes, Portugal*
Sofia Diniz	*Federal University of Minas Gerais, Belo Horizonte, Minas Gerais, Brazil*
You Dong	*Hong Kong Polytechnic University, Hong Kong, China*

Bruce Ellingwood	*Colorado State University, Fort Collins, CO, USA*
David De Leon	*Escobedo Autonomous University of Mexico State, Toluca, Mexico*
João Almeida Fernandes	*National Civil Engineering Laboratory, Lisbon, Portugal*
Yozo Fujino	*Yokohama National University, Yokohama, Japan*
Yaojun Ge	*Tongji University, Shanghai, China*
Chan Ghee Koh	*National University of Singapore, Singapore*
Jesse Grimson	*BDI, Boulder, CO, USA*
Andrea Del Grosso	*University of Genoa, Genoa, Italy*
Nenad Gucunski	*Rutgers, The State University of New Jersey, Piscataway, NJ, USA*
Rade Hajdin	*University of Belgrade, Belgrade, Serbia*
Rosemarie Helmerich	*Federal Institute for Materials Research and Testing, Berlin, Germany*
Riyadh Hindi	*Saint Louis University, Missouri, US*
Naeem Hussain	*ARUP, Hong Kong, China*
Ichiro Iwaki	*Nihon University, Koriyama, Japan*
Jens Sandager Jensen	*COWI A/S, Lyngby, Denmark*
Ahsan Kareem	*University of Notre Dame, Notre Dame, IN, USA*
Sunyong Kim	*Wonkwang University, Iksan, Jeonbuk, Korea*
Ho-Kyung Kim	*Seoul National University, Seoul, Korea*
Sang-Hyo Kim	*Yonsei University, Seoul, Korea*
Leo Klatter	*Public Works & Water Management, Utrecht, The Netherlands*
Jung Sik Kong	*Korea University, Seoul, Korea*
Jurgen Krieger	*Bundesanstalt für Straßenwesen (BASt), Bergisch Gladbach, Germany*
Chad Kusko	*Lehigh University, Bethlehem, PA, USA*
Eva Lantsoght	*Politécnico Universidad San Francisco de Quito, Quito, Equador and Delft University of Technology, Delft, The Netherlands*
Jun Li	*Curtin University, Perth, Australia*
Jerome Lynch	*University of Michigan, Ann Arbor, MI, USA*
Ayaz Malik	*Rensselaer Polytechnic Institute, Troy, NY, USA*
Barney Martin	*Modjeski & Masters, Poughkeepsie, NY, USA*
Takashi Matsumoto	*Hokkaido University, Sapporo, Japan*
Hiroshi Matsuzaki	*Tohoku University, Sendai, Japan*
Ayaho Miyamoto	*Yamaguchi University, Ube, Japan*
Claudio Modena	*University of Padua, Padua, Italy*
Hani Nassif	*Rutgers, The State University of New Jersey, Piscataway, NJ, USA*
Andrzej Nowak	*Auburn University, Auburn, AL, USA*
Eugene Obrien	*University College Dublin, Dublin, Ireland*
Alan J. O'Connor	*Trinity College Dublin, Dublin, Ireland*
Nader Okasha	*Hail University, Hail, Saudi Arabia*
André D. Orcesi	*Laboratoire Central des Ponts et Chaussées, Paris, France*
Jamie Ellen Padgett	*Rice University, Houston, TX, USA*
Shamim Pakzad	*Lehigh University, Bethlehem, PA, USA*
Alessandro Palermo	*University of Canterbury, Christchurch, New Zealand*
Livia Pardi	*Autostrade per l'Italia, Rome, Italy*
Xin Ruan	*Tongji University, Shanghai, China*
Mehdi Saiidi	*University of Nevada, Reno, NV, USA*
Arunprakash M. Shirolè	*Arora and Associates, P.C., Robbinsdale, MN, USA*
Mohamed Soliman	*Oklahoma State University, Stillwater, OK USA*
Bill Spencer	*University of Illinois, Urbana-Champaign, IL, USA*
Mark Stewart	*University of Newcastle, Newcastle, Australia*
Luc Taerwe	*University of Ghent, Ghent, Belgium*
Man-Chung Tang	*T.Y. Lin International, San Francisco, CA, USA*
Paul Thompson	*Bellevue, WA, USA*
Yiannis Tsompanakis	*Technical University of Crete, Chania, Greece*
Matias A. Valenzuela	*Pontificia Universidad Católica de Valparaiso, Valparaiso, Chile*
Pedro Vellasco	*State University of Rio de Janeiro, Rio de Janeiro, Brazil*
Chunsheng Wang	*Chang'an University, Xi'an, China*
Zhishen Wu	*Ibaraki University, Hitachi, Japan*
You-Lin Xu	*The Hong Kong Polytechnic University, Hong Kong, China*

Yongbin Yang	*Chongqing University, Chongqing, China*
Hiroshi Yokota	*Hokkaido University, Sapporo, Japan*
Chung-Bang Yun	*Ulsan National University of Science and Technology, Ulsan, Korea*
Riccardo Zandonini	*University of Trento, Trento, Italy*
Yunfeng Zhang	*University of Maryland, College Park, MD, USA*
Jinsong Zhu	*Tianjin University, Tianjin, China*
Ales Znidaric	*Slovenian National Building and Civil Engineering Institute, Ljubljana, Slovenia*

NATIONAL ORGANIZING COMMITTEE

Chairs

Nigel Powers	*VicRoads, Melbourne, Australia*
Geoff Taplin	*Swinburne University of Technology, Melbourne, Australia*

Members

Riadh Al-Mahaidi	*Swinburne University of Technology, Melbourne, Australia*
Colin Caprani	*Monash University, Melbourne, Australia*
Ricky Chan	*RMIT University, Melbourne, Australia*
Javad Hashemi	*Swinburne University of Technology, Melbourne, Australia*
David Huggett	*WSP, Melbourne, Australia*
Robin Kalfat	*Swinburne University of Technology, Melbourne, Australia*
Donna Maloney	*VicRoads, Melbourne, Australia*
Hessam Mohseni	*Transport for Victoria, Melbourne, Australia*
Andy Ng	*VicRoads, Melbourne, Australia*
Sujeeva Setunge	*RMIT University, Melbourne, Australia*
Javier Silla-Sanchez	*John Holland Group, Melbourne, Australia*
Scott Taylor	*SMEC, Melbourne, Australia*
Xiao-Ling Zhao	*Monash University, Melbourne, Australia*

IABMAS 2018 SECRETARIAT
ICMS Australasia
PO Box 5005, South Melbourne
Victoria, Australia, 3205
Phone: (+61) 3 9682 0550

CONFERENCE WEBSITE
www.iabmas2018.org

IABMAS WEBSITE
www.iabmas.org



Taylor & Francis
Taylor & Francis Group
http://taylorandfrancis.com

T.Y. LIN LECTURE

Maintenance, Safety, Risk, Management and Life-Cycle Performance of Bridges – Powers, Frangopol, Al-Mahaidi & Caprani (Eds)
© 2018 Taylor & Francis Group, London, ISBN 978-1-138-73045-8

Bridge maintenance, renovation and management - Research and Development of governmental program in Japan

Y. Fujino
Institute of Advanced Sciences (IAS), Yokohama National University, Yokohama, Kanagawa, Japan

ABSTRACT: The collapse of over-130m suspended roof with casualties of nine people in Sasago Tunnel of one of the major highways near Tokyo in 2012 has led to strong doubts about the current quality and safety of infrastructure, and immediately brought public attention to the issue of infrastructure degradation in Japan. Japanese government decided to invest on research and development for efficient management of infrastructure through implementation of science and advanced technology. The emphasis is placed on bridges. The new research and development (R&D) program named "Infrastructure maintenance, renovation and management" was started in 2014 under the Council of Science, Technology and Innovation (CSTI)'s Strategic Innovation Program (SIP). The 5-years program covers various subjects of infrastructure maintenance with key technologies in condition assessment using non-destructive testing, monitoring and robotics; long-term performance prediction of infrastructure, development of durable high-quality of material for repair and replacement, and management of large amount of bridges and other infrastructure data using advanced information and communication technologies (ICT). The program consists of about 60 research projects involving universities, government research institutes and industries. This initiative is expected to prevent further accidents and setting an example for efficient bridge and infrastructure maintenance by reducing the burden of maintenance works and cost. In the lecture, outline and major output of this SIP program are explained.

1 INTRODUCTION

The economic sustainability, security and well-being of a nation depend heavily on the reliable functioning of infrastructure typically such as roads, highway and bridges. After five decades of development, the stocks of infrastructure in Japan have reached enormous amount of over US$7000 billion as shown in Figure 1.

A comparison of construction age of highway bridges in USA and Japan is given in Figure 2. In USA, large volume of construction started in 1930s. Bridge accidents like the complete collapse of Silver Bridge in 1967 due to poor maintenance took place around 1970s and bridge inspection became mandatory in early 1970s. Bridge management based on inspection data has been developed (Yanev, B, 2007). On the other hand, in Japan large volume of bridge construction started in 1960s as shown in Figure 2.

Built between the 1960s and 1980s, majority of infrastructure have stood for three to four decades (Fujino & Siringoringo 2011). Most works on highways started in late 1960s, bridges in early 1970s, dams and harbors in early 1980s. Some of the infrastructures are not in good condition now. Demand for rapid availability of infrastructure in the past sometimes might have led to poor design; poor construction quality or structures built using undeveloped technology. Some of bridges are deteriorating due to increasing traffic volumes, the use of anti-freezing salts and humid environment. Figure 3 shows a RC bridge deck with cracks due to salt and a bridge deck with holes. Figure 4 shows a RC wall with many cracks due to Alkali-Silica Reaction (ASR).

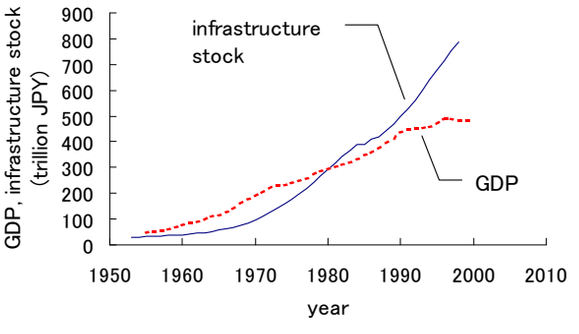


Figure 1. Accumulating infrastructure stock and GDP in Japan.

Suspended roof for air ventilation in Sasago Tunnel (Figure 5) on the Chuo Expressway near Tokyo collapsed over 130m in length in Dec. 2, 2012 and

fortunately involved only 9 deaths because of very low traffic volume at that time. This is the first maintenance-related accident with involvement of human loss. The accident has brought serious public attention to the issue of infrastructure degradation and led to strong doubts about their current quality and safety.

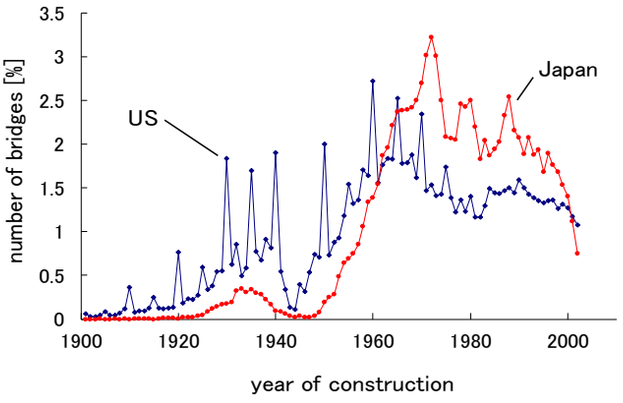


Figure 2. Comparison of yearly changes of construction of highway bridges in USA and Japan

Realizing this condition, Japanese government decided to invest on research and development for efficient infrastructure management. A new R&D program named "Infrastructure maintenance, renovation and management" was launched in 2013 under the Japanese Council of Science, Technology and Innovation (CSTI)'s Cross-ministerial Strategic Innovation Promotion Program (SIP). The 5-years program covers various subjects with key technologies in condition assessment, non-destructive testing, monitoring and robotics; long-term performance prediction, development of high-quality durable material for repair and replacement, and infrastructure management using advanced information and communication technologies (ICT). The program consists of over 60 research projects involving universities, research institutes and industries. This initiative is expected to prevent further accidents and setting an example for efficient infrastructure maintenance by reducing the burden of maintenance works and cost (SIP 2014 a).



Figure 3. Deteriorated RC bridge decks

2 INFRASTRUCTURE CONDITION IN JAPAN

After the Sasago Tunnel accident, Ministry of Land, Infrastructure, Transport and Tourism (MLIT) declared that 2013 was the first year of the maintenance era, and is trying to put more emphasis on the maintenance rather than the construction. However, no one knows how much is needed for the infrastructure maintenance entirely, because there has not been such an experience in the past.



Figure 4. Cracked RC retaining wall due to Alkali-Silica Reaction(ASR)



Figure 5. Accident in Sasago highway tunnel in Japan Dec. 2nd, 2012

In the past couple of years, expressway companies in Japan released their large-scale repair and renovation plans, and the costs for the repair and renovation were estimated. The Metropolitan Expressway's estimate was about US$ 5 billion and three NEXCO companies' (East Nippon Expressway Co. Ltd., Central Nippon Expressway Co. Ltd. and West Nippon Expressway Co. Ltd.) estimate was about US$ 25 billion. It was the first time that the concrete cost estimates were shown and it was considered to be very significant. Followings are the breakdown of the NEXCO's estimate: US$ 4 billion for earthworks, US$ 3 billion for tunnels and US$ 17 billion for bridges. Ninety percent of the bridge costs go to concrete bridge deck slabs. The reason behind this high percentage is that bridge deck slabs all over the country are heavily damaged. This condition is mainly caused by overloaded trucks and the actual loads that are significantly heavier than the design live loads. Deterioration of concrete bridge deck slabs did not attract many attentions from research-

ers in the past, because they were not considered as major structural members.

Generally, locations of the large-scale repair work and renovation were determined roughly considering factors such as inspection results, periods after completion and deterioration rates. However, after detailed investigations the repair and renovation plans might change considerably. Therefore, it is of great interests of civil engineering communities to find a roadmap in reducing the cost, for example US$ 25 billion for the NEXCO Expressway companies,



while at the same time reducing the burden of infrastructure deterioration to the next generations.

Figure 6. Ten SIP projects and their Program Directors

3 CROSS-MINISTERIAL STRATEGIC INNOVATION PROMOTION PROGRAM (SIP)

Based on Japan revival strategy and the science, technology and innovation comprehensive strategy, the Council for Science, Technology and Innovation(CSTI), Cabinet Office, Government of Japan, has founded “Cross-ministerial Strategic Innovation Promotion Program (SIP)”, and included “Science, Technology and Innovation Promotion Expense” in the budget of Cabinet Office for fiscal year 2014 (SIP 2014).

There are five most important task for the Science Technology Innovation Policies, namely: (1). Realization of clean and economical energy system (Energy), (2). Realization of healthy long life society (Healthy Long Life),(3). Development of next generation infrastructure (Next Generation Infrastructure), (4). Community revival by utilization of community resources (Community Resources), and(5). Quick reconstruction and recovery from Great East Japan Earthquake disaster (Reconstruction and Recovery). Among the five most important tasks the SIP selected Energy, Next Generation Infrastructure, Community Resources to promote one of the most urgent issues that is the economic revival and set up 10 subjects. Afterwards, they nominated a talent representing the industry/academy as a Program Director (PD) for each subject (see Figure 6).

Each PD, who has been assigned at the cabinet office, prepared and promoted research and development plans. They include several important issues from basic research to exit strategies (practical applications and commercialization) and this was conducted in close cooperation with relevant ministries and agencies.

4 IMPLICATION OF SELECTION OF INFRASTRUCTURE THEMES FOR SIP – FUSION OF CIVIL ENGINEERING AND ADVANCED TECHNOLOGIES CONDITION IN JAPAN

The Ministry of Land, Infrastructure, Transport and Tourism (MLIT) has recognized the importance of the stock management of infrastructure for some years now, but many local governments do not carry out infrastructure inventories and inspections satisfactorily. However, after the abovementioned Sasago Tunnel collapse incident, “inspection” as a basis for management became compulsory for road infrastructure starting from July 2014. This can be seen as a great momentum for recognition of the importance of infrastructure maintenance in all over the country.

Under such circumstances, the CSTI that usually deals with advanced technologies such as biotechnology and nanotechnology, has selected “Infrastructure maintenance, renovation and management” as one of ten subjects of the SIP.

It is specially mentioned that infrastructure is selected for the SIP subjects, besides the Energy and Community Resources. In the SIP research and development, innovation by the application of research outputs to the society is expected, and the infrastructure is considered to be one of the important fields for that.

Selection of maintenance related topics, which was widely considered inconspicuous before, for the SIP among many topics of Next Generation Infrastructure remarks a new era in the science and technology policy in our country. And this may yet indicate that the time is now changing.

Furthermore, the program promotion system is clearly different from the one that we had before. One of the keywords for the SIP is “innovation by the cooperation,” and the infrastructure related research and development is conducted based on close cooperation among miniseries, such as Ministry of Land, Infrastructure, Transport and Tourism (MLIT), Ministry of Education, Culture, Sports, Science and Technology (MEXT), Ministry of Economy, Trade and Industry(METI), Ministry of Internal Affairs and

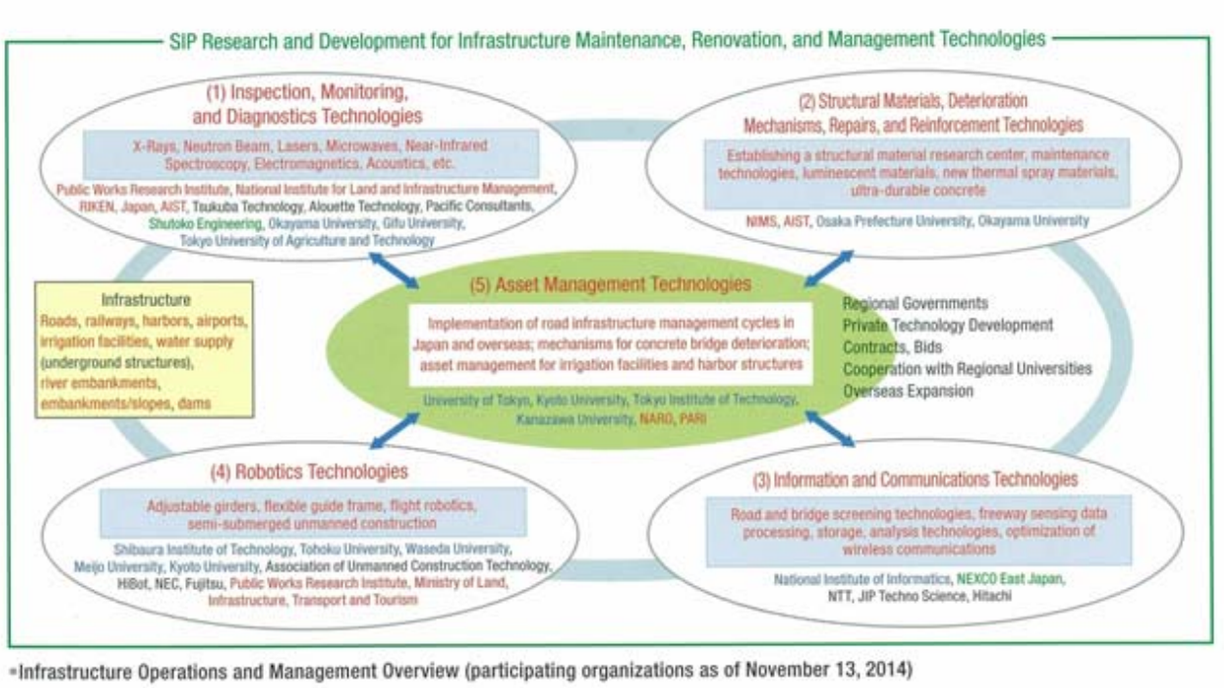


Figure 7. Five fields of R&D in SIP-Infrastructure

Communications (MIC), and Ministry of Agriculture, Forestry, and Fisheries(MAFF), national laboratories, universities, and private enterprises, for the total of five years, of which 3.5 years are remaining.

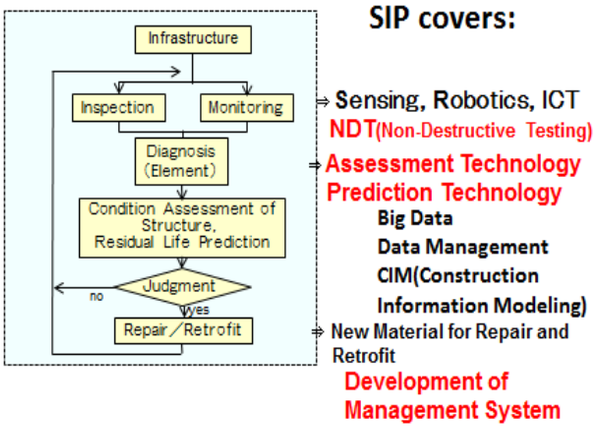


Figure 8. Flow of infrastructure maintenance and management

So far, miniseries, such as MEXT, METI, MIC, are generally interested in advanced technologies since they believed that advanced technologies will create new industries. It is commonly said that "civil engineering is far from the frontier of advanced technologies or that it is on the opposite side of advanced technologies." However, now there is a genuine perception that the time is changing. In order to know the conditions of existing infrastructures, latest technologies in robot and sensing are needed. Communication and data treatment technologies dealing with enormous amount of information of infrastructures obtained by sensors are important, and to discuss deteriorations of structural materials, most advanced material technologies are necessary. For repair, strengthening and replacement, new materials should be used. Therefore, advanced technologies are becoming increasingly important to civil engineering, and the mixture between advanced technologies and civil engineering has created new establishment (Fujino et al 2009).

5 RESEARCH THEMES FOR INFRASTRUCTURE MAINTENANCE, RENOVATION AND MANAGEMENT

In SIP "Infrastructure Maintenance, Renovation and Management Technology R&D", the following five R&D fields are set up as shown in Figure 7, and R&D proposals were invited;

1. R&D for inspection, diagnosis and monitoring technologies. To develop efficient and effective inspection or monitoring technologies that can gather data showing infrastructures deterioration levels.
2. R&D for structural materials, deterioration mechanisms, repair and strengthening technologies. To develop and establish simulation technologies for deterioration mechanisms of structural materials or the deterioration process prediction systems for structures.
3. R&D for information and communication technologies. To develop data management technologies that can utilize enormous information on infrastructure maintenance, renovation and repair.
4. R&D for robot technologies. To develop maintenance or repair robots that can implement efficient and effective inspection/diagnosis. To

develop the robots that allow investigation and/or work needed at dangerous disaster sites.

5. R&D for asset management technologies.

In parallel with R&D 1-4, outcomes of each R&D are applied to the real infrastructure management. Furthermore, asset management technologies that allow efficient maintenance with limited budgets and human resources are developed.

6 INNOVATION OF INFRASTRUCTURE MANAGEMENT CYCLE BY SIP

The R&D for asset management technologies includes development of systematic management technologies aiming at minimization of lifecycle costs, development of asset management technologies applicable to local governments and nationwide, and establishment of basis for overseas expansion by organizing technical exchange platform with overseas infrastructure owners and individuals with relevant knowledge and experience.

The flowchart of the asset management is shown in Figure 8. Technical developments and managing circulation of technology outcomes for local governments and other infrastructure owners would be the important role of an SIP Program Director. If the use of sensors and robots are necessary at the locations, then implementation of these technologies would greatly change the style of development.

Following the SIP policy that highly regards the exit strategies we are trying to lead the basic research to the better direction, to expand various R&D from the basic to the outcomes and to innovate the infrastructure management cycle.

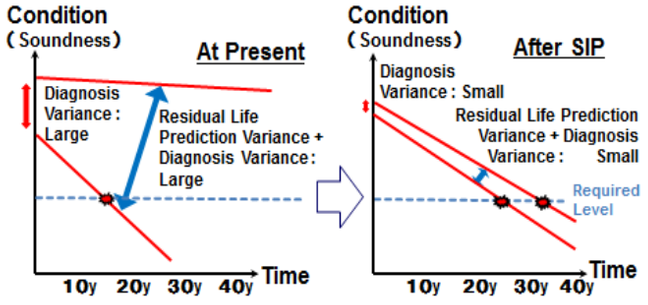


Figure 9. Residual life prediction of deteriorated infrastructure at present(left) and after SIP (right)

Furthermore, we aim at realizing resilient infrastructure systems that utilize the most advanced ICT (Information and Communication Technology) and IRT (Information and Robot Technology) developed in Japan. This is expected to help in reducing the required costs. As shown in Figure 9, the present residual life prediction is not accurate because diagnosis and prediction variance are large. However, after completion of SIP projects the residual life prediction is expected to be more accurate because diagnosis and prediction variance will be smaller, which mean reduction in the required cost. And this may lead to further expansion of the products to South-east Asian countries having similar problems, which means great opportunities for overseas business expansion.

Selected themes were determined last year from many proposals received in the categories of 5 R&D fields mentioned above. The budget of about 30 million US$ per was allocated to all of these themes every year since 2014.

We appreciate understanding and cooperation from all participants and other relevant experts involved.

7 SOME OF ONGOING SIP-INFRASTRUCTURE PROJECTS

7.1 *UAV for bridge inspection –Drones and others-*

After the Sasago tunnel accident, visual and hands-on inspection of bridges, tunnels and other facilities in highways and roads became mandatory. The interval is 5 years and hammering is to be done if necessary.

Hands-on bridge inspection of bridge from the back side and high piers needs special equipment and hence can be very expensive. It is also labor consuming. To overcome these problems, applying UAV to bridge inspection, at least to its screening is a natural choice. In SIP-infrastructure, various types of UAV including drones are being developed for inspection of bridges and tunnels (Figure 10).

One of the advantages of use of UAV is to capture the surface conditions of bridge components such as RC bridge decks by video and/or camera and can be stored in digital data. Automatized process to identify cracks in concrete surface from the photos is also being developed.

7.2 *Ultrasensitive magnetic nondestructive testing for evaluation of steel infrastructure*

Professor Tsukada's team is developing a non-destructive testing (NDT) method using highly-sensitive magnetic measurements for evaluation of steel infrastructure such as bridges. To ensure the safety of infrastructure, simple and accurate inspection methods are essential. Conventional magnetic testing techniques are simple and inexpensive; however, they can only detect surface defects. In this study, we developed a magnetoresistance (MR) sensor based on two types of NDT instruments that can detect not only surface defects but also inner defects.

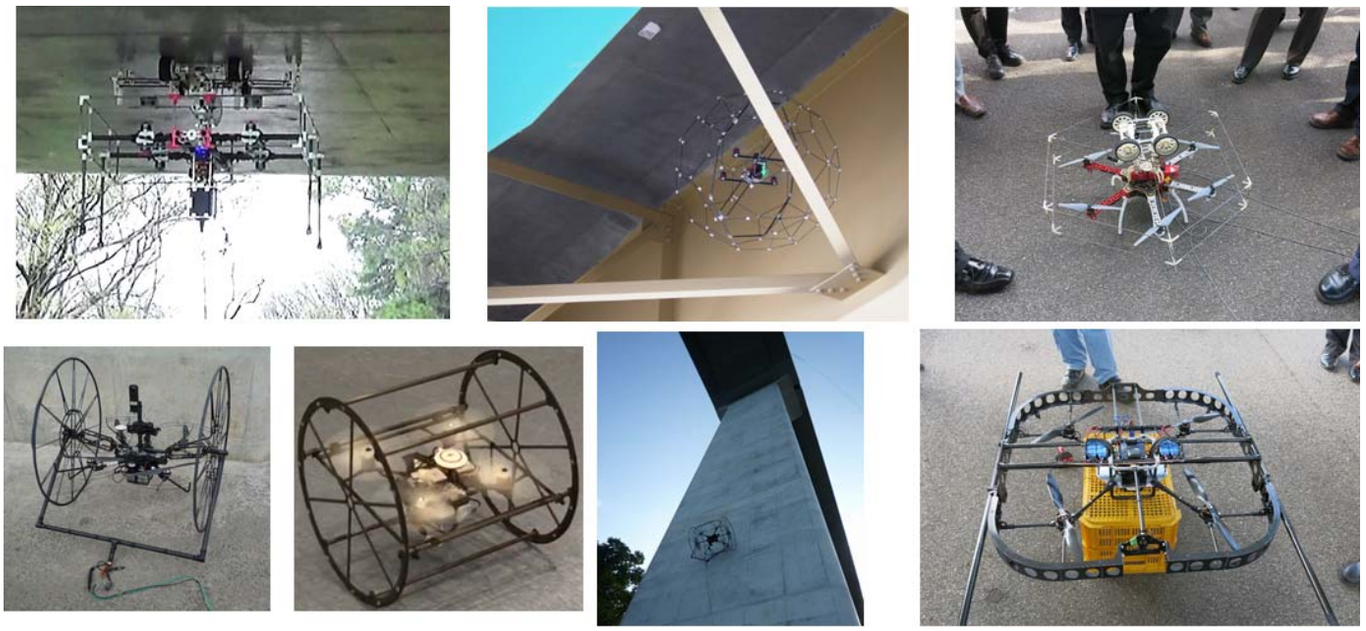
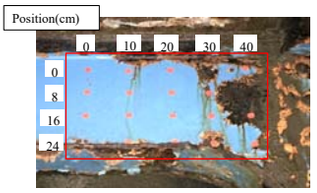


Figure 10. Drones being developed in SIP for inspection of bridge girders and piers

To detect the thinning depth caused by corrosion of thick steel plate, extremely low-frequency eddy current testing (ELECT) with an applied magnetic field ranging from 1 Hz to 1 kHz was developed. The steel thickness was estimated by analysis of the magnetic spectroscopy, which was traced using the obtained multi-frequency magnetic vector signals as shown in Figure 11.

As a result, steel plate thinner than 20 mm could be measured within 0.1 mm resolution. Moreover, the shape of the back-side corrosion was determined by scanning with a magnetic probe. Compared with ultrasonic testing, ELECT has the advantage of non-contact, which enables detection even on rough, corroded or coated surfaces.





Position (cm)	Estimated thickness (%)				
	y = 0	10	20	30	40
x = 0	86	73	59	53	53
8	53	73	59	57	40
16	53	59	56	56	39
24	43	50	54	45	46

Figure 11. Bridge corrosion investigation using ELECT

To detect an inner crack in steel, we developed unsaturated AC magnetic flux leakage (USAC-MFL) testing using an MR gradiometer. Conventional MFL methods need a strong applied magnetic field to ensure that the magnetization characteristic of the steel becomes saturated so that the magnetic field leakage is measurable. They need a strong power source, and therefore they are not suitable for field testing. To solve this problem, a gradiometer with two highly sensitive MR sensors to detect weak magnetic field intensity and the change in the phase-shifted signal caused by the crack were applied. A sharp signal change was detected just above not only the surface but also the inner crack without being influenced by the variations in steel remnant magnetization. As the frequency of the applied magnetic field was decreased, a deeper inner crack was observed, and then an inner crack at a depth of 10 mm could be detected. USAC-MFL is helpful for covering undetectable regions of the surface and subsurface (the dead zone) of ultrasonic testing.

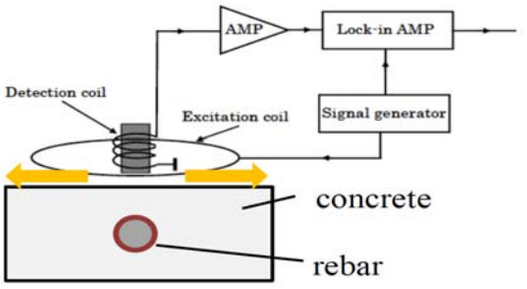


Figure 12. Schematic illustration of EM-NDE method

7.3 *Advanced Nondestructive Evaluation Technology for RC structures*

Novel nondestructive evaluation (NDE) technology using electromagnetic (EM) methods has being developed to assess the degradation of RC structures. Target of the EM NDE technology is to detect the covering depth, diameter of rebars as well as degree of their corrosion in RC structures. Figure 12 is the schematic illustration of the method being developed. The probe composed of an excitation coil and a detection coil. AC magnetic field is produced by an excitation coil and applied to the con-

crete. In response to the excitation field, magnetic field is produced by the rebar due to magnetization and eddy current, which lead to the output signals with 90-degree phase difference. The output signals contain the information on magnetic permeability and electric conductivity of the rebar and corrosion products on the surface. By scanning the surface of the RC structure by the prove, degree of corrosion of rebar can be evaluated.

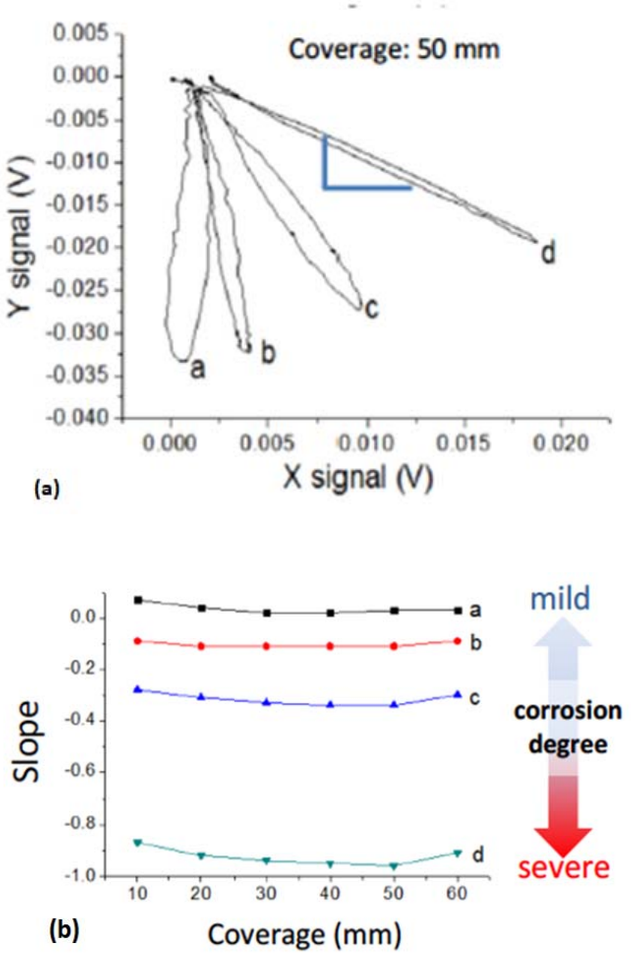


Figure 13. Example of measurement data by EM-NDE method.

Figure 13(a) is an example of the data obtained from the developed EM-NDE for four rebars with different degree of corrosion. (a) is data for the rebar without corrosion and (d) for the most severely corroded one. With increasing the degree of corrosion, the slope of the loops changes. According to the slopes the degree of corrosion can be classified as shown in Figure 13. By changing the frequency of an excitation field, it is also possible to detect the position of the rebar and to measure the coverage. This technique may be useful for the efficient planning of the repairing and/or replacement of the RC structures and will lead to reduction of maintenance cost.

7.4 *Nondestructive Measurement Method to Detect Water/Void inside Slabs using Compact Neutron Source*

Neutrons have the power to penetrate metals or heavy elements such as calcium, silicon, and iron, while they have high sensitivity to detect such light elements as hydrogen, boron. An accelerator-driven compact neutron system has been developed in RIKEN for practical use on job sites. Nondestructive inspection methods which is in type using transmission imaging and backscattered neutrons to detect void and water in concrete are developed with using RANS (RIKEN Accelerator-driven Compact Neutron Source). The backscattered neutron imaging of the water and the void in different position under 6cm thick concrete are shown as in Figure 15, and experimental set up is shown as in Figure 14. The water distribution under the concrete can be seen four times brighter than common concrete. This method is quite sensitive to detect water under such thick concrete as from 1cm until 30cm (Ikeda et al.2017)

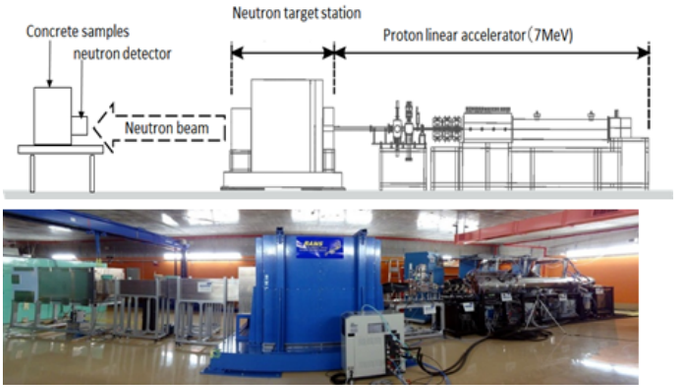
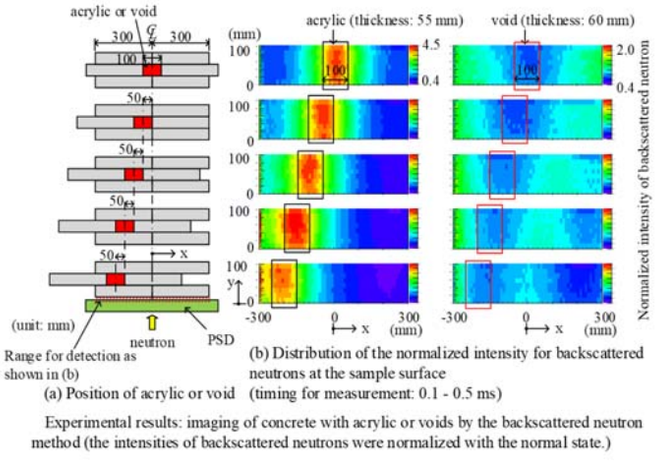


Figure 14. Backscattering experimental set up of compact neutron system



Experimental results: imaging of concrete with acrylic or voids by the backscattered neutron method (the intensities of backscattered neutrons were normalized with the normal state.)

Figure 15. Back scattering neutron imaging method

7.5 *Damage Detection by Advanced Digital Signal Processing of UHF-Band Ground Penetrating Radar Data*

Maintenance costs of bridge slab have been increasing especially in developed countries. As an essential part of the structure, current condition evaluation of bridge slab using dense hammering test requires extensive manpower and is time-consuming. To overcome this difficulty, a non-contact radar-based inspection technique is proposed using (Mizutani et al. 2017). In contrast to visually-based reflected-wave image inspection technique commonly used in the fields of mining, oil and geology that is strongly depends on the inspectors' ability and expertise; in this research bridge slab condition is evaluated by automatic reflected wave signals analysis in a fast and objective manner. This is important because the technique should be applicable to many inspected bridges.

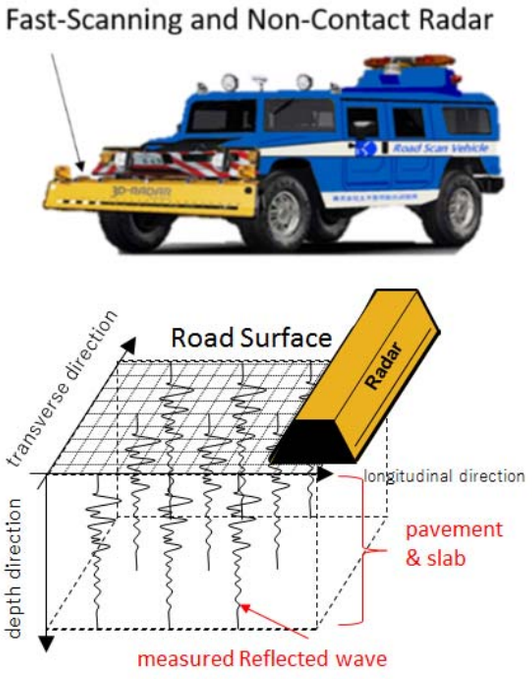


Figure 16. Ground penetrating radar (GPR) mounted on inspection car and its measuring principle.

To detect the damage of slab, an advanced signal processing technique for the reflected wave signal measured by UHF-band Ground Penetrating Radar (GPR) was proposed (Mizutani et al. 2017). A university of Tokyo research group by Dr. T. Mizutani utilizes a vehicle-mounted GPR that can obtain three-dimensional data (transverse direction, depth direction and longitudinal direction) at max. 80 km/h (Figure16). The proposed damage detection algorithm proposed can process the 100 m-length data in just a few seconds, and the damage area can be automatically detected (Figure 17(a)). To validate the algorithm in detail, a real scale bridge slab in which ideal damage was embedded was constructed. Employing the algorithm to the measured data, damage area was clearly detected especially after fulfilling the damage with water because water that has entered the concrete reflects electromagnetic waves more strongly (Figure 17 (b)) (Mizutani, T. et al., 2017)). Measurement on a number of actual bridges are currently being conducted to verify accuracy of the method. In addition, a new radar system suitable for detecting the damage of the deck is also being developed (Yamaguchi, T. et al., 2017).

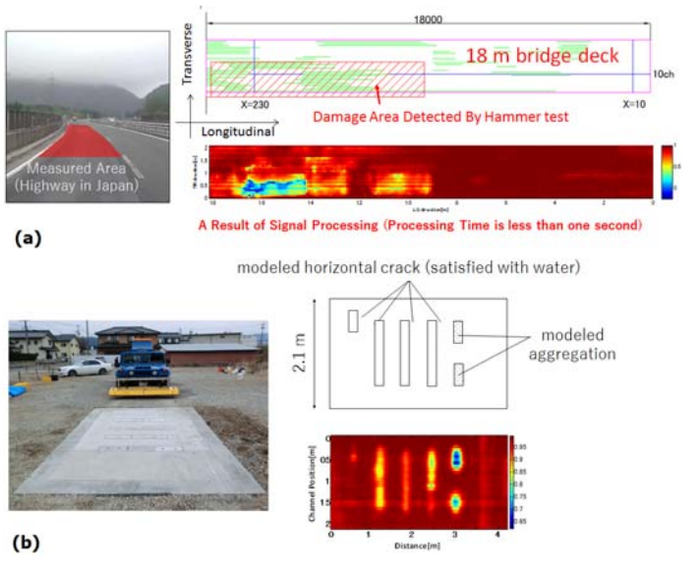


Figure 17.(a) Detection of damaged area by advanced signal processing technique, (b) validation by damage-embedded bridge slab model.

7.6 *Survival analysis of risk factors affecting deterioration of RC deck slabs in Northeast Japan*

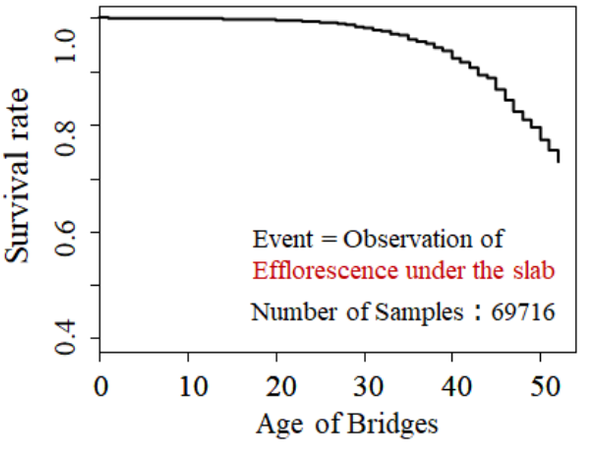


Figure 18. An example of Estimated Kaplan-Meier survival curves

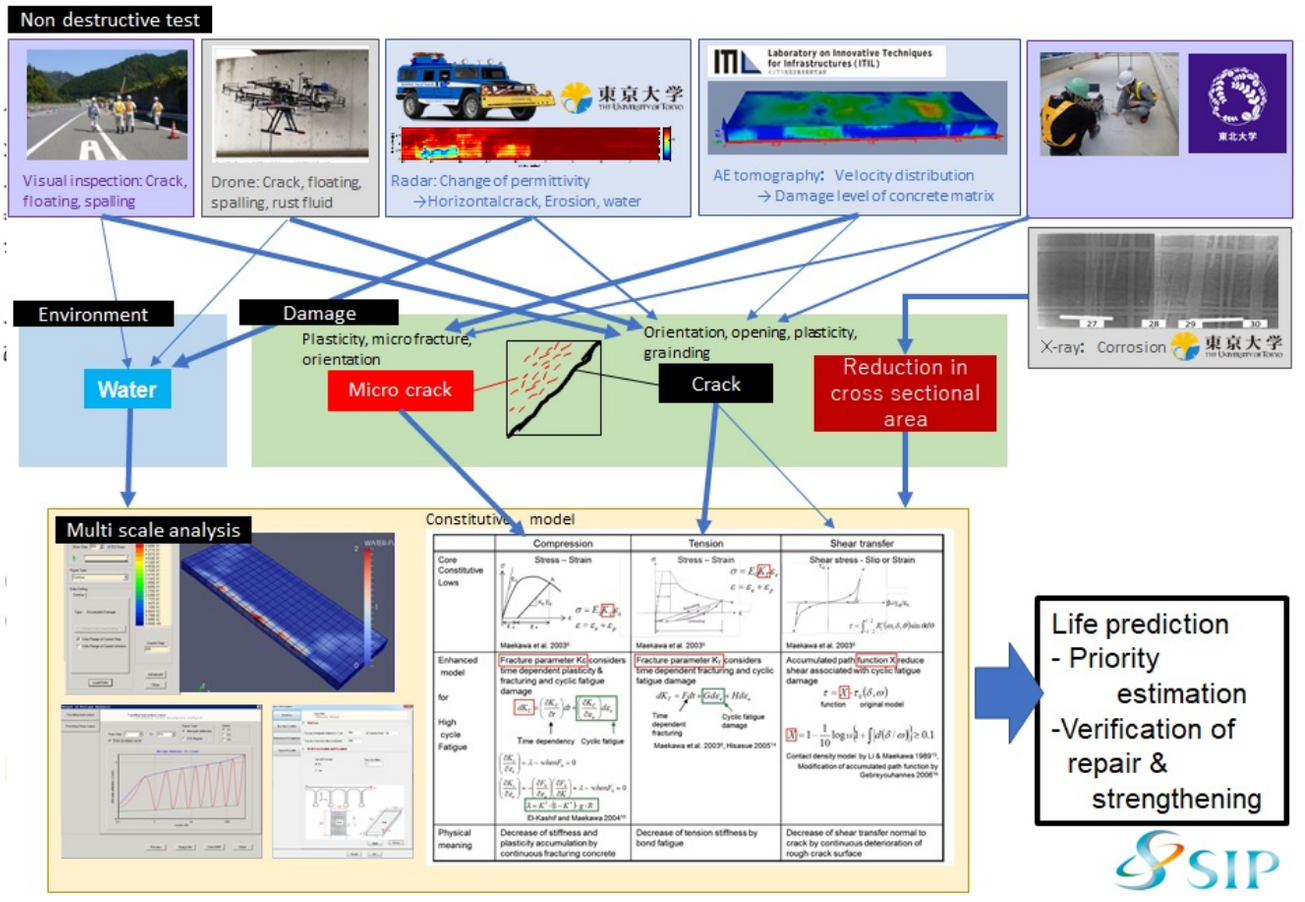


Figure 19. Schematic process of data assimilation to estimate remaining life of existing road bridge decks.



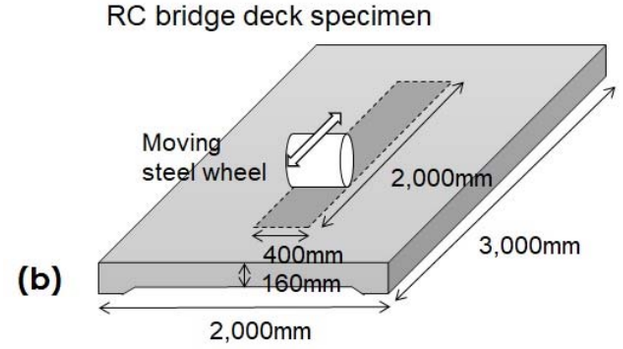


Figure 20. (a) wheel running test machine, (b) dimensions of RC deck specimen and position of wheel load.

Implementation of data-driven efficient maintenance that supports decision making by engineers is absolutely expected for rational infrastructure management. A university of Tokyo group led by Professor T. Ishida applied survival analysis to identify dominant deterioration risk factors of RC deck slab in Northeast Japan by analyzing 80,000 inspection records of national roads. Firstly, Kaplan-Meier estimator analysis for estimating the survival curve of time-to-event data is applied (Figure 18).

By estimating the survival curve, salt damage is indicated as a major cause of deterioration. Secondly, the group applied Cox regression analysis to quantify structural and environmental deterioration factors (Table 1). As a result, the predominant risk factors are explained as the rainfall in specific seasons and the movement of water on the surface of slabs. Additionally, a comparative study using 60,000 records of highway inspection data is done to check the congruence of the analytical results for two datasets distributed in the same area. A methodology for estimating future risk is also proposed (Yamazaki and Ishida 2015).

7.7 *Remaining Fatigue Life Assessment of Damaged RC Decks -Data Assimilation of Multiscale Model and Site Inspection-*

For predicting remaining fatigue life of RC bridge decks subjected to traveling wheel-type loads, Pro

Figure 21. Data assimilation with crack patterns in wheel running test.

fessor K. Maekawa at the University of Tokyo group is developing a data assimilation procedure coupled life-span simulation with inspection data at site as shown in Figure 19 (Tanaka, Y. et al., 2017a). Multi-scale analysis with hygro-mechanistic models, developed by the group is used for the platform of data assimilation on which the visual inspection of cracking on the members' surfaces and/or non-destructive test such as the acoustic emission (AE) tomography are numerically integrated.

For verification, the wheel running load experiments of slabs (Figure 20) were conducted with continuous data acquisition of both crack patterns and the acoustic emission data over the life till failure (Tanaka, Y. et al., 2017b). Visually inspected cracks are converted to space-averaged strains with Bernoulli-Euler theory. Imbalance in deformation and forces are compensated by numerical predictor-corrector cycles and non-inspected internal cracks are re-produced. Consequently, data assimilation succeeded to predict remaining fatigue life as shown in Figure 21. The 3D field of elastic wave identified by AE tomography is also converted to the fracture parameter of concrete. Although no information on cracking is available, the proposed assimilation method successfully reproduces most probable internal cracks over the volume of analysis domains, and the remaining life of the deck slabs inspected was successfully predicted.

8 INNOVATION

Since the industrial revolution in the late 18th century, technological developments have been continuously advancing. For the past few decades, information technologies based on computers have added in the technological development and we are now in the stage of the second industrial revolution. Integration of various technologies including information technologies can generate new values in the society. This is the Innovation and innovation is becoming a very important keyword.

Table 1. Result of Cox regression analysis of RC bridge decks in Tohoku area (Total records: 78697; damaged records:15821)

Name of variable	RC*	HR**	LL[#1)]	UL[#2)]
Numerical covariates				
No. of normal traffic	-0.268	0.765	0.741	0.789
No. of heavy traffic	-0.329	0.719	0.697	0.743
Span Length	0.193	1.213	1.191	1.236
Slab thickness	0.348	0.706	1.393	1.439
Mean lowest temperature in winter	0.058	0.944	1.033	1.088
Spring rain	0.490	1.633	1.559	1.710
Summer rain	-0.738	0.478	0.459	0.497
Autumn rain	-0.385	0.680	0.642	0.720
Winter rain	0.528	1.695	1.624	1.769
Winter sunshine hours	0.030	1.030	1.008	1.050

*) Regression coefficients **) Hazard Ratio
#)95% confidence limit; 1) Lower Limit; 2) Upper Limit

In SIP infrastructure, to solve problems related to infrastructure maintenance, renovation and management, not only civil engineering but also other disciplines such as material sciences, mechanical engineering(robotics), electrical engineering and electronics(sensors), informatics are essentially important and proper integration of various disciplines is absolutely needed to produce new and valuable outcomes. As the program director, I always encourage the SIP players to interact with group of other disciplines and emphasize interaction as the key to produce innovative products.

Civil engineering is often considered to be rather traditional and conservative for are number of reasons. Civil engineering structures are exposed to harsh environment for a long time like 50 years or even more than 100 years, involving very large uncertainties and their replacement are very difficult. Civil engineering structures are mostly owned by public sectors such as central and local governments and they are very sensitive to the safety and accidents of civil structures such as bridges and tunnels. All these circumstances, requirements and challenges naturally make civil engineers conservative.

However, conservative and traditional view do not always hinder innovation. In history, we have seen many prominent civil engineers who are proved to be very innovative Isambard Kingdom Brunel, Gustave Eiffel and John A. Roebling (Figure 22) are the notable examples. Isambard Kingdom Brunel for example is known as one of the most ingenious figures in engineering history. He is widely respected in UK, because his projects contained many innovative solutions to long-standing engineering problems. Brunel achieved many engineering firsts, including new technique for construction of bridges, viaducts and tunnels. Brunel is perhaps best remembered for designs for the Clifton suspension bridge in Bristol, but his works spanned beyond civil engineering as he was also involved in development of SS Great Britain, the first propeller-driven iron ship.



Figure 22. Great engineers known for their innovations that have shaped the engineering world (left to right: Isambard Kingdom Brunel-UK (1806–1859), Gustave Eiffel – France (1832-1923), John Augustus Roebling – Germany -US (1806-1869)

History also witnesses the raise of Gustave Eiffel from France. His innovative metal-structure design still supports buildings, bridges and even statues that last until now. He started to work on a system of standardized prefabricated bridge which was very innovative at the time. He was also a pioneer in combining analytical approach with an insistence on a high standard of accuracy in drawing and manufacture. John A. Roebling, an American engineer who invented an innovative wire rope that aided in revolutionizing modern long-span cable-suspended bridge in the world. He is known for daring to try an untried problem, without a precedent and undertaken with his innovation and great engineering solution. These are several world's renowned engineers who have made engineering breakthrough and accomplishments through their innovative solutions.



Figure 23. Great engineers from Japan known for their innovation and leadership, left Dr. Isamu Hiroi (1862- 1928) and right Dr. Kouichi Furuichi (1854-1938)

I would like to introduce Dr. Isamu Hiroi (1862-1928) whom I believe that is one of the great and innovative civil engineers in Japan (Figure 23). Even though he was born in a small town of southern island, he chose Sapporo Agricultural College in Sapporo, Hokkaido which the northern part of Japan. The reason is that he wanted to contribute the development of new area, Hokkaido. Teachers in the college were all American and the college was full of American-style. After the graduation, he went to the United States and joined a bridge company to learn advanced steel bridge engineering. After coming back to Japan, he was appointed a professor of Sapporo Agricultural College.



Figure 24. North breakwater in Otaru Port, Hokkaido completed in 1909

In 1894, he was assigned to be adjunct engineer at Hokkaido Development Bureau and he was asked to supervise construction of 500m breakwater in Otaru Port in Hokaiddo in 1894 (Figure 24). To accelerate the construction efficiently, he concluded that the project need to utilize a mechanized construction system and the breakwater was constructed by machine he ordered from the UK (Figure 25). Note that machine had never been used in construction before in Japan. Cement was very expensive at that time, and to reduce the cost, he developed concrete with volcanic ash. He was confident with strength of this new concrete, but not fully confident about its 100-year long-term durability (Figure 25(c)). So, he made 50,000 test pieces of this concrete and ordered them to be tested for strength a piece a year to make sure that that the strength of concrete used in the breakwater is adequate. This method resembles a monitoring without using sensors. I think that Dr. I. Hiroi was really innovative.



Figure 25. North breakwater in Otaru Port. (a) Large machine used for construction of breakwater, (b) completed breakwater, (c) concrete pieces for long-term performance evaluation

Dr. Kouichi Furuichi (1854-1938) (Figure 23), the first professor in Dept. of Civil Engineering and the first president of Imperial College of Tokyo, thought Dr. Hiroi was so excellent in engineering and research, and recruited him to a professor of bridge engineering chair at Imperial College of Tokyo in 1899. This is a very prestigious position. He continued to pursue new technologies and produced many eminent researchers and engineers. He published a steel bridge book which had a very high reputation internationally and he proposed a formula on the wave pressure, namely Hiroi Formula which has been used widely in the world until recently. He also started research on wave power generation 100 years ago.

Prof. K. Furuichi became the first president of the Japan Society of Civil Engineering (JSCE) when it was founded in 1914. In his inaugural speech, he said that civil engineers had to be leaders of leaders. This means that civil engineers are expected to be coordinators of projects. In his speech, he said to researchers should "widen/extend your research as far as possible according to your interest and the societal need, but make civil engineering be in the center of your research". I feel strongly that Prof K. Furuichi is appealing to all civil engineers to be innovative. I feel strongly that Prof K. Furuichi is appealing to all civil engineers to be innovative and this idea was followed closely by Dr. Hiroi.

Civil Engineering is basically problem-oriented, need-driven and needs to seek for methods, tools and knowledge of other disciplines, hence interdisciplinary is genuinely the nature of civil engineers. The spirit of innovation and interdisciplinary was instilled and manifested in the SIP projects mentioned here. We expect that this spirit will bring out the maximum outcome that can be implemented in infrastructure maintenance, renovation and management.

It should be mentioned that in addition to maintenance, renovation and management using non-destruction evaluation techniques mentioned above, in the past few decades we have seen monitoring evolved to a continuous and permanent installations throughout a structure's lifetime (Abe et al 2014, Fujino et. al. 2009). Continuous monitoring provides data on a structure's behavior under various loading and environment conditions, including unexpected extreme events. Monitoring has been shown to be particularly useful for understanding real structural behaviors in depth, revealing unknown factors that were not considered in design and providing structural information for necessary retrofits after extreme events (Fujino et al 2016, 2018). Therefore, best practices in monitoring, maintenance, renovation and management will hopefully allow us to maintain our infrastructure in their best qualities in an effective and efficient manner.

9 CONCLUDING REMARKS

This paper describes the new research and development (R&D) program named "Infrastructure maintenance, renovation and management" was started in 2014 under the Japan Council of Science, Technology and Innovation (CSTI)'s Strategic Innovation Program (SIP). covers various subjects of infrastructure maintenance with key technologies in condition assessment using non-destructive testing, monitoring and robotics; long-term performance prediction of infrastructure, development of durable high-quality of material for repair and replacement, and management of large amount of bridges and other infrastructure data using advanced information and communication technologies (ICT). The program consists of about 60 research projects involving universities, government research institutes and industries. Stared in 2014, the SIP-Infrastructure project is now coming into its 5th year and will conclude at 2019 spring.

As explained in this paper, all sub-projects deal with emerging problems in evaluation of civil infrastructure conditions in an interdisciplinary and innovative manner. They are now in the final stage the projects and working hard to maximize the final output. The common goal is to have all the outcomes finally implemented in infrastructure maintenance, renovation and management. It is also expected that the outcomes of SIP-Infrastructure would be implemented outside Japan.

ACKNOWLEDGEMENT

The author would like to acknowledge the following individuals for their tremendous support. Dr. Dionysius Siringoringo (Yokohama National University) for the help in preparing the manuscript. Prof. K. Maekawa, Prof. T. Ishida, Dr. H. Tanaka, Dr. T. Mizutani (University of Tokyo), Prof. K. Tsukada (Okayama University), Dr. D.He, Dr. M. Shiwa, Dr. K. Tsuchiya (NIMS), Satoshi Takaya (Kyoto Univ.) and Dr. T. Otake (RIKEN) for providing very valuable data and information.

REFERENCES

Abe, M, Fujino, Y. and Shimamura, M. (2014) Risk management and monitoring of Japanese railway bridges, Proceedings of the Institution of Civil Engineers – Forensic Engineering Vol.167(2), pp. 88–98.

Fujino, Y., Siringoringo, D. M. and Abe, M. (2009) The needs for advanced sensor technologies in risk assessment of civil infrastructures, Smart Structure and System, Vol. 5, No. 2, pp. 173-191.

Fujino, Y. and Siringoringo, D. M. (2011) Bridge monitoring in Japan: the needs and strategies, Structure and Infrastructure Engineering, Vol. 7, No. 7-8, pp. 597-611.

Fujino, Y., Siringoringo, D. M. and M. Abe (2016) Japan's experience on long-span bridges monitoring, Journal of Structural Monitoring and Maintenance, Vol. 3(3), pp. 233-257.

Fujino Y., (2018). Vibration-based monitoring for performance evaluation of flexible civil structures in Japan, Proceedings of the Japan Academy, Ser. B, Physical and Biological Sciences (Review paper) , Vol. 94, Issue 2, pp.1-31, 2018

Ikeda,Y. Otake ,Y., Mizuta, M. (2017), Nondestructive Measurement Method to Detect Water/Void inside Slabs using Compact Neutron Source by "Backscattered Neutrons" Journal of Advanced Concrete Technology Vol.15 No.10 (2017) pp.603-609.

Mizutani,T, Nakamura,N., Yamaguchi,T, Tarumi, M., Ando, Y. and Hara,I, (2017), Bridge slab damage detection by signal processing of UHF-band ground penetrating radar data, Journal of Disaster Research, vol. 12, no.3, pp. 415 - 421, Aug. 2017.

SIP (Cross-ministerial Strategic Innovation Program), Pioneering the Future: Japanese Science, Technology, and Innovation, Council for Science, Technology and Innovation, Cabinet Office, Government of Japan, 2014 (http://www8.cao.go.jp/cstp/gaiyo/sip/index.html, access Feb 18th, 2018)

SIP (Cross-ministerial Strategic Innovation Program), Pioneering the Future: Japanese Science, Technology, and Innovation, Council for Science, Technology and Innovation, Cabinet Office, Government of Japan, 2014.

Tanaka, Y., Maekawa, K., Takahashi, Y., and Ishida, T. (2017a), Life assessment of bridge decks by data assimilation and survival analysis, Proceedings of the 2nd ACF symposium 2017.

Tanaka, Y., Maekawa, K., and Takahashi, Y. (2017b), Remaining fatigue life assessment of damaged RC decks-Data assimilation of multi -scale model and site inspection-, Journal of Advanced Concrete Technology, Vol.15, pp.328-345.

Yanev, B. 2007. *Bridge management*. Hoboken, NJ: Wiley,

Yamaguchi,T, Mizutani T,Tarumi M, and Su,D (2018). Sensitive Damage Detection of Reinforced Concrete Bridge Slab by Time-Variant Deconvolution of SHF-Band Radar Signal, IEEE Transactions on Geoscience and Remote Sensing, 2018 (under peer review)

Yamazaki, T. and Ishida, T. 2015. *Application of Survival Analysis to Deteriorated Concrete Bridges in East Japan*. J. JSCE, Ser.F4, Vol. 71, No.4, 2015, pp. I_11-I_22.

KEYNOTE LECTURES

Maintenance, Safety, Risk, Management and Life-Cycle Performance of Bridges – Powers, Frangopol, Al-Mahaidi & Caprani (Eds)
© 2018 Taylor & Francis Group, London, ISBN 978-1-138-73045-8

Life-cycle reliability of bridges under independent and interacting hazards

Mitsuyoshi Akiyama
Waseda University, Tokyo, Japan

Dan M. Frangopol
Lehigh University, Bethlehem, PA, USA

ABSTRACT: After recent large earthquakes, field investigations confirmed that several bridges were severely damaged and collapsed not only due to the earthquake, as an independent hazard, but also to the subsequent tsunami, landslide or fault displacement. In addition, material deterioration might cause further seismic damage to bridges. Therefore, it is important to study both independent and interacting hazards and their effects on the reliability of bridge and bridge networks. Although earthquake is still a dominant hazard to bridges in many earthquake-prone countries, a life-cycle reliability approach has to consider both independent and interrelated hazards causing bridge failure. Such an approach is presented in this keynote paper. In addition, issues related to life-cycle analysis, design, risk, resilience and management of bridges under earthquake and other hazards are discussed. Finally, the concepts and methods presented are illustrated on both single bridges and bridge networks.

1 INTRODUCTION

Bridges may be susceptible to damage during an earthquake event, particularly if they were designed without adequate seismic detailing. Bridge columns built using earlier design codes (i.e., without proper seismic detailing) often lack adequate flexural strength and ductility capacity, and/or shear strength. When subjected to strong ground motions, they have the potential to exhibit brittle failure. Several destructive earthquakes in Japan shown in Figure 1 inflicted various levels of damage on the structures and infrastructures. The investigation of these negative consequences gave rise to serious discussions about seismic design philosophy and to extensive research activity on the retrofit of as-built bridges (Akiyama et al. 2014).

There are several performance indicators that can be related to the possible occurrence of local and global failures, including system ductility, redundancy, failure times, redundancy, robustness, and resilience (Biondini & Frangopol 2016). These performance indicators need to be included into the practical design for bridges (Biondini & Frangopol 2018). A review of performance indicators and metrics is available in Ghosn et al. (2016). These performance indicators are expected to change over time due to structural deterioration and time-variant resistance (Zhu & Frangopol 2012, Barone & Frangopol 2014, Frangopol & Saydam 2014).

System ductility is the ratio of ultimate displacement at collapse to the corresponding displacement at first failure. This performance indicator is related to the energy dissipation capacity of the structural system and is generally a key factor in seismic design concept based on capacity design criteria (Akiyama et al. 2012a). Structural redundancy denotes the ability of the system to redistribute among its members the loadings that can no longer be sustained by damaged members after the occurrence of a local failure (Frangopol & Curley 1987, Frangopol & Nakib 1991). The load distribution capacity is a desirable structural feature to ensure suitable system performance under the strong excitations (Bertero & Bertero, 1999). Structural robustness can be viewed as the ability of the system to suffer an amount of damage not disappropriate with respect to the causes of the damage itself (Saydam & Frangopol, 2011).

Reliability-based performance indicators, which account for the uncertainty in both resistance and load, have been the basis for establishing the safety levels of structural design codes. Although reliability-based performance indicators can provide adequate information on the safety of bridge components and individual bridges, they lack the ability to reflect the

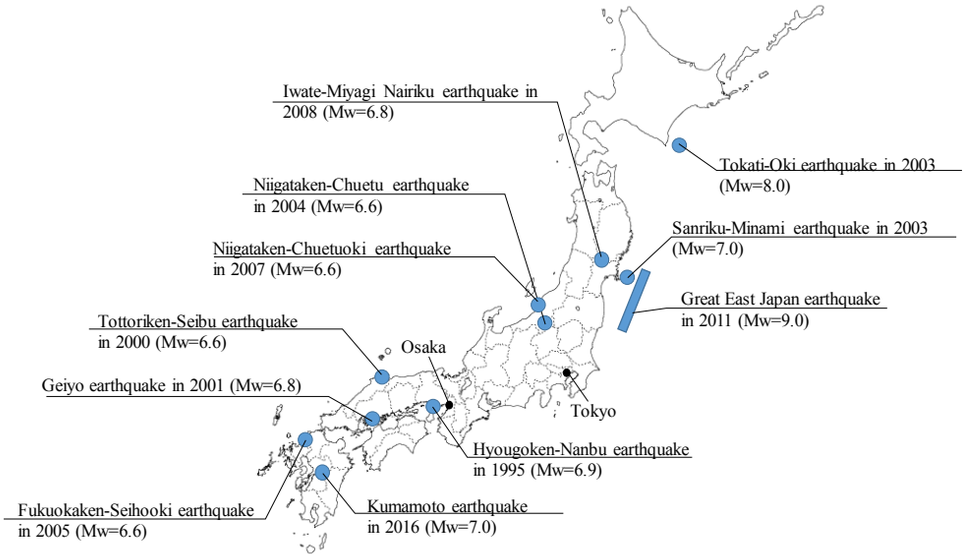


Figure 1. Recent large earthquakes in Japan after the 1995 Hogoken-Nanbu (Kobe) earthquake

outcome of a failure event in terms of economic losses. On the other hand, risk and risk-based performance indicators offer additional information on the performance of structural systems under various hazards. Risk allows combining the probability of component or system failure with the consequence of the event.

As observed in recent catastrophic disasters (e.g. 2011 Great East Japan earthquake and 2016 Kumamoto earthquake), because the transportation network, including bridges, plays a crucial role in the evacuation of affected people and the transportation of emergency goods and materials, the functionality of the network after a disaster must be investigated (Unjoh 2012). A significant amount of research efforts has shifted the focus from the analytical of individual components of the infrastructure to the investigation of entire distributed civil infrastructure systems and networks (Stergiou & Kiremidjian 2010, Bocchini et al. 2011, Saydam et al. 2013, Torbol & Shinozuka 2014, Dong & Frangopol 2017).

Transportation systems are needed to perform economic and strategic activities, and, immediately, after a catastrophic event, they allow rescue operations to be initiated. However, the flow capacity of a transportation network would be reduced significantly if its constituent bridges are damaged. Bridges are considered as weakest links in road transportation system because of their vulnerability to hazards (Lee et al. 2011, Frangopol & Bocchini 2012). Robustness and recovery of the transportation network as a whole highly depends on the performance of its individual bridges. Large-scale hazards can damage many bridges in a transportation system simultaneously, and the loss resulting from this damage can be classified into two categories: initial direct loss caused by structural damage and indirect loss caused by downtime of the network before its full recovery. The initial loss is determined by the vulnerability of the components in the system to the hazard event. The indirect loss due to downtime largely depends on the overall recovery time and trajectory of the network (Zhang et al. 2017). Indirect losses as a consequence of cascading failures (i.e. negative economic, social and environmental consequences) are key factors that affect the restoration time of a community from the event. In order to account for these cascading failures in the community, network dependency and cross-dependency should be included in the risk assessment of the community (Masoomi & van de Lindt 2018), although they are outside of the scope of this paper.

The prompt restoration of critical infrastructure facilities after an extreme event is always a goal of paramount importance (Bocchini & Frangopol 2012a, b). To quantify the promptness of the restoration, it has become customary to use the concept of resilience. Even though there are several definitions of resilience in the literature, the most widely accepted definition is provided by Bruneau et al. (2003): "resilience is defined as the ability of social units (e.g., organizations, communities) to mitigate hazards, contain the effects of disasters when they occur, and carry out recovery activities in ways that minimize social disruption and mitigate the effects of future earthquake." For example, the definition of seismic resilience combines information from technical and organizational fields, from seismology and earthquake engineering to social science and economics (Cimellaro et al. 2010).

Hutt et al. (2016) and Tirca et al. (2016) considered downtime and recovery of existing steel buildings and proposed the seismic strategies in order to achieve increased resilience. Previous efforts to investigate the functionality of networks have proven that damage to components directly cause a major degradation in the functionality of the entire network. Bocchini & Frangopol (2012a) considered resilience as a measure of the ability to recover the functionality of bridges along a highway segment, subjected to an extreme event of any kind, in a fast and economically efficient way.

The environmental, social, and economic impacts of structural activities have become an increasingly significant issue in modern sustainability conscious design, assessment and management methodology

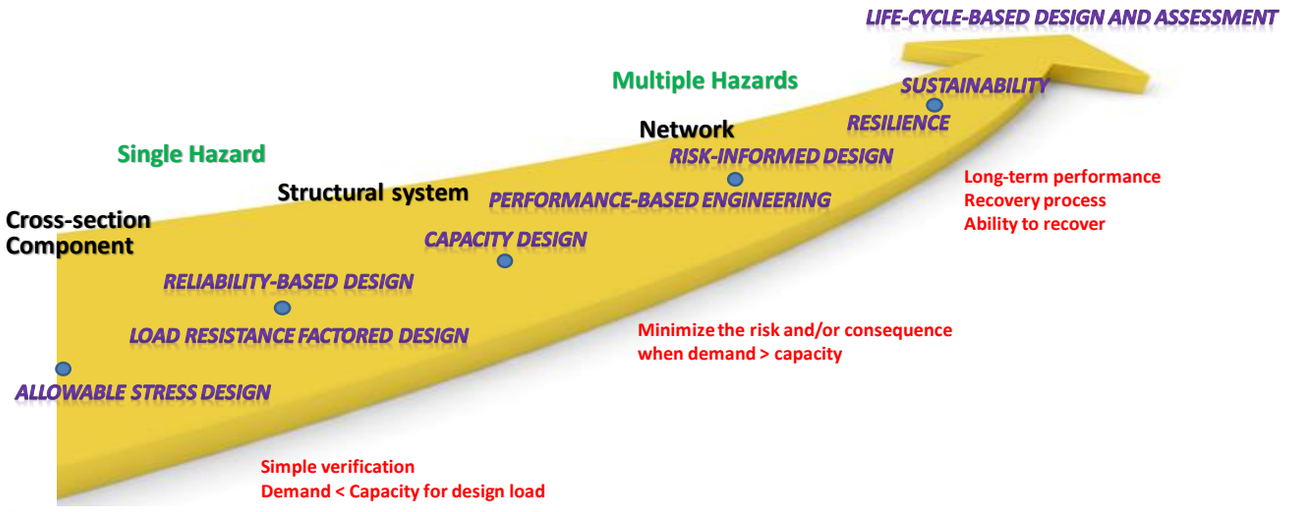


Figure 2. Progress of structural design methodology: From the classical allowable stress design method toward the life-cycle-based design and assessment of network involving bridges under multiple hazards

aiming to ensure structural sustainability in a life-cycle context (Du and Karoumi 2013, 2014, Wang et al. 2018). Sustainability includes social, economic, and environmental metrics to evaluate structural performance and can serve as a useful tool in decision making associated with civil infrastructure systems (Dong et al. 2014). Wang et al. (2018) proposed a novel life-cycle design methodology consisting of six steps: Level 1 -safety and reliability design, Level 2 -durability design, Level 3 -economic evaluation, Level 4 -local environmental evaluation, Level 5 -social evaluation, and Level 6 -global environmental environment. Gencturk et al. (2016) developed a life-cycle sustainability assessment framework which can be used for sustainability quantification of reinforced concrete (RC) buildings subjected to earthquakes. The sustainability through various stages of the lifetime of an RC building was obtained in terms of cost and downtime (related to the economy component), environmental emissions and waste generation (related to the environmental impact component), and deaths (related to society component).

Resilience emphasizes the impact of infrastructure damage, failure, and societal recovery when subject to hazards with a low probability of occurrence and potentially high consequences. On the other hand, sustainability concentrates on current and future resource management, and addresses the impacts of planning and development on the economy, society, and the environment. A sustainable infrastructure system needs to include resilient and adaptive capabilities to ensure its long-term sustainability. Some of the most promising solutions for resilience are actually also sustainable in nature (Mackie et al. 2016). Meanwhile, Bocchini et al. (2014) proposed a unified approach by combining resilience and sustainability and concluded that a systematic unification of resilience and sustainability is mandatory.

Design and assessment of structures have been geared towards addressing the most dominant hazard at the location of interest. However, the possibility of structures experiencing multiple hazards of different types during their service life needs to be considered. The design methodology of bridges must shift towards a more comprehensive approach of addressing multiple hazards to ensure adequate performance under different loading scenarios (Chulahwat & Mahmoud 2017, Gidaris et al. 2017). Quantification of the reliability and risk associated with damage to each bridge considering multi-hazard exposure helps in prioritizing retrofit activities for bridges in a network. There are different types of hazard such as: independent hazards, correlated hazards, concurrent hazards, and cascading hazards (Asprone et al. 2010, Akiyama & Frangopol 2012b, 2013a, Kameshwar & Padgett 2014).

Life-cycle performance approaches of RC structures exposed continuously to the attack of chloride ions in seismic prone regions were proposed by several investigators (Akiyama et al. 2011, Alipour et al. 2011, Biondini et al. 2014, Rao et al. 2016a, b, among others). Several researchers estimated the seismic risk or resilience of road network taking into consideration the effect of corrosion on the bridge performance deterioration (Rokneddin et al. 2013, Biondini et al. 2015, Kurtz et al. 2016, Alipour & Shafei 2016, Zanini et al. 2017).

Zhang et al. (2013) presented a holistic framework for fatigue reliability analysis of long-span bridges under combined dynamic loads from vehicles and wind. Even though the stresses from either the vehicle loads or wind loads may not be able to induce serious fatigue problems alone, the superposed dynamic stress ranges cannot be ignored for fatigue reliability assessment of long-span bridges.

Scour plays an important role in the seismic response of bridges since it weakens the foundation of the structure. A multihazard reliability-based or risk-based framework for evaluating the structural response of bridge under the combined effects of scour and earthquake events has been investigated (Banerjee & Prasad 2012, Dong et al. 2013, Alipour et al. 2013, Yilmaz et al. 2016, Chandrasekaran & Banerjee 2016).

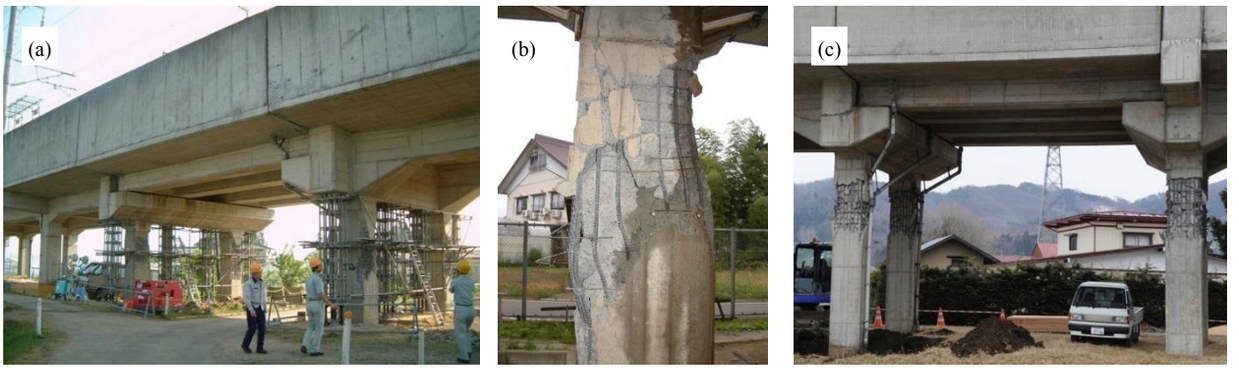


Figure 3. Typical failure mode of RC columns designed before the 1990s: Shear failure of RC columns of Shinkansen viaducts (phots (a) and (b) taken by the first author; and phot (c) courtesy of Dr. Takahashi at Kyoto University)



Figure 4. Typical failure mode of RC columns designed before the 1990s: Damage to RC columns with the cut-off of the rebars (photos (a) and (b) taken by the first author; and photo (c) courtesy of East Japan Railway Company)

A multi-hazard optimization framework for wind and seismic loading for two suspended floor slab isolation system was developed by Chulahwat & Mahmoud (2017). Their results highlighted the effectiveness of tuning the suspended slab system to meet the wind and seismic performance objectives.

Structural damage accumulation resulting from the action of sequences of seismic excitations has been investigated in the assessment of life-cycle system reliability and performance (e.g. Esteva et al. 2011, Esteva et al. 2016). Meanwhile, since it may take a time to repair the bridges after a mainshock, the aftershocks have the potential to cause more severe damage to bridges. Seismic hazards associated with aftershocks are not explicitly accounted for in modern bridge design codes, nor in emerging methodologies such as performance-based seismic design. Nazari et al. (2015) developed a methodology that can quantify the changes that would be needed in the structural design of a building to account for aftershock hazards and illustrate it by using a basic nonlinear model of a building. Probabilistic risk and resilience of highway bridges under mainshock and aftershock sequences were estimated for implementing risk mitigation strategies and equipping decision makers with a better understanding of structural performance under seismic hazards (Dong & Frangopol 2015).

Significant advances have been accomplished in the field of earthquake engineering. However, there is a need to promote further research for developing concepts and methods in order to design and assess resilient and sustainable bridges and bridge networks in a life-cycle context. This paper provides an

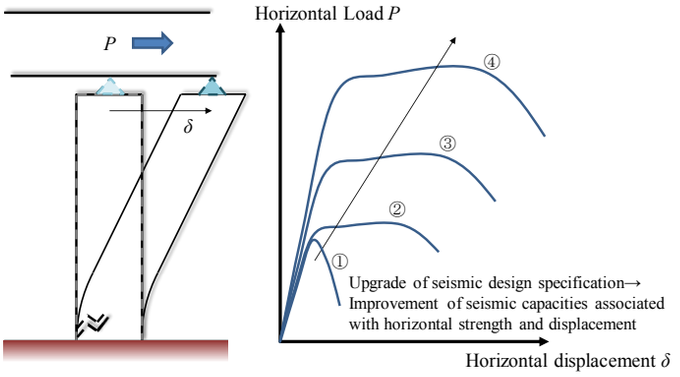


Figure 5. Improvement of seismic capacities associated with horizontal strength and displacement

overview of bridge design methodology progress together with the lessons from recent large earthquakes in Japan. Several performance indicators necessary to be implemented into the practical design and importance of taking into consideration the effect of multiple hazards on the life-cycle performance deterioration of bridges are introduced. Finally, the concepts and methods presented are illustrated on both single bridges and bridge networks under single and multiple hazards.

2 TOWARD LIFE-CYCLE BASED DESIGN AND ASSESSMENT OF BRIDGES UNDER MULTIPLE HAZARDS

Figure 2 shows progress of structural design methodology from the deterministic allowable stress design



Figure 6. No. 5 Inohana viaduct taken after the 2003 Sanriku-Minami earthquake and after the 2011 Great East Japan earthquake (Note: the viaduct was retrofitted before the 2011 Great East Japan earthquake) (both photos taken by the first author)

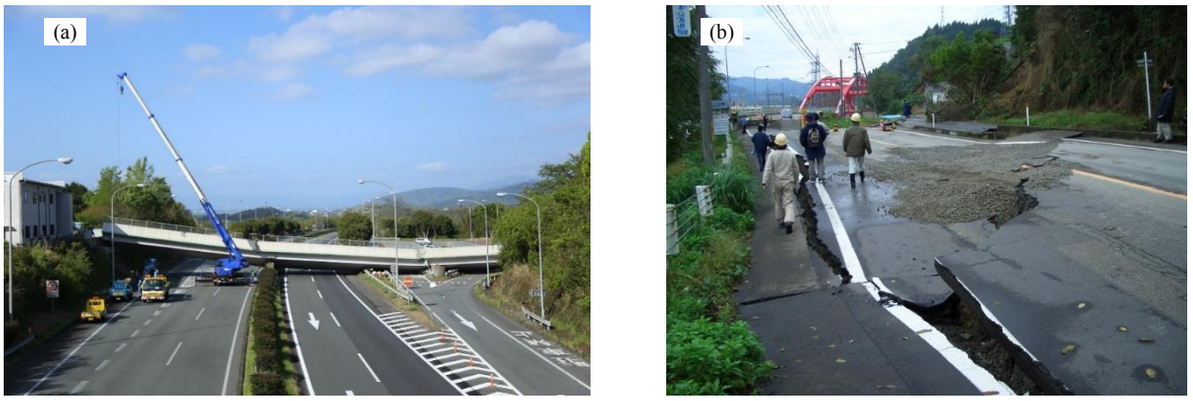


Figure 7. Example of post-disaster functionality deterioration of road network (photo (a) courtesy of Mr. Matsunaga at Kyodo Engineering Consultant Co. LTD.; and (b) taken by the first author)

method toward the life-cycle-based design and assessment of transportation networks involving bridges under multiple hazards. The structural safety in design is traditionary quantified by comparing the structural capacity, *R*, with the load effect, *L*. The uncertainties in *R* and *L* are implicitly considered when assigning the minimum allowable safety factor. Static and linear elastic analysis were performed to estimate *R* at the component-level. The designers did not predict the whole behavior of bridges under excitation and did not identify the possible failure mode when subject to the unexpected seismic action. Also, there is a lack of proper knowledge on structural details. Figures 3 and 4 show typical failure modes of RC columns designed according to the old design code. RC bridge piers had insufficient shear reinforcement and/or have cut-offs of longitudinal rebars without adequate anchorage length at the midpoint of bridge pier.

Based on the experience of seismic damage to bridges and research progress on earthquake resistance, shear and ductility designs of RC components were modified. Figure 5 shows the relationship between horizontal load and displacement of a bridge pier. According to the revisions of seismic design codes, lateral strength and displacement ductility have been improved (Kawashima 2000). Also, several seismic retrofitting methods have been developed. Figure 6 shows the damaged states of the Shinkansen viaducts taken after the 2003 Sanriku-Minami earthquake and the 2011 Great East Japan earthquake. The retrofitted columns of the viaducts performed well, with almost no damage during the 2011 Great East Japan earthquake (Akiyama & Frangopol, 2012b). There have been no reports on the damage of retrofitted RC columns or on the undesirable consequences elsewhere in the retrofitted bridge.

In current semi-probabilistic load resistance factored design, the concept of the reliability index is introduced in code calibration. The uncertainties in *R* and *L* are considered separately by assigning different load factors and resistance factors through rational calibration procedures, where target reliability index for each type of structural element is assigned to maintain an acceptable probability of failure (Liu et al. 2009). The structural components are designed based on either ultimate limit states or serviceability limit states or both (Estes & Frangopol 2001).

Evolution of structural design methodologies from allowable design method to load resistance factored design method has revealed the importance of uncertainty consideration in balancing economical and safety aspects of structural designs (Liu et al. 2009). With the development of computer technology, *R* and *L* at the structure-level could be evaluated by the nonlinear and dynamic analysis considering uncertainties and correlations. A reliability-based capacity design procedure was proposed to obtain the hierarchy of resistance of the various structural components and failure modes necessary to ensure a suitable plastic mechanism and avoid brittle modes (Akiyama et al. 2012a). Although the capacity design method has been developed to maximize post-event operability and minimize the cost of repairing bridges after a



Figure 8. Matsurube Bridge collapsed due to the land slide during the 2008 Iwate-Miyagi earthquake (both photos taken by the first author)



Figure 9. Koizumi Bridge collapsed due to the tsunami during the 2011 Great East Japan earthquake (both photos taken by the first author)

severe earthquake, consequences associated with functionality and recovery cannot be explicitly incorporated in the reliability-based capacity design method.

Figure 7 (a) shows the collapse of as-build bridges over the Kyushu Expressway preventing traffic passage after the 2016 Kumamoto earthquake. Figure 7 (b) shows the damage to embankment. Although the nearby bridge did not have any damage, the functionality of the post-disaster road network deteriorated severely. In addition, field investigations after recent large earthquakes in Japan confirmed that several bridges were severely damaged and collapsed not only due to the earthquake, as an independent hazard, but also to the subsequent tsunami, landslide or fault displacement. Figure 8 shows the collapse of Matsurube bridge during the 2008 Iwate-Miyagi Nairiku earthquake. The abutment was displaced by the landslide due to the strong ground motion. Figures 9 and 10 show the photos of Koizumi Bridge and Utatsu Bridge taken after the 2011 Great East Japan earthquake. Koizumi Bridge had the superstructure supported by five RC bridge piers. The superstructure was displaced more than 400 m from the original position. The concrete superstructure of Utatsu Bridge was washed away. Koizumi Bridge had been retrofitted by a seismic damper to prevent the excessive superstructure response under strong excitations. Also, RC bridge piers of the Utatsu Bridge were retrofitted by jacketing to improve their capacity against the strong ground motions (Akiyama et al. 2013b). Retrofitted bridges could prevent the failures from the strong ground motion; however, they could not prevent the washout of superstructure due to a giant tsunami. For these bridges, tsunami was the dominant hazard.

Figure 11 shows Aso Bridge taken before and after the 2016 Kumamoto earthquake. Aso Bridge was constructed in 1970. The center of Aso Bridge was an arch with a simple span and continuous three-span girders on both sides. The Aso Bridge would be completely destroyed due to a huge landslide or fault displacement caused by the 2016 Kumamoto earthquake. The Aso Bridge was retrofitted before the 2016 Kumamoto earthquake; however, for this bridge, the ground motion was not the dominant hazard. Figure 12 shows Okirihata Bridge taken after the 2016 Kumamo earthquake. This bridge was designed based on the design code revised after the 1995 Hyogoken-Nanbu earthquake. Rubber bearings, including elastomeric bearings and seismic isolators, had been installed to improve the seismic performance. All rubber bearings at the abutments and three piers were ruptured. Since the landslide occurred in the mountains directly beside the bridge, this damage might have been caused by not only the ground motion but also landslide effects. Please note that the cause of the Aso Bridge and Okirihata Bridge collapses is still under investigation.

Reliability-based approach for bridges under multiple hazards considers uncertainties associated with loads, resistance and modelling. However, this approach is not able to account for the consequences incurred from bridge failure. A framework for quantifying the functionality loss of road networks involving bridges and other road structures (e.g. tunnels and embankments) is needed based on the occurrence of a main shock and subsequent cascading



Figure 10. Utatsu Bridge collapsed due to the tsunami during the 2011 Great East Japan earthquake (all photos taken by the first author)

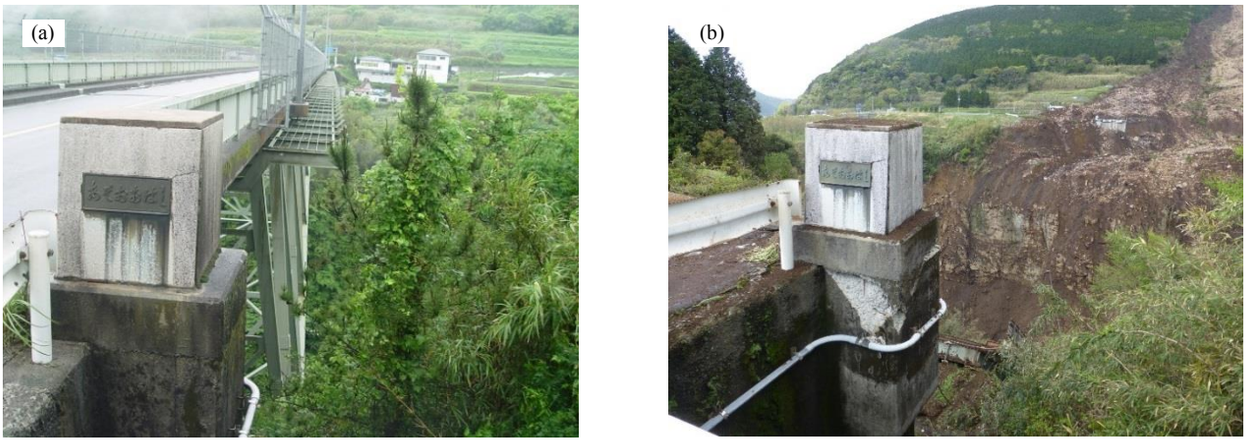


Figure 11. Aso Bridge collapse due to the ground motion, land slide and/or fault displacement during the 2016 Kumamoto earthquake (photo (a) courtesy of Dr. Yabe at Chodai Co. LTD.; and photo (b) taken by the first author)



Figure 12. Okirihata Bridge damaged due the ground motion and/or land slide (all photos taken by the first author)

hazard events (i.e., aftershocks, landslides, fault displacements or tsunamis). Constructing all structures with high-performance requirements that prevent any damage or failure due to severe earthquakes, giant tsunamis and/or huge landslides would be too expensive and impractical. A risk-based decision-making approach at the network-level needs to be developed for identifying the dominant hazard, most vulnerable structures and determining the priority of upgrade and/or repair actions.

Performance-based engineering has gained significant attention and is being used in many areas of structural engineering. Performance-based earthquake engineering has been at the frontier among natural hazards (Attary et al. 2017). This framework is based on the total probability theorem and can be disaggregated into different analysis phases that include hazard analysis, structural analysis, fragility analysis, and loss analysis. When the limit states of the structure are mutually exclusive, the probability of losses due to failure can be determined by multiplying the probability of failure by the probability of losses which is provided by (Ellingwood 2006a, b)

$$P[Loss > L] = \sum_{LS}\sum_{H} P[Loss > L|LS]\,P[LS|H]\,P[H] \quad (1)$$

$$P[Loss > L] = \sum_{LS} P[Loss > L|LS]\,P[LS|H_s] \quad (2)$$

where $P[H]$ is the probability of occurrence of hazard H, $P[LS \mid H]$ is the conditional probability of the limit state LS given the occurrence of H, $P[Loss > L \mid LS]$ is the probability of loss exceeding L given the limit state LS, and $P[LS \mid H_s]$ is the conditional probability of the limit state LS given the postulated hazard scenario.

Lounis & McAllister (2016) reported that the consequences associated with sustainability can be grouped as follows:

- Social consequences: fatalities, injuries, illnesses, psychological trauma, reputation damage, reduction/loss of service, public fear, loss of political support;
- Economic consequences: deterioration of structural system, damage to contents, loss of income, loss of productivity, delays in service delivery, user's costs; and
- Environmental consequences: irreversible environmental damage (depletion of resources, extinction) and reversible environmental damage (pollution, oxygen depletion in bays).

With regards to resilience, there may be similar social and economic consequences of failure. Additional consequences associated with resilience may include (Lounis & McAllister 2016):

- Functionality consequences: loss of community service, loss of facility use for its intended function, loss of other systems or services due to dependence on damages system; and
- Recovery consequences: time to restore system functionality results in delays and losses in restoration of



Figure 13 Debris generated by the tsunami due to the 2011 Great East Japan earthquake (photo (a) taken by the first author; and photo (b) courtesy of Dr Takahashi at Kyoto University)



Figure 14. Material deterioration observed in the field investigation after the 2011 Great East Japan earthquake (all photos taken by the first author)

other systems, costs to restore system reduce or delay funding for other services and systems.

In addition to the above consequence, the impacts of disaster waste management systems, in particular economic and social impacts, need to be investigated in terms of sustainability (Brown & Milke 2016). The environmental impacts of the disaster were substantial. For example, following the tsunami due to the 2011 Great East Japan earthquake, large areas of farmland were flooded with salty water and contaminated by sea sediments, which led to long-term soil contamination of high fertile agricultural land by metal and metalloid compounds (Portugal-Peperia & Lee 2016). As a result of the earthquake and subsequent tsunami, approximately 23 million tons of disaster debris was generated (see Figure 13), with more than 12 million m^3 of tsunami deposits left in the flooded area. The structural and geotechnical utilization of the concrete and soil fraction in the disaster debris and tsunami deposits has presented a huge challenge to engineers since (1) the clearance of debris and tsunami deposits is an urgent task which must be completed within a few years, and (2) although a large amount of waste-mixed concrete and soil can be recycled and used in the reconstruction, their properties have temporal and spatial variations (Inui et al. 2012). If poorly managed, the waste can have significant environmental and public health impacts and can affect the overall recovery process (Brown et al. 2011).

Field investigation conducted after the 2011 Great East Japan earthquake confirmed that some of RC structures and bridge steel bearings were severely deteriorated due to chloride-induced corrosion as shown in Figure 14. A life-cycle approach is needed in the risk assessment, mitigation procedure, and quantification of resilience and sustainability, because the effect of aging and environmental aggressiveness can reduce the structural performance and functionality, and it depends on the time of occurrence of the event (Biondini et al. 2015). The classical time-invariant structural design and assessment methods need to be revised to account for a proper modeling of the structural system over its entire life-cycle by taking into account the effects of deterioration process, time-variant loadings, and maintenance and repair interventions, among others (Biondini & Frangopol 2016). It is crucial to implement rational management strategies that maintain performance of bridges within acceptable levels through their life-cycle. As shown in Figure 2, life-cycle design and assessment methodology can encompass all the key concepts such as risk, resilience, sustainability, and multiple hazards learning from the past disasters. However, there is still a need to fill the gap between theory and practice by incorporating life-cycle concepts in structural design and assessment codes (Frangopol & Kim 2014, Biondini & Frangopol 2018).

As mentioned earlier, there have been many studies investigating the risk and resilience through quantitative approaches and application to case studies, among others, to bridge structures in transportation networks. They highlighted the importance of resilience for reducing the consequences of failures and



Figure 15. Rigid frame in the tsunami affected region taken after the 2011 Great East Japan earthquake (all photos taken by the first author)



Figure 16. Rigid frame in the landslide affected region taken after the 2016 Kumamoto earthquake (both photos taken by the first author)

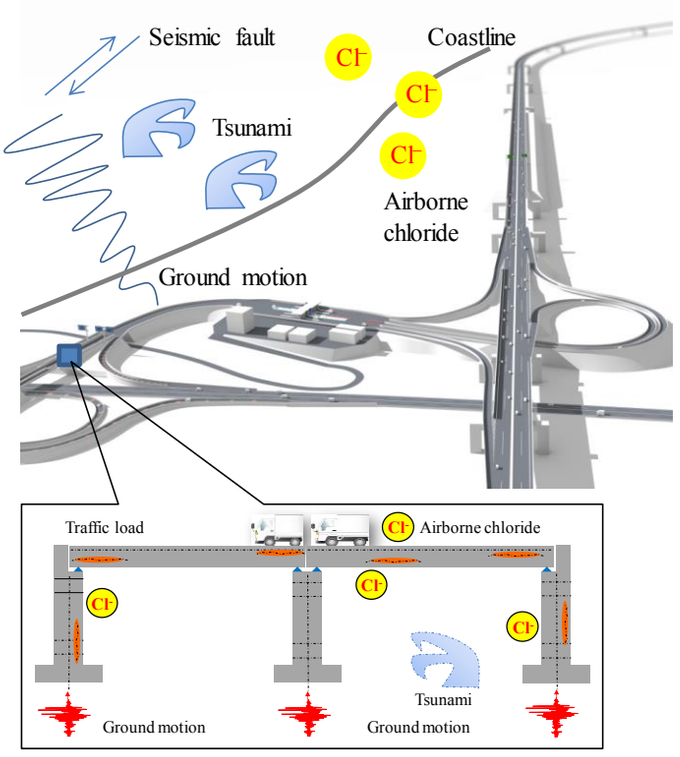


Figure 17. Bridges belonging to a network under independent and interacting hazards

enhancing serviceability subsequent to the occurrence of damage. However, the current literature is lacking studies and researches on the contribution to resilience coming from structural control. It is important to recognize that the capacity design approach is to carefully manage plastic deformations for ensuring life safety for the design event and collapse prevention for the maximum considered earthquake. Postearthquake restoration of damaged piers is challenging, time-consuming and cause traffic disruptions. Simple ductile structures are neither robust, nor do they exhibit rapidity as they are not easily repaired. Enhancing the robustness of bridge can improve the resiliency of the bridge itself and the surrounding community by reducing repair costs and downtime after an extreme event. Several interesting robust and resilient structures have been developed experimentally and computationally (Akiyama et. al. 2012c, Lehman et al. 2015, Echevarria et al. 2016, Domaneschi & Martinelli 2016, Rodgers et al. 2016, Iqbal et al. 2017, Mitoulis & Rodriguez 2017).

Compared with the conventional girder bridges, a rigid frame structure had less damage due to the effect of tsunami or landslide as shown in Figures 15 and 16. The rigid frame structure could be appropriate for the bridge under the hazards associated with tsunami and landslide. Figure 16 shows that the abutment of Aso-Choyo Bridge could not support the PC box girder after it was transversely displaced by the landslide. However, since both the superstructure and substructure were rigidly connected and behaved as a continuous unit, the severe damage to the Aso-Choyo Bridge due to this landslide was not observed. Further research is needed to investigate the robust and resilient bridges under multiple hazards.

Figure 17 shows an individual bridge and road network near a coastal line. Seismic and tsunami hazards have to be considered in the design and assessment of bridges and road structures belonging to the network. Also, bridges in the coastal area were deteriorated due to chloride-induced corrosion. When estimating the life-cycle reliability of bridges, it is important to consider the spatial distribution associated with the

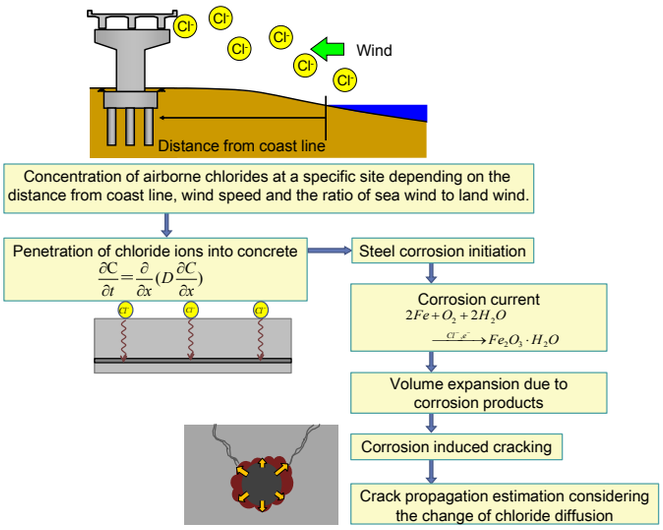


Figure 18. Flowchart for evaluating the deterioration process of RC structures in a marine environment (adapted from Akiyama et al. 2015)

seismic intensity of ground motion, hydrodynamic features, and the amount of airborne chloride. Comparing life-cycle reliabilities among structures belonging to a network under seismic and tsunami hazards and hazards associated with continuous deterioration (such as those associated with corrosion and fatigue) is useful for identifying significant threat scenarios and for assessing and mitigating the risk associated with structural damage and collapse.

In the following sections, several challenges for enhancing the life-cycle reliability and for mitigating the risk of both single bridges and bridge networks under multiple hazards are introduced.

3 LIFE-CYCLE RELIABILITY OF BRIDGES UNDER INDEPENDENT HAZARDS: MECHANICAL AND ENVIRONMENTAL HAZARDS

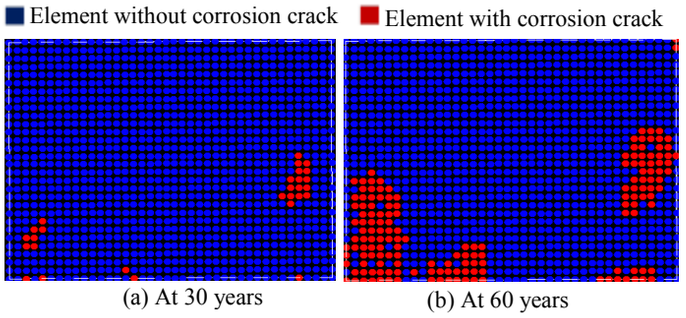
A time-dependent model has been developed that can simulate all stages of corrosion including corrosion initiation, crack initiation and propagation (Akiyama et al. 2010, 2012d, 2017, Papakonstantinou & Shinozuka 2013). Regarding the life-cycle reliability estimation of RC structures in an aggressive environment, the exact influence of environmental factors affecting degradation mechanisms is difficult to predict as they vary in time and space. Probabilistic hazard assessment associated with environmental stressors has to be included in the life-cycle reliability analysis of RC structures. Figure 18 shows the flowchart for evaluating the degradation process of RC slab in a marine environment.

It is well recognized that the material properties of a RC structure and structural dimensions are random due to the spatial variability associated with workmanship and other factors. This randomness cause spatially corrosion damages such as corrosion cracks and cover spalling. It is of great importance to simulate deterioration processes in a stochastic field context. Modeling the spatial variability of model parameters gives one the ability not only to quantify the probability of degradation but the extent of damage as well. As an example, based on the formulations presented by Papakonstantinou & Shinozuka (2013), spatial variability associated with the random variables used in the degradation process of a RC slab is represented by a 2D Gaussian stochastic field. The power spectral density is

$$S_{f_0 f_0}(\kappa_1,\kappa_2)=\sigma^2\frac{b_1 b_2}{4\pi}\exp\left[-\left(\frac{b_1\kappa_1}{2}\right)^2-\left(\frac{b_2\kappa_2}{2}\right)^2\right] \quad (3)$$

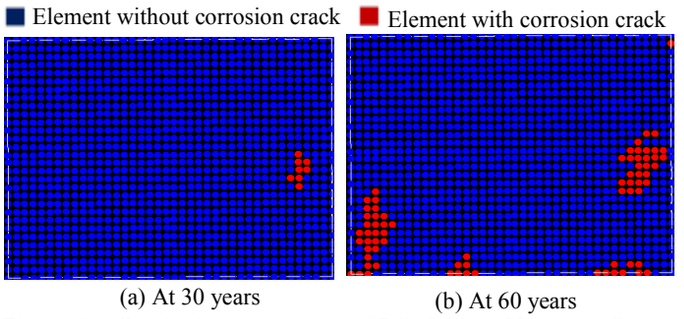
where b_1 and b_2 are proportional to the correlation distance of the stochastic fields along the x_1 and x_2 axes, respectively. In this illustrative example, it is assumed that b_1 and b_2 are both equal to 1.0. Further research is needed to investigate how power spectral density and its parameters can be determined to represent the spatial distributions of variables used in the degradation model.

Figures 19 and 20 show examples of RC slab plan views in Niigata City and Uwajima City, respectively, and illustrates the elements with corrosion cracks from a random realization at 30 years and 60 years after the construction (Miyamoto et al. 2015). Due to the difference of airborne chloride hazard, RC slab in Niigata City has more elements with corrosion cracks. For this case study, it was simply assumed that the concrete element cracks when the tensile stresses due to the volume expansion of corrosion products reach the tensile strength of concrete. If a bridge is located in earthquake-prone region or heavy traffic route, or both, it is necessary to consider the effect of material corrosion on life-cycle structural performance considering the spatial distribution associated



(a) At 30 years (b) At 60 years

Figure 19. Cracked area patterns of RC slabs in Niigata City



(a) At 30 years (b) At 60 years

Figure 20. Cracked area patterns of RC slabs in Uwajima City

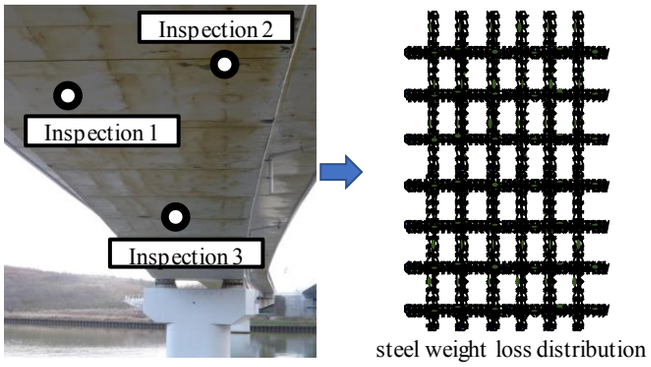


Figure 21. Estimation of steel weight loss distribution based on limited inspection results

with the material properties and mechanical stressors. Flexural and shear strength, and ductility capacity cannot be correctly estimated by using a very simple structural model (e.g. cross-section analysis using the reduced area of rebars).

Also, for existing bridges, what is actually important and difficult in their life-cycle reliability estimation is how to accurately predict the degree and location of the current material deterioration and how to adequately quantify this deterioration in terms of input data in the fragility analysis (Akiyama & Frangopol 2014, Yanweerasak, et al. 2016). As shown in Figure 21, identifying the possible spatial distribution of material corrosion over a large structure based on the limited number of inspection results and updating the life-cycle reliability are demanding and challenging problems. Owing to the uncertainties, the predicted life-cycle performance, despite how accurate or advanced the tools used to obtain this performance were, may deviate from the actual performance exhibited by the structure over time. A frequent updating of the life-cycle performance is required as new information become available (Okasha & Frangopol 2011).

In the seismic probabilistic risk assessment, the annual probability of exceedance of seismic capacity is

$$p_{fa} = \int_0^\infty -\frac{dp_0(\gamma)}{d\gamma} \cdot P\left[D_e \geq C_a \middle| \Gamma = \gamma\right] d\gamma \qquad (4)$$

where $p_0(\gamma)$ is the annual probability that the seismic intensity, Γ, at a specific site would exceed a value γ; and $P\left[D_e \geq C_a \middle| \Gamma = \gamma\right]$ is the fragility, which is the conditional probability of the seismic demand D_e exceeding the seismic capacity C_a conditioned upon the seismic intensity γ.

In the calculation of the conditional probability $P\left[D_e \geq C_a \middle| \Gamma = \gamma\right]$ of bridge piers in a marine environment, the effect of corrosion has to be taken into consideration. The demand depends on the results of seismic hazard assessment; however, the seismic capacity depends on the results of hazard associated with airborne chlorides. As the steel weight loss of rebars increases, the seismic capacity decreases. Using the total probability theorem, the annual probability of exceedance of seismic capacity C_a under earthquake excitation at t years after construction can be expressed as

$$p_{fa}(t) = \int_0^{100} \int_0^\infty -\frac{dp_0(\gamma)}{d\gamma} \cdot P\left[D_e \geq C_a \middle| \Gamma = \gamma, C_w = c_w(t)\right] \cdot f\left(c_w(t)\right) d\gamma \, dc_w \qquad (5)$$

where $P\left[D_e \geq C_a \middle| \Gamma = \gamma, C_w = c_w(t)\right]$ is the probability of the seismic demand D_e exceeding the seismic capacity C_a conditioned upon the seismic intensity γ and steel weight loss $c_w(t)$; and $f(c_w(t))$ is the probability density function (PDF) of $c_w(t)$.

Based on the comparison of the experimental and computational results of corroded RC columns subjected to cyclic loading, Akiyama et al. (2011) confirmed that the accuracy of the results of corroded columns is approximately the same as that of noncorroded columns. To ensure the computational accuracy of δ_u as shown in Figure 22, the average steel weight loss in the plastic hinge of a RC bridge pier must be estimated correctly.

For an existing RC bridge pier, this could be estimated based on the discrete inspection results associated with the steel weight loss. Yanweerasak et al. (2016) presented a procedure for estimating the mean and variance of steel weight loss in the plastic hinge of corroded RC structures based on inspection results. Variance of steel weight loss depends on the number and space interval of inspection locations based on the statistical estimation error process (Honjo & Otake 2013). The variance is used as the observation noise during the updating process. $P\left[D_e \geq C_a \middle| \Gamma = \gamma, C_w = c_w(t)\right]$

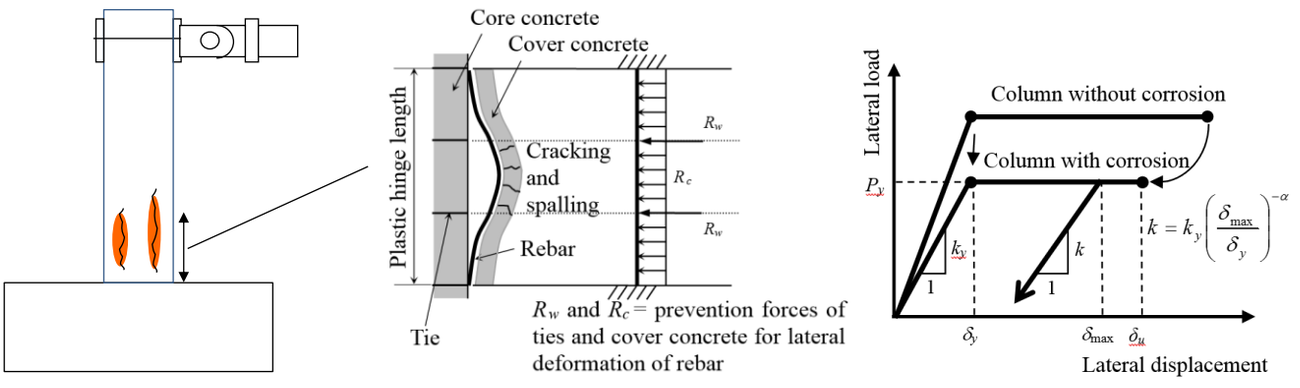


Figure 22. Buckling model of a longitudinal rebar in the plastic hinge of corroded RC column subjected to cyclic loading

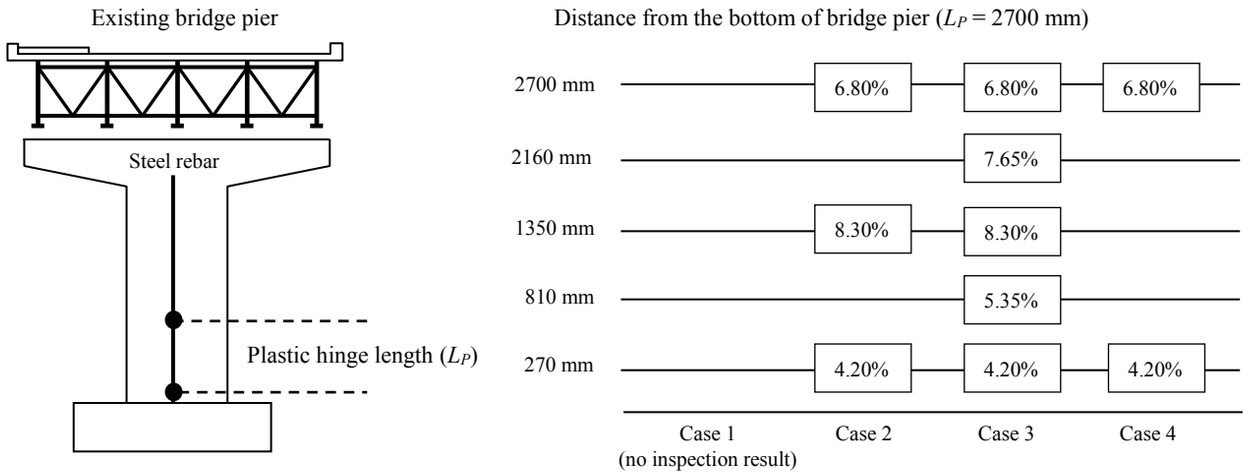


Figure 23. Assumed location of the steel weight loss measurements in the plastic hinge

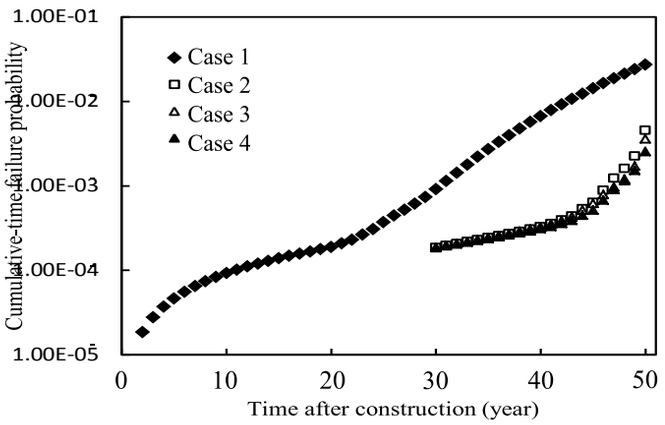


Figure 24. Relationship between the cumulative-time failure probability and the time after construction (years)

in Equation 5 is estimated using the updated random variables.

As an illustrative example, the locations of the steel weight loss measurements are assumed as shown in Figure 23. The simple average is almost the same among Cases 2, 3 and 4, but, the number of inspection points are different. Figure 24 shows the updated cumulative-time failure probability based on the inspection data using Sequential Monte Carlo Simulation (SMCS) (Akiyama et al. 2010). The cumulative-time failure probabilities of Cases 2, 3 and 4 at year 30 are smaller compared with that of Case 1. From Figure 24, although the cumulative-time failure probabilities are nearly identical for Cases 2, 3 and 4 because the magnitudes of steel weight loss from the inspection results are almost identical, a significant difference in the correlation among random variables can be confirmed. Figure 25 shows the correlations between x_3 and x_5 using 100,000 samples of SMCS, where x_3 and x_5 are random variables associated with airborne chloride and surface chloride concentration relation, and associated with estimation by diffusion equation, respectively. Before updating, the random variables are assumed statistically independent. After updating, all random variables related with the prediction of the steel weight loss were updated simultaneously by SMCS. These results illustrate that, as expected, having more inspection locations can provide a more accurate reliability assessment.

For a RC bridge pier subjected to the cyclic loading, the plastic hinge is formed at the bottom of the pier. The ductility capacity depends strongly on the corrosion level of plastic hinge. Meanwhile, it's difficult to identify the possible failure region of corroded concrete girder subjected to traffic load. The severity of damage due to corrosion of RC structures primarily

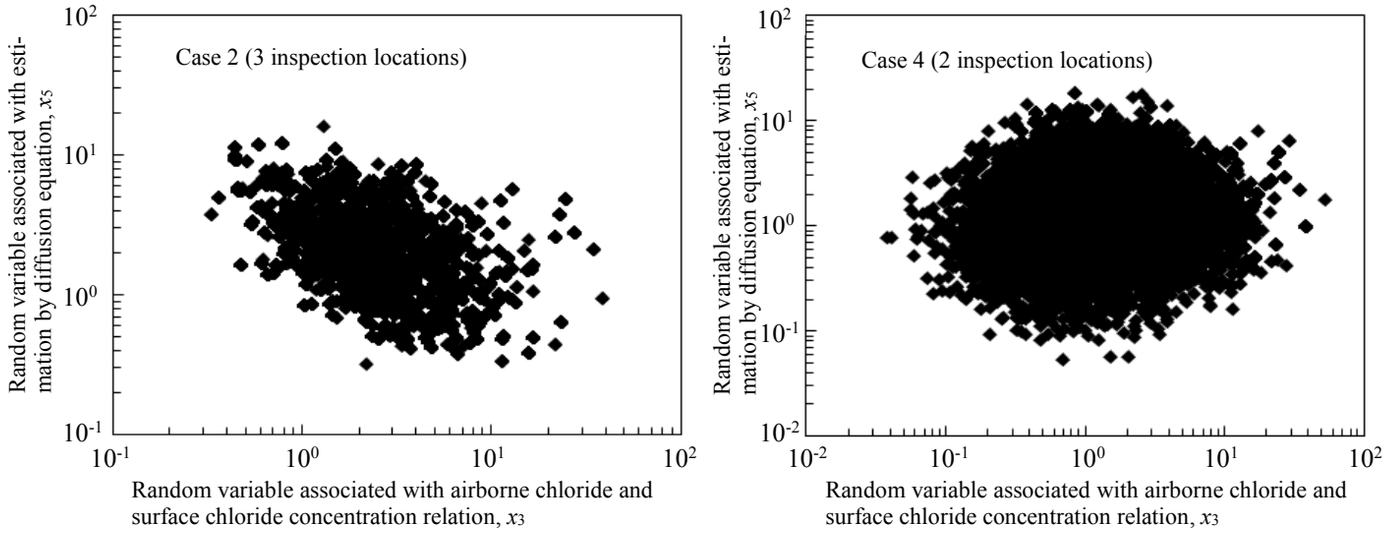


Figure 25. Effect of the number of inspection locations on the variability associated with random variables used in the prediction of steel weight loss (adapted from Yanweerasak et al. 2016)

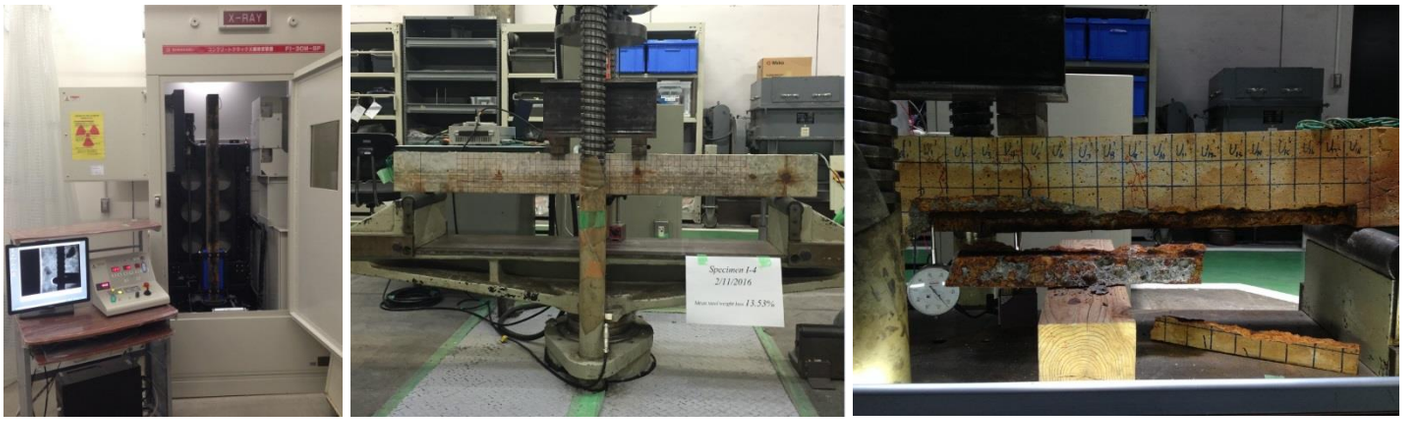


Figure 26. X-ray machine at Waseda University to visualize the corroded rebars embedded in the concrete beam

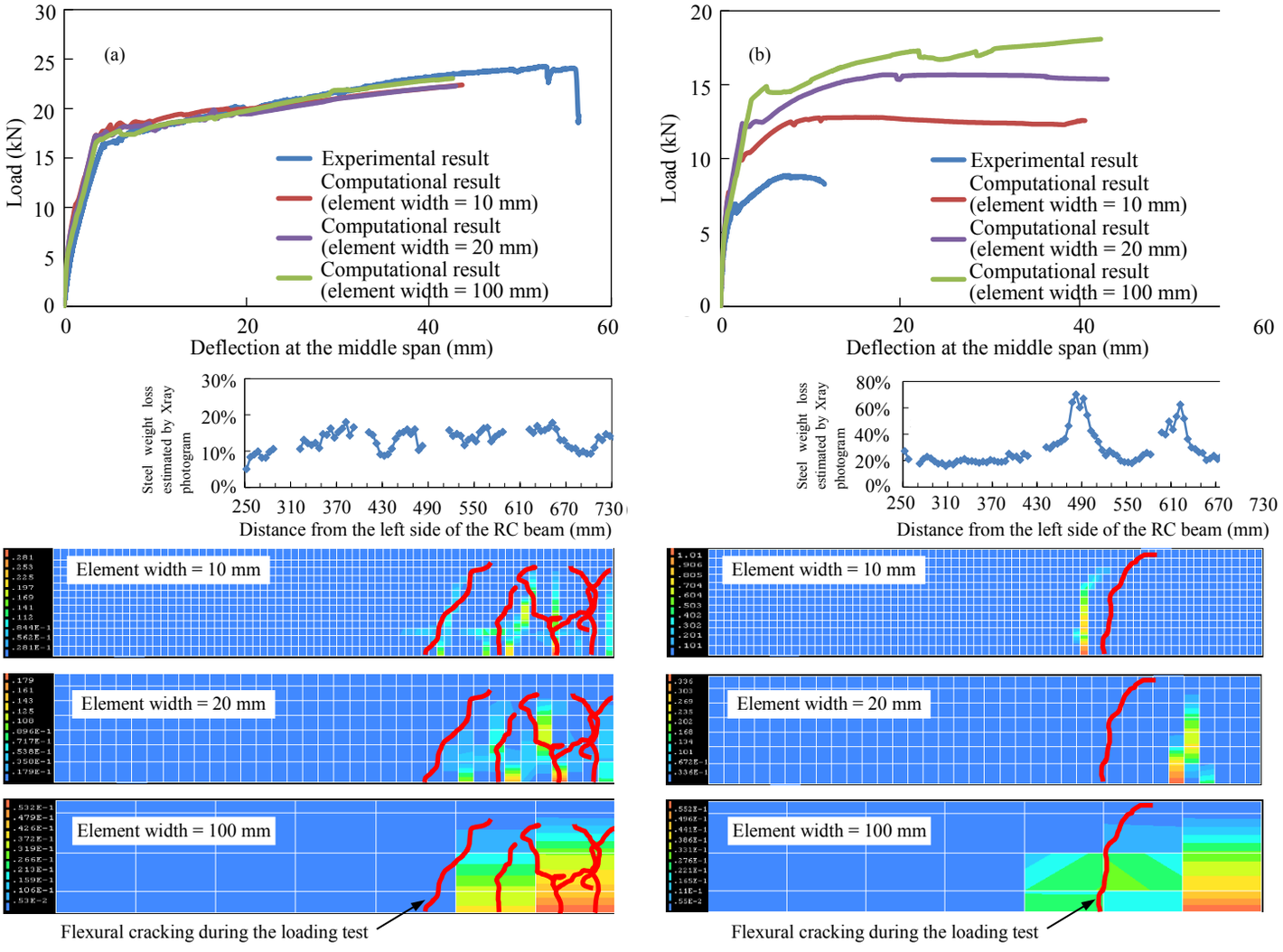
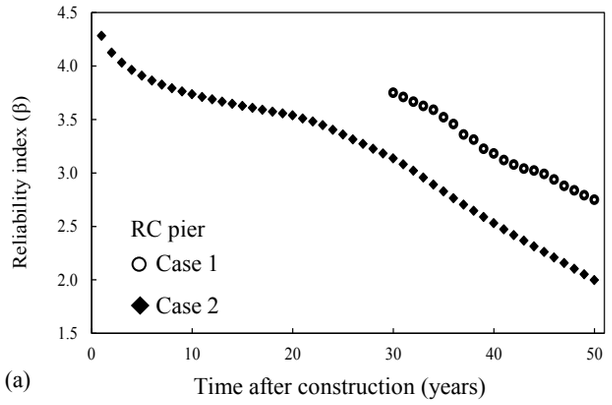


Figure 27. Effect of element size in FE model on the computational results of corroded RC beam: (a) average steel weight loss over RC beam = 12.1%; and (b) average steel weight loss over RC beam = 25.5%

depends on the magnitude and location of the steel corrosion. Spatial distribution associated with the material corrosion in concrete girder has to be investigated.

To understand the steel corrosion growth process and the change in the spatial variability of steel corrosion with time, continuous monitoring is necessary. X-ray photography has been applied to observe steel corrosion in RC beams (Akiyama & Frangopol 2014, Lim et al. 2016, 2017). They estimated the steel weight loss by the digital image processing of the X-ray photograms. The nonuniform distribution of steel weight loss along rebars inside RC beams determined using X-ray radiography and its correlation with longitudinal crack widths and loading capacity were experimentally investigated (see Figure 26). A finite element (FE) analysis method has been used to simulate the structural responses of the corroded beams when considering two different inputs (i.e., uniform and non-uniform cross-sectional area of rebars over the beam). Comparing the numerical results of the flexural responses of the simulated beams to those of the test beams in the experimental study, the effect of mesh size on the accuracy of the FE model was investigated.



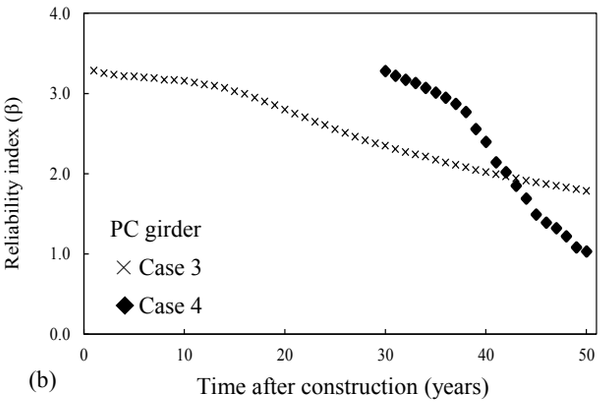


Figure 28. Life-cycle reliabilities: (a) RC pier; and (b) PC girder

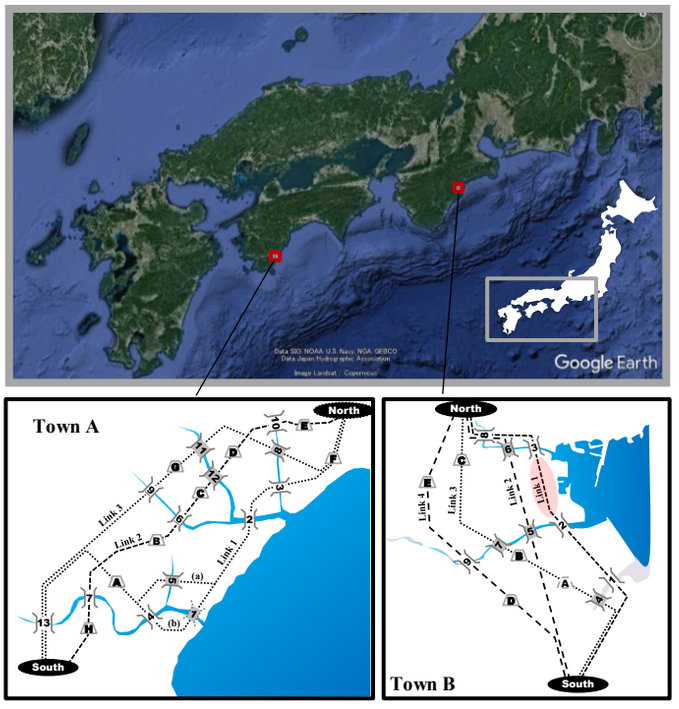


Figure 29. Example of road network affected by the anticipated Nankai Trough earthquake

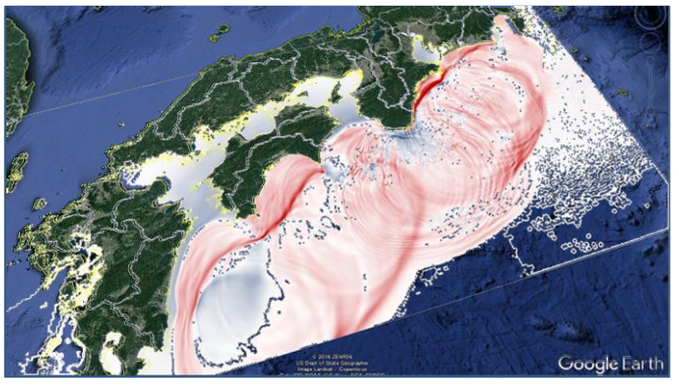


Figure 30. Propagation analysis of tsunami caused by the anticipated Nankai Trough earthquake

Figure 27 shows the comparison of computational and experimental results of the relationship between load and deflection, and the comparison of contour of the principal tensile strain obtained from the FE analysis, flexural cracking caused during the bending test, and steel weight loss. Average steel weight losses over RC beam shown in Figures 27 (a) and (b) are 12.1 % and 25.5%, respectively. As shown in Figure 27, when the spatial distribution of steel weight loss seems to be more uniform, the effect of mesh size on the computational results can be ignored. However, when the spatial variability becomes larger, the computational results depend on the mesh size. Spatial distributions associated with the bond properties and internal and external cracks due the volume expansion of corrosion products are not considered in the computational results shown in Figure 27. More studies on this topic are needed for further improvements in FE modeling.

Figure 28 shows the comparison of life-cycle reliability of bridge pier under seismic and airborne chloride hazards with that of bridge girder under traffic load and airborne chloride hazards. Comparing life-cycle reliabilities among the bridge components under multiple hazards can make the determination of the priority of intervention actions possible.

4 LIFE-CYCLE RELIABILITY OF BRIDGES UNDER INTERACTING HAZARDS: SEISMIC AND TSUNAMI HAZARDS

Frameworks for multihazard risk assessment have been reported in the literature as described earlier. Tsunami intensity is correlated with the magnitude of the oceanic earthquake, and a bridge may have severe damage due to the strong ground motion before the tsunami arrives. Difficulties in estimating the reliability of bridges under tsunami hazards are similar to those associated with bridges under aftershocks. Strong aftershocks have the potential to cause extensive structural damage. Damaged structures due to mainshock are even more susceptible to incremental damage due to aftershocks because their reduced structural capacity decreases the threshold of the ground motion intensity needed to cause further damage.

Yeo and Cornell (2005) divided the seismic performance assessment and design process into simpler components in terms of the description, definition and quantification of earthquake intensity measures (*IM*s), engineering demand parameters (*EDP*s), damage measures (*DM*s) and decision variables (*DV*s). Commonly used examples of the above parameters are peak ground acceleration (PGA) and first-mode

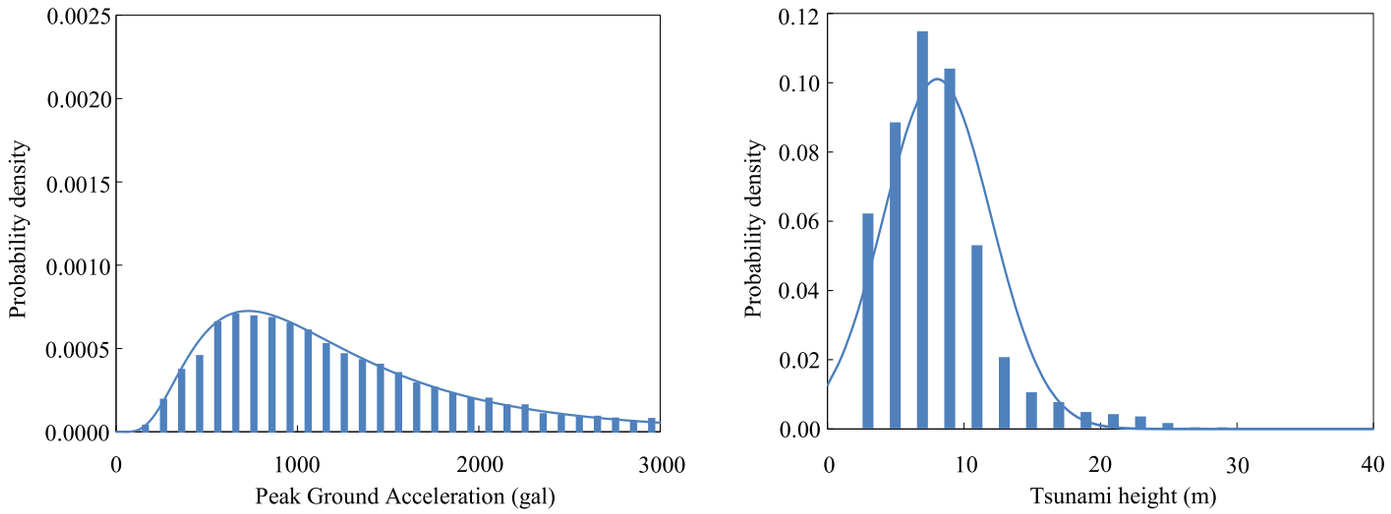


Figure 31. Example of probability densities of peak ground acceleration and tsunami height at the Town A in Figure 29

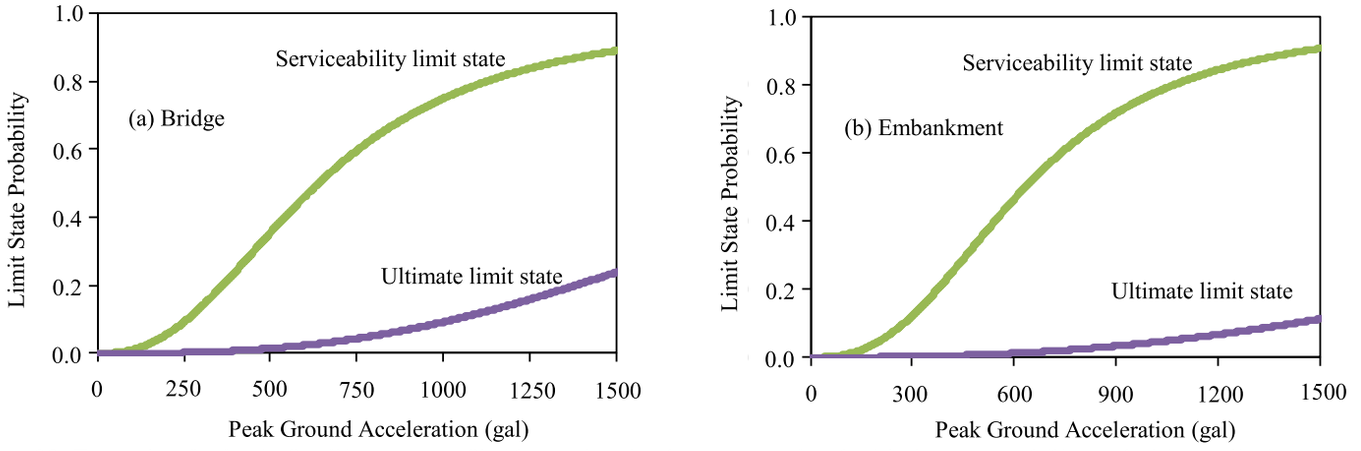


Figure 32. Example of seismic fragility curves of bridge and embankment associated with the serviceability and ultimate limit states

spectral acceleration (*IM*s), interstory drift ratios, inelastic component deformations and floor acceleration spectra (*EDP*s), damage states of structural and nonstructural elements (*DM*s) and fatalities, financial losses and downtimes (*DV*s). Based on the total probability theorem, the mean annual rate $v(DV)$ of exceeding a given level of $DV = x$, is (Yeo and Cornell 2005)

$$\upsilon(DV) = \iiint G\left(DV|DM\right) dG\left(DM|EDP\right) dG\left(EDP|IM\right)\left| d\lambda\left(IM\right)\right| \qquad (6)$$

where λ (IM) is the mean annual rate of exceeding a given IM and is obtained from a conventional probabilistic hazard analysis. $G(EDP|IM)$ is the complement of the cumulative distribution function of EDP conditioned by a given level of IM (i.e., $G(EDP|IM) = P[EDP \geq y|IM = x]$ while in the continuous case $G(EDP|IM) = f_{EDP|IM}(y|x)dy$ is the conditional probability density function times dy).

Based on Equation 6, Yeo and Cornell (2005) discussed the reliability of structures under aftershock hazard. If a structure had the mainshock with the intensity MI and damage state SI due to the mainshock, the mean rate exceeding a given DV in post-mainshock time interval $[0, t_{max}]$ is (Yeo and Cornell 2005)

$$\upsilon_a^{t_{\max}}\left(DV \mid MI, SI\right) = \int_{DM}\int_{EDP}\int_{IM}\sum_{i} G_a(DV \mid DM, i)\, dG_a(DM \mid EDP, i)\, dG_a(EDP \mid IM, i)\, d\lambda_a^{t_{nax}}\left(IM, i \mid MI\right) dG_a(i \mid MI, SI) \qquad (7)$$

where the subscript a refers to the aftershock environment, $\lambda^{tmax}{}_a$ is the mean number of aftershocks exceeding a given IM in post-mainshock time interval, and $G_a(i|MI, SI)$ is the probability that the structure is in damage state i after the mainshock given MI and SI. The inclusion of $G_a(i|MI, SI)$ means an additional integral over all possible post-mainshock damage states i.

Equation 7 can be used for estimating the reliability of bridges under tsunami hazards. IM could be the hydrodynamic features such as tsunami wave velocity and height, and EDP and DM could be the tsunami demands and structural damage states due to the tsunami in the estimation of dG_a in Equation 7. In addition, if reliability will be estimated given the occurrence of the earthquake, Equations 6 and 7 can be simplified because it is not necessary to consider the earthquake occurrence rate.

It is expected that the damage and the economic loss resulting from the anticipated Nankai Trough earthquake and its associated tsunami would be larger

Table 1 Failure probability of the bridge and embankment at the Town B in Figure 29

Extreme Event	Bridge			Embankment		
	2	5	9	A	B	E
Ground motion	0.106	0.106	0.106	0.157	0.157	0.157
Tsunami	0.648	0.629	0.573	0.857	0.742	0.157

than those resulting from the 2011 Great East Japan earthquake. As an illustrative example, reliabilities, life-cycle cost and recovery time of road networks including bridges and embankments in Town A in Kochi-Prefecture and Town B in Mie-Prefecture under both seismic and tsunami hazards due to the anticipated Nankai trough earthquake are computed. Figure 29 shows the schematic layouts of the investigated network. The parameters associated with the fault movement caused by the anticipated Nankai trough earthquake are determined based on Central Disaster Management Council (2003).

It is difficult to evaluate the exact fault movement during the seismic event since uncertainties associated with fault movement vary in time and space. The average stress drop at the seismic fault is assumed to be random. Seismic intensity at the bridge site given seismic event is estimated by the attenuation relation. In this case study, the PDF of the PGA given the occurrence of the anticipated Nankai Trough earthquake is calculated. Figure 30 shows an example of tsunami propagation computation to obtain the PDF of the tsunami wave height and velocity at the locations of bridges and embankments analyzed. Horizontal 2D tsunami analysis based on non-linear long-wave theory (Goto et al. 1997) is performed in this simulation. The PDF is calculated by Monte Carlo Simulation (MCS) using the random variables associated with the seismic fault and considering the difference of roughness coefficient among the locations of interest.

Figure 31 shows an example of probability densities of PGA and tsunami height at the Town A in Figure 29. Also, Figure 32 shows the seismic fragility curves of bridge and embankment for the serviceability and ultimate limit states.

The PDF of the hydrodynamic forces given the tsunami height can be identified based on MCS. Then, the hydrodynamic horizontal and uplift forces are applied to bridges. When estimating the tsunami fragility of bridges, a push-over analysis using hydrodynamic forces given tsunami height is performed to compare the tsunami capacity with the tsunami demand. Tsunami fragility of embankments can be estimated by comparing the heights of embankment and tsunami.

Table 1 lists the failure probabilities of Bridge 2, Bridge 3, Bridge 9, Embankment A, Embankment B, and Embankment C at the Town B shown in Figure 29. It can be confirmed that the failure probabilities of bridges due to tsunami decrease with the distance from the coastline. As listed in Table 1, the seismic and tsunami reliabilities depend on the locations of bridge and embankment in the road network. When the structure is located near the coast line, the failure probabilities need to be estimated considering the effect of both seismic and tsunami hazards on the structural performance.

The ground motion induced- and/or tsunami induced damage to bridges cause the deterioration of the post-disaster road network functionality. The

Table 2 Damage state and residual percentage relation (after Guo et al. 2017)

Damage State	*LDI*	Residual Percentage (%)	
		Traffic-carrying capacity	Free-flow speed
None	$0 \le LDI < 0.5$	100	100
Slight	$0.5 \le LDI < 1.0$	100	75
Moderate	$1.0 \le LDI < 1.5$	75	50
Excessive	$1.5 \le LDI < \infty$	50	50
Complete	∞	0	0

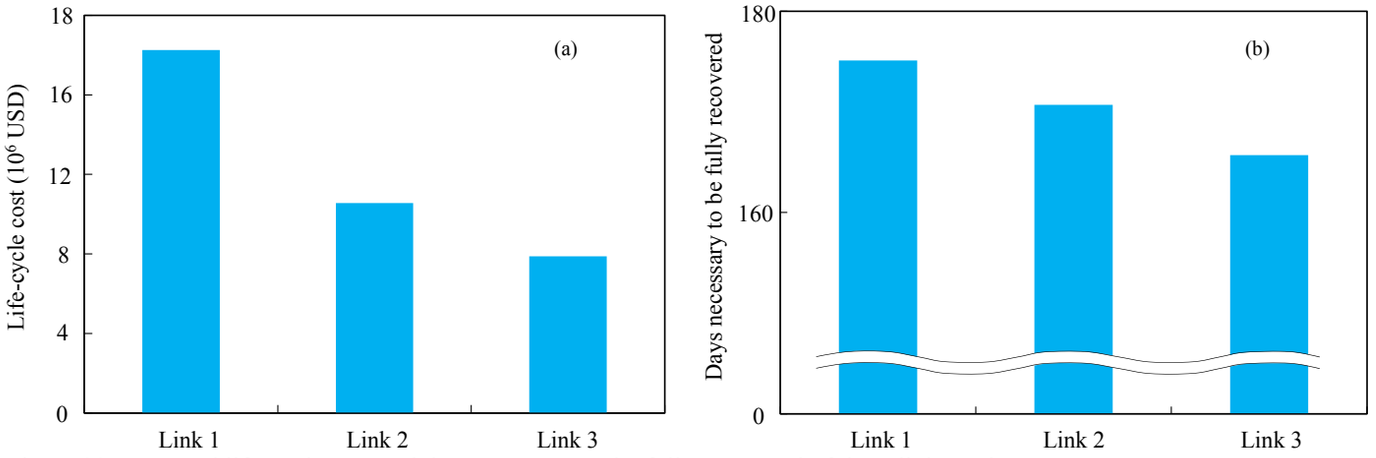


Figure 33. Expected life-cycle cost and days necessary to be fully recovered of three links at the Town B

damaged bridges can be open, closed or partially open within a bridge network. Consequently, traffic flow in the links can be different and speed limits might be reduced for various damage conditions of the link (Frangopol et al. 2017). As there may be several bridges located on the link, the damage state of each bridge can affect the functionality of the investigated link. The performance of a link after an earthquake can be expressed in terms of link damage index (*LDI*) provided by (Chang et al. 2002)

$$LDI(t) = \sqrt{\sum_{j=1}^{n} BDI_j((t))^2} \tag{8}$$

where n is the number of the bridges located in the link, and BDI_j is the expected damage index of bridge j.

After earthquakes, the damage states of individual bridges are generally divided into five levels: none, slight, moderate, extensive and complete damage states. The damage states with these linguistic descriptions are quantified by the bridge damage index (*BDI*) with discrete values of 0, 0.10, 0.25, 0.75 and 1, respectively. A value of 0 corresponds to no damage, while 1 corresponds to the complete collapse of the bridge. The none, slight, moderate and major damage states are associated with $LDI \leq 0.5$, $0.5 < LDI \leq 1.0$, $1.0 < LDI \leq 1.5$, and $LDI > 1.5$, respectively (Chang et al., 2000). The increase in the damage state of the link will reduce the link traffic capacity and speed limit. In this case study, the relationship between damage state and residual percentage of traffic-carrying capacity and free-flow speed listed in Table 2 (Guo et al. 2017) was used.

Figures 33(a) and 33(b) show, respectively, the expected life-cycle cost and days necessary to be fully recovered from the event of three links, Link 1, Link 2 and Link 3 at the Town B. As shown in Figure 29, the bridges and embankments belonging to Link 1 have higher failure probabilities, implying higher life-cycle cost and days necessary to be fully recovered, because both ground motion and tsunami can cause the damage to structures. Reliability and risk approaches are useful to identify the dominant hazard and most vulnerable structure, and to make the decision on the priority for upgrade and/or repair actions.

5 CONCLUSIONS

This keynote paper overviewed the progress of structural design methodology from the deterministic allowable stress design method toward the life-cycle-based design and assessment of bridges and bridge networks under multiple hazards. Field investigations after recent large earthquakes in Japan confirmed that several bridges were severely damaged and collapsed not only due to the earthquake, as an independent hazard, but also to the subsequent tsunami, landslide or fault displacement. In addition, the collapse of as-build bridges over highways prevented the traffic passage. Even if the bridge has no damage during the seismic event, damage to embankment can deteriorate the functionality of the post-disaster road network. A probabilistic life-cycle framework for quantifying the functionality loss of road networks involving bridges and other road structures is needed for the occurrence of a main shock and subsequent cascading hazard events. A risk-based decision-making approach at the network-level is necessary for identifying the dominant hazard and vulnerable structures requiring the strengthening and retrofit.

Because the transportation networks play important roles for the evacuation of affected people and the transportation of emergency goods and materials, it is necessary to recover the functionality of these networks as soon as possible after a severe natural disaster. To quantify the promptness of the restoration, it has become customary to use the concept of resilience. In addition, the economic, environmental and social impacts of disaster waste management systems need to be investigated in terms of sustainability. If the disaster waste is poorly managed, this can have significant environmental and public health impacts and can affect the overall recovery process. Consequences associated with the resilience and sustainability must be studied and implemented into the risk estimation of bridge network under multiple hazards. Life-cycle design and assessment methodology can encompass all the key concepts such as risk, resilience, sustainability, and multiple hazards learning from the past disaster lessons.

Finally, the concepts and methods presented are illustrated on both single bridges and bridge networks with an emphasis on earthquake, tsunami and continuous deterioration. Further research is needed to enhance the framework for estimating the reliability and risk of bridges under interacting hazards. Specifically, the integration of bridge performance under multiple independent or interacting hazards in a comprehensive life-cycle infrastructure network in terms of performance, management and optimization under uncertainty (Frangopol 2011, Frangopol & Soliman 2016) must be investigated.

ACKNOWLEDGEMENTS

The authors express sincere appreciation to Dr. Masayuki Yoshimi, National Institute of Advanced Industrial Science and Technology of Japan, for his suggestions related to seismic fault parameters. The authors also thank Prof. Shunichi Koshimura at Tohoku University for many suggestions on the topic of tsunami propagation analysis. Special appreciation is extended to Dr. Sopokhem Lim and Mr. Kengo Nanami at Waseda University. This work was supported by JSPS KAKENHI Grant Number JP 16H02357 and 16KK0152 and the Institute for

Research on Safety and Security of Greater Tokyo. The support by grants from U.S. National Science Foundation Award CMMI-1537926 and the U.S. Federal Highway Administration Cooperative Agreement Award DTFH61-07-H-00040 is also gratefully acknowledged.

The opinions and conclusions presented in this paper are only those of the authors.

REFERENCES

Akiyama, M., Frangopol, D.M. & Yoshida, I. 2010. Time-dependent reliability analysis of existing RC structures in marine environment using hazard associated with airborne chlorides. *Engineering Structures* 32: 3768-3779.

Akiyama, M., Frangopol, D.M. & Matsuzaki, H. 2011. Life-cycle reliability of RC bridge piers under seismic and airborne chloride hazards. *Earthquake Engineering and Structural Dynamics* 40(15): 1671-1687.

Akiyama, M., Matsuzaki, H., Dan, H.T., Suzuki, M. 2012a. Reliability-based capacity design for reinforced concrete bridge structures. *Structure and Infrastructure Engineering* 8(12): 1096-1107.

Akiyama, M. and Frangopol, D.M. 2012b. Lessons from the 2011 Great East Japan earthquake: Emphasis on life-cycle structural performance. *Proceedings of the Third International Symposium on Life-Cycle Civil Engineering* (A. Strauss. D. M. Frangopol, K. Bergmeister eds.), Vienna, Austria, Oct. 3-6, 2012, CRC Press, 13-20, and DVD: 18-35.

Akiyama, M. Abe, S., Aoki, N. & Suzuki, M. 2012c. Flexural test of precast high-strength reinforced concrete pile prestressed with unbonded bars arranged at the center of the cross-section. *Engineering Structures* 34(1): 259-270.

Akiyama, M., Frangopol, D.M. & Suzuki, M. 2012d. Integration of the effects of airborne chlorides into reliability-based durability design of reinforced concrete structures in a marine environment. *Structure and Infrastructure Engineering* 8(2): 125-134.

Akiyama, M. & Frangopol, D.M. 2013a. Life-cycle design of bridges under multiple hazards: Earthquake, tsunami, and continuous deterioration. *Proceedings of the Eleventh International Conference on Structural Safety and Reliability*, ICOSSAR2013, New York, NY, USA, June 16-20, 2013; in Safety, Reliability, Risk, and Life-Cycle Performance of Structures and Infrastructures, G. Deodatis, B.R. Ellingwood, and D. M. Frangopol, eds., CRC Press, Taylor & Francis Group, Boca Raton, London, New York, Leiden, 2013, 3-4, and full paper on USB stick, Taylor and Francis Group, London, 2014, 3-16.

Akiyama, M., Frangopol, D.M., Arai, M. & Koshimura, S. 2013b. Reliability of bridges under tsunami hazards: emphasis on the 2011 Tohoku-oki earthquake. *Earthquake Spectra* 29(S): S295-S314.

Akiyama, M., Frangopol, D.M. & Mizuno, K. 2014. Performance analysis of Tohoku-Shinkansen viaducts affected by the 2011 Great East Japan earthquake. *Structure and Infrastructure Engineering* 10(9): 1228-1247.

Akiyama, M. & Frangopol, D.M. 2014. Long-term seismic performance of RC structures in an aggressive environment: emphasis on bridge piers. *Structure and Infrastructure Engineering* 10(7): 865-879.

Akiyama, M., Frangopol, D.M. & Takenaka, K. 2017. Reliability-based durability design and service life assessment of reinforced concrete deck slab of jetty structures. *Structure and Infrastructure Engineering* 13(4), 468-477.

Alipour, A., Shafei, B. & Shinozuka, M. 2011. Performance evaluation of deteriorating highway bridges located in high seismic areas. *Journal of Bridge Engineering* 16(5): 597-611.

Alipour, A., Shafei, B. & Shinozuka, M. 2013. Reliability-based calibration of load and resistance factors for design of RC bridges under multiple extreme events: scour and earthquake. *Journal of Bridge Engineering* 18(5): 362-371.

Alipour, A. & Shafei, B. 2016. Seismic resilience of transportation networks with deteriorating components. *Journal of Structural Engineering* 142(8): C4015015.

Asprone, D., Jalayer, F., Prota, A. & Manfredi, G. 2010. Proposal of a probabilistic model for multi-hazard risk assessment of structures in seismic zones subjected to blast for the limit state of collapse. *Structural Safety* 32: 25-34.

Attary, N., Unnikrishnan, V.U., van de Lindt, J.W., Cox, D.T. & Barbosa, A.R. 2017. Performance-based tsunami engineering methodology for risk assessment of structures. *Engineering Structures* 141: 676-686.

Banerjee, S. & Prasad, G.G. 2012. Seismic risk assessment of reinforced concrete bridges in flood-prone regions. *Structure and Infrastructure Engineering* 9(9): 952-968.

Barone, G. & Frangopol, D.M. 2014. Reliability, risk and lifetime distributions as performance indicators for life-cycle maintenance of deteriorating structures. *Reliability Engineering & System Safety*, 123: 21-37.

Bertero, R.D. & Bertero, V.V. 1999. Redundancy in earthquake resistant design. *Journal of Structural Engineering* 125(1): 81-88.

Biondini, F. Camnasio, E. & Palermo, A. 2014. Lifetime seismic performance of concrete bridges exposed to corrosion. *Structure and Infrastructure Engineering* 10(7): 880-900.

Biondini, F., Camnasio, E. & Titi, A. 2015. Seismic resilience of concrete structure under corrosion. *Earthquake Engineering and Structural Dynamics* 44(14):2445-2466.

Biondini, F. & Frangopol, D.M. 2016. Life-cycle performance of deteriorating structural systems under uncertainty: Review. *Journal of Structural Engineering* 142(9): F4016001.

Biondini, F. & Frangopol, D.M. 2018. Life-cycle performance of civil structure and infrastructure systems: survey. *Journal of Structural Engineering* 144(1): 06017008.

Bocchini, P., Frangopol, D.M. & Deodatis, G. 2011. A random field based technique for the efficiency enhancement of bridge network life-cycle analysis under uncertainty. *Engineering Structures* 33: 3208-3217.

Bocchini, P. & Frangopol, D.M. 2012a. Optimal resilience- and cost-based postdisaster intervention prioritization for bridges along a highway segment. *Journal of Bridge Engineering* 17(1): 117-129.

Bocchini, P. & Frangopol, D.M. 2012b. Restoration of bridge networks after an earthquake: Multi-criteria intervention optimization. *Earthquake Spectra*, 28(2): 426-455.

Bocchini, P., Frangopol, D.M., Ummenhofer, T. and Zinke, T. 2014. Resilience and sustainability of civil infrastructure: Toward a unified approach. *Journal of Infrastructure System* 20(2):04014004.

Brown, C. & Milke, M. 2016. Recycling disaster waste: feasibility, method and effectiveness. *Resources, Conservation and Recycling* 106: 21-32.

Brown, C., Milke, M. & Seville, E. 2011. Disaster waste management: A review article. *Waste Management* 31: 1085-1098.

Bruneau, M., Chang, S., Eguchi, R., Lee, G., O'Rourke, T., Reinhorn, A.M, et al. 2003. A framework to quantitatively assess and enhance the seismic resilience of communities. *Earthquake Spectra* 19(4): 733-752.

Central Disaster Management Council. Conference document 16th conference of the spatial board of inquiry on Tonankai, and Nankai earthquake. 2003. (in Japanese)

Chandrasekaran, S. & Banerjee, S. 2016. Retrofit optimization for resilience enhancement of bridges under multiple scenario. *Journal of Structural Engineering* 142(8): C4015012.

Chang, S.E., Shinozuka, M. & Moore J.E. 2002. Probabilistic Earthquake Scenarios: Extending Risk Analysis Methodologies to Spatially Distributed Systems. *Earthquake Spectra* 16(3): 557-572.

Chulahwat, A. & Mahmoud, H. 2017. A combinational optimization approach for multi-hazard design of building systems with suspended floor slabs under wind and seismic hazards. *Engineering Structures* 137:268-284.

Cimellaro G.P., Reinhorn, A.M. & Bruneau M. 2010. Framework for analytical quantification of disaster resilience. *Engineering Structures* 32: 3639-3649.

Domaneschi, M. & Martinelli, L. 2016. Earthquake-resilience-based control solutions for the extended benchmark cable-stayed bridge. *Journal of Structural Engineering*, 142(8): C4015009-1-9.

Dong, Y. & Frangopol, D.M. 2015. Risk and resilience assessment of bridges under mainshock and aftershocks incorporating uncertainties. *Engineering Structures* 83: 198-208.

Dong, Y. & Frangopol, D.M. 2017. Probabilistic assessment of an interdependent healthcare-bridge network system under seismic hazard. *Structure and Infrastructure Engineering* 13(1): 160-170.

Dong, Y., Frangopol, D.M. & Saydam, D. 2014. Pre-earthquake multi-objective probabilistic retrofit optimization of bridge networks based on sustainability. *Journal of Bridge Engineering* 19(6): 04014018.

Dong, Y., Frangopol, D.M. & Saydam, D. 2013. Time-variant sustainability assessment of seismically vulnerable bridges subjected to multiple hazards. *Earthquake Engineering and Structural Dynamics* 42(10): 1451-1467.

Du, G. & Karoumi, R. 2013. Life cycle assessment of a railway bridge: comparison of two superstructure designs. *Structure and Infrastructure Engineering* 9(11): 1149-1160.

Du, G. & Karoumi, R. 2014. Life cycle assessment framework for railway bridges: literature survey and critical issues. *Structure and Infrastructure Engineering* 10(3): 277-294.

Echevarria, A., Zaghi, A.E., Christenson, R. & Accorsi, M. 2016. CFFT bridge columns for multihazard resilience. *Journal of Structural Engineering* 142(8): C4015002-1-16.

Ellingwood, B.R. 2006a. Mitigating risk from abnormal loads and progressive collapse. *Journal of Performance of Constructed Facilities* 20: 315-323.

Ellingwood, B.R. 2006b. Strategies for mitigating risk to buildings from abnormal load events. *International Journal of Risk Assessment and Management* 7: 828-845.

Estes, A.C. & Frangopol, D.M. 2001. Bridge lifetime system reliability under multiple limit states. *Journal of Bridge Engineering* 6(6): 523-528.

Esteva L., Campos, D. & Diaz-Lopez, O. 2011. Life-cycle optimization in earthquake engineering. *Structure and Infrastructure Engineering* 7: 33-49.

Esteva, L., Diaz-Lopez, O., Vasquez, A. & Leon, A. 2016. Structural damage accumulation and control for life cycle optimum seismic performance of buildings. *Structure and Infrastructure Engineering* 12: 848-860.

Frangopol, D.M., Dong, Y. & Sabatino, S. 2017. Bridge life-cycle performance and cost: analysis, prediction, optimization and decision-making. *Structure and Infrastructure Engineering* 13(10): 1239-1257.

Frangopol, D.M. & Soliman, M. 2016. Life-cycle of structural systems: recent achievements and future directions. *Structure and Infrastructure Engineering* 12(1): 1-20.

Frangopol, D.M. & Kim, S. 2014. Life-cycle analysis and optimization. Chapter 18 in *Bridge Engineering Handbook* - Second Edition, Vol. 5 *Construction and Maintenance*, W-F. Chen and L. Duan, eds., CRC Press: 537-566.

Frangopol, D.M. & Saydam, D. 2014. Structural performance indicators for bridges. Chapter 9 in *Bridge Engineering Handbook* - Second Edition, Vol. 1 Fundamentals, W-F. Chen and L. Duan, eds., CRC Press: 185-205.

Frangopol, D.M. & Bocchini, P. 2012. Bridge network performance, maintenance, and optimization under uncertainty: Accomplishments and challenges. *Structure and Infrastructure Engineering*, 8: 341-356

Frangopol, D. M. 2011. Life-cycle performance, management, and optimization of structural systems under uncertainty: Accomplishments and challenges. *Structure and Infrastructure Engineering* 7: 389-413.

Frangopol, D.M. & Nakib, R. 1991. Redundancy in highway bridges. *Engineering Journal*, AISC 28(1): 45-50.

Frangopol, D.M. & Curley, J.P. 1987. Effects of damage and redundancy on structural reliability. *Journal of Structural Engineering* 113(7): 1533-1549.

Gencturk, B., Hossain, K. & Lahourpour, S. 2016. Life-cycle sustainability assessment of RC buildings in seismic regions. *Engineering Structures* 110: 347-362.

Ghosn, G., Duenas-Osorio, L., Frangopol, D.M., McAllister, T.P., Bocchini, P., Manuel, L., Ellingwood, B.R., Arangio, S., Bontempi, F., Shah, M., Akiyama, M., Biondini, F., Hernandez, S. & Tsiatas, G. 2016. Performance indicators for structural systems and infrastructure networks. *Journal of Structural Engineering* 142(9): F4016003.

Gidaris, I., Padgett, J.E., Barbosa, A.R., Chen, S., Cox, D., Webb, B. & Cerato, A. 2017. Multiple-hazard fragility and restoration models of highway bridges for regional risk and resilience assessment in the United States: state-of-the-art review. *Journal of Structural Engineering* 143(3): 04016188.

Goto, C.; Ogawa, Y.; Shuto, N; Imamura, F. Numerical method of tsunami simulation with the leap-frog scheme. IUGG/IOC Time Project, 1997.

Guo, A., Liu, Z., Li, S. & Li, H. 2017. Seismic performance assessment of highway bridge networks considering post-disaster traffic demand of a transportation system in emergency conditions. *Structure and Infrastructure Engineering* 13(12): 1523-1537.

Honjo, Y. & Otake, Y. 2013. Statistical estimation error evaluation theory of local averages of a geotechnical parameter. Safety reliability risk and life-cycle performance of structure and infrastructure, G. Deodatis, B. R. Ellingwood, and D. M. Frangopol, eds., CRC Press, London, 1987-1994.

Hutt, C.A., Almufti, I., Willford, M. & Deierlein, G. 2016. Seismic loss and downtime assessment of existing tall steel-framed buildings and strategies for increased resilience. *Journal of Structural Engineering* 142(8): C4015005.

Inui, T., Yasutaka, T., Endo, K. & Katsumi, T. 2012. Geo-environmental issues induced by the 2011 off the Pacific Coast of Tohoku Earthquake and tsunami. *Soils and Foundations* 52(5): 856-871.

Iqbal, A., Fragiacomo, M., Pampanin, S. & Buchanan, A. 2017. Seismic resilience of plywood-coupled LVL wall panels. *Engineering Structures*, DOI: 10.1016/j.engstruct. 2017.09.053

Kameshwar, S. & Padgett, J.E. 2014. Multi-hazard risk assessment of highway bridges subjected to earthquake and hurricane hazards. *Engineering Structures* 78: 154-166.

Kawashima, K. 2000. Seismic design and retrofit of bridges. *Proceedings of 12th World Conference on Earthquake Engineering* (*WCEE*), Keynote paper. Auckland, New Zealand.

Kurtz, N., Song, J. & Gardoni, P. 2016. Seismic reliability analysis of deteriorating representative U.S. west coast bridge transportation networks. *Journal of Structural Engineering* 142(8): C4015010.

Lee Y.-J., Song, J., Gardoni. P. & Lim, H.-W. 2011. Post-disaster flow capacity of bridge transportation network considering structural deterioration of bridges. *Structure and Infrastructure Engineering*, 7: 509-521.

Lehman, D.E., Kuder, K.G., Gunnarrson, A.K., Roeder, C.W. & Berman, J.W. Circular concrete-filled tubes for improved sustainability and seismic resilience. *Journal of Structural Engineering* 141(3): B4014008.

Lim, S., Akiyama, M. & Frangopol, D.M. 2016. Assessment of the structural performance of corrosion-affected RC members based on experimental study and probabilistic modeling. *Engineering Structures* 127: 189-205.

Lim, S., Akiyama, M., Frangopol, D.M. & Jiang, H. 2017. Experimental investigation of the spatial variability of the steel weight loss and corrosion cracking of RC members: Novel X-ray and digital image processing techniques. *Structure and Infrastructure Engineering* 13(1): 118-134.

Liu, M., Frangopol, D.M. & Kim, S. 2009. Bridge safety evaluation based on monitored live load effects. *Journal of Bridge Engineering* 14(4): 257-269.

Lounis, Z. & McAllister. Risk-based decision making for sustainable and resilient infrastructure systems. *Journal of Structural Engineering* 142(9): F4016005.

Mackie, K.R., Kucukvar, M., Tatari, O. & Elgamal, A. 2016. Sustainability metrics for performance-based seismic bridge response. *Journal of Structural Engineering* 142(8): C4015001.

Masoomi, H. & van de Lindt, J.W. 2018. Restoration and functionality assessment of a community subjected to tornado hazard. *Structure and Infrastructure Engineering* 14(3): 275-291.

Mitoulis, S.A. & Rodriguez, J.R. 2017. Seismic performance of novel resilient hinges for columns and application on irregular bridges. *Journal of Bridge Engineering* 22(2): 04016114.

Miyamoto, S., Akiyama, M. & Frangopol, D.M. 2015. Life-cycle reliability estimation of large-scale reinforced concrete slabs in a marine environment considering spatial variability. *Proceedings of Symposium on Reliability of Engineering System*, *SRES'2015*, Hangzhou, China.

Nazari, N., van de Lindt, J.W. & Li, Y. 2015. Quantifying changes in structural design needed to account for aftershock hazard. *Journal of Structural Engineering*, 04015035.

Okasha, N.M & Frangopol, D.M. 2011. Computational platform for the integrated life-cycle management of highway bridges. *Engineering Structures* 33: 2145-2153.

Papakonstantinou, K.G. & Shinozuka, M. 2013. Probabilistic model for steel corrosion in reinforced concrete structures of large dimensions considering crack effects. *Engineering Structures* 57: 306-326.

Portugal-Pereira, J. & Lee, L. 2016. Economic and environmental benefits of waste-to-energy technologies for debris recovery in disaster-hit Northeast Japan. *Journal of Cleaner Production* 112: 4419-4429.

Rao, A.S., Lepech, M.D. Kiremidjian, A.S. 2016a. Simplified structural deterioration model for reinforced concrete bridge piers under cyclic loading. *Structure and Infrastructure Engineering* 13(1): 55-66.

Rao, A.S., Lepech, M.D., Kiremidjian, A.S. 2016b. Development of time-dependent fragility functions for deteriorating reinforced concrete bridge piers. *Structure and Infrastructure Engineering* 13(1): 67-83.

Rodgers, G.W., Mander, J.B., Chase, J.G & Dhakal, R.P. 2016. Beyond ductility: parametric testing of a jointed rocking beam-column connection designed for damage avidance. *Journal of Structural Engineering*, 142(8): C4015006.

Rokneddin, K., Ghosh, J., Duenas-Osorio, L. & Padgett, J.E. 2013. Bridge retrofit prioritization for ageing transportation networks subject to seismic hazards. *Structure and Infrastructure Engineering* 9(10): 1050-1066.

Saydam, D. & Frangopol, D.M. 2011. Time-dependent performance indicators of damages bridge superstructures. *Engineering Structures* 33(9): 2458-2471.

Saydam, D., Bocchini, P. & Frangopol, D.M. 2013. Time-dependent risk associated with deterioration of highway bridge networks. *Engineering Structures* 54: 221-233.

Stergiou, E.C. & Kiremidjian, A.S. 2010. Risk assessment of transportation systems with network functionality losses. *Structure and Infrastructure Engineering* 6:111-125.

Tirca, L., Serban, O., Lin L., Wang, M. & Lin, N. 2016. Improving the seismic resilience of existing braced-frame office buildings. *Journal of Structural Engineering* 142(8): C4015003-1-14.

Torbol, M. & Shinozuka, M. 2014. The directionality effect in the seismic risk assessment of highway networks. *Structure and Infrastructure Engineering*, 10(2): 175-188.

Unjoh, S. 2012. Tsunami damage to bridge structures in Rikuzen-Takada City and the emergency road network recovery actions. *Proceedings of the International Symposium on Engineering Lessons Learned from the 2011 Great East Japan Earthquake*, Tokyo, Japan.

Wang, Z., Jin. W., Dong, Y. & Frangopol, D.M. 2018. Hierarchical life-cycle design of reinforced concrete structures incorporating durability, economic efficiency and green objectives. *Engineering Structures* 157: 119-131.

Yanweerasak, T., Akiyama, M. & Frangopol, D.M. 2016. Updating the seismic reliability of existing RC structures in a marine environment by incorporating the spatial steel corrosion distribution: application to bridge piers. *Journal of Bridge Engineering* 21(7): 04016031.

Yeo G.L. & Cornell, C.A. 2005. Stochastic characterization and decision bases under time-dependent aftershock risk in performance-based earthquake engineering. The John A. Blume Earthquake Engineering Center, Stanford University.

Yilmax, T., Banerjee, S. & Johnson, P. 2016. Performance of two real-life California bridges under regional natural hazards. *Journal of Bridge Engineering* 21(3): 04015063.

Zanini M. A. Faleschini, F. & Pellegrino, C. 2017. Probabilistic seismic risk forecasting of aging bridge networks. *Engineering Structures* 136: 219-232.

Zhang, W., Cai, C. S. & Pan, F. 2013. Fatigue reliability assessment for long-span bridges under combined dynamic loads from winds and vehicles. *Journal of Bridge Engineering* 18(8): 735-747.

Zhang, W., Wang, N. & Nicholson, C. 2017. Resilience-based post-disaster recovery strategies for road-bridge networks. *Structure and Infrastructure Engineering* 13(11): 1404-1413.

Zhu, B. & Frangopol D.M. 2012. Reliability, redundancy and risk as performance indicators of structural systems during their life-cycle. *Engineering Structures* 41: 34-49.

Maintenance, Safety, Risk, Management and Life-Cycle Performance of Bridges – Powers, Frangopol, Al-Mahaidi & Caprani (Eds)
© 2018 Taylor & Francis Group, London, ISBN 978-1-138-73045-8

Assessment of the dynamic behaviour of railway bridges for high-speed traffic

R. Calçada
University of Porto – Faculty of Engineering, Porto, Portugal

ABSTRACT: To make a rigorous analysis of the dynamic behaviour of railway bridges a method for 3D analysis of the train-structure dynamic interaction, developed by the centre of competence in railways of the Faculty of Engineering of the University of Porto (CSF-FEUP), is described. Subsequently, several case studies developed by CSF-FEUP are presented, showing the efficiency and the usefulness of the developed method and enabling the achievement of different objectives, such as: i) the running safety assessment of trains moving over long bridges subjected to earthquake actions; ii) the track stability and wheel-rail contact stability safety assessment on short span railway bridges; iii) the running safety assessment of trains for settlement of the backfill at transition zones to railway bridges.

1 INTRODUCTION

In railway bridges the dynamic effects induced by high speed traffic can be very significant due to the rapid rate of loading, the passage of successive loads with uniform spacing which can create resonance and the variations in wheel loads resulting from track irregularities. The assessment of these dynamic effects is of the utmost importance because excessive vibrations and deformations can endanger traffic by creating unacceptable changes in track geometry, can lead to ballast instability, unacceptable reductions in wheel-rail contact forces and create conditions which cause passenger discomfort. The dynamic effects induced by the simultaneous action of traffic and earthquakes loads should also be considered in some scenarios. Transitions to railway bridges are zones where significant dynamic effects also occur due to the rapid degradation of the track, mostly due to the development of settlements in the backfill.

In this lecture an accurate, efficient and robust algorithm to analyse the vehicle structure dynamic interaction, is described. The formulation takes into account the vertical and lateral dynamic interaction between railway vehicles and structures. Most of the existing methods treat the contact forces in the normal and tangential directions as external forces, whereas the proposed formulation uses a finite element to model the behaviour in the contact interface. The formulation is divided into three main parts: the geometric problem, consisting of the detection of the contact points; the normal contact problem, in which the forces are determined based on the Hertz nonlinear theory; the tangential contact problem, in which the creep forces, that appear due to the rolling friction contact, are calculated. The proposed method is based on the finite element method, which allows the analysis of structures and vehicles with any degree of complexity and the consideration of the deformations undergone by the two systems.

The method is applied to study the running safety of a railway vehicle moving over a viaduct subjected to earthquakes. The viaduct is based on an existing flyover type structure of the Portuguese railway network composed by simply supported box girders. The influence of the seismic intensity, track irregularities and train speed in the train running safety is evaluated. Unlike the majority of the studies in this field, in which the earthquake is assumed to start at the instant the train enters the bridge, the randomness of the earthquake has been accounted for by considering different time offsets between the beginning of the excitation and the entry of the vehicle in the viaduct. Furthermore, four levels of seismic intensity and two levels of track quality have been considered in the study. Regarding the seismic loads, artificial accelerograms have been generated from the elastic spectra described in Eurocode 8 Part 1 (CEN, 1998) with peak ground accelerations corresponding to moderate events with return periods less than 475 years, which is the reference return period of the design seismic action associated with the no collapse requirement. Since no significant nonlinearity is likely to be exhibited in the columns for these levels of seismicity, all the analysis have been per-

formed in the elastic domain with a reduction in the stiffness of the columns to account for the concrete cracking. The track irregularities have been also generated based on analytical power spectral density functions. The running safety of the train is evaluated based on the safety criteria existent in the literature, such as Nadal, Prud'homme and wheel unloading criteria.

The method is also applied in a probabilistic study to understand how the variability of the train, track and bridge parameters affects the dynamic behaviour of a short span bridge. Since the limit state functions are extremely complex when a large number of variables are considered, simulation techniques were applied. Simulations techniques allow a large number of experiments to be performed, taking into account the real variability of the train-track-bridge system parameters. A bridge with six simply supported spans of 12 m each was selected as case study. The accelerations at several points of the span and the wheel-rail contact forces were analysed for several hypothetical scenarios. The Monte Carlo method will allow the evaluation of how the dynamic response of the train-bridge system is affected by changes in its properties and which variables play the most important role in the dynamic behaviour. Besides determining which variables are the most important for the dynamic response, a safety assessment of the bridge, based on the simulation results, was also performed in order to establish train speed limits on the bridge.

The method is also applied to develop a more efficient and robust numerical approach to study the effect of differential settlements on the dynamic train-track interaction. In addition, the numerical approach is innovative in that in takes into account: i) all the relevant components of the track, bridge and backfill; ii) the train model with primary and secondary suspensions; iii) the train-track interaction at the wheel-rail interface and between the sleepers and the ballast layer – a fundamental aspects to account for the development of hanging sleepers and the negative effects in the dynamic train-track interaction; iv) a previous calibration and validation procedure that used extensive field measurements obtained in the track, presented in earlier studies (Alves Ribeiro et al. 2014; Paixão et al. 2014; Paixão et al. 2015a); v) realistic longitudinal level profiles of the track that resulted from settlement profiles (based on earlier studies (Schooleman 1996; England et al. 2000; Kempfert & Stadel, 2000; Luomala & Nurmikolu, 2012; Abu-Farsakh & Chen, 2014) imposed on the track.

Within the scope of a research project on transition zones, the authors have used an earlier version of this model, which proved to be very accurate for simulating the dynamic behaviour of the train-track system at a transition zone to a bridge in a Portuguese railway line (Paixão et al., 2014). That study comprised an extensive validation of the model using field measurements, but it did not address the topic of differential settlements. As a result of that work, the model was adapted to assess the influence of the shape and amplitude of the settlement profiles of the backfill, thus contributing to a better understanding of the dynamic behaviour of the train-track system at transition zones.

2 TRAIN-STRUCTURE DYNAMIC INTERACTION

2.1 *Introduction*

The wheel-rail contact model and the vehicle-structure coupling method used for the 3D analysis of the train-structure dynamic interaction are described. The wheel rail contact model is divided into three main parts: 1) the geometric problem, consisting of the detection of the contact points; 2) the normal contact problem, in which the forces are determined based on the Hertz nonlinear theory; 3) the tangential contact problem, in which the creep forces, that appear due to the rolling friction contact, are calculated. The vehicle-structure coupling formulation is based on the finite element method, which allows the analysis of structures and vehicles with any degree of complexity and the consideration of the deformations undergone by the two systems.

2.2 *Wheel-rail contact model*

The wheel-rail contact model is the key point of the train-structure interaction method, since the position of the contact point between wheel and rail significantly influence the contact forces and, consequently, the behaviour of the vehicle moving over the structure. The model is based on a contact finite element developed specifically for this purpose that takes into account the behaviour in the contact interface and guarantees the coupling between the vehicle and structure when contact occurs (see Neves et al. 2012; Neves et al. 2014; Montenegro et al. 2015 and Montenegro et al. 2016 for details). The contact formulation of the element consists of the geometric problem, the normal contact problem and the tangential contact problem, which are described in Sections 2.2.1 to 2.2.3, respectively.

2.2.1 *Geometric contact problem*

The geometric contact problem consists of determining the location of the contact points between wheel and rail. In order to do this, the wheel and rail profile surfaces are first parameterized as a function of two surface parameters that define its geometry. Then, the location of the potential contact points is determined online during each step of the dynamic analy-

sis using the following set of nonlinear equations (see Fig. 1).

$$\begin{cases} \mathbf{t}^t_{r,y} \cdot \mathbf{d}^t_{wr} = 0 \\ \mathbf{t}^t_{w,y} \cdot \mathbf{n}^t_r = 0 \end{cases} \tag{1}$$

where $\mathbf{t}^t_{r,y}$ and $\mathbf{t}^t_{w,y}$ are the tangent vectors to the rail and wheel surfaces, respectively, at the potential contact point along the lateral direction, $\mathbf{n}^t_r$ is the normal vector to the rail surface at the same point and $\mathbf{d}^t_{wr}$ is the vector that defines the relative position of the potential contact point of the wheel with respect to the potential contact point of the rail, given by

$$\mathbf{d}^t_{wr} = \mathbf{u}^t_W - \mathbf{u}^t_R \tag{2}$$

where $\mathbf{u}^t_W$ and $\mathbf{u}^t_R$ are the positions of the potential contact points of the wheel and rail, respectively. The superscripts *t* indicate that the vectors are defined with respect to the target element coordinate system presented in Montenegro et al. (2015). The first condition described by Eq. (1) ensures that the tangent vector to the rail is perpendicular to the vector defining the relative position of the point of the wheel with respect to the point of the rail. The second condition ensures that the normal vector to the rail is perpendicular to the tangent vector to the wheel, as shown in Fig. 1.

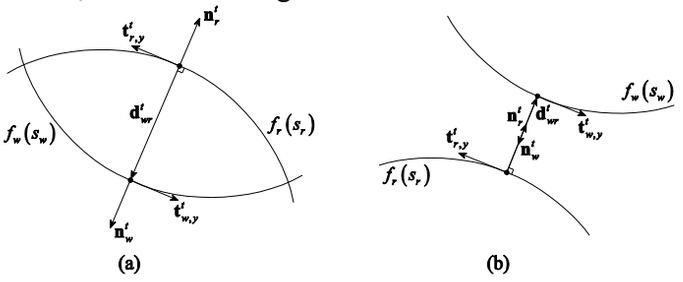


Figure 1. Potential contact points between the two surfaces: (a) actual contact and (b) no contact.

It is important to notice that the system of equations (1) may have multiple solutions if one of the contact surfaces is not convex. Therefore, the concave region in the transition zone between the tread and flange is neglected, and an approximation to the surface is adopted.

The potential contact points determined with the procedure described above have to fulfil a last condition, that is, the parametric surfaces have to intersect each other. As shown in Fig. 1b, the conditions described in Eq. (1) are satisfied but there is no contact. This condition can be expressed mathematically as

$$\mathbf{d}^t_{wr} \cdot \mathbf{n}^t_r \leq 0 \tag{3}$$

which means that the intersection between two bodies is guaranteed only if the vectors $\mathbf{d}^t_{wr}$ and $\mathbf{n}^t_r$ point in opposite directions, as depicted in Fig. 1a. The penetration *d* is given by

$$d = \left\| \mathbf{d}^t_{wr} \right\| \tag{4}$$

This procedure is performed for both the tread and flange region, thus allowing the detection of one contact point in each region of the wheel

2.2.2 *Normal contact problem*

When two non-conforming bodies are compressed against each other, they will deform around the first point of contact and form a contact area. In the present investigation, the nonlinear Hertz contact theory (Hertz, 1882) is used to analyse the normal contact problem. Although this theory can only deal with non-conformal contact, where the contact area is small when compared with the dimensions of the two bodies and the relative radii of curvature of the surfaces, this assumption is acceptable in railway applications, since the wheel and rail have considerably different shapes. However, more complex contact shapes, namely, multi-Hertzian and non-Hertzian, may be necessary for analysing local problems such as wear, in which a detailed analysis of the local stresses in the contact area is essential. Thus, the normal contact force F_n between the wheel and rail is given by

$$F_n = K_h \, d^{\frac{3}{2}} \tag{5}$$

where d is the penetration defined in Eq. (4) and K_h is a generalized stiffness coefficient that depends on the material properties of the bodies in contact, such as the Young modulus and the Poisson ratio, and on the curvatures of the surfaces at the contact point.

2.2.3 *Tangential contact problem*

Due to the elasticity of the bodies and the external applied normal load, some points on the contact area may slip while others may adhere when the bodies are allowed to roll over each other. The difference between the tangential strains of the bodies in the adhesion area leads to a small apparent slip, called creep, which is crucial for the determination of the tangential forces that develop in the contact area.

These forces, called creep forces, can be calculated through the creepages, which consist in the relative velocities between wheel and rail at the contact point, normalized to the vehicle forward speed. In the present work, the longitudinal and the lateral creep forces are precalculated and stored in a lookup table, based on USETAB (Kalker, 1996), to be later interpolated during the dynamic analysis as a function of the creepages and the semi-axes ratio of the contact ellipse. This table has been calculated with the software CONTACT (2011) which is based on Kalker's exact three-dimensional rolling contact theory (Kalker, 1990).

2.3 *Vehicle-structure coupling*

The train-structure dynamic interaction problem is solved using the direct method developed by Neves et al. (2014). In this method, the governing equilibrium equations of the vehicle and structure are complemented with additional constraint equations that relate the displacements of the contact nodes of the vehicle with the corresponding nodal displacements of the structure. Montenegro et al. (2015) extended the formulation to take into account the geometry of the wheel and rail and the behavior of the contact interface by using the finite contact element referred in Section 2.2. Hence, the vehicle-structure coupling is mathematically expressed as

$$\begin{bmatrix} \overline{\mathbf{K}} & \overline{\mathbf{D}} \\ \overline{\mathbf{H}} & \mathbf{0} \end{bmatrix} \begin{bmatrix} \Delta \mathbf{a}^{i+1} \\ \Delta \mathbf{X}^{i+1} \end{bmatrix} = \begin{bmatrix} \boldsymbol{\psi}\left(\mathbf{a}^{t+\Delta t,i}, \mathbf{X}^{t+\Delta t,i}\right) \\ \bar{\mathbf{r}} \end{bmatrix} \tag{6}$$

where $\overline{\mathbf{K}}$ is the current effective stiffness matrix of the vehicle-structure system, $\overline{\mathbf{D}}$ is a matrix that relates the contact forces, defined with respect to the target element coordinate system, with the nodal forces defined in the global coordinate system, $\overline{\mathbf{H}}$ is the transformation matrix that relates the nodal displacements of the target elements, defined in the global coordinate system, with the displacements of the auxiliary points defined with respect to the target element coordinate system, $\boldsymbol{\psi}$ is the residual force vector that depends on the nodal displacements $\mathbf{a}$ and on the contact forces $\mathbf{X}$ and $\bar{\mathbf{r}}$ the vector with the irregularities in the contact interface. The superscript $t+\Delta t$ indicates the current time step, while i and $i+1$ denotes the previous and current Newton iteration, respectively. Equation (6) consists of a mixed system of equations composed by equilibrium equations of motion and constraint equations to couple the vehicle to the structure. These equations, whose unknowns are incremental nodal displacements and contact forces, are solved using a Newton-type iterative scheme. The detailed formulation of the direct method, and in particular of the system of equations (6), may be found in Neves et al. (2014) and Montenegro et al. (2015).

3 ASSESSMENT OF TRAIN RUNNING SAFETY ON BRIDGES SUBJECTED TO EARTHQUAKES

3.1 *Introduction*

In the present section, a study regarding the running safety of a railway vehicle based on a Shinkansen train moving over a viaduct subjected to earthquakes (Montenegro et al. 2016). The viaduct is based on an existing flyover type structure of the Portuguese railway network composed by simply supported box girders (Malveiro et al. 2013). The main objective of the present study consists of evaluating the influence of the seismic intensity, track irregularities and train speed in the train running safety.

3.2 *Train-structure dynamic model*

The structure used in the present study is based on the Alverca viaduct, a flyover structure that belongs to the Northern Line of the Portuguese railway network (see Fig. 2a). The actual structure consists of several simply supported spans with lengths of 16.5 m, 17.5 m and 21 m supported by columns with heights ranging from, approximately, 5 m to 15 m (Malveiro et al. 2013). In the present study, the actual mechanical and geometrical properties of the cross sections of the deck and columns have been adopted. However, for simplicity of the model, the span lengths and column heights have been kept constant in the whole structure. Therefore, the viaduct considered in the present work has a total length of 630 m divided into 30 simply supported spans with 21 m length each, supported by columns with 10 m height.

The deck consists of a prefabricated and prestressed U-shaped beam on which pre-slabs serving as formwork to the concrete upper slab cast in situ were placed, forming a single-cell box girder deck (see Fig. 2b). The deck is directly supported in the columns and abutments by elastomeric-reinforced bearings. Each span is fixed in one extremity and longitudinally guided in the other, being the transverse direction fixed on both edges. The track in the existent viaduct consists on UIC60 rails with an Iberian gauge of 1.688 m, elastomeric rubber pads, prestressed concrete monoblock sleepers and a 25 cm ballast layer under them. However, since the study is carried out with a Japanese high-speed train, the standard gauge of 1.435 m has been considered in the numerical model, as well as the JIS60 rail profiles. The columns have a rectangular solid cross-section with dimensions 2×1 m^2.

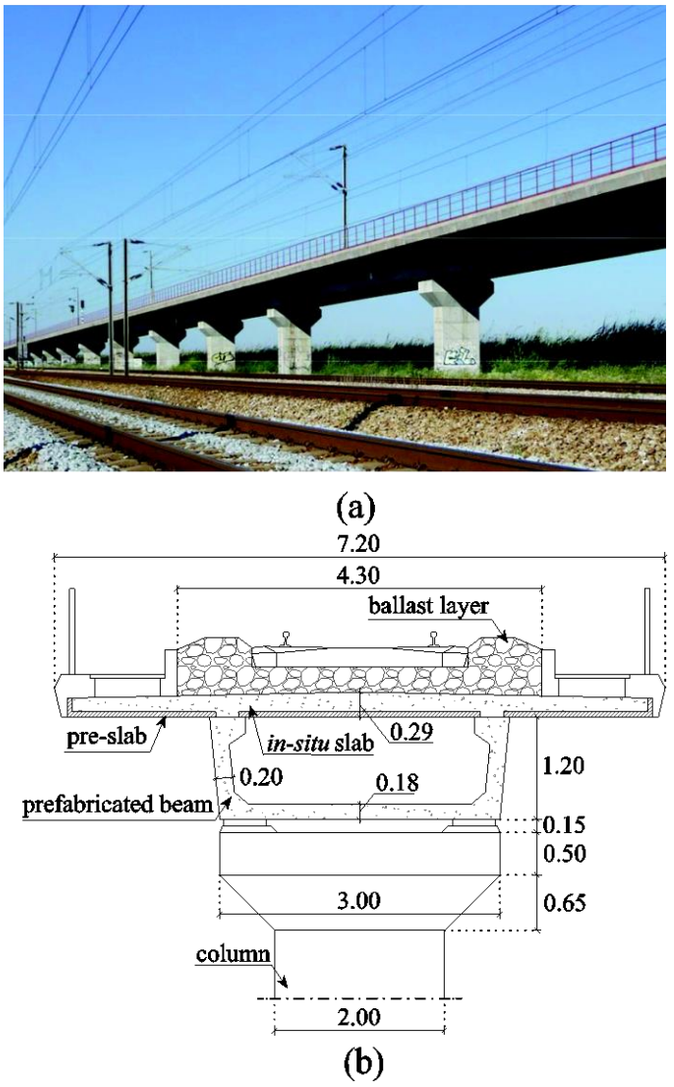


Figure 2. Alverca viaduct: (a) perspective view and (b) deck cross-section.

The numerical model of the viaduct has been developed in ANSYS. The deck, columns, sleepers and rails are modelled using beam finite elements, while the bearing supports, ballast and pads are modelled using linear spring dampers. Mass point elements are also used to model the ballast mass and the non structural elements such as safeguards and edge beams of the deck. The connection between the top of the columns and deck, as well as the connection between the deck and the track, is accomplished by rigid frame elements. In order to guarantee a correct representation of the transition zones between the structure and the embankment, an extension of the track has been modelled in both extremities of the viaduct. A schematic representation of the numerical model together with a detail of the cross section and the deck joint above the columns is illustrated in Fig. 3 (the track is not included in Fig. 3a for simplicity). Although the spans are disconnected from each other, the track confers a certain amount of transversal stiffness to the deck, as can be seen in the detail depicted in Fig. 3c.

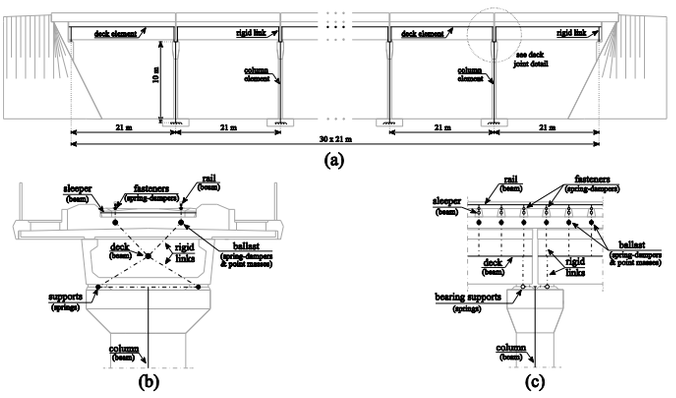


Figure 3. Numerical model of the viaduct: (a) elevation view, (a) cross-section and (b) deck joint.

The vehicle used in the present work for the dynamic analysis is based on a Japanese conventional type high-speed Shinkansen train with all the cars independent from each other. A schematic representation of the dynamic model of the railway vehicle is illustrated in Fig. 4. The springs and dampers of the suspensions are denoted by k and c and the masses and rotary inertias are indicated by m and I. The longitudinal, lateral and vertical distances are denoted by a, b and h, respectively, s refers to the lateral distance between the initial contact points and R_0 is the nominal rolling radius. The subscripts cb, b and w indicate carbody, bogie and wheelset.

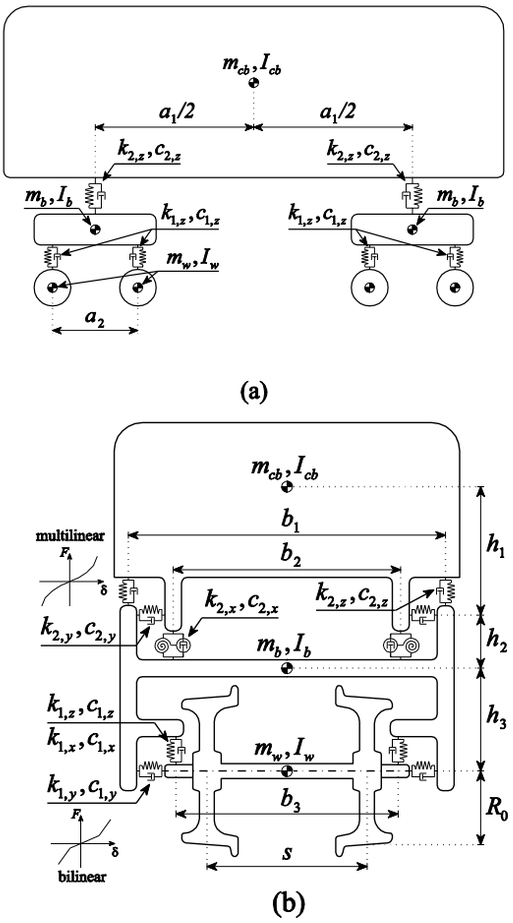


Figure 4. Dynamic model of the railway vehicle: (a) lateral view and (b) front view.

The carbody, bogies and wheelsets are modelled using beam finite elements, and the suspensions are modelled using spring dampers in the three directions. The springs used to model the suspensions are characterized by bilinear laws, except the one used to model the secondary transversal suspension. This suspension follows a multilinear law to simulate the presence of rubber stoppers whose stiffness increases gradually. These stoppers are used to avoid large lateral displacements of the carbody not only during normal operation, but especially during earthquake. The masses and rotary inertias are modelled using mass point elements, located at the center of mass of each component.

3.3 *Seismic excitation*

The seismic excitations adopted in the present study consist of artificial accelerograms generated from the elastic spectra described in EN 1998-1 (2004), with PGA corresponding to moderate events with relatively high probability of occurrence and return periods less than 475 years, which is the reference return period of seismic action for the no collapse requirement.

This type of seismic actions is of the utmost importance, since the running safety of trains might be jeopardized not only by intense earthquakes, but also by moderate seismic events, which may not cause significant damage to the structure. Therefore, four levels of seismic intensity with return periods of 95 (proposed return period for the damage limitation requirement of Eurocode 8), 150, 225 and 310 years have been considered in the present study.

The seismic excitation is imposed along the lateral direction and, since the data regarding the soil properties is scarce, the spatial variability of the seismic action is not considered in this work.

The artificial accelerograms have been generated with the software SeismoArtif, which uses a random process of adjustment by correction in the frequency domain. The target elastic spectra have been defined for the seismic zone 2.3 of the Portuguese territory and for a soil type A (NP EN 1998-1, 2009), with an importance factor of 1.0, as proposed by EN 1998-2 (2005) for railway bridges.

3.4 *Analysis scenario*

For each level of irregularity and seismic intensity, the safety of the vehicle is evaluated for running speeds ranging from 200 to 350 km/h with 10 km/h steps. Furthermore, for each speed, five scenarios with different time offsets between the beginning of the earthquake and the entry of the vehicle in the viaduct are considered in order to cover a wider range of combinations. The coordinate of the first wheelset xi at the instant the earthquake starts is schematized in Fig. 5. The coordinate xi is defined with respect to the coordinate system (x,y) positioned at the beginning of the viaduct and the subscripts i = 1, 2, ..., n indicate the scenario number

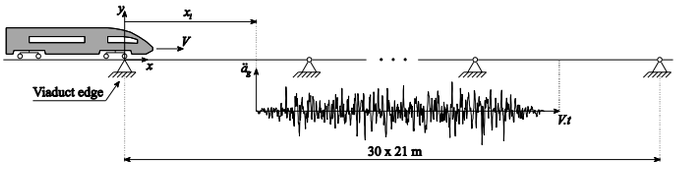


Figure 5. Coordinate of the first wheelset at the instant the earthquake starts.

Track irregularities have also been accounted for, since they may be an important source of excitation for both the structure and the vehicle. In the present work the track irregularities have been generated based on the stochastic Gaussian ergodic process described in Claus & Schiehlen (1998).

Two levels of track quality have been considered: 1) regular operation limit.; 2) alert limit defined in the EN 13848-5 (2008). In all the scenarios, the effect of the irregularities has been accounted from the beginning of the analysis. The profiles have been generated with 2000 discrete frequencies with wavelengths ranging between 3 and 25 m.

3.5 *Running safety analysis*

Fig. 6 shows the vertical and lateral contact forces in the left wheel of the second wheelset calculated for the aforementioned scenario.

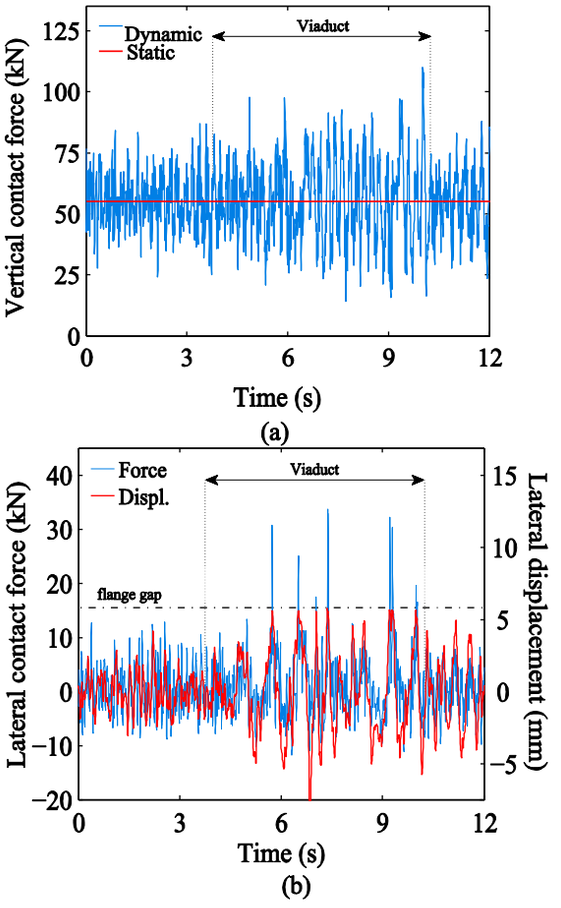


Figure 6. Contact forces in the left wheel of the second wheelset: (a) vertical and (b) lateral.

The lateral contact forces in Fig. 6b are superimposed on the relative lateral displacements between wheel and rail. It is clear that the peaks observed in the lateral force are due to the wheel flange impacts, since they occur at the same moment as the gap between the flange and rail closes (approximately 6 mm).

Fig.7 shows the Nadal and wheel unloading criteria obtained for the left wheel of the first wheelset when the vehicle is running at 200 km/h and 350 km/h. It is clear that both the lateral and the vertical dynamics are affected by the running speed of the vehicle.

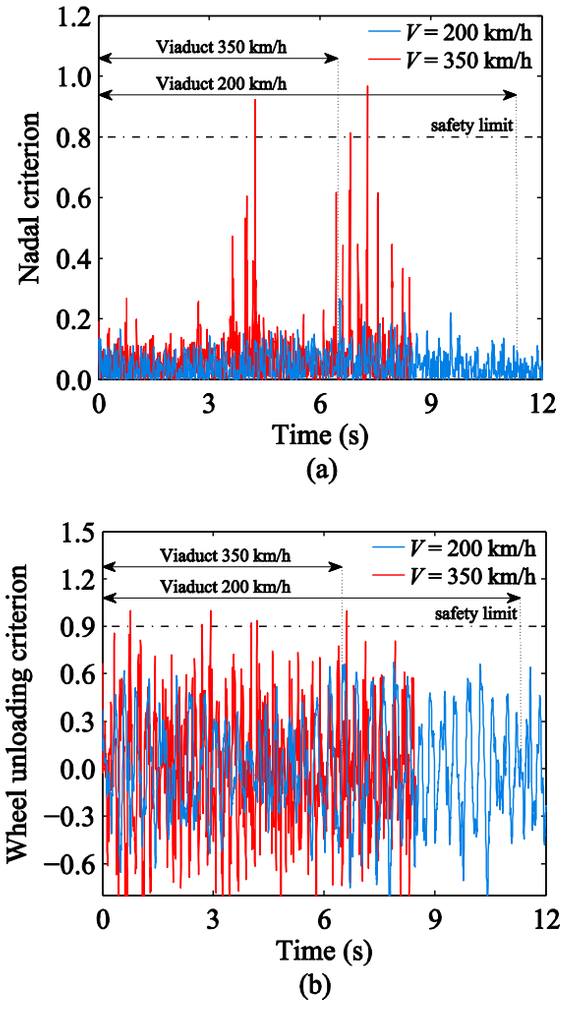


Figure 7. Safety criteria for the left wheel of the first wheelset in a scenario with an earthquake with $T = 150$ years and track quality corresponding to the alert limit: (a) Nadal and (b) wheel unloading

The Nadal and wheel unloading criteria obtained for the left wheel of the first wheelset when the vehicle crosses the viaduct at 350 km/h with the two levels of track quality and without any earthquake load, are depicted as an example in Fig. 8. Several peaks can be observed in the Nadal criterion time-history when the vehicle runs on the track with worse quality. These peaks are mostly related with lateral impacts between the wheel flange and rail, which can lead to wheel flange climbing or track panel shift and subsequent derailment.

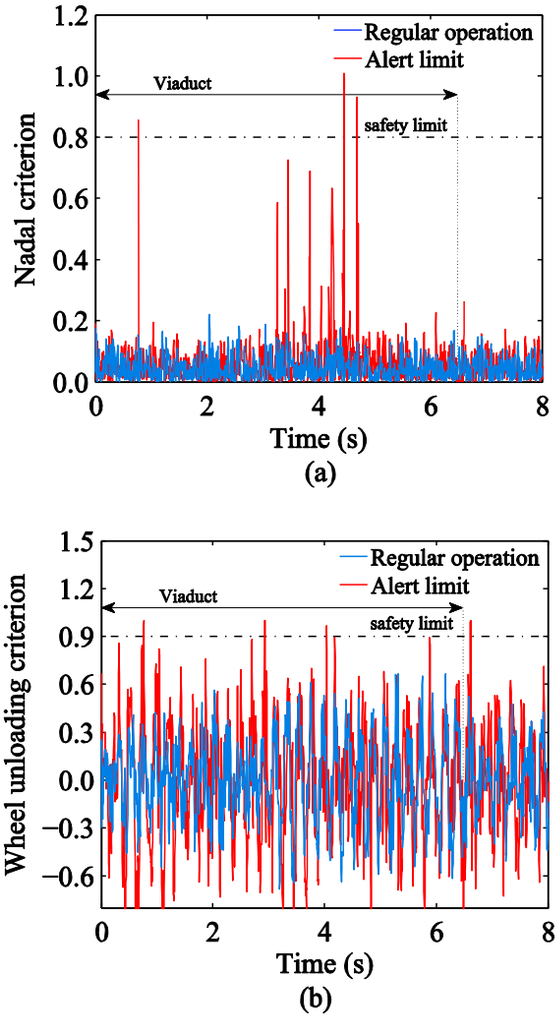


Figure 8. Safety criteria for the left wheel of the first wheelset in a scenario with $V = 350$ km/h and without seismic excitation: (a) Nadal and (b) wheel unloading

The global envelope of each of the analysed safety criterion, as function of the running speed of the vehicle and of the seismic intensity, calculated for the two track quality levels considered in the present work, is plotted in Fig. 9. Each point corresponds to the maximum seismic intensity that guarantees the safety of the vehicle for each running speed, considering the envelope of the five scenarios to account for the time offset between the beginning of the earthquake and the entry of the vehicle in the viaduct.

As expected, the tendency observed in all the criteria is similar, indicating that the risk of derailment increases with the increasing of the running speed and seismic intensity. It may be observed that the risk of derailment due to the wheel unloading is null when the train runs over a track whose quality corresponds to the regular operation limit. For this level of irregularities, the Prud'homme criterion proved to be the most conservative, since it controls the derailment risk for all the speeds. However, this tendency changes for poorer quality tracks, in which the

Nadal and wheel unloading criteria define the safety zone, as may be seen in Fig. 9b. Hence, for the track with better quality, the vehicle remains safe at every speed if no earthquake occurs, while for the track with poorer quality, the derailment risk predicted with the wheel unloading criterion and with the Nadal and Prud'homme criteria significantly increases for speeds above 270 km/h and 300 km/h, respectively.

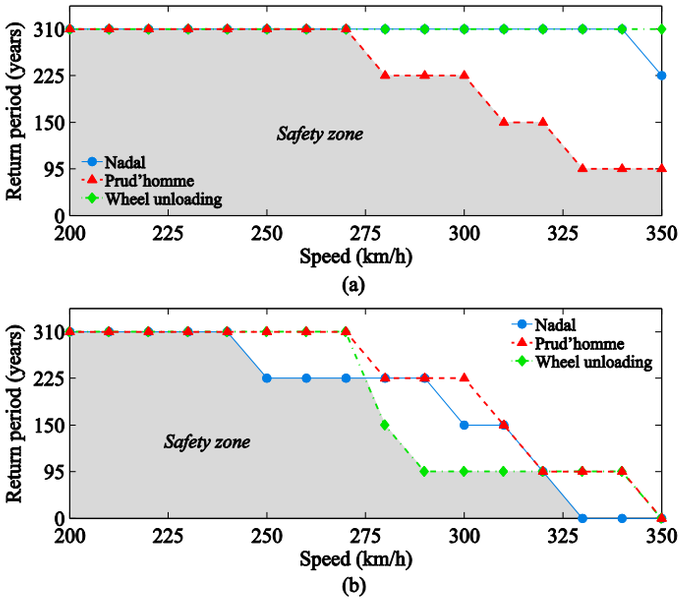


Figure 9. Running safety charts obtained for levels of irregularities corresponding to the (a) regular operation limit and to the (b) alert limit.

4 PROBABILISTIC ASSESSMENT OF THE DYNAMIC BEHAVIOUR OF A SHORT SPAN RAILWAY BRIDGE

4.1 *Introduction*

The safety assessment of a short span composite high-speed railway bridge is presented. Two different failure modes are assessed: the running safety of trains due to loss of contact between the wheel and the rail and track instability due to excessive deck vibrations. This provides examples of limit state functions with different degree of complexity and enables the understanding of how this complexity affects the efficiency of the assessment.

4.2 *Train-structure dynamic model*

Canelas Bridge (Fig. 10) is located in the Northern line of the Portuguese railway and is composed of six simply supported spans of 12 m each, with a total length of 72 m. The bridge deck is a filler beam consisting of two half concrete slab decks, each supporting a single ballasted track, with nine embedded rolled steel profiles HEB 500, which is a typical deck solution for short span high-speed railway bridges.

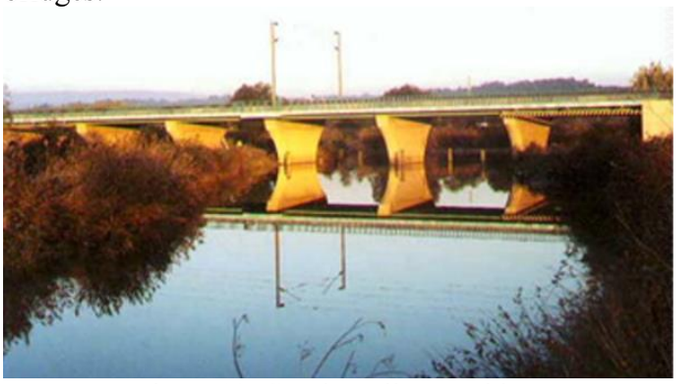


Figure 10. Canelas railway Bridge.

A 2D model was developed and was discretized using beam elements. A single span was modelled and only one track was analysed, as the two half slab decks are independent. The deck was modelled as a beam positioned at the corresponding centre of gravity. The bearings were also included in the numerical model as springs positioned at the corresponding centre of rotation. Regarding the ballasted track, the rails were modelled as beams with the properties of a UIC 60 rail. The beam representing the rail is connected in parallel to a set of springs and dampers, with stiffness k_{pa} and damping c_{pa}, respectively, simulating the rail pads. Below the spring-dashpot set a series of lumped masses, with mass M_s, simulate the sleepers. These lumped masses are also connected in parallel to another set of springs and dampers, with stiffness k_b and damping c_b, respectively, simulating the ballast layer. The shear behaviour of the ballast layer due to composite effects was also accounted for through horizontal springs with stiffness s_r.

A schematic representation of the track-bridge numerical model is shown in Fig. 11.

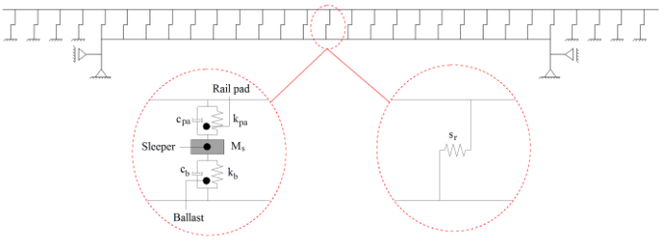


Figure. 11. Track-bridge numerical model.

Track irregularities were randomly generated using power spectral density functions using the SNCF proposal. the wavelength range D1 defined by EN13848-5 (2005) was considered, limiting the analysis to wavelengths between 3 m and 25 m. In order to comply with the quality demands of CEN the maximum standard deviation of the generated track irregularities profiles was limited to 1.5 mm over a track extension of 200 m.

The dynamic behaviour of the bridge was assessed for the crossing of a TGV double high-speed train, which is an articulated train. It is composed by a total of 20 coaches: four power cars, four power passenger cars and twelve passenger cars. The articulated structure only comprises the power passen ger cars and the passenger cars. In the articulate part of the train the bogies are located between ca bodies and are connected by car body–bogie joints In Rocha et al. (2014) the influence of the train mod el was analysed and it could be concluded that a simplified model allows obtaining accurate results A schematic representation of the train and the cor responding numerical model is illustrated in Figur 12.

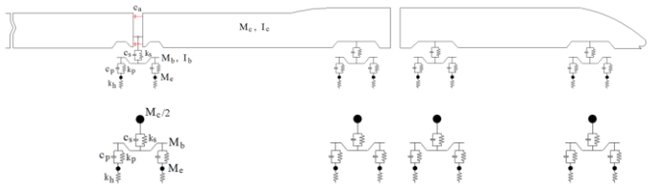


Figure 12. Schematic representation of the TGV double train numerical model.

4.3 *Train-structure dynamic response*

To provide a better understanding of the dynamic behaviour of the train-bridge system the response is analysed for speed ranging from 200 km/h to 450 km/h.

For the particular case study of this lecture two of the main critical safety aspects of dynamic response are the bridge deck accelerations and the wheel unloading coefficients.

Regarding the bridge deck accelerations, the ¾ span was identified as the critical one. The maximum acceleration obtained at this section for increasing train speeds is presented in Figure 13. The black line represents the results for the case where all the variables take their mean value whereas the circles correspond to results obtained from MC simulation, illustrating the variability of the dynamic response for different train speeds.

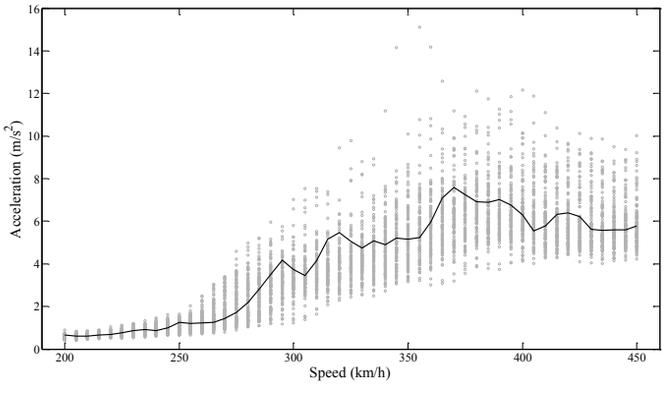


Figure 13. Maximum bridge deck acceleration at the ¾ span section.

With respect to the wheel unloading, the maximum unloading coefficient for increasing train speeds is presented in Fig. 14. Similarly, the black line corresponds to the average scenario whereas the circles correspond to results obtained from MC sim-

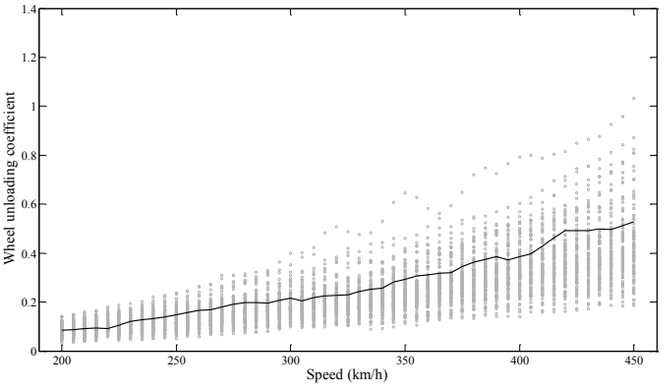


Figure 14. Maximum wheel unloading.

Both the maximum value and the dispersion of the unloading rate show a tendency to increase with speed. However, this is a rather complex phenomenon that depends on a large number of parameters. It is influenced not only by the dynamic response of the bridge (which is affected by both the bridge and track properties) but also by the track irregularities profile.

4.4 *Train running safety*

The running safety of the train is assessed through the analysis of the wheel unloading coefficients.

In its most usual form the wheel unloading, η_U, is calculated by:

$$\eta_U = 1 - \frac{Q_{dyn}}{Q_{sta}} \tag{7}$$

where Q_{sta} is the static load of each wheel and Q_{dyn} is the dynamic wheel load. CEN limits the unloading to 90% of the static wheel load, corresponding to a 10% safety margin. Since a stochastic analysis is performed and the variability of the train, the track and the bridge is accounted for, no safety margin was used to assess the train running safety. Thus, in this paper the limit for the wheel unloading coefficient is 1. The train is considered to run safely on the bridge if the estimated probability of failure due to wheel unloading is lower than 10^{-4}, which corresponds to a reference value in the Joint Committee on Structural Safety Probabilistic Model Code (JCSS, 2001).

In Fig. 15 the distribution of the wheel unloading coefficient is represented for several wheels of the train crossing the bridge at 425 km/h for a sample of 20,000 Monte Carlo simulations.

The results for the several train wheels regarding the distribution are very similar, as can be confirmed by the shape of the curves for each wheel and also by the obtained mean and standard deviation.

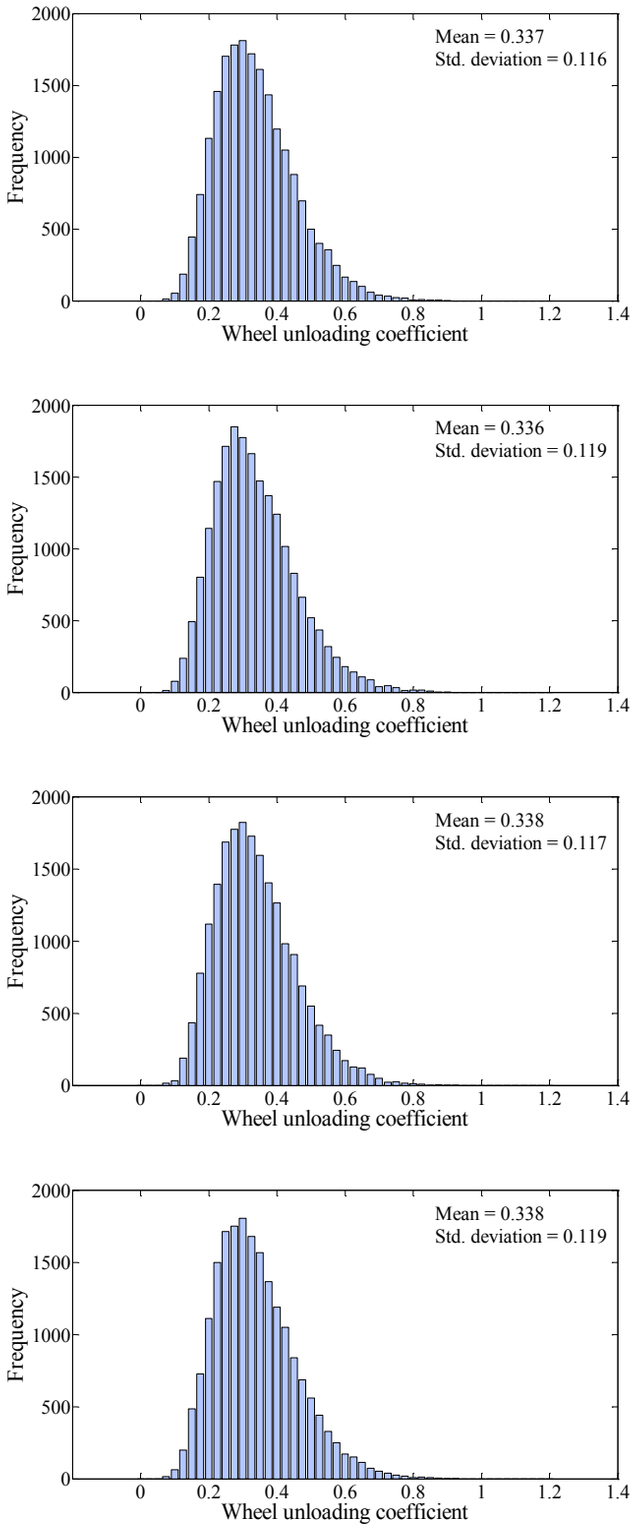


Figure 15. Wheel unloading coefficient distribution for individual wheels.

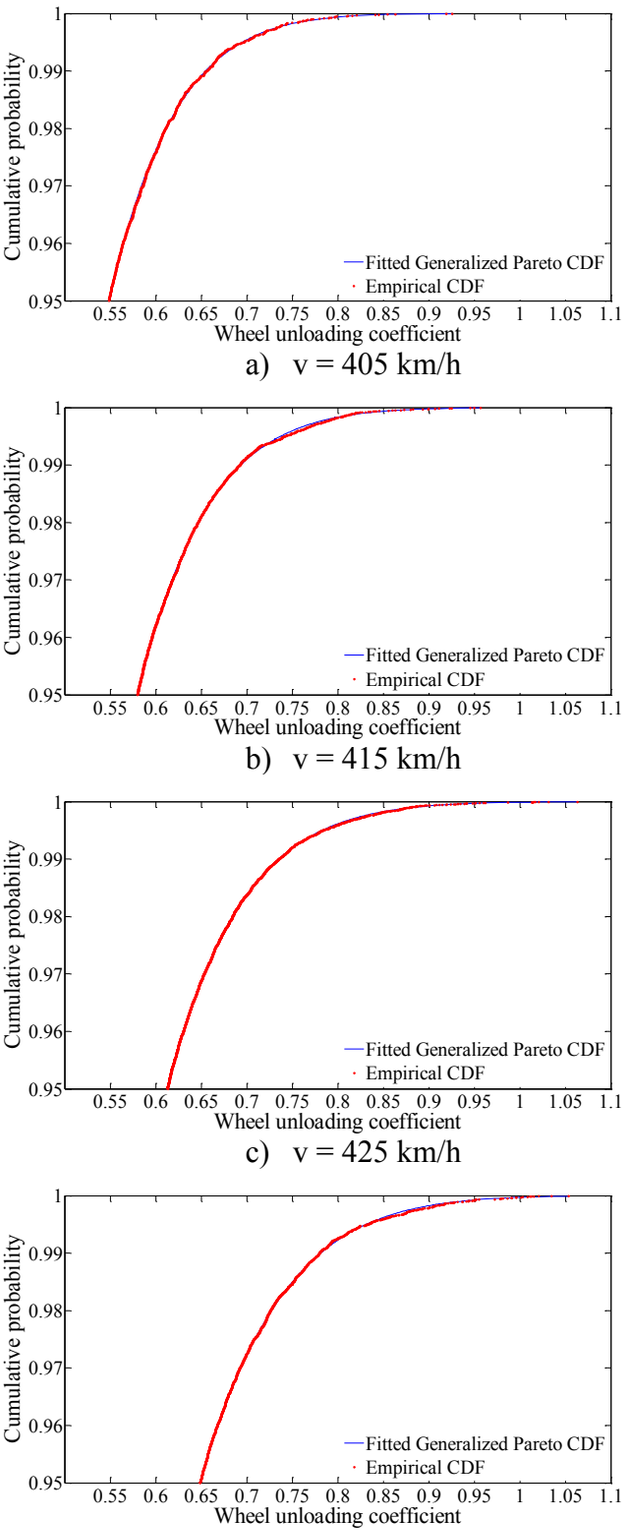


Figure 16. GPD fit to the upper tail of the wheel unloading coefficient distribution.

An example of the fit of the GPD to the data obtained from the simulations is shown in Fig. 16 for different train speeds.

The fit to the data is very good and this is confirmed by the obtained R^2 index values for the several fits performed, which are always above 0.99, regardless of the train speed that is analysed. Therefore, the accuracy of the estimates is assured.

The probability of failure was estimated for increasing train speeds and these results are shown in Fig. 17.

The depicted results correspond to the global analysis. It can be observed that the safety threshold (dashed line) is not exceeded for speeds up to 420 km/h, which make this the train speed limit to ensure the running safety.

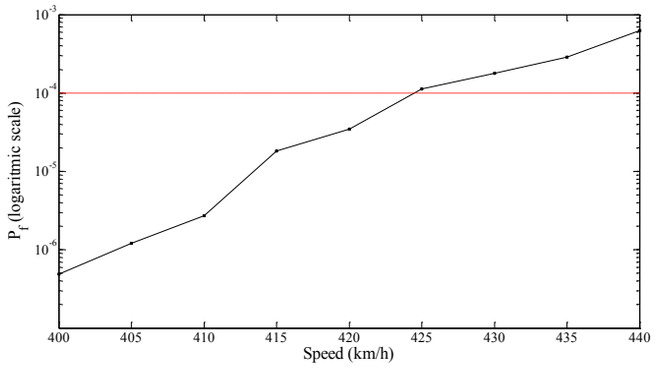


Figure 17. Evolution of the estimated probability of failure with the train speed.

For most train speeds in the vicinity of the failure region less than 20,000 simulations were sufficient to accurately estimate the probability of failure. However, for the critical train speed of 425 km/h, 50,000 simulations were performed. This is explained by the fact that the estimated probability for this train speed is extremely close to the safety threshold. As the sample size increased the value kept varying between the safe and the unsafe side. Even though this was not strictly necessary, as the estimated probability of failure had stabilized fairly well and the confidence intervals were always above the safety limit, for accuracy purposes the number of simulations was increased until the estimated probability stabilized on one of the sides for a sufficient number of sample size increments.

In the critical range of speed the dynamic response of the train-bridge system is governed by the impulsive loading due to the passage of the train at high-speed rather than resonant effects, as had been shown in Rocha et al. (2014). Therefore, the wheel unloading, and consequently the probability of failure, shows a tendency to increase with speed. However, the unloading rate is also dependent of the track properties and of the track irregularities. For this reason, it can be said that the estimated probability of failure depends on a rather complex combination of both the bridge and track dynamic properties and the irregularities profile.

4.5 *Track instability*

The safety due to track instability is assessed by the bridge deck acceleration. For each simulation the maximum acceleration along the bridge deck is identified and selected as representative to assess the safety. The track instability is characterized by the loss of interlock between ballast grains, leading to the loss of the lateral resistance of the sleepers. Laboratory tests confirmed that the ballast instability only tends to occur for deck accelerations higher than 7 m/s^2 (Zacher & Baeβler, 2009). Below this limit the sleeper hardly moves and no loss of lateral resistance is observed. However, EN1991-2 (2003) limits deck acceleration to a maximum of 3.5 m/s^2 for ballasted tracks, which indicates that a safety factor of 2 is applied. Since the safety of the train-bridge system is only at risk when deck accelerations are over 7 m/s^2, the probability of failure of the train-bridge system is established as the probability of the bridge deck reach this acceleration level.

Similarly to what was done in the assessment of the train running safety, to begin the discussion of this failure mode the maximum acceleration is presented for a sample of 50,000 Monte Carlo simulations for a train speed of 285 km/h in Fig. 18.

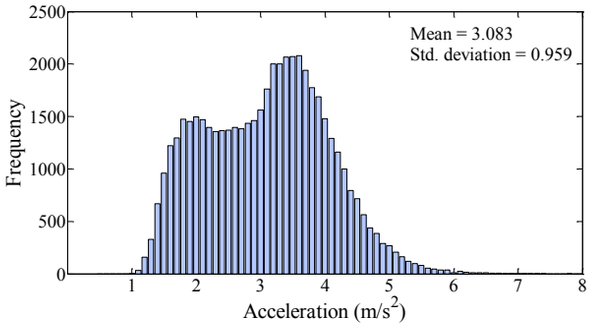


Figure 18. Maximum bridge deck acceleration distribution.

In this case, however, the obtained distribution is not unimodal, due to the existence of two distinct types of response: resonant and non-resonant behaviour. Fig. 19 illustrates the evolution of the estimated probability of failure for increasing train speeds.

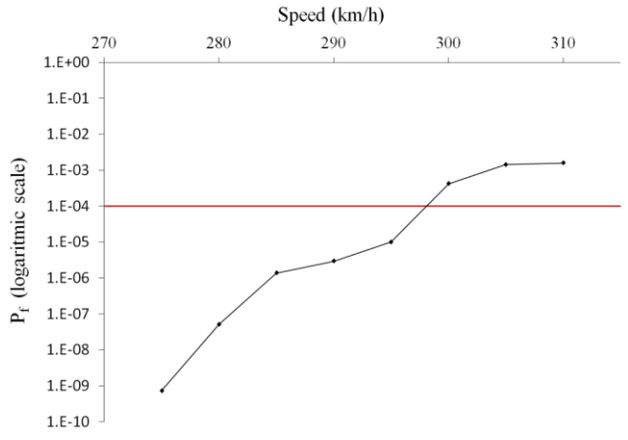


Figure 19. Estimated probability of failure for increasing speeds.

As mentioned before, probability values up to 10^{-4} are considered to be acceptable to measure failure due to the instability of the ballast layer. Analysing Fig. 19 it can be seen that this value is not exceeded for speeds lower than 295 km/h which, therefore, can be seen as an estimate of the train speed limit to be imposed on the bridge.

From the analysis of Fig. 19 it can also be observed that if a more conservative approach was performed, lowering the limit for the probability of failure to values up to 10^{-5}, the speed limit would not be very different, decreasing only 5 km/h to 290 km/h.

5 ASSESSMENT OF THE DYNAMIC BEHAVIOUR OF THE TRAIN-TRACK SYSTEM AT RAILWAY TRANSITION ZONES

5.1 *Introduction*

Within the scope of a research project on transition zones, an earlier version of this model, which proved to be very accurate for simulating the dynamic behaviour of the train-track system at a transition zone to a bridge in a Portuguese railway line (Paixão et al., 2014), was used. That study comprised an extensive validation of the model using field measurements, but it did not address the topic of differential settlements. As a result of that work, the model to assess the influence of the shape and amplitude of the settlement profiles of the backfill, thus contributing to a better understanding of the dynamic behaviour of the train-track system at transition zones, was adopted.

5.2 *Train-track dynamic model*

The numerical model was developed in ANSYS. It comprises a track stretch of about 57 m on the embankment (on the backfill of the bridge's abutment) and a stretch of approximately 115.5 m on the bridge (on the abutment and on the deck), as illustrated in Fig. 20a.

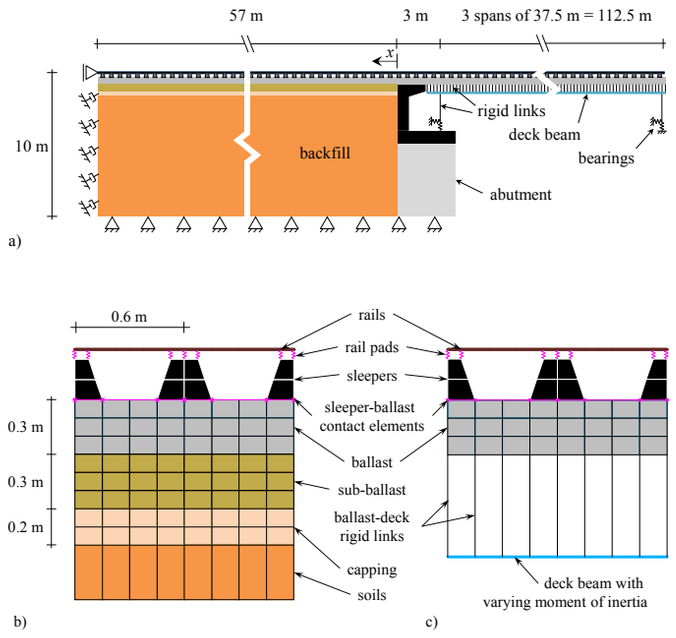


Figure 20. Schematic representation of the numerical model (a), and detailed aspects of the track on the backfill (b) and on the bridge (c).

Although it is a 2D model, the numerical method was developed to represent the behaviour of a full track cross-section and it has successfully been applied to the study of transition zones, following extensive calibration and validation works with field measurements (Alves Ribeiro et al., 2014; Paixão et al., 2014).

The model developed for this study, in particular, considers various aspects of the track superstructure, its substructure and the bridge, using 24,537 nodes and 28,096 elements. The two rails (type UIC60) were modelled as one continuous beam with 0.075 m long elements, with a cross-section area of $2\times7.7\times10^{-3}$ m^2 and a moment of inertia of $2\times30.55\times10^{-6}$ m4. The pairs of rail pads on each sleeper were modelled as three independent vertical spring-damper elements, as depicted in Figure 20b-c. Following previous experimental and numerical studies (Alves Ribeiro et al., 2014; Paixão, 2014; Paixão et al., 2014; Paixão et al., 2015a), the rail pads were considered to have a vertical stiffness of k_{rp}=160 kN/mm and a vertical damping value of c_{rp}=17 kN.s/m.

Plane-stress elements with 4 nodes were used to represent the sleepers, the bridge abutment and the layers of ballast, sub-ballast, capping and embankment soils (Figure 20b). In ANSYS it was possible to define the width values of each plane-stress element, which were initially calibrated using reduced 3D static models. This process basically uses an optimization algorithm to minimize the differences in the vertical displacements between the 3D and the 2D models.

Contact elements on the bottom node of the sleepers and on the surface of the ballast layer were included at the sleeper-ballast interface to account for the eventual separation of these two track components and to study the development of the hanging sleepers (Figure 20b-c).

Viscous boundary conditions were included in the left vertical boundary of the model (Figure 1a), to minimize the effect of wave reflections. The displacements of the bottom nodes of the model were vertically restrained.

The deck of the bridge was modelled as one continuous beam with 0.15 m-long elements located at the centre of gravity of the deck's cross section. Initial tests showed that it was necessary to model at least three spans of the bridge to account for the influence of the bending of the deck on the behaviour of the train-track system.

Bearing in mind that this study addressed transition zones in the Portuguese railway network, the dynamic analysis was performed taking into consideration the fastest passenger train in service in Portugal - the tilting "Alfa Pendular" train, travelling at 220 km/h (Figure 21a). Figure 21b shows the train model considered in the study (Ribeiro et al. 2013). The bogies and car bodies were considered as rigid bodies.

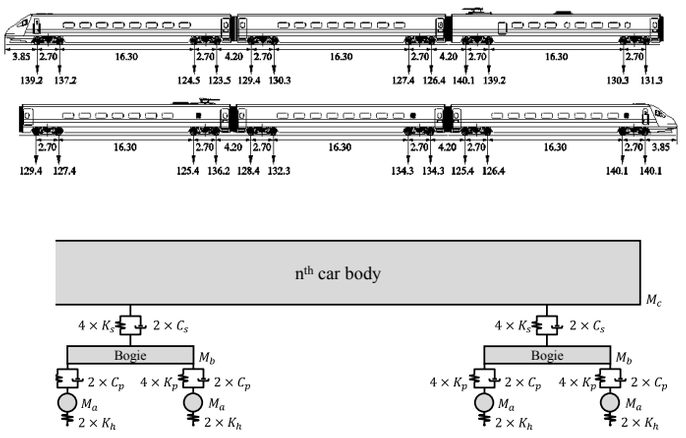


Figure 21. The "Alfa Pendular" train: a) distances between axles (in m) and approximate loads (in kN); b) model of one of the 6 coach cars.

5.3 *Backfill settlement scenario*

In an attempt to simulate scenarios in which settlements occurred in the backfill, at the substructure level, the authors altered the mesh of the model to reproduce those conditions. Four hypothetical scenarios of uniform settlement of the backfill were studied, considering a maximum settlement value of δ_max= 1, 5, 10 and 15 mm in each case (Fig. 22).

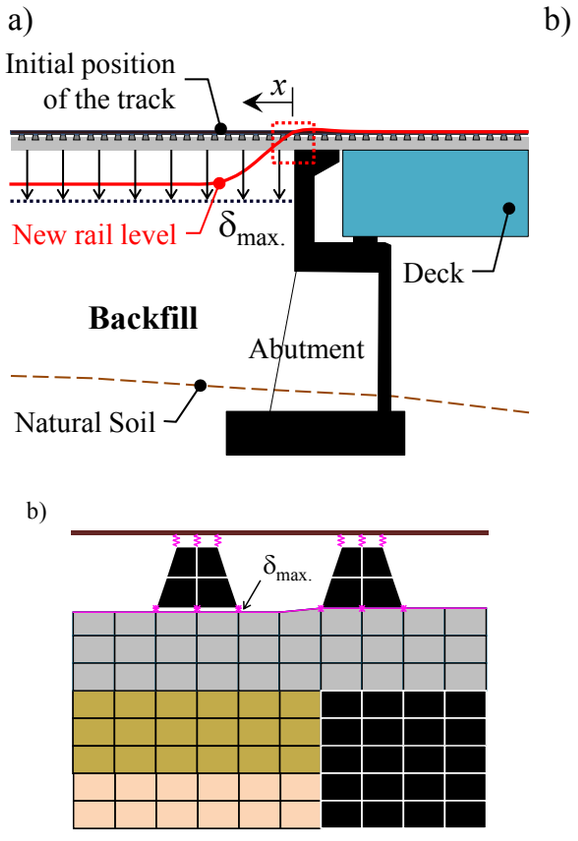


Figure 22. Backfill settlements: a) schematic representation; b) detail of the top nodes of the ballast layer moved downwards by δ_{max}.

Aiming at assessing the influence of different settlement profiles on the levelling of the track and on the dynamic response of the train-track system, four shapes of hypothetical settlement profiles were studied, as depicted in Fig. 23:

U – uniform settlement of the track substructure along the approach;

W – settlement profile resulting from a wedge-shaped backfill using materials with improved mechanical properties (Paixão et al., 2015b): unbound granular material (UGM) and cement-bound mixture (CBM);

S – sharp settlement variation at the bridge approach;

G – gradual settlement variation at the bridge approach.

For each shape (U, W, S and G), four settlement profiles were analysed corresponding to different maximum amplitudes of settlement, δ_{max}: 1, 5, 10 and 15 mm. The first profile shape, U, regards the scenarios presented earlier in section 3.1. The settlement profiles were also applied to the top nodes of the ballast layer in the model (Fig. 22).

The four profile shapes under study were determined in resemblance with profiles reported by railways infrastructures managers (ERRI, 1999; Nicks, 2009) and based on previous studies (Schooleman, 1996; England et al., 2000; Kempfert & Stadel, 2000; Luomala & Nurmikolu, 2012; Abu-Farsakh & Chen, 2014).

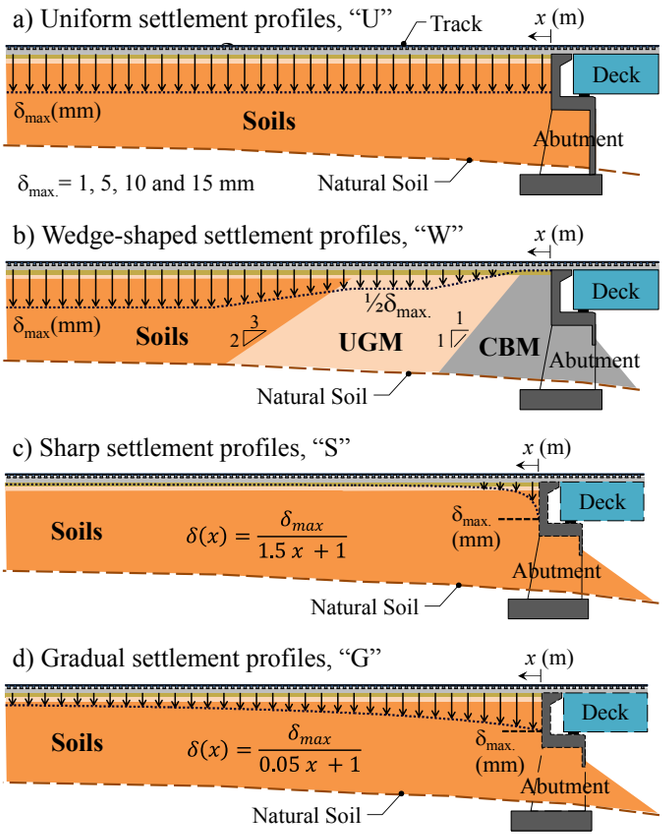


Figure 23. Schematic representation of the settlement profile shapes U, W, S and G.

As mentioned earlier, due to the bending stiffness of the rails, some sleepers were hanging from the rails with gaps under them. For each profile shape,

the number of hanging sleepers increased with the value of δ_{max}. The position of the hanging sleepers is identified in Fig. 24 with the respective size of the gap.

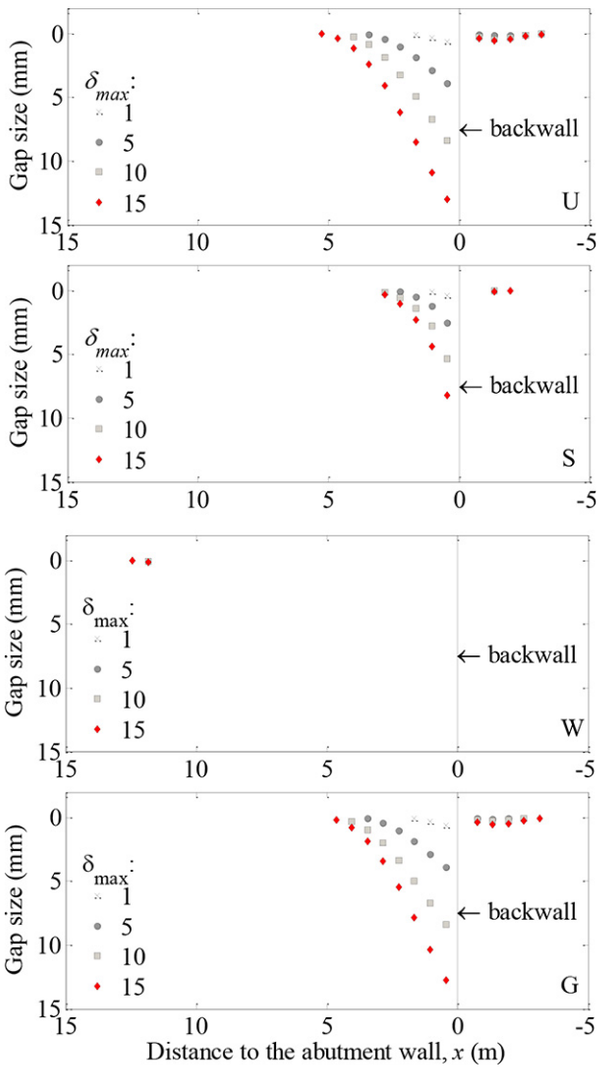


Figure 24. Location of hanging sleepers and respective gap sizes in unloaded conditions.

As expected, profile shapes U and G yielded the highest number of hanging sleepers and the largest gaps for each value of δ_{max}, for example: in shapes U and G, with δ_{max}=15 mm, the results revealed 9 and 8 consecutive hanging sleepers, respectively, and maximum gap sizes of about 13 mm.

Fig. 25 shows peak variations of the normal train-track interaction force (in percentage) for the first eight axles of the train, calculated as $\Delta P_p=(P_p-P_s)/P_s$, where P_s is the static axle load of 132 kN and P_p is the peak axle load. The results confirm that very low variations of the train-track interaction can be expected for profiles with shape W, suggesting reduced track degradation. On the other hand, the amplitude of the interaction force in the remaining profile shapes seems to increase significantly with the settlement, due to the sharp variations of the rail's position at the approach to the abutment. Some variability is observed, depending on the profile's shape and value of δ_{max}, and there are a few cases where the load increased by 100 to 150% in profiles with shapes U and G.

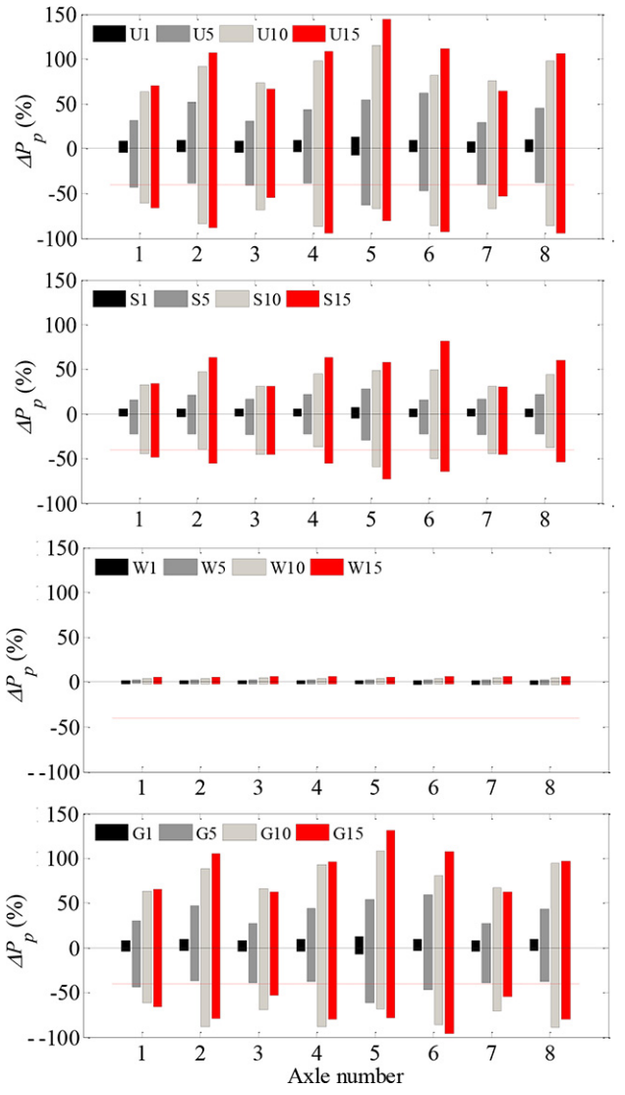


Figure 25. Peak variations of the dynamic train-track interaction force.

To illustrate the severity caused by the hanging sleepers, Fig. 26 shows peak values of the total contact force obtained between the underside of each sleeper and the ballast layer, depending on the value of δ_{max} and the distance from the sleeper to the abutment wall, x. Profile shapes U and G produced comparable results and seem to yield very severe situations, amplifying the load on the ballast by about 1.7, 3.6, 5.0 and 5.8 times, under the sleeper aligned with the abutment wall, when δ_{max}= 1, 5, 10 and 15 mm, respectively. This aspect suggests a significant increase in the degradation of the ballast layer with increasing δ_{max}. On the other hand, profiles with shape W did not evidence significant amplifications of the contact forces – the peak values were kept between 55-65 kN for all the sleepers in the different cases. Numerical studies by Lundqvist and Dahlberg (2005) using 3D models reported that the case of one unsupported sleeper with a gap of 1 mm can increase loads onto the ballast from approximately 50 kN to

70 kN - about 1.4 times - considering a static axle load of 107.5 kN travelling at 216 km/h. A similar result was obtained in a profile with shape S with δ_{max}= 1 mm, which had two hanging sleepers with smaller gap sizes of 0.4 and 0.1 mm, but considered a higher axle load of 132 kN, travelling at about 220 km/h, and resulted in a force increment from 55 kN to 79 kN - also by about 1.4.

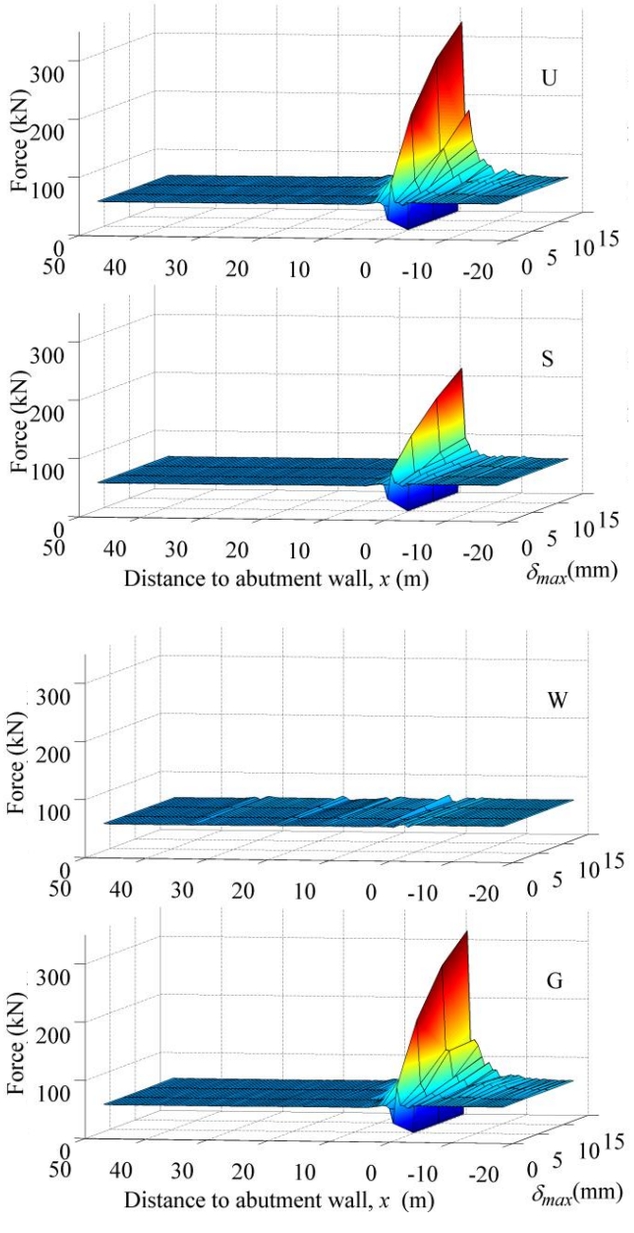


Figure 26. Peak contact forces between sleepers and ballast layer.

The authors also noticed that, in each tested case, the highest peak loads occurred at the sleepers that were not hanging, but were adjacent to the hanging sleepers that had the largest gaps (in these cases, the first sleeper behind the abutment wall, at about x=-0.15m). This can be explained by the fact that the static weight of the rail and of the hanging sleepers, plus part of the axle load, was directly transferred to those sleepers that were not hanging. Similar observations were reported in other numerical studies (Lundqvist & Dahlberg, 2005; Varandas et al., 2014).

Fig. 27 shows peak vertical accelerations of the sleepers along the transition. Again, profile shapes U and G seem to produce similar results with increasing acceleration values of δ_{max}, not only near abutment wall, but also in a zone stretching by about 10 m on the backfill and on the bridge

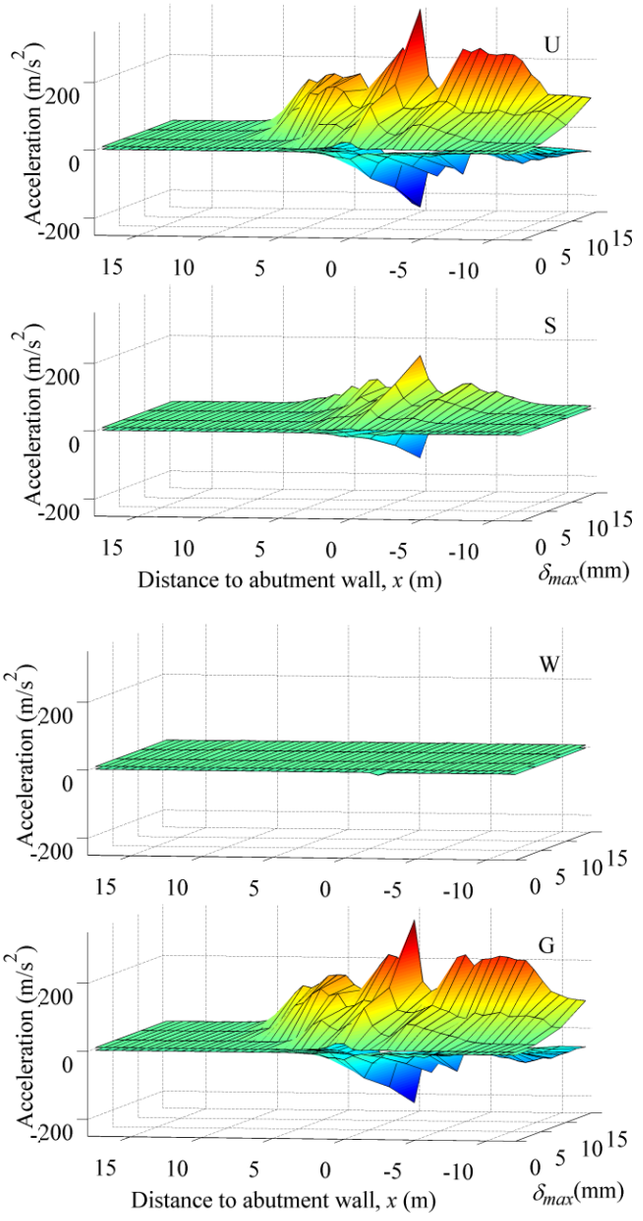


Figure 27. Peak vertical accelerations of the sleepers, along the transition zone.

6 CONCLUSIONS

A wheel rail contact formulation for analysing the nonlinear dynamic interaction between vehicles and structures is presented. This method takes into account the geometry of the wheel and rail surfaces in order to accurately evaluate the vertical and lateral interaction. An enhanced node to segment contact element is used for modelling the behaviour in the

contact interface in the normal and tangential directions. This approach is generally more efficient than treating the normal and tangential contact forces as external forces. The constraint equations that relate the displacements of the vehicle and structure are imposed using a direct method. In contrast with other contact formulations such as the penalty method, the proposed formulation does not require additional penalty parameters and is less likely to lead to ill conditioned systems.

A study regarding the running safety assessment of trains moving over bridges subjected to earthquakes is presented. Since the running safety of trains might be jeopardized not only by intense shakings, but also by moderate earthquakes, which may not cause significant damage to the structure, only seismic events with relatively low return periods and high probability of occurrence have been considered. Nevertheless, although the columns do not experience significant damage for these levels of seismic intensity, a methodology to account for the reduction in their stiffness due to concrete cracking is proposed. The influence of the seismic intensity level, running speed and track quality in the running safety of a high speed railway vehicle moving over a viaduct is discussed. Unlike the majority of studies, in which the earthquake is assumed to start at the instant the train enters the bridge, the randomness of the earthquake is accounted for by considering different time offsets between the beginning of the earthquake and the entry of the vehicle in the viaduct. The results have shown that, even for the moderate seismic intensities considered in the present study, the train safety is put at risk in a considerable number of scenarios, especially due to the risks of derailment caused by wheel flange climbing. These results prove the importance of taking low intensity earthquakes into account in the design of railway bridges, even if they do not represent a major threat to the structure integrity. The track quality has also a strong influence on the running safety, since, even without considering the effect of the earthquake, the values of the Nadal and Prud'homme criteria increased approximately 5 times for the track with poorer quality.

The assessment of the running safety of high-speed trains over a short span railway bridge using a probabilistic approach was also presented. A filler beam bridge with spans with a length of 12 m was selected as case study. The existence of track irregularities was accounted for along with the variability of parameters related to the bridge, the track and the train. The obtained distribution for the wheel unloading coefficient was unimodal. For this reason, attempts were made to fit known distributions to the data obtained from the simulations. The lognormal distribution was the most likely to fit the data, however, adequate tests led to the rejection of this hypothesis. Consequently, the modified Monte Carlo method, which combines Monte Carlo simulations with the classical GPD, was used to assess the running safety of the trains over the bridge. The analysis allowed concluding that the train speed must be limited to 420 km/h in order to ensure the running safety of the trains over the bridge. The speed limit to guarantee the running safety is significantly higher than that obtained when analysing the track stability, 295 km/h. Therefore, it can be concluded that when no lateral actions are taken into account the safety of the train-bridge system is governed by the deck acceleration, which is related to the track stability. In future developments lateral actions will be included in order to provide a better understanding of the influence of such actions on the running safety of high-speed trains.

A numerical study on the influence of the settlement profiles of the backfill in the dynamic train-track interaction at the approach to railway bridges - the transition zone – was presented. To that aim, a numerical model was used to simulate the effect caused by different shapes of settlement profiles and different settlement amplitudes (up to 15 mm). It was possible to conclude that the number of hanging sleepers and the gap between the sleepers' underside and the ballast layer depend not only on the maximum settlement amplitude, but also on the shape of the profile. In addition, the development of differential settlements on the backfill can lead to critical situations in terms of track degradation (due to excessive load on the track) and safety requirements (offload limits and loss of axle-rail contact). In some scenarios, the vertical accelerations of the axles may exceed maintenance-related limits, established by some railway infrastructure managers. In general, peak axle loads and accelerations increased with the amplitude of the settlement, but it may also depend on the shape of the settlement profile. Normally, the greater the number of hanging sleepers and gap sizes, the higher the vertical accelerations of the sleepers and the larger the vertical contact forces between the sleepers and the ballast layer. Despite these downside aspects, a very good level of passenger comfort was observed in all tested scenarios. The cases of settlement profiles associated with wedge-shaped backfills indicate an adequate behaviour of the train-track system because none of the limits related to track degradation or safety were exceeded. This finding supports the conclusion that wedge-shaped backfills seem adequate to address the problems related to abrupt variations of the track's stiffness and differential settlements normally found at transition zones. Although this study comprises a theoretic approach, the obtained results may be regarded as recommendations for the design of bridge approaches, particularly, with the suggestion to include wedge-shaped backfills at these locations of the railway tracks. To account for the variability of the development of settlement profiles at transition

zones, further research is necessary and improvements in the model need to be introduced. For example, future developments could include the incorporation of the plastic deformation behaviour of the geomaterials, aiming at predicting the development of more realistic settlement profiles, and testing and comparison of other structural solutions for transition zones, such as approach slabs, under sleeper pads or different backfill designs.

7 ACKNOWLEDGEMENTS

This work was financially supported by: Project POCI-01- 0145-FEDER- 007457 - CONSTRUCT - Institute of R&D in Structures and Construction funded by FEDER funds through COMPETE2020 - Programa Operacional Competitividade e Internacionalização (POCI) – and by national funds through FCT - Fundação para a Ciência e a Tecnologia; The support of the centre of competence in railways of the Faculty of Engineering of the University of Porto (CSF-FEUP) and of IP – Infraestruturas de Portugal, the Portuguese railway infrastructures manager, is also acknowledged.

REFERENCES

Abu-Farsakh, M.Y. & Chen, Q. 2014. Field Demonstration of New Bridge Approach Slab Designs and Performance; Baton Rouge, LA: Louisiana Transportation Research Center; FHWA/LA. 13/520;

Alves Ribeiro, C.; Paixão, A.; Fortunato, E. & Calçada, R. 2015. Under sleeper pads in transition zones at railway underpasses: numerical modelling and experimental validation; Structure and Infrastructure Engineering. Vol. 11, 2015 - Issue 11, pp. 1432-1449.

Claus H. & Schiehlen W. 1998. Modeling and simulation of railway bogie structural vibrations. Vehicle System Dynamics; 29 (1): pp. 538-552.

CONTACT 2011. Release 11.1, VORtech Computing, Delft, the Netherlands.

EN 13848-5 2005. Railway applications - Track - Track geometry quality - Part 5: Geometric quality assessment, European Committee for Standardization (CEN), Brussels.

EN 14067-6 2010. Railway applications - Aerodynamics - Part 6: Requirements and test procedures for cross wind assessment, European Committee for Standardization (CEN), Brussels.

EN 1998-1 2004. Eurocode 8: Design of structures for earthquake resistance-Part 1:General rules, seismic actions and rules for buildings, European Committee for Standardization (CEN), Brussels.

EN 1998-2 2005. Eurocode 8: Design of structures for earthquake resistance - Part 2: Bridges, European Committee for Standardization (CEN), Brussels.

EN13484-5 2008. Railway applications - Track - Track geometry quality - Part 5: Geometric quality levels. European Committee for Standardization (CEN), Brussels.

EN1991-2 2003. Eurocode 1 - part 2: Actions on structures - traffic load on Bridges. European Committee for Standardization (CEN), Brussels.

England, G.L.; Tsang, N.C.M. & Bush, D.I. 2000. Integral bridges: A fundamental approach to the time-temperature loading problem; Ed. 3; Prague: Thomas Telford; ISBN: 0-7277-2845-8.

Hertz H. 1882. Ueber die Berührung fester elastischer Körper [On the contact of elastic solids], Journal für die reine und angewandte Mathematik 1882; 92: 156-171.

Joint Committee on Structural Safety (JCSS). Probabilistic Model Code – 12th draft, 2001. (http://www.jcss.ethz.ch/).

Kalker JJ. 1990. Three-Dimensional Elastic Bodies in Rolling Contact. Kluwer Academic Publishers, Dordrecht, The Netherlands.

Kalker JJ. 1996. Book of tables for the Hertzian creep-force law, in Proceedings of the 2nd Mini Conference on Contact Mechanics and Wear of Wheel/Rail Systems, I. Zobory (Ed.), Budapest, Hungary.

Kempfert, H.-G. & Stadel, M. 2000. Geotechnische Konstruktionen am Übergang Brücke-Erdbauwerk; Vorträge der Baugrundtagung 2000; Hannover, Germany; 18-21 Sep. 2000; pp. 295-301.

Lundqvist, A. & Dahlberg, T. (2005) Load impact on railway track due to unsupported sleepers; Proceedings of the Institution of Mechanical Engineers, Part F: Journal of Rail and Rapid Transit; Vol. 219; n.º 2; pp. 67-77;

Luomala, H. & Nurmikolu, A. 2012. Railway Track Stiffness Measurements at Bridge Transition Zones; Advances in Transportation Geotechnics II; Hokkaido University, Japan; 10-12 Sep. 2012; pp. 811-816.

Malveiro J, Ribeiro D, Calçada R, Delgado R. 2013. Updating and validation of the dynamic model of a railway viaduct with precast deck. Structure and Infrastructure Engineering: Maintenance, Management, Life-Cycle Design and Performance, Volume 10, 2014 - Issue 11, pp.1484-1509.

Montenegro PA, Neves SGM, Calçada R, Tanabe M, Sogabe M. 2015. Wheel-rail contact formulation for analyzing the lateral train-structure dynamic interaction. Computers & Structures 2015; 152: pp. 200-214.

Montenegro, P.A., Calçada, R., Vila Pouca, N., Tanabe, M. 2016. Running safety assessment of trains moving over bridges subjected to moderate earthquakes, Earthquake Engineering and Structural Dynamics, 45 (3), pp. 483-504.

Nadal J. 1908 Locomotives à vapeur, Collection Encyclopédie Scientifique, Bibliotèque de Mecanique Appliquée et Genie, Vol. 186, in Paris, France.

Neves SGM, Montenegro PA, Azevedo AFM, Calçada R. 2014. A direct method for analyzing the nonlinear vehicle–structure interaction. Engineering Structures, 69: pp. 83-89.

Neves, S.G.M., Azevedo, A.F.M., Calçada, R. 2012. A direct method for analyzing the vertical vehicle-structure interaction, Engineering Structures, 34, pp. 414-420.

NP EN 1998-1 2009. Eurocode 8: Design of structures for earthquake resistance - Part 1: General rules, seismic actions and rules for buildings - Portuguese National Annex, European Committee for Standardization (CEN), Brussels.

Paixão, A. & Fortunato, E. 2010. Rail track structural analysis using three-dimensional numerical models; 7th European Conference on Numerical Methods in Geotechnical Engineering; Trondheim; 02-04 Jun. 2010.

Paixão, A.; Alves Ribeiro, C.; Pinto, N.M.P.; Fortunato, E. & Calçada, R. 2015a. On the use of under sleeper pads on transition zones at railway underpasses: experimental field testing; Structure and Infrastructure Engineering; Vol. 11; n.º 2; pp. 112-128.

Paixão, A.; Fortunato, E. & Calçada, R. 2014. Transition zones to railway bridges: track measurements and numerical modelling; Engineering Structures; Vol. 80; pp. 435-443.

Paixão, A.; Fortunato, E. & Calçada, R. 2015b. Design and construction of backfills for railway track transition zones; Proceedings of the Institution of Mechanical Engineers, Part

F: Journal of Rail and Rapid Transit; Vol. 229; n.º 1; pp.58-70.
Prud'homme A. 1967 La résistance de la voie aux efforts transversaux éxercés par le material roulant, in Revue Generale des Chemins de Fer.
Ribeiro, D.; Calçada, R.; Delgado, R.; Brehm, M. & Zabel, V. 2013. Finite-element model calibration of a railway vehicle based on experimental modal parameters; Vehicle System Dynamics; Vol. 51; n.º 6; pp. 821-856.
Rocha, J. M., Henriques, A. A., Calçada, R. 2012. Safety assessment of a short span railway bridge for high-speed traffic using simulation techniques. Engineering Structures 2012; 40: pp. 141-154.
Rocha, J. M., Henriques, A. A., Calçada, R. 2014. Probabilistic safety assessment of a short span high-speed railway bridge. Engineering Structures 2014; 71: pp. 99-111.
Rocha, J. M., Henriques, A. A., Calçada, R. 2016. Probabilistic assessment of the train running safety on a short span high-speed railway bridge. Structure and Infrastructure Engineering 2014; Vol. 12, 2016 - Issue 1, pp. 78-92.
Rocha, J.M., Henriques, A.A., Calçada, R., Rönnquist, A. 2015. Efficient methodology for the probabilistic safety assessment of high-speed railway bridges, Engineering Structures, 101, pp. 138-149.
Schooleman, R. 1996. Overgang kunstwerk-aardebaan voor de hoge-snelheidslijn; M.Sc Thesis; Delft: Technische Universiteit Delft.
Varandas, J.N.; Paixão, A.; Fortunato, E.; Hölscher, P. & Calçada, R. 2014. Non-linear elastic behaviour of unbound aggregates in FEM representing railway transition zones; The Second International Conference on Railway Technology: Research, Development and Maintenance (Railways 2014); Ajaccio, Corsica, France; 8-11 Apr. 2014.
Zacher, M., Baeβler, M. 2009. Dynamic behaviour of ballast on railway bridges. In: Proceedings of Dynamics of High-Speed Railway Bridges. London: Taylor & Francis.

Maintenance, Safety, Risk, Management and Life-Cycle Performance of Bridges – Powers, Frangopol, Al-Mahaidi & Caprani (Eds)
© 2018 Taylor & Francis Group, London, ISBN 978-1-138-73045-8

A Vision for Vision-based Technologies for Bridge Health Monitoring

N. Catbas, C.Z. Dong, O. Celik & T. Khuc
University of Central Florida, Orlando, Florida, USA

ABSTRACT: Condition assessment of bridges evolved over the years with the advances in non-destructive evaluation technologies, field tests and structural health monitoring. As a result, technological advances changed the resources that bridge engineers can tap into; however, the requirement for practical, low-cost and effective approaches has remained the same. The writer and his research team have explored vision-based technologies to fulfill such requirements. In this paper, first the vision-based technologies will be presented along with capabilities and limitations. A review of basic concepts, available camera, lens and other peripherals are reviewed along with some of the algorithms for analyzing computer vision data. A framework of image-based structural identification is proposed to obtain structural parameters by using a full con-contact method on vision related techniques. By using a camera system, traffic over the bridge will be identified and classified into classes and sub-classes for vehicle weight estimation. Finally, some solutions and example applications from a laboratory bridge, a footbridge and a railroad bridge are presented.

1 INSTRUCTIONS

Structural health monitoring (SHM) has been employed as an effective approach for structural assessment and decision making for bridges. Due to the advances in technology, SHM has received attention from researchers and civil infrastructure owners over the last several decades. Decision making by means of SHM data in real-life structures has some challenges and discussed extensively by Catbas & Kijewski-Correa (2013). Especially for bridge engineering applications, certain challenges have been presented and discussed such as challenges in field-work for sensor instrumentation, cable wiring, data acquisition, power and transmission arrangement for wired and wireless sensing. These challenges can make certain SHM applications inconvenient, time consuming, and expensive. Additional considerations that need to be resolved are as follows: the inspection and monitoring of existing structures may require service interruptions due to traffic closure; it may be difficult to obtain access for instrumentation work for some large or sensitive bridges; some bridges or network of ordinary highway bridges may warrant just intermittent monitoring with portable systems instead of permanent and continuous monitoring systems. As a result, the development of effective, convenient and inexpensive monitoring tools for situations outlined above and also for large populations of bridges has become more important.

To address the limitations of conventional sensor-based SHM, imaging and computer vision methods have been considered as potential alternatives due to advances in related technologies (Webb et al. 2014). Unquestionably, the main advantage of vision-based approaches is contactless implementation that accelerates monitoring and reduces maintenance cost of structural assessments. As examples for bridge applications, a hybrid sensor-camera St-Id system for bridge monitoring has been developed and demonstrated in the laboratory (Zaurin & Catbas 2010) and also for real bridges (Catbas et al 2012). Although some of these challenges related to structural assessments have been addressed by utilizing image processing and computer vision methods such as detection and quantification of cracks and surface damages of structures (Abdel-Qader et al. 2003, Gul et al. 2013, Yamaguchi & Hashimoto 2010), and displacement measurement of structures (Khuc & Catbas 2014, Kim et al. 2013, Lee et al. 2007), a very few of complete studies in the context of structural identification (St-Id) have been presented (Khuc & Catbas 2017). Structural identification (St-Id) is a transformation of system identification that focuses on creating a numerical or nonphysics-based model of a dynamic system based on its measured response.

2 BASICS FOR VISION-BASED MONITORING

The main idea of vision-based monitoring is to convert the target motion in an image to the actual motion in a physical quantity such as millimeter. In recent literature, many researchers proposed their procedures of vision-based displacement measurement methods. In this study, the authors first summarize the state-of-the-art and then give a general procedure as illustrated in Figure 1. There're four steps in this procedure, including: 1) camera calibration; 2) initial image capture and feature extraction; 3) visual tracking and 4) displacement calculation.

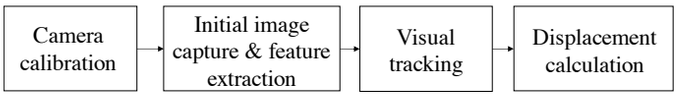


Figure 1. General procedure of the vision-based displacement measurement.

In the first step, there're two prevailing methods: the planar homography matrix method and the scale factor method. Using the planar homography matrix between the image and physical world, it is possible to convert the image entities to the physical world objects (Zhang 2002). In this study, instead of planar homography matrix, for convenience, the authors use the scale factor to convert the target motion in pixels to physical metric such as millimeter. More details about the scale factor calculation can be found from the literatures (Dong et al. 2015, 2017a, b, Khuc & Catbas 2016, 2017, Ye et al. 2016a, b, c). In the second step, one needs to select the tracking region, which includes the measurement targets in the field of view of the initial image. According to the visual tracking methods used in the third step, image preprocessing is utilized to extract useful features from the tracking region. Researches, who use digital image correlation (DIC) in frequency domain or space domain, just select the target regions as the patterns, and the image intensities of the patterns play the role of visual tracking features. Other researchers extract key points and descriptors such as Shi-Tomasi corners, SURF, SIFT, FREAK, etc. as the tracking features and the corresponding visual tracking method includes Lucas-Kanade optical flow estimation (Dong et al. 2017a) and key point matching based on nearest neighborhood approximation (Khuc & Catbas 2017). The third step is to track the selected targets in the subsequent images captured by the camera continuously and locate the targets' new positions. Here except the tracking algorithms mentioned above, dense optical flow algorithms and phase-based optical flow algorithms are also good choices. Finally, with the scale factor, s, applied to the displacements in pixels, the actual displacements at time t with a physical unit are obtained: $(x_t - x_0)$s, horizontally, and $(y_t - y_0)$s, vertically.

3 SYTEM CONFIGURATIONS

It is important to pick and choose the right cameras, lens and software as well as other associated peripherals for a particular bridge engineering application. The vision-based displacement measurement system consists of a suite of image acquisition device and image processing software. In general, the image acquisition device includes a camera and a lens. As shown in Table 1, some typical components including cameras, zoom lenses and synchronization modules. The selection of image acquisition device depends on the application scenarios and requirements for real-time monitoring or post processing. If one just wants to acquire the images during the experiments and do post processing, portable cameras are good options, because they are easy to setup and don't need external power supply. Also, portable cameras have on board storage mechanism, which means that the videos or images can be directly stored in the built-in storage or SD card. And the exposure time can easily be controlled and fixed to a specific value, which makes the cameras have the uniform sample rates. However, the portable cameras are not programmable so that connecting with computers and working with other sensors synchronously can be very hard to achieve. The 4K action camera (Z camera E1) listed in Table 1 can be synchronized with several cameras via a master-slave series connection. The industrial cameras are programmable and have input-output interface, which can be connected with computers and controlled by software. These cameras can work with other sensors synchronously. The synchronization can be achieved by the external controlling system. Here NI 6343 Multifunction I/O Device and MindVision trigger module are listed as the external controlling system. There are two video/image output interface for industrial cameras: USB 3.0/2.0 and GigE. USB2.0 is becoming out of date and most of the USB camera are using USB 3.0. USB3.0 has a higher transmission speed and higher volume bandwidth (5 Gbit/s) than GigE cameras (1000 Mbit/s). And in general, the frame rate of USB3.0 cameras are higher than GigE camera. But there is a tradeoff: the transmission distance of the USB3.0 cameras is much shorter (less than 5m) than the GigE cameras (100m). Camera arrangement and synchronization in a wide range is very hard for USB3.0 camera. Even though this problem can be solved by adding fiber optic cable or using the zoom lens with longer focal length, the cost would be increased greatly. For long span bridge monitoring with the requirement of multi-point and wide range distributed camera arrangement where the sample rate is not very high, GigE

may be more suitable. Since most of the industrial cameras and lenses are separated, the selection of zoom lenses is determined according to different measurement distance and requirement of accuracy. Remarks are noted in Table 1.

Table 1. Components of vision-based displacement system.

Item		Model	Technical Specifications	Remarks
Camera	Portable camera	 Sony HDR-SR10	Resolution: 1920 × 1080; Frame rate: 30 fps; On board image storage; Carl Zeiss Vario-Sonnar T Lens; 15x Optical Zoom, 3.1-46.5 mm;	High resolution, with own zoom lens, suitable for close range measurement
		 Canon VIXIA HF R42	Resolution: 1920 × 1080; Frame rate: 60 fps; On board image storage; Zoom Ratio: 53x Advanced*/32x Optical/1060x Digital; Focal Length: 2.8-89.6mm.	High resolution, with own zoom lens, suitable for close range measurement
	4K action camera	 Z camera E1	Multiple video resolutions: 4096x2160 @24fps; 3840x2160 @24fps/25fps/30fps; 2880x2160 @24fps/25fps/30fps; 1920x1920 @24fps/25fps/30fps; 1920x1440 @24fps/25fps/30fps; 1920x1080 @24fps/25fps/30fps; 1920x1080 @50fps/60fps; 1280x720 @50fps/60fps/**240fps**; 840x480 @25fps/30fps; Mount: Micro Four-Third; On board image storage.	High resolution and can be switched to different video resolution and frame rate according to the application scenarios, portable, easy to set up
	Industrial camera	 Basler ace-acA2040-120um	Resolution: 2048 × 1536; Frame rate: 120 fps; Pixel Size (H × V): 3.45 μm × 3.45 μm; Mono/ Color: Mono; Sensor Type: CMOS; Shutter: Global Shutter; Interface: USB 3.0; Mount: C mount; Synchronization: software trigger/hardware trigger/free-run.	High sample rate and high resolution, can be controlled by computer, real-time displacement monitoring and image acquisition for post processing, programmable
		 MindVision- MV-GE131gc-t	Resolution: 1280 × 960; Frame rate: 72 fps; Pixel Size (H × V): 3.75 μm × 3.75 μm; Mono/ Color: Color; Sensor Type: CMOS; Shutter: Global Shutter; Interface: GigE; Mount: CS mount; Synchronization: software trigger/hardware trigger/free-run.	High sample rate, can be controlled by computer, real-time displacement monitoring and image acquisition for post processing, programmable, cost-effective
Lens		 Olympus M.Zuiko ED 75-300 II	Zoom: 75-300mm; Manual zoom; Aperture: F4.8-607; Mount: Micro Four-Third.	Long distance, high resolution
		 Navitar 12x zoom lens	24X Zoom with 2X extender; High magnification; Mount: C mount;	Super long-distance zoom, long span bridge displacement measurement
		 6-60mm lens	Zoom: 6-60mm; Manual zoom; Aperture: F1-1.6; Sensor size: 1/3"; Mount: C/CS mount	Light and easy to control; with luminosity control
		 5-100mm lens	Zoom: 5-100mm; Aperture: F1-1.8; Sensor size: 1/3"; Manual zoom; Mount: C/CS mount	Light and easy to control; with luminosity control
Synchronization			32 AI (16-Bit, 500 kS/s);	It need to connect with

module	NI 6343 Multifunction I/O Device	4 AO (900 kS/s); 48 DIO USB Multifunction I/O Device.	computer and can synchronize conventional sensors and cameras via LabVIEW
	 MindVision Tigger module	Four channel output trigger; Flash control.	On board control, programmable, digital output, can trigger industrial camera.
	 Z camera master-slave Synch module	Master-slave control; input-output series connection.	For portable camera with I/O function, wire control gives high synchronization accuracy

4 COMPUTER VISION-BASED STRUCTURAL IDENTIFICATION

In this paper, a new St-Id framework for bridge monitoring using computer vision technologies is presented, and subsequent computer vision-based bridge monitoring examples are developed within the context of St-Id. In brief, traffic loading induced from multiple vehicles is estimated including axle loads and load locations by utilizing a combined detection and localization computer vision algorithm on image data from a traffic-camera. Simultaneously, other cameras (response-cameras) are deployed under the bridge to measure bridge displacements at multiple locations to those vehicles by means of a non-target vision-based displacement monitoring. Then, the input data (traffic loading) and output data (displacement responses) are processed with an image-based structural identification (iSt-Id) system to obtain a new indicator for bridge damage detection, named the displacement Unit Influence Surfaces, UIS (Khuc & Catbas 2017). Similar to natural frequencies and mode shapes of structures, the UIS is one of a few structural parameters that can be derived as a function of only structural characteristics. It means that the UIS can be employed as a powerful structural indicator for the assessment of bridges. The UIS of a laboratory bridge have been successfully obtained and illustrated on subsequent sections. Those UIS that were obtained have shown consistence and reliability, and enabled a new fully contactless iSt-Id implementation.

In this research, traffic vehicles are categorized into classes for example sedan, SUV, minivan, bus, truck, semi-trailer, etc., and the weight distribution of each class can be studied based on the manufacture's vehicle specification and/or using Weigh-In-Motion (WIM) database. In order to detect each type of vehicle in a scene, for instance the semi-trailer class, the Haar (Viola & Jones 2001) and/or HOG (Dalal & Triggs 2005) features corresponding to semi-trailer trucks are extracted to represent for this class. Thus, those object features are used to develop a classification algorithm based on booting technique (Viola & Jones 2001), which can rapidly find regions where a particular class may occur. The initial and successful implementation for detecting and classifying small-scale vehicles has been demonstrated in the UCF Structural Lab, which is illustrated in Figure 2.

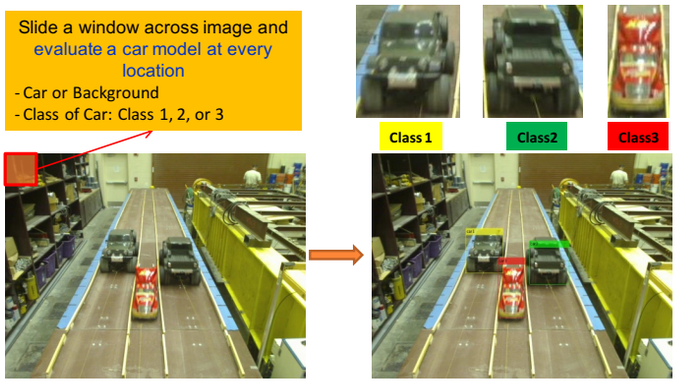


Figure 2. Three types of vehicles detection and classification.

5 NON-TARGET DISPLACEMENT MEASUREMENT BASED ON VISION APPROACH

While using some certain of sensors such as linear variable differential transformers (LVDTs) and slide wire potentiomers are the most common sensors to collect displacement data, those conventional sensors are not convenient in the field as they require a fixed reference frame. In addition to conventional sensors, use of cameras as special sensors that can collect motion of targets attached at structures in distance, has gained attention recently. As a novel sensing approach, a new vision based method is proposed and will be exploded to measure bridge displacement without using any attached target on the structures. To implement this idea, the authors will extract key-points from the images of the measurement location, to match those key-points between the consecutive frames to determine the pixel based displacement, and to convert the pixel displacement

to the engineering unit (e.g. inch, mm). Although there are several robust methods related to extracting key-points, some well-established algorithms such as Scale Invariant Feature Transform (SIFT) (Lowe 2004), Speed-up Robust Feature (SURF) (Bay et al. 2008), Binary Robust Invariant Scalable Keypoints (BRISK) (Leutenegger et al. 2011), and Fast Retina Keypoint (FREAK) (Alahi et al. 2012) have been explored in a comparative fashion to obtain the measurement location key-points and match them across images. The proposed non-target displacement measurement method has been implemented in the UCF Structures Lab as shown in Figure 3.

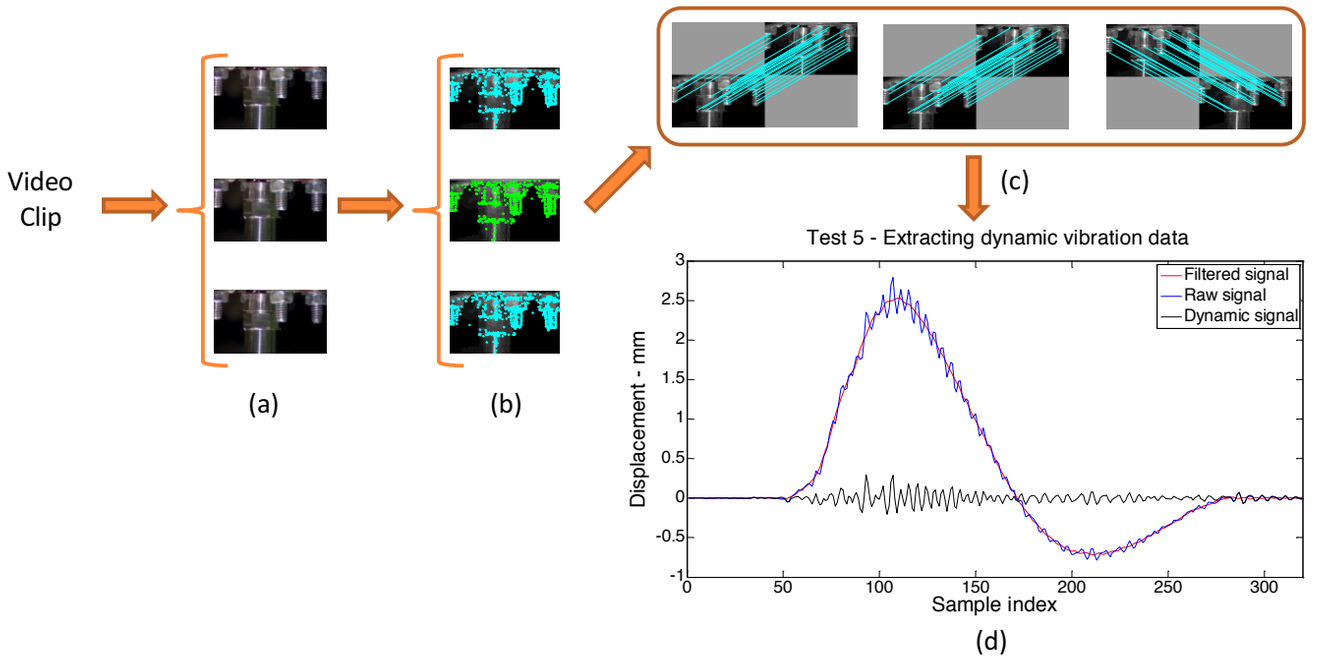


Figure 3. Overview of non-target displacement measurement method; (a) Measurement locations, (b) Extracted key-points as virtual makers, (c) Matching key-points, (d) Get dynamic displacements

6 RESULTS FROM LABORATORY TESTS

The proposed iSt-Id framework has been conducted in a bridge model at the University of Central Florida (UCF) Structures Lab. The experimental bridge called UCF 4-Span Bridge Model consists of two 304.8cm main continuous spans and two 120cm approach spans. The bridge deck includes a 3.18mm steel sheet at 120cm wide which is composited with two HSS 25x25x3mm girders separated 60.96cm from each other. As a bridge test set-up for SHM studies at the UCF, there are a number of sensors attached in the model such as strain gages, accelerometers, LVDTs, tilt-meters, and Fiber Bragg Grating (FBG) sensors. Moreover, some common damage scenarios can be simulated in the model by changing stiffness of the structural system and/or of the supports. The result from one test is shown in Figure 4. It is seen that each blue dot location (*x*-bridge length, *y*-bridge width) presents for a combined position of multi-vehicles on the bridge deck. The z-unit displacement value of a particular blue dot is a normalized response (displacement herein) to effects of multi-vehicles loadings. In time domain, each blue dot corresponds to the frame of the video clip recorded by the traffic-camera, and the response of z value must be obtained synchronously.

The UIS is determined by fitting a number of discrete data points (e.g., blue dots in Figure 4). Therefore, combination of several tests is a need for the regression analysis. Figure 5 shows a displacement UIS obtained from several random data sets for one-fifths-span locations of the bridge girder for the undamaged condition (Baseline). To confirm consistency of the proposed method results, a total of fifteen (15) UIS are obtained for each measured position by randomly selecting five (5) tests out of forty (40) tests database. Consequently, some characteristics of those 15 UIS including volume, maximum and minimum values are calculated to compare with the ones of the mean-UIS. It is seen that the characteristics from those UIS are very close (± 6% error interval for maximum values, and only ± 3% error interval for minimum and volume values), which confirms the outcomes of are consistency and reliability of the proposed method (the unit influence surfaces, UIS). Consequently, the UIS can be utilized for damage detection purpose.

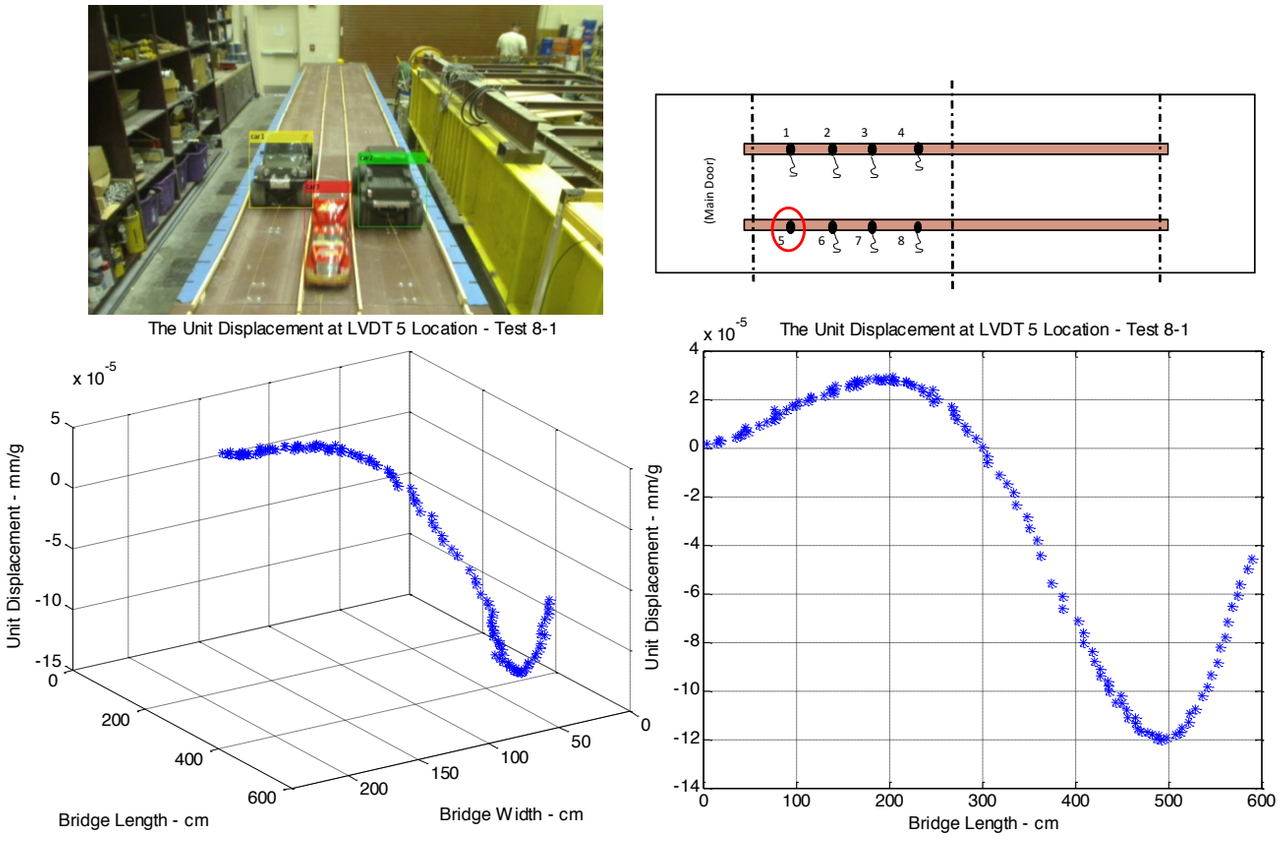


Figure 4. The unit displacement data at a certain measured location

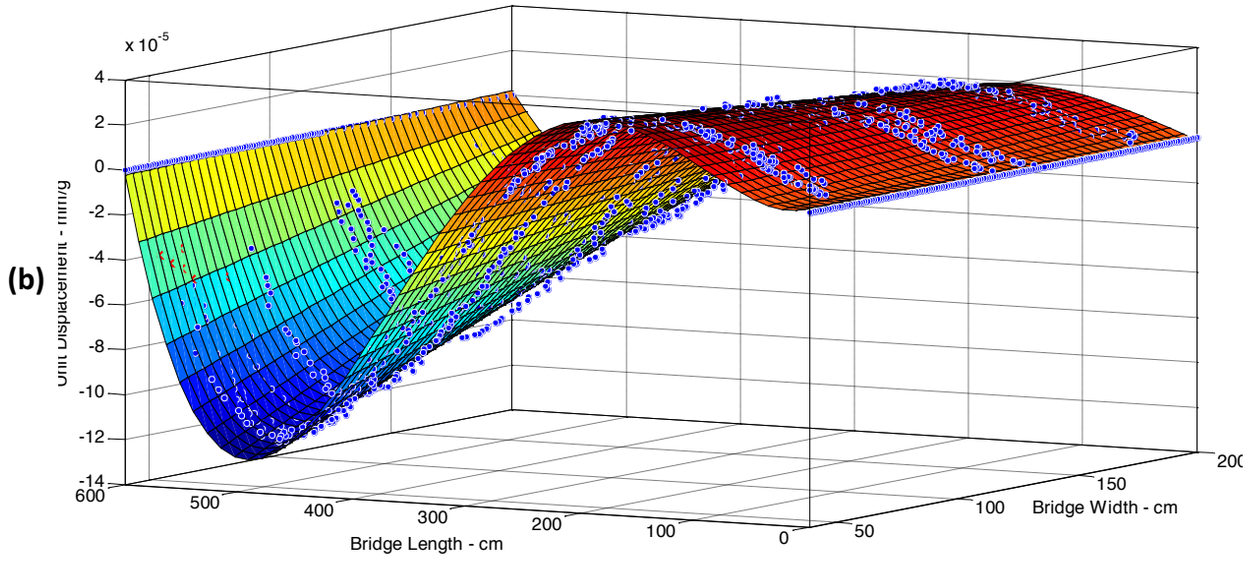
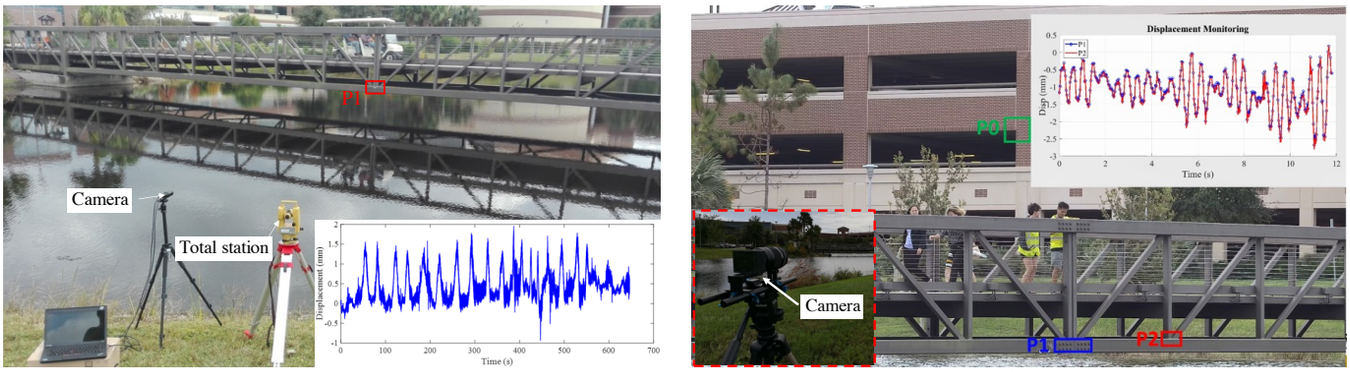


Figure 5. The displacement unit influence surface obtained by fitting from several test data sets

7 REAL LIFE IMPLEMENTATION EXAMPLES

In this section, two examples of real life examples, one from a footbridge and one from a railroad bridge are presented. Figure 6 illustrates the displacement measurement of a footbridge on UCF campus. For this footbridge, golf cart and human loading (walking and jumping) are the two main loads. In the first scenario as shown in Figure 6a, an industrial camera and a total station were set up to measure the bridge displacement at P1 induced by the golf cart when it travelled back and forth on the bridge. The distance

from the location of the camera and the total station and P1 is 18.3 m. The displacement time history was obtained by processing the image sequence acquired by the camera and the maximum displacement was about 1.5 mm. The total station gave 1.75 mm as the maximum displacement and it was almost the minimum resolution. Here, the total station can only measure the static displacement not dynamic one. Comparing the results from vision-based method and total station, it can be seen that the vision-based method shows good performance for dynamic structural displacement measurement. Figure 6b shows the bridge displacements of two points (P1 and P2) under human loads. The camera used here was an 4k action camera which was placed 60 m away from the P1. Since this camera was placed further away at a location with ground vibration, it could easily be disturbed by the wind and ground vibration. As a result, a stationary point P0 was selected to eliminate the camera motion. The revised displacements, which were obtained by subtracting the displacement of P0 from P1 and P2 respectively, were assumed the corrected ones. The measurement results not only show the whole process of human loading but also give a high accuracy. The precision here was smaller than 0.01 mm.



a) b)

Figure 6. Displacement measurement of a footbridge under: a) golf cart loading; b) human walking and jumping

Figure 7 shows a railway bridge in the city of Winter Park near Orlando, Florida. A 4K action camera was placed about 40 m away from the measurement point, P1. To eliminate the camera motion, a stationary point P0 was selected as the reference point. The camera recorded the whole process when the trained crossed the bridge. As shown in Figure 7, the displacement time history of P1 clearly indicates the bridge deformation at midspan. The red dash line box shows the moments starting from the train getting on the bridge and departure from the bridge. The maximum displacement is around 11.5 mm.

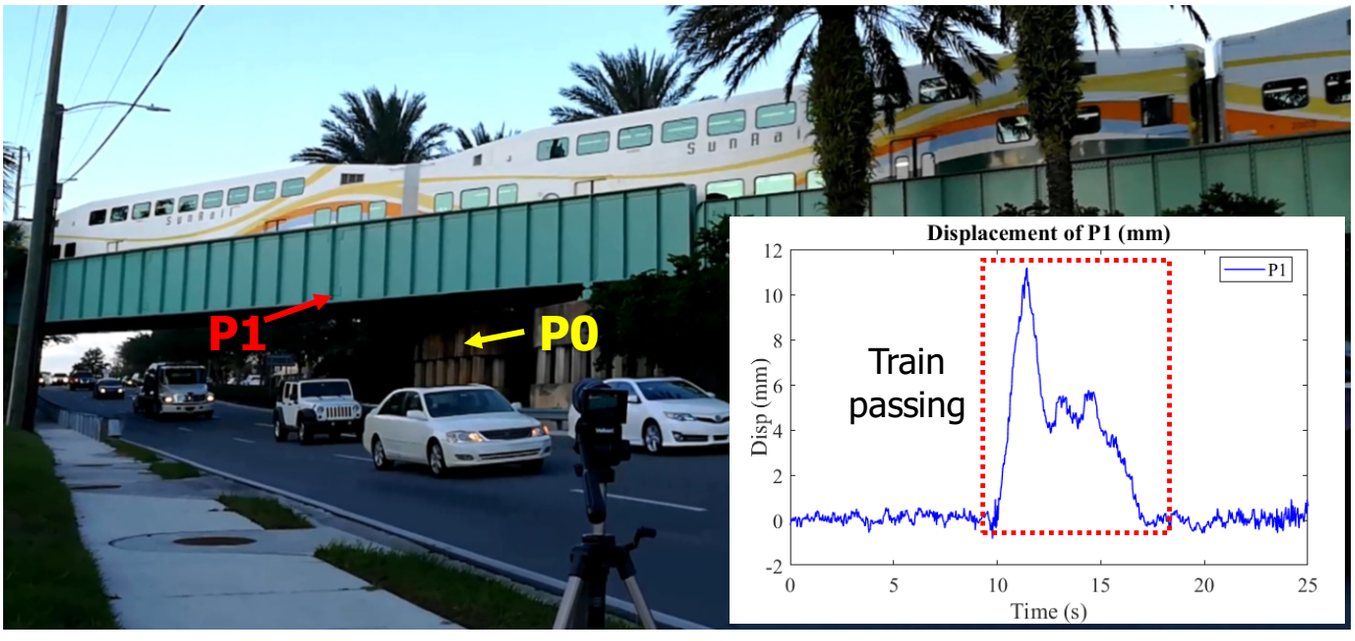


Figure 7. Displacement measurement of a railway bridge when a train passing through

8 CONCLUSIONS

This paper introduces an overview of vision-based monitoring of structures. Prevailing algorithms are briefly reviewed, and image acquisition devices are discussed according to various application scenarios. First, a laboratory study is presented where structure is monitored using cameras and sensors within the context of structural identification. A new indicator for bridge damage detection, entitled Unit Influence Surfaces, UIS, is presented and demonstrated. UIS is a powerful index that can be obtained using cameras that monitor vehicle traffic on bridges and also responses of the critical locations of the structure. The dynamic displacements of bridge girders to those vehicle loads at several measured locations can be obtained. The input effects including vehicle loadings, vehicle locations, and output displacements of the bridge structures can be obtained to determine a series of displacement unit influence surfaces (UIS). Quantitative analysis of the UIS have confirmed its consistency and reliability that enables applications of using the UIS in damage detection and damage localization. Next, a footbridge and a railroad bridge monitoring study as real life examples are presented. These studies were conducted without interrupting the traffic and without the need to have access for sensor or target installation.

Computer vision based monitoring of bridges has major positive impacts for structural safety and assessment of especially large population of bridges. The sensor based structural health monitoring (SHM) technologies have somewhat matured and are available; yet, permanent and continuous of such SHM may be economically feasible for only a small fraction of bridges such as structurally critical or landmark bridges. In the meantime, a large population of routine highway bridges will still rely on visual inspection by the inspectors/engineers. Cost-effective and easy to use camera based technologies can support field inspections of such structures while also eliminating time-taking field installation of sensors. Besides, the data obtained using computer vision-based monitoring can be further employed for structural damage detection, condition assessment, etc., which are also currently carried out using conventional sensors. As a result, cost and time could be saved for the SHM of ordinary bridges. It is anticipated that such SHM would support decision-making and planning for structure management and maintenance.

9 ACKNOWLEDGMENTS

The authors would like to acknowledge several members of the Civil Infrastructure Technologies for Resilience and Safety (CITRS) research group at University of Central Florida for their endless support in creation of this work. In addition, several discussions and meetings have been conducted with colleagues and former students who worked in areas related to the ideas presented in this paper. The financial support for this research was provided by NSF Division of Civil, Mechanical and Manufacturing Innovation [grant number 1463493] and the statements made herein are solely the responsibility of the authors

REFERENCES

Abdel-Qader, I., Abudayyeh, O. & Kelly, M.E. 2003. Analysis of edge-detection techniques for crack identification in bridges. *Journal of Computing in Civil Engineering* 17(4): 255-263.

Alahi, A., Ortiz, R. & Vandergheynst, P. 2012. Freak: Fast retina keypoint. *Proc., Computer Vision and Pattern Recognition (CVPR), 2012 IEEE Conference on, IEEE*: 510-517.

Bay, H., Ess, A., Tuytelaars, T. & Van Gool, L. 2008. Speeded-Up Robust Features (SURF). *Computer Vision and Image Understanding* 110(3): 346-359.

Catbas, F.N. & Kijewski-Correa, T. 2013. Structural identification of constructed systems: Collective effort toward an integrated approach that reduces barriers to adoption. *Journal of Structural Engineering ASCE* 139(10): 1648-1652.

Catbas, F.N., Gokce, H.B. & Gul, M. 2012. A Practical Methodology for Load Rating of Existing Highway Bridges: Demonstration on Reinforced Concrete T-Beam Bridges. *Journal of Bridge Engineering ASCE* 17(4): 652–661.

Dalal, N. & Triggs, B. 2005. Histograms of oriented gradients for human detection. *Proc., Computer Vision and Pattern Recognition, 2005. CVPR 2005. IEEE Computer Society Conference on, IEEE*: 886-893.

Dong, C.Z., Celik, O. & Catbas, F.N. 2017a. Long-term structural displacement monitoring using image sequences and spatio-temporal context learning. *Structural Health Monitoring 2017, Proceedings of the 11th International Workshop on Structural Health Monitoring, IWSHM 2017*.

Dong, C.Z., Ye, X.W. & Jin, T. 2017b. Identification of structural dynamic characteristics based on machine vision technology. *Measurement: Journal of the International Measurement Confederation*.

Dong, C.Z., Ye, X.W. & Liu, T. 2015. Non-contact structural vibration monitoring under varying environmental conditions. *Vibroengineering Procedia* 5: 217 - 222.

Gul, M., Catbas, F. N. & Hattori, H. 2013. Image-based monitoring of open gears of movable bridges for condition assessment and maintenance decision making. *Journal of Computing in Civil Engineering*, 04014034.

Khuc, T. & Catbas, F.N. 2017. Structural identification using computer vision-based bridge health monitoring. *Journal of Structural Engineering ASCE* 144(2): 04017202.

Khuc, T. & Catbas, F.N. 2014. Non-target displacement measurement of structures using vision based approaches. *IABMAS 2014 International Conference on Bridge Maintenance, Safety and Management*. Shanghai, China.

Khuc, T. & Catbas, F.N. 2016. Computer vision-based displacement and vibration monitoring without using physical target on structures. *Structure and Infrastructure Engineering* 13(4): 505-516.

Khuc, T. & Catbas, F.N. 2017. Completely contactless structural health monitoring of real-life structures using cameras

and computer vision. *Structural Control and Health Monitoring* 24(1): e1852.

Kim, S.W., Jeon, B.G., Kim, N.S., & Park, J. C. 2013. Vision-based monitoring system for evaluating cable tensile forces on a cable-stayed bridge. *Structural Health Monitoring* 12(5-6): 440-456.

Lee, J.J., Fukuda, Y., Shinozuka, M., Yun, C.B. & Cho, S. 2007. Development and application of a vision-based displacement measument system for structural health monitoring of civil structures. *Smart Structures and Systems* 3(3): 373-384.

Leutenegger, S., Chli, M. & Siegwart, R.Y. 2011. BRISK: Binary robust invariant scalable keypoints. *Proc., Computer Vision (ICCV), 2011 IEEE International Conference on, IEEE*: 2548-2555.

Lowe, D.G. 2004. Distinctive image features from scale-invariant keypoints. *International journal of computer vision* 60(2): 91-110.

Viola, P. & Jones, M. 2001 Rapid object detection using a boosted cascade of simple features. *Proc., Computer Vision and Pattern Recognition, 2001. CVPR 2001. Proceedings of the 2001 IEEE Computer Society Conference on, IEEE* I-511-I-518 vol. 511.

Webb, G., Vardanega, P. & Middleton, C. 2014. Categories of SHM Deployments: Technologies and Capabilities. *Journal of Bridge Engineering ASCE* 20(11): 04014118.

Yamaguchi, T. & Hashimoto, S. 2010. Fast crack detection method for large-size concrete surface images using percolation-based image processing. *Machine Vision and Applications* 21(5): 797-809.

Ye, X.W., Dong, C.Z. & Liu, T. 2016a. Image-based structural dynamic displacement measurement using different multi-object tracking algorithms. *Smart Structures and Systems* 17(6): 935–956.

Ye, X.W., Dong, C.Z. & Liu, T. 2016b. A Review of Machine Vision-Based Structural Health Monitoring: Methodologies and Applications. *Journal of Sensors* 2016.

Ye, X.W., Dong, C.Z. & Liu, T. 2016c. Force monitoring of steel cables using vision-based sensing technology : methodology and experimental verification. *Smart Structures and Systems* 18(3): 585–599.

Zaurin, R. & Catbas, F.N. 2010. Structural health monitoring using video stream, influence lines, and statistical analysis. *Structural Health Monitoring* 10(3): 309-332.

Zhang, Z. 2002. A Flexible New Technique for Camera Calibration (Technical Report). *IEEE Transactions on Pattern Analysis and Machine Intelligence* 22(11): 1330–1334.

Maintenance, Safety, Risk, Management and Life-Cycle Performance of Bridges – Powers, Frangopol, Al-Mahaidi & Caprani (Eds)
© 2018 Taylor & Francis Group, London, ISBN 978-1-138-73045-8

The engineering and management of major steel box girder bridges; lessons from West Gate Bridge.

I. Firth
COWI, London

ABSTRACT: Steel box girder bridges are in use for long spans all over the world. They represent an economic solution for such structures, but must be properly conceived and carefully detailed if they are not to be a long-term maintenance burden for their owners. Ten years ago, the West Gate bridge in Melbourne (Figure 1) was substantially strengthened and upgraded to accommodate an extra traffic lane in each direction and to deal with a variety of problems that had arisen since its construction in the 1970's. This paper describes the background to the development of the steel box girder genre, and outlines some of the strengthening, refurbishment and ongoing maintenance work on the bridge. It also touches on some lessons learnt from other similar major steel box girder bridge structures.

1 INTRODUCTIONS

Steel box girders provide an efficient and economic solution for long span bridges, and are frequently used for more modest spans as well. After a rather shaky start, their behaviour and design are now well understood, and when properly detailed and constructed, with well-conceived operation and maintenance plans in place from the outset, modern steel box girder bridges provide an economic long term solution for most long span situations.

Early examples from the 1960's have suffered due to insufficient understanding of design or maintenance issues at the time and frequently because of poor attention to detail. In addition, the enormous increase in traffic since then has placed extra demands which were not envisaged at the time of their design. As a result, several have subsequently undergone substantial refurbishment and repair. The lessons that have been learnt have informed and thereby improved the practices and procedures now generally adopted in design, construction and maintenance for more modern steel box girder bridges, such that they are not expected to exhibit maintenance problems to the same degree in future.

However, memories are frighteningly short, and those charged with teaching engineering students or training young professionals are in some cases ignorant of the tragic events of the past, with the dangerous consequence that old mistakes are in danger of being repeated. Whether it is to avoid tragic collapse or more likely costly repair and maintenance, it is vital that those involved in the design and construction of steel box girder bridges, and those responsible for teaching and training younger engineers, are aware of what has gone before so that the mistakes of the past are not merely repeated.



Fig. 1 - The West Gate Bridge, Melbourne

2 THE STEEL BOX GIRDER STORY

Some of the earliest examples of modern steel box girder bridges were constructed across the River Rhine in the 1950's to replace bridges destroyed during World War Two, although the origins of the form go back much further to the wrought iron and eventually steel tubular bridges of the mid to late 19th century, mainly in the UK. [1] The development of welding technology in the 1920's and 1930's and the desire to reduce weight, particularly on longer spans, led to the emergence of lightweight girders with an orthotropic deck comprising a thin

steel plate with longitudinal stiffeners welded underneath.

This form of stiffened deck plate, with closed, torsionally stiff trough stiffeners for improved transverse dispersion of local wheel loads, has evolved over the years partly through theoretical analysis and partly through empirical development from first-hand experience. Huge leaps in the understanding of the fatigue performance of the welded details in orthotropic decks have been made since those early days, but it is surprising how much variation still exists, even now, given that by and large they all do the same job.

A major step-change for the long span story occurred with the Severn suspension bridge, designed by Freeman Fox and Partners and completed in 1966. (Figure 2) This aerodynamically streamlined closed box girder was the first of its kind and substantially lighter than the foregoing steel truss designs. It has been copied in a variety of forms ever since for long span structures, and even for some shorter spans



Fig. 2 - The Severn Bridge, England

The Severn bridge started a flurry of activity which saw many new steel box girder structures emerging in the mid to late 1960's. But then tragedy struck in 1970 with the collapse during construction of the Milford Haven bridge on 2nd June and the West Gate bridge on 15th October. The investigations that followed in the UK [2] and Australia [3] pointed to a combination of errors in design and construction, and led to feverish activity to develop new design and workmanship rules as well as improved procedures for design and construction control. There is much more to be said about this particular episode in the box girder story, but mostly in connection with design and construction, rather than operation and maintenance, which is the principal theme of this conference. Nevertheless, the lessons learnt from that time still reverberate today, and influence all modern steel box girder bridge projects.

After a significant appraisal and re-design process (particularly extensive for West Gate which was originally designed with a concrete deck but rebuilt with an orthotropic steel deck [4]), both failed bridges were rebuilt, as was the Koblenz bridge over the Rhine which had also collapsed during construction in November 1971. Other steel box girder bridges already built or under construction at the time were strengthened, usually by the addition of extra stiffening and plating to webs, diaphragms and bottom flanges, in what became known as the Merrison Strengthening programme.

In the ensuing years, experience with the bridges in operation began to reveal weaknesses of a different kind. Fatigue cracks were observed after only a few years in details subject to high local stress fluctuations due to passing traffic. In particular, the welds attaching the longitudinal trough stiffeners to the deck plate and transverse diaphragms were susceptible, as were other locations where live load stress concentrations occurred. The situation was exacerbated by the rapid growth in vehicle weights and numbers during the 1970's and 1980's.

In the UK, the structures of the Severn Crossing were assessed and substantially strengthened [5], in which a significant aspect was the improvement of the orthotropic deck weld details. The research carried out and the lessons learnt as part of that programme have informed steel box girder design ever since, and have resulted in much improved long life performance of orthotropic deck designs.

Steel box girders are also used increasingly with a composite concrete deck instead of an orthotropic deck in cases where the disadvantage of added weight in the concrete deck is outweighed by the long-term advantage of reduced maintenance demand in the steelwork. That is not to say that composite concrete decks are maintenance-free, but the absence of the fatigue-prone weld details in a steel orthotropic deck is a distinct benefit.

But for the longest spans, all-steel box girders still hold sway, and will continue to do so at least until we gain greater confidence in the use of lighter weight carbon and glass fibre composites, whose long term performance and maintenance issues are as yet not fully appreciated.

3 DESIGN AND ASSESSMENT STANDARDS

The collapses in 1970 triggered an extraordinary amount of research and development into the behaviour of thin steel plated structures. The previous relevant design standard in the UK, BS153 [6], was already known to be inadequate in such cases. Requests for urgent research funding had been made to the UK Government in the 1960's but sadly funds had not been forthcoming. Now, in the light of the tragic circumstances, the money was suddenly miraculously available and it is said that about 30 years

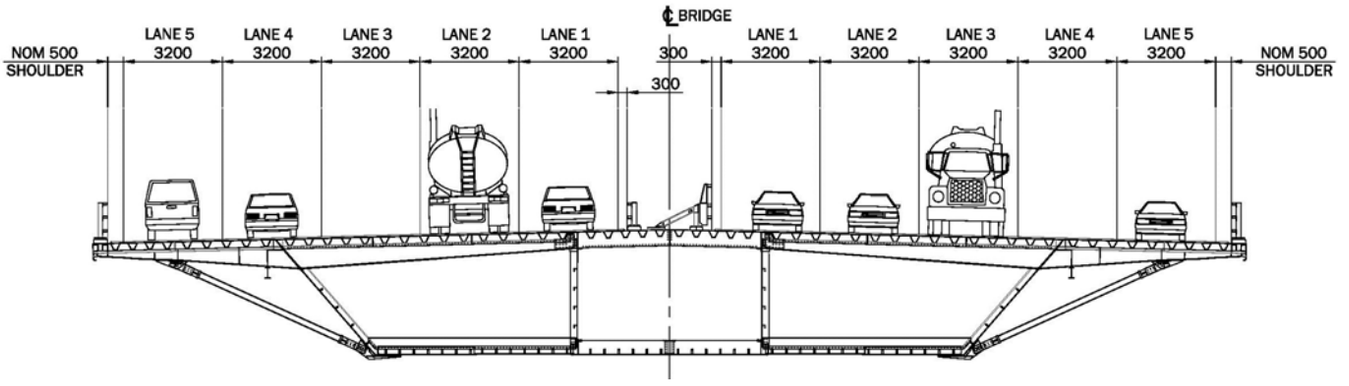


Fig. 3 – Typical Cross Section showing lane layout

of research was carried out in three years, such was the urgency and importance of the work.

Under the auspices of the Merrison Committee of Inquiry, new design and workmanship rules were rapidly developed, and the urgency was such that designers were being issued with amendments to design clauses for them to incorporate as their designs evolved. The new rules, known as the Interim Design and Workmanship Rules (IDWR) [7] were comprehensive, treating aspects such as residual stresses due to welding, imperfections, orthotropic behaviour and other issues explicitly in a rigorous way not found elsewhere. However, the rules were also complicated and demanded a certain degree of expertise and specialist knowledge in their interpretation, so eventually a simpler design standard was called for. In his Gold Medal Address to this Institution of Structural Engineers in 1989 [8], Dr. A.R. Flint, a key member of the Merrison Committee, reflected that in the race to find solutions there was no time to be brief in the code drafting. This required more time, and it wasn't until 1982 that the new steel bridge code BS5400 parts 3 and 6 [9] finally emerged to replace the now obsolete BS153. This was a simpler document, easier to apply and more suited to design, but with the simplification came some conservatism.

In Europe, the Eurocodes have since largely taken over for the design of new bridges. The inevitable and inherent conservatism built into the codes has little impact on the economic outcomes for the project when used in the design of new bridges. But for the assessment of existing bridges, and in particular those designed before the mid 1980's, the use of such conservative design standards would result in an under-estimate of residual structural capacity in some instances and thus potentially lead to unnecessarily costly strengthening. Consequently, for the assessment of steel bridges in the UK, the applicable standard is BD56 [10] which applies the relevant clauses of BS5400 part 3 [9] but with modifications to suit assessment. At the time of writing, the author is involved with updating BD56 in line with the wide-ranging review of the whole of the UK's Design Manual for Roads and Bridges. [11]

Thus, for the assessment of major steel box girder structures older than about 30 years, it is recommended that a Bridge Specific Assessment approach should generally be adopted. Benefits of this approach arise from the improvements in structural capacity obtainable by using appropriate assessment standards, and the IDWR is still considered by many to be the most appropriate for treating the actual behaviour in most cases. And also in certain cases, the adoption of a Bridge Specific Assessment Live Load model (BSALL) can have a marked benefit where this is less onerous than the standard codified loading model. This was the approach taken in the West Gate Bridge assessment referred to below.

4 OPERATION AND MAINTENANCE

Designers today are thankfully much more conscious of the need to design for ease of operation and maintenance than they were 50 years ago. Early steel box girders were typically provided with very poor access provisions by designers who naively thought that their creations would not need regular, routine inspection and maintenance. Operators found that they needed to close busy traffic lanes to gain access to the interior because the designers had simply not considered such things.

Today, this is thankfully one of the most important items on the list of essential considerations in the design of a major steel bridge, but it was not always so. It is not until you have experienced first-hand the awful shortcomings of a bridge where this has not been a priority that you can really appreciate how important this is. As a bridge designer, the author is grateful that his early experience concerned the assessment, strengthening and upgrading of bridges which were all deficient in the matter of easy access and maintenance. A good bridge designer needs to understand the needs of those responsible for the long term management and maintenance of the bridge, and must ensure that easy access to all parts requiring inspection is provided.

In recent years there has been a trend towards using vehicle-mounted telescopic working platforms to

gain access to the underside of the bridge instead of a travelling gantry running on rails permanently fixed to the bridge. Such travelling gantries themselves need maintenance, and their relatively infrequent use means that considerable costs can be incurred just ensuring that the gantry is safe to use each time. A vehicle dedicated to this activity has to be constantly checked and certified as safe to use, so is often preferred by bridge owners, particularly as the vehicle can generally be used on many bridges in their network. Such a vehicle was made specifically to suit the geometry of West Gate Bridge by Moog in Germany and can also be used on other bridges in Victoria. (Figure 4)

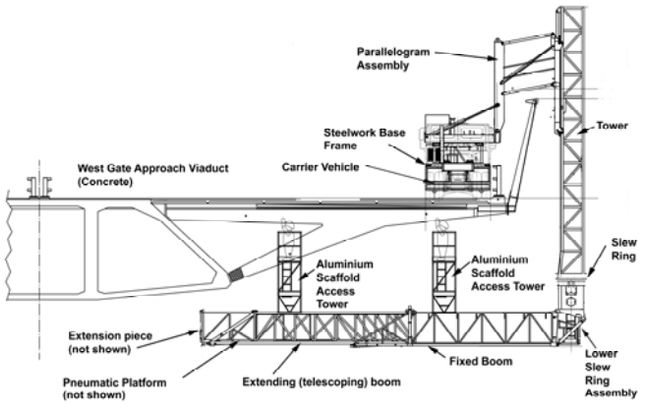


Fig. 4 – Vehicle-mounted telescopic platform (MBIP)

The use of drones for close-up inspection of inaccessible part of bridge is also now commonplace, and coupled with intelligent systems using GPS with the camera, it is possible to generate inspection reports quickly and semi-automatically, pinpointing the location of defective or suspect details requiring further close-up investigation. The pace of change is very rapid in this area.

Access for inspection is fundamental, but even more so is the need for very careful detailing in the first place. Stress concentrations, sharp changes in direction in load paths experiencing fluctuating stresses, and corners where it is not possible to see critical welds and details up close are all examples of the kind of issues which should be avoided. Sadly, too often such details are overlooked by inexperienced designers or subsequently changed by contractors, without proper oversight by someone familiar with the challenges of steel bridge maintenance. There is no doubt that the little extra cost and effort required to get such things right at the outset will save a fortune in long term maintenance costs and avoid all sorts of difficulties for the owner later.

On West Gate bridge, as on other steel box girder structures in the author's experience, there are many problematic details which tend to be repeated throughout the bridge. We have identified a family of repetitive details in need of regular inspection and occasional intervention on the transverse cross-frames, which occur generally every 3.2m. (Figure 5). Every detail is categorised according to its vulnerability – how susceptible it is to high fluctuating stresses, for example – and its criticality – the potential significance for the integrity of the bridge if the detail is found to contain a defect. This is arrived at by detailed finite element analysis and evaluation, and in some cases actual instrumentation and monitoring over an extended period.

Such a system has the benefit of allowing the bridge management team to deploy limited resources most effectively by focusing on the most vulnerable and most critical details. So for example, a detail which is vulnerable but not critical may be allowed to develop a defect without too much concern, and one that is critical but not vulnerable probably does not require very regular inspection. But those that are both vulnerable and critical receive the greatest scrutiny, and procedures have been pre-determined so that the maintenance team knows what to do in the event that a defect needing repair is found in such a location.

Having worked hard to establish this system, it is now only necessary for the bridge managers to seek

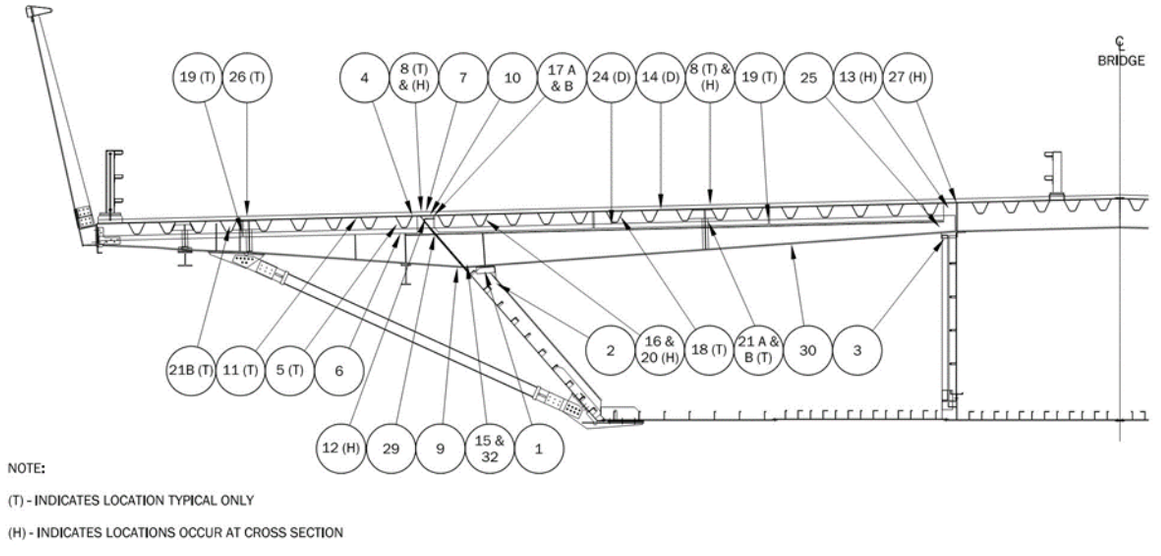


Fig. 5 – Critical details on a typical cross-frame in West Gate bridge outer cell.

advice from the assessment team if a new type of defect is encountered of if something unexpected occurs that needs to be evaluated. The majority of the inspection and repair work is thus relatively routine.

Modern instrumentation and monitoring techniques are developing all the time, and it is now commonplace to specify the inclusion of relatively sophisticated structural health monitoring systems on major new bridges. These are intended to assist the bridge maintenance team by enabling them to focus attention on those parts of the bridge most needing it and reducing the need for regular intervention elsewhere.

In some situations, intelligent systems are being introduced to automatically trigger an alert in the event that certain strain or displacement thresholds are exceeded in critical details. This would be a very extensive and costly exercise for a major bridge, and is unlikely to be economic when there the structure has the luxury of full time maintenance staff as at West Gate. Such systems are more likely to be justifiable for smaller structures which do not have a resident or frequently visiting inspection team. In such circumstances, an intelligent early warning system can alert a network management team that an inspection is needed, and such systems are set to become much more commonplace in the years ahead.

5 LESSONS FROM WEST GATE BRIDGE

The West Gate bridge carries the busy M1 motorway across the Yarra River just south west of Melbourne city centre. It is nearly 50 years since the tragic collapse during construction that killed 35 people, and the reverberations of that event are still felt today. Originally designed with four lanes in each direction and a hard shoulder, the increase on traffic demand through the 1980's and 1990's was such that widening to 2x5 lanes became essential. At the same time, assessments of the bridge had shown that it was in need of strengthening and upgrading to meet future demands.

The structure is a five span cable stayed bridge, 848m long, with a main span of 336m. It has a 3-cell steel box girder which is supported by the cable stays along the centreline. The whole structure, including the long curving post-tensioned concrete box girder approach viaducts, was upgraded and strengthened to carry the extra traffic lanes between 2007 and 2011. The work was carried out by an Alliance comprising VicRoads, main contractor John Holland, and designers Flint & Neill (now COWI) for the steel bridge and SKM (now Jacobs) for the concrete approaches.

The work was extremely challenging, not least because of the logistics of keeping the motorway open and the traffic flowing at all times, getting men and materials inside the bridge to carry out the work safely and efficiently, and dealing with hazards such as removing red lead paint before certain works could progress. Details of the works on the steel bridge are covered more fully elsewhere [12], but in a nutshell, they mainly entailed:

- additional stiffening of webs and flanges,
- reinforcement of existing plates and stiffeners,
- adding steel props to support the cantilevers,
- replacing waisted shank "Gilbert Roberts" bolts with conventional parallel shank HSFG bolts, and reinforcing bolted splice joints by the addition of extra bolts, typically using Tension Control Bolts,
- strengthening the internal diaphragms in places,
- reinforcing the steel box section towers, and
- substantial improvements in internal access provisions to enable all of the above and facilitate future ongoing maintenance.

The works also included the addition of a high fence to deter would-be suicides, as well as upgrading the vehicle containment barriers along the edges of the deck.

Following the main strengthening works, attention turned to dealing with the ongoing maintenance issues, and the classification of potentially defective details referred to above was carried out. Specific repair procedures were developed, with operatives trained in the particular and sometimes complex welding procedures necessary in certain cases.

Fatigue cracking is commonplace with bridges of this type and age, and a specific fatigue management strategy always needs to be developed in order to ensure the ongoing long term integrity of the structure. Most critical are any fatigue cracks that if left to grow could propagate into the parent plate and cause more extensive damage and/or become much more difficult to repair.

In some cases, the detail is such that the only solution is to provide an alternative load path so that high stress concentrations, typically at corners of the ends of welded connections, are removed. In others, it is simply a matter of grinding out and re-welding if a crack extends beyond a pre-determined critical length. In still others it may be possible simply arrest the crack growth by drilling a hole to encompass the crack tip, or even just to leave it alone and not worry about it (as in cases of low vulnerability and low criticality). Every detail has its own peculiar characteristics, which is why each type has been assessed on its merits considering the fluctuating stress state, any alternative load paths, the steel material quality and so on, and the generic monitoring and repair procedures agreed.

Sometimes, in carrying out the repair, the welders encounter poor quality steel plate, which can significantly hamper their ability to carry out a sound repair. These days we tend to be much more aware of the dangers of accepting poor plate material into

steel bridges and we have quality control procedures in place to prevent it (or should have) in new steel bridge construction. But back in the 1970's the procedures and the understanding were not quite so advanced as they are today, and as a result some poor plate can be encountered from time to time. This then requires special treatment, and sometimes the pre-agreed repair procedure will no longer suffice. Either the damaging stress state needs to be improved by creating an alternative load path or in some other way, or some of the poor parent plate may need to be removed and the detail reconstructed in a more invasive intervention.

In all of this work, it is necessary to use a considerable amount of experience and engineering judgement to arrive at the appropriate solution. This is because the analysis of crack growth rates and residual life can be very uncertain due to the uncertainties in:

- the true state of stress (including locked-in fabrication stresses)
- the actual cyclic live load stresses
- the idealisation of a complex and changing stress field close to the weld tip
- the material properties in general and the fracture toughness properties in particular

By working closely together between the inspectors, welders and the design and analysis team the best solution for each observed defect can be developed.

The details of the fatigue cracking and the management of crack repairs has been covered in a previous IABMAS paper [13] so it is not proposed to go into them again here. The West Gate team has completed the repair of the majority of the important observed defects, and the ongoing monitoring and management processes in place will ensure the long term integrity of the bridge.

6 OTHER LESSONS

Generally speaking, and with the exception of the well-known orthotropic steel deck issues, the majority of fatigue-prone details occur in transverse elements of the bridge. Cross-beams, cross-frames, diaphragms and cantilevers which support the deck are loaded mainly by transient live loads (there is relatively little permanent load stress in such elements) and are therefore much more likely to suffer fatigue damage than those elements which are also designed to carry significant permanent loads. So such elements need particular careful treatment in the design and should receive extra scrutiny in maintenance inspections. However, it is not only such locations that generate problems.

One unexpected problem which we have encountered elsewhere, not on West Gate, concerned the behaviour of unstiffened bottom flange panels in the middle of the span where the flange is in tension. When designing a tension flange which is never expected to experience compression, it would be tempting to leave out any longitudinal stiffeners. Why add the extra stiffening material and workmanship when the plate can carry the tension quite satisfactorily without? However, when the flat bottom flange plate is welded, such as to transverse cross-frames or stiffeners, the weld distortion can result in the panel becoming bowed upwards in an inverted classic "hungry horse" profile. Then when additional tension appears in the flange due to transient loads, the flange tries to straighten out. In the case we were asked to investigate, this straightening out was sufficient to cause relatively high local bending stresses at the cusp of the profile where the welds were, leading eventually to fatigue damage.

This case was further complicated because the upwards bowed profile acted rather as if it was pushed upwards under compressive forces. When loaded out of plane and then released the plate "popped" back up rather like if you push down on the roof of your car and then release your hand. There was no external compression applied to the flange, but the boundary restraints and residual stresses in the system created a stress state similar to that as if there were.

So the lesson from this example was firstly that going for flat, thin, unstiffened tension flange plates in a box girder in an attempt to save weight may be a false economy, and secondly that nothing is quite what it seems. We frequently come up against reminders, like this, that the apparently obvious behaviour is not necessarily what is actually going on when it comes to steel box girders. The actual stress state in this flange was much more complex than a simple analysis would predict. Again, experience counts for a lot in this field.

7 CONCLUSION

This paper has shown the importance of diligent and effective inspection and maintenance in the management of major steel box girder structures such as West Gate Bridge. Modern materials and design and workmanship practices are such that when properly applied by experienced designers, with particular care being taken over small details, steel bridges will not experience the same maintenance challenges faced by their predecessors.

Close liaison between inspection and maintenance teams on the bridge and the design and assessment teams in the office is essential to derive an effective and efficient system for long term economic management of such bridges.

8 REFERENCES

Allen, C. et al. 2012. Concrete Viaducts. *The West Gate Bridge Strengthening Project special session*. 18th IABSE Congress on Innovative Structures, Seoul – South Korea.

Balfe, P. J. et al. 1986. Redesign of West Gate Bridge. In Toakley, A. R. (ed.). Melbourne: Road Construction Authority Victoria Australia.

British Standards Institution. 1958. BS153 Part 1: Materials and Workmanship. *Steel girder bridges*. London: BSI.

British Standards Institution. 1958. BS153 Part 2: Weighing, shipping and erection. *Steel girder bridges*. London: BSI.

British Standards Institution. 1958. BS153 Part 3: Loads. *Steel girder bridges*. London: BSI.

British Standards Institution. 1958. BS153 Part 4: Design and construction. *Steel girder bridges*. London: BSI.

British Standards Institution. 1958. BS153 Part 5: Stresses, construction and erection. *Steel girder bridges*. London: BSI.

British Standards Institution. 1982. BS5400 Part 3: Code of practice for design of steel bridges. *Steel, concrete and composite bridges*. London: BSI.

British Standards Institution. 1982. BS5400 Part 6: Specification for materials and workmanship, steel. *Steel, concrete and composite bridges*. London: BSI.

Cunningham, J. 2012. Context and Project Objectives. *The West Gate Bridge Strengthening Project special session*. 18th IABSE Congress on Innovative Structures, Seoul – South Korea.

Firth, I.P.T. 2010. Lessons from history - the steel box girder story. *The Structural Engineer*. 88(5): 18-24.

Flint, A.R. 1989. Matters of balance. *The Structural Engineer*. 67(10): 189-191.

Flint, A. R. 1992. Strengthening and refurbishment of the Severn Crossing. *Proceedings of the Institution of Civil Engineers*. 92(2): 57-65.

Government of the State of Victoria. 1971. Report of the Royal Commission of Inquiry into the Failure of West Gate Bridge. Melbourne: C. H. Rixon.

Her Majesty's Stationary Office. 1971. Inquiry into the Basis of Design and Method of Erection of Steel-Box Girder Bridges. *Interim Report of the Merrison Committee of Inquiry*. London: HMSO.

Her Majesty's Stationary Office. 1973. Inquiry into the Basis of Design and Method of Erection of Steel-Box Girder Bridges. *Final Report of the Merrison Committee of Inquiry and the Interim Design and Workmanship Rules*. London: HMSO.

Her Majesty's Stationary Office. 2010. BD56 - The Assessment of Steel Highway Bridges and Structures. *Design Manual for Roads and Bridges*. London: HMSO.

Firth, I. P. T. et al. 2012. Responding to the Logistical Challenge. *The West Gate Bridge Strengthening Project special session*. 18th IABSE Congress on Innovative Structures, Seoul – South Korea.

McFadyen, N. et al. 2012. Strengthening of Bolted Splices and the use of Tension Controlled Bolts. *The West Gate Bridge Strengthening Project special session*. 18th IABSE Congress on Innovative Structures, Seoul – South Korea.

Murphy, C. et al. 2012. Development of Novel Stiffened Panel Solutions. *The West Gate Bridge Strengthening Project special session*. 18th IABSE Congress on Innovative Structures, Seoul – South Korea.

Murphy, C. et al. 2012. Strengthening of the Main Cable Stayed Bridge. *The West Gate Bridge Strengthening Project special session*. 18th IABSE Congress on Innovative Structures, Seoul – South Korea.

Percy, R. et al. 2012. Operation and Maintenance Strategies. *The West Gate Bridge Strengthening Project special session*. 18th IABSE Congress on Innovative Structures, Seoul – South Korea.

Silla-Sanchez, J. et al. 2014. West Gate Bridge – Fatigue Cracking Treatment Works. *Bridge Maintenance, Safety, Management and Life Extension*. 899-908.

Williams, G. et al. 2012. Carbon Fibre Application. *The West Gate Bridge Strengthening Project special session*. 18th IABSE Congress on Innovative Structures, Seoul – South Korea.

Maintenance, Safety, Risk, Management and Life-Cycle Performance of Bridges – Powers, Frangopol, Al-Mahaidi & Caprani (Eds)
© 2018 Taylor & Francis Group, London, ISBN 978-1-138-73045-8

Managing Existing Bridges – On the Brink of an Exciting Future

R. Hajdin
Infrastructure Management Consultants GmbH, Zurich, Switzerland
and
Faculty of Civil Engineering, University of Belgrade, Serbia

ABSTRACT:
It is widely accepted that safety and serviceability are primary concerns in bridge design. However, for the most of bridges' service life, these concerns are addressed indirectly by a qualitative measure, defined herein as condition state, which is based upon observable damages recorded during inspections. Condition state is at best, only loosely correlated to safety and serviceability. It would be more reasonable to address safety and serviceability in inspection process directly, using the information on bridge performance obtained during the design and construction. The future Bridge Management Systems (fBMS) should therefore include this information allowing assessment of safety and serviceability based on inspection results. By including Bridge Information Models that are currently being developed and Structural Health Monitoring, the fBMS will become an invaluable decision-support tool not only for maintenance planning but also for issuing special permits, specification of heavy vehicle corridors, risk assessment due to natural hazards, etc.

Keywords: Bridges, Service life, Reliability, Safety, Serviceability, Performance Indicators, Maintenance

1 INTRODUCTION

There is a broad consensus that the benefits of road infrastructure for the society cannot be overestimated. The investments in road infrastructure raise the growth potential of a national economy, which can be fully exploited by efficient utilization of the road infrastructure. It is difficult to quantify the economic benefit of road infrastructure but its lower bound is estimated to be between 4% (U.S. DOT, 2015) and 10% (Kurte & Esser, 2008, ARE, ASTRA, 2006) of Gross Domestic Product (GDP). Apart from purely economic benefit, the road infrastructure enables road users to be involved in various activities that yield private, public, and social benefits (Frischmann, 2012). Maintaining these benefits on the long run in economically efficient, environmentally responsible, and socially reconcilable manner is the fundamental task of road authorities. They are bound to provide fast, safe, comfortable, and affordable travel.

Bridges are critical components of the road infrastructure as they ensure fast and safe passages over otherwise hardly surmountable obstacles. From the users' perspective, it is irrelevant whether a road is carried by a bridge or being in a tunnel or merely resting on soil, so long it provides safe and fast travel from origin to destination. In this context, it is necessary to define what is meant by fast and safe.

There are codes of practice that apply to the design of a road infrastructure and they are related to clearance, speed, and weight allowance. The design travel speed defines the minimum legal travel time on an arbitrary road link. In reality, this minimum travel time can be achieved only in the case of unrestricted traffic flow i.e. if road capacity is sufficiently higher than traffic volume. Based on the current or future traffic, one can specify some travel time – exceeding the minimum travel time - as the "**fast travel**". Clearly, the actual travel times will scatter significantly and the measure of this scatter needs to be consider when defining "fast travel". In this context, one often refers to travel time reliability.

The **safe travel** however is somewhat difficult to define since it doesn't imply absolute protection from undesired events. When travelling, there is always a probability of undesired events, which can harm life and limb, induce economic losses and damage environment. The sufficiently low probability of such undesired events defines "safe travel".

The bridges can play significant role regarding the travel time since their posting can lead to detours and therefore to increased travel time. Furthermore, bridges or parts of them can fail harming life and limb and inducing adverse consequences for economy and environment. A failed bridge can also cause detours and therefore impact travel times. In some cases, a failed bridge can render a region completely inaccessible with disastrous economic effects. It is therefore not surprising that the **structural safety** is the primary concern of bridge owners since it affects both safe and fast travel. Besides structural safety the bridge owners care about **serviceability**, which relates to user comfort that can be affected by deflections and vibrations of a bridge. If safety or serviceability requirements are not met, the bridge will be posted or even closed affecting adversely road users and the whole economy.

Following the definition of the "safe travel", a bridge is regarded as structurally safe if the probability of failure during its service life doesn't exceed some nominal value. Similar approach applies to serviceability in which the exceedance probability of some service limits (deflection, frequency, etc.) must be sufficiently low. Most modern codes of practice for bridge design have adopted this concept (e.g. CEN EN 1990, 2002). In addition, the bridge riding surface must also fulfill the requirements applicable to pavements.

The owners need to ensure that their bridge inventory fulfills the safety and serviceability requirements during their service life and therefore maintain the benefits of road infrastructure. Considering the extent of the road infrastructure in developed countries, this is increasingly challenging task. The tools currently available to owners to fulfill this task seem not to be adequate and, in this paper, recommendations are made that may facilitate the management of existing bridges in future.

2 CHALLANGES

Safety and serviceability were always the primary concerns in bridge design. However, in course of time the requirements have changed significantly and the existing bridges are characterized by the several generations of design codes. In course of time, the codes of practices have changed both regarding actions and resistance models. It is therefore not surprising that the old, otherwise undamaged bridge may not fulfill safety and/or serviceability requirements for the current traffic loading.

Furthermore, safety and serviceability can be jeopardized by deterioration processes or sudden events. The resistance of deteriorated bridges can in time reach a level, at which there is an immediate danger of structural failure. In addition to it, the new insights (e.g. statistical analysis) in frequencies and magnitude of sudden events can render some bridges as unsafe and require posting or even their closure.

The increasing traffic volume and traffic loads are probably the most significant challenge regarding the existing bridges. The traffic mix is shifting toward the larger share of heavy weight vehicles, effectively increasing the occurrence probability of load situations that exceed current design loads. Furthermore, there is an increasing number of special transports, i.e. the ones that exceed legal limits and require special permits. In Switzerland, some of these transports cannot be regarded as accidental actions but rather frequent actions as passages occur on weekly or even daily basis. Similar situation is also in the USA as reported in (Lou, et al., 2018). This trend will increase in the future as the transportation industry is interested in using larger trucks with higher axle loads in order to improve economies of scale. The stiff competition will also lead to platooning i.e. to the trains of wirelessly coupled trucks. The wireless coupling allows to significantly reduce the safety distance between the trucks. This seems to result in a particularly aggressive load situation as these trucks also break simultaneously. The break forces that are mostly neglected in road bridges must be considered in the future and existing bridges need to be assessed for this load situation.

Finally, climate change may lead to more frequent and intensive gravitational hazards, such as flooding, avalanches, landslides, rockfalls, etc.

In summary, the prudent bridge owner needs to plan and execute timely intervention in order to cope with following challenges:

- Potentially unsafe bridges that are designed using bygone codes of practice.
- Bridges with reduced resistance due to deterioration or mechanical damage.
- Bridges exposed to natural hazards that are not or not adequately considered in design.
- Increasing traffic volume and loads that can render some bridges unsafe.
- Increased exposure of bridges to natural hazards due to climate change.

The current approach and tools available to bridge managers in practice seem to be hardly adequate to cope with these challenges. In the following chapters the gradual evolution of these tools towards more efficient bridge management is outlined.

3 CURRENT ASSESSMENT AND DECISION-MAKING

Bridge Management practice differs quite significantly from country to country, but the common denominator is that it relies on visual inspections. The visual inspections are – if performed by a qualified structural engineer – cost efficient and very valuable

source of information. During the inspection, the observation is recorded and evaluated. The result of inspections is qualitative indicator, which is named differently from country to country as condition rating, condition state, condition class, etc. Herein, the term condition state is used. Whereas in the design phase the safety and serviceability concerns are addressed directly in quantitative manner, in the service phase, based on inspection results the condition state is determined. The condition state is a vague measure for the deviation of inspected bridge from the "as new" condition. The direct assessment of safety and serviceability is regarded as not cost efficient since it is commonly assumed that it always requires an in-depth material investigations and structural analysis.

Based on condition state, owners trigger often costly in-depth investigations or even maintenance actions. In practice, once an in-depth investigation based on condition state is triggered, the maintenance intervention is very likely to follow, even if a bridge can still be used without restrictions. The reasons are different from country to country, but one is surely the visual appearance and related perception of safety that entice owners to remove all visible damages with appropriate maintenance interventions. In some (rare) cases, a maintenance action is triggered if a bridge fails structural safety and serviceability checks, with the load and resistance models for the design of new bridges. This is clearly inadequate and uneconomical, given the remaining service life and possibilities to reduce uncertainties on existing bridges. Thus, some countries have introduced safety and serviceability checking formats for existing bridges in their code of practice (e.g. SIA, 2011).

The above-mentioned approach seems not to be very logical. In the design phase, the wealth of information about safety and serviceability for different load situations is created. This information is unstructured and mostly in paper form. After the commissioning of newly constructed bridge, the documents containing this information is handed over to the bridges' owners or operators that act further on as trustees of the bridges assigned to them. The documents are mostly in archives and in general not easily accessible. During the service life, inspections are performed with no consideration of safety and serviceability information produced during the design phase. It only within the in-depth investigation that the safety and serviceability are assessed again. There is a substantial gap during the service life of a bridge, in which decision are made based on qualitative indicators, that are sometimes unrelated to the key concerns of bridge owners: safety and serviceability.

In most countries, bridge management is supported by databases, in which the results of inspections are stored, sometimes in great detail. The information from design phase i.e. critical load combinations, safety factors, assumed traffic loads is usually not stored in these databases. In some road agencies, there are load rating software that facilitate evaluation of special transports, but it is rarely used in conjunction with inspection results.

Even more surprising is that the relevant information on safety and serviceability is often not stored in the database after maintenance interventions. It can be assumed that the provisions of the current code of practice are fulfilled due to maintenance interventions, but it is not recorded if these are exceeded and by what margin.

It should be noted that within the in-depth investigations a substantial work effort is necessary to find information from the design phase or previous maintenance activities. In some cases, the information on existing bridges is lost due to negligence or some accident (e.g. fire, flooding).

In some ways, the current bridge management undergoes amnesia because

- relevant information from the design phase and/or in-depth investigation is not stored and/or
- information is stored only in paper form and is lost due to negligence or accidents.

It is not that bridge owners and operators are not aware of this deficiency, but to remedy it, they need to be provided tools and resources to efficiently store and access the elaborated information on their bridge inventory. In the time of growing awareness of data importance and big data, it is high time to establish an organizational setting for business processes to ensure the benefit of collected data on the long term.

4 ASSESSMENT

The challenges listed in chapter 2 can be only efficiently coped with, if the bridge owners have all necessary information at their fingertips. This means that the current databases need to be significantly improved to accommodate all relevant information either from design phase, inspections, or maintenance interventions. This transition can be quite costly and therefore needs to be performed gradually in several phases as outlined in the following chapters.

4.1 *Safety and serviceability of undamaged bridges*

The information on safety and serviceability margin of an undamaged (virgin) bridge is essential in the service phase. This information should be structured and include all relevant load cases, which would also allow owners to have a clear picture of possible failure modes and related vulnerable zones that need to be observed in more detail.

The current databases are not structured to accommodate the graphical representation of structural systems and load situations. The material properties and load effects need also to be included in the database

as searchable data and coupled with graphical representations. The same apply to load models and provisions of current and previous codes of practice.

A large effort is required to obtain and store information for all existing bridges and this cannot be done within a short time period. Ideally, it could be done together with inspections or in-depth investigations and in this way, one can gradually fill the database.

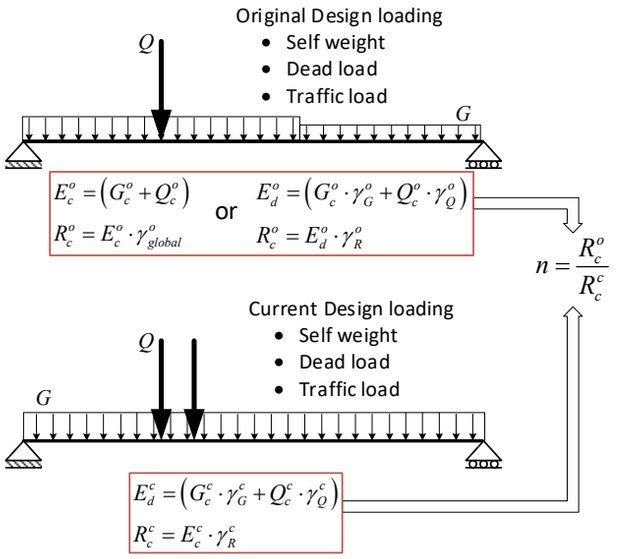


Figure 1: Assessment of safety and serviceability margins

Fortunately, there is a simplified method to assess safety and serviceability margins due to traffic loads. If the load model used originally for the design of a bridge is known, one can assume that the bridge is designed according to it. This means that the bridge resistance is in minimum as high as to sustain the internal forces due to the load model multiplied with the safety factor. In some sense, the originally used design load model is a proxy for the resistance (or service limit) of the bridge. However, to obtain internal forces, one still need a structural system.

Based on the experience from the load rating software (Hajdin & Despot, 1999) and (BMVI, 2016) most non-landmark bridges can be simplified with a series of simply supported beams. Somewhat more sophisticated alternative is to model a bridge with a continuous girder as used in traffic simulations (Freundt & Bönning, 2011, Meystre & Hirt, 2006, Enright & O'Brien, 2013). The simplified model considers only the load transfer in longitudinal direction. The load transfer in traverse direction i.e. across the deck is indirectly considered by defining appropriate effective widths. If the bygone codes of practice didn't require dimensioning in traverse direction, the presented simplification can be problematic. Furthermore, modelling of skew decks or girders with skewed support with simply supported beams is challenging and requires good understanding of the load carrying paths in these structures.

The current load model, i.e. the one that represent current traffic is to be applied on the same simplified structural system and maximum moment and shear forces are compared with the ones of the original design code. This concept is explained in Figure 1 following the notation of the (CEN EN 1990, 2002). For the loading situation used in design, the load effect E_c^o is computed. For the bygone codes of design this value is multiplied with the global safety factor to obtain the characteristic value of required resistance R_c^o against the computed load effect. If the design is performed correctly one can assume that the real resistance value (i.e. allowable stress) will not be lower than R_c^o. For the newer code with partial safety factors, the load effect E_d^o need to be evaluated and this value is multiplied with the partial factor γ_R^o covering the uncertainty in the resistance model to obtain R_c^o. The current design loading is assumed to mirror the current traffic loading sufficiently well and therefore one can expect that the load effects from the real loading will not exceed the load effect of design loading E_d^c. The required resistance due to the current design R_d^c can be computed by multiplying E_d^c with γ_R^c. The degree of compliance is the ratio of required resistances R_c^o and R_d^c. The values below 1 indicate that the bridge may have a safety deficit.

Clearly, using this simplified method, safety and serviceability reserves that stem from bridge specific detailing and dimensioning decisions cannot be assessed. To this end one needs to perform a thorough structural analysis on more sophisticated structural system. Nevertheless, the simplified method can be efficiently used for screening purposes.

Owners can decide, based on their needs to store

– the actual structural system as used in analysis or
– a continuous girder model as used often used in simulation to obtain maximum load effect or
– a series of simply supported beams as in some load rating software.

Independent of this choice, the results of a thorough structural analysis on an adequate structural system can be used to update the resistance (or service limits) of the model stored in the database. The safety or serviceability margins against the current design loads can be expressed therein either as

– the degree of compliance n, that can be evaluated for each load situation as a ratio between the available resistance/service limit and resistance/service requirements based on the total factored load effect, or as
– the traffic load capacity factor with which the traffic load can be multiplied and still fulfill the safety and serviceability requirements.

The latter seems to be more useful for owners to assess special transports or future traffic load.

4.2 *Reliability*

The modern codes define the safety and serviceability in terms of reliability i.e. the probability that a bridge will be fit for purpose during its service life. The partial safety factors in modern codes are calibrated to satisfy these reliability requirements. In (CEN EN 1990, 2002) the target annual reliability index β for safety is 4.7 (corresponds to occurrence probability of $1.3 \cdot 10^{-6}$) and for serviceability 2.9 (corresponds to occurrence probability of $1.9 \cdot 10^{-3}$). The bridge is considered as safe and serviceable if specified reliability indexes are not below these target values. If for an existing bridge the degree of compliance is above 1,

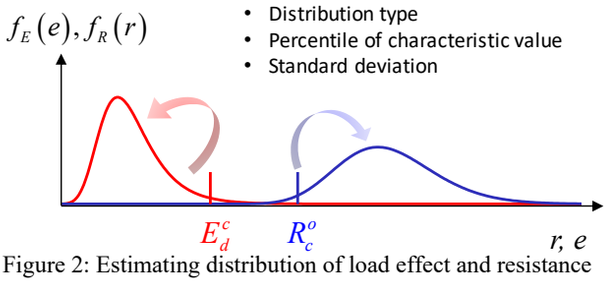


Figure 2: Estimating distribution of load effect and resistance

one can assume that the reliability index for safety exceeds the target value. However, the degree of compliance below 1 doesn't necessarily mean that the bridge doesn't meet reliability requirements. In (Das, 1999) traffic load capacity factor is evaluated based on reliability assessment for 15 similar concrete bridges in UK that are constructed in 1960's and 1970's to the same design requirements. Nevertheless, the traffic load capacity factors – derived from reliability assessment - vary between 1.9 and 5.2. Given that at that time the design was based on global safety factor, the results are not surprising. For the bridges that are designed or examined using modern codes of practice the scatter is significantly smaller as demonstrated in (Mertz, 2005). However, even for these bridges the evaluation of reliability may be economically beneficial if existing bridges can still be used without restrictions.

Assessing the reliability of existing bridges can be tedious task as one needs to model all actions and material properties as stochastic variables. However, based on experience and available data, a simplified reliability assessment can be performed using the similar approach to the one in chapter 4.1 (see also Braml & Wurzer, 2012). The original design load situation can be used to assess the characteristic value of resistance against the chosen failure mode. For the example in Figure 1, the characteristic value of resistance is R_c^o. If the percentile of the characteristic value R_c^o and the type of its distribution is known, one can obtain the resistance distribution for a chosen failure mode. The recommendations for percentiles of characteristic values, standard deviations and distribution types based on construction materials can be found in literature (e.g. JCSS, 2013). To compute load effects current design loading needs to be used. In general, several actions contribute to load effect and their characteristic values represent different percentiles of their distributions. In addition, the actions are modeled with different distribution types. For instance, the load effect due to the traffic load is normally modeled by extreme distributions. This is supported by measurements and simulation that are performed within research projects all over the world (e.g. Freundt & Bönning, 2011, Meystre & Hirt, 2006, Mertz, 2005, Caprani, 2013). After all, traffic load models are derived from probabilistic analysis based on traffic simulations and weigh-in-motion measurements (e.g. Calgaro & Sedlacek, 1992). The distributions for the self-weight and dead load as well as for other actions can be derived based on percentile assumption of their characteristic values following the recommendations from literature (e.g. JCSS, 2013). The derivation of distribution for load affect *e* and resistance *r*, for the chosen failure mode is illustrated in Figure 2.

The load effect can be determined on the simplified structural system and the reliability index can be computed. The reliability obtained in this manner can be regarded as a rough estimate as the material and action uncertainties are modeled based on literature and experience data. These results can be improved if reliability analyses would be performed on the relevant sample of the bridges of same type. The systematic detailed reliability analyses can be also used to update assumptions regarding distribution of stochastic variables.

The traffic load capacity factor can be also obtained based on reliability assessment as in (Das, 1999). It is a deterministic coefficient with which the stochastic effect of traffic load can be multiplied and still fulfill the reliability criterion.

4.3 *Inspections and impact of damages*

The inspection procedures need not to change significantly. However, there is some additional information that is indispensable if the effect of deterioration and damages is to be appropriately considered in assessment of bridges:

– Based on the design documentation, relevant failure modes need to be defined. These failure modes correspond to the critical load situations used in design and
– for each failure mode, vulnerable zones (Linneberg, et al., 2017 and NYSDOT, 1997) are to be defined, in which damages have the largest impact on safety and serviceability.

Experienced inspectors know intuitively where are these zones, but they can confirm themselves with the readily available information (Hajdin, 2017a). The damages outside vulnerable zones can also trigger failures, but for them to occur the extent of damage needs to be significantly larger than in the vulnerable

zones. If this seems likely, one needs to define an additional failure mode that can be triggered by the observed damages.

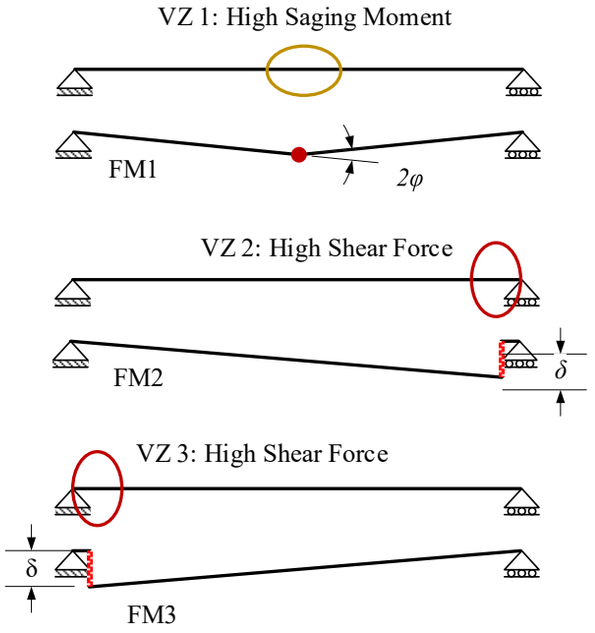


Figure 3: Vulnerable zone and failure modes

For a simply supported beam the vulnerable zones and corresponding failure modes are illustrated in Figure 3. In this example failure modes (FM1, FM2 and FM3) are chosen to be collapse mechanisms. However, other failure modes can be selected based on owner's preferences. For instance, the extent of spalling or crack width can be chosen to be failure criteria.

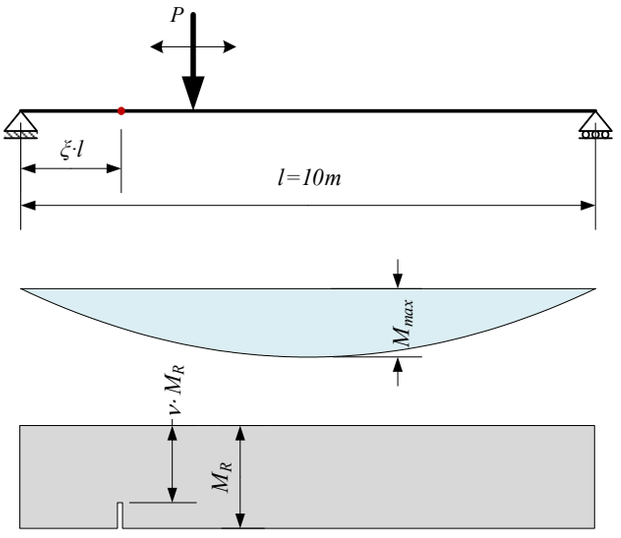


Figure 4. Load and resistance of damaged beam

For each failure mode, the corresponding degree of compliance, if semi-probabilistic format is used, or reliability, if probabilistic assessment is required, is to be evaluated for an undamaged bridge. This can be done beforehand either using the simplified approach described in chapter 4.1 and 4.2 or by in-depth examination as described in chapter 4.4. For illustration purposes of this procedure, a simply supported beam with the span of *10m* as in Figure 4 is assumed to be loaded only by live load *P,* whose maximum annual value is normally distributed with the mean value of *100kN* and the standard deviation of *12kN*. Permanent loads are neglected in this example. The resistance to bending moment is assumed constant along the beam and normally distributed with the mean value of *500kNm* and the standard deviation of *40kNm*. Only failure mode FM1 is considered. Since both load effect and resistance are normally distributed, the reliability index and corresponding probability of failure can be computed as follows:

$$\beta = \frac{\mu_{M_R} - \frac{\mu_P \cdot l}{4}}{\sqrt{\sigma_{M_R}^2 + \left(\frac{\sigma_P \cdot l}{4}\right)^2}} = \frac{500 - 250}{\sqrt{40^2 + \left(\frac{120}{4}\right)^2}} = \frac{250}{40 \cdot \sqrt{\frac{25}{16}}} = \frac{1000}{200} = 5.0 \quad \Rightarrow P_f = 2.87 \cdot 10^{-7} \tag{1}$$

The à priori reliability i.e. the reliability of undamaged bridge meets the criteria according to (CEN EN 1990, 2002).

Once an observation has been collected, the impact of this observation on safety and serviceability is to be evaluated. Based on the observation the rough estimate of resistance reduction can be made, even if the uncertainty is large. The same damage and related resistance reduction can have different impact on reliability of different bridges. If the safety margin of undamaged bridge is large, it can clearly withstand much larger damage than the one with slim margin. It is therefore that the same damage i.e. the same condition state can lead to different decisions, based on the safety margin of the undamaged bridge.

In the illustrative example it is assumed that the observed damage lead to reduction of resistance, but there is uncertainty regarding the magnitude of this reduction. This uncertainty can be expressed by a discrete distribution as in Table 1.

Table 1. Likelihood of resistance reduction – an example

Resistance reduction (1-ν)	5%	10%	15%	20%
Likelihood	60%	20%	10%	10%

In most databases the location of damages is not recorded. This means that the location of damage is not known and therefore a uniform distribution along the whole length must be assumed. The reliability index can be expressed as a function of damage location as follows:

$$\beta(\xi) = Min\left(\frac{\nu \cdot \mu_{M_R} - \mu_P \cdot \xi \cdot (1-\xi) \cdot l}{\sqrt{\sigma_{M_R}^2 + (\sigma_P \cdot \xi \cdot (1-\xi) \cdot l)^2}}, 5\right) \quad (2)$$

With available information one can evaluate the probability of failure as follows,

$$P_f = \sum_{i=1}^{4} \vartheta_i \int_0^1 \Phi(-\beta(\xi)) \cdot d\xi \quad (3)$$

where ϑ_i represents the likelihood values of discrete distribution from Table 1. The resulting reliability index is

$$P_f = 3.15 \cdot 10^{-5} \Rightarrow \beta = 4.00 \quad (4)$$

which means that à posteriori (after inspection) reliability index doesn't meet the requirements of (CEN EN 1990, 2002). However, this assessment can be improved with some additional information: The reliability index can be plotted as a function of damage location ξ as in Figure 5. In this plot, the zone with an effect on reliability index is clearly visible. If the damage location is known, the reliability index can be updated. For instance, if the damage is in the far left quarter of the span, the reliability index is not affected i.e. the bridge meets the reliability criterion. On the other hand, if the damage is in the middle of the span the reliability index would be

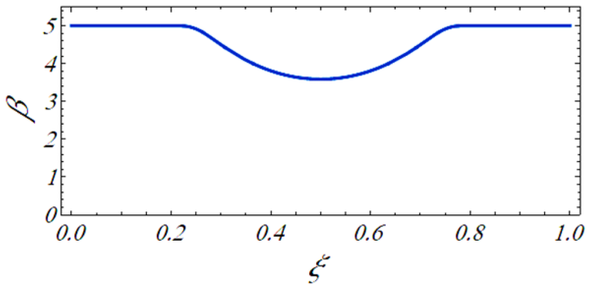


Figure 5. Safety index in function of damage location

$$P_f = 1.66 \cdot 10^{-4} \Rightarrow \beta = 3.59 \quad (5)$$

which means that the bridge doesn't meet the reliability requirements. With this approach the inspection data can be rationally used in reliability assessment taking into account the uncertainty associated with it. The likelihoods as in Table 1 can be refined as more data are collected.

In the example above, an isostatic system is chosen, which means that a local failure in one of the vulnerable zones is sufficient to trigger collapse of a bridge. For hyperstatic systems several local failures are required to trigger the collapse. It is therefore necessary to associate vulnerable zones to collapse mechanism. For a frame bridge a possible collapse mechanism and associated vulnerable zones are indicated in Figure 6 with orange ovals. It is assumed that the hogging plastic moments over the columns are 40% higher than the sagging plastic moment in mid-span. The inspection revealed that the damages in the mid-span lead to a plastic moment reduction of 15% and the ones over the columns are responsible for the plastic moment reduction of 5%. However, to assess reliability, one needs to estimate the reduction of resistance for the whole bridge and not only of vulnerable zones. In this case the resistance is equal to the internal dissipation work and the resistance reduction can be obtained by comparing the dissipation work of undamaged frame with the dissipation work of damaged frame:

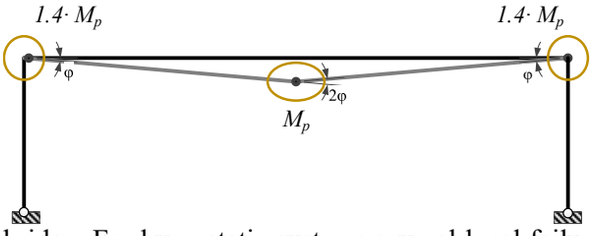


Figure 6: Vulnerable zones and a collapse mechanism of a frame bridge

$$r = \frac{0.95 \cdot 2 \cdot 1.4 \cdot M_p + 0.85 \cdot 2 \cdot M_p}{2 \cdot 1.4 \cdot M_p + 2 \cdot M_p} = \\ = \frac{4.36}{4.8} = 0.91 \quad (6)$$

The resistance reduction amounts to 9%, which is significantly smaller that 15% plastic moment reduction in the mid-span. The relationship between the vulnerable zones and failure modes is conceptionally described in section 5.3.

Finally, it should be noted that the presented approach can be implemented as Bayesian net as in (Hajdin, et al., 2018). Bayesian nets are particularly useful in combination with Structural Health Monitoring (SHM) (Cawley, 2018). The monitoring data can be used on-the-fly to assess reliability of bridges.

4.4 *In-depth investigations*

If the results of an inspection raise doubts regarding acceptable safety and serviceability, the in-depth investigation should be triggered. The in-depth investigation should include all measures that may reduce uncertainties such as testing of material properties, checking of dimensions, stiffness measurements, etc. Furthermore, archive documents must be duly examined since they may reveal assumption made regarding load situations and material properties. For hidden

structural elements such as foundations and reinforcements, old plans are the only source of information. Finally, the exposure of bridge to natural hazard needs to be investigated based on the newest findings (e.g. update of magnitudes, re-assessment of site condition).

The structural analysis needs to be performed with nonlinear methods that address failure modes appropriately and yield realistic failure probabilities. This doesn't necessarily mean that sophisticated analysis is necessary, in most cases the skillful application of the limit theorems of the theory of plasticity, as in previous section, is sufficient.

The bridge should be examined for all relevant load situations and the results need to be stored in the database in a structured form. Gradually, by means of in-depth investigations, high quality information on all bridges will be stored in the databases allowing bridge owner to manage their inventory efficiently.

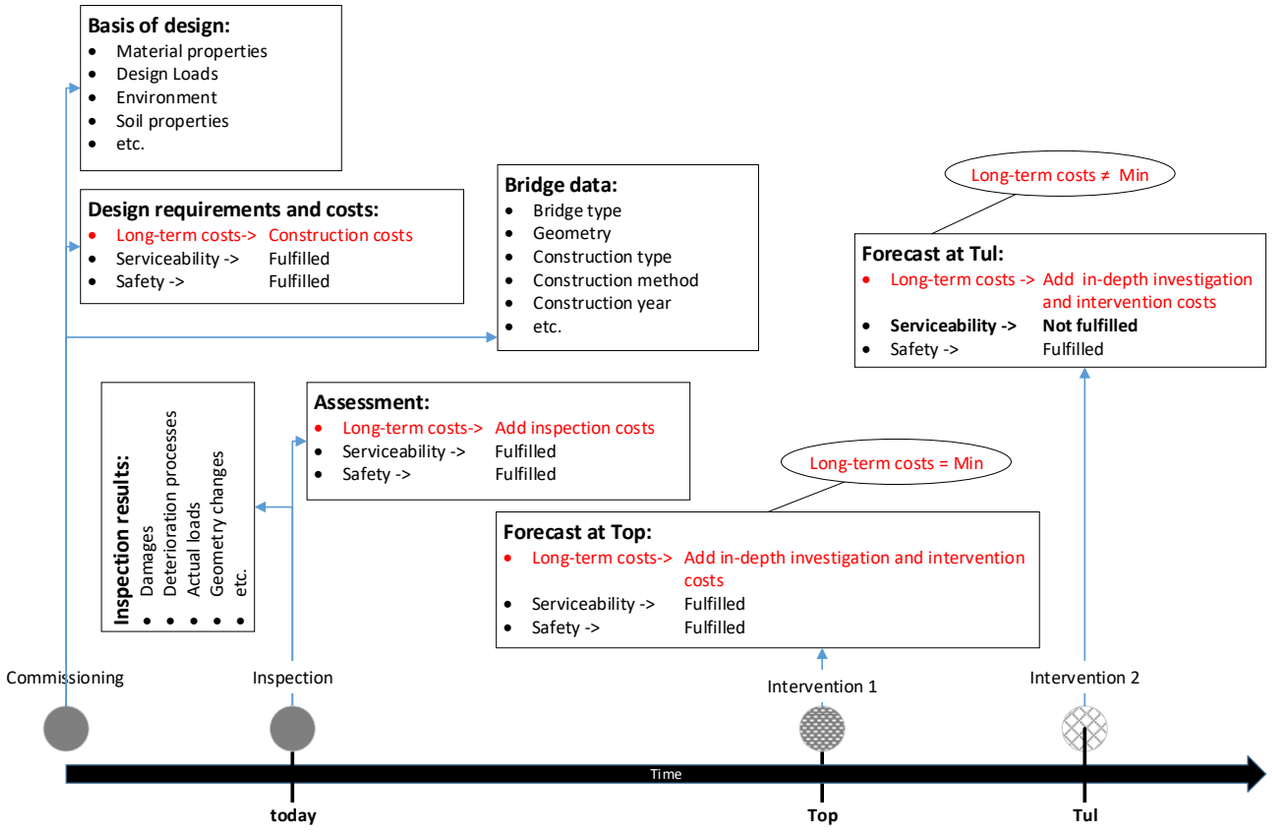


Figure 7: General approach to mid- to long-term maintenance planning

The growing experience will also allow for more accurate assessment of reliability based on inspections as Bayesian nets can be updated introducing new high-quality data.

4.5 *Special transports and corridors*

The outlined approach, which allows the assessment of safety margins and reliability level for each bridge can be a basis for issuing of permits for special transports or to define dedicated corridors for typical special transports. In the future one can think of defining several road classes based on the traffic load model for which they fulfill safety and serviceability requirements. It is very likely that in the future that vehicles or trains of wirelessly coupled vehicles will be registered for certain road classes. This also means that several traffic load models in codes of practice need to be defined. It is intuitively clear that current "one size fits all" approach is not economical. The requirement for roads need to be tailored according to the traffic that they need to accommodate.

5 MAINTENANCE PLANNING

Bridge Management is not confined to bridge assessment following inspections but also includes maintenance planning. The short-term maintenance planning is based on in-depth investigations and structural analysis and include detailed specification of interventions that are to be taken shortly thereafter. The mid- to long-term maintenance planning is a process, in which different intervention scenarios are developed. The interventions are not specified in detail and their costs are rough estimates backed by experience. The goal is to estimate financial and other needs well

in advance and avoid unpleasant surprises. Furthermore, early planning allows to choose the optimum time for interventions and reduce long-term costs.

The general approach is presented in Figure 7, where it is assumed that an inspection is performed "today". The results from the inspection revealed some damages that in conjunction with the actual loads lead to worsening of the safety and serviceability levels that, however, still meet the requirements for existing structures. This procedure is explained in previous chapters. For mid- to long-term maintenance, planning forecasts for serviceability and safety are performed predicting that serviceability criterion will be not fulfilled at the time instance marked "Tul". This means that the intervention needs to be executed no later than at that point in time, if serviceability requirements are not to be violated. However, it may well be that a scenario that includes an intervention at the time instance "Top", has lower long-term costs than the one with the intervention at the time instance "Tul". The Figure 7 doesn't show any interventions after "Tul", but normally the ensuing interventions are considered in long-term costs.

The forecasts of safety and serviceability over time defines the time instance at which, at the latest, an intervention is necessary. However, these forecasts cannot be used to define the type and the costs of the interventions. To this end afore-mentioned qualitative indicators (e.g. condition rating, condition state, condition class, etc.) are used. The application of qualitative indicators to generate interventions is well-established in current approaches to maintenance planning as explained in the following chapter. The problem lies with the usage of these qualitative indicators as proxies for safety and serviceability. The worst condition state represents herein the safety and serviceability threshold. To remedy this problem of mid- to long-term maintenance planning adaptations are suggested that are explained in the following chapters.

5.1 *Current approach to maintenance planning*

Currently, maintenance planning is based on qualitative indicators. The procedure can vary quite significantly from country to country, but the main distinction lies in the choice of **assessment unit**. The assessment unit is the physical entity of the lowest granularity that is assessed during inspections. The assessment units can be whole bridges, bridge components (super-, substructure and equipment), bridge elements, group of damages or even single damages. All these different assessment units can be found in current BMS, based on the owner or operator's needs.

The scale of condition state is chosen in such a manner that only if an assessment unit is assigned into the worst condition state – being a proxy for safety and serviceability thresholds - immediate interventions are required. The maintenance planning considers therefore only interventions that are to be initiated before the worst condition state is reached. The optimum maintenance intervention(s) is/are the ones that minimize the long-term agency costs and in some cases user costs during these interventions, as in (Schiffmann & Hajdin, 2017).

The interventions are performed on **planning units** that in some BMS coincide with assessment units and in the others, they differ from them. If assessment units are damages, then it is often more reasonable to plan interventions on affected bridge element or the whole bridges than on a single damage. Based on the condition state of assessment units, the intervention on planning units are determined based mostly on heuristic rules. To this end, technically feasible maintenance intervention on planning units are catalogued together with their unit costs and effectiveness. For instance, for the same condition states of assessment units, both rehabilitations on elements as well as replacement of the whole bridge are technically feasible. The choice of the optimum intervention is subject to minimization of the long-term costs as in (Adey & Hajdin, 2011).

This approach has significant drawbacks since it focuses solely on restoring damage-free bridges, without considering directly the safety and serviceability or consequences of possible failures. It is therefore that mid- to long-term maintenance planning can significantly deviate from the short-term planning and executed interventions, which are often triggered by safety and serviceability criteria.

5.2 *Deterioration models*

The key ingredient of mid- to long term maintenance planning is a deterioration model. The deterioration model allows condition state forecasts of assessment units and determine possible maintenance interventions in the future. The deterioration models can be derived from physico-chemical deterioration processes, and there is significant research in this area (e.g. Roelfstra, et al., 2004, Alnaggar, et al., 2017). Notwithstanding the undeniable progress in this research, most deterioration models in current BMS are based on statistical analysis of past condition data (e.g. Lethanh, et al., 2017, Hajdin & Peeters, 2008). Many BMS use Markov chains to model deterioration as it supports the discrete scale for condition states and transition probabilities can be easily derived from condition data. Finally, with Markov decision process, which is based on Markov chains and catalogued interventions, the optimum set of intervention can be estimated with modest computational effort. However, Markov chains are mostly employed for elements or components, whereas their applicability for individual damages waits to be proven.

5.3 *Improvements to current approach*

The current approach to mid- to long-term maintenance planning based on condition states of assessment units is used quite successfully to define maintenance scenarios and estimate long-term costs. However, it doesn't consider safety and serviceability directly and therefore the estimation of the optimum time instance to perform intervention can be quite wrong. A bridge with high safety and serviceability margin may be used significantly longer than suggested by an assessment unit in the worst condition state. The opposite is also true: A bridge barely meeting serviceability requirements may need to undergo an intervention even before a single assessment unit reaches the worst condition state.

age or a damage group. Consequently, the deterioration models need to be developed for these assessment units and based on the evolution of these assessment units, the safety and serviceability can be evaluated. The current deterioration processes used for elements and components can be quite useful as baseline for calibration of deterioration models for damages and damage groups.

The improved approach is presented in Figure 8 with damage group as assessment unit as in Swiss Bridge Management System KUBA. An individual damage can also be a damage group, so there is no loss of generality if a damage group is used as an assessment unit. The basic bridge data include apart from element data also the most probable failure

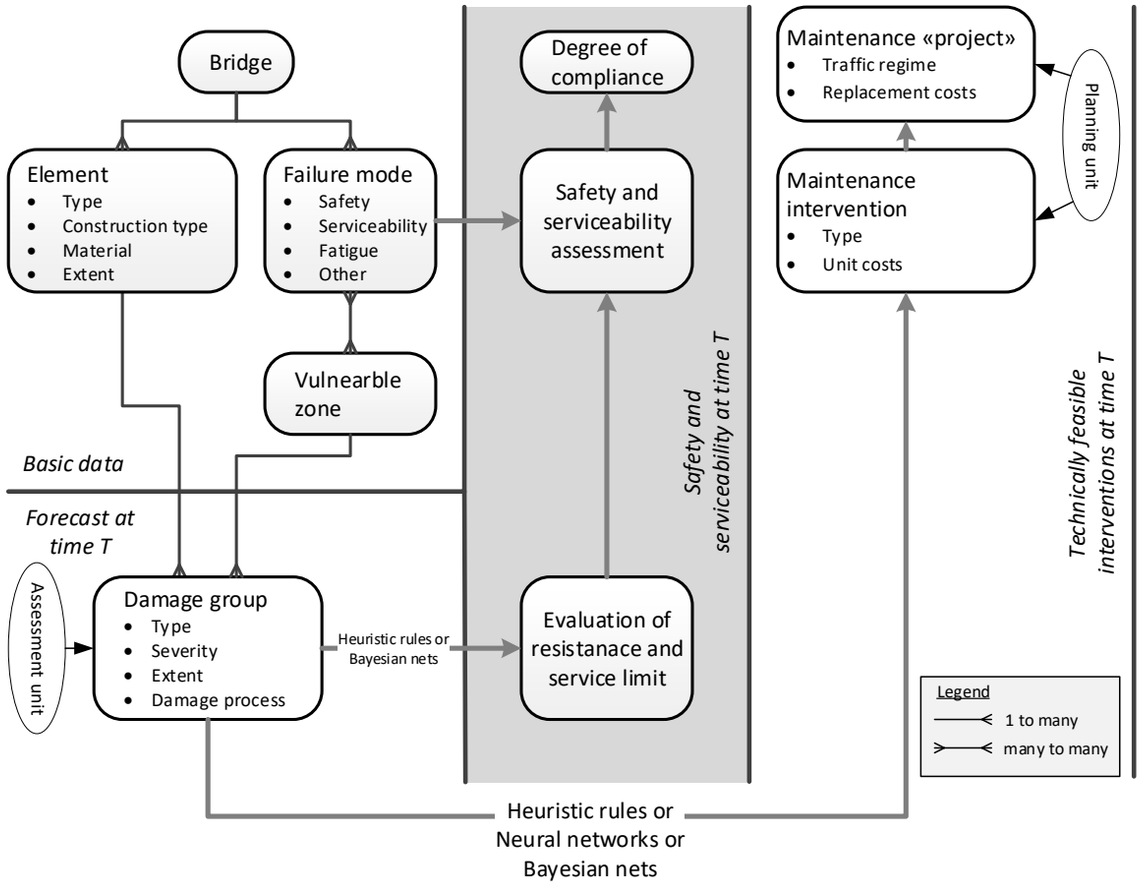


Figure 8: Assessment of degree of compliance related to safety and serviceability and determination of maintenance intervention at time T

On one side, it is necessary to estimate both condition states of assessment units and based on them define intervention scenarios on planning units and related costs. On the other side, the reliable forecast of safety and serviceability are needed to estimate the remaining service life without interventions. It is shown in the previous sections that meaningful safety and serviceability assessment is possible only if individual damages or damage groups underlying the same damage process are assessed. This means that the assessment unit must be either an individual damage or a damage group.

modes. These failure modes can be determined from bridge design documents as explained in 4.3. A bridge can have several elements and several failure modes. A failure mode can include several vulnerable zones as shown in 4.3. For instance, a collapse mechanism of an hyperstatic structure has always several places where rupture or yielding occurs and these are vulnerable zones. These vulnerable zones can also participate in several failure modes. Hence, there is many-to-many relationship between the "Failure mode" and "Vulnerable zone".

Using the deterioration model for an assessment unit, the severity and extent of the damage group can be predicted at some time point T. The impact of the damage group on resistance and/or service limits in vulnerable zones can be estimated using heuristic rules or Bayesian nets (Hajdin, et al., 2018). Following the same procedure as in 4.1, the degree of compliance for safety and serviceability at the time T can be assessed. These steps are represented in the gray column in Figure 1 to highlight the addition to current maintenance planning procedure.

The path from damage group forecast at time T to maintenance interventions is already implemented in KUBA and many other BMS. Herein, the catalog of technically feasible maintenance interventions for each damage type and severity of a given element type is of pivotal importance. The cataloged interventions are characterized by their unit costs and effectiveness. The cost predictions are generated by the heuristic rules and optimization depend on these data. The catalog is the result of a statistical analysis of executed preservation projects and is subject to changes reflecting developments in construction industry. The unit costs refer to a specific measurement unit. The unit for maintenance work on steel elements, for example, is the square meter [m^2], i.e. the surface area. This unit must be the same unit used to measure the extent of damage groups.

The technically feasible maintenance interventions are then aggregated using heuristic rules and threshold values in maintenance "projects" on bridge level. The quotation marks indicate that these are no engineering "project", but rather a very general outline of the maintenance work that is feasible at the time T. In addition to "projects" aggregated from elements, a replacement "project" is added as an option, as it can be assumed that it is the costliest maintenance option. For the high-volume bridges, a traffic regime and eventual closures during the execution of the maintenance works needs to be defined. This information is needed to evaluate societal costs. The interested reader can find further details on estimation of user costs in (Adey, et al., 2012).

A maintenance intervention results in improvement in degree of compliance regarding safety and serviceability. Currently, the estimation of this improvement is not possible, since there are only data on improvement in condition states. Also, similar refers to the effectiveness of the intervention. Still, the effectiveness of intervention related to condition states can be useful: If the condition state is restored to the best condition state after the intervention, one can assume that also the degree of compliance of the undamaged bridge is restored.

In summary, the proposed improvements allow decision maker to

- estimate remaining intervention-free service life of a bridge in rational manner, using safety and serviceability assessment,
- consider the improvement in safety and serviceability and compare with the costs to obtain this improvement, and
- plan reliable financial needs and needs for other resources on mid to long-term, considering the forecasts of traffic loads.

The data collection effort to implement these improvement is quite modest. However, the data needs to be collected conscientiously and the procedure to evaluate degree of compliance related to safety and serviceability needs to be updated to match performed in-depth investigations.

One step further would be to replace the degree of compliance with reliability assessment at some time T as explained in 4.2. The estimation of reliability over time (e.g. Mandić Ivanković, et al., 2017) is just a stepping stone to estimation of risk over time. This topic will be discussed in 6.2.

6 OUTLOOK

6.1 *Application of BIM in assessment*

It is foreseeable that in not so distant future, Building Information Models (BIM) of both newly built and existing bridges will be available (see e.g. Chipman, et al., 2016 and BMVI, 2015). These models will be included into the Bridge Management System (BMS) and will significantly enhance the quantity of useful information in fBMS. A BIM can embed realistic structural system of a bridge as well as the relevant load situations (buildingSMART, 2018). The evaluation of the reliability or safety/serviceability would be therefore possible quasi, on-the-fly within the fBMS, provided that the observations and results from SHM can be adequately integrated in BIM.

In principle, the inspection results can be directly captured in the BIM using photogrammetry or some other procedure. Cracks, spalling, deformation, and other defects will be a part of a BIM, which in most cases alter the BIM geometry. An information model and a candidate binding to Industry Foundation Classes (IFC) has been developed by (Hüthwohl, et al., 2018). This study demonstrated that that IFC provides sufficient functionality to serve as a basis for integrating relevant defect information and imagery.

In Figure 9, this future approach to bridge management is illustrated. A column as a part of a BIM is shown on the far left. On this column, a spalling area is observed (second from left). This spalling area is captured photogrammetrically as a 3D model and merged with the BIM of an intact column. The result is shown in BIM (third from left). The embedded structural system is also updated: The resistance of the column can be reduced due to spalling and the internal forces i.e. bending moment (M) and axial force (N) can be compared with the reduced resistance (e.g. using interaction diagram). In this manner, the degree

of compliance can be updated. Clearly, also the uncertainty of the material properties and spalling effect on resistance can be taken into account, so that the probability of failure can be determined.

The results of past inspections, e.g. damages are stored in a temporal BIM, which is an enhancement of the existing temporal databases. This would enhance possibility to statistically estimate deterioration models. Furthermore, the temporal BIM is a valuable data source that will allow researchers to better understand physical deterioration processes. The data stored in fBMS include also other changes that a bridge experience during its life span. This includes strengthening, widening, seismic retrofit and other structural changes. In short fBMS is similar to the 6D BIM or Asset Information Model (Wikipedia, 2017), which continues to be updated during the whole service life of a bridge.

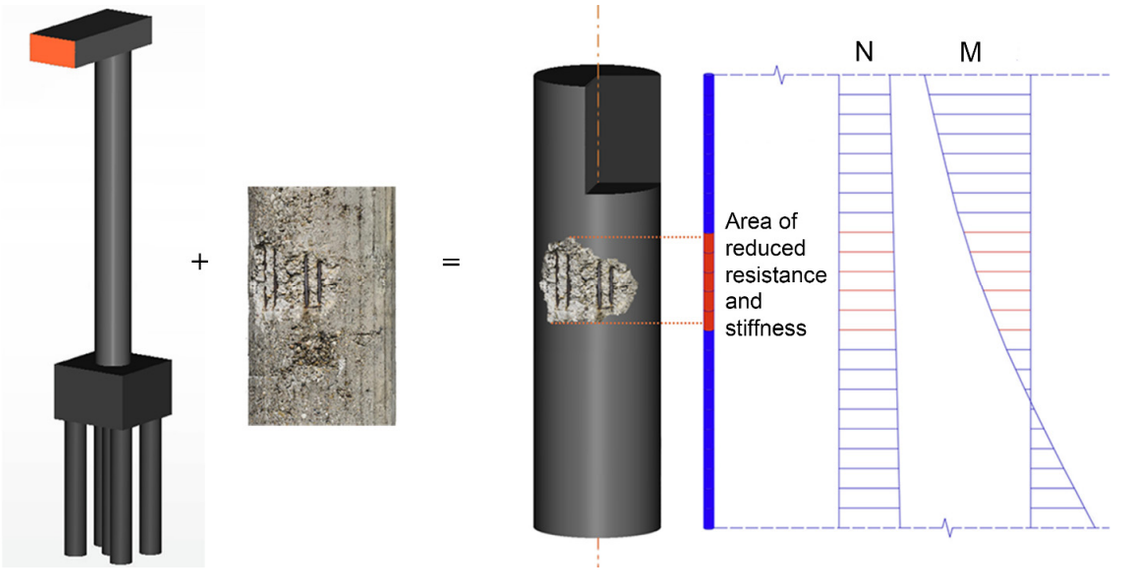


Figure 9: Integration of damage into BIM

For purposes of maintenance planning, the BIM with damages can be used as the basis for the deterioration simulation, which can provide significantly more accurate forecast that the current methods. The reasons for this are twofold:

- The resistance and loads i.e. probability of failure of an intact structure is duly taken into account.
- The exact location of a defect is known so that its effect on the safety and serviceability can be assessed in a more accurate manner.

The same applies to maintenance scenarios, which can be determined more accurately, both regarding their types as well as regarding their costs rdtimates.

There are still large obstacles that need to be overcome to develop fully functional fBMS. In particular, the modeling of cracks, spallings, chemical degradation and internal damages is still in infancy. It is also feasible to include fBMS into a GIS Systems, which would open further analytical possibilities regarding the natural hazards or advanced deterioration (Heitzler, et al., 2017).

6.2 *Risk-based maintenance planning*

The reliability thresholds related to safety and serviceability as defined in (CEN EN 1990, 2002) are values that apply to all bridges disregarding the traffic volume they carry or their environment. This can be questioned for two reasons. In sections 2 and 4.5, the one reason regarding traffic was discussed: The traffic load used in assessment procedure needs to correspond to real traffic situation at the bridge site. This can be done using nowadays abundantly available weigh-in-motion data or by instrumenting bridges with simple structural systems (e.g. Treacy & Brühwiler, 2014). This customized traffic load that is developed for each road section can allow significant number of low volume bridges to meet requirements in the codes of practice.

The second reason not discussed so far, relates to consequences of potential failures. It is questionable that the same safety index (reliability) is required for the failure with small consequences as for the ones with high consequences. It seems that this one-size-fits-all is not economical. Indeed, in (SIA, 2011) the required safety indices are graded according to the consequences of failure. Given that the risk is defined as expected consequences of a failure, the provisions in (SIA, 2011) are actually replacing reliability thresholds with risk thresholds. Risk thresholds are not new in engineering: They are used to evaluate road accidents, exposure to natural hazards and in many other areas. In most cases, the risk thresholds are not given as a single value, but rather as an acceptable area in a risk matrix that spans occurrence rate and consequences of failure. This acceptable area is often called ALARP-area, which stands for risk that

is "**a**s **l**ow **a**s **r**easonably **p**racticable". The term "practicable" raises a suspicion whether the risk thresholds are really needed. It implies that there should be a balance between the effort (e.g. money, resources) to reduce risks and the outcome of this effort i.e. risk reduction. If both the effort and the achieved risk reduction are expressed in monetary terms, then they can be compared and if risk reduction is higher than the effort to achieved it, then this effort is beneficial. In context of this paper, the effort can be understood as maintenance intervention costs to reduce risks. Theoretically, all maintenance interventions, whose costs are lower than the achieved risk reduction are beneficial and should be undertaken. This means that the acceptable risk is dependent on the available, technically feasible maintenance interventions to reduce it. This is nothing else but **proportionality** principle that often governs human behavior. In (SIA, 2011), the proportionality principle finds it application as it requires to evaluate the ratio between discounted, monetized risk reduction and the discounted costs of maintenance interventions for the remaining service life. This long-term perspective can directly be applied to risk-based maintenance planning.

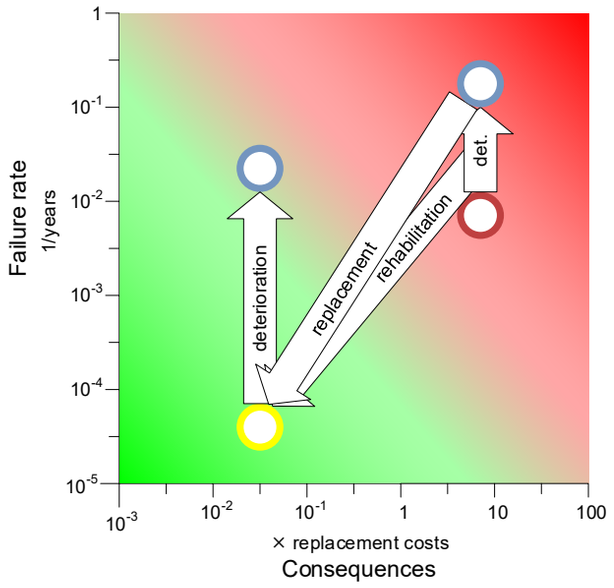


Figure 11: Maintenance scenario and basis scenario

For each maintenance scenario, a corresponding monetized risk (or rather its rate) as function of time can be developed and its discounted value at some arbitrary time instance can be evaluated. This absolute value cannot be used directly as it needs to be compared with the one of basis scenarios, which can be also a "do nothing" scenario. It is the difference in discounted value of risk between these two scenarios that is of interest. The costs of sequence of intervention that are included in maintenance scenario can be also discounted to the same time instance, and the difference to the basis scenario is evaluated. Assuming that the basis scenario has higher discounted value of risk but lower maintenance costs, the maintenance scenario is more beneficial than the basis scenario if risk reduction exceeds the higher costs of maintenance scenario. It should be therefore favored over the basis scenario.

The above reasoning is illustrated in Figure 11. The risk of a bridge is evaluated based on the failure rate and the related consequences with the red circle in a risk matrix. Within 10 years, the structure would reach blue circle, in which the failure rate is so high that the structure has to be replaced due to the immediate danger of failure. In this case this is assumed to be the basis scenario. In order to prevent the immediate danger of failure, a rehabilitation intervention in 5 years is considered. This rehabilitation represents the maintenance scenario. Both interventions reduce the risk to the same level and the risk after the interventions is represented with the yellow circle. This means that replacement and rehabilitation reduce both the failure rate and the consequences. In course of time the deterioration proceeds further 65 years. In year 70 the cut-off is set and afterwards neither maintenance costs nor risk are being considered.

The same colour coding applies to Figure 10. The benefit (=risk reduction) of the rehabilitation intervention compared to replacement is represented with the shaded area above horizontal axis. Both interventions costs and risk are normalized by replacements

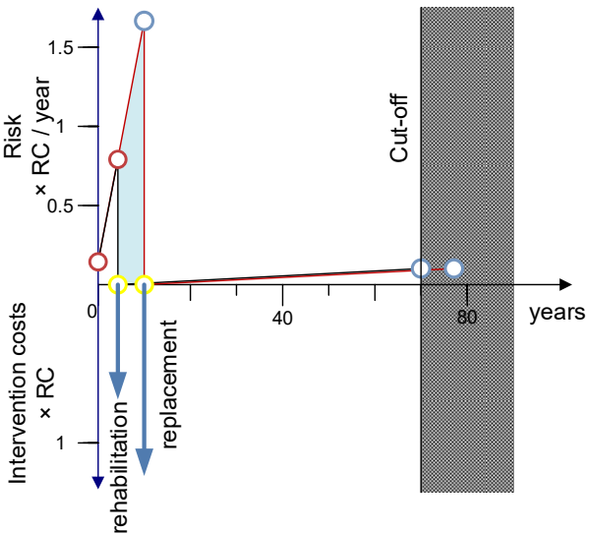


Figure 10: Risk and cost comparison

costs (RC) in Figure 10. The risk reduction can be computed as follows

$$\Delta R = \int_0^{70} \Delta r(t) \cdot e^{-\gamma t} dt \qquad (7)$$

where r is risk, γ is the compound discount rate and t is time. The difference in the costs of two scenarios can be evaluated with following expression:

$$\Delta C = C_{Rehab} \cdot e^{\gamma \cdot 5} - C_{Repla} \cdot e^{\gamma \cdot 10} \quad (8)$$

Finally, the net benefit of the maintenance (rehabilitation) strategy versus basis (replacement) strategy is as follows:

$$NB = \Delta R + \Delta C \quad (9)$$

It is obvious in this example that the rehabilitation strategy should be chosen since it both incurs higher risk reduction and lower intervention costs.

The outcome of maintenance intervention i.e. the risk reduction at some time instance T, needs to be assessed. To this end, both the effect of maintenance intervention on reliability as well as on consequences needs to be evaluated. In this manner, one can evaluate, for the chosen maintenance scenario, the risk development over time, and compare it with the basis scenario.

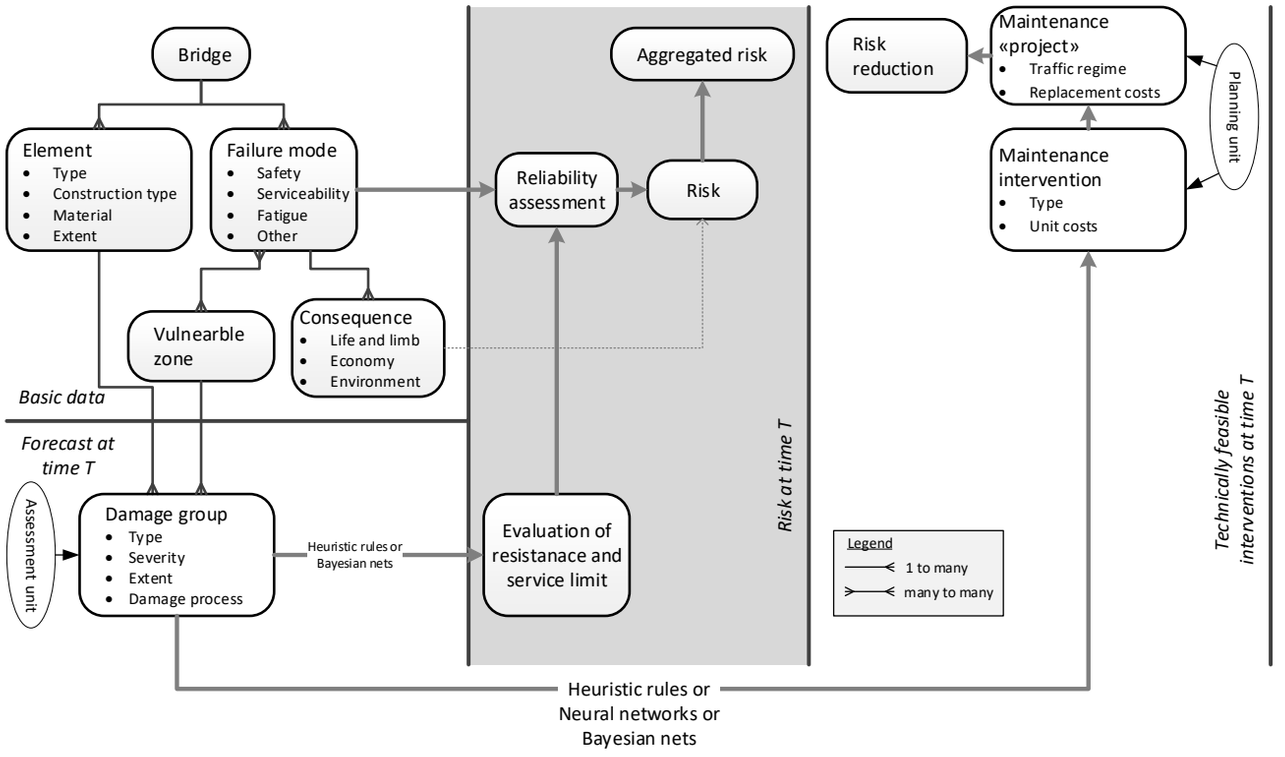


Figure 12: Assessment of risk and risk reduction due to maintenance intervention at the time T

The decision whether the maintenance scenario should be followed even if the achieved risk reduction is higher than the additional costs of maintenance scenario depends also on the available financial means and other resources. The set of interventions within the maintenance scenarios needs to fit into available resources and the scenario that have the maximum net benefit (risk reduction – costs) will be executed. This also means that the acceptable risk is directly dependent on the amount of available resources.

Based on the explanations above, one can adapt the current mid- to long-term maintenance planning that is to be supported by fBMS as shown in Figure 12. Each failure mode can have different consequences, which can be divided in three main categories and several subcategories (Faber, et al., 2009). These consequences are used for the risk evaluation related to each failure mode. The risks due to different failure modes need to be aggregated taking into account the correlation between these failure modes. Strictly taken, only risks of failure modes that are mutually exclusive can be summed together.

6.3 *Natural hazards*

The one of the challenges listed in section 2 are the natural hazards. On one hand, older bridges are often not or not adequately designed for natural hazards and on the other hand it is likely that the climate change has an adverse impact on frequency and intensity of gravitational hazards.

The risk-based maintenance planning explained in previous section is actually developed for natural hazards and is being used by agencies world-wide (e.g. ASTRA, 2014). It allows therefore to treat natural hazards in the same way as, for instance, traffic loads. The failure modes and corresponding probabilities of failure must be defined in the same manner as it is described for traffic loads. This task can be more difficult than the one for traffic loads, since some bridges are not design for extreme loadings. These bridges must be examined for different frequency and intensity of hazard events. Based on this analysis the

failure probability can be assessed as a function of hazard intensity.

This approach for local scour induced by flooding events as the predominant cause of bridge collapses is discussed in (Tanasic & Hajdin, 2017). Herein, the failure modes are based on water-soil-structure interaction. This means that the resistance of a bridge and its ability to prevent collapse of river bed under the foundation is duly considered. The failure modes and the associated vulnerable zones are determined both for the structure and soil below foundations.

Following the need to improve the behavior of bridges in an earthquake event, a risk-based approach, similar to the one explained in this chapter was developed by (Padgett, et al., 2010) for girder bridges.

6.4 *Risk and social equity*

The risk-based maintenance planning explained in previous chapter has a significant drawback. The consequences for life and limb needs to be monetized, which is highly controversial ethical issue. The virulence of this issue can be lingered if the mortality and/or injury rate is evaluated for each maintenance scenario. Based on this data one can require that the incremental investment i.e. the difference in investment between an arbitrary maintenance scenario and the next more expensive scenario needs to exceed some value for additionally saved human life or for additionally avoided injury (Adey, et al., 2009). This value, also called marginal costs of saving lives, can be coupled to GDP and therefore can be different from country to country. By setting a threshold to marginal costs of saving lives, the social equity can be reinforced as the scarce resources to save human lives can be justly distributed if the same marginal costs of saving lives are used not only across different regions, but also across different live saving activities (health, crime prevention, etc.).

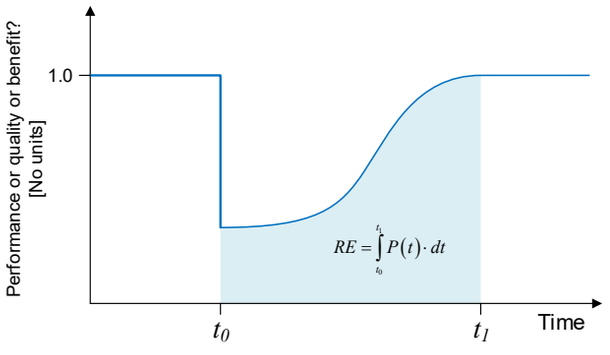


Figure 13: Recovery curve and resilience

The concept of marginal costs can also apply to other types of consequences such as user costs, travel time, environmental impact etc. This can foster sensitivity analysis and improve the accepted value system within communities.

6.5 *Resilience and risk-based maintenance planning*

Given the current interest of research community in resilience coupled with public call for more "resilient" road infrastructure, there is an open question if and how the resilience should influence decision-making in bridge management.

The term itself comes from Latin "resilens", which is the present participle of the verb "resilire" or in English "to spring (bounce) back" or "to rebound". In realm of civil engineering it was firstly adopted in seismic engineering to describe the "ability of social units to mitigate hazards, contain the effects of disasters when they occur, and carry out recovery activities in ways that minimize social disruption and mitigate the effects of future earthquakes" (Bruneau, et al., 2003). The effect of a natural disaster such as earthquake is described in Figure 13. At the time instance t_0 the earthquake occurs with an adverse effect on the performance, quality or benefit of infrastructure. The recovery starts immediately after the earthquake and at the time instance t_1 the infrastructure is fully restored. The dynamics of this recovery is represented with a recovery function $P(t)$ and the resilience is computed as a definite integral of the recovery function between t_0 to t_1. If the recovery function is expressed as a performance function, then the resilience is average performance between t_0 to t_1 (Bocchini, et al., 2014).

To analyze the resilience of a bridge (or any other entity) the criterion on the ordinate in Figure 13 and recovery function for different hazards needs to be defined. Given that the benefit of a bridge is in ensuring fast and safe passages for road traffic over otherwise hardly surmountable obstacles, the impact of a damaging event would be a good criterion to analyze resilience. Following the reasoning in section 1, the impact of a damaging event can be quantified by user costs. They emerge from the change in traffic pattern that result in additional travel time and change in accident rates. Conversely, the benefit of a bridge can be quantified by user costs of its complete closure as in (VSS, 2003). It should be noted that strictly taken this benefit applies only for a single bridge on otherwise fully operational road network. This means that the benefit of the bridge under consideration can significantly change in already damaged network (Adey, et al., 2003). For instance, the benefit of a bridge on the only remaining road connection between two regions after the failure of all other connections can hugely increase. Given that, for the resilience analysis only the recovery function is of interest and the above problem can be efficiently solved by normalizing benefit to values between 0 and 1. The recovery function is therefore independent from the network condition before the onset of a damaging event. Consequently, it can be regarded as technically feasible recovery function. Actually, the recovery function is

subject to availability of resources (Faber, et al., 2017) and in case of major damaging event they might not be available, leading to waiting time for recovery to begin. This effect is out of the scope of this paper. In summary, the resilience is defined an average normalized benefit of a bridge from the onset of damaging event to the full recovery.

The damaging events can occur at some rate governed for instance by a Poisson process. A possible realization of this Poisson process with different event intensity is shown in Figure 14. The resilience

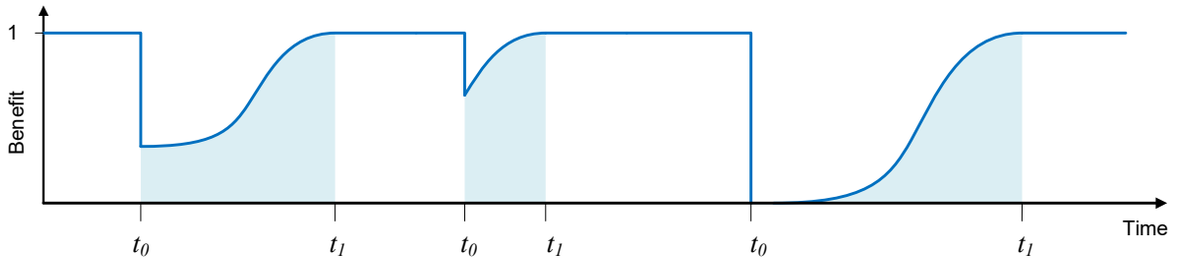


Figure 14: Possible realization of the sequence of damaging events

can be evaluated for each event, or an average can be computed for any given time horizon including infinity. In most cases, the time interval between the damaging events is large enough to accommodate time needed for recovery, as illustrated in Figure 14. If this can be assumed, as it is implicitly done for risk-based maintenance planning in which the user costs are explicitly considered in decision-making process, the resilience is additional information that can hardly influence decision making. It can however be used for communication purposes, stating that a bridge exhibits its resilience of, for instance, 90% meaning that the damaging events has reduced its benefit to the users by 10%.

If the probability that a damaging event occurs before a bridge is recovered from previous one cannot be neglected, then it must be considered in estimation of the consequences. This will also have an impact on the decisions regarding maintenance scenarios, preferring the ones that are more expensive i.e. the ones with shorter recovery times. The resilience can be very useful information to justify the need for more resources since it is easy to communicate. With the resilience the owner can also illustrate the point-of-no-return i.e. the resource threshold at which no full recovery is possible. Furthermore, resilience hat an undoubted positive connotation, which is not the case with the term “risk”, and therefore more acceptable to general public.

The resilience analysis of a bridge can be enhanced with deterioration that can gradually decrease benefit of a bridge or lead to a larger drop in benefit when damaging event occur. The interdependency between the sudden damaging events and gradual deterioration and its impact on resilience is studied in (Hajdin, 2017b).

In summary, the resilience is a very useful information, more easily understood than risk. However, the change in resilience need to be accompanied with associated costs and other resources. Furthermore, owners can set threshold values for resilience that enter decision-making process. This is equivalent to setting constraints on user costs and eliminating maintenance scenarios that don’t meet these constraints, similar to limiting the marginal costs of saving lives discussed in section 6.4.

7 CONCLUSIONS

The need for more economic utilization of transportation infrastructure is also a challenge for bridge owners. They need to have readily available, high quality information on their bridge inventory in order to cope with gradual deterioration, growing traffic demands and increased frequency and magnitude of natural hazards. To obtain and store this information is a task that cannot be accomplished in a short time. In this paper, the methods are proposed that use data that is already available and allow their gradual refinement. They allow better exploitation of inspection results to assess safety and serviceability and improved decision making regarding in-depth investigations and maintenance interventions. The assessment of safety and serviceability during the whole service life allows also more responsive processing of special permits and established corridors for heavy weight vehicles.

The presented methods are only stepping stones toward a new generation of BMS that will integrate BIM and allow more accurate and prompt information on bridge behavior. Current databases need to be enhanced with BIM. The data generated during the design and construction process must be handed to the owner or operator that act henceforth as their trustees. It is essential that this data can be transparently and intuitively used in the exploitation phase. To this end, the owners need to set requirements that are independent of software packages used in design and construction phase.

Finally, the owners and/or operators must provide both financial and personal resources to maintain a

fBMS and its data. Owners need in-house competence both in structural and decision engineering as well as in information technology similar to the banking sector, where competence in information technology, financial and decision engineering is required. It is not a coincidence that in both sectors the term "Asset Management" is widely used.

8 ACKNOWLEDGEMENTS

This paper is partially based upon work supported by the German Federal Highway Research Institute under grant FE 15.0628/2016/LRB. Parts of paper address the work from COST Action TU-1406, Quality specifications for roadway bridges, standardization at a European level (BridgeSpec), supported by COST (European Cooperation in Science and Technology). The author is the leader of the Working Group 3 of the COST Action TU1406.

REFERENCES

Adey, B. & Hajdin, R., 2011. Methodology for determination of financial needs of gradually deteriorating bridges. *Journal of Structure and Infrastructure Engineering,* 77-8, pp. 645-660.

Adey, B., Hajdin, R. & Brühwiler, E., 2003. Supply and Demand System Approach to the Development of Bridge Management Strategies. *ASCE Journal of Infrastructure Systems,* 3(3), pp. 117-131.

Adey, B., Hajdin, R., van Linn, A. & Welte, U., 2009. *Effectiveness and efficiency of interventions on highway structures (in German),* Zurich: VSS, Report 625.

Adey, B. et al., 2012. Methodology and Base Cost Models to Determine the Total Benefits of Preservation Interventions and Road Sections in Switzerland. *Journal of Structure and Infrastructure Engineering,* 8(7), pp. 639-654.

Alnaggar, M., Di Luzio , G. & Cusatis, G., 2017. Modeling Time-Dependent Behavior of Concrete Affected by Alkali Silica Reaction in Variable Environmental Conditions. *Materials,* 10(5), p. 471.

ARE, ASTRA, 2006. *The benefit of transportation – Subproject: Contribution of transportation to value creation in Switzerland (Der Nutzen des Verkehrs – Teilprojekt: Beitrag des Verkehrs zur Wertschöpfung in der Schweiz),* Bern: Federal Office for Spatial Development and Federal Roads Office.

ASTRA, 2014. *Management of natural hazards on NHS (in German: Management von Naturgefahren auf den Nationalstrassen), Guidelines,* Bern: Swiss Federal Roads Office.

BMVI, 2015. *Phase Plan for Digital Planning and Constructing (Stufenplan Digitales Planen und Bauen),* Berlin: Federal Ministry of Transport and Digital Infrastructure.

BMVI, 2016. Part 3: Analysis of existing road bridges due to special transports. In: *Provisions and Guidelines for Analysis and Diemsnioning of structures (in German).* Bonn: Fedral Ministry of Transport and Digital Infrastructure.

Bocchini, P., Frangopol, D. M., Ummenhofer, T. & Zinke, T., 2014. Resilience and Sustainability of Civil Infrastructure: Toward a Unified Approach. *ASCE Journal of Infrastructure Systems,* 20(2).

Braml, T. & Wurzer, O., 2012. Probabilistic analysis methods as an additional component for the integrated assessment of existing bridges (in German). *Beton- und Stahlbetonbau,* 10710, pp. 654-668.

Bruneau, M. et al., 2003. A Framework to Quantitatively Assess and Enhance the Seismic Resilience of Communities. *Earthquake Spectra,* 19(4), pp. 733-752.

buildingSMART, 2018. *IfcStructuralAnalysisModel.* [Online] Available at: http://www.buildingsmart-tech.org/ifc/IFC2x3/TC1/html/ifcstructuralanalysisdomain/lexical/ifcstructuralanalysismodel.htm [Zugriff am 02 01 2018].

Calgaro, J.-A. & Sedlacek, G., 1992. EC1: Traffic loads on road bridges. *IABSE reports,* Band 65.

Caprani, C., 2013. Lifetime highway bridge traffic load effect from a combination of traffic states allowing for dynamic amplification. *ASCE Journal of Bridge Engineering,* 189, pp. 901-909.

Cawley, P., 2018. Structural health monitoring: Closing the gap between research and industral development. *Structural Health Monitoring,* Volume : doi.dox.org/10.1177/1475921717750047, pp. 1-20.

CEN EN 1990, 2002. *Basis of structural design,* Brussels: European Committee for Standardisation.

Chipman, T. et al., 2016. *Bridge Information Modeling Standardization. Report No. FHWA-HIF-16-011,* Washington D. C.: FHWA.

Das, P., 1999. Development of a comprehensive structures management methodology for the Highways Agency. In: *Management of highway structures.* London: ICE, Highways Agency.

Enright, B. & O'Brien, E. J., 2013. Monte Carlo simulation of extreme traffic loading on short and medium span bridges. *Structure and Infrastructure Engineering,* 912, pp. 1267-1282.

Faber, M. H. et al., 2009. *Methodological basis for comparative risk assessment (in German),* Zurich: VSS, Report 618.

Faber, M. H., Qin, J., Miraglia, S. & Thöns, S., 2017. On the Probabilistic Characterization of Robustness and Resilience. *Procedia Engineering,,* 198, Special issue: Urban Transitions Conference, Shanghai, September 2016, pp. 1070-1083.

Freundt, U. & Bönning, S., 2011. *Traffic load models for recalculation of existing (Verkehrslastmodelle für die Nachrechnung von Straßenbrücken im Bestand),* Bonn: Federal Highway Institute.

Frischmann, B. M., 2012. *Infrastructure - the social value of shared resources.* New York: Oxford University Press.

Hajdin, R., 2017a. Visual inspections and key performance indicators - Bridging the gap. *Transportation Research Circular, 11th International Bridge and Structures Management Conference*, October, Issue E-C224.

Hajdin, R., 2017b. *Bridge Resilience,* Zurich: IMC GmbH (unpublished manustript).

Hajdin, R. & Despot, Z., 1999. TRUCK – Bridge Rating Software. In: *International Bridge Management Conference, Denver, Colorado, April 26-28, 1999.* Washington D. C.: Transportation Research Board.

Hajdin, R., Holst, R., Büchel, B. & Rabe, R., 2018. A new practice-oriented approach for relibability-based bridge inspections (to be published). *The Sixth International Symposium on Life-Cycle Civil Engineering*.

Hajdin, R. & Peeters, L., 2008. Bridging Data Voids: Advanced Statistical Methods for Bridge Management in KUBA. *10th International Bridge and Structure Management Conference, Buffalo, New York, TRB Circular E-C128*, October, pp. 90-104.

Heitzler, M. et al., 2017. A Simulation and Visualization Environment for Spatiotemporal Disaster Risk Assessments of Network Infrastructures. *Cartographica: The International Journal for Geographic Information and Geovisualization ,* 52(4), pp. 349-353.

Hüthwohl, P., Brilakis, I., Borrmann, A. & Sacks, R., 2018. Integrating RC Bridge Defect Information into BIM Models. *ASCE Journal of Computing in Civil Engineering ,* 32(3), p. 04018013.

JCSS, 2013. *Probabilistic Model Code,* Lyngby: Joint Committee for Structural Safety.

Kurte, J. & Esser, K., 2008. Benefit of road traffic (Nutzen des Straßenverkehres). In: *ADAC study on mobility (in German).* Munich: ADAC (Ed.).

Lethanh, N., Hackl, J. & Adey, B., 2017. Determination of Markov Transition Probabilities to be Used in Bridge Management from Mechanistic-Empirical Models. *ASCE Joournal of Bridge Engineering,* 22(10), p. Published online.

Linneberg, P., Mašović, S. & Hajdin, R., 2017. Quality Control Plans for Girder and Frame Bridges. *IABSE Symposium, Vancouver*.

Lou, P., Nassif, H. & Truban, P., 2018. Development of live load model for strenght II limit state in AASHTO LRFD design specifications. *Transportation Reserach Board, Annual meeting*.

Mandić Ivanković, A., Skokandić, D., Žnidarič, A. & Kreslin, M., 2017. Bridge performance indicators based on traffic load monitoring. *Structure and Infrastructure Engineering,* Volume : doi.org/10.1080/15732479.2017.1415941 (published onlilne), pp. 1-13.

Mertz, D., 2005. *Load rating by load and resistance factor evaluation method,* Washington D. C.: Transportation Research Board.

Meystre, T. & Hirt, M., 2006. *Examination of existing road bridges with updated road loads (Überprpfung bestehnder Strassenbrücken mit aktualisierten Strassenlasten),* Bern: Swiss Federal Roads Office.

NYSDOT, 1997. *Concrete Details Vulnerability Manual.* Albany, NY: New York State Departement of Transportation.

Padgett, J., Dennemann, K. & Ghosh, J., 2010. Risk-based seismic life-cycle cost–benefit (LCC-B) analysis for bridge. *Structural Safety,* 32(3), pp. 165-173.

Roelfstra, G., Hajdin, R., Adey, B. & Brühwiler, E., 2004. Condition Evolution in Bridge Management Systems and Corrosion-Induced Deterioration. *ASCE Journal of Bridge Engineering,* 9(3), pp. 268-277.

Schiffmann, F. & Hajdin, R., 2017. Lont-term work zone planning for highway infrastructure. *World Conference on Pavement and Asset Management, WCPAM2017*, June.

SIA, 2011. *SIA 269 - Maintenance of existing structures,* Zurich: Swiss Engineers and Architects Association.

Tanasic, N. & Hajdin, R., 2017. Management of Bridges with Shallow Foundations Exposed to Local Scour. *Journal of Structure and Infrastructure Engineering, Special issue on IABMAS 2016,* Issue doi: 10.1080/15732479.2017.1406960, pp. Published online, print in 2018.

Treacy, M. A. & Brühwiler, E., 2014. Are current bridge load modelling techniques realistic for existing road bridges?. In: F. &. R. Chen, Hrsg. *Bridge Maintenance, Safety, Management and Life Extension, 7th International Conference on Bridge Maintenance, Safety and Management (IABMAS)* . London: Taylor & Francis Group, pp. 340-347.

U.S. DOT, 2015. *Industry Snapshots: Uses of transportation,* Wahsington D.C.: U.S. Departement of Transportation.

VSS, 2003. *Swiss Norm 640 904: Evaluation of pavements, road structures and equipment: substance and utilization values,* Zurich: Swiss Association of Road and Transport Experts.

Wikipedia, 2017. *6D BIM.* [Online]
Available at: https://en.wikipedia.org/wiki/6D_BIM
[Accessed 21 February 2018].

Maintenance, Safety, Risk, Management and Life-Cycle Performance of Bridges – Powers, Frangopol, Al-Mahaidi & Caprani (Eds)
© 2018 Taylor & Francis Group, London, ISBN 978-1-138-73045-8

Timber bridges in Australia, where to from here?

J.A. Hilton
Global Service Leader Bridges and Civil Structures, Aurecon, Sydney, Australia

ABSTRACT: There is estimated to be over 11,000 timber road bridges owned by Local Government in Australia today. The majority were constructed in the second half of the 19th century and the first half of the 20th century as simple girder bridges with spans up to around 10-12m. Bridge lengths varied from single spans up to viaducts several kilometres in length. The bridges utilised Australia's then plentiful supply of exceptional quality hardwood which could generally be sought close to the bridge site. Today, a substantial number have fallen into disrepair. This is particularly so for the timber bridges owned by Local Government due principally to lack of sufficient funds and increasing shortage of good quality hardwood. The fact that until recently there has been no Australian Standard for the design of timber bridges has also been an issue. Recent studies have indicated that approximately 30% of Local Government timber bridges are in a "poor" to "very poor" condition. To make the required step change a collaborative public-private solution is recommended. These defective bridges represent a "Whole of Government" long-term community safety risk. The reality is that timely replacement of Local Government bridges is simply not provided for in Local, State or Federal Government capital programmes. The author is chairman of Australian Standards Committee BD090-08, responsible for the technical input to the new bridge design standard, AS 5100.8 "Bridge Rehabilitation and Strengthening". This is the first Australian Design Standard to address the rehabilitation of timber bridges. This paper draws on the learnings from the development of this Standard.

1 DEVELOPMENT IN AUSTRALIA

1.1 *Historical context*

The first timber bridges in Australia were constructed by the aborigines. There is ample documented evidence of felled trees used as creek crossings, as dams for collecting fish and as vantage points for catching fish.



Figure 1 Typical bridge constructed by aborigines

The first bridge built by European settlers was also a timber structure, across the Tank Stream near the corner of what is now Bridge and Pitt Streets, in Sydney in October 1788. John Meehan's "Plan of the Town of Sydney, 1807" also shows two others, one near Hunter Street, and another in King Street (O'Connor 1985).

Each of these bridges comprises longitudinal timber girders, supporting timber planking and supported on timber trestles and abutments.

Although none of these early bridges survives today, they form the rudimentary forerunners of tens of thousands of similar timber structures constructed in Australia in the 19th century.

Coming in to the first half of 20th century, when both structural steel and reinforced concrete bridges were being developed throughout the western world, timber bridges could in many cases still be constructed cheaper and quicker in Australia than the steel and concrete alternatives, particularly in country areas.

Essentially structural timber members did not have to be transported from factories very distant from the bridge site and particularly for long or multiple bridges, concurrent activities of timber felling, dressing and erection implied speedy construction.

Refer Figure 2 for a typical timber trestle bridge example.



Figure 2 Typical timber trestle bridge

Bridge designers in the 19th century drew on British bridge-carpentry traditions which we can now trace back to Roman times. Refer Figure 3 for an artistic image of Caesar's bridge across the Rhine constructed during the Gallic War in 55 BC. The Roman technique comprised machine driven raking timber pile supporting a timber headstock to form piers, in turn supporting a timber superstructure comprising longitudinal girders and cross decking, all very similar to the timber bridges in Australia today.



Figure 3 Roman bridge over the Rhine (artists impression)

Using this form of construction with discrete spans of around 6-8m the Romans constructed small creek crossings and viaducts several hundred metres long. A key component of the construction is the use of driven timber piles. The Romans developed a special drop hammer for this process, as reconstructed in the image in Figure 4.

There are more than 40,000 bridges in Australia. It is estimated that approximately 27,000 of these are timber bridges. Most of these are simple timber trestle bridges similar to the original Roman concept, the majority constructed at least 80-120 years ago.

1.2 *Structural form*

Typical superstructure details for the Australian bridges are noted in Figure 5, and typical substructure details are noted in Figure 6. Sizes shown are typical only.

Superstructures generally comprise longitudinal (usually round) girders spanning between trestle piers. The girders are spaced at around 1.4m centres, and support transverse timber decking. In more recent designs it was found more cost effective to install longitudinal timber sheeting across the decking to both act as a wearing surface and provide a degree of water tightness to the timber below. Timber barrier railing was originally constructed, although in many cases it has been replaced with steel guardrail.



Figure 4 Roman drop hammer for piles (reconstructed)

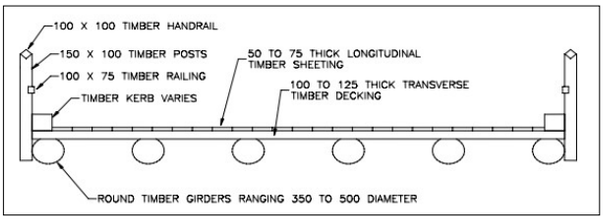


Figure 5 Typical Australian bridge cross section

Piers and abutments comprise timber piles usually driven to refusal on competent material. These are braced diagonally in plane. Longitudinally stability is obtained by a combination of the piles together flexing, plus abutment soil pressure. The piles are notched to allow installation of twin capwale (headstock) beams, configured to support the longitudinal girders. Abutments are similar in form to piers with timber sheeting behind for fill retention.

A common feature is the use of corbels between girders and pier headstocks. Though there are potential structural benefits to girder capacity by introducing partial structural continuity at piers (provided the

bolt system is tight) the main reason provided by early sources was that the time for girder replacement due to end deterioration could be extended.

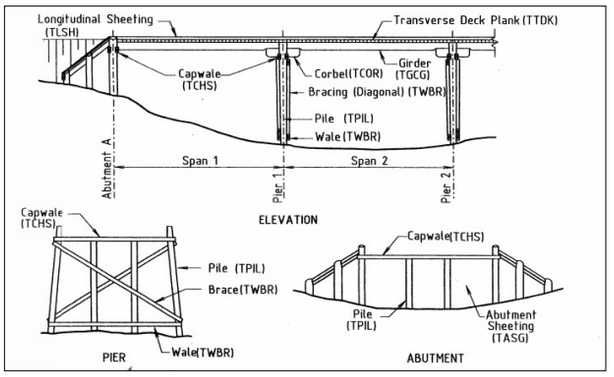


Figure 6 Typical Australian bridge elevation and plan

Except for the subsequent installation of SLT (stress laminated timber) or plywood decking in specific instances all timber used for these bridges is hardwood. In particular the heartwood of the hardwood, the inner region of the trunk, and comprised of dead cells as the sapwood growth front has moved out. Because sapwood is rich in nutrients such as starch, it is very susceptible to fungal attack when it remains on structural timber, and is generally removed when the timber is dressed.

There are a number of reasons for the success of timber bridges in Australia. Eucalypt timbers available were far superior to northern hemisphere softwoods in their ability to survive long term exposure to the elements. The strongest and most enduring Australian bridge timber, ironbark, was known in Britain as a superior ship-building timber by at least the mid-nineteenth century.

For valley crossings timber viaducts were cheaper than embankments with real advantages in low afflux under flood conditions. Two of the longest timber viaduct bridges in Australia were the rail structures at Yarra Glen (2296m) and Wagga Wagga (3106m).

1.3 *Typical defects*

Typical defects of these bridges are noted.



Figure 7 Splitting at snipe for bearing



Figure 8 corbel crushing due to fungal or insect attack



Figure 9 Pile deterioration at ground level



Figure 10 Structural overload due to excessive fill



Figure 11 General deterioration



Figure 12 typical crushing of headstock



Figure 13 Deteriorated piles



Figure 14 Typical bearing failure

1.4 *Case study: Tharwa bridge*

Tharwa Bridge is a four-span timber Allan truss bridge originally constructed around 1895. It is the only four span structure of its type in the world and is considered to be of exceptional national heritage significance. It is now being fully restored. This work has been undertaken with careful consultation to a very detailed conservation management plan, and in full conformance with the AS5100 to T44 loading.



Figure 15 Tharwa bridge

The work included the following;

- Provision of a steel underslung girders to temporarily support the existing bridge deck and provide continued traffic access during the refurbishment operation
- Complete reconstruction of the four Allan truss spans, enhanced for T44 loading
- Erection of a new stress laminated timber (SLT) deck. The deck was over 100m in length and was constructed off the bridge and then launched into position over temporary rollers. This is understood to be over double the longest SLT deck span previously erected by launching.
- Strengthened main span piers using jet grouting and micropiles
- Development and installation of heritage style traffic barriers designed to AS5100 crash loading
- Strengthened approach span piers using new generation carbon fibre technology



Figure 16 Tharwa bridge during construction

Construction of the timber superstructure was undertaken by RMS's own construction personnel us-

ing specialist techniques to replicate the original methods of construction.

The work was undertaken by Roads ACT who engaged ACT Procurement Solutions as project managers, Aurecon for the bridge design, RMS for the timber superstructure construction, Guideline Constructions for the substructure strengthening and Arenco for the supply and installation of the temporary bridging. Specialist advice on the timber engineering was provided by Prof Keith Crewes of UTS and Ray Taylor provided construction advice on the SLT.

2 LOCAL GOVERNMENT CONTEXT

2.1 *Extent of bridges*

The National Local Roads Data System (NLRDS) reports in 2011 that there are 27,939 bridges under Local Government management. This is distributed between the States as noted in Figure 17.

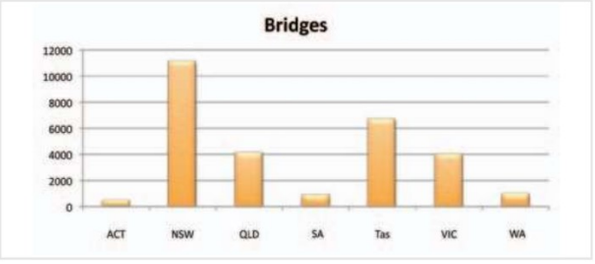


Figure 17 Distribution between states

There appears to be no consolidated national survey of the exact number or condition of timber bridges owned by Local Government. However, it is estimated that approximately 11,000 Local Government owned bridges are of timber construction. Adequate maintenance of these bridges has been problematic. A recent national survey (Roorda 2013) was undertaken to review the condition of Local Council roads and bridges. The survey was responded to by Councils covering $87B of an estimated $144B of total Local Government owned road assets. The survey showed 30% of timber bridges were reported as being in poor to very poor condition.

2.2 *Shortfall in maintenance*

Problems Local Government asset owners are confronted with;

- Increasing shortage of quality large section hardwood. In the early days of timber bridge construction there appeared to be an inexhaustible supply of good quality, high strength hardwood timbers. Today, some 100-150 years later, much of the high-quality timbers have disappeared and other regions of forest reserves have restrictions to logging for environmental and ecological reasons.
- Insufficient funds to construct replacement structures. It is understood that funding to Local Government for timber bridge replacement has been nominally linked to CPI increases at best, at a time when deterioration of these structures is accelerating
- Ongoing need for the assets to remain in safe and usable conditions under increasing design axle loads associated with the higher mass limits. For example, the same TMR bridges with a design load for 16 tonnes trucks in 1925 are load rated for 42.5 tonnes semi-trailers today.
- Until recently no available Australian standard for the design of timber bridges

In 2015 the Institute of Public Works Engineering Australia (IPWEA) identified 474 timber bridges in regional NSW as being in "poor condition" and "representing a high-risk profile for likelihood of failure and high consequences". Refer Table 1.

Table 1

Region	Good	Fair	Poor	Total
North Coast	238	581	309	*1128*
New England	63	108	42	*213*
Hunter	62	76	27	*165*
South East	49	65	21	*135*
South West	22	27	24	*73*
Illawarra	9	38	13	*60*
Orana	1	14	28	*43*
Sydney	2	2	10	*14*
Total	*446*	*911*	*474*	*1831*

It is noted that this report is simply based on a survey of 1831 timber bridges, and does not reflect the total number of Council owned timber bridges in NSW, estimated to be over 3500.

A further study initiated by the Australian Local Government Association (ALGA 2013) noted as follows;

"Bridges link people and jobs, children and schools, patients and hospitals and businesses and markets. Bridges literally bring communities together, yet so many of our regional communities are struggling because of the challenge of maintaining tens of thousands of older bridges. Local Government's own studies have revealed the parlous state of some of our bridges and have highlighted the need for a partnership with other levels of government in dealing with what is a national issue. It's an issue which touches on questions of equality, national productivity and safety."

A specific example is Kyogle Council in northern NSW. Kyogle Council have approximately 200

timber bridges, around 30% of which are rated in "poor" condition. The 2013 Kyogle Council published *Fact Sheet 4 – Bridges* states;

"Council's current funding levels for bridges are $880,000 per year for replacements and $556,000 per year for maintenance. At this level of expenditure, it will take another 58 years to replace the remaining timber bridges. In this time period, many of these will need to have weight limits imposed, or be closed altogether. This could have significant impacts on the local economy and the health and well-being of the affected communities."

2.3 *Need for a new approach*

There is a clear need for a new approach to deal with the large and increasing number of timber trestle bridges in "poor" or "very poor" condition owned by local government. This new approach should include the following;

- Use of the new Bridge Standard, AS 5100.8 which for the first time covers the design and rehabilitation of timber bridges. It is considered that the lack of an Australian Standard for timber bridges has inhibited timber bridge upgrades.
- A better understanding of both the reasons that Australian timber bridges deteriorate and reliable long-term types of repair
- A better understanding of replacement bridge forms available for timber bridges sufficiently deteriorated that repair solutions are not an option. Care is required here. Typical highway bridge structural forms used for bridges on local roads can be very costly, and unwarranted. Conversely there are very low-cost bridge forms in the market which do not comply with the requirements of AS 5100 and are anticipated to require a high level of maintenance in the medium to long term.

To make the required step change a collaborative public-private solution is recommended. These defective bridges represent a "Whole of Government" long-term community safety risk. The reality is timely replacement is simply not provided for in Council, State or Federal Government capital programmes. It is noted that there are examples overseas where this approach has been adopted.

2.4 *Case study: Pennsylvania RBR Project*

The Pennsylvania Rapid Bridge Replacement (RBR) Project is the first multi-asset public-private partnership (PPP) project to be undertaken in the US, using a "bundled" contract approach to replace 558 structurally deficient (SD) bridges across Pennsylvania.

The project is being delivered as a Design-Build-Finance-Operate-Maintain (DBFOM), availability payment, PPP concession, between the Pennsylvania Department of Transportation (PennDOT) and the Plenary Walsh Keystone Partners (PWKP) consortium. The consortium was awarded the contract in October 2014.



Figure 18 Typical replacement bridge in Pennsylvania

The RBR Project will make a substantial contribution to reducing the large backlog of SD bridges in the state. PWKP is managing the financing, design and construction of the replacement bridges and will then be responsible for their maintenance for 25 years after construction. Construction is expected to take approximately four years from commercial close. The project will involve the full demolition and replacement of all 558 replacement bridges, which are primarily single and multi-span bridges on smaller state highways, many located in rural areas. The bridges in the project are of a similar size and design, allowing for prefabrication, mass production, equipment reutilisation and standardisation.

3 DESIGN STANDARDS

3.1 *General*

In April 2017 the new Australian Design Standard for bridges, AS 5100 was released. For the first time, it included a Part for rehabilitation of bridges, and in addition, for the first time included a Part for the design of timber elements on bridges.

AS 5100 was originally developed for the design of new bridges. Although Part 7 of the Standard relates to the strength rating of existing bridges, the previous AS 5100 generally did not refer to the specific applications of design and construction for the repair, rehabilitation, strengthening or widening of existing bridges. Following numerous requests from industry, this has been addressed with the introduction of Part 8, "Rehabilitation and strengthening of existing bridges", which forms part of the new revised AS 5100.

Specifically, Part 8 sets out minimum requirements and procedures to:

- Repair or rehabilitate to restore a structure to its original or intended level of service

– Extend the remaining service life of the structure
– Strengthen to restore capacity due to structural deterioration
– Strengthen to increase capacity for live load (such as in response to a proposed increase in vehicle loads), barrier loading, collision loading, earthquake loading and other loading
– Change the function of a structure (such as a road bridge to a pedestrian/cyclist bridge)
– Widen an existing structure

3.2 *Design specifics*



Figure 19 typical timber bridge

Firstly, the dynamic behavior of timber bridges is very different to steel or concrete structures. This is recognised with a reduction in the dynamic load allowance to be not less than 0.2 (0.25 for timber bridges with SLT decks), compared to a DLA of 0.3 to 0.4 noted in Part 2 of the Standard.

Timber elements in a bridge can vary considerably from design drawings, certainly more than for either steel or concrete structures. This is recognised in the nominated load factors. Refer Table 2, which also provides requirements from Part 2 of the Standard for comparison.

Table 2

Material	Ultimate Limit State	
	Load reduces safety	Load increases safety
Timber	1.4	0.8
Concrete	1.2	0.85
Steel	1.1	0.9

Capacity reduction factors are generally lower than equivalent values for steel or concrete, to reflect the inherent relative variably of timber. In addition, a distinction is made between primary structural elements (whose failure could result in collapse of a significant portion of the structure, such as girders) and secondary structural elements (whose failure would result in a localized collapse, such as stringers and decking). Details are noted in Table 3.

Table 3

	Secondary structural element	Primary structural element
Sawn timber F17 grade or higher	0.85	0.75
Round timber	0.70	0.60

The design capacity of a timber member in bending is also a function of duration of load, size and extent of timber shaving. Timber is a resilient material, can withstand significantly higher loads when applied of a short duration.

Typical reduction factors for member capacity for different loadings are as follows;

– Permanent actions, 0.57
– Serviceability live load, 0.80
– Ultimate design live load (T44), 0.97
– Other ultimate actions (eg braking, log impact), 1.00

Characteristic strength and stiffness properties for common replacement timber elements are designated in Table 4.

Table 4

Stress	Bending	Tension	Shear	Comp'n	E
F27	67	42	5.1	51	18
F22	55	34	4.2	42	16
F17	42	25	3.6	34	14

4 DETERIORATION

4.1 *General*

The main reasons that Australian timber bridges deteriorate are noted below. We have incorporated this into the Design Standard.

4.2 *Splitting due to shrinkage*

Moisture can exist in wood as water or water vapour in the cell cavities and as chemically bound water within the cell walls. As green timber loses moisture to the surrounding atmosphere, a point is reached when the cell cavities no longer contain moisture, but the cell walls are still completely saturated with chemically bound water. This point is called the 'fibre saturation point'. Wood is dimensionally stable while its moisture content remains above the fibre

saturation point, which is typically around 30% for most timbers. Refer Figure 20.

Bridges are normally constructed from green timber which gradually dries below its fibre saturation point until it reaches equilibrium with the surrounding atmosphere. As it does so, the wood shrinks but because it is anisotropic, the maximum shrinkage occurs parallel to the annular rings, about half as much occurs perpendicular to the annular rings.



Figure 20 Splitting due to shrinkage

The relatively large cross section timbers used in bridges lose their moisture through their exterior surfaces so that the interior of the member remains above the fibre saturation point while the outer layers fall below and attempt to shrink. This sets up tensile stresses perpendicular to the grain and when these exceed the tensile strength of the wood, a check or split develops, which deepens as the moisture content continues to drop. As timber dries more rapidly through the ends of the member than through the sides, more serious splitting occurs at the ends. Deep checks provide a convenient site for the start of fungal decay.

Shrinkage also causes splitting where the timber is restrained by a bolted steel plate or other type of fastening. This splitting can be avoided by allowing the timber to shrink freely by using slotted holes. As timber shrinks, it tends to lose contact with steel washers or plates, so the connection is no longer tight. Checking the tightness of nuts in bolted connections is therefore a standard item of routine maintenance for timber bridges.

4.3 *Insect attack (termites and marine borers)*

Australia has a large number of different species of termites which are widely distributed. Most termite damage to timber bridges occurs through subterranean termites which require contact with the soil or some other constant so urce of moisture. Termites live in colonies or nests which may be located below ground in the soil, or above ground in a tree stump, hollowed out bridge member or an earth mound. Attack by subterranean termites originates from the nest, but may spread well above ground level, either inside the wood or via mud walled tubes called galleries which are constructed on the outside of bridge members. These galleries are essential for termites as they require an absence of light, a humid atmosphere and a source of moisture to survive.



Figure 21 Insect attack

An example is shown in Figure 21. Termite attack, once established, usually degrades timber much more quickly than fungi, but termite attack in durable hardwoods normally used in bridge construction is usually associated with some pre-existing fungal decay. This decay accelerates as the termites extend their galleries through the structure, moving fungal spores and moisture about with their bodies. Termites can be controlled either by eradication of the nest (by direct chemical treatment or by separation of the colony from its sustaining moisture) or by installation of chemical and physical barriers to prevent termites from entering a bridge or attacking timber in contact with the ground.

Damage to underwater timber in the sea or tidal inlets is usually caused by marine borers, and is more severe in tropical and sub-tropical waters than in colder waters. They are controlled by reducing the oxygen content. The two main groups of animals involved are:

molluscs (teredinindae) these borers destroy timber at all levels from the mudline to high water level, but the greatest intensity of the attack is just below water level. While only a few small holes may be visible on the surface of the pile, it is possible that the interior of the pile may be completely eaten away.

crustaceans these attack the wood on its surface, making many narrower and shorter tunnels than those made by the teredines. The timber is steadily

eroded from the outside. Attack is generally limited to the tidal zone in water containing at least 1% salinity, but they can survive at lower temperatures than the teredines.

4.4 *Fungal attack (rot)*

Both internal and external decay (commonly known as rot) of timbers used for bridges is often caused by fungi.



Figure 22 Fungal attack

Fungal growths will not develop unless there is a source of infection from which the plants can grow. Fungi procreate by producing vast numbers of microscopic spores which may float through the air for long periods and can be blown for considerable distances. These spores will not germinate and develop unless there is—

- an adequate supply of food (wood cells);
- an adequate supply of air or oxygen (immersion in water inhibits fungal growth);
- a suitable range of temperatures (highest risk between 20°C and 25°C); and
- a continuing supply of moisture (highest risk in unseasoned timber).

Once established, the decay fungi continue to grow at an accelerating rate as long as favourable conditions prevail. Depriving the fungi of any one of these required conditions will effectively curtail the spread of decay. Moisture change can affect decay indirectly because drying often leads to surface checks, which may expose untreated parts of timber or create water traps. The most common rotting areas in timber bridges are internally in log girders, corbels and piles (piping), and in sawn timbers with exposed ends and at interfaces.

4.5 *Weathering*

Weathering is the gradual deterioration of sawn or log timber due to its exposure to sun, wind and rain. Refer Figure 23.



Figure 23 Weathering

Weathering can be a serious problem especially to the exposed end grain of untreated or unprotected wood, where severe rotting can occur around the connections. The exposed ends of transverse deck planks are susceptible to this defect.

4.6 *Fire*

Wood itself does not burn. The effect of heat is firstly to decompose the wood (a process known as 'pyrolysis') and it is some of the products of this decomposition that burn if conditions are suitable. In theory, wood decomposes even at temperatures as low as 20°C (at the rate of 1% per century). At 93°C the wood will become charred in about 5 years.

Large section round timbers, as used in bridge construction, have good resistance to fire, and, except during a severe bush fire, usually survive quite successfully.

5 TYPES OF REPAIR

5.1 *General*

The following presents a number of reliable long-term types of repair. We have incorporated these into the Design Standard. These should be considered before deciding that a bridge replacement is required.

5.2 *Splicing of piles*

While splices can provide a solution to local deterioration of timber piles, splices should not be applied to too many piles in the same structure, especially near ground level. Splicing should be limited to no more than 1 in 4 piles in a group unless a detailed

engineering assessment of the overall substructure is carried out.

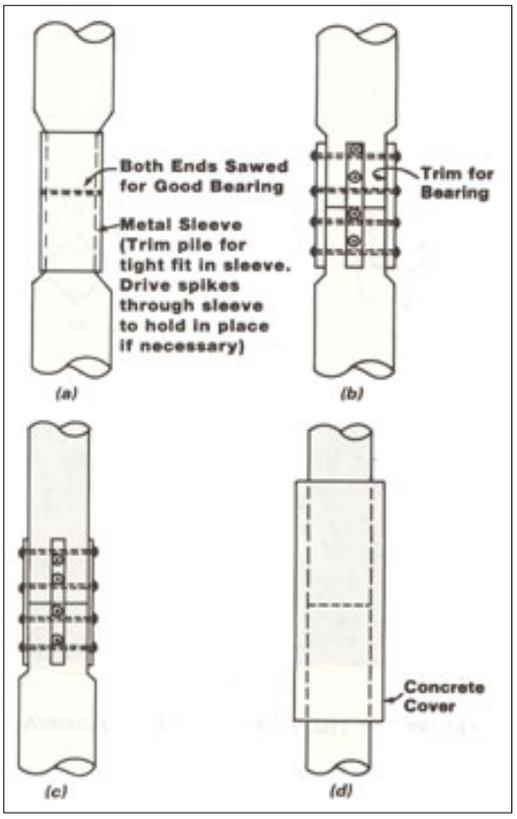


Figure 24 Pile splices

Typically, deterioration of piles occurs at or near ground lev el where both moisture and oxygen are abundant. Without oxygen, the potential for deterioration is low. Splices in piles should be located a minimum of 1.2 m below ground level and ideally below a permanent water table. Splicing will generally be more durable in a low permeability soil than a granular soil.

The interface should be liberally coated with a gel or grease type remedial preservative and wrapped with a geotextile fabric to help contain the treatment, and secured with galvanised steel plates and bolts.

5.3 *Additional girders*

Two additional girders can be installed directly adjacent to a damaged or under-strength member (one on each side). It is important to provide additional girders on both sides so that the correct load distribution between the girders in the span is maintained.

5.4 *Concrete overlay*

Due to uncertainties in long-term composite action between overlays and timber decks, concrete overlays are not considered to contribute to strength or stiffness in the longitudinal direction, and should ignore in strength calculations for the timber girders. However, they improve the transverse distribution of load, and therefore should be modelled in the transverse direction in the grillage model. Concrete overlays are considered structural when assessing the local effects of the transverse timber decking. Refer Figure 25.

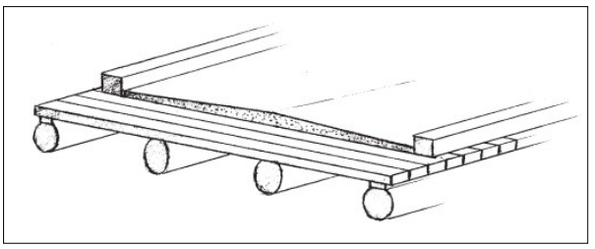


Figure 25 Concrete overlay

Early concrete overlays were designed as thin, flexible running surfaces providing a weatherproof cover to the timber deck. Consequently, many of the overlays carried out in the early 1970s are now failing, having badly cracked due to timber flexibility under traffic loading, and are leaking water. Concrete overlays designed today are thicker and contain more steel reinforcement than the earlier overlays. With increasing guardrail requirements, another important consideration for the concrete overlay is to provide adequate connection for a guardrail appropriate to the current standards

5.5 *Timber concrete composite bridge decks*



Figure 26 Timber concrete composite construction

The timber concrete composite (TCC) system can be used to replace deteriorated timber girder superstructures of spans up to 12 m. refer Figure 15.

These are built in panels with each panel having two round timber girders which are made semi-composite with a concrete deck by steel shear connectors. Generally, the TCC decks do not have a wearing surface applied and the vehicles travel directly on the concrete. These modules should, in effect, be treated as disposable units, as there is little that can be done to repair them once they lose

strength through damage or deterioration. The timber girders cannot be replaced, nor can the shear connection between the components be properly reinstated.

5.6 *Replacement of timber piers*

Typically, deterioration of timber piles occurs at or near ground level where both moisture and oxygen are abundant. It is possible to substantially increase the durability of a timber pier by providing a concrete pile cap below ground level which extends at least 300 mm above ground level, with a timber trestle pier founded on top of the concrete pile cap.

However, the connection between the concrete and the timber at the base of the pier is not able to take substantial bending moments, and so this solution should be limited to those bridges with four or less spans, which are not subjected to high flood or debris loading, and where both abutments have sufficient capacity to take all forces due to braking loads.

5.7 *Stress laminated timber bridge decks*

The stress laminated timber (SLT) system uses 35 to 45 mm thick timber laminates of widths from 140 to 290 mm (and wider where manufactured wood products are utilised). These laminates are oriented on edge (upright) and stressed together using high strength bars or prestressing strands to form a solid structural slab. The SLT decks re quire both a waterproofing system as well as a wearing surface. Since the SLT system provides a strong structural slab, these decks can support any bitumen based wearing surface without cracking.



Figure 27 Installation of an SLT

For spans up to 8 m, the SLT deck system generally represents a reduction in overall dead load as the deck replaces the stringers, decking and sheeting.

5.8 *Replacement of members*

There are two practical methods of strengthening and upgrading existing timber girder bridges and deck systems using the same general design style. The size of the girders can be increased or additional girders added. In most cases, obtaining larger girders is becoming more difficult. Therefore, in a bridge where the existing girders are sound, additional girders should be added between the existing members to strengthen the superstructure. If there is variability in the sizes of the timber girders then a proper engineering evaluation must be performed as the load carried by the girders is related to their stiffness.

All timber components should be ordered by specifying the size, strength grade, seasoning requirements (green, 12 months air dried or kiln dried) and durability class. If unseasoned or air-dried timber is ordered then a larger size must be specified (add 5%) to cover shrinkage of the timber as it seasons with time.

6 CONCLUSIONS

Timber bridges are the most common form of bridge construction in Australia. There is ample evidence that the first timber bridges were constructed by the aborigines. With European settlement, this number increased. It is estimated that there are now over 11,000 timber bridges owned by Local Government. Recent studies have indicated that approximately 30% of these bridges are in a “poor” to “very poor” condition. To make the required step change a collaborative public-private solution is recommended. These defective bridges represent a “Whole of Government” long-term community safety risk. The reality is timely replacement is simply not provided for in Council, State or Federal Government capital programmes.

7 REFERENCES

AS 5100.8 2017, Rehabilitation and strengthening of existing bridges

AS 5100.9 2017, Timber

Australian Local Government Association (ALGA). 2013. Bridges to a stronger future

Balendra, T et al. 2007. Review of condition assessment and retrofitting techniques for timber bridge assets in Australia

Chambers, D et al. 1998. Victoria’s timber bridges. 9th National Conference on Engineering Heritage, Melbourne, Australia

Department of Main Roads, Queensland. 2005. Timber bridge maintenance manual

O'Connor, C. 1985. Spanning two centuries. University of Queensland Press

Roorda, J et al. 2013. National state of the assets. Australian Local Government Association

Smith, E et al. 2010. Load rating of timber bridges in Western Australia

Westcott, C. 2008. Timber bridge heritage. Queensland Roads, Edition No 5

Yttrup, P et al. 1991. The mechanics of timber beam bridges. Austroads Bridge Conference, Melbourne, Australia

Maintenance, Safety, Risk, Management and Life-Cycle Performance of Bridges – Powers, Frangopol, Al-Mahaidi & Caprani (Eds)
© 2018 Taylor & Francis Group, London, ISBN 978-1-138-73045-8

Innovative and sustainable operation and maintenance of bridges

Jens Sandager Jensen
COWI A/S, Kongens Lyngby, Denmark

ABSTRACT: How can learnings from innovative and sustainable operation and maintenance (O&M) of bridges contribute to improved planning for and design of bridges? The present paper will highlight how important it is to consider O&M issues already in the planning and design phase. Durable solutions as well as easy access for inspection, repair and renewal projects together with considerations regarding necessary traffic regulating measures are vital to cost optimal operation. Likewise, asset management systems that are able to provide precise and current performance information are vital to cost optimal operation.

Today's society demands solutions that maximise reliability and availability as well as minimise costs, environmental impacts and the probability of loss of life and limb. To accommodate this it is important both to take into account experience from O&M and the possibilities that comes with application of new technologies.

1 INTRODUCTION

Transportation infrastructure support economic growth and a satisfactory quality of life for the citizens. Optimal technical and economic planning, design, execution and operation of transportation infrastructure, such as bridges, is crucial in order to support these goals.

It is important to consider operation and maintenance (O&M) aspects already in the design phase. Durable solutions as well as easy access for inspection, repair and renewal projects together with considerations regarding necessary traffic regulating measures are vital to cost optimal operation. Today's society demands cost optimal, safe and sustainable solutions. To accommodate this it is important both to take into account experience from O&M of existing bridges and the possibilities that comes with new technologies (Jensen, 2010, Jensen, 2016 and Paulsson et al, 2016).

It is well known that decisions made early in a project has the greatest impact on performance and Life Cycle Costs, see Figure 1.

Planning is important. Such planning may comprise Corrosion Protection Plans (CPP), Building Information Modelling (BIM), O&M-manuals, Structural Health Monitoring Systems (SHMS), Life Cycle Cost (LCC) studies, Operational Risk Analyses (ORA) and Asset Management System. These tasks shall be tailored to the individual bridge or a portfolio of bridges. Naturally, the scope of work varies from small size culverts to major suspension bridges.

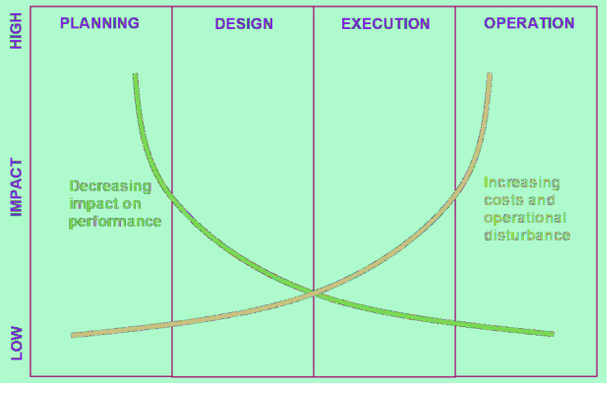


Figure 1. Impact on performance and costs during different project stages (Linneberg et al, 2016).

CPP's comprise corrosion protection strategies that takes into account durability (service life models), access and O&M instructions for the bridge management. Durability shall be ensured through a design with the right material specifications, proper drainage details etc. as well as high quality execution. Furthermore, service life models shall be robust and transparent so that they may be verified during operation and updated in order to reflect current per-

formance. This argument is valid for a great number of components, where hands-on knowledge on long-term performance is a key to successful planning. Asset management systems should be able to provide these long-term performance data in a structured and transparent way. This may also allow for extrapolation of data within a portfolio of bridges.

The principle of Building Information Modelling (BIM) is used in modern asset management systems to manage all stages of new infrastructure projects, i.e. design, construction and operation. Many bridge owners would like to use this technology for existing bridges also. The first step would be to establish a 3-D model of the geometry. Often a combination of scanning and imagery has proved successful. In this way owners move from "dead" data in paper records to "live" and fully digital data based on the principle of BIM, which can be used in asset management.

Major bridges call for bridge specific O&M manuals. They will provide the necessary basis for safe and cost optimal O&M for such a large investment by the society. A lean Structural Health Monitoring System (SHMS) is also a vital component for a major bridge as a mean for obtaining data describing the exposure conditions and performance of the structure.

A systematic identification of Life Cycle Costs facilitates a holistic approach to cost optimal design. Similar to current O&M planning this could include user costs (delays etc.) and possible sustainability indicators.

Finally, application of risk analyses in design as well as during O&M has proven beneficial (Linneberg et al, 2013). In this way, the likelihood or occurrence rate is considered alongside the consequence. One example is bridge-specific Operational Risk Analyses (ORA) that have been performed for many existing major bridges. Often they recommend risk mitigating measures such as fire protection of main cables, improved drainage and strengthening of barriers and railings. ORA's are reviewed and updated on a regular basis, say every 10th year, or when significant accidents occur. Also, risk review, risk assessment and risk management is used when hidden defects in existing bridges are investigated (CIRIA, 2017).

2 CORROSION PROTECTION PLANS

2.1 *Introduction*

CPP's comprise corrosion protection strategies that takes into account durability (service life models), access and O&M instructions for the bridge management. Durability shall be ensured through a design with the right material specifications, proper drainage details etc. as well as high quality execution. Furthermore, service life models shall be robust and transparent so that they may be verified during operation and updated in order to reflect current performance. This argument is valid for a great number of components, where hands-on knowledge on long-term performance is a key to successful planning. Asset management systems should be able to provide these long-term performance data in a structured and transparent way. This may also allow for extrapolation of data within a portfolio of bridges.

2.2 *Outline of a CPP*

The benefit of a bridge design based on a CPP is two-fold. Firstly, for each type of component, the plan provides the required corrosion protection and durability measures to achieve a satisfactory service life with due attention towards varying exposure conditions. The implementation is carried out through adequate design, quality control and assurance incl. control of suppliers and manufacturers and the entire construction work process. For major bridges, a project specific O&M Manual implements the required caretaker principles of operation, inspection and maintenance.

Secondly, through the overall concept of the bridge design, attention is given to limit future operational restrictions and to keep the amount of inspection and maintenance at an appropriate level through a number of durability enhancing features.

The CPP shall demonstrate that the design will achieve the required service life. This includes optimisation of e.g.:

- Drainage
- Concrete cover (and possible use of membranes)
- Concrete mix
- Use of admixtures to reduce cracking (permeability)
- Reinforcement type
- Fibre reinforcement of concrete
- Steel grade (fatigue)
- Steel coating system
- Preparation for cathodic protection

For non-replaceable components the service life is typically in the range of 100-150 years.

For replaceable components easy access for inspection, repair and renewal projects together with considerations regarding necessary traffic regulating measures shall be considered. Cost-benefit analyses / Life Cycle Costs studies may assist economic optimal design of replaceable components. In Denmark typical service lives for bridge components under normal operation has been developed as a joint task between Danish Owners, Consultants and Contractors, see Table 1.

For concrete structures, the CPP shall detail deterioration mechanisms and the strategies that will be used to mitigate the deterioration to ensure that service life requirements are met.

Table 1. Typical service lives for bridge components under normal operation (Håndbog, 2014).

Bridge Component	**Service Life (years)**
1. Asset in general	50-100
2. Wing walls	50-100 10-15 (coating)
3. Slopes	25-50 20-30 (gabion and sheet piling)
4. Abutments	50-100 25-50 (parement) 10-15 (coating)
5. Piers incl. foundations	50-100 25-50 (parement) 10-15 (coating)
6. Bearings	25-50
7. Load carrying superstructure	50-100 10-15 (coating of concrete) 25-40 (hot-dip galvanizing) 15-25 (coating of steel)
8. Waterproofing	30-50
9. Edge beams	30-50 (in-situ cast) 20-40 (prefabricated) 10-15 (joints and coating of concrete)
10. Parapet / railing	30-50 20-40 (hot-dip galvanizing) 10-20 (coating of steel)
11. Bridge surfacing	30-50 (asphalt base layer) 15-25 (asphalt top layer) 15-20 (polymer surfacing) 20-30 (tiles) 10-15 (bitumen joints) approx. 30 (track and sleeper) 15-25 (ballast)
12. Expansion joints	30-50 (general) 50-100 (cast-in parts) 15-25 (sealers) 10-15 (joints)
13. Drainage	20-30 (grating) 10-15 (suspension) 25-50 (pump pit)
Other elements	20-30 (signals, lighting) 25-50 (e.g. stairs, sluice elements)

For reinforced concrete structures, the following deterioration mechanisms are often considered:

- Alkali Aggregate Reaction (AAR)
- Sulphate attack
- Delayed Ettringite Formation (DEF)
- Freeze-thaw
- Carbonation induced corrosion
- Chloride induced corrosion

As seen from the above list, one of the design objectives is to slow the transport of chlorides from the environment through the concrete cover to the reinforcement location. Durability modelling according to Fib Bulletin 34 (Fib, 2006) provides the technical background for analysing depassivation over the target service life in a probabilistic framework. One of the major advantages of probabilistic models is that they are excellent for sensitivity studies as well as for updating based on on-site data, ref. (Engelund et al, 2008).

For steel structures, the objective is to minimise number of joints, avoid fatigue prone details, use dehumidification where beneficial (e.g. suspension cables, box girders), apply state of the art materials (e.g. wear parts in bearings) and specify excellent coating with a long service life. Thus, it is essential to consider operation during design. The design should be able to answer questions such as: how to replace sliding material in bearings (ref. Figure 2), partial or full replacement of expansion joints and does outer steel tower or deck area promote inspection and recoating using robots? It is evident that Inspection and Maintenance (I&M) supported by robots is the future. They may provide accurate data, reduce labour costs, reduce risk exposure of staffing (primarily work environment related) and accelerate execution. Even though this technology develops rapidly, current state-of-the-art has to be considered during design, e.g. unobstructed travelling paths.

The same principles also apply for design of electrical and mechanical (E&M) systems, especially that they shall be easy to inspect, maintain and replace as they have shorter service lives than the bridge structure.

A key part of any major bridge design is also to provide ready access for inspection and maintenance. Providing ready access will significantly reduce long-term costs associated with I&M. Furthermore, access equipment is much cheaper for the Owner if provided during construction than during operation. Often such facilities may be of benefit for both the construction and the operation phase. Access facilities will be used in combination with drones, robots etc., i.e. access facility design has to consider current state-of-the-art in these related areas.



Figure 2. Replacement of sliding material at the Sjaelland-Faroe bridge.

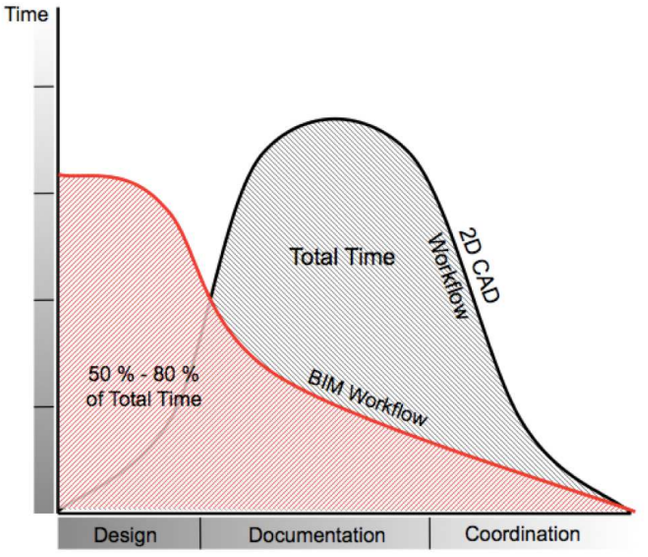


Figure 3. Potential for savings with a BIM workflow.

3 BUILDING INFORMATION MODELLING

3.1 *Introduction*

Building Information Modelling (BIM) is a data-enriched collaborative process that utilises intelligent, object orientated, three-dimensional (3D) parametric models to realise efficiencies throughout the lifecycle of a facility or asset, ref. (McKenna et al, 2016). These years BIM awareness in architecture, engineering and construction sector increases significantly.

The BIM model is used in a workflow where different model characteristics are used for different purposes. The workflow for a standard concrete bridge design may comprise a 3D general model, an analytic model, a Finite Element model, formwork/arrangement drawings, reinforcement drawings and a steel bending schedule.

There is a huge potential for savings when utilizing a BIM workflow, see Figure 3. When owners, architects, engineers and contractors have access to the same model many clashes between the different stakeholders can be handled early in the program/planning and design phase. Also the level of automation releases more time for design, when compared to tradition CAD use, where 2D drawings documented the design in a way, so that the contractor was able to construct the project.

Furthermore, 3D models may be used for generating 3D PDF files that can be used for dynamic verification of constructability etc.

The 3D models may be extended with information related to time (scheduling), costs, as-built documentation and operation. This is sometimes referred to as 4D, 5D, 6D (etc.) BIM models; however, 3D+ models may be the most suitable term.

In COWI, we have developed the 'COWI BIM Wheel', which we use when discussing information exchange with Clients and other project stakeholders, ref. Figure 4. Based on the 'COWI BIM Wheel' we align expectations and tailor the BIM setup to the Client needs and outlook for the future.

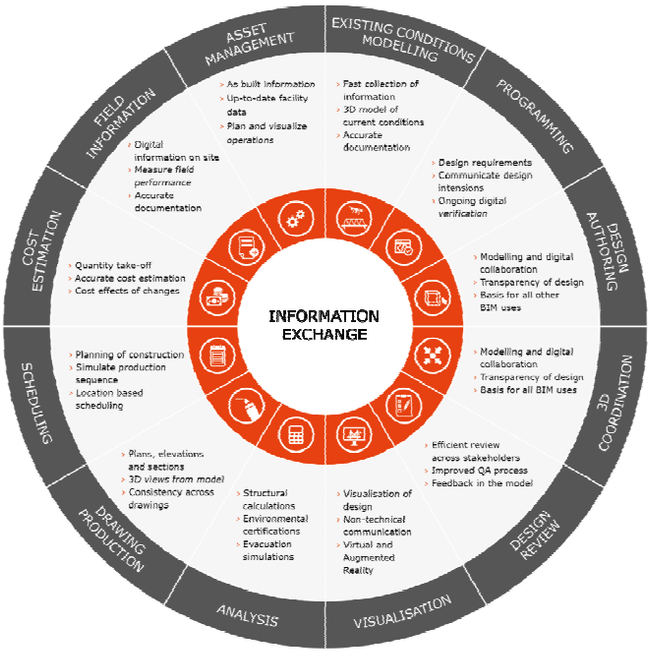


Figure 4. COWI BIM Wheel © COWI A/S.

It isexpected that the next generation of bridge inspector's work using augmented reality glasses in the same way as e.g. Caterpillar is using augmented reality during repairworks. In this way, the bridge inspector may have material descriptions, execution records, previous inspection results, operation and maintenance requirements etc. all relevant for the element right in from of him and displayed on top of the physical reality.

3.2 *Existing bridges*

The principle of Building Information Modelling (BIM) is used in modern asset management systems to manage all stages of new infrastructure projects, i.e. design, construction and operation. Many bridge owners would like to use this technology for existing bridges also. The first step would be to establish a 3-D model of the geometry. Often a combination of scanning and imagery has proved successful. In this way owners move from "dead" data in paper records to "live" and fully digital data based on the principle of BIM, which can be used in asset management.

UAV technology (unmanned aerial vehicle) is one of the possible technical developments that can be used to generate a 3D model of the geometry. Increased stability and control combined with lower prices has resulted in a booming industry within this area. In addition, the mobile industry has pushed the development for sensor and camera technology (thermography etc.); therefore, a more advanced tool package can be carried by UAVs.

COWI has performed a number of UAV inspections on Danish bridges. The first trials where performed to establish a common understanding between bridge inspectors and drone pilots. The bridge inspectors quickly realized the challenge of locating each observation by video, due to the comprehensive size of the structure and the many identical surfaces. Therefore, COWI developed a new easy-to-use, web-based tool "COWI Virtual Inspection" (CVI) where a 3D model can be created based on the images from the UAV inspection. On top of this surface model, images are applied. All data collected are automatically tagged with geographical, axial and time information.

Damage intensity, extend and location should be described during an inspection. The CVI tool has made it easy to locate each visual damage. In Figure 5, a snapshot of the CVI screen is shown for an anchor block. In the CVI model it is possible to mark/highlight defects, write defect specific text, assign condition rating and click anywhere on the structure and get close-up pictures of defect or other information of interest. In Figure 6, a close-up of a drainage pipe is shown. Furthermore, comparison of close-ups of defects taken at different point in time is possible. This provide a powerful tool for performance prediction.

This approach will for large structures reduce the hours spend significantly and reduce the amount of traffic interruption. In the future, it is foreseen that structures can automatically be screened by UAVs, where image recognition software will be able to point out relevant areas, where a hand-near inspection is needed.

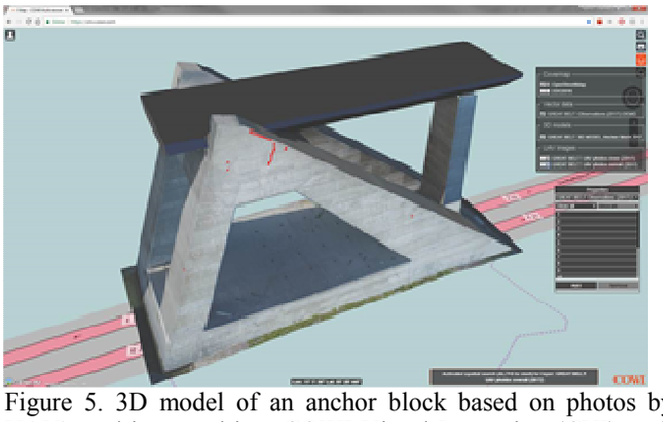


Figure 5. 3D model of an anchor block based on photos by UAV's and imported into COWI Visual Inspection (CVI) tool. Minor defects are highlighted in red color.

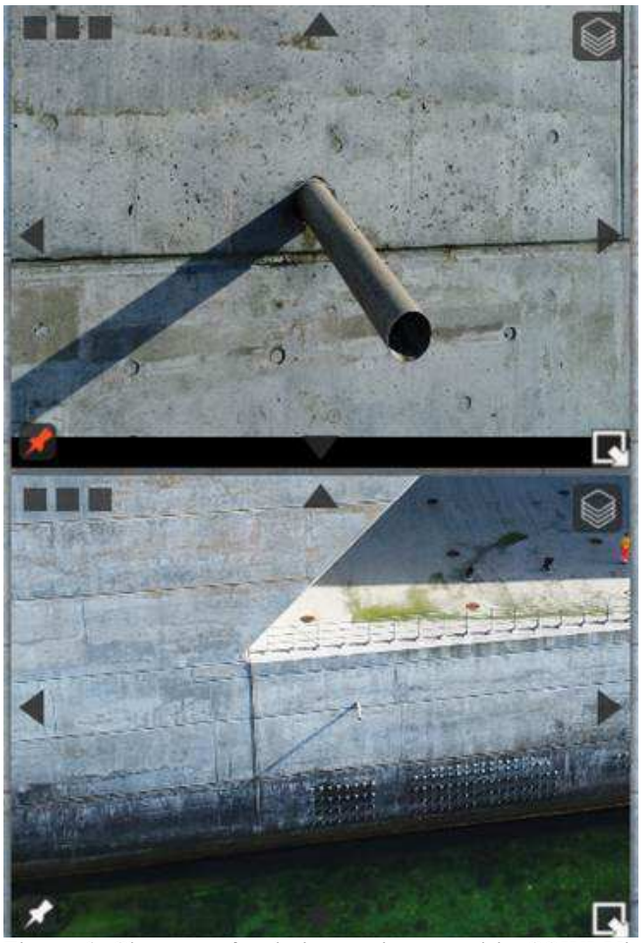


Figure 6. Close-up of a drainage pipe stored in COWI Visual Inspection (CVI) tool.

4 O&M 'MANUALS' FOR MAJOR BRIDGES

4.1 *Introduction*

Major bridges call for bridge specific O&M 'manuals'. The term manuals has been stated within punctuation marks (' '). The reason is that the term manuals should be understood in a very broad way. As reasoned in the previous chapter, O&M of bridges are moving away from paper records into real-time data-driven O&M and possibly into augmented reality, i.e. the term manuals is to be understood as data and structures that allow for supplementing new data.

'Manuals' shall provide the necessary basis for safe and cost optimal O&M for such a large investment by the society. A lean Structural Health Monitoring System (SHMS) is also a vital component for a major bridge as a mean for obtaining data describing the exposure conditions and performance of the structure.

4.2 *Outline of a O&M 'Manual'*

A O&M 'manual' for a major bridge shall be applicable for use in the following ways:

- As a basis for scheduling and planning of O&M
- As a basis for training of inspection and maintenance (I&M) personnel
- As a source for forms, instructions, check-lists and other information
- As a basis for audits according to the quality management system implemented for bridge
- Linking and ensuring consistency with existing rules, instructions and procedures at the local authority

The O&M 'manual' is recommended to comprise the following minimum information:

- Table of content
- Scope
- Description of the bridge
- Operational instructions
- Instructions for principal inspections
- Replacement procedures
- Spare part inventory
- Appendices

The O&M 'Manual' shall be based on as-built information incl. possible birth certificates. Furthermore, the O&M 'Manual' shall be in a format that is easy to update.

5 STRUCTURAL HEALTH MONITORING SYSTEM

A Structural Health Monitoring System (SHMS) is essential for optimising O&M of major bridges. It shall provide input for a safe and cost-efficient bridge management with minimal traffic restrictions or disturbance.

Initial analyses of hazards and deterioration mechanisms map the requirements for the SHMS. From this, on-structure installations and functions of data management and control can be specified in a reliable, easy-to-operate and cost-efficient way. As our industry becomes more and more technical and economic comfortable with large quantities of data (big data), transparency and easy operation become essential characteristics.

By monitoring the actual exposure conditions and performance of the bridge through the SHMS, the bridge manager can compare the data collected against the fundamental design assumptions and make an assessment of the remaining service life and plan inspections if required. The data can also be used to identify areas where mitigation may be necessary before significant deterioration occurs, minimising future maintenance costs and enhancing the bridge's service life.

Bridge SHMS consists in general of 4 important technical elements:

- Sensors placed on the structure. These modules house various sensors, depending on the nature of the structure.
- A data communication system for the transfer of the collected data to a remote computer.
- A database application, which collects, stores and processes the sensor data in real time, providing an evaluation of the condition of the structure based on application areas such as user safety, trouble shooting, natural disaster follow-up and maintenance optimisation.
- Processed data can be used to derive service life models, enabling the bridge owner to decide if structural components shall be replaced or whether the service life of the component can be prolonged. As usual, it shall be highlighted that results are no better than the underlying model and the quality of input.

In Figure 7 shows an example of a simple measurement campaign that is used for re-estimating the remaining fatigue life of an orthotropic steel deck. The campaign was only running for a limited period of time.

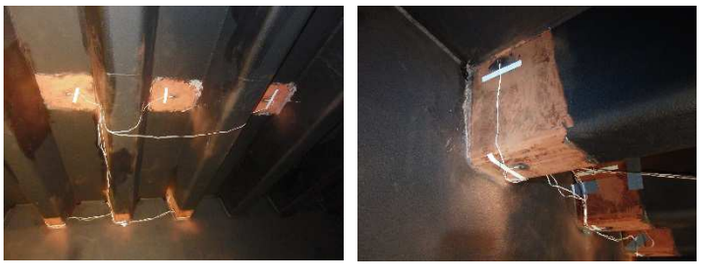


Figure 7. Simple measurement campaign in order to re-estimate remaining fatigue life in an orthotropic steel deck.

6 LIFE CYCLE COSTS

6.1 *Introduction*

A systematic identification of Life Cycle Costs facilitates a holistic approach to cost optimal design. Similar to current O&M planning in some countries this could include user costs (delays etc.) and possible sustainability indicators.

Life Cycle Cost (LCC) studies are performed for nearly all major bridges at some stage of their service life. Such studies are typically based on net present values. LCC studies are considered as part of an overall assessment in parallel with other important issues such as risk assessment, environmental assessment (incl. LCA), traffic impact assessment etc.

LCC may be carried out as part of feasibility studies to find the most cost-efficient solution, as part of detailed design to determine and possible minimize an in-service budget for the owner, as part of the tender to evaluate the most attractive bid proposal, or as part of the operation to evaluate the optimum operation and maintenance strategy. For the latter case, monetization of user costs (e.g. delays) may become the decisive factor.

The society's increasing awareness of whole life environmental impact related to infrastructure is reflected by the fact that some Infrastructural Managers now also request Life Cycle Assessments to assist their decision-making. Two recent research projects reflect this awareness: MAINLINE (MAINtenance, renewaL and Improvement of rail transport iNfrastructure to reduce Economic and environmental impact, EU 7th framework programme) and ETSI (Nordic research project on Life Cycle Cost, Environment and Aesthetics for road bridges). Reference is made to (Linneberg et al, 2014 and Linneberg et al, 2016) on key parameters needed in order to provide reliable and possibly integrated LCC and LCA results. In that reference, it is highlighted that some of these parameters need detailed as well as governmental considerations. Intervention strategies driven by performance profiles, where:

- degradation
- monitoring and examination techniques
- availability of real data
- life extension by refined structural models and/or strengthening
- new construction methods and logistics

may add complexity into the decision making.

A widely used approach for comparing environmental, financial and social impacts is the so-called triple bottom line accounting approach. However, some countries has developed cost equivalents associated with environmental impacts. For instance, Rijkswaterstaat (part of the Dutch Ministry of Infrastructure and Enviroment) has published a list of corresponding shadow prices. With these it is possible to integrate financial and environmental impacts. However, such shadow priced should be country specific and their implementation should be supported by the government. Another approach would be the application of multi-objective optimization models, which is a systematic approach to evaluate multiple conflicting criteria in decision making. Analytical Hierarchy Processes and Multi-Attribute Utility Functions is two approaches that tackled this goal. Both methods has been adopted within infrastructure decision making on network level by e.g. the COST TU1406 action (COST TU1406).

6.2 *Good news for concrete structures*

In order to aid owners, operators and their consultants, a task group under fib (Fédération Internationale Du Béton) has been established to prepare a

state-of-the-art report regarding LCC analyses of concrete assets. The state-of-the-art report will contain a description of existing LCC standards and guidelines, their applicability, the definition of different cost elements, the treatment of uncertain information in a reliability or risk based framework, etc. providing the reader with background information and methodology for preparation of such analysis. Moreover, the report will contain case studies, presenting the applicability of the methodology presented in the report. The state-of-the-art report is due by the end of 2018, ref. (Matos et al, 2017).

6.3 *O&M drivers*

O&M drivers are actions related to elements that consume a major part of the maintenance budget during the bridge service life. Typically, these elements have a high unit price, short service life when compared to the bridge service life and are difficult to maintain or replace.

LCC studies typically confirm that it is cost optimal to specify premium quality for these O&M drivers. For some components, such as surfacing, it is even more evident if LCC estimates consider indirect or society costs such as costs related to traffic interruption (delay due to congestion, speed limitation and/or possible detour).

Components belonging to this category of elements are edge beams, coating, bearings (major bridges), expansion joints (and joints in general) and surfacing (incl. waterproofing). As seen, poor performance of some of these elements are not critical in relations to structural safety.

Identification of O&M drivers is furthermore dependant on the O&M strategy. LCC of a well maintained coating is not the same as LCC of coating that has been allowed to degrade to technical failure. In general, preventive maintenance is superior to corrective maintenance.

Through search criterions, O&M drivers may be obtained from the data gathered in a Bridge Management System (BMS).

6.4 *Tendering*

Low LCC require early planning. One of the important decisions during this planning is the contractual setup. Contracts shall support low LCC, stable budgets, right timing and innovation where appropriate (Simonsson et al, 2016).

When offering design and build contracts functional requirements shall ensure low LCC. Implementation of other constraints in a design and build tender material is not easy or at least it requires a robust evaluation model that favours minimal future O&M costs.

Design, Build, Operate and Maintenance (over a certain period) contracts favours low O&M costs during the period of operation. The contract shall describe robust and transparent requirements (performance thresholds) as well as performance indicators and models that shall document satisfactory performance. Chloride ingress in concrete structures is one example, where extensive description of performance models and thresholds is needed.

When entering a Public-Private-Partnership contract the risk over a certain period is split between the partners. Because of this mutual involvement over a certain period, Public-Private-Partnership often promote low LCC during the contract period as well as during the total life of the bridge.

Functional requirements in a tender document addresses requirements to the performance of components. Most often functional requirements only deal with the initial quality of the component. One of the reason is that supplier warranty has a time limitation that typically covers immediate construction faults that materialize within the first 5 years. A 10% reduction of a stated service life is typically outside such warranties. It is the author's experience that requirements to the initial quality of components may not be sufficient in order to obtain optimal LCC.

Initial performance shall be supplemented with requirements to component performance during the entire service life where possible.

However, functional requirement shall not be a technical barrier in EU-terms, i.e. the Owner cannot specify a certain manufacturer where he has good experience. Functional requirements shall allow more than one supplier to be qualified. As an example, bearings for major bridges are high cost elements, the wear parts (sliding material) have short service lives (especially if dirt enters and result in extensive friction) and their replacement may require closing of the bridge towards traffic. Because of this, one of the functional requirements is improved and documented resistance of the sliding material.

A LCC model as part of the tender evaluation model could supplement functional requirements. Such a model could, on a component level, favour low initial cost, low maintenance costs, low replacement costs, low quantity and/or high service life. The model should match the degree of freedom to the component in question. When considering bearings, maybe the only degree of freedom should be the quantity (supplementing functional requirements), i.e. this will favour bridge types with minimum amount of bearings. As seen, such a degree of freedom has nothing to do with quality.

Only allowing the Contractor to freely estimate LCC associated with his bid does not provide objective information that can be used in a tender evaluation. If it is purely up to the Owner to perform a LCC study of each bid, and rank them according to a simple evaluation model, the evaluation model shall be robust, transparent and part of the tender material. The Swedish Transport Administration has initiated such work (Safi et al, 2015). However, further work

is needed to robustly integrate it with their established procedures.

6.5 *Key parameters*

As defined in ISO 15686-5, the discount rate is used to convert cash flows occurring at different time to a common time to reflect the time value of money (Net Present Value, NPV). ISO 15686-5 suggests using the real discount rate in order to exclude the impact of future inflation in the LCC evaluation.

It is stressed that the discount rate probably has the most significant impact to the final results in a LCC evaluation and hence the selection of a suitable discount rate is crucial for the decision-making. A high discount rate will tend to favour options with low capital cost, short life and high recurring cost; whilst a low discount rate will have the opposite effect.

In many countries, the government regulates discount rates. However, research and development projects also provide guidance, such an example is INNOTRACK that provided guidance in adopting discount rate for European rail projects.

A general constraint is the fact that the public tend to value immediate returns; the concept of optimal design selection based on LCC is, therefore, fundamentally at odds with political systems. This conflict is further detailed in (Corotis, 2009).

The time period studied (also known as analysis period, time horizon or mission time) is the period of time over which LCC is to be evaluated. The length of the analysis period is dependent on the nature of the project. The following are the factors, suggested by INNOTRACK, for consideration when determining the duration of the study period for LCC analysis:

- The time period studied should be at least equivalent to the life-span of a great part of the components, at least one entire life-span of the majority of the replaceable components.
- When comparing alternatives where the majority of the components have different life cycles, the time horizon should be long enough to avoid distortions, at least one cycle of the most long-lasting components.
- Too long a time period will increase the uncertainties and risks on the project appraisal (difficulties to forecast technological scenarios, economy trends and social welfare issues over very long periods).
- The range of values to be adopted for the time period in rail should be in clear consensus with most recent guidelines and practices on the project appraisal standards.
- The definition of any time period studied for comparison of alternatives with very different life span should address homogeneous and consensus criteria to estimate the residual values.

Although INNOTRACK focus on tracks the same arguments are valid for other infrastructure assets.

7 OPERATIONAL RISK ANALYSES

Application of risk analyses in design as well as during O&M has proven beneficial. Application of risk analysis ensure that the likelihood or occurrence rate is considered alongside the consequence. One example is bridge-specific Operational Risk Analyses (ORA) that have been performed for many existing major bridges. Often they recommend risk mitigating measures such as fire protection of main cables, improved drainage and strengthening of barriers and railings. ORA's are reviewed and updated on a regular basis, say every 10th year, or when significant accidents occur.

Another initiative is to develop and maintain a risk log to mitigate risks during the lifetime of a bridge or a portfolio of bridges. It is in the interest of the society to have an overall picture of which hazards influences e.g. traffic safety and maybe even passability.

The purpose of an operational risk analysis is:

- to assess risks related to operation of the bridge
- to compare these to the risk acceptance criteria, and, if these criteria cannot be fulfilled, to propose risk reducing measures

A systematic approach will lead to identification of risks as well as requirements and recommendations on operational measures. A follow up on the risk distribution as well as requirements and recommendations may then be performed at certain intervals.

An example of recommendations for an existing suspension bridge in Sweden was:

- Improved drainage. Open channels should be closed, so that flammable liquid cannot burn in the channel with due consequence for the bridge deck. In addition, drainage capacity should be increased, so that flammable liquids are drained way from the bridge, which decreases the risk associated with a fire from a tank transporter.
- Strengthening of crash barriers. Renewal of crash barriers so that they fulfill current standards,

The above recommendations was implemented in 2016-2017.

Another example of application of an ORA is related to ship impact analysis. If the probability of a critical failure is larger than 10^{-6} per year, an ALARP (As Low As Reasonable Practicable) procedure has to be performed. The procedure consist of identification of risk mitigating measures (reduction of frequency or reduction of loss of lives), review of measure effectiveness, and estimation of mitigation costs. On that basis an acceptable solution may be identified, ref. (Dansk Standard, 2016).

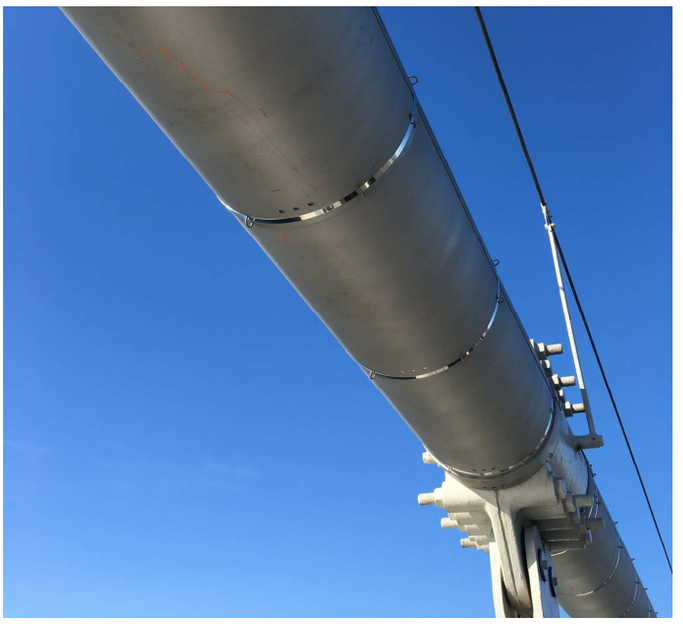
When accidents on major bridges occur, it is relevant to revisit the ORA. When a truck caught fire at the New Little Belt Bridge in Denmark, ref. Figure 8, a protective or risk mitigation measure was suggested.



Figure 8. Fire on the New Little Belt suspension bridge.

In 2017 main cable protection was installed consisting of insulation material and a protective cover, ref Figure 9.

Also, risk review, risk assessment and risk management is used when hidden defects in existing bridges are investigated. Sudden weight restrictions and emergency closures on roadway bridges are often because of hidden defects. Hidden defects are defects that are hidden from sight (inspection within touching distance) or not obvious on first observation. CIRIA has provided a guidance for detection and management of hidden defects in bridges, ref. CIRIA, 2017. The recommended practice consist of a three-step procedure comprising risk review, risk assessment and risk management. As part of the risk-review two key questions has to be asked during review of existing information: What do the records say? and What is not recorded? Also two questions has to be asked on site during inspections: What can I see? and What can I not see?


Figure 9. Protective cover (against fire) installed on the New Little Belt suspension bridge.

The CIRIA guideline provides extensive guidance on identifying key hazards, their consequences, associated deterioration mechanism and their control measures. An example of a somewhat hidden defect is the AAR affected bridge slab (supported by columns), where a cut-though is shown in Figure 10. Clearly, this is a undesirable situation since the bridge has no shear reinforcement.


Figure 10. AAR affected bridge slab (supported by columns) with no shear reinforcement.

8 ASSET MANAGEMENT SYSTEM

Asset management systems should among other things be able to provide long-term performance data in a structured and transparent way. Asset management systems should also allow for extrapolation of data within a portfolio of bridges.

8.1 *Major Bridges*

Major Bridges are often born with a Bridge Management System (BMS) tailored for the bridge in question. This system is the anchor point for data handling. Data may come from:

- SCADA (Supervisory Control And Data Acquisition) system
- Structural Health Monitoring System (sensors, images etc.)
- Building Information Modelling (BIM) system
- Documents
- GIS data
- etc.

Among other things, such a system should be able to provide easy storage and data-retrieval for operation and maintenance of the bridge.

8.2 *Regular bridges and portfolio of bridges*

Quality Control Plans (QPCs) should define at which interval the quality controls are necessary and for which conditions more detailed investigations or interventions are necessary.

In case of regular bridges, performance indicators are established for their components. These indicators can be qualitative or quantitative and they can be obtained during principal inspections, through a visual examination, a non-destructive test or a temporary or permanent monitoring system. Then, obtained indicators are compared with performance goals, in order to evaluate whether the quality control plan is accomplished.

It is verified that there is a large disparity in Europe regarding the way these indicators are quantified and how such goals are specified. Therefore, COST Action TU1406 has brought together, both research and practicing community in order to accelerate the establishment of a European guideline in this subject, ref. (COST TU1406).

The desired quality of the whole bridge can be affected by a single dysfunctional component or by the combination of several dysfunctional components. The decrease in bridge quality clearly depends on the degree of components' dysfunctionality.

However, in order to assure a desired quality with minimum traffic interruptions, bridge owners launch preventative actions when the risk of service impairment, interruption or increase in life cycle costs reaches some predefined level. Implicitly the owners define herewith the accepted risk. This accepted risk depends upon the established performance goals for each component or combination of bridge components.

COST TU1406 has established a procedure, which would allow the bridge owner to define a QCP for each individual bridge. The QCP operates on component and system level (one bridge at a time). The QCP methodology may be implemented in a BMS.

Managing a portfolio of bridges is somewhat different from managing one bridge at a time. For a portfolio of bridges, downstream or network level consequences may become essential. Such consequences may include the importance of the bridge within the network, i.e. maximising network functionality.

8.3 *Some notes on next generation of asset management systems*

In recent years, cognitive analytics and Internet of Things (IoT) has emerged also in bridge management. Cognitive computing is a tool that brings structure in unstructured data (often of huge amounts) in order to find new patterns, relations and interpretations. Cognitive computing has also found its way into the health sector and financial services to name but a few.

9 CONCLUSION

When we design new bridges, it is important that we learn from decades of operation and maintenance of bridges. Likewise, it is important to realise that consideration of operation and maintenance in the planning and design phase has the greatest impact on bridge performance and life cycle costs.

Understanding and prediction of bridge performance during its service life is essential. Agreeing on performance predictive models and how they are verified in a robust and transparent way is important for all stakeholders dealing with operation and maintenance of bridges.

Today's society demands solutions that maximise reliability and availability as well as minimise costs, environmental impacts and the probability of loss of life and limb. To accommodate this it is important both to take into account experience from O&M and the possibilities that comes with new technologies.

New technologies may comprise e.g. probabilistic performance models, operational risk assessment and Building Information Modelling in design of new bridges or established for existing bridges using e.g. photos taken by UAV's (Unmanned Aerial Vehicles). Such photos may be used for establishment of a 3D-model (a digital twin) and mark-up of damage location. These mark-ups are then basis for detailed inspection (within arms-reach), possibly using the benefit of Augmented Reality. The use of UAV's has proven beneficial also for bridge inspection but legislation on the use of UAV's and other robots (over/near the traffic) needs some adjustment with due attention towards the risks associated.

Life Cycle Costs studies are widely adopted within design of major new bridges as well as analysing

different maintenance strategies for existing bridges. Once environmental impacts are capitalized by the government, e.g. in a similar way as detour and waiting time for cars and trucks in done in Denmark, they will become need to know information also for the bridge society. For now we may use the triple bottom line accounting approach, i.e. prepare three different and separate bottom lines: profit (costs), people (social) and planet (environment), ref. (Elkington, 1997). These three bottom lines may be combined using multi-objective optimisation models in order to make a comparison of impacts.

In recent years, cognitive analytics and Internet of Things (IoT) has emerged in the health and financial sectors. We now also see that it has emerged into bridge management. Operated by people with a solid experience within operation and maintenance these new technologies has very interesting perspectives.

10 REFERENCES

CIRIA C764, 2017, Hidden defects in bridges – guidance for detection and management, ISBN 978-0-86017-779-1

Corotis, R., 2009 Societal issues in adopting life-cycle concepts within the political system, *Structures and Infrastructure Engineering*. 2009, **5**(1): 59-65.

COST TU1406, Quality specifications for roadway bridges, standardization at a European level, www.tu1406.eu

Dansk Standard, 2016 Nationalt anneks til Eurocode 1: Last på bygværker - Del 1-7: Generelle laster-Ulykkeslast, DS/EN 1991-1-7DK NA:2013, 2016

Elkington, J., "Cannibals with Forks: the Triple Bottom Line of 21st Century Business", Capstone, 1997

Engelund et al, 2008 Optimization of special inspections of concrete bridges, IABMAS *2008*.

ETSI Project, 2013, Bridge Life Cycle Optimization Stage 3, http://etsi.aalto.fi/Etsi3/PDF/Reports/ETSI_Stage3.pdf

fib, 2006 Fib Bulletin 34, Model Code for Service Life Design, 2006, ISBN: 978-2-88394-074-1

Håndbog, 2014 *Eftersyn af bygværker, Drift, Vejdirektoratet*, 2014 (in Danish)

ISO 15686-5 *Buildings and Constructed Assets Service Life Planning – Life Cycle Costing*, 2008, Geneva, Switzerland

Jensen, J. S., 2010, Cable supported bridges – design, maintenance, rehabilitation, and management, *IABMAS 2010*.

Jensen, J. S., 2016, Trends within Sustainable Bridge Operation and Maintenance, *IABSE 2016*

Linneberg et al, 2013, Optimising inspection and maintenance using risk and reliability. *ICSBOC 2013*

Linneberg et al, 2014 Challenges within Life Cycle Cost (LCC) Studies and Life Cycle Assessment (LCA), *IABMAS 2014*.

Linneberg et al, 2016 Prefabricated vs. in-situ concrete bridges in a whole life perspective, *IABMAS 2016*.

Linneberg et al, 2017 Quality Control Plans for Girder and Frame Bridges, *IABSE 2017*.

MAINLINE, 2013, MAINtenance, renewaL, and Improvement of rail transport iNfrastructure to reduce Economic and environmental impacts, www.mainline-project.eu

McKenna et al, 2016, Bridge information modelling (BrIM) for a listed viaduct, *Bridge Engineering, Vol. 170, Issue BE3*

Matos et al, 2017 Life cycle costs, as a tool for decision making on concrete infrastructure, *fib Symposium 2017*

Paulsson et al, 2016, Results and Experiences from European Research Projects on Railway Bridges, IABSE 2016.

Safi et al, 2015 Cost-Efficient Procurement of Bridge Infrastructure by Incorporating Life-Cycle Cost Analysis with Bridge Management Systems, *Journal of Bridge Engineering, 2015, 20(6)*

Simonsson et al, 2016 Bridge performance and tendering based on Life Cycle Costs, IABSE 2016.

Maintenance, Safety, Risk, Management and Life-Cycle Performance of Bridges – Powers, Frangopol, Al-Mahaidi & Caprani (Eds)
© 2018 Taylor & Francis Group, London, ISBN 978-1-138-73045-8

Long Term Bridge Performance Program Status and Preliminary Results

Bruce V. Johnson
Oregon Department of Transportation, Salem, Oregon, USA

Jeffrey E. Purdy
Pennoni Associates Inc., Philadelphia, Pennsylvania, USA

Daniel Haotian Liu
Center for Advanced Infrastructure & Transportation, Rutgers University, Piscataway, New Jersey, USA

ABSTRACT: The United States Department of Transportation, Federal Highway Administration's Long-Term Bridge Performance (LTBP) Program is a 20-year minimum research program that will produce a comprehensive database on bridge condition and performance based on data collected from over 1,000 bridges assembled in 14 data collection clusters and 10 national highway corridors. The systematic research approach of the Program includes a development phase which provided guidance and tools for the operational or data collection phase. Key to the program is the LTBP Bridge Portal which is a web-enabled interface to the database being developed. To provide cost-effective and efficient data collection, the LTBP Program developed innovative data collection and analysis technologies; specifically the RABIT™ was an early product of the Program enabling bridge evaluation and research quality data collection while reducing time on the bridge. Data collected using RABIT™ and other nondestructive (NDE) test results are used to enhance bridge performance knowledge and to develop more accurate bridge element deterioration models. The LTBP Program will include a variety of research projects to address the influence of a multitude of factors on bridge performance such as vehicular live loads and other environmental factors. The products from this program will be data-driven tools, including predictive and forecasting models, which will enhance the abilities of bridge owners to optimize their management of bridges. Concrete bridge deck performance was identified as one of the key bridge performance issues in the LTBP Program. The overall objective of the LTBP Program is to inspect, evaluate, and periodically monitor representative samples of bridges nationwide to collect, document, maintain, and manage high-quality quantitative performance data over an extended period of time by taking advantage of sensing and nondestructive evaluation (NDE) tools and technologies such as impact echo (IE), ground penetrating radar (GPR), half-cell potential (HCP), ultrasonic surface waves (USW), and electrical resistivity (ER). This paper presents the condition change of a bridge deck in Virginia over a 6 year period. The assessment covered corrosive environment and corrosion processes, concrete degradation, and deck delamination. Deterioration progression from periodic NDE surveys is illustrated qualitatively by condition maps and quantitatively by condition assessment numbers. The results demonstrate the ability of NDE technologies to capture and quantify progression of deterioration. Strong agreement between different NDE technology results improves the confidence level of the condition assessment of the deck. The LTBP has the capability for establishing a direct relationship between data-driven condition measures in the form of NDE test results and bridge performance. The Program is striving to do this first for bridge decks and then will address steel and concrete superstructures, substructures and foundations. Along with detailed inspections and NDE tests, the program is assessing the influence of truck weights and overall bridge stiffness on bridge performance. While definitive conclusions will not be available for several years, preliminary benefits of the program include a web-based data storage application, hundreds of protocols for systematic data collection and testing, and systematic collection and cataloging of reference bridge plans, preservation actions, costs, and historical design standards. This program presents a unique opportunity to collaborate with other similar efforts to leverage other research that is focused on understanding how various factors influence bridge performance.

1 INRODUCTION

1.1 *Program Background*

The Long-Term Bridge Performance (LTBP) Program is a 20-year (minimum) research effort to collect scientific performance field data from a representative sample of bridges nationwide that will help the bridge community better understand bridge deterioration and performance. The products from this program will be a collection of data-driven tools, including predictive and forecasting models, which will enhance the abilities of bridge owners to optimize their management of bridges.

The program was created by legislation as the Safe, Accountable, Flexible, and Efficient Transportation Equity Act: A Legacy for Users (SAFETEA-LU) for surface transportation, and was enacted by the United States Congress in 2005.

Aging and deterioration of bridges in the United States (USA) mandates developing efficient strategies for bridge maintenance, rehabilitation, and repair. Bridge decks deteriorate faster than all other bridge components because of the routine application of deicing salts, repeated freeze-thaw cycles, direct application of traffic loading, and other damaging effects. Concrete bridge deck performance was identified as one of the key bridge performance issues in the FHWA's Long Term Bridge Performance (LTBP) Program (Brown, 2014). To improve the understanding of the mechanisms and timing of bridge deck deterioration because of the effects of age, material types, traffic loading, and climatic conditions, high quality performance data should be collected over an extended period of time, and condition assessment should be conducted periodically.

Given the large, diverse population of bridges throughout the USA, one of the most significant challenges to the LTBP Program was selecting representative bridges. The sampling challenge was mitigated by selecting “reference bridges” and representative clusters of bridges in the same vicinity of the “reference bridges” that have similar characteristics (age, type, climate, and maintenance practices). This selection helps compare the performance of concrete bridge decks of a similar type geographical area but, for instance, carry different traffic loads to ascertain the influence of traffic load on deck performance.

The common practices of State transportation departments for condition assessment and monitoring of concrete bridge decks have been visual inspection, sounding methods, and destructive methods. While visual inspection and sounding methods have their merits, they are limited when used for the early detection and characterization of defects. Similarly, while destructive testing usually provides reliable assessment of the structure, the time and effort needed make this type of test impractical. As a result, the need emerged for nondestructive evaluation (NDE) technologies that can qualitatively and quantitatively assess the condition of concrete decks. The qualitative nature of NDE data helps capture deterioration progression, and its quantitative nature assists in developing more reliable deterioration, predictive, and life cycle cost models. Since concrete decks are affected by various deterioration processes, multiple NDE technologies should be used for condition assessment. The commonly used NDE technologies to assess and monitor the condition of bridge decks include impact echo (IE), ground penetrating radar (GPR), half-cell potential (HCP), ultrasonic surface waves (USW), and electrical resistivity (ER). In addition to providing comprehensive information about the deck condition, combining the results of different NDE technologies increases the confidence level of detection.

1.2 *Vision*

The LTBP Program will serve as the national platform for strategic long-term investigation of in-service bridge performance.

1.3 *Mission*

Foster improved bridge performance, health, stewardship, and management through the analysis of research-quality data collected over a minimum of 20-year period on a large representative sample of U.S. highway bridges. To achieve this, the Program is designed to:

- Improve knowledge of bridge performance.
- Advance research in deterioration and predictive models.
- Apply life-cycle cost analysis effectively.
- Improve inspection/condition information through nondestructive evaluation (NDE) and structural health monitoring (SHM).
- Further the advancement of technology used for the assessment of critical but hidden bridge elements and components.
- Support development of improved bridge design methods and maintenance/preservation practices.
- Quantify the effectiveness of various maintenance, repair, and rehabilitation strategies.
- Improve the operational performance of bridges with the potential to reduce congestion, delay, and accidents.
- Promote the next generation of bridge management systems.

1.4 *The Meaning of Bridge Performance*

One simple definition of performance is that performance equates to accomplishment of a specified purpose or set of purposes. For the purposes of the LTBP Program, the following definition is used: Bridge performance encompasses how bridges function and behave under the complex and interrelated factors they are subjected to day in and day out—traffic volumes, loads, deicing chemicals, freeze-thaw cycles, rains, or high winds. Bridge design, construction, materials, age, and maintenance history also play roles in performance. Performance is usually associated with some set of standards, whether absolute or relative, and performance can be measured against those standards. In baseball, for example, one purpose of a batter is to hit safely, and a measure of the batter's performance is the batting average—the number of hits divided by the number of at-bats. A batter hitting over 0.300 is considered to be performing very well.

The purpose of a bridge is inherent in the NBIS definition: to carry vehicular traffic or other moving loads over a depression or obstruction such as water, highway, or railroad.

Transportation users expect a given bridge to accomplish its purpose in a satisfactory manner as measured against several objectives. Bridges should do the following:

- Present a minimal safety hazard to users during normal service.
- Present minimal obstruction to the free flow of traffic at all times.
- Have a minimal negative impact on the local and global environments.
- Present an acceptable level of risk against catastrophic failure.
- Present an aesthetically pleasing appearance.
- Accomplish all of the preceding elements with minimal life-cycle costs.

As a performance indicator for a baseball batter, batting average is a simple index with a range of 0.000–1.000. The batting average is a useful measure, but it does not reflect the value of the batter to the baseball team in a complete manner. Other related factors are also important, including hits with runners in scoring position; number of bases reached via singles, doubles, triples, and home runs; percentage of times reaching base safely; or even the outcome of at-bats in which the batter does not hit safely. In the same manner, the overall performance of a bridge cannot be described by any one rating, index value, or other individual parameter.

The differences in batters' levels of performance are analogous to the differences in bridges' levels of performance. Imagine bridge A is located in an arid (dry, no-freeze) climate and bridge B is located in a northern (wet, freeze) climate. The bridges are steel multi-girder simple span bridges that were built in the same year. The girders on bridge A are rated 8 on the NBI scale, nearly new condition. The girders on bridge B are rated 4, for poor condition with advanced section loss and deterioration. In comparing the relative performance of each bridge, factors such as annual snowfall, amount of deicing salts applied, and condition of the joints must be considered. Also of importance are the type and frequency of preservation treatments applied to the bridge (e.g., sealing joints, washing the superstructure, etc.). Continuing the analogy, baseball factors such as hits with runners in scoring position could be the equivalent of traffic and heavy trucks carried on the bridges.

There are many different ways to measure bridge performance. Some of these measures are in the form of an index value calculated from a defined formula using input data such as NBI condition ratings and traffic volumes. Numerical indices such as the Federal Sufficiency Rating (SR), California Bridge Health Index and Finnish National Road Administration (Finnra) Repair Index have been used for quite some time to define bridge performance. (FHWA, 2005, Sheppard & Johnson, 1999) For example, SR is an index calculated from an established formula and has a range of 100 (representing an entirely sufficient bridge) to 0 (representing an entirely insufficient or deficient bridge). An SR value of less than 50 indicates a low level of performance but does not reveal the specific characteristics of the bridge that render it deficient.

Other measures are based on whether or not a bridge meets some defined criteria. These include classification as Structurally Deficient (SD) or Functionally Obsolete (FO) and whether a bridge meets or exceeds defined deflection limits. Still other measures reflect a level of operational capacity or service, including posted load, load rating, rideability of the bridge wearing surface, traffic congestion near or on the bridge, number of accidents on the bridge, and percentage of rain events and floods that overtop the bridge. Most of these measures can be applied to an individual bridge or to a population of bridges, such as bridges on the NHS or bridges of a certain type and material.

Each measure has value depending on the person using the measures and the purpose for using it. For example, commercial interests, shippers, and drivers can use simple measures of posted weight limits or geometrical dimension limitations to weigh performance in terms of durability, operational capacity, and roadway safety, all important factors in supporting a free flow of goods and services. These measures do

not readily support a better understanding of bridge performance because it is difficult to correlate changes in these measures with underlying causes of changes in performance. Additional work is needed to better understand and develop solutions to improve bridge performance.

Experience has shown that the performance of any specific bridge is dependent on complex interactions of multiple factors, many of which are closely linked, including the following:

- The original design parameters and specifications such as bridge type, materials of construction, geometry, and load capacity.
- The initial quality of materials and of the as-built construction.
- The varying environmental conditions of climate, air quality, and surrounding soil.
- The extent and severity of corrosion or other deterioration processes that affect component strength or structural behavior (e.g., bearings locked up due to corrosion products).
- The traffic volumes and frequency and the weight of truck traffic carried by the structure.
- The type, timing, and effectiveness of preventive maintenance, minor and major rehabilitation actions, and ultimately, replacement actions.

All of these factors combine to affect the condition and operational capacities of the bridge and its structural elements at any given point in the life of the bridge. While simple measures such as those described in this chapter are currently used to evaluate overall performance, a better performance measure would be an indicator of the qualitative or quantitative impact of a parameter or set of parameters on some specific aspect of bridge performance.

Because bridge performance is a complex issue, it is useful to organize the primary issues relating to bridge performance into general categories. As shown in Figure 1, the primary issues in bridge performance can be divided into four general categories: structural condition (for durability and serviceability), functionality (safety and traffic capacity), structural integrity and risk (for safety and stability), and costs to the user and to the agency.

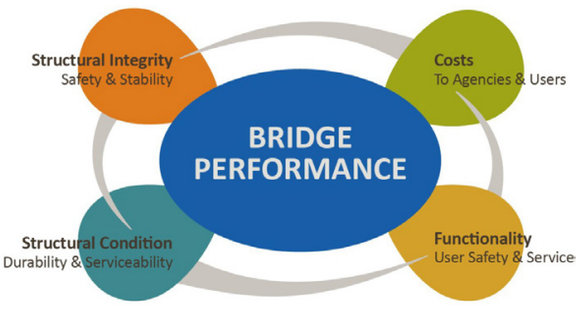


Figure 1. Main Categories of Bridge Performance Issues

Many relevant factors combine to affect performance under each of these four main categories. The LTBP Program will focus on the relevant factors related to structural condition listed in Table 1. Within this category are many specific performance issues that could be studied over the long term to achieve better understanding. For each of these specific performance issues, there are multiple data items that may be gathered to evaluate performance.

Table 1. Performance Issues for Structural Condition

Category	Important Data or Factor
Structural condition—durability and serviceability	Structure type
	Structural materials and specifications
	Structure age
	As-built material qualities/conditions
	As-built const. qualities/conditions
	Truck loads and other live loads
	Environment—climate, air quality, and marine atmosphere
	Snow and ice removal operations
	Type, timing, and effectiveness of preventive maintenance
	Type, timing, and effectiveness of maintenance and rehabilitation
	Flooding, hydraulic design, and scour
	Subsurface soils and settlement

2 SYSTEMATIC APPROACH

2.1 *Designing the Experiment*

The work included in this step provides the detailed framework for each experimental study that will address one of the high-priority bridge performance issues. The thought process behind each study also provides input into the final stage of step 2 (adopting and developing specific data protocols for each of the chosen data collection methodologies). Once each specific study is designed, the final approach to data collection on the critical parameters can be revised as necessary. The revision might mean eliminating or adding parameters to fine-tune the data collection protocols and/or modify the testing frequencies.

A well-designed experimental program is the key to collecting data that will support a better understanding of bridge performance. The design begins with postulating the critical questions about what governs the performance issue being studied. For example, when considering bridge decks that are untreated (that

is, have not been overlaid with a wearing course or treated with a sealing compound), critical questions might include the following:

1. What is the current condition of the deck concrete?
2. What is its permeability?
3. What is the rate of deicer application on the deck?
4. What is the existing chloride profile in the deck?
5. What is the rate of corrosion, if any, on the reinforcing steel?
6. What are the annual climate fluctuations in the vicinity of the bridge?
7. What is the truck load history that this deck has been exposed to?

In addition to current values, how will the value of these parameters or measurements change over time? A proper experimental study can be developed only after such questions are addressed.

Each experimental study will be developed to assess the relationships of one or more of these critical issues to some aspect of the performance of the deck. For example, studying annual climate fluctuations might elicit data that suggest a significant relationship between freeze-thaw cycles and a measured level of scaling of the surface of a concrete deck.

Each study's parameters will include types of testing to be done and the instrumentation and sensors to be deployed. For example, answering the question about the condition of concrete decks might require a field survey of a deck using the conventional chain drag method (chain dragged across deteriorated concrete makes a hollow sound) or mapping cracks visible on the surface or taking advantage of technology such as ground penetrating radar (high-frequency electromagnetic waves detect cracks, voids, and delamination).

The LTBP researchers also will develop data collection protocols, such as standard test methods, frequency of testing, and duration of the study. Finally, the researchers will select a representative sample of bridges for the study.

2.2 *Pilot Study*

The LTBP Program adopted a systematic approach including a developmental phase and an operational phase. A pilot study in the developmental phase was a key part of implementing Federal Highway Administration's (FHWA) Long-Term Bridge Performance (LTBP) Program. This study involved the detailed inspection and testing of bridges representative of the most common superstructure types, physical bridge layouts, and environmental conditions likely to be considered within the program. The seven bridges selected for the pilot phase are located in California, Florida, Minnesota, New Jersey, New York, Utah, and Virginia (Fig. 2). These different bridges provided a platform for the LTBP Program research team to test data collection protocols in a variety of settings that may pose technical or logistical challenges, such as the presence of an overlay on the deck, high traffic volumes on and/or under the bridge, or a waterway under the bridge.



Figure 2. Seven Bridge Pilot Program

2.3 *Development Phase*

The backbone of the LTBP Program is a data management system. The LTBP Bridge Portal, currently available via FHWA's website and continually undergoing enhancement serves as the data management system for the Program (Fig. 3). The portal currently includes readily available data sources such as historical National Bridge Inventory (NBI) data, augmented with National Bridge Element (NBE) level data as it becomes available, as well as data collected from field efforts, legacy data mining, weather data, as well as cost and maintenance data as these become available. The LTBP Bridge Portal provides visualization of data through a Geographic Information System (GIS) interface with robust searching and filtering capabilities as well as tools for data analytics. Eventually the portal will incorporate data-driven tools for the analysis of both raw data and processed data developed throughout the program's duration.

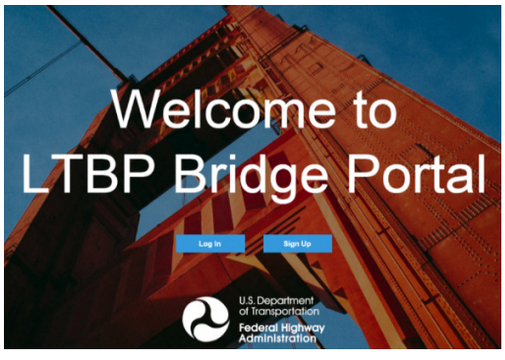


Figure 3. Bridge Portal

Following the pilot study, a legacy data mining data collection approach was developed. Legacy data mining is the collection of bridge documentation (design plans, specifications, standards, and more) and extraction of data and information that is relevant to the determination of bridge performance and condition. The bridges in this sample were selected to provide context, assess variability, and ensure that the bridges selected for field data collection are representative.

Legacy data mining is nationwide, covers 965 bridges, with 445 bridges complete with statistical analysis. For each bridge between 684 to 707 data elements are collected depending on the type of bridge. These data elements are statistically analyzed leading to the selection of bridges for field data collection in the operational phase of the program.

The developmental phase is complete and produced the following:

- LTBP Bridge Performance Primer Report (FHWA-HRT-13-051, LTBP Bridge Performance Primer).
- High Priority issues were identified with input from State transportation departments include untreated and treated decks, bearings, joints, prestressing steel strands, and steel beam coatings.
- Legacy data mining initiated using existing data sources.
- Bridge portal developed and FHWA LTBP Program External SharePoint site established.
- 51 data collection protocols published and distributed to LTBP Program contractors and State Coordinators for use and dissemination. (FHWA-HRT-16-007, Long-Term Bridge Performance (LTBP) Program Protocols, Version 1).
- 170 additional data collection protocols in development and under peer review.
- Strategic and Operational Research Matrices were developed.

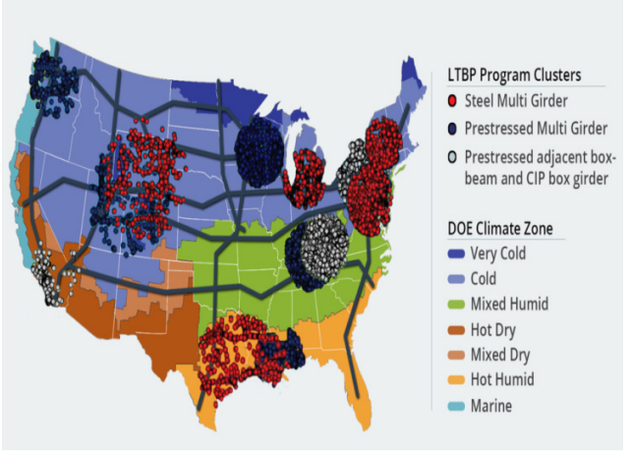


Figure 4. LTBP Program

2.3 *Operational Phase*

The operational phase of the program is on-going and will be ramping up in the near future. A structured approach has been established that groups bridges of similar characteristics (design and environmental exposure) into 14 clusters and nine corridors (Fig. 4). Cluster bridges are selected to allow the investigation of various inputs and attribute influences on pe rformance.

Bridge performance is measured (data collection) and tracked through targeted use of technology and enhanced visual inspection procedures.

Three rounds of data have been collected on 24 Mid-Atlantic cluster bridges with data collected in 2013, 2015 and 2017. Data collection, guided by the data collection protocols, has been achieved through visual inspection, material testing, nondestructive evaluation technology, and modal testing.

It is evident from the data collection effort that development and implementation of new technologies is warranted to achieve the required data quality on a cost-effective basis. Maintaining data quality over time requires that the data collection effort is reliable and repeatable, while minimizing disruption to travelers caused by traffic control while providing safety to the public and to the data collection teams.

To achieve the quality of data needed and to reduce cost and disruption to traffic, the LTBP program is developing new technologies. To date, a Robotic Assisted Bridge Assessment Tool or RABIT™ has been developed. This technology, first developed as a prototype (Fig. 5) has demonstrated its effectiveness in providing multiple NDE technologies mounted on a single platform to assess the condition of bridge decks.



Figure 5. RABIT™ Prototype

Based on the performance of the prototype version of RABIT™, the program has invested in the development of four additional RABIT™s that improve on the prototype design with more reliable performance and improved software. This technology assesses bridge condition while the bridge remains open to traffic using lane closures only. Prior NDE data collection efforts would require complete bridge closure.

Currently, the Program is evaluating a modal testing technology (Fig. 6) that produces calibrated finite element models and analysis of modal performance of bridges. This technology allows for the identification and quantification of load distribution on a bridge through finite element analysis. The testing of a bridge span is performed in approximately 30 minutes and like RABIT™ required only lane closures. Traditional modal testing procedures require closures and over 8 hours of data collection setup, collection and tear down.



Figure 6. Automated Modal Testing

2.4 *Deterioration Modeling*

Initial deterioration model development has employed three sets of deck condition data collected on the Virginia Pilot Bridge using manual NDE technique and RABIT™. 2-D contour maps of deck condition determined using Impact Echo, Electro-Resistivity, and other NDE technologies have been instrumental in the development of an initial bridge deck deterioration model.

The modeling effort is now expanding to utilize bridge element condition data provided by the Oregon Department of Transportation from 2009 to today, complementing the research conducted on the Virginia Pilot Bridge. California, New Jersey, New Hampshire, and Massachusetts Departments of Transportation are also providing bridge element condition data for deterioration model development. Exponential- and Weibull-based deterioration curves are being tested with variables for average daily truck traffic (ADTT), structure age, skew, deck structure type, deck protection and others to determine deck condition today, matching field data collection and projecting into the future.

2.5 *The Influence of Vehicular Live Loads on Bridge Performance*

A pooled fund study of the influence of vehicular live loads on bridge performance is underway and combines resources from seven states with LTBP program funds with the goals to:

- Develop a National Bridge Traffic Database
- Determine and quantify influence of trucks on bridge component performance

There are two fundamental questions that the research program is addressing:

- What are the current truck loads on our nation's bridges?
- What are the impacts of increased truck loads on the durability of the nation's bridges?

There have been changes in truck geometry, axle configurations, suspension, and tire characteristics. Common loaded truck weights are stipulated to have increased in some cases from 32,660 kg (72 kips) (design truck) to more than 49,900 kg (110 kips). (FHWA, 2016)

The research study is beginning by instrumenting a bridge in Oregon to evaluate both bridge response to environment (primarily temperature) and to truck live load. The instrumentation system is collecting data on bridge response for every foot of travel by a truck over the bridge requiring data to be collected at 150 Hz. A weigh-in-motion system is being placed 200 ft. upstream of the bridge with a video camera to capture single and multi-presence of trucks and individual truck gross vehicle weight, axle weight and axle spacing.

By knowing both environmental response and live load response, researchers will be able to identify which bridge elements are especially affected by truck loads.

By answering these two questions, bridge deterioration models attributed to truck loads are being developed to assist bridge owners in developing bridge maintenance, preservation, and rehabilitation strategies.

2.6 *Collaboration and Outreach*

Critical to the success of the Program is the partnerships and collaboration that occurs between State Departments of Transportation, researchers and academia (universities and the Transportation Research Board) and industry. Collaboration occurs through a variety of methods inclusive of in-person and virtual meetings of the State Coordinators and Special Activities Committee of the Transportation Research Board (TRB) to provide technical guidance to the Program, the TRB Long-Term Infrastructure Performance Committee to provide programmatic guidance to the Program and through Technical Advisory Committees and Expert Panels that address specific technical program content at a grass roots level. Attendance and presentation of progress by FHWA representatives at technical committee meetings of the American Association of State Highway and Transportation Officials (AASHTO) provide a forum for industry collaboration and guidance.

Each of these collaborative initiatives keeps the Program focused on its vision, goals, and objectives and assures that the products of the research program are relevant to the needs of bridge owners.

3 DATA DRIVEN, REPEATABLE CONDITION ASSESSMENT USING NON-DESTRUCTIVE EVALUATIOM (NDE)

3.1 *Example Data Collection Effort for Bridge Decks*

This section of the paper demonstrates the ability of NDE technologies to monitor deck performance and capture deterioration progression with time.

3.2 *Description of the Bridge*

This study was performed on a bridge carrying southbound U.S. Route 15 over Interstate 66 (I-66) in Haymarket, Virginia. The bridge (structure number 14178) is 84.1 m (276 ft.) long and 12.8 m (42 ft.) wide and was built in 1979. The bridge is a two-span, six-girder steel built-up superstructure (Figure 6) with a bare, cast-in-place 200 mm (8 in.) thick reinforced concrete deck constructed with removable forms. The southbound carries two lanes of traffic.

The deck condition (including corrosion, deterioration, delamination, and concrete degradation condition maps) of the deck has been monitored four times since 2009, most recently in May 2015 (in years 2009, 2011, 2014 and 2015). The NDE results from the periodic surveys will be used to better understand deck performance and monitor deck deterioration progression with time.



Figure 7. (top) Side view of the bridge and (bottom) the deck surface of the southbound U.S. Route 15 bridge, Haymarket, VA.

All the NDE measurements were collected on a 0.6 m by 0.6 m (2 ft. by 2 ft.) grid, except for the GPR surveys which were conducted in the longitudinal direction of the bridge with survey lines 0.6 m (2 ft.) apart. It took two 5-hour (total 10 hours) lane closures to survey the deck. In other words, considering that the surveyed deck area was about1020 m^2 (11000 ft^2), the surveys were conducted at production rates of about 102 m^2 (1100 ft^2) per hour. A section of the deck surface with clearly visible patches and spalling is shown in Figure 7.

3.3 *NDE Technologies Description and Results*

3.3.1 *Electrical Resistivity (ER)*

The electrical resistivity of concrete decreases as the moisture and chloride concentration increases (Whiting & Nagi, 2003). It has been observed that a resistivity of less than 5 kOhm-cm supports very rapid rebar corrosion (Brown, 1980). A four-point Wenner probe is used for resistivity measurements (Fig. 8).

The assessment of the corrosion progression is illustrated in Figure 9. The ER maps in Figure 9 describe concrete resistivity in kOhm-cm. The threshold for corrosive environment was identified to be 30 kOhm-cm based on correlations with other NDE methods. It can be clearly observed qualitatively that ER captured corrosion progression during the 6 year period. Expansion of corrosion affected areas and increase of severity of corrosive environment in 2015 occurs in the same areas identified as corrosive in 2009.



Figure 8. Electrical resistivity survey

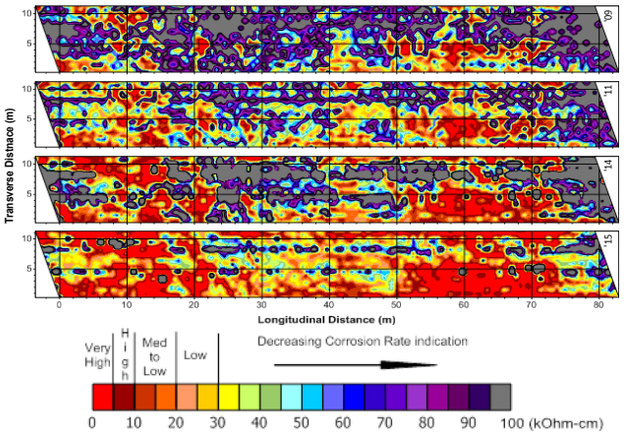


Figure 9. Corrosion assessment maps from ER surveys conducted on the bridge deck from 2009 (top) to 2015 (bottom).

Since the data obtained from NDE technologies are quantitative, they can be used to assess the condition of decks quantitatively and compute a condition assessment number. The condition assessment number combines the effect of the extent and severity of deterioration obtained from the NDE surveys. The NDE measurements and the calculated condition assessment numbers, which vary from 100 for the best condition to 0 for the worst, could be entered to the bridge management systems to assist bridge owners in data-driven decision making regarding maintenance, rehabilitation, or replacement of the deck. The condition assessment number of each type of defect is calculated as a weighted average of percentages of the deck area, with different severity levels of that specific defect. The area described as sound is assigned a weight factor of 100, fair to poor grade is 50, and severe is a factor of 0.

The ER-based corrosion condition assessment numbers and the percentages of the decks areas are compared in Table 2 for the 2009 and 2015 ER surveys. The four corrosion states are defined by four electrical resistivity ranges: less than 10 kOhm-cm as high, 10 to 20 kOhm-cm as moderate, 20 to 30 kOhm-cm as low, and above 30 kOhm-cm as very low. The corrosion condition assessment number for the deck dropped from 86 to 41 in 6 years. The overall decrease in condition assessment numbers is well-reflected in the increase of deck area in different severity levels of corrosion. The majority of the deck area had very low corrosion rates in 2009, while the majority of the same had high to moderate corrosion rates in 2015.

Table 2. Corrosion Assessment from ER: Condition Assessment Number and Percentages of Deck Area.

		Distribution			
Bridge -Year	**Condition Assessment Number**	**Very Low (%)**	**Low (%)**	**Moderate (%)**	**High (%)**
2009	86.3	72	15	10	3
2015	40.9	22	17	17	44

3.1.2 *Ground Penetrating Radar (GPR)*

A qualitative assessment of the deck condition can be made using a GPR survey through measuring the attenuation of electromagnetic waves on the top rebar level (Barnes & Trottier, 2000). The amplitude of the reflection will be highest when the deck is in a good condition. Moisture, chloride ions, iron oxide, cracks, and air-filled delaminations alter dielectric properties and increase the attenuation of electromagnetic waves. Thus, zones of highly-attenuated signal in GPR attenuation maps indicate locations of likely concrete dete-

rioration, delamination, and/or corrosive environment. A GPR survey conducted using a 1.5 GHz ground coupled antenna is shown in Figure 10.



Figure 10. GPR survey using a 1.5 GHz ground coupled antenna.

GPR condition maps obtained from GPR surveys of the deck in 2009 to 2015 are shown and compared qualitatively in Figure 11. The GPR threshold levels of deterioration are specific to the bridge conditions and equipment used and were obtained from correlations with other NDE technologies. The correlations between the attenuation levels and condition grades are indicated in the figure. A serious condition is described for both bridges with attenuation level of below -20 dB. Similar to ER, GPR qualitatively captured deterioration progression in the deck during the 6 year period. The progression and level of deterioration correlate well with the corrosion progression captured during the ER surveys. The similarity can be attributed to the fact that both measurements are primarily affected by the same elements affecting the electrical conductivity and dielectric value of concrete: moisture, chlorides, salts, etc.

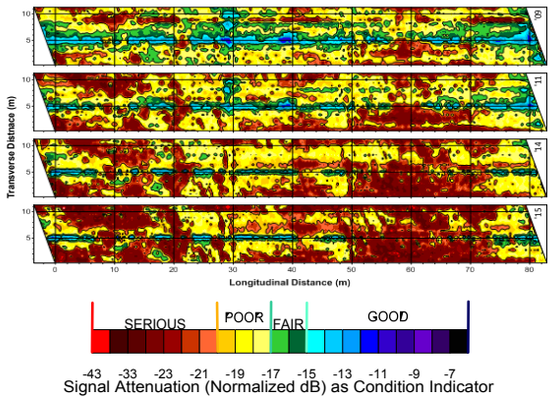


Figure 11 Deterioration condition maps from GPR survey on the bridge deck in 2009 (top) and 2015 (bottom).

To quantify deterioration progression, the condition assessment numbers along with the percentages of the decks areas at various severity levels of deterioration are compared in Table 3 for the 2009 and 2015 GPR surveys. The GPR condition assessment number for the deck dropped from 48 in 2009 to 22 in 2015. A large percentage of the deck area was in a poor condition in 2009, while most of the deck area is currently in a serious condition.

Table 3. GPR Assessment: Condition Assessment Number and Percentages of Deck Area

		Distribution			
Bridge-Year	Condition Assessment Number	Good (%)	Fair (%)	Poor (%)	Serious (%)
2009	48.1	14	24	41	21
2015	22.4	5	5	35	55

3.1.3 *Impact Echo (IE)*

IE has been successfully implemented in detecting and characterizing delamination in bridge decks (Sansalone, 1993).

IE measurements can be made by using a single IE probe, consisting of an impactor and a receiver (Fig. 12 (top)) or by using multiple IE probes (Fig. 12 (bottom)), each consisting of an impactor and a sensor.

The primary objective of IE testing is to locate reflectors (bottom of the deck or a delamination) in the deck. The extent and position of reflectors can be estimated by analyzing the frequency response of the waves reflected from the reflector.



Figure 12. Two types of IE testing systems: (top) an IE cane and (bottom) a stepper.

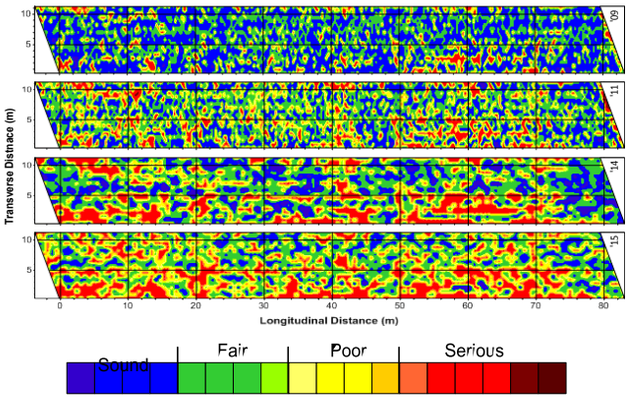


Figure 13. Delamination maps from IE surveys conducted on the bridge deck from 2009 (top) to 2015 (bottom).

The results from IE surveys on the deck are shown in Figure 13. The condition is described as good or sound when the depth of the reflector based on the measured response frequency matches the thickness of the deck. In the case of a delaminated deck, reflections of the compression wave occur at shallower depths, causing a shift in the response spectrum towards higher frequencies. Depending on the extent and continuity of the delamination, the partitioning of energy of waves being reflected from the bottom of the deck and delamination may vary. Initial delamination (fair condition) is described as occasional separations between the two deck zones. Thus it will have two distinct peaks corresponding to reflections from the bottom of the deck and the delamination. Progressed delamination (poor condition) is characterized by a single peak at a frequency corresponding to the depth of the delamination. Finally, in cases of wide or shallow delaminations, the dominant response of the deck to an impact is characterized by a low frequency response of flexural mode oscillations of the upper delaminated portion of the deck. This condition is graded as a serious condition and is always in the audible frequency range.

Figure 13 depicts the condition of the deck obtained from the IE surveys conducted from 2009 to 2015. The maps illustrate progression of delamination during the 6 year period.

Similar to the ER and GPR results, the condition assessment numbers from the 2009 and 2015 IE surveys, along with the percentages of the decks areas at various severity levels of delamination, are compared quantitatively in Table 4. The delamination condition assessment number for the deck dropped from 69 in 2009 to 40 in 2015. While a large percentage of the deck area was sound in 2009, the majority of the deck was extensively delaminated in 2015.

Table 4. Delamination Assessment from IE: Condition Assessment Number and Percent of Deck Area.

		Distribution			
Bridge-Year	Condition Assessment Number	Sound (%)	Fair (%)	Poor (%)	Serious (%)
2009	69.5	54	26	4	15
2015	39.9	21	31	7	41

3.1.4 *Ultrasonic Surface Waves (USW)*

Other deterioration processes may lead to expansive stresses (cracks) within the concrete and either reduce mechanical properties or alter dielectric properties. The USW method is effective for detecting and measuring changes in mechanical properties. Surface waves are stress waves traveling along the surface of the deck, with their body extending to the depth of approximately one wavelength (Nazarian, 1993). Therefore, as long as the USW testing is limited to the wavelengths comparable to the deck thickness, the surface wave velocity will be controlled by concrete properties (elastic modulus). Devices like the portable seismic property analyzer (PSPA), shown in Figure 14, can be used in the evaluation of concrete modulus by the USW method.

Figure 15 depicts the condition of the deck obtained from the USW surveys conducted in 2009 and 2015. The maps illustrate progression of delamination during the 6 year period. Table 5 compares the condition assessment numbers and percentages of USW results from 2009 and 2015.

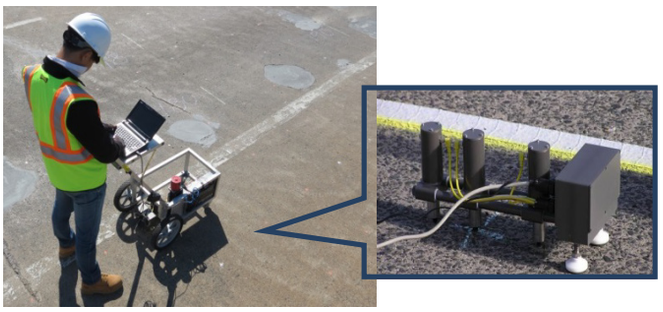


Figure 14 Surface wave testing using a PSPA.

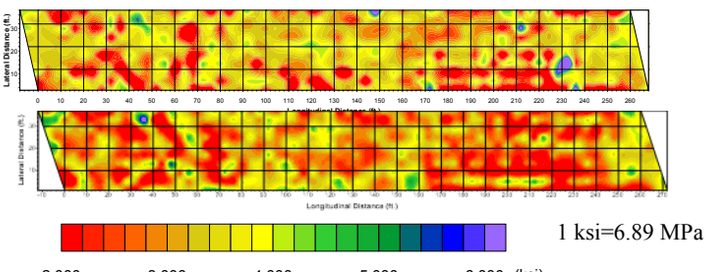


Figure 15 Concrete modulus maps from USW surveys conducted on the bridge deck in 2009 (top) and 2015 (bottom).

Table 5. Concrete Quality Assessment from USW: Average Modulus and Standard Deviation.

	Distribution				
Bridge-Year	**< 3,500 ksi (%)**	**3,500 – 4,500 ksi (%)**	**> 4,500 ksi (%)**	**Mean *E* (ksi)**	**STDEV (ksi)**
2009	66	29	5	3,286	705
2015	68	27	5	3,008	988

3.4 *NDE Summary*

The condition of the deck of the southbound U.S. Route 15 Bridge in Haymarket, Virginia was monitored over a period of 6 years to improve knowledge about the bridge deck performance and to better understand progression rates of different deterioration and defect types over an extended period of time.

Results of the surveys over a 6 year period show that NDE technologies have the ability to monitor deterioration progression with time, whether qualitatively through increase of deteriorated areas or quantitatively through changes in condition assessment numbers. Expanding deterioration and increasing severity of deterioration in 2015 occurs in the same areas as identified as deteriorated in 2009 in all NDE condition maps. The condition assessment numbers facilitate development of more objective and realistic deterioration and prediction models for the bridge deck.

The complementary use of multiple NDE technologies identifies corrosion as the primary cause of damage in the deck. The NDE results provide strong correlation between the ER and GPR condition maps, explained by similar electrical properties affecting the two. Additional correlations are established regarding delamination detection between GPR and IE, and USW and IE, and concrete degradation between USW and GPR. These correlations also point to corrosion as the primary cause of deterioration for these decks.

4 DETERIORATION MODELING

Since its initialization in 2008, the Federal Highway Administration (FHWA) Long-Term Bridge Performance (LTBP) Program has been collecting valuable quantitative data for bridges, such as visual inspection data, non-destructive evaluation (NDE) data and legacy data, etc. As the data continually grow in dimension, size and depth, the development of a scientific data analysis module to complement this unprecedented bridge research effort is critical. In this section a novel statistical approach, *LTBP Data-Driven Deterioration Modeling Method* (D^3M^2), is described for scientific analyses of LTBP data. It is comprehensible, flexible and accurate.

This section covers the following topics: A description of the challenges with the traditional approach for deterioration modeling; an introduction of the LTBP D^3M^2 and its strengths; questions and answers about the LTBP approach; a working example with electrical resistivity (ER) data is provided to demonstrate the application of the learning methodology; and a prototype is provided.

4.1 *Challenges Faced By Traditional Deterioration Modeling*

The traditional approach of deterioration modeling in the literature consists of two steps:

1) Select a model *functional form* (MFF). Select a model functional class (MFC), e.g. linear, hazard-based, Markovian, etc. Select a set of deterioration variables (e.g. traffic, age), and determine how they would be incorporated into the selected MFC (e.g. perhaps decide that traffic and age form an interactive factor, traffic age, aside from their individual impacts on deterioration). The variables are most commonly incorporated into the selected MFC through assigning variable coefficients, and the result is an MFF. Take the following formula for example:

$$P(7|7) = \frac{1}{1+\exp(\beta_0+\beta_{ADTT}\cdot ADTT+\beta_{AGE}\cdot AGE+\beta_{ADTT\&AGE}\cdot ADTT\cdot AGE)},$$

where P(7|7) is the probability of a bridge (element) having a condition rating of 7 in the next year given that in the current year it is 7; exp is the natural exponent; ADTT is average daily truck traffic; and the βs are coefficients to be estimated. The MFF in the Equation is of Markovian-logit class; and

2) Model estimation. Perform statistical estimation[1] on data and determine the means and variances of the coefficients. This might include MFF refinement, which investigates if some variables should be removed based on certain statistical criteria.

This approach, while prevalently used in the literature and practice, is rather restrictive in the following senses:

- By selecting an MFF, one inherently assumes that it describes data the best, or better than other candidates. It is only when a very poor fit is produced that the engineer would consider choosing a different MFF;
- This approach can potentially lead to compromised estimation accuracy. New selections of MFF are only initiated when the fits are very poor, while relatively poor fits may be considered acceptable.

[1] Parameter updating is considered to be a form of model estimation.

○ The approach has limited flexibility. A new selection means a new iteration of the entire process, with no memory of previous results. Furthermore, the integration of different opinions (e.g. different MFFs or coefficient values) is challenging since only one MFF can be selected each time, especially when the opinions are drastically different.

4.2 *The LTBP D3M2: How Does It Work?*

The LTBP data analysis module takes a different approach. Instead of selecting an MFF prior to data mining, it incorporates the learning of MFF into the analytical process. This improves deterioration modeling efficacy and allows incorporation and competition of different opinions.

Before further discussion, it is worthwhile pointing out the difference between two terms that will be used repeatedly throughout the rest of the whitepaper: MFF and *model*. An MFF consists only of structural denotations and its coefficients have no numerical values. (For example, Equation 1 is an MFF and the βs have no numerical values.) Once model estimation assigns its coefficients numerical values, an MFF becomes a model. Therefore, the distinction lies in whether the coefficients have numerical values (Fig. 16).



Figure 16. Distinction between "MFF" and "model"

The LTBP data analysis module consists of two steps (demonstrated from a hypothetical agency's point of view): (1) proposing candidate models and (2) Statistical Learning. A discussion of each step follows.

4.2.1 *Step 1: Proposing Candidate Models*

As an example, in developing potential models, first a particular agency decides that two MFFs, A and B, are desirable for its inventory, and proposes multiple candidate models (*not* MFFs). Experienced bridge practitioners within the agency propose models I, II and III, which are of MFF A, B and A, respectively. In the meantime, the agency also has close collaboration with academia and its research partners propose models IV, V and VI, of MFF B, A, B, respectively. Furthermore, it can also develop a model VII of MFF A solely based on data. The pool of candidates is summarized in Table 6.

Table 6. Summary of Candidate Models for the Hypothetical Agency

Source	Practitioner Experience			Research Community			Statistical Estimation
Model #	I	II	III	IV	V	VI	VII
MFF Category	A	B	A	B	A	B	A
Initial Weights	10 %	20 %	10 %	20 %	10 %	20 %	10%

By including both MFFs in the candidate pool, the LTBP data analysis module explicitly allows MFF to become a learning component; therefore, the restriction of a fixed MFF has been lifted and different opinions can be flexibly integrated. In fact, the module allows as many MFFs to be included as the agency desires.

It is worth noting that learning the impact of a certain deterioration variable also can be considered during the formation of the candidate pool. For example, if II and III differ in nothing but the coefficient of ADTT, the comparison between the two models essentially provides information on the impact of ADTT on deterioration.

The agency then proceeds to assign model-specific weights, as shown in Table 6. The weights are interpreted as prior probabilities of the models being the underlying truth. For example, model III has an initial weight of 10%, which means:

$$\Pr(\textit{model III is the true model}) = 10\%.$$

The weights offer the agency further flexibility in deterioration modeling, as it can choose how much it favors each model initially (and even adjust the weights in the process of learning). The relative magnitudes of the model weights provide information on the relative significances of the models, e.g. the agency considers model II to be twice as important as model III.

4.2.2 *Step 2: Statistical Learning*

Once the candidate pool is formed, the agency proceeds to learning, which uses to another novel feature of the LTBP D^3M^2: learning is not achieved through model estimation, but rather selection of one or more models from the candidate pool based on their fits to

data. The selection is done through updating the weights of the models. And intuitively, models that agree with data gain weights, while those that do not lose weights. The updating for probabilistic models is derived from conditional probability theories, as explained below.

- After each data collection, the agency evaluates the likelihood of observing the collected data under model i ($i \in \{I, II, III, \dots, VII\}$), which can be interpreted as how much data is agreeing with model i:

  $$likelihood(data|model\ i) = \Pr(observed\ data\ if\ model\ i\ was\ true);$$

- Then the joint probability that the collected data are observed and that model i is the true model is given by:

  $$\Pr(model\ i\ was\ the\ true\ model\ observed\ data) = \Pr^{old}(model\ i\ was\ the\ true\ model) * likelihood(data|model\ i)$$

- The probability of observing the collected data simply becomes:
  $\Pr(observed\ data) = \sum_{i=I}^{VII} \Pr(model\ i\ was\ the\ true\ model)$; and

- Finally, the new weight of model i given the collected data can be calculated as:

  $$\Pr^{new}(model\ i\ is\ the\ true\ model|data) = \frac{\Pr(model\ i\ was\ the\ true\ model\ \&\ observed\ data)}{\Pr(observed\ data)}.$$

It follows that the entire updating process is data-driven.

4.3 *The Strengths Of The LTBP D^3M^2 Method*

The strengths of the LTBP D^3M^2 are:

- Built-in MFF learning. Agencies can choose to include as many MFFs as they desire, even when they are drastically different, as long as they can be assessed in a common metric. Likelihood immediately emerges as a fit choice, since deterioration is most often described by probabilistic models due to its stochasticity arising from unaccounted variables, measurement errors, etc. The traditional approach does not allow learning of MFFs;
- Agencies ability to fully utilize their resources. Agencies have rich in-house practitioner experience and/or academic support. By including multiple models, they can maximize the utility of available resources. They also assign the initial model weights as they see fit and adjust them in future learning, offering them more flexibility;
- Flexibility in Accommodate Changes: Error-tolerant. With the LTBP D^3M^2, agencies can add or remove candidate models at any given time, to accommodate changes in bridge design, new/outdated materials, etc. and preserve learning results at the same time;
- Learning/fine-tuning the impacts of certain deterioration variables. By proposing proper candidate models, agencies can fine-tune the impact of a deterioration variable; and
- Guaranteed improvement in deterioration model accuracy. Liu and Madanat (2015) showed that the LTBP D^3M^2 is guaranteed to improve deterioration model accuracy through successive updating.

4.4 *Questions About The LTBP D^3M^2 Method*

Question: Can the LTBP D^3M^2 erroneously delete a model due to the randomness in data in its early phase?

Answer: No. If a model was deleted in the early phase of learning, the likelihood of it might have diminished significantly compared to those of the other models. Therefore deletion is statistically significant. Nonetheless, an agency can add back the model anytime if it has concerns about erroneous deletion, simply by giving the model a new weight α, and timing the other model weights by $1 - \alpha$.

Question: Can the LTBP D^3M^2 give predictions of bridge (element) condition ratings when it has numerous models?

Answer: Yes. The LTBP D^3M^2 can generate bridge element condition ratings by weighing the individual predictions of each model. This is because the model weights are essentially probabilities. Therefore agencies can use the LTBP D^3M^2 to predict deterioration.

Question: If none of the candidate models is the true model, how does the LTBP D^3M^2 arrive at the true model?

Answer: The LTBP D^3M^2 can provide the right direction to test new models. For example, if three models differ in nothing but the coefficient of ADTT, which are 0.1, 0.2, and 0.3 respectively. Suppose that learning assigns the most weight on the model with ADTT coefficient = 0.3, second on 0.2 and least on 0.1. It is an indication that the coefficient is bigger

than 0.3 and agencies can accordingly sample new models and keep improving model accuracy.

Question: How does the LTBP D^3M^2 take into consideration the maintenance history of a bridge when modeling its deterioration?

Answer: First, it is necessary to distinguish two concepts: *deterioration curve* and *deterioration history*. Deterioration curve depicts a mathematical relationship that describes how the condition of a bridge (e.g. NBI deck condition rating) naturally degrades with time by accounting for a set of explanatory variables. Hence, it is monotonically non-increasing and can be considered a (relatively) objective "fact" that does not alter with respect to the maintenance actions performed on the bridge. Deterioration history, on the other hand, is the trajectory of the condition of a bridge, considering *both* condition degradations due to natural deterioration and condition improvements due to maintenance actions. Graphically, one would observe jumps associated with maintenance actions and pieces of deterioration curves in between.

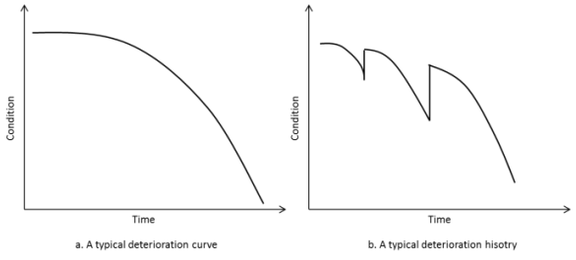


Figure 17: Comparison between a typical deterioration curve and a typical deterioration history

Therefore, the LTBP D^3M^2 is intended for the learning of deterioration curves. Deterioration histories are critical concepts in the discussions of life-cycle costs.

4.5 *A Working Example: Learning Deterioration Models With ER Data*

In this section, the LTBP D^3M^2 is demonstrated with ER data collected on the Virginia (VA) LTBP pilot bridge. (ER data represents a simple example of basis for modeling deterioration.)

4.5.1 *Proposing Candidate Models*

It is first assumed that the true deterioration model (representing nature) is:

$$ER^{t+1} = \frac{ER^t}{1+\exp(\alpha+\beta\cdot ADT+\varepsilon)}, \text{ with } \alpha = -5.5,$$

$$\beta = 0.0001 \text{ and } \varepsilon \sim N(0, \sigma = 0.5^2)$$

Therefore, deterioration modeling should: 1) identify the MFF; and 2) learn the values of α, β *and* σ. Our hypothetical agency, however, is not aware of either, and is choosing between two MFFS:

A) $ER^{t+1} = \frac{ER^t}{1+\exp(\alpha+\beta\cdot ADT+\varepsilon)}, \varepsilon \sim N(0, \sigma^2)$; and

B) $ER^{t+1} = 0.9 \cdot ER^t - 2 + \vartheta,\ \vartheta \sim N(0, \mu^2)$.

The candidate models that it accordingly proposes are:

	MFF A					MFF B
Source	Practitioner Experience		Research Community		Statistical Estimation	
α	-5.25	-5.25	-6.25	-6.25	-6.25	ϑ = 0.25
β	0.0001	0.0000	0.0001	0.0000	0.0001	
σ	0.5	0.5	0.4	0.4	0.5	
Weight	18%	18%	18%	18%	18%	10%
No.	1	2	3	4	5	6

Figure 18: Hypothetical agency's candidate models

It follows that the agency proposed five models of MFF A, and one model of MFF B. The *Weight* row sums up to 100%, with the heights of the boxes representing the magnitudes of the weights.

4.5.2 *Statistical Learning*

2009 ER data from the VA pilot bridge is used as the "seed" data for the initialization of the learning process, and all subsequent ER data is simulated according to the above Equation on a biannual basis. It is important to point out that *simulated data is strictly for demonstration purposes*; once field data are collected, they will be used for practical deterioration learning. The updated results for 2011 ER data (simulated from 2009 ER data) are in Figure 19.

It follows that model 6 is ruled out after one update, due to its inconsistency with the underlying truth. Its weight (10%) is accordingly distributed to all the other five candidate models, whose weights also changed according to how well they describe the simulated data. After 17 updates, the results are given in Figure 20.

No.	1	2	3	4	5	6
α	-5.25	-5.25	-6.25	-6.25	-6.25	ϑ=0.25
β	0.0001	0.0000	0.0001	0.0000	0.0001	
σ	0.5	0.5	0.4	0.4	0.5	
Weight +Δ	18%+8.35%	18%+0.94%	18%+2.44%	18% -2.53%	18%+0.77%	10%-10%

Figure 19: Updating results with 2011 simulated ER data

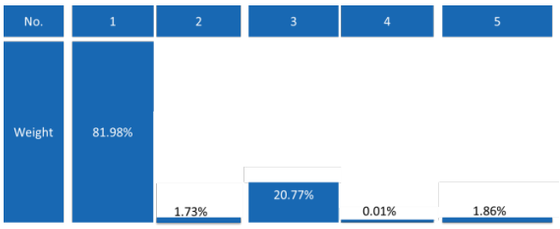


Figure 20: Learning results after 17 updates

After 17 updates, model weights are drastically different from their initial values. We can accordingly draw the following conclusions:

1) Model 6 is quickly ruled out in the updating process; therefore it is not a good candidate; and
2) Models 1 and 2 (or models 3 and 4) differ only in the coefficient for ADT. With model 1 taking significantly heavier weight than model 2, one can conclude that a coefficient of 0.0001 is more suitable to describe ADT's impact on deterioration than a coefficient of 0.0000 (which means traffic has no impact). Likewise for σ, 0.4 is possibly a more appropriate value than 0.5 by comparing the weights of models 3 and 5.

How does the LTBP D^3M^2 fit into the big picture? With the learning and prediction capabilities of the LTBP D^3M^2, an agency can generate parallel predictions for multiple indices, e.g. ER, half-cell potential (HCP), impact echo (IE), ground penetrating radar (GPR), etc. Therefore the agency can use predicted information to calculate a fused[2] condition index anytime without having to worry about loss of information, as illustrated in Figure 21.

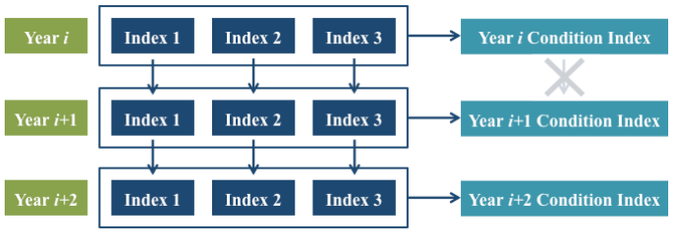


Figure 21: Closing the loop: using the LTBP D^3M^2 to do data prediction and fusion

When the agency feeds multiple indices in year i into a designed formula to generate year i's condition index, a fraction of information contained in {Index 1, Index 2, Index 3} will be inevitably lost. (An alternative interpretation is loss of definition). If it only uses year i's condition index to do prediction, the loss of information will propagate, and eventually predictions will be unacceptably inaccurate. In contrast, with the LTBP D^3M^2, the agency can generate predictions for individual indices, and just apply the fusing formula anytime that it needs a condition index.

4.6 *The Prototype Of The LTBP D^3M^2*

In Figure 22, a prototype web-based interface for the LTBP D^3M^2 is illustrated. The most noteworthy strength of the prototype is its simplicity. Instead of eliciting MFFS and numerical coefficients from practitioners, it allows them to visually examine if a deterioration model is matching their experience by simply looking at the graph on the right-hand side. It also offers the flexibility of inputting the user's own deterioration model(s) if preferred. Therefore, the LTBP D^3M^2 is not only a statistically sound and comprehensible data analysis module, but also has the potential to be developed into a useful, practical tool.

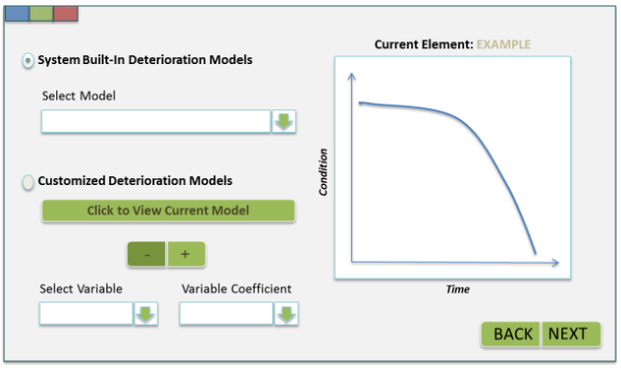


Figure 22: Prototype of the LTBP D^3M^2

5 PRELIMINARY RESULTS

5.1 *Data Collection Consistency*

The use of NDE as the primary measure of deterioration and performance has been shown to provide a consistent basis for modeling.

5.2 *Deterioration Modeling*

The results of three rounds of NDE data for bridge decks have been demonstrated to provide a useful basis for estimating deterioration rates. Additional testing is planned to assess the margin of increased reliability if more than three rounds are used. A LTBP Deterioration Modeling Learning tool has been developed to assure the most accurate model is fitted to the NDE data collected in the Program.

[2]Index fusing herein refers to process of integrating information contained in an array of indices to generate one index, or an index array of reduced dimensions.

5.3 *Sample Size and Reliability*

The use of reference bridges correlated to cluster bridges over a range of bridge types, climatic conditions, and truck traffic will provide a reliable basis for modeling condition and performance of bridge elements.

6 CONCLUSIONS

6.1 *Data-driven Bridge Performance Program*

One simple definition of *performance* is that performance equates to accomplishment of a specified purpose or set of purposes. For the purposes of the LTBP Program, the following definition is used: Bridge performance encompasses how bridges function and behave under the complex and interrelated factors they are subjected to day in and day out—traffic volumes, loads, deicing chemicals, freeze-thaw cycles, rains, or high winds. Bridge design, construction, materials, age, and maintenance history also play roles in performance. Virtually everyone in the United States, from bridge maintenance engineers to the everyday road user, has a stake in ensuring that the performance of bridges is good or excellent in terms of durability, operational capacity, roadway safety, resistance against failure, environmental neutrality, and life-cycle costs. Each group needs to have confidence in their understanding of the indicators by which they measure bridge performance. For the everyday commuter or casual user, an indicator such as Federal SR may suffice. For commercial interests, shippers, and drivers, a simple measure of bridges with posted weight limits or geometrical dimensions may suffice. These groups also need assurance that satisfactory bridge performance is being provided at reasonable costs, as reflected in gasoline taxes, tolls, other roadway fees, and other revenue sources devoted to maintaining performance.

Members of the bridge community such as designers, construction engineers, inspectors, maintenance engineers, and bridge management personnel who are responsible for maintaining performance must be able to properly and effectively evaluate bridge performance in more precise and targeted manners. They must break down bridge performance into very specific issues that can be adequately evaluated in terms of cause and effect. This will allow them to identify actions or programs that will ensure a high level of performance at a reasonable cost. This report describes a breakdown of bridge performance issues into four categories of performance: structural condition (for durability and serviceability), functionality (safety and traffic capacity), structural integrity (for safety and stability), and risk and costs to the user and to the agency. This breakdown helps isolate the most critical aspects of bridge performance and provides the basis for long-term research studies that will improve understanding of these issues.

Making a proper evaluation of bridge performance can be a formidable task given the many factors that can govern performance under different circumstances. The LTBP Program is being implemented to identify the most critical aspects of bridge performance and conduct studies that will result in the high-quality data necessary to better understand how multiple, variable factors govern those aspects of performance. This effort should ultimately lead to the ability to implement policies and actions for bridge programs that will improve performance and extend the life of bridges at minimum cost.

The LTBP has the capability for establishing a direct relationship between data-driven condition measures in the form of NDE test results and bridge performance. The Program is striving to do this first for bridge decks and then will address steel and concrete superstructures, substructures and foundations. Along with detailed inspections and NDE tests, the program is measuring truck weights and overall bridge stiffness to determine how those factors influence bridge performance. While definitive conclusions will not be available for several years, preliminary benefits of the program include a web-based data storage and retrieval application, hundreds of protocols for systematic data collection and testing, and systematic collection and cataloging of reference bridge plans, preservation actions, costs, and historical design standards.

This program is a unique opportunity to collaborate with other similar efforts to leverage other research that is focused on determination of factors that influence bridge performance.

6.2 *Acknowledgements*

This publication was supported by a grant from the U.S. Department of Transportation, Office of the Secretary of Transportation (OST), and Office of the Assistant Secretary for Research and Technology under Grant no. DTRT12-G-UTC16. The authors are grateful to the data collection team from Rutgers' Center for Advanced Infrastructure and Transportation (CAIT) for their help during the data collection. The authors are also grateful to the Virginia Department of Transportation (VDOT) for its cooperation in providing access to the Haymarket Bridge.

6.3 *Disclaimer Statement*

The contents of this report reflect the views of the authors, who are responsible for the facts and the accuracy of the information presented herein. The U.S. Government assumes no liability for the contents or use thereof.

7 REFERENCES

Barnes, L., and J.F., Trottier. Ground Penetrating Radar for Network Level Concrete Deck Repair Management. *Journal of Transportation Engineering*, ASCE, Vol. 126, 2000, pp. 257-262.

Brown, R.D. Mechanisms of Corrosion of Steel in Concrete in Relation to Design, Inspection, and Repair of Offshore and Coastal Structures. *SP-65: Performance of Concrete in Marine Environments*, American Concrete Institute, 1980, pp. 169-204.

Brown, M.C., J.P., Gomez, M.L., Hammer, and J.H., Hooks. *Long-Term Bridge Performance High Priority Bridge Performance Issues*. Publication No. FHWA-HRT-14-052. FHWA, U.S. Department of Transportation, 2014.

FHWA International Scan, "*Bridge Preservation in Europe*," FHWA Office of International Programs, Report FHWA – PL-05-002, American Trade Initiatives, Federal Highway Administration, April 2005.

FHWA, *Report to Congress, Comprehensive Truck Size and Weight Limits Study,* US DOT, FHWA, Washington DC. 2016

Hooks, John M. and Frangopol, Dan M. *LTBP Bridge Performance Primer.* Report FHWA-HRT-13-051, FHWA Office of infrastructure Research and Development, FHWA, McLean, VA, 2013.

Hooks, John M. and Weidner, Jeff. *Long-Term Bridge Performance (LTBP) Program Protocols, Version 1.* Report FHWA-HRT-16-007, 2016.

Liu H. and Madanat S., "*Adaptive Optimization Methods in System-Level Bridge Management*", accepted for publication in Structure and Infrastructure Engineering: Maintenance, Management, Life-Cycle Design and Performance, 2015

Nazarian, S., M.R. Baker, and K. Crain. *Development and Testing of a Seismic Pavement Analyzer*. Report SHRP-H-375, Strategic Highway Research Program, NRC, Washington, D.C., 1993.

Sansalone, M.J. Detecting Delaminations in Concrete Bridge Decks with and without Asphalt Overlays Using an Automated Impact-Echo Field System. In *Proceedings of the BINDT International Conference NDT in Civil Engineering*, Liverpool, U.K., April 1993, pp. 807-820.

Shepard, R.W., Johnson, M.B. (1999),"*California Bridge Health Index"*, Eighth Transportation Research Board Conference on Bridge Management, Transportation Research Board Library, Washington, DC.

Whiting, D.A., and M.A., Nagi. (Eds.) 2003. *Electrical Resistivity of Concrete – A Literature Review*. PCA R&D Serial No. 2457, PCA, Skokie, Illinois, USA, 57 pages.

Maintenance, Safety, Risk, Management and Life-Cycle Performance of Bridges – Powers, Frangopol, Al-Mahaidi & Caprani (Eds)
© 2018 Taylor & Francis Group, London, ISBN 978-1-138-73045-8

Value of monitoring data for long-span bridge operation – Aerodynamic point of view

Ho-Kyung Kim, Sunjoong Kim, Sejin Kim & WoongHee Jung
Seoul National University, Seoul, Korea, Rep.

ABSTRACT: Wind-induced unexpected events for cable-supported bridges are introduced for the purpose of sharing authors' experiences regarding to data utilization for cause investigation, securing countermeasures, and design feedbacks. The events include two cases of vortex-induced vibration and one case of rollover accident of running vehicle over the bridge deck. The utilized data include the basic acceleration and wind speed data, but wind tunnel tests, data processing techniques, system identification with operational modal analysis (OMA), Measure-Correlate-Predict analysis, and Long Short-term Memory were applied to increase the value of data obtained. The results demonstrate that the damping identification from OMA is an essential issue as a serviceability performance index for flexible long-span bridge. Also, the vulnerability assessment procedure of running vehicle to strong side wind can be utilized for the effective traffic control by utilizing long-term and short-term wind speed data. By these way, examples of increasing the value of data for long-span bridge operation are demonstrated in an aerodynamic point of view.

1 INTRODUCTION

Structural health monitoring (SHM) systems are commonly used in most long-span bridges. Although a lot of data are being accumulated from various sensors, there are relatively few examples the monitored data are used directly in bridge operation judgement and decision-making process. In this study, the authors share their experiences of using the monitoring data in the process of identifying incidents, finding causes and countermeasures for long-span bridges in operation over the past years. The reviewed cases are the vortex induced vibration (VIV) observed in two cable-supported bridges, the estimation of the damping ratio through operational modal analysis in the cause identification procedure, and the rollover accidents during strong winds experienced in another bridge. Since all the cases were caused by wind, the wind speed data as well as the wind tunnel test results were used together. The data used were simple and basic ones such as the measured acceleration and wind speed data, but the data analysis techniques such as system identification, wind tunnel tests, and a deep learning algorithm were utilized to increase the value of data. By demonstrating the procedure, the authors would like to share their experiences and knowledges on the value of data by which one can assess and operate the flexible sea-crossing bridges with more confidence in aerodynamic point of view.

2 CONCEPTUAL APPROACH

In many cases, the expansion of knowledge begins with the observation of unexpected events. Events related to winds on bridges can include vibration of bridges or damage to facilities. Since the data acquired through the SHM system during specific events on the bridge is limited, it is common to carry out wind tunnel tests or computational fluid dynamics analysis for better understanding the phenomenon. At the same time, data processing techniques are utilized to mine useful information from data.

The approach to the VIV event begins with a review of the oscillating wind speed region, vibration mode and amplitude. This can be easily determined from the wind speed and acceleration response data of the SHM system. VIV is caused by vortex trails falling from the trailing or leading edges of the deck. Since VIV is prevented from the design stage through wind tunnel tests combined with deck shape adjustment, if the VIV is observed in the field, the wind tunnel test should be performed again to determine the cause. Note that VIV is a resonant phenomenon that occurs due to the tuning between the frequencies of deck motion and harmonic load from vortex trails, hence the amplitude varies depending on the modal damping ratio. Since the wind tunnel tests are per-

formed at the design stage following the assumed design damping ratio, the VIV amplitude can be larger than expected when the damping ratio of the actual bridge is below the design damping ratio. Therefore, it is necessary to evaluate the damping ratio after completion of the bridge for the modes for which VIV is potentially triggered.

Damping can be estimated from the operational modal analysis (OMA) by utilizing ambient vibration data, but it requires knowledges in setting the parameters for data processing and system identification. Because the basic assumptions of OMA are based on white noise excitation and stationary response, appropriate modulating is required when the measurement data shows nonstationarity. Through this process, it is possible to evaluate the damping ratio even to the higher-order modes with higher accuracy. This is a procedure to increase the value of the data provided.

Running vehicles can be exposed to strong horizontal winds for sea-crossing cable-supported bridges with decks installed at high altitudes to ensure sufficient space under the bridge. It is necessary to control vehicle passage over a specific wind speed according to the result of risk assessment to side wind, or to install windshields to secure vehicle safety. Even in this case, long-term wind speed data can be importantly utilized. The frequency data of wind speed according to wind direction is preferably obtained from the SHM system on the bridges. If these data are not sufficient in terms of duration, it may be necessary to convert long-term data obtained from nearby weather stations onto bridges. Since the wind velocity distribution for each lane cannot be obtained directly from the SHM system, it is necessary to secure more sophisticate data through the wind tunnel tests using the deck model. Using these data, it is possible to evaluate the vulnerability of the running vehicle by considering the specific wind condition of the bridge, and to take effective measures to control the traffic.

At least a few hours are necessary to implement an operational decision such as a bridge closure. Also, the time to re-open the bridge operation is also an issue to bridge operators as well as passengers. Therefore, the bridge operator needs a technique to predict the wind speed over the deck a few hours earlier. The prediction of wind speed by the Meteorological Agency is generally available for the typhoon events, but the prediction of wind speed over the deck, which is located in the boundary layer, is physically more complicated. In this case, if short-term wind speed prediction based on a deep learning algorithm becomes possible, it will increase the value of existing wind data for a more reliable decision-making.

The authors would like to introduce the case of increasing the value of the measurement data for each subsequent event and expanding the engineering knowledge therefrom.

3 EVENT 1: VORTEX-INDUCED VIBRATION OF A PARALLEL CABLE-STAYED BRIDGE

3.1 *Observed VIV*

The Jindo Bridge consists of two parallel-disposed cable-stayed bridges. Two similar decks are located with a net distance of 9.9m. While the unexpected VIV was observed at Bridge 2 which was located upstream, the wind velocity was maintained as 9.8-11.5 m/s for two hours (Seo et al. 2013). Since the VIV amplitude exceeded the allowable level, as shown in Figure 1, a series of wind tunnel tests and operational modal analysis were performed to identify the main causes of VIV.

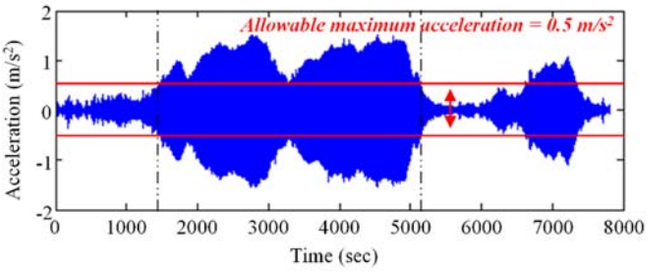


Figure 1. Vertical acceleration of the deck in Bridge 2 at the center of main span

3.2 *Cause investigation via wind tunnel test*

The main purpose of wind tunnel tests was to identify 1) the reason why VIV amplitude was amplified in tandem arrangement by applying a particle image velocimetry, and 2) the relationship between amplitude of VIV and damping ratio.

Figure 2 showed the VIV amplitude of single and parallel disposition together. The VIV in the upstream deck is clearly amplified due to the effect of downstream deck.

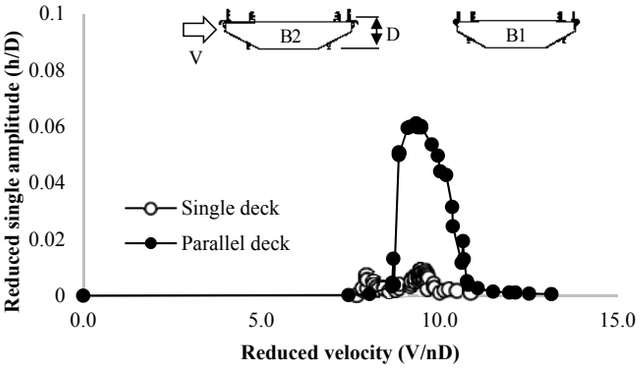


Figure 2. Amplitude of VIVs in both a single deck and parallel decks

Figure 3 shows the reason of amplitude amplification. In this phase-averaged flow streams between two decks at the lock-in wind velocity, the Karman-type vortex trails behind the upstream deck was magnified to motion-induced vortices, which induced interference VIV in upstream deck (Seo et al. 2013).

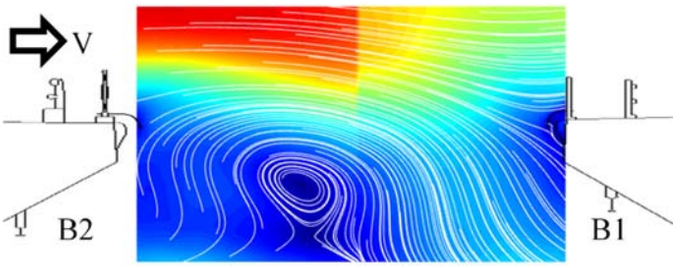


Figure 3. Phase-averaged flow streams at the phase of π/2

Since this phenomenon was not well reported to bridge engineers before, continuing investigations followed by variating the gap distance between two decks (Park et al. 2017). The effect of relative differences in the natural frequencies of two bridges was also investigated (Park & Kim 2017).

Figure 4 shows the relationship between the amplitude of VIV in upstream deck to the damping ratio in wind tunnel setup (Seo et al. 2013). It clearly shows the high sensitivity of VIV amplitude to damping ratio. Based on this graph and observed amplitude of 0.19m, a potential damping ratio of Bridge 2 can be approximated as 0.21%, which is much less than the design damping ratio of 0.40% recommended in design guidelines (KSCE, 2006).

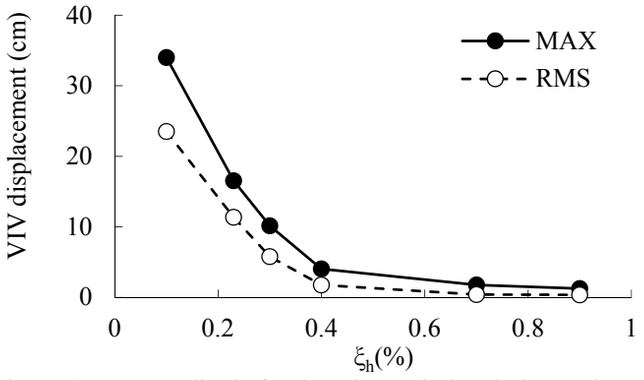


Figure 4. VIV amplitude for damping ratio in wind tunnel

3.3 *Damping identification via operational modal analysis*

Based on thorough wind tunnel tests, two main causes were indicated. The first cause was the amplification of VIV in upstream deck owing to the close parallel disposition between two decks, and the second one was unexpected low damping ratio of Bridge 2. The Natural Excitation Technique combined with Eigen Realization Algorithm (NExT-ERA) technique (Caicedo, 2004) was applied as an OMA to three-day acceleration data measured at the center of mid-span in both bridges (Kim et al. 2013). Figure 5(a) shows the identified damping ratios for each segmented 20-min data. A large scattering was observable, but the mean value of the damping ratio was 0.28%, which showed a somehow agreement with the predicted one in wind tunnel tests. However, the damping ratios for Bridge 1 was identified much higher than those for Bridge 2 by showing around 0.69%, as shown in Figure 5(b). In fact, the damping ratio is an inherent property of bridge and, even two similar bridges in terms of materials and overall shapes show a quite different level of damping ratio.

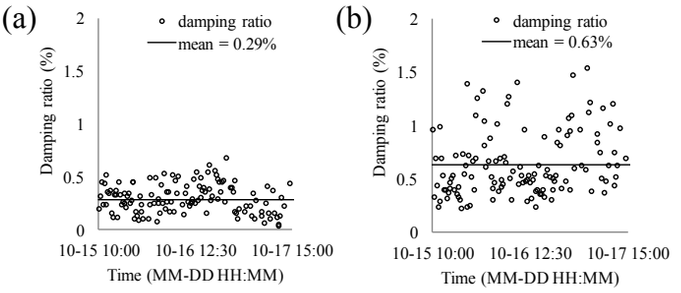


Figure 5. Estimated damping ratio of (a) Bridge 2 and (b) Bridge 1

3.4 *Automated parameter selection and signal stationarization process for NExT-ERA*

The automated proper parameter selection process for NExT-ERA was suggested to reduce the large error bound due to poor parameter selection and achieve similar level of correctness of heuristic parameter selection. To make suitable criteria for each algorithm parameter, a series of parametric studies using numerical simulation and operational monitoring data was performed, respectively. It was found that the number of FFT (NFFT) of 2^{15} with 60 min data provided the accurate estimation in terms of mean and coefficient of variance (COV). A size of Hankel matrix was determined corresponding to the shape of calculated impulse response function (IRF). To overcome the limitation of non-structural model-based algorithm, the sensitivity analysis was performed using each estimated value according to a system order. The median value of estimated damping ratios provided a converged value successfully. This automated parameter selection process accomplished more accurate damping estimation compared to the result of heuristic parameter selection (Kim et al., 2016).

When the number of traffic lane over the bridge is only one or two for one direction and the traffic volume is not high, the ambient vibration signal at the sensor position show an envelope as a vehicle is approaching and fading away. Since OMA assumes that the signal to be analyzed is a stationary white-noise process, the envelop-like signal obtained from running vehicles can also contribute the scattering in structural identification. Kim & Kim (2017) confirmed that the over/underestimated damping ratio due to nonstationarity in traffic-induced vibration can recovered and the uncertainty of the estimated damping ratios was reduced by applying the signal stationarization process based on amplitude-modulating (AM) function.

Figure 6 illustrates the estimate damping ratio according to parameter selection according to three

comparative approaches. Blue circles (denoted as 'Basic') indicated the primitively estimated damping ratios, and red circles (denoted as 'Proper parameter selection') meant the result after a proposed parameter selection procedure. An identified damping ratio with signal stationarization is referred to as 'P.P.S + Stationarization' or 'w/ stationarization'.

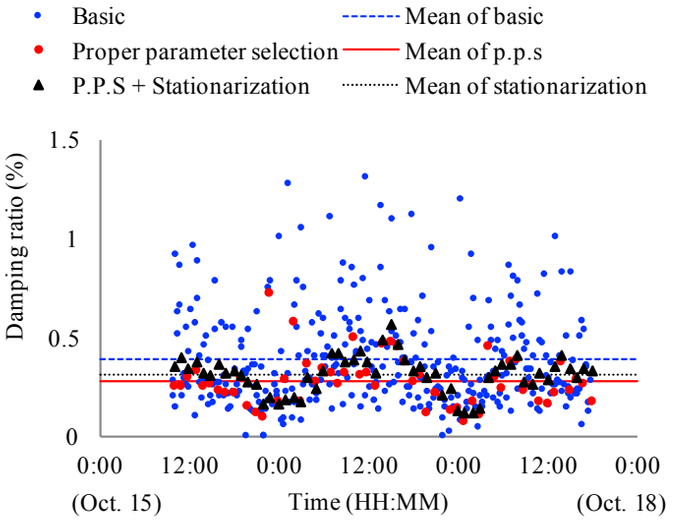


Figure 6. Estimated damping ratio of the Jindo Bridge corresponding to proper parameter selection

As can be seen, a large scattering in damping estimates due to the over/underestimated damping ratio was significantly reduced. By applying a proper parameter selection, a mean value of estimated damping ratios slightly decreases from 0.37% to 0.28%, while COV dramatically reduced from 69.44% to 43.29%, which was acceptable value compared to the COV of heuristic parameter selection. It is clear that the proposed proper parameter selection of NFFT, data length, size of Hankel matrix and system order was automated as well as effective to enhance the accuracy of damping estimation based on operational modal analysis (Kim et al. 2016). Furthermore, by applying the signal stationarization process, COV also reduced as a level of 31.84% from P.P.S of 43.29% while mean value was almost same with the case of P.P.S. This COV of combined case was slightly larger than the COV of stationarization case. In the consideration of the result of free vibration test of 0.33%, the case of stationarization gave more accurate identification in terms of bias and variance error.

3.5 *Environmental effect on the identified damping ratio*

The previous section shows the reduced uncertainty in OMA-based damping estimation by proper parameter selection with signal stationarization process. Nevertheless, the variation of damping ratio was still found with a large range of 0.1% to 0.6%. The reason for these variations should be further identified.

Interestingly, the change in estimated damping ratio shows a repeating pattern with a duration of 24 hours. The damping ratio started to increase in the morning and maintained a constant value until the evening. After that, it decreased and showed a relatively low value until dawn. This tendency was repeated for 3 days.

In order to assess the effect of environmental factors on the variation of damping ratio, correlation analysis was performed for root-mean-square (RMS) amplitude, the number of vehicle and temperature. While a RMS amplitude of acceleration was calculated from a monitoring data, the number of vehicle and temperature were not obtained from the SHM system. Therefore, instead of the number of traffic, the number of peaks in the measured acceleration was counted inevitably. Figure 7 showed that the number of local maxima was successfully counted from the measurement acceleration of the bridge. For the temperature of the bridge, the atmosphere temperature measured at an automatic weather station (AWS) at 10 km from the bridge was used for correlation analysis.

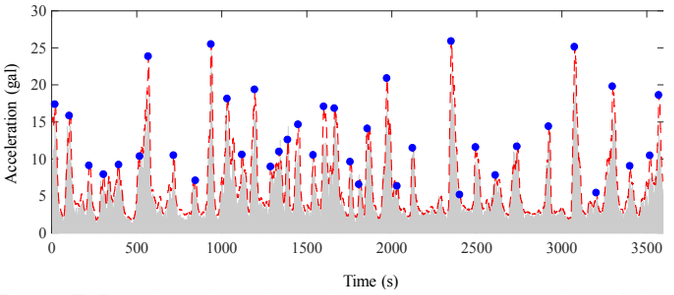


Figure 7. Local maxima from the measured acceleration of the Jindo Bridge

Since each unit is different, the normalized (average of 0 and standard deviation of 1) distribution of four parameters over 3 days was shown in Figure 8. It is clear that the trends of the four variables were much similar. The correlation analysis results for the damping ratio were shown in Table 1. As can be seen from Table 1, it can be confirmed that the variable with the highest correlation was the number of the vehicle while the tendency toward temperature was the lowest. Interestingly, unlike vehicle numbers, the RMS amplitude is not high. This is presumably due to the amplified response to the lock-in range.

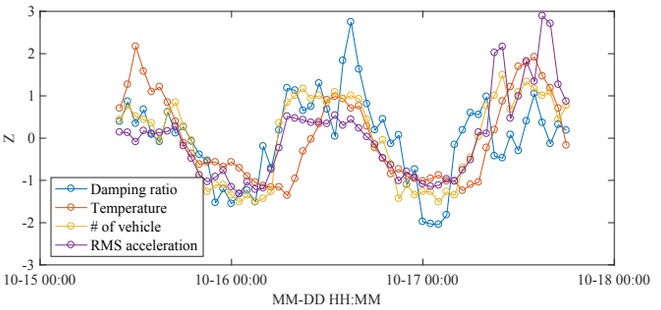


Figure 8. Normalized distribution of damping ratio and representative environmental factors according to time evolution (3 days)

Table 1. Correlation coefficient between identified damping ratios and environmental factor

	Damping ratio	RMS Acceleration	Number of vehicle	Temperature
Damping ratio	1.000	0.475	0.735	0.438
RMS acceleration		1.000	0.850	0.682
Number of vehicle			1.000	0.708
Temperature				1.000

In the lock-in range, the bridge was subjected to a vortex-shedding force, which amplified the vibration amplitude of the bridge deck. Figure 9(a) shows that the number of vehicle is identical for 3 days, but the RMS amplitude rapidly increased on October 17 when the corresponding mean wind speed was within the lock-in wind velocity. However, these VIVs seem not to contribute to damping identification in NExT-ERA. As shown in Figure 9(b), regardless of larger amplitude due to VIVs, identified damping ratios did not increase as much.

A correlation analysis between estimated damping ratio and environmental factors was re-performed without lock-in range data set. Table 2 also summarizes the correlation coefficients between identified damping ratios and environmental factor without lock-in range data set. Also, in this case, the factor that has the highest correlation with the damping ratio was the number of vehicles. Note that the correlation coefficient between damping ratio and RMS amplitude increased rapidly from 0.475 to 0.761. As a result, the coefficient between RMS acceleration and the number of vehicle was also enhanced from 0.850 to 0.968 which is almost 1.0.

3.6 *Discussions*

VIV observed in the upstream deck was induced by the magnified motion-induced vortex trails generated behind the deck due to the blockage effect by the downstream deck. Accordingly, the interactive VIV was identified to be sensitive to the open gap width between two decks.

Another issue of low damping ratio also attracted keen interest of engineers. The damping ratios for both bridges were identified from OMA for the field-monitored data. Even though both bridges were designed as a concept of twin bridges, the estimated damping ratios showed a wide difference. The damping ratio for the upstream bridge, subjected to interactive VIV, was estimated to be 0.28%, while that of the downstream bridge was more than 0.6%.

Since the design damping ratio of the steel cable-supported bridge was set to 0.4% in a design guideline, the estimated damping ratio was much lower than expected. Therefore, if necessary, the level of design damping ratio can be lowered to accommodate a potential possibility of low damping ratios of flexible structures, which adopt higher-strength materials and simpler connections.

Accordingly, it is recommended for bridge owners to secure initial damping ratios for dominant modes and to confirm the validity of wind-resistance design in terms of design damping ratios. The proposed parameter selection process allows to automate damping estimation process from operational monitoring data, so that it can lead to obtain a reliable damping estimation in real time without the controlled experiment or engineering judgements.

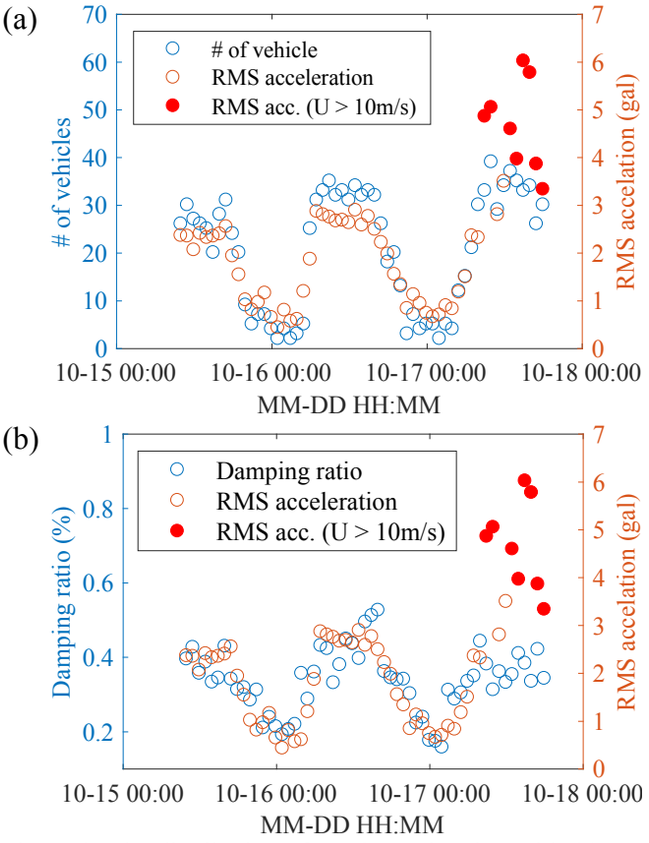


Figure 9. The distribution of RMS acceleration with (a) corresponding the number of vehicle and (b) identified damping ratios

Table 2. Correlation coefficient between identified damping ratios and environmental factor without lock-in range data set

	Damping ratio	RMS Acceleration	Number of vehicle	Temperature
Damping ratio	1.000	0.761	0.805	0.447
RMS acceleration		1.000	0.968	0.674
Number of vehicle			1.000	0.663
Temperature				1.000

4 EVENT 2: VORTEX-INDUCED VIBRATION OF THE YI-SUNSHIN BRIDGE

4.1 *Observed VIV*

The investigation bridge, the Yi Sun-shin Bridge (YSS Bridge) is a suspension bridge with a main span length of 1,545m with a streamlined twin-deck section. A large VIV was observed for two hours on Oct. 26, 2014. At that time, the temporal screens were applied on the bridge railings for maintaining curing temperature of the replaced wearing surface as shown in Figure 10.

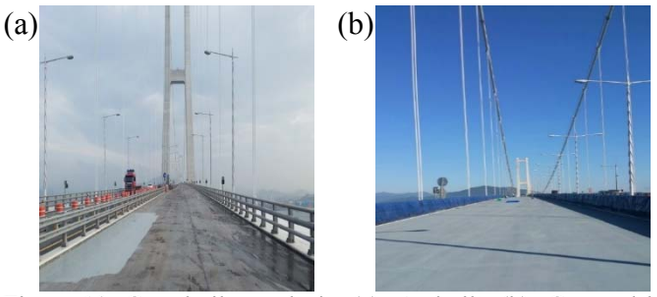


Figure 10. Guardrails on decks (a): As-built, (b): Covered by temporal screens

Unfortunately, the built-in SHM system was not work properly at that time, and only a global navigation satellite system (GNSS) sensor at the center of the main span worked. As a result, the time history of displacement could be obtained from the GNSS sensor, as shown in Figure 11. The maximum vibration amplitude reached 0.52m in double amplitude and the motional frequency was identified to be 0.3176Hz, which was the 4th symmetric vertical mode, as shown in Figure 12.

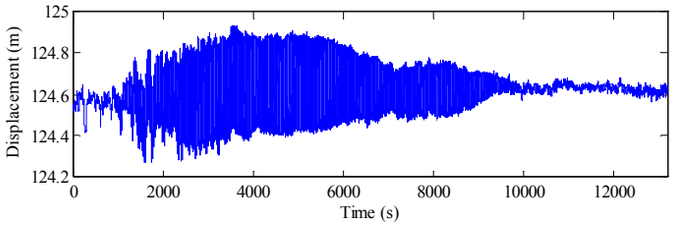


Figure 11. Measured displacement of VIV

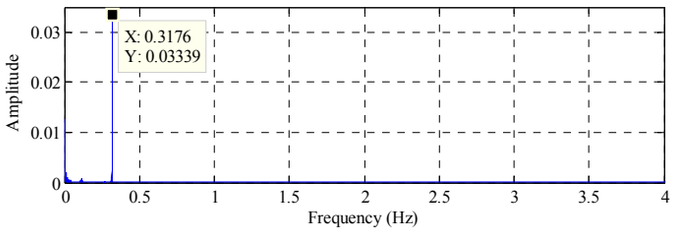


Figure 12. PSD of measured VIV

4.2 *Cause investigation via wind tunnel test*

A series of wind tunnel test was performed using a 1:70 scale model to reproduce the observed VIV. The detail dimensions of set-up model are described in Figure 13.

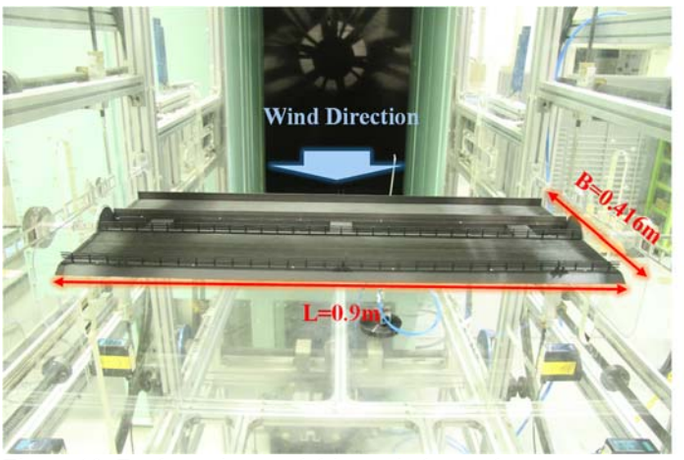


Figure 13. Deck section model in a wind tunnel

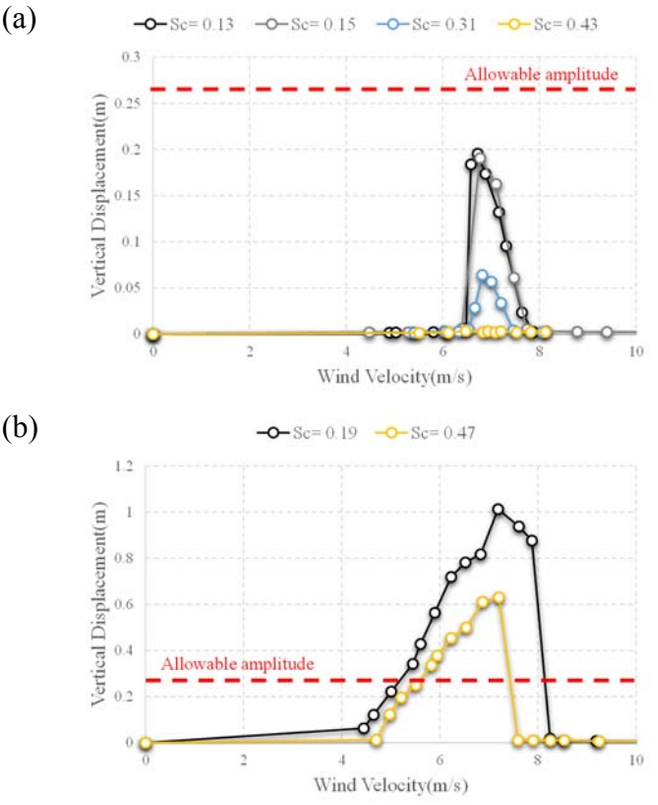


Figure 14. V-A curve: (a) original section, (b) original section with temporal screens

A two of comparative railing configurations was considered for a cause investigation. The first case was an as-built section, while the second one was a section with a temporal screen on the railings. Figures 14(a) and 14(b) illustrate V-A curve for the vertical displacement of two cases, in which S_c denotes the Scruton number. All responses are calculated in double-amplitude. As can be seen, the amplitude of VIV exceeded an allowable limitation only for a case with temporal screens. The amplitude of VIV was strongly influenced by Scruton number. Even in the case of original section, a relatively high level of vibration was observed with low S_c. For the case of a temporal screen on railings, a VIV amplitude still exceeded the limitation even with the design damping level.

4.3 *Cause investigation via operational modal analysis*

The interesting aspect is that the bridge deck was oscillated in the 4th vertical mode, in which the damping ratio (or Scruton number) of 4th vertical mode seems to be substantially less than other modes. Thus, the modal damping ratio was identified from the ambient vibration data measured from built-in accelerometers.

The ambient vibration data obtained for a duration of 1 hour was utilized. PSD of measured acceleration shown in Figure 15 indicates that the 4th vertical mode (0.32Hz) was well developed in ambient vibration data. Two output-only system identification methods, the frequency domain decomposition (Brinker, 2000) and NExT-ERA, were implemented to estimate the modal damping ratio.

At first, the frequency domain decomposition was applied. Frequency response function for each mode were obtained by the peak picking method from the singular values of the spectral matrix. Then, the auto correlation function of each mode could be obtained via inverse FFT of selected frequency response function (FRF). The natural frequency was calculated by counting of zero crossing and the modal damping ratio was estimated from logarithmic decrements.

For the NExT-ERA, a correlation function was calculated with the number of FFT of 2^{16} points with the overlapping of 2^{15}. A size of 3,500 by 3,500 was used to build a Hankel matrix. A calculated auto correlation function and implemented one are illustrated in Fig 16.

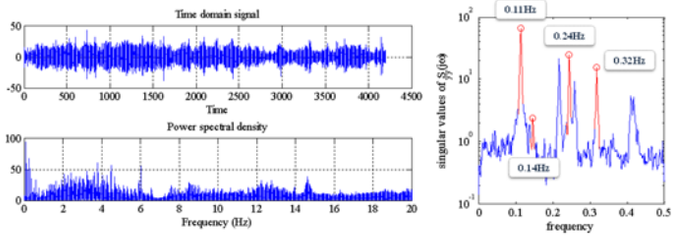


Figure 15. Measured ambient vibration data: (a) acceleration, (b) PSD and (c) components of symmetric vertical modes.

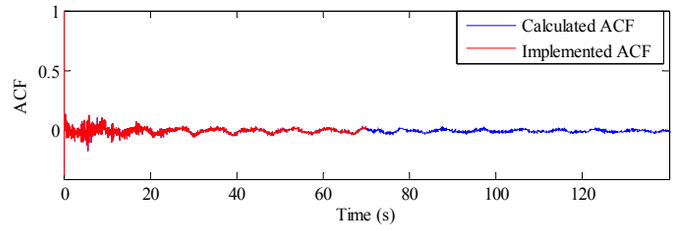


Figure 16. Auto-correlation functions

Table 3 summarizes the results of OMA, in which VS1 denotes the "1st Vertical Symmetric mode". The modal damping ratio of the 4th vertical mode is 0.42% that is the level of design guideline, while 1st, 2nd and 3rd modal damping ratios are 1.26%, 2.42% and 0.44%, respectively. This result clearly shows that the occurrence of the 4th vertical mode VIV would be related to a relatively low modal damping ratio.

Table 3. OMA result (frequency and damping ratio)

Methodology	VS1	VS2	VS3	VS4
FDD	0.11Hz 1.26%	0.15Hz 2.42%	0.24Hz 0.44%	0.32Hz 0.42%
NExT-ERA	0.11Hz 1.17%	-	0.24Hz 0.45%	0.32Hz 0.38%

4.4 *Discussions*

The source of the unexpected vibration observed in 2014 on a suspension bridge was the temporal screens used for curing the epoxy-coated pavement. The bridge was subjected to the vortex-induced vibration tuned to the 4th vertical mode, for which the modal damping ratio was identified to be relatively small than other modes. The bridge at the current normal operational condition, without the temporal screens, is identified to be aerodynamically stable as it was thoroughly verified via the wind tunnel tests at the design stage.

5 EVENT 3: OVERTURNING ACCIDENT ON GWANGAN BRIDGE

5.1 *Two trailer accidents on bridge*



Figure 17. The 2nd trailer overturning accident on a suspension bridge (Retrieved from http://news20.busan.com/controller/newsController.jsp?newsId=20120404000160)

On April 3rd, 2012, two consecutive trailer overturning accidents were observed on the approaching span of a suspension bridge with double deck, as shown in Figure 17. The recorded 10-minute averaged wind speed when these accidents happened were 14.3m/s and 11m/s at the height of accident site, which were much lower than the limit wind speed of 25m/s for bridge closure. Since the trailer is relatively vulnerable to wind as well as the accidents occurred in a curved section, the limit wind speed of 25m/s seems not to be enough for this condition. In order to figure out cause of these accidents and to assess vulnerability of vehicle safety, vehicle analysis and probabilistic risk assessment are proceeded based on collected data.

5.2 *Estimation of critical wind speed via vehicle analysis*

In order to calculate critical wind speed of trailer, vehicle analysis is performed based on a quasi-static theory (Batista & Perkovic 2014; Kim et al. 2016). Static model of trailer is constructed with one axle and one hitch point considering reaction forces of tire and hitch point, as shown in Figure 18. Also effect of cant and curvature are reflected during analysis by including gravity and centrifugal forces into equilibrium equations.

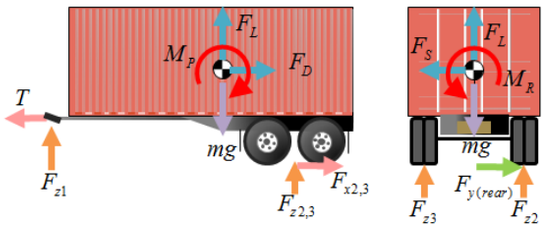


Figure 18. Established static model of trailer

Based on pictures of accident and collected information, basic information of the overturned trailer such as weight and dimension are assumed as shown in Table 4.

Table 4. Information of investigated trailer

Distance between hitch point and C.O.G*	3.6m
Distance between axle and C.O.G*	3.0m
Height of hitch point	1.4m
Height of C.O.G*	1.7m
Track width	1.86m
Weight of trailer	6.7t

* Center of gravity

Through vehicle analysis, vertical reaction forces of tires can be estimated for any wind condition, and critical wind speed is determined when one of vertical reaction forces becomes zero. Critical wind speed is determined for 16 wind directions with 22.5-degree interval.

Two straight road sections are located at both side of the curved section, and critical wind speed curves (CWCs) which show variation of critical wind speed for wind direction are determined for each section. Vehicle speed is assumed to be 50km/h, and curvature and cant of curved road are 450m and 2%, respectively. Since vehicle experiences various wind direction on curved section, minimum critical wind speed is selected for each wind direction. Estimated CWCs are shown in Figure 19.

A shift of CWC about 70 degree between two straight roads can be found due to change of travel direction, as shown in Figure 19. This difference indicates that accident possibility can be largely influenced by the vehicle location even under the same wind condition. In case of curved road, a flat portion could be observed in CWC due to the change of travel direction on the road. In other words, possibility that vehicle meets most critical wind direction on curved road is much larger than that on straight road. Also, even centrifugal force can make vehicle unstable if wind load acts in the same direction. These characteristics of curved road might be the reason of the overturning accidents, and particular traffic control strategy is required considering these points.

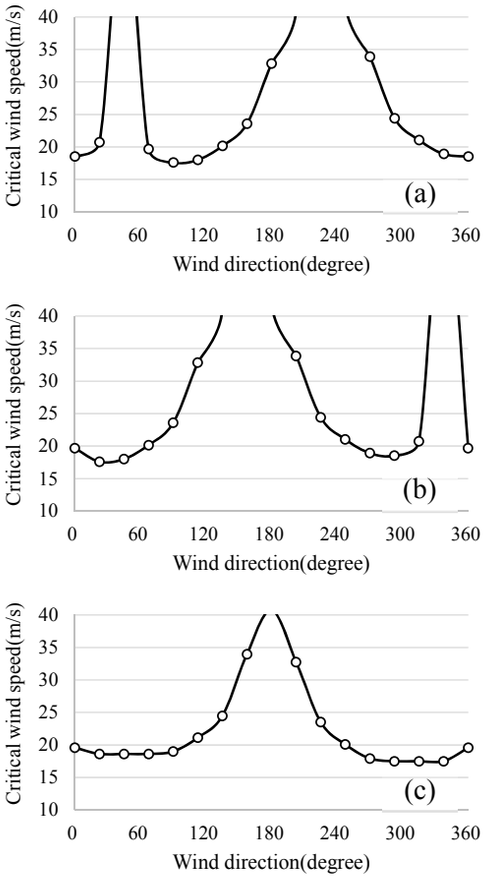


Figure 19. Critical wind speed curves for three sections: (a) straight road 1, (b) straight road 2 and (c) curved road

5.3 *Risk assessment using long-term measured data*

Probabilistic analysis is also performed to assess the frequency of daily maximum wind speed that exceeds CWC. Long-term wind data measured at nearby weather station are obtained to estimate probabilistic model of wind speed for each wind direction. Period of obtained data is 20 years and data type is 10-minute averaged daily maximum wind speed.

In order to reflect wind properties, Measure-Correlate-Predict (MCP) method (Carta et al. 2013) is applied which modifies long-term data based on field-monitored data. Field-monitored data of one year could be obtained which was measured from 2012.01.01 to 2012.12.31 at top of the tower of the bridge (see Figure 20).

Both of wind data have almost linear relation that correlation coefficient is estimated about 0.78 (see Figure 21). First-order regression model in equation (1) is utilized to convert long-term data which considers mean and standard deviation of wind speed.

$$U_T = \frac{\sigma_T}{\sigma_W} U_W + m_T - \frac{\sigma_T}{\sigma_W} m_W = 2.89 U_W - 3.34 \quad (1)$$

where U, σ, m are wind speed, standard deviation and mean of wind speed, respectively. Subscript W refers to the weather station and subscript T refers to the top of the tower.

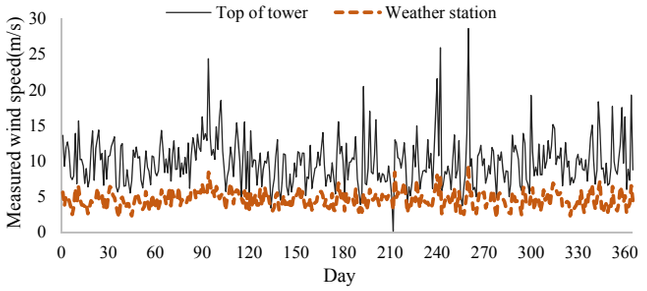


Figure 20. Wind data measured at bridge site and weather station

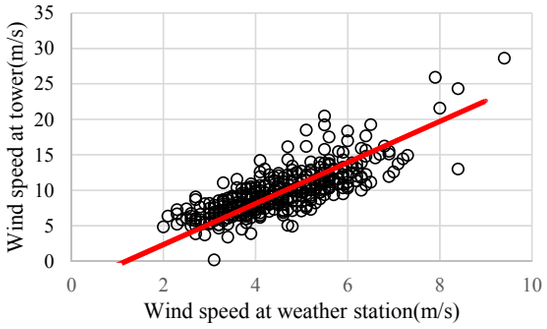


Figure 21. Correlation between two wind data sets (R=0.78)

The wind speed data measured at the top of the tower was transformed to those at the deck level by the exponential law for the wind profile in boundary layer.

Probabilistic distribution function is estimated using Generalized Extreme Value (GEV) distribution model. All wind data is classified into 16 directions with 22.5-degree interval, and three coefficients, location, scale and shape parameters, are estimated for each direction by the maximum likelihood method (Coles 2001). Figure 22 demonstrates an example of estimated cumulative distribution function.

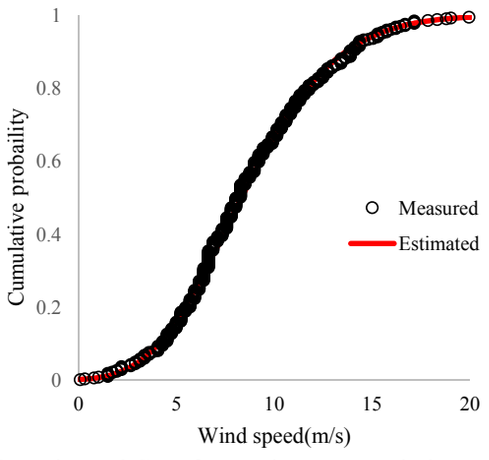


Figure 22. Estimated CDF for south-western wind

After estimation, a probability that wind speed exceeds CWC, P_E, is evaluated by considering 16 wind directions as equation (2) (Kim et al. 2016).

$$P_E = \sum_{all\ direction} P_i \times P_{E|dir=i} \quad (2)$$

where P_i is the probability that the direction of the wind is i, and $P_{E|dir=i}$ is the conditional probability that wind speed exceeds the critical wind speed for i.

Finally, by multiplying 365 days to P_E, number of days for traffic control, N_C, which is the risk index can be estimated. N_C is estimated for three road sections - two straight roads and one curved road. Additionally, in order to compare with other vehicle types, large van and passenger car are also investigated (Kim et al. 2016), and assumed vehicle speed is 60km/h. The results are shown in Figure 23.

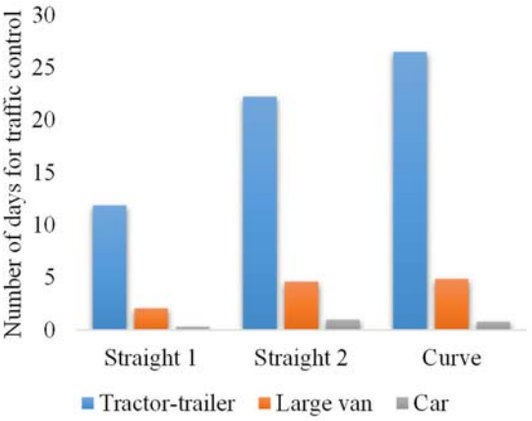


Figure 23. Estimated N_C for 3 sections and 3 vehicle types

According to Figure 23, straight 1 is safer than other sections, and the main reason for this difference is wind direction. Based on the wind rose of the bridge site, main wind direction is south-western which is almost parallel to direction of straight 1 section.

Another interesting point is that tractor-trailer is much vulnerable than other types of vehicle. It exceeds 5 days, a criterion for side-wind vulnerability, in all section. This result indicates the necessity of appropriate measure to secure trailer safety such as traffic control strategy.

Two parameters, vehicle speed and loading ratio, are investigated for traffic control strategy. According to Figures 24 and 25, both parameters can affect on risk index dramatically. The operator of the bridge has applied a limit vehicle speed as 40km/h when mean wind speed exceeds 10m/s. By decreasing the vehicle speed to 40km/h, the risk index for Straight 1 also decreases less than 5 days. Another efficient option to secure safety is increasing vehicle weight. If loading ratio, a ratio between loading weight and vehicle weight, increases to 50%, the risk indices for all directions reduce to 5 days.

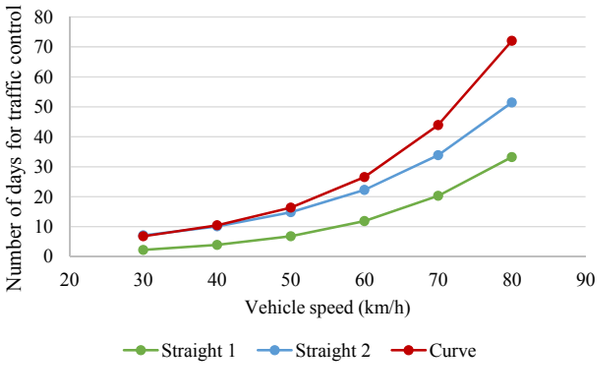


Figure 24. Variation of N_C according to vehicle speed

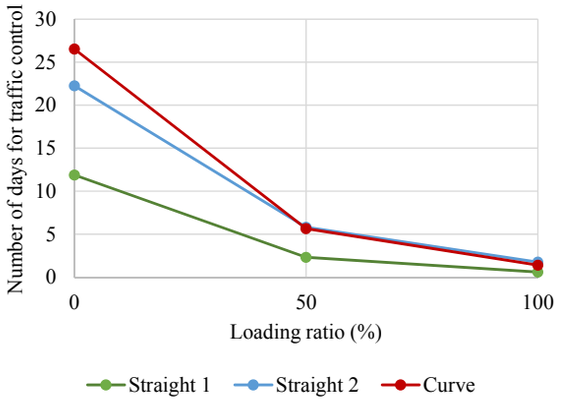


Figure 25. Variation of N_C according to loading ratio

5.4 *Short-term prediction of wind speed*

Operational actions such as closing the bridge require times to prepare it. Also, it should be important to predict when a normal operation can be restored. Accordingly, the short-term prediction of wind speed over the bridge deck is another issue in bridge operation during strong side wind.

Since wind speed data has nonstationarity, prediction model, which can handle nonstationary data, is required to increase prediction accuracy. Long Short-term Memory (LSTM), which is known to be suitable for dealing with time series, is applied to predict wind speed. LSTM is a deep learning algorithm, which is proposed by Hochreiter & Schmidhuber (1997). The basic structure of the LSTM is called LSTM Block, as shown in Figure 26. LSTM block consists of a cell state(c_t) and three gates, which are input(i_t), forget(f_t), and output gate(o_t).

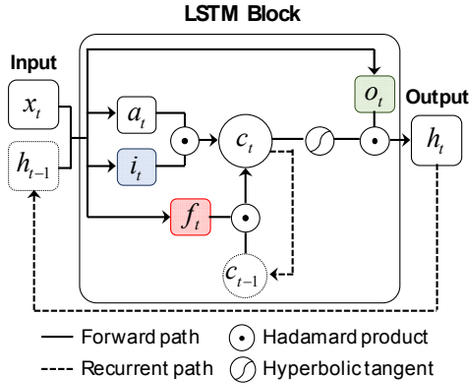


Figure 26. Structure of LSTM Block

Wind speed data measured at top of the tower of the bridge from 2003 to 2013 were obtained. The wind speed data is processed to 1-hour maximum wind speed from 10-minute wind speed. Wind speed during the typhoon Sanba is targeted to predict. In order to increase prediction accuracy, three typhoons, which are similar to the typhoon Sanba, are selected and wind speed data during those typhoons are utilized as training data. Wind speed is predicted from 1 hour to 6 hours in advance and prediction results are presented in Figure 27.

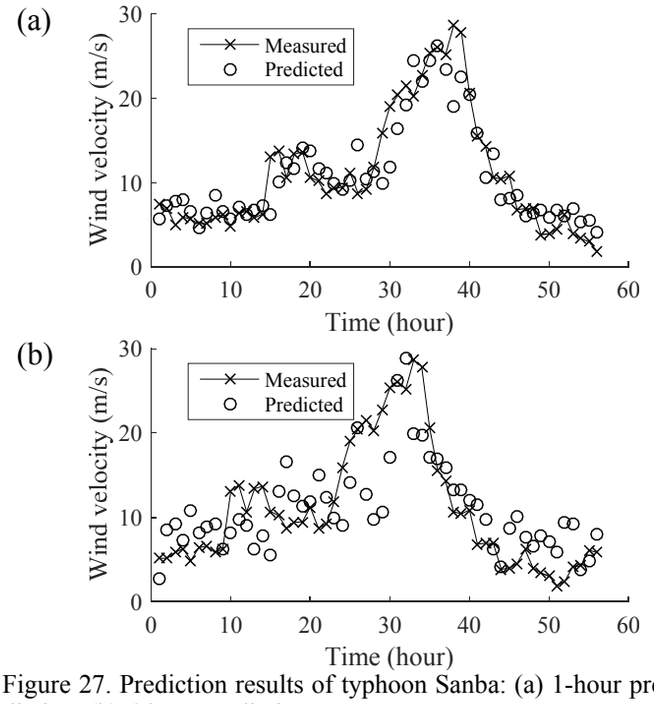


Figure 27. Prediction results of typhoon Sanba: (a) 1-hour prediction, (b) 6-hour prediction

As shown in Figure 25, the prediction accuracy is satisfactory, although the accuracy tends to become lower from 1-hour to 6-hour prediction in advance. Furthermore, the prediction model can capture the time of increasing and decreasing of wind speeds.

5.5 *Discussions*

Since vulnerability of vehicle from strong wind highly depends on not only wind speed but also other factors such as wind direction, vehicle speed and weight, traffic control strategy should be previously specified by considering these factors and road conditions in order to secure vehicle safety. Also, wind prediction based on deep learning algorithm can be a useful measure for prompt action during strong wind. All these procedures are parts of the best practices of increasing value of data available.

6 CONCLUSIONS

The data obtained from the field include much more information as demonstrated in case studies. However, soft technologies such as data processing, system identification with operational modal analysis (OMA), Measure-Correlate-Predict analysis, and Long Short-term Memory are also required to mine more accurate information from available data. Also, wind tunnel test is indispensable to compensate unmeasured areas of certain physics from field monitoring data, particularly for the aerodynamic events as demonstrated.

The findings from operational monitoring and corresponding analysis can feedback to enhance the current design practice, as demonstrated for the importance of design modal damping ratios of completed bridges. The damping identification from OMA is an essential issue as a serviceability performance index for flexible long-span bridge. Also, the vulnerability assessment procedure of running vehicle to strong side wind can be utilized for the effective traffic control by utilizing long-term and short-term wind speed data. By these way, examples of increasing the value of data for long-span bridge operation are demonstrated in an aerodynamic point of view.

7 ACKNOWLEDGEMENTS

This research was supported by a Grant (18SCIP-B119964-03) from the Ministry of Land, Infrastructure and Transport of the Korean Government through the Korea Bridge Design and Engineering Research Center (KBRC) at Seoul National University. This work was also supported by the National Research Foundation of Korea (NRF) grant funded by the Korean government (MSIP) (2017R1A2B4008973).

8 REFERENCES

Batista, M., Perkovič, M., 2014. A simple static analysis of moving road vehicle under crosswind. *Journal of Wind Engineering and Industrial Aerodynamics,* 128, 105–113.

Brincker, R., Zhang, L., & Andersen, P. (2000, February). Modal identification from ambient responses using frequency domain decomposition. In *Proc. of the 18*'International Modal Analysis Conference (IMAC), San A ntonio, Texas*.

Caicedo, J. M., Dyke, S. J., & Johnson, E. A. 2004. Natural excitation technique and eigensystem realization algorithm for phase I of the IASC-ASCE benchmark problem: Simulated data. *Journal of Engineering Mechanics*, *130*(1), 49-60.

Carta, J. A., Celazquez, S. & Cabrera, P. 2013. A review of measure-correlate-predict (MCP) methods used to estimate long-term wind characteristics at a target site. *Renewable and Sustainable Energy Reviews, 27*, 362-400.

Coles, S., 2001. *An Introduction to Statistical Modeling of Extreme Values*. Springer, London.

Kim, S., & Kim, H. K. 2017. Damping Identification of Bridges Under Nonstationary Ambient Vibration. *Engineering*, *3(6),* 839-844.

Kim, S. J., Kim, H. K., Calmer, R., Park, J., Kim, G. S., & Lee, D. K. 2013. Operational field monitoring of interactive vortex-induced vibrations between two parallel cable-stayed bridges. *Journal of wind engineering and industrial aerodynamics*, *123*, 143-154.

Kim, S., Park, J., & Kim, H. K. 2016. Damping identification and serviceability assessment of a cable-stayed bridge based on operational monitoring data. *Journal of Bridge Engineering*, *22*(3), 04016123.

Kim, S.J., Yoo, C.H. & Kim, H.K. 2016. Vulnerability assessment for the hazards of crosswinds when vehicles cross a bridge deck. *Journal of Wind Engineering and Industrial Aerodynamics* 156: 62-71.

Korean Society of Civil Engineers 2006. Design Guidelines for Steel Cable-Supported Bridges, Korea.

Hochreiter, S. & Schmidhuber, J. 1997. Long short-term memory. *Neural computation* 9(8): 1735-1780

Greff, K., Srivastava, R. K., Koutník, J., Steunebrink, B. R., & Schmidhuber, J. 2017. LSTM: A search space odyssey. *IEEE transactions on neural networks and learning systems* 28(10): 2222-2232.

Park, J., & Kim, H. K. 2017. Effect of the relative differences in the natural frequencies of parallel cable-stayed bridges during interactive vortex-induced vibration. *Journal of Wind Engineering and Industrial Aerodynamics*, *171*, 330-341.

Park, J., Kim, S., & Kim, H. K. 2017. Effect of gap distance on vortex-induced vibration in two parallel cable-stayed bridges. *Journal of Wind Engineering and Industrial Aerodynamics*, *162*, 35-44.

Seo, J. W., Kim, H. K., Park, J., Kim, K. T., & Kim, G. N. 2013. Interference effect on vortex-induced vibration in a parallel twin cable-stayed bridge. *Journal of wind engineering and industrial aerodynamics*, *116*, 7-20.

Maintenance, Safety, Risk, Management and Life-Cycle Performance of Bridges – Powers, Frangopol, Al-Mahaidi & Caprani (Eds)
© 2018 Taylor & Francis Group, London, ISBN 978-1-138-73045-8

Design Concept of the Twin River Bridges in Chongqing

M.C. Tang
T.Y. Lin International, San Francisco, California, USA

ABSTRACT: Chongqing is bisected by the Yangtze and Jialing Rivers, into three parts: Nanan in the south, Yuzhong in the middle and Jiangbei in the north. The Twin River Bridges are two cable-supported girder bridges: the Dongshuimen Bridge crosses the Yangtze River from Nanan to Yuzhong, while the Qianximen Bridge crosses the Jialing River from Yuzhong to Jiangbei. A tunnel under the entire Yuzhong District connects the two bridges. The bridge site offers the best vantage point of the City, so aesthetics were critically important for the design. The bridges carry four lanes of city traffic and two rapid transit tracks with very stringent design requirements. The girders are steel truss structures with orthotropic plates and the towers are made of concrete. The bridges were designed based on the concept of partially cable-supported girder bridge. This paper describes the development of two alternative design concepts and the final construction of these bridges.

1 INTRODUCTION

Chongqing is located in the middle of China. It is one of four municipalities in the country. The other three are Beijing, Shanghai and Tianjin. In China, a municipality is a city that directly reports to the central government, equivalent to a province. With a population of 32 million, Chongqing is the largest among the four municipalities. It is probably the largest city in the world with respect to population.

Chongqing is very hilly. It also has many rivers. The Yangtze River passes through the entire city diagonally. Besides the Yangtze, there are other rivers such as the Jialing, Wujiang, and Fujiang, etc. They all flow into the Yangtze River. With so many hills and rivers, Chongqing needs many bridges. It has also built many bridges. As of the end of 2017, the Municipality has over 15,000 bridges.

Metropolitan Chongqing is bisected by two major rivers, the Yangtze River in the south and the Jialing River in the north. These two rivers divide the metropolitan into three parts: the southern district, the northern district and the Yuzhong Peninsula in the middle, where the central business district is located. The southern district is called Nanping, the northern district is called Jiangbeijui. The Jialing River flows into the Yangtze at the tip of the peninsula.

The Twin River Bridges consist of two bridges: the Dongshuimen Bridge crosses the Yangtze connecting the southern district to the Yuzhong Peninsula and the Qianximen Bridge crosses the Jialing River connecting the Yuzhong District to the northern district. A tunnel under the Yuzhong Peninsula connects the two bridges so through traffic can flow from the Southern District directly to the Northern District without going through the streets of the Yuzhong Peninsula. (See Figure 1.) However, there are ramps at the peninsula to allow traffic to enter the Yuzhong District as well.

Both bridges have two decks. The upper deck carries four lanes of city traffic and the lower deck carries two tracks of transit trains. Chongqing will ultimately have 13 transit routes totaling over 500 km in length. The Twin Bridges are on Route #6.

Because of the bridges' high visibility, aesthetics were an important consideration during the bridge type selection process.

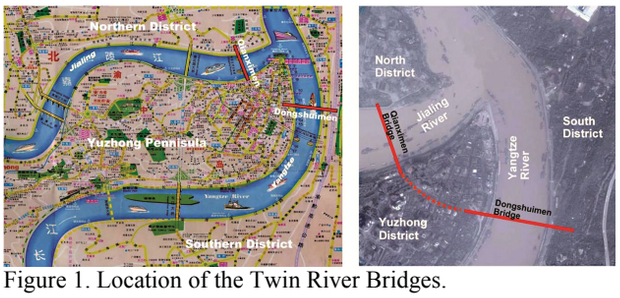


Figure 1. Location of the Twin River Bridges.

In 2008, the owner held an international design competition to select the final design concept. More than 20 bridge schemes were submitted by consulting firms encompassing all types of bridges includ-

ing girder, suspension, cable-stayed, arch, and extradosed bridges, and combinations thereof. The owner finally selected the partially cable-stayed girder bridge scheme proposed by the joint venture of Chongqing Communication & Research Institute and T.Y. Lin International. The joint venture had also submitted a suspension bridge scheme, which, incidentally, was the runner-up to the partially cable-stayed girder bridge scheme. As the technical director for the joint venture, the writer was responsible for the conceptualization of both bridge schemes.

2 BRIDGE TYPE SELECTION

The configuration of the Dongshuimen and Qianshimen Bridges had to satisfy aesthetic, geographic, and technical criteria. Because they were to be located between three city districts, they had to be harmonious with three disparate surroundings. They had to complement one another and they had to stand on their own. Finally, the bridges could not obstruct views of the city from various vantage points.

Navigational requirements and local geology demanded minimum main span lengths of 445m and 340m for the Dongshuimen and Qianximen Bridges respectively. The lack of a side span at the Yuzhong side of the Qianximen Bridge limited the number of towers to a single tower. Both span requirements influenced the type selection process.

In addition, the girder bridge had to be at least 12m deep to accommodate transit tracks on its lower deck. Such a deep girder has to be a truss for two reasons: to offer transit passengers a more open view of the area and to increase the transparency of the bridges themselves. A solid girder would look much too heavy in this area.

Another key factor during type selection was that the city had just constructed two major arch bridges not far away: the Caiyuanba Bridge and the Chaotianmen Bridge. Therefore, an arch bridge was not a favorable choice.

The choice of a conventional cable-stayed bridge was discarded because it would obstruct one's view of the city. A 340m span single tower cable-stayed bridge must have a tower protruding approximately 170m above the deck level. The bridge would be roughly 60m above normal water level so the total height of such a tower would be approximately 230m tall—taller than almost every building in the city. A conventional cable-stayed bridge would also have too many cables, further hindering the view of the city.

A regular girder bridge was also discarded because of the bridges' relatively long spans.

Consequently, it was decided that the bridges should be either a pair of partially cable-stayed girder bridges or a pair of suspension bridges for their relatively shorter towers and fewer cables. Both minimalist designs that would least disturb the surrounding space.

Keeping in mind the locations of the bridges in relation to the Yuzhong Penninsula, it was natural that the two bridges should be similar. Therefore, the writer conceptualized two schemes—a pair of suspension bridges and a pair of partially cable-stayed girder bridges.

3 SUSPENSION BRIDGE SCHEME

The suspension bridge scheme is comprised of two single tower suspension bridges with 496m main spans each, as shown in Figure 2. The side spans of both bridges are 250m long. They both have two planes of cables. The towers are 100m above the deck.



Figure 2. Renderings of a pair of suspension bridges.

On the Yuzhong Penninsula, where the rock formation is very fractured, it would be difficult to anchor the main cables in the soil, unless an extremely large anchor block and a major tie back system to transfer the cable force deep into the ground was used. Because there are numerous buildings in the area, the tie-back anchors would compromise the foundations of these buildings. Therefore, conventional suspension bridges were deemed unsuitable for these two bridges.

Self-anchored suspension bridge scheme was also studied. A 496m span self-anchored suspension bridge is technically possible, despite its record-setting length. However, it would be very expensive. To build a self-anchored suspension bridge, the girder must be erected before the cables can be suspended. This would require placing costly temporary piers in the river. The busy river traffic and swift current during the high water season would pose a danger to any temporary intermediate supports due to possible ship collisions. Besides, it would be much more expensive. Consequently, the idea of self-anchored suspension bridges was discarded.

To resolve this problem of anchorage, a special concept was introduced.

As mentioned above, the fractured rock is not good for tension. But it is capable of resisting compression. Thus it would be perfect if we could change the anchoring force from a tension force into a compression force.

The transit tunnel that connects the two bridges runs under a street on the Yuzhong Peninsula. The tunnel is about 600m long with a subway station in the middle, as shown in Figure 3.

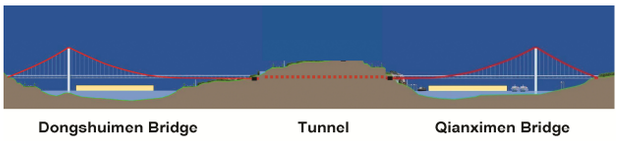


Figure 3. Connecting the main suspension cables through the Yuzhong Pennisula.

Making use of this arrangement, we had studied three anchoring schemes:

1 Instead of having to anchor the cables to an anchor block at the end of the bridge, it is possible to extend the main cables of each suspension bridge over the length of the tunnel and anchor them on the other face of the peninsula so the cables would exert a compression force on the rock, Figure 4a. In this scheme, the anchoring force is always equal to the cable force. Each bridge is an independent structure that does not affect the behavior of the other.
2 Because the two suspension bridges have the same span length and girder configuration, the cable force of the two bridges should be approximately equal all the time. If we use a pair of cables to connect the main cables of the two suspension bridges together, the combined structure will be similar to a suspension bridge with two towers, Figure 4b. In such an arrangement, loading on one bridge will affect the behavior of the other bridge. This will make the analysis much more complicated, especially because the tunnel is on a horizontal curve so there will be friction force along the curve the magnitude of which is difficult to predict.
3 To solve this problem we proposed to use a pair of connection cables, which are slightly larger than the main cables to connect to two anchor blocks which are located at the outer faces of the tunnel, Figure 4c. The connection cables are stressed to a force slightly higher than the maximum force in the main cables. If C_p is the cable force under permanent load, C_L is the cable force due to live load and other loads, and C_R is the minimum residue compression force we want to keep at the anchor blocks, the force in the connection cables, C_C, should be $C_C = C_p + C_{L,\,max} + C_R$ where C_p , and $C_{L,\,max}$ are known values while C_R is a value selected by the engineer. To assure that there is always a compression force acting on the rock, we proposed $C_R \approx 0.2\ (C_p + C_{L,\,max})$. Thus, under service conditions, the minimum compression force at the interface between the anchor block and the rock surface would be C_R, while the maximum compression force at the interface would be $C_R + C_{L,\,max} - C_{L,\,min}$ where $C_{L,\,min}$ is negative. Because the main component of cable force in a suspension bridge is due to its permanent load, the actual anchor force required is much smaller than the force in the main cables.

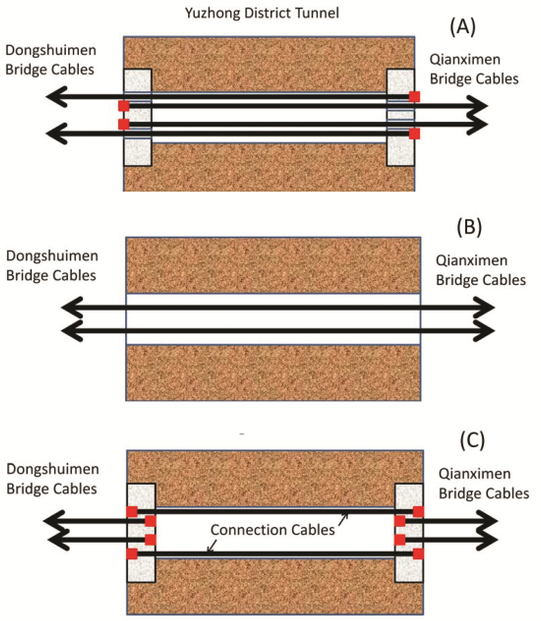


Figure 4. Anchorage schemes of the main cables.

Thus, the anchor blocks will always exert a compression force on the rock formation of the Yuzhong Peninsula. This is preferable for the fractured rock in the area. The connecting cables can run through a separate chamber underneath the transit tunnel. The chamber can be excavated and constructed simultaneously with the transit tunnel. Because this cable chamber is directly underneath the transit tunnel, there will be no right-of-way issues and the cost will be minimal. This anchorage arrangement basically separate the structure into two individual suspension bridges so the structural behavior of one bridge will not affect the behavior of the other bridge.



Figure 5 Rendering of the Suspension Bridge Scheme

The shape of a suspension bridge is usually very graceful. Therefore, a simple portal configuration for the towers of both bridges will fit well with the suspension cables, as shown in Figure 5. From afar, it looks like the two bridges are holding up the Yuzhong Peninsula. It would have been a very spectacular view!

Aesthetically, the pair of suspension bridges were attractive and compatible with one another. As well, they complemented the landscape and were transparent in elevation.

4 PARTIALLY CABLE-STAYED GIRDER BRIDGE SCHEME

Compared to the tower of a suspension bridge, the tower of a conventional cable-stayed bridge is typically twice as tall. In this scenario, while the span of the bridge may be reduced to 340m, its tower would remain 170m above the deck. Such a tall tower would not complement the surrounding landscape. Furthermore, a conventional cable-stayed bridge has many cables. They obstruct views of the city. Therefore, conventional cable-stayed bridges are not suitable for this bridge site. In order to satisfy all design requirements and aesthetic expectations, a pair of partially cable-stayed girder bridges was selected, as shown in Figure 6.



Figure 6. Renderings of the partially cable-stayed girder bridge scheme.

At the time of this proposal, the concept of a partially cable-stayed girder bridge, (Tang 2007), has been applied successfully to the design of several medium-span bridges in China, most notably the Taijiang Bridge in Sanming and the Sanhao Bridge in Shenyang. While the spans of the Twin River Bridges are much longer, the girder depths of these two bridges, at 12m, are also much deeper. Thus, the span to girder depth ratio is comparable to that of the previously designed medium-span partially cable-supported girder bridges.

The minimum main span length of the Dongshuimen Bridge is 445m. Thus, the span to girder depth ratio is 445/12 = 37. The minimum main span length of the Qianximen Bridge is 340m. Its span to girder depth ratio is 340/12 = 28.3. These ratios are within the workable range of partially cable-stayed girder bridges.

The Dongshuimen Bridge has two towers while the Qianximen Bridge has one tower. All three towers are 100m high above the upper deck. Each tower of the Dongshuimen Bridge carries nine pairs of cables. The tower of the Qianximen Bridge has ten pairs of cables. All of the cables are located on a single plane on the center line of the bridge. The upper deck is an orthotropic steel deck with a minimum deck plate thickness of 16mm. The main floor beams are 2.00m deep. The lower deck consists of four longitudinal beams located directly under the rails. Transverse girders are 1.20m deep. The lower floor system is also an orthotropic deck with open ribs. The orthotropic deck serves as a platform next to the tracks. It acts monolithically with the lower chord of the main truss.

It is the desire of the owner that these two bridges are to be signature structures of the City. With a single plane of cables in the middle of the box girder, the towers can be either a diamond shape or an inverted Y shape. However, those tower shapes would not have been sufficiently distinctive to satisfy the aesthetic requirement. After extensive studies, the very special tower shape as shown was adopted. It simulates the shuttle of a Chinese weaving machine. The writer had studied this tower shape for a long time but has not been able to find a suitable bridge for it. Most bridges in China have six lanes or more, a six-lane bridge girder would be too wide for this tower shape. It would loss its elegant slenderness. The Twin River Bridges are four lane bridges, which are perfect for this slender tower configuration!



Figure 7. Renderings of the partially cable-stayed girder bridges.

As shown in Figure 7 above, the bridges are located at the tip of the peninsula. Both bridges can be seen from various view points of the city. Therefore, it is more harmonious if all three towers have the same shape. Figure 8 shows the basic dimensions of the tower. Because the ground elevation of each tower is different, the very bottom portion of the towers can be slightly different from each other. For the tower with lower ground elevation the tower shape is extended longer. However, at normal water level, all three towers look the same.

The lower portion of the tower has an oval cross section, as shown in Figure 8. The two ends are circular and the middle part consists of two flat surfaces. The upper portion of the tower has the same basic shape except the middle part is cut out to receive the girder. The radius of the circular surface is constant over the entire height of the tower. Thus, we can reuse most of the formwork, which is a major cost in concrete construction.

Both the Yangtze and the Jialing are busy waterways. Therefore, ship and barge collision must be carefully considered. The lower portion of each tower has relatively thick walls to resist any possible impact by barges or ships. The smooth oval shape of the tower cross section is also beneficial in redirecting the ship impact forces away from the tower.

Even though the tower looks curvy, the center of gravity of the members in the towers are close to straight lines.

The top of the tower is separated into two symmetrical arms by a vertical slit. All cables are anchored to inclined steel anchor plates inside the slit. The anchor plates are welded to two large vertical steel plates, each of which is attached to the face of the slit in the concrete tower head by means of shear studs. There are two concrete blocks that connect the two tower arms together, one at the top and one at the bottom. These two concrete blocks are to resist the bending of the tower arms due to the eccentricity of the cable anchorage to the arms. Light can shed through the slit to give the tower head a much lighter appearance. The concrete blocks can also serve as anchorage blocks for temporary cables during possible rehabilitation. It is envision that the temporary cable strands can just wrap around the concrete block, which has a round surface. They can be reinforced using a curved steel plate on top of the concrete surface, if required.

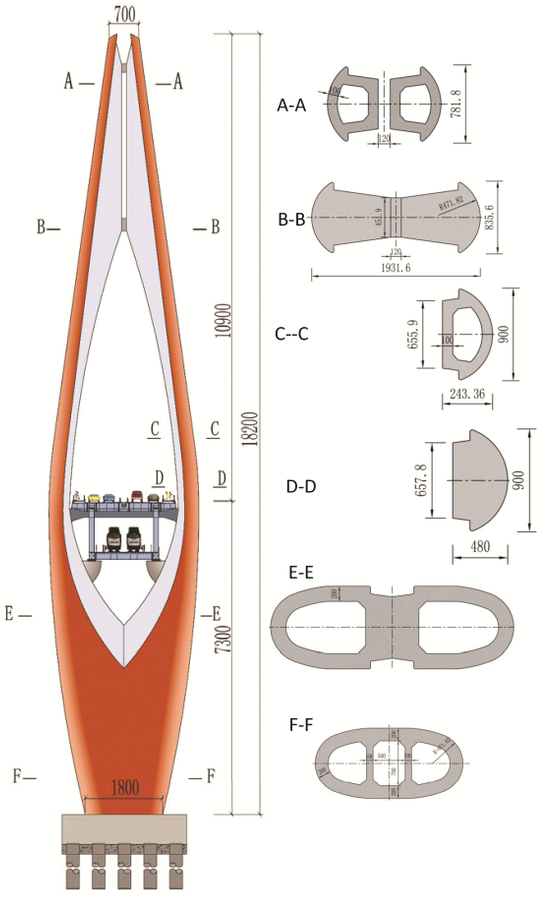


Figure 8. Tower and tower cross sections.

5 THE GIRDER

The main girder of the two bridges is a steel truss. The girder is about 12m deep except at the end of the Qianximen Bridge where the girder is deepened to accommodate additional cross beam for the transition. This girder depth was required for the transit tracks. Such a deep girder would be a disturbance to the river view if it were solid. Therefore, a steel truss was selected to make the girder look more transparent.

The cross section of the truss is as shown in Figure 9. It carries four lanes of city traffic and two pedestrian paths on the upper level and two tracks of transit on the lower level. The upper level has an orthotropic steel bridge deck with flat ribs.

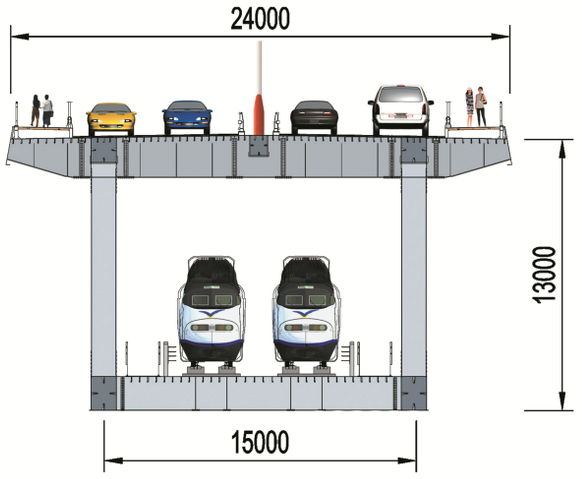


Figure 9. Truss girder cross section

There are several possible ways to support the rails of the transit tracks in a bridge. For these two bridges, the owner decided on a concrete supporting plate version, which is very heavy. In a cable-stayed bridge, the axial force in the girder is directly proportional to the weight of the girder. Therefore, the axial force in the girder of these two bridges is very high.

The reason to use flat ribs instead of the more popular trapezoidal ribs is a better guarantee of welding quality of the ribs to the deck plate. The Twin River Bridges are cable-stayed girder bridges, which have very high longitudinal axial forces in addition to the high bending moment in the girder. They cause high stresses in the orthotropic deck. In addition, the lower level of the Twin River Bridges was designed to carry trains, which are very heavy. To resist the high axial force and bending moment it is necessary to have more steel area in the deck. Therefore, a heavier orthotropic steel deck is actually beneficial for the structure. The beefier open rib orthotropic deck is not a disadvantage to the bridge. The other reason for using open ribs is that the Twin River Bridges have a single plane of cables located in the center line of the bridge girder. The transverse bending moment of the girder causes tension in the top deck in the transverse direction. This transverse tensile stress in the deck plate must be designed for fatigue stresses. Therefore, it is more desirable to make sure that higher quality welds between the ribs and the deck plate can be readily achieved. Thus, open ribs are a better choice.

Another important consideration in the selection of open rib is due to the quality control of the fabrication. Welding in an orthotropic deck with trapezoidal ribs requires very high quality control. If this cannot be assured, open ribs are a better choice.

The partially cable-stayed girder bridge scheme was selected by the owner for the final design.

6 DESIGN CONCEPT – THE PARTIALLY CABLE-STAYED GIRDER BRIDGE

Partially cable-supported girder bridge is a subset of partially cable-supported girder bridge. Because a 12m deep girder is required to accommodate the transit tracks on the lower level, the main truss girder itself provides a relatively high capacity for carrying the loads. The concept of partially cable-stayed girder bridge, as described in “Rethinking Bridge Design: A New Configuration,” (Tang 2007), can be applied here with great advantage. The idea is to design a girder bridge, the load capacity of which is to be supplemented by cable forces. The cable forces are selected so as to provide what is needed to bring the total capacity of the bridge to the required level. Therefore, the cable forces can be assigned with relative freedom.

Figure 10 portrays the design procedure of a partially cable-stayed girder bridge. For simplicity, we use a uniform steel girder under uniform load as example. Figure 10a illustrates a three-span uniform steel girder under a uniform load. Figure 10b shows the positive and negative bending moment in the girder under the given uniform load and the moment capacities of the girder. Portions of the girder do not have a sufficient capacity to resist the bending moment caused by the load on the girder. Figure 10c shows the shortage in capacity. To address this issue, a cable-stay system, as shown in Figure 10d can be used to produce an additional bending moment capacity, as shown in Figure 10e, to make up the difference can be added as indicated by Figure 10f.

There are many combinations of cable forces that can produce bending moments that will satisfy or exceed the demand requirements not assumed by the girder’s moment capacity as shown in Figure 10e. It will be advisable to assign cable forces in such a way as to gain certain advantages in fabrication and/or in construction. For example, to simplify construction of the girder, we can select a set of cable forces that will have the same vertical component. This will allow us to have one design for all cable anchorage points in the girder. Alternatively, we can assign the same force to all cables to simplify cable manufacturing.

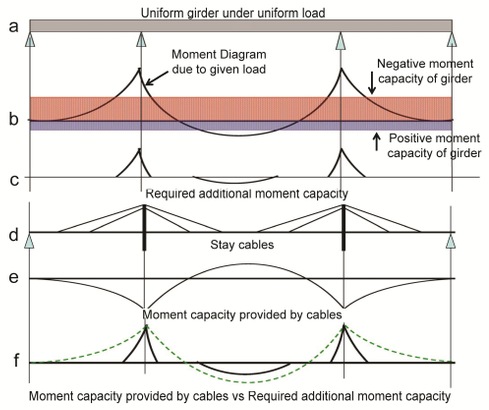


Figure 10 The Concept of Partially Cable-Stayed Girder Bridge

A partially cable-stayed girder bridge is an economical solution in that it fully utilizes the capacities of both the deep girder and the stay cable system. In addition, a single plane of cables has a transparent appearance and satisfies the aesthetic criteria for this location.

7 CONSTRUCTION

China has built many long span cable-stayed bridges in the last 30 years. Today, construction of cable-stayed bridges is relatively routine. The towers of both bridges are located at shallow water or rock outcrop so foundations can be constructed rather easily. However, foundation construction of bridges in Chongqing must be carefully scheduled to avoid the high water season, which runs from about May to October each year. The water level can rise over 30 meters above the normal water level. Therefore, the foundation of the towers was constructed within one low water season to eliminate the need of high cofferdams.

The towers were constructed using jump forms with 2m lifts. Wood forms were used to better suit the curvature of the surface. Wood forms are also sturdier so the resulting surface is smoother.

The girders were built as cantilevers. The method is rather routine.

8 COLOR SCHEMES

We have done an extensive study on the color of the bridge. Figure 11 shows a few color combinations we originally proposed. During the design stage, the latest color scheme was chosen. However, after the bridge was complete, the owner decided to have the color combination as shown in Figure 12. Red is a rather popular color in China.

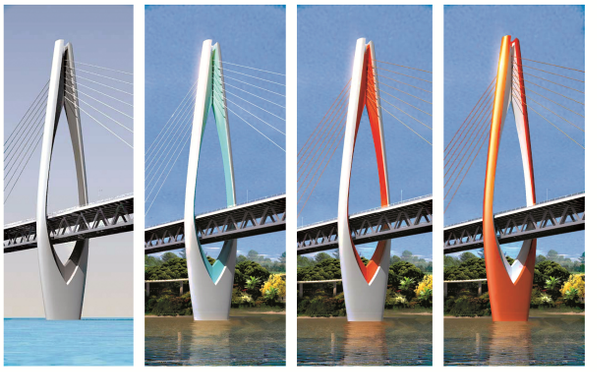


Figure 11. Various color schemes of the towers.



Figure 12 The completed bridges.

9 A BEAUTIFUL ADDITION TO THE BRIDGE CAPITAL OF CHINA

Since the opening up of China 30 years ago, bridge construction has been a focus of infrastructure developments there. In 1996, the City of Chongqing was separated from Sichuan province and became a special municipality, reporting directly to the central government. Chongqing has since become one of China's most vibrant cities. The city's rapid development has led to the construction of many new bridges. Indeed, Chongqing is often called the "Bridge Capital of China" because of its plethora and variety of bridges. The Dongshuimen Bridge and the Qianximen Bridge are two more beautiful additions to this "Bridge Capital of China."

REFERENCES

Tang, M.C., "Rethinking Bridge Design: A New Configuration." *Civil Engineering Magazine*, *American Society of Civil Engineers,* Volume 77, Number 7, July 2007. pp28-45.

MINI SYMPOSIA

MS01: Innovations and world leading research and practice in bridge management systems

Organizers: N. Powers & S. Joshi

Maintenance, Safety, Risk, Management and Life-Cycle Performance of Bridges – Powers, Frangopol, Al-Mahaidi & Caprani (Eds)
© 2018 Taylor & Francis Group, London, ISBN 978-1-138-73045-8

Experience of Management of Bridges Prior to and Post Evaluation of BMS on NH network of India

Sachidanand Joshi
Team Leader, IBMS, IDDC Engineers Pvt. Ltd., India

Nagaraju Naga
Assistant Bridge Engineer, IBMS, IDDC Engineers Pvt. Ltd., India

Unnam Rajesh
Assistant Bridge Engineer, IBMS, IDDC Engineers Pvt. Ltd., India

1 ABSTRACT

India has second largest road network in the world having a Road Network of over 5,472,144 kilometres (3,400,233 mi) which comprises 1,00,087.02 km National Highways which includes over 35,733 Bridges. If we want to repair and rehabilitate these Bridges, current information looks inadequate, also Indian scenario needs trained and responsive manpower to be proactive to repair and rehabilitate the Bridges. Fund allocation required is huge. There is lack of training and manpower to handle the work of this magnitude. Even in recent past before Indian Bridge Management System (IBMS), Digital Inventory of Structures (Bridges & Culverts) including year of construction of various structures and criteria for defining condition of structures did not look feasible. The historical data of inspections and maintenance works was recorded which was piecemeal and thus it founds to be the main hurdle in developing a scientific management system. If the same scenario continues further which may not provide a better trait for Improving the life span of structures existing on National Highways of country, which in turn will have a direct impact in the development of Country.

Importance of maintenance of any infrastructure to keep it in serviceable condition during its entire service life needs no emphasis. In fact the huge cost invested in creating the infrastructure loses its significance and becomes irrelevant if due attention is not given towards its regular maintenance. A timely and appropriate intervention can only be planned if relevant data and tool for logical & scientific analysis is available.

Indian Bridge Management System (IBMS) is developed to create an inventory of all bridge assets in India and apply a technical logic to manage the Bridge asset during its life cycle. It generates detailed inventory data and condition ratings of assets to ensure that dynamics of deterioration process are captured and this dynamism in the deterioration process guides the inspection and rehabilitation of bridges. The system allows the user to assign priority to maintenance activity based on the present condition of the Bridge.

Indian Bridge Management System (IBMS) is the largest platform in the world with a database of more than 1,61,739 bridge structures owned by single owner.

2 MANAGEMENT OF BRIDGES PRIOR TO AND POST IBMS

2.1 *Pre-IBMS:*

In the earlier days management and maintenance of bridges were done by collecting the data by using the bridge register which were manually written with the technical details and identify the distress visually by standing on the structure by the respective authorities which are kept in the form of hard copies and they can't be able to access and identify the distress that occur in the bottom side of the structure via., girders, bearings, pedestal, substructure etc. Likewise they were collected the data of the bridges which are falling in their respective boundaries, which makes very difficult to access for further references and for further comparison of data to the ministry in order to take the decision. If the same phenomena continues then the management and maintenance of thousands of bridge data had become a real challenge for bridge engineers without having a systematic approach for a decision making. Repairs, Rehabilitation and Retrofitting need authentic, reliable and factual data in real time to enable efficient solutions. In order to overcome these problems a digital platform came into picture which is called IBMS.

The following mishaps which happened in the past one and half year in the country had highlighted for the need of IBMS.

Case:-1 – British Era Bridge Collapse on Mumbai-Goa Highway, Maharashtra

British Era Bridge which is over 100 years old bridge connecting from Mumbai to Goa and is crossing over Savitri River in Raigad district in the state of Maharashtra had collapsed on the mid night of 02.08.2016. Because of this tragic accident around 22 people from two buses had swept away.

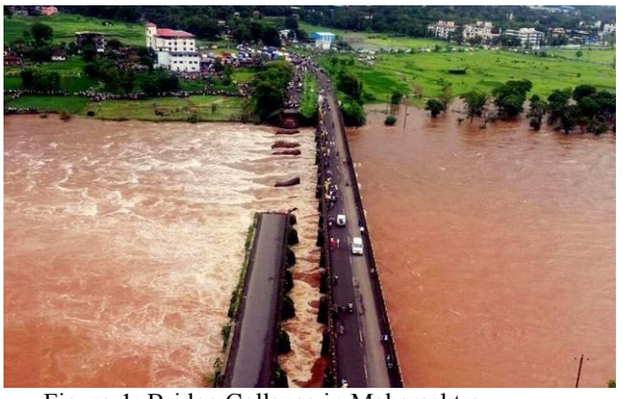


Figure-1: Bridge Collapse in Maharashtra

Case:-2 – Collapse of Bridge in Araria District, Bihar

Collapse of a Bridge which is connecting a village in Araria district of Bihar state on 18.08.2017 had feared drowned 3 people (1-Woman, 1-Girl & 1-Man).



Figure-2: Bridge Collapse in Bihar

2.2 *IBMS System:*

Development of the system posed its own challenge as the system to manage asset had to be developed in a manner where the field studies could be conducted with minimum effort and in which maximum details could be collected. The volume of the database was also posing a challenge; it is anticipated that the overall data base will consist of over 1,61,739 culverts and bridge data. This is a huge volume to handle for a management platform. The bridges have to be given a unique identity number which was the first step of inventory creation. Then their precise location details in form of Latitude and Longitude had to be collected in an Auto mode using the Ground Positioning system. Once these details are collected, the engineering properties of the bridge design, material and other technical details of the bridge are being collected. These are essential components of inventory collection process. On completion of inventory data, the structural component rating is done using a 0 to 9 scale to define the status of various bridge components like Foundation, Piers, Super structure, Deck, Scour rating, waterway adequacy, structural status and also Socio- Economic parameter which decide the importance of the bridge in relation to its contribution to daily social and economic activity of the area in its immediate vicinity. A scale of 0 to 9 was used to ensure that the in-experience of Field engineers (Over 2000) in using rating system does not critically affect our analysis once the inventory is complete.

3 POST IBMS

Data collection is in real time and should have on site stamping for location (Latitude and Longitude) to embed for all bridge data collected. Collection system is capable of uploading photos and data collected by User in Auto mode. On completion of all entries, the bridge data shifts from bridge for Update to Bridge for Submit. The software needs the user to remain online or logged in till the time the data is uploaded or transferred to the server. Classification of bridge is done by a series of alpha numeric strings which is based on specific details of the bridge. There are 5 such strings used to classify the bridge. They being

Table:-1 Classification of Strings

S.No.	Strings used to classify the Bridge	Parameters considered
1	National Identity number	State Code, RTO Zone, Type of road, Road/Highway Number, Chainage and Bridge Cumulative Number
2	Bridge Location number	Latitude & Longitude
3	Bridge Classification number	Structural Form, Material of Construction, Type of Bridge, Loading as per IRC, Age of Bridge, Traffic Lanes on Bridge, Bridge Structure Crossing Feature, Length of the Bridge & Width of the Bridge
4	Bridge Structural and Functional Rating number (SR and FR)	Rating for Deck, Rating for Superstructure, Rating for Substructure, Rating for Bank & Channel, Rating for Structural Evolution, Rating for Vertical Clearance, Rating for Waterway Adequacy & Rating for Scour Efficiency
5	Bridge Socio- Economic rating number (SER)	Rating for Connectivity between two Cities, Rating for Average Daily Traffic, Rating for Social Importance, Rating for Economic Growth, Rating for Alternate Route & Rating for Environmental Importance

Inventory compiles Structural rating (SR), Functional rating (FR) & Socio- Economical rating (SER).Below chart depicts the logical flow of event and decision making within IBMS Inspection and testing module.

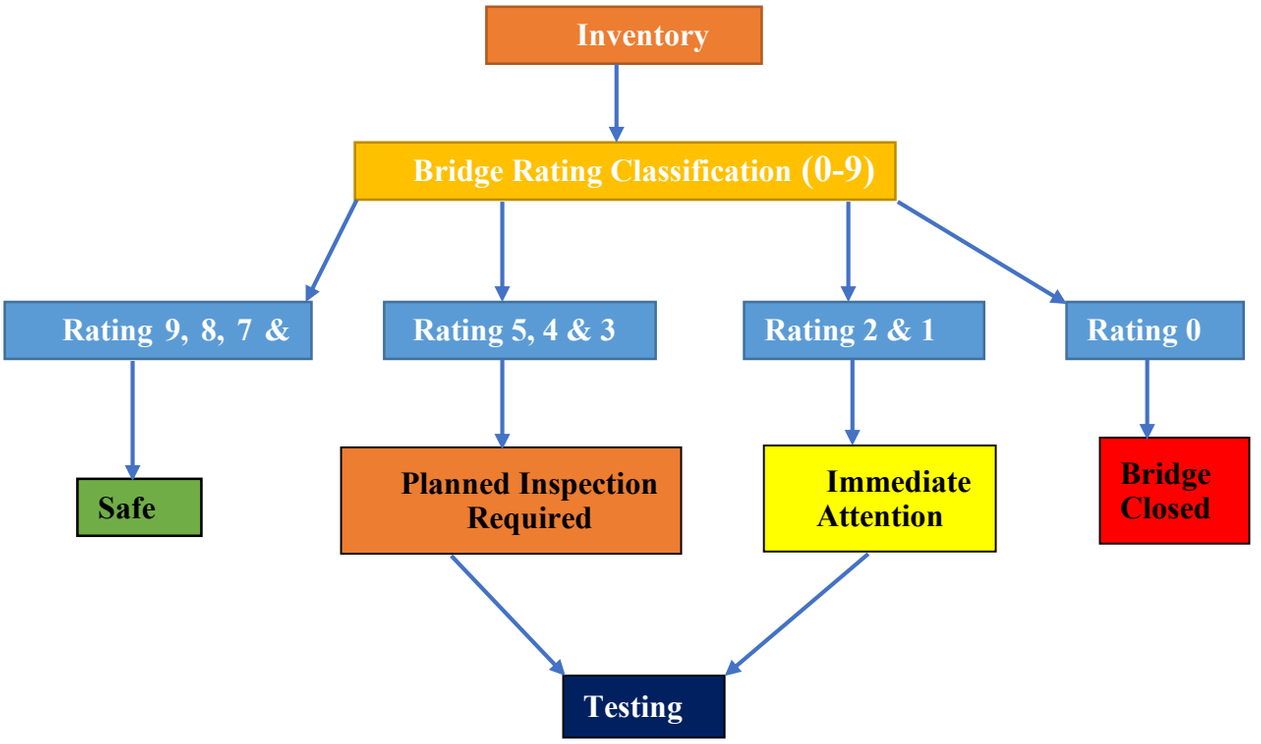


Figure-3: Flow of event and decision making within IBMS (Source: Author)

In the first task, inventory data and rating is completed, the same is required to be validated during the inspection stage.

The second task during Bridge Inspection, the Bridge Inspection Engineer has to ascertain the ratings provided during inventory. This provides for in built validation of data collected during inventory. Based on the observations of the bridge parameters and the environment and traffic condition existing at bridge location, it is essential for the bridge Inspection engineer to reassess the rating provided by the Inventory engineer. This procedure fulfils the need for self-validation of all data that ensures that data used by IBMS in processing is correct and validated.

The third task during the inspection process is to complete the prognosis of distress in bridge if any distress is observed. To be able to do this, it is critical that the Bridge Inspection Engineer to understand the various deterioration processes and what type of distress causes this deterioration process to happen.

3.1 *Identification of Distress Bridges:*

In order to distinguish the distress bridges (Structurally inadequate) in this category we had considered the following components into account,

- Rating for Integral & Non-Integral Deck.
- Rating for Superstructure.
- Rating for Substructure.
- Rating for Scour Efficiency.

By considering the above components into account we had found 6551 number of bridges that are structurally inadequate and their details are given below,

As per the Type of Bridge

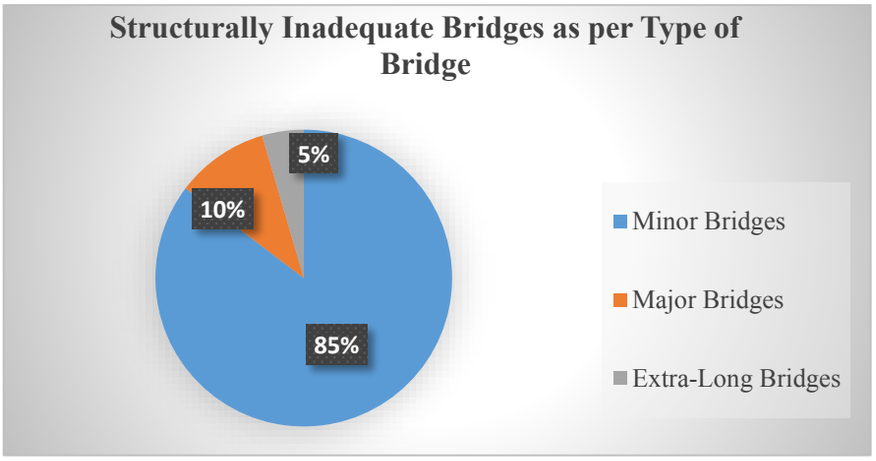


Figure:-4 Structurally Inadequate Bridges as per Type of Bridge (Source: Author)

As per the Age of Bridge

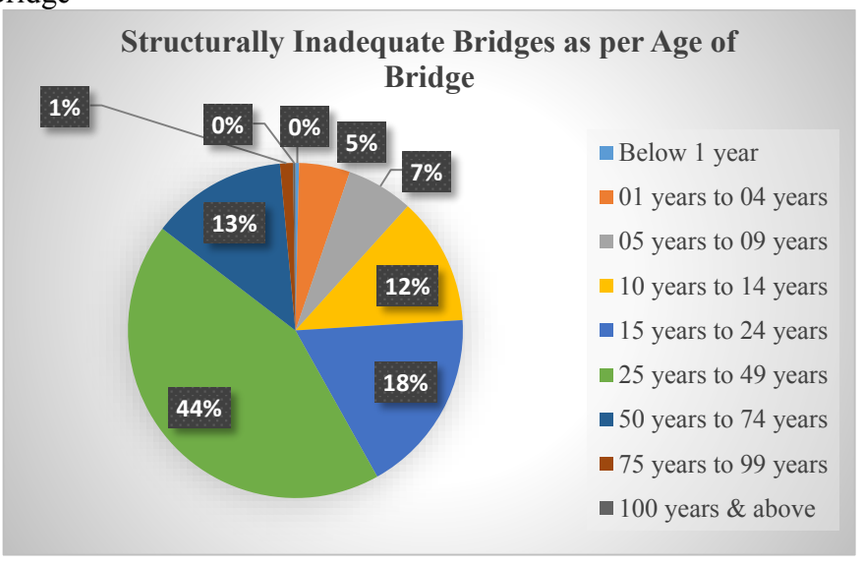


Figure:-5 Structurally Inadequate Bridges as per Age of Bridge (Source: Author)

In order to distinguish the distress bridges (Functionally inadequate) in this category we had considered the following components into account,

- Rating for Bank & Channel.
- Rating for Waterway Adequacy.
- Rating for Vertical Clearance.

By considering the above components into account we had found 4807 number of bridges that are functionally inadequate and their details are given below,

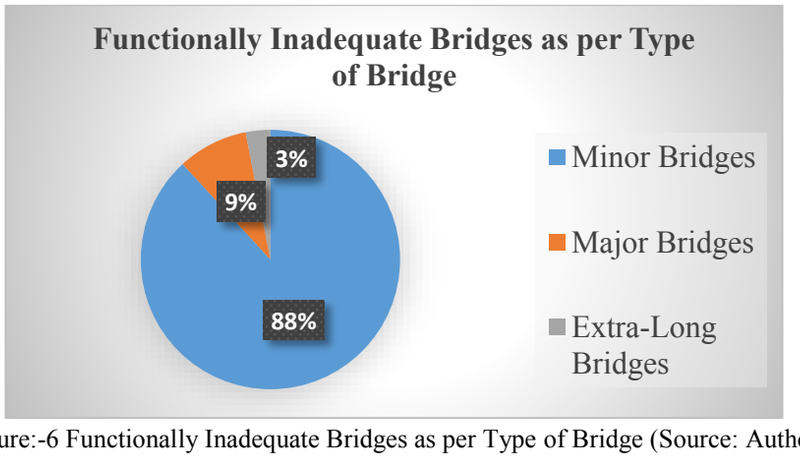


Figure:-6 Functionally Inadequate Bridges as per Type of Bridge (Source: Author)

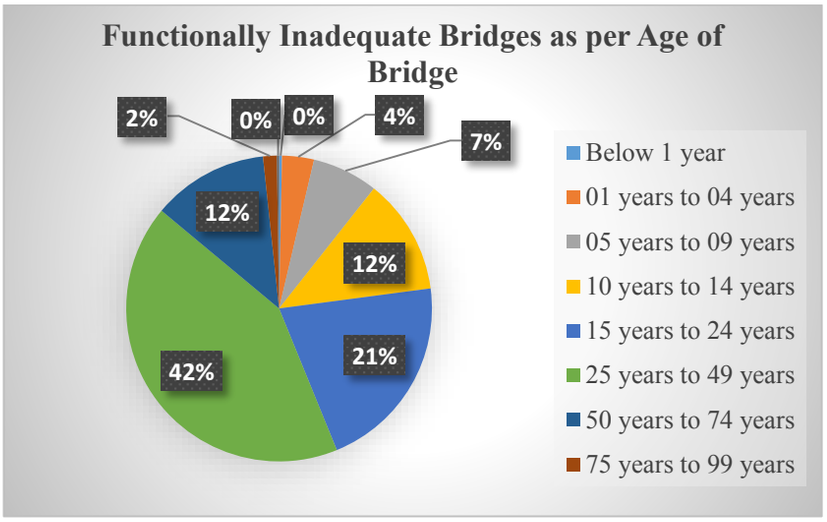


Figure:-7 Functionally Inadequate Bridges as per Age of Bridge (Source: Author)

The Distress in bridge is any situation that is not designed and has occurred. Deterioration is the manifestation or propagation of this distress in a continuous manner to cause alarm. Bridge Inspection Engineer based on his expertise and knowledge will judge the reason for the distress to have occurred and this form the prognosis of distress. The main cause of distress which sometimes results in manifestation of other type of distress or is severe is called the primary cause of distress. The subsequent distress that gets manifested or resultant due to primary distress is called secondary distress. Distress can occur in specific and localized manner as much as it can occur in the overall structure. The final distress map of the bridge may be a result of multiple causes (primary cause and secondary cause) and combined effect of both primary and secondary causes. This could at times make it difficult to determine the correct primary cause. Primary cause can be defined as the cause that is seen to the maximum and has resulted in most extensive distress from among the all the other causes.

Ideally it is better to eliminate the causes rather than identify the cause. This could result in a matrix of causes. From among these identified causes, the primary cause can be confirmed if not properly identified initially.

Based on the cause the following parameters need to be assigned a rating. This assignment is based on the various symptoms observed and for which a rating scale of 0 to 9 is used. 0 rating is assigned for very severe condition and 9 is assigned to no distress condition.

The parameters identified for compilation of deterioration matrix are as defined in below table. These three causes are further classified based on the cause as under and ratings are assigned to each of the parameters from 0 to 9.

Table:-2 Causes of Deterioration

S.No.	Causes	Parameters	Ratings
1	Aggression by Mechanical	Impact	
		Abrasion	
		Erosion, Cavitation & Wear	
		Over load	
		Fatigue	
2	Aggression by Physical	Temperature	
		Shrinkage induced Distress	
3	Aggression by Chemical	Aggression by Carbon dioxide & Chlorides	
		Aggression by Sulphates	
		Aggression by Carbonation	
		Alkali-aggregate reaction	

Once the assignment of rating is done for distress, this is used to identify the method of testing to be adopted. The application of test on the component of bridge is decided by the Structural ratings matrix.

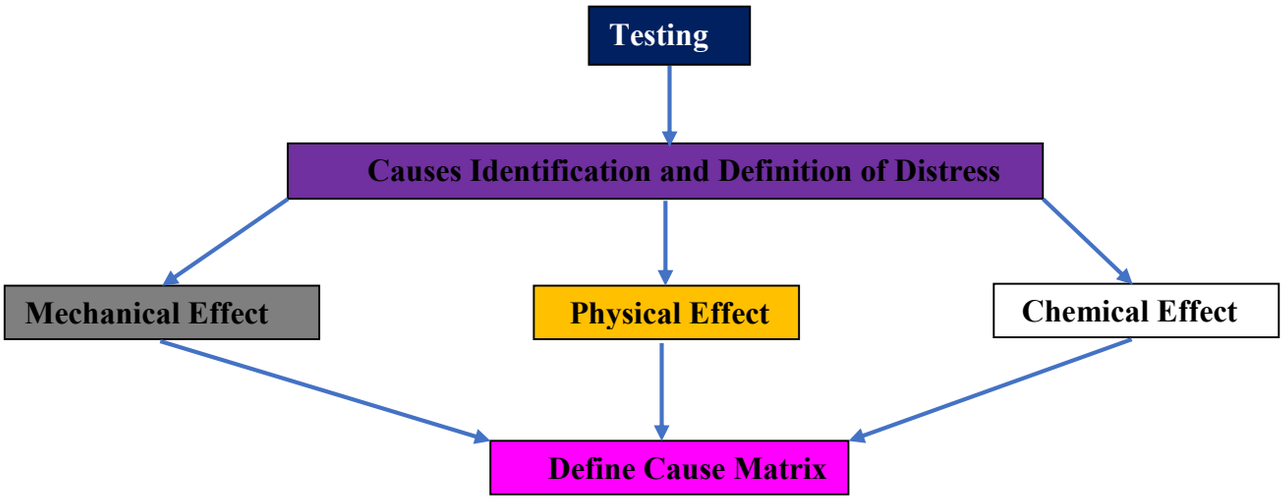


Figure-8: Decision making post testing within IBMS (Source: Author)

3.2 *Define Cause Matrix:*

By defining cause matrix to be able to capture the combined effect of each of the process, we assign rating number to each of the process and then combine these rating in the form of a Deterioration Matrix P.

$$P = \begin{pmatrix} \text{Mechanical} & \text{Physical} & \text{Chemical} \end{pmatrix}$$

This creates the deterioration matrix which identifies the main cause of deterioration and also the secondary cause of deterioration

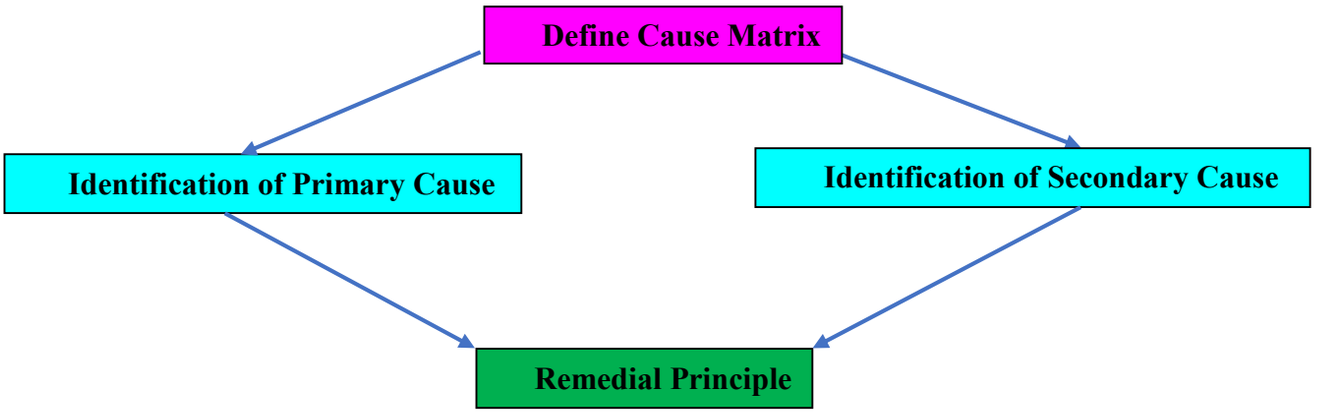


Figure:-9 Decision making post Cause identification within IBMS (Source: Author)

3.3 *Principle Adoption:*

During identification of the cause of distress, laminar behavior of the bridge is to be accounted for most the distress affects the lamina of the bridge component. Such effect causes the surface lamina of the component to deteriorate faster than the section. Such effects are to be recorded and accordingly the repair strategy is to be selected.

Once the principle cause is identified, certain principles only can be adopted to address that cause. However as the bridge structure is massive, contributory factors and principle factor could be affecting the bridge in certain specific areas/ locations. In such cases the locations cause will dictate the repair principle. Certain principle of repair need to applied to the whole bridge structure and such principles have to be applied post all other repair principles are applied.

4 CONCLUSION

IBMS had completed two years of implementation and one major cycle of inventory and inspection had been completed. The first year's work required 20 months to complete due to large volumes of structures to be managed.
The findings of first cycle has resulted in completion of inventory of over 169758 Structures on the National Highway network in India. Of these there are 36,673 bridges. From these bridges IBMS has identified over 6551 bridges to have structural inadequacy and over 4807 bridge to be functionally inadequate.

IBMS aims to render all bridges safe by application of Maintenance Repair/Rehabilitation Strengthening & Replacement (MRSR) modules to the bridges few at a time (presently using the First Repair Worst Damage (FRWD) protocol to bridges whose rating is below 3) and once all bridges are rendered safe (rating above 5), the efforts would be directed to improve on the efficiency of the management of bridges by ensuring all bridges have repeat rating above 6 and would only require timely maintenance.

The above method provides for a logical sequence to decision making and eases the process of decision making till the point where the principles for remedial measures are defined for application. The only thing that is left for the field engineer to do is to be able to properly estimate the correct extend of distress and then define the application area for the suggested remedial measure.

The quantification can also be automated once the as built drawings of the bridges are available and then on this drawing we superimpose the distress. The future of IBMS shall involve application of BIM (Bridge Information Modelling) to IBMS. Technology exploitation is the motto of our IBMS and hence we are looking for future trends that can be applied to this process.

5 REFERENCES

- *Bridge Inspector's Reference Manual Publication No. FHWA NHI 03-001 October, 2002, US Federal Highway Department.*
- *Pontis Bridge Inspection Coding Guide, October 1998.*
- *Guidelines for Bridge Management – Structure Information,ISBN 0 85588 704 4,Austroads Project Nos. BS.B.C.008 and BS.B.C.024 Austroads Publication No. AP.R252/04.*
- *Bridge Management Systems — the State of the Art, First Published 2002, Austroads Inc. 2002.*
- *Improved Bridge Deterioration Models, Predictive Tools and Costs, Austroads 2015.*
- *Diagnostic evaluation and repair of deteriorated concrete bridges, the University of Mississippi University, Mississippi December 2004.*
- *Bridge Inspection Field Manual, Version 2.0 – February 16, 2016, Minnesota Department of Transportation.*
- *Modelling Bridge Deterioration with Markov Chains, Research Gate Publications, November 1992,*
- *Determination of Bridge Deterioration Models and Bridge User Costs for the NCDOT Bridge Management System*
- *Figure:-1 and 2 are from the e-papers of India Today and NDTV.*

Maintenance, Safety, Risk, Management and Life-Cycle Performance of Bridges – Powers, Frangopol, Al-Mahaidi & Caprani (Eds)
© 2018 Taylor & Francis Group, London, ISBN 978-1-138-73045-8

BIM related workflow for an image-based deformation monitoring of bridges

N. Hallermann, J. Taraben & G. Morgenthal
Bauhaus-Universität Weimar, Weimar, Germany

ABSTRACT: Conventional inspections are based on intensive visual investigations. Though, the process of data capturing and post processing for extracting significant structural information, i.e. geometrical changes, is a complex task. Unmanned Aircraft Systems (UAS) offer a significant improvement of inspection and guarantee high quality images which are essential for reliable inspection results. The gathered data can be geo-referenced which offers the possibility of a highly accurate 3D modelling of structures in relation to a direct referenced visualization of detected changes or damages. The paper shows a case study of UAS-based monitoring of bridge pier deformations. An approach for a simplified extraction of basic geometries from 3D point clouds for a quantification of deformations generated from aerial images by the use of Computer Vision methods is introduced. A reproducible workflow for the recording, processing and evaluation of a change detection and condition documentation is provided with regard to Building Information Modelling (BIM).

1 INTRODUCTION

The conventional inspection of critical structures as bridges is based on intensive visual periodical investigations performed by specially trained inspectors. Though, the process of data capturing and post processing for extracting significant structural information, i.e. geometrical changes, is a very complex task. Due to the immense size of large structures, the inspection and thereby the data acquisition is time consuming, technically complex and cost intensive. In particular the inspection of critical structural components and hot spots that are hard to reach is mostly done by specially skilled workers trained as industrial climbers or by the use of specialized equipment.

Unmanned Aircraft Systems (UAS) or often called as drones equipped with high-resolution cameras can simplify and accelerate inspection tasks (Morgenthal et al. 2015). The extreme wind stability of the flight system and the fully compensated camera guarantee high quality images which are essential for reliable inspection results. The gathered data can be geo referenced relating inspection results to locations on the structure. This offers the possibility of a highly accurate 3D modelling of structures in relation to a direct referenced visualization of the detected changes or damages, like deformations or distortions (Hallermann et al. 2014).

The paper shows a possible application and case study of UAS-based inspection and monitoring of bridges or bridge elements. In regard to the post processing, an approach is introduced for simplified extraction of basic geometries from 3D point clouds generated from high resolution images by the use of modern Computer Vision methods. The extraction results are further used for a quantification of displacements, deformations or distortions of the surveyed structure. A reproducible workflow for the recording, processing and evaluation of high quality image-based damage detection and structure condition documentation is provided with regard to an implementation in Building Information Modelling (BIM).

2 DRONE BASED SURVEY OF INFRASTRUCTURE

2.1 *Drone technology*

The rapid technological development of UAS to professional high-end systems in the last years offer the potential for various applications in the infrastructure sector especially for the inspection and monitoring of large and complex structures such as bridges. Based on interdisciplinary research of the authors and project partner Intel, small but powerful drones were developed and designed with the scope on aerial image-based survey and monitoring of structures for supporting the bridge inspectors directly in simplifying and accelerating their data capturing pro-

cess. Aim and result of these projects were the definition of technical requirements for an UAS which are suitable for applications in civil engineering sector. The Intel Falcon 8+, shown in Figure 1, is such a highly professional rotary-wing UAS designed for survey, inspection and monitoring applications.



Figure 1. Unmanned Aircraft System Intel Falcon 8+.

This extremely wind stable up to wind speeds of 15m/s, but very light weight (2.8 kg takeoff weight) and electrical operating system is based on a multi-rotor platform with eight rotors in V-shape configuration. The special configuration with the centered high-performance flight control unit allows for a unique field of view in all flight situations. Equipped with triple redundant Autopilot (AscTec Trinity) a highly accurate stabilization, positioning and orientation of the flight system is guaranteed, also during complex wind conditions and in short distances to the structure. Position accuracy and stability, in addition to the redundancy of each motor-rotor combination guarantee a maximum of safety and allow for complex outdoor and also indoor flight missions. The payload of 800g allows for the use of high resolution system cameras like the Sony Alpha7R (full-frame sensor, 36MP). The camera is mounted on an actively stabilized and compensated camera mount with an adjustable camera tilt of 90° up and down. Flight operation for an automatic data acquisition can be performed by the support of an advanced GPS-based navigation software tool. High-performance battery packs enable flights up to 15 minutes. Current research of the authors and technological developments focus on structure orientated flight missions based on optimized flight paths in relation to a minimized number of images and active collision avoidance systems based on Intel RealSense technology.

2.2 *Pilot studies and former research*

Former investigations of the authors have shown that high quality and high resolution aerial images taken by professional UAS can be used for 3D-reconstructions and also detailed visual damage detection of structures based on modern photogrammetric and computer vision methods. These studies focused on large retaining walls or heritage structures with a well textured surfaces (natural stone) shown in Figure 2.



Figure 2. Investigated structures in former research projects, top: large retaining wall along Highway 4, Germany, bottom: Anna-Ebert-Bridge, Magdeburg, Germany.

The potential and applicability of UAS in the field of civil engineering are shown in different case studies (Morgenthal & Hallermann 2014a, Morgenthal & Hallermann 2014b, Hallermann et al. 2015a, Hallermann et al. 2015b,).

Furthermore, UAS can also help to enhance the different steps in regard to the BIM lifecycle of planning, construction, operation and maintenance and rehabilitation of structures. Other than the above mentioned inspection and maintenance during operation especially the planning process could be supported by current geo-referenced 3D data of construction sites based on aerial images for an interactive and transparent planning process (Fruchter et al 2016).

3 CASE STUDY DEFORMATION MONITORING OF BRIDGE PIERS

The applicability of high accurate UAS and aerial image based survey and deformation monitoring of bridges or bridge element was investigated on a modern semi-integral railway bridge. Due to the special type of construction, the pier heads show large displacements in the longitudinal direction essentially caused by changes in temperature. Therefore, special attention has to be paid for the monitor-

ing of these pier displacements and deformations during the periodical inspection over the whole lifetime.

The case study focused on the UAS-based data acquisition and the determination of the longitudinal pier head displacements and entire deformations of the extreme slender piers at different times respectively different temperatures. Based on high resolution aerial images taken by the UAS close to the structure one pier was reconstructed twice in 3D for the extraction and comparison of displacements and deformations. For this, a simplified approach from high detailed geo-referenced point clouds to single displacement information of the pier was developed.

3.1 *Case study object Scherkonde Viaduct*

The Scherkonde Viaduct is a 576.5 m long and 4 m high semi-integral railway bridge of the new ICE high speed railway track from Berlin to Munich, shown in Figure 3. The bridge was built in 2011 and is situated in Thuringia in the center of Germany.



Figure 3. Scherkonde Viaduct (railway bridge), Germany.

The 14-span girder bridge manufactured in prestressed concrete has a construction height of 2 m at the spans and 3.5 m at the supports. The superstructure is monolithically linked to the western abutment and the piers. The piers are wall slabs with a constant thickness of 1.50 m and have a width of 5.50 m at the top and a constant taper ratio of 1:40. These very slender and flexible piers allow for the compensation of large deformations in the longitudinal direction due to temperature, creep and shrinkage. Due to the construction type and the constraint forces in the system, the piers cannot be connected to the superstructure monolithically in the axes 11, 12 and at the eastern abutment in axis 13. Consequently, bearings that move longitudinally are used there. The western abutment in axis 0 is a fixed point to carry the longitudinal forces. At the eastern end of the bridge there is an expansion joint that compensates the large deformations. The foundations of the piers were constructed with large-bore piles of up to 19 m in length, so that can be assumed a fixed support of the piers.

3.2 *Data acquisition and 3D-reconstruction of a bridge pier for deformation monitoring*

For the investigation of the pier head displacements due to temperature changes on the longest piers with a length of approx. 32 m was recorded twice, first in August 2016 (mean temperature of 19°C) and second in April 2017 (mean temperature of 6°C), in team operation from all sides by using an Intel Falcon 8. The investigated pier is shown in Figure 4 left and the data recording in team operation (one UAS-pilot and one camera operator) in Figure 4 right.



Figure 4. Investigated pier of the Scherkonde viaduct. Data recording in team operation (right).

Due to the safety features of the flight system and the very experienced pilot team, the recording could perform under complex weather conditions and under running traffic without any disturbances. The aerial images should be used for a highly accurate 3D-reconstruction. Furthermore, they should also be used for automatic surface analysis, e.g. for an automatic detection of anomalies like cracks or stainings. This requires a very high resolution of the pier surface in the aerial images. That leads to a maximum recording distance of 4.5 m to the structure. The recorded images with a mean object resolution of 0.6 mm/pixel were used for a geo-referenced, true scale and color fidelity 3D-reconstruction using modern Computer Vision methods like Structure-from-Motion (SfM) explained in (Hallermann et al. 2015a). SfM requires a minimum image overlap of 70% in the horizontal direction and 30% in vertical direction which leads to a very high number of aerial images. The 1250 images were recorded on 10 vertical lines around the pier only from bottom to the top of the pier shown in a schematic view Figure 5. It shows that the manual data recording leads to a various distance and angles of view to the object which influences the accuracy and quality of the 3D reconstruction of the pier directly. To avoid such position variations in data recording structure orientated flight path and reliable collision avoidance systems has to develop and implemented directly on the UAS.

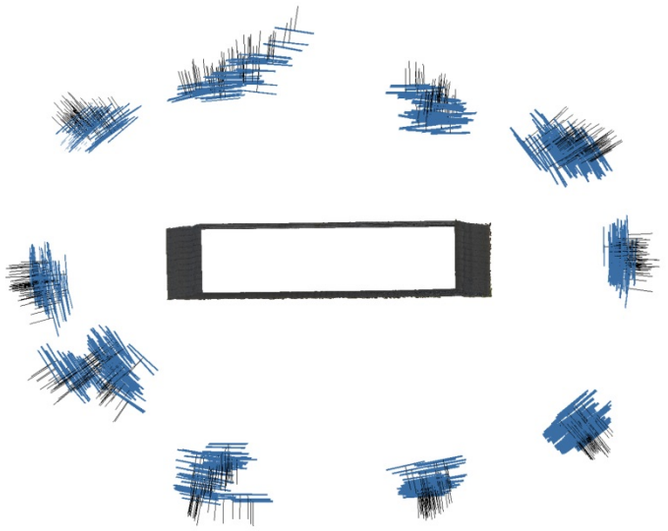


Figure 5. Reconstructed image positions around the pier, view from above.

The whole process of data capturing of one pier was completed in only 25 minutes.

The geo-referencing of the images respectively the point cloud was carried out by only 4 ground control points attached next to the food of the pier and determined by conventional tachometry. These ground control points or often called markers have to be well recognizable in the aerial images and measured as accurately as possible. Based on the high image quality and resolution (RAW-data processing) a dense RGB-coded point cloud could be generated for 3D-modelling of the pier in detail. Figure 6 shows the color-coded 3D-point cloud of the pier.



Figure 6. RGB color coded roughly cut 3D point cloud of the investigated pier (110,000,000 points, height approx. 29 m).

For the 3D-reconstruction of the pier, only a quarter of the maximum image resolution was used. The generated point cloud contains approx. 110,000,000 3D color-coded measurement points. Table 1 summarizes the recording parameters and the results of the 3D-recontrution of the pier of the measurement campaigns.

Table 1. Record parameters and reconstruction results.

No. of images	1250
mean Object distance	4.50 m
mean image resolution	0.6 mm/pixel
3D point cloud	approx.110,000,000
accuracy	± 1.7 mm
3D-object resolution	2.4 mm/pixel
point density	17 points/ cm²

Further tests and analysis with the generated data sets show that much more dense 3D reconstructions were possible by using the half (approx. half a billion points) or the full resolution (approx. 2 billion points) of the images. That leads to billions of measurement points which help to detect small geometrical defects on the pier surface (concrete spellings) but leads also to a rapidly increasing amount of data. So cloud to cloud or cloud to mesh comparisons are extremely computationally extensive and time consuming.

3.3 *Information extraction – pier displacements and deformations*

The extraction of significant information regarding displacements and deformations based on 3D point clouds leads to a possible structural evaluation of the structural condition. Depending on the accuracy and density of the given point cloud, the complexity of the geometry and the parameters for a certain analysis the extracted information can differ in terms of significance. The case study on the previously explained bridge proposes a method for the analysis of point clouds from bridge piers and highlights some of the main adjustments that can influence the analysis results. The aim of the method is the extraction of the displacement at the pier head and the deformations along its height. To show the analysis steps two piers were recorded in different seasons and therefore different temperature conditions are used.

3.3.1 *Point cloud analysis*

The developed method requires a rectangular cross section of the test object that can change the dimensions along the height of the pier as in the example. To enable a comparison of more than one analysis the point clouds should be geo-referenced or at least

have an equal start and end point. Before starting the automatically process of displacement extraction the generated roughly cut point cloud has to be preprocessed in that way that the pier is cropped exactly at the joined between pier and superstructure. Due to the soil covered pier foot of approx. 2 m, it has to be considered that the starting point of the pier could not be recorded by images and also is not reconstructed.

Step 1 divides the point cloud in a defined number of sections S along the longitudinal axis. The result is an array of cross sections where the four edges and the center point have be extracted. Depending on the ratio of S to the absolute number of points in the cloud n results the number of points contained in a section that should be enough for the following edge reconstruction. Figure 7 shows exemplarily selected sections from the original point cloud which has a total height of 28.750 m. Divided into 200 sections each section covers a height of 14.375 cm containing average 500000 points. The values x and y are indicating the position in the local coordinate system of the entire bridge itself. That means y describes the longitudinal and x the transverse direction of the bridge.

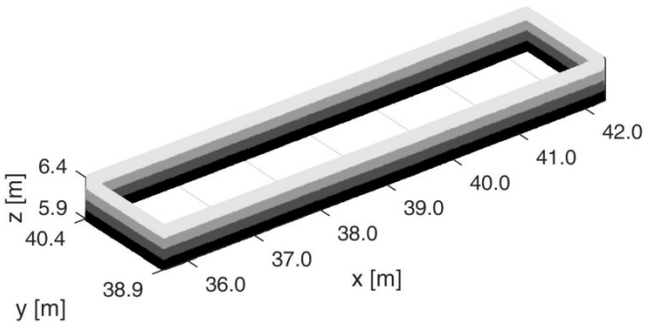


Figure 7. Exemplary view on a subset of 4 sections separated from the original point cloud of 100,000,000 points with a height of 14.375 cm each

Step 2 takes each section and fits a linear function on a defined percentage of points p contained in the single sides of the cross section. The resulting intersections form all edges of the cross section and accordingly the intersection of the diagonals is generating its center point. It is not recommended to take the edge points directly from the raw point cloud, i.e. by a bounding box. In this case the missing accuracy while reconstructing sharp edges using image based reconstruction methods leads to significant reduction of analysis precision and increases the number of outliers in the longitudinal axis. Furthermore, typical edges on concrete structures are beveled that a direct picking of the edge in the point cloud is not possible. Important for the selection of relevant points is to balance a preferably high percentage of possible points excluding the influence of the noised edge areas as shown in Figure 8. For each face, 80% of the possible points were selected which is expressed by the points colored in black.

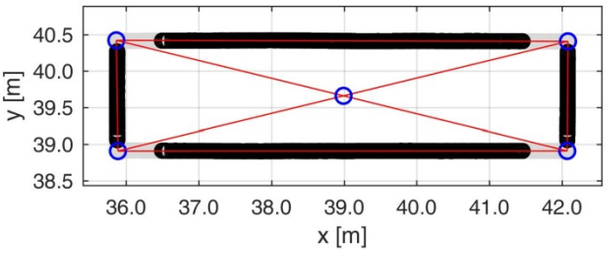


Figure 8. Raw points of a cross section (grey) reduced from 475,417 to 389,112 relevant points used for the linear fit (black) and the constructed edges and center points (circles) of the 100th of 200 sections at a height of 14.55 m at the bridge pier.

Step 3 merges the constructed center points of each cross section. A figure of the real position of these points along the longitudinal axis with a discretization directly related to S is assembled. After this step, outliers could be identified and eliminated before a comparison of two different states respectively point clouds. Figure 9 shows a mapping of the constructed edges by the described method. On height 27.2 m reconstruction outliers due to anomalies in edge detection can be identified and eliminated before further comparisons.

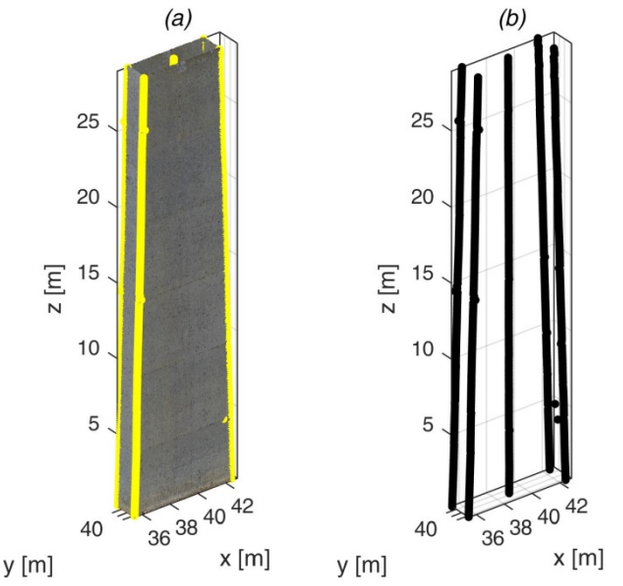


Figure 9. (a) Original point cloud with constructed edges composing 200 sections (grey) and (b) view on single edges including the longitudinal center axis which is used for further comparison

Step 4 includes the comparison of results regarding the differences of center points of different states to get the deformations along the longitudinal axis of the bridge pier and the total displacement at the pier head. The average amount of relevant points n_r that

were used for the reconstruction process are estimated by

$$n_r = \frac{p \cdot n}{S}$$

This value can be used to evaluate the significance of possible results regarding the complexity of the analyzed geometry. Figure 10a shows the comparison of the longitudinal center axes positions of two states with a ΔT = 13 K and Figure 10b the related differences of the positions configuring the deformation figure (grey) of the bridge pier in longitudinal direction combined with a smoothed function.

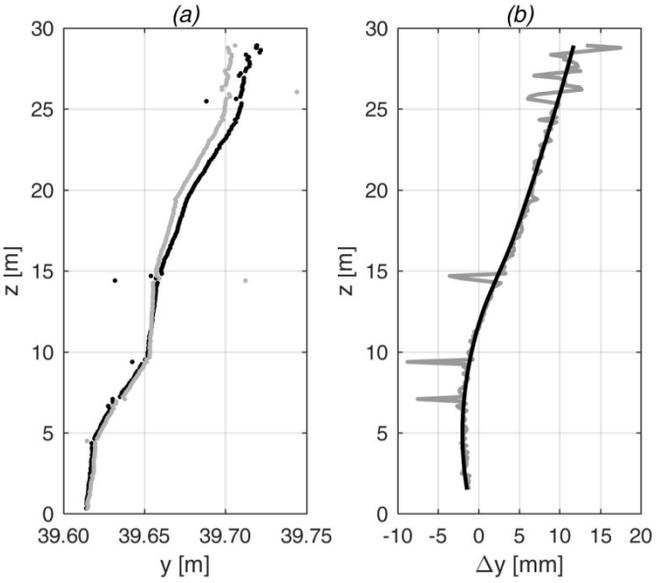


Figure 10. (a) Comparison of the longitudinal center axes positions of two states with a ΔT = 13 K and (b) the related differences of the positions configuring the deformation figure (grey) of the bridge pier in longitudinal direction combined with a smoothed function (black).

3.3.2 *Parameter study*

For the point cloud analysis the main parameter n, S and p were investigated regarding their influence on the single analysis steps and the results. Therefore the original point clouds of 100,000,000 points were subsampled with random distribution to four considerably smaller point clouds. The incremental reduction should represent a minimum number of points or minimum point density to get reliable results.

Figure 11 shows the compared cross sections of randomly subsampled point clouds considering (a) a section of a 200,000 points cloud reduced from 963 to 780 relevant points, (b) a section of a 100,000 points cloud reduced from 476 to 390 relevant points, (c) a section of a 50,000 points cloud reduced from 239 to 196 relevant points and (d) a section of a 25,000 points cloud reduced from 118 to 92 relevant points

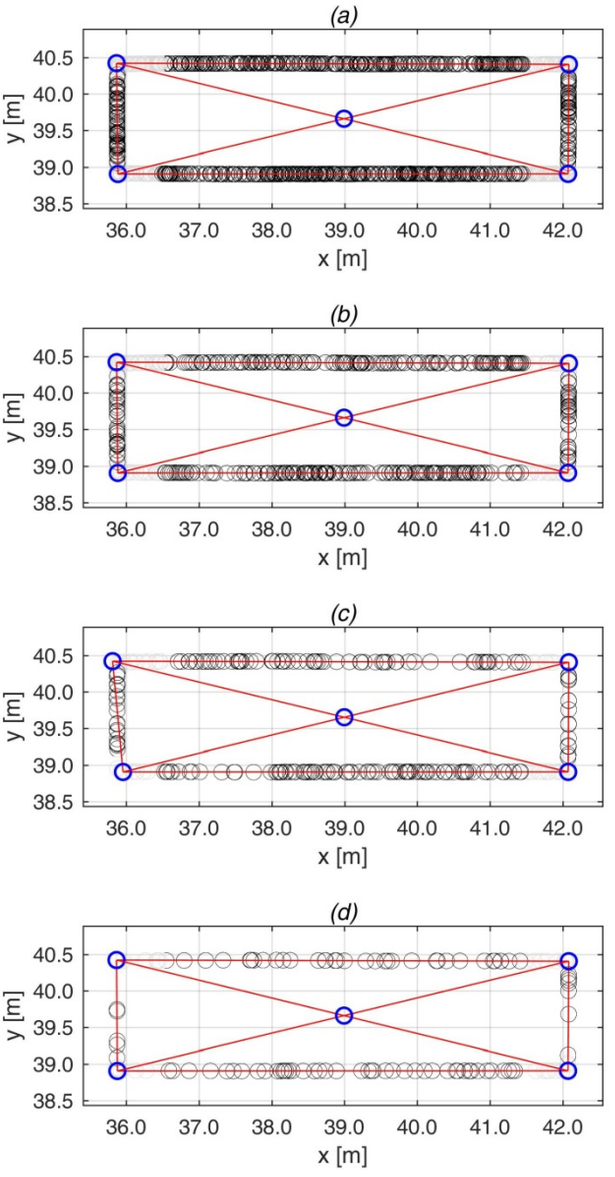


Figure 11. Compared cross sections of randomly subsampled point clouds considering (a) a section of a 200,000 points cloud reduced from 963 to 780 relevant points, (b) a section of a 100,000 points cloud reduced from 476 to 390 relevant points, (c) a section of a 50,000 points cloud reduced from 239 to 196 relevant points and (d) a section of a 25,000 points cloud reduced from 118 to 92 relevant points.

The comparison was done by the previously described states from August 2016 with an average temperature of 19°C and from April 2017 with an average temperature of 6°C. As Table 2 shows it is possible to achieve comparable results even if the size of the original point cloud was reduced to 0.025%. Of course the simple rectangular geometry of the cross section is supporting this effect, but it shows that the detection of deformations is already possible at a small amount of data which effects also a small amount of needed storage.

Table 2. Characteristic values and the displacements at the top of the pier from analyses of the given point clouds with the parameters p = 80 % and S = 200 on the bridge pier of h = 28.75 m height, a surface area of A = 445.34 m² and a temperature difference of ΔT = 13 K.

Total points (point cloud)	Point density [pts/m²]	average n_r/section	Δx [mm]	Δy [mm]
100,000,000	224,549	400,000	-6	10
200,000	449	800	-6	13
100,000	225	400	-7	13
50,000	112	200	-8	11
25,000	56	100	-9	10

For point clouds smaller than 25,000 points the reconstruction of most sections was incomplete and thus the edges not extractable using the developed algorithm. In the shown case the growing uncertainty of reconstruction is the consequence of a less detailed described surface. The points itself keep their precision as previously described. Additionally reducing the number of points gives more weight to outliers or defective reconstructed points.

4 CONTEXTUAL DATA MODELING

During the entire workflow for image based deformation analysis, a high amount of heterogeneous data compared to a single recording of reference points is accumulated that should be somehow connected to a related building model for further monitoring and evaluation. Namely the flight path for the UAS data recording, recorded high resolution images, point clouds and the analysis outcome including the inputs for each processing step should be context related and time-referenced stored to have a well-documented inspection report. To link this extremely high amount of data to building models it requires a certain level of compression and filtering for effective access in the future. Open data bases which keep the main part of non-interpreted data in a common readable structure linked to an inspection object in a building model could be one approach. The outcome of point cloud analyses that covers only the pure deformation data could be written directly in a building information model to keep the relevant information for inspections exchangeable with the building element information. This method enables the separate use of the entire monitored data and other building information while having a logical link among them which enables a comparison and evaluation of consecutive inspections.

5 ACKNOWLEDGEMENTS

This work was supported by the Free State of Thuringia and the European Social Fund (ESF) under the project number 2016 FGR 0026. Furthermore, the authors would like to thank the Deutsche Bahn Netz AG for their support of the flight campaigns and Intel for the technical support.

6 CONCLUSIONS

This paper presented a promising approach and the capability of using Unmanned Aircraft Systems (UAS) for the aerial image-based deformation monitoring of bridges or bridge elements including geo-referenced highly accurate survey. The high-end flight systems provide a fast and safe data acquisition without causing disturbances in usability of the structure. Here the bridge inspectors will be noticeably relieved. The high-quality image data can be used for geo-referenced analysis of the structure based on modern photogrammetric computer vision methods. This could drastically increase the efficiency of monitoring. The modern computer vision methods described allow the fully automatic generation of a dense 3D reconstructions from digital imagery. After performing successful test on real structures future research should be focused on methods for automatic damage detection and quantification of damage. Automated evaluation process could lead to an objective and improved damage detection.

7 REFERENCES

Hallermann N. & Morgenthal G. 2016, From Aerial Photography to 3-Dimensional Inspection of Bridges. *Proc. of IABSE Conference 2016, Bridges and Structures Sustainability – Seeking Intelligent Solutions, Guangzhou, 2016*: 546-553.

Fruchter R., Herzog S., Hallermann N. & Morgenthal G. 2016, Drone Site Data for Better Decisions in AEC Global Teamwork, *16th International Conference on Computing in Civil and Building Engineering, Osaka, 2016.*

Morgenthal G., Hallermann N. & Achtelik M. 2015, Unbemannte Fluggeräte zur Zustandsermittlung von Bauwerken. *Zukunft Bau, ISBN: 978-3816795896.*

Hallermann N., Morgenthal G. & Rodehorst V. 2015a, Unmanned Aerial Systems (UAS) – Survey and monitoring based on high-quality airborne photos. *IABSE Conference 2015 Structural Engineering Providing Solutions to Global Challenges, Geneva, 2015.*

Hallermann N., Morgenthal G. & Rodehorst V. 2015b, Unmanned Aerial Systems (UAS) – Case studies of vision based monitoring of aging structures. *NDT-CE 2015, International Symposium Non-Destructive Testing in Civil Engineering, Berlin, 2015.*

Hallermann N. & Morgenthal G. 2014a, Visual inspection strategies for large bridges using Unmanned Aerial Vehicles (UAV). *Proc. of 7th IABMAS, International Conference on Bridge Maintenance, Safety and Management, Shanghai, 2014*: 661-667.

Morgenthal G. & Hallermann, N. 2014b, Quality Assessment of Unmanned Aerial Vehicle (UAV) Based Visual Inspection of Structures. *Advances in Structural Engineering* 17 (3): 289-302.

Hallermann N., Morgenthal G. & Rodehorst V. 2014, Vision-based deformation monitoring of large scale structures using Unmanned Aerial Systems. *Proc. of 37th IABSE Symposium, Engineering for Progress, nature and People, Madrid, 2014*: 2852-2859.

Maintenance, Safety, Risk, Management and Life-Cycle Performance of Bridges – Powers, Frangopol, Al-Mahaidi & Caprani (Eds)
© 2018 Taylor & Francis Group, London, ISBN 978-1-138-73045-8

Utilizing BMS to Develop Programs and Reports for PEI Transportation

D.J. Evans
Department of Transportation, Infrastructure and Energy, Charlottetown, Prince Edward Island, Canada
R.M. Ellis
Stantec Consulting Ltd, Edmonton, Alberta, Canada

ABSTRACT: The Prince Edward Island Department of Transportation, Infrastructure and Energy (TIE) is responsible for the densest network of roadway and bridges per capita. Over the last 11 years, TIE has taken steps to implement bridge management processes including implementing an advanced bridge management system (BMS) which has enabled the department to make significant improvements in the management of inventory and inspection data, the inspection process, tracking and reporting condition thru a standard condition index, performing asset valuation, and in handling of inspection photos, videos, plans and other documents.

TIE are optimizing treatment costs for maintenance and replacement costing models as well as utilize the BMS's powerful analytical tools in determining their Capital Program for five years and ten years, including placing limits on available budgets. Risk principles are being applied using Bridge Criticality and Urgency (BCU) and Risk Analysis to determine structures which pose significant risk. TIE have also adopted a bridge asset valuation methodology and are in the process calibrating Sufficiency Index (SI), which includes appraisals of load carrying capacity, scour, flood, seismic, safety as well as condition and risk, all of which are handled by BMS.

The department utilizes the BMS to analyze the inspection data and develop a five year capital program based on lifecycle cost analysis, and correlating the results of the network bridge condition index and risk profiles produced by the BMS.

The department also utilizes the data produced by the BMS to report on the current and forecasted overall condition of the network to the Minister and Deputy Minister of TIE, as well as other key performance indicators.

This paper will look at the methods the department uses in order to determine their capital program as well as review information that is reported to the Minister and Deputy Minister on an annual basis.

1 INTRODUCTION

The Province of Prince Edward Island (PEI) is situated on the east coast of Canada and is the smallest of all the Canadian Provinces.

The Province has 5660 km of natural waterways throughout its land mass and is crossed at various locations by 5600 km of roadway network with over 1500 structures.

The Province has three main sources of income, which include tourism, agriculture and aquaculture.

The Province has spent the last 9 years developing and maintaining a Bridge Management System (BMS) for the provincial network of structures. Of the 1575 structures, only 266 are inspected on a biennial basis (IE. Once every two years). As of the end of 2015, the department will have completed a fifth full round of biennial inspections.

This paper discuss how the Province is tracking the overall Bridge Condition Index (BCI) and Risk Profile (BCU) over time based on the current budget constraints by utilizing some of the analytical tools which are incorporated into the BMS for their forecasting and budgetary considerations.

2 BRIDGE INSPECTION ON PEI

2.1 *Inventory*

The department has roughly 1575 structures province wide that we are responsible for. Of these, we have only inspecting 266 larger, bridge type structures with a few larger buried structures.

Like most jurisdictions across Canada, our inventory is a product of the construction boom from the late 50's to the early 90's. A good portion of the Province's inventory is at or very near its intended design life and many structures are nearing the end of service life.

Like most all jurisdictions, the department continues to struggle with condition of the inventory

and the available capital dollars which are available to address these issues.

More information regarding the evolution of bridge inspections and bridge management in Prince Edward Island can be found in Evans et.al, 2014 and Evans, et.al, 2012.

3 BRIDGE MANAGEMENT SYSTEM

3.1 *Evolution of BMS on PEI*

Like most other jurisdictions, PEITIE have historically relied on hard paper copies of our safety inspections with a rudimentary spreadsheet for asset management data. This housed such information as structure ID, structure type, material, span length, age (if known), location, route number, and other basic information.

After a literature review, the department decided on the best fit BMS for our inspection program, which was Ontario Bridge Management System (OBMS) (Thompson et.al, 2003).

The department's consultant had been working on significant improvements to the OBMS and in 2010 the department licensed and implemented the new Stantec BMS 2010 platform as the new PEI BMS (Evans et.al, 2010).

3.2 *BMS 2010*

The PEI BMS accepts inspection data in the OSIM format, calculates the Bridge Condition Index (BCI), produces all of the reports the previous system produces, and provides several other significant enhancements. The BMS meets or exceeds all the requirements of documents such as the AASHTO Guide to Bridge Management (AASHTO, 1994) and Bridge Management in Europe (BRIME 2002).

BMS2010 offers the following capabilities that were of interest to the Department:

1. Improved photo, video, document management including search capabilities,
2. Automated project scoping and treatment selection using engineering models and benefit-cost analysis ,
3. Element, project and network level risk analysis,
4. Network-level priority programming and budgeting,
5. Network and individual bridge target performance analysis,
6. Risk-based decision making (See Figure 1),
7. Risk-based setting of inspection frequencies.
8. Bridge asset valuation
9. Tracking Critical Findings
10. Automated reporting of key performance indicators (KPI)

For further information regarding the capabilities of BMS2010 and other features, please refer to Evans et.al, 2014, Evans et.al, 2012, Ellis et.al, 2012 and Dalziel et.al, 2012.

4 TRACKING AND FORECASTING BRIDGE CONDITION AND RISK VERSUS BUDGETS OVER TIME USING ANALYTICAL TOOLS

The Province uses the analytical tools available in the BMS in order to greatly assist with the capital programming, for an annual and 5 year basis, to determine what projects should be completed first and what can be deferred until after the 5 year period.

The Province is also tracking the condition and risk profile across the entire network of inspected structures and reports on the overall trend as to whether or not we are seeing improvement in the overall network condition and risk, or if more resources are required.

Additional information regarding BMS2010's analytical tools can be found in Evans et.al, 2014.

4.1 *Tracking Condition and Risk versus Budgets over time*

4.1.1 *2016 Bridge Condition Index (BCI) Results*

The results of the condition inspections conducted in 2017 yield an overall Bridge Condition Index (BCI) for each structure. BCI is grouped into three categories corresponding to GOOD (BCI>70), FAIR (60<BCI<70), and POOR (BCI<60). Structures that are in POOR condition generally are found to have maintenance or rehabilitation needs with near term timing (now or within 5 years). Structures with FAIR condition can be expected to not have needs for more than 5 years, while structures in GOOD condition have no needs in the next 10 years.

PEI TIE are also able to review the BCI distribution over the entire inspected network and see where our threats are moving forward in the very near future.

4.1.2 *Risk Profile*

The department has been inspecting structures using a BCU rating since 2011 and we have been tracking the risk profile of the inspected network since this time. In general, the higher the BCU rating, then the higher risk category the structure is in.

We currently have a matrix of risk from low, medium, medium–high and high risk category. The matrix is indicated in Figure 7 for all inspected structures. As can be seen, the tables and graphs indicate

that the department is currently at risk, as over 25% of the network is in High risk, and over 27% is in Medium-High risk. PEI TIE is currently reviewing our five year capital bridge construction plan to include these structures in the program. The department is also looking at conducting more periodic reviews of our higher risk structures in order to maintain an acceptable level of safety across the network. The Risk Profile is specifically designed to address risks associated with structure element condition and considers element type, structural behavior and failure mode, condition, defects and criticality of defects, together with structure importance, traffic volume. More details are available in Ellis et al, 2012.

4.1.3 *Structure Sufficiency Index*

PEI TIE has been experimenting with a prototype Sufficiency Index. The structure Sufficiency Index (SI) is a compilation of the BCI, BCU as well as other important operational factors; such as, load rating; scour potential; flood potential; fatigue critical elements; approach road geometry; structure lane width; barrier index; etc..

Additional information can be found in Evans et.al, 2016

4.2 *Condition and Risk Tracking vs. Budgets*

We have been tracking the BCI breakdown of the network of structures since 2012. We have also tracked the risk profile of the structures since 2011. The following table outlines the BCI Breakdown from 2012 through to 2016. So, the natural question becomes, “How are we doing?”

More information can be found in Evans et.al 2016.

5 REPORTING CONDITION, RISK AND PROGRAMMES TO DEPARTMENT HEADS

The Bridge Management Software is an excellent tool in providing high level information to the department heads and directors.

The department reports annually to the senior management both in written form and through presentation.

5.1 *Reporting to Senior Management*

Once TIE staff are satisfied that the inspections are complete and closed, the analysis is completed and verified and the prioritization is complete, we are then comfortable with reporting this to senior management.

Reports typically begin with the evolution of our bridge inspection and bridge management program. Since senior management changes from time to time, this is always included.

Reporting will then dive into our network, our inspections for the previous season and the results of our Bridge Management Software as well as out proposed 5 year program (discussed in Sec. 5.2).

In general we report on the inspection results, including: BCI (see Tab. 1 and Fig. 1); BCI Distribution (see Fig. 2); Risk distribution (see Fig. 3); BCI and Risk trending (See Figs 4, 5); and Sufficiency index (See figure 6).

The BCI has been found to be useful not only as an excellent condition reporting tool; but, also as a performance measure. For example, the condition of an inventory can be entirely represented with the following figures:

- average BCI = 70.3
- distribution of G/F/P equal to 47% / 27% / 26%.

Table 1 – BCI Breakdown of All Inspected Structures

Condition State	Percentage of Inspected Structures
Good (BCI > 70)	47 %
Fair (60 < BCI < 70)	27 %
Poor (BCI < 60)	26 %
Average BCI	70.3

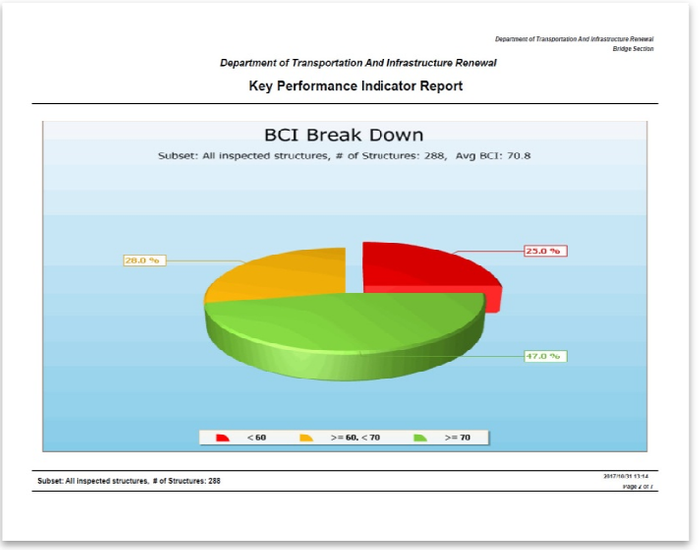


Figure 1- BCI Breakdown All Inspected Structures

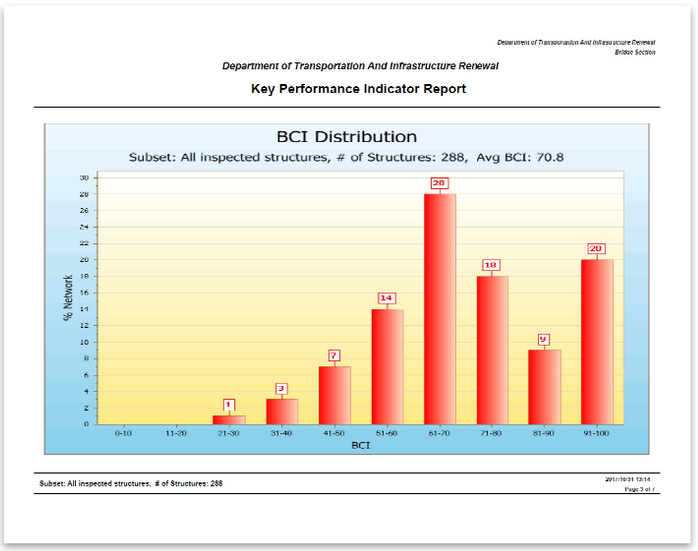


Figure 2 – BCI Distribution All Inspected Structures

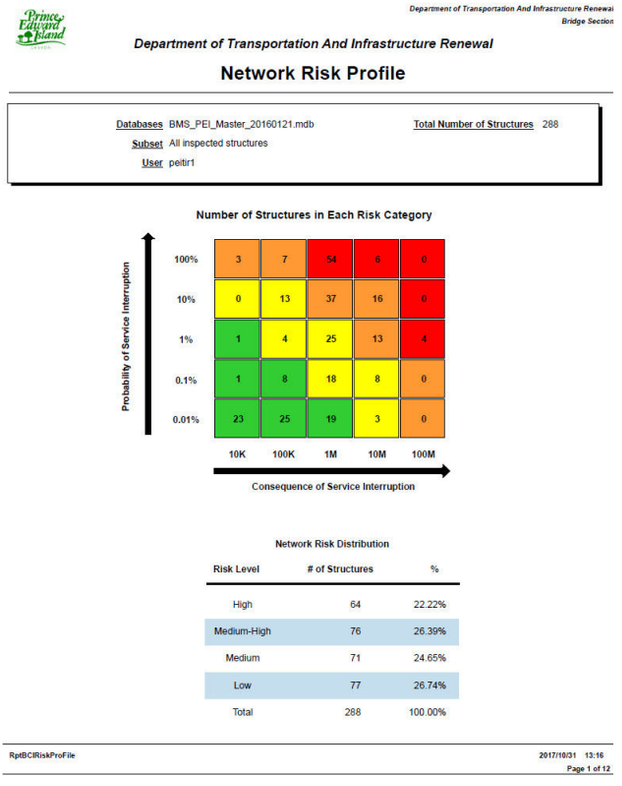


Figure 3 – Network Risk Profile

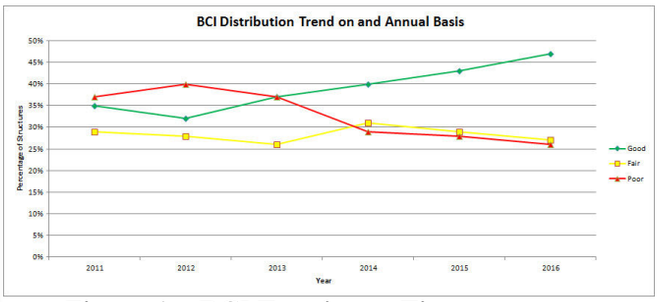


Figure 4 – BCI Trend over Time

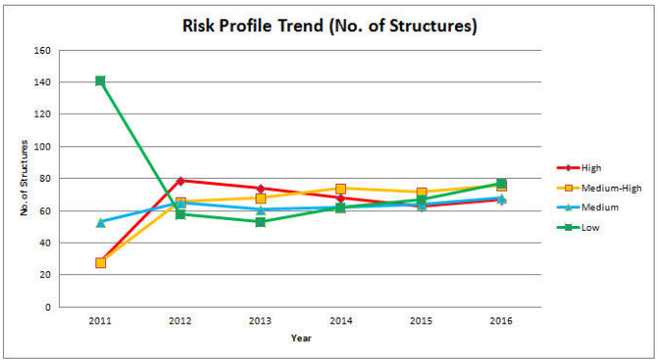


Figure 5 – Risk Profile Trend over Time

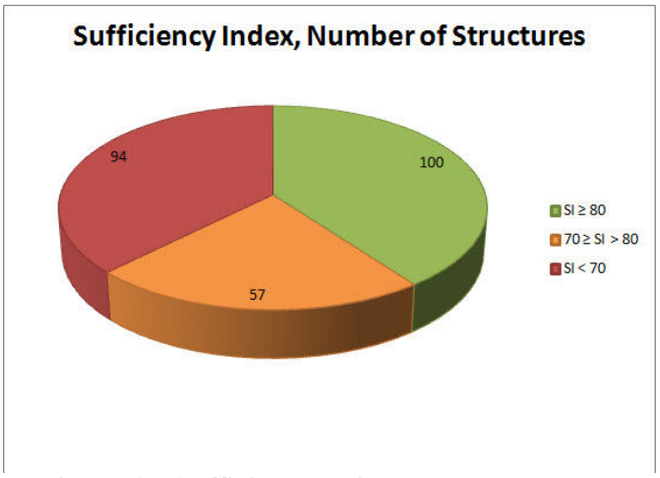


Figure 6 – Sufficiency Index

In conjunction with this, we also report on suspected performance deficiencies and associated maintenance needs or recommended works. See Tables 2, 3 and 4 for a summary of the inspection findings.

Table 2 – Performance Deficiencies

Performance Deficiency	No. of Occurrences
1-Load Carrying Capacity	1033
2-Excessive Deformations	86
3-Continuing Settlement	45
4-Continuing Movements	124
5-Seized Bearings	8
6-Brng. not Unif.Load/Unstbl.	20
7-Jammed Expansion Joint	9
8-Pedestrian/Vehicular Hazard	280
9-Rough Riding Surface	101
10-Surface Ponding	21
11-Deck Drainage	20
12-Slippery Surfaces	0
13-Flooding/channel Blockage	15
14-Undermining of Foundation	40
15-Unstable Embankments	77
16-Other	233
TOTAL	2112

Table 3 – Maintenance Needs

Maintenance Need	Timing			No. of Occurances
	Now	1 Year	2 Years	
1-Lift/Swing Bridge Maintenance	0	0	0	0
2-Bridge Cleaning	13	44	25	83
3-Bridge Handrail Maintenance	43	157	156	357
4-Painting Steel Bridge Struc	0	20	42	62
5-Bridge Deck Joint Repair	0	14	12	26
6-Bridge Bearing Maintenace	0	1	7	8
7-Repairs to Structural Steel	1	6	11	18
8-Repair of Bridge Concrete	1	30	270	303
9-Repair of Bridge Timber	22	107	364	495
10-Bailey Bridge Maintenance	0	0	0	0
11-Animal/Pest Control	2	2	1	5
12-Bridge Surface Repair	5	32	61	98
13-Erosion Control at Bridges	22	42	58	123
14-Concrete Sealing	0	0	2	2
15-Rout and Seal	1	16	64	81
16-Bridge Deck Drainage	2	12	9	23
17-Other	92	116	165	377
TOTALS	204	599	1247	2061

Table 4 – Recommended Works

Timing	No. of Occ.	Cost
Urgent	28	$904,440
< 1 year	116	$2,639,857
1 - 5 year	463	$9,521,860
6 - 10 year	98	$1,810,235
None	4	$20,200
Total	709	$14,896,592

Based on the information above, we utilize the BMS' forecasting tools to report on future condition of the network, in Periods 1 and 2, based on three scenarios. These are: 1) Do nothing (shown in figure 7); 2) Unconstrained budgets (shown in Fig. 8); and 3) Constrained Budget (shown in Fig. 9).



Figure 7 – BCI Forecast Summary – Do Nothing

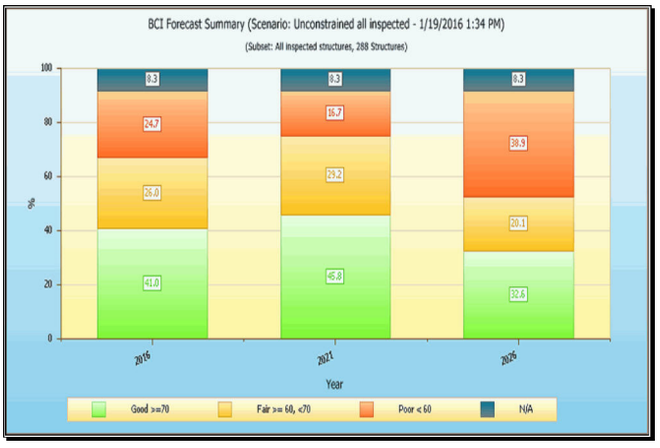


Figure 8 - BCI Forecast Summary – Unconstrained Budgets

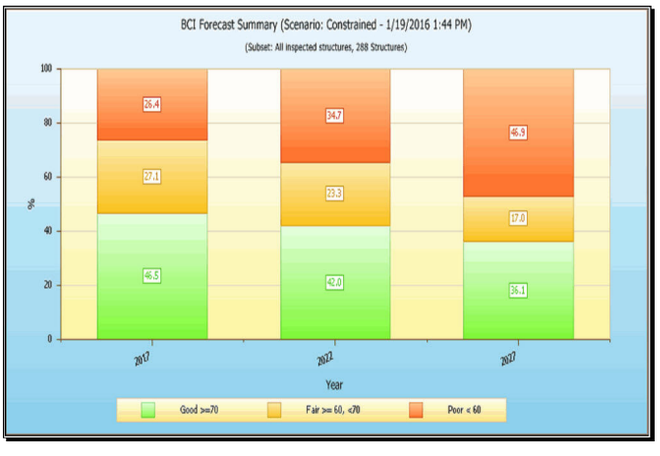


Figure 9 - BCI Forecast Summary – Constrained Budgets

5.2 *Program Development*

Once the annual inspections are complete and the consultants have reviewed them critically, the department reviews the inspection information for completeness, accuracy and consistency. Early inspection reports required 3 to 4 iterations of this; however, due to time and experience, the department

has only very minor comments on each inspection cycle.

Once the inspections are finalized and closed, only then do department staff begin to develop the bridge program, looking at Period 1 (Years 1 through 5) and Period 2 (Years 6 through 10); however, we only report on Period 1.

The bridge program is formulated by the following routine:

- *Review of the BCI values and determine the risk factors associated which each structure that are in fair to poor condition state.*
- *Conduct a Project Analysis for the structures with unconstrained budgets to determine the actual need in any given period P1 or P2. Conduct an analysis with constrained budgets, setting the Risk analysis factors to 100 (IE do not include risk).*
- *Conduct an analysis to include constrained budgets and risk parameters.*

Once all of the program analyses are complete, we can then correlate the results and determine the best course of action based on the inspection data only.

We then look at factors such as geometric and functional obsolescence, importance of highway network (local road, collector, arterial, etc.) as well as Average Annual Daily Traffic (AADT) and Average Daily Truck Traffic (ADTT) on each of the structures on the program in P1. Since the system is not capable of allocating budgets to account for the socio-economic impacts of the proposed structure replacement(s), the department needs to do this manually.

After this is done, we can then start prioritizing the program based on the project analysis conducted by the system, the highway classification, the AADT and ADTT and the condition and risk parameters set forth through the inspection program. This will become our 5 year program and this is what gets reported to senior management (see Fig. 10).

2017/18 Bridge Projects

Region	Project Name	District	Route/ Section	Bridge ID	Description of Work
East	Fortune Bridge	1	31001	K1-001	Replacement
East	Graham's Road	4	01702	K5-004	Replacement
East	York Road	9	02501	Q3-024	Carry Over
West	Stanley Bridge	18	00610	Q1-020	Deck Repairs
West	Cairns Road	19	11003	P4-044	Replacement
West	Margate	20	00611	Q1-056	Replacement
West	Margate	20	00611	P4-014	Replacement
West	Bideford Arch	23	01208	P2-017	Replacement
West	Wellington	24	17701	P3-024	Replacement
West	Egmont Bay	24	01105	P3-047	Replacement
West	Gully Bridge	26	14003	P1-047	Dredging
West	Cascumpec Bridge	26	01212	P1-015	Carry Over

2018/19 Bridge Projects

Region	Project Name	District	Route/ Section	Bridge ID	Description of Work
East	Woodville Mills	2	33401	K5-017	Replacement
East	Lorne Valley Road	2	35501	K3-051	Replacement
East	Hazelgreen Road	2	32901	K3-049	Replacement
East	Peakes Road	7	32001	K2-026	Replacement
East	Peakes Road	7	32001	K2-039	Replacement
West	Tryon	19	11603	P4-055	Replacement
West	Gains Creek	25	17401	P2-093	Replacement
West	Alaska	25	13801	P2-029	Replacement
West	Coleman	26	13701	P1-010	Replacement

2019/20 Bridge Projects

Region	Project Name	District	Route/ Section	Bridge ID	Description of Work
East	Five Houses	2	32701	K2-037	Replacement
East	Sorrey Bridge	3	13701	K3-038	Replacement
West	Simpson Mill	18	Maint. ID 50325	Q1-071	Replacement
West	Cabot Park	20	10501	P3-009	Replacement
West	Ox River	25	01102	P2-035	Replacement
West	Sheep River	25	13501	P2-034	Replacement

2020/21 Bridge Projects

Region	Project Name	District	Route/ Section	Bridge ID	Description of Work
East	Little Sands	4	00409	Q4-012	Replacement
East	County Line Road	2/5	01102	K3-032	Replacement
East	St. Peters Road	8/9	00207	Q5-001	Replacement
West	Riverdale Bridge	17	01102	Q1-074	Replacement
West	Portage Bridge	25	00219	P2-046	Replacement
West	Enmore Bridge	25	Maint. ID 40127	P2-039	Replacement
West	Oyster Creek	26	01211	P1-009	Replacement

2021/22 Bridge Projects

Region	Project Name	District	Route/ Section	Bridge ID	Description of Work
East	Wood Islands (Mt. Vernon)	4	31501	P2-035	Replacement
East	Little Sands	4	00409	Q4-059	Replacement
West	Crapaud	17	01301	Q1-052	Replacement
West	Searletown Bridge	19	01003	P4-048	Replacement
West	Bideford Bridge	23	01207	P2-016	Replacement
West	Campbellton Bridge	25	14302	P1-093	Replacement
West	St. Felix	27	15301	P1-041	Replacement

Figure 10 – 5 Year Program List

6 CONCLUSIONS AND CLOSING REMARKS

Since 2007, the department has come a long way in how we manage our highway bridge assets, from virtually nothing to implementing and using a state-of-the-art bridge management software system. The system is capable not only of collecting basic information of each structure; but, integrating the inspection data and developing a bridge condition index (BCI) for each structure.

Using the network-level priority tool and automatic project scoping tool, the BMS will conduct life cycle cost analyses and benefit/cost rations for each structure, based on the element condition data entered into the BMS. The system will then calculate a capital program for a variety of user defined scenarios; such as, ‘do nothing, unlimited budget, constrained budgets, or key performance targets.

In concert with this, we have trained our inspectors to identify the criticality and urgency of any given element on the structure and the system will

conduct a risk analysis on the entire network to determine those in the high risk categories versus those in the lower to medium risk categories.

The department now relies very heavily on the inspections and BMS analysis in determining its capital program for the next 5 years and forecasting to 10 years. It must be stated; however, that while this tool is extremely useful in determining our capital program, it is not a replacement for engineering judgment, which we exercise on a routine basis.

The BMS output and subsequent reports to Senior Management outlines the need for additional funding in order to maintain a serviceability of the highway structure network. There are areas of significant risk that the department is assuming on a number of structures that are currently being inspected. We have no real indicator on how this translates into the remaining portion of the highway network that is not currently being inspected; however we are beginning to include these structures in our inspection program It will take several years for this data to be input into the system and calibrated.

With the reports and graphical representations that are reported to Senior Management, we have been successful in obtaining additional funds for capital investments across our network of bridge structure. Senior management can quickly visualize the importance of the bridge structure network, the condition and risk parameters associated with the network and what the consequences are if budgets remain stagnant or decrease over time.

We are reducing the number of structures on our network by closing or severing non-essential or seasonal roads as required.

In closing, we will continue to conduct routine inspections on our network of structures and are beginning to include all our smaller structures. We realize that budgets are constrained and we will continue to work within these confines as required; however, the reports show that there will be consequences as a result.

7 ACKNOWLEDGMENTS

The Department would like to acknowledge Stantec Consulting Ltd., the consultant for the bridge management program, the BMS implementation project, inspection training courses, and support of the bridge management system.

8 REFERENCES

Dalziel et al, 2012 Application of bridge management system to determine preservation and improvement budgets, meet condition targets, and manage risk for the City of Hamilton. 6th International Conference on Bridge Maintenance, Safety and Management, IABMAS2012, Stresa, Lake Maggiore, Italy: Balkema

Ellis, R.M., et al, 2012. Incorporating Risk and Criticality in Bridge Management Decision Making and Project Prioritization. 6th International Conference on Bridge Maintenance, Safety and Management, IABMAS2012, Stresa, Lake Maggiore, Italy: Balkema

Evans, D.J. & Ellis, R.M., 2016. Tracking bridge conditions versus budgets using bridge management system tools in Prince Edward Island Department of Transportation and Infrastructure Renewal. 8th International Conference on Bridge Maintenance, Safety and Management, IABMAS2016, Foz do Iguaçu, Brazil: Balkema

Evans, D.J. & Ellis, R.M., 2014. Use of Advanced Bridge Management System Analytical Tools in Prince Edward Island Department of Transportation and Infrastructure Renewal. 7th International Conference on Bridge Maintenance, Safety and Management, IABMAS2014, Shanghai, China: Balkema

Evans, D.J. & Ellis, R.M., 2012. Development, implementation and application of Bridge Management Systems in Prince Edward Island. 6th International Conference on Bridge Maintenance, Safety and Management, IABMAS2012, Stresa, Lake Maggiore, Italy: Balkema

Evans, D.J.& Ellis, R.M., 2010. Development, implementation and application of Bridge Management in Prince Edward Island, Canada. International Short and Medium Span Bridge Conference, Niagara Falls: Canada Canadian Society of Civil Engineers

Maintenance, Safety, Risk, Management and Life-Cycle Performance of Bridges – Powers, Frangopol, Al-Mahaidi & Caprani (Eds)
© 2018 Taylor & Francis Group, London, ISBN 978-1-138-73045-8

Creating the basis for implementing BIMS in existing infrastructure components

J. S. Jensen & F. R. Gottfredsen
COWI A/S, Denmark

ABSTRACT: In recent years the concept and use of a Building Information Modelling System (BIMS) has acquired increasing attention in asset management. The core of BIMS is a 3D-model of the assets under consideration. For new structures this is not a problem as they will usually be designed by means of 3D models. For existing structures on the other hand, this poses a challenge, as 3D models of the structures will usually not exist. In recent years COWI has been involved in a number of projects where different approaches have been used to establish 3D-models of existing infrastructure assets. Two such projects will be described in this paper. Further prerequisites for using BIMS on existing structures are also presented. This includes existence of an object hierarchy as well as availability of relevant as-built documentation. Further, this paper discusses the similarities and differences between a BIM system and an Asset Management System (AMS).

1 INTRODUCTION

The principles of Building Information Modelling System (BIMS) is widely used to manage all stages of new building projects, i.e. design, construction and maintenance. Hence, BIMS have many of the same features as a traditional Asset Management System (AMS).

Usually the basis for an asset management system were mainly documents: specifications and drawings from the construction stage, reports from inspections and rehabilitation proposals from the operation stage. Today, the basis for a modern asset management system is usually an information system developed and updated during the design and construction stages. Many general asset management systems supports automated, optimal maintenance management using the data as stored in an infrastructure database.

Recently, COWI has been involved in projects for two major clients where it has been the objective to create the basis for applying the principles of BIMS for existing infrastructure facilities as a basis for an asset management system:

- The Storebelt Link in Denmark
  This link comprises a major suspension bridge, a low bridge and a twin tube railway tunnel.
- The Montenegrin Railway authorities.
  The project comprised the 106 tunnels on the main railway through Montenegro from the Adriatis Sea in the south to the border to Serbia in the north.

In both cases the first step in the process – to create a BIMS in the operations stage - has been to establish a 3D-model of the infrastructure. This goal has been obtained by using a combination of laser scanning and video imagery. Further, provisions have been made to register all data concerning the present condition of the infrastructure in a structured manner, and in formats, that allows data to be fed into a BIMS based asset management system.

2 SHORT INTRODUCTION TO BIM(S)

Building Information Modelling (BIM) and Building Information Modelling System (BIMS) as subjects have received much attention in recent years. There is, however, some confusion with respect to what it actually means.

The National Building Information Model Standard Project Committee defines BIM as:

> *Building Information Modeling (BIM) is a digital representation of physical and functional characteristics of a facility. A BIM is a shared knowledge resource for information about a facility forming a reliable basis for decisions during its life-cycle; defined as existing from earliest conception to demolition.* (NBIMS-US 2017)

BIMS is presently used mainly on new construction projects as part of Computer Aided Engineering (CAE). In BIMS each object is assigned a unique code describing type and location. The type code will also show the object's hierarchal position within

the structure, the object assemblage. A number of attributes containing information about the object are then assigned to all the objects. Attributes could be material properties, supplier information, date of purchase/delivery, specification on spare parts, etc.

Retrieving a list of objects from the CAE model can be used by the procurement office to estimate quantities. It can also be used as basis for an Operation and Maintenance Manual, but with one major reservation: Items (i.e. objects) that are normally not maintainable as separate objects, like reinforcement inside a concrete structure, are consequently not covered by the manual.

Similarly the implementation of BIMS on an existing structure should handle maintainable objects only.

It is also important to note, that object breakdown should only be performed to the level of the smallest object that is being maintained "on its own" by the maintenance organization.

3 RELATIONSHIP BETWEEN BIMS AND AMS

An Asset Management System (AMS) is a system – usually based on a software package – that is used to carry out asset management, which in turn can be defined as:

> *Asset Management is the combination of management, financial, economic, engineering and other practices applied to physical assets with the objective of providing the required level of service in the most cost effective manner. It includes the management of the whole life cycle (design, construction, commissioning, operating, maintaining, repairing, modifying, replacing and decommissioning/disposal) of physical and infrastructure assets.* (LGAM 2017)

BIMS and AMS clearly share a number of common features but also there are some clear differences.

The main similarities are found to be that the same information is stored and handled:

- information on the design and construction of the structural assets (materials data, suppliers data, etc.)
- information on the geometry of objects (dimensions, quantities, etc.)
- etc……

In the present context the major differences in the way BIMS and AMS are traditionally used is:

- BIMS is used from the first conceptual design of a structure and the core of BIMS is a 3D model of the structure which may be extended to 4D (fourth dimension is time) and 5D (fifth dimension is cost/economy). Also, a major aspect in BIMS is that it shall support and promote the exchange of information between the different parties (owners/architects/designers/contractors) involved during design and construction of structures.
- AMS is usually launched after the design and construction stages, or – in recent cases - during the last stages of construction, one of the main purposes being to manage economy and operational services.

4 USING BIMS ON EXISTING INFRASTRUCTURE COMPONENTS

For existing structures, not having a BIM associated to it, a 3D model need to be established in order to effectively implement BIM as this model shall act as the link between the object hierarchy and the information related to each object.

For an existing structure, a basic BIM system would contain the following information:

- Object Identification Number (OIN) (Being part of an Object Identification System (OIS))
- Basic structural information (material data, production information (supplier, date of manufacture, etc.)),
- O&M-related documents (manuals inspection plans, inspection reports, etc.)
- As build documentation (especially drawings).

All the above information may be linked to the relevant objects (as attributes) in a 3D representation of the structure. Hence, it is essential to have a detailed 3D representation of the structure.

5 TWO CASE STUDIES

In the two case studies presented below the objective has been, as a first step to establish a BIMS, to establish a 3D model of the existing structures.

Further, an object hierarchy needs to be established and existing information that shall be fed into the BIMS shall be identified.

5.1 *Description of structural assets*

5.1.1 *The Storebelt Link*

The Storebelt Link is situated in the center of Denmark, as shown on Figure 1, and connects the two main islands Zealand and Funen. The link comprises five main parts:

- the East Bridge: a 6,8 km long suspension bridge (road only)
- the West Bridge: two parallel 6,6 km long box girder bridges (railway and road)
- the East Tunnel: a 8 km long twin tube bored railway tunnel
- The Sprogoe Island: an island forming the transition between the East and West Bridge (road) and the East Tunnel and the West Bridge (rail).

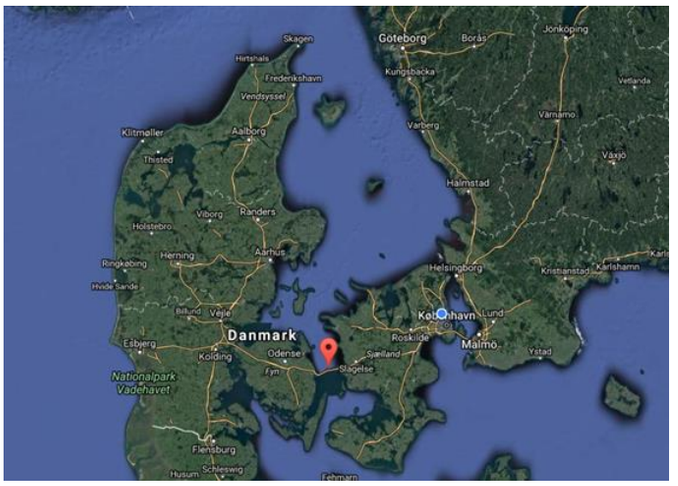


Figure 1 The Storebelt Link (at red marker) is placed in the center of Denmark. It connects the two major islands Zealand and Funen by road and rail. © Google Maps.

– area for toll station and administration at Halsskov (On Zealand at eastern approach to the link)

The link was constructed in the years from 1988 to 1998. The railway link opened in June 1997 and the road link opened in June 1998.

5.1.2 *The Vrbnica – Bar railway line in Montenegro*

This railway line runs through the central part of Montenegro from the Adriatic Sea at Bar to the border to Serbia at Vrbnica in the north as shown in Figure 2.

The railway line is app. 100 km in length and includes 106 tunnels with a total length of app. 53 km.

The shortest tunnel is 40 m long and the longest is 6.171 m.

The railway line is a single-track line except at a few stretches around stations where it comprises up to 3 tracks. Three tunnels are so close to a station that they also comprise three tracks – two in full and one in part.

5.2 *Data collection*

The way of collecting data for the two referenced projects have been somewhat different in nature. However, the starting point for both projects, BIMS wise, has been from scratch.

5.2.1 *The Storebelt Link*

For the Storebelt Link the collection of data needed to establish a 3D model of the main structures is a process that is foreseen to take years due to the mere size of the assets.

To date (autumn 2017) data for 3D-models has been collected for the following parts of the Storebelt link:

– the two anchor blocks,
– the Sprogoe Island,



Figure 2 The main railway line in Montenegro going between Bar at the Adratic Sea (south) and Vrbnica at the Serbian border (north).

– Tollstation area and administrative center at Halsskov.

Data has been collected by means of UAV's that fly around the anchor blocks in a predefined pattern taking a large number of high resolution photographs – app. 5.000 for each anchor block.

At present COWI is using two different types of unmanned aerial vehicles (UAV's) for data collection. The newest of the two types is shown in Figure 3.

As the recorded photographs are overlapping they can be processed digitally to produce a 3D model of the anchor blocks. The model is georeferenced and measurements can be made directly on the model.

5.2.2 *Montenegro Railways*

For the project in Montenegro a somewhat different approach has been adopted. Data was sampled by two means:

– 360° camera (a la street view images),
– laser scanning

The camera inspections were used to perform an initial visual inspection in the office of all the tunnels. This initial inspection was used to get the first impression of the current state of the tunnels and data from the initial inspection was used to plan the detailed on-site inspection that was carried out later in the project.



Figure 3. UAV type Matrice 210 RTK from DJI. The UAV can be equipped with two cameras.



Figure 4. Mobile mapping system placed on a flatbed wagon and pulled by a dresine.

The detailed outcome of this part of the project is presented in another paper at this conference.

The Mobile Mapping System used for the laser scanning of the tunnels consisted of the following components:

- 2 laser scanners,
- GNSS System (Global Navigation Satellite System),
- INS (Inertial Navigation System).

The equipment was installed on a flatbed wagon and driven through the tunnels by means of a dresine at a moderate speed of app. 20 km/h. The setup is shown in Figure 4.

The laser scanning resulted in a point cloud for each tunnel. The point clouds are so detailed that they almost resemble a black/white 3D image of the tunnels. A small example is shown in Figure 5. Due to the use of GNSS and INS the point clouds can be positioned globally in absolute terms, i.e. by means of global xyz-coordinates.

5.3 *1.1 Object hierarchy*

An object hierarchy was developed for the Storebelt Link when it was designed. This original hierarchy is still being used.

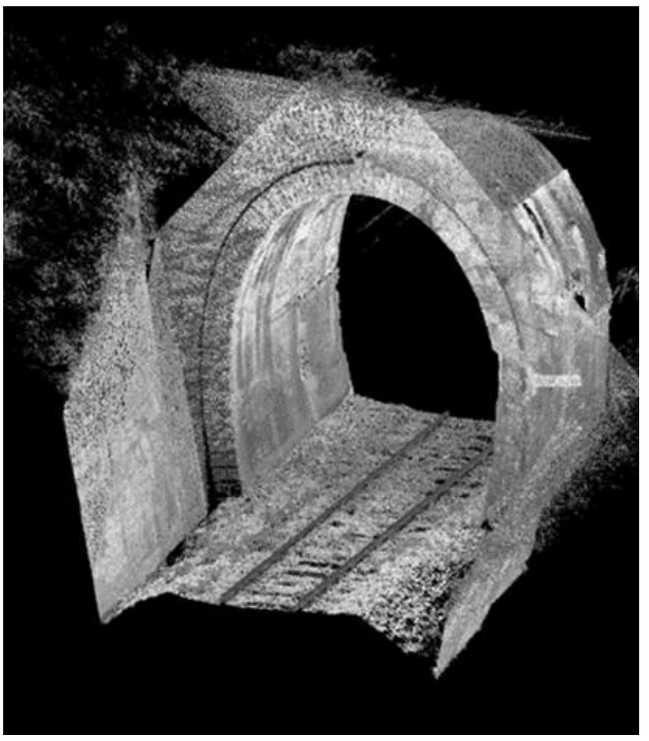


Figure 5. Example of outcome of point cloud from laser scanning. Only the tunnel portal is shown.



Figure 6. Example showing how the eastern anchor block of the Storebelt East Bridge is subdivided into objects at level 4: foundation, front leg(s), spreading chamber(s) and saddle house.

The East Bridge is at level 1 and the anchor blocks at level 3. The division of an anchor block into next level objects is illustrated in Figure 6.

For the tunnels on the railway in Montenegro no object hierarchy has been developed previously.

A simple hierarchy was developed:

- level 1: Tunnel no./name
- level 2: relative stationing within tunnel (each tunnel was divided into a number of virtual "rings" – each 1 m wide.)



Figure 7. Image from COWI Multiviewer showing the 3D-model of an anchor block from the Storebelt East Bridge (right), an overview picture (bottom left) and a close-up of observed crack (top left). The red and blue annotations are used to identify different types of observations.

6 DATA HANDLING

6.1 *Digital images*

As a versatile tool for handling different kinds of georeferenced data COWI has developed a special tool. The tool, entitled COWI Multiviewer, is fully web based and can be used to store and present data in a number of different formats. An image of one of the anchor blocks – taken from COWI Multiviewer - is presented in Figure 7.

A special application of the COWI Multiviewer – known as COWI Virtual Inspection Tool (CVI) – can be used to carry out desk inspections of structures based on digital images fed into the viewer.

The COWI Multiviewer is just shown here as an example of an application able to handle digital images. It is assumed that standard BIMS applications can handle this kind of information in a similar manner.

6.2 *Inspection data*

For 20 years COWI has developed and used dedicated databases to register observations from inspections carried out on large infrastructure.

The use of databases has a number of advantages over a paper-based system:

- Predefined defects
  A core component of the databases is a hierarchy of predefined defects. Usually the predefined defects will cover more than 95% of the observations. The use of predefined defects assure a uniform registration of defects even when 5 or more inspectors are involved in an inspection.
- Easy registration in the field
  The database is installed on a tablet pc so that registration can be done directly in the database. Hence, a full and final registration is made on the spot.
- Optimal data handling
  As 95% of the defects (or more) are described by means of a rather limited number of predefined defects it is easy to handle the data and do reports directly from the database.
- Easy exchange of data between systems
  Data from the inspection databases may be easily interchanges with higher level Asset Management Systems or BIMS by means of standardized data formats such as Excel, csv-format, txt-format or the like.

Further in BIMS a direct link can be established between a main structural component and the inspection database containing

Currently COWI is involved in the development of tools that may combine data in such inspection databases with the COWI Virtual Inspection Tool in COWI MultiViewer.

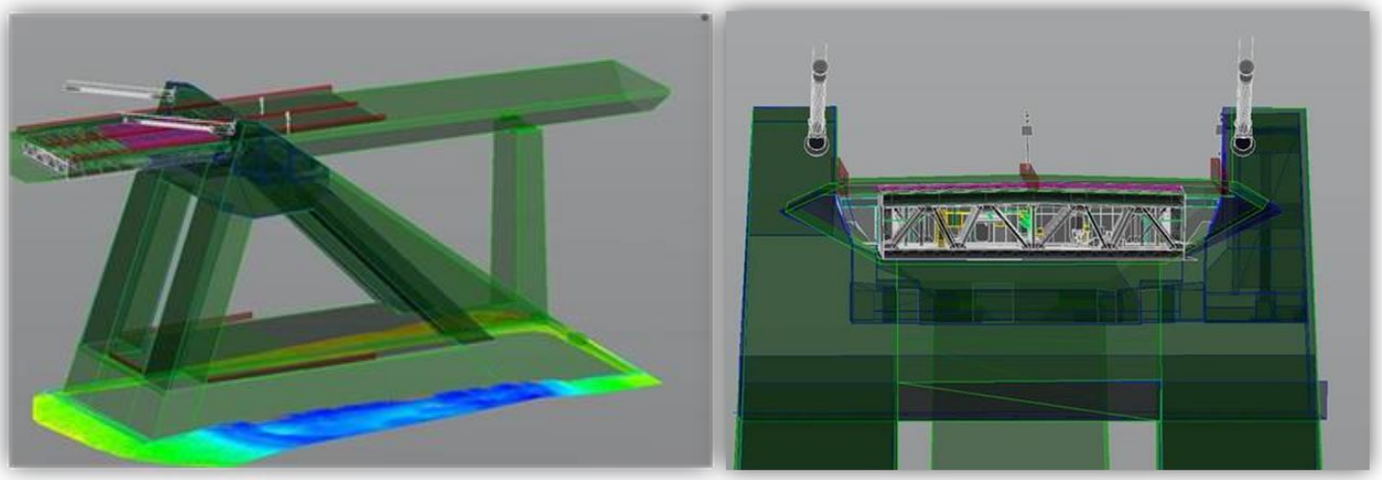


Figure 8. 3D-model of anchor block based on images taken by a UAV combined with the 3D-model of an interior part of the bridge deck based on a point cloud from laser scanning.

6.3 *Monitoring data*

Most modern infrastructure is equipped with a number monitoring equipment that can carry out automated monitoring and also

As the level of monitoring increases also the need for effective handling and processing of data increases.

Over the last 10 years COWI has been involved in the development of systems and tools that can handle and process data from monitoring systems such as

- Cathotic protection systems
- dewatering system for tunnel ramps at Storebelt East Tunnel,
- inspection of bridge bearings,
- hanger fluctuation.

It is foreseen that the handling of monitoring data will soon be an integral part of BIMS.

7 SHORT TERM PERSPECTIVES

Video recordings and high resolution digital images can be used to prepare inspection, structural assessment and reporting in the office.

Repeating full video inspection at regular intervals is an effective way to monitor changes in the condition of infrastructure that are often large in size and a challenge to access in all details.

Information from different sources may be combined, which is shown in the example in Figure 8. This example combines a 3D-model of one of the anchor blocks on the Storebelt East Bridge with the result of a laser scanning of the interior of the bridge deck at the same location.

8 LONG TERM PERSPECTIVES

Automatic image processing can be used to monitor changes in the condition of structures based on changes in visual appearance.

Also it will be possible soon to detect some defects by means of automated image processing. This may include:

- development and changes in crack patterns,
- spalling concrete,
- ingress of water in concrete structures,
- corrosion on steel surfaces,
- degradation of surface treatment on steel structures.

Further, the data may be gathered by UAVs that are remotely controlled from an office to inspect (visually) specific and remote parts that may be difficult to access in person or UAVs that are programmed to fly a prescribed route in order to inspect a structure at certain intervals.

All of the above information will (probably) be handled, documented and communicated by means of BIMS. That is why BIMS is such an interesting issue also for existing structures.

9 CONCLUSION

The main advantage of implementing an asset management system incorporating the special features of BIMS on existing infrastructure components, compared to traditional AMS, is the fact that a direct and intuitive link between the components and the related information can be obtained by means of a 3D model.

Another, and in fact very important advantage is that most AMS available on the market in the future will be incorporating features from BIMS. Systems

that are based on an alphanumerical object identification system are foreseen to die out. Hence, the need for 3D models of existing infrastructure components will increase in the coming years.

This paper has given some examples on rational ways to establish a functional 3D-model for existing assets.

The future will show how AMS and BIM can co-exist and be combined to promote a more effective and rational way to handle the huge amount of information related to infrastructure components from the first conceptual studies, over commissioning, operation and final decommissioning.

Some of the basic features of BIMS – the fact that it is visually based and intuitively and easy to interpret - makes it a strong and versatile tool when it comes to communicating information such as inspection data or graphics based on monitoring.

REFERENCES

NBIMS-US. 2017. National BIM Standard-United States - FAQ (https://www.nationalbimstandard.org/faqs#faq1)

LGAM. 2017. Local Government & Municipal Knowledge Base (http://www.lgam.info/asset-management/)

Maintenance, Safety, Risk, Management and Life-Cycle Performance of Bridges – Powers, Frangopol, Al-Mahaidi & Caprani (Eds)
© 2018 Taylor & Francis Group, London, ISBN 978-1-138-73045-8

Creation of "live data" for existing infrastructure

F. R. Gottfredsen & H. Pedersen
COWI A/S, Denmark

ABSTRACT: A recent project concerning the central railway line in Montenegro comprised visual, detailed and special inspection, condition evaluation and action plan for rehabilitation works on all tunnels and galleries. This generated a huge amount of information and data to be structured and processed for various objectives. It was requested that data should be delivered in a format suitable for future incorporation in a BIM system. Therefore, it was decided to adopt a "fully digital" approach. An initial visual inspection was performed based on a full video recording of all tunnel surfaces. Geodetic survey was performed by laser scanning and continuous 3D point clouds of the inside of the tunnels were obtained. Defect registration was performed by pre-defining of a number of typical defects. A purpose made inspection database was used for registration of observations on the spot. Afterwards, an Action Plans for Rehabilitation Works weas generated directly from data in the Inspection Database.

1 INTRODUCTION

The objective of this paper is to provide an example on how a vital part of an Asset Management System for an infrastructure component can be effectively established, being far into the operational phase.

COWI has been involved in a recent project in Montenegro "Special inspection of 106 tunnels and development of the Main Designs for their rehabilitation (urgent measures on the tunnels according to the priority established based on the special inspection findings) on the railway line "Vrbnica-Bar" (SEETO Rail Route 4), Component 1 – Inspection of Tunnels", that provides a good basis for such an example. The main characteristics of the basis of this project are the following:

- there exists no information system for the component: railway tunnels and galleries, civil works
- data as captured in the inspection phase of the project is requested to be "provided in accordance with a format suitable for easy transfer to a future Building Information Modelling System (BIMS)"
- the results obtained from the inspection activities should also be used by:
  1) a Consultant to prepare Main Design,
  2) the Montenegrin Railway to select tunnel rehabilitation works to be executed urgently,
  3) the Montenegrin Railway to develop detailed rehabilitation strategies ,
- information gathered during the inspection, survey, evaluation and further recommendation of rehabilitation strategies comprises a huge amount of data, that can only be handled in an effective way by use of computer applications.

This paper describes the selected main approach and methodology, the activities for capturing, structuring, evaluating, processing and delivering data that are prepared for entering into an Asset Management System (AMS) (or a BIM system).

Further, the paper describes in brief how the data can be used directly in the coming phases for operation and maintenance of the railway infrastructure, with or without implementation of an AMS. Finally, some thoughts are given onhow benefit of the data could be improved by implementation of a few, simple data processing tools.

2 STRUCTURAL ASSETS

The railway line between Bar and Vrbnica runs through the central part of Montenegro from the Adriatic Sea at Bar to the border to Serbia at Vrbnica in the north as shown in Figure 1. The railway line is app. 100 km in length and includes 106 tunnels and 14 galleries with a total length of app. 53 km.

The shortest tunnel is 40 m long and the longest is 6.171 m. The galleries are between 10 and 100 m in length.



Figure 2 The main railway line in Montenegro going between Bar at the Adratic Sea (south) and Vrbnica at the Serbian border (north).

The railway line is a single-track line except at a few stretches around stations where it comprises up to 3 tracks. Three tunnels are so close to a station that they also comprise three tracks – two in full and one in part.

3 METHODOLOGY

3.1 *Main project tasks*

The main project parts, that was dealing with inventory data, comprised:

1 Inspection of 106 tunnels and 14 galleries
- an initial visual inspection of all components,
- a detailed inspection of all components, for in depth inspection of observed defects and damages,
- special inspection of selected structural parts.

2 Geodetic Survey
Laser scanning of all tunnel and gallery surfaces

3 Defect Registration
Performed during detailed inspection. Observation of all defects (innate as well as inflicted damages). Registration according to type of damages and location of each defect.

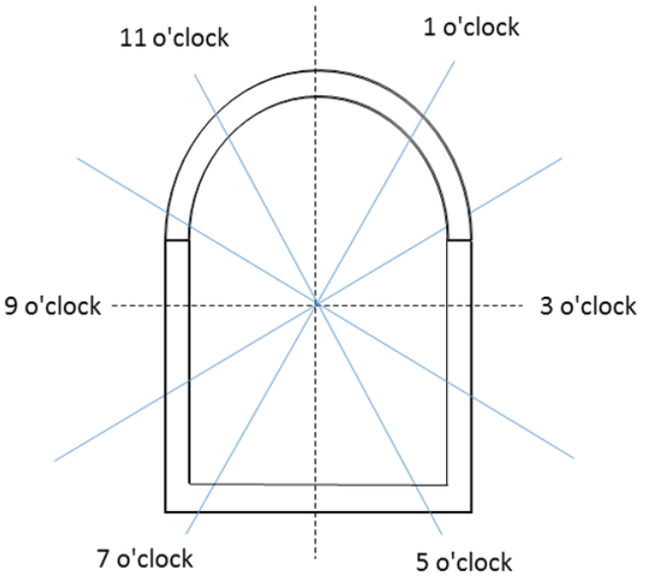


Figure 2. Definition of "clock wise" system to define placement of defects within the tunnel cross section.

4 Action Plan for Rehabilitation Works
Recommendation of types of rehabilitation works related to observed defects and estimated degradation rates.
Composition of rehabilitation works into Rehabilitation Projects related to individual tunnels or set of tunnels.
Estimates of costs and time for each tunnels rehabilitation works
Development of Rehabilitation Strategies

3.2 *Selected approach*

In order to assure that the data achieved from inspections could be available for various usages and be readily entered into a future BIMS, the following was decided:

– all data should be in digital form and should be live data (in native format, not pdf-files),
– most general system formats should be used:
  - Microsoft Office (Excel, Access, etc)
  - AutoCad and Microstation

Based on these decisions the following performance of project activities were selected:

– Visual inspections based on video recordings,
– Geodetic survey based on mobile laser scanning to obtain 3D point clouds,
– Digital Defect Registration using an Access database developed for this project
– Monitoring of temperatures in selected tunnels: (as frost resistance was a major issue)
– Preparation of an Action Plan for Rehabilitation Works for all tunnels and galleries. Data is structured from defect registration according to tunnel numbers and processed in ordinary Excel sheets.

As no BIMS for the infrastructure exists the following, very simple structure of the element hierarchy was selected:

– Level 1: Tunnel number
  The tunnels are numbered from Vrbnica (at Serbian border) to Bar (at Adriatic Sea), starting with number 147.
– Level 2: Ring number in tunnel (construction section number), or portal number (A or B)
– Level 3: Definition of local system for data registration.
  - A "clock-wise" system for local registration of data within a tunnel was used (See Figure 2).
  - The tunnel is seen in the direction of increasing chainage (i.e. in the direction Vrbnica – Bar).

4 DESCRIPTION OF ACTIVITIES

4.1 *Visual inspection*

The requested visual inspection was performed as a CPV recording of all tunnels and galleries.
(CPV is an acronym for COWI Panoramic View which is a 360° recording based on the same technology as Google Street View©)

The CPV recording device was installed on top of a car that was positioned on a flatbed rail wagon driven through all tunnels and galleries by a dresine. The installation is shown in Figure 3.

CPV images were recorded in a cooperation between the project team and the Montenegrin Railways (ŽICG).

Panoramic images were recorded with 5 frames/sec, which gives an image for each app. 28 cm while driving 5 km/h and app. 39 cm while driving 7 km/h.

For each tunnel and gallery, a file containing the CPV-recording was created.

The outcome of the CPV was a full 360° image of the tunnel surface (lining) of all tunnels and galleries.

In a dedicated viewer, it was possible to look through all the recordings. The viewer made it possible to pan and zoom so that all parts of a tunnel section could be viewed in detail. Single images (screen dumps) of certain details can be generated and saved.

From the CPV all defects above a certain size could be observed. This meant that signs of water ingress could be seen – typically as dark patches. However, it was not possible solely from the recordings to evaluate the amount of water entering the tunnel.

Furthermore, spalled concrete and areas with deteriorated concrete could be identified from the CPV. Larger cracks (w > 0,5 mm) could also be observed, especially if they were accompanied with water ingress. At the same time, medium size cracks (width between 0,2 mm and 0,5 mm) could under certain conditions be identifiable, whereas smaller cracks (w < 0,2) could not be observed from the CPV.

From the CPV the size of identified damages were initially assessed simply by assessing the size directly from the images.

Although the GPS installed on the recording device is not working in tunnels, it is anticipated that the chainage can be determined within a tolerance of app. 0,5 m, which was found to be adequate to reliable re-find in the tunnels damages identified from the recordings.

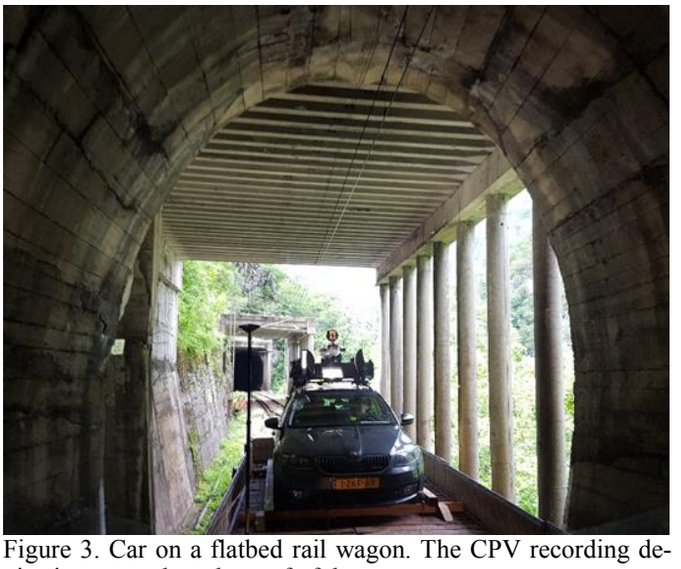


Figure 3. Car on a flatbed rail wagon. The CPV recording device is mounted on the roof of the car.

4.2 *Geodetic survey*

The geodetic survey of the interior of the tunnels was performed with a mobile laser scanning, running on a flatbed wagon. From the mobile mapping high density continuous 3D point clouds of the inside of the tunnels were obtained. The 3D point clouds have a very high relative accuracy. Furthermore, the point clouds can be used for any measurements inside the tunnels for any future work and in that way they are considered an asset for the railway company and all maintenance / rehabilitation works to be undertaken in the future. Cross sections and longitudinal profiles are generated from the point clouds. Clearance profiles are imposed on cross sections for evaluation of tunnel geometry.

The laser scanning recording system was installed on a flatbed wagon driven by a diesel dresine. The installation is shown in Figure 4.

Main components of the mobile mapping system are:
– Two laser scanners, positioned tilted along driving direction to collect as many objects as possible. Each laser scanner can collect up to 1.016 Mio. points per sec.



Figure 4. Flatbed rail wagon with laser scanning equipment mounted on it. The wagon is moved with help from a dresine.

– One GNSS (Global Navigation Satellite System)/GPS (Global Positioning System), receiving satellite observations for United State satellite system and European satellite system. Satellite observations are stored each second.
– One INS (Inertial Navigation System), tracking changes in speed movement together with rotation of the vessel. Data motion is stored twice every second.
– Odometer/wheel sensor, tracks the amount of distance travelled by the wheels.
– Computer for tracking and storing information.

Original output from the laser scanning is a 3D point cloud. For each single point in the point cloud, an intensity value is collected depending on the surface. The point cloud can be imported and viewed in different standard CAD and GIS (Geographical Information System) software.

Derived presentation from the point cloud can be a 2D cross sections with specified intervals along the alignment or wherever there are interesting features, which have to be investigated.

The left part of the figure shows the original point cloud. The right part shows a generated cross section. Within this cross section is shown four clearance profiles defined by the project. The objective was to identify possible clashes between the required clearance profiles and the tunnel lining. In this project clash test was done every 20 m where the length profile was straight and every 5 m where the length profile was curved.

The point cloud were also used as basis for the development of longitudinal profiles with indication of the stationing. Figure 6 shows an example of this.

The 3D image that is also the outcome of the point cloud from the laser scanning is illustrated in Figure 7.

4.3 *Defect registration*

Defect registration is composed of three parts:
– Overall registration (Inspector, weather …),
– Location of the defect (tunnel number, section number, local "watch" coordinate,
  Characterization of the defect.

The core of the registration methodology is the definition of a number of predefined defects.

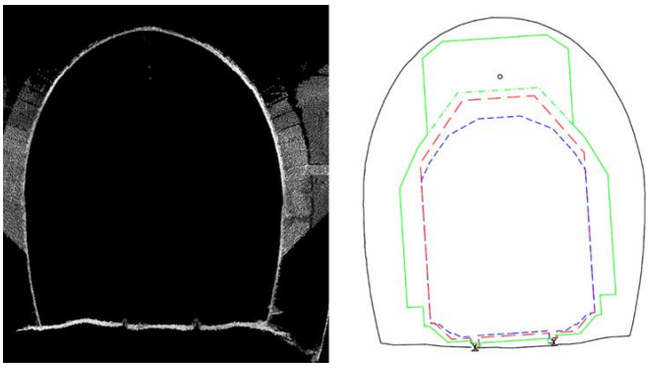


Figure 5. Point cloud of tunnel on the left. A cross section with different clearance profiles included are shown on the right.

Each predefined defect is characterized by means of the following parameters:
– defect type,
– cause,
– level of water ingress,
– size,
– extent.

Each defect was given a defect mark by the inspector. The defect mark reflects the inspectors engineering judgment concerning the severity of the defect. The definition of the defect marks that were used are given in Table 1.

Table 1. Definition of defect marks (DM).

DM	Description
1	Severe defect (heavily deteriorated concrete and/or extensive water ingress) that may endanger structural safety (failure/overload) or safety of passing trains (e.g. due to falling concrete).
2-	Significantly deteriorated concrete (up to 0,5 m in depth) and extensive water ingress, but no immediate risk of structural failure or safety of passing trains. Damages will probably cause disturbance to train traffic e.g. due to ice forming.
2	Significantly deteriorated concrete and/or significant water ingress, but no risk of structural failure or safety of passing trains. Damages may cause some disturbance to train traffic e.g. due to ice forming.
2+	Deteriorated concrete (up to 0,2 m in depth) and significant water ingress, but no risk of structural safety or safety of passing trains. Water ingress is unlikely to cause disturbance to train traffic.
3	Smaller, less significant defect.

Defect recording was done on the spot by use of a tablet loaded with an Access database prepared for the project. The database is entitled Inspection Database.

The registration was done by choosing relevant values for type, water ingress, size and extent as well as the defect mark in a number of drop down menus in the input page of the database.

Further, the input page allows the inspector to register any pictures related to the defect and finally it is possible to add relevant remark in a free text box.

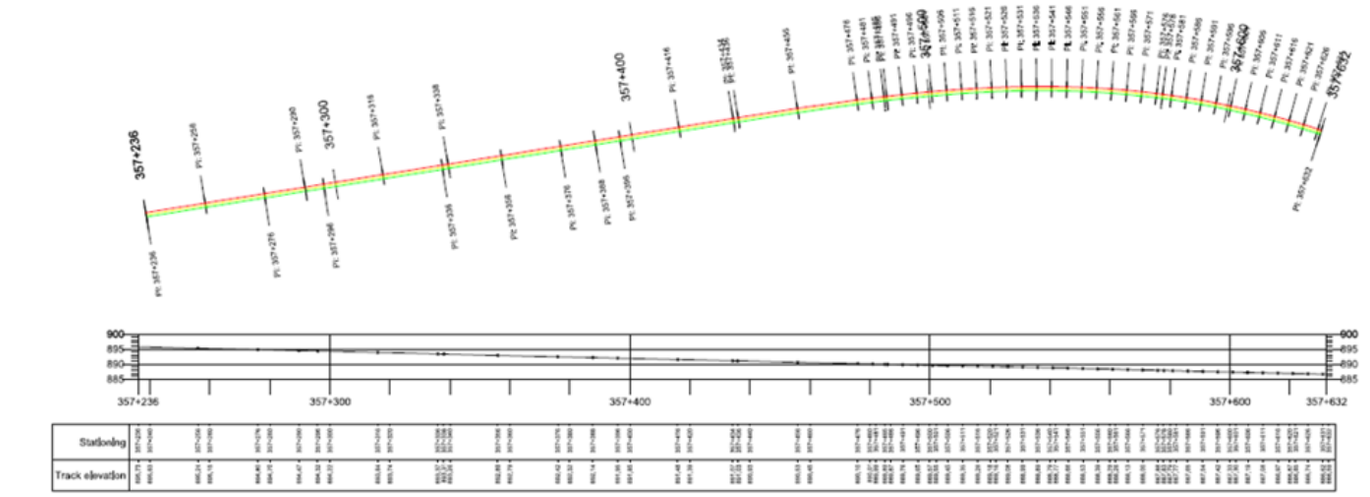


Figure 6. Horizontal and vertical profile of a single tunnel obtained from the laser scanning (example). On the vertical profile the chainage where cross sections have been defined (as shown to the right in Figure 5) is indicated.

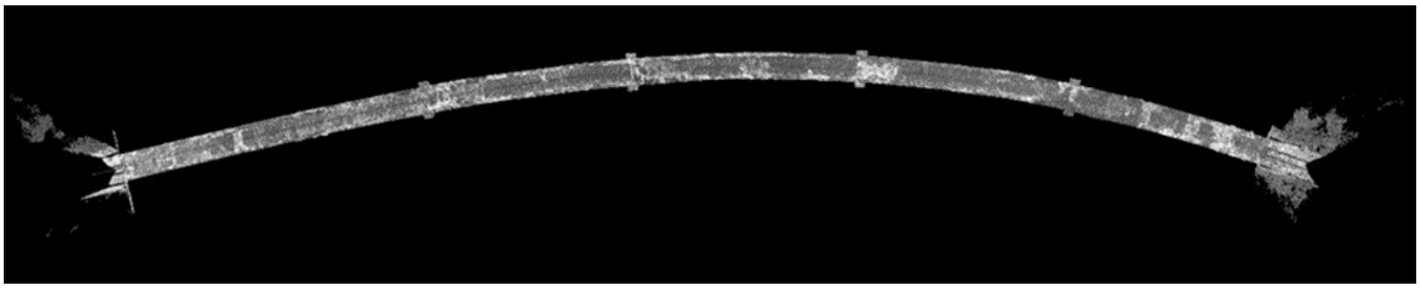


Figure 7. Point cloud of a single tunnel (example) – seen from above.

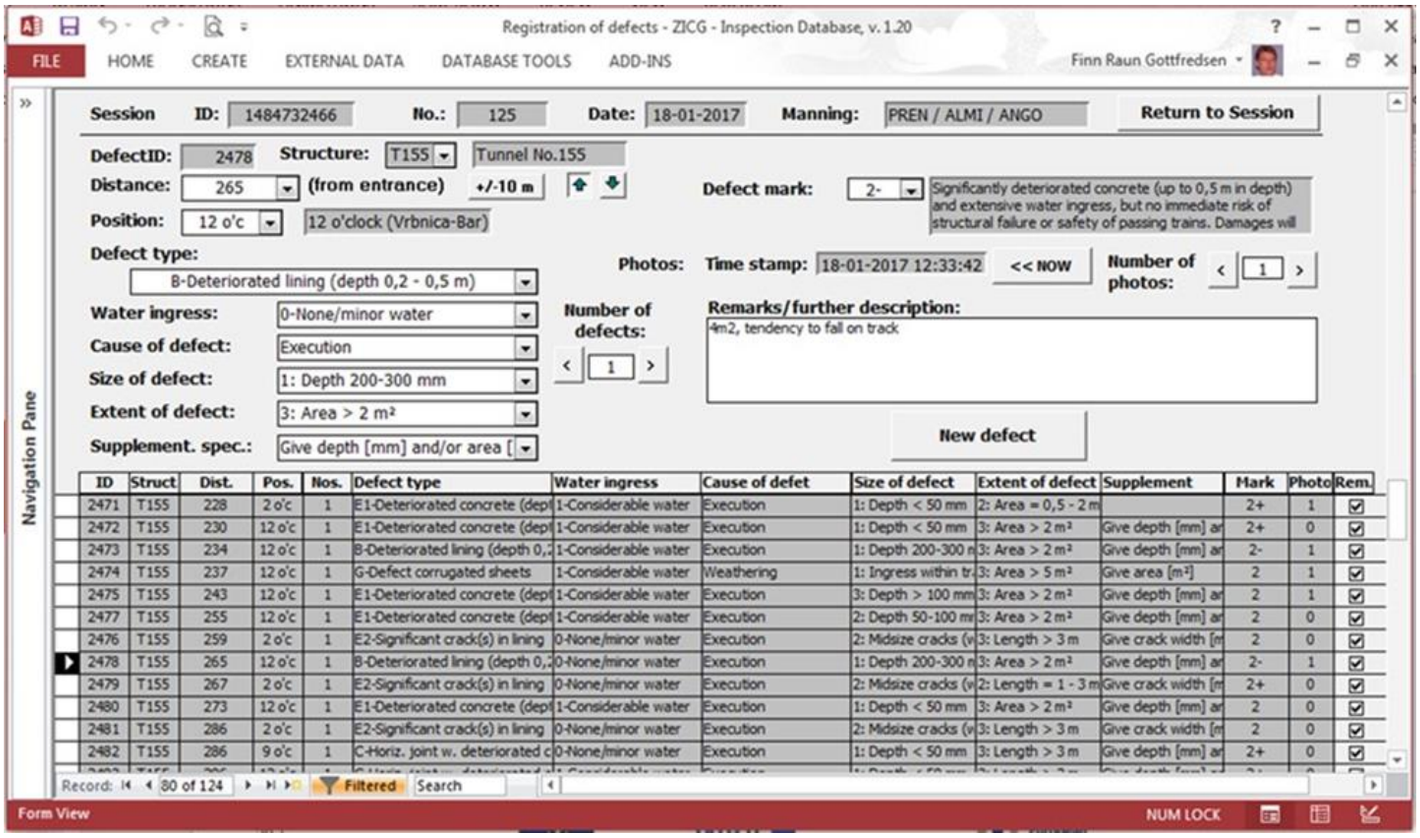
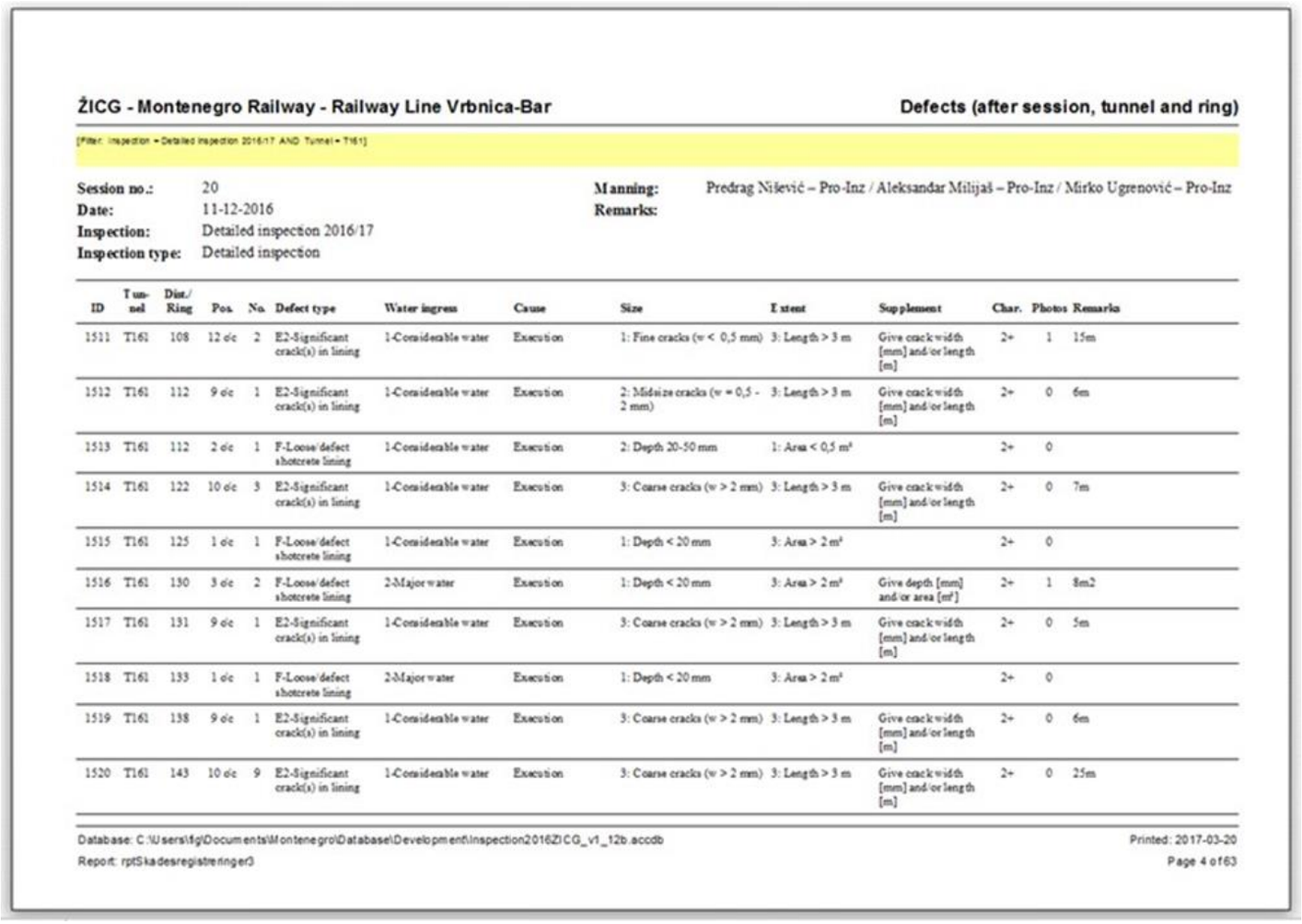


Figure 8. Input page in the Inspection Database. Input is done in the upper part of the page – mainly using drop-down menus. In the lower part of the page, observations already registered in the database can be seen.



ŽICG - Montenegro Railway - Railway Line Vrbnica-Bar — Defects (after session, tunnel and ring)

[Filter: Inspection = Detailed inspection 2016/17 AND Tunnel = T161]

Session no.: 20 **Manning:** Predrag Nišević – Pro-Inz / Aleksandar Milijaš – Pro-Inz / Mirko Ugrenović – Pro-Inz
Date: 11-12-2016 **Remarks:**
Inspection: Detailed inspection 2016/17
Inspection type: Detailed inspection

ID	Tunnel	Dist./ Ring	Pos.	No.	Defect type	Water ingress	Cause	Size	Extent	Supplement	Char.	Photos	Remarks
1511	T161	108	12 o'c	2	E2-Significant crack(s) in lining	1-Considerable water	Execution	1: Fine cracks (w < 0,5 mm)	3: Length > 3 m	Give crack width [mm] and/or length [m]	2+	1	15m
1512	T161	112	9 o'c	1	E2-Significant crack(s) in lining	1-Considerable water	Execution	2: Midsize cracks (w = 0,5 - 2 mm)	3: Length > 3 m	Give crack width [mm] and/or length [m]	2+	0	6m
1513	T161	112	2 o'c	1	F-Loose/defect shotcrete lining	1-Considerable water	Execution	2: Depth 20-50 mm	1: Area < 0,5 m²		2+	0	
1514	T161	122	10 o'c	3	E2-Significant crack(s) in lining	1-Considerable water	Execution	3: Coarse cracks (w > 2 mm)	3: Length > 3 m	Give crack width [mm] and/or length [m]	2+	0	7m
1515	T161	125	1 o'c	1	F-Loose/defect shotcrete lining	1-Considerable water	Execution	1: Depth < 20 mm	3: Area > 2 m²		2+	0	
1516	T161	130	3 o'c	2	F-Loose/defect shotcrete lining	2-Major water	Execution	1: Depth < 20 mm	3: Area > 2 m²	Give depth [mm] and/or area [m²]	2+	1	8m2
1517	T161	131	9 o'c	1	E2-Significant crack(s) in lining	1-Considerable water	Execution	3: Coarse cracks (w > 2 mm)	3: Length > 3 m	Give crack width [mm] and/or length [m]	2+	0	5m
1518	T161	133	1 o'c	1	F-Loose/defect shotcrete lining	2-Major water	Execution	1: Depth < 20 mm	3: Area > 2 m²		2+	0	
1519	T161	138	9 o'c	1	E2-Significant crack(s) in lining	1-Considerable water	Execution	3: Coarse cracks (w > 2 mm)	3: Length > 3 m	Give crack width [mm] and/or length [m]	2+	0	6m
1520	T161	143	10 o'c	9	E2-Significant crack(s) in lining	1-Considerable water	Execution	3: Coarse cracks (w > 2 mm)	3: Length > 3 m	Give crack width [mm] and/or length [m]	2+	0	25m

Database: C:\Users\fg\Documents\Montenegro\Database\Development\Inspection2016ZICG_v1_12b.accdb Printed: 2017-03-20
Report: rptSkadesregistreringer0 Page 4 of 63

Figure 9. Sample page of a standard report from the Inspection Database.

The input page is shown in Figure 8 The input part of the page is at the top. The lower part shows observations already registered in the database. It is observed that most data are chosen from drop down menus. That makes registration very quick and intuitive. The registration database also contains a versatile report facility, by which a number of specialized reports can be easily defined and retrieved.

All basic parameters of the defects are shown in one of the standard reports defined in the Inspection Database. An example of this report type is shown in Figure 9. As can be seen the defects are sorted according to tunnel and "ring"-number.

4.4 *Temperature registration*

As part of the special inspections carried out during the project a number of temperature loggers where installed in four tunnels during the winter period. Five loggers where installed in each of the tunnels: one close to each end, one logger app. ¼ of the tunnel length from each portal and one in the middle. It was considered of interest to monitor and map the temperature within the tunnels, due to the fact that:

- The number of freeze-thaw cycles may have a considerable impact on the degrading of the concrete lining.
- The risk of ice building, due to ingress of water in the tunnels, is dependent on the temperature inside the different tunnels.

Four tunnels were chosen for temperature monitoring in order to be representative for both the geography as well as the length of tunnels.

Very simple (and cheap) data loggers type EL-CC-1-FG from Lascar Electronics were used to log the temperature. These loggers can only be used once.

An example of logged temperature data is shown in Figure 10. It is clearly recognized how temperatures fluctuate during the day –especially close to the portals. Also, it can be seen that the temperature only changes moderately over the length of the tunnel.

For tunnel T232 – which is situated just south of the center of Montenegro – only a few freeze/thaw cycled could be observed during the winter of 2016/17.

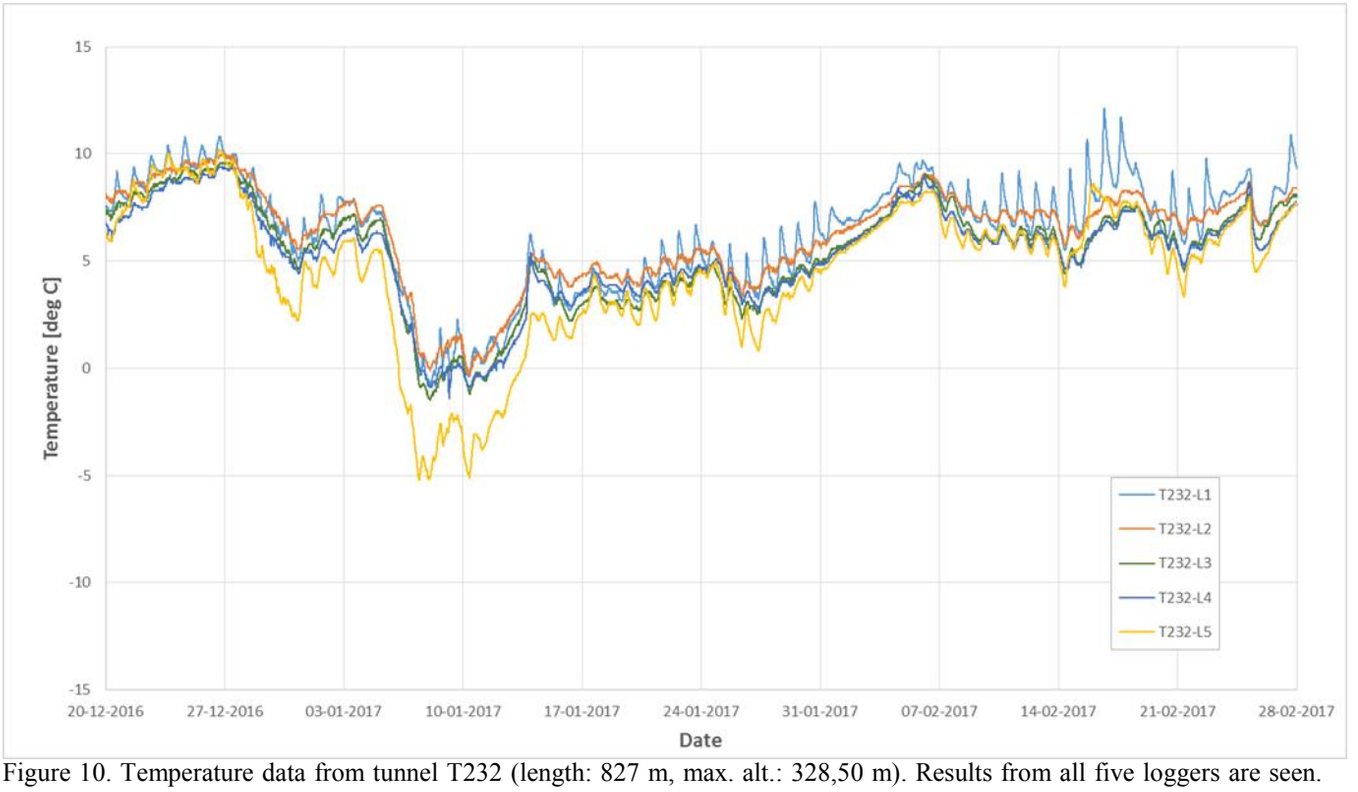


Figure 10. Temperature data from tunnel T232 (length: 827 m, max. alt.: 328,50 m). Results from all five loggers are seen. Loggers L1 and L5 were placed close to each of the portals, L2 and L4 were placed ¼ of the tunnel length inside the tunnel, L3 was placed in the middle of the tunnel.

4.5 *Action Plan for Rehabilitation Works*

Based on the findings from the detailed inspection carried out in all 106 tunnels 12 standard repair types where defined.

Based on the detailed registrations in the Inspection Database, which were exported to Excel, a repair was assigned to all defects having a Defect Mark of 2, 2- or 1, i.e. the three most severe categories, cf. table 1. From the individual registrations the type and extent of repair was defined for each defect.

Defects and the associated repairs where summarized for each tunnel, resulting in an Action Plan for Rehabilitation Works for each tunnel.

The spreadsheet system was expanded to include cost estimates and construction time estimates related to each repair type. Again, the estimates were summarized for each tunnel. Influence of railway operation was included in the estimate of construction time.

In this way an Action Plan for the whole railway line was developed containing a rehabilitation plan for each tunnel or for a set of tunnels positioned on a certain railway section. For each Rehabilitation Project was estimated a total cost, a total construction period and manning from Contractors.

Based on these Rehabilitation Projects was developed a set of rehabilitation strategies.

As an example Figure 11 shows the estimated duration of rehabilitation works and the estimated "number of men" necessary for various scenarios.

Scenario number	Works included	Length of railway closure	No. of ineff. hours	Duration of rehab. works [years]	Estimated number of men
A1	All structural repairs. No TSI-SRT related works.	12 hours	2	10,0	11
A2		8 hours		16,7	
A3		5 hours		33,3	
B1	All structural repairs. All TSI-SRT related works.	12 hours	2	10,0	30
B2		8 hours		16,7	
B3		5 hours		33,3	
C1	Structural repairs type RA1 + RA2. No TSI-SRT related works	12 hours	2	6,0	12
C2		8 hours		10,0	
C3		5 hours		20,0	
D1	Structural repairs type RA1 + RA2. TSI works TSI06-TSI08	12 hours	2	6,0	38
D2		8 hours		10,0	
D3		5 hours		20,0	

Figure 11. Estimated duration of railway closure and estimated number men for different rehabilitation scenarios. It is interesting to note that the available length of tunnel closure has a significant impact on the estimated duration.

It is interesting to note how the length of available railway closures has a significant impact on the estimated duration of rehabilitation works.

5 DELIVERABLES

5.1 *Workshops*

In order to promote the Beneficiary's (Montenegrin Railways) use and benefit of the data a number of workshops with participation of potential users from Montenegrin Railways were performed.

On these workshops possibilities of enhanced use of the data acquired during the project was discussed. Further, possibilities and plans for future implementation of an AMS was discussed. The Montenegrin Railways are still considering what available standard system to invest in.

5.2 *Data*

A hard disk with all the collected data was delivered to the Montenegrin Railways at the end of the project. The following data were included on the hard disk:

- CPV recordings (including a freeware viewer),
- Laser scanning recordings,
- Cross sections with clearance profiles, incl. facility for easy access to selected tunnels,
- Defect Registration Access Database, which can be accessed and used (but not altered) on any Windows-based pc,
- Spreadsheets containing plans for Rehabilitation Works and Strategies.

The total amount of data collected during the project amounted to app. 3,5 TB equal to 3.500.000 MB.

6 LESSONS LEARNED

The project presented in this paper had an effective duration of 15 months. As described previously the project comprised 106 tunnels and 14 galleries situated on a single-track railway line going across Montenegro. The total length of tunnels/galleries is about 53 km.

During the fairly short period of time available for the project the following tasks were carried out:

- 360° recordings of all tunnels and galleries (called CPV),
- laser scanning of all tunnels and galleries,
- cross sections where determined and compared to clearance profiles for all tunnels at short intervals (max. 20 m distance),
- initial visual inspection based on CPV,
- detailed inspection of all tunnels and galleries (almost 20.000 observations where registered in the Inspection Database),
- a rehabilitation plan was established for each tunnel. The plan included cost estimate and time needed for rehabilitation.

The task described above could only be carried out in a rational and effective way by extensive use of digital data registration and data handling.

The project has shown that video recordings can be used as an effective tool when performing a visual inspection of infrastructure components such as tunnels and galleries.

Video recordings should not stand alone, as some defects cannot be effectively observed without being close to the structures. However, it is possible to use the video recordings effectively as a screening tool to optimize the planning of detailed inspections.

Effective handling of data from the detailed inspection, by means of a purpose made Inspection Database, has made it possible to develop individual rehabilitation plans for all the 106 tunnels.

7 ACKNOWLEDGEMENTS

The technical assistance described in this paper was financed under the Western Balkans Investment Framework (WBIF) which is a joint initiative of the EU, International Financial institutions, bilateral donors and the governments of the Western Balkans which supports socio-economic development and EU accession across the Western Balkans through the provision of finance and technical assistance for strategic investments, particularly in infrastructure, energy efficiency and private sector development.

COWI wants to acknowledge the funding that made this project possible.

Further, COWI wants to express its appreciation of the positive collaboration shown by the Montenegrin Railways during the project, which made it possible to get the access to the tunnels needed to carry out the project in an efficient manner.

Maintenance, Safety, Risk, Management and Life-Cycle Performance of Bridges – Powers, Frangopol, Al-Mahaidi & Caprani (Eds)
© 2018 Taylor & Francis Group, London, ISBN 978-1-138-73045-8

A simulated maintenance costing using a Markov deterioration model for bridge components

H.D. Tran & S. Setunge
RMIT University, Melbourne, Australia

Y-C. Koay & H. Luczak
VicRoads, Melbourne, Australia

ABSTRACT: Road bridges are life line structures essential to ensure community mobility. Bridge management agencies currently adopt streamlined and cost-effective approaches to facilitate maintenance of their aging and deteriorating bridge assets. One typical approach is based on different levels of inspection before making a decision on repair or replacement. In such approach, the deterioration level of bridge component is expressed through time-varying discrete condition states (e.g. use of 4 condition states with 1 being good and 4 being poor) which are defined by type and severity of structural deterioration and damages at the time of inspection. In utilizing the inspected condition data, past studies successfully applied the Markov deterioration model to understand and predict the rate of deterioration of bridge components. Based on that, optimal rehabilitation and replacement policies for bridge components have been developed in several past studies. However, one important management problem, which has not been addressed in previous studies of bridge maintenance, is to identify the next inspection time for a bridge component with known current condition that will result in lowest operational cost over a planning horizon. Furthermore, the effect of early intervention on inspection and maintenance cost has not been well investigated. From cost-saving and risk perspective, finding the optimal inspection time and repair intervals, while keeping bridges at a reasonable level of service, is of interest to the bridge management agencies. The model proposed here integrates the Markov deterioration model and a cost rate function through a computational procedure for deriving the lowest-cost inspection time of bridge components with various known condition states. A case study with bridge condition data is presented to demonstrate the benefit of this study.

1 INTRODUCTION

1.1 *Background*

Road Bridges are part of essential infrastructure assets to the human living. They are long life structures expectedly exceeding 100 years of service life as required by the latest version 2017 of bridge design standard AS 5100 in Australia. During their service life, road bridges are subjected to various deterioration processes and random damage events that adversely affect their serviceability and structural safety. For the example of commonly used reinforced concrete (RC) bridge components, the structural deterioration processes have been known due to a number of phenomena including corrosion of concrete, corrosion of reinforcement, concrete creep and fatigue resulting in excessive cracking, loss of strength and material (Jamali et al., 2013, Stewart, 2010). The random damage events include traffic and collision accidents, and natural hazards such as bushfire, flooding, earthquake (Gidaris et al., 2017, Agbelie et al., 2017, Frangopol et al., 2017). As a result, road bridges can be subjected to various maintenance, rehabilitation and replacement (MRR) actions during their lifetime.

Industries such as bridge management agencies are expected to adopt more streamlined and cost-effective MRR management approaches to facilitate structural safety, and service performance under constraints of limited funding, and reduced environmental footprint. The common management practice is based on different levels of inspection before making a decision on MRR actions (Sonnenberg, 2014). In such approach, the visual inspection with inspection interval of 2-3 years is commonly adopted (Rashidi et al., 2016). The deterioration level of bridge component is considered to be captured through time-varying discrete condition states (e.g. 4 condition states with 1 being good and 4 being poor). The condition state is rated by type and severity of structural defects such as cracking, corroded steel and spalling, which are found during inspection (Principal Bridge Engineers, 2014).

In the past and even in some current bridge management systems, the MRR decisions are often based the knowledge and experience of bridge engi-

neers after evaluating observed defects (Safia et al., 2013, Parr et al., 2010). With the advance of deterioration modelling and simulation technology, it is desirable to use prediction from deterioration models and simulated costing to further streamline inspection frequency and annual budget and understand cost-benefit of various MRR options.

As far as deterioration is concerned, the data-driven deterioration models using Markov chain theory (Moomen, 2016, Bu, 2013) is often adopted as compared to the mechanism-based deterioration models (Vatteri et al., 2016, Jamali et al., 2013) because the former modelling approach can utilize the available inspection data while the later modeling approach, despite more accurate, requires data that are not available and costly and difficult to obtain.

Based on deterioration models, several inspection and maintenance approaches have been developed. Robelin and Madanat (2007) developed a Markov decision process to determine optimal maintenance and replacement policies for bridge decks in their worked examples. Saydam and Frangopol (2015) proposed an innovative risk-based maintenance optimisation methodology for existing deteriorating bridges to find the optimum maintenance options and timing.

However, one important management problem, which has not been addressed in previous studies of bridge maintenance, is to identify the next inspection time for a bridge component with known current condition that will result in lowest operational cost over a short planning horizon. Furthermore, the comparative cost saving of various early intervention strategies have not been well studied.

1.2 *Aims and objectives*

This study develops a computational procedure to find the inspection interval with lowest cost for asset management of bridge components. The Markov chain theory is used to model the change of discrete condition states and Monte Carlo simulation is used to find optimal inspection interval with the lowest cost. A case study with actual inspection data is presented to demonstrate the benefit of this study.

With the trend of embracing sustainable development for increased population, the challenge to bridge management agency is to prove the efficiency in asset management during the expected service life. The proposed procedure demonstrated through one example with specific assumptions would contribute to improve MRR strategy for bridge program, and reliability analysis for prioritization and long-term management.

2 METHODOLOGY

2.1 *Overview*

The methodology is developed to obtain the simulated inspection and maintenance strategies over the planning horizon. It is based on the widely adopted routine inspection with 4 rated conditions. The methodology contains the four following steps:

1. Calibrate the Markov model
2. Generate N simulated pathways of condition change over the selected planning horizon by using the calibrated Markov model
3. Define cost rate function
4. Apply cost rate function to the simulated pathways of condition changes to obtain the average cost rates for various scenarios.

2.2 *Markov model*

The Markov model is based on the stochastic theory of Markov chain (Madanat et al., 1995), which describes a system that can be in one of several condition states at any time, and it can stay still or move to another state at each time step with some transition probabilities. This theory is well suited for observation of level 2 condition data of bridge elements because the snapshot inspection reveals the condition state at the time of inspection and the unchanged and changed condition states over time can be captured with the transition probabilities.

The most important property of the Markov chain is that the probability of movement depends only on the current condition regardless of the history of movement, called memoryless property. This means that a) the currently known condition can represent for the accumulated deterioration up to the current time and b) the future condition does not depend on how long it stays in previous conditions. This property is well suited for long life assets such as concrete. In the opposite is usage-based assets such as light bulbs and machineries in which their future condition depends on how long they have been used in the past.

The Markov model is mathematically expressed as a matrix M of transition probabilities:

$$M = \begin{bmatrix} P_{11} & P_{12} & P_{13} & P_{14} \\ P_{21} & P_{22} & P_{23} & P_{24} \\ P_{31} & P_{32} & P_{33} & P_{34} \\ P_{41} & P_{42} & P_{43} & P_{44} \end{bmatrix} \quad (2)$$

where P_{ij} is the probability of moving from a condition state i to a condition state j over a unit time step. In this study, P_{ij} is assumed zero if i>j meaning improved condition is not modeled due to lack of maintenance data.

The memoryless property can be used to predict the probability vector [P_1 P_2 P_3 P_4] at any future time

T, given the known current condition with certainty or probabilities [C_1 C_2 C_3 C_4] as shown in the Kolmogorov Equation:

$$[P_1\ P_2\ P_3\ P_4]_T = [C_1\ C_2\ C_3\ C_4] * M^T \quad (3)$$

Several calibration techniques have been used to calibrate the Markov model, this study uses the proven Bayesian Monte Carlo simulation technique (Micevski et al., 2002) to estimate the transition matrix M of the Markov model.

The predictive performance of the Markov model is commonly validated using the Chi-square test on a separate dataset that is not used in the calibration of the Markov model (Micevski et al., 2002). The validation dataset is often randomly selected from 15-20% of the entire dataset.

2.3 *Simulated condition changes*

The evidence of inspection data and the theory of Markov chain show that for the same group of bridge component (e.g. group of concrete girders). Each member of group can experience any of many possible sequences of condition changes during their expected lifetime, saying 100 years. For example, staring from condition 1 as a newly constructed concrete girder in 1980, a possible sequence of condition change could be demonstrated as follows:

Start from year 0,
Condition 1 continues from year 0 to year 20,
Condition 2 continues from year 21 to year 34,
Condition 3 continues from year 35 to year 69,
Condition 4 starts at year 70.
End at failure at year 75.

From the demonstrated sequence, several observational points are: a) the conditions 1-4 are rated condition from the routine inspection, b) the exact timing of condition change is not known with the snapshot inspection approach (as compared to continuous monitoring approach) but can be detected by the closest inspection, c) the condition 4 often is not meant an immediate and actual failure but can be seen as the most likely leading to an actual failure, d) the time to enter condition 4 is uncertain and can be before or beyond the expected life of 100 years.

The 2000 sequences of random condition changes as demonstrated above can be simulated by using the calibrated Markov model as follows:

1. Start as condition 1 at current year 0 with current probability distribution [1 0 0 0]
2. Use Equation 3 to compute the probability distribution as next year (i.e. current year+1)
3. Randomly select the condition at the current year+1 from the probability distribution
4. The selected condition becomes the current condition and repeat the process until planning horizon T is reached.

2.4 *Cost rate function*

For an inspection-based asset management strategy, the cost rate function for such sequence of condition changes can be defined as shown in Equation 4 (Hong et al., 2014, Yanaka et al., 2016, Frangopol et al., 2017).

$$CR(TI) = \frac{1}{T}\left\{\begin{array}{l} \sum_{i=1}^{ni} a_i b_i * CI * e^{-\varepsilon * i * TI} + \\ + \sum_{j=1}^{nj} CM * e^{-\varepsilon * tMj} + \\ + \sum_{k=1}^{nk} CF * e^{-\varepsilon * tFk} \end{array}\right\} \quad (4)$$

where CR (dollar/year) is the average cost per year over a planning horizon of T years;

CI is unit inspection cost (dollar/structure), CM is repair cost (dollar/structure), CF is replacement cost (dollar/structure),

ni is number of inspection, nj is number of repair/rehabilitation, nk is number of replacement;

TI is inspection interval, tMj is time at the jth repair, tFk is time at the kth replacement,

T is planning horizon, ϵ is annual interest rate with typical value of 5%;

a_i, b_i are ≥ 1 and are the penalty costs acting on inspection cost due to the inspection interval is too large to detect the occurrence of poor conditions for repair or replacement.

Equation 4 shows the MRR cost over the service life of any existing bridge component. The MRR cost includes the inspection cost, repair cost and replacement cost. The capital cost can be added to Equation 4 for life cycle cost design of new component.

The exponent function in Equation 4 is to transform cost value at various future time into cost value at present time as per the concept of interest rate for proper comparison.

The key decision variable of Equation 4 is the inspection interval that should be optimised to have the lowest cost rate. A too short interval results in numerous inspection, which have higher chance of detecting poor conditions but come with higher inspection cost. A too long interval results in lower inspection cost but often fail to detect when repairable defects or failures occur.

A penalty is therefore applied for too long inspection interval that misses the repairable defects or worst condition. For example, it can be chosen that repair action will be taken if component condition is

3 or 4. A penalty of an inspection cost can be applied if that condition is not detected for a given inspection interval. Obviously, without penalty, the inspection interval will tend to be longer so that cost rate decreases. The penalty can also be viewed as a cost difference between planned and emergency repair/replacement in which user cost is also included. The user cost can contain time cost, vehicle cost, accident cost and so on.

2.5 *Applications*

From the simulated sequences of condition changes in Section 2.3, the average time from condition 1 to poor conditions can be calculated. This information can be seen as the average service life of the structures for financial accounting. It is noted that some structures might have longer service life and others have shorter life.

When the above simulated sequences are applied with cost rate function, two management strategies can be formed.

The first strategy is to search for lowest inspection cost over the short-term planning. This strategy can be applied for non-critical structures such as kerb and railing whose consequences of failure and repair are minor. In this case, the Equation 4 is applied with CM and CF assigned to zero. The search for lowest cost is conducted by using Monte Carlo simulation as follows. The inspection intervals from 1 to 20 years are fed into the 2000 simulated sequences of condition change. For each inspection interval, the average of inspection cost is calculated from the 2000 simulated sequence and is recorded. The inspection interval with lowest inspection cost can be found among different inspection intervals.

The second strategy is whether early intervention should be applied to reduce the total life cost because when inspection and MRR actions are included, the random sequence of condition changes can be revised as follows:

Start from year 0,
  Condition 1 continues from year 0 to year 20,
  Condition 2 continues from year 21 to year 34,
  Condition 3 continues from year 35 to year 69,
  Condition 4 starts at year 70,
  Detected by inspection at year 72,
  MRR action,
  Becoming Condition 1 at year 73 or new year 1,
  Condition 1 continues from year 73 to year 100 or new year 1 to new year 27,
End at design year 100.

The search to find the lowest MRR costs can be found in the similar manner with that of inspection cost.

3 CASE STUDY

The concrete open girder coded VR2C from level 2 inspection database of VicRoads is used to demonstrate the benefit of this study. This component is associated with 200 bridge structures.

One issue is called the first inspection because the average built year is 1972 with standard deviation of 21 years. However, the first recorded inspection year was 1995. It is not sure whether any maintenance action had been conducted from built year until first inspection record. Taking example of the 2C open girder, it has been found that there are 239 first inspections out of 757 inspections and 144 out of 239 cases shows 100% in condition 1. This means the use of first inspection data would likely to reduce the rate of deterioration as compared to second and third and later inspections (hereafter called second-up inspection data)

Another study (Ackah 2016) has found the similar issue. To ensure reliable data, the effect of first inspection records on the outcome of MRR costing is investigated in this study by comparing all-inspection containing first-inspection with second-up inspection.

The average cost of level 2 inspection is $150 AUD per bridge structure. This inspection cost is taken as unit cost and other cost is represented as relative to this cost. The costs of repair and replacement are not available in the database and thus are assumed to be 20 and 60 times of inspection cost, respectively.

4 RESULTS

4.1 *Comparison of deterioration rates*

The Markov models are calibrated and pass validation test with the level 2 inspection data. The calibrated transition matrix for old bridge is shown as a demonstration in equation 5 and 6 for all-inspection and second-up inspection.

$$M(all)=\begin{bmatrix} 0.9934 & 0.0052 & 0.0008 & 0.0006 \\ 0 & 0.9984 & 0.0009 & 0.0007 \\ 0 & 0 & 0.9972 & 0.0028 \\ 0 & 0 & 0 & 1 \end{bmatrix} \quad (5)$$

$$M(\text{second})=\begin{bmatrix} 0.9894 & 0.0082 & 0.0018 & 0.0006 \\ 0 & 0.9889 & 0.0104 & 0.0007 \\ 0 & 0 & 0.9991 & 0.0009 \\ 0 & 0 & 0 & 1 \end{bmatrix} \quad (6)$$

Table 1 shows the average time from condition 1 to condition 4 for various cases. The effect of first inspection is on the recently built bridge structures, which is more significant than on the low traffic.

Table 1. Average time from condition 1 to condition 4 for built year and traffic volume.

Factor	All Inspection	Second Up inspection
Old age	187	187
Young Age	174	125
Low Traffic	180	168
High Traffic	168	167

4.2 *Whole life maintenance strategy*

The whole life maintenance strategy can be whether to repair at condition 2 or 3 that would produce lowest annual cost. Table 2 shows the results for different factors with input parameters as follows. The expected service life is 100 years, the interest rate is 5%, the repair cost is 20 times inspection cost, the replacement cost is 60 times inspection cost and the penalty cost is the same with inspection cost.

The results of Table 2 indicate that the repair at condition 3 with shorter inspection interval can still have better cost-saving than at condition 2 with longer inspection interval. This finding can help focusing inspection strategy on detecting condition 3, which is addressed in the subsequent section.

Table 2. Effect of repair at condition 2 and 3 on the lowest annual cost and inspection interval for second up inspection data.

Factors	Repair at condition 2		Repair at condition 3	
	Lowest annual cost*	Inspection Interval	Lowest annual cost*	Inspection Interval
Old age	0.021	50	0.0156	48.6
Young Age	0.055	35.8	0.047	22.8
Low Traffic	0.032	49	0.026	32.6
High Traffic	0.032	49.2	0.029	37.5

* Based on unit cost of $1 for inspection cost.

4.3 *Inspection strategy*

Given the preferred condition 3 for early intervention as identified in the previous section of whole life maintenance, the inspection strategy can be focused on detecting condition 3. Figure 1 shows the annual cost rates for different inspection intervals for the case of detecting condition 3 from condition 1 under low traffic volume over the short planning of 20 years with penalty of twice inspection cost and zero interest rate.

From this figure, the lowest inspection cost rate as 11 years can be found for both cases of All inspection and Second-Up inspection. The highest inspection cost obviously occurs at 1-year interval. As the inspection interval time increases, the annual cost rate decreases until the lowest because after that point, the annual inspection cost starts increasing due to the effect of penalty. The lowest cost rate of second-up inspection is slightly higher than the all-inspection.

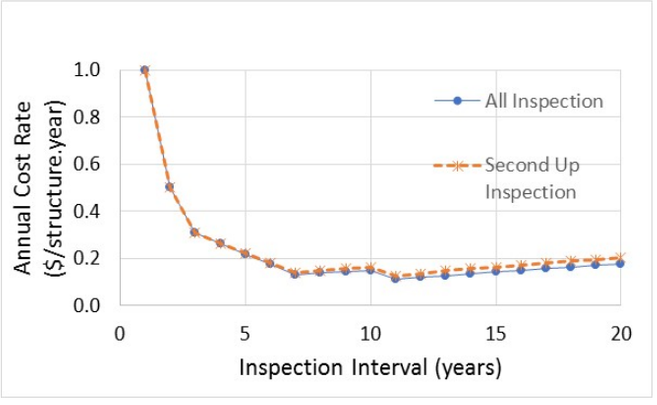


Figure 1. Annual cost rate for different inspection intervals.

Figure 2 shows the number of undetected poor conditions (i.e. the selected condition 3 in this study) for the same case of low traffic volume with second-up inspection. As expected, the lowest number of zero undetected occurs at the inspection interval of 1 years. As the inspection interval increases, the annual number of undetected cases also increases. This is the risk associated with longer inspection interval and lower inspection cost.

As a result of Figures 1 and 2, asset engineers should be aware of the cost and benefit of various inspection intervals and the effect of first inspection.

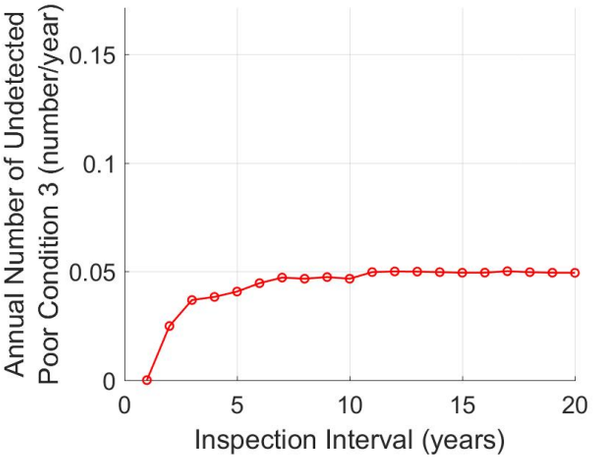


Figure 2. Annual number of undetected poor conditions for various inspection intervals

Table 3 shows the lowest cost, inspection intervals and annual numbers of un-detected poor condition 3 for different factors on Second-up inspection data.
All four factors have the same inspection interval but the lowest inspection cost and number of undetected poor condition are found with old structures. The other extreme is surprisingly found with young structures. This could be due to the implication of old design and construction methods as compared with the newer ones.

Table 3. Lowest cost inspection interval for different factors on Second up inspection data.

Factors	Lowest annual cost*	Inspection interval	Number of undetected poor condition 3
Old age	0.060	11	0.011
Young Age	0.071	11	0.036
Low Traffic	0.067	11	0.020
High Traffic	0.068	11	0.021

* Based on unit cost of $1 for inspection cost.

5 DISCUSSION

This study is limited to the case of concrete material with a demonstration on open girder 2C. However, the methodology can be extended to all bridge elements with different material.

The effect of traffic volume and age are investigated in this study. Further studies can look at the impact of interest rate and other contributing factors such as exposure class and percentage of truck.

The detailed costing for user cost, which constitutes the penalty used in this study, and maintenance cost together with discount rate will be established in future works.

The comparison between Markov model and other stochastic models such as Gamma process model (Edirisinghe et al., 2013) will be further investigated.

6 CONCLUSION

Deterioration models can significantly improve the efficiency of asset management of bridge networks. This study demonstrated an application of Markov deterioration model for determining risk-based inspection and maintenance strategies through development of a computational methodology. The methodology incorporates Markov deterioration model with cost rate function and Monte Carlo simulation to search for the inspection interval with lowest inspection cost, and whole life maintenance cost.

The major innovation of this methodology is the ability to simulate the condition changes of bridge elements due to deterioration over a planning horizon. Furthermore, the methodology also allows to capture the condition improved due to rehabilitation actions and the restart of deterioration process after rehabilitation for inspection and maintenance strategies.

The findings are that the inspection interval with lowest inspection cost can be used with informed risk. Early intervention can be done on condition 3 instead of condition 2 for lower maintenance cost. The outcomes of this study can provide understanding of risk and cost-saving when making decision on inspection and whole life maintenance strategies.

7 REFERENCES

Ackah , K. E. 2016. *Weibull-Based Deterioration And Preservation Models For Florida Bridges.* Master, Florida State University

Agbelie, B. R. D. K., Labi, S. & Sinha, K. C. 2017. Estimating The Marginal Costs of Bridge Damage Due To Overweight Vehicles Using A Modified Equivalent-Vehicle Methodology And In-Service Data On Life-Cycle Costs And Usage. *Transportation Research Part A: Policy And Practice,* 95**,** 275-288.

Bu, G. 2013. *Development of An Integrated Deterioration Method For Long-Term Bridge Performance Prediction.* Phd Thesis, Griffith University.

Edirisinghe, R., Setunge, S. & Zhang, G. 2013. Application Of Gamma Process For Building Deterioration Prediction. *Journal of Performance of Constructed Facilities,* 27**,** 763-773.

Frangopol, D. M., Dong, Y. & Sabatino, S. 2017. Bridge Life-Cycle Performance And Cost: Analysis, Prediction, Optimisation And Decision-Making. *Structure And Infrastructure Engineering,* 13**,** 1239-1257.

Gidaris, I., Padgett, J. E., Barbosa, A. R., Chen, S., Cox, D., Webb, B. & Cerato, A. 2017. Multiple-Hazard Fragility And Restoration Models Of Highway Bridges For Regional Risk And Resilience Assessment In The United States: State-of-The-Art Review. *Journal of Structural Engineering (United States),* 143.

Hong, H. P., Zhou, W., Zhang, S. & Ye, W. 2014. Optimal Condition-Based Maintenance Decisions For Systems With Dependent Stochastic Degradation of Components. *Reliability Engineering And System Safety,* 121**,** 276-288.

Jamali, A., Angst, U., Adey, B. & Elsener, B. 2013. Modeling of Corrosion-Induced Concrete Cover Cracking: A Critical Analysis.

Construction And Building Materials, 42**,** 225-237.
Madanat, S., Mishalani, R. & Ibrahim, W. H. W. 1995. Estimation Of Infrastructure Transition Probabilities From Condition Rating Data. *Journal of Infrastructure Systems, Asce,* 1**,** 120-125.
Micevski, T., Kuczera, G. & Coombes, P. 2002. Markov Model For Storm Water Pipe Deterioration. *Journal of Infrastructure Systems,* 8**,** 49-56.
Moomen, M. 2016. *Deterioration Modeling of Highway Bridge Components Using Deterministic and Stochastic Methods.* Master Thesis, Purdue University.
Parr, M. J., Connor, R. J. & Bowman, M. 2010. Proposed Method For Determining The Interval For Hands-On Inspection Of Steel Bridges With Fracture Critical Members. *Journal of Bridge Engineering,* 15**,** 352-363.
Principal Bridge Engineers 2014. Road Structures Inspection Manual Melbourne: Vicroads.
Rashidi, M., Samali, B. & Sharafi, P. 2016. A New Model For Bridge Management: Part A: Condition Assessment And Priority Ranking Of Bridges. *Australian Journal of Civil Engineering,* 14**,** 35-45.
Robelin, C. & Madanat, S. 2007. History-Dependent Bridge Deck Maintenance And Replacement Optimization With Markov Decision Processes. *Journal of Infrastructure Systems,* 13**,** 195-201.
Safia, M., Sundquista, H., Karoumia, R. & Racutanu, G. 2013. Development Of The Swedish Bridge Management System By Upgrading And Expanding The Use Of Lcc. *Structure And Infrastructure Engineering,* 9**,** 1240–1250.
Saydam, D. & Frangopol, D. M. 2015. Risk-Based Maintenance Optimization Of Deteriorating Bridges. *Journal of Structural Engineering (United States),* 141.
Sonnenberg, A. 2014. Australian Bridge Inspection Processes. *6th Australian Small Bridges Conference 2014.* Sydney: Commstrat.
Stewart, M. G. 2010. Reliability Safety Assessment Of Corroding Reinforced Concrete Structures Based On Visual Inspection Information. *Aci Structural Journal,* 107**,** 671-679.
Vatteri, A. P., Balaji Rao, K. & Bharathan, A. M. 2016. Time-Variant Reliability Analysis Of Rc Bridge Girders Subjected To Corrosion – Shear Limit State. *Structural Concrete,* 17**,** 162-174.
Yanaka, M., Hooman Ghasemi, S. & Nowak, A. S. 2016. Reliability-Based And Life-Cycle Cost-Oriented Design Recommendations For Prestressed Concrete Bridge Girders. *Structural Concrete,* 17**,** 836-847.

Maintenance, Safety, Risk, Management and Life-Cycle Performance of Bridges – Powers, Frangopol, Al-Mahaidi & Caprani (Eds)
© 2018 Taylor & Francis Group, London, ISBN 978-1-138-73045-8

Maintenance Cost Evaluation based on Bridge Performance Degradation Model

S. H. Kim, W. H. Heo, J. G. Choi & M. Gombosuren

School of Civil and Environmental Engineering, Yonsei University, Seoul 03722, Korea

ABSTRACT: This study proposes the future life cycle cost evaluation method, in which the future performance degradation models are adopted to estimate the future maintenance cost and the expected loss due to the bridge safety. A procedure to adjust the future performance degradation model is proposed based on the bridge inspection records and considering the site environments. The basic degradation model is adopted from the previous research results, which are developed through the regression works with many local bridge inspection records. When the previous inspection records are not available, the current performance level is the only information to adjust the degradation model. The effect of previous inspection records is examined in the study. The expected loss in LCC is estimated through the reliability evaluation based on the local traffic load effect evaluation and the future performance degradation model. The case study has been performed with a PSC girder highway bridge.

1 INTRODUCTION

As the number of aged and deteriorated bridges that require proper maintenance and rehabilitation is increasing globally, the reasonable maintenance planning and budget allocation for such bridges is necessary. The performance degradation of a highway bridge may be depending diversely on both the construction quality and its local site environments, such as traffic condition, corrosion environment, maintenance level, etc. The most reasonable maintenance plan should be set based on the current performance level and future degradation pattern. The future deterioration model may be adjusted properly utilizing the performance degradation history based on the bridge inspection records, which may represent the site environments as well as the initial construction quality.

This study assesses the maintenance cost arising from the performance degradation of a PSC girder bridge. Bridge performance evaluation based on its reliability is used to estimate the maintenance cost. The performance degradation of bridge can be assumed to be attributable to diverse conditions in the site environment. This study proposes a method of developing a performance degradation model that considers traffic characteristics and corrosion environments as the site environment and that is based on the result of previous evaluations of an in-service bridge. It also explains the result of the maintenance cost analysis for the purpose of setting a reasonable repair schedule based on the performance degradation model.

2 TRAFFIC LOAD MODEL

The probabilistic traffic load characteristics such as daily traffic volume, heavy vehicle proportion, heavy vehicle weight model, and heavy vehicle consecutive traveling mode may play an important role in the highway bridge performance reliability during the service life of the bridge. The consecutive travelling characteristics of heavy vehicles are widely understood to cause the unintentional high load effects, especially on medium span bridges. The Markov transition probability matrix models are developed based on the site traffic load survey data to include the consecutive travelling effects in the estimation of maximum traffic load effects in the intended service period. Table 1 lists the consecutive traveling coefficients and proportions of single vehicles to heavy vehicles, which is the very important parameter in the models (Kim et al., 2017). Table 2 explains how the consecutive travelling models affect the extreme traffic load effects on a simple model bridge (30m span). The values in Table 2 are the annual 95% extreme live load effects normalized with the design live load effect.

Table 1. Transition probability matrix models.

(a) Heavy vehicle proportion : 25%

Type	Consecutive traveling coefficient (Consecutive traveling probability: %)					Simple vehicle proportion (%)	
	P	B	T	TT	ST		
P	1.06 (76.36)	0.97 (2.92)	0.85 (10.59)	0.80 (7.64)	0.83 (2.49)	72.0	
B	0.98 (70.40)	2.32 (6.97)	0.83 (10.43)	1.02 (9.68)	0.84 (2.52)	3.0	
T	0.84 (60.33)	0.94 (2.82)	1.71 (21.32)	1.27 (12.05)	1.16 (3.48)	12.5	
TT	0.83 (59.47)	0.88 (2.63)	1.20 (15.01)	1.98 (18.84)	1.35 (4.04)	9.5	25.0
ST	0.80 (57.39)	0.97 (2.90)	1.25 (15.66)	1.45 (13.75)	3.43 (10.30)	3.0	

(b) Heavy vehicle proportion : 35%

Type	Consecutive traveling coefficient (Consecutive traveling probability: %)					Simple vehicle proportion (%)	
	P	B	T	TT	ST		
P	1.11 (69.10)	1.01 (2.62)	0.83 (14.58)	0.77 (10.28)	0.82 (3.43)	62.4	
B	1.01 (63.31)	2.38 (6.20)	0.81 (14.19)	0.97 (12.88)	0.81 (3.42)	2.6	
T	0.82 (51.02)	0.90 (2.34)	1.53 (26.79)	1.17 (15.53)	1.03 (4.31)	17.5	
TT	0.81 (50.29)	0.84 (2.18)	1.08 (18.98)	1.76 (23.47)	1.21 (5.08)	13.3	35.0
ST	0.77 (48.06)	0.93 (2.41)	1.12 (19.62)	1.28 (16.98)	3.08 (12.94)	4.2	

(c) Heavy vehicle proportion : 45%

Type	Consecutive traveling coefficient (Consecutive traveling probability: %)					Simple vehicle proportion (%)	
	P	B	T	TT	ST		
P	1.21 (62.02)	1.09 (2.33)	0.84 (18.45)	0.77 (12.87)	0.82 (4.33)	52.8	
B	1.09 (56.37)	2.54 (5.45)	0.81 (17.85)	0.96 (16.04)	0.81 (4.29)	2.2	
T	0.83 (42.59)	0.90 (1.93)	1.45 (31.96)	1.10 (18.37)	0.97 (5.14)	22.5	
TT	0.81 (41.87)	0.84 (1.80)	1.03 (22.60)	1.66 (27.70)	1.14 (6.03)	17.1	45.0
ST	0.77 (39.67)	0.92 (1.97)	1.06 (23.19)	1.19 (19.90)	2.90 (15.27)	5.4	

Table 2. Comparison of simple model and consecutive travelling model (single lane).

Heavy Vehicle proportion	Model	Average daily traffic volume			
		5,000	10,000	20,000	40,000
25%	Simple	1.37	1.38	1.42	1.48
	Consecutive	1.71	1.72	1.75	1.75
	Consecutive model effect (↑)	25.3%	24.2%	23.1%	18.5%
45%	Simple	1.39	1.44	1.47	1.49
	Consecutive	1.77	1.88	1.93	2.01
	Consecutive model effect (↑)	27.7%	30.7%	31.9%	34.5%

3 PERFORMANCE DEGRADATION MODEL BASED ON INSPECTION HISTORY

3.1 *Calibration of performance degradation model considering inspection results*

The performance degradation of a PSC girder bridge is believed to be influenced by various site environments. Future performance degradation is estimated by calibrating a representative degradation model using past inspection results of the bridge. Figure 1 shows an example of the degradation model corrected by inspection history. Table 3 shows an example of the inspection history. In Table 3, 1-W and 2-W show the cases of regular inspections. 1-W/O and 2-W/O present cases with no past inspection reports. Figure 2 shows the calibrated degradation function. A degradation model may provide inaccurate estimation of future performance degradation depending on the availability of past inspection results. However, a degradation model that has been corrected by past inspection results is not so sensitive to the availability of previous inspection data as long as the current performance status is included. This implies that the proposed calibration method can provide a stable degradation model that does not rely too much on past inspection data.

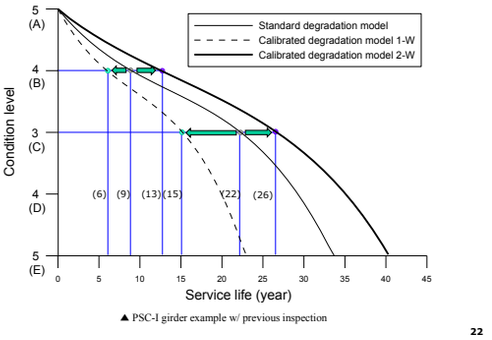
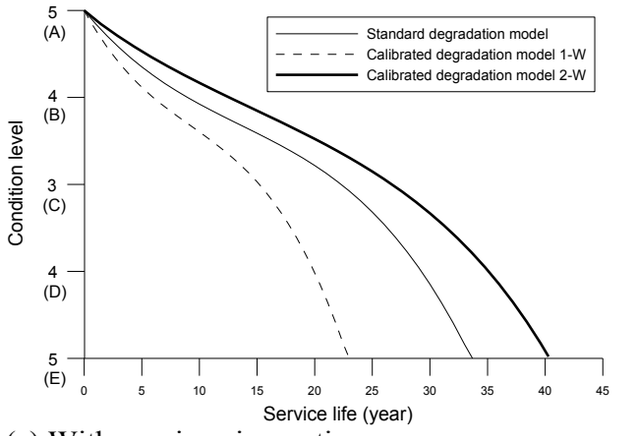


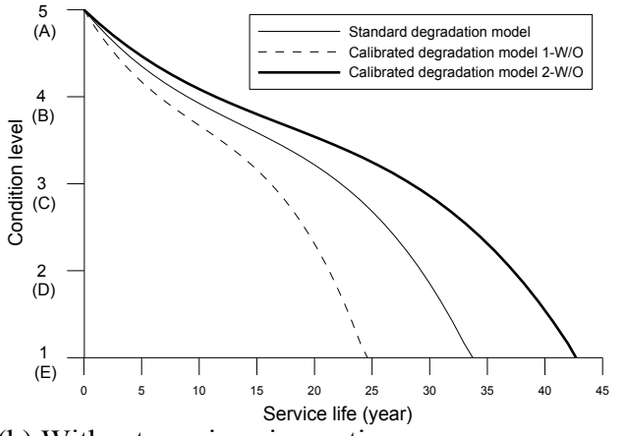
Figure 1. Calibration of performance degradation model

Table 3. Example inspection histories of PSC-I girder.

History	Year of inspection															
	2	4	6	8	10	11	13	15	16	18	20	21	23	25	26	28
1-W	A	A	B	B	B	B	B	C	C	-	-	-	-	-	-	-
1-W/O	-	-	-	-	-	-	-	-	C	-	-		-	-	-	-
2-W	A	A	A	A	A	A	B	B	B	B	B	B	B	B	C	C
2-W/O	-	-	-	-	-	-	-	-	-	-	-	-	-	-	-	C



(a) With previous inspections



(b) Without previous inspections

Figure 2. Calibrated performance degradation models

3.2 *Performance-based resistance deterioration model based on corrosion environments*

The existing concrete cracks should be considered when evaluating the deterioration of resistance capacity due to a corrosion environment. The corrosion environments of bridges are classified as mild, normal, and severe. Figure 3 presents the cross-sectional profiles of the example bridge (Kim et al., 2016). The performance-based resistance deterioration model is developed by combining a resistance deterioration model and performance degradation model (Figure 4). Figure 5 shows the resistance capacity of PSC girder bridges in various site environments. The estimated decrease in resistance capacity varies according to the crack width measured at the bridge.

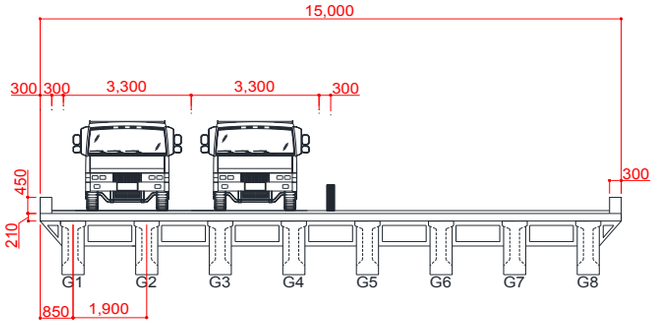


Figure 3. PSC-I bridge (span=30m)

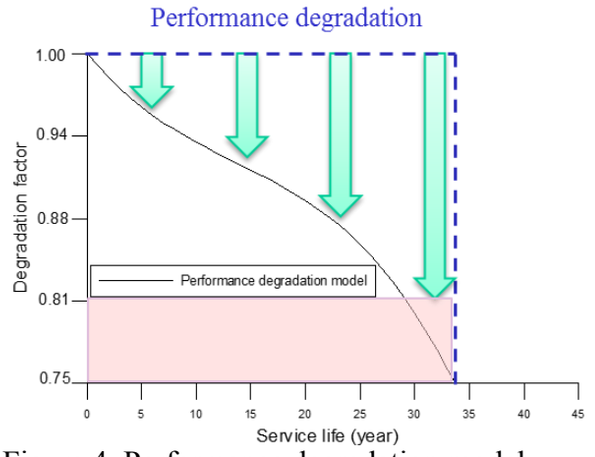
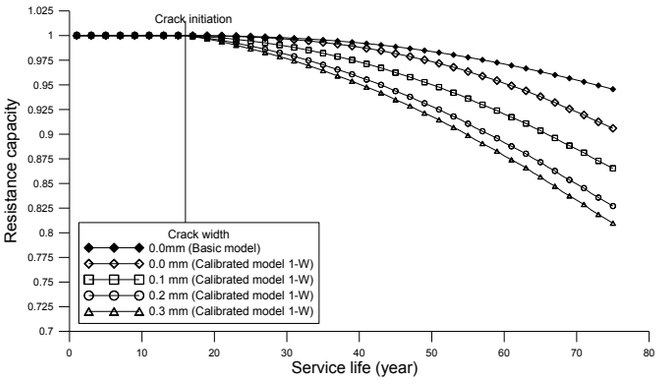
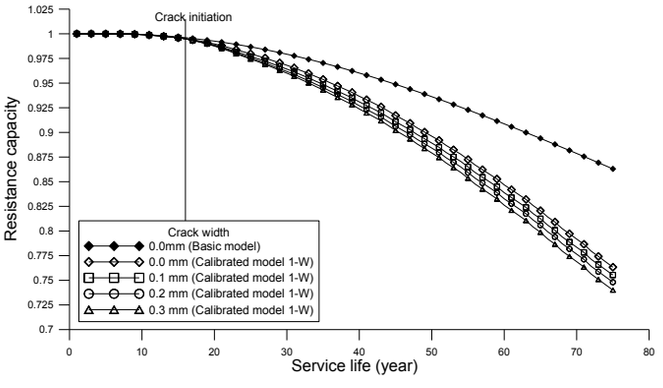


Figure 4. Performance degradation model



(a) Mild corrosion environment

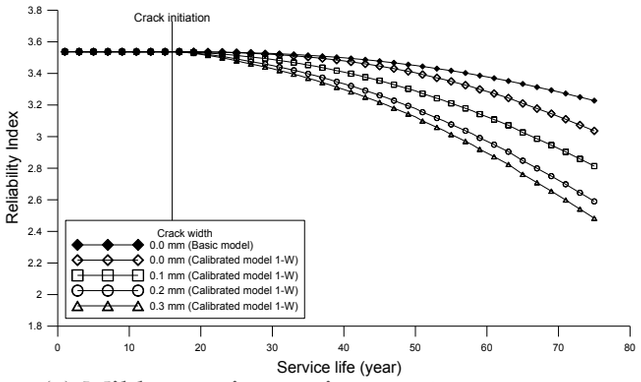


(b) Severe corrosion environment

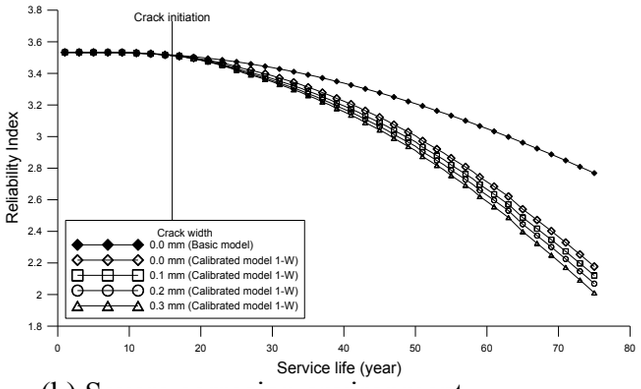
Figure 5. Performance-based resistance deterioration model

3.3 *Reliability evaluation considering resistance deterioration model*

The expected performance degradation is evaluated in terms of the reliability level as shown in Figure 6, in which the probabilistic models of the bridge resistances and loadings are included. The traffic load effect model has been developed through the Monte Carlo simulations based on the traffic models mentioned above for the inventory bridge.



(a) Mild corrosion environment

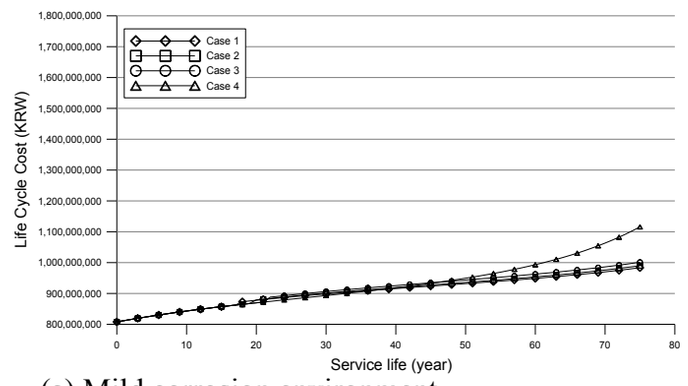


(b) Severe corrosion environment

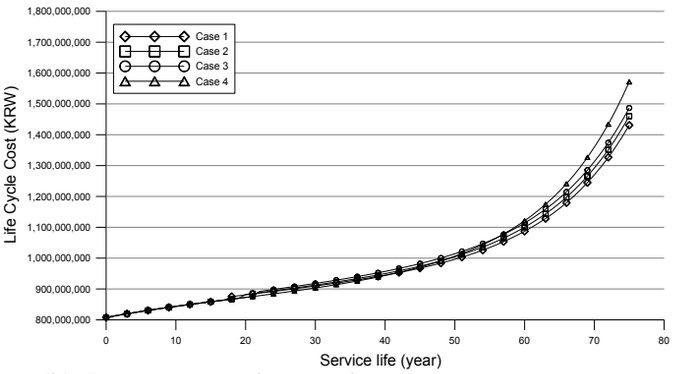
Figure 6. Reliability evaluation considering performance-based resistance deterioration model

4 MAINTENANCE COST EVALUATION BASED ON PERFORMANCE DEGRADATION OF BRIDGE

Figure 7 shows the maintenance costs of bridges that were evaluated based on the performance-based resistance deterioration model by considering traffic characteristics and corrosion environment. When the corrosion environment is mild and the traffic characteristics is normal, performance degradation slows down and maintenance costs decrease. By contrast, when the corrosion environment is severe and the traffic characteristics is normal, performance declines rapidly and maintenance costs increase accordingly. These results indicate that site environments influence the performance degradation characteristics and maintenance costs of bridges.



(a) Mild corrosion environment



(b) Severe corrosion environment

Figure 7. Maintenance cost evaluation

5 CONCLUSION

In this study, the maintenance cost based on performance degradation was evaluated for PSC girder bridges. A method of developing a performance-based resistance deterioration model by considering traffic characteristics, corrosion environment, and inspection history was proposed to analyze the performance degradation of bridges. The proposed method was found to be very efficient in considering systematically the performance degradation characteristics based on bridge inspection results as well as site environmental characteristics, such as traffic conditions and others factors that contribute to structural deterioration. If the proposed method is applied to the development of maintenance plans, it is expected to be helpful in establishing a rational plan.

6 ACKNOWLEDGMENTS

This work was supported by the Korea Institute of Energy Technology Evaluation and Planning (KETEP) and the Ministry of Trade, Industry & Energy (MOTIE) of the Republic of Korea (No. 20174030201480).

This research was supported by Basic Science Research Program through the National Research Foundation of Korea (NRF) funded by the Ministry of Education, Science and Technology (2017R1D1A1B03028262).

7 REFERENCES

Kim. S. H., Heo, W. H., Yu, D.W., and Choi, J. G. (2017). Vehicle Loads for Assessing the Required Load Capacity Considering the Traffic Environment, Applied Sciences, 7, 1-15.

Kim. S. H., Choi, J. G., Ham, S. M., and Heo, W. H. (2016). Reliability Evaluation of a PSC Highway Bridge based on Resistance Capacity Degradation Due to a Corrosive Environment, Applied Sciences, 6, 1-16.

Korea Infrastructure Safety and Technology Corporation (2012). Standard for structure safety inspection: Bridge structure, RD-12-E6-024, Korea Infrastructure Safety and Technology Corporation, Korea.

Maintenance, Safety, Risk, Management and Life-Cycle Performance of Bridges – Powers, Frangopol, Al-Mahaidi & Caprani (Eds)
© 2018 Taylor & Francis Group, London, ISBN 978-1-138-73045-8

An Integrated Model-Based Bridge Management System

S.T. Hou, G. Wu & H.L. Li
College of Civil Engineering in Southeast University, Nanjing, Jiangsu, China

ABSTRACT: How to manage and maintain aging bridges becomes a critical issue in both engineering research and practice. This paper presents an integrated bridge management system for tracking and assessing the structural condition of bridges. First, the system supported by JAVA software platform collected model-based data of bridges. Second, the authority management and task dispatch were established for transport agencies. Next, the interactive 4D models of the bridges with structural information and history record of multiple data can be visualized. 3D panorama created by special cameras provided the surrounding environment of each bridge in website browser. Furthermore, inspectors can use mobile apps to capture and update bridge damages. It is found that the interactive 4D models can facilitate data sharing and avoid the barriers from other Building Information Modeling software. The developed system can lead to a more automated and powerful practice for bridge management and similar applications in bridge management.

1 INTRODUCTION

Recently, the rehabilitation and management of bridges has become a big concern in China. According to the Report from ASCE, as of 2016, America's Infrastructure Scores is D+, and C+ for bridges, the U.S. has 614387 bridges, almost four in ten of which are 50 years or older, and 9.1% of the nation' s bridges were structurally deficient in 2016 (ASCE, 2017). In Japan, many highway bridge were built in 1950s, many of which have seriously deteriorated over the years. China has experienced the golden age of infrastructure construction, the total number of bridges is 805300. However, due to the factors such as the increase in traffic volume and weight, almost 90000 bridges were structural deficient.

While the number of bridges that are in such poor condition as to be considered structurally deficient is decreasing, bridge maintenance method are approached to keep bridges safe. Since the collecting data generated from the inspection and monitoring, and the demand to predict the bridge condition and decision making is urgent using these numerous data. The necessity of developing a practical bridge management system points out.

The development of a comprehensive bridge management system is essential (Akgul, 2017). Such a system should enable not only store the data, and evaluate the condition of bridges, but also the capacity to make the decision which takes into account the limits funds that are available for bridge maintenance.

The Pontis bridge management system of a AASHTO product, includes the inspection data, recommends the preservation policy and predicts the needs and performance for the agency. It also supports the agency-specific needs (Robert & Marshall, 2003). Pontis provide the assessment function mainly based on the inspection data, and 3D model has not widespread used until now. J-BMS is applied to existing reinforced concrete bridges, it provides the performance evaluation of bridges and the maintenance strategies considering the cost minimization and quality (Miyamoto et al. 2001). Ongoing efforts to develop to the road management system based on Pontis have resulted in KUBA-MS in Swiss, several distinguished features have exploited including condition assessment and forecast, elaboration of working program (Hajdin, 2000). For current bridge management system especially in China, the documents are stored in print version or textual comment in database. Chan & Guan (2016) defined a integrated framework for modeling and imaging, and ultimately highlighted the need for alternative approaches to bridge inspection to more accurately monitor the current condition of key structural elements in a model-based method. McGuire (2016) presents a method and prototype implementation for bridge inspection and evaluation in Bridge information modeling, using BIM software can analyze and present that information to help make decisions on the basis of the damage location and provide maintenance recommendations.

This paper presents an integrated bridge management system for tracking and assessing the structural condition of bridges, the system links the information about several stages of a bridge (e.g., design, inspection, and maintenance) to an interactive 4D model incorporating different record events, 3D panorama created by the special cameras was supported in this system, and the surrounding environment of each bridge can be seen in the website browser. In addition , a rule-based expert system to support the decision-making is provided in this system. The methodology in this system will be describes from user perspective.

2 PROPOSED FRAMEWORK

Current BMS provide different modules to perform their functions (Marzouk & Hisham, 2012). Figure 1 shows the proposed framework of the integrated BMS and Figure 2 shows the connectivity between different functions in this system. The full description of the proposed framework is provided in the below section.

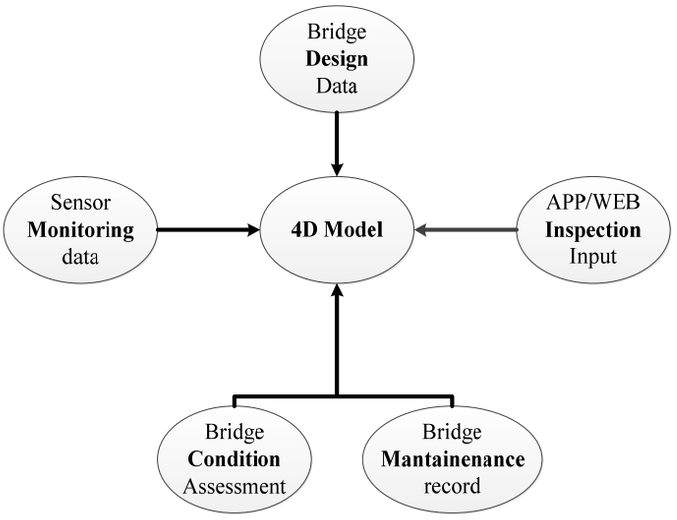


Figure 1. Proposed framework of the integrated BMS

The system supported by the Java software platform mainly contains five modules, and web-based property guarantees no proprietary software needed. The MVC design pattern is selected for the present framework. This pattern enforces the separation between the input, processing and output of an application. Each of these components handles a discrete set of tasks, enabling loose coupling and the ability to change one component without affecting the others (Potel, 1996).

Java database connectivity (JDBC) is a programming framework for Java developers writing programs that access information stored in databases. The system connects with MySQL to present bridge information of the name, type, location, properties, components and other data in specific functions. MangoDB system is designed to store the sensor data in corresponding tables (Hammad et al. 2006). Android application is developed in Java software platform for the inspection, the data captured on mobile phones could be stored in the MySQL database mentioned above.

4D model in this system means the 3D model of bridges with multiple information in element level, interactivity makes the element labeled with the corresponding data, it is supported by the WebGL which is a JavaScript API for rendering interactive 3D graphics within any compatible web browser without the use of plug-ins. WebGL based on the OpenGL can be used in HTML5 elements.

2.1 *System right management*

This system designed for the bridge owner and agencies to manage bridges in China efficiently, and inspection departments are granted permission to login their account for recording and browsing bridge deterioration in appointed modules. Research institutes could consult the inspection and monitoring data by means of the permission given by managers. The construction staff could upload the reinforcement or maintain plan in their account in this system. Super administrators are set up to manage the whole users as shown below.

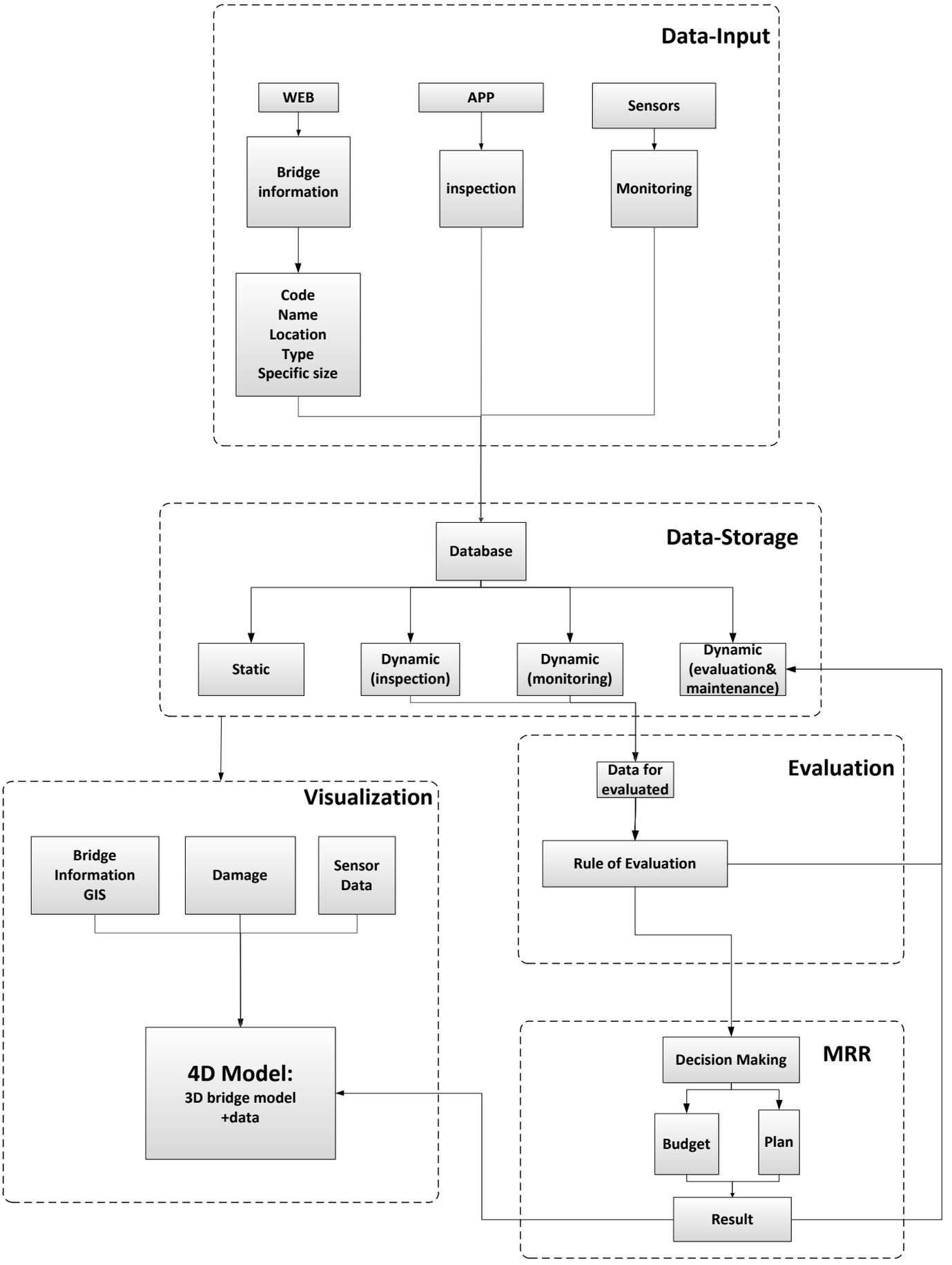


Figure 2. Connectivity between different functions

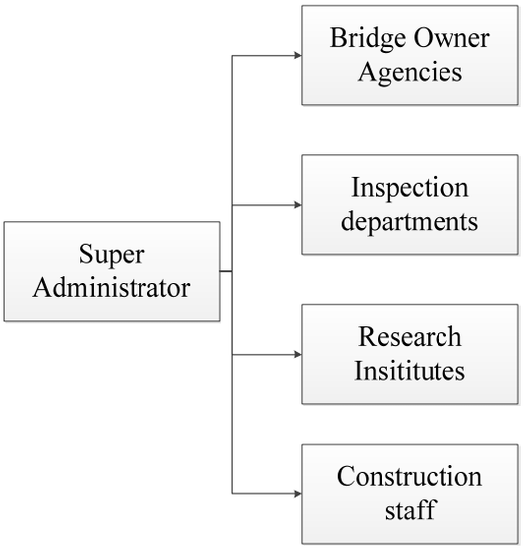


Figure 3. User roles in system

2.2 *Location-based bridge selection*

Due to the superior spatial data handling capabilities, geographic information system (GIS) technology is increasingly being considered for implementation in many BMS (She et al. 1999), Bridge location information from the MySQL database is selected for the GIS visualization in this system, Baidu map used in China provides an open API wrapper for drawing objects onto maps, bridges represented by their center points could be seen in the map based on the location information, bridge distribution is perfectly shown in the BMS.

2.3 *Mobile-based inspection*

In the proposed method below, an inspector uses a mobile install the app to capture the damage information about type, amount, severity, location and photo during the inspection period, and the data could be used and visualized on the website based on the shared database (Lee & Yi, 2004).

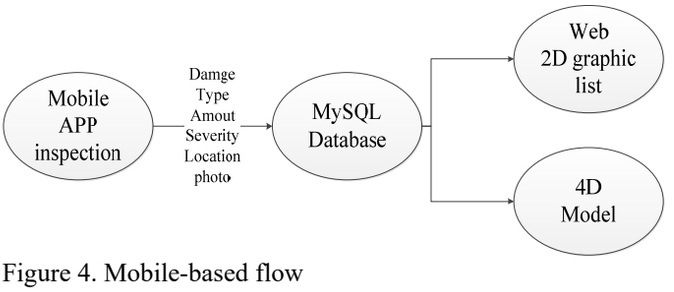


Figure 4. Mobile-based flow

2.4 *Monitoring*

The system provides several sensor interfaces based on the material and transmission type. For the wireless connection, UDP or TCP/IP ports and programs are developed to receive data in high or low frequency depend on the sensor sample rate. The data received from wire sensors mainly sent by the base station in Internet, related path folders are created to store in the BMS. Piezoelectric, optical fiber and electromagnetic type are considered, and corresponding algorithms are applied to manage different kinds of sensor.

2.5 *Evaluation and maintainnence*

According to the Evaluation Criteria of Highway Bridge Technical Status in China, bridge scores and ratings are calculated by the relevant algorithm based on the inspection data in the system. After that, deficient bridges with low scores are listed and maintenance information is sent to the bridge owners, the budget and plan for these bridge could be recorded in this system (Hai, 2008).

2.6 *Integrated model*

A 4D *model* of every bridges in this system is developed for visualizing different types of data, for example, displaying the damage changes in a bridge3D model at a specific time or during a specific period of its lifecycle. Visualization has powerful functions for interacting with the system in a virtual reality modes, inspection and condition data can be integrated in the 4D model. At the same time, 3D panorama show the real environment around the bridge which facilitates the inspection or construction work if necessary. The integration of 4D model with the 3D panorama builds a powerful function for virtual reality.

3 CAPACITY OF MODEL-BASED BMS

The structure of the prototype system follows the framework architecture explained above, the system integrates an interactive 3D model of a bridge with an object-relational database, GIS and tracking components, and multimedia equipment to develop a 4D model for BMS that can be used, on-site mobile application is developed for capturing and updating damage information, 3D panorama function provide the real environment around the bridge. the specific function of every module is explained below.

3.1 *Basic information*

The first menu in system is basic information. The login interface contains a GIS-based map which show the distribution and condition of bridges in system, the label which represent the center point of bridge location has six colors, express the class 1, 2, 3, 4, 5 and unclassified condition. The condition of bridges depends on the evaluation scores in the

Evaluation Criteria of Highway Bridge Technical Status (ECHBTS). The total number of bridges and the historical curve included in this system can be queried, and the summarizing of bridge condition and bridges to be repaired could also be queried in this page. Modal window is created to show the code, location, and scores of bridges when the color label clicked in GIS map.

Another submenu is the list with condition or fuzzy search of bridge information contains name, type, time, location and department, user could add, delete or modify the bridge basic information in this page. It should be pointed out that the specific information about the structure and element is shown in several lists with a modal window which contains the link to 4D model and 3D panorama.

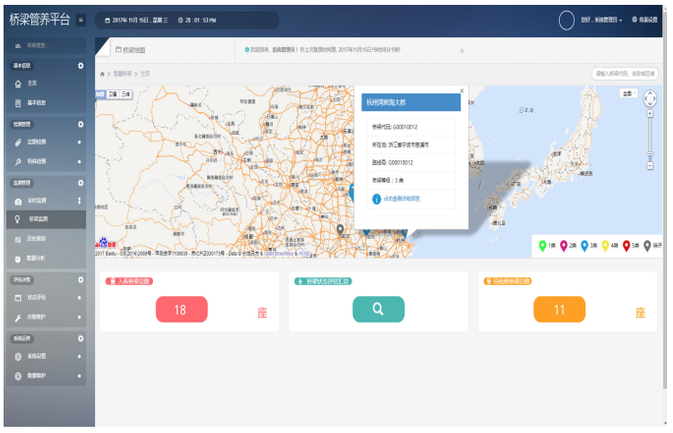


Figure 5. GIS-based map

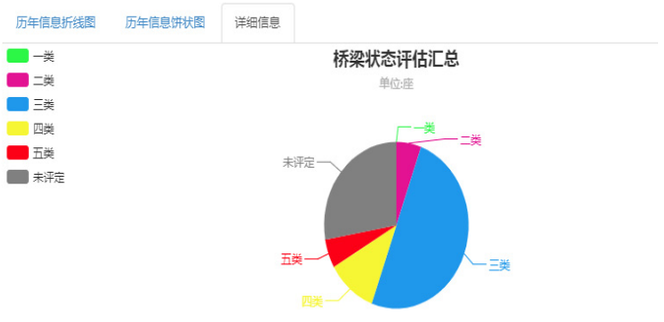


Figure 6. Summarizing of bridge condition in pie chart

3.2 *Inspection management*

In this menu, task dispatch and damage input are the main function. User of bridge owner could designate staff with regular inspection task of which the condition and collection could be referred in this page. Each task for capturing and updating damage of bridges could be utilized both in Web or mobile phone. The web provides the list the bridge code, task code, bridge name and the staff, user could record the damage by element level of bridges as shown below. Inspection record of damage could be seen in the submenu ordering by time, and the connection of 4D model with damage information also contained, the colored element shows the severity of damage in this region as shown in Figure 8.



Figure 7. Mobile application for damage inputting

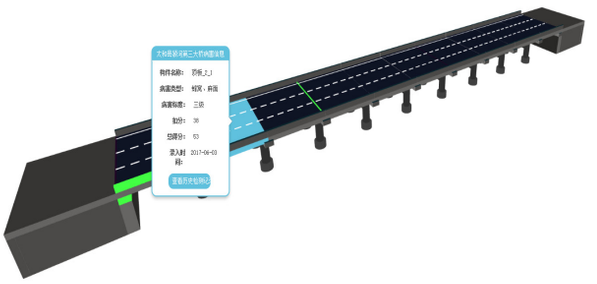


Figure 8. 4D interactive model with damage information

3.3 *Monitoring management*

This menu mainly focuses on the three monitoring type of bridges, including long-term real-time monitoring, construction monitoring, and special monitoring. The bridge list of monitoring in each type could be searched which contains bridge code, name, location and department. Sensors in each monitoring bridge could be set, and the real-time data in curve could be seen in each sensor page as shown in Figure 9.As with inspection management, the historical data could be queried with condition search option.



Figure 9. Real-time monitoring data of displacement sensor

3.4 *Evaluation and decision-making*

With the inspection data recorded in database, the condition scores could be displayed in this menu, details of damage and evaluation also recorded within list and 4D model as is shown later. After evaluation finished, corresponding maintenance work including replacement of abutment, main grider reinforcement, expansion joint replacement, etc. will be recorded in this menu.



Figure 10. Evaluation information in pie chart

3.5 *System operator*

This menu is opened only for the super administrator, the authority of using functions mentioned above and user management could be facilitated, and new type of department for special work could be created as well.

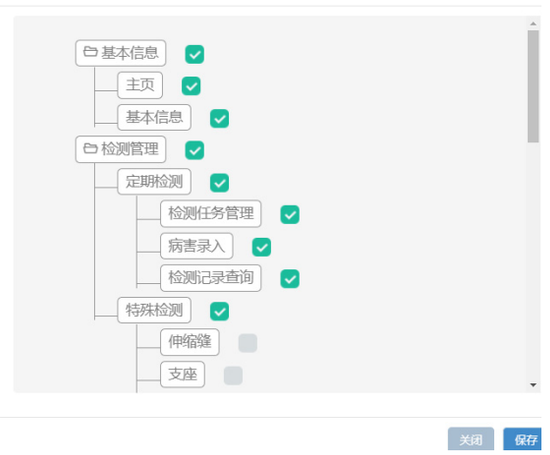


Figure 11. Authority and user management

3.6 *4D model and 3D panorama*

The 4D model mentioned above built after the basic information completed, virtual universes in WebGL can be created from scene graphs. Scene graphs are assembled from objects to define geometry, location, orientation, and the appearance of objects. The model contains the necessary element of bridges including main grider, pier, abutment, bearing, expansion joint, foundation and the merchandising. All element information obtained from MySQL database, and cloud picture is applied to identify the detail about damage severity, sensor location and the maintenance record. As Figure 11 shown, 5 options represent basic, damage, evaluation, maintenance and sensor model respectively. The basic model shows the type of bridges and the detail of every element, details in damage, evaluation and maintenance are shown in element level which could be referred by the interactive function. Last model displays the sensor layout on the bridge, and the real-time data curve could be seen by click the link on the modal window.



Figure 12. 4D interactive model

3D panorama theory in this system is shown below, six photos mapping six cube face taken with special lens created a 360-degree cylindrical panorama. Environment around bridges can be known in this function which facilitates the on-site inspection and construction.

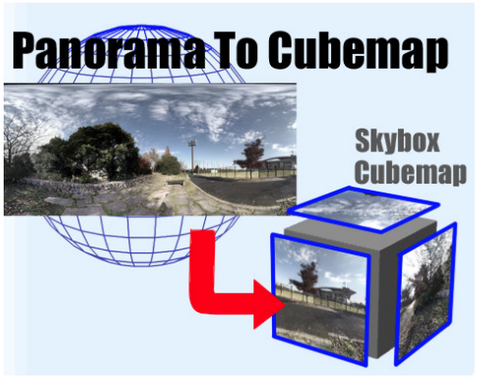


Figure 13. 3D panorama Theory

4 CONCLUSION

This paper proposed a new type bridge management system applied in China, and discussed the features of this system. The first attempt is to establish the database to support the integrate 4D bridge models, on-site mobile application for damage capturing and updating also mentioned. the following conclusions can be stated:

(1) the authority management and task dispatch including inspection, monitoring and maintenance were established for transport agencies. The related officials can be informed of dangerous bridges via e-mail.

(2) 4D models of the bridges were created using model-based data. The structural information and history record of inspection data, monitoring data, sensor location, evaluation data and maintenance data can be visualized by the interactive interface. 3D panorama created by the special cameras was supported in this system, and the surrounding environment of each bridge can be seen in the website browser. The integration of 4D model with the 3D panorama builds a powerful function for virtual reality.

(3) port expansion was exploited with hardware interface. Inspectors can use mobile apps to capture the bridge damages, and inspection data and reports are automatically recorded according to the prescribed form.

It is found that this system can effectively improve the work efficiency of bridge management, and the interactive 4D models can facilitate data sharing and avoid the barriers from other Building Information Modeling software. Further testing of the developed components of the system in practical situations is necessary to improve the functionalities and usability of the system. It should be noted that this research is still in progress and many aspects are still to be implemented and tested.

5 ACKNOWLEDGEMENTS

Funding for this research was supported by the National Natural Science Fund of China under award number 51708112.

6 REFERENCES

ASCE. (2017). “2017 report card for America’s infrastructure.” https://www.infrastructurereportcard.org/.

Akgul, F. 2012. Development of a bridge management system incorporating a newly developed model for element condition evaluation based on damage effects. *Structure and Infrastructure Engineering* 9(12):1206-1224.

Chan, B., Guan, H., Hou, L., Jo, J., Blumenstein, M. & Wang, J. 2016. Defining a conceptual framework for the integration of modelling and advanced imaging for improving the reliability and efficiency of bridge assessments. *Journal of Civil Structural Health Monitoring* 6(4):703-714

Hai, D.T. 2008. Computerized Database for Maintenance and Management of Highway Bridges in Vietnam. *Journal of Bridge Engineering* 13(3).

Hajdin, R. 2000. BMS Development in Switzerland. *Advanced Technology in Structural Engineering; Philadelphia, 8-10 May 2000.*

Hammad, A., Zhang, C., Hu, Y.X. & Mozaffari, E. 2006. Mobile Model-Based Bridge Lifecycle Management System. *Computer-Aided Civil and Infrastructure Engineering* 21(7):530-547.

Lee, T.S. & Yi, S.H. 2012. Efficiency Improvement of Korean Bridge Management System (KOBMS) : Via Mobile Internet. *Fourth Joint International Symposium on Information Technology in Civil Engineering; Nashvile, 15-16 November 2003.*

Miyamoto, A., Kawamura, K. & Nakamura, H. 2001. Development of a bridge management system for existing bridges. *Advances in Engineering Software* 32(10-11): 821-833.

McGuire, B., Atadero, R., Clevenger, C. & Ozbek, M. 2016. Bridge Information Modeling for Inspection and Evaluation. *Journal of Bridge Engineering* 21(4)

Marzouk, M. M. & Hisham, M. 2011. Bridge Information Modeling in Sustainable Bridge Management. *International Conference on Sustainable Design and Construction; Kansas city, 23-25 March, 2011.*

Potel, M. (1996), MVP: Model-View-Presenter, The Taligent Programming Model for C++ and Java. Retrieved from: <ftp://www6.software.ibm.com/software/developer/library/mvp.pdf>.

Robert, W.E., Marshall, A.R., Shepard, R.W. & Aldyuz J., 2003. Pontis Bridge Management System State of the Practice in Implementation and Development. *9th international bridge management conference*; *Florida, 28-30 April 2003*.

She, T.H., Aouad, G. & Sarshar, M. 1999. A Geographic Information System (GIS)–Based Bridge Management System. *Computer-Aided Civil and Infrastructure Engineering* 14(6):417-427.

Maintenance, Safety, Risk, Management and Life-Cycle Performance of Bridges – Powers, Frangopol, Al-Mahaidi & Caprani (Eds)
© 2018 Taylor & Francis Group, London, ISBN 978-1-138-73045-8

Indian Bridge Management System - Overview and Way forward

Sachidanand Joshi
Team Leader- Research on IBMS project
Director- IDDC Engineers Pvt. Ltd.

Sitarama Sagi Raju
Co- Researcher IBMS project
Managing Director- IDDC Engineers Pvt. Ltd.

ABSTRACT
Indian Bridge Management System (IBMS) was initiated by Ministry of Road Transport and Highways, Government of India in September 2015. In a country where no formal bridge management system exists, the task to get IBMS going in a short time was a herculean task. Initial development was based of the practicality of the implementation. Some basic parameters essential to define the bridge and ensure sufficient data is collected to digitize the management system was put in place.

Inventory and Inspection module of the system was commissioned in October 2015 and first cycle of various bridges inventorized and inspected,.

Table 1. Inventory of structures – IBMS October 2017

Sr. No.	Type of Bridge	Total Number
1	Culvert < 6 (CV)	133085
2	Extra-long Bridge length above 150m (EL)	1744
3	Major Bridge length above 60m (MA)	3395
4	Minor Bridge length 6m to 60m (MI)	31534
	Total	169758

We had found 6551 number of bridges that are structurally inadequate and their details are given below

Table-2 Distress bridges - IBMS June 2017

Sr. No.	Type of Bridge	Number
1	Minor Bridges	5591
2	Major Bridges	664
3	Extra-Long Bridges	296
Total		6551

Bridges and a structure was completed within 14 months. The paper outlines the challenges and solutions provided during the initial period. It outlines the various modules that are under implementation post this inventory and inspection module. Testing and definition of remedial measures is the next module which aims to make safe all bridges on Indian National Highways (NH).

Once safety issues of the bridges are addressed, the efficient management policies will be implemented. Such an approach has enabled us to identify bridges which need rehabilitation intervention to make them safe in a short span of 18 months. Work on bridge repairs will begin post monsoon season.

IBMS will ensure the birth of Indian Bridge Rehabilitation Industry as none exists today. IBMS seeks expertise in this area. Volume of work is estimated to be USD 750 Million.

IBMS at present covers only 3% of road network and soon will cover about 45% road network when it is implemented in all 29 regional states of the country.

REFERENCES

Indian Road Congress, 1993, Guidelines on Techniques for Strengthening and Rehabilitation of Bridges, India, IRC SP: 40

Joshi Sachidanand, 1995, FRWD Expounded- International Conference on Retrofitting and Rehabilitation of Structures, London, UK

Office of Research Development and Technology, 2001, Highway Bridge Inspection: State of Practice, USA, FHWA-RD-01-033

Matos Jose, 2016, Quality Specifications for roadway bridges standard at European level: TU 1406, Europe, COST Action publication

Prof. Dr. Michael Raupach, 2016, Concrete Repair EN-1504; Diagnosis, Design, Principles and Practices, Europe

Maintenance, Safety, Risk, Management and Life-Cycle Performance of Bridges – Powers, Frangopol, Al-Mahaidi & Caprani (Eds)
© 2018 Taylor & Francis Group, London, ISBN 978-1-138-73045-8

Bridge management implemented by the South African National Roads Agency

E.J. Kruger
The South African National Roads Agency SOC Limited, Pretoria, South Africa

A.A. Nyokana
The South African National Roads Agency SOC Limited, Pretoria, South Africa

ABSTRACT: Bridge management methods are becoming more and more sophisticated and costly. However, the goal of bridge management is sometimes lost in the desire to collect more and more data. The basic aim should always be to identify critical defective bridges to implement timely interventions. The cost of inspections must be balanced against budgets actually allocated towards repair. Prioritization lists of defective bridges must make sense or else the credibility of the management system will be brought into disrepute. The South African national Roads Agency SOC Ltd in common with other state institutions, uses a defects based system, referred to as the DER System, for inspections and not a condition based system. Outlined in the paper is inspection requirements and how structures are categorized from good to critical using the "deduct method" of prioritization. The simple calculation of how the asset values of bridges are determined is also outlined.

1 INTRODUCTION

The The South African National Roads Agency SOC Limited (SANRAL) is a state-owned company that was formed in 1998 with a mandate to finance, improve, manage and maintain the national road network in South Africa. The national road network consists of approximately 22000 km of paved roads with a total of about 3750 bridges. Unlike road pavements structures, bridges generally have a longer design life and so the pressure to delay bridge repairs in budgets is evident. Institutions need to be aware that the repair and rehabilitation of structures cannot be delayed indefinitely as this sometimes leads to disastrous failures with all the associated negative consequences.

Bridges are important elements of the national road network making effective management and proper maintenance of these structures essential. An appropriate systems approach to the management of bridges should assist the managing authority in identifying the best time for maintenance intervention and the most appropriate allocation of funds.

2 THE STRUCTRES MANAGEMENT SYSTEM DEVELOPED FOR SANRAL

Prior to 1998 an overall condition based system was used for the management of bridges for the national roads. It was found to be ineffective in that bridges in need of repair were not high on priority lists whilst bridge not in need of repair were higher up the priority lists. This lead to resistance against relying on results from the then bridge management system. Under this old condition based system the inspector had to rate each and every element of a structure regardless if there are defects or not. The ratings were then combined for similar members to get an overall condition rating for the members and then for the overall structure.

The inability to identify critical structures needing urgent repair resulted in SANRAL's management to decide to scrap the old condition based management system and to develop a totally new system. In 1998 SANRAL contributed to research into a new defects based system by the Council for Scientific and Industrial Research (CSIR) and a consulting engineer a defects based system. The CSIR system became known as STRUMAN (Structures Management) and was

further developed and refined in collaboration with SANRAL. This system, also referred to as DER System, is now used for the management of bridges on the national road and provincial road, and some metropolitan road networks.

The priority lists for repair that are obtained using this system have been refined and now give good believable priority lists. As a result, regional management now accepts that the right bridges have been identified for repair.

The decision to move from an old system with years of accumulated data was brave one in that the old data had to be scrapped.

3 THE DANGER OF UNEXPECTED FAILURES

When failures occur inevitably there is an accusation by the public and politicians that the authority did not inspect the structures or do repairs.

SANRAL recently on the 9th August 2017 at 01h15 had such a case where a pedestrian bridge structure collapsed onto the busy N3. Fortunately, the collapse occurred on a public holiday and nobody was killed. The bridge did not collapse onto any vehicle. However, three trucks and a car did drive into the bridge as can be seen in Figure 1. The initial reaction of the public was that SANRAL did not maintain the bridge and that was the reason for the collapse. It was fortuitous that a full inspection of the bridge had been done in Late July 2016, the previous year, with no defects of any significance being noted, by the accredited and appropriately qualified bridge inspector. Refer to Section 6 of this paper for the requirements for inspectors.



Figure 1. Collapsed Pedestrian Bridge into highway

SANRAL appointed independent consultants who were on site within 3 hrs of the collapse to investigate and report on the cause of the collapse. The report indicated that the collapse was caused by an 8.1 ton roll of steel that was not secured to a truck coming off and impacting the pier at about 90km/hr. Statistically the accident was an extremely rare event. The point of including this incident in this paper is that the bridge had been inspected. This helped in answering media questions and parliamentary questions. Regular bridge inspections are important.

4 THE DEFECTS BASED SYSTEM KNOWN AS THE DER SYSTEM

As mentioned previously the system used by SANRAL is a defects based system or DER system.

DER refers to the degree; extent and relevancy of a defect as described below:

D = Degree of defect: How bad or severe the defect is
E = Extent of defect: How widespread is the defect on the inspection item being inspected
R = Relevancy of defect: The consequence of the defect with regards to the structural/functional integrity of the inspection item or the safety of the user of the structure.
U= Urgency of repair item

The worst defect per element is rated for the Degree (D), Extent (E) and Relevancy (R) (to the bridge element in question). The ratings are done for each sub-item and only the worst defect on the inspection sub-item is rated. Only defects are rated as to their effect on the element under consideration. The importance of the element with the defect in relation to the structural integrity is taken into account by applying weighting factors which range from 0 to 5, for example guardrails have a weighting of 0 and abutments have a weighting of 5.

The DER rating system is essentially a four-point rating system on a scale of 0 to 4 as shown in Table 1 below:

Table 1. Valid DER values.

Rating	D (Degree)	E (Extent)	R (Relevancy)	
X	Not applicable			
U	Unable to inspect			
0	No visible defects			
1	Minor	Local	Minimum	No structural integrity or safety issues
2	Moderate	More than local	Moderate	Some possible structural integrity or safety issues
3	Warning	Less than general	Major	Structural integrity or safety compromised
4	Severe	General	Critical	Potentially a serious impact on structural integrity and/or user safety

The Relevancy (R) rating is critical and it is important that the inspector understands the effect of a defect on the member in question. Inspectors also indicate the Urgency (U) of the repair needed. The Urgency ratings are shown in Table 2 below.

Table 2. Urgency values

U - URGENCY					
Record	Monitor	Routine	< 10 yrs	< 5 yrs	ASAP
R	0	1	2	3	4

There are defects that will never be repaired and are thus marked as R (record purposes only). If defects need monitoring then U=0. U=1 (Routine) means that the repairs are routine such as replacement of damaged guardrails.

Figure 2 below shows a sample photo from an inspection defects report of a bridge with a vertical crack in the abutment. The rating for this defect is a follows:

D = 4; E = 2; R = 4 and U=4 (ASAP)



Figure 2. Vertical crack in abutment wall

This bridge was on the priority list but because there were two authorities involved agreement as to who will pay for the repair is ongoing. The procurement process to appoint a contractor is underway at the time of writing this paper.

In a one year period the crack has widened further as can be seen in Figure 3 below but the rating remains as D=4 E=2 and R=4. The urgency remains U=4. Fortunately the wall is far enough from the railway line not to endanger trains if it totally collapses. The road above will be affected but not catastrophically. The bridge is being continuously monitored by the SANRAL routine maintenance contractor whilst a contractor is being procured to repair the wall. The bridge will be widened at the same time.



Figure 3. Vertical crack widened further after one year.

5 THE INSPECTION PROCEDURE

The DER rating system is characterized by a simple inspection procedure which consists of:

a) A practical visual inspection of the following twenty-one (21) standard bridge items as shown in Tables 3. For major culverts fourteen (14) items are inspected and are as shown in Table 4.

Table 3. Standard bridge inspection items and their weight

Inspection Item	Weight
01. Approach Embankment	2
02. Guardrail	0
03. Waterway	2
04. Approach Embankment Protection Works	2
05. Abutment Foundations	5
06. Abutments	5
07. Wing/ Retaining Walls	4
08. Surfacing	1
09. Super-structure Drainage	1
10. Kerbs / Sidewalks	1
11. Parapet	3
12. Pier Protection Works	1
13. Pier Foundations	5
14. Piers & Columns	5
15. Bearings	3
16. Support Drainage	1
17. Expansion Joints	2
18. Longitudinal Members	5
19. Transverse Members	3
20. Decks & Slabs	5
21. Miscellaneous Items	0

Table 4 Standard major culvert inspection items and their weight

Inspection Item	Weight
01. Apron slab & cut off walls	3
02. Wing/retaining/head walls	4
03. Scour protection works	3
04. Embankment/s	2
05. Waterway	5
06. Road slabs	3
07. Roadway joints	1
08. Guardrails	1
09. Parapets/handrails	3
10. Walls	5
11. Top slab	5
12. Invert slab/foundations	5
13. Cell deformation	5
14. Miscellaneous items	0

b) A single bridge inspection sheet is used and one defects photo's sheet. All photos are geotagged.
c) Estimated quantities of the repair work for each defect are estimated during the inspection. Each of the repair activities has a unit rate that is used in the budget module to determine an estimated budget for the repair of the structure.
d) The urgency of each repair item is also recorded including the time limits. The BSMS can separate out what is termed routine road maintenance (RRM) repair items (U=1) that do not require specialists' knowledge, such as grass cutting or guardrail repair. If U=1 for a repair item it is allocated to RRM section for repair.
e) If an item is marked as Routine (R), it is reported as for record purposes only and will not be repaired.
f) If any defect poses an immediate danger to the public the inspector is required to rate the defect as "Make Safe" and to notify SANRAL to address the defect immediately.

For the larger bridges, the inspection of decks and bearings is done using an Under Bridge Inspection Unit (UBIU) to enable inspectors to get close to items. Figure 4 shows the use of the UBIU during inspections.

The use of drones has been investigated but their use has some disadvantages. If for instance videos are taken of all bearings and other elements these videos still need to be viewed by inspectors who are qualified engineers. This will take an inordinate amount of time. In addition, the drone operators must be licenced by the civil aviation authorities. Awkward locations are also not able to be inspected using drones.

Thus presently SANRAL presently does not make use of drones for inspection but acknowledges that their use has certain advantages. The big disadvantage in South Africa is that drones are presently not allowed to be operated over roads.



Figure 4. Under bridge inspection unit used for inspection

6 THE CLASSIFICATION OF BRIDGES AND MAJOR CULVERTS

A bridge is classified as a structure with a span equal to or greater than 6 m, or a total length of 20 m or more or an opening of 36 m^2 or greater. A major culvert is classified as a structure with dimensions less than those defining a bridge but with clear span (as measured horizontally at the soffit perpendicular to the faces of its supports) length equal to or larger than 2.1 m, or diameter equal to or larger than 2.1 m, or total cross-sectional opening area equal to or larger than 5 m^2. Another structure type called a cellular bridge has also been introduced. This is a structure that classifies as a bridge based on its dimensions but looks like a culvert in that is it has the typical features of a major culvert and is inspected as such. All service culverts (including all agricultural lined irrigation canals) are classified as major culverts regardless of size except if they fall within the bridge classification. The maintenance of lesser culverts falls under road maintenance contract and does not presently form part of the BSMS priority list. This may change in the future.

7 TRAINING AND QUALIFICATION OF INSPECTORS

Principal inspections play a vital role in the BSMS and are carried out by inspectors that are suitably qualified and experienced in bridge design and rehabilitation. Bridge inspectors must have a minimum of 5 years relevant bridge design experience for engineers or minimum of 10 years relevant bridge design experience for technologists. They must be registered as professional engineers or technologists in South Africa.

For culvert inspectors, the only requirement is that they shall have a diploma or degree with a minimum

of 5 years relative experience. Verification inspections and strategic bridges inspections are conducted by senior bridge inspector who must be Professional Engineers with a minimum of 15 years full time bridge design experience and have made bridges as their full-time career. For large strategic bridges a under bridge inspection unit is used obtain better access as shown in Figure 4.

In addition to the above experience and qualification an inspector must have attended a two day Technical Methods for Highways (TMH) 19 DER Methodology course in bridge and culvert inspections accredited by the Committee of Transport Officials (COTO) Structures Subcommittee. Case studies are presented by experienced engineers to give examples of the rating of defects and the lessons learnt from previous inspections as to when inspectors got ratings wrong or correct. Emphasis is placed on the actual design experience of inspectors so they can correctly interpret defects and their relevancy in the field. Thus it is impossible to use lower qualified persons to do inspections unless a more rigorous course lasting months is done. This approach although used in other countries has not be adopted in South Africa.

In order to be accredited as COTO certified inspectors, applicants must pass the exam written at the end of the training workshop. Slide presentations and lectures are presented on the first day and a practical bridge inspection field trip is undertaken on the second day as shown in Figure 5.



Figure 5: Course attendants at the practical bridge inspection field trip.

8 BRIDGE MANAGEMENT SYSTEM AS PART OF THE INTEGRATED TRANSPORT INFORMATION SYSTEM (ITIS)

The bridge and structures management system (BSMS) is one component of SANRAL's Integrated Transport Information System (ITIS) for the management of its assets and information. The BSMS contains of inventory and location information on the approximately 10000 different structures types that form part of the national road network, these include major culverts, lesser culverts, service culverts, bridges, tunnels, retaining walls and sign gantries.

The BSMS is used for the analysis of structures data to identify out of a large number of structures, a single serious degree (D=4) of defect that has high relevancy (R=4) on one element that can cause failure of a structure. For example, if a single beam of a bridge deck is severely damaged but all the other beams are undamaged, then it must be this beam that is used in the prioritization model.

Network level principal inspections are conducted every five years on the bridges and major culverts. This provides network-based results which allows for undertaking of repairs of individual bridges based on the results of the whole bridge network. At a network level, the bridges with the highest risk will be identified and appear at the top of the priority list. SANRAL uses the priority list generated, bridges and other structures are grouped into projects which could be done by a single contractor. Single outlier bridges or structures in need of repair are put out as single projects if they are large enough otherwise they are combined into road rehabilitation or upgrade projects in the area.

9 IMPLEMENTATION OF THE BRIDGE INSPECTION PROGRAMME

The bridges on the network are split into inspection packages based on their location and route description. Packages are created in BSMS which is on the Integrated Transport Information System (ITIS) web portal. On the BSMS, inspectors have access to the previous inventory and photo reports but not the previous inspection reports. Blank inspection reports are available for download for use during the field inspection. The work carried out by the inspector during the inspection programme comprises of following:

a) Compilation of previous inventory sheets and blank inspection report;
b) Field inspections;

c) Input of the inventory and inspection data (including geotagged photographs) into the computer using specially programmed ITIS software.

Inspectors are issued with the TMH 19 Manual for the visual assessment of road structures and are assigned rights to access the bridges and submit inspection and inventory data to SANRAL using the ITIS software. The inspection information is first approved by SANRAL before it is published to the BSMS.

10 CALCULATION OF OCI SCORE USING DER RATING SYSTEM

Once inspections have been properly captured and approved the overall condition index (OCI) for each structure is calculated using the values of DER rating system. This is a multi-level method applied to first to inspection sub-items (1) and then inspections items (2) to calculate the total structure deduct points.

The deduct points for the inspection sub-items is calculated using Equation 1 below:

$$dp_{ij} = DP_{max} \times \frac{(D+0.25E)\times R^{1.5}}{40} \quad (1)$$

where D, E and R are the degree, extent and relevancy ratings for inspections sub-item j of item i respectively and DP_{max} is the maximum deduct points for inspection sub-item. The agreed value for DP_{max} is 65, resulting in the worst OCI score of 9. Previously the agreed DP_{max} value was 75 but this resulted in structures with negative or zero OCI scores. As such when the OCI score was applied to the structure asset value, structures with negative or zero OCI scores had a negative or zero asset value which cannot be the case.

The inspection sub-item with the highest deduct point is used to calculate the deduct points for the inspection item as shown in Equation 2 below:

$$DP_i = \frac{w_i}{w_{max}} \times dp_{imax} \quad (2)$$

where DP_i is the calculated deduct points for inspection item i; w_i is the weight for inspection item i; w_{max} is the highest weight for the inspection items making up the structure up and dp_{imax} is the highest deduct points calculated for any inspection sub-item j making up inspection item i. For example the inspection Item 13 – 'pier foundations' for a three span bridge will have two inspection sub-items for the two pier foundations.

The five inspection items with the highest deduct point are used to calculate the deduct points (DPs) for the structure as shown in Equation 3 below:

$$DP_S = DP_{i1} + 0.3DP_{i2} + 0.1DP_{i3} + 0.05DP_{i4} + 0.05DP_{i5} \quad (3)$$

where DP_{ij} is the deduct points for the inspection item such that DP_{i1} is the primary inspection item with the highest deduct point and DP_{i5} is the inspection item with the fifth highest deduct point. The contribution to the total deduct point of a structure from the five highest inspection items is based on the similar deduct method applied in pavement management where the primary, secondary, tertiary and additional inspection items contribute 100%, 30%, 10% and 5% respectively.

The overall condition index for the structure is calculated using Equation 4 below:

$$OCI = 100 - DP_S \quad (4)$$

OCI ratings can range from 9 (worst condition) to 100 (best condition) with a structure falling into one of the five condition categories described Table 4 below.

Table 5. Condition and functional categories

Condition Category	Index Range	Condition Category Description	Functional Category Description	Colour Code
Very Good	85 - 100	Asset is still like new and no problems are expected.	Good service levels at all times	Blue
Good	70 – 85	Asset is still in a condition that only requires routine maintenance to retain its condition.	Mostly good service levels with isolated problems occurring at certain times.	Green
Fair	50 – 70	Some clearly evident deterioration and would benefit from preventative maintenance or requires renewal of isolated areas.	Reasonable service but with intermittent poor service.	Orange
Poor	30 – 50	Asset needs significant renewal or rehabilitation to improve its structural integrity	Generally poor service levels with occasional very poor service being provided.	Red
Critical	9 - 30	Asset is in imminent danger of structural failure and requires substantial renewal or upgrading with less than 10% of EUL remaining.	Very poor service levels at most times.	Purple

The previous system used to calculate the OCI score resulted in structures in a poor condition falling in the 50 -75% condition category. However, when it came to allocating funds for projects, the accountants did not understand why structures with an OCI score greater than 50% were considered to be in poor condition and in need of repair.

The condition and functional categories shown in Table 5 are based on the DER system and are in line with the ones applied to the pavement management systems. These categories allow for structures in a poor and critical condition (less than 50%) to be easily identifiable by all and included in the priority list of bridge repair projects. Based on the inspection and

inventory information, the system generates live reports and dashboards containing:

a) Detailed Inventory and Inspection reports
b) Inventory and defects photo reports
c) Priority Index for all structures
d) Routine maintenance activities for each structure

The figures below show some of the dashboards output generated by the BSMS:

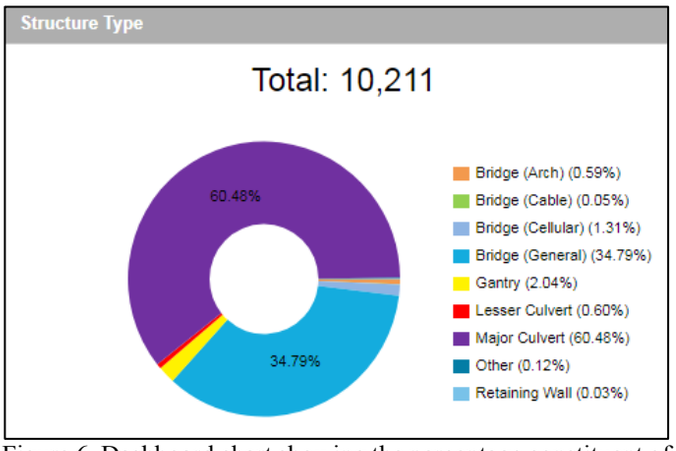


Figure 6. Dashboard chart showing the percentage constituent of the different structure types

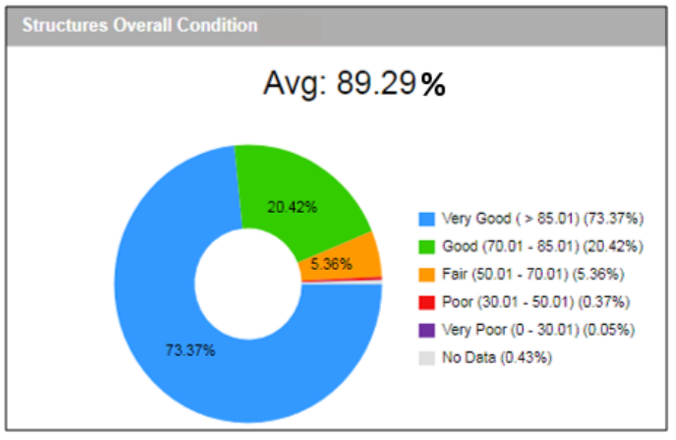


Figure 7. Dashboard chart showing the percentage of bridges in the different condition categories

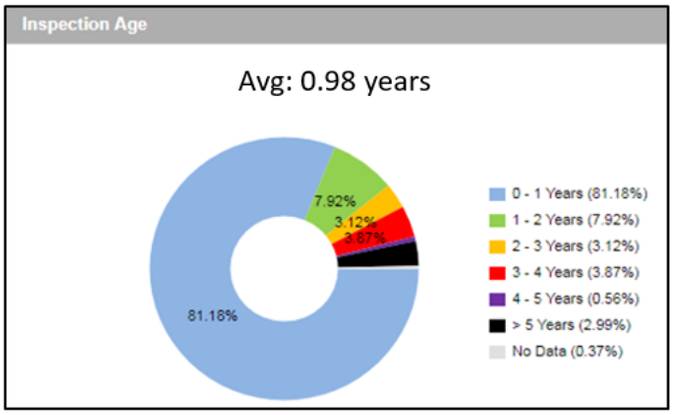


Figure 8. Dashboard chart showing average inspection age of the bridges of less than a year.

11 THE BRIDGE ASSET VALUE CALCULATION

The asset value of bridges is determined by calculating the depreciated replacement cost of the structure that is based on the Overall Condition Index of a bridge.

Firstly, the Gross Replacement Cost (GRC) for each bridge (this is the cost of the bridge if built new) is calculated using Equation 5 below:

$$\text{GRC} = \text{Deck Area} * \text{Mat. Unit Rate} * \text{Adj. factor} \quad (5)$$

The Material Unit Rate (this is the rate per m^2 of deck area) is recalculated each year using the average of 3 standard sample bridges that are given to an experienced contractor quantity surveyor to price. The same 3 bridges are used each year. This is also compared to recent construction projects and the rate per m^2 of deck area.

For structures with a pier or abutment height of less than 8m the unit rate per m^2 value is kept constant. This accounts for approximately 90% of all bridges. For bridge with abutments or piers greater than 8m high the unit rate adjustment shown in Equation 6 below:

$$\text{Material Unit Rate} = A + B * \max[0, (C - 8)^{0.6}] \quad (6)$$

where A is the base unit rate (for bridges with piers or abutments up to 8m high), B is the pier height adjustment rate and C is the maximum pier height on the bridge.

A perpetual life is assumed for bridges and the depreciation is related to bridges OCI score with the Depreciated Replacement Cost (DRC) for bridge calculated using Equation 7 below:

$$\text{DRC} = \text{GRC Bridge} * (\text{OCI}/100) \quad (7)$$

If a bridge is repaired and rehabilitated then the Depreciated Replacement Cost (DRC) will increase. Any change in the bridge deck area due to bridge widening or lengthening will obviously increase the replacement cost of the structure. The formula avoids the detailed depreciation of individual elements of a bridge such as joints, bearings, piles etc. It is the view of the authors that more complex valuations should be avoided so as not to overly complicate the calculation of asset values. The method used by SANRAL is realistic and has yielded good results.

After repairs or work is done on bridges fresh inspections are required by the consulting engineers so as to keep the data current. This updating of data although important has in the past been neglected and

penalties on consultant fees have had to be introduced to force compliance.

12 CONCLUSION

The BSMS is an invaluable tool in assisting SANRAL to carry its mandate which is to manage and control the national road network infrastructure. The inspection procedure is simple and effective as it only focuses on defects, thus elements in good condition are not rated reducing the data capture time required. The defects based deduct point system has led to a better allocation of bridge repair projects and a more appropriate allocation of funds for bridge repair projects. The system is able to streamline the function of the RRM as defects that do not require specialists' attention are allocated RRM.

REFERENCES

Committee of Transport Officials. (2013). *TMH 22 Road Asset Management Manual.* Pretoria: Committee Draft (not published).

Committee of Transport Officials. (2016). *THM19 Manual for the visual assessment of road structures. Part A: Road structure management information.* Pretoria: Committe Draft Final (not publised).

13 ACKNOWLEDGEMENTS

The authors acknowledge the contribution from Paul Nordengen and Michael Roux from the Council of Scientific and Industrial Research (CSIR) who over the past 20 years have intimately been involved with the development and enhancements to the DER system of structures management. Also acknowledged is Eric de Fleuriot, a consulting engineer, who was the main contributor in in the earlier years prior to 2000, to the development of the DER method of inspections for some clients.

Maintenance, Safety, Risk, Management and Life-Cycle Performance of Bridges – Powers, Frangopol, Al-Mahaidi & Caprani (Eds)
© 2018 Taylor & Francis Group, London, ISBN 978-1-138-73045-8

The Optimal Maintenance Strategy of Bridge using Bayesian Approach

Jin Hyuk Lee, Kyung Yong Lee, Sang Mi Ahn & Jung Sik Kong
School of Civil, Environmental and Architectural Engineering, Korea University, Seoul, Korea

ABSTRACT: For the efficient life-cycle maintenance of bridge, prediction of future bridge performance based on the current performance must be required and it is possible more rational decision-making through the higher accuracy of the prediction model of bridge deterioration.

In other words, predicting a performance of bridges is important to reduce the costs of maintenance, repair, rehabilitation and replacement of bridges. To establish the optimal maintenance strategy and planning, there are needs to consider bridge performance history and prediction of maintenance time. In this study, performance models of bridges are developed on the basis of condition index of the bridges by a statistical and probabilistic method. The condition index(or grade) resulted from visual inspection and are associated with bridge damage. (corrosion, fatigue, crack, water leak, scaling, etc.) Factors causing these defects are considered in bridge element performance model. Also, the predicted performance includes a lot of uncertain factors because the condition index of bridge elements were observed by person. So, when inspector determine the bridge condition index(or grade), it is essential to perform In-depth inspection and monitoring using device.

While performing a detailed inspection of all parts of a bridge and/or assigning an experienced inspector have reduced a significant part of errors contained in the prediction model, such personnel-based existing maintenance may result in enormous maintenance costs since it is difficult for a bridge administrator to estimate the bridge performance exactly at a targeting management level, thereby disrupting a rational decision making for bridge maintenance.

In this study, to solve this problem, a Bayesian updating method which is related to updating prior information of bridge deterioration is used to the optimal maintenance strategy in Bridge Management System(BMS) considering the uncertainty of inspection data. Also, examples of application are presented, showing the effects of inspection and updating on domestic(Korea) bridge maintenance strategies.

That is, we propose a bridge maintenance scenario model based on Bayesian updating and discuss the uncertainty of inspection data obtained from a bridge. The main purpose of this research is to verify advantages of the Bayesian-updating-driven preventive maintenance in terms of the cost efficiency in contrast to the conventional periodic maintenance.

1 INSTRUCTIONS

Predicting a performance of bridges is important to reduce the costs of maintenance, repair, rehabilitation and replacement of bridges. To establish the optimal maintenance strategy and planning, there are needs to consider bridge performance history and prediction of maintenance time.

In bridge maintenance, the method having been used broadly is inspection, but it is not free from uncertainty and error. Also, most people just know intuitively that doing accurate prediction of performance by inspecting status of structure.

This study is done in order to certify that predicting performance by updating data gained from inspection of bridge using Bayesian method.

The main purpose of this study is to verify, that updating performance model related to optimal repair and rehabilitation cost have sufficient advantages in an aspect of bridge maintenance.

2 UPDATING EXISTING PERFOMANCE MODEL USING BAYESIAN APPROACH

2.1 *Development of element life cycle performance model*

To develop element performance models of the bridges, a multiple regression analysis is carried out

on the basis of a database of condition indices and influence factors making the structures deteriorated. A detail procedure is shown in Figure 1. The multiple regression analysis is a statistical process for estimating relationships between a dependent variable and one or more independent variables.
Prior to the multiple regression analysis, deteriorating rates for each element of the bridges according to changing time were calculated by univariate regression analysis. The deteriorating rates are considered by a dependent variable in the multiple regression analysis. A length of the bridge, traffic volume, amount of surface chloride and humidity are regarded as independent variables.

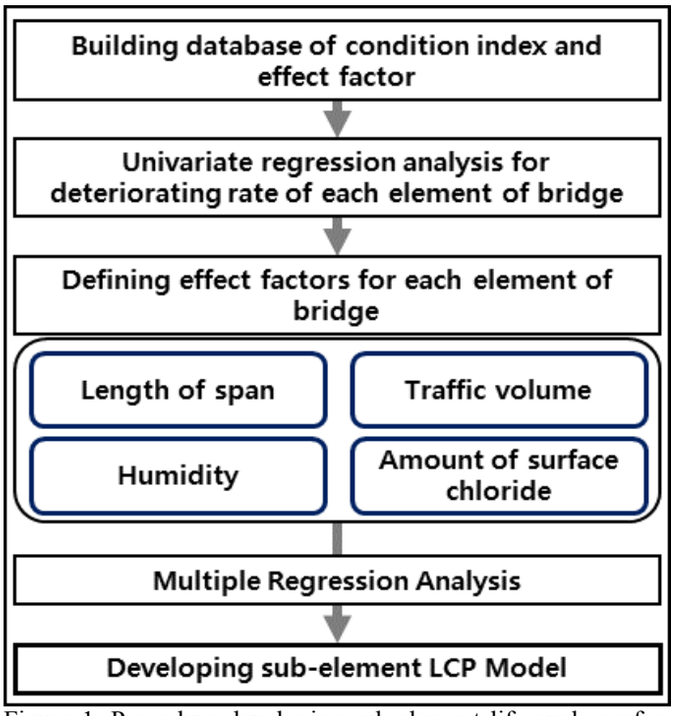


Figure 1. Procedure developing sub-element life cycle performance model

Additionally, these independent variables have correlation between them.
In consideration of the correlation terms, the deteriorating model equation is defined as Equation 1 below:

$$y = a_0 + a_1x_1 + a_2x_2 + a_3x_3 + a_4x_4 + a_5x_1x_2 + a_6x_1x_3 + a_7x_1x_4 + a_8x_2x_3 + a_9x_2x_4 + a_{10}x_3x_4 \quad (1)$$

Where y is life-cycle performance model and it means deteriorating rate proposed by the multiple regression analysis, a_0 is constant, a_1~a_{10} are coefficients about the independent variables, x_1 is the length of the bridge, x_2 is the traffic volume, x_3 is the amount of surface chloride and x_4 is the humidity.

2.2 *Updating models using Bayesian probability theory*

Predicting performance through LCP models that are suggested based on statistical method needs to be updated by applying monitoring data in order to improve prediction accuracy. New monitoring information obtained by inspection can often include errors and uncertainty as to the quality of the inspection, experience of the inspectors, and environmental conditions during inspection. To reduce uncertainty in the information, an update method was utilized based on the Bayes' theorem as proposed by Frangopol et al. (2008). Bayes' theorem is to estimate the posterior when given the prior and likelihood function. In this study, the new information measured by the inspector is regarded as likelihood function that can be approximated by a normal distribution with mean and standard deviation. At the time of the inspection, the developed performance model of the structures is considered prior information. As a result, the posterior becomes information updating the models. The procedure of updating deterioration model based on Bayes' theorem is shown in Figure 2.

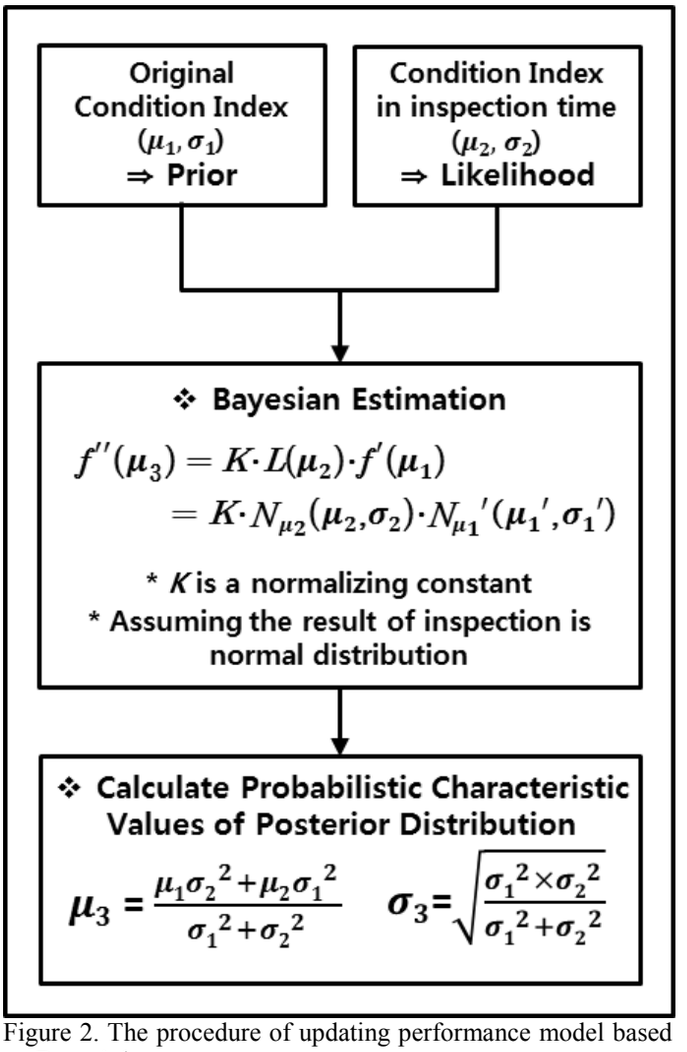


Figure 2. The procedure of updating performance model based on Bayes' theorem

Through Figure 2., μ_1, σ_1 can be defined in probabilistic characteristic values of prior, which means original condition information. And μ_2, σ_2 can be defined in likelihood information when inspection is

applied in particular time. After updating in monitoring time, the existing performance model is updated by Bayes' theorem.

It is important to observe that the posterior variance of μ, as given by σ_2 in Figure 2., is always less than σ_1^2 or σ_2^2; that is, the variance of the posterior distribution is always less than that of the prior distribution or of the likelihood function (Ang, A., W. Tang., 2007). And procedure of verification can be seen in Figure 3.

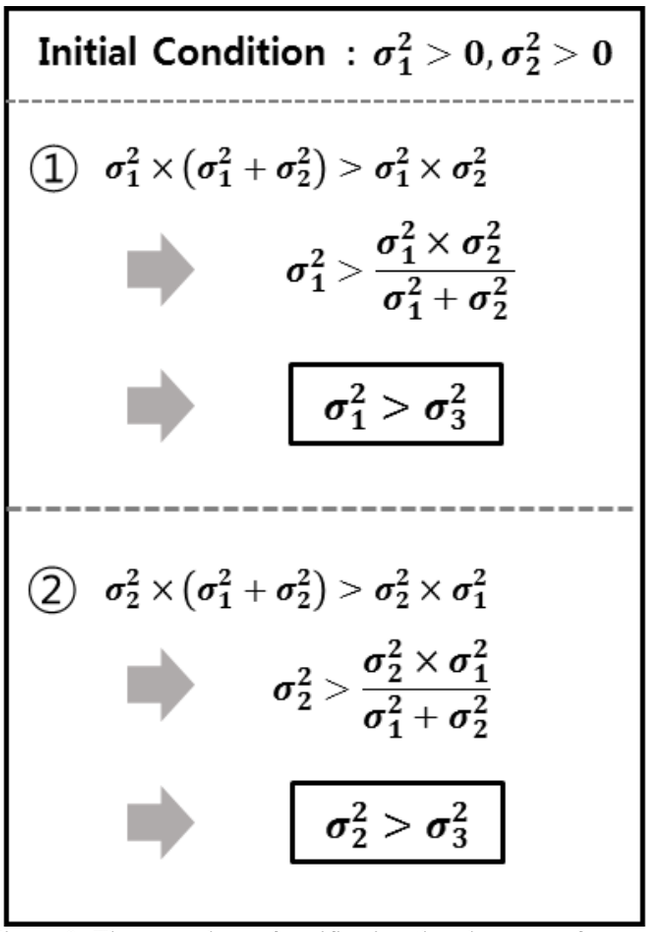


Figure 3. The procedure of verification that decrease of uncertainty of updating performance model based on Bayes' theorem

3 VALIDATION OF BAYESIAN UPDATING SCENARIO

3.1 *Application to domestic bridge element*

Consider the fatigue crack monitoring technology of the youngjong grand bridge steel girder. And target bridge element information is indicated in Table 1.

Table 1. Analysis condition of target bridge element.

Division	Quantity
Span length	300m(6@50)
Width	2m(Two Lane)
Area	600㎡
Discount rate(q)	3%

In Figure 4, performance model of a steel girder are shown. the y-axis means condition index and x axis means service life (years). Also, full line is mean(μ_1) slope of steel girder, dotted line is standard deviation(σ_1) slope.

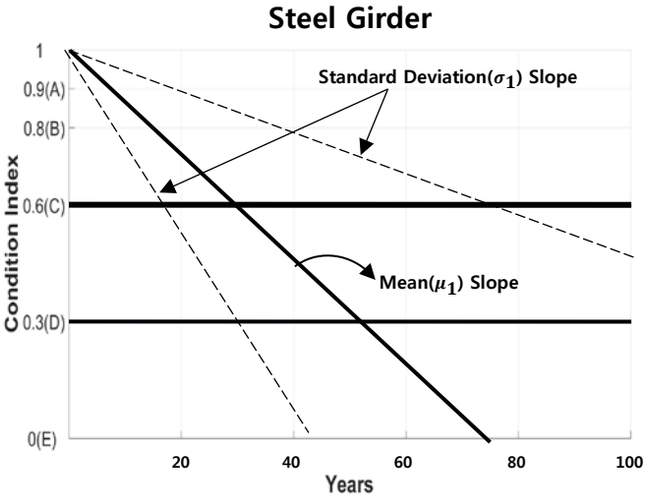


Figure 4. Condition index model for steel girder.

In Figure 5, d ecreased standard deviation slope of steel girder after inspection time is shown.

According to quality of the new information obtained by the inspection, quality of the updated models is different. For instance, in Table 2. case1~4 are set depending on variability of inspection accuracy. In the case of performance model of steel girder, the prior's mean is 0.709 and standard deviation is 0.188. Based on Baye's theorem, the updated model is calculated in the Table 2. After updating the models, the posterior's standard deviations are smaller than the prior. It means that updating models through reflecting the result of the inspection can reduce the uncertainty that is included in the performance model.

Table 2. Case study according to the quality of the inspection's result.

Case	Prior		Likelihood		Posterior	
	Mean	Std. Dev.	Mean	Std. Dev.	Mean	Std. Dev.
Case1	0.871	0.188	0.871	0.05	0.871	0.048
Case2	0.871	0.188	0.871	0.1	0.871	0.088
Case3	0.871	0.188	0.871	0.15	0.871	0.117
Case4	0.871	0.188	0.871	0.2	0.871	0.137
Case5	0.871	0.188	0.915(5%↑)	0.05	0.912	0.048
Case6	0.871	0.188	0.827(5%↓)	0.05	0.830	0.048
Case7	0.871	0.188	0.915(5%↑)	0.2	0.892	0.137
Case8	0.871	0.188	0.827(5%↓)	0.2	0.850	0.137

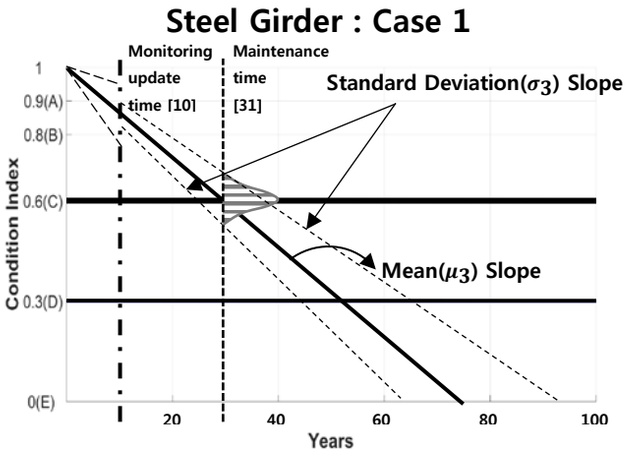


Figure 5. Condition index model for steel girder based on Bayesian(monitoring) updating at 10years

Also, for comparing the posterior by Case, a total maintenance cost is calculated. The total maintenance cost equation in this study is defined as equation 2 below:

$$C_{MAI}^{Total}(t) = \sum_{t=1}^{T} \frac{1}{(1+q)^t}\{C_{INS}^{rins}(t) + C_{INS}^{pins}(t) + C_{INS}^{psdia}(t)\} + \frac{1}{(1+q)^t} \times C_{MAI}^{C-grade}(t) \times P_{MAI}^{C-grade}(t) \quad (2)$$

Where $C_{MAI}^{Total}(t)$ is the total maintenance cost at time t, q is discount rate, $C_{INS}^{rins}(t)$ is regular inspection cost at time t, $C_{INS}^{pins}(t)$ is precise inspection cost at time t, $C_{INS}^{psdia}(t)$ is precise safety diagnosis cost at time t, $C_{MAI}^{C-grade}(t)$ is maintenance cost distribution when mean(μ_1) slope reaches C grade, and $P_{MAI}^{C-grade}(t)$ is probability distribution of maintenance when mean(μ_1) slope reaches C grade. The steel girder cost of maintenance function (In this case only) is shown in Figure 6.

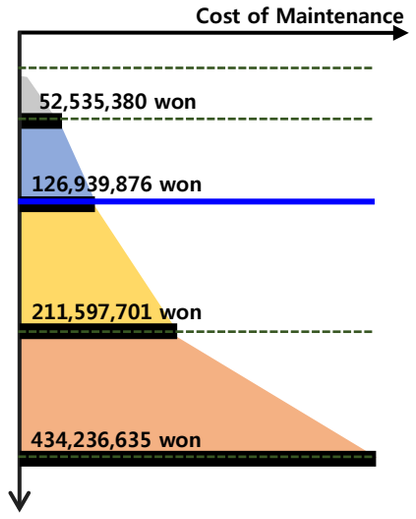


Figure 6. The steel girder cost of maintenance function.

Such as above information, it is possible to calculate each maintenance cost at time t (31years) by case.

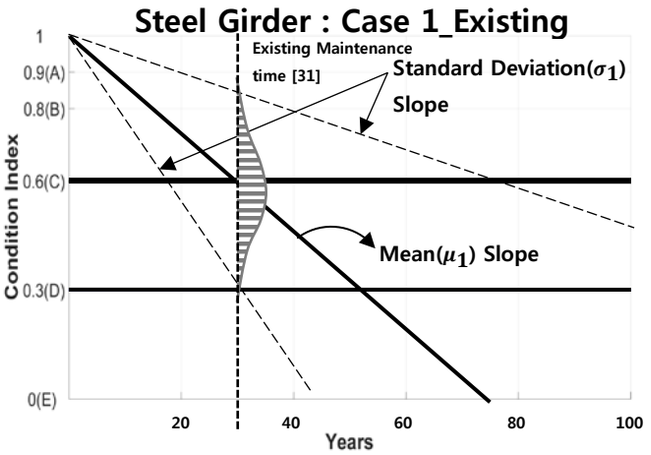


Figure 7. Existing condition index model for steel girder

And compare to existing case $C_{MAI,existing}^{Total}(31)$ (Figure 7.), it is possible to predict about 15% cost savings in case 1.

Through cost analysis by case, it shows that the more quality of the inspection is good, the more cost efficiency of the total maintenance is higher.

That is, by reducing the uncertainty of probability distribution at specific time(t) through Bayesian updating, matching cost of maintenance areas are decreased.

4 CONCLUSION

This study propose the methods of updating existing LCP models of the bridge elements by using the result of the inspection. In reliability analysis and cost efficiency of inspection, if condition is poor compared with the initial predicted condition, the probability of failure is increased as a result cost of failure is increased. Even though the result about condition from bridge inspection is presented worse than prediction, the execution of bridge inspection should be done because the supervisor can estimate the bridge condition and sets maintenance scenario for safety of bridge until the target bridge life. If researchers can use the real damage detection data and errors of inspection method, these result would be more reasonable and powerful.

In further study, considering the optimal maintenance algorithm would be updated for helping decision-making.

5 ACKNOWLEDGEMENT

This research was supported by a grant(13SCIPA01) from Smart Civil Infrastructure Research Program funded by Ministry of Land, Infrastructure and Transport(MOLIT) of Korea government and Korea Agency for Infrastructure Technology Advancement(KAIA).

6 REFERENCES

Ang, A., W. Tang., 2007. Probability concepts in Engineering : Emphasis on applications in Civil & Environmental Engineering. Wiley.

Cha, K.H., Kim, S.W., Kim, J.H., Park, M.Y. & Kong, J.S., 2015. Development of the deterioration Models for the port structures by the multiple regression analysis and Markov Chain. Journal of Computational Structural Engineering Institute of Korea, 28(3): 229-239.

C. Xing, M. Van Kerhove, R. Caspeele & L. Taerwe, 2017. Use of Bayesian updating of time-dependent performance indicators for prediction of structural lifetime and critical inspection points in time, The Fifth International Symposium on Lifecycle Engineering..

Frangopol, D.M., Neves, L.C., 2008. Structural performance updating and optimization with conflicting objectives under uncertainty. Structures Congress-Crossing Borders.

Lee, J.H., Cha, K.H., Ahn. S.M., Kong, J.S., 2017. Updating Life-Cycle Performance Model of Bridge based on Inspection Data, 39th IABSE(International Association for Bridge & Structural Engineering) SYMPOSIUM, 19-23 September 2017:300-303. Vancouver, Canada.

Lee, J.H., Lee, K.Y., Ahn, S.M., Kong, J.S., 2017. Development of Bridge Maintenance Scenario Model using Bayesian Approach, Korean Society of Civil Engineers, 18-20 October 2017:35-36. Busan, Korea.

Park, K.H., Kong, J.S., Hwang, Y.K., Cho, H.N., 2006. Development of Bridge Maintenance Method based on Life-Cycle Performance and Cost, Korean Society of Civil Engineers, 26(6): 1023-1032

Maintenance, Safety, Risk, Management and Life-Cycle Performance of Bridges – Powers, Frangopol, Al-Mahaidi & Caprani (Eds)
© 2018 Taylor & Francis Group, London, ISBN 978-1-138-73045-8

Development and implementation of digital bridge management systems in the Gulf region

D.E. Moore
Qatar Country Manager, Aurecon
S. Naelini
Managing Director, AMX Solutions

ABSTRACT: The dramatic expansion of road and rail infrastructure in the Gulf region serves as a barometer for the rapid economic growth that has taken place in the region since 2006. Until 1999, there were approximately 40 operational bridges in the Emirate of Dubai and since then more than 400 new bridges have been constructed and brought into service. Similar stories can be told for Abu Dhabi and Qatar. Although few in number, aging road infrastructure also needs to be maintained, such as the Shindagha Tunnel (ca. 1975) and Maktoum Bridge (ca. 1963) in Dubai, which serve as critical transportation links in the community. This paper describes the modules of the bridge management systems developed for these Gulf states, including the inspection rating system and calculations for estimating asset condition and prioritizing repairs. We touch upon the lessons learnt in developing systems, future developments and the need for bridge management systems to be adaptable in order to remain relevant to business operations and asset managers.

1 INTRODUCTION

1.1 *The need for a digital BMS*

Over the last two decades, cities in the Gulf region have experienced a construction boom in buildings, aviation and transportation infrastructure. Up until 1999 there were approximately 40 operational bridges in the Emirate of Dubai and since then more than 400 road bridges have been built and opened. Similarly in Qatar, there are currently 200 operational bridges, with future expansion set to provide more than 1000 bridges over the next 5 years.

Due to the rapid expansion in physical infrastructure and improvements in technology, government authorities in the Gulf are increasingly looking for ways to create efficiencies in managing maintenance activities, integrate bridge maintenance with other enterprise systems, and maximize the value of maintenance spending.

Traditional, paper-based methods of maintaining infrastructure are no longer viable. Governments now expect digital tools which leverage information and communication technology (ICT) and which are aligned with the country's digital strategy for economic improvement (Qatar General Secretariat of Development Planning. 2011). An integrated digital asset management system is an asset management tool which will help to meet these objectives.

1.2 *Diversity of Structures*

Road structures and assets in the Gulf region are extremely varied and therefore any asset management solution needs to be highly flexible and adaptable.

A single asset management solution is needed to manage a variety of structure types for different government departments. Typical road assets in the Gulf region include concrete and steel bridges, bascule bridges, cable stay bridges, floating concrete pontoon bridges, a variety of footbridge types, long tunnels and underpasses, and camel crossings. Other structure types include wharf structures, pump stations, fountains, as well as street furniture and lighting.

The maintenance of electromechanical systems for transportation assets also needs to be addressed in a single asset management system.

Since electromechanical systems are inspected and maintained differently to structural systems, this can be challenging to implement in one BMS.

1.3 *Regional considerations*

Another point to note in the development of asset management systems in the Gulf is that structures in the region typically have to contend with severe exposure conditions. Summer in the Gulf is extremely hot and humid, with temperatures reaching 45 degrees C and a humidity of 90%. Ground investigations have also found that the soil is comprised almost

entirely of crushed shells and sea coral, making the groundwater highly saline and the concentrations of chlorides and sulfates extremely high (Sherif, 2011).
The extreme environmental conditions in which road assets are constructed means that design standards and details are often different to those used in Europe and other parts of the world. Concrete structures are designed to have very small crack widths to help prevent carbonation and ingress of chloride ions. This often means that steel reinforcement quantities in concrete structures are higher, with an increased concrete cover to reinforcement. Exposed concrete surfaces are also often coated with multi-part coating systems which are designed to help prevent ingress of carbons and chlorides through the concrete surface.
For the inspector, a coating on the exposed concrete surface makes it difficult to interpret the true condition of the concrete underneath. In addition, the inspector needs to be familiar with the Gulf design standards and the impact this may have on interpreting the defects which have been identified. The BMS also needs to be customized in consideration of the design and construction methodologies in the Gulf, to take account of the repair methods and procedures used by local authorities and contractors.

2 SYSTEM MODULES

2.1 *Internal integration*

For a BMS to function efficiently, system modules need to be integrated internally to minimize duplication and user inputs, and to achieve optimal performance in line with effective operational asset management.
The inventory module is considered to be the foundation off which the rest of the BMS operates. Inventory contains data on the elements of the asset, which is effectively a digital version of the physical asset. The inventory drives the rest of the BMS modules.
The inspection module is derived from the inventory module. The digital elements of the asset are pushed into the inspection module to form the basis of the inspection sheet. Inspection ratings are allocated to asset elements and sub-elements. The inspection rating procedure and methodology need to be robust and relevant to scoring of defects assigned to the asset sub-elements, in order to calculate structural condition and prioritize the repair of defects.
System calculations need to be tailored to be relevant to the business enterprise, which will calculate condition and prioritize repairs in accordance with business requirements.
Cost of works need to be estimated based on enterprise rates, or bill of quantities, so that estimated costs are relevant to the government authority implementing the BMS.
Finally, the rating and condition of sub-elements, defects and cost of repairs, all need to be linked back to the inventory module for a complete integration.
The following sections describe the system modules in detail.

2.2 *System dashboard*

It is important that the BMS has a customizable dashboard displaying summary information for the user, and to provide quick links to relevant modules. The dashboard should display information such as the last structure accessed by the user, including Structural Condition Index (SCI), lists of structure types, GIS map information and quick-access links to reports, charts and filters.
From the dashboard the user should be able to quickly find relevant information for his daily work and access other modules.
The dashboard display and content should be user role based to streamline operational requirements and system navigation.

2.3 *Inventory Module*

Establishment of the inventory database is crucial for integration with all other BMS modules, and forms the foundation off which the other modules operate. The inventory framework drives the inspection elements, the condition calculations, the prioritization of structures and ultimately the works management.
The inventory module is structured to contain the asset types applicable to the government authority, such as bridges, tunnels, underpasses, footbridges, etc. At this point, the user needs to map elements and sub-elements for each of the asset types, similar to the way an asset would be categorized in a BIM (Building Information Model).
The inventory module also captures details such as general photographs, location information, contact information, ancillary elements and electromechanical equipment related to the asset.
The elements and sub-elements contained in the inventory module brought into the inspection module, which effectively creates a unique inspection form for each individual structure, and stays with that structure until alterations warrant a new or modified element or sub-element mapping. A typical breakdown of elements and sub-elements is shown in Table 1.
The BMS contains a standard list of sub-elements per element, according to the unique structure type, which automates the input of the structure sub-elements. If a sub-element is not relevant to a particular structure, then a quantity of zero is allocated or not included.

Table 1. Examples elements and sub-elements for a typical bridge structure.

Location	Element	Sub-element
Approach	North approach	Embankment
		Retaining walls
		Road surface
Superstructure	Span 1	Deck
		Girders / Beams
		Traffic barriers
Substructure	North abutment	Front wall
		Bearing seat
		Bearings
		Expansion joint

Sub-elements are measured to correlate with the inspections methodology, which is generally in m^2 for exposed surface areas, linear meters for expansion joints and a unit count for items such as bearings.

2.4 *Inspection Module*

Past or future inspections are scheduled in the inspection module, as a General Inspection, Principle Inspection or an Electromechanical inspection. The inspection is created in the system by the user and a unique reference number is generated by the system.
Structure elements and sub-elements are imported from the inventory module. Sub-elements are rated by the inspector according to the DERU (Degree, Extent, Relevancy and Urgency) scoring methodology, which is described in detail in the next section.
Defect ratings are input primarily through the inspection summary screen, which is a tabulated representation of the asset sub-elements. The values of degree, extent and relevancy are entered into the table for each sub-element. A color-coding aligned with the value of relevancy (green, amber and red) gives the user a visual sense of the overall condition of the structure.
At this stage the inspector also inputs the description of the defect, along with photographs and an estimation of the urgency (maximum timeframe) to repair the defect. The work required to repair the defect back to "as-new" condition is also estimated at this stage by the inspector, via a Bill of Quantities in the system library.

2.5 *Works management*

In the BMS, 'works' refers to identified work that needs to be carried out on assets. This work is necessary in order to ensure the structures operate in a safe manner and provide the required level of service to the road network users.
Generally, works are identified during the condition inspection of structures and are primarily repair works that eliminate identified defects and restore structure elements to the original, or as-new working condition.
Works may also arise from the need to upgrade the structure, such as widening or strengthening, to provide the required level of service.
Further, works may arise from taking preventative measures to ensure longer service life of structures is achieved at low cost to the users.
In all of the above-mentioned cases, and regardless of the source, all identified works are added to the BMS 'Work Bank' either as part of the inspection data or as an individual work item added to each structure.
A comprehensive, objective and time-based prioritization process is applied to all works in the BMS, which ensures the works management team schedules maintenance works objectively and in line with corporate policies of the maintaining authority.

2.6 *Budget module*

The BMS budget module is designed to ensure budget allocation and expenditure are monitored as works are planned and performed on the assets.
In the region, it is quite common to have multiple maintenance contracts in place to carry out routine and preventative work on groups or even individual structures. Each maintenance contract needs to be budgeted and monitored and, most importantly, accommodate variations during contract period.
The budget module presents the expenditure profile of each maintenance contract across all types of works such as accidents, preventative, special requests and any other. It also manages multiple budget sources such as additional budget allocation for special events or unforeseen events such as major bridge strikes.
The budget module, while allowing each contract to be monitored and managed separately, also presents a comprehensive budgetary performance across all contracts to illustrate authority's overall performance.
Generally due to budget constraints, not all planned works are carried out as intended and while maintenance works are carried out new, and sometimes very urgent, works are identified either from inspections or even during maintenance works.
The BMS budget module accommodates unforeseen and new works and reallocates works across multiple years dynamically.

2.7 *Deterioration module and Life Cycle Costing*

Life cycle costing (LCC) utilizes deterioration models that are assigned at sub-element level. There is a library of deterioration models for materials types such as concrete or steel, and for components such bearings and expansion joints. Users can modify existing or add new deterioration models to the library as required. Each model has a number of performance strategies that are linked to service levels and trigger maintenance works.

Based on the BMS inventory and system customization, each structure type sub-element inherits a deterioration model and is analyzed for the duration of the life cycle analysis. Sub-element projected conditions are presented together with works identified during the analysis. Overall asset condition is then calculated and compared for various maintenance strategies with actual asset conditions from inspection history also superimposed.
A monitoring regime is in place to compare actual maintenance works with that predicted for each maintenance strategy from the LCC analysis. This will allow users to compare and improve the LCC analysis at asset level.

3 INSPECTION RATING PROCEDURE

3.1 *DERU Inspection Rating Procedure*

A simple yet robust inspection rating procedure, and the accurate capture of inspection information, is the foundation of a good Bridge Management System. For the Dubai BMMS the DERU (degree-extent-relevancy-urgency) procedure has been adopted. Inspection forms are created from the inventory module, which minimizes the risk of not capturing important inspection data in the field.
The DERU rating procedure is based the DER rating system (degree-extent-relevancy), as documented by de Fleuriot et al. (1995), with the later addition of urgency by Nordengen et al. (2000).
The DERU procedure forces the inspector to focus on each characteristic of the defect at a time, eliminating the need to combine defect characteristics (for example degree and relevancy) and applying one score for both characteristics. De Fleuriot (1995) considers that the DER procedure results in more precise inspection information being captured, and thereby a more accurate determination of overall condition.
The DERU is defined as:

- D refers to the Degree of severity (how bad is the defect?)
- E refers to the Extent of the defect (how common is the defect or what percentage of the sub-element is affected?)
- R refers to the Relevancy of the defect (what is the effect on structural integrity and safety of the user?)
- U refers to the Urgency to carry out the remedial work to repair the defect, measured as a time limit (when does it need to be repaired?).

The relevancy rating is considered the most important rating (Moore et al. 2011). The relevancy rating coerces the inspector to review the defect while considering the consequences of the defect concerning the safety and serviceability of the system as a whole. For example, identical defects may be present at two locations on an asset; for example, severe concrete cracking on the bridge approach retaining wall as well as to the bridge deck soffit at mid-span. While the defect may be the same the relevancy of these defects differs, while the degree and extent of the defects may be identical. A higher relevancy score forces the defect to be prioritized over defects of the same severity level.
The degree and relevancy ratings are based on a five-point system, from 0 (no defect) to 4 (most severe). Limits are defined for degree based on the relevancy rating; degree can be greater than, but never be less than the relevancy rating. It is possible to have a very severe defect which has a low relevancy to the overall integrity of the structure, however a defect with a high relevancy, which may impact structural integrity or safety to users, should not be rated as having a low degree of severity.
The extent rating takes consideration of how common the defect is on the given sub-element, and is generally expressed as a percentage of the sub-element area or unit.
The urgency rating is also a five-point rating, from 0 (routine maintenance) to 4 (should be repaired as soon as possible, within the next 12 months). The urgency rating is based on the inspector's view on the maximum timeframe of when the defect should be repaired, considering probable future events.

3.2 *System calculations*

Based on the DERU ratings provided in the inspection module, the BMS calculates the following indices:

- Structural Condition Index (SCI)
- Priority Index (PI)
- Relevancy Index (RI)

These indices are used to rank structures in different ways and we find that using a combination of indices provides the best results when prioritizing repairs to assets.

3.2.1 *Structural Condition Index (SCI)*

The structural condition index (SCI) is provides an estimation on the overall condition of the asset and is measured as a percentage. SCI is the weighted summation of the condition of all the sub-elements on a particular asset and provides an average condition for the structure.
The sub-element condition index *Icii* and is calculated for all sub-elements of the structure as follows:

$$Icii = 100 - \frac{100\left(D+\frac{E}{25}\right)R}{32} \quad (1)$$

where D = degree; R = relevancy; and E = extent.

The value of 25 is used to normalize the extent rating back to a value of 4 when $E = 100\%$, and the value of 32 is used to normalize the equation overall; i.e. $(D_{max}+E_{max})R_{max} = (4+4)4 = 32$.
The result of *Icii* is given as an integer between 0 and 100. The division condition index *Ici* is calculated as the weighted average of all sub-elements:

$$Ici = \sum_{i=0}^{n} IciiWi \,/\, \sum Wi \qquad (2)$$

where W = the weighting given to sub-elements based on perceived importance, as a five-point scale.

The structural condition index SCI is calculated as:

$$SCI = \sum_{i=0}^{n} Ici/n \qquad (3)$$

where n = total number of divisions assigned to the structure. The result of the SCI calculation is an integer number between 0 and 100.
One disadvantage of the structural condition index is that for larger and more complex assets which contain many sub-elements, the averaging of the conditions across all elements may cause critical defects to be lost in in the overall SCI.

3.2.2 *Priority Index (PI)*

The priority index (PI) is used to rank assets in order of defect criticality and is based on a modified *Icii* for each asset sub-element condition. Each sub-element is placed into a range according to the *Icii* condition rating of that sub-element. Four ranges are available and are defined as *Icii* of less than 50 (poor), between 51 and 74 (warning), between 75 and 99 (acceptable) and 100 (excellent).
A series of calculations are performed whereby the priority index is anchored by the lowest *Icii* sub-element condition rating of the asset and the higher *Icii* ratings are weighted downwards to make them less relevant in the overall calculation.
The aim of the priority index is to amplify the asset sub-elements which are considered to be in a critical condition, reducing the effects of averaging the condition of the asset, which occurs in the SCI calculation. The outcome of the priority index calculation is that structures with a higher number of *poor* or *warning* sub-element conditions will obtain a higher priority index than those with relatively few poor condition ratings and a higher number of less severe sub-element conditions.
The result of the priority index calculation is an integer number between 0 and 100.

3.2.3 *Relevancy Index (RI)*

The relevancy index is another method of ranking structures with a focus on the relevancy ratings for each sub-element of the asset. One disadvantage in using this method is that the relevancy index score is not capped to any range and it is not possible to give the asset an effective score out of one hundred, making it difficult to monitor the asset's deterioration over time. The index is used to rank assets in a network in relation to one another.
The relevancy index is calculated by counting the number of R = 4, R = 3, R = 2 and R = 1, then ranking the structures in that order. The structures with higher numbers of high relevancy ratings will have a higher relevancy index. This is a simple but effective approach to prioritizing structures.

3.3 *Combining Indices*

The system user can employ a single index or a combination of indices to determine an overall prioritization of works. The user should first examine the results derived from each index and determine which index provides the result which best suit the desired outcomes and preference. The prioritization of defects then feeds into the annual maintenance budgets. From our experience across government authorities in the Gulf region we generally recommend the following combination and order of indices:

1. Structure Priority Index rating (PI) rating
2. Sub-element Relevancy Index rating (RI)
3. Sub-element urgency rating (U)

We have found that the overall Structure Condition Index (SCI) is generally not a good indicator of priority for the repair of defects, since the averaging of sub-element conditions over the structure tends to reduce the impact of high criticality defects.

4 SYSTEM SOFTWARE

The bridge management systems implemented in the Gulf region began as desktop versions. Through user interaction and feedback, as well as a measure to make the system future ready, the desktop versions were developed into web-based asset management systems to accommodate all the operational business processes including integration with other corporate systems.
Detailed quality control and assurance approvals were implemented both for inspection and for work ordering business processes. Corporate GIS map services are also consumed on both PCs and Android mobile devices.

4.1 *System architecture*

High level system architecture is presented in Figure 1 below.

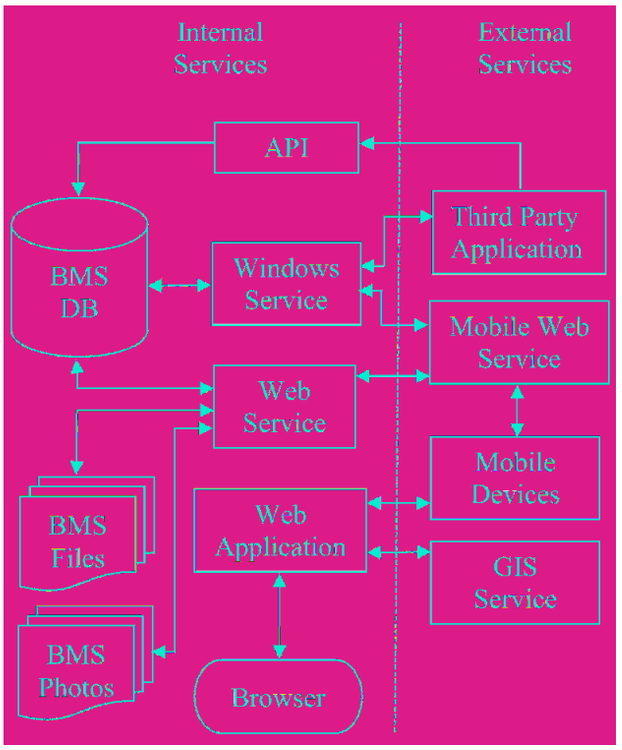


Figure 1. BMS system architecture.

A number of servers are in place delivering system operations in line with client's IT governance policies.

4.2 *Web-based system*

Using a web-based solution allows the user to access the BMS from any computer with internet access. Previously, desktop systems were based on Microsoft Windows platforms but this can be cumbersome to manage for information technology departments. A web-based system allows tailoring of a multitude of security and system maintenance requirements and maintenance of all asset management needs. The look and feel of a web-based system can be adapted to particular design requirements and remains responsive under all operational scenarios.

4.3 *Separation of structural and electromechanical systems*

As new construction methods, materials and equipment are incorporated into new assets, maintaining authorities are faced with unique challenges in the maintenance management of both structural and electromechanical systems. The management of structures and electromechanical systems should be handled separately, ideally by splitting them into two distinct modules. Independent inventory, inspection and maintenance processes should be developed for both, then recombined at the reporting level to deliver a unified approach to management operations.

4.4 *Integration with other enterprise systems*

Using multiple software systems is commonplace in large government departments and seamless integration between them is essential to delivering correct contextual information and avoiding data duplication. Government authorities in the Gulf region are typically implementing advanced enterprise architecture solutions in order to provide a single enterprise integration platform. The enterprise service bus (ESB) provides a means of communication between interacting software applications. It is essential that a modern asset management system be able to integrate rapidly and safely across multiple data resources.
Through the ESB the BMS is able to integrate with other enterprise systems such as IBM Maximo for works execution and management, enterprise GIS services, electronic document management systems and other specialized systems such as abnormal loads management systems.

4.5 *Mobile Inspection devices*

An effective BMS allows field staff to use mobile devices for inventory and inspection data collection. Allowing field data to be downloaded and uploaded via mobile devices minimizes inspectors' time in the office, reduces error, as well as allowing for the faster identification of any potential safety concern.
Dedicated BMS web services are in place to facilitate all data exchanges between BMS database and the field devices. Mobile devices must continue to function without internet connection and seamlessly update as soon as connection is reestablished. Multi factor authentication confirm user identities and complies with client's security policies.

5 LESSONS LEARNED

While highway asset management processes are the core requirements of a BMS, efficient delivery of these processes is of paramount importance in ensuring optimum use of available resources.
Through our experience in developing and implementing bridge management systems in the region, we have come to learn the importance of implementing a BMS that is client-operations focused, aligned with best asset management practices. The system must be adaptable to future business process, which may be envisaged by the client, but not yet implemented. Government departments are looking to continuously improve performance across all levels of operation and they are looking for a BMS that will

assist in delivering the key performance indicators established by the organization.
We have also learned that early stakeholder engagement and change management advisory services are critical success factors when developing and implementing a new asset management system into an existing organization. The implementation of a BMS will impact on a broad range of stakeholders inside and outside the maintaining authority, including other departments, senior management, inspectors and contractors. Any one of these stakeholder could derail the implementation process if they have not been included in the engagement process.
Similarly the authority will certainly undergo some form of internal change with respect to workflows, roles and organizational structure. The early recognition of these changes is important for a successful implementation of a BMS.

6 FUTURE DEVELOPMENTS

6.1 *Building Information Modelling (BIM)*

Future developments for the BMS include the adoption of Building Information Modelling (BIM) as an enhancement to the graphical user interface. A BIM is a 3D graphical model, or intelligent digital version of a physical thing, which can be assigned metadata, or attributes and information, regarding particular model sub-elements.
We envisage that the BIM of an asset will be created or imported into the BMS and the inventory sub-elements will be linked to the corresponding sub-elements of the BIM. In order to make the BMS future ready, the sub-elements in the inventory module need to be designated and assigned attributes while keeping in mind that BIM will one day be incorporated. Eventually the inventory module will be populated simply by importing the BIM into the BMS, which contains all of the correct divisions and attributes needed for the BMS to function.
The benefits of making the step to integrate BIM into the BMS are many. The user experience will be enhanced by seeing the virtual asset in 3D and having the ability to examine elements of the structure or system in a visual way. Defects can be displayed on the digital structure, providing the user with an overview not possible in a data table. Commentators such as McGuire et al (2016) also note that BIM is an effective tool in facilitating the inspection and evaluation of bridges.
The adoption of BIM into BMS is to ultimately provide a reality context to the user in using the right maintenance decisions (Moore et al. 2017).

7 CONCLUSIONS

In a world that is continuously changing, and changing at an ever-increasing rate, improvement to business operations is a perpetual process as is improvement to the asset management systems that facilities short and long term operational planning.
It is imperative that BMS applications remain adoptable and relevant well into the future, which serve to maintain operational continuity and promote operation improvements.
Digital asset management systems must be built on system architecture that can adapt to change and remain relevant into the future. In addition, the inspection rating systems and calculations performed in the BMS for condition and prioritization must be robust and reliable.
The asset management systems implemented in the Gulf region have been designed and customized with these attributes in mind in order to meet client expectations. Future developments in the BIM interface are the next step in the digital evolution of BMS applications in the region.

8 REFERENCES

de Fleuriot, E., Nordengen, P.A., Li, Y-F. & Lin.A-Y. 1995. A bridge management system for the Taiwan area national freeway bureau (TANFB). International Symposium in Hong Kong, October 1995.

El-Sayed M.S. 2011. Corrosion and Corrosion Inhibition of Aluminum in Arabian Gulf Seawater and Sodium Chloride Solutions by 3-Amino-5-Mercapto-1,2,4-Triazole, International Journal of Electrochemical Science, Vol. 6: 1479–1492.

McGuire, B., Atadero, R. et al. 2016. Bridge Information Modeling for Inspection and Evaluation. Journal of Bridge Engineering (ASCE), 21(4).

Moore, D., Refaat, M., de Fleuriot, E. & Nordengen P. 2011. Implementation of a bridge management system for Dubai, United Arab Emirates. 8th Austroads Bridge Conference, Sydney, Australia.

Moore, D., Naelini, S. 2017. Digital Evolution of Bridge Management Systems in the Gulf Region. 10th Austroads Bridge Conference, Melbourne, Australia.

Nordengen, P.A., Welthagen D., de Fleuriot, E. 2000. A bridge management system for the South African National Road Agency. Bridge Management Four – Inspection, Maintenance, Assessment and Repair, pp.38-46.

Qatar General Secretariat of Development Planning. June 2011. Qatar National Development Strategy 2011 ~ 2016. Qatar

Maintenance, Safety, Risk, Management and Life-Cycle Performance of Bridges – Powers, Frangopol, Al-Mahaidi & Caprani (Eds)
© 2018 Taylor & Francis Group, London, ISBN 978-1-138-73045-8

Research on Bridge Management System Based on BIM Technology

Y.D. Qin & R.C. Xiao
Department of bridge engineering, Tongji University, Shanghai, China

ABSTRACT: To promote the efficiency of bridge management work, the advanced BIM technology is applied in bridge management system (BMS), and thus the life cycle performance of bridge structure could improve. In the process of establishing the BMS based on BIM, the first step is to parameterize the bridge structure information during its whole life cycle, including geometric and physical information, load information, detection information, evaluation information and maintenance information of bridge. Then the logical relationships between the parameters are analyzed, and the BIM model used for bridge management is built. The BIM model in design stage contains structural static information and load information, with extensible information schema. The information in the design model is inherited and developed by the one in the construction stage. This model is more accurate because the component model is modified according to the manufacturing process, and the structure model is modified according to construction monitoring data. Finally, the as-built BIM model is close to the practical structure and is used as the BIM model in the maintenance and management stage. The durability of the bridge is precisely evaluated in BIM model combined with data of the structural health monitoring system and the bridge structural technical condition inspection results. Moreover, the maintenance plan could be simulated and tested in the BIM model. This new BMS could guide the bridge structural rehabilitation work more effectively and economically. The bridge management system based on BIM technology enables collaborative management of life-cycle information of bridge, and thus allocate manpower, material and financial resources with high efficiency.

1 INRODUCTION

Bridges suffer deterioration problems caused by the initial defects, the deterioration of natural conditions, the vehicle overload, etc., during the operation stage. So reasonable management and maintenance are needed to improve the life cycle performance (Frangopol and Liu, 2007). It is commonly believed that the bridge management system (BMS) is one of the best measures to improve the life-cycle performance of bridge due to the success of several BMS, such as the AASHTOWare Bridge Management (formerly named PONTIS) in the USA (Golabi and Shepard, 1997). Another BMS in the USA, the BRIDGIT, was developed under the AASHTO-sponsored National Cooperative Highway Research Program (Hawk, 1999). Japan developed the J-BMS for damaged concrete bridges (Miyamoto and Motoshita, 2015). In addition, Switzerland, Arabia, the United Arab Emirates, Sweden, Italy, Turkey and other countries have also developed their BMS according to local bridge management situation (Hajdin, 2004, Yehia et al., 2012, Safi et al., 2013, Fruguglietti et al., 2014, Akgul, 2016).

The rapid development of information technology provides the bridge management system with technical support for upgrading. The combination of civil engineering and information technology is Building Information Modeling (BIM), which manages the whole process of design, construction, and operation of building project efficiently through the digital description of physical and functional characteristics of structural components. To share all kinds of information across architecture, engineering, construction, and owner-operator industries, the interoperability of exchanging information is the base for BIM technology (Steel et al., 2010). IFC (Industry Foundation Classes) is the most widely adopted BIM data format standard at this moment (Solihin et al., 2016).

In analogy to BIM, bridge information modeling (BrIM) is introduced for design, construction, maintenance and operation of bridges (Chen and Shirole, 2006). The first step of establishing BrIM model is the 3D spatial model. Ji proposed a data format based on IFC to describe complex geometric

information of bridge, but this method can only be used in the bridge design stage (Ji et al., 2013). Karaman *et al.* suggest a 3D geometric representation of highway bridge for design and construction stages (Karaman et al., 2013). Ali studied the application of BIM technology in concrete and bridge parametric design model of the beam, bridge deck, and bearing (Ali et al., 2014). Nagarajan investigated and developed the XML format for steel bridge design and construction work (Nagarajan, 2010). Furthermore, Hu deepened Nagarajan's work by establish an efficient and extensible data exchange protocol to exchange bridge data, which is called OpenBrIM (Hu, 2014).

However, the application of BIM/BrIM in operation and maintenance stage is less than that in design or construction stage. Yalcinkaya applied latent semantic analysis to the abstract of 975 academic articles, and the results revealed that researches related to maintaining and managing are less than 10% (Yalcinkaya and Singh, 2015).

If BrIM technology is introduced into bridge operation work, the sharing and integration of monitoring and inspection information would improve the efficiency of bridge management and maintenance work. Jeong proposed a BrIM framework for supporting bridge monitoring and management applications (Jeong et al., 2017b). This framework is based on attempts of introducing emerging information technology into bridge monitoring, such as NoSQL database (Jeong et al., 2016b) to handle time-series data and unstructured bridge information, and cloud-based platform (Jeong et al., 2017c) to store and process enormous volume of data such as sensor information and traffic video images. The formation of BMS based on BIM technology is of great significance for the improvement of life cycle performance of bridges. The main content of this paper is the function modules of BMS based on BIM and brief research framework of combining BIM and BMS.

2 BRIDGE MANAGEMENT SYSTEM

2.1 *The development of BMS*

Bridge management work includes structural inspection and monitoring, performance evaluation, and maintenance and repair in operation phase. BMS is a comprehensive system related to bridge engineering, disease mechanism, detection technology, data acquisition technology, geographic information system (GIS) technology.

In 1988, the Federal Highway Administration of US developed the first BMS in the world, the National Bridge Inventory (NBI) database (Small et al., 1999). NBIS collected and maintained inspection information and gave appraisal ratings for allocating federal funds. After the success of NBI, the Federal Highway Administration developed the PONTIS bridge management system. In PONTIS BMS, bridges are described as sets of elements, such as decks, beams, bearings, columns, etc. The data format of these elements are developed by several State highway agencies and the Federal Highway Administration so that the information could be shared across agencies and bridge management systems (Fruguglietti et al., 2012). The PONTIS bridge management system supports network-level and project-level decision making on the condition and functional obsolescence of bridges (Inkoom et al., 2017). Another BMS in the USA is the BRIDGIT, which has many similarities with PONTIS (Hawk, 1999).

The development of bridge management system in China began in the mid-1980s. The CBMS developed by the Ministry of Transportation Highway of China contained 4 databases and 7 subsystems. The 4 databases are bridge static information database, dynamic information database, document database and evaluation decision database, and the 7 subsystems provide different functions such as analytic hierarchy process evaluation, cost analysis, statistical analysis, maintenance plan, etc.

The Tongji University has developed the urban bridge management system of Shanghai, which includes six function modules, which are the geographic information module, the file management module, bridge monitoring module, technical condition evaluation module, maintenance countermeasure module and heavy vehicle route plan module.

2.2 *The function modules of BMS*

The function of BMS depends on the requirement of the agencies of highway management. Take the urban bridge management system of Shanghai as an example to introduce the typical function modules of BMS.

2.2.1 *Database Module*

The bridge database is used for the storage, query, modification, and analysis of static and dynamic information of the bridge, such as the structural dimensions, material properties, inspection information, evaluation data, maintenance history, etc.

It is the cornerstone of BMS that it determines the reliability and availability of bridge management system.

2.2.2 *Evaluation Module*

The core function of BMS is the evaluation of bridge technical condition. Using the analytic hierarchy process (AHP) and the variable weight assessment method, the bridge condition is evaluated with appropriate indexes according to collected inspection and monitoring data. Moreover, the structural health monitoring system is integrated to realize forecast-

ing function. According to the results of evaluation, the bridge technical performance trend could be further predicted.

2.2.3 *Prediction Module*

This module aims to predict the deterioration trend of bridge technical condition. The theory of time series analysis is brought in to establish seasonal prediction model based on monitoring data. The prediction result simulates structural degradation trends and forecast critical moment, and then clarifies the demand for bridge maintenance and repair plan.

2.2.4 *Maintenance Plan Module*

The BMS can provide maintenance plan decision support. At the project level, the bridge maintenance plan decision is based on the damage inspection, monitoring data and the prediction model. The maintenance plan module selects appropriate management measures, including maintenance, repair, reinforcement, and even reconstruction. At the network level, that is to determine the maintenance priority of the bridges and the funds allocating based on the severity of bridge technical condition, the urgency of repair and the amount of disposable funds.

2.2.5 *Auxiliary functions*

The BMS provides the administrative departments with some specific functions required to improve the applicability. For example, the file management module stores drawings, photographs and other related documents of bridge projects. The GIS module displays geographic data visually. The mobile technology assists the field man in the query and input of information.

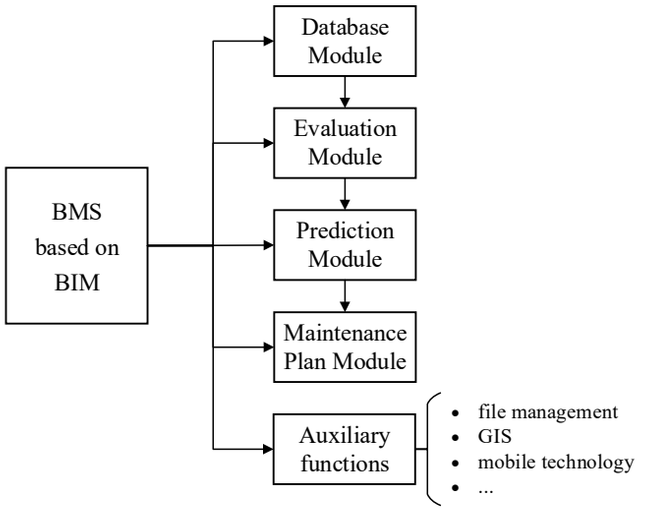


Figure 1. Function modules of BMS.

2.3 *Technology to be improved*

However, due to various reasons, the BMS does not play its proper role in the process of bridge management at the present stage. Firstly, the bridge condition is not simulated accurately because the tedious bridge data input work is manual in many cases and different types of information are processed by isolated systems of design, construction, and operation. This results in a lack of consistency of data exchange because the data source is not traceable. Secondly, the current evaluation method is experience-based, and thus it is subjective to a large extent. At last, the authorities lack preventive maintenance measures for bridges. Before the repair or reinforcement work is carried out, the bridge damage has happened.

To sum up, the core problem of current BMS is the unavailability of necessary data during the lifecycle of the bridge. The prerequisite of the success of bridge management work is a comprehensive description of the bridge structure, including construction conditions, structural geometric and physical data, design standards, etc.

To obtain and integrate all the information needed for bridge management, it is necessary for BMS to collect and update information from all date source automatically, instead of inefficient and imprecise manually input. After that, BMS establishes static and dynamic information database of the bridge. The static information refers to the information that is unchangeable after the bridge is built, such as the geometry dimension and material properties, etc. The dynamic information refers to that related to time, including the load data, the structural damage type and location, and health monitoring data, etc. Only if the static and dynamic information database of the bridge is built, the goals of other functions in BMS could be achieved.

3 BRIDGE MANAGEMENT SYSTEM BASED ON BIM TECHNOLOGY

As for the evaluation, prediction and decision support function, the basis is a comprehensive database of the bridge. There are some limitations in the current information management of BMS. The solution to this problem is the application of BIM technology to establish a life cycle integrated information database.

To create such a BIM-based database, the first step is to parameterize the bridge structural and non-structural information and develop the logical relationship among the parameters, including structural geometry and physical information, load information, detection information, monitoring information, evaluation information, and maintenance information in design, construction and operation stages.

3.1 *In design stage*

The BIM model in design stage mainly contains structural geometry information, physical information, and load information. The typical data model in design is the finite element model used for the calculation and analysis, and the CAD drawings of the project.

Firstly, the proper encoding method of components of the bridge structure is designed. So, both the bridge structural and non-structural components are identified into reasonable hierarchy levels. After the component is numbered, the geometric model is created by the bridge designers. The bridge structure is different from the traditional architecture as the locating axis of a bridge is usually spatial curved and the section type is more complex and variable. Because the bridge structure is suitable for parametric design, at present, we are working on a parametric design method in which the bridge structure is divided into the three layers of axis, form, and component.

3.2 *In construction stage*

The BIM model in construction stage inherits from and deepens that in design.

On the one hand, the BIM model LOD (level of details) is increased according to the component manufacturing process as the prefabrication technology has been widely used in civil engineering. The bridge BIM model get information from the component model used by the factory and integrates the manufacturing data. On the other hand, as for the whole structure of the bridge, the position information of each component and election history in the BIM model are updated according to the construction monitoring system. Finally, the as-built BIM model conforms to the actual situation of the bridge. That means the static information of design and construction stage is preserved completely in the BIM model, which is used as the initial BIM model in the subsequent operation stage.

3.3 *In operation stage*

In the operation stage, dynamic data is generated by structural health monitoring system and bridge technical status inspection results, and is used to update the BIM model.

Several methods of using BIM technology to store and analyze the detected damage or monitoring information of bridge structure has been proposed (McGuire et al., 2016, Jeong et al., 2017a). However, because the amount of data during the operation of the bridge is enormous (Jeong et al., 2016a), so the pre-processing technology and storage method requires further study, such as the cluster analysis of the similarity of sensor data. The BIM model is capable of evaluating the durability of the bridge structure and then simulating the implementation effect of maintenance and repair more accurately than before.

3.4 *Life-cycle BIM*

BIM technology can unite all the involved industries during the life-cycle of a bridge project and share all the information among them. The consistency of all the static and dynamic information of the bridge is the solution to the isolation problem of design, construction, and operation. It is obvious that this aim of a building information model with a continuous flow of information needs data transfer method among tens of kinds of modeling and analysis software. Only after that, the BMS could create the bridge database with all the information offered by the BIM model to evaluate and predict the performance of the bridge structure and then give a reasonable maintenance plan decision support.

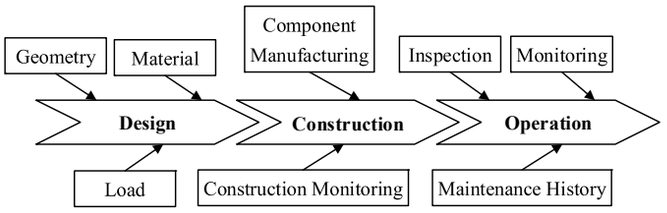


Figure 2. Information Source of BIM model during life cycle of bridge.

To achieve the goal of sharing BIM data, it is necessary to establish the BIM data format standard which meets the needs of each industry in the whole of the bridge. Models at different stages can inherit component and structure data from the earlier stages, and participants of bridge engineering, such as suppliers and contractors, also share data with the others.

At this moment, one of the main limitation that restricts the application of BIM technology in bridge management is that there is no applicable as-built BIM model. With the help of BIM, the static information of design and construction stages will be well recorded. Then in operation stage, the dynamic data is used to update the BIM model so that the integrated database of BMS is established. After that, the other functions could be more efficient and accurate.

4 CONCLUSION

The establishment of BMS based on BIM technology can comprehensively manage information in the whole life cycle of the bridge and achieve the goal

of allocating manpower, material, and funds economically and coordinately.

Firstly, the information of the whole life cycle of the bridge is parameterized, including structural geometry and physical information, load information, inspection information, evaluation information and maintenance history information.

Secondly, establish the proper BIM data format standard suitable for bridge management. The point is that the static and dynamic data in BIM models of the design, construction and operation stages can be reused by following stages.

Finally, the BMS evaluate the structural durability and simulate of the maintenance effect taken the structural health monitoring data and inspection results into account and guide the bridge management work.

REFERENCE

AKGUL, F. 2016. Bridge management in Turkey: a BMS design with customised functionalities. *Structure and Infrastructure Engineering,* 12**,** 647-666.

ALI, N., CHEN, S. S., SRIKONDA, R. & HU, H. J. 2014. Development of Concrete Bridge Data Schema for Interoperability. *Transportation Research Record***,** 87-97.

CHEN, S. S. & SHIROLE, A. M. 2006. Integration of information and automation technologies in bridge engineering and management - Extending the state of the art. *Design of Structures 2006***,** 3-12.

FRANGOPOL, D. M. & LIU, M. 2007. Maintenance and management of civil infrastructure based on condition, safety, optimization, and life-cycle cost. *Structure and Infrastructure Engineering,* 3**,** 29-41.

FRUGUGLIETTI, E., PASQUALATO, G. & SPALLAROSSA, E. Bridge management system implementation in Italy: Pontis&reg and other BMS application in Italy. 6th International Conference on Bridge Maintenance, Safety and Management, IABMAS 2012, July 8, 2012 - July 12, 2012, 2012 Stresa, Lake Maggiore, Italy. Taylor & Francis - Balkema, 3052-3057.

FRUGUGLIETTI, E., PASQUALATO, G. & SPALLAROSSA, E. Bridge management system implementation for Italian highways: From Pontis towards SIOS (Sistema Ispettivo Opere Sineco) and new generation systems. 7th International Conference on Bridge Maintenance, Safety and Management, IABMAS 2014, July 7, 2014 - July 11, 2014, 2014 Shanghai, China. Taylor and Francis - Balkema, 2087-2091.

GOLABI, K. & SHEPARD, R. 1997. Pontis: A system for maintenance optimization and improvement of US bridge networks. *Interfaces,* 27**,** 71-88.

HAJDIN, R. BMS development in Switzerland. Structures Congress 2000: Advanced Technology in Structural Engineering, May 8, 2000 - May 10, 2000, 2004 Philadelphia, PA, United states. American Society of Civil Engineers.

HAWK, H. 1999. BRIDGIT: User-friendly approach to bridge management. *Transportation Research Circular,* 498.

HU, H. 2014. *Development of Interoperable Data Protocol for Integrated Bridge Project Delivery.*

INKOOM, S., SOBANJO, J. O., THOMPSON, P. D., KERR, R. & TWUMASI-BOAKYE, R. 2017. Bridge Health Index Study of Element Condition States and Importance Weights. *Transportation Research Record***,** 67-75.

JEONG, S., HOU, R., LYNCH, J. P., SOHN, H. & LAW, K. H. 2016a. Cloud-based Cyber Infrastructure for Bridge Monitoring. *The 14th International Symposium on Structural Engineering.*

JEONG, S., HOU, R., LYNCH, J. P., SOHN, H. & LAW, K. H. 2017a. A big data management and analytics framework for bridge monitoring. *International Workshop on Structural Health Monitoring 2017 (IWSHM 2017).* Stanford University, Stanford, CA, USA.

JEONG, S., HOU, R., LYNCH, J. P., SOHN, H. & LAW, K. H. 2017b. An information modeling framework for bridge monitoring. *Advances in Engineering Software,* 114**,** 11-31.

JEONG, S., HOU, R., LYNCH, J. P., SOHN, H. & LAW, K. H. 2017c. A Scalable Cloud-based Cyberinfrastructure Platform for Bridge Monitoring.

JEONG, S., ZHANG, Y. L., O'CONNOR, S., LYNCH, J. P., SOHN, H. & LAW, K. H. 2016b. A NoSQL data management infrastructure for bridge monitoring. *Smart Structures and Systems,* 17**,** 669-690.

JI, Y., BORRMANN, A., BEETZ, J. & OBERGRIESSER, M. 2013. Exchange of Parametric Bridge Models Using a Neutral Data Format. *Journal of Computing in Civil Engineering,* 27**,** 593-606.

KARAMAN, S. G., CHEN, S. S. & RATNAGARAN, B. J. 2013. Three-Dimensional Parametric Data Exchange for Curved Steel Bridges. *Transportation Research Record,* 2331**,** 27-34.

MCGUIRE, B., ATADERO, R., CLEVENGER, C. & OZBEK, M. 2016. Bridge Information Modeling for Inspection and Evaluation. *Journal of Bridge Engineering,* 21**,** 9.

MIYAMOTO, A. & MOTOSHITA, M. 2015. Development and Practical Application of a Bridge Management System (J-BMS) in Japan. *Civil Engineering Infrastructures Journal-Ceij,* 48**,** 189-216.

NAGARAJAN, K. 2010. *Development of Framework for Extending TransXML to Steel Bridge Construction.* Doctor of Philosophy, The State University of New York at Buffalo.

SAFI, M., SUNDQUIST, H., KAROUMI, R. & RACUTANU, G. 2013. Development of the Swedish bridge management system by upgrading and expanding the use of LCC. *Structure and Infrastructure Engineering,* 9**,** 1240-50.

SMALL, E. P., PHILBIN, T., FRAHER, M. & ROMACK, G. P. Current status of bridge management system implementation in the United States. 8th International Bridge Management Conference, 1999.

SOLIHIN, W., EASTMAN, C. & LEE, Y. C. 2016. A framework for fully integrated building information models in a federated environment. *Advanced Engineering Informatics,* 30**,** 168-189.

STEEL, J., DROGEMULLER, R. & TOTH, B. 2010. Model interoperability in building information modelling. *Software & Systems Modeling,* 11**,** 99-109.

YALCINKAYA, M. & SINGH, V. 2015. Patterns and trends in Building Information Modeling (BIM) research: A Latent Semantic Analysis. *Automation in Construction,* 59**,** 68-80.

YEHIA, S., ABDELFATAH, A. & ABU DABOUS, S. 2012. A conceptual framework for a bridge management system for the United Arab Emirates. *Bridge Structures,* 8**,** 67-79.

Maintenance, Safety, Risk, Management and Life-Cycle Performance of Bridges – Powers, Frangopol, Al-Mahaidi & Caprani (Eds)
© 2018 Taylor & Francis Group, London, ISBN 978-1-138-73045-8

Bridge Maintenance Strategies – A brief comparison among different countries around the world

M. C. Scutaru
Department of Civil and Industrial Engineering, Faculty of Civil Engineering, Technical University "Gh. Asachi" of Iasi, Iasi, Romania

C. C. Comisu
Department of Bridges, Faculty of Civil Engineering, Technical University "Gh. Asachi" of Iasi, Iasi, Romania

G. Boacă
Department of Bridges, Faculty of Civil Engineering, Technical University "Gh. Asachi" of Iasi, Iasi, Romania

N. Țăranu
Department of Civil and Industrial Engineering, Faculty of Civil Engineering, Technical University "Gh. Asachi" of Iasi, Iasi, Romania

ABSTRACT: Both national and international agencies have attempted over time to implement inspection and maintenance systems to ensure an accurate assessment of bridge structures in administration. Due to the development of the road network around the world, but also due to the historical contexts, bridge inspections, assessment and maintenance strategies differ from country to country, with managed structures being maintained under different technical conditions. With the development of the transport network, budgets allocations have become unsatisfactorily, with the number of structures growing. This has increased the importance of carrying out regular inspections and maintenance work from the very first stages of the emergence and development of degradation. Thus, researchers and managers have come with the conclusion of the need to create and implement an integrated, trustworthy system responsible for providing the data needed to make the best decisions regarding the inspection, assessment and maintenance of patrimony structures. The implementation of this system leads to ensuring user safety, optimal traffic, budget allocation and efficient use of available funds. Another reason for applying an efficient bridge assessment and maintenance system is the need to estimate the strength of patrimony structures needed to calculate the current and future safety levels of the transport network. This system aims at avoiding the execution of maintenance and rehabilitation works that are not a priority for those structures, leading to high costs, delays in the delivery of goods and services, and increased waiting times in traffic.

The present paper aims to carry out a comparative critical analysis of the inspection and intervention strategies implemented in several countries in Australia and Europe, including Romania. This comparison would like to highlight the strengths of several bridge maintenance strategies and methods to provide an overview of them.

1 INTRODUCTION

In operation, roads and bridges are permanently undergoing a degradation process from the time of their construction and commissioning. This is mainly due to traffic, exceeding the permissible axle weight and the action of environmental agents (Comisu et.al., 2017). In order to prevent trafficking from being affected by inappropriate conditions of the road network, different ways of permanent surveillance and overhaul of roads and bridges have been implemented throughout the world. The main purpose is to identify, from the very first stages, the emergence and development of degradation and to repair it in the shortest possible time (AND 504, 2007).

Regular technical inspections are the most useful and effective tools implemented by engineers in charge with road network management; they are used to assess any structural damage or loss of resistance caused by various factors, both internal and external. The complexity of the analyses carried out during the technical inspections varies depending on the structural type, the static scheme and the material from which the bridge is built. This is because it is necessary to provide the most accurate answers, which are then used to make decisions on budget planning and the execution of the maintenance work required for the structure (Pavelescu, 2013).

Since any administrator of a road network is forced to deal with budgetary constraints, maintaining bridge structures in optimal conditions becomes a priority. Researchers from all over the world have come to their aid by creating different progressive testing methods. They start from visual inspections, evaluating to the most detailed computer added analysis or laboratory analysis.

The most important advantages of implementing a regular bridge evaluation system through regular inspections are the possibility of detecting any defects from the early stages of their development, the investigation of the causes of their occurrence and optimal decision making on how to remediate them and prevent expensive repair work.

Inspection of an in-service structure is required in order to:

- Check its technical state and whether traffic can be carried out in optimal conditions both in the present and in the near future
- Identify the presence of any degradation or defect that may affect the user's safety
- Draw up a plan of the measures that need to be taken in order to maintain the safety and the execution of maintenance work

The main purpose of inspections is to observe and record the technical state of the entire structure or just some of its components in order to provide engineers responsible for its administration with the necessary data to make the best decisions in time. These decisions concern both the timely implementation of the intervention work and the extension of these works.

The main objectives of the bridge structure inspection are:

- Determining the occurrence of degradation from the earliest signs and monitoring their development;
- Determining the appearance, extent and causes of degradation of the materials used in the structure execution;
- Determining the appearance of any changes that will affect the safety and durability of the structure over its life span;
- Assessing the efficiency of various maintenance and repair works;
- Data recording for uploading capacity evaluation;
- Determining the technical state of the entire structure or of certain components.

2 INSPECTION TYPES USED IN SEVERAL COUNTRIES

Currently, the most commonly used methodology for monitoring the technical condition of bridges is visual inspection. Depending on the extent of degradation and how it affects the traffic safety, the structure manager will decide to use non-destructive tests during the inspections. The types of inspections used in various countries in the European Union and around the world are described below.

2.1 *Australia*

There are several road administrations operating in this country; some of them have overall state responsibilities, others only territorial. These administrations are:

- -Main Roads Western Australia – Western Australia (WA);
- -Department of Infrastructure, Planning and Logistics – Northern Territory (NT);
- -Department for Planning, Transport and Infrastructure – South Australia (SA);
- -Department of Transport and Main Roads (TMR) – Queensland (Qld),
- -Roads and Maritime Services at Ministry of Roads, Maritime and Freight – New South Wales (NSW);
- -VicRoads or the Roads Corporation of Victoria – Victoria (Vic);
- -Department of State Growth – Tasmania (Tas);
- -At the Australian Government level, road administration is the responsibility of Department of Infrastructure, Regional Development and Cities – Infrastructure and Regional Development.

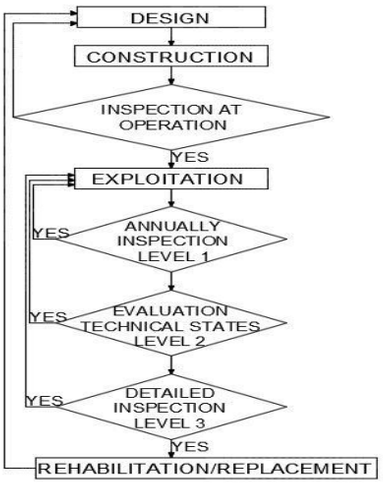
Each road administration has set up its own inspection system for the administration of structures with spans of more than 3 m. However, these systems are quite similar. All manuals are based on the Pontis bridge maintenance system, which is used by the US road administration.

The manuals describing how and how often inspections should be done are *Bridge Inspection Manual* (2004) in Part IV – *Procedures* and *Manual Part one – Bridge Inspection Policy* (2014). Thus, the verification of the bridge degradation degree is divided into 3 levels as follows (Fig. 1):

- Level 1 is represented by the inspection carried out during the periodic maintenance works execution. It is primarily aimed at checking the degradation state of the structure, in particular the safety of the road users, and identifying any degradation that would create resistance and safety issues in the future. This type of inspection is carried out annually on any bridge, regardless of the material, the static scheme and/or the degradation state. Level 1 consists of a visual inspection of all the visible and easily accessible elements of the structure, being integrated into the execution of the current maintenance work. It is necessary for the inspection to be carried out by a person with a rather extensive experience in the field of road and bridge maintenance. Any work performed at this stage is recorded in the Structure Maintenance Program, where the type, nature and cost of these works are identified
- Level 2 of inspection is primarily intended to estimate the current technical state of the structure under consideration. The data collected at this stage is used to: identify structural defects and quantify their extent, estimate the cost of repair, rehabilitate or replace the structure according to the degradation extent, determine the remaining

life of the structure, assess the load capacity, assess the entire structure or just some of its elements after the periodic maintenance or rehabilitation works. Level 2 inspections are carried out by qualified personnel (accredited by road administrations dealing with that structure) with extensive experience in the design, construction, inspection, maintenance or rehabilitation of bridges. The verification of the technical condition at this stage takes place only visually, covering all components of the structure located above the water. Foundation elements below the water level require trained divers specialized in structure analysis.

– Level 3, the most detailed inspection, is coordinated by a structural engineer. These inspections include, besides the visual examination of the structure, non-destructive tests and the structural analysis of the bridge. The main objectives of these inspections are to analyse structural behaviour, degradation status and load bearing capability, evaluate the remaining lifetime of the structure and determine the appropriate intervention strategy. The Australian authorities have imposed that the personnel responsible for carrying out inspections at level 3 should be engineers, members of the Australian Institute of Engineers or any other equivalent institution accredited by the State. At the same time, at least 5 years of experience in the field of bridge design and construction are required. From the frequency point of view, level 3 inspections take place only on the recommendation of the level 2 inspection reports, on the discovery of the load bearing capacity decrease or on a technical audit program. The inspection included in level 3 is composed of a close visual examination of all structural elements. When the inspector in charge deems necessary, different non-destructive tests are performed to highlight the presence and quantify the extent of degradation on the analysed structure.



– Figure no. 1. Inspection chart in Australia

The data resulting from the above inspections are collected, processed and stored through 2 specially designed programs. Thus, WA used the system called MRWA (Main Roads Western Australia) Bridge Management System, and ACT used the NSW Bridge Management System (Mirzaei et al., 2014). However, in 2014, not all road authorities in Australia had implemented information management systems. These systems would be developed and implemented in the future.

2.2 *Austria*

In Austria, the inspections are carried out by the Road Administration for all bridges whose spans reach or exceed the length of 2 m. The data from these inspections are used to assess both the structure state and how the entire in-service road network is affected. There are three types of inspections:

– Superficial inspections carried out by the personnel responsible for the structure maintenance. They report any occurrence of a defect or degradation of easily observable structural parts.
– General inspections are carried out by qualified staff, under the direction of a bridge engineer. These inspections take place every two years and after an extreme event in the life of the structure (e.g. earthquake, flood, etc.). Only the accessible elements of the structure are inspected.
– Major inspections are performed every six years for all structures. Their main objective is to provide detailed information on the state of the bridge. Based on these data, it is recommended to carry out various maintenance or rehabilitation works, depending on the needs of the structure.

2.3 *Denmark*

Bridges are managed by the Danish Road Directorate. Those with spans greater than 5 m are subject to 3 types of inspections:

– Superficial or routine inspections are carried out during on-site maintenance by the personnel responsible for their execution, with the aim of detecting major degradation and changes in the operating conditions of the structure.
– Main inspections are carried out by qualified personnel, every three years. However, depending on the technical state of the structure, this period may vary between 1 and 6 years. Within them, there is a visual check of all the accessible elements of the structure.
– Special inspections are carried out according to the recommendations made by the qualified personnel during the main inspections. Those inspections are made to evaluate the technical condition of all structural elements. In-situ or laboratory tests are also included, if necessary. Special inspections must always be carried out before regular maintenance works or capital repairs.

In Denmark, the road administration developed a computerized data collection and management program for bridge structure inspections called the DANBRO Bridge Management System. The first version of this program was carried out around 1975; since 2010 an improved version has been utilized. The only drawback of this program is that it is used only by the structure administration on the national and regional roads, consultants and builders (Mirzaei et al., 2014, Hearn et al., 2005).

2.4 *France*

The French Road Administration (Ministry of Ecology, Energy, Sustainable Development and the Sea, Transport Infrastructure Directorate) carries out the following inspections of all bridges with an opening of more than 2 m:

- Superficial inspections take place annually. They are done during the annual maintenance work and finalize with a report. This report contains the necessary data to identify the bridge, the date of the inspection, along with any observed defect or change in the structure.
- Assessment inspections consist of the rapid visual inspection of all bridge elements. These inspections are carried out by qualified personnel every three years.
- Detailed periodic inspections are carried out on bridges with medium and large spans every six years. However, the inspection period may vary between 1 and 9 years, depending on the technical condition and age of the structure. On this type of inspection, all structural elements are checked by qualified personnel in order to determine the different bridge-specific pathologies.
- There are two types of detailed inspections: preliminary inspections, before the execution of the main repair works and inspections carried out at the end of the warranty period.
- Exceptional inspections are made after the occurrence of various major events in the life of the bridge (e.g. earthquakes, floods, execution of various construction in the vicinity of the construction)

The program that manages data from field inspections is called LAGORA. Bridges, culverts, tunnels and retaining walls are recorded under this program (Hearn et al., 2005).

2.5 *Germany*

The German Highway Research Institute implemented the DIN 1076 program to monitor the technical condition of all bridges through 4 types of inspection:

- Surface inspections take place annually, with the main purpose of discovering the occurrence and development of major flaws that affect the safe operation of the structure. These inspections are carried out by the personnel responsible for managing the structure.
- General inspections take place every three years and consist of visual inspections of all accessible elements of the structure. In exceptional cases, various in situ non-destructive tests are permitted to monitor and capture different data about the degradation evolution or extent.
- Major inspections are visual assessments of all bridge elements. Various tests are carried out to determine the physical and chemical properties of the materials from which the structure is built. These inspections take place every six years from the bridge opening.
- Special inspection is carried out when the data from the structure indicates the necessity of carrying out various maintenance works.

The same research institute also recommended the use of the GBMS (Bauwerk Management System) program to manage data on the approximately 10.000 bridge structures under the German Federal Ministry of Transport. This program was implemented from the beginning of 2015 (Mirzaei et al., 2014, Hearn et al., 2005).

2.6 *Norway*

In this country, the first inspections done by the road manager (the Norwegian Public Road Administration) over a bridge are admission inspections (at the end of the structure execution or at the end of the main repair works) and end-of-warranty inspections. The main purpose of this inspection is to check the good behaviour of the newly built structure or of the repairs. It should be noted that in Norway, bridges are considered to be the structures whose span is equal to or greater than 2.5 m.

In exploitation, bridges are subjected to the following 3 types of inspections:

- The overall inspection is a visual inspection of all bridge components in order to detect any degradation that will affect the load capacity, traffic safety and the environment. This type of inspection takes place annually and it is carried out by the staff responsible for maintaining the structure.
- Major inspections are aimed at verifying the functionality of the analysed structure and determining the type of periodic maintenance work required to repair or maintain the bridge in optimal operating condition. These inspections take place every five years and are executed by qualified personnel.
- Special inspections specifically target any degradation or displacement of the structure that affects its technical condition. These works are performed when the previous inspections identified different defects that need to be monitored at shorter intervals of time than with the general inspection. The qualified personnel responsible for

conducting these inspections shall visually examine the affected area, while performing different in-situ tests, particularly with regard to the physical and chemical properties of the materials used to build the structure.

To ease decision-making on the maintenance and rehabilitation need and for easier management of data, the Norwegian Public Roads Administration developed the BRUTUS program in 1995. It contains data on bridges and various other types of structures of particular importance, managed by the Norwegian Public Roads Administration and local municipalities (Mirzaei et al., 2014, Hearn et al., 2005). At this point, the version implemented in 2013 of the BRUTUS program can be considered to be one of the best performing programs of its kind.

2.7 *Poland*

There are four types of inspection of all bridges, regardless of span, in public administration (Polish Railways and Local Roads Administrations) in Poland. These types of inspections are:

- Routine inspection takes place 4 times a year, being carried out by the personnel responsible for maintaining the structure. The purpose of these inspections is to confirm the safety and functionality of the analysed structure and to discover those defects that require the immediate execution of the remediation work.
- General inspection takes place annually, after an extreme event in the structure life, or on the recommendation of the routine inspection, with the aim of identifying any changes of the structure. These inspections are carried out by qualified personnel, namely an engineer responsible for managing bridges, with special training.
- Main inspection is carried out every five years or following a general inspection. It is performed by a specially prepared team, under the guidance of an experienced engineer.
- Special inspection is carried out only when necessary, at the suggestion of the inspections presented above.

In Poland, two transport infrastructure management programs have been developed. Thus, in the case of bridges tracking and other construction within the railway network, PKP Polish Railway Lines SA, their administrator, implemented the SMOK program responsible for managing the data from the inspections presented above. The first version of this program was implemented in 1997, the current version dating back to 2001 (Mirzaei et al., 2014).

Equivalent to the presented program, regional and local road administrations have developed and implemented for the first time in 2001 the SZOK program. The version currently in use dates back to 2010. Under the current version data on both bridges, tunnels, supporting walls and other work related to the road area are managed.

2.8 *Romania*

In Romania, roads are divided into 3 categories, each with an administrator (National Company for Road Infrastructure Administration, Country Councils and Local Councils). The Romanian norms in force at the time of publication of this article stipulate the submission of the entire road network to 5 types of inspections or revisions, each with different complexities (AND 504, 2007). The minimum regulated span of the bridge structures that is included in the national inspection system is 5 m (STAS 5629, 1992).

According to the standards, road and bridge revisions are (Fig 2):

- Supervision revision is the verification of the integrity and safety of the road through the entire management sector, including bridges and visual observations of road infrastructure. In the case of bridges, only visible track elements are inspected. This type of revision is carried out by the personnel responsible for the maintenance work currently employed in the road administration. Theoretically, surveillance revisions take place daily on the European roads, every 2 days on the national roads and twice a week on other public roads.
- Current revision is carried out by the head of the unit directly responsible for managing the bridge under review, once a month. The recommendations resulting from the visual inspections at this stage are recorded in the Administrator's Register and it is required that they be remediated in the shortest possible time.
- Periodical review takes place twice a year (usually in the spring and autumn), being carried out by a committee consisting of 3 members of the administrator. The checks in this revision are similar to those performed in the current revisions, and consist of visual examinations of the structure. In addition, cross-sections of the bedrock are also provided to assess bed obstruction.
- Special revisions are done after the occurrence of calamities (floods, earthquakes, landslides, etc.) or extreme events (accidents, changes in structural behaviour) by committees appointed by the structure manager.

All revisions presented above are performed by visually examining the analysed structure. According to AND 522 – 2006, every 5 years administration specialists or bridge experts perform the calculation of the technical status index of the analysed structures in order to classify the structure and plan the funds needed for the structural repair or rehabilitation. At this stage, non-destructive tests on the bridge, which are not mandatory, may also be carried out.

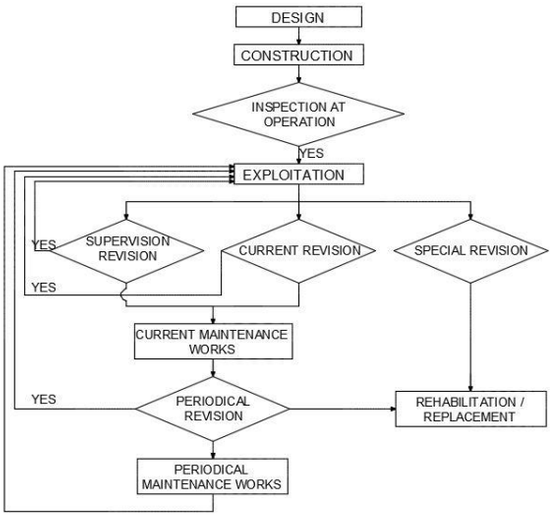


Figure no. 2. Inspection chart in Romania

2.9 *Slovenia*

In Slovenia, the Ministry of Infrastructure performs 4 types of inspections on all bridges with span of at least 5 m, as follows:

- Surface inspection is carried out annually by the personnel responsible for the structure management, along with the maintenance work. This inspection is a visual examination of all structural elements
- General inspection consists of a visual inspection of all accessible elements of the structure and takes place every 2 years. It is done by qualified personnel, under the strict guidance of an engineer responsible for verifying the framing structure.
- Major inspection takes place every six years, being a visual inspection of all structural elements. Specially trained staff prepares reports for all observed degradations and a list of recommendations for performing the required repairs.
- Special inspection is carried out on the recommendation of the staff responsible for the previous inspections. The purpose of this type of inspection is to produce a map of all recorded defects. If necessary, in-situ non-destructive tests are recommended to easily classify defects discovered and determine the best ways to correct them.

2.10 *Spain*

The road administrators of this country (Spanish Ministry of Public Works) have implemented 3 types of inspections, namely:

- Surface inspection is carried out at the initiative of the personnel responsible for the maintenance work. This type of inspection is used to verify the functionality of the structure and to discover the possible degradation that will affect traffic safety and load capacity over time. Due to the fact that, in the superficial inspections, the personnel does not have access to the use of the various tools for inspecting all the elements of the structure, the verification will be limited to the accessible components.
- Main and general inspections are carried out by qualified personnel, and consist of visual checks of the bridge components. These inspections take place every 2 to 5 years, depending on the structure maintenance policy, degree of degradation and age.

In this country, the Spanish Management System (SGP) was implemented to assist road network administrators in planning and carrying out the maintenance work required for bridge structures. The main users of this program are Ministerio de Fomento (Ministry of Development), Road Demarcations and Road Maintenance Areas. The current version of this program was implemented in 2013, but the program dates back to 2005 (Mirzaei et al., 2014).

2.11 *Sweden*

The bridge inspection in this country is carried out by the Swedish Road Administration as follows:

- Regular inspection is designed to detect and report the occurrence of any degradation that may affect the load-bearing structure's capacity and the safety of traffic participants. This inspection is visually carried out by the specially qualified personnel of the contractor performing the maintenance on the part of the road on which the structure is located.
- Surface inspection is carried out by the same staff as regular inspection at specific time intervals (once every 6 months for highways and national roads and once a year for the rest of public roads). The main purpose of these inspections is to identify in the early stages those degradations which, with their development, will affect structural safety.
- General inspection is carried out every three years for all structures having a span larger than 5 m. It consists of a visual inspection of all the structural elements of the bridge. The main objectives of these inspections are to evaluate the performance of previous work, to discover degradations which, if not remedied in a timely manner, will lead to a decrease in load capacity and safety of road users and increased remediation costs.
- Major inspection is the verification of the technical condition of all the elements of the bridge under consideration, including through non-destructive tests. These inspections are carried out every six years, with the objective of detecting and assessing degradations which will affect traffic safety and structure functionality in the following 10 years if no intervention is carried out, and also those degradations whose development will lead to remediation costs.

– Special inspection is carried out only when the situation requires it and when it is assumed that there is certain rapid degradation that would seriously affect traffic safety until the following inspection.

The Swedish Road Administration has implemented the BaTMan (Bridge and Tunnel Management System) program responsible for data management from the above-mentioned inspections. This program is used in the entire country by the Swedish Transport Administration, the Swedish Association of Local Authorities (about 70 out of a total of 290 authorities), the Stockholm administration, the Stockholm-based transport, the State-subsidized private Roads, the Gothenburg harbour, consultants and private firms that carry out maintenance work. The first version of BaTMan dates back to 1987. Nowadays the Swedish administration is using the 4.2 version, implemented in 2011 (Mirzaei et al., 2014).

2.12 *Switzerland*

In Switzerland, the Federal Roads Office (FEDRO) has implemented 3 types of inspections to determine bridge degradation and remedy it in the shortest possible time:

– Main inspection takes place every 5 years, consisting of a visual inspection of the entire structure.
– Intermediate inspection is carried out between two consecutive main inspections aiming at verifying the technical condition of a structure component or the evolution of a degradation process.
– Special inspection is carried out whenever the institutions responsible for the administration of the structure consider it necessary, especially after the occurrence of extreme events in the structure life.

In addition to these inspections, observations are done on bridges as part of the road network monitoring system. These observations consist of the visual check of the degradation state and the serviceability of the structure, and they are carried out by qualified personnel.

KUBA is the computerized data collection software from field inspections developed and implemented by the Swiss Federal Roads Authority. In 2014, version 5.1.2 was implemented, the first version dating back to 1989. In Switzerland, the KUBA program is used by both the Swiss Federal Roads Office and other road administrations in the country (Mirzaei et al., 2014).

2.13 *United Kingdom*

Road administrations in the UK (e.g. local authorities, Scottish, Northern Ireland and Wales authority, but especially Highways England) have implemented 4 types of inspections applicable to all bridges whose span exceeds 3 m. These inspections are (Fig 3):

– Surface inspection carried out by the road maintenance personnel takes place at regular intervals. The main purpose is to check the structure and discover those defects that affect or will affect structural safety in the near future or those that lead to significant increase of the remediation costs.

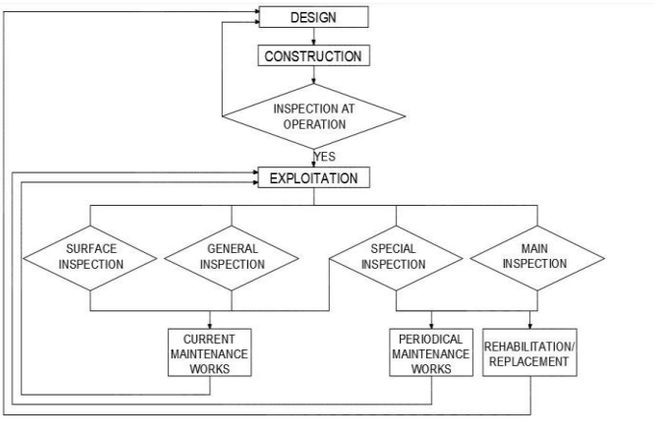


Figure no. 3. Inspection chart in United Kingdom

– General inspection consists of a visual examination of both the structure itself and the easily accessible parts of the supporting members and the river bed. This type of inspection does not use special equipment or non-destructive tests. The periodicity established by the administrators is approximately 2 years after the main inspection or since the last general inspection.
– Main inspection consists of a very precise check of structural elements in accessible areas. The examination is carried out by qualified personnel at specific time intervals, which were established in the bridge construction phase. Most often, these inspections take place every six years; but the range can be extended up to 10 years for new structures. The first main inspection takes place one month before the bridge is put into operation
– Special inspection is carried out only when:
  * it is necessary to examine the various types of degradation discovered during the previous inspection and which could endanger the traffic safety;
  * a structure is built with innovative materials or designed with special solutions;
  * it is necessary to investigate specific elements of the structure;
  * the structure has been subjected to exceptional loads.

In the United Kingdom, the reports of all previous inspections are entered into an electronic database called SMIS where they can be accessed by the personnel concerned with the structure (Hearn et al., 2005).

3. CONCLUSIONS

The methods for assessing the bridge degradation degree differ from country to country, although they all seek to provide similar information. The main differences are mainly represented by the format in which the information of the structure manager and the framing of the bridges in different technical classes are presented.

As it can be seen from the information presented above, the inspection and verification methods of the bridge technical condition used in different countries around the world present a number of advantages, but also various disadvantages. With this in mind, the following can be concluded:

- The most complete system for assessing management structures is the system applied in Germany. The main advantage is the use of non-destructive tests at all levels of inspection, except for superficial inspections.
- Due to the obvious advantages, it is recommended to develop and implement data collection, processing and storage programs in as many countries as possible. These programs make it easier for people to assess all of the available data on the management structures, leading to more efficient design and execution of maintenance and repair work. In the literature (Mirzaei et al., 2014, Bevc et al., 2009, Everett et al., 2008), the BRUTUS program developed and used in Norway is considered to be one of the most advanced data processing programs from the structures inspection.
- In order to better assess the bridge technical condition and to discover and remedy the degradations still in their early stages of development, it is advisable to use non-destructive tests. This leads to an efficient management of the limited budget funds available, due to the fact that remediation of degradation in the early stages of development requires less expense than when degradation affects structural safety. Also, for the same reason, it is recommended that various systems be implemented to continuously monitor the technical condition for the most important bridges in administration.

This paper presents a comparative analysis of strategies for carrying out inspections in different countries around the world, such as Australia or countries in the European Union. This comparison aims to highlight the existing differences, providing support to road managers in studying and developing the most effective way to carry out bridge inspections. Also, the main BMS systems are responsible for preventive measured information from the inspection and verification of structures.

This paper is part of a complex research program developed within the Technical University ”Gheorghe Asachi”, The Faculty of Civil Engineering and Building Services of Iasi, Romania. This research concerns the study and development of Structural Health Monitoring (SHM) systems for bridges.

REFERENCES

* * *, *Bridge Inspection Manual Part Three – Procedures,* Department of Transport and Main Roads Queensland Government, 2004.

* * *, *Manual, Part one – Bridge Inspection Policy,* Department of Transport and Main Roads Queensland Government, 2014.

* * *, http://www.australia.gov.au/information-and-services/transport-and-regional/roads-and-road-transport

* * *, *AND 504 – 2007 – Normative for public road revision,* Technical Road Newslatter (in Romanian), year V, nr. **11**, 51 – 82 (2006).

* * *, *AND 522 – 2002 – Technical instructions for determining the technical condition of a bridge,* Technical Road Newslatter (in Romanian), year II, nr. **16**, 77 – 103 (2002).

* * *, *Manual, Part one – Bridge Inspection Policy,* Queensland Government,, 2014.

Bevc L., Krieger J., Simon-Talero J. M., Wierzbicki T., Delattre L., Woodward R., Cases J. R., Olaszek P., Turk M. R., Vacek J., Vogel T., Lassen B., 2009, COST 345 - Procedures Required for Assessing Highway Structures – Joint report of Working Groups 2 and 3: Methods used in European Stated to inspect and assess the condition of highway structures, *European Commission, Directorate general Transport and Energy,* Bruxelles Belgium.

Comisu C. C., Taranu N., Boaca G., Scutaru M. C. *Structural health monitoring system of bridges,* Procedia Engineering 199, 2054 – 2059, 2017.

Everett T. D., Weykamp P., Capers H. A., Cox W. R., Drda T. S., Hummel L., Jensen P., Juntunen D. A., Kimball T., Washer G. A., FHWA-PL-08-016 - Bridge Evaluation Quality Assurance in Europe, US Department of Transportation Federal Highway Administration, Georgetown, US, 2008.

Hearn G., Puckett J., Friedland I., Everett T., Hurst K., Romack G., Christian G., Shepard R., Thompson T., Young R., *Bridge Preservation and Maintenance in Europe and South Africa,* Report Submitted to Office of International Programs, Office of Policy, Federal Highway Administration, U. S. Department of Transportation, FHWA-PL-05-002, April 2005.

Mirzaei Z., Adey B. T., Klatter L., Thompson P. D., *The IABMAS Bridge Management Committee – Overview of existing bridge management systems,* Rijkswaterstaat, Olanda, 2014.

Pavelescu L., *Study on the implementation of a bridge management system on Romania,* PhD Diss. (in Romanian), Technical University of Civil Engineering Bucharest, Bucharest, 2013.

Maintenance, Safety, Risk, Management and Life-Cycle Performance of Bridges – Powers, Frangopol, Al-Mahaidi & Caprani (Eds)
© 2018 Taylor & Francis Group, London, ISBN 978-1-138-73045-8

The development of a modern bridge asset management system

A. Sonnenberg
Pitt&Sherry, Melbourne, Australia

ABSTRACT: An asset management system has been developed to manage bridge infrastructure. The system includes risk assessment, predictive modelling, load assessment, capital renewal prioritisation and optimisation algorithms. The system is a valuable tool for Universities and other interested parties to apply their deterioration models as well as extract data required to develop deterioration curves. For asset owners it holds the intellect required for them to efficiently manage the life cycle of their infrastructure from commissioning, inspection, maintenance, rehabilitation and renewal.

1 INTROCUTION

The demand for good asset management tools is increasing as the number assets under management increases and the staffing of organisations decreases. There is also increased expectations from the community to achieve greater levels of service without increasing expenditures.

To tackle these increased demands Pitt&Sherry engineers and programmers have been working on the development of an asset management system over the last 15 years. Although the system allows the management of all types of assets the system includes a number of specific modules, such as the bridge module.

1.1 *Key features*

Key features provided by the asset management system include:

1. Inventory data
2. Condition Assessment
3. Risk assessment
4. Financial management
5. Predictive modelling
6. Optimisation
7. Level of service tracking
8. Heavy Vehicle route assessment
9. Capital renewal
10. Reporting

A benefit of capturing data for a range of asset classes in the one system is that the system seamlessly interrelates the data between various asset classes, such as the bridge assets utilising information from the road assets when determining bridge barrier risks.

2 INVENTORY DATA

2.1 *Location*

The system provides multiple methods to cross reference location information. The primary method is via the longitude and latitude of the asset. Using this information the location of assets and defects are displayed on a map within the software.

Location referencing in the form of chainage along the road or path on which the bridge is located is also provided. The software automatically determines the road segment on which the structure is located.

As assets are modified the location of widenings, lengthening and strengthening's can also be recorded.

A proof of concept was developed to automatically generate 3D models of bridges by using the component data collected from inspections to show where each component is located with respect to the other. Although it was found possible to generate a 3D model automatically there was little benefit for most bridges as they aren't complex.

2.2 *Structure data*

The asset owner records the size and date of construction of the original structure, any widenings and lengthening. The software then determines the plan dimensions of the structure.

Other data about the assets is recorded such as the owner, span material, span type, what it crosses, the

clearance above, clearance below and the traffic width.

Information about the age of structures is feed through by the software to the components of the structures. Users are able to modify the age of each and every component if required. For example a component may be replaced on part of the original structure and its date of replacement can be recorded.

3 INSPECTIONS

A requirement of bridge asset management system is the ability to schedule and record inspections. The system needs flexibility to cater for various inspection practices across jurisdiction's. The software can accommodate the inspection manuals of various road authorities in Australia including VicRoads, Roads and Maritime Services and Queensland Department of Transport and Main Roads. The authority manuals use similar inspection methodologies and are based on practices developed in America. The main deference's between each manual is how components are described and measured. For example the State of Queensland (2016) manual describes the condition of components based on the quantity of each component in each condition, of each span, while Vicroads Technical Services (2014) utlises the percentage of each component, in each condition, in the structure as a whole.

The ability be mobile with the asset management system is important for cost efficient and accurate inspections. The software supports inspections using android, IOS and win10 mobile devices. The inspector can choose to have inspection information available as well as information regarding the asset. In this way inspectors can audit asset generic information, such as the name of the river which an asset crosses will in the field.

For larger structures it is important to be able to inspect only part of the structure at a time. Moreover large bridges have structural, electrical and mechanical systems that require regular inspections to be undertaken by separate specialists. The software is coded so that each specialist can do their work acting independently of others while the data is synchronised into one location.

4 RISK ASSESSMENT

The system allows the estimation of risk based on a variety of parameters, including risks related to:

1. Poor condition leading to bridge failure
2. Inadequate load capacity
3. Barriers substandard
4. Flood immunity

4.1 *Bridge Condition*

In 2011 the inconvenience of bridge closure was highlighted when over 200 campers along with their vehicles were stranded in Wilsons Promontory National park. The only route in and out of the park was cut by a wash away of a bridge approach requiring the campers to be Heli-evacuated a great expense. Such sites should be treated as having a high consequence should failure occur.

The risk of a structure of poor condition failing is managed by the system using a risk assessment procedure that creates a risk score which is used to rank the risk of bridge site to another. The risk is derived by the system using the consequence of failure and the probability of failure. A structure with components with unfavorable consequence of failure are provided with a high weighting. The system also assumes higher probabilities of failure to components that are in poor condition. This is an area in which further research could be undertaken to determine appropriate values to be used in the assessment. At this stage the parameters are based on engineering judgement. It is hoped that with larger and more complete data sets the data may be mined in order to determine more accurate estimates for the probability of failure.

Components within areas of the network that are critical to the functioning of the network are given a greater consequence weighting reflecting the cost and inconvenience when these areas of the network are out of service.

4.2 *Inadequate load capacity*

In 2016 a bridge failed in Italy under the passage of a 108 tonne permit vehicle killing one person. Although the bridge was found defective prior to the collapse the bridge was not closed and the operator of the permit vehicle not informed of the hazard. Having a good asset management system which stores load capacity and permit information can assist in the response time in these circumstances thereby reducing the probability of failure leading to loss of life.

The Risk of overload in the asset magnement system Pitt&Sherry has developed is managed by way of a load assessment tool. The configuration of permit vehicles is entered into the system, along with capacities so that a range of vehicles and bridges can be checked. The checks are used to determine if the bridges have sufficient capacity to cater for the vehicles.

The tool is used to identify bridges that require posted load limits to mitigate the risk of failure. Another use of the tool is that if damage occurs to a bridge it is possible to assess the seriousness of the damaged and review what permits are currently outstanding on a bridge. This mitigates the risk that a

permit vehicle may inadvertently travel of a bridge that has been recently damaged.

4.3 *Barrier Risk*

The asset management system greats risk scores for each bridge component and ranks them. The user then selects the highest ranking scores to contribute to an overall risk score. Typically, the highest risk component is assumed to be reflective of the overall risk of an asset but there is the option to use a collection of high ranking components to be reflective of the overall risk of the asset.

Barriers are assessed using both the chart based and site specific requirements of the bridge design code, Austroads (2017). Every barrier on each bridge performance level is stored and compared with the ideal performance level suggested by the bridge design code. The process is automated as the data such as annual average daily traffic and percentage heavy vehicles is shared from the road asset information within the asset management system. By sharing this information from the road asset to the bridge asset avoids duplication of data and allows for the automatic update of barrier risk information once road usage data is updated.

4.4 *Flood immunity*

At this stage flood immunity is simply stored as a recurrence interval to prevent inundation. With advances in technology it should be possible to associate a bridge with a river / catchment and make prediction using meteorology data in real time.

5 FINANCIAL MANAGEMENT

Asset owners need to report annually on their financial status to ensure compliance with regulatory requirements. Fainical data also assists in making prudent decisions with the management of assets. Beside keeping track of work order expenses the software enables users to record the construction cost, replacement cost, current cost and written down value of assets. The software assists the users in this process by allowing unit rates for both the structures current cost and replacement cost to be stored. These unit rates are multiplied by the structures plan area to determine the total costs or the user can enter the costs directly.

The deprecation of assets can be undertaken utilising one of three options. The first option is a traditional straight line depreciation methodology where deprecation is made a linear rate assuming a useful life of the asset which was estimated when it was first put into service. The second methodology is to adjust the useful life based on calculations through the software's predictive modelling capability. The last method is to use the predictive modelling capability of the software to undertake an asset revaluation of the asset.

6 PREDICTIVE MODELLING

The predictive modelling module of the software helps asset owners determine the useful life of their assets. The modelling utilises information from various aspects of the software including, generic data, financial data and condition data as diagrammatically displayed in Figure 1.

The condition data obtained from bridge inspections is used in conjunction with a deterioration curves to predict the useful life of components. The software allows for the export of condition data from the database. The condition data enables the development of deterioration curves. Sample data from bridge abutments inspected in Victoria, Australia is provided in figure 2. The data indicates considerable scatter in the results. The general trend is for bridge abutments to deteriorate with age, consistent with expectations. The data suggests that abutments could be expected to last on average more than 120 years provided they are considered serviceable at 70% or more of new condition.

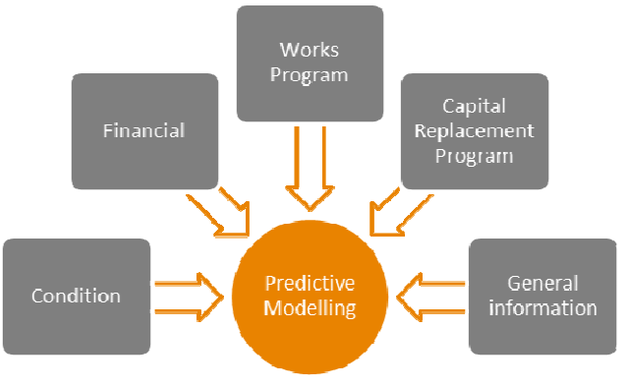


Figure 1. Inputs into predictive modelling

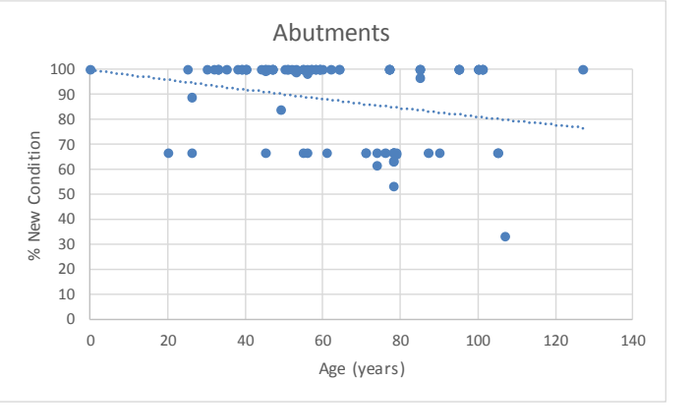


Figure 2. Deterioration curve for bridge abutments

A sample of condition data for compression joint seals is provided in Figure 3. The data indicates considerable scatter in results. The trend is for seals to deteriorate with age. After approximately 40 years the seal are expected to be in 70% of new condition in contrast to abutments reach this condition after approximately 120 years of age. The data is consistent with expectations that expansion joints are

less durable than main structural components of a bridge.

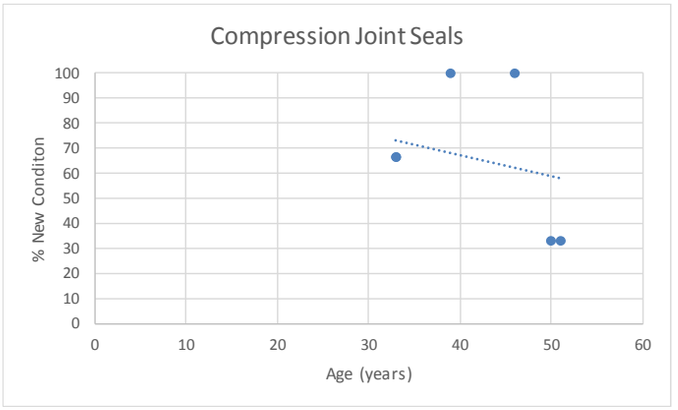


Figure 3. Deterioration curve for compression joint seals

The quality of the deterioration curve is affected by the base data used to generate it. Some asset owners don't accurately record the age of their bridges or the time at which works are done on their components. By making it easy to collect data and by utilising data from a range of clients should provide valuable data for researchers to create accurate deterioration curves. Plans are in place to allow the asset management system to use the data collected to self learn deterioration curves.

Due to a lack of reliable data the software allows the user to enter theoretical deterioration curves such as on the one displayed in Figure 4.

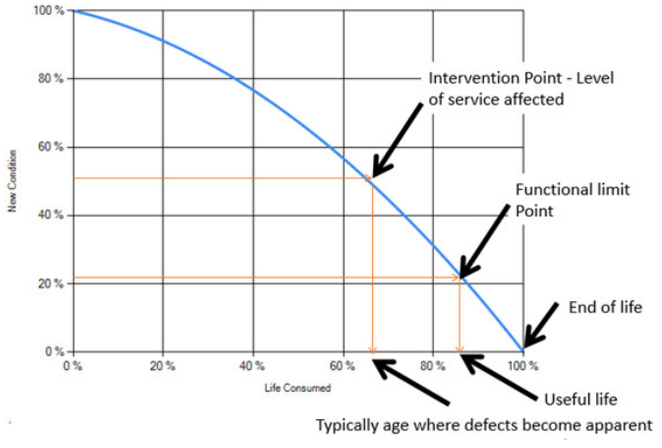


Figure 4. Theoretical deterioration curve

The software stores intervention levels for each component and functional limits. The intervention level is defined as the condition at which an asset owner considers undertaking works while the functional limit is the point at which the component reaches it useful life.

The software utilises the stored condition after repair of a component to forecast the life extension achieved by the proposed repair. The software also summaries the condition based valuation of the structure before and after the repair. The cost of a repair can be compared with the benefit obtained from the repair.

7 OPTIMISATION

7.1 *Works Management*

The works management system has two types of works order, Basic and Advanced. Basic work orders allow for the collection of defects onto a work order. These defects are found by the end user using search tools and then appended by them to a work order.

An advanced work order allows for the automatic allocation of defects to a work order provided the User selects the structures and the defect types they would like the software to monitor. With this type of work order as soon as the inspector identifies a defect that matches the criteria then the defect is allocated to the work order by the software.

Another function of advanced work orders it that preventative works can be scheduled. In the case of preventative works the user determines that part or parts of structures that require works. The user can also confirm the condition after repair work is done and the nature of the work eg. Maintenance or Capital expenditure.

The predictive modelling tool estimates the value of the assets components before and after works. In this way the asset owner can observe the cost benefit of the proposed works and undertake works on assets that provide the best cost benefit. At this stage the risk reduction benefit of undertaking works isn't factored into the software but works are underway to do this. The risk reduction may take the form of safety, economic and political risks.

8 LEVEL OF SERVICE

Level of service provided by structures varies depending on a range of factors. Factors to consider include

- Load capacity
- Barrier performance level
- Flood immunity
- Clearance for over height vehicles
- Volume of traffic catered for
- Number of lanes

At this stage the software doesn't link these service levels together however an algorithm has been developed to do so. The algorithm is based on the premise that there is benefit in providing a service which is largely dependent on the number of people utilizing the asset.

8.1 *Load Capacity*

Load capacity is important not only for safety but also important so that the structure can meet the community's needs. For some bridges only pedestrian

traffic is required to be catered for while for others heavy load platforms need to be catered for.

To determine the benefit a structure provides or could provide three classes of travel are consider. Light vehicles, Heavy vehicle (travelling without permit) and Oversize and Over mass vehicles traveling under permit. By understanding the quantity of each type of vehicle currently using a structure and the number of these vehicles that could potentially use a replacement structure enables an estimation of the benefit a replacement structure may provide.

8.2 *Barrier performance level*

Barriers provide protection to road users. The level of protection to be afforded is specified by the bridge design codes. The Austroads Bridge Design Code is based on providing a level of protection based on a cost benefit analysis. For low risks sites the code specifies lower, less cost costly barriers.

Levels of protection less than that specified by the design code are view as undesirable with respect to level of service. The benefit between one type and another barrier type can be determined by estimating the cost differential between the installation of those types of barriers.

8.3 *Flood immunity*

Flood immunity protection afforded to road users is important for the safety of road users as well as for productivity.

Every year lives are lost due to vehicles being swept off structures and towns are isolated from supplies due to the inundation of roads. The cost the isolation of roads is estimated by storing the detour length for bridges closed by flooding and by estimating the flood return interval for structures.

For structures know to inundate regularly procedures can be put in place through the software to search for these during times of expected flooding and to ensure appropriate safety measures are but is place to protect road users.

8.4 *Clearance for over height vehicles*

The software records the clearance above and below assets. It is anticipated in the future this information will be utilised to automatically check oversize vehicle request across the network.

8.5 *Volume of traffic*

Bridges are designed to cater for a certain volume of traffic. When this volume is exceeded the bridge is not meeting the level of service expectations and there will be increased benefit in either widening, duplicating or replacing the bridge to provide the desired level of service.

9 HEAVY VEHICLE ROUTE ASSESSMENT

9.1 *Permit requirements*

Under relevant legislation General Mass Limit (GML) vehicles such as buses, semi trailers and B-Doubles don't need specific permits to cross most bridges.

Higher Mass Limit (HML) vehicles need to observe relevant designated networks during their travel. Most State Government roads provide access to HML vehicles, while there is limited access to local roads.

All vehicles need to observe posted load limit signs for bridges.

Permit assessments are required for oversize and over mass vehicles, along with Special Purpose Vehicles. Over mass vehicles may have an axle tonnage greater than that allowed for under general operation or a mass density (close axle spacing) exceeding the provisions of a GML vehicle. In these instances, the Heavy Vehicle Operator needs to apply for a permit through the National Heavy Vehicle Regulator (NHVR). The permit requests are made online with the Heavy Vehicle Operator keying in the types of vehicle and their relevant registration details, axle masses, axle spacing and wheel configuration. The Operator is also required to state the route for which they desire the permit.

The NHVR distributes permit request through to the relevant authorities so that they can undertake the permit assessment. The authorities determine whether it is safe to grant access and if such access would cause a detrimental effect to other road users. A request may be denied if it would lead to an unsafe situation or adversely affect the functionality of a bridge or culvert asset.

9.2 *Benefits of permits*

The permit system provides operators with reassurance regarding the safety of their proposed vehicle to travel on the network, the safety of other road users and the wider community.

In 1996, the National Road Transport Commission (NRTC) Australia determined that even allowing minor increases of axle masses to GML vehicles could lead to significant saving to the community. The benefits included the ability to carry heavier loads, lower export costs, fewer vehicles, improved safety and improved environmental performance.

Like the benefits obtained from GML to HML vehicles, similar benefits extend to granting of permit vehicles access, provided the bridges have sufficient capacity to support the loading. Permit vehicles often carry indivisible loads that can't simply be split and are common place in heavy construction such as mining and civil infrastructure.

9.3 *What needs to be assessed*

When a heavy vehicle operator requests a permit there is an associated list of bridges and culverts that need to be assessed. These structures can be expected to take a range of forms since bridge construction technology has evolved.

Pre 1940 structures were designed for loads typical of a steam roller of 15 tonnes hauling a number of wagons. Due to the comparatively light loading structures where typically designed from short spans of timber girders.

It was not until 1946 that the design load increased to design vehicle representing approximately 32 tonnes. At that stage cast in place and precast concrete bridges become popular.

In 1967 there was a 30% increase in the design loads to approximately 44 tonnes. New precast concrete forms of structures were developed to accommodate the increased loading along with the ability to span further.

In 2004 the design load increased to approximately 160 tonnes with the intent of catering for increases in loading requirements of another 100 years.

9.4 *Inputs into the assessment*

To undertake an analysis in the asset management sytem the following inputs are required.

- Customer details.
- Vehicle configuration
- Structure capacity information
- Vehicles and structures to be analysed

The software has been configured to take the information provided by the NHVR or to be manually entered by the end user.

The structure capacity information is entered into the asset management system by a bridge engineer. Information is required relating to the shear capacity, positive and negative bending moment capacities. The capacities are provided at points of interest along each span. Support capacities and arrangement are also entered.

To streamline the process a generic capacity input can be used whereby the capacity information is modelled off the assumption that the original design load capacity is achieved.

Once structure information is entered by the Bridge Engineer the asset owners permitting officer may enter the vehicle details for assessment and choose the structures to be analysed on the route.

9.5 *Results*

Assuming a vehicle passes all checks then it would be permitted to travel. The assessment may indicate a travel restriction is required, such as marked lane or centreline travel. If the checks aren't passed then the outcome is either not to permit the vehicle to travel or to undertake further engineering assessment.

9.6 *What are the benefits of automation*

Automation provides a range of benefits to the network wide assessment of permits. These benefits include

- Information from previous assessments can be used for future assessments
- Using an automated process provides for consistency of results
- Undertaking assessment in an asset management system allows for integration with other systems and allows for the history of permits to be stored against each customer and asset
- Less experience staff may participate in the heavy vehicle checks

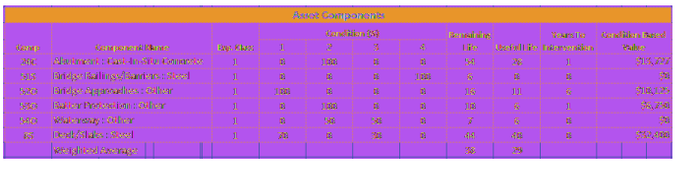
Perhaps the greatest benefit of implementing a rigorous automated process is to minimise the potential of death or injury caused by inadvertently permitting a vehicle to cross a bridge with inadequate capacity.

10 CAPITAL RENEWEAL

Asset renewals occur for a variety of reasons. First and foremost consideration should be given to the service level expected from the assets by the community. Service levels vary by asset class. But common to all classes is the need to maintain assets in a serviceable condition.

In order to assist in the asset renewal programming process the software stores the proposed replacement date the asset owner chooses. Where the replacement date is not provided by the user, the software's predictive modelling will estimate the replacement date based on the remaining useful life for the asset. This value is obtained from the weighted average useful life of the asset components. Table 1 provides an example report from the software to demonstrate the process. The table shows how a bridge has a range of components with varying useful lives. Short lived items often are of low value and may be maintained compared to components with longer lives that tend to be more expensive and difficult to maintain. When the long life items begin to fail the useful life is typically reached. The exception is when the useful life is limited by other service level factors. In this instance the asset owner may desire to replace the asset sooner, in which case they would not utilise the software automatically calculated useful life.

Table 1. Useful life.



The software is capable of predicting 100 years forward, well exceeding most asset owner's re-

quirements, as asset management planning's are normally for a 10 to 20 year period. The software is clever in that it utilises both work order and condition information.

11 REPORTING

The software includes a range of tailored reports to address specific asset management needs. Should users find that software's tailored reports don't meet their needs user defined reporting is also provided. User defined reporting gives access to all database fields and the option to modify how data is presented. Queries/reports can be saved and shared with other users/or run later allowing for changes in asset data to be tracked.

The user defined reporting makes visible the SQL queries run so that those accustomed to SQL can automate the sharing of software's data with other databases and software. Tailored reports typically include the option for the insertion of attachments into Microsoft word documents and/or spreadsheets. In the case of spreadsheets attachments are conveniently extracted and labelled by the software utilising descriptors such as asset number, date etc. and then hyperlinked back to the spreadsheet.

Tailored reports include:

- Asset reports
- Inspection program reports
- Inspection detail reports
- Defect summary reports
- Works reports
- Financial summary reports
- Depreciation reports
- Risk reports
- Predictive modelling reports (both at the asset level and network level).

12 CONCLUSION

Modern bridge asset management systems are required to enable asset owners to manage large asset basis with limited funds and staff. A system has been developed over the last 15 years which allows asset owners to apply engineering and scientific judgement to predict future outcomes and manage the associate risks with bridge assets.

13 REFERENCES

Austroads, 2017. *AS5100 Bridge Design*. Standards Australia.

State of Queensland, 2016. *Structures inspection Manual*. Brisbane. Transport and Main Roads.

Vicroads Technical Services, 2014. *Road Structures inspection manual*. Victoria. VicRoads.

Maintenance, Safety, Risk, Management and Life-Cycle Performance of Bridges – Powers, Frangopol, Al-Mahaidi & Caprani (Eds)
© 2018 Taylor & Francis Group, London, ISBN 978-1-138-73045-8

Risk assessment for bridge management systems

P.D. Thompson
Consultant

ABSTRACT: A National Cooperative Highway Research Program (NCHRP) project was commissioned to develop a Guideline for Risk Assessment for Bridge Management Systems (BMS), to be used within a BMS to estimate the beneficial effects of bridge risk mitigation and replacement on transportation performance, as a part of BMS methods for project utility and benefit/cost analysis. The Guideline describes methods for developing service disruption scenarios, and then estimating the likelihood and consequences of these scenarios. Likelihood probability models are provided for 16 hazards including earthquake, landslide, storm surge, high wind, flood, scour, wildfire, temperature extremes, permafrost instability, overload, over-height collision, truck collision, vessel collision, sabotage, advanced deterioration, and fatigue. These models are based on published research gathered from a wide variety of sources, and consistent with the AASHTO Guide for User and Non-User Benefit Analysis for Highways (the "Red Book").

1 INRODUCTION

Transportation Asset Management uses data and analysis to improve decision making, with the goal of providing the desired level of service in the most cost-effective manner. A Bridge Management System (BMS) contains features to apply bridge inventory and condition data to assess the costs and benefits of preservation, risk mitigation, and replacement activities, to support management decision making processes such as project definition, priority setting, resource allocation, and programming.

BMS have long had functionality to estimate the effects of agency actions on the long-term cost of maintaining the desired level of service. Recent BMS innovations have opened the door to multi-objective assessment of additional stakeholder concerns including safety, mobility, and environmental sustainability (Patidar et al 2007). Bridges affect these concerns by means of their functional characteristics, and by means of the risk that natural or man-made hazards might disrupt transportation service.

National Cooperative Highway Research Program (NCHRP) Project 20-07, Task 378 was commissioned by the American Association of State Highway and Transportation Officials (AASHTO) Subcommittee on Bridges and Structures to develop a Guideline for Risk Assessment for Bridge Management Systems, to be used within a BMS to estimate the beneficial effects of bridge risk mitigation and replacement on transportation performance, as a part of BMS methods for project utility and benefit/cost analysis. AASHTOWare Bridge Management was explicitly targeted, but the methodology is intended to be usable with any BMS using the data typically collected by, or available to, US highway agencies.

The final Guideline describes methods for developing service disruption scenarios, and then estimating the likelihood and consequences of these scenarios. Likelihood probability models are provided for 16 hazards including earthquake, landslide, storm surge, high wind, flood, scour, wildfire, temperature extremes, permafrost instability, overload, over-height collision, truck collision, vessel collision, sabotage, advanced deterioration, and fatigue. Consequences of service disruption are estimated in dollars for recovery cost, safety, mobility, and environmental sustainability. All of these models are based on published research gathered from a wide variety of sources, and consistent with the AASHTO Guide for User and Non-User Benefit Analysis for Highways (the "Red Book"). The economic basis for risk assessment is designed to be compatible with existing use of life cycle cost analysis in BMS, as well as with the

utility framework provided in AASHTOWare Bridge Management.

1.1 *Risk in bridge management systems*

Bridge management systems (BMS) typically provide functions to capture inventory and inspection data for each bridge, and then provide a set of mathematical models to analyze each bridge to forecast future conditions, performance, and costs (Figure 1). As a part of this functionality, BMS apply a set of decision rules to generate one or more alternative projects intended to relieve performance deficiencies and/or to reduce future costs. The software forecasts future performance and costs conditional on a project alternative and implementation year. A do-nothing scenario is also analyzed using similar models. By comparing each project alternative with the do-nothing alternative, a project benefit is estimated.

Typically a BMS will generate far more project candidates with positive benefits than can be funded under anticipated resource constraints. It then becomes necessary to prioritize. Practically all modern BMS use a benefit/cost ratio as the priority-setting criterion. Given a list of selected projects in a fiscally-constrained program, the BMS estimates future network condition and performance outcomes. Such estimates can be used for evaluating and comparing program alternatives, and for establishing performance targets and resource allocations.

Most fully-developed bridge management systems compute project benefits using a life cycle cost analysis, as depicted in Figure 1. In some cases, this life cycle cost analysis can include the user costs associated with functional deficiencies. Risk assessment that is fully integrated with this BMS analysis framework adds a second model to accompany the life cycle cost analysis in computing project benefits. The risk assessment uses information about the project and the effects of the project on future bridge characteristics, to compute a portion of the project benefit.

1.2 *Performance concerns and measures*

Transportation agencies typically list their major goals and objectives in their enabling legislation, mission statements, strategic plans, or other broad policy documents that communicate with stakeholders and the public. For transportation asset management in general, a set of national goals have been defined by the US Congress in 23 USC 150(b):

- Safety
- Infrastructure condition
- Congestion reduction
- System reliability
- Freight movement and economic vitality
- Environmental sustainability
- Reduced project delivery delays

Congestion reduction, system reliability, and freight movement are often considered together as "mobility." Elsewhere in the legislation, agencies are also called upon to minimize long-term costs and manage risks. Each state DOT typically has a similar list of goals. In bridge management decision making, the most relevant concerns are cost, safety, mobility, and environmental sustainability, with condition and risk potentially influencing all of the other goals.

When conditions of individual bridges are compared with each other, or when one bridge is tracked over time, it is common practice to use a bridge health index (Shepard and Johnson 2001). To characterize risk on a comparable basis, it is possible to use a concept of resilience or vulnerability (NYSDOT 2013). Network conditions or resilience can be characterized as the percent good or percent poor, perhaps weighted by deck area.

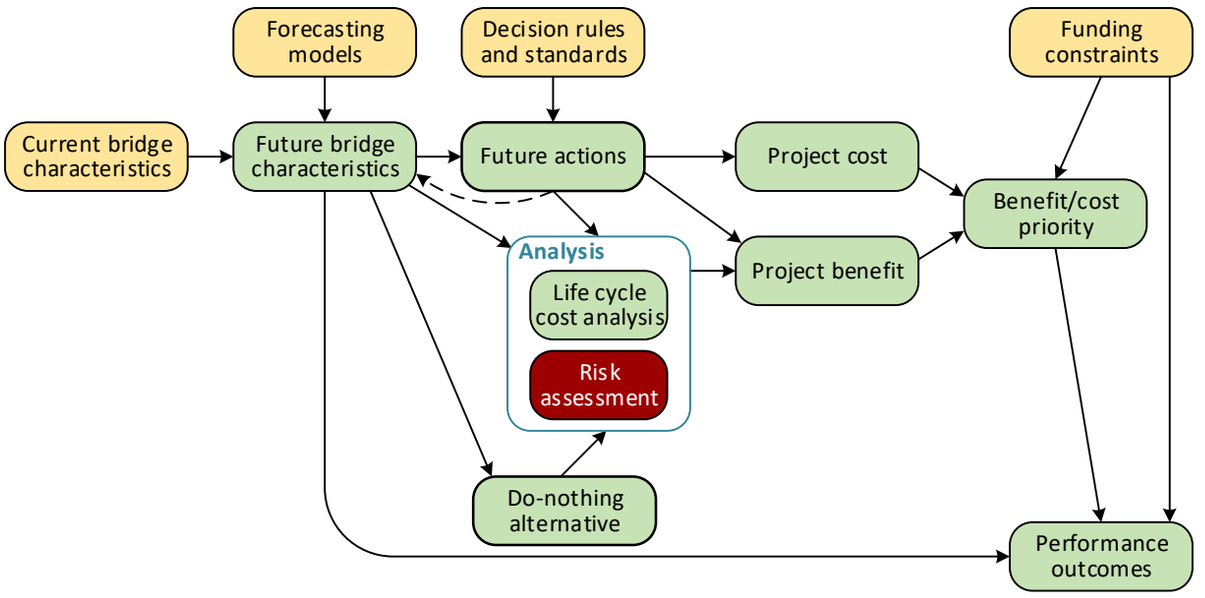


Figure 1. Role of risk in a bridge management system framework.

For benefit/cost priority-setting, it is necessary to describe performance of the network as affected by a given bridge. Cost varies from one bridge to another based on size and potentially other factors. Risk mitigation benefits also vary from bridge to bridge because of traffic volume, detour length, and potentially other factors. NCHRP Report 590 explores ways of combining safety, mobility, and other project benefits, taking traffic and detour length into account, to estimate project benefits as a type of utility function (1). As an alternative, it is possible to estimate project benefits in the form of user costs, as is done in Florida DOT's analytical process (Sobanjo and Thompson 2013). This latter approach simplifies the means of combining risk benefits with life cycle cost reduction. The Guideline described in this paper supports both methods.

2 OVERALL FRAMEWORK

The Guideline presents the risk assessment procedure as a series of worksheets. While the worksheets could in principle be filled out by hand, most agencies will want to implement them either by entering corresponding data in a bridge management system, or by creating a spreadsheet or other software to run the calculations. The worksheet format is intended to make the structure and data requirements as transparent as possible.

Each agency will want to choose which hazards and performance criteria to address, and customize the procedures to fit their own needs and resources. The modular worksheet structure is designed to allow agencies to "mix and match," to plug in the modules which best fit their needs (Figure 2).

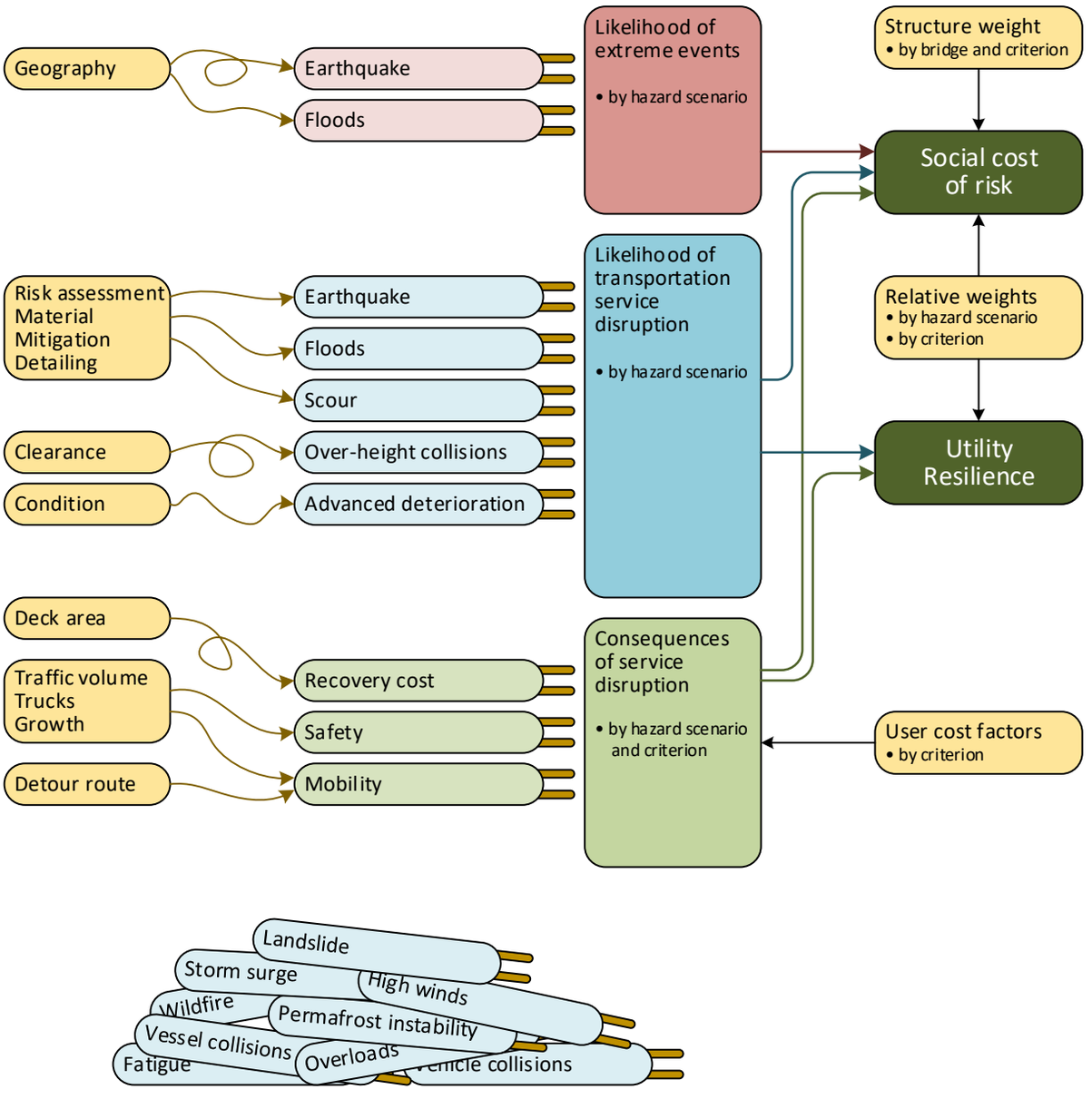


Figure 2. Plug-in architecture of the risk analysis.

Depending on the hazards to be addressed, the agency will choose among plug-in modules for the likelihood of extreme events, the likelihood of service disruption, and the consequences of service disruption. The agency defines a set of hazard scenarios and applies the modular analysis to compute social cost and/or utility for use in the priority-setting and resource allocation functions of the BMS.

2.1 *Hazard scenarios and performance criteria*

The disutility of an adverse event depends on the nature and magnitude of the hazard, and on the effect on each performance concern. In order to reflect these influences in a reasonable way, the following concepts are defined:

- Hazard scenarios, denoted in the equations using the subscript *h*, entail extreme events of a specific magnitude (if applicable), or the cumulative effect of an ongoing adverse process, causing a defined impact on transportation service. For example, a hurricane of at least magnitude 4 that destroys a bridge.
- Performance criteria, denoted using the subscript *c*, represent agency objectives that may be compromised by a hazard scenario. Examples are cost, safety, mobility, and environmental sustainability.

Each agency will select the hazard scenarios and performance criteria to be analyzed consistently across all bridges. An important decision is the level of disruption that should be incorporated into the threshold for recognition of a hazard scenario. Some of the options are:

- The structure is damaged to at least a defined damage level, typically corresponding to the agency's distinction between routine work orders for repair, and programmed capital projects for mitigation, rehabilitation or replacement.
- Near-term or long-term costs are increased.
- Transportation service is disrupted, causing a loss of performance in terms of safety or mobility.
- Environmental resources or the property of others are damaged.

Any or all of the above could have a role in defining the criteria for a hazard scenario. For an understandable and consistent analysis, however, it is important to be consistent in definitions across all hazard types. The Guideline is flexible in allowing agencies to adopt any reasonable set of criteria. However, the service disruption criterion is recommended for primary emphasis, for the following reasons:

- Most of the states having existing risk management capabilities as part of bridge management use this as their criterion.
- For most hazard classes, events that cause service disruption also cause structure damage.
- Service disruption events are typically regarded as more severe than damage-only events, and are more likely to be captured in historical records.
- Damage that is significant enough to disrupt service is typically more expensive to repair and more urgent than damage that does not disrupt service.
- Events belonging to some of the hazard types are not typically recognized as risk consequences unless they disrupt service. Examples are extreme temperature, settlement, advanced deterioration, and fatigue.

In considering which hazards to include in the BMS risk analysis, the following questions should be considered:

- Within the agency's jurisdiction, does the hazard occasionally cause service disruptions or otherwise meet the criteria for a hazard scenario? "Occasionally" should be interpreted in a consistent way, such as at least once every 100 years for a given bridge.
- Do the likelihood or consequences of the hazard scenario differ from one structure to another or one part of the jurisdiction to another? This likelihood could apply to extreme events, to structure damage, or to service disruption. Consequences could apply to any agency objective such as cost, safety, mobility, or environmental sustainability.
- Does the hazard apply to a significant number of bridges? If only a handful of bridges can experience the hazard, then it might be more appropriate to perform site-specific analyses rather than including a model within the BMS.
- Does the agency have treatments available to mitigate the hazard that would be programmed using the BMS? Bridge replacement is a relevant treatment, but in that case the question is, does the magnitude of the hazard make a difference in the choice of replacement or in the priority of replacement?
- Is the hazard significant enough in decision making to justify the additional data collection, particularly field assessment that may be required in order to consider the hazard within the BMS?

The level of detail represented in hazard scenarios can vary based on agency preference. It is likely that most agencies will want to keep the model simple by defining only a small number of scenarios to represent the broader range of possible adverse events. Increasing the number of scenarios increases the development and computational effort, but gives a more precise estimate of outcomes and risk.

If a hazard scenario includes the occurrence of an extreme event, it is desirable to use the event magnitude for which agency's structures are typically designed. For example, if bridges are typically designed to withstand a 100-year flood, then the 100-year flood is the extreme event magnitude to use, and the extreme event probability is one percent.

2.2 *Project Summary Worksheet*

Figure 3 shows the Project Summary Worksheet, presenting intermediate and final results of the risk calculations for a single bridge and project as developed in the Guideline. Input data requirements are provided in the upper two blocks of cells.

The lower two blocks of cells are calculation results. Green cells are results, in thousands of dollars, gathered from worksheets provided for each type of consequences. Red cells are extreme event probabilities gathered from worksheets for each type of hazard scenario. Blue cells are service disruption probabilities gathered from worksheets for each type of hazard scenario. Gray cells are configuration parameters set on a separate worksheet. White cells in the lower two blocks are calculated on the worksheet itself.

2.2.1 *Likelihood of service disruption*

The likelihood of service disruption in this framework varies by bridge, based on bridge characteristics, and also varies by hazard scenario. It has two parts:

LE_{bh} = likelihood of occurrence of the extreme event of given magnitude that is specified by hazard scenario h, estimated for bridge b.

LD_{bh} = likelihood of a specific magnitude of service disruption, conditional on the occurrence of the extreme event specified in hazard scenario h, estimated for bridge b.

The total likelihood of hazard scenario h on bridge b is $LE_{bh} \times LD_{bh}$. The two likelihood estimates are separated because different data sources and methods are used to calculate them, as described below. These likelihoods are the probability of the indicated event occurring in any one year. Agencies using AASHTOWare Bridge Management may want to use the Assessments feature of that system as a basis for estimating one or both of the likelihoods. Other bridge management systems may also have features to allow inspectors to record risk assessments made in the field.

NCHRP 20-07 (378) Risk Analysis

Sheet B - Project summary

Bridge ID	**010001**			
Alternative	**Do nothing**	Deck area (sq.ft)	20,000	
Program year	**2017**	Program cost ($000)	12,345	

Roadways	On structure				Under structure			
Func class	11 - Urban interstate				14 - Urban other principal arterial			
Utilization	ADT	54,000	Trucks	5.50%	ADT	21,000	Trucks	3.00%
Roadway	Length (ft)	200	MPH	55	Length (ft)	100	MPH	45
Detour	Miles	2.1	MPH	45	Miles	1.0	MPH	45

From BMS data. If multiple roadways, use the total ADT and most significant roadway, projected to program year.
Length on-structure is bridge length. Length under-structure is bridge width..

Hazard scenarios		Consequences ($000)				Likelihood			Risk
ID	Scenario	Cost	Safety	Mobility	Environment	Extreme	Disruption	Weight	Cost ($k)
1	Earthquake-100	12,345	50	6,000	600	1.00%	5.00%	1.00	9.50
2	Flood 100a	12,345	50	6,000	600	1.00%	10.00%	1.00	19.00
3	Flood 100b	100	0	2,000	200	1.00%	20.00%	1.00	4.60
4	Flood 500	12,345	50	6,000	600	0.20%	50.00%	1.00	19.00
5	Overheight	100	70	200	40	--	5.00%	1.00	20.50
6	Deterioration	50	0	200	40	--	10.00%	1.00	29.00
7	Fracture	12,345	0	6,000	600	--	0.50%	1.00	94.73
8								1.00	0.00
9								1.00	0.00
10								1.00	0.00

Risk cost and vulnerability	Cost	Safety	Mobility	Environment
Struc weight	20,000	75,000	134,400	134,400
Criteria weight	1.00	1.00	1.00	1.00
Risk cost ($k)	102.79	3.63	79.00	10.90
Vulnerability	5.1394	0.0483	0.5878	0.0811

Risk analysis results	
Maximum unit risk cost:	100.00
Vulnerability index:	0.0586
Utility:	**94.14**
Social cost of risk ($000):	**196.31**

Figure 3. Project Summary Worksheet.

2.2.2 *Consequences of service disruption*
Consequences are defined as an economic quantity, that varies by bridge, based on bridge and network characteristics. It also varies by hazard scenario and performance criterion.

CQ_{bhc} = consequence, estimated in dollars per disruption event, to performance criterion c on bridge b, conditional on the occurrence of the service disruption specified in hazard scenario h.

Consequences include the agency costs of disaster recovery as well as an economic value assigned to safety, mobility, and environmental impacts. The dollar value of recovery cost is typically estimated using economic models and normal agency cost estimation practices, or by classifying potential losses in ranges using judgment. Methods for other types of consequences are described below.

2.3 *Performance measures*

The basic ingredients described in the preceding section are used to compute performance measures for decision support purposes. The following performance measures are needed:

RC_b = Social cost of risk for bridge b. This variable should be structured and scaled so a savings in cost can be used in the benefit of a benefit/cost ratio for priority-setting, and so the BMS resource allocation and optimization models can minimize it network-wide. It may increase over time due to deterioration, traffic growth, or increased hazard likelihood; and it may decrease if an agency action improves bridge characteristics such that life cycle costs, risks, or road user inconvenience are reduced. Its values can range from 0 to positive infinity.

U_b = Utility for bridge b. This variable should be structured and scaled so it can be understood as the degree of resilience of an individual bridge. It provides a uniform unitless scale for comparing the status of one bridge with other bridges, or for tracking performance of a bridge over time. Its values can range from 0 to 100, where 0 is the worst possible performance and 100 is the best possible performance.

2.3.1 *Social cost*
In the recommended methodology, social cost of risk is the weighted sum of the social costs of all hazard scenarios and all performance criteria:

$$RC_b = \sum_h \sum_c RC_{bhc} \quad (1)$$

RC_{bhc} = statistical expected value of weighted social cost, in dollars per year, of hazard scenario h on bridge b for criterion c.

$$RC_{bhc} = W_c \times W_h \times LE_{bh} \times LD_{bh} \times CQ_{bhc} \quad (2)$$

The variable W_c is a weight given to each performance criterion in the cost equation. It should be 1.0 by default, but can be more or less than 1.0 to increase or decrease the contribution of a criterion in the calculation. For example, if W_c=1.2 for c=safety, then safety is given 20% additional cost in the risk calculation. Similarly, W_h is a weight given to each hazard scenario. For example, if W_h=1.1 for h=earthquakes, then earthquakes are given 10% additional cost, perhaps to reflect the difficulty of incident response and the importance of supporting evacuation plans. The other variables in this equation are computed from bridge and network characteristics as introduced above.

2.3.2 *Utility*
Utility is a concept related to social cost, but is designed to be used when making a direct comparison between bridges (disregarding their relative size), or when tracking performance over time. It is equivalent to resilience. The scale is intentionally designed so each bridge can potentially score a perfect 100 or a worst-case 0 depending on its ability to resist hazards. By definition, agency actions should be able to improve this resilience to nearly 100 on any bridge, given sufficient resources.

Depending on the structure of the bridge management system, there may or may not be a mathematical relationship between utility and social cost. AASHTOWare Bridge Management, for example, is designed to compute utility first, at the work candidate level, and then convert this to social cost at the program level for computation of the benefit/cost ratio. Other systems may compute utility from social cost, or treat the two concepts as equivalent, or compute the two measures independently. Utility is meant primarily as a communication tool, while social cost is more rigorously defined for priority-setting and resource allocation.

To compute utility, it is common to first compute vulnerability as the product of likelihood and consequence of each separate adverse scenario for each separate performance criterion. Then the results are additive, and utility is:

$$U_b = (1 - V_b) \times 100 \quad (3)$$

The quantity V_b can be called the vulnerability index, on a scale where 1.0 is maximum vulnerability and 0 is no vulnerability. One way to compute vulnerability is:

$$V_b = \frac{URC_b}{MaxURC} \tag{4}$$

where

$$URC_b = \sum_h \sum_c \frac{RC_{bhc}}{SW_{bc}} \tag{5}$$

The value URC_b can be called the unit risk cost. It is the same risk cost as in equation 2 except that it is normalized to remove the effects of consequence scale. *MaxURC* is determined by computing URC_b for every bridge (or a representative set of bridges) in the database and finding the maximum value, which then defines the worst end of the vulnerability scale for the agency. SW_{bc} is called the structure weight, and is computed in different ways for different performance criteria, as follows:

Cost	Deck area (sq.ft.)	
Safety	Average daily traffic (ADT)	(6)
Mobility	ADT × Detour length (miles)	
Environmental sustainability	ADT × Detour length (miles)	

After an agency first computes or estimates its *MaxURC*, this quantity is not likely to change very quickly over time. Therefore it might not be necessary for the agency to re-compute this constant unless it makes significant changes in its risk assessment process, such as by adding more hazards.

The advantage of having a linear relationship between vulnerability and social cost is the fact that social cost can be computed from vulnerability, which is a necessity for AASHTOWare Bridge Management and is desirable for keeping any BMS framework relatively simple.

3 SUBMODELS

The Guidelines provide recommended methods and alternatives for likelihood of extreme events, likelihood of service disruption, and consequences of service disruption. The study collected methods from existing literature and did not have resources to develop new methods. There are significant opportunities for future research to develop new and better methods for many of the hazards and criteria that can be assessed within this framework.

3.1 *Likelihood of extreme events*

Certain hazards, specifically earthquake, landslide, storm surge, high wind, flood, wildfire, extreme temperature, and truck collisions, are triggered by short-duration events which are unusual and unexpected at any given site, but which occur with regularity across the inventory. Some of these hazards, such as earthquakes, are so abrupt that they have unavoidable safety consequences. Others, such as floods, occur with some advance warning, allowing operational practices which may improve safety in exchange for a compromise in cost and/or mobility.

What all the extreme events have in common is that a portion of the likelihood of service disruption is unaffected by normal agency actions, but is related more to bridge location. This can be significant for decision making because, for example, an agency is powerless to prevent earthquakes, but can, with appropriate resource allocation, make programmatic decisions that increase the ability of bridges to resist earthquakes.

3.1.1 *Natural extreme events*

For a given agency, geographically-referenced data on extreme event likelihood is available from several sources. Ideally, such a data set has polygons representing zones where the event return period is estimated to be 100 years. This return period is most appropriate for bridge risk analysis since it is most likely to approximate or exceed the remaining service lifespans of most bridges. It is equivalent to a probability of one percent. Such data sets often have polygons for alternative return periods such as 20 years or 500 years, which can form the basis for defining additional hazard scenarios if this is applicable for decision making. Alternative return periods also can be used for interpolating extreme event probabilities for locations between polygon boundaries.

As an example, the U.S. Geological Survey (USGS) National Seismic Hazard Maps display earthquake ground motions for various probability levels across the United States. They represent a uniform probability (either 2% or 10%) that the ground acceleration will exceed the given value over 50 years. These can translate directly to an event likelihood for a corresponding hazard scenario. FEMA, NOAA, USFS, and various state agencies are potential sources of geographic hazard data.

3.1.2 *Man-made extreme events*

The Guideline also provides suggested methods for gathering incident data that might be used for human-caused extreme events such as overloads, over-height truck or tanker truck collisions, vessel collisions, and sabotage. In some cases existing data sources can be used to gain insight into the overall statewide probability of some of these hazards, which can form the basis for individual site estimates.

3.2 *Likelihood of service disruption*

For hazard classes that involve extreme events, the likelihood of service disruption is the probability that service is impacted, conditional on the occurrence of

the related extreme event scenario. While the extreme event probability depends mainly on location or other exogenous factors, the service disruption probability typically depends on structure characteristics. Certain hazards, such as advanced deterioration, are not associated with extreme events but have service disruption probabilities (e.g. restricted load ratings requiring posting) that depend only on structure characteristics. Models are provided for the following hazards:

Earthquake	Permafrost instability
Landslide	Overload
Storm surge	Over-height collision
High wind or tornado	Tanker truck collision
Flood	Vessel collision
Scour	Sabotage
Wildfire	Advanced deterioration
Temperature extremes	Fatigue

The Guideline presents worksheets and examples for several generic methods to approximate the disruption probability, that can be applied to most hazard classes even with minimal data availability. These include a judgment-based risk assessment; scoring tables; analogies to other known risks; polling of maintenance personnel; and allocation of statewide long-term incident experience.

These methods can be used separately or in combination, exploiting whatever data the agency can locate, to bracket reasonable risk estimates for each hazard class.

The Guideline also documents methods developed from past research studies that are specific to certain hazard classes, most notably for scour, overloads, over-height collisions, tanker truck collisions, terrorism, advanced deterioration, and fatigue. In some cases, such as scour, multiple alternative models can be found in the literature.

3.3 *Consequences of service disruption*

The likelihood models described above provide the typical probability or frequency, each year, that a service disruption event can be expected to take place. Consequence models then assign a dollar value to each disruption event. The monetization methods are already standardized in the AASHTO Red Book, which is widely used in life cycle cost, value engineering, and regulatory analyses (AASHTO 2010). The Red Book provides unit costs for accidents, travel time, and vehicle operations. The Guidelines provide worksheets and examples of research-based procedures to estimate the safety and mobility impacts, in terms of excess accidents, hours of delay, and miles of detour. These can then be converted to dollars using AASHTO Red Book parameters.

In addition to recovery cost, safety, and mobility, the Guideline also presents an environmental sustainability model based on estimates of vehicular emissions. It uses the approach from FHWA's Highway Economic Requirements System (FHWA 2005). This methodology, updated from earlier research in California, relies on a study that simulates vehicular air pollution emissions under various scenarios of congestion, speed, and volume. Six pollutants are included in the analysis: carbon monoxide, volatile organic compounds, oxides of nitrogen, sulfur oxides, small particulate matter, and road dust. To establish a dollar value and relative weights of the pollutants, the study uses earlier research on the economic impact on health and property damage caused by these pollutants.

4 CONCLUSIONS

The Guidelines document produced by NCHRP 20-07(378) will be of considerable help to agencies wishing to incorporate realistic risk assessment models into the decision support functions of bridge management systems. Based on a wide range of existing research studies, the models have been simplified as needed so they are compatible with the data and software commonly available to transportation agencies. When bridge management systems such as AASHTOWare Bridge Management are configured to use these models, no significant additional effort is required in order to consider risk routinely in combination with life cycle cost in decision making.

REFERENCES

AASHTO 2010. *User and Non-User Benefit Analysis for Highways*. Washington: American Association of State Highway and Transportation Officials.

FHWA 2005. *Highway Economic Requirements System – State Version: Technical Report*. Washington: US Federal Highway Administration.

NYSDOT 2013. *Bridge Safety Assurance Manuals: Hydraulic, Steel Details, Overload, Collision, Concrete Details, and Seismic*. Albany: New York State Department of Transportation.

Patidar, V., S. Labi, K. Sinha, and P.D. Thompson 2007. *Multi-Objective Optimization for Bridge Management Systems*. National Cooperative Highway Research Program Report 590, Washington: Transportation Research Board of the National Academies.

Shepard, R.W., and M.B. Johnson 2001. "California Bridge Health Index: A Diagnostic Tool to Maximize Bridge Longevity, Investment". *TR News* 215.

Sobanjo, J.O., and P.D. Thompson 2013. *Development of Risk Models for Florida's Bridge Management System: Final Report*. Tallahassee: Florida Department of Transportation Contract BDK83 977-11.

Maintenance, Safety, Risk, Management and Life-Cycle Performance of Bridges – Powers, Frangopol, Al-Mahaidi & Caprani (Eds)
© 2018 Taylor & Francis Group, London, ISBN 978-1-138-73045-8

What are the attributes of a superior bridge management system?

H.D. Tran & S. Setunge
RMIT University, Melbourne, Australia

Y-C. Koay & H. Luczak
VicRoads, Melbourne, Australia

ABSTRACT: Many projects are in progress to enhance the current capabilities of Bridge Management Systems (BMSs). This paper investigates the BMS from its expectations relating to transparent policy, decision support and improved organizational work to its core components including inventory database, inspection and condition rating, deterioration models, cost and optimization models, and risk assessment. Major features and capabilities of different bridge management systems in the world are presented and the gaps in the current systems have been identified.

1 INTRODUCTION

1.1 *Background*

Bridge network is a complex system because it often contains thousands of bridge structures with different materials (e.g. concrete and steel), designs (e.g. girder and cable stayed) and sizes. Each bridge structure has a hierarchy of component types, component groups and components (e.g. component group can be substructure and components will be pile and abutment) and is subjected to various management activities (e.g. funding, inspection and load rating) that constantly require storage, analysis and communication of mass data.

To manage such complex bridge network, the bridge management systems (BMS) have evolved significantly from paper-based to computerized systems. It is common to define the BMS as a rational and systematic approach to organize and carry out all activities related to managing a network of bridges (Woodward et al., 2001, Akgul, 2013). The aim of BMS is to assist bridge asset managers and engineers to provide cost effective decisions for planning of maintenance and rehabilitation and replacement (MRR) and for identifying the future funding requirements. In this sense, the BMS is a complex and interactive system between objects (data and information), actions (decision making) and outcomes (performance measures).

The importance of the BMS was further recognized in 1993 when a US legislation outlined the compulsory requirements for a BMS model, which consists of 5 decision support components. The sixth component, risk model, is later added by the industry. The six components of the current BMS are:

i. Database (inventory, inspection data, maintenance data etc.)
ii. Condition rating model (field evaluation of bridge condition)
iii. Deterioration model (prediction of condition of bridge components)
iv. Cost model (identification of cost and benefit)
v. Optimization model (search of optimal MRR strategies)
vi. Risk model (risk ranking and risk assessment)

The US-initiated BMS models can be viewed as a basis for further developments leading to current BMS models used by bridge management agencies around the world.

1.2 *Aims and contributions*

The aims of this study are two folds. First, it reviews the goals and objectives that are expected from the BMS by all stakeholders of bridge networks. Second, it compares decision support components of the current BMS supplied by commercial-vendors, self-developed by bridge agencies or advanced by research projects.

The major contribution of this study is to identify the current gaps in BMS and to support bridge industry in improving asset management of bridge networks.

2 EXPECTATIONS FROM BMS

2.1 *Creating transparent management policy*

Thompson et al. (2012) described all stakeholders of bridge networks, which are grouped into outside stakeholders (e.g. public, specific user groups and regulators) and internal management team (e.g. asset managers, bridge engineers and maintenance technicians). The expectations from all stakeholders can be summarized as follows (Sobanjo and Thompson, 2011, Thompson et al., 2012):

1. Knowledge of current condition of bridge networks
2. Accounting and financial reports
3. Cost-benefit based funding options
4. Importance or risk ranking of individual bridges
5. Long-term cost-effective management plans

2.2 *Assisting improved decision making*

Condition state data provides quantitative data about the physical condition and performance of bridge elements. Element level data is an essential part of the BMS functions. Element level inspections can track the effectiveness of action over time by showing the various condition states and how they may change over time after the bridge element is either repaired, replaced, or left alone. Potential applications for short and long term asset management of bridge networks agencies includes (Thompson et al., 2012, Woodward et al., 2001):

6. Justifying the timing and scope of rehabilitation and replacement.
7. Justifying funding for preventive or early maintenance.
8. Planning adequate resources, parts and equipment to meet maintenance needs.
9. Reducing the overall frequency of rehabilitation and maintenance work zones.
10. Estimating life expectancy and the life-extension effects of preventive maintenance activities on constructed facilities such as pavements and bridges.
11. Comparing two or more alternative maintenance, repair, and rehabilitation alternatives on a facility, under differing assumptions and discount rates.
12. Determining the optimal preventive maintenance interval for constructed facilities.
13. Determining the optimal annual expenditure level on periodic maintenance activities.
14. Comparing design alternatives based on their relative lifecycle costs; for example, comparing a conventional material with a more expensive low-maintenance material.
15. Determining the price point where a low-maintenance material becomes cost-effective.
16. Proactively grouping future preservation work on multiple assets into projects based on the anticipated convergence of their end-of-life conditions.
17. Selecting design alternatives for the various assets on a corridor, such that preservation and replacement interventions likely can be synchronized and long-term traffic disruptions can be minimized.
18. Multi-objective prioritization of programmed projects, using life extension as one of the criteria.
19. Allocating funding.
20. Determining the effect on asset life and long-term costs for variations in near-term funding levels.
21. Establishing research priorities for improved life spans of bridge assets.

2.3 *Enhancing efficiency of agency/organization*

The BMS can be part of a journey towards improved performance in the bridge agency/organization by supporting and enhancing the operational flow and work efficiency as follows (Thompson et al., 2012):

22. Improving the consistency of accounting reports.
23. Improving management guidance and accountability.
24. Building credibility with oversight bodies and elected officials.
25. Increasing the level of cooperation vertically and horizontally among the units of the organization,
26. Increasing the shared understanding of agency objectives and constraints across the agency and with its customers and stakeholders,
27. Increasing the use of quantitative measures of performance,
28. Being more proactive in using agency decisions and actions to improve future performance,
29. Using performance measurement for accountability,
30. Gaining more effective support from decision support tools, and
31. Increasing the drive among all employees to improve the agency's performance.

3 COMPARISION OF CURRENT BMS

3.1 *Inventory Database*

The inventory database is aimed to store and allow exchange of data and information generated during service life of bridges (Akgul, 2013). The traditional 2-D relational tables with structured query language are currently popular among BMSs including self-developed RAS of VicRoads of Australia, research-translated PONTIS of US and commercial dTIMS of Canada. Recently, for building assets 3D visualization is enabled using building information model (BIM), which hasn't yet been used for bridges. BIM is a database model with virtual 3D objects of the structures and multiple-stakeholder collaboration platform (Pärn et al., 2017, Guillen et al., 2016). BIM not only significantly improves the visualization of hierarchy structures such as bridges but also allow seeing through the whole service life with additional time –based (4D) changes and cost-based (5D) activities by related stakeholders.

BIM is first applied to construction of buildings and infrastructures and some commercial providers include ZUUSE in Australia and ACONEX worldwide.

One obvious benefit of BIM is that the location of inspection defects can be quickly entered into the 3D images of bridges without going through the complex numbering code of the 2D Tables. However, the major challenge for BIM application to BMS is the cost-effective conversion of many existing structures and 2-D drawings into 3D BIM. Several solutions such as 3D laser scanning and image-based technique have been reported by researchers (Gimenez et al., 2015, Lu and Lee, 2017).

3.2 *Inspection practice*

The key task of the bridge management process is inspection and condition rating because it provides the basis for subsequent assessment and evaluation of a bridge. The inspection is the first line of safety, and can report when dangerously deficient conditions of structures are found (Hurt and Schrock, 2016).

Only US is found to have legislation requiring regular inspection of 2-year interval to be conducted for each bridge. In other countries, it is considered as the responsibility of the asset managers to conduct regular bridge inspection. The Road Management Act in 2004 in Victoria State of Australia dramatically changed the legal liability of public agencies for road design, operation and maintenance, and having in place a process for reducing reasonable risks. This removed the immunity previously, government officials had under the concept of nonfeasance (Geiger et al., 2005).

A brief summary of inspection practices among Australia, US and Europe is presented as follows.

3.2.1 *US*

There are 5 types of inspections such as routine inspection, damage inspection and so on. The AASHTO recommends using 4 condition states with percentage distribution approach for condition rating of bridge elements such as piles, bearing as compared to brand-new condition. The FHWA specifies 9 condition states with single-condition approach for condition rating of 3 bridge components, namely, deck, superstructure and substructures from inspection reports of their elements. In addition, 9 condition states are also used to appraise the 3 bridge components with regards to serviceability, i.e. under current traffic demand and requirements.

3.2.2 *Australia*

The inspection practice is to conduct 3 levels of inspection as compared to brand-new condition, in which level 1 is screening, level 2 is routine visual and level 3 is detail. Based on inspection reports, four condition states from 1-4 are used to rate condition of bridge elements such as piles, girders by using condition state percentage distribution approach. A detailed comparison of inspection practices between major road agencies in Australia can be found in the work by Sonnenberg (Sonnenberg, 2014).

3.2.3 *Europe*

A detailed investigation into inspection practices of bridges in Europe has been conducted under an international scanning program of best practice by the US FHWA (Hearn, 2005, Hurt and Schrock, 2016). The results show that 3 levels of inspections are often adopted by European countries. They are cursory or safety inspection (annually or quaterly), general or routine inspection (2-3 years) and principal or detail inspection (5-6 years).

The condition rating of bridge component often uses 4 rating scales; however, it is different with US and Australia in a way that the rating scale is associated with recommendation of repair urgency and assessment of damage effect of element on the whole bridge.

3.3 *Element condition rating*

As reviewed in the previous section on inspection practice, bridge elements are commonly rated using percentage distribution from defects found during inspection. For example, a reasonable rating for concrete deck would be [0% 15% 75% 10%] for 1 (good) to 4 (worst) condition states. An unexpected case would be [75% 15% 0% 10%] because there is a significant difference in conditions for the deck which are operated in exactly the same environment. However, bridge engineers could argue that the difference can be due to the location of defects which are subjected to direct and more loadings than other

locations. Another reason could be due to a construction defect that allows occurring of corrosion.

The element condition rating with percentage distribution makes it difficult to report, prioritized comparing and be utilized for deterioration models. Several methods have been used to convert percentage distribution into a single condition rating as far as defects are concerned and their impacts to the whole bridge are treated separately. The common method is called weighted average (Rashidi et al., 2016):

$$Single_Cond = \frac{\sum_{i=1}^{4} i * perc_i}{100} \quad (1)$$

where i is condition state from 1 to 4 (for example) and $perc_i$ is percentage in condition i.

Table 1 shows the outcome of conversion from 4-state percentage distribution into single condition rating from 1-4 as an example for several methods including the one proposed in this study. The conservative or worst first method produces single condition rating according to the worst condition found regardless the value of its percentage. The semi-conservative or worst percentage takes into account the percentage value of the worst condition. It does not rate at condition 4 because condition 4 is not fully developed. This method however, does not recognize the difference between two cases. This can be acceptable given that the analysis of inspection data of VicRoads reveal that such unexpected case occurs less than 5% of inspection data.

The remaining 2 methods produce single condition rating that can be misleading because both cases of example are rated below condition 3 while part of condition 4 is already present. The method developed by Sobanjo et al. (2011) actually produces condition index from 0 (failure) to 1 (good), which is then converted into 1-4 for ease of comparison in this study.

Table 1. List of methods converting condition state percentage distribution into single condition rating (1 to 4 as an example)

Methods	Reasonable case [0% 15% 75% 10%]	Unexpected case [75% 15% 0% 10%]
Weighted average	2.95	1.45
Sobanjo at al. (2011)	2.95	1.45
Conservative	4	4
Semi-conservative (proposed)	3.1	3.1

3.4 *Deterioration models*

"We had bags of data, but not much information." —Maintenance Concessionaire (Geiger et al., 2005) explains the typical situation of a bridge asset manager. A bridge deterioration model is a mathematical model that is calibrated with inspection data to provide current and future prediction of asset condition as well as their deterioration rate, which is crucial information for planning of maintenance and rehabilitation and renewal programs. One advantage of a good deterioration model is that when the rate of deterioration is predicted as slow, the interval of routine inspection and the service life can be extended resulting in significant savings.

The predictive accuracy of deterioration models is a challenging issue. Sweden BMS is one of a few that does not actually adopt deterioration models. Instead, the knowledge and experience are used to decide future inspection and maintenance (Safia et al., 2013, Fu and Devaraj, 2008). Many more BMSs use deterioration model as a core module for planning and optimization. The stochastic deterioration models have been recommended to replace the deterministic models to improve accuracy and to account for uncertainty of deterioration process (Cavalline et al., 2015, Sobanjo and Thompson, 2011, Fu and Devaraj, 2008). Figure 1 shows the poor fitness of deterministic models for modelling the decreasing percentage in condition 1 (good) over time when condition data have large variation or uncertainty.

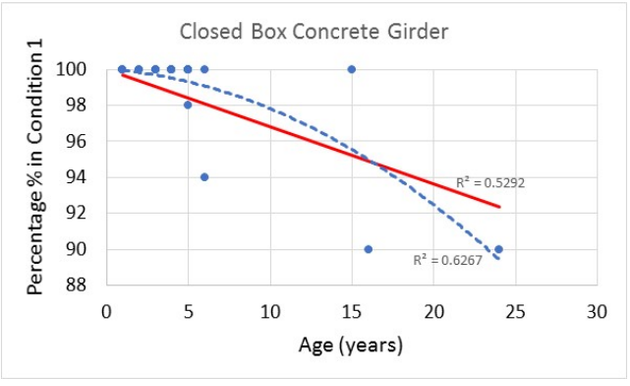


Figure 1. Fitting of deterministic models with condition data

Among stochastic models, the Markov chain model is commonly used for modelling deterioration of bridge. The major attractive feature of Markov is the memoryless property, meaning the future condition is dependent on the current condition, regardless of how it arrived at the current condition. This is suitable for long-life structures such as bridges. In the opposite, is usage-based structures such as pavements and machinery, where future condition depends on past conditions, i.e. how long they have been used.

The Markov model is the built-in deterioration model of PONTIS BMS, while others still use the deterministic models. In the latest version of PONTIS, the Weibull survival model is used to capture the time spent in condition 1 before moving into condition 2 because it is found that Markov model has higher rate of deterioration in condition 1. Figure 1 shows such a pattern of staying in condition 1 for 5 years before the deterioration process starts. From condition 2, the deterioration process is captured by the Markov model in PONTIS. To allow more user choices, the commercial dTIMS BMS allows to input user-defined deterioration models as deterministic or stochastic models.

3.5 *Cost models*

Cost models are an important component in the BMS because they affect short and long-term management decision through cost-benefit analysis. Various cost models have been developed in the literature such as MRR cost, life-cycle cost, user cost and MRR cost. The MRR cost can be easily calculated from the inventory database, which often includes the operating cost of bridge, monitoring cost, repair cost and rehabilitation cost.

The lifecycle cost (LCC) model is commonly available in the commercial BMS. The LCC model includes not only the MRR cost but also the failure cost (Vacheyrouxa and Corotis, 2013), which relates to user cost. The repair and rehabilitation cost in the LCC model can take into account the costs incurred from deterioration, accidents and hazards (Vacheyrouxa and Corotis, 2013).

The user cost model describes the user cost as a cost incurred by the users as a result of bridge deficiencies related to load postings, inadequate, deck width, poor alignment, and limited vertical clearance and accidents. The user cost models are adopted in the PONTIS BMS, which is the well-known model developed by Chen and Johnston and is currently adopted in the BMS of North Carolina State (US) (Cavalline et al., 2015). The user cost can be broken down into 3 main components: travel time cost, vehicle operating cost and accident risk cost. The user cost can also be calculated for the case of detour and no detours (Sobanjo and Thompson, 2011).

3.6 *Optimization models*

The current optimization models in BMS of bridges agency focus on single objective optimization to search for the optimal MRR actions and management strategies over a planning horizon. The common optimization tasks include:

- Minimization of the expected cost of MRR actions over planning time by using probabilistic prediction (Hong et al., 2013)
- Search for repair or replace option to a specific bridge structural component given different life-spans of repair and replacement by minimizing lifecycle cost (Safia et al., 2013).
- Minimize the rehabilitation cost in order to optimize the allocation of the available budget (Darbani and Hammad, 2007)

The approaches to maintenance optimisation implemented in the current bridge management systems are based on single objective optimisation, and more specifically on the minimisation of life cycle maintenance costs, which represents the present value of all the costs incurred throughout the life cycle of a bridge structure, including the costs of design, construction, maintenance, repair, rehabilitation, replacement, demolition and, in some instances, the user costs.

In considering sustainable management of highway bridges, the single-objective approach becomes inadequate and other objective functions should be considered, such as structural reliability and user cost (Shim et al., 2017). Several researches are undertaken in these areas aiming to add other optimization criteria. This can be replaced by a multi-objective optimisation problem as the bridge owner or manager seeks to satisfy implicitly and simultaneously several objectives, such as the minimisation of life cycle costs to owners and users, improvement of public safety, security and serviceability, improvement of bridge functionality, minimisation of environmental impacts and maximisation of economic benefits (Lounis and Daigle, 2013).

3.7 *Risk models*

The general perception of risk is assessing both probability and severity of a loss to a system. Risk is often quantified as a product of likelihood of failure and consequence of failure. Risk is often estimated for bridge element and risk of the whole bridge is often obtained through system reliability analysis in which the serial system (failure of any element becomes system failure) is commonly adopted for simplicity.

Likelihood of failure can be based on condition-based deterioration models, physical-based structural reliability models and fragility curves of bridge elements. The deterioration models are described in the previous section.

The physical-based structural reliability models are often based on deterioration mechanisms such as corrosion and cracking for reliability estimation (Vu and Stewart, 2000, Yogalakshmi et al., 2017, Stewart and Val, 2003, Stewart, 2010).

The fragility curves are defined as cumulative probability function of exceeding limit state condi-

tional on the human-induced (e.g. accident collision and fire) and/or nature-induced (e.g. earthquake, flooding, scour) hazards and attributes of bridges (e.g. length, width) (Gidaris et al., 2017).
The consequence of failure can be based on cost models described above.

Risk assessment is aimed to identify all possible hazards and threats to the system and is then used in risk management, which is to reduce the likelihood of failure and to mitigate the consequence of failure.

In several commercial BMS, risk ranking based on prediction of deterioration models is often used for prioritized planning of maintenance. In the PONTIS BMS, risk ranking model is implemented by the Bridge Health Index (BHI) developed by California State, which is a single number bridge index that measures the health condition of a bridge. This scale index is based on percentages that range from 0 to 100 percent. The basic principle of BHI is driven by the condition and the weight of each component of the bridge. Furthermore, in PONTIS, risk assessment model is also available for various hazards such as fire, flooding, scouting and earthquake.

Risk management can be implemented through inspection and maintenance. For example, Reising (2014) developed a risk-based inspection procedure for determining the inspection interval as follows:

i. Selecting a bridge for analysis,
ii. Determining the damage modes for the bridge components based upon engineering experience, design characteristics, material characteristics, and environment using the information obtained from the Risk Assessment Panel. The result is known as the occurrence factor.
iii. Evaluating the consequence factor concurrently, but independently
iv. Combining the occurrence factor and consequence factor in a risk matrix, the inspection interval can be determined. The longest inspection intervals occur when both the occurrence factor and consequence factor are low. Bridges with high occurrence and high consequence factors are inspected the most often.

This rational approach focuses inspection efforts on bridges where safety or serviceability are likely to be disrupted by targeting the scope of the inspection on the most likely and high consequence damage modes. Following the inspection, bridges that exhibit deteriorating conditions are reassessed to determine a new occurrence factor and a new inspection interval. Once established, consequence factor typically remains constant throughout the life of the bridge because the worst-case scenario remains constant. The developed procedure was applied to the Indiana bridge network in US.

Al-Wazeer (2007) developed a risk-based bridge maintenance methodology to find optimal maintenance strategies for individual bridge elements and for individual bridges in the network that can best utilize limited resources allocated for maintenance. The methodology can be summarized in the following steps:

a. Defining the system for risk analysis and management,
b. Modeling the element-level data needed for developing the methodology,
c. Evaluating the probabilities of failure in the condition states of the elements,
d. Estimating the failure consequences for the elements,
e. Estimating the risk associated with the condition states of the elements based on the probabilities and consequences of failure,
f. Determining the optimal maintenance actions in the condition states based on the maintenance cost and risk associated with the elements,
g. Identifying the element maintenance scenarios of implementing and/or delaying the optimal maintenance actions within the planning horizon,
h. Evaluating the cost and risk associated with the element maintenance scenarios,
i. Filtering the maintenance scenarios based on budget constraints and target risk,
j. Ranking the element maintenance scenarios based on their effectiveness of risk reduction,
k. Selecting the optimal maintenance scenario for each bridge element,
l. Selecting the best maintenance strategy for a bridge based on the available resources allocated for bridge maintenance, and
m. Prioritizing the bridges for maintenance.

4 DISCUSSION

This study investigated the BMSs and their components that are currently available or being developed. One important aspect of BMS that has not been mentioned in the previous sections, is the user-interface with mobile technology. It is observed that most commercial BMS allows web-based access, mobile-apps data input with touchscreen ability. This means end-users can communicate with BMS anywhere and anytime. The report from BMS is now supported by advanced data analytics tool such as Qlik sense that can link with GIS map and can produce real-time visual reports. The increasing trend of adopting BIM in BMS and the advancement of smart sensors poses a new challenge. Real-time integration of smart sensors for structural health monitoring will be future features in BMS

A gap observed in existing systems is the ability to link the structural capacity or load rating to the BMS. In the risk based methodology proposed by

Al-Wazeer (2014) opportunity exists for the capacity to be integrated in to decision making when calculating the probability of failure.

Another missing aspect is the ability to use material durability models to predict deterioration of components of bridges where a known mechanism (eg: chloride ingress in concrete) may initiate degradation.

A superior BMS could use the condition data driven deterioration models for bridge components as the base system with durability driven models superseding the data driven models where applicable. A risk based methodology can incorporate the structural capacity in to the decision making.

5 CONCLUSIONS

A number of comprehensive BMSs are being used by major road authorities in the developed world. Major features of these systems include inventory, deterioration prediction models, cost benefit or life cycle cost and optimised decision making. Superior systems may integrate risk and resilience under hazards in to decision making as well. Following gaps have been identified in current BMSs:

a. The use of 3D visualization BIM models
b. The multi-objective optimization
c. The integration of smart sensors
d. The relation between load rating with inspection data, structural health monitoring and current demands.
e. Use of mechanistic deterioration models for components vulnerable to known mechanisms of degradation to improve accuracy.

6 REFERENCES

Akgul, F. 2013. Development of A Bridge Management System Incorporating A Newly Developed Model For Element Condition Evaluation Based on Damage Effects. *Structure And Infrastructure Engineering,* 9**,** 1206–1224.

Al-Wazeer, A. A.-R. 2007. *Risk-Based Bridge Maintenance Strategies.* Phd Thesis, University of Maryland.

Cavalline, T. L., Whelan, M. J., Tempest, B. Q., Goyal, R. & Ramsey, J. D. 2015. Determination of Bridge Deterioration Models And Bridge User Costs For The Ncdot Bridge Management System. Charlotte, North Carolina, Us.: Department of Civil And Environmental Engineering, University of North Carolina At Charlotte.

Darbani, B. M. & Hammad, A. Critical Review of New Directions In Bridge Management Systems. Congress on Computing In Civil Engineering, Proceedings, 2007. 330-337.

Fu, G. & Devaraj, D. 2008. Methodology of Homogeneous And Non-Homogeneous Markov Chains For Modelling Bridge Element Deterioration. Michigan, Us: Wayne State University, Us.

Geiger Et Al. 2005. Transportation Asset Management In Australia, Canada, England, And New Zealand. Fhwa, Us.

Gidaris, I., Padgett, J. E., Barbosa, A. R., Chen, S., Cox, D., Webb, B. & Cerato, A. 2017. Multiple-Hazard Fragility And Restoration Models Of Highway Bridges For Regional Risk And Resilience Assessment In The United States: State-Of-The-Art Review. *Journal of Structural Engineering (United States),* 143.

Gimenez, L., Hippolyte, J. L., Robert, S., Suard, F. & Zreik, K. 2015. Review: Reconstruction of 3d Building Information Models From 2d Scanned Plans. *Journal of Building Engineering,* 2**,** 24-35.

Guillen, A. J., Crespo, A., Gómez, J., González-Prida, V., Kobbacy, K. & Shariff, S. 2016. Building Information Modeling As Assest Management Tool. *Ifac-Papersonline,* 49**,** 191-196.

Hearn, G. E. A. 2005. Bridge Preservation And Maintenance In Europe And South Africa. Fhwa, Us.

Hong, T., Chae, M. J., Kim, D., Koo, C., Lee, K. S. & Chin, K. H. 2013. Infrastructure Asset Management System For Bridge Projects In South Korea. *Ksce Journal of Civil Engineering,* 17**,** 1551-1561.

Hurt, M. & Schrock, S. 2016. *Highway Bridge Maintenance Planning And Scheduling,* Kansas, Us, Butterworth-Heinemann.

Lounis, Z. & Daigle, L. 2013. Multi-Objective And Probabilistic Decision-Making Approaches To Sustainable Design And Management of Highway Bridge Decks. *Structure And Infrastructure Engineering,* 9**,** 364–383

Lu, Q. & Lee, S. 2017. Image-Based Technologies For Constructing As-Is Building Information Models For Existing Buildings. *Journal of Computing In Civil Engineering,* 31.

Pärn, E. A., Edwards, D. J. & Sing, M. C. P. 2017. The Building Information Modelling Trajectory In Facilities Management: A Review. *Automation In Construction,* 75**,** 45-55.

Rashidi, M., Samali, B. & Sharafi, P. 2016. A New Model For Bridge Management: Part A: Condition Assessment And Priority Ranking Of Bridges. *Australian Journal of Civil Engineering,* 14**,** 35-45.

Reising, R. S. 2014. *Risk-Based Bridge Inspection Practices.* Master Thesis, Purdue University.

Safia, M., Sundquista, H., Karoumia, R. & Racutanu, G. 2013. Development Of The Swedish Bridge Management System By Upgrading And Expanding The Use of Lcc. *Structure And Infrastructure Engineering,* 9**,** 1240–1250.

Shim, H. S., Lee, S. H. & Kang, B. S. 2017. Pareto Front Generation For Bridge Deck Management System Using Bi-Objective Optimization. *Ksce Journal of Civil Engineering,* 21**,** 1563-1572.

Sobanjo, J. O. & Thompson, P. D. 2011. Enhancement of The Fdot's Project Level And Network-Level Bridge Management Analysis Tools Final Report. Florida State University.

Sonnenberg, A. 2014. Australian Bridge Inspection Processes. *6th Australian Small Bridges Conference 2014.* Sydney: Commstrat.

Stewart, M. G. 2010. Reliability Safety Assessment of Corroding Reinforced Concrete Structures Based On Visual Inspection Information. *Aci Structural Journal,* 107**,** 671-679.

Stewart, M. G. & Val, D. V. 2003. Multiple Limit States And Expected Failure Costs For Deteriorating Reinforced Concrete Bridges. *Journal of Bridge Engineering,* 8**,** 405-415.

Thompson, P. D., Ford, K. M., Arman, M. H. R., Labi, S., Sinha, K. C. & Shirole, A. M. 2012. Estimating Life Expectancies of Highway Assets, Volume 1: Guidebook. Purdue University

Vacheyrouxa, G. & Corotis, R. 2013. Strategies Of Investment In The Management Of Urban Bridges: A Life-Cycle Approach Illustrated For Paris. *Structure And Infrastructure Engineering,* 9**,** 1080–1093.

Vu, K. & Stewart, M. G. 2000. Structural Reliability Of Concrete Bridges Including Improved Chloride-Induced Corrosion Models. *Structural Safety,* 22**,** 313-333.

Woodward Et Al. 2001. Brime – Bridge Management In Europe. Trl, Uk.

Yogalakshmi, N. J., Balaji Rao, K. & Anoop, M. B. 2017. Safety Assessment of In-Service Reinforced Concrete T-Girders of Bridge Decks. *Structural Concrete,* 18**,** 733-746.

Maintenance, Safety, Risk, Management and Life-Cycle Performance of Bridges –
Powers, Frangopol, Al-Mahaidi & Caprani (Eds)
© 2018 Taylor & Francis Group, London, ISBN 978-1-138-73045-8

Using Petri-Net Modelling for a Data-Driven Approach to Bridge Management and Safety

P. C. Yianni
Asset Management and Systems Assurance, Jacobs,
Wokingham, Berkshire, RG41 5TU, United Kingdom.

L. C. Neves, D. Rama, J. D Andrews
Resilience Engineering Research Group, University of Nottingham,
Faculty of Engineering, University Park, Nottingham, NG7 2RD, United Kingdom.

R. Dean
Network Rail, The Quadrant:MK, Elder Gate, Milton Keynes,
Buckinghamshire, MK9 1EN, United Kingdom.

ABSTRACT: Bridge portfolio managers have a difficult task managing a large, varied portfolio of aging assets in a squeezed financial climate and on networks with increasing usage. Therefore, decision support tools are becoming more and more integral in managing portfolios of this scale. The model presented in this paper is designed to show a modern, data-driven approach to modelling which would sit as the base for the predictive module of a Bridge Management System (BMS). Extensive research has been carried out in this area however, it has usually resulted in bridge deterioration models; the approach taken in this research is to create a unified system model to encapsulate deterioration, inspection and maintenance to make a Whole Life-Cycle Costing (WLCC) model to offer new insight for bridge portfolio managers. The model in this research uses a Petri-Net (PN) approach which was decided upon as it is flexible enough to incorporate a complex deterioration module, calibrated with over a decade of historic inspection records, corporate policies regarding inspection and maintenance and even certain maintenance practices that are often overlooked. Using the model as a robust foundation, an investigation in the stressors which affect bridge deterioration is carried out. A low-cost, rapid approach to identifying which stressors are driving bridge deterioration is presented. The results indicate which stressors are a safety concern by accelerating the deterioration of bridge assets. Additionally, the results can be used in the PN model to create enhanced deterioration profiles. The resulting model is able to provide more accurate forward prediction capabilities of the assets condition over time, enhancing asset safety predicitons.

1 INTRODUCTION

Railway networks are often critical to the economy as they facilitate the movement of a both freight and commuters. This reliance creates an enormous amount of pressure on the railway and those who manage it. In the UK, a step change is due to occur with the roll-out of the European Train Control System (ETCS) which will introduce moving block signalling, allowing trains to run closer together for greater network throughput (Technical Strategy Leadership Group (TSLG) 2012). Although this development will improve passenger experience, it increases the pressure on the backbone infrastructure. This research focuses on bridge management using the example of the UK railway network, which is owned and managed by Network Rail (NR), however the techniques and results presented would be of interest to any organisation managing similar assets. With increasing asset usage, there is reduced opportunity for asset possession which means analytics and decision support tools are becoming increasingly more important. An investigation into the key stressors which cause deterioration is presented, along with their financial and operational effects, which allows bridge managers to more efficiently allocate resources to avoid assets falling below the safety critical threshold.

2 STOCHASTIC BRIDGE MODELS

A number of studies have been carried out to understand the deterioration behaviour of bridges. Stochastic models seem to be the preferred choice for modelling structural deterioration as they mimic the "micro-response" observed with structural deterioration (Morcous, Lounis, & Cho 2010, Ditlevsen 1984), as well as the deterioration behaviour being naturally stochastic (Frangopol, Kallen, & van Noortwijk 2004).

The most popular technique for stochastic modelling of structural deterioration is the Markov model (Frangopol, Kallen, & van Noortwijk 2004). Jiang & Sinha 1989 was one of the first studies to use this approach for bridge deterioration. The authors carried out a study in Indiana, USA, on a population of 5,700 bridges where 50 where chosen as random samples to calibrate the model with. The authors convert the condition of the assets to a scoring system used by the Federal Highway Administration (FHWA) which ranges from 0-9 with 0 being an element in poor condition and 9 being an element in a new condition. The authors discuss the methodology which they use to calibrate the Markov Transition Probability Matrices (TPMs) using the historic condition data of the bridges. The authors found that the deterioration rate varied over the lifetime of the asset. The approach used in this study was utilised by the AASHTO in the creation of PONTIS, which is one of the most successful BMSs (Sobanjo & Thompson 2011).

Scherer & Glagola 1994 studied a population of 13,000 bridges in Virginia, USA. The authors develop a 7-state Markov model to predict the condition of bridge assets. To increase the computational efficiency, the authors group similar assets based on the structure type, age, number of spans, climate and loading. This reduced the number of Markov model states from $7^{13,000}$ to 7^{216}. The paper is pioneering in grouping assets by operational and structural attributes. Although there is little justification as to why those attributes were chosen, it demonstrates that creating groups of assets with similar deterioration profiles is a successful approach.

Agrawal, Kawaguchi, & Chen 2010 also utilised a 7-state Markov model to study a population of 17,000 bridges in New York, USA. The authors use historic data of bridge elements to calculate the effect of stressors using probabilistic lifetime distributions. One of their main comparisons was between bridges built with standard structural steel and those built with weathering steel. The results of the comparison was that the rates of deterioration were similar for the first 20 years of the assets life, but beyond that the weathering steel demonstrated lower levels of deterioration than the standard steel. Investigating the stressors that affect bridge deterioration were key to this study, however the focus was mostly on the construction materials rather than external environmental stressors.

Huang, Mao, & Lee 2010 focused on the external stressors that affect bridge deterioration on a population of 2,128 reinforced concrete structures in Taiwan. Analysis was carried out on the structures deterioration behaviours to identify major and minor stressors by the types of defects that they cause. The authors identify traffic loading as a major stressor in the deterioration of the reinforcement bars and distance from the coast as a factor in causing spalling and fragmentation. Cracking seems to be one of the most prevalent types of defects as the results show that it is affected by 8 of the 10 stressors. The authors also identify that the peak monthly rainfall seems to be a major cause of concrete honeycombing. Finally, the distance from the coast is identified as a factor that affects structural deterioration, but was categorised as a minor stressor. However, the authors recognise that there were very few bridges in the population which would be classified as coastal.

Le & Andrews 2014 created a PN-based WLCC bridge model using a modularised sub-net approach. A sub-net was created to model the deterioration of each major bridge component, each sub-net was then calibrated with historic bridge data. The authors focused on metallic bridges with specialised sub-nets relating to the condition of the element coating and the condition of the underlying steel. The authors develop the model further to introduce Coloured Petri-Nets (CPNs) which enables a variety of features including the ability to perform state resets and enable tokens to hold tuple information about their respective bridge element. Monte Carlo (MC) simulation is performed using the model from which WLCC outputs are calculated. The paper demonstrated the flexibility of the PN approach and the suitability of CPNs to the application.

A number of studies have been evaluated which can be categorised into two main groups: 1) the studies which use historic bridge data to develop a bridge deterioration or WLCC model and 2) the studies which analyse historic bridge data to try to deduce the factors affecting bridge deterioration rates. The approach in this paper is to investigate the main external environmental factors affecting bridge deterioration and combine them into a WLCC model to understand the financial, operational and safety implications of the stressors over the lifetime of the asset.

3 CONDITION ASSESSMENT AND INDUSTRY POLICIES

3.1 *Condition Scores*

The industry guidelines on the examination of bridges (Network Rail 2012b) explain that bridge elements are inspected according to a matrix condition scoring system relating to the severity and extent of the defect, known as Severity Extent Rating (SevEx). The scores are alpha-numeric (e.g. B3) and range from

A-G where A is no visible defect to G which is permanent structural deterioration and from 1-6 where 1 is no extent to 6 where the defect extent is greater than 50% of the element surface area.

3.2 *Condition Assessment*

Condition assessments are used to schedule inspections as well as decide upon maintenance actions. SevEx is used to score each element during an inspection, but these are then converted to a numerical Structure Condition Marking Index (SCMI) afterwards. A good SevEx score would result in a high SCMI score e.g. an element in a new condition would be allocated an A1 SevEx score which would then be converted to an SCMI score of 100. The industry policies on future inspections and maintenance actions (Network Rail 2012a) describe SCMI thresholds which have been back-converted to SevEx scores for the purpose of this research to keep the method of condition assessment consistent.

3.3 *Maintenance and Inspection Policies*

The inspection frequency is dependant upon condition, an element in a good condition (A1 to D2) would only need to be inspected every 12 years, an element in moderate condition (B6 to F3) would need to be inspected every 6 years and an element in poor condition (D6 to G6) would need to be inspected every 3 years (Network Rail 2012a).

Maintenance follows a similar pattern, with an element in good condition (B2 to D2) only being eligible for a Minor Repair, an element in moderate condition (B5 to F3) being eligible for a Major Repair. Elements in a worse state are deemed to be below the Basic Safety Limit (BSL) and would need to be replaced, relating to SevEx condition states D6 to G6. It should be noted that the A1 condition state is the only condition state which is not eligible for any maintenance (Network Rail 2010).

4 DATA SOURCES

A number of different data sources were used for this work, all of which were provided by NR. These include the asset register, known as CARRS, the historic inspection data and the historic maintenance data, which is split between the Cost Analysis Framework (CAF) and MONITOR depending on the party that carried out the maintenance. In total the datasets cover 1998 to 2014 with inspection data for 25,949 bridges which breaks down into 273,427 major elements inspected and 1,397,748 inspections of minor elements.

Railway bridges are often comprised of either concrete, masonry or metallic elements. Concrete bridges are becoming increasingly common which means the management of them is becoming more important too. For this reason, concrete was chosen as the material type focused on in this research with the main girder elements chosen as the exemplar element. The dataset includes 4,434 concrete bridges, with 407,708 inspection of concrete main girders. Elements with a single inspection were discounted as at least two inspection are required to calculate a condition delta.



Figure 1: Basic PN components presented from left to right: 1) transition, 2) place, 3) marked place, 4) arc.

5 PETRI-NETS

Although Markov models have traditionally been the preferred technique for modelling bridge deterioration (Morcous 2006), they suffer from limitations including: difficulties in calibrating the TPMs (Frangopol, Kallen, & van Noortwijk 2004), difficulty considering maintenance actions in the model (Morcous, Rivard, & Hanna 2002b, Robelin & Madanat 2007) and state based explosion issues (Agrawal, Kawaguchi, & Chen 2010, British Standards Institution 2012). Although it is still understood that structural deterioration is a stochastic process and therefore, a stochastic model will best capture that behaviour, (Frangopol, Kallen, & van Noortwijk 2004), the model enhancements presented in this research benefit from the flexibility of the PNs approach.

PNs are directed bipartite graphs created from places and transitions. Tokens occupy places and indicate the system state e.g. a token in the place "Requires Maintenance" would indicate that the system is in a state requiring maintenance. Transitions move tokens between places and are calibrated with a firing criterion known as a guard. For example, a transition configured with a firing delay equal to the Mean Time to Repair (MTTR), could move a token from a "failed" place to a "working" place to model a system being repaired after a failure. Arcs are used to illustrate the dependencies between places and transitions. No two places or two transitions can be directly connected.

5.1 *Coloured Petri-Nets*

CPNs offer numerous features over simple PNs which are useful for modelling more complex systems (British Standards Institution 2004) including: 1) enabling tokens to contain tuple information e.g. asset age 2) allowing the use of reset arcs which help simplify the model and 3) allowing more complex transition guards including stochastic and programmatic guards (Jensen 1997).

Figure 2 shows a CPN where transition Ω is inhibited by the marked place β. If the transition were able

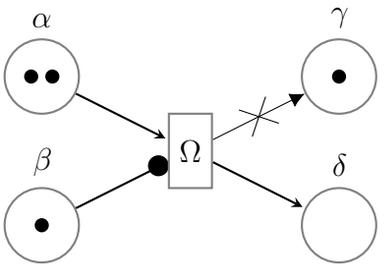


Figure 2: CPN example with both inhibitor arc and reset arc.

to fire, it would remove all tokens in place γ, this is represented by the arc with cross.

6 CPN WLCC MODEL

The CPN model which has been developed is at a Tier 3 level i.e. it focuses on asset and sub-asset level. The model follows the modular sub-net approach which is common with this type of modelling technique. The modules connect in a cyclic way, broadly describing the life-cycle of an asset: starting with the component condition module which contains the deterioration characteristics, through to the inspection module that triggers the maintenance module which, in turn, improves the condition of the bridge components in the deterioration module.

6.1 *Component Condition Module*

The component condition module, which can be seen in Figure 3, mimics the SevEx matrix described in Section 3. The decision to retain the 2-D condition matrix rather than convert to a linear scale, as is the de-facto standard (Cesare, Santamarina, Turkstra, & Vanmarcke 1992, Morcous 2006, Le & Andrews 2014, Network Rail 2010), was that: 1) structural defects have individualistic characteristics and converting defects to a linear scale would involve weightings which introduces subjectivity and 2) the source inspection data uses the SevEx framework so using this data directly avoids any transformations which enables a more accurate calibration of the deterioration profile.

In the module, transitions move tokens, representing bridge components, between the condition states. Lifetime distributions could not be reliably calculated as the inspection data was of insufficient frequency. Therefore, the transitions are calibrated with a constant failure rate where failure is defined as moving to a worse condition state. For example, in Figure 3, there are two tokens representing two different bridge components at different levels of deterioration. These components are considered individually and move through the condition states independently i.e. triggered at different times, along different routes.

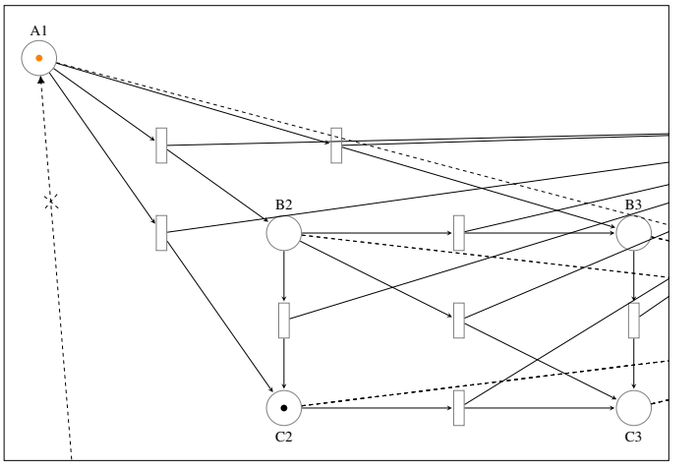


Figure 3: CPN component condition module. A reduced number of condition states are shown for illustrative purposes. The total number of states is 31 which cover SevEx conditions A1 to G6.

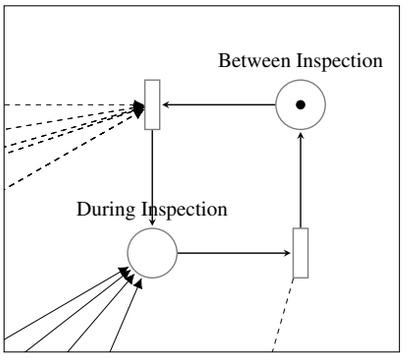


Figure 4: The condition assessment module.

6.2 *Condition Assessment Module*

The condition assessment module schedules inspections on the bridge components. The transition which initiates inspections is calibrated to fire in accordance with the industry guidelines for inspection (Network Rail 2012b). The industry policies describe how the condition relates to the frequency of inspection; the way this is represented in the model is with dashed arcs to the transition, which uses the marking of places to deduce the condition and then calculate the appropriate firing delay. The transition which fires to indicate the completion of an inspection is calibrated with the average length of time required for inspections according to industry experts. Tokens in this module do not contain tuple information and simply indicate the system state by their presence/absence e.g. “between inspection”.

6.3 *Rehabilitation Module*

Once an inspection occurs, a decision about element rehabilitation is made. The industry guidelines detail the type of rehabilitation to rectify different defects (Network Rail 2012a). The rehabilitation options, Minor rehabilitation, Major rehabilitation and Replacement, have each been calibrated with historic data from CAF and MONITOR for both cost and durations which were then verified by industry experts. These attributes were used to calibrate the transitions in Fig-

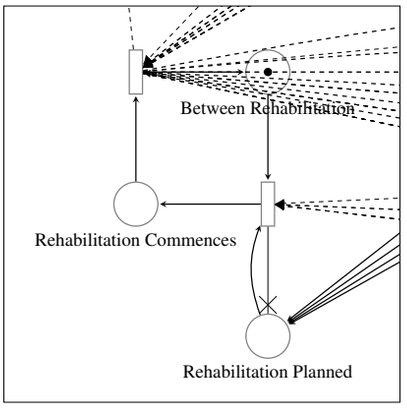


Figure 5: The rehabilitation module makes extensive use of CPN features to closely mimic the complex processes involved.

ure 5.

One major feature which was incorporated into the model required detailed expert judgement of the rehabilitation process. This situation occurs when the element has deteriorated into a worse state during the time between inspection and rehabilitation where the planned rehabilitation is no longer sufficient. This normally would only occur when then condition is near the boundary of rehabilitation actions or the element deteriorates particularly quickly. In Figure 5 this is represented by dashed arcs which are used to deduce whether the rehabilitation action is still appropriate based on the condition of the element. If the rehabilitation action is no longer appropriate the maintenance teams would have to return to that element at a later date to carry out the appropriate rehabilitation action; this delays the repair, increases WLCC and increases pressure on maintenance teams.

6.4 *Model Simulation and Outputs*

With the use of stochastic transitions and complex guards in the CPN model, simple PN analytics are unavailable which means the model must be simulated to understand its behaviour. A MC approach was used for this. The model outputs shown in this section result from a simulation starting with a concrete beam element in an A1 condition over a 100 year period. To simulate an entire bridge asset, a token would be added for each bridge element. A single element was chosen for this example for illustrative purposes to avoid conflicting deterioration profiles and enable a visually clear behavioural trend. A total of 10,000 iterations were carried out to ensure consistent results.

Figure 6 shows the condition of the element over time. The model, in this configuration, uses the standard industry maintenance policies, described in Section 3. The condition starts the simulation with a deterministic A1 condition, hence the high probability of residing in an A1 condition at the end of the first year. The downward slope of the condition continues until the 12th year when an inspection and subsequent maintenance action take place, resulting in an uplift in condition. This process starts the saw-tooth

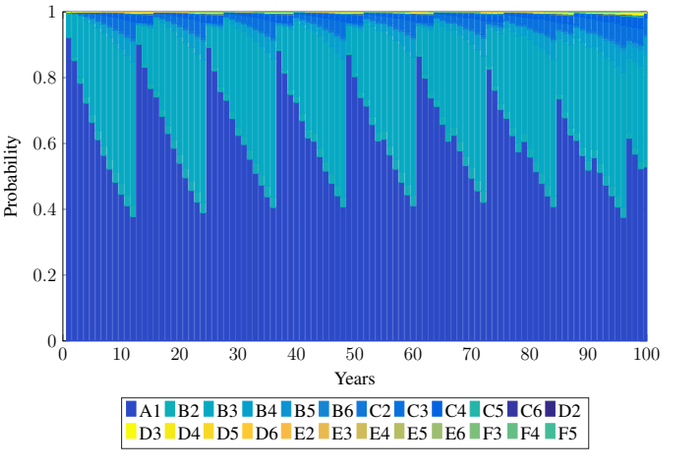


Figure 6: Model simulation outputs showing the condition over time of a concrete girder element.

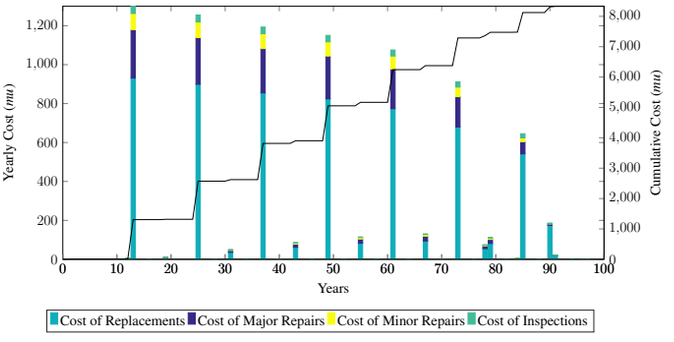


Figure 7: Model simulation outputs showing the cost per year and cumulative cost over time of a concrete girder element.

cycle which continues over the life of the simulation describing the cycle of deterioration, inspection and maintenance.

Figure 7 shows a similar cycle, but from a financial perspective. It can be seen that costs are only realised in years when inspections and maintenance occurs, which coincide with the condition uplifts seen in Figure 6. It should also be noted that when the maintenance teams are required to return to an element, as described in Section 6.3, a second set of expenditure is realised, which can be seen in the figure as the smaller bars between the normal cycles.

7 INVESTIGATION INTO STRESSORS

The model presented so far considers generic bridge elements. From the literature reviewed, there seem to be a number of external environmental factors which can cause varying rates of deterioration in bridge elements. A number of studies have highlighted that there are “other” factors which can contribute to bridge deterioration (Morcous, Rivard, & Hanna 2002a, Sobanjo 1997, Arditi & Tokdemir 1999), but to be able to investigate these a sufficiently large portfolio of bridges and wide enough dataset is required.

As mentioned in Section 3, during inspections the element conditions are recorded using the SevEx system. Rather than convert these alpha-numeric scores to a linear system to carry out stressor analysis, it was

decided that retaining their format would avoid the need for weightings which can introduce subjectivity. Therefore, an approach was developed which considers each of the 31 condition states as nodes with the "length" of the paths connecting the nodes to be equivalent to the Mean Time to Failure (MTTF), following the approach of the deterioration module seen in Section 6.1. The most likely route from node to node through the network is the route which has he lowest MTTF. This allows the use of a classic routing algorithm (Dijkstra 1959) to calculate the time it would take for an element to reach a condition requiring Major Rehabilitation or Replacement from its current condition.

The methodology would be to select an attribute which could be a contributor to structural deterioration (e.g. amount of rainfall), and divide up the population into equal groups e.g. structures exposed to $<$700mm of rainfall per year or $\geq$700mm of rainfall per year. Then calibrate a network diagram for each of the groups, calculating the shortest path for each condition state to the thresholds for Major Rehabilitation or Replacement. The results can be compared as a quick visual indicator to identify if that particular attribute may be a significant factor in structural deterioration.

7.1 *Structure Configuration*

Structural configuration was analysed to ascertain if it is a key factor in deterioration. Railway bridges are usually configured as either underline bridges or overline bridges. Underline bridges carry the railway over obstacles, for example a roadway or river.

The population of underline and overline bridges were taken as two groups and analysed using the methodology described in the previous section. The results can be seen in Figure 8. The results give a visual indication that underline bridges deteriorate faster than overline bridges in general, which can be seen by the lower amount of time required to reach the threshold requiring rehabilitation. The difference highlighted by these results is most likely caused by the different stress profiles caused by the different types of vehicular traffic. The results indicate that these two bridge configurations should be treated as separate groups.

7.2 *Distance to Sea*

The distance of each bridge asset to the sea could be calculated using the assets location, provided in the CARRS dataset, with a shorelines database (National Oceanic and Atmospheric Administration (NOAA) 2015). The approach used in this paper was to divide the population of bridges from the coast inland i.e. a split at 10Km would create two groups of assets, bridges within 10Km to the sea and bridges 10Km or further from the sea. The population was split every

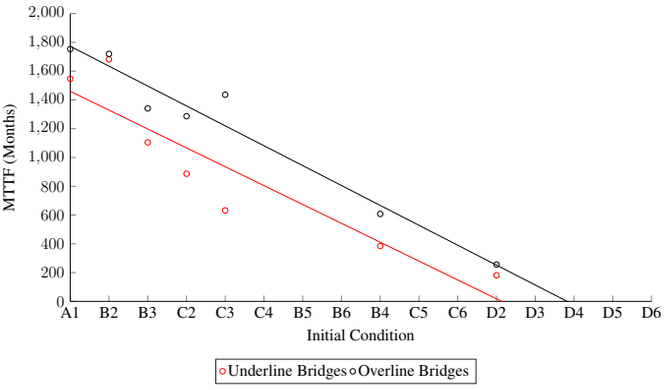


Figure 8: Analysis results of different bridge configurations to deteriorate to the Major rehabilitation threshold.

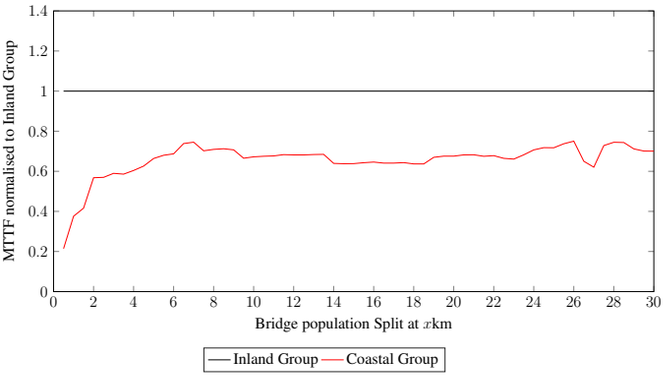


Figure 9: Bridge behaviour at different points from the sea, tested to a condition state requiring Major rehabilitation.

0.5Km up to 30Km inland. The groups would then be analysed with the methodology described in the previous section.

The results can be seen in Figures 9 and 10. They show the inflection point between inland and coastal bridge behaviour. This was tested with a concrete girder element starting in an A1 condition and deteriorating to a state requiring Major rehabilitation in Figure 9 and a state below the BSL, requiring element replacement in Figure 10. The results show that there is, in general, a significant difference in the deterioration rate between the coastal and inland bridge groups with the MTTF being around 30% lower for the coastal group than the inland group. From these results, it can be seen that the distance to the sea is a factor affecting deterioration and the data suggests that the groups should be split with: 1) assets severely affected by the sea at 0-5Km, 2) assets in moderate exposure to the sea at 5-25Km and 3) assets with minimal/no exposure to the sea beyond 25Km.

8 WLCC MODEL CONSIDERING STRESSORS

Although the identification of stressors is useful for portfolio grouping, a greater advantage is gained by bridge managers by understanding the financial and safety implications of bridges exposed to those stressors is. Therefore, it is possible to enhance the component condition module, seen in Section 6.1, which controls the rate of element deterioration, with the results from previous section. The way this works in

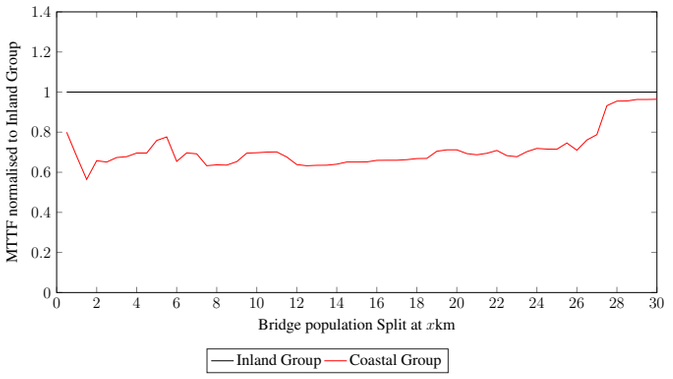


Figure 10: Bridge behaviour at different points from the sea, tested to a condition state below the BSL, requiring element replacement.

practice is to embed the stressor information in the tuple of the bridge element token in the CPN model. The transitions are calibrated with each of the deterioration profiles based on the different stressors. The transitions use a stressor identifier in the token tuple to determine the appropriate firing delay to replicate the appropriate deterioration profile for an element exposed to that particular environmental factor.

A simulation has been carried out with a concrete girder element, starting in an A1 condition, inspected and maintained to the industry standard "managed" maintenance regime over a 100 year period. The results have been summarised in Table 1. It can be seen that the generic deterioration profile (ID1), in which stressor information is not considered, costs 7,900*mu* over a 100 year period, which correlates to the model output seen in Figure 7. When running the simulation of the concrete girder element with different structure configurations, IDs 2 and 3 are the model WLCC outputs, corresponding to overline and underline bridges. It can be seen that overline bridges cost considerably less than underline bridges. It should be noted that there are other structure configurations, but overline and underline bridges make up 94% of the portfolio. When simulating the concrete girder element on structures at different coastal proximities, the results are more divergent (IDs 4, 5 and 6). It can be seen that the WLCC of an inland bridge (ID6) is comparatively low whereas a structure which is closer to the sea (ID5) costs significantly more at 1.7 times that if ID1. Furthermore, structures that are very close to the sea, at maximum exposure to the saline atmosphere, cost almost twice the baseline WLCC seen in ID1. The variation in capital expenditure between these groups varies significantly and reveals a great deal to bridge portfolio managers.

As well as increased financial burden, factors which cause rapid deterioration can also cause issues with maintainability. This is evident when comparing Figures 8 and 8. In Figure 8, the deterioration rate is slower and so the delay time between inspection and maintenance is acceptable. However in Figure 8 the sawtooth curve begins to deviate suggesting that intermediate rehabilitations are beginning to occur. The

Table 1: Stressor simulation WLCC results.

ID	Structure Configuration	Distance to Sea (km)	WLCC (nearest 100*mu*)	Relative Cost to ID 1
1	All	0 - Inf	7,900	1.000
2	Overline Bridges	0 - Inf	3,600	0.460
3	Underline Bridges	0 - Inf	7,100	0.906
4	All	<5	15,100	1.918
5	All	5-25	13,700	1.736
6	All	>25	2,800	0.355

situation under which this occurs is when the element has deteriorated further than expected on an initial rehabilitation attempt and so the maintenance teams must return. This causes an increase in WLCC, increases possession time of the asset and reduces maintenance efficiency. The safety implications are that assets exposed to stressors which cause rapid deterioration are more difficult to manage and therefore there is a higher likelihood of the element straying below the BSL.

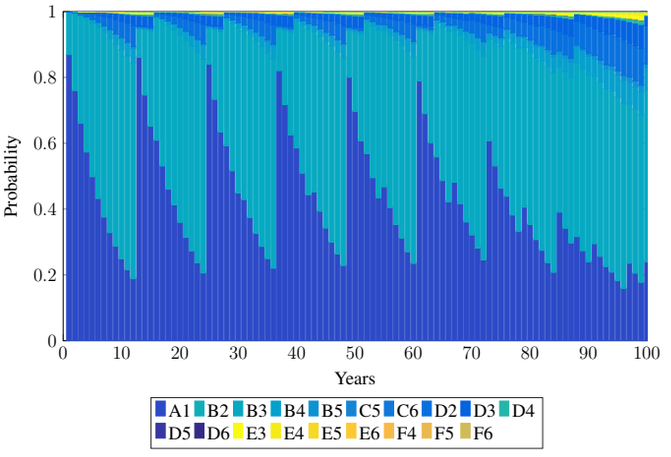


Figure 11: Simulation of a concrete girder element <5Km from the sea.

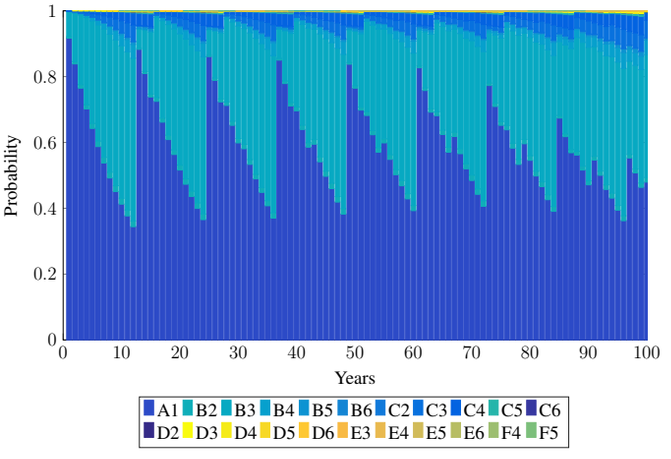


Figure 12: Simulation of a concrete girder element >25Km from the sea.

9 CONCLUSION

The international standards for Asset Management (AM) discuss safety as a key aspect of good AM (International Organization for Standardization 2014). With an aligned AM strategy and objectives, understanding the main risks that can cause an asset to breach the safety threshold can be avoided. In the work presented, a robust WLCC model was presented which develops new insight into how the policies which govern the management bridge assets affect them using historic condition data. Then an analysis into the main factors affecting deterioration allow bridge managers to understand the environmental factors which are the highest risk of causing rapid deterioration. Finally, by combining the stressor analysis and the WLCC model, a financial, safety and maintainability insight can be gained about the stressors, all of which can improve the AM understanding and help mitigate risks of assets falling below the BSL.

10 ACKNOWLEDGEMENTS

John Andrews is the Royal Academy of Engineering and Network Rail Professor of Infrastructure Asset Management. He is also Director of The Lloyds Register Foundation (LRF) Resilience Engineering Research Group at the University of Nottingham. Robert Dean is a Principal Engineer within the Safety, Technical and Engineering team at Network Rail. Luis Canhoto Neves is an Assistant Professor in the Resilience Engineering Research Group at the University of Nottingham. Dovile Rama is the Network Rail Research Fellow in Asset Management. Panayioti Yianni is an Asset Management Consultant within Jacobs' Asset Management and Systems Assurance team. The research was supported by Network Rail and the Engineering and the EPSRC grant reference EP/L50502X/1. They gratefully acknowledge the support of these organizations.

REFERENCES

Agrawal, A. K., A. Kawaguchi, & Z. Chen (2010). Deterioration rates of typical bridge elements in New York. *Journal of Bridge Engineering 15*(4), 419–429.

Arditi, D. & O. Tokdemir (1999). Comparison of Case-Based Reasoning and Artificial Neural Networks. *Journal of Computing in Civil Engineering 13*(3), 162–169.

British Standards Institution (2004). Systems and software engineering. High-level Petri nets. Concepts, definitions and graphical notation. Technical report, British Standards Institution.

British Standards Institution (2012). Analysis techniques for dependability — Petri net techniques. Technical report.

Cesare, M. A., C. Santamarina, C. Turkstra, & E. H. Vanmarcke (1992). Modeling bridge deterioration with Markov chains. *Journal of Transportation Engineering 118*(6), 820–833.

Dijkstra, E. W. (1959). A note on two problems in connexion with graphs. *Numerische Mathematik 1*(1), 269–271.

Ditlevsen, O. (1984). *Probabilistic Thinking: An Imperative In Engineering Modelling*. Department of Structural Engineering, Technical University of Denmark.

Frangopol, D. M., M.-J. Kallen, & J. M. van Noortwijk (2004). Probabilistic models for life-cycle performance of deteriorating structures: review and future directions. *Progress in Structural Engineering and Materials 6*(4), 197–212.

Huang, R.-Y., I.-S. Mao, & H.-K. Lee (2010). Exploring the Deterioration Factors of RC Bridge Decks: A Rough Set Approach. *Computer-Aided Civil and Infrastructure Engineering 25*(7), 517–529.

International Organization for Standardization (2014). ISO 55001:2014 Asset management – Management systems – Requirements. Standard, Geneva, CH.

Jensen, K. (1997). A brief introduction to coloured Petri Nets. In E. Brinksma (Ed.), *Tools and Algorithms for the Construction and Analysis of Systems*, Number 1217 in Lecture Notes in Computer Science, pp. 203–208. Springer Berlin Heidelberg.

Jiang, Y. & K. C. Sinha (1989). Bridge service life prediction model using the Markov chain. *Transportation Research Record* (1223), 24–30.

Le, B. & J. Andrews (2014). Modelling Railway Bridge Asset Management using Petri-Net Modelling Techniques. In *Proceedings of the Second International Conference on Railway Technology: Research, Development and Maintenance*.

Morcous, G. (2006). Performance prediction of bridge deck systems using Markov chains. *Journal of Performance of Constructed Facilities 20*(2), 146–155.

Morcous, G., Z. Lounis, & Y. Cho (2010). An integrated system for bridge management using probabilistic and mechanistic deterioration models: Application to bridge decks. *KSCE Journal of Civil Engineering 14*(4), 527–537.

Morcous, G., H. Rivard, & A. Hanna (2002a). Case-Based Reasoning System for Modeling Infrastructure Deterioration. *Journal of Computing in Civil Engineering 16*(2), 104–114.

Morcous, G., H. Rivard, & A. Hanna (2002b). Modeling bridge deterioration using case-based reasoning. *Journal of Infrastructure Systems 8*(3), 86–95.

National Oceanic and Atmospheric Administration (NOAA) (2015). GSHHG - A Global Self-consistent, Hierarchical, High-resolution Geography Database. *https://www.ngdc.noaa.gov/mgg/shorelines/gshhs.html*.

Network Rail (2010). Handbook for the examination of Structures Part 11A: Reporting and recording examinations of Structures in CARRS. *NR/L1/CIV/006/11A*.

Network Rail (2012a). Policy on a Page: Structures.

Network Rail (2012b). Structures Asset Management Policy and Strategy. pp. 219.

Robelin, C.-A. & S. M. Madanat (2007). History-dependent bridge deck maintenance and replacement optimization with Markov decision processes. *Journal of Infrastructure Systems 13*(3), 195–201.

Scherer, W. & D. Glagola (1994). Markovian Models for Bridge Maintenance Management. *Journal of Transportation Engineering 120*(1), 37–51.

Sobanjo, J. (1997). Neural network approach to modeling bridge deterioration. In *Proceedings of the 1997 4th Congress on Computing in Civil Engineering, June 16, 1997 - June 18, 1997*, Computing in Civil Engineering (New York), pp. 623–626. ASCE.

Sobanjo, J. O. & P. D. Thompson (2011). Enhancement of the FDOT's Project Level and Network Level Bridge Management Analysis Tools.

Technical Strategy Leadership Group (TSLG) (2012). Rail Technical Strategy. Technical report, Rail Research UK Association.

Maintenance, Safety, Risk, Management and Life-Cycle Performance of Bridges – Powers, Frangopol, Al-Mahaidi & Caprani (Eds)
© 2018 Taylor & Francis Group, London, ISBN 978-1-138-73045-8

Network Importance of Melbourne's Metropolitan Bridges – Development of a Strategic Bridge Prioritisation Framework

S. Di Cicco
Manager Structures, VicRoads Metropolitan North West Region

ABSTRACT: VicRoads manages a network of some 1,700 bridges across metropolitan Melbourne. Many of these bridges are critical for the safe operation of the transport network which provides for the movement of passenger and freight vehicles and public transport users. The development of bridgeworks programs, to address maintenance, repair and bridge capacity deficiencies therefore requires careful prioritisation.

VicRoads has typically prioritised its bridgeworks programs based on the age and condition of a bridge as well as any changes in performance requirements that inevitably occur over time, such as the introduction of heavier freight vehicles and/or trams.

While the above approach has also taken into account factors such as the importance of the bridge to the transport network, there has not been to date an explicit framework upon which bridgework priorities could be based on. As a result, VicRoads has had mixed success in procuring funding for its bridgeworks program.

In response, VicRoads is developing a prioritization methodology, referred to as a 'Strategic Bridge Prioritisation Framework' (or "Framework" for short) to ensure that the broader needs of the transport network are seen to be strategically and effectively accounted for.

This paper presents the key features and benefits of the 'Framework' which include:

• Adoption of a rational methodology for the prioritisation of bridge projects based on maximising benefits to the overall transport network and the community.
• Priorities to be seen to clearly and transparently addressing the criticality and strategic value of the bridge project to the overall transport network and reflecting both short and long term bridge asset management strategy.
• Implications for the community clearly identified, should the works not be funded. These implications could include service reductions, load limits, increased travel times, environmental effects and associated economic costs.
• Development of consolidated business cases for the management of VicRoads bridges which maximise benefits to the overall transport network and the community.

Keywords: bridge assessment, bridge maintenance, asset management strategy, prioritisation methodology.

1 INTRODUCTION

VicRoads manages a network of some 1,700 bridges across metropolitan Melbourne. Many of these bridges are critical for the safe operation of the transport network which provides for the movement of passenger and freight vehicles and public transport users.

The development of bridgeworks programs, which specify works based on the assessment of maintenance and repair needs as well as bridge load capacity deficiencies therefore requires careful prioritisation.

This paper reports on the development of a prioritisation methodology, to ensure that bridgework programs are prioritised to ensure that the broader needs of the transport network and the associated benefits to the community are strategically and effectively accounted for.

2 BACKGROUND

VicRoads has typically prioritised its bridgeworks program (which includes assessment, maintenance,

repair and/or bridge strengthening activities) based on the age of the bridge, its load capacity and its condition.

While this approach has also taken into account factors such as the importance of the bridge to the passenger and freight networks, (as well as economic costs to the community should any identified works not be carried out) there has not been to date an explicit framework against which bridge assessment and maintenance could be prioritised.

Additionally, internal reviews within VicRoads business areas responsible for managing bridge assets have identified this basic reliance on bridge condition data as a potential weakness of funding submissions.

This paper reports on a prioritisation methodology currently being developed. The methodology is referred to as a 'Strategic Bridge Prioritisation Framework' or "Framework" for short.

Details of the methodology are provided including its aims, what criteria it is based on, its limitations and finally, following stakeholder review, additional enhancements have been identified..

3 STRATEGIC BRIDGE PRIORITISATION FRAMEWORK

3.1 *General*

In recent years, VicRoads has had mixed success in obtaining funding for bridge repair, maintenance and bridge strengthening projects. Key reasons for this mixed success include:

- A lack of clarity about why certain bridges were put forward for funding over others. In particular, the way in which bridge projects were being prioritised as part of a long term asset management strategy, was not clear.
- Uncertainty regarding the criticality of the bridges to the overall transport network, particularly the implications for the community if the proposed works were not carried out.

The development of the Framework which addresses these issues encapsulates several components:

- Identification and weighting of criteria which were considered for bridge prioritisation purposes. These included factors such as access to local facilities, volume of traffic, congestion, and importance of the bridge to the public transport network.
- Identification of data sources for each of the criteria.
- Development of a Geographical Information System (GIS) to provide geographical data for all bridges (eg. how close a bridge is to a school or hospital)

The Framework provides a mechanism for VicRoads to prioritise all of the bridges in the metropolitan area for the purposes of determining which bridges are most significant to the transport network. "Significance" is a difficult concept to define for the purposes of the Framework. What it means in essence is that a "significant bridge" is one that plays an important role in a local or whole of metropolitan capacity for a mix of user groups, including freight, commuter, private vehicles, public transport and others. In particular, the Framework identifies the network importance of the bridge should an incident occur which causes the bridge to be shut for a period of time to undertake repairs.

The Framework encapsulates a range of weighted factors or inputs which together are used to create a priority list for all bridges in the metropolitan network. This is a strategic approach which seeks to tell us which bridges, on balance, are most important for the network.

There is no 'scientific' approach to the weighting and scoring process, instead it relies on experienced judgment combined with an iterative approach which takes into account Government priorities, experience and expertise within VicRoads and other agencies about how the transport network operates, and an understanding of bridge users and their needs.

The Framework and GIS is intended to support existing VicRoads management tools and interface with the existing VicRoads' bridge condition information.

The Framework, addresses the significant challenges faced by VicRoads with regard to identification and prioritisation of the required maintenance, repair and/or strengthening works and will take into account economic impact factors in the prioritisation process. Specifically, the Framework will:

- Provide a transparent, coherent and cohesive process to assist VicRoads to prioritise the assessment and maintenance of its metropolitan bridge network.
- Be used as a decision making tool by VicRoads to identify and demonstrate remedial or strengthening priorities.
- Provide a basis by which to plan and prioritise future data collection including periodic inspection of bridges.

The Framework can usefully address the potential weaknesses of previous funding bids by identifying the bridges' relative network importance, supple-

menting condition data and the economic case by providing a justification of why one bridge requiring works may be prioritised for funding over another.

3.2 *Framework*

3.2.1 *Framework Methodology - Categories*

In this Framework, five categories have been identified. These categories cover key issues that should be considered when deciding the importance of a bridge to the network. They also provide a strategic fit with VicRoads priority networks such as the Principal Freight Network (PFN). These five categories are weighted, and drive the overall bridge rankings. The five categories are:

- Freight movement – this refers to the importance of a bridge for the movement of freight within the metropolitan area and beyond.
- Vehicle movement – this refers to the significance of the bridge for all road vehicles and the congestion on the route.
- Features below bridge – the feature below the bridge may be important in the event of a disruption to the bridge or major maintenance. An event of this nature has the potential to disrupt whatever activities take place below the bridge in question, be that a road, rail or a major asset such as the Port of Melbourne.
- Community access – this refers to the significance of a bridge for the local community to gain access to local services such as a hospital, school or emergency provider.
- Commuter movement – this refers to the importance of the bridge for the public transport network. This focuses on the impact for road based services such as trams and buses.

3.2.2 *Framework Methodology – Criteria*

These include factors such as proximity to services such as hospitals, volume of traffic, and whether the bridge is on a freight route or public transport route. These have all been weighted, and data sets have been identified and assigned to each of these measures.

An overall 'score' for each bridge can then be calculated which reflects the data and weightings for each criterion and for each category. The proposed Framework is illustrated in Figure 1 (next page).

Refer to Figure 1-The Framework, criteria and weightings

3.3 *Framework Outputs*

The table below shows the Top 30 bridges based on their network importance rank considering all VicRoads bridges in the Metropolitan area database.

Refer to Figure 2 for table

The bridges at the top of the list with high scores are generally those which:

- Cater for a number of transport modes combined with high traffic volumes
- Are included on the strategic freight network
- Are on a preferred traffic route

Bridges with a low traffic volume which do not have a public transport mode do not appear at the top of the list.

Note that the Westgate Bridge was not scored as the most important bridge on the network (refer Cl 3.4.3 - Stakeholder Views, below).

3.4 *Framework Enhancements*

3.4.1 *Economic Impacts*

Another factor which needs to be taken into account when prioritising bridge projects is the economic cost to the community if maintenance or rehabilitation work is not carried out. Service reductions such as the imposition of a load limit or emergency lane closures (to carry out unplanned repair) carry a measurable cost to the community and the environment in the form of additional travel time and vehicle km travelled.

It is intended to incorporate a theoretical economic cost for each bridge into the Framework. All prospective bridge repair, maintenance or strengthening projects will incorporate an economic impact element demonstrating the costs to the community should the project not proceed. These costs can be considered an economic benefit of the project if implemented. It is therefore beneficial that the economic value in completing the required work is known.

This can be achieved by assuming traffic restrictions would be applied on the bridge until maintenance could be completed. The economic cost of the scenarios considered can then be calculated from the direct cost of the reductions in level of service as well as the impact of this on other road users.

The scenarios generally considered fall into two categories as follows, on the basis that avoidance of maintenance could result in either a planned, long-term load restrictions or an unplanned, short-term closure to allow emergency remedial maintenance to occur.

• A load restriction, forcing articulated vehicles to divert around each bridge and where applicable, restricting trams from crossing the bridge. This scenario provides the likely impact on the community in the event that bridge capacity was found to be deficient and heavy vehicles were diverted. It can be assumed that lighter commercial and private vehicles, pedestrians and cyclists are not affected by the load restriction.
• A total bridge closure, forcing all vehicles to divert around the bridge. This scenario provides the likely impact on the community in the event that bridge condition required the bridge to be closed for a short period to undertake emergency repairs in the event of a structural failure.

The table below shows an example of the annual avoided costs of imposing a 12 month load limit and restricting trams on Victoria Street Bridge over the Yarra River. Articulated vehicles will primarily divert around this bridge, under the load limit scenario using Studley Park Drive and Bridge Road, resulting in articulated vehicles spending more time on the road and travelling further distance. This frees up capacity on Victoria Street such that light vehicles travel a shorter net distance but spend more time on the road.

Restricting trams results in public transport users spending more time travelling to their destination. The effect is a net cost to the economy if a load limit and tram restrictions are imposed on Victoria Street Bridge over the Yarra River.

Victoria Street - SN6248			
	Light	Articulated	Tram
Daily Δ Hours	0	20	2,000
Daily Δ KMs	-240	-210	N/A
Annual Cost - 12 month load limit + tram restrictions			
Travel time	$ 36,000	$ 519,000	$ 7,110,000
Vehicle operating costs	$ 21,000	-$ 157,000	N/A
Externalities	-$ 5,000	-$ 73,000	N/A
Total per vehicle Class	$ 52,000	$ 289,000	$ 7,110,000
Capital costs	N/A	N/A	$ 2,000,000
Total Annual Cost			$ 9,451,000

The costs were calculated using the Austroads Guide to Project Evaluation (AGPE04-12) including:
- Road user costs (travel time costs and vehicle operating costs)
- Non-user costs (environmental externality costs)
- Capital costs.

It is proposed to include an element of the economic impact as a criterion within the bridge prioritisation Framework. The GIS can facilitate this by calculating the best diversion route for each bridge and multiplying this by traffic volume. This factor when viewed independently of the Framework will give an accurate ranking of the expected economic costs of imposing a load limit or diversion for each bridge. However this factor will also be weighted and added to the Framework and overall ranking of each bridge.

3.4.2 *Bridge conditions*

Bridge condition is not included in the Framework. The current intent of the Framework is to assess the bridges importance within the overall road network from a traffic and community point of view.

Using condition data to determine which projects should receive funding has traditionally been based on the technical need or urgency of the condition. Carrying out repairs and maintenance as a result of condition based assessment only will not necessarily serve the community efficiently, although it may be required to maintain the current level of service of a particular bridge. However if that bridge is not critically important to the network or the community, then accepting a lower level of service (load restriction) may be a better use of resources.

Effective asset management requires tools such as this Framework to more accurately target scarce resources.

Adding bridge data such as condition data to the GIS is a process which is proposed to be part of a wider Bridge Management System. This is a system where all data related to a bridge including drawings, reports, previous inspections, photographs etc. is housed in a database along with its geographical and condition information. The database and geographical information can then be filtered and queried according to user priorities. Advanced and well maintained Bridge Management Systems can alarm when inspections or maintenance is due. With the addition of maintenance cost rates it is possible for such systems to forecast future expenditure.

3.4.3 *Stakeholder Views*

A series of workshops in August and September 2014 were held to showcase the methodology of the Framework and seek feedback regarding its applicability and accuracy. The current Framework was also presented to key internal VicRoads stakeholders and their views have been taken into consideration in the

development of the Framework, however further work remains.

One of the main outstanding issues concerned the lack of consideration for future growth, which is not currently scored under any of the weighted factors. The importance of the Principal Freight Network was also raised and how the development of freight corridors can be captured in the Framework.

The applicability of the Framework to regional areas was also an issue for concern. Current factors considered, and their weightings, could skew the scoring of bridge assets in favor of the metropolitan regions. This could possibly lead to unequal funding allocations. How to fairly apply the principle of connectivity to the scoring of assets was discussed at many of the workshops. It was noted that connectivity in regional areas may be more important than in metropolitan areas where a readily available alternative route exists. The nature of connectivity is different in rural areas given that community facilities need not be close to a bridge to impact on its importance. Quite often no readily available alternative route is available to a school / hospital etc. The Framework needs to be amended somehow to reflect this.

The fact that the Westgate Bridge was not scored as the most important bridge on the network was noted. The Westgate is generally considered the most important bridge on the network from a strategic point of view. It's scoring falls down on community and public transport factors. The importance of the connectivity of the bridge, given that an alternative route is not readily available, appears to be the key factor in the framework requiring attention.

3.4.4 *Future Steps*

A number of the following modifications are planned in the future based on feedback from users and funding agencies:

- Investigate the addition of a GIS route calculation to determine the distance required to take an alternate route around the bridge in the event of a closure or load restriction. This factor, when multiplied by traffic or freight volume, can be considered as an economic impact criterion and weighted accordingly.
- The development and rollout of a web based GIS interface to allow VicRoads staff to use and develop the tool. For example this will allow users to query the database which bridges are on a Principal Freight Network and rank this subset according to priority for targeted inspections or maintenance.
- Adopting the GIS to calculate Framework criteria more suited to rural locations. For example, bridges within 1-2km of a school or hospital to be given the same score as a bridge within 50m of a hospital in urban areas. These kinds of modifications will reduce disadvantage to rural areas for project funding.
- The investigation and development of additional categories and criteria based on bridge replacement value and complexity. This can be achieved by weighting criteria associated with bridge dimensions (length, height etc.)
- Increase ratings for traffic flow to 5 categories to incorporate roads which have the very highest traffic volume on the network and ensure they have a sufficiently high ranking (e.g. Westgate Bridge).
- The investigation and development of additional categories and criteria based on bridge heritage value. This can be achieved by using data from the Heritage Victoria database.
- Future Growth in traffic volumes to be determined from Victorian Integrated Transport Model (VITM) and incorporated into the Framework under the vehicle movement category – a future VITM model will incorporate expected changes to the network in the future.
- Future growth in Commercial vehicles (%CV) to be determined and added to the freight movement category.
- Bus passenger numbers per route to be added in the Commuter Movement category.
- Development of route priority classes within the GIS such as the Principal Bike Network and future Freight Network classes.

4 CONCLUSIONS

1. VicRoads has had mixed success in obtaining funding for bridge repair, maintenance and bridge strengthening projects. Key reasons for this mixed success include:

   - A lack of clarity about why certain bridges were put forward for funding over others. In particular, the way in which bridge projects were being prioritised as part of a long term asset management strategy, was not clear.

   - Uncertainty regarding the criticality of the bridges to the overall transport network, particularly the implications for the community if the proposed works were not carried out.

2. As a response, VicRoads commissioned AECOM (1) to develop a 'Strategic Bridge Prioritisation Framework' methodology.

3. The key features and benefits of the 'Framework' include:

   - Adoption of a rational methodology for the prioritisation of bridge projects based on maximizing benefits to the overall transport network and the community.

   - Priorities to be seen to clearly and transparently addressing the criticality and strategic value of the bridge project to the overall transport network and reflecting both short and long term bridge asset management strategy.

   - Implications for the community clearly identified, should the works not be funded. These implications could include service reductions, load limits, increased travel times, environmental effects and associated economic costs.

   - Development of consolidated business cases for the management of VicRoads bridges which maximise benefits to the overall transport network and the community.

4. Future improvements to the 'Framework' being considered include:

- Integration of the Framework with existing VicRoads management tools and bridge condition information.

- Possible addition of a GIS route calculation to determine the distance required to take an alternate route around the bridge in the event of a closure or load restriction. This factor, when multiplied by traffic or freight volume, can be considered as an economic impact criterion and weighted accordingly.

- The development and rollout of a web based GIS interface to allow VicRoads staff to use and develop the tool. For example this will allow users to query the database which bridges are on a Principal Freight Network and rank this subset according to priority for targeted inspections or maintenance.

- Adopting the GIS to calculate Framework criteria more suited to rural locations. For example, bridges within 1-2km of a school or hospital to be given the same score as a bridge within 50m of a hospital in urban areas. These kinds of modifications will reduce disadvantage to rural areas for project funding.

- The investigation and development of additional categories and criteria based on bridge replacement value and complexity. This can be achieved by weighting criteria associated with bridge dimensions (length, height etc.)
- The investigation and development of additional categories and criteria based on bridge heritage value. This can be achieved by using data from the Heritage Victoria database.
- Increase ratings for traffic flow to 5 categories to incorporate roads which have the very highest traffic volume on the network and ensure they have a sufficiently high ranking (e.g. Westgate Bridge).

- Future Growth in traffic volumes to be determined from Victorian Integrated Transport Model (VITM) and incorporated into the Framework under the vehicle movement category – a future VITM model will incorporate expected changes to the network in the future.

- Future growth in Commercial vehicles (%CV) to be determined and added to the freight movement category.

- Bus passenger numbers per route to be added in the Commuter Movement category.

- Development of route priority classes within the GIS such as the Principal Bike Network and future Freight Network classes.

5 ACKNOWLEDGMENTS

- Strategic Bridge Prioritisation Framework developed by AECOM [1]
- Assistance from Karsten Forsterling , Principal Engineer AECOM [1]
- Luay Butrus – Team Leader Structures VicRoads MNW

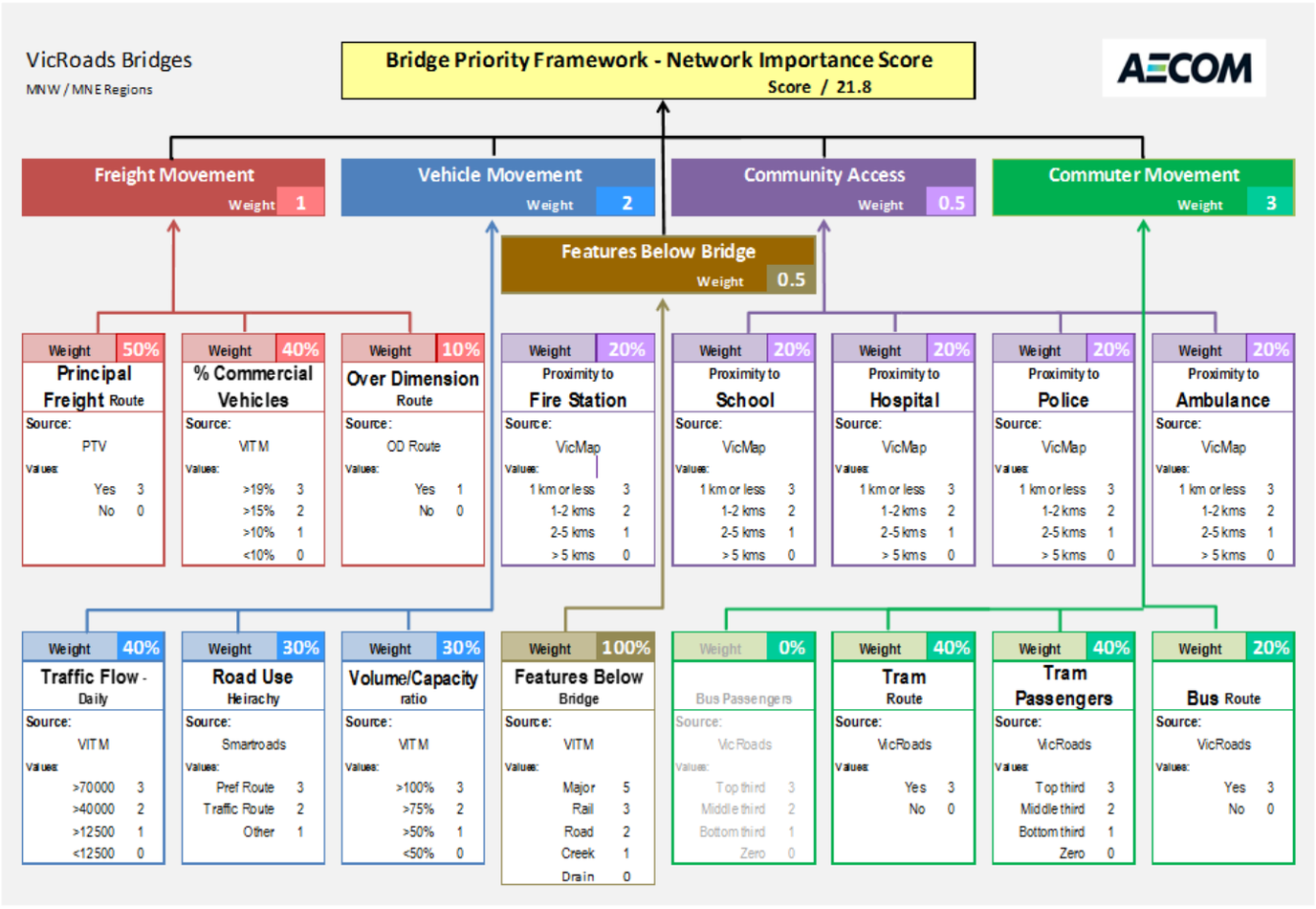
The authors wish to thank the Regional Director Metro North West of VicRoads for permission to publish this paper. The views expressed are those of the authors and not necessarily those of VicRoads

6 REFERENCES

1. AECOM, Network Importance of metropolitan Bridges (Strategic GIS Framework), 2014

7 APPENDIX

7.1 *Figure 1*



7.2 *Figure 2*

Rank	Structure ID	Road Name	Featured Cr	Weighted Score	Freight Movement	Community Access	Vehicle Movement	Feature be-low	Commuter movement	Year con-structed
1	SN6520	West Gate Fwy	2510 Princes Hwy East	19.9	2.7	2.8	4.0	2	2.6	1987
1	SN6521	West Gate Fwy	Princes Hwy/Fwy (East) [F+R]	19.9	2.7	2.8	4.0	2	2.6	1988
3	SN3298	Hoddle Hwy	2510 Princes Hwy East	18.3	1.5	2.4	3.3	2	3.0	1967
4	SN8973	Princes Hwy East	St Kilda Junction	18.1	1.5	2.4	3.2	2	3.0	1979
5	SN0477	Western Link Tollway Fwy	Yarra Riv To Flem. R	17.6	2.7	2.2	3.6	2	2.2	0
5	SN2775	Princes Hwy West	Upfield Railway Line Over Bo	17.6	2.7	2.2	3.6	2	2.2	1930
7	SN3312	St Kilda Rd	Princes Hwy/Fwy (East) [F+R]	17.5	1.5	2.4	2.9	2	3.0	1967
8	SN8845	Metropolitan Ring Rd	Plenty Valley Hwy	17.1	1.9	2.0	3.2	2	2.6	1996
9	SN1710	Mount Alex-ander Rd	Moonee Ponds Creek	16.7	2.8	2.2	3.1	1	2.2	1997
10	SN2672	Princes Hwy West	Moonee Ponds Creek	16.6	2.7	2.2	3.1	1	2.2	1920
11	SN8846	Metropolitan Ring Rd	Plenty Valley Hwy	16.5	1.9	2.0	2.9	2	2.6	1996
12	**SN6225**	**West Gate Fwy**	**Yarra River/Todd Rd/Rail**	**16.1**	**2.7**	**1.2**	**5.5**	**5**	**0.6**	**1978**
13	SN8985	Burke Rd	2000 Monash Fwy	15.8	2.7	1.8	3.7	2	1.6	1996
14	SN8376	Victoria St	Railway Over Victo-ria St	15.5	0.0	3.0	2.5	2	3.0	1930
15	SN8619	Yarra Bank Hwy	St Kilda Rd	15.4	0.0	2.4	2.6	2	3.0	1969
16	SN9443	Docklands Hwy	Yarra River	15.2	2.0	2.4	2.1	1	2.6	2000
17	SN6272	Glenferrie Rd	Gardiners Creek	15.2	2.7	1.8	2.5	1	2.2	1912
18	SN8398	Queens Pde	Railway Over Queens Pde	15.1	0.0	1.8	3.2	2	2.6	1930
19	SN0959	Docklands Hwy	Collins Street	14.7	2.0	2.2	1.9	0	2.6	0
20	SN3010	Princes Hwy East	Brighton Rail (Dan-denong R	14.7	0.0	2.6	3.4	3	2.2	1957
21	SN2583	West Gate Fwy	Newport-Sunshine Rail/Foga	14.5	2.7	2.0	4.5	3	0.6	1970
21	SN2586	West Gate Fwy	Newport-Sunshine Rail/Foga	14.5	2.7	2.0	4.5	3	0.6	1970
23	SN6344	Royal Pde	Royal Park-Fitzroy Rail(Disus	14.4	0.0	2.0	3.4	3	2.2	1960
24	SN6237	Spencer St	Yarra River	14.3	0.0	2.6	2.0	1	3.0	1930
25	SN8386	Burwood Hwy	Railway Over Bur-wood Hwy	14.2	0.0	2.4	3.2	2	2.2	1930
26	SN2802	Princes Hwy West	Melbourne-Broadmeadows R	14.1	0.0	2.2	3.2	2	2.2	1930
26	SN2809	Princes Hwy East	Brighton Rail (Dan-denong R	14.1	0.0	2.6	3.1	3	2.2	1930
28	SN0523	Church St	Yarra River	14.1	2.7	2.0	2.5	1	1.8	1923
29	SN6248	Victoria St	Yarra River	13.9	0.0	2.6	2.4	1	2.6	1884
29	SN6340	Bridge Rd	Yarra River	13.9	0.0	2.6	2.4	1	2.6	1861

MS02: Innovative methods in strengthening of concrete bridges

Organizers: R. Kalfat, R. Al-Mahaidi & B. Pham

Maintenance, Safety, Risk, Management and Life-Cycle Performance of Bridges – Powers, Frangopol, Al-Mahaidi & Caprani (Eds)
© 2018 Taylor & Francis Group, London, ISBN 978-1-138-73045-8

Experimental investigation into the fatigue life of patch anchors used to anchor FRP laminates bonded to concrete

A. Al-Saoudi, R. Al-Mahaidi & R. Kalfat
Swinburne University of Technology, Melbourne, Australia

ABSTRACT: During the recent decades, the number of vehicles passing the bridges has dramatically increased in many many countries around the world compared with initial design consideration. Excessive cycling loading lead to fatigue degradation in the structural element and if untreated, severe damage may occur. Externally bonded Fiber Reinforced Polymers (FRPs) has become one of the successfully methods of upgrading and retrofitting reinforced concrete RC structures such as bridges and highways. Although extensive research has been carried out to investigate the performance of this exterior strengthening systems, the majority of report studies addressed the effectiveness of this technique under monotonic loading. However, to date, no unique design guidelines specified the fatigue life behaviour of this externally FRP anchorage devices when subjected to cyclic loading. This paper presents the experimental results of externally FRP bidirectional sheets bonded to RC beams and subjected to different cyclic load application. The results demonstrated on the basis of maximum stress ratio and relative fatigue number of cycles. The outcomes of this study showed that there is no fatigue degradation when the maximum stress ratio is 60% of the ultimate static capacity, and the fatigue test remained running until 5.6 million cycles without observing any crack initiation along the bond line. Further details of the test results with recommendation for future research study are also outlined.

1 INTRODUCTION

All bridges and highways experience numerous levels of cyclic loading throughout their lifetime. This is due to loading and unloading cycles caused by the passage of heavy trucks and vehicles. Excessive cyclic loading has been found to result in fatigue degradation in structural members. Externally-bonded FRP composites adhered to the concrete had become a popular method for strengthening RC structures, typically highway and railway bridges. Many existing concrete bridges are being strengthened with FRP composites due to increased loading or deterioration.

External application of FRP material provides a practical solution for improving the overall performance of reinforced concrete structures. This application can also be used in a repair capacity for structures that have undergone moderate earthquake damage or to reinforce structures that are considered vulnerable or sub-standard. The effectiveness of using externally-bonded FRP in the retrofitting process depends primarily on the interface bond behaviour between the FRP sheets and the concrete substrates. The major role of the interface between FRP externally bonded to concrete is the mechanism of shear stress transfer between the two materials. Research has shown that the bond interface between FRP and concrete in concrete beams strengthened with externally-bonded FRP plays a crucial role (Chen and Teng 2001). FRP debonding failure is very frequently observed in these structures under both static and fatigue loadings. Previous studies have shown that stresses in CFRP laminates are transferred to concrete beams via the adhesive interfaces, and the effectiveness of the strengthening technique is largely determined by the bond behaviour between the CFRP material and the concrete (Kalfat and Al-Mahaidi 2011).

Although extensive research has been conducted on the behaviour of the externally FRP-concrete bond interface, the vast majority of the work has been concerned with monotonic static loading, and few studies have been concerned with the bond behaviour under cyclic loading that can be caused by seismic tremors or traffic loads (Martinelli and Caggiano 2014). Different test methods were conducted by Belarbi (2011) to assess the average interfacial bond strength, including single-lap, double-lap, bending, and inserted tests. These strengthening methods were used in many research studies. For instance, Chen and Teng (2001), Chen et al. (2012) and Xie et al. (2016) performed fatigue tests on beams strengthened in flexure using one

and two strips of CFRP on the soffit surface. The authors found that the beams strengthened with two strips had greater fatigue life than beams with a single strip of strengthening due to the effectiveness of the dual strips in restraining crack opening

The aim of this research study is to investigate the fatigue life performance of externally bonded FRP-to-concrete joints anchored with bidirectional fabric patch anchors. Anchorage devices are typically used to mitigate the longitudinal shear stresses and peeling stresses that often initiate at fibre termination points inducing premature debonding failure of FRP-to-concrete joints. Generally, anchors have several types, however, the patch anchor is the main type considered in this research study which utilizes bidirectional fabric sheets. In particular, anchors are used in this research to achieve higher strain in the FRP prior to debonding and allow a higher degree of strengthening to be achieved using less material. The main problem with bonding and debonding is the mechanism and mode of failure that can occur between the FRP and the concrete surface, while debonding issues play an important role in member performance and safety. This paper presents the experimental results of investigating the fatigue life performance of externally FRP bidirectional sheets bonded to concrete surface and subjected to different static and cyclic load application. The results demonstrated on the basis of maximum stress and relative fatigue number of cycles. The results showed that no fatigue degradation was observed when the maximum stress is 60% of the ultimate static capacity, and the fatigue test remained running up to 5.6 million cycles without failure occurred. Further details of the test results and summary of conclusion are outlined in the following sections.

2 EXPERIMENTAL WORK

2.1 *Specimen design*

Six specimens of RC blocks with dimensions of 400 × 400 × 250mm were prepared for this experimental study. Each specimen was reinforced with steel cages of N4 Φ12mm closed ties through each direction. A spacing of 120mm was allowed between the bars with a reinforced cover of 30mm.

2.2 *Specimen preparation*

After casting the concrete, all specimens were painted with water-based wax emulsion (cure compound), as this liquid material provides efficient curing in minimum time. Following the curing stage, sand-blasting was implemented on the larger faces of the concrete blocks (400 x 400mm). This is to ensure that both surfaces had an adequate level of roughness so that ideal bond application could be achieved between the FRP material and the concrete surface.

2.3 *Use of FRP application*

The specimen had two layers of bidirectional fabric sheets applied to the concrete, with CFRP laminate strip placed between each fabric layer. The fabric sheet with dimensions of 400 x 300mm was applied to the concrete surface. The first fabric layer and its saturant component were applied using the wet-lay-up method and left for a sufficient time to reach a tacky state. The specimens were then cured for 72 hours using a set of 250W heat lamps to maintain a curing temperature of 35C. When the specimens were cured, strain gauges were attached at selected locations evenly along the CFRP laminate surfaces and across the bidirectional sheet, as shown schematically in Figure 1. A typical photograph of the anchored model inside the test machine is depicted in Figure 2.

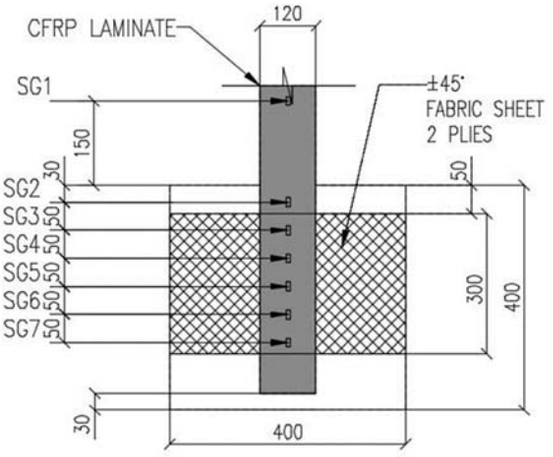


Figure 1. Sketch of the anchored model



Figure 2. Anchored model inside the MTS machine

2.4 *Material properties*

Most of the material properties supplied by the manufacturers were tested experimentally to verify the properties prior to their use in the FRP application. However, some parameters were used as per manufacture' specification, noted with (*). A summary of the materials properties used in the experimental tests is presented in Table 1.

Table 1. Summary of material properties.

Properties	Concrete	Saturant	CFRP laminate	CFRP sheets
Compressive strength, (MPa)	32	-	-	-
Tensile strength (MPa)	2.7	>50*	21	3790*
Young's modulus, (GPa)	42	>3.0*	181	230*

3 EXPERIMENTAL WORK

3.1 *Instrumentation of the test frame*

The experimental work was conducted on a steel frame first designed by Kalfat et al. (2011). However, the frame was developed further to comply with fatigue test considerations. The rig configuration was arranged so that it could perform the near end-supported single-pull test. The test frame has two steel plates top and bottom where the specimen can be placed and secured by bolts. As the fatigue test includes applying loads at high frequency, some modifications to the test frame were adopted in order to increase its stiffness. These included replacing the top and bottom plates with thicker plates of 50mm thickness each, and the addition of extra vertical thread bars to ensure high levels of resistance to the cyclic loads with minimal movement and vibration. Figure 3 shows a sketch of test frame.

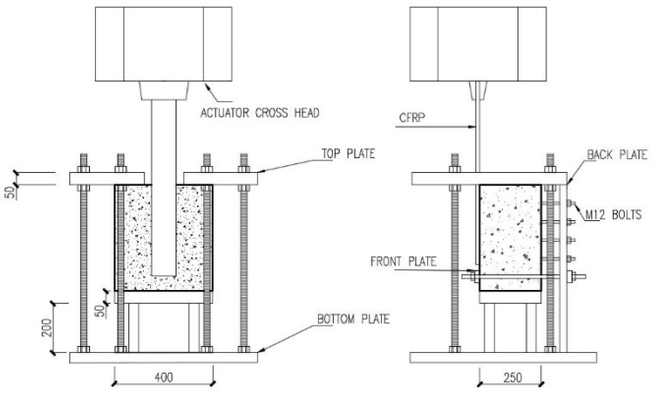


Figure 3. Sketch of the test frame

3.2 *Results*

In total, two static tests and four fatigue tests were performed on the anchored model. The average static failure load was used to assess the maximum and minimum stress of fatigue loading. Two points were used to study the fatigue life behaviour on the basis of maximum stress ratios and corresponding fatigue number of cycles, S-N relationship. These points were 70 and 60% of the ultimate static capacity. Each point represents a fatigue test which was repeated on an identical specimen for comparison and validation purposes. The details of the experimental results with conclusion outcome are presented below.

The two static tests showed good agreement in the failure load, and the first anchored specimen failed at 157kN and the second failed at 163kN. The average ultimate static failure load was therefore considered to be 160kN. It is important to note that the two static tests presented good correlation results in the strain distribution during the applied load as shown in Figure 4 and 5.

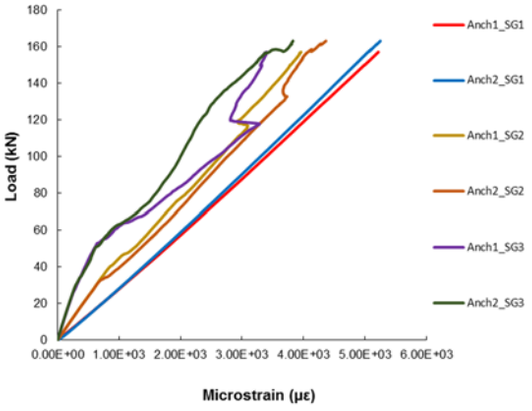


Figure 4. Static test: Load vs. micro-strain (SG1; SG2; SG3)

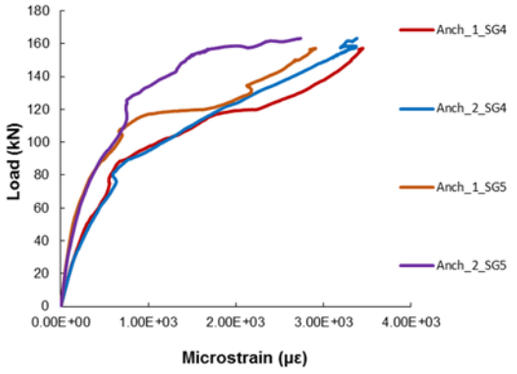


Figure 5. Static test: Load vs. micro-strain (SG4; SG5)

Based on the two static test results, the fatigue test matrix was set to test four specimens under cyclic loading. Two maximum stress ratios were used to reveal the fatigue life behaviour on the basis of the S-N relationship. These maximum stress ratios were 70 and 60% of ultimate monotonic strength. Each test was repeated on an identical specimen so that the results could be compared. Table 2 presents the fatigue test matrix with the results obtained.

Table 2. Experimental test results

Fatigue test ID	Stress ratio %	Load range (kN)	Fatigue no. of Cycles	Stopped without failure (No. of Cycles)
AF1	(20-70%)	(32-112)	1,355,000	
AF1-R	(20-70%)	(32-112)	607,100	
AF2	(20-60%)	(32-96)		5.6M*
AF2-R	(20-60%)	(32-96)		4.0M*

* M: Million

The first fatigue test (AF1) was run with minimum and maximum stresses of 20-70% and 32-112 kN respectively. Five strain gauges were attached to the laminate and fabric sheet to measure the strain distribution along the bonding line. The results showed a steady increase in strains (SG1-SG3) as the number of cycles increased. However, strain gauges SG4 and SG5 had gradual increment during the fatigue loading, as shown in Figure 6(a). The test was run until failure occurred at 1,355,000 cycles, when the full patch anchor delaminated from the concrete surface. No global signs of debonding were observed under the cyclic loading. Figure 6(b) demonstrates the measurement of peak micro-strain versus the distance along the bond line under cyclic loading. The results showed that the strains exhibited a linear decrease between strain gauge SG1 and SG2, and once the distance exceeded 180mm, the reductions in the micro-strains commenced to be a non-linear trend over the bonding area. This indicates that delamination was initiated at the edge of the block. At 280mm from SG1, the strains started to reduce dramatically until full patch anchor separation occurred at failure

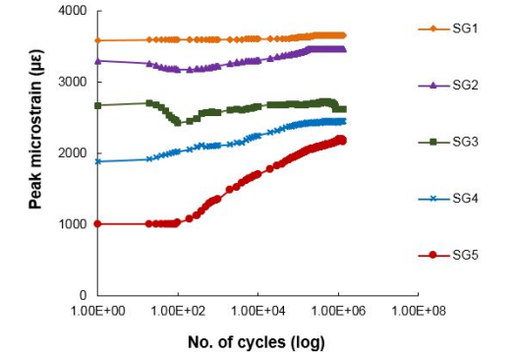
The repeated tested (AF1-R) showed very good correlations with the peak micro-strain over the fatigue number of cycles and distance along the bond line compared to the first fatigue test (AF1). However, the test failed at 607,100 cycles, which is approximately half the fatigue number of cycles recorded in fatigue test one (AF1). Despite this difference in the fatigue number of cycles, both tests failed in the same failure range (below 2 million cycles). The maximum strain measured in the first fatigue test and the repeated test was very close, with 3900με and 3660με respectively. Figure 7(a) demonstrates the peak micro-strain versus the number of cycles. The strain distribution along the bond line measured from SG1 exhibited the same behaviour as that observed in the first fatigue test, as presented in Figure 7(b)

The second fatigue test (AF2) was run with minimum and maximum stresses of 20- 60% and 32-96kN respectively. Six strain gauges were used along the bonding area to reveal the strain distribution under fatigue loading. The first strain gauge (SG1) located at the free end of the laminate exhibited a steady trend during the entire test. However, the peak micro-strains of the other five gauges (SG2-SG6) showed an almost regular increase with increased number of cycles. The maximum strain reached was approximately 3250με, which is slightly below the maximum strain recorded in the first fatigue test when subjected to a maximum stress of 70% of the ultimate static strength. The test continued cycling until 5.6 million cycles without any global signs of crack propagation observed. The test was then stopped and the specimen failed by static tensile loading. Figure 8(a) presents the peak micro-strains of six gauges with the logarithm number of cycles. All the six strain gauges showed a steady trend along the bond line, as depicted in Figure 8(b). Gradual reduction was captured until about 180mm from SG1 where the gauges commenced to diverge. This indicates that cracks started to generate along the bonding area after more than 5 million cycles.

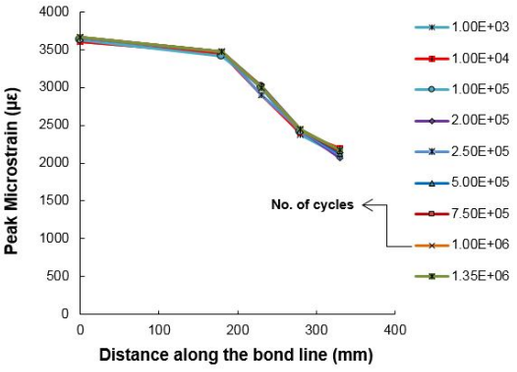
The repeated test of the second fatigue test (AF2-R) was run for 4 million cycles without any debonding initiation or degradation in the bonding zone observed. The test was then stopped and failed by static test. The strain gauge readings present a steady trend in most gauges; however, after a million cycle loadings, some gauges exhibited a slight increase in the strain measurement as the number of cycles increased, as shown in Figure 9(a). When the behaviour of strain gauges was examined along the bond line, it was found that during the first million cycles, the peak micro-strain of most gauges had a divergent trend until 180mm. The divergence behaviour remained constant and levelled off when approaching the farthest distance of strain gauge, SG6. This is because the applied tensile fatigue load generates shear stresses between the bonding layers, which decrease when moving from strain gauges SG2 and SG6. These shear stresses resist the tendency of debonding and as a result cause a reduction in the micro-strain readings. Figure 9(b) shows the peak micro-strain measurements in relation to the distances along the bond line.

3.3 *Mode of failure*

The experimental tests showed that the mode of failure of all static and fatigue tests occurred in the concrete cover with full separation of the patch anchors from the concrete surface. No slippage of the laminate was observed between the two fabric sheets, which confirmed that good bonding was achieved. Figure 10 depicts the mode of failure of the anchorage model.

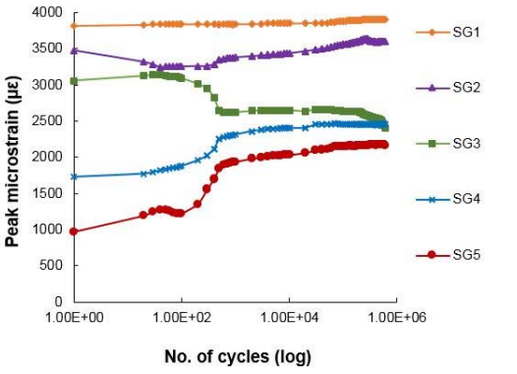


(a)

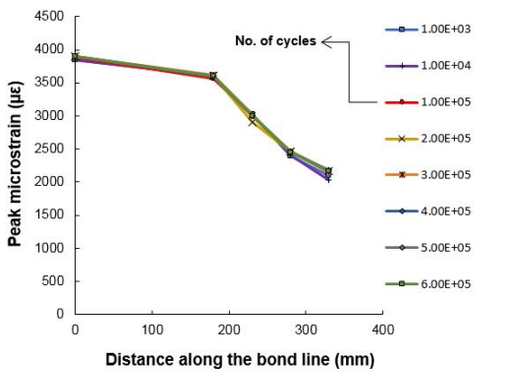


(b)

Figure 6. Test AF1: (a) Peak micro-strain vs. no. of cycles; (b) Peak micro-strain vs. distance along the bond line.

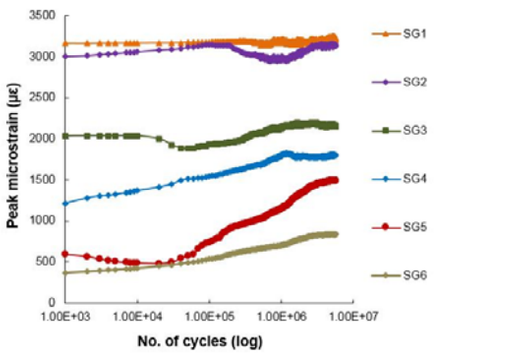


(a)

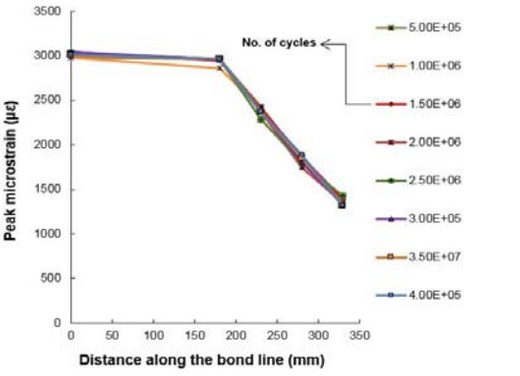


(b)

Figure 7. Test AF-R: (a) Peak micro-strain vs. no. of cycles; (b) Peak micro-strain vs. distance along the bond line.

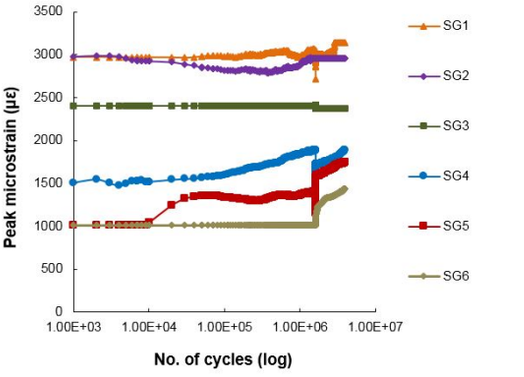


(a)

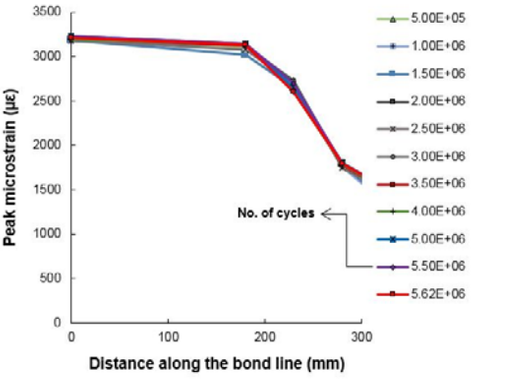


(b)

Figure 8. Test AF2: (a) Peak micro-strain vs. no. of cycles; (b) Peak micro-strain vs. distance along the bond line.



(a)



(b)

Figure 9. Test AF2-R: (a) Peak micro-strain vs. no. of cycles; (b) Peak micro-strain vs. distance along the bond line.



Figure 10. Mode of failure

4 CONCLUSION

In summary, the experimental investigation of anchored model indicate that the use of anchorage devices of CFRP laminate with two fabric sheets provides additional strength to RC structures. When these anchorage strengthening systems were examined under fatigue loading, the results showed that a maximum stress ratio of 70% of the ultimate static failure had a low fatigue life and failure occurred before 2 million cycles. However, when the anchored specimen was subjected to a maximum stress of 60% of the static strength capacity, no fatigue degradation occurred up to 5.6 million cycles. The results indicated that there is no fatigue issues with externally-bonded FRP anchorage systems when the maximum stress ratio is 60% and below. In addition, further research needs to be conducted to validate the results and to enable design guidelines to be proposed for practical engineers

5 REFERENCES

Belarbi, Abdeldjelil. *Design of Frp Systems for Strengthening Concrete Girders in Shear*. Vol. 678, Washington D.C, USA: Transportation Research Board, 2011.

Chen, JF, and JG Teng. "Anchorage Strength Models for Frp and Steel Plates Bonded to Concrete." *Journal of Structural Engineering* 127, no. 7 (2001): 784-91.

Chen, Tao, Qian-Qian Yu, Xiang-Lin Gu, and Xiao-Ling Zhao. "Study on Fatigue Behavior of Strengthened Non-Load-Carrying Cruciform Welded Joints Using Carbon Fiber Sheets." *International Journal of Structural Stability and Dynamics* 12, no. 01 (2012): 179-94.

Kalfat, R, and R Al-Mahaidi. "Investigation into Cfrp Laminate Anchorage Systems Utilising Bi-Directional Fabric Wrap." *Composite Structures* 93, no. 4 (2011): 1265-74.

Kalfat, R, R Al-Mahaidi, and G Williams. "Investigation of Efficient Anchorage Systems for Shear and Torsion Retrofitting of Box Girder Bridges." *ACI Special Publication* 275 (2011).

Martinelli, Enzo, and Antonio Caggiano. "A Unified Theoretical Model for the Monotonic and Cyclic Response of Frp Strips Glued to Concrete." *Polymers* 6, no. 2 (2014): 370-81.

Xie, Yan, Kunhua Guan, Lei Zhan, and Qichen Wang. "Mechanical Behavior and Chloride Penetration of Precracked Reinforced Concrete Beams with Externally Bonded Cfrp Exposed to Marine Environment." *International Journal of Polymer Science* 2016 (2016): 8 pages.

Maintenance, Safety, Risk, Management and Life-Cycle Performance of Bridges – Powers, Frangopol, Al-Mahaidi & Caprani (Eds)
© 2018 Taylor & Francis Group, London, ISBN 978-1-138-73045-8

Mathematical analysis of an innovative method for strengthening concrete beams using pre-stressed FRP laminates

S.R. Atashipour, J. Yang, R. Haghani & M. Al-Emrani
Chalmers University of Technology, Gothenburg, Sweden

ABSTRACT: This paper presents mathematical modeling and analytical solution of an innovative method for strengthening of flexural concrete members using pre-stressed carbon fiber reinforced polymer (CFRP) laminates without the need for mechanical anchorage. Bonding CFRP laminate in a pre-stressed state to the tensile part of flexural members is an effective method to improve their bending performance. The elimination of end anchors is found to be possible by using an innovative pre-stressing device capable of creating a step-wise decreasing profile of pre-stressing force towards each end of the CFRP laminate. The proposed innovative pre-stressing device consists of a multiple of aluminum tabs interconnected by steel bars having different diameters. The pre-stressing force is applied to the end tab and evenly distributed among all tabs. Each tab is mechanically fastened to the CFRP laminate. Two 10-mm-thick GFRP plates are used as force-transfer medium to connect the pre-stressing device to the CFRP laminate. An efficient mathematical modeling of the innovative system is developed and corresponding governing equations are solved analytically. A comparative study is conducted between the stress and displacement results of the step-wise pre-stressing method and that of conventional methods where pre-stressing is performed in one step.

1 INTRODUCTION

Fiber reinforced polymer (FRP) composite materials have been increasing used in the retrofitting of civil infrastructure since the research efforts started in the mid-1970s. The range of applications, at the present, has expanded from concrete members to masonry, timber, and iron structures (Bakis et al., 2002). When it comes to flexural strengthening of reinforced concrete (RC) structures, using bonded carbon fiber reinforced polymer (CFRP) laminates as the externally bonded reinforcement (EBR) has become a common technique (Meier, 1995). Compared to previously used steel plates, CFRP composites offer advantages such as light-weight, superior tensile strength and corrosion resistance.

A major drawback of bonded FRP laminates is debonding, i.e. separation of the strengthening laminate from the structure due to high interfacial stresses at stress raisers such as intermediate cracks or ends of the laminate. To utilize the CFRP laminates more efficiently, it is suggested to pre-stress them before bonding to concrete members (Meier, 1995; El-Hacha et al., 2001). In case of flexural strengthening of RC members, using pre-stressing in EBR instead of passive EBR offers the following benefits:

– Significant increase of ultimate load bearing capacity;
– provide active strengthening in terms of carrying a portion of the self-weigh in addition to the live load;
– Further improve the serviceability performance by enhancing the bending stiffness and delaying the onset of cracks;
– Enhance the durability of cracked RC members by reducing the width of existing cracks and delaying the formation of new cracks;
– Increasing the utilization ratio of the CFRP material, since introducing the pre-stress either changes the failure mode from premature debonding of CFRP due to intermediate cracks to the tensile rupture of the laminate or delays the debonding.

The major challenge of using pre-stressed CFRP is the need for anchorage at the ends of CFRP laminates. High shear stress, due to so called shear lag effect, would develop—at the moment of pretension release—in the bond line between the CFRP laminate and the concrete substrate at the end zones (Al-Emrani and Kliger 2006, Haghani et al., 2009). Without end anchorage, immediate shear failure of concrete substrate would occur and consequently the debonding of the CFRP laminate. Previous study by (Meier, 1995) indicated that without end anchorage the CFRP laminate may be debonded from the con-

crete substrate at a pre-stressing levels as low as 5% of the ultimate strength of CFRP. A case study of interfacial shear stress analysis based on the closed solution developed by Al-Emrani and Kliger (2006) showed that the typical anchorage length of bonded CFRP laminates can be as short as 50 mm. The same equations showed that upon removing an 80-kN-prestressing force, interfacial shear stress of about 94 MPa would be built up at the end of the laminate. Therefore, in the conventional pre-stressing technique the mechanical end anchorage is necessary to avoid premature debonding by transferring the peak shear stress from bond line into the concrete beam. The most commonly used mechanical anchor system is composed of two steel plates installed on the concrete with help of bolt fasteners, clamping the CFRP laminate before the pre-stressing force is released.

There are, however, some shortcomings associated with using mechanical anchors. Doubts about the long-term performance of such anchors, the need for further modification of the concrete element to fit the steel plates and inspect-ability of anchors are among the most important challenges. To resolve the problem, developing non-metallic anchors was studied by Kim et al. (2008). However, non-metallic anchors have not yet been commercialized and are not available on market.

Researchers in EMPA (Stöcklin and Meier, 2001; Meier and Stöcklin, 2006) first put forward a pre-stressing method—the gradient anchorage method—without the need for mechanical anchorage system. This method introduces a gradually decreasing pre-stressing force toward the ends of CFRP reinforcement, which is realized by releasing the pretension force using a computer controlled system in a number of segments. In each segment, the adhesive in the bond line is fast cured by means of elevating the temperature in the adhesive layer. The reduscton continues until the pre-stressing force is reduced to zero at the end of the laminate. The major benefit of gradient anchorage is the aesthetic and durability which is comparable with regular passive CFRP strengthening. Even though this method eliminates the need for mechanical anchors, it is too complicated to be realized in practice as it involves use of a sophisticated electro mechanical system to make the curing and gradual force release possible.

2 DEVELOPMENT OF AN INNOVATIVE SOLUTION

Setting the same goal of eliminating the end anchorage, an innovative stepwise pre-stressing method and a device were proposed and developed by Haghani et al. (2015). This pre-stressing method is the focus of this paper. Different from EMPA's approach, the stepwise pre-stressing method is able to—within one jacking action—achieve a stepwise decreasing profile of pre-stressing force in the CFRP laminate towards the ends (Haghani and Al-Emrani 2016). Previous experimental verification (Yang et al., 2017) showed that the application of this new pre-stressing method can realize the 'self-anchorage' of CFRP laminate at pre-stressing levels equivalent to 27% of ultimate tensile strength without using end anchors, and the ultimate CFRP laminate utilization ratio of ca. 80% before the separation failure of CFRP reinforcement.

The pre-stressing device, shown in Figure 1, consists of eight aluminum tabs that are inter-connected with a series of springs—steel bars with different designed diameters. The tabs are connected to the CFRP laminates via a medium (GFRP plate with dimensions of 1250 mm x 80 mm x 10 mm). The GFRP plates were bonded to CFRP laminate using a specially designed epoxy adhesive. The GFRP plate has embedded nuts that enables a bolted connection to the device.

The function of the pre-stressing device is to evenly distribute the total amount of pre-stressing force through these tabs to the CFRP laminate. The pretension force transferred from the pre-stressing device to the CFRP plate in each segment is dependent on the ratio of cross-sectional stiffness between the CFRP and springs (steel bars). Considering the increasing diameter of steel bars towards the CFRP ends, the pre-stressing force transferred to the CFRP is decreasing gradually segment by segment toward the end. Aided by this mechanism, it is possible —with merely one jacking action—distribute the pre-stressing force into CFRP laminate in a step-wise manner decreasing the force profile towards the CFRP ends.

The pre-stressing device would be maintained for 24 hours to assure that the epoxy develops sufficient strength to transfer the interfacial stresses to concrete beam. The pre-stressing force would then be released and the device removed. Upon the release of the pre-stressing device (aluminum tabs and steel bars), the pre-stressing force in CFRP would be transferred to concrete through cured adhesive layer. The magnitude of shear stress developed along the bond line, in this manner, is directly related to the gradient of axial pretension force in the CFRP laminate. Considering the gradient of the decreasing pre-stressing force within 1250 mm anchorage length, the developed shear and peeling stress were controlled to such a level that the adhesive bond line and adjacent concrete had sufficient strength to withstand the interfacial stress. Previous numerical and experimental studies proved that it was possible to reduce the shear and peeling stresses in the bond line below 1.0 and 0.2 MPa, respectively, given a pre-stressing force of 80 kN distributed by ten steps (tabs) (Haghani et al., 2015).

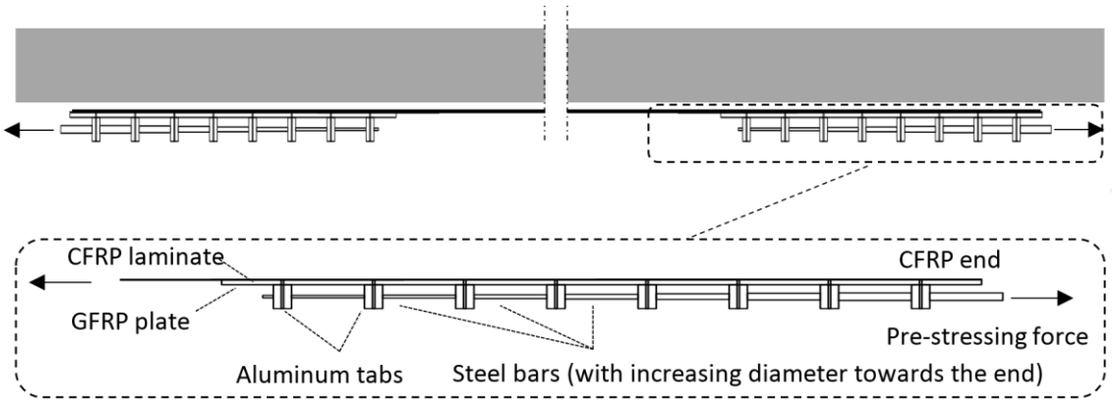


Figure 1. Configuration of pre-stressing device connected to CFRP laminate via GFRP plate.

3 MATHEMATICAL MODELING OF THE INNOVATIVE METHOD

Mathematical simulation of the strengthened concrete beam with composite pre-stressing method is here divided into two distinguished steps: the first, static displacement and stress distribution within the CFRP and GFRP layers as well as the shear stress in the adhesive layer in between them; and the second, the static response of the equilibrium state of the adhesive layer bonding the strengthening laminate to the beam.

3.1 *Step 1: Tension in the strengthening CFRP-GFRP layer*

Consider a thin layer of CFRP of length L, having two GFRP layers of length L_0 bonded to its ends. Due to symmetry of the system with respect to its middle point, the origin of the coordinates system is assumed in the middle and only half of it is considered. N number of local loads will be applied into the GFRP through N discretized points (i.e. where the pre-stressing device is connected to the GFRP). Therefore, N+2 distinguished parts (i = 1,2,…, N+1) will be assumed for each half-length as follows

Only CFRP part ($i=1$):

$$0 \le x \le L/2 - L_0$$

CFRP bonded to GFRP ($i = 2,3,...,N+2$):

Distance between n-th anchorage point to the next ($0 \le n \le N$); $n+2 \equiv i$: (1)

$$L/2 - L_0 + \frac{n}{N+1} L_0 \le x \le L/2 - L_0 + \frac{n+1}{N+1} L_0$$

It should be clarified that n = 0, N indicate the start point of GFRP bonded to CFRP, and the end point near the beam end location, respectively. Clearly, for i = 1, the displacement function:

$$\delta_{c,1} = \frac{P_0}{EA_c} x, \quad 0 \le x \le L/2 - L_0 \tag{2}$$

where P_0 is the total axial load applied to the pre-stressing layer before bonding to the beam, and EA_c is the axial stiffness of the CFRP laminate.

To analyze the portions corresponding to the CFRP-bounded-to-GFRP parts (i.e. i = 2,3,…,N+2), an infinitesimal differential element is considered, as shown in Figure 2. From equilibrium equations of each differential part we have

$$\frac{\mathrm{d}P_{g,i}}{\mathrm{d}x} = B_a \tau_i \tag{3.1}$$

$$\frac{\mathrm{d}P_{c,i}}{\mathrm{d}x} = -B_a \tau_i \tag{3.2}$$

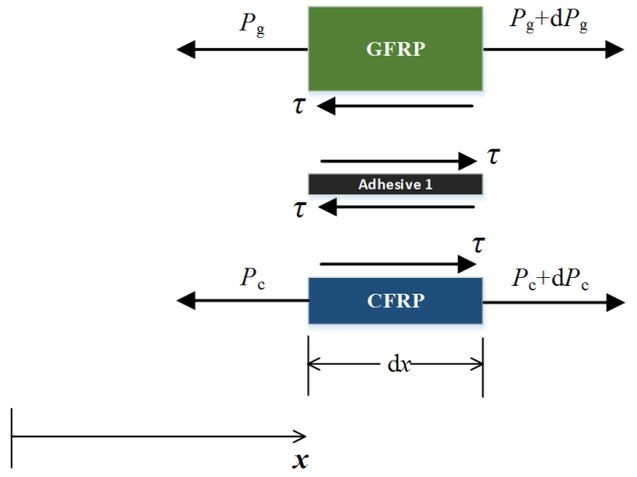


Figure 2. Differential element of GFRP-bonded-to-CFRP parts.

Using the definition of the shear strain in the i-th part of the thin adhesive layer, one can write

$$\tau_i = \frac{G_a}{t_a}(\delta_{g,i} - \delta_{c,i}) \tag{4}$$

where G_a and t_a are the shear modulus and thickness of the adhesive layer between the GFRP and CFRP (we nominate it here adhesive type-1), respectively. Also, $\delta_{g,i}$ indicates the axial displacement of the GFRP part in the i-th part at the x level, whereas $\delta_{c,i}$ is that of the CFRP part. Indeed, the differentiation of the aforementioned displacement functions are expressed as

$$\frac{\mathrm{d}\delta_{g,i}}{\mathrm{d}x} = \frac{P_{g,i}}{EA_g} \tag{5.1}$$

$$\frac{\mathrm{d}\delta_{c,i}}{\mathrm{d}x} = \frac{P_{c,i}}{EA_c} \tag{5.2}$$

in which $P_{g,i}$ and $P_{c,i}$ are respectively the axial load in the i-th part of the GFRP and CFRP. Apparently, EA_g and EA_c are the axial stiffness of the GFRP and CFRP parts, respectively. Differentiating Eq. (5) with respect to x and substituting Eqs. (5.1,2) into it yields

$$\frac{\mathrm{d}\tau_i}{\mathrm{d}x} = \frac{G_a}{t_a}\left(\frac{P_{g,i}}{EA_g} - \frac{P_{c,i}}{EA_c}\right) \tag{6}$$

Differentiating Eq. (6) with respect to x and replacing Eqs. (3.1,2) into it, leads to a differential equation in terms of the shear stress as follows

$$\frac{\mathrm{d}^2\tau_i}{\mathrm{d}x^2} - \omega^2\tau_i = 0 \tag{7}$$

where

$$\omega = \sqrt{\frac{B_a G_a}{t_a}\left(\frac{1}{EA_g} + \frac{1}{EA_c}\right)} \tag{8}$$

The solution of Eq. (7) can be represented as

$$\tau_i = c_{1,i}\cosh(\omega x) + c_{2,i}\sinh(\omega x) \tag{9}$$

By substitution of the obtained solution from Eq. (9) into Eqs. (3.1,2) and integrating the results, the axial loads in the GFRP and CFRP parts are determined as follows

$$P_{g,i} = \frac{B_a}{\omega}\left[c_{1,i}\sinh(\omega x) + c_{2,i}\cosh(\omega x)\right] + c_{3,i} \tag{10.1}$$

$$P_{c,i} = -\frac{B_a}{\omega}\left[c_{1,i}\sinh(\omega x) + c_{2,i}\cosh(\omega x)\right] + c_{4,i} \tag{10.2}$$

The constants $c_{3,i}$ and $c_{4,i}$ are not independent of each other, and their relationship can be obtained, after substituting Eqs. (9) and (10.1,2) into Eq. (6) in the form

$$c_{4,i} = \frac{EA_c}{EA_g}c_{3,i} \tag{11}$$

Now, we determine the mathematical functions for the displacements in CFRP and GFRP parts by substituting Eqs. (10.1,2) into Eqs. (5.1,2) and integrating the results, as follows

$$\delta_{g,i} = \frac{B_a}{EA_g\omega^2}\left[c_{1,i}\cosh(\omega x) + c_{2,i}\sinh(\omega x)\right] + \frac{c_{3,i}}{EA_g}x + c_{5,i} \tag{12.1}$$

$$\delta_{c,i} = -\frac{B_a}{EA_c\omega^2}\left[c_{1,i}\cosh(\omega x) + c_{2,i}\sinh(\omega x)\right] + \frac{c_{4,i}}{EA_c}x + c_{6,i} \tag{12.2}$$

Substitution of Eqs. (9) and (12.1,2) into Eq. (4) yields

$$c_{6,i} = c_{5,i} \tag{13}$$

It is evident that for each portion of the GFRP-bonded-to-CFRP, as described in Eq. (1), four boundary conditions are required to be satisfied to determine the four independent constants: $c_{1,i}$, $c_{2,i}$, $c_{3,i}$ and $c_{5,i}$. Assuming symmetry of the beam with respect to its middle point, it is expected that the axial displacement at $x = 0$ to be zero. Thus, using Eq. (2) and considering the free edge of the GFRP, at the location of bonding to CFRP, the two boundary conditions at this location are represented as

$$\text{at } x = L/2 - L_0 : \begin{cases} \delta_{c,2} = \dfrac{P_0(L/2 - L_0)}{EA_c} \\ P_{g,2} = 0 \end{cases} \tag{14}$$

The first part of Eq. (14) relies on the continuity condition in the displacement in the CFRP laminate before and after the edge of GFRP layer.

At the end point of the pre-stressed laminate, the axial load would be zero in both GFRP and CFRP; i.e.,

$$\text{at } x = L/2 : \begin{cases} P_{c,N+2} = 0 \\ P_{g,N+2} = 0 \end{cases} \tag{15}$$

Also, the following four continuity conditions must be satisfied at any location of the N tab anchorages:

$$\text{at } x = X_i : \begin{cases} P_{g,i-1} - P_{g,i} = P_0/N \\ \delta_{g,i-1} - \delta_{g,i} = 0 \\ P_{c,i-1} - P_{c,i} = 0 \\ \delta_{c,i-1} - \delta_{c,i} = 0 \end{cases} \tag{16}$$

$(i = 2, 3, ..., N+1)$

Obviously, X_i indicates the horizontal coordinate of the i-th tab location, and is expressed as

$$X_i = L/2 - L_0 + \frac{i-1}{N+1}L_0 \tag{17}$$

Eqs. (15), (16) and (17) gives a set of 4×(N+1) algebraic equations in terms of the same number of constant coefficients.

The outcome of the described analytical solution will be implemented into the second step to determine the stress distribution as well as displacements in the beam, adhesive layer and the pre-stressing composite layer in an equilibrium state.

3.2 *Step 2: Bonding the prestressing composite layer to the concrete beam*

Assume that the pre-tensioned composite laminate is bonded to the concrete beam. In an equilibrium state, the beam will be under compression and a negative

bending moment (i.e. the bottom surface of the beam under compression). The pre-stressing layer will lose some of its tensile stress. To analyze this step, a differential element of the beam together with the composite layer and the adhesive in between is considered, as illustrated in Figure 3.

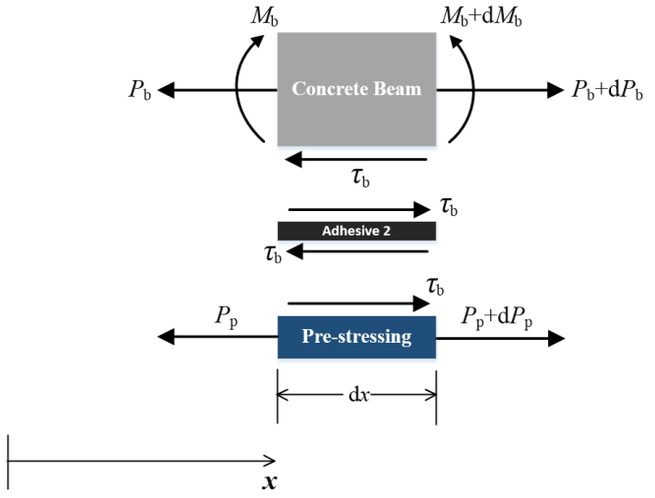


Figure 3. A differential element of the concrete beam, strengthened with the composite pre-stressing layer.

From the static equilibrium state of each part of the differential element shown in Fig. 3, the following equations are obtained

$$\frac{\mathrm{d}P_{b,i}}{\mathrm{d}x} = B_A \tau_{b,i} \tag{18.1}$$

$$\frac{\mathrm{d}P_{p,i}}{\mathrm{d}x} = -B_A \tau_{b,i} \tag{18.2}$$

$$\frac{\mathrm{d}M_{b,i}}{\mathrm{d}x} = Y_c B_A \tau_{b,i} \tag{18.3}$$

where $\tau_{b,i}$ is the shear stress in the i-th portion of the beam after installing the pre-stressing layer; $M_{b,i}$ and $P_{b,i}$ are the bending moment and axial load appears in the i-th part of the beam, in an equilibrium situation after installation of the pre-stressing layer; $P_{p,i}$ is the final equilibrium value of the axial load in the i-th part of the pre-stressing layer after losing some of its initial tensile load. Also, B_A is the width of the adhesive type-2 which is used for bonding the pre-stressing layer to the concrete beam, and Y_c is the transverse distance between the beam neutral-axis to the bottom surface, where the pre-stressing layer is glued. Using the definition of the shear strain in the adhesive layer, the following expression is obtained for the shear stress function in that layer:

$$\tau_{b,i} = \frac{G_A}{t_A}(\delta_{p,i} - \delta_{b,i}) \tag{19}$$

in which G_A and t_A are the shear modulus and thickness of the adhesive type-2.

It is evident that the pre-stressing layer will lose a part of its initial axial stretching load after it is bonded to the beam. The loss in the pre-stressing axial load, in the i-th part, is represented as

$$\Delta P_p = P_{0,i} - P_{p,i} \tag{20}$$

where $P_{0,i}$ in the function of the initial pre-stressing load before bonding to the beam, at the i-th part; and $P_{p,i}$ is the final axial load after installing the pre-stressing layer to the beam. Therefore, the axial strain of the pre-stressing layer in the second stage can be expressed as

$$\frac{\mathrm{d}\delta_{p,i}}{\mathrm{d}x} = \frac{P_{0,i} - P_{p,i}}{EA_{p,i}} \tag{21}$$

in which $EA_{p,i}$ is the axial stiffness of the pre-stressing layer at the i-th part. The strain at the bottom surface of the concrete beam, corresponding to the second stage, due to the bending action and the compression, can be represented as

$$\frac{\mathrm{d}\delta_{b,i}}{\mathrm{d}x} = \frac{-P_{b,i}}{EA_b} + \frac{-M_{b,i}Y_c}{EI_b} \tag{22}$$

where EA_b and EI_b are the axial and bending stiffness of the beam, respectively. Now, we differentiate Eq. (19) and substitute Eqs. (21) and (22) into it and obtain:

$$\frac{\mathrm{d}\tau_{b,i}}{\mathrm{d}x} = \frac{G_A}{t_A}\left(\frac{P_{0,i}}{EA_{p,i}} - \frac{P_{p,i}}{EA_{p,i}} + \frac{P_{b,i}}{EA_b} + \frac{M_{b,i}Y_c}{EI_b}\right) \tag{23}$$

Differentiating Eq. (23) one more time and inserting Eqs. (18.1,2,3) into it will result in an uncoupled differential equation in terms of the adhesive shear stress (adhesive type-2) in the form

$$\frac{\mathrm{d}^2\tau_{b,i}}{\mathrm{d}x^2} - \Omega_i^2 \tau_{b,i} = \lambda_i \frac{\mathrm{d}}{\mathrm{d}x} P_{0,i} \tag{24}$$

where

$$\Omega_i = \sqrt{\frac{B_A G_A}{t_A}\left(\frac{1}{EA_{p,i}} + \frac{1}{EA_b} + \frac{Y_c^2}{EI_b}\right)}$$
$$\lambda_i = \frac{G_A}{t_A EA_{p,i}} \tag{25}$$

Similar to the first step, here we consider N+2 separate regions for each half of the strengthened beam. The first region (i = 1) is related to the part of the beam which is strengthened with the CFRP; and other regions (i = 2,3,…,N+2) indicate N+1 distinguished regions in the strengthened beam with CFRP-bonded-to-GFRP layer, from the inner edge of the GFRP till the end of that, in between the N tab connection points. For the case i = 1, we have:

$$P_{0,i} = P_0 = \text{const.} \tag{26}$$

Therefore, Eq. (24) may be rewritten, for this case, as follows

$$\frac{\mathrm{d}^2\tau_{b,1}}{\mathrm{d}x^2}-\Omega_1^2\tau_{b,1}=0 \tag{27}$$

where

$$\Omega_1=\sqrt{\frac{B_A G_A}{t_A}\left(\frac{1}{EA_c}+\frac{1}{EA_b}+\frac{Y_c^2}{EI_b}\right)} \tag{28}$$

The solution of Eq. (27) is represented in the form

$$\tau_{b,1}=d_{1,1}\cosh(\Omega_1 x)+d_{2,1}\sinh(\Omega_1 x) \tag{29}$$

Substituting Eq. (29) into Eqs. (18.1-3) and integrating the results yield

$$P_{b,1}=\frac{B_A}{\Omega_1}\left[d_{1,1}\sinh(\Omega_1 x)+d_{2,1}\cosh(\Omega_1 x)\right]+d_{3,1} \tag{30.1}$$

$$P_{p,1}=-\frac{B_A}{\Omega_1}\left[d_{1,1}\sinh(\Omega_1 x)+d_{2,1}\cosh(\Omega_1 x)\right]+d_{4,1} \tag{30.2}$$

$$M_{b,1}=\frac{Y_c B_A}{\Omega_1}\left[d_{1,1}\sinh(\Omega_1 x)+d_{2,1}\cosh(\Omega_1 x)\right]+d_{5,1} \tag{30.3}$$

Only two of the constant coefficients $d_{3,1}$, $d_{4,1}$ and $d_{5,1}$ are independent. Therefore, by substituting Eqs. (26), (29) and (30.1-3) into Eq. (23), the following relationship is obtained between the aforementioned constants:

$$d_{5,1}=\frac{EI_b}{Y_c}\left(-\frac{1}{EA_b}d_{3,1}+\frac{1}{EA_c}d_{4,1}-\frac{P_0}{EA_c}\right) \tag{31}$$

Now, we substitute Eqs. (30.1-3) into Eqs. (21) and (22), and integrating the results and obtain:

$$\begin{aligned}\delta_{p,1}=&\frac{B_A}{EA_c\Omega_1^2}\left[d_{1,1}\cosh(\Omega_1 x)+d_{2,1}\sinh(\Omega_1 x)\right]\\&-\frac{1}{EA_c}d_{4,1}x+d_{6,1}+\frac{P_0}{EA_c}x\end{aligned} \tag{32.1}$$

$$\begin{aligned}\delta_{b,1}=&-\frac{B_A}{\Omega_1^2}\left(\frac{1}{EA_b}+\frac{Y_c^2}{EI_b}\right)\left[d_{1,1}\cosh(\Omega_1 x)+d_{2,1}\sinh(\Omega_1 x)\right]\\&-\frac{1}{EA_b}d_{3,1}x-\frac{Y_c}{EI_b}d_{5,1}+d_{7,1}\end{aligned} \tag{32.1}$$

It should be pointed out that Eqs. (32.1,2) rely on the fact that $EA_{p,1} = EA_c$. Easily, it could be shown, by substituting Eqs. (29) and (32.1,2) into Eq. (19), that:

$$d_{7,1}=d_{6,1} \tag{33}$$

Now, we develop the analytical solution for the cases i = 2,3,…,N+2. To this end, we obtain the complete solution of the inhomogeneous Eq. (24) by inserting the function of the axial load in the stretched composite layer from Eq. (10.2) in the first stage. Consequently, for the cases i = 2,3,…,N+2 we obtain:

$$\begin{aligned}\tau_{b,i}=&\frac{\lambda_i B_a}{\Omega_i^2-\omega^2}\left[c_{1,i}\cosh(\omega x)+c_{2,i}\sinh(\omega x)\right]\\&+d_{1,i}\cosh(\Omega_i x)+d_{2,i}\sinh(\Omega_i x)\end{aligned} \tag{34}$$

where

$$\Omega_i=\sqrt{\frac{B_A G_A}{t_A}\left(\frac{1}{EA_g+EA_c}+\frac{1}{EA_b}+\frac{Y_c^2}{EI_b}\right)},\qquad \lambda_i=\frac{G_A}{t_A(EA_g+EA_c)},\qquad (i=2,3,...,N+2) \tag{35}$$

and ω is given by Eq. (8). Substituting Eq. (34) into Eqs. (18.1-3) and integrating the results lead to

$$\begin{aligned}P_{b,i}=&\frac{\lambda_i B_a B_A}{(\Omega_i^2-\omega^2)\omega}\left[c_{1,i}\sinh(\omega x)+c_{2,i}\cosh(\omega x)\right]\\&+\frac{B_A}{\Omega_i}\left[d_{1,i}\sinh(\Omega_i x)+d_{2,i}\cosh(\Omega_i x)\right]+d_{3,i}\end{aligned} \tag{36.1}$$

$$\begin{aligned}P_{p,i}=&-\frac{\lambda_i B_a B_A}{(\Omega_i^2-\omega^2)\omega}\left[c_{1,i}\sinh(\omega x)+c_{2,i}\cosh(\omega x)\right]\\&-\frac{B_A}{\Omega_i}\left[d_{1,i}\sinh(\Omega_i x)+d_{2,i}\cosh(\Omega_i x)\right]+d_{4,i}\end{aligned} \tag{36.2}$$

$$\begin{aligned}M_{b,i}=&\frac{\lambda_i B_a B_A Y_c}{(\Omega_i^2-\omega^2)\omega}\left[c_{1,i}\sinh(\omega x)+c_{2,i}\cosh(\omega x)\right]\\&+\frac{B_A Y_c}{\Omega_i}\left[d_{1,i}\sinh(\Omega_i x)+d_{2,i}\cosh(\Omega_i x)\right]+d_{5,i}\end{aligned} \tag{36.3}$$

In a similar manner, we identify relationship between the three coefficients d3,i, d4,i and d5,i though substituting Eqs. (36.1-3) into Eq. (23) and obtain

$$d_{5,i}=\frac{EI_b}{Y_c}\left(-\frac{1}{EA_b}d_{3,1}+\frac{1}{EA_g+EA_c}d_{4,i}-\frac{EA_c c_{3,i}}{EA_g(EA_g+EA_c)}\right) \tag{37}$$

The displacement functions are determined by substituting Eqs. (36.1-3) into Eqs. (21) and (22) and integrating the results, as follows

$$\begin{aligned}\delta_{p,i}=&\\&\frac{1}{EA_c+EA_g}\left\{\frac{B_a}{\omega^2}\left(\frac{\lambda_i B_A}{\Omega_i^2-\omega^2}-1\right)\left[c_{1,i}\cosh(\omega x)+c_{2,i}\sinh(\omega x)\right]\right.\\&\left.+\frac{EA_c}{EA_g}c_{3,i}+\frac{B_A}{\Omega_i^2}\left[d_{1,i}\cosh(\Omega_i x)+d_{2,i}\sinh(\Omega_i x)\right]-d_{4,i}x\right\}+d_{6,i}\end{aligned} \tag{38.1}$$

$$\delta_{b,i} =$$
$$-\frac{\lambda_i B_a B_A}{(\Omega_i^2-\omega^2)\omega^2}\left(\frac{1}{EA_b}+\frac{Y_c^2}{EI_b}\right)\left[c_{1,i}\cosh(\omega x)+c_{2,i}\sinh(\omega x)\right]$$
$$-\frac{B_A}{\Omega_i^2}\left(\frac{1}{EA_b}+\frac{Y_c^2}{EI_b}\right)\left[d_{1,i}\cosh(\Omega_i x)+d_{2,i}\sinh(\Omega_i x)\right]$$
$$-\frac{1}{EA_b}d_{3,i}x-\frac{Y_c}{EI_b}d_{5,i}x+d_{7,i} \qquad (38.2)$$

Substituting Eqs. (38.1,2) into Eq. (19) indicates that

$$d_{7,i}=d_{6,i} \qquad (39)$$

In the above equations, five independent constant coefficients $d_{1,i}$, $d_{2,i}$, $d_{3,i}$, $d_{4,i}$ and $d_{5,i}$ are to be determined from five boundary conditions for each region. As it was mentioned earlier, assuming N number of tab anchorage points, N+2 number of distinguished regions are considered for the second stage. Therefore, the total number of 5(N+2) boundary and continuity conditions should be established. Considering the symmetry of the strengthened beam, the boundary conditions at the center is set as follows

$$\text{at } x=0: \begin{cases}\delta_{b,1}=0\\ \delta_{p,1}=0\end{cases} \qquad (40)$$

Also, three boundary conditions are to be satisfied at the free end of the strengthened layer and the beam as follows,

$$\text{at } x=L/2: \begin{cases}P_{p,N+2}=0\\ P_{b,N+2}=0\\ M_{b,N+2}=0\end{cases} \qquad (41)$$

At each level of the anchored tabs as well as the level of the interior GFRP start point, the following continuity conditions must be satisfied:

$$\begin{aligned}&P_{b,i-1}-P_{b,i}=0,\\ &\delta_{b,i-1}-\delta_{b,i}=0,\\ &P_{p,i-1}-P_{p,i}=0,\\ &\delta_{p,i-1}-\delta_{p,i}=0, \qquad (i=2,3,...,N+2)\end{aligned} \qquad (42)$$

4 NUMERICAL RESULTS & DISCUSSION

In this section, numerical results of the developed mathematical modelling are presented using a simple programming code in MAPLE. Geometrical dimensions and material properties of the concrete beam, the two types of adhesives, CFRP and GFRP layers are presented in Table 1.

The concrete beam has a rectangular cross section of height 300 mm and width 200 mm. The CFRP composite laminate is stretched through eight tabs, using the innovative device, and totally, it will be subjected to 80 kN initial tensile load before bonding to the concrete beam.

Table 1. Geometric dimensions and material properties of the beam and the strengthening layer's constituents.

Material properties		Geometric properties	
E_g (GPa)	6.2	A_g (mm^2)	80×10
E_c (GPa)	214	A_c (mm^2)	82×1.45
E_b (GPa)	36	A_b (mm^2)	200×300
G_a (GPa)	0.23	t_a (mm)	1.0
		B_a (mm)	80
G_A (GPa)	2.7	t_A (mm)	1.0
		B_A (mm)	82
		Y_c (mm)	150
		L (mm)	3800
		L_0 (mm)	1250

In Figure 4, comparison of axial load distribution in the strengthening layer, in the equilibrium state, is shown between the innovative method and the conventional method with uniform stretching. It should be noted that, in the conventional way of strengthening concrete beams, the composite layer is simply stretched at the ends which results in a uniformly distributed pattern for the axial stress before its installation. It can be seen from Figure 4 that there exists an edge effect; or so-called boundary layer phenomenon at the axial stress. This will cause a high shear stress value at the adhesive layer between the beam and the strengthening layer at the end (i.e. at x = L/2), as shown in Figure 5. Therefore, this would be the origin of failure in the structure under a low value of external load, compared to its real load capacity.

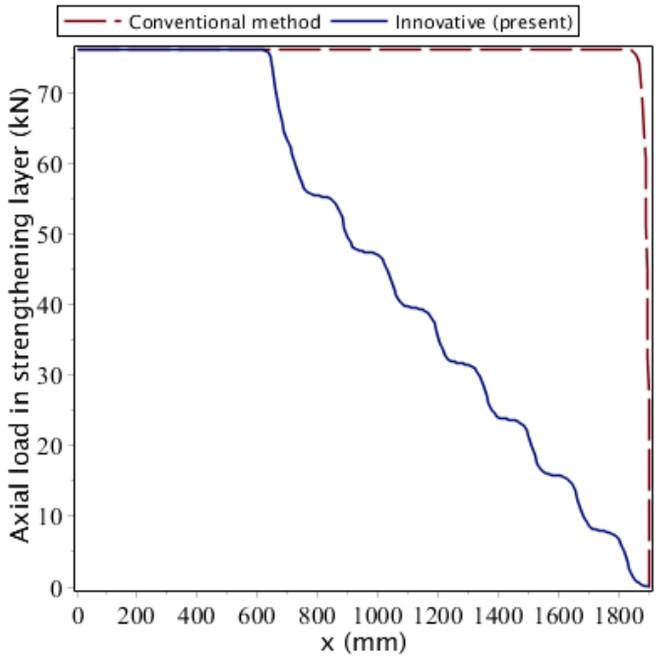


Figure 4. Variation of the axial tensile load in the strengthening layer in an equilibrium state, based on the present innovative and conventional methods.

It can be observed from Figure 4 that, unlike the conventional method of strengthening the concrete beam, the innovative method of strengthening the beam will result in a step-wise increase in the axial load to the maximum value at a location far from the ends. It enables the possibility of self-anchoring of the CFRP laminate to the beam; so, unlike the conventional method, there would be no need for using mechanical end anchors.

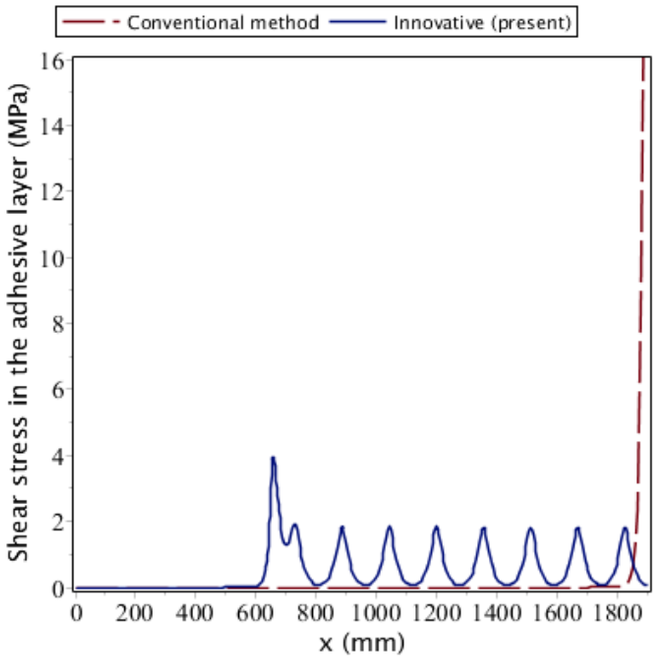


Figure 5. Shear stress distribution in the adhesive layer between the concrete beam and the strengthening layer in an equilibrium state, based on the innovative and conventional methods.

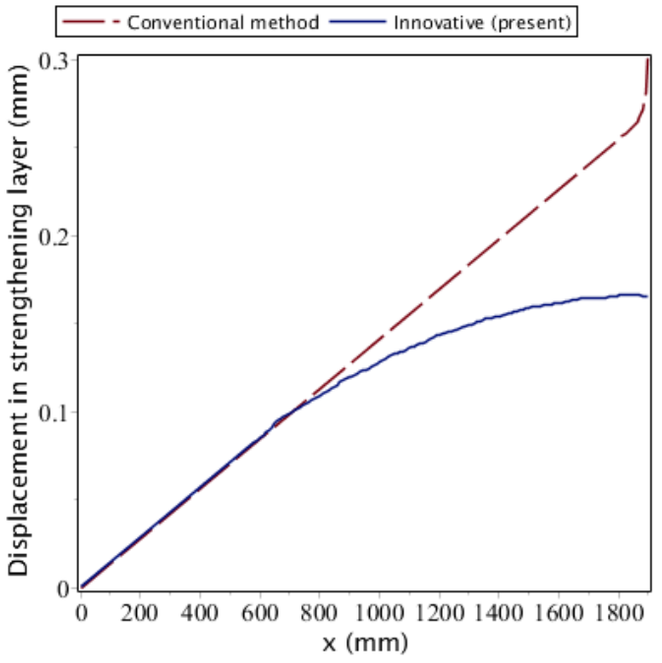


Figure 6. Variation of the axial displacement in the strengthening layer in an equilibrium state, based on the present innovative and conventional methods.

It can be observed from Figure 5 that the maximum shear stress in the adhesive layer, based on the innovative method, is less than ¼ of the corresponding value in the conventional method.

Another remarkable observation that might be drawn from Figure 5 is a peak value of the shear stress at the inner end point of the GFRP. In order to diminish this peak stress value, a tapered end is suggested for the inner end region of the GFRP bonded to the CFRP, instead of a sudden change in the geometry and axial stiffness of the strengthening layer.

Comparison of the axial displacement of the composite strengthening layer, based on the conventional method and the innovative method, are illustrated in Figure 6.

5 CONCLUSIONS

In this paper, a mathematical model and corresponding analytical solution were established for an innovative method to use pre-stressed CFRP laminates for strengthening of concrete beams without the need for mechanical anchorage. The elimination of the end anchors was found to be possible by using the proposed innovative pre-stressing device. Using the new innovative pre-stressing device, a step-wise decreasing profile of pre-stressing force towards each end of the CFRP laminate was obtained. It was observed that the maximum shear stress at the adhesive layer between the concrete beam and the composite strengthening laminate would be decreased significantly to a level which could be taken by the strength of the adhesive layer and the concrete substrate.

ACKNOWLEDGEMENT

The work in the paper is a part of SUREBridge project which has received funding from the European Union's Seventh Framework Programme for research, technological development and demonstration. SUREBridge project is co-funded by Funding Partners of the ERA-NET Plus Infravation program.

REFERENCES

Al-Emrani, M., Kliger, R., 2006. Analysis of interfacial shear stresses in beams strengthened with bonded prestressed laminates. Compos. Part B Eng. 37, 265–272.

Bakis, C., Bank, L., Brown, V., Cosenza, E., Davalos, J., Lesko, J., Machida, A., Rizkalla, S., Triantafillou, T., 2002. Fiber-Reinforced Polymer Composites for Construction—State-of-the-Art Review. J. Compos. Constr. 6, 73–87.

El-Hacha, R., Wight, R., Green, M., 2001. Prestressed fibre-reinforced polymer laminates for strengthening structures. Prog. Struct. Eng. Mater. 3, 111–121.

Haghani, R., Al-Emrani, M., 2016. A New Method for Application of Pre-stressed FRP laminates for Strengthening of Concrete Structures. Presented at the 19th IABSE Congress 2016, Stockholm, Sweden.

Haghani, R., Al-Emrani, M., Kliger, R., 2015. A new method for strengtheng concrete structures using prestressed FRP laminates. Presented at the ISEC 2015 - 8th International Structural Engineering and Construction Conference: Implementing Innovative Ideas in Structural Engineering and Project Management, pp. 1153–1158.

Haghani, R., Al-Emrani, M., Kliger, R., 2009. Interfacial stress analysis of geometrically modified adhesive joints in steel beams strengthened with FRP laminates. Constr. Build. Mater. 23, 1413–1422.

Kim, Y., Gordon Wight, R., Green, M., 2008. Flexural Strengthening of RC Beams with Prestressed CFRP Sheets: Using Nonmetallic Anchor Systems. J. Compos. Constr. 12, 44–52.

Meier, U., 1995. Strengthening of structures using carbon fibre/epoxy composites. Constr. Build. Mater., Application of Polymeric Materials to the Construction Industry 9, 341–351.

Meier, U., Stöcklin, I., 2006. A novel Carbon Fiber Reinforced Polymer (CFRP) system for post-strengthening. Presented at the Concrete Repair, Rehabilitation and Retrofitting - Proceedings of the International Conference on Concrete Repair, Rehabilitation and Retrofitting, ICCRRR 2005, pp. 477–479.

Stöcklin, I., Meier, U., 2001. Strengthening of concrete structures with prestressed and gradually anchored CFRP strips, in: FRPRCS-5: Fibre-Reinforced Plastics for Reinforced Concrete Structures Volume 1. Thomas Telford Publishing, pp. 291–296.

Yang, J., Haghani, R., Al-Emrani, M., 2017. Flexural strengthening of reinforced concrete beams using externally bonded FRP laminates prestressed with a new method. Presented at the 4th International Conference on Smart Monitoring, Assessment and Rehabilitation of Civil Structures, SMAR 2017, Zurich, Switzerland.

Maintenance, Safety, Risk, Management and Life-Cycle Performance of Bridges – Powers, Frangopol, Al-Mahaidi & Caprani (Eds)
© 2018 Taylor & Francis Group, London, ISBN 978-1-138-73045-8

Bond Performance of FRP-Strengthened Reinforced Concrete In Aggressive Environmental Conditions

R.J. Gravina, J. Li, H. Aydin, S Setunge
School of Engineering, RMIT University, Melbourne, Australia

P.Visintin
Adelaide University

S.T. Smith
Southern Cross University

R. Al-Mahaidi
Swinburne University

ABSTRACT: Bonding fibre-reinforced polymers (FRP) to reinforced concrete (RC) members has become a popular means for enhancing load carrying capacity and extending service life of bridge structures. However, there is uncertainty surrounding the long-term durability of flexurally strengthened members. This paper presents work on an experimental program to determine the debonding resistance of FRP-to-concrete interface considering environmental conditions and material durability. Further a mechanics based model that considers the intermediate-crack (IC) debonding behavior at the FRP-concrete interface as both a local and global mechanism along the length of a beam is also presented. The model is shown to be able to accurately predict the load-deflection response of FRP-strengthened beams considering the bond properties at the FRP-to-concrete interface.

1 INTRODUCTION

Externally bonded (EB) FRP as a simple and cost-effective means, has been widely used to strengthen/rehabilitate RC structures deteriorated over time due to exposure to harsh environments and/or increased load demands. To strengthen underperforming RC structures, adhesively bonded steel platewere firstly utilised (Hamoush & Ahmad 1990), however, the corrosion of the steel plating material exposed directly under variety of environmental conditions including wet/dry cycles, thermal cycles, alkaline attack, acid attack and chloride attack has resulted in long-term durability issues (Bertolini et al. 2013). Therefore, fibre-reinforced polymers (FRPs) were introduced to combat the steel corrosion issue. FRP is material that has several advantages compared to steel including its superior corrosion resistance, high tensile strength-to-weight ratio and non-magnetic nature (Teng et al. 2002, Teng et al. 2007). Despite the excellent mechanical and chemical properties, the long-term bond durability is still susceptible to environmental exposure.

Recently, large amount of research has been conducted on short-term and long-term bond durability of external bonded FRP plate to concrete substrate, including wet/dry cycling (Li et al. 2010, Shrestha et al. 2014, Hassan et al. 2015), water consistent immersion (Barger 2000, Pack 2003, Au & Büyüköztürk 2006, Lai et al. 2009, Nishizaki & Kato 2011, Huang & Ye 2013, Shi et al. 2012, Aydin et al. 2014, Shrestha et al. 2014), chemical attack (Mukhopadhyaya et al. 1998, Barger 2000, Homam et al. 2001, Pack 2003, Alfar et al. 2006, Fava et al. 2007, Abbas 2010, Pan et al. 2010, Al-Rousan et al. 2013, Aydin et al. 2014, Hassan et al. 2015, Zhou et al. 2015), thermal cycling (Mukhopadhyaya et al. 1998, Barger 2000, Green et al. 2000, Homam et al. 2001, DohnAlek 2006, Hu et al. 2007, Subramaniam et al. 2007, Colombi et al. 2010, Li et al. 2010, Yun & Wu 2011, Kabir et al. 2016, Shi et al. 2012, Hong et al. 2014) and elevated temperatures (Blontrock 2003, Pack 2003, Wu et al. 2005, Dai et al. 2012, Leone et al. 2009, Klamer et al. 2005, Li et al. 2010, Adelzadeh 2013).

Reviewing the experimental studies has revealed that the environmental conidtion of thermal cycling based on freeze/thaw, moderate temperature and sustained temperature has been studied comprehensively, however, a knowledge gap exsits in the area of cycling under moderate temperature.

A wide range of simulated environmental conditions was also recently summarized by Aydin et al. (2016). Geometric, material and conditioning regime differences in test procedures have been widely explored with the general outcome being that the degradation of joint strength is dependent on the change in shear strength of the adhesive relative to the concrete shear strength with prolonged exposure. Further the maturity of the concrete specimens was also found to effect the performance of the long-term durability test. Specimens exposed to harsh environments when compared to 0 day control

samples experience a significant increase of concrete strength, observed even after as little as 28 days and as long as 20 years (Wood 1992).

The environmental conditions that effect durability of FRP strengthened concrete structures are natural and artificial degrading conditions such as temperature variation, moisture effect, sulphate, and/or acid environments. An extensive experimental program to investigate the durability and debonding resistance of composite based strengthening techniques for deteriorated structures is currently underway. The experimental program considers the following environmental conditions, temperature cycle, wet-dry cycle, salt water/ chloride content, sulphate attack and acid attack.

In this paper the influence of thermal cycling on CFRP strengthened concrete elements is only presented. A total of 27 CFRP plates and sheets strengthened concrete specimens were casted and tested. Three different types of adhesives were applied. The thermal cycling was selected ranged between 10 °C and 40 °C, which is most common average lower-bound and upper-bound daily service temperature can be found on concrete structures.

2 EXPERIMENTAL PROGRAM

2.1 *Materials*

An FRP plate externally strengthened concrete system consists of three important components including FRP plate, adhesive layer and concrete substrate. An FRP plate is bonded to concrete substrate depending on adhesive.

Two FRP systems were used in this study, pultruded plate and wet-layup systems with a dimension of 50 mm (width)* 400 mm (length). The thickness of the pultruded plate is 1.4 mm and for the wet layup sheet, 3 layers were used, each layer has thickness of 0.139 mm. The mechanical properties of CFRP plate and sheet were provided by the supplier which is shown in Table 1.

Table 1:Summary of Mechanical Properties of the CFRP

FRP Type	f_{ut} *(MPa)*	E_{frp} *(GPa)*	ε_{ut} *(%)*
FRP Laminate	2800	160	1.7
FRP Sheets	4300	234	1.8

A total of three types of adhesives were used in this study, including two adhesives for FRP laminate system (high and low viscosity ones) and one adhesive for FRP wet layup systems, the details of the adhesive are found in Table 2.

Table 2: Summary of Adhesives' Properties

Property	*High Viscosity*	*Low Viscosity A*	*Low Viscosity B*
Tensile Modulus	4500 MPa	4500 MPa	1495 MPa
Tensile Strength	33 MPa	30 MPa	32 MPa
Shear Strength	>15 MPa (Concrete Failure)	-	35 MPa
Elongation at Break	1.00 %	0.90 %	4.60 %
Glass Transition Point	62 °C	58 °C	56 °C
CTE	$9*10^{-5}$ per °C	$4.5*10^{-5}$ per °C	-

Note: "-" means information is not available.

The concrete blocks that used for strengthening base were pre-mixed and delivery to the site on the date of pouring. The concrete was pouring into 45 customized plywood moulds which have inner dimensions of 150×150×300 mm. And another 18 concrete cylinders with a diameter of 100mm and height of 200 mm were also casted by the same batch of concrete at the same time. The detail properties of the concrete are given in Table 3 and Table 4.

Table 3: Concrete Mix Design

Component	*Volume*
Cement	300 kg/m3
Water	200 L/m3
Sand	890 kg/m3
14mm Aggregate	865 kg/m3

Table 4: Concrete Compressive Strength

Sample ID	*Conditioning Duration (Month)*	*Age under Ambient Environment (Month)*	f_{cm} *(MPa)*
CT-0	0	0	26.05
CT-3	0	3	26.53
T-3	3	0	25.35

3 TEST PREPARATION

3.1 *Sample Preparations*

The concrete blocks were demould after 24 hours after casting and wrapped with an insulation blanket for 28 days. To ensure proper curing environment, water was sprayed every second day. After 28 days, the concrete blocks were then sent for sandblasting to remove a thin top mortar layer and expose the underlying aggregates to assure a good quality bond. The CFRP plate and sheet were cut into 50 mm (width)*400 mm (length) strips. The surface of the

CFRP plates was gently wiped with sandpaper to remove a thin layer of fibre dust, and it was then cleaned with liquid ethanol, whereas, the CFRP sheets need merely cleaned by liquid ethanol. Before the attachment, an air gun was used to clean the dust and losing parts from the concrete surface, and a layer of release film was glued on the boundary of the bond region to avoid misplacement of adhesive in an unwanted area. The bond area was 50 mm (width)* 220 mm (length) located at the center of the concrete surface, a 40 mm unbonded section was left on the front to prevent the wedge failure. The detail bond scheme is found on Figure 1.

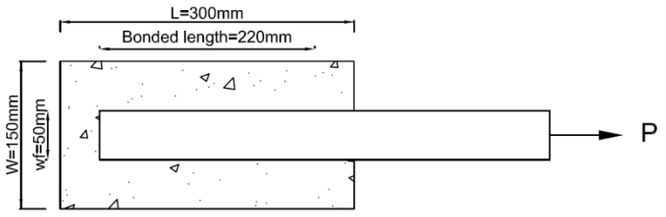


Figure 1: Specimens Details

3.2 *Environmental Conditioning*

A total of 45 samples were scheduled for this experimental investigation, including 9 control samples, 18 aged control samples and 18 conditioning samples. The normal and aged control samples were left out from environmental exposure and kept in an ambient laboratory environment with average 22 °C. The conditioning samples were exposed to temperature cycling between 10 °C to 40 °C inside a temperature controlled chamber with 50 % humidity setting (Figure 2). Each cycle takes 24 hours (12 hours at 10 °C and 12 hours at 40 °C). The conditioned samples were tested after 84 cycles (3 months) and 336 cycles (12 months). At the end of each conditioning duration, the samples which were planned to be tested were removed from the temperature chamber and leave in ambient laboratory condition for 7 days before conducting the pull-out test.
The details for each specimen was listed in Table 5. The the sample ID can be interpreted; the first group letters C stands for control, T stands for temperature cycling, the second group of letter A for low viscosity B, S for high viscosity, W for FPR sheet bonded with low viscosity A sample, the following number are the testing sequence, the third group is stands for the conditioning duration, 0 for control, 3 for 3 months and 12 for 12 months.



Figure 2: Temperature Chamber

3.3 *Test Setup*

The single lap shear test (SLS) was set up horizontally. The Concrete specimen was placed on a metal base. In front of the metal base, a positioning frame was established to ensure the alignment of the specimens with hydraulic actuator and also avoid horizontal movement of the concrete prism. Additionally, an overhead restrain was placed on the rear top of the specimen to prevent the concrete specimens from vertical movement due to pull-out force. Two aluminium plates (50 mm×100 mm) which were applied to prevent CFRP from splitting were attached on both sides of the CFRP on the loaded end. Two LVDTs were set up, one was placed on the rear end of the concrete blocks to monitor the displacement of the concrete, another LVDT was placed on the top of the concrete specimens against an L-shaped metal which is close to the loaded end which was glued on the CFRP plate to measure the CFRP and concrete relative slip. The SLS test performed using a hydraulic actuator which can provide a maximum of 200kN pull-out force. A displacement control program was used for this experiment, a speed rate of 0.2 mm/min was selected. The SLS tests were stopped only the completely interfacial debonding was observed.

4 RESULT AND DISCUSSION

The 0 and 3 months' test results can be found in Table 5, and the specimens designed for 12 months' conditioning are still ongoing.

4.1 *Failure Mode*

Most of the specimens have its failure plane remained at the concrete substrate. A few specimens were found to have failure plane between adhesive

and FRP plate, which is resulting from poor workmanship, so these were excluded from this analysis. The typical failure mode can be observed on Figure 3.



(a) CT-S1-0



(b) CT-A1-0



(c) CT-W1-0

Figure 3: Failure Plane

Table 5: Summary of Test Results

Specimens ID	*P.max (kN)*	*S.max (mm)*	*P.ulti (kN)*	*S.ulti (mm)*	*Avg.P.max (kN)*	*Failure*
CT-S1-0	31.63	0.47	29.50	0.62		CD
CT-S2-0	33.78	0.38	30.80	0.60	31.71	CD
CT-S3-0	29.79	-	27.54	-		CD
CT-W1-0	20.67	0.45	-	-		CD
CT-W2-0	23.06	0.31	16.66	0.61	21.90	CD, A
CT-W3-0	21.97	0.41	19.27	0.89		CD, A
CT-A1-0	32.50*	0.17	30.05	0.48		CD, W
CT-A2-0	34.53	0.48	0.50	0.53	32.79	C
CT-A3-0	31.04	0.42	30.34	0.48		CD
CT-S1-3	39.14	0.61	38.29	0.64		CD
CT-S2-3	33.82	0.47	31.42	0.57	36.48	CD, A
CT-S3-3	39.42*	0.42	39.12	0.44		CD, W
T-S1-3	34	0.5	32.8	0.58		CD
T-S2-3	42.08*	0.63	41.32	0.68	33.28	CD, FD
T-S3-3	32.55	0.56	32.55	0.56		CD
CT-W1-3	23.8	0.73	23.8	0.73		CD, A
CT-W2-3	24.22	0.75	24.22	0.75	23.33	CD, A
CT-W3-3	21.98	0.3	18.73	0.75		CD, A
T-W1-3	27.62*	0.73	23.8	0.75		CD, A
T-W2-3	19.82	0.41	17.98	1.11	21.26	CD, A
T-W3-3	22.70	0.39	22.43	0.95		CD, A
CT-A1-3	33.47	0.26	28.81	0.51		CD
CT-A2-3	25.84*	0.49	25.22	0.53	33.91	CD
CT-A3-3	34.35	0.29	33.77	0.52		CD
T-A1-3	30.94	0.29	27.22	0.48	30.88	CD
T-A2-3	30.60	0.37	29.87	0.40		CD
T-A3-3	31.11	0.30	27.60	0.53		CD

Note:

- *means the results were omitted due to operation errors.
- Failure Modes: CD: Concrete Substrate, A: Concrete and Adhesive interface, W: Wedge Failure, FD: FRP delamination

4.2 *Change of Load vs Slip Curve*

When comparing the peak load of the control samples to that of 3 months' aged samples, the obvious increase was found in the aged ones. The increase in peak load for high viscosity, low viscosity A and low viscosity B samples were 13 %, 6 % and 3 % respectively. The increase can be explained by the concrete maturity; the compressive strength of concrete was observed increased over 3 months from 26.05 Mpa to 26.53 Mpa. On the contrary, the debonding load of the speicmens under 84 temperature cycling decreased, the peak loads of all the conditioned specimens were found lower than the 3 m onths' aged samples, however, the low viscosity B and low viscosity A bonded specimens have their peak loads even lower than the 0 months controlled samples. This may indicate that the high Viscosity was potentially working as a p rotective coating that prevents the influence of the thermal cycling from the concrete substrate, whereas, low viscosity B adhesive was found severely deteriorated which may contribute to its lower T_g value (Table 1). The changes of the peak loads are found on Figure 4.

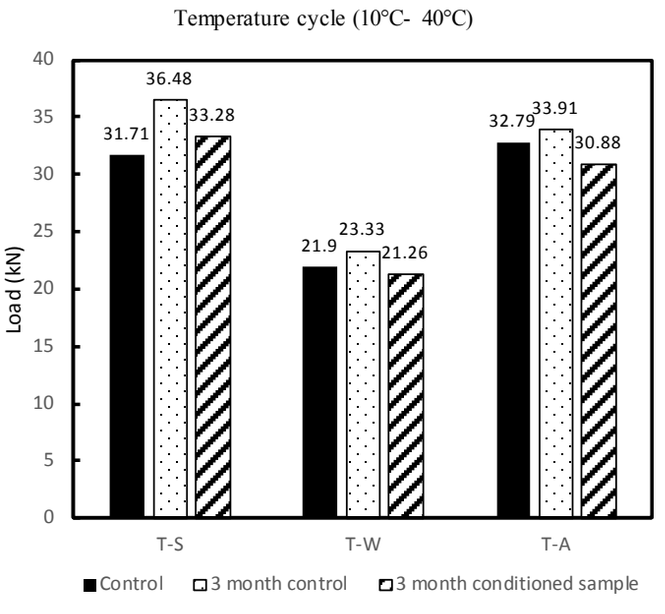


Figure 4:Comparison of Control, Aged and Conditioned Samples

Additionally, the ultimate slip of all the specimens were compared (Figure 5). It can be observed that the ultimate slip for most of the controls experienced no noticeable changes compared to 3 month aged prisms, nevertheless, reduction on the ultimate slip was found on high viscosity and low viscosity B bonded specimens after 3 months' temperature cycling. On contrast, the low viscosity A adhesive bonded wet layup samples had larger slip after temperature cycling.

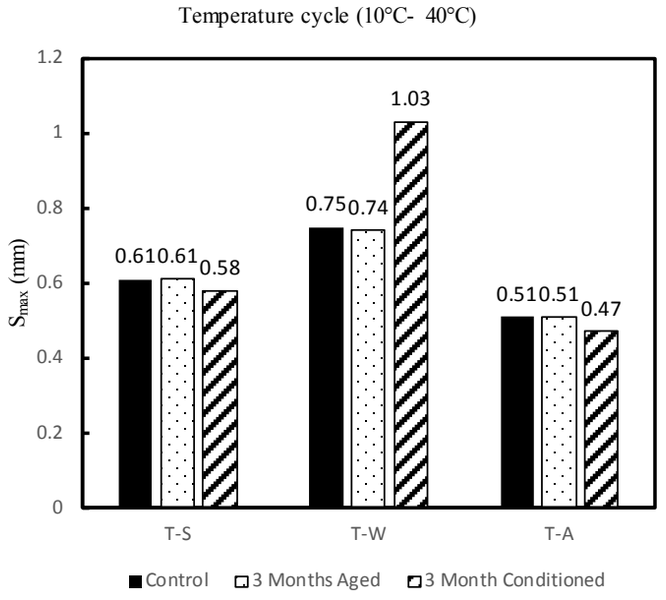


Figure 5:Summary of Ultimate Slip

EXTRACTION OF BOND PROPERTY

A numerical model based on the partial-interaction theory can be applied to extract the bond property of the tested samples. Its accuracy and efficiency has been proved by many previous literatures (Zhang et al. 2016, Haskett et al. 2008, Visintin et al. 2013). In this study, a bilinear bond-slip relationship (Figure 6) was chosen, which is considered as a simple and accuracy model to simulate the shear stress and slip relationship between concrete and FRP (Wu & Yin 2003). The bilinear model can be divided into three sections including ascending, softening and friction components, the governing equation for mentioned components can be presented as the follows:

Ascending $$\tau = \frac{\delta}{\delta_{\max}} \tau_{\max} \quad (1)$$

Softening $$\tau = \left(\frac{\tau_{\max} - \tau_f}{\delta_1 - \delta_{\max}} \right) (\delta_1 - \delta) \quad (2)$$

Friction $$\tau = \tau_f \quad (3)$$

It needs to be noted that this presented mechanics based partial interaction behaviour model can cope with any bond-slip relationship, material property and shape. The fundamental concept of this model has been explained on (Haskett et al. 2008). The correct force and strain value at each stage can be determined by its boundary conditions. In the case, the bonded length is greater than the effective bond length, the boundary condition is $\frac{ds}{dx} = 0$ (Slip strain) and s (Slip) =0 at the free end. If the bonded length is shorter than the effective bond length, the boundary condition becomes $\varepsilon_{frp} = 0$ at the free end.

The input parameters are including mechanical properties of FRP and concrete, and selected bond-slip relationship, in this case, the bilinear relationship (δ_1, δ_2, τ_{max} and τ_f). The main output includes slip, strain, stress and force at a different position along the bonded length, a global force-slip curve simulated by this model shown in Figure 7.

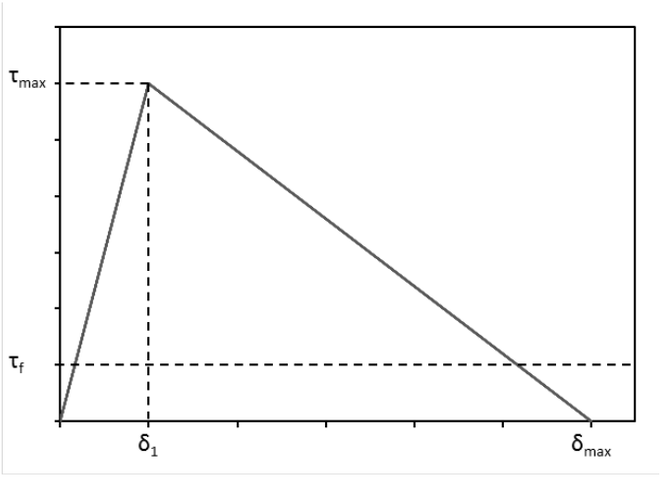


Figure 6:Bilinear Bond slip relationship

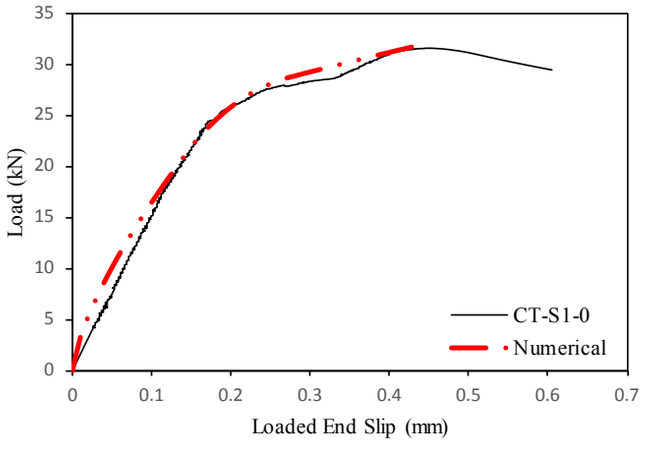


Figure 7:Global Force vs Slip Curve

When comparing the interfacial fractural energy (G_f) of the control samples which is the area under

the stress-slip curve with the aged ones and the aged specimens with conditioned ones, G_f in most of the cases increased, except for the low viscosity B bonded samples which remained almost no changes. However it is obvious that the interfacial energy significantly dropped when comparing aged samples with conditioned ones, 30.1 %, 14.6 % and 15 % for high viscosity, and low viscosity B bonded specimens. The bond-slip properties extracted from experiment results from this study can be found in Table 6.

Table 6: Summary of Bond Slip Property

Sample ID	δ_1 *(mm)*	δ_2 *(mm)*	δ_3 *(mm)*	τ_{max} *(Mpa)*	τ_f *(Mpa)*	*G (N/mm)*
CT-S1-0	0.1	0.27	0.46	4.4	1.48	1.001
CT-S2-0	0.03	0.17	0.36	6.8	1.5	0.968
CT-W2-0	0.14	0.22	0.58	6.6	0	0.726
CT-W3-0	0.13	0.25	0.68	6.4	0	0.800
CT-A2-0	0.1	0.23	0.5	5.5	1.65	1.185
CT-A3-0	0.18	0.24	0.48	6.3	0.47	0.883
CT-S1-3	0.22	0.33	0.63	5.2	2.4	1.710
CT-S2-3	0.22	0.23	0.49	5.3	2.1	1.166
T-S1-3	0.16	0.3	0.54	6.7	0	1.005
CT-W1-3	0.13	0.26	0.72	6.8	0	0.884
CT-W2-3	0.1	0.33	0.69	4.4	0.6	1.011
CT-W3-3	0.1	0.29	0.68	5.6	0	0.812
T-W2-3	0.06	0.37	0.57	3.6	0	0.666
T-W3-3	0.06	0.35	0.68	5	0	0.875
CT-A1-3	0.17	0.27	0.54	7.2	0	0.972
CT-A3-3	0.08	0.3	0.52	6.7	0	1.005
T-A1-3	0.05	0.32	0.44	5.2	0	0.832
T-A2-3	0.18	0.34	0.4	4.6	0	0.782
T-A3-3	0.2	0.37	0.5	4.9	0	0.907

5 CONCLUSION

To investigate the influence of thermal cycling on externally bonded CFRP plate or sheet to concrete bond, a total of 27 specimens were tested. Based on the results, some conclusion may draw:

1. No obvious change in failure plane thickness was observed.
2. The maximum joint strengths decrease after 3 months' thermal cycling comparing to 3 months' aged samples. The strength of conditioned low viscosity A and low viscosity B adhesives bonded specimens are even lower than the non-aged control samples.
3. Change of ultimate slip was found after the conditioning, for the high viscosity and low viscosity B strengthened specimens, the ultimate slips were reduced. The low viscosity A bonded specimens have their ultimate slip increased significantly.
4. The mechanics based partial interaction model has shown its effectiveness in extracting the bond property of the sample with and without environmental conditioning.
5. The interfacial fractural energy was reduced after 3 months' 10 °C to 40 °C temperature cycling when compared to 3 months' aged specimens.

6 REFERENCE

Abbas, B. M. M. (2010) Durability of CFRP-concrete bond under sustained load in harsh environment. Melbourne, Australia, Monash University.

Adelzadeh, M. (2013) *Structural and thermal behaviour of insulated FRP-strengthened reinforced concrete beams and slabs in fire*, Queen's University (Canada).

Al-Rousan, R., Haddad, R. & Al-Sa'di, K. (2013) Effect of sulfates on bond behavior between carbon fiber reinforced polymer sheets and concrete. *Materials & Design,* 43**,** 237-248.

Alfar, A., Rostary, F., Budelmann, H. & Hadid, T. A. (2006) Durability of reinforced concrete members strengthened with CFRP plates and subjected to moisture and salts. *Fiber-reinforced polymer reinforcement for concrete structures (FRPRCS-8): Proceedings of the 8th international symposium.*

Au, C. & Büyüköztürk, O. (2006) Peel and shear fracture characterization of debonding in FRP plated concrete affected by moisture. *Journal of Composites for Construction,* 10**,** 35-47.

Aydin, H., Gravina, R. & Visintin, P. (2014) Effects of moisture, chlorides and sulphuric acid attack on CFRP to concrete bond interfaces.

Barger, J. D. (2000) Effects of aging on bond between FRP and concrete. West Virginia University.

Bertolini, L., Elsener, B., Pedeferri, P., Redaelli, E. & Polder, R. B. (2013) *Corrosion of steel in concrete: prevention, diagnosis, repair*, John Wiley & Sons.

Blontrock, H. (2003) Analysis and modeling of the fire resistance of concrete elements strengthened with externally bonded FRPs. Master's thesis, Ghent University, 414 pp (in Dutch).

Colombi, P., Fava, G. & Poggi, C. (2010) Bond strength of CFRP–concrete elements under freeze–thaw cycles. *Composite Structures,* 92**,** 973-983.

Dai, J.-G., Gao, W. & Teng, J. (2012) Bond-slip model for FRP laminates externally bonded to concrete at elevated temperature. *Journal of Composites for Construction,* 17**,** 217-228.

DohnAlek, P. (2006) Environmental durability of FRP bond to concrete subjected to freeze-

thaw action. Massachusetts Institute of Technology.
Fava, G., Mazzotti, C., Poggi, C. & Savoia, M. (2007) Durability of FRP-concrete bonding exposed to aggressive environment. *Proc., 8th Int. Symp. on Fiber Reinforced Polymer Reinforcement for Concrete Structures, Univ. of Patras, Patras, Greece, 1–10.*
.
Green, M. F., Bisby, L. A., Beaudoin, Y. & Labossière, P. (2000) Effect of freeze-thaw cycles on the bond durability between fibre reinforced polymer plate reinforcement and concrete. *Canadian Journal of Civil Engineering,* 27**,** 949-959.
Hamoush, S. A. & Ahmad, S. (1990) Debonding of steel plate-strengthened concrete beams. *Journal of Structural Engineering,* 116**,** 356-371.
Haskett, M., Oehlers, D. J. & Ali, M. M. (2008) Local and global bond characteristics of steel reinforcing bars. *Engineering Structures,* 30**,** 376-383.
Hassan, S. A., Gholami, M., Ismail, Y. S. & Sam, A. R. M. (2015) Characteristics of concrete/CFRP bonding system under natural tropical climate. *Construction and Building Materials,* 77**,** 297-306.
Homam, S. M., Sheikh, S. A. & Mukherjee, P. (2001) Durability of fibre reinforced polymers (FRP) wraps and external FRP–concrete bond. *Proceedings of the 3rd international conference on concrete under severe conditions.*
Hong, L., Duo, R. M., Wang, S. Y. & Li, L. X. (2014) Influence of freeze-thaw cycles on bonded interface performance between CFRP and high strength concrete. *Applied Mechanics and Materials.* Trans Tech Publ.
Hu, A., R, H. & Y, Q. (2007) Durability of concrete structures strengthened with FRP laminates. *Journal of Harbin Institute of Technology,* 14**,** 571-576.
Huang, S.-q. & Ye, B. (2013) Effect of Moisture on Shear Bond Properties of FRP-Concrete Interface. *Applied Mechanics and Materials,* 405**,** 2635.
Kabir, M. I., Shrestha, R. & Samali, B. (2016) Effects of applied environmental conditions on the pull-out strengths of CFRP-concrete bond. *Construction and Building Materials,* 114**,** 817-830.
Klamer, E. L., Hordijk, D. A. & Janssen, H. J. (2005) The influence of temperature on the debonding of externally bonded CFRP. *Special issue of ACI,* 230**,** 1551-70.
Lai, W. L., Kou, S. C., Poon, C. S., Tsang, W. F. & Lai, C. C. (2009) Effects of elevated water temperatures on interfacial delaminations, failure modes and shear strength in externally-bonded CFRP-concrete beams using infrared thermography, gray-scale images and direct shear test. *Construction and Building Materials,* 23**,** 3152-3160.
Leone, M., Matthys, S. & Aiello, M. A. (2009) Effect of elevated service temperature on bond between FRP EBR systems and concrete. *Composites Part B: Engineering,* 40**,** 85-93.
Li, L., Shao, Y. & Wu, Z. (2010) Durability of wet bond of hybrid laminates to cast-in-place concrete. *Journal of Composites for Construction,* 14**,** 209-216.
Mukhopadhyaya, P., Swamy, R. N. & Lynsdale, C. J. (1998) Influence of aggressive exposure conditions on the behaviour of adhesive bonded concrete–GFRP joints. *Construction and Building Materials,* 12**,** 427-446.
Nishizaki, I. & Kato, Y. (2011) Durability of the adhesive bond between continuous fibre sheet reinforcements and concrete in an outdoor environment. *Construction and Building Materials,* 25**,** 515-522.
Pack, J. R. (2003) Environmental durability evaluation of externally bonded composites. University of Cincinnati.
Pan, J., Huang, Y. & Xing, F. (2010) Effect of chloride content on bond behavior between FRP and concrete. *Transactions of Tianjin University,* 16**,** 405-410.
Shi, J., Zhu, H., Wu, Z., Seracino, R. & Wu, G. (2012) Bond behavior between basalt fiber–reinforced polymer sheet and concrete substrate under the coupled effects of freeze-thaw cycling and sustained load. *Journal of Composites for Construction,* 17**,** 530-542.
Shrestha, J., Ueda, T. & Zhang, D. (2014) Durability of FRP concrete bonds and its constituent properties under the influence of moisture conditions. *Journal of materials in civil engineering,* 27**,** A4014009.
Subramaniam, K. V., Carloni, C. & Nobile, L. (2007) Width effect in the interface fracture during shear debonding of FRP sheets from concrete. *Engineering Fracture Mechanics,* 74**,** 578-594.
Teng, J., Chen, J.-F., Smith, S. T. & Lam, L. (2002) FRP: strengthened RC structures. *Frontiers in Physics***,** 266.
Teng, J., Yu, T., Wong, Y. & Dong, S. (2007) Hybrid FRP–concrete–steel tubular columns: concept and behavior. *Construction and Building Materials,* 21**,** 846-854.
Visintin, P., Oehlers, D. J. & Haskett, M. (2013) Partial-interaction time dependent behaviour of reinforced concrete beams. *Engineering Structures,* 49**,** 408-420.
Wu, Z., Iwashita, K., Yagashiro, S., Ishikawa, T. & Hamaguchi, Y. (2005) Temperature effect on bonding and debonding behavior between FRP sheets and concrete. *Journal of the Society of Materials Science,* 54**,** 474-480.
Wu, Z. & Yin, J. (2003) Fracturing behaviors of FRP-strengthened concrete structures. *Engineering Fracture Mechanics,* 70**,** 1339-1355.
Yun, Y. & Wu, Y.-F. (2011) Durability of CFRP–concrete joints under freeze–thaw cycling.

Cold Regions Science and Technology, 65**,** 401-412.

Zhang, H., Smith, S. T. & Gravina, R. J. (2016) Analysis of FRP-to-concrete interfaces using a displacement driven partial interaction model. *International Journal of Mechanical Sciences*.

Zhou, Y., Fan, Z., Du, J., Sui, L. & Xing, F. (2015) Bond behavior of FRP-to-concrete interface under sulfate attack: An experimental study and modeling of bond degradation. *Construction and Building Materials,* 85**,** 9-21.

Maintenance, Safety, Risk, Management and Life-Cycle Performance of Bridges – Powers, Frangopol, Al-Mahaidi & Caprani (Eds)
© 2018 Taylor & Francis Group, London, ISBN 978-1-138-73045-8

Developments in External Post Tensioning Strengthening – An update of latest innovations and applications

D. Cecan & P.Y. Souesme
Freyssinet, Sydney, Australia

ABSTRACT: In recent years external post-tensioning technology has been revolutionized to a point where it is commonly considered as the most cost effective, durable, and efficient strengthening solution for civil and industrial structures. This paper describes the latest developments in strengthening by external post-tensioning and reviews main applications on various recent projects with a particular focus on challenging technical aspects.

1 INTRODUCTION

1.1 *Context*

Any civil engineering structure is intended to perform one or more functions which are not necessarily constant over time. The initial functions, i.e. those for which the structure has been built, could potentially be modified either voluntarily because of a desired change of the functions or an extension of the lifetime, or involuntarily because of external actions. Three main causes can lead to the loss of the structure's initial intended purposes:

a) *Aging of the structure* – sudden or gradual loss of resistance (degradation of materials, section losses);
b) *External factors* - overloading, earthquakes, pollution, aggressive environmental factors, vehicle or vessel impact, flood events, soil movements…;
c) *Human related factors* - design errors, poor construction quality, lack of maintenance, act of terrorism …

Considering the current global context of cost control and sustainable development policies there is a constant requirement to increase the service period of these structures. Therefore, the need for modern and effective measures to optimize their service life, while respecting their value, represent a challenging objective for the project. There is currently a diverse range of strengthening and repair techniques available for different scenarios that have proven their reliability. However, the strengthening measures must fulfill a very restrictive set of constraints for each specific case.

1.2 *Strengthening considerations*

The success of the operation essentially relies on the quality of the diagnosis, the clear identification of the purpose of strengthening and its solution. If one or another is not completed appropriately, the operation might lead to a poor cost performance or even new type of structural disorders after few years of works completion.

When a structure has been identified to be understrength, it is important to design an engineering solution that fulfils the following requirements:

a) Structural requirements

- Restore or improve structural integrity;
- Increase the load carrying capacity without excess stress or strain in the structure;
- Avoid a major change in the behavior of the structure as a result of over-strengthening or over-stiffening;
- Improve the in-service performance;
- Avoid increasing the self-weight of the structure;
- Accommodate a variety of existing defects such as cracks, extensive loss of corrosion, etc.;
- Improve the robustness and ductility;
- Provide sufficiently rapid gains in strength;
- Avoid creating maintenance liabilities;
- Improve the resistance to fire events;
- Improve or preserve the architectural value and aesthetics;

– Provide a durable and sustainable solution.

b) Construction requirements

– Create a safe working environment for the workforce on site;
– Minimize disruption to the traffic, canal, road or railway system;
– Perform the works in a minimum time;
– Minimize the impact on the environment (noise, pollution, …)

c) Be cost-effective within the constraints identified above.

1.3 *Main Structural Disorders and Deficiencies Scenarios*

The disorders that affect a structure or one of its elements may be due either to a deterioration of its materials, or to a structural problem.
One of the most common material disorders is corrosion. Unlike reinforced concrete structures, where the corrosion can be detected by simple visual inspection (cracking, peeling, spalling, corroded steels, etc.), in prestressed concrete, once the corrosion reached the tendon, it is often generalized and the disorders are often serious without being visible.

There are several types of structural disorders and its associated capacity deficiencies. The most common ones are listed below:

– Flexural deficiency capacity;
– Shear deficiency capacity;
– Torsional deficiency capacity;
– Disorders due to the concentrated loads;
– Disorders due to lateral thrusts.

Structural failures are usually caused by excessive tension leading to cracking. Therefore, the most appropriate repair and strengthening method is to improve the tensile strength of the structure and its resistance to cracking without causing a significant change in the fundamental structural behavior. Although many of the existing structures have been damaged in the form of extensive cracking, experience shows that these structures could regain substantial capacity with limited degree of strengthening.

In this context, the research in materials and development of strengthening systems opened up many opportunities for structural strengthening by external prestressing. The paper presents below different scenarios and innovative strengthening by external post-tensioning techniques which addressed the requirements and challenges of the structure.

2 EXTERNAL POST-TENSIONING STRENGTHENING SYSTEM

2.1 *General Principles*

Post-tensioning is based around the principal of applying compressive loads into a structure once it has reached an appreciable strength (i.e. concrete has hardened), in order to increase the compression to a level that compensates the tension stresses generated by any service or construction load scenario.

These external loads that induce the structure into compression are developed by means of post-tensioned tendons consisting of one or more 7 wire strands.

Tendon profiling is typically evaluated with respect to bending moments in the structure. The tendons can be straight or profiled depending on the extent, location, and orientation of the loads. It is therefore possible to generate radial to the tendon reactions on the existing structure by changing its profile through a careful arrangement of deviators and anchor blocks, see Figure 1.

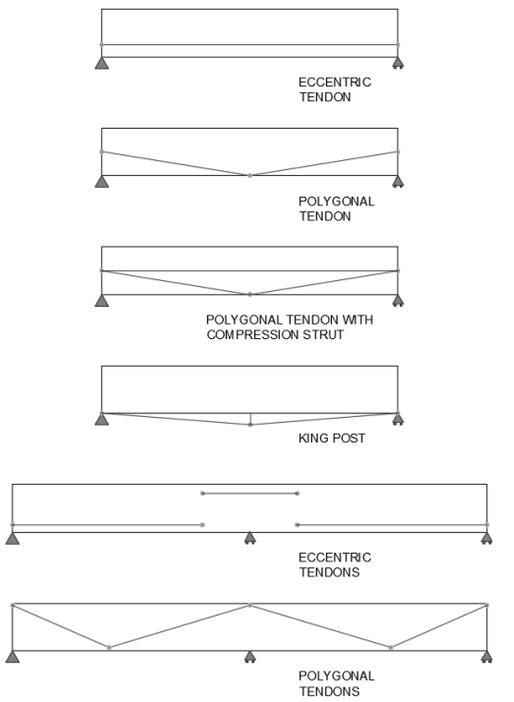


Figure 1: Example of feasible tendon lay-outs with external post tensioning

2.2 *Scope of application*

External post tensioning strengthening is applicable to a wide range of existing constructions provided that the structure has enough capacity to withstand the additional external forces applied by the prestressing for all the load scenarios. The local resistance due to the presence of the anchorages is rarely an issue because it can be overcome by providing an appropriate anchorage design or local strengthening which will enhance the load diffusion. External post-tensioning can be used to improve the performance of any kind of construction or structural

component, be it timber, reinforced or prestressed concrete, steel or composite.

- Concrete bridges and civil structures



Figure 2: Hammersmith Flyover Bridge, Source: Freyssinet

- Steel bridges and civil structures



Figure 3: Gora Kalwari Bridge, Warsaw, Poland, Source: Freyssinet International

- Timber structures



Figure 4: Timber Structure Strengthen with External Post Tensioning System, Source: Freyssinet

- Circular Reservoir



Figure 5: Silos strengthening with external PT, Geraldton, Australia, Source: Freyssinet

- Buildings

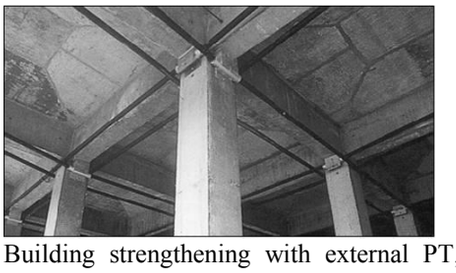


Figure 6: Building strengthening with external PT, Source: Freyssinet

2.3 *Tendons*

Generally, the most relevant type of tendons for strengthening applications with external post-tensioning, consists of greased and sheathed strands (15.7", 1860 MPa, 279 kN breaking load) placed in a HDPE duct injected with cement grout before tensioning of the tendon. This has the advantage of increasing the durability of the prestressing by increasing the number of barriers against corrosion. Also, by making each strand independent from each other, the breakage of one strand doesn't affect the force in the remaining strands allowing for each strand to be replaced if needed.

2.4 *Anchoring to the structure*

Depending on the structural configuration, construction constraints and quantity of strands in each tendon there are several options available for the anchorage detailing.

The most innate solution, whenever possible, would consist of directly anchoring the additional external tendons to elements of the existing structure. For instance, housing the additional tendons anchorage units in new cast-in-situ concrete blocks at deck-ends as shown in the Figure 7, or diaphragms, would ensure a direct compressive force load transfer into the existing structure. However, in practice, this solution is not always the most appropriate due to the amount of works and constraints associated with the preparation of cast-in-situ works, access works behind the girder ends or abutments, and associated traffic disruptions in case of bridge applications.

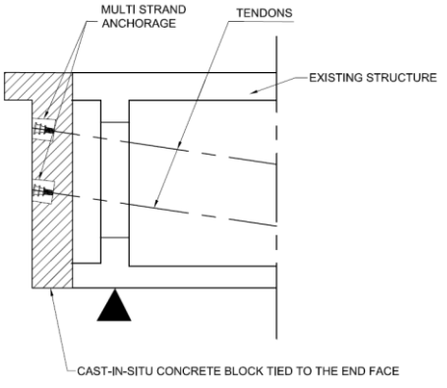


Figure 7: Anchoring the tendons on the face end

In practice, most of the time, the project requirements do not allow the addition of supplementary concrete members, walls to the existing structure. For such cases, the anchorages are housed inside a reinforced concrete or steel "blister" which is connected and secured to the main structure using either standard reinforcing bars working in shear or prestressed bars utilizing friction between the blister and the substrate, see Figure 8.

In the latter case, the prestressing solution offers the most benefit because it provides a confining

force to the anchorage trumplate preventing the spalling and bursting effects, reduced time for concrete surface preparation (light scabbling completed by 3-pin scabblers for concrete grooves instead of deep scabbling), and minimizing the number of core holes in the vertical web wall (lower risk to cut existing reinforcing steel or post-tensioning), particularly when using large diameter stress bars.

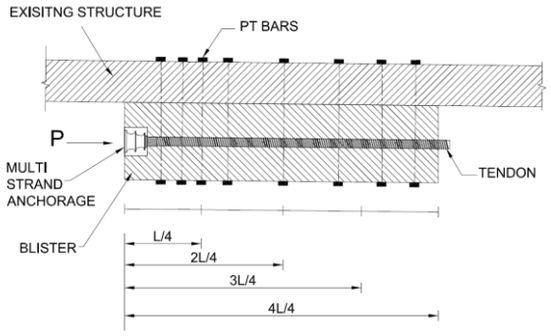


Figure 8: Anchoring the tendons sideways by means of PT bars

2.4.1 *Design - General Requirements*

There are different standards covering the design of shear transfer at the interface between dissimilar materials or two concrete cast at different times.

For instance, AASHTO 2012 Section 5.8.4 "Interface Shear Transfer – Shear Friction" provides a set of rules based on a model which accounts for interface reinforcement, cohesion, and shear-friction resistance contributions for different scenarios:

$$V_{ni} = c.A_{cv} + \mu(A_{vf}.f_y + P_c)$$

V_{ni}	Nominal interface shear resistance
c	Cohesion factor (for corbels, brackets applications: c = 0)
A_{cv}	Area of concrete considered in interface shear transfer
μ	Friction coefficient, depending on the blister / concrete interface
A_{vf}	Area of interface shear reinforcement crossing the shear plan within the area A_{cv}
f_y	Yield stress of reinforcement, design value limited to 413 MPa
P_c	Permanent net compressive force normal to the shear plan

It should also be noted, this design is based on extreme limit state events and it does not specifically cover the service limit states requirements (SLS). For structural elements such as blisters, deviators, etc. anchored to the concrete through a prestressed friction interface, it is prudent to satisfy the absence of tension zone developments (crack opening) at service limit states.

For instance, the French norm NF P 95-104, specifically intended for the design of strengthening by additional prestressing, requires the following conditions to be justified for applications without shear reinforcement:

1) Ultimate Limit State (ULS):

$$\gamma_p.N_p.\frac{\mu}{\gamma_\mu} \geq 1.35.P_m$$

2) Service Limit State (SLS):

$$\gamma_p.N_p.\mu \geq P_m$$

$\gamma_p \leq 1$	Safety coefficient to account for uncertainty related to the transverse prestressing load, commonly used 0.85
γ_μ	Safety coefficient to account for uncertainty related to the friction coefficient, commonly used 1.2
μ	Friction coefficient, depending on the blister / concrete interface
N_p	Total PT Bars residual stressing force
P_m	Tendon prestressing force

Table 1. Commonly used friction coefficient values following NF P 95-104

Designation	Friction coefficient μ
Cast-in-situ concrete blister against old concrete, scabbling up to rebars	1.00
Cast-in-situ concrete blister against old concrete, simply cleaned	0.75
Precast concrete blister with an interposed resin	0.50
Steel blister with a striated face against fresh concrete	0.45
Steel blister with a striated face with an interposed resin or mortar on the old concrete	0.37

For example, in application of the NF P95-104 norm, anchoring a precast blister housing an anchorage of 13 strands (15.7", 1860 MPa) (~2720 kN) would require approximatively 6 x Ø40mm PT bars (1030 MPa).

For cast-in-situ blisters anchored to the existing structure by means of shear reinforcement and prestressed bars the following conditions, as amended by the article No. 501 of ITBTP 1992, should be satisfied:

1) Ultimate Limit State (ULS):

$$(\gamma_p N_p + A_{cv} \times \frac{f_y}{\gamma_s}) \times \frac{\mu}{\gamma_\mu} \geq 1.35.P_m$$

γ_s	Reinforcement strength reduction factor

2) Service Limit State (SLS):

$$\gamma_p.N_p.\mu \geq P_m$$

Different friction coefficient values can be adopted by the project, providing that, a series of tests are carried out in accordance with the design assumptions, construction methodology and material used.

2.4.2 *Cast-in-situ concrete blister*

The blocks can be cast either internally or externally to the structure. This method offers the advantage of blister construction in a confined space or for applications where the access and handling is limited. In practice, connecting the new blister by means of passive reinforcement to the existing structure is not always possible as the required length for anchoring the shear reinforcement is greater than the member depth. Also, if anchoring a blister by means of reinforcing bars only, increases the overall size of the blister. The option of anchoring the blister to the existing structure by means of PT bars or combining it with reinforcing bars offers a more compact solution.



Figure 9: Cast-in-situ concrete blister anchored with PT bars, Westgate Bridge Strengthening, Source: Freyssinet

2.4.3 *Precast concrete blister*

Precast concrete blocks present an interesting solution where the minimum time for intervention is required. Also, this option guarantees a better quality as the precast block is manufactured in a controlled casting environment.

For instance, several advanced initiatives in precast concrete blister design and more generally in strengthening by external post-tensioning have been achieved as part of the Hammersmith Flyover project in London, where the existing post tensioning system of a 630 meter long concrete precast segmental bridge built in the 1960's has been fully replaced. The project requirements, mainly related to the congested urban environment, tight programme and maintaining the traffic on the deck at all times, challenged the engineers to develop new solutions to meet the client's key objectives. As a result, the new post-tensioned tendons were anchored to the existing structure through precast Ultra-High Performance Fibre Reinforced Concrete (UHPFR) blisters fixed to existing structure with Freyssibars+HTSR (High Tensile Strength Resistance bars, f_{pk} = 1200 Mpa). The choice of UHPFRC combined with Freyssibars+HTSR allowed the design to be compact enough to preserve the headroom under the deck (reduction of 50% of concrete quantities and 30% of number of bars compared to traditional anchors blocks fixed with traditional PT bars fpk = 1030 MPa) and to optimize the tendons' eccentricity. The friction coefficient between UHPFRC blister and existing concrete, as well as the design of the blisters were validated by tests.

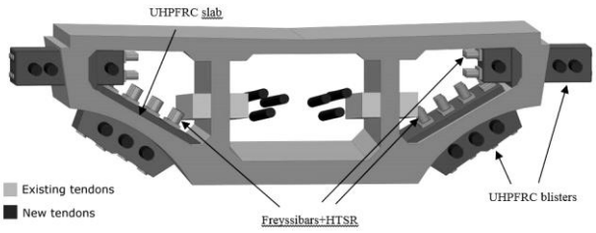


Figure 10: Hammersmith Flyover project, London- Complete strengthening system, Source: Freyssinet



Figure 11: Hammersmith Flyover project, London – External post-tensioning strengthening system, Source: Freyssinet



Figure 12: Hammersmith Flyover project, London – Installation of precast blisters, Source: Freyssinet

2.4.4 *Steel blister*

Steel blocks can be an interesting option for configurations where there is a lack of space to place a concrete block. This solution offers rapid installation however constructability (heavy to install) and durability can be a trade off to the concrete blister solution. Also, anchoring a steel blister requires a greater clamping force (more PT bars) when comparing with a concrete blister as a result of reduced friction factor.



Figure 13: Example of steel blister, Source: Freyssinet

2.4.5 *Bond-friction Anchorage Freyssinet 1R15*

For monostrand applications an efficient and innovative system developed by Freyssinet is the 1R15 bond-friction anchorage, see Figure 15. This system eliminates the provision for the supply, design and fabrication of the blisters detailed above which might result in a substantial savings for the project.

The 1R15 anchorage is a bond-friction type anchorage made of cast iron. The bottom surface at the back end of the anchorage, is provided with steel indentations to create shear interlock with concrete through epoxy resin.

Initially, the system has been developed for building works but further applications revealed that it can offer a cost-effective alternative solution for multistrand applications by combining the anchors in an appropriate arrangement.

For example, the 1R15 system was an alternative solution adopted for Cobbadah Creek Bridge strengthening in NSW, Australia (see Figure 14), which enabled the elimination of major road works involving significant traffic disruption. For this project, all the external post tensioning components were installed by use of hand tools below the roadway without impeding the traffic flow.



Figure 14: Cobbadah Creek Bridge, Strengthening with 1R15 external post-tensioned system, Source: Freyssinet



Figure 15: Cobbadah Creek Bridge, 1R15 anchorages arrangement, Source: Freyssinet

2.5 *Deviators*

The tendon deviation is provided by additional elements 'deviators', the function of which is to transfer the resulting component from tendon deviation into the existing structure. The deviator brackets are detailed in function of the project constraints and are dependent on the type of strand system being used (multistrand vs monostrand), curvature of the deviation, site constraints, and so forth. For multistrand deviators similar detailing to the anchor blocks can be used with either concrete blisters or steel brackets.

The deviators need to be designed to ensure that the radius of tendon in deviators, generally comprising bent steel tubing, shall comply with the minimum required values.



Figure 16: Westgate Bridge, Melbourne - Combined deviator / blister concrete block, Source: Freyssinet

For monostrand applications, it is important to ensure that the correct bend radius and separation of strands is achieved by designing the blister specifically to meet these requirements. Otherwise, within the bundle of strands, the transverse pressure arising from stressing the tendon on a curve leads to ripping of the individual HDPE sheath which is too thin to withstand the corresponding strains. In practice, a multitube saddle with flared ends to allow for strand angular misalignment is generally provided.

HDPE deviators as shown in the Figure 17, are also feasible providing they are designed to withstand the transverse pressure arising from tension in the tendons.



Figure 17: HDPE Deviator for monostrand application, Source: Freyssinet

2.6 *Advantages of External Post-Tensioning Strengthening*

External post-tensioning is generally more effective than passive strengthening methods including steel bands, concrete thickening, additional reinforcement, and carbon fiber for structural strengthening. It provides an active force that does not require further deflection to activate the strengthening system, and provides negligible additional structural mass to the structure.

The advantages of strengthening by external post tensioning systems are summarized below:

- High structural efficiency;
- Capability of applying the desired load conditions and its amount to the structure in a controlled manner;
- Insignificant increase in deadweight;

- Reduces the live load stresses and deflections;
- Cost-effective, low cost of strengthening works;
- Ease of installation and overall speed of construction;
- Limited or no disruption to the traffic;
- Adaptable, replaceable and controlled strengthening system (ability to adjust or to replace the strengthening in the future);
- Durable (active system).

3 REVIEW OF STRENGTHENING APPLICATIONS – CASE STUDY

3.1 *Flexural deficiency capacity*

External post-tensioning strengthening is in the most cases associated with flexural deficiency capacity either in the longitudinal or transversal direction of the main structural components.



Figure 18: SLU, Burnley Viaduct, 1R15 strengthening system, Source: Freyssinet

However, it can also be used for members such as decks, diaphragms, headstocks (see Figure 19), or more generally any structural elements requiring an increase in flexural capacity.

The strengthening by post-tensioning is normally designed as in the case of a new structure, assuming an ordinary prestressed member due to the fact that it's an active strengthening system (the loads are applied to the structure with the stressing of the tendons). It should be noted that the effect of creep and shrinkage may generally be less significant due to the age of the existing concrete.



Figure 19: M2U, Terry's Creek Bridge – Pier headstock strengthening, Australia, Source: Freyssinet

3.2 *Shear deficiency capacity*

Disorders due to a lack of shear and potentially combined with torsion resistance are usually sever but rather rare. Generally, if the structure is deficient in flexure then strengthening by external post-tensioning with a polygonal tendon layout makes the strengthened structure compliant with respect to the shear capacity. In some situations, the longitudinal post-tensioning strengthening is not enough to provide the required additional shear capacity. For such cases, the existing structure is reinforced with additional vertical stirrups usually made of post tensioned bars.

The design of shear reinforcement needs to be undertaken after a careful structural diagnosis and appreciation of the crack widths. If the structure presents a significant cracking then it is very likely that the existing stirrups have been plasticized. It is therefore prudent to size the additional prestressing to equilibrate the total required shear load.



Figure 20: Pont du Royaume, - Shear strengthening of the webs by stress bars combined with transverse prestressing of the bottom slab, Avignon, France

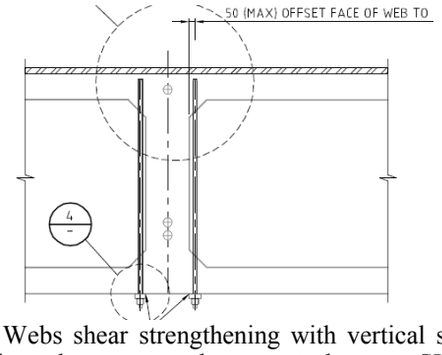


Figure 21: Webs shear strengthening with vertical stress bars anchored through epoxy anchorage at the top, SLU, Yarra Bridge, Australia, Source: Freyssinet

3.3 *Modification of initial scheme*

3.3.1 *M2 Motorway, Sydney, Australia*

The following example, based on the M2 Motorway widening operation in Sydney, illustrates a successful and cost efficient modification of the initial static scheme of existing bridges with external post-tensioning. For this project, the motorway widening was associated with relocation of the substructures of overpasses. Profiled external post tensioning tendons were designed to provide the required increased capacity as well as to achieve the load transfer from the old to the new supports during the stressing.

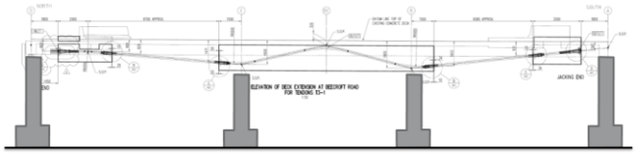


Figure 22- M2 Motorway, Sydney, Initial Static Scheme, before stressing of external post tensioned tendons

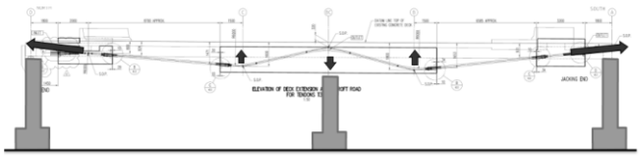


Figure 23- M2 Motorway, Sydney - Final arrangement

3.3.2 *Binh Trieu Bridge, Ho Chi Minh, Vietnam*

The 560 meter long crossing composed of a main steel bridge (3 spans measuring 160 meters) and two simply supported prestressed beam girders approach spans (10 spans measuring 250 meters on one side and 6 spans measuring 150 meters on the other was built in the 1960s.



Figure 24: Binh Trieu Bridge – Concrete approach spans & Steel Bridge, Source: Freyssinet

The aim of the strengthening was to widen the bridge in order to create a specific lane for cycles on one side only and to make the bridge complying with new construction codes (vehicles and seismic loads).

As a consequence of the increased loads, the solution was to make both access viaducts continuous by grouping the 5 or 6 spans together, using external prestressing. To ease execution, the cables were chosen to be 2 to 3 spans in length and were crossed on piers. Transverse blocks were built to ensure correct deviation and proper anchorage of new longitudinal cables.

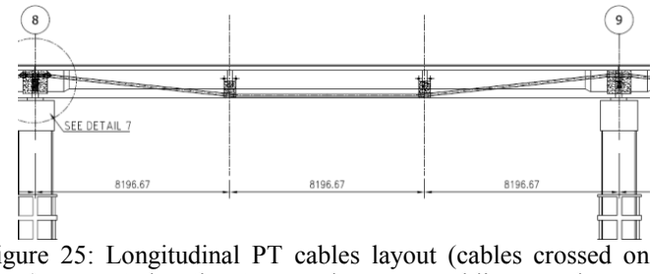


Figure 25: Longitudinal PT cables layout (cables crossed on piers) connected to the structure by concrete blisters and transversal PT cables

The chosen and implemented engineering solution for this projected which consisted in a complete change of the static behavior of the bridge, allowed the reduction of the material quantities when compared to alternative solutions, as well as completion of the strengthening works with a minimum disruption to the traffic.

4 CONCLUSIONS

With the recent development in structural analysis, design and post-tensioning systems, external post-tensioning has become one of the most cost effective, constructible and relatively simple methods for strengthening concrete bridges available today. It is relatively quick to install, has low aesthetic impact and can be designed to be retrofitted to accommodate almost all concrete bridge structure types. In addition, the following provides the key conclusions that can be drawn from the recent experiences:

- External post tensioning provides a wide range of solutions to address different types of disorders and deficiencies on concrete, steel or timber structures. Several options and systems are available depending on the final intent, types of corrosion protection, construction requirements, etc.;
- A careful assessment is essential prior the design phase in order to ensure that all the strengthening in conjunction with the project and environmental requirements have been considered;
- The strengthening projects leads to strong mutual dependence between all the parties involved (Client, Main Contractor, Designer, specialist Subcontractor). As such, it is recommended to have a careful balance between the design and the constructability. Furthermore, the project management structure in place should ensure strong links between the key players.

5 REFERENCES

V. Buchin-Roulie, N. Kaczkowski, C. de Courcelles, M. Toth. 2017. Innovative solutions for Bridge strengthening (widening and compliance to new codes) by modification of initial static scheme, *39th IABSE Symposium – Engineering the Future, 21-23 September 2017.* Vancouver, Canada

B. Cousin, V. Buchin-Roulie, C. Vandevoorde, N. Fabry. 2017. Hammersmith Flyover: A Complete Innovative Renovation, *AFGC-ACI-fib-RILEB Int. Symposium on Ultra-High Fibre-Reinforced Concrete, 02-04 October 2017.* Montpellier, France

NF P 95-104. December 1992. Masonry Construction, Specifications Pertaining to the Prestressing Technique

AASHTO LFRD Bridge Design Specifications. 2012

Maintenance, Safety, Risk, Management and Life-Cycle Performance of Bridges – Powers, Frangopol, Al-Mahaidi & Caprani (Eds)
© 2018 Taylor & Francis Group, London, ISBN 978-1-138-73045-8

S-N curves for RC beams strengthened with FRP

L.C. Meneghetti
University of São Paulo, São Paulo, Brazil
M.R. Garcez
Federal University of Rio Grande do Sul, Porto Alegre, Brazil
R. M. Teixeira
Federal University of Pará, Belém, Brazil

ABSTRACT: Externally bonded FRP may increase the fatigue life of RC beams due to the reduction of the steel stress level if compared to unstrengthened beams. In general, fatigue failure is marked by the gradual deterioration of the steel rebars, which leads a stress transfer to the Fiber Reinforced Polymer (FRP), until failure. Steel stresses higher than 80% of yield stress are associated with FRP debonding, while steel stresses below the fatigue limit will never lead to fatigue failure. The lack of data regarding fatigue life of FRP strengthened beams, mainly when related to low stress levels, leads to general fatigue analysis with S-N curves developed for different FRP systems and stress ranges. Aiming to improve the fatigue life analysis of RC beams strengthened with FRP this paper aims to develop specific S-N curves for different FRP systems, through the Maximum Likelihood Estimation Method (MLE). Experimental data with runouts of fatigue tests found in literature and generated through an experimental program were used to adjust the fatigue model aiming to characterize the large scatter between the results of fatigue tests from the different sources. The proposed fatigue models for the different FRP systems represent accurately the declivity of the fatigue curves for FRP strengthened RC beams.

1 INTRODUCTION

Cyclic loading are one of the main causes of RC deterioration in bridges because repeated loading and unloading cycles may lead to fatigue (Demers 1998, Ye et al. 2014, Song & Yu 2015). A typical RC highway bridge deck with a design life of 40 years may experience a range of 10^7 to 10^8 cycles (Barnes and Mays 1999), or, according to the Canadian Standard Association, a minimum of 58 x 10^8 loading cycles of varying intensities (CSA, 2014). In this perspective, fatigue may significantly reduce the expected lifetime of a RC structure, resulting in catastrophic failure even with applied loads below the structural capacity of the elements (Demers 1998).

Fatigue life becomes a crucial question since the lack of data regarding FRP post-strengthened elements leads to superficial analysis that consider the same S-N curves for different FRP systems and stress ranges. Thus, although FRP strengthening design methods are now established and many guidelines exist, fatigue design procedure is still an ongoing research topic.

Fatigue analytical models can link theory with observed data to provide a good prediction of future observations (Ye et al. 2014) or even can be useful for deciding aspects to be explorated in real scale fatigue tests. Fatigue tests are, in general, expensive, and curve fitting of fatigue data is time-consuming, as well as fatigue tests. On the other hand, engineering designers need to make safe use of these complex fatigue life data, especially for unconventional materials like composites (Meneghetti et al. 2017).

Aiming to improve the fatigue life assessment of RC beams strengthened with FRP, the goal of this paper is to adjust specific S-N curves for different FRP systems. An extensive database, with experimental data gathered from the literature, have been used to adjust fatigue models through Maximun Likelihod Estimation (MLE) aiming to characterize the large scatter between the results of fatigue tests from the different sources.

The MLE allows the use of runout data that are not used in classical regression analysis due to the fact that the number of load cycles at failure is unknown or even because the number of load cycles at which the test was interrupted is completely arbitrary (Taras & Greiner 2009). Runout data, in fact, are not as complete as test data resulting from a fatigue test up to failure, but also show that the tested member

could achieve more than the number of load cycles at the test interruption.

Distinct fatigue models have been developed considering four post-strengthening categories of FRP Externally Bonded Reinforcement (EBR) with FRP strips and sheets with and without additional anchorage.

2 MAXIMUM LIKELIHOOD ESTIMATION

The relation between the nominal steel stress range ($\Delta\sigma$) and the number of cycles at failure (N) is given by the well-known form expressed in Equation 1, where m>0 and k>0 are real numbers that can be estimated by linear regression of under the constant-amplitude fatigue regime.

$$N = \Delta\sigma^{-m}\, k \tag{1}$$

Equation 1 can be written in log-log scale with $x = logN$, $y = log\Delta\sigma$, $B = -m$, and $A = log(k)$, resulting Equation 2.

$$x = By + A \tag{2}$$

In the log-log system B represents the slope of the S-N curve and A denotes the intersection with the horizontal axis, as it can be seen in Figure 1.

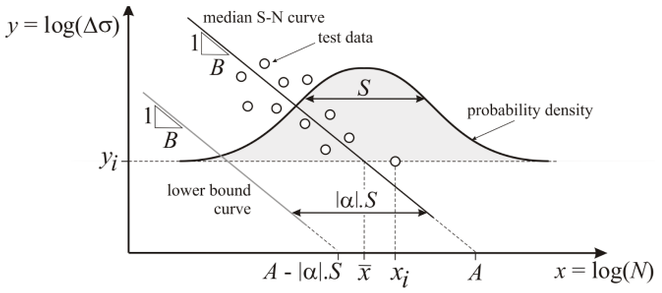


Figure 1. Variables used in the S-N model.

Considering the statistical nature of N, Equation 2 can be rewritten, according to ASTM E739-10 (2015), as Equation 3, which means that for a given $\Delta\sigma$, $x = logN$ obeys a normal distribution with median $\bar{x}$ with a non-exceedance probability of 50%.

$$\bar{x} = E\,[x][y] = By + A \tag{3}$$

For other probabilities, the standard deviation (S) for log(N) must be multiplied by α and computed as shown in Equation 4. The factor α defines different non-exceedance probabilities of the normal distribution and can be defined as $\alpha = \Phi^{-1}(p)$, where $\Phi^{-1}(p)$ is the standard normal inverse cumulative distribution function for a specific probability of failure.

$$x = By + (A + \alpha S) \tag{4}$$

International codes, such as CEP-FIP (2010), recommend the 5% fractile S-N curves for fatigue assessment and design of RC members if failure happens in steel rebars.

Linear regression analysis is frequently used to fit experimental datasets collected from the literature, through the Least-Square Method. In such case, only failure points are considered and runouts are excluded from the analysis. Apart from that, the Constant Amplitude Fatigue Limit (CAFL) position is, in general, arbitrarily chosen and prediction bounds of linear regression curves are based on fatigue data scatter in the finite-life region, which results less accuracy in the high cycle fatigue region (D'Angelo et al., 2014).

The application of the Maximum Likelihood Estimation (MLE) in the fatigue field, through a five-parameter random fatigue model, was first proposed by Pascual and Meeker (1999). A generalised methodology based on MLE for the inclusion of runouts, as well as different probability distributions of fatigue life, was proposed by Sarkani et al. (2007), based on a Weibull distribution. When applied to fatigue, MLE determines the S-N curve that describes the most likely location of each fatigue test result, including runouts.

For a given set of x_i independent observations obtained in different y_i levels, and considering the transformation $z_i = [x_i - \bar{x}(y_i)]/S$, the likelihood function is given by Equation 5 , in which $\delta_i = 1$ for failure, $\delta_i = 0$ for runout, $f(z_i;\theta)$ is the probability density of z_i, $F(z_i;\theta)$ is the cumulative probability distribution of z_i, and $\theta = [\,A\ B\ S]$ is the vector of parameters of the fatigue model.

$$\Gamma(\theta) = \prod_{i=1}^{n} [f(z_i;\theta)]^{\delta 1} [1 - F(z_i;\theta)]^{1-\delta i} \tag{5}$$

Assuming that data may be adjusted through a normal distribution in log-log scale, the likelihood function $L_i(\theta)$ for a single test result is given by Equation 6, where $\varphi(z_i;\theta)$ is the standard normal probability density of z_i and $\Phi(z_i;\theta)$ is the standard normal cumulative probability function of z_i.

$$L_i(z_i;\theta) = \delta_i \{log[\varphi(z_i;\theta)] - log[SN_i]\} + (1 - \delta_i) log[1 - \Phi(z_i;\theta)] \tag{6}$$

The log-likelihood function of the entire dataset is given by the contribution of each dataset, according to Equation 7.

$$\Lambda(z_i;\theta) = \sum_{i=1}^{n} L_i(z_i;\theta)] \tag{7}$$

The set of parameters θ that maximizes the function $\Lambda(z_i;\theta)$ can be determined using popular optimization algorithms, such as the native *fmincon* function of the Matlab Optimization Toolbox (Mathworks 2010), for instance. In this case,

algorithms are used to minimise $-\Lambda(z_i;\theta)$ which is the same as maximizing $\Lambda(z_i;\theta)$, when initial constraints are given to θ to limit the search space within a feasible region.

3 FATIGUE DATABASE

Experimental data of fatigue tests with runouts, reported by Barnes and Mays 1999, Meier 2000, Al Rousan & Issa 2001, Masoud et al. 2001, Papakonstantinou et al. 2001, Wight & Erki 2003, Aidoo et al. 2004, Heffernan & Erki 2004, Gussenhoven & Breña 2005, Masoud et al. 2005, Quattlebaum et al. 2005, Silva Filho 2005, Ekenel et al. 2006, Rosemboon & Riskalla 2006, Toutanji et al. 2006, Al Saraj 2007, Gheorghiu et al. 2007, Meneghetti 2007, Wang et al. 2007, Ferrier et al. 2011, Charalambidi et al. 2016, Mahal et al. 2016, Peng et al. 2016, and Huang et al. 2017 have been used to generate the proposed fatigue models.

Fatigue test data were generated through cyclic loading tests carried in reinforced concrete beams post-strengthened with different FRP systems and techniques. The following assumptions were considered to generate the proposed fatigue models: i) database collected constitutes a random sample from a population of all possible test results; ii) individual results, in terms of fatigue life, are random samples from a log-normal population. A random sample is required for a meaningful evaluation of population parameters, confidence limits, and tolerance intervals (Meneghetti et al., 2011).

Data have been classified in four post-strengthening categories, according to the FRP system and application technique, as shown in Table 1.

Table 1. Data categories.

Category	FRP System	Technique
1	FRP strips	EBR, anchorage
2	FRP strips	EBR, no anchorage
3	FRP sheets	EBR, anchorage
4	FRP sheets	EBR, no anchorage

Tables 2 to 6 show the reported fatigue tests used to generate the proposed fatigue models with data that reasonably represent the actual vehicular loading and frequency experienced in practice.

Table 2. Reported fatigue test results for category 1, FRP strips, EBR, additional anchorage.

Author	Specimen	Δσ	N	F
Wang et al. 2007	C1	200	10000	0
	C2	200	1000000	0
Charalambidi et al. 2016	REX20-L	220	2000000	0
	TEX20-L	220	1300000	0
	REX20-H	352	990147	1
	REX40-H	365	1450105	1
Mahal et al. 2016	B1-EE1-F	258	520733	1
	B6-EE2-F	258	438592	1
	B9-EE1-F-C	258	600000	0
Quattlebaum et al. 2005	P-L	169	1320000	1
Barnes and Mays 1999	3	274	508500	1
	4	222	1889087	1
	5	180	11968200	0
Rosemboon & Riskalla 2006	EB1F	514	625000	1
Peng et al. 2016	RF	117	658000	1
Ekenel et al. 2006	S4F	210	2000000	0

Δσ : Stress Steel Range, in MPa; N: No of cycles; F: Failure

Table 3. Reported fatigue test results for category 2, FRP strips, EBR, no anchorage.

Author	Specimen	Δσ	N	F
Aidoo et al. 2004	RS1	338	308879	1
	RS2	279	1280000	1
Gheorghiu et al. 2007	L400A	254	400000	0
	L400B	254	400000	0
	L800A	254	800000	0
	L800B	254	800000	0
	L800C	254	800000	0
	L2000A	254	2000000	0
	L2000B	254	2000000	0
	H400A	267	400000	0
	H400B	267	243000	0
	H800A	267	800000	0
	H800B	267	203000	1
	H2000A	267	710000	0
	H2000B	267	2000000	1
Quattlebaum et al. 2005	C-H	211	600000	1
	C-L(a)	156	2000000	0
Wang et al.2007	F6	200	10000	0
Silva Filho 2005	FB6	142	347145	1
	FB7	143	150415	1
Al Rousan & Issa 2001	B4A	103	2000000	0
	B4b	186	2000000	0
	B5	186	1115000	1
Ekenel et al. 2006	S3F	210	2000000	0
Meier 2000	T	131	14090000	1

Δσ : Stress Steel Range, in MPa; N: No of cycles; F: Failure

Table 4. Reported fatigue test results for category 3, FRP sheets, EBR, additional anchorage.

Author	Specimen	Δσ	N	F
Toutanji et al. 2006	3FI-5	226	2000000	0
	3FI-6	226	2000000	0
	3FI-7	226	2000000	0
	3FI-8	226	2000000	0
	3FI-9	283	259432	1
	3FI-10	283	314728	1
	3FI-11	283	197954	1
	3FI-12	367	74383	1
	3FI-13	367	74579	1
	3FI-14	399	2122	1
	3FI-15	399	2375	1
	3FI-16	399	4480	1
	3FI-17	399	5047	1
Meneghetti et al. 2007	Carbono A	310	210217	1
	Carbono B	246	378499	1
	Aramida A	312	234368	1
	Aramida B	247	665609	1
	Vidro A	258	832517	1
	Vidro B	204	3662726	1
	AA1	387	212201	1
	CB1	338	258515	1
	CB2	338	208928	1
	CB3	338	217026	1
	VB1	347	137250	1
	VA3	208	2384018	1
	VC2	208	885000	1
	VA1	208	5000000	0
	VC2	208	5000000	0
	CA1	202	4999750	0
	CC1	68	4871000	0
	CD1	202	5000000	0
	AA1	232	5000000	0
	AC2	232	5081300	0
	AD1	77	5000000	0
Silva Filho 2005	FB8	168	142904	1
Rosemboon & Riskalla 2006	EB2F	635	2000000	0
Masoud et al. 2001	T II F	275	517976	1
Wight & Erki 2003	SF-N	325	169000	1
	SF-SN	190	1519000	1
Masoud et al. 2005	11-R1	323	232000	1
Ekenel et al. 2006	S2F	188	2000000	0

Δσ : Stress Steel Range, in MPa; N: No of cycles; F: Failure

Table 5. Reported fatigue test results for category 4, FRP sheets, EBR, no anchorage.

Author	Specimen	Δσ	N	F
Papakonstantinou et al. 2001	S-2	266	880000	1
	S-5	268	800000	1
	S-6	359	126000	1
	S-7	299	570000	1
	S-8	454	30500	1
	S-9	325	235000	1
	S-10	246	685000	1
Heffernan & Erki 2004	CF-2	215	312000	1
	CF-4	202	627000	1
	CF-6	191	1049000	1
	LCFa	160	4890000	1
	LCFb	160	6440000	1
	MCFa	201	900000	1
	MCFb	201	890000	1
	HCFa	241	340000	1
	HCFb	241	390000	1
Aidoo et al. 2004	RF1	306	193160	1
	RF2	279	960000	1
Gussenhoven & Breña 2005	A-1-4-80	295	131619	1
	A-1-4-70	272	287594	1
	A-1-4-60	224	778734	1
	B-1-2-80	300	290307	1
	B-1-2-70	268	336873	1
	B-1-2-60	236	4000000	0
	B-2-2-70	270	150000	1
	B-2-2-60	199	2000000	0
	C-1-2-80S	326	326775	1
	C-1-2-70S	226	4401793	1
	C-1-2-60S	189	4000000	0
Ferrier et al. 2011	B5	294	1000000	0
	B6	294	1000000	0
Huang et al. 2017	SB2	178	2000000	0
Al Rousan & Issa 2001	B1	41	2000000	0
	B2a	83	2000000	0
	B2b	103	2000000	0
	B3	103	2000000	0
	B6	186	2000000	0
Al Saraj. 2007	N4	205	2000000	0
	N5	237	2000000	0
	N8	269	650000	1
	N3	296	275000	1
	N6	360	155000	1
	N7	433	80000	1
	S11	196	6000000	0
	S10	220	685000	1
	S2	237	880000	1
	S5	239	800000	1
	S7	267	570000	1
	S9	291	235000	1
	S6	320	126000	1
	S8	406	30500	1
Ekenel et al. 2006	S1F	188	2000000	0

Δσ : Stress Steel Range, in MPa; N: No of cycles; F: Failure

4 S-N CURVES

Specific S-N curves were obtained through the native *fmincon* function of the Matlab Optimization Toolbox (Mathworks 2010). The MLE solution was found considering a start point $\theta_0 = [16\ 3.7\ 0.5]$ and data were first classified in four categories, as shown in Figures 2 to 5.
Table 6 presents the MLE detected parameters of the four fatigue models and estimates of $\Delta\sigma$ at 2 million cycles.

Table 6. MLE parameters of the four fatigue models for different probabilities at 2,000,000 cycles.

Cat.	Intercept A	Slope B	St. Dev. S	Δσ at 2mi cycles	
				$p = 25\ \%$	$p = 5\ \%$
1	8.59	-1	0.45	34.85	25.08
2	8.71	-1	0.65	21.62	13.41
3	20.66	-6.08	0.89	131.55	118.96
4	17.51	-4.85	0.35	155.25	147.31

Black dots on Figures 2 to 5 represent data associated to tests that were interrupted when before fatigue failure, and, therefore, indicate that the specimen could support a higher number of cycles, with the possibility to achieve infinite fatigue lifetime.

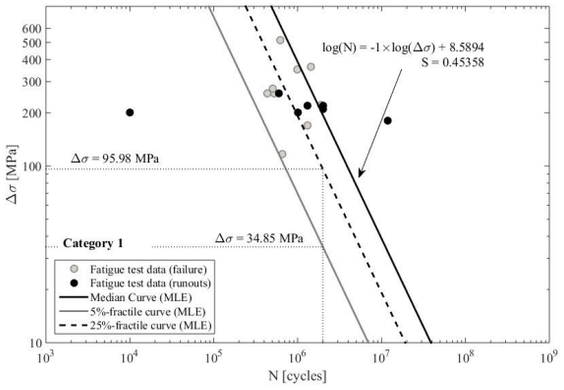


Figure 2. Maximum Likelihood Estimation for Category 1, FRP strips, EBR, additional anchorage.

The MLE model estimates quite different S-N curves for strips (Figures 2 and 3) and sheets (Figures 3 e 4) at 2 million cycles, which is confirmed by the huge change in the slope of the curves.

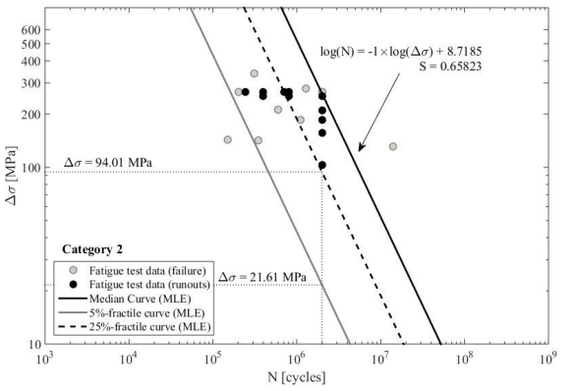


Figure 3. Maximum likelihood estimation for Category 2, FRP strips, EBR, no additional anchorage.

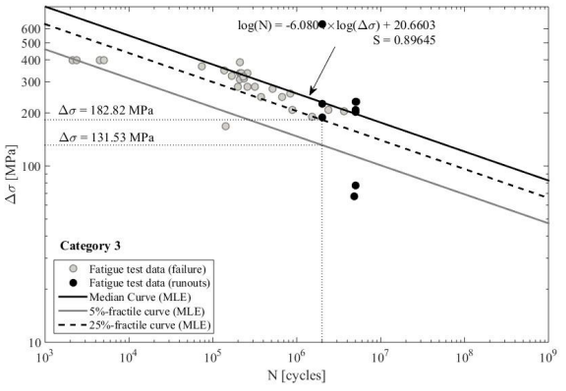


Figure 4. Maximum Likelihood Estimation for Category 3, FRP sheets, EBR, additional anchorage.

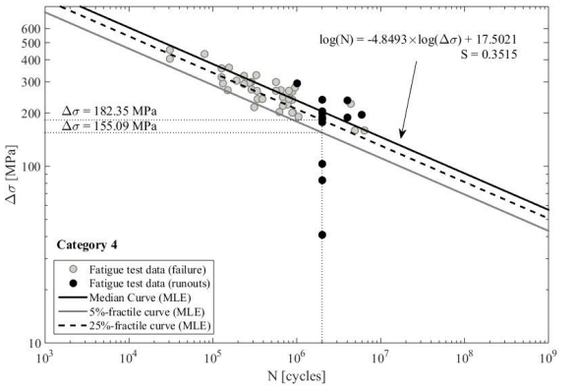


Figure 5. Maximum Likelihood Estimation for Category 4 , FRP sheets, EBR, no additional anchorage.

In the case of FRP strips, results of 5% fractile curves at 2 million cycles seems to confirm the positive effect of the additional anchorage, which is not endorsed by the results of FRP sheets. In fact, one of the most common anchorage system for FRP EBR, especially sheets, is the use of uni or multidirectional FRP U-wraps. If not perfectly executed, the radius of the FRP U-wraps may experience stresses concentration that induce premature failures at the anchorage system (Figure 6). Experimental results of Skuturna & Valivonis 2016 revealed that steel clamps are the most

effective anchorage system for FRP EBR, when compared to steel pins, U-wraps, and over support.



Figure 6. Premature failure at the FRP U-Wrap anchorage.

Aiming to ratify this findings, specific S-N curves were obtained considering 2 categories, strips (Figure 7), sheets (Figure 8), and curves that consider all data (Figures 9), whose MLE parameters and estimates of at 2 million cycles are presented in Table 7.

Table 7. MLE parameters of the four fatigue models for different probabilities at 2,000,000 cycles.

Cat	Intercept A	Slope B	St. Dev. S	Δσ at mi cycles	
				p = 25 %	p = 5 %
strips	8.644	-1	0.56	91.65	25.99
sheets	18.97	-5.43	0.63	180.09	138.89
all	15.85	-4.10	0.69	162.63	111.67

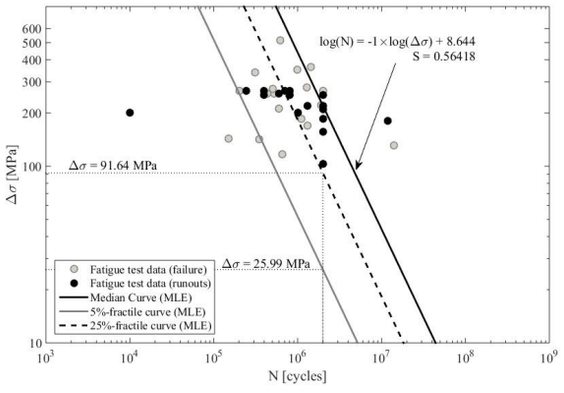


Figure 7. Maximum Likelihood Estimation for FRP strips, categories 1 and 2.

Figures 7 and 8 that aggregate data of anchored and unanchored FRP strengthening, confirm the findings of S-N curves for each category, presented in Figures 2 to 5, especially for the case of FRP sheets. S-N curves of FRP strips may be underestimated the fatigue life due to the lack of fatigue data for beams post-strengthened with FRP strips in the high cycles region.

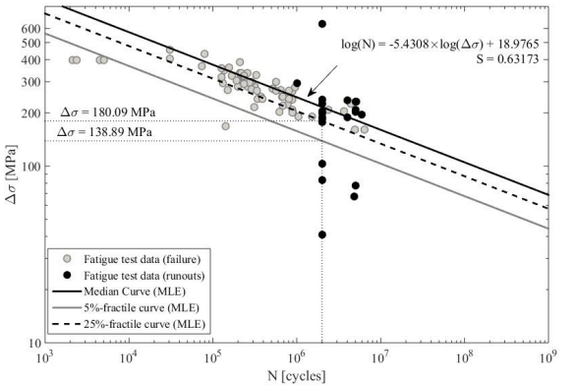


Figure 8. Maximum Likelihood Estimation for FRP sheets, categories 3 and 4.

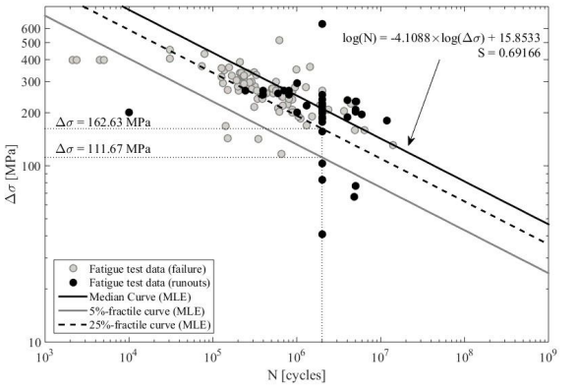


Figure 9. Maximum Likelihood Estimation for FRP strips and sheets, all categories.

S-N curves of Figure 9 with data of all categories show that the use of the same model for all types of FRP and techniques may underestimate the fatigue limit for FRP sheets and overestimate the results for FRP strips.

It is important to highlight that the fatigue design in the current bridge design specifications is based in the CAFL, the stress range below which the constant amplitude fatigue tests do not exhibit cracks after millions of cycles. The CAFL is, in general, arbitrarily chosen: 5% fractile curves are frequently used to determine the stress range that corresponds to a specified number of cycles, i.e. AASHTO allowable fatigue stress range for highway bridge design specifications, that depends on the structural element and redundancy of loading paths (AASHTO 2002).

On the other hand, in real life, structural elements are subjected to varying fatigue loads, and not to constant amplitude fatigue loadings. Fatigue models based in linear log-log S-N curves, frequently used if fatigue assessment, however, are not able to predict the fatigue limit. For this, fatigue models originated from non linear log-log SN curves are needed.

The fatigue limit, endurance limit, or fatigue strength for unstrengthened beams (ACI 215R 1997), may be estimated using the equation 8 where σ_{min} is the minimum steel stress level, pointing out that stress amplitudes lower than 138MPa could be ignored.

$$\Delta\sigma = 161 - 0.33\sigma_{min} \quad (8)$$

Apart from the results of Category 4 (sheets, no additional anchorage), the fatigue models do not show any positive effect on the endurance limit of the original steel rebars at 5% fractile curve. However, given the large scatter of fatigue data and the reduced size of the database available, especially regarding the use of FRP strips and data related to low steel stress ranges, further tests and confirmation of this tendency are necessary before any consideration on the endurance limit for FRP strengthened beams is made.

5 CONCLUSIONS

Based on data gathered from the literature, it was possible to adjust models based MLE method. Different declivities have been found for the adjusted fatigue life models, which highlight specific aspects of each category.

The declivity of the fatigue curves accurately represent the fatigue behavior of FRP strengthened RC beams, especially for FRP sheets, and can be used to support proper post-strengthening design, to avoid future unnecessary interventions.

The anchorage system may influence the fatigue behaviour of FRP strengthened beams especially in U-wraps anchorages, since if minimum radius is not respected, eventual stress concentrations on the anchorage system may induce premature failures.

More fatigue tests data with post-strengthened RC beams submitted to different higher and lower steel stress ranges may be useful, in the future, to ratify these findings.

ACKNOWLEDGEMENTS

Authors would like to acknowledge CNPq (Portuguese acronyms of the Brazilian Ministry of Science and Technology Agency) and CAPES (Portuguese acronyms of the Brazilian Ministry of Education Agency) for providing part of the financial support needed to develop this project.

REFERENCES

ACI 215R. 1997. Considerations for design of concrete structures subjected to fatigue loading. American Concrete Institute, Farmington Hills, MI, USA.

Aidoo, J. et al. 2004. Fatigue behavior of carbon fiber reinforced polymer strengthened reinforced concrete bridge girders. *Journal of Composites for Construction* 8(6): 501-509.

Al Rousan, R. Z. & Issa, M. A. 2011. Fatigue performance of reinforced concrete beams strengthened with CFRP sheets. *Construction and Building Materials* 25(8):3520-3529.

Al Saraj, W. K. A. 2007. Fatigue Behavior of reinforced concrete beams strengthened with GFRP sheets. *Journal of Engineering and Development*, 11(2):1-18.

ASTM E739-10. 2015. Standard Practice for Statistical Analysis of Linear or Linearized Stress-Life (S-N) and Strain-Life (ε-N) Fatigue Data. ASTM International, West Conshohocken, PA.

Barnes, R. A. & Mays, G. C. 1999. Fatigue performance of concrete beams strengthened with CFRP plates. *Journal of Composites for Construction* 3(2): 63-72.

CEB-FIP. 2010. Model Code 2010: First Complete Draft Volume 2. International Federation for Structural Concrete (fib). Lausanne, Switzerland.

Charalambidi, B.G. et al. 2016. Fatigue behavior of large-scale reinforced concrete beams strengthened in flexure with fiber-reinforced polymer laminates. *Journal of Composites for Construction* 20(5): 69-78.

CSA S6-14. 2014. Canadian Highway Bridge Design Code. Canadian Standard Association, Ontario, Canada.

D'Angelo, L. et al. 2014. S–N–P fatigue curves using maximum likelihood method for fatigue resistance curves with application to straight and welded rebars. In: *Proceedings of the 7th European Conference on Steel and Composite Structures: ECCS European Convention for Constructional Steelwork*, Brussels, Belgium.

Demers, C. E. 1998. Fatigue strength degradation of E-glass FRP composites and carbon FRP composites. *Construction and Building Materials* 12: 311-318.

Ekenel, M. et al. 2006, Flexural fatigue behavior of reinforced concrete beams strengthened with FRP fabric and precured laminate systems. *Journal of Composites for Construction* 10(5): 433-452.

Ferrier, E. et al. 2005. Fatigue of CFRPs externally bonded to concrete. *Materials and Structures* 38: 39-46.

Ferrier, E. et al. 2011. Fatigue-loading effect on RC beams strengthened with externally bonded FRP.

Construction and Building Materials 25 (2): 539-546.

Gheorghiu, C. et al. 2007. Response of CFRP-strengthened beams under fatigue with different load amplitudes. *Construction and Building Materials* 21: 756-763.

Gussenhoven, R. & Breña, S. F. 2005. Fatigue Behavior of Reinforced Concrete Beams Strengthened with Different FRP Laminate Configurations. American Concrete Institute, Farmington Hills, MI, USA, SP 230-36, 613–630.

Heffernan, P. J. & Erki, M. A. 2004. Fatigue behavior of reinforced concrete beams strengthened with carbon fiber reinforced plastic laminates. *Journal of Composites for Construction* 8(2): 132-140.

Huang, H. et al. 2017. Fatigue Behavior of Reinforced Concrete Beams Strengthened with Externally Bonded Prestressed CFRP Sheets. *Journal of Composites for Construction* 21(3): 04016108-1-13.

Mahal, M. et al. 2016. Experimental performance of RC beams strengthened with FRP materials under monotonic and fatigue loads. *Construction and Building Materials* 122:126-139.

Masoud, S. et al. 2005, Postrepair fatigue performance of frp-repaired corroded RC beams: Experimental and analytical investigation. *Journal of Composites for Construction* 9(5): 441-449.

Masoud, S. et al. 2001 CFRP-strengthened and corroded rc beams under monotonic and fatigue loads. *Journal of Composites for Construction* 5(4): 228-236.

Mathworks. 2010. Optmization Toolbox™ User's Guide (Release 2010b). The Mathworks Inc, Natick, Massachusetts, United States.

Meier U. 2000. Composite materials in bridge repair. *Applied Composite Materials* 7: 75-94.

Meneghetti LC. 2007. Análise do comportamento à fadiga de vigas de concreto armado reforçadas com PRF de vidro, carbono e aramida. Thesis. Department of Civil Engineering, Federal University of Rio Grande do Sul, Porto Alegre, Brazil.

Meneghetti LC, Garcez MR, Teixeira RM and Silva Filho LCP. 2017. Stress–cycle curves for concrete beams with fibre-reinforced polymer using runout data. *Proceedings of the Institution of Civil Engineers - Structures and Buildings* in press.

Papakonstantinou, C. G. et al. 2001. Fatigue behavior of RC beams strengthened with GFRP sheets. *Journal of Composites for Construction* 5(4): 246-253.

Pascual, F. G. & Meeker, W. Q. 1999. Analysis of Fatigue Data with Runouts Based on a Model with Nonconstant Standard Deviation and a Fatigue Limit Parameter. Statistics Preprints. See http://lib.dr.iastate.edu/stat_las_preprints/3 (accessed 25/07/2016).

Peng. H. et al. 2016. Experimental study of flexural fatigue performance of reinforced concrete beams strengthened with prestressed CFRP plates. *Engineering Structures* 127: 62–72.

Quattlebaum, J. B. et al. 2005. Comparison of three flexural retrofit systems under monotonic and fatigue loads. *Journal of Bridge Engineering* 10(6): 731-740.

Rosemboon, O. & Riskalla, S. 2006. Behavior of prestressed concrete strengthened with various CFRP systems subjected to fatigue loading. *Journal of Composites for Construction* 10(6): 492-502.

Sarkani, S. et al. 2007. Runout analysis in fatigue investigation. *Engineering Fracture Mechanics* 74: 2971–2980.

Silva Filho, J. N. 2005. Análise experimental de vigas “T” em concreto armado reforçadas à flexão com FRP submetidas a carregamentos pseudo-estáticos e cíclicos. Thesis. Department of Civil Engineering, University of Brasilia, Brasilia, Brazil.

Skuturna, T. & Valivonis, J. 2016. Experimental study on the effect of anchorage systems on RC beams strengthened using FRP. *Composites Part B* 91:283-290.

Song, L. & Yu, Z. 2015. Fatigue performance of corroded reinforced concrete beams strengthened with CFRP sheets. *Construction and Building Materials* 90: 99–109.

Taras, A. & Greiner, R. 2009. Development and application of a fatigue class catalogue for Riveted Bridge components. Institute for Steel Structures and Sheel Structures. Graz University of Technology, Graz, Austria, ECCS TC6-2009, 1–47.

Toutanji, H. et al. 2006. Cyclic behavior of RC beams strengthened with carbon fiber sheets bonded by inorganic matrix. *Journal of Materials in Civil Engineering* 18(1): 28-35.

Wang, Y. C. et al. 2007. Experimental study of FRP-strengthened RC bridge girders subjected to fatigue loading. Composites Structures 81(4): 491-498.

Wight, R. G. & Erki, M. A. 2001. CFRP strengthening of severely damaged reinforced concrete slabs. In: *3rd International Conference on Concrete Under Severe Condition, Environment, and Loading (CONSEC’01)*. Vancouver, Canada, 18-20, 2191-2198.

Ye, X.W. et al. 2014. A state-of-the-art review on fatigue life assessment of steel bridges. *Mathematical Problems in Engineering*: 1-13.

Maintenance, Safety, Risk, Management and Life-Cycle Performance of Bridges – Powers, Frangopol, Al-Mahaidi & Caprani (Eds)
© 2018 Taylor & Francis Group, London, ISBN 978-1-138-73045-8

UHPFRC Technology to enhance the performance of existing concrete bridges

E. Brühwiler
Swiss Federal Institute of Technology (EPFL), Lausanne, Switzerland

ABSTRACT: "UHPFRC" stands for Ultra-High Performance Fibre Reinforced Cementitious Composite materials. UHPFRC – complemented with steel reinforcing bars – serves as an external reinforcement increasing the ultimate flexural and shear resistances as well as the fatigue resistance and stiffness of the RC members, thus strengthening for higher live loads. UHPFRC is waterproof and crack-free under service conditions and thus improves the durability. The concept of the UHPFRC Technology consists in adding a thin layer of UHPFRC to an existing member in reinforced concrete (RC) in order to enhance its structural resistance and durability. The UHPFRC Technology is applied in Switzerland for more than 10 years. Basic principles are presented and the characteristics of the UHPFRC Technology are highlighted by two applications to enhance the performance of two large existing highway bridges.

1 THE UHPFRC TECHNOLOGY

"UHPFRC" stands for Ultra-High Performance Fibre Reinforced Cementitious Composite material produced from cement and other reactive powders, additions, fine hard particles, water, admixtures and high amount of short and slender steel fibres. UHPFRC does not comply with the definition of "concrete", and therefore, UHPFRC should not be called "concrete" as is evidenced in Figure 1a. It is fundamental to understand UHPFRC as an individual material with specific properties leading to a technology with own features. This is the first basic principle when designing with UHPFRC to enhance existing structures.

The second principle is that UHPFRC is complemented in a targeted manner with reinforcing steel in order to enhance structural performance and economy of applications. Subsequently, the terms reinforced UHPFRC (or short: R-UHPFRC) are used.

Reinforced concrete (RC) structures like bridges, retaining walls or buildings often show insufficient performance in terms of structural resistance and durability when exposed to severe environmental influences and high mechanical loading. Interventions to improve deteriorated concrete structures are a heavy burden from the socio-economic viewpoint since they lead to significant intervention costs and user costs. (RC structures are cheap at construction but turn out to be costly during their use because of premature repair and rehabilitation.) Many conventional "retrofitting" using concrete and repair mortar are not durable, and therefore, novel concepts for the improvement of RC structures must be developed.

This leads to the 3rd principle of the UHPFRC Technology. The targeted addition of a thin layer of strain-hardening UHPFRC to an existing member in reinforced concrete (RC) enhances the structural resistance and the durability of existing RC structures. The two basic concepts are shown in Figure 1b; they lead to the structural system of composite R-UHPFRC – RC elements.

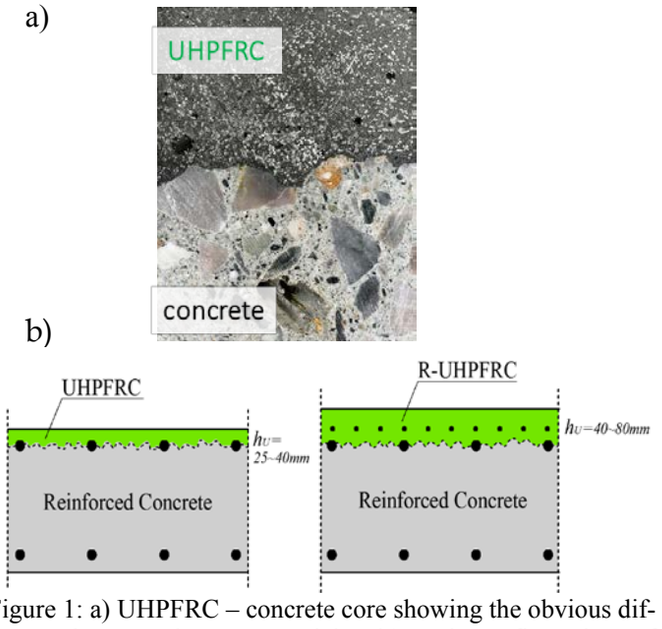


Figure 1: a) UHPFRC – concrete core showing the obvious difference between the two materials; b) Basic configurations of structural elements combining UHPFRC and RC: left: UHPFRC layer (25 to 40mm) has a protective function only; right: R-UHPFRC layer (40 to 80mm or more) has structural resistance and protective functions.

This paper presents the design of the strengthening of (1) the box girder and (2) multiple beam girder of existing concrete bridges. Simple analytical formulas are provided for the preliminary design of the strengthening, i.e. determination of the increase in structural resistance. The UHPFRC Technology to enhance structural performance of these two frequent types of bridge girders are highlighted by application cases.

2 PERFORMANCE OF UHPFRC

The required performance of currently used strain-hardening UHPFRC is summarized in [1-3]. Other fibre reinforced cementitious materials with lower performance – also designated as "UHPC" or high-strength concrete – do not qualify for the designs and applications described in this paper.

The tensile behaviour of strain-hardening UHPFRC is of first importance for strengthening purposes presented in this paper. The uniaxial tensile behaviour of plain UHPFRC has to comply with the indications and values given in Figure 2a. The significant strain-hardening deformation ε_U of more than 2‰, while the (uniaxial) tensile strength f_{Ut} reaches values ranging from 8 to 14 MPa, can only be obtained with fibre contents of more than 3 volume-% of straight steel fibres with an aspect ratio of at least 65.

The main reasons to complement UHPFRC with steel reinforcing bars to obtain R-UHPFRC are a significantly improved tensile behaviour and reduced scatter of UHPFRC properties [4, 5]. Small diameter steel reinforcing bars (arranged with relatively small spacing) provide in-plane continuity to the UHPFRC layer and ensure its monolithic action with the RC element in flexural members. The rebars not only significantly increase the resistance but also improve the deformation capacity and strain-hardening behaviour of UHPFRC. The mechanical behaviour in tension of R-UHPFRC is described by linear superposition of the reinforcing steel and the UHPFRC tensile behaviours (Fig. 2b).

Relatively modest UHPFRC compressive strength of 130 MPa is generally sufficient in the context of the present strengthening concept. The modulus of elasticity of UHPFRC in tension and compression is 45 to 50 G Pa which is not significantly higher than the one of concrete. For composite R-UHPFRC – RC members, this is advantageous with respect to deformation-induced stresses due to temperature and shrinkage effects.

UHPFRC has extremely low permeability and water conductivity due to the extremely dense matrix making strain-hardening UHPFRC impermeable for liquids, crack-free under service conditions and thus durable.

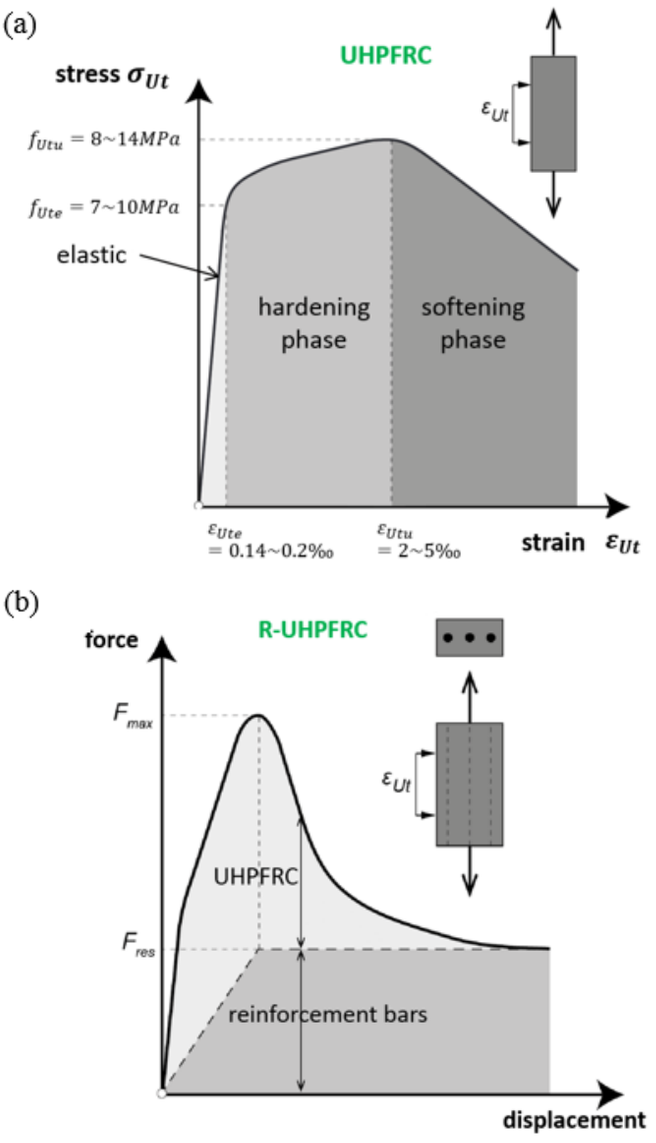


Figure 2: Characteristic tensile behaviour of a) plain UHPFRC and b) R-UHPFRC

3 STRUCTURAL RESPONSE OF R-UHPFRC – RC COMPOSITE BEAMS

The author and his team have investigated the structural concept of composite R-UHPFRC – RC elements (Fig. 1b) over more than 18 years (see [1] and references in [2, 3]).

3.1 *Behavior in bending*

When in tension, the R-UHPFRC layer principally acts as an added flexural reinforcement chord for the RC element. Both the steel rebars and the UHPFRC contribute to the resistance. RC beams strengthened with an R-UHPFRC layer are characterized by a significant increase in elastic stiffness and ultimate resistance when compared to the initial concrete element.

The bond between UHPFRC and concrete is obtained by preparing the concrete substrate surface by high pressure water jetting or sand blasting. The concrete substrate has to be wetted and needs to be wet when the layer of UHPFRC is cast. This surface

preparation provides full bond be tween UHPFRC and concrete substrate. In fact, pull-out fracture tests (force applied perpendicular to the surface) show the expected fracture in the concrete (and not at the interface or in the UHPFRC). Thus, the composite R-UHPFRC – RC section behaves monolithically.

The plastic post-peak rotation capacity of strengthened RC beams is maintained with an appropriate design of the rebars in the UHPFRC layer. Also, smooth high yield strength reinforcing bars in the UHPFRC layer offer high increase in resistance while the post-peak rotation capacity remains ductile. The structural behaviour in terms of moment – curvature relation and the ultimate bending moment are calculated using the conventional sectional model with the extension to account for the R-UHPFRC layer in the monolithic section (Fig. 3).

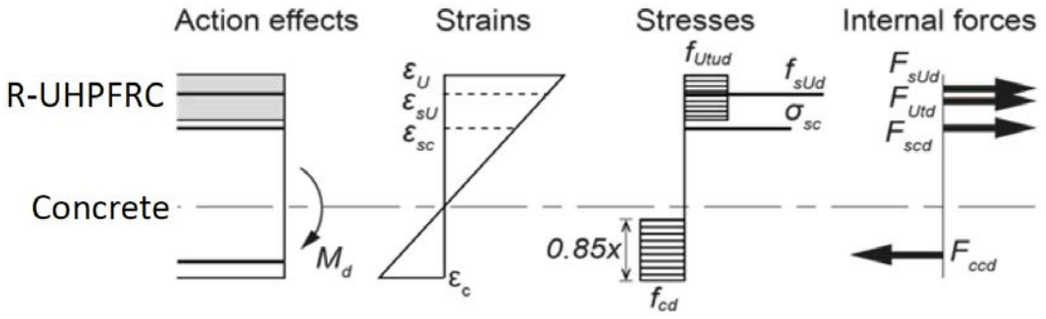


Figure 3: Plane section analysis for bending resistance at Ultimate Limit State ULS.

When subjected to compressive stresses, the R-UHPFRC layer acts as a compression flange but the high UHPFRC compressive strength cannot be fully exploited. This is because the compressive strength of the adjacent concrete below the UHPFRC layer often is 3 to 6 times lower, and thus concrete would crush prior to the UHFPRC reaching its compressive strength.

3.2 Behaviour in combined bending and shear

As was shown by tests on composite beams, the addition of a layer of UHPFRC delays the formation of the inclined shear crack in the concrete section. For many geometric configurations, the layer of UHPFRC modifies the failure mode from shear failure with little deformation to a ductile flexural failure mode.

A shear failure is observed in a composite section only for specific geometric and material configurations. Due to the experimentally observed failure mechanism (Fig. 4), the ultimate shear strength is composed of the contributions due to (1) concrete web crushing V_{Rc}, (2) vertical steel reinforcement yielding V_{Rs} and (3) the two hinge-bending mechanism of the R-UHPFRC layer V_{RU}. Accordingly, analytical expressions have been deduced to calculate the ultimate shear strength [6, 7].

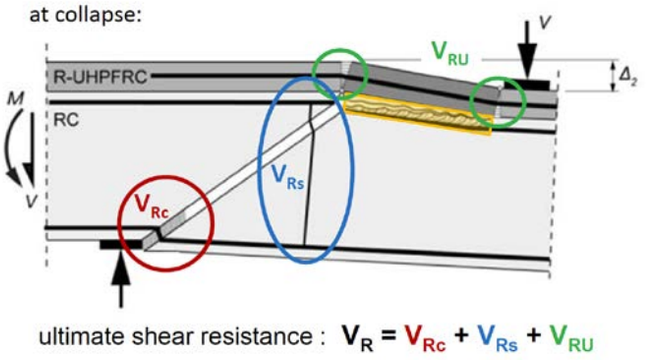


Figure 4: Shear failure mechanism at ULS

3.3 Fatigue behaviour

The results of bending fatigue tests on R-UHPFRC – RC beams revealed the existence of a fatigue limit at 10 million cycles at a fatigue stress level of about 50 % of the ultimate static resistance of the R-UHPFRC – RC beams [8]. Consequently, fatigue design rules for R-UHPFRC – RC members under bending fatigue need to account for steel rebar and UHPFRC fatigue resistances. Fatigue stresses are calculated using an elastic sectional model similar to the one shown in Figure 3.

4 TWO APPLICATIONS

4.1 Introductory remark

In Switzerland, the technology of enhancing the structural performance of existing RC structures by a layer of R-UHPFRC was applied for the first time in October 2004. Since then, more than 50 structures have been strengthened using the UHPFRC Technology. Subsequently, the conceptual design for the enhancement of two large highway viaducts is presented.

4.2 Improvement of the Chillon Viaducts [9]

4.2.1 Motivation and objectives

Located in Switzerland, the Chillon viaducts are two parallel posttensioned concrete highway bridges built in the late 1960s (Fig. 5). To insure structural safety for future traffic demands, it was decided to strengthen the slab by adding a layer of R-UHPFRC acting as an external tensile reinforcement for the slab and main girder.



Figure 5: Chillon Viaducts along Lake Geneva.

4.2.2 Motivation and objective

The concept implemented in 2014/15 consisted in casting one layer of R-UHPFRC on the deck slab (Fig. 6) to achieve the following beneficial effects:

- increase the slab's ultimate (bending and shear) resistance in the transverse direction
- increase the slab's stiffness to reduce fatigue stresses in steel rebars in the concrete
- increase the hogging bending moment resistance and the stiffness of the box girder
- provide waterproofing to protect the existing concrete of the slab from water and chloride ingress, thus improving durability
- limit duration of the intervention.

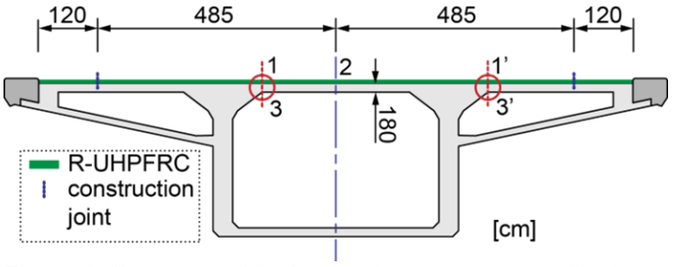


Figure 6: Geometry of the box girders cross-section (thickness of R-UHPFRC layer: 50mm over piers and 40mm in the spans).

4.2.3 Pre-dimensioning

As illustrated in Figure 6, the concrete bridge deck slab has a total thickness h_c of 180 mm. The transversal 16-mm diameter top steel rebars are positioned at a height d_{sc} of 152 mm from the intrados and spaced at 125 mm. There is no transversal prestressing in the bridge deck slab. The layer of UHPFRC has a thickness of h_U of 40 mm and is reinforced transversally with 12-mm diameter rebars also spaced at 125 mm. The centre of these rebars is at 16 mm from the top of the concrete. Over the piers, the thickness of the UHPFRC layer was increased to 50mm, and 12 mm rebars spaced at 125mm were placed in the longitudinal direction (in addition to the transverse rebars) to increase the negative (hogging) moment resistance of the box girder in the longitudinal direction.

The *transversal bending resistance of the deck slab* was calculated using the resistance model according to 3.1. For negative bending moment, the ultimate bending resistance m_{Rd} for sections 1 and 1' (Fig. 6) is equal to 165.5 kN m/m. The ultimate bending resistance of the strengthened slab is 73% higher than the resistance of the RC section alone. For positive bending moments, the layer of UHPFRC is in compression and mainly contributes to the resistance by reducing the height of the compression zone and thus increasing the static height. The ultimate positive bending resistance at section 2 is increased by 33%.

The deck slab does not have any shear reinforcement. *Ultimate shear resistance* v_{Rd} of the composite element was thus calculated as the sum of the concrete contribution v_{Rc} and the UHPRRC contribution v_{RU} according to Chapter 3.2. With an angle of the inclined crack estimated at 35°, the shear resistance of the composite slab section is 265 kN /m. The UHPFRC layer contributes to 33% of the total shear resistance. Due to the R-UHPFRC reinforcement, the increase in shear resistance is 40% according to the resistance model presented in [7].

The increased shear resistance is significantly higher than for the flexural failure mode, and the flexural failure mode is predominant even in shear prone loading situations.

4.2.4 Execution

All listed requirements and structural functions were realized by the casting of just one layer of R-UHPFRC using a machine (Fig. 7) on the concrete surface prepared by removal of 10mm by hydrojetting. The large volume of 2'350m^3 of fresh UHPFRC was produced on-site in a ready-mix plant. During the summers 2014 and 2015, the UHPFRC layer was cast over the two 2'120 m long viaducts, each in less than 30 working days.

Testing according to quality assurance given in [1] revealed that the UHPFRC complied with the requirements for strain-hardening UHPFRC. The fresh UHPFRC had to show thixotropic behaviour as it was cast on slopes of up to 7%. An asphalt layer and bituminous pavement, overall 6-cm thick, were finally placed on the UHPFRC surface to obtain the drivable road surface. The overall self-weight of the structure was not increased significantly.



Figure 7: UHPFRC casting machine (up) and fresh UHPFRC layer after casting (down)

4.3 Improvement of three highway viaducts consisting of multiple PC precast girders

4.3.1 Motivation and objective

Three 45 years old highway twin viaducts of identical construction follow each other in a hilly area in Central Switzerland to form a total length of 1'050m (Fig. 8a). The superstructure of the viaducts is composed of four slender precast prestressed girders with lengths of 40m. These girders have been designed as simple span beams, but during construction, they were monolithically joined over the piers (to avoid joints) to form a continuous girder. The realized hogging moment capacity (over the piers) is relatively low. In view of future traffic demands, the viaducts need to be strengthened to increase the load bearing capacity. They also need to be rehabilitated because of rebar corrosion damage.

4.3.2 Conceptual design

The basic idea of the strengthening of the superstructure is the following: since the original hogging moment capacity is low, it can be increased significantly by adding a strong R-UHPFRC layer on top of the slab (Fig. 8b).

Allowing for plastic moment redistribution from mid-span (sagging moment range) to the piers (hogging moment range) at ULS, the required load bearing capacity of the superstructure is obtained (Fig. 8c). This moment distribution is however only possible if the relevant cross sections allow for plastic hinges of sufficient ductility. This condition has been verified in the present case.

The 100 mm thick R-UHPFRC flange extends by 6 m on each side of the pier such that the strong R-UHPFRC layer also increases the shear resistance of the girder near the piers according to the mechanism shown in Fig. 6.

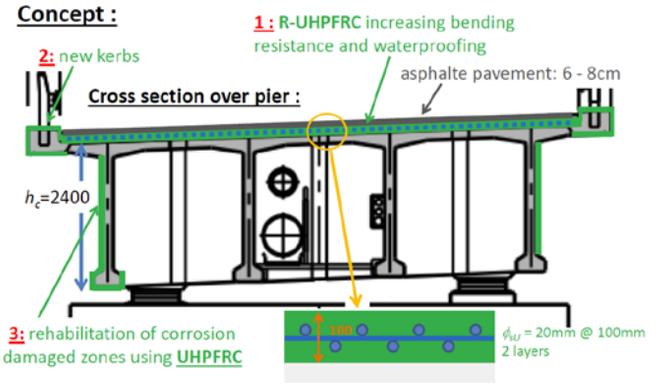
The rest of the deck slab (sagging moment region) is strengthened by a 45 mm thick UHPFRC layer with rebars in the transverse direction such as to increase the torsional stiffness of the open cross section allowing for more effective distribution of high concentrated forces in the transverse direction of the cross section while reducing moment peaks.

In addition, the UHPFRC layer on the deck slab provides the waterproofing, and UHPFRC is also used to rehabilitate local rebar corrosion damage on the outer girders and bottom flanges because of superior performance compared to repair mortars.

a)



b)



c)

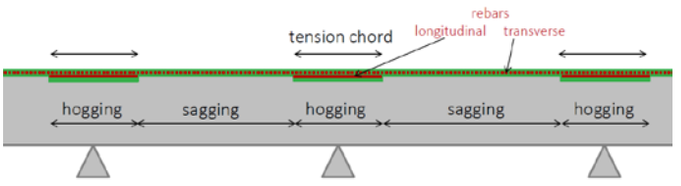


Fig. 8 a) View of one of the three twin viaducts; b) Intervention concept (cross section at pier); c) concept of strengthening: increasing the hogging moment capacity.

4.3.3 Pre-dimensioning

Bending moment capacity: With design values for the tensile strength of UHPFRC and steel rebars of respectively 8 MPa and 435 MPa, and the UHPFRC cross section and rebar area as given in Figure 8b, the tensile force developed at ULS by the R-UHPFRC flange is F_{RUd} = 3'480 kN per meter width. (78% of this tensile force is due to the steel rebars; 22% is due to the UHPFRC.) The internal lever arm y_U of the cross section (i.e. distance between the resultant tensile force and compression force), plastified at ULS, is estimated to be about 1.8 m, and thus, the additional hogging (negative) moment capacity in the longitudinal direction is: $\Delta M_{RUd} = y_U \cdot F_{RUd} = 1.8m \cdot 3.48MN = 6.3MNm/m$.

This additional moment capacity is sufficient to obtain the required moment bearing capacity of the superstructure. Obviously, increasing the tensile reinforcement leads to higher compressive stresses in the lower part of the cross section over the pier. In the present case, the compression zone was not fully exploited before strengthening and the compressive strength increased over time to reach after 45 years a compressive strength about 30% higher than the 28-day-compressive strength assumed in the initial design. These are the reasons why the dimensions of the compression zone are sufficient also after strengthening.

Shear resistance: The resistance model (Fig. 4) was applied to the 2.5m high girder. The following contributions to the ultimate shear resistance of one strengthened girder were obtained: (1) concrete web crushing V_{Rc} = 426 kN; (2) two hinge mechanism of the R-UHPFRC layer V_{RU} = 305 kN; (3) steel reinforcement: vertical rebars (stirrups) and vertical component of two inclined post-tensioning cables in the concrete girder web: V_{Rs} = 813 kN. Thus, the ultimate shear resistance of the strengthened girder is the sum of (1) to (3): V_{Rd} = 1'544 kN. This ultimate shear resistance is 90% higher than the shear resistance before strengthening and 34% higher than the acting shear force. Actually, the shear resistance is enhanced to such an extent that bending failure will prevail. In addition, non-linear FE analysis was performed confirming the formation of the expected failure mechanism and the analytically determined ultimate shear resistance.

Slab strengthening in the transverse direction: The R-UHPFRC layer leads to a thicker slab of higher stiffness allowing for more effective transverse distribution of concentrated loads. This favourable effect was considered and precisely determined in the detailed dimensioning.

The pre-dimensioning was used to validate the feasibility of the intervention concept. Detailed design by means of non-linear FE analyses gave deeper insight into the performance of the R-UHPFRC strengthening concept.

4.3.4 Execution

The works to improve the three viaducts are currently conducted. In 2017, chloride induced rebar corrosion damage at outer girder webs and bottom flanges were rehabilitated using UHPFRC. In addition, suitability tests have been performed to validate the UHPFRC material and the machine-made UHPFRC casting. In 2018 and 2019, UHPFRC layer is cast on the deck slab of the viaducts using a casting machine.

5 VALIDATION

The presented UHPFRC Technology for the enhancement of existing concrete bridges is validated by qualitative comparison with the traditional method using concrete, instead of strain-hardening UHPFRC, leading to the following arguments:

UHPFRC has an optimised compact matrix consisting of particles and a water/binder ratio typically lower than 0.20, which results in a material that has no free water, and no (communicating) capillary pores; consequently UHPFRC is waterproof and thus durable. On the contrary, concretes show significant amounts of communicating capillary pores because of the relatively high w/c-ratio larger than 0.40; consequently, concrete cannot be considered as durable, i.e., durability problems like rebar corrosion, frost damage or alkali-aggregate reaction are likely to occur even for improved concrete.

UHPFRC shows much higher tensile strength with significant deformation capacity (ductility) compared to concretes; consequently, the tensile strength of UHPFRC is considered in the design of strengthening interventions (like the ones presented in this paper). This significantly enhances the ultimate resistance and also the stiffness of strengthened R-UHPFRC – RC structural members. On the contrary, the tensile strength of concrete must not be taken into account in the determination of structural resistance, also because of brittleness.

The compressive strength of UHPFRC is about 3 - 5 times higher the one of high strength concretes. This is a further reason why relatively thin additional layers in UHPFRC are sufficient.

Because of the aforementioned differences in mechanical performance of the two materials, a strengthening layer in concrete (following similarly the concept presented in this paper) would result in a thicker concrete cover and overall layer thickness, more rebars and additional measures (like waterproofing membranes) to guarantee durability. Overall, the additional relatively thick layer in high strength concrete would lead to an important increase in dead weight of the bridge structure which is likely to trigger additional (costly and time consuming) strengthening interventions.

In addition, additional measures, f.ex. to guarantee durability, and more complex works in the case of traditional methods are time-consuming and offer more sources of errors. This leads to more important restrictions for the user of the structure and thus significantly higher (indirect) user costs.

Overall, despite the fact that concrete is a cheap material compared to UHPFRC, the overall cost of a UHPFRC strengthening intervention on existing structures is significantly lower … which is actually

the main reason why in Switzerland numerous applications have already been realised. Obviously, it is erroneous to compare the material cost only of concrete and UHPFRC, since in many countries labour and machine costs are significantly higher than material costs. The cost for the overall intervention finally counts, and the material cost is only a (minor) part of it.

6 CONCLUSIONS

The strengthening method using a layer of strain-hardening UHPFRC is an effective method in terms of technical performance. Significant tensile strain-hardening and high tensile strength of the UHPFRC is required for the improvement of concrete bridges.

The design of the strengthening intervention is based on a clear concept with a targeted consideration of the structural behaviour and performance of the given structure to be improved as well as the UHPFRC material properties.

The UHPFRC strengthening concept has been demonstrated in this paper by means of two large viaducts of common design, i.e. box girder and multiple beam cross sections. Simple analytical formulas are sufficient to validate this intervention concept.

The presented R-UHPFRC technology to improve the resistance and durability of existing concrete structures is cost-effective at execution and economic. Actually, lower intervention costs (when compared to traditional methods) are the main reason for the increasing number of applications of the R-UHPFRC technology in Switzerland.

7 REFERENCES

Technical Leaflet SIA 2052 UHPFRC – Materials, design and construction, March 2016. (in German and French; for English translation: eugen.bruehwiler@epfl.ch)

Brühwiler E, Denarié E. Rehabilitation and Strengthening of Concrete Structures Using Ultra-High Performance Fibre Reinforced Concrete. *Structural Engineering International*. 2013;23(4):450-7.

Brühwiler E. "Structural UHPFRC": Welcome to the post-concrete era ! Proceedings, Keynote Lecture, *1st International US-UHPC Symposium*, Des Moines, Iowa, USA July 18-20 2017.

Bastien-Masse, M., Denarié, E., Brühwiler, E., Effect of fiber orientation on the in-plane tensile response of UHPFRC reinforcement layers, *Cement and Concrete Composites* 67, 2016, pp.111-125.

Oesterlee, C. Structural response of reinforced UHPFRC and RC composite members, *Doctoral Thesis No 4848, Swiss Federal Institute of Technology Lausanne (EPFL)*, 2010.

Noshiravani T., Brühwiler E., Analytical Model for Predicting Response and Flexure-Shear Resistance of Composite Beams Combining Reinforced Ultra-high Performance Fiber-Reinforced Concrete and Reinforced Concrete, *Journal of Structural Engineering*, 2014;140(6): 10 pp.

Bastien Masse, M., Brühwiler, E., Contribution of R-UHPFRC Strengthening Layers to the Shear Resistance of RC Elements, *Structural Engineering International*, Nr. 4, 2016, pp.365-374.

Makita, T., Brühwiler, E., Model for describing the fatigue behaviour of bridge deck slab elements strengthened with reinforced UHPFRC, *IABMAS Shanghai 2014: "Bridge Maintenance, Safety, Management and Life Extension" (Chen, Frangopol & Ruan (Editors))*, Proceedings published by Taylor & Francis Group, London, 2014, pp. 2472-2479.

Brühwiler E., Bastien-Masse M., Mühlberg H., Houriet B., Fleury B., Cuennet S., Schär P., Boudry F., Maurer M., Design of the strengthening of the Chillon viaducts deck slabs with reinforced UHPFRC, *IABSE Conference, Geneva*, September 23-25 2015.

Maintenance, Safety, Risk, Management and Life-Cycle Performance of Bridges – Powers, Frangopol, Al-Mahaidi & Caprani (Eds)
© 2018 Taylor & Francis Group, London, ISBN 978-1-138-73045-8

Strengthening of concrete bridges girders using FRP and patch anchors

Reem Jumaah
PhD candidate, Faculty of Science, Engineering and Technology, Swinburne University of Technology
Robin Kalfat
Lecturer, Faculty of Science, Engineering and Technology, Swinburne University of Technology
Riadh Al-Mahaidi*
Professor, Faculty of Science, Engineering and Technology, Swinburne University of Technology

ABSTRACT: Factors such as population growth, higher volumes of commuter and freight traffic and heavier vehicles have increased the demands placed on existing bridges throughout Australia. Alongside the necessity for structural rehabilitation and strengthening in order to prolong the service life and increase the safety of existing bridges, many innovative materials such as advanced fibre reinforced polymer composites (FRPs) have become popular as a means to strengthen existing reinforced concrete (RC) members in flexure, shear and torsion, via bonding of the FRP to the external surface of the member. Despite the many advantages of FRP materials, a commonly documented failure mode is premature debonding of the FRP from the concrete substrate. It is well understood that the bond strength between the FRP and concrete members can be improved when sufficient anchorage is provided thereby preventing the critical mode of FRP failure. Anchorage systems have the potential to significantly improve the bond performance of FRP systems thus permitting higher levels of strengthening at a fraction of the cost. To date the authors have researched the patch anchors concept which consists of bi-directionally oriented fibre sheets bonded to the surface of the FRP strengthening and the adjacent primarily through a series of FRP-to-concrete joint direct shear tests. More recently, the patch anchors were implemented in the shear strengthening of a large scale prestressed beams for the first time which takes into account omitted factors in joint assemblies such as: size effect, combined flexural/shear stresses, diagonal shear cracking (potentially intersecting the FRP within the anchorage zone) and other failure modes such as web shear crushing or concrete crushing. An evaluation of patch anchor performances in large-scale beam applications will be presented in this paper long side a comparison of results between joint assemblies and full-scale implementations.

1 INTRODUCTION

A major problem that has been emerging in recent years is the need for strengthening of existing infrastructures due to factors such as: increased loading, corrosion of reinforcing steel, design defect or deterioration. Many technologies have been presented to solve this problem which included the use of composite materials, such as Fibre Reinforced Polymers (FRP) as externally bonded reinforcement. The materials lend them selves as excellent for strengthening applications due to their high tensile strength, light weight, high durability and ease of installation (Koutas & Triantafillou 2013). As a result, FRP's have been used successfully to strengthen members in flexure, shear and torsion (Panigrahi, Biswal & Barik 2014).

Despite the many advantages of FRP's for strengthening applications, the occurrence of prema-ture debonding currently limits the level of material utilizations to 15-30% for most shear strengthening applications. Debonding for shear strengthened members typically occurs at the intersection of the FRP with a propagated diagonal shear crack which initiates a debonding failure at the crack which propagates towards the nearest FRP free end. One of the most effective techniques to suppress or delay the occurrence of FRP debonding is the use of FRP anchorage systems (Grelle & Sneed 2013). The types of anchorage systems available for shear strengthened members were summarized by Kalfat et al. (2013) as: FRP (spike) anchors, NSM anchors, me-chanical substrate strengthening, patch anchors, hybrid anchors, mechanically fastened steel plates or FRP embedment into concrete flanges.

Patch anchors were developed by Kalfat and Al-Mahaidi (2014) and showed promising results in increasing the utilization of the CFRP laminate when tested on the level of FRP-to-concrete joints. In this method, the ends of the laminate are sandwiched between two CFRP bidirectional fabric sheets, the anchors are applied externally and no drilling is re-

quired. Therefore, in this study patch anchors performance is tested on large scale beams strengthened with externally bonded CFRP laminates in shear.

2 EXPERIMENTAL PROGRAM

2.1 *Specimen Details*

Three full scale post-tensioned T-beams were constructed with span length of 5000 mm and a depth of 1050 mm. The properties of the beam are depicted in Figure 1. The beam was reinforced with eight Ø32 mm diameter longitudinal reinforcement and one Ø32 mm post-tensioned threaded bar in the bottom and 2N20 bars in the top. Shear reinforcement consisted of 2 legs of N10 ligatures at 475mm spacing throughout the span. Both the longitudinal and shear reinforcement were chosen in order to ensure that the beam failed in shear.

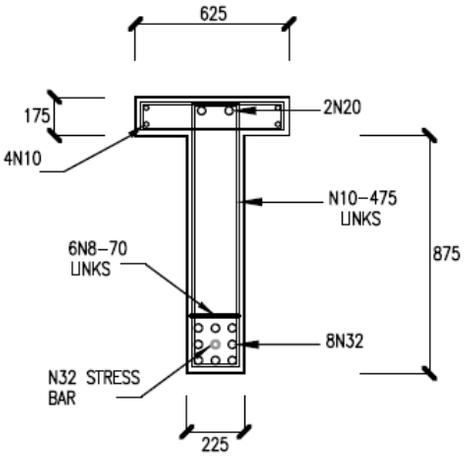


Figure 1. The beams cross-section details.

Three T-Beams were tested using three point bending configuration. The first specimen was strengthened and functioned as a control beam as depicted in Figure (2.a). The second specimen (ST series) was strengthened using CFRP side bonded laminates. Twelve strips were installed at each end of the beam with spacing of 300 mm c/c as shown in Figure (2.b). The third beam (STA series) used the same strengthening configuration as the ST series beams with the addition of patch anchors at each end of the laminates. Hence, the laminate was anchored at both ends using two plies of CFRP bi-directional sheets with ± 45° fabric as shown in Figure (2.c).

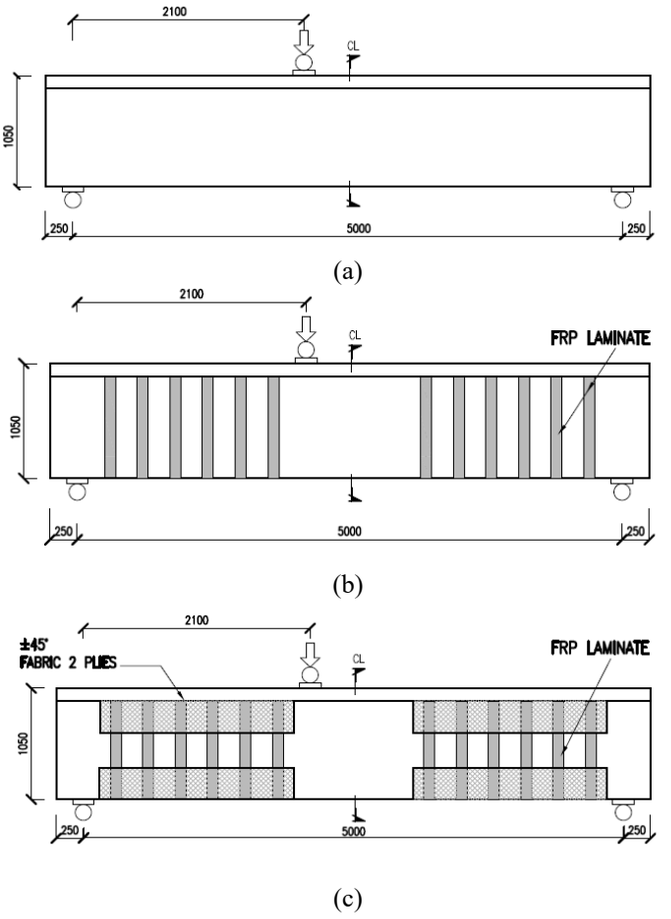


Figure 2. (a) Control Specimen, (b) Strengthened Specimen, and (c) Strengthened Specimen with CFRP Sheets Anchors.

2.2 *Patch Anchor Application Process*

The patch anchoring method consisted of using CFRP bi-directional sheets with $\pm 45^{\circ}$ fabric as anchors at the ends of the laminate. This involved sandwiching each laminate in between two layers sheet. The application process included surface preparation where webs of each beam were sandblasted to achieve a surface roughness corresponding to 60 grit sandpaper. The first layer of sheet was saturated with epoxy resin and applied to the concrete surface over the 1800 mm bond length. This was followed by applying the pultruded CFRP laminate strips in the required locations. lastly, the second layer of the CFRP bidirectional sheet was applied to complete the installation of the patch anchors. Figure 3 shows the patch anchors with the laminates after finishing the application. The curing process took 7 days, and heat lamps were used to provide a 40 °C curing environment to accelerate the curing process as shown in Figure 4.

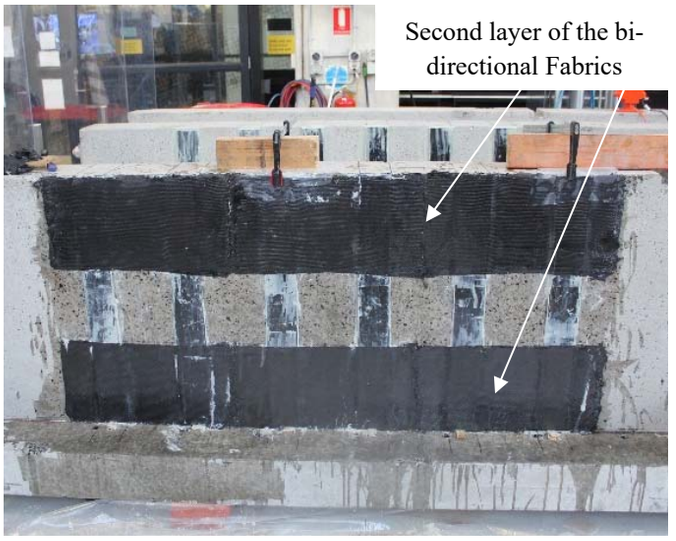


Figure 3. Patch anchors application.

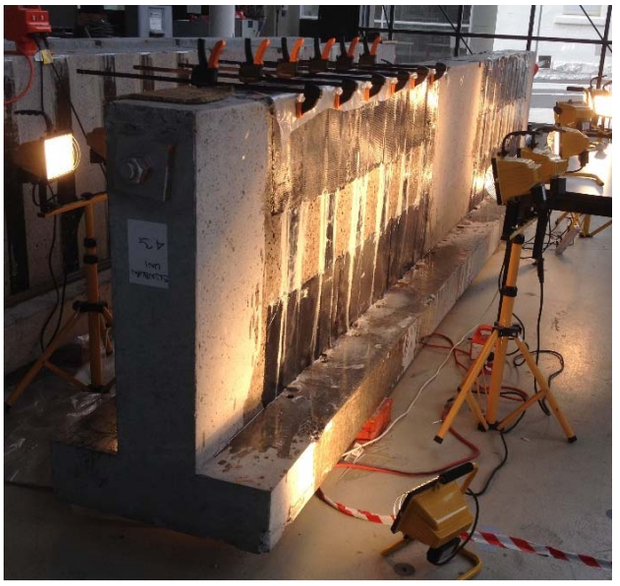


Figure 4. Curing using projectors.

3 TEST DETAILS

The beams were tested in the Smart Structures Laboratory at Swinburne University of Technology using a 5 MN universal testing machine as shown in Figure 5. Each beam was tested twice in order to extract more results from the beams. This was achieved by forcing the failure on one half of the beam only. Extra external clamping was provided in the second half of the beam, in order to increase the shear capacity and keep it unharmed during the test. Prior to testing the beams, 18 holes with a diameter of 22mm were drilled on each side of the flange, this was followed by installing 20 mm diameter high tensile all thread through these holes. Steel bearing plates were used at the top and bottom of the beam with a thickness of 30 mm as shown in Figure 6. Each bar was stressed to a force of 100 kN using a hydraulic jacks as shown in Figure 7.



Figure 5. The beam inside the 5MN machine.



Figure 6. The beam with the all thread bars and the steel plates.



Figure 7. Stressing the bars using the hydraulic jack.

Image correlation photogrammetry was used to monitor the strain in the laminates during the tests as shown in Figure 8. Additionally, strain gauges were also installed on the laminates for additional verification. Six laminates were instrumented with strain gauges, thirteen strain gauges were used for each test.

Nine strain gauges were installed at the middle of the fourth laminate along its length, with gauge spacing of 100 mm. The rest of the laminates were instrumented with one strain gauge at the middle. The results, which have been obtained from the strain gauges, were later compared with the strains obtained from the Correlated Solutions device.

Table 1 presents the martial properties of the FRP laminates and sheets used in the tests, and table 2 shows the adhesive and staurant properties; in addition, table 3 plots the compressive strength of the three beams.

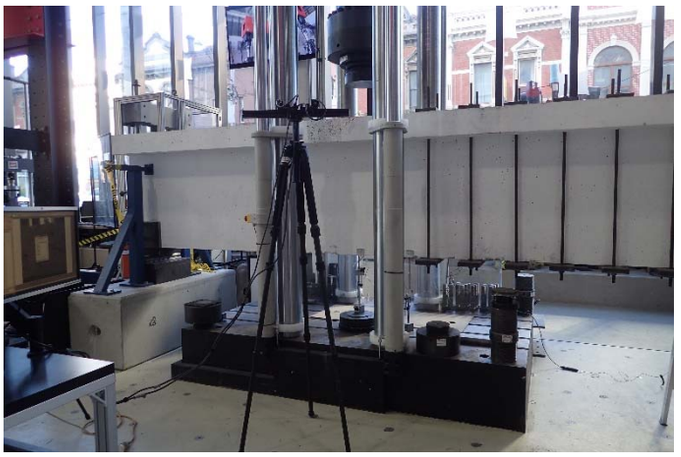


Figure 8. Correlated solutions Cameras.

Table 1. FRP Properties.

Properties	*Fyfe Bi-directional FRP (±45°)*	*Fyfe FRP Laminate*	*Units*
Tensile Strength	3.79	2.54	GPa
Tensile Modulus	230	150	GPa
Ult. Elongation	2.1	1.86	%
Thickness	0.55	1.4	mm
Width		100	mm

Table 2. Adhesive and saturant properties.

Product	*Tensile Strength (MPa)*	*Tensile Modulus (GPa)*
Laminate Adhesive Tyfo-TC 1 Epoxy	15.8	1.04
Saturant Tyfo S Epoxy	44.2	3.2

Table 3. The compressive strength of the Concrete beams.

Beams	*Compressive Strength Value (MPa)*
Control Beam	59.8
Strengthened Beam	62.4
Strengthened Beam with Anchors	64.7

4 TEST RESULTS

4.1 *Load-Displacement*

The use of Patch anchors has increased the load carrying capacity of the beam by 63.9% when comparing the maximum load reached of the beam with anchors and the peak load of the control beam as shown Table 4. Figure 9 presents the load-displacement curves of the tested beams. Moreover, using the unanchored CFRP laminate in the ST series beams resulted in a maximum load increase of 32.7% when comparing to the control beam.

Table 4. Maximum load for the tested beams.

Beam	*Symbol*	*Maximum Load Value kN*	*Percentage increase over control beam*
Control Beam	C	1216	
Strengthened Beam Test 1	ST1	1454	(19.6%)
Strengthened Beam Test 2	ST2	1614	(32.7%)
Strengthened Beam with Anchors Test 1	STA1	1967	(63.9%), (35.3%)
Strengthened Beam with Anchors Test 2	STA2	1948	(60.2%), (20.7%)

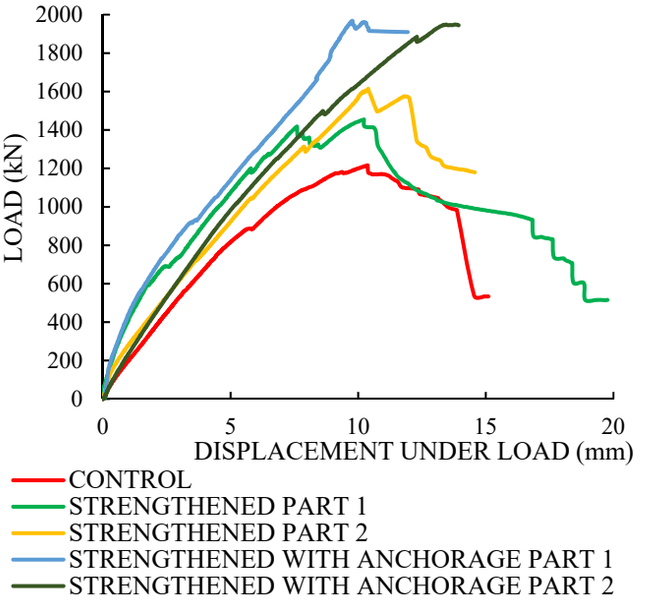


Figure 9. Load-Displacement diagram for the all beams.

4.2 *CFRP Strains*

The CFRP Strains in the strengthened beams were observed and measured, in order to study the effect of the patch anchors on the CFRP Laminates strains and their role in improving the ultimate shear capacity of the beams. Figure 10 displays the strains in the critical three laminates of the strengthened beam with anchors. The maximum strains in the laminates (in the tested beams) which have been obtained from using the image correlation photogrammetry system have been compared with the strains of the laminates in the joints that have been tested by Kalfat and Al-Mahaidi (2014), these joints are shown in Figure 11; in addition, table 2 presents a comparison between these strains. The average of the strain along the observed laminates has been examined and plotted in Figures 12 for the strengthened Beam. In this figure the strain is plotted with different loadings, in order to distinguish the load at which the maximum strain is recorded and the load at which the laminate debonded. From the obtained results it can be concluded that the use of the patch anchors has increased the strain in the laminates and they enhanced the utilization of the laminates strength.

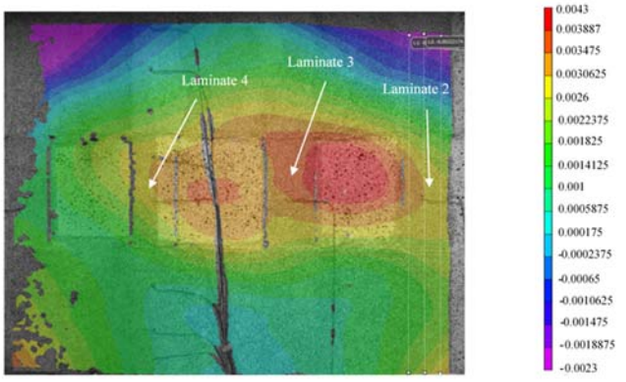
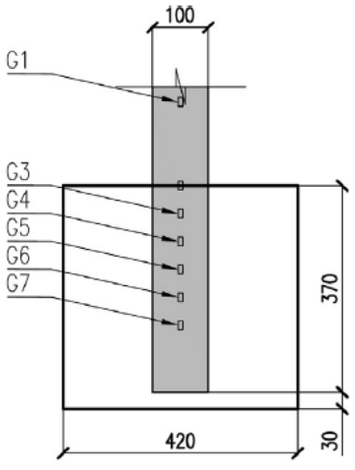
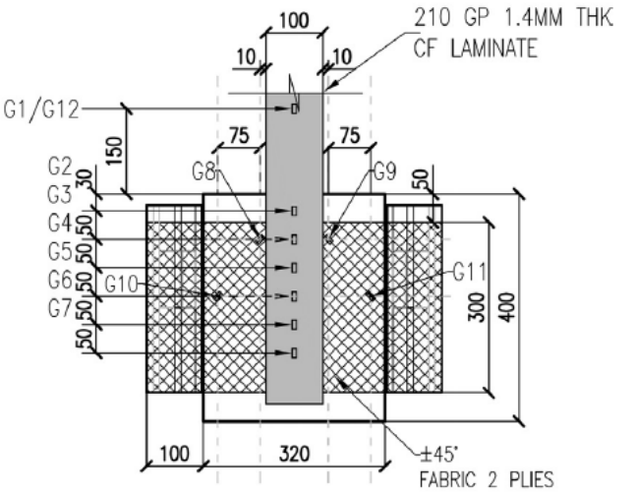


Figure 10. Plot of the CFRP laminates' strains in the strengthened beam with Anchors part 1 (Photogrammetry).



(a)

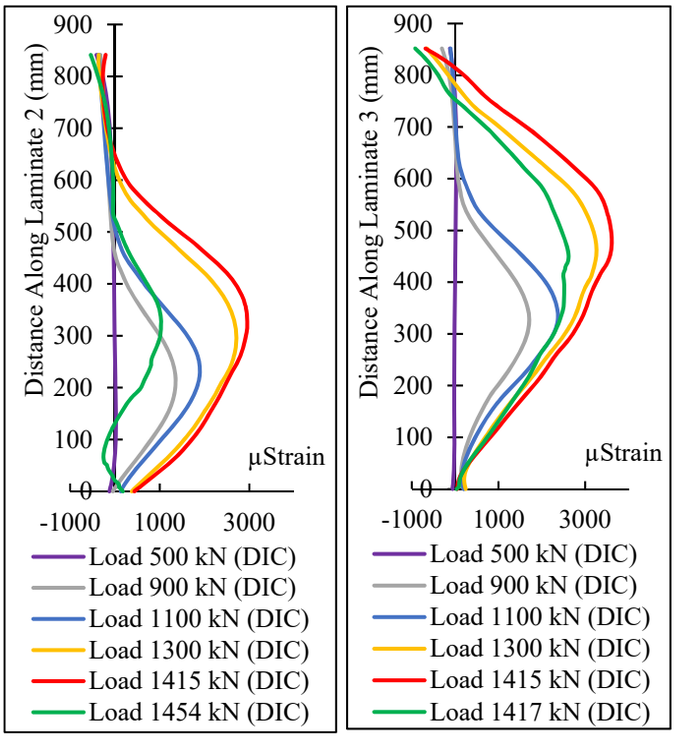


(b)

Figure 11. (a) Strengthened Specimen, (b) Specimen with the Patch Anchors (Bidirectional Fabrics) (Kalfat and Al-Mahaidi 2014).

Table 2. Maximum strains obtained from the experimental results of (Kalfat and Al-Mahaidi 2014), and Maximum strains obtained from the experimental tests of the beams.

Tested beams	*Max Laminate 2 Strain*	*Max Laminate 3 Strain*	*Max Laminate 4 Strain*	*(Kalfat and Al-Mahaidi) Joints Strain*
	(με)	*(με)*	*(με)*	*(με)*
ST1	2953	3614	2443	3012
ST2	3578.87	3435.45	4445.40	3012
STA1	4114	3744	3111	5218
STA2		4960.085	4586.49	5218



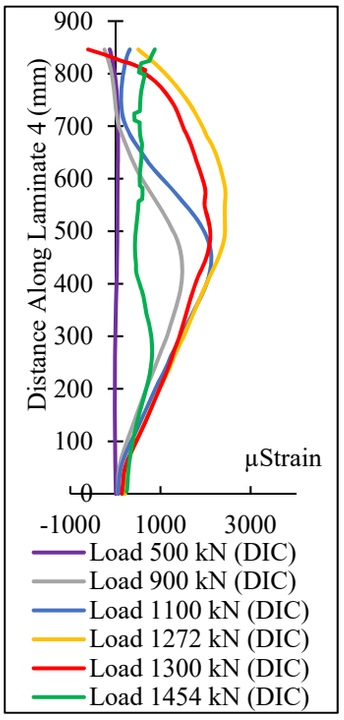


Figure 12. Strain along laminates 2, 3, and 4 in the strengthened beam test 1, at different loadings.

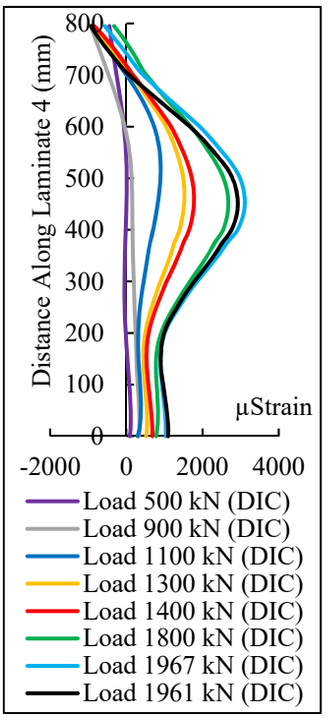
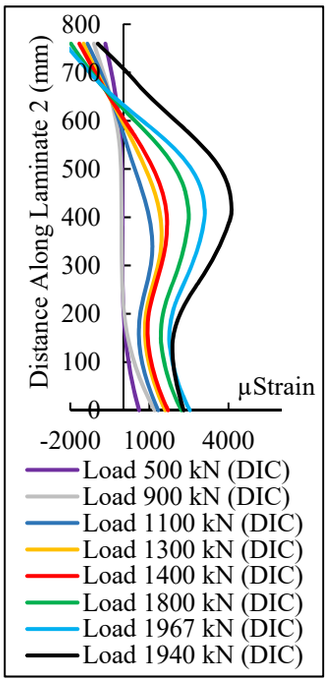
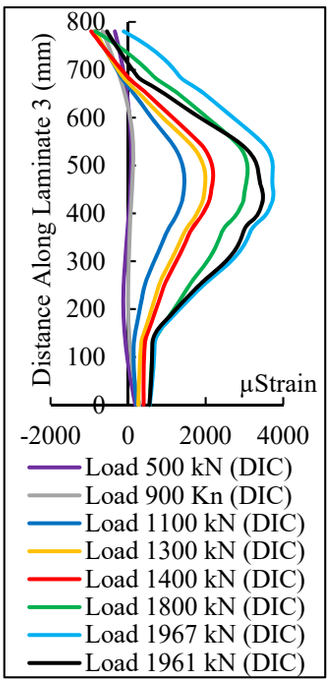


Figure 13. Strain along laminates 2, 3, and 4 in the strengthened beam with anchors test 1, at different loadings.

It should be noted that the use of the patch anchors increased the strain in the CFRP Laminates, from 2953 micro-strain (obtained from the CFRP in the strengthened beam without anchorage first test) to 4114 micro-strain (obtained from the anchored beam first test), these readings represent the strain in laminate 2 in the beams. Laminate 3 strain was 3614 micro strain in the strengthened beam and was 3744 micro strain in the anchored beam. Moreover, the strain in laminate 4 increased from 2443 micro strain to 3111 micro strain as noted before in the previous table and charts; moreover, from Figure 13 which shows the strain along the laminates for the strengthened beam with anchors first test.





CONCLUSION

In the current paper, the effectiveness of the patch anchors as an anchorage system for the CFRP laminates in the shear strengthened large scaled post-tensioned T-beams was investigated experimentally. In this anchoring method, the CFRP laminates strip, at the web part of the T-beam, was sandwiched with two layers of bi-directional CFRP sheets with ±45° fabrics. Theses anchors were used at both ends of the laminate strip. It can be concluded from the achieved results that:

- Using the patch anchors has delayed the premature debonding of the laminate, and that has resulted in enhancing the utilization of the laminates, which has been proven by the increase in the laminate strain in the anchored specimens.

- The shear capacity in the tested beams has been considerably enhanced with the use of the CFRP laminate strips as an external strengthening method for the shear deficient beams; in addition, the anchors also improved it further beyond the unanchored specimens. This can be noted with the increase of the load carrying capacity of the tested beams.

ACKNOWLEDGEMENT

The support of FYFE Asia Ltd is gratefully acknowledged for sponsoring this project and supplying all the CFRP material used.

REFRENCES

Grelle, S & Sneed, L 2013, 'Review of Anchorage Systems for Externally Bonded FRP Laminates', *International Journal of Concrete Structures and Materials*, vol. 7, no. 1, pp. 17-33.

Kalfat, R., et al. (2013). Anchorage Devices Used to Improve the Performance of Reinforced Concrete Beams Retrofitted with FRP Composites: State-of-the-Art Review. J. Compos. Constr. **17:** 14-33.

Kalfat, R. and Al-Mahaidi, R. (2014). "Experimental investigation into the size effect of bidirectional fiber patch anchors in strengthening of concrete structures." Composite Structures 112: 134-145.

Koutas, L & Triantafillou, TC 2013, 'Use of Anchors in Shear Strengthening of Reinforced Concrete T-Beams with FRP', *Journal of Composites for Construction*, vol. 17, no. 1, pp. 101-107.

Panigrahi, A, Biswal, K & Barik, M 2014, 'Strengthening of shear deficient RC T-beams with externally bonded GFRP sheets', *Constr. Build. Mater.*, vol. 57, pp. 81-91.

Maintenance, Safety, Risk, Management and Life-Cycle Performance of Bridges – Powers, Frangopol, Al-Mahaidi & Caprani (Eds)
© 2018 Taylor & Francis Group, London, ISBN 978-1-138-73045-8

FRP strengthening of concrete structures using AS5100-2017

H. B. Pham
SMEC Australia

ABSTRACT: The new Australian Bridge Design Standard AS5100-2017 provides guidance on the design of reinforced and prestressed concrete structures using fibre reinforced polymer composites (FRP). This is the first design standard for FRP strengthening in Australia which cover many relevant topics including material specification, installation, inspection and maintenance, flexural strengthening, shear and torsional strengthening, and axial strengthening. The paper provides some background information for some of those topics. Relevant Australian and international researches are reviewed and summarized. As noted in the paper, understanding of the mechanic and theories behind FRP strengthening is important before a safe and efficient design can be achieved.

1 INTRODUCTION

1.1 *General*

Strengthening of concrete structures using fibre reinforced polymer (FRP) is gaining popularity in Australia. This is due to not only many advantages that this technique can offer but also the increasing awareness among asset owners, engineers and contractors. The new AS5100-2017 was released early 2017 marked another significant step in FRP strengthening in Australia where a state-of-the-art guidance is provided in AS5100.8 Clause 3.6.2 and Appendix A.

This paper describes a background for some of the information provided in this standard. What presented here is the author's own interpretation and the reader should contact Standards Australia if he/she wishes to send queries on the standards.

1.2 *References*

The guidance on FRP strengthening in AS5100 is the result of the works by many people. It is based on VicRoads Standard Specification 688, international design guides, and international and Australian researches. Inputs from local suppliers were also incorporated.

2 GENERAL REQUIREMENTS FOR FRP STRENGTHENING

Clause 3.6.2 provides a very brief summary of the general requirements for FRP strengthening.

The strength of the existing concrete surface affects the bond and the performance of the FRP system. The minimum tensile and compressive strengths required by AS5100 are1.5 MPa and 17 MPa, respectively. This is consistent with the recommendation from AS 440.2R. These requirements should apply for the concrete adjacent to the bond only and for bond-critical applications only.

FRP bond performance is sensitive to other factors including adhesive properties, environmental conditions and workmanship. As a result, a comprehensive and strict inspection scheme is a must.

While a 30 year design life is mentioned in the standard, a longer design life can be achieved and ensured by routine inspections and maintenance. FRP system can be repaired relatively easily using techniques as outlined in Pham (2009) and TR 57 Report.

Validation of FRP composite system by testing is typically not required provided it is designed and proof engineered by qualified personnel who have proven track records of working with FRP materials and bridge strengthening.

3 MATERIALS

AS5100.8 Clause A2 defines general requirements for constituent materials. It is important that sufficient details are provided for all materials. They must be of a satisfactory standard with evidence of acceptable quality control procedures, test methods and results.

An attempt was made in the standard to categorise carbon laminates, carbon fabrics, glass fabrics, aramid fabrics as well as adhesive and resin materials. In the author's opinion, the properties stated should be for guidance only and materials with different engineering properties might be allowed provided that they satisfy the general requirements mentioned above and the system has been appropriately engineered.

Table 1. Typical reinforcing fibre material property ranges

Property	CFRP Laminates	CFRP Fabrics	GFRP Fabrics	AFRP Fabrics
E (GPa)	140-245	215-600	60	100
f_t (MPa)	2000-2800	2600-4300	2800	2800
Fibre fraction	~65%			
Fibre density (g/cm3)		1.6	2.2	1.3

Resin materials need to be compatible with reinforcing materials and substrates and are able to transfer the shear force between the two materials. One important property is the bond strength which must not be less than 1.5 MPa for bond-critical applications.

It is worth noting that the typical resin material glass transition temperature is between 60 to 80 degree C. This means the FRP system will become ineffective when the temperature reaches that level. Insulation can be provided to ensure service appropriate temperatures.

4 INSTALLATION, INSPECTION AND MAINTENANCE

AS5100.8 Clause A3 provide requirements for surface preparation, application and trials. These requirements appear to be based on existing specifications and FRP system provider's application guides. As the effectiveness and durability of FRP a system are dependent on many factors, a trial is highly recommended. Trials can be inexpensive and very effective method to ensure a successful application of FRP.

Clause A4 sets out the requirements for inspection, performance testing and maintenance. These requirements are self-explanatory. They are again based on existing specifications, FRP system provider's application guides and the writers' experiences.

Pull-off tests are relatively easy to be carried out and shall be conducted in addition to component testing. A successful test would have the failure surface in the concrete as shown in Figure 1.



Figure 1. A pull-off test dolly

5 DESIGN

General design requirements are covered in Clause A5 of the standard.

The minimum strength requirement is consistent with ACI 440.2R. This limit is to ensure the non-strengthened structural member have sufficient strength to sustain permanent loads and 75% of service transient loads. Coupled with ductility requirement specified in Clause 6.3.3, this ensure that if debonding occurs for any reasons (vandalism, overloading…), the structure is still ductile and allows sufficient warning before total collapse. It is worth noting that for bridge structures, the live loads that are typically on the bridge are less than 75% of the design live loads.

The environmental reduction factors are based on the recommendations by ACI 440.2R. These are considered appropriate at this moment. Recently, there has been much research on this topic and it is expected that these factors would be revised.

6 FLEXURAL STRENGTHENING

The basic principles and design assumptions of flexural strengthening are similar to those for normal-reinforced or prestressed sections. The FRP strengthened section is assumed to follow beam theory. However, there are fundamental differences in the behavior of normal reinforced or prestressed girders to FRP strengthened girders. These are explained below.

6.1 *Importance of construction staging and long-term effects*

For a typical ductile bridge girder section, the section strength at ultimate is reached when the steel reinforcements have yielded and the top concrete fibre strain reaches the crushing strain (3000 microstrain). A typical strain distribution at ultimate is shown below (Figure 2).

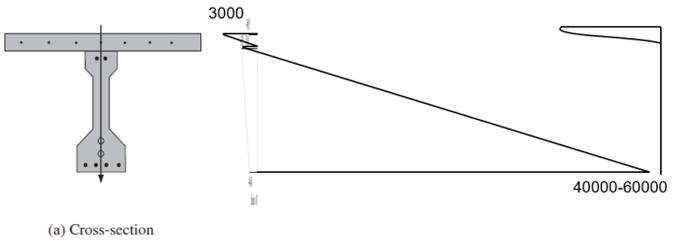


Figure 2. Strains in a typical bridge girder at ultimate (microstrains)

The strains at ultimate are therefore well defined and much higher that the strains developed using service limit state. As a result, the effects of construction staging, and creep and shrinkage are often ignored in the calculation of the girder ultimate capacity. This also means that the calculation is relatively straight forward.

For FPR strengthened girders, the concrete and reinforcement (steel and FRP) strains at ultimate can be much lower than those in normal reinforced or prestressed girders (Figure 3). This is due to the fact that the controlling strain is often the FRP debonding strain which is often less than 6000 microstrain.

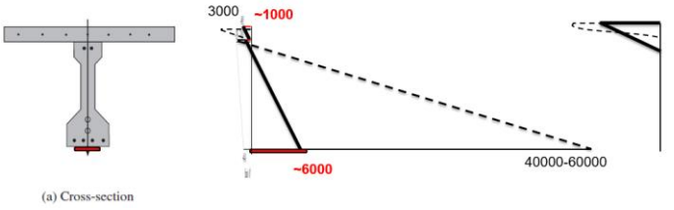


Figure 3. Strains in a typical FRP strengthened bridge girder at ultimate (microstrains) (shown as solid lines) as compared to those in normal underreinforced girder (shown as dotted lines)

As a result, effects of construction staging are significant and cannot be ignored in the calculation of the girder ultimate capacity. It is worth noting that permanent effects are already locked in prior to FRP is bonded introducing another stage. While the effects due to creep, shrinkage and relaxation might be ignored at ultimate, they would alter the strain levels and affect the calculation of the capacity reduction factor.

Accounting for construction staging and long-term effects is not straight forward. However, if it is ignored, the strain in the FRP might be underestimated by up to 50% and therefore the moment ultimate capacity might be overestimated significantly. Calculation of strains would involve an iterative progress.

6.2 *Material stress-strain curves*

When the compression strain in the concrete top fibre is much less than 3000 microstrain, the use of Whitney rectangular stress block may not be accurate. The recommended concrete stress strain relationship as decribed in AS5100.8 Clause A6.2.3 is taken from Desayi and Krishnan (1964) and by Todeschini et al. (1964).

A full stress strain relationship for prestressing steel is also required to determine the strengthened capacity. Due to potential low strains at ultimate, the ultimate tensile strength of prestressing steel might not be achieved and the strength gain might be sensitive to the assumed stress-strain curve. Stress-strain models are available in ACI440-2R or Skogman et al. (1988).

6.3 *Failure modes*

Unlike normal reinforced or prestressed concrete girders, FRP strengthened girders have much more failure modes. These modes are summarized in Clause A6.3.1 which is adapted from Pham and Al-Mahaidi (2002) and Pham (2005).

6.4 *Capacity reduction factors*

Equation A6.3.2 is based on ACI 440.2R Equation 10.2.7 which is in turn based on ACI 318. In this equation, it is taken that the section is ductile when the steel yields at ultimate. This was developed for normal reinforced concrete beams. This approach is generally different to AS5100 approach which defines ductility based on the depth of the neutral axis. Due to the reasons noted in Section 6.2, if Equation A6.3.2 is used, it is possible that the strengthened section has lower strength than the non-strengthened section due to lower reduction factor. In the author's opinion, a capacity reduction factor of 0.8 should be adopted for the following reasons:

- Ductility is the capacity to see warning signs (large deflection, cracking…) before collapse. Pham (2005) has shown that after debonding of FRP, the tested beams retain its original strength and ductility.
- AS5100.8 Clauses A5.3, A6.1 and A6.3.3 have ensured that in the scenarios when FRP debonding occurs (with or without low strains in steel reinforcement at ultimate), the structure does not collapse. Total failure would only occur if the non-strengthened girder reaches its ductility limit.

Other benefits of using the 0.8 factor are:

- This is consistent with AS5100 approach regarding capacity reduction factors. The ACI approach is not consistent with Australian standards (for example, we do not have capacity reduction factor of 0.9 when a section is highly ductile).
- This would avoid many difficulties/confusions among designers.
- This approach is safe because we have only allowed ductile sections to be strengthened and we have ensured that unstrengthened

sections have adequate capacity to avoid total collapse without early warmings.

Equation A6.3.2 does not apply for prestressed sections. The reader needs to refer to Clause 10.3.1.3 in ACI 440.2R for the equation for prestressed sections. This would be added to AS5100 in the next revision.

6.5 *FRP debonding strains*

The common failure modes are FRP IC debonding which is initiated from a flexural crack, and FRP end interfacial debonding and concrete cover separation that both occur from the FRP end due to high shear stresses there. The failure mechanisms are illustrated below.

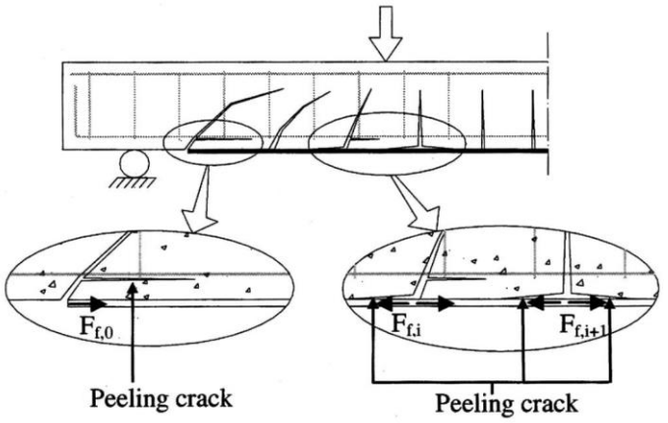


Figure 4. FRP debonding mechanisms

Equation A6.3.5.2 is based on the work by Teng et al. (2003). This equation has been verified by Pham and Al-Mahaidi (2004) and proven to be accurate. It is worth noting that the debonding strain is inversely proportional to the square root of FRP stiffness. As shown below, FRP becomes less effective as its thickness is greater than 2mm. It is recommended that the number of FRP layers is limited to 2 or 3.

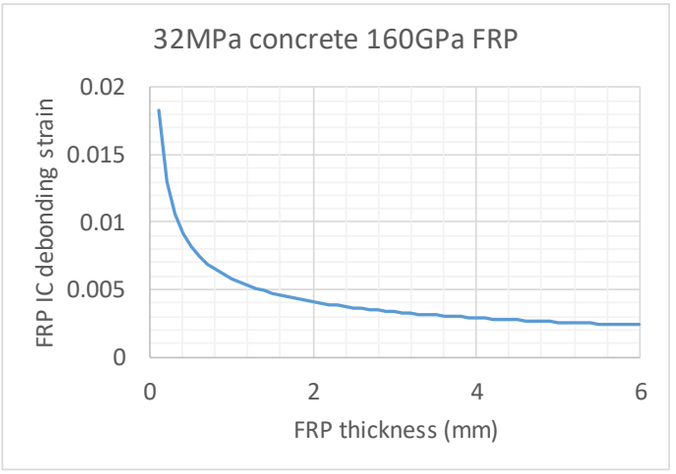


Figure 5. FRP IC debond strains versus thickness

Equation A6.3.5.3(1) is based on the work by Pham and Al-Mahaidi (2006). The longitudinal shear stresses in the adhesive layer or in the concrete level of the nearest reinforced should be limited to a shear strength limit of 0.17 sqrt(f'_c). This is consistent with the recommendation in AASHTO Guide Specification (2012).

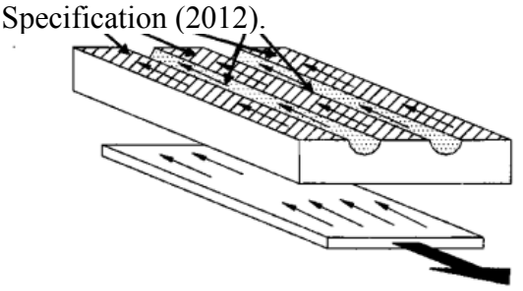


Figure 6. Surfaces where longitudinal shear stresses act

For near surface mounted FRP strengthened beams, the IC debonding strain is higher. The limit is based on ACI 440.2R. Interfacial debonding should not be critical and cover separation can be checked in the same way as surface bonded FRP.

Near surface mounted FRP is often used on the top of a deck to strengthen the hogging region. Recommendations for detailing is not available in AS5100 but can be found in ACI440.2R. In addition, a layer of cementitious grout is recommended to provide insulation from hot asphalts. A layer of coloured asphalt could also be used as an indicator for future pavement work. It is worth noting that a wide FRP laminate bonded in a shallow recess does not behave similarly to a near surface mounted FRP rod or narrow strip.

6.6 *Serviceability Limit State*

The creep rupture and fatigue stress limits are based on ACI 440.2R. The serviceability stress limits are modifications form the requirements in ACI 440.2R.

6.7 *Notes*

- Simplified code equations do not apply for complex bridge girder strengthening.
- Calculation of the capacity of a retrofitted composite prestressed section requires an iterative process considering of construction staging. This is often done by specialised spreadsheets or softwares.
- Increasing FRP thicknesses does necessarily increase the capacity as thicker FRP would debond at a lower strain.
- Using thinner FRP and increasing bond areas would improve the strength enhancement.

The level of strengthening will depend greatly on the element existing level of reinforcing, geometry and section buildup. However, as a guide, the typical in-

creases in flexural strength due to bonding FRP are as below.

Table 2. Typical increases in moment capacity

Section	Potential increase in moment capacity
Non-composite reinforced sections	50%
Composite reinforced sections	40%
Non-composite prestressed slabs	30%
Non-composite prestressed box girders	15%
Composite pretensioned I girders	10%
Composite Teeroff girders	5%

7 SHEAR AND TORSIONAL STRENGTHENING

Shear strengthening is often carried out by bonding laminates on both the soffit and the sides of the beam. The laminates on the sides act like steel stirrups to cross diagonal cracks. They can be narrow strips placed at certain spacing or wide plates covering the entire shear span. The main direction of the fibres can be vertical or inclined to intersect shear cracks. The shear laminates can also be anchored by being wrapped around the beam or by mechanical anchorage (Figure 7).

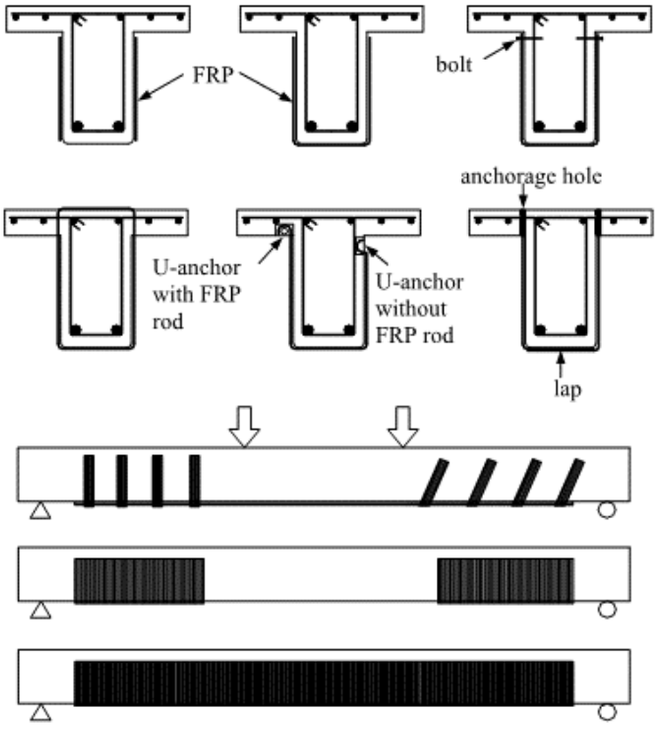


Figure 7. Shear strengthening using FRP

Several shear related failure mechanisms of FRP shear laminates have been identified including tensile rupture, debonding through the concrete near the bond interface or localised failures. The ultimate shear strength can be calculated as the sum of the portions contributed by concrete, steel stirrups and FRP shear laminates. Expressions used to calculate the portion of the shear force contributed by FRP laminates were based on the truss analogy or more rigorous compression field theory. To predict the maximum force that FRP shear laminates can undertake, a reduction in the FRP capacity due to stress concentration or debonding needs to be considered.

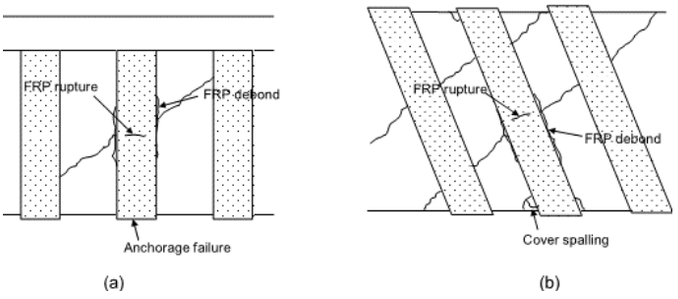


Figure 8. Failure modes in RC beams strengthened in shear and torsion

Equation A7.2.2 is based on the truss analogy. The effective strain equations in Clause 7.2.3 are based on ACI 440.2R and researches by Priestley et al. (1996) and Khalifa et al. (1998). These strains can be as low as 0.0015 which is much lower than the FRP ultimate limit strain (the standard specifies an upper limit of 4000 microstrain for shear strengthening). This highlights the fact that the higher strength FRP does not necessarily results in higher shear strength. Providing more layers of FRP would increase the FRP shear contribution slightly. However, it is recommended that the number of plies/laminates is kept below 3.

Torsional strength of concrete beams with bonded FRP can be determined using the principles set out in AS5100.5 Clause 8.2.5. with T_{us} replaced by (T_{us} + T_{uf}). The angle θ_t is as calculated in AS5100 Clause 8.2.4, and the area A_t can be taken as the area of a polygon with vertices at the centre of the longitudinal bars.

Equation A7.3.3 is based on a torsional truss analogy. This approach is consistent with fib Bulletin 14 with some modification as described in Adrian and Al-Mahaidi (2007). This formula has been verified and proven to be conservative.

8 AXIAL STRENGTHENING WITH CONFINEMENT

Equations for axial strengthening are based on ACI 440-2R. Wrapping concrete columns with FRP provides confining stresses that result in higher concrete strength as well higher strain at ultimate. N-M moment interaction diagrams will need to be constructed taking into account the concrete confined stress-strain curve.

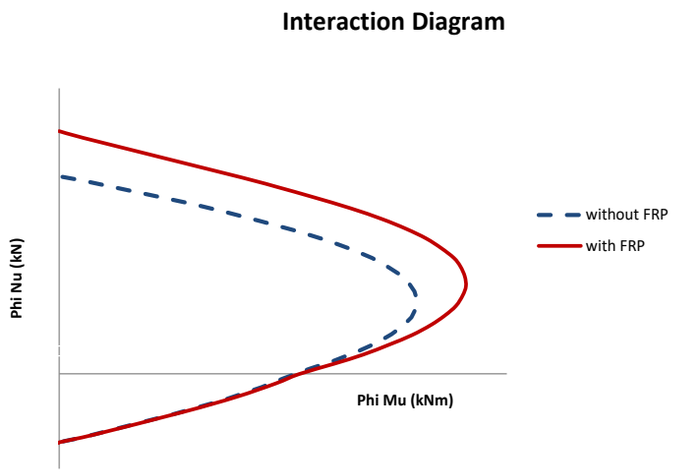


Figure 8. N-M curves for a concrete column with and without FRP

9 ANCHORAGE OF FRP

Detailed knowledge of the bond behaviour between FRP and concrete is fundamental in designing structures retrofitted by bonding FRP strips or sheets. The bond failure interface occurs in a thin concrete layer just under the adhesive layer. There have been great difficulties in developing a simple and accurate method to predict the bond strength. An inherent challenge is the fact that the shear strength of the failure interface can vary significantly due to variation in concrete properties (cement paste properties, aggregate properties and distribution near the bond surfaces). These properties can be sensitive to concrete mix, concrete casting, type of cement and aggregate and surface preparation. As a result, the more reliable prediction formulas tend to be empirical or semi-empirical.

Another challenge in deriving a strength model is due to variations in the test set-ups and a variety of failure modes. Past studies have indicated that tension is transferred to the concrete mainly via shear stress in a short length nearest to the loaded end called the effective bond length. The bond load does not increase once the bond length exceeds the effective bond length.

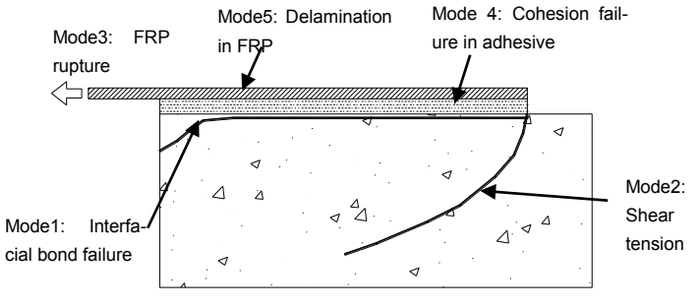


Figure 9. Possible failure locations in a shear-lap test

There have been a number of models developed to predict the bond strength. These models were summarized and verified by Pham and Al-Mahaidi (2014). AS5100.8 Formula A9.1 is based on TR55 report which appears to be modification of the formulas developed by Neubauer and Rostary (1999). These formulas were verified and found to be reasonably accurate (Figure 10).

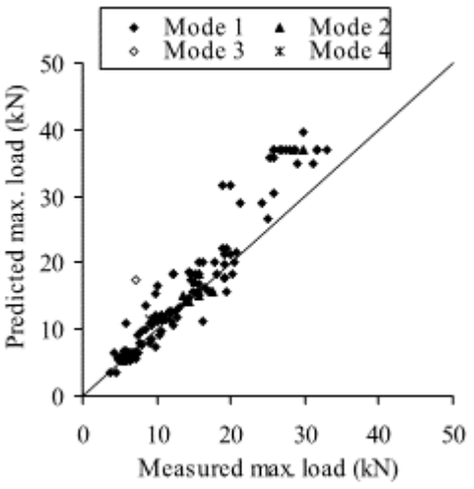


Figure 10. Verification results for Neubauer and Rostary's model by Pham and Al-Mahaidi (2014)

Anchorage devices for FRP are often designed from first principles. These can be made of FRP or steel.

There appears to be a lack of guidance in AS5100-2017 on detailing for FRP flexural strengthening. It is recommended that designers refer to ACI-440 for guidance in detailing.

10 SUMMARY

AS5100.8-2017 provides a detailed guidance into FRP strengthening. A good understanding of FRP strengthening is essential during the design and selection of the system. Much of complexity is due to the fact that FRP tends to debond from concrete prematurely. As a result, stringent installation and inspection requirements are a must. The design often involves complex calculations and a thorough assessment of the system. It is recommended that both the design and construction of FRP strengthening are reviewed by experienced personnel.

11 ACKNOWLEDGEMENT

The author would like to acknowledge other members of the Standards Australia Working Group BD-090-08 FRP Strengthening Sub-Group who, together with the author, developed Appendix A of AS5100.8-2017. The author would also like to acknowledge Professor Riadh Al-Mahaidi who led the research in FRP strengthening in concrete structures at Monash University.

12 REFERENCES

ACI 440.2R-17 (2017) *Guide for the design and construction of externally bonded FRP systems for strengthening concrete structures*. American Concrete Institute.

Concrete Society (2003) *Strengthening of Concrete Strutures Using Fibre Composite Materials: Acceptance, Inspection and Monitoring*, TR 57, Camberley, UK, The Concrete Society.

fib Bulletin 14 (2001) *Design and use of externally bonded FRP reinforcement for RC structures*.

American Association of State Highway and Transportation Officials, *Guide specifications for design of bonded FRP systems for repair and strengthening of concrete bridge elements*, AASHTO, 2012, Washington.

VicRoads Technical Specification Section 688 (2013) *Fibre reinforced polymer composite strengthening of concrete structures*.

Skogman et al. (1988) Flexural Strength of Prestressed Concrete Members *PCI Journal* Sep-Oct 1988.

Pham, H. and Al-Mahaidi, R. (2002) Anchorage zones of FRP lamiates bonded to concrete beams – State-of-the-Art review. *ACUN-4*, Sydney , Australia.

Pham, H.B. (2005) *Debonding failure in concrete members retrofitted with carbon fibre reinforced polymer composites*. PhD thesis, Department of Civil Engineering, Monash University.

Teng, J. G., Smith, G., Yao, J. and Chen, J. F. (2003) Intermeidate Crack Induced Debonding in RC Beams and Slabs *Construction and Building Materials*, V.17 No. 6-7 pp. 447-462.

Pham and Al-Mahaidi, R. (2004) Assessment of Available Prediction Models for the Strength of FRP Retrofitted RC Beams. *Journal of Composite Structures*, American Society of Civil Engineers, No. 66 pp. 601-610.

Pham, H. and Al-Mahaidi, R. (2006) Prediction Models for Debonding Failure Loads of CFRP retrofitted RC Beams. *Journal for Composites for Construction*, American Society of Civil Engineers, Vol. 10, No. 1, pp. 48-59.

Hii, A. and Al-Mahaidi, R. (2007). Torsional Capacity of CFRP Strengthened Reinforced Concrete Beams. *Journal of Composites for Construction*, Vol 11 No. 1.

Priestley, M., Seible, F., and Calvi, G., (1996) *Seismic Design and Retrofit of Bridges*, John Wiley and Sons, New York, 704 pp.

Khalifa, A., Gold, W., Nanni, A., and Abel-Aziz, M., (1998) Contribution of Externally Bonded FRP to the Shear Capacity of RC Flexural Members. *Journal of Composites for Construction*, V. 2, No. 4, pp. 195-203

Pham, H. and Al-Mahaidi, R. (2014) A study of the bond of FRP-concrete using shear-lap tests in Australia. *IABMAS 2014* Shanghai, China.

Concrete Society (2004) *Design guidance for strengthening concrete structures using fibre composite materials* TR 55, Camberley, UK, The Concrete Society.

Neubauer, U. and Rostasy, F. S. (1999) Bond failure of CFRP plates at inclined cracks - experiments and fracture mechanics model. *Fourth International Symposium - Fiber Reinforced Polymer Reinforcement for Reinforced Concrete*, American Concrete Institute, pp. 369-381.

Pham H. B. *Durability of Concrete Structures retrofitted with CFRP composites- State of the Art Review and Inspection Guide* AECOM, 2009.

Maintenance, Safety, Risk, Management and Life-Cycle Performance of Bridges – Powers, Frangopol, Al-Mahaidi & Caprani (Eds)
© 2018 Taylor & Francis Group, London, ISBN 978-1-138-73045-8

Flexural FRP Strengthening of Concrete Bridges Using an Innovative Concept

Jincheng Yang[1], Reza Haghani[1], Mohammad Al-Emrani[1]
[1]*Chalmers University of Technology, Gothenburg, Sweden*

ABSTRACT: This paper presents an innovative method for flexural strengthening of reinforced concrete (RC) bridges using pre-stressed carbon fiber reinforced polymer (CFRP) laminates as externally bonded reinforcement (EBR) and glass-fiber reinforced polymer (GFRP) deck panels. The work was a part of an EU-funded project called sustainable refurbishment of existing bridges (SUREBridge). The innovative features of this concept include the tensile reinforcement of the section using self-anchored pre-stressed CFRP laminates and compressive reinforcement of the section using tailor-made GFRP deck panels at the same time. The flexural behavior of RC T-section beams, strengthened using this concept, has been studied experimentally. Four 6-meter-long beams—three strengthened with bonded pre-stressed CFRP laminates in bottom with a pre-stressing force of 100 kN and GFRP deck panels on the top side and one as control beam—were tested in four-point bending configuration. The results indicated a substantial increase of ca. 160% in ultimate load carrying capacity of the strengthened beams as well as considerable improvements in flexural stiffness and cracking loads. The strengthened beams also displayed a ductile behavior after debonding of externally bonded CFRP laminates while maintaining the maximum load level before debonding due to the strong bond between the GFRP decks panels and the concrete beam. It was concluded that the proposed method has the potential to be introduced as a reliable method for strengthening of old concrete bridges.

1 INTRODUCTION

1.1 *Existing challenges and demands*

There exist about one million bridges in Europe. Over 90% of these bridges have concrete decks. 65% of concrete and steel/concrete composite bridges are older than 50 years. Bridge owners and traffic authorities in European countries, therefore, are dealing with a substantial number of old bridges which are turning structurally deficient and geometrically insufficient. Results of surveys from SUREBridge project reveal that 70% of the reported damage in concrete bridges are related to decks and edge beams. A study conducted within the European project "Sustainable Bridges" (PANTURA Project, 2012) revealed that a top priority from the bridge management point of view is to develop non-disruptive strengthening and repair techniques for bridges. It also indicated that two major problems involved with existing bridges are (i) the aging and lack of load bearing capacity of the superstructure, and (ii) the need for wider decks to accommodate the increased traffic volume. Therefore, the refurbishment of existing bridge structures, in this context, includes not only strengthening, repair and upgrading, but also geometric changes such as widening the bridge deck to provide more traffic volume capacity.

1.2 *SUREBRIDGE concept*

SUREBridge stands for sustainable refurbishment of existing bridges and was an EU funded project within the framework of Infravation program. To meet the demands put forward by road authorities and bridge owners, the SUREBridge refurbishment concept chose to take a holistic approach to further upgrade the structural capacity and geometry of bridge superstructures beyond what traditional refurbishment methods offer. In brief, it consists of using bonded carbon fiber reinforced polymer (CFRP) laminates (in pre-stressed or passive state) as externally bonded reinforcement (EBR) on the bottom side of the bridge deck or girders in sagging moment areas and simultaneously installing prefabricated light-weight glass-fiber reinforced polymer (GFRP) deck panels installed on the top of the original concrete deck. The idea is to create a "sandwich" strengthening scheme in which the amount of tensile and compressive strengthening is balanced. Taking advantage of the superior tensile strength of CFRP and possibility for geometric widening using tailor-

made GFRP deck panels, the SUREBridge solution aims to upgrade the existing old concrete bridges to the desired load and service capacity levels.

The major innovations of the SUREBridge solution to be addressed in this paper include (i) a new pre-stressing method developed for EBR technique without mechanical anchorage system at CFRP ends, and (ii) developing a tailor-made GFRP composite decking system providing a desired amount of stiffness and strength to the existing cross-section.

1.2.1 *Innovative CFRP pre-stressing method*

Bonded CFRP laminates using EBR technique in passive (i.e. un-prestressed) has become widely accepted as a structurally effective and cost-efficient method for strengthening of concrete structures. Thousands of structures have been strengthened and repaired using this technique in the past three decades. However, one problem associated with using passive CFRP strengthening laminates is the debonding of the laminate at fairly low strains from the concrete substrate. The separation of the laminate is attributed to so-called "intermediate cracks" which are points of stress concentration along the bond line. Debonding phenomenon significantly reduces the cost efficiency of the strengthening as it usually takes place at strains well below the ultimate strength of the laminate. It is believed that the utilization ratio of bonded CFRPs for flexural strengthening is limited to 40%. To increase the efficiency, researchers have suggested to use pre-stressing in the laminate before bonding. It has been shown that using pre-stressing not only increases the utilization of the material but also offers advantages such as postponing the yielding of the internal reinforcement, reducing the crack width and thus improved durability, and improved fatigue behavior. However, a problem associated with pre-stressed bonded FRP laminates is the emerge of very high interfacial stresses close to the ends of the laminate which necessitate the use of mechanical anchors. Using mechanical anchors, so far, has been considered as the biggest hindrance towards widespread use of pre-stressed CFRP laminates despite the advantages they offer.

A new concept developed at Chalmers University of Technology allows for using pre-stressed laminates without the need for mechanical anchorage (Haghani and Al-Emrani 2015).

This innovative method is based on gradient introduction of the pre-stressing force in the CFRP laminate by means of a device (see Figure 2) and thus controlling the magnitude of the interfacial shear stress. A recent experimental study (Yang et. al 2017) showed that the application of the new pre-stressing method can realize the 'self-anchorage' of CFRP laminate at a pre-stressing level equivalent to 25% of ultimate tensile strength of the strengthening laminate without end anchors, and achievable ultimate utilization ratio of approximately 80% before debonding of the CFRP reinforcement.

1.2.2 *Tailor-made GFRP deck panels*

Another innovative feature of SUREBridge solution is to install prefabricated GFRP sandwich panels as a reinforcement on top of the existing concrete deck, creating a new FRP-concrete composite decking system. The major benefits of installing the GFRP deck panels on the existing concrete deck include:

- providing the possibility to widen the original concrete deck to meet the demand from clients regarding the geometric insufficiency;
- The GFRP deck helps to relax the compressive stress in the concrete deck;
- Enhancing the sectional resistance by contributing to the overall bending stiffness of the section.

2 EXPERIMENTAL PROGRAM

2.1 *Test specimens*

Four 6-meter long RC beams with T-shape cross-section were cast. The reference specimen, B1, was left without strengthening while specimens B2 to B4 were strengthened suing SUREBridge concept—by applying pre-stressed CFRP on the bottom side of the beams and GFRP deck panels on the top. The cross-sectional configuration of specimens is shown in Figure 1.

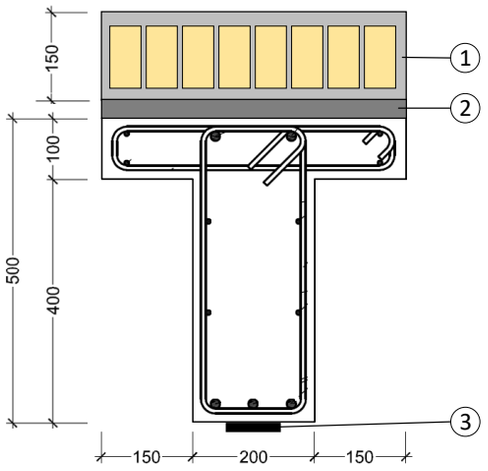


Figure 1. Cross-section of the beam specimens. Notes: 1—GFRP panel in B2-B4; 2—10-mm-thick bond layer using epoxy adhesive in B2 and 30-mm-thick bond layer using low-shrinkage mortar in B3 and B4; 3—pre-stressed CFRP plate

The concrete of grade C35/45 was used to cast the T-beams, as later was verified by compressive cube tests. The CFRP laminates were 5.3-meter long with a nominal cross-section of 81.98 mm × 1.45 mm. The designed pre-stressing force was 100 kN. Tensile tests on CFRP coupons were conducted according to ASTMD3039 to characterize the mechan-

ical properties of laminates. The material properties are listed in Table 1.

Table 1. Summary of material properties

Concrete	Steel bars			CFRP	
$f_{c.m}$	$E_{s.m}$	$f_{s.y.m}$	$f_{s.t.m}$	$E_{cfrp.m}$	$\varepsilon_{cfrp.u}$
MPa	GPa	MPa	MPa	GPa	$\times 10^{-3}$
59,5	197,6	580	672	214	13
GFRP					
E_{11}	$f_{t.11.u}$	$f_{c.11.u}$	E_{22}	$f_{t.22.u}$	$f_{c.22.u}$
GPa	MPa	MPa	GPa	MPa	MPa
29,0	738*	447*	15,3	314*	221*

* values provided by suppliers

The difference between B2, B3, and B4 specimens was mainly due to (i) the connection method between the GFRP deck and the T-beam, and (ii) the orientation of GFRP decks installed on top of the beams (Table 2). In specimen B2 and B3, the GFRP deck panels were oriented with webs in the longitudinal direction (i.e. strong direction) along the beam while the panels in specimen B4 had webs in the transverse direction of the beam. The GFRP deck panels were manufactured with vacuum assisted resin transfer molding (VARTM) method. The prefabricated sandwich decks were 6-meter long and 0.5-meter wide. The nominal thickness of top and bottom skins was 19.1 mm, while the webs were 8.5 mm thick and 112 mm high with a spacing of 110 mm.

Table 2. GFRP GFRP panel and connection method in specimen B2, B3 and B4

Specimen	Type of GFRP deck/panel	Connection method	Bond material
B2	GFRP panel with longitudinal webs	Epoxy-based adhesive bonding	Sto SK 41
B3	GFRP panel with longitudinal webs	Low-shrinkage mortar bonding	Weber 702
B4	GFRP panel with transverse webs	Low-shrinkage mortar bonding	Weber 702

2.2 *Pre-stressing method and implementation*

The innovative pre-stressing device (Figure 2) consists of eight aluminum tabs, which are interconnected with a series of springs (i.e. steel bars with different diameters). The tabs are then connected to the CFRP laminate via a medium (a 10-mm-thick GFRP plate in Figure 2). The GFRP plates (length of 1200 mm) with built-in steel nuts were bonded to the CFRP plate in advance. The pre-stressing device was then bolted to the GFRP plate using high strength M6 bolts. The function of the pre-stressing device is to evenly distribute the total amount of pre-stressing force via these tabs over the length of the CFRP laminate.

Aided by this innovative mechanism, it was possible to—with merely one jacking action—distribute the total pre-stressing force in the CFRP laminate in a step-wise manner and control the gradient of the pre-stressing force in the laminate as intended in the design. A detailed description of the pre-stressing process can be found in Haghani and Al-Emrani (2016) and Yang et al. (2017).

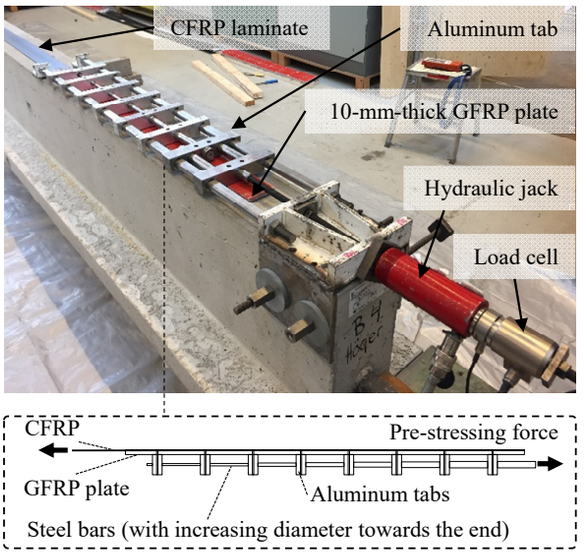


Figure 2. Pre-stressing device mounted on the bottom side of web during tensioning the CFRP laminate

The pre-stressing device was mounted on the concrete beam using temporary anchors. After pre-stressing and curing of the epoxy for 24 hours, the device was removed (Figure 2). Upon the release of the pre-stressing device (aluminum tabs and steel bars), the pre-stressing force in CFRP was transferred to the concrete through the adhesive layer. Previous experimental studies by Yang et al. (2017) proved that it was possible to control the shear and peeling stresses in the bond line below 0.5 and 0.1 MPa, respectively, given a pre-stressing force of 80 kN distributed by eight steps (i.e. tabs).

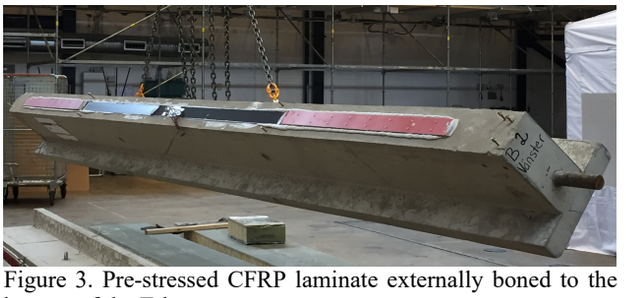


Figure 3. Pre-stressed CFRP laminate externally boned to the bottom of the T-beam

2.3 *Installation of GFRP deck*

Before installation, the top surface of flanges in each T-beam was coarsened with sandblasting in the workshop. In specimen B2 the GFRP deck was

bonded to concrete beam with 10-mm-thick epoxy adhesive, see Figure 4. In specimen B3 and B4, the surfaces of the GFRP deck panels were pre-coated with coarse aggregates with help of an epoxy adhesive. The aggregates were emery stones with a diameter size of 1 mm to 3 mm. The distribution density was 12 kg per square meter. The GFRP panels were first connected to concrete beam with M24 dowels. The dowels served as an extra safety measure in case the cement-based mortar between the GFRP and concrete fails. They also provided a 30-mm gap (i.e. thickness of the mortar layer) through using adjustment washers and nuts before laying down the deck panels on concrete beams. After building the formwork around the beam flange, a low-shrink mortar was used to cast the 30-mm-thick bond layer. The well-mixed mortar was poured into the gap from one side along the beam (Figure 5). Meanwhile, the mortar was vibrated to assure a good flow of the mortar and uniform distribution. The cement-based mortar was left for curing of 28 days before the flexural test.

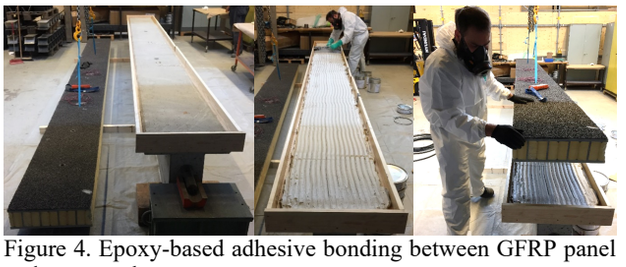


Figure 4. Epoxy-based adhesive bonding between GFRP panel and concrete beam



Figure 5. Low-shrinkage mortar bonding between GFRP panel

2.4 *Test setup and monitoring devices*

The beam specimens were simply supported with a clear span of 5.7 meters (Figure 6). The monotonic loads from two hydraulic jacks were applied in the displacement-control manner to form a four-point bending configuration. The loading speed was 1 mm/min before the yielding of tensile reinforcement bars (B1) or the failure of the CFRP laminates (B2-B4), and then increased to 6 mm/min after that. The distance (center-to-center) between two hydraulic cylinders was 1.3 meter. The size of load prints under the hydraulic cylinders was 400 mm × 400 mm × 30 mm. A rubber pad was used between the load print and the top of the GFRP panels to transfer the load. In each specimen six linear variable differential transformers (LVDT) were used to obtain the mid-span deflection during the tests. Two strain gauges were installed on the bottom surface of each CFRP laminate at the mid-span to monitor the tensile strain from the pre-stressing process till the end of the flexural test.

3 TEST RESULT AND ANALYSIS

3.1 *Load-deflection curves*

The load vs. mid-span deflection curves were plotted for all four beams and are illustrated in Figure 7. They indicate the critical states of specimens from the onset of cracks, through the yielding of tensile steel reinforcement bars, to the failure of externally bonded CFRP laminates, till the end of the tests. The control specimen B1 exhibited a typical behavior expected from an RC beam.

The yielding of the internal reinforcement was obtained at a load of ca. 134 kN. Accounting for the strain hardening of the steel reinforcement, the ultimate load carrying capacity of the beam was determined to be ca. 155 kN. It was decided to terminate the test at deflection of 120 mm. The test result for this specimen matched well with the theoretical prediction of yielding load at 130 kN and ultimate load at 159 kN. In specimens B2-B4, there is a significant

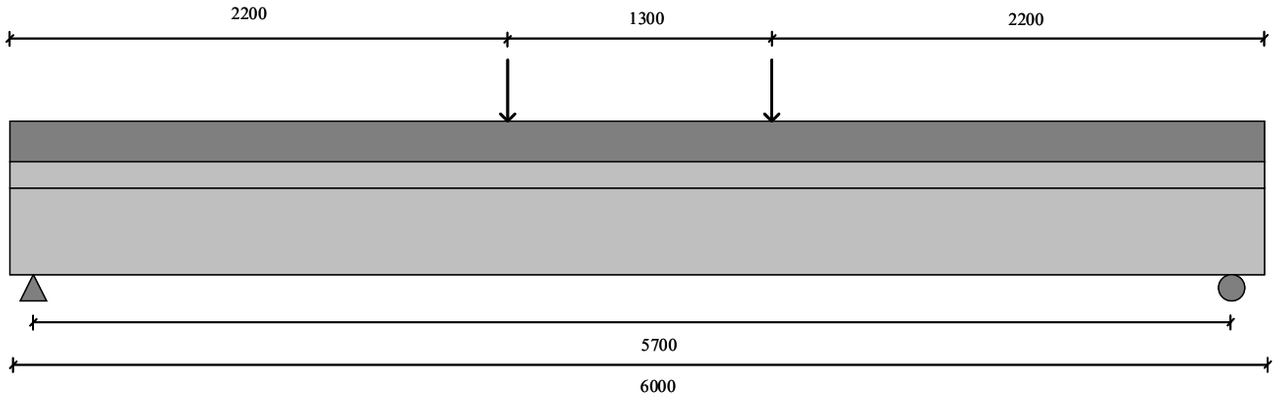


Figure 6. Configuration of specimens with location of loads. The GFRP panel on top of T-beam is only for specimen B2, B3 and B4 (Dimensions are in mm).

Table 3. Improvement in SLS and ULS behavior of strengthened specimens B2-B4 compared with the reference specimen

Specimen	P_{cr} *1	K*2	Δ_{imp} *3	$P_{max.def}$ *4	Δ_{imp} *3	$P_{max.cr}$ *5	Δ_{imp} *3	P_u *6	Δ_{imp} *3
	kN	kN/mm		kN		kN		kN	
B1	19	4.9	NA	113	NA	108	NA	155	NA
B2	75	9.4	93%	261	130%	201	85%	398	157%
B3	77	9.7	99%	275	143%	167	52%	406	162%
B4	61	8.9	82%	242	114%	141	30%	373	141%

*1 Cracking load
*2 Bending stiffness
*3 Improvement compared with reference specimen B1
*4 Load at deflection of 22.8 mm (equals to 1/250 of net span)
*5 Load at maximum crack width reaching 0.3 mm in B1 and 0.2 mm in B2, B3 and B4
*6 Ultimate load

drop of the load due to debonding of the CFRP laminate at a deflection of ca. 50 mm. What is to be highlighted is the contribution of the GFRP deck panel in the load carrying capacity of the beam after CFRP debonding resulting in substantial load bearing capacity. In specimens B2 and B3, the load increased and even exceeded the maximum load achieved in the presence of CFRP laminates. It was decided to terminate the tests due to safety reasons (the tests were continued to deflections up to 210 mm).

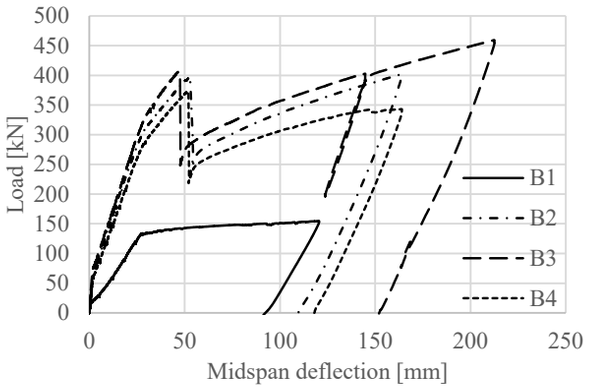


Figure 7. Load-deflection curves of specimens B1-B4

3.2 *Improvements in SLS and ULS*

The behavior of the beams in serviceability and ultimate limit states were studied. The criteria for comparison include the cracking load, stiffness and the ultimate load bearing capacity as reported in Table 3.

3.2.1 *Delayed onset of cracks*

Contribution from the increased stiffness by adding the GFRP deck panels and the pre-stressing force in the CFRP laminate, it significantly increased the cracking loads in strengthened sections. According to Table 3, the cracking load of specimen B1 increased from 18.7 kN to ca. (61~77) kN in specimens B2-B4.

3.2.2 *Improvement of bending stiffness*

The bending stiffness was estimated based on a certain section of load-deflection curves with deflection values between 10 mm (after cracking initiated) and 20 mm (before yielding of rebars). It showed that the estimated bending stiffness of the strengthened specimens increased by 82~99% compared with the reference specimen without strengthening.

In Eurocode 2 the maximum allowed deflection of RC beams is L/250 of the net span, which equals to ca. 23 mm for the tested beams. The load bearing capacity at this deflection increased from 114 kN in Specimen B1 to 261 kN, 275 kN and 242 kN in specimens B2-B4, equivalent to 114~143%, respectively.

3.2.3 *Control of maximum crack width*

In Eurocode 2 the maximum allowed crack width is limited to 0.3 mm for normal RC beams in XC2. The crack widths were measured along the full-span at different load levels starting from 30 kN to 120 kN (for B1) and to 180 kN (for B2-B4) to evaluate the effect of strengthening on crack width. The maximum crack width at each monitored load step is plotted in Figure 8.

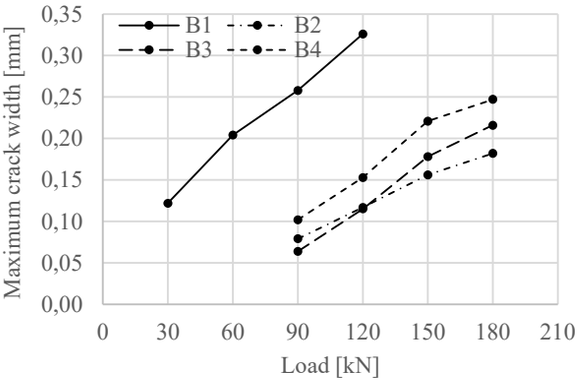


Figure 8. Maximum crack width monitored at different load levels

The load at a maximum crack width of 0.3 mm in specimen B1 was estimated to be ca. 108 kN using linear interpolation. In the strengthened specimens, the cracks did not exceed a width of 0.25 mm. It is worth to mention that the strengthened beams can

satisfy the limit of 0.2 mm for XC3 and 4 at significantly higher loads. The load at a crack width of 0.2 mm in specimen B1 was ca. 60 kN while it was increased to ca. 135, 165 and 180 kN in specimens B2-B4 respectively.

3.2.4 *Ultimate load bearing capacity*

The comparison of ultimate load bearing capacity among the specimens is shown in Table 3. Specimen B1 reached the maximum load of ca. 155 kN. The ultimate loads of specimen B2-B4 were determined at loads when debonding of the CFRP laminate took place. The comparison showed a significant improvement (141~162%) of the ultimate load capacity after the strengthening.

It is worth mentioning that the strengthened beams continued to increase the load levels beyond this limit after CFRP debonding. Even though the design for strengthening shall be based on debonding of the CFRP laminate, the ultimate load carrying capacity resulting from the composite action of the concrete beam and the GFRP deck panels would provide a suitable safety margin in a semi-ductile behavior.

3.3 *Ultimate utilization ratio of CFRP laminate*

In EBR technique using passive CFRP laminate, the maximum strain in the laminate is often limited to ca. 5‰) due to the risk of intermediate crack debonding. In specimens B2-B4, a pre-stress level equivalent to ca. 25% of the ultimate strain (3.23‰) was used. When the failure of CFRP took place (Figure 9), the tensile strain in the CFRP laminates reached 10.94‰, 10.37‰ and 10.87 ‰ in B2-B4, respectively. The ultimate utilization ratio of CFRP in terms of tensile strength therefore reached 80~84% indicating a 100% increase in the utilization ratio.

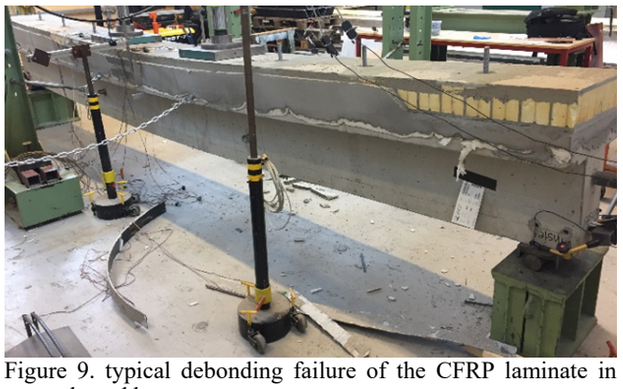


Figure 9. typical debonding failure of the CFRP laminate in strengthened beams

4 CONCLUSIONS

The four-point bending tests were carried out on concrete beams strengthened with bonded pre-stressed CFRP laminates and GFRP deck panels. Tests results indicate significant improvements in the behavior of the beams in SLS and ULS.

The innovative method for pre-stressing CFRP laminate as EBR could successfully eliminate the need for mechanical anchorage system at the ends of CFRP for a pre-stressing force of 100 kN. It could realize the 'self-anchorage' of CFRP laminate with a pre-stressing level equivalent to 25% of the tensile strength, and obtain an ultimate utilization ratio up to 80~84% when debonding of CFRP occurs.

The flexural behavior of strengthened specimens (B3&B4) using mortar bonding method exhibited satisfying performance compared to that of (B2) using traditional epoxy adhesive bonding. The used low-shrinkage mortar is a promising alternative to cast the bond layer between the RC section (with the sandblasted surface) and GFRP component (coated with coarse aggregates).

The specimens implemented with SUREBRIDGE solution demonstrated significant improvement in SLS and ULS:

- The onset of cracks was delayed from 19 kN of B1 to 61~77 kN in B2-B4.
- The estimated bending stiffness of cracked section increased by 82~99% after strengthening compared to the reference specimen.
- The crack width in strengthened beams at the same load level (120 kN) was ca. 35~47% of that in B1.
- In ultimate limit state, the capacity of strengthened specimens at CFRP failure was 141~162% greater than that of the reference beam

5 NOTATION

The following symbols are used in this paper:

E_{11} = mean value of young's modulus of GFRP skin of the sandwich panel along the direction of webs

E_{22} = mean value of young's modulus of GFRP skin of the sandwich panel perpendicular to the direction of webs

$E_{cfrp.m}$ = mean value of young's modulus of CFRP laminate

$E_{s.m}$ = mean value of young's modulus of steel reinforcement bars with diameter of 16 mm

$f_{c.11.u}$ = mean value of compressive strength of GFRP skin of the sandwich panel along the direction of webs

$f_{c.22.u}$ = mean value of compressive strength of GFRP skin of the sandwich panel perpendicular to the direction of webs

$f_{c.m}$ = compressive strength of concrete cubes (side length of 150 mm) cured for 140 days in the same condition with the RC beams

$f_{s.t.m}$ = mean value of tensile strength at rupture of steel reinforcement bars

$f_{s.y.m}$	=	mean value of yielding stress of steel reinforcement bars
$f_{t.11.u}$	=	mean value of tensile strength of GFRP skin of the sandwich panel along the direction of webs
$f_{t.22.u}$	=	mean value of tensile strength of GFRP skin of the sandwich panel perpendicular to the direction of webs
K	=	bending stiffness
P_{cr}	=	cracking load
$P_{max.cr}$	=	load at maximum crack width reaching 0.3 mm in B1 and 0.2 mm in B2, B3 and B4
$P_{max.def}$	=	load at deflection of 22.8 mm (equals to 1/250 of net span)
P_u	=	ultimate load
Δ_{imp}	=	improvement compared with reference specimen B1
$\varepsilon_{cfrp.u}$	=	mean value of ultimate tensile strain of CFRP laminate

6 ACKNOWLEDGEMENT

The work in this paper is a part of SUREBridge project which has received funding from the European Union's Seventh Framework Programme for research, technological development and demonstration. SUREBridge project is co-funded by Funding Partners of the ERA-NET Plus Infravation program.

7 REFERENCE

Haghani, R., Al-Emrani, M., 2016. A New Method for Application of Pre-stressed FRP laminates for Strengthening of Concrete Structures. Presented at the 19th IABSE Congress 2016, Stockholm, Sweden.

Haghani, R., Al-Emrani, M., Kliger, R., 2015. A new method for strengthening concrete structures using prestressed FRP laminates. Presented at the ISEC 2015 - 8th International Structural Engineering and Construction Conference: Implementing Innovative Ideas in Structural Engineering and Project Management, pp. 1153–1158.

PANTURA Project, Deliverable D5.3, Needs for maintenance and refurbishment of bridges in urban environments, FP7 Program, 2011-2014.

Yang, J., Haghani, R., Al-Emrani, M., 2017. Flexural strengthening of reinforced concrete beams using externally bonded FRP laminates pre-stressed with a new method. Presented at the 4th International Conference on Smart Monitoring, Assessment and Rehabilitation of Civil Structures, SMAR 2017, Zurich, Switzerland.

Maintenance, Safety, Risk, Management and Life-Cycle Performance of Bridges – Powers, Frangopol, Al-Mahaidi & Caprani (Eds)
© 2018 Taylor & Francis Group, London, ISBN 978-1-138-73045-8

CFRP Strengthening of ASR affected concrete piers of railway bridges

M. Lima, R.Salamy, D.Miller
Sterling Group Consultants

ABSTRACT: Alkali-Silica Reactions (ASR) occur in concrete due to chemical reactions between the alkali (sodium and potassium) hydroxides in the concrete pore solution. Under certain circumstances, these reactions cause internal expansion (commonly known as "concrete cancer"). The swelling within the concrete can potentially result in cracking of the concrete impairing its function and shortening its service life. This paper presents the outcomes of engineering inspections, material properties investigation and strengthening design of concrete piers and abutments of four railway bridges located on the Mildura Line in Victoria. The inspection findings are discussed in detail and engineering interpretation is presented including the potential remediation options for the observed defect including steel/concrete jacketing and CFRP wrapping. The cons and pros of these methods are discussed and CFRP wrap is selected as a suitable method. The assumptions for CFRP strengthening design and challenges during application of concrete epoxy injection and CFRP are highlighted.

1 INTRODUCTION

The Alkali Silica Reaction (ASR) refers to the formation of an expansive gel through the reaction of alkalies and silicates in concrete (Monette, Gardner et al. 2002, Fournier, Bérubé et al. 2004). In the presence of sufficient moisture, the gel expands and puts pressure on the surrounding cement paste and aggregates, which can lead to cracking (Fournier, Bérubé et al. 2004). Three factors are required for the reaction: a) sufficient moisture; b) the presence of reactive aggregate and c) a high level of alkalinity. The reaction cannot occur without any of these elements (Talley 2009).

The mechanism of ASR is as follows: a high level of alkaline ions in the pore solution will essentially attack the silica bonds in the aggregate and cause the silica to dissolve. Then, the silica goes into the concrete pore solution and it reacts with the alkaline ions present in the solution. The chemical reaction between the silica and the alkali ions form an alkali-silica gel around the edge of the aggregate. In presence of sufficient moisture, the gel expands and pushes against the surrounding concrete causing high localised pressure. This pressure can result in micro-cracking of the concrete, and over time with exposure to moisture, the cracks expand and can be visible with the naked eye (Farny and Kosmatka 1997, Talley 2009). This schematic of this process is showed in Figure 1.

The type of aggregate, exposure environment and alkali content of concrete affects the severity of reaction. Having cracks in structure adversely affects the durability of concrete by exposing the interior portions of concrete to environmental agents. Several cases of ASR have been reported in Australia in dams and bridges (Shayan and Lancucki 1986, Shayan 1988, Shayan and Quick 1992, Ross and Shayan 1996, Shayan 1999, Shayan, Wark et al. 2000, Shayan, Al-Mahaidi et al. 2008, Shayan, Xu et al. 2015). Several cases of ASR affected structures are presented in HB79 'Guidelines on minimizing the risk of damage to concrete structures in Australia' (StandardsAustralia 2015).

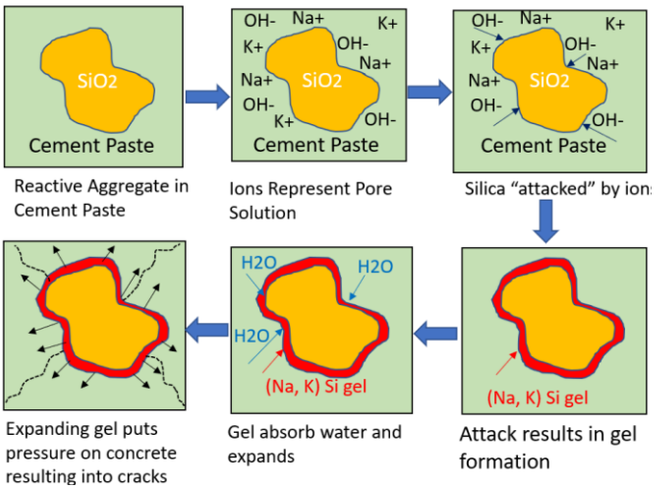


Figure 1 . Schematic of ASR mechanism

Previous investigation indicates that the cracking of the concrete affects the strength properties of concrete (Mohammed, Hamada et al. 2004, Shayan, Al-Mahaidi et al. 2008, Shayan, Xu et al. 2015); however, the load carrying capacity of the of the structure might not be proportionally reduced (Monette, Gardner et al. 2000, Shayan, Al-Mahaidi et al. 2008, Shayan, Xu et al. 2015). In addition, the deterioration effects are more significant for small elements in comparing to large elements due to the larger ratio of crack depth to dimension of the element (Shayan 2016). The impact of different factors in ASR affected structures has also been investigated (Shayan, Xu et al. 2015, Shayan 2016). Considering the history of ASR issues in Australia, this paper presents the engineering inspection outcome and strengthening design of four railway bridges with brief overview of the crack injection and repair.

2 STRUCTURAL DESCRIPTION

Four bridges with 56 total piers and abutments were inspected and evaluated. All bridges were simply supported girders on plain concrete piers comprised of four main girders with timber transoms on top. A brief description of each structure is provided herein.

Bridge A: the bridge has 17 spans in total consisting of two different span lengths - 9m (15 spans) and 12m (2 spans). One span of this bridge was over a creek. The average height and width of the piers were approximately 2.6m and 3.4 m respectively. The year of construction was 1957.

Bridge B: the bridge has 15 identical spans of 9m in length. Three spans of this bridge were located over a pooled water area/pond. The average height and width of the piers were approximately 2.5m and 3.3 m respectively. The year of construction is 1957. A general photo of this bridge is shown in Figure 2.

Bridge C: the bridge has 7 identical spans, each 9m in length. The height of the piers varies from 0.5m to 4.4m, while the width of the piers is constant (approximately 3.6m). The year of construction was 1958.

Bridge D: the bridge has 13 spans in total with span lengths of 12.2m (4 spans), 9.1m (7 spans) and 9.7 m (2 spans). Two spans of this bridge are located over a river. The width of the piers was 3.3m and 5.4m and average height of the piers was 2.5m. The year of construction was 1957.



Figure 2 . General view of piers – Bridge B

3 ENGINEERING INSPECTION AND MATERIAL TESTING

The inspection revealed that the piers of all bridges included in this investigation were mass concrete without reinforcement. To investigate the concrete properties and provide appropriate solution for the potential ASR, five concrete samples were taken from the middle piers of each bridge to conduct laboratory investigation. The length of the samples was about 170mm and the diameter was 75mm (Figure 3).

Four out of five concrete samples from each bridge were tested for compressive strength AS 1012.14 (Standards Australia 2014) and Alkali Silica Reactivity ASTM C856 (ASTM C856 2017) and one sample was kept as reference. These samples were taken from a minimum of three different piers to capture the overall behaviour/condition of the concrete piers. The concrete strength of the samples in both dry and wet condition were obtained to provide a better insight of the concrete properties considering various environmental conditions. Dry and wet conditions best represent the actual environment of the piers as only a few of them were located at the middle of creeks (within water) while some of them were in dry land. The result of the concrete compressive strength tests for these samples are presented in Table 1.

Petrography analysis was based on the treatment of thin cross-sections of the core samples with a laboratory prepared Uranyl Acetate solution and examination both pre-treatment and post-treatment under Ultra-Violet light. The grey coloured concrete cross sections of the cores are shown in Figure 4. The lab results revealed that the concrete was generally well compacted and has a high proportion of large aggregate. Some orange coloured staining and minor voids were observed within the concrete cores.



Figure 3 . Concrete coring of Bridge A

The petrography analysis revealed that the coarse aggregate is predominantly Carbonatite. The maximum sizes of the aggregates and voids are presented in Table 1. Severe microcracking was observed in and around the aggregate, however, no visible macrocracking was evident in the analysis. The cores show the presence of crystal formation within the voids of the concrete. There was evidence of Ettringite Formation, Alkali Silica Reactivity (ASR) and delayed Ettringite Formation. Crystalline needles were evident in the voids. The Ettringite Formation appeared to be in early stages and may continue to increase, although the extent and timeframe for this is unknown. There was also ASR gel visible in some cracks surrounding the aggregate. Severe microcracking is present both within the aggregate and throughout the surrounding concrete.

Table 1. Concrete material properties for bridges

BRIDGE	COMPRESSIVE STRESS (MPA)			SIZE (MM)	
	S1 (dry)	S2 (wet)	S3 (wet)	Aggregate	Voids
A	34.5	19.0	26.0	≥50	≤3
B	45.5	33.0	26.0	≥50	≤3
C	43.5	18.5	30.5	≥25	≤5
D	31.5	12.5	24.5	≥ 25	≤7

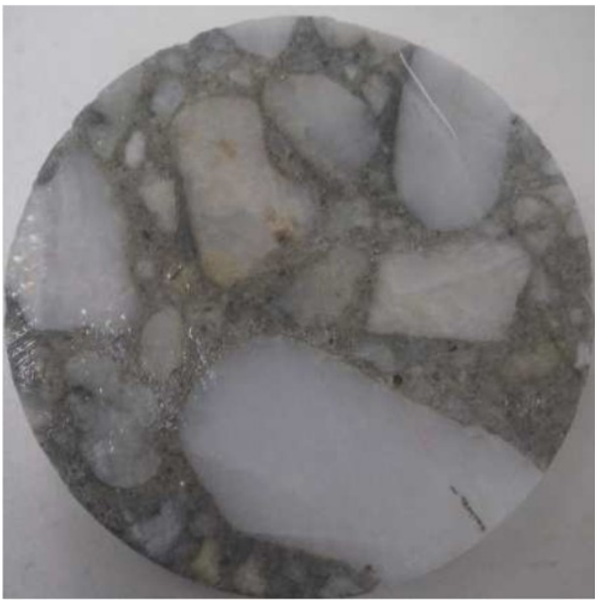


Figure 4 . Cross section of concrete core for petrography analysis of Bridge A

Extensive cracking was observed within most of the concrete piers of the bridges. The width and length of the cracks varied between 0.1mm to 10mm. A sample of pier crack mapping is presented in Figure 5.

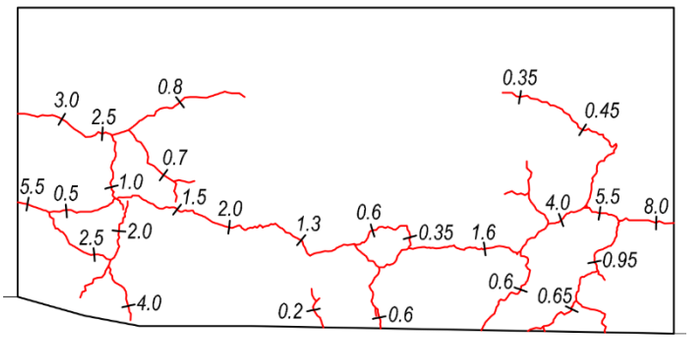


Figure 5 . Crack mapping of Pier 2 – Bridge C

4 CFRP STRENGTHENING DESIGN AND APPLICATION

Considering the condition of the piers and the existence of ASR, injection of the cracks and waterproofing was recommended for all affected piers. Also, for piers with severe cracking, a strengthening design was provided. A few alternatives were considered for strengthening of these piers including CFRP wrapping; concrete jacketing, and steel jacketing. The pros and cons of these methods are as follows:

- Steel/ concrete jacketing usually requires heavy machinery.
- The total labour cost for concrete/steel jacketing are likely to be equal or even higher than CFRP wrapping method. However, the required

time and line interruption for concrete jacketing is more than CFRP application.
- The curing time for concrete jacketing is more than CFRP wrapping.
- The access constraints are also challenging for jacketing option as the bridges; located off the road.
- For those cracks that are propagated below the ground level, more soil excavation is required for jacketing for scaffolding purposes.
- CFRP has unique properties, including high strength-to-weight ratio, high fatigue endurance, environmental degradation and corrosion resistance (Lima, Doh et al. 2016).

Therefore, the CFRP wrapping was favoured due to the budget and construction time constraints during occupation of the rail corridor.

Several investigations have been completed on CFRP strengthening of ASR affected structures and various levels of success are reported for different types of structures and environmental conditions (Haddad, Shannag et al. 2008, Talley 2009). The geometry of an element has a key role in the ultimate performance of the CFRP application in concrete columns/piers and maximum efficiency achieved in wrapping of circular columns/piers (Shayan, Xu et al. 2009). AS5100.8 (2017) provides some guidance for design of CFRP strengthening of elements with various shapes and materials. The formula provided for CFRP strengthening of concrete columns/piers is based on the stress-strain curve of an FRP confined section. The maximum confinement pressure (f_l) is as follows:

$$f_l = \frac{2E_f t_f \epsilon_{fe}}{D} \geq 0.08 f'_c$$

Where D is either the diameter of a circular cross section or the dimension as shown of Figure 6; E_f is the average FRP modulus of elasticity; t_f is the total FRP thickness of all layers; ϵ_{fe} is the effective strain level in the FRP at failure.

For different cross sections, AS 5100.8 provides efficiency factors (κ_a and κ_b) and for circular cross section, the shape factors may be taken as 1. For rectangular cross section, the shape factors are as follows:

$$\kappa_a = \frac{A_e}{A_c}\left(\frac{b}{h}\right)^2; \qquad \kappa_b = \frac{A_e}{A_c}\left(\frac{h}{b}\right)^2$$

Where b and h are the section dimensions as shown in Figure 6. Based on AS5100.8, the aspect ratio (h/b) shall be less than or equal to 2. The dimensions h and b shall be less than 900 mm.

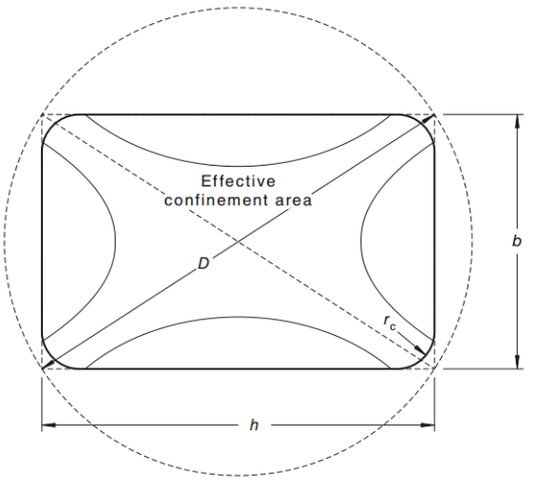


Figure 6 . Equivalent circular cross section (AS 5100.8)

A_e/A_c is the ratio of the effective confinement area and the concrete cross sectional area as follows:

$$\frac{Ae}{Ac} = \frac{1 - \frac{\left[\left(\frac{b}{h}\right)(h-2r_c)^2 + \left(\frac{h}{b}\right)(b-2r_c)^2\right]}{3A_g}}{1-\rho_g}$$

Where r_c is the radius if rounded corners and ρ_g is the longitudinal steel reinforcement ratio.

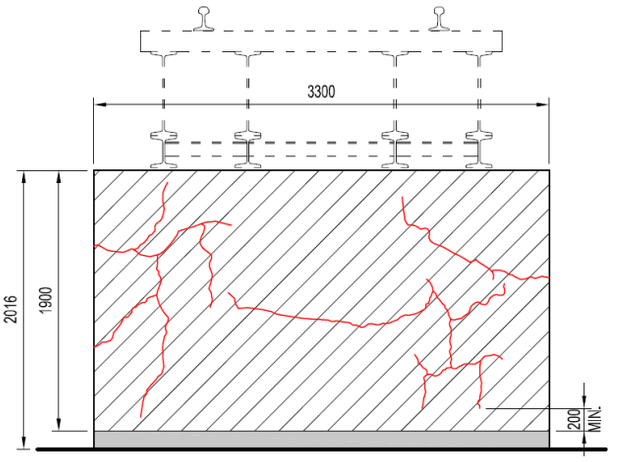


Figure 7 . CFRP strengthening scheme for Pier 2 – Bridge C (dimensions are in mm)

The aspect ratio for the piers in this project was b= 1200mm and h=3300mm which is beyond the specification of AS5100.8. However, the crack injection and CFRP strengthening in this project was mainly to improve the durability, integrity of the structure by minimising the water ingress into concrete and control the crack expansion. The enhancement of axial load carrying capacity of the piers was not the main purpose of this project. For design purposes, it was assumed that the cracks are epoxy injected, strengthened by CFRP, are coated and water ingress in insignificant or minimal. However, the design of the CFRP wrapping was completed based on the conservative assumption that the lifetime expansion of concrete

piers will not exceed 0.5%. This assumption was made in absence of monitoring data for the concrete piers. Based on this assumption, the design consists of one layer of vertical and one layer of horizontal CFRP sheets (Figure 7). The thickness of each layer of CFRP was t_f = 0.129mm and the modulus of elasticity was E_f = 230GPa. The combination of vertical and horizontal layers was proposed in order to constrain the scattered cracks and those that propagated diagonally. Strengthening of the piers was completed in four stages as follows:

Concrete patch repair: delamination ("drummy") survey using a hammer was completed for detection of incipient spalls and delamination. The defective concrete was then removed and repaired with approved mortar (Figure 8).



Figure 8 . concrete patch repair of abutment – Bridge A

Crack injection: a summary of the crack injection procedure is as follows: a) all impurities including dirt, dust, loose particles, oils, grease, coatings, and efflorescence was cleaned from the surface of the concrete for 50mm either side of the crack; b) injection entry ports were installed along the cracks at intervals no greater than 200mm (Figure 9-10); c) injection ports were located on all pier faces and exposed abutments faces; d) bonded-on injection fittings or injection fittings placed into drilled holes were also acceptable; e) the surface of the cracks were sealed between the injection ports.

Injection of the epoxy initiated at the lowest entry port and continued until it appeared at the closest horizontally adjacent port; f) once all horizontally adjacent ports were injected, then injections continued until epoxy appeared at the closest vertically adjacent port; g) two to four cores (maximum one core from each side of the pier) were extracted from the piers with the largest size of crack (greater than 1mm). Each core had a diameter of at least 50mm and depth of at least 400mm and was positioned centrally between injection ports with a crack located centrally at the surface of the core; h) the bond strength of the injection epoxy to the inside surfaces of the crack and the depth of the penetration (Figure 11) was verified by using the extracted core samples trough the repaired cracks; i) the injection pressure was between 150Psi to 200Psi. Low viscosity material was used for cracks under 5mm width while a medium to high viscosity material was used for wider cracks. For crack that were extended to the ground level, minimum soil excavation of 500mm was completed in order to ascertain that the cracks are epoxy injected properly (Figure 12).

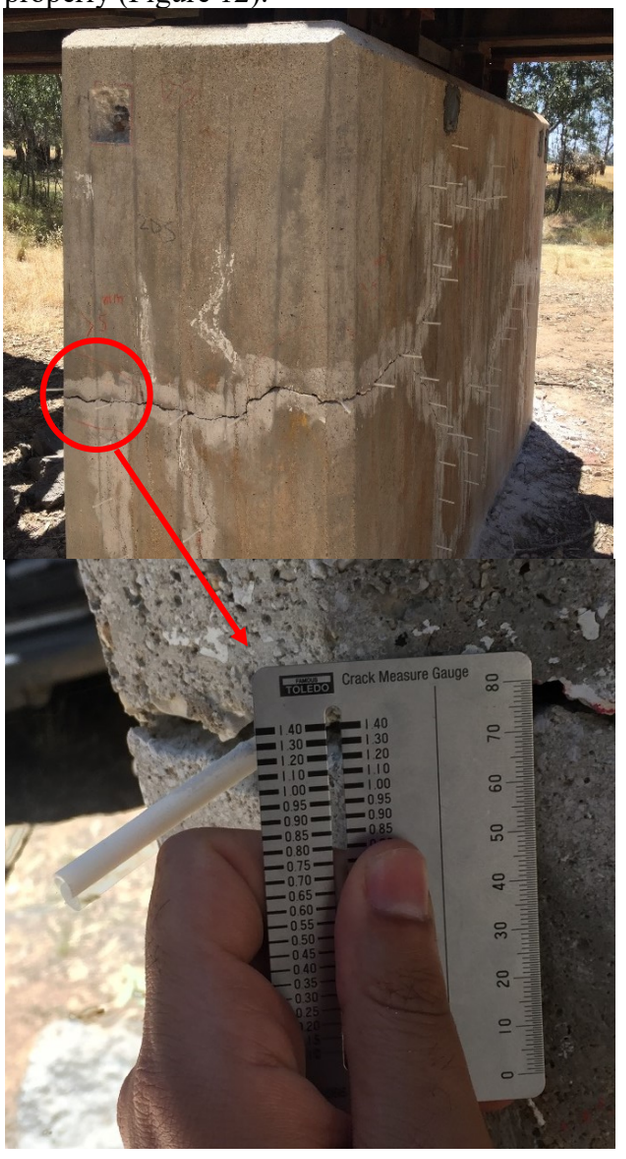


Figure 9. Installation of injection entry points - Bridge B



Figure 10. crack sealing prior to injection - Bridge A



Figure 11 . Depth of epoxy penetration – Bridge A



Figure 12. Soil excavation for extended cracks below ground level

Due to the nature of ASR cracks and inadequate sealing in limited cases (Figure 13), there were air traps (Figure 14) revealed after coring. In these cases, a layer of wax was applied over the leakage point and the injection was continued as normal.

CFRP wrapping: a summary of CFRP wrapping procedure is as follows: a) abrasive blast cleaning equipment was used to mechanically prepare the surface of the concrete within the CFRP wrap application areas; b) corners which the CFRP wrap was to be applied around were rounded or chamfered to a minimum radius of 25mm by grinding; c) the application of vertical layers of CFRP were completed, then another layer of horizontal CFRP was wrapped around the piers continuously; d) the CFRP wrap was extended at least 200mm beyond the crack location; e) the manufacturer's instructions were used for mixing and applying the Carbon Fibre Wrap Primer to the prepared substrate; f) the resin was applied to all areas of the fabric without any dry spots, trapped air, bubbles or blisters; g) once application was completed, a protective sheet was applied to ensure safety against rain, sand, dust and other contaminants.



Figure 13 . Inadequate sealing over the crack and epoxy leakage - Bridge A



Figure 14 . Air trap in crack injection- Bridge A

Coating and sealing: a summary of coating and sealing procedure is as follows: a) the surface was cleaned prior to coating to maximise bonding; b) previously painted surfaces were cleaned and sound and all traces of peeling or loose paint were removed; c) primer was applied as a single coat over the entire surface, and then a top coat was applied in accordance with the manufacturer's instructions over the base

coat; d) application of the final coating system was implemented on continuous and pin-hole free surfaces. A minimum dry film thickness (DFT) of 160 microns was required after achieving full cure. The quality control testing of all stages was in accordance with AS 5100.8 or relative standards/guidelines.

A monitoring period of 2 to 3 years was recommended to validate the assumed value for expansion rate and modify the CFRP wrapping design where required. If monitoring reveals that the recorded expansion rate of the concrete exceeds the assumed value of 0.5% within the structure's remaining service-life, then a new evaluation based on the observed condition will be required to identify any requirement to the modification of the proposed CFRP wrapping design.

5 CONCLUSION:

This paper presents the CFRP strengthening of the piers of four railway bridge with a summary of inspection findings and material testing as well as the design approach and assumptions. Also, a summary of CFRP application steps is provided for engineers' references. The crack injection and some of the challenges during application is also highlighted. the following points are the significance of this project:

- The CFRP wrap was selected as a suitable material for strengthening of ASR affected piers due to its superb properties, time and budget of the project as well as handling and transportation of the material to site.
- The design of CFRP assumed that the lifetime expansion of concrete piers will not exceed 0.5%. This assumption was made in absence of monitoring data for the concrete piers. Further monitoring and measurement is required in order to validate this assumption. If monitoring reveals that the recorded expansion rate of the concrete exceeds the assumed value of 0.5% within structure's remaining service-life, then a new evaluation based on the observed condition will be required to identify any requirement to the modification of the proposed CFRP wrapping design in necessary.

- It is critical for this application that crack injection to be conducted properly by a qualified contractor and active supervision. During the construction phase, there were some challenges for crack injection and CFRP application. The crack sealing should be properly completed prior to injection. Even though, due to the nature of ASR cracks that are interconnected inside the concrete piers, there are always a chance of leakage from some areas that seems no cracks exists. In these cases, the contractor should apply wax or other appropriate material to prevent any leakage and continue the injection.

6 REFERENCES

ASTM C856-17 (2017). ASTM C856-17. Standard Practice for Petrographic Examination of Hardened Concrete, ASTM International, West Conshohocken, PA, 2017.

Farny, J. A. and S. H. Kosmatka (1997). Diagnosis and control of alkali-aggregate reactions in concrete, Portland Cement Association.

Fournier, B., et al. (2004). Evaluation and Management of Concrete Structures Affected by Alkali–Silica Reaction—A Review. Seventh CANMET/ACI International Conference on Recent Advances in Concrete Technology.

Haddad, R., et al. (2008). "Repair of reinforced concrete beams damaged by alkali-silica reaction." ACI Structural Journal **105**(2): 145.

Lima, M. M., et al. (2016). "The effects of CFRP orientation on the strengthening of reinforced concrete structures." The Structural Design of Tall and Special Buildings **25**(15): 759-784.

Mohammed, T., et al. (2004). ASR expansion of concrete beams with various restrained conditions–612 days of accelerated marine exposure. Proceedings of the 12th International Conference on Alkali-Aggregate Reaction in Concrete.

Monette, L., et al. (2000). "Structural effects of the alkali-silica reaction on non-loaded and loaded reinforced concrete beams."

Monette, L., et al. (2002). "Residual strength of reinforced concrete beams damaged by alkali-silica reaction—Examination of damage rating index method." Materials Journal **99**(1): 42-50.

Ross, I. and A. Shayan (1996). Alkali aggregate reaction in Western Australia: investigations on the causeway bridge and some aggregate sources. International Conference on Alkali-Aggregate Reaction in Concrete,, Melbourne, AARC Australia.

Shayan, A. (1988). "Alkali aggregate reaction in a 60-year-old dam in Australia." International Journal of Cement Composites and Lightweight Concrete **10**(4): 259-266.

Shayan, A. (1999). Characterisation of AAR-affected concrete from a dam structure for rehabilitation purposes. Infrastructure regeneration and rehabilitation improving the quality of life through better construction. International conference.

Shayan, A. (2016). "Effects of alkali–aggregate reaction on concrete and structures." Proceedings of the Institution of Civil Engineers - Construction Materials **169**(3): 145-153.

Shayan, A., et al. (2008). Durability and strength assessment of AAR-affected bridge deck planks. International Conference on Alkali-Aggregate Reaction in Concrete (ICAAR), 13th, 2008, Trondheim, Norway.

Shayan, A. and C. Lancucki (1986). Alkali-aggregate reaction in the Causeway Bridge, Perth, western Australia. Proceedings of the 7th International Conference on Alkali-Aggregate Reaction in Concrete, Ottawa.

Shayan, A. and G. Quick (1992). "Microscopic features of cracked and uncracked concrete railway sleepers." Materials Journal **89**(4): 348-361.

Shayan, A., et al. (2000). Diagnosis of AAR in Canning dam, characterisation of the affected concrete and rehabilitation of the structure. Proc. 11th Inter. Conf. on Alkali-aggregate Reaction in Concrete.

Shayan, A., et al. (2015). "Assessment of alkali-aggregate reaction in three bridges and its implications for maintenance of the structures." Road & Transport Research: A Journal of Australian and New Zealand Research and Practice **24**(2): 54.

Shayan, A., et al. (2009). Effectiveness of CFRP wrapping in confining the expansion of AAR-affected concrete. Austroads 7th Bridge Conference, Auckland, New Zealand, May.

Standards Australia (2014). AS 1012.14-1991 Methods of testing concrete Method for securing and testing cores from hardened concrete for compressive strength, Standards Australia.

StandardsAustralia (2015). Alkali Aggregate Reaction— Guidelines on Minimising the Risk of Damage to Concrete Structures in Australia, SA HB 79:2015, Standards Australia, Sydney.

Talley, K. G. (2009). Assessment and strengthening of ASR and DEF affected concrete bridge columns, The University of Texas at Austin.

Maintenance, Safety, Risk, Management and Life-Cycle Performance of Bridges – Powers, Frangopol, Al-Mahaidi & Caprani (Eds)
© 2018 Taylor & Francis Group, London, ISBN 978-1-138-73045-8

Feasibility of reinforcement in Brazilian concrete highway bridges using carbon fiber-reinforced polymer

A. Medeiros & W. Mazer
Technological Federal University of Paraná, Curitiba, Brazil

C. E. Rossigali
Center for Marine Studies, Federal University of Paraná, Pontal do Paraná, Brazil

T. N. Bittencourt
University of São Paulo, São Paulo, SP, Brazil

ABSTRACT: *Due to increase of traffic weight, there is a need to check if the bridges designed and built in the 1960s support current traffic load effects. In this context, some bridges in a ring road around Curitiba city in southern Brazil were revised. They were designed for 36-ton class and the requirement of the Brazilian design code raised to 45-ton. The research reported in this paper focus on the feasibility of carbon fiber reinforced polymers on the reinforcement of three highway bridges. The reinforcement design proved to be feasible in two bridges, with flexural and shear reinforcement in up to three layers of carbon fiber composites. However, in one of the bridges the reinforcement was technically infeasible, as it would require up to seven layers of carbon fiber composites. According to the manufacturers of the FRP it is not possible to apply more than four layers.*

1 INTRODUCTION

Design of Brazilian highway bridges meet the design code ABNT NBR 7188 (2013), in which the live load model is composed of a 3-axle vehicle and a distributed crowd load (Fig. 1). The configuration of this design loading follows the pattern of the ancient Brazilian design code ABNT NB-6 (1960), which was based on the German design code DIN 1072 (1952). The weight of the main load model have been increased over time, from 36-ton in the 1960s to the current heavier vehicle load equal to 45-ton. This change occurred in 1982, the magnitude updates occurred to follow the increasing allowable gross vehicle to transit in Brazilian highways, mainly from the 1970s. The current version of the ABNT NBR 7188 (2013) kept the 450 kN total weight of the load model (Rossigali et al. 2015).

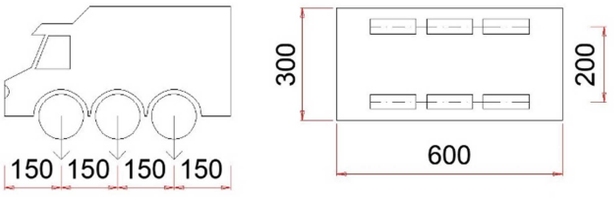


Figure 1. Side view if the current Brazilian load model vehicle (ABNT NBR 7188, 2013). Units: cm.

According to Mendes (2009), most highway Brazilian bridges were design in the 1960s and the 1970s and have the following features: 83% are reinforced concrete deck girder bridges; 93% have maximum length lower or equal to 40 meters; 64% were designed according to NB-6 36-ton vehicle. It means that a large amount of the Brazilian highway bridges are low-span reinforced concrete RC structures.

Usual problems identified in existing reinforced concrete bridges are the diagonal cracks that identify shear deficiency (Higgins et al. 2012). In reinforced concrete, cracks are caused either by the applied loads or by shrinkage and thermic stresses (Mostafa et al. 2010). After flexure cracks initiate in a reinforced concrete structure and turn diagonal, besides the reduction of the flexural stiffness there is a considerable reduction of the capability in transfer the shear forces: the shear stiffness is not elastic (Ramezansefat et al. 2017). These lead to the conclusion that the Brazilian bridges designed according to the 1960 Brazilian code NB-6 do not bear current traffic effects and necessarily must be reinforced (El Debs & Malite 2002).

Besides these facts, some ancient highway bridges are reaching their design lives. The overestimation of the concrete contribution to shear resistance during design (Higgins et al. 2012), the continuous growth in traffic volume of commercial vehicles, shrinkage, fatigue of the reinforcement bars, temperature effects and the lack of a maintenance policy of these structures also play a role on their deterioration. The cracking arising and growth cause the prolonged exposition of the steel, which means in some bridges a considerable level of corrosion of steel re-

inforcement. Corrosion might increase the volume of steel by until six times, damaging the concrete at the vicinity (Grace et al. 2012).

In this scenario, many strategies are available to reinforce the RC bridges. One of the most usual is the epoxy injection to vanish the cracks followed by an increase of the transverse section and of the reinforcement. The main disadvantage of this measure is that it is time-consuming. Other alternatives are steel plate reinforcement, that is worldwide available, but increases weight, but the gain in stiffness is low; post-tension that requires careful work and its very useful contain or reverse displacements. In this sense, new strategies are needed. For instance, the surface-bonded strips of carbon fiber reinforcement polymers (CFRP) are becoming a widely useful alternative to strengthen concrete members like columns, slabs, beams and piers (Liu et al. 2011, Vosooghi & Saiid 2013).

The main goal of this paper is to describe the CFRP reinforcement design of three highway bridges locates at Paraná State, Brazil. They are located at the Curitiba's city ring road. The CFRP reinforcement was a request of the Transportation Ministry in 2012, looking for a fast and light solution.

2 FEATURES OF CFRP

2.1 *The main advantages of using CFRP*

According to Vosooghi & Saiid (2013) the CFRP increases the concrete confinement and then prevents splice failure even at large deformations. It increases the ductility and ultimate strength capacity of the structural member. The stiffness is also increased, although not to the initial values of the undamaged reinforced concrete element.

At high service loads after rehabilitation with CFRP, a brittle fracture may occur after delamination (Mostafa et al. 2010). Partial delamination led to an initial drop in the strength capacity of a CFRP-reinforced beam, but subsequently it acquires a high deformation capacity. Besides, the corrosion resistant, the great pullout strength, the installation relatively simple and the fabric very thin and thus light, increasing little dead load to the RC members are many reasons the motivate the use of CFRP to RC bridge reinforcement.

2.2 *Limitations on the use of CFRP*

On the other hand, Liu & Sun (2010) and Ramezansefat et al. (2017) point some characteristics of the CFRP can be disadvantages. The carbon fibers cannot bear compression, only tension; small curvature radius or edges are difficult places to apply the CFRP; the application of CFRP requires a very careful and meticulous work.

There is a limit, depending on the manufacturer, of CFRP layers that can be superimposed. Generally, more than four layers are very difficult to execute. In this case, the carbon fiber and the epoxy resin would fall by its self-weight during application. Because of its high price, the application of CFRP is not worth in large strengthening areas.

2.3 *Other features of the CFRP*

The shear strength of the CFRP strips depends on the flexural details, besides concrete and the reinforcement. In general, the smaller the CFRP wrap thickness, the grater the pullout strength. The application of longitudinal CFRP in beams does not increase shear capacity, thus is not effective to diagonal crack locations (Higgins et al. 2012). The application in columns in the hoop direction is quite effective (Grace et al. 2012). The debonding of the CFRP generally occurs at the vicinity of the cracks.

In terms of a life-cycle analysis, the initial construction costs of a CFRP reinforced bridge is quite higher than the traditional steel bars reinforcement, but the substantial reduction in maintenance costs makes this alternative more cost-effective in a long-term comparison (Grace et al. 2012). The CFRP strips can be placed to furnish flexural or shear strengthen. Its Young's modulus is comparable to steel and its rupture strength is huge in comparison to concrete and steel: a typical value is 3 GPa.

Application of CFRP in general follows the steps (Vosooghi & Saiid 2013): remove the loosing concrete (with an impact hammer); clean the area (with compressed air); repair the concrete with grout, mortar etc. (recommended only high-early-strength, low-shrinkage grout); perform the epoxy injection; smooth the element surface; apply a prime layer; apply the CFRP fabric carefully; apply a cover resin layer; repeat CFRP if necessary; curing of the system.

3 REINFORCEMENT DESIGN USING CFRP

In terms of design using CFRP as reinforcement in RC structures, it is reasonable to assume that a certain fraction (e.g. 50%) of the original shear strength of the transverse steel to avoid conservative results in terms of number of layers of CFRP (Vosooghi & Saiid 2013).

Due to the lack of a Brazilian code for the use of CFRP, one can adopt the traditional RC calculus of the Brazilian code for design of reinforced concrete structures, ABNT NBR 6118 (2014). Other strategies are use the American code ACI 318 (2008) or the CEB-FIP Model Code (2010) manual. In this paper, it was used the ACI 318 procedure to design the CFRP reinforcement of the RC bridges.

4 BRIDGES INFORMATION AND REINFORCED DESIGNS

Three bridge designs are presented, all of them being part of the Curitiba City´s ring road in southern Brazil, according to Table 1.

Table 1. Bridges' information.

Bridge over	num. of spans	Span
	units	m
Eduardo Sprada St.	1	37.5
José Luis St.	3	27.0
		22.0
		27.0
Cyro Correia St.	1	35.0

All bridges have the same one-cell box type cross section as Figure 2.

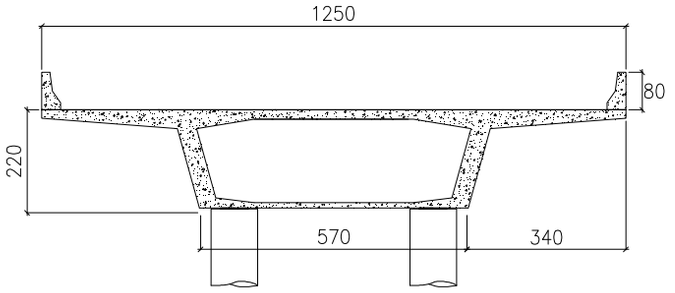


Figure 2. Transverse section of the bridges. Units: cm.

4.1 *Bridge reinforcement design*

To calculate the amount of CFRP necessary to reinforce each bridge, the soliciting bending moment M_{sd} and shear force Q_{sd} was obtained for the vehicle load equal to 45-ton envelope of stresses. The resistant bending moment M_{rd} and shear force Q_{rd} were calculated considering the real concrete cross section (25MPa) and the steel reinforcement. According to the ACI 318 procedures, the area of fibers A_f is calculated considering a fiber thickness of 0.165 mm, that leads to the number of layers of CFRP for the bending reinforcement. The relation width/spacing w_f/s_f was calculated to obtain the number of layers of CFRP for the shear reinforcement. This data is present in Table 2 for bending and Table 3 for shear reinforcement.

Table 2. Bridge CFRP bending reinforcement

Bridge over	M_{rd}	M_{sd}	A_f	n. CFRP layers
	kN.m	kN.m	cm^2	units
Eduardo Sprada St.	21091	13065	61.3	7
José Luis St.	22134	18540	26.5	3
Cyro Correia St.	11224	12839	-	-

For the bridge over Eduardo Sprada Street, the number of seven layers of carbon fiber reinforced polymers was technically infeasible. According to the manufacturers of the CFRP, it is not possible to apply more than four layers. In this case, the carbon fiber and the epoxy resin would fall by its self-weight during application. For the bridge over José Luis Street the CFRP for bending reinforcement is feasible. For the bridge over Cyro Correia Street the bending reinforcement was not necessary due to the soliciting bending moment is lower than the resisting bending moment.

Table 3. Bridge CFRP Shear reinforcement

Bridge over	Q_{rd}	Q_{sd}	w_f/s_f	n. CFRP layers
	kN	kN		units
Eduardo Sprada St.	8489	4340	6.0	3
José Luis St.	6748	4999	1.4	3
Cyro Correia St.	7762	4260	5,1	3

Shear reinforcement was necessary for all the bridges. According to ACI 318 (2008) procedure for shear reinforcement using CFRP, when the relation w_f/s_f is greater than 1, one single layer of carbon fiber is not enough. To calculate the number of layers necessary Equation 1 is used.

$$\frac{w_f}{s_f} = \frac{V_f}{2.n.t_f.f_f.d_f} \quad (1)$$

Where V_f = the extra shear force that the CFRP will support; n = the number of layers; t_f = the thickness of the carbon fiber blade; f_f = the ultimate tensile stress of the carbon fiber; and d_f = depth of the carbon fiber blade for shear reinforcement.

5 CONCLUSIONS

A maintenance policy is imperative to guarantee the safety level of the Brazilian bridges.

In some cases the number of necessary CFRP layers is high enough to turn this reinforcement alternative unfeasible; in these cases there is a need to investigate other solutions like traditional reinforcement, post-tensioning and others. Nevertheless the CFRP is a remarkable reinforcement alternative.

It was a request of the Transportation Ministry in 2012 to verify the economic and technical feasibility of the CFRP reinforcement in those three bridges. Surprisingly, after five years, the bridges are still active and no reinforcement was made in none of them. Considering this, two assumptions can be made: (i) the weight of the main load model of 45-ton is maybe overestimated and the safety factors used for bridges' design (for both loads and resistances), according to Brazilian design codes, contribute for an additional safety margin; and (ii) the service life of these bridges is reaching their end.

6 REFERENCES

ACI Committee 318 2008. *Building Code Requirements for Structural Concrete and Commentary*. Farmington Hills, USA: American Concrete Institute.

Brazilian Association of Technical Standards 1960 NB-6: *Live load on highway bridges* (in Portuguese). Rio de Janeiro, Brazil: ABNT.

Brazilian Association of Technical Standards 2013 NBR 7188: *Live load on highway bridges and footbridges* (in Portuguese). Rio de Janeiro, Brazil: ABNT.

Brazilian Association of Technical Standards 2014 NBR 6118: *Design of concrete structures - Proceeding* (in Portuguese). Rio de Janeiro, Brazil: ABNT.

CEB-FIP 2010. *Model Code: Final Draft*. Lausanne, Switzerland: Fédération Internationale du Betón / International Federation for Structural Concrete (du Béton, Fédération Internationale).

DIN 1072. 1952. *Straßen – und Wegbrücken*. Berlin, Germany: Deutsche Institut für Mormung.

El Debs, M.K. & Malite, M. 2002. A study of the consequences of the traffic of special load vehicles on the highway bridges of the DER-SP. *XXX Jornadas Sul-americanas de Engenharia Estrutural*. Brasília, Brazil.

Grace, N.F. & Jensen, E.A. & Eamon, C.D. & Shi, X. 2012. Life-cycle cost analysis of carbon fiber-reinforced polymer reinforced concrete bridges. *ACI Structural Journal* 109 (5): 105-114.

Higgins, C. & Williams, G.T. & Mitchel, M.M. & Dawson, M.R. & Howell, D. 2012. Shear strength of reinforced concrete girders with carbon fiber-reinforced polymer: experimental results. *ACI Structural Journal* 109(6): 805-814.

Liu, H. & Zheng, J. & Sun, Y. 2011. Theoretical research on ultimate bearing capacity of pier strengthened using carbon fiber reinforced polymer. *Polymers and Polymer Composites* 131(6): 177-182.

Mendes, P.T.C. 2009. *Contributions to a RC bridge management model applied to Brazilian highways network* (in Portuguese) D.Sc. Thesis. São Paulo, Brazil: University of São Paulo.

Mostafa, A.A.B. & Razaqpur, A.G. 2010. Finite element model for predicting post delamination behavior in FRP-retrofitted beams in flexure. *Construction and Building Materials* 131(6): 195-204.

Ramezansefat, H. & Barros, J. & Rezazadeh, M. 2017. A model for the simultaneous prediction of the flexural and shear deflections of statically determinate and indeterminate reinforced concrete structures. *Structural Concrete* 18: 618-633.

Rossigali, C.E. & Pfeil, M.S. & Battista, R.C. & Sagrilo, L.V. 2015. Towards actual Brazilian traffic load models for short span highway bridges. *Ibracon Structures and Materials Journal* 8(2): 124-139.

Vosooghi, A. & Saiid Saiid, M. 2013. Shake-table studies of repaired reinforced concrete bridge columns using carbon fiber-reinforced polymers. *ACI Structural Journal* 110(1): 105-114.

Maintenance, Safety, Risk, Management and Life-Cycle Performance of Bridges – Powers, Frangopol, Al-Mahaidi & Caprani (Eds)
© 2018 Taylor & Francis Group, London, ISBN 978-1-138-73045-8

Influence of arch bridge skewness

A. Outtier, E. Van Puymbroeck & H. De Backer
Ghent University, Ghent, Belgium

ABSTRACT: Designers try to find new ways to make landmark bridges slenderer and distinctive. A new trend for arch bridges is placing the arch not co-linear with the bridge axis, but slightly skew. While visually attractive, this concept introduces a number of design problems which are not normal for arch bridges: the arch becomes subjected to significant out of plane bending moments, a permanent torsional effect develops, hangers are not possible in certain areas because of conflict with traffic and the tied arch concept becomes quite difficult to realize. The aim of this research is to study the skew arch concept using finite element modelling. A parametric study is undertaken to investigate the main design problems and to find an allowable application area in terms of bridge span, bridge deck width and skewness of the arch. Hereby, two different skew arch hanger configurations are considered including also a minimization of the number of hangers.

1 INTRODUCTION

For centuries, bridges have played an important role in the traffic system to allow passage across a body of water, a valley or a road.

The construction material for bridges evolved from timber in the early ages, to stone masonry during the Roman period and the Middle Ages. In those periods, compressive strength of the materials could be relied upon whilst tensile strength could not. Hence, an arch bridge structure was often the logical choice as it transfers the loads towards a horizontal thrust at the abutment by means of compression forces in the arch shape. With the invention of iron during the industrial revolution, larger span bridges became possible containing elements with a significant tension strength.

Nowadays several designs of bridges exist. They vary depending on the nature of the terrain where the bridge is located, the function of the bridge, the required span length, the materials used to build it and the available funds for the bridge construction. As a consequence, a distinction can be made between beam bridges, truss bridges, arch bridges, suspension bridges, cable stayed bridges and movable bridges. Concrete and steel are the most frequently used materials for bridges. Steel is preferred for longer span bridges due to a larger strength to weight ratio compared to concrete.

Over the years, several configurations for arch bridges have been developed. Old arch bridges are associated with fairly massive brickwork structures. In this way, the possibility of tension forces could be minimized. The last century, the use of steel and reinforced concrete allowed more slender and elegant arches. Depending on the position of the deck with respect to the arch and the load transfer from the deck to the arch, different arch type bridges can be distinguished. The deck can run below, through or above the arch. A tied arch can be used to minimize the horizontal thrust forces on the abutment. In arch bridges where the deck runs below a single arch, lateral loading of the arch can be critical for the bridge design. Therefore, the single arch is often split in two arches which are interconnected to get a better resistance against lateral loading.

Designers try to find new ways to make landmark bridges slenderer and distinctive. A new trend for arch bridges is placing the arch not co-linear with the bridge axis, but slightly skew. Besides aesthetical benefits, the skew position makes the single arch more resistant against lateral loading and the arch abutments do not form an obstruction for the road traffic. Nevertheless, while visually attractive, this bridge concept introduces a number of design problems which are not normal for arch bridges: hangers are not possible in certain areas because of conflict with traffic, the tied arch concept becomes quite difficult to realize, the arch is besides axial compression also loaded by significant bending moments and the arch becomes subjected to a permanent torsional effect.

2 STATE-OF-THE-ART

Currently, only a few skew arch road bridges have been constructed. This implies the absence of a large number of studies concerning the skew placement of the arch in single span road bridges.

Most of the bridges are located in the United Kingdom. The two most known projects are the Hulme Arch Bridge in Manchester and the Clyde Arc in Glasgow. According to Warren 2009 and Apostolidis 2011, both bridges form a gateway into the city and thereby symbolize a plan to increase the quality in the neighboring urban environment. The skew placement of the arch results in an asymmetric cable arrangement. These cables generate significant out of plane bending moments in the arch rib. These bending moments are the most determinant factor for the arch design. Therefore, the arch no longer behaves like a conventional parabolic arch which is in pure compression under a uniformly distributed load. Due to the out of plane bending moments, the arch behaves more like a laterally loaded bending member.

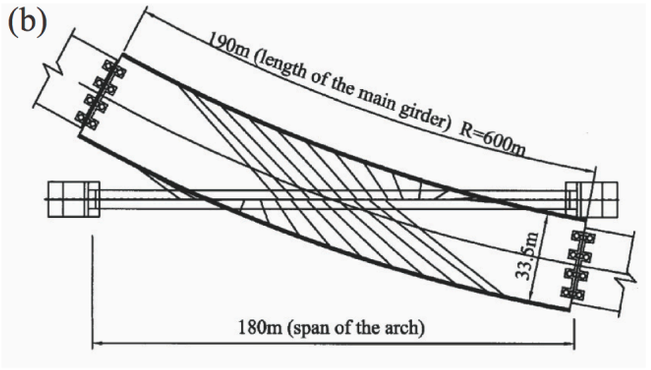


Figure 1. Arch bridge

Qiu et al. 2010 performed a stability analysis of a specific shaped arch bridge (Figure 1), namely a straight arch suspending a curved deck. Therefore, it will exhibit similar properties as a skew placed arch carrying a straight deck. Due to the skew position of the arch compared to the deck, the hangers are placed in a diagonal position contrary to the standard vertical direction in straight arch bridges. They cause large bending moments, compression forces, shear forces and torsion in the arch rib. Nevertheless, the new slanting direction of the hangers tends to resist any deformation of the arch out of its plane and hence increases the structure stability. Similar to straight placed arches, the restraining boundary conditions at the arch spring and the rise-to-span ratio significantly influence the overall structural stability. The stability coefficients for fixed arch springs are more than twice the coefficients for pin-ended arch springs. The stability is found to decrease drastically for very small or large rise-to-span ratios. An optimal rise-to-span ratio for the considered bridge is found to be about 0.37. They noted that this value is larger than the optimal ratio for normal, non-skewed arches analyzed in other studies. The more the design of the bridge deviates from a rise-to-span ratio of 0.37, the less reliable the bridge design, Qiu et al. 2010.

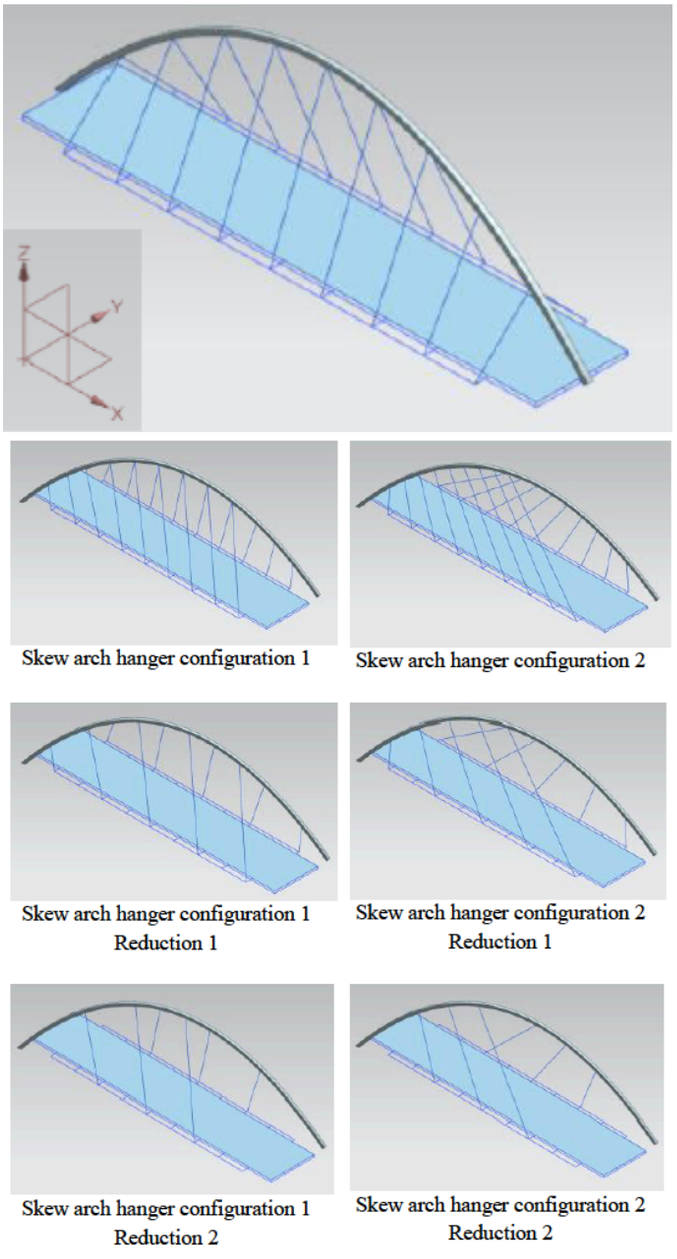


Figure 2. Straight arch bridge model and the different variations

3 REFRENCE BRIDGE MODELS

3.1 *Design*

The aim of this research is to study the skew placement of arches for single span road bridges using finite element modelling. Therefore, a parametric study is undertaken to determine the main design problems and to find an allowable application area

in terms of bridge span, bridge deck width and skewness of the arch. The investigated ranges for each parameter are based on existing skew placed arch bridges. All the results are compared to a straight arch bridge configuration (Figure 2) with the same bridge length, deck width and number of hangers as the skew arch bridges.

When the arch in the straight arch model is placed in a skew position the hangers would come in conflict with traffic. Hence, the hanger configuration for straight arch bridges is not practically applicable for skew arch models. Therefore, for the skew arch bridge concept, appropriate cable configurations need to be developed. Hereby, the cables inclining across the bridge deck have to provide enough headroom above the carriageway in order to allow the largest design vehicles to pass safely below the hangers. Therefore, a minimum free height of 5 m is assumed, based on guidelines in EN 1991-1-7. Even with special developed hanger arrangements, outriggers for hanger connection and pedestrian provisions are a necessity to avoid vehicle-cable impact. It can be concluded that the required clearance has a significant influence on the overall design of skew arch bridges. It imposes criteria to both the bridge dimensions as to the hanger configuration. Therefore, it indirectly has an effect on the internal force distribution and hence on the structural behavior. A hanger configuration which limits the out of plane bending, the determining design factor for skew arch bridges, has a disadvantageous effect on the provided clearance and vice versa. This resulted in two configurations: skew arch hanger configuration 1 inducing minimal bending moments in the arch and skew arch hanger configuration 2 providing the largest possible vehicle clearance (Figure 2). Based on aesthetical preferences the number of hangers is often chosen as small as possible. Therefore, the effect of reducing the number of hangers in configuration 1 and 2 is investigated (Figure 2). A second reduction in the number of hangers is also considered, as for the removed outer hangers often problems arise with vehicle-cable conflict.

The skew arch reference bridges have a span length of 100 m, an 18 m wide deck and an arch skewed over 16° with respect to the bridge axis. The arch has a parabolic shape and its crown is located 30 m above the deck. The arch has a square box section with a side of 1 m and a thickness of 50 mm. The arch is modelled using 2D elements and is considered fixed at its ends. The deck is made up out of a 20 cm thick concrete layer supported by longitudinal and transverse steel girders. The four longitudinal girders are spaced 6 m while a transverse girder is foreseen each 10 m. The girders are modelled as I profiles with a height of 1500 mm, width of 750 mm and web and flange thicknesses of 50 mm. The transverse girders extend 2 m outwards of the longitudinal girders to provide a connection with the hangers. To avoid locally high deformations at the connection, the outriggers are interconnected by 500 mm diameter tubes with a thickness of 50 mm. The bearings at the bridge deck ends restrain vertical motions. Moreover, at one side also longitudinal motions are resisted. The deck is fixed in the transverse displacement direction at one of the outer points for each of the two edge transverse girders. The hangers are implemented as rod elements without compressive strength. They have a diameter of 100 mm and a tensile strength of 1500 N/mm². Each time a cable is connected to the arch, a diaphragm is provided in the arch cross section. The steel for the deck and arch is S355 and the concrete used in the deck has a quality of C40/50.

3.2 *Analysis of the reference models*

In comparison to straight arch bridges, uniform loads in combination with a skew arch position and skew arch hanger configuration lead to out of plane bending moments in the arch rather than the development of axial compression forces. Hence, the arch is used more as a beam then as an arch. Hereby, the self weight of the bridge components and the uniform traffic loads dominate the bridge design. The presence of significant bending moments illustrates that the arch is not used efficiently in skew arch bridges. Based on the occurring stresses and deformations, skew arch configuration 1 and 2 use the arch material less efficient than a straight arch model, respectively with a factor 1.35 and 3.

The most loaded arch section is located at the crown for the reference model with configuration 1. On the other hand, it is positioned horizontally a distance 0.33 times the span length from the arch ends when configuration 2 is considered. An opposite behavior is observed for the critical deck section. The middle of the deck deflects the most for configuration 2, while for configuration 1 the critical deck section is situated 10% of the span length more towards the abutment.

The arch behavior is determined by the X, Y and Z force components that each cable transfers to the arch. The magnitude of each component is determined by the geometric arrangement of the cables and by the load distribution on the deck. Hence, the bridge design is rather limitedly affected by the skew arch position but by a larger extent determined by the hanger configuration which accompanies the skew arch. The Y and Z force component create respectively out and in plane bending moments. As the cables insert their forces into the bottom plate of the box section, the resulting force component works with some eccentricity with respect to the center of gravity of the arch cross section. This develops some torsion in the arch. The arch in the reference model with skew arch hanger configuration 2 is subjected to at least three times larger in plane, out of plane and torsional moments than the arch in configuration

1. Hereby, the out of plane bending moments dominate the design of the arch. The importance of the out of plane bending moments is much more pronounced for the arch in the model with configuration 2. While the arch for the skew arch configuration 1 remains nearly completely in compression, the arch for the skew arch configuration 2 is subjected to significant tensile forces. As the out of plane bending moments are the critical internal forces, the lateral deformations are the dominant deflection component. Skew arch bridges with configuration 1 are much more resistant against asymmetric mobile loads than straight arch bridges. The arch deflections under asymmetric loads in the reference model with skew arch hanger configuration 1 and 2 are respectively 0.5 and 0.85 times the deformations in straight arches. As a consequence, skew arch bridges work, based on the arch deformations, more efficient than straight arch bridges if the proportion of the live to dead load is rather large. This is because the live load can induce significant load differences on the two deck halves.

It can be concluded that configuration 1 is a more structurally efficient skew arch bridge concept than configuration 2. Nonetheless, configuration 2 is less prone to vehicle-cable conflicts than configuration 1 and therefore corresponds to less stringent requirements to provide enough clearance.

4 PARAMETRIC STUDY

When a bridge parameter is investigated, all the other parameters are considered to be fixed to the corresponding value in the reference bridge design. In this way, all the resulting changes in bending moments, stresses and deformations are completely dedicated to that single parameter adaptation.

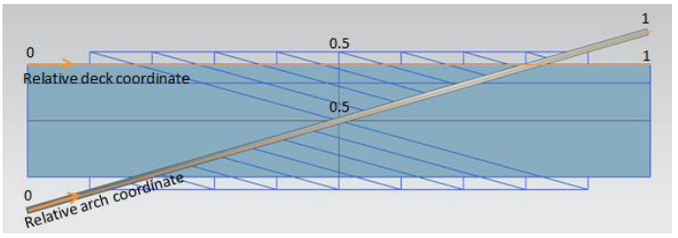


Figure 3. Definition of relative arch and deck coordinate

4.1 *Influence of the span length*

As the bridge span increases, the distance between two successive hangers enlarges, the cable inclination changes, the rise-to-span ratio diminishes, the ratio of the lateral distance between the arch abutments and the bridge length decreases, the relative stiffness of the deck and arch reduces, the application area of the mobile loads enlarges, the effect of the dead load increases and the clearance below the hangers reduces. As a consequence, the bending moments increase quadratic when the bridge becomes longer. As the span length increases, the relative importance of the out of plane bending moments compared to in plane bending reduces. This indicates a more efficient use of the arch structure.

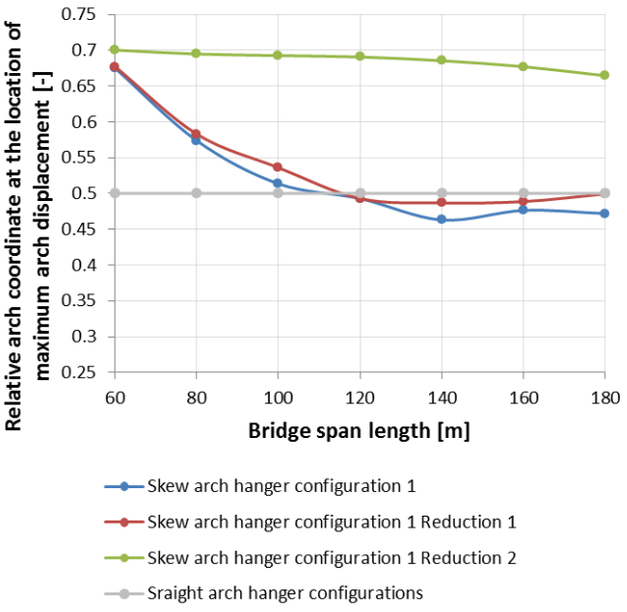


Figure 4. Relative arch coordinate of maximum arch displacement in configuration 1 for varying span length

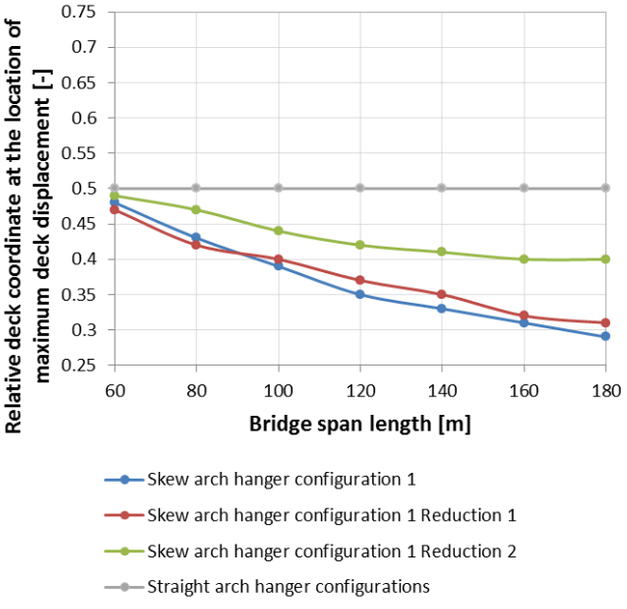


Figure 5. Relative deck coordinate of maximum deck displacement in configuration 1 for varying span length

For longer bridges with configuration 1, the critical arch section shifts horizontally from a location 0.3 times the span length separated from the abutment towards the arch crown. The critical deck section shifts from the middle of the deck towards a distance 0.3 times the deck length from the deck ends. The shifts are illustrated in Figure 4 and Fig-

ure 5, respectively for the arch and the deck. The graphs display a relative coordinate which is defined in Figure 3.

In the reference design with configuration 2, the critical arch and deck section shift from the same original sections to respectively 0.33 and 0.45 times the bridge length from the abutment.

For the reference model with varying span length, the out of plane bending moments show a maximum value for the model with the skew arch hanger configuration 1 with a deck length of 160 m (Figure 6). To avoid failure of the reference bridge, design the span length has to be limited to 120 m for the model with skew arch hanger configuration 1. Nevertheless, the length should be below 100 m to reduce the risk of vehicle-cable conflict in the reference model. For the reference bridge design with skew arch hanger configuration 2, the span length has to be limited to 70 m in order to avoid yielding of the arch. The difference in behavior between configuration 1 and 2 reduces as more hangers are left out of the model.

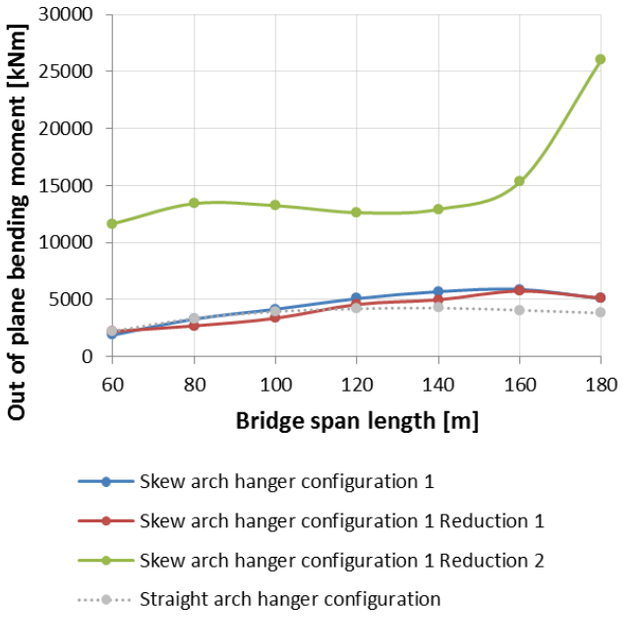


Figure 6. Out of plane bending moments in arch with hanger configuration 1 for varying span length

For all the investigated span lengths for the model with skew arch hanger configuration 1, the first reduction in number of hangers has only a limited influence on the bending moments (Figure 6), stresses, deformations and hence on the global arch behavior. The second reduction for the number of cables on the other hand has a much more pronounced influence (Figure 6), leading to unacceptable arch stresses and deck deformations. The outer cables, which are removed for the second reduction in number of hangers, tend to restrain lateral arch deflection and only limitedly affect the vertical arch motion. It should be noted that although the most outer cables play an important role to minimize the deformations and stresses, they cause problems with respect to clearance for driving vehicles on the other hand.

Contrary to the results for configuration 1, a first reduction of the number of hangers in configuration 2 causes already a significant increase in critical bending moments in both the arch (Figure 7) and the deck.

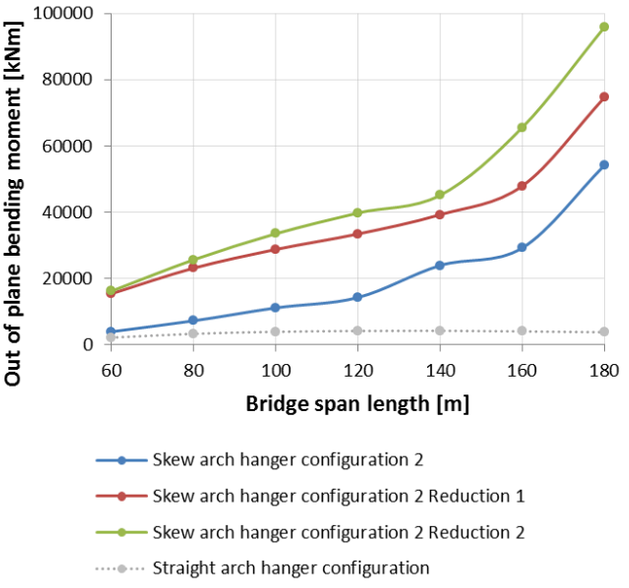


Figure 7. Out of plane bending moments in arch with hanger configuration 2 for varying span length

Similar observations about minimizing the number of hangers in configuration 1 and 2 are valid for changing the deck width or the angle of skewness.

4.2 *Influence of the deck width*

Compared to the modification of the span length, a more linear increase in bending moment is observed when the deck width is enlarged. As the rise-to-span ratio does not change for varying deck widths, the relative importance of the out of plane bending compared to the in plane bending moment remains large for each deck width. Hence, out of plane bending remains determining for the bridge design.

For increasing deck widths, the position of the critical arch and deck sections respectively shifts from 0.25 and 0.3 times the span length distanced from the deck extremity towards the center of the bridge. On the other hand, for each investigated deck width, the most loaded arch and deck sections in the reference models with skew arch hanger configuration 2 remain respectively 0.3 and 0.5 times the bridge length horizontally separated from the abutment.

When varying the deck width, or span length, the bending moments in both the arch and the deck are much more critical when hanger configuration 2 is

considered compared to the use of hanger configuration 1. To avoid yielding of the steel in the arch, the bridge deck width has to be limited. For the geometry and arch thickness considered in the reference model, the deck width has to be below 21 m for the models with skew arch hanger configuration 1 or configuration 1 reduction 1 and below 10 m for the models with skew arch hanger configuration 2 or configuration 2 reduction 1. Nevertheless, to prevent vehicle-cable conflict, the deck width should be limited to 18 m in the model with configuration 1. An upper boundary of 14 m and 6 m applies for the model with skew arch hanger configuration 1 reduction 2 and skew arch hanger configuration 2 reduction 2 respectively.

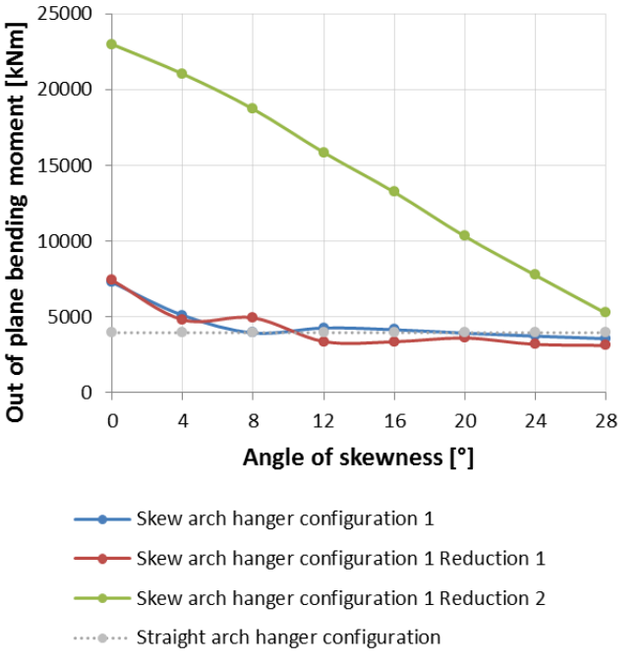


Figure 78. Out of plane bending moments in arch with hanger configuration 1 for varying angle of skewness

4.3 *Influence of the angle*

When changing the angle of skewness, nearly all the changes in the arch and deck behavior can be assigned to the modification of the cable inclinations and hence to the force transfer by the hanger arrangement. In the reference models with skew arch hanger configuration 1 and reduction 1, the arch is used most efficiently for angles of skewness larger than 12°. Hereby, an upper boundary of 25-30° applies for practical and realistic applications. Nevertheless, for angles larger than 16°, the minimum required vehicle clearance is no longer present in the reference model. In reality, this translates to arch abutments which will be located next to the bridge deck, indicating that the angle of skewness is often related to the deck width. For angles larger than 12°, the out of plane bending moments are minimal (Figure 8) as are the resulting maximum arch and deck deformations. Nevertheless, the out of plane bending moments remain determining in the bridge design and the contribution of the axial compression in the force transfer through the arch remains limited. For angles in between 12° and 16°, the design out of plane bending moment is similar to the design moment for straight arch bridges with the same dimensions as the reference models (Figure 8).

For the range 12-16° of skewness angles, the location of the critical arch section is situated near the arch crown. This is because the critical section shifts in between an angle of 8° and 12° horizontal from 0.25 to 0.5 times the bridge length separated from the arch end. This is observed in Figure 9.

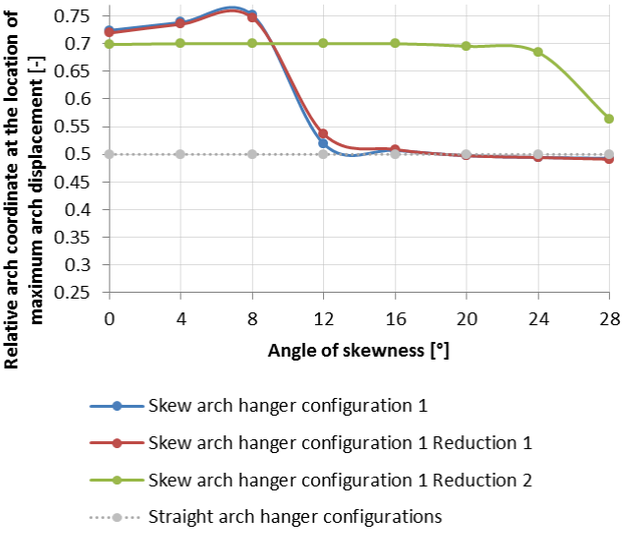


Figure 9. Relative arch coordinate of maximum arch displacement in configuration 1 for varying angle of skewness

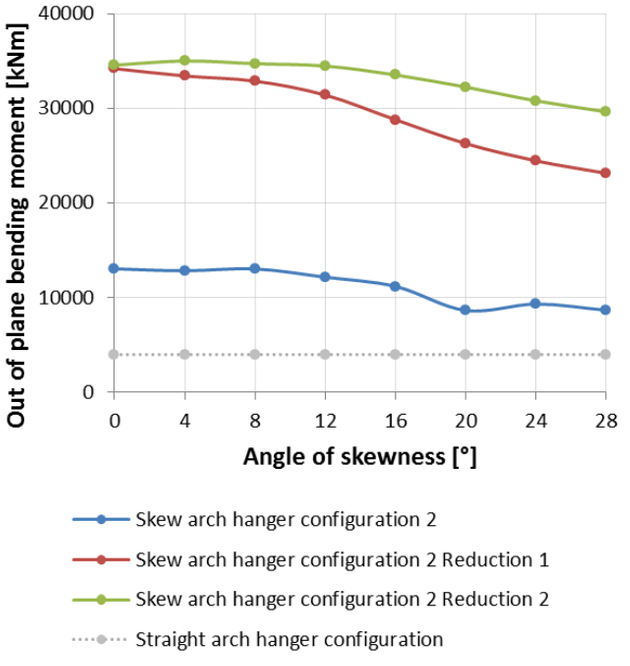


Figure 10. Out of plane bending moments in arch with hanger configuration 2 for varying angle of skewness

For angles in between 6° and 28°, the critical deck location shifts from the bridge center towards a distance 0.3 times the span length from the abutment.

For the bridge structure where the number of hangers is reduced a second time, the optimum angle of skewness lies beyond practical and realistic angles of skewness (>30° in Figure 8).

In comparison to configuration 1, no optimum angle of skewness exists for bridges with skew arch hanger configuration 2. For increasing angles of skewness, the inclination of the cables becomes more and more advantageous. Hence, the largest practically applicable angle of skewness that is still realistic should be chosen in order to minimize the bending moments (Figure 10).

Nonetheless, the bending moments in configuration 2 remain always a factor 2-3 larger than the design moments in arrangement 1. Consequently, configuration 2 is at least a factor 2-3 less efficient compared to straight arch bridges. As the arch abutments are in reality often located immediately next to the bridge deck, configuration 2 can be used for relatively wide bridges compared to the span length. The reason is that for those bridges the angle of skewness of the arch is large. For large but realistic angles of skewness, the critical arch and deck section are located at a horizontal distance of 0.33 and 0.45 times the span length from the abutment.

5 BUCKLING ANALYSIS

In comparison to straight arch bridge models which buckle in an out of plane sine wave due to large axial arch compression, no global arch buckling is observed for skew arch bridges. The reason is that no relevant load combinations exist which load the arch mainly in axial compression. Under the effect of the deadweight and uniform mobile loads, the arch is subjected to significant in and out of plane bending moments. At the locations where bending moments are maximal, the arch has the largest deformations and is subjected to the most severe curvature. Due to this maximal arch curvature, critical compression forces develop within the webs of the arch box section. Eventually this compression can induce local plate buckling of a web of the arch box. The most efficient way to prevent the local plate failure is increasing the shell thickness of the arch or adding stiffeners. The difference in buckling behavior between the models with skew arch hanger configuration 1 and 2 and the effect of changing the bridge span length, bridge deck width and angle of skewness is determined by the difference in magnitude and location of maximal arch deformations. For the reference skew arch models 1 and 2 from Figure 2, the loads in the critical load combination can increase respectively with a factor 12.81 and 11.25 before inducing local plate buckling. Hence, buckling will only be observed when the stress levels in the arch steel have already largely exceeded the yield strength. This indicates that buckling is not a stringent requirement for the design of skew arch bridges. Consequently, no sudden failure due to buckling is expected. (Figure 11)

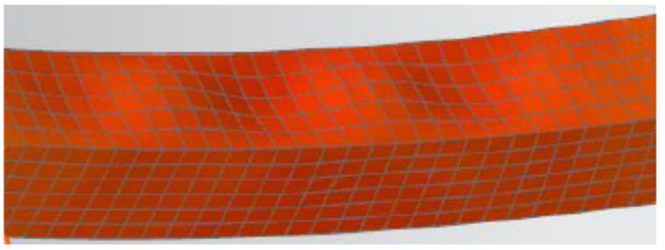


Figure 11. Local plate buckling in a web of the arch box

6 CONCLUSIONS

Skew arch bridges deform less than straight arch bridges under asymmetric live loads and can therefore be useful when the live to dead load ratio is large.

Furthermore, it can be concluded that a skew arch bridge with hanger configuration 1 is structurally more efficient than a skew arch concept with cable configuration 2. Nevertheless, the useful deck width in configuration 1 is lower than for configuration 2 due to vehicle-cable clearance requirements.

In bridges with skew arch hanger configuration 1, the number of hangers can be quite low without inducing more stringent design conditions than for a bridge with a lot of cables.

In order to use the bridge material most efficiently, the angle of skewness should be at least 12° when opting for hanger configuration 1 or should be designed as large as possible for a bridge with hanger configuration 2. For both bridge concepts an upper boundary in the range of 16°-30° is assumed for practical and realistic applications. Nevertheless, for configuration 1 the upper limit is often induced by vehicle clearance regulations. Practically, arch abutments next to the bridge deck form a good design.

7 REFERENCES

Warren, L.B. 2009. A critical analysis of the Hulme arch bridge, Manchester. In Proceedings of Bridge Engineering 2 Conference 2009, University of Bath, UK.

Apostolidis, C. 2011. A critical analysis of the Clyde arc bridge. In Proceedings of Bridge Engineering 2Conference 2011, University of Bath, UK.

Qui, W.-L., Kao, C.-S., Kuo, C.-H., Tsai, J.-L.n& Yang, G. 2010. Stability Analysis of Special-Shape Arch Bridge. *Tamkang Journal of Science and Engineering* 13(4): 365-373.

European Committee for Standardization. (2006). *Actions on structures - Part 1-7: General actions – Accidental actions*. Eurocode 1, Brussels

Maintenance, Safety, Risk, Management and Life-Cycle Performance of Bridges – Powers, Frangopol, Al-Mahaidi & Caprani (Eds)
© 2018 Taylor & Francis Group, London, ISBN 978-1-138-73045-8

Ensuring safety and assessment of life-cycle costs using SHM for concrete bridges

J. Creighton & S.N. Kazi
Mageba (Australia) Pty. Ltd, Sydney, Australia

K. Islami
Mageba SA, Bulach, Switzerland

ABSTRACT: The application of Structural Health Monitoring (SHM) systems to structures has proven to provide key performance statistics of bridges post-construction, which was not previously possible. Analysis of statistics logged by SHM is very useful in understanding the behaviour of these structures under various sets of circumstances.

This paper discusses a variety of recently implemented SHM systems on concrete bridges. Implementation of SHM systems greatly reduces ambiguity in relation to material properties and structural capacity, and optimises inspection and maintenance programmes. The versatile range of applications presented was developed with the input of structure owners and design engineers, and an in-depth case study on concrete box girder bridges in a subsidence area is included.

Both static and dynamic approaches were adopted, and they successfully demonstrated the necessity and ease of use of such systems. The immense gains in efficiency that SHM systems offer over alternative manual monitoring methods are also discussed.

1 INTRODUCTION

The ability to observe, monitor and understand the behaviour of built structures is paramount in order to avoid critical or perhaps even catastrophic occurrences. As such, there is a definite need for the implementation of technologies that enable key stakeholders, whether they be asset owners or engineers, to examine structures in real-time and hence be able to respond efficiently and effectively in the event that undesirable situations transpire.

Structural Health Monitoring (SHM) systems enable physical parameters of interest to be measured and analysed, with the intention of assessing the actual condition of a structure. These systems utilise advanced electronic devices in the form of measuring instruments (sensors and cables), data collection units and data evaluation software to continuously record both local and global structural properties, and ultimately provide the end user with the information that they require to make the assessment.

The finite element method (FEM) approach has been employed successfully in recently designed structures, and enables the properties of the materials used for construction to be fully exploited. Hence, by undertaking comparison between the design expectations and actual performance of a structure, one can be assured that it is functioning satisfactorily. However, it is evident that many existing structures presently in service were designed before the implementation of current design standards and specifications, and hence there is an obligation to carry out the necessary work to ensure that their performance fulfils the requirements of today. This becomes even more important when considering the general trend of ever-increasing vehicle loads and traffic volumes over time.

This paper will examine the safety advantages and life cycle optimisation opportunities that are made possible by SHM systems. Two key case studies will be presented to demonstrate the benefits for both existing and recently-constructed concrete bridges.

2 ENSURING SAFETY OF CRITICAL INFRASTRUCTURE - COMPARISON OF SHM WITH MANUAL INSPECTION & MONITORING METHODS

Bridges are undoubtedly crucial pieces of infrastructure responsible for the safe passage of immeasurable numbers of people around the world every day. Due to this, there is an inherent obligation to monitor the integrity of these structures, as unavoidable deterioration due to external influences combined with the potential effects of insufficient

design can certainly compromise their safety, stability and usability.

Asset management teams have the responsibility of performing routine inspections of bridges to observe and report their condition, and consequently identifying necessary maintenance or repair actions. In Australia, this is typically managed by the state road authorities. The frequency and degree of inspections would generally be dictated by the following factors at minimum:

- Previously observed and reported structural condition
- Complexity of the structure
- Environmental surrounds, which may result in accelerated deterioration; for example, the potential for subsidence described in Section 3 of this paper for the Hunter Expressway Bridges

Some questions that could be asked of manual inspection and monitoring regimes are:

- Is the correct amount and type of data being gathered?
- Is the data being processed and output in a way that is conducive to effective maintenance and remediation strategies?

Whilst contemplating the above questions, it is also important to note that the cost and time investment required to carry out manual inspections increases significantly when a structure is located in a remote or difficult-to-access place. The Ponte Nanin bridges are situated near the town of Mesocco in the Swiss Alps, a region of relatively undeveloped rugged terrain, as shown in Figure 1. Modification work was undertaken on these bridges in 2004 to increase their load capacity, which was achieved by adapting the bearings and pier-to-deck connections. There was an inherent requirement to deliver continuing validation that the revamped design of the structure and its resulting performance was acceptable. Due to the isolated location of the bridges, a permanent automated monitoring system was selected to accomplish this (Moor et. al., 2013).

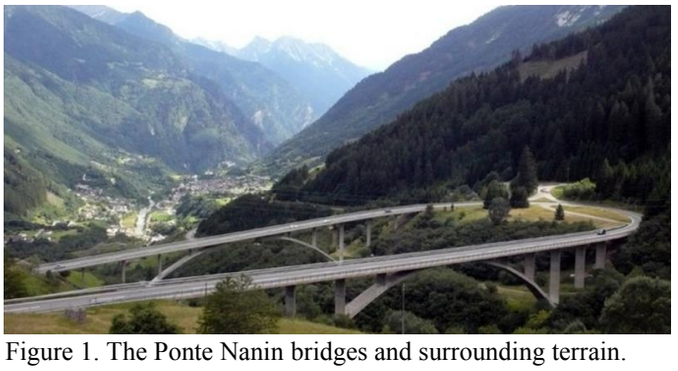


Figure 1. The Ponte Nanin bridges and surrounding terrain.

In Figure 2, a diagram illustrating the simplified process of data acquisition, analogue to digital conversion, transmission to the monitoring station and finally receipt by the end user is provided.

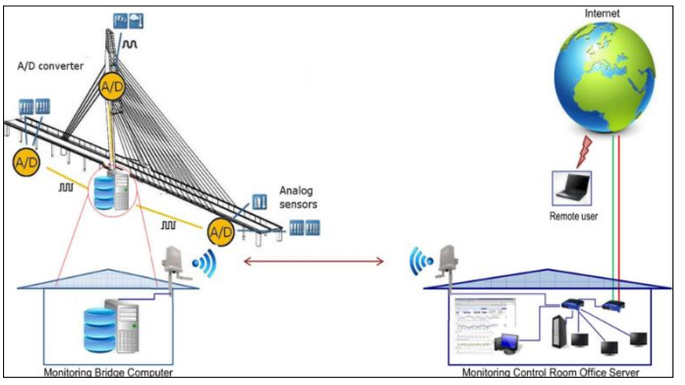


Figure 2. Data acquisition scheme used for SHM systems

Data is collected by a range of sensors and conveyed by the SHM system's computer to a monitoring server, from which a user can view information via their personal computer or mobile devices. From a flexibility perspective, SHM systems have much to offer. The reduced requirement for physical inspection has a positive effect on safety and costs over the life of the structure.

The SHM system for Ponte Nanin was designed to function under the constraints imposed by the bridges' site, namely the non-existence of electricity and telecommunications systems. A solar panel was employed to deliver power to the monitoring system, as shown in Figure 3.



Figure 3. Solar panel of the Ponte Nanin monitoring system.

A low-frequency solution was adopted in order to provide adequate information whilst working under the aforementioned limitations. Gathered data is transmitted to the user via the mobile telephone network. If necessary, the user can adjust the sampling rate from the standard 15 minute frequency to provide more information as required. The parameters measured for these bridges consist of:

- Expansion joint movements
- Bearing loads
- Temperature (ambient and structural)
- Humidity

Expansion joints and bearings are some of the most often overlooked yet critical components of a bridge. Bridges are dependent on the performance of expansion joints to create a safe trafficable riding surface, and on bearings for transferring loads, movements and rotations from the superstructure to the substructure. If the functionality of a bearing is impeded for any reason, its inability to transfer loads, movements and rotations would result in accumulation of forces at some point in the surrounding structure, which could result in the onset of major damage and hence compromise the safety of the structure and its users (Islami et. al., 2016).

The Ponte Nanin bearings feature pressure sensors, which enable the SHM system to calculate the loads sustained due to the forces imposed by the bridge deck. The motivation for utilising these monitoring devices was the need to understand the change in load paths caused by the structural modifications made to the bridges, and hence to certify that the actual behaviour post-modification met design expectations. An image of the bearing monitoring setup is given in Figure 4. If load measurements were to be taken manually instead of via automated monitoring, data would only be available for specific points in time, the accuracy of the measured data would be hard to verify, and therefore it would be much more difficult to gain confidence in the performance of the structure and the bearings. Additionally, the need to make multiple journeys to manually inspect the structure would definitely contribute to increasing its life-cycle costs.



Figure 4. Bridge bearing capable of load measurement.

The data records for the Ponte Nanin Bridges over a period of approximately 9 years are presented in Figure 5.

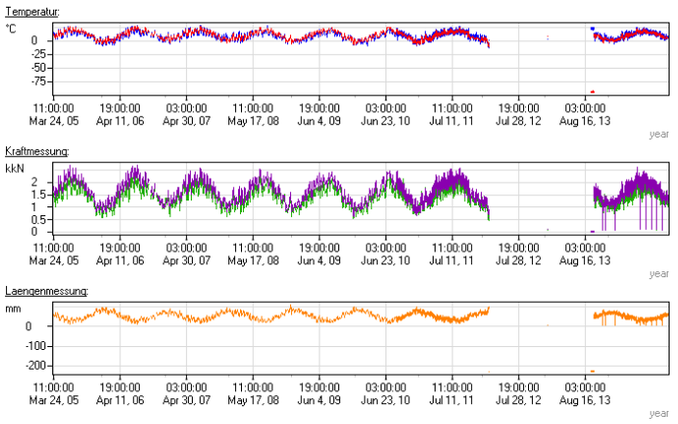


Figure 5. Temperature, bearing loads and expansion joint movements from a period of approximately 9 years.

The forces recorded by the bearings are seen to correlate reasonably well with the temperature profile. That is, the highest loads are experienced at the highest temperatures, and vice versa. The SHM software allows graphs to be generated to illustrate the relationship between two variables of interest, allowing conclusions to be drawn about the behaviour of the structure. In the case of force and temperature, force is a measured variable and temperature is an influencing variable. This is shown in more detail in Figure 6. A linear relationship between these two variables is apparent.

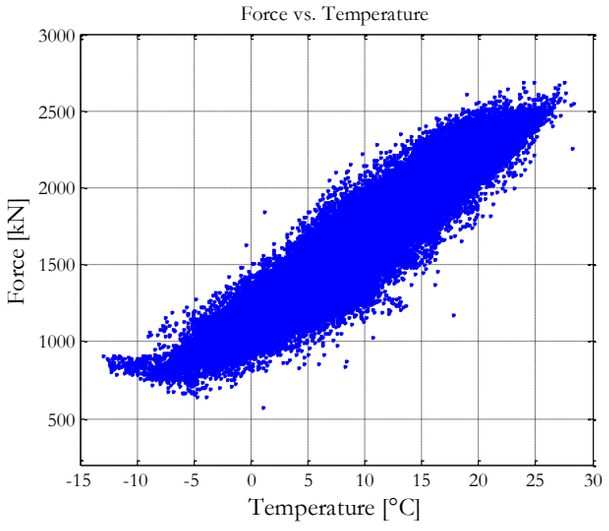


Figure 6. Plot of force measured in bearings vs. temperature.

In Figure 7, the relationship between displacement of the structure at the expansion joints and temperature is shown. It can be seen that the bridge experiences maximum longitudinal displacement (deck contraction) at the lowest temperatures, which fits well with anticipated behaviour.

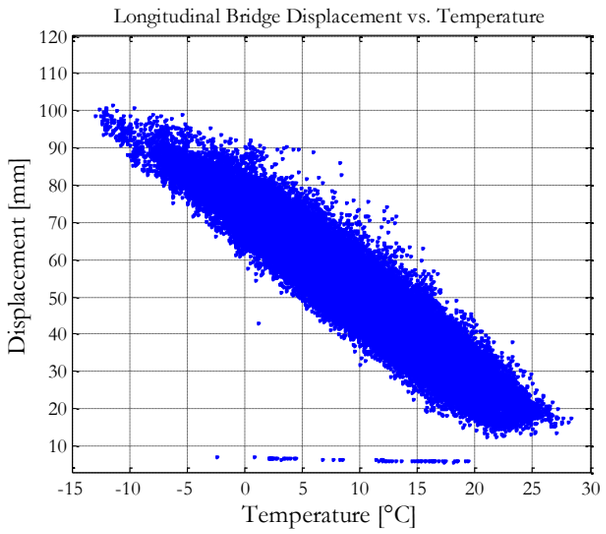


Figure 7. Plot of longitudinal displacement vs. temperature.

From an analysis of the output data from the SHM system presented in Figures 5-7, the user can make judgements regarding structural performance and determine whether any corrective actions are required. If the data shown here was to be collected via manual monitoring and measurement methods, the following points would be apparent:

- Manual setup of the measuring equipment would be time-consuming and cumbersome
- Access to the relevant parts of the structure, for example under the bridge deck to measure bearing loads, would be difficult and potentially dangerous to the inspection team
- Accuracy of data collected via manual means is dependent on the inspector's experience and proficiency, and as such may be questionable. This can result in subjective assessments, which are not useful for proposing efficient maintenance measures
- Manual inspection and monitoring provides data at a discrete point in time, whereas automated monitoring provides continuous data, making it easier to identify and track abnormalities in the performance of the structure over time

The intention of this case study is not to discount the need for physical inspection and monitoring of structures, but rather to demonstrate that a correctly designed SHM system can offer many benefits to the user, by providing objective and accurate information in an efficient manner.

An optimum duration of frequency for determining the condition of bridges can be reached through the combined use of monitoring and conventional inspections (Wenzel, 2008). This brings together the precise quantitative data delivered by automated monitoring and the qualitative data obtained by visual and physical inspection of bridge elements. Thus, with the ability to increase the safety of a structure and its users, automated monitoring systems shall complement and augment the standard inspection practices followed by asset owners.

3 ASSESSMENT OF LIFE-CYCLE COSTS

Bridges are long-term investments that will inevitably require ongoing expenditures in order for them to remain in service. A key challenge for asset managers is to determine the most cost-effective way in which to achieve this (Hawk et. al., 2003). In Figure 8, the relative distribution of costs for a bridge is shown, categorised into the five key areas of design, construction, maintenance, rehabilitation, and user costs (due to diversions, traffic congestion etc. while maintenance or renovation work is carried out).

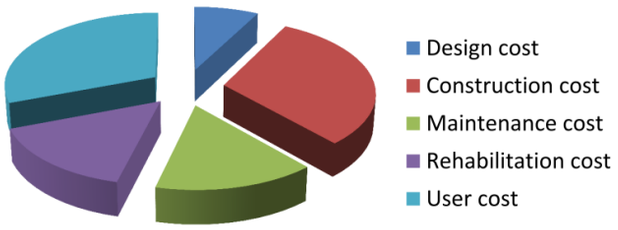


Figure 8. Cost distribution graph for a typical bridge.

From Figure 8, it is evident that the combined maintenance and rehabilitation costs for a bridge comprise approximately 40% of its overall cost. This figure is vast, especially when considering the known magnitude of bridge construction costs (typically in the tens to hundreds of millions of dollars). Therefore, any opportunity to reduce maintenance and rehabilitation costs would be highly advantageous.

The use of SHM systems can result in substantial reduction of life-cycle costs associated with maintenance and rehabilitation, and hence optimisation of service life for a given structure. By providing precise up-to-date information related to present condition, the user is able to more efficiently deal with issues before they become problematic and require exhaustive remediation.

Additionally, the data collected by automated monitoring systems can be input back into statistical deterioration models to provide a more accurate prognosis of the structure's future requirements (Cho et. al., 2007). This allows for more effective planning and scheduling of upcoming maintenance activities.

In Figure 9, a general depiction of the comparison of life-cycle costs over a 50-year period for structures with and without monitoring and maintenance is presented.

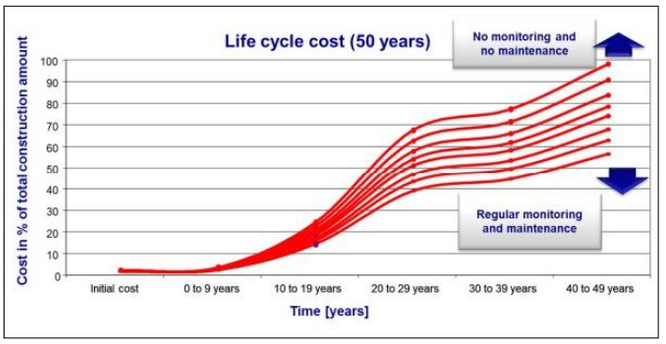


Figure 9. Comparison of life-cycle costs over a 50-year period.

It can be seen that over time, the difference in life cycle cost (expressed in Figure 9 as percentage of total construction amount) between unmonitored and monitored structures increases steadily. After 50 years, the life-cycle costs for structures with no monitoring or maintenance are approximately 80 percent higher than their counterparts. Based on this relationship and considering that bridges are often designed for a service life of 100 years or more, the importance of SHM systems becomes apparent.

Seven concrete box girder bridges of varying lengths (ranging from 155m to 337m) were constructed as part of the Hunter Expressway project in New South Wales and opened to traffic in 2014. Views of the bridges are shown in Figures 10 & 11.


Figure 10. Underside views of some of the seven bridges with SHM systems installed.

Located approx. 170 km north of Sydney in a mining region, the risk of settlement due to ground subsidence prompted the use of SHM systems on these bridges (Islami et. al., 2014). An aerial view of the terrain surrounding the structures is presented in Figure 11.


Figure 11. Topography surrounding the Hunter Expressway, a region with potential for subsidence due to mining activities.

Bridges form critical links as part of the transport infrastructure network. If any structural elements are damaged, there will likely be severe consequences which will always result in amplification of costs, to the detriment of the asset owner and users. The potential settlement and resulting undesirable movement of structural elements on the Hunter Expressway Bridges could require costly rectification measures post-construction, with the likelihood that the bridge would have to be closed to traffic to undertake these works. This would pose additional direct financial costs for the labour, equipment and machinery required, as well as economic and social costs to the local community.

The use of automated structural monitoring was deemed to mitigate these risks significantly, with the ability to inform the relevant personnel of any unexpected movements at the exact time of their occurrence. This provides greater control over the risk management of the structure without the need for regular engagement of inspection teams, which would allow maintenance and/or remediation to be carried out as and when required, thus minimising life-cycle costs.

The monitoring systems utilised on the Hunter Expressway Bridges are depicted in Figure 12, and were designed to capture the following parameters of interest:

- Settlement of piers with respect to the abutments
- Settlement of abutments
- Movement of the abutments with respect to the longitudinal and transverse axes of the structure
- Temperature at piers and abutments

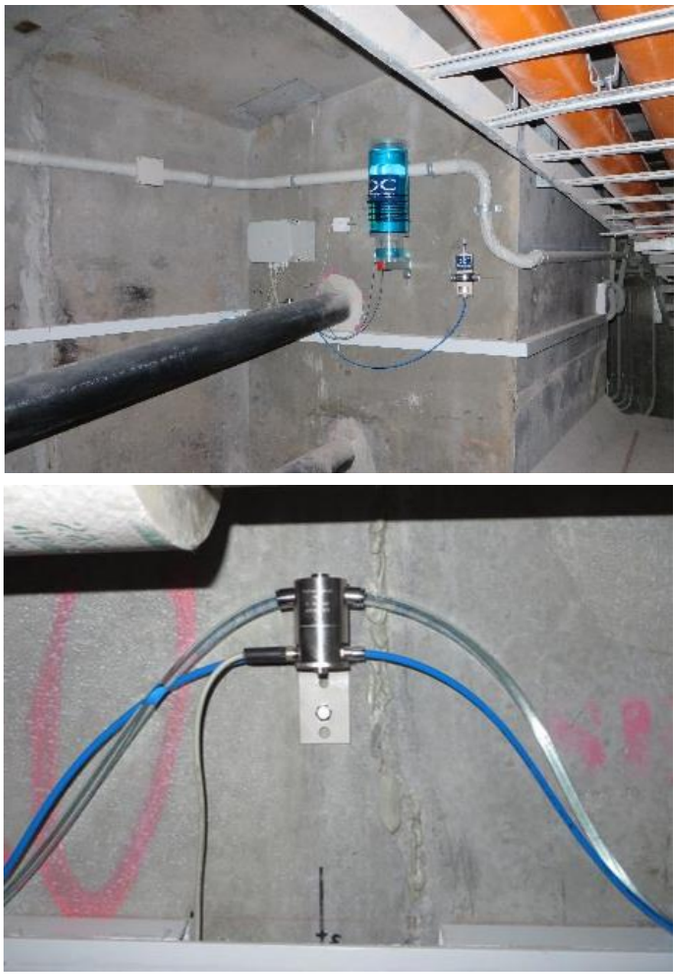


Figure 12. Close-up view of SHM system components.

The data collected by the SHM system is transmitted in real-time to the "monitoring cockpit" which is accessible remotely via the Internet. This means that data can be viewed at any time and from almost any location. From this platform, the user is able to analyse the actual values measured by each sensor on the given structure, which are able to be compared with minimum and maximum permissible values to give an indication of current performance. There are also "alarm values" programmed to alert the user of atypical behaviour. This functionality enables the user to make an informed decision about the necessity to implement further inspection, maintenance or repairs. A sample of the monitoring cockpit for the Hunter Expressway Bridges is shown in Figure 13.

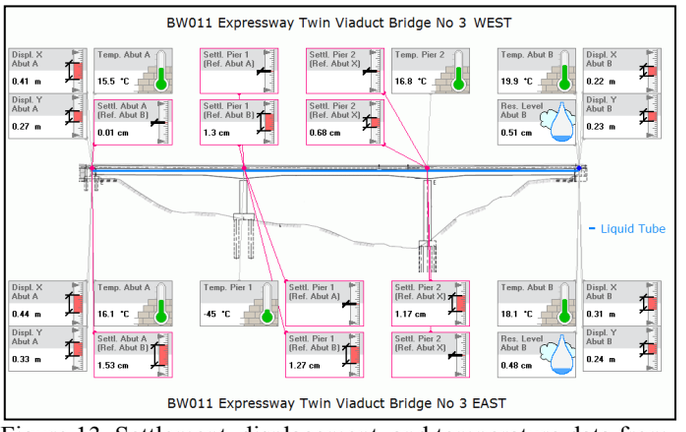


Figure 13. Settlement, displacement, and temperature data from the east and west sections of one bridge – Cockpit view.

From Figure 13, the user is able to gain an insight into the parameters of interest for this structure. The measured values are shown alongside the location of the respective sensors for data collection on the bridge, making it easy for the user to isolate the particular values that they are interested in observing. A quick glance would be sufficient to indicate that settlements, displacements and temperatures are within acceptable limits. The cost and inconvenience of measuring these values at the multiple relevant locations using alternative manual methods of monitoring would be significant for a single inspection, let alone for regular inspections. This emphasises the efficiency gains that SHM systems can offer to users.

All data and tables generated by the SHM system can be downloaded for further analysis. Data can be exported as a CSV file to enable processing, manipulation and presentation to achieve required outcomes, as shown in Figure 14.

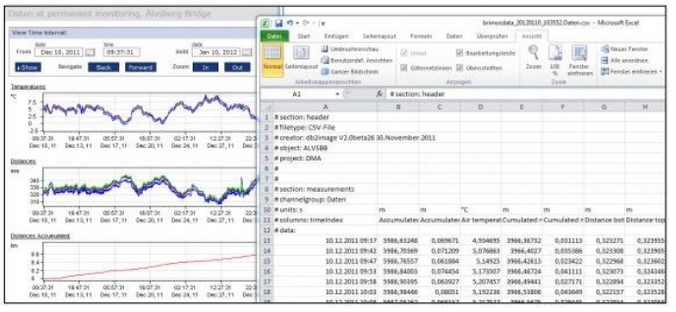


Figure 14. Data presented in CSV form.

Figure 15 shows that there is a relationship between environmental factors (in this case temperature) and the settlements experienced by the piers. The largest settlements measured by the SHM system occurred at the higher end of the temperature spectrum. In Figure 16, the relationship between longitudinal displacement and temperature is shown.

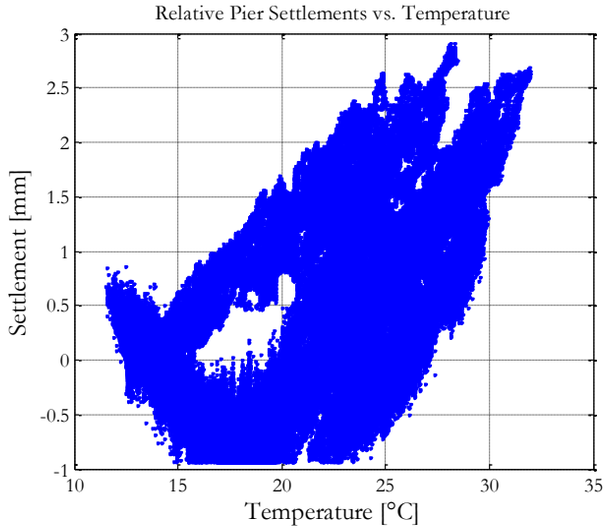


Figure 15. Relative pier settlements vs. abutment temperature.

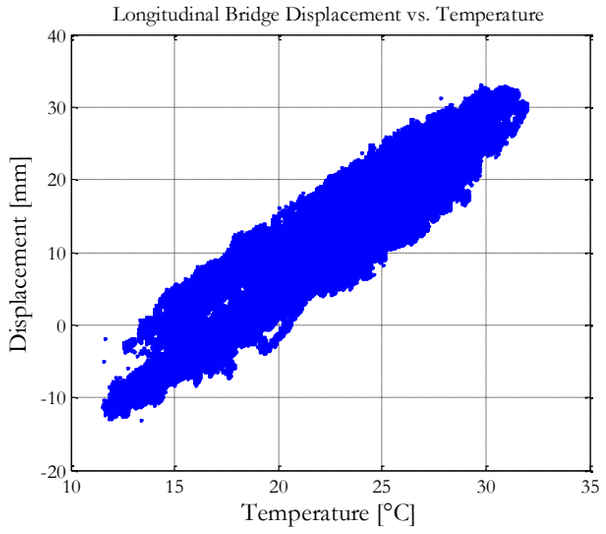


Figure 16. Longitudinal displacement vs. temperature.

Figure 16 shows that there is a distinct linear relationship between longitudinal displacement and temperature. Intuitively, the bridge experiences the largest displacements at higher temperatures, and minimal displacements within a temperature range of approximately 15-20°C. From both Figures 15 and 16, it can be seen how strongly temperature variations influence the various movements occurring in the structure.

There are situations where it may be desirable to eliminate specific influencing factors, such as temperature, in order to gain a better understanding of the relationships between less dominant variables. This can be achieved through the use of regression modelling, which is beyond the scope of this paper, but is described in detail by Islami & Modena (2013).

Further data from one of the Hunter Expressway Bridges is presented in Figure 17. This represents behaviour of the structure over a 19-month period.

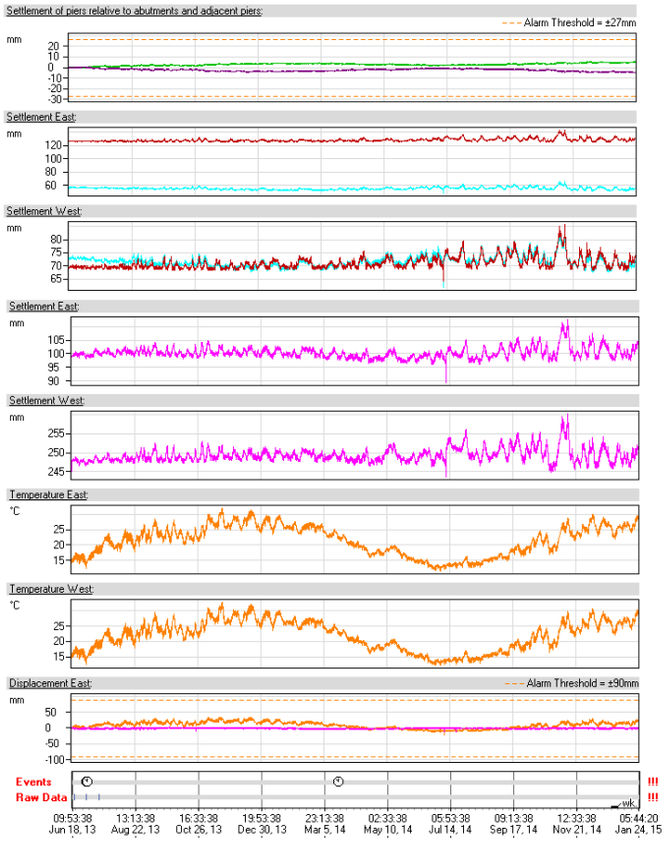


Figure 17. Settlement, temperature and displacement recorded over a period of 19 months.

It can be seen that relative settlement of the piers is quite stable and reaches a maximum value of approximately 7 mm, well below the indicated alarm threshold value of 27 mm. The temperature profile matches the expected seasonal fluctuation (peak in November-January and trough in June-August), and the settlements and displacements follow this profile as commented previously for Figures 15 & 16.

The implementation of SHM systems on the Hunter Expressway Bridges from the beginning of their service lives will allow any required corrective measures to be taken proactively rather than reactively, effectively decreasing life-cycle costs. These bridges form a key part of the road network in New South Wales, and it is therefore necessary to ensure that they remain in a safe and serviceable condition. It can be confirmed that since the SHM systems were installed on the bridges, there has been no evidence of substantial settlements. The ability to monitor the structures constantly over time safely allows this judgement to be made, and it would be difficult, if not impossible, to arrive at the same conclusion if monitoring was undertaken solely via manual methods.

4 CONCLUSIONS

It is evident that Structural Health Monitoring systems can effectively increase safety and optimise life-cycle costs for concrete bridges. This is achieved by making it possible to identify and deal with issues before they can result in structural damage and require costly repair works.

Whether employed on existing or newly-built structures, automated monitoring enables collection of useful data in a manner that is extremely accurate, safe, efficient and cost-effective. The potential to reduce the need for expenditure on maintenance and repair, and therefore allow structures to remain safely in service for years to come, reinforces the need to implement this essential technology on a wider scale.

REFERENCES

Cho, H.N., Frangopol, D.M. & Ang, A.H.S. 2007. *Life-Cycle Cost and Performance of Civil Infrastructure Systems.* London: Taylor & Francis.

Hawk, H. et. al. 2003. National Cooperative Highway Research Program. *NCHRP Report 483: Bridge Life Cycle Cost Analysis.* 483(2):4

Islami, K., Meng, N. & O'Suilleabhain, C. 2016. 19th IABSE Congress Stockholm. *Smart bridge components (expansion joints, bearings and seismic devices) for intelligent infrastructure.*

Islami, K. & Modena, C. 2013. 6th International Conference on Structural Health Monitoring of Intelligent Infrastructure, Hong Kong. *Life cycle assessment by dynamic diagnosis and long term monitoring of old bridges in northeastern Italy.*

Islami, K. et. al. 2014. Istanbul Bridge Conference. *Life-cycle monitoring and maintenance of bridges: The role of remote SHM systems.*

Moor, G., Meng, N. & O'Suilleabhain, C. 2013. SMAR 2013. *Remote structural health monitoring systems for bridge expansion joints and bearings*.

Wenzel, H. 2008. *Health Monitoring of Bridges.* Chichester: John Wiley & Sons.

MS03: Developments and trends in composite steel-concrete structures

Organizers: S.H. Kim, K.F. Chung & G. Ranzi

Maintenance, Safety, Risk, Management and Life-Cycle Performance of Bridges – Powers, Frangopol, Al-Mahaidi & Caprani (Eds)
© 2018 Taylor & Francis Group, London, ISBN 978-1-138-73045-8

Push-out test on shear behavior of joint structure between corrugated steel web and concrete lower slab

Sihao Wang & Yuqing Liu
Tongji University, Shanghai, China
Jun He & Chuanxi Li
Changsha University of Science & Technology, Hunan, China

ABSTRACT: Pre-stressed concrete girder with corrugated steel web is one of the promising steel and concrete hybrid structures which are widely applied to highway bridges. The joint structure between concrete and steel is an important part of such structure. Firstly, the application of various shear connectors for joint structure was introduced and compared for the mechanical performance, such as headed stud and perfobond strips shear connectors weld on the flange or the corrugated steel web embedded in the concrete slab directly. In order to improve the construction quality of concrete and durability of joint structure, a new joint structure that placing lower slab on the inner side of corrugated steel webs with perforated plate connector is proposed in this study. Then, push-out tests with different parameters including plate height, plate thickness, and plate shape were carried out to study shear strength, shear stiffness, failure modes and relative slip characteristics of proposed joint structure. Finally, on the basis of test results, the calculation formula of shear capacity for proposed joint structure is proposed, which can accurately predict the shear strength. All the findings of proposed joint structure in present study can provide reference for its application in practical bridge.

1 INTRODUCTION

A pre-stressed concrete girder with corrugated steel web is one of the promising concrete and steel hybrid structures applied to highway and railway bridges. The way to substitute corrugated steel webs for concrete webs of a box-girder bridge will result in no restraint among the slabs and webs, which will alleviate influences on the box girder due to concrete creep, drying shrinkage and temperature differences. Pre-stressing can be efficiently introduced into the top and bottom concrete slabs due to the so-called "accordion effect" of the corrugated webs (He *et al.* 2012a). Based on the promising new type hybrid structure, their flexural, shear and torsional behavior, fatigue performance and engineering applications have been experimentally and analytically studied (Sause and Braxtan 2011; Mo and Fan 2006; Ibrahim *et al.* 2006; He *et al.* 2012b,c; He *et al.* 2014 a, b).

The connection between concrete and steel is an important part of composite structure. The shear studs, perfobond strips (PBLs) and angle shear connectors welded on the flange or the corrugated steel webs embedded in the concrete slab directly are generally used for the joint part. He (2011) investigated composite bridges with corrugated web domestic and abroad to analyze the number and proportion of different kinds connectors, and found that headed studs were adopted most for corrugated web bridge in early time, such as Shinkai Bridge (Kondo *et al.* 1994) in Japan and Altwipfergrund Bridge (Novák *et al.* 2007) in Germany. And angel connector was the most popular one used in such kind bridges in France and Japan, U-shape reinforcements welded on the angel help the connector deform ductile, and the longitudinal reinforcements bear out-of-plane moment. The PBL connector was developed in the eighties by the German company for the design of the third bridge over the Caroni River in Venezuela (Leonhardt *et al.* 1987). Push out test results show that PBL shear connectors are advantageous from the viewpoint of fatigue strength (Hosaka *et al.* 2002). However the out-of-plane moment performance for single perforated plate is relatively weak, so studs welded on both sides of the perforated plate or Twin PBL connectors were used to improve this condition. Ebina *et al.* (2004) conducted an extensive research to obtain the mechanical characteristics (shear and out-of-plane bending behavior) of twin perforated ribs connector, also the force transmission mechanism and fatigue characteristics under out-of-plane bending moments caused by transverse deflection of concrete slab were discussed. Corrugated steel webs have very low axial rigidity, which requires relatively flexible shear connectors. Corru-

gated steel web embedded in the concrete as shear connector without using a top steel flange was initiated in Hondani Bridge. Nakasu *et al.* (2000) carried out the experiments and finite element (FE) analysis for several types of specimens changing plate thicknesses and embedded depths of corrugated steel webs to investigate a long-term behavior of embedded connector. Kosa *et al.* (2006) carried out experimental and analytical investigations on flexural and shear behavior of composite girders with corrugated steel webs to make clear ultimate behavior and failure mechanism of embedded connection. Novák & Röhm (2009, 2010), investigated the load bearing behavior of an embedded corrugated steel web in combination with concrete dowels under longitude shear and transverse bending respectively. On the basis of these studies, simple design rules for shear connection in the ultimate limit state were developed. Kim *et.al.* (2011) carried out push-out test of corrugated perfobond rib shear connections. Test results showed that the failure was determined by concrete bearing with small deformations of inclined panel, and shear strength increased much than standard perfobond rib connector due to the shear resistance of the inclined rib panel.

When stud or embedded connections used for the joints between corrugated steel webs and concrete lower slab, construction quality of concrete and water proofing of the joints requires special attention. With a view to these problems, Ono *et al.* (2006) prepared some specimens modeled the embedded connection and carried out accelerated corrosion tests of the specimens. The results showed that durability of the embedded connection is increased by sealing the border between steel and concrete and by embedding paint in concrete. Shiji *et al.* (2008), He (2011) adopted the joint structures as shown in Fig.1, and the validity of placing lower slab on the inner side of corrugated steel webs was confirmed. It was proved that the bottom flange was beneficial to the concrete construction quality, as well as the durability of the interface between concrete slab and corrugate web.

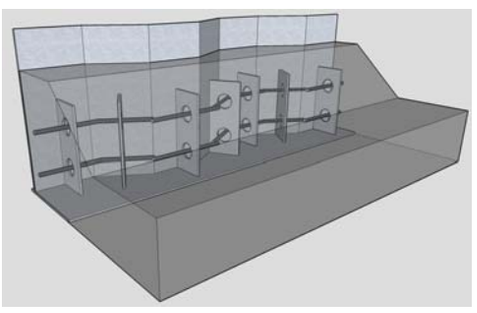


Figure 1. Joint structure between lower slab and corrugated web

Since shear loading capacity, failure modes and relative slip characteristics of proposed joint structures are different from those of conventional ones. Therefore, standard push-out tests are carried out to investigate the influence of different parameters (thickness, height and shape of perforate plate) on the shear behavior. Based on the results of model tests, a formula for calculating shear strength is proposed. All the findings of experimental works at present study may provide reference for the application of such joint structure in bridge construction.

2 EXPERIMENTAL PROGRAM

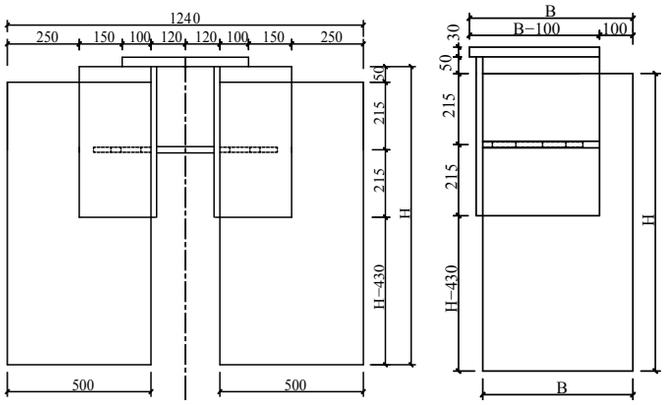
2.1 *Test specimen*

Referring to standard push-out test of headed stud connector, punching shear tests of perforated plate connectors in out-of-plane direction were carried out to verify the shear strength and relative slip. There are four test specimens prepared to investigate the influence of the geometrical parameters of perforated plate including the height, thickness and shape (L-shape or Trapezoidal shape) on shear behavior of joint structure. The push-out test specimens are shown in Fig.2, and the test parameters are list in Tab.1. The thickness of concrete block for all the specimens is 500mm, the width of concrete block is 450mm for DPS1 and DPS 3, while 500 for DPS2 and DPS 4. The distance from perforated plate to bottom of concrete block should be large enough to prevent local damage of concrete block, which was adopted as 685 and 785mm for DPS1,3 and DPS2,4, respectively. These push-out tests focus on shear strength of perforated plate in perpendicular direction, so the diameter of penetrating reinforcement through 70mm- diameter holes is chosen as 20mm to meet the minimum reinforcement requirements.

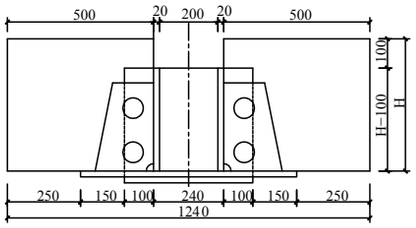
In order to prevent tension failure of concrete block, 16mm-diameter reinforcements with spacing of 100mm and 8mm-diameter stirrups with spacing of 150mm were arranged in concrete block.

Table 1. Parameters of test specimens (unit: mm)

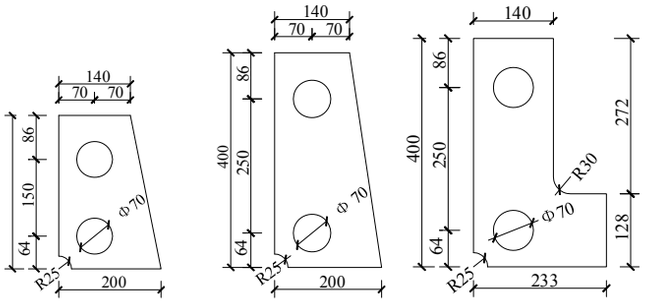
No.	PBLs					Concrete block	
	h	b_1	b_2	t	shape	B	H
DPS1	300	140	200	16	Trapezoidal	450	900
DPS2	400	140	200	16	Trapezoidal	500	1000
DPS3	300	140	200	10	Trapezoidal	450	900
DPS4	400	140	233	16	L	500	1000



(a) Elevation view (b) Side view



(c) To view



(d) PBL of DPS1and 3 (e) PBL of DPS2 (f) PBL of DPS4

Figure 2. Push-out test specimens

2.2 *Material properties*

The material properties including compressive strengths, tensile strengths and Young's modulus of three cubes at 28 days after the casting of the concrete with nominal strength of 55MPa are given in Tab.2. The mean tensile properties of samples cut from the steel component (Q345) such as perforated plate, the flange, loading plate and the reinforcements (HRB400) of the specimens are summarized in Tab.3.

Table 2. Material properties of concrete (unit: MPa)

Sample	Compressive strength	Tensile strength	Young's modulus ($\times 10^4$)
1	54.46	3.87	4.28
2	52.71	4.32	4.41
3	54.58	4.55	4.09
Mean	53.92	4.25	4.26

Table 3. Material properties of steel (unit: MPa)

Component		Yield strength	Tensile strength	Young's modulus
Plate	10mm	430	558	1.99×10^5
	16mm	400	531	2.02×10^5
	20mm	410	526	1.96×10^5
	30mm	423	551	2.01×10^5
Rebars	16mm	527	644	1.97×10^5
	20mm	499	664	2.00×10^5

2.3 *Loading and measurements*

Push-out specimens are tested in a hydraulic testing machine. A loading plate was installed at the top of the steel beam, in order to achieve a uniformly distributed load among all the connectors of each specimen. At the bottom of the concrete slabs, a layer of fine sand was paved to reduce concentrated reaction forces between specimens and the test bench. For the loading process, force control was applied with a rate of 5kN/min till 40% of the expected failure load, in this stage loading and unloading for 5 times to check the stiffness degradation of specimen. Subsequently, displacement control is used until the load dropped to 80% of the maximum load or obvious failure of the specimen was observed. The loading rate for the latter stage is 0.01 mm/s.

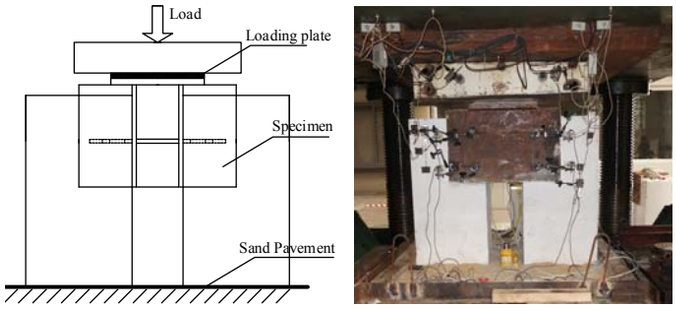


Figure 3. Test set-up

Four linear variable differential transformers (LVDTs) were symmetrically mounted at both the front and back sides of the specimen, and fixed at the same height to the perforated plate, as shown in Fig. 4. The transversal and vertical relative slip between the steel beam and the concrete block was measured by four gauges T1~T4 and D1~D4 respectively. The applied load and relative slips were recorded continuously and automatically. Besides the measurement of displacement for specimens during loading process, cracking initiation and propagation on the surface of concrete block were observed.

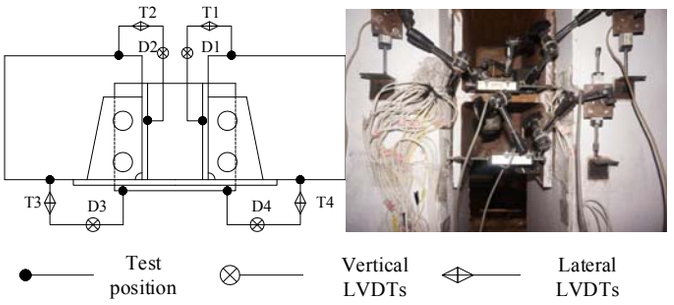
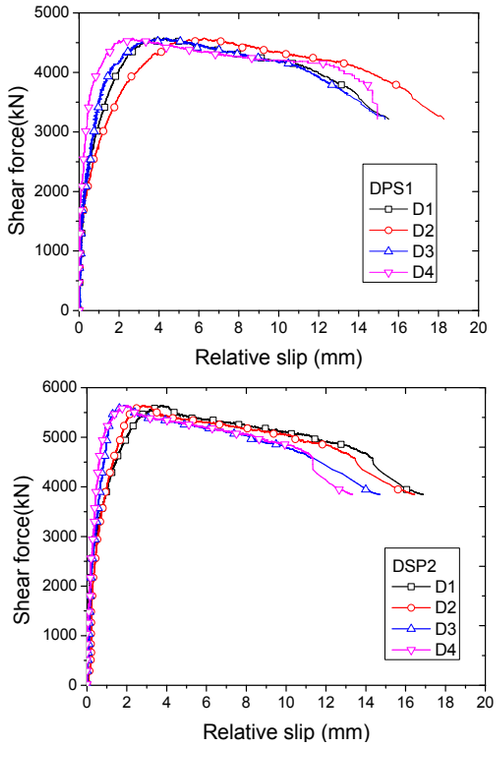


Figure 4. Relative slip measurement

3 EXPERIMENTAL RESULTS AND DISCUSSION

3.1 *Load-slip relationship*

The slip between steel plate and concrete slab occurred as the applied load increased. The slip from four LVDTs versus the shear load is plotted in Fig.5. It can be found that the load-slip relationship of plate dowel is nearly linear up to 1/3 of the maximum load (the relative slip is about 0.2mm). Besides, the shear force of perforated plate connector under serviceability limit states is usually not greater than 1/3 of the maximum load (V_u). Hence the shear stiffness, k_s, is defined as the secant modulus at the point where the applied load (V_y) related to the relative slip of 0.2mm in this study. Then, with the increase of shear load, the concrete under perforate plate damaged, load-slip curve became nonlinear, shear stiffness of perforated plate reduced gradually. When the applied load reached the limit state, relative slip increased rapidly until failure, and the slip at specimen failure is 2 times more than the slip corresponding to ultimate load, showing good ductility.



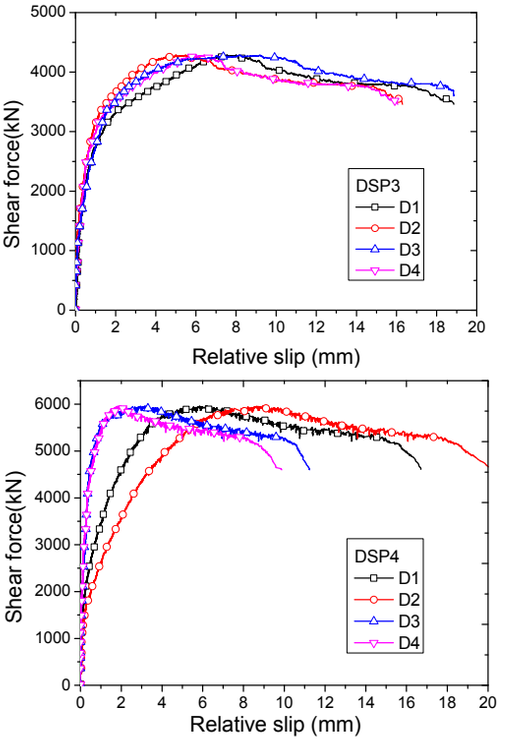


Figure 5. Load-slip curve

3.2 *Failure mode*

The failure modes of test specimens involved failure of concrete slab and deformation of perforate steel plate. The concrete punching shear failure was occurred on the corner of shear connector for all specimens, specimen DPS3 was selected as an example, as shown in Fig.6. The initial crack appeared on the concrete slab near the position of perforated plate connector. As the load increased, cracks gradually spread out toward the top and bottom of the concrete slab, mostly in the neighborhood of the steel beam.



Figure 6. Typical failure mode (Specimen DPS3)

After loading of push-out tests, the specimens were dismantled and concrete block was cut off directly under perforated plate to investigate the inner failure modes. The concrete under perforated plate damaged in the zone of approximate triangle shape near steel flange, which was similar to rectangular perforated plate connector in previous study (He 2011). Concrete in the disassembly specimen was

removed to investigate the deformation of perforated plate. The perforated plates for all the specimens were almost intact after loading of the test. In addition, no cracks or fracture were found in the perforated plates and weld seam for all the specimens.

3.3 *Shear strength and stiffness*

The push-out test results are summarized in Table 4, including the shear strength, shear stiffness and slip deformation. The shear strength (V_u) is defined as the maximum load during the tests; the relative slip at maximum load is defined as peak slip (s_p). The shear stiffness (k_s) represents the secant slope at applied load V_y corresponding to relative slip of 0.2mm, as mentioned before.

Table 4. Shear strength and shear stiffness

Specimen	Shear strength		Shear stiffness		
	V_u/kN		s_p/mm	k_s/kN·mm^{-1}	V_y/kN
	Test	*Cal.*			
DPS1	2273	2148	4.8	4190	838
DPS2	2821	2864	2.8	6100	1220
DPS3	2143	2148	5.5	3420	684
DPS4	2977	2860	2.3	6970	1394

Note: the value of shear strength and stiffness represent the related value for one perforated plate connector

The shear stiffness which reflects deformation capacity of perforated plate connector changed from 3000 to 7000kN/mm. The shear stiffness of specimen DPS3 with thinner thickness is smaller than that of specimen DPS1. And shear stiffness of specimen DPS4 with L-shape is slightly larger than that of specimen DPS2 with trapezoidal shape.

From Table 4, it can be found that: the shear strength of specimen DPS2 with the perforated plate height of 400mm increased about 24% in comparison to that of specimen DPS1 with the perforated plate height of 300mm, also the shear stiffness enhanced about 1.45 times. With the increasing of perforated plate height, the compression area of concrete under perforated plate also increased, therefore the shear strength and stiffness were improved. When the thickness of perforated plate increased form 10mm (DPS3) to 16mm (DPS1), the shear strength and stiffness increased about 6% and 18% respectively, indicating increase of plate thickness can also improve the shear strength and stiffness to a certain degree. When the plate shape change from trapezoidal shape (DPS2) to L-shape (DPS4), the ratio of shear strength for DPS4 to that for DPS2 is 1.05, while the ratio of shear stiffness for DPS4 to that for DPS2 is 1.14, which indicate that the plate shape with the same area has slight effect on shear strength, but certain effect on shear stiffness.

4 SIMPLIFIED ANALYTICAL METHOD

4.1 *Calculation of shear strength*

The calculation of punching shear strength was deduced referring to the calculation method of angel shear connector (PCTS 2005) with the similar resistant mechanism, which includes the compressive strength of concrete and the shearing strength of welding part. The perforated plate connector and steel web were welded in double side, and the compressive area of concrete is effective in triangle part around the welding line, which was verified by experimental failure mode, the shear capacity of plate dowel is calculated as follows:

$$V_u = \min(R_1,\ R_2,\ R_3) \tag{1}$$

$$R_1 = A f_{ck}^{'} / k \tag{2}$$

$$R_2 = \sum a L_1 f_y / \sqrt{3} \tag{3}$$

$$R_3 = t\left(b + h\right) f_y / \sqrt{3} \tag{4}$$

Where R_1 is compressive resistance of concrete; R_2 is shear resistance of welding part; R_3 is shear resistance of plate material; A is area of perforated plate; f_{ck}' is compression strength of concrete; b, h, t is the width, height and thickness of perforated plate respectively; k is the reduction coefficient, k=1.28 refer to He *et al.* (2011); a is theoretical thickness of welding; L_1 is effective length of welding; f_y is yielding strength of steel.

4.2 *Comparison and discussion*

Table 4 also shows the calculated shear strength of push-out test specimens. All the specimens are failure due to concrete crush at the position of perorated plate connector. So the compressive resistance R1 represents shear strength for all the test specimens. And the ratio of calculate shear strength to test one for specimens DPS1~4 is 0.95, 1.02, 1.00, 0.96 respectively, the mean value of these ratios is 0.98, with the corresponding coefficients of variations of 0.03. Therefore, the proposed calculation equations (1~4) can reasonably predict shear strength of perorated plate connector with high accuracy.

The shear strength ratio of calculation value to test one for specimen DSP1 has the same degree comparing with specimen DSP3, indicating that the increase of plate thickness slightly affected shear strength, if perforate plate is thick enough.

The shear strength ratio of calculation value to test one for specimen DSP4 is slightly lower than that for specimen DSP2. The concrete compressive resistance is inclined to decrease with slender shape, since only specimen DSP4 is applied for studying the influence of plate shape, more specimens with different width and height should be tested in the future.

The shear strength from previous test (He 2011) and present test results are compared with calculation ones, as shown in Fig. 7. The average value of the ratio of the test shear strength to theoretical calculation one is 0.98, with the corresponding coefficients of variations of 0.1, indicating that the shear strength of perforate plate connector can be predicted according to theoretical calculation formula (1~4). Also, the value of parameter k=1.28 is verified by the comparison between tested and calculated results.

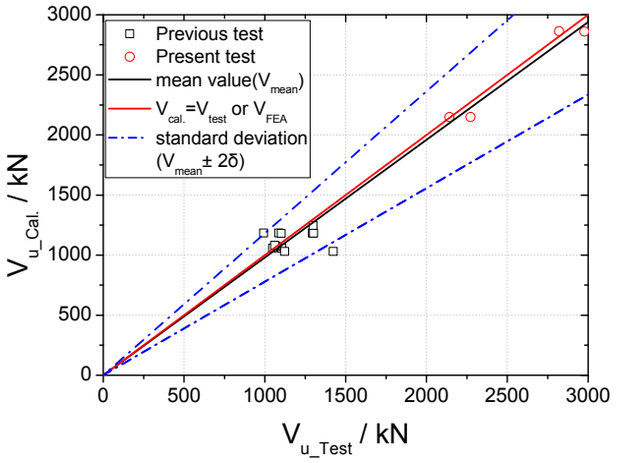


Figure 7. Comparison of shear strength from test and calculation

5 CONCLUDING REMARK

Push out tests of perforate plate connector were conducted, typical failure mode under punching shear load was observed, and the effects of key parameters including material properties, the shape and thickness of the perforated plate on shear capacity and stiffness were clarified: the increase of the plate thickness and area can improve the shear strength. Concrete damage took place adjacent welding edge under failure loading. Shear strength calculation based on effective compressive area of concrete is deduced. The theoretical analysis results are in good agreement with the experimental results. And reduction coefficient k is verified as 1.28 from test results for safe side.

All the experimental and theoretical calculation results can provide a reference for the design of joint between corrugated steel web and lower concrete slab. Since this paper ignores the contribution of the corrugated web itself to shear bearing capacity, the magnitude of its influence needs to be further studied.

ACKNOWLEDGMENTS

This research is sponsored by National Nature Science Foundation of China under Grant No. 51308070, National Basic Research Program of China (973 Program, No. 2015CB057702); Open Fund of Hunan Province University Key Laboratory of Bridge Engineering (13KA04); Key Discipline Fund of Creative Project of Bridge and Tunnel Engineering (13ZDXK04) from Changsha Univ. of Science and Technology, and The Applied Basic Research Program of Shanxi Province. These supports are gratefully acknowledged.

6 REFERENCES

Ebina, T., Higashida, N., Nakamura, H., Tategami, H., and Sonoda, K. (2004). "Study on out-plane bending behavior of corrugated steel web with twin- perfobond strip connections." *Journal of Structural Engineering, JSCE*, 50A, pp.1191-1202.

He, J. (2011), "Mechanical performance and design method of composite bridge with corrugated steel webs." Ph.D. dissertation, Tongji University, Shanghai, China.

He, J., Liu, Y., Chen, A., and Yoda, T. (2012a). "Mechanical behavior and analysis of composite bridges with corrugated steel webs: State-of-the-art." *International Journal of Steel Structures*, 12(3), 321-338.

He, J., Liu, Y., Chen, A., and Yoda, T. (2012b). "Shear behavior of partially encased composite I-girder with corrugated steel web: Experimental study." *Journal of Constructional Steel Research*, 77, 193-209.

He, J., Liu, Y., Lin, Z., Chen, A., and Yoda, T. (2012c). "Shear behavior of partially encased composite I-girder with corrugated steel web: Numerical study." *Journal of Constructional Steel Research*, 79, 166-182.

He, J., Liu, Y., Chen, A. Wang, D. and Yoda, T. (2014a) "Bending behavior of partially encased composite I-girder with corrugated steel web." *Thin-walled Structures*, 74: 70–84.

He, J., Liu, Y., Xu, X. and Li, L. (2014b). "Loading capacity evaluation of composite box girder with corrugated webs and steel tube slab." *Structural Engineering and Mechanics,* Vol. 50, No. 4 : 501-524

Hosaka, T., MItsugi, K., Hiragi, H. and Ushijima, H.(2002), "Study on shear strength and design method of perfobond strip." *Journal of Structural Engineering A. JSC E*, 48(3), pp.1265-1272.

Ibrahim, S. A., El-Dakhakhni, W. W., and Elgaaly, M. (2006). "Fatigue of corrugated-web plate girders: Experimental study." *Journal of Structural Engineering, ASCE*, 132(9), 1371-1380.

Kim, S., Ahn, J., Choi, K., and Jung, C. (2011), "Experimental evaluation of the shear resistance of corrugated perfobond rib shear connections." *Advances in Structural Engineering,* Vol. 14 No. 2. Pp. 249-263.

Kondo, M., Shimizu, Y., Kobayashi, K., and Hattori, M. (1994). "Design and construction of the Shinkai Bridge-Prestressed concrete bridge using corrugated steel webs." *Bridge Found. Eng.,* pp.13-20.(in Japanese).

Kosa, K., Awane, S., Uchino, H., and Fujibayashi, K. (2006). "Ultimate behavior of prestressed concrete bridge with corrugated steel webs using embedded connection." *Proceeding of JSCE,* 62(1), 202-220.

Leonhardt,F., Andrae, W., and Andrae, H.P.(1987), "New, improved bonding means for composite load bearing structure with high fatigue strength." *Beton-und Stahlbetonbau*,82(12), pp.325-331.

Mo, Y. L., and Fan, Y. (2006). "Torsional design of hybrid concrete box girders." *Journal of Bridge Engineering, ASCE*, 11(3), 329-339.

Nakasu, K., Yoda, T., and Sato, K. (2000). "Study on out-of-plane bending of concrete dowels in a composite girder with corrugated steel web." *Proceeding of JSCE*, 647(I-51), 267-279.

Novák, B., Denzer, G., and Reichert, F. (2007), "Validation of the structural behaviour of the Altwipfergrund Bridge." *Bautechnik*, 84, pp.289-300.

Novák, B., and Röhm, J. (2009). "The use of corrugated steel webs in bridge constructions -Load bearing behaviour of concrete dowels in combination with corrugated steel webs under longitudinal shear." *Beton- und St ahlbetonbau*, 104(9), pp. 562-569.

Ono, K., Osada, K., Sakurada, M., and Ohura, T. (2006) "Corrosion characteristics of embedded connection for pre-stressed concrete bridges with corrugated steel webs." *6th Symposium of hybrid structure*, Japan, pp. 29(1-6).

Pre-stressed concrete technological society, PCTS. (2005) Composite bridge design and construction standard. (In Japanese)

Röhm, J., and Novák, B. (2010). "Behavior of composite structures with corrugated steel webs under transverse bending using concrete dowels." *Beton- und St ahlbetonbau*,105(3), pp.176-185.

Sause, R., and Braxtan, T. N. (2011). "Shear strength of trapezoidal corrugated steel webs." *Journal of Constructional Steel Research*, 67(2), 223-236.

Shiji, A., Ooyama, H., and Yoda, T. (2008). "Experimental Study on the New Joint Structures of a Bridge with Corrugated Steel Webs." *Journal of structural engineering, JSCE*, 54A, 759-768.

Maintenance, Safety, Risk, Management and Life-Cycle Performance of Bridges – Powers, Frangopol, Al-Mahaidi & Caprani (Eds)
© 2018 Taylor & Francis Group, London, ISBN 978-1-138-73045-8

Effect of rebar strength in Y-type perfobond rib shear connectors

S. H. Kim, O. Han & K. S. Kim
School of Civil and Environmental Engineering, Yonsei University, Seoul 03722, Korea
S. J. Kim
Bridge Technology Co.,Ltd., Seongnam-si, Gyeonggi-do 13201, Korea
J. Y. Shin
NICE Co.,Ltd., Seongnam-si, Gyeonggi-do 13488, Korea

ABSTRACT: Rebars improve composite structure constructability and efficiency. Transverse rebars in the Y-type perfobond rib shear connector influence both shear strength and ductility. Performance characteristics of Y-type perfobond rib shear connectors with various transverse rebar strengths and diameters need to be identified. Push-out tests were done with Y-type perfobond rib shear connectors with various transverse rebars. Strain gauges monitored the strain histories with both push force and relative slip between the perfobond rib and composite concrete block. The concrete block surface was photographed to confirm the surface crack formation time and pattern. Strain histories indicate that surface cracks initiated after the nominal yield strains of the rebars were exceeded. Shear resistance can be increased and the surface crack formation delayed by using high-strength transverse rebars. However, a balanced design is needed to achieve shear resistance and ductility. Excessive strength transverse rebars may cause early damage on, and failure of, the Y-ribs.

1 INTRODUCTION

Composite structures, which use varied materials in one structure, are being researched extensively because of their structural efficiency. Steel-concrete composite structure is a representative composite structure that is widely used in diverse infrastructures and buildings around the world. The steel-concrete composite structure has effectively combined the characteristics of steel, which is robust against tension, and the characteristics of concrete, which is robust against compression. The composite behavior of shear connectors is essential to manifest the structural rigidity and strength of the composite structure effectively. A shear connector is a mechanical device that prevents vertical and horizontal separation and connects the steel and concrete to transmit stress effectively. To improve the efficiency of composite structures, various shear connectors have been researched and developed, such as stud shear connectors (Viset et al., 1956), perfobond rib shear connectors (Leonhardt et al., 1987), and Y-type perfobond rib shear connectors (Kim et al., 2013).

The stud shear connector, which is the most widely used shear connector in the world, was developed by Viset et al. (1956), and its usability was verified through experiments. However, stud shear connectors are vulnerable to fatigue and strength degradation due to weld quality. To address this problem, a German design company developed the perfobond rib shear connector in 1987 (Leonhardt et al., 1987). The perfobond rib shear connector has advantages over the stud shear connector, such as excellent shear performance and the possibility of mass production. However, it also has disadvantages such as the troublesome arrangement of transverse rebars in the dowel holes, lower ductility than that of studs, and susceptibility to brittle fracture. To overcome these shortcomings of the perfobond rib shear connector, Kim et al. (2013) developed the Y-type perfobond rib shear connector, which is a new type of shear connector. This Y-type perfobond rib shear connector has greater shear resistance performance and ductility compared to the conventional perfobond rib shear connector, and has improved the constructability problem of the transverse rebars of the perfobond rib shear connector (Kim et al., 2014; 2015).

Owing to the recent increase in demand for large structures, the performance requirements of structures are increasing; from the perspectives of economy and safety, there is a gradual increase in the strength of materials used in composite structures. Past experiments on the Y-type perfobond rib shear

connector evaluated the shear resistance performance and ductile behavior to examine its applicability to highway bridges and composite frame structures with general structural steel and concrete. Although the need for high-strength materials is under the spotlight owing to the increasing demand for large structures, research on the Y-type perfobond rib shear connector is insufficient. Therefore, additional behavior analysis of the Y-type perfobond rib shear connector should be conducted according to the characteristics of the high-strength materials. This study aims to identify the effect of transverse rebar strength on shear resistance of Y-type perfobond rib shear connector. For this purpose, the behavior of shear connectors is verified through experimental studies with various transverse rebars: SD400-D16, D500-D16, SD500-D19, and SD500-D22.

2 SPECIMENS AND MATERIAL PROPERTIES

2.1 *Push-out test specimen*

The twelve specimens were made in accordance with Eurocode-4 to evaluate the shear resistance and ductility of the Y-type perfobond rib shear connector. The Y-type perfobond rib used SS400 as the steel plate with a height of 100 mm, width of 80 mm, thickness of 10 mm, and dowel hole diameter of 40 mm. The arrangement interval of the transverse rebars was 120 mm, and three types of specimens were made with the diameters of 16 mm, 19 mm, and 22 mm. The concrete block used concrete with a compressive strength of 50 MPa, and was designed with the following dimensions: thickness of 280 mm, width of 600 mm, and length of 750 mm. Fig. 1 shows the dimension of the push-out test specimens according to the diameter of the transverse rebars.

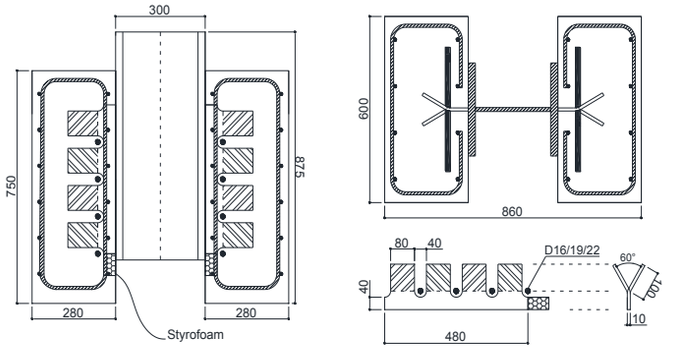


Figure 1. Dimension of push-out test specimen with Y-type perfobond rib shear connectors (unit: mm).

In order to examine the effect of transverse rebar strength, strain gauges were attached to the transverse rebars before being embedded in concrete parts. As shown in Fig. 2 the strain gauges (SG-1 and SG-2) were attached at the critical point of the transverse rebars.

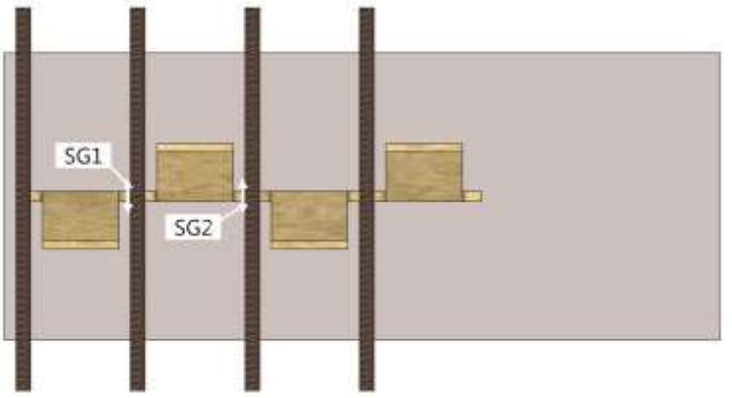


Figure 2. Attached position of strain gauges.

2.2 *Material properties*

Concrete with designed compressive strength of 50 MPa was employed for the push-out test specimens. The 12 concrete cylindrical specimens were manufactured, cured under the same conditions, and compressive strength tests were conducted to check the quality of the materials. There are four groups of test specimens which had different curing periods and each group contains three test specimens. Three groups of test specimens had standard curing period of 14 days, 21 days, and 28 days respectively and the other group had test-day standard curing. Table 1 lists the results of compressive tests of concrete. Steel material properties of SS400 steel for structural steel, SD400/SD500 steel for transverse rebar steel, and SD400 steel for reinforcement steel were obtained from the test reports. Steel material properties of the push-out test specimens are shown in Table 2.

Table 1. Concrete compressive strength.

Curing time	Test results	Average
14-days	41.5 MPa	42.9 MPa
	42.8 MPa	
	44.5 MPa	
21-days	48.2 MPa	49.2 MPa
	49.3 MPa	
	50.2 MPa	
28-days	49.7 MPa	50.1 MPa
	50.2 MPa	
	50.5 MPa	
Before test	50.3 MPa	50.7 MPa
	50.8 MPa	
	51.1 MPa	

Table 2. Properties of structural steel and rebar.

	Yield strength	Tensile strength	Elongation
SS400	288 MPa	470 MPa	29.0%
SD500	560 MPa	700 MPa	14.7%
SD400	510 MPa	610 MPa	21.0%

3 PUSH-OUT TEST

The push-out test proposed by Eurocode-4 was conducted using the 5,000 kN universal testing machine (UTM) to evaluate the shear resistance and ductility of Y-type perfobond rib shear connector and analyze the structural behaviors with strength of transverse rebar as variables. To measure the relative slip between the concrete and structural steel, L-shaped aluminum angles were attached 350 mm below the top of the concrete block and four linear variable differential transformers (LVDTs) were installed. The load was applied by controlling the displacement and the load rate was set to 0.02 mm/s to prevent the failure of specimen within 15 minutes according to the method proposed by Eurocode-4. White paint and grid lines were applied on the surface of concrete block to observe initial crack occurrence. Fig. 3 shows the test set-up of push-out tests.



(a) Front view (b) Side view

Figure 3. Push-out Test set-up.

4 PUSH-OUT TEST RESULTS

Test results of SD400-D16, SD500-D16, SD500-D19 and SD500-D22 specimens are evaluated based on the load-relative slip characteristics obtained by push-out tests. Fig. 4 shows the determination of relative slips for ductility assessment. The characteristic resistance P_{RK} refers to a value that corresponds to 0.9 times the peak shear resistance P_u with regard to relative slip capacity δ_u. The characteristic slip, δ_{uk}, refers to a relative slip that corresponds to 0.9 times δ_u. In Eurocode-4, δ_{uk} is recommended as 6 mm or higher. In this study, P_u and δ_{uk} according to Eurocode-4 were used to evaluate the peak shear resistance and ductility of Y-type perfobond rib shear connectors. To consider initial stiffness, the ductility ratio (δ_u/δ_{90}) proposed by Kim et al. (2013) was used when evaluating the ductility of the Y-type perfobond rib shear connectors. δ_u/δ_{90} refers to the ratio of relative slip capacity to the initial relative slip. Furthermore, δ_{pu} and δ_{cr} were used to compare the shear behavior of each specimens. δ_{Pu} refers to relative slip with regard to the peak shear resistance P_u and δ_{cr} refers to relative slip with regard to initial surface crack formation.

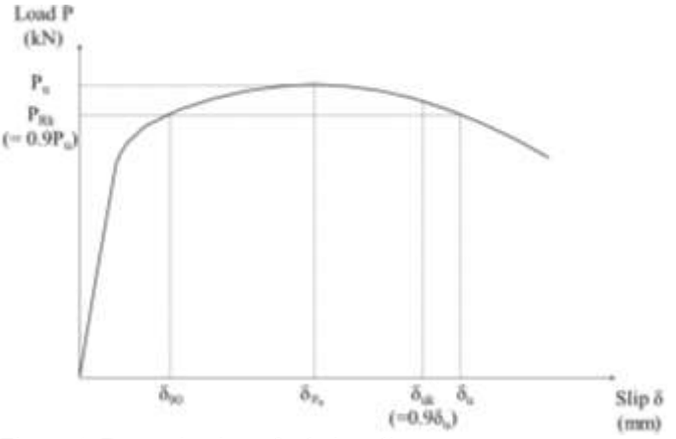
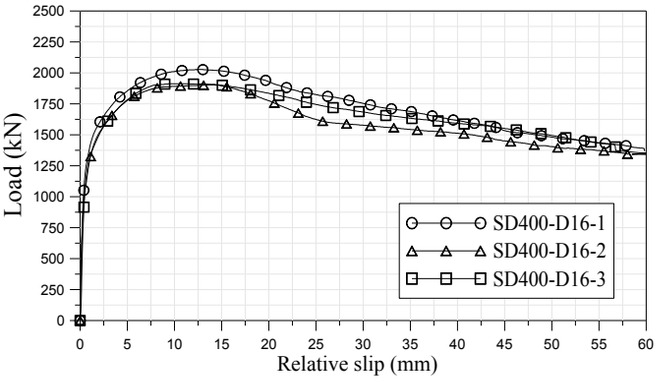


Figure 4. Determination of relative slips

4.1 *Shear resistance and ductility*

In the case of specimens with SD400-D16, the average P_u and δ_{Pu} measured were 1,948 kN and 12.5 mm. In terms of ductility, the average values of δ_{uk} and the δ_u/δ_{90} were calculated as 22.0 mm and 5.8, respectively. In the case of specimens with SD500-D16, the average P_u and δ_{Pu} measured were 1,970 kN and 12.4 mm. In terms of ductility, the average values of δ_{uk} and the δ_u/δ_{90} were calculated as 20.5 mm and 5.4, respectively. In the case of specimens with SD500-D19, the average P_u and δ_{Pu} measured were 2,076 kN and 12.7 mm. In terms of ductility, the average values of δ_{uk} and δ_u/δ_{90} were calculated as 24.3 mm and 5.3, respectively. In the case of specimens with SD500-D22, the average P_u and δ_{Pu} measured were 2,175 kN and 19.5 mm. In terms of ductility, the average values of δ_{uk} and the δ_u/δ_{90} were calculated as 34.6 mm and 5.8, respectively. Fig. 5 shows the load-relative slip curves of each specimen.



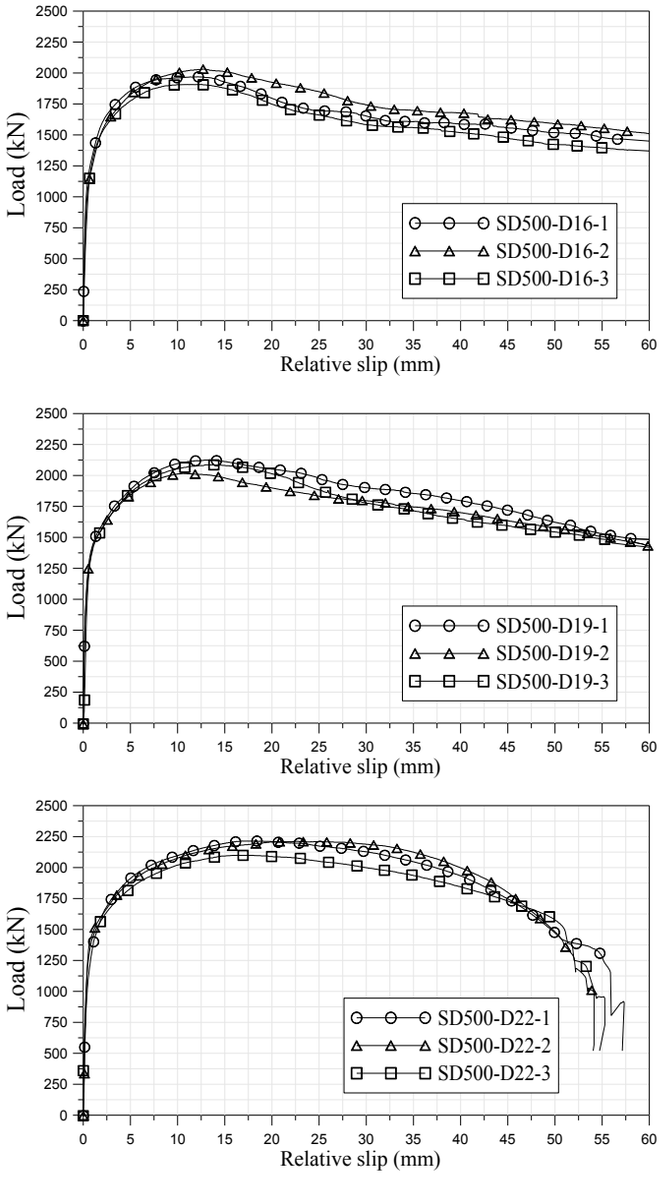


Figure 5. Load-relative slip curves

The results of the specimens of SD500-D16 do not exhibit significant changes from SD400-D16 in terms of P_u, δ_{pu}, δ_{uk}, and δ_u/δ_{90}. On the other hand, the P_u increased with the rebar diameter in SD500: the rate of increase from SD500-D16 to SD500-D22 was approximately 10.5 % and that from SD500-D16 to SD500-D19 was 5.4 %. The shear connectors with D16 and D19 of SD500 developed peak shear resistance at similar δ_{pu} whereas the SD500-D22 developed P_u at the δ_{pu} of 19.5 mm. In terms of ductility, δ_{uk} also increased significantly by 18.5 % from SD500-D16 to SD500-D19 and by 68.8 % from SD500-D16 to SD500-D22. The ductility ratio decreased by 1.9 % from SD500-D16 to SD500-D19, and increased by 7.4 % from SD500-D16 to SD500-D22. It can be observed that the Y-type perfobond rib shear connectors with D22 rebars of SD500 shows different shear behavior as compared to D16 and D19.

4.2 *Initial crack occurrence and failure modes*

Through the occurrence time of crack on the concrete surface and strain of transverse rebars, the effect of strength and diameter of transverse rebar on the concrete crack was confirmed. As shown in Fig. 2, the strain gauges (SG1 and SG2) attached to the critical strain point of transverse rebars. The Fig. 6 shows the strain histories monitored at the SG1 and SG2 and relative slip of initial surface crack occurrence time.

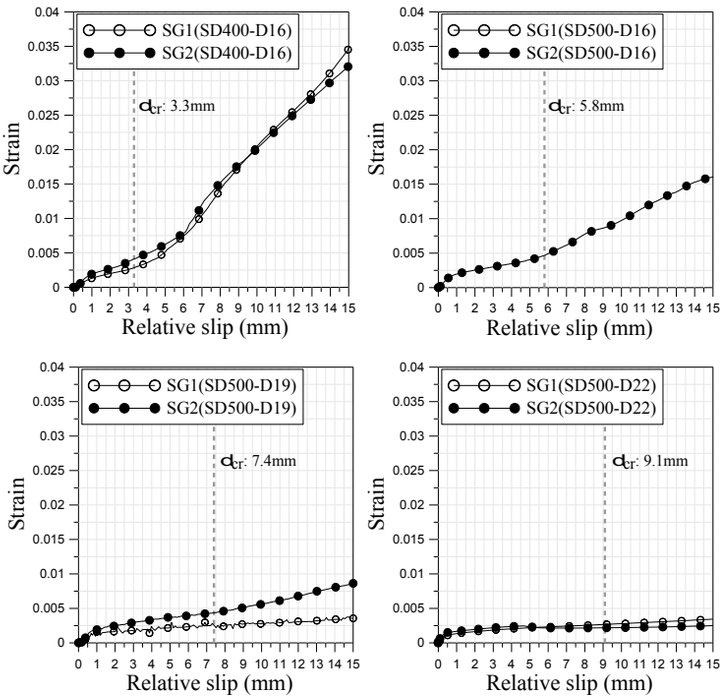


Figure 6. Strain history and δcr of transverse rebars

The initial surface crack occurred at the relative slips of 3.3 mm in the SD400-D16, and 5.8 mm in the SD500-D16 rebars of SD500. Also, the initial surface crack occurred at the relative slips of 7.4 mm in the SD500-D19, and 9.4 mm in the SD500-D22. Therefore, the initial surface crack is significantly influenced by the tensile strength and the increase in diameter of the rebars.

After the push-out tests were completed, concrete blocks were removed to confirm the deformation of the Y-ribs. As shown in Fig. 7, the deformation of the dowel hole of the Y-rib adjacent to the transverse rebar increases with increasing diameter of transverse rebar. In the case of SD500-D16 and SD500-D19, some damage occurred to the Y-ribs, and as shown in Fig. 6, significant deformation occurs in the transverse rebars as well. However, the Y-ribs were cut in SD500-D22, and the transverse rebars were much less deformed. In the curve after the δ_u in Fig. 5, the behavior characteristics for each failure mode can be confirmed. The mixed failure modes for SD500-D16 and SD500-D19 show a gradual decrease in shear force after δ_u, while the Y-rib failure for SD-D22 shows a decrease in shear force after δ_u and a decrease in the occurrence of Y- ribs failures.

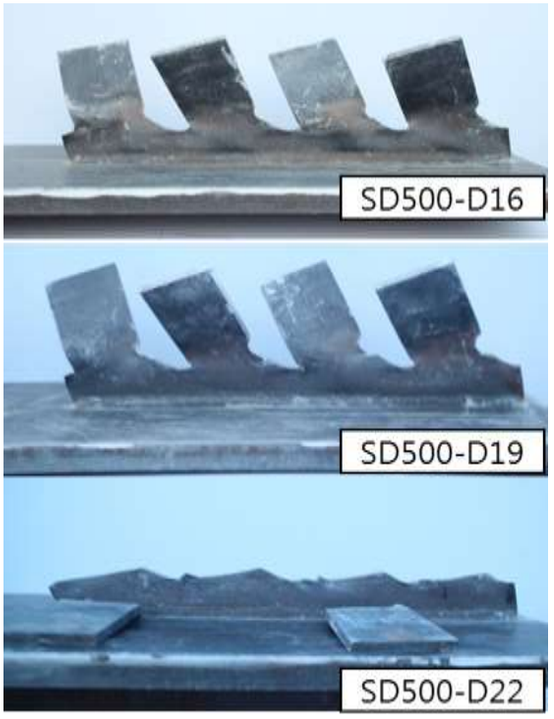


Figure 7. Deformed shape of Y-ribs.

5 CONCLUSION

The performance characteristics of Y-type perfobond rib shear connectors have been evaluated to identify the effect of transverse rebar on shear resistance, ductility, failure mode, and initial surface crack occurrence. Push-out test specimens with Y-type perfobond rib shear connectors were manufactured with various rebar strengths and diameters. The strength and diameter of the transverse rebar are found to be very important to control the behavior of shear connector. It was confirmed that the increase of the diameter of transverse rebar improves the shear strength (P_u) and ductility (δ_{uk}) of the shear connection part. The P_u increased about 5.4 % from SD500-D16 to SD500-D19 and about 10.5 % from SD500-D19 to SD500-D22. The δ_{uk} also increase significantly, 18.5 % from SD500-D16 to SD500-D19, and 68.8 % from SD500-D16 to SD500-D22. Also, it was confirmed that when the transverse rebar diameter increased as compared with Y-rib section, it changed from a mixed failure mode to a Y-rib failure mode.

The increase in strength of transverse rebar did not affect P_u and δ_{uk}, but had an effect of delaying initial crack occurrence. This effect also occurred when the transverse rebar diameter increased. Therefore, the balanced design between the transverse rebar and Y-rib is found to be very significant in controlling the shear behavior of Y-type perfobond rib shear connector.

6 ACKNOWLEDGMENTS

This work was supported by the Korea Institute of Energy Technology Evaluation and Planning (KETEP) and the Ministry of Trade, Industry & Energy (MOTIE) of the Republic of Korea (No. 20174030201480).

This research was supported by Basic Science Research Program through the National Research Foundation of Korea (NRF) funded by the Ministry of Education, Science and Technology (2017R1D1A1B03028262).

7 REFERENCES

Kim, S. H., Choi, K. T., Park, S. J., Park, S. M., & Jung, C. Y. (2013). Experimental shear resistance evaluation of Y-type perfobond rib shear connector. Journal of constructional steel research, 82, 1-18.

Kim, S. H., Heo, W. H., Woo, K. S., Jung, C. Y., & Park, S. J. (2014). End-bearing resistance of Y-type perfobond rib according to rib width–height ratio. Journal of Constructional Steel Research, 103, 101-116.

Kim, S. H., Park, S. J., Heo, W. H., & Jung, C. Y. (2015). Shear resistance characteristic and ductility of Y-type perfobond rib shear connector. Steel and Composite Structures, 18(2), 497-517.

Leonhardt, F., Andrä, W., Andrä, H. P., & Harre, W. (1987). New advantageous shear connection for composite structures with high fatigue strength. Beton und Stahlbetonbau, 62(12), 325-331.

Viest, I. M. (1956). Investigation of stud shear connectors for composite concrete and steel T-beams. Journal of the American Concrete Institute, 27(8), 875-891.

Maintenance, Safety, Risk, Management and Life-Cycle Performance of Bridges – Powers, Frangopol, Al-Mahaidi & Caprani (Eds)
© 2018 Taylor & Francis Group, London, ISBN 978-1-138-73045-8

Energy dissipating characteristics of Y-type perfobond rib shear connectors

S. H. Kim, K. S. Kim, O. Han & J. G. Choi
School of Civil and Environmental Engineering, Yonsei University, Seoul 03722, Korea

ABSTRACT: This study involves investigating the Y-type perfobond rib shear connector to reveal its superior ductile capacity when compared with those of the traditional stud-type shear connectors. It is expected that the excellent ductile behavior of the Y-type perfobond rib shear connectors can be utilized for energy dissipating devices in seismic structural excitations. In this study, the energy dissipating characteristics of the Y-type perfobond rib shear connectors are evaluated. Monotonic loading tests and cyclic loading tests of the Y-type perfobond rib shear connector are conducted. The specimens with various rebar diameters are fabricated, and the accumulated energy dissipations in each cyclic loading are evaluated. The decreasing characteristics of both energy dissipating capacity and shear resistance stiffness of Y-type shear connections during the cyclic loadings are examined.

1 INTRODUCTION

Steel-concrete composite structures have been used in various infrastructures and buildings for decades. In order to achieve composite action in a steel–concrete structure, it is necessary to install shear connectors between the steel and concrete. The shear connections of structures under seismic loading play an important role in load distribution, collapse prevention, and energy dissipation (Bursi et al., 1999). Therefore, the structural performance of the shear connection under a high displacement cyclic loading significantly influences the seismic performance of a composite structure.

An investigation of the Y-type perfobond rib shear connector revealed its superior ductile capacity when compared to those of traditional stud-type shear connectors as well as traditional flat-type perfobond rib shear connectors (Kim et al., 2013). Additionally, the hysteretic behavior of Y-type perfobond rib shear connectors exhibits superior energy dissipating capacity and residual strength (Kim et al., 2017(b)). This study involved evaluating the hysteretic behaviors of the Y-type perfobond rib shear connectors. Monotonic loading tests and fully reversed cyclic loading tests with high deformation of the Y-type perfobond rib shear connector were conducted. Specimens with various diameters (D10, D13, and D16) of transverse rebars were fabricated.

2 SPECIMENS AND MATERIAL PROPERTIES

2.1 *Push-out test specimen*

The six specimens were fabricated based on a previous study (Kim et al., 2017(b)) to evaluate the hysteretic behavior of the Y-type perfobond rib shear connectors with various transverse rebar diameters. The Y-type perfobond rib consisted of a steel plate with a height of 50 mm, width of 70 mm, thickness of 8 mm, and dowel hole diameter of 30 mm (Kim et al., 2017(a)). The arrangement interval of the transverse rebars was 100 mm, and three types of specimens were fabricated with diameters of 10 mm, 13 mm, and 16 mm. A concrete slab with a compressive strength of 30 MPa was used and was designed with dimensions including a thickness of 150 mm. Given the loading cases and diameter of the transverse rebar, the names of the specimens were defined as M-D10 (monotonic loading and 10 mm diameter rebar), C-D10 (cyclic loading and 10 mm diameter rebar), M-D13 (monotonic loading and 13 mm diameter rebar), C-D13 (cyclic loading and 13 mm diameter rebar), M-D16 (monotonic loading and 16 mm diame-

ter rebar), and C-D10 (cyclic loading and 16 mm diameter rebar). Figure 1 shows the dimension of the specimens based on the diameter of the transverse rebars. In order to apply load in the pull-out direction, a [ㅂ]-shaped steel plate with sufficient stiffness was installed and attached to the specimen as shown in Fig. 2.

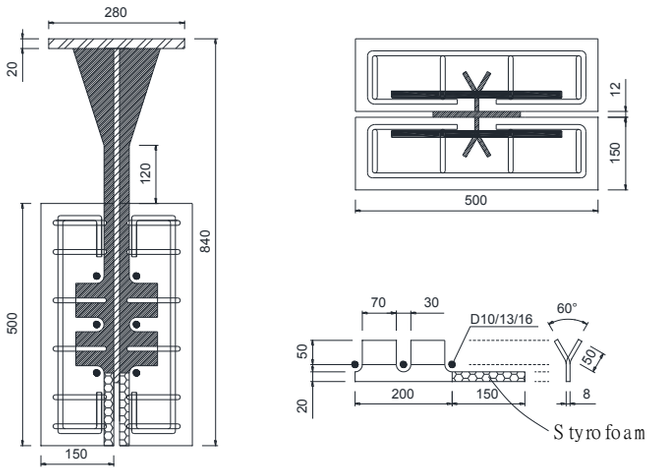


Figure 1. Dimension of the specimen with Y-type perfobond rib shear connectors (unit: mm).

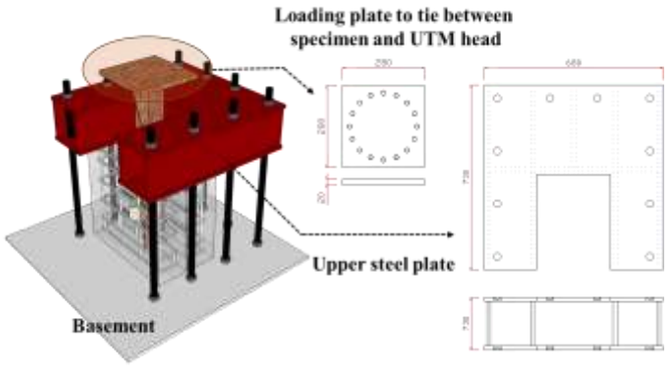


Figure 2. Illustration of the test set-up.

2.2 *Material properties*

Concrete with a designed compressive strength of 30 MPa was employed for the specimens. Twelve concrete cylindrical specimens were manufactured and cured under the same conditions, and compressive strength tests were conducted to check the quality of the materials. Table 1 summarizes the results of the compressive tests of concrete. The test results revealed the material properties of SS400 steel for the structural steel and SD400 rebar for the transverse rebar. The material properties of the push-out test specimens are listed in Table 2

Table 1. Concrete compressive strength.

Curing time	Test results	Average
28 days	29.7 MPa	30.6 MPa
(Test day)	30.5 MPa	
	31.5 MPa	

Table 2. Properties of the structural steel and rebar.

	Yield strength	Tensile strength	Elongation
SS400	389 MPa	451 MPa	25%
SD400-D10	515 MPa	613 MPa	20%
SD400-D13	516 MPa	611 MPa	19%
SD400-D16	446 MPa	639 MPa	17%

3 CYCLIC LOADING TEST

The push-out tests and cyclic loading tests were conducted by using a 1,000 kN universal testing machine (UTM) to evaluate the shear behavior under monotonic loading and cyclic loading of the Y-type perfobond rib shear connector with respect to various diameters of the transverse rebar. The load was applied by controlling the displacement. The displacement and load data of the tests were measured via UTM, and were recorded. Figure 3 shows the fully reversed cyclic loading conditions to evaluate the hysteretic behavior of the shear connection. The pull–push loadings corresponding to ±0.2, ±0.4, ±0.6, ±0.8, ±1.0, ±1.5, ±2.0, ±3.0, ±4.0, ±5.0, ±7.5, ±10, ±15, ±20, ±30, and ±40 mm were applied for three cycles at a time.

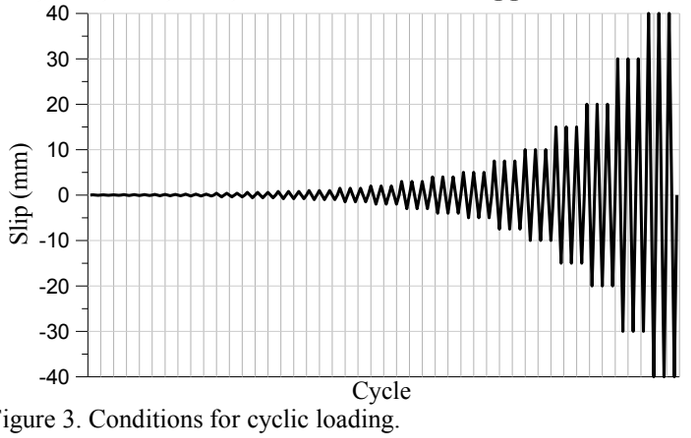


Figure 3. Conditions for cyclic loading.

4 TEST RESULTS

The monotonic loading test results of M-D10, M-D13, and M-D16 are shown in Fig. 4. The shear strengths of M-D10, M-D13, and M-D16 were measured as 596 kN, 650 kN, and 684 kN, respectively.

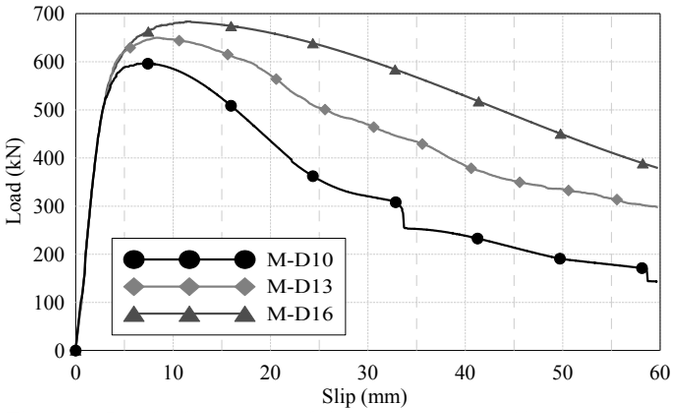
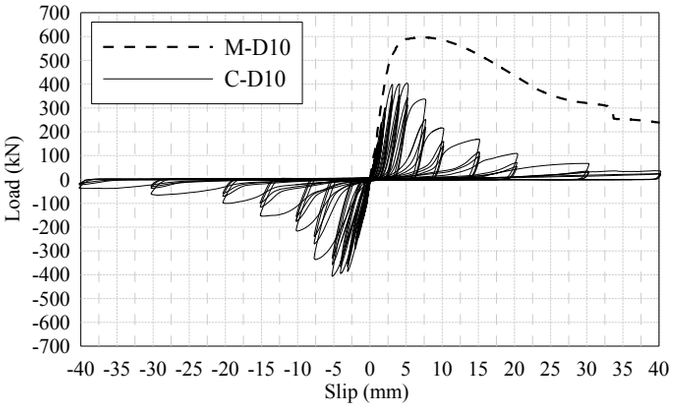
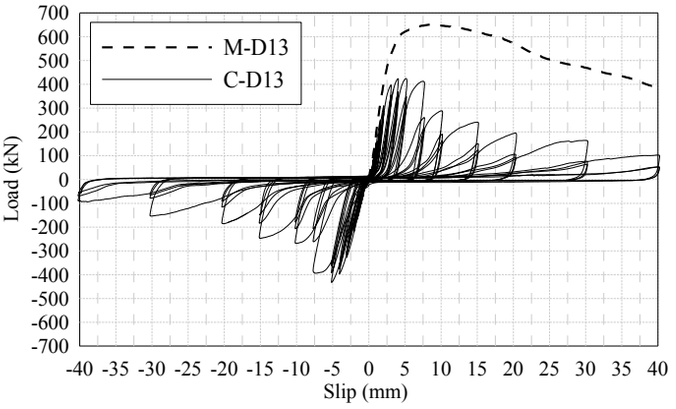


Figure 4. Load–slip curves of the monotonic loading tests

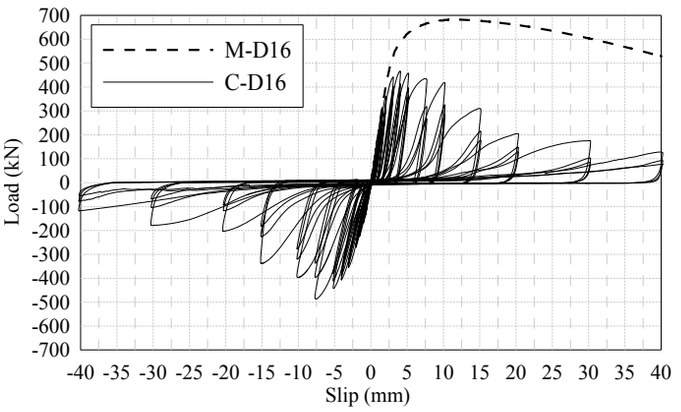
The load–slip curves of the monotonic loading test and cyclic loading test of specimens with the same transverse rebar diameter are shown in Fig. 5. As shown in Fig. 5, the shear strength determined by the backbone curve of the Y-type perfobond rib shear connectors with D10, D13, and D16 decreased by 32.2%, 34.7%, and 31.7%, respectively. Figure 6 shows the dissipated energy of C-D10, C-D13, and C-D16 with respect to cyclic loading in each cycle. The cumulated dissipated energies for C-D10, C-D16 was 22,497kN·mm, 35,558kN·mm and 43,982kN·mm respectively.



(a) M-D10 and C-D10



(b) M-D13 and C-D13



(c) M-D16 and C-D16

Figure 5. Load–slip curves of the monotonic loading test and cyclic loading test.

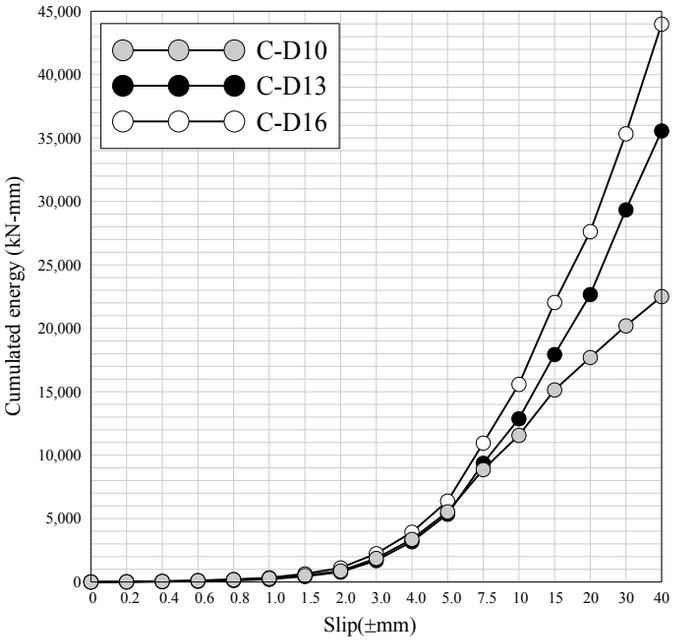


Figure 6. Dissipated energy after each loading cycle.

5 CONCLUSION

In this study, the hysteretic behavior of Y-type perfobond rib shear connectors with various diameters of transverse rebars was experimentally evaluated. The energy dissipation and shear strength degradation were evaluated by using the load–slip curves obtained from monotonic and cyclic tests. The test results of the specimen with a high diameter transverse rebar revealed superior residual shear strength and energy dissipating capacity. Additionally, sudden failure of the shear connection was not observed in any specimen. It is expected that the superior hysteretic behavior of the Y-type perfobond rib shear connectors can be utilized for energy dissipating devices in seismic structural excitations.

6 ACKNOWLEDGMENTS

This study was supported by the Korea Institute of Energy Technology Evaluation and Planning (KETEP) and the Ministry of Trade, Industry & Energy (MOTIE) of the Republic of Korea (No. 20174030201480).
The study was also was supported by Basic Science Research Program through the National Research Foundation of Korea (NRF) funded by the Ministry of Education, Science and Technology (2017R1D1A1B03028262).

7 REFERENCES

Kim, S. H., Choi, K. T., Park, S. J., Park, S. M., & Jung, C. Y. 2013. Experimental shear resistance evaluation of Y-type perfobond rib shear connector. *Journal of constructional steel* research 82: 1-18.

Bursi, O. S., & Gramola, G. 1999. Behaviour of headed stud shear connectors under lowcycle high amplitude displacements. *Materials and Structures* 32(4): 290-297.

Kim, S. H., Kim, K. S., Han, O., Lee, D. H., & Park, J. S. 2017. Analysis of the shear behavior of stubby Y-type perfobond rib shear connectors for composite frame structure.

Kim, S. H., Kim, K. S., Park, S., Jung, C. Y., & Choi, J. G. 2017. Comparison of hysteretic performance of stubby Y-type perfobond rib and stud shear connectors. *Engineering Structures* 147: 114-124.

Maintenance, Safety, Risk, Management and Life-Cycle Performance of Bridges – Powers, Frangopol, Al-Mahaidi & Caprani (Eds)
© 2018 Taylor & Francis Group, London, ISBN 978-1-138-73045-8

Strengthening of Steel Girder Flanges with Concrete-Filled Ribs

S. H. Kim, J. Shin, O. Han & K. Hwang
School of Civil and Environmental Engineering, Yonsei University, Seoul 03722, Korea
K. B. Rho
Wookyung Construction Co.,Ltd., Seongnam-si, Gyeonggi-do 13558, Korea

ABSTRACT: The flanges of steel girders in the compressive region are strengthened with the longitudinal steel stiffeners in general practices. The new details of concrete-filled longitudinal ribs have been proposed to strengthen the compressive flanges in steel girders in this study and its behaviors have been evaluated through both experimental and numerical studies. The concrete-filled longitudinal ribs may contain the special type perfobond rib shear connectors to increase the composite action between the steel flange and concrete part in the rib. The transverse rebars are installed through the U-type dowel spaces in the perfobond ribs to improve the composite action between the concrete part and longitudinal steel rib also. The both ends of transverse rebar are welded to the insides of steel rib. The transverse rebars are found to play important roles for the composite strengths of the proposed details in the section under the bending moment. When the longitudinal ribs are welded to the compressive steel flanges, the thermal-prestressed tensile stresses may be introduced to the flanges that will experience the compressive stress due to the service actions. The longitudinal ribs may be designed with high-strength steel than the flange steel, because the longitudinal ribs will be subjected to the thermal-prestressed compressive stresses.

1 INTRODUCTION

The continuous steel box girder bridges have negative moment regions. To strengthen bottom flanges, the longitudinal stiffeners are used or the bottom flange may get thicker.

In this study, the concrete filled steel tube (CFT) is proposed to strengthen the bottom flanges in the negative moment region. This method guarantees the structural performance with low amount of steel. The design concept is that the steel tube confines the concrete, and the concrete resists the compression. And by combining the Y-type perfobond rib shear connector, the compressive stress can be distributed effectively in the concrete.

2 PROPOSED DESIGN SECTION

The section of AASHTO steel box girder is shown in Figure 1. The dimension of the T-section stiffener is in Figure 1. The concrete filled steel tube has been designed in 4 cases.

The proposed steel box girders are shown in Figure 2 and 3, and the section of the concrete filled steel tube and the Y-type perfobond rib shear connectors are shown in Figure 4.

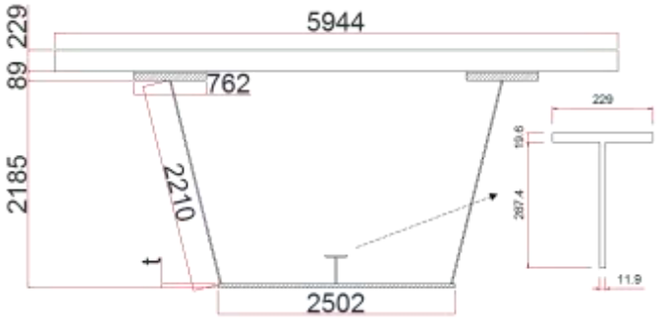


Figure 1. AASHTO steel box girder (AASHTO, 2012) (Unit: mm)

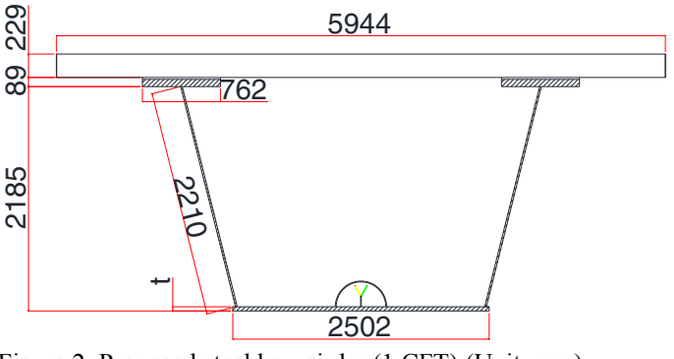


Figure 2. Proposed steel box girder (1 CFT) (Unit: mm)

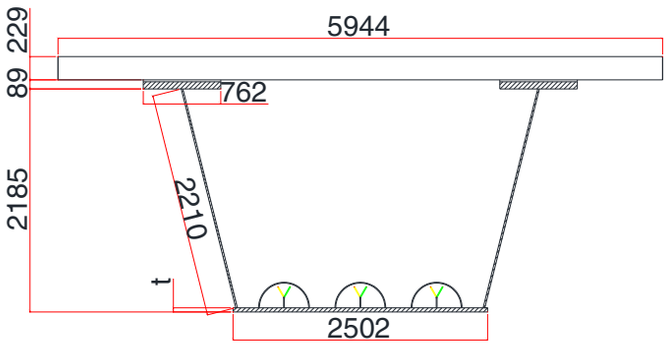
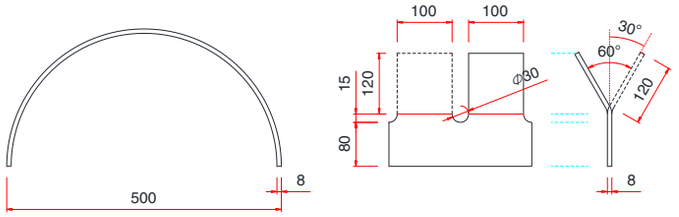


Figure 3. Proposed steel box girder (3 CFTs) (Unit: mm)



(a) steel tube (b) Y-type perfobond rib shear connector

Figure 4. Dimensions of the concrete filled steel tube and the Y-type perfobond rib shear connector (Unit: mm)

3 PERFORMANCE EVALUATION

The trial models are 4 cases which are summarized in Table 1. The model, TS, represents the section in Figure 1 with usage of T-section stiffener, and CFT-1, 2, and 3 are the sections with the concrete filled steel tubes as shown in Figure 2 and 3. The proposed girder model shown in Figure 5 is evaluated under varying load using the FEM analysis.

Table 1. Model cases

Model	Bottom flange thickness (t) [mm]	Steel Area [mm^2]	Number of stiffener/CFT
TS (AASHTO)	41.3	103,266	1
CFT-1 (1 CFT)	41.3	103,266	1
CFT-2 (3 CFT)	34.7	103,266	3
CFT-3 (3 CFT)	25.0	78,247(0.76)	3

The compressive stresses at the bottom flange at the interior support are compared in Table 2 and plotted on Figure 5. Table 2 contains the stress levels under the loading which generates either 150MPa or 200MPa in the model, TS.

Table 2. Compressive stresses in Bottom Flange

Model	Stage 1 [MPa]	Stage 2 [MPa]
TS	150	200
CFT-1	136	182
CFT-2	117	162
CFT-3	137	195

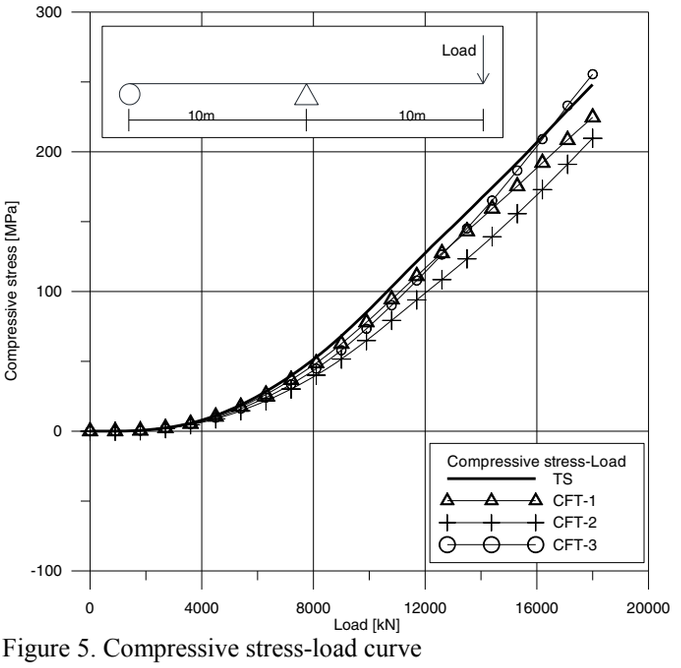


Figure 5. Compressive stress-load curve

4 NEW COMPRESSION TEST FOR CFT

It is hard to build the whole model such as steel box girders to evaluate a structural behavior of CFT. The new type of model is proposed to minimize the analysis for a structural behavior of CFT. It describes bottom flange and CFT in compression and negative moment region. Figure 6 shows the model specification.

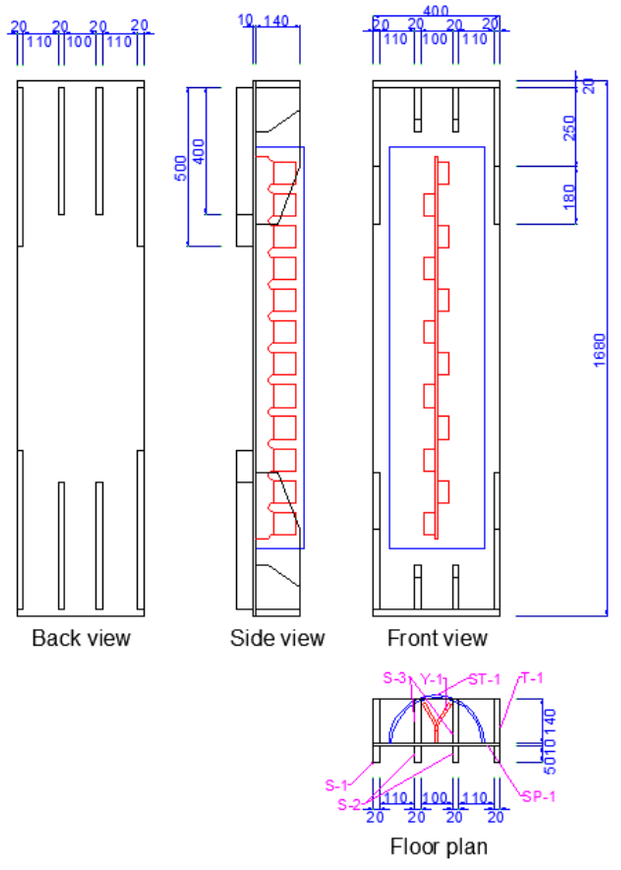


Figure 6. New type analysis model

This model has the concept that the compressive force is applied vertically to the model, and assumes

that the whole area is on compressive zone. There are four types of models that are composed of H20L100-30, H40L80-30, AASHTO-Stiffener, and No shear connector (Y-type rib dimension; H: Height, L: Length, Y-shape angle; Unit: mm).

The model is performed with linear analysis to compare the performance of CFT and stiffener in the same conditions. The analysis method is that the stress caused by the external compressive force sets equal for each model. And the value is extracted when the stresses are in same statement for each model. Table 3 and Figure 6 show the results. The results using Y-type perfobond rib shear connectors are almost same, and thus there is not the effect of the size of the shear connector. And the compressive force on the bottom flange is 55.7% of the force on the no shear connector specimen. But in case of AASHTO-Stiffener, it shows that 60% of the compressive force for Y-type perfobond rib shear connector, is needed to occur in the same stress. Thus, the CFT type has more advantage to secure the structural stiffness than AASHTO-Stiffener.

Table 3. Compressive force in same stress

Model	Compressive force [kN]
H20L100-30	292.81
H20L100-30	295.13
AASHTO-STIFFENER	173.40
No shear connector	163.62

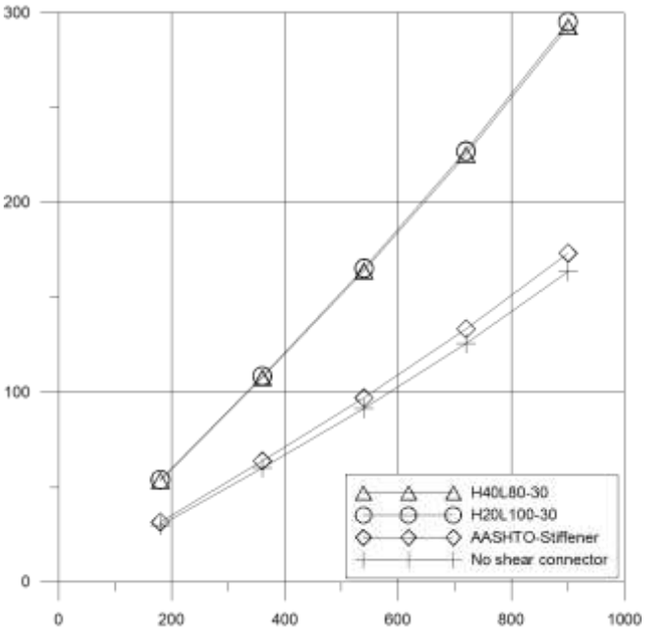


Figure 6. Analysis results on the new type model

5 CONCLUSION

The concrete filled steel tube are found to be applied effectively to the bottom flanges of the steel box girder in the negative moment region near the interior supports, and reduce the amount of the steel used.

The new type of CFT model minimizes the procedure of the analysis. And through the analysis of the model, Y-type perfonbond rib shear connector is the more efficient stiffener than the existing AASHTO-Stiffener in compressive area.

6 ACKNOWLEDGMENTS

This work was supported by the Korea Institute of Energy Technology Evaluation and Planning (KETEP) and the Ministry of Trade, Industry & Energy (MOTIE) of the Republic of Korea
(No. 20174030201480).

This research was supported by Basic Science Research Program through the National Research Foundation of Korea (NRF) funded by the Ministry of Education, Science and Technology
(2017R1D1A1B03028262).

7 REFERENCE

American Association of State Highway and Transportation (AASHTO) (2012). AASHTO LRFD bridge design specifications 6th edition. American Association of State Highway and Transportation (AASHTO)

Kim, S. H., Choi, K. T., Park, S. J., Park, S. M., & Jung, C. Y. (2013). Experimental shear resistance evaluation of Y-type perfobond rib shear connector. Journal of constructional steel research, 82, 1-18.

Zhan, Y., Zhao, R., Ma, Z. J., Xu, T., & Song, R. (2016). Behavior of prestressed concrete-filled steel tube (CFST) beam. Engineering Structures, 122, 144-155.

Maintenance, Safety, Risk, Management and Life-Cycle Performance of Bridges – Powers, Frangopol, Al-Mahaidi & Caprani (Eds)
© 2018 Taylor & Francis Group, London, ISBN 978-1-138-73045-8

Redundancy Evaluation of Composite Twin I-Girder Bridges in Fractured Condition

H. Lam, W. Lin, T. Yoda & K. Ono
Waseda University, Tokyo, Japan

ABSTRACT: Despite commonly used in highway bridge design in Japan, composite twin I-girder bridge system is currently classified as non-redundant mainly due to the oversimplified assumption in the current bridge design. In this study, two composite twin I-girder bridge models are tested to investigate the mechanical behavior and redundancy analyses of the composite twin I-girder bridge system in fractured condition. Numerical models were first validated based on the experimental results. Hereafter, numerical study was carried out to investigate the effect of fracture location and the effect of concrete slab on the redundancy level of the composite twin I-girder bridge system. Results show that the fracture at the mid-span section is the most critical damage condition comparing to other fracture locations. In addition, the concrete slab is found as the main structural component that ensures the survivability of the composite twin I-girder bridge system in fracture condition.

1 INTRODUCTION

Comparing to non-composite steel girder bridges, the composite twin I-girder bridge structure is highly beneficial from its composite action due to the use of connections between top flange of the steel and concrete slab which allow the bridge to have higher span to depth ratio and much lighter bridge structure (load carrying capacity per unit weight). For this reason, steel-concrete composite twin I-girder bridge system is commonly used in highway bridge system. Particularly in Japan, the number of the twin I-girder bridges has been increasing significantly in comparison with other bridge types in recent twenty years mainly due to the low construction cost required for this type of bridge, as shown in Figure 1 (Nagai 2006). On the other hand, such a bridge is rarely used in the United States because all two girder bridges are classified as non-redundant and fracture critical (AASHTO 2012). However, several past experiences have shown that composite twin I-girder bridge systems do not collapse in the severe fracture condition and thus should not be classified as non-redundant bridge system. This is due to the effect of the concrete slab in three-dimensional space which is served as an alternative load path in redistributing the load from one girder to the other girder in the twin I-girder bridge system under fracture condition (Lam et al. 2014). In current research trends, redundancy is considered as a very important measure to prevent the bridge structure from collapse. Researchers sometimes considered redundancy as a criterion for bridge rating. Moreover, by introducing the term redundancy in the structural design, fully collapse of the bridge structures can be highly avoidable. For this reason, a study was carried out to evaluate the redundancy level and mechanical behavior of the Composite Twin I-girder Bridge Systems in critical fractured condition.

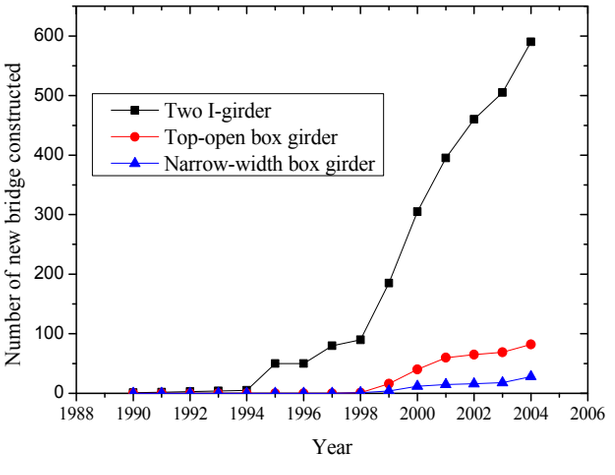


Figure 1. Number of bridges constructed in Japan

2 DETAILS OF TEST SPECIMENS

This study focuses on the redundancy analysis of the composite twin I-girder bridge in damage condition. Two test specimens of composite twin I-girder bridges were fabricated including an intact specimen and a damaged specimen. The intact specimen, hereafter called Specimen-1, is used for investigating the behavior and response of the bridge without any damage. The damage specimen, hereafter called Specimen-2, is used for investigating the behavior and response of the bridge in critical fracture condition. In both specimens, girder-1 refers to the main girder side subjected to loading, and girder-2 refers to the other main girder. The dimensions of the two specimens are identical. For Specimen-2, artificial fracture of full web and bottom flange had been imposed on mid-span section of girder-1 as can be seen in Figure 2. The cross-section of the bridge model is shown in Figure 3(a). The details of the main girder and transverse beams are shown in Figure 3(b). Two rows of shear stud connectors with the diameter of 19 mm and the height of 80 mm were employed on top of the flanges of the main girders to ensure the composite action between the concrete slab and the steel girders. The side view and top view are shown in Figure 4 and Figure 5, respectively. To comply with JRA specification (2002), two layers of reinforcement are installed in the slab. As shown in Figure 6, reinforcing bar type SD345 with 10 mm in diameter is used with the 100 mm spacing in both longitudinal and transversal direction. Further details of the test specimens can be found at Lam et al. (2017).

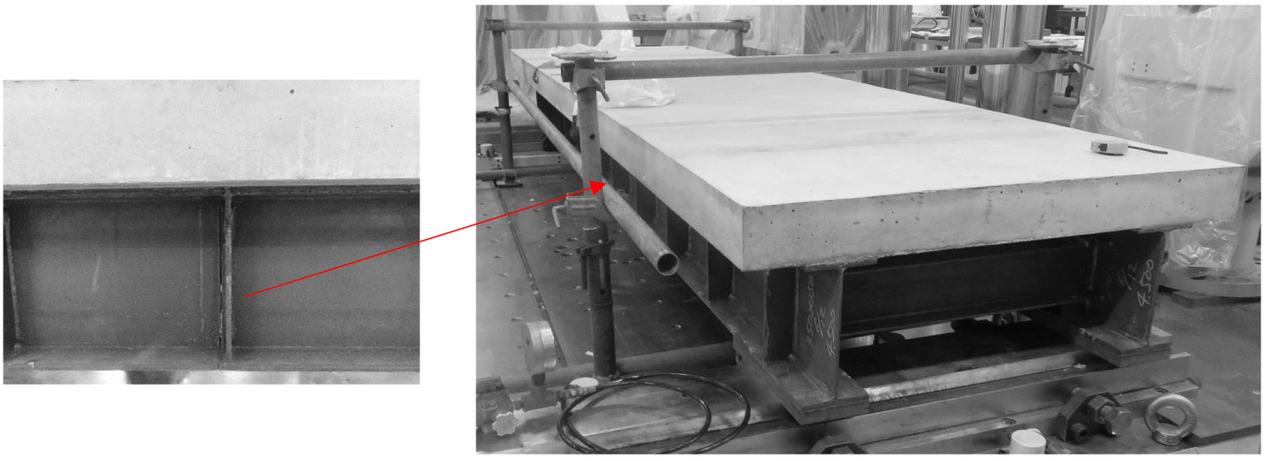
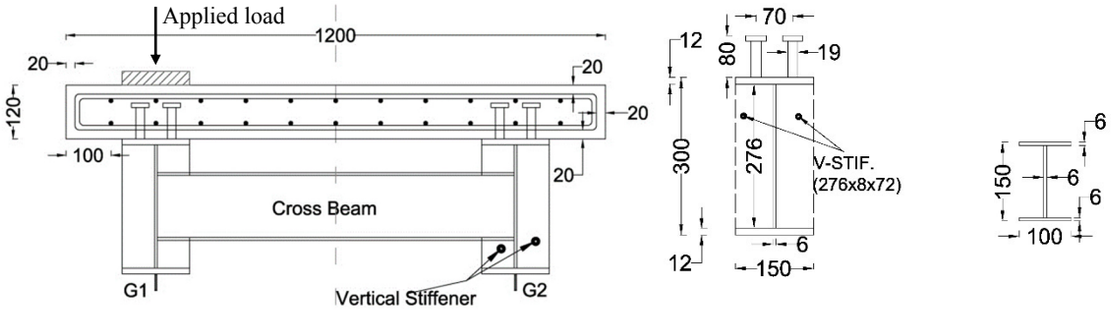


Figure 2. Overview of damaged specimen (Specimen-2)



(a) Cross section **(b)** Details of girders and studs

Figure 3. Cross section of the bridge model

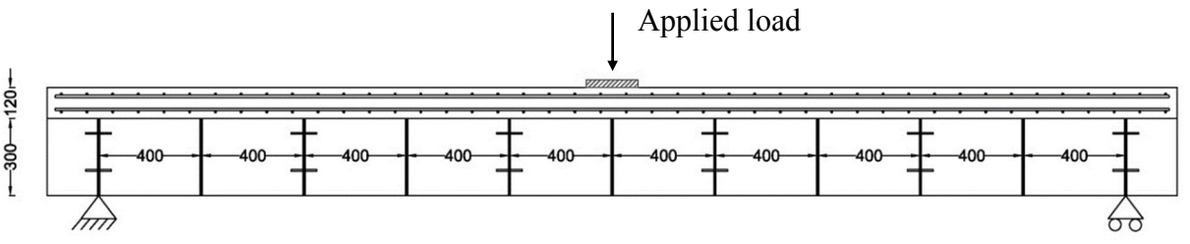


Figure 4. Side view of the test specimens (mm)

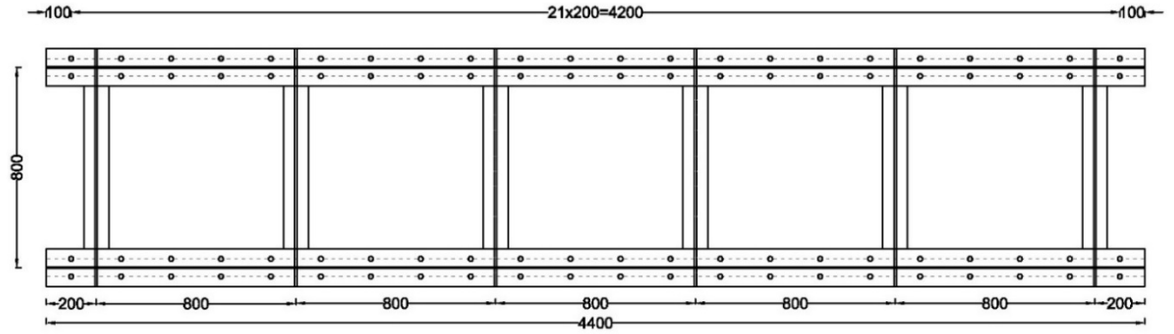


Figure 5. Top view of the steel girders (mm)

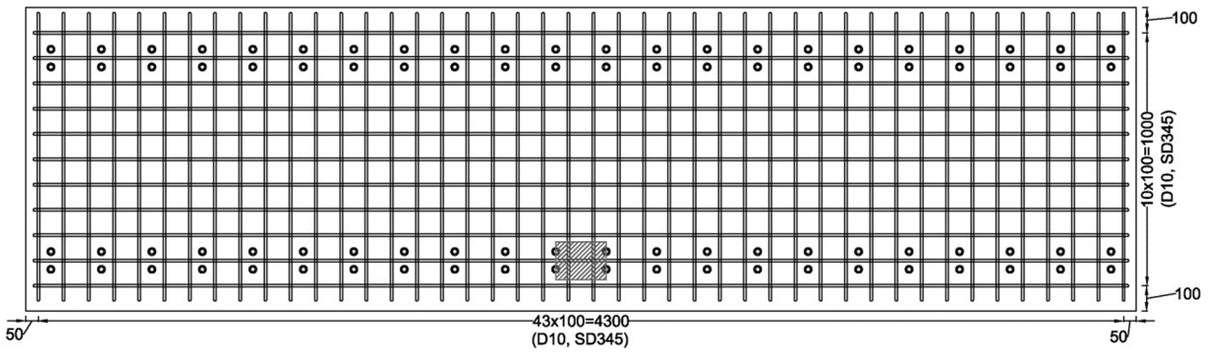


Figure 6. Layout of the reinforcement (mm)

3 NUMERICAL MODELS

3.1 *Numerical simulation*

In the numerical model, Finite Element Method with the aid of TNO Diana 9.4.4 software was employed for modeling and analyzing the bridge model. Both material nonlinearity and geometrical nonlinearity were included in the nonlinear analyses. The concrete slab is modeled by using the 8-node solid elements with 24 degrees of freedom. The reinforcement bar is modeled by using embedded bar elements. The steel girders, transverse beams, and vertical stiffeners are modeled by 4-node curve shell elements. Spring elements were used for modeling the shear studs and interface elements were used for simulating the interface friction between the concrete slab and main girders top flanges. Phase analyses and load increment method were employed to analyze the bridge model. Perfect bond between reinforcement bars and concrete was assumed to simplify the numerical model. The dead load (self-weight) is analyzed in the first phase following by the applied live load in the second phase. The overview of the numerical model is shown in Figure 7. The fracture is modeled by reducing the young modulus of the element at the fracture section to near zero value.

3.2 *Materials properties*

3.2.1 *Concrete*

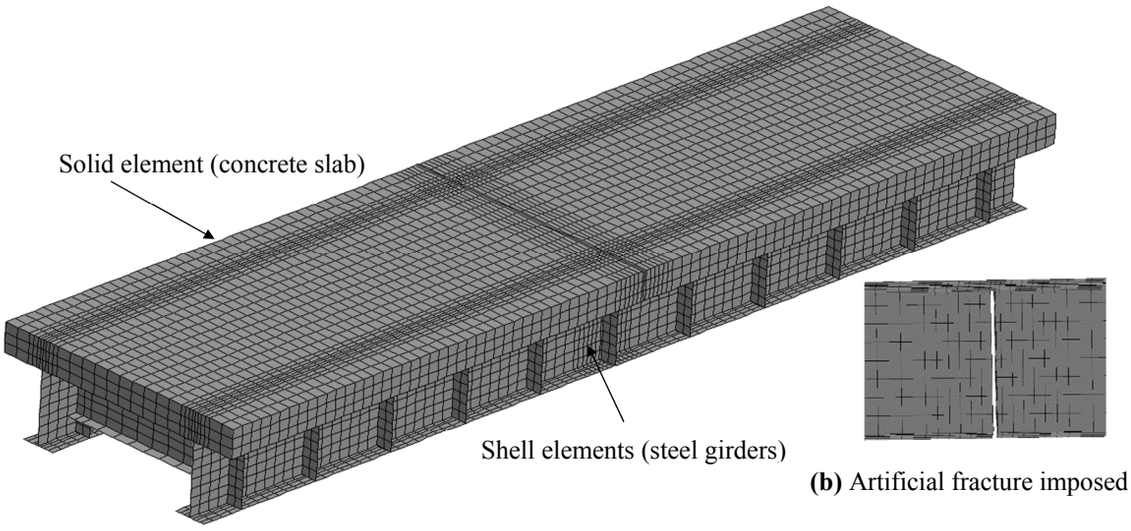
Smeared cracking model was employed for the cracking of concrete slab. The concrete compressive strength is taken as 33 MPa. The tensile strength of the concrete was calculated according to Equation 1 suggested by JSCE (2002), in which the f_t and f_c' denote tensile and compressive strengths of concrete, respectively. The stress-strain curve due to JSCE (2002) was employed to simulate the compression behavior of concrete, as shown in Figure 8. The factor of k_1 and ultimate compression strain ε_{cu} was determined according to Equation 2 and Equation 3. Experimental tension-stiffness curve proposed by Nakasu et al. was used in the numerical analyses to reflect the softening of concrete.

$$f_t = 0.28 f_{ck}^{'\,2/3} \tag{1}$$

$$k_1 = 1 - 0.003 f_{ck}^{'} \le 0.85 \tag{2}$$

$$\varepsilon_{cu}^{'} = \frac{155 - f_{ck}^{'}}{3000}; 0.0025 \le \varepsilon_{cu}^{'} \le 0.0035 \tag{3}$$

In which $\sigma_c^{'}$, $\varepsilon_c^{'}$ and $f_{cd}^{'}$ denote the compressive stress, strain, and design compressive stress of concrete, respectively.



(a) Overview of numerical model

(b) Artificial fracture imposed on girder

Figure 7. Numerical models

3.2.2 *Structural steel and reinforcing bars*

The stress-strain relationship for structural steel and reinforcing bars shown in Figure 9 and Figure 10 were adopted in numerical models (JSCE 2006). The ultimate strain for steel and rebar is taken as 20 %. Table 1 provides details of material properties of reinforcing bar and steel plate including yield strength and ultimate strength.

3.2.3 *Shear stud*

To model the shear stud inside the concrete slab, 3D nonlinear spring elements are employed. For each stud, one spring is used to model the behavior in the normal direction and two other springs are used to model the behavior in tangential directions. The constitutive relationship of the spring is given by Equation 4 suggested by Ollgaard et al. (1971) and illustrated in Figure 11, in which the ultimate shear force loading capacity of studs was specified by JSCE (2002), as shown in Equation 5.

$$Q=Q_u(1-e^{-0.7S})^{0.4} \tag{4}$$

$$Q_u = \min.\begin{pmatrix} (31A_{ss}\sqrt{(h_{ss}/d_{ss})f_{cd}^{'}}+10000)/\gamma_b \\ A_{ss}f_{ss}/\gamma_b \end{pmatrix} \tag{5}$$

where S: slip of the shear stud (mm), A_{ss}: area of the shank of the stud (mm^2), d_{ss}: diameter of the shank of the stud (mm), h_{ss}: height of the stud (mm), f_{cd}: design compressive strength of concrete (N/mm^2) (=f_{ck}/γ_c), f_{ck}: the characteristic compressive strength of concrete (N/mm^2), f_{ss}: design tensile strength of the stud (N/mm^2) (=f_{sk}/γ_s), f_{sk}: characteristic tensile strength of the stud (N/mm^2), γ_c: material factor of concrete (=1.3), γ_s: material factor of stud (=1.0), γ_b: member factor (=1.3).

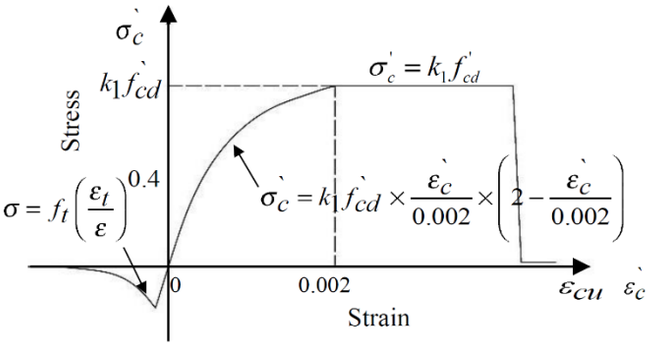


Figure 8. Stress-strain relationship of concrete

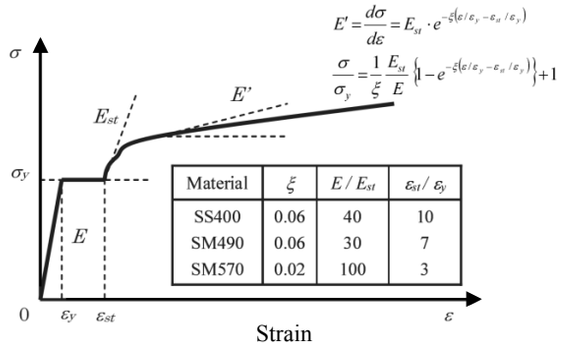


Figure 9. Stress-strain relationship of structural steel

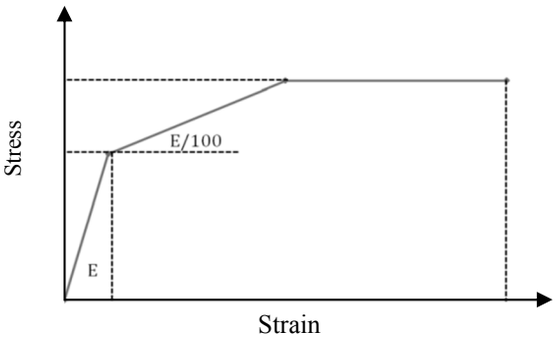


Figure 10. Stress-strain relationship of reinforcing bar

Table 1. Yield strength and ultimate strength of structural steel and reinforcing bar.

Material	Yield Strength (MPa)	Ultimate Strength (MPa)
Steel Plate (6mm)	450	577
Steel Plate (8mm)	389	548
Steel Plate (12mm)	389	548
Reinforcing Bar(D10)	406	544

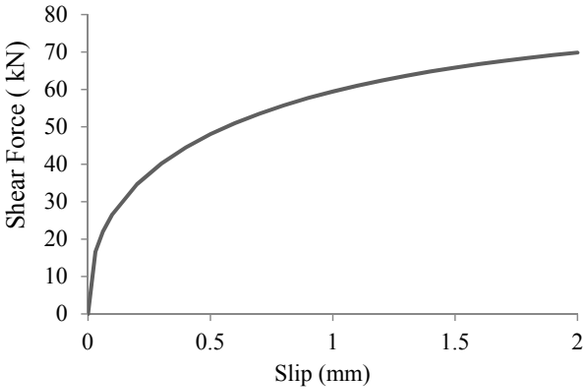


Figure 11. Shear force-slip relationship of shear stud

3.2.4 *Interface between steel and concrete*

In this study, the experimentally based bond-friction interface model suggested by Okada et al. (2006) was employed to simulate the composite action between the steel girder and the concrete slab, as shown in Equation 6 and Equation 7. The maximum bond stress f_{bo} and the corresponding slip was taken as 0.5 N/mm^2 and 0.06 mm, respectively.

$0 \le \Delta u_t \le \Delta u_t^0$:

$$f_{\tan} = \frac{f_{bo}}{1.9}\left(5\left(\frac{\Delta u_t}{\Delta u_t^0}\right) - 4.5\left(\frac{\Delta u_t}{\Delta u_t^0}\right)^2 + 1.4\left(\frac{\Delta u_t}{\Delta u_t^0}\right)^3\right) \quad (6)$$

$\Delta u_t > \Delta u_t^0$:

$$f_{\tan} = f_{bo} \quad (7)$$

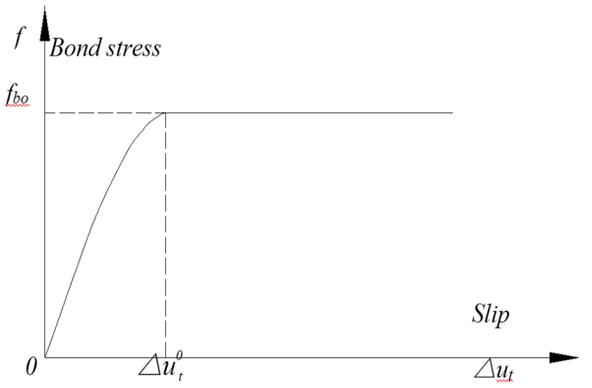


Figure 12. Bond stress slip relationship of interface between the steel and the concrete

3.3 *Numerical model validation*

The load-deflection curves from numerical analyses and experimental results were shown in Figure 13 for Specimen-1and Figure 14 for Specimen-2. Consistent results between experimental models and numerical models can be observed. The numerical models used in this study are proved to be accurate to predict the performance of both intact specimen and damaged specimen under vertical loading condition. The system stiffness of the experimental specimen and numerical model is well agreed for the elastic stage.

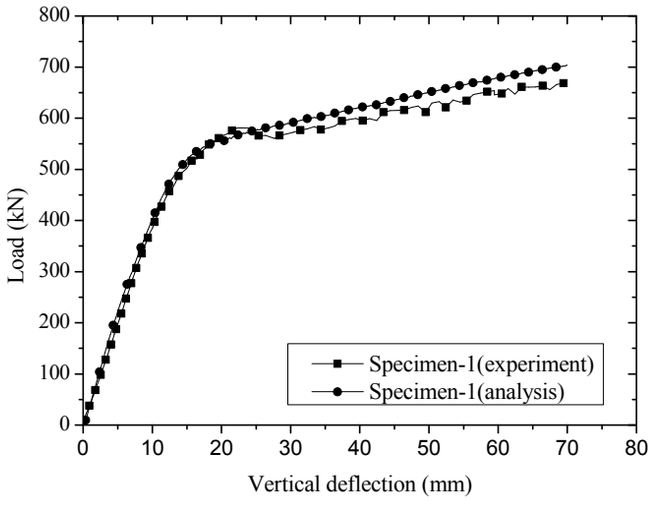


Figure 13. Load-deflection curves of Specimen-1

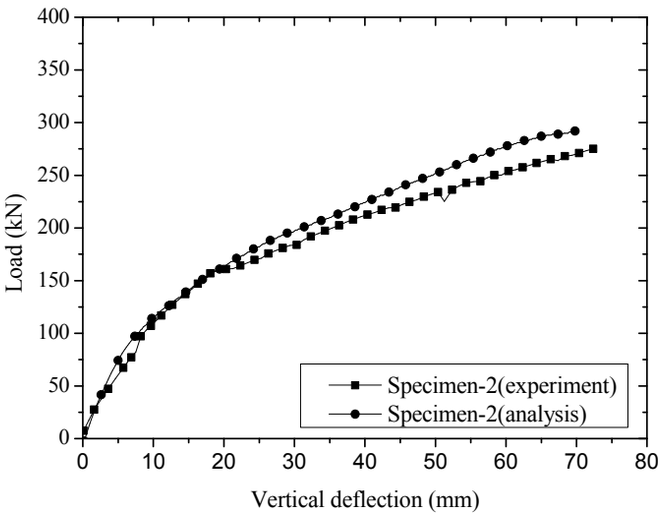


Figure 14. Load-deflection curves of Specimen-2

4 PARAMETRIC STUDY

4.1 *Redundancy evaluation of bridge models*

To ensure the safety of the bridge in critical damage condition, using redundant bridge system is the most effective way because a redundant bridge system generally resists the collapse caused by the failure of one of its structural members. In this study, redundancy is defined as the property of the bridge structure itself that guarantees its survival after an incident initiated by partial or full damage on the critical member of the bridge system. The redundancy level in this study is determined by comparing the remaining load carrying capacity of the bridge in damage condition (Specimen-2) with the design load of the bridge in intact condition. The equation 8 below is used to determine the redundancy level in this study:

$$R_d = \frac{P_{damage}}{P_{design}} \tag{8}$$

where:
R_d: Redundancy level of the bridge system
P_{damage}: Load carrying capacity of the damaged bridge
P_{design}: Design load of the bridge system

In this study, the load carrying capacity of the damaged bridge is determined by FEM with the nonlinear analyses (P_d *=292 kN*). Meanwhile, as the test specimens were designed according to Japanese specification (JRA, 2002), the design load for the intact bridge system is taken as the applied load level corresponding to the allowable stress level of the steel provided by JRA (2002), which means:

$$P_{design} = P(\sigma_{allowable}) \tag{9}$$

According to the Japanese specifications (JRA, 2002), $\sigma_{allowable}$ for the steel SM490 used for the test specimen in this study is 185 MPa corresponding to the $\varepsilon_{allowable}$ of 925 μ. According to the analyses results of the intact specimen, the design load is taken as follow:

$$P_{design} = P(\varepsilon_{allowable} = 925\mu) = 210kN \tag{10}$$

$$\mathrm{R}_d = \frac{P_{damage}}{P_{design}} = \frac{292\ kN}{210\ kN} = 1.39 \tag{11}$$

The R_d*>1* indicates that the remaining load carrying capacity of the bridge in the critical damaged condition in this study is large enough to sustain the design load and thus can be considered as redundant bridge system.

4.2 *Effect of fracture on the redundancy level of the bridge*

In this section, the redundancy level of the bridge system in relation to the fracture location is determined. Fracture at the mid-span section, near the support, and at the 1/4 span section were compared to determine the most critical damaged location. A total of five different scenarios (including one associated with experiment program) are included in determining the most severe fracture condition, as shown in Table 2. The redundancy level for each damaged case is determined according to Equation 8 and summarized in Table 3. The results indicated that, compared with the fracture near the support (Case-2 and Case-3) and fracture at one-fourth span section (Case-4 and Case-5), the fracture at the mid-span section is the most critical fracture location for the test specimen in this study as assumed in the experimental program.

Table 2: Details of each damaged case

	Fracture section	Loading section
Case-1	Mid-span	Mid-span
Case-2	Near support	Damaged section
Case-3	Near support	Mid-span
Case-4	1/4 span	Damaged section
Case-5	1/4 span	Mid-span

4.3 *Alternate load path and the effect of concrete slab*

Previous study shows that the transverse beam alone in the twin I-girder bridge model has no effect on the behavior of the bridge in fracture condition (Lam et al. 2014). By comparing the twin girder model with one girder model with the same design, the effect of concrete slab on the redundancy level of the twin girder bridge model when the bridge in fracture critical damage condition can be determined. The fracture section is assumed at the mid-span section, which is determined as the most critical fracture location. The cross section of one girder model is shown in Figure 15. The overview of the numerical model is shown in Figure 16.

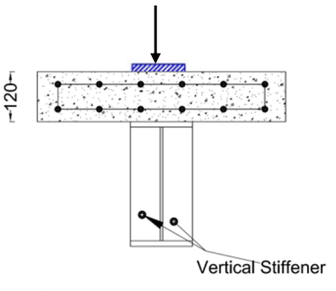


Figure 15. Cross section of one girder model

Table 3: Redundancy level for each damaged case

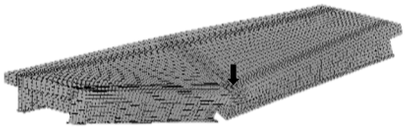
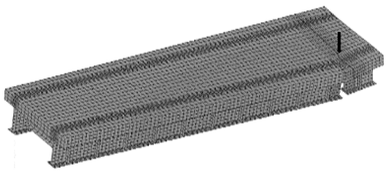
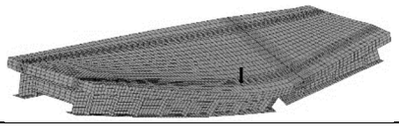
Damage Cases	Loading and damaged conditions	P_{damage} (kN)	P_{design} (kN)	R_d
Case-1		292		1.39
Case-2		532		2.53
Case-3		464	210	2.21
Case-4		417		1.98
Case-5		537		2.55

Figure 17 shown the load-deflection curves of the one girder and twin girder model in both intact and damaged conditions. The redundancy level of both models is determined according to Equation 8 and presented in Table 4. Results show that the load carrying capacity of the one girder model is much smaller than the design load, which deems the one girder as non-redundant. Meanwhile, by comparing one girder and twin girder model, based on the assumption that transverse beam is not effective as reported in the previous study, it can be clearly seen that the composite twin I-girder bridge can be classified as redundant bridge system totally depend on the alternative load path produced by the concrete slab that transfers the load from damaged girder to the intact girder.

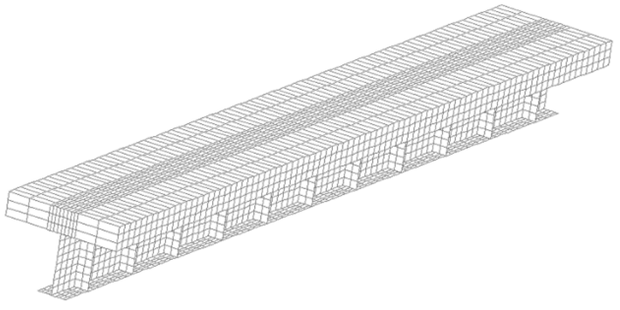


Figure 16. Overview of one girder model

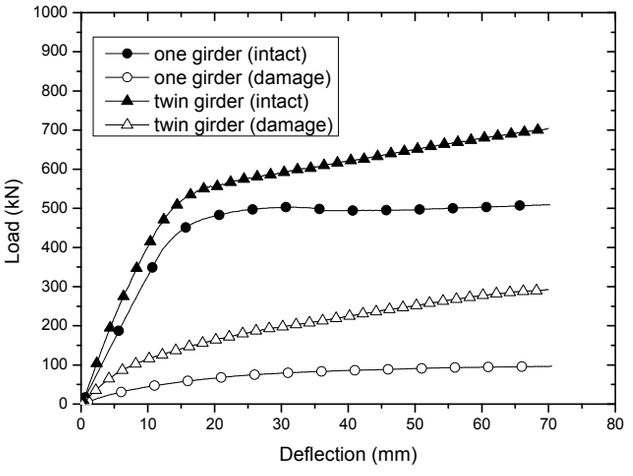


Figure 17. Load-deflection curves of the one girder and twin girder models

Table 4: Redundancy level of one girder and twin girders models

Models	P_{damage} (kN)	P_{design} (kN)	R_d
One girder	97	187	0.52
Twin girders	292	210	1.39

5 CONCLUSIONS

This study was carried out to investigate the effect of the fracture on the redundancy level of the composite twin I-girder bridge system. Finite element method with nonlinear analyses is used to determine the behavior of the bridge models in different damage cases. The validity of the numerical models is achieved by comparing with the experimental results. The finding of this study can be summarized as follow:

- The composite twin I-girder bridge models used in this study can be classified as redundant bridge system in critical fracture condition.
- It was confirmed that the fracture at the midspan section is the most critical fracture location comparing to the fracture near the support and at one-fourth span section.
- The concrete slab is determined as the alternative load path in composite twin I-girder bridge system which guarantees the redundancy level of the bridge in fracture critical condition.

ACKNOWLEDGEMENT

This research is sponsored by Waseda University Grant for Special Research Project-A (The key funding, Project number: 2015A-503). This financial support is gratefully acknowledged.

REFERENCES

American Association of State Highway and Transportation Officials. 2012. *LRFD bridge design specifications, 6th Ed*ition. Washington: AASHTO.

Japan Road Association. (2002). *Specifications for highway bridges*. Tokyo: JRA.

Japan Society of Civil Engineers. 2002. *Standard specification for concrete structures.* Tokyo: JSCE.

Japan Society of Civil Engineers. 2007. *Standard specifications for steel and composite structures*. Tokyo: JSCE.

Lam, H., Lin, W., & Yoda, T. 2014. Effect of bracing systems on redundancy of three-span composite twin I-girder bridge." *JSCE J. Struct. Eng.*, JSCE, 60A, 59–69.

Lam, H., Lin, W., & Yoda, T. 2017. Performance of Composite Twin I-Girder Bridges with Fatigue Induced Crack. *ASCE Journal of Bridge Engineering*, 22(9).

Nagai, M. 2006. Steel bridges in Japan—Rationalized design methods in Japan, *Magazine of Japan Society of Steel Construction*, 15, Tokyo.

Nakasu, M., & Iwatate, J. 1996. Fatigue experiment on bond between concrete and reinforcement. *Trans. JSCE*, 426, 852–853.

Okada, J., Yoda, T., & Lebet, J. P. 2006. A study of the grouped arrangement of stud connectors on the shear strength. *JSCE Journal of Struct. Eng. Earthquake Eng.,* 23(1), 75–89.

Ollgaard, J. G., Slutter, R. G., & Fisher, J. W. 1971. Shear strength of stud connectors in lightweight and normal weight concrete." *AISC Eng. J.,* 8(2), 55–64.

Maintenance, Safety, Risk, Management and Life-Cycle Performance of Bridges – Powers, Frangopol, Al-Mahaidi & Caprani (Eds)
© 2018 Taylor & Francis Group, London, ISBN 978-1-138-73045-8

Group effect of Y-type perfobond rib shear connectors

O. Altanzagas & E. Ganzorig
School of Civil & Architectural Engineering, Mongolian University of Science and Technology, Ulaanbaatar, Mongolia

S. H. Kim & O. Han
School of Civil and Environmental Engineering, Yonsei University, Seoul 03722, Korea

T. S. Kim
Consumer Product Business Division, Korea Conformity Laboratories, Seoul 08503, Korea

ABSTRACT: Many shear connectors may need to be arranged together in group to achieve the required shear strength in the design stage of the composite connection. In most practical situations the space to install the shear connectors may be limited. The shear strength of the individual Y-type perfobond rib shear connector may not be obtained if the Y-type perfobond rib shear connector layers are placed too much close to other adjacent layers. It has been investigated in the previous study that the total shear resistance of the flat-type perfobond rib shear connector group may either increase or decrease depending on the spacing between the adjacent layers.

This study is designed to verify the effect of the spacing between the adjacent layers of Y-type perfobond rib shear connectors and propose the proper design rule to estimate the shear strength in the multi-layer shear connectors. The double layer specimens with various spacings have been push tested. The minimum adjacent spacing for the specimens has been selected considering the limited distance due to the inclined Y-ribs to each other. The Y-ribs in the standard Y-type perfobond rib shear connector are inclined with 30-degree, and may bother the Y-ribs from the adjacent shear connector. Two different spacings of 120 mm and 300 mm are selected as the minimum and maximum distances. The maximum 300 mm spacing is selected considering the height of the shear connector. The parametric study for the spacings between 120 and 300 mm have been performed using the numerical FEM models. The numerical FEM model has been verified and improved based on the experimental test results. The effect of transverse rebar diameters is also examined. The shear resistance formula is proposed for the double layer shear connectors.

Keywords—Y-type perfobond rib shear connector, push-out test, group shear connector, rib arrangement and spacing

1. INTRODUCTION

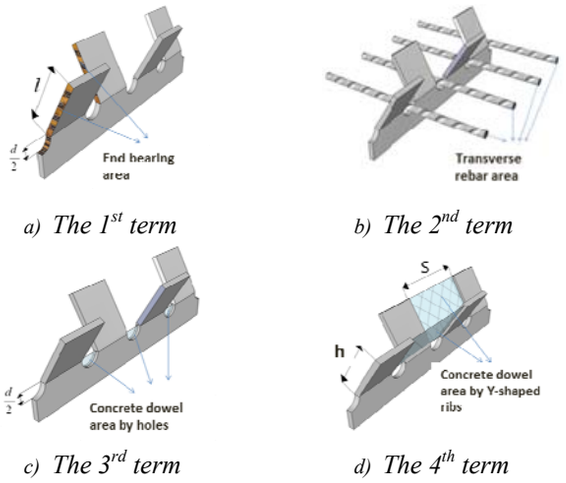
Steel-concrete composite structures are one of the advanced solutions, by combining steel and concrete advantages: steel provides the resistance to tension stresses, while concrete is associated to compressive stresses and enhances the stability and fire capacities of the steel section. To achieve this structural behavior in a steel-concrete composite structure, shear connector's needed to be designed accurately and economically. There are many types of shear connectors that have been studied by previous researchers. One of the latest advanced shear connector type is Y-type shear connector developed by Kim at al., 2013 [1], in which combines advantages of both stud types and the conventional flat type perfobond rib shear connectors [2].

Kim et al. (2013), first obtained shear resistance formula for single Y-type perfobond rib shear connector by consider four variables, which those are concrete strength, rebar, rib thickness, and Y-shaped angle. The proposed shear resistance formula is described in Eq. (1.1).

$$Q = 3.428 \cdot \left(\frac{d}{2} + 2h\right) \cdot t \cdot f_{ck} + 1.213 \cdot r \cdot A_{tr} \cdot f_y + \\ + 1.9 \cdot n \cdot \pi \cdot \left(\frac{d}{2}\right)^2 \sqrt{f_{ck}} + +0.428 \cdot m \cdot h \cdot s \cdot \sqrt{f_{ck}} \quad (1.1)$$

In equation (1.1), the first term indicates the end bearing resistance of the concrete by the Y-type

perfobond rib. The second term represents transverse rebars placed between the Y-shape ribs affects the shear resistance (see Fig. 1 (b)). The third term explains concrete dowel resistance caused by the holes and affects the shear resistance (see Fig. 1 (c)). The fourth term represents the concrete dowel resistance by Y-shaped ribs and affects the shear resistance (see Fig. 1 (d)).



a) The 1st term *b) The 2nd term*

c) The 3rd term *d) The 4th term*

Fig.1. *Mechanical characteristics of Y-type perfobond rib shear connector* [1]

Kim et al. (2014) and Kim et al. (2015), improved the shear resistance formula by considering additional push-out tests involving the rib width and height, concrete strength, number of transverse rebar, rib thickness, height, which can be significant when influence of shear resistance of Y-type perfobond rib shear connectors.

Lastly, Kim et al. (2017), modified shear resistance-equation for Y-type perfobond rib shear connector by performing push-out tests with additional design variables considered in previous study. An important modification was introduced by excluding the 3rd term, because the hole in Y-type perfobond rib connectors is semi-circular and has lesser effect on the total shear capacity of connector's, only 0.85% [3]. In addition, the yield strength of the transverse rebar was replaced the compressive strength of concrete due to considering predominant failure of concrete.

Furthermore, the authors found that, when the number of ribs increases the shear resistance increases, but the increasing rates are decreased and converged to 44% from two-four, four-six, six-eight rib systems. To reflect this effect the authors introduced a reduction factor R_n, and the shear resistance equations focusing on multiple ribs expressed as Eq.(1.2) and Eq.(1.3).

$$Q_u = 11500\, f_{ck}{}^{0.3} \cdot S_{rib} + R_n \cdot f_{ck}{}^{0.3} \left[700 \cdot n \cdot A_{tr}{}^{0.75} + 2600\,(n-2) \cdot S_{rib}\right] \quad (1.2)$$

In previous expressions:

$$S_{rib} = (w/80)^{0.95} \cdot (h'/120)^{0.3} \cdot (d/40)^{0.3} \quad (1.3)$$

$h' = h + 0.5 \cdot d$

R_n is the reduction factor, $R_n = 1/(n-1)^{0.12}$

Several attempts have been made to consider multiple arrangements of perfobond rib shear connector in shear resistance equations.

Studnika et al. (2004), studied the twin parallel arrangement perfobond connectors. Author found that some interaction between them leads to an overall resistance that is less than the sum of the resistance of the individual connectors. In their study they proposed Eq. (1.4) and (1.5) to predict this overall resistance P_{twin} from the resistance of each individual connector P_{RK} that placed side by side with an axial placing b (mm):

$$P_{twin} = k_d \cdot P_{RK} \quad (1.4)$$

$$k_d = 1.66 + \frac{b-100}{14000} \le 1.85 \quad (1.5)$$

Jun Okada, Teruhiko Yoda and Jean-Paul Lebet (2004) [5], investigated shear strength reduction equations (η) of the grouped arrangement of stud connectors. Based on the analytical results, the shear strength reduction equations of the grouped arrangement are proposed in Eq. (1.6) - (1.8).

$$P_{group} = \eta \cdot P_{sin\,gle} \quad (1.6)$$

$3 \le C_1 < 13$ уед

C25/30: $\eta = 0.023\ C_1 + 0.70$ (1.7)

$C_1 \ge 13$ уед

C25/30 – C50/60: $\eta = 1.0$ (1.8)

Liu Yang-qing, Liu Yu-qing, Zheng Shuang-jie (2016) [6], investigated effects of plate spacing on shear stiffness of perfobond rib shear connector. The main influence factor for the shear stiffness of perfobond connector is the spacing-diameter ratio, which is suggested to be no less than 3.3 when multi perfobonds are arranged in parallel. Authors developed new formula Eq (1.9) and Eq. (1.10) for perfobond shear stiffness (k_s), which accounts for the influence of plate spacing (α_e).

$$k_s = \alpha_e \left(0.27 + 0614\, n_E n_d^2\right) E_c d \quad (1.9)$$

$$\alpha_e = \begin{cases} 0.5 + 0.15\dfrac{e}{d}, & \dfrac{e}{d} < 3.3 \\ 1.0, & \dfrac{e}{d} \geq 3.3 \end{cases} \qquad (1.10)$$

2. PUSH-OUT TEST

Push-out tests were undertaken to examine group effects of the Y-type shear connector, considering distance between adjacent shear connectors. The distances were selected as 120 mm and 300 mm. For the shape of the bent rib configuration of group-Y-type shear connectors, the minimum acceptable spacing is 120 mm. Series of test specimens are denoted as S1, G2-120, G2-300 respectively. Table 1 describes conditions of variables for each series of specimen. For each series, three specimens with the same specifications are manufactured to make sure that the tests results are reliable.

Table 1. Push-out test series

Division/ Name	*S (mm)*	*Shape dimensions $W \times H \times t$ (mm)*	*Transverse rebar diameter d_{tr} (mm)*	*Hole diameter d_h (mm)*
S1	-	80 x 100 x 10	16	40
G2 - 200	120	80 x 100 x 10	16	40
G2 - 300	300	80 x 100 x 10	16	40

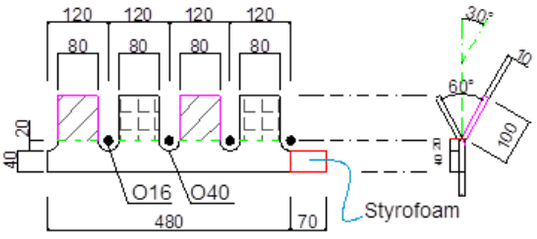


Fig. 1. *Dimensions of Y-shape rib*

The concrete compressive strength of 53.7 MPa, steel beam and Y-shape ribs SPHC (JIC G 3131 standard) steel grade with nominal yield stress of 307.2 MPa, all rebars of SD400 steel grade with a nominal yield stress of 400 MPa was used for the test.

2.1. Test set up

Push-out tests are performed at the KCL (Korea Conformity Laboratory) laboratory which is the top testing and inspection laboratory. After the specimens had been cured for about 28 days, they were placed in the "seismic isolation devices test & evaluation system" machine (see Fig. 2) with loading capacity of 30000. A monotonic load was applied in the displacement control method, and the load rate was set to 0.03 mm/s to prevent failure for less than 15 min, according to Eurocode 4 [7].

The push-out test stopped when the load decreased by 20% of the ultimate load. The load was applied until the displacement reached 50 mm. Each push-out specimen was equipped with eight LVDTs. Grid lines were drawn on the concrete surface of all specimens (Fig. 2), and a high-resolution camera was used to record the crack paths during the test. Push-out test set-ups are shown in Fig. 2.

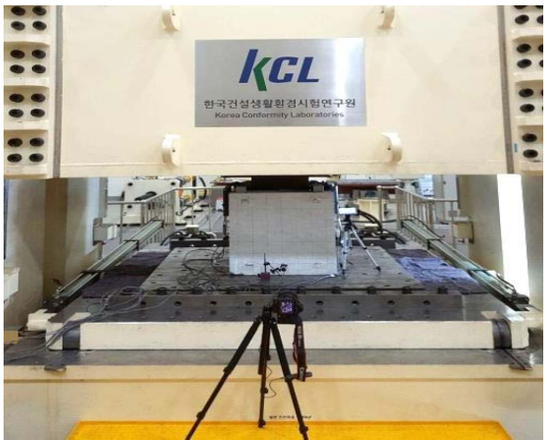


Fig.2. *Push-out test set up*



a) Front side of the specimen *b) Left side of the specimen*

Fig. 3. *Push-out test set up*

2.2. Test results

Results of push-out test series of a single Y-type perfobond rib shear connector S1, for group connector series G2 - 120 and G2- S300 are presented in Table II. The load-slip curve for all the series of specimens is shown in Fig. 3. The average ultimate load for single S1 was 1682.66 kN, and G2-120 had an ultimate load of 3320.33 kN that was approximately 1.97 times higher, compared with the single S1 specimen. For G2-300, the average ultimate load was 3830.18 kN, which is approximately 2.28 times, higher than that of a single S1 specimen. In case of an average characteristic slip is 19.5 mm, 35.2 mm and 34.5 mm respectively, the test results are much higher than that is required by "Eurocode 4" [7]. As

shown in Fig. 3, the series of specimens exhibit a similar load-slip behavior. These results indicated that the Y-type shear connector has a high ductile behavior both in single and grouped test series.

Table 2. Push-out test results

Types	*S (mm)*	*Average Ultimate Load* P_u *(kN)*	*Average Relative slip* δ_u *(mm)*	*Average Characteristic slip* δ_{uk} *(mm)*
S1	-	1682.66 (1.0)	21.4 (1.0)	19.3
G2-120	120	3320.33 (1.97)	28.8 (1.34)	25.9
G2-300	300	3830.2 (2.28)	38.3 (1.79)	34.4

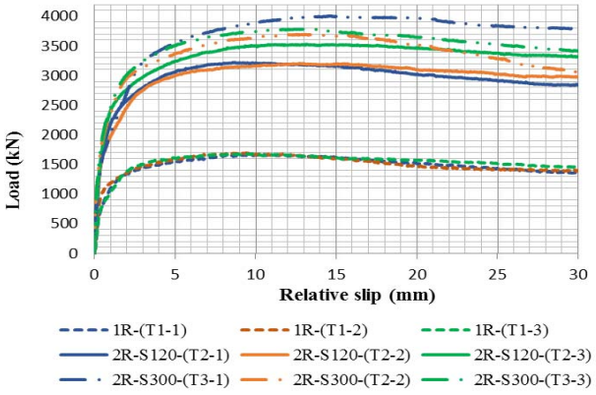


Fig .3. *Load-slip curves of experimental tests*

3. NUMERICAL ANALYSES

A 3D finite element model of the push-out test was developed using ABAQUS/Explicit software. Firstly, FE models were built with the use of exact geometry, analysis method, suitable contact interactions, constraints, boundary conditions, load application, material models, and a mesh to accurately model the actual push-out test specimens. Both geometric and material nonlinearity are also included in the analytical model.

3.1. Numerical modeling

A FE model consists of six parts as used in push-out tests: concrete slab, Y-type perfobond rib shear connector, steel beam, reinforcement rebars, transverse rebar, and rigid basement. Taking advantage of symmetry to reduce the size of the problem, only one-half of the specimens are modeled. A concrete damage-plastic model (CDPM) was used to simulate the non-linear behavior of the concrete, and a non-linear elastic-plastic model was used in the steel beam, Y-shape ribs and rebars. The concrete slab was meshed with a three-dimensional solid element C3D10M. Then the steel beam and Y-type perfobond rib shear connector were modeled into a three-dimensional reduced solid element C3D8R, while rebar elements were modeled into three-dimensional tress element T3D2.

Material properties of the steel and concrete are presented in Table 3 and Table 4 [8], [9].

Table 3. Steel material input in ABAQUS

Material	*Parameter*	*Value (MPa)*
Structural steel	E_s – Elastic modulus	210,000
	σ_{ys} – Yield stress	307.2
	σ_u – Ultimate stress	379.3
	ν – Poisson's ratio	0.3
Reinforcement rebar	E_s – Elastic modulus	200,000
	σ_{ys} – Yield stress	500
	σ_u – Ultimate stress	600

Table 4. Concrete material input in ABAQUS

Material	*Parameter*	*Value*
Concrete	E_{cm} – Elastic modulus	36426.3 (MPa)
	f_{ck} – Concrete compressive strength	53.7 (MPa)
	f_{ct} – Concrete tensile strength	5.37 (MPa)
CDPM	ρ – Density	2350 (kg/m^3)
	ψ – Dilation angle	40°
	$\in$ – flow of potential eccentricity	0.1
	σ_{b0}/σ_{c0} – ratio of the strength in the biaxial state to the strength in the uniaxial state	1.16
	K_c – shape of deviatory trace	0.667
	μ – Cohesion	0
	ν – Poisson's ratio	0.3

All parts are positioned together to form an assembly, and appropriate constraints and contact interactions are defined between them. Therefore, to ensure similar conditions for the tests conducted, FE models were used in a displacement-controlled method for loading steps. The applied displacement is linearly increased by the amplitude function. The relative slip in accordance with the loading steps was measured as the displacement of the end of the steel beam node. Nodes of elements on the bottom face of the rigid-base part which was fully constrained to the reference point at the bottom are named as "RP".

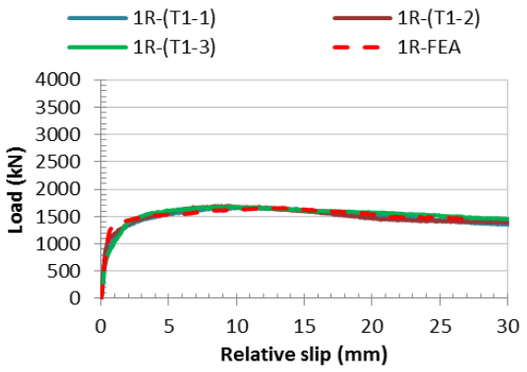
3.2. Validation numerical model

The finite element model developed in this study is validated against experimental test results. The load-slip behaviors obtained from the finite element

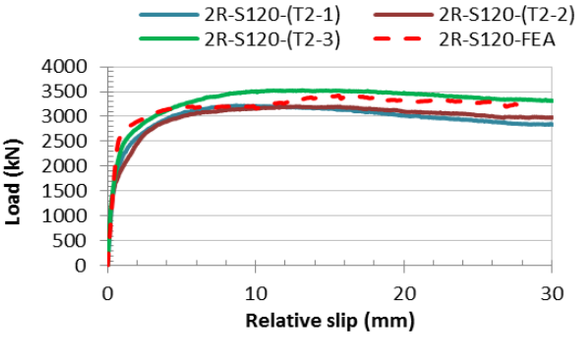
Table 5. Concrete material

№	*Push-out test results (A)*		*FEA results (B)*		*A/B*	*A/B*
Types	P_u	δ_u	P_u	δ_u	P_u	δ_u
S1	1670.91	21.1	1658.63	21	1.01	0.83
	1695.66	18.9			1.02	0.77
	1681.41	25.0			1.01	1.27
Aver	**1682.66**	**21.4**			**1.01**	**0.96**
G2-120	3225.58	25.8	3394.04	28	0.95	0.80
	3206.83	41.6			0.94	1.22
	3528.57	50.0			1.04	1.27
Aver	**3320.33**	**28.8**			**0.98**	**1.09**
G2-300	4008.92	50.0	3352.78	30	1.13	1.21
	3696.56	24.1			1.04	0.70
	3785.05	40.9			1.07	1.33
Aver	**3830.18**	**38.3**			**1.08**	**1.08**

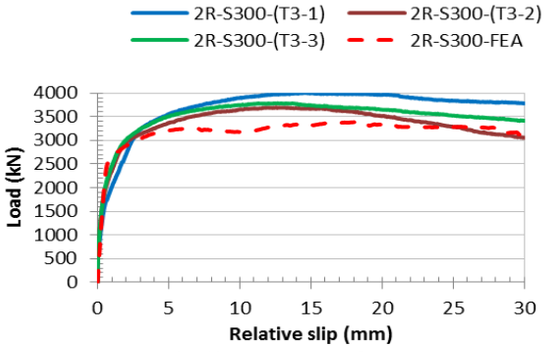
analyses are compared with experimental studies are shown in Fig. 9. Table 5 summarizes load-relative slip characteristics of obtained from the FEA and experimental tests. It can be observed that both FE analyses and experimental results match excellently in terms of curve shapes, ultimate shear strength and ductility. According to the Table 5, the average ratio of ductility obtained in the test to the numerical simulation, indicate a range from 0.96 to 1.09. Mismatches of numerical results compared to experimental results for slip capacity, are approximately 8% and considered to be correct. Mismatching ratios of shear resistance were 1.4%, 2.2 % and 7.2% for 1R, 2R – S120 and 2R – S300 specimens respectively. Therefore, taken together, the numerical model simulated in this study can be used to evaluate and predict not only the ultimate shear capacity but also the ductility of the Y-type perfobond rib shear connector having various specifications.



a) Load-slip curves of 1R-W80H100



b) Load-slip curves of 2R - S120



c) Load-slip curves of 2R - S300

Fig. 9. *Load-slip curves of experimental tests*

3.3. Parametric study

A spacing between parallel arrangement of adjacent shear connectors were varied within the range from S = 80 mm to S = 350 mm. The results of analytical study were presented in Table 6 and Fig. 4, as load-relative slip curves of the specimen with different spacing. Shear reduction factors represented in Table 6, are 1.86 - 2.0 times higher than in a single shear connector. Therefore, it is indicated that the influence of the grouped arrangement is negligible, when spacing is greater than 300 mm.

Table 6. Results of parametric study

Spacing	Results of parametric study (FEA)					
	P_u	P_{RK}	δ_u	δ_{uk}	k	Inc (%)
S1	1808.4	1627.56	21.2	19.1	1.0	-
G2-120	3369.94	3032.91	7.6	6.8	1.86	86
G2-150	3422.3	3080.07	11.0	9.9	1.89	89
G2-200	3560.08	3204.09	14.5	13.1	1.97	96
G2-300	3732.72	3359.43	21.0	18.9	2.0	100

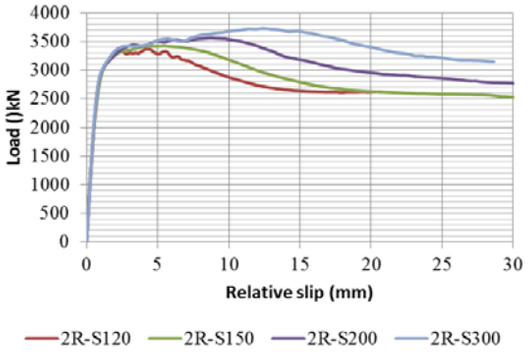


Fig. 4. *Load slip curves of parametric study*

4. DEVELOPMENT OF SHEAR RESISTANCE FORMULA FOR GROUP Y-TYPE PERFOBOND RIB SHEAR CONNECTOR

4.1. Shear strength reduction factor

Shear strength reduction factor k is determined by ratio of spacing between the adjacent shear connector (S) and transverse rebar diameter (d_s).

Numerical results indicate that the influence of adjacent shear connector can be estimated from acceptable minimum spacing of 120 mm to the maximum possible spacing of 300 mm. The shear resistance linearly increases as the spacing increases, gradually approaching the behavior of a single shear connector resistance. The beta values are acquired by regression analysis. Based on evaluation of $\beta_0 = 1.811,\ \beta_1 = 0.009$, the new formula for the group Y-type shear connector is given by Eq. (4.1) and Eq. (4.2).

$$k\left(\frac{S}{d_s}\right) = \begin{cases} 1.87, & \frac{S}{d_s} \le 7.5 \\ 1.81 + 0.009\left(\frac{S}{d_s}\right); & 7.5 < \frac{S}{d_s} < 22 \\ 2.0 & \frac{S}{d_s} \ge 22 \end{cases} \quad (4.2)$$

$$Q_u^G = k\left(\frac{S}{d_s}\right) \cdot Q_u^S \quad (4.3)$$

In previous expression:

Q_u^G - Shear resistance of a group Y-type perfobond rib shear connector (кН)

Q_u^S - Shear resistance of a single Y-type perfobond rib shear connector (кН)

k - Shear reduction factor, considering the spacing and transverse rebar diameter ratio

Based on Eq. 4.1 shear strength reduction factor can be calculated as shown in Fig. 5. The main influence factor for the shear resistance of a group Y-type perfobond rib shear connector is the spacing-transverse rebar diameter ratio (S/d_s), which is suggested to be no less than 7.5. When the spacing factor (S/d_s) increases shear strength increases and peaks at 22.

The shear resistances obtained from the numerical analysis are compared to verify the proposed shear resistance evaluation formula, Equation (4.2). Fig. 6. compares the shear resistances of the numerical analysis and given formulas.

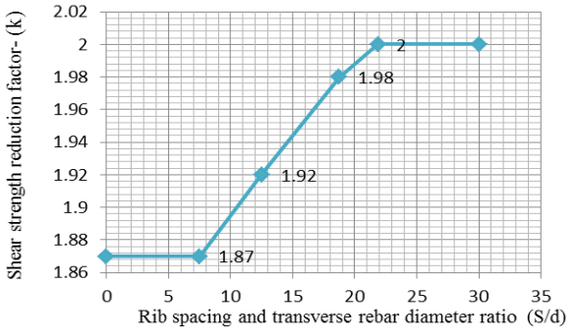


Fig. 5. *Shear strength reduction factor*

In Fig. 6, dots are placed closer to the diagonal dash line, meaning that the formula is fairly accurate in estimating the shear resistance of the group Y-type perfobond rib shears connectors. Table 7 summarizes the comparisons between the numerical simulation and estimated shear resistance of a group Y-type perfobond rib shear connector.

Table 7. Comparison shear resistance of numerical analysis and proposed formula

S MM	Eq 1.4 Q_u^S	$k\left(\frac{S}{d_s}\right)$	$\frac{S}{d_s}$	Eq 4.3 Q_u^G (EQ)	Q_u^G (NUM)	$\frac{NUM}{EQ}$
SPHC – C50						
80	1792.22	1.87	5.0	3345.6	3314.0	1.01
120		1.88	7.5	3365.7	3394.0	0.99
200		1.92	12	3446.1	3453.4	1.00
300		1.98	19	3546.7	3552.7	1.00
350		2.01	22	3597.0	3587.1	1.00
SS400 – C40						
120	1766.6	1.88	7.5	3373.9	3394.4	0.99
150		1.92	9.4	3454.6	3422.3	1.01
200		1.98	12	3555.4	3560.1	1.00
300		2.01	22	3655.8	3732.7	0.98

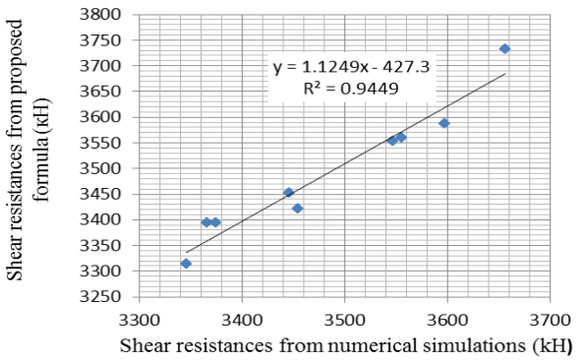


Fig. 6. *Evaluation of proposed formula*

5. CONCLUSION

Effects of spacing between adjacent shear connector on the shear resistance of group Y-type shear connectors is analyzed through the push-out test and numerical analysis. Following conclusions were drawn:

1) Push-out test results indicated that shear strength evaluation factor is 1.97 in double row specimens with 120 mm spacing, due to some overlapped stresses around a shear connector area. In double row specimens with spacing of 300 mm, shear strength evaluation factor is determined by 2.28 points.
2) Concrete damage-plastic model (CDPM) was used to simulate the non-linear behavior of the concrete, non-linear elastic-plastic model was used in steel beam, Y-shape ribs and rebars. The numerical analyses showed good agreement with experimental results.
3) The main influence factor for the shear resistance of group Y-type perfobond rib shear connector is the rib spacing-transverse rebar diameter ratio (S/d_s), which is suggested to be no less than 7.5. When spacing factor (S/d_s) increases shear strength increases and peaks at 22.
4) Based on numerical and experimental results shear strength evaluation formula for group Y-type shear connector is developed.

ACKNOWLEDGEMENTS

This research project was conducted in Structure & Bridge Engineering Lab. at Yonsei University. The authors would also like to acknowledge cooperation from members of Structure & Bridge Engineering Lab. at Yonsei University.

REFERENCES

[1] S.-H. Kim, K.-T. Choi, S.-J. Park, S.-M. Park, and C.-Y. Jung, "Experimental shear resistance evaluation of Y-type perfobond rib shear connector," *J. Constr. Steel Res.*, vol. 82, pp. 1–18, 2013.

[2] S. Kim, S. Park, W. Heo, and C. Jung, "Shear resistance characteristic and ductility of Y-type perfobond rib shear connector," vol. 2, pp. 497–517, 2015.

[3] S.-H. Kim, W.-H. Heo, K.-S. Woo, C.-Y. Jung, and S.-J. Park, "End-bearing resistance of Y-type perfobond rib according to rib width–height ratio," *J. Constr. Steel Res.*, vol. 103, pp. 101–116, 2014.

[4] S.-H. Kim, S. Park, K.-S. Kim, and C.-Y. Jung, "Generalized formulation for shear resistance on Y-type perfobond rib shear connectors," *J. Constr. Steel Res.*, vol. 128, pp. 245–260, 2017.

[5] J. Okada, T. Yoda, and J.-P. Lebet, "A STUDY OF THE GROUPED ARRANGEMENTS OF STUD CONNECTORS ON SHEAR STRENGTH BEHAVIOR," *Struct. Eng./Earthquake Eng., JSCE*, vol. 23, pp. 75–89, 2006.

[6] L. I. U. Yang-qing, L. I. U. Yu-qing, and Z. Shuang-jie, "Analysis on Effect of Plate Spacing on Shear Stiffness of," vol. 33, no. 9, 2016.

[7] Eurocode 4, "EN 1994-1-1: Eurocode 4: Design of composite steel and concrete structures – Part 1-1: General rules and rules for buildings," 2004.

[8] S. V.Chaudhari and M. A. Chakrabarti, "Modeling of Concrete for Nonlinear Analysis using Finite Element Code ABAQUS," *Int. J. Comput. Appl.*, vol. 44, no. 7, pp. 14–18, 2012.

[9] J. Zhang, Z. Zhang, and C. Chen, "YIELD CRITERION IN PLASTIC-DAMAGE MODELS FOR CONCRETE," *China Acta Mech. Solida Sin.*, vol. 23, no. 3, pp. 220–230, 2010.

Maintenance, Safety, Risk, Management and Life-Cycle Performance of Bridges – Powers, Frangopol, Al-Mahaidi & Caprani (Eds)
© 2018 Taylor & Francis Group, London, ISBN 978-1-138-73045-8

Evaluation of the ultimate response of post-tensioned composite slabs

G. Ranzi
School of Civil Engineering, The University of Sydney, Australia

ABSTRACT: Post-tensioned composite slab systems consist of concrete slabs poured on thin-walled profiled sheeting and prestressed soon after casting. This paper presents a theoretical model aimed at evaluating the ultimate moment resistance of this form of construction. In the first part of the paper the key equations describing the model are introduced and these are then followed by the model validation carried out against experimental results available in the literature. The comparisons carried out between the experimental measurements and the calculated capacities show good agreement.

1 INTRODUCTION

Post-tensioned composite steel-concrete slabs are widely used in Australia for floor systems in building applications. These represent an economical form of construction which consist of thin-walled profiled steel sheeting, post-tensioning strands and concrete (Figure 1). While the use of post-tensioned concrete floor solutions has been widely adopted over the last decades, the use of steel sheeting as permanent formwork for this type of application has been proposed in the last few years as a replacement for conventional plywood formwork. From a structural viewpoint, once the concrete has hardened, the contribution of the profiled sheeting as external reinforcement depends on the interaction between the steel sheeting and the concrete and, as such, this form of construction is classified as a composite system. With the use of post-tensioning, concrete cracking is significantly reduced, therefore enhancing the flexural stiffness and strength when compared with conventional composite slabs.

In 1990, Schravendeel et al. (1990) pointed out the potential advantages in adopting post-tensioned composite slab solutions based on strength considerations. A few years later, Koukkari (1999, 2001) investigated the behaviour of unbonded post-tensioned slabs. A composite prestressed slab system was proposed using the Tekdek steel deck which was prestressed prior to delivery to site. (Bailey et al., 2006) Three ultimate tests were carried out by Patrick and Lloyde (2008) to compare the structural response of a composite slab, a post-tensioned solid slab and a post-tensioned composite slab prepared with Fielders KF57 steel deck. The samples were simply-supported with a total length of 5 m and a distance between roller supports of 4 m.

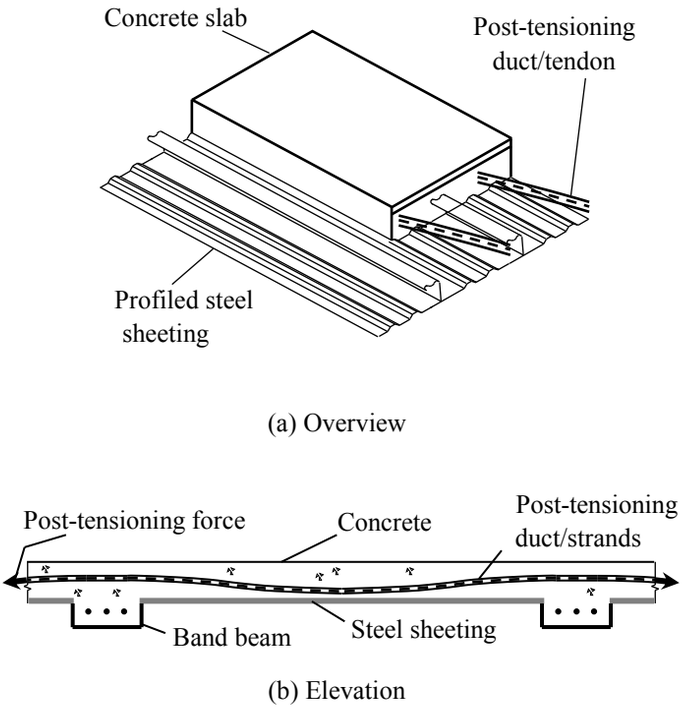


Figure 1. Typical post-tensioned composite slab.

They reported a significant increase in strength of the post-tensioned composite slab when compared to the capacities exhibited by the composite and post-tensioned solid samples, with the latter exhibiting premature bond failure between the strands and surrounding grout. For the post-tensioned composite

sample they highlighted that the test was terminated due to the fracture of the steel deck at the nearly estimated full shear connection capacity, calculated making use of a nonlinear cross-sectional analysis while ignoring slip effects. (Patrick and Lloyde, 2008) Experimental work on post-tensioned composite slabs was also proposed by considering their ultimate response, e.g. (Ranzi et al., 2013a; Ranzi and Ostinelli, 2017) and their time-dependent behavior produced by creep and shrinkage effects, e.g. (Ranzi et al., 2013b, 2013c).

In this context, this paper presents a theoretical model for the evaluation of the ultimate resistance of post-tensioned composite slabs that is validated against test results available in the literature, e.g. (Ranzi et al., 2013a; Ranzi and Ostinelli, 2017). The comparisons carried out between the predictions obtained with the proposed theoretical model and those measured during the experiments show good agreement.

2 THEORETICAL MODEL

A theoretical approach is briefly presented in the following to determine the ultimate resistance of post-tensioned composite slabs. The model builds on current design practice for composite slab design, e.g. (EN 1994-1-1, 2004), and on the design procedure adopted for prestressed floors, e.g. (Gilbert et al., 2016). The assumptions of the proposed model can be summarized as follows (Ranzi et al., 2017): (i) no tensile stresses are resisted by the concrete; (ii) plane sections remain plane and perpendicular to the member axis before and after loading; (iii) a rectangular stress block is used to depict the concrete stresses (here introduced, without any loss of generality, based on Australian guidelines (AS3600, 2009); (iv) full and partial shear connection is used to describe the interface behaviour between the sheeting and the slab (where the partial shear connection depicts the condition in which the shear connection represents the critical component at a particular cross-section); (v) the response of the prestressing is described using a simplified procedure; and (vi) the components forming the structural member are assumed to be ductile and possible failure due to limited ductility needs to be verified separately, e.g. rupture of the steel sheeting as observed in the composite post-tensioned test reported in reference (Patrick and Lloyde, 2008).

With the proposed approach, the ultimate moment of the post-tensioned composite section is determined as follows:

$$M_u = N_c z_c - N_{pre} z_{pre} + M_{pr} \tag{1}$$

where N_c and N_{pre} describe the axial forces resisted by the concrete component and by the prestressing strands, respectively, the lever arms z_c and z_{pre} depict the distances of the concrete and prestressing forces, respectively, from the line of action of the force resisted by the profiled steel sheeting N_p, and M_{pr} is the plastic resistance of the profiled steel sheeting. (Ranzi and Ostinelli, 2017) The calculations of the terms contributing to the ultimate moment capacity M_u is outlined in the following and the associated stress and strain diagrams are illustrated in Figure 1.

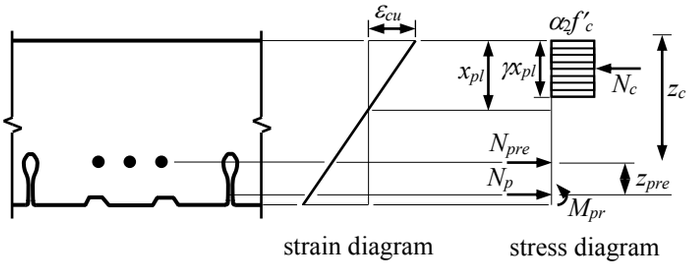


Figure 1. Stress and strain distribution considered in the design model.

The concrete response at ultimate conditions has been described, without any loss of generality, based on Australian design recommendations (AS3600, 2009), while material representations of other design standards could be specified as well. In this manner, the concrete strain ε_{cu} in the extreme fibre of the slab at the ultimate moment condition is assumed to equal 0.003. The compressive resistance of the concrete can then be calculated as: (AS3600, 2009)

$$N_c = \alpha_2 f'_c \gamma x_{pl} b \tag{2}$$

which assumes a stress equal to $\alpha_2 f'_c$ (with f'_c being the characteristic strength of the concrete and α_2 being defined in Equation 3a) to be resisted by the concrete over a height of γx_{pl}, x_{pl} defines the distance between the neutral axis and the slab top fibre (reduced by γ provided in Equation 3b), and b depicts the width of the slab. The parameters γ and α_2 are used to define the concrete stress block to be used in design and is determined in the following based on Australian guidelines (AS3600, 2009):

$$\alpha_2 = 1.0 - 0.003 f'_c \qquad 0.67 \le \alpha_2 \le 0.85 \tag{3a}$$

$$\gamma = 1.05 - 0.007 f'_c \qquad 0.67 \le \gamma \le 0.85 \tag{3b}$$

The axial contribution of the prestressing strands N_{pre} is here accounted for as follows:

$$N_{pre} = \sigma_{pu} A_{pre} \tag{4}$$

where A_{pre} depicts the area of the strands located at a distance d_{pre} from the top fibre of the cross-section to the centroid of the prestressing steel, and σ_{pu} can be determined using a simplified expression (applicable when the minimum effective stress in the strands is not less than $0.5 f_{bc}$) available in reference (AS3600, 2009). For the 7-wire ordinary strands commonly specified for composite post-tensioned

floors the following properties apply: A_{pre} = 98.6 mm^2, f_{preb} = 1870 MPa, f_{prey} = 1533 MPa and f_{preb} / f_{prey} = 0.81978609. σ_{pu} is determined based on Australian guidelines as (AS3600, 2009):

$$\sigma_{pu} = f_{pb}\left(1 - \frac{k_1 k_2}{\gamma}\right) \tag{5}$$

with f_{pb} being the characteristic minimum breaking load of the prestressing strand, and parameters k_1 and k_2 being calculated from:

$$k_1 = 0.28 \qquad \text{for } f_{ypre}/f_{pb} \geq 0.9 \tag{6a}$$

$$k_1 = 0.4 \qquad \text{for } f_{ypre}/f_{pb} < 0.9 \tag{6b}$$

$$k_2 = \frac{1}{b_{ef} d_{pre} f_c'}\left[A_{pre} f_{pb} + A_{pe} f_{yp} + \left(A_{st} - A_{sc}\right) f_{ys}\right] \tag{7}$$

where A_{st} and A_{sc} define the tensile and compressive reinforcement (i.e. steel reinforcing bars) with f_{ys} being its yield strength, b_{ef} represents the effective concrete width, and f_{ypre} and f_{yp} describe the yield strength of the prestressing strands and of the steel sheeting, respectively.

Partial shear connection theory is used to consider the influence of the profiled steel sheeting in the analysis. With this approach, the force resisted by the sheeting N_p is determined as follows:

$$N_p = \min\left(N_\tau, N_{FSC}\right) \tag{8}$$

in which N_τ depicts the shear connection force relying on mechanical interlock, and N_{FSC} defines the axial force that the profiled steel sheeting could resist in the case of full shear connection (i.e. when the interface between the concrete and the sheeting is not the weak component of the member). The value for N_τ is calculated with respect to the interface shear strength τ_u that depicts an experimental representation of the shear-bond response exhibited between the sheeting and the concrete that needs to be identified experimentally for each profiled sheeting to be used for post-tensioned floor applications. The terms N_τ and N_{FSC} can be expressed as:

$$N_\tau = \tau_u b L_x \tag{9}$$

$$N_{FSC} = \min\left(N_{yp}, N_{c(\max)} - N_{pre(\max)}\right) \tag{10}$$

where τ_u is the interface shear strength between the sheeting and the concrete obtained from experimental tests, L_x represents the distance of the cross-section under consideration to the nearest support, $N_{c(max)}$ and $N_{pre(max)}$ describe compressive and tensile capacities of the concrete and prestressing components, respectively, and N_{yp} depicts the axial force resisted by the profiled sheeting at yield. These terms can be calculated as:

$$N_{c(\max)} = \alpha_2 f_c' \gamma D_c b \tag{11a}$$

$$N_{pre(\max)} = f_{pb} A_{pre} \tag{11b}$$

$$N_{yp} = f_{yp} A_{pe} \tag{11c}$$

in which A_{pe} is the area of the profiled steel sheeting. Obviously, the maximum compressive force available in the post-tensioned solid slab (i.e. $N_{c(max)}$ - $N_{pre(max)}$ in Equation 10) depend on the prestressing force level and a check might need to be carried out at the end of the calculations to ensure that the adopted N_{FSC} is within the available prestressed solid slab capacity.

For the profiled steel sheeting considered in the validation presented in this study, τ_u equals 210 kPa. The flexural contribution of the profiled steel sheeting is then determined using:

$$M_{pr} = 1.25 M_{pa}\left(1 - \frac{N_p}{N_{yp}}\right) \leq M_{pa} \tag{12}$$

where M_{pa} represents the plastic moment of the profiled sheeting.

3 VALIDATION

The proposed model is applied in in this section to predict the ultimate moment resistance of the specimens outlined in references (Ranzi et al., 2013a; Ranzi and Ostinelli, 2017). The material and geometric properties adopted in the numerical calculations are those obtained from material testing and from measurements of the samples, therefore reflecting the condition of the tested specimens. Details regarding the samples and the testing can be found in references (Ranzi et al., 2013a; Ranzi and Ostinelli, 2017).

The ultimate moments evaluated using the proposed approach are summarized in Table 1.

Table 1. Summary of comparisons between experimental and calculated ultimate moment resistances.

Sample ID	Experimental ultimate moment (M_{exp})	Calculated ultimate moment (M_u)	M_u / M_{exp}
	kNm	kNm	
S1*	152.1	140.2	0.92
S2*	124.2	105.1	0.85
S3*	170.0	159.8	0.94
S4*	174.9	155.3	0.89
S5*	250.9	239.2	0.95
S6*	265.9	250.8	0.94
CK1**	132.8	127.2	0.96
CK2**	144.6	137.7	0.95

* from reference (Ranzi and Ostinelli, 2017)
** from reference (Ranzi et al., 2013a)

The comparisons between the experimental and the predicted values show good agreement. This can be observed considering the ratios of the estimated ultimate moments (i.e. M_u) over the measured capacities (i.e. M_{exp}) reported in Table 1, where M_u / M_{exp} and remained in the range of 0.89-0.96 for all test samples except specimen S2. In the case of sample S2, the specimen exhibited a flexural shear failure and its ultimate moment prediction was $M_u/M_{exp} = 0.85$.

4 CONCLUSIONS

This paper has presented a theoretical model for the evaluation of the ultimate resistance of post-tensioned composite slabs. The main equations describing the model have been presented and have been validated against experimental measurements available in the literature. The comparisons between predicted and experimental moment resistances showed good agreement.

5 ACKNOWLEDGEMENTS

The experimental work in this article was supported under Australian Research Council's Linkage Projects funding scheme (project number LP0990190) and by Stramit Building Products and Arup as Partner Organisations. The design model and numerical predictions developed as part of this study were supported by the Australian Research Council through its Future Fellowship scheme (FT140100130). Support from the University of Sydney (Materials & Structures Research Cluster) is gratefully acknowledged.

6 REFERENCES

Bailey, C.G., Currie, P.M. & Miller, F.R. 2006. Development of a new long span composite floor system, *The Structural Engineer* 84(21): 32-38.

EN 1994-1-1. 2004. *EUROCODE 4: Design of composite steel and concrete structures - Part 1-1: General rules and rules for buildings*, European Committee for Standardization.

Gilbert, R.I., Mickleborough, N.C. and Ranzi, G. 2016. *Design of prestressed concrete to AS3600-2009*, 2nd edition, Spon Press, London, UK.

Koukkari, H. 1999. Steel sheet in a post-tensioned composite slab, *Proceedings of Eurosteel 99*, Prague, Czech Republic, 26-29 May 1999.

Koukkari, H. 2001. Anchorage zone in a steel-concrete composite slab with unbonded tendons, *Proceedings of the International Symposium on Connections between Steel and Concrete*, Stuttgart, Germany, 10-12 September 2001.

Patrick, M. & Lloyde, M. 2008. Development of Moment Capacity Tables for Post-Tensioned Composite Slabs incorporating High-Tensile Steel Decking, Validated by test Data, *Proceedings of the Australasian Structural Engineering Conference (ASEC)*, Melbourne, Australia, 26-27 June 2008.

Ranzi, G., Al-Deen, S., Hollingum, G., Hone, T., Gowripalan, S. & Uy, B. 2013a. An experimental study on the ultimate behaviour of simply-supported post-tensioned composite slabs, *Journal of Constructional Steel Research* 89: 293-306.

Ranzi, G., Al-Deen, S., Ambrogi, L. & Uy, B. 2013b. Long-term behaviour of simply-supported post-tensioned composite slabs, *Journal of Constructional Steel Research* 88: 172-180.

Ranzi, G., Leoni, G. & Zandonini, R. 2013c. State of the art on the time-dependent behaviour of composite steel-concrete structures, *Journal of Constructional Steel Research* 80: 252-263.

Ranzi, G. & Ostinelli, A. 2017. Ultimate behaviour and design of post-tensioned composite slabs, *Engineering Structures* 150: 711-718.

Schravendeel, P.L., De Sitter, W.R. & Klop, G.R.. 1990. Prestressed post-tensioned composite floor slabs, *IABSE Conference*, 1990.

Standards Australia. 2009. *Australian Standard for Concrete Structures AS3600-2009*, Standards Australia, Australia.

Maintenance, Safety, Risk, Management and Life-Cycle Performance of Bridges – Powers, Frangopol, Al-Mahaidi & Caprani (Eds)
© 2018 Taylor & Francis Group, London, ISBN 978-1-138-73045-8

Service behaviour of composite steel-concrete slabs with a simplified approach and a hygro-thermo-chemical-mechanical model for the non-uniform shrinkage evaluation

M. Bocciarelli
Architecture, Built Environment and Construction Engineering Department, Politecnico di Milano, Italy

G. Ranzi
School of Civil Engineering, The University of Sydney, Australia

ABSTRACT: Composite steel-concrete floors are widely used throughout the world for building applications. These floors usually consist of composite slabs supported by steel beams in steel framed construction and of post-tensioned composite slabs carried by band beams in concrete buildings. The design of composite floors is commonly governed by serviceability limit state associated with deflection limits. Recent research has pointed out that a non-uniform shrinkage profile occurs in slabs cast on profiled steel sheeting. In this context, this paper provides a brief overview of the main factors influencing the service behavior of composite slabs and of a model capable of predicting their long-term deflections considering two approaches for the evaluation of the non-uniform shrinkage profiles, i.e. a simplified approach and a hygro-thermo-chemical-mechanical model. The adequacy of the proposed prediction models is then outlined by comparing the long-term deflections calculated with the proposed approach and those measured experimentally from long-term tests carried out on selected composite and post-tensioned composite slab samples that have been reported in the literature.

1 INTRODUCTION

Composite steel-concrete floors are widely used throughout the world for building applications. Their design is commonly governed by serviceability limit state associated with deflection limits. Recent research has pointed out that a non-uniform shrinkage profile occurs in slabs cast on profiles steel sheeting, i.e. composite slabs, due to the inability of the concrete to dry from its underside because of the presence of the sheeting, e.g. (Al-deen et al., 2011, 2015; Al-deen and Ranzi, 2015; Gholamhoseini et al., 2014; Gilbert et al., 2012; Ranzi et al., 2013a, 2013b). In this context, this paper provides a brief overview of the main factors influencing the service behavior of composite slabs and of a model capable of predicting their long-term deflections considering two approaches for the evaluation of the non-uniform shrinkage profiles, i.e. a simplified approach and a hygro-thermo-chemical-mechanical model. Their main differences relies on the fact that the simplified procedure uses a linearly-varying shrinkage profile as input in the design steps (Ranzi 2017), while the refined multi-physics model needs the evaluation of the temperature and relative humidity distributions for the determination of the non-uniform shrinkage effects (Bocciarelli et al., 2017). The use of the hygro-thermo-chemical-mechanical model requires an inverse analysis procedure to be carried out for the characterisation of the numerous parameters that it needs in input. The adequacy of the deflection prediction model is then briefly outlined by comparing the long-term deflections calculated and those measured experimentally from long-term tests carried out on selected composite and post-tensioned composite slab samples that have been reported in the literature.

2 CONCRETE BEHAVIOUR: NON-UNIFORM SHRINKAGE PROFILES

The service behavior of concrete structures is influenced by concrete time effects, such as creep and shrinkage. This section intends to outline the key features describing the development of non-uniform shrinkage profiles in composite floors. For this purpose, two unreinforced and unloaded concrete slabs are considered and differ for their exposure conditions, i.e. one slab being exposed to dry on both sides (Figure 1a) and one being exposed on one side and sealed on the other (Figure 2a). In the former case (Figure 1a), the slab is able to dry from both its top and bottom faces and it exhibits constant total deformations over time (Figure 1b). For design purposes, it is well accepted to simplify the problem and to assume that these total deformations can represent the shrinkage distributions. In reality, the real shrinkage distribution is nonlinear, e.g. (Gilbert and Ranzi 2011). When considering the unreinforced slab with exposure conditions similar to those of a composite slab (Figure 2a), the asymmetric drying

conditions produce a linearly varying total deformation profile over time (Figure 2b). Under the assumption of using linear shrinkage profiles for design purposes, it is possible to relate the total deformations to a simplified shrinkage distribution. Also in this case, the real shrinkage profile would be nonlinear.

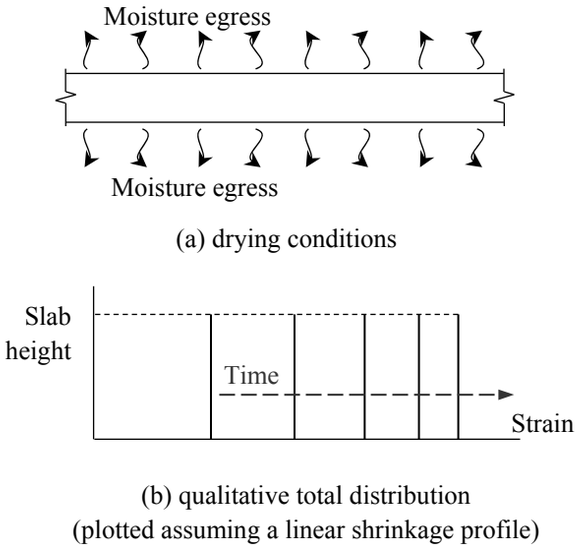


Figure 1. Drying conditions and qualitative total deformations for slab exposed on both sides.

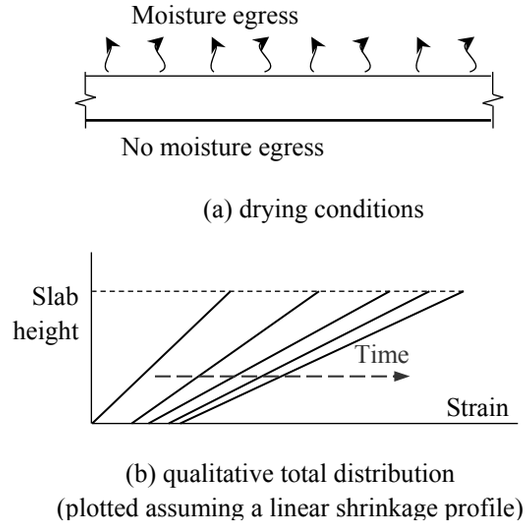


Figure 2. Drying conditions and qualitative total deformations for slab exposed on one side only.

3 MODELLING

3.1 *Model description*

The deflection predictions at service conditions account for the contribution of a number of components. These usually consist of the instantaneous deflection δ_0 produced by the short-term service loads, of the deflection δ_{cc} produced by creep effects and of the component δ_{cs} induced by shrinkage. Details of the design model can be found in (Ranzi 2017). In particular, the instantaneous deflection is determined performing an analysis of the composite slab adopting an effective flexural rigidity. The latter can be evaluated following common design specifications recommended for reinforced concrete slabs, as performed in the Australian guidelines (AS3600 2009). The creep deflection is calculated relying on the effective modulus method, e.g. (Gilbert and Ranzi 2011), and considering only the sustained part of the short-term service load. The remaining shrinkage deflection is obtained by evaluating the effects produced by a shrinkage-induced curvature κ_{cs} at different locations and calculated as a weighted value between the curvature exhibited under uncracked condition $\kappa_{cs.uncr}$ and the one developed for cracked conditions $\kappa_{cs.\,cr}$. The weighting term in this case is the distribution coefficient γ_{cs} that considers the degree of cracking exhibited in the slab for the applied service load. Based on this, the shrinkage-induced curvature at a particular cross-section is determined as follows:

$$\kappa_{cs} = (1 - \gamma_{cs}) \kappa_{cs.cr} + \gamma_{cs} \kappa_{cs.uncr} \quad (1)$$

The evaluation of the shrinkage profile is carried out in this paper considering two procedures, i.e. one based on a simplified approach and one relying on the use of a hygro-thermo-chemical-mechanical model.

3.1.1 *Simplified approach for the evaluation of the non-uniform shrinkage*

The shrinkage profile to be used in the design (assumed to be linearly varying) is determined based on a reference shrinkage value ε_{sh} obtained from reinforced concrete guidelines, e.g. (AS3600 2009), by adopting a hypothetical thickness equal to the thickness of the composite slab and assuming both sides of the slab to be exposed. The non-uniform shrinkage distribution is then defined considering a linearly varying profile possessing values of 1.2 ε_{sh} and 0.2 ε_{sh} at the top (exposed) and bottom (sealed) sides of the slab, respectively. The definition of the shrinkage reference strain is a consequence of the fact that the top and bottom values of the non-uniform shrinkage profile have been calibrated experimentally against those exhibited by companion concrete slab samples exposed on both sides with same thickness as the composite specimens.

3.1.2 *Use of a hygro-thermo-chemical-mechanical model for the evaluation of the non-uniform shrinkage*

The determination of the non-uniform shrinkage distribution to be used for the evaluation of the shrinkage deformations and deflections can be carried out using a hygro-thermo-chemical-mechanical model, such as the one presented in (Bocciarelli et al., 2017). Such a multi-physics approach requires an extensive set of parameters to be used in input

that can be identified by means of inverse analysis techniques. Examples of how this model is suitable for the representation of shrinkage effects has been described in (Bocciarelli et al., 2017).

3.2 *Model validation*

The proposed deflection model has been validated against long-term tests available in the literature on composite slabs and post-tensioned composite slabs. For the purpose of this paper only selected experimental tests have been selected and presented in Figures 3-6.

In particular, Figure 3 reports a comparison between the values calculated with the design model (using the simplified approach for the definition of the non-uniform shrinkage effects) and the experimental measurements recorded in a long-term test of a composite slab whose details can be found in (Gholamhoseini et al 2014, Gholamhoseini 2014). In this case, the results relate to a sample cast on a Fielders' KF70 profiled steel sheeting. A second long-term test carried out on a composite slab is depicted in Figure 4. (Al-deen et al 2015) Also in this case the non-uniform shrinkage profile has been obtained with the simplified approach. In this case, a Stramit Condeck HP profiled sheeting was used in the preparation of the specimen. The third comparison presented in this paper relates to a post-tensioned composite slab also cast on a Stramit Condeck HP profile and its comparisons are illustrated in Figure 5 by using the simplified approach for the non-uniform shrinkage representation (Ranzi et al 2013b). The same profiled steel sheeting is used for the post-tensioned sample whose measurements and comparisons with predicted values are shown in Figure 6 (Ranzi et al., 2012) . In this case both simplified and hygro-thermo-chemical-mechanical model have been used for the evaluation of the non-uniform shrinkage distributions. Both approaches are shown to provide good predictions.

In summary, the deflection predictions based on the use of a non-uniform shrinkage profile well match the experimental deflections recorded over time, while the use of a constant shrinkage distribution underestimates the deformation.

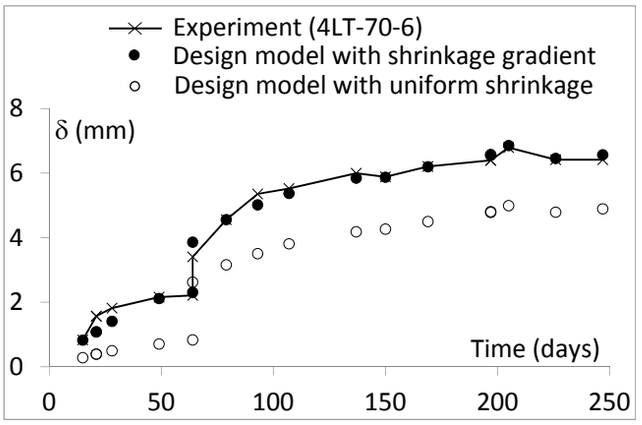


Figure 3. Comparisons between experimental measurements and calculated values: sample 4LT-70-6. (Gholamhoseini et al 2014, Gholamhoseini 2014)

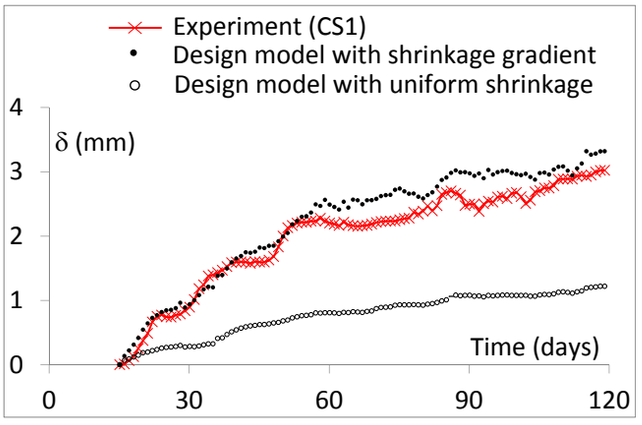


Figure 4. Comparisons between experimental measurements and calculated values: sample CS1. (Al-deen et al 2015)

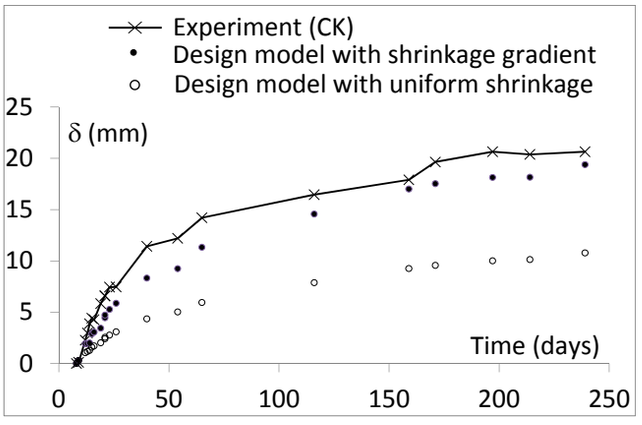


Figure 5. Comparisons between experimental measurements and calculated values: sample CK. (Ranzi et al 2013b)

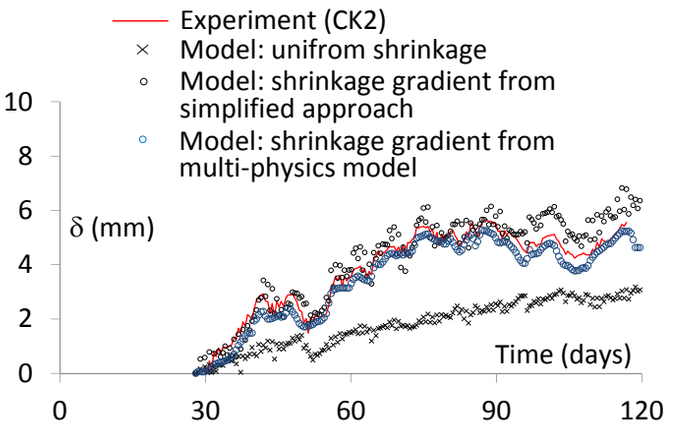


Figure 6. Comparisons between experimental measurements and calculated values: sample CK2. (Ranzi et al 2012)

4 CONCLUSIONS

This paper has provided a brief overview of recent advances related to the serviceability limit state design of composite floor systems. In particular, it has presented a design model for the evaluation of deflections at service conditions. The particularity of this work relies on the ability of the proposed formulation to account for the development of a non-uniform shrinkage profile, observed in recent long-term experimental tests carried out on composite slabs and post-tensioned composite slabs, to occur due to the inability of the concrete to dry from its underside. The evaluation of the shrinkage profile has been carried out considering two procedures, i.e. one based on a simplified approach and one relying on the use of a hygro-thermo-chemical-mechanical model. The validity of the proposed approach has been validated by comparing the numerical calculated values to the measured deflections of selected composite and post-tensioned composite samples. In all cases, the adopted model implemented with a non-uniform shrinkage profile has shown to well match the experimental data while the use of a uniform shrinkage has underestimated the deformations.

5 ACKNOWLEDGEMENTS

The work presented in this paper was supported by the Australian Research Council through its Future Fellowship scheme (FT140100130). Support from the University of Sydney (Materials & Structures Research Cluster) is gratefully acknowledged.

REFERENCES

Al-Deen, S. & Ranzi, G. 2015. Effects of non-uniform shrinkage on the long-term behaviour of composite steel-concrete slabs, *International Journal of Steel Structures,* 15(2): 415-432.

Al-Deen, S., Ranzi, G. & Uy, B. 2015. Non-uniform shrinkage in simply-supported composite steel-concrete slabs, *Steel and Composite Structures* 18(2): 375-394.

Al-deen, S., Ranzi, G. & Vrcelj, Z. 2011. Full-scale long-term and ultimate experiments of simply-supported composite beams with steel deck, *Journal of Constructional Steel Research* 67(10): 1658-1676.

AS3600. 2009. *Australian Standard for Concrete Structures AS3600-2009*, Standards Australia.

Bocciarelli, M., Ranzi, G. and Rahman, M.M. 2017. A hygro-thermo-chemical-mechanical model for the shrinkage prediction in composite steel-concrete floors, *Proceedings of the Concrete 2017 Conference*, Adelaide (Australia), 22-25 October 2017.

Gholamhoseini, A. 2014. *Time-dependent behaviour of composite concrete slabs*, PhD Thesis, The University of New South Wales, Australia.

Gholamhoseini, A., Gilbert, R.I., Bradford, M.A. & Chang, Z.T. 2014. Time-dependent deflection of composite concrete slabs, *ACI Struct Journal* 111(4): 765-776.

Gilbert, R.I., Bradford, M.A., Gholamhoseini, A. & Chang, Z.-T. 2012. Effects of Shrinkage on the Long-Term Stresses and Deformations of Composite Concrete Slabs, *Engineering Structures* 40:, 9-19.

Gilbert, R.I. & Ranzi, G. 2011. *Time-dependent behaviour of concrete structures*, Spon Press.

Ranzi, G. 2017. Service design approach for composite steel-concrete floors, *Structures and Buildings, Proceedings of the Institution of Civil Engineers - Structures and Buildings*, https://doi.org/10.1680/jstbu.16.00196.

Ranzi, G., Leoni, G. & Zandonini, R. 2013a. State of the art on the time-dependent behaviour of composite steel-concrete structures, *Journal of Constructional Steel Research* 80: 252-263.

Ranzi, G., Al-Deen, S., Ambrogi, L. & Uy , B. 2013b. Long-term behaviour of simply-supported post-tensioned composite slabs, *Journal of Constructional Steel Research* 88: 172-180.

Ranzi, G., Ostinelli, A. & Uy, B. 2012. An experimental study on the shrinkage and ultimate behaviour of post-tensioned composite slabs, *Proceedings of the 22nd Australasian Conference on the Mechanics of Structures and Materials (ACMSM22), Sydney (Australia), 11-14 December 2012.*

Maintenance, Safety, Risk, Management and Life-Cycle Performance of Bridges – Powers, Frangopol, Al-Mahaidi & Caprani (Eds)
© 2018 Taylor & Francis Group, London, ISBN 978-1-138-73045-8

Behavior of an innovative demountable steel-concrete connector under static loading

Fei Yang, Yuqing Liu
Department of Bridge Engineering, Tongji University, Shanghai, People's Republic of China

ABSTRACT: Using suitable bolted connectors in lieu of conventional welded stud connectors may have great advantages in terms of the accelerated construction of composite bridges and the concrete slab replacement considering the life-cycle design of composite bridges. An innovative demountable steel-concrete connector, which mainly consists of a short bolt, a long bolt and a coupler, is proposed in this paper. Compared with other existing demountable bolted connectors, the proposed innovative demountable connector could render the dismantling of concrete slabs more convenient. Static push-out tests are carried out on three groups of demountable bolted connector specimens for investigating their failure mode and the fundamental mechanical behavior. The test results demonstrate that the failure mode of proposed demountable connectors is that the shank of short bolts is sheared off directly without local concrete crushing under couplers. The shear bearing capacity can be approximately estimated as 0.8 times of the tensile strength of short bolts. The peak slip of the steel-concrete interface grows with the increase of the bolt shank diameter. The clearance between bolt shank and bolt hole has an effect on the shear stiffness of innovative demountable connectors. The fundamental mechanical behavior of the innovative demountable connector can be a reference for the connector arrangement in the steel-concrete interface of composite bridges employing the proposed innovative bolted connector.
Keywords: composite bridge; demountable connector; shear behavior; push-out test; accelerated construction

1 INTRODUCTION

Steel-concrete composite superstructures have a great advantage in terms of the structural performance and the accelerated bridge construction especially exhibited in short to medium span continuous girder bridges (Brozzetti 2000; Nakamura et al. 2002; Hanswille 2011). In the construction of steel-concrete composite bridges, the welded headed stud connector has become the most prevailing connector for achieving the composite action between steel girders and concrete slabs owing to its outstanding mechanical performance and rapid welding technique. There also has been a comprehensive research production focusing on the mechanical behavior of the welded stud connector (Xue et al. 2012; Lin et al. 2014; Lin et al. 2016). On the other hand, if the concrete slabs of composite bridges deteriorate seriously under overloaded traffic scenarios and environmental actions, dismantling or strengthening of deteriorated concrete slabs are supposed to be implemented for extending the service life of composite bridges. However, it would be rather costly and time-consuming to dismantle the damaged concrete slabs which are fully attached to the upper flange of steel girders by welded stud connectors (Lachemi et al. 2007; Umphrey et al. 2007). In the design stage of the composite bridges, therefore, the issue of replacing the concrete slabs should be taken into account to improve the structural sustainability of composite bridges and to reduce the structural life-cycle cost.

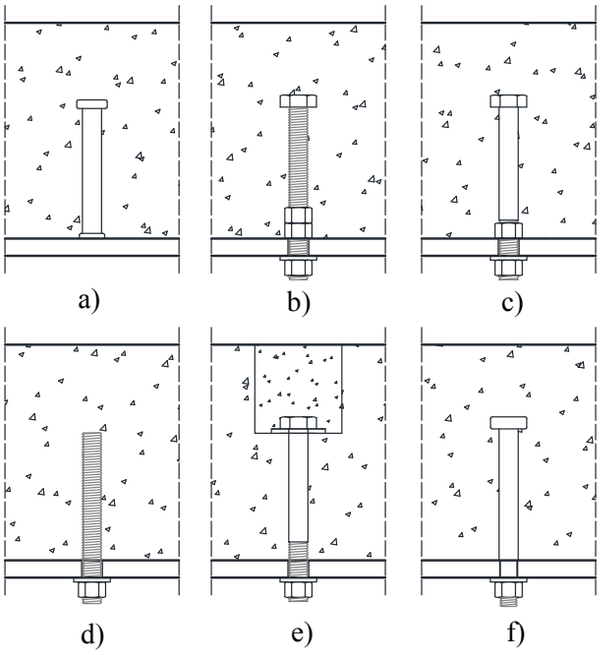
Bolted connectors can be an option for the connection between steel girders and concrete slabs in composite bridges. A concrete slab attached to steel girders using bolted connectors could be dismantled more conveniently than using the most prevailing welded stud connector. Therefore, a reasonable configuration for the steel-concrete bolted connector is necessary and significant to realize the dismantling work of concrete slabs effectively. Currently, bolted connectors are rarely employed in the construction of steel-concrete composite bridges due to lack of detailed research and design specifications.

In this paper, an innovative demountable steel-concrete bolted connector is proposed after examining the existing researching on the demountable bolted connectors and comparing their configurational characteristics. The innovative demountable connector mainly consists of a long bolt, a short bolt and a coupler, which could render the dismantling of concrete slabs more convenient. Static push-out tests are carried out on three groups of demountable bolted connector specimens for investigating their failure mode and the fundamental mechanical behavior including shear bearing capacity, slip performance and shear stiffness. The experimental results for the innovative demountable connector can be a reference for the connector arrangement in the steel-concrete interface of composite bridges employing the proposed innovative bolted connector.

2 CONFIGURATION OF BOLTED CONNECTORS

2.1 *Existing bolted connectors*

Recently, there has been some research work in terms of using demountable bolted connectors to achieve the composite action between steel girders and concrete slabs. Figure 1 shows the configuration of the conventional welded stud connector and five types of existing demountable bolted connectors, and the configurational characteristics of those bolted connectors will be given a detailed explanation as follows.



a) Welded headed stud connector
b) Type I Double-nut bolt
c) Type II High-strength bolt
d) Type III Adhesive anchor
e) Type IV High-tension friction-grip bolt
f) Type V Headed stud bolt

Figure 1. Configuration of bolted connectors.

Kwon et al. (2010) proposed three types of post-installed bolted shear connectors for achieving the composite action in existing non-composite bridges built in America before the 1970s. Those three types of post-installed bolted connectors were called Double-Nut Bolt (Type I, Figure 1b), Adhesive Anchor (Type III, Figure 1d) and High-Tension Friction-Grip Bolt (Type IV, Figure 1e). The pretension in Type I bolted connector was only induced on the bolt shank between the upper and the bottom nuts, and the initial shear stiffness of this bolted connector could be improved by the pretension. The bolt in Type III bolted connector could not be pretensioned because of its special geometry configuration, and eventually this bolted connector was selected for application in strengthening the non-composite bridge owing to its simple configuration and low-cost installation. The through high strength bolt was exploited in Type IV bolted connector, which could attach the concrete slab to the top flange of steel girders. But the concrete adjacent to the bolt shank has to bear local compressive stress induced by the pretension of the high strength bolt.

Pavlović et al. (2013) investigated the shear behavior of Type II demountable bolted connector through push-out experimental tests, and Figure 1c exhibits the configuration of this bolted connector. He believed the competitiveness of the prefabricated concrete slab could be improved through embedding Type II bolted shear connectors into the prefabricated concrete slab, and the prefabricated concrete slab could benefit the accelerated construction and of composite bridges. Moynihan & Allwood (2014) thought that a demountable connection between steel girders and concrete slabs could not only develop the composite action in the constructional stage but also permit the reuse of steel girders and concrete slabs after the dismantling the composite bridges at the end of their service life. Type II demountable bolted connector was utilized in the construction of the experimental composite beams, which were implemented in static loading tests for investigating the performance of the demountable bolted connector and the composite beam.

Chen et al. (2014) believed that a suitable bolted connector was needed to achieve composite action between steel girders and precast concrete slabs from the perspective of the accelerated construction of composite bridges. High-strength through-bolt connectors, whose configurations just like the High-Tension Friction-Grip Bolt (Type IV, Figure 1e) proposed by Kwon, were examined under static push-out tests. Liu et al. (2015) thought that an innovative demountable high-strength friction-grip bolt shear connectors (Type IV, Figure 1e) in composite beams could greatly enhance the sustainability of building infrastructures. Some practical design recommendations were proposed for predicting the shear bearing capacity and the load-slip curve of the bolted connector. The configuration of the last type bolted connector was proposed by Dai et al. (2015) They reformed the conventional welded headed studs into demountable bolted connectors which are depicted in Figure 1f. The configurational characteristic of Type V demountable bolted connector was that its shank diameter in the bolt hole was 1 to 3 mm less than the diameter of the shank embedded in concrete slabs. The mechanical performance of this type bolted connector is closer to that of the conventional welded stud connector.

2.2 *Proposed demountable connector*

An innovative demountable steel-concrete bolted connector as shown in Figure 2 is proposed for facilitating the dismantling work of concrete slabs in

composite girder bridges. There are two configurations for the demountable bolted connector which are exhibited in Figure 3. As is shown in Figure 3a, the proposed demountable bolted connector with Type I configuration consists of a short bolt, a long bolt, a washer and a coupler. The long bolt and coupler for Type I demountable connector could be manufactured as one component which could be seen in Figure 3b. The configuration of the proposed demountable bolted connector could be much simplified in Type II configuration, but the long bolt embedded in concrete slabs need to be specially produced by the manufacturer. In this research, the demountable bolted connector with Type I configuration will be examined since all components of Type I demountable connector could be obtained.

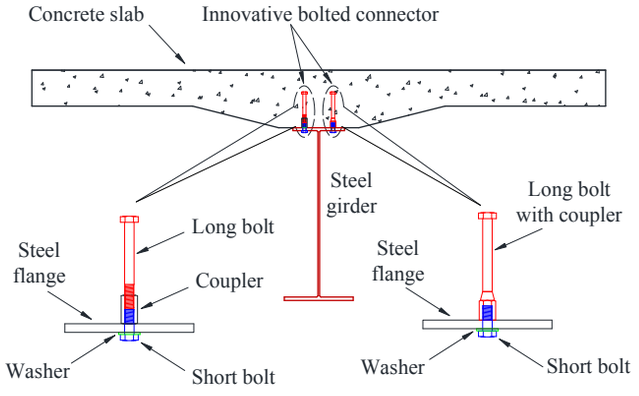
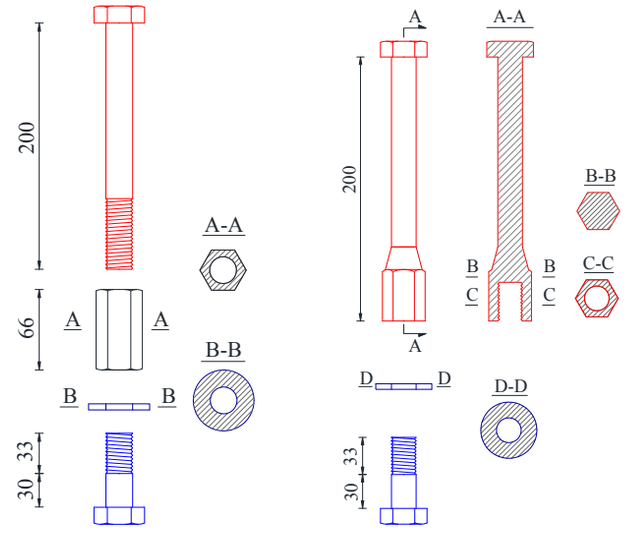


Figure 2. An innovative demountable bolted connector.



a) Type I configuration b) Type II configuration

Figure 3. Configurations of the innovative connector.

If the proposed demountable bolted connector is used in composite bridges with cast-in-place concrete slabs, the short bolt, washer and coupler should be installed firstly on the top flange of steel girders, and then the long bolt could be screwed into the coupler. Lastly, concrete slabs could be cast after the installation of the demountable bolted connectors. Whether imposing pretension on the short bolt or not depends on the mechanical requirement of the steel-concrete interface of composite bridges.

If the proposed demountable bolted connector is used in composite bridges with prefabricated concrete slabs, all components of the proposed demountable bolted connector should be installed on concrete slab formworks before pouring the concrete of slabs firstly. When the concrete strength of prefabricated slabs gets to the design target, formworks of concrete slabs should be dismantled along with short bolts and washers, and long bolts and couplers of demountable connectors are embedded in prefabricated slabs. When assembling the prefabricated slab on steel girders, shorts bolts and washers should again be screwed into couplers from the underside of the top flange of steel girders. Therefore, the position of short bolt holes in the top flange of steel girders should be drilled much accurately for the use of the demountable bolted connector in the prefabricated concrete slabs.

As is shown in Figure 2, when dismantling concrete slabs of composite bridges using demountable bolted connectors, screwing out the short bolts from the underside of the steel flange could separate steel girders and concrete slabs completely. However, if concrete slabs are attached to steel girders with the existing bolted connectors as shown in Figure 1, the nut below the steel flange should be removed first, and then concrete slabs need to be lifted up with the bolted connector embedded in concrete slabs to implement the dismantling work, which may be feasible but rather complicated. Consequently, the innovative demountable bolted connector could render the dismantling of concrete slabs more convenient.

In the following, static push-out tests will be introduced for investigating the failure mode and fundamental mechanical performance of the innovative bolted connector. The shear bearing capacity, load-slip curve and the shear stiffness of the innovative bolted connector will be discussed in detail.

3 DESIGN OF PUSH-OUT TESTS

3.1 *Program of push-out tests*

Table 1 exhibits the main variables for each group of push-out tests. There are three bolt diameters in total including M18, M22 and M27, and all their strength are grade 8.8 which means that the characteristic tensile strength of the bolt is 800 MPa and the yield-strength ratio of the bolt is 0.8. Type I configuration in Figure 3a shows the dimension of the long bolt, coupler and short bolt of the M22 demountable bolted connector. All the shank length of M18, M22 and M27 long bolts are 200 mm. The height of M18, M22 and M27 couplers are 3 times of their internal diameters, which are 54 mm, 66 mm and 81 mm, respectively. The shank length of M18, M22 and M27 short bolts are 57 mm, 63 mm and 70.5 mm, respec-

tively. To ensure the reliability of shear performance and tensile performance of the demountable bolted connector simultaneously, both the long bolt and the short bolt should be screwed into the coupler 1.5 times length of their internal diameters.

Table 1. Program of push-out tests.

Specimen	Strength	Diameter (mm)	Clearance (mm)	Concrete Age (days)
B1	Grade 8.8	18	0.15	57
B2			0.26	58
B3		22	0.31	60
B4			0.30	70
B5		27	0.51	68
B6			0.47	72

There exists clearance between the bolt shank and the bolt hole in the steel plate. The installation of short bolts may be difficult if the clearance is too small, while the shear stiffness of demountable bolted connectors may decrease if the clearance becomes much larger. So the clearance between the bolt shank and the bolt hole is set to be 0.2 mm up to 0.5 mm when drilling the bolt hole in steel plates. In the fabrication process of each bolted connector push-out specimen, the diameter of each bolt shank and the interior diameter of the corresponding bolt hole were measured for obtaining the clearance between the bolt shank and the bolt hole of each demountable bolted specimen. Table 1 lists the average clearance of four bolted connectors for each bolted push-out specimen. The actual average clearance for B1 to B6 specimens is between 0.1 mm and 0.5 mm. The average clearance for B5 and B6 specimens with M27 bolted connectors is much larger which is closer to 0.5 mm.

During casting the concrete of push-out specimens, standard prisms (150 mm × 150 mm × 300 mm) and cubes (150 mm × 150 mm × 150 mm) were cast at the same time. The concrete compressive strength was obtained from both the prism and the cube compressive tests, the concrete tensile strength was obtained from the cube splitting tests, and the modulus of elasticity of the concrete was determined using the prism compressive tests. The test material properties of the concrete are listed in Table 2. During the static push-out loadings, as shown in Table 1, specimen B1 was loaded with the shortest concrete age which was 57 days and specimen B6 with the longest concrete age which was 72 days. Therefore, it could be inferred that the concrete actual compressive strength of each specimen might exceed 50 MPa.

Table 2. Material properties of concrete.

Testing Age	Cube Strength (MPa)	Prim Strength (MPa)	Tensile Strength (MPa)	Young's Modulus (GPa)
7 days	34.8	32.9	—	38.75
28 days	48.9	43.4	4.62	40.63

3.2 *Strength of short bolts*

The axial tensile tests were carried out on M18, M22 and M27 short bolts of the innovative demountable bolted connector. Figure 4 shows the final appearance of M22 short bolts, and it can be seen that the necking deformation in the threaded part of each shot bolt is significantly obvious after the load-displacement enters into the descending branch.

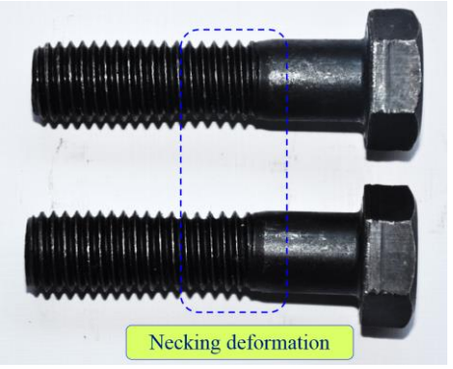


Figure 4. Failure model of tensile test for short bolts.

3.3 *Strength of connecting sleeves*

For investigating the connecting performance of the coupler in the proposed demountable bolted connector, axial tensile specimens were fabricated through using M18, M22 and M27 couplers to connect two long bolts whose diameter were consistent with corresponding couplers. In each axial tensile specimen, the long bolt threaded shank which was screwed into the coupler was 1.5 times of the bolt diameter. Figure 5 shows the failure mode of axial tensile tests for M22 axial tensile connecting specimens, and it can be seen that the fractured section locates in the threaded part of the long bolt. It can be concluded that the axial connecting performance of the bolt coupler whose height is 3 times of its internal diameter is reliable in the proposed demountable bolted connector.

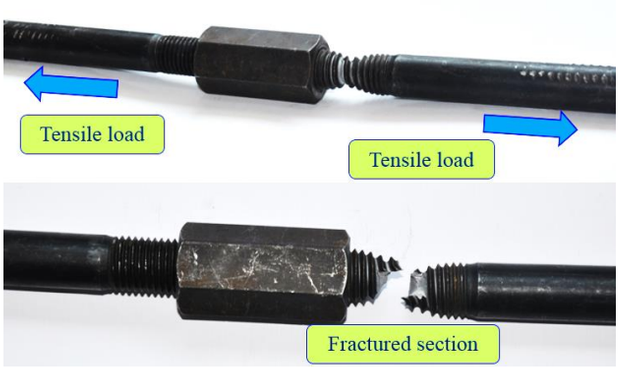


Figure 5. Failure models of tensile tests for couplers.

3.4 *Push-out specimens*

Figure 6 demonstrates the configuration of demountable bolted connector push-out specimens. There are four bolted connectors for each specimen. The trans-

verse spacing for bolted connectors is 200 mm, and the spacing to top and bottom of the concrete block both are 250 mm. The thickness of the concrete slab in the specimen for standard push-out test recommended in EN 1994-1-1 is only 150 mm, and the thinner concrete slab may result in a splitting failure mode of the concrete slab rather than the fracture of connectors due to their much higher shear bearing capacity (Pavlović et al. 2013). Therefore, the concrete blocks in push-out specimens are designed as a cube with 500 mm edge. In the concrete block, some HRB 335 (Hot-rolled Ribbed Bar with 335 MPa yielding strength) rebar with 16 mm diameter reinforces the concrete block, whose transverse, longitudinal and vertical spacing all is 400 mm.

The thickness of the steel plate adjacent to the concrete block is set to be 30 mm for preventing that the wall of the bolt hole occurs bearing failure mode. The thickness of the web of the push-out steel member is also 30 mm. The height of the push-out steel member is 500 mm, and the width of the flange and web are 400 mm and 200 mm, respectively. The distance from the bottom of the push-out steel member to that of the concrete block is 50 mm considering that the maximum slip would not exceed 20 mm.

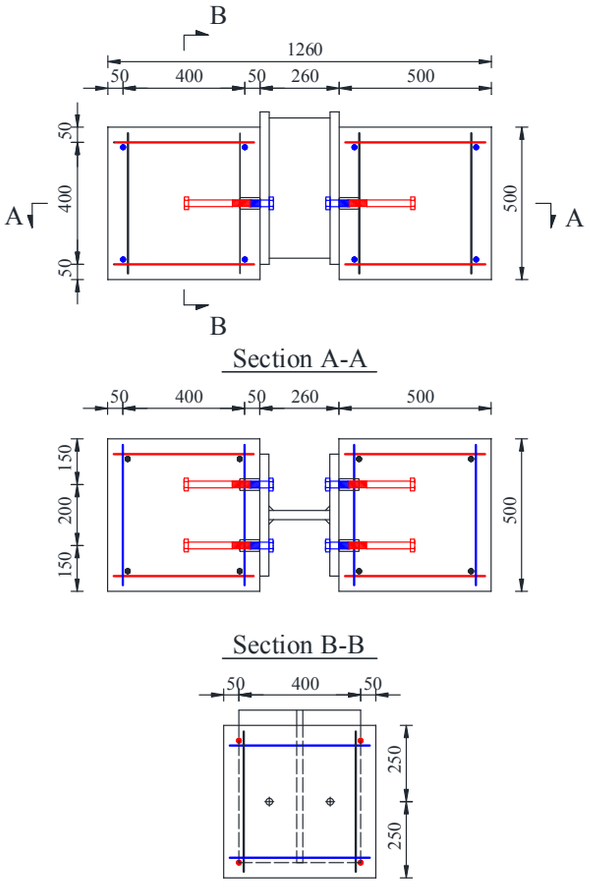


Figure 6. Details of push-out specimens / mm.

The push-out specimen with M18 and M27 bolted connectors before casting concrete is shown in Figure 7. In the installation of bolted connectors, an ordinary wrench was used to screw short bolts and long bolts into couplers. Therefore, there is almost no pretension induced in short bolts. The concrete of all the specimens was cast using the ready mixed C50 concrete.

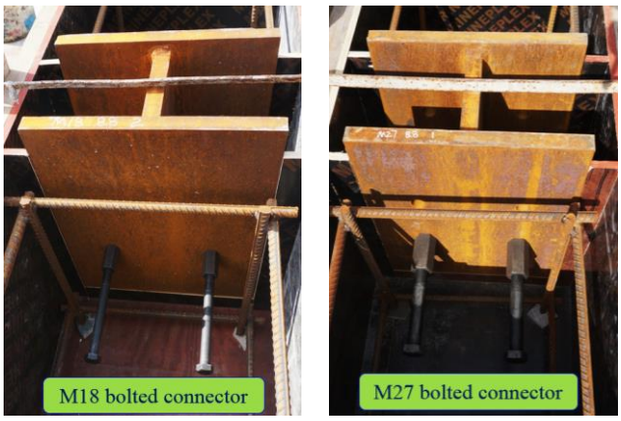


Figure 7. Push-out specimens before casting concrete.

3.5 *Schedule for loading and measurement*

Figure 8 shows the test set-up of push-out experimental tests. The push-out tests were performed through a hydraulic jack with a total capacity of 2000 kN. At the bottom of the concrete blocks, a layer of fine sand was paved to reduce the concentrated reaction force between the specimen and the testing ground. Each push-out specimen was equipped with four displacement transducers to monitor the vertical slip between the concrete block and the steel plate. In the following analysis of the slip data, the average value of the four vertical displacements was taken as the representative slip for each specimen.

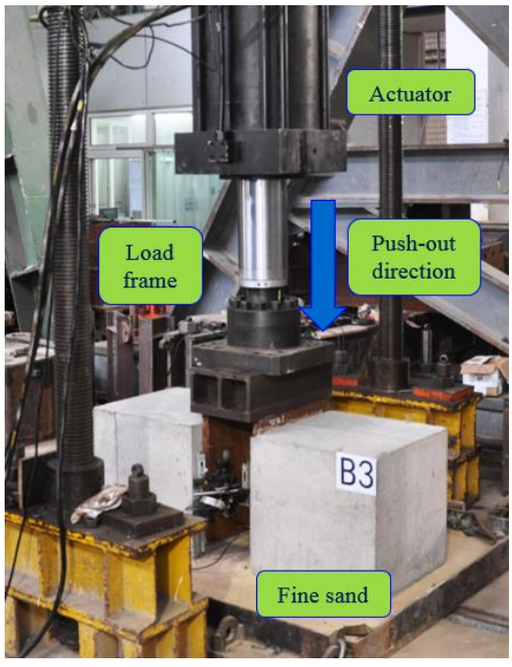


Figure 8. Loading set-up of push-out tests.

The loading schedule recommended in EN 1994-1-1 was followed for investigating the shear behavior of steel-concrete connectors. In the loading schedule, the push-out load was first applied in increments up to 40% of the expected failure load and

then cycled 25 times between 5% and 40% of the expected failure load for examining the service performance of the connector. After the cycling load, subsequent load increment was imposed until the fracture of the shear connector for investigating the failure mode and the mechanical behavior of the connector in the ultimate shear state. Force-controlled loading was applied in the cyclic loading, and the loading rate was approximately 5 min/cycle which was assumed to be quasi-static loading. Displacement-controlled loading was applied in the last stage loading, and the displacement loading rate was 0.3 mm/min.

4 ANALYSIS FOR PUSH-OUT TESTS

4.1 *Failure mode*

Figure 9 shows the failure mode of the demountable bolted connector specimen under static push-out tests. The failure mode of three groups of demountable bolted connector specimens all is that the short bolts are sheared off directly. As is shown in Figure 9a, there are only a few small cracks without local concrete crushing phenomena under couplers after the shearing off of the short bolts for each specimen. The coupler embedded in the concrete of bolted connector specimens enlarges the interface area between bolt shank and the ambient concrete, resulting in that the local compressive stress of the concrete under the connecting sleeve is much lower and that the interface slip also decreases. As is shown in Figure 9b, the final failure mode of the short bolts for each bolted connector specimen that the fractured section of the short bolts are extremely even, therefore, the bolted connectors could be considered to be a brittle facture mode.



Figure 9. Failure modes of bolted connectors.

4.2 *Test results*

Figure 10 shows the load-slip curve of each push-out specimen, and the vertical axis represents the average load of the four demountable bolted connectors. There are five stages in the load-slip curve of the innovative bolted connector including bolt shank slipping stage, cyclic loading stage, linear stage, nonlinear stage, and the descending stage.

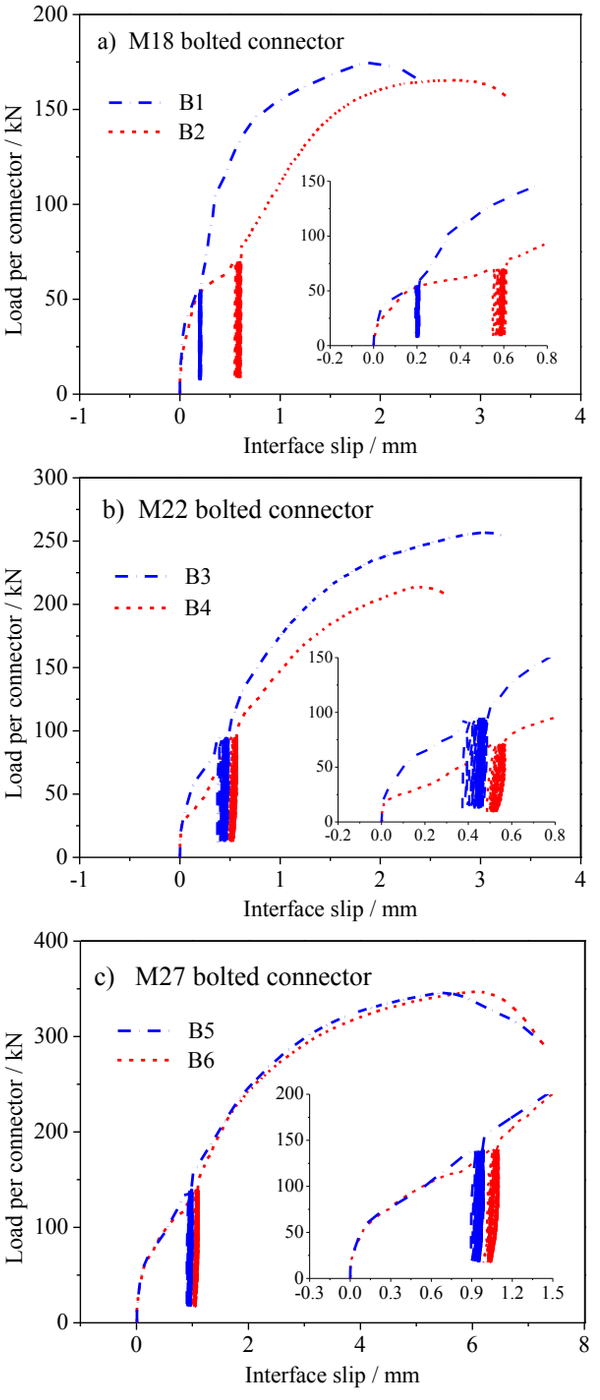


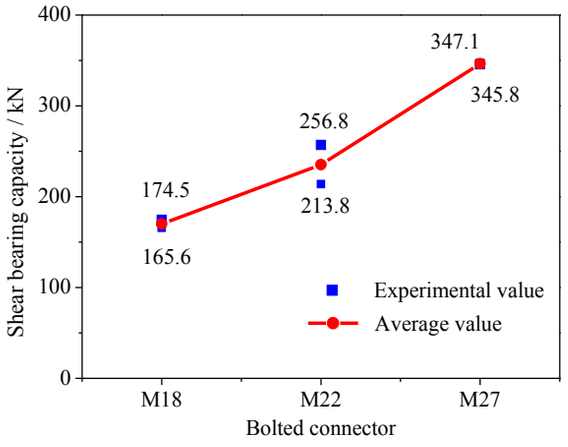
Figure 10. Load-slip curves of push-out specimens.

Due to the clearance between the bolt shank and the bolt hole of the innovative bolted connectors, it can be observed that the clearances have a significant effect on the shape of the load-slip curves of the push-out specimens especially for B2 and B4 specimen. When the initial loading gets to the 40% of the expected failure load, the slip between the bolt shank

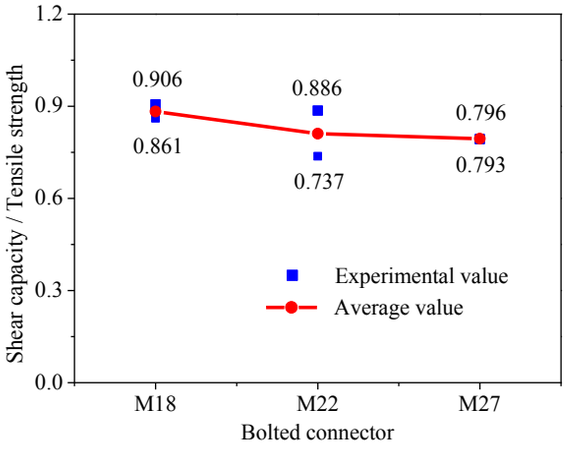
and the bolt hole for each push-out specimen all has occurred. The load-slip curve in reciprocating loading is much closer to that in unloading process, and the shear stiffness in the cyclic loading stage is obviously larger than that in the initial loading stage. After the cyclic loadings, the load-slip curves for each bolted connector push-out specimen could increase linearly and then enter into the nonlinear stage until the ultimate shear bearing capacity. The descending branches of the load-slip curve for each bolted connector push-out specimen is rather short. Besides, there was loud sound when short bolts were sheared off, demonstrating that the failure mode of the innovative bolted connectors is much brittle compared with that of welded headed stud connectors.

4.3 *Shear bearing capacity*

Figure 11 exhibits the distribution of the shear bearing capacity of three groups of demountable bolted connectors. All the shear bearing capacity experimental results of six push-out specimens are illustrated in Figure 11a. The ratio distribution of the shear bearing capacity of the corresponding tensile strength for each push-out specimen is shown in Figure 11b.



a) Shear bearing capacity



b) Comparison with tensile strength

Figure 11. Shear bearing capacity of bolted connectors.

For M18 bolted connectors, the shear bearing capacity is about 0.88 times of their tensile capacity, which is the maximum ratio in three groups of demountable bolted connectors. The average ratio of the shear bearing capacity to the tensile capacity for M22 and M27 bolted connectors is approximately 0.80.

4.4 *Peak slip*

The peak slip for each push-out specimen is defined as the slip corresponding to the ultimate shear bearing capacity. Figure 12 shows the peak slip for three groups of demountable bolted connectors. The peak slip would grow gradually as the bolt diameter increases. The average peak slip for M27 bolted connectors is 5.77 mm, which is closer to the ductile connector's minimum slip requirement specified in EN 1994-1-1. In addition, due to the peak slip of the demountable bolted connector is much smaller than that of conventional welded stud connector, the maximum slip of the steel-concrete interface used demountable bolted connector should be limited strictly.

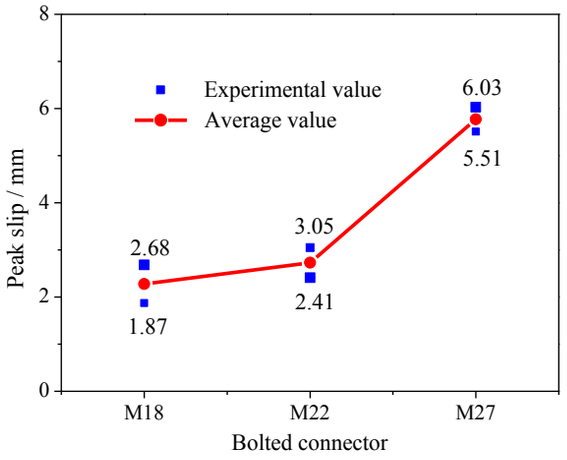
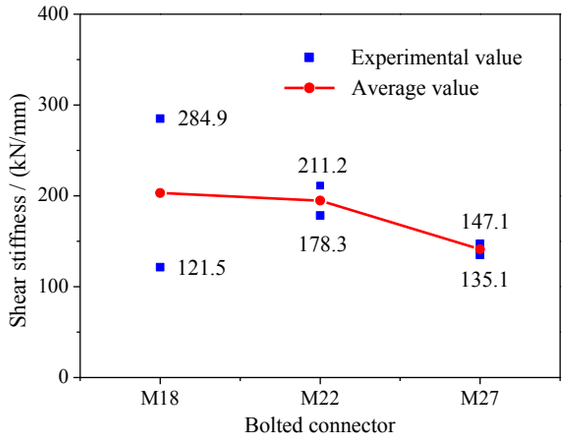


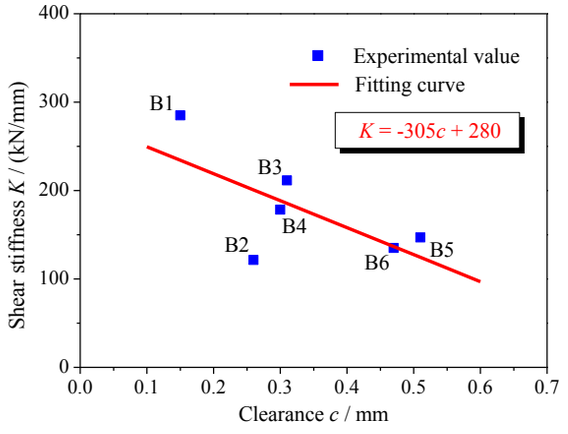
Figure 12. Peak slip of bolted connectors.

4.5 *Shear Stiffness*

The shear stiffness for the demountable bolted connector is defined as the ratio of the half of the shear bearing capacity to the corresponding slip value. Figure 13 shows the shear stiffness distribution of the innovative bolted connectors. It can be seen from Figure 13a that the shear stiffness of M18 bolted connectors are extremely discrete, and the shear stiffness of other two groups bolted connectors are approximately similar. Therefore, it can be concluded from Figure 13a that there is little correlation between the shear stiffness and the diameter of demountable bolted connectors.



a) Shear stiffness



b) Comparison with bolt hole clearance

Figure 13. Shear stiffness of bolted connectors.

Figure 13b illustrates the relationship between the shear stiffness of demountable bolt connectors and their corresponding bolt hole clearance. The shear stiffness of each bolted connectors exhibits a decreasing tendency with the increase of the clearance between the bolt shank and the bolt hole. The average clearance for B5 and B6 specimens is about 0.5 mm, and the shear stiffness for those two specimens is in the order of 140 kN/mm. Much lower stiffness of connectors may result in that the slip in the steel-concrete interface may need to be considered in composite beam deflection calculations.

5 CONCLUSION

1) An innovative demountable steel-concrete connector, which mainly consists of a short bolt, a long bolt and a coupler, was proposed for rendering the dismantling of the concrete slab in composite bridges more conveniently.

2) The failure mode of four groups of bolted connector specimens is that the short bolts are sheared off directly. There are only a few small cracks without local concrete crushing phenomenon under the coupler after the fracture of the short bolts for each specimen.

3) The shear bearing capacity of each bolted connector can be predicted as 0.8 times of the bolt characteristic tensile strength. The peak slip of each bolted connector specimen grows with the increase of the bolt diameter of grade 8.8 bolted connectors.

4) There is little correlation between the shear stiffness and the diameter or strength of the bolted connector, while the shear stiffness of each bolted connector exhibits a decreasing tendency with the increase of the clearance between the bolt shank and the bolt hole.

REFERENCES

Brozzetti J, Design development of steel-concrete composite bridges in France. Journal of Constructional Steel Research, 2000, 55: 229–243.

Chen Y T, Zhao Y, West J S, et al. Behavior of steel-precast composite girders with through-bolt shear connectors under static loading. Journal of Constructional Steel Research, 2014, 103: 168-178.

Dai X H, Lam D, Saveri E. Effect of concrete strength and stud collar size to shear capacity of demountable shear connectors. Journal of Structural Engineering, 2015, 141(11): 04015025.

EN 1994-1-1: 2004. Eurocode 4: design of composite steel and concrete structures, Part 1-1: general rules and rules for buildings. Brussels: European Committee for Standardization (CEN); 2004.

Hanswille G. Composite bridges in Germany designed according to Eurocode 4-2. Composite Construction in Steel and Concrete VI. 2011: 391-405.

Kwon G, Engelhardt M D, Klingner R E. Behavior of post-installed shear connectors under static and fatigue loading. Journal of Constructional Steel Research, 2010, 66: 532-541.

Lachemi M, Hossain K M A, Ramcharitar M, et al. Bridge deck rehabilitation practices in North America. Journal of Infrastructure Systems, 2007, 13(3): 225-234.

Lin Z, Liu Y, He J. Behavior of stud connectors under combined shear and tension loads. Engineering Structures, 2014, 81(81): 362-376.

Lin Z, Liu Y, Roeder C W. Behavior of stud connections between concrete slabs and steel girders under transverse bending moment. Engineering Structures, 2016, 117: 130-144.

Liu X P, Bradford M A, and Lee M S S. Behavior of high-strength friction-grip bolted shear connectors in sustainable composite beams. Journal of Structural Engineering, 2015, 141(6): 04014149.

Moynihan M C, Allwood J M. Viability and performance of demountable composite connectors. Journal of Constructional Steel Research, 2014, 99: 47-56.

Nakamura S, Momiyama Y, Hosaka T, et al. New technologies of steel/concrete composite bridges. Journal of Constructional Steel Research, 2002, 58(1): 99-130.

Pavlović M, Marković Z, Veljković M, et al. Bolted shear connectors vs. headed studs behavior in push-out tests. Journal of Constructional Steel Research, 2013, 88: 134-149.

Umphrey J, Beck D, Ramey G E, et al. Rapid replacement of four GDOT bridge decks. Practice Periodical on Structural Design & Construction, 2007, 12(1): 48-58.

Xue D, Liu Y, Yu Z, et al. Static behavior of multi-stud shear connectors for steel-concrete composite bridge. Journal of Constructional Steel Research, 2012, 74(8): 1-7.

Maintenance, Safety, Risk, Management and Life-Cycle Performance of Bridges – Powers, Frangopol, Al-Mahaidi & Caprani (Eds)
© 2018 Taylor & Francis Group, London, ISBN 978-1-138-73045-8

A new era of steel bridge service life

F. Piccoli, R. Pavan, E. Siviero
AP&P srl, Italy

ABSTRACT: European bridges need refurbishment and strengthening to meet new demands of higher loads and new codes. Three distinctive ideas with potential of saving costs for the European community, reducing the environmental impact for the same result and minimizing the traffic disturbance. New composite action or strengthening of existing shear connectors by post installed shear dowels. Box action by horizontal trusses between the bottom flanges of I-girder bridges, transferring the very fatigue-sensitive I-girders into box girders. Effective strengthening of old truss bridges.

1 INTRODUCTION

Since the road traffic and the loads have increased in a much more significant way than for rail traffic, there are not so many steel road bridges left from the first half of the 20:th century. Early steel bridges for road traffic with concrete deck were often not built as composite ones, but during the last decades composite bridges have become a popular solution in many countries around Europe. The competitiveness of composite bridges depends on several circumstances such as site conditions, local costs of material and staff and the contractor's experience. However many bridges for road traffic will have to be either strengthened or replaced the next decades, where the first alternative can save not only investment costs but also less disturbance for the traffic running on or under the bridge, a fact that is often neglected when deciding for different options for a bridge. The European railway network is one of the busiest in the world and it is necessary to have a reliable railway system. In order to prevent disruptions, the track must be in perfect shape. Preventing rail track maintenance is of extreme importance. Preventing corrosion protection maintenance is another important aspect. Also, in very densely populated areas, noise emission of existing steel railway bridges, forms a serious problem. Preventing maintenance and noise emission strongly influence the competitiveness of steel bridges. At the end of the 19th century up to about 20 years ago, steel bridges were built without any attention paid to noise emission, long-life exercise, increasing traffic magnitude and quantity. It was more or less accepted that steel bridges needed also a lot of maintenance. Therefore, we have in Europe, as probably elsewhere in the world, a heritage of steel bridges with high maintenance costs. These bridges have therefore a very bad reputation from environmental point of view. The upgrading of the European infrastructural system for more and heavier traffic show that the designs of many existing bridges are critical and therefore actions are necessary. In Europe, many bridges were built just before and after the Second World War. These bridges have in most cases a traditional deck design consisting of girders or trusses. In order to prevent incrementing costs of maintenance, easy and fast solutions to repair these bridge types are needed.

2 LITERATURE ANALYSIS

As reported in the aforementioned step level classification, various stages of analysis could be adopted by bridge owners or managing agencies. Some examples have been developed by the author and could be found in detail in Pipinato (2016) the assessment of a new bridge is presented in order to evaluate different typologies of construction alternatives to gain different lifetime; while in Pipinato (2014) the assessment and rehabilitation of steel railway bridges using fibre-reinforced polymer (FRP) composites in the particular situation of the rehabilitation of metallic civil infrastructure using fiber reinforced polymer (FRP) composites is evaluated. The residual life of historic riveted steel bridges could be also assessed with an analytical approach or introducing an orthotropic steel deck design to extend the lifetime of plate and box girder bridge and viaducts, as explained in Pipinato et al. 2014 and in Pipinato (2014a). And however steel bridge exhibited in the past a wide amount of problems not evi-

denced in other bridges (Pipinato 2014b), for this particular type of structure a variety of technologies to repair and retrofit are available: this is the case reported for the fracture propagation and life cycle design of girders (Pipinato 2014c), or for advanced solutions of the corrosion protection (Pipinato 2014d). For network of bridges, however, an integrated solution has been presented in order to understand what is the possibility of prioritize the bridge retrofit (Pipinato 2013a). A particular asset of bridges in which the lifecycle assessment should be performed from the design stage is the case of long span bridges, where the traffic is represented also from exceptional moving loads and the consequent fatigue expected lifetime could fail in less than ten years from the construction stage if a correct detailing is not perceived (Pipinato 2013b-2013c-2010d); similar issues comes also from the original construction alternative choses, as demonstrated in Pipinato et al. 2012a. The particular case of fatigue sensitive materials of course is more recurrent in steel bridges where retrofit and assessment alternatives are in part applied (Pipinato 2012b), in part not well investigated, as is the case of coupled damages (seismic and fatigue, Pipinato 2012a,b, Pipinato et al. 2012c,d,e,f, Pipinato et al. 2011c,d). Wherever there is the possibility to investigate with full scale tests existing bridges, e.g. where managing agencies are interested to know the structural behavior of recurrent structures along their network, this could be an interesting occasion to understand how materials decay could influence the static and fatigue behavior of bridges: this is the case both of railway (Pipinato et al. 2011a,b, Pipinato 2011, Pipinato 2010b, Pipinato et al. 2010a,b,c,e Pipinato 2010, Pipinato et al. 2009, 2008a,b, Pipinato et al. 2007) and roadways (Pipinato 2010a). A particular and further subset is represented by monumental and large bridge structures (Pipinato & Modena 2010): in this case, a long and time-consuming but useful procedure should be performed, by evaluating al the assessment steps described before, in order to understand in detail the aforementioned problems that could influence the final retrofit design decision.

3 RETROFIT PROPOSALS

3.1 *New composite action or strengthening of existing shear connectors by post installed shear dowels*

Many older steel bridges are constructed with a non-composite concrete slab over steel girders. A potentially economical means of strengthening these floor systems is to connect the existing concrete slab and steel girders to permit the development of composite action. Composite action means that the steel girder and concrete can help each other out carrying the loads more efficiently than in the original nanocomposite condition. To achieve the benefits of composite action, the existing steel girder must be connected to the existing concrete slab to permit the transfer of shear forces at the steel-concrete interface. For new bridges, composite action is achieved by welding shear studs to the top of the steel girder prior to casting the concrete slab. In the case of an existing bridge, this approach is not possible, since the slab is already in-place. One alternative is to make holes in the slab and weld studs to the top flange, but that interrupts the traffic and means that the water proofing and asphalt of the bridge must be done once again. Perhaps even worse, the transversal re-bars of the deck will be broken when making holes for shear connectors, and that means that e.g. the cantilevers will loose their capacity in bending since they are depending on the top layer of the re-bars in tension. Hence, the best thing would be to develop methods for post-installing shear connectors. In the case of existing bridges, strengthening by welded shear studs is only suitable if the bridge can be closed for quite a long time. The strengthening work often involves the following steps: removal of pavement and waterproofing, water jetting to remove the concrete, welding of new shear studs, casting concrete, re-waterproofing and resurfacing. Spring pins or coiled spring pins (Figure 2), offer the possibility of performing the whole installation from below the bridge deck without interrupting the traffic on the bridge. This is possible since the pins are connected to the steel and concrete only by a force created by the compressed coiled spring pin itself. This is a major advantage of interference fit shear connectors in bridge applications, compared to the other types of shear connectors. Coiled spring pins can be used as shear connectors either to create or to strengthen the shear connection between steel and concrete. In the first case, there will be only one type of shear connector at the shear interface, which makes it easy to establish design assumptions. However, since there are no heads on the coiled spring connectors, the uplift forces must be considered in design. In the second case, there will be at least two different kinds of shear connectors at the shear interface. This implies that the distribution of shear forces between the different shear connectors must be established. This is essential when a structure is strengthened due to insufficient fatigue capacity in the shear connection. It is, however, less important for static load in the ultimate limit state.

An application has been performed onto the Pitsund bridge in Sweden: the Pitsund-bridge is a seven span bridge, with a total length of 399 m and a free width of 9 m, see Figure 3. The superstructure consists of steel girders with a concrete deck slab on top, in six out of seven spans. The seventh span is a movable span, designed as a bascular bridge with two leafs. In 2006, coiled spring pins were installed in a part of the bridge in order to create composite action and to avoid sudden movements in the steel-concrete interface, which created loud bangs in wintertime.



Figure 1 Pitsund-bridge (Collin et. al 2015).

In the area marked with red, there are no shear connectors, only a few anchoring steel bars that connect the steel and the concrete over the supports. In the blue area, the bridge was designed and constructed as a composite structure (year 1984). The shear connection was created by welded headed shear studs. The green area was originally designed with no composite action and remained so until year 2006. Then 1200 coiled spring pins were installed in order to create composite action. Then the bridge was monitored under known loads, to understand differences in the structural behavior: one conclusion from the measurements is that the coiled spring pins can be used to create composite action in non-composite steel concrete bridges, even though they behave a bit different compared to shear studs at low load levels. The tests indicate that that there is a need of a small initial slip, or compression of the pins, before the coiled spring pins starts to transfer shear forces to a greater extent. FE-models have been created for the bridge, simulating different types of shear connections. A comparison between FE-models and the field monitoring will be presented in a future paper.

3.2 *Box action by horizontal trusses between the bottom flanges of I-girder*

For I-girder bridges the loads from the weight of the steel and concrete generally are evenly distributed between the girders, just like for box girder bridges. For I-girder bridges however, that is not the case. For smaller bridges with two I-girders the concrete deck is often assumed to be simply supported on the girders, meaning that a concentrated load on top of one girder is designed to carry all loads, with no help from the other girder. In reality the torsional stiffness of the deck and the warping stiffness of the whole composite section however transfer some of the load so the real distribution can be something like 85% for the loaded girder and 15 % for the other girder. Tests on the bridge over Rokån have shown good agreement with FEM simulations (Hällmark et al, 2013). For a box section however, the two parts of the section (left-right) will deflect almost the same, thus sharing the load almost equally When strengthening old I-girder bridges in composite action, one of the most powerful concepts is to simply make the cross section act like a box section, by adding a horizontal truss between the bottom flanges. This means that the eccentric loads produce a torsional moment that will be carried be shear forces around the section. The preferred type of truss is a K-truss, since other types will force the diagonals to take part in the global bending, which will make them sensible to buckling between the joints. This means a lot in the Ultimate Limit State, but even more in the Fatigue Limit State. For example, a reduction of the bending stresses in the bottom flange with 50%, and m=5 in the Wöhler diagram, could very roughly make the remaining life time 32 times longer. The top flanges in midspan on the other hand do get very low fatigue stresses after the concrete has hardened, so fatigue is usually not a problem here. In France this technique is used for new railway bridges, in order to make the dynamic behavior for the torsional mode much better. In Finland the concept has been used for new road bridges to lower the stresses in each I-girder from the traffic (Collin et. al 2015).

3.3 *Effective strengthening of old truss bridges*

Almost all steel truss railway bridges that have been built some decades ago, are with open decks. The open deck has the following disadvantages from nowadays point of view:

- The load bearing capacity of deck elements is sometimes not sufficient for nowadays increasing axle loads and train speeds although the main load bearing parts usually have some reserves
- High level of noise emissions during passing of the trains, which is unacceptable in rural areas;
- Difficulties during maintenance of the track;
- Significant differences between the elastic properties of the track on the bridge and outside the bridge discontinuity;
- Increased vibrations;
- High risk of fatigue crack initiation in deck elements and connections;

These are mainly problems not considered at the time these bridges were designed. Sometimes the above mentioned disadvantages become a reason for the railway administrations to replace these bridges even though the main trusses might have enough bearing capacity to face the increased live loads or are still in good condition to be kept for some decades in service. This was the case in Forsmo Railway Bridge (Sweden), built in 1912, in which the main structure was able to carry higher loads than the design loads, but the deck elements (longitudinal beams and cross beams) could not. As a result of that a replacement, invented and designed by Ramböll, of the deck was done (see Figure 2), which has led to considerable saving of money (appr. 25 MEuro), compared to a new bridge and also prolonged the lifetime of the bridge. The exchange of the bridge deck was carried out in 20 stops 8 hours each, which means that the trains could roll as usual. This was especially important since a stop would have cut off the train traffic (Collin et. al 2015).



Figure 2 Forsmo bridge deck substitution (Collin et. al 2015).

The fatigue problems of the directly loaded structural elements (longitudinal deck beams) and their connection details were also identified during upgrading programme of the Dutch railway system. The proposed strengthening approach is replacing the bridge sleepers by especially designed silent bridge® decks, a design with an acoustically optimal plate thickness configuration and rails embedded in a trough using corkelast, developed by de Silent Bridge Group, the stresses in the longitudinal girders can be reduced and therefore the lifetime increased (see Figure 3).



Figure 3 Silent bridge® deck new installation (Kuhn et al. 2010).

Other applications deals with the substitution of existing steel deck with new UHPFRC decks, in order to extend the life of railway trusses. The chosen sample bridge is a steel truss railway bridge designed in 1896 situated in the town of Vienna over the river Wien. It is 120 years old and it is still in operation. Originally designed for railway traffic, but at the moment the bridge is operated by town's metro line No. 4. The superstructure is twin steel truss beams simply sup- ported with a span of 50,92m. This retrofit solution is proven to be effective in "compensating" the additional dead load not only for ULS checks of the main truss element, but also for fatigue behavior and SLS checks. For retrofitted bridge, in this case, it is shifted from 4,2Hz to 3,4Hz, which is well in the middle between upper and lower limits. In terms of deflections, due to the higher stiffness, the deflection from vertical traffic load is reduced from 66mm to 40mm (with 40%). Both values satisfy the traffic safety criteria of L/600=85mm Figure 4



Wien truss railway bridge (Collin et. al 2015).

4 CONCLUSION

European bridges need refurbishment and strengthening to meet new demands of higher loads and new codes. Three distinctive ideas with potential of saving costs for the European community, reducing the environmental impact for the same result and minimizing the traffic disturbance. New composite action or strengthening of existing shear connectors by post installed shear dowels. Box action by horizontal trusses between the bottom flanges of I-girder bridges, transferring the very fatigue-sensitive I-girders into box girders. Effective strengthening of old truss bridges. All these solutions have been demonstrated to be effective to reduce the common procedure to demolish existing bridges, by adopting conservation procedures able to retrofit and prolong the lifetime of relevant infrastructures along European.

5 ACKNOWLEDGMENTS

This research was supported by the European Union, represented by the European Commission—Directorate General for Research and Innovation, Research Fund for Coal & Steel (RFCS) program, under grant agreement no. RFSR-CT-2015-00025. This funding is gratefully acknowledged.

6 REFERENCES

Kühn B., M. Lukić, A. Nussbaumer, H.-P. Günther, R. Helmerich, S. Herion, M.H. Kolstein, S. Walbridge, B. Androic, O. Dijkstra, Ö. Bucak (2010). Assessment of Existing Steel Structures: Recommendations for Estimation of Remaining Fatigue Life. Joint Report Prepared under the JRC – ECCS cooperation agreement for the evolution of Eurocode 3 (programme of CEN / TC 250).

Collin P., Rebelo C., Nunez E., Geier R., Pipinato A., Hesselink B. (2015). PROLIFE-Prolonging the life of steel and steel composite bridges. Research Fund for Coal and Steel Call:

RFCS-2014 Topic: RFCS-02-2014 Type of action: RFCS-RPJ Proposal number: SEP-210202537 Proposal acronym: PRO-LIFE.

Pipinato, A. (2016). Structural analysis and design of a multispan network arch bridge. Proceedings of the Institution of Civil Engineers: Bridge Engineering, 169 (1), pp. 54-66. DOI: 10.1680/jbren.14.00013

Pipinato, A. (2014). Assessment and rehabilitation of steel railway bridges using fibre-reinforced polymer (FRP) composites. Rehabilitation of Metallic Civil Infrastructure Using Fiber Reinforced Polymer (FRP) Composites: Types Properties and Testing Methods, pp. 373-405. DOI: 10.1533/9780857096654.4.373

Pipinato, A., Pellegrino, C., Modena, C. (2014). Residual life of historic riveted steel bridges: An analytical approach. Proceedings of the Institution of Civil Engineers: Bridge Engineering, 167 (1), pp. 17-32. Cited 9 times. DOI: 10.1680/bren.11.00014

Pipinato, A. (2014a). Orthotropic steel deck design to extend the lifetime of plate and box girder bridge and viaducts. Bridge Maintenance, Safety, Management and Life Extension - Proceedings of the 7th International Conference of Bridge Maintenance, Safety and Management, IABMAS 2014, pp. 1329-1336.

Pipinato, A. (2014b). Steel bridges: Codes, design specifications and construction issues. Bridge Maintenance, Safety, Management and Life Extension - Proceedings of the 7th International Conference of Bridge Maintenance, Safety and Management, IABMAS 2014, pp. 1891-1898.

Pipinato, A. (2014c). Longitudinal web stiffening in steel girders: Fracture propagation and life cycle design
(2014) Bridge Maintenance, Safety, Management and Life Extension - Proceedings of the 7th International Conference of Bridge Maintenance, Safety and Management, IABMAS 2014, pp. 1886-1890.

Pipinato, A. (2014d). Steel bridge coatings and corrosion protection. Bridge Maintenance, Safety, anagement and Life Extension - Proceedings of the 7th International Conference of Bridge Maintenance, Safety and Management, IABMAS 2014, pp. 1899-1905.

Pipinato, A. (2013a). Retrofit procedures of bridge networks against seismic actions in Italy. Durability of Bridge Structures, pp. 215-228.

Pipinato, A. (2013b). Moving load and fatigue analysis of a long span high speed railway bridge.Advanced Materials Research, 629, pp. 403-408.

Pipinato, A. (2013c). Moving loads bridge response: Structural analysis and eurocode provisions (2013) Advanced Materials Research, 629, pp. 409-417. 10.4028/www.scientific.net/AMR.629.409

Pipinato, A., Pellegrino, C., Modena, C. (2012a). Structural Analysis of the Cantilever Construction Process in Cable-Stayed Bridges (2012) Periodica Polytechnica: Civil Engineering, 56 (2), pp. 141-166. DOI: 10.3311/pp.ci.2012-2.02

Pipinato, A., Pellegrino, C., Modena, C. (2012b). Fatigue behaviour of steel bridge joints strenghtened with FRP laminates. Modern Applied Science, 6 (10), pp. 1-15. DOI: 10.5539/mas.v6n10p1

Pipinato, A., Pellegrino, C., Modena, C. (2012c). Coupled damage in assessing the lifetime of bridge and viaducts. Life-Cycle and Sustainability of Civil Infrastructure Systems - Proceedings of the 3rd International Symposium on Life-Cycle Civil Engineering, IALCCE 2012, pp. 2292-2297.

Pipinato, A. (2012a). Coupled safety assessment of cable stay bridges. Modern Applied Science, 6 (7). DOI: 10.5539/mas.v6n7p64

Pipinato, A., Pellegrino, C., Modena, C. (2012d). Assessment procedure and rehabilitation criteria for the riveted railway Adige Bridge (2012) Structure and Infrastructure Engineering, 8 (8), pp. 747-764. Cited 21 times. DOI: 10.1080/15732479.2010.481674

Pipinato, A. (2012b). Assessment procedures and strengthening of an existing metal bridge. (2012) Bridge Maintenance, Safety, Management, Resilience and Sustainability - Proceedings of the Sixth International Conference on Bridge Maintenance, Safety and Management, pp. 3651-3655.

Pipinato, A., Pellegrino, C., Modena, C. (2012e). Life cycle assessment of existing steel bridges considering corrosion and fatigue coupled problems. Bridge Maintenance, Safety, Management, Resilience and Sustainability - Proceedings of the Sixth International Conference on Bridge Maintenance, Safety and Management, pp. 1003-1007.

Pipinato, A., Pellegrino, C., Fregno, G., Modena, C. (2012f). Influence of fatigue on cable arrangement in cable-stayed bridges. International Journal of Steel Structures, 12 (1), pp. 107-123. DOI: 10.1007/s13296-012-1010-5

Pipinato, A., Molinari, M., Pellegrino, C., Bursi, O.S., Modena, C. (2011a). Fatigue tests on riveted steel elements taken from a railway bridge (2011) Structure and Infrastructure Engineering, 7 (12), pp. 907-920. DOI: 10.1080/15732470903099776

Pellegrino, C., Pipinato, A., Modena, C. (2011b). A simplified management procedure for bridge network maintenance. Structure and Infrastructure Engineering, 7 (5), pp. 341-351. DOI: 10.1080/15732470802659084

Pipinato, A. (2011). Assessment of existing bridges: Safety and security issues [Problemi di sicurezza nelle valutazioni strutturali di ponti esistenti] (2011) Ingegneria Ferroviaria, 66 (4), pp. 355-371.

Pipinato, A., Pellegrino, C., Modena, C. (2011c). Fatigue assessment of highway steel bridges in presence of seismic loading (2011) Engineering Structures, 33 (1), pp. 202-209. DOI: 10.1016/j.engstruct.2010.10.008

Pipinato, A., Pellegrino, C., Modena, C. (2011d). Correlation between fatigue effects and seismic actions in highway steel bridges (2011) Proceedings of the 8th International Conference on Structural Dynamics, EURODYN 2011, pp. 1118-1123.

Pipinato, A. (2010a). Structural analysis and fatigue life assessment of the Paderno Arch Bridge. Bridge Maintenance, Safety, Management and Life-Cycle Optimization - Proceedings of the 5th International Conference on Bridge Maintenance, Safety and Management, pp. 3480-3484.

Pipinato, A. (2010b) Structural analysis and fatigue life assessment of the Paderno Arch Bridge Bridge Maintenance, Safety, Management and Life-Cycle Optimization - Proceed-

ings of the 5th International Conference on Bridge Maintenance, Safety and Management, pp. 3486-3490.

Pipinato, A., Pellegrino, C., Modena, C. (2010a) Residual service life of existing railway bridges Bridge Maintenance, Safety, Management and Life-Cycle Optimization - Proceedings of the 5th International Conference on Bridge Maintenance, Safety and Management, pp. 1444-1452.

Pipinato, A., Pellegrino, C., Modena, C. (2010b) Structural analysis of historical metal bridges in Italy Advanced Materials Research, 133-134, pp. 525-530. DOI: 10.4028/www.scientific.net/AMR.133-134.525

Pipinato, A., Pellegrino, C., Modena, C. (2010c). Residual service life of existing railway bridges Bridge Maintenance, Safety, Management and Life-Cycle Optimization - Proceedings of the 5th International Conference on Bridge Maintenance, Safety and Management, pp. 1455-1462.

Pipinato, A., Modena, C. (2010). Structural analysis and fatigue reliability assessment of the paderno bridge (2010) Practice Periodical on Structural Design and Construction, 15 (2), pp. 109-124. DOI: 10.1061/(ASCE)SC.1943-5576.0000037

Pipinato, A. (2010). Step level procedure for remaining fatigue life evaluation of one railway bridge. Baltic Journal of Road and Bridge Engineering, 5 (1), pp. 28-37. DOI: 10.3846/bjrbe.2010.04

Pellegrino, C., Pipinato, A., Freno, G., Modena, C. (2010d). Arranging geometric configuration of cable-stayed bridges taking fatigue into account (2010) Large Structures and Infrastructures for Environmentally Constrained and Urbanised Areas, pp. 692-693.

Pipinato, A., Gueli, M., Pellegrino, C., Modena, C. (2010e). Innovative methods for railway steel bridge remaining life estimation (2010) Large Structures and Infrastructures for Environmentally Constrained and Urbanised Areas, pp. 384-385.

Pipinato, A., Pellegrino, C., Bursi, O.S., Modena, C. (2009). High-cycle fatigue behavior of riveted connections for railway metal bridges. Journal of Constructional Steel Research, 65 (12), pp. 2167-2175. DOI: 10.1016/j.jcsr.2009.06.019

Pipinato, A., Pellegrino, C., Modena, C. (2008a). Evaluation of fatigue strength of one riveted historical railway bridge. Bridge Maintenance, Safety, Management, Health Monitoring and Informatics - Proceedings of the 4th International Conference on Bridge Maintenance, Safety and Management, pp. 283-290. DOI: 10.1201/9781439828434.ch148

Pipinato, A., Pellegrino, C., Modena, C. (2008b). Scheduled maintenance actions and residual life evaluation of railway infrastructures for metallic structure bridges [Interventi di manutenzione programmata e valutazione della vita residua delle infrastrutture ferroviarie da ponte a struttura metallica]. Ingegneria Ferroviaria, 63 (2), pp. 125-134.

Pipinato, A., Pellegrino, C., Modena, C. (2007). Static load tests on a historical steel railway bridge (2007) Proceedings of the 9th International Conference on Steel, Space and Composite Structures, pp. 217-224.

Maintenance, Safety, Risk, Management and Life-Cycle Performance of Bridges – Powers, Frangopol, Al-Mahaidi & Caprani (Eds)
© 2018 Taylor & Francis Group, London, ISBN 978-1-138-73045-8

DESIGNING LONG INTEGRAL BRIDGES FOR ENVIRONMENTAL LOADING IN SOUTH AFRICA

S.A. Skorpen
Lecturer, Department of Civil Engineering, University of Pretoria, South Africa.
E.P. Kearsley
Professor, Department of Civil Engineering, University of Pretoria, South Africa.
E.J. Kruger
Bridge Network Manager, The South African National Roads Agency SOC Ltd, South Africa.

ABSTRACT: This paper focuses on how environmental loads should be taken into account in the design and construction of durable integral bridges with reference to South African conditions. Specific reference will be made to the Van Zylspruit River Bridge, a 90m long, fully integral bridge located on the South African National Roads Agency SOC Ltd (SANRAL) National Route N1. The bridge has been extensively instrumented and since the end of 2015 the structural response to the environmental conditions have been recorded. Some of the trends observed are discussed in this paper.

1 INTRODUCTION

In an effort to promote the design and construction of reduced maintenance bridge structures in South Africa, The South African National Roads Agency SOC Ltd (SANRAL) together with the Civil Engineering Department at the University of Pretoria, has instrumented a newly built long (90m) concrete integral bridge. This structure will be monitored for the next few years to assess the effect of environmental factors on the behaviour of integral bridges taking the South African climate (hot and dry) into account.

Integral abutment and pier bridges have been designed for a number of years to replace traditional jointed bridges because expansion joints and bearings can affect the durability of bridges. Not only are water leaking and maintenance issues of expansion joints minimized, but the use of integral structures can also result in good resistance to earthquakes; quicker construction; and lower total life-cycle costs (initial construction costs and maintenance costs) when compared to jointed bridges. However, there are some design challenges that need to be addressed.

Eliminating joints and bearings from a bridge deck not only introduces restraining forces into the deck which can cause cracking, but also results in a complex soil-structure interaction problem into bridge design involving the relative movement between the bridge abutment and the retained soil behind the abutment. Consequently integral construction is susceptible to similar problems common to the construction and maintenance of jointed bridges for decades, such as early age transverse bridge cracking, especially in areas of top slab tension such as over pier supports. This is generally more evident is reinforced concrete bridges, such as Van Zylspruit River Bridge, as opposed to prestressed concrete bridges.

Some of the causes of early age transverse cracking in bridge decks include differential thermal gradients in fresh concrete due to heat of hydration conditions that take place during concrete placement; finishing and curing as well as initial differential shrinkage. The adoption of integral-type bridges does thus not eliminate some of the troublesome problems in highway bridge construction (Burke, 2009).

It is also important that construction site staff are informed of the differences between integral bridge behaviour and jointed bridges. If the structural concepts are appreciated this can result in specific attention to the important details during construction such as backfill material behind integral abutments.

This paper will discuss some of the observed environmental loading in the Van Zylspruit bridge up to October 2017 which could contribute to deck cracking such as:

- Heat of hydration,
- Changes in effective bridge temperatures,
- Transverse temperature variation, and
- Deck shrinkage.

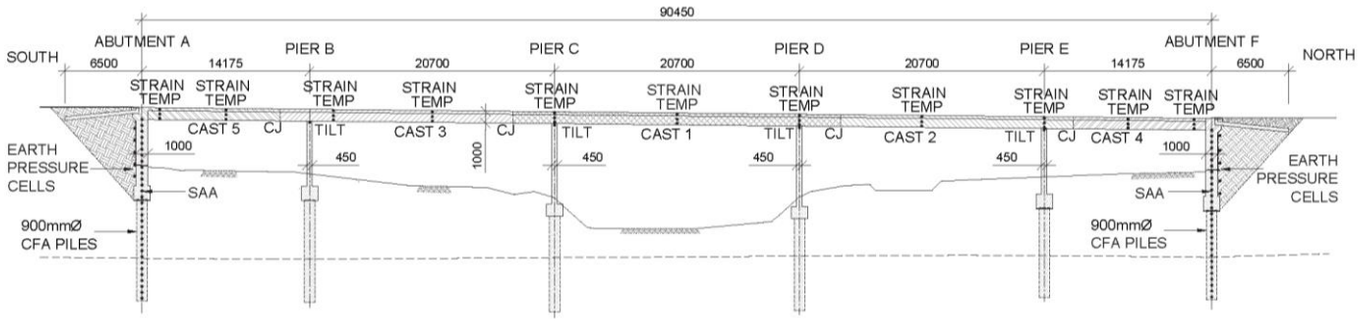
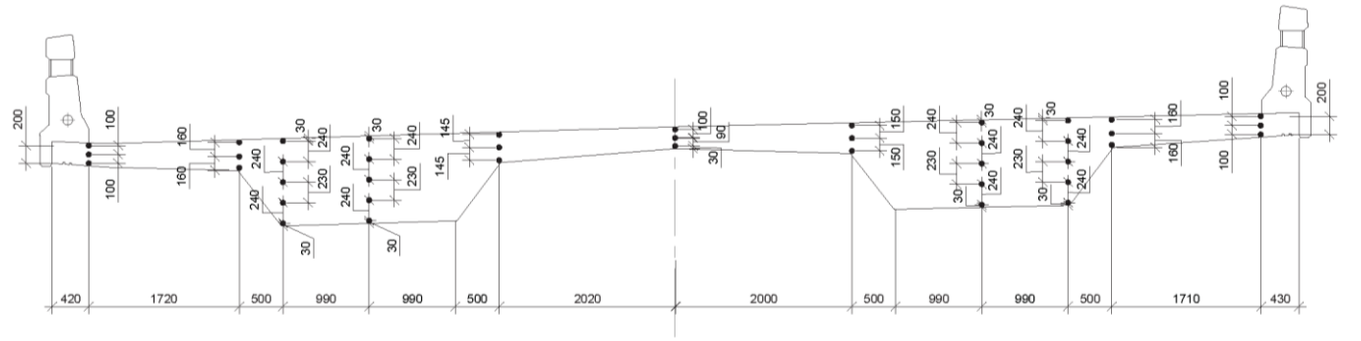


Figure 1. Typical Bridge Long section showing sensor positions



- Thermistor

Figure 2. Typical deck cross section showing the thermistor layout in Span A-B

2 BRIDGE MONITORING

The Van Zylspruit River Bridge is a reinforced concrete, 5 span, 90.45m long, integral bridge with spans as shown in the long section in Figure 1. The deck is solid (i.e. no voids), 14m wide and varies in thickness, with two 1m deep beams connected to 250mm thick flanges (see Figure 2). The deck is monolithic with the piers and fully integral with the abutments. The bridge is located on the SANRAL National Route N1 in central South Africa (about 1000 km North of Cape Town), an area known for its harsh climate with both high and low temperatures. The bridge has been extensively instrumented to measure the environmental effects on the structure, and numerous samples taken to determine the material properties.

The instrumentation was installed during construction, and the data from this instrumentation has been logged continually during the construction phase and onwards. Instrumentation includes over 200 thermistors and 110 vibrating wire strain gauges, as well as earth pressure cells, shape-accel-arrays at both abutments and tilt meters on all piers. The data from these sensors together with data from 6 shrinkage reference structures (built adjacent to the structure) provides a complete picture of the bridge deck and abutment behaviour.

The deck was cast in five (5) pours, starting with the central span CD, and moving outwards towards the abutments (See Figure 1). The first deck pour was on the 19th of September 2015, and the final deck pour on the 8th of December 2015. A cross section through the deck showing the position of some of the thermistors can be seen in Figure 2. The final sensor count is just over 550 with readings taken at 15 minute intervals, and all the data is logged remotely.

The bridge is part of a larger road construction project, and has thus remained closed to traffic and unsurfaced until August 2017 when it was surfaced with a 60mm asphalt layer and then opened to traffic shortly afterwards. In addition fibre optic instrumentation was also installed on the top and bottom surfaces of the deck to measure strain. However this paper does not deal with these results. A photograph of the competed structure is shown in Figure 3.

The measured concrete material properties of the specified concrete with 19mm Dolerite stone and CEM II/A-M (V-L) 42.5R cement is as follows:

28 day compressive cube strength: 60MPa
(Specified as 40MPa)

28 day split cylinder strength: 3.6MPa

28 day Modulus of Elasticity: 37GPa
(Design Assumption was 31GPa)

Coefficient of thermal expansion: $8.5x10^{-6}$/°C
(TMH7 Part 2 recommends 12 x 10^{-6})

250 Cylinder drying Shrinkage: 300με

Backfill sand density: $19kN/m^3$

The bridge abutment was backfilled between April and July 2016 using a wedge of single sized sandy material with an internal angle of friction of 35°. However prior to this the contractor's site staff mistakenly changed the backfill material to a cemented backfill. This was removed and the correct backfill material was then placed. This is mentioned to emphasise that all site staff must be aware of the requirements so as to eliminate uninformed changes on site.



Figure 3. Completed Van Zylspruit River Bridge

3 HEAT OF HYDRATION

The heat of hydration observed for the final deck pour in December 2015 (summer in South Africa) is shown in Figure 4. This graph was typical for all five deck pours, and an increasing trend was observed as the ambient temperature increased (see Table 1). The centre of the 1m thick beam heats up to almost 80°C during the hydration process, and takes just over 10 days to cool down. The flanges however only heat up to just over 50°C and cool down within 3 days of casting. The temperature in the flanges is already varying with the daily temperature while the beam concrete is still cooling down. For this section there is a maximum difference of 38°C between the centre of the deck and the flanges, which occurs as the flanges cool down at night while the beam heat of hydration is still high. These significant temperature differences could cause micro-cracking to occur in the flanges and they cool faster than the central beam.

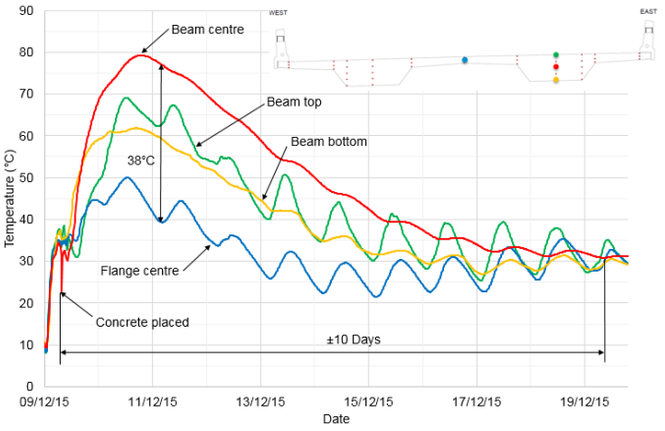


Figure 4: Heat of hydration observed in the deck (8 December 2015)

Table 1. Maximum and Minimum Ambient Temperature compared to Maximum Heat of Hydration.

Date Cast	Ambient Temperature		Max Heat of Hydration Temp	
	Max	Min	Beam	Flange
17/09/2015	10	25	68.65	42.47
16/10/2015	10	26	75.39	47.51
06/11/2015	15	32	73.54	43.18
02/12/2015	24	30	78.73	55.28
09/12/2015	23	33	81.31	57.28

Table 1 shows an increase of 12.7°C in maximum heat of hydration in the beams, and 14.8°C increase in maximum heat of hydration in the flanges as the maximum ambient temperature increase by ±8°C. The reason for a difference between the flanges and the beams could be attributed to the proximity of the formwork. The flanges are more affected by the steel shutters, which can heat up significantly on a hot day before concrete is placed and so affect the thinner sections more than the thicker sections. This could result in the increased maximum heat of hydration temperatures.

The maximum temperature difference between the middle of the beam and the flange generally occurred on the second night after the deck was cast, as the flanges decreased in temperature with the decrease in ambient temperature. Figure 5 shows how the maximum temperature difference between the beam and flange temperatures is dependent on

the maximum change in ambient temperature in a day-night cycle.

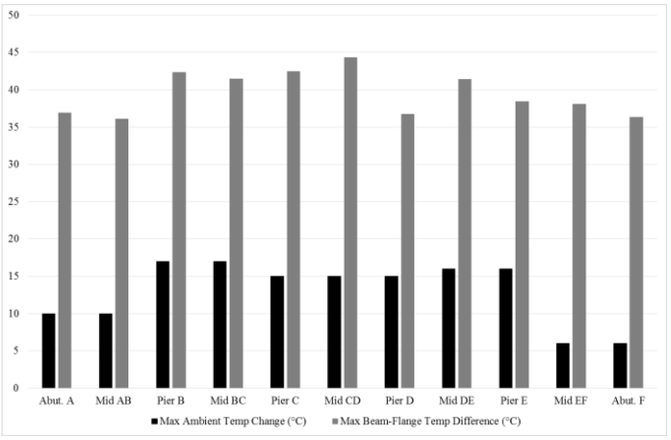


Figure 5. Maximum ambient temperature change compared to Maximum Difference in Temperature between the Flange and Middle of the Beam.

Work done by Kraus et.al. (1996) on transverse cracking in newly constructed bridge decks reports that a 28°C temperature change in the deck relative to the girder can cause stresses greater than 1.38MPa when the concrete has an early effective modulus of elasticity of only 3.5GPa, and greater than 6.89MPa when the early effective modulus is 17.2GPa.

Using an average 38°C temperature difference between the beam and flange:

$$\varepsilon_T = \Delta T \alpha = 323\mu\varepsilon \qquad \text{(Equation 1)}$$

Where:

ε_T = thermal strain
ΔT = change in deck temperature = 38°C
α = coefficient of thermal expansion = 8.5×10^{-6}/°C

Early age testing of the concrete shows a concrete tensile strength of 2.1MPa after 48hours, which is when the maximum temperature difference normally occurs. If the concrete is to remain uncracked the early are E value of the concrete is required to remain below 6.5GPa for 48 hours, which is highly unlikely.

$$E = \sigma/\varepsilon = 2.1\text{MPa} / 323\mu\varepsilon = 6.5\text{GPa} \qquad \text{(Equation 2)}$$

The data points towards the following preventative measures that can reduce early are cracking and reduce the maintenance requirements due to cracking of the structure:

- Limits on maximum and minimum ambient temperatures for casting bridge decks.
- Casting bridge decks while ambient temperatures are cool (i.e. at night) during summer.
- Delaying a deck pour if sudden changes in ambient temperature are expected (i.e. if a cold front is expected to pass through the area)
- Including additional secondary reinforcement, preferably smaller bar sizes and close spacing to limit crack widths.

4 EFFECTIVE BRIDGE TEMPERATURE AND AMBIENT TEMPERATURE

Temperature differences through the thickness of the deck can cause significant stresses and need to be considered in the design of the deck, however they do not have much effect on the bridge abutment design. Integral bridge abutments are affected by the change in the overall effective bridge temperature. The effective bridge temperature is defined as the temperature, which governs the longitudinal movement of the deck (Emerson, 1976). It is calculated from the sum of the product of area between isotherms and their mean temperatures, divided by the total area of the cross section of the deck. In practice it is difficult to locate the isotherms exactly and an approximation is made by dividing the cross section into areas. In essence it is a weighted average of the bridge temperature.

Figure 6 shows a normal distribution of the effective bridge, flange and beam temperatures separately, compared to the ambient temperature.

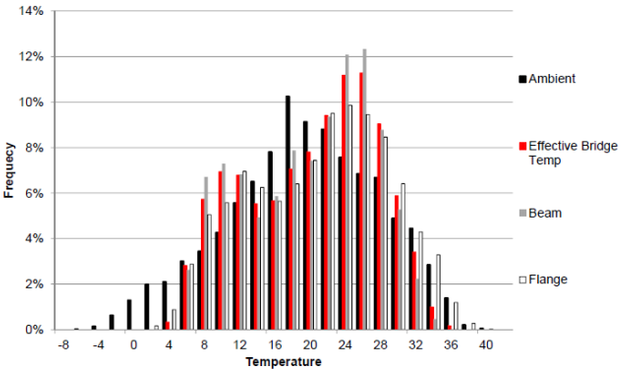


Figure 6. Normal distribution of effective bridge temperatures

One can notice the damping effect of the large solid beam on the thermal effects, which is consistent with work done by Black et al., 1976 when they investigated the influence of the shape of the cross section on the bridge effective temperature. They suggest that the effective bridge temperature is related to the area of the cross section of the deck per meter width of the deck.

Table 2 summarizes the maximum, minimum, average and standard deviation for the ambient temperature as well as deck, beam and flange effective temperatures.

Table 2. Maximum and Minimum Ambient Temperature compared to Maximum Heat of Hydration.

Date Cast	Ambient	Deck	Beam	Flange
Max	40.3	35.3	34.0	38.2
Min	-7.9	2.7	3.6	0.7
Average	18.4	17.7	17.5	18.2
Std. Deviation	8.5	7.4	7.1	7.8

5 TRANSVERSE TEMPERATURE VARIATION

Most design codes have detailed information on the vertical temperature gradient, but very little, if any, on transverse temperature variation. Lee (2012) investigated the effect of extreme environmental conditions of temperature gradients during construction of prestressed concrete bridge girders and found this temperature difference to be as high as 30°C in some States in America. Transverse temperature differences are effected by the cross sectional depth of the deck.

Thinner sections heat up and cool down faster than thicker sections, and if these differences are large enough transverse cracking can occur in the thinner sections of the deck. The effects of the solid concrete parapets should also be considered. The deck temperature measured 30mm below the surface at Van Zylspruit is plotted at 6 different points across the half of the deck for 5 days in January 2017 in Figure 7 as a cold front moved through the area. On a hot day the parapet caused the edge flanges to lag in temperature by up to 8°C, but as the ambient temperature cause the bridge temperature to drop so the parapet dampened the effect of the decrease in temperature so that there was a fairly uniform transverse temperature distribution during the cold period. Immediately after the cold spell the temperature difference re-occurred.

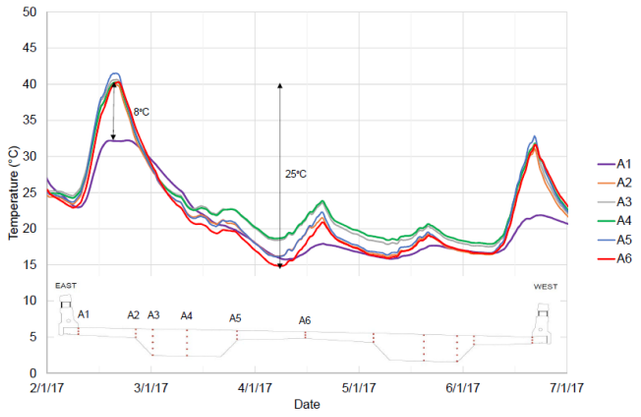


Figure 7. Top transverse temperature profile in summer

The deck temperature measured 30mm below the surface at Van Zylspruit is plotted at 11 different points across the deck for a typical hot day (Figure 8) and cold day (Figure 9), with and without parapets.

On a hot day the parapet caused the edge flanges to lag in temperature by up to 8°C, and on a typical cold day the parapet dampens the effect in the outside flanges resulting in a more even distribution of transverse temperature in the top of the deck

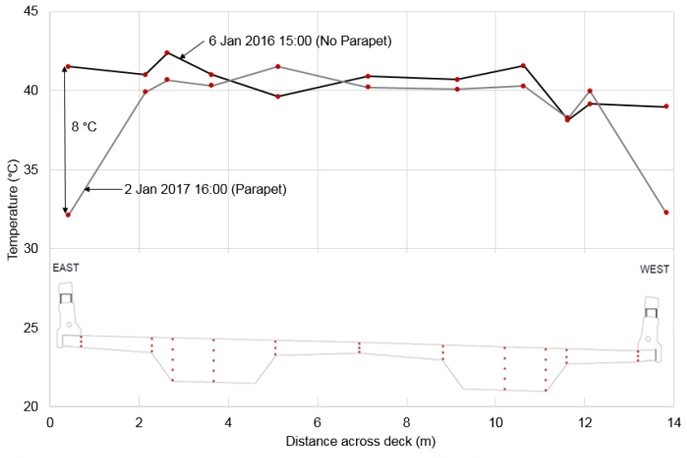


Figure 8. Top transverse temperature profile in summer

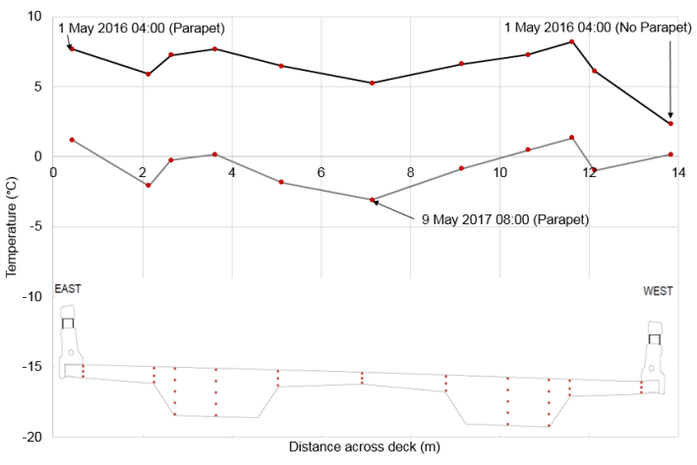


Figure 9. Top transverse temperature profile in winter

The temperature difference on hot days combined with the stiffening effect of the parapets could result in cracking of the edge flanges at the parapet joints. This type of cracking was observed at Van Zylspruit, particularly on the Western side of the deck, which gets the hottest in the afternoon. Additional secondary reinforcement, preferably smaller bars at close spacing could be considered at the flanges edges over the parapet joints. This has also been observed on another SANRAL bridge with thin cantilever slabs and concrete parapets.

6 MEASURED SHRINKAGE

The shrinkage at Van Zylspruit was measured with 6 reference structures:

- Two (2) unreinforced 250mm diameter, 500mm long cylinders were cast and placed in the shade under the bridge at Piers B and D, (see Figure 10).
- Two (2) 2000mm x 1000mm x 250mm thick panels (see Figure 11). One was unreinforced, and the other reinforced with the same percentage reinforcement as the bridge deck flanges. This is representative of the bridge deck flanges which are approximately 2m long and 0.25m thick. These panels are supported on 4 stub columns, one at each corner, with frictionless supports to allow free movement.
- Two (2) 1000mm x 1000mm x 1000mm thick blocks (see figure 11). One was unreinforced, and the other reinforced with the same percentage reinforcement as the bridge deck beams. This is representative of the bridge deck beams which are 1m thick. These blocks are supported on 4 stub columns, one at each corner, with frictionless supports to allow free movement.



Figure 10. Cylinder reference structure



Figure 11. Thin panel and thick block reference structures

Vibrating wire strain gauge were cast into all of these structures to measure strain and temperature. They were cast while the deck was poured, with concrete from the deck pour. They have remained on site for the entire project, thus being exposed to the same environmental conditions as the deck. The self-weight load on the reference shrinkage structures is so small that the effect of creep can be ignored and the strain readings are assumed to be purely shrinkage. There are again some gaps in the data where the batteries ran out of charge and where the logging systems had to be switched off to do the final configuration of the loggers. The shrinkage strain for the reference structures is shown in Figure 12.

The 250mm panels show a shrinkage after approximately 1.5 years of 180με, compared to 100με in the 1m thick blocks. The shrinkage of the panels and blocks occurred over a much longer period (compared to the cylinders). After approximately 1.5 years, both the panel and the block appear to have stopped shrinking

There was also no marked difference between the reinforced and unreinforced reference panels. The design shrinkage values according to TMH7 Part 2 are 290με for the thin panel (250mm) and 205με for the thick section (1000mm), thus the measured shrinkage is less than the values used for design purposes. However the shrinkage is significantly size dependent, and additional secondary reinforcement may be required at positions of restraint (i.e. a pier) where the cross section changes in size.

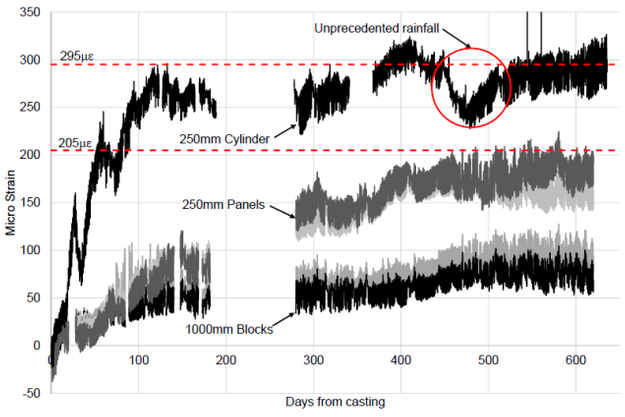


Figure 12. Reference structure shrinkage

7 CONCLUSIONS

This is an ongoing monitoring project and changes in the behaviour are expected now that the deck is surfaced and the bridge is opened to traffic, however the data points towards aspects that can help designers of integral bridges including:

- Heat of hydration is significantly dependant on the depth of the section, and on the ambient weather conditions. To prevent early age transverse cracking limits should be placed on maximum and minimum ambient temperatures for casting bridge decks; bridge decks should be cast while ambient temperatures are cool (i.e. at night) during summer; and deck pour should be delayed if sudden changes in ambient temperature are expected (i.e. if a cold front is expected to pass through the area). Additional secondary reinforcement, preferably smaller bar sizes at close spacing should be included to limit crack widths.
- In concrete slab and beam type construction a large solid beam damps the thermal effects, thus reducing the daily and season movement of the abutment.
- The transverse temperature variations in the deck are also dependant on the depth of the cross section.
- Concrete parapet causes greater transverse temperature variation in hot weather, and less in cold weather.
- Concrete shrinkage is significantly size dependent, and additional secondary reinforcement may be required at positions of restraint (i.e. a pier) where the cross section changes in size and where the thinner top slab of the deck is in tension over supports due to negative bending moments, however the concrete shrinkage measured to date is less than the design values.

8 ACKNOWLEDGEMENTS

The following organizations are gratefully acknowledged for their assistance during the course of the study:

- The South African National Roads Agency SOC Ltd;
- Mott Macdonald PDNA
- Aveng Grinaker-LTA

9 REFERENCES

Black, W., Moss, D.S., and Emerson, M., (1976), "Bridge Temperatures Derived from measurement of movement," TRRL Report LR 748, Transport and Road Research Laboratory, Crowthorne, Berkshire

Burke MP. Integral and Semi-Integral Abutments. John Wiley and Sons Inc.: Ames, Iowa, USA: 2009.

Emerson, M., (1976), "Bridge Temperatures Estimated from the Shade Temperature," TRRL Report LR 696, Transport and Road Research Laboratory, Crowthorne, Berkshire

Krauss, P.D., Rogalla, E.A., Transverse Cracking in Newly Constructed Bridge Decks, NCHRP Report 380, Transportation Research Board of the National Academies, 1996

Lee, J., 2012, Investigation of extreme environmental conditions and design thermal gradients during construction for prestressed concrete bridge girders. ACSE Journal of Bridge Engineering, Vol 17, Pages 547 – 556

TMH 7, 1989. Code of Practice for the Design of Highway Bridges and Culverts in South Africa, Part 1, 2 and 3. Department of Transport, Pretoria.

Maintenance, Safety, Risk, Management and Life-Cycle Performance of Bridges – Powers, Frangopol, Al-Mahaidi & Caprani (Eds)
© 2018 Taylor & Francis Group, London, ISBN 978-1-138-73045-8

SEISMIC PERFORMANCE AND RETROFIT EVALUATION OF HOLLOW-CORE COMPOSITE BRIDGE COLUMNS

Mohanad M. Abdulazeez[1]; Ahmed Gheni[2]; Nicholas Colbert[3]; and Mohamed A. ElGawady[4§], PhD, M. ASCE

[1]Graduate Research Assistance and PhD student, Dept. of Civil, Architectural, and Environmental Engineering, Missouri University of Science and Technology, Rolla, MO. 65401; Email: mma548@mst.edu
[2] PhD Candidate, Dept. of Civil, Architectural, and Environmental Engineering, Missouri University of Science and Technology, Rolla, MO. 65401; Email: aagmr6@mst.edu
[3] Graduate Research Assistance, Dept. of Civil, Architectural, and Environmental Engineering, Missouri University of Science and Technology, Rolla, MO. 65401; Email: nbcwd2@mst.edu
[4] Benavides Associate Professor, Dept. of Civil, Architectural, and Environmental Engineering, Missouri University of Science and Technology, Rolla, MO. 65401; Email: elgawadym@mst.edu
§Corresponding author

ABSTRACT: This paper presents the seismic behavior of large-scale hollow-core fiber-reinforced polymer-concrete-steel (HC-FCS) bridge column. The HC-FCS column consists of a concrete wall sandwiched between an outer fiber-reinforced polymer (FRP) tube and an inner thin-walled steel tube. The width-to-diameter ratio for the steel tube was 147. The column had an outer diameter of 24 inches and a height-to-diameter ratio of 4.0. The steel tube was embedded into reinforced concrete footing with an embedded length of 1.25 times the steel tube diameter, while the FRP tube only confined the concrete wall thickness and curtail at the top of the footing level. The column was first tested as a vertical cantilever by applying cyclic horizontal and constant axial loads to the top of the column. Then, the column was repaired using a rapid repair technique within 6 hours duration and retested under the same seismic loading condition. The retrofitting technique includes wrapping three glass FRP layers around the outer bottommost FRP tube that ruptured at the interface joint between the column and the footing during the first test. The results revealed that the HC-FCS column achieved the ductile behavior with good inelastic deformation capacity under seismic loads. While, repaired column performed relatively well under cyclic loading, recovering 34% flexural strength and 80% of the lateral displacement capacity compared to the virgin tested column.

1 INTRODUCTION

It's estimated that Americans spend 14.5 million hours per day on traffic. 10 to 15% of that congestion is caused by work zones even when it occurs in the off-peak, they increase traffic congestion [1,2]. Therefore, new bridge construction techniques are required to reduce the amount of time it takes to build our roads and bridges from months to days. Accelerated bridge construction (ABC) is a proposed technology to minimize earthquake-induced residual deformations, damage, and associated repair costs.

According to the US Federal Highway Administration, ABC is a paradigm shift where minimizing the mobility impacts of on-site and speed up the construction process. ABC includes such elements as prefabricated modular units that are built off-site in a controlled environment and then transferred to the construction area for rapid installation. ABC reduces traffic disruptions and life-cycle costs and improves construction quality and safety, resulting in more sustainable development [3]. One technique to accelerate bridge construction is to use precast bridge columns with excellent seismic performance.

Recently, interest has been rapidly growing in using fiber reinforced polymer (FRP) tubes in construction as a replacement for the outer steel tube of double skin tubular (DSTCs) column [4, 5]. The proposed column, hollow core FRP-Concrete-Steel (HC-FCS), consists of an inner steel tube and an outer FRP tube, with a concrete shell placed in-between the two tubes [Fig. 1].

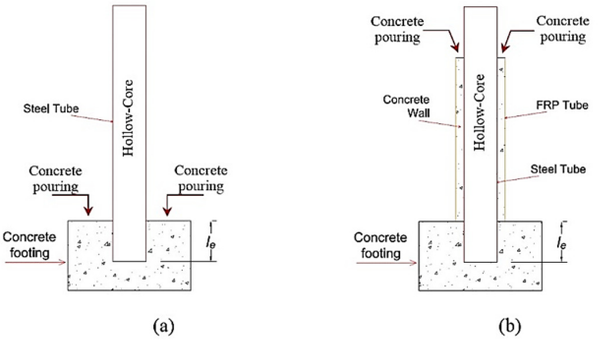


Figure 1. General arrangement of the construction of the HC-FCS column (a) inserting the steel tube and casting the footing, (b) installing the FRP tube and pouring the concrete shell

HC-FCS composite columns have several advantages as a precast element over conventional reinforced concrete or structural steel. The concrete infill is confined by both FRP and steel tubes, which results in a triaxial state of compression that increases the strength and strain capacity of the concrete infill and enhances the seismic performance of such columns [6-9]. The concrete shell reduces the susceptibility of the local and global buckling of the steel tube.

Fiber-reinforced polymer (FRP) is outstanding in its high strength-to-mass ratio, and has been used weidly for retrofitting existing structures during the past decades [10,11].

2 RESEARCH SIGNIFICANCE

The main objective of this study is to investigate the performance of HC-FCS column having thin-walled steel tube under seismic loads. The column had a steel tube diameter-to-thickness ratio (D_i/t_s) of 147. The column first tested under axial and quasi-static cyclic loads, then repaired rapidly and retested under the same loads condition.

3 EXPERIMENTAL PROGRAM

3.1 *Specimen Description*

In this study, a 0.4-scale HC-FCS column, F4-24-P1(0.8)4 was tested under constant axial load and lateral cyclic load. The F4-24-P1(0.8)4 column had a circular cross section with an outer diameter (D_f) of 24 inches and a clear height of 80 inches. The lateral load was applied at a height of 95 inches with a shear span-to-depth ratio of approximately 4.0.

The column consisted of an outer filament-wound GFRP tube with a thickness of 0.125 inches. The inner steel tube had an outer diameter of 16 inches and a thickness of 0.109 inches corresponding to inner-diameter-to-thickness D_i/t_s of 147. The steel tube was manufactured in The Highbay laboratory of Missouri University of Science and Technology by performing a seam-welding (full-penetration groove weld according to AWS 2000) for a 0.109-inches steel sheet cut and rolled to the required dimensions (length x circumference) prior to the welding. A concrete shell with a thickness of 4 inches was sandwiched between the steel and FRP tubes [Fig. 2].

The inner steel tube had yield stress of 56,240 psi, ultimate stress of 62,800 psi, yield strain of 2.15%, and an ultimate strain of 5.4%. The steel rebar had yield stress of 60,000 (psi), ultimate stress of 90,000 (psi), and ultimate strain of 0.08. The rebar properties are based on the manufacturer's data sheet while the steel tube properties were determined through tensile steel-coupon testing according to ASTM A 1067.

The used GFRP tube, was made with a matrix of Iso-polyester with a wall thickness of 0.125 inch, and based on the manufacturer's datasheet, had an axial elastic modulus of 1,400 ksi, hoop elastic modulus of 2,200 ksi, axial ultimate stress of 17,900 psi, and hoop rupture stress of 40,000 psi.

The columns' label used in the current experimental work consisted of four segments. The first segment is a letter F in reference to flexural testing, followed by the column's height-to-outer diameter ratio (H/D_f). The second segment refers to the column's outer diameter (D_f) in inches. The third segment refers to the GFRP matrix using "P" for Iso-Polyester base matrices; this is followed by the GFRP thickness in 1/8 inch, steel thickness in 1/8 inch, and concrete shell thickness in inches.

The steel tube of the column was embedded into the footing while the FRP tube truncated at the face of the footing without any embedment. The embedment depth, l_e, was determined using equation 1 [12].

$$\frac{D_i t_s F_u}{\left(l_e{}^2\right)} \leq 3.3\sqrt{f'_{c,FT}} \quad (1)$$

where D_i is the steel tube outer diameter (being 16 inches), t_s is the steel tube thickness (being 0.109 inches), and F_u is the ultimate stress of steel tube (being 62,800 psi) , and $f'_{c,FT}$ is the unconfined cylindrical compressive strength of the concrete footing (being 5,500 psi). Using these values an embedded length of 20 inches was deduced. Therefore, during the experimental work, l_e of 20 inches corresponding to 1.25 D_i (D_i is the inner diameter of the steel tube) was used to achieve the full embedment of the HC-FCS column [Fig. 1].

The concrete footing that was used in this study had a length x width x depth of 60-inches x 48-inches x 34 inches with bottom reinforcements of 7-#7, top reinforcements of 6-#7, and shear reinforcement of #4 at 2.5 inches [Fig. 2]. The steel cage of the footing was installed into the formwork.

The construction steps were as follows: 1) preparing and installing the reinforcement cages of the footings; 2) installing the steel tube into the footing cage with an embedded length of 20 inches; 3) pouring the concrete of the footing; 4) installing the GFRP tube and pouring the concrete of the concrete shell; 5) installing the reinforcement cage of the column head with dimensions of length x width x depth of 30-inches x 30- inches x 32 inches around the and concrete pouring.

Pea gravel with a maximum aggregate size of 3/8 inches was used for concrete mixtures. The unconfined concrete strengths ($f'c$) for F4-24-P1(0.8)4 at 28 days and at the day of the test were 6,305 (psi)

and 6,575 (psi) for the concrete wall, while 5,960 (psi) and 6,295 (psi) were obtained for the footing at the same ages, respectively.

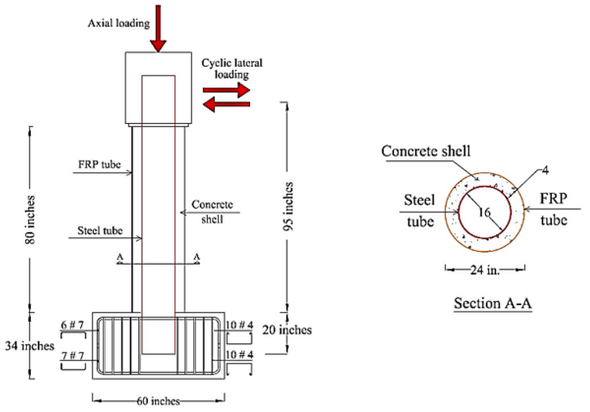


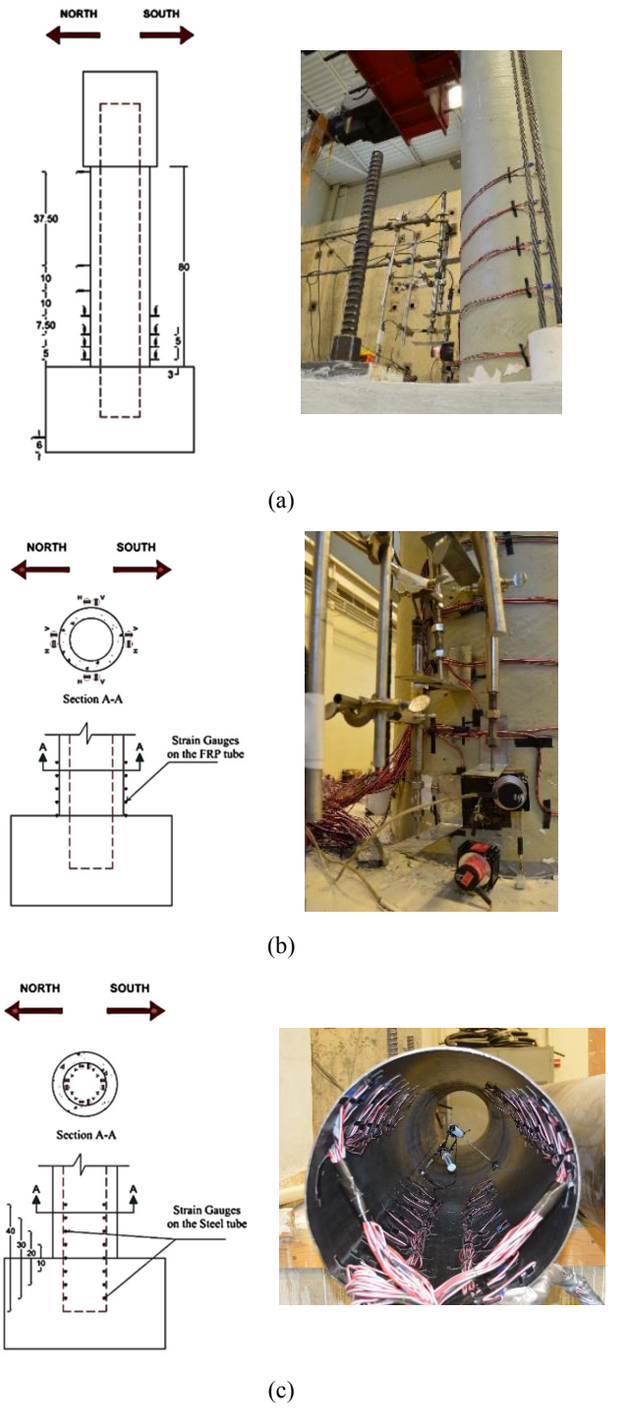
Figure 2. Construction layout of the column (a) elevation, (b) column cross-section (A-A)

3.2 *Test setup and instrumentations*

Sixteen linear variable displacement transducers (LVDTs) and string potentiometers (SPs) were assigned for measuring different displacements in each test specimen [Fig. 3 (a)]. Four LVDTs were mounted on each of the north and south faces of the column to measure the vertical displacements along the potential plastic hinge region. Two more LVDTs were attached to the footing for measuring the uplift and sliding of the footing during the test. The effects of the footing uplift and sliding were considered before calculating the lateral displacement and curvature of the column.

Forty strain gauges were installed on the FRP tube at five levels with 5 inch spacing between them. Four horizontal and four vertical strain gauges were installed at each level [Fig. 3 (b)]. Sixty-four strain gauges were installed inside the steel tube at seven levels with a spacing of 5 inches [Fig. 3 (c)]. Four horizontal and four vertical strain gauges were installed at each level. A high definition webcam was placed inside the steel tube 20 inches from the top of the footing level to film any potential buckling of the steel tube and any internal damage.

Three string Potentiometers (SPs) were assigned for measuring the slip between the FRP tube, concrete wall, and the steel tube. To achieve that, a 0.75 inches in diameter hole was drilled at hieght of 5 inches (from the top level of the footing) all the way to the steel tube [Fig. 4]. Then, the SPs were mounted in three positions : 1) on FRP tube to meaure the FRP tube, 2) connected to metal rods fixed on the concrete wall to measure it's movement, and 3) connected to metal rods fixed on the steel tube from inside (opposite to the hole from outside) throug an opening into the head to measure the relative movement at the same level (5 inches from the top level of the footing) [Fig. 4 (b)].

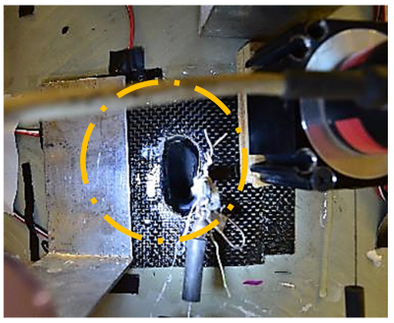


(a)

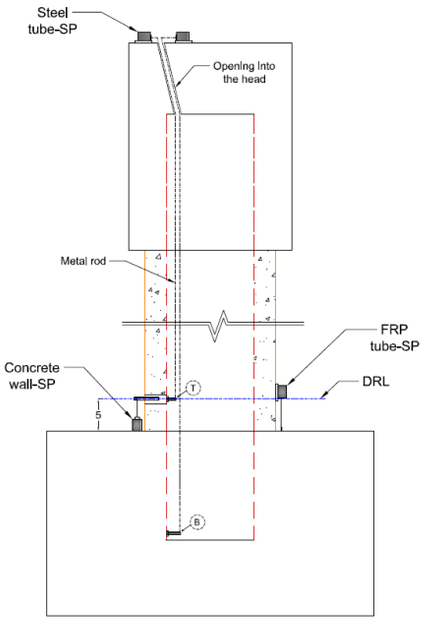
(b)

(c)

Figure 3. Strain gauges layout: (a) LVDT's and SP's installed, (b) mounted on GFRP tube, (c) mounted on steel tube



(a)



(b)

Figure 4. (a) Hole into the F4-24-P1(0.8)4 column for the relative movements measuring of the FRP tube, concrete wall, and inner steel tube, (b) hole and instrumentation layout

3.3 *Loading protocol*

Constant axial load, P, of 110 kips corresponding to 5% of the axial load capacity of the equivalent RC-column, P_o, with the same diameter and 1% longitudinal reinforcement ratio was applied to the column using six external prestressing strands [Fig. 5]. The P_o was calculated using Eq. 2 (AASHTO-LRFD 2012):

$$P_o = A_s F_y + 0.85(A_c - A_s)f'c \qquad (2)$$

where A_s = the cross-sectional area of the longitudinal steel reinforcements, A_c = the cross-sectional area of the concrete column, and F_y = the yield stress of the longitudinal steel reinforcements. The prestressing strands were supported by a rigid steel beam atop the column and the column's footing. The prestressing force was applied using two servo-controlled jacks that kept the prestressing force constant during the test.

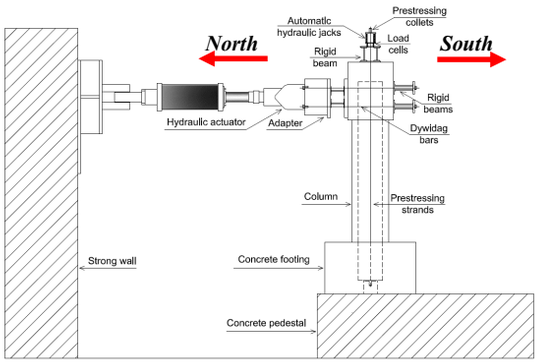


Figure 5. Layout of the test setup

After applying the axial load, a cyclic lateral load was applied in a displacement control mode using two hydraulic actuators connected to the column loading stub. The loading regime was based on the recommendations of FEMA 2007, where the displacement amplitude a_{i+1} of the step i+1 is 1.4 times the displacement amplitude of the proceeding step (a_i). Two cycles were executed for each displacement amplitude. Fig. 6 illustrates the loading regime of the cyclic lateral displacement. Each loading cycle was applied in 100 sec. corresponding to a loading rate that ranged from 0.01 inch/sec. to 0.05 inch/sec.

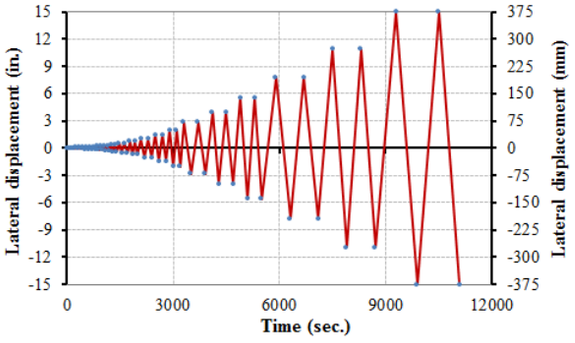


Figure 6. Lateral displacement loading regime

4 RESULTS AND DISCUSSION

Generally, the embedded length and thickness of the steel tube have significant effects on the behavior of HC-FCS columns under cyclic loads [12]. The tested column in this study had thin steel tube that was susceptible to inward buckling instabilities, and thereby steel tube slippage led to degradation of the bending strength.

Fig. 7 shows the moment drift ratio response of F4-24-P1(0.8)4 column. The lateral drift (δ) was calculated by dividing the lateral displacement measured from the actuators displacement transducers by the shear span of 95 inches. The moment (M) at the

interface joint was obtained by multiplying the force measured by the actuators' load cells by the column's height of 95 inches.

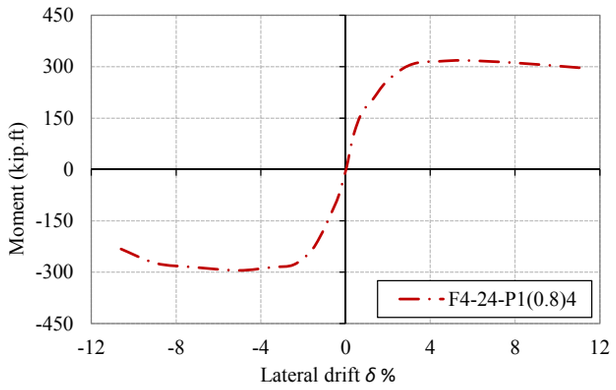


Figure 7. Moment drift ratio envelop curve

The attained moment capacity and the lateral drift were 312 kip.ft and 11.2% for column F4-24-P1(0.8)4.

Fig. 8 shows the relative movements of the FRP tube, concrete wall, and inner steel tube measured at the same level (5 inches above the interface joint, as shown in Fig. 4). As shown in the figure, at lateral drift of almost 8%, the relative movement was increased up to 1 inches between the FRP tube-concrete wall. The reason was at late lateral drift ratios, the FRP tube exhibited more lateral pressure as a result of the concrete wall dilation, and thereby, degradation of the bond interface was occurred.

While, it was in 0.6 inches at the same lateral drift between the concrete wall-steel tube indicating that the interface bond was decreased due to the steel tube local buckling. The interfacial bond failure and relative slip gradually developed at early lateral drift stage, which is related mainly to the steel tube large diameter-to-thickness ratio that influences the bond-slip performance.

Eventually, as shown in Fig. 9, the F4-24-P1(0.8)4 failed by the steel tube diamond local buckling mode of deformation followed by FRP tube rupture [Fig. 9 (b)] on the north side at 11% lateral drift.

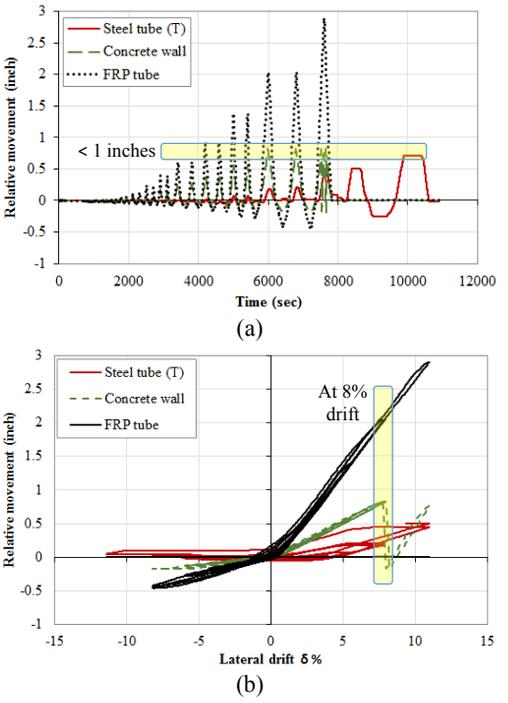


Figure 8. The relative movements of the FRP tube, concrete wall, and inner steel tube measured at 5 inches level above the interface joint (a) vs. time, (b) vs. lateral drift (%)



(a)



(b)

Figure 9. F4-24-P1(0.8)4 column (a) during the test, (b) FRP tube rupture and steel tube buckling (at 11% lateral drift)

5 RETROFITTING WORK

The economical retrofitting techniques using FRP jackets can be used to improve the seismic performance of bridge columns by increasing confinement and avoiding failures near the base of existing columns. The retrofitting schemes in this study consist of using GFRP systems, wrapped in the damaged region near the interface joint.

FRP composite jackets fabricated from GFRP by wet layup were used to rehabilitate the tested HC-FCS column. The fibers in the composite laminates were oriented in the hoop direction so that the contribution of the composites to the flexural strength of the columns was small. The composites were formed using a single sheet of GFRP with an overlap of 20 inches in the hoop direction of the columns to avoid a localized failure at the fabric ends. The jackets were started at the footing top face level and extended 40 inches above the base of the columns.

Fig. 10 illustrates the rapid repairing process of column F4-24-P1(0.8)4. The repaired column named F4-24-P1(0.8)4-R by adding the letter "R" which stands for "repair". This repairing process was selected to minimize cost of implementation for columns subjected to moderate displacement demands and was finished within 6 hours (1.5 hour GFRP wrapping, 3 hours GFRP curing, and 1.5 hour concrete mortar injection). Properties of the composite materials used in this study are listed in Table 1.

Table 1. Properties of Saturated GFRP Wrapping (Data from Fyfe Co. LLC., 2002)

Nominal thickness/layer (inches)	0.05
Young's modulus, E (ksi)	3,790
Tensile strength (ksi)	83.4
Ultimate strain	2.2%

The F4-24-P1(0.8)4-R column tested under the same lateral and axial loads that applied to the F4-24-P1(0.8)4 column. Fig. 11 shows the moment capacity versus lateral drift response of F4-24-P1(0.8)4-R column. The moment capacity and the lateral drift were 104 kip.ft and 8%, respectively (66% and 20% lower than those for column F4-24-P1(0.8)4) [Fig. 11].

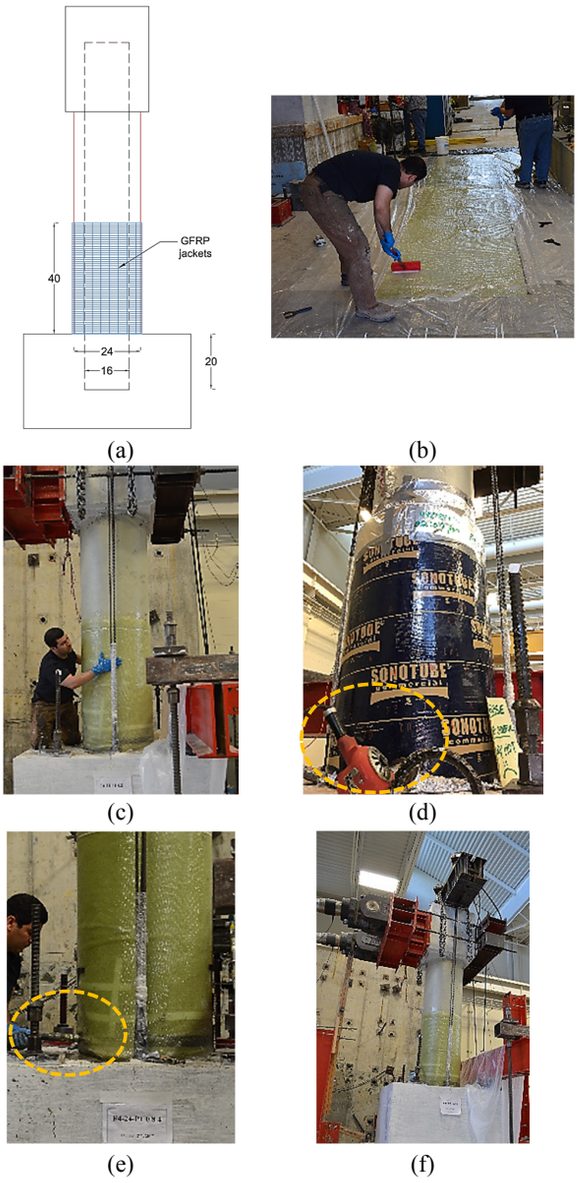


Figure 10. Retrofitting process of F4-24-P1(0.8)4 column (a) layout, (b) GFRP wet layup preparing, (c) GFRP wet layup wrapping, (d) GFRP layers curing using the heat-gun, (e) grout injecting, and (f) F4-24-P1(0.8)4-R column

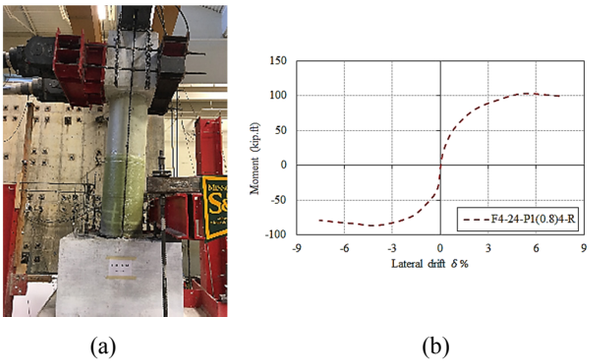


Figure 11. F4-24-P1(0.8)4-R column (a) during the test, (b) Moment drift ratio envelop curve

Careful examination of the tested column's concrete wall as well as steel tube have been conducted after peeling the FRP tube. As shown in Fig. 12 (a), the concrete wall cracked longitudinally (up to 40 inches above the footing top level) on the west side. While, it was crashed (up to 10 inches above the footing top level) on the both south and north sides where the concrete wall suffered high compression stresses. The steel tube was severely buckled locally near the footing-column interface joint [Fig. 12 (b)] as well as steel tube ductile tearing [Fig. 12 (d)], which is gradually extended 20 inches downward and upward leading to bond interface deterioration between the steel tube and the surrounding concrete. As shown in Fig. 12 (c), the end cross-section of the steel tube did not keep its circular shape. Thus, early initiation of the steel tube pull-out (slip) was observed at 2.7% lateral drift followed by bending strength dropping.

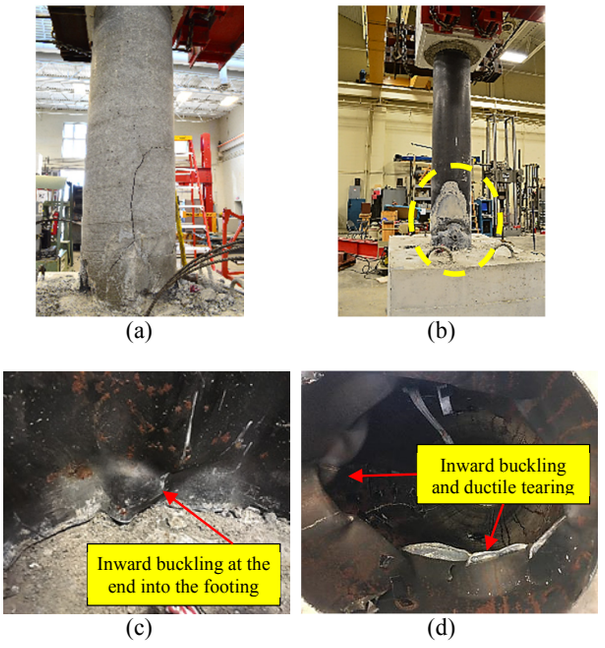


Figure 12. F4-24-P1(0.8)4-R column forensic structural (a) concrete wall cracks, (b) steel tube buckling, (c) steel tube inward buckling at the end into the footing, (b) steel tube inward buckling and ductile tearing at the interface joint

6 CONCLUSIONS

This paper presents the experimental results of a hollow-core fiber reinforced polymer concrete steel (HC-FCS) precast column. The HC-FCS column consists of a concrete hollow cylinder sandwiched between an outer fiber-reinforced polymer (FRP) tube and an inner steel tube. The column had an outer diameter of 24 inches, an inner steel tube diameter of 16 inches with D_i/t_s=147, and a height-to-diameter ratio of 4.0. The steel tube was embedded into reinforced concrete footing with an embedded length of 20 inches corresponding to 1.25 D_i, while the FRP tube acted as a formwork and provided a continuous confinement for the concrete shell, and was curtailed at the top surface of the footing. The column was subjected to constant axial load and lateral cyclic load during this study and then repaired rapidly using GRFP wet layup technique and retested under the same seismic loading regime. The tested column in this study has a thin-walled steel tube that was susceptible to inward buckling instabilities observed at small lateral drift of 2.7% led to initiate the dropping the bending strength. Therefore, steel tube slippage occurs due to the combination of the insufficient development length and the contact interface deboning with the surrounding footing and column concrete. Finally, after steel tube sever buckling at the interface joint, FRP tube rupture occurred at 11% lateral drift. The repaired column by GRFP wet layup technique displayed good lateral displacement behavior. However, the bending strength less enhanced due to the severe local buckling deformations of the inner steel tube.

7 PREFERENCES

1. Schrank, D., B. Eisele, and T. Lomax, *TTI's 2012 urban mobility report.* Texas A&M Transportation Institute. The Texas A&M University System, 2012: p. 4.
2. Schrank, D.L. and T.J. Lomax, *2009 urban mobility report*. 2009: Texas Transportation Institute, Texas A & M University.
3. Dawood, H., M. ElGawady, and J. Hewes, *Factors affecting the seismic behavior of segmental precast bridge columns*. Frontiers of Structural and Civil Engineering, 2014. 8(4): p. 388-398.
4. Teng, J. and L. Lam, *Behavior and modeling of fiber reinforced polymer-confined concrete.* Journal of structural engineering, 2004. 130(11): p. 1713-1723.
5. Teng, J., et al., *Hybrid FRP–concrete–steel tubular columns: concept and behavior.* Construction and Building Materials, 2007. 21(4): p. 846-854.
6. Abdelkarim, O.I. and M.A. ElGawady, *Analytical and Finite-Element Modeling of FRP-Concrete-Steel Double-Skin Tubular Columns.* Journal of Bridge Engineering, 2014.
7. Abdelkarim, O.I. and M.A. ElGawady, *Behavior of hollow FRP–concrete–steel columns under static cyclic axial*

compressive loading. Engineering Structures, 2016. 123: p. 77-88.
8. Abdulazeez, Mohanad M., Omar I. Abdelkarim, Ahmed Gheni, Mohamed A. ElGawady, and Greg Sanders. *Effects of Footing Connections of Precast Hollow-Core Composite Columns*. No. 17-01256. 2017.
9. Abdelkarim, O.I. and M.A. ElGawady, *Concrete-Filled-Large Deformable FRP Tubular Columns under Axial Compressive Loading*. Fibers, 2015. 3(4): p. 432-449.
10. Seible, F., et al., *Seismic retrofit of RC columns with continuous carbon fiber jackets*. Journal of composites for construction, 1997. 1(2): p. 52-62.
11. Jia, J., et al., *Cyclic load responses of GFRP-strengthened hollow rectangular bridge piers*. Advances in Materials Science and Engineering, 2014. 2014.
12. Abdelkarim, O. I., ElGawady, M. A., Gheni, A., Anumolu, S., and Abdulazeez, M. (2016). *"Seismic Performance of Innovative Hollow-Core FRP–Concrete–Steel Bridge Columns." Journal of Bridge Engineering, 04016120.*

MS04: Strengthening, monitoring and life-cycle assessment of steel bridges

Organizers: E. Ghafoori, R. Al-Mahaidi, X.L. Zhao, M. Motavalli & M. Dawood

Maintenance, Safety, Risk, Management and Life-Cycle Performance of Bridges – Powers, Frangopol, Al-Mahaidi & Caprani (Eds)
© 2018 Taylor & Francis Group, London, ISBN 978-1-138-73045-8

Fatigue improvement of welded bridge details in stainless steel using High-Frequency Mechanical Impact treatment

M. Al-Emrani & P. Shams-Hakimi
Chalmers University of Technology, Göteborg, Sweden

C. Schneider
Swerea - Kimab, Stockholm, Sweden

Z. Barsoum
Royal Institute of Technology, Stockholm, Sweden

H. Groth
Outokumpu, Degerfors, Sweden

ABSTRACT: This paper reports the results from fatigue testing on welded non-load-carrying transverse attachments made of C-Mn (S460) and stainless (LDX2101) steels. The tests are done on 40 mm thick specimens in as-welded and HFMI-treated specimens. Measurements on weld toe radius and weld residual stresses are also reported. The results show that the improvement of fatigue strength that can be achieved by HFMI-treatment on welded LDX2101 steel is similar to what is obtained for equivalent C-Mn steels. Also in the as-welded condition do these two types of steel show similar fatigue strength. HFMI-treatment gives more than 5 steps increase in fatigue strength for both steels, which is higher than what specified, for example by the recommendations of the International Institute of Welding.

1 INTRODUCTION

The design of steel and composite (steel-concrete) bridges is generally determined by the Fatigue Limit State. This has practically meant that high strength steels are very seldom – if ever – relevant in bridge applications. In fact, even for conventional construction steels, such as S355, the strength of the material is often not fully utilized in design as the fatigue strength of welded details sets the roof in term of utilization ratios. Being able to "bypass" this limitation opens for interesting possibilities in term of material saving, weight reduction and more optimized designs. This has been the driving force behind the rather extensive research conducted in recent years in the field of fatigue strength enhancement of welded bridge details by means of various post-weld treatment method. In this respect, High Frequency Mechanical Impact (HFMI) techniques have gained most attention. This category of methods promises high efficiency to relatively low cost and can be applied both in workshop and in situ. In addition, HFMI treatment has proven to be particularly effective in the high-cycle fatigue regime where bridges usually operate. Several previous studies have demonstrated considerable material and weight saving with HFMI treatment applied to critical, fatigue governing details in steel and composite bridges. Shams Hakimi et al. (2015) showed for example that for simply-supported railway bridges with spans ranging between 10 and 30 m a weight saving between 30 and 20% can be achieved if fatigue critical details are treated with HFMI. This material saving was partly enabled by upgrading the steel strength from S355, which is most common in steel railway bridges, to S460. Several other studies show similar results on C-Mn steels. Today, the use of HFMI treatment for enhancing the fatigue strength of welded steel bridges is gaining increasing applicability and the method has been used both in the design of new bridges and for the rehabilitation of existing ones, see for example Shams Hakimi & Al-Emrani (2014).

It should be mentioned that post-weld treatment of the weld toe can shift the fatigue failure site to other areas, for instance to the root of the same weld or to other weldments in the structure. In new structures, non-load-carrying welds which are post-weld treated can be produced as fully penetrated in order to avoid root failure.

To date, almost all research related to HFMI has been conducted on C-Mn steels. Particularly high strength steels in relatively thin plates (mostly up to 16 mm even if some work exist on thicker plates) have been in focus, see e.g. Shams-Hakimi et al. (2017a) where 582 fatigue test results are compiled and evaluated.

Recently, the interest in using stainless steel as structural material in bridges has increased both in Sweden and elsewhere in the world. The main driving force has often been the lower total life cycle costs promised by stainless steels compared to conventional C-Mn steels.

There are two reasons why fatigue strength enhancement of welded details in stainless steel is of high interest. On the one hand, stainless steels are

typically several times more expensive than conventional constructions steels. Material saving in stainless steel is therefore expected to have a larger impact on the total cost of a steel bridge compared to bridges made of conventional steels. In addition, stainless steels, such as Duplex and Lean Duplex have higher strength than conventional construction steel used in bridge applications (S355 or even S420) and can thus better meet the potential offered by the increase in fatigue strength after HFMI-treatment.

Studies on fatigue improvement of welded details in stainless steels are very limited. Toe grinding was investigated by Baptista et al. (2008) on stainless steels subjected to salt water corrosion. Xu et al. (2014) studied the efficiency of weld toe dressing with low transformation temperature (LTT) welding wires on 304L (1.4306) stainless steel specimens with welded transverse attachments. The only extensive experimental study known to the authors where HFMI treatment (in addition to grinding, TIG- and plasma dressing) was investigated on welded details in stainless steel is the one reported by Marquis & Maddox (2009). Relatively thin plates were used in this investigation (3 and 10 mm) and in many cases fatigue cracking in the tested specimens initiated elsewhere than in the treated area at the weld toe.

This paper presents the results from an extensive testing program done within the research Project INNODEFAB. The entire testing program included 74 fatigue tests. Focus here is however on test results obtained on specimens made of LDX2101 stainless steel. Results from similar tests from specimens made of S460 steel are also presented for comparison. In addition to fatigue testing, measurements of weld toe profile and weld residual stresses have also been conducted. A more detailed reporting of the test program with focus on C-Mn steels is given by Shams-Hakimi et al. (2017b).

2 EXPERIMENTAL PROGRAM

The entire experimental program for bridges within INNODEFAB included 74 fatigue tests, 54 of C-Mn steel and 20 of LDX2101 stainless steel. In this paper, the results from the stainless steel specimens (series 7 and 8) are presented and compared to the corresponding results for C-Mn steel (series 1 and 4), see Table 1. The test specimens resemble typical welded connections of vertical stiffeners in steel bridges, see Figure 1.

Fatigue testing was performed in 4-point bending in two different testing rigs with frequencies that varied between 3 and 20 Hz. The distance between loading points was chosen so as to avoid local effects from loading close to the welded detail. Strain gauges were used to obtain the nominal stress in the main plate between the loading points. The target

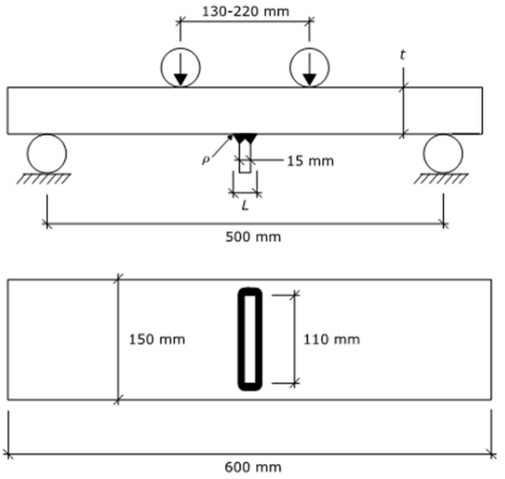


Figure 1. Test specimen dimensions and loading arrangement, Shams-Hakimi et al. (2017b).

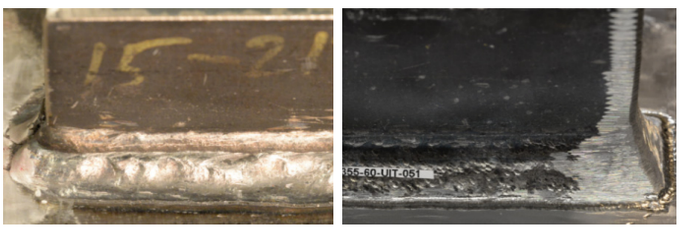
stress ratio in the tests was 0.1. However, the actual stress ratio varied between 0.01 and 0.2 depending on load level and testing rig.

Table 1. Overview of the experimental program.

Series	Specimens	Steel type	Min. yield stress [MPa]	*k*
1	460-38-AW	S460M	460	7
4	460-40-HFMI	S460M	460	11
7	LDX-40-AW	LDX2101	450	10
8	LDX-40-HFMI	LDX2101	450	10

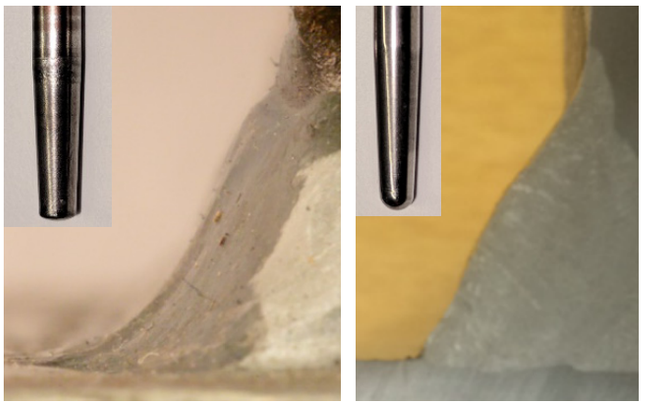
2.1 *Manufacturing*

The C-Mn and LDX specimens were welded in two different workshops and some important production aspects differed between the two different specimen batches. The C-Mn specimens were welded in a bridge production workshop and common procedures were followed to reproduce a weld quality similar to that found in bridges. Therefore, the C-Mn HFMI-treated specimens were ground prior to HFMI-treatment to obtain a weld quality of class B according to ISO 5817. The as-welded C-Mn specimens were on the other hand not ground. A view of the welds in the as-welded and HFMI-treated specimens is given in Figure 2 for the C-Mn series. Welding of the C-Mn specimens was conducted in vertical position of the specimens which resulted in large radius for the weld toe at the main plate side.



As-welded (C-Mn) Ground then HFMI-treated (C-Mn)

Figure 2. Difference between the as-welded and HFMI-treated specimens of the C-Mn speicmens, Shams-Hakimi et al. (2017b).



As-welded (C-Mn) As-welded (LDX)

Figure 3. Difference of toe radius due to vertical positioning of the C-Mn specimens and horizontal positioning of the LDX specimens during welding. Different indenter tip radii for HFMI-treatment were therefore used.

For the LDX specimens, welding was performed as the specimens were lying in a horizontal position, as would be the case in bridge production. As a result, the weld toe radius on the main plate side was smaller. The effect of specimen positioning during welding on the weld toe radius is illustrated in Figure 3 for the two different cases. Furthermore, none of the LDX specimens were ground at any point.

The HFMI-treatment was conducted using an Ultrasonic Needle Peening device with a sonotrode (internal vibration component) frequency of 20 kHz and a vibration range of 40 µm. Due to the difference of the weld toe radii of the C-Mn and LDX specimens, an indenter tip radius of 3 mm was used for the C-Mn specimens while an indenter with a radius of 1.5 mm was used for the LDX specimens. The average treatment speed varied between 200-300 mm/min.

In all specimens, full-penetration K-welds were used to join the transverse attachment to the main plate in order to avoid root failure in the joints. The length of the transverse attachment was chosen so that at least 10 mm free distance was obtained between the ends of the welds and the edges of the main plates, see Figure 1.

2.2 *Weld scanning*

All specimens were laser-scanned to provide average weld toe radii and standard deviations. Post-processing of the scanning raw data was performed by an algorithm developed by Stenberg et al. (2012). As expected, due to vertical positioning, the as-welded C-Mn series was found to have a large average toe radius. In addition, relatively large variations were registered for the different C-Mn specimens. For the ground and subsequently HFMI-treated C-Mn series, an average toe radius similar to the indenter radius (3mm) was measured with considerably more consistent values for the individual specimens, see Figure 4.

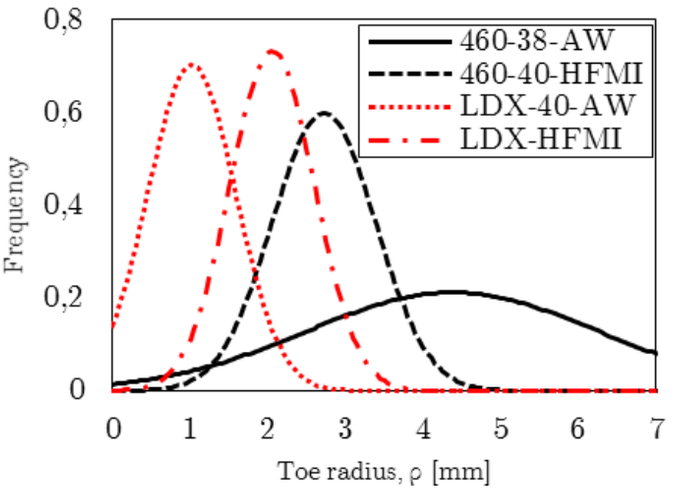


Figure 4. Weld toe scanning results. Normality test were not conducted since the purpose only was illustrative. The C-Mn results are reported in Shams-Hakimi et al. (2017b).

The as-welded LDX series had significantly smaller average toe radius than the as-welded C-Mn specimens. The average weld toe radius increased as a result of HFMI-treatment of the LDX series, however, smaller values were registered as compared to the C-Mn HFMI series due to the smaller indenter radius used (1.5 mm). The measurement results are also given in Table 2.

Table 2. The average value, µ, and standard deviation, σ, of the weld toe radii.

Series	Specimens	μ_ρ [mm]	σ_ρ [mm]
1	460-38-AW	4.38	1.88
4	460-40-HFMI	2.72	0.67
7	LDX-40-AW	1.02	0.57
8	LDX-40-HFMI	2.05	0.54

2.3 *Residual stress measurements*

Residual stress measurements were performed by X-ray diffraction with an X3000 device from Stresstech Oy. The details of various measurement parameters have been reported by Shams-Hakimi et al. (2017b). Measurements were performed both at the surface and in the depth direction, however, only the depth measurements at the weld toes (HFMI-grooves) are presented here. The measurements in the depth direction were performed by successive etching (saturated aqueous NH_4Cl solution) and electropolishing (13 V) in the centre of the HFMI groove on one side of the attachment.

For the C-Mn ground specimen (i.e. prior to HFMI treatment), the transverse residual stresses at the weld toe were approximately -100 MPa, see Figure 5. After HFMI treatment these values changed to ca -300 MPa, successively approaching zero at a depth of approximately 1.5 mm below the weld toe surface. Similar values were measured for the LDX specimens which were not ground. However, it is

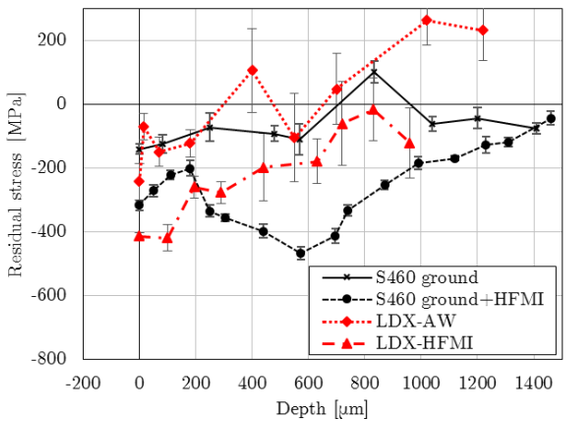


Figure 5. Through-thickness residual stresses profiles from the weld toes. The C-Mn results are reported in Shams-Hakimi et al. (2017b).

observed in Figure 5 that the measurement uncertainties were larger for the LDX specimens. It can also be seen that the compressive stresses induced by HFMI treatment in the LDX specimens approached zero at a smaller depth, less than 1 mm.

3 FATIGUE TEST RESULTS

Figure 6 shows the fatigue test results of all specimens that failed from weld toe. Runouts are excluded as well as one HFMI-treated stainless steel specimen which failed in the base material. The results of the stainless steel specimens are also listed in Table 3. It is observed that HFMI treatment of the stainless steel resulted in a quite similar fatigue strength as that of treated C-Mn specimens, although somewhat lower. For the stainless steel, an average fatigue strength of 249 MPa at 2 million cycles was obtained with a fixed slope of $m = 5$, whereas for the C-Mn steel, the corresponding value was 272 MPa.

The results of HFMI-treated specimens are all well above the S-N curve suggested by the International Institute of Welding (IIW), FAT140, which corresponds to an increase of five FAT-classes. Furthermore, looking at the runout specimens, the average stress range at which these specimens were tested was 258 MPa, which is similar to the runout stress ranges reported by Shams-Hakimi et al. (2017b).

For the as-welded test results, a much more significant difference in fatigue strength is observed between C-Mn and LDX steels. The stainless steel specimens had a fatigue strength of 111 MPa which is closer to the design *S-N* curve of FAT80, relevant for this detail. The fatigue strength for the specimens in C-Mn steel was 149 MPa.

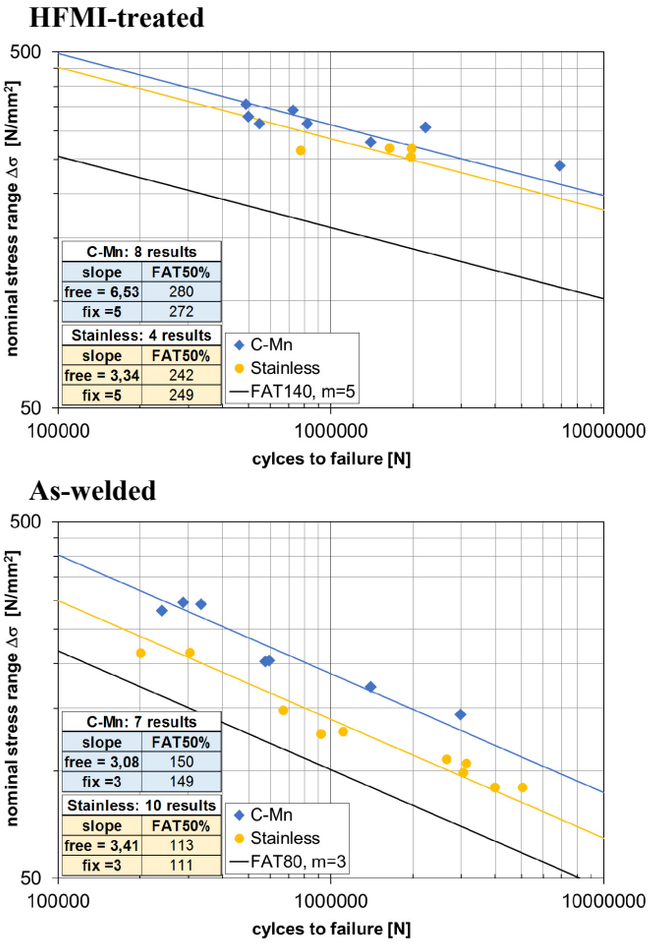


Figure 6. Fatigue test results. The C-Mn results are reported in Shams-Hakimi et al. (2017b).

Table 3. Fatigue test results of the LDX series.

Type	Steel	Δσ	N	Site
AW	LDX2101	108	2 651 108	Toe
AW	LDX2101	105	3 136 992	Toe
AW	LDX2101	148	668 148	Toe
AW	LDX2101	127	920 049	Toe
AW	LDX2101	214	200 609	Toe
AW	LDX2101	215	304 048	Toe
AW	LDX2101	129	1 108 135	Toe
AW	LDX2101	99	3 051 425	Toe
AW	LDX2101	90	5 047 341	Toe
AW	LDX2101	90	3 987 746	Toe
HFMI	LDX2101	254	1 959 311	Toe
HFMI	LDX2101	265	774 354	Toe
HFMI	LDX2101	269	1 641 897	Toe
HFMI	LDX2101	268	1 978 639	Toe
HFMI	LDX2101	254	11 488 755	Runout
HFMI	LDX2101	254	9 387 489	Runout
HFMI	LDX2101	254	9 764 355	Runout
HFMI	LDX2101	268	10 348 390	Runout
HFMI	LDX2101	258	10 213 693	Runout
HFMI	LDX2101	270	2 552 427	Base

4 DISCUSSION AND FINAL REMARKS

The fatigue strength of all HFMI-treated specimens presented in this study was much higher than what is given in the IIW recommendation for the studied detail and steel strength classes. One reason for this might be the fact that, unlike most of other available test - Leitner et al. (2014), Kuhlmann & Günther (2009), Kuhlmann et al. (2005) and Tehrani (2012) – the attachment plates were here terminated at a distance from the edges of the main plate. This should give a better fatigue strength compared to cases where the weld is extended to the edge of the load-carrying plate. Also, the test specimens in this study were HFMI-treated individually, whereas in some other experimental studies, the treatment was first done on wider plates which were then sliced into smaller specimens after the HFMI treatment. This may result in partial relaxation of the beneficial local compressive stresses generated by the HFMI-treatment. Similar observation was lately reported by Zhang et al. (2017).

The fatigue strength of the HFMI-treated stainless steel specimens was on par with that obtained for C-Mn specimens. The difference in derived fatigue strength for the two materials (271 vs 249 MPa in Figure 6) should be seen in view of the limited number of failures obtained for the LDX specimens. Even if this difference holds statistically, it could very well be a result of the difference in weld toe radii after HFMI-treatment in these two types of specimens (3 vs 2 mm for C-Mn and LDX respectively). The difference in yield stress may also provide some answers. The actual minimum yield stress of the batch of C-Mn was actually 566 MPa. Similar information is not available for the stainless steel, but a lower proof stress should usually be expected for LDX2101. For the comparison of the as-welded test results, the significant difference in fatigue strength is mainly attributed to the difference in toe radii as a result of specimen position during welding.

5 ACKNOWLEDGEMENT

The work described in this paper has been funded through the Swedish Vinnova office within the program LIGHTer. The authors would like to acknowledge the contribution of all partners in the INNODEFAB project (Dnr 2014-05133). Special thanks to Lars-Åke Bylund from Böhler Welding Group. Sonats is also acknowledged for helping with the HFMI-treatment and the residual stress measurements.

6 REFERENCES

Baptista, R., Infante, V. & Branco C.M.: “Study of the fatigue behavior in welded joints of stainless steels treated by weld toe grinding and subjected to salt water corrosion.” International Journal of Fatigue 30 (2008) 453–462.

ISO standard, “Welding – Fusion-welded joints in steel, nickel, titanium and their alloys (beam welding excluded) – Quality levels for imperfections (ISO 5817:2014).” European Committee for Standardization, 2014.

Kuhlmann, U. & Günther, H. P.: “Experimentelle untersuchungen zur ermüdungssteigernden wirkung des PIT-verfahrens,” Vers. Univ. Stuttg. Inst. Für Konstr. Entwurf, 2009.

Kuhlmann, U., Bergmann, J., Dürr, A., Thumser, R., Günther, H.-P. & Gerth, U.: “Erhöhung der Ermüdungsfestigkeit von geschwei\s sten höherfesten Baustählen durch Anwendung von Nachbehandlungsverfahren,” Stahlbau, vol. 74, no. 5, pp. 358–365, 2005.

Leitner, M., Stoschka, M. & Eichlseder, W.: “Fatigue enhancement of thin-walled, high-strength steel joints by high-frequency mechanical impact treatment,” Weld. World, vol. 58, no. 1, pp. 29–39, Jan. 2014.

Marquis, G. B. & Barsoum, Z. “IIW Recommendations for the HFMI Treatment - For Improving the Fatigue Strength of Welded Joints.” Singapore: Springer Singapore, 2016.

Marquis, G. & Maddox, S. J.: "Post-weld Fatigue Improvement Technologies for Stainless Steel Welds". 20th International Conference on Structural Mechanics in Reactor Technology (SMiRT 20) Espoo, Finland. SMiRT 20-Division II, Paper 2032. August 9-14, 2009

Shams Hakimi, P. & Al-Emrani, M.: “Post weld treatment - Implementation on bridges with special focus on HFMI,” Chalmers University of Technology, Report, 2014.

Shams Hakimi, P., Mosiello A., Kostakakis K. & Al-Emrani M.: ”Fatigue life improvement of welded bridge details using high frequency mechanical impact (HFMI) treatment,” Proceedings of the 13th Nordic steel construction conference, 2015.

Shams-Hakimi, P., Yıldırım, H. C. & Al-Emrani, M.: “The thickness effect of welded details improved by high-frequency mechanical impact treatment,” Int. J. Fatigue, vol. 99, Part 1, pp. 111–124, Jun. 2017a.

Shams-Hakimi, P., Zamiri, F., Al-Emrani, M. & Barsoum, Z.: “Experimental study of transverse attachment joints with 40 and 60 mm thick main plates, improved by high-frequency mechanical impact treatment (HFMI),” Eng. Struct., Nov. 2017b.

Stenberg, T., Lindgren, E. & Barsoum, Z.: “Development of an algorithm for quality inspection of welded structures,” Proc. Inst. Mech. Eng. Part B J.

Eng. Manuf., vol. 226, no. 6, pp. 1033–1041, Jun. 2012.

Tehrani Yekta, R.: “Acceptance Criteria for Ultrasonic Impact Treatment of Highway Steel Bridges,” University of Waterloo, 2012.

Xu, L. Y., Wang, Y. F., Jing, H. Y. & Han, Y. D.: “Fatigue strength improvement of stainless steel using weld toes dressing with low transformation temperature welding wire.” Science and Technology of Welding and Joining, 19:8, 664-672, 2014.

Zhang, H., Wang, D., & Deng, C.: “Optimal Preparation Process for Fatigue Specimens Treated by Ultrasonic Peening,” Exp. Tech., pp. 1–9, Oct. 2017.

Maintenance, Safety, Risk, Management and Life-Cycle Performance of Bridges – Powers, Frangopol, Al-Mahaidi & Caprani (Eds)
© 2018 Taylor & Francis Group, London, ISBN 978-1-138-73045-8

The effect of the CFRP properties on the fatigue strengthening of steel plates in multiaxial loading

N.J. Aljabar & X. L. Zhao
Department of Civil Engineering, Monash University, Clayton, VIC 3800, Australia.

R. Al-Mahaidi
Faculty of Science, Engineering and Technology, Swinburne University of Technology, Melbourne, Australia.

E. Ghafoori & Masoud Motavalli
Empa, Swiss Federal Laboratories for Materials Science and Technology, Dübendorf, Switzerland.

Yew-Chin Koay
VicRoads, Level 3, 60 Denmark Street, Kew, VIC, 3101, Australia

ABSTRACT: Employing advanced material such as Carbon-fiber-reinforced-polymer (CFRP) in tension fatigue strengthening of aged bridges shows a great capability of arresting or delaying the crack propagation in steel structures. Extending the current knowledge of the CFRP strengthening to the case of the multiaxial cyclic loading will broaden its application in Civil Engineering. The aim of this paper is to investigate the fatigue behavior of the CFRP strengthening of central-cracked steel plates subjected to the combined action of tensile (mode-I) and shear (mode-II) loading with a focus on the effect of the CFRP properties. The key parameters in this study are the mixed-mode ratio (crack angle), the crack length ratio (crack length to the plate width), patching configurations, and mechanical properties of the composite material. A comparative study was conducted on steel plates strengthened with different composite properties (thickness, Young's modulus) and types (plates vs. sheets).

1 INTRODUCTION

Complex details and connections in ageing steel bridges often contain defects and also it is prone to fatigue failure. Restoring such structural elements to the service requires upgrading its strength and stiffness. Carbon-fiber-reinforced-polymer (CFRP) composites offer a competitive solution in terms of its light weight and the high tensile strength (Zhao 2013; Hollaway & Cadei 2002). The composite material has launched in the construction industry with different Young's modulus, thickness, types (sheet vs. laminate) providing a wide range of its applications, namely improving the tensile strength and stiffness of the upgraded components. Much research has been investigated the higher strengthening efficacy of the adhesively bonded systems that can be obtained from various mechanical properties of the composite material and the strengthening scheme (Ghafoori *et al.* 2015; Wu et *al.* 2012; Liu et *al.* 2009). The majority of these studies have been carried out on CFRP-strengthened cracked steel plates. Furthermore, The fatigue performance of the CFRP strengthening systems was studied at different load conditions (Amraei et *al.* 2017; Aljabar et *al.* 2016; Feng et *al.* 2014), for strengthening at different stages of the fatigue life of the strengthened elements (Aljabar et *al.* 2017), and for a range of the steel grades (Hu et *al.*2016). It showed that the tension fatigue strengthening of steel plates with tensile crack increased proportionally to the tensile stiffness of the unidirectional composites. Several researchers (i.e.; Ghafoori *et al.* 2015; Liu *et* al. 2009, Wu *et al.* 2012) revealed that the in-plane stiffness of the CFRP strengthening systems was improved by utilizing a composite material with higher Young's modulus, thickness (plates over sheets), and strengthening method (double-sided vs single-sided strengthening methods). However, it is not clear whether the investment in composite materials with superior properties yields the same benefits when the crack or defects in the steel components exhibits a state of mixed-mode loading of tensile and shear stresses. A preliminary study of the authors of the present paper investigated the fatigue behavior of CFRP strengthening system of steel plates with inclined cracks (Aljabar et *al.* 2016, & Aljabar et *al.* 2017). The steel plates were notched with a crack starter of different orientation to introduce different ratios of the shear to tensile stresses at the crack starter tip. The CFRP-strengthened specimens had initial crack lengths of 2%, and 30% of the width of the steel plate simulating specimens with different damage levels. CFRP laminates with Young's modulus of 477GPa and thickness of 1.5mm were patched on a single side

of the steel plates by adopting two strengthening configurations. The test results revealed that the crack propagation curves of CFRP strengthened steel plate with inclined crack can be simulated by the curves of the same specimens with flat (tensile) crack. The crack propagation curves of steel plates with inclined crack showed a proportional shift in the number of cycles to the smaller crack angles. This shift represented the increase in the number of cycles under mixed-mode conditions before the crack kinks to model-I (tensile dominated). The fatigue behavior of steel plates with severe damage level was almost the same but with a lesser increase in the total number of cycles due to the effect of higher tensile stresses at the tip of the initial crack. Having the same test specimen, initial crack lengths, and strengthening configurations, in this paper the fatigue behavior of steel plates with inclined cracks has been investigated further for strengthening with sheet composites of Young's modulus of 640GPa, and thickness of 0.19mm. The test results of the current work were presented and compared with the previous one in terms of the behavior and fatigue performance. This paper constitutes a part of a large research program on the CFRP strengthening of metallic bridges under mixed-mode fatigue loading at Monash University in collaboration with Swinburne University of Technology, and the Swiss Federal Laboratories for Materials Science and Technology (Empa).

2 FATIGUE EXPERIMENT DETAILS

2.1 *Test specimens*

For comparison purpose, the experimental program was kept the same as the recent experimental study that conducted on strengthening with CFRP plates. The dimension, notch details, and the strengthening configurations of the test specimens are presented in Figure 1. The test specimens either fully (configuration A) or partially covered (configuration D) with the composite material. The steel plates with a minimum yield strength of 300MPa were strengthened with 3 layers of S&P C-sheet 640 composite. The composite sheets have a cross section of 300mm*0.19mm whereas the composite laminates have a cross section of 50mm*1.5mm. The tensile test results for the steel plates were 500MPa, 204GPa, and 330 for the tensile strength, Young's modulus, and yield stress, respectively. The tensile strength and Young's modulus of the composite materials were 1603MPa, and 478GPa for the CFRP laminates, and 2650MPa, and 640GPa for the CFRP sheets. In the literature, the researchers used to classify the composite materials based on their Young's modulus in different groups as normal-modulus CFRP, high-modulus CFRP, and ultra-high-modulus CFRP (Zhao 2013). For comparison between the strengthening systems of different composites in this study, it referred to the plate composites with higher Young's modulus as ultra-high-modulus composites UHM-CFRP, whereas it referred to the sheet composite as high-modulus composites HM-CFRP.

The components of the strengthening system were adhered together by a bonding layer of Araldite 420. The tensile strength and elastic modulus of the adhesive were 28.6MPa and 1.9GPa, respectively (Fawzia 2007). To simulate a state of mixed-mode loading (tensile and shear stresses) at the initial crack tip, steel plates were notched with a centrally oriented crack starter. The test specimens have Initial crack lengths ratio of 2%, and 30% and crack angles (β) of 90°, 60°, 45°, and 30°. The bonding surface of the steel plates was cleaned first from the grease by the sandblasting method. Then treated with the acetone solution before a uniform layer of the adhesive was applied. Afterward, the composite sheets were patched to the steel surface. The CFRP strengthened specimens were cured at room temperature for more than two weeks.

2.2 *Test procedure*

The fatigue tests were carried out in an Instron 8802 servo-hydraulic testing machine in the Civil Engineering laboratory at Monash University. The tension fatigue tests were conducted on all specimens

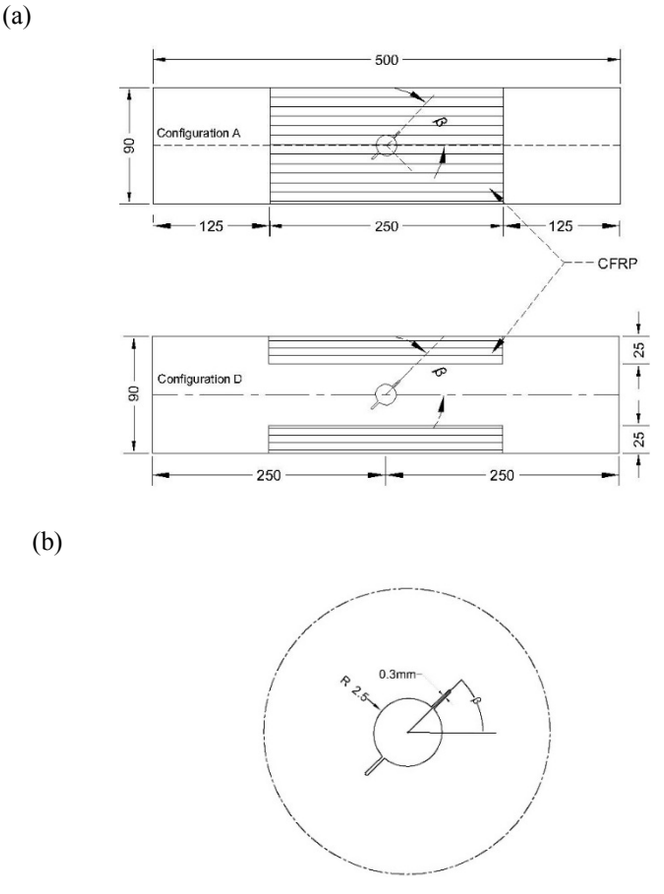


Figure 1. (a) Specimen dimensions and patching configurations; (b) Notch details (dimension in mm, not to scale).

Table 1. Experiment results for CFRP-strengthened steel plates with damage level of 2%.

Specimen Symbol	Fatigue life (HM-sheets)	Fatigue life* (UHM-plates)	Extension ratio (HM-sheets)	Extension ratio* (UHM-plates)	N_m (HM-Sheets)	N_m* (UHM-plates)
US-90°	202784	202784	-	-		
US-60°	251221	251221	-	-	48437	48437
US-45°	402436	402436	-	-	199652	199652
US-30°	2743384	2743384	-	-	2540600	2540600
SHD-90°	294347	319724.3	1.45	1.58		
SHD-60°	349800	388029.8	1.39	1.54	55453	68306
SHD-45°	709438	669034.5	1.76	1.66	415091	349310
SHD-30°	-	-		1.19		-
SHA-90°	345665	460684	1.70	2.27		
SHA-60°	523785	529940	2.08	2.11	178120	69256
SHA-45°	965299	881791.8	2.39	2.19	619634	421108
SHA-30°	-	-		1.22		-

*Aljabar et *al.* 2016

Table 2. Experiment results for CFRP-strengthened steel plates with damage level of 30%.

Specimen Symbol	Fatigue life (HM-sheets)	Fatigue life* (UHM-plates)	Extension ratio (HM-sheets)	Extension ratio* (UHM-plates)	N_m (HM-sheets)	N_m* (UHM-plates)
US-90°	25995	25995	-	-	0	0
US-60°	32000	32000	-	-	6,005	6,005
US-45°	41119	41119	-	-	15,124	15,124
US-30°	79314	79314	-	-	53,319	53,319
SHD-90°	42,638	52,905	1.64	2.04		0
SHD-60°	52,911	64,579	1.65	2.02	10,273	11674
SHD-45°	64,155	81,555	1.56	1.98	21,517	28,650
SHD-30°	116,110	129,496	1.46	1.63	73,472	76,591
SHA-90°	62,686.5	66,442	2.41	2.56		0
SHA-60°	78,575	85,941	2.46	2.69	15,889	19499
SHA-45°	109,528	118,372	2.66	2.88	46,842	51,930
SHA-30°	183,793	181,945	2.32	2.29	121,107	115,503

*Aljabar et *al.* 2017

with a constant amplitude, 0.1 stress ratio, and 20Hz frequency. Such a loading ratio are commonly used for fatigue tests on the CFRP strengthened specimens (Liu *et* al. 2009, Wu *et* al. 2012). It is usually advised to use a frequency between 20-35Hz to shorten the total test time and cost. However, the frequency should not increase the temperature of the tested specimens by more than room temperature plus 2°C, according to ASTME606 (Yung-Li et *al.* 2005). Feng et *al*. (2014) reported that increasing the temperature has a slight effect on the fatigue life of the adhesively bonded composites as long as the temperature is below the glass transition temperature (T_g) of the adhesive. In this study, all specimens were subjected to a fatigue loading fluctuated between 150MPa and 15MPa. The maximum load level was nearly 46% of the yield tensile stress of the steel plates. The beach marking method was adopted in measuring the crack length on the fractured surface and recorded with the corresponding fatigue cycles. The adopted procedure of calculating the length of the kinked cracks are detailed by Aljabar et *al*. (2016).

3 FATIGUE TEST RESULTS

Experimental details and test results are presented in Tables 2, and 3 for specimens with crack length ratios of 2%, and 30% respectively. For comparison reason, the current test results were presented with the recent experimental study of strengthening with UHM-CFRP material (Aljabar *et* al. 2016 & Aljabar *et* al. 2017). The tables show the specimens and the corresponding symbols i.e. strengthening method, strengthening configuration, and crack angles. US stands for un-strengthened specimens, whereas SHA, and SHD identify single-sided strengthening for specimens with full and partial configurations, respectively.

The recorded fatigue life represents the number of cycles that counted till the crack propagated through the whole steel plate width. The strengthening efficacy of the CFRP sheets and laminates for steel plates with different crack orientation is presented in terms of the fatigue life extension factor. This factor represents the ratio of the fatigue life of the steel plates

strengthened with different composite materials to that of the same specimens without CFRP strengthening. The effect of the crack orientation on the fatigue life introduced in terms of the number of cycles counted under the effect of mixed-mode loading (*Nm*). The fatigue life under mixed-mode conditions presented as the difference between the fatigue life of specimens with inclined cracks and the specimens with flat tensile cracks (β<90°). Strengthening with composite sheets and laminates show a comparable increase in the fatigue life of the steel plates with inclined cracks. As the current tests are ongoing the test results of the specimens of β=30° and damage level of 2% were not presented in this paper. HM-CFRP strengthening system of steel plates with damage level of 2% improved the fatigue life by an average factor of 1.54 and 2.1 for full (SHA) and partial (SHD) strengthening schemes. It is clear that there is almost similar increase observed for specimens with configuration A and severe damage. In general, the average difference in the fatigue life extension ratio of strengthening with HM-CFRP sheets and UHM-CFRP laminates was less than 6%. However, the CFRP partially-strengthened specimens with crack length ration of 30% showed the higher difference with advantage for UHM-CFRP strengthening by 18%.

4 MIXED-MODE CRACK PROPAGATION CURVES

The effect of the crack orientation on the fatigue behavior of steel plates strengthened with HM-CFRP sheets was investigated in this study through the crack propagation curves obtained from the test data. Figures 2-5 show the crack propagation curves of steel plates with different damage level and strengthening schemes. Test specimens with inclined cracks exhibit a state of mixed-mode loading condition at the crack tip due to the effect of crack orientation whereas specimens with β=90° exhibit a state of pure tensile stresses.

The difference of the stresses at the crack tips of the two sets of specimens is obvious in the crack propagation curves. The difference is clearly shown in terms of a proportional increase in the fatigue life of specimens with smaller crack angles (β). The relative increase in the total number of cycles of specimens with β<90° was explained by the shifting phenomenon in mixed-mode crack propagation curves (Aljabar et *al*. 2016). The shift in crack propagation curves represents an increase in the number cycles under mixed-mode condition (*Nm*). Furthermore, the shift in *a-N* curves could be a function of the mixed-mode ratio; the ratio of the shear to tensile stresses at the crack tip.

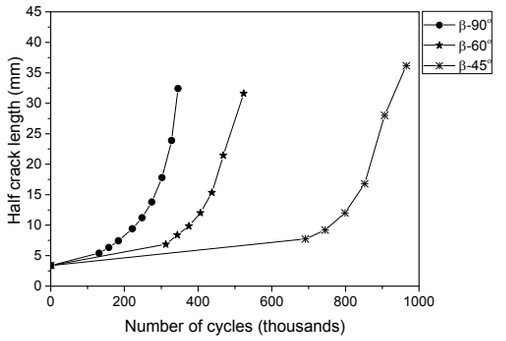


Figure 2. Crack length vs. number of cycles for fully-strengthened specimens with crack length ratio of 2%

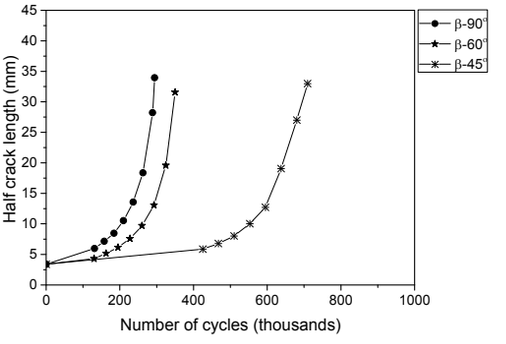


Figure 3. Crack length vs. number of cycles for partially-strengthened specimens with crack length ratio of 2%

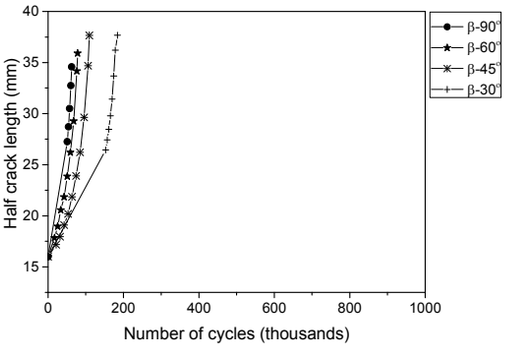


Figure 4. Crack length vs. number of cycles for fully-strengthened specimens with crack length ratio of 30%

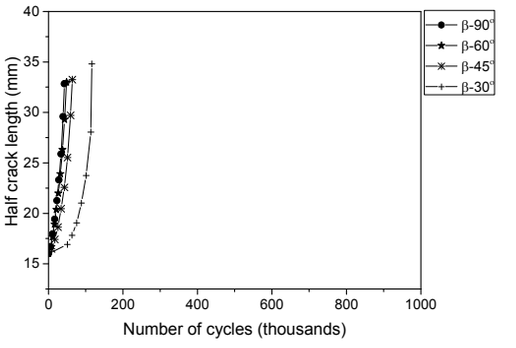


Figure 5. Crack length vs. number of cycles for partially-strengthened specimens with crack length ratio of 30%

Strengthened specimens with higher damage level exhibited a smaller amount of shift due to the increase of the tensile stresses for longer initial cracks and consequently reduced the mixed-mode ratio, the function of *Nm*. The same trend observed for SHD specimens

compared to SHA specimen. The former has smaller strengthening stiffness and then higher tensile stress compared to the latter. It should be noted that the mixed-mode fatigue behavior was almost independent of the type and properties of the CFRP. The tensile strengthening stiffness of the unidirectional composites does not seem to have a significant effect on the fatigue behavior of specimens with initially inclined crack. However, the mechanical properties of the composite material showed the higher influence as the crack initiated as it dominated by the tensile stresses. Therefore, the difference between the fatigue life of the same specimen strengthened with UHM-CFRP and HM-CFRP reflects the effect of the tension strengthening on the tensile stress at the crack tip.

5 EFFECT OF THE COMPOSITE MATERIAL ON THE MIXED-MODE FATIGUE BEHAVIOR

The current knowledge of utilizing CFRP material in tension strengthening of steel components with tensile crack is that the more investment in the mechanical properties of the composted material the longer the fatigue life. Also, the higher the damage level of the CFRP reinforced elements, the more pronounced the fatigue life extension ratio. However, it is not clear whether the fatigue performance of the composite strengthening of steel components with inclined cracks has a similar trend or not. In the current study, the steel plates were patched with composite sheets and laminates of different mechanical properties. The strengthening stiffness of CFRP laminates (one plate of 1.5mm) was clearly higher than the mechanical properties of the CFRP sheets (3 sheets of 0,19mm). Figures 6-9 show that the fatigue improvement of strengthening systems with different composite material was nearly comparable with the relatively small advantage of the CFRP laminates. Both the tension strengthening systems influenced the number of cycles counted for the phase where the propagated crack exhibits tensile dominated stress. The specimen with higher tensile stress showed the higher difference between the fatigue lives of specimens with different CFRP composites. For example, the average increase in the fatigue life of specimens strengthened with UHM-CFRP was higher by 11 %, and 5% for steel plates with damage level of 30%, and 2%, respectively. However, the advantage of strengthening with the composite material of higher tensile stiffness was almost marginal for different strengthening schemes as shown in Figures 6-9.

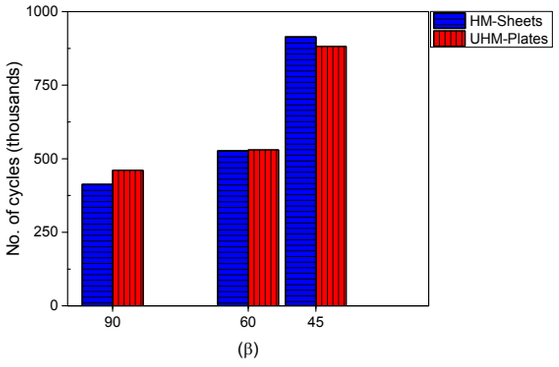


Figure 6. Comparison between the fatigue lives of steel plates fully-strengthened with HM-CFRP and UHM-CFRP with crack length ratio of 2%

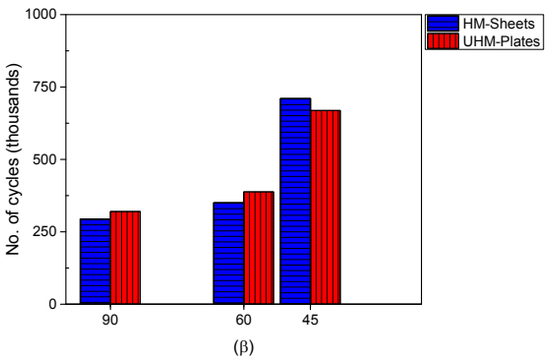


Figure 7. Comparison between the fatigue lives of steel plates partially-strengthened with HM-CFRP and UHM-CFRP with crack length ratio of 2%

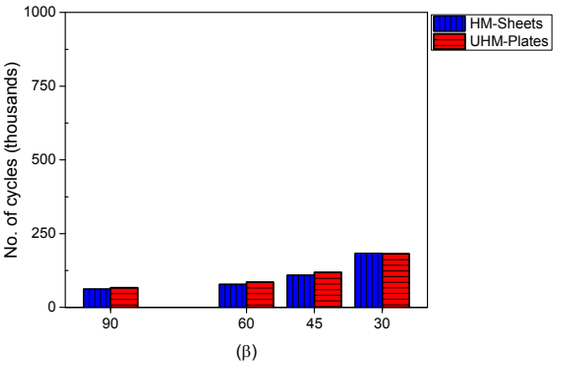


Figure 8. Comparison between the fatigue lives of steel plates fully-strengthened with HM-CFRP and UHM-CFRP with crack length ratio of 30%

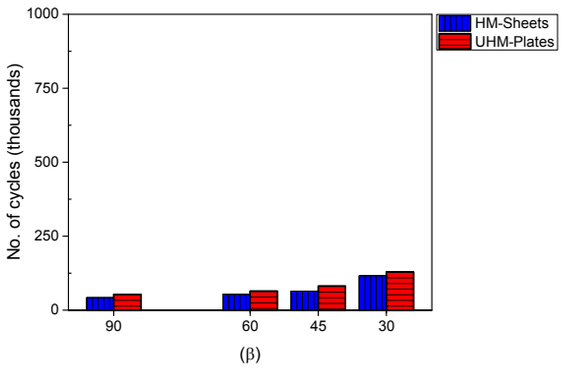


Figure 9. Comparison between the fatigue lives of steel plates partially-strengthened with HM-CFRP and UHM-CFRP with crack length ratio of 30%

6 CONCLUSIONS

In this study, the fatigue behavior of steel plates with inclined crack was investigated under the effect of different variables, i.e.; the crack angle, the crack length, and the strengthening scheme, with a focus on the fatigue performance of strengthening systems of different composite material. A total of 14 specimens were strengthened with 3 layers of the sheet composite of high modulus (E=640, t=0.19mm). The test results were presented and compared to the recent study of similar specimen strengthened with CFRP laminates of the higher modulus (E=477GPa, t=1.5mm). The following conclusions were drawn based on the available test results:

1. The average increase in the fatigue life of steel specimens strengthened with composite sheets was between 150%-210% for smaller damage level. Almost similar increase was observed for the case of specimens with severe damage.
2. The fatigue life extension ratio of strengthening systems of different composite type (sheets vs. laminates) and properties (Young's modulus, thickness) was almost comparable with only a difference less than 6%. However, the UHM-CFRP strengthening system shows a higher improvement in the fatigue life by 18% for partially-strengthened specimens with a crack length ratio of 30%.
3. For strengthening systems of different composite materials, the crack propagation curves of steel plates with inclined crack showed a proportional shift (increase in fatigue life) to smaller crack angles. The fatigue life increase was inversely correlated with the tensile stress components at the crack tip. For example, the higher the damage level, and the higher the tensile stress the smaller the shift and the fatigue life. Similarly, the shift in crack propagation curves of the partially-strengthened specimen was less significant than that of fully-strengthened specimens.
4. The difference between the fatigue life of the same specimen strengthened with UHM-CFRP and HM-CFRP reflects the effect of the tension strengthening on the tensile stress component at the crack tip. The higher this component (the less mixed-mode ratio) the more pronounced the effect of strengthening stiffness on the fatigue life of steel plates with inclined cracks. For example, the average increase in the fatigue life of specimens strengthened with UHM-CFRP was higher by 11 %, and 5% for steel plates with damage level of 30%, and 2%, respectively.

ACKNOWLEDGEMENTS

The authors gratefully acknowledge the financial support provided by the Australian Research Council through an ARC Linkage Grant (LP140100543) with VicRoads and S&P Clever Reinforcement Company AG as Industry Partners. The first author wishes to thank the Higher Committee for Education Development in Iraq for sponsoring his research at Monash University. Thanks are given to all technical staff in the Civil Engineering laboratory at Monash University.

REFERENCES

Aljabar, N.J., Zhao, X. L, Al-Mahaidi, R., Ghafoori, E., Motavalli, M. and Powers, N. 2016. Effect of crack orientation on fatigue behavior of CFRP-strengthened steel plates. *Composite Structures*, 152 295-305.

Aljabar, N.J., Zhao, X. L, Al-Mahaidi, R., Ghafoori, E., Motavalli, M. and, Koay, Y.C. 2017. Fatigue tests on UHM-CFRP strengthened steel plates with central inclined cracks under different damage levels. *Composite Structures*, 160, 995-1006.

Amraei, M., Jiao, H., Zhao, X. L, Tong, L-W. 2017. Fatigue testing of butt-welded high strength square hollow sections strengthened with CFRP. *Thin-Walled Structures*, 120, 260-268.

Fawzia S. 2007. Bond characteristics between steel and carbon fibre reinforced polymer (CFRP) composites, [Ph.D. thesis]. Melbourne, Australia: Monash University.

Feng, P., Hu, L.L., Zhao, X. L, Cheng, L., Xu, S.H. 2014. Study on thermal effects on fatigue behavior of cracked steel plates strengthened by CFRP sheets. *Thin-Walled Structures*, 82, 311-320.

Ghafoori, E. & Motavalli, M. 2015. Normal, high and ultra-high modulus carbon fiber-reinforced polymer laminates for bonded and un-bonded strengthening of steel beams. *Materials & Design,* 67: 232-243.

Hollaway, L. C. & Cadei, J. 2002. Progress in the technique of upgrading metallic structures with advanced polymer composites. *Progress in Structural Engineering and Materials,* 4(2): 131-148.

Hu, L.L., Zhao, X. L, and Feng, P. 2016. Fatigue behavior of cracked high-strength steel plates strengthened by CFRP sheets. *Journal of Composites for Construction* 20(6): 04016043.

Liu, H., Al-Mahaidi, R. & Zhao, X. L. 2009. Experimental study of fatigue crack growth behaviour in adhesively reinforced steel structures. *Composite Structures,* 90(1): 12-20.

Lee, Y. L., Jwo, P., Richard , H., Mark, B. (2005). *Fatigue testing and analysis - theory and practice*. (pp. 187). Elsevier. Online version available at: https://app.knovel.com /hotlink/toc/id:kpFTATP002/fatigue-testing-analysis/fatigue-testing-analysis

Wu, C., Zhao, X. L., Al-Mahaidi, R., Emdad, M. & Duan, W. 2012. Fatigue tests of cracked steel plates strengthened with UHM CFRP plates. *Advances in Structural Engineering,* 15(10): 1801-1816.

Zhao, X. L. 2013. *FRP Strengthened Metallic Structures,* Boca Raton, FL., CRC Press, Taylor & Francis Group.

Maintenance, Safety, Risk, Management and Life-Cycle Performance of Bridges – Powers, Frangopol, Al-Mahaidi & Caprani (Eds)
© 2018 Taylor & Francis Group, London, ISBN 978-1-138-73045-8

Improving the fatigue design of orthotropic steel decks

H. De Backer, W. Nagy & A. Outtier
Ghent University, Ghent, Belgium

ABSTRACT: Orthotropic steel decks (OSDs) consist of a complex network of longitudinal stiffeners, transverse stiffeners and the deck plate itself. Working as a whole, it takes part in the structural working of the overall bridge concept, resulting in an extremely lightweight and durable deck concept. Orthotropic steel decks are very sensitive to fatigue damage, because of the large number of welded connections in the deck. Historically, designers have tried to improve upon the concept by focusing on: optimization of the overall dimension of the steel plates, determining the shape of the stiffeners and possible cut-outs and investigating the possible influence of the wearing courses in distributing vehicle loads. Most of these approaches have proven successful. However, combined with the ever-increasing vehicular loads and traffic volumes, designers still feel the need to increase the plate thicknesses. A deck plate thickness of 18mm or more has become quite common. This is mainly caused since regulations stick to the existing fatigue concepts. Innovative research focuses on the application of fracture mechanics as well as the influence of residual stresses on the fatigue lifetime. An analysing tool using Linear Elastic Fracture Mechanics (LEFM) is proposed in this paper. Crack propagation and crack growth direction are evaluated with an eXtended Finite Element Model (XFEM), on macro- and meso-scale. In addition, thickness effects are evaluated for both longitudinal stiffener and deck plate. These calculations result in a better understanding of the increased fatigue properties compared to the increased dead load of the structure. Manufacturing processes such as welding operations cause residual stresses, which are present in most civil structures. They are causing plastic deformations without any external loads and are therefore often overlooked during design. Nevertheless, residual stresses can have profound influences on the material strength and the fatigue life. Overall, it can be stated that the OSD remains a valuable bridge concept, especially for larger span bridges, that can be understood better using modern research techniques.

1 INTRODUCTION

Due to their contribution to the general resistance of the structure, by significantly reducing the total weight of the construction, orthotropic steel deck plates are one of the most commonly used deck systems for larger span bridges. This contribution also allows the design of tied arch bridges of a more moderate span but with an extremely low structural depth, e.g. a structural depth of only 1 m for a double track railway bridge with a length just over 110 m. The recent design practice in Belgium has used this advantage for about 13 arch bridges, most of them a part of the development of the European network of High Speed Lines where a considerable number of short to medium span bridges for the high-speed railway lines have been designed. Other applications include movable bridges crossing the lock doors of the Port of Antwerp, Belgium. However, orthotropic deck plates are also highly sensitive to fatigue damage, requiring an in-depth fatigue analysis, ensuring it fulfills all fatigue criterions. This problem is mainly caused by the many stress concentrations and the large amplitudes of stress variations, caused by road traffic in particular. Recent international research has extensively studied this phenomenon.

The complex stress field in an orthotropic road bridge can be attributed to three different actions working in union. The first of these actions is caused by the membrane stresses arising because of the bending of the lateral main girders of the bridge, with the bridge deck itself acting as their upper flanges. This action represents in fact the main action of the overall bridge concept. The orthogonal anisotropy (i.e. orthotropic behavior) of the deck with the distribution of the load working on the deck corresponding to the different rigidities of the ribs and the crossbeams is responsible for the second action existing in the deck plate. Finally, the local

bending along longitudinal or transversal axis of the deck plate elements under direct wheel loading causes the third action existing in an orthotropic road bridge. The largest stress concentrations for this deck concept are found at the ribs where longitudinal stiffeners are connected to the deck plate and both hogging and sagging bending effects are found, as well as at the intersection of both longitudinal and cross stiffeners.

Road pavements on the deck plate may contribute to the dispersal of concentrated wheel loads from road traffic. This has also been observed for railway loading, where the ballast may disperse the track loads. However, wearing courses and pavements are not always available or sufficient to reduce the heavy traffic loads, for instance in the case of movable bridges.

An example of this is the Calandbridge in Rotterdam, which was examined more closely and where severe damage due to cracking and fatigue has been found. In Belgium, large span bridges with orthotropic plated deck (for instance the Vilvoorde viaduct in Brussels) do not suffer from this cracking, but smaller movable bridges also show this sensitivity. This situation has to be considered in view of the ever-increasing axle loads and more compact wheel loads introduced by road traffic.

The design and fatigue loads as mentioned by Eurocode 1, which were intended as higher bond values of European traffic, may well be circulating frequently at present. In view of these considerations, the conclusion must be to find systems to decrease the aggressive effects of concentrated wheel loads on orthotropic plated decks, or to eliminate these effects.

This paper focuses on the connection of the deck plate to the trapezoidal closed longitudinal ribs (Figure 1) and more in particular at the location mid span two transverse stiffeners. This is one of the most common locations where fatigue problems occur. At the manufacturing level, welding details have to make use of the available standards. Following the recommendations of Eurocode 3, Part 2 2015, a weld penetration of minimum 67%-75% should be achieved.

In addition, the AASHTO Specification note even describes a weld penetration of 80%. Despite the latter, the manufacturers already try to achieve full weld penetration as much as possible. When welds are executed with care, the reference value $\Delta\sigma_c$ for the fatigue strength increases. However, when taking into account current construction technologies, Eurocode is still considering the outdated reference values $\Delta\sigma_c$, as shown in Eurocode 3, part 1-9 2015. Therefore, present fatigue calculations are very conservative. For the weld detail of the stiffener-to-deck plate connection (right-hand side of Figurer 1), a reference value $\Delta\sigma_c$ of 71 MPa applies. According to recent fatigue tests, higher reference values up to 140 MPa are found, Kolstein M.H. 2007, indicating that the fatigue resistance could be higher than expected.

Unfortunately, the designer has to use the Eurocode guidelines resulting in a tendency to use thicker deck plates and stiffeners, thus reducing the advantage of having a light weighted construction. To investigate and quantify the real fatigue behavior, a much more in-depth method is used, based on Linear Elastic Fracture Mechanics (LEFM). With this method, a detailed crack behavior can be evaluated and the total fatigue life can be estimated as well as the expected crack pattern. The latter can be very useful for weld details similar to the one presented in this paper because the crack could start at positions invisible to any visual inspection tool. In the case of a stiffener-to-deck plate connection, the crack would start at the weld root, which is on the inside of the longitudinal stiffener. Therefore, when a fatigue crack becomes visible in such details, there is already sufficient damage to cause failure, Nagy W. et al. 2014.

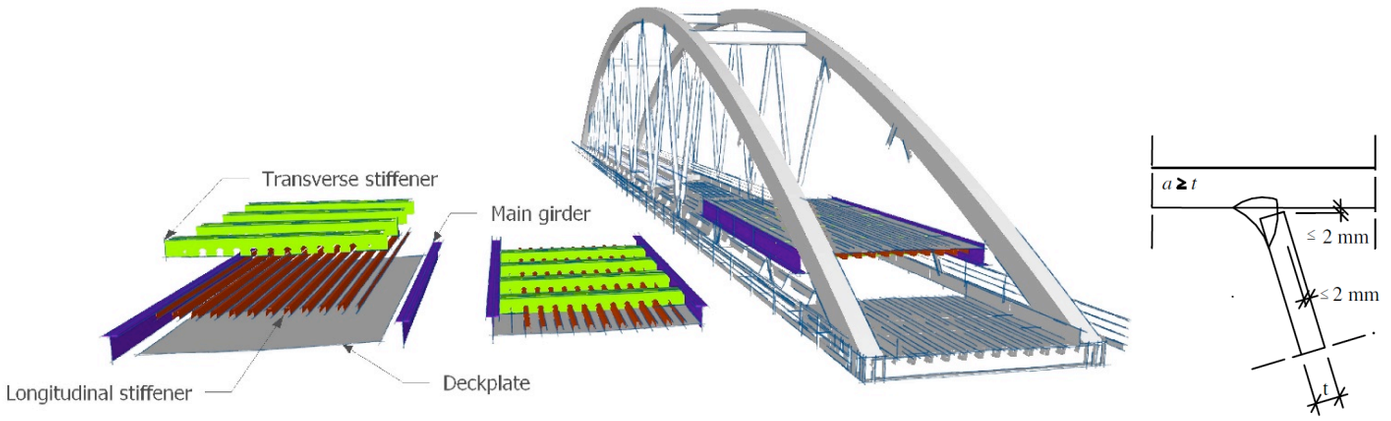


Figure 1. Orthotropic steel bridge deck and welding procedure according to NBN EN 1993-2:2009

2 XFEM AND THE INFLUENCE OF RESIDUAL STRESSES

2.1 *eXtended Finite Element Models*

To evaluate the fatigue life of steel bridges, stress cycles due to traffic are calculated with detailed FEM-models. However, when LEFM is introduced, standard FEM models cause many practical and computational problems, especially if automatic crack propagation is required. In such cases, eXtended Finite Element Models (XFEM) can offer a solution. When using XFEM, it is possible to evaluate automated crack propagation with all its LEFM calculated parameters without adapting the initial model and corresponding mesh for every crack propagation step. However, the downside of this is the heavy computational effort. In order to have realistic and accurate results, the mesh in the vicinity of the crack tip has to be sufficiently small to capture the stresses. In addition, the larger the crack tip, the more degrees of freedom are generated. Due to the latter, XFEM simulations are often limited to simulating a small crack front when considering automatic crack propagation methods. This is however not a problem, as the XFEM calculations can give a clear visualization of the initial crack propagation up to stable crack growth.

In 2004, a fatigue crack was detected in a stiffener-to-deck plate connection of an orthotropic steel bridge deck in Belgium, Nagy W. et al. 2014. This was in the Temse Bridge, a movable truss across the river Scheldt. To verify the fatigue life of this bridge deck, a full-scale FEM-model was developed based on its dimensions. The Temse Bridge has a span of 53.90 m and a width of 7.00 m. The deck plate of the bridge is only 12 mm thick and the closed trapezoidal stiffeners are 8 mm thick. The stiffeners are 350 mm high and 300 mm wide on top and have a width of 90 mm at the lower soffit. The distance between the longitudinal stiffeners equals 300 mm.

$$\frac{da}{dN} = C \cdot (\Delta K_{eff})^m \qquad \Delta K_{eff} = f(a) \cdot \Delta\sigma \cdot \sqrt{\pi \cdot a}$$

$$N_f = \int_{a_i}^{a_f} \frac{da}{C \cdot \Delta K_{eff}^m} = \int_{a_i}^{a_f} \frac{da}{C \cdot \left(f(a) \cdot \Delta\sigma \cdot \sqrt{\pi \cdot a}\right)^m}$$

The used FEM-model consists of shell elements and beams. The advantage of using a full FEM-model is to have boundary conditions as close as possible to the real structure. In a next step, this model is linked to a much more detailed XFEM model. This XFEM model is a small piece of a stiffener-to-deck plate connection and is made out of volume elements. To link both models together, the displacements from the large FEM-model are introduced on the edge of the XFEM model. As mentioned before, thicker plates are used when trying to increase the fatigue life of the structure. To validate whether this is justified, the dimensions of the Temse Bridge are also adapted with different stiffener web thicknesses and deck plate thicknesses. Therefore, a comparison could be made.

Fatigue crack growth is mainly defined by three different phases: crack initiation, crack propagation and crack failure. The first phase depends on the execution of the weld. For example, bad weld penetration, weld defects and partially rewelded tack welds can reduce or eliminate the crack initiation phase and therefore reduce the fatigue life of the structure. Looking for example at some weld macros of recently executed stiffener-to-deck plate welds, relevant lack of penetration can be noticed (Figure 2). This lack of penetration is a perfect initial crack with a length of approximately 1.5 mm. It is assumed in the XFEM model that the initial crack has a semi-elliptical shape with a half-length of 1.5 mm along the minor axis and a half-length of 3 mm along the major.

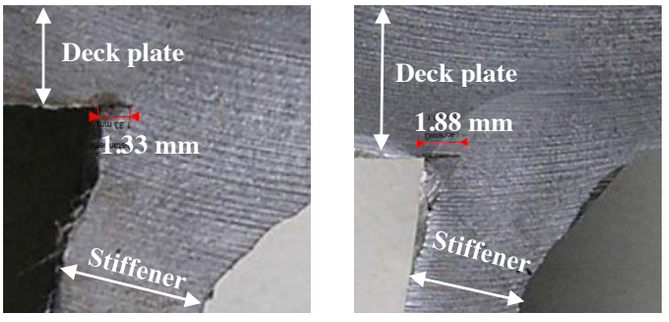


Figure 2. Influence of wearing course type on the fatigue life

2.2 *Residual weld stresses*

Residual stresses are present in all civil structures due to manufacturing steps, causing plastic deformation. Nevertheless, these stresses are not often implicitly taken into account when considering the design of structures. Similar as for the dead load of the bridge deck, this is true when focusing on the stress variations, which eliminate the initial stress state of the structure. However, the effect of residual stresses may either be beneficial or detrimental, depending on their magnitude, sign and distribution with respect to the load-induced stresses. Therefore, the initial stress state due to a welding operation is also introduced into the FEM/XFEM-model.

Literature results from similar fillet welds as those in the orthotropic bridge deck are used to implement residual stresses into the model. These results stated that tensile yield stresses are present in the deck plate and the stiffener spread out in the heat affected zone, FHWA-IF-12-027 2012. Outside this area, compressive compensating stresses are found. To simulate residual stresses into the model, external forces and bending moments are inserted with respect to the global equilibrium. Therefore, N_{deck} is chosen in order to have tensile yield stresses in the deck plate at the weld. For the stresses in the stiffener, an additional bending moment $M_{stiffener}$ and normal force $N_{stiffener}$ are also introduced. The bending moment is necessary because the joint is welded from one side only and the filler metal and the corresponding heat area is larger at the weld toe com-

pared to the weld root. For the magnitude of this bending moment and normal force, an assumption is made based on the distribution of the filler metal.

2.3 *LEFM parameters*

As is generally accepted, the evaluation of the geometry dependent parameter f(a), which combines the influence of the weld and specimen geometry on the crack behaviour, is of major importance to quantify the fatigue behaviour of the detail being studied. As illustrated in Figure 3, the XFEM calculations result in a detailed visualization of the crack propagation behaviour through the deck plate. For every time step and curvilinear location along every crack front, the SIF-values are determined. Due to computational or convergence problems, the crack propagation could only be simulated up to a half-length of approximately 18 mm in longitudinal direction which is complying with the welding direction. To overcome this problem, larger initial crack fronts are evaluated with a half-length of 25 mm and 50 mm. It is assumed that at this point, the crack has already fully penetrated the deck plate. Therefore, the crack front inside the material is reduced and less degrees of freedom are necessary.

To investigate the influence of different thicknesses used for the deck plate and the longitudinal stiffeners, different plate thicknesses are used: 6 mm, 7 mm and 8 mm for the longitudinal stiffener and 12 mm, 14 mm and 16 mm for the deck plate. Figure 4 illustrates all the calculated f(a) values for these thicknesses. For the evaluation of the fatigue life and the corresponding crack length, a best-fit curve has to be fitted to these data points.

In addition to the plotted best-fit curves Figure 4, Table 1 gives the corresponding R-square values. A clear trend is visible and the best-fit curves have a great reliability.

In the f(a) curves, it is clear that the longitudinal stiffener thickness has no major influence on the profile of the curve. In the deck plate however, a large shift is sometimes noticeable. Although higher values of f(a) result in a faster crack propagation, these higher values apply to thicker deck plate cases only. In these deck plates, the stresses at the weld root are much smaller and will therefore result in a lower crack propagation than smaller deck plates.

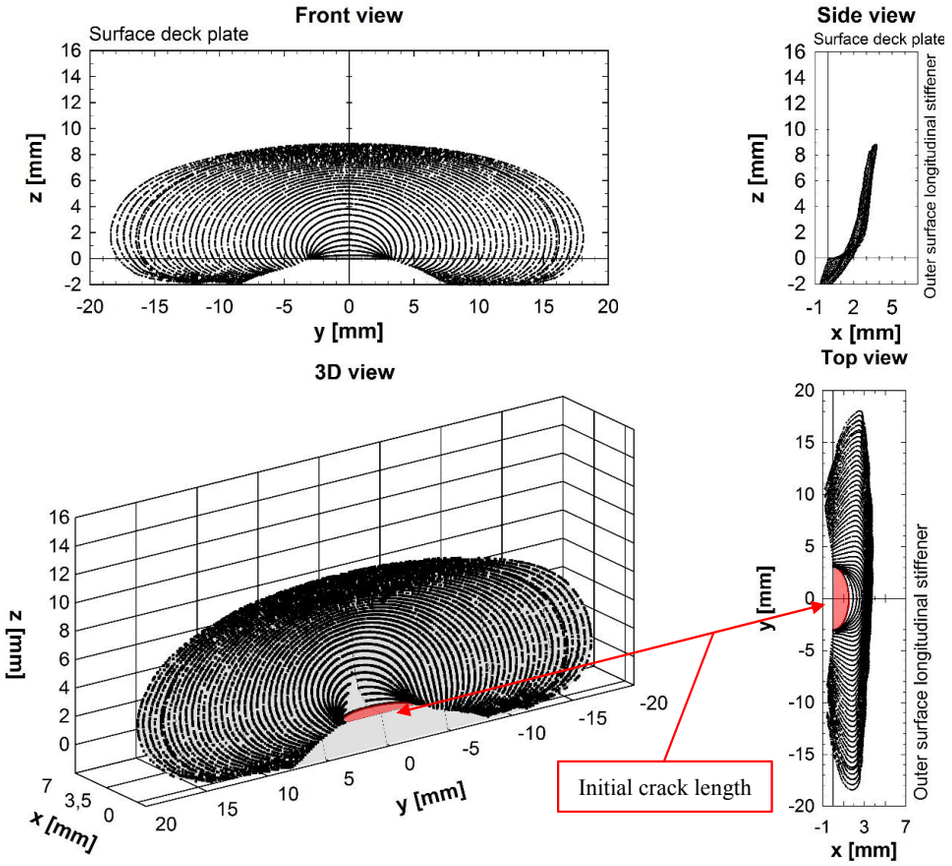


Figure 3. XFEM crack simulation including the initial semi-elliptical crack length

Table 1. R-square value of best-fit curves. Stiffener-to-deck plate detail: S = stiffener - number = thickness of the stiffener - D = deck plate - number = thickness of the deck plate.

Stiffener-to-deck plate detail	S6_D12	S6_D14	S6_D16	S7_D12	S7_D14	S7_D16	S8_D12	S8_D14	S8_D16
R-square	0.95	0.99	0.99	1.00	0.97	0.98	0.99	1.00	0.99



2.4 *Fatigue life*

When combining the best-fit curves of f(a) with equations for crack length, the crack length in function of time can be plotted. According to the same graphs of f(a), the fatigue life up to a service life of 100 years is illustrated in Figure 5. When looking at the left graphs where the curves are grouped by the thickness of the longitudinal stiffener, the crack grows much faster in thinner deck plates. This results from the reduced applied stress at the weld root due to the capability of spreading the loads over multiple longitudinal stiffeners. When looking at the graphs on the right where the curves are grouped based on the thickness of the transverse stiffener, the opposite is true. The crack seems to grow faster when the thickness of the stiffener is increased. A possible explanation is the increased stiffness of the closed trapezoidal stiffener. Therefore, the stiffener close to the applied load attracts the stresses in the deck plate. As illustrated in Figure 4, the f(a) curves for the same deck plate thickness are almost identical. A small difference in the stresses at the weld root causes large differences in the crack growth due to the cubic equation.

The calculated fatigue life is summarized in Table 2. This corresponds with the time where the crack has fully penetrated the deck plate. Although not included in this paper, also the f(a) curves for the direction through the deck plate was calculated. With these curves, the total crack length through the deck plate could be validated next to the longitudinal ones.

Stiffener-to-deck plate detail	S6_D12	S6_D14	S6_D16	S7_D12	S7_D14	S7_D16	S8_D12	S8_D14	S8_D16
R-square	0.95	0.99	0.99	1.00	0.97	0.98	0.99	1.00	0.99

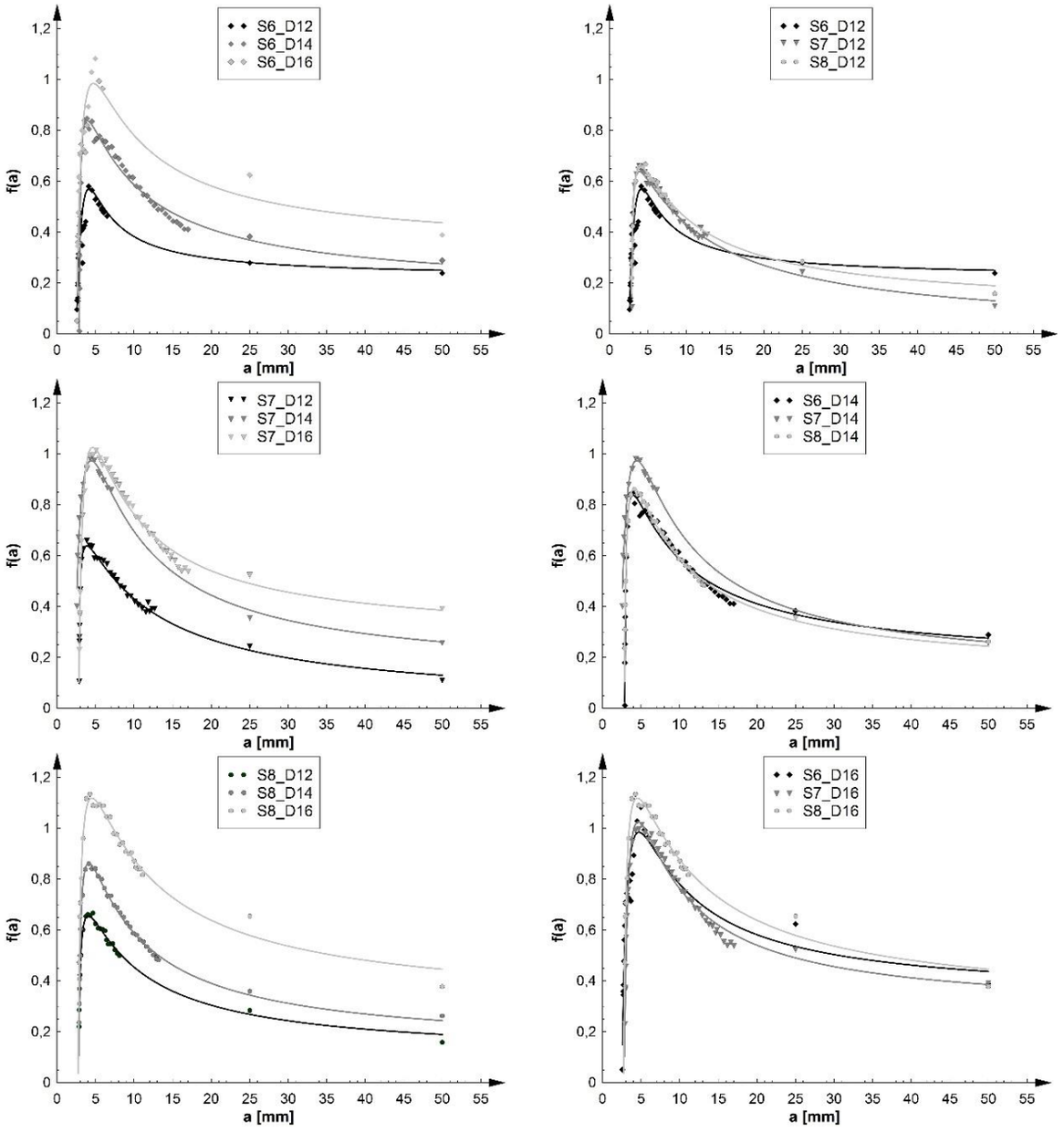


Figure 4. Geometrical dependent parameters f(a) for different deck plate and stiffener thicknesses. Legend: S = stiffener - number = thickness of the stiffener - D = deck plate - number = thickness of the deck plate. Left: f(a) curves grouped per stiffener thickness. Right: f(a) curves grouped per deck plate thickness

Within the service life of 100 years, this was only the case for a stiffener thickness of 8 mm and a deck plate thickness of 12 mm. The fatigue life in this case is 41.84 years. This rather low result corresponds with the fatigue crack that was observed in the Temse Bridge. In all the other cases, the crack still has not penetrated the deck plate. Table 2 also lists the amount of crack propagation through the deck plate after 100 years of service life in percentage. According to these results, the best option in a truss bridge is to have a thick deck plate and a slender stiffener. But in the case of the Temse Bridge, a solution can already be found in using a stiffener of 7 mm instead of 8 mm.

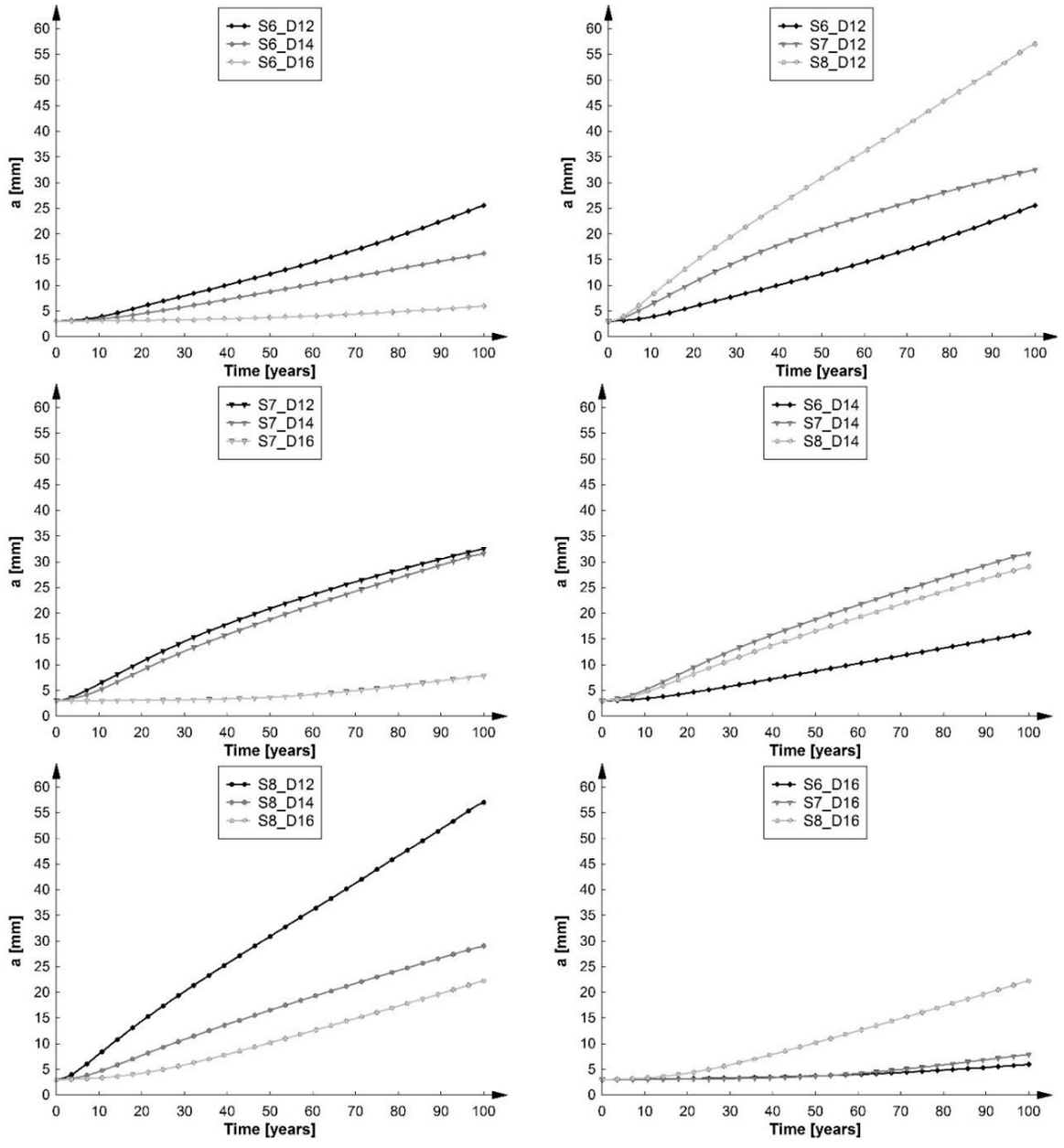


Figure 5. Fatigue life for different deck plate and stiffener thicknesses. Legend: S = stiffener - number = thickness of the stiffener - D = deck plate - number = thickness of the deck plate. Left: fatigue life curves grouped per stiffener thickness. Right: fatigue life curves grouped per deck plate thickness.

Table 2. Amount of crack propagation through the deck plate at 100 years and the corresponding fatigue life. Stiffener-to-deck plate detail: S = stiffener - number = thickness of the stiffener - D = deck plate - number = thickness of the deck plate.

Stiffener-to-deck plate detail	S6_D12	S6_D14	S6_D16	S7_D12	S7_D14	S7_D16	S8_D12	S8_D14	S8_D16
Crack propagation through deck plate at 100 years [%]	-	63	10	75	70	31	100	77	66
Fatigue life [years]	-	>100	>100	>100	>100	>100	41.84	>100	>100

Therefore, the effect of using a light weighted construction is really present. This also confirms that using thicker deck plates increases the fatigue life. However, this is not always the necessary, especially when thick plates of 15 mm are used in new orthotropic bridge deck designs.

Finally, the effect of random loads is compared to fixed sequences. With the current fatigue design methods, the Palmgren-Miner method is used. This method is not very accurate since the load history and the load sequences do not have any effect on the fatigue resistance. With LEFM however, it is possible to take the load sequence into account. In Figure 6 a comparison is made between a random sequence and two fixed sequences. Sequence 1-2-3-4-5 corresponds with the set of equivalent lorries described in Eurocode using the same order. This agrees with using the smaller lorries first and ending with the heavy lorries. Sequence 5-4-3-2-1 is the opposite.

It is clear that the load sequence has an influence on the crack propagation. When first using lower loads and ending with heavy loads, the crack propagation is much lower at the beginning when compared with first using heavy loads and ending with lower loads. Remarkably, at the end of the calculated service life, it does not matter if a random sequence or a fixed one is used. This means that no real memory effect is present in the fatigue calculation with LEFM.

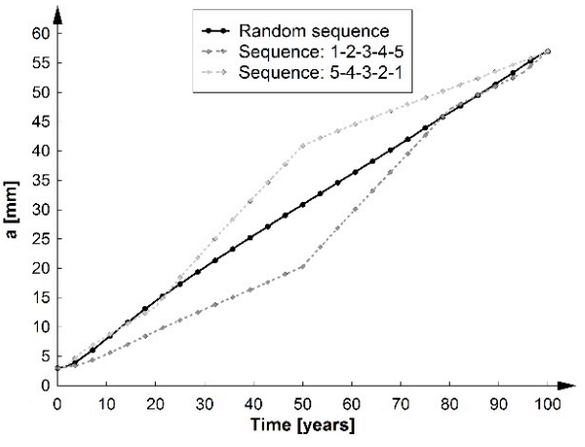


Figure 6. Random sequence of applied loads versus fixed sequences

3 CONCLUSIONS

Using LEFM as a fatigue assessment tool has many benefits compared to the current fatigue designs with Eurocode. It is a more in-depth method resulting in the evaluation of both the crack growth direction and the crack propagation. The advantages of this method can be combined with the implementation of the initial stress state due to dead load and residual stresses. By doing this, a more realistic crack path can be evaluated. For all different stiffener-to-deck plate geometries studied in this paper, all cracks propagated through the deck plate.

When comparing the crack propagation for all different geometries, it can be concluded that an increased deck plate thickness increases the fatigue life of the stiffener-to-deck plate detail. However, this is not the case when looking to the thickness of the stiffeners web. Thicker stiffeners attract more stresses at the weld root resulting in faster crack propagation. The solution of keeping the advantages of a light weighted construction relies on reducing the thickness of the closed trapezoidal stiffeners and increasing the thickness of the deck plate, although the latter should be limited as well. In addition, the reduced thickness of the closed trapezoidal stiffeners is limited as well when looking the global displacements of the deck plate.

Using the Palmgren-Miner method in current design methods does not allow for accounting for the actual load sequences. When using LEFM, such an analysis can be performed. The effect of using fixed load sequences can have a major influence on the crack propagation. Although, when looking at the final crack at the estimated service life of the bridge deck, the crack propagation curves for both random and fixed sequences are coinciding in the end. Therefore, the load sequence has no influence when looking at the final stage of the fatigue life.

4 REFERENCES

De Backer, H. 2006. *Optimization of the fatigue behavior of the orthotropic plated bridge deck concept through better dispersion of traffic loads (in Dutch)*, Ghent University, Belgium.

Eurocode 3, Part 2 2015, Design of steel structures – Part 3: steel bridges, EN 1993-2:2007/AC:2009, CENT/TC 250 – Structural Eurocodes.

Eurocode 3, Part 1-9 2015, Design of steel structures – Part 1-9: fatigue, EN 1993-1-9:2005/AC:2009, CENT/TC 250 – Structural Eurocodes.

FHWA-IF-12-027 2012. Manual for Design, Construction, and Maintenance of Orthotropic Steel Deck Bridges, US Department of Transportation, Federal Highway Administration.

Kolstein, M. H. 2007. *Fatigue classification of welded joints in orthotropic steel bridge decks*, PhD thesis, Delft University of Technology, The Netherlands.

Nagy, W., Diversi, M., Van Bogaert, Ph. & De Backer, H. 2014. Improved fatigue assessment techniques of connecting welds in orthotropic bridge decks. In *Proceedings of Eurosteel 2014 – 7th European Conference on Steel and Composite Structures*, ECCS European Convention for Constructional Steelwork, Brussels.

Maintenance, Safety, Risk, Management and Life-Cycle Performance of Bridges – Powers, Frangopol, Al-Mahaidi & Caprani (Eds)
© 2018 Taylor & Francis Group, London, ISBN 978-1-138-73045-8

Flat Prestressed Unbonded Reinforcement (FPUR) System for Strengthening of Steel I-Beams

Ardalan Hosseini
Structural Engineering Research Laboratory, Empa, Dübendorf, Switzerland; Resilient Steel Structures Laboratory, EPFL, Lausanne, Switzerland

Elyas Ghafoori
Structural Engineering Research Laboratory, Empa, Switzerland; Smart Structures Laboratory, Swinburne University of Technology, Melbourne, Australia

Masoud Motavalli
Structural Engineering Research Laboratory, Empa, Dübendorf, Switzerland; Department of Civil Engineering, University of Tehran, Iran; Department of Civil Engineering, Monash University, Australia

Alain Nussbaumer
Resilient Steel Structures Laboratory, EPFL, Lausanne, Switzerland

Xiao-Ling Zhao
Department of Civil Engineering, Monash University, Australia

Riadh Al-Mahaidi
Department of Civil and Construction Engineering, Swinburne University of Technology, Melbourne, Australia

ABSTRACT: This paper proposes a novel retrofitting system for the strengthening of steel I-beams using prestressed unbonded carbon fiber reinforced polymer (CFRP) plates. The system relies on a pair of mechanical clamps. Each clamp holds two flat CFRP plates (each 50 × 1.4 mm) and anchors their prestressing forces to the steel I-beam via friction. The proposed system does not require any adhesive between the CFRP plates and the steel substrate; therefore, surface preparation and adhesive curing are not needed, which reduces the time and cost of retrofitting. The design considerations of the mechanical clamps, the most important elements of the proposed unbonded system, are explained. A finite element (FE) model was established to optimize the design of the required mechanical parts, and a set of pull-off tests was performed to evaluate the capacity of the optimized system. The experimental results show that the proposed system is capable of transferring almost the entire tensile capacity of the normal modulus CFRP plates to the steel substrate via friction, while no sliding of the joint was observed. Moreover, the proposed flat prestressed unbonded reinforcement (FPUR) system was applied on a 6.4-m-long steel I-beam and the high performance of the system was confirmed based on the results of a set of four-point static and fatigue tests. Relying on the laboratory experimental tests, the proposed FPUR system was applied on the cross-girders of an almost 120-year-old steel bridge in Australia to monitor its long-term performance as a strengthening solution to increase the capacity and/or fatigue life of existing metallic I-beams.

1 INTRODUCTION

The unique advantages of carbon fiber reinforced polymer (CFRP) composites have made CFRP reinforcement a suitable material for strengthening of steel structures (Zhao 2013). It has been shown that the application of nonprestressed bonded ultra-high modulus CFRP reinforcement can prolong the fatigue life of steel members. However, crack prevention or crack arrest is only possible when prestressed CFRP reinforcement with a certain level of prestressing is used (Ghafoori et al. 2015a, Hosseini et al. 2017a). On the other hand, due to the limitations of prestressed bonded reinforcement systems, such as their time-consuming and costly surface preparation, inability to withstand relatively high prestressing forces, and premature debonding failure of bonded reinforcements (Hosseini et al. 2017b,c), a novel trapezoidal prestressed unbonded reinforcement (TPUR) system was developed by Ghafoori & Motavalli (2015) and used to strengthen a 120-year-old railway metallic bridge in Switzerland (Ghafoori et al. 2015b). It was shown by the authors that the proposed TPUR system has certain advantages, including ease of application, elimination of any surface preparation, and high performance of the system in terms of prestressing levels (Ghafoori & Motavalli 2015).

In the current study, another configuration of a prestressed unbonded reinforcement system, i.e. a flat prestressed unbonded reinforcement (FPUR) system is introduced for the strengthening of metal-

lic I-beams using prestressed CFRP plates. The design concept and finite element simulation are discussed. Furthermore, sets of static and fatigue tests were performed as part of the current study to evaluate the performance of the proposed system. A brief discussion of the laboratory test results and the field application of the proposed FPUR system are provided in the current paper.

2 CONCEPT AND OVERALL VIEW OF THE PROPOSED STRENGTHENING SYSTEM

As illustrated in Figure 1, the FPUR system relies on two sets of mechanical clamps i.e. a *fixed clamp* on one side, and a *movable clamp* on the other side of the beam. The two mechanical clamps are capable of transferring the prestressing force of the CFRP plates to the lower flange of a metallic I-shaped girder via friction. Each set of mechanical clamps holds two prestressed normal modulus (NM) CFRP plates with cross-sectional dimensions of 50 × 1.4 mm (width × thickness). The strengthening procedure using the proposed FPUR system consists of the following three steps:

1) Installation of the mechanical clamps and the nonprestressed CFRP plates (see Fig. 1a): on both sides of the beam, the nonstressed CFRP plates are sandwiched between 16-mm thick toothed plates installed inside the *lower plate* and *upper plate* with five M16 (grade 12.9) and ten M10 (grade 12.9) prestressed bolts. The bolts generate a total gripping force of about 1230 kN. On one side of the beam (the left side in Fig. 1a) the beam bottom flange is sandwiched between the *upper plate* and the *over-flange plate* by fastening eight M20 (grade 12.9) bolts tightened with a torque of 605 Nm, to generate a prestressing force of 223 kN per bolt. This results in a full gripping force between the *fixed clamp* set and the beam bottom flange. On the other side of the beam, the nonstressed CFRP plates are sandwiched in the *movable clamp*, and this clamp set is free to move horizontally along the beam axis for prestressing.
2) Installation of the prestressing system, applying the required prestressing force, and fastening the movable clamp (see Fig. 1b): two 120-kN hollow plunger cylinders are installed adjacent to the *movable clamp* using a special cylinder housing. The cylinder housing is anchored to the beam bottom flange in a similar way to the *fixed clamp* set. With the help of two M16 threaded rods, the *movable clamp* can be pulled using the hollow plunger cylinders connected to a manual hydraulic pump, and consequently, the CFRP plates can be prestressed. Upon reaching the desired prestressing level in the CFRP plates, all the eight M20 bolts of the *movable clamp* can be tightened with a torque of 605 Nm, which leads to the designed gripping force between the mechanical clamping system and the beam flange.
3) Removing the prestressing system to realize the final configuration as depicted in Figure 1c: after reaching the desired prestressing force in the CFRP plates, the hydraulic pressure can be released and the entire prestressing system consisting of the two hollow plunger cylinders and the cylinder housing can be removed.

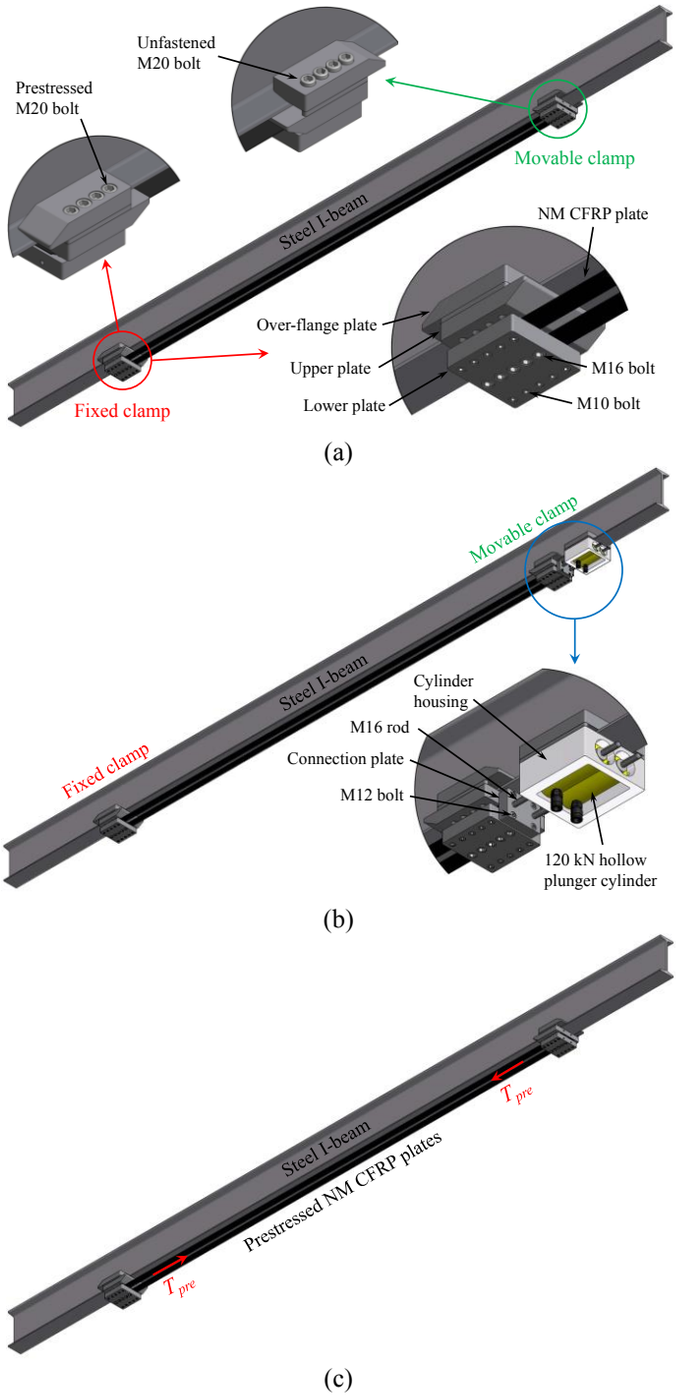


Figure 1. Strengthening a steel I-beam using flat prestressed unbonded reinforcement (FPUR) system: (a) Installation of the mechanical clamps and non-prestressed NM CFRPs; (b) Installation of the prestressing system and applying the required prestressing level; (c) Fastening the movable clamp and removing the prestressing system.

3 FINITE ELEMENT SIMULATION

3.1 *Model description*

In order to optimize the geometry of the mechanical components of the FPUR system and estimate the required number and diameter of prestressed bolts, a finite element (FE) simulation was performed using ABAQUS (2016). Due to symmetry, only half of the proposed mechanical clamping system, installed on a 1.5-m-long INP300 steel profile was assembled in ABAQUS (Fig. 2). The FE model consisted of a NM CFRP plate (50 × 1.4 mm) gripped in the proposed mechanical clamping system, while the clamp is anchored on the bottom flange of the INP300. All the steel parts and the CFRP plate were modelled as isotropic linear elastic materials with an elastic modulus of 210 and 160 GPa, respectively, and a Poisson's ratio of 0.3. A hard contact was used between all the individual parts in the normal direction; however, using the penalty formulation, an isotropic tangential friction was introduced between the CFRP plate and toothed hard plates, as well as between the clamping system and the steel I-beam. Coefficients of friction equal to μ_s = 0.5 and 0.3 were used in the case of CFRP-to-hard plate and steel-to-steel, respectively (see Hosseini et al 2017a,c for further details). The CFRP and the steel substrate were modelled using 8-node linear brick elements of type C3D8R with reduced integration and hourglass control, while the entire clamping system was modelled using 4-node linear tetrahedrons of type C3D4. A total number of about 365,000 elements was generated.

In addition to the symmetry boundary condition, horizontal and vertical support boundaries were introduced into the model to stabilize the assembly (Fig. 2). In the first step, static uniform pressures of 395 and 540 MPa per bolt location were introduced on the upper and lower plates to simulate the prestressing force of 52.1 and 142.4 kN per bolt generated in M16 and M10 high-strength bolts, respectively. In the next step, a static uniform pressure of 546 MPa per bolt location was introduced on the over-flange and upper plates to simulate the prestressing force of 223 kN per bolt generated in M20 high-strength bolts. Finally, a uniform surface traction of 2800 MPa (equal to the nominal tensile strength of the CFRP, $\sigma_{f,u}$) was applied to the free edge of the CFRP plate to observe any probable slippage of the joint before reaching $\sigma_{f,u}$.

3.2 *FE results*

Figure 2 shows the von Mises stresses in the FE model when the full bolt prestressing load is applied on the clamping system and the CFRP plate is pulled up to its tensile strength $\sigma_{f,u}$. It can be seen that by using 40mm-thick lower and upper plates manufactured from M200 steel with the nominal yield strength of f_y = 1000 MPa, the maximum stresses in the clamping system remain below 0.6 f_y.

Using the optimized FE model of the mechanical clamp, the load–displacement response of the CFRP plate was obtained and is provided in Figure 3. It can be seen from the figure that the proposed mechanical clamping system is capable of transferring the entire tensile capacity of the CFRP plate ($\sigma_{f,u}$ = 2800 MPa) to the steel I-beam before any slippage of the clamp occurs. It is worth mentioning here that an approximately uniform contact pressure between the toothed hard plates and the CFRP reinforcements needs to be obtained by fastening the prestressed bolts; otherwise probable stress concentration on the CFRP edges can result in longitudinal delamination of the CFRP during prestressing (Hosseini et al. 2017c). A uniform distribution of contact pressure can be obtained by careful design of the toothed hard plates (see Hosseini et al. 2017c for further details).

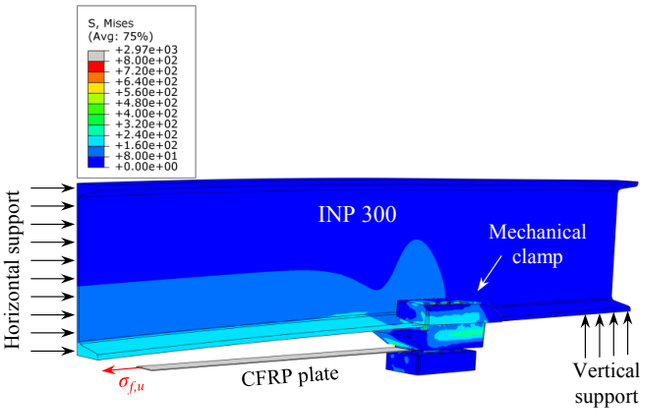


Figure 2. ABAQUS model of half of the FPUR system and von Mises stress distribution at the nominal tensile capacity of CFRP plate (deformation scale factor = 10).

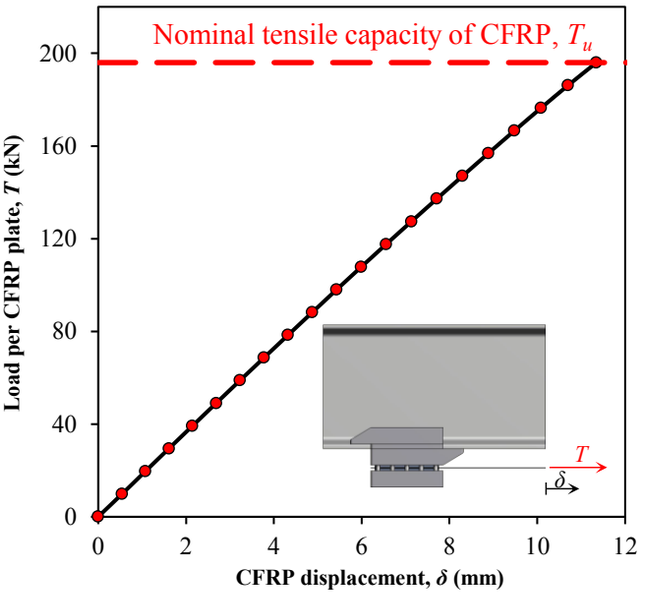


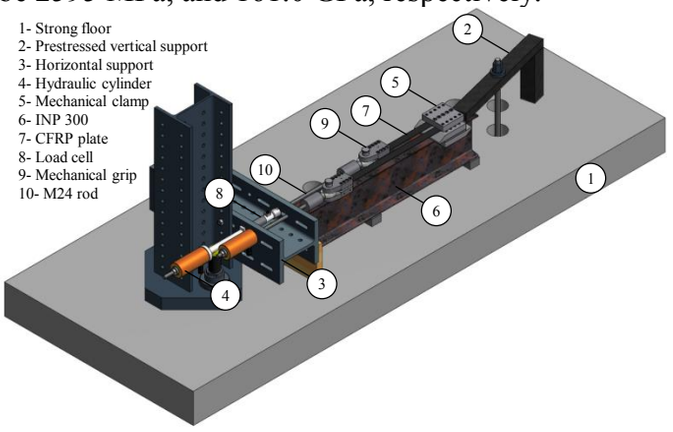
Figure 3. FE results: Load–deformation response of mechanically-clamped CFRP plate up to ultimate tensile capacity.

4 EXPERIMENTAL VERIFICATION

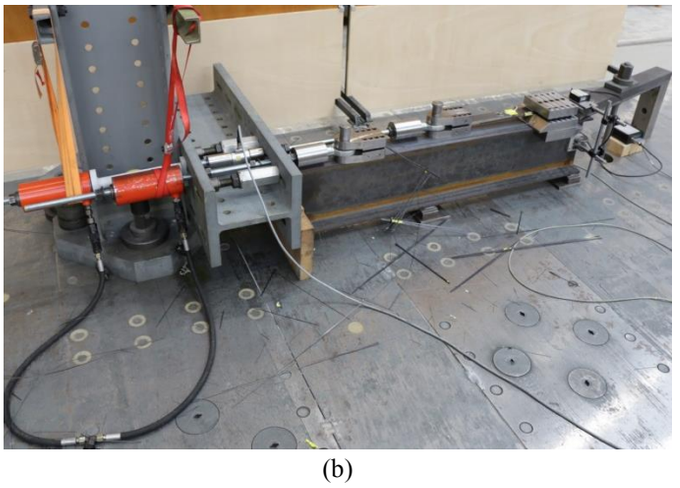
4.1 *Pull-off test*

4.1.1 *Test set-up and material properties*

All the required mechanical parts with the optimized geometry were manufactured from high-strength steel M200 with a nominal yield strength of 1000 MPa. A special *pull-off* test set-up was then designed to evaluate the ultimate capacity and failure mode of the proposed mechanical clamping system and a pull-off test was performed on the optimized configuration of the system (Fig. 4a). Note that NM CFRP plates of type S&P 150/2000-50/1.4 were used in all the tests, and the tensile strength and elastic modulus of the utilized CFRP composite were determined to be 2595 MPa, and 161.0 GPa, respectively.



(a)



(b)

Figure 4. (a) Pull-off test set-up; (b) Tensile rupture of CFRP plate.

4.1.2 *Experimental results*

The strain level generated in the CFRP plates vs. the applied load per hydraulic cylinder is provided in Figure 5. It can be seen from Figure 5 that the strain response of the CFRP plates was almost linear with respect to the applied load up the tensile rupture of one of the CFRP plates. It should be mentioned that the force was generated in the hydraulic cylinders using a manual hydraulic pump. Therefore, as the test was performed under load-control conditions, any slippage of the clamp would have occurred as a sudden drop in the load level, which was not the case in the test conducted. Figure 4b shows the tensile rupture of the CFRP plate.

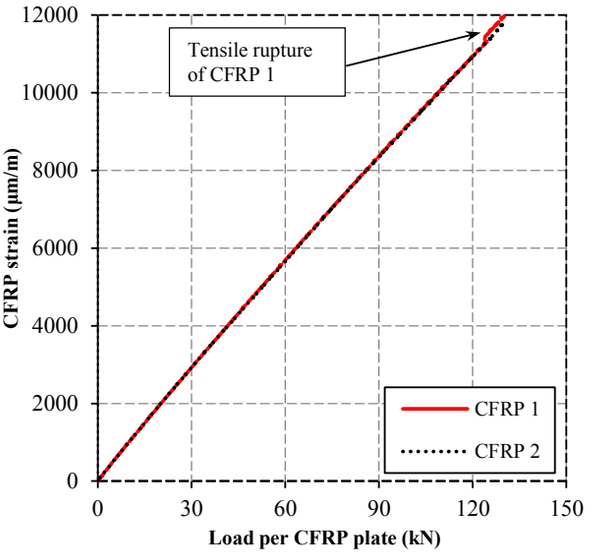


Figure 5. Strain in CFRP plates vs. applied load in pull-off test.

4.2 *Static and fatigue four-point bending test*

4.2.1 *Test set-up and material properties*

In order to evaluate the performance of the proposed FPUR system for the strengthening of metallic I-beams, sets of static and fatigue tests were performed at the Structural Engineering Research Laboratory of Empa on a 6.4-m long steel I-beam under four-point bending. The centre-to-centre distance of the supports was 5.3 m, while the centre-to-centre distance of the 250 kN hydraulic actuators was 1.8 m. An Amsler pulsator of type P131 was used to perform both static and fatigue tests. The steel I-beam utilized in the four-point bending tests was of type S275JR with an elastic modulus of 203.3 GPa, and yield and ultimate strength of 328 and 465 MPa, respectively. The CFRP plates were taken from the same batch of material as for the pull-off test. The four-point bending test set-up is shown in Figure 6.

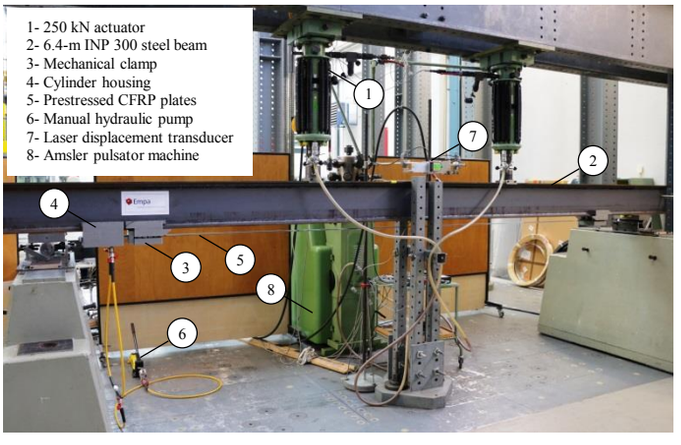


Figure 6. Static and fatigue four-point bending test set-up.

4.2.2 *Experimental results*

First a reference unstrengthened INP300 beam was loaded in the linear regime up to 75 kN per cylinder. Next, the proposed flat unbonded reinforcement (FUR) system, without any prestressing force, was installed on the beam and the beam was reloaded up to 75 kN per cylinder. Note that the intention of using the FUR system was to observe the efficiency of nonprestressed CFRP reinforcements for the strengthening of the steel I-beam. Finally, the CFRP plates were prestressed (see Section 2 for the prestressing process) up to 10, 20, 30, 40% of tensile strength $\sigma_{f,u}$, and each time the beam was loaded up to 75 kN per cylinder. Figure 7 shows the strain history of the CFRP plates and the top and bottom flanges of the INP300 during the prestressing process for the case of FPUR with 40% prestressing level. Figure 7 illustrates that with a 40% prestressing level in the CFRP reinforcement, a compressive stress of 70.3 MPa is generated in the bottom flange of the beam, while the top flange experiences 23.6 MPa tensile stress when the beam is unloaded.

As indicated by the experimental results in Figure 8, the application of the nonprestressed FUR system slightly increases the stiffness of the strengthened member; however, the deflection/strain reduction in the member is not significant, owing to the fact that the utilization of nonprestressed CFRPs cannot considerably increase the stiffness of a real-scale steel member. On the other hand, Figure 8 illustrates that using the proposed FPUR system with higher prestressing levels can significantly decrease the maximum deflection and strain level in the strengthened steel I-beam under service loads. Consequently, the proposed system may be a very efficient strengthening solution to increase the yield strength and/or fatigue life of existing metallic I-beams.

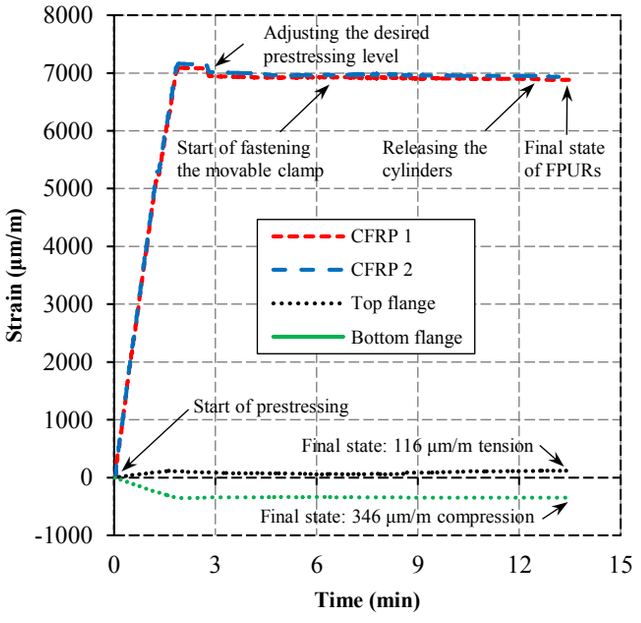


Figure 7. Strain history of CFRP plates, and top and bottom flanges of INP 300 during prestressing up to $0.4\sigma_{f,u}$.

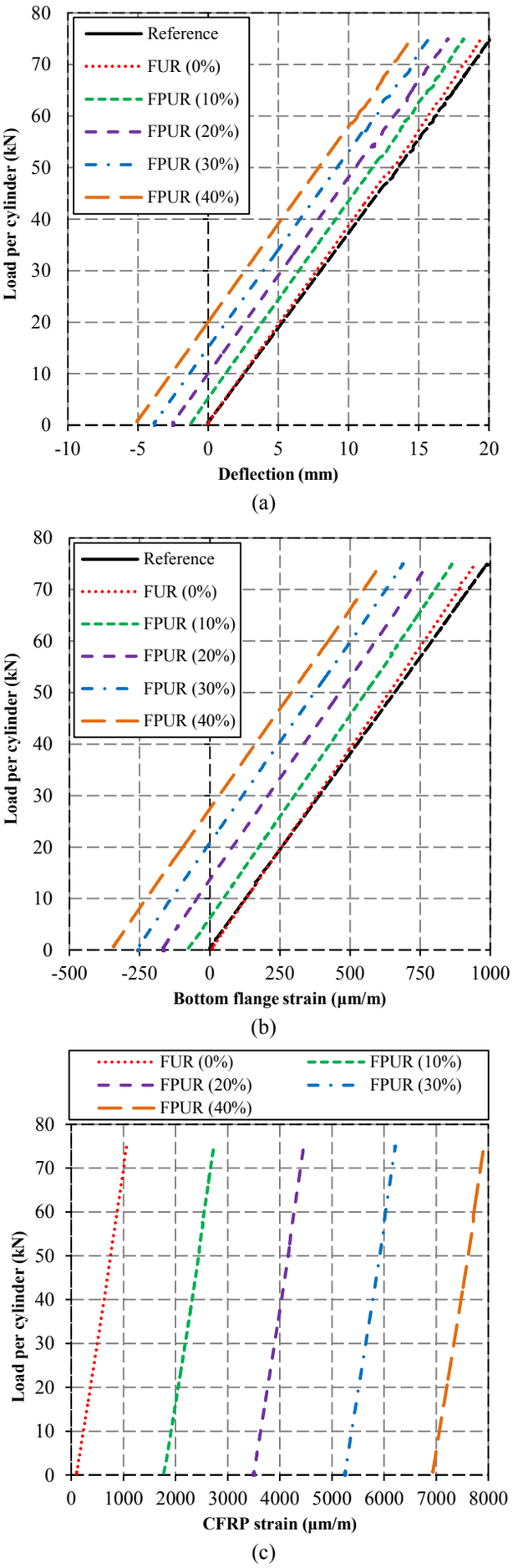


Figure 8. Static test results: (a) Load-deflection diagrams; (b) Load-strain response of bottom flange; (c) Load-strain response of CFRPs.

In addition to the four-point static tests, the performance of the proposed FPUR system was also evaluated under fatigue loading for 10 million fatigue cycles, while the CFRP plates were prestressed up to almost 40% of their ultimate strength. The four-point fatigue test was performed under load-control conditions with a load ratio ($R = P_{min}/P_{max}$) of 0.2 and a loading frequency of 4.35 Hz. The maximum load level during the fatigue test on the INP 300 beam was equal to P_{max} = 40.2 kN per cylinder, corresponding to $0.33f_y$ in the top and bottom flanges of the unstrengthened beam.

Figure 9 illustrates the evolution of the maximum and minimum strain levels in the FPUR system and the bottom flange of the INP300 with respect to the elapsed fatigue cycles. It can be seen from the figure that during the four-point fatigue test the maximum strain in the prestressed CFRP plates remained constant for the 10 million loading cycles. This proves that the proposed FPUR system experienced no slippage during fatigue loading, as no reduction in prestrain level was observed. Furthermore, Figure 9 shows that by applying the FPUR on the INP 300 beam, the bottom flange of the beam remains in compression for almost half of the loading range, which can significantly improve the fatigue performance of the strengthened member.

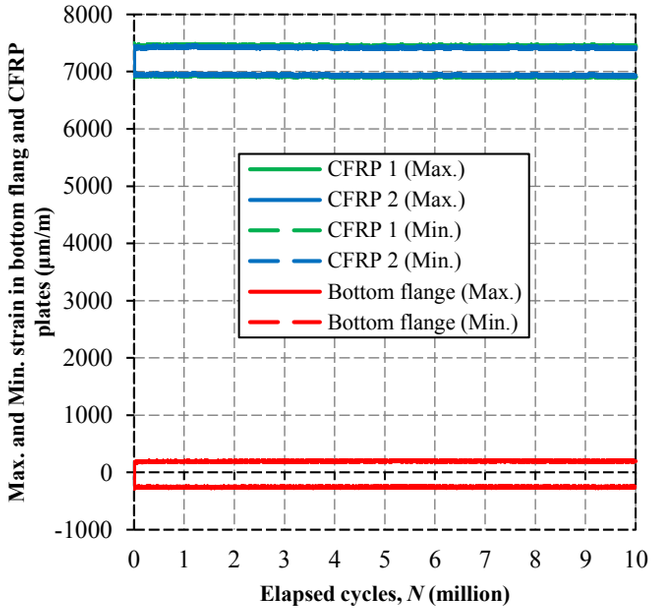


Figure 9. Fatigue test results: evolution of maximum and minimum strain in CFRP plates in response to elapsed fatigue cycles.

5 FIELD APPLICATION OF THE PROPOSED FPUR SYSTEM

After successful laboratory tests performed on the proposed FPUR system, the system was applied on two cross-girders of a roadway metallic bridge called *SN6091 Bridge* over Diamond Creek on the Heidelberg-Kinglake Road in Victoria, Australia. The steel I-shaped cross-girders were strengthened with the proposed FPUR system with a prestressing level of about 38%. A wireless sensor network (WSN) system is installed on the bridge for long-term monitoring of the strain levels in prestressed CFRP plates. Figure 10 shows the FPUR and the WSN systems applied on the cross-girders of the *Diamond Creek Bridge*. Sets of truck loading were performed before and after strengthening of the bridge, which showed excellent performance of the FPUR system, as the bending stresses in the bottom flanges of the girders were reduced to almost half after application of the FPUR system. The long-term performance of the system will be monitored for at least one year using the installed WSN system. As a detailed explanation of the field application of the FPUR system on the *Diamond Creek Bridge* is beyond the scope of the current paper, readers are referred to Ghafoori et al. (2018) for a comprehensive discussion of the topic.

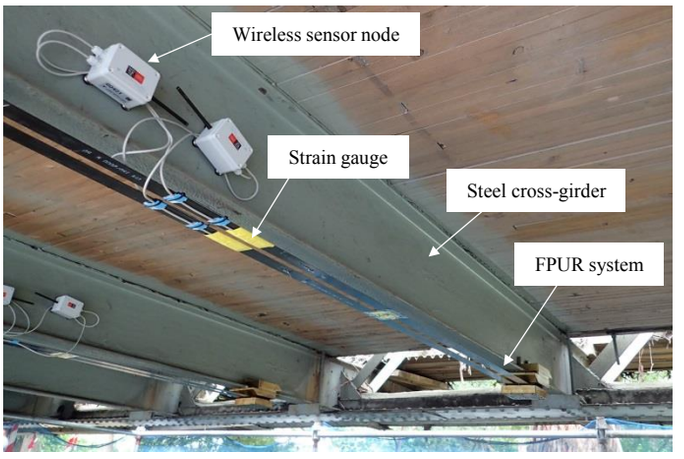


Figure 10. Application of proposed flat prestressed unbonded reinforcement (FPUR) system for strengthening of cross-girders of Diamond Creek Bridge, Victoria, Australia.

6 SUMMARY AND CONCLUSIONS

In the current study, a novel friction-based mechanical clamping system, called the FPUR system, for the strengthening of metallic I-beams with prestressed CFRP plates was designed, manufactured, and tested under static and fatigue loading. Experimental results revealed that the proposed system is capable of transferring the entire tensile capacity of the CFRP plates to the steel I-beam via friction, while the performance of the system is not affected by fatigue loading, as no slippage of the clamping system was observed over 10 million fatigue cycles. The advantages of the proposed FPUR system can be summarized as follows:

- Ease of installation and prestressing,
- Elimination of surface preparation required for any bonded reinforcement,
- Prevention of any installation damage to existing members,

- Capability of modifying (decreasing or increasing) the prestressing level at any time,
- Capability of easy removal of the entire system without damage to existing members,
- Insensitivity of the system to high service temperatures which might be a significant issue for adhesively bonded reinforcements, and
- High performance of the system in terms of prestressing levels.

Based on the laboratory test results and the advantages of the proposed FPUR system, it is concluded that the system may be an efficient strengthening solution to increase the yield strength and/or fatigue life of existing metallic I-beams. The proposed FPUR system has been applied on the *Diamond Creek Bridge* in Victoria, Australia, and its long-term performance will be monitored using a wireless sensor network (WSN) system.

7 ACKNOWLEDGMENTS

The authors gratefully acknowledge the financial support provided by the Swiss National Science Foundation (SNSF Project No. 200021-153609) and the Australian Research Council (ARC) Linkage Grant (LP140100543). They would also like to thank the technicians of the Structural Engineering Research Laboratory of Empa for their exceptional cooperation in performing the experiments. Finally, the support of S&P Clever Reinforcement Company AG, and Mettler Mech. Produkte GmbH, Switzerland, which provided the materials and manufactured the mechanical parts for the current study is acknowledged.

8 REFERENCES

ABAQUS U. 2016. Version 6.16. Dassault Systèmes Simulia Corp., Providence, RI.

Ghafoori, E. & Motavalli, M. 2015. Innovative CFRP-prestressing system for strengthening metallic structures. *Journal of Composite for Construction* 19(6): 04015006.

Ghafoori, E., Motavalli, M., Botsis, J., Herwig, A. & Galli, M. 2012. Fatigue strengthening of damaged metallic beams using prestressed unbonded and bonded CFRP plates. *International Journal of Fatigue* 44: 303–15.

Ghafoori, E., Motavalli, M., Nussbaumer, A., Herwig, A., Prinz, G.S. & Fontana, M. 2015. Design criterion for fatigue strengthening of riveted beams in a 120-year-old railway metallic bridge using pre-stressed CFRP plates. *Composites Part B: Engineering* 68:1–3.

Ghafoori, E., Hosseini, A., Al-Mahaidi, R., Zhao, X. L., Motavalli, M. & Koay, Y.C. 2018. Strengthening steel girders of an Australian bridge with CFRP laminates. *9th International Conference on Bridge Maintenance, Safety and Management (IABMAS2018), Melbourne, 9-3 July 2018.*

Hosseini, A., Ghafoori, E., Motavalli, M., Nussbaumer, A. & Zhao, X.L., 2017. Mode I fatigue crack arrest in tensile steel members using prestressed CFRP plates. *Composite Structures* 178: 119-134.

Hosseini, A., Wellauer, M., Ghafoori, E., Marzaleh, A.S. & Motavalli, M., 2017. An experimental investigation into bond behavior of prestressed CFRP to steel substrate. *In Fourth Conference on Smart Monitoring, Assessment and Rehabilitation of Civil Structures (SMAR 2017), Zurich, 13-15 September 2017*.

Hosseini, A., Ghafoori, E., Motavalli, M., Nussbaumer, A., Al-Mahaidi, R. & Terrasi, G., 2017. A novel mechanical clamp for strengthening of steel members using prestressed CFRP plates. *In Fourth Conference on Smart Monitoring, Assessment and Rehabilitation of Civil Structures (SMAR 2017), Zurich, 13-15 September 2017*.

Zhao, XL. 2013. FRP-strengthened metallic structures. CRC Press.

Maintenance, Safety, Risk, Management and Life-Cycle Performance of Bridges – Powers, Frangopol, Al-Mahaidi & Caprani (Eds)
© 2018 Taylor & Francis Group, London, ISBN 978-1-138-73045-8

Prestressed FRP-Strengthening and Wireless Monitoring of a Metallic Bridge in Australia

Elyas Ghafoori
Swinburne University of Technology, Hawthorn VIC 3122, Melbourne, Australia
Empa, Swiss Federal Laboratories for Materials Science and Technology, Duebendorf 8600 Switzerland

Ardalan Hosseini
Empa, Swiss Federal Laboratories for Materials Science and Technology, Duebendorf 8600 Switzerland

Riadh Al-Mahaidi
Swinburne University of Technology, Hawthorn VIC 3122, Melbourne, Australia

Xiao-Ling Zhao
Monash University, Clayton 3800, Australia

Masoud Motavalli
Empa, Swiss Federal Laboratories for Materials Science and Technology, Duebendorf 8600 Switzerland

Yew-Chin Koay
VicRoads, 60 Denmark Street, Kew, VIC 3101, Australia

ABSTRACT: This paper presents the first application of pre-stressed carbon fibre-reinforced polymer (CFRP) material for strengthening of a metallic bridge in Australia. The study also describes the application of a wireless sensor network (WSN) system for long-term structural health monitoring (SHM) of the installed retrofit system. A flat pre-stressed un-bonded reinforcement (FPUR) system was developed to apply pre-stressed CFRP strips to the steel girders of Diamond-Creek Bridge. The bridge is a 121-year-old metallic roadway bridge in Melbourne, which is subjected to daily passenger and heavy truck vehicles. Sets of laboratory tests were performed to examine the efficiency of the proposed FPUR system, prior to its installation on the bridge. Furthermore, in order to demonstrate the efficiency of the proposed retrofit technique, the bridge was instrumented with different types of sensors (including strain gauges, temperature and humidity sensors) and short- and long-term measurements were performed. As for short-term measurements, the bridge was loaded by a 42.5-tonnes semi-trailer before and after strengthening. For the long-term monitoring, a WSN system was used to monitor the prestress level in the CFRP reinforcements for at least one year. The CFRP plates were pre-stressed up to about 980 MPa (≈38% of the CFRP ultimate strength), which resulted in about 50% reduction in the maximum tensile stress in the bridge girders. The results of the short- and long-term measurements in this study showed that the FPUR system was very effective for flexural and fatigue strengthening of the bridge girders.

1 INTRODUCTION

Carbon fibre-reinforced polymer (CFRP) as a light material with a wide range of strength and Young's moduli has been used for strengthening concrete and steel members. The CFRP materials have high corrosion and fatigue resistance (Zhao 2013). Several studies have shown the effectiveness of using CFRP materials for flexural (e.g., Al-Emrani and Kliger 2006, Ghafoori and Motavalli 2013) and fatigue (e.g., Bassetti et al. 1998, Colombi and Fava 2015, Schnerch et al. 2006, Wu et al. 2012) strengthening of steel members.

The majority of the existing studies on this topic have used a bonded retrofit (BR) system to attach CFRP material to steel substrates. Ghafoori et al. 2012 have suggested an un-bonded retrofit (UR) system for strengthening of metallic girders. Unlike the BR systems, the UR systems work without any glue, and instead use a pair of mechanical clamps, which works based on friction, to attach the CFRP plates to steel I-beams. The UR systems have several advantages compared to BR systems: they can be applied to rough (e.g., corroded) or obstructed (e.g., riveted) surfaces and offer fast installation (i.e., no surface preparation prior to bonding and glue application). The UR systems are particularly good for strengthening heritage/old structures, where the reversibility of the retrofitted elements to the original unstrengthened form is important. The UR systems can be easily removed from the original structure by disassembling the mechanical clamps.

Ghafoori and Motavalli 2015c have performed the first systematic study to compare the behavior of the steel members strengthened by the BR and the UR systems. The results of extensive laboratory tests have shown that when metallic beams are strengthened by pre-stressed CFRP laminates, the performance of the CFRP-strengthened steel beams is more sensitive to the magnitude of pre-stress level rather than the presence of the bond (Ghafoori and Motavalli 2015b).

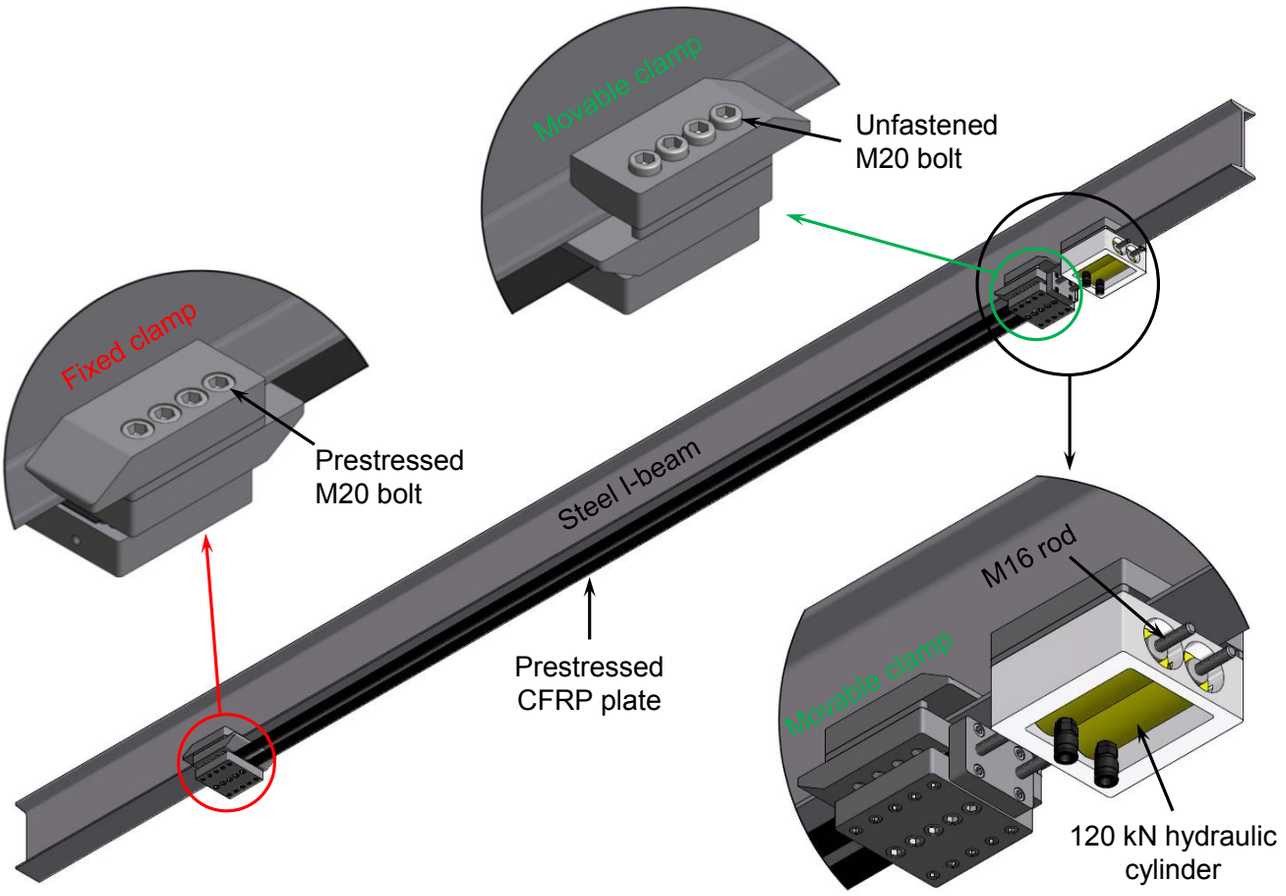


Figure 1. Different components of the flat prestressed unbonded reinforcement (FPUR) system.

Furthermore, Kianmofrad et al. 2017 have suggested different shapes and configurations of the pre-stressed UR (PUR) system. A trapezoidal PUR (TPUR) system was developed and tested under static (Ghafoori and Motavalli 2015a) and fatigue loading (Ghafoori et al. 2015a). The system has been used for fatigue strengthening of a 120-year-old railway riveted bridge in Switzerland (Ghafoori et al. 2015b, Ghafoori et al. 2014). More recently, Hosseini et al. 2018 have developed and tested a flat PUR (FPUR) system in the laboratory subjected to static and fatigue loading.

This paper presents the application of the FPUR system for strengthening of an old metallic roadway bridge in Victoria, Australia. Furthermore, a wireless sensor network (WSN) system was used to monitor the long-term behavior of the bridge after strengthening. The current paper aims to briefly explain different aspects of the bridge strengthening project and summarize the most important results of short-term and long-term measurements.

2 DEVELOPMENT OF THE FPUR SYSTEM

2.1 *Design basis and pull-off tests*

A FPUR system was designed, manufactured, and tested at the Structural Engineering Research Laboratory of the Swiss Federal Laboratories for Materials Science and Technology (Empa). As it is shown in Figure 1, the FPUR system relies on two sets of mechanical clamps, which transfer the pre-stressing force of the CFRP plates to the lower flange of the steel girders via friction. Each set of the mechanical clamps holds two prestressed normal modulus (NM) CFRP plates with cross-sectional dimensions of 50 × 1.4 mm (width × thickness). The strengthening procedure using the proposed FPUR system is as follows:

(1) the unstressed CFRP plates are anchored on one side of the beam using the so called *fixed clamp* with the help of eight M20 high-strength (grade 12.9) bolts, which are tightened with a torque of 605 N·m, to generate a prestressing force of 223 kN per bolt. (2) On the other side, the unstressed CFRP plates are gripped in the so called *movable clamp*, while the clamp set is free to move horizontally along the beam axis. (3) Two 120-kN hollow plunger cylinders are then installed adjacent to the *movable clamp* using a cylinder housing. (4) With the help of two prestressing M16 rods, the movable clamp is pulled using the hollow plunger cylinders connected to a manual hydraulic pump, and, subsequently, the CFRP plates are prestressed. (5) Upon reaching the desired prestressing level in the CFRP plates, all the eight M20 bolts of the movable clamps are tightened.

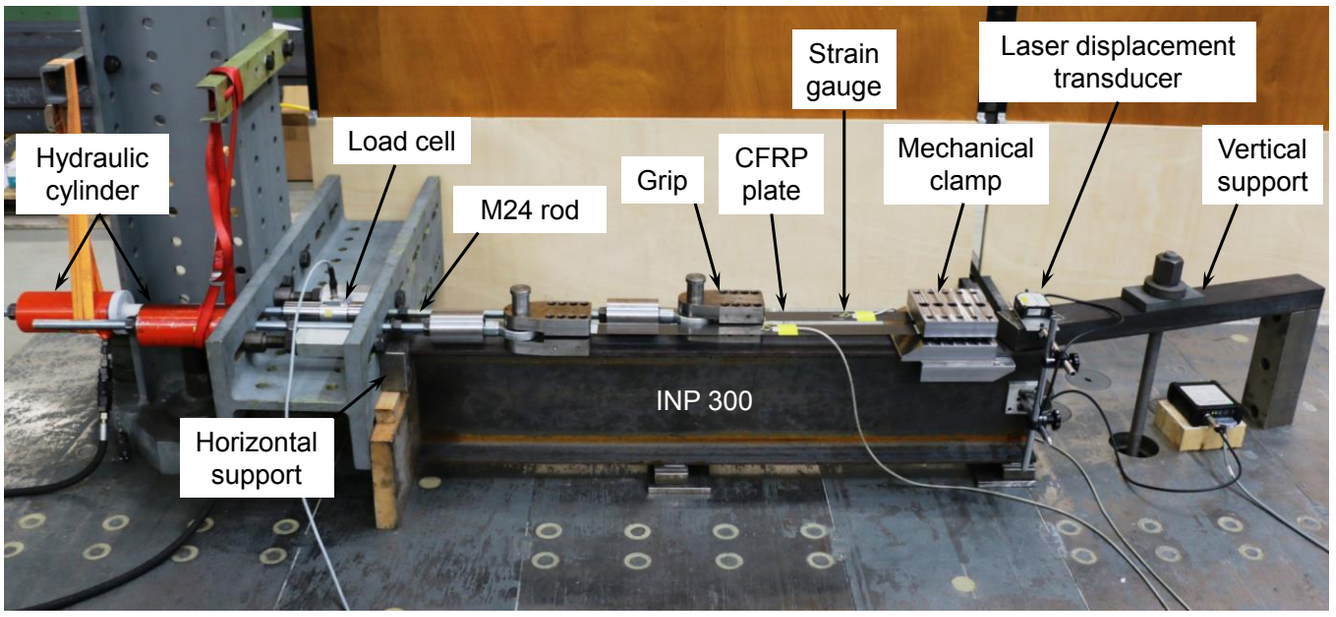


Figure 2. Pull-off test setup.

(6) Finally, the hydraulic pressure is released and the prestressing system consisting of the two hollow plunger cylinders and the housing are removed.

In order to optimize the geometry of the mechanical clamping system and estimate the number and diameter of the prestressed bolts (to generate the required friction force between the clamps and tensile flange of the beam), an FE simulation was performed using ABAQUS FE Package. Further details regarding the FE simulation of the FPUR system can be found in Hosseini et al. 2018. All the required mechanical parts, with the optimized geometry, were then manufactured from high strength steel M200 with a nominal yield strength of 1000 MPa.

In order to determine the ultimate capacity of the mechanical clamps before slippage, a pull-off test setup was designed and a set of pull-off tests were performed on the optimized configuration of the system. Different components of the test setup are shown in Figure 2. Figure 3 shows the strain level generated in both the CFRP plates versus the applied load per hydraulic cylinder. It can be seen from Figure 3 that CFRP rupture occurred as the governing failure mode of the system, and no slippage of the clamp was observed. The NM CFRP plates of type S&P 150/2000-50/1.4 were used in all the laboratory tests. The tensile strength and elastic modulus of the utilized CFRP composite were 2595 MPa and 161 GPa, respectively.

2.2 *Static and fatigue four-point bending tests*

In order to evaluate the performance of the proposed FPUR system for strengthening of steel I-beams, a set of static and fatigue tests was performed at the Structural Engineering Research Laboratory of Empa on 6.4-m long steel I beams under four-point bending. Figure 4 shows different elements of the test set-up and the FUR system. First a reference unstrengthened INP 300 beam was loaded in the linear regime (up to 75 kN per cylinder). Afterwards, the FPUR system was installed on the beam, and the beam was reloaded up to 75 kN per cylinder. As Figure 5 shows, the application of the non-prestressed CFRP plates increased the stiffness of the steel beam slightly, however, the deflection/strain reduction in the member is not significant.

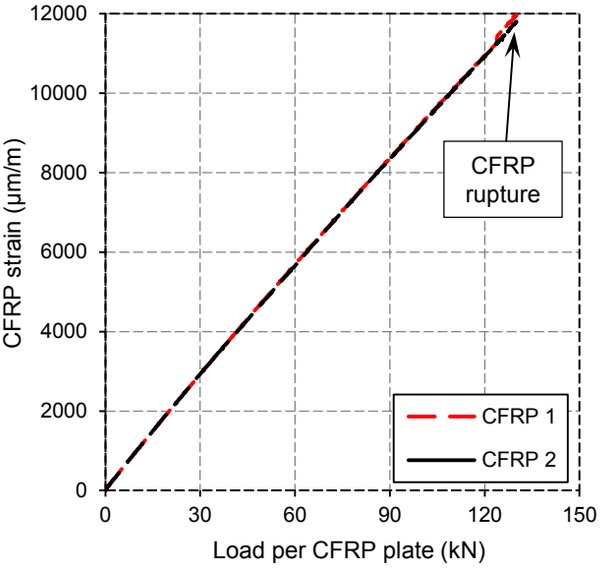


Figure 3. CFRP strain versus load in pull-off tests.

Furthermore, it can be seen from Figure 5 that application of the FPUR system with 20% or 40% prestressing level can significantly decrease the deflection and strain/stress level in the strengthened steel I-beam under service loads.

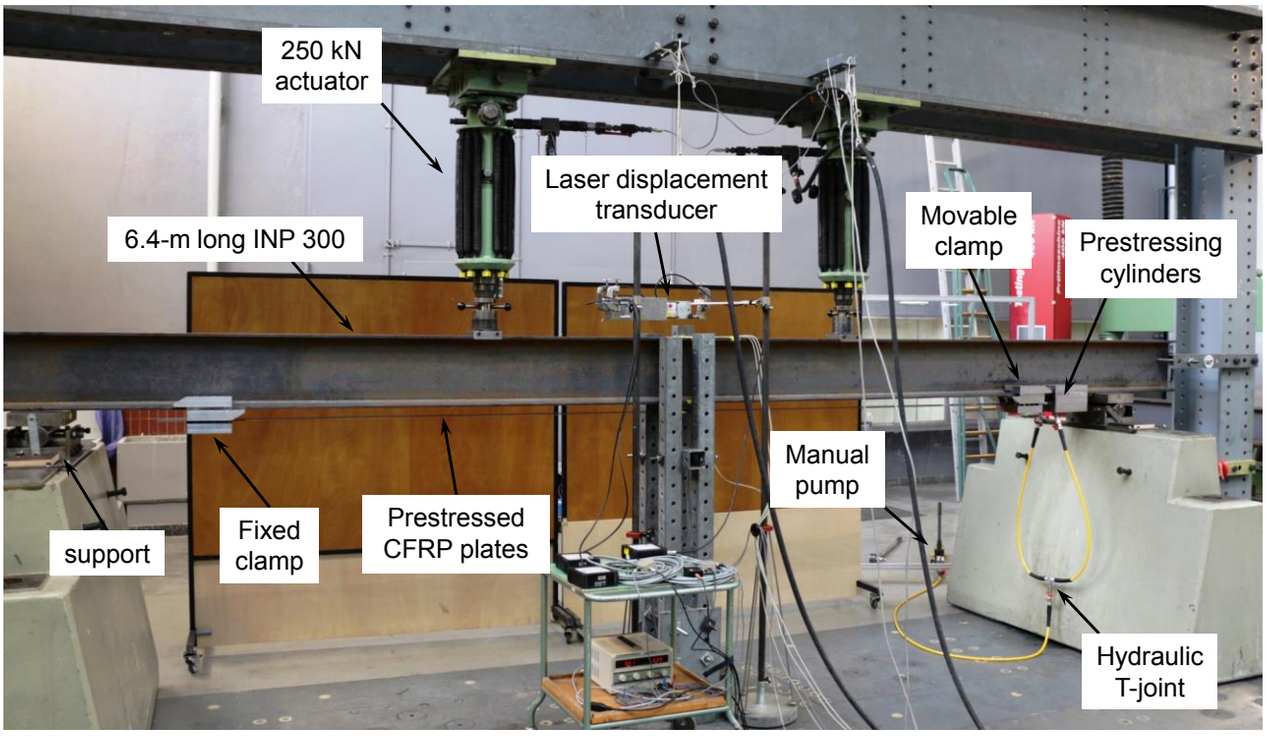
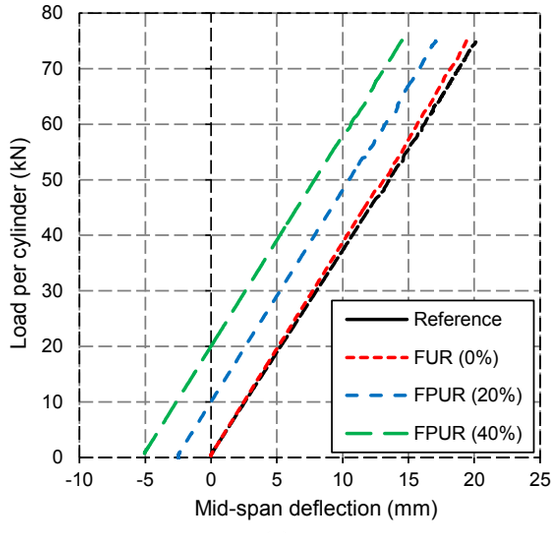
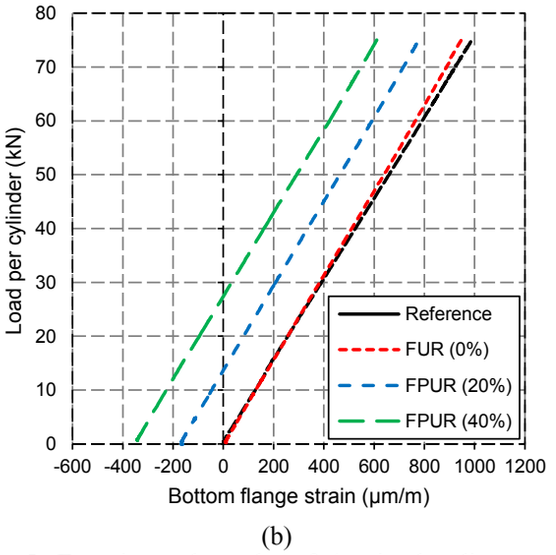


Figure 4. Static and fatigue four-point bending test setup.



(a)



(b)

Figure 5. Experimental results of 4-point bending tests: (a) load-deflection response; (b) load-strain response of bottom flange.

It should be mentioned that the utilized steel I-beams in the four-point bending tests was of type S275JR with a measured elastic modulus of 203.3 GPa, and yield and ultimate strength of 328 and 465 MPa, respectively.

In addition to the four-point static tests, the performance of the FPUR system was also evaluated under 4-point fatigue loading for 10 million fatigue cycles, while the CFRP plates were prestressed up to 40% of their ultimate tensile capacity. No slippage neither reduction in the prestressing level was observed over 2 million fatigue cycles, which demonstrates a superior performance of the system. After testing the system under static and fatigue loading, the system was shipped to Victoria, Australia.

More information about the FE modeling and laboratory tests on the FPUR system can be found in Hosseini et al. 2018.

3 STRENGTHENING OF DIAMOND-CREEK BRIDGE

SN6091 Bridge over Diamond-Creek along Heidelberg-Kinglake Road (constructed in 1896) is a double-span metallic roadway bridge in Victoria, Australia. The total length of the bridge is approximately 33 m with a width of 6.4 m and a height of 2.3 m. The bridge was constructed approximately 6.4 m above the river water level. The bridge is subjected to daily passenger and heavy truck vehicles. It consists of two longitudinal wrought iron trusses (i.e., as main girders) connected by several steel cross-girders, as shown in Figures 6 and 7.

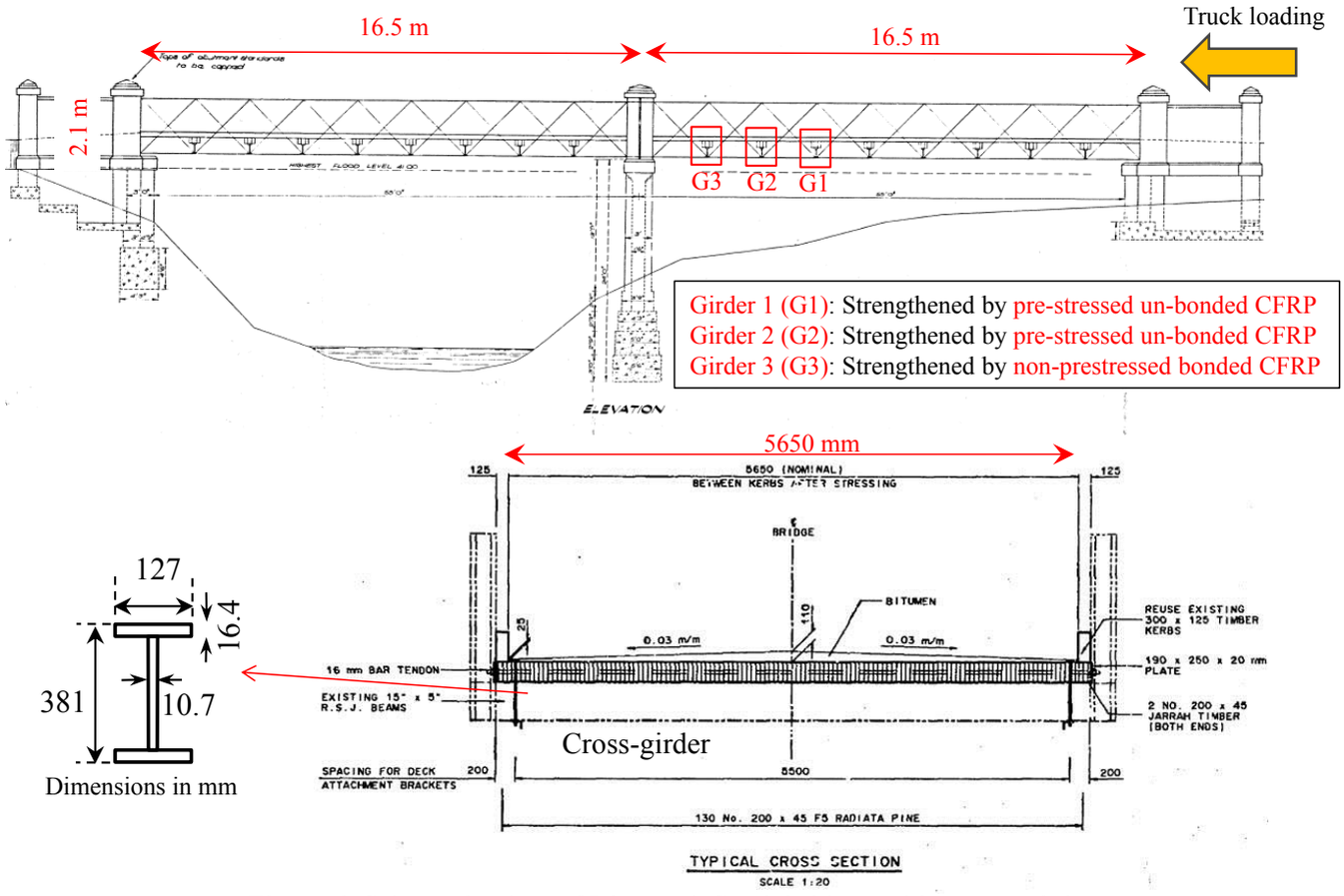


Figure 6. Schematic view of Diamond-Creek bridge and its cross-girders.

Figure 6 shows the bridge elevation as well as the details and dimensions of the cross-girders. The bridge belongs to VicRoads, which is the road and traffic authority in the state of Victoria.

Two girders of the bridge (i.e., girders G1 and G2) were strengthened by the FPUR system, and girder G3 was strengthened with non-prestressed bonded CFRP plate. For the sake of brevity, this paper only discusses the part of the work related to CFRP strengthening of girders G1 and G2.

3.1 *Strengthening of the bridge girders*

After successful accomplishment of the laboratory tests, presented in Section 2, the FPUR system was applied on two cross-girders of the bridge with a prestressing level of about 38%. The CFRP plates had the same geometrical and mechanical properties as those explained in Section 2.1. Based on the bridge documents, the steel cross-girders were of type B.S.B. 25 from the Dorman, Long & Co. Limited Company in UK. A Young's modulus, yielding and ultimate strength of 210 GPa, 250 and 320 MPa, respectively, were assumed for mechanical properties of the steel girders. Different elements of the strengthening and monitoring systems on girders G1 and G2 are shown in Figure 8.

As for short-term measurements, the bridge was subjected to a 42.5-tonnes semi-trailer before and after strengthening, as shown in Figure 7.

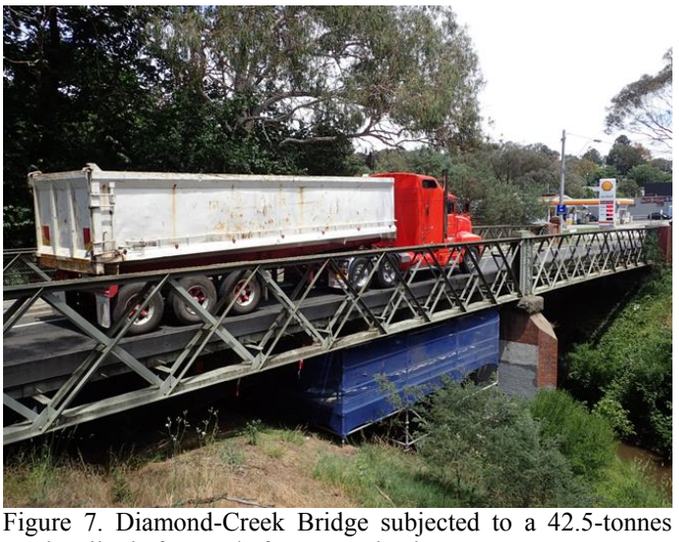


Figure 7. Diamond-Creek Bridge subjected to a 42.5-tonnes semi-trailer before and after strengthening.

Figure 9 shows the state of stresses in the CFRP plates and the top and bottom flanges of the steel girders during pre-stressing procedure. The CFRP plates were gradually pre-stressed up to about 38% (of its ultimate strength) using a set of hydraulic actuators, as explained in Section 2. From Figure 9, it can be seen that an increase in the CFRP pre-stress level results in an increase in the magnitude of the compressive stress at the beam bottom flange. After prestressing, a maximum compression of about 30 MPa was achieved at the beam bottom flange. Note that in Figure 9, the sudden jumps in the stresses

show the passages of vehicles (regular daily traffic) over the bridge during the pre-stressing process. Furthermore, it can be seen that pre-stressing process took place in less than 300 s. A truck loading test was then performed (as for short-term measurements) right after strengthening. Figure 10 shows the stresses at the top and bottom flanges of the mid-span of girder G2 due to the passages of the 42.5-tonnes semi-trailer with a slow speed of about 5 km/h.

The tensile maximum stress in the beam bottom flange before strengthening was about 80 MPa, which was then reduced to about 40 MPa after strengthening with the FPUR system. This shows a reduction of about 50% (i.e., ≈40 MPa) of the maximum tensile stress in the cross-girder. Out of 40 MPa decrease in the tensile stress, it can be shown that -30 MPa was because of the application of pre-stressing (see Figure 9) and -10 MPa was due to the increased stiffness of the girders after the CFRP strengthening. Furthermore, it can be seen from Figure 10 that the magnitude of the compressive stress in the top flange of the cross-girder was also slightly decreased after strengthening. Therefore, it can be concluded that strengthening with the FPUR system could decrease the magnitude of the stresses in the both top and bottom flanges, and, therefore, can result in an increase in flexural capacity of the bridge girders.

3.2 *Fatigue strengthening criterion*

It has been shown by Ghafoori et al. 2015c that application of pre-stressed CFRP can increase the fatigue life of the steel girders substantially. Ghafoori and Motavalli 2016 have suggested a constant life diagram (CLD) approach to estimate the pre-stressing level that results in a complete prevention of fatigue crack initiation. The CLDs are used to demonstrate the combined effect of stress range, mean stress level and material properties. CLDs can foresee the fatigue life of metals at different mean stress levels. For a given maximum stress (σ_{max}) and minimum stress (σ_{min}), the stress amplitude (σ_a) and the mean stress (σ_m) are expressed by

$$\sigma_a = (\sigma_{max} - \sigma_{min}) / 2 \quad (1)$$

$$\sigma_m = (\sigma_{max} + \sigma_{min}) / 2 \quad (2)$$

Figure 11 shows a CLD diagram which shows the fatigue strengthening approach used for strengthening of the bridge girders. In Figure 11, the vertical axis is the stress amplitude, σ_a, and the horizontal axis is the mean stress, σ_m. This figure also presents the yield line and the Gerber fatigue criterion, which is often used for ductile metals. Furthermore, Figure 11 shows the Modified Johnson line, which was proposed by Ghafoori et al. 2015b, as a fatigue design criterion for determination of the safe service stresses of old metallic bridge members.

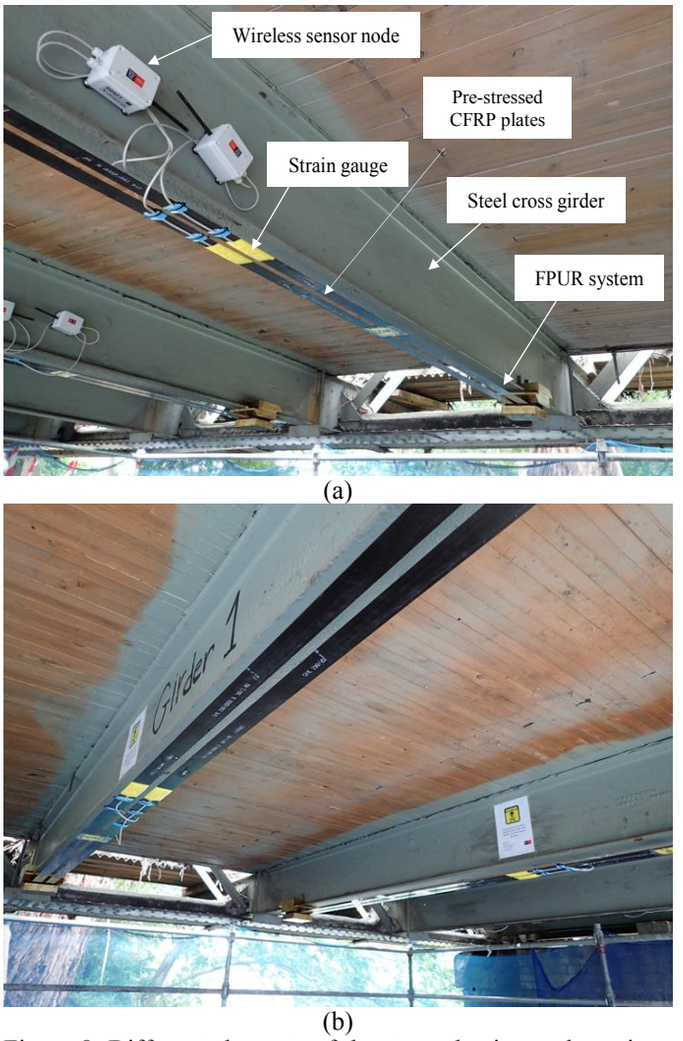


Figure 8. Different elements of the strengthening and monitoring system installed on (a) girder G2 and (b) girder G1.

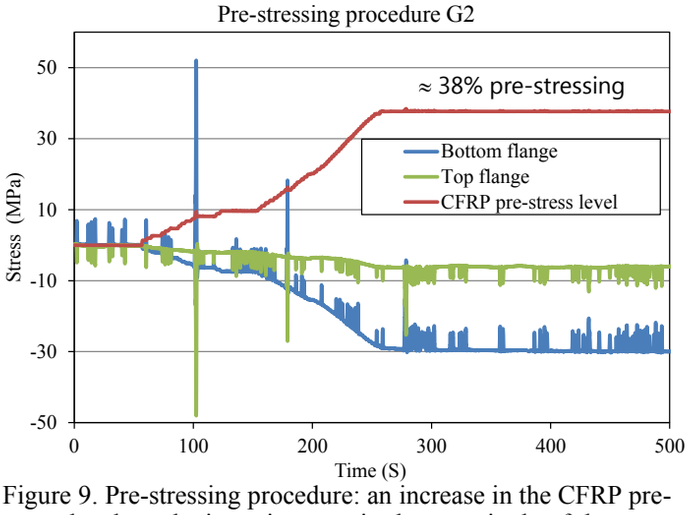


Figure 9. Pre-stressing procedure: an increase in the CFRP pre-stress level results in an increase in the magnitude of the compressive stress at the beam bottom flange.

Stress points A and B in Figure 11 refer to the state of the stresses in the beam bottom flange before and after strengthening, respectively. As it can be seen in this figure, point A, which refers to the stress state in the girder prior to strengthening, is marginally outside of the safe region.

After strengthening using the FPUR system, the working stress in the girder bottom flange was shift-

ed from the at-risk region (i.e., point A) to the safe-life region (i.e., point B) based on the modified Johnson criteria.

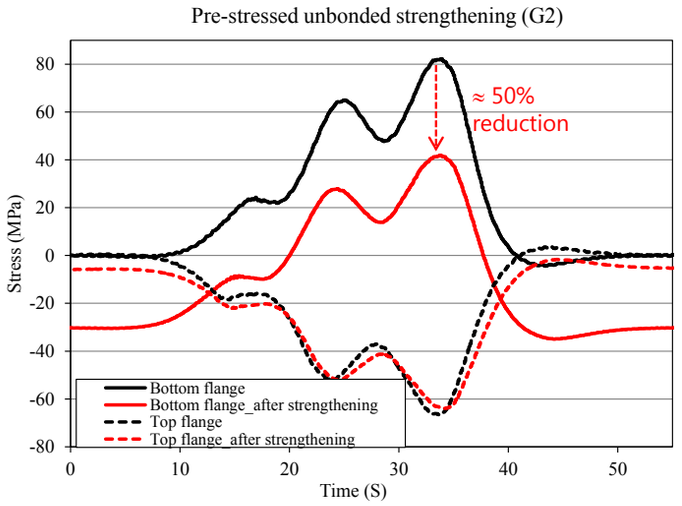


Figure 10. Stress at the top and bottom flanges in the mid-span of girder G2 due to the passages of a 42.5-tonnes semi-trailer before and after strengthening.

4 WIRELESS MONITORING SYSTEM

In the recent years, the WSN technology has been used for structural health monitoring (SHM) of different types of civil structures (Feltrin et al. 2013). The WSN system offers many attractive features, such as cable-free and easy deployment, which minimize the installation time and cost (Flouri et al. 2012). Figure 12 shows a scheme of the architecture of the WSN system, which includes several sensor nodes, a base station and a server. The sensor nodes work with battery and are directly connected to the sensors on the bridge. The housing of the WSN nodes and those of the temperature and humidity sensors, shown in Figure 8a, were equipped with four magnetic footings, which allows for a simple and fast mounting of the nodes. These nodes read the data of the sensor every 10 min and send them to the base station, which can be placed within 1-km away from the bridge. The base station is connected to the electricity power and has a data sim card.

The base station works similar to a modem and receives the data from the sensor nodes and sends them to a server through internet connection. The server then makes the data online on a website and accessible to the public. The electronic modules of the WSN monitoring system were provided by Decentlab GmbH, Switzerland.

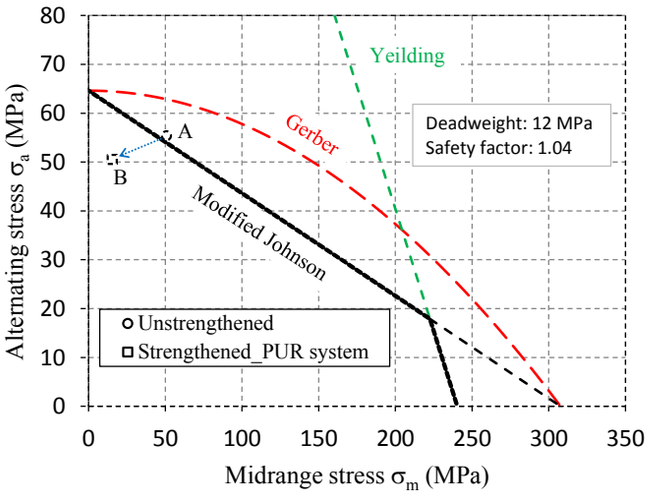


Figure 11. Fatigue strengthening approach: shifting the working stresses in the girder bottom flange from the at-risk region to the safe-life region based on the modified Johnson criteria (Ghafoori 2015).

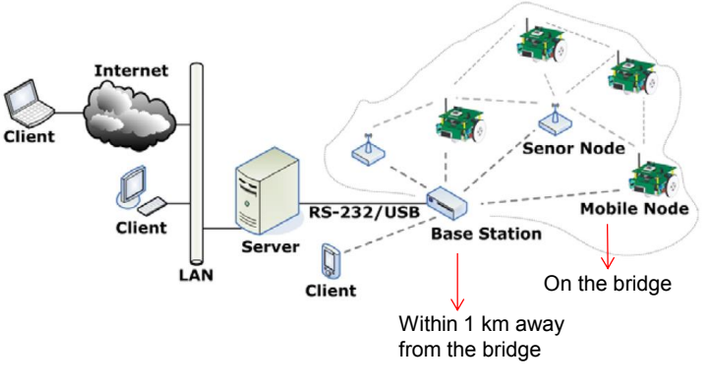


Figure 12. A scheme of the architecture of the WSN system for SHM.

4.1 *Monitoring CFRP pre-stressing using the WSN*

In order to ensure that no slippage occurs between the CFRP plates and the clamps, neither between the friction clamps and the steel beam flange, one resistance strain gauge was mounted on each CFRP plate, coated with long-term protection layers, and was then connected to a sensor node (see Figure 8a). Because strain gauges do not automatically compensate for temperature, for each active strain gauge, a dummy strain gauge was used to compensate for the effects of temperature variations. The dummy strain gauges, which are identical to the active strain gauges, were mounted on pieces of unstrained CFRP plates and placed next to the active gauges. To account for the temperature effects, the dummy strain gauges were wired into a half Wheatstone bridge on an arm adjacent to the active strain gauge. All the strain gauges used for the WSN system were of type 6/700 LY46 with a k-factor of 2.03 ± 1.5% and an electric resistance of 700 Ω ± 0.30% and were provided by the HBM Company, Germany. All of the strain gauges as well as the humidity and temperature sensors were connected to the WSN nodes.

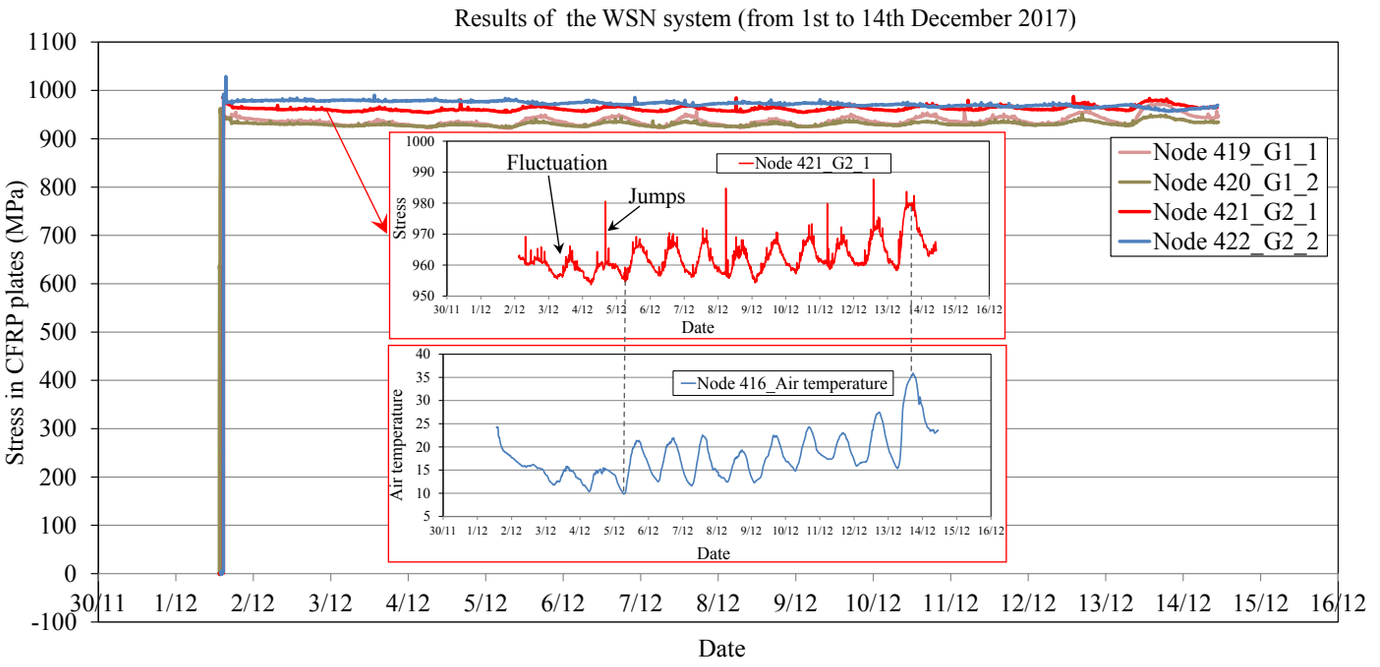


Figure 13. Results of wireless monitoring system: time-history of the pre-stress level in the four CFRP plates from 1st to 14th December 2017.

4.2 *Preliminary results of the wireless monitoring*

Figure 13 shows the time history of the on-site air temperature and the stress level in all CFRP plates mounted on G1 and G2 girders of the bridge from 1st to 14th December 2017 (for two weeks). Nodes 419 and 420 show the stress in the two prestressed CFRP plates attached to G1 girder, while nodes 421 and 422 refer to the CFRP plates on G2 girder. Figure 13 also shows an enlarged view of the results of node 421 (i.e., one of the CFRP plates on G2 girder). This figure shows a pattern of stress fluctuations during day and night, and also some sudden jumps with small and large stress amplitudes. The stress fluctuations can be attributed to the temperature change. As the temperature increases, the CFRP pre-stress level increases due to the fact that CFRP material has a negligible thermal expansion coefficient in its fiber direction compared to that for steel.

As shown in Figure 13, with an approximately 25 degrees Celsius increase in the ambient temperature, the CFRP pre-stress level increases by approximately about 25 MPa, which is less than 1% of CFRP ultimate strength. Furthermore, the sudden small and large jumps that can be observed in the CFRP pre-stress level in Figure 13 are due to the passages of small passenger vehicles and heavy trucks, respectively. The change in humidity did not have any influence on the CFRP pre-stress level and therefore has not discussed in this study. The WSN system will remain on the bridge for at least one year to monitor possible pre-stress loss and also to study the probable effects of the temperature. The results related to this long-term monitoring will be reported in a future publication. The results from the wireless monitoring system have shown that no slip or pre-stress loss has occurred in the system so far.

5 CONCLUSIONS

This study presents the work on the strengthening of Diamond-Creek Bridge (121 years-old) in Victoria, Australia. Two steel cross-girders of the bridge were strengthened using pre-stressed un-bonded CFRP plates. The feasibility and effectiveness of pre-stressed FRP composites for strengthening of metallic bridges have been demonstrated. Furthermore, a wireless monitoring system was used to monitor the pre-strain level in each CFRP plate as well as the on-site temperature and humidity.

The results of the short-term measurements showed that after pre-stressing the CFRP plates up to about 980 MPa (which is ≈38% of the CFRP ultimate strength), the maximum tensile stress in the bridge cross-girders decreased about 50%. Furthermore, it was shown that the application of the FPUR system can substantially decrease the mean tensile stress in the bridge girders, and therefore, increase the fatigue life of the structure (in this case to an infinite fatigue life). Therefore, the results of strain measurements show that the proposed FPUR system is very effective for flexural and also fatigue strengthening of metallic bridge girders.

The preliminary results of the WSN system have shown no loss in the CFRP pre-stressing level so far. Furthermore, the WSN results showed that because of the low thermal expansion coefficient of the

CFRP material (in the fiber direction) compared to steel, an increase in ambient temperature results in an increase in the stress in the CFRP plates. The effect of thermal mismatch between CFRP and steel structure is not necessarily negligible and should be considered in the design.

6 ACKNOWLEDGMENTS

The authors gratefully acknowledge the financial supports provided by the Australian Research Council (ARC) Linkage Grant (LP140100543), the Swiss National Science Foundation (SNSF Project No. 200021-153609) and the S&P Clever Reinforcement Company AG in Switzerland.
Thanks also go to Marko Horvat and Jon-Paul Marrow from Aeramix Company, Martin Hüppi from S&P AG, Hai Luong from VicRoads, Sanjeet Chandra and Alaa Al-Mosawe from Swinburne University of Technology and Herb Kuhn from Simpson Strong-Tie for their exceptional help and cooperation during the installation of the system on the bridge. The authors would also like to thank Slavko Tudor, Robert Widmann and Dimitri Ott from Empa for their supports and help in development, testing and shipment of the retrofit system.

7 REFERENCES

Al-Emrani, M. & Kliger, R. 2006. Analysis of interfacial shear stresses in beams strengthened with bonded prestressed laminates. *Composites - Part B,* 37**,** 265-272.

Bassetti, A., Liechti, P. & Nussbaumer, A. 1998. Fatigue resistance and repairs of riveted bridge members. *Fatigue Design and Reliability,* II**,** 535-546.

Colombi, P. & Fava, G. 2015. Experimental study on the fatigue behaviour of cracked steel beams repaired with CFRP plates. *Engineering Fracture Mechanics,* 145**,** 128-142.

Feltrin, G., Jalsan, K. E. & Flouri, K. 2013. Vibration monitoring of a footbridge with a wireless sensor network. *JVC/Journal of Vibration and Control,* 19**,** 2285-2300.

Flouri, K., Saukh, O., Sauter, R., Jalsan, K. E., Bischoff, R., Meyer, J. & Feltrin, G. 2012. A versatile software architecture for civil structure monitoring with wireless sensor networks. *Smart Structures and Systems,* 10**,** 209-228.

Ghafoori, E. 2015. Fatigue strengthening of metallic members using un-bonded and bonded CFRP laminates. *PhD Thesis, ETH-Zurich (http://dx.doi.org/10.3929/ethz-a-010453130).*

Ghafoori, E. & Motavalli, M. 2013. Flexural and interfacial behavior of metallic beams strengthened by prestressed bonded plates. *Composite Structures,* 101**,** 22-34.

Ghafoori, E. & Motavalli, M. 2015a. Innovative CFRP-Prestressing System for Strengthening Metallic Structures. *Journal of Composites for Construction,* 19**,** 04015006.

Ghafoori, E. & Motavalli, M. 2015b. Lateral-torsional buckling of steel I-beams retrofitted by bonded and un-bonded CFRP laminates with different pre-stress levels: experimental and numerical study. *Construction and Building Materials,* 76**,** 194–206.

Ghafoori, E. & Motavalli, M. 2015c. Normal, high and ultra-high modulus CFRP laminates for bonded and un-bonded strengthening of steel beams. *Materials and Design,* 67**,** 232–243.

Ghafoori, E. & Motavalli, M. 2016. A Retrofit Theory to Prevent Fatigue Crack Initiation in Aging Riveted Bridges Using Carbon Fiber-Reinforced Polymer Materials. *Polymers,* 8**,** 308.

Ghafoori, E., Motavalli, M., Botsis, J., Herwig, A. & Galli, M. 2012. Fatigue strengthening of damaged metallic beams using prestressed unbonded and bonded CFRP plates. *International Journal of Fatigue,* 44**,** 303-315.

Ghafoori, E., Motavalli, M., Nussbaumer, A., Herwig, A., Prinz, G. & Fontana, M. 2015a. Determination of minimum CFRP pre-stress levels for fatigue crack prevention in retrofitted metallic beams. *Engineering Structures,* 84**,** 29–41.

Ghafoori, E., Motavalli, M., Nussbaumer, A., Herwig, A., Prinz, G. S. & Fontana, M. 2015b. Design criterion for fatigue strengthening of riveted beams in a 120-year-old railway metallic bridge using pre-stressed CFRP plates. *Composites Part B: Engineering,* 68**,** 1-13.

Ghafoori, E., Motavalli, M., Zhao, X. L., Nussbaumer, A. & Fontana, M. 2015c. Fatigue design criteria for strengthening metallic beams with bonded CFRP plates. *Engineering Structures,* 101**,** 542-557.

Ghafoori, E., Prinz, G. S., Mayor, E., Nussbaumer, A., Motavalli, M., Herwig, A. & Fontana, M. 2014. Finite element analysis for fatigue damage reduction in metallic riveted bridges using pre-stressed CFRP plates. *Polymers,* 6**,** 1096-1118.

Hosseini, A., Ghafoori, E., Motavalli, M., Nussbaumer, A., Zhao, X. L. & Al-Mahaidi, R. 2018. Flat Prestressed Unbonded Reinforcement (FPUR) System for Strengthening of Steel I-Beams. *9th International Conference on Bridge Maintenance, Safety and Management (IABMAS2018), Melbourne, 9-3 July.*

Kianmofrad, F., Ghafoori, E., Elyasi, M. M., Motavalli, M. & Rahimian, M. 2017. Strengthening of metallic beams with different types of pre-stressed un-bonded retrofit systems. *Composite Structures,* 159**,** 81-95.

Schnerch, D., Dawood, M., Rizkalla, S., Sumner, E. & Stanford, K. 2006. Bond behavior of CFRP strengthened steel structures. *Advances in Structural Engineering,* 9**,** 805-817.

Wu, C., Zhao, X. L., Al-Mahaidi, R., Emdad, M. & Duan, W. 2012. Fatigue tests of cracked steel plates strengthened with UHM CFRP plates. *Advances in Structural Engineering,* 15**,** 1801-1816.

Zhao, X. L. 2013. *FRP-Strengthened Metallic Structures,* Boca Raton, FL, Taylor and Francis.

Maintenance, Safety, Risk, Management and Life-Cycle Performance of Bridges – Powers, Frangopol, Al-Mahaidi & Caprani (Eds)
© 2018 Taylor & Francis Group, London, ISBN 978-1-138-73045-8

The Peak Stress Method for fatigue analysis of welded details

G. Meneghetti*, A. Campagnolo & B. Atzori
Department of Industrial Engineering, University of Padova, Via Venezia, 1 – 35131 Padova (Italy)
**Corresponding author: giovanni.meneghetti@unipd.it, tel. 0039 049 8276751, fax 0039 049 8276785*

ABSTRACT: In fatigue design of welded joints according to the notch stress intensity factor (NSIF) approach, the weld toe profile is assumed to be a sharp V-notch having tip radius equal to zero, while the root side is assumed to be a pre-crack in the structure. The Peak Stress Method (PSM) represents an engineering, simplified method which allows a rapid calculation of the NSIFs on the basis of the singular linear elastic peak stresses evaluated at the notch tip by means of FE analyses with coarse FE meshes. The advantages of the PSM can be summarized as follows: (i) coarse meshes can be adopted, the required FE size being some orders of magnitude larger than that necessary to evaluate the NSIFs from the local stress distributions; (ii) only a single stress value is sufficient to estimate the NSIFs instead of a number of stress-distance numerical results. First, the PSM has been calibrated by analysing several mode I and mode II problems with Ansys FE code. Recently, the PSM has been also calibrated by adopting six commercial FE packages other than Ansys, taking advantage of a Round Robin between some Italian Universities. After having recalled the calibration of the method, the paper presents some applications of the PSM relevant to partial-penetration butt joints made of aluminum alloys as well as load-carrying cruciform joints and tube-to-flange joints made of structural steels under uniaxial fatigue loadings. Because of the relatively coarse FE analyses required and simplicity of post-processing the calculated peak stresses, the PSM might be useful in the everyday design practice.

1 INTRODUCTION

On the basis of the fundamental contribution of Williams (1952), who studied two-dimensional notch problems under mode I (opening) and mode II (sliding) loadings, the singular linear elastic stress distributions in the neighborhood of a sharp V-notch tip, see the example of a welded joint in Fig. 1, can be written as functions of the NSIFs, which quantify the intensity of the asymptotic stress fields. The following equations define the mode I and mode II NSIFs, respectively according to Gross & Mendelson (1972):

$$K_1 = \sqrt{2\pi} \cdot \lim_{r\to 0}\left[\left(\sigma_{\theta\theta}\right)_{\theta=0} \cdot r^{1-\lambda_1}\right] \quad (1)$$

$$K_2 = \sqrt{2\pi} \cdot \lim_{r\to 0}\left[\left(\tau_{r\theta}\right)_{\theta=0} \cdot r^{1-\lambda_2}\right] \quad (2)$$

In Eqs. (1) and (2), λ_1 and λ_2 are the mode I and II eigenvalues, respectively, being dependent on the opening angle 2α (Williams 1952), while $\sigma_{\theta\theta}$ and $\tau_{r\theta}$ represent the stress components evaluated along the notch bisector line, which is defined by the angular coordinate θ=0 according to Fig. 1.

In the literature, the NSIF approach has been used to analyse the medium as well as the high-cycle fatigue strength of specimens weakened by sharp V-notches and made of structural materials (Kihara & Yoshii 1991; Boukharouba et al. 1995). Focusing on welded joints, NSIFs allow to correlate the fatigue strength under uniaxial (Verreman & Nie 1996; Lazzarin & Tovo 1998; Lazzarin & Livieri 2001; Atzori & Meneghetti 2001) as well as multiaxial loadings (Lazzarin et al. 2004).

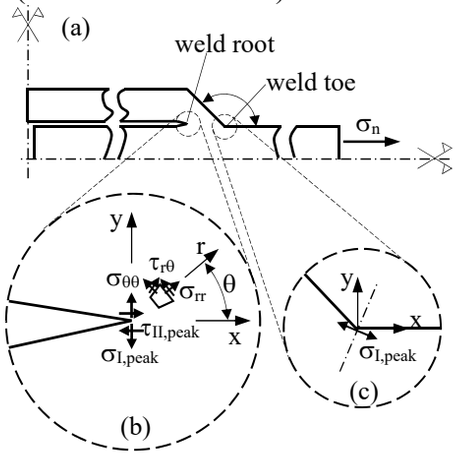


Figure 1: Sharp V-shaped notches in a welded joint (a) at the weld root (2α = 0°) (b) and at the weld toe (2α typically equal to 135°) (c) sides. Definition of peak stresses $\sigma_{I,peak}$ and $\tau_{II,peak}$.

Nevertheless, it should be noted that the calculation of NSIFs on the basis of the results of numerical analyses shows a major drawback in engineering applications, since very refined FE meshes (element size on the order of 10^{-5} mm) are required in order to apply definitions (1) and (2) to calculate the NSIFs. When dealing with three-dimensional notched components, both the solution of the FE model and the post-processing of numerical results could be even more time-consuming.

In order to overcome this issue, an engineering and rapid technique, the so-called Peak Stress Method (PSM), has been proposed, which allows to speed up the calculation of the NSIFs by adopting coarse FE analyses, the element size being some orders of magnitude larger than that required to apply definitions (1) and (2). The method takes inspiration from the contribution by Nisitani & Teranishi (2001; 2004), who proposed a technique to readily estimate the mode I Stress Intensity Factor of a crack propagating from an ellipsoidal cavity. The PSM has been theoretically justified and extended to allow the rapid calculation also of the NSIF relevant to sharp and open V-notches under mode I (Meneghetti & Lazzarin 2007; Meneghetti & Guzzella 2014), the SIF of cracks under mode II (Meneghetti 2012) and, finally, the NSIF of open V-notches under mode III (Meneghetti 2013).

Practically, the NSIFs K_1 and K_2 can be readily estimated according to the PSM by adopting the singular, linear elastic, opening (mode I) and sliding (mode II) peak stresses $\sigma_{I,peak}$ and $\tau_{II,peak}$, respectively, calculated at the V-notch tip (see definition of peak stresses in Fig. 1) from FE analyses with coarse meshes. The estimated NSIF values can be obtained from the following expressions (Meneghetti & Lazzarin 2007; Meneghetti 2012):

$$K_1 \cong K^*_{FE} \cdot \sigma_{I,peak} \cdot d^{1-\lambda_1} \quad (3)$$

$$K_2 \cong K^{**}_{FE} \cdot \tau_{II,peak} \cdot d^{0.5} \quad (4)$$

where *a* represents the characteristic size of the considered sharp V-notch, as an example it is the notch depth in Fig. 2, *d* is the so-called 'global element size', i.e. the average FE size adopted by the free mesh generation algorithm available in the numerical software. Finally, parameters K^*_{FE} and K^{**}_{FE} depend on the following calibration options (see also the detailed discussion in (Meneghetti et al. 2017c)):

- the *element type* and *formulation*;
- the *mesh pattern* of finite elements;
- the procedures for *stress extrapolation* and *principal stress calculation at FE nodes.*

The comparison between Eqs. (3) and (4) and previous Eqs. (1) and (2) shows that the PSM has a further advantage in addition to the coarse FE mesh: only a single stress value is necessary to estimate the NSIFs, instead of a number of *stress-distance* results, which require a post-processing analysis.

It is worth noting that thanks to Eqs. (3) and (4), any NSIF-based approach for the structural strength assessment can in principle be reformulated on the basis of the PSM. Recently, the PSM has been applied in combination with the approach based on the averaged strain energy density (SED) to assess the fatigue strength of welded joints under axial (Meneghetti & Lazzarin 2011; Meneghetti 2012), torsion (Meneghetti 2013) and multiaxial (Meneghetti et al. 2017a; Meneghetti et al. 2017b) loading conditions.

First, the PSM has been calibrated by analysing notched problems with Ansys FE code and parameters K^*_{FE} and K^{**}_{FE}, to be used in Eqs. (3) and (4), resulted equal to 1.38 and 3.38, respectively. Such values are valid under the conditions discussed in the relevant literature (Meneghetti & Lazzarin 2007; Meneghetti 2012), to which the reader is referred.

Recently, parameters K^*_{FE} and K^{**}_{FE} have been calibrated by adopting six commercial FE packages other than Ansys (Meneghetti et al. 2017c), taking advantage of a Round Robin between some Italian Universities. Essentially, it has been checked whether or not the parameters $K^*_{FE} \cong 1.38$ and $K^{**}_{FE} \cong 3.38$, valid for Ansys code, can be adopted also with other FE software. The main results of such calibration exercise are reported in the following. After that some application examples are illustrated.

2 CALIBRATING THE PEAK STRESS METHOD

The PSM has been calibrated by analysing several 2D notch problems under pure mode I as well as crack problems under pure mode II loadings with different commercial software packages. After having calculated the peak stresses, the parameters K^*_{FE} and K^{**}_{FE} have been evaluated from Eqs. (3) and (4), re-arranged as follows:

$$K^*_{FE} \cong \frac{K_1}{\sigma_{I,peak} \cdot d^{1-\lambda_1}} \quad (5)$$

$$K^{**}_{FE} \cong \frac{K_2}{\tau_{II,peak} \cdot d^{0.5}} \quad (6)$$

The calibration of the PSM for each FE code has been carried out by fixing the following stress analysis conditions: (i) element type and element formulation, (ii) mesh pattern of the finite elements and (iii) procedures for stress extrapolation and principal stress calculation at FE nodes.

The Round Robin involved ten Universities and all in all seven commercial FE codes have been calibrated, as reported in detail in Table 1.

The different FE codes have been adopted to analyse several 2D notched and crack problems under mode I or mode II loading conditions. Geometries, material properties, boundary conditions and FE type were obviously the same in all adopted FE codes. In more detail, the considered material was a structural steel, having Young's modulus equal to 206000 MPa and a Poisson's ratio of 0.3. On the other hand, whenever possible, specific options relevant to the element formulation, free mesh generation algorithms, stress extrapolation and stress averaging criteria at FE nodes have been set to *default options* in each code. For details about the settings adopted in each software package, the reader is referred to (Meneghetti et al. 2017c). Only the key aspects of the analyses performed and the main results are summarized in the following.

Table 1: List of participants and FE codes.

Universities	**FE codes**
• Bologna • Genova • Messina • Modena and Reggio Emilia • Padova • Palermo • Parma • Pisa • Politecnico di Torino • Trento	• Ansys 16 and 17 • Abaqus 6.13 and 6.14 • Hypermesh 14*/Optistruct 14 implicit/Hyperview 14** • Hypermesh 13*/Ls-Dyna R7.1.3 implicit/Hyperview 13** • Lusas 14.6-2 • MSC Patran/Nastran 2014 and 2016 • Straus 7 R.2.4.6

*: pre-processor; **: post-processor

2.1 *2D problems (plane strain), mode I loading, $0° \le 2\alpha \le 135°$*

Several two-dimensional notch and crack problems under pure mode I (Fig. 2) have been analysed. All these case studies are the same adopted in the first calibration of the PSM under mode I loading which has been carried out with Ansys numerical software (Meneghetti & Lazzarin 2007).

Linear elastic analyses under plane strain conditions have been performed by adopting a pattern of four-node linear quadrilateral elements, in order to calculate the peak stress values (Meneghetti et al. 2017c). Only a quarter of each geometry has been modeled by using the double symmetry condition. The free mesh generation algorithm available in each code has been used after having input the average element size *d*. The mesh density ratio *a/d* has been varied between 1 and 50, by varying either the notch depth *a* or the element size *d*. Moreover, three values of the notch opening angle, i.e. 2α=0°, 90°, 135° have been considered. A nominal gross-section stress equal to 1 MPa has been applied to each FE model.

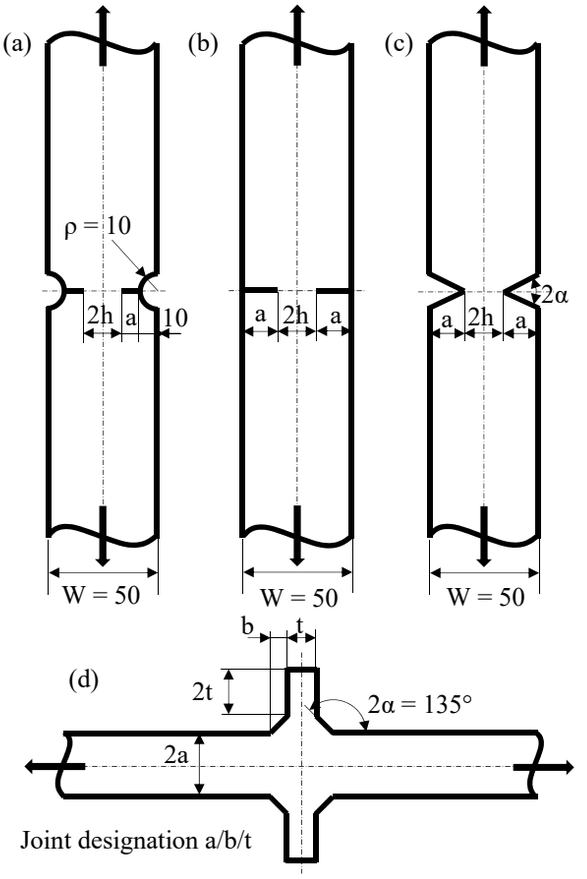


Figure 2: Geometries of 2D problems (plane strain) under mode I loading. Dimensions in [mm].

After having solved the FE model, the peak value of the maximum principal stress $\sigma_{I,peak}$ has been calculated at the FE node located at the V-notch tip. It is worth noting that stress averaging at FE nodes has been activated in all adopted FE codes. Accordingly, only a single stress value for $\sigma_{I,peak}$ has been obtained per node by averaging the nodal stresses from all elements sharing the node. To this aim, as far as possible, the default options of each FE code have been adopted (Meneghetti et al. 2017c).

2.2 *2D problems (plane strain), mode II loading, $2\alpha = 0°$*

A plate having the geometry shown in Fig. 3, weakened by a central crack (2α = 0°) and subjected to pure mode II loading has been analysed. The case study has been taken from the first calibration of the PSM under mode II loading carried out by using Ansys numerical software (Meneghetti 2012).

Linear elastic analyses under plane strain conditions have been carried out by adopting a pattern of four-node linear quadrilateral elements, in order to calculate the peak stress values. The mesh density ratio *a/d* has been varied in a wide range from 1 to 200, being $2<2a<200$ mm. Only a quarter of the plate geometry has been modeled by using the double anti-symmetry boundary conditions.

The external load has been applied to the model by means of displacements $u_x=u_y=1.262\cdot10^{-3}$ mm at

the plate free edges, which correspond to a nominal gross shear stress of 1 MPa when no crack is present. After having solved the numerical model, the peak value of the (mode II) shear stress $\tau_{xy,peak} = \tau_{II,peak}$ has been calculated at the node located at the crack tip. It is worth noting that stress averaging at FE nodes has been activated in all adopted FE codes, similarly to mode I analyses. For additional details about the numerical analyses the reader is referred to (Meneghetti et al. 2017c).

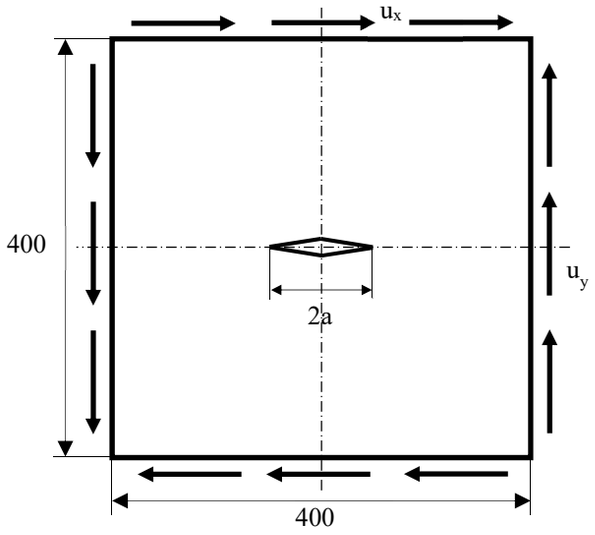


Figure 3: Geometry of 2D problems (plane strain) under mode II loading. Dimensions in [mm].

Finally, the exact values of the mode I NSIF K_1 and mode II SIF K_2 to be input in Eq. (5) and (6), respectively, have been calculated by applying definitions (1) and (2) to the stress-distance numerical results obtained by using Ansys FE code and adopting very refined FE meshes (the size of the smallest element being on the order of 10^{-5} mm).

As mentioned above, two-dimensional, four-node, linear quadrilateral elements have been used in all FE analyses. The numerical integration has been carried out by adopting 2x2 Gauss points. Once selected the proper element type and formulation, the FE analyst has input the average FE size *d*, which has been the sole parameter used to drive the automatic free mesh generation algorithm. Details concerning element type/options along with the adopted mesh generation settings have been reported for each FE code in (Meneghetti et al. 2017c).

3 RESULTS OF FE ANALYSES

The results obtained from the calibration of different FE codes and relevant to mode I and mode II problems are shown in Figs. 4a and b, respectively. The figures report the parameters K^*_{FE} and K^{**}_{FE}, calculated from Eqs. (5) and (6), respectively, as functions of the mesh density ratio *a/d*. All results reported in Figs. 4a and b were obtained by adopting the *default options* of the post-processing environment of each FE code (see details in (Meneghetti et al. 2017c)).

In the case of 2D problems under mode I loading, Fig. 4a shows that most of the adopted FE codes, i.e. Abaqus, Straus 7, MSC Patran/Nastran and Lusas, present the same constant $K^*_{FE} \cong 1.38$ that had been previously calibrated with Ansys (Meneghetti & Lazzarin 2007). Convergence is obtained when $a/d \geq 3$ for all FE codes. A slightly larger scatter band of ±5% should be accepted, as compared to that of ±3% found for Ansys (Meneghetti & Lazzarin 2007). Moreover, it can be observed from Fig. 4a that the calibration of the FE packages Hypermesh/Optistruct /Hyperview and Hypermesh/Ls-Dyna/Hyperview results in a different value of the parameter K^*_{FE}, i.e. 1.84. This peculiar behaviour depends on stress extrapolation rules at FE nodes as extensively discussed in (Meneghetti et al. 2017c). Moreover, the scatter ±8% is higher as compared to ±5% obtained with the other FE codes.

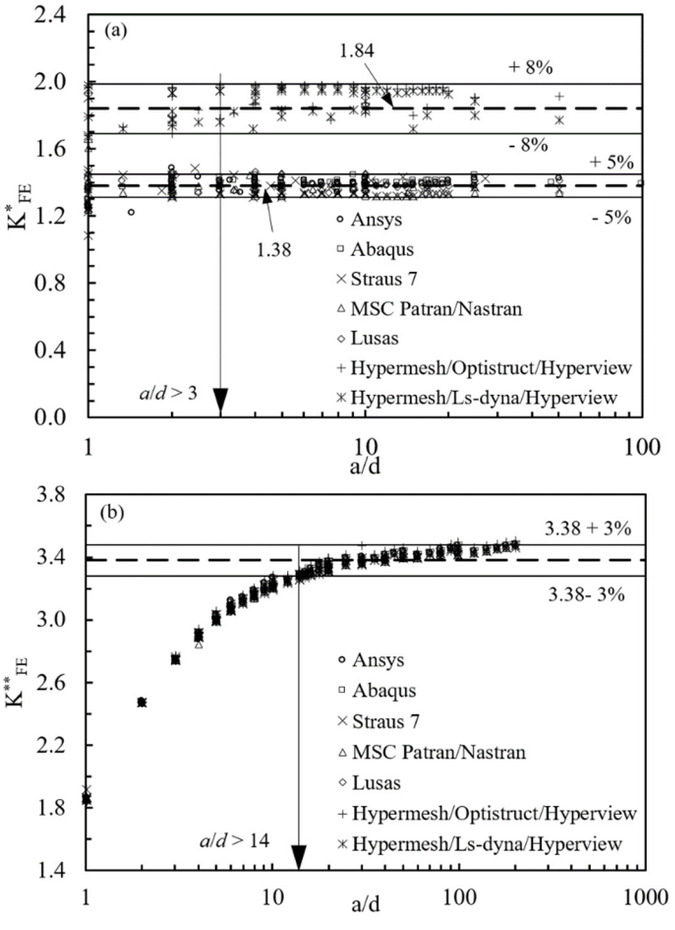


Figure 4: Results for (a) mode I and (b) mode II loading: K^*_{FE} and K^{**}_{FE}, respectively, for each FE code.

Dealing then with mode II loading, the obtained results are reported in Fig. 4b, which shows that all considered FE codes converge to $K^{**}_{FE} \cong 3.38 \pm 3\%$, i.e. the values obtained previously with Ansys FE code (Meneghetti 2012). Convergence is obtained when the ratio $a/d \geq 14$, which is again consistent with the first calibration (Meneghetti 2012).

4 FATIGUE STRENGTH ASSESSMENTS ACCORDING TO THE PEAK STRESS METHOD

To illustrate the PSM in practical design situations, the fatigue strength assessment of conventional arc-welded joints made of aluminum alloys and structural steels is reported below.

The strain energy density (SED) averaged over a structural volume of radius R_0 surrounding the weld root or the weld toe (see the example in Fig. 5) was adopted as fatigue damage parameter, as proposed by Lazzarin and co-workers (Lazzarin & Zambardi 2001; Livieri & Lazzarin 2005). The averaged SED under mode I+II loading can be expressed in closed-form as a function of the relevant NSIFs according to Eq. (7).

$$\Delta\overline{W}=c_w\left[\frac{e_1}{E}\left(\frac{\Delta K_1}{R_0^{1-\lambda_1}}\right)^2+\frac{e_2}{E}\left(\frac{\Delta K_2}{R_0^{1-\lambda_2}}\right)^2\right] \quad (7)$$

where R_0 represents the control radius, ΔK_1 and ΔK_2 are the ranges of the NSIFs relevant to mode I and mode II, respectively, E is the Young's modulus, while e_1 and e_2 are known parameters depending on the notch opening angle 2α and the Poisson's ratio ν (Lazzarin & Zambardi 2001). The size of the structural volume R_0 was calibrated on experimental fatigue test data and resulted equal to 0.28 mm and 0.12 mm for welded joints made of structural steel and aluminum alloys (Livieri & Lazzarin 2005), respectively. Finally, the coefficient c_w depends on the nominal load ratio R (Lazzarin et al. 2004): it equals 0.5 for R = −1 and 1 for R = 0. It should be noted that welded joints loaded in the as-welded conditions are almost not sensitive to mean stresses, according to design standards (Eurocode 3), therefore Eq. (7) with c_w =1 should be applied.

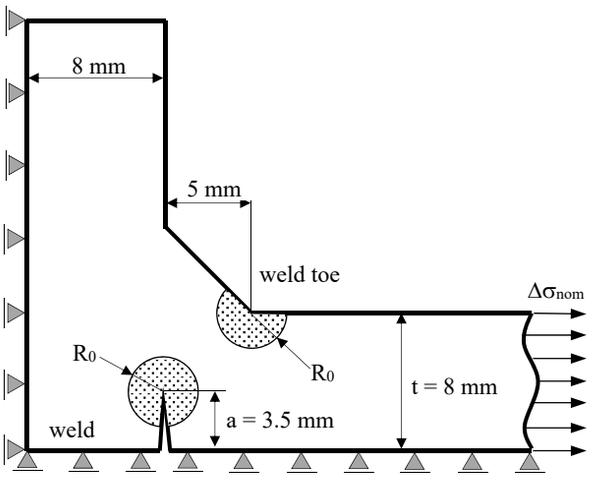


Figure 5: Geometry of the load-carrying steel weld joint tested in (Ouchida & Nishioka 1964). Control volumes for the averaged SED evaluation at the weld toe and the weld root sides.

Taking advantage of the equality $W=(1-\nu^2)\cdot\sigma^2_{eq,peak}/2E$ valid under plane strain conditions, an equivalent peak stress, $\sigma_{eq,peak}$, can be derived as follow (Meneghetti 2012):

$$\Delta\sigma_{eq,peak}=\sqrt{\frac{2\cdot c_w}{1-\nu^2}\cdot\left[e_1\left(\frac{\Delta K_1}{R_0^{1-\lambda_1}}\right)^2+e_2\left(\frac{\Delta K_2}{R_0^{1-\lambda_2}}\right)^2\right]} \quad (8)$$

If ΔK_1 and ΔK_2 are evaluated directly at the weld toe and at the weld root by means of definitions, Eqs. (1) and (2), the mesh density must be very refined with a minimum element size on the order of 10^{-5} mm as shown in (Meneghetti et al. 2017c).

By using the PSM-based relationships (Eqs. (3) and (4)), Eq. (8) can be rewritten as a function of the singular, linear elastic FE peak stresses $\sigma_{I,peak}$ and $\tau_{II,peak}$ (Meneghetti & Lazzarin 2011):

$$\Delta\sigma_{eq,peak}=\sqrt{c_w}\cdot\sqrt{f_{w1}^2\cdot\Delta\sigma_{I,peak}^2+f_{w2}^2\cdot\Delta\tau_{II,peak}^2} \quad (9a)$$

$$f_{wi}=K_{FE}\cdot\sqrt{\frac{2e_i}{1-\nu^2}}\cdot\left(\frac{d}{R_0}\right)^{1-\lambda_i} \quad \text{where} \quad i=1,2 \quad (9b)$$

Equation (9) can be applied to the fatigue strength assessment of conventional arc-welded joints made of structural steels and aluminum alloys. In the following, some applications of the PSM are reported, which are relevant to:

1. 25-mm-thick partial-penetration butt welded joints made of aluminum alloys (see Fig. 6), which were fatigue tested by Sonsino et al. (Brandt et al. 1999; Sonsino et al. 1999) in the stress-relieved conditions under axial loading with nominal load ratios R=0 and -1;
2. load-carrying cruciform welded steel joints (see the geometry in Fig. 7), which were fatigue tested by Ouchida and Nishioka (1964) in the as-welded conditions under axial loading with a nominal load ratio R = 0;
3. tube-to-flange welded joints with 3.2-mm-thick tube made of structural steel (see Fig. 8), which were fatigue tested in (Razmjoo 1996) in the as-welded conditions under axial loading with a nominal load ratio R = 0.

The detailed analyses according to the PSM are reported in (Meneghetti et al. 2015; Meneghetti & Lazzarin 2011; Meneghetti et al. 2017b), to which the reader is referred. Only the main steps of the analysis are reported here. Ansys FE code has been adopted, however, according to the calibration described above, the same results could be obtained by adopting FE codes other than Ansys, provided that the proper calibrated constants K^*_{FE} and K^{**}_{FE}, as reported in Fig. 4, were used in Eq. (9). The peak stresses were calculated by using the FE meshes reported in Figs. 6a, 7a and 8a, respectively, according to the following steps:

- A 2D FE analysis was performed by adopting 4 node quadrilateral elements (PLANE 182 of Ansys element library, with K-option 1 set to

3, i.e. '*simple enhanced strain*' formulation activated);

- Plane strain conditions were adopted for both butt and cruciform joints (cases 1 and 2, see Fig. 6 and 7), while axisymmetric conditions were applied for the tube-to-flange joint (case 3, Fig. 8).
- The mesh density ratio a/d was established as follows:
  1. Fig. 6a: a is the pre-crack length at the root side, so that the maximum FE size d is equal to $a/3 = 3.75/3 \rightarrow \approx 1.25$ mm is appropriate to apply Eq. (9); at the toe side, a is half the plate thickness, i.e. $a = 12.5$ mm, therefore the maximum FE size is $12.5/3 \approx 4$. In conclusion d = 1.25 mm is appropriate both at the root and at the toe side;
  2. Fig. 7a: a is the pre-crack length at the root side, so that the maximum FE size d is equal to $a/3 = 3.5/3 \rightarrow \approx 1$ mm is appropriate to apply Eq. (9); at the toe side, a is half the main plate thickness, i.e. $a = 8$ mm, therefore the maximum FE size is $8/3 = 2.66$. In conclusion d = 1 mm is appropriate both at the root and at the toe side;
  3. Fig. 8a: a is the tube thickness, i.e. $a = 3.2$ mm, therefore the maximum FE size is $a/3 = 3.2/3 \approx 1.0$ mm. Finally, d = 0.8 mm has been adopted to apply Eq. (9) at the toe side;
- The *free-mesh* patterns, see Figs. 6a, 7a and 8a, were generated by setting a 'global element size' parameter d = 1.25, 1 and 0.8 mm, respectively, in the free mesh generation algorithm;
- The maximum principal stress $\Delta\sigma_{I,peak}$ was evaluated at the FE nodes located at the weld toe and root, mode II being not singular at weld toe and negligible at weld root in all cases;
- Figures 6b, 7b and 8b show the results according to the PSM:
  1. the weld root is more critical than the weld toe, since $\Delta\sigma_{eq,peak}$ is higher at the root (5.28 MPa) than at the toe (2.87 MPa). This is in agreement with the fatigue crack initiation point experimentally observed by (Brandt et al. 1999; Sonsino et al. 1999).
  2. the weld root is more critical than the weld toe, since $\Delta\sigma_{eq,peak}$ is higher at the root (3.07 MPa) than at the toe (2.54 MPa). This is in agreement with the fatigue crack initiation point experimentally observed by Ouchida and Nishioka (1964).
  3. the weld toe is the only critical point of the joint ($\Delta\sigma_{eq,peak}$=2.25 MPa) since stresses are not singular at the weld root. This is in agreement with the fatigue crack initiation point experimentally observed in (Razmjoo 1996).

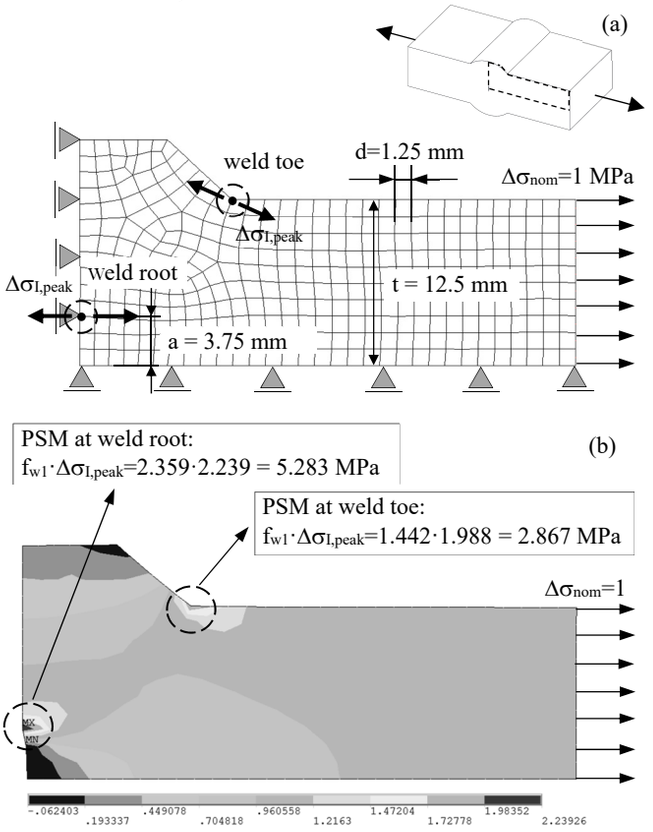


Figure 6: Application of the PSM to the fatigue strength assessment of a partial-penetration butt welded joints made of aluminum alloys (Brandt et al. 1999; Sonsino et al. 1999).

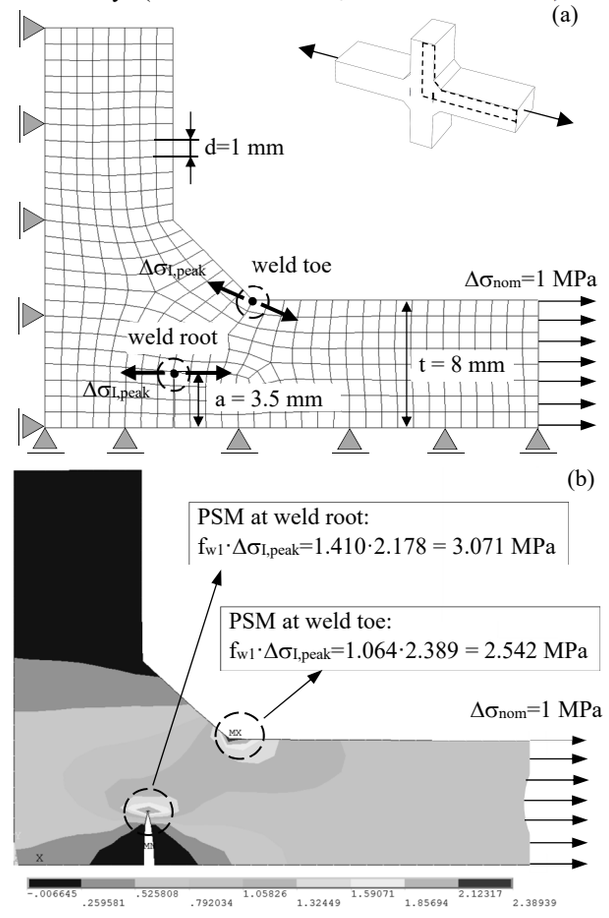


Figure 7: Application of the PSM to the fatigue strength assessment of a load-carrying arc-welded joint made of structural steel and tested in (Ouchida & Nishioka 1964).

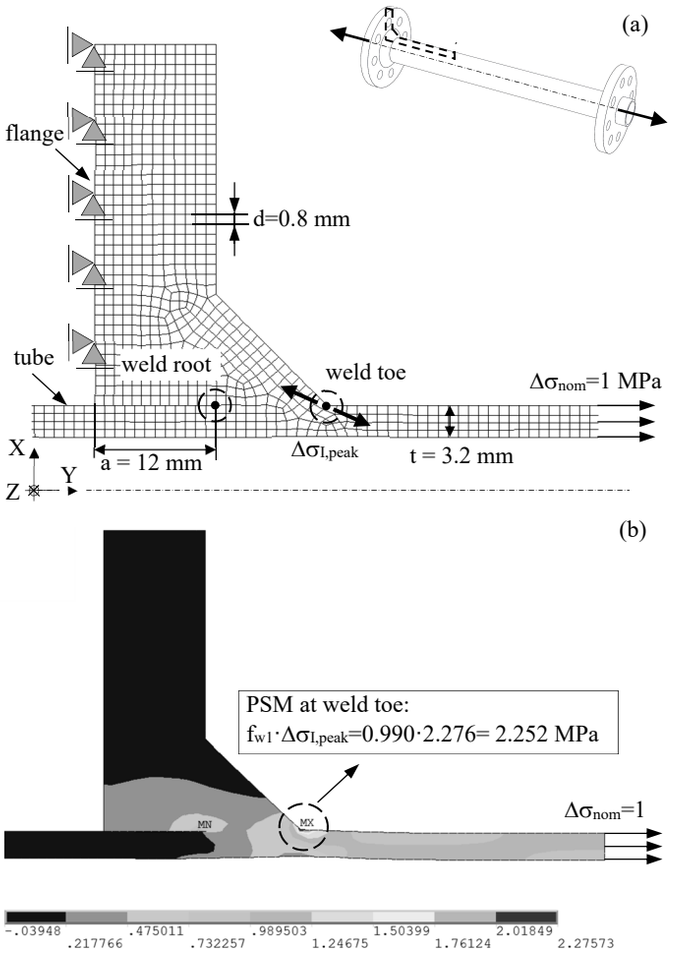
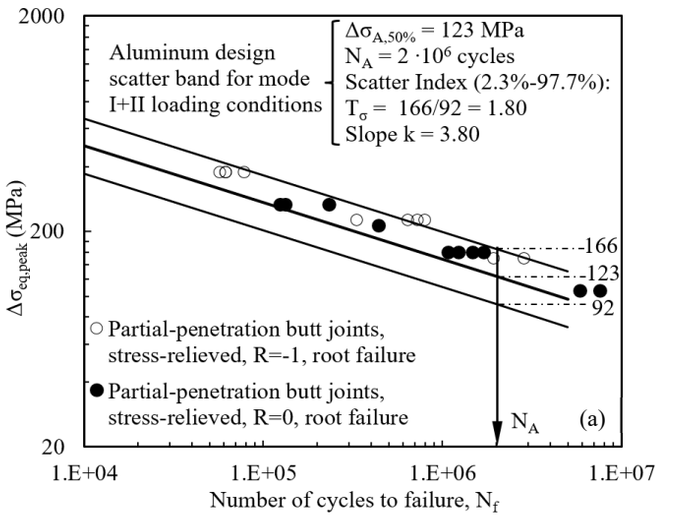


Figure 8: Application of the PSM to the fatigue strength assessment of a tube-to-flange welded joint made of structural steel and tested in (Razmjoo 1996).

Subsequently, the original experimental data have been reconverted in terms of equivalent peak stress evaluated by means of Eq. (9) at the experimental fatigue crack initiation point, i.e. weld root for cases 1 and 2 (Figs. 6 and 7) and the weld toe for case 3 (Fig. 8). Finally, Figures 9a and b show the comparison between the experimental results and the fatigue design scatter bands previously calibrated in (Meneghetti et al. 2015) and in (Meneghetti & Lazzarin 2011) for welded joints made of aluminum alloys and structural steels, respectively.



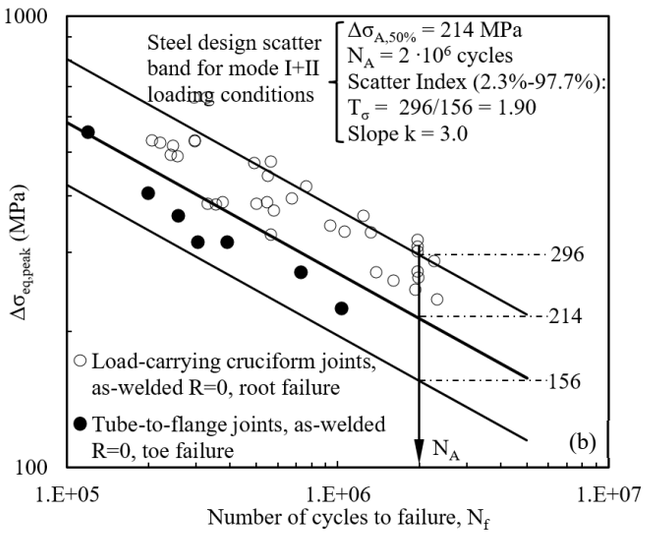


Figure 9: Comparison between the experimental fatigue results and the fatigue design scatter bands of the PSM valid for welded joints made of (a) aluminum alloys and (b) structural steels.

5 CONCLUSIONS

The peak stress method (PSM) employs the singular, linear elastic peak stresses evaluated at the toe and root sides by means of FE analyses with coarse meshes to rapidly estimate the mode I and mode II NSIFs. Two calibration constants are needed, namely K^*_{FE} (Eq. (3)) and K^{**}_{FE} (Eq. (4)), respectively.

Originally, the PSM has been calibrated by using the Ansys FE code. Recently, a Round Robin has been carried out in order to calibrate the PSM by using also commercial FE codes different from Ansys.

By using the PSM in combination with the averaged Strain Energy Density (SED) as a fatigue strength criterion, a so-called equivalent peak stress (Eq. (9)) can be defined to assess either weld toe or weld root fatigue failures in conjunction with a properly calibrated design curve.

The following conclusions can be drawn from the present study:

- Based on the calibration of the PSM with different commercial FE codes, it has been shown that under mode I loading the constant K^*_{FE} to be used either in Eq. (3) or (9) is the same for Ansys, Abaqus, Straus 7, MSC Patran/Nastran and Lusas FE codes, i.e. $K^*_{FE} \cong 1.38$; while it assumes a different value for Optistruct and Ls-Dyna FE codes, i.e. $K^*_{FE} \cong 1.84$. The convergence is guaranteed when the mesh density ratio $a/d \geq 3$ for all FE codes.
- Dealing with mode II loading, it has been shown that the constant K^{**}_{FE} to be used either in Eq. (4) or (9) is the same for all FE codes involved in the calibration, i.e. $K^{**}_{FE} \cong 3.38$. The convergence occurs for a mesh density ratio $a/d \geq 14$ for all FE codes.
- Finally, the PSM has been applied in practical design situations by adopting the equivalent

peak stress to assess weld toe as well as weld root fatigue failures in some examples of welded joints made of aluminum alloys and structural steels tested under axial fatigue loadings. Comparison between experimental fatigue results and the relevant design scatter bands was satisfactory. Because of the simplicity of a point-like method combined with the robustness of the NSIF approach, the PSM might be useful to design engineers engaged in fatigue assessments of welded joints.

REFERENCES

Atzori, B. & Meneghetti, G., 2001. Fatigue strength of fillet welded structural steels: finite elements, strain gauges and reality. *International Journal of Fatigue*, 23(8), pp.713–721.

Boukharouba, T. et al., 1995. The use of notch stress intensity factor as a fatigue crack initiation parameter. *Engineering Fracture Mechanics*, 52(3), pp.503–512.

Brandt, U. et al., 1999. *Anwendung des Kergrundkonzeptes für die schwingfeste Bemessung von Schweissverbindungen aus Aluminiumknetlegierungen*, Darmstadt.

Eurocode 3: Design of steel structures – part 1–9: Fatigue, CEN.

Gross, B. & Mendelson, A., 1972. Plane elastostatic analysis of V-notched plates. *International Journal of Fracture Mechanics*, 8(3), pp.267–276.

Kihara, S. & Yoshii, A., 1991. A Strength Evaluation Method of a Sharply Notched Structure by a New Parameter, "The Equivalent Stress Intensity Factor." *JSME international journal. Ser. 1, Solid mechanics, strength of materials*, 34(1), pp.70–75.

Lazzarin, P. & Tovo, R., 1998. A notch intensity factor approach to the stress analysis of welds. *Fatigue & Fracture of Engineering Materials & Structures*, 21(9), pp.1089–1103.

Lazzarin, P. & Livieri, P., 2001. Notch stress intensity factors and fatigue strength of aluminium and steel welded joints. *International Journal of Fatigue*, 23(3), pp.225–232.

Lazzarin, P. & Zambardi, R., 2001. A finite-volume-energy based approach to predict the static and fatigue behavior of components with sharp V-shaped notches. *International Journal of Fracture*, 112, pp.275–298.

Lazzarin, P., Sonsino, C.M. & Zambardi, R., 2004. A notch stress intensity approach to assess the multiaxial fatigue strength of welded tube-to-flange joints subjected to combined loadings. *Fatigue & Fracture of Engineering Materials & Structures*, 27(2), pp.127–140.

Livieri, P. & Lazzarin, P., 2005. Fatigue strength of steel and aluminium welded joints based on generalised stress intensity factors and local strain energy values. *International Journal of Fracture*, 133(3), pp.247–276.

Meneghetti, G. & Lazzarin, P., 2007. Significance of the elastic peak stress evaluated by FE analyses at the point of singularity of sharp V-notched components. *Fatigue & Fracture of Engineering Materials and Structures*, 30(2), pp.95–106.

Meneghetti, G. & Lazzarin, P., 2011. The Peak Stress Method for Fatigue Strength Assessment of welded joints with weld toe or weld root failures. *Welding in the World*, 55(7–8), pp.22–29.

Meneghetti, G., 2012. The use of peak stresses for fatigue strength assessments of welded lap joints and cover plates with toe and root failures. *Engineering Fracture Mechanics*, 89, pp.40–51.

Meneghetti, G., 2013. The peak stress method for fatigue strength assessment of tube-to-flange welded joints under torsion loading. *Welding in the World*, 57(2), pp.265–275.

Meneghetti, G. & Guzzella, C., 2014. The peak stress method to estimate the mode I notch stress intensity factor in welded joints using three-dimensional finite element models. *Engineering Fracture Mechanics*, 115, pp.154–171.

Meneghetti, G., Campagnolo, A. & Berto, F., 2015. Fatigue strength assessment of partial and full-penetration steel and aluminium butt-welded joints according to the peak stress method. *Fatigue & Fracture of Engineering Materials & Structures*, 38(12), pp.1419–1431.

Meneghetti, G., Campagnolo, A. & Rigon, D., 2017a. Multiaxial fatigue strength assessment of welded joints using the Peak Stress Method – Part I: Approach and application to aluminium joints. *International Journal of Fatigue*, 101, pp.328–342.

Meneghetti, G., Campagnolo, A. & Rigon, D., 2017b. Multiaxial fatigue strength assessment of welded joints using the Peak Stress Method – Part II: Application to structural steel joints. *International Journal of Fatigue*, 101, pp.343–362.

Meneghetti, G. et al., 2017c. Rapid evaluation of notch stress intensity factors using the peak stress method: comparison of commercial finite element codes for a range of mesh patterns. *Fatigue & Fracture of Engineering Materials & Structures*, in press. DOI: 10.1111/ffe.12751

Nisitani, H. & Teranishi, T., 2004. K_I of a circumferential crack emanating from an ellipsoidal cavity obtained by the crack tip stress method in FEM. *Engineering Fracture Mechanics*, 71(4–6), pp.579–585.

Nisitani, H. & Teranishi, T., 2001. K_I value of a circumferential crack emanating from an ellipsoidal cavity obtained by the crack tip stress method in FEM. In M. Guagliano & M. H. Aliabadi, eds. *Proceedings of the 2nd international conference on fracture and damage mechanics*. pp. 141–146.

Ouchida, H. & Nishioka, A., 1964. A study of fatigue strength of fillet welded joints. In *IIW Doc. XIII-338-64*.

Razmjoo, G., 1996. Fatigue of Load-Carrying Fillet Welded Joints Under Multiaxial Loadings. In Abington, ed. *TWI REF. 7309.02/96/909*. Cambridge, UK.

Sonsino, C.M. et al., 1999. Fatigue assessment of welded joints in AlMg 4.5Mn aluminum alloy (AA 5083) by local approaches. *International Journal of Fatigue*, 21(9), pp.985–999.

Verreman, Y. & Nie, B., 1996. Early development of fatigue cracking at manual fillet welds. *Fatigue & Fracture of Engineering Materials and Structures*, 19(6), pp.669–681.

Williams, M.L., 1952. Stress singularities resulting from various boundary conditions in angular corners of plates in tension. *J Appl Mech*, 19, pp.526–528.

Maintenance, Safety, Risk, Management and Life-Cycle Performance of Bridges – Powers, Frangopol, Al-Mahaidi & Caprani (Eds)
© 2018 Taylor & Francis Group, London, ISBN 978-1-138-73045-8

Prolonging the service life of steel truss bridges

A.Pipinato, R. Pavan
AP&P srl, Italy
P. Collin, R. Hallmark
Lulea University of Technology, Sweden
S. Ivanov, R. Geier
Schimetta Consult, Austria
M. van der Burg
Movares, The Netherlands

ABSTRACT: Prolonging the life of existing steel trusses all over the world is a incoming necessity for all managing authorities wherever these structures have reached a particular state of use. The unsatisfactory behavior of these structures under the current type and increasing number of loads make clearer that innovative solutions are needed. For this purpose, the realization of different techniques are presented, in order to retrofit the actual load onto a structure conceived with historical codes, characterized by lower design live loads. The possibilities of retrofitting bridges with different solution studied in a recent research program are presented and compared in this study.

1 INTRODUCTION

Increasing traffic density and vehicle weight have been increasing in recent decades. Many existing truss bridges, all over the world, were not designed for the high service loads and the increased number of load cycles that they are exposed to today. Some bridges will have to be either strengthened or replaced in the next decades. As late as the 1980s, steel truss bridges in Europe were often constructed with a non-composite concrete slab on top of steel girders. Different alternatives of interventions for truss bridges are presented in this paper, according to the different truss type to be reinforced. Sometimes the bridge should be retrofitted by deck replacing, other times a new structural configuration should be adopted, or in some cases only little interventions are needed in order to strengthen a truss. This paper presents a brief overview of different alternatives to strengthen existing trusses, ever considering the optimization of costs and material savings.

2 STRENGHTENING SOLUTIONS

2.1 Upgrading the load carrying capacity of a cultural heritage arched-truss bridge by deck replacing

The utilization of the railway capacity in the center of Stockholm has been high for a long time, resulting in delays and congestions. The Old Årsta Bridge is a part of the railway directly south of the new Stockholm City Line, and will mainly carry increasing number of trains in the future. The bridge was opened in year 1929 and has two tracks.



Figure 1. Lowering of the old Ărsta midspan section.

In 2005 the capacity was doubled in this section, when the parallel New Årsta Bridge was finished. To secure the future traffic the old bridge has been rehabilitated in several stages. In this section the latest upgrading of the main span of the bridge are presented. The Old Årsta Bridge is 753 m long and was built in 1923-1929. The bridge is a "*listed construction*", which means a legal cultural and historical protection of a structure in Sweden. This means, for example, that rehabilitations work has to be done without affecting the original appearance of the bridge. The majority of the length is spanned by twenty concrete arches, meanwhile a movable bridge respectively a steel truss arch is used over the two waterways, see Figure 2. During the last decade, the movable span has been replaced by a non-movable simply supported steel span, while the concrete arches and the concrete foundations for the steel truss arch have been strengthened. The 151 m long main span was designed as a through arch bridge, with two tracks with rails

lying on wooden sleepers directly in contact with the steel deck. The open steel deck consisted of four rail girders and two edge girders in the longitudinal direction. The latter acted as tied rods in the part of the bridge where the horizontal deck is located below the arch. All connections were riveted and rigid. In the transversal direction there were cross girders at every steel deck support, and horizontal trusses connecting the upper flanges of rail girders to the cross girders.

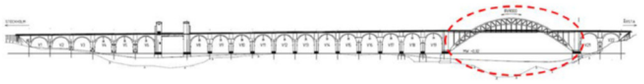
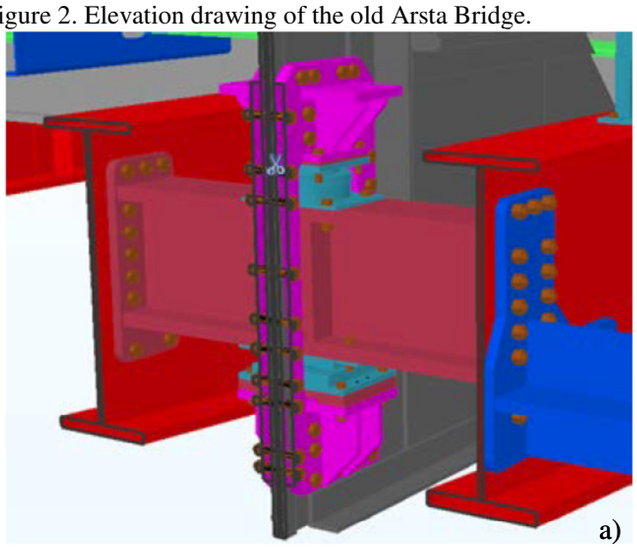
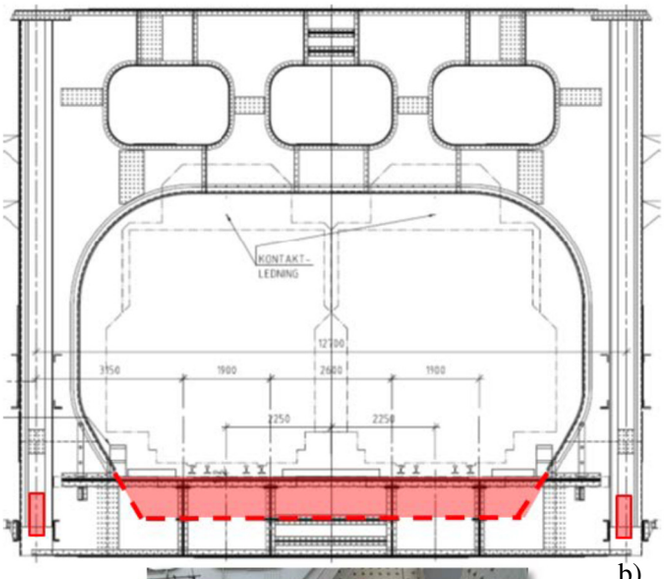


Figure 2. Elevation drawing of the old Arsta Bridge.





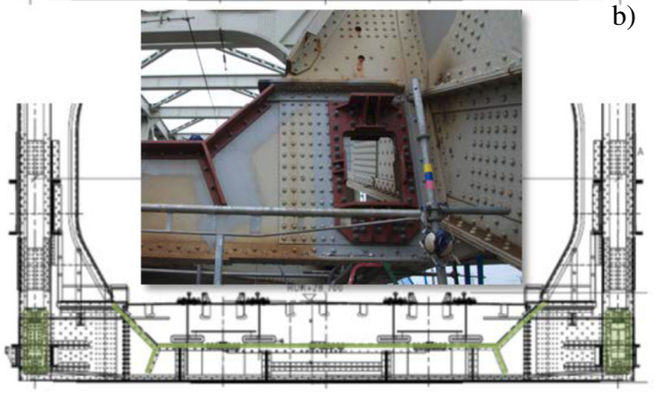


Figure 3. Connection beam at a portal frame (a), modifications of the existing portal frames (b).

With respect to fatigue, the steel arch is in good condition. The rail girders and the cross girders are structural parts with shorter determinant lengths compared to the arch. These parts were in focus in a study performed in year 2006-2008 (James and Paulsson 2008), in which the fracture toughness and the chemical composition were tested. The test results indicated poor fracture toughness, and a risk of brittle failure in both rail girders and cross girders. The tests were also combined with a fatigue assessment calculation, based on measured strains. This calculation showed, depending on the degree of corrosion and choice of detail category, a remaining fatigue life of 0 – 50 years. Based on the study presented in the former section, a decision was taken to replace the steel grillage deck and to leave the rest of the structure as intact as possible. The fatigue requirement on the total structure was an extended lifetime of 60 years, and the new parts were designed for 120 years. The bridge was also designed for an increased maximum axle load, from 25 t to 30 t. Three different rehabilitation alternatives were proposed by the bridge designers that were doing the pre-design (Lundmark and Nilsson 2013). At an early stage, before the detailed design was started, the complete structure was laser-scanned in order to get a digital 3D-modell of the existing bridge. The model, consisting of a point-cloud, was later used as a digital reference when the new bridge deck was modelled in a 3D-software. By using laser-scanning, together with surveying of critical detail in the existing structure, it was possible to use demanding tolerances throughout the structure and to avoid deck sections acting as fitting pieces that had to be cut on site. The deck sections were installed from above, before the bottom plates of the cross girders were welded on-site. In the 3D-model, the free space between new and old parts was about 3 cm in the most critical points. The new bridge deck was designed as a full width steel deck, without any gratings, that can carry the horizontal forces between the end-supports and the intersections with the arch, without horizontal trusses. In order to avoid welding on site, the connections between different deck elements and other steel parts were all bolted. The connections to the existing steel had to be bolted connections as well, since the old steel is not weldable. The national bridge code (TRVK 2011) requires fit bolts in bolted connections in a rail bridge main structure, which makes the drilling and reaming of the holes time consuming. The fatigue assessment indicated that the connection between the arch and the columns, as well as the hangers, would be critical if the connection remained rigid. To avoid strengthening of these details, due to the stresses caused by bending moments, the formerly stiff connections were replaced with joints (bearings) that mainly transfer normal forces. The new midspan deck section has a length of 60 m and a weight of 350 t. Unlike the other deck sections, the large midspan section was transported by barges on the water, lifted and built (Lundmark et al. 2016).

2.2 *Strengthening old truss railway bridges with a new HPC deck*

The chosen sample bridge is a steel truss railway bridge designed in 1896 situated in the town of Vienna over the river Wien (Figure 4). It is 120 years old and it is still in operation. Originally designed for railway traffic, but at the moment the bridge is operated by town's metro line No. 4. The superstructure is twin steel truss beams simply sup- ported with a span of 50,92m. The alignment on the bridges is partially in transition curve and partially in straight line. The maximum design speed, governed by the small radius of the horizontal curve R=160m is 40km/h. Typical bridge cross section is shown in Figure 5.

Three-dimensional finite element model of the existing bridge was created in order to investigate the utilization level of the bridge elements (Figure 6). The geometry of the bridge and the cross sections are modelled according to the original design drawings.



Figure 4. Hütteldorf bridge.

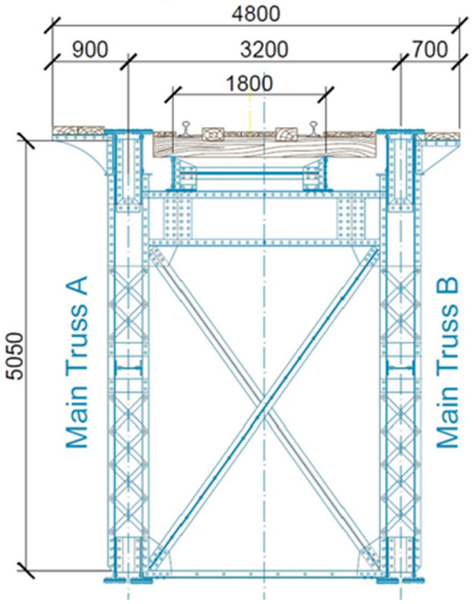


Figure 5. Cross section of the bridge.

The material properties are designed according to Annex B of (ONR 24008 2006), where for bridges built before 1900 the following values are recommended – Es=200000MPa, G=77000MPa, fyk=220MPa and fuk=320MPa. In order to take into account all eccentricities, coming from different levels of the deck elements and local effect of the traffic loads the open deck is modelled with "shell" elements, whereas the main trusses are modelled with "beam" elements. All truss nodes are modelled as stiff. Evaluation of the load bearing capacity of existing railway and highway bridges in Austria is made according to ONR 24008 (2006), where four levels are prescribed. The first level is recalculating the structure according to the recent valid standards. This level was used in this case, where the Eurocode loads and procedures are used for the evaluation. The load model LM71 is reduced with α-factors, according to ÖNORM B 1991-2, for tram and metro loads.



Figure 6. FEM of the steel truss over the Wien river.

Elastic normal stress checks (utilization) of the stringers' top and bottom flanges for different values of α are presented in Figure 7. For open decks of railway bridges the dynamic factor Φ3 is recommended (ÖNORM B 1991-2). The utilization factor exceeds 1 for the top flange, due to local bending generated by transversal loads like centrifugal and nosing force.

Components of the normal stresses in the top flange from different loads are illustrated in Figure 8, wind load is not included.

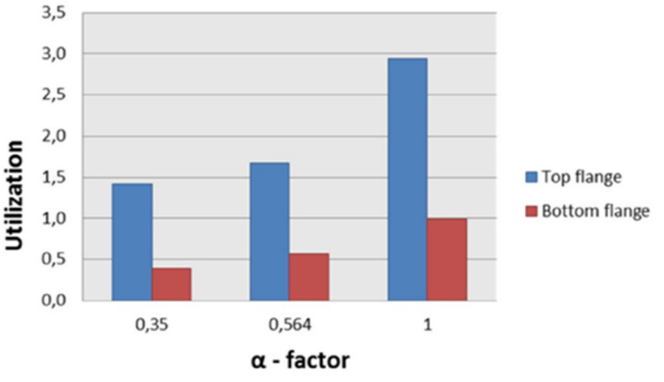


Figure 7. Utilization of top and bottom flange for different α factors.

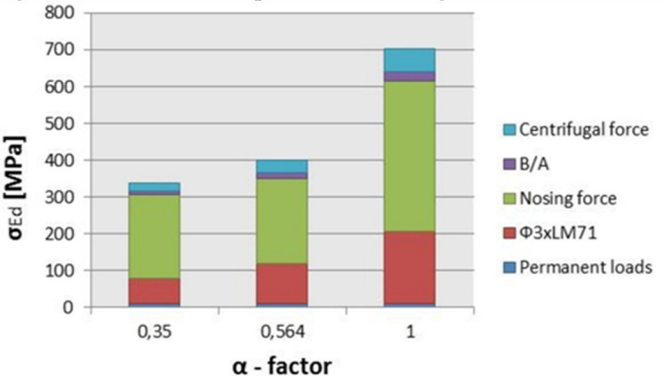


Figure 8. Components of the normal stress in the top flange.

In summary the result from the evaluation showed that the open deck elements (stringers and cross girders) are

exposed to high stress levels. The main reason for their under dimensioning is due to the fact, that in the time of their original design, only vertical loads were considered ignoring secondary bending moments and local eccentricities.

Instead of strengthening these elements, an innovative solution for their replacement by new UHPC deck slab is proposed (Figure 9). This retrofit solution is proven to be effective in "compensating" the additional dead load not only for ULS checks of the main truss element, but also for fatigue behavior and SLS checks. Utilization checks of the truss elements, after linear elastic analysis, for both cases original situation and retrofitted bridge are presented (Figure 10).

In terms of deflections, due to the higher stiffness, the deflection from vertical traffic load is reduced from 66mm to 40mm (with 40%). Both values satisfy the traffic safety criteria of L/600=85mm.

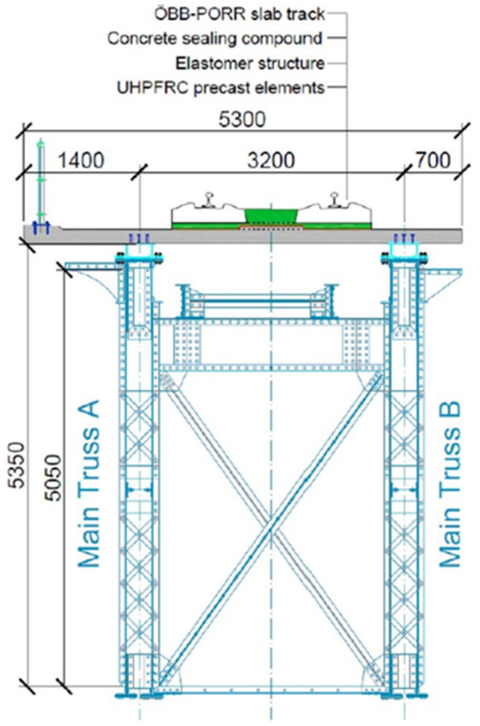


Figure 9. Retrofit alternative chosen: prestressed precast UHP-FRC slab 160mm thick and ballast-less track.

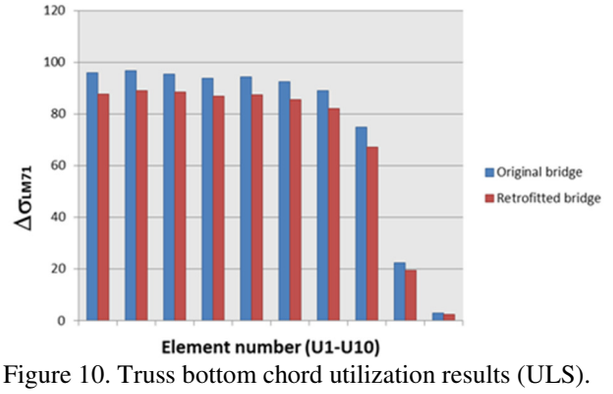


Figure 10. Truss bottom chord utilization results (ULS).

2.3 *Prolonging the fatigue life an old truss railway bridge with innovative direct track deck solution*

The bridge chosen for this case study is the bridge over the river Waal in the Netherlands (Van Der Burg et al. 2017). This bridge is situated in the railway line between Utrecht and 's Hertogenbosch, the main connection for south traffic in the Netherlands.



Figure 11 The bridge over the river Waal.

The east bridge today consists of three main spans (124,3 m each), six single spans (59,6 m) and a double span bridge (2x 60,4 m). The span used as a case study is the third span, which is built in 1932 and is a simply supported truss bridge spanning 59,6 meters. The total height of the truss is 7,5 m. Crossbeams are placed every 4,97 m. Big gusset plates and rivets connect all the elements together. The first FEM model consists of beam elements only, using the original drawings (Figure 12). All beams are modeled with the correct eccentricities, which mainly comes in effect with the wind bracing. These are connected to the flange of the lower and upper cord. From the results it can be concluded that the crossbeams and stringers are governing for the fatigue life of the bridge. This means this case study bridge is a good candidate to have its service life increased by strengthening with deck sections. In order to calibrate the FEM, strain gauges measurements have been performed on top and bottom flanges of cross beam and main girder. The real load of the passing train have been derived from the "*Quo Vadis*" WIM-weight in motion system adopted by the railway authority (Figure 13). When comparing the measurements with the first FEM model, it is noticed that for some strain gauges the results seem to match quite well, while others are far off. Another important observation is that with three stress measurements of one cross-section, the fourth one cannot be calculated by assuming a linear stress distribution. This means that plane sections do not remain plane as assumed in a classic Euler-Bernoulli beam, and no linear stress distribution is present over a cross-section. Consequently, a more refined FEM has been delivered (Fig.14) considering: the transition from beam elements to shell elements, for the first 7,5 meter of the stringers, cross-beams and lower chord; a second refinement is found in the support conditions. From the measurements it was found that when a point load is half-way across the bridge, the end cross-beam still has vertical bending moments. Since the cross-beam itself is not loaded at that time, bending moments arise due to small eccentricities in support conditions. The retrofit solution of the deck implies the adoption of a direct fastened rail incorporating an anti-derailment device instead of an embedded rail (Figure 15). By the adoption of this strengthening option, an interesting improvement on the fatigue life of the

most affected hot-spot fatigue sensitive details of the bridge are achieved (Figure16).

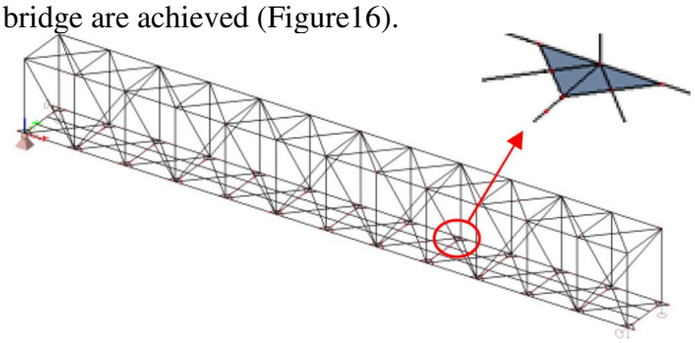


Figure 12 3D view original FEM model, beam elements.

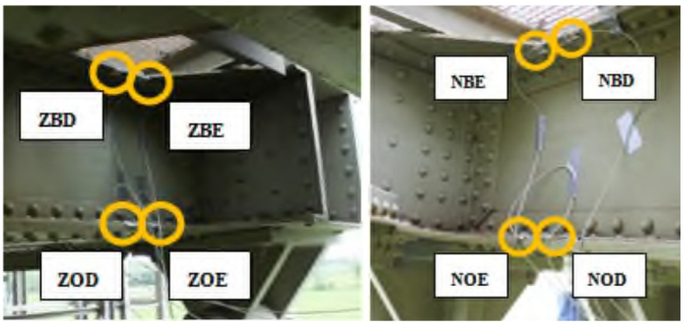


Figure 13 3D Overview of the instrumentation of the bridge.

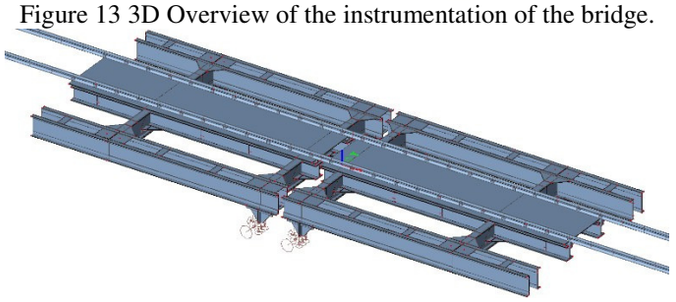


Figure 14 3D Overview of the refined FEM of the retrofitted-bridge.

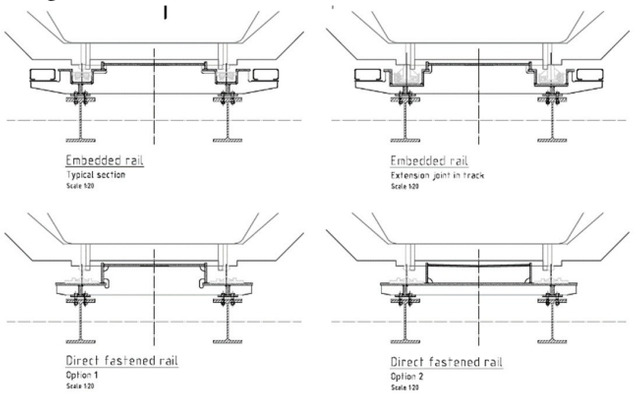


Figure 15 Original rail solution vs. direct fastened rail.

	Current fatigue damage	Yearly damage increase	Remaining fatigue life
5: Crossbeam (end of span)	$D_{2017} = 0.5$	$D_{yearly,original} = 0.00570$	$RFL_{original} = 88$
		$D_{yearly,plastic} = 0.00303$	$RFL_{plastic} = 165$
		$D_{yearly,elastic} = 0.00004$	$RFL_{elastic} = \infty$ Inf
6: Stringer (sagging moment)	$D_{2017} = 0.5$	$D_{yearly,original} = 0.04396$	$RFL_{original} = 11$
		$D_{yearly,plastic} = 0.01176$	$RFL_{plastic} = 43$
		$D_{yearly,elastic} = 0.01133$	$RFL_{elastic} = 44$
7: Stringer (hogging moment)	$D_{2017} = 0.5$	$D_{yearly,original} = 0.03663$	$RFL_{original} = 14$
		$D_{yearly,plastic} = 0.00000$	$RFL_{plastic} = \infty$ Inf
		$D_{yearly,elastic} = 0.00005$	$RFL_{elastic} = \infty$ Inf
8: CB-stringer (rivets in web)	$D_{2017} = 0.5$	$D_{yearly,original} = 0.03591$	$RFL_{original} = 14$
		$D_{yearly,plastic} = 0.00875$	$RFL_{plastic} = 57$
		$D_{yearly,elastic} = 0.00875$	$RFL_{elastic} = 57$

Figure 16 Fatigue analysis of the original deck vs. direct fastened rail.

2.4 Strengthening old truss road bridges with innovative solutions: a parametric analysis

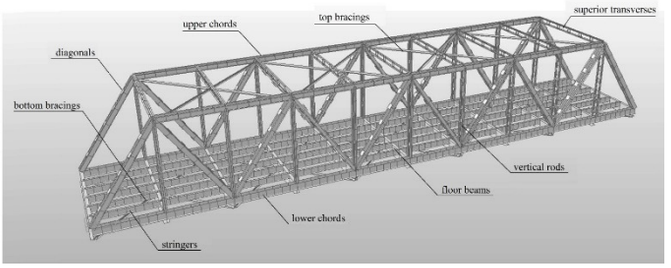


Figure 17 The bridge over the river Adige.

The investigated structure is a two-lane roadway steel bridge truss. The overall bridge length is 120 m through three spans (40 m each one). The superstructure consists of riveted built-up truss members. Lower chords are inverse T-shaped sections, diagonals and upper chords are C-built-up elements with battens (stiffening brackets), while struts are I-section shaped built-up elements composed of four L-shaped elements and a plate. The deck is realized with longitudinal stringers and transverse floor beams. The floor beams have a fixed distance of 4 m, while the stringers are at 1.15 m one to the other. Top and bottom double-L bracings provide adequate stiffening of the structure. Built-up members, realized with plates, L- profiles or C profiles, are connected by hot riveting and connection joints are made of gusset riveted plates. The main structure and the member details have been completely revealed by an on-site geometrical survey. The bridge structure was modeled using the finite element method (FEM) software Midas (2005), using only beam elements. Rigid links (rigid body) were used to represent eccentricities of the elements. Overall, the entire bridge model consists of about 2000 beam elements. A Young's modulus of 210,000 MPa (N/mm2), Poisson's ratio of 0.3 and a material density value of 7850 kg/m3 (weight density of 76.98 kN/m3) were used for the analyses. All beam member sections were modeled as the as-built structure, as measured during the geometrical survey. The bridge is subjected to permanent loads, such as the self-weight of steel elements and of nonstructural elements and to variable loads such as temperature and traffic. At first, the bridge was checked referring to the Italian Ministerial Decree 09/06/1945, n. 6018 (DM 6018, 1945) and then to current Italian and Eurocode. Historical tests on the bridge have been used to calibrate the FEM model. In this study, retrofit alternatives chosen from the following solutions are considered:

a. making composite an existing non-composite deck;
b. building an orthotropic deck;
c. building a new concrete deck, directly connected to the main trusses.

All these strategies are normally combined with steel-only interventions (including cover-plating, element replacement). The described procedures are finalized to redistribute the live loads adequately onto the deck with a new or modified deck. As can be observed in

the following, the beneficial use of a rigid deck is often the best solution able to extend the bridge life adequately. In the case of Italy, the bridge category shifts from the 1st to the 2nd class:

- AD1 Load, 1st category: Load Model 1, EN 1991-2:2003 or
- AD2 Load, 2nd category: Load Model 1, EN 1991-2:2003 taking a reduction of 20% for all loads of Lane number 1.

In the present study, the reference retrofit solutions considered are:

• BR00) The existing bridge is calculated with the historical live load, HS-LOAD, without any retrofit intervention;
• BR01) The existing bridge is calculated with the actual code live load, AD1-LOAD, without any retrofit intervention;
• BR02) The existing bridge is calculated with the actual code live load, AD2-LOAD, without any retrofit intervention;
• RROOR1-2) The bridge is retrofitted with the introduction of an orthotropic deck laying between stringers, with open ribs considering both the AD1-Load and AD2-Load;
• RROCR1-2) The bridge is retrofitted with the introduction of an orthotropic deck laying between stringers, with closed ribs considering both the AD1-Load and AD2-Load;
• RRA1-2) The bridge is retrofitted with the introduction of a concrete deck considering both the AD1-Load and AD2-Load; welded shear studs are introduced in the bridge to connect the new concrete deck with the stringers (three ϕ20 mm studs/m along all stringers, except for stringers along sections 1, 9–13, 19–23, 29–31 where six ϕ20 mm studs/m have been placed); a parametric analysis is developed varying both the concrete deck thickness (with a fixed strength of C40/50) among 10 cm (RRA1, 2–10), 15 cm (RRA1, 2–15), 20 cm (RRA1, 2–20), 25 cm (RRA1, 2–25), 30 cm (RRA1, 2–30) and the deck concrete strength (fixing the deck thickness at the lowest value of 10 cm) among C30/37 (RRA1, 2-R1), C35/45 (RRA1, 2-R2), C40/50 (RRA1, 2-R3), C45/55 (RRA1, 2-R4), C55/67 (RRA1, 2-R5);
• RRA1-2-I) The bridge is retrofitted with the introduction of a concrete deck considering both the AD1-Load and AD2-Load, fixing the concrete strength at C40/50 and the deck thickness at 100 mm; moreover, the steel-to-steel intervention -cover plating- are introduced adopting S355 new members;
• RRB1-2-I) The bridge is retrofitted with the introduction of a concrete deck considering both the AD1-Load and AD2-Load, introducing a UHPC concrete of C90/105 strength class and fixing the deck thickness at 50 mm; moreover, the steel-to-steel intervention -cover plating- are introduced adopting S355 new members;
• RRC1-2-I) The bridge is retrofitted with the introduction of a concrete deck considering both the AD1-Load and AD2-Load, introducing a UHPC concrete of C150/160 strength class and fixing the deck thickness at 30 mm; moreover, the steel-to-steel intervention are introduced adopting S355 new members. According to the analysis performed, the optimal solution is represented by the RRB1-I, which has been compared in terms of utilization rate to the main solution descripted above (maximum ratios Ed/Rd de- fined as the minimum safety factor of all ultimate limit state-ULS checks) (Figures 18-20).

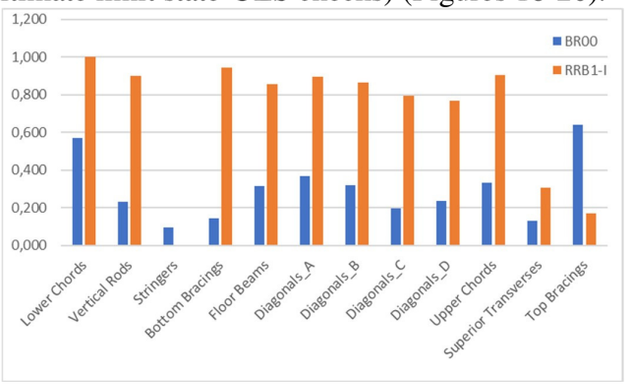


Figure 18: Comparison of B00 vs. RRB1-I model.

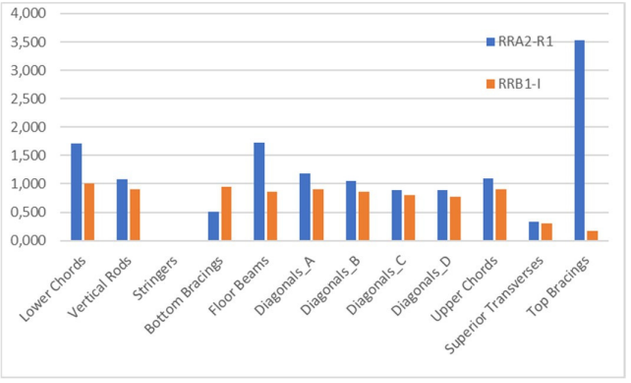


Figure 19: Comparison of RRA2-R1 vs. RRB1-I model.

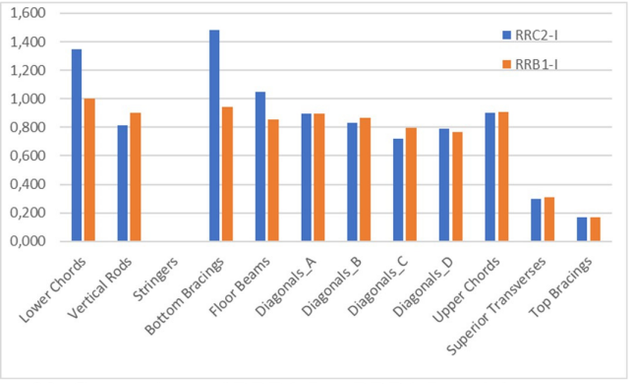


Figure 20: Comparison of RRB1-Ivs. RRB1-I model.

2.5 Strengthening for fatigue induced damages in trusses: a parametric analysis

Traffic running on bridges produces a stress spectrum that may cause fatigue damage. This stress spectrum depends on the geometry of the vehicles, the axle loads, the vehicle spacing, the composition of the traffic, and its dynamic effects. However, the increasing loads on truss bridges (magnitude and quantity), both railways and roadways, imply the increasing accumulation of damage in iron or steel member, that could lead to sudden failure. A parametric analysis has been performed onto two existing bridges in Italy, the case study of the par. 2.4 (Br1) and the railway Adige bridge (Figure 21) (Br2), in order to check which are the more

suitable and effective solution for bridge repair, in order to prolong their fatigue life. After the retrofit solution proposed, all bridges are checked according EN1993-1-9:2005.

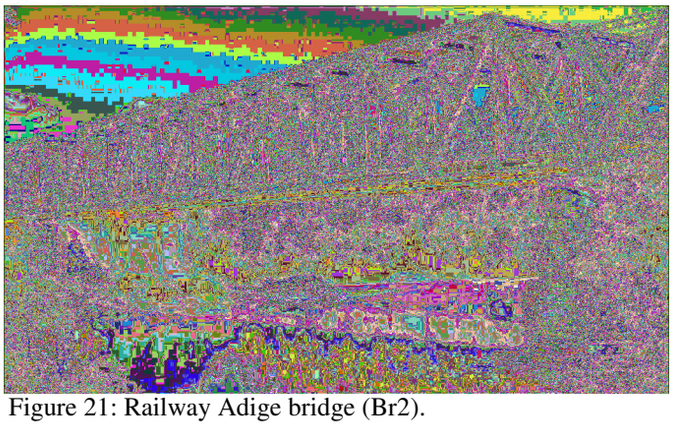


Figure 21: Railway Adige bridge (Br2).

The following solutions have been considered:

- RRF1: the bridge is retrofitted with the introduction of a concrete deck, made of UHPC concrete; the cover-plating technique is adopted in hot spot fatigue stresses;
- RRF2: the bridge is retrofitted with the introduction of a concrete deck, made of UHPC concrete; hot spot stress truss-nodes are encased in new UHPC nodes;

For every RRFi (i=1, 2) retrofit solution, a limit of adding no more new material than the 25% of the original weight of the bridge is fixed.

For railway bridges, an unballasted solution is provided for RRF1-RRF2.

A wide number of other parameters are varied in order to analyze the sensitivity of the model to these variations. According to the analysis performed, the optimal solution depends on the bridge type, which has been compared in terms of utilization rate to the main solution descripted above (maximum ratios Ed/Rd defined as the minimum safety factor of all ultimate limit state-ULS checks) (Figures 22-29).

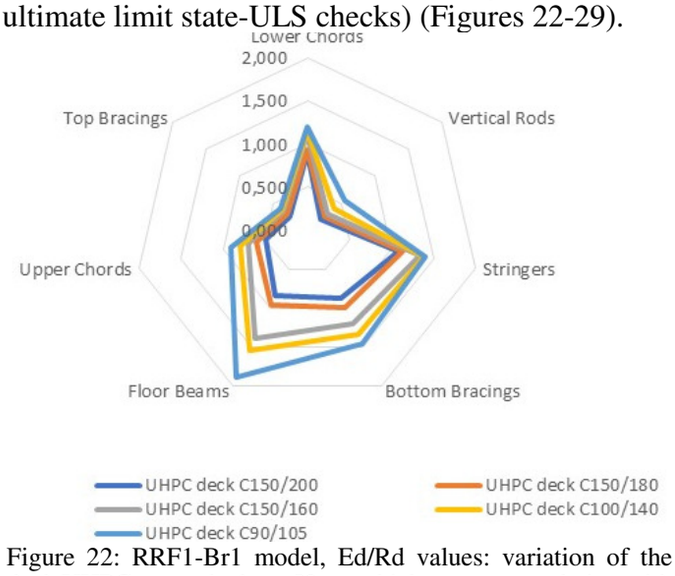


Figure 22: RRF1-Br1 model, Ed/Rd values: variation of the deck UHPC strength class, 50 mm thickness; cover-plating with S275 steel grade.

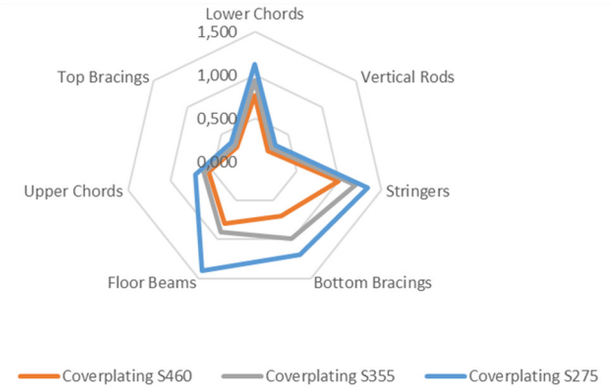


Figure 23: RRF1-Br1 model, Ed/Rd values: variation of the cover plating steel strength class; UHPC deck grade C150/160, 50 mm thickness.

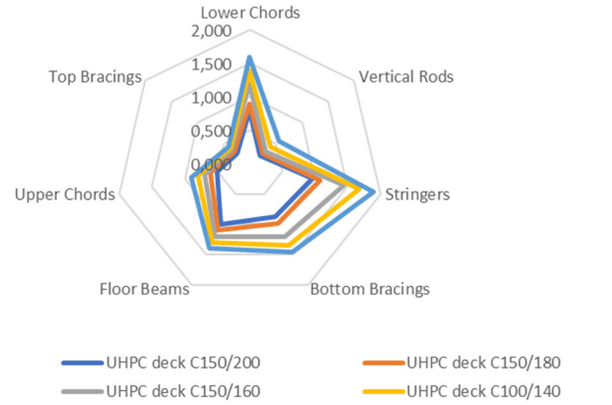


Figure 24: RRF1-Br2 model, Ed/Rd values: variation of the deck UHPC strength class, 80 mm thickness; cover-plating with S275 steel grade.

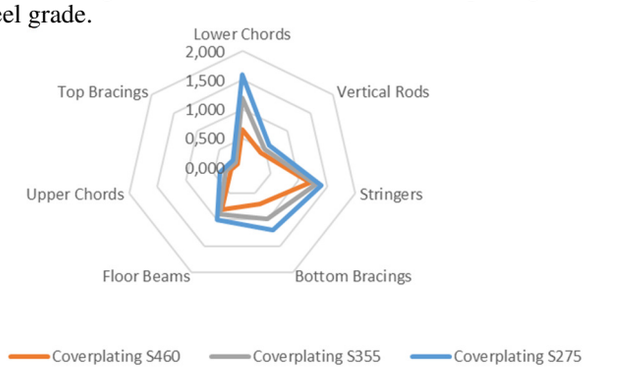


Figure 25: RRF1-Br2 model, Ed/Rd values: variation of the cover plating steel strength class; UHPC deck grade C150/160, 80 mm thickness.

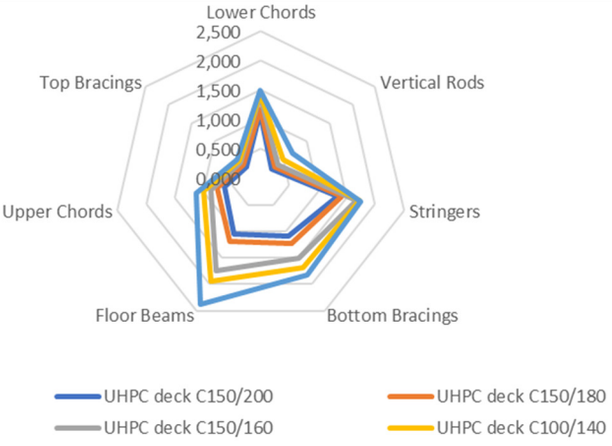


Figure 26: RRF2-Br1 model, Ed/Rd values: variation of the deck UHPC strength class, 50 mm thickness; cover-plating with S275 steel grade.

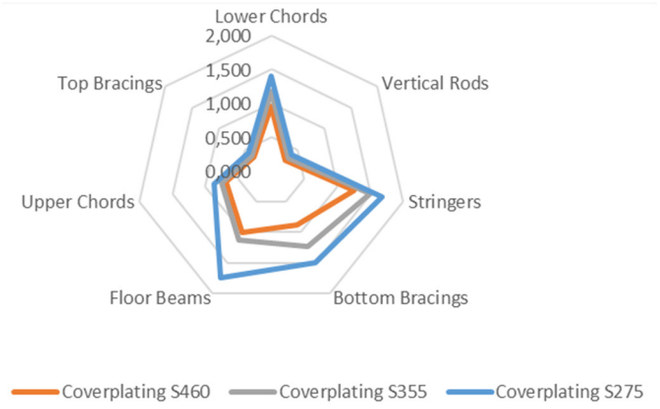


Figure 27: RRF2-Br1 model, Ed/Rd values: variation of the cover plating steel strength class; UHPC deck grade C150/160, 50 mm thickness.

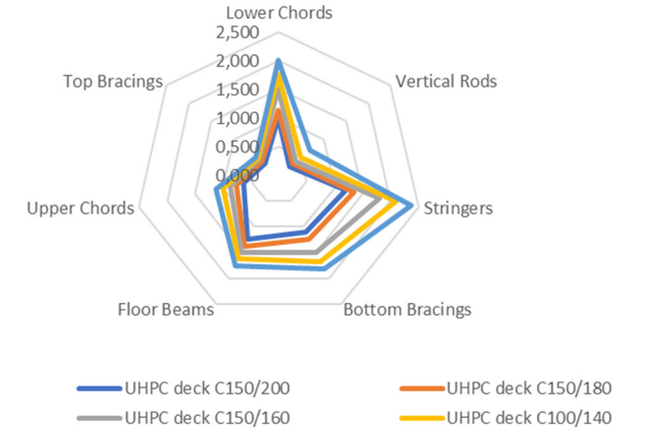


Figure 28: RRF2-Br2 model, Ed/Rd values: variation of the deck UHPC strength class, 80 mm thickness; cover-plating with S275 steel grade.

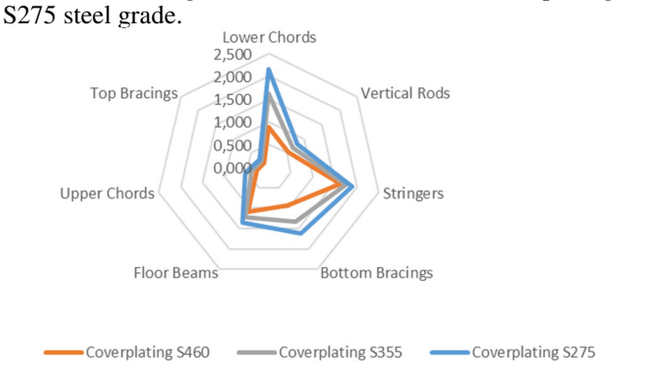


Figure 29: RRF2-Br2 model, Ed/Rd values: variation of the cover plating steel strength class; UHPC deck grade C150/160, 80 mm thickness.

3 CONCLUSION

In this paper different strategies in order to prolong the lifetime of existing steel truss bridges have been presented. The first technique deals with the possibility to upgrade the load carrying capacity of a cultural heritage arched-truss bridge by deck replacing, maintaining the existent architectural profile, but increasing at the same time the structural strength and reliability; the second technique explored the possibility to build a new UHPC deck onto existing metro-railway trusses, calculating the beneficial reduction of stressed and deformations of the whole existing structure; the third solution provide refined calibrated FEM finalized to build a direct fastened rail incorporating an anti-derailment device, able to reduce the stress amplitude dealing with fatigue, and consequently prolonging the life of the whole truss; the fourth solution presented a parametric analysis of a road truss, to discover the most suitable retrofit solution, represented by the realization of a thin UHPC 50mm deck together with cove- plating applications; the last solution presented a parametric analysis to prolong the fatigue strength of existing bridges, to discover the most suitable retrofit solution, and to compare different retrofit techniques. As a matter of fact, the whole solutions presented are finalized to demonstrate that it is possible to prolong the life of existing trusses, with the innovative techniques illustrated herein.

4 ACKNOWLEDGMENTS

This research was supported by the European Un- ion, represented by the European Commission—Directorate General for Research and Innovation, Research Fund for Coal & Steel (RFCS) program, under grant agreement no. RFSR-CT-2015-00025. This funding is gratefully acknowledged.

5 REFERENCES

DM 6018 (1945). Italian Ministerial Decree 09/06/1945 n. 6018, Ministero dei Lavori Pubblici, Roma

EN 1993-1-9 (2006). Eurocode 3: Design of steel structures - Part 1-9: Fatigue. CEN-European Committee for Standardization, Brussels, Belgium

EN 1991-.2 (2003). Eurocode 1: Actions on structures - Part 2: Traffic loads on bridges. CEN-European Committee for Standardization, Brussels, Belgium

Lundmark T., Hallmark R., Dahlman L., Collin P. (2016) Upgrading of an old railway bridge – the old Arsta bridge. Proceeding from IABSE: Challenges in Design and Construction of an Innovative and Sustainable Built Environment, 19th IABSE Congress Stockholm, 21-23 September 2016

Lundmark T., Nilsson M (2013). Förstudie av möjlighet till utbyte av spårplan för G:a Årstabron - Bågspannet. Stockholm/Luleå: Ramböll; 2013. Trafikverket – project report

MIDAS (2016). Midas User Manual. MIDAS Information Tech- nology Co., Korea.

Ivanov S., Geier R., (2016). Retrofitting of old steel railway truss bridges by implementing new concrete deck. Proceeding from IABSE: Challenges in Design and Construction of an Innovative and Sustainable Built Environment, 19th IABSE Congress Stockholm, 21-23 September 2016

Van der Burg M., Steenbrink A., Hesselink B. (2017). Recalculating a steel railway bridge for determining the strengthening measures measurements using updated FEM model and measurements. Proceeding from IABSE: 39th IABSE Sym- posium – Engineering the Future September 21-23 2017, Vancouver, Canada

James G., Paulsson T. (2008). Gamla Årstabrons fackverksbågen – Sammanställningsrapport av trådtöjningsmätning, utmattningsberäkning och brottseghetsprovning 2006-2008. Stockholm: Projektengagemang.; 2008. Banverket – project report no: 600013:A

TRVK Bro 11(2011). Trafikverket tekniska krav Bro. Borlänge: Trafikverket; 2011. Trafikverket – TRV publ nr 2011:085

Maintenance, Safety, Risk, Management and Life-Cycle Performance of Bridges – Powers, Frangopol, Al-Mahaidi & Caprani (Eds)
© 2018 Taylor & Francis Group, London, ISBN 978-1-138-73045-8

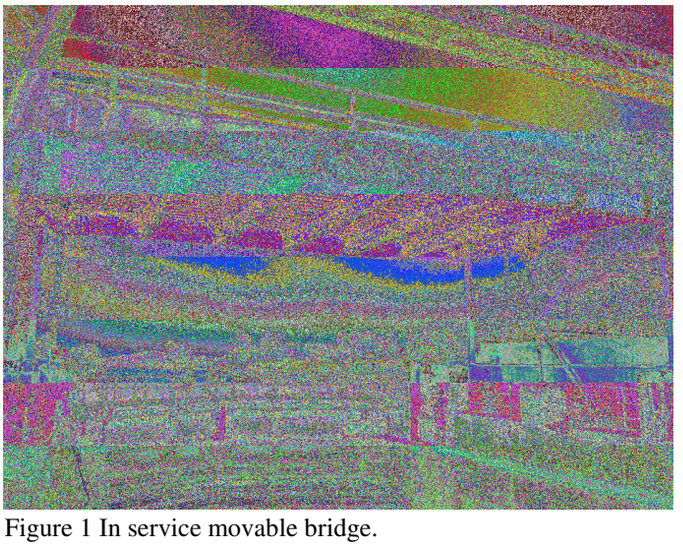
Steel bridge retrofit solution for movable cases

R. Pavan A. Ruzzante
AP&P srl, Italy

ABSTRACT: Prolonging the life of existing steel movable bridges is a paramount problem for managing authorities, where these specific types of bridges have reached a prolonged state of use. The unsatisfactory behavior of these structures under the current type and increasing number of loads make clearer that innovative solutions are needed. For this purpose, the realization of lightweight composite decks is needed, in order to redistribute the common actual load onto a structure conceived with historical codes, characterized by lower design live loads. The possibilities of retrofitting bridges with this solution studied in a recent research program are presented and compared in this study.

1 INTRODUCTION

Increasing traffic density and vehicle weight have been increasing in recent decades. Many existing movable bridges, all over the world, were not designed for the high service loads and the increased number of load cycles that they are exposed to today. Some bridges will have to be either strengthened or replaced in the next decades. Movable bridges have proved to be an economical solution to the problem of how to carry a rail line or highway across an active waterway. A "closed" movable bridge has closed the waterway to marine traffic, while an "open" bridge has opened the waterway to marine traffic. Highway bridges are typically designed to remain in the closed position and only to be opened when required by marine traffic. However, movable railroad bridges can be designed to remain in either the open or closed position, depending on how frequently they are used by train traffic. The difference is important as different wind and seismic load design conditions are used to design for a bridge that is usually open vs. one that is usually closed. The three major categories of movable bridges are swing, bascule, and vertical lift. This list is not exclusive and there are other types, such as jackknife, reticulated, retracting, and floating that are not common and will not be described here. Movable bridges are designed to be operated following a set protocol, and this protocol is incorporated into the control system as a series of permissive interlocks. The normal sequence of operation is as follows. Vessel signals for an opening, usually through a marine radio but it can be through a horn. For a highway bridge the operator sounds a horn, activates the traffic signals, halting traffic, lowers the roadway gates, then lowers the barrier gates. For a rail bridge the operator needs to get a permissive signal from the train dispatcher. After the barrier gates are lowered, a permissive signal allows the operator to withdraw the locks and/or wedges and lifts and, once that is completed, to open the span. The vessel then can proceed through the opening. To close the bridge, the steps are reversed. The controls are operated from a control desk and Note that the control desk includes a position indicator to demonstrate the movable span(s) position as well as an array of push buttons to control the operation. A general objective in designing such a desk is to have the position of the buttons mimic the sequence of operations. Typically, the buttons are lit to indicate their status. or every type of movable bridge there are a wide amount of interventions needed both


Figure 1 In service movable bridge.

every year, both during long time scheduling maintenance. The most frequent interventions lie on the moving equipment maintenance and checks, while the structural maintenance and eventual retrofit refers to longer period.

2 RETROFIT SOLUTIONS

2.1 *Literature review*

A special category of steel structures where the fatigue induced damage is relevant for the life cycle of the structure, deals with movable bridges. These are daily subjected to high level stresses induced by load cycles of passing vehicles: the incrementing speeds and concurring dynamic amplifications, and the incremental number of loads and number of vehicles, represented a critical structural situation especially for those bridges in principle lines and with some decades of exercise. The literature for these detailed analysis and damage assessment is not so extensive, and relegated to a small number of specialists: guidelines for the assessment of historical existing steel structures are deepen in Kuhn et al. (2008) and Brühwiler et al. (2012), in a sort of pre normative design document, respectively in the European and Swiss context; while well-established authorities in this framework have studied riveted bridges Fisher et al. (1984), Brühwiler et al. (1990), other studies are focused on large scale experimentations and damage assessment procedures (Pipinato et al 2008b; Pipinato et al. 2009; Pipinato et al. 2010a; Pipinato et al 2011c; Pipinato 2011; Pipinato 2012a); a detailed procedures for accounting for remaining fatigue life is provided in Imam et al. (2005), while other studies are more focused on the structural analysis of single bridges (Pipinato et al. 2012a; Pipinato et al. 2012a; Pipinato 2010b; Pipinato et al. 2012e; Pipinato et al. 2010a; Pipinato and Modena 2010 Pipinato et al. 2008) even considering special combination of external loadings, and damage accumulation including fatigue and seismic loads (Pipinato 2012b); or FRP interventions for build up new structures or repairing solutions Pipinato (2012d); particular cases of damages are included also in some hint studies (Pipinato et al. 2012e; Pipinato et al. 2012c) reporting particular analysis solutions that can help to solve bridge damaged systems; retrofit procedures and load analysis also for high speed bridges are reported in (Pipinato 2013a,b,c), also coupling damage as in the aforementioned studies (Pipinato 2012c; Pipinato et al 2011a; Pipinato et al 2010b) a particular subset of these studies includes damage analysis and control of existing and historical bridges (Pipinato 2012d; Pipinato et al. 2013); reliability analysis also considering dynamic effects are described in (Imam et al. 2012; Imam et al. 2012; Kaliyaperumal et al. 2011; Imam and Righiniotis 2010), while a more focused study on the probabilistic fatigue evaluation of riveted bridges is included in Imam et al (2008); the fatigue analysis of riveted bridge connections using the theory of critical distances and relative numerical modelling are described in (Righiniotis et al. 2008; Imam et al. 2007); while a general introduction on the specific argument could be found in (Imam et al. 2006; Imam et al. 2005); more focused and specialist deepens deals with the fracture reliability of a typical Northridge steel moment resisting connection (Righiniotis and Imam 2004), the fatigue reliability of riveted connections in bridges (Imam et al. 2006, 2008), the effect of climate change on the deterioration of steel bridges (Kallias and Imam 2013), the risk assessment of steel bridges under the influence of changing environmental conditions (Kallias and Imam 2012), the fatigue assessment of a bridge detail using dynamic analysis and probabilistic fracture mechanics (Imam and Kaliyaperumal 2012), the modelling of failure consequences for robustness evaluation (Chryssanthopoulos et al. 2011), the review of metallic bridge failure statistics (Imam and Chryssanthopoulos 2010), the effects on the fatigue reliability of deteriorating riveted bridges (Imam et al. 2009a), the global-local finite element analysis of riveted bridge connections for fatigue evaluation (Imam et al. 2009b), the probabilistic fatigue load spectra for riveted bridges (Imam et al. 2007), the probabilistic fatigue life estimates for riveted bridges (Imam et al. 2006), the effect of fracture on the reliability of a moment resisting frame under earthquake loading (Righiniotis and Imam 2006), the probabilistic fatigue life estimates for riveted bridges (Imam et al. 2006), the remaining fatigue life estimates for riveted bridges (Imam et al. 2005), and the connection fixity effects on stress histories in riveted rail bridges (Imam et al. 2004).

2.2 *Movable bridge deck intervention*

As a fact, the most damaged structure of movable bridges is represented by the deck. A crucial part of the design of movable bridges is to limit the moving dead load which affects the size of the counterweight, the overall size of the main structural members, and, to a lesser extent, the machinery depending upon the type of movable bridge. For movable railroad bridges this is typically not a problem, as movable span decks are designed with open decks (timber ties on stringers) and the design live load is such a large part of the overall design load that the type of deck is not an issue. For highway bridges, however, the type of deck needs to be carefully selected to provide a minimum weight while providing an acceptable riding surface. Early movable spans used timber decks, but they are relatively heavy and have poor traction and wear. Timber was replaced by open steel grid, a good solution that is both lightweight and long wearing. In addition, the open grid reduced the exposed wind area, particularly for bas-

cule bridges in the open position. However, with higher driving speeds, changes in tires and greater congestion, steel grid deck has become the source of accidents, particularly when wet or icy. Now most new movable bridge decks are designed with some type of solid surface. Depending on the bridge, this can be a steel grid partially filled with concrete or epoxy, an orthotopic deck, lightweight concrete, or the "exodermic" system. Aluminum and composite decks are also now being developed and may prove to be a good solution. While orthotropic decks would seem to be a good solution, as the deck can be used as part of the overall structural system, they have not yet seen widespread use in new designs.

2.3 *Light deck intervention*

Consequently, a number of factors that should be considered in the selection of a lightweight solid deck system to replace steel open grid deck on typical movable bridges. These factors include (URS 2012):

- Costs including:

o Deck fabrication and installation,
o Modifications to the bascule leaf steel framing, bascule pier, flanking spans,
counterweight, and trunnion assemblies required to implement the new deck system,
o Design and construction inspection for the new deck system,
o Future maintenance and inspection.

- Functionality and Safety including:

o Load capacity (i.e. support of legal loads and permitted overloads),
o Improved riding surface and skid resistance for vehicular and bicycle traffic,
o Reduced traffic generated noise.

-Maintenance including:

o Ease of repair and/or replacement of all or portions of the deck,
o Need for periodic maintenance (e.g. reapplication of coatings and/or replacement of
wearing surfaces).

-Service-life and Durability including:

o Deck and/or deck component (e.g. wearing service, fasteners, etc.) service-life,
o Resistance to corrosion, fatigue, wear, impact, fire, ultraviolet light, and chemicals,
o Accommodation of thermal movements.

-Constructability including:

o Disruption to traffic (e.g. overall construction duration, maintenance of traffic),
Ability to accommodate fabrication and installation tolerances,
o Sensitivity to environmental conditions during construction,
o Shipping, storage and handling,
o Specialized inspection requirements during fabrication and installation.

- Other Risks including:

o Familiarity of the product and technology (e.g. years' experience, previous bridge installations, quantity and quality of applicable research, endorsement by bridge design community),
o Availability of design tools and construction techniques,
o Financial and technical support from supplier(s),
o Product availability (e.g. opportunities for competitive bidding, sole source and/or patents).

These new lightweight solid decks to replace steel open grid decks on typical movable bridges include:

a) Sandwich Plate System

The Sandwich Plate System is a proprietary and patented composite laminate plate material consisting of thin metal faceplates continuously bonded to a polyurethane elastomer core. The elastomer core transfers forces between the metal faceplates by way of shear, analogous to an I-beam when subjected to flexure with the steel plates acting as the flanges and the elastomer core as the web. The elastomer core also prevents local buckling of the metal faceplates in compression, which permits development of full yield of the metal faceplates. Panels are very thin (1 to 2 inches thick) compared to traditional bridge decks. The use of these thin panels is possible through a combination of panel bending and membrane action (i.e. in-plane tension). Separation of the thin metal plates with a lightweight elastomer core more efficiently increases strength and stiffness of the plate, while minimizing the increase in weight of the plate (URS 2012).

b) Aluminum Orthotropic Deck

Aluminum alloys have much to offer for bridge deck applications, and continue to be used, primarily overseas, where their lightweight, high strength-to-weight ratio and excellent corrosion resistance satisfy service requirements. Aluminum is manufactured by an extrusion process, which permits highly customized sections that can be optimized for a given application. The lack of widespread use of aluminum, despite the structural and maintenance advantages, is primarily due to the high initial cost of the material (URS 2012).

c) Fiber Reinforced Polymer (FRP) Composite Deck

Fiberglass reinforced plastic (FRP) is a composite material that has a number of characteristics that makes it a good alternative to replace steel open grid deck on bascule bridges. FRP composites can be designed to provide a wide range of mechanical properties including tensile, flexural, impact and compressive strengths. FRP composites are generally lightweight (i.e. approximately 20% of steel) with high strength-to-weight ratio and are generally resistant to creep and fatigue. FRP composites are ver-

satile and can be fabricated in many different configurations, customized specifically for a given application (e.g. bridge decks), designed and fabricated such that the strength is oriented to meet specific configuration and loading demands, made into larger more complex structural components and systems that simplifies connections and minimizes the number of components that must be handled. The relatively low modulus of elasticity of FRP composites make them relatively flexible compared to other bridge deck materials and thus deflections generally control the design of FRP bridge decks. FRP composite materials are susceptible to degradation from ultraviolet light and chemicals; however, the materials can be formulated with additives to improve the resistance to these effects (URS 2012).

d) Ultra-high Performance Concrete (UHPC) thin deck

Ultra-High Performance Concrete (UHPC) is a material that has recently gained attention in the bridge industry. UHPC provides a combination of superior properties including strength, ductility, durability that permits design and construction of thinner sections and longer spans that are lighter and more efficient, while providing improved durability and impermeability against corrosion, abrasion and impact. UHPC has potential to be used in an alternative deck design to replace steel open grid deck. The high concrete compressive and tensile strength allows design and construction of a lightweight waffle slab bridge deck with thin elements (slab and ribs) (URS 2012).

e) Making composite existing non-composite decks

Many older steel bridges are constructed with a non-composite concrete slab over steel girders. A potentially economical means of strengthening these floor systems is to connect the existing concrete slab and steel girders to permit the development of composite action. Composite action means that the steel girder and concrete can help each other out carrying the loads more efficiently than in the original nanocomposite condition. To achieve the benefits of composite action, the existing steel girder must be connected to the existing concrete slab to permit the transfer of shear forces at the steel-concrete interface. For new bridges, composite action is achieved by welding shear studs to the top of the steel girder prior to casting the concrete slab. In the case of an existing bridge, this approach is not possible, since the slab is already in-place. One alternative is to make holes in the slab and weld studs to the top flange, but that interrupts the traffic and means that the water proofing and asphalt of the bridge must be done once again. Perhaps even worse, the transversal re-bars of the deck will be broken when making holes for shear connectors, and that means that e.g. the cantilevers will loose their capacity in bending since they are depending on the top layer of the re-bars in tension. Hence, the best thing would be to develop methods for post-installing shear connectors. In the case of existing bridges, strengthening by welded shear studs is only suitable if the bridge can be closed for quite a long time. The strengthening work often involves the following steps: removal of pavement and waterproofing, water jetting to remove the concrete, welding of new shear studs, casting concrete, re-waterproofing and resurfacing. Spring pins or coiled spring pins (Figure 2), offer the possibility of performing the whole installation from below the bridge deck without interrupting the traffic on the bridge. This is possible since the pins are connected to the steel and concrete only by a force created by the compressed coiled spring pin itself. This is a major advantage of interference fit shear connectors in bridge applications, compared to the other types of shear connectors.

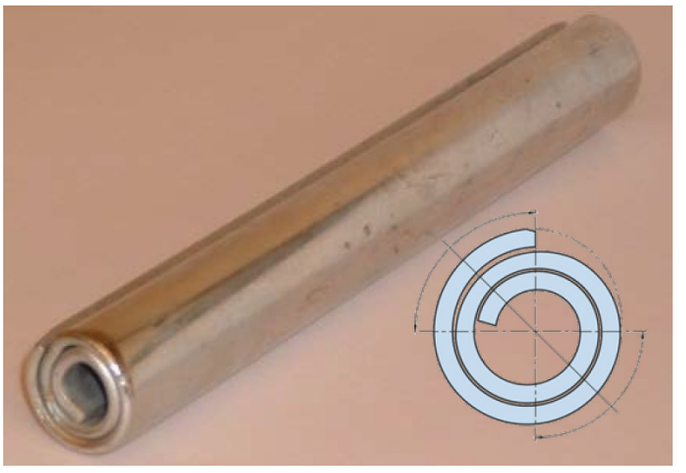


Figure 2 A coiled spring pin, and a schematic sketch of its cross-section.

Coiled spring pins can be used as shear connectors either to create or to strengthen the shear connection between steel and concrete. In the first case, there will be only one type of shear connector at the shear interface, which makes it easy to establish design assumptions. However, since there are no heads on the coiled spring connectors, the uplift forces must be considered in design. In the second case, there will be at least two different kinds of shear connectors at the shear interface. This implies that the distribution of shear forces between the different shear connectors must be established. This is essential when a structure is strengthened due to insufficient fatigue capacity in the shear connection. It is, however, less important for static load in the ultimate limit state.

An application has been performed onto the Pitsund bridge in Sweden: the Pitsund-bridge is a seven span bridge, with a total length of 399 m and a free width of 9 m, see Figure 3. The superstructure consists of steel girders with a concrete deck slab on top, in six out of seven spans. The seventh span is a movable span, designed as a bascular bridge with two leafs. In 2006, coiled spring pins were installed in a part of the bridge in order to create composite action and to avoid sudden movements in

the steel-concrete interface, which created loud bangs in wintertime.

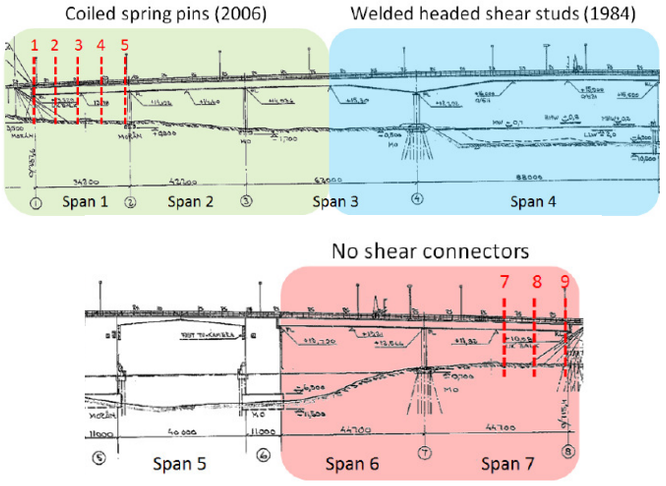


Figure 3 Pitsund-bridge sections.

In the area marked with red, there are no shear connectors, only a few anchoring steel bars that connect the steel and the concrete over the supports. In the blue area, the bridge was designed and constructed as a composite structure (year 1984). The shear connection was created by welded headed shear studs. The green area was originally designed with no composite action and remained so until year 2006. Then 1200 coiled spring pins were installed in order to create composite action. Then the bridge was monitored under known loads, to understand differences in the structural behavior: one conclusion from the measurements is that the coiled spring pins can be used to create composite action in non-composite steel concrete bridges, even though they behave a bit different compared to shear studs at low load levels. The tests indicate that that there is a need of a small initial slip, or compression of the pins, before the coiled spring pins starts to transfer shear forces to a greater extent. FE-models have been created for the bridge, simulating different types of shear connections. A comparison between FE-models and the field monitoring will be presented in a future paper.

3 CONCLUSION

Many existing movable bridges, all over the world, were not designed for the high service loads and the increased number of load cycles that they are exposed to today. Some bridges will have to be either strengthened or replaced in the next decades. For this reason, in this paper specific intervention are presented, including the following: bridge deck traditional intervention; light deck intervention (including SPS systems, aluminum orthotropic deck, FRP composite deck UHPC thin deck, making composite existing non composite solutions). According to the specific situation, span, loads, traffic, service life to be maintained, the proper solution or a combination thereof should be designed.

4 ACKNOWLEDGMENTS

This research was supported by the European Union, represented by the European Commission—Directorate General for Research and Innovation, Research Fund for Coal & Steel (RFCS) program, under grant agreement no. RFSR-CT-2015-00025. This funding is gratefully acknowledged.

5 REFERENCES

Brühwiler E., Smith I. F. C., Hirt M. A., 1990. Fatigue and Fracture of Riveted Bridge Members. Journal of Structural ngineering (ASCE), 116 (1), 198-214.

Brühwiler E., Vogel T., Lang T., Lüch P., 2012. Swiss Standards for Existing Structures. Structural Engineering International 2/2012 Technical Report, pp. 275-280.

Chryssanthopoulos MK, Janssens V, Imam B., 2011. Modelling of Failure Consequences for Robustness Evaluation'. IABSE/IASS London, UK: IABSE–IASS Symposium: Taller, Longer, Lighter

Fisher J. W., Yen B. T., Wang D., 1984. NCHRP Report No 302 : Fatigue and Fracture Evaluation for Rating Riveted Bridges. Transportation Research Board, National Research Council, Washington, D.C.

Imam B, Chryssanthopoulos MK, Frangopol DM., 2009b. System effects on the fatigue reliability of deteriorating riveted railway bridges'. CRC Press Safety, Reliability and Risk of Structures, Infrastructures and Engineering Systems: Proceedings of the Tenth International Conference on Structural Safety and Reliability, Osaka, Japan: ICOSSAR2009

Imam B, Chryssanthopoulos MK., 2010. A review of metallic bridge failure statistics'. CRC Press Bridge Maintenance, Safety and Management: Proceedings of the Fifth International IABMAS Conference, Philadelphia, USA: IABMAS 2010, pp. 3275-3282.

Imam B, Righiniotis TD, Chryssanthopoułos MK, Bell B., 2006. Analytical fatigue assessment of riveted rail bridges'. Proceedings of the Institution of Civil Engineers: Bridge Engineering, 159 (3), pp. 105-116.

Imam B, Righiniotis TD, Chryssanthopoulos MK, Bell B., 2006. Probabilistic fatigue life estimates for riveted railway bridges'. Taylor & Francis Advances in Bridge Maintenance, Safety Management, and Life-Cycle Performance: Proceedings of the Third International Conference, Porto, Portugal: IABMAS '06

Imam B, Righiniotis TD, Chryssanthopoulos MK., 2004. Connection fixity effects on stress histories in riveted rail bridges'. Taylor & Francis Bridge Maintenance, Safety, Management and Cost: Proceedings of the 2nd International Conference on Bridge Maintenance, Safety and Management, Kyoto, Japan: Iabmas'04.

Imam B, Righiniotis TD, Chryssanthopoulos MK., 2005. Fatigue assessment of riveted railway bridges'. Korean Society Of Steel Construction Steel Structures, 5 (5), pp. 485-494.

Imam B, Righiniotis TD, Chryssanthopoulos MK., 2005. Remaining fatigue life estimates for riveted railway bridges'. Thomas Telford (ICE Publishing) Bridge Management Five: Proceedings of the 5th International Conference on Bridge Management, Guildford, UK: 5th International Conference on Bridge Management, pp. 417-425.

Imam B, Righiniotis TD, Chryssanthopoulos MK., 2009b. Global-local finite element analysis of riveted railway bridge connections for fatigue evaluation'. Taylor and Francis Bridge Maintenance, Safety Management, Health Monitoring and Informatics - IABMAS '08, Seoul, Korea: Proceedings of the 4th International Conference on Bridge Maintenance

Imam B, Righiniotis TD, Chryssanthopoulos MK., 2014. Fatigue crack initiation in riveted railway bridge connections. Philadelphia, USA: Proceedings of the 1st International Conference on Fatigue and Fracture in the Infrastructure, Bridges and Structures of the 21st Century

Imam B, Righiniotis TD, Chryssanthopoulos MK., 2006. Fatigue reliability of riveted connections in railway bridges. American Society of Mechanical Engineers Glasgow, UK: 3rd ASRANet International Colloquium

Imam B. M., Chryssanthopoulos MK, Frangopol DM., 2012. Fatigue system reliability analysis of riveted railway bridge connections. Structure and Infrastructure Engineering, 8 (10), pp. 967-984.

Imam BM, Chryssanthopoulos MK., 2012. Causes and consequences of metallic bridge failures. Structural Engineering International: Journal of the International Association for Bridge and Structural Engineering (IABSE), 22 (1), pp. 93-98.

Imam BM, Kaliyaperumal G., 2012. Fatigue assessment of a railway bridge detail using dynamic analysis and probabilistic fracture mechanics. Taylor & Francis Group Bridge Maintenance, Safety, Management, Resilience and Sustainability - Proceedings of the Sixth International Conference on Bridge Maintenance, Safety and Management, Lake Como, Italy: The 6th International Conference on Bridge Maintenance, Safety and Management (IABMAS 2012), pp. 3206-3213.

Imam BM, Righiniotis TD, Chryssanthopoulos MK, Bell B. 2006. Probabilistic fatigue life estimates for riveted railway bridges'. Proceedings of the 3rd International Conference on Bridge Maintenance, Safety and Management - Bridge Maintenance, Safety, Management, Life-Cycle Performance and Cost, , pp. 499-500.

Imam BM, Righiniotis TD, Chryssanthopoulos MK., 2007. Numerical modelling of riveted railway bridge connections for fatigue evaluation'. ELSEVIER Engineering Structures, 29 (11), pp. 3071-3081.

Imam BM, Righiniotis TD, Chryssanthopoulos MK., 2007. Probabilistic fatigue load spectra for riveted railway bridges'. Taylor & Francis Proceedings of the 10th International Conference on Applications of Statistics and Probability in Civil Engineering, Tokyo, Japan: 10th International Conference on Application of Statistics and Probability in Civil Engineering, pp. 73-74.

Imam BM, Righiniotis TD, Chryssanthopoulos MK., 2008. Probabilistic fatigue evaluation of riveted railway bridges'. Journal of Bridge Engineering, 13 (3), pp. 237-244.

Imam BM, Righiniotis TD., 2010. Fatigue evaluation of riveted railway bridges through global and local analysis'. Elsevier Journal of Constructional Steel Research, 66 (11), pp. 1411-1421.

Imam, B., Righiniotis, T.D., Chryssanthopoulos, M.K., 2005. Remaining fatigue life estimates for riveted railway bridges. Proceedings of the 5th International Conference on Bridge Management, p 417-425, 2005, Bridge Management 5: Inspection, Maintenance, Assessment and Repair - Proceedings of the 5th International Conference on Bridge Management

Kaliyaperumal G, Imam B, Righiniotis T., 2011. Advanced dynamic finite element analysis of a skew steel railway bridge'. Elsevier Sci Ltd Engineering Structures, 33 (1), pp. 181-190.

Kallias AN, Imam B., 2012. Risk assessment of steel bridges under the influence of changing environmental conditions'. Faculty of Construction and Environment & Research Institute for Sustainable Urban Development, Hong Kong Polytechnic University Proceedings of the First International Conference on Performance-based and Life-cycle Structural Engineering (PLSE 2012): 5-7 December 2012, Hong Kong, China, Hong Kong, China: First International Conference on Performance-based and Life-cycle Structural Engineering

Kallias AN, Imam B., 2013. Effect of climate change on the deterioration of steel bridges. International Association for Bridge and Structural Engineering IABSE Symposium Report, Rotterdam, The Netherlands: IABSE Rotterdam Spring Conference 2013: Assessment, Upgrading and Refurbishment of Infrastructures, pp. 1731-1738.

Kuhn, B., Lukic´ , M., Nussbaumer, A., Gunther, H.-P., Helmerich, R., Herion, S., Kolstein, M.H., Walbridge, S., Androic, B., Dijkstra, O. and Bucak, O., 2008. Assessment of existing steel structures: Recommendations for estimation of remaining fatigue life. Joint report prepared under the JRC-ECCS cooperation agreement for the evolution of Eurocode 3 (programme of CEN/TC 250). Editors: G. Sedlacek, F. Bijlaard, M. Ge´radin, A. Pinto and S. Dimora. Background documents in support to the implementation, harmonization and further development of the Eurocodes First Edition, February 2008 EUR 23252 EN-2008.

Pipinato A., 2010b. Structural analysis and fatigue life assessment of the Paderno Arch Bridge. IABMAS 2010 - Bridge Maintenance, Safety, Management, Resilience and Sustainability - Proceedings of the Sixth International Conference on Bridge Maintenance, Safety and Management , pp. 1003-1007. Philadelphia, USA, 11-15 July 2010. ISBN: 9780415877862.

Pipinato A., 2012a. Life cycle assessment of existing steel bridges considering corrosion and fatigue coupled problems. IABMAS 2012 - Bridge Maintenance, Safety, Management, Resilience and Sustainability - Proceedings of the Sixth International Conference on Bridge Maintenance, Safety and Management , pp. 1003-1007. Stresa, Lake Maggiore, Italy, 8-12 July 2012. ISBN: 9780415621243.

Pipinato A., 2012b. Coupled damage in assessing the lifetime of bridge and viaducts. Life-Cycle and Sustainability of Civil Infrastructure Systems - Proceedings of the 3rd International Symposium on Life-Cycle Civil Engineering, IALCCE

2012 , pp. 2292-2297. Vienna, Austria, October 3-6, 2012. ISBN 9780415621267.

Pipinato A., 2012d. Assessment procedures and strengthening of an existing metal bridge. IABMAS 2012 - Bridge Maintenance, Safety, Management, Resilience and Sustainability - Proceedings of the Sixth International Conference on Bridge Maintenance, Safety and Management , pp. 3651-3655. Stresa, Lake Maggiore, Italy, 8-12 July 2012.

Pipinato A., Pellegrino C. and Modena C., 2010b. Residual service life of existing railway bridges. IABMAS 2010 - Bridge Maintenance, Safety, Management, Resilience and Sustainability - Proceedings of the Sixth International Conference on Bridge Maintenance, Safety and Management , pp. 1003-1007. Philadelphia, USA, 11-15 July 2010.

Pipinato A., 2010a. Step level procedure for remaining fatigue life evaluation of one railway bridge. Baltic Journal of Road and Bridge Engineering, 5(1), pp. 28-37. DOI: 10.3846/bjrbe.2010.04

Pipinato, A., 2011. Assessment of existing bridges: Safety and security issues [Problemi di sicurezza nelle valutazioni strutturali di ponti esistenti]. Ingegneria Ferroviaria, 66(4), 355-371.

Pipinato, A., 2012c. Coupled safety assessment of cable stay bridges. Modern Applied Science, 6(7), pp. 64-78. DOI: 10.5539/mas.v6n7p64

Pipinato, A. 2013a. Retrofit procedures of bridge networks against seismic actions in Italy. Durability of Bridge Structures , pp. 215-228. Proceedings of the 7th New York City Bridge Conference, 26-27 August 2013. Edited by Khaled M . Mahmoud, CRC Press 2013 Print ISBN: 978-1-138-00112-1

Pipinato, A. (2013b). Moving load and fatigue analysis of a long span high speed railway bridge. Advanced Materials Research 629 , pp. 403-408. 10.

Pipinato, A. 2013c. Moving loads bridge response: Structural analysis and eurocode provisions. Advanced Materials Research 629 , pp. 409-417. 10.

Pipinato, A., & Modena, C., 2010. Structural analysis and fatigue reliability assessment of the Paderno bridge. Practice Periodical on Structural Design and Construction, 15(2), 109-124. DOI: 10.1061/(ASCE)SC.1943-5576.0000037

Pipinato, A., Molinari, M., Pellegrino, C., Bursi, O. S., & Modena, C. 2011c. Fatigue tests on riveted steel elements taken from a railway bridge. Structure and Infrastructure Engineering, 7(12), 907-920. DOI: 10.1080/15732470903099776

Pipinato, A., Pellegrino, C., & Modena, C. (2008). Scheduled maintenance actions and residual life evaluation of railway infrastructures for metallic structure bridges [Interventi di manutenzione programmata e valutazione della vita residua delle infrastrutture ferroviarie da ponte a struttura metallica]. Ingegneria Ferroviaria, 63(2), 125-134.

Pipinato, A., Pellegrino, C., & Modena, C., 2008b. Evaluation of fatigue strength of one riveted historical railway bridge. Bridge Maintenance, Safety Management, Health Monitoring and Informatics IABMAS '08 Proceedings of the Fourth International IABMAS Conference, Seoul, Korea, July 13-17 2008. Edited by Hyun-Moo Koh and Dan M . Frangopol, Taylor & Francis 2008, Print ISBN: 978-0-415-46844-2.

Pipinato, A., Pellegrino, C., & Modena, C., 2010a. Structural analysis of historical metal bridges in Italy. Advanced Materials Research, 133-134, 525-530. DOI: 10.4028/www.scientific.net/AMR.133-134.525

Pipinato, A., Pellegrino, C., & Modena, C., 2011a. Fatigue assessment of highway steel bridges in presence of seismic loading. Engineering Structures, 33(1), 202-209. DOI: 10.1016/j.engstruct.2010.10.008

Pipinato, A., Pellegrino, C., & Modena, C., 2012a. Assessment procedure and rehabilitation criteria for the riveted railway Adige Bridge. Structure and Infrastructure Engineering, 8(8), 747-764. DOI: 10.1080/15732479.2010.481674

Pipinato, A., Pellegrino, C., & Modena, C., 2012c. Structural Analysis of the Cantilever Construction Process in Cable-Stayed Bridges. Periodica Polytechnica: Civil Engineering 56 (2) , pp. 141-166. DOI: 10.3311/pp.ci.2012-2.02

Pipinato, A., Pellegrino, C., & Modena, C., 2012d. Fatigue behaviour of steel bridge joints strenghtened with FRP laminates. Modern Applied Science 6 (10) , pp. 1-15. ISSN: 1913-1844. DOI: 10.5539/mas.v6n10p1

Pipinato, A., Pellegrino, C., & Modena, C., 2013. Residual life of historic riveted steel bridges: an analytical approach. ICE-Bridge Engineering, UK Institution of Bridge Engineers. DOI: 10.1680/bren.11.00014

Pipinato, A., Pellegrino, C., and Modena, C., 2012e. Fatigue Damage Estimation in Existing Railway Steel Bridges by Detailed Loading History Analysis. ISRN Civil Engineering, 2012, 1-13. Volume 2012 (2012), Article ID 231674, 13 pages.

Pipinato, A., Pellegrino, C., Bursi, O. S., & Modena, C., 2009. High-cycle fatigue behavior of riveted connections for railway metal bridges. Journal of Constructional Steel Research, 65(12), pp. 2167-2175. DOI: 10.1016/j.jcsr.2009.06.019

Pipinato, A., Pellegrino, C., Fregno, G., & Modena, C., 2012b. Influence of fatigue on cable arrangement in cable-stayed bridges. International Journal of Steel Structures, 12(1), 107-123. DOI: 10.1007/s13296-012-1010-5

Pritchard B., 1992. Bridge Design for Economy and Durability – Concepts for new, strengthened and replacement bridges. London: Thomas Telford Service Ltd.

Righiniotis TD, Imam B., 2004. Fracture reliability of a typical Northridge steel moment resisting connection. Engineering Structures, 26 (3), pp. 381-390.

Righiniotis TD, Imam B., 2006. Effect of fracture on the reliability of a moment resisting frame under earthquake loading. Millpress Proceedings of 9th International Conference on Structural Safety and Reliability, Rome, Italy: ICOSSAR '05

Righiniotis TD, Imam BM, Chryssanthopoulos MK., 2008. Fatigue analysis of riveted railway bridge connections using the theory of critical distances'. Elsevier Engineering Structures, 30 (10), pp. 2707-2715.

URS, 2012. Bascule bridge lightweight solid deck retrofit research project. Deck Alternative Screening Report Final Fpid 419497-1-B2-01, Florida

Maintenance, Safety, Risk, Management and Life-Cycle Performance of Bridges – Powers, Frangopol, Al-Mahaidi & Caprani (Eds)
© 2018 Taylor & Francis Group, London, ISBN 978-1-138-73045-8

Steel Box-Girder Bridge Diseases Identification Based on Computer Vision System

Dalei Wang, Yue Pan & Bo Peng
Department of Bridge Engineering
Tongji University, China

ABSTRACT: Bridge diseases, including steel corrosion, protective material flaking off, etc., lead performance deterioration of material and risk increasing of structure failure. To understand well where a disease is and which level it is as the stipulation of maintenance specification, lots of manual inspection works are performed every year. Manual visual inspection method is reliable and useful, but it is time-consuming and high-cost, also not suitable for a standardized tracking of a disease development. In this study, a computer vision system is developed for long-span steel box-girder bridge inspection. Correspondingly, an automatic framework of disease identification based on deep learning is proposed. Finally, an experiment of this system on Jiangyin Bridge is introduced. This systemized solution is a novel methodology to instead of manual visual inspection and it can be attached to an existed bridge inspection installation. The results indicate that it is reliable and has a high robustness in real scenarios.

1 INTRODUCTION

To prevent the early failures of long-span bridge in service, the healthy status of bridges need to be monitored and evaluated. Thus, diseases identification is necessary for supporting the proper management strategies.

There are various diseases on steel box-girder of a long-span bridge, including steel corrosion, protective material flaking off, coating spalling, cracking etc. With the lack of advanced information-based auxiliary equipment and automated inspection system, people usually record and analysis each type of diseases manually and separately, which leads to low efficiency and difficulty in standardization, or long-term disease tracking.

To handle the drawbacks of manual inspection, based on computer vision, a steel box-girder bridge diseases inspection system is developed in this study.

Considering using an image recognition algorithm for the steel box-girder disease identification, the key point is the standardized image data acquisition. Thus, an image acquisition system is developed firstly for scanning the bottom of the steel box-girder, which moved by the inspection gantry at deck soffit. Then, to preferably present the position of diseases, the images captured per second are stitched into a large-scale panorama. Finally, a deep learning based steel diseases identification algorithm is performed, achieves average precision of 82.91%.

The image acquisition system as well as strategies are described in Section 3. Then the diseases identification algorithm based on deep learning is introduced in Section 4. Section 5 presents an experiment of this system on Jiangyin Bridge. Finally, summaries and conclusions are in Section 6.

This study is useful and meaningful in the developing of informationalized bridge maintenance.

2 RELATED WORKS

Corrosion, coating spalling and fatigue cracking are major diseases in steel box-girder bridges, and these diseases may lead to deterioration of structure performance as well as the increasing risk of failure. At present, the corresponding manual detection methods are adopted for various diseases. For instance, manual visual inspection is widely accepted in steel corrosion and coating deterioration detection, while ultrasonic and magnetic particle inspection has become a common practice in detecting fatigue cracks. The major limitations of these traditional manual inspection are the hardness of digitization and standardization due to the detection and evaluation results of diseases depend on the experience of inspectors to a large extent. In addition, it is costly and unachievable in the long-term monitoring of diseases especially in the inaccessible regions.

Many researchers set about detecting structural diseases with advanced equipment owing to the development of computer and sensor technologies in recent years. In the field of corrosion detection, corrosion segmentation can be achieved considering the color difference between corrosion regions and non-corrosion regions in early studies (Chen PH et al. 2009); other studies combined color with texture information to improve the applicability of corrosion segmentation (Shen HK et al. 2013); researchers test several machine learning algorithms including SVM, decision tree, naïve Bayes etc. in corrosion detection and achieved automatic evaluation of steel corrosion with detection results (Son H et al. 2014); a SVM classifier is trained to enhance segmentation effects in recent studies (Liao KW et al. 2016);. In the field of fatigue cracks detection, studies show that cracks detection can be realized with ultrasonic guided waves (Pahlavan L et al. 2016); other studies show that strain sensors can be arranged on a steel girder and train a SVM classifier to read the signals as well as evaluate fatigue state of steel girder (Hasni H et al. 2017). These studies expand the disease detection approaches and promote the process of standardized and automatic detection. But unfortunately, most of these advanced methods are still in research stage instead of applied stage considering the high equipment cost or strict site limitation.

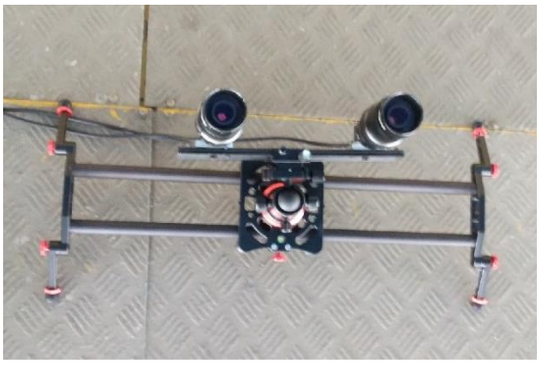


Figure 1 Hardware system.

3 IMAGE ACQUISITION

3.1 *Hardware*

The image acquisition system consists of a sliding rail, gimbal controller and industrial cameras, as shown in Figure 1. In practice, two Basler acA2040-120uc industrial cameras and two 8 mm lenses are applied in this study. The resolution of each camera is 2048 px × 1536 px and the frame rate is up to 120 fps with full resolution.



3.2 *Camera Calibration*

To counteract the effects of camera distortion and determine the relation between the camera's natural units (pixels) and the real-world units (for example millimeters), camera calibration is necessary to be carried out. Camera distortion are usually taken into account as a combination of radial and tangential distortion.

The radial distortion can be solved as:

$$x_{corrected} = x(1 + k_1 r^2 + k_2 r^4 + k_3 r^6) \quad (1)$$

$$y_{corrected} = y(1 + k_1 r^2 + k_2 r^4 + k_3 r^6) \quad (2)$$

where x, y = the distorted image point coordinates; $x_{corrected}$, $y_{corrected}$ = the undistorted image point coordinates; r = the distance from distorted image point to the distortion center; k_1, k_2, k_3 = distortion coefficients for radial distortion.

The tangential distortion can be solved as:

$$x_{corrected} = x + [2p_1 xy + p_2(r^2 + 2x^2)] \quad (3)$$

$$y_{corrected} = y + [p_1(r^2 + 2y^2) + 2p_2 xy] \quad (4)$$

where p_1, p_2 = distortion coefficients for tangential distortion.

OpenCV library, an open-source library, is applied for camera calibration in this study, the distortion coefficients are listed in Table 1, where we use chessboard to estimate distortion coefficients and then counteract camera distortion.

Table 1 Distortion coefficients for camera calibration.

Distortion Coefficients	Value
k_1	-1.095
k_2	10.325
k_3	-200.578
p_1	2.979×10^{-3}
p_2	-3.933×10^{-3}

3.3 *Image Stitching*

Disease identification commonly has two works:

1) Recording the position of diseases.

2) Classifying and evaluating the diseases.

To preferably present the position of diseases, large-scale panoramas are commonly required. Image stitching technique is widely used to obtain a panorama.

In this study, a phase correlation based image stitching approach (Reddy BS & Chatterji BN. 1996) is applied, which is widely used in remote-sensing images registration, considering the small sampling

interval and the surfaces of steel are usually less context.

Suppose there are two images: the fixed image $f_1(x,y)$ and the moving image $f_2(x,y)$ respectively, and the only difference between moving image and fixed image is a translation in spatial domain, which means:

$$f_2(x,y)=f_1(x-x_0,y-y_0) \tag{5}$$

Then the corresponding Fourier transforms of the two images are:

$$\begin{aligned} F_1(\xi,\eta) &= F[f_1(x,y)] \\ &= \int_{-\infty}^{\infty}\int_{-\infty}^{\infty} f_1(x,y)e^{-j2\pi(\xi x+\eta y)}dxdy \end{aligned} \tag{6}$$

$$\begin{aligned} F_2(\xi,\eta) &= F[f_2(x,y)] \\ &= \int_{-\infty}^{\infty}\int_{-\infty}^{\infty} f_2(x,y)e^{-j2\pi(\xi x+\eta y)}dxdy \end{aligned} \tag{7}$$

According to Fourier shift theorem, the Fourier transforms F_1 and F_2 are related by

$$F_2(\xi,\eta)=e^{-j2\pi(\xi x_0+\eta y_0)}F_1(\xi,\eta) \tag{8}$$

Then the normalized cross power spectrum is given by

$$\frac{F_1(\xi,\eta)F_2^*(\xi,\eta)}{|F_1(\xi,\eta)F_2^*(\xi,\eta)|}=e^{-j2\pi(\xi x_0+\eta y_0)} \tag{9}$$

where * indicates the complex conjugate.

By taking inverse Fourier transform, the normalized cross power spectrum in spatial domain is expressed as

$$F^{-1}(e^{-j2\pi(\xi x_0+\eta y_0)})=\delta(x-x_0,y-y_0) \tag{10}$$

Hence, the spatial response of cross power spectrum is a Dirac delta function centered at (x_0,y_0), from which the spatial translation is obtained. As to rotation and scale change, the translation can also be identified if we represent the image in log polar coordinate. Figure 2 shows the stitching results of steel box-girder images.

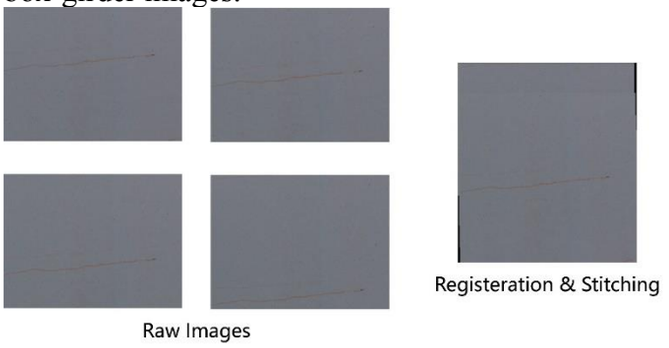


Figure 2 Image stitching result using phase correlation method.

4 DISEASES IDENTIFICATION

Considering the characteristic of the distribution and shapes of surface diseases of steel box-girder, a semantic segmentation deep neural network (DNN) is studied, which can achieve the "end-to-end" disease identification. Based on that, disease identification works are carried out automatically by just feeding a scanning image into the network and then the network will be output a segmentation mask as the result, which presents the diseases position and its class index for each single pixel.

4.1 *Network Architecture*

There are two types segmentation methods, one is called "decoder variants" and another one is "integrating context knowledge". Considering the computing efficiency and facilitating in network training DeepLab architecture (Chen LC et al. 2017), belongs to integrating context knowledge type, is selected.

Figure 3 shows the overall architecture of our segmentation DNN. this network can be divided into four blocks: to down-sample the input image, the first and second blocks are composed of two convolution layers with a max pooling layer behind; the third block is similar to the first and second blocks but the ordinary convolution layers are replaced by atrous convolution layers and pooling layers are discarded; In block 4, an atrous spatial pyramid pooling (ASPP) is used to achieve feature fusion; finally a transpose convolution is added as the last layer to up-sample the resolution reduced feature map and obtain a segmentation mask with the same size as the input image. More details are introduced in followings.

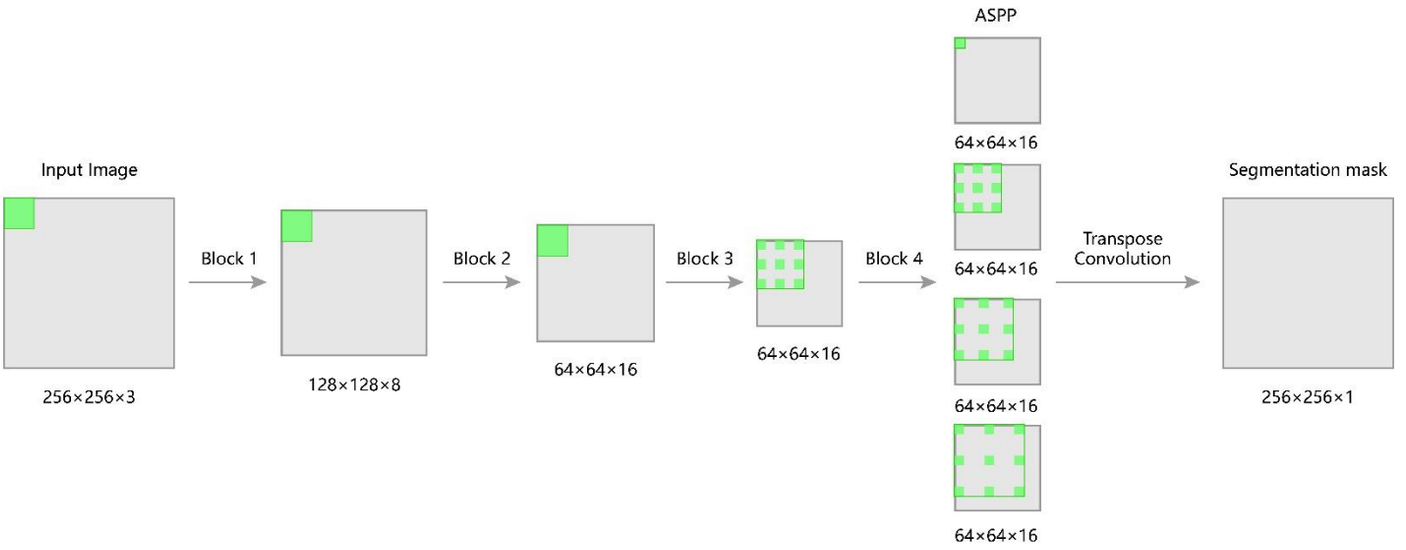


Figure 3 The architecture of segmentation deep neural network.

4.1.1 *Atrous Convolution*

The core of DeepLab network architecture lies in the utilization of atrous convolution (or dilated convolution) instead of ordinary convolution in feature extraction. In comparison with ordinary convolution, a parameter called "dilate rate" is proposed in atrous convolution to perform down-sampling with intervals, as is expressed:

$$I'(x,y)=\sum_{m}\sum_{n} I(x+r\cdot m, y+r\cdot n)K(m,n) \tag{11}$$

where $I'(x,y)$ = output value in (x,y); $I(x+r\cdot m, y+r\cdot n)$ = input value in $(x+r\cdot m, y+r\cdot n)$; $K(m,n)$ = kernel value in (m,n); r = dilate rate.

It can be proved that the atrous convolution result in high resolution feature map contains ordinary convolution result in low resolution, besides the feature map becomes much denser in atrous convolution compared with ordinary convolution. Thus, atrous convolution is applied in our network to keep the resolution of feature map and preserve spatial information to a certain extent.

4.1.2 *ASPP*

There are two variants in DeepLab architecture: DeepLab LargeFOV which lays out convolution layers in cascade and DeepLab ASPP which combines features in multi-scale. The essence of ASPP lies in parallel atrous convolutions with different atrous rates, which is equivalent to construct multi-scale space in feature map. The authors of DeepLab indicate that DeepLab ASPP demonstrates better performance in segmentation task, so DeepLab ASPP architecture is referred in designing our network.

The ASPP block is composed of four layers: the first layer is a linear combination of the input feature map, while in the other three layers atrous convolution is applied parallel with dilate rate of 4, 8 and 16. Each of the layer consists of 16 channels and they are concatenated to achieved a final feature map with 64 channels.

4.1.3 *Network Details*

The size of convolution kernels is fixed as 3×3 in all the convolution layers, and the pooling window size is fixed as 2×2 with non-overlapping to down sample the feature map. As to atrous convolution layer, the dilate rate is set as 2 in block 3 and 4,8,16 in ASPP to construct multi-scale space. The activation functions are fixed as ReLU function in all the convolution layers except the final transpose convolution layer, and sigmoid function is used in the final layer to predict whether a pixel corresponds to disease.

Batch normalization is set before convolution layers, which could modify the original distribution of the input data to accelerate network convergence. The process of batch normalization is shown as follows: firstly, the original distribution is modified with zero mean and unit variance,

$$\hat{x}^{(k)}=\frac{x^{(k)}-\mu_B}{\sqrt{\sigma_B^2+\varepsilon}} \tag{12}$$

where $x^{(k)}$ = the kth sample of the batch; μ_B = the expectation of the batch; σ_B^2 = the variance of the batch; ε = a minimum preventing zero denominator; $\hat{x}^{(k)}$ = the kth modifier sample.

Then, there are two trainable parameters to construct a linear transform of the modified distribution:

$$y^{(k)}=\gamma\hat{x}^{(k)}+\beta \tag{13}$$

where γ, β = trainable parameters; $y^{(k)}$ the kth normalized sample after batch normalization.

Therefore, the original distribution of the input batch is normalized with β mean and γ^2 variance, and these two parameters can be updated in the training process just like other parameters.

In terms of loss function, binary cross-entropy is major component. The loss of each pixel in the output segmentation mask is defined as:

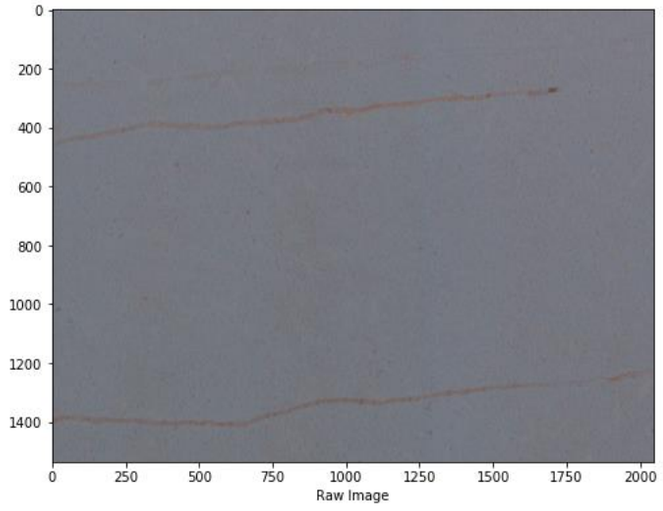
$$J(\theta)=\sum_{i=1}^{m}-y^{(i)}\ln p-(1-y^{(i)})\ln(1-p) \tag{14}$$

where $J(\theta)$ = the loss function; θ = parameters in the segmentation network; $y^{(i)}$ = label of the i th pixel, where 1 indicates disease and 0 indicates non-disease; p = the probability whether the i th pixel corresponds to disease, which is also the output of this pixel in segmentation network.

A regularization term is added to the loss function to prevent overfitting. L2 norm of convolution kernels, biases, etc. are added as regularization and the final loss function is:

$$\begin{aligned}\tilde{J}(\theta) &= J(\theta) + \lambda \|\theta\|_2^2 \\ &= \sum_{i=1}^{m} -y^{(i)} \ln p - (1-y^{(i)}) \ln(1-p) + \frac{\lambda}{2}\theta^T\theta\end{aligned} \tag{15}$$

where $\tilde{J}(\theta)$ = the final loss function; λ = regularization term factor representing the significance of regularization term, and is set to 0.01 by default; $\|\theta\|_2$ = the L2 norm of parameters including convolution kernels, biases, etc.



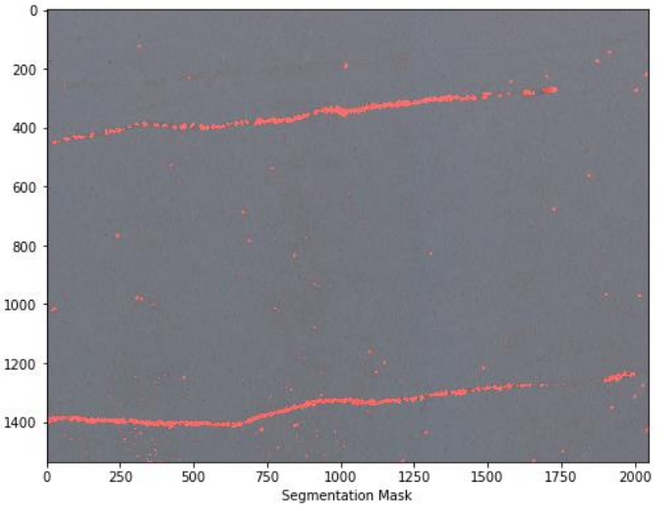


Figure 4 Raw image and segmentation mask.

4.2.2 *Training*

The segmentation network is implemented with TensorFlow framework. Adam algorithm (Kingma DP & Ba J 2014) is applied in training segmentation network to minimize the loss function. The initial learning rate is set as 1×10^{-3}, and the learning rate will be reduced by half when the accuracy in validation set does not drop any more. Only one image with its segmentation mask is trained in one training epoch. All the tasks are performed on a workstation with 16 GB RAM, Intel Xeon E3-1505M v5 @2.80GHz CPU and Nvidia Quadro M2000M GPU. The training process includes 50 epochs, which spends about 10 minutes. The loss curves and learning rate curves in training process are shown in Figure 5 and Figure 6.

4.2 *Network training*

4.2.1 *Dataset*

A training dataset involving Jiangyin bridge disease images is employed in this paper. The dataset contains 100 2048 px × 1536 px images captured at the bottom of girder. The region of corrosion is labeled manually on each single image. The raw image and segmentation mask are shown in Figure 4.

In training processing, to prevent out of memory problem (OOM) in training process, each of the raw images are split to 48 patches with the size of 256 px × 256 px. Thus, the original dataset is extrapolated to 4,800 images for training. This dataset is used for training, validation and testing with the ratio of 8.1:0.9: 1, respectively. which means 3888 images and 432 images are used in training and validation, and finally the other 480 images are used in testing.

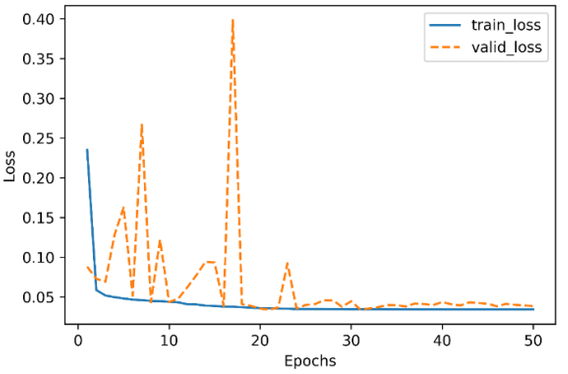


Figure 5 Loss curve.

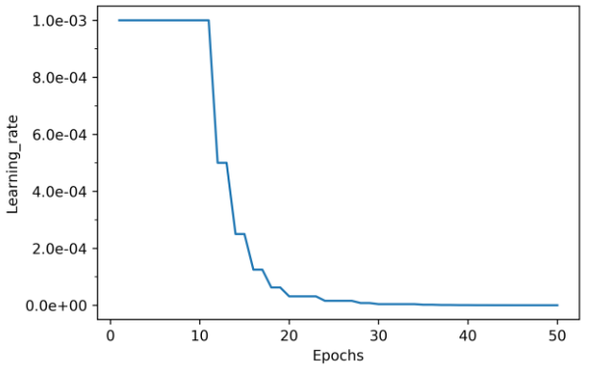


Figure 6 Learning rate curve.

4.2.3 *Validation*

To evaluate the model, precision, recall and accuracy are commonly used. They are defined as :

$$P = \frac{p_{11}}{p_{11} + p_{01}} = \frac{TP}{TP + FP} \tag{16}$$

$$R = \frac{p_{11}}{p_{11} + p_{10}} = \frac{TP}{TP + FN} \tag{17}$$

$$A = \frac{\sum_{i=0}^{1} p_{ii}}{\sum_{i=0}^{1}\sum_{j=0}^{1} p_{ij}} = \frac{TP + TN}{TP + FP + FN + TN} \tag{18}$$

where P = precision; R = recall; A = accuracy; p_{ij} = the number of pixels that belongs to class i but inferred to class j. In other words, p_{11} refers to TP, which is the number of pixels belonging to disease and inferred to disease; p_{10} refers to FN which is the number of pixels belonging to disease but inferred to background; p_{01} refers to FP which is the number of pixels belonging to background but inferred to disease; p_{00} refers to TN which is the number of pixels belonging to background and inferred to background.

With these evaluation indictors, the final binary accuracy, which is the accuracy for binary classification problems, achieves 98.93% on training set and 98.98% on validation set, and their relevant curves are shown in Figure 7.

To obtain the advised threshold value, which also is very important in final application of DNN, precision and recall (PR) curve are illustrated based on testing set, see Figure 8. It shows that it achieves average precision of 82.91% and the classification threshold can be set to 0.5 according to 5% error principle, which means a pixel will be classified as disease if it gets score higher than 0.5 in the final layer, otherwise it will be classified as background.

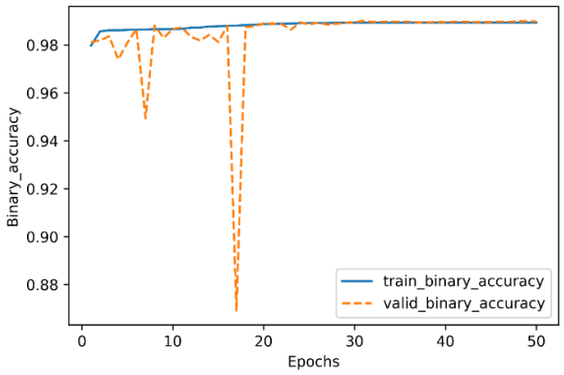


Figure 7 Binary accuracy curve.

We also test our segmentation network on the raw images with resolution of 2048 px × 1536 px, and the testing result shows that the segmentation network could recognize the major part of diseases, as is shown in Figure 9 where TP regions are painted green, FP regions are painted blue and FN regions are painted red.

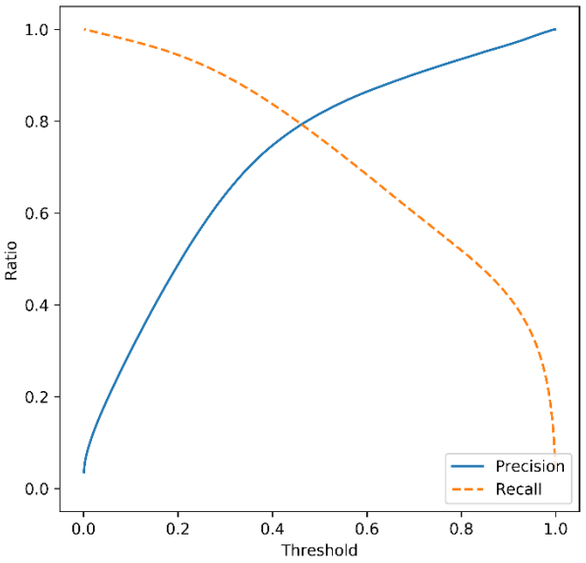


Figure 8 PR curve with threshold.

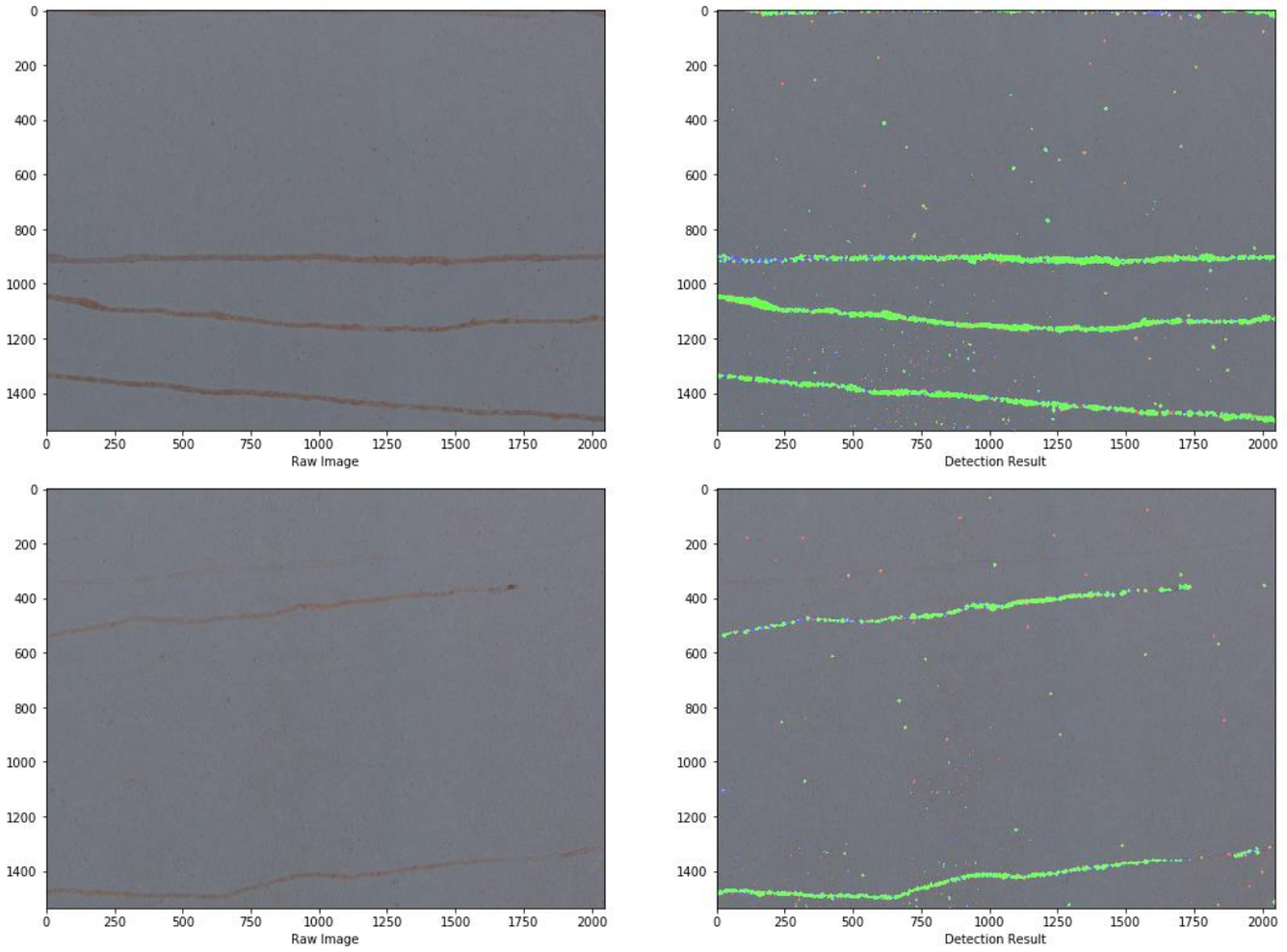


Figure 9 Testing on raw images.

5 EXPERIMENT

5.1 *General information*

The visual inspection system is tested on Jiangyin Bridge to detect surface diseases at the bottom of steel box girder. Jiangyin Bridge is a suspension bridge with a main span of 1,385 meters and 33.8 meters wide deck over the Yangtze River in Jiangsu, China. The hardware system consists of cameras, lens and sliding rails to capture actual images, and the software system consists of image registration program and segmentation network to obtain panoramic image and detect diseases, as pre-mentioned.

Cameras and lens are fixed on the inspection gantry at deck soffit and the layout is shown in Figure 10. The actual view field is measured as 97 cm×69 cm and the scale of view field and image is then calculated as 1: 136.62, which can be converted as one pixel on the image corresponds to 0.47 mm on the bridge. Considering the speed of inspection gantry, the sampling frequency is set as 0.5 fps, meaning that an image is captured per two second.

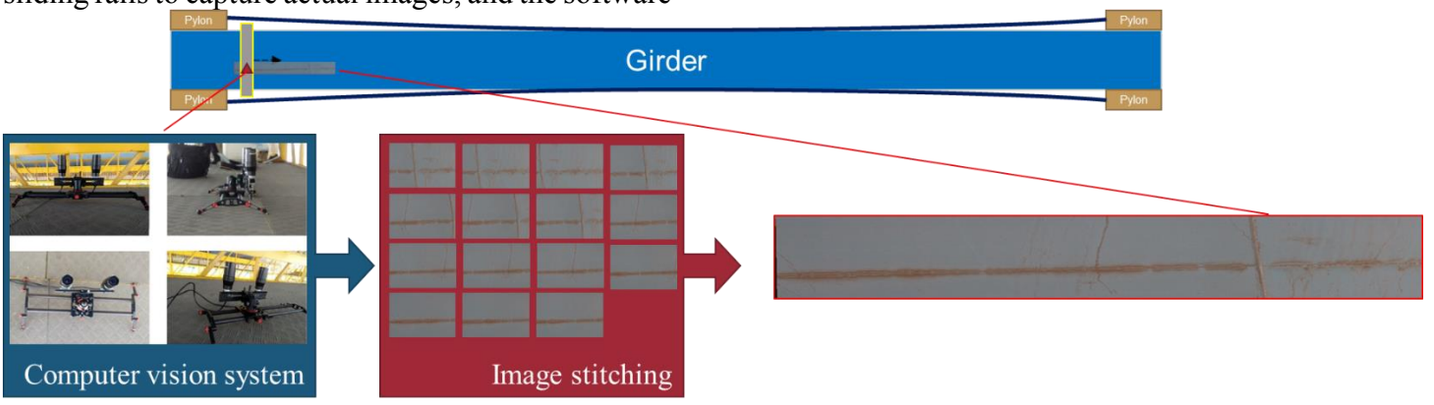


Figure 10 GIS based corrosion inspection management.

5.2 *Segmentation Result*

The segmentation network is applied after image capture. For example, a panorama with resolution of 1816 px ×19832 px is obtained through image stitching and manually cropping, then the panorama is split to 10 patches and fed to segmentation network in case of OOM. The panorama together as well as its segmentation result are shown in Figure 11. The disease area can be easily calculated after the segmentation mask is obtained. In this example, the area of steel disease is 2,607,192 pixels, which corresponds to 0.576 m^2 in total, occupy a 7.24% of the overall inspection region.

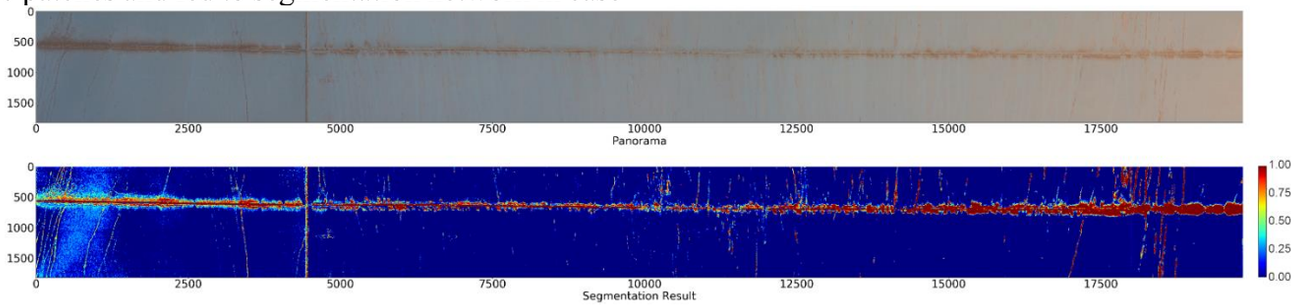


Figure 11 Panorama and segmentation result.

6 CONCLUSION

A novel disease inspection system based on computer vision technology is proposed in this study, and is tested on Jiangyin Bridge to detect surface diseases at the bottom of steel box girder standardized. The inspection system consists of two parts: the hardware system including cameras, lens and sliding rails to capture girder bottom images and software system including image stitching and segmentation network to obtain panorama image and identify diseases, separately. The experiment results indicate that disease identification together with panorama of disease distribution can be realized automatically.

It is believed that the inspection system could provide useful and standardized data for the daily management and maintenance of bridges. In addition, this inspection system can be installed on other platforms to identify diseases in the inaccessible regions for traditional methods, which could improve the level of standardization and extend the application scope of disease inspection to a certain extent.

ACKNOWLEDGMENTS

The work described in this paper was financially supported by National Natural Science Foundation of China (Grant No. 51778472). The authors also would like to express the thanks to Jiangsu Yangzi Bridge Co., Ltd., for the supports and assistances during the experiments.

REFERENCE

Chen PH, Yang YC, Chang LM. Automated bridge coating defect recognition using adaptive ellipse approach. Automation in Construction. 2009;18(5):632-43.

Shen HK, Chen PH, Chang LM. Automated steel bridge coating rust defect recognition method based on color and texture feature. Automation in Construction. 2013;31(5):338-56.

Liao KW, Lee YT. Detection of rust defects on steel bridge coatings via digital image recognition. Automation in Construction. 2016;71:294-306.

Son H, Hwang N, Kim C, Kim C. Rapid and automated determination of rusted surface areas of a steel bridge for robotic maintenance systems. Automation in Construction. 2014;42(2):13-24.

Hasni H, Alavi AH, Jiao P, Lajnef N. Detection of fatigue cracking in steel bridge girders: A support vector machine approach. Archives of Civil & Mechanical Engineering. 2017;17(3):609-22.

Pahlavan L, Blacquière G. Fatigue crack sizing in steel bridge decks using ultrasonic guided waves. Ndt & E International. 2016;77:49-62.

Zhang Z. A flexible new technique for camera calibration. IEEE Transactions on Pattern Analysis & Machine Intelligence. 2000;22(11):1330-4.

Zitová B, Flusser J. Image registration methods: a survey. Image & Vision Computing. 2003;21(11):977-1000.

Reddy BS, Chatterji BN. An FFT-based technique for translation, rotation, and scale-invariant image registration. IEEE Transactions on Image Processing A Publication of the IEEE Signal Processing Society. 1996;5(8):1266.

Garcia-Garcia A, Orts-Escolano S, Oprea S, Villena-Martinez V, Garcia-Rodriguez J. A Review on Deep Learning Techniques Applied to Semantic Segmentation. 2017.

Chen LC, Papandreou G, Kokkinos I, Murphy K, Yuille AL. DeepLab: Semantic Image Segmentation with Deep Convolutional Nets, Atrous Convolution, and Fully Connected CRFs. IEEE Transactions on Pattern Analysis & Machine Intelligence. 2017;PP(99):1-.

Chen LC, Papandreou G, Schroff F, Adam H. Rethinking Atrous Convolution for Semantic Image Segmentation. 2017.

Ioffe S, Szegedy C. Batch Normalization: Accelerating Deep Network Training by Reducing Internal Covariate Shift. 2015:448-56.

Kingma DP, Ba J. Adam: A Method for Stochastic Optimization. Computer Science. 2014.

Maintenance, Safety, Risk, Management and Life-Cycle Performance of Bridges – Powers, Frangopol, Al-Mahaidi & Caprani (Eds)
© 2018 Taylor & Francis Group, London, ISBN 978-1-138-73045-8

Bond behaviour of CFRP-steel double-lap shear joints exposed to marine atmosphere

Q.Q. Yu
State Key Laboratory for Disaster Reduction in Civil Engineering, Tongji University, Shanghai, China
Department of Structural Engineering, Tongji University, Shanghai, China

R.X. Gao
Department of Structural Engineering, Tongji University, Shanghai, China

X.L. Gu
State Key Laboratory for Disaster Reduction in Civil Engineering, Tongji University, Shanghai, China
Department of Structural Engineering, Tongji University, Shanghai, China

X.L. Zhao
Department of Civil Engineering, Monash University, Melbourne, Australia

ABSTRACT: Fibre reinforced polymer (FRP) materials are currently more and more widely applied in structural engineering attributed to the high strength-to-weight ratio and good resistance to environmental attack. Carbon FRP (CFRP) has been demonstrated great potential in fatigue strengthening of defected steel components, because it could help to share the far-field load, to constrain the crack opening, and to reduce the crack propagation rate. The strengthening efficiency relies on the load transfer between steel and CFRP and consequently the interfacial behaviour of CFRP-to-steel joints. Generally, a structural adhesive is adopted to attach CFRP to a steel substrate and it takes one to two weeks to achieve the full strength. However, the potential risk of environmental attack at the curing stage of the adhesive has not been well understood. In this paper, a series of experimental studies on the interfacial behaviour of CFRP-steel double-lap joints were carried out. The specimens were cured in different environmental conditions for two weeks and then statically loaded to failure. The performance of specimens subjected to room condition, salt fog and high relative humidity (RH) was compared. Effects of CFRP material type and surface treatment were also considered. The bond strength was decreased by 2-17% in comparison with the control specimens. Proper silane treatment could help to maintain the integrity of the specimen. This study extends the understanding of the environmental durability of CFRP-to-steel joints and provides some useful suggestions for the strengthening technique.

1 INTRODUCTION

Fatigue damage is a major concern of steel structures and fatigue cracks may emanate from stress concentration zone. Lifecycle management of these infrastructure has been one of the most important issues in the civil engineering community.

Traditionally, these damage is either stopped by hole drilling at the crack tip or replaced by new plate through welding or fastening. These techniques are time-consuming and complex to fix, and the most important, the rehabilitation is still prone to fatigue damage (Zhao & Zhang 2007).

Currently, externally bonding with fibre reinforced polymer (FRP) composite materials have attracted much attention as an alternative in retrofitting of aged infrastructure (Teng et al. 2012, Zhao 2013). For fatigue repair of defected steel structures, extensive studies have been carried out to investigate the fatigue behaviour of initially damaged steel plate strengthened by CFRP overlays (Jones & Civjan 2003, Liu et al. 2009, Yu et al. 2013, 2014, Colombi et al. 2015, Hu et al. 2016). The crack propagation life was significantly prolonged which demonstrated a great potential of CFRP bonding.

Research was also performed on the effectiveness of this strengthening approach applied to steel beams and welded joints (Kim & Harries 2011, Wu et al. 2012, Colombi and Fava 2015, Yu et al. 2015, Yu & Wu 2017).

Most infrastructure endures both service load and environmental attack during their life cycle, and therefore, durability of the CFRP-steel system has become a new concern in recent years (Dawood & Rizkalla 2010, Nguyen et al. 2012, Bai et al. 2014, Borrie et al. 2015). Since the retrofitting scheme relies on load transfer between FRP and substrate, different harsh environmental conditions were selected to investigate their effects on the interfacial bond behaviour and double-lap shear joints were commonly adopted.

Dawood & Rizkalla (2010) tested 44 steel-CFRP double-lap shear joints, among with 30 specimens were exposed to wet/dry cycles in a 5% NaCl solution at a temperature of 38 °C, up to 6 months. Different methods to enhance the bond durability were compared including silane coupling agent, glass fibre layer and a combination of both methods. The results showed that the silane treatment was preferred to improve the bond durability whereas glass

fiber layer was helpful to increase the initial bond strength.

In Nguyen et al. (2012), more complicated environmental conditions were taken into consideration, including, simulated sea-water at 20 °C and 50 °C up to one year, constant and cyclic temperatures with a high level of relative humidity (RH) up to 1000 h. It was demonstrated that simulated sea-water after one year of exposure was more detrimental to both the strength and stiffness of the joints compared to combinations of temperature and humidity for 1000 h of exposure. A prediction model on the degradation was also proposed.

Borrie et al. (2015) presented a study on the combined effect of marine environment and fatigue loading. The CFRP laminate and sheeting patched double-lap shear joints were exposed to a 5% by weight NaCl solution at 20, 40 and 50 °C as well as a certain static tensile load. Afterwards, these specimens were applied by fatigue load for up to 6 million cycles. The residual static strength of the joints witnessed a maximum 28% loss in strength.

To the best knowledge of the authors, there have been limited attempts to perform an experimental study exposed to salt fog to simulate the marine atmosphere which is frequently occurred to steel cross-sea bridges. According to manufactures' datasheet, the structural adhesive Araldite 420 A/B gels in three to four hours at 25 °C and is sufficiently cured to allow handling after 5 hours. 90% of the full strength could be achieved by four to five days and the full strength development takes one to two weeks at room temperature. Currently, the aforementioned research generally first cured the specimens at room condition and then exposed them to aggressive conditions. The effect of environmental exposure during the curing stage of adhesive hasn't been well understood.

This paper presents a series of experimental studies on the performance of CFRP-steel double-lap shear joints. The effect of harsh environment condition on the curing stage was focused and specimens were subjected 5% by weight NaCl fog or 80% RH at 35 °C for two weeks. Normal/high modulus CFRP sheets and normal modulus CFRP laminate were selected. The effect of saline treatment was also carefully checked. Later, all the specimens were statically loaded to failure and the ultimate tensile strength witnessed a reduction of 2-17% in comparison with the normally cured joints.

2 EXPERIMENTAL PROGRAM

The test program was conducted in the Laboratory of Performance Evolution for Engineering Structures at Tongji University, China. A total of 22 specimens were designed and tested, as listed in Table 1.

2.1 *Configuration of test specimens*

Double-lap shear joint specimens shown in Figure 1 were used for the experimental program. Two steel plates with dimensions of 180 × 50 × 5 mm were connected by CFRP materials. A bond length of 100 mm was adopted to ensure the load transfer. The specimen configuration and dimensions were chosen to be similar to those reported in Borrie et al. (2015) for comparison purposes.

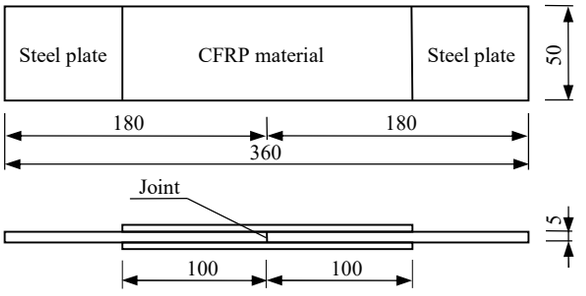


Figure 1. Specimen geometry (dimensions in millimeters, not to scale).

2.2 *Material properties*

The steel plates used in the tests were Q345b (according to Chinese Standard GB 50017-2003). The mechanical properties were determined based on coupon tensile tests. The average yield strength, ultimate tensile strength and Young's modulus were 274.3 MPa, 401.6 MPa and 201 GPa, respectively. The authors realized that the yield strength was much lower than expected. Fortunately, the specimens did not fail due to yield of steel and it was therefore believed that the yield strength had little effect on the experimental program. Different types of CFRP materials were selected for the patching system, i.e., normal modulus CFRP laminate, normal modulus CFRP sheet and high modulus CFRP sheet with a nominal thickness of 1.4 mm, 0.167 mm and 0.217 mm, respectively. Flat coupon tests were also performed to investigate their technical data. The normal modulus CFRP laminate exhibited a Young's modulus of 200.4 GPa, an ultimate tensile strength of 3022.4 MPa, and an ultimate strain of 15081 με, respectively (Yu & Wu 2017). The normal modulus CFRP sheet showed a Young's modulus of 254 GPa, an ultimate tensile strength of 4192 MPa, and an ultimate strain of 1.84% (Wu & Jiang 2013). The high modulus CFRP sheet had a Young's modulus of 532 GPa, an ultimate tensile strength of 2647 MPa, and an ultimate strain of 4976 με. The CFRP materials were bonded to the steel plate by structural adhesive Araldite 420. Its tested Young's modulus, ultimate tensile strength, and ultimate strain were 28.6 MPa, 1901 MPa, and 24000 με, respectively (Fawzia 2007).

2.3 *Specimen preparation*

The steel plate was sandblasted and cleaned by acetone to remove the weak oxidation layer and to expose a chemically active surface. Afterwards, they were lightly bonded together to create a flat and continuous substrate for CFRP application. Araldite 420 was mixed by a weight ratio of 5:2 and laid evenly on the steel substrate and CFRP. The specimens were bonded by one layer of normal modulus CFRP laminate, three layers of normal modulus CFRP sheet, or one layer of high modulus CFRP sheet. The thickness of the bond layer was controlled to be approximately 0.5 mm (Yu & Wu 2017).

Silane treatment has been proven a potential approach to improve the interfacial behaviour between CFRP and steel (Dawood & Rizkalla 2010, Borrie 2016). Four specimens were tried in this experimental program using the glycidoxypropylmethoxysilane supplied by Dow Corning. Two formulas were adopted, i.e., 4% silane by volume with 96% methanol by volume mix (N, representing nonhydrolysed), and 4% silane by volume, 90% methanol by volume and 6% deionised water by volume mix (H, representing hydrolysed). The silane solution was prepared by stirring for 1 hour followed by aging for 20 hours. After brushed by the solution, the steel plates were either aged in room temperature for 1 hour (A, representing ambient temperature) or dried by a hot air stream (80 °C) with dryer for 15 minutes (C, representing hot cured) as suggested by suppliers to achieve a better hydrolytic action. For the specimens with silane treatment, those procedures were taken before application of epoxy and CFRP.

2.4 *Environmental exposure and load condition*

With concern of the effect of curing condition on the bond behaviour of CFRP-steel double-lap shear joints, three different environmental exposure conditions were adopted in the experimental program, i.e., laboratory room condition, an environmental chamber with salt fog generated by 5% by weight NaCl, 35 °C (Figure 2a) and an environmental chamber with a RH of 80%, 35 °C (Figure 2b).



(a) (b)

Figure 2. Environmental chambers: (a) with salt fog, (b) with high humidity.

All the specimens were cured for two weeks since normally the structural adhesive takes two week to achieve the full strength in room condition. Afterwards, they were gripped on both ends and tensioned to failure at a rate of 2 mm/min.

3 EXPERIMENTAL RESULTS AND DISCUSSIONS

Table 1 presents a summary of the test results of all the specimens. The specimen nomenclature is as follows: L = CFRP laminate, 3S = three layers of normal modulus CFRP sheet, 1S = one layer of high modulus CFRP sheet, R = room condition, M = marine atmosphere, i.e., 5% NaCl salt fog and 35 °C, H = 80% RH and 35 °C. Two identical specimens were designed for one scenario to reduce the scatter of the experimental program and the number after the hyphen indicates the number of them. Four specimens with three layers of normal modulus CFRP sheet were intended to examine the performance of silane treatment when subjected to the salt fog, among which, N and H indicate the mixed solutions with and without deionised water, respectively; A and C represent the preparation procedures in room condition and hot air stream, respectively.

Table 1. Experimental program and results.

Specimen	Ultimate tensile strength (kN)
LR-1	95.1
LR-2	98.0
LM-1	90.6
LM-2	89.4
LH-1	94.4
LH-2	86.8
3SR-1	94.8
3SR-2	91.3
3SM-1	90.6
3SM-2	91.7
3SH-1	89.3
3SH-2	91.7
1SR-1	55.1
1SR-2	56.6
1SM-1	44.3
1SM-2	57.4
1SH-1	47.2
1SH-2	45.7
3SMNA	94.1
3SMNC	81.9
3SMHA	93.1
3SMHC	80.2

3.1 *Failure modes*

After two weeks' exposure, obvious corrosion was found in specimens exposed to salt fog while those exposed to high RH witnessed a much slighter corrosion. Figure 3 showed a typical group of cured specimens.

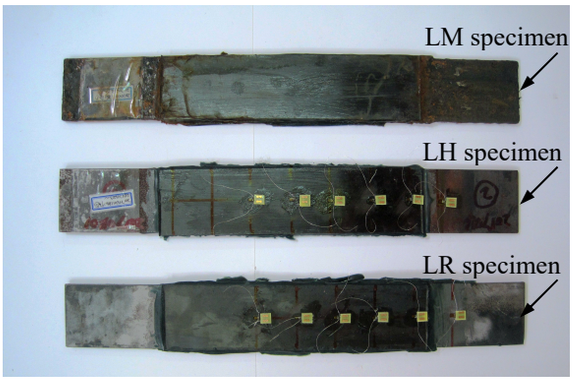


Figure 3. Specimens after environmental exposure.

Specimens with one layer of normal modulus CFRP laminate witnessed adhesion failure between steel and adhesive accompanied by CFRP delamination. Similar failure mode was observed for specimens with three layers of normal modulus CFRP sheet whereas CFRP rupture was found in those with one layer of high modulus CFRP sheet. It is mainly because of the difference of deformability between normal modulus and high modulus CFRP sheet, which is in conformance with the phenomenon reported in Liu et al. (2009). For the specimens with the same patch configuration exposed to different conditions, the failure modes were approximate to each other. With respect to the specimens with silane treatment before CFRP application, similarly, no apparent difference was observed in comparison with un-treated specimens and the specimens all failed with interfacial debonding and CFRP delamination, regardless the zone of delamination was slightly different. Typical failure modes are shown in Figure 4.

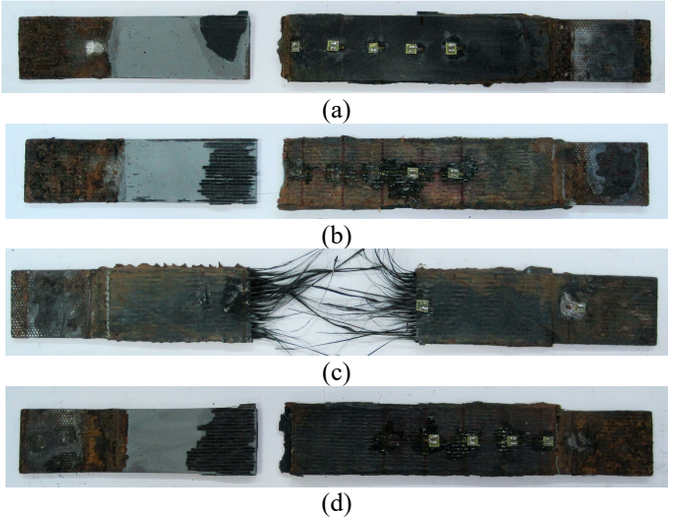


Figure 4. Failure modes: (a) LM-1; (b) 3SM-1; (c) 1SM-1; (d) 3SMNA.

3.2 *Bond strength*

The bond strength ratio defined as the ratio of the average bond strength of two identical specimens to that of the specimens cured at the room condition is displayed in Figure 5. It is shown that the bond strength decreased by 2%-17%. The specimens with three layers of normal modulus CFRP sheet appeared to be the most resilient among the specimens with different patch schemes. Comparing the effects of environmental conditions during the curing stage of structural adhesive, the degradation of specimens with CFRP laminate and normal modulus CFRP sheet was approximately the same when subject to salt fog and 80% RH. However, the specimens with high modulus CFRP sheet seems more vulnerable to high RH condition.

In Borrie et al. (2015), the specimens were first cured at room condition for two weeks and then immersed into sea-water up to six months and fatigue cycles up to 6 million, the bond strengths of the joints generally decreased by 10-15%, and the most severe reductions reached to 20 and 28% occurred to laminate and sheeting specimens respectively. It was therefore implied that the deterioration due to the environmental exposure during the curing stage of structural adhesive was comparable to the long-term attack.

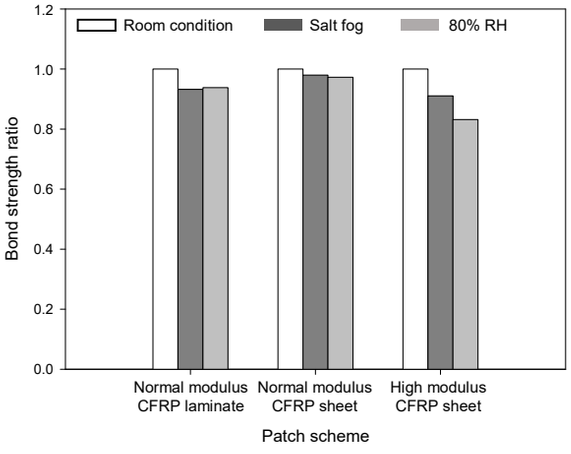


Figure 5. Bond strength ratio.

Figure 6 plots the test results of the specimens with silane treatment as well as the control specimens. It was interesting to find that the procedure of aging in room condition is sufficient to maintain the integrity of the specimen while those dried by the hot air stream which was expected to have a better performance led to an adverse effect. Future research was planned to study the effectiveness of surface treatment.

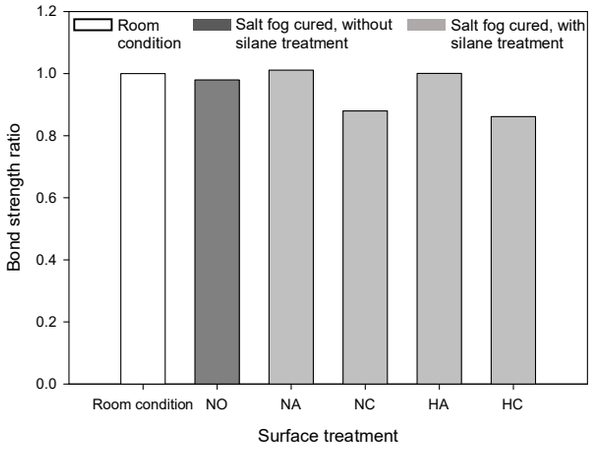


Figure 6. Effect of silane treatment.

4 CONCLUSIONS

This paper presents an experimental study of CFRP-steel double-lap shear joints subjected to environmental exposure at curing stage of structural adhesive. The following is concluded.

After cured in salt fog or high RH for two weeks, bond strengths decreased by 2-17%, which was comparable with the previous study on the effect of long-term exposure.

For specimens with one layer of normal modulus CFRP laminate and three layers of normal modulus sheets, the effects of salt fog and high RH salt did not have an apparent difference. Based on the current test results, the deterioration of the specimens with one layer of high modulus CFRP sheet was the most significant.

Specimens with CFRP laminate and three layers of normal modulus sheets failed with fibre delamination while specimens with one layer of high modulus sheet failed with fibre fracture. The failure mode did not change with the curing condition.

Silane treatment with proper application procedure could be used to improve the interfacial behaviour.

5 ACKNOWLEDGMENTS

The work described in this paper was supported by the National Natural Science Foundation of China (NSFC Grant No. 51508406). The authors are grateful for the program.

6 REFERENCES

Borrie, D. 2016. *Carbon fibre reinforced polymer patched steel under fatigue loading and pre-exposure to extreme environmental conditioning*. PhD thesis, Monash University, Melbourne, Australia.

Borrie, D., Liu, H.B., Zhao, X.L., Singh Raman, R.K. & Bai Y. 2015. Bond durability of fatigued CFRP-steel double-lap joints pre-exposed to marine environment. *Composite Structures* 131: 799-809.

Colombi, P. & Fava, G. 2015. Experimental study on the fatigue behaviour of cracked steel beams repaired with CFRP plates. *Engineering Fracture Mechanics* 145: 128-142.

Colombi, P., Fava, G. & Sonzogni, L. 2015. Effect of initial damage level and patch configuration on the fatigue behaviour of reinforced steel plates. *Fatigue & Fracture of Engineering Materials & Structures* 38(3): 368-378.

Dawood, M. & Rizkalla, S. 2010. Environmental durability of a CFRP system for strengthening steel structures. *Construction and Building Materials* 24: 1682-1689.

Fawzia S. 2007. *Bond characteristics between steel and carbon fibre reinforced polymer (CFRP) composites*. PhD thesis, Monash University, Melbourne, Australia.

Hu, L.L., Zhao, X.L. & Feng, P. 2016. Fatigue behavior of cracked high strength steel plates strengthened by CFRP sheets. *Journal of Composites for Construction* 20(6): 04016043.

Jones, S.C. & Civjan, S.A. 2003. Application of fiber reinforced polymer overlays to extend steel fatigue life. *Journal of Composites for Construction* 7(4): 331-338.

Kim, Y.J. & Harries, K.A. 2011. Fatigue behavior of damaged steel beams repaired with CFRP strips. *Engineering Structures* 33(5): 1491-1502.

Liu, H.B., Al-Mahaidi, R. & Zhao, X.L. 2009. Experimental study of fatigue crack growth behaviour in adhesively reinforced steel structures. *Composite Structures* 90(1), 12-20.

Nguyen, T.C., Bai, Y., Zhao, X.L. & Al-Mahaidi, R. 2012. Durability of steel/CFRP double strap joints exposed to sea water, cyclic temperature and humidity. *Composite Structures* 94(5): 1834-1845.

Teng, J.G., Yu, T. & Fernando, D. 2012. Strengthening of Steel Structures with Fiber-Reinforced Polymer Composites. *Journal of Constructional Steel Research* 78: 131-143.

Wu, Y.F. & Jiang, C. 2013. Effect of load eccentricity on the stress-strain relationship of FRP-confined concrete columns. *Composite Structures* 98: 228-241.

Wu, G., Wang, H.T., Wu, Z.S., Liu, H.Y. & Ren, Y. 2012. Experimental study on the fatigue behavior of steel beams strengthened with different fiber-reinforced composite plates. *Journal of Composites for Construction* 16(2): 127-137.

Yu, Q.Q., Chen, T., Gu, X.L., Zhao, X.L. & Xiao, Z.G. 2013. Fatigue behaviour of CFRP strengthened steel plates with different degrees of damage. *Thin-Walled Structures* 69: 10-17.

Yu, Q.Q., Chen, T., Gu, X.L., Zhao, X.L. & Xiao, Z.G. 2015. Boundary element analysis of fatigue crack growth for CFRP-strengthened steel plates with longitudinal weld attachments. *Journal of Composites for Construction* 19(2): 04014044.

Yu, Q.Q. & Wu, Y.F. 2017. Fatigue strengthening of cracked steel beams with different configurations and materials. *Journal of Composites for Construction* 21(2): 04016093.

Yu, Q.Q., Zhao, X.L., Al-Mahaidi, R., Xiao, Z.G., Chen, T. & Gu, X.L. 2014. Test on cracked steel plates with different damage levels strengthened by CFRP laminates. *International Journal of Structural Stability and Dynamics* 14(6): 1450018.

Zhao, X.L. 2013. *FRP-strengthened metallic structures*, CRC Press, Boca Raton, FL.

Zhao, X.L., Bai, Y., Al-Mahaidi, R. & Rizkalla, S. 2014. Effect of dynamic loading and environmental conditions on the bond between CFRP and steel: State-of-the-art review. *Journal of Composites for Construction* 18(3): A4013005.

Zhao, X.L. & Zhang, L. 2007. State-of-art review on FRP strengthened steel structures. *Engineering Structures* 29(8): 1808-1823.

Maintenance, Safety, Risk, Management and Life-Cycle Performance of Bridges – Powers, Frangopol, Al-Mahaidi & Caprani (Eds)
© 2018 Taylor & Francis Group, London, ISBN 978-1-138-73045-8

Drilling-Hole Shape for Retarding the Fatigue Crack Propagation

Z.Y. YuanZhou & B.H. Ji & Z.Q. Fu
College of Civil and Transportation Engineering, Hohai University, Nanjing, Jiangsu, P.R. China

ABSTRACT: The study focuses on the drilling hole shape for retarding the crack propagation, on the basis of finite-element method. A lumbar-round hole was proposed, and compared with normal-round hole. The stress concentration factor (SCF) was analyzed, as well as the drilling parameters. The results show that the stress concentration at crack tip can be further decreased when comparing with the normal-round hole. The performance of lumbar-round hole can be further improved by decreasing the radius of arc. When applying the spiral transition curve to design the lumbar-round hole, a better stress distribution can be obtained, resulting in better crack retarding effects.

1 INTRODUCTION

Stop-hole, which is also called drilling-hole, is usually be regarded as a temporary method for preventing crack propagation in mechanical or structural components, such as the orthotropic steel deck (OSD). It is widely applied throughout the steel bridges, due to its excellent structural performance, while it is susceptible to fatigue crack under cyclic traffic load (Ya et al. 2013; Choi & Kim 2009), causing serious damage if left the crack unconcerned. Thus, a proper method should have been conducted before the crack becoming unstable.

When the crack emanates, a high stress concentration area generated near the crack tip, where the stress value may exceed the material yield strength, forming a plastic zone. Some micro-cracks and -holes began to appear with the accumulation of plastic deformation, resulting in crack rapid propagation (Zhu et al 1995). The plastic zone can be removed if drilling holes with a certain size near the crack tip, and the stress concentration can be also reduced, resulting in a delay on crack propagation or stop crack propagation thoroughly. However, the issues that when to drill the hole, what is the drilling size, how is the shape need to be figure out before conducting the drilling-hole method on the operation.

There are numerous on-going research efforts to address these issues. Guo suggested that the proper diameter of drilling-hole should be 0.6 times of the fatigue crack length (Guo et al 2008) by comparing the relationship between crack length and drilling-hole diameter, based on the maximum stress, while other researchers proposed that the diameter of drilling-hole should be 0.4 times of the fatigue crack length (Xiong et al 2016), or about 5.57mm~7.14mm (He et al 2004). The relationship between the drilling-hole diameter and plate thickness were discussed (Ji et al 2016). Though the proper diameter of drilling-hole has not come to an agreement, the similar regulation that the drilling-hole with large diameter has better reduction on stress concentration near crack tip, is confirmed.

Since the stress concentration (Peterson et al 2010) mainly depends on the shape, or structural feature, it can be modified when changing the detail shape parameters. The curvature (Bates et al 1980) is defined as the state of being curved, or the degree to which something is curved. As for the drilling-hole, the reciprocal value of radius equals to the curvature, therefore smaller the curvature is, better stress concentration reduction can be obtained. Fanni M proposed a new crack stop-hole shape, and the analysis results approved that it is better than round hole (Fanni et al 2015). However, it is quite complicated to drill the hole like this type, or even impossible on service structure.

If reducing the curvature continuously to zero, the straight line appears near the hole edge, then the round hole gradually becoming the lumbar-round hole. Therefore, the lumbar-round hole was proposed by considering the curvature reduction. The investigation of lumbar-round hole was carried out in this paper, based on the stress concentration factor by finite-element method (FEM).

2 FINITE-ELEMENT MODEL

2.1 *Model size*

A linear elastic analysis was carried out with the software package ABAQUS, considering the material's young modulus 210 GPa, poisson ratio 0.3. The quarter shell model was established by taking advantages of symmetric model geometry and boundary conditions. The size of whole model was 100mm by 50mm, and the crack length was arranged in the center of the model with 12mm long. The drilling-hole was set at the crack tip, with the diameter 6mm.

Since the drilling-hole may weaken the bearing capacity of the remaining section, the hole shapes with lumbar-round and round are compared under the similar drilling area, as shown in Fig.1. The radius of lumbar-round hole is 2mm, and the horizontal length L is about 2mm.

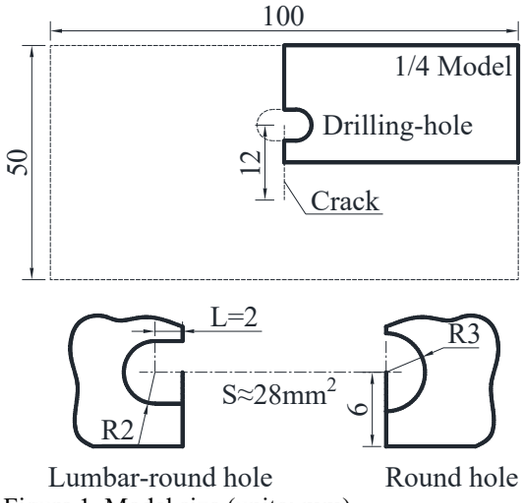


Figure 1. Model size (unite: mm)

2.2 *Modeling details*

Fig.2 shows the modeling details of lumbar-round hole. The tensile stress was applied at the edge the model, with the magnitude of 1MPa. The symmetry boundary was set at the axis both in X and Y direction. In order to deal with the stress concentration, the element type of CPS8 was used in the model, and the minimum mesh size is 0.5mm round the drilling-hole. The parameters of round hole model are the same.

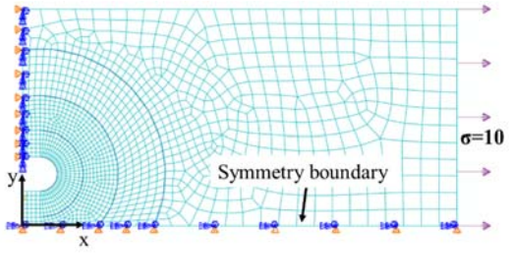


Figure 2. Modeling details of lumbar-round hole

3 RESULTS COMPARING

The stress distribution alone the hole edge was investigated, as shown in Fig.3. It is found that the maximum stress value of lumbar-round hole is a little smaller than that of round hole, and the maximum point is not locate on the crack predicted extension path, i.e. the stress concentration point moves a new location. However, at the predicted extension point (θ=0), the stress value of lumbar-round hole is much lower than that of round hole, due to the reduction on curvature. Therefore, when comparing with the round hole, the lumbar-round hole has better stress distribution.

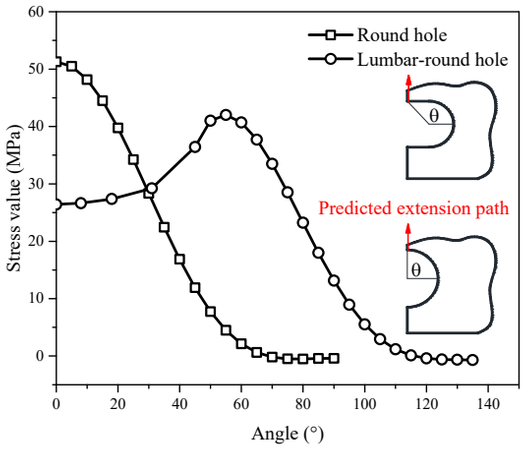


Figure 3. Stress distribution alone the hole edge

The range of effective section will decrease, when drilling a hole near the crack tip, weaken the bearing capacity to an extent. The stress distribution at the remaining bearing section is important for fatigue crack initiation and propagation. Fig.4 shows the stress solution at the remaining section. It turns out that the stress distribution becomes more uniform when using the lumbar-round hole, instead of round hole, while the affected range of stress concentration seems similar. Large stress gradient of round hole can be obtained from the figure, resulting in poor fatigue performance (Montebello et al 2016).

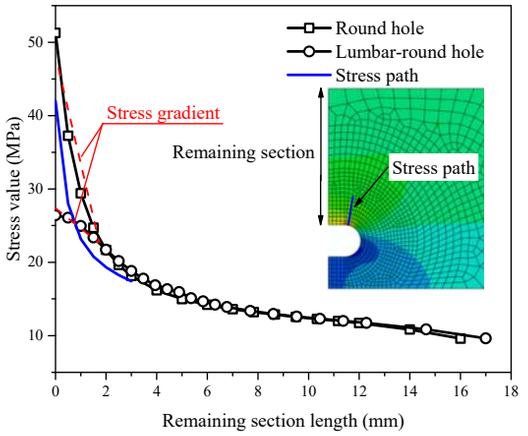


Figure 4. Stress distribution alone the remaining section

Since the stress concentration appears at the place where the curvature is mutated, the stress distribution along path (the straight line in Fig.4) is also compared. Results show that the stress distribution is similar with the round hole, but the

value is a little smaller. This critical position has potential risk on fatigue cracking.

4 PARAMETERS EFFECT ON LUMBAR-ROUND HOLE

4.1 *Definition parameters*

The parameters of lumbar-round hole consist of two aspects, the horizontal length 2L and the radius R, as shown in Fig.5. Thus, the lumbar-round hole with different parameters can be denoted, for example L2R2 stands for the model described in the Fig.2.

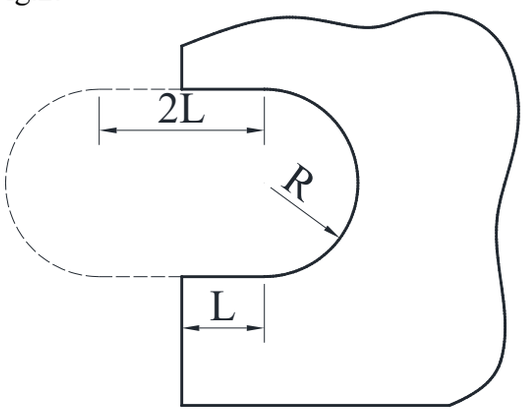


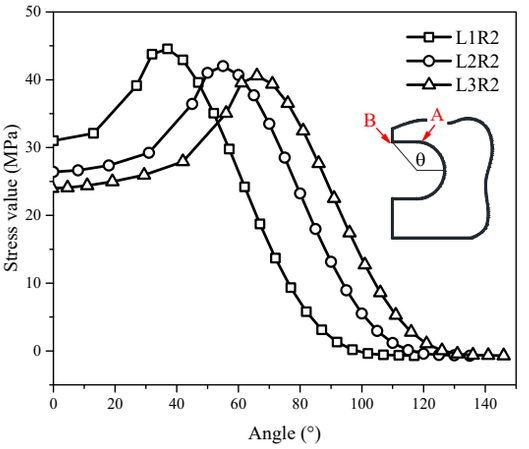
Figure 5. Definition of lumbar-round hole parameters

4.2 *Comparison with different parameters*

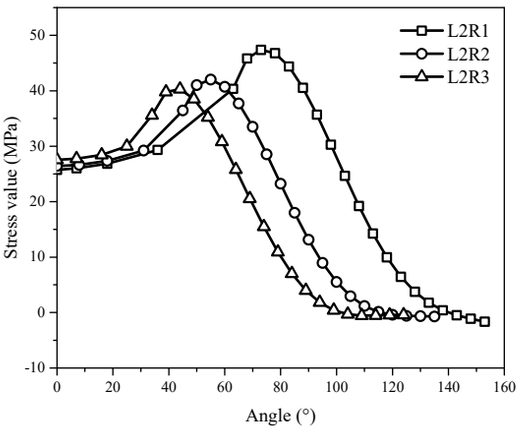
Regarding the previous model as the reference set, five different cases were calculated by FEM with same load condition, mesh size and element type. Solutions are plotted in the Fig.6. It is found that with the increasing of L, the maximum stress value at critical position (A) decreases, as well as the stress value at position B. However, the decreasing tendency slows down when keeps L increasing. Therefore, excessive increasing the lumbar-round hole length is not suggested, due to the low beneficial for stress reduction.

If changing the radius R, a different stress distribution can be obtained in Fig.6b. With the increasing of R, the maximum stress value at position A decreases, while the stress value at position B seems more stable. Since the curvature equals to the reciprocal value of radius, the curvature thus decreases when increasing the radius R, resulting in lower stress values at position A.

In order to acquire the main influence factors on parameters, the relative stress variation was calculated based on the standard model (L2R2), and the results were shown in Fig.7. It is seen that, the stress variation degree with radius R changes is a little larger than that with L changes, indicating that the radius R may be the main factor influencing the maximum stress around the lumbar-round hole edge. The regulation seems same with the round hole, despite the fact that there is only one parameter for the round hole.



(a) Variation with L



(b) Variation with R

Figure 6. Stress distribution with different parameters

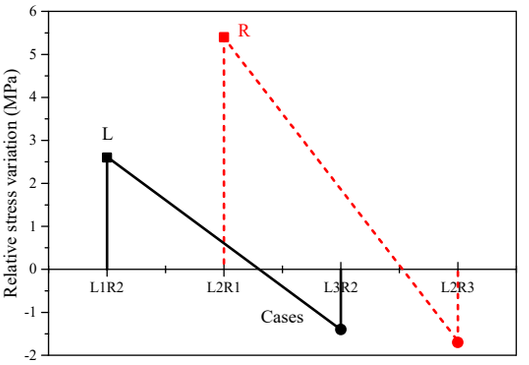


Figure 7. Stress variation degree comparing

5 LUMBAR-ROUND HOLE SHAPE OPTIMIZING

The curvature is mutated at the joint of straight line and curve, resulting in a new stress concentration along the lumbar-round hole. In order to reduce the degree of stress concentration, the spiral transition curve (STC), used in the design of the alignment of road (Yu et al 2011), was considered in the lumbar-round hole shape optimizing. The purpose of using STC is to stabilize the curvature variation, thus resulting in a gentle stress variation. The formulation of STC used for shape optimizing is based on the cubic parabola, shown as follows:

$$y = \frac{1}{6Rl_s}x^3 \qquad (1)$$

where l_s is the length of STC, R is the radius of lumbar-round hole.

The detailed lumbar-round hole shape after optimizing is shown in Fig.8. The STC was added between the straight line and circular curve, resulting a gentle curvature variation.

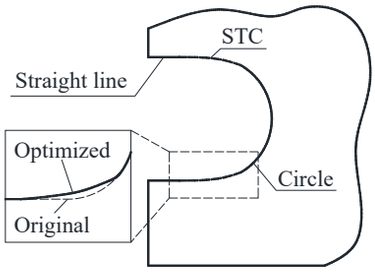


Figure 8. Optimized lumbar-round shape

Fig.9 shows the comparison results after the lumbar-round hole optimized. It is found that the stress peak clipped, when using STC to deal with the mutation of curvature. Meanwhile, the stress values at predicted crack propagation path are almost the same. Therefore, a better stress distribution can be obtained if further optimizing the STC. Although, it is quite difficult to drill the hole when the shape was optimized, it does reflect a fact that proper burnishing to drilled hole is beneficial for stress concentration reduction, resulting in better crack retarding effects.

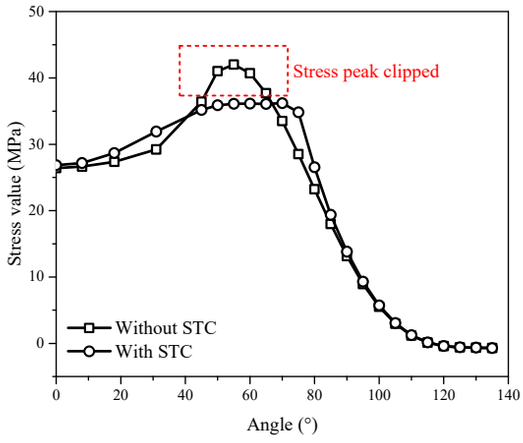


Figure 9. Stress peak reduced by STC

6 CONCLUSIONS

The drilling-hole shape was discussed in the paper, and a lumbar-round hole shape was proposed. The finite-element analysis was carried out to investigate the performance of this shape. The following conclusions may be drawn from this study.

1) The lumbar-round hole has better stress distribution than that of round hole.

2) Increasing the horizontal length and the radius of lumbar-round hole can both beneficial for stress reduction.

3) The lumbar-round hole shape can be further optimized when using the spiral transition curve to deal with the mutation of curvature.

ACKNOWLEDGEMENT

The authors thank the support of National Natural Science Fund (No. 51478163), and Transport Science Research Project of Jiangsu Province (No.2017Y09). The assistances are gratefully acknowledged.

REFERENCES

Bates, D. M., and Watts, D. G. (1980). “Relative curvature measures of nonlinearity.” Journal of the Royal Statistical Society, 42(1), 1-25.

Choi, J. H., and Kim, D. H. (2009). “Stress characteristics and fatigue crack behaviour of the longitudinal rib-to-cross beam joints in an orthotropic steel deck.” Advances in Structural Engineering, 11(2), 189-198.

Fanni, M., Fouda, N., Shabara, M. A. N., and Awad, M. (2015). “New crack stop hole shape using structural optimizing technique.” Ain Shams Engineering Journal, 6(3), 987-999.

Guo, A. M., Wang, L. Z., and Tian, Q. Y. (2008). “Study on fatigue repair with stop hole techniques.” Sichuan Building Science, 34(4),107-109.

He, Y. S., Chen, L. J., and Du, H. Z. (2004). “Effectiveness varying in dimension of crack-stopping holes.” Journal of Civil Aviation University of China, 22(3), 29-31.

Ji, B. H., Yuanzhou Z. Y., Liu T. J., and Fu Z. Q. (2016). “Influencing factors of stop-hole method for fatigue crack of steel box girder.” Journal of Jiangsu University(Natural Science Edition), 37 (1), 97-102.

Montebello, C., Pommier, S., Demmou, K., Leroux, J., and Meriaux, J. (2016). “Analysis of the stress gradient effect in fretting-fatigue through nonlocal intensity factors.” International Journal of Fatigue, 82(3), 188-198.

Peterson, R. E., and Plunkett, R. (2010). “Stress concentration factors.” Naval Engineers Journal, 67(3), 697-708.

Xiong, Z. Z., and Yi, L. (2016). “Research of steel structure crack arrest drilling based on extended finite element.” China Rubber/ Plastics Technology and Equipment (Plastics), 42(8),80-82.

Ya, S., Yamada, K., and Shikawa, T. (2013). “Fatigue evaluation of rib-to-deck welded joints of orthotropic steel bridge deck.” Journal of Bridge Engineering, 18(5), 492-499.

Yu, L., Zhen, Y., and Pan, X. (2011). “Effect of spiral transition curve length on vehicle path.” Journal of Southwest Jiaotong University, 46(2), 200-204.

Zhu, R. Y., Zhou, J. Z., and Yi, G. X. (1995). “The way of increasing the fatigue life of welding components—On the mechanism of crack-cutting Holes.” Journal of Hubei Polytechnic University, 10 (S1), 133-136.

Maintenance, Safety, Risk, Management and Life-Cycle Performance of Bridges – Powers, Frangopol, Al-Mahaidi & Caprani (Eds)
© 2018 Taylor & Francis Group, London, ISBN 978-1-138-73045-8

Study on crack stop holes in weld of orthotropic steel bridge decks

Z.Q. Fu; G.Y. Sun; Y. Yao; B.H. Ji
College of Civil and Transportation Engineering, Hohai University, Nanjing, Jiangsu, P.R. China

ABSTRACT: The technique of drilling stop holes in fillet weld of orthotropic steel bridge decks to arrest fatigue cracking was studied. The stress distribution characteristics at the crack tips were analyzed according to the compact tension model and the local bending model. The variation of stress concentration and gradient were compared to obtain the stress characteristics before and after drilling the holes. Fatigue tests of specimens were also conducted to verify the effects of stop holes. The results shows that drilling a stop hole at the tip of the cracks decreased the stress concentration without changing stress distribution trends while the mean stress of the cracking section increased. The largest stress around the hole appeared at the extending direction of the original crack, which was also the re-cracking position. Stop holes delayed the crack propagation but with no effects on the crack propagation rate of re-cracking.

1. INTRODUCTION

Orthotropic steel bridge decks have been widely used with the advantages in light weight, high ultimate bearing capacity, short construction period and so on(Lu and Li 2014). However, fatigue cracks always occur in the process of bridge operation under the wheel load because of the complex welded structural details and manufacturing defects(Deng *et al*. 2015; Maljaars *et al*. 2013). Some investigation results about bridge collapse shows that fatigue fracture is one of the main reasons(Connor and Fisher 2001). It is difficult to avoid the fatigue cracks of the steel bridge deck because of its structural details and load characteristics. Therefore, fatigue of the steel bridge is paid more attention in the maintenance work. Especially, the crack repair work affects the operation safety of steel bridges. Crack stop holes are a temporary maintenance measure(Choi and Kim 2008), which entail drilling a hole at the crack tip to eliminate the stress concentration, thus the extension of the crack is prevented or postponed and the service life of the structure is prolonged. The crack stop hole is simple to install, and cheap, so it is widely used in the maintenance of metal structures(Makabe, Kaito and Ferdous 2014; Wang *et al*. 2014).

A crack stop hole was verified as having enhanced the fatigue service life of a structure(Wu *et al*. 2010; Crain *et al*. 2010). The effect of hole diameter on the recycled service life of a fatigue crack was also analysed by Song and Shieh.(2004). The effect of hole diameter on crack arrest behaviour was analysed by He, Chen and Du(2004), who proposed a reasonable hole diameter. In addition, the crack arrest behaviour is also influenced by the mechanical behaviour of the structure(Ya, Yamada and Shikawa 2013), as found by (Ayatollahi. Razavi and Chamani 2014; Avatollashi *et al*. 2015), who focused on crack arrest behaviour under pure bending and pure shear. As an accurate location of crack tips was required in crack stop hole design, some scholars proposed that the effects of a single stop hole could be enhanced by improvement of hole shape as well as their arrangement. Fanni *et al*.(2015) simulated a reasonable stop hole shape in view of optimizing the structural stress. The compact tension models were mostly studied for the cracks in both numerical and experiment. However, few researchers studied about the crack stop hole considering the actual steel bridge structure details, especially about the cracking on the fillet welds of bridge decks. Meanwhile, the cycle load of tension and compression stress was adopted mainly.

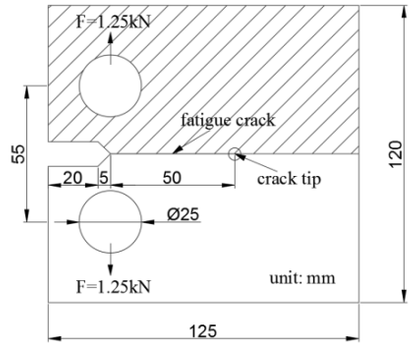
Nevertheless, the fillet welds of bridge decks were under bending load. The applicability of the results also need more demonstration.

The standard sample recommended by ASTM(American Society for Testing Materials, 2007) and fillet weld in steel bridge deck were adopted in this research to analyse the stress characteristics of crack stop holes. The performance of the stop hole was assessed by stress changes after drilling, which was verified by an experiment involving fatigue cracks on vertical stiffening rib welds in steel bridge deck.

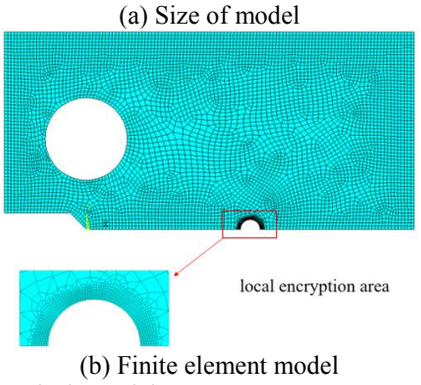
2. ANALYSIS OF THE CT MODEL

2.1 *CT model*

According to the standard samples recommended by ASTM, the compact tension model (CT model) in Fig. 1 was adopted for a finite element model. As the model is symmetrical, only half of the model was analysed. The length of the crack was 50 mm, on the tip of which a crack stop hole was set with a diameter of 6 mm. Coinciding with the centre of the hole, lay the crack tip. The modulus of elasticity E = 206 GPa and Poisson's ratio ν = 0.3; the load F = 1.25 kN; the thickness of the plane t = 5 mm. The singular element was set in the vicinity of the crack tip in the process of mesh generation while the plane quadrilateral element PLANE183 with eight nodes was used in other regions. The mesh size of the model was 5mm globally. Along the diameter of the stop hole, mesh size refined to be 0.25mm in 6mm length.



(a) Size of model



(b) Finite element model

Figure 1. Analysis model

2.2 *Stress around the hole*

The crack usually grows perpendicular to the principal stress and is generated from the position where the local stress concentration is maximized. To obtain the points of local stress concentration, the distribution of stress at the edge of the hole was studied. The major principal stress σ_1 around the edge of the hole was calculated (Fig. 2), so was the slope K of the curve, where 0° was the positive direction of the X-axis.

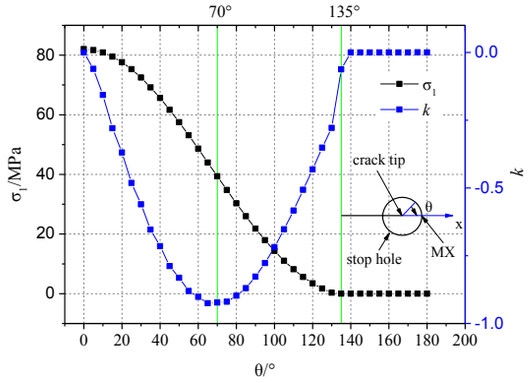


Figure 2. Major principal stress distribution at the edge of a crack stop hole

The distribution of major principal stress in Fig. 2 shows that the major principal stress is symmetrical along the hole wall. It decreases as the angle of the tip ranges from 0° to 135° and remains zero from 135° to 180°. The slope of the curve reaches the minimum at an angle of 70°, which is the inflection point of the curve and the rate of decrease of stress also decelerates. The maximum stress, namely MX, occurs at 0°. New fatigue cracks will generate at 0° under cyclic loading.

The growth path of the crack is obtained according to the stress condition in the vicinity of MX. Stress of Points along the X-axis near MX was shown in Fig. 3: the sample is under tension, the value of stress σ_y in the Y-direction is much the same as that of the major principal stress σ_1 and the value of shear stress τ_{xy} is about zero, while the value of σ_x in the X-direction is between that of σ_y and τ_{xy}. Therefore, the direction of the major principal stress around MX lies along the Y-axis and crack grows along the positive X-axis.

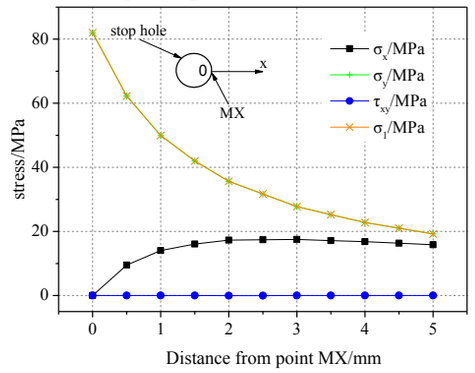


Figure 3. Stress state in the vicinity of a stress concentration

2.3 *Stress gradient*

The influence of stress concentration on the fatigue strength is decided by the fatigue gap coefficient K_f which represents the decline time of fatigue strength, instead of the stress concentration coefficient K_t, showing the increase of peak stress of the gap. Compared with the stress concentration coefficient, the fatigue gap coefficient takes both geometric condition of any gaps and types of material into consideration.

The crack stopping performance of the hole was assessed by K_t and K_f of model. K_t and K_f can be obtained, respectively, by Eqs. (1) and Eqs. (2).

$$K_t = \frac{\sigma_{\max}}{\sigma_{nom}} \tag{1}$$

Where, σ_{max} is the practical maximum stress obtained by calculation; σ_{nom} is the nominal stress obtained by Eqs. (3).

$$K_f = 1 + \frac{K_t - 1}{1 + \left(\frac{c}{\rho}\right)} \tag{2}$$

$$\sigma_{nom} = \frac{2F(2W + L)}{t(W - L)^2} \tag{3}$$

Where, c is a constant related to the material: for steel of type Q345qD, c = 0.45, ρ is the radius of curvature and diameter of the hole, F is the applied load, W is the width of the model, t is the thickness of the model, and L is the length of the crack.

A crack stop hole was set in the path of the crack growth and stress σ_y at the crack tip before, and after, drilling, in the Y-direction, was substituted into (1) as σ_{max}, and the calculated results are shown in Table 1. The stress at MX is only 50 MPa without cracks under the same conditions, while local stress increases to 179.0 MPa, showing remarkable stress concentration at the crack tip. The stress amplitude at MX decreases to 82.0 MPa after drilling: the stress at the crack tip falls by 54.2%, relieving this stress concentration.

Table 1 Comparison of mechanical behavior before and after drilling

Item	Stress on crack tip/MPa	Stress concentration coefficient K_t	Gap fatigue coefficient K_f
Non-crack	50	/	/
Before drilling	179.0	3.58	3.24
After drilling	82.0	1.64	1.56

The stress gradient of σ_y before, and after, drilling, in the Y-direction and with crack growth, is shown in Fig. 4: the stress was larger in the vicinity of the crack tip than that at a distance from crack tip and the stress concentration is prominent in the crack tip before drilling. Stress within 1 mm of the crack tip after drilling decrease and the stress concentration is relieved, while the stress 1 mm from the crack tip was slightly larger, showing that crack stop holes eliminate the influence of the plastic zone around a crack tip and result in some stress redistribution. The average stress across the section increases owing to the crack stop hole and all materials work together to bear load. Here, the average stress 1 mm from the crack tip increased from 11.63 MPa to 13.58 MPa, an increase of 16.8%.

3. ANALYSIS OF THE BENDING MODEL

3.1 *Bending model*

The fillet weld of steel deck is one of the most vulnerable details to fatigue cracks under the bending load. The local model of deck and U-rib weld in steel bridge decks is shown in Fig. 5.

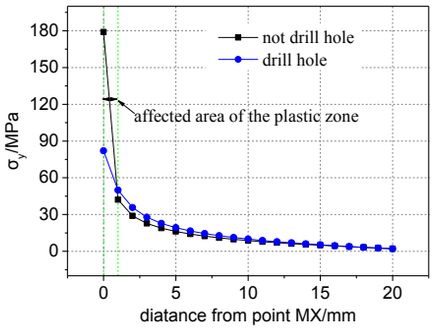
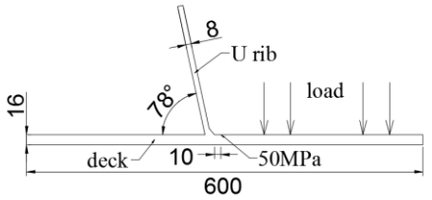


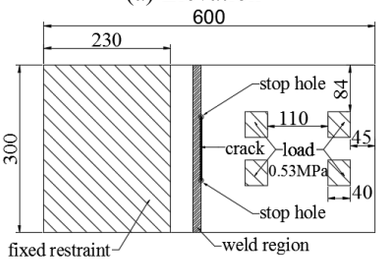
Figure 4. Stress gradient

Q345qD steel was adopted with elastic modulus E = 206GPa, Poisson's ratio υ = 0.3. The model length was 600mm and width was 300mm. The deck thickness was 16mm and U rib thickness was 8mm. Full penetration welding was considered. According to the fatigue test in previous studies by authors, loads of 0.53 MPa were added at the bolt hole positions of the vibration fatigue machine(Fu *et al*. 2017). It caused 50MPa stress at the model center (no crack) with 10mm from the weld toe. All freedom degrees of the area which was 230mm from the

edge were restrained to simulate the fixed end.



(a) Elevation



(b) Plan

Figure 5. Model sizes (Unit: mm)

According to the welding accuracy, the cracks are always not just at the weld toe. Meanwhile considering to the convergence of finite element calculation, the crack was set 0.5mm from the weld toe in the model. The fatigue crack section can be considered to be a semi ellipse(Zeng, Tian and Liao 2016). Therefore, the simulated crack section is shown in Fig. 6, in which a is semi-major axis length and b is semi-minor axis length. The ratio of minor to major axis(b/a) is 0.2 with a=50mm and b=10mm for the model. The endpoints of major axis are crack tips and the curve of crack depth is crack front. The position on the depth curve is indicated by the angle of the radial direction as shown in Fig. 6. It is called position angle in this study. The 0° direction position is located at left crack tip. The angle increases counterclockwise.

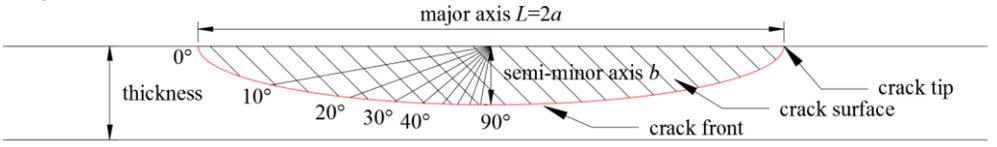


Figure 6. Position angle in crack section

ABAQUS model was built and extended finite element method was used to deal with stress singularity. Elements of C3D8R and C3D10 were adopted. The mesh size of the model was 20mm globally. The mesh size refined to be 0.5mm at the weld. In the width of 20mm out of weld, the 5mm and 10mm mesh sizes were adopted for transition region. Along the crack, mesh size refined to be 1mm in 25mm length range near the crack tips and 2mm at other parts. The position of the stop hole was near the crack tip. The specific positions and parameters were considered according to the analysis condition. The stop holes were formed by Boolean subtraction operation of the cylinder and model without reduction in the division accuracy of mesh sizes. The finite element model is shown in Fig. 7.

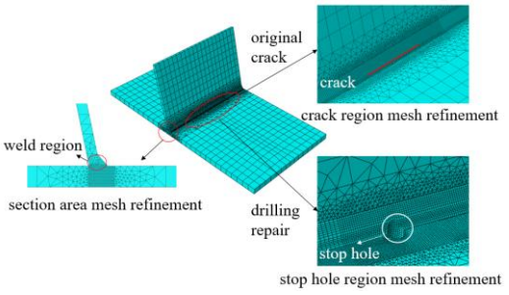


Figure 7. Finite element model

3.2 *Stress distribution*

The surface Mises stress along the crack section was obtained as shown in Fig. 8. As the stress distribution was symmetrical by the medial axis of the model, only half of the curve was drawn. The stresses with or without crack were compared. Due to the crack, obvious stress concentration is appeared at the crack tips. The stress on the crack (L=100mm)is close to 0 because of the releasing after cracking. The crack surface almost has no stress resulting by the stress redistribution. The stress at the crack tip reaches 234.8MPa while the stress at model edge is 44.9MPa. However, the stress distributes without obvious change for the model without crack. The maximum stress is 64.9MPa which located in the center and the stress is 42.3MPa at the two side of model edge. The stress distribution is generally uniform without stress mutations. The stress concentration factor of the crack tip is 3.69 when stress of model without crack is nominal stress.

Fig. 9 is the stress distribution of model with a 100mm crack after drilling stop holes(D=8mm). The center of stop hole locates at the crack tips. Stress on the surface caused by the fracture is small near the crack. The stress concentration

area at the crack tips is removed by the stop holes. However, the maximum stress also appears near the stop hole. It is located at the converge positions of crack and stop hole. The stress concentration is also presented but with a reduction in the peak stress value. In general, the trend of stress distribution is not changed by stop holes.

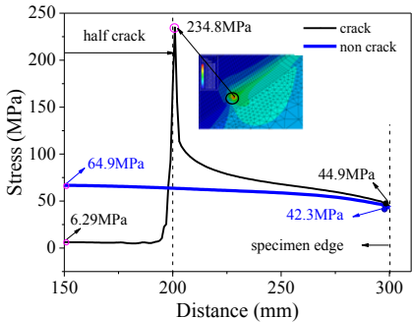


Figure 8. Mises stress along the crack

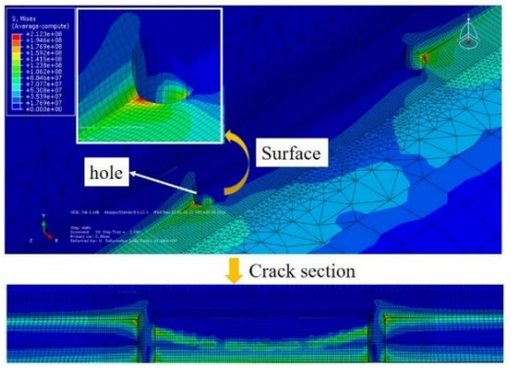


Figure 9. Stress distribution after drilling

The stop hole is a temporary treatment for the crack prevention. The cracks have a possibility to cracking again. Taking the stop hole center as the origin of coordinates, the stress around the stop hole edge is shown in Fig. 10. In the side with crack (90°~270°), the stress is close to 0. The stress in 90°~180° is less than that in 180°~270° because the local stiffness of the weld is greater than that of deck. The maximum stress appears at the extension direction of crack (180°) with a value of 213.0MPa. It is the most probable position to crack again.

4. EXPERIMENTAL VERIFICATION

4.1 *Experiment introduction*

It is hard to simulate fatigue cracks in real conditions on a plate deck, thus a crack stop hole was set in samples featuring a real bridge at full-scale to provide a more favourable reference for real bridge application. The fillet weld connecting the steel bridge deck and its vertical stiffener was adopted: both member sizes and welding technology replicated that of the actual bridge (Fig. 11), i.e., special steel Q345qD and a weld foot of 6 mm for all steel fillet welds were used. Fatigue cracks were obtained by fatigue experiment at an early stage with a crack length on both sides of 30 mm.

Mechanical vibration fatigue testing was used and after fatigue arresting, fatigue loading was carried out. The cyclic loading provided by the apparatus was sinusoidal. The stress amplitude was 120 MPa.

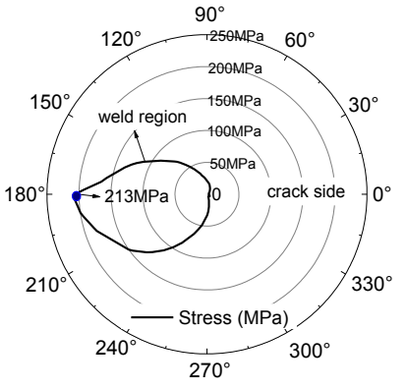


Figure 10. Stress around the hole edge

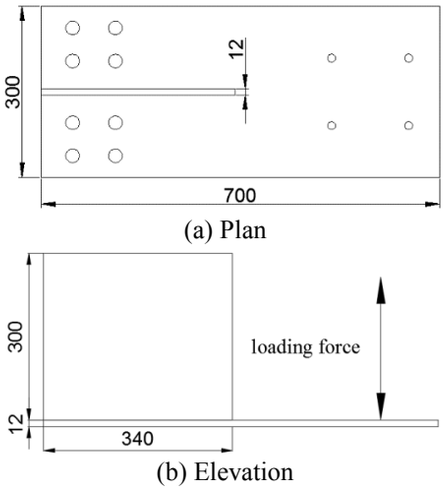
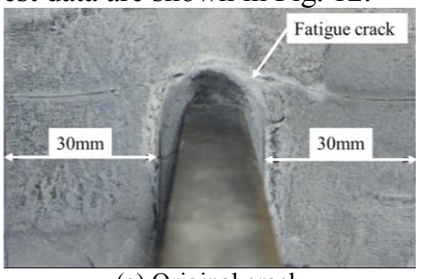


Figure 11. Specimen size(Unit: mm)

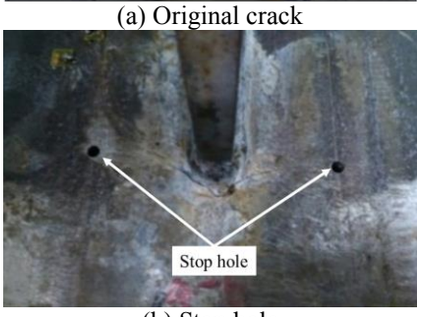
4.2 *Processing of crack arresting*

Crack stop holes with diameters of 0mm(meaning without stop hole), 4mm, 6mm and 8mm were selected for this crack arrest experiment considering the diversity of crack arrest behaviour of different diameters. The four samples were named as SJ1, SJ2, SJ3 and SJ4 in

the order of the hole diameter. As each crack has two tips, the same processing was carried out on them both. Aligning the edge of the hole with the crack tip, the inner wall and edges were polished by round file and sandpaper after drilling. The crack arrest data are shown in Fig. 12.



(a) Original crack



(b) Stop hole

Figure 12. Drilling method

4.3 *Experimental phenomenon and results*

Crack forms of all samples were reflected by magnetic tester after fatigue loading. Fig. 13 shows a cross-sectional view of the sample. Fatigue cracks in samples SJ1 and SJ2 grew at both sides of the crack stop hole while those in samples SJ3 and SJ4 grew at one side of the hole (Fig. 14).

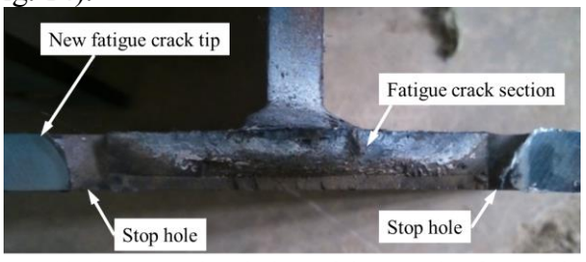


Figure 13. Cross-sectional view of the sample after crack arrest processing

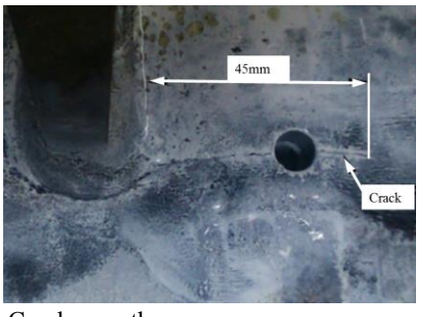


Figure 14. Crack growth

Cycle times for fatigue loading corresponding to regeneration, 5 mm, and 15 mm of crack growth were recorded (Table 2). The total length of crack growth was 45 mm.

Table 2 Loading cyclic times corresponding to growth of cracks(×100 times)

Growth of new crack	SJ1	SJ2	SJ3	SJ4
Regeneration	/	1029	2468	3100
To 5mm-long	/	2921	4237	4968
To 15mm-long	3559	4866	5880	6870

As seen in Table 2, the cyclic times for crack regeneration increased with increasing hole diameter in SJ2, SJ3, and SJ4, thus extending their fatigue life. This verified the conclusion above, i.e., the larger diameter crack stop holes prevented cracks from growing and provided better crack arrest behaviour.

The process of crack growth was divided into two stages: crack growth from regeneration to 5 mm-long, and that from 5 mm-long to 15 mm-long. The growth rate of each stage is shown in Table 3.

Table 3 Crack growth rate in two stages(×10^{-8} m/C)

d_a/d_N	SJ1	SJ2	SJ3	SJ4
The first stage (0-5mm)	-	2.64	2.83	2.68
The second stage(5-10mm)	-	5.14	6.09	5.26
Average	4.21	3.89	4.46	3.97

As seen in Table 3, crack growth rates in both stages were in the 10-8 m/C order of magnitude, namely, a moderate rate. The crack growth rate in the second phase is much larger than that in the first stage. The average rate of crack growth was similar for both stages, i.e., crack stop holes can only prevent cracks from growing, yet have little influence on their growth rate after regeneration.

5. CONCLUSION

The CT model and bending model were adopted in this research to analyse the stress characteristics of crack stop holes. The performance of the stop hole was verified by the fatigue experiment and it could be concluded as following:

(1) Stress in the vicinity of the crack tip after

drilling decreased remarkably and the stress concentration was relieved, while the stress of cracking section was slightly larger, showing that crack stop holes eliminated the influence of the plastic zone around a crack tip and resulted in some stress redistribution.

(2) The stress around the hole edge reached the maximum along the propagation direction of the original crack, which was the initiation cracking again.

(3) The experiment showed that a crack stop hole could prevent cracks from growing and the stop holes with larger diameter provided better crack arrest behaviour. The crack growth rate at later stages was faster than that in the earlier stage after regeneration. Thus a stop hole and its diameter had no influence on crack growth rate.

ACKNOWLEDGMENTS

The authors appreciate the support of the National Natural Science Fund of China (No.51678215) and the Fundamental Research Funds for the Central Universities (2015B17414).

REFERENCES

ASTM E2472-06 (2007), Standard test method for determination of resistance to stable crack extension under low constraint conditions. Annual book of ASTM Standards, Vol.03.01. ASTM International, West Conshohocken, USA.

Ayatollahi, M.R., Razavi, S.M.J., and Chamani, H.R. (2014), Fatigue life extension by crack repair using stop-hole technique under pure mode-i and pure mode-ii loading conditions. *Procedia Engineering*, 74, 18-21.

Ayatollahi, M.R., Razavi, S.M. J., and Yahya, M.Y. (2015), Mixed mode fatigue crack initiation and growth in a ct specimen repaired by stop hole technique. *Engineering Fracture Mechanics*, 145, 115-127.

Choi, J.H and Kim, D.H. (2008), Stress characteristics and fatigue crack behaviour of the longitudinal rib-to-cross beam joints in an orthotropic steel deck. *Advances in Structural Engineering*, 11(2):189-198.

Connor, R.J and Fisher, W.J (2001), Results of Field Measurements on the Williamsburg Bridge Orthotropic Deck-Final Report. Lehigh University, Bethlehem.

Crain, J., Simmons, G., Bennett, C., Barrett-Gonzalez, R., Matamoros, A., and Rolfe, S. (2010), Development of a technique to improve fatigue lives of crack-stop holes in steel bridges. *Transportation Research Record Journal of the Transportation Research Board*, 2200(2200), 69-77.

Deng, Y., Liu, Y., Feng, D., and Li, A. (2015), Investigation of fatigue performance of welded details in long‐span steel bridges using long‐term monitoring strain data. *Structural Control & Health Monitoring*, 22(11), 1343-1358.

Fanni, M., Fouda, N., Shabara, M.A.N., and Awad, M. (2015), New crack stop hole shape using structural optimizing technique. *Ain Shams Engineering Journal*, 6(3), 987-999.

Fu, Z.Q., Ji, B.H., Kong, X.M., and Chen, X. (2017), Grinding treatment effect on rib-to-roof weld fatigue performance of steel bridge decks. *Journal of Constructional Steel Research*, 129, 163-170.

He, S.Y., Chen, L.J. and Du, H.Z. (2004), Effectiveness varying in dimension of crack-stopping holes. *Journal of Civil Aviation University of China*, 2004, 22(3):29-31. (in chinese)

Lu, P.M. and Li, D.T. (2014), Fatigue research on bridge deck-plate of orthotropic steel bridge deck. *China Journal of Highway & Transport*, 27(2), 84-89+97.

Makabe, C., Kaito, N., and Ferdous, M.S. (2014), Method of arresting crack growth for application at a narrow working space. *Mechanical Engineering Journal*. 1(6):1-12.

Maljaars, J., Gration, D., Vonk, E., and Van Dooren, F. (2013), Crack growth prediction of deck plate-stiffener joints in orthotropic steel bridge decks. *IABSE Symposium Report*, 99(8), 1571-1578.

Song, P.S., and Shieh, Y.L. (2004), Stop drilling procedure for fatigue life improvement. *International Journal of Fatigue*, 26(12), 1333-1339.

Wang, Y.L., Pan, Q.L., We, L.L, Li, B. and Wang, Y. (2014), Fracture toughness and fatigue crack growth analysis of 7050-T7451 alloy thick plate with different thicknesses. *Journal of Central South University*, 2014, 21(8):2977-2983.

Wu, H., Imad, A., Benseddiq, N., Castro, J.T.P.D. and Meggiolaro, M.A. (2010), On the prediction of the residual fatigue life of cracked structures repaired by the stop-hole method. *International Journal of Fatigue*, 32(4), 670-677.

Ya, S., Yamada, K., and Shikawa, T. (2013), Fatigue evaluation of rib-to-deck welded joints of orthotropic steel bridge deck. *Journal of Bridge Engineering*, 18(5), 492-499.

Zeng, C., Tian, W., and Liao, W.H. (2016), The effect of residual stress due to interference fit on the fatigue behavior of a fastener hole with edge cracks. *Engineering Failure Analysis*, 66, 72-87.

Maintenance, Safety, Risk, Management and Life-Cycle Performance of Bridges – Powers, Frangopol, Al-Mahaidi & Caprani (Eds)
© 2018 Taylor & Francis Group, London, ISBN 978-1-138-73045-8

Fatigue Performance of Hammer-peened Diaphragm-to-rib Welds in Orthotropic Steel Decks

Q.D. Wang, B.H. Ji, Z.Q. Fu
College of Civil and Transportation Engineering, Hohai University, Nanjing, Jiangsu, P.R. China

ABSTRACT: Diaphragm-to-rib welds are easily subjected to fatigue cracking under cyclic traffic loads. To evaluate the effect of hammer peening technique, the simplified finite element model (FEM) of hammer-peened specimen was developed to investigate the local stress variation after hammer peening. The effective stress was also analysed by another simplified FEM. Besides, three local specimens were peened and the subsequent fatigue test was conducted for comparison. The results show that the crack initiation life of hammer-peened specimen is enhanced significantly, while the crack propagation pattern still remains unchanged. Significant compressive stress is induced by hammer peening, and the effective tensile stress under bending load could be decreased effectively, which is beneficial to the fatigue performance of diaphragm-to-rib welds.

1 INTRODUCTION

Orthotropic steel bridge decks (short for OSBDs) has been widely used in long-span cable-supported bridges because of lightweight, excellent stability, high bearing capacity and some other advantages (Fu Z, et al. 2017). However, the structure of OSBDs is complex and main components are welded with each other, which lead to short influence lines of OSBDs and considerable welding residual stress (Kainuma S, et al. 2016). With the increase of services years, the OSBD is easily subjected to fatigue cracking under cyclic traffic load (Xiao Z G, et al. 2008). The stress state near diaphragm-to-rib welds are rather complex because of both in-plane and out-plane deformation, where fatigue cracks are usually found (Choi J H and Kim D H). Fatigue cracks are unavoidable and hard to be detected at its initial stage (Xie, et al.2015) Besides, the detection and repair work of fatigue cracks is expensive (Yamada K, et al. 2015) Therefore, it is meaningful to take measures to improve the local mechanical properties of welded joints, which will also help to reduce the life cycle cost of bridges.

Recently, the methods for improving the mechanical properties of welded joints could be divided into three types: improving the geometric profile of welds, decreasing the welding residual stress and optimizing the structural bearing. Grinding, peening and local strengthening methods are usually adopted thereof (Fisher J W, et al. 2015a). Ultrasonic hammer peening (UHP) and Air hammer peening (AHP) are the main peening methods sharing the similar fundamentals: minor defects of the welds could be eliminated during the impacting process and compressive residual stress will be induced there (Fisher J W et al.1979b; Janosch J J, et all. 1996). For AHP, the compressed air is the source energy of the impacting system. The air pressure of AHP is usually no more than 300 kPa, indicating limited plastic deformation and residual compressive stress (Fisher J W, et al. 2015a). Recently, a new technique called Impact crack-closure Retrofit (ICR) was developed based on AHP, with a much higher air pressure (0.6MPa~0.8MPa) and impacting frequency (Yamada K, et al. 2015). In view of higher impacting energy induced by ICR, the technique was mainly used to retrofit cracked components, and the relative experimental results showed that the fatigue life of cracked specimens was significantly improved after ICR treatment (Zhiyuan Y Z, et al.2016). If the welds are treated by ICR technique before the crack initiation, the fatigue performance might also be improved due to the decrease of effective tensile stress under fatigue load.

Therefore, the simplified ICR process and the out-plane deformation of diaphragm-to-rib welded specimen were both modeled, and the local deformation and stress variation were analysed. Besides, three local diaphragm-to-rib welded specimens were adopted here, and the weld toe near the arc-sharped notch was treated by ICR technique. Then the treated specimens were fatigue tested subsequently using vibrating fatigue test machine. The crack initiation life, crack propagation and stress variation were analysed to evaluate the improvement

in fatigue performance of ICR treated diaphragm-to-rib welds.

2 FINITE ELEMENT ANALYSIS

2.1 *Analytical model*

The finite element model was developed by *ANSYS* to analyse the residual stress variation after peening process. Considering that the distribution of residual stress was limited to a small range, a local model was developed for saving time, as shown in Fig.1.

SOLID185-type element was used to simulate both the specimen and the chisel. The model was meshed with a refined mesh size of 1mm. The bilinear kinematic hardening model (BKIN), with a yield strength of 345MPa and a tangent modulus of 0, was adopted. Element types of TARGE170 and CONTA174 were adopted at the surface of chisel and weld respectively. To keep the same boundary conditions with the specimen, nodes at the cut surface between the local and whole model were fixed. The angel between the chisel and the diaphragm was set as 60°.

Displacement-controlled loading was adopted here instead of load-controlled loading. To obtain the displacement of the chisel, preliminary peening was conducted to the diaphragm-to-rib welded specimen, and reverse molding was applied to the peened zone, of which the surface was covered rapidly by hot-melt glue. Then the cold glue was removed and cut into two pieces to measure the peening depth. As the peening depth was 0.2mm~0.3mm, the displacement of the chisel was set as 0.2mm in the model. The peening process was divided into two steps: the pressing and lifting of the chisel. The whole peening process was completed in 0.01s with each step taking 0.005s.

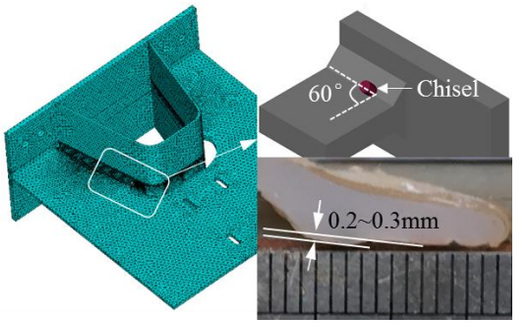
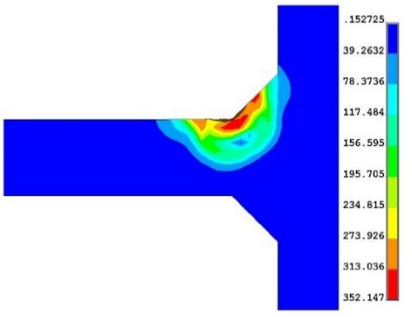


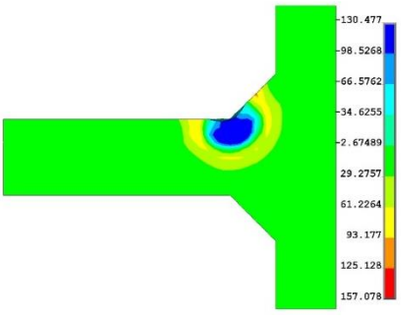
Figure 1. Analytical model

2.2 *Residual stress nephogram*

The nephogram of Mises equivalent stress after peening was shown in Fig.2a, of which the deformation was at its original scale. According to Fig.2a, plastic deformation and significant residual stress was generated in hammer peened zone presenting a radial distribution centred on the weld toe. The maximum residual stress located near the hammer peened surface reaching a value of 352MPa, which indicated that the relevant metal was yield. Because of the plastic deformation, the geometric profile of weld toe was improved, which was beneficial to the local mechanical behavior. The first principle stress near the peening center was compressive and reached a value of -130MPa, which demonstrate that significant residual compressive stress was induced therein.



(a) Mises equivalent stress

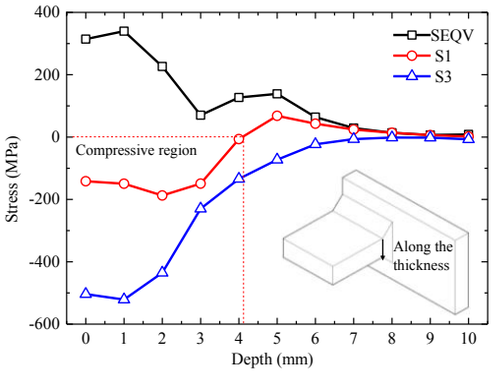


(b) The first principle stress

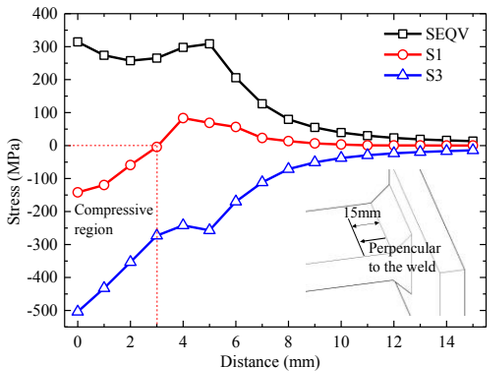
Figure.2 Residual stress nephogram

2.3 *Residual stress variation*

The Mises equivalent stress (SEQV), the first and third principle stress (S1 and S3) in hammer peened region were analysed, as shown in Fig.3. The maximum SEQV was located at the position 1mm under the surface, and the relevant influence depth was about 7mm. S1 was compressive at the weld toe, and became tensile stress while the depth reached 4mm and the distance at the surface exceeded 3mm, which was consistent with the deformation compatibility condition. S1 induced by peening process was about -150MPa at the surface of weld toe indicating the improvement in local mechanical properties therein. It could be assumed that higher residual compressive stress might be generated if the ICR process is improved (e.g. an optimal hammerhead radius is adopted).



(a) Stress variation along the thickness



(b) Stress variation on the surface

Figure.3 Residual stress variation

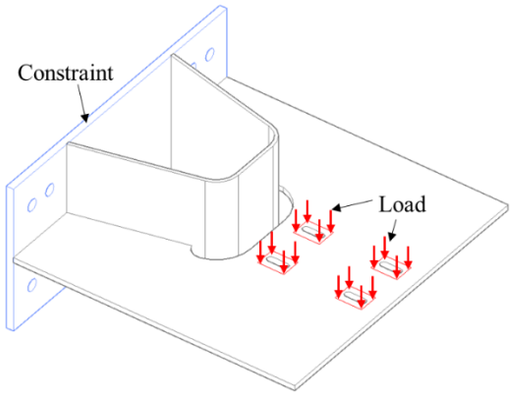
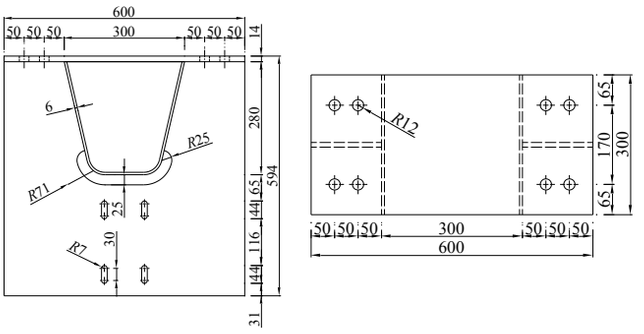


Figure.4 Loading method



(a) Front view (b) Top view

Figure.5 Geometric size of the model (unit: mm)

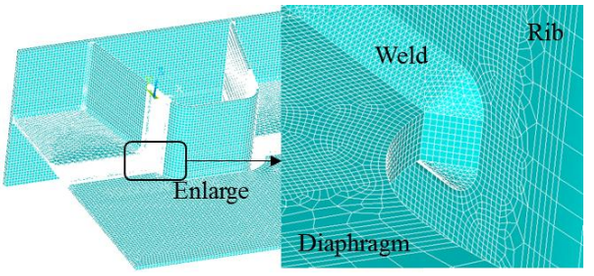


Figure.6 Local refining

3 ANALYSIS OF EFFECTIVE STRESS

3.1 *FE model*

The vibrating fatigue test machine was adopted by the authors' research group to conduct fatigue tests of rib-to-deck welds, diaphragm-to-rib welds and plate edge gusset welds. For diaphragm-to-rib welded specimens, former experimental results showed that the fatigue crack caused by out-plane deformation in the test was similar with the one in real suspension bridges. Therefore, the loading method in the FE model was the same with that in fatigue test as illustrated in Fig.4. The geometric size of the model was given in Fig.5.

In the model, the region near the arc-shaped notch was meshed with a refined mesh size of 1mm (shown in Fig.6), and other regions were meshed with a course mesh size of 6mm. The deck in the model was constraint, and four surface loads of 0.5 N/mm^2 were applied to the model. Other parameters of the model were the same with the former one as illustrated in Section 2.1.

3.2 *Stress concentration*

Significant stress concentration region was located at the junction of diaphragm and diaphragm-to-rib welds near the arc-shaped notch, as shown in Fig.7. It demonstrates that fatigue cracks will initiated therein if cyclic fatigue loads are applied. Fig.8 showed the crack source regions in diaphragm-to-rib welds both in fatigue tests and a suspension bridge in China. It demonstrated that the analytical results were consistent with the experimental results and the actual situation.

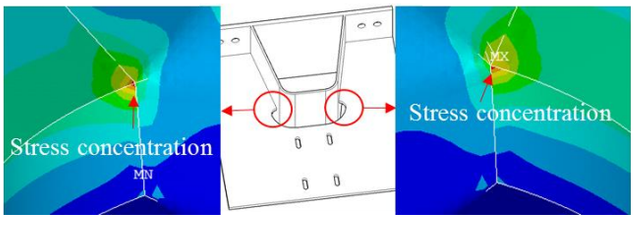


Figure.7 Stress concentration under bearing load

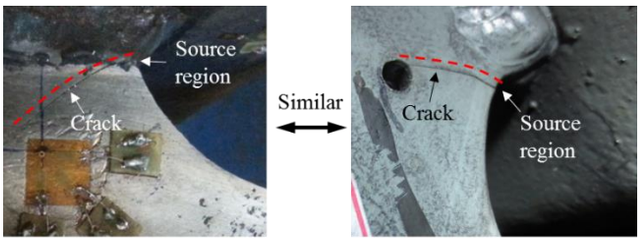


Figure 8. Crack source region of diaphragm-to-rib welds (imaged by the author)

3.3 *Effective stress*

Simulation of peening process was not applied to this model for simplifying. However, superposition principle was adopted here to analyse the effective tensile stress at the weld toe of diaphragm-to-rib welds, where the value of residual compressive stress (-150MPa) was considered. The results were illustrated in Fig.9.

According to Fig.8, the stress amplitude at the junction between the diaphragm-to-rib weld and diaphragm was about 220MPa as the model was subjected to bearing load. However, due to the residual compressive stress induced by peening process, the stress level was decreased by nearly 70%. After hammer peening, the effective stress decreased rapidly and became compressive when the distance was about 2.5mm away from the junction. The effective stress at the surface of junction was only about 60MPa indicating the significant improvement of local mechanical properties.

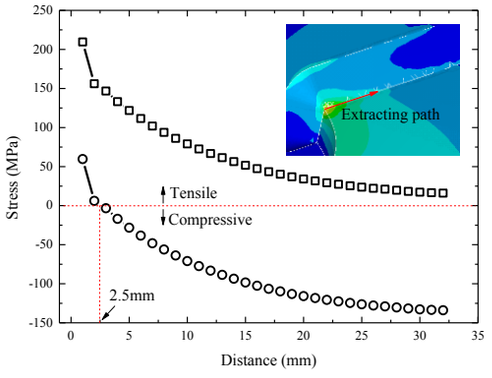


Figure.9 Effective stress

4 EXPERIMENTAL INVESTIGATION

4.1 *Specimen*

Q345qD was adopted to manufacture the specimens shown in Fig.10. The geometric sizes of the specimen were the same with the FE model (shown in Fig.5), which were also consistent with the geometric sizes in real bridges. All specimens were welded by CO_2 gas metal arc welding technology. Three specimens, labelled S-P-1, S-P-2 and S-NONE-3, were tested. S-P-1 and S-P-2 were hammer peened and subsequent fatigue test was conducted, while S-NONE-3 was fatigue tested without peening. Fig.10 showed the appearance of the specimen.



Figure.10 The appearance of the specimen

4.2 *Test procedure*

Considering that the diaphragm-to-rib welds near the arc-shaped notch were easily subjected to fatigue cracking, peening process was conducted therein before fatigue loading. The hammer peening was performed until obvious plastic deformation was induced at the weld toe.

Vibrating fatigue test machine was used to apply fatigue loads. The loading force was controlled by the vibrating frequency of the machine, which was adjusted according to the strain at the angle of 45 degree. The initial stress amplitude was set as 100MPa in the test, while the relative frequency was 9.32Hz. The experimental details were illustrated in Fig.11.

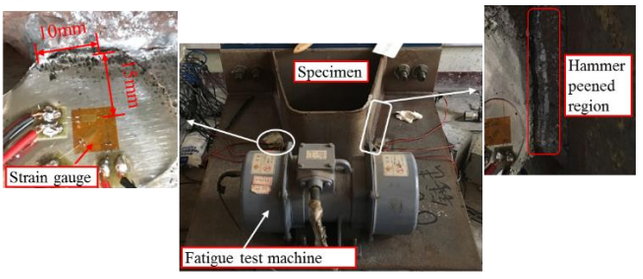


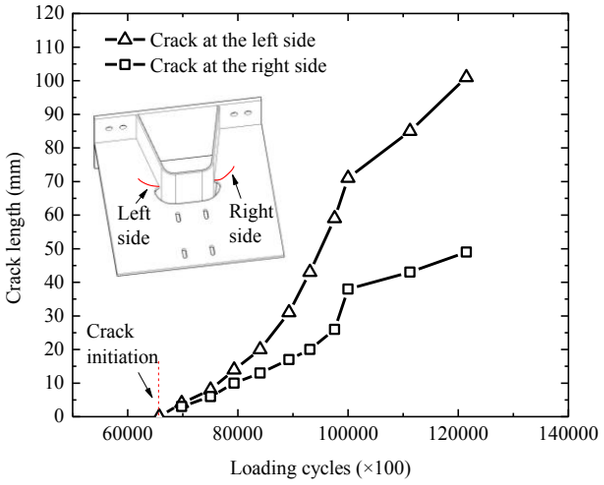
Figure.11 Experimental details

4.3 *Crack propagation*

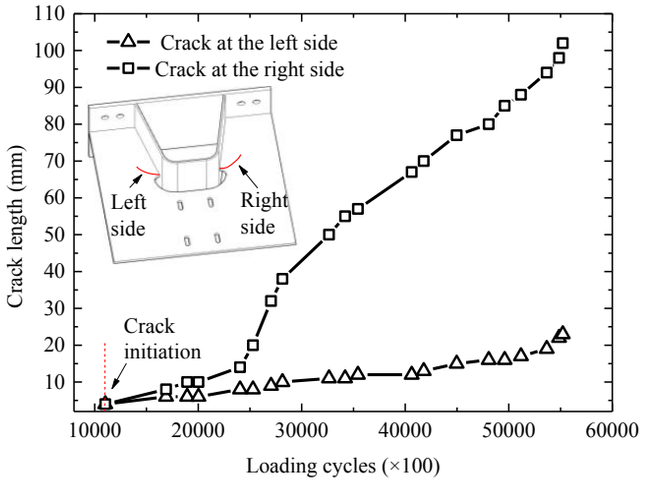
For diaphragm-to-rib welded specimens, the welds at both sides of the U-shaped rib are easily subjected to cracking. Therefore, the fatigue test was finished once the crack reached a length of 100mm, or the specimen was not cracked with the loading cycles exceeding 10 million times. In the test, S-P-2 was not cracked, while fatigue cracks were both detected at both sides of the U-shaped rib. The source region of the fatigue cracks was the same with the one shown in Fig.8, and propagated at an angle of about 45° along the diaphragm.

Fig.12 showed the crack propagation curves of S-P-1 and S-NONE-3. Even though two cracks

propagated concurrently, the relative propagation rates were different: one propagated rapidly with the other propagated slowly due to the stress release. The crack propagation curves of the two specimens were similar, indicating that the crack propagation pattern of hammer peened specimen remained unchanged. However, the crack initiation life of S-P-1 was about 6.5 million cycles, which was about 10 times higher than that of S-NONE-3 (about 1 million cycles).



(a) S-P-1



(b) S-NONE-3

Figure12. Crack propagation curve

4.4 *Crack initiation life*

The test results of six additional specimens without hammer peening in the former fatigue test conducted by the authors' group was adopted for comparison (labelled from S-C-1 to S-C-6 respectively). The crack initiation life was compared in Fig.13. The crack initiation life of S-NONE-3 was similar with the former test result, which was about 1million loading cycles. However, the crack initiation life of hammer peened specimens was much higher than the one of untreated specimens (6.5million for S-P-1 an0d more than 10million for S-P-2). It demonstrated that the crack initiation life could be significantly enhanced by hammer peening technique.

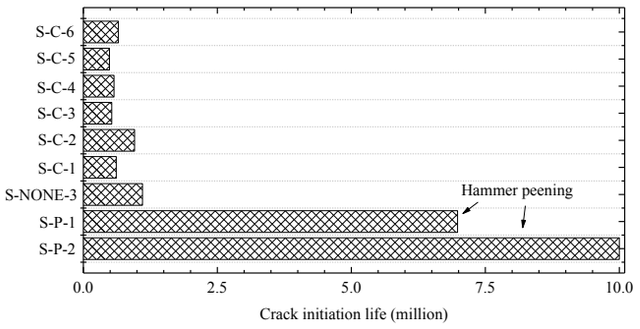


Figure.13 Comparison of crack initiation life

5 CONCLUSIONS

FE models were developed to analyse the residual stress variation induced by ICR process, and the effective stress at the weld near the arc-shaped notch was analysed. Then, the ICR process and the subsequent fatigue test were applied to local specimens to evaluate the effect of peening treatment on the performance of local mechanical properties. The following conclusions may be drawn from this study.

1) Considerable compressive stress was induced by peening process centred on the weld toe, and the effective stress at peened surface was significant decreased.

2) The position of crack source region was not changed after peening process, and the crack propagation path was similar with the one of untreated specimen.

3) The crack initiation life of peened specimens was enhanced by more than six times than that of untreated specimens in the test. It demonstrates that the fatigue performance of diaphragm-to-rib welds could be significantly improved by ICR technique.

ACKNOWLEDGEMENT

The authors thanks the support of National Natural Science Fund (No. 51478163); Transport Science Research Project of Jiangsu Province (No.2017Y09).

REFERENCES

Fu Z, Ji B, Zhang C, et al. (2017). Experimental study on the fatigue performance of roof and U-rib welds of orthotropic steel bridge decks. KSCE Journal of Civil Engineering, (3), 1-9.

Kainuma S, Jeong Y S, Yang M, et al. (2016). Welding residual stress in roots between deck plate and U-rib in orthotropic steel decks. Measurement, 92, 475-482.

Xiao Z G, Yamada K, Ya S, et al. (2008). Stress analysis and fatigue evaluation of rib-to-deck joints in steel

orthotropic decks. Internal Journal of Fatigue, 30(8), 1387-1397.

Choi J H, Kim D H. (2009). Stress characteristics and fatigue crack behavior of the longitudinal rib-to-cross beam joints in an orthotropic steel deck. Advances in Structural Engineering, 11(2), 189-198.

Xie, F. X., Ji, B. H., YuanZhou, Z. Y., Fu, Z. Q., and Ge, H. B. (2015). "Ultrasonic Detecting Method and Repair Technology Based on Fatigue Crack Features in Steel Box Girder." Journal of Performance of Constructed Facilities, 04015006.

Yamada K, Ishikawa T, Kakiichi T. (2015). Rehabilitation and improvement of fatigue life of welded joints by ICR technique. Advanced Steel Construction, 11(3), 294-304.

Fisher J W, Roy S. (2015a). Fatigue damages in steel bridges and extending their life. Advanced Steel Construction, 11(3), 250-268.

Fisher J W, Hausammann H, Sullivan M D and Pense A W. (1979b). Detection and repair of fatigue damage in welded highway bridges. NCHRP Report 206, Washington D.C, Transportation Research Board.

Janosch J J, Koneczny H, Debiez S, et al. (1996). Improvement of fatigue strength in welded joints (in HSS and in aluminium alloys) by ultrasonic hammer peening. International Journal of Fatigue, (10), 725.

Zhiyuan Y Z, Ji B, Fu Z, et al. (2016). Fatigue Performance of Cracked Rib-Deck Welded Joint Retrofitted by ICR Technique. International Journal of Steel Structures, 16(3), 735-742.

Maintenance, Safety, Risk, Management and Life-Cycle Performance of Bridges – Powers, Frangopol, Al-Mahaidi & Caprani (Eds)
© 2018 Taylor & Francis Group, London, ISBN 978-1-138-73045-8

Fatigue stress analysis of diaphragm-U-rib welding joints and local optimization

Ye Zhi , Y.X. Wang , H.B. Sun , B.H. Ji
College of Civil and Transportation Engineering, Hohai University, Nanjing, Jiangsu, P.R. China
Jiangsu Yangtze River Bridge Ltd, Jingjiang, Jiangsu, P.R. China

ABSTRACT: To study the fatigue problem of diaphragm-U-rib welding joint and diaphragm arc gap in steel box girder of Yangtze River Bridge, analysis of stress range and service life were carried out on fatigue details mentioned above based on the strain data collected from sensors in real bridge. Meanwhile, in order to improve fatigue behavior of the diaphragm, two new types of diaphragm structure were proposed, including transverse stiffener between major diaphragms and stiffener set on the arc gap. The finite element model of the steel bridge deck was established to analyze influence of the new structure on the fatigue stress. The result shows that the fatigue lives of diaphragm-U-rib weld ending and diaphragm arc web gap are, respectively, 3 years and 10.5 years. The optimized structures proposed in this study can effectively reduce stress range and the possibility of fatigue cracking in these two fatigue details.

1 INTRODUCTION

In recent years, the orthotropic steel bridge deck is widely used for its advantages in low self-weight, rapid construction, good load-carrying capacity. But the complicated structure of the steel deck and welds connecting components lead to the prominent residual stress and stress concentration in critical details, which are vulnerable to fatigue damage and failure under the long-term traffic loading (Cao et al.2015; Li et al.2001). At present, fatigue cracks of various propagations and types have been observed in orthotropic steel bridge deck at home and abroad.

Fatigue cracks propagated from the arc gap in the connection of diaphragm and U-rib is one of the most common cracking types in orthotropic steel bridge deck (Grundy et al.1990; Leendertz et al.1995; Bocchieri et al.1998; Connor et al.2001). The complicated structure results in unfavourable stress in the connection of diaphragm and U-rib (Leendertz et al.1995; Bocchieri et al.1998; Connor et al.2001), and the manual welding is of poor quality during the welding processing considering different welding conditions (taking overhead welding and down-hand welding) and welding sequences. Therefore, residual stress generated from weld is uncertain in the connection of diaphragm and U-rib and fatigue cracks tend to propagate around the arc gap. There are two kinds of cracking types in the diaphragm, including cracks initiated from the diaphragm-U-rib weld ending and the arc gap.

The bridge monitoring was carried out on the cracks initiated from diaphragm-to-rib weld ending and the arc gap of the diaphragm in Jiangyin Yangtze River Bridge. Fatigue life of different details was estimated based on measured data. Besides, two kinds of optimized structures were applied on di aphragm and effects on its fatigue performance were analyzed by the finite element method.

2 REAL BRIDGE LOAD TESTING SCHEME

The fatigue stress monitoring was carried out on the diaphragm measurements under the normal traffic conditions of Jiangyin Yangtze River Bridge. The strain gauge data were sampled at a frequency of 50 Hz for 1-day using the Data Acquisition & Signal Processing system (DASP). The field test was mainly comprised of six stages, namely, measurements arranging, diaphragm polishing, strain gauge sticking, temperature compensating, device debugging and strain testing. The gauges were attached to the ending of the rib-diaphragm weld and arc gap on t he U-rib 6#, which is located on t he slow lane of the downstream direction and 1/4 span of Jiangyin Yangtze River Bridge. It is suggested by IIW that stress at the distance of 1.5t (t is the thickness of deck) from the weld toe was measured as the nominal stress (Hobbacher,2015). The layout of the measurements is shown in Figure1 and Figure2.

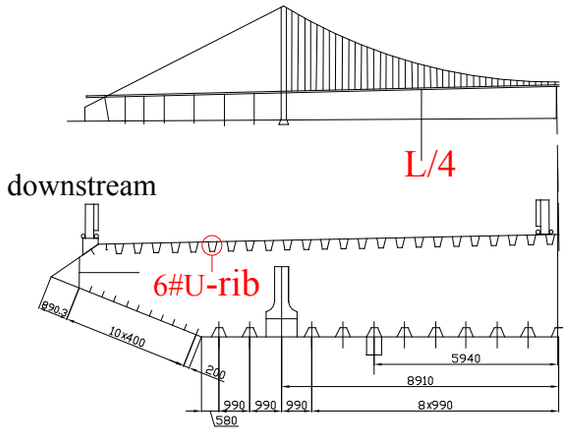


Figure1 Testing position of girder.

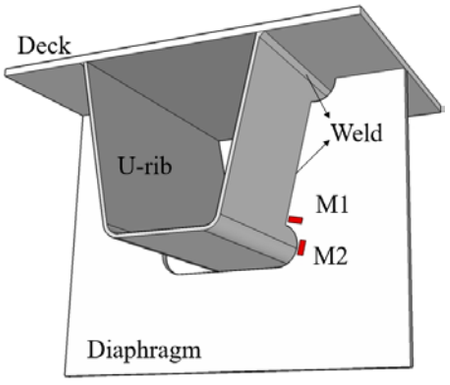
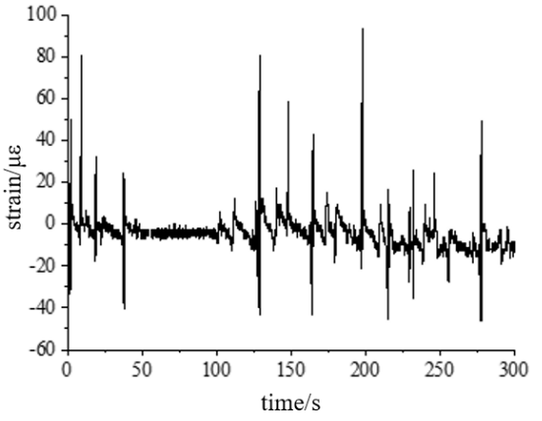
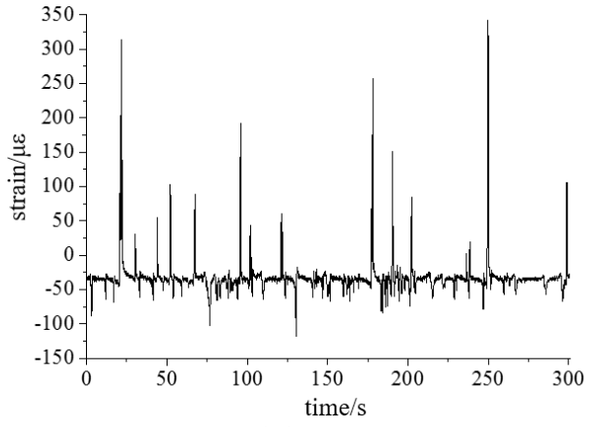


Figure2 Layout of strain gauges on the diaphragm



（a）M1



（b）M2

Figure3 The strain time curve of measurements (300s)

3 ANANLYSIS OF MEASURED DATA

3.1 *Strain histogram*

Measurement errors are inevitable during the field testing due to the effects of temperature loading, wind loading and various noises. In order to guarantee the reliability of the measured data, the zero drift and signal filtering processing were carried out using the DASP system. Therefore, effects generated from various environment factors were reduced and modified strain histogram curves were extracted under traffic loadings. 300s of strain data were extracted from 24h histogram because of its large volume. Strain changes at the diaphragm-U-rib weld ending and arc gap were shown in Figure3.

The monitoring data show that time periods, namely 9:00~12:00 and 14:00~17:00, are of the most strain cycles, indicating the heavy traffic during these two periods. According to strain histogram curves of diaphragm, strain of the diaphragm-U-rib weld ending changes within 40 με, and strain of diaphragm arc gap changes in a relatively great ranges, mostly within 100 με.

3.2 *Strain spectrum*

The data of stress histogram were obtained through multiplying the strain histogram by the elasticity modulus of steel. Stress of details changing with time can be analyzed according to the stress histogram curves, but fatigue stress spectrums are necessary as the cycles of stress ranges at each levels are still uncertain. By executing the rainflow ananlysis algorithm to the stress histogram data, cycles corresponding to each level of stress ranges were calculated and fatigue stress spectrums were obtained by specifying a resolution of 1.0 MPa for the stress range interval. The stress cycles with amplitudes less than 2.0 MPa were discarded because they had little effect on the results of fatigue life and added extra workload. The stress spectrums of two measurements are shown in Table 1.

Table1 The stress spectrum of measurements

Stress range /MPa	Stress cycles/ N	
	M1	M2
2~3	2914	2400
3~4	530.5	387
4~5	182.5	174
5~6	122.5	113.5
6~7	88.5	52
7~8	73	39
8~9	76.5	31
9~10	72.5	28
10~20	174	93
20~30	58	22
30~40	32	5.5
40~50	15	3
50~60	10	0.5

Table 1 shows that with the increase of stress range, the corresponding stress cycles gradually reduce. The stress range of 2~8MPa accounts for more than 90% of stress cycles, which indicates that low-amplitude cycles are mostly included in stress spectrum of two details. According to the BS5400 specification, the greater stress range will enlarge the initial defects of the component, thus reducing the fatigue limit. As time goes by, the stress range that is lower than fatigue limit of the components can play a part in the accumulation of damage.

The BS5400 (2009) specification provides the fatigue resistance of classified welded details in steel bridges, in which diaphragm-U-rib weld ending and diaphragm arc gap are classified as level F2 and level B with the fatigue limits of 35MPa and 100MPa respectively. Table 1 shows that the peak stress ranges of M1 and M2 are greater than the fatigue limit, thus M1 and M2 are prone to fatigue damage under the accumulation of vehicle loads.

3.3 *Fatigue reliability*

The equivalent stress ranges of 1-day were calculated and fatigue damage per hour was analyzed based on the fatigue stress spectrum. It's deduced that fatigue damage follows the log-normal distribution. Fatigue reliability of M1 and M2 was calculated by Eq. (1) (Dan M F et al. 2008; Kwon K et al.2010), where D_C=critical damage; D_T =cumulative damage; u=average damage; δ^2 =variance. The target reliability of 3.5, w hich is recommended by the European steel structure association(2010), was adopted with corresponding failure probability is 10^{-4}.

$$\beta = \frac{\ln\left[\frac{u_{D_C}}{u_{D_T}}\left(\frac{1+\delta_{D_T}^2}{1+\delta_{D_C}^2}\right)^{1/2}\right]}{\left[\ln(1+\delta_{D_C}^2)+\ln(1+\delta_{D_T}^2)\right]^{1/2}} \quad (1)$$

Fatigue reliability of M1 and M2 changing with service years was shown in Figure4. The reliability decreases noticeably in the early years but the decline slows down later on. The reliability of M1 is always smaller than that of M2. The reliability index of M2 is estimated as 3.48 in the 10.5 years of service and reliability index of M1 decreases to 3.44 after only 3 years of service, both failing to meet the β_{target}.

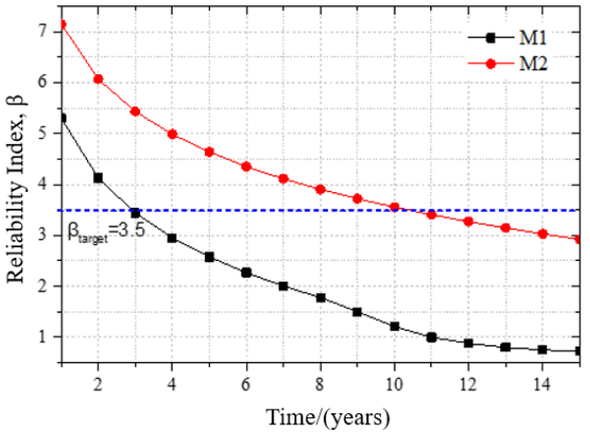


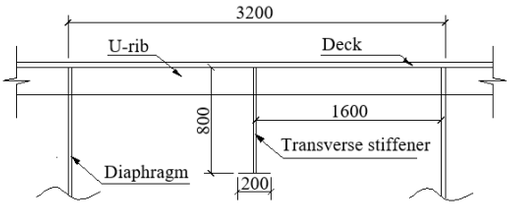
Figure4 Fatigue reliability evaluation of two measurements

4 ANALYSIS OF OPTIMIZED STRUCTURE

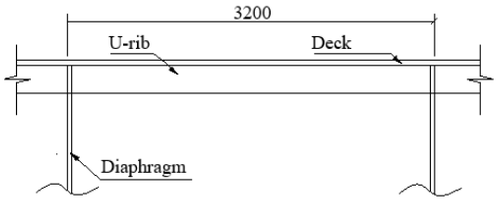
4.1 *Two optimized constructures*

Two forms of optimization were proposed to improve the fatigue problem of diaphragm, namely, setting of the transverse stiffener between diaphragms and stiffener on the arc gap.

Type 1: Setting of the transverse stiffener between diaphragms (Dan M F et al.2008). There are two kinds of diaphragm setting in the steel box girder nowadays.Taking Ikushi Bridge and Minggang Bridge as examples, the transverse stiffener is set between diaphragms in the steel box girder. For Nanjing Yangtze River Bridge and Humen Bridge (Zhou et al.2004), there's no such structure as setting of the transverse stiffener between diaphragms. Two kinds of diaphragms setting were studied in reference to the former design experience, which were shown in Fig.5. Type1: the space between two diaphragms was 3.2m and transverse stiffener with height of 0.8m and thickness of 0.012m was set between diaphragms. Type2: the space between two diaphragms was 3.2m and there's no transverse stiffener.



(a) type 1



(b) type 2

Figure5 Two kinds of diaphragms setting

Type 2: Setting of the stiffener on the arc gap. An stiffener sharing the same shape with the arc gap was set and welded with U-rib. The stiffener was perpendicular to diaphragm and the width on bot h sides of the U-rib were 100mm, which was shown in Fig.6.

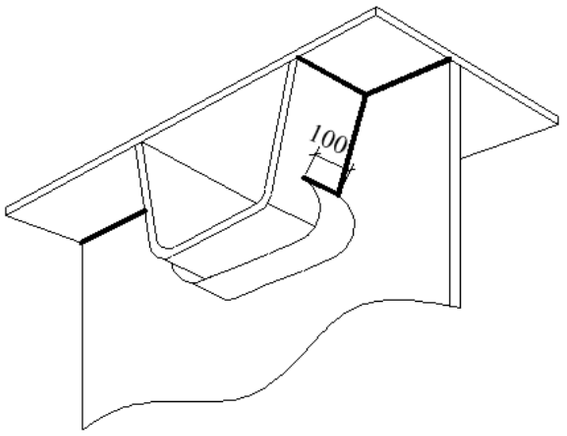
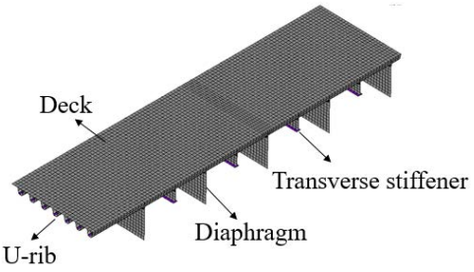


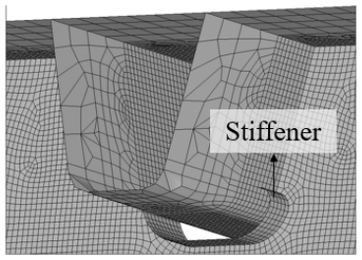
Figure6 Setting stiffener on the arc gap

4.2 *Finite element model and loading*

Seven U-ribs were fitted in the transverse direction and five diaphragm distances were adopted in the longitudinal direction to reduce the influence of boundary conditions on the stress value in calculating area. The total length of the model is 16000mm and space between diaphragms is 3200mm. The width of the model is 3900mm, the space between U-rib is 600mm and the size of U-rib is 300mm×280mm×8mm. The thickness of deck and diaphragm were 16mm and 12mm respectively. The local model was simulated by Shell63 elements. The bilinear kinematic hardening plasticity model was adopted. The elastic modulus E of steel is 2.0×10^5MPa and the poisson ratio is 0.3. T he finite element models of two optimized structures were adjusted on the basic model, as shown in Fig.7.



(a) model with transverse stiffener



(b) model with stiffener on the arc gap

Figure7 Finite element model of two optimized structures

Stress increment caused by change of geometrical shape was only considered in the calculation of the nominal stress. The weld and partial penetration gap could be overlooked and the rough grid size was acceptable for FEM analysis. Therefore, the nominal stress method was adopted for fatigue assessment of the diaphragm-U-rib weld ending and the arc gap (Hobbacher A et al.2016; Martinsson J et al.2005; Yamada K et al.2008).

In order to calculate stress ranges of fatigue measurements, the double-wheel loading was applied on the local model of steel bridge deck. According to General Specifications for Design of Highway Bridges and Culverts(in Chinese), the acting length of the double wheel was 0.6m and 0.2m respectively along the transverse and longitudinal direction, and the wheel loading was 70kN. The stress influence line was calculated by moving area loading on the local steel bridge model. The transverse layout of the loading was shown in Fig.8.

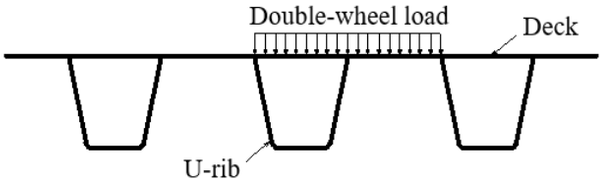
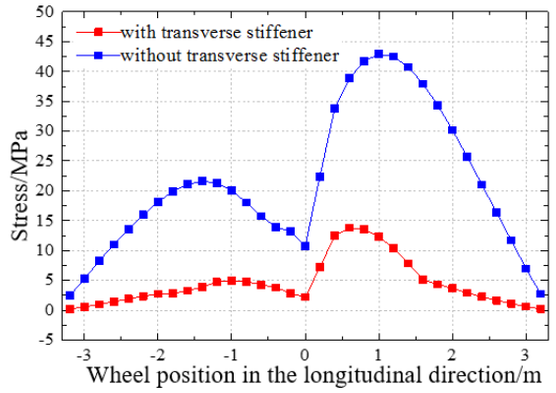


Figure8 The position of wheel loading

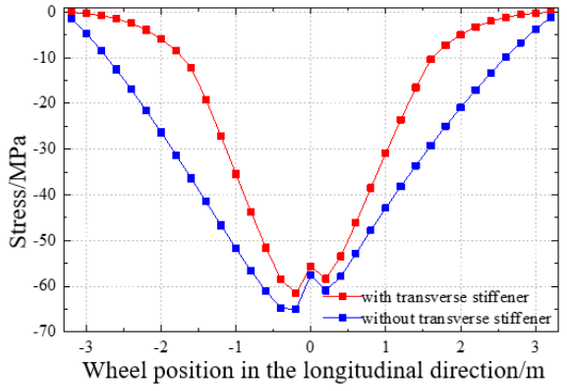
4.3 *Analysis of calculation results*

The stress influence line of two measurements, with the transverse stiffener setting between diaphragms was shown in Fig.9. Stress of critical M1 and M2 is noticeably declined. The maximum tensile stress of diaphragm-U-rib weld ending are reduced by 67%, having the specific value decreases from approximately 32.33MPa to 10.40MPa. Likewise, maximum tensile stress of the arc gap are reduced by 5%, having the specific value decreased from

approximately 65.05MPa to 61.58 MPa. The setting of transverse stiffener leads to greater decline in stress of diaphragm-U-rib weld ending than that of the arc gap, indicating diaphragm-U-rib weld ending is more susceptible to the transverse stiffener. The decrease of the tensile stress of diaphragm-U-rib weld ending can effectively reduce the possibility of fatigue cracking. By the stress influence line of two measurements, stress of diaphragm-U-rib weld ending shows barely no changes and compressive stress of diaphragm arc gap increases gradually before arrival of wheels on the transverse stiffener. When the wheels cross transverse stiffener, stress of diaphragm-U-rib weld ending changes in great amplitude and compressive stress of diaphragm arc gap increases linearly. This is because loadings transferred from the deck are shared by the diaphragm and transverse stiffener after the setting of the transverse stiffener between diaphragms.



(a) diaphragm-U-rib weld ending



(b) arc gap of the diaphragm

Figure9 Stress influence line of fatigue details

The stress influence line of two fatigue details in the bridge deck is equivalent to the stress histogram under vehicle loadings, The stress range and cyclic number were calculated by using the rainflow analysis algorithm. The Miner's cumulative damage rule, as shown in Eq. (2), was applied to calculate stress ranges corresponding to one stress cycle(AASHTO 1990; Miner MA et al.1945). where σ_{eq}= equivalent stress range; n_i= cycles corresponding to σ_i; N_T= the total cyclic numbers of all the stress cycles ; m= the slope of the *S-N* curve, for most of the fatigue details, m=3.

$$\sigma_{eq}=\sum\left[a_i\sigma_i^m\right]^{\frac{1}{m}}=\left[\frac{1}{N_T}\sum n_i\sigma_i^m\right]^{\frac{1}{m}} \quad (2)$$

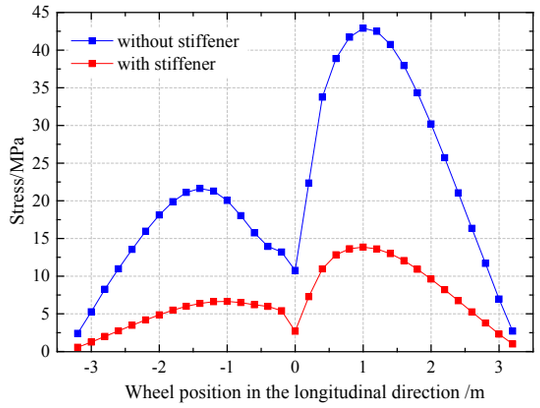
The transverse stiffener was set between diaphragms and the equivalent stress ranges of these two measurements were shown in Table2. The transverse stiffener exerts no effects on stress ranges of the arc gap, which decreases less than 4% after the setting of transverse stiffener. The stress ranges of diaphragm-U-rib weld ending are susceptible to the transverse stiffener and reduces by 66%, having the specific value decreased from approximately 32.33MPa to 10.85MPa.

Table 2. Stress range of details with the transverse stiffener

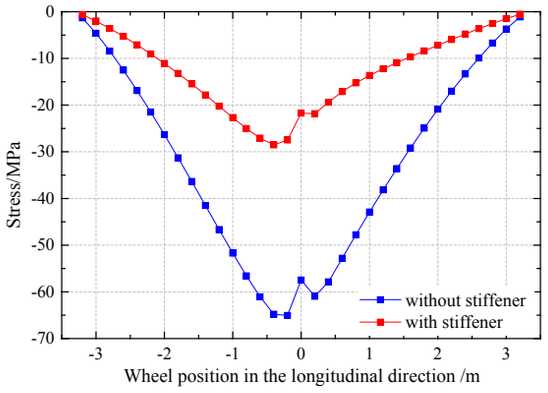
Forms	Stress range/MPa	
	U-rib - diaphragm weld ending	arc gap of the diaphragm
with transverse stiffener	10.85	48.81
without transverse stiffener	32.33	50.40

According to the stress analysis of two measurements, setting of the transverse stiffener between the diaphragms can effectively decrease stress ranges and the maximum tensile stress and compressive stress are reduced to different degrees. Therefore, setting of the transverse stiffener not only improves fatigue performance of diaphragm, but also reduces the possibility of fatigue cracking.

The stress influence line of two details with the stiffener setting on the arc gap was shown in Fig.10. The maximum tensile stress of diaphragm-U-rib weld ending are reduced by 67%, having the specific value decreased from approximately 42.89MPa to 13.85MPa. Likewise, maximum tensile stress of the arc gap are reduced by 58%, having the specific value decreased from approximately 65.05MPa to 27.47 MPa. This is mainly because the bending and torsional deformation of the U-rib are restrained by the shear force and bending moment of weld connecting the U-rib and diaphragm. The shear force and bending moment reach the maximum on the arc gap. Therefore, the stiffener not only improves the flexural rigidity of arc gap, but also improves its fatigue performance.



(a) diaphragm-U-rib weld ending



(b) arc gap of the diaphragm

Figure10 Stress influence line of fatigue details

The equivalent stress range with the setting of stiffener on the arc gap was calculated according to the aforementioned method and the results were shown in Table 3. The maximum tensile stress of diaphragm-U-rib weld ending are reduced by 67%, having the specific value decreased from approximately 32.33MPa to 10.40MPa. Likewise, maximum tensile stress of the arc gap are reduced by 45%, having the specific value decreased from approximately 50.40MPa to 27.50 MPa. The stress ranges of diaphragm-U-rib weld ending and arc gap are both susceptible to the stiffener setting on the arc gap. Therefore, setting of the stiffener on the arc gap can improve the fatigue performance of diaphragm as the stress range is one of the main factors of steel structure failure.

Table 3. Stress range of details with stiffener on the arc gap

Form	Stress range/MPa	
	U-rib - diaphragm weld ending	arc gap of the diaphragm
With stiffener on the arc gap	32.33	50.40
Without stiffener on the arc gap	10.40	27.50

5 CONCLUSIONS

1) The reliability index of arc gap was estimated as 3.48 in the 10.5 years of service and reliability index of diaphragm-U-rib weld ending decreased to 3.44 after only 3 years of service, both failing to meet the target reliability index.
2) Setting of the transverse stiffener between the diaphragms could effectively decrease stress ranges of two details. The stress ranges of diaphragm-U-rib weld ending were more susceptible to the optimized structure and declined more than that of the arc gap.
3) Setting of the stiffener on the arc gap decreased stress ranges of the diaphragm-U-rib weld ending and arc gap, thus reducing the possibility of fatigue cracking.

ACKNOWLEDGEMENT

The authors thanks the support of National Natural Science Fund (No.51678216).

REFERENCES

Cao, V. D., Sasaki, E., Tajima, K., & Suzuki, T. (2015). Investigations on t he effect of weld penetration on fatigue strength of rib-to-deck welded joints in orthotropic steel decks. International Journal of Steel Structures,15(2), 299-310.

Cao V D, Sasaki E, Tajima K, et al. (2015). Investigations on the effect of weld penetration on fatigue strength of rib-to-deck welded joints in orthotropic steel decks[J]. International Journal of Steel Structures, 15(2): 299-310.

Li Z X, Chan T H T, Ko J M. (2001). Fatigue damage model for bridge under traffic loading: application made to Tsing Ma Bridge[J]. Theoretical & Applied Fracture Mechanics, 35(1):81-91.

Grundy P. (1990). Measurements and interpretation of strains on Westgate Bridge. In: Monash University Report. Australia, 1-49.

Leendertz J , Kolstein M H. (1995). The behaviour of trough stiffener to crossbeam connections in orthotropic steel bridge decks[J]. Heron, 40.

Bocchieri W J, Fisher J W. (1998). Williamsburg Bridge replacement orthotropic deck as built fatigue test. In: Lehigh University Report. Bethlehem, 1-161

Connor R J, Fisher W J. (2001). Results of field measurements on the Williamsburg Bridge orthotropic deck. In: Lehigh University Report. Bethlehem, 1-198.

BS5400-10-1980 Steel, concrete and Transportion Research and Development,2009,26(6):69-73.

Dan M F, Strauss A, Kim S. Bridge Reliability Assessment Based on Monitoring[J]. Journal of Bridge Engineering, 2008, 13(3):258-270.

Kwon K, Dan M F. Bridge fatigue reliability assessment using probability density functions of equivalent stress range based on field monitoring data[J]. International Journal of Fatigue, 2010, 32(8):1221-1232.

Eurocode 3: Design of steel structures, Part 1.9.

Zhou Mengbo. Cable-stayed Bridge Handbook[M]. Beijin: China communication press, 2004.

Hobbacher A. Recommendations for Fatigue Design of Welded Joints and Components[M]. Springer International Publishing, 2016.

Martinsson J. Fatigue Assessment of Complex Welded Steel Structures[J]. 2005.

Yamada K, Samol Y. Plate bending fatigue tests for root crack of trough rib of orthotropic steel deck[J]. Kozo Kogaku Ronbunshu A, 2008, 54:675-684.

JTG D60—2004, General Specifications for Design of Highway Bridges and Culverts [S]. Beijing： China standards press, 2004.

AASHTO. Guide specifications for fatigue evaluation of existing steel bridges. In: Specifications. Washington(DC): American Association of state Highway and Transportion Official;1990.

Miner MA. Cumulative damage in fatigue. J Appl Mech 1945; 12(3):A-159-A164.

Maintenance, Safety, Risk, Management and Life-Cycle Performance of Bridges – Powers, Frangopol, Al-Mahaidi & Caprani (Eds)
© 2018 Taylor & Francis Group, London, ISBN 978-1-138-73045-8

Grouting compactness monitoring of concrete-filled steel tube arch bridge using electro-mechanical impedance technique

Q. Feng & Y.B. Liang
Hubei Key Laboratory of Earthquake Early Warning, Institute of Seismology, CEA, Wuhan, China.
Wuhan Institute of Earthquake Engineering Co Ltd, Wuhan, China

T.H. Yi
School of Civil Engineering, Dalian University of Technology, Dalian, China

ABSTRACT: Concrete-Filled Steel Tube (CFST) structures have been widely applied in civil infrastructures. The grouting compactness in the steel tube will seriously influence the loading capacity and structural behavior for the CFST structures. In this paper, the electro-mechanical impedance technique was developed to monitor the grouting compactness of CFST arch bridges. In the study, a small-scale steel tube specimen was fabricated to simulate the actual CFST arch bridge structure, all the experimental results demonstrated that the developed method can clearly reveal the structural changes during the grouting in the steel tube, and can be used to monitor the grouting process and detect the occurrence of debonding disease in real-time.

1 INTRODUCTION

Due to their distinguish advantages, such as high load-carrying capability, perfect ductility, convenience and economy in construction, Concrete-Filled Steel Tube (CFST) structures, which combine the advantages of both steel and concrete, have been widely applied in infrastructure construction. Figure 1 presents the applications of the CFST in two arch bridges. In practical applications, the steady cooperative work between the concrete and steel materials in the tube is crucial to guarantee the structural safety during its service period. However, the incomplete grouting of CFST structures during its construction period, may induce the debonding between the concrete core and the steel tube, and will seriously influence the load-carrying ability, reduce the structural integrity, and leave a serious threaten to the vehicle and pedestrian (Su, 2009). Figure 2 presents the detection photos of the surface deformation of the steel tube because of the incomplete grouting of CFST structure.



(a) (b)

Figure 1. The arch bridges using concrete-filled steel tube (a) The first bridge of Yangzi river in Hejiang county (Xhf0293, 2014), (b) Taiping lake bridge in Anhui province (He, 2014).

In order to deal with this problem, some routine detection methods had been applied in actual bridges to detect this defect on the tube, such as the drilled core specimen (Lu et al., 2011), artificial knocking (Chen, 2011), ultrasonic detection (Liu, 2004) and etc. However, these techniques still face a lot of challenges, especially involve the manual inspections, for example, it is always inconvenient or difficult for the workers to reach to the detection region of the bridges, besides, the inspection results usually strongly depend on the worker's experience. On the other hand, for drilled core specimen method, it is inevitable to induce the second artificial damage for the test structure, and may help the disease development. Therefore, developing a new Non Destructive Testing (NDT) technique for the CFST structures to detect the debonding disease in real time, is very necessary and meaningful.



Figure 2. Tube surface deformation caused by incomplete grouting

Electro-mechanical impedance (EMI) technique, which utilizes high-frequency signal as the structural excitation sources, presents great potential for structural health monitoring (Liang et al., 2016a, Liang et al., 2016b). At the same time, the distinguish advantages of piezoceramic materials, such as wide bandwidth, dual sensing and actuation abilities, and availability in different size and shapes, also make the EMI-based method an attractive technique to damage diagnose. The basic idea of this technique is to use high frequency vibrations to locally monitor the desired structure for finding any structural damage especially at the incipient stage. Physical changes in the host structure cause changes in the structural mechanical impedance, which may induce changes in the electrical impedance of the surface bonded PZT patch of the structure. Lots of researcher have successfully applied this technique to monitor the structural health condition, including an aircraft structure (Chaudhry et al., 1995), a massive steel bridge joint (Ayres et al., 1996), complex precision parts (Park et al., 1999), and several applications under significant varying-temperature condition (Park et al., 2000).

In this paper, the electro-mechanical impedance technique was employed here to monitor and detect the grouting process and the quality of grouting compactness of the steel tube. At the beginning, the theoretical description of the EMI technique is briefly introduced, then a small-scale steel tube was designed and fabricated to simulate the real CFST arch bridge structure. A distributive sensor network, including eight piezoceramic patches, was developed in the specimen. The specimen was grouted through a reserved grouting hole in four stages, and each stage extended three days for cement hydration. For each stage, the eight patches will be connected with a high precious impedance analyzer to acquire the electrical impedance, and then the acquired signals in different location under different stages will be compared and analyzed. Finally, all the experimental results demonstrate that the EMI-based method can effectively detect the occurrence of the debonding disease and evaluate the compactness quality of the CFST arch bridge.

2 DETECTION PRINCIPLE

2.1 *Electro-mechanical impedance*

The electro-mechanical coupling of piezoelectric (PZT) actuator/sensor patch is the key for the impedance-based qualitative health monitoring technique. This technique was first proposed by Liang (Liang, 1997) and subsequently developed by other researchers (Ayres et al., 1999, Park and Inman, 2007). The coupling effect of the EMI for a system with a PZT patch and a host structure can be conceptually investigated by using an idealized 1D electro-mechanical system, as shown in Figure 3. From the figure, a PZT is bonded to the surface of the structure by adhesive, and is considered as a thin bar that vibrating axially due to an applied alternating voltage. Thus, the integrated electro-mechanical system may be electrically represented by an electrical impedance which is affected by the dynamics of the PZT and the host structure.

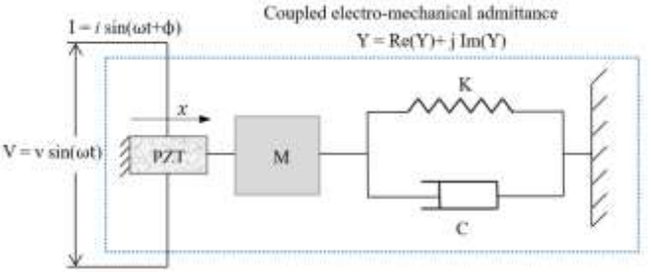


Figure 3. 1D electro-mechanical impedance system (Liang et al. 2016b)

From the figure, assuming the mechanical impedance of PZT patch Z_A is defined as the ratio of a harmonic input voltage $V(\omega)$ at an angular frequency ω to the current response $I(\omega)$ in frequency domain. Similarly, the mechanical impedance of the host structure that is idealized as a SDOF system, can be represented by Z_S and is defined as the ratio of a harmonic excitation force $F_0(\omega)$ at an angular frequency ω to the velocity response $\dot{x}(\omega)$ in frequency domain.

Thus, the solution of the wave equation for the PZT bar that is connected to the structure leads to the following equation for a frequency-denpent electrical admittance:

$$Y(\omega) = j\omega \frac{wl}{h}\left[\frac{Z_A(\omega)}{Z_A(\omega)+Z_S(\omega)}\frac{d_{31}^2 \bar{Y}_{11}^E \tan(\kappa l)}{\kappa l} + \bar{\varepsilon}_{33}^T - d_{31}^2 \bar{Y}_{11}^E\right] \quad (1)$$

where ω is the angular frequency of the driving voltage; $Y(\omega)$ is the electrical admittance (inverse of impedance) of the PZT patch at angular frequency ω, κ is a wave number ($=\omega/c_t^E$); c_t^E is a wave velocity ($=\sqrt{\bar{Y}_{11}^E/\rho}$); ρ is density; Z_A and Z_s are the mechanical impedance of the PZT and the host structure, respectively; w, l and h are the width, length and thickness of the PZT transducer, respectively; $\bar{Y}_{11}^E = Y_{11}^E(1+\eta j)$ is the complex Young's modulus of the PZT transducer at zero electric field; d_{31} is the coupling piezoelectric constant between the z and x direction at zeros stress; $\bar{\varepsilon}_{33}^E = \varepsilon_{33}^E(1-\delta j)$ is the complex dielectric constant at zero stress along the z direction, η and δ are the mechanical loss factor and dielectric loss factor.

From the equation, it indicates that electrical impedance of the PZT patch is directly related to the mechanical impedance of the host structure. Therefore, the EMI technique can be employed to identify the structural diseases, including the grouting compactness changes and the debonding defect of the concrete-filled steel tube for arch bridge.

2.2 *Grouting compactness and debonding detection using the EMI technique*

In this study, the impedance technique was employed to monitor the grouting compactness and detect the occurrence of debonding disease of the CFST structure. The PZT patch was bonded on the outside surface of the steel tube, and then connected with a high precious impedance analyzer, thus the electrical impedance signal of the PZT patch can be acquired in real-time.

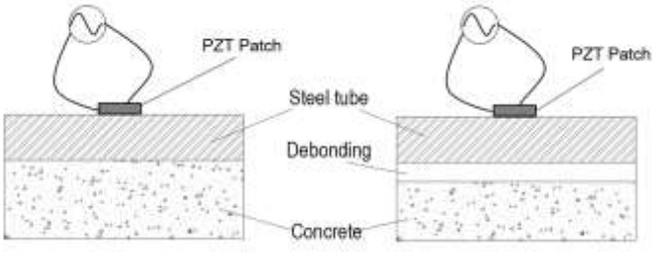


Figure 4. Principle of impedance-based debonding detection for CFST structure

As shown in Figure 4, when grouting is incomplete during its construction, a debonding occurs between the core concrete and the outside steel tube. This disease induces the structural physical characteristic change, including the local stiffness decrease, dampling ratio variation and etc. Therefore, following the description of EMI technique in last section, this structural physical parameters changes will influence the mechanical impedance of structure, and then induce the variation of the electrical impedance of the PZT patch. Thus, by acquiring the electrical impedance of the PZT patch, the health condition of the structure can be monitored, and the debonding disease of the steel tube can also be identified by monitoring and analyzing the variation of the impedance signal acquired from the surface bonded PZT patches.

2.3 *Compactness monitoring index*

After the electrical impedance signals of the PZT sensors were acquired under different grouting compactness conditions, in order to conveniently compare and analyze these signals, a monitoring index was proposed here to monitor the compactness of the steel tube, and diagnose if there is a debonding occurrence. The monitoring index is given as

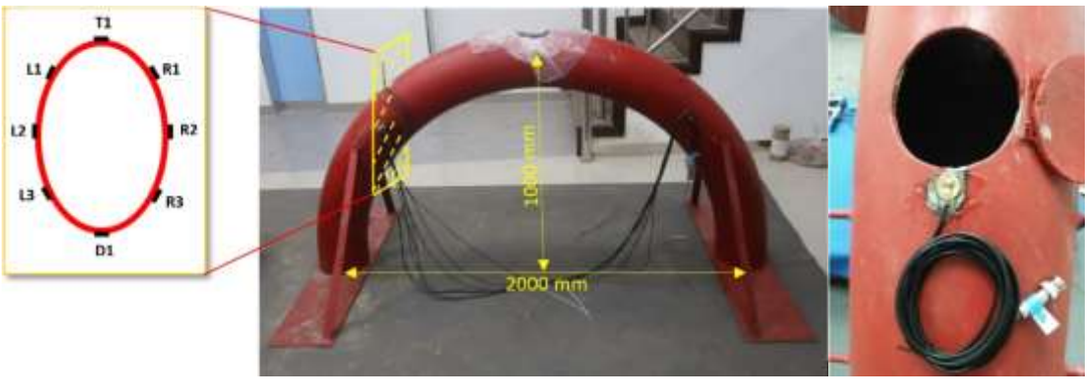
$$I_{RMSD} = \sqrt{\frac{\sum_{i=1}^{N}\left(Y(\omega_i) - Y_0(\omega_i)\right)^2}{\sum_{i=1}^{N}\left(Y_0(\omega_i)\right)^2}} \quad (2)$$

where $Y(\omega_i)$ is the admittance signature at the ith measurement point, and $Y_0(\omega_i)$ is baseline (empty condition) admittance signature at the ith measurement point, N is the total measurement points in a signature. As the structural compactness monitoring index indicates, when the current structural status is close to its empty condition $Y(\omega_i)$, and the IRMSD is close to 0.

3. EXPERIMENTAL SETUP AND PROCEDURES

3.1 *Specimen and sensor location*

In order to verify the effectiveness of proposed method in this paper, a small-scale steel tube specimen was designed and fabricated, as shown in Figure 5. The construction material of the steel tube is Steel Q235. The diameter of the tube is 200 mm, and three holes with the diameter of 150 mm were reserved on the tube for grouting in the test, as shown in Figure 5(b). In the study, eight PZT patches were bonded on the outside surface of the steel tube along the vertical section near one of the reversed holes, as shown in Figure 5(a), in which, two PZT patches located on the top and down side denoted as T1 and D1, respectively, and three patches locate on left side, denotes as L1-L3, and three are right, denoted as R1-R3.



(a) (b)

Figure 5. Specimen (a) the small-scale steel tube specimen and sensor location (b) the reserved grouting hole and the PZT patch

3.2 *Experimental setup and procedures*

In the experiment, a high precious impedance analyzer was connected to the bonded PZT patch using a BNC line, and it was then connected to a laptop with supporting software to control the signal acquisition and the following data analysis, as shown in Figure 6. When the test is beginning, the left side of the steel tube specimen was grouted through the grouting hole by four times, as shown in Figure 7. The grouting cement is C40 which is a typical type of construction concrete. Shortly after grouting, compaction was performed by tapping a rubber mallet at the exterior of the steel tube. In each grouting stage, the impedance signal was acquired for each PZT patch by using the impedance analyzer, then these signals were compared and analyzed by the processing terminal. It should be noted that the each grouting stage holds for three days and the measurements conducted at the 3rd day of each grouting stage.

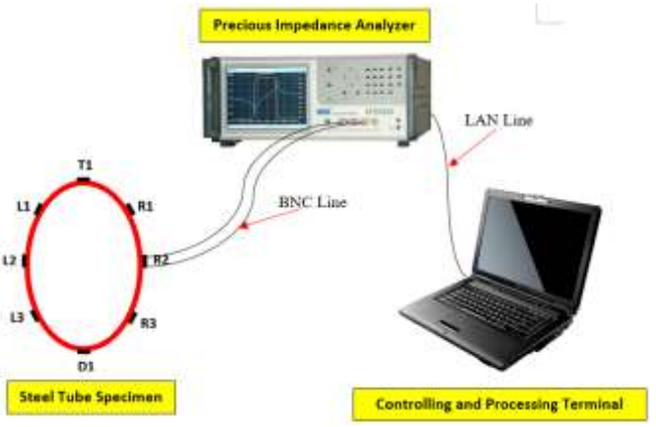


Figure 6. Experimental setup

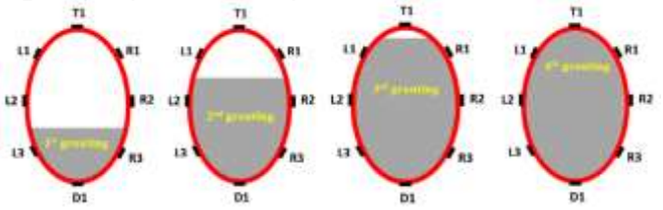


Figure 7. Four times grouting for the steel tube

4. TEST RESULTS AND ANALYSIS

4.1 *The acquired impedance signals*

In the study, the electrical admittance signal was acquired by the impedance analyzer with a frequency range from 300 kHz to 500 kHz. Even though both the real and imaginary admittances were measured, only the real admittance measurements were analyzed and presented in the following analysis due to the fact that the real admittance has a large interaction with the structure than the imaginary admittance (Ayres et al., 1999, Park and Inman, 2007). Because of the space limitation, only the electrical admittance signal acquired by the top sensor was presented and analyzed in the following study, as shown in Figure 8.

From the figure, it is clear that with the increase of the concrete grouting into the steel tube, the real part of the acquired admittance signals have an obvious increase compared to the signal acquired under the empty condition. This phenomenon may be explained by the increase of grouting compactness of the specimen during the experiment. Thus, the structural mechanical parameters change, including the local stiffness and damping ratio, and finally induce the variation of the structural mechanical impedance, which can be caught by the changes of the electrical impedance acquired by the PZT patch on the specimen.

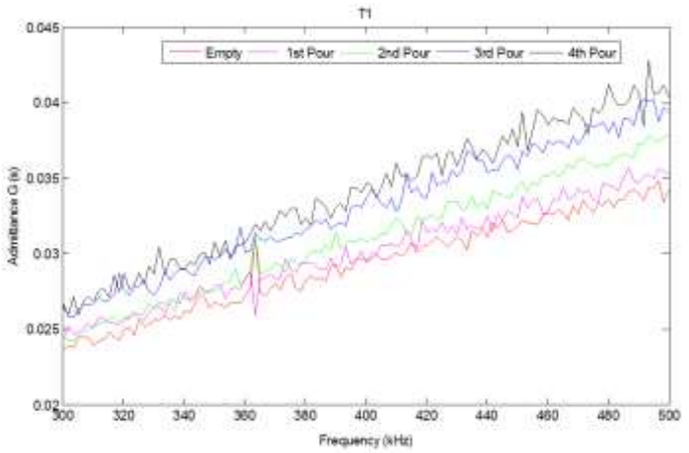


Figure 8. Admittance (real part) versus frequency chart for top PZT patch

4.2 *Impedance-based compactness monitoring index*

In order to clearly quantify the variation of the admittance signal acquired under four different pour conditions, a compactness monitoring index, was employed here to evaluate the grouting compactness and detect the debonding occurrence. The final calculation results was shown in Figure 9. From the figure, it is clear that with the increase of the concrete grouting, i.e. from empty to 4th pouring, the RMSD index increases monotonously, which demonstrates that the developed impedance-based method can effectively monitor the concrete grouting process during the construction, and accurately diagnose the debonding disease between the core concrete and the outside steel tube.

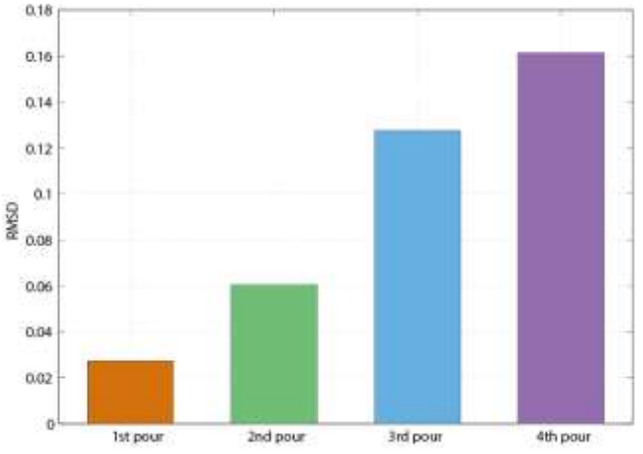


Figure 9. Admittance-based debonding index for the top PZT patch

5. CONCLUSIONS

In this paper, an electro-mechanical impedance based technique combining with piezoceramic transducers, was developed to monitor the grouting process during the structure construction, at the same time, to detect the occurrence of the debonding disease between the core concrete and the outside steel tube for Concrete-Filled Steel Tube (CFST) structures. In order to validate the effectiveness of the developed method, a small-scale steel tube specimen was designed and fabricated in the laboratory, and then eight PZT patches were attached along the outside steel section in the selected location. During the test, concrete was filled the steel tube through the reversed hole on the specimen by four times. For each pouring, the eight PZT sensors were successively connected with a higher impedance analyzer to acquire the electrical admittance of the sensors bonded on the specimen in different location. Then, all the acquired admittance signals were compared and analyzed with the one acquired in the empty condition. Finally, all the test results demonstrated that the developed method can monitor and evaluate the cement grouting process effectively, and also has the ability to evaluate the compactness severity and detect the occurrence of the debonding for the specimen.

ACKNOWLEDGEMENT

This work was partially supported by National Natural Science Foundation of China (grant number 51608493, 51708520), Natural Science Foundation of Hubei Province of China (Grant number 2017CFB509), and Director's Foundation of Institute of Seismology, China Earthquake Administration (Grant number IS201626258, IS201626268 and IS201616250). The authors would like to thank for these financial supports.

REFERENCES

Ayres, J. W., Lalande, F., Chaudhry, Z. & Rogers, C. A., 1998. Qualitative impedance-based health monitoring of civil infrastructures. *Smart Materials and Structures*, 7(5), 599-605.

Ayres, J. W., Rogers, C. A. & Chaudhry, Z. A., 1996. Qualitative health monitoring of a steel bridge joint via piezoelectric actuator/sensor patches. Nondestructive Evaluation of Bridges and Highways. International Society for Optics and Photonics, 2946: 211-219.

Chaudhry, Z. A., Joseph, T., Sun, F. P. & Rogers, C. A., 1995. Local-area health monitoring of aircraft via piezoelectric actuator/sensor patches. *Smart Structures and Integrated Systems. International Society for Optics and Photonics*, 2443: 268-277.

Chen, L., 2011. Debonding defect detection for concrete filled steel tubular using knocking technique. *China Concrete*, 01, 54-56.

He B., 2014, Taiping lake bridge in Anhui province, Guangxi Road and Bridge Engineering Group Co. Ltd. Website: http://www.gxlq.com.cn/html/2014/qiaolianggong-cheng_0612/5741.html. 2014.06.12

Liang, C., 1997. Coupled Electro-Mechanical Analysis of Adaptive Material Systems Determination of the Actuator Power

Consumption and System Energy Transfer. *Journal of Intelligent Material Systems and Structures*, 8(4), 335-343.

Liang, Y., Li, D., Parvasi, S. M., Kong, Q. & Song, G., 2016a. Bond-slip detection of concrete-encased composite structure using electro-mechanical impedance technique. *Smart Materials and Structures*, 25(9), 095003.

Liang, Y., Li, D., Parvasi, S. M. & Song, G., 2016b. Load monitoring of pin-connected structures using piezoelectric impedance measurement. *Smart Materials and Structures*, 25(10), 105011.

Liu, Q., 2004. Compactness detection research for concrete filled steel tube arch bridge using ultrasonic technique. *Non Destructive Testing*, 02, 13-15.

Lu, X.-W., Xu, R., & Wang, G.-L., 2011. Common Defects in the Concrete-filled Steel Tube and Its Detection Methods. *Construction Technology*, 40, 46-48.

Park, G., Cudney, H. H. & Inman, D. J., 2000. An integrated health monitoring technique using structural impedance sensors. *Journal of Intelligent Material Systems and Structures*, 11, 448-455.

Park, G. & Inman, D. J., 2007. Structural health monitoring using piezoelectric impedance measurements. *Philosophical transactions-Royal Society. Mathematical, Physical and engineering sciences*, 365, 373-392.

Park, G., Kabeya, K., Cudney, H. H. & Inman, D. J., 1999. Impedance-based structural health monitoring for temperature varying applications. *JSME International Journal Series A Solid Mechanics and Material Engineering*, 42, 249-258.

Su, J., 2009. Survey on CFST arch bridges and research on their void problem. Chengdu, Sichuan, Southwest Jiaotong University.

Xhf0293, 2014, China solve the problem of building technology for large-scale concrete-filled steel tubes arch bridge. News of road and beidge municipal, Zhulong.com, website http://bbs.zhulong.com/102020_group_3000015/detail19187780.

Maintenance, Safety, Risk, Management and Life-Cycle Performance of Bridges – Powers, Frangopol, Al-Mahaidi & Caprani (Eds)
© 2018 Taylor & Francis Group, London, ISBN 978-1-138-73045-8

Study on soil-steel bridge response during backfilling

T. Maleska & D. Beben
Opole University of Technology, Opole, Poland

ABSTRACT: The paper presents the results of the numerical study and field testing of shell steel structure under backfilling. For these purposes a soil-steel bridge with span of 17.67 m and height of 6.05 m was chosen. The steel shell is made of corrugated steel plate of thickness 0.007 m and has a corrugation depth of 0.14 m and pitch 0.38 m. The assembled shell structure was backfilled with soil layers of thickness ranging from 0.2–0.3 m, which were then properly compacted (min. $I_D = 0.97$). Numerical analysis was conducted using the DIANA program based on finite element method. The assumptions of computational 3*D* model of shell structure with linear interface layer are also described. The corrugated steel plate elements are defined by shell-type elements as an elastic-plastic material and the backfill will be modelled using the non-linear elastic hyperbolic Duncan-Chang model. The highest axial force and stresses in the shell structure observed on additional ribs near the supports and at 1/4 height of shell. Maximum axial forces and stresses were compressive. The greatest bending moments are also compressive and they occurred at the additional ribs (at the 1/4 of height) and at shell crown. The maximum displacements situated near the shell crown and at the end of structure. The displacements obtained from the measurements and finite element analysis are generally quite close to each other. The maximum strains were observed near the support of shell and at 1/3 of shell height. The calculated values are smaller than those obtained from the field test (maximum differences were ca. 20%).

1 INTRODUCTION

Corrugated steel plate (CSP) structures are used to build engineering objects for many years around the world. In Europe, this type of structures began the more popular over the 80s and in the following years saw rapid growth of further investments with the use of corrugated sheets. The reasons for such a rapid increase in the number of structure made from CSP are: (i) the simplicity of construction, (ii) relatively low construction costs, (iii) short construction period and (iv) small expenditure related to maintenance of the object. Soil-steel bridges usually have a span in the range of 3 to 25 m, and they are used to construct bridges, culverts, railway passes, etc. (Machelski 2008).

The durability of soil-steel bridges determines the resistance of the steel to corrosion, which is related to: (i) the abrasion of the inner part due to the rapid flow of water, (ii) the salinity of the water flowing from the road and (iii) the strength and aggressiveness of the backfill. Due to the character of the behaviour of soil-steel bridges, the procedures related to the design as well as selection and execution of backfill are very important issues for the proper and safe operation of the entire structure. This is especially valid during the backfilling process (compaction of the backfill). Suitable backfill characteristics, such as density index, aggregate grain size, density intensity, thickness of compacted layers, backfill range, type of soil and soil cover height are the basic elements affecting the strength of the soil-steel bridges. In addition, the following have to be checked: (i) the weight of the moving equipment near the structure, (ii) the size of the structure deformations during the backfilling, and (iii) the tightening of the connecting bolts.

Strict observance to the technological regime and control of construction processes as well as the application of appropriate enforcement procedures is required. Even a good designed structure can be damaged as a result of an incorrect compaction procedure, the use of unsuitable backfill, lack of appropriate equipment, and lack of control the structure during backfilling (Janusz & Madaj 2009)

So far, attempts have been made to analyse the impact of backfilling for soil-steel bridge (Pittino & Gosler 2006, Manko & Beben 2005). It was found that during the backfilling, the displacements and the bending moments exceeds the maximal values, especially in the initial layers of backfilling of the CSP structure. Koruszewicz & Kunecki (2011) analysed

the backfill densities in the laboratory conditions and the obtained results were compared with the numerical ones. The differences between the laboratory and the numerical results were at the level of 16%, which can be considered an acceptable error. Sanaeiha et al. 2017 present a field test of a soil–steel bridge during backfilling. The case study involved a CSP that was stiffened by concrete rings. The test results show that both maximum deflection and the maximum bending moment occurred at the crown when the soil reached the crown level. Conversely, the maximum axial force occurred at the bottom of the arch when the soil reached its maximum level above the arch. Influence of backfill quality and RC relieving slab on soil-steel bridges was analysed by Beben (2017) and Beben & Stryczek (2016), respectively.

The design of this type of structure has also been verified according to the applicable standards, where the various soil cover heights (in the range of 0.45–1.5 m) were considered (Elshimi et al. 2011). Significant differences of bending moments were observed up to 70% between the values obtained using the Canadian standard (CHBDC 2006) and the measured ones. These results were also compared with finite element analysis (FEA). The difference between the FEA and the measured values was a few percent. Bayoglu Flener (2010) analysed the Canadian standard in comparison to the FEA, but the height backfill over the shell crown was in the range of 2.5–4.08 m. Significant discrepancies were observed, which reached over 50%. Brachaman et al. (2012) investigated the influence of manner of CSP modelling (orthotropic and corrugated). The obtained results were compared to the measured values. The received results show that the difference between the simplified model (orthotropic steel plate) and the result obtained in the tests differs by few percent (for displacements – 4%, and for strains – 13%). The highest discrepancies amounting to 40% occurred in bending moments. 2*D* numerical studies of soil-steel bridge during backfilling were presented also by Beben (2012) and Taleb & Moore (1999). The results are quite reasonable, however they are not show the behaviour of whole structure.



Figure 1. Side view of soil-steel bridge during backfilling.

Some design methods, such as Sundquist-Pettersson (2014) and CHBDC (2006) allow calculating the maximum internal forces in these structures also during the backfilling process. However, these methods give appropriate results for the bridges with small spans up to 8.0 m. Additionally, Bayoglu Flener (2010) received conservative results using these design methods in comparison to experiments. Taking into account these experiences it was decided to focus elaborating an own finite element model, which do not include conservative safety factors and too preservative approach for modelling the interaction between steel shell and backfill. This paper analysed the soil-steel bridge with a large span (almost 18 m) during the backfilling (Fig. 1). Backfilling process is one of the most important stages in this type of structures due to the bridge safety. The obtained results were verified with test values received during the construction of the analysed object. The obtained results can be helpful for designers and practitioners.

2 DESCRIPTION OF THE SOIL-STEEL BRIDGE

The analysed soil-steel bridge constitutes the overpass for animals. The structure have a span of 17.67 m, and vertical height of 6.05 m (Fig. 2). The shell structure was made from corrugated steel plate with depth of 0.14 m, pitch of 0.38 m and plate thickness of 0.007 m. The corrugated sheets were joined together on the span using the high strength bolts. The CSP structure is based on two massive footing with a base width of 4.00 m and a length of 57.83 m, made of C25/30 concrete. The CSP shell is reinforced using additional ribs of the same corrugated plates in an axial spacing of 1.524 m. Additional ribs consist of two wave over the entire length of the bridge (Fig. 2a). The interior of the ribs was filled with concrete mix without bars after backfilling process, therefore it was not included in the numerical analysis.

The length of shell structure at the top is 40.39 m, while the lower part of the structure is 53.83 m. The assembled shell structure was backfilled with soil layers of thickness ranging from 0.2–0.3 m, which were then compacted (I_D = 0.97). The basic dimensions of the soil-steel bridge are shown in Figure 2. The predicted soil cover depth at the shell crown is 1.80 m, which makes it possible to plant various types of vegetation. Such backfill depth also results in a good damping of the shell structure and a reduction of the noise level coming from the vehicles ride under the bridge. Both ends of the shell structure (the inlet and outlet sides) were secured and reinforced using the RC collars with dimension of 0.40 × 0.60 m.

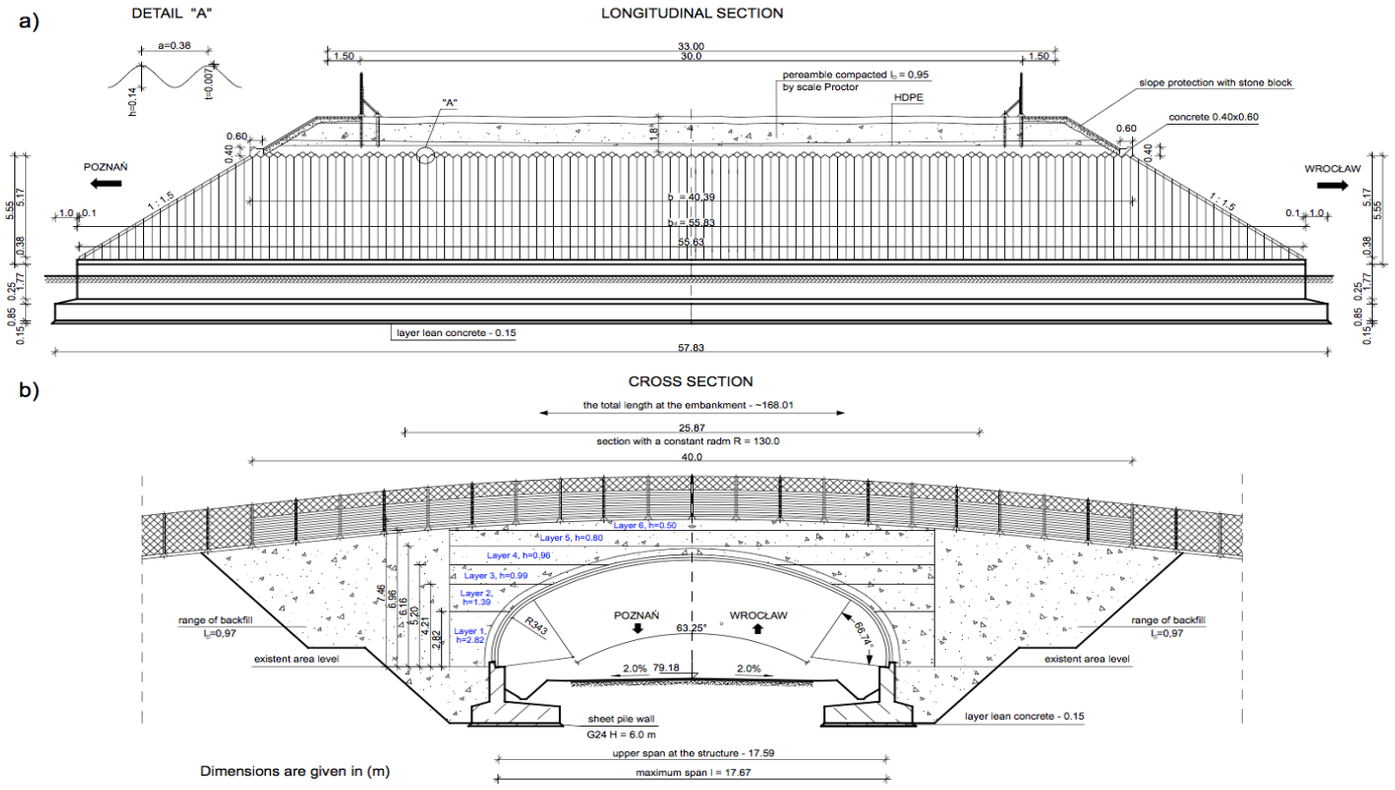


Figure 2. Soil-steel bridge: a) longitudinal section, and b) cross-section with analysed backfill heights.

3 NUMERICAL MODEL DESCRIPTION

3.1 *General remarks*

For the numerical analysis of the soil-steel bridge, a DIANA program was used (DIANA FEA 2017). This program is based on finite element method (FEM). The bridge was modelled as a 3*D* object using shell curved elements (Q24IF) for shell structure and solid elements (HX24L) for soil (backfill) medium. Figure 3 shows the numerical model in DIANA.

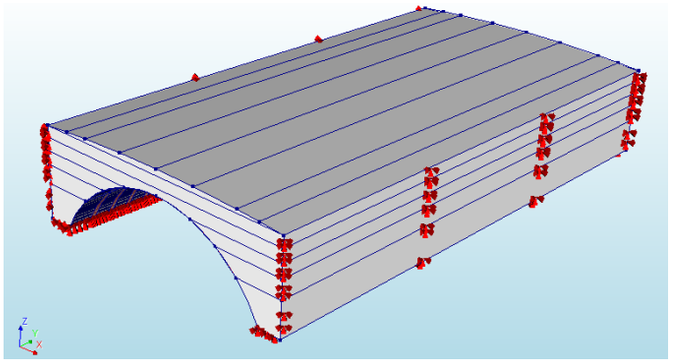


Figure 3. Numerical model created in DIANA.

Table 1 and Figure 2b present the thicknesses and weight of backfill for what the numerical analysis and field measurements were conducted.

Table 1. Weight and thickness of backfill layers.

Layers number	Thickness* (m)	Weight * (kN/m^2)
1	2.82	57.8
2	4.21	86.3
3	5.20	106.6
4	6.16	126.3
5	6.96	142.7
6	7.46	153.0

* - thickness of backfill is counted from top level of foundation (please see Fig. 2b).

3.2 *Material characteristics*

For the numerical analyses following material were used:

- backfill was modelled as solid element (HX24L) with Duncan-Chang nonlinear elastic hyperbolic model with material density of 2050 kg/m^2, Young's modulus of 1e^8 N/m^2, Poisson ration of 0.2, angle of internal friction of 39^o, dilation angle of 5^o, cohesion of 3000 N, unloading-reloading stiffness E_{ur} = 1000 N/m^2, failure ratio R_f = 0.7, reference pressure P_{ref} = 101350 N/m^2, exponent for backbone curve n = 1.1, exponent for unloading reloading curve m = 0.25, minimum tangential stiffness of backbone curve $E_{t.min}$ = 1200 N/m^3, and minimum compressive stress 350 N/m^2,
- steel plate was described as shell element (Q24IF), elastic-plastic model with density of 7850 kg/m^3, Young's modulus of 205e^9 N/m^2,

Poisson ratio of 0.3, the yield strength of steel of $235e^6$ N/m^2, plate thickness of 0.007 m, cross section area of $8.867e^{-6}$ m^2, and moment of inertia of $2.189745e^{-5}$ m^4,

- connections of the backfill and steel shell structure were made by using an interface as automatic interface by applied function "Coulomb friction" with rigidity of $1e^8$ N/m^3, angle of internal friction of 39º, dilation angle of 5º, and cohesion of 3000 N,
- boundary conditions were assumed as non-transferable supports on all boundary walls of the soil and support of the shell walls for x, y, z directions (Fig. 3),
- quadratic finite elements with dimension of 0.5×0.5 m for flat shell and backfill were applied.

The corrugated steel plate of the shell structure was modelled as shell elements using variable material characteristic plates. An orthotropic shell (Fig. 4) was used to calculate the equivalent parameters such as:

- equivalent thickness of plate:

$$t_{equ.} = \sqrt{12(1-\nu^2)\frac{I}{A}}, \tag{1}$$

where I = moment of inertia; A = cross-sectional area; ν = Poisson ratio ($\nu = \nu_x = 0.3$),

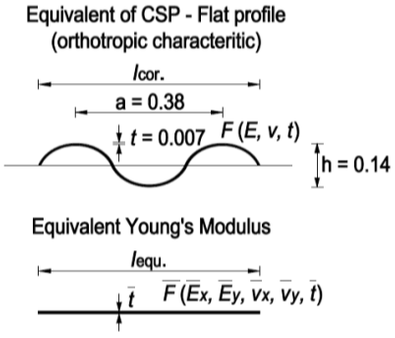


Figure 4. Orthotropic characteristics of flat plates used in numerical model of shell (dimensions are given in m).

- equivalent elastic modulus of material (Young modulus) in circumferential direction of shell thickness of plate:

$$E_{x\,equ.} = E\frac{A}{a\,t_{equ.}}, \tag{2}$$

where a = a pitch of corrugation,

- equivalent elastic shear modulus:

$$E_{y\,equ.} = E\left(\frac{t}{t_{equ.}}\right)^3, \tag{3}$$

- equivalent Poisson ratio:

$$\nu_{equ.} = \nu\frac{E_{y\,equ.}}{E_{x\ equ.}}. \tag{4}$$

4 EXPERIMENTAL TESTING

Four Leica self-levelling levels with a reading accuracy of 0.01 m were used for the displacement measurements of shell structure during backfilling. Due to the relatively long shell structure (about 60 m), four measuring stations were set up (Fig. 5). So, such approach allowed that each measuring point was controlled by at least two independent measuring instruments.

Three transverse cross-sections and four longitudinal cross-sections were selected to provide accurate information about the displacements of the CSP

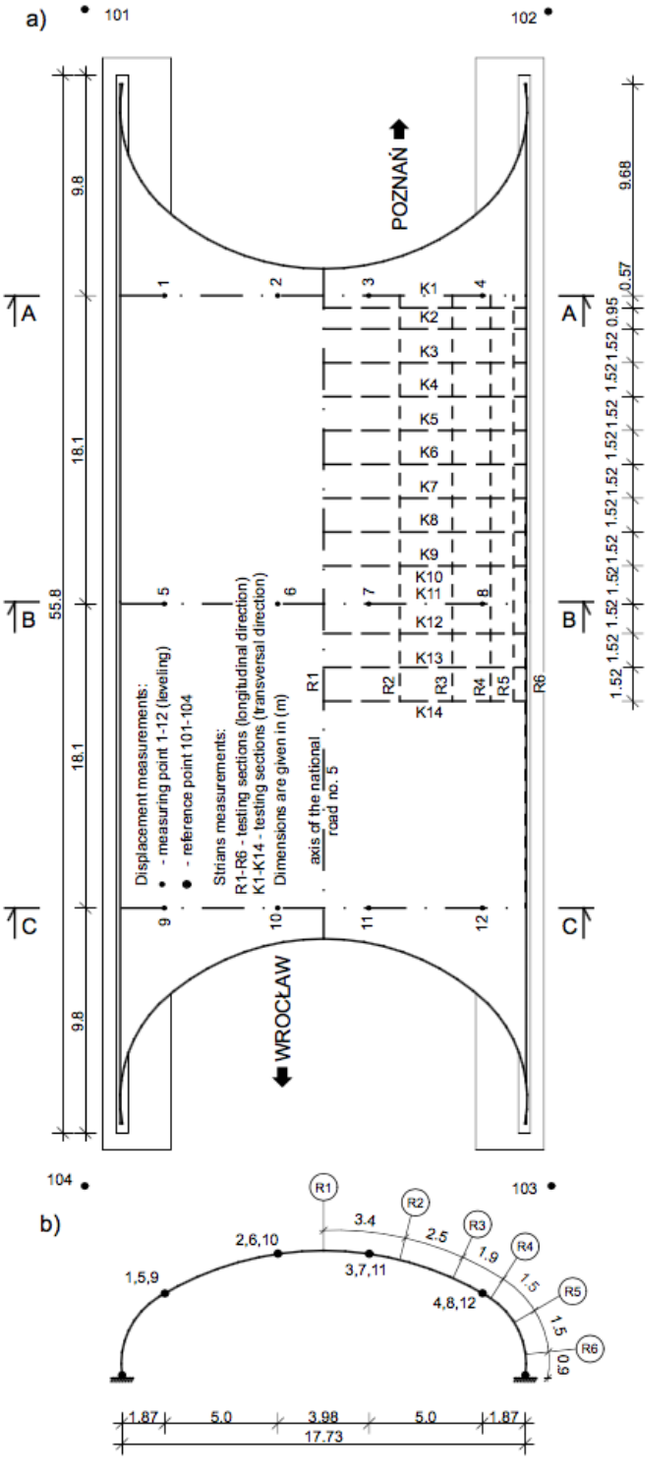


Figure 5. Location of measurement points and testing sections.

shell structure (Fig. 5). Measurement points were stabilized from the bottom of the shell structure to allow for the exact way to make the measurements.

Measurements of the height network of bench marks # 101, 102, 103 and 104 were performed by geometric levelling in the main and return direction. An assessment of the constancy of the bench marks was also conducted. Displacement and strain measurements were executed between 18.00 and 22.00, i.e. after completion of all building work on the facility to obtain actual deformation of the shell structure after full day loading and compacting of the backfill around the structure. The testing was started with the output measurements, i.e. the analysis of the state of the structure before loading (without backfill) to obtain the so-called measurement base (comparative). Vertical displacements of the examined points were calculated on the basis of changes in altitude differences.

Additionally, in selected points and sections of CSP shell structure, the strains were measured (Fig. 5). In cross-section, six testing points (R1-R6) were predicted (only on the half of shell – due to the symmetric of structure). In longitudinal section fourteen testing sections (K1-K14) were chosen (to half of the structure). The strain gauges were located at the top and bottom of the corrugation of basic shell structure and additionally on the reinforcing ribs.

5 ANALYSIS OF RESULTS

Analysis of results at this stage of construction of soil-steel bridges is very important, i.e. taking into account that the steel shell structure was first uploaded by the backfill and technological equipment (roller, vibratory plates). The measurements were carried out after compaction of each of the analysed backfill layers. Therefore, the direct impact of forces coming from the vibration plates has been omitted in calculations. However, some influence of these equipment's exists. Performing a thorough analysis of the state of displacement and internal forces in the CSP structure allows us to determine the strength and behaviour of the thin steel shell structure. Additionally, the first phase of cooperation between the backfill and steel shell can be also evaluated.

It has been observed that the values of the vertical displacements obtained in most cases are similar to the measured ones during backfilling process (Table 2). The highest displacements in the numerical program were obtained for the case of backfill layer # 6, where the maximum value was 21.3 mm (Fig. 6a), near the measurement points # 2, 3, 10 and 11 (end of shell structure).

Slightly smaller displacement (18.6 mm) occurred in the middle of the shell length in the vicinity of measurement points # 6 and # 7. The smallest calculated displacements from the numerical calculations for the backfill layer # 6 occurred at the lower part of

Table 2. Maximum displacements (mm) of CSP structure obtained from testing and numerical analysis.

Measurement point number:	Value:	Number of backfill layers: 1	2	3	4	5	6
1	d_m	–1	4	–4	–6	–15	–
	$d_{cal.}$	2.8	2.9	3	4.2	5.1	2.6
2	d_m	–2	2	3	–9	13	–
	$d_{cal.}$	6.5	5.9	11.3	16.7	20.5	21.3
3	d_m	–2	4	3	7	24	–
	$d_{cal.}$	6.5	5.9	11.3	16.7	20.5	21.3
4	d_m	1	6	–2	–2	–6	–
	$d_{cal.}$	2.8	2.9	3	4.2	5.1	2.6
5	d_m	–2	1	–6	–6	–22	–
	$d_{cal.}$	2.8	2.9	3	4.2	5.1	2.6
6	d_m	–2	1	5	12	8	–
	$d_{cal.}$	6.5	4.4	8.5	14.5	17.9	18.6
7	d_m	–2	6	2	8	26	–
	$d_{cal.}$	6.5	4.4	8.5	14.5	17.9	18.6
8	d_m	–4	–3	–2	–10	–14	–
	$d_{cal.}$	2.8	2.9	2.5	4.2	5.1	2.6
9	d_m	–3	–2	–9	–11	–21	–
	$d_{cal.}$	2.8	2.9	2.5	4.2	5.1	2.6
10	d_m	3	12	17	16	20	–
	$d_{cal.}$	6.5	5.9	11.3	16.7	20.5	21.3
11	d_m	–3	6	5	7	29	–
	$d_{cal.}$	6.5	5.9	11.3	16.7	20.5	21.3
12	d_m	–4	4	–8	–10	–15	–
	$d_{cal.}$	2.8	2.9	2.5	4.2	5.1	2.6

Note: d_m – measured displacements, $d_{cal.}$ – calculated displacements from DIANA.

shell (the measuring points # 1, 4, 5, 8, 9, and 12) and it was 2.6 mm (Table 2).

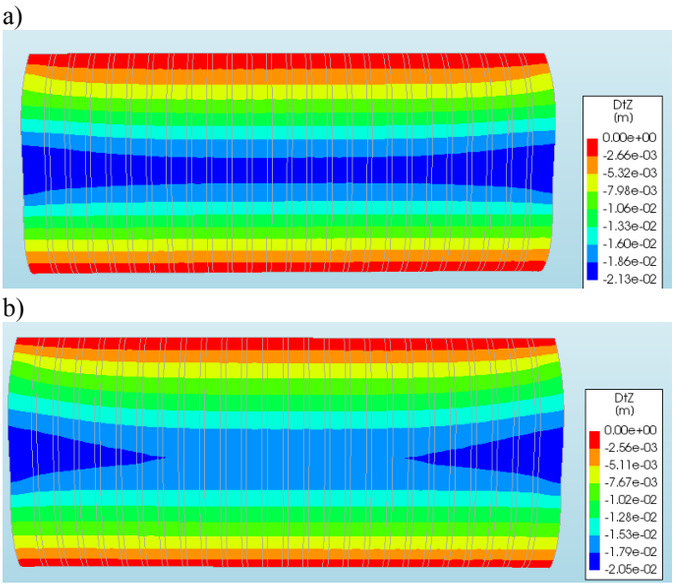


Figure 6. Maximum displacement of CSP shell structure from backfilling of layers: a) # 6, and b) # 5.

However, the largest measured displacements amounted to 29 mm and it was located at measurement point # 11, located at one end of the CSP shell structure. In the adjacent measurement point # 10 the displacement was 20 mm. In the numerical analysis for points # 11 and # 10, the displacements were at the level of 20.5 mm (Fig. 6b), which constitutes of 71% and 102.5% of measured ones for points # 11 and # 10, respectively. The same calculated values were obtained in opposite points # 2 and # 3. They are 158% higher and 85% lower than the measured value. In the middle of shell structure, the displacements do not exceed 19.0 mm. The greatest discrepancies between numerical and measured values were observed in case of backfill layer # 3, where the difference in displacements were 377%, i.e. the calculated displacements were strongly higher than measured ones. Generally, the smallest displacements were observed during loading of backfill layer # 1. They are no exceed 6.5 mm at the measuring points # 2, 3, 10, and 11 as well as at points located in the middle of span, i.e. # 6 and # 7. All displacements of shell structure are presented in Table 2.

It was also observed that the largest axial forces Nxx obtained from the numerical analysis were caused by backfill layer # 5 and they amounted to –3336 kN/m (Fig. 7). They were observed on additional ribs near the supports and 1/4 height of shell. The backfill depth was on level of the crown of the shell structure. During backfilling of the layer # 6 (over the crown shell) the axial forces Nxx were smaller and equalled to –2656 kN/m, which represents 80% value of axial force from layer # 5. In the remaining backfill layers (# 1–4), the axial forces were strongly reduced. For example, the first analysed backfill layer caused that the axial forces in the shell structure were on the level of –1088 kN/m. It constitutes only 33% of the axial force from layer # 5. The remaining maximum axial forces are shown in Table 3. It should be also mentioned that all maximum axial forces are compressive.

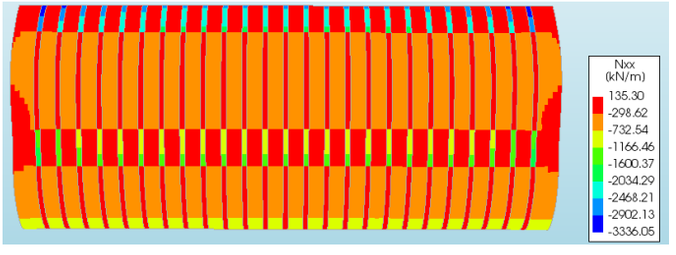


Figure 7. Maximum axial forces in shell structure during backfilling of layer # 5.

The highest bending moment amounted to Mxx = –34.91 kNm/m and it was observed during compacting backfill layer # 1 (Fig. 8). The maximum bending moments occurred at the additional ribs (at the 1/4 of its height) and the a little smaller values (ca. 31 kNm/m) at the shell crown. It means that at the beginning of the backfilling process the top of shell structure lifts up. Bending moments during backfilling of backfill layer # 5 do not exceed –29 kNm/m (Fig. 9a) which represents ca. 80% of the bending moment caused by backfill layer # 1. After completion of backfilling process (layer # 6 – Fig. 9b) the bending moments decrease to the level of –22 kNm/m which constitutes ca. 62% of the bending moment caused by first analysed backfill. The smallest bending moment occurred during backfilling of layers # 2–4, and they are not exceed –16 kNm/m. The difference between these layers was a few percent. Maximum results of bending moments are shown in Table 3.

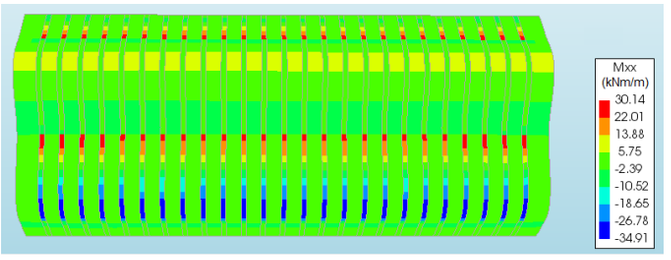
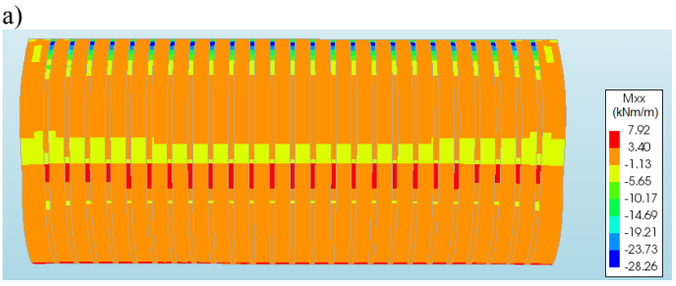


Figure 8. Maximum bending moments in shell structure caused by backfill layer # 1.

Table 3. Maximum results of axial forces, bending moments and stresses.

Backfill layers:	Axial forces Nxx (kN/m)	Bending moments Mxx (kNm/m)	Stresses Szz (MPa)
1	–1088	–34.91	–6.70
2	–1324	–11.26	–4.50
3	–1491.7	15.57	–5.67
4	–2037	–15.9	–7.58
5	–3336	–28.26	–11.20
6	–2656	–21.59	–10.10

a)



b)

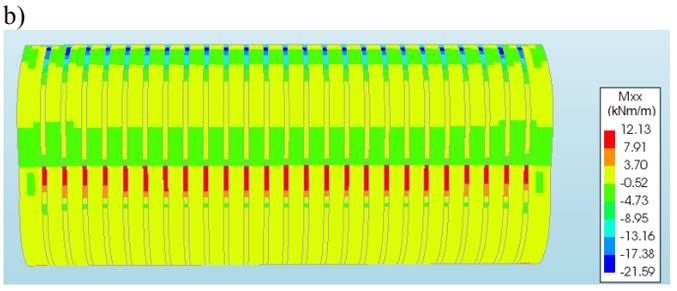
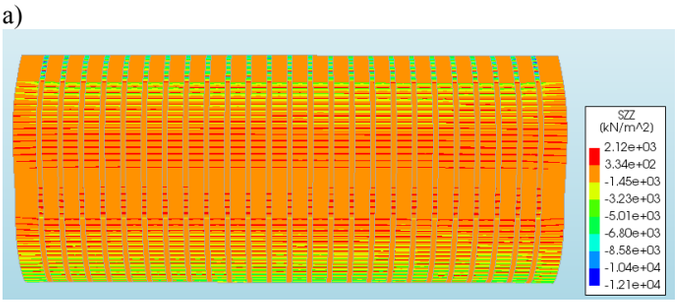


Figure 9. Maximum bending moments in shell structure during backfilling of layers: a) # 5 and b) # 6.

The highest stresses occurred similarly as the axial forces during compacting the backfill layer # 5 (Fig. 10a). Maximum values amounted to –11.20 MPa and they were located at additional ribs near the supports and at 1/4 height of shell. After finish of backfilling process (layer # 6), the stresses were slightly reduced (–10.10 MPa) and they were observed at in the quarter points (Fig. 10b). It is worth underlined that first three analysed backfill layers did not strongly affect on the level of stresses in the shell structure. The maximum stresses do not exceed –8 MPa during backfilling of these layers. It should be also added that all stresses are compressive and generally increases together with the backfill height (with except of layers # 2 and # 6). Maximum stresses of the shell structure are shown in Table 3.

a)



b)

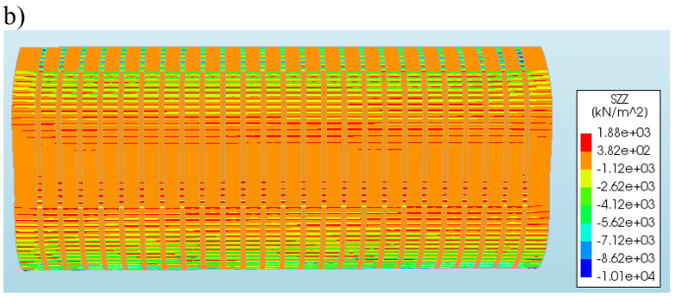


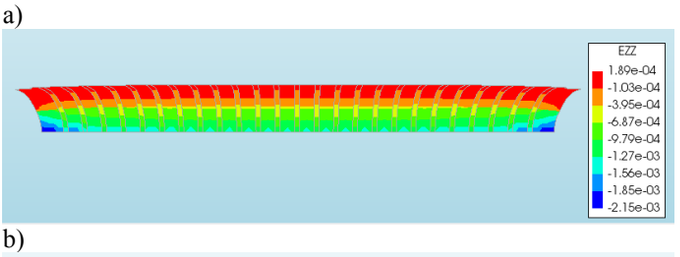
Figure 10. Maximum stresses in shell structure during backfilling of layers: a) # 5 and b) # 6.

Table 4. Maximum strains in shell structure obtained from numerical calculations and measurements.

Number of backfill layer:	Strains (10^{-6})		Differences (%)
	Calculation	Field test	
1	–709	–854	20.5
2	–818	–950	16.1
3	–908	–1005	10.7
4	–1220	–1359	11.4
5	–2150	–2256	4.9
6	–1590	–1690	6.3

It was also noted that the maximum strains in the CSP shell occurred during backfilling the layer # 5 (Fig. 11). Very similar strain maps of the shell structure were obtained for backfill layer # 6 (Fig. 12), while the values were a little smaller than those received from backfill # 5. In both cases, maximum values were observed near the support of shell and at 1/3 of shell height. The maximum strains obtained from numerical calculations and measurements are presented in Table 4. It should be underlined that the calculated values in all cases of backfill loading are smaller than those obtained from field test. However, they were occurred at the same sections of the shell structure. The largest differences were observed in the first backfill layer and they were about 20%. In the remaining layers, the differences were between a few and a dozen percent. This can be caused by some construction works, which had to done (not stopped during testing), for example the movement of vibratory plates.

a)



b)

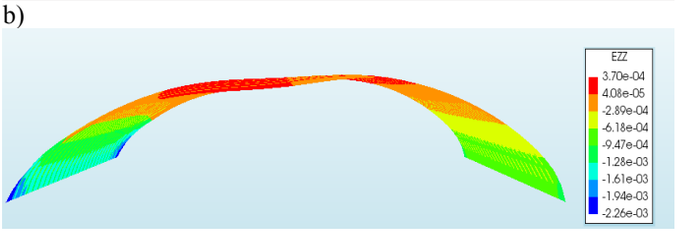


Figure 11. Maximum strains of shell structure for backfill layer # 5 in section: a) longitudinal, and b) transversal.

6 CONCLUSION

Taking into account the numerical analysis and experimental tests, carried out on the soil-steel bridge during backfilling process the following general conclusions can be drawn:

– the highest axial force and stresses in the CSP shell structure occurred during backfilling of layer # 5 (backfill height was on the level of shell

crown). Maximum axial force was –3336 kN/m and highest stress was at the level of –11.20 MPa. They were observed on additional ribs near the supports and at 1/4 height of shell. Maximum axial forces and stresses were compressive.

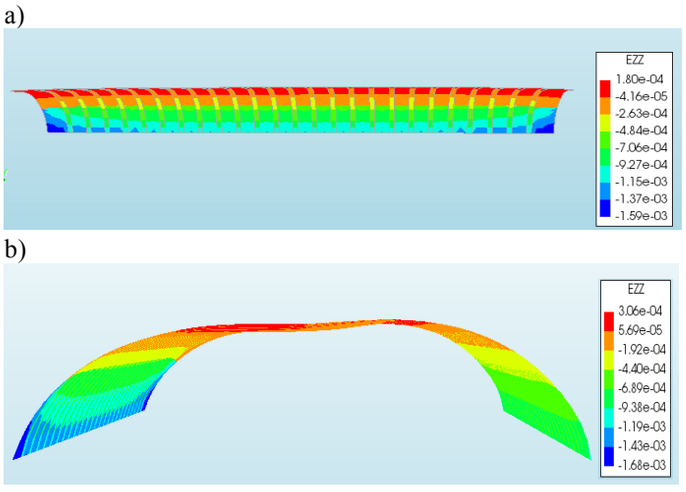


Figure 12. Maximum strains of CSP shell after completion of backfilling process (layer # 6) in section: a) longitudinal, and b) transversal.

– the greatest bending moments were caused by compaction of backfill layer # 1 (–34.91 kNm/m). In the results of the lateral soil pressure, the top of CSP shell structure lifts up. The maximum compressive bending moments occurred at the additional ribs (at the 1/4 of their height) and at shell crown.
– the maximum measured and calculated displacements were 29 mm and 20.5 mm, respectively. They were situated at the point # 11 (near the shell crown and at the end of structure). Generally, the highest displacements were observed at the structure ends during backfilling of layers # 5 and # 6 (shell was completely backfilled). The displacements obtained from the measurements and finite element analysis are generally quite close to each other.
– the maximum calculated and measured strains occurred during backfilling of the layer # 5 and they were observed near the support of shell and at 1/3 of shell height. The calculated strains in all cases of backfill loading are smaller than those obtained from the field test (maximum differences were ca. 20%). This can be caused by some construction works, which had to be carried out (works has not been stopped during testing), for example, the movement of vibratory plates.
– the observed differences between calculations and measurements would be probably smaller for more density of finite element mesh. At this stage of analysis, there was no need for the greater density of the finite elements because the obtained results are quite reasonable.

To provide more general conclusions, further analyses are needed for this type of structure. These analyses should be included the various type of backfill, various corrugation profiles, and modelling of the shell without using the additional stiffening ribs.

REFERENCES

Bayoglu Flener, E. 2010. Soil-steel interaction of long-span box culverts-performance during backfilling. *Journal of Geotechnical and Geoenvironmental Engineering* 136: 823-832.

Beben, D. 2012. Numerical study of performance of soil-steel bridge during soil backfilling. *Structural Engineering and Mechanics* 42(4): 571-587.

Beben, D. 2017. The role of backfill quality on corrugated steel plate culvert behaviour. *The Baltic Journal of Road and Bridge Engineering* 12(1): 1-11.

Beben, D. & Stryczek, A. 2016. Numerical analysis of corrugated steel plate bridge with reinforced concrete relieving slab. *Journal of Civil Engineering and Management* 22(5): 585-596.

Brachman, R. W. I. & Elshimi, A. C. 2012. Testing and analysis of a deep-corrugated large-span box culvert prior to burial. *Journal of Bridge Engineering* 17: 81-88.

CHBDC. 2006. *Canadian Highway Bridge Design Code*. CAN/CSA-S6-06, Canadian Standards Association International, Mississauga, Ontario.

DIANA FEA. 2017. Available online from URL:*www.dianafea.com/.*

Elshimi, T. M., Mak, A.C., Brachman, R.W.I. & Moore, I.D. 2011. Behaviour of a deep-corrugated large-span box culvert during backfilling, *Pan-American Conference on Teaching and Learning of Geotechnical Engineering; Toronto, 2-6 October 2011.*

Janusz, L. & Madaj, A. 2009. *Engineering Structures from Corrugated Plates. Design and Construction.* Warsaw: Transport and Communication Publishers.

Koruszewicz, L. & Kumecki, B. 2011. Behaviour of steel box-type culvert during backfilling. *Archives of Civil and Mechanical Engineering* 11(3): 637-650.

Machelski, Cz. 2008. *Modelling of Soil-Shell Bridge Structures*. Wroclaw: The Lower Silesian Educational Publishers.

Manko, Z. & Beben, D. 2005. Research on steel shell of a road bridge made of corrugated plates during backfilling. *Journal of Bridge Engineering* 10(5): 592-603.

Pettersson, L. & Sundquist H. 2014. *Design of Soil-Steel Composite Bridges*. TRITA-BKN Rep. No. 112, Stockholm: Royal Institute of Technology.

Pittino, G. & Gosler, J. 2006. Structural plate steel underpasses during backfilling - how to minimize the bending moment. In Varona, P. & Hart, R. D (eds), *FLAC and numerical modeling in geomechanics; 4th Intern. FLAC Symp.; Madrid, 29-31 May 2006.* Minneapolis: Itasca Consulting Group.

Sanaeiha, A., Rahimian, M. & Sadegh Marefat M. 2017. Field test of a large-span soil-steel bridge stiffened by concrete rings during backfilling. *Journal of Bridge Engineering* 22(10).

Taleb, B. & Moore, I.D. 1999. Metal culvert response to earth loading. Performance of two-dimensional analysis", Transportation Research Record, No. 1656, *Journal of Transportation Research Board*, pp. 25-36.

Maintenance, Safety, Risk, Management and Life-Cycle Performance of Bridges – Powers, Frangopol, Al-Mahaidi & Caprani (Eds)
© 2018 Taylor & Francis Group, London, ISBN 978-1-138-73045-8

EXPERIMENTAL INVESTIGATION OF RETROFITTED WEB-GAP REGIONS IN STEEL BRIDGE GIRDERS

Mehdi Motaleb, Mohammad Rahman, Riyadh Hindi
Saint Louis University, St. Louis, MO 63103
Will Lindquist
William Jewell College, Liberty, MO 64068
Ahmed Ibrahim
University of Idaho, Moscow, ID 83844

ABSTRACT: This paper describes an experimental study on retrofitting web-gap regions in steel girder bridges. The retrofit aims at reducing the stress concentrations at the intersection of connection plates and the web which can potentially be where distortion induced fatigue cracking initiates. In this study, a laboratory investigation was performed on a small-scale steel bridge bay under displacement-control vertical loading to simulate the differential deflection between two girders in actual bridges. A new method to retrofit the web-gap is proposed by modifying the existing slot-method by connecting the connection plate and web with steel angles on either side of the connection plate. The performance of the newly-developed retrofit technique, called the slot-angle technique, is compared with existing retrofit techniques. Results showed that the newly-developed slot-angle technique has significant potential for effectively reducing the stress concentrations in the web-gap region which by moving the location of the initial stress concentrations and potentially redistributing those stresses over a wider area.

1 INTRODUCTION

The design specification for steel bridges built in the United States prior to the mid-1980s discouraged welding of connection plates (CPs) to the tension flange to avoid cracking issues due to primary longitudinal stresses (Jajich and Schultz, 2003, Khalil et al., 1998).

The resulting flexible connection resulted in reducing the torsional resistance of bridge girder webs leading to stress concentrations in the unstiffened web-gap under out-of-plane forces. In many cases, these stress concentrations led to distortion-induced fatigue cracking after only a limited number of cycles. Several experimental studies (Hartman et al., 2013, Alemdar et al., 2013) and field-test measurements (Shifferaw and Fanous, 2013, Connor and Fisher, 2006, Tarries, 2002, Khalil et al., 1998) have been conducted to investigate distortion-induced fatigue cracking and to propose effective repair measures. However, selection of an appropriate repair strategy is complicated and depends on many factors (Alavi et al., 2017). A previous study (Lindquist et al., 2015) elaborated on one such case where girders developed web-gap cracking shortly after completion of a comprehensive seismic repair which consisted of replacing existing "K"-type diaphragms with much stiffer ×-type diaphragms. This repair resulted in increasing the web-gap stresses above the constant amplitude fatigue threshold (CAFT) and led to significant cracking (Motaleb et al., 2016). The current study shows that stresses in these regions can be mitigated with additional retrofit measures prior to the development of distortion-induced fatigue cracks. This paper examines the effectiveness of this newly developed web-gap retrofit method by comparing stresses with two existing and popular retrofit techniques.

This paper presents laboratory test results of three beams utilizing different web-gap retrofit techniques. The testing was performed on a small-scale steel bridge bay by applying a vertical displacement to the free end of a cross-frame diaphragm to simulate the differential deflection between two adjacent girders in bridges.

2 RETROFIT MEASURES

There are two retrofit options frequently used to reduce stress in web-gap regions including (1) increasing the stiffness of the web-gap region by providing a positive attachment between the CP and the longitudinal girder flanges, or (2) increasing the flexibility of the web-gap region in order to reduce the concentration of stresses. In this study, variations of these common retrofit techniques, along with an innovative strategy, are compared to measure effectiveness in reducing stress concentrations in the web-gap region.

The proposed retrofit technique consisted of a slot and an angle section connecting the disconnected

part of the CP to the web to reduce stresses by softening the web-gap region as well as distributing lateral forces, transferred by cross-frames, over a wider area of the web (slot-angle retrofit). This technique can be implemented to upgrade existing slot repairs that failed to sufficiently address distortion-induced fatigue cracking in the web-gap region. Two other common retrofit methods are also considered in this study so that the effectiveness of the newly developed technique can be compared with the most popular techniques. The first retrofit strategy provided a positive connection between the CP and the girder flange (referred to as the top-angle retrofit). The second retrofit created an 89-mm (3.5-in.) slot where approximately one-sixth of the CP depth is cut from the web (slot-retrofit) thereby softening the web-gap. The slot was created by cutting the stiffener while still providing enough room for handling the grinder. Thus, there was a thin part of stiffener (about 0.25 in.) that remained on the girder web. Figures 1 through 4 show the retrofit measures investigated in this paper. The main advantage of the slot-angle technique over top-angle option is that traffic interruption and lane closures are not necessary for implementation.



Fig. 1 – Instrumentation of Control beam



Fig. 2 – Instrumentation of Top-angle retrofit



Fig. 3 – Instrumentation of Slot retrofit



Fig. 4 – Instrumentation of Slot-angle retrofit

3 EXPERIMENTAL PROGRAM

A small steel bridge prototype consisting of a 1-m [3-ft] long standard hot-rolled W24×55 girder connected to a 0.2-m (8-in) thick 3.05 m × 2.13 m (10 ft. × 7 ft.) concrete deck was used for testing. The cross-frame consisted of 2 L2×2×¼ angles connected to a CP through a welded gusset plate, as shown in Figure 5.

The bottom flange of the beam was fixed to the deck using twelve A325 12.7 mm (5/8 in.) diameter structural bolts to simulate an inverse steel-concrete composite beam, as shown in Figure 6. The load was applied with a portable gantry crane used to apply a tension force through a load cell to the free end of the diaphragm. The loading system was intended to approximately simulate the differential deflection between two girders in actual bridges by applying a differential upward vertical displacement. All specimens were subjected to a deflection of approximately 20.3 mm (0.8 in). The system remained intact during the tests while the retrofit measures were implemented.



Fig. 5 – Test setup



Fig. 6 – Inverted steel-concrete beam

4 STRAIN GAGES LAYOUT

A total of eight strain gages were attached to the girder to measure the strain in this experimental study based on the predicted strain concentration locations before and after implementing the retrofit methods. A schematic view of the strain gage layout is shown in Figs. 7 and 8. The control beam was instrumented with three strain gages while gages 2 and 3 recorded the strains that originated 12.7 mm (0.5 in.) and 19.1 mm (0.75 in.) left of the stiffener where it intersects the web, as shown in Fig.7. Strain gage "a" was positioned on the opposite side of the stiffener 5.08 mm (0.2 in.) from the stiffener.

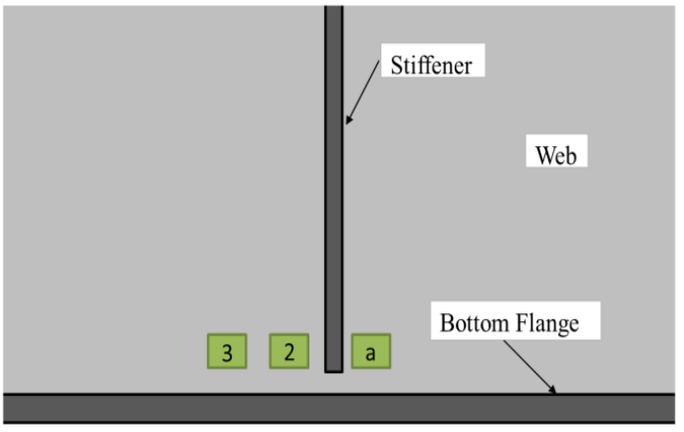


Fig. 7 – Starin gage layouts for control beam and top-angle retrofit

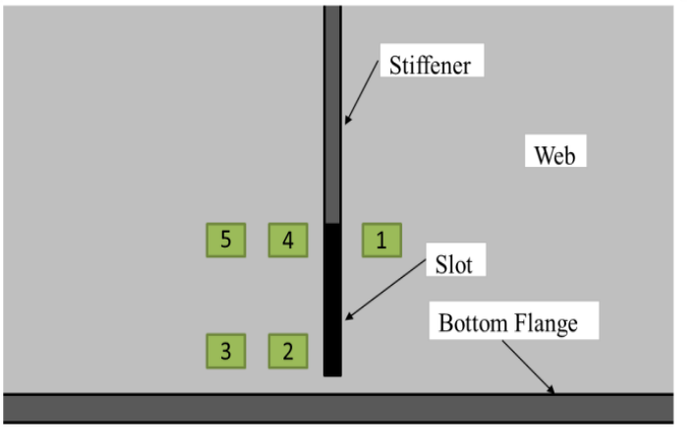


Fig. 8 – Strain gage layouts for slot retrofit and slot-angle retrofit method

5 EXPERIMENTAL RESULTS

Each strain gage provided three values for strain in three directions which was converted to a principal stress for each rosette gage. The principal strain was converted to stress using Hooke's law and a steel elastic modulus of 29,000 ksi. Each test was repeated three times to ensure consistency, and the results for each test are summarized in Table 1. The stresses reported in this table correspond to the strain readings for the control and retrofitted beams under a 20.3 mm (0.8 in.) differential deflection. Various reductions in the elastic stresses were observed with respect to the control beam which varied between 14.8% and 62.0%. An L2×2×1/8 angle was first used to connect the CP to the flange using two bolts on each leg. The top-angle option showed the lowest reduction among the investigated options as it decreased the stresses from 14.8% to 16.8%. The slot technique reduced the stress in the original web-gap region by 62.0% and stress at the new CP-web intersection did not exceed 100 MPa (14.5 ksi) – far below the stress range in the control beam. The slot-angle retrofit method experienced 137 MPa (19.8 ksi) which corresponds to a 44.4% reduction compared to the control.

Table 1 – Laboratory test results

Web-gap stress (MPa) corresponding to 20.3 mm (0.8 in.) deflection							
Gase#	Control	Top-angle (units)	Reduction (%)	Slot	Reduction (%)	Slot -angle	Reduction (%)
a	272	226	***-16.8***				
1				88.3		43.5	
2	246	203	***-17.4***	93.8	***-62.0***	137	***-44.4***
3	206	175	***-14.8***	86.9	***-57.8***	123	***-40.4***
4				100		60.3	
5				95.1		61.1	
Distortion $x10^{-3}$ (mm)	40.6	115		11.8		28.7	

6 CONCLUSIONS

In this study, a method to retrofit web-gap distortion and upgrade existing retrofits was introduced. The effectiveness of the proposed technique is compared with two other common retrofit techniques. This study was based on structural tests performed on a small portion of a bridge designed to simulate the actual condition presented in the field. The slot retrofit option removed the stress concentrations from the CP ending and introduced new stress concentrations at the slot termination, while in terms of the magnitude, the highest stresses are not as large as for the control beam. On the other hand, results from the newly-developed slot-angle technique has significant potential for effectively reducing stress concentrations in the web-gap region by eliminating the location of initial stress concentrations and potentially redistributing those stresses over a wider area. The slot-angle method does not require disruption to the concrete deck and consequently does not disrupte traffic flow. This technique can also be used to upgrade slot retrofits already implemented if they are ineffective.

7 REFERENCES

ALAVI, A. H., HASNI, H., JIAO, P., BORCHANI, W. & LAJNEF, N. 2017. Fatigue cracking detection in steel bridge girders through a self-powered sensing concept. *Journal of Constructional Steel Research,* 128**,** 19-38.

ALEMDAR, F., NAGATI, D., MATAMOROS, A., BENNETT, C. & ROLFE, S. 2013. Repairing distortion-induced fatigue cracks in steel bridge girders using angles-with-plate retrofit technique. I: Physical simulations. *Journal of Structural Engineering*.

CONNOR, R. J. & FISHER, J. W. 2006. Identifying Effective and Ineffective Retrofits for Distortion Fatigue Cracking in Steel Bridges Using Field Instrumentation. *Journal of Bridge Engineering,* 11**,** 745–752.

HARTMAN, A., BENNETT, C., MATAMOROS, A. & ROLFE, S. 2013. Innovative retrofit technique for distortion-induced fatigue cracks in steel girder web gaps. *Bridge Structures,* 9**,** 57-71.

JAJICH, D. & SCHULTZ, A. E. 2003. Measurement and Analysis of Distortion-Induced Fatigue in Multigirder Steel Bridges. *Journal of Bridge Engineering,* 8**,** 84–91.

KHALIL, A., WIPF, T. J., GREIMANN, L., WOOD, D. L. & BRAKKE, B. Retrofit solution for out-of-plane distortion of X-type diaphragm bridges. Transportation Conference Proceedings, Iowa Department of Transportation, 1998. 99-102.

LINDQUIST, W., IBRAHIM, A., TUNG, Y., MOTALEB, M., TOBIAS, D. & HINDI, R. 2015. Distortion-Induced Fatigue Cracking in a Seismically Retrofitted Steel Bridge. *Journal of Performance of Constructed Facilities,* 30**,** 04015068.

MOTALEB, M., DUONG, N., LINDQUIST, W. & HINDI, R. 2016. Investigation of Distortion-Induced Web-Gap Cracking in a Seismically Retrofitted Steel Bridge: Repair Measures. *Journal of Bridge Engineering,* 0**,** 04016139.

SHIFFERAW, Y. & FANOUS, F. S. 2013. Field testing and finite element analysis of steel bridge retrofits for distortion-induced fatigue. *Engineering Structures,* 49**,** 385–395.

TARRIES, D. J. 2002. Diaphragm bolt loosening retrofit for web gap fatigue cracking in steel girder bridges.

Maintenance, Safety, Risk, Management and Life-Cycle Performance of Bridges – Powers, Frangopol, Al-Mahaidi & Caprani (Eds)
© 2018 Taylor & Francis Group, London, ISBN 978-1-138-73045-8

Investigation of live load deflection limit for steel cable stayed and suspension bridges

E.-S. Hwang & D.-Y. Kim
Kyung Hee University, Yongin, Korea
K.J. Park
Department of Structural Engineering, Yooshin Engineering Corporation, Korea

ABSTRACT: Sea-crossing bridges connect islands to secure the sea and road traffic in the area. For the construction of sea-crossing bridges, bridge engineers should plan to secure the safety of large ships passing under the bridge. In particular, clearance of cable-stayed bridges and suspension bridges is determined considering the height of the ship master from the surface of the water, the trim of the ship, the psychological free space, the tide height, and live load deflection. Of these, bridge engineers should calculate the deflection of bridges by live loads. The purpose of this study is to investigate the suitability of live load deflection limit for cable-stayed and suspension bridges over main span length of 200m. For the design of long span cable stayed and suspension bridges, limitations are L/400 and L/350 respectively in the Korean Bridge Design Code (2010) and Korean Bridge Design Code (LSD) (MLIT, 2015). Saadeghvaziri (2012) also suggested deflection limit based on natural frequency, acceleration limit of 0.5 m/s^2 and vehicle speed. In this study, the theoretical analysis of Yi Sun-Sin grand bridge (suspension bridge, main span length=1,545m) and Young-Hung grand bridge (cable stayed bridge, main span length=240m) were carried out and compared with these limits. The results of the study on the limitation of live load deflection are expected to be useful reference for the design, the proper planning and deflection review of the long span bridges around the world.

1 INTRODUCTION

1.1 *Backgrounds and objective of this study*

Sea-crossing bridges are being constructed to connect islands to secure the sea and road traffic in the area. They are also being constructed for the purpose of bypassing the center of a complex port city. For the construction of sea crossing bridges, bridge engineers should plan the vertical profile to secure the safety of large ships passing under the bridge. Clearance of cable-stayed bridges and suspension bridges is determined considering the height of the ship master from the surface of the water, the trim of the ship, the psychological free space, the tide height, and live load deflection, as shown in Figure 1.

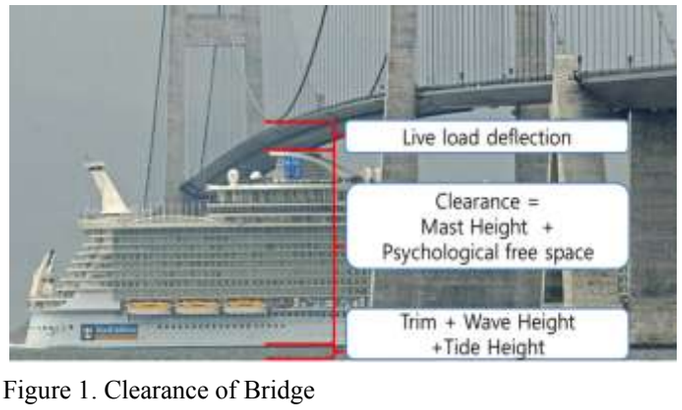


Figure 1. Clearance of Bridge

In line with the worldwide trend of constructing longer and slender bridges, limiting live load deflection becomes more important issue for the safety and serviceability of bridges. In design codes for long span bridges, there is no consensus on the deflection or vibration criteria even though L/400 and L/350 are specified in Korean Bridge Design Code (LSD) (MLIT, 2015), respectively for cable stayed and suspension bridges.

On Oct. 26, 2014, traffic on the Yi Sun-Sin Grand Bridge, a suspension bridge located in Korea, was controlled due to the civil complaint against the vibration of the bridge. Later, it was found out that the amplitude of the vertical acceleration was increased by 20 to 30% and the frequency of the vibration was changed from 0.1171 Hz (the 1st vertical mode) to 0.3173 Hz (the 4th vertical symmetrical mode). The deflection was not increased. the vibration was related with the changes of the relations between displacement amplitude and natural frequency.

The purpose of this study is to investigate the suitability of live load deflection limit for cable-stayed and suspension bridges over main span length of 200m. Since the new live load model is adopted in Korea Bridge Design Code (Limit State Design) (MLIT, 2015), it is necessary to make a comparison between old live load model (DB24, DL24) in Korea

Bridge Design Code (MLTM, 2010) and new live load model (KL-510) in Korea Bridge Design Code (Limit State Design)(MLIT, 2015). Results are compared with deflection limit in the code and equation proposed by Saadeghvaziri. For this study, two long span bridges (a suspension bridge with the main span length of 1,545m and a cable stayed bridge with the main span length of 240m) are analyzed.

1.2 *Literature review*

In this section, the design criteria in various codes, human comfort criteria and previous researches on deflection and/or vibration serviceability are reviewed.

1.2.1 *Deflection Limits in Design Codes*

Deflection limits for road bridges were first introduced by AASHTO for the purpose of controlling the vibration using the span ratio. However, these limits were found to have insufficient technical foundations (ASCE, 1958). In order to supplement such technical inefficiency, the Ontario Highway Bridge Design Code (OHBDC, 1983) and the Canadian Code (CSA, 1990) adjusted deflection limits based on the natural frequency. However, these criteria are specifically for short to medium span bridges and cannot be applied to long span bridges. Korea Bridge Design Code (Limit State Design) (MLIT, 2015) describes the optional deflection limit for short to medium span bridges as 1/800~1/1200 of the bridge spans. The deflections are calculated as the larger value of standard truck load only and the combination of 25% of the standard truck load and the standard lane load. In the commentary of the code, the limits of the span ratio are 1/400 for cable-stayed bridges, 1/350 for suspension bridges, and 1/600 for other types of bridges.

1.2.2 *Human comfort criteria and other studies on vibration assessment*

Diverse studies have been carried out across the world on displacement and vibration in order to ensure vibration serviceability. In 1931, Reiher and Meister(1931) suggested a vibration response curve following the natural frequency. Postlethwaite(1944) suggested acceleration limits of 0.03g for a natural frequency level below 1Hz. Acceleration and displacement amplitude limits dictated by the natural frequency were studied by Goldman(1948) and by Wright and Green(1964). Wright and Walker(1971) proposed a new design method that defined the acceleration limits as 100 in/sec^2 based on reflecting the static deflection, the natural frequency, and vehicle speed. Recently Barker (2011) developed an approximate relationship based on a graph of the "Approximate & Actual Deflection vs. 1st Natural Frequency Log-Log Axis" as a way of supplementing the deflection limitation of OHBDC, which does not include any formulas. Saadeghvaziri et al. (2012) suggested deflection limit standards calculated based on the natural frequency in terms of a formula that defines the relationship between speed coefficient, deflection, and acceleration. Their formula was found to generate similar values to the deflection limits for bridge span ratios of 1/1000 suggested by AASHTO.

Most studies of vibration serviceability for long span bridges are limited to deflection and vibration limits, which require displacement and acceleration vibration amplitudes calculated during lab tests or structural analysis. There are not a sufficient number of experimental studies on the vibration serviceability of bridges that have frequencies below 1Hz like steel cable-stayed bridge (Hwang et al., 2014).

2 EXAMPLE BRIDGES

2.1 *Yi Sun-Sin Grand Bridge*

For the purpose of this study, two steel cable bridge are selected for the analysis. Yi Sun-Sin Grand Bridge is the longest suspension bridge in Korea with the main span length of 1,545 m. It connects Gwangyang city to Yeosu Industrial Complex. It has steel decks and steel box girders as shown in Figure 2(a). The longitudinal cross section of Yi Sun-Sin Grand Bridge is shown in Figure 2(b). The box girder cross section of Yi Sun-Sin Grand Bridge is shown in Figure 2(c).

2.2 *Young-Hung Grand Bridge*

Another bridge is Young-Hung Grand Bridge which is a cable-stayed bridge with the main span length of 240m, as shown in Figure 3(a). This bridge connects YoungHung island with SunJae island that is part of Incheon City. The longitudinal cross section of Young-Hung Grand Bridge is shown in Figure 3(b). The box girder cross section of Young-Hung Grand Bridge is shown in Figure 3(c).

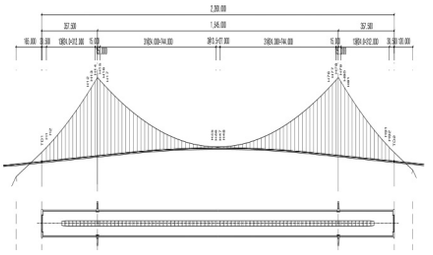
3 STRUCTURAL MODELING AND ANALYSIS

3.1 *Structural modeling of example bridges*

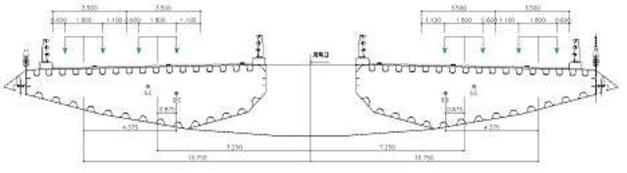
Structural analysis was carried out to examine deflection limits for example bridges.



(a) Yi Sun-Sin Grand Bridge (Suspension Bridge)



(b) Longitudinal section



(c) Cross section

Figure 2. Example Suspension Bridge

Yi Sun-Sin Grand Bridge is modeled by RM Bridge V8i, as shown in Figure 4(a). Young-Hung grand bridge is modeled by MIDAS CIVIL 2012 LSD V300, The FE model for structural analysis of the test bridge was composed of 274 nodes and 248 elements as shown in Figure 4(b). The steel girders and steel pylons are modelled with beam elements, and cable is modelled with truss (tension only) elements.

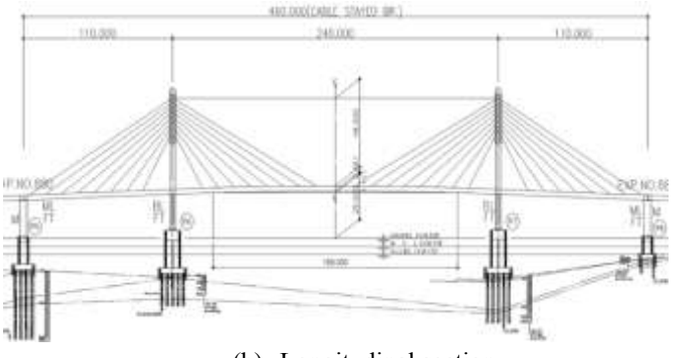
3.2 *Live load model*

Live load model for the calculation of deflection of the bridges includes DB24/DL24 model in Korea Bridge Design Code (MLTM, 2010), as shown in Figure 5(a) and (b). KL-510 model in Korea Bridge Design Code (Limit State Design) (MLIT, 2015), are shown in Figure 5(c) and (d).

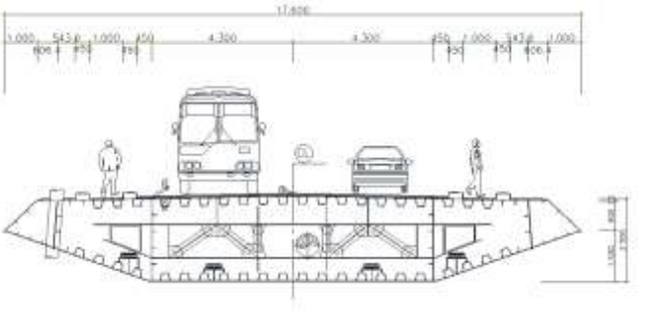
In DB/DL model, design deflections are selected as the larger deflection of DB24 and DL24. For long span bridges, DL24 usually produce larger deflection.



(a) Young-Hung Grand Bridge (Cable-Stayed Bridge)



(b) Longitudinal section



(c) Cross section

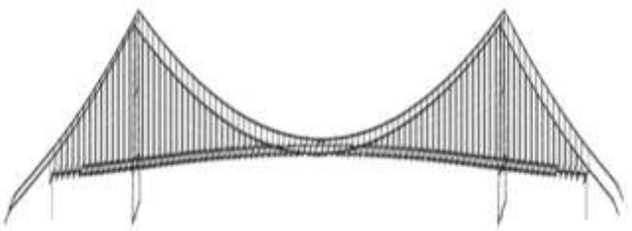
Figure 3. Example Cable-Stayed Bridge

In KL-510 model, design deflections are selected as the larger deflection of KL-510 standard truck load and standard lane load combined with 25% of standard truck load.

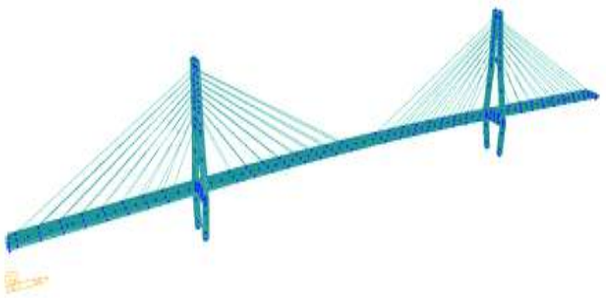
4 ANALYSIS RESULTS AND COMPARISON

4.1 *Deflections*

Deflections for the long span cable bridges are calculated based on the influence line of the bridge. Figure 6 shows the influence line for deflection at midspan of the main span. The maximum deflections at each section of Yi Sun-Sin grand bridge by DL24 and KL-510 model is shown in Figure 7. As shown in the figure, the maximum deflection does not occur at midspan.



(a)FE model of Yi Sun-Sin grand bridge



(b) FE model of Young-Hung grand bridge

Figure 4. FE model of example bridges

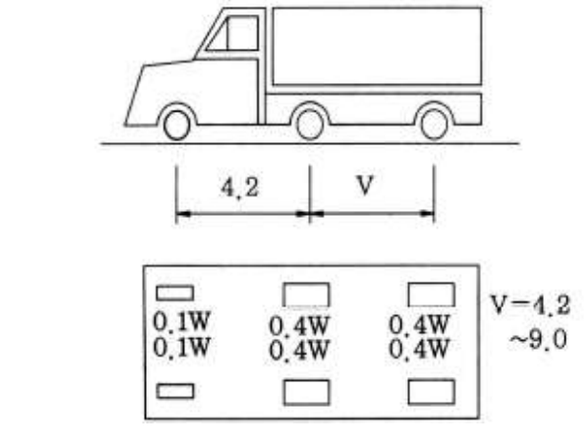
For example, in case of Yi Sun-Sin grand bridge, maximum deflection of center span is 3.448 m but deflection at midspan of center span is 2.759 m. Maximum deflections at center span of each bridge by two design live load models are shown in Table 1.

For Yi Sun-Sin grand bridge, maximum deflections at center span are 3.877 m by DL24 and 3.448 m by KL-510. For Young Hung grand bridge, deflections at midspan are 0.302 m by DL24 and 0.242 m by KL-510. Deflections by KL-510 shows smaller values than by DL24.

4.2 *Natural frequencies*

From the structural modeling, natural frequencies of each bridge are also calculated. Figure 8 shows the mode shapes of the first vertical natural frequency. The first natural frequency of the vertical mode is 0.113Hz and 0.435Hz for Yi Sun-Sin Grand Bridge and Young Hung Grand Bridge, respectively. Natural frequency of the bridge is an important parameter since some code (CSA, 2000) specify the dynamic load allowance or impact factors as the function of the natural frequency. ISO2631-2(1989) and some other passenger comfort criteria specify the displacement or acceleration limit as the function of the natural frequency also.

Some researchers (Saadeghvaziri (2012), Irwin(1978)) suggested the deflection/vibration limit as the function of the natural frequency of the bridge. In this study, the criteria suggested by Saadeghvaziri are used and explained below.



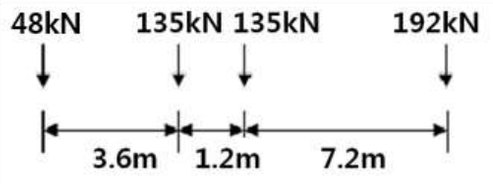
W=240kN

(a) DB24 truck load

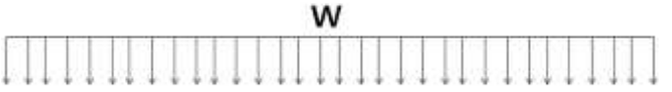


W=12.7kN/m, Ps=156kN, Pm=108kN

(b) DL24 lane load



(c) KL-510 Standard truck load

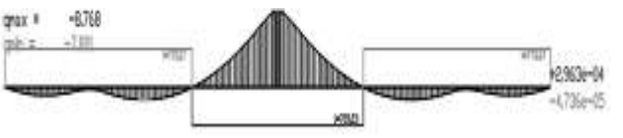


L≤60m; W=12.7 (kN/m),

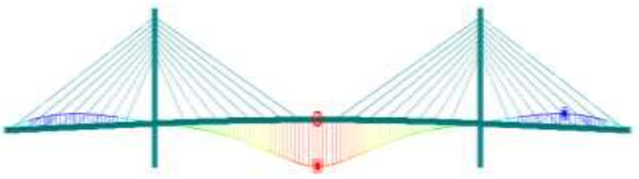
L>60m; $W=12.7\times(\frac{60}{L})^{0.10}$ (kN/m), L=Span length

(d) KL-510 Standard lane load

Figure 5. Live load models



(a) Yi Sun-Sin Grand Bridge



(b) Young Hung Grand Bridge

Figure 6. Deflection influence line of the midspan of the main span

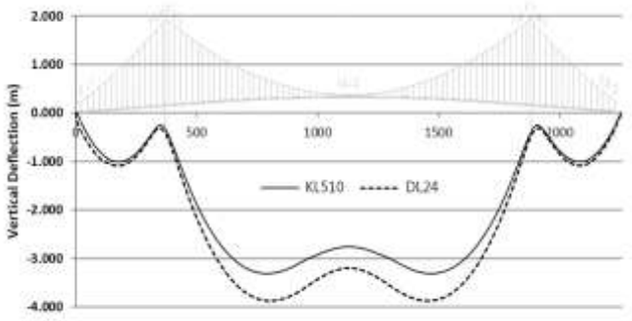
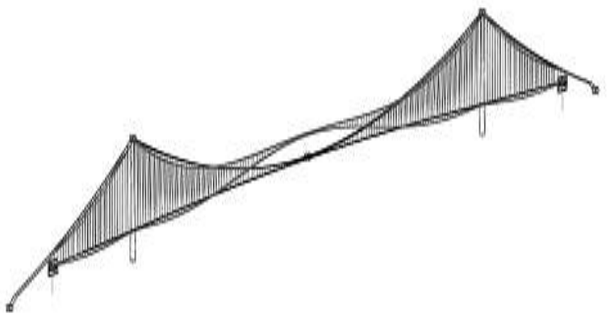


Figure 7. Deflection Result for Yi Sun-Sin Grand Bridge



(a) Yı Sun-Sın grand brıdge



(b) Young Hung grand bridge (Park & Hwang, 2016)

Figure 8. Mode shape corresponding to the first vertical natural mode

4.3 *Comparison with deflection limit*

Deflection limits in Korean codes are L/400 and L/350 for cable-stayed and suspension bridges, respectively. Another deflection limits are proposed by Saadeghvaziri (2012), as shown in Eq. (1) and Eq. (2).

$$\delta_{limit} = \frac{A_{max}}{(2\pi f)^2 \times 1.2\alpha} \quad (1)$$

$$\alpha = V/2Lf \quad (2)$$

In this equation, A_{max}, the acceleration limits of the girder are 0.5 m/s^2 and 1.0 m/s^2. The design speed(V) are 60km/h, 80km/h, 100km/h. α is the speed coefficient as shown in Eq. (2), L is main span length, and f is the primary natural frequency for vertical direction. Deflection limits proposed by Saadeghvaziri (2012) of Yi Sun- Sin grand bridge is shown in Figure9 and Table 1. Deflection limits proposed by Saadeghvaziri (2012) of Young-Hung grand bridge is shown in Figure10 and Table 2.

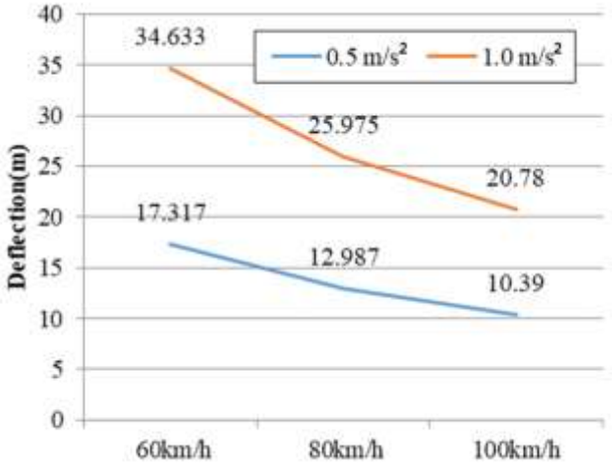


Figure 9. Deflection limits proposed by Saadeghvaziri (2012) of Yi Sun- Sin grand bridge

Table 1. Deflection limits proposed by Saadeghvaziri (2012) of Yi Sun- Sin grand bridge

A_{max}	0.5 m/s^2	1.0 m/s^2
Deflection under 60km/h (m)	17.317	34.633
Deflection under 80km/h (m)	12.987	25.975
Deflection under 100km/h (m)	10.390	20.780

Both Yi Sun- Sin grand bridge and Young-Hung grand bridge are designed as 0.5 m/s^2 with 60km/h. By the equation, deflection limits proposed by Saadeghvaziri (2012) on 0.5 m/s^2 with 60km/h for Yi Sun-Sin and Young Hung grand bridge are 17.317m and 0.699m, respectively and are shown in Table 3.

Calculated deflections and design limits are summarized in Table 3 and Figure 11 for both example bridges. Deflections by both live load model satisfy all limit or criteria. However, deflection limit by Saadeghvaziri is very large compared to other criteria and this criterion may not be suitable for very long span bridges.

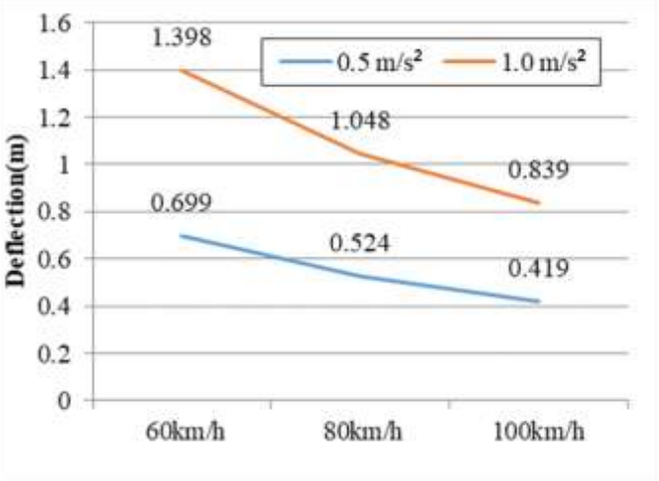


Figure 10. Deflection limits proposed by Saadeghvaziri (2012) of Young-Hung grand bridge

Table 2. Deflection limits proposed by Saadeghvaziri (2012) of Young-Hung grand bridge

A_{max}	0.5 m/s^2	1.0 m/s^2
Deflection under 60km/h (m)	0.699	1.398
Deflection under 80km/h (m)	0.524	1.048
Deflection under 100km/h (m)	0.419	0.839

Table 3. Natural Frequency and Live Load Deflection of example bridges

Bridge	Yi Sun- Sin grand bridge	Young-Hung grand bridge
Structural type	Suspension bridge	Cable-Stayed bridge
Main Span Length(m)	1,545	240
First Vertical Natural Frequency (Hz)	0.113	0.435
Deflection by DL24 (m)	3.877	0.302
Deflection by KL-510 (m)	3.448	0.242
Deflection limit in the code (m)	4.414 (L/350)	0.600 (L/400)
Deflection limit proposed by Saadeghvaziri under 0.5 m/s^2 with 60km/h(m)	17.317	0.699

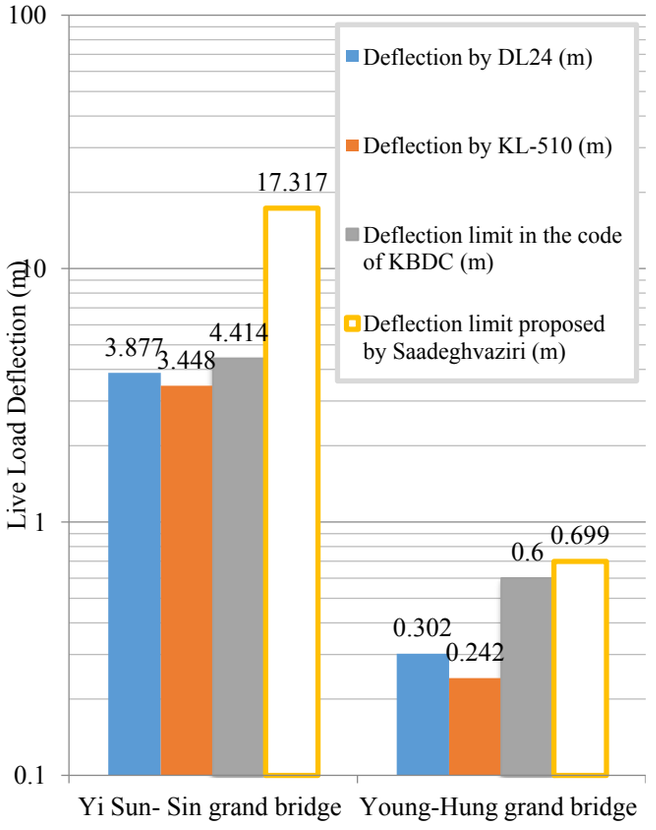


Figure 11. Comparison of Live load deflection and limitation of live load

Table 4. Ratio of Deflection limit proposed by Saadeghvaziri for Yi Sun-Sin grand bridge

Bridge	Yi Sun- Sin grand bridge	Ratio of Deflection limit proposed by Saadeghvaziri
Deflection by DL24 (m)	3.877	22.4%
Deflection by KL-510 (m)	3.448	19.9%
Deflection limit in the code (m)	4.414 (L/350)	25.5%
Deflection limit proposed by Saadeghvaziri under 0.5 m/s^2 with 60km/h(m)	17.317	100.0%

Table 5. Ratio of Deflection limit proposed by Saadeghvaziri for Young-Hung grand bridge

Bridge	Young-Hung grand bridge	Ratio of Deflection limit proposed by Saadeghvaziri
Deflection by DL24 (m)	0.302	43.2%
Deflection by KL-510 (m)	0.242	34.6%
Deflection limit in the code (m)	0.600 (L/400)	85.8%
Deflection limit proposed by Saadeghvaziri under 0.5 m/s^2 with 60km/h(m)	0.699	100.0%

4.4 *Ratio of the deflection limit proposed equation*

Ratio of deflection limit proposed by Saadeghvaziri on Yi Sun-Sin grand bridge for Deflection by DL24, Deflection by KL-510 and Deflection limit in the code are 22.4%, 19.9% and 25.5%, respectively and are shown in Table 4.

Ratio of deflection limit proposed by Saadeghvaziri on Young-Hung grand bridge for Deflection by DL24, Deflection by KL-510 and Deflection limit in the code are 43.2%, 34.6% and 85.8%, respectively and are shown in Table 5.

Deflection limit are proposed by Saadeghvaziri (2012) may not be suitable for very long span bridges like Yi Sun Sin grand bridge.

5 CONCLUSION

Deflection of the sea-crossing bridges by live loads is very important since it controls the clearance and the overall elevation of the bridge. It also controls the passenger or pedestrian comfort criteria. In this study, the theoretical analysis of long span suspension and cable stayed bridge are performed to investigate the live load deflection limit specified in the code. Two live load models (DL24 and KL-510) are used. Other deflection limit based on the natural frequency is also investigated. Following conclusions can be made based on results of this study:

1) For example bridges, deflection by live load model satisfies deflection limit specified in the code, which is the function of the span length.

2) Deflections by two live load models, namely DL24 and KL-510, show similar values but KL-510 gives smaller deflections.

3) The example bridges satisfy deflection limits suggested by Saadeghvaziri, which is based on the natural frequency of the bridge. This limit shows larger limits than the code values, but for very long span bridge such as Yi Sun-Sin grand bridge, the limit is too generous.

Further researches are required to find the optimum deflection or vibration criteria for long span bridge and their effects on bridge clearance and elevation. Also many other long span bridges should be considered in the analysis.

ACKNOWLEDGEMENT

This study and presentation were supported by grants(18SCIP-B119964-03) from the Ministry of Land, Infrastructure and Transport of the Korean Government. The authors wish to express their gratitude for the financial support.

REFERENCES

American Society of Civil Engineering. 1958. “Deflection Limitation of a Bridge”. *Journal of the Structural Division*, 84, (Rep. No. ST3).

Barker, M.G., Staebler, J., Barth, K.E., 2011. “Serviceability limits and economical steel bridge design.” FHWA-HIF-11-044

Bentley Systems.2010. “Analysis user guide”, RM Bridge V8i, October.

CSA .2000. CAN/CSA. S6-00. Canadian Highway Bridge Design Code, Canadian Standards Association

Gethin, W.R., Emily, C., Xiaolin, M., Alan, D. 2004. High Frequency Deflection Monitoring of Bridges by GPS, Journal of Global Positioning Systems, Vol.3, No. 1-2, pp.226-231.

Goldman, D. E. 1948. “A Review of Subjective Responses to Vibratory Motion of the Human Body in the Frequency Range 1 to 70 Cycle per second.” Naval Medical research Institute, National Naval Medical Center, Bethesda, MD.

Hwang, E.S., Kwon, Y.C., Park, K.J. and Kim, D.Y. 2014. “Serviceability Assessment of Deflection for Long Span Suspension Bridge”, 2014 KIBSE Annual Meeting and Conference, pp 129-130

Hwang, E.S., Kim, D.Y., Gil, Y.S., Park, K.J. .2016. “Analysis of Live Load Deflection Limitation against Natural Frequency of Cable Stayed Bridge and Suspension Bridge”, 2016 KIBSE Annual Meeting and Conference

International Standard .1989. *ISO 2631-2:1989*, The International Organization for Standardization’s standard

Irwin .1978. “Human response to dynamic motion of structures.” *Structural Engineers*, 56A:237-44.

Park, K.J., Hwang, E.S.2016. “Assessment of Vibration Serviceability for Steel Cable-Stayed Bridges Using GNSS Data”, International Journal of Steel Structures, 16(4), 1251-1262.

Saadeghvaziri,Ala M., Darjani, S., Saigal,S., and Khan, A. 2012. “Design for deflection control vs. use of specified span to depth ratio limitations”, FHWA-NJ-2012-009, Final Report.

Midas Information Technology Co., Ltd. 2016. “Midas User Support System”, Retrieved January 31, 2016, from http://kor.midasuser.com/civil/index.asp

Ministry of Land, Infrastructure and Transport .2015. Korean Bridge Design Code, Limit State Design

OHBDC .1983. *Design of Highway Bridges*, Ontario Highway Bridge Department, Ontario, Canada.

Postlethwaite, F. 1944. “Human Susceptibility to Vibration”, Engineering, Vol. 157 pp.61-63

Reiher, H. and Meister, F. J. 1931. StatEmpfindlichkeit des Menschen gegen Erschütterungen.teForschung auf dem Gebiet des Ingenieurwesens A ,Volume 2, Issue 11, pp 381-386

Saadeghvaziri, M.A., Darjani, S., Saigal, S. and Khan, A. 2012. “Design for deflection control vs. use of specified span to depth ratio limitations”, FHWA-NJ-2012-009, Final Report.

Wright, D.T. and Green, R. 1964. Highway Bridge Vibration. Part II: Report No. 5 Ontario Test Program. Ontario Department of Highways and Queen’s University Kingston, Onrario

Wright, R.N. and Walker, W.H. 1971. “Criteria for the deflection of steel bridges”, American Iron and Steel Institute, Bulletin No.19, November 1971

MS05: Advancements in performance assessment, monitoring, and management of bridges under fatigue deterioration

Organizers: M. Soliman & D.M. Frangopol

Maintenance, Safety, Risk, Management and Life-Cycle Performance of Bridges – Powers, Frangopol, Al-Mahaidi & Caprani (Eds)
© 2018 Taylor & Francis Group, London, ISBN 978-1-138-73045-8

Large-scale strain sensing approach for detecting fatigue cracks in steel bridges

X. Kong, J. Li, C. Bennett & W. Collins,
Department of Civil, Environmental and Architectural Engineering
University of Kansas, Lawrence, KS, USA

S. Laflamme
Department of Civil, Construction, and Environmental Engineering
Department of Electrical and Computer Engineering
Iowa State University, Ames, IA, USA

H. Jo
Department of Civil Engineering and Engineering Mechanics
University of Arizona, Tucson, AZ, USA

ABSTRACT: Fatigue cracking in steel highway bridges presents major safety and maintenance concerns for bridge owners: if bridges are not regularly inspected and maintained, fatigue cracks can lead to structural failure. It is of key importance to detect and assess fatigue crack activity in steel bridges in a timely and holistic manner. This study presents a novel strain sensing technology for fatigue crack monitoring based on soft elastomeric capacitors (SECs). SECs are inexpensive, easy to fabricate, highly stretchable, and mechanically robust capacitance-based strain gauges. Additionally, SECs are a highly-scalable technology, capable of monitoring deformations over a much larger area than can be achieved with traditional metal foil strain gauges. This characteristic enables SECs to be applied over and around entire fatigue details in steel bridges to detect, localize, and monitor fatigue cracks. Here, we first review previous experimental work using the SEC as a crack monitoring device for in-plane fatigue crack detection on small-scale compact, C(T), specimens. Then, we extend the SEC technology for sensing fatigue damage in a large-scale structural surface through dense SEC arrays. An effective data visualization method is proposed to convert a fatigue damage feature, termed crack growth index (*CGI*), from individual SECs to a 2-dimensional *CGI* map, which depicts the fatigue damage over a large-scale area. It is possible to monitor fatigue damage evolution by observing the change in intensity in *CGI* maps during the fatigue test. The effectiveness of this approach was validated through an experimental test on a bridge girder-to-cross-frame connection subjected to out-of-plane fatigue loading. Overall, the results of this study indicate that the SEC technology has great potential for detecting and monitoring fatigue crack growth in practical applications.

1 INTRODUCTION

Fatigue cracking in steel highway bridges presents major safety and maintenance concerns for bridge owners. If bridges are not regularly inspected and maintained, fatigue cracks can lead to structural failure. According to a recently released report by the American Society of Civil Engineering (ASCE) in 2017 (ASCE 2017), 9.1% of the 614,387 bridges in the United States are structurally deficient. Significant maintenance or retrofitting can be expected to be required for these bridges due to deterioration or damage occurring in load-carrying structural members. Currently, bridge owners in the United States such as state departments of transportation (DOTs) generally rely on visual inspections at typical two-year intervals (Phares et al. 2001). However, due to variations in inspector interpretation of inspection results, objective evaluations of fatigue cracks are not guaranteed (Zhao & Haldar 1996).

Many advanced sensing technologies have been proposed for detecting and/or monitoring fatigue cracks in domains of both structural health monitoring (SHM) and non-destructive evaluation (NDE) over the past decades. Examples include: piezoelectric actuators (Ihn & Chang 2004), lamb wave (Staszewski et al. 2007), digital image correlation (DIC) technology (Poncelet et al. 2010), machine vision method (Kong & Li 2018), laser lock-in thermography (An et al. 2014), impulse response method (Keller el al. 2017), and others. However, these methods may require extensive efforts in sensor deployment, human operation, and signal processing, which may present significant practical challenges for detecting and monitoring fatigue cracks in steel bridges.

Recently, novel large-scale strain sensing technologies have shown potential as a cost-effective solution for monitoring structural damage. Sharing the same feature of large-scale sensing, several types of sensors have been reported in the literature including: resistance-based sensing sheets (Yao & Glisic 2015), carbon nanotube-based sensors (Kang et al. 2014), antenna sensors (Mohammad & Huang 2010), and soft elastomeric capacitors (SECs) (Laflamme et al. 2012). In particular, the SEC technology, previously developed by the authors, is a large-scale flexible strain gauge, capable of sensing up to 20% strain (Laflamme et al. 2013) over a large area (e.g. typical research on the SEC used 63.5 mm by 63.5 mm area sensors). The SEC is mechanically-robust and suitable for long-term monitoring. Our previous research established a numerical method to predict the SEC's response under fatigue crack growth (Kong et al. 2016), and experimentally validated the SEC's performance for sensing in-plane fatigue cracks on small-scale compact, C(T), specimens (Kong et al. 2017b, Kharroub et al. 2017a, Kong et al. 2017b).2015).

To extend the SEC fatigue sensing technology from small-scale specimens to realistic large-scale structural components, a challenge must be overcome: detecting fatigue cracks over a large fatigue-susceptible region without prior knowledge of the locations of crack initiation and propagation paths. One solution is to deploy multiple SECs in the form of dense sensor arrays over a structural surface to greatly increase the chance of capturing fatigue damage over the large area.

In this article, we describe a deployment of dense SEC arrays on a bridge girder-to-cross-frame connection subjected to out-of-plane distortion induced fatigue in the girder web gap regions (the region near the web to flange connection, when the connection plate is not attached to the flange). Fatigue damage in web gap regions commonly exists in many aged steel bridges in the United States, and hence are of primary concern to state DOTs. A sensing algorithm was formulated to extract fatigue damage feature, termed crack growth index (*CGI*), from each individual SEC in the sensor arrays. Then a data visualization method is created to convert the extracted *CGIs* into a 2-dimensional *CGI* map, depicting the fatigue damage over a large structural surface. More importantly, the fatigue crack growth can be identified through monitoring the change in intensity from a series of *CGI* maps during the fatigue test. The results in this article form the basis for applying the SEC technology in field sensing of fatigue cracks in steel bridges.

The rest of this article is organized as follows: Section 2 begins with an introduction of the SEC technology and its sensing principle, followed by a review of previous SEC-based experimental work on in-plane fatigue crack detection; Section 3 describes the experimental methodology and test setup, the algorithm for constructing the *CGI* map, and the test procedure; Section 4 summarizes conclusions.

2. BACKGROUND

2.1 Soft elastomeric capacitor

The sensing principle of the SEC has been reported in Laflamme et al. (2012). A brief summary is provided here. Shown in Figure 1*a*, the SEC is a flexible capacitor comprised of a dielectric layer sandwiched between two conductive layers. Equation 1 describes the SEC's sensing principle, where C is the capacitance of the SEC; ε_0 and ε_r are the permittivity of air and the dielectric, respectively; l, w and h are the length, width, and thickness of the SEC as denoted in Figure 1*b*.

The SEC can serve as a large-area strain gauge (Figure 1*a*). Variations in surface strains on the monitored structure induce changes in the geometric dimensions of the SEC (i.e. l, w, and h), leading to a capacitance change C of the SEC according to Equation 1. The capacitance C can be measured through two copper tapes attached on the top and bottom conductive layers (Figure 1*b*). A photograph of the SEC is shown in Figure 1*c*.

$$C = \frac{\varepsilon_0 \varepsilon_r l w}{h} \tag{1}$$

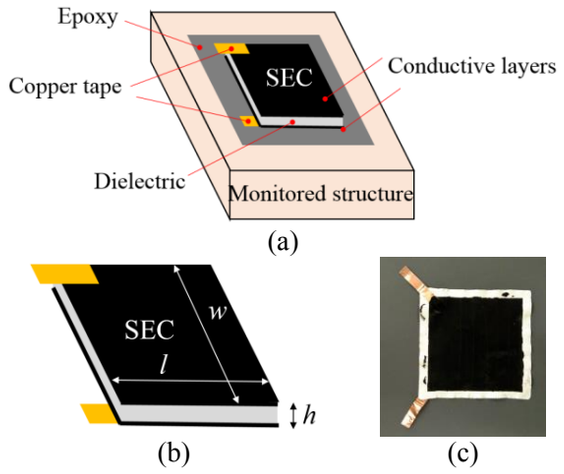


Figure 1. (a) Schematic of the SEC; (b) dimensions of the SEC; and (c) a picture of the SEC. Figures are reproduced from Kong et al. (2017a).

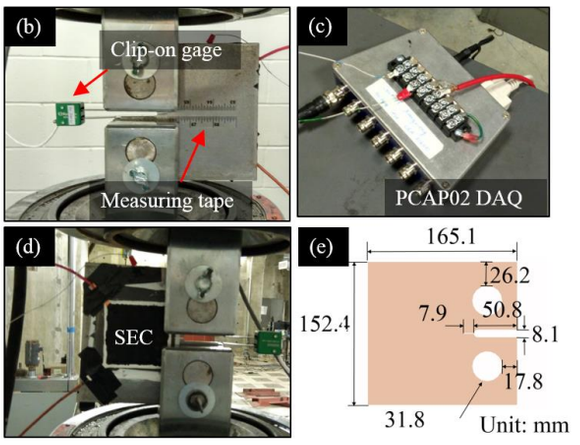


Figure 2. (a) Test setup; (b) front view of the specimen; (c) the DAQ system; (d) back view of the specimen; and (e) dimensions of the specimen. Figures are adapted from Kong et al. (2017a).

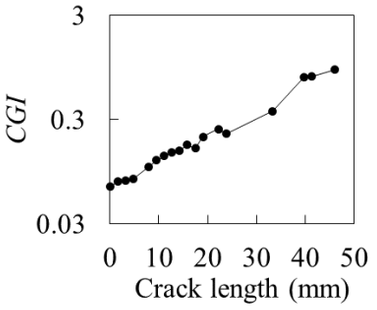
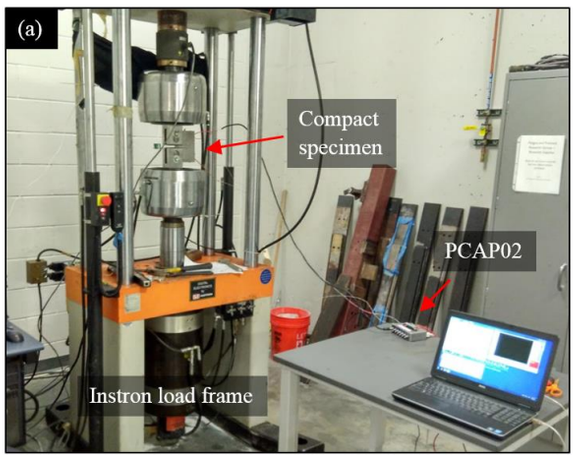


Figure 3. CGI versus crack growth. Figure is adapted from Kong et al. (2017a).

2.2 SEC-based in-plane fatigue crack detection

Use of the SEC for detecting in-plane fatigue cracks has been previously investigated in Kong et al. (2017a, 2017b). A brief summary of the experimental results is described here. Figure 2 shows the test setup using a steel compact, C(T), specimen. The dimensions of the specimen are presented in Figure 2*e* where the thickness of the specimen is 6.35 mm. As shown in Figure 2*b*, the C(T) specimen was installed in a closed-loop servo-hydraulic universal test frame (Instron model 1334) via two clevises. Two adhesive measuring tapes were attached to the specimen for visually identifying the crack growth. On the other side of the specimen, an SEC was adhered using JB-weld epoxy (Figure 2*d*). An off-the-shelf DAQ system (ACAM PCAP02) was used to collect capacitance data from the SEC, as shown in Figure 2*a* and 2*e*.



Both the applied load and the SEC's response were collected during the test as the crack propagated to different lengths, visually identified using the adhesive measuring tapes. Then, the fatigue damage features, termed the crack growth index (*CGI*), were extracted from the measurements as a robust indicator of crack growth. As demonstrated in Figure 3, an increasing trend of *CGI* was observed when the crack propagated. This indicates that as a single sensing unit, the SEC can detect and monitor the fatigue crack growth in a small-scale specimen. More discussions on this test including the loading protocol can be found in Kong et al. (2017b).

3. METHODOLOGY

This section introduces the test setup, test procedure, and the approach used to extract fatigue damage over a large-scale structural area using dense SEC arrays. Due to space limitations, the test procedure for the top portion of the connection (the top web gap) is presented in this section.

3.1 Test setup

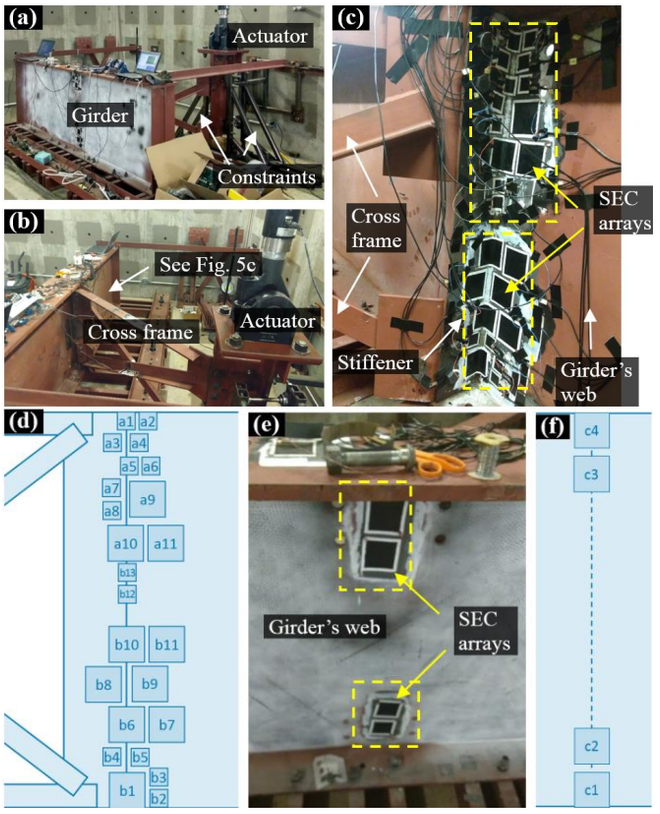


Figure 4. (a) Exterior view of the test model; (b) interior view of the test model; (c) SEC arrays and (d) sensor layout at the interior side of the connection; and (e) SEC arrays and (f) sensor layout at the exterior side of the connection.

The test setup includes three components: 1) the test model; 2) the loading system; and 3) dense SEC arrays. The test model is a bridge girder-to-cross-frame connection as shown in Figure 4*a* and 4*b*. The bridge girder was mounted upside-down on the floor and a cross frame was connected to the girder through a connection plate as shown in Figure 4*c*. The connection plate was only welded to the girder web while the top and bottom of the connection plate were not attached to the flanges. This configuration mimics typical connection details in many aged steel bridges in the United States. Detailed discussion on this connection detail can be found in Yu et al. (2017). By testing the girder upside-down, the restraint offered to the bottom flange by the laboratory strong floor simulated the restraint provided to the top flange of a bridge girder by the laterally-stiff deck.

Cyclic fatigue loading was applied through the actuator attached at the far end of the cross frame (Figure 4*a* and 4*b*). Load cycles were applied at a frequency of 0.5 Hz with a load range of -4.9 kN to 4.9 kN. To prevent out-of-plane movement of the cross frame when applying the load cycles, additional lateral constraints were added so that only vertical movement would occur at the cross frame, as illustrated in Figure 4*a*.

Figure 4*c* shows the arrangement of the dense SEC arrays at the top and bottom web gaps, where two sizes of SECs were used, including large SECs (63.5 x 63.5 mm), and small SECs (25.4 x 25.4 mm). A total of 24 SECs were deployed over the interior side of the connection. On the exterior side of the connection, 4 SECs were attached in the top and bottom web gaps, respectively (Figure 4*e*). Figure 4*d* and 4*f* show the layout and the sensor labels for the SEC arrays.

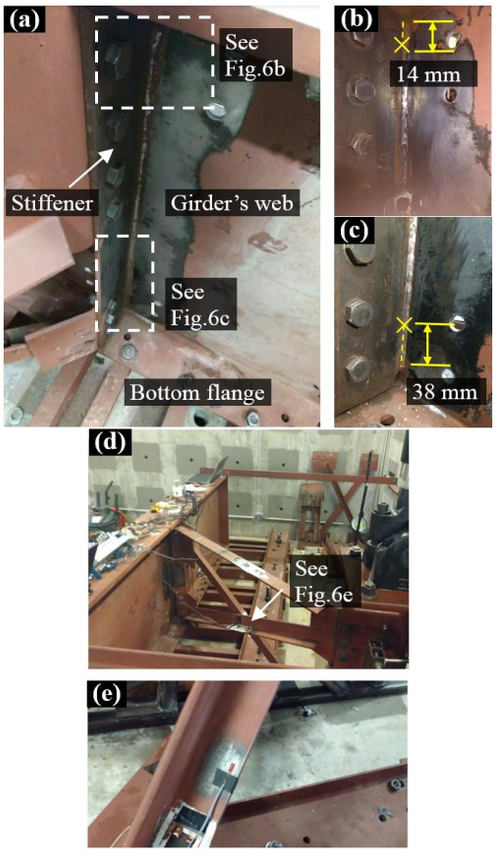


Figure 5. (a) Test model prior to sensor deployment; (b) an existing fatigue crack at the top web gap; (c) an existing fatigue crack at the bottom web gap; (d) and (e) a strain gauge was deployed on a diagonal member of the cross frame.

Prior to installation of the SEC arrays, the test model had been loaded with 2.7 million cycles using a load range of 0 to 11.2 kN. Two out-of-plane fatigue cracks had generated between the connection plate and web as shown in Figure 5*a*, *b*, and *c*. The top

fatigue crack was approximately 14 mm (Figure 5*b*) long, while the bottom fatigue crack was about 38 mm (Figure 5*c*) long. The tips of the fatigue cracks are denoted using a yellow "x" in Figure 5*b* and *c*.

In field applications, the load magnitudes caused by traffic may not be always known. One solution to deal with this challenge is to deploy strain gauges along the load path to indirectly infer the magnitude of loads. Because distortion-induced fatigue cracks are driven by differential vertical movements between two adjacent girders, strains in the cross frame members are proportional to the external load. For this reason, a foil strain gauge was deployed on a diagonal member of the cross frame to indirectly capture the applied load as shown in Figure 5*d* and *e*.

3.2 Test procedure

During the test, 71,000 new cycles were applied to the test model and eight datasets were collected when the cycle count reached 0; 15,000; 21,500; 30,000; 43,100; 53,800; 64,900; and 71,000 cycles; respectively. After 71,000 cycles, SEC a1 was removed to closely inspect the propagated crack. As shown in Figure 6*a*, the length of the fatigue crack was 14 mm at the beginning of the test prior to the installation of the SEC arrays. When the test was completed, the crack had propagated to its new length of 42 mm, indicating that the fatigue crack propagated within the eight data collection intervals.

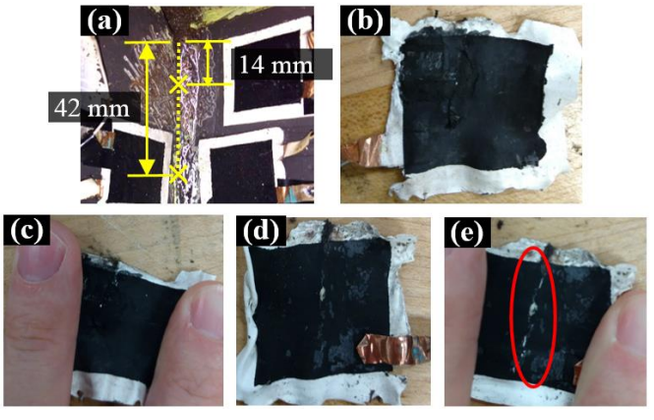


Figure 6. (a) The fatigue crack grew from 14 mm to 42 mm during the test; (b) front side of the SEC a1; (c) front side of the SEC a1 under stretching; (d) back side of the SEC a1; and (e) back side of the SEC a1 under stretching.

3.3 Fatigue damage features

The authors previously established a robust algorithm for extracting fatigue damage features, termed the crack growth index (*CGI*), described in Kong et al. (2017b) based on a single SEC applied on a small-scale C(T) specimen. Here, we have extended this algorithm for extracting the fatigue damage feature in dense SEC arrays. As illustrated in Figure 7, first the short-time measurements of capacitance C from the SEC and strain ε from the strain gauge (Figure 5*e*) were collected. Then, the peak-to-peak amplitude of strain measurement, denoted as Amp_ε, was obtained. The peak-to-peak amplitude of the capacitance measurement is challenging to directly identify in the time-series signal due to high noise content. Thus, the power spectral density (PSD) is proposed, where the peak of the PSD curves $Peak_C$ would indicate the peak-to-peak magnitudes in the time-series signals of capacitance C. Next, the *CGI* was established by computing the square root of $peak_C$ over Amp_ε.

The *CGI* is a normalized strain indicator under fatigue cracking. If the crack propagates into the SEC, the SEC can directly capture the crack growth by showing an increasing *CGI*. On the other hand, if the crack propagates but does not grow into the SEC, the SEC functions as a large area strain gauge to monitor the strain field migration caused by crack propagation.

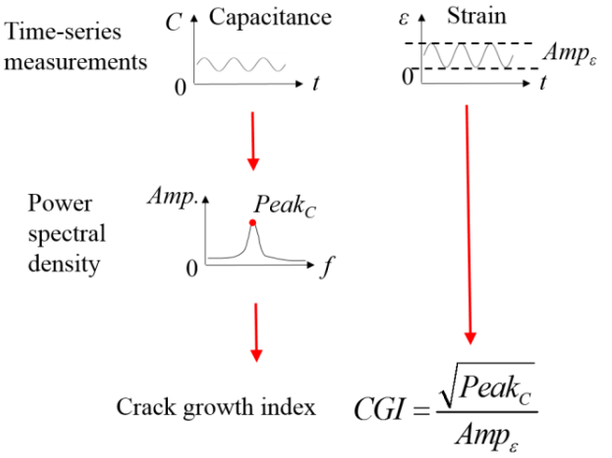


Figure 7. Fatigue damage sensing algorithm based on CGI from a single SEC.

Utilizing the procedure in Figure 7, the *CGIs* of all the SECs deployed over a large fatigue-susceptible region were computed. Figure 8*a* shows an example of *CGIs* computed from the 11 SECs in the top web gap of the connection. Linear interpolation was applied to these *CGIs* over the spatial dimensions x and y (denoted in Figure 8*a*) to create a 3D *CGI* surface as shown in Figure 8*b*. Essentially, the 3D *CGI* surface is a matrix containing the interpolated *CGIs* within the red-dashed zone in Figure 8*a*. Next,

the 3D *CGI* surface was presented in terms of a 2D image, termed the *CGI* map, in Figure 8*c*. The intensity of each pixel (x, y) in the CGI map is an interpolated *CGI*. The *CGI* map offers a clear presentation of the spatial distribution of *CGI* and serves as the basis for fatigue damage sensing using dense SEC arrays.

Finally, by periodically collecting short-time measurements from the monitored structure under the fatigue load cycles, a series of *CGI* maps was constructed through the above procedure. If the fatigue crack did not propagate during the data collection intervals, the corresponding *CGI* maps would exhibit similar spatial intensities. Conversely, if the fatigue crack grew during the data collection intervals, it would result in changes to the intensity distribution of the CGI map.

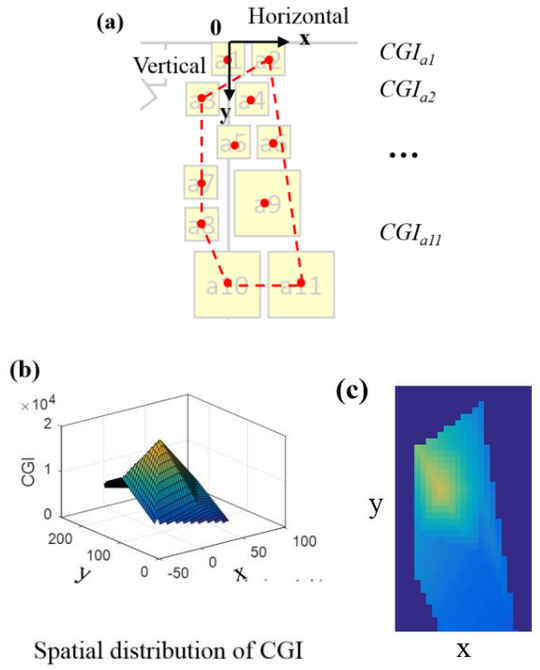


Figure 8. Construction of the *CGI* map.

4. RESULTS AND DISCUSSIONS

This section provides the test results and discussions. Results from the top web gap of the connection are discussed.

4.1 CGIs of single SECs

Following the *CGI* extraction algorithm presented in Section 3.2, the CGI responses of SEC arrays on the top of the connection are shown in Figure 9. Generally, SEC a1 exhibited the largest CGI response in the top web-gap region. This is because SEC a1 was deployed directly over the existing fatigue crack. The out-of-plane distortion-induced fatigue crack provoked a significant change in capacitance in this particular SEC. In addition, a significant increase of CGI was observed in SEC a10 at approximately 60,000 cycles.

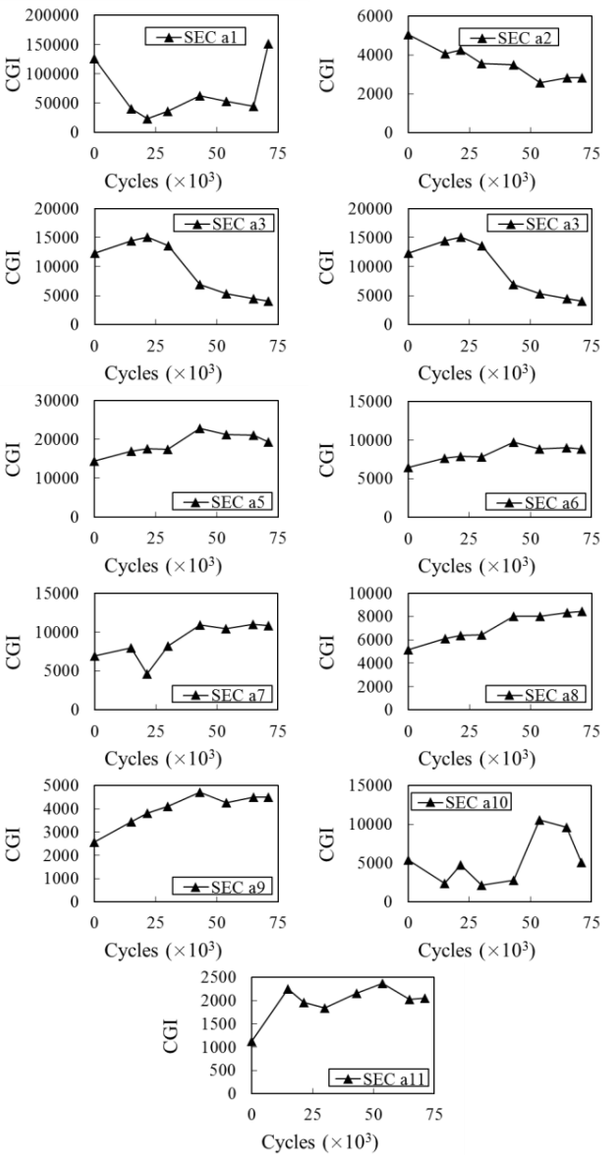


Figure 9. CGI response of the SEC arrays on the top region of the connection. The sensor numbers are shown in legends.

Figure 10 shows the CGIs of all the top web-gap SECs except SEC a1 and a10. By correlating the CGI changes with the spatial distribution of the SEC arrays (Figure 4*d*), some observations can be made as follows: 1) during the crack propagation as shown in Figure 6*a*, the concentrated strain field migrated

along with the crack tip. In particular, the strain level continuously dropped along the two sides of the crack path due to stress relief. As a result, decreasing trends in *CGIs* were observed for SEC a2, a3, and a4; 2) crack growth provoked increased strain levels in the sensor that covered the crack, leading to increasing trends for *CGIs* at SEC a5, a6, a7, a8, and a9. Interestingly, the above phenomenon became clearer between 30,000 cycles and 40,000 cycles, as highlighted in the black dashed block in Figure 10, indicating a period of significant crack growth.

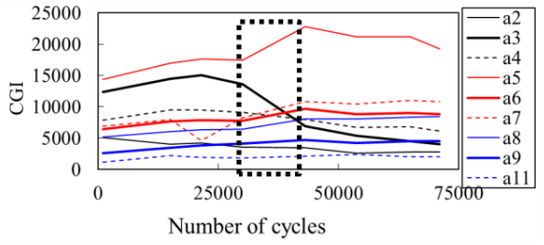


Figure 10. Comparison of CGIs in SEC a2 to a9, and a11.

4.2 CGIs maps

Utilizing the method proposed in Figure 8a, the *CGI* responses of the SEC arrays were used to further construct *CGI* maps. Figure 11 shows the spatial distribution of the *CGIs* obtained by linearly interpolating all the *CGIs* from the SEC arrays in the top web gap of the connection. The results clearly show the distribution of *CGI* magnitudes of the SEC array, enabling a clear depiction of the fatigue damage over a large area. As shown in the figure, as the number of load cycles increased, the fatigue crack grew causing the shape of the *CGI* surface to change. Monitoring such changes enables detection of the fatigue damage. Briefly, the largest *CGI* magnitude was observed near x=0 mm and y=100 mm, which is the location of SEC a5. The same information could also be obtained through Figure 10. In addition, the *CGI* maps show changes in intensity as the cycle count increased. The local region around SEC a5 (x=0 mm, y=100 mm) gradually became brighter (more intense) from 0 to 30,000 cycles, as shown in the first row in Figure 12. Then the intensity was significantly increased when the test reached 43,100 cycles, indicating significant fatigue crack growth in this particular interval.

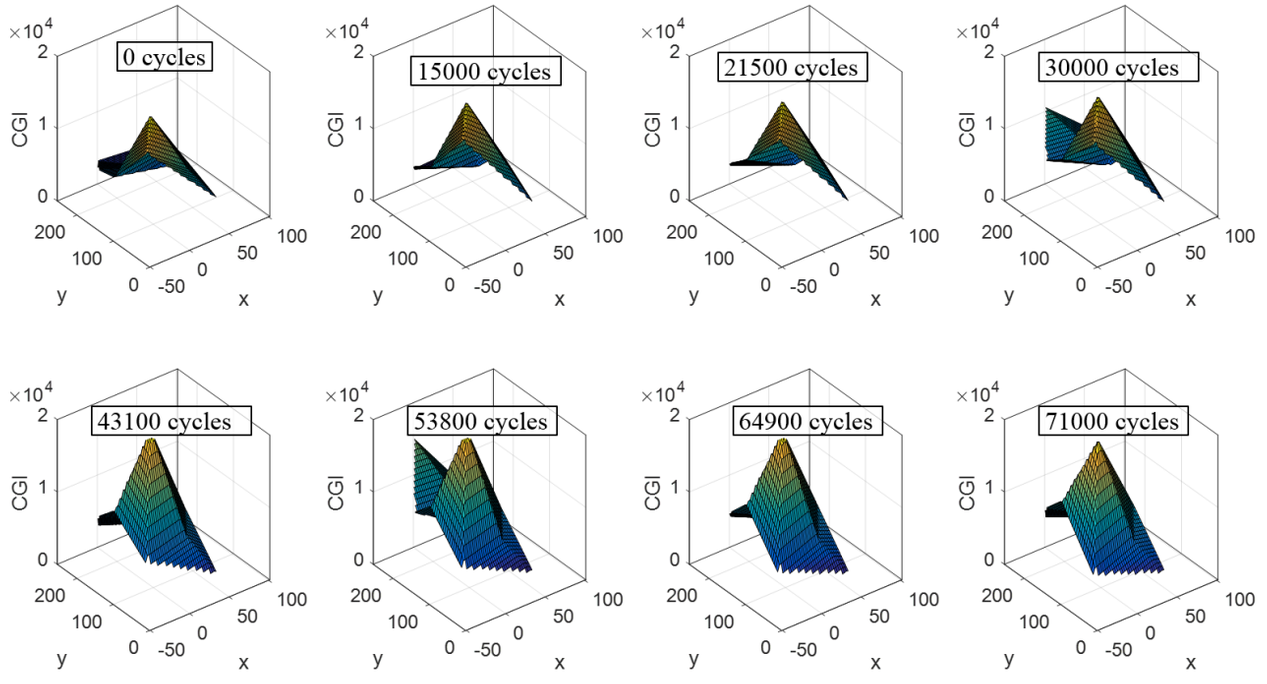


Figure 11. Spatial distribution of CGIs with different load cycles.

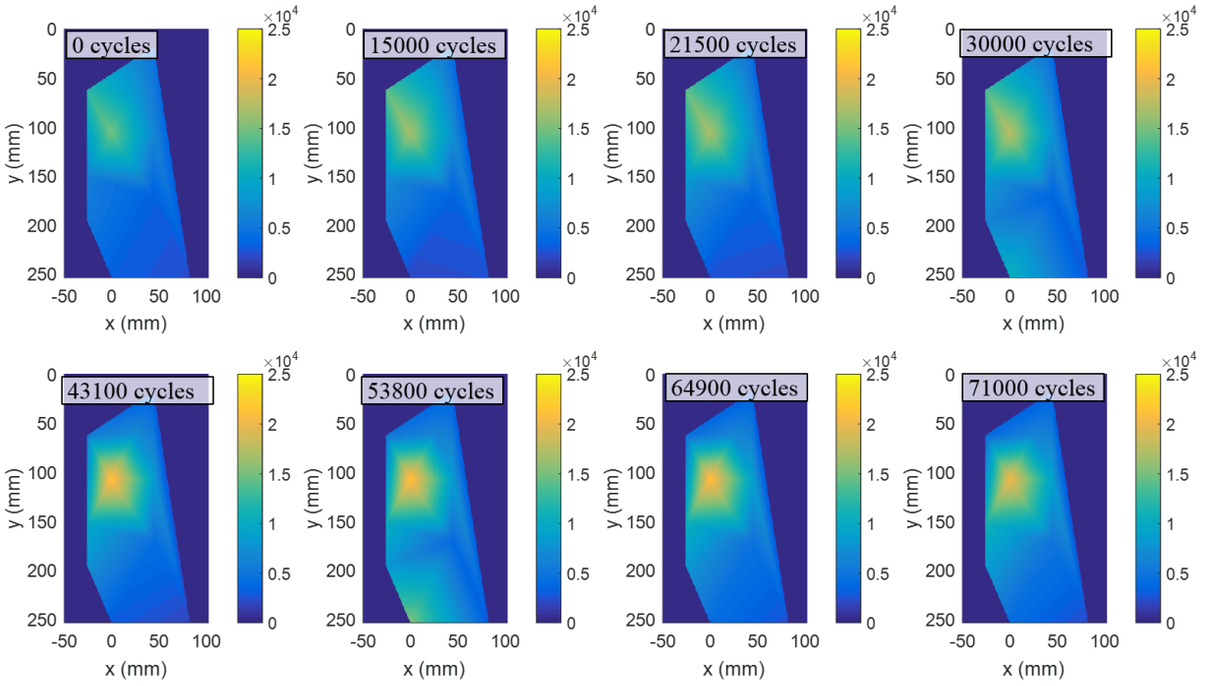


Figure 12. CGIs maps with different load cycles.

5. CONCLUSION

In this paper, we proposed strain-based dense sensor arrays to monitor fatigue cracks over large structural surfaces. The strain sensing technology, termed soft elastomeric capacitor (SEC), is a large-area flexible strain gauge, serving as the basic sensing unit in this study. A fatigue damage feature extraction algorithm was established based on the SEC arrays, through which the development of fatigue damage can be visualized with *CGI* maps. By observing the changing pattern of intensities in the *CGI* maps, the fatigue damage occurring in a large structural surface can be monitored. The effectiveness of this approach has been validated through an experimental test using a large-scale steel girder-to-cross-frame connection. The success of the proposed *CGI* map concept will serve as the enabling tool for field applications of the SEC technology for sensing fatigue damage in steel bridges.

ACKNOWLEDGEMENTS

This work was supported by Transportation Pooled Fund Study TPF-5(328), which includes the following participating state DOTs: Kansas (lead state), Iowa, Minnesota, North Carolina, Pennsylvania, Texas, and Oklahoma; and Iowa Department of Transportation grant #RT454-494. Their support is gratefully acknowledged. The authors also want to thank Austin Downey from Iowa State University for providing support regarding the data acquisition system, and Justin Ocel at FHWA for providing valuable feedback to the test program.

REFERENCES

American Society of Civil Engineers (ASCE). (2017). *2017 Infrastructure Report Card, Bridges,* https://www.infrastructurereportcard.org/cat-item/bridges/

An, Y. K., Kim, J. M., & Sohn, H. (2014). Laser lock-in thermography for detection of surface-breaking fatigue cracks on uncoated steel structures. *Ndt & E International*, 65, 54-63.

Ihn, J. B., & Chang, F. K. (2004). Detection and monitoring of hidden fatigue crack growth using a built-in piezoelectric sensor/actuator network: I. Diagnostics. *Smart materials and structures*, 13(3), 609.

Kang, M. H., Choi, J. H., & Kweon, J. H. (2014). Fatigue life evaluation and crack detection of the adhesive joint with carbon nanotubes. *Composite Structures*, 108, 417-422.

Keller, W., Cohen, R., Pakzad, S., & Pessiki, S. (2017). *Rapid Detection of Fatigue Cracking in Steel Anchor Rods Using the Impulse Response Method* (No. NCHRP Idea Project 175).

Kharroub, S., Laflamme, S., Song, C., Qiao, D., Phares, B., & Li, J. (2015). Smart sensing skin for detection and localization of fatigue cracks. *Smart Materials and Structures*, 24(6), 065004.

Kong, X. and Li, J. (2018). Vision-based fatigue crack detection using feature tracking. *Computer-Aided Civil and Infrastructure Engineering*. In revision.

Kong, X., Li, J., Bennett, C., Collins, W., & Laflamme, S. (2016). Numerical simulation and experimental validation of a large-area capacitive strain sensor for fatigue crack

monitoring. *Measurement Science and Technology*, 27(12), 124009.

Kong, X., Li, J., Collins, W., Bennett, C., Laflamme, S., & Jo, H. (2017a). A robust signal processing method for quantitative high-cycle fatigue crack monitoring using soft elastomeric capacitor sensors. *Proc. SPIE 10168, Sensors and Smart Structures Technologies for Civil, Mechanical, and Aerospace Systems 2017, 101680B*

Kong, X., Li, J., Collins, W., Bennett, C., Laflamme, S., & Jo, H. (2017b). A large-area strain sensing technology for monitoring fatigue cracks in steel bridges. *Smart Materials and Structures*, 26(8).

Laflamme S, Kollosche M, Connor JJ, and Kofod G. (2012). Robust flexible capacitive surface sensor for structural health monitoring applications *Journal of Engineering Mechanics*. 139 879-85.

Laflamme S, Saleem HS, Vasan BK, Geiger RL, Chen D, Kessler MR, and Rajan K. (2013). Soft elastomeric capacitor network for strain sensing over large surfaces *IEEE/ASME Transactions on Mechatronics.* 18 1647-54

Mohammad, I., & Huang, H. (2010). Monitoring fatigue crack growth and opening using antenna sensors. *Smart Materials and Structures*, 19(5), 055023.

Phares, B. M., Rolander, D. D., Graybeal, B. A., & Washer, G. A. (2001). Reliability of visual bridge inspection. *Public Roads*, 64(5).

Poncelet, M., Barbier, G., Raka, B., Courtin, S., Desmorat, R., Le-Roux, J. C., & Vincent, L. (2010). Biaxial High Cycle Fatigue of a type 304L stainless steel: Cyclic strains and crack initiation detection by digital image correlation. *European Journal of Mechanics-A/Solids*, 29(5), 810-825.

Staszewski, W. J., Lee, B. C., & Traynor, R. (2007). Fatigue crack detection in metallic structures with Lamb waves and 3D laser vibrometry. *Measurement Science and Technology*, 18(3), 727.

Yao, Y., & Glisic, B. (2015). Detection of steel fatigue cracks with strain sensing sheets based on large area electronics. *Sensors*, 15(4), 8088-8108.

Yu, D., Bennett, C., & Matamoros, A. Retrofitting Distortion-Induced Fatigue in Skewed Girders to Cross-Frame Connections. *In Structures Congress 2017* (pp. 149-161).

Zhao Z, and Haldar A. (1996). Bridge fatigue damage evaluation and updating using non-destructive inspections. *Engineering fracture mechanics*. 53(5), 775-88.

Maintenance, Safety, Risk, Management and Life-Cycle Performance of Bridges – Powers, Frangopol, Al-Mahaidi & Caprani (Eds)
© 2018 Taylor & Francis Group, London, ISBN 978-1-138-73045-8

Fatigue Assessment of Concrete Girder Bridges Based on Traffic Information

P. J. Zhang, C. S. Wang, Q. Wang, L. Duan
Engineering Research Center for Large Highway Structure Safety of Ministry of Education, College of Highways, Chang'an University, Xi'an, China

ABSTRACT: With the increasing of traffic volume and carrying capacity of vehicles, fatigue failure of concrete girder becomes the one of the most serious problem. A better way to evaluate the fatigue performance of concrete girder bridges is using existing information instead of taking field test. As the main load fatigue load of concrete girder bridges, vehicle load affects the fatigue life of concrete bridges significantly. Traffic information can be changed into fatigue load when bridge information is known. So a process is proposed to evaluate the fatigue performance of concrete girder bridges by using traffic information. An assessment method contains five parts including gathering vehicle load information, setting up fatigue load model, calculating stress spectrum, correcting the calculated stress spectrum and doing fatigue life calculation is proposed. To verify the effectiveness of the method, a small box girder bride is chosen as the case bridge. The weigh in motion system (WIM) and manual counting were used under the real traffic conditions. And in order to give the correction factor, dynamic strain monitoring data was taken to provide comparative results.

1 INTRODUCTION

Concrete girder bridges are the most widely used bridge style around the world. Before 1970, fatigue problems were rarely found in concrete girder bridges because of allowable stress design method adopted in earlier design specifications, smaller design load, and the lower material stress. With the development of social economy, the traffic volume and gross vehicle weights of trucks are increasing continuously. Thus, concrete bridges are subject to serious fatigue problems(Wang et al. 2012, Feng et al. 2003 Aggarwal et al. 2015). Combined with the environmental corrosion impact, concrete material aging and mechanical behaviour deterioration appear gradually. These all leads to reduction of strength and fatigue damage accumulation of reinforcing and prestressing steel (Akgül & Frangopol. 2004, Sarveswaran et al. 2000, Darmawan & Stewart 2007). But existing standards and specifications rarely focused on it. The common practice is taking long term monitoring and using measured stress spectrum to calculate fatigue life for concrete bridge, which is costly and time-consuming. To solve this question, it will require a method that uses fatigue load model to reduce the complexity and expense of fatigue evaluation.

Fatigue load model has been researched a lot for evaluating fatigue performance conveniently and economically, and most of the researches are for steel bridges. The fatigue load includes measured load spectrum, standard load spectrum and standard fatigue load model. The measured load spectrum data obtained from actual traffic volume statistics are complex and cumbersome, and are generally simplified to standard load spectrum. Based on this, a standard fatigue load model with universal applicability is established. The currently research on the fatigue load model mainly taken overall bridge structure as the research object (Wang et al. 2005, Zhou et al. 2010, Zong et al. 2013). Taken a vulnerable detail in the steel bridge deck of Hong Kong Zhuhai Macao Bridge as the research object, and adopted the traffic statistics data of Humen bridge and Lantau link, Bu and his collaborators have established the four axle fatigue load model with total weight 300kN (Bu et al. 2014). Based on the dynamic weighing data of Guizhou Baling Bridge within one week, Sun Xiuya has established three kinds of axle load spectra suitable for the steel bridge deck (Sun et al. 2014). Due to the difference between various fatigue stress behaviors of steel deck, the fatigue load model established with someone detail may not be suitable for other details, and the adaptability of fatigue load model only established with few data samples still need to be verified. Standards and specifications also give the suggested models for fatigue evaluation. Based on British highway traffic load information, a four axle standard fatigue load model with total weight 320kN was proposed by British BS5400 standard (BS 5400-2: 2006

2006); the four axle standard fatigue load model with total weight 480kN was adopted by Eurocode (BS EN 1993-1-9: 2005 2005); the three axle standard fatigue load model with total weight 325kN was recommended by AASHTO code (AASHTO LRFD 2010); and the four axle standard fatigue load model with total weight 480kN was suggested in China latest specification for highway steel bridge design implementation (JTG D64-2015 2015), the vehicle type and axle load of which is consistent with the European Eurocode 3.

For concrete girder bridges, most of standard and specification only give a stress limit for fatigue design. And little researchers focus on the fatigue load models of concrete bridges. Although from some fatigue load model researches of steel bridges can be used in fatigue assessment for concrete girder bridges, the structure un-symmetry, existing structural damage and other factors can lead to an incorrect consequence because measured stress amplitude may have difference from the calculated stress amplitude which uses fatigue load model.

In this paper, the proposed assessment method contains five parts including gathering vehicle load information, setting up fatigue load model, calculating stress spectrum, correcting the calculated stress spectrum and doing fatigue life calculation. A small box girder bride is chosen to calculate the fatigue life. The weigh in motion system (WIM) and manual counting were used under the real traffic conditions. And to verify the effectiveness of the proposed method and give the correction factor, dynamic strain monitoring data was taken to provide comparative results.

2 ASSESSMENT METHOD USING TRAFFIC INFORMATION

For steel bridges, using fatigue load model to evaluate fatigue life is a common practice. But for concrete, most of standard and specification only give a stress limit for fatigue design.

It is much convenient and economical to use fatigue load model when calculate fatigue life. So, the method to be proposed is a way to using fatigue load model. Similarly to the establishment of fatigue load model for steel bridges, the procedures for calculating fatigue load model for concrete girder bridges contain two main steps which are collecting vehicle load information and calculating fatigue load model by using equivalent damage theory.

However, structure un-symmetry and existing structural damage will lead to bigger stress amplitude than that of ideal model. This will result in a wrong consequence. That means the original stress which calculated by fatigue load model needs a correction factor. The correction factors for calibrating the calculated stress spectrum can be obtained through statistical vehicle information or field test of bridges. After that, fatigue life evaluation can be carried out. The whole

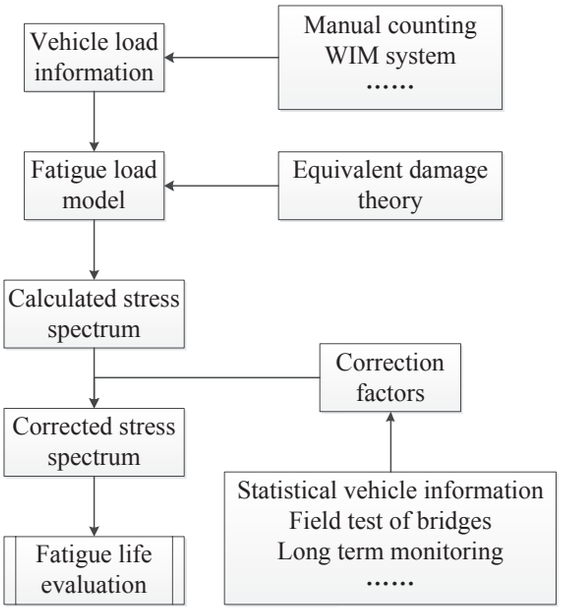


Figure 1. Assessment method using traffic information

3 FATIGUE VEHICLE LOAD MODEL

3.1 *Information of Case Bridges*

Shown in Figure 1, a small box girder bridge which located in Shaanxi Province (China) was chosen as case study bridges. Traffic information was gathered and long-term stress monitoring was adopted for the three bridges. Information of three bridges is listed in Table. 1.

Table 1. Information of case bridges

Section form	Span layout	Structure type	Steel bar grade
Small box girder bridge	4×30m+4×30m	Continue bridge	d=16mm; f_y=335MPa



Figure 1. External view of case bridges

3.2 *Vehicle Load Information*

Before taking the observation of traffic information, it is necessary to classify the vehicle types. Figure 2 shows the various types of vehicles: 'a' and 'b' are 2 axle vehicles; 'c' to 'g' are 2, 3, 4, 5 and 6 axle trucks respectively. Also, two ways to gather traffic information are shown as 'h' and 'i' which 'h' is WIM system and 'i' is manual collection of traffic information. WIM system is the system that can collect the information such as vehicle types, axle numbers, gross weight, axle distance and so on. By using manual counting, manual collection is a method collecting vehicle types, driving directions and loading condition. Considering the features of the two methods and the field situation, observations using the two methods were carried out at different observation site. Based on the two ways above, vehicle information of three case bridges in this paper were gathered as follows.

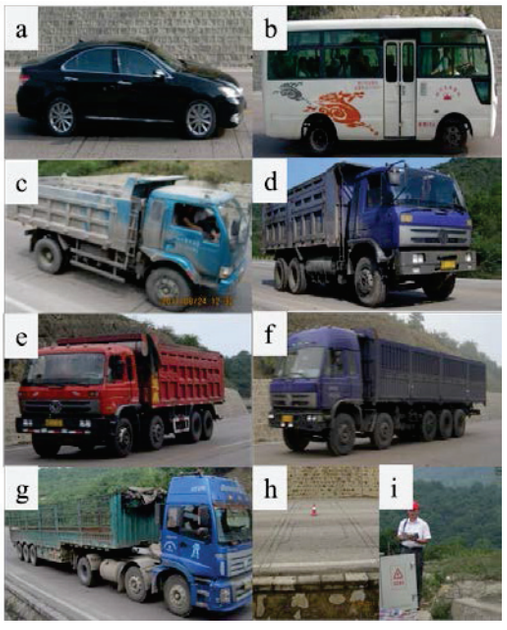


Figure 2. Different types of vehicles and WIM system

For the small box girder bridge, observation was carried out from Aug. 22nd to Sep. 22nd in 2011. Taken the vehicle data gathered from WIM system as case sample, the values of occupation ratio of different types of vehicles are shown in Figure 3. It can be seen that the largest number of vehicles is trucks for both uplink and downlink. Compared with the hollow slab girder bridge, the main type of trucks is 4-axle truck which occupies over a quarter of all kinds of vehicles.

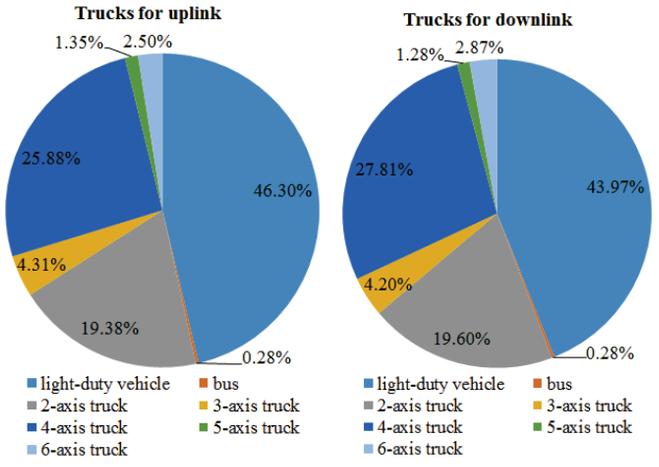


Figure 3. Occupation ratio of different types of vehicles for small box girder bridge

Based on the statistical analysis of measured data, the daily average value, variation coefficient, maximum and minimum values were obtained. As shown in Table 2, take the seven-day vehicle information of the small box girder bridge as an example, the variation coefficient of vehicle types in this measuring point is relatively large, which was above 1.0. The results showed that the vehicle load discreteness was larger, the vehicle type was various, and the load weight was difference. While the average values and variation coefficient of vehicle load in each day showed that there were little difference on the average values and variation coefficients of daily vehicle load. It suggested that the traffic load was stable in short term and can represent the situation of vehicle load in a period of time.

Table 2. Seven-day vehicle information of the case small box girder bridge

Date	Vehicle number	Gross weight	Maximum weight	Minimum weight	Average weight	Variation coefficient
		ton	ton	ton	ton	
2011-8-24	595	4368.17	53.40	0.66	7.34	1.01
2011-8-25	919	6113.17	37.90	0.27	6.65	1.00
2011-8-26	906	6387.67	46.80	0.21	7.05	1.06
2011-8-27	831	5729.72	43.60	0.39	6.89	1.09
2011-8-28	928	6775.04	63.20	0.36	7.30	1.13
2011-8-29	908	7949.81	53.80	0.17	8.76	1.11
2011-8-30	808	5232.90	58.30	0.34	6.48	1.26

3.3 *Fatigue Load Model*

Because the vehicle types are various and the gross weight of single vehicle has big range of variation. It is necessary to set up a fatigue load model by using vehicle load information. Common practice is:
1) Using the Equation (1), merge the vehicles which have same axle numbers into a submodel.

$$W_{ej} = \left[\sum\left(f_i W_{ij}^m\right)\right]^{\frac{1}{m}} \tag{1}$$

where f_i is the relative frequency of *i*th vehicle in same vehicle class; W_{ij} is the *j*th axle weight (axle distance) of *i*th vehicle; W_{ej} is the *j*th equivalent axle weight (equivalent axle distance) for the corresponding submodel; *m* is the slop of the S-N curve.
2) Based on equivalent damage assumption, the equivalent axle weight can be calculated for each submodel as Equation (2) and Equation (3);

$$\alpha = \frac{W_S}{W_B} \tag{2}$$

where α is the correction factor of the axle weight; is W_S the axle weight of the fatigue load model, W_B is the axle weight of the submodel.

$$\alpha = \frac{\left(\frac{n_T \Delta\sigma_T}{N_T n_B'}\right)^{\frac{1}{m}}}{\Delta\sigma_B} \tag{3}$$

where n_B' is the number of the stress cycles which caused by one submodel; n_T is the number of the stress cycles which caused by one fatigue load model; $\Delta\sigma_T$ is the sum of the equivalent stress amplitude; $\Delta\sigma_B$ is the equivalent stress amplitude caused by submodel.

3) Chose the main truck type as the basic model of the fatigue load model;
4) Using the sum of equivalent axle weight of each submodel, the equivalent gross weight of fatigue load model can be obtained through.

According to the vehicle information of the case small box girder bridge, the following conclusions were summarized:

(1) Trucks made up the largest proportion of all vehicles; 4-axle truck accounted for the largest proportion in all trucks, which was the basic model of the fatigue load model.

(2) Impact of light-duty vehicles such as sedan car and small agricultural machinery should be ignored because the lighter weight cause little fatigue damage.

(3) Through the dynamic strain monitoring test on the part of bridge, we found that when the vehicles (including buses and trucks) were passing, the stress curve usually occurred two peaks, which was the structure response of two axle groups in the front and in the back of vehicles.

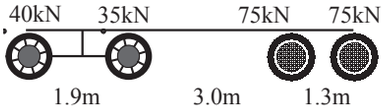


Figure 4. Diagram of fatigue load model of the case small box girder bridge

Based on the gathered data and the dimensional details, the four axle truck was recommended as the fatigue load model in this place, and the values of axle weight and wheelbase truck were averaged and rounded according to the data provided by the manufacturer of truck and the measured data, the values were. The suggested fatigue vehicle load model as shown in Figure 4:

4 FATIGUE ASSESSMENT FOR CASE BRIDGES

For case small box girder bridge, validation of equivalent stress was carried out firstly. By using the influence lines, the fatigue load model was loaded on the structure and its equivalent force amplitude was calculated, and compared with the stress produced by the actual traffic flow which was gathered from WIM system. The vehicle driving direction for the case small box girder bridge was divided into two directions, namely uplink direction and downlink direction.

Table 3. The stress amplitude comparison between fatigue vehicle and actual vehicle

Stress amplitude	Number of stress cycles	
	Loaded by fatigue load model	Loaded by measured vehicle axle weight
MPa	*n*	*n*
1	580	1444
2	33	109
3	36	93
4	49	210
5	679	22
6	40	4
7	20	7
8	20	16
9	10	8
10	\	13
11	\	7
12	\	3

The measured data showed that in the measured strain data of the case bridge girders, the stress of external girders is larger than the internal girders.

And because the bridge was a continue girder, the critical steel bar was in the 0.4L section of side span than the other parts of the bridge. Therefore, the 0.4L section of side span was selected as the control section. And the steel bar in the bottom plate of the control section was chosen as the critical member which needs to be assessed. Through influence line, the fatigue load model and the measured vehicle load were loaded to the structure to calculate the equivalent force amplitude, and the results were compared and showed in Table 3.

Ideally, the equivalent stress amplitude which caused by fatigue load model should be same with the equivalent stress amplitude which caused by actual vehicle. However, round-off error from each steps cause a little deviation as Table 4 shows. But the result still shows good agreement with expected the equivalent stress amplitude.

Table 4. The equivalent stress amplitude loaded by fatigue load Model and actual vehicle

Load type	Equivalent stress amplitude MPa	Ratio of Fatigue load model to actual vehicle
Fatigue load model	4.88	1.03
Actual vehicle	4.74	

In order to valid the effectiveness of the method, the long term stress monitoring for critical part of the case bridge was conducted for the case small box girder bridge. The strain measurement point layout as shown in Figure 5.

Diameter of critical steel bars in the bottom plate is 16mm, and specification of prestressing steel at the measured position is 4×15.2. The layout of steel bar and prestressing steel are shown in Figure 6.

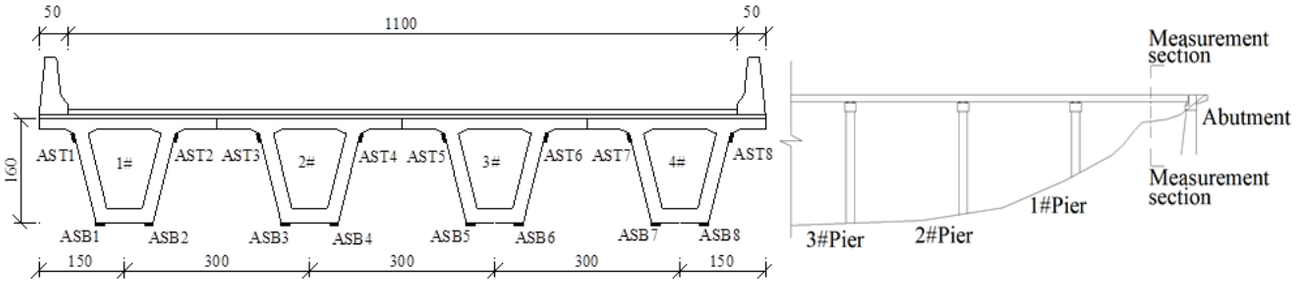


Figure 5. The measuring points layout at side span 0.4L cross section (unit: cm)

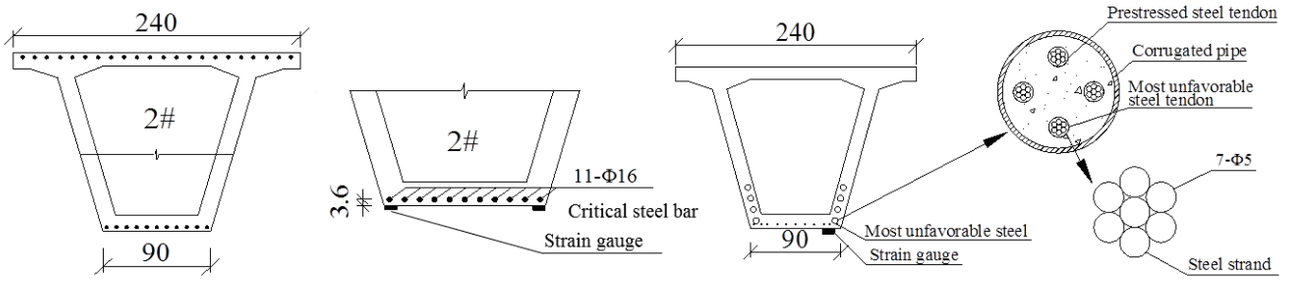


Figure 6. The layout of critical steel bar and prestressing steel at side span 0.4l cross section (unit: cm)

In the field monitoring, the maximum internal force section is selected, and the longitudinal strain gauges were arranged on the surface of the bottom plate of the box girder. Based on the plane cross-section assumption, the strain of critical steel bar and most unfavorable prestressing steel can be calculated by using the measured strain. The stress spectrum of the steel bar is obtained by the rain flow counting method. According to Eurocode[28], the detail category of steel bar is close to level 100 for normal steel bar.

In the measured stress data, the test point which had larger accumulated damage was selected as the evaluation object. After comparing, the measuring points with maximum cumulative damage at the most unfavorable section is selected, that is, the measure point of ASB3. The stress spectrum of ASB3 is shown in Table 5.

Neglect the stress which is in stress level 0~2MPa where has lots of noise and has no effects on fatigue life calculation. Based on plane section computational assumption, the stress spectrums for both steel bar and prestressing steel were obtained. By comparing the stress amplitude of the two spectrums, prestressing steel and steel bar were both in low stress

level. So, for convenience, only chose steel bar as calculation object.

Table 5. The stress spectrum of measure point ASB3

Stress amplitude	Number of cycles	Stress amplitude	Number of cycles
MPa	*n*	MPa	*n*
0<S≤2	/	24<S≤26	18
2<S≤4	4868	26<S≤28	12
4<S≤6	390	28<S≤30	15
6<S≤8	457	30<S≤32	13
8<S≤10	176	32<S≤34	10
10<S≤12	546	34<S≤36	3
12<S≤14	414	36<S≤38	2
14<S≤16	74	38<S≤40	2
16<S≤18	78	40<S≤42	3
18<S≤20	59	42<S≤44	3
20<S≤22	39	44<S≤46	0
22<S≤24	25	46<S≤48	1

Linear cumulative damage theory is the most widely used to assess fatigue performance. Considering the high randomness of fatigue damage initiation position and shape, linear cumulative damage theory is adopted in this paper. According to linear fatigue cumulative damage theory, damage caused by one cycle is presented as Equation (4).

$$D = \frac{1}{N} \tag{4}$$

where N means cycles within the action of stress amplitude level S. Under the effect of constant amplitude stress, the fatigue damage caused by n cycles is as Equation (5).

$$D = \frac{n}{N} \tag{5}$$

Under the effect of variable amplitude stress S_i of n_i cycles, the fatigue damage is as Equation (6).

$$D = \sum_i D_i = \sum_i \frac{n_i}{N_i} \tag{6}$$

where N_i is cycle within the action of stress amplitude level S_i until failure.

Based on above analysis, during the monitoring period, actual stress amplitude $\Delta\sigma_i$ and cycles are obtained and the fatigue accumulation damage can be calculated by Equation (7).

$$D_T = \sum_i \frac{n_i}{N_i} \tag{7}$$

Fatigue life Y of structure can be calculated by Equation (8).

$$Y = \frac{D_{cr}}{D_T} \times T \tag{8}$$

where D_{cr} is critical fatigue damage, T is monitoring time and D_T is fatigue damage during time T. Previous experiments show that, under random loading, D_{cr} is around 1, so the value of D_{cr} is taken as 1.

The fatigue damage within the monitoring duration is 4.256×10-6 and the monitoring duration is 21-day long. So, based on the measured stress spectrum, the fatigue life is calculated as follow:

$$Y = \frac{21}{4.256\times10^{-6}\times365} = 13518 \quad \text{years} \tag{9}$$

As mentioned above, the real structure is different from the ideal model. Structure un-symmetry and existing structural damage will lead to bigger stress amplitude than that of ideal model. According to the fatigue load model calculated in Section 3.3, the stress spectrum corresponding to the fatigue load model is smaller than the measured stress spectrum. So, it is required correct the stress spectrum which was obtained by loading fatigue load model, and amplify the stress range into a reasonable scale.

Take measure point ASB3 as the research object, the stress spectrum of the probability distribution fitting field monitoring of bridge, the mixed Gauss model is simulated, the distribution function as shown Equation (10) and the fitting curve as shown in Figure 7.

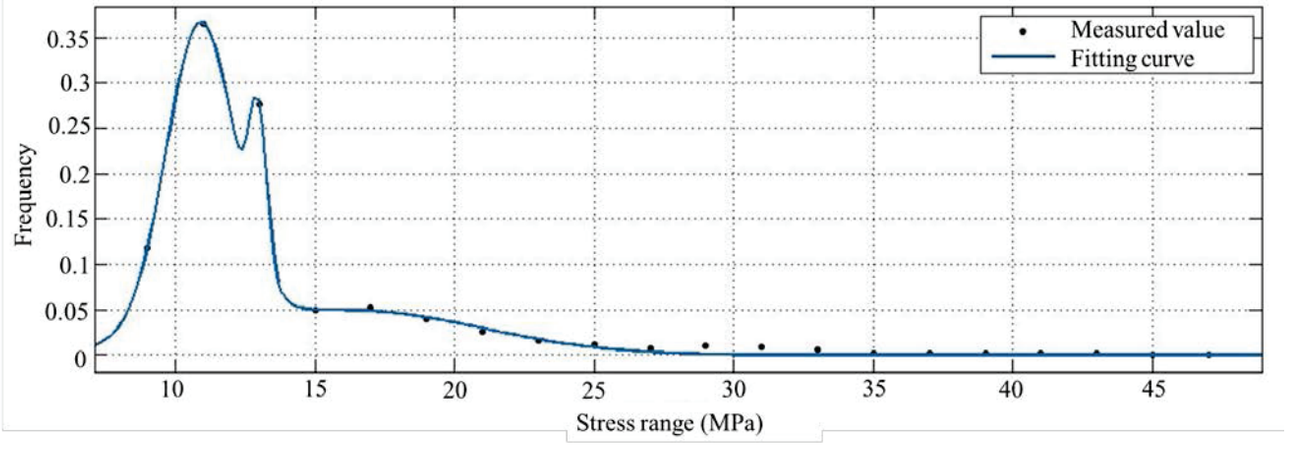


Figure 7. Fitting curve for the frequency of measured stress spectrum

$$f_f(\sigma) = 0.1613\exp\left\{-\left[(\sigma-12.96)/0.4393\right]^2\right\} + 0.009794\exp\left\{-\left[(\sigma-11.17)/3.557\right]^2\right\} + 0.3334\exp\left\{-\left[(\sigma-10.89)/1.713\right]^2\right\} + 0.04838\exp\left\{-\left[(\sigma-16.46)/6.483\right]^2\right\} \quad (10)$$

where f_f is probability density function of the measured stress spectrum.

Considering the possible overloading in the actual operation of the bridge, the upper limit of the stress amplitude is taken as the upper cut-off frequency when the integral value of the frequency distribution function is 0.9. Therefore, the equivalent stress amplitude of the fatigue car model is modified as Equation (11):

$$\sigma_c = (\sigma_{\varepsilon-\mathrm{sd}} \cdot \mu) \cdot \left[\frac{\sigma_{0.9\mathrm{f-max}}}{(\sigma_{\mathrm{s\text{-}max}} \cdot \mu)}\right] \quad (11)$$

where σ_c is the corrected equivalent stress amplitude; $\sigma_{\varepsilon-\mathrm{sd}}$ is the equivalent stress amplitude which was calculated by fatigue load model; $\sigma_{0.9\mathrm{f-max}}$ is the maximum stress of the measured stress spectrum when the upper cut-off frequency equals to 90%. $\sigma_{\mathrm{s\text{-}max}}$ is the maximum stress amplitude of the measured stress spectrum; μ is the impact factor.

Through calculation, the corrected equivalent stress amplitude is calculated as:

$$\sigma_c = 4.88 \times \left(\frac{18.66}{12}\right) = 7.588 \quad \mathrm{MPa} \quad (12)$$

Similarly, the corresponding number of stress cycles also need to be zoomed on account of the relationship between actual traffic flow and simulation loading. The number of stress cycles corresponding to corrected equivalent stress amplitude was calculated as 637097 times. Thus, fatigue life of the case small box girder bridge was calculated as follow:

$$Y = \frac{21}{4.499 \times 10^{-6} \times 365} = 12787 \quad \mathrm{years} \quad (13)$$

The calculated fatigue life of the fatigue load model calculated by Equation (7) is close to the calculated fatigue life which is 13518 years based on the measured stress spectrum as Equation (4). And the result using fatigue load model reaches 94.6% of the fatigue life using the measured value. Furthermore, because it is smaller than the fatigue life calculated by measured stress spectrum, it is a safe result.

At the same time it can be seen that the parameter and variables are sensitive to load and structure factors. For instance, $\sigma_{0.9\mathrm{f-max}}$ and $\sigma_{\mathrm{s\text{-}max}}$ are easily affected by traffic volume, structure type of bridge, pavement roughness and some other factors. Taking these factors into account, every bridge should have its own scaling factor. This paper only gives the calculating example of the case small box girder bridge.

5 CONCLUSIONS

An assessment method that uses traffic information to evaluate fatigue life was proposed. And it was applied for a case small box girder bridge. Based on the results and analysis of the measured and calculated data, conclusions can be drawn as follows:

(1) The assessment method of fatigue life evaluation for concrete girder bridge was established. The method needs traffic information and correction factor.

(2) Compared with the equivalent damage that calculated by WIM data, fatigue damage calculated by fatigue load model has error due to round-off error, however, the error was small which did not affect the result of fatigue life calculation.

(3) Structure un-symmetry and existing structural damage will lead to bigger stress amplitude than that of ideal model, which needs a correction factor to scale the stress amplitude calculated by fatigue load model.

(4) Using the proposed method, the fatigue life calculated by using corrected stress spectrum show good agreement with fatigue life calculated by using measured stress spectrum.

(5) Because the features of each concrete girder bridges are different, the scaling factors using proposed method are not likely to be the same. The regularity of the factors still needs to be analyzed.

6 ACKNOWLEDGEMENTS

The authors gratefully acknowledge the financial support provided by Construction Technology Projects of Ministry of Transport (2013318223040), the Special Fund for Basic Scientific Research of Central Colleges of the P.R. China (310821153401, 310821161021), Project of Key Laboratory of Shaanxi Province (213021150235e), Construction Technology Projects of Ministry of Transport (2014318223030) and China Postdoctoral Science Foundation (2014M552394).

7 REFERENCES

AASHTO LRFD. 2010. *Bridge Design Specifications*. Fifth Edition.

Aggarwal, V. & Parameswaran, L. 2015. Effect of overweight trucks on fatigue damage of a bridge. Advances in Structural Engineering, Matsagar V (Ed), Vol. 3. Springer India: New Delhi, 2015; pp 2483-2491.

Akgül, F. & Frangopol, D. M. 2004. Lifetime performance analysis of existing prestressed concrete bridge superstructures. *Journal of Structural Engineering*. 2004; 130 (12): 1889-1903.

BS 5400-2. 2006. 2006. *Steel, Concrete and Composite Bridges-Part 2: Specification for Loads*.

BS EN 1993-1-9: 2005. 2005. *Eurocode 3: Design of Steel Structures-Part 1-9: Fatigue*. European Committee for Standardization, Brussels

Bu, Y. Z. et al. 2014. Study of Fatigue Load for Orthotropic Bridge Deck in Highway Steel Box Girders. *Highway* 10:22-29.

Darmawan, M. S. & Stewart, M. G. 2007. Spatial time-dependent reliability analysis of corroding pretensioned prestressed concrete bridge girders. *Structural Safety* 29(1): 16-31.

Feng, J. 2003. *Reinforced concrete bridge deck fatigue under truck wheel load.* Michigan: University of Wayne State.

JTG D64-2015. 2015. *Specifications for Design of Highway Steel Bridge.* Beijing: The People Transportation Publish House. (in Chinese)

Sun, X. Z. et al. 2014. Random Axle Frequency Value Spectrum Deduction of Steel Deck Based on WIM. *Highway Engineering* 39(6):297-301.

Sarveswaran, V. et al. 2000. Reliability assessment of deteriorating reinforced concrete beams. *Structures & Buildings* 152(1): 83-84.

Wang, C. S. et al. 2012. Fatigue Life and Service Safety Assessment for Existing Concrete Bridges. *China Journal of Highway & Transport* 25(6): 101-107.

Wang, T. L. et al. 2005. Truck Loading and Fatigue Damage Analysis for Girder Bridges Based on Weigh-in-Motion Data. *Journal of Bridge Engineering* 10(1): 12-20.

Zhou, Y. T. et al. 2010. Study of standard fatigue design load for steel highway bridges. *China Civil Engineering Journal* 43(11): 79-85.

Zong, Z. H. et al. 2013. Study of vehicle load models for Xinyi River Bridge based on WIM data. *Bridge Construction* 43(5): 29-36.

Maintenance, Safety, Risk, Management and Life-Cycle Performance of Bridges – Powers, Frangopol, Al-Mahaidi & Caprani (Eds)
© 2018 Taylor & Francis Group, London, ISBN 978-1-138-73045-8

Historical load effects on fatigue of metallic railway bridges

B. Imam
Department of Civil and Environmental Engineering, University of Surrey, Guildford, UK
P.A. Salter
Ramboll UK Ltd, Carlton House, Ringwood Road, Woodlands, Southampton, SO40 7HT, UK

ABSTRACT: This paper presents load models for quantifying the effect of historical rail traffic on the remaining fatigue life of riveted bridges in the UK. Three types of load models, based on realistic trains, accounting for differences in rail traffic composition, are developed and subsequently used for investigating their effect on the accumulation of fatigue damage in typical old metallic bridge structures. The overall findings show that the increase within train axle loads from 1900 to 2010 is the main attributor to the significant increase in fatigue damage caused from the modern trains compared to the residual fatigue damage from the historic trains. These findings are particularly relevant to the majority of existing metallic rail bridges on the rail network, which are known to have a span length less than 10 m. These findings show the importance of considering the effects of historical loading for more reliable fatigue assessment purposes, leading towards more efficient planning of bridge maintenance and renewal programmes.

1 INTRODUCTION

A vast number of the existing metallic bridges in the British railway network, as well as many parts of Europe and North America, are either wrought iron or early mild steel riveted bridges. According to the Sustainable Bridges European Demography, out of the 47,000 metallic railway bridges in Europe, approximately 12,000 of these are made of wrought-iron (Bell, 2007). About 30% of the metallic bridges are exceeding 100 years of age. These existing bridges can be considered as fatigue sensitive structures as they significantly precede any design methodology that is inclusive of fatigue damaging effects. Although fatigue has been studied for over 100 years, the explicit inclusion of fatigue effects within the performance of bridges has only occurred since the 1970s in the UK (BS5400, 1980). During the last few decades, there have been significant amounts of research carried out on understanding and quantifying the fatigue behaviour of riveted bridges (Akesson, 1994; Al-Emrani, 2005; Al-Emrani and Kliger, 2003; Imam, 2006; Imam *et al*., 2008; 2012; Righiniotis *et al*., 2008). These investigations provided valuable insight by identifying, both experimentally as well as numerically, the factors that affect their fatigue performance and the modes of initiation and propagation of fatigue damage in this type of bridges.

A fundamental part of keeping the existing railway network operating without having to replace existing structures, unless absolutely necessary, is to be able to accurately calculate their performance. In the case of metallic bridge structures, fatigue is one of the critical elements to the performance of the structure, especially as the only live loading experienced by these is train loading which, inherently by its nature, is one of the most fatigue damaging types of loading process. However, unlike other fatigue damaging live loading, for example wind loading or highway loading, rail loading can be accurately predicted and modelled, as it is a controlled process. The axle loads are known for all train types on the network and an estimation of the frequency of trains over a particular structure is possible; therefore, a reasonably accurate method can be used to gauge the fatigue damage within the bridge member being considered.

One of the key steps during fatigue analysis of bridge structures is the prediction of load effects; it is well known that fatigue damage is highly sensitive to the stress range estimates. Accurate estimation of the remaining fatigue life of old metallic bridges, considering a safe life approach, is highly dependent on the accurate prediction of the past, current and future damage accumulation. This is, in turn, reliant on accurate estimation of the load effects caused by railway traffic in each of these periods. The codes of practice for fatigue design and assessment often provide good information regarding modern (current-day) train loading and traffic. However, they lack information and guidance about historical (past) rail

traffic which is essential for quantifying the fraction of fatigue damage that has already accumulated in existing bridges. There is limited literature that considers the variation between historic (1900s) and modern train loading trends and the effects this has upon these old metallic bridge structures.

This paper concentrates on the fatigue effects due to these variations in train loading upon riveted plate girder bridges with the aim of understanding the differing effects of historic to modern train loading. The aim of this study is to identify where the majority of the fatigue damage originates in old metallic bridges to allow a greater accuracy of fatigue analysis and therefore enable more accurate prediction of their remaining fatigue life. To this end, examples of historical train load models are reviewed first and a novel load model that captures variations in rail traffic composition from passenger-dominated to freight-dominated is developed. The load model, which is based on realistic trains, is used on a number of typical case-study bridge structural models to investigate the effects of historical loading on the fatigue damage of old metallic bridges and identify other parameters that affect fatigue behaviour.

2 HISTORICAL RAIL TRAFFIC MODELS

For historic railway bridges that have not been designed for fatigue, to assume that they have been subjected to modern train loading since their initial construction, circa 1900, is an extremely conservative method to be using, considering how sensitive fatigue damage is to small variations within the load trends. On the other hand, neglecting completely the effects of historical rail traffic on their fatigue behaviour is likely to overestimate their remaining fatigue life. This demonstrates that there is a genuine requirement to provide a standardised historical train load model for the purposes of more reliable fatigue assessment.

A detailed history of the train locomotive development and the significant changes of the freight wagons and passenger coaches over time are presented by Hayward (2010; 2013). The 1960s saw the introduction of fuel tanker bogie wagons weighing 100 tons loaded. These were followed by 100-ton mineral tipper wagons and coal hopper bogie wagons. Presently, modern freight trains typically induce 25-ton repetitive axle loads which have considerably increased outside the bounds of the historical design envelope, potentially having serious implications on the fatigue performance of the existing bridges in the rail network.

A practical way of considering the cumulative effect of historical loading on bridge structures has been suggested by Akesson (1994). According to his method, the amount of damage that historical trains have caused to date can be estimated by transforming the freight tonnage amount per year into a number of equivalent freight train passages over the bridge. This approach provides a simplified conservative way of quantifying the fatigue damage based on a known statistical tonnage per year, without taking into account the variation in train layouts or axle spacings that have occurred during the lifetime of the bridge. However, in many cases, axle weights and spacings, rather than train frequencies, can be the governing factors that control the remaining fatigue life of bridges.

A past traffic load model is suggested by the International Union of Railways (UIC, 1988). The model is divided into six different time periods and each period is represented by a number of representative trains for passenger and freight traffic, including their daily frequency. This load model has been used for the fatigue assessment of a real case study metallic railway bridge in Italy where it was shown that the fatigue damage produced by the historical trains is not insignificant (Pipinato *et al*., 2012).

One of the few load models that have been developed in the past to capture historical rail traffic and its effect on the fatigue damage of old metallic bridges is the one proposed by Imam and Righiniotis (2010). The basis of this model, which has been developed in collaboration with Network Rail based on realistic train configurations, was taken from BS5400: Part 10 (BS5400, 1980) which includes the modern train load models. BS5400 defines three variations of fatigue loading, light, medium and heavy which correlate to passenger-only lines, mixed passenger and freight lines and dedicated freight lines, respectively, and provides details about the types and frequencies of the trains to be used in each model. The load model developed by Imam and Righiniotis (2010) is divided into three distinct periods between 1900 and 1970 and considers the medium traffic variation only. It has been developed from the number of trains per year of the medium traffic variation suggested in BS5400. As opposed to the model developed by Akesson (1994), this historical load model not only takes into account changes in train frequencies over time but it also captures changes in axle loads as well as axle spacings.

In this paper, this model is further extended allowing it to be used for passenger-only and freight dedicated lines corresponding to light and heavy fatigue loading conditions according to BS5400. For example, a bridge which is located on a freight route that has been used to transport heavy freight such us iron ore or coal is likely to have experienced heavy traffic type; on the other hand, a bridge which is located in the vicinity of a city centre is more likely to have experienced passenger traffic only.

There is a distinct difference between the haulage capacity of modern and historical freight trains. For example, the freight train defined in the load model

developed by Imam and Righiniotis (2010) for the period 1900-1920 has a capacity of 570 tonnes whereas the modern heavy freight train (No 7) has a capacity of 1,120 tonnes. Due to this difference in tonnage the formation of the heavy historical train load model has been based on the tonnage per train rather than the frequency of trains per year. The modern total tonnage has been divided by the haulage capacity of the historic freight train to calculate the frequency of historic freight trains required to haul the tonnage annually. The tonnage hauled per year for each historic period has been proportionally adjusted against the modern tonnage provided in BS5400 using historic freight data (Coucher *et al*., 2008; IMechE, 2009; Leach, 2002; Whiteing, 2003). The heavy historical train load model is presented in Figure 1.

The light historic train load model, unlike the heavy model, is not created from the annual tonnage of trains as the weight of passenger coaches have not changed significantly through the periods (Hayward, 2010; 2013). The light model is created by considering the amount of coaches required per year to move the volume of passengers. This is proportionally adjusted from the known historic passenger volume data (Coucher *et al*., 2008) against BS5400 (1980) to back calculate the annual train frequency required for each period. The historic passenger volume data that has been used to create the adjusted weighting for each historical period has been obtained from (Coucher *et al*., 2008). The light historical train load model is presented in Figure 2. The layout of all the historical trains shown in Figures 1 and 2 can be found in Imam (2006) and Imam *et al*. (2006). The layouts of the modern trains for the period 1970- can be found in BS5400 (1980). All the load models developed in this paper are based on realistic train configurations.

Period	Traffic Type	Locomotive Type	Wagon Axle Weight	No of Wagons	Train speed	Annual Frequency
1900-1920	F	0-6-0 Superheater Freight Engine	2×8 t	30	30mph	48,421
1920-1940	F	0-6-0 Superheater Freight Engine	2×10 t	40	40mph	45,505
1940-1970	F	2-8-0 Freight Engine	2×10 t	40	40mph	48,825
1970-	F	Mixed freight (BS5400 no 9)	2×7, 4×20, 6×20 t	12	120 km/h	4,821
	F	Heavy Freight Train (BS5400 no 7)	4×25 t	10	120 km/h	7,232
	F	Heavy Freight Train (BS5400 no 8)	2×25 t	20	120 km/h	15,845

Figure 1. Heavy traffic historical and modern train load model.

3 FATIGUE ASSESSMENT

Historically, within the rail network, there were a few typical bridge designs that were commonly used for their construction. In general, these can be categorised by the span length of the bridge. Short span bridges consist mainly of either masonry arches or plate girder bridges. For medium span bridges, truss girders or plate girder arches were preferred, with plate girder arches and large box section bridges being preferred for longer spans (Hayward, 2010; 2013). The majority of the bridges on the rail network have a span around or less than 10 m (Hayward, 2010; 2013; Imam, 2006) and are of plate girder construction. For example, about 45% of the metallic bridges in Europe have a span less than 10 m (Bell, 2007). Of the metallic bridge types used, the truss girder bridges and box section bridges are less fatigue sensitive in terms of their main truss members due to their long span lengths; the dead load dominates a high percentage of the available capacity and therefore reduces the fluctuating live load stress range on those elements. On the other hand, plate girder bridges and stringers and cross-girders of truss bridges work in bending and therefore sections see high fluctuating tensile stresses as the live load dominates the available capacity due to the shorter span length. As a consequence, short span plate girder bridges can be considered as the most fatigue sensitive bridge type on the railway network.

Period	Traffic Type	Locomotive Type	Wagon Axle Weight	No of Wagons	Train speed	Annual Frequency
1900-1920	P	4-4-0 Passenger Engine	4×8 t	30	50 mph	41,163
	LS	0-4-4 Tank Engine	4×8 t	8	30 mph	82,326
1920-1940	P	4-6-0 Superheated Mixed Traffic Engine	4×9 t	12	60 mph	58,888
	LS	0-4-4 Tank Engine	4×8 t	4	30 mph	44,165
1940-1970	P	4-6-0 Superheated Mixed Traffic Engine	4×9 t	15	70 mph	44,217
	LS	0-4-4 Tank Engine	4×8 t	6	40 mph	41,454
1970-	F	Steel Train (BS5400 no 1)	6×18.5 t	15	80 km/h	752
	P	Electric multiple unit (BS5400 no 2)	4×10 t	8	145 km/h	14,516
	LS	Southern region suburban (BS5400 no 3)	9.5, 11 & 13 t	12	145 km/h	23,546
	LS	Southern region suburban (BS5400 no 4)	9.5, 11 & 13 t	6	145 km/h	47,093
	P	Diesel Hauled Passenger Train (no 5)	4×10 t	12	160 km/h	4,500
	P	Electric Hauled Passenger Train (no 6)	4×10 t	12	160 km/h	2,360

Figure 2. Light traffic historical and modern train load model

For the purposes of comparing the effect of varying historical loading on fatigue, single span riveted plate girder bridges are considered in this paper. These comprise of two girders with equal load share supporting a single track via a simple ballasted troughing deck. For the analysis of the main girders a standard bridge set consisting of 17 bridges has been created to represent riveted plate girder bridges with spans ranging from 4 m to 20 m in one metre increments. These bridges are based on a standard cross section layout; a simply supported bridge with a trough deck supporting ballast and single track, connected to two plate girders as shown in Figure 3.

The parameters that are being investigated in this paper in terms of their influence on the fatigue behaviour of these bridges are:

- The axle spacing of the trains and the bridge span length.
- The differences between the modern and historical trains within the train load models.

- The variance created between the three train load models, light, medium and heavy.
- The comparison between wrought iron and mild steel riveted bridges.
- The year of construction of the bridge

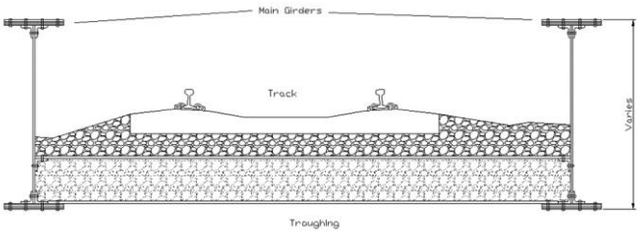


Figure 3. Standard bridge set cross-section at midspan.

To ensure the analyses are representative, each bridge has been designed from the working stress limit of 77.5 MPa for wrought iron and 100 MPa for mild steel, which were typical values employed circa 1900s for design (Fitzmaurice, 1895). Live loading is based on the equivalent uniform distributed load (EUDL) curve design model defined in (Hayward, 2010; 2013). The bridges have been designed so that the combination of live load stress and total dead load stress sums to the working stress limit (Fitzmaurice, 1895; Hayward, 2010; 2013). This method may provide higher utilisation within the main girders than existing bridges. However, the aim of the analyses is to find correlation within the results from the bridges rather than explicitly quantifying the fatigue failure point of these bridges.

The design process is based on only varying the strength of the main girders between each bridge. As the span length increases the bending moment due to the total dead and live load will also increase. To ensure that the combined maximum total dead load and live stress on the main girder at midspan equals to the working stress limit for each span length, the strength of the girder must increase. Therefore, an iterative process has been used to calculate the strength of the girder. The combined live and total dead load stress is equated to the working stress limit by iterating through standard riveted girder section sizes (Fitzmaurice, 1895).

The DAFs for each train and for each span are taken into account within the assessment procedure by multiplying the DAFs obtained from (Network Rail, 2006) with the static stresses obtained from the bridge analysis. An overview of the effect of dynamic amplification on fatigue damage of metallic bridges and the range of values expected in such bridges can be found in Imam *et al*. (2006).

The standard bridge set is assessed for fatigue damage occurring within the bottom flange detail of the main girder at the location of the rivet holes. This detail is classified as Class D according to BS5400: Part 10 (BS5400, 1980). The analysis of the bridge set is carried out by developing a structural model of each bridge within the finite element program, STRAP 2010. These models comprise of line (beam) elements to represent the bridge members with each element having a representative section and material property. Linear static analysis was carried out to extract the stress histories resulting from the passages of the trains over each bridge span. An influence table for the bending moment at the midspan due to a unit load traversing across the bridge representing one train axle has been obtained from the analysis; these have then been combined through the superposition rule to produce the train stress histories. These are then converted into stress range histograms through rainflow counting and are used for the calculation of fatigue damage. The fatigue damage is estimated through the Miner Rule (Miner, 1945), which forms the basis of a major part of fatigue assessment codes worldwide, including the UK fatigue assessment code for metallic railway bridges (Network Rail, 2006) which is used in this paper.

For the purposes of the fatigue damage calculations, the fatigue limit has not be considered and all stress ranges, even below the fatigue limit, have been assumed to contribute to fatigue damage accumulation, which is a conservative assumption.

4 RESULTS AND DISCUSSION

4.1 *Effect of train axle spacing*

It can be expected that there is a fatigue damage relationship between the span length of the bridge and the axle spacing of the train. Key trends can be identified within the layout of the train axles and the critical effects these trends have upon fatigue damage. The locomotive engines make up only a small percentage of the total axles within an entire train. The engine and tender axles are typically between 1.5 m and 3 m spacing and generally are the heaviest loaded axles. Due to this close axle spacing the engine loading often acts as a uniformly distributed load rather than individual axles. For this reason, the engine locomotive produces only one stress cycle per train journey, which predominantly is the single largest stress range within the load spectrum for that train, as can be seen in Figure 4.

For both the historical and modern trains within the train load model, the passenger train represents a key identifiable axle trend. The passenger coach is formed of four axles, two axle pairs at either end of the coach. The axles within the pairs are spaced 1.5 m to 3 m apart and between 1 m and 3 m from the end couplers of the coach. The central spacing between the axle pairs is between 11.5 m and 13 m. This creates four axles evenly spaced between 1.5 m to 3 m then a significant gap of between 11.5 m and 13 m before the next set of four closely spaced axle. Similarly to the engine and tender trend, the axles of

the coaches are closely grouped together and do not cause large stress range amplitudes themselves. However, the increased spacing between the axle groups will cause large stress range amplitudes caused by the full loading and complete unloading of the bridge.

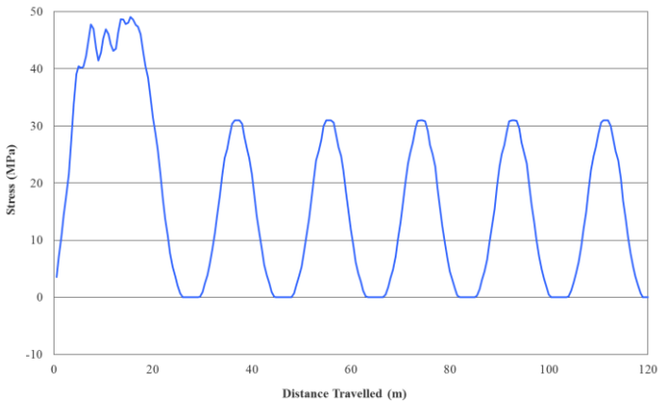


Figure 4. Stress history in main girder for passenger train 1900-1920.

Figure 4 shows the stress history obtained from the passage of the 1900-1920 passenger train over the 9 m span standard bridge and provides examples of the axle trends described above. The first stress cycle from 0 m to 30 m represents the engine and the front of the first coach travelling over the bridge. Each stress cycle of the evenly spaced equal amplitude stress cycles from 30 m to 160 m represents the grouping of the four coach axles. The four meters of zero stress between each coach cycle represents the difference between the central coach axle spacing and the span length which, in this case, is equal to four metres (13 minus 9).

In addition to the passenger coach axle trend, the effects of the freight train No 7 wagon can be added. This wagon represents the 100 tonne coal and mineral wagon used since the 1970s (Hayward, 2010; 2013). The axle spacing for these wagons falls within the bounds discussed above. The axle loads for these wagons are approximately double the axle loads of the passenger coaches, causing significantly greater fatigue damage than the equivalent coach.

The final key axle trend identified represents the historic freight wagons and the modern freight train No 8 wagons, which have short wagon length. The historic freight wagons consist of two axles spaced at 3 m with 2 m spacing between adjoining wagon axles. This trend extends to 5.5 m spacing between wagon axles and 3.5 m between adjoining wagon axles for the modern freight train No 8 wagons. The historic freight wagons produce the smallest amplitude stress fluctuations of all the trains and, for most bridges, can be treated as a uniformly distributed load for fatigue assessments. For longer span bridges over 17 m the modern freight wagon can also be considered as a uniformly distributed load for fatigue assessments. However, for spans under 10 m, the axle spacing to span length ratio becomes critical to the scale of the fatigue damage that the freight train No 8 wagons causes. Figure 5 shows the stress histories for the freight train No 8 wagon on three varying spans less than 10 m in length. The variance within the amplitude of the stress cycles between the span lengths is critical to the change in fatigue damage between the spans.

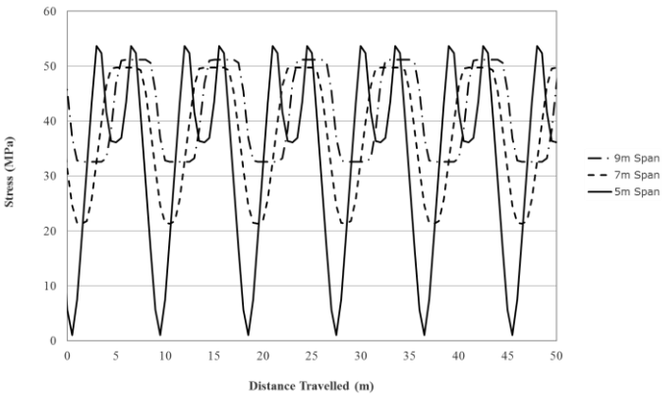


Figure 5. Stress histories of freight train No 8 wagons for different spans.

4.2 *Comparisons between modern and historic trains*

Comparison of the fatigue damage between the historic and modern train types has been carried out using the standard bridge set. Figure 6 shows the total fatigue damage caused from the historic trains against the modern trains within the medium traffic load model. The historic trains are representative of the period from 1900 to 1970 and account for all the fatigue damage within this period; the modern trains represent fatigue damage from 1970 onwards until the present. The results in Figure 6 and all subsequent figures have been normalised to the highest peak point in order to identify the trends and relative differences between the different types of loading rather than providing an explicit estimate of the fatigue damage.

The results in Figure 6 show that for bridges around 100 years old that have been subjected to medium traffic conditions, modern trains cause the majority of the fatigue damage for bridge spans ranging between 4 m and 14 m. In particular, fatigue damage in bridge spans under 9 m can be seen to be heavily dominated by modern trains which demonstrates the criticality of short span bridges being particularly fatigue sensitive to modern train loads (Hayward, 2010; 2013). For bridge spans greater than 14 m, historic trains can be seen to produce the highest proportion of the fatigue damage. For example, for a 9 m bridge, approximately 70% of the fatigue damage can be attributed to modern loading and the remaining 30% to historical trains. On the other hand, for a 16 m bridge, approximately 60% of

the damage is attributed to historical trains whereas the remaining 40% to modern rail traffic.

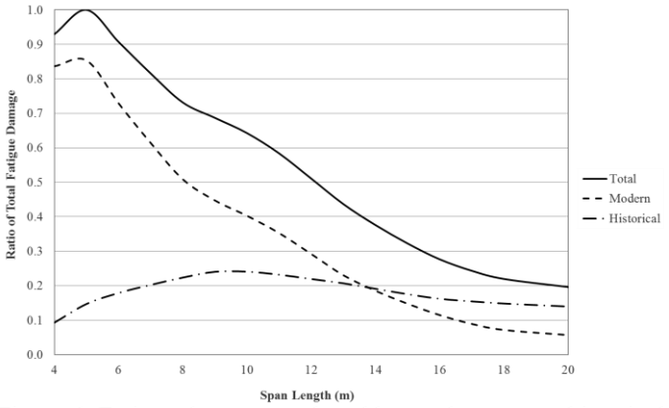


Figure 6. Fatigue damage produced by modern versus historical loading.

The variables that create this distinct difference in fatigue damage between modern and historic trains are:

- The length of service for each train type.
- The physical length of the trains i.e. the number of wagons/coaches.
- The engine locomotive axle loads.
- The wagon and coach axle loads.
- The annual frequency of the train types.
- The train speeds which affect the applied dynamic amplification factor.
- The type of axle grouping trains within each period (short axle spacing versus long axle spacing).

To understand which trains cause the most fatigue damage for particular span lengths, the critical variables have been removed to create a standardised train set for comparison. The standardised variables across this train set are:

- The train length; the train consists of the engine and five trailing units only.
- A period of one year for all trains has been used for the comparison.
- 10,000 trains per year for each train type has been assumed.
- The remaining variables have been left independent for each train type.

As can be seen in Figure 7, the standardised train results show that, for span lengths less than 10m, the modern trains BS5400 No 1 to 8 cause significantly greater fatigue damage than their historical counterparts. Between span lengths of 10 m and 18 m the modern trains, excluding the BS5400 No 7 freight train, cause relatively similar fatigue damage to the historic trains with both sets having a slow linear change between span lengths. BS5400 No 7 and 8 freight trains have the greatest axle load of 25 tonnes per axle for all the trailing unit types (BS5400, 1980). All other units range between eight and thirteen tonnes per axle. The damaging effect of these high axle loads can be seen within the results in Figure 7. The increased magnitude of axle load within the modern freight trains creates similarly increased stress ranges within the bridge spans of the same spacing magnitude. However, the relationship between stress range and fatigue damage is cubed or higher, therefore any increase in stress range is vastly magnified for the corresponding fatigue damage.

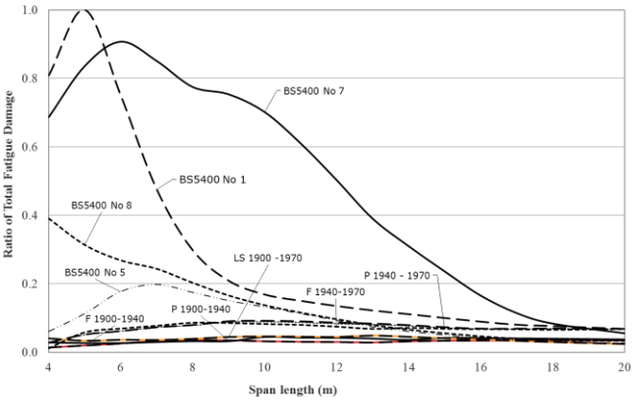


Figure 7. Individual train fatigue damage for the standardised train set.

4.3 *Light, medium and heavy historic load models*

The light and heavy train load models presented in Figures 1 and 2 have been developed based on the modern load models within BS5400: Part 10 (BS5400, 1980), which represent bridges that solely see either passenger trains or freight trains respectively. A bridge subjected to the light train load model could be representative of a bridge located just outside one of the main London terminus stations and would only ever see passenger trains. On the other hand, a bridge located outside a busy freight terminal, away from a major city, would only be subjected to the heavy freight train load model.

The difference between the light and the heavy traffic load models can be seen in Figure 8 which shows the fatigue damage for all three models (medium, light and heavy traffic). The light load model consists solely of large axle spacing trains. The significant increase in fatigue damage caused by the historic trains with respect to the damage caused by the modern trains, in comparison to the medium train load model is created due to the much higher frequency of the extremely damaging passenger locomotive engine. For example, for the 6 m span bridge the locomotive engine causes 33% of the total damage from the historic passenger train, whereas for the 18 m span bridge the percentage contribution increases to 82% of the total damage by the passenger train.

The results from the heavy train load model have a high correlation with the medium train load model, showing that the freight trains predominantly create the fatigue damage with the medium train load model.

It should be noted that the load models suggested in this paper are based on representative UK rail traffic. However, comparison of the train suggest here with other historical load models, such as the one suggested by UIC (1988), displays similarities in terms of the evolution of the axle loads over time and the configuration of the trains. The historical traffic experienced by bridges located in different parts of the railway network is likely to be different; for example, an old railway bridge that is located close to a coal/iron mine is likely to have experienced heavier historical loads due to freight trains as compared to a typical bridge located on a main passenger route, where traffic may be more passenger-dominated. The proposed load models with the light and heavy variations can be representative of upper and lower bounds of fatigue damage originating from historical trains. Obviously, in the availability of detailed historical traffic data for a specific region, further detailed traffic load models can be developed.

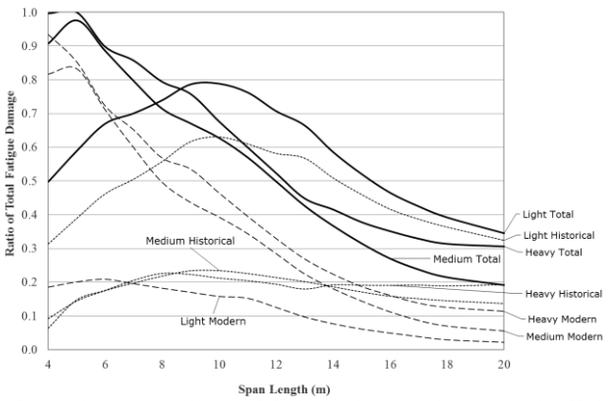


Figure 8. Comparison of fatigue damage between the light, medium and heavy traffic load models.

4.4 *Wrought-iron vs mild steel riveted bridges*

It is known that during the mid-19th century the Board of Trade imposed design strength limits upon the use of wrought iron of 77.5 MPa within tension members and additionally a limit to mild steel in tension of 100 MPa two decades later (Fitzmaurice, 1895; Hayward, 2010; 2013). The implication from these design limits is the additional strength of mild steel, which creates a lighter design than the equivalent wrought iron bridges, therefore having a higher maximum live load limit and increased equivalent amplitude of stress cycles due to trains travelling across the structure. This increased stress range would, under the same fatigue detail, produce significantly more fatigue damage for the steel bridges than the wrought iron counterparts.

However, the fatigue detail categories vary for riveted plate girders in steel compared to wrought iron. BS5400 Class D (BS5400, 1980) is suggested for the former whereas a separate classification exists for wrought iron girders (Network Rail, 2006).

Another standard bridge set has been created so that both steel and wrought iron bridges are represented; the steel and wrought iron bridge sets have been designed to the same working stress method (Fitzmaurice, 1895; Hayward, 2010; 2013). From comparing the fatigue damage results for both bridge material types, it can be seen in Figure 9 that the reduction in stress cycle amplitude between the steel and wrought iron bridges is more significant than the increased fatigue category sensitivity of the wrought iron. The early mild steel riveted plate girder bridges are between 15% to 30% more fatigue sensitive across the span range than the equivalent wrought iron riveted plate girder bridges.

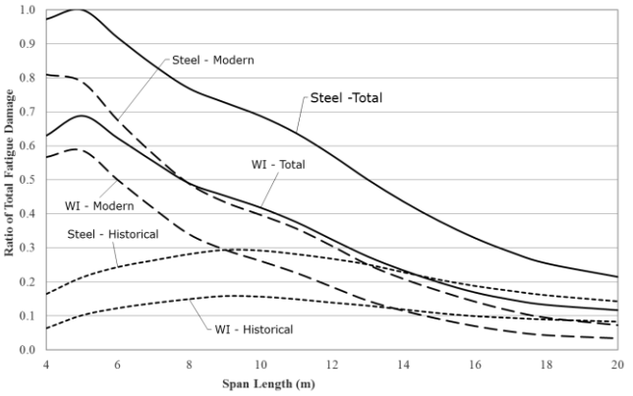


Figure 9. Comparison of fatigue damage between steel and wrought iron bridges.

4.5 *Comparison of bridges between 1900 and 1940*

A comparison of the fatigue damage for the standard bridge sets constructed between 1900 to 1940 is shown in Figure 10. For comparison purposes, the fatigue damage produced solely by the modern (1970-) trains is also presented. The historic load models for each bridge era have been created by excluding any fatigue damage from trains representing earlier periods. It can be seen from that figure that as the standard bridge sets become younger, the modern trains increasingly dominate the proportion of fatigue damage caused. For any riveted plate girder bridge constructed in wrought iron or steel up to 1940, modern train loads based on the medium train load model dominate the fatigue performance of short and medium span bridges.

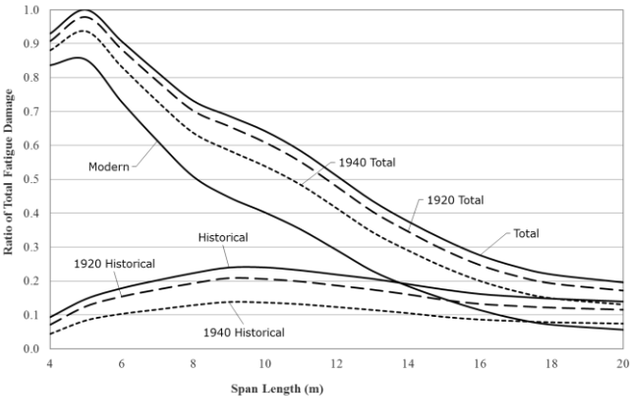


Figure 10. Comparison of bridges constructed between 1900-1940.

5 CONCLUSIONS

This paper focused on fatigue effects due to the variations in train loading over time upon riveted plate girder bridges, with the aim of understanding the differing fatigue effects of historic to modern train loading. Three historical load model variations, accounting for passenger-dominated, freight-dominated and combined railway lines have been proposed. These were then applied to a set of typical riveted plate girder bridges to investigate trends on fatigue loading. The parameters that have been investigated were the type of the trains passing over the bridge, the bridge span, the material of the bridge (mild steel vs. wrought iron) and the date of construction of the bridge.

The results show that, for the majority of existing riveted plate girder bridges, which have been constructed circa 1900, the modern trains from 1970 to 2010 cause the majority of the fatigue damage for bridge spans less than 14 m in length, as compared to the historical trains from 1900 to 1970. The fundamental effect of increasing axle loads over time was observed to override the other identified effects of variation in train frequency, train length and loading lifetime. The results presented in this paper can be easily used during fatigue assessment in identifying and quantifying the significance of historic loading on fatigue damage accumulation for different bridge spans. Obviously, the configuration as well as the intensity of historical rail traffic will can vary in different railway lines (routes) where some routes can be more freight-dominated, whereas other routes can be more passenger-dominated. Nevertheless, the results presented in this paper show that, in some cases, the effect of historical traffic may not be insignificant.

Comparison between wrought iron and mild steel main girders has shown that due to the increased strength found within early mild steel compared to wrought iron, higher fatigue damage is accumulated within the steel girders compared to an equivalent wrought iron detail. This increased fatigue sensitivity of steel riveted plated girders varies from 20% for the short span bridges to 10% for the longer span riveted bridges. Furthermore, by investigating the influence of the year of construction of the bridge it was found that the younger a riveted plate girder bridge is, the more dominant the effect of the modern trains becomes on the overall fatigue damage caused.

REFERENCES

Akesson, B. 1994. *Fatigue life of riveted railway bridges*, Publ. S94:6. PhD Thesis, Chalmers University of Technology, Sweden.

Al-Emrani, M. & Kliger, R. 2003. FE analysis of stringer-to-floor-beam connections in riveted railway bridges. *Journal of Constructional Steel Research* **59(7)**: 803-818.

Al-Emrani, M. 2005. Fatigue performance of stringer-to-floor-beam connections in riveted railway bridges. *Journal of Bridge Engineering ASCE* **10(2)**:179-185.

Bell, B. 2007. European Railway Bridge Demographics – Deliverable D2.1. *Sustainable Bridges Project: Assessment for Future traffic Demands and Longer Lives*.

BS 5400, 1980. *Steel, concrete and composite bridges: Part 10: Code of practice for fatigue*. BSI, London, UK.

Coucher, I., Austin, C., Leunig, T. *et al.* 2008. *The Billion Passenger Railway Lessons From the Past: Prospects for the Future*, ATOC, London, UK.

Fitzmaurice, M. 1895. *Plate-Girder Railway Bridges*. E. & F. N. SPON, London, UK.

Hayward, A.C.G. 2010. Trains loads on Bridges 1825 to 2010. *International Journal for the History of the Engineering & Technology* **81(2)**:159-191.

Hayward, A.C.G. 2013. Train loading on bridges since Stephenson's Rocket. *Proceedings of the Institution of Civil Engineers - Bridge Engineering* **167(4)**: 326-337

Imam, B. 2006. *Fatigue analysis of riveted railway bridges*. PhD Thesis. University of Surrey, UK.

Imam, B., Righiniotis, T.D., Chryssanthopoulos, M.K., Bell, B. 2006. Analytical fatigue assessment of a typical riveted UK rail bridge. *Proceedings of the Institution of Civil Engineers - Bridge Engineering* **159(3)**: 105-116.

Imam, B.M., Righiniotis, T.D., Chryssanthopoulos, M.K. 2008. Probabilistic fatigue evaluation of riveted railway bridges. *Journal of Bridge Engineering ASCE* **13(3)**:237-244.

Imam, B.M., Righiniotis, T.D. 2010. Fatigue evaluation of riveted railway bridges through global and local analysis. *Journal of Constructional Steel Research* **66(11)**:1411-1421.

Imam, B.M., Chryssanthopoulos, M.K., Frangopol, D.M. 2012. Fatigue system reliability analysis of riveted railway bridge connections. Structure and Infrastructure Engineering **8(10)**:967-984.

IMechE. 2009. *Rail Freight Getting on the Right Track*. Institution of Mechanical Engineers, London, UK.

Leach, G. 2002. *Evolution not revolution – the Future of the Railways*. The Institute of Directors, London, UK.

Network Rail. 2006. *NR/GN/CIV/025: The Structural Assessment of Underbridges*. Issue 3, Network Rail.

Righiniotis, T.D., Imam, B.M., Chryssanthopoulos, M.K. 2008. Fatigue analysis of riveted railway bridge connections using the theory of critical distances. Engineering Structures **30(10)**:2707-2715.

Whiteing, A. 2003. *Multimodal Freight Transport in Great Britain*. University of Huddersfield in association with The Institute of Logistics and Transport, UK.

Maintenance, Safety, Risk, Management and Life-Cycle Performance of Bridges – Powers, Frangopol, Al-Mahaidi & Caprani (Eds)
© 2018 Taylor & Francis Group, London, ISBN 978-1-138-73045-8

Multi-Objective Optimum Service Life Bridge Management Based on Fatigue Damage Detection

Sunyong Kim
Wonkwang University, Iksan, South Korea
Dan M. Frangopol
Lehigh University, Bethlehem, PA, USA

ABSTRACT: This paper deals with the inspection planning for service life management of deteriorating bridges based on efficient multi-objective optimization. The damage detection based-objectives presented in this paper are (a) minimizing the expected fatigue damage detection delay, (b) minimizing the probability of fatigue failure, (c) maximizing the expected extended service life, and (d) minimizing the expected total life-cycle cost. The effect of fatigue damage detection on the probability of failure, service life extension, and life-cycle cost is considered. Using the objective reduction approach, the effects of adding or removing particular objectives among these four on the Pareto front are investigated, and the redundant objectives, which have no effect on the Pareto front, are identified. By removing the redundant objectives, the efficiency in decision making and visualization of the multi-objective optimization for inspection planning are improved.

1 INTRODUCTION

Damage detection and identification are the first phase to ensure the structural safety and extend the service life of deteriorating bridges (NCHRP 2006). During the last few decades, the techniques associated with damage detection and identification have been extensively developed (Frangopol 2011, Frangopol et al. 2011, Frangopol & Soliman 2016). However, due to the uncertainties associated with the damage initiation and propagation prediction, and damage detection, damage may not be detected on time (Mohanty et al. 2009, Kwon & Frangopol 2011). Therefore, inspection plans have to be applied at uniform or non-uniform time intervals (Frangopol et al 1997). Inspection plans can be established through single or multi-objective optimization (Kabir et al. 2014). It has been known that the increase of the number of objectives to be optimized simultaneously can lead to more rational and well-balanced solutions (Deb 2001, Arora 2012). However, more effort is required for computation to find the Pareto solutions, visualization of these solutions, and decision making to select the well balanced solution (Deb 2001, Brockhoff & Zitzler 2007, Saxena et al. 2013, Jaimes et al. 2014).

Recently, the optimum inspection planning based on four objectives was investigated for deteriorating reinforced concrete structures by Kim & Frangopol (2017a). Based on this study, the five objectives for the optimum structural health monitoring planning were developed, and applied to a fatigue-sensitive ship hull structure in Kim and Frangopol (2017b). However, the multi-objective optimum inspection planning for a steel bridge under fatigue needs to be investigated considering the correlation among the objectives based on damage detection.

This paper deals with the inspection planning for service life bridge management based on fatigue damage detection. The objectives considered are (a) minimizing the fatigue damage detection delay, (b) minimizing the probability of fatigue failure, (c) maximizing the extended service life, and (d) minimizing the expected total life-cycle cost. They are formulated considering the effect of damage detection on probability of failure, service life extension, and life-cycle cost. Using the objective reduction approach, the effect of adding or removing particular objectives among these four on the Pareto front are investigated, and the redundant objectives, which have no effect on the Pareto front, are identified. By removing the redundant objectives, the efficiency in decision making and visualization of the multi-objective optimization for NDT planning are improved.

2 DAMAGE DETECTION-BASED OBJECTIVES

Service life management of deteriorating structures should be based on multi-objective optimization. The formulation of the objectives for fatigue management intervention considers the damage initiation and propagation prediction, probability of damage

detection, service life prediction, and cost estimation (Kim et al 2013).

2.1 *Fatigue damage detection delay*

When the time t_{oc} for damage to occur is deterministic, and the damage is detected at time t_{de}, the damage detection delay t_{dl} is $t_{de} - t_{oc}$. However, due to the uncertainties associated with damage occurrence/propagation and the inspection methods, damage detection delay cannot be estimated deterministically. The expected fatigue damage detection delay $E(t_{dl})$ is expressed as (Kim & Frangopol 2011a)

$$E\left(t_{dl}\right) = \sum_{i=1}^{N_{in}} \left[\int_{t_{in,i-1}}^{t_{in}} t_{dl,i} \cdot f_T\left(t\right) dt \right] \quad (1)$$

where N_{in} = number of inspections; $t_{in,i}$ = ith inspection time; $t_{dl,i}$ = damage detection delay when the damage occurs between $t_{in,i-1}$ and $t_{in,i}$; and $f_T(t)$ = probability density function (PDF) of the damage occurrence time. The optimum inspection planning can be based on the minimization of the expected damage detection delay. Improvement of inspection quality and increase of number of inspections can result in reduction of the expected damage detection delay (Kim & Frangopol 2011a).

2.2 *Probability of fatigue failure based on damage detection*

Fatigue cracks have to be detected and repaired before reaching critical sizes to reduce the probability of failure and extend the service life. The time-based safety margin can be expressed as the difference between the time associated with the occurrence of the critical crack size t_{cr} and damage detection time t_{de} (Kim & Frangopol 2011b). By treating t_{cr} and t_{de} as random variables, the probability of fatigue failure P_{fail} is defined as

$$P_{fail} = P\left(t_{cr} < t_{de}\right) \quad (2)$$

The optimum inspection planning can be based on minimizing the probability of fatigue failure. Increasing the number of inspections and/or improving inspection quality results in reduction of the probability of failure (Kim & Frangopol 2011b).

2.3 *Extended service life*

The service life can be extended through the timely and appropriate maintenance actions, which have to be applied after damage detection and identification. The formulation of the extended service life is based on the decision tree, where the relation among damage detection, maintenance and service life extension is addressed. The extended service life $t_{sv,ex}$ is expressed as (Kim et al. 2013)

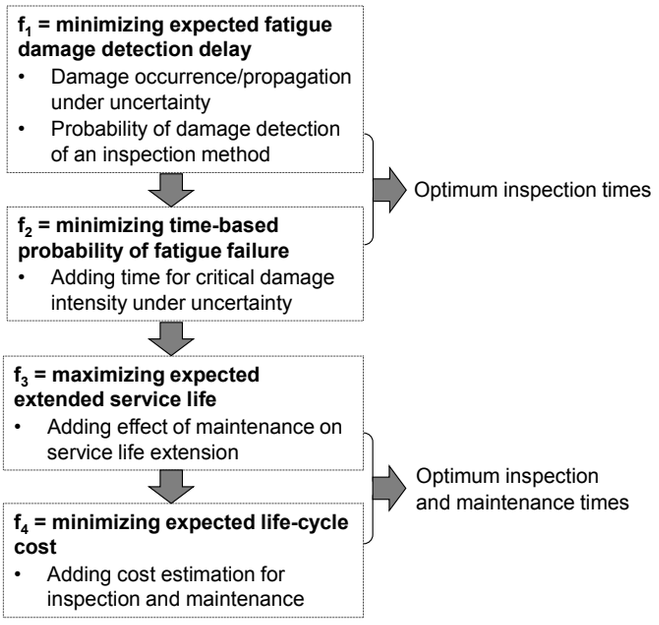


Figure 1. Required estimation for the formulation of objectives f_1, f_2, f_3 and f_4.

$$t_{sv,ex} = t_{sv,o} \quad \text{for } t_{in} > t_{sv,o} \quad (3a)$$

$$t_{sv,ex} = \left(1 - P_{in}\right) \cdot t_{sv,o} + P_{in} \cdot \left(t_{sv,o} + t_{ex}\right) \quad \text{for } t_{in} > t_{sv,o} \quad (3b)$$

where $t_{sv,o}$ = initial service life; P_{in} = probability of damage detection; and t_{ex} = extended service life. The service life extension t_{ex} in Eq. (3b) depends on the type of maintenance. The maintenance type is determined based on the degree of damage (Kim et al 2013). It should be noted that late inspection (i.e. $t_{in} > t_{sv,o}$) or no damage detection (i.e. $1 - P_{in}$) results in no service life extension (i.e. $t_{ex} = 0$) as indicated in Eq. (3).

2.4 *Expected life-cycle cost*

Damage detection and maintenance to reduce the probability of failure and extend the service life are generally cost related. In order to consider direct and indirect costs of deteriorating structures, and establish the optimum inspection and maintenance plans, life-cycle cost analysis has to be applied (Frangopol et al 1997). The expected life-cycle cost C_{lc} during the predefined service life of a deteriorating structure is expressed as (Frangopol et al. 1997, Wallbank et al. 1999, NCHRP 2003)

$$C_{lc} = C_{ma} + P_{fail} \cdot C_{fa} \quad (4)$$

where C_{ma} is the cost for inspection and maintenance, and C_{fa} is the monetary loss induced by the structural failure.

3 ESTIMATION OF RELATION AMONG OBJECTIVES

In this paper, the optimum service life management is based on four objectives of (a) f_1 = minimizing the fatigue damage detection delay (see Eq. (1)), (b) f_2 = minimizing the probability of fatigue failure (see Eq. (2)), (c) f_3 = maximizing the extended service life (see Eq. (3)), and (d) f_4 = minimizing the expected total life-cycle cost (see Eq. (4)). As shown in Figure 1, the formulations of the objectives f_1, f_2, f_3 and f_4 includes estimating the probabilistic damage occurrence and propagation, and probability of damage detection of an inspection method. Therefore, the objectives may be correlated.

In order to quantify the linear relationship between the objectives f_i and f_j, the Pearson's coefficient of correlation ρ (f_i, f_j) is computed as (Ang & Tang 2007)

$$\rho_p\left(f_i, f_j\right) = \frac{E\left[\left\{f_i(\mathbf{x}) - E\left[f_i(\mathbf{x})\right]\right\} \cdot \left\{f_j(\mathbf{x}) - E\left[f_j(\mathbf{x})\right]\right\}\right]}{\sigma_i \cdot \sigma_j} \quad (5)$$

where $\mathbf{x}$ is the vector of the design variables, and σ_i and σ_j are the standard deviations of the objective values of f_i and f_j in the design space, respectively. The monotone relation between the objectives f_i and f_j is represented by the Spearman's coefficient correlation as (Myers et al. 2003)

$$\rho_s\left(f_i, f_j\right) = 1 - \frac{6\sum_{i=1}^{n} d_i^2}{n\left(n^2 - 1\right)} \quad (6)$$

where n = number of values of objective f_i or f_j in the design space; and d_i = difference between the ranks of objective values of f_i and f_j.

Furthermore, the relation among objectives can be represented by using the dominance relation-based objective reduction approach. If and only if $\forall f_a \in \Omega_R : f_a(\mathbf{x_1}) \leq f_a(\mathbf{x_2})$, a solution $\mathbf{x_1}$ dominates another solution $\mathbf{x_2}$ for $\Omega_R \subseteq \Omega_O$, where Ω_R and Ω_O are the reduced and original objective sets, respectively. $\forall f_a \in \Omega_R$ denotes any objective f_a of Ω_R. The purpose of this approach is to investigate the dominance relation among the objective values, and the change of the Pareto front by removing a particular objective. Finally, the redundant and essential objectives are identified. The dominance relation is represented by the normalized degree of conflict γ_{nm} ranging from 0 (non-conflict) to 1 (full-conflict). γ_{nm} between Ω_R and Ω_O equal to zero indicates that there is no change in the dominance relation and Pareto front when the original objective set Ω_O is replaced by the reduced objective set Ω_R. Detailed information on this approach is available (Brockhoff & Zitzler 2006, 2007).

4 ILLUSTRATIVE EXAMPLE

The approach presented is applied to an existing highway bridge, which is the I-64 bridge over the Kanawha River in West Virginia, USA, and was opened for traffic in 1974 (Connor & Fisher 2001). This application focuses on the gap between the bottom flange and the end of the transverse connecting plate as shown in Figure 2. The fatigue propagation under uncertainty is predicted based on the information provided in Soliman et al (2013). In this illustrative example, it is assumed that (a) the ultrasonic inspection method is applied to detect the fatigue crack, (b) the initial condition before cracking occurred is expected by applying the maintenance such as cutting out and re-fabricating parts of elements, and (c) the cost for each inspection and maintenance and monetary loss due to the structural failure are \$65000 and \$100000, respectively.

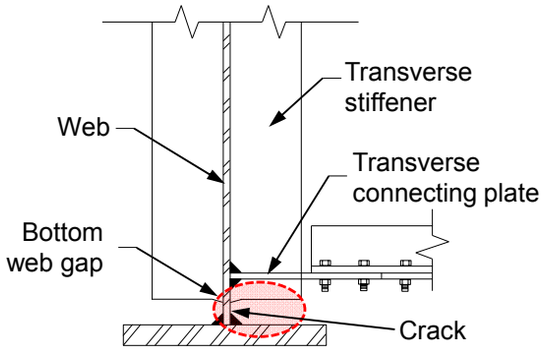


Figure 2. Fatigue sensitive detail of steel bridge (adapted from (Soliman et al 2013)).

Table 1. Correlation coefficients among the objectives $E(t_{dl})$, P_{fail}, $E(t_{sv,ex})$ and C_{lc} for N_{in} = 2.

		$E(t_{dl})$	P_{fail}	$E(t_{sv,ex})$	C_{lc}
Pearson's coefficient of correlation ρ_p	$E(t_{dl})$	1	0.991	0.423	-0.004
	P_{fail}	0.991	1	0.403	-0.001
	$E(t_{sv,ex})$	0.423	0.403	1	-0.694
	C_{lc}	-0.004	-0.001	-0.694	1
		$E(t_{dl})$	P_{fail}	$E(t_{sv,ex})$	C_{lc}
Spearman's coefficient of correlation ρ_s	$E(t_{dl})$	1	0.989	0.119	0.348
	P_{fail}	0.989	1	0.068	0.374
	$E(t_{sv,ex})$	0.119	0.068	1	-0.727
	C_{lc}	0.348	0.374	-0.727	1

The coefficient of correlation between the expected damage detection delay $E(t_{dl})$ and probability of failure P_{fail} is the largest (i.e., $\rho_p = \rho_s = 0.99$) as indicated in Table 1. Figure 3 illustrates this relation for two inspections N_{in} = 2. Since $E(t_{dl})$ and P_{fail} are highly correlated, $E(t_{dl})$ or P_{fail} may be redundant (Kim & Frangopol 2017a).

The multi-objective optimization formulation using the objectives f_1 to f_4 for a given number of inspections N_{in} is

$$\textit{Find } \boldsymbol{t_{in}} = \{t_{in,1},\ t_{in,2}, \ldots t_{in,Nin}\} \tag{7a}$$

$$\textit{for } f_1 = \text{minimizing } E(t_{dl}), \tag{7b}$$
$$f_2 = \text{minimizing } P_{fail},$$
$$f_3 = \text{maximizing } E(t_{sv,ex}),$$
$$f_4 = \text{minimizing } C_{lc}$$

$$\textit{subject to } 1 \text{ year} \leq t_{in,i} - t_{in,i-1} \leq 20 \text{ years} \tag{7c}$$

where $\boldsymbol{t_{in}}$ is the vector consisting of the design variables of inspection times. In order to solve the multi-objective optimization problem defined in Eq. (7), the genetic algorithm provided in MATLAB R2016b (MathWork 2016) is used. The Pareto solution set obtained from the multi-objective optimization problem is used to compute the normalized degree of conflict γ_{nm} between the original objective set.

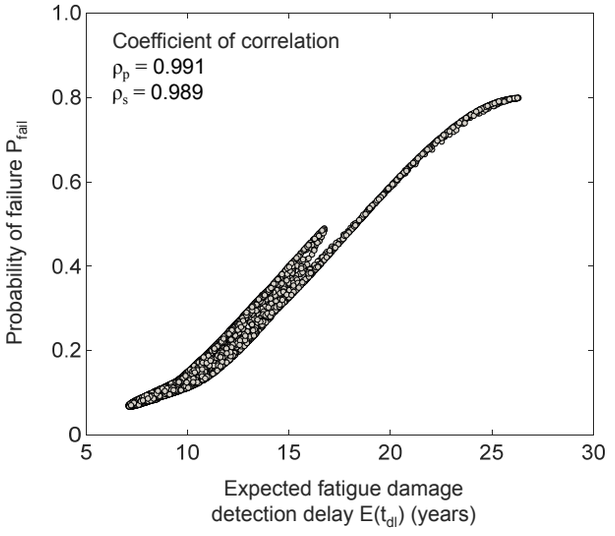


Figure 3. Relation between $E(t_{dl})$ and P_{fail} for $N_{in} = 2$.

Table 2. Normalized degree of conflict γ_{nm} between original objective set $\Omega_O = \{f_1, f_2, f_3, f_4\}$ and reduced objective set Ω_R.

Reduced objective set Ω_R	$N_{in} = 1$	$N_{in} = 2$
$\{f_1, f_3\}$	0.001	0.992
$\{f_2, f_3\}$	0.0	0.992
$\{f_2, f_4\}$	1.0	1.0
$\{f_3, f_4\}$	0.001	0.953
$\{f_1, f_2, f_3\}$	0.0	0.992
$\{f_1, f_3, f_4\}$	0.001	0.001
$\{f_2, f_3, f_4\}$	0.0	0.038

The representative γ_{nm} for the number of inspection N_{in} =1 and 2 is presented in Table 2. Figure 4 compares the Pareto solution sets of the original objective set $\Omega_O = \{f_1, f_2, f_3, f_4\}$ and reduced objective sets $\Omega_R = \{f_2, f_3\}$, $\{f_1, f_2, f_3\}$ and $\{f_2, f_3, f_4\}$ for N_{in} =

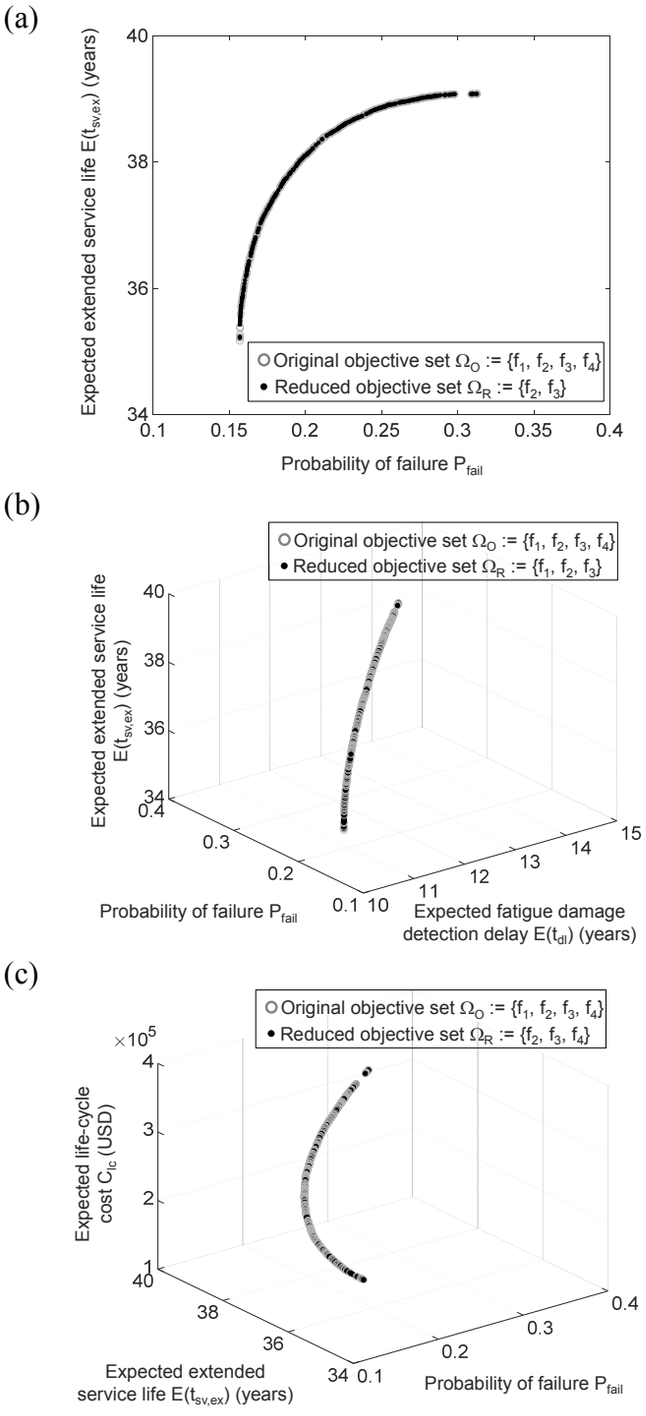


Figure 4. Pareto solution sets for $\gamma_{nm} = 0$ and $N_{in} = 1$: (a) $\Omega_R = \{f_2, f_3\}$; (b) $\Omega_R = \{f_1, f_2, f_3\}$; (c) $\Omega_R = \{f_2, f_3, f_4\}$.

1. From Fig. 3, it can be seen that the reduced objective sets $\Omega_R = \{f_2, f_3\}$, $\{f_1, f_2, f_3\}$ and $\{f_2, f_3, f_4\}$ result in the identical Pareto set with the one of Ω_O, since γ_{nm} is equal to zero. $\Omega_R = \{f_2, f_3\}$ associated with the minimum number of objectives is the essential objective set, and f_1 and f_4 are redundant.

For $N_{in} = 2$, the comparison between the Pareto-solution sets of Ω_O and $\Omega_R := \{f_1, f_3, f_4\}$ is illustrated in Figure 5. Since γ_{nm} between these objective sets is approximately zero (i.e. $\gamma_{nm} = 0.001$), the Pareto front of Ω_O is similar to that of $\Omega_R := \{f_1, f_3, f_4\}$. For this reason, it can be concluded that the objective set $\{f_1, f_3, f_4\}$ is the essential objective set, and is used

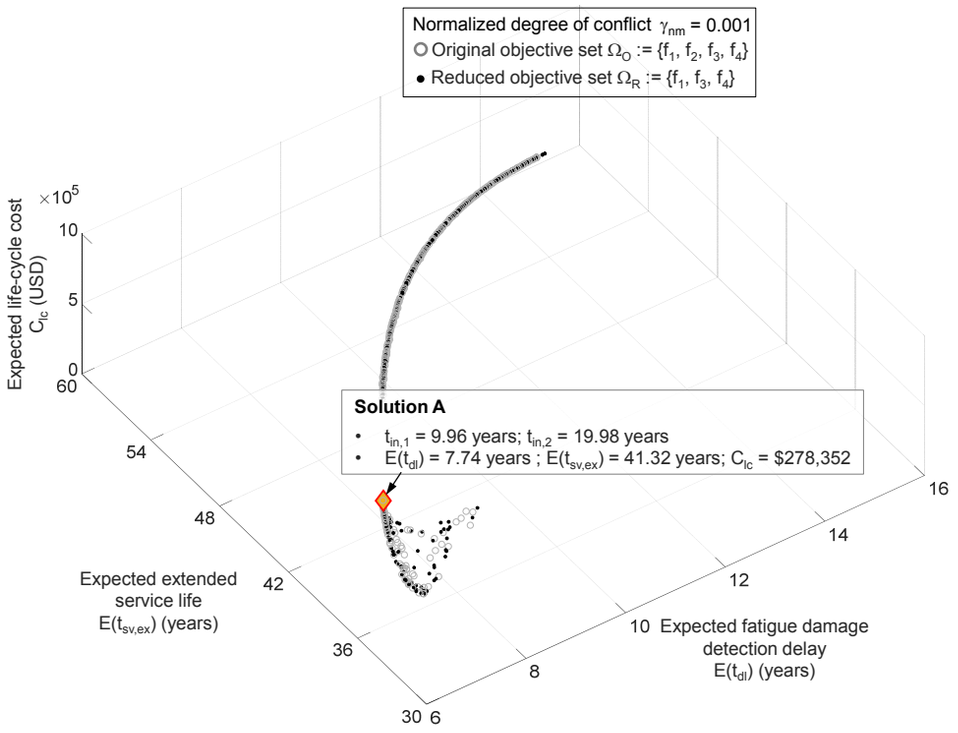


Figure 5. Pareto solution sets of Ω_O = {f_1, f_2, f_3, f_4} and Ω_R = {f_1, f_3, f_4}.

for optimum inspection planning instead of using all the four objectives f_1 to f_4. The solution A in Figure 5 requires two inspections applied at time $t_{in,1}$ = 9.96 years and $t_{in,2}$ = 19.98 years, and the associated $E(t_{dl})$, $E(t_{sv,ex})$ and C_{lc} are 7.74 years, 41.32 years, and $278352, respectively.

5 CONCLUSIONS

This paper presents the damage detection–based objectives including minimizing the expected fatigue damage detection delay, minimizing the probability of fatigue failure, maximizing the expected extended service life, and minimizing the expected life-cycle cost. These objectives are used for multi-objective optimum service life management of deteriorating highway bridges under fatigue. The correlations among the four objectives are investigated. In order to identify the redundant and essential objectives, the dominance relation-based objective reduction approach is used. The approach proposed is applied to a highway bridge under fatigue. The approach can be extended to include system reliability, redundancy, sensitivity, and lifetime maintenance (Frangopol 1985, Frangopol & Nakib 1991, Frangopol & Estes 1997, Onoufriou & Frangopol 2002, Okasha & Frangopol 2009).

ACKNOWLEDGEMENTS

The support by grants from (a) the National Science Foundation (NSF) Award CMMI-1537926, (b) the Commonwealth of Pennsylvania, Department of Community and Economic Development, through the Pennsylvania Infrastructure Technology Alliance (PITA), (c) the U.S. Federal Highway Administration (FHWA) Cooperative Agreement Award DTFH61-07-H-00040, (d) the U.S. Office of Naval Research (ONR) Awards N00014-08-1-0188, N00014-12-1-0023, and N00014-16-1-2299, (e) the National Aeronautics and Space Administration (NASA) Award NNX10AJ20G, and (f) the Regional Development Research Program by Ministry of Land, Infrastructure and Transport of Korean government Award 16RDRP-B076564-03 is gratefully acknowledged. The opinions presented in this paper are those of the authors and do not necessarily reflect the views of the sponsoring organizations.

REFERENCES

Ang, A.H.-S. & Tang, W.H. 2007. *Probability Concepts in Engineering: Emphasis on Applications to Civil and Environmental Engineering.* 2nd edn. New York, Wiley.

Arora, J.S. 2012 Introduction to Optimum Design, London: Elsevier.

Brockhoff, D. and Zitzler, E. 2006. *Dimensionality reduction in multiobjective optimization with (partial) dominance structure preservation: Generalized minimum objective subset problems.* TIK Report 247, *ETH Zurich*, Switzerland.

Brockhoff, D. & Zitzler, E. 2007. Improving hypervolume-based multiobjective evolutionary algorithms by using objective reduction methods, *2007 IEEE Congress on Evolutionary Computation*, *IEEE Press, Singapore*, 2086–2093.

Connor, R.J, and Fisher, J.W. (2001). *Report on field measurements and assessment of the I-64 Kanawha River Bridge at Dunbar, West Virginia.* Report No.01-14, Lehigh University's Center for Advanced Technology for Large Structural Systems (ATLSS), Bethlehem, PA.

Deb, K. 2001. *Multi-objective Optimization using Evolutionary Algorithms*, New York, NY: Wiley.

Frangopol, D.M. 1985. Sensitivity of reliability-based optimum design. *Journal of Structural Eng.*, 111(8): 1703-1721.

Frangopol, D.M. 2011. Life-cycle performance, management, and optimization of structural systems under uncertainty: Accomplishments and challenges. *Structure and Infrastructure Engineering*, 7(6): 389-413.

Frangopol, D.M. & Estes, A.C. 1997. Lifetime bridge maintenance strategies based on system reliability. *Structural Eng. International, IABSE*, 3: 193-198.

Frangopol, D.M. & Nakib, R. 1991. Redundancy in highway bridges. *Eng. Journal, American Institute of Steel Construction*, 28(1): 45-50.

Frangopol, D.M., Saydam, D., & Kim, S. 2011. Maintenance, management, life-cycle design and performance of structures and infrastructures: a brief review. *Structure and Infrastructure Engineering*, 8(1): 1–25.

Frangopol, D.M. & Soliman, M. 2016 Life-cycle of structural systems: Recent achievements and future directions, *Structure and Infrastructure Eng*., 12(1): 1–20.

Frangopol, D.M., Lin, K.Y. & Estes, A.C. 1997. Life-cycle cost design of deteriorating structures. *Journal of Structural Eng*., 123(10): 1390-1401.

Jaimes, L.A., Coello, C.A.C., Aguirre, H., & Tanaka, K. 2014. Objective space partitioning using conflict information for solving many-objective problems. *Information Sciences*, 268: 305-327.

Kabir, G., Sadiq, R., & Tesfamariam, S. 2014. A review of multi-criteria decision-making methods for infrastructure management. *Structure and Infrastructure Engineering*, 10(9): 1176–1210.

Kim, S., & Frangopol, D.M. 2011a. Optimum inspection planning for minimizing fatigue damage detection delay of ship hull structures, *International Journal of Fatigue*, 33(3): 448-459.

Kim, S. & Frangopol, D.M. 2011b. Cost-based optimum scheduling of inspection and monitoring for fatigue sensitive structures under uncertainty, *Journal of Structural Eng*., 137(11): 1319− 1331.

Kim, S., & Frangopol, D.M. 2017a. Efficient multi-objective optimisation of probabilistic service life management. *Structure and Infrastructure Engineering*, 13(1): 147–159.

Kim, S., & Frangopol, D.M. 2017b. Multi-objective probabilistic optimum monitoring planning considering fatigue damage detection, maintenance, reliability, service life and cost. *Structural and Multidisciplinary Optimization*, https://doi.org/10.1007/s00158-017-1849-3.

Kim, S. Frangopol, D.M. & Soliman, M. 2013. Generalized probabilistic framework for optimum inspection and maintenance planning, *Journal of Structural Eng.,* 139(3): 435-447.

Kwon, K., & Frangopol, D.M. 2011. Bridge fatigue assessment and management using reliability-based crack growth and probability of detection models. *Probabilistic Engineering Mechanics*, 26(3): pp. 471–480.

MathWorks 2016. *Optimization Toolbox™ User's Guide*, MathWorks, Natick, MA.

Mohanty, J. R., Verma, B. B., & Ray, P. K. 2009. Prediction of fatigue crack growth and residual life using an exponential model: Part I (constant amplitude loading). *International Journal of Fatigue*, 31(3): 418–424.

Myers, J. L.; Well, A. D., & Lorch, Jr. R.F. 2003. *Research Design and Statistical Analysis*. Routledge, NY.

NCHRP. 2003. *Bridge life-cycle cost analysis.* (NCHRP-report 483), *Washington, DC: Transportation Research Board, National Cooperative Highway Research Program.*

NCHRP. 2006. *Manual on service life of corrosion-damaged reinforced concrete bridge superstructure elements* (NCHRP-Report 558), Washington, DC: Transportation Research Board, National Cooperative Highway Research Program.

Okasha, N. M. and Frangopol, D.M. 2009. Lifetime-oriented multi-objective optimization of structural maintenance considering system reliability, redundancy and life-cycle cost using GA. *Structural Safety*, 31(6): 460–474.

Onoufriou, T. & Frangopol, D.M. 2002 Reliability-based inspection optimization of complex structures: a brief retrospective. *Computers & Structures*, 80(12): 1133-1144.

Saxena, D.K., Duro, J.A., Tiwari, A., Deb, K. & Zhang, Q. 2013. Objective reduction in many-objective optimization: linear and nonlinear algorithms, *Evolutionary Computation*, 17: 77–99.

Soliman, M., Frangopol, D.M. & Kim, S. 2013. Probabilistic optimum inspection planning of steel bridges with multiple fatigue sensitive details, *Eng. Structures*, 49: 996-1006.

Wallbank, E. J., Tailor, P., & Vassie, P. R. 1999. Strategic planning of future maintenance needs. *Management of highway structures*, P. C. Das, ed., Thomas Telford, London: 163–172.

Maintenance, Safety, Risk, Management and Life-Cycle Performance of Bridges – Powers, Frangopol, Al-Mahaidi & Caprani (Eds)
© 2018 Taylor & Francis Group, London, ISBN 978-1-138-73045-8

Probabilistic fatigue life prediction employing an advanced crack propagation model

Y.-J. Lee, J.H. Lee & S. Lee
Ulsan National Institute of Science and Technology (UNIST), Ulsan, Republic of Korea

ABSTRACT: Steel railway bridges are exposed to repeated train loads that often result in fatigue failure. As critical nodes of a transportation network, railway bridges should be designed and maintained to prevent fatigue failure for a predetermined period of time. However, as this would mandate accurate prediction of the fatigue life of railway bridges, the various sources of uncertainty associated with aging bridges, train loads, and the environment considerably complicate this task. In addition, for accurate fatigue life prediction, it is necessary to introduce an appropriate model for crack propagation. Although various studies have been conducted to predict the probabilistic fatigue life of steel railway bridges, many of them are based on a relatively simple model of crack propagation that assumes zero minimum stress and constant loading amplitude, thereby limiting the application scope and reducing the result accuracy. Thus, in this study, a new probabilistic method employing an advanced crack propagation model is proposed for the fatigue life prediction of steel railway bridges. A series of formulations are derived from an advanced crack propagation model such that probabilistic fatigue failure probability can be calculated through reliability analysis using the derived formulations as limit-state functions. Additionally, the formulations are derived such that the model can handle variable amplitude loading, which is the most common loading pattern for railway bridges. To demonstrate the proposed method, it is applied to a numerical example of a steel railway bridge, and the effects of an advanced crack propagation model and various loading amplitudes on bridge fatigue life is discussed through a parametric study.

1 INTRODUCTION

Railway bridges, which play an important role in the daily lives of numerous people, are known to be highly susceptible to fatigue failure. Many structural systems are subjected to the risk of fatigue-induced failure as due to repeated loading over their life cycle; consequently, this is an important safety concern for railway bridges. Thus, it is essential that fatigue life is accurately predicted such that an effective bridge design and maintenance plan can be developed. However, this is not an easy task, as there are various sources of uncertainty associated with aging bridges, train loads, and environmental conditions. Moreover, it is also necessary to introduce an appropriate model for crack propagation.

Two approaches are commonly employed for the fatigue damage evaluation and life prediction of bridge structures. The first approach is the traditional stress-life (S-N) curve method in which the relationship between the constant-amplitude stress range, S, and the number of cycles to failure, N, is determined via appropriate fatigue experiments and described by an S-N curve. In this approach, the Palmgren-Miner linear damage hypothesis, which is also referred to as Miner's rule (Miner 1945), extends this approach to variable amplitude loadings. The second approach is the fracture mechanics approach, which is primarily dedicated to exploring the features and disciplines of crack initiation and growth, while also considering the stress field at the crack tip.

These two approaches are generally applied in sequence, with the S-N curve method being implemented first at the bridge design stage, or for the preliminary evaluation of fatigue life; the fracture mechanics approach is subsequently used to refine the crack-based assessment of remaining fatigue life, or to promote effective inspection and maintenance strategy-related decision-making (Chryssanthopoulos & Righiniotis 2006). However, the S-N curve can only be obtained via experimentation, and is limited in its ability to estimate the probabilistic bridge life as based on the current condition of a bridge.

Alternatively, the fracture mechanics approach is often applied to predict the propagation life as based on an initial crack or defect. More specifically, linear elastic fracture mechanics (LEFM)-based methods relate the growth of an initial crack of a certain size

to the number of fatigue cycles. To date, there has been many investigations into fracture mechanics-based bridge fatigue condition assessment. For example, Fisher (1984) illustrated more than 25 case studies on fatigue crack phenomena in steel bridges using the fracture mechanics approach and other theories. Agerskov and Nielsen (1999) investigated fatigue damage accumulation in steel bridges under the condition of random loading and determined the fatigue life of welded joints in steel highway bridges by carrying out fracture mechanics analysis. By using an LEFM model to predict crack growth, MacDougall et al. (2006) quantified the effects of successive passages of a steel-sprung vehicle and an air-sprung vehicle, respectively, on the differences between the fatigue lives of a short-span bridge and a medium-span bridge. Using experimental data obtained via the structural components of Kinuura Bridge, and LEFM-based theoretical predictions, Xiao et al. (2006) found that the lack of 2–3-mm penetration zones resulted in the low fatigue strength of butt-welded joints. Imam et al. (2008) proposed a probabilistic fatigue assessment methodology for riveted railway bridges, and subsequently applied this method to predict the fatigue occurring in a typical short-span riveted railway bridge in the UK by using train loading data. Similarly, Park et al. (2005), Zhao et al. (1994), and Madsen (1983) used a fracture mechanics approach to estimate the fatigue reliability of bridges. Additionally, Lukić & Cremona (2001) proposed a crack growth model for the probabilistic assessment of steel components damaged by fatigue, and applied the results to a typical steel bridge.

Although there are numerous studies proposing models for fatigue failure prediction of railway bridge components, many of the studies focused on probabilistic fatigue life implement a relatively simple model of crack propagation that assumes zero minimum stress and constant loading amplitude, and thereby limits the application scope and reduces the result accuracy. Thus, in this study, a new probabilistic method implementing an advanced crack propagation model is proposed for the fatigue life prediction of steel railway bridges. The proposed method entails derivation of a series of formulations that allows the model to appropriately manage non-zero minimum stress and variable amplitude loading. To validate the method, it is applied to a numerical model of a railway bridge, and the fatigue life of the bridge is subsequently evaluated.

2 PROPOSED METHODOLOGY

In a structural reliability problem, the failure probability calculation requires construction of an appropriate limit-state function, which represents the failure event of interest as an analytical function of random variables (RVs) and deterministic parameters (Agerskov & Nielsen 1999, Xiao et al. 2006). As was mentioned in Section 1, many researchers have developed various S-N-based or LEFM-based methods for the fatigue reliability analysis of bridges. A widely used LEFM-based numerical model for crack propagation is the Paris equation (Lee & Cho 2016, Lee et al. 2017). Building on this equation, Lee and Cho (2016) and Lee and Song (2014) derived a series of formulations to estimate the structural risk of fatigue-induced failure. However, because the formulations are based on the Paris equation (Paris and Erdogan 1963), which assumes zero minimum stress and constant-amplitude loads, they cannot be practically applied to a railway bridge, as non-zero minimum stress and variable amplitude loading is the realistic pattern generated by train traffic. Therefore, in this study, the limit-state functions proposed by Lee and Cho (2016) and Lee and Song (2014) are modified to enable practical application as a method to evaluate the fatigue life of a railway bridge.

First, consider the following Walker equation (Dowling et al. 2009):

$$\frac{da}{dN} = C_0 \left(\frac{\Delta K}{(1-R)^{1-\gamma}} \right)^{m_0} \tag{1}$$

where a denotes the crack length, N denotes the number of loading cycles, C, m, and γ are the material properties, R is the stress ratio, and ΔK is the range of the stress intensity factor. The stress ratio R is defined by the ratio of the minimum stress σ_{min} to the maximum stress σ_{max} of the cyclic load.

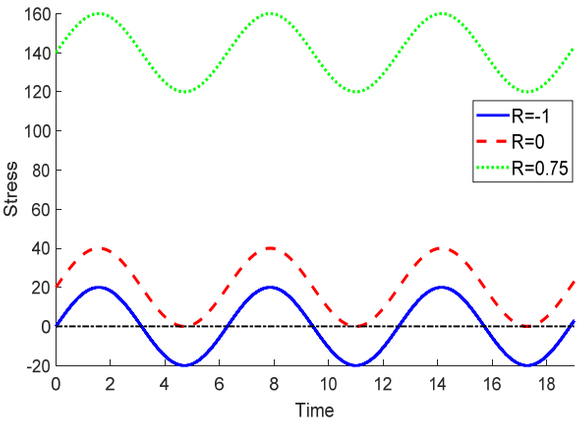


Figure 1. Cyclic loading for various values of R

Figure 1 shows cyclic load examples for different values of R (i.e., −1, 0, 0.75). R = −1 represents a load in both compression and tension. Alternatively, tension loading is dominant when R is zero, which represents a special case; under these conditions, the Walker equation is equivalent to the Paris equation, which yields a widely-known model of crack propagation. In addition, if the ratio of live load (i.e., train

load) to dead load (i.e., self-weight) is 1/3, the stress ratio R becomes 0.75, and the bridge will experience an oscillating stress such as that illustrated in green in Figure 1.

In Equation (1), the stress intensity factor range ΔK can be estimated via Newman's approximation (Newman and Raju 1981):

$$\Delta K = \Delta S \cdot Y(a) \cdot \sqrt{\pi a} \tag{2}$$

where ΔS denotes the stress amplitude and $Y(a)$ is the geometry function, which is a dimensionless parameter that varies according to the crack geometry. The following equation can be obtained by substituting Equation (2) into Equation (1):

$$\frac{1}{\left[Y(a)\sqrt{\pi a}\right]^{m_0}} da = C_0 \left(\frac{\Delta S}{\left(1-R\right)^{1-\gamma}} \right)^{m_0} dN \tag{3}$$

If the load amplitude is constant, Equation (3) can be developed into an equation for the fatigue life evaluation of a structure, as has been described by Lee and Song (2014) and Lee and Cho (2016). However, when a train passes over a bridge, the stress experienced by a structural member has been confirmed to oscillate, thereby enabling the use of the formulations devised for constant amplitude loading.

The rainflow cycle counting algorithm (Nieslony 2009) is commonly used to handle such variable amplitude loading and assess the fatigue life of structures, particularly in the field of mechanical engineering. Generally, the algorithm extracts cycles from the load, stress, or strain history as obtained via measurement or simulation results. Then, several cycles and half-cycles with varying amplitude and mean values are obtained subsequent to cycle counting. Because this counting algorithm implements a fatigue damage accumulation hypothesis (e.g., Paris equation and Miner's rule), it offers the advantage of enabling theoretical computation of the expected fatigue life under random loading conditions (Nieslony 2009).

The stress amplitude ΔS_i and the corresponding number of cycles and stress ratios n_i and R_i are used for the integration of Equation (3) from the initial condition to the current time point, thereby providing the following relationship between the current crack length and the time duration as follows:

$$\begin{aligned} &\int_{a^0}^{a} \frac{1}{\left[Y(a)\sqrt{\pi a}\right]^{m_0}} da \\ &= C_0 \cdot \nu_0 \cdot T \cdot \sum_{i=1}^{N_{amp}} \left[n_i \left(\frac{\Delta S_i}{\left(1-R_i\right)^{1-\gamma}} \right)^{m_0} \right] \end{aligned} \tag{4}$$

where a^0 is the initial crack length, ν_0 is the frequency of train loading, T is the time duration, and N_{amp} is the total number of stress amplitude values. If a crack failure is assumed to occur when the crack length exceeds the critical crack length a^c, the time required for crack growth from a^0 to a^c, T, is expressed as follows:

$$T = \frac{1}{C_0 \nu_0 \sum_{i=1}^{N_{amp}} \left[n_i \left(\frac{\Delta S_i}{\left(1-R_i\right)^{1-\gamma}} \right)^{m_0} \right]} \int_{a^0}^{a^c} \frac{1}{\left[Y(a)\sqrt{\pi a}\right]^{m_0}} da \tag{5}$$

The limit-state function for the failure of the j-th structural member within a given time interval $[0, T_s]$ is expressed via the following equation:

$$g(\mathbf{X}) = T_j^0 - T_s = \frac{\int_{a^0}^{a^c} \frac{1}{\left[Y(a)\sqrt{\pi a}\right]^{m_0}} da}{C_0 \nu_0 \sum_{i=1}^{N_{amp}} \left[n_i \left(\frac{\Delta S_i}{\left(1-R_i\right)^{1-\gamma}} \right)^{m_0} \right]} - T_s \tag{6}$$

where $\mathbf{X}$ denotes the vector of random variables, and T_j^0 is the time to fatigue failure of the j-th structural member. In structural reliability problems, $g(\mathbf{X}) \leq 0$ typically indicates the occurrence of a failure event.

Multiple considerations must be considered if a railway bridge is considered to be a structural system comprising multiple structural members. First, the failure of the bridge system should be expressed by a Boolean function of the failure events of individual members; to obtain such a function, system reliability analysis is required. Thus, in this study, a bridge is considered to fail if any of its members experience fatigue failure; the probability of this system event, P_{sys}, is described as

$$P_{sys} = P\left[\bigcup_{j=1}^{N_{mem}} \left(T_j^0 < T_s \right) \right] \tag{7}$$

Reliability analyses need to be performed to calculate fatigue failure probabilities by using these formulations (i.e., Equation (6) at a component level and Equation (7) at a system level). Therefore, among numerous methods developed to date for reliability analysis, the first-order reliability method (FORM) and second-order reliability method (SORM) (Der Kiureghian 2005) are implemented in this study to perform component reliability analysis. As a computational platform, FERUM (Finite Element Reliability Using MATLAB; Sudret and Der Kiureghian 2000), which is a reliability software package developed at the University of California, Berkeley, was modified and then introduced to perform reliability analysis. Secondly, for a structural system comprising multiple structural members, a failure event must be expressed as a system event; this requires system reliability analysis (SRA). In

this study, because it is assumed that the railway bridge system fails if any of its structural members fail, a multivariate normal integral method (Genz 1992), which enables us to efficiently and accurately calculate the probabilities of large-size parallel systems, is employed to calculate the system probability.

3 NUMERICAL EXAMPLE

3.1 *Numerical example of a steel railway bridge*

The proposed method of fatigue life estimation is tested by applying it to a simple numerical example shown in Figure 2. The bridge is assumed to be 95 m long, 21 m tall, 10 m wide, and made of A36 American Society for Testing and Materials (ASTM) steel.

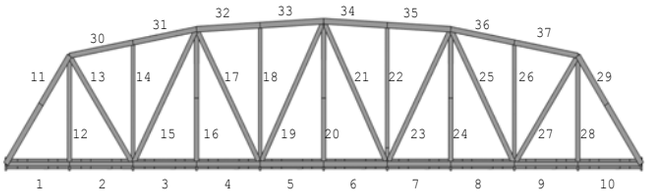


Figure 2. Steel railway bridge example

When a test train, which is assumed to be an ordinary American Amtrack train, passes over the bridge, the axial stresses of the members can be analyzed via dynamic analysis. The results reveal that the following five members, as is labeled in Figure 2, yield the highest stress values (in decreasing order of maximum stress): Members 13, 27, 8, 6, and 7. Table 1 respectively lists the maximum stresses of the five members induced by the train load. It can be seen that the stress levels of Members 13 and 27 are significantly higher than those of the other members. Thus, for further analysis, how the stress changed over time was examined. Figure 3 shows the stresses of Members 13 and 27 as a train passed over the bridge.

Table 1. Maximum stress values of the five structural members with the overall highest stress values.

Member No.	13	27	8	6	7
Maximum stress (MPa)	32.82	32.48	21.26	20.73	20.73

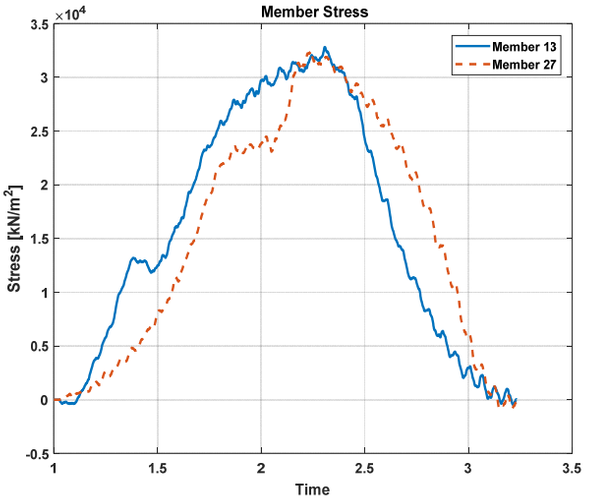


Figure 3. Stress history for Members 13 and 27

Next, the rainflow counting algorithm is applied to the stress responses of the five selected members. The rainflow cycle counting algorithm is widely used for the fatigue life assessment of machine components or structures under the condition of variable amplitude loading. Although the algorithm typically extracts cycles by using the load, stress, or strain history obtained via measurement or simulation, in this study, a code for rainflow counting developed by Nieslony (2009) is used and applied to the simulated results using the model developed by Kim et al. (2016) to obtain the number of amplitudes and cycles. The data are then used to calculate failure probability via Equation (6).

Here, the stress ratio R in Equations (1) and (6) can be determined as based on the ratio of the maximum live load to the dead load; this facilitates consideration of the effects of the mean stress on the fatigue life evaluation of the bridge. In this example, for the sake of simplicity, the ratio R is assumed as 0.75, which represents the ratio of the dead load to the total load (i.e., both the dead and live loads). This means that the live load is one-third of the dead load. In addition, a parametric study implementing various values of R is conducted to investigate the effects of the mean stress on bridge fatigue life.

3.2 *Random variables and deterministic parameters*

In this study, the applied statistical properties of random variables are determined as based on a comprehensive literature review (Lee & Cho 2016, Lee & Song 2014, Moan & Song 2000, Tada et al. 2000, Yazdani & Albrecht 1989, Lee & Song 2012); the means, coefficients of variation (c.o.v.s), and distribution types of the random variables are summarized in Table 2. Although each of the random variables in this numerical case study is assumed to be normally, lognormally, or exponentially distributed, other dis-

tributions, such as Gumbel and Weibull distributions, can also be applied if they more accurately represent the uncertainty of a random variable. This variety of distributions is possible because the proposed method employs FERUM, which ensures reliability for up to a total of 16 different probability distributions, including normal, lognormal, exponential, Gumbel, and Weibull distributions.

In this example, only C is considered as a random variable, and m, and γ are respectively assumed to be 3.344 and 0.7352, as determined subsequent to a comprehensive literature review.

Table 2. Statistical properties of random variables (RVs).

RVs	Mean	c.o.v.	Distribution type	# of RVs
C	1.537×10^{-12} m/cycle/ (MPa·mm)^m	0.2258	Lognormal	5
a^0 (mm)	0.11 mm	1.0	Exponential	5
I	1.0	0.1	Lognormal	1

(#: number)

Statistical independence is assumed for all random variables except the following: (1) values of the Paris equation parameter C for the ten members (correlation coefficient: 0.6), and (2) initial crack lengths (a^0) in the ten members (correlation coefficient: 0.6). Because the correlation coefficients in these cases are unknown, they are initially assumed to be 0.6; this indicates that the five members have been manufactured by the same manufacturer, and thus have material properties that are highly correlated.

In addition, the following deterministic parameters are used: L-bracket width (b) = 650 mm, critical crack length (a^c) = 12.7 or 19.05 mm, and average train traffic = 20 per day. For the geometric function $Y(a)$ in Equation (2), the following function for I-beams is applied as based on the findings of Tada et al. (2000).

$$Y(a) = 1.122 - 0.231\left(\frac{a}{b}\right) + 10.550\left(\frac{a}{b}\right)^2 - 21.710\left(\frac{a}{b}\right)^3 + 30.382\left(\frac{a}{b}\right)^4 \quad (7)$$

4 ANALYSIS RESULTS

Figure 4 shows the reliability indices at various periods throughout the service life for the five selected members. Overall, the reliability indices for the bridge decrease as the time of service increases; this means that the probability of failure increases with increased bridge use.

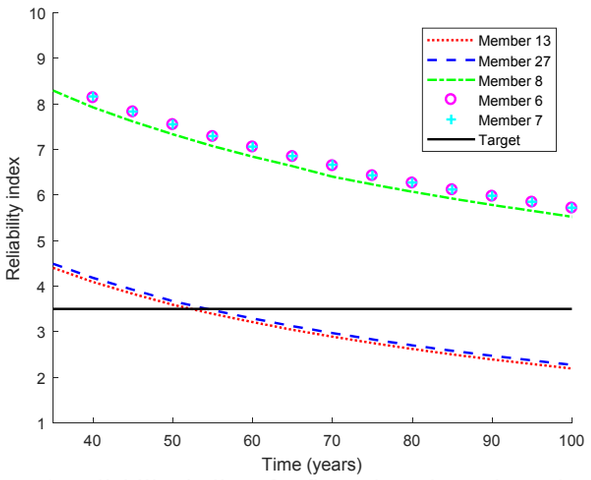


Figure 4. Reliability indices for five selected members obtained via proposed method (R = 3/4).

The American Association of State Highway and Transportation Officials (AASHTO) Bridge Design Code recommends a target reliability index of 3.5, which equates to a failure probability of 2.33×10^{-4}, (Lee & Cho 2016, Lee et al. 2017). The fatigue lives of the five selected members are estimated using this target reliability index as a reference (Target line in Figure 5). Accordingly, the fatigue lives of Members 13 and 27 are evaluated as 52.3 and 54.3 years, respectively, whereas the fatigue lives of the other members are estimated to exceed 100 years. As was mentioned in Section 3.1, this difference is primarily attributed to the significantly higher stress levels of Members 13 and 27 relative to the other members. Because Members 13 and 27 have the shortest fatigue life, only the analysis results of these two members are hereafter presented.

By considering the 0.6 correlation coefficient value for the Walker equation parameters and initial crack lengths of the five members, and the target reliability index of 3.5, the fatigue life of this bridge system is evaluated as 70.7 years.

In this manner, the fatigue lives at component and system levels can be estimated for different values of R. In this study, the R values for parametric analysis are 0, 2/3, 3/4, 4/5, and 5/6. The corresponding analysis results are shown in Figure 5, and the associated fatigue lives are summarized in Table 3. It is observed from the table that the fatigue lives of the members and the railway bridge system decrease significantly as R increases.

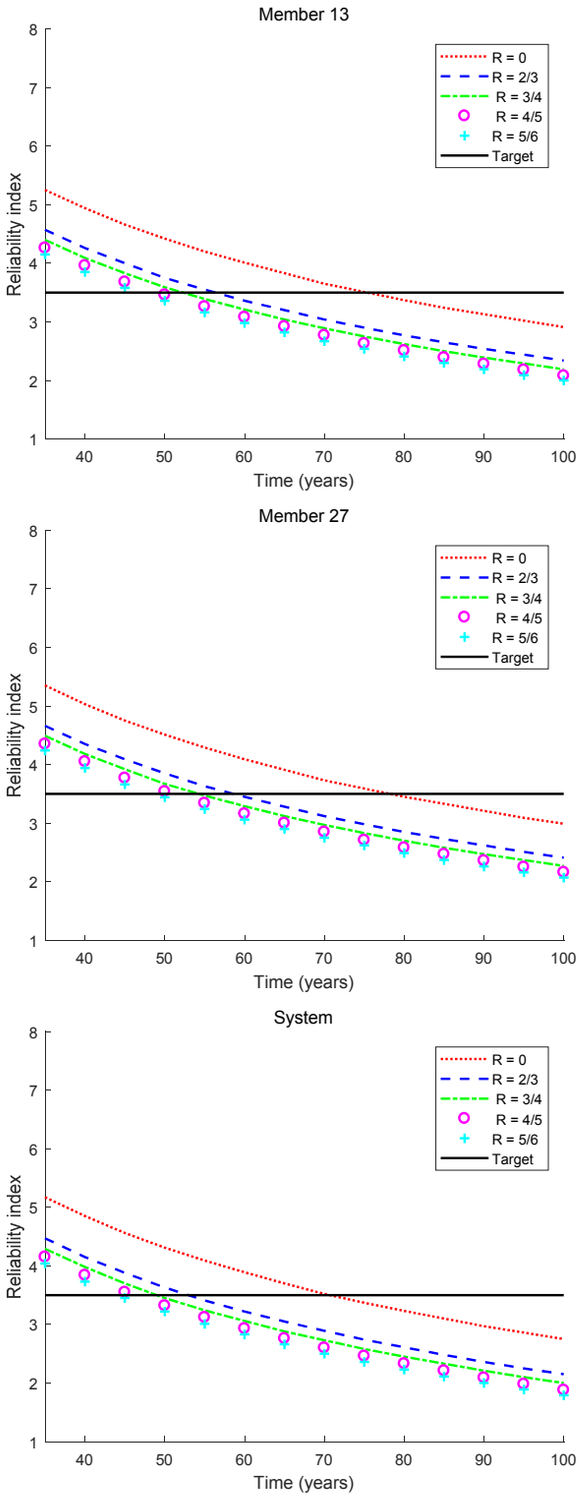


Figure 5. Reliability indices for two selected members and the entire system, as derived via the proposed method.

Table 3. Proposed method results: fatigue lives of two selected members and entire system.

	Fatigue life (years)		
	Member 13	Member 27	System
$R = 0$	75.4	78.2	70.7
$R = 2/3$	56.3	58.6	53.0
$R = 3/4$	52.3	54.3	49.0
$R = 4/5$	49.1	51.0	46.1
$R = 5/6$	46.8	48.6	44.1

5 CONCLUSIONS

This study presents a new probabilistic method employing an advanced crack propagation model to be applied for the fatigue life prediction of steel railway bridges. Specifically, to overcome the limitations of previous studies and accurately predict the fatigue life of a steel railway bridge, an advanced crack propagation model that is able to account for non-zero minimum stress and variable amplitude loading is implemented. A series of formulations are derived via the advanced crack propagation model such that probabilistic fatigue failure probability can be calculated via reliability analysis by implementing the formulations as limit-state functions. To validate the proposed method, it is applied to a numerical model of a steel railway bridge, and the corresponding results are analyzed via reliability indices and fatigue life evaluations. Consequently, the proposed method is shown to accurately estimate the fatigue life of a steel railway bridge. Furthermore, it has been confirmed that the fatigue life decreases with increasing mean stress, and that the proposed method is able to quantify the effects of mean stress on fatigue life.

ACKNOWLEDGEMENT

This study was supported by a grant (18SCIP-B066018-06) from the Smart Civil Infrastructure Research Program funded by the Ministry of Land, Infrastructure and Transport (MOLIT) of the Korean government and the Korea Agency for Infrastructure Technology Advancement (KAIA). This study was also supported by a grant (18SCIP-B128570-02) from the Smart Civil Infrastructure Research Program funded by the Ministry of Land, Infrastructure and Transport (MOLIT) of the Korean government and the Korea Agency for Infrastructure Technology Advancement (KAIA).

REFERENCES

Agerskov, H. & Nielsen, J.A. 1999. Fatigue in steel highway bridges under random loading. *ASCE Journal of Structural Engineering* 125(2): 152-162.

Chryssanthopoulos, M.K. & Righiniotis, T.D. 2006. Fatigue reliability of welded steel structures. *Journal of Constructional Steel Research* 62(11): 1199-1209.

Der Kiureghian, A. 2005. First- and second-order reliability methods. *Engineering Design Reliability Handbook* . CRC Press, Boca Raton, FL, USA, Chapter 14.

Dowling, N.E., Calhoun, C.A., & Arcari, A. 2009. Mean stress effects in stress-life fatigue and the Walker equation. *Fatigue & Fracture of Engineering Materials & Structures* 32(3): 163-179.

Fisher, J.W. 1984. *Fatigue and Fract ure in Steel Bridges: Case Studies*. JohnWiley & Sons, New York, NY, USA.

Genz, A. 1992. Numerical computation of multivariate normal probabilities. *Journal of Computational and Graphical Statistics* 1: 141-149.

Imam, B.M., Righiniotis, T.D., & Chryssanthopoulos, M.K. 2008. Probabilistic fatigue evaluation of riveted railway bridges. *Journal of Bridge Engineering* 13: 237-244.
Kim, R.E., Moreu, F., & Spencer, B.F. 2016. Hybrid model for railroad bridge dynamics. *Journal of Structural Engineering* 142(10): 01046066.
Lee, Y.-J. & Cho, S. 2016. SHM-based probabilistic fatigue life prediction for bridges based on FE model updating. *Sensors* 16(3): 317.
Lee, Y.-J. & Song, J. 2012. Finite-element-based system reliability analysis of fatigue-induced sequential failures. *Reliability Engineering & System Safety* 108: 131-141.
Lee, Y.-J. & Song, J. 2014. System reliability updating of fatigue-induced sequential failures. *Journal of Structural Engineering* 140(3): 04013074-1~16.
Lee, Y.-J., Kim, R.E., Suh, W., & Park, K. 2017. Probabilistic fatigue life updating for railway bridges based on local inspection and repair. *Sensors* 17(4): 936.
Lukić, M. & Cremona, C. 2001. Probabilistic assessment of welded joints versus fatigue and fracture. *Journal of Structural Engineering* 127: 211-218.
MacDougall, C., Green, M.F., & Shillinglaw, S. 2006. Fatigue damage of steel bridges due to dynamic vehicle loads. *Journal of Bridge Engineering* 11(3): 320-328.
Madsen, H.O. 1983. *Probabilistic and deterministic models for predicting damage accumulation due to time varying loading*. Danish Engineering Academy, Lyngby, Denmark.
Miner, M.A. 1945. Cumulative damage in fatigue. *Journal of Applied Mechanics* 12(3): 159-164.
Moan, T & Song, R. 2000. Implications of inspection updating on system fatigue reliability of offshore structures. *Journal of Offshore Mechanics and Arctic Engineering* 122(3): 173-180.
Newman, J.C. & Raju, I.S. 1981. An empirical stress intensity factor equation for the surface crack. *Engineering of Fracture Mechanics* 15: 185-192.
Nieslony, A. 2009. Determination of fragments of multiaxial service loading strongly influencing the fatigue of machine components. *Mechanical Systems and Signal Processing* 23(8): 2712-2721.
Paris, P.C. & Erdogan, F. 1963. An effective approximation to evaluate multinormal integrals. *Structural Safety* 20: 51-67.
Park, Y.-S., Han, S.-Y., & Suh, B.-C. 2005. Fatigue reliability analysis of steel bridge welding member by fracture mechanics method. *Structural Engineering and Mechanics* 19: 347-359.
Sudret, B. & Der Kiureghian, A. 2000. *Stochastic finite element methods and reliability: a state-of-the-art report* . Berkeley, CA: Department of Civil and Environmental Engineering, University of California, CA, USA.
Tada, H., Paris, P.C., & Irwin, G.R. 2000. *The stress analysis of cracks handbook*. ASME. New York, NY, USA.
Xiao, Z.-G., Yamada, K., Inoue, J., & Yamaguchi, K. 2006. Fatigue cracks in longitudinal ribs of steel orthotropic deck. *International Journal of Fatigue* 28(4): 409-416.
Yazdani, N. & Albrecht, P. 1989. Crack growth rates of structural steel in air and aqueous environments. *Engineering Fracture Mechanics* 32(6): 997-1007.
Zhao, Z., Haldar, A., & Breen, F.L. 1994. Fatigue-reliability evaluation of steel bridges. *Journal of Structural Engineering* 120: 1608-1623

Maintenance, Safety, Risk, Management and Life-Cycle Performance of Bridges – Powers, Frangopol, Al-Mahaidi & Caprani (Eds)
© 2018 Taylor & Francis Group, London, ISBN 978-1-138-73045-8

Development of Calibration Factor for Fatigue Assessment

J. Y. Park & H.K. Kim
Department of Civil and Environmental Engineering, Seoul National University, Seoul, South Korea
Y. C. Park
Institute of Construction and Environmental Engineering, Seoul National University, Seoul, South Korea

ABSTRACT: Based on linear elastic fracture mechanic (LEFM), stress cycles non-contributing crack growth from stress range spectrum is truncated for fatigue assessment. Calibration which make fatigue life N_c representing total applied stress cycle to failure instead of stress cycle contributing crack growth is considered for realistic fatigue assessment. Effectiveness of truncation and calibration is identified through actual fatigue reliability assessment case using weigh in motion measurement data. The result shows importance of considering stress spectrum truncation and calibration for N_c simultaneously for realistic fatigue reliability assessment.

1 INTRODUCTION

In linear elastic fracture mechanic (LEFM), crack growth can be divided by three phase. Phase I is non-propagation stage which fatigue crack cannot propagate under stress intensity factor (SIF) ranges below fatigue crack propagation threshold (ΔK_{th}). Phase II is linearized propagation stage which fatigue crack propagation rate and SIF in log-log scale (Paris & Erdogan, 1963). Phase III is fracture stage which fatigue crack propagate to a critical crack size. In welded details, propagation life only exist due to large initial crack and can be estimated from linearized propagation stage of phase II although fatigue life is generally defined as sum of initiation and propagation life of crack.

SIF at the crack tip which is essential factor for crack growth can be defined by applied stress range, crack length or depth and correction factors. Therefore, only stress ranges over ΔK_{th} are contributed to crack growth and stress ranges below ΔK_{th} are neglected for fatigue crack growth as shown in Figure 1. This concept is similarly applied to bridge evaluation procedure through S-N approach as shown in Figure 2. S-N curves defined for fatigue details consists of finite and infinite life regimes. In order to estimate finite fatigue life using S-N approach, stress ranges in a stress range histogram below half of constant amplitude fatigue threshold (CAFT/2) should be truncated not to underestimate the fatigue life(AASHTO, 2013).

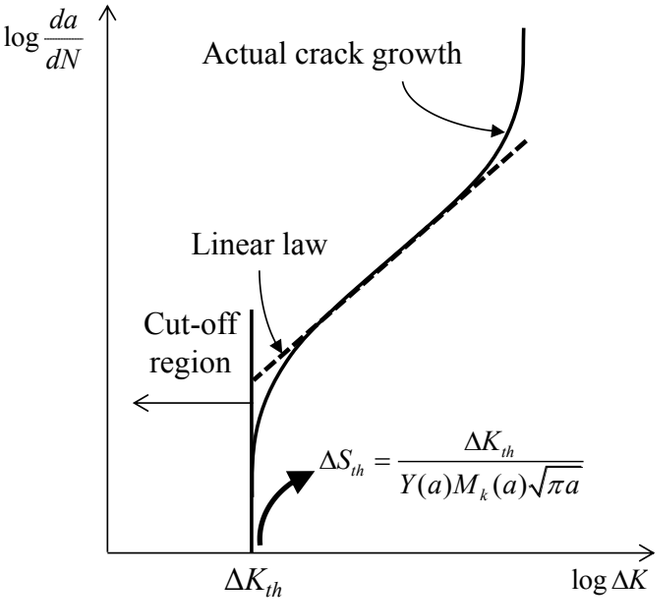


Figure 1. Fatigue crack growth model in LFEM

Therefore, it is important to truncate stress cycles non-contributing crack growth from stress range histogram for realistic fatigue assessment. Moreover, it must be considered that the threshold of stress ranges (ΔS_{th}) contributing crack growth changes according to crack grows. When this is not considered, fatigue life can be underestimated since every stress cycle is effectively applied to crack growth.

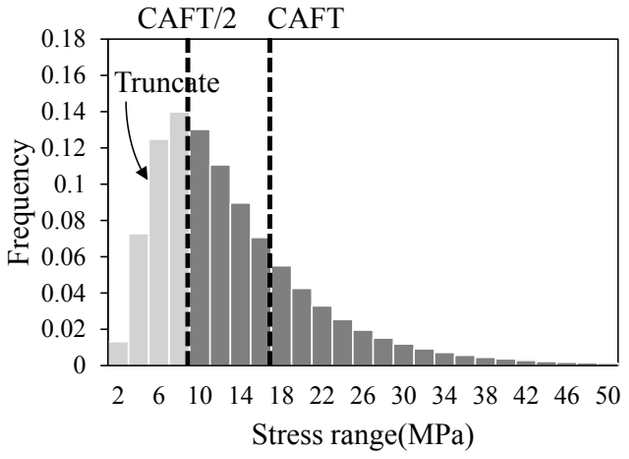


Figure 2. Stress range truncation in S-N approach

Fatigue reliability analysis is performed using stress spectrum itself. Otherwise, each stress blocks should be considered separately for the fatigue analysis. Whole spectrum is represented by effective stress range and reliability analysis is performed using first order reliability analysis (FORM).

Fatigue limit state is consisted by expected fatigue life and current fatigue life. Expected fatigue life can be represented by stress cycles to failure, N_c. Current fatigue life can be represented by number of applied stress cycles at the time of evaluation, $N(t)$. Since only stress ranges over ΔK_{th} contribute to crack propagation, N_c only includes stress cycles contributing crack growth. The stress cycles which contribute to crack growth will be called "contributing stress cycles". $N(t)$ is usually estimated by traffic information, weigh in motion (WIM) data and so on, which includes both contributing and non-contributing stress cycles. In order to eliminate difference between N_c and $N(t)$, calibration should be applied to N_c or $N(t)$. It may be reasonable to calibrate N_c because it is difficult to separate contributing stress cycles in $N(t)$ without identifying exact history of crack growth and traffic information.

In this paper, stress spectrum truncation and calibration for N_c is proposed for fatigue reliability assessment using FORM. Effectiveness is identified through case study of actual bridge assessment.

2 PROPOSED PROCEDURE FOR FATIGUE RELIABILITY ASSESSMENT

2.1 *Fatigue assessment based on LEFM*

A linearized crack growth model proposed by Paris & Erdogan (1963) is utilized for fatigue crack growth in Equation (1).

$$\frac{da}{dN} = \begin{cases} 0 & for\ \Delta K < \Delta K_{th} \\ C(\Delta K)^m & for\ \Delta K_{th} \le \Delta K \end{cases} \tag{1}$$

where a is fatigue crack depth, N is number of applied stress cycles, da/dN is fatigue crack growth rate, C and m are material parameters in Paris' law, ΔK is range of stress intensity factor at the crack tip and ΔK_{th} is fatigue crack propagation threshold.

Since crack growth in depth direction is considered, stress intensity factor is only calculated at the deepest point of crack as shown in Figure 3. Range of SIF could be calculated by:

$$\Delta K = Y(a) \cdot F_g(a) \cdot S_r \cdot \sqrt{\pi a} \tag{2}$$

where $Y(a)$ is geometry correction factor which is function of the aspect ratio of crack and size and geometry of detail, $F_g(a)$ is stress gradient correction factor which considers the stress distribution through thickness and S_r is applied nominal stress range.

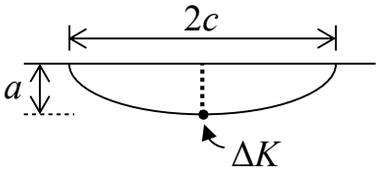


Figure 3. Semi-elliptical surface crack and location of maximum ΔK

Since stress intensity factor is function of crack size and stress range, threshold of the stress range, $S_{r,th}$, changes as the crack grows. Effective stress range, S_{re}, also changes as:

$$S_{r,th}(a) = \frac{\Delta K_{th}}{Y(a) \cdot F_g(a) \cdot \sqrt{\pi a}} \tag{3}$$

$$S_{re}^m = \frac{\int_{S_{r,th}(a)}^{S_{r,\max}} S_r^m f_S(S_r) dS_r}{\int_{S_{r,th}(a)}^{S_{r,\max}} f_S(S_r) dS_r} \tag{4}$$

where f_S is stress range spectrum and $S_{r,max}$ is maximum stress range.

In order to calculate the effective stress range which changes as crack growth, $S_{r,max}$, $S_{r,th}$ should be determined. In this paper, $S_{r,max}$ is determined as measured maximum value of WIM data. $S_{r,th}$ is determined by fatigue crack propagation threshold ΔK_{th} and crack size (a) according to crack growth as Equation (3).

Expected stress cycles to failure can be obtained by integrating the crack growth rate as

$$\begin{aligned} N_c &= \int_{a_0}^{a_c} \frac{1}{C \cdot (\Delta K)^m} da \\ &= \int_{a_0}^{a_c} \frac{1}{C \cdot \left(Y(a) \cdot F_g(a) \cdot S_{re} \cdot \sqrt{\pi a} \right)^m} da \end{aligned} \tag{5}$$

where a_0 is the initial crack depth, a_c is predefined critical crack depth. Expected stress cycles to failure is calculated using effective stress range for general variable amplitude loading condition.

2.2 *Calibration factor for N_c*

When expected fatigue life, N_c, is estimated by LEFM considering effective stress, fatigue life only includes contributing stress cycles. On the other hand, $N(t)$ includes of contributing and non-contributing stress cycles since $N(t)$ usually estimated by WIM data or counting truck traffic or counting stress cycles at fatigue details. In order to make N_c representing total applied stress cycle to failure instead of contributing stress cycle, calibration factor (Ω) is applied to crack growth rate and then calibrated stress cycle to failure can be obtained as

$$\Omega(a) = \frac{N_t(a)}{N_e(a)} = \frac{1}{\int_{S_{r,th(a)}}^{S_{r,\max}} f_S(S_r)dS_r} \tag{6}$$

$$\begin{aligned} \overline{N_c} &= \int_{a_0}^{a_c} \frac{1}{C(\Delta K)^m} \cdot \Omega(a)\, da \\ &= \int_{a_0}^{a_c} \left[\frac{1}{C \cdot (\Delta K)^m \cdot \int_{S_{r,th(a)}}^{S_{r,\max}} f_S(S_r)dS_r} \right] da \end{aligned} \tag{7}$$

where N_e is contributing stress cycles in stress spectrum, N_t is total applied stress cycles including both contributing and non-contributing stress cycles in stress spectrum.

3 CASE STUDY: FATIGUE EVALUATION ON ACTUAL BRIDGE

3.1 *Fatigue detail*

Investigated bridge is part of a test road of the expressway in Korea, which is composite box girder bridge. Among the fatigue details of the bridge, fillet-welded connection of gusset plate to girder web plate classified as AASHTO Fatigue Category E is evaluated, shown in Figure 4. Detail information of the bridge can be referred to Park & Kim (2014).

Semi-elliptical surface crack is assumed and then geometry correction factor, Y, is referred to Newman & Raju (1981) as

$$Y(a) = \left[M_1 + M_2 \left(\frac{a}{t}\right)^2 + M_3 \left(\frac{a}{t}\right)^4 \right] \frac{g f_\phi f_w}{\sqrt{Q}} \tag{8}$$

where t is thickness of web plate, Q is shape factor for elliptical crack, f_φ is angular function, f_w is finite-width correction factor. f_φ and g is one when crack growth in depth direction is considered. Stress gradient correction factor, F_g, for investigated fatigue detail is referred to Norris & Fisher (1981) as

$$F_g = \frac{SCF}{1 + 0.88a^{0.576}} \tag{9}$$

where SCF is stress concentration factor which varies between 5.5 and 7.0, 7.0 is applied in this assessment.

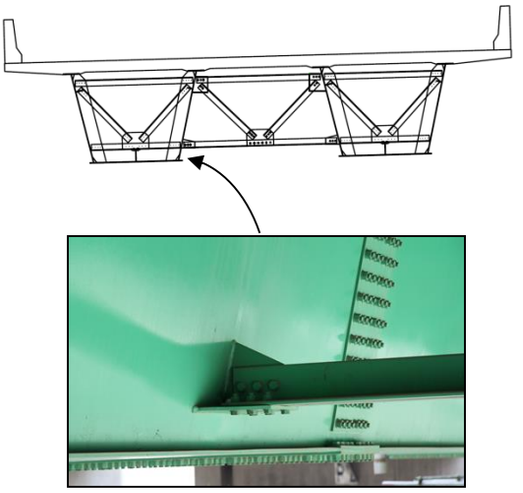


Figure 4. Investigated fatigue detail

3.2 *Probabilistic variables and assumptions*

Crack-related variable, material-related variables and uncertainty of loading condition is considered for fatigue reliability assessment. Detailed information of variables utilized for reliability analysis is shown in Table 1.

Table 1. Probabilistic variables.

Variables	Distribution	Mean	COV
Initial crack depth[1], a_0 (mm)	Lognormal	0.125	0.36
Critical crack depth, a_c (mm)	Deterministic	12	-
Aspect ratio[2], a/c	Lognormal	0.39	0.41
Material constant[3], m	Deterministic	3.1	-
Material constant[3], ln$C$	Normal	-29.84	0.02
Crack propagation threshold[4], (MPa-m$^{1/2}$)	Lognormal	140	0.4
Load effect uncertainty factor[5]	Normal	1.0	0.20

1) Referred to Engesvik & Moan (1983)
2) Referred to Yamada et al. (1989)
3) Referred to BSI (2015)
4) Referred to JCSS (2011)
5) Referred to Hwang et al. (2013)

3.3 *Determining stress spectrum*

Truck weight is measured by weigh in motion (WIM) study and then Truck weight histograms are converted to stress range histogram using result of dynamic loading tests performed in investigated bridge. Stress range spectrum can be fitted with

stress range histogram. In order to determine suitable stress spectrum based on histogram, Lognormal, Weibull, Gaussian mixture model (GMM) and so on are utilized. Each distribution model is evaluated through root mean square error (RMSE) with histogram and fatigue life estimation. As a result, GMM with three components are well fitted than other distributions. Therefore, GMM which reflect the global shape of histogram is considered as representative distribution.

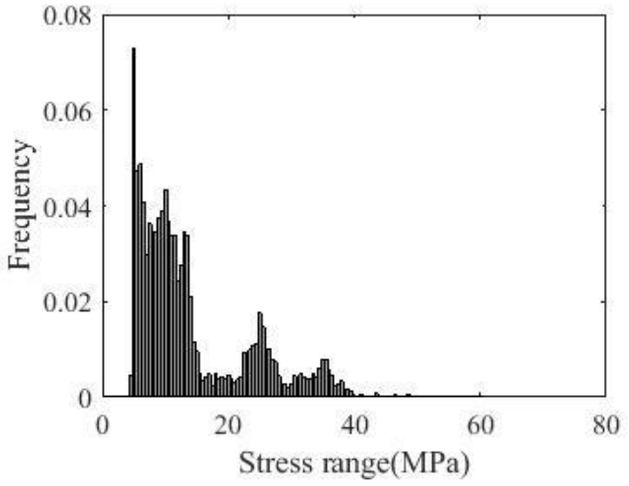


Figure 5. Stress range histogram based on measured truck weight

4 RESULTS

Three analysis cases were compared to identify the effect of stress spectrum truncation and calibration factor. Case 1 is performed without considering stress spectrum truncation, which assume that all stress cycles are effectively applied to crack growth. Case 2 is performed with stress spectrum truncation. Case 3 is performed with stress spectrum truncation and calibration factor simultaneously.

Table 2. Mean fatigue life of investigated detail.

Case	Mean fatigue life (year)
1:W/o truncation	72
2:W/ truncation	20
3:W/ truncation and calibration	96

Table 2 shows the mean fatigue life which represent the zero of reliability index. When stress spectrum truncation is not applied, mean fatigue life is underestimated than Case 3 since all of region in stress spectrum is effectively applied to crack growth from initial crack stage. When only stress spectrum truncation is applied, mean fatigue life is considerably underestimated than Case 3 since very few stress cycles only effectively applied to crack growth are considered as fatigue life. Therefore, stress spectrum truncation and calibration should be considered simultaneously for reasonable assessment.

5 CONCLUSIONS

Procedure for fatigue assessment considering stress spectrum truncation and calibration for N_c is proposed. When stress spectrum truncation and calibration is not considered, fatigue life and reliability can be underestimated. For realistic fatigue reliability analysis, stress spectrum truncation and calibration for crack growth rate should be applied to assessment simultaneously.

6 ACKNOWLEDGEMENTS

This research was supported by a grant (17SCIP-B128568-01 2) from Smart Civil Infrastructure Research Program and a grant (17SCIP-B119960-02). Both grants were funded by the Ministry of Land, Infrastructure and Transport of the Korean government.

REFERENCES

AASHTO. (2013). The manual for bridge evaluation(2nd ed.). Washington, D.C., USA.: AASHTO.

BSI. (2015). BS 7910: Guide to methods for assessing the acceptability of flaws in metallic structures. London: BSI.

Engesvik, K. M., & Moan, T. (1983). Probabilistic Analysis of the Uncertainty in the Fatigue Capacity of Welded-Joints. *Engineering Fracture Mechanics, 18*(4), 743-762. doi:Doi 10.1016/0013-7944(83)90122-4

Hwang, E. S., Nguyen, T. H., & Kim, D. Y. (2013). Live load factors for reliability-based bridge evaluation. *Ksce Journal of Civil Engineering, 17*(3), 499-508. doi:10.1007/s12205-013-0561-0

JCSS. (2011). JCSS Probabilistic model code *Part 3: Resistance models*: Joint Committee on Structural Safety (JCSS).

Newman, J. C., & Raju, I. S. (1981). An Empirical Stress-Intensity Factor Equation for the Surface Crack. *Engineering Fracture Mechanics, 15*(1-2), 185-192. doi:Doi 10.1016/0013-7944(81)90116-8

Norris, S. N., & Fisher, J. W. (1981). The fatigue behaviour of welded web attachments. *Journal of Constructional Steel Research, 1*(2), 27-38.

Paris, P., & Erdogan, F. (1963). A Critical Analysis of Crack Propagation Laws. *Journal of Basic Engineering, 85*(4), 528-533.

Park, J. Y., & Kim, H. K. (2014). Fatigue life assessment for a composite box girder bridge. *International Journal of Steel Structures, 14*(4), 843-853. doi:10.1007/s13296-014-1215-x

Yamada, K., Nagatsu, S., & Mitsugi, Y. (1989). Evaluation of scatter of fatigue life of welded details using fracture mechanics.

Maintenance, Safety, Risk, Management and Life-Cycle Performance of Bridges – Powers, Frangopol, Al-Mahaidi & Caprani (Eds)
© 2018 Taylor & Francis Group, London, ISBN 978-1-138-73045-8

Fatigue assessment of deteriorated steel bridge members considering corrosion

Y.C. Park
Institute of Construction and Environmental Engineering, Seoul National University, Seoul, Republic of Korea

L.S. An & H.K. Kim
Department of Civil and Environmental Engineering, Seoul National University, Seoul, Republic of Korea

ABSTRACT: Fatigue crack and corrosion are two significant factors which could affect fatigue performance of steel bridge members. In this study, a reliability based assessment procedure for determining remaining fatigue life is proposed. Both fatigue crack propagation and progress of corrosion are simultaneously considered for the assessment. Three scenarios simulating progress of steel bridge deterioration are established and fatigue assessment was performed accordingly. As corrosion progresses, stress concentration effect around the corroded area increases and may cause fatigue crack initiation. By utilizing stress-strain approach and linear elastic fracture mechanics, pit depth threshold which can be transformed as fatigue crack is determined. To develop relation between pit depth threshold and fatigue crack initiation, an equation estimating the stress concentration factor for corrosion pit is formulated by parametric study based on finite element analysis Proposed fatigue assessment method could establish reliability based deterioration levels, which may lead to reasonable and efficient maintenance strategy.

1 INTRODUCTION

Bridge assessment is significant for maintenance of deteriorated steel bridge. Initial step for assessing steel bridge is inspection of each member. Condition assessment of the steel bridge could be conducted based on the inspection results. Various bridge assessment manuals and guidelines have been published from North America, Europe and other countries. However, most of them recommends quantitative evaluation rather than qualitative evaluation. For example, in *AASHTO Bridge Element Inspection Guide Manual*, inspector's judgment dominates the structural member's rating (AASHTO 2010). *Ontario Structure Inspection Manual* provides quantitative criteria for corrosion, but does not suggest criteria for crack (Ontario Ministry of Transportation 2000). Korea Infrastructure Safety & Technology Corporation (KISTEC 2012) categorizes levels of steel elements into five steps (A to E) to evaluate deterioration of steel bridges (Table 1). Categorizing deterioration level of steel members is conducted based on measuring data, i.e. crack length, uncoated and corroded area or section loss due to corrosion. However, ranges of the damages were somehow determined without any rational judgement.

This study developed preliminary study for reliability-based fatigue life assessment for deteriorated steel bridge member. Realistic scenarios which indicate results of inspection were established and case studies were conducted.

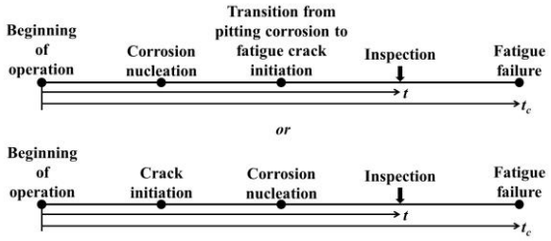
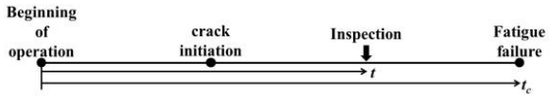
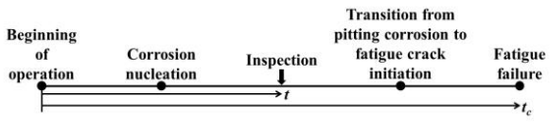
Table 1. Categories of Deteriorations for Steel Member (KISTEC 2012)

Level	Types of Deteriorations	
	Corrosion	Crack
A	-None	-None
B	-Uncoated area<10% -Corroded area<2%	-Local crack in secondary member
C	-Uncoated area>10% -2%<Corroded area<10%	-Large crack in secondary member -Local crack in primary member
D	-Corroded area<10% -Section loss<10%	-Large crack in primary member
E	-Section loss>10%	-Large crack in primary member (>20% of its depth)

2 DETERIORATION SCENARIOS OF STEEL MEMBERS

Following Table 1, corrosion and fatigue crack are considered to develop the fatigue assessment procedure. When inspecting crack and corrosion, three scenarios of inspection results can be assumed. Since this study only focuses on fatigue assessment, corrosion failure is not considered. The deterioration scenarios are established based on the inspection results and presented in Table 2.

Table 2. Fatigue Life Assessment Scenarios based on Inspection Results

Scenarios	Expected Time Line
I	
II	
III	

Detail information of each scenarios is following:

• Scenario I: This scenario represents the case that both fatigue crack and corrosion pit are found at the same location. If both fatigue crack and corrosion exist simultaneously, fatigue crack dominates fatigue life of the member. According to Kondo (1989), corrosion does not proceed if fatigue crack is initiated from corrosion. Therefore, although it is unknown that which deterioration among corrosion and crack occurred earlier, it is reasonable that the member will be failed due to fatigue crack.

• Scenario II: This scenario represents the cases when fatigue crack is found only.

• Scenario III: This scenario represents the cases when corrosion is found only. In this case, fatigue crack was transformed from corrosion pit.

3 ESTABLISHING FATIGUE LIMIT STATE

As per the scenarios, both corrosion and fatigue crack propagation should be considered for defining fatigue limit state. The parameter which commonly represent both fatigue crack propagation and corrosion is time. Therefore, fatigue limit state function is defined in terms of time as shown in Equation 1

$$g = t_c - t \tag{1}$$

where, t_c and t denote expected fatigue life of steel member and years of operation, respectively.

3.1 *Scenario I and Scenario II*

Fatigue limit state is defined based on crack propagation for Scenarios I and II. Although corrosion is also found in the case of Scenario I, fatigue crack is related with fatigue failure directly and it dominates fatigue failure. Thus, the limit state function of these two scenarios is founded based on linear elastic fracture mechanics (LEFM) concept using Paris' Law (Paris & Erdogan 1963).

$$\frac{da}{dN} = C\left(\Delta K\right)^m \tag{2}$$

where, a and N indicate fatigue crack length and the number of cycles, respectively. C and m are material coefficients. ΔK is stress intensity factor range at the crack tip. It can be calculated as follows.

$$\Delta K = Y\left(a\right) S_{re} \sqrt{a\pi} \tag{3}$$

where, Y and S_{re} denote correction factor and equivalent stress range, respectively.

If initial crack length (a_0) and critical crack length (a_c) are determined, expected number of cycles to fatigue failure (N_f) can be calculated by integrating Equation 3 as follows.

$$N_f = \int_{a_0}^{a_c} \frac{da}{C\left(\Delta K\right)^m} \tag{4}$$

Since the fatigue limit state is defined in terms of time, the number of cycles has to be converted into time divided by average daily stress cycles (*ADSC,* cycles/day). Finally, fatigue limit state function for Scenario I and II can be set as follows.

$$g = t_c - t = \int_{a_0}^{a_c} \frac{da}{C \cdot \Delta K^m \cdot 365 \cdot ADSC} - t \tag{5}$$

3.2 *Scenario III*

This scenario represents the case only corrosion was found from the inspection. Stress concentration effect due to corrosion pit and micro-cracks around the pit could initiate fatigue crack under repeated loading. Therefore, possibility of initiating fatigue crack could become larger as corrosion pit grows. According to Kondo (1989), corrosion pit stops growing when fatigue crack initiated from the pit. The maximum size of corrosion pit, which may initiate fatigue crack is defined as pit depth threshold (d_{th}).

Expected life of steel member, t_c should include expected time to form corrosion nucleation (t_0), required time for growing corrosion pit to pit depth threshold (t_{cg}) and required time to failure by fatigue crack propagation (t_{cg}). Accordingly, fatigue limit state function for Scenario III is defined as follows.

$$g = t_c - t = t_0 + t_{cg} + t_{cp} - t \tag{6}$$

The first part of this scenario (t_0) is not well understood yet, because it depends on factors such as electrolytes, loads, materials (Shi & Mahadevan 2001). Therefore, the first part, t_0, is assumed as a random variable.

Pit depth threshold is determined by estimating fatigue threshold proposed by Roy & Fisher (2005). It was developed based on the stress-strain approach suggested by Smith et al. (1970). Roy & Fisher's

study successfully estimated maximum stress range which may not initiate fatigue crack under constant stress range for UIT treated welded cover plate connection. The result of this study was adopted by Park (2015) and applied to estimate fatigue threshold for various tube-to-transverse plate welded connection. In order to find pit depth threshold, the critical condition which may initiate fatigue crack is defined as per stress-strain approach (Equation 7).

$$\sqrt{(\sigma_{\max}\sigma_a)} = \sqrt{(\sigma_a+\sigma_0)\sigma_a} = \frac{F_u}{2} \tag{7}$$

where, σ_{max}, σ_a, σ_0 and F_u denote maximum stress, stress amplitude, mean stress and ultimate strength of steel, respectively. Stress concentration effects around corrosion pit can be reflected by utilizing fatigue notch factor (K_f) which is the function of stress concentration factor (K_t), material parameter (a) and pit radius (d). Thus, stress concentration factor developed by corrosion pit should be applied. Cerit et al. (2009) proposed a stress concentration factor for corrosion pit, but it could not be applied because the pit depth considered for this study was too small. Thus, stress concentration factor for corrosion pit is developed by a parametric study based on finite element analysis for various pit sizes. Result of the parametric study is shown in Figure 1.

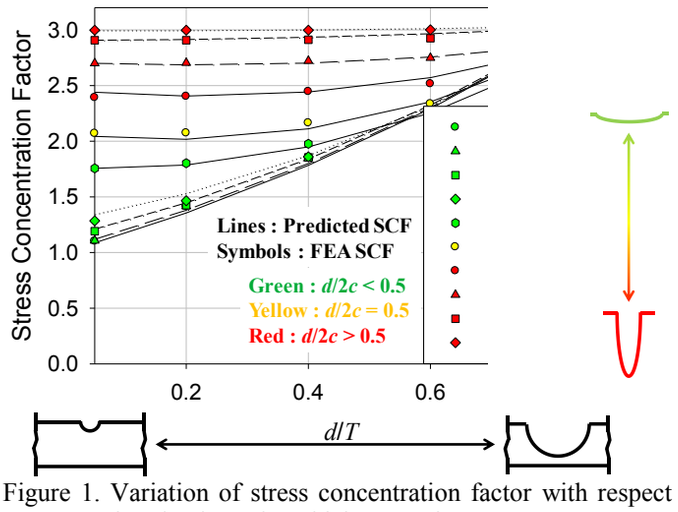


Figure 1. Variation of stress concentration factor with respect to penetration depth to plate thickness ratio.

Finally, pit depth threshold could be obtained by solving Equation 8.

$$1+\frac{K_t-1}{1+\frac{a}{d}} = \sqrt{\frac{F_u^{\,2}}{4(S_a+S_0)S_a}} \tag{8}$$

where, S_a and S_0 are nominal stress amplitude and mean stress, respectively.

Komp (1987) proposed a corrosion growth model, which corrosion growth can be determined against time.

$$t_{c,cg} = \left(\frac{d_{th}}{p}\right)^{\frac{1}{q}} \tag{9}$$

where, p and q are environmental parameters.

For fatigue crack growth, pit depth threhold can be considered as an initial crack length. Finally, fatigue limit state function for Scenario III is defined as follows.

$$\begin{aligned} g &= t_c - t = t_0 + t_{cg} + t_{cp} - t \\ &= t_0 + \left(\frac{d_{th}}{p}\right)^{\frac{1}{q}} + \int_{d_{th}}^{a_c} \frac{da}{C\cdot\Delta K^m \cdot 365\cdot ADSC} - t \end{aligned} \tag{10}$$

4 CASE STUDY

Case study is conducted for existing 80 year-old bridge by applying the fatigue assessment procedure suggested in this study. Actual measurement of stress range for fatigue critical detail is used for reliability analysis. The fatigue critical detail was fillet-welded cover plate welded connection at the bottom of main girder. AASHTO fatigue detail category of cover plate detail is E′, which is the lowest among other welded details in the bridge.

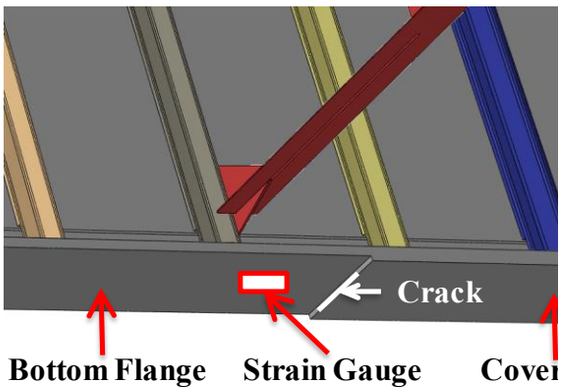


Figure 2. Case study: the location of a fatigue crack.

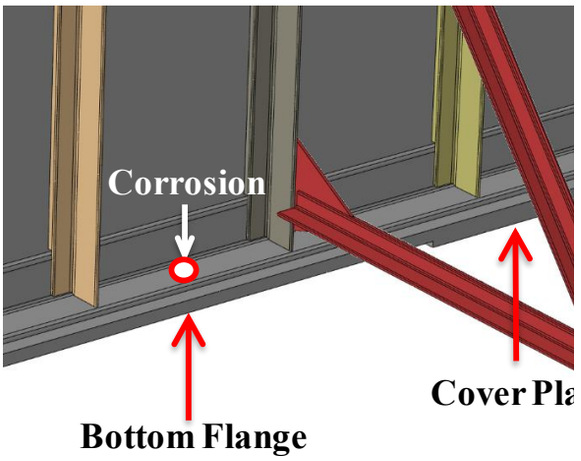


Figure 3. Case study: the location of a pit corrosion.

First-order reliability method (FORM) is utilized for the reliability analysis. Variables used for the reliability analysis are presented in Table 3.

Result of fatigue reliability analysis for Scenarios I and II is shown in Figure 4. Reliability indices decrease from approximately 5.0 to 2.0 for the operation time (t) from 10 to 100 years. The trend of the reliability indices shows a sharper decrease at the early years of operation than the later years of operation.

Results of fatigue reliability analysis for scenario III is shown in Figure 5. Time to corrosion nucleation (t_0) is considered for reliability analysis. It was assumed as a random variable due to a lack of information about the phenomenon. Even though coefficient of variance (COV) is changed from 0.01 to 0.95, reliability indices do not show significant discrepancies. It indicates that the time to corrosion nucleation does not have significant influence on fatigue failure of scenario III.

Table 3. Variables used for a case study.

Variable	Mean	C. O. V.	Type	Reference
T (mm)	51	-	Deterministic	Girder flange thickness
F_u (MPa)	400	-	Deterministic	Ultimate strength of steel
S_0 (MPa)	145	-	Deterministic	Actual measurement
S_a (MPa)	30	-	Deterministic	Actual measurement
a_c (mm)	51	-	Deterministic	Girder flange thickness
m	3	-	Deterministic	Rolfe and Barsom (1977)
$ADSC$ (cycles/day)	3323	0.3550	Lognormal	Actual measurement
t_0 (day)	1500	0.01/0.5/0.95	Lognormal	Shi and Mahadevan (2001)
C ($\mathrm{MPa}\sqrt{mm}$ MPa·m $m^{1/2}$)	7.12×10^{-9}	0.63	Lognormal	Fisher (1984)
p (10^{-6} m)	80.2	0.42	Lognormal	Albrecht and Naeemi (1984)
q	0.593	0.4	Lognormal	

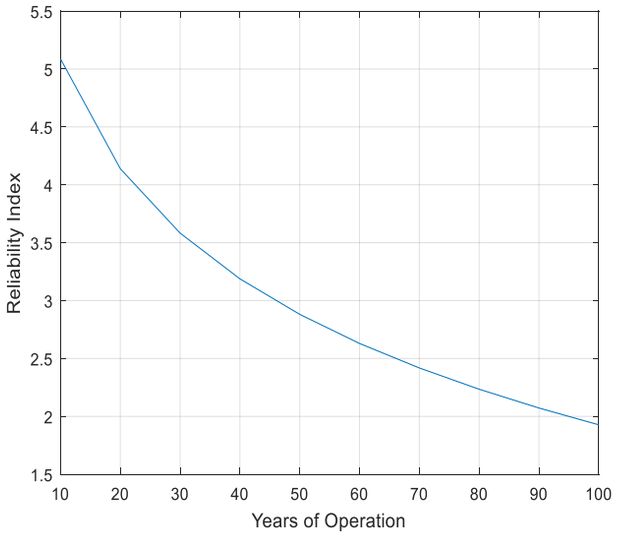


Figure 4. Reliability index for Scenario I and Scenario II.

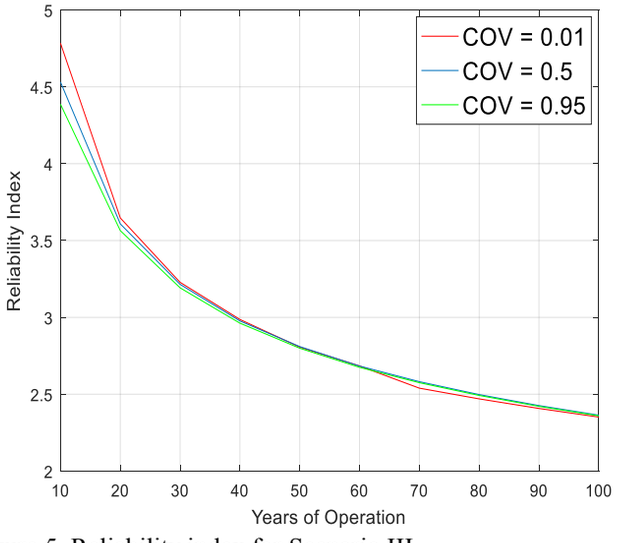


Figure 5. Reliability index for Scenario III.

5 CONCLUSIONS

As a preliminary study for developing reasonable guideline for evaluating deteriorated steel bridge member, fatigue reliability assessment procedures were studied. Since fatigue crack propagation corrosion are the two major damages of deteriorated steel members, fatigue limit state functions which reflects corrosion and crack propagations simultaneously are developed. Stress-strain approach is used to determine a limit penetration depth of a corrosion pit. Case studies were conducted to verify effectiveness of proposed assessment procedure.

ACKNOWLEDGEMENTS

This research was supported by a grant (17SCIP-B128568-01 2) from Smart Civil Infrastructure Research Program and a grant (17SCIP-B119960-02). Both grants were funded by the Ministry of Land, Infrastructure and Transport of the Korean government.

REFERENCES

AASHTO. 2010. *Bridge Element Inspection Guide Manual*, AASHTO, USA.

Cerit, M., K. Genel, & S. Eksi. 2009. Numerical investigation on stress concentration of corrosion pit. *Engineering Failure Analysis*, 16(7): p. 2467-2472.

Komp, M. 1987. *Atmospheric corrosion rating of weathering steel.* Calculations and significance.

Kondo, Y. 1989. Prediction of fatigue crack initiation life based on pit growth. *Corrosion*, 45(1): p. 7-11.

Korea Infrastructure Safety and Technology Corporation. 2011. *Safety Inspection and Precision Safety Diagnosis Detailed Guide(Bridge)*, Go-yang, Korea.

Ministry of transportation. 2000. *Ontario Structure Inspection Manual*, Ministry of transportation, Ontario, Canada.

Paris, P.C. and F. Erdogan. 1963. *A critical analysis of crack propagation laws*. ASME.

Park, Y.C. 2015. *Developing Fatigue Resistant Tube-to-transverse Plate Welded Connections for Highway Sign, Signal, and Luminaire Support Structures*. Ph.D. Dissertation, Lehigh University.

Roy, S. & J.W. Fisher. 2005. Enhancing fatigue strength by ultrasonic impact treatment. *International Journal of Steel Structures*, 5(3): p. 241-252.

Shi, P. & Mahadevan, S. 2003. Corrosion fatigue and multiple site damage reliability analysis. *International Journal of Fatigue*, 25, pp. 457-469.

Smith, K.N. 1970. A stress-strain function for the fatigue of metals. *J mater*, 5: p. 767-778.

Maintenance, Safety, Risk, Management and Life-Cycle Performance of Bridges – Powers, Frangopol, Al-Mahaidi & Caprani (Eds)
© 2018 Taylor & Francis Group, London, ISBN 978-1-138-73045-8

Reliability Analysis of Steel Bridges under Propagating Fatigue Cracks

H. Ali & M. Soliman
School of Civil and Environmental Engineering; Oklahoma State University, Stillwater, Oklahoma, USA

ABSTRACT: Fatigue is one of the major factors that may influence the safety of civil and marine structures. The presence of significant uncertainties related to loads, geometry, and material properties affects our ability to reliably predict the time-dependent performance of structures under fatigue deterioration. Probabilistic approaches can aid in predicting the time-dependent performance of structures under fatigue deterioration considering uncertainties. Moreover, reliability and risk-based management techniques can be used to predict the safe service life of fatigue sensitive structures, plan for their future inspections and support the decision-making process regarding maintenance and repair actions. This paper applies a probabilistic approach to quantify the reliability of a box-girder bridge against fatigue failure. The approach establishes a relationship between the maximum live load that can be sustained and the crack size. This relationship is next used to compute the time-variant bridge reliability against fatigue failure. The approach is applied to an existing steel box-girder bridge.

1 INTRODUCTION

Fatigue damage poses a significant threat to the integrity and safety of steel structures. This damage can lead to significant risks if overlooked during regular bridge inspection and maintenance activities. Fatigue cracks can occur at regions of high stress concentrations in a structural member subjected to load fluctuations. These stress concentrations are inherently present in a member due to the presence of initial imperfections induced during manufacturing and fabrication or due to residual stresses occurring in the heat affected zones during welding (Osgood 1954). The stress fluctuations under working loads causes plastic deformations at the crack tip (Lu and Liu 2010). In case of bridges, the stresses due to regular traffic loads at the fatigue critical details causes the initially microscopic imperfections to grow into macroscopic cracks which start to propagate at greater rates. These growing cracks can cause structural failure if not repaired on time (Han and Ramulu 2005). The increase in truck weights and traffic volume over time can lead to accelerated crack growth. Under time-variant increasing demand and diminishing capacity (see Figure 1), the service life and optimum maintenance and repair activities can be established based on reliability analysis.

The AASHTO code (AASHTO 2008) outlines the S-N (stress-life) curve approach for designing bridge components to minimize fatigue damage. In this approach, different structural configurations (i.e., details) are grouped based on their fatigue resistance into several categories each with its own stress-life relationship. These generalized curves are most commonly used in the design phase to predict the safe fatigue life. However, this method cannot be used to study the state of the crack at any point during the

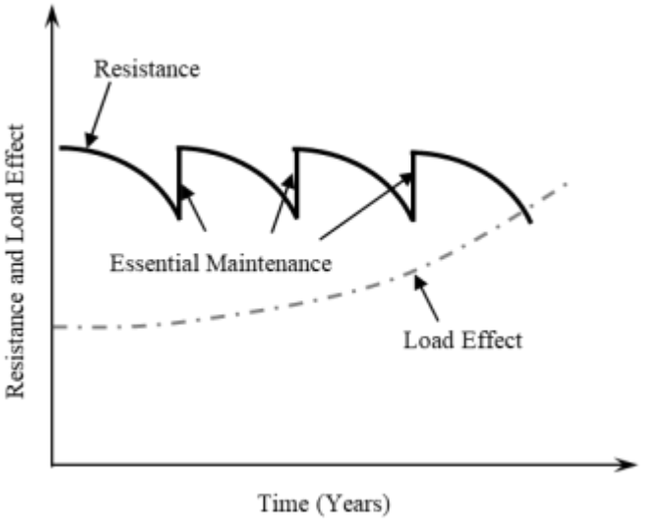


Figure 1. Load effect and resistance of bridge over time with maintenance actions

service life of the structure. Such problems can be solved by utilizing approaches based on the linear elastic fracture mechanics (LEFM). This approach can predict the crack growth against the number of cycles or time given the geometry and stress conditions at the investigated detail. LEFM is used in this paper to predict the crack growth in box-girder bridges. The bridge reliability considering fatigue crack growth is quantified by combining LEFM with information on the loads acting on the bridge during its service life.

Numerous research studies have been conducted on the prediction of crack growth in steel structures. McMillan and Pelloux (1967) experimentally investigated the growth of cracks under random and pseudo-random loadings. Their work has since served as a basis for research on random fatigue loading and crack growth. Lu and Liu (2010) developed a method for predicting the cycle-by-cycle crack growth over any timescale and over any crack length. Their model can analyze fatigue problems under variable amplitude loading. Mahmoud and Dexter (2005) investigated the crack growth behavior in stiffened panels under flexure loading. Cheung and Li (2003) performed probabilistic analysis using LEFM crack growth model and obtained the reliability of welds in steel bridges.

Kim et al. (2013) used LEFM to establish the optimum inspection and maintenance schedules of fatigue prone details in ship structures. Soliman et al. (2013) also used LEFM in a probabilistic model that can establish optimum inspection plans for bridges with multiple fatigue critical details. Finally, Soliman et al. (2016) proposed an approach based on LEFM for establishing the optimum inspection, monitoring, and maintenance times and types for fatigue critical locations. However, these probabilistic studies did not cover the overall reliability of the structural system against failure due to cracks, but rather, they focused on establishing the reliability with respect to the crack reaching a critical size.

In this paper, a probabilistic approach is proposed to quantify the bridge reliability considering global flexure failure under the presence of cracks. The crack growth is predicted using an LEFM model which considers the effect of residual stresses and provides the probabilistic descriptors of the crack size along the service life of the bridge. A finite element (FE) model of the structural system is constructed and used to find the live load carrying capacity of the bridge considering the loss of stiffness due to the growing cracks. Finally, a performance function is established to quantify the bridge reliability against global flexure failure under growing cracks. The approach is illustrated on an existing box-girder bridge.

2 CRACK GROWTH MODEL

The linear elastic fracture mechanics encompasses the stresses and their effects around a crack. The stress acting at the vicinity of the crack tip are expressed in terms of the stress intensity factor as

$$K = Y(a) \cdot S \cdot \sqrt{\pi \cdot a} \tag{1}$$

where K is the stress intensity factor, S is the stress, a is the crack size, and $Y(a)$ is the geometry correction factor which accounts for finite width or thickness, stress gradients, surface cracks, and crack shape (Fisher and Martz 1984).

Paris and Erdogan (1963) developed a relationship between the crack growth rate and stress range of the intensity factor as

$$\frac{da}{dN} = C \cdot (\Delta K)^m \tag{2}$$

where N is the number of cycles, C and m are material dependent parameters, and

$$\Delta K = \Delta S \cdot \sqrt{\pi \cdot a} \tag{3}$$

in which ΔS is the stress range.

Hence, the number of cycles required for the crack to grow from an initial crack size a_0 to a size a_c (i.e., critical crack size) is

$$N = \frac{1}{C \cdot \Delta S^m} \cdot \int_{a_0}^{a_c} \frac{1}{(Y(a) \cdot \sqrt{\pi \cdot a})^m} da \quad (4)$$

Each of the parameters in Equation (4) can be considered as a random variable with its own probabilistic distribution; therefore, the crack growth problem should be performed using probabilistic analysis in order to account for uncertainties associated with these input parameters (Cheung and Li 2003).

2.1 *Crack Growth in Stiffened Panels*

In stiffened bridge box girders, the crack growth is restricted compared to unstiffened plates, due to the presence of the longitudinal stiffeners. The crack growth in stiffened panels has been studied for stiffened box girders and a model to obtain the stress intensity factor accounting for the effects of stiffener restraint and residual stresses has been established in Dexter and Pilarski (2000). This approach is adopted in this paper to predict the crack growth in a bridge box girder with longitudinal stiffeners.

In welded box girders, the residual stresses play an important part in the crack growth. If the crack is in a zone with residual compressive stresses, the crack would require higher stresses (or larger number of cycles) to grow; whereas in case of tensile residual stresses, the crack growth would be rapid.

The stress intensity factor for the crack growth in a stiffened panel with stiffener restraint effect and residual stress effect is given by Dexter and Pilarski (2000)

$$K_{total} = 1 + K_1 + K_2 + K_{residual} \quad (5)$$

where $K_1 = f_1 \sigma \sqrt{\pi a}$ and $K_2 = f_2 \sigma \sqrt{\pi a}$ are stress intensity factors due to stiffener restraint, f_1 and f_2 are stiffener restraint coefficients and $K_{residual} = \frac{2}{\pi} \sqrt{\pi a} \int_0^a \frac{\sigma_{res}(x)}{\sqrt{a^2 - x^2}} dx$ is the residual stress intensity factor (Dexter and Pilarski 2000).

By combining Equation (5) and (4), the number of cycles required for a crack to grow from an initial crack size a_0 to a given crack size in the stiffened panel a_f can be established.

3 BRIDGE CAPACITY AND RELIABILITY PREDICTION

Due to the growing cracks, the flexural stiffness of the bridge box girder will decrease. This reduction can be quantified by computing the reduced live load carrying capacity of the box girder under the presence of the growing cracks. In this paper, the bridge resistance at time t is computed as the HL-93 loading (AASHTO 2008) multiplied by a factor $LLM(t)$, which results in the load that causes bridge collapse or large deflections to occur. In this paper, this deflection limit is assumed to be 0.0075L following the recommended values in Ghosn et al. (2010). Accordingly, the probability of failure can be represented as (Okasha and Frangopol 2010)

$$P_f(t) = \mathrm{P}[LLM(t) < LL(t)] \quad (6)$$

where $LLM(t)$ is the live load multiplier representing the resistance and $LL(t)$ is the expected normalized maximum live-load effect acting on the structure within the appropriate time t.

The input parameters required to establish the relationship between the live load multiplier and the crack size is obtained through executing finite element (FE) analysis of the investigated bridge. An iterative process has been established to quantify the maximum live load that could be placed on the bridge before it reaches the limiting deflection for a given crack size.

In order to estimate the time-variant probability of failure and reliability, the expected normalized live load $LL(t)$ can be computed using extreme value statistics as outlined in (Frangopol et al. 1997). This model is based on available truck survey data performed by the Ontario Ministry of Transportation which covered 10,000 trucks (Nowak 1993). The model can provide the distribution of the maximum truck loads with respect to time. The time-variant increasing rate of occurrence of these maximum loads can also be established following the approach proposed by the National Cooperative Highway Research Program Report 538 (NCHRP 2005).

Given the uncertainties associated with the different crack growth model input parameters (Rolfe and Barsom 1977; Connor and Fisher 2001), Monte Carlo simulation is used to establish the probabilistic distribution of the time required to reach a certain

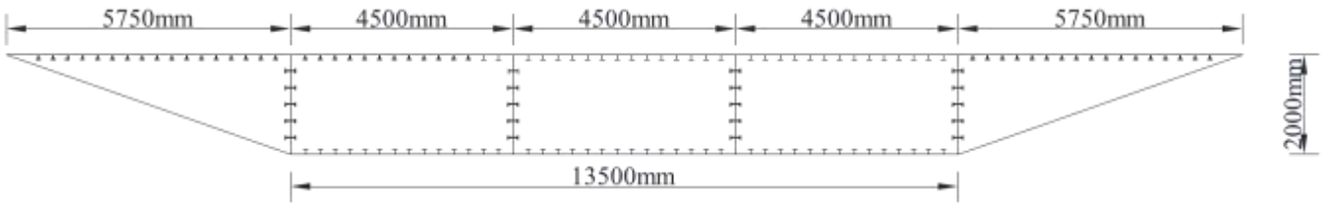


Figure 2. Bridge section

crack size, and subsequently, the time required to reach a certain live load capacity. The probability of failure can be used next to quantify the reliability using Equation (7) as shown in Figure 7.

$$\beta(t) = \Phi^{-1}[1 - P_f(t)] \quad (7)$$

Where Φ is the CDF of normal distribution.

4 ILLUSTRATIVE EXAMPLE

A three-lane steel box girder bridge, the Xianyue Road Bridge in Xaimen City, China, is selected as the case study in this paper. The superstructure of the bridge is a 25m wide thin walled box girder consisting of two 45m long spans. The cross-section has three box cells and two external lenticular cells shaped cantilever extensions as shown in Figure 2. Since the lenticular cells do not play a significant role in the load resisting mechanism of the bridge (Zhang et al. 2010), they were replaced in this study by triangular cells for simplicity. Figure 3 shows the details of the longitudinal stiffeners of the box girder.

The FE model (Figure 4) of the bridge is constructed using non-linear finite element code SAP2000® v.19 (SAP2000 2016). The FE model provides the bridge deflections and live load multipliers for different crack sizes. The model was developed for one span of the bridge assuming pinned support conditions. The model is constructed using a combination of shell and frame elements. The flanges and webs of the box girder are modelled as shell elements and the longitudinal stiffeners are modelled as frame elements.

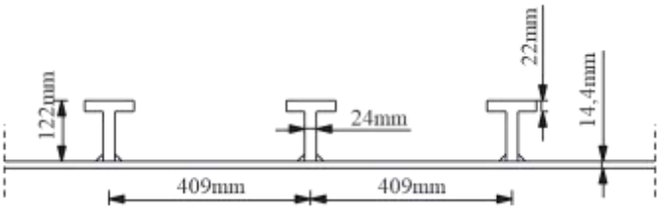
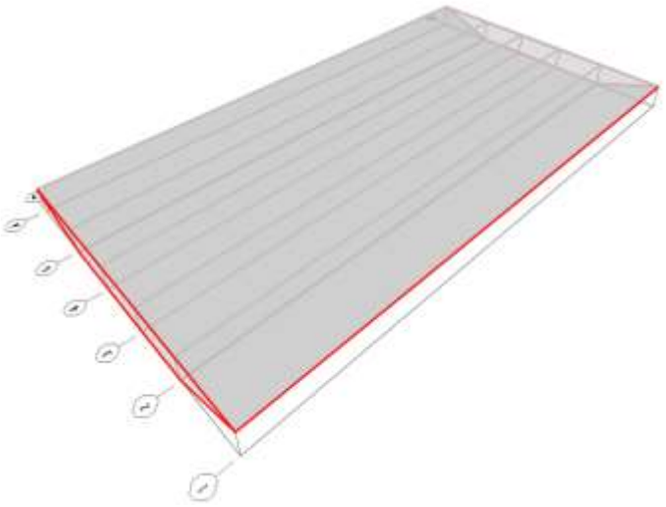


Figure 3. Stiffener Detail

The AASHTO HL-93 (AASHTO 2008) loading, consisting of a distributed lane load and a standard truck, was placed on the bridge to obtain the largest deflection at mid-span. Next the live load is increased incrementally until the established deflection limit is reached.


Figure 4. FEM model of bridge

4.1 *Probabilistic Crack Growth Analysis*

A transversal crack is initiated and propagated in the lower flange of the box girder. The initial crack size is assumed 400 mm and the crack propagation is studied up to crack size of 4200 mm. The values of material constants C and m are considered as 9.5×10^{-12} and 3 respectively. The number of cycles is assumed a random variable with mean 3500 and coefficient of variation of 0.1. The maximum and minimum stress values are obtained from the finite element model under dead load and total loads. The probabilistic crack growth profile is established using Monte Carlo simulation based on Equations (4) and (5) and shown in Figure 5.

For each crack size, the live load multiplier required to reach a deflection of 337.5 mm (i.e., 0.0075L) is computed using the non-linear finite element analysis. Accordingly, a probabilistic time-variant live load multiplier can be established as

shown in Figure 6. By setting the reliability threshold, optimum maintenance and repair times can be identified as the time to reach the reliability threshold.

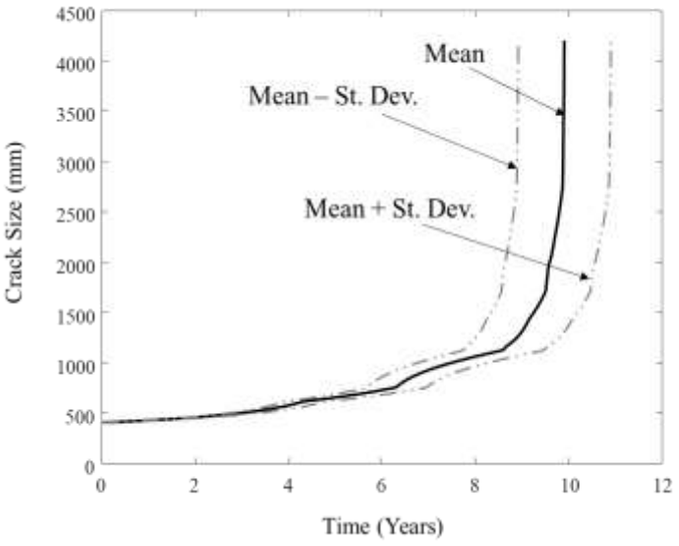


Figure 5. Probabilistic crack growth profile through stiffened panel

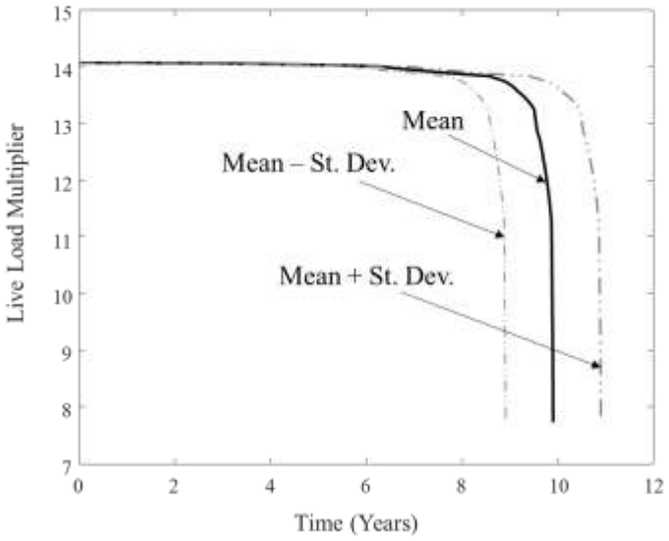


Figure 6. Change in live load multiplier with time due to crack growth

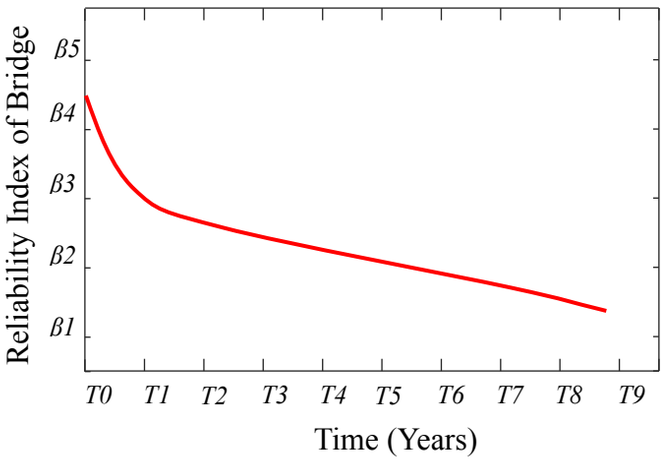


Figure 7. Time variant bridge reliability under growing cracks

This live load multiplier combined with information on time-variant live loads acting on the bridge can be used to establish the probability of failure representing the probability the actual live load will exceed the live-load capacity of the bridge. This is shown conceptually in Figure 7.

5 CONCLUSIONS

This paper presented an approach for establishing the time-variant global reliability profile of bridges considering the reduction in resistance due to fatigue cracks. The approach employs LEFM to establish the crack growth profile and integrates it into a finite element model to quantify the maximum live load that can be applied to the bridge until a certain deflection limit is reached. The maximum live loads are quantified as a function of the number of cycles (or time).

The approach is proven efficient in considering ductile failure due the reduction of the cross-sectional resistance. However, more analysis is required to include failure modes associated with uncontrolled crack growth. This can be performed using the failure assessment diagram as outlined in the guide to methods for assessing the acceptability of flaws in metallic structures (British Standard 2005).

6 ACKNOWLEDGMENTS

The authors gratefully acknowledge the financial support from (a) the Southern Plains Transportation Center (SPTC) award number 15.1-12 and (b) the Transportation Consortium of South Central States (Tran-SET) project number 17STOKS01. The opinions and conclusions presented in this paper are those of the authors and do not necessarily reflect the views of the sponsoring organizations.

7 REFERENCES

AASHTO. 2008. *"AASHTO LRFD Bridge Design Specifications."* 4th Ed., AASHTO, Washington, DC.

British Standard, B.S. 2005. 7910. *Guide on methods for assessing the acceptability of flaws in metallic structures*.

Cheung, M. S. & Li, W. C. 2003. Probabilistic fatigue and fracture analyses of steel bridges. *Structural Safety,* 25**,** 245-262.

Connor, R. J. & Fisher, J. W. 2001. Report on field measurements and assessment of the I-64 Kanawha River bridge at Dunbar, West Virginia.

Dexter, R. J. & Pilarski, P. J. 2000. Effect of welded stiffeners on crack growth rate. Ship Structure Committee Report SSC-413, Washington DC.

Fisher, J. W. & Martz, D. Fatigue and fracture in steel bridges. Proceedings 1st International Bridge Conference, 1984, Pittsburgh, Pennsylvania.

Frangopol, D. M., Lin, K.-Y. &, A. C. 1997. Life-Cycle Cost Design of Deteriorating Structures. *Journal of Structural Engineering,* 123**,** 1390-1401.

Ghosn, M., Moses, F. & Frangopol, D. M. 2010. Redundancy and robustness of highway bridge superstructures and substructures. *Structure and Infrastructure Engineering,* 6**,** 257-278.

Han, M. K. & Ramulu, M. Fatigue Life Prediction of Ship Welded Materials. Key Engineering Materials, 2005. Trans Tech Publ, 743-749.

Kim, S., Frangopol, D.M. And Soliman, M., 2013. Generalized probabilistic framework for optimum inspection and maintenance planning. Journal of Structural Engineering, 139(3), pp.435-447.

Lu, Z. & Liu, Y. 2010. Small time scale fatigue crack growth analysis. *International Journal of Fatigue,* 32**,** 1306-1321.

Mahmoud, H. N. & Dexter, R. J. 2005. Propagation rate of large cracks in stiffened panels under tension loading. *Marine Structures,* 18**,** 265-288.

McMillan, J. C. and Pelloux, R. M., "Fatigue Crack Propagation Under Program and Random Loads," STP47241S Fatigue Crack Propagation, STP47241S, J. Grosskreutz, Ed., ASTM International, West Conshohocken, PA, 1967, pp. 505-535.

National Cooperative Highway Research Program (NCHRP). (2005). "Traffic data collection, analysis, and forecasting for mechanistic pavement design." Rep. No.538, Washington, D.C.

Nowak, A. S. 1993. Live load model for highway bridges. *Structural safety,* 13**,** 53-66.

Okasha, N. M. & Frangopol, D. M. 2010. Advanced modeling for efficient computation of life-cycle performance prediction and service-life estimation of bridges. *Journal of Computing in Civil Engineering,* 24**,** 548-556.

Osgood, W. R. 1954. *Residual stresses in metals and metal construction*, Reinhold Publishing Corporation.

P. Paris, F. E. 1963. A Critical Analysis of Crack Propagation Laws. *Journal of Basic Engineering,* 85 (Series D)**,** 528-534.

Rolfe, S. T. & Barsom, J. M. 1977. *Fracture and fatigue control in structures: applications of fracture mechanics*, ASTM International.

SAP2000 Analysis Reference Computers and Structures, Inc, Berkeley (CA) (2016)

Soliman, M., Frangopol, D. M. & Kim, S. 2013. Probabilistic optimum inspection planning of steel bridges with multiple fatigue sensitive details. *Engineering Structures,* 49**,** 996-1006.

Soliman, M., Frangopol, D. M. & MONDORO, A. 2016. A probabilistic approach for optimizing inspection, monitoring, and maintenance actions against fatigue of critical ship details. *Structural* Safety, 60, 91-101.

Zhang, H., Desroches, R., Yang, Z. & Liu, S. 2010. Experimental and analytical studies on a streamlined steel box girder. *Journal of Constructional Steel Research,* 66**,** 906-914.

Maintenance, Safety, Risk, Management and Life-Cycle Performance of Bridges – Powers, Frangopol, Al-Mahaidi & Caprani (Eds)
© 2018 Taylor & Francis Group, London, ISBN 978-1-138-73045-8

A non-concurrent multiscale simulation of fatigue crack on orthotropic steel decks

B. Wang
Department of Bridge Engineering, Tongji University, Shanghai, China
H. De Backer
Department of Civil Engineering, Ghent University, Zwijnaarde, Belgium
A. Chen
Department of Bridge Engineering, Tongji University, Shanghai, China

ABSTRACT: The numerous welded joints on orthotropic steel deck lead to high probability to the emerge of fatigue cracks. Numerical simulation based on linear elastic fracture mechanics has been proven to be effective on reproducing the crack growth process. When put into practice on actual projects, however, its accuracy and feasibility are largely dependent on features in various scales. This paper presents a non-concurrent multiscale method on investigating the crack on orthotropic steel decks. According to the fatigue test, the rib-to-deck weld toe crack that penetrates the deck plate was addressed, and the key factors were the crack shape and size, especially for the shallow and long early-stage cracks. Therefore, a two-dimensional local model of rib-to-deck weld toe crack was built using extended finite element method, by which the stress intensity factors for early-stage cracks can be calculated. Based on the similar concept of nominal stress, it can be easily linked to the macroscopic model, and forms a non-concurrent multiscale method that enables to simulate the crack growth at rib-to-deck weld toe. As a result, a detailed analysis on different stages in crack growth rate curve were given with respect to Paris law, implying the influences from welding process on early-stage fatigue cracks. The results will benefit the fatigue assessment and life estimation of orthotropic steel decks, and may further be introduced to the maintenance work by combining with inspections.

1 INTRODUCTION

As a common structural type in steel bridge, the orthotropic steel deck (OSD) is favored for its mechanical efficiency in terms of load carrying capacity per unit weight. Whilst its fatigue performance is always the issue, as it is one of the most-reported structures that suffer from fatigue problems. According to previous studies (Fisher 1970, Wolchuk 1990, de Jong 2004), the most fatigue-prone areas of OSDs are the welded joints and adjacent areas. Experimental and numerical studies were conducted on this issue (Kolstein 2007; Sim & Uang 2012; Xiao et al. 2008; Aygül et al. 2012). These studies were mainly based on the stress-life relations that overlook the exact crack growth in the fatigue process. With respect to that, the introduction of linear elastic fracture mechanics will provide a way to further investigate the fatigue problem on OSDs (Kiss & Dunai 2012, Nagy et al. 2015). In addition, this kind of method is capable of evaluating the remaining life of OSDs, in case the fatigue-oriented inspection was given.

Nevertheless, since the initial cracks in welded joints are tiny when compared with the structure size, the multiscale problem is one of the biggest concerns when focusing on the fatigue crack growth on OSDs. For multiscale problems, two kinds of models, i.e. the concurrent model and the non-concurrent (or hierarchical) one, were usually adopted (Li et al. 2009, Sumi & Inoue 2011, Silani et al. 2014). Generally speaking, the concurrent model may obtain results with higher accuracy. But on the issue of fatigue on large-scale engineering works, the concurrent model is quite difficult to put into practice as it requires to solve various scale simultaneously. Therefore, the non-concurrent model seems to be a better option, since the trivial coupling effects between the cracked part and the whole model can be neglected.

This paper presented a multiscale study with respect to the fatigue test that reveals the crack growth behavior on rib-to-deck welded joint of OSDs. The multiscale method was established in a non-concurrent way and obtained the crack growth rate (CGR) curve. For the final step, different stages of the fatigue process of the rib-to-deck welded joint of OSDs were addressed and analyzed.

2 FATIGUE TEST

As the most convincing way, the fatigue test is always the first option for fatigue studies. Kolstein (2007) summarized 245 fatigue tests on rib-to-deck welded joints of OSDs, and the stress-life relations were obtained and compared with the S-N curves in Eurocode. However, the information about the crack growth process in these fatigue tests is limited. Hence, a fatigue test designed with respect to that was conducted. A brief introduction is given in this

section, and more details can be found in (Nagy et al. 2017).

2.1 *Test scheme*

Given the scatter results from the fatigue tests in previous studies, it is preferred that the test can be repeated as many times as possible. In that case, fatigue test on small-scale specimens is a good option for cost concerns. The designed test specimen was, therefore, consisted of one trapezoidal stiffener and the deck plate, as shown in Figure 1. It was simply supported at the distance between longitudinal stiffeners, i.e. 300mm, to the concerned welded joint, and fixed at the distance of 150 mm to the welded joint on the other side. The load was a line load applied at the distance of 70 mm to the left of the welded joint. The length of the specimen is 370 mm. According to the common way of OSD production, the test specimens were welded by submerged arc welding (SAW).

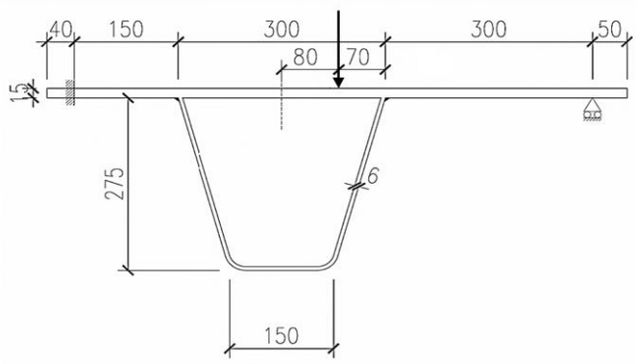


Figure 1 Test specimen and boundary conditions (unit in mm)

To understand the fatigue crack growth, the beach mark on the fracture face offers a simple way to trace the entire process. The only concern is that according to some of the fatigue tests on OSDs (Ya et al. 2011, Kainuma et al. 2016), the obtained beach marks were either with limited quantities, or can hardly be identified visually. Hence, it was planned to apply the loading sequences designed for this fatigue test specifically, which can help to produce clear beach marks on the fracture face.

The loading sequences consisted of two parts, i.e. the base cycles and beach mark cycles. The beach mark cycles were designed following the principle that the maximum load equals to the base cycle to prevent the effect of overload retardation. Whilst the minimum load, noted as $P_{beachmark}$, will determine the load range ratio between beach mark cycles and base cycles, which is about 0.2~0.4 in this test.

2.2 *Test results*

In total eleven specimens were tested, among which nine specimens were designed to produce beach marks. The exceptions were Specimen 2 which did not apply beach mark cycles, and Specimen 8 which stopped after more than 1.5 million cycles as no sign of failure occurred. The summary of the applied loads and the cycles till failure for all test specimens were given in Table 1.

By this fatigue test, results show that the crack initiation at the weld toe was predominant in every specimen. The cracks propagated vertically towards the top face of deck plate and longitudinally followed the weld toe strictly.

Table 1 Summary of loading conditions and fatigue cycles on test specimens

No.	P_{max} (kN)	P_{min} (kN)	$P_{beachmark}$ (kN)	R	N_{base}	$N_{beachmark}$
1	27	-27	-10.8	-1	156 535	119 220
2	40	-40	/	-1	62 844	/
3	40	-40	-24	-1	46 737	168 692
4	0	-40	-24	0	147 425	19 500
5	0	-27	-16.2	0	484 782	178 149
6	0	-35	-21	0	247 762	99 067
7	0	-31	-18.6	0	272 852	337 525
8	40	0	24	-∞	>1 527 492	640 000
9	40	-40	-8	-1	40 809	24 402
10	0	-31	-18.6	0	270 544	307 902
11	30	-30	-18	-1	101 394	148 871

2.3 *Crack growth process analysis*

The beach marks were observed with naked eyes in the first place. One of the test specimens with most beach marks on its fracture face was Specimen 10, as shown in Figure 2, which is also analyzed as the typical case hereinafter. Clearly, only a few beach marks can be observed on such a global view. The first few beach marks can only be identified from magnified local view from scanning electron microscope (SEM) and/or stereo microscope. According to the beach marks, it can be addressed that the shape of a single crack was basically semi-elliptical.

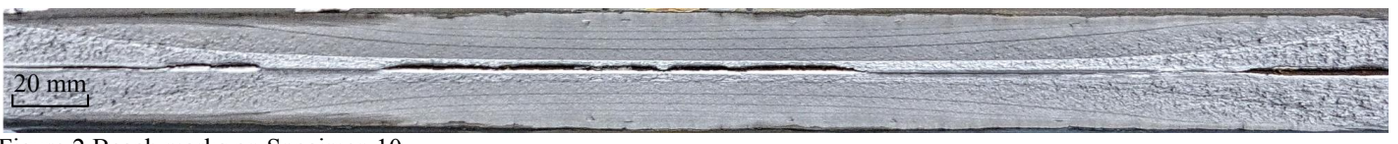


Figure 2 Beach marks on Specimen 10

The size of the semi-elliptical cracks was measured afterwards. The crack depth *a* with respect to the fatigue cycle numbers *N* was given in Figure 3. Table 2 further presented the elliptical long axis length, namely the half crack length *c*, and the aspect ratio *a/c* for Specimen 10. The results show that the crack is quite long and shallow in the beginning, and grows mainly in the depth direction as the aspect ratio gets larger.

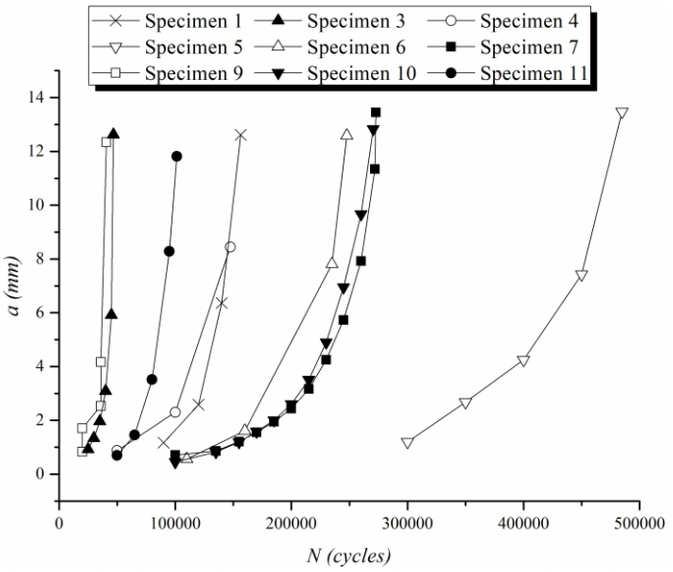


Figure 3 Crack growth process according to the beach marks

Table 2 Crack sizes on Specimen 10 according to the beach marks

Beach mark	N	*a* (mm)	*c* (mm)	*a/c*
0*	0	0.288	93.6	0.003
1	100000	0.451	100.7	0.004
2	135000	0.825	111.1	0.007
3	155000	1.188	117.9	0.010
4	170000	1.578	123.5	0.013
5	185000	2.002	128.4	0.016
6	200000	2.601	134.0	0.019
7	215000	3.514	137.5	0.026
8	230000	4.900	142.5	0.034
9	245000	6.952	152.5	0.046
10	260000	9.663	159.0	0.061
11	270544	12.827	172.5	0.074

* Beach Mark 0 means the initial crack measured according to the different fractography feature in SEM.

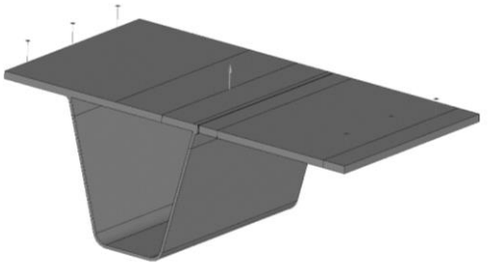
3 NON-CONCURRENT MULTISCALE STUDY BASED ON BEACH MARKS

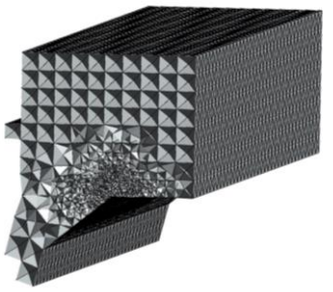
3.1 *Macroscopic model*

With respect to the fatigue test setup, a macroscopic model was firstly built in finite element software SAMCEF, as shown in Figure 4a). The element type used was solid element, and the total number of elements was 144 966. The supportive system was modeled as the test scheme, which means to fix the deformation on all directions on the left, and the deformation on the longitudinal and vertical directions on the simple-supported line.

With the eXtended Finite Element Method (XFEM) module in SAMCEF, a user-defined XFEM domain that contains a crack can be defined in the model, and the mesh around the crack will be refined in an adaptive way to generate elements that are fine enough to calculate the stress intensity factors (SIFs) along the crack front. Ideally, it is possible to verify or reproduce the fatigue process in the test based on all beach marks. Nevertheless, the computations were too heavy to conduct for small cracks in early stages. The main reason could be attributed to the shallow and long crack shape, which requires an enormous number of elements in the XFEM domain.

Figure 4b) presents the refined mesh of the XFEM domain for a semi-elliptical crack with the depth of 2mm and length of 128.4 mm, in accordance with the 5th beach mark on Specimen 10. It can be seen that the element shape is converted into tetrahedra for adaptive refinement first, and the region around the crack, especially the crack front, is refined. It added 107 910 elements to the model, and pushed the total element number to more than 250 000. However, for an initial crack with a depth smaller than 0.3 mm and a length more than 90 mm, the density of the elements would be too high to achieve. Since the XFEM has already provided the advantage by allowing the crack body to intersect the elements, the refinement of the mesh is only determined by the requirement of calculating stress field around the crack front. It means that the mesh around the crack cannot be optimized anymore.


a) Macroscopic model


b) XFEM domain for the 5th beach mark of Specimen 10
Figure 4 Cracked model in SAMCEF

All the beach marks were tested to calculate with the macroscopic model, and it turns to be feasible for those with the depths larger than 1.5mm only. For

smaller cracks, it is, therefore, necessary to build a multiscale way.

3.2 *Local model*

This model was built focusing on the early-stage cracks with the depth smaller than 1.5mm. As the aspect ratios for these cracks were quite small, the crack length was much larger than the depth, which means the stress field for the crack front could be approximated by plane strain assumption in two-dimensions. On the other hand, a two-dimensional model is also the only feasible way with the current computational ability, as the macroscopic model in SAMCEF has almost reached its limit.

An XFEM program coded in MATLAB was adopted to build the two-dimensional model in plane strain status, as shown in Figure 5. It was built for the weld toe region, and the geometry was determined with respect to the full thickness of the deck plate and the weld toe flank angle.

As a local model, the boundary conditions should be in accordance with the global model, i.e. the macroscopic one. Normally, the displacement-based sub-model could give a relatively accurate solution. However, the sub-model is kind of a refined model that zooms into the macroscopic one, which requires the exact same geometry. As in two-dimensions, the boundary displacements can comply with only one section of the three-dimensional model, and this essential difference could lead to inevitable errors. In that case, the stress boundary conditions were applied to this local model instead of the displacement boundary conditions. The bending/membrane stresses were applied on the right edge of the model, while full fixations were used on the left edge. But it should be noted that, in most cases, the membrane stresses were so small that can be ignored (Wang et al. 2017), and only the bending stresses were applied.

The stress to be applied should be far away enough to the weld toe, which makes it more or less similar to the nominal stress. Two benchmarks were given to validate this local model by comparing the Mode-I SIFs. To be comparable with the results obtained by stress intensity factor handbook (Murakami & Hasebe 2001) and Newman-Raju Equation (Newman & Raju 1981), it was built without considering the flank angle first, as shown in Figure 6a). As long as the distance between the crack and boundary, namely the half width of the local model *w/2*, is large enough, the adopted boundary conditions agreed with previous studies that using nominal stress. In case that the flank angle is considered, this distance should be further verified, since the flank angle itself will lead to stress concentration. Therefore, a set of local models with the flank angle equals 40 degrees and various values of *w/2* were built to calculate and compare the SIFs, as shown in Figure 6b). The SIFs obtained by *w/2* larger than 5mm are quite close, indicating the small error using this model.

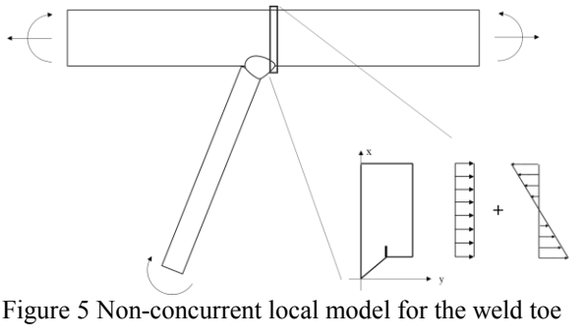
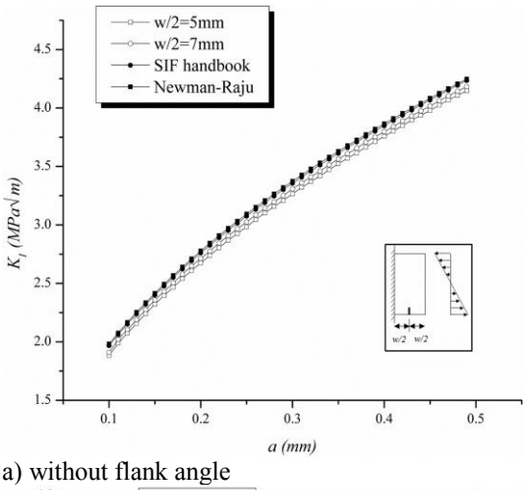
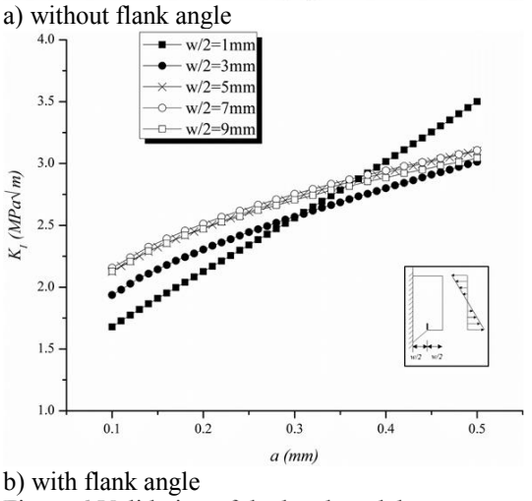


Figure 5 Non-concurrent local model for the weld toe



a) without flank angle



b) with flank angle

Figure 6 Validation of the local model

On the other hand, the stress to be applied should also be free from the influence of the growth of early-stage cracks, so that the local model could be easily linked to the macroscopic one, and this non-concurrent method will be applicable on this issue. According to the strain ranges measured on Specimen 10 (see Table 3), it can be addressed that early-stage cracks (till the 4th beach mark) will hardly affect the strain ranges if *w/2* is larger than 7mm. With consideration of both requirements and computational abilities, *w/2* was set to be 8 mm. Hence, the size of the local model was 16 × 15mm. The element size of 20 μm was adopted, leading to more than 600,000 elements in the local model. The applied

bending stress on the local model was 172.21MPa, provided by the non-cracked macroscopic model.

Table 3 The reductions of strain range at different strain gauges

w/2 (mm)	$\Delta\varepsilon_1$ (με)	$\Delta\varepsilon_2$ (με)	$\Delta\varepsilon_3$ (με)	$\Delta\varepsilon_4$ (με)	$(\Delta\varepsilon_4-\Delta\varepsilon_1)/\Delta\varepsilon_1$
3	981	862	738	610	-37.80%
5	980	934	881	818	-16.53%
7	984	967	943	914	-7.19%
9	911	903	891	876	-3.82%
11	758	753	746	737	-2.75%

* $\Delta\varepsilon_i$ is the average value of the strain ranges before the *i*-th beach mark

3.3 *Results*

The results were verified in the first place by comparing the SIFs for three cracks, i.e. S10BM4, S7BM4, S6BM2, that are possible to solve by both the SAMCEF model and the local model, as given in Table 4. The S10BM4, for example, refers to the 4th beach mark identified on Specimen 10, and so on. Clearly, the results from the local model are slightly smaller with acceptable errors.

Table 4 Verification of results obtained by the local model

Beach mark	Crack dimensions		K (MPa·√m)		
	a (mm)	*c* (mm)	Local model	SAMCEF model	diff.
S10BM4	1.578	123.5	13.81	14.31	-3.52%
S7BM4	1.551	123.2	13.74	14.15	-2.90%
S6BM2	1.611	147.5	15.70	16.26	-3.46%

Eventually, the macroscopic SAMCEF model combined with the local model was applied to obtain the SIFs for cracks indicated by beach marks, as shown in Table 5. It should be noted that the crack growth rate can only be achieved by the distance between two beach marks and the cycles, and thus is an average value for one period. Therefore, the SIF for each beach mark cannot be used directly for the CGR curve. Instead, a representative SIF range for one period is required. As the Paris law indicated, the CGR changes with SIF range in power law, and therefore a linearity can be expected when taking the logarithm of them,

$$log_{10}(\frac{\Delta a}{\Delta N})_i = log_{10}C + m log_{10}\overline{\Delta K_i} \quad (1)$$

where *i* refers to the period before the *i*-th beach mark; *C* is the Paris constant and *m* is the Paris exponent; $\overline{\Delta K_i}$ is the representative SIF range for this period. Being a linearity, it is easy to get $\overline{\Delta K_i}$ as follows,

$$log_{10}\overline{\Delta K_i} = (log_{10}\Delta K_{i-1} + log_{10}\Delta K_i)/2 \quad (2)$$

where ΔK_i is the SIF range for the *i*-th beach mark. Accordingly, the CGRs and the corresponding SIF ranges were given in Table 5. Consequently, the relationship between CGR and the SIF range can be drawn for Specimen 10 in logarithm coordinates, as shown in Figure 7.

Table 5 Summary of calculation on specimens

Beach mark	K (MPa·√m)	$\Delta a/\Delta N$ (m/cycle)	$\overline{\Delta K}$ (MPa·√m)
0	8.89	-	-
1	9.87	1.628E-09	9.37
2	11.46	1.069E-08	10.64
3	12.67	1.815E-08	12.05
4	14.31	2.600E-08	13.23
5	15.57	2.827E-08	14.66
6	17.23	3.993E-08	16.38
7	19.65	6.087E-08	18.40
8	23.24	9.240E-08	21.37
9	28.57	1.368E-07	25.77
10	34.60	1.807E-07	31.44
11	32.85	3.001E-07	33.71

In accordance with Paris law, the entire progress of crack growth is generally described by three stages: I) threshold region; II) Paris region; III) stable tearing crack growth region. However, one interesting observation in Figure 7 is that there exists a slight reduction in Stage II, which makes a "pit" on the curve. Thus two sub-stages could be addressed, named as Stage II-a and Stage II-b hereinafter. The stages of crack growth can then be elaborated as follows.

Stage I: the initial crack stage, in which the crack growth rate is low but increases sharply. In this stage, microscopic and mesoscopic heterogeneities will affect the crack growth. From the test results, this stage lasts till the crack goes to the depth about 0.5 mm.

Stage II-a: the transition stage, in which the increment of CGR, i.e. the slope of the curve, slows down gradually. In the meantime, the uncertainty induced by the microscopic and mesoscopic heterogeneities still affect the CGR. In the end of this stage, as the crack (around 2-mm-depth) is getting further away from the heat-affected zone, the reduction of CGR can be identified on the curve instead of a smooth transition to the next one.

Stage II-b: the stable crack propagation stage. The classical Paris law is expected to be applicable, and the uncertainty induced by the heat-affected zone fades in this stage.

Stage III: the unstable crack propagation stage.

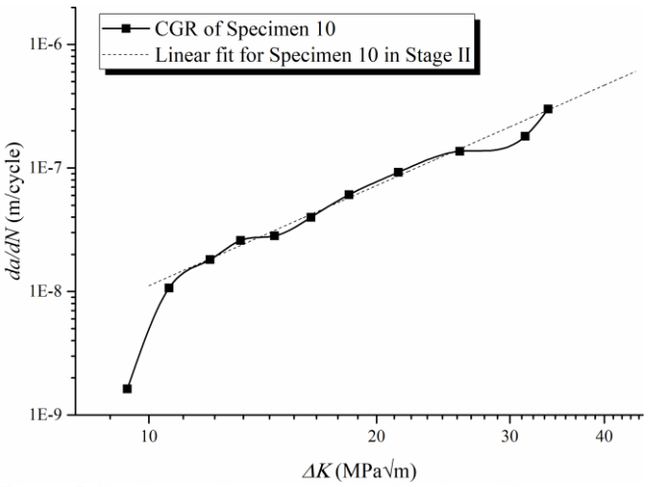


Figure 7 Crack growth rate curve for Specimen 10

4 CONCLUSIONS

This paper established a multiscale method that enables to compute the SIFs in a numerical way with respect to the fatigue test. Firstly, the crack growth process was traced using beach mark method in the test, and then the corresponding SIFs should be calculated with respect to the crack shape and size. The three-dimensional macroscopic model built in SAMCEF was proved to not applicable on the early-stage cracks due to computational ability limits. Hence, a two-dimensional local model was built and linked to the macroscopic one using a non-concurrent way. The applicability and the accuracy were validated by comparing with previous studies and with the SAMCEF model. Afterwards, the SIFs for the whole crack growth process can be obtained. As a result, different stages of crack growth can be addressed, which are basically follows the Paris law. However, part of Stage II seemed to have fluctuations of CGRs, which could be the effect induced by the heat-affected zone or weld defects in welded joints. The results will benefit the fatigue assessment and the maintenance work for OSDs when combining with inspections. But due to the limited data points in Stage I and Stage II-a, future research is still needed as the majority of fatigue life will be spent on these stages.

ACKNOWLEDGEMENTS

The authors are grateful for the support provided by National Natural Science Foundation of China (grant number 51678437).

REFERENCE

Aygül, M., Al-Emrani, M., & Urushadze, S. 2012. Modelling and fatigue life assessment of orthotropic bridge deck details using fem. *International Journal of Fatigue, 40*, 129-142.

De Jong, F. 2004. *Overview fatigue phenomenon in orthotropic bridge decks in the Netherlands*. Paper presented at the 2004 Orthotropic bridge conference, Sacramento.

Fisher, J. W. 1970. *Effect of weldments on the fatigue strength of steel beams*: Highway Research Board, National Research Council.

Kainuma, S., Yang, M., Jeong, Y.-S., Inokuchi, S., Kawabata, A., & Uchida, D. 2016. Experiment on fatigue behavior of rib-to-deck weld root in orthotropic steel decks. *Journal of Constructional Steel Research, 119*, 113-122.

Kiss, K., & Dunai, L. 2002. Fracture mechanics based fatigue analysis of steel bridge decks by two-level cracked models. *Computers & Structures, 80*(27), 2321-2331.

Kolstein, M. H. 2007. *Fatigue classification of welded joints in orthotropic steel bridge decks*: TU Delft, Delft University of Technology.

Li, Z. X., Chan, T. H. T., Yu, Y., & Sun, Z. H. 2009. Concurrent multi-scale modeling of civil infrastructures for analyses on structural deterioration—part i: Modeling methodology and strategy. *Finite Elements in Analysis and Design, 45*(11), 782-794.

Murakami, Y., & Hasebe, N. 2001. *Stress intensity factors handbook*. Elsevier Science.

Nagy, W., Van Bogaert, P., & De Backer, H. 2015. LEFM based fatigue design for welded connections in orthotropic steel bridge decks. *Procedia Engineering, 133*, 758-769.

Nagy W., Wang B., Culek B., Van Bogaert P., & De Backer, H. 2017. Development of a fatigue experiment for the stiffener-to-deck plate connection in Orthotropic Steel Decks. *International Journal of Steel Structures.* 17(4), 1353-1364.

Newman, J. C., & Raju, I. S. 1981. An empirical stress-intensity factor equation for the surface crack. *Engineering Fracture Mechanics, 15*(1), 185-192.

Silani, M., Ziaei-Rad, S., Talebi, H. & Rabczuk, T. 2014. A semi-concurrent multiscale approach for modeling damage in nanocomposites. *Theoretical and Applied Fracture Mechanics,* 74**,** 30-38.

Sim, H.-B., & Uang, C.-M. 2012. Stress analyses and parametric study on full-scale fatigue tests of rib-to-deck welded joints in steel orthotropic decks. *Journal of Bridge Engineering, 17*(5), 765-773.

Sumi, Y., & Inoue, T. 2011. Multi-scale modeling of fatigue crack propagation applied to random sequence of clustered loading. *Marine Structures, 24*(2), 117-131.

Wang, B., Zhou, X.-Y., De Backer, H., Chen, A., & Schmidt, F. 2017. Macro-crack initiation life for orthotropic steel decks considering weld heterogeneity and random traffic loading. *Structure and Infrastructure Engineering, 13*(12), 1639-1652.

Wolchuk, R. 1990. Lessons from weld cracks in orthotropic decks on three european bridges. *Journal of Structural Engineering, 116*(1), 75-84.

Xiao, Z.-G., Yamada, K., Ya, S., & Zhao, X.-L. 2008. Stress analyses and fatigue evaluation of rib-to-deck joints in steel orthotropic decks. *International Journal of Fatigue, 30*(8), 1387-1397.

Ya, S., Yamada, K., & Ishikawa, T. 2011. Fatigue evaluation of rib-to-deck welded joints of orthotropic steel bridge deck. *Journal of Bridge Engineering, 16*(4), 492-499.

Maintenance, Safety, Risk, Management and Life-Cycle Performance of Bridges – Powers, Frangopol, Al-Mahaidi & Caprani (Eds)
© 2018 Taylor & Francis Group, London, ISBN 978-1-138-73045-8

Numerical Fracture Mechanics Analysis of Distortion-Induced Fatigue in Steel Bridges

C. S. Wang, B. Cui, N.X. Ma, L. Duan, Y.Z. Wang
Engineering Research Center for Large Highway Structure Safety of Ministry of Education, College of Highways, Chang'an University, Xi'an, China

ABSTRACT: Aimed to study the propagation mechanism of steel bridge distortion-induced fatigue cracks, a finite element model was built to calculate the residual stresses by simulating the entire welding process of the horizontal-gusset-plate web gap detail. Numerical fracture mechanical models were built based on eXtended Finite Element Method to analyze the crack propagation behavior. The results of the welding process show that there are large residual tensile stresses at stiffener-to-web weld toes, which are close to the yield stress. Static numerical fracture mechanical analysis results show that the crack propagation modes are greatly affected by initial propagation angles, and the crack mode is Mode I leading mixed cracks of Mode I, II and III. Dynamic numerical fracture mechanical analysis shows that the detail is in the state of tension under the test loading. When the residual stress was introduced, the numerical fatigue crack propagation form is consistent with the fatigue test results, and the fatigue crack growth rate is faster.

1 INTRODUCTION

Steel bridges have been widely adopted by the countries all over the world. However, because of combined action of many factors like inadequate consideration about fatigue problems in design phase, low quality of welding and the objective existence of overloaded vehicles, steel bridges have high stress level, more times stress cycle under the action of axle load of vehicles, and the fatigue crack problems are relatively outstanding (Wang et al. 2015, 2017a). Fatigue of steel bridges can be divided into two categories: loading induced fatigue and distortion induced fatigue. Loading induced fatigue only needs to calculate the internal stress of steel girders under the action of fatigue loads, so that the design and analysis of the fatigue resistance can be carried out. However, distortion-induced fatigue has no direct relation with loads but depends on local out-of-plane distortions in key details. Research from American scholars shows that about 90% of fatigue cracks in steel bridges are caused by out-of-plane distortions (Connor & Fisher 2006).

Many researches for steel bridge web gap distortion-induced fatigue have been carried out by scholars. In 1987, a large number of actual bridge tests by Fisher, et al. (1987) show that the size of web gaps is an important factor that influences the distortion in web gaps and stress at corresponding welding details. In 2006, Berglund, et al. (2006) analyzed factors which have influence on stress distribution and size in web gaps affected by out-of-plane distortion, and they found that web gap sizes and bridge spans have great influence on the stress at gaps of webs, while the other factors have less influence. Hassel, et al. (2013) established a large number of 3D finite element models, and analyzed the influence on distortion-induced fatigue in steel bridges by factors like oblique angle, lateral brace spacing, transverse brace shape, brace stiffness and loading position, and the results show that the stiffness of the cross bracing and the shape of the cross brace have important influences on web gaps. From 2010 to 2016, Wang, et al. analyzed web gap distortion-induced fatigue in different kinds of bridges; steel bridge web gap distortion-induced full-scale fatigue tests were carried out, and the distortion-induced detail fatigue strength was determined based on hot-spot stress method; effective cold maintenance for web gap distortion-induced fatigue crack details were carried out (Wang & Cheng 2010, Cheng 2010, Yan 2013, Cheng 2013, Wei 2014, Sun 2015, Wang et al. 2017b). Researchers commonly use fatigue tests and theoretical analysis to study the fatigue performance and fatigue design of steel bridge web gap distortion-induced details. The results of fatigue tests with large dispersion and high test cost cannot meet the engineering demands of fatigue design and maintenance. Therefore, new technological approaches should be explored to study the distortion-induced fatigue behavior.

In this paper which is based on linear elastic fracture mechanics (LEFM) theory and extended finite element (XFEM) technique, numerical fracture mechanics models of the horizontal-gusset-plate web gap detail were established by ABAQUS software platform, and the welding residual stress field was introduced, then the web gap distortion-induced fatigue crack mechanism and propagation law were revealed, which can give theory and technology support to fatigue performance research, fatigue design and maintenance of steel bridges.

2 NUMERICAL METHOD FOR SIMULATION OF FATIGUE CRACK GROWTH

2.1 *Calculating stress intensity factors using the interaction integral method*

In the extended finite element method, the basic principle is that the extension function is introduced in the conventional finite element displacement model to reflect the discontinuity, and the level set function is used to track the crack surface (Moës et al. 1999). The extended finite element displacement function can be expressed as follows:

$$u(x)=\sum_{\mathrm{I}\in K}N_{\mathrm{I}}(x)\left[u_{\mathrm{I}}+\underbrace{H(x)a_{\mathrm{I}}}_{\mathrm{I}\in K_{\Gamma}}+\underbrace{\sum_{\alpha=1}^{4}F_{\alpha}(x)b_{\mathrm{I}}^{\alpha}}_{\mathrm{I}\in K_{\Lambda}}\right] \tag{1}$$

where u_{I} is continuous node displacement vector, a_{I} is improved degree of freedom passed by cracks, b_{I}^{α} is improved degree of freedom in crack-tip, K is collection of every discrete node, K_{Γ} is collection of elements and nodes passed by cracks, K_{Λ} is collection of elements and nodes on crack-tip, $H(x)$ is jump function which represent discontinuous displacement field of cracks, and its expression is:

$$H(x)=\begin{cases}1 & (x-x^{*})n\geq 0\\ -1 & (x-x^{*})n<0\end{cases} \tag{2}$$

where x is Gauss point，x^{*} is x point's projection in nearest point from the crack, n is unit exterior normal vector.

$F_{\alpha}(x)$ in formula (1) is a progressive function to describe crack-tip displacement, and it includes following 4 base functions:

$$F_{\alpha}(x)=\left[\sqrt{r}\sin\frac{\theta}{2},\sqrt{r}\cos\frac{\theta}{2},\sqrt{r}\sin\theta\cos\frac{\theta}{2},\sqrt{r}\cos\theta\sin\frac{\theta}{2}\right];\quad \alpha=1\sim 4 \tag{3}$$

Where (r,θ) is polar coordinate of crack-tip. The governing equations of the extended finite element method are derived based on the virtual work principle, and the total stiffness matrix and load matrix are obtained. Finally, the nodal displacements are solved. When solving the stiffness matrix, Gauss integral method is generally used for the conventional elements; for elements with cracks, usually, these units in the crack edge are taken to the boundary, and it is divided into many sub-elements, then each sub-element will be integrated and summed respectively.

2.2 *The achievement of crack propagation in ABAQUS*

When fatigue crack propagation is being simulated under the iterative action of cycle loading, the Paris formula expressed by ABAQUS is as follows (Paris 1963):

$$\frac{\mathrm{d}a}{\mathrm{d}N}=c_1\left(\Delta G\right)^{c_2} \tag{4}$$

where c_1, c_2 are material parameters, ΔG is strain energy release rate, a is crack length, N is time of cycles; when the crack tip meets $G_{\mathrm{th}}<\Delta G<G_{\mathrm{pl}}$, cracks begin to grow, G_{th} is threshold value of energy release rate, G_{pl} is upper limit value of energy release rate.

When dynamic crack propagation is being simulated by ABAQUS, the use of crack tip asymptotic function is given up, and jump function is only used. After N cycles, the crack propagation direction is determined by the maximum shear stress criterion according to the stress state of the element at the front edge of the crack tip. It is assumed that the jth element in crack tip front edge cracks completely in the crack propagation direction, the virtual crack propagation length is identified according to the shape of the element, strain energy release rate is calculated using virtual crack closure technique (VCCT), then the cycle value ΔN_{j} is calculated according to the formula (4), so the fracture element is the element with the minimum required number of cycles, where $\Delta N_{\min}=\min(\Delta N_{\mathrm{j}})$, finally, the cycle times and the crack length are updated and it can be in next cycle.

3 STATIC NUMERICAL FRACTURE MECHANICS ANALYSIS OF WEB GAP DISTORTION-INDUCED FATIGUE CRACKS

3.1 *Finite element model*

In this paper, using ABAQUS finite element analysis software, based on XFEM, multi-scale static crack analysis models of the horizontal gusset plate web gap details in the full-scale fatigue test specimens were established. The specimens were made of steel plate girder 600mm segments including flanges, webs, and stiffeners. The size of flanges (L×W×H) is 600×300×24mm, and the size of webs (L×W×H) is 600×870×8mm. Among them, the size of the stiffener (L×W×H) is 870×120×6mm, and the size of horizontal gusset plates (L×W×H) is 360×230×10mm, and the width of rectangle digging holes is 86mm, and the size of correspondingly nominal web gaps is 40mm. The diagram of the specimen is shown in Figure 1.

Using mutil-scale modeling method, the finite element model including 3 levels which are segmental

steel plate girder shell model, solid sub-model, and block model with cracks. The local shell model is modeled by shell elements S4R; solid sub-model

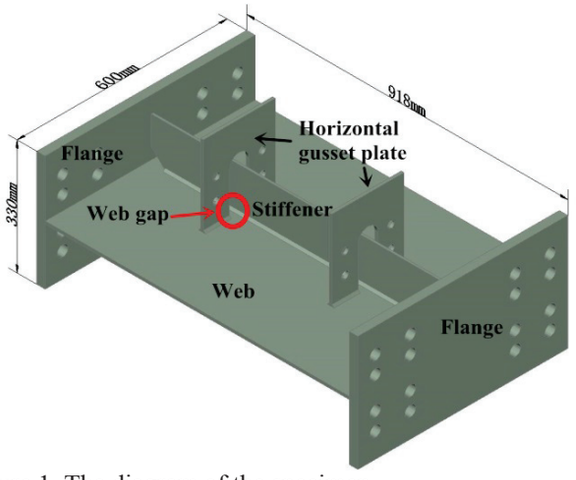


Figure 1. The diagram of the specimen

is modeled by solid elements C3D8R; the block model with cracks is modeled by elements introducing enrichment function. “Shell-solid” coupling restraint is used between segmental shell model and solid sub-model; “binding” restraint is used between solid sub-model and block element with cracks. The shape of cracks is semi-ellipse and $a_0/2c_0$=1mm/3mm. Special treatment is used to make the elements of the block with cracks well divided, and the first 15 fracture parameter values of the crack tip were outputted, and values after numerical values were stable were treated as corresponding fracture parameters. According to the test condition, nodal concentrated forces were exerted in totally 4 bolt hole positions on 2 horizontal gusset plates, and the direction is down; the resultant force of the applied load is 30KN, and the individual concentrated force should be 3.75KN. The finite element model and the mesh generation are shown in Figure 2.

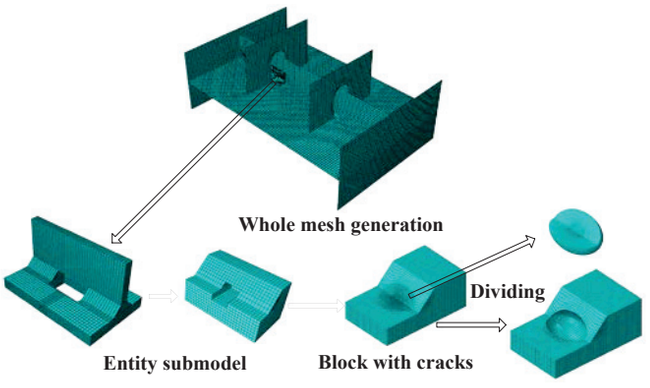


Figure 2. Finite element models and mesh generations

3.2 *Stress intensity factor analysis*

Because the initial defects in the manufacturing process of the steel plates are random, the initial propagation angle of the crack is also random. This paper adopted different initial expansion angles to analyze its impact on the cracking mode. Due to the mesh generation of the critical details, namely the locations of the cracks, is denser, the number of XFEM points are larger at the crack front. In order to obtain a more stable crack fracture parameter, the 15 line integral paths are chosen to output it. This section selects 13 reference points (P0 ~ P12) of the crack propagation front to describe the crack front position. The reference points divide the arc length of the semi-elliptical arc into 12 equal parts, and the ratio of the elliptical arc length (S_1) of the reference point to P6 and 1/4 elliptical arc length (S_0) represents the reference point position (x=S_1/S_0).The numerical value of x of the left side and the right side are equal, and the sign is opposite, as shown in Figure 3.

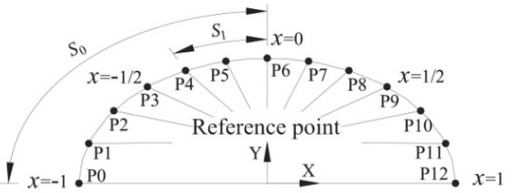
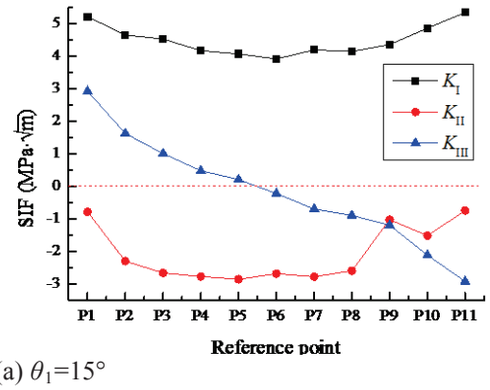
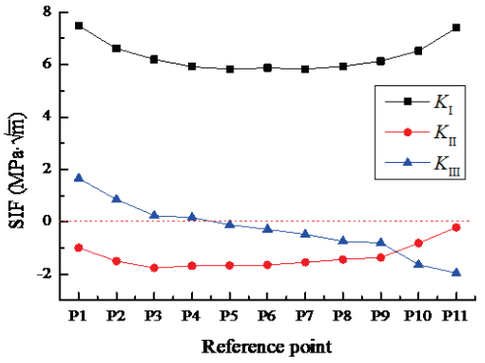


Figure 3. Position of crack propagation stage reference points

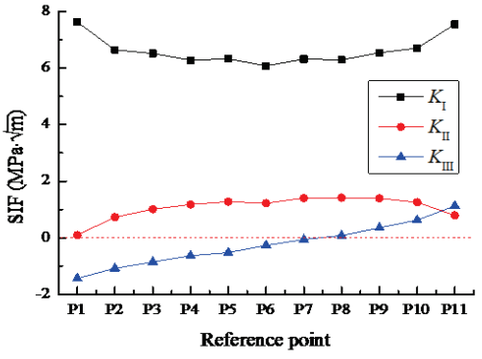
Fatigue cracks were set in advance at the location where the typical horizontal gusset plate web gap fatigue cracks are easy to form. In this section, the initial expansion angle θ_1 is selected to be 15 °, 45 ° and 90 °, so as to obtain the curve, as shown in Figure 4.



(a) θ_1=15°



(b) θ_1=45°

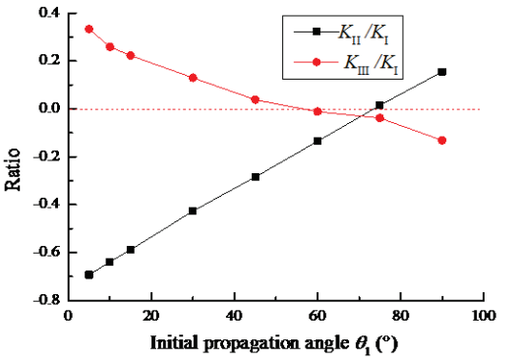


(c) θ_1=90°

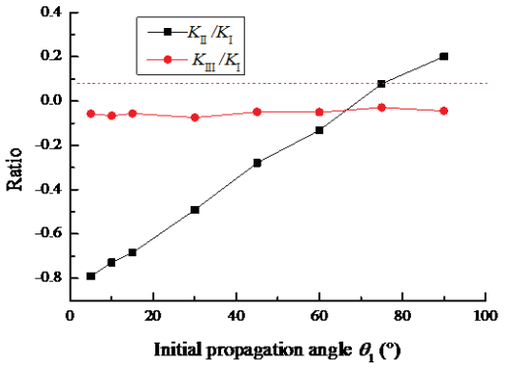
Figure 4. Position of crack propagation stage reference points

Figure 4 shows that the values of K_I of the reference point positions are larger than that of K_{II} and K_{III} of different initial propagation angles. The distribution curve of the value of K_I is concave along the crack front reference points. K_I of the reference point positions that is close to the two ends of the long axis is larger. And the distribution curve of K_{II} gradually changes from negative concave curve to positive convex curve with the increase of θ_1. The slope of the distribution curve of the value of K_{III} converts from positive to negative with the increase of θ_1, and the K_{III} near P6 is approximately zero. As for different initial propagation angle θ_1, both K_{II} and K_{III} occupy certain proportions, indicating that the crack at this point is a combination of Mode I, Mode II, and Mode III cracks, which is predominant Mode I.

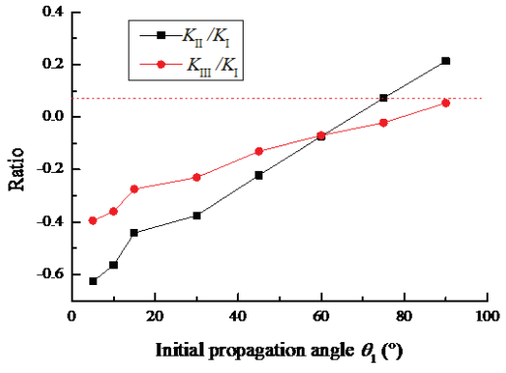
Three representative reference points are selected according to the variation of stress intensity factor values along the crack front at different initial expansion angles, namely P3, P6, and P9. The effect of initial propagation angles on the cracking modes of fatigue cracks was analyzed based on the proportions of K_I, K_{II}, and K_{III}, as shown in Figure 5.



(a) P3



(b) P6



(c) P9

Figure 5. K_{II}/K_I and K_{III}/K_I of different initial propagation angles

Figure 5 shows that the K_{II}/K_I distribution curve of P3, P6 and P9 is approximately linear and the slope is positive. And its value is close to zero when the initial propagation angle θ_1 near 70°. During the process of the initial propagation angle θ_1 increases from 0 ° to 90 °, the proportion of K_{II}/K_I increases. The K_{III}/K_I distribution curve at P6 is always small. The K_{III}/K_I distribution curve decreases at P3 and increases at P9 as the initial expansion angle θ_1 increases from 0 ° to 90 °. Therefore, the initial propagation angle θ_1 has a great influence on the initial

crack propagation mode. In general, the proportions of K_{II}/K_I and K_{III}/K_I decrease at first and then increase. And the effects of the Mode II and Mode III cracks at different initial propagation angle cannot be ignored.

4 WELDING RESIDUAL STRESS ANALYSIS OF DISTORTION-INDUCED FATIGUE DETAILS

Residual stress is considered to be an important factor influencing the fatigue cracking in the weld zone of steel bridges. There is a large residual stress in the weld zone, and even reach to the yield strength of the material. In this paper, simulation analysis of residual stress of welds in steel bridge web gap details was carried out to prepare for the numerical fracture mechanics analysis of fatigue mechanism in steel bridge web gap details.

4.1 *Finite element model of welding analysis*

The stress field produced in welding process involves the nonlinear problems of material, geometry nonlinearity, and the heating source is also highly concentrated and inputted into welding component instantly. Because of the complexity of welding thermo-mechanical coupling behavior, at the same time, in order to simulate accurately, nonlinear transient problems based on the incremental theory is used in the numerical simulation of welding. In this paper, a sequentially coupled thermal analysis method is used to analyze the residual stress. Based on ABAQUS software platform, the horizontal gusset plate web gap detail joint weld is established (Fig.6).

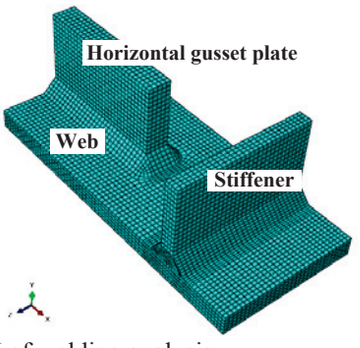


Figure 6. FEM of welding analysis

The length of stiffener in residual stress analysis model in horizontal gusset plate web gap fatigue detail is 60mm, and the length in the direction of horizontal gusset plate is 130mm. There are 20986 elements and 25536 nodes. DC3D8 eight node linear hexahedron elements are used in the thermal analysis, and heat transfer transient analysis steps are used in analysis steps. C3D8R eight node linear hexahedron elements are used in the thermo-mechanical analysis, and static-general analysis steps are used in analysis steps. No boundary condition was performed in the thermal analysis; in order to avoid inaccuracy caused by too many welding constraints and to guarantee the convergence in the model calculation, the boundary conditions should be exerted as little as possible according to actual welding conditions.

At present, the thermal physical and thermal mechanical parameters of steel are not complete. According to the value in the research from Zhao & Wu (2012), and some data were modified, mechanical parameters of Q345 steel are shown in Figure 7. Three kinds of heat transfer form (heat conduction, heat convection, and heat radiation) are considered. Heat convection and heat radiation areas are divided into the area below the CO_2 nozzle, the gas flow area and the cooling zone. The parameters of thermal transmission were referred from the paper of Zheng et al. (2007). The radiation Stefan-Boltzmann constant is 5.67×10^{-8}W/(m$^2\cdot$°C^4), and the absolute zero is -273.15°C.

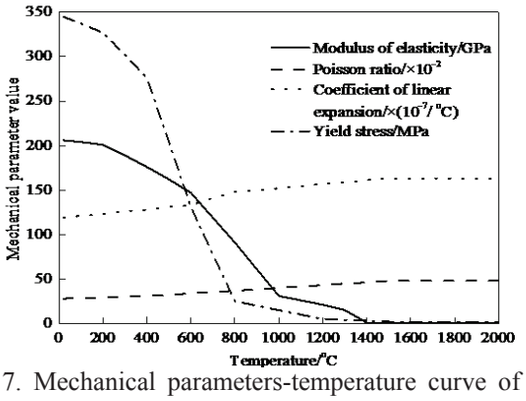


Figure 7. Mechanical parameters-temperature curve of Q345 steel

4.2 *Welding residual stress analysis*

Figure 8 shows routes P1 (P1'), P2 (P2') to extract residual stress in the flange to web welding area. Figure 9 shows distribution curves of transverse and vertical residual stress in the direction of welding seam. As can be seen from figures: (1) the residual stress changes largely in arc and arc blowout stages, and the transition in the middle is gentle; (2) residual stress located in the weld toe in web side is large, and the residual stress in the weld toe in the stiffener side is smaller; (3) residual tensile stress nearby the center of the direction of weld length, meanwhile, under the action of experimental load, stiffener to web end weld toe is mainly in cyclic tension, so fatigue cracks in this detail are easy to initiate and propagate.

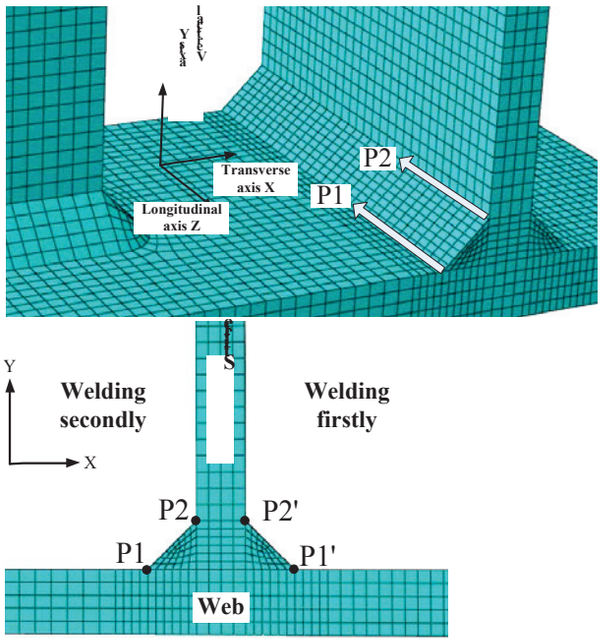
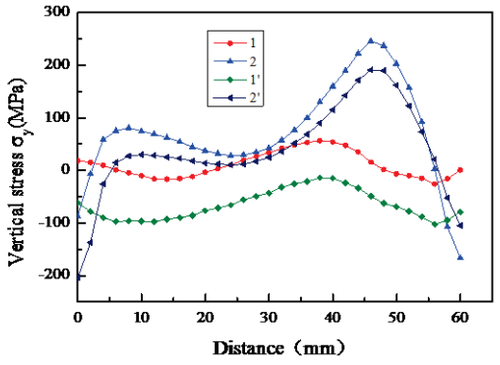
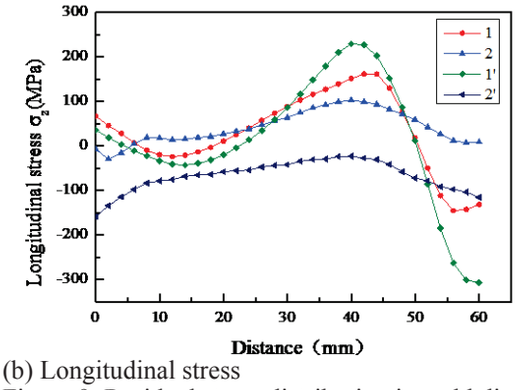


Figure 8. Mechanical parameters-temperature curve of Q345 steel



(a) Vertical stress



(b) Longitudinal stress

Figure 9. Residual stress distribution in weld direction

Figure 10 shows the residual tensile stress distribution curve in the vertical weld direction of horizontal gusset plate to web (route P3 and P3'). As is shown in Figure 10, residual tensile stress close to horizontal gusset plate to web weld toe area is large, and is close to the yield strength of steel. As the distance with the weld increases, the residual tensile stress decreases gradually.

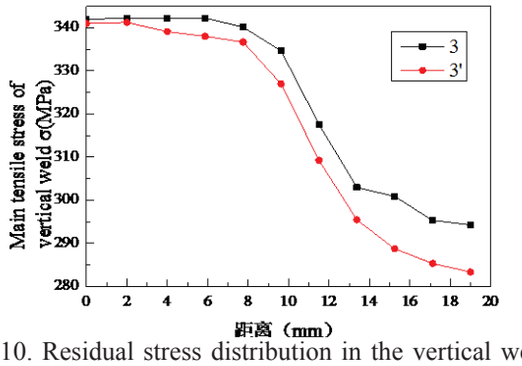


Figure 10. Residual stress distribution in the vertical weld direction

Figure 11 shows the residual stress distribution curve on the web in horizontal gusset plate to stiffener gap (route P4). As is shown in Figure 11, large residual main tensile stress is located in the position close to horizontal gusset plate to web end weld toe in horizontal gusset plate web gap, and is close to the yield strength of steel. Residual tensile stress decreases rapidly within 15mm distance of this weld toe, and the residual tensile stress increases in a position close to stiffener to web weld toe. Because of the action of testing loads, horizontal gusset plate to web weld toe endure compressive stress, so cracks cannot initiate in this position easily. However, stiffener to web weld toe endure cyclic tensile stress under testing loads, and the damage continues to accumulate, so fatigue cracks can initiate and propagate easily.

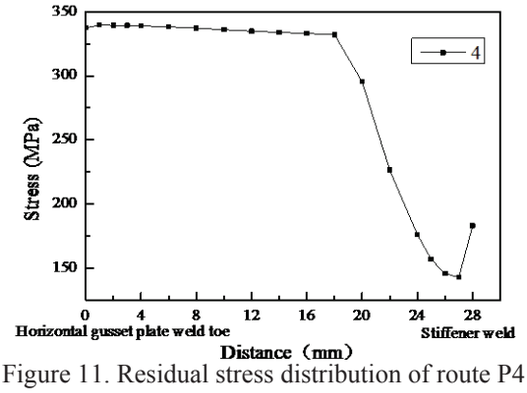


Figure 11. Residual stress distribution of route P4

5 CRACK PROPAGATION BEHAVIOR ANALYSIS OF DISTORTION-INDUCED FATIGUE

5.1 *Finite element model*

As is shown in Figure 12 is the finite element analysis model for the web gap fatigue detail of horizontal gusset plate considering residual stress field. The model consists of 2 sections: segmental steel plate girder shell model and local solid sub-model. The introduction of the residual stress field needs three steps: firstly, the welding temperature field is obtained by welding thermal analysis of the local solid

sub-model; secondly, the welding temperature field results are introduced into the welding thermal stress analysis model of the local solid, and the welding residual stress field is obtained; thirdly, the welding residual stress field is introduced into the dynamic crack growth analysis model.

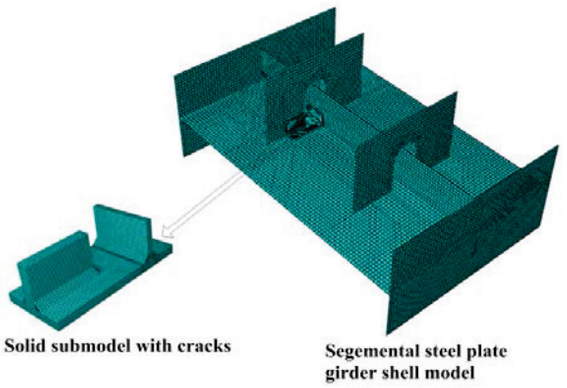
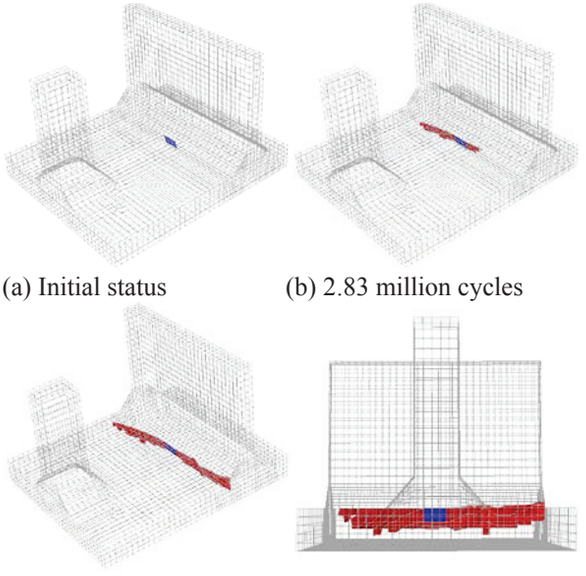


Figure 12. The finite element model with the introduction of residual stress field

5.2 *Dynamic fatigue crack propagation simulation*

The initial crack size of stiffener end weld toe position is assumed as $a_0/2c_0$=2mm/6mm, and the propagation behavior of the fatigue crack is shown in Figure 13. The crack propagates along the direction of weld toe to both sides of the horizontal gusset plate. Crack propagation in both sides of the horizontal gusset plate has a lesser difference, which coincides with the fatigue test.

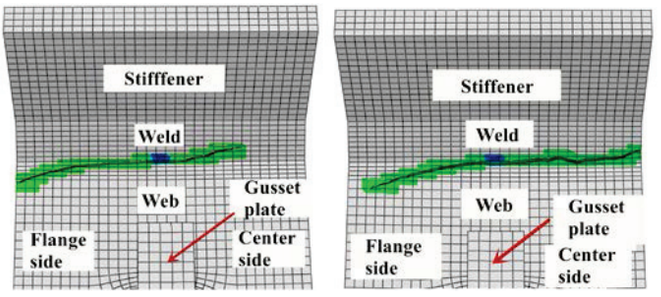


(a) Initial status (b) 2.83 million cycles

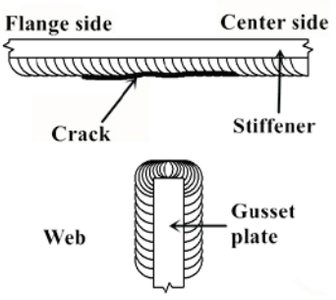
(c) 5.91 million cycles

Figure 13. Dynamic fatigue crack propagation in stiffener end weld toe

Figure 14 shows the comparison between fatigue test results and numerical analysis results for the surface crack forms of the web with and without considering residual stress. As is shown in Figure 14a is the crack form without considering residual stress after the action of 9.03 million cycles, and the long axis of the crack propagates from 6mm to 47mm; as is shown in Figure 14b is the crack form considering residual stress after the action of 591 million cycles, and the long axis of the crack propagates from 6mm to 58mm. Therefore, the existence of residual stress can influence the form of crack propagation, meanwhile, because of the larger residual tensile stress, under the same load amplitude, the crack propagation rate is faster.



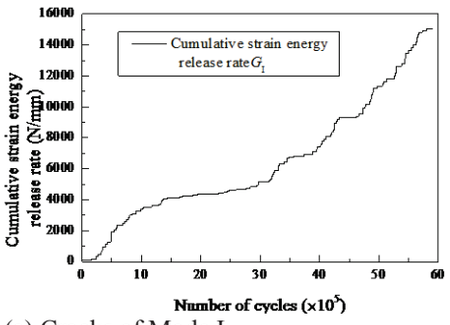
(a) Without the residual stress (b) With the residual stress



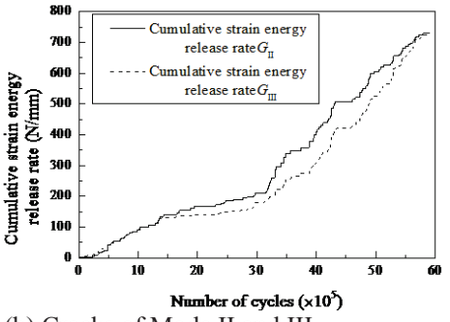
(c) Crack in the fatigue test specimen

Figure 14. Comparison of crack propagation

As is shown in Figure 15 is cumulative strain energy release rates G_{I}, G_{II} and G_{III} in crack propagation process with the consideration of residual stress. Obviously, cracks of Mode I are dominant, meanwhile, cracks of Mode II and III are similar. After conversion, $K_{\mathrm{II}}/K_{\mathrm{I}}$ and $K_{\mathrm{III}}/K_{\mathrm{I}}$ are both about 0.22, which is larger than the value without considering residual stress, and forms of cumulative strain energy release rates are different, which indicates that the influence of Mode II and III cracks increases and crack propagation forms have difference with the consideration of residual stress. Crack propagation form reflected by the cumulative strain energy release rate curve is basically consistent with the results obtained by static crack analysis, which is that cracks at the end of the stiffener web weld toes are Mode I leading mixed mode cracks of Modes I, II and III.



(a) Cracks of Mode I



(b) Cracks of Mode II and III

Figure 15. Cumulative strain energy release rate of crack propagation

6 CONCLUSION

Typical cracks at stiffener to web weld toe in the horizontal gusset plate to stiffener web gap detail are Mode I leading mixed mode cracks of Modes I, II and III. When fracture mechanics is used for analysis and assessment, cracks of Modes II and III cannot be ignored.

Great residual tensile stress exists at stiffener to web weld toe in the horizontal gusset plate to stiffener web gap detail, and the value is reach to the yield strength of steel; the residual tensile stress is one of the major factors that control the fatigue crack initiation and propagation form in such details.

After considering the influence of residual tensile stress, crack propagation form in the dynamic crack propagation analysis model of the horizontal gusset plate to stiffener web gap is similar to the fatigue test results. The rate of crack propagation increases because of the existence of residual tensile stress, and the influence of residual tensile stress cannot be ignored when analysis and assessment of steel bridge web gap distortion-induced fatigue behavior.

7 ACKNOWLEDGEMENTS

The authors gratefully acknowledge the financial support provided by National Natural Science Foundation of China (Grant 51578073, 51078039), the Major State Basic Research Development program of China (973 Program) Subprogram (Grant 2015CB057703), and the Special Fund for Basic Scientific Re-search of Central Colleges of the P.R. China, Chang'an University (Grants 10821153501, 310821153401 and 310821153314).

REFERENCES

Berglund, E. M. & Schultz, A. E. 2006. Girder differential deflection and distortion-induced fatigue in skewed steel bridges. *Journal of Bridge Engineering* 11(2): 169-177.

Cheng, F. 2010. *Numerical Analysis of Fatigue Behavior Caused by Web Gap Out-of-Plane Distortion for Steel Bridges*. Xi'an: Chang'an University. (in Chinese)

Cheng, J. 2013. *Research on Retrofit Techniques and Overload Effects on Out-of-Plane Distortion-Induced Fatigue of Steel Bridges*. Xi'an: Chang'an University. (in Chinese)

Connor, R. J. & Fisher, J. W. 2006. Identifying effective and ineffective retrofits for distortion fatigue cracking in steel bridges using field instrumentation. *Journal of Bridge Engineering* 11(6): 745-752.

Fisher, J. W. et al. 1987. *Review of Field Measurements for Distortion Induced Fatigue Cracking in Steel Bridges*. Washington D.C.: Transportation Research Board.

Hassel, H. L. et al. 2013. Parametric analysis of cross-frame layout on distortion-induced fatigue in skewed steel bridges. *Journal of Bridge Engineering* 18(7): 601-611.

Moës, N. et al. 1999. A finite element method for crack growth without remeshing. *International Journal for Numerical Methods in Engineering* 46(1): 131-150.

Paris, P. C. et al. 1963. A critical analysis of crack propagation laws . *Journal of Basic Engineering* 85(4): 528-533.

Sun, Y. J. 2015. *Researches on the Performance of Out-of-Plane Distortion Induced Fatigue at Web Gaps in Steel Bridges Based on Hot Spot Stress*. Xi'an: Chang'an University. (in Chinese)

Wang, C. S. & Cheng, F. 2010. Out-of-plane distortional fatigue stress analysis at web gaps of steel bridges. *Journal of Architecture and Civil Engineering* 27(1), 65-72. (in Chinese)

Wang, C. S. et al. 2017a. Steel bridge long-term performance research technology framework and research progress." *Advances in Structural Engineering* 20(1): 1-18.

Wang, C. S. et al. 2017b. Experiment on the effect of stress ratio on out-of-plane distortion-induced fatigue performance of web gaps in steel bridges." *China Journal of Highway and Transport* 30(3): 72-81. (in Chinese)

Wang, C. S. et al. 2015. Fatigue service life evaluation of existing steel and concrete bridges. *Advanced Steel Construction* 11(3): 305-321.

Wei, M. C. 2014. *The Research of the Fatigue Mechanism and Retrofitting Methods for Distortion-Induced Fatigue in Steel Bridges*. Xi'an: Chang'an University. (in Chinese)

Yan, S. L. 2013. *Experimental Study on Out-of-Plane Distortion Induced Fatigue Mechanism of Web Gaps for Steel Bridges*. Xi'an: Chang'an University. (in Chinese)

Zhao, Q. & Wu, C. 2012. Numerical analysis of welding residual stress of u-rib stiffened plate. *Engineering Mechanics* 29(8): 262-268. (in Chinese)

Zheng, Z. T. et al. 2007. Numerical simulation of CO_2 arc welding temperature field. *Journal of Tianjin University* 40(2): 234-238. (in Chinese)

Maintenance, Safety, Risk, Management and Life-Cycle Performance of Bridges – Powers, Frangopol, Al-Mahaidi & Caprani (Eds)
© 2018 Taylor & Francis Group, London, ISBN 978-1-138-73045-8

Fatigue life assessment of reinforced concrete bridges from monitoring data

P. Junges
Federal University of Mato Grosso, Cuiabá, Matro Grosso, Brazil
R.C.A Pinto & L.F. Fadel Miguel
Federal University of Santa Catarina, Florianópolis, Santa Catarina, Brazil

ABSTRACT: The majority of Brazilian bridges are made of reinforced concrete with spans smaller than 50 m. These bridges are reaching their design service life and, thus, have already been submitted to the passage of millions of vehicles. Furthermore, there have been an increase in the load traffic and in the number of trucks in the highways. Trucks with up to nine axles are usually seen nowadays. As a result, fatigue assessment is needed to ensure safety. Therefore, two reinforced concrete bridges were monitored with time intervals in order to assess their structural safety. The monitoring lasted 120 days in each structure. In this paper, the signals acquired at the midspan of the girders during the monitoring were used to assess the fatigue life of the bridges. Equivalent stresses were calculated from stress bin histograms for several variable amplitude fatigue limits (VAFL). In order to estimate the life cycle, it was used the tension-life (S-N) approach, using S-N curves from international standards. Moreover, it was considered a linear accumulation damage through the Palmgren-Miner rule with the counting of stress cycles given by the Rainflow method. Uncertainties about maximum stresses and bridge degradation were taken into account in a simplified way based on international standards recommendations. It is concluded that the consideration of VAFL value between 10% to 33% of the constant amplitude fatigue limit (CAFL) would better describe the actual state of conservation of the evaluated bridges. Also, it is not expected that fatigue will be the failure mechanism of these bridges.

1 INTRODUCTION

The majority of Brazilian bridges have been built in the last century, and thus, are reaching their service lives. They are typically 50 m long reinforced concrete bridges. For these small span bridges, live loads due to traffic are the ones that bring in stresses with larger amplitudes.

The normal traffic usually induces cyclical stresses below the resistance stresses of the bridge materials. Nonetheless, a large number of repetitions of these cyclical stresses may lead to failure of a structural component by fatigue.

In addition, the traffic on the highways has changed significantly in the past decades. There has been an increase in the number of trucks and in the load traffic. Trucks with up to nine axles are usually seen nowadays.

Consequently, the bridges have been submitted to the passage of millions of vehicles which are constantly increasing their gross weight. Thus, these structures have already supported a large number of stress cycles, and even stress cycles that were not taken into account during the design. Hence, it is necessary to perform a fatigue assessment in order to ensure their actual safety level.

Although fatigue assessment is often done for steel bridges, several researches have addressed this assessment to reinforced concrete bridges (Schläfli & Brühwiler 1998, Higgins et al. 2006, Kumpoopong & Herabat 2010, Forrest et al. 2010, Sasaki et al. 2010, Zanuy et al. 2011, Junges et al. 2016).

The estimation of the remaining fatigue life is usually deterministic, using stress-service life approaches supported by S-N curves given by international standards together with a particular damage accumulation rule. The stress ranges applied are obtained from numerical models with the use of design traffic loads, which may or may not represent the reality of the current traffic.

To improve this approach, some researchers have been using traffic data from weigh-in-motion (WIM) measurements (Wang et al. 2005, Sasaki et al. 2010, Guo et al. 2012, Zhang & Cai 2012) while others have continuously monitored bridges for some period of time (Higgins et al. 2006, Zhou 2006, Kwon & Frangopol 2010, Junges et al. 2016).

To perform more accurate evaluations, it is of the utmost importance the use of real data in order to correctly characterize the actual structural behavior of the bridge. Consequently, it has become more common to use Bridge weight-in-motion (B-WIM)

techniques to verify traffic loads and to evaluate the structural safety of bridges (Žnidarič & Lavrič 2010, Junges et. al. 2017).

In this study, a B-WIM system was used to acquire strain data due to traffic load yielding the stress ranges supported by two bridges. These stress ranges were then used to evaluate the bridge service life to fatigue. This evaluation was performed solely for the reinforcing bars, thus assuming that fatigue failure in concrete is unlikely (Schläfli & Brühwiler 1998). Service life was estimated based on the S-N curves provided by the Eurocode 2 (2004). Uncertainties about maximum stresses and bridge degradation were taken into account in a simplified way based on Eurocode 2 (2004) and AASHTO LRFD (2014) recommendations.

2 FATIGUE ASSESSMENT

2.1 *Fatigue analysis based on S-N curves*

An S-N curve (Figure 1) relates the nominal stress required to cause a fatigue failure after some number of cycles. This curve is derived from experimental tests on specimens subjected to harmonic loads at different amplitudes.

As can be seen in Figure 1, when plotted in a log-log graph, the S-N curve shows a bi-linear typical behavior. The initial linear part of the curve is described by Basquin's equation, provided in Equation (1), relating the number of cycles to failure.

$$S_a = A(N)^m \tag{1}$$

where A represents the linear coefficient of a S-N curve, m is the slope of the curve in a log-log scale, and N_f is the number of cycles to failure.

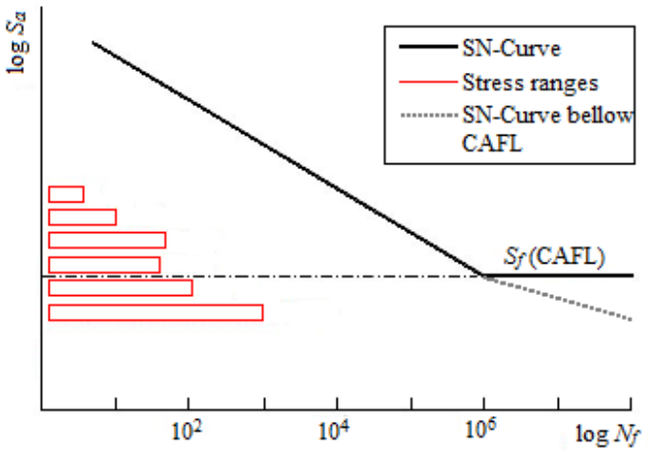


Figure 1. Typical S-N Curve.

Unlike the harmonic loads used to build an S-N curve, traffic loading on bridges leads to variable amplitude stresses. Thus, it is necessary to consider a cumulative damage model in order to take into account the damage derived from cycles at different amplitudes.

Fatemi & Yang (1998) have analyzed several cumulative damage models and concluded that there is no model that is widely accepted. The most popular model is the Palmgren-Miner model. It does not consider sequence effect and damage accumulation, being regarded as independent of the stress level.

This model evaluates total damage as the sum of damage given at each stress level, as indicated by Equation (2).

$$D = \sum n.d_i = \sum_{i=1}^{k} \frac{n}{N_{f,i}} \tag{2}$$

where D is the total damage in the structure; n is the number of cycles accumulated at a stress level S_i; di is the individual damage due to stress level S_i; k is the number of stress cycles analyzed; $N_{f,i}$ is the average number of cycles to failure at stress level S_i.

The lack of consideration of sequence effects is one great disadvantage of the Palmgren-Miner damage model. As a result, when stress levels below the fatigue limit S_f, also known as constant amplitude fatigue limit (CAFL), are applied, there is no damage caused. This may be true when harmonic loads are applied. However, when variable amplitude loading is applied, cycles with amplitudes greater than the fatigue limit may induce the initiation of cracking. Subsequent cycles, even at lower amplitudes, may propagate such cracks leading to damage (Schijve, 2003).

One possibility to reduce this disadvantage is to extrapolate the S-N curve to values below the fatigue limit. In this case, stress levels below CAFL would be considered in the damage model (Figure 1). This consideration is adopted by several international standards, such as the Eurocode 2 (2004). Usually, the slope of the line bellow CAFL is proportional to the slope of the original S-N curve (Schijve 2003).

However, not all cycles below CAFL have to be taken into consideration. In fact, it is necessary to define a variable amplitude fatigue limit (VAFL), below which the cycles will not propagate the fatigue crack. Usually the VAFL is defined as a percentage of CAFL. Zhou (2006), Kwon & Frangopol (2010), and Guo et al. (2012) present values of 25%, 33% e 50% applied to evaluate fatigue of steel bridges. Junges et al. (2016) used the same values to evaluate fatigue in a reinforced concrete bridge. In the present study, VAFL values varying between 1% and 50% are considered, as can be seen on Table 1. This table gives the corresponding stress levels considering the CAFL indicated by Eurocode 2.

Table 1. VAFL used in the analysis

CAFL (Eurocode 2)	162.50 MPa
CAFL (Medium stress)	79.01 MPa
VAFL (% CAFL)	VAFL (MPa)
1	0.79
2	1.58
3	2.37
4	3.16
5	3.95
10	7.90
15	11.85
20	15.80
25	19.75
30	23.70
33	26.07
35	27.65
40	31.60
45	35.55
50	39.50
60	47.40
70	55.30
80	63.20
90	71.10
100	79.01

As Table 1 presents, the VAFL values are calculated using the CAFL corrected by the mean stress value. Stephens et al. (2011) recommend to correct the stress amplitude values depending on the mean stress value, so the non-stationary state of stresses are taken into account. One possibility to correct the stress levels is to use the Goodman method, as introduced in Equation (3).

$$\frac{S_a}{S_f} + \frac{S_m}{S_u} = 1 \tag{3}$$

where S_a is the stress semi amplitude; S_f is the fatigue limit stress; S_m is the mean stress; and S_u is the ultimate strength.

Each VAFL value shown in Table 1 leads to a different stress histogram. From these histograms it is possible to calculate an equivalent stress range (S_{re}) as presented in Equation (4).

$$S_{re} = \left[\sum \frac{n_i}{N} S_{ri}{}^{m} \right]^{\frac{1}{m}} \tag{4}$$

where S_{re} is the equivalent stress range; S_{ri} is the predefined stress range bin; n_i is the number of observations in the predefined stress range; N is the total number of cycles; and m is the angular coefficient of the S-N curve above CAFL.

Even though several researchers have been using Equation (4) (Higgins et al. 2006, Zhou 2006, Kwon & Frangopol 2010, Guo et al. 2012, Zhang & Cai 2012), this equation ignores the second slope and the stress cycles below CAFL. It only takes into account the first slope of the S-N curve, above CAFL. To overcome this, the stress cycles above and below CAFL can be treated separately, as given in Equation (5).

$$S_{re} = \left[\left(\sum_{S \geq CAFL} \frac{n_i}{N_1} S_{ri}{}^{m_1} \right)^{\frac{1}{m_1}} \frac{N_1}{N_T} \right] + \left[\left(\sum_{S < CAFL} \frac{n_i}{N_2} S_{ri}{}^{m_2} \right)^{\frac{1}{m_2}} \frac{N_2}{N_T} \right] \tag{5}$$

where S_{re} is the equivalent stress range; S_{ri} is the predefined stress range bin; n_i is the number of observations in the predefined stress range; N_1 is the total number of cycles above CAFL; N_2 is the total number of cycles below CAFL; N_T is the total number of cycles (N_1+N_2); and m_1 and m_2 are the angular coefficient of the S-N curve, above and below CAFL respectively.

Equation (5) takes into account the stress cycle amplitude and the amount of cycles above and below CAFL to calculate the equivalent stress range.

The non-stationary nature of the resultant stresses also makes difficult to easily count the cycles of each stress level. Therefore, a specific algorithm, such as the rainflow-counting algorithm, must be used (ASTM E1049-85, 2011). This algorithm was developed to take into consideration slow, as well as fast stress variations, forming pairs of maximum and minimum values (Johannesson, 1999).

3 PROPOSED METHOD

The two bridges analyzed in the present study, were monitored by a Bridge Weigh-in-motion (BWIM) system in order to evaluate their structural safety. The strain data acquired during the monitoring are used here to evaluate the service life related to fatigue failure of the reinforcing steel of bridge girders (Schläfli & Brüwiler 1998, Zanuy, Alabajar & Fuente 2009).

The B-WIM system transducers were mounted on the inner surface, close to the mid span of the girders. As pointed out by Zanuy et al. (2011) and Higgins et al. (2013), the tension stiffening effects decreases as the number of cycles increases. Accordingly, the girder section must be considered as a pure cracked section.

The evaluation of service life due to fatigue is performed by the S-N approach with VAFL varying as displayed on Table 1. The rainflow counting algorithm, and the Goodman method are also used to consider the non-stationary state of stress as provided by Equation (3). Finally, the equivalent stress range (S_{re}) is calculated for each VAFL using Equantion (5). The service life, in years, is estimated considering damage due to each stress cycle together with the average daily number of cycles, as given by Equation (6).

$$Y = \frac{1}{365 \times ADC \times D_C} \quad (6)$$

where Y is the service life to fatigue in years; ADC is the average number of cycles per day; D_C is the damage due to one cycle for the equivalent stress range. Stress range

During the monitoring period, maximum stress range is unlikely to be captured. Therefore, AASHTO LRFD Bridge Design Specifications (2014) assume that the maximum stress range is twice the effective stress range. In addition, it is expected that reinforced concrete structures lose stiffness due to degradation, especially when subjected to corrosion. Thus, Eurocode 2 (2004) permits the extrapolation of the S-N curve below CAFL using the same slope coefficient as the one above CAFL. This way, bridge degradation is taken into account in a simplified way. These two considerations (maximum stress range and degradation due to corrosion) are used in the present study.

4 APPLICATIONS

The bridges assessed in the current study are located at highway BR-153, between the cities of Uruaçu and Porangatu in the state of Goiás. This highway is subjected to a significant heavy trucks traffic.

Among the several bridges in this portion of BR-153, the Lambari and Itinguijada bridges were chosen since their location permits easy access to inspection, as well as to mount B-WIM transducers. Also, the girders of Lambari Bridge exhibit some cracking and exposed corroded reinforced steel, while Itinguijada Bridge seems to be in good conditions.

For both bridges, the design drawings were not available. Then, the reinforcing steel area was estimated from Brazilian standard at the expected time of construction (NB 1, 1960), together with information gathered during bridge inspection.

4.1 *Lambari Bridge*

4.1.1 *Description of the bridge*

Lambari Bridge is composed of four main simple supported girders; with main span around 15 m and two unsupported spans at each end, which leads to 22.5 m girder length. There are, also, five transverse beams, one in the mid-span, two over the piers and two others at the free ends of the girders. More details of the structure can be seen on Figures 2 to 5.

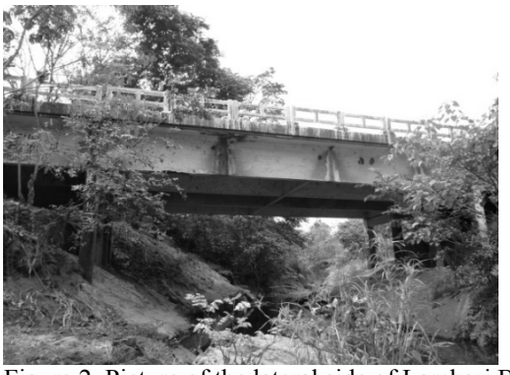


Figure 2. Picture of the lateral side of Lambari Bridge.

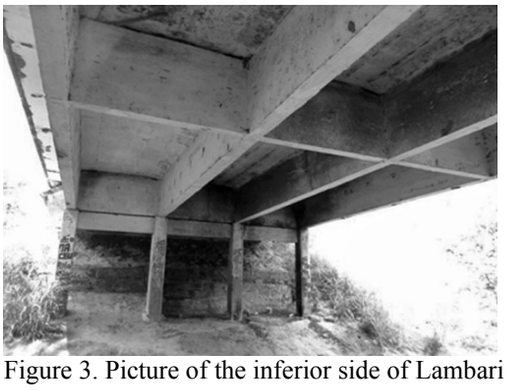


Figure 3. Picture of the inferior side of Lambari Bridge.

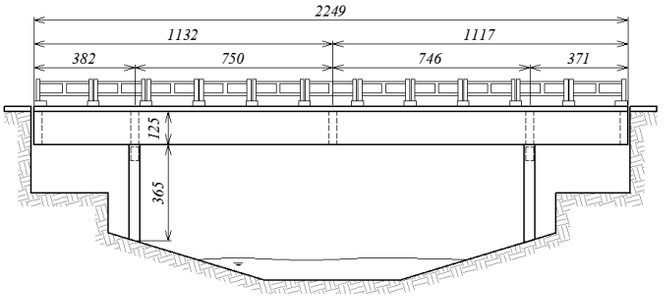


Figure 4. Side view of Lambari Bridge (in cm).

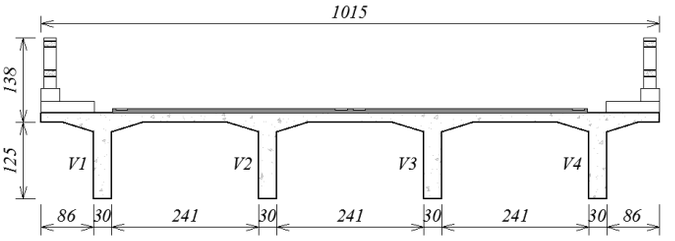


Figure 5. Lambari Bridge transversal section at mid-span (in cm).

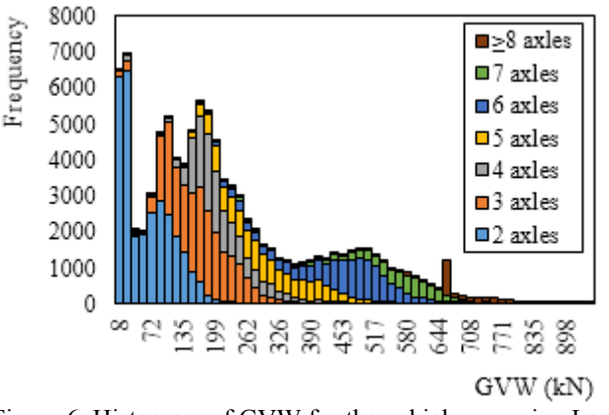


Figure 6. Histogram of GVW for the vehicles crossing Lambari Bridge during the monitoring period.

Lambari Bridge was monitored between November of 2013 and January of 2014, for a total of 42 days. The B-WIM transducers were placed on the bottom surface of the girders near to the mid-span in order to evaluate the bending moments of the bridge. During the monitoring time, more than 100,000 vehicles crossed the bridge. Figure 6 illustrates a histogram of gross vehicle weight (GVW) of these vehicles. As can be seen in this figure, vehicles up to 326 kN are the majority. However, vehicles heavier than the Brazilian design live load (450 kN) sum 15%.

4.1.2 *Results of expected service life to fatigue*

Figure 7 depicts an example of the obtained histograms of stress ranges of the four girders. As can be seen, the great concentration of cycles in low stress ranges makes important the adequate choice of the VAFL values to be used in the analysis. This figure also emphasizes that girders V2 and V3 were the most demanded, with almost the same number of stress cycles.

Nevertheless, the damage suffered by girder V3 is quite higher than the damage of girder V2, as can be seen in Figure 8. This figure shows the equivalent stress ranges with its respective number of cycles for each VAFL cut-off levels. Damage is evaluated by the distance between dots and the thick line (S-N Curve). In this way, girder V2 has roughly the same damage as girder V4, which has half number of cycles.

According to Figure 8, girder V3 is the most damaged and, if traffic is constant for all service life, it will be the first one to fail. Accordingly, the service life of Lambari Bridge will be limited by girder V3. Table 2 brings the estimated service life of Lambari Bridge for each VAFL cut-off value considering the stress ranges histograms as measured.

In order to take into account the effect of maximum stresses and bridge degradation, the stress ranges histograms were multiplied by a factor of 2 (AASHTO, 2014) and the second slope of the S-N Curve, below CAFL, was taken as the first one (Eurocode 2, 2004). Therefore, Table 3 presents the results of estimated service life for Lambari Bridge considering the worst case scenario.

Figure 8, Table 2 and Table 3 establish that below a certain level, there is no improvement in the estimation of service life in spite of a larger number of cycles. In fact, as the equivalent stress range decreases, it matches the inclination of the S-N curve and the number of cycles does not matter anymore. For the worst case scenario of Lambari Bridge, the VAFL value below which this happens is VAFL45. Thus, it can be said that the service life of this bridge is 53 years.

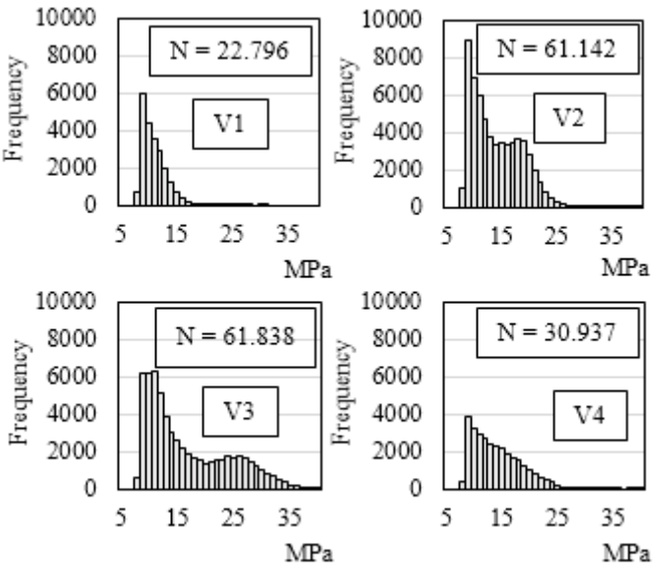


Figure 7. Measured stress ranges histograms of each girder for VAFL10 cut-off level for Lambari Bridge.

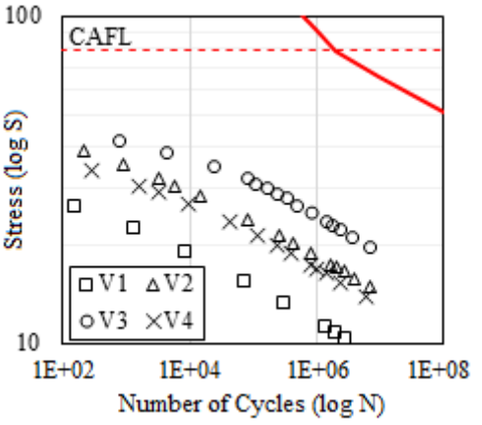


Figure 8. Equivalent stress range and number of cycles for each VAFL level for Lambari Bridge.

Table 2. Estimated service life of Lambari Bridge for each VAFL level, as measured.

VAFL	N_{sol}	S_{re} (MPa)	N_{res}	$N_{cycles/day}$	Estimated service life (years)
1	75355	24.60	8.41E+10	2691.25	85659
2	68464	24.86	7.65E+10	2445.14	85661
3	65021	25.01	7.26E+10	2322.18	85659
4	61755	25.15	6.90E+10	2205.54	85659
5	56952	25.38	6.36E+10	2034.00	85659
10	39253	26.45	4.38E+10	1401.89	85660
15	27787	27.48	3.10E+10	992.39	85665
20	21500	28.28	2.40E+10	767.86	85709
25	17347	28.95	1.94E+10	619.54	86001
30	12130	30.03	1.40E+10	433.21	88341
33	8295	31.11	1.02E+10	296.25	93990
35	5927	32.01	7.86E+09	211.68	101748
40	1870	34.77	3.74E+09	66.79	153438
45	340	38.37	1.54E+09	12.14	347179
50	60	42.03	6.78E+08	2.14	867446

Table 3. Estimated service life of Lambari Bridge for each VAFL level considering bridge degradation and maximum stresses.

VAFL	N_{sol}	S_{re} (MPa)	N_{res}	$N_{cycles/day}$	Estimated service life (years)
1	81930	40.60	5.58E+07	2926.07	52
2	75355	41.29	5.13E+07	2691.25	52
3	70609	41.83	4.81E+07	2521.75	52
4	68464	42.09	4.66E+07	2445.14	52
5	66424	42.35	4.52E+07	2372.29	52
10	56952	43.68	3.87E+07	2034.00	52
15	44660	45.86	3.03E+07	1595.00	52
20	39253	47.06	2.67E+07	1401.89	52
25	34064	48.41	2.32E+07	1216.57	52
30	27787	50.40	1.89E+07	992.39	52
33	25317	51.33	1.73E+07	904.18	52
35	24115	51.81	1.65E+07	861.25	52
40	21500	52.95	1.48E+07	767.86	53
45	19415	53.94	1.35E+07	693.39	53
50	17347	54.98	1.23E+07	619.54	54
60	12130	57.88	9.48E+06	433.21	60
70	5927	62.52	6.44E+06	211.68	83
80	1870	68.39	4.12E+06	66.79	169
90	340	75.69	2.48E+06	12.14	559
100	60	83.70	1.50E+06	2.14	1916

4.2 *Itinguijada Bridge*

4.2.1 *Description of the bridge*

The superstructure of Itinguijada Bridge is formed by two girders, simple supported on four circular columns, with a mid-span of about 20 m and two unsupported spans at each end, which give girders of 29.70 m long. There are five transverse beams. Figures 7 to 10 display more details of this structure.

Itinguijada Bridge was monitored between September and November of 2016, for a total of 68 days. The B-WIM transducers were placed on the bottom surface of the girders near to the mid-span in order to evaluate the bending moments of the bridge. During the monitoring time, more than 150,000 vehicles crossed the bridge. Figure 13 reveals a histogram of gross vehicle weight (GVW) of these vehicles. This figure indicates a great concentration of vehicles with GVW between 70 and 370 kN. Furthermore, around 14% of the total vehicles are heavier than 450 kN (live load for Brazilian standards).

4.2.2 *Results of expected service life to fatigue*

Figure 14 depicts an example of the obtained histograms of stress ranges of the two girders of Itinguijada Bridge. Similarly to Lambari Bridge, there is a great concentration of cycles in low stress ranges, which makes important the adequate choice of the VAFL values. It is easily seen that girder V1 was the



Figure 9. Picture of the lateral side of Itinguijada Bridge.

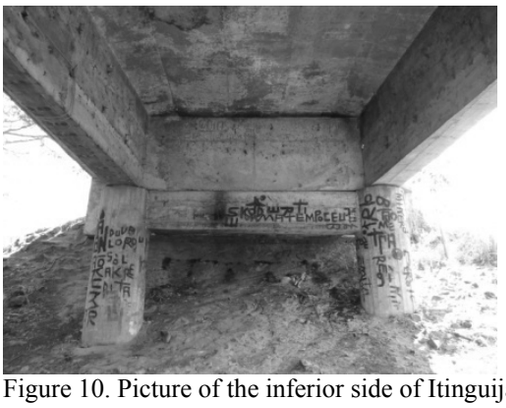


Figure 10. Picture of the inferior side of Itinguijada Bridge.

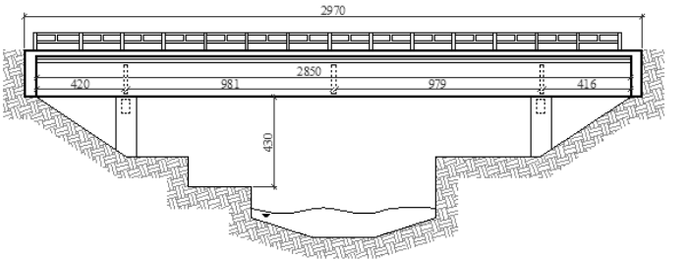


Figure 11. Side view of Itinguijada Bridge (in cm).

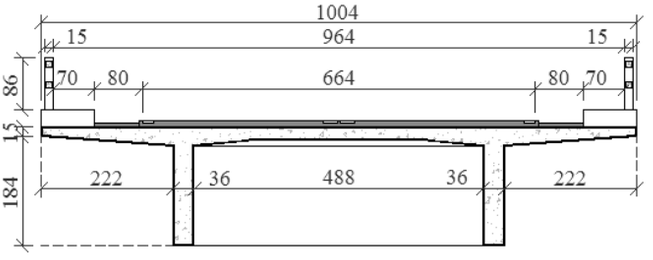


Figure 12. Itinguijada Bridge transversal section at mid-span (in cm).

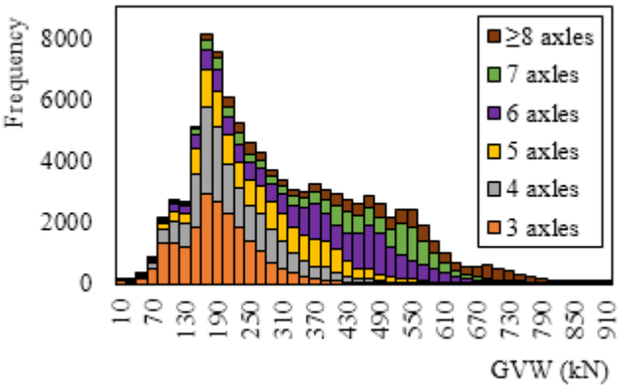


Figure 13. Histogram of GVW for the vehicles crossing Itinguijada Bridge during the monitoring period.

most required during the monitoring, as can be also seen in Figure 15. This figure exhibits the equivalent stress ranges with its respective number of cycles for each VAFL cut-off levels.

Considering that the service life of Itinguijada Bridge will be limited by girder V1, Table 4 brings the estimated service life of this bridge for each VAFL cut-off value considering the stress ranges histograms as measured.

Table 4. Estimated service life of Itinguijada Bridge for each VAFL level, as measured.

VAFL	N_{sol}	S_{re} (MPa)	N_{res}	$N_{cycles/day}$	Estimated service life (years)
1	117898	9.52	3.74E+14	4210.64	243417775
2	94060	9.76	2.98E+14	3359.29	243420843
3	80049	9.94	2.54E+14	2858.89	243418876
4	67266	10.13	2.13E+14	2402.36	243409523
5	56.451	10.33	1.79E+14	2016.11	243416536
10	15.536	11.91	4.99E+13	554.86	246532656
15	2.610	14.29	9.65E+12	93.21	283731714
20	180	17.54	1.53E+12	6.43	650904724
25	6	21.05	2.96E+11	0.21	3785591528

Bridge degradation and the effect of maximum stresses were also taken into account as said before. The stress ranges histograms were multiplied by a factor of 2 (AASHTO, 2014) and the second slope of the S-N Curve, below CAFL, was taken as the first one (Eurocode 2, 2004). Thus, Table 5 exhibits the results of estimated service life for Itinguijada Bridge considering this worst-case scenario.

In Figure 15, differently from Figure 8, one cannot see a clear difference between the slope of the equivalent stress range points. This happens because of the low levels of stress that Itinguijada Bridge is subjected. In spite of that, in Tables 4 and 5 is possible to identify the cut-off limit.

For the worst case scenario of Itinguijada Bridge, the VAFL value below which the slope of the points matches the slope of the S-N curve, and the number of cycles does not matter anymore, is VAFL10. Thus, it can be said that the service life of this bridge is 5511 years. Therefore, it is considered that Itinguijada Bridge has infinite fatigue life.

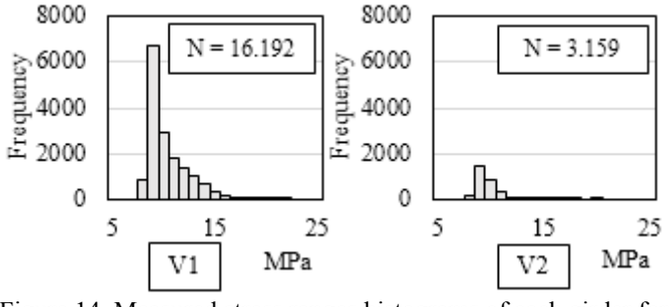


Figure 14. Measured stress ranges histograms of each girder for VAFL10 cut-off level for Itinguijada Bridge.

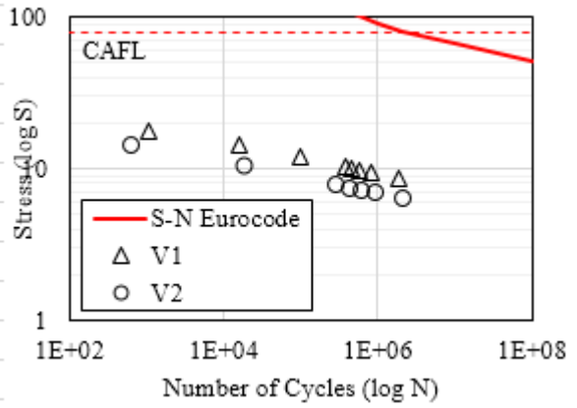


Figure 15. Equivalent stress range and number of cycles for each VAFL level for Itinguijada Bridge.

Table 5. Estimated service life of Itinguijada Bridge for each VAFL level considering bridge degradation and maximum stresses.

VAFL	N_{sol}	S_{re} (MPa)	N_{res}	$N_{cycles/day}$	Estimated service life (years)
1	124205	14.72	8.89E+09	4435.89	5493
2	117898	14.88	8.44E+09	4210.64	5493
3	106093	15.20	7.60E+09	3789.04	5493
4	94060	15.57	6.73E+09	3359.29	5493
5	86008	15.85	6.16E+09	3071.71	5493
10	56451	17.23	4.06E+09	2016.11	5511
15	35717	18.79	2.63E+09	1275.61	5651
20	15536	21.58	1.32E+09	554.86	6495
25	5734	25.08	6.20E+08	204.79	8296
30	2610	27.63	3.82E+08	93.21	11234
33	1383	29.39	2.81E+08	49.39	15580
35	819	30.74	2.24E+08	29.25	21023
40	180	34.61	1.24E+08	6.43	52866
45	44	37.98	7.79E+07	1.57	135849
50	6	42.00	4.71E+07	0.21	601902

5 CONCLUSIONS

In the present study, the fatigue service life of two simple supported short-span reinforced concrete bridges were evaluated. The equivalent stress ranges used were calculated from monitoring data given by a BWIM system.

The proposed method estimates the service life due to fatigue using S-N curves offered by international standards, with the correction of medium stress, and equivalent stress ranges produced by actual traffic conditions calculated in a novel way. This analysis was performed for several VAFL cut-off values in order to identify which one would be more suited to evaluate those bridges. The main conclusions are:

- The extension of the S-N curve below CAFL must be considered for cycled loading. Without an adequate VAFL cut-off level, the calculated service life would be quite optimistic;

- VAFL between 25 to 33% of CAFL, normally used in the literature, can give a good and conservative estimative of the service life when degradation and maximum stresses are taken into account;
- From the results of both bridges, it is expected infinite fatigue life for bridges with estimated life above 100 years when VAFL50 cut-off level and the worst-case scenario are considered.

The results obtained in the current study contribute to the state-of-the art of fatigue in reinforced concrete bridges. However, they are not definitive.

The assumptions made regarding maximum stress range and bridge degradation, are conservative. They do not describe perfectly the effects of degradation and traffic conditions.

Although the period of monitoring was quite long, it was not long enough to characterize the seasonal nature of traffic. Hence, it is not possible to state that the actual traffic was well-defined. In addition, it cannot be stated that the traffic will remain the same over the next years. Therefore, a better model should include an expected increase in traffic.

All these aforementioned issues may be addressed by a reliability model, which considers all the problem variables as random.

ACKNOWELEGMENTS

The authors would like to express their gratitude to the Brazilian National Department of Infrastructure (DNIT) for having financially supported such research.

REFERENCES

ABNT. 2014. NBR 6118: *Projeto de estruturas de concreto – procedimento*.

ABNT. 2013. NBR 7188: *Carga móvel rodoviária e de pedestres em pontes, viadutos, passarelas e outras estruturas*.

ACI Committee 215. 1997. *Considerations for design of concrete structures subjected to fatigue loading*.

ASTM. 2011. E1049-85: *Standard practices for cycle counting in fatigue analysis*.

AASHTO. 2014. *LRFD Bridge Design Specifications*. 7 ed, Washington.

EUROCODE. 2004. Eurocode 2. *Design of concrete structures – Part 1-1: General rules and rules for buildings*.

Forrest, R.W.B. Higgins, C. & Ekin Senturk, A. 2010. Experimental and analytical evaluation of reinforced concrete girders under low-cycle shear fatigue. *ACI Structural Journal* 107(2): 199-207.

Guo, T. Frangopol, D.M. & Chen, Y. 2012. Fatigue reliability assessment of steel bridge details integrating weigh-in-motion data and probabilistic finite element analysis. *Computers and Structures* 112-113: 245-257.

Higgins, C. Farrow, W.C. Nicholas, B.S. & Potisuk, T. 2006. High-cycle fatigue of diagonally cracked reinforced concrete bridge girders: field tests. *Journal of Bridge Engineering* 11(6): 699-706.

Higgins, L. Forth, J.P. Neville, A. Jones, R. & Hodgson, T. 2013.Behaviour of cracked reinforced concrete beams under repeated and sustained load types. *Engineering Structures* 56: 457-465.

Johannesson, P. 1999. *Rainflow analysis of switching Markov loads*. Doctoral Theses. Lund Institute of Technology.

Junges, P. Pinto, R.C.A. & Fadel Miguel, L.F. 2016. Fatigue analysis of reinforced concrete bridges from monitoring. In A.T. Beck, D.M. Frangopol, T.N. Bittencourt (ed.), *Maintenance, Monitoring, Safety, Risk and Resilience of Bridges and Bridge Networks; Proc. 8th intern. conf. IABMAS 2016, Foz do Iguaçu, 26-30 June 2016.* CRC Press: Balkema.

Junges, P. Pinto, R.C.A. & Fadel Miguel, L.F. 2017. B-WIM systems application on reinforced concrete bridge structural assessment and highway traffic characterization. *IBRACON Structural and Materials Journal* 10(6): 1338-1365.

Kumpoopong, R. & Herabat, P. 2010. Finite element analysis for fatigue evaluation of reinforced concrete bridge deck. *Advances in Structural Engineering* 13(6): 1017-1031.

Kwon, K. & Frangopol, D. M. 2010. Bridge fatigue reliability assessment using probability density functions of equivalent stress range based on field monitoring data. *International Journal of Fatigue* 32: 1221-1232.

Moses, F. 1979. Weigh-in-motion system using instrumented bridges. *ASCE Transp. Eng. J.* 105(3): 233-249.

Rocha, M. Brüwiler, E. & Nussbaumer, A. 2015. Microstructural influence on the scatter in the fatigue life of steel reinforcement bars. *International Journal of Fatigue* 75: 205-212.

Sasaki, K.K. Paret, T. Araiza, J.C. & Hals, P. 2010. Failure of concrete T-beam and box-girder highway bridges subjected to cyclic loading from traffic. *Engineering Structures* 32(7): 1838-1845.

Schijve, J. 2003. Fatigue of structures and materials. *International Journal of fatigue* 25: 679-702.

Schäfli, M. & Brühwiler, E. 1998. Fatigue of existing reinforced concrete bridge deck slabs. *Engineering Structures* 20(11): 991-998.

Wang, T. Liu, C. Huang, D. & Shahawy, M. 2005. Truck loading and fatigue damage analysis for girder bridges based on weigh-in-motion data. *Journal of Bridge Engineering* 10(1): 12-20.

Zanuy, C. Albajar, L. & Fuente, P. 2009. Sectional analysis of concrete structures under fatigue loading. *ACI Structural Journal* 106(5): 667-677.

Zanuy, C. Maya, L.F. Albajar, L. & Fuente, P. 2011. Transverse fatigue behaviour of lightly reinforced concrete bridge decks. *Engineering Structures* 33: 2839-2849.

Zhang, W. & Cai, C. 2012. Fatigue reliability assessment for existing bridges considering vehicle speed and road surface conditions. *Journal of Bridge Engineering* 17(3): 443-453.

Zhang, W. Cai, C.S. & Pan, F. 2013. Nonlinear fatigue damage assessment of existing bridges considering progressively deteriorated road conditions. *Engineering Structures* 56: 1922-1932.

Zhou, Y. 2006. Assessment of bridge remaining life through field strain measurement. *Journal of Bridge Engineering* 11(6): 737-744.

Žnidarič, A. & Lavrič. 2010. Applications of B-WIM technology to bridge assessment. In *Maintenance, Monitoring, Safety, Risk and Resilience of Bridges and Bridge Networks; Proc. 5th intern. conf. IABMAS 2010, Philadelphia, 11-15 July 2010.* CRC Press: Balkema.

Maintenance, Safety, Risk, Management and Life-Cycle Performance of Bridges – Powers, Frangopol, Al-Mahaidi & Caprani (Eds)
© 2018 Taylor & Francis Group, London, ISBN 978-1-138-73045-8

Measurement of time-dependent corrosion of steel bridge from corrosion monitoring

Seok-Hyeon Jeon, Jun Min You & Jin-Hee Ahn,
Gyeongnam National University of Science and Technology, Jinju, Republic of Korea

Kwang-Il Cho
Product Application Center, POSCO, Inchon, Republic of Korea

Young-Soo Jeong
Seismic Testing Center, Pusan National University, Yangsan, Republic of Korea

ABSTRACT: Steel structures have been generally exposed atmospheric corrosion environments such as humidity, temperature, airborne salt from the sea and chemical components in regional areas etc. to function as structural members of infrastructures. These atmospheric corrosion environments have naturally generate the corrosion problem of steel structures based on oxidational characteristics of structural steel materials. Therefore, it is important to measure the corrosion environment and condition for steel structure. In this study, thus, corrosion environment and condition were examined using atmospheric corrosion monitoring sensors, monitoring steel plate(MSP) and environmental data as temperature, humidity etc. Then compare corrosivity grade was calculated and compared to use basic data for proposing mean corrosion depth estimation method depending on structural members using monitoring data.

1. INTRODUCTION

1.1 Research outline

In various infrastructures, steel members have been generally used as main structural element to resist or transmit the service load and forces. These steel structural members can be easily damaged and failure by corrosion and fatigue phenomena related to their maintenance process for their service periods. For fatigue problem of steel structure, many studies and reviews were reported and researched for its failure mechanism and related causes. For corrosion problem of steel structure, however related studies and researches have been limited up to now. Corrosion problem of steel structures could be related to environmental conditions as wet time, sedimentation of chloride etc. affected by installed and structural locations of steel structural members. Thus, different corrosion problems and rates can be occurred in the same structure. Therefore, it is useful to examine corrosion environment of steel structures depending on its installed environmental characteristics to estimate corrosion rate of steel structure. For steel bridges, however, it is difficult to examine the corrosion environment for each bridge member of steel bridges determined by structural shape using general corrosion test method, since its installed condition and structural condition. In this study, therefore, corrosion condition and environment of each structural direction were measured for test steel box structure similar to real steel box bridge from corrosion monitoring sensors and monitoring steel plate (MSP) to estimate corrosion rate instead of typical carrion tests.

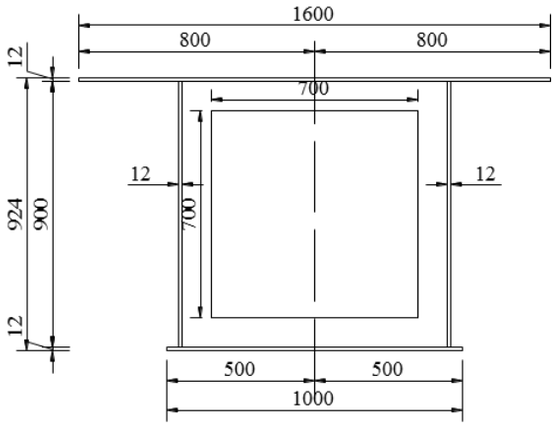
1.2 Research objectives

In this study, corrosion condition and environment were examined depending on structural characteristics of steel box from corrosion monitoring sensors and monitoring steel plates. To examine corrosion environments, atmospheric corrosion monitoring sensors were used as corrosion environmental monitoring sensors (Shinohara. 2015). This sensor data will be used to compare the difference between structural direction in the same structure. And monitoring steel plate (MSP) was additionally installed to examine each corrosion conditions and its weight loss level and mean corrosion depth were measured according to installed environment of each monitoring steel plate (Kainuma at al. 2013, 2014). For monitoring steel plate (MSP), carbon steel and weathering steel were used to compare corrosion level and condition under same corrosion environment and structural characteristics, since corrosion rate can be main design factor in steel bridges. Additionally, temperature and humidity, precipitation were also compared to confirm the corrosivity grade. From these corrosion environment condition monitoring method and MSP monitoring, corrosion environment was examined depending on structural direction of steel box member.

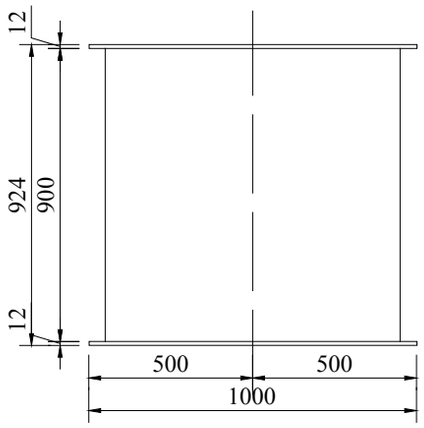
2. TEST METHOD

2.1 Test specimen

To examine the corrosion environment effect depending on structural direction in same structure, steel box specimen was fabricated with 900mm height, 1,000mm width and 1,000mm length. To make the similar corrosive environment of steel box bridge, its upper flange of the steel box specimen was fabricated with 1,600mm. Figure 1 shows the dimensions of the steel box specimens used in this study. These steel box specimens were installed to south and north direction in the steel frame with 900mm height. Figure 2 shows the test steel box specimens, attached monitoring sensors and attached monitoring steel plates (MSP) in the exposure test.



(a) Front view of test steel box



(b) Side view of test steel box

Figure 1. Dimension of exposed test steel box specimen.



(a) Test set up for atmospheric exposure test

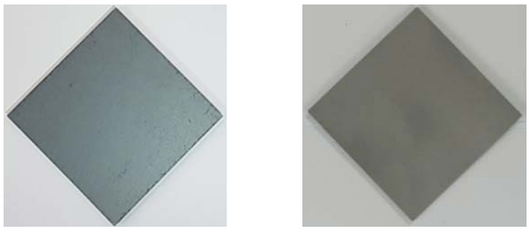


(b) Front view of test set-up

Figure 2. Exposure test set-up.

2.2 Monitoring steel plate (MSP)

The monitoring steel plate (MSP) used in this study was manufactured with a height of 60mm, a width of 60mm, and a thickness of 3mm, and carbon steel(SM490A) and weathering steel(SM490AW) were used (KS D 3515. 2016; JIS G 3114. 2008). Before attaching the monitoring steel plate to the structure, SSPC SP 10 standard was applied and surface treatment was performed to remove foreign substances such as mill scale on the surface of steel and to form a uniform corrosion product. Figure 3 shows the monitoring steel plate before and after the surface treatment. Double-sided tape for industrial was used to install the monitoring steel plate in the bottom of the monitoring steel plate. In order to equalize the corrosion rate of the actual structure and the monitoring steel, a heat conduction sheet was also attached to the bottom of the steel.



(a) Before surface treatment (b) After surface treatment
Figure 3. Before and after surface treatment.

2.3 Atmospheric corrosion environment sensor

The atmospheric corrosion monitoring sensor with the characteristic of generating galvanic currents between dissimilar metals (Fe/Ag) was used. Figure 4 shows the mechanism of galvanic cell of the atmospheric corrosion monitoring sensor. As shown in Fig. 4, double metal layers were placed on the surface of the sensor, it measures the galvanic current between Fe and Ag when a water film is formed on the sensor surface. From measured corrosion current, the corrosion environment and thus the corrosion rate of the steel can be evaluated (Cheng et al 1997). Figure 5 shows the atmospheric corrosion monitoring sensor.

For raining atmospheric corrosion environment, the amount of electric charge output from the atmospheric corrosion monitoring sensor can be highly generated. For evaluating the corrosion rate of steel using atmospheric corrosion monitoring sensor, its highly generated electric charge output results should be considered. Thus, in order to obtain the correlation between the mean corrosion depth of the steel and the sensor output, it is necessary to convert the amount of electric charge measured by the atmospheric corrosion monitoring sensor in consideration of the influence of rainfall (Kainuma at al. 2010; Shinohara at al. 2005).

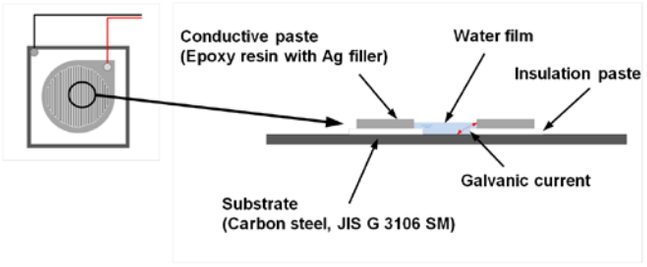


Figure 4. Mechanism of galvanic cell.

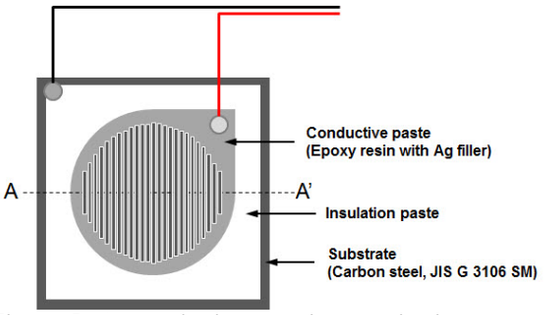


Figure 5. Atmospheric corrosion monitoring sensor schematic diagram.

2.4 Corrosivity grade

For general steel and alloy steel, corrosion grade is defined as following factors such as time of wetness (τ) by relative humidity, pollution by sulfur dioxide (SO_2) (P) and salinity of the atmosphere (S) in ISO 9223. For each corrosion factors, atmospheric corrosivity is defined as the ability to cause corrosion in a given corrosion system. Time of wetness is defined as time during which the steel surface is covered by the liquid film of the electrolyte and the absorbability. For pollution grade, it is also defined as calculated grades based on quantitative measurements of certain chemically active substances, corrosive gases or suspended particles in the atmosphere (both natural and artificial results) different from the normal components of the atmosphere. Wetness of steel surface is caused by various factors such as dew, rainfall, melting snow and high humidity. Thus, time of wetness is classified as Table 1 in ISO 9223 (ISO 9223. 2003).

Table 1. Classification of time of wetness (Tow) (ISO 9223. 2003).

Grade	Time of wetness (Tow)	
	h/a(hour/year)	%
$\tau 1$	$\tau \leq 10$	$\tau \leq 0.1$
$\tau 2$	$10 < \tau \leq 250$	$0.1 < \tau \leq 3$
$\tau 3$	$250 < \tau \leq 2{,}500$	$3 < \tau \leq 30$
$\tau 4$	$2{,}500 < \tau \leq 5{,}500$	$30 < \tau \leq 60$
$\tau 5$	$5{,}500 < \tau$	$60 < \tau$

The pollution grade assessed by sulfur dioxide and salinity in the atmosphere can be affected by atmospheric condition such as rural, urban, industrial and marine environments. In case of sulfur dioxide, its grade is divided into four classes (from P_0 to P_3) according to its deposition rate and concentration. The rate of SO_2 is P_d, and the concentration of SO_2 is represented by Pc. Table 2 shows the pollution classification by sulfur-containing substances. In case of salinity generated in the marine atmosphere, airborne salt developed from seawater evaporation can accelerate the corrosion of the nearby steel structure. Therefore, it is necessary to evaluate the atmospheric salinity. Table 3 shows the pollution clas-

sification by amount of salt under atmospheric (ISO 9223. 2003).

Table 2. Pollution classification by sulfur-containing substances (ISO 9223. 2003).

Attachment rate of SO_2	Concentration of SO_2 μg/m3	Grade
$P_d \leq 10$	$P_c \leq 12$	P_0
$10 < P_d \leq 35$	$12 < P_c \leq 40$	P_1
$35 < P_d \leq 80$	$40 < P_c \leq 90$	P_2
$80 < P_d \leq 200$	$90 < P_c \leq 250$	P_3

Table 3. Pollution classification by amount of salt under atmospheric (ISO 9223. 2003).

Attachment rate of Chloride mg/($m^2 \cdot$ d)	Grade
$S \leq 3$	S_0
$3 < S \leq 60$	S_1
$60 < S \leq 300$	S_2
$300 < S \leq 1{,}500$	S_3

The corrosivity grade of steel exposed to the atmospheric environment can be evaluated according to the ISO 9223. It is a method to estimate the corrosive grade by measuring its weight loss from corrosion and its thickness reduction. Table 4 shows the criteria for measuring and reducing the weight loss of the corrosion tested steel and the criteria for measuring the reduction in the thickness of the steel. It is classified as C1 ~ C5, with a very low corrosion rate for C1, a low corrosion rate for C2, a normal corrosion rate for C3, a high corrosion rate for C4, and a very high corrosion rate for C5.

Table 4. Corrosion rate for initial 1 year exposure (ISO 9223. 2003).

Corrosivity Grade	Corrosion rate of carbon steel(γ_{corr})
	Carbon steel
C1	$\gamma_{corr} \leq 10$ [g/(m2·a)] $\gamma_{corr} \leq 1.3$ [μm/a]
C2	$10 < \gamma_{corr} \leq 200$ [g/(m2·a)] $1.3 < \gamma_{corr} \leq 2.5$ [μm/a]
C3	$200 < \gamma_{corr} \leq 400$ [g/(m2·a)] $25 < \gamma_{corr} \leq 50$ [μm/a]
C4	$400 < \gamma_{corr} \leq 650$ [g/(m2·a)] $50 < \gamma_{corr} \leq 80$ [μm/a]
C5	$650 < \gamma_{corr} \leq 1{,}500$ [g/(m2·a)] $80 < \gamma_{corr} \leq 200$ [μm/a]

3. EXPOSURE TEST RESULTS

From atmospheric corrosion expose test of steel box structure, corrosion rate and corrosion condition of carbon steel and weathering steel were examined depending on structural direction as south and north of steel box structure. Atmospheric corrosion expose tests were conducted for six months. From atmospheric corrosion monitoring sensors and monitoring steel plate (MSP), corrosion environments and weight loss rate were measured and mean corrosion depth etc. were calculated. And also there results were explained related to corrosivity grade depending on structural direction of test steel box.

3.1 Visual inspection results

To evaluate corroded condition of each monitoring steel plate (MSP) installed on the structural direction of steel box. Firstly, visual inspection of each monitoring steel plate was conducted such as rust examination through surface color change. In this study, color of rust was examined by its installed direction and exposed test period, since several test specimens were attached depending on direction and location of test steel box. Figure 5 s hows tested monitoring steel plates. When comparing initial specimen and six months specimen, it can be confirmed that monitoring steel plate exposed to the atmospheric environment has corroded on the plate surface due to repetition of the wet state depending on each installed corrosion environment due to increase in the exposure test periods as shown in Figure 5.

From visual inspection for monitoring steel plates, the rust color of every monitoring steel plate gradually becomes yellowish brown depending on the increase in the exposure test periods. This color is similar to the color of α-FeOOH (Goethite) among the components of rust which determines rust. The characteristics of goethite are chemically stable among the rust formed from general atmospheric corrosion environment, it is inactive rust with low possibility of corrosion because it is difficult to dissolve oxidized Fe^{3+} ions due to low solubility. Thus, it is considered that this atmospheric corrosion environment is likely to form a relatively stable rust layer.



(a) South (Start)



(b) North (Start)



(c) South (Six months)



(d) North (Six months)

Figure 5. Surface condition of test steel box and MSP.

3.2 Evaluation of corrosion rate of monitoring steel plate (MSP)

The measured values of the weight of the monitoring steel plate in the south direction and the north direction were obtained and the mean corrosion depth was calculated using the weight loss method. Figure 6 and 7 shows the weight loss and mean corrosion depth. From Fig. 7, the weight loss and mean corrosion depth of north direction is greater than those of south direction. And also, it shows that the different weight loss and mean corrosion depth depending on the steel type; carbon steel and weathering steel. In results was obtained from six months exposure tests, therefore it can be more clearly evaluated after long-term measurement.

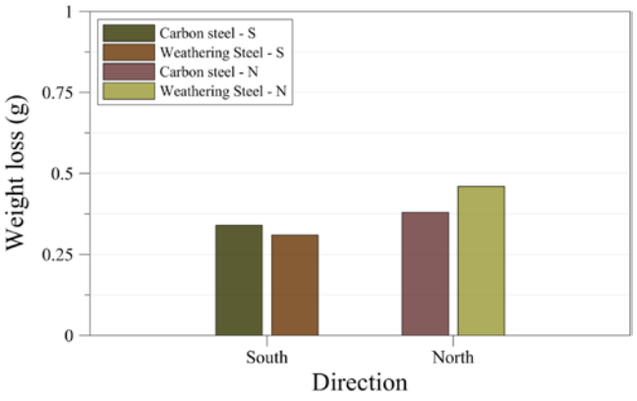


Figure 6. Weight loss – structural direction of the test period.

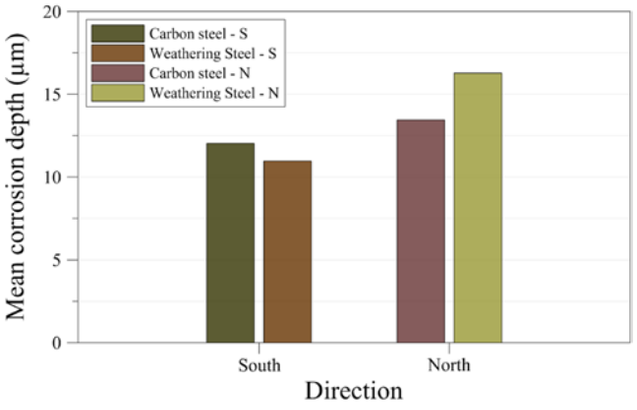


Figure 7. Mean corrosion depth – structural direction of the test period.

3.3 Assessment of corrosivity grade by weight loss method

According to ISO-9223 (Corrosion of metals and alloys - corrosivity of atmospheres - classification), from Fig. 6 and 7, corrosivity of atmospheres were evaluated as C2 in the south direction and C3 in the north direction. Table 5 summarized the annual corrosion rate conversion results and corrosivity grades for each tested direction.

Table 5. Result according to the ISO-9223 – corrosion of metals and alloys – corrosivity of atmospheres – classification

Steel	Mean corrosion depth (μm)	Annual corrosion rate g/(m2·a)	Annual corrosion rate (μm/a)
Carbon steel-S	12.03	188.89	24.06
Carbon steel-N	13.45	211.11	26.89
Weathering steel-S	10.97	172.22	21.94
Weathering steel-N	16.28	255.56	32.56
Corrosivity grade			
Carbon steel-S	C2	Carbon steel-N	C3
Weathering steel-S	C2	Weathering steel-N	C3

3.4 Corrosivity grade from test results

To identify atmospheric corrosion environmental grades based on atmospheric corrosion environmental data, temperature and humidity data of the exposed test region were taken from meteorological office for exposure test periods (17.01.12~17.07.12). Figure 8 and Table 6 summarized monthly mean temperature and humidity in the exposed test region. From these atmospheric corrosion environmental data, time of wetness (τ) was calculated as 22.50% for over 80% humidity with over 0℃ temperature. The concentration of sulfur dioxide (μg / m3) and the deposition rate of chloride (mdd) were obtained from "Air Korea" internet site which provides information on the atmospheric environment. (http://www.airkorea.or.kr/index). Table 7 summarized the classified corrosion grade and corrosivity grade of the atmosphere for this exposed condition due to time of wetness and pollution according to ISO-9223. As shown in Table 7, this atmospheric corrosive grade was evaluated as C2 or C3 from combining the classified grades and this result is similar to those of atmospheric corrosivity calculated using the weight loss method.

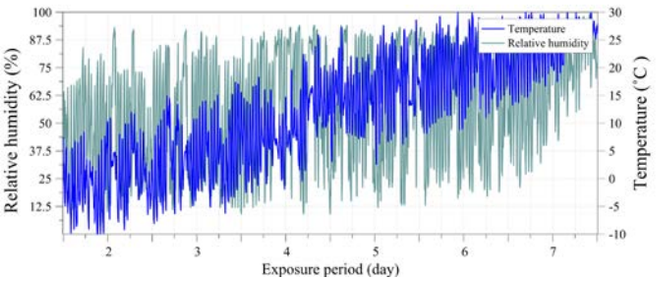


Figure 8. Mean Temperature and Humidity during the period(17.01.12~17.07.12).

Table 6. Average temperature and humidity during the test period

Average temperature (ºC)				
Test Period	Month			
	1	2	3	4
	-0.6	2.8	6.5	14.3
	Month			
	5	6	7	8
	18.4	21.7	26	-
Average humidity (%)				
Test Period	Month			
	1	2	3	4
	47	47.7	55	56.6
	Month			
	5	6	7	8
	58.9	61.8	82.2	-

Table 7. Result according to the KS D ISO-9223 – corrosion of metals and alloys – corrosivity of atmospheres – classification.

Time of wetness (%)	Time of wetness grade (τ)	SO_2 grade	Chloride grade
22.50	τ_3	P_0	S_0
Corrosivity grade			
C2 or C3			

3.5 Evaluation of corrosion environment through atmospheric corrosion monitoring sensor

The atmospheric corrosion monitoring sensors were attached to the south and north direction of the web along the monitoring steel plates in the steel box specimens. Figure 9 shows the measured corrosion current. Table 8 summarized the measured atmospheric corrosion monitoring sensor data. As shown in Figure 9, the amount of electric charge was gradually increased depending on exposure test period. For installed direction, the amount of electric charge in the north direction was higher than that of the south direction. Figure 10, shows the difference in the amount of electric charge in the south and

north direction of the web. From these results, it can be considered that corrosion environment is different and affected depending on s tructural direction of steel box.

Table 8. Result of the corrosion current during the test period (17.01.12~17.07.12)

Atmospheric corrosion monitoring sensor of south				
Daily average electricity (Q/day)	Month			
	1	2	3	4
	0.0000	0.00059	0.00052	0.00928
	Month			
	5	6	7	8
	0.00539	0.01021	0.00961	-
Atmospheric corrosion monitoring sensor of north				
Daily average electricity (Q/day)	Month			
	1	2	3	4
	0.0000	0.00083	0.00636	0.01350
	Month			
	5	6	7	8
	0.00575	0.00980	0.00974	-

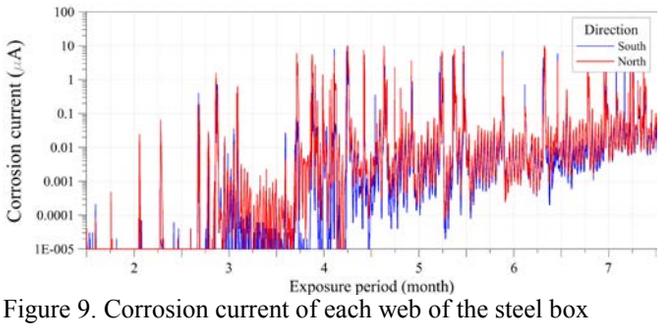


Figure 9. Corrosion current of each web of the steel box

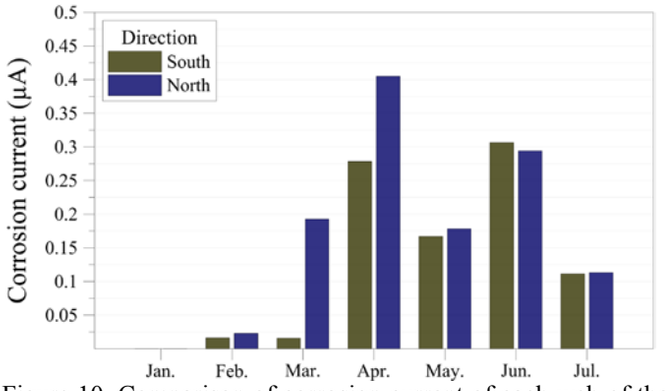


Figure 10. Comparison of corrosion current of each web of the steel box

4. CONCLUSION

This study dealt with relative corrosion condition and environment of each structural direction for a steel box structure using corrosion monitoring sensors and monitoring steel plates (MSP). For this purpose, the daily mean current achieved from atmosphere corrosion sensor affected by corrosion environment was measured. And weight loss and mean corrosion depth of MSP were calculated according to installed environment of each structural direction. Additionally, corrosivity grade of tested region was evaluated using environmental data. Thus, these results were compared to estimate corrosion condition and corrosion environment. For this test region and structural direction was evaluated as C2 or C3 corrosivity grade. It can be confirm the corrosion condition is different depending on structural member and direction. This result can be explained from atmosphere corrosion sensor data. This comparison and measured data can be used to propose mean corrosion depth estimation method depending on structural members or direction etc. from correlation between rate of corrosion and amount of the daily average electricity in the future.

ACKNOWLEDGEMENTS

This research was supported by Basic Science Research Program through the National Research Foundation of Korea (NRF) funded by the Ministry of Education(NRF-2017R1D1A1B03028755).

REFERENCES

Cheng, Y.F. & Luo, J.L. & Zheng, L.Q. & Du, Y.L. & Cao, C.N. 1997. Monitoring of galvanic current of dual electrode ACM covered with thin electrolyte film. Bull. Electrochem. 13 : 280–283.

ISO 9223. 2003. Corrosion of metals and alloys – Corrosivity of atmospheres – Classfication.

JIS G 3114. 2008. Hot-rolled atmospheric corrosion resisting steels for welded structure. *Japan Industrial standards, (in Japanese)*.

Kainuma, S. & Sugitani, K. & Ito, Y. & Kim, I. T. 2010. Evaluation method for time-dependent corrosion behavior of carbon steel plate using atmospheric corrosion monitoring sensor. Key Engineering Materials : 417-418, 417-420.

Kainuma, S. & Yamamoto, Y. & Itoh, Y. & Oshikawa, W. 2011. Prediction method for mean corrosion depth of uncoated carbon steel plate subjected to rainfall effect using Fe/Ag galvanic couple ACM-Type corrosion sensor. Corros. Eng. (Translation of Zairyo-to-Kankyo) 60 : 498-503.

Kainuma, S. & Yamamoto, Y. & Hayashi, H. & Itoh, Y. & Oshikawa, W. 2013. Practical method for estimating time-dependent corrosion depth of uncoated carbon steel plate under atmospheric environment using Fe/Ag galvanic couple ACM-type corrosion sensor. Corros. Eng. (Translation of Zairyo-to-Kankyo) 63 : 1-8.

Kainuma, S. & Yamamoto, Y. & Hayashi, H. & Ito, Y. 2014. Practical method for estimating corrosion depth of uncoated

carbon steel using thickness of the corrosion-product layer. Key Engineering Materials : 577-578, 201-204.
KS D 3515. 2016. Rolled steels for welded structures. *Korea Industrial standards, (in Korea)*.
Shinohara, Shin. & Shinichi, Motohida. & Wataru, Ogawa. 2005. Environmental corrosion evaluation by ACM sensor. Materials and environment. 54 : 375-382.
Shinohara, T. 2015. Evaluation and monitoring methods for atmospheric corrosion. Corros. Eng. (Translation of Zairyo-to-Kankyo) 64 : 26-33.

Maintenance, Safety, Risk, Management and Life-Cycle Performance of Bridges – Powers, Frangopol, Al-Mahaidi & Caprani (Eds)
© 2018 Taylor & Francis Group, London, ISBN 978-1-138-73045-8

Structural monitoring of Eltham Rail Trestle Bridge using advanced non-destructive testing techniques

Maizuar Maizuar[1,2], Lihai Zhang[1], Saeed Miramini[1], Priyan Mendis[1]
[1]*Department of Infrastructure Engineering, University of Melbourne, VIC 3010, Australia*
[2]*Department of Civil Engineering, Malikussaleh University, Indonesia*

ABSTRACT: This present a series of bridge condition assessment methods using innovative nondestructive testing tech-niques (i.e. microwave interferometry radar IBIS-S and 3D optical measurement system ARAMIS). Using a timber bridge in Australia as a case study (i.e. Eltham Rail Trestle Bridge), it demonstrates that IBIS-S can ef-fectively capture the dynamic behaviour of the bridge under train loading, such as natural frequencies, maxi-mum vertical and horizontal displacements, while ARAMIS optical measurement system has the capability for accurately measuring the deformation of the critical members of the bridge.

.

1 INTRODUCTION

There are around 29,000 timber bridges in Australia with most over fifty years old (Samali, Li, Dackermann, & Choi, 2011). Some are still being used to carry heavy traffic loads (e.g., train loading). Consequently, ageing bridges and the induced dynamic effects caused by the passage of trains could accelerate the structural deterioration of the bridges, ultimately the reduced service life of the bridges (Moreu et al., 2015; Terry Wipf, Ritter, & Wood, 2000). Thus, the development of innovative methods for condition monitoring of bridges becomes critical important.

1.1 *Monitor the dynamic behaviour of the bridges*

Traditional measuring devices for dynamic behaviour of bridges (e.g., accelerometer) may be limited the bridge accessibility, time and budgets (Gentile, 2010). Other monitoring devices i.e. laser sensor, also have limitation in detecting the overall deformation of a bridge and are very sensitive to enviromental conditions (Pieraccini et al., 2007). When full-field monitoring real-time dynamic behaviour of bridges is required, the recent advanced IBIS-S radar interferometry technique provides a solution.

A typical IBIS-S system primarily consists of three parts: a sensor module, a user control PC and a power supply unit. The sensor module consists of two horn antennas and is supported by a rotating head tripod, sends and receives the electromagnetic waves. The data acquisition and interpretation are handled by a laptop which is connected to the sensors (IDS, 2013).

The IBIS-S radar sensor is designed for remote monitoring of structural vibrations from a distance up to 1km with high accuracy. Vibration frequencies can be measured as high as 100 Hz. In operational condition, the radar is suitable for measuring displacement of a structure with accuracy better than 0.1mm, a range resolution of 0.5m and a sampling rate up to 200Hz.

The performance of IBIS-S radar sensor technology is founded on the combined use of the interferometry technique and the stepped-frequency continuous wave technique (SF-CW). While SF-CW detects the positions of different target points in the range direction, the interferometry technique provides the displacement of each target point by analysing the back-scattered electromagnetic waves reflected by the targets at different time points. Detail of these techniques can be found in (Kafle et al., 2017; Maizuar, Zhang, Miramini, Mendis, & Thompson, 2017; Zhang, Maizuar, Mendis, Duffield, & Thompson, 2016). It should be noted that IBIS-S technique enables a measurement of the line-of-sight displacement or the radial displacement of structures. Once the radial displacement has been obtained, the actual displacement of the measured points can be easily calculated by applying a simple geometric projection.

1.2 *Monitor the deformation profile of the bridge members*

The deformation of bridge structural members (e.g., column) has conventionally been measured using strain gauges. However, the use of these devices generally consists of localized measurements since only at preselected points information and in one direction could be obtained (Schmidt, Tyson, & Galanulis, 2003). Further, the quality of measurement essentially depends on the contact surface of a structure and its accuracy could be greatly affected by changing environmental conditions (Motra, Hildebrand, & Dimmig-Osburg, 2014). When a full-field non-contact deformation measurement profile is required, the non-contact 3D optical measurement (e.g., ARAMIS) system has the capability of capturing the time-dependent deformation profile of critical bridge members. This technique allows unique non-contact measurements of 3D deformations and analyzes the displacement and strain fields through 3D digital image correlation methods (DIC). It is robust technique which enables large data capturing and accurate model validation (Miramini, Zhang, Richardson, Mendis, & Ebeling, 2016; Zhang et al., 2017).

The ARAMIS system consists of a pair of digital CCD cameras (1280 x 1024 pixels) with a 3D resolution of around 3.0μm, specimen lightings, laser pointer, tripod, data acquisition box and a laptop PC installed with commercial ARAMIS software package. While the digital CCD cameras capture the images of an object from different angles when the object is subject to external loading, the time-dependent deformation of the object is obtained through image processing using ARAMIS post-processing software (GOM, 2017).

2 CASE STUDY

The IBIS-S and ARAMIS described in the Sections 1.1 and 1.2 were implemented to monitor the structural performance of Melbourne's only wooden Eltham Rail Trestle Bridge in Australia. The Eltham bridge is one of few timber heritage bridges in Australia that are still providing train service for Melbourne's metropolitan electric railway network. This timber bridge was built in 1902 with a length of approximately 200m and is possibly the longest curved wooden bridge for commuter railway in the southern hemisphere (VHD, 2005).

The IBIS-S radar sensors were configured to a horizontal distance of 5.2m and a height (h) of 3m with a distance resolution of 0.75m and a sampling frequency of 100Hz (Figure 1). Simultaneously, the deformation of a timber column of the bridge was measured using ARAMIS system, the selected column areas for deformation analysis were approximately 1.5m above ground level with measurement area was set to be 100×75mm, and camera lens were located 810mm from measurement surface (Figure 2).



Figure 1. Monitoring dynamic behaviour of bridge using IBIS-S



Figure 2. Monitoring deformation of timber column using ARAMIS

3 RESULTS AND DISCUSSION

3.1 *Dynamic behaviour of the bridge captured by IBIS-S*

The quality of the electromagnetic signals captured by IBIS-S can be obtained from the range profile of the test scenario as shown in Figure 3. P2 indicates the target measurement point while P1 and P3 are the neighbourhood of the target point. It can be seen that peaks with a good electromagnetic reflectivity (*i.e.,* SNR over 50dB) can be used as measurement points.

Figure 4 shows the vertical displacement time history of the bridge girder resulting from a passing

train. The results show that the observed maximum vertical displacement was around 10mm.

As shown in Figure 5 the natural frequency is identified using the displacement spectrum data analysis in frequency domain by a peak point at 4.6 Hz. This result is consistent with other previous studies (T Wipf, Wood, Phares, Ritter, & Bigelow, 2004). It also indicates that the bridge is in good condition.

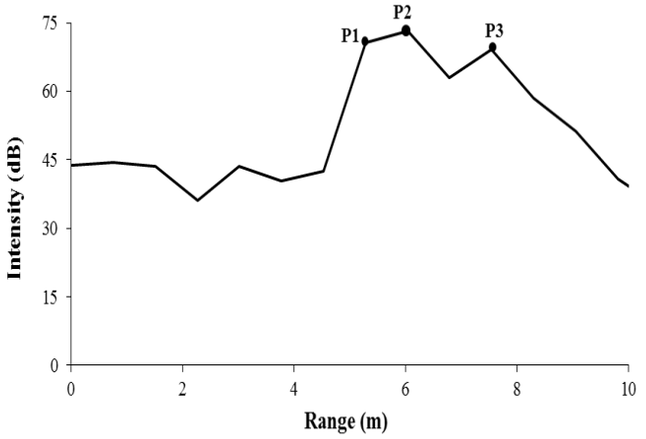


Figure 3. Range profile of the bridge

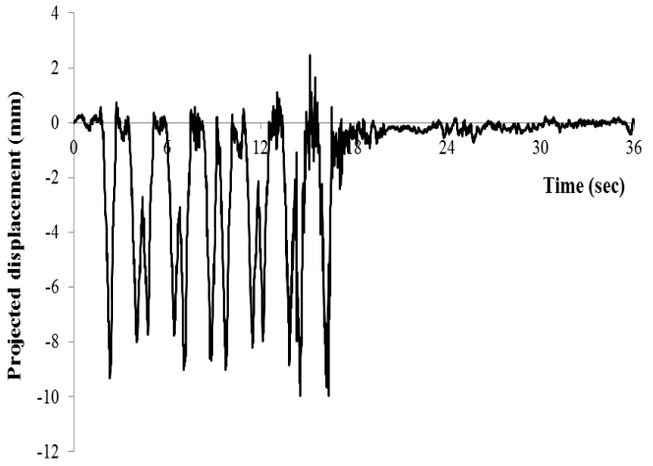


Figure 4. Displacement time history of a bridge girder

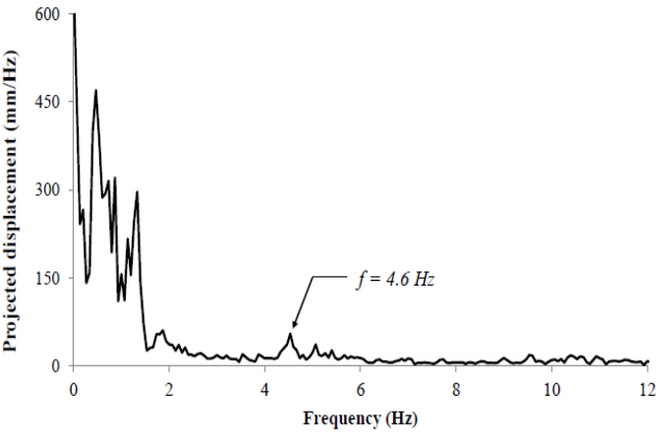


Figure 5. Natural frequency of the bridge

3.2 *Deformation of bridge member captured by ARAMIS*

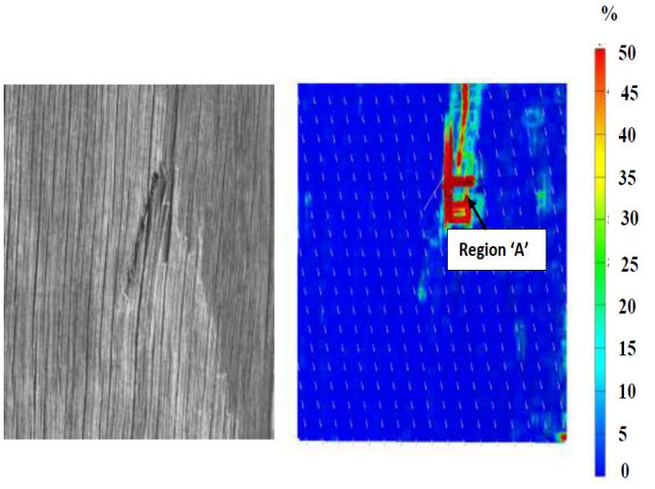


Figure 6. Surface of a timber column and von Mises strain distribution in region 'A'

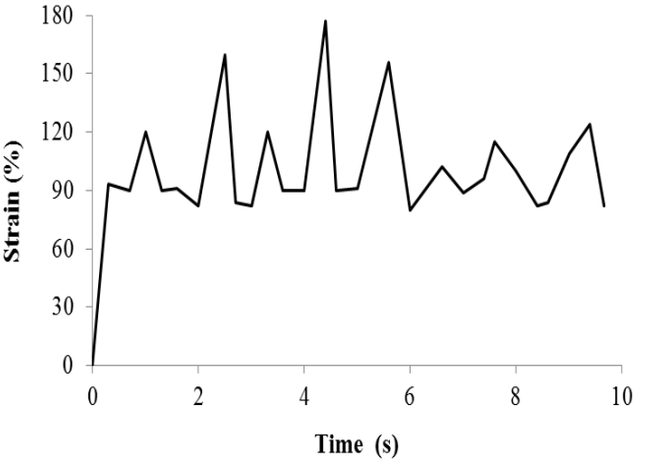


Figure 7. Time-dependent Von Mises strain in region 'A'

The von Mises strain distribution and the image of the column surface with a region of defect 'A' are illustrated in Figure 6. The results show that, under train loading, the strain in most area of column surface is relatively small (around 5%), and there is a strain concentration in the region of defect (i.e. region 'A'). It also demonstrates that, under a passing train, the maximum strain and vertical displacement in the defect region of the column surface (region 'A') could reach larger than 177% (Figure 7) and 0.7mm (Figure 8), respectively. The results also show that ARAMIS has the capability in capturing the column surface strain with a region of defect demonstrating its potential use for bridge structural health monitoring and assessment.

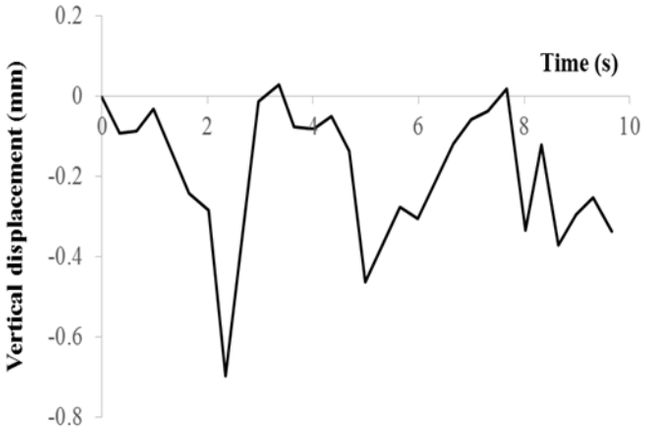


Figure 8. Time dependent vertical displacement in region 'A'

4 CONCLUSION

A structural monitoring of timber bridges under train loading using the recent advanced non-destructive testing (NDT) involving interferometric radar IBIS-S and ARAMIS optical measurement system was performed. The results of the study demonstrate that IBIS-S can effectively capture the dynamic behaviour of the bridge under train loading such as its natural frequency, maximum vertical and horizontal displacements. In addition, it shows that the 3D ARAMIS optical measurement system has the capability for assessing the structural performance of the critical members of the bridge (e.g., column) caused by a passing train, particularly in the region with surface defect.

5 REFERENCES

Gentile, C. 2010. Application of radar technology to deflection measurement and dynamic testing of bridges. In G. Kouemou (Ed.), *Radar Technology*. 141-162: InTech.

GOM. 2017. Precise industrial 3D metrology. RL

IDS. 2013. *IBIS surveyor v. 1.00 - user manual*. Pisa, Italy: IDS.

Kafle, B., Zhang, L., Mendis, P., Herath, N., Maizuar, M., Duffield, C., & Thompson, R. G. 2017. Monitoring the dynamic behavior of the merlynston creek bridge using interferometric radar sensors and finite element modeling. *Int J Appl Mech* 9(1): 1750003-1750020

Maizuar, M., Zhang, L., Miramini, S., Mendis, P., & Thompson, R. G. 2017. Detecting structural damage to bridge girders using radar interferometry and computational modelling. *Struct Control Health Monit* 24(10): 1-6

Miramini, S., Zhang, L., Richardson, M., Mendis, P., & Ebeling, P. R. 2016. Influence of fracture geometry on bone healing under locking plate fixations: A comparison between oblique and transverse tibial fractures. *Med Eng Phys* 38(10): 1100-1108

Moreu, F., Jo, H., Li, J., Kim, R. E., Cho, S., Kimmle, A., . . . LaFave, J. M. 2015. Dynamic assessment of timber railroad bridges using displacements. *J Bridge Eng* 20(10): 1-12

Motra, H. B., Hildebrand, J., & Dimmig-Osburg, A. 2014. Assessment of strain measurement techniques to characterise mechanical properties of structural steel. *Engineering Science and Technology* 17(4): 260-269

Pieraccini, M., Parrini, F., Fratini, M., Atzeni, C., Spinelli, P., & Micheloni, M. 2007. Static and dynamic testing of bridges through microwave interferometry. *NDT & E Int* 40(3): 208-214

Samali, B., Li, J., Dackermann, U., & Choi, F. 2011. Vibration-based damage detection for timber structures in Australia. In T. Chan & D. Thambiratnam (Eds.), *Structural Health Monitoring in Australia*. 81-108: Nova Science Publishers Inc.

Schmidt, T., Tyson, J., & Galanulis, K. 2003. Full-field dynamic displacement and strain measurement using advanced 3D image correlation photogrammetry: Part 1. *Exp Techniques* 27(3): 47-50

VHD. 2005. Eltham rail trestle bridge. RL

Wipf, T., Ritter, M., & Wood, D. 2000. Evaluation and field load testing of timber railroad bridge. *Transport Res Rec* 1696(1): 323-333

Wipf, T., Wood, T., Phares, B., Ritter, M., & Bigelow, J. 2004. *Dynamic field performance of timber bridges, final report: summary and conclusions* USA: B. E. Center

Zhang, L., Maizuar, M., Mendis, P., Duffield, C., & Thompson, R. 2016. Monitor the dynamic behaviour of concrete bridges using non-contact sensors (IBIS-S). *Adv Mater Res: Trans Tech Publ* 846: 225-230

Zhang, L., Miramini, S., Richardson, M., Ebeling, P., Little, D., Yang, Y., & Huang, Z. 2017. Computational modelling of bone fracture healing under partial weight-bearing exercise. *Med Eng Phys* 42: 65-72

Maintenance, Safety, Risk, Management and Life-Cycle Performance of Bridges – Powers, Frangopol, Al-Mahaidi & Caprani (Eds)
© 2018 Taylor & Francis Group, London, ISBN 978-1-138-73045-8

Fatigue life assessment of damaged steel strands

Y.C. Park
Institute of Construction and Environmental Engineering, Seoul National University, Seoul, Republic of Korea

S.M. Yoo, C.Y. Kim & M.S. Park
Myongji University, Yong-in-si, Gyung-gi-do, Republic of Korea

ABSTRACT: Fatigue assessment was conducted for damaged strands collected from corroded tendons to evaluate their structural safety and serviceability. Fatigue test was conducted for the nominal stress range of 190 MPa and maximum nominal stress of 1100 MPa. All corroded strand specimens could not satisfy two million stress cycles recommended by Eurocode. Five specimens were tested under 70 MPa stress range which was known to be actual stress range in tendons under live load. Except one specimen, all of them were fractured and had fatigue lives lower than seven million stress cycles. On the other hand, the specimen without defect did not developed fatigue crack. It was observed that remaining fatigue life of corroded strand does not have any correlation with the size of corroded section. The lowest fatigue life was found from the least corroded strand.

1 INTRODUCTION

One of the external tendon of a pre-stressed concrete box girder bridge in Seoul, Korea was failed in 2016 (Figure 1). It was the first tendon failure in Korean history. As per in-depth investigation of the failure, it was found that corrosion of steel strands in the tendon was the major reason of the failure. Accordingly, other tendons were also inspected. Many tendons in the same section where the failure was found were also corroded. The reasons of the corrosion were investigated and those were:

1) Air vents were located underneath the bridge deck and those were not properly sealed or damaged. From the opened air vents, water with high level of chloride infiltrated. Abnormally higher moisture and chloride contents were found from the grout under the air vents.

2) Transverse and longitudinal gradients of the bridge deck was very low at the failure location which were almost close to zero degree. The low gradients caused drainage problem and could accelerated corrosion.

3) Large void was found at the saddle of the tendons, which were located underneath the damaged air vents.

4) Although the bridge was inspected regularly, only visual inspection was conducted. Any deterioration inside of the tendon could not be inspected by visual inspection.



Figure 1. Photograph of the failed external tendon.

Once the preliminary inspection was completed, all the external tendons in the bridge were inspected and many corroded tendons were found. As a result, serviceability of the corroded tendon was concerned and the fatigue tests for the corroded tendons were conducted.

2 EXPERIMENTAL STUDIES

2.1 *Description of fatigue tests*

Corroded strand specimens for fatigue testing was obtained from the tendon which had been in service. After the in-depth investigation was completed,

owner of the bridge decided to replace corroded tendons. Twelve strands having 1 m length were collected from the replaced tendons. Corroded strands with various section loss were collected. (Figure 2). Configuration of the corrosion was various such as pitting corrosion and wide surface corrosion. In order to prevent breaking wire in the wedge or the boundary of the wedge, it was intended to place corroded part at the center of the specimen.

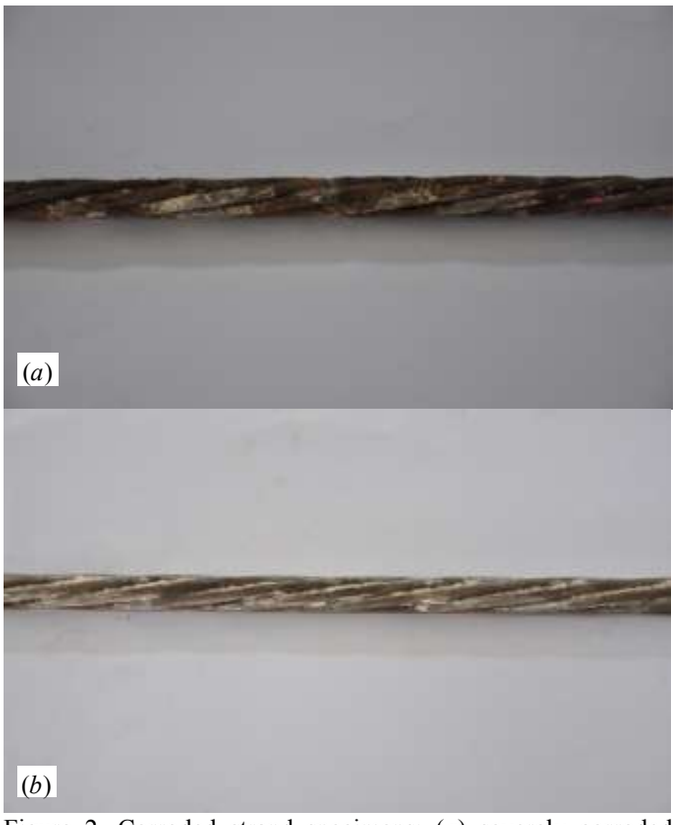


Figure 2. Corroded strand specimens: (*a*) severely corroded strands; and (*b*) less corroded strands.

Fatigue test were conducted at the multi-direction testing facility in the Hybrid Structural Testing Center (HYSTEC) in Myongji University, Korea. Two grips were fabricated to hold the wedges and connect to the foundation block and actuator, respectively. The loads were applied using 50 tone hydraulic actuator as shown in Figure 3.

Fatigue test was conducted under constant amplitude sinusoidal loading. The test was load controlled and load and displacement were recorded.

As per Eurocode (1994), post-tensioning strands should achieve two million stress cycles under nominal maximum stress of 0.7 GUTS (guaranteed ultimate tensile strength) and nominal stress range of 190 MPa, which are equivalent to respectively 1300 MPa and 190 MPa for the strands having GUTS of 1860 MPa. The nominal stress range of 190 MPa is much higher than the actual stress range in tendons develops by heavy trucks (Lee 2015). However, the maximum stress range was set to 1100 MPa, because the first specimen was broken at the corroded section while it was loaded to the maximum stress. Loading frequency was varied between 10 to 14 Hz depending on the responses from the specimens. Testing was continued until at least one wire fail due to fatigue crack (ASTM 2016).

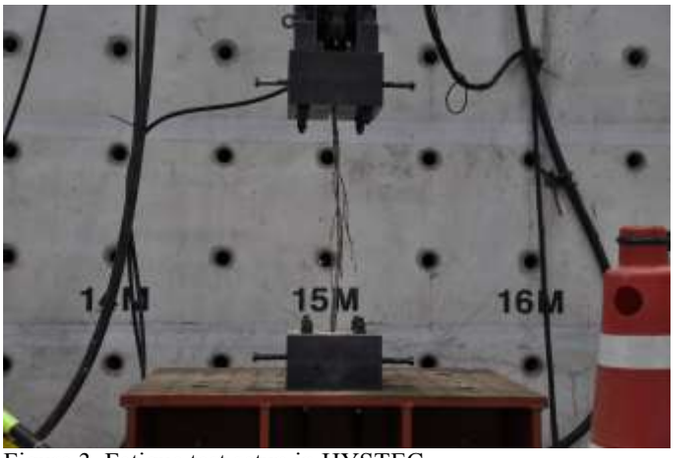


Figure 3. Fatigue test setup in HYSTEC.

2.2 *Fatigue test results*

Three specimens were failed while the specimens were loaded to the maximum stress range. Thus, only nine specimens were valid for fatigue testing. One specimen developed fatigue crack inside of the wedge, so that the results of the specimen was excluded from the test results. The wires in some specimens were broken multiple times during testing. Initial wire fracture was verified by the record of displacement and number of cycles. As it is shown in Figure 4, sudden drop in displacement was recorded when a wire was fractured. In this case, fatigue life of the specimen was determined at the time of the drop.

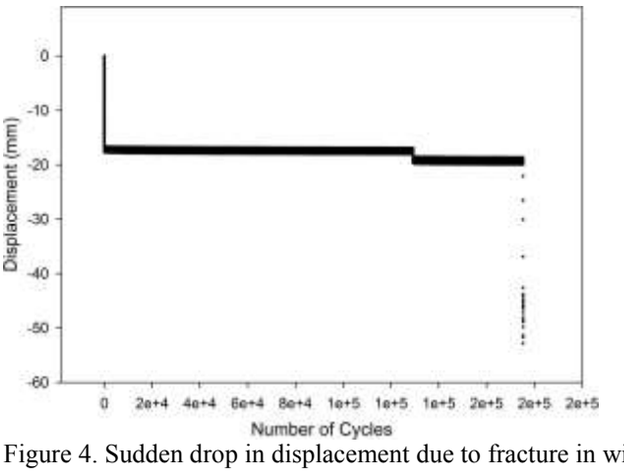


Figure 4. Sudden drop in displacement due to fracture in wires.

After the test was completed, fracture surfaces of the specimens were carefully observed. It was found that all specimens developed fatigue cracking at the corroded section. None of the center wire was frac-

tured and only outer wires developed fatigue cracks. Fatigue lives of the corroded strands were ranged between 0.13 to 0.52 million cycles, which could not achieve the requirement of two million cycles at the stress range of 190 MPa.

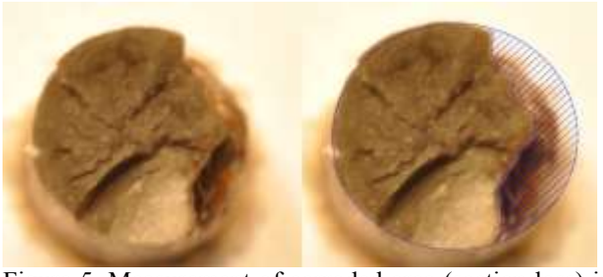


Figure 5. Measurement of corroded area (section loss) in fractured surface.

Section losses in wires were measured from the fracture surfaces. The wires which did not develop fatigue crack were cut at the section where fatigue crack was found. Sections of each wire were photographed to measure corroded area in the fractured section using AutoCAD. The section loss was defined by the ratio of corroded area and non-corroded area of strand. Section loss of fatigue tested specimens were in range of 7.7% and 33.2%. For the specimens which fracture during static loading, section loss was 39.6% or higher. Photograph of fractured section demonstrates section loss due to corrosion, fatigue crack surface and tensile fracture surface (Figure 5). Gray shiny surface presents fatigue crack surface. On the other hand, dark rough and wrinkled surface presents tensile fracture surface, which is generally shown from the tensile fractured surface of high strength steel. Fatigue crack initiated from the bottom side of the corroded surface and propagated towards left. None of the specimens developed fatigue cracking initiated from non-corroded surface.

3 DISCUSSION OF TEST RESULTS

The S-N plot of the fatigue test results are presented in Figure 6, along with the fatigue design curves from the *AASHTO LRFD Bridge Design Specification*s (AASHTO 2012) and design curve suggested by Paulson et al. (1983). The fatigue test results are plotted against nominal stress, which was computed based on non-corroded section of a strand.

Fatigue life of corroded strands distributed between AASHTO Fatigue Category B and D, which was much lower than target fatigue life of two million cycles. The fatigue lives are also lower than Paulson et al.'s design curve. Therefore, corroded strand could cause fatigue problem during service.

Fatigue test results always demonstrate spread due to inconsistent distribution of micro-discontinuities, residual stress or notch severity. However, the spread in the test results is larger than other connection details. It may be because applied stresses of each strand at the cracked section were diverse due to difference in remaining section. Variability in the configuration of corroded surface could also develop different stress concentration, which may change stress condition.

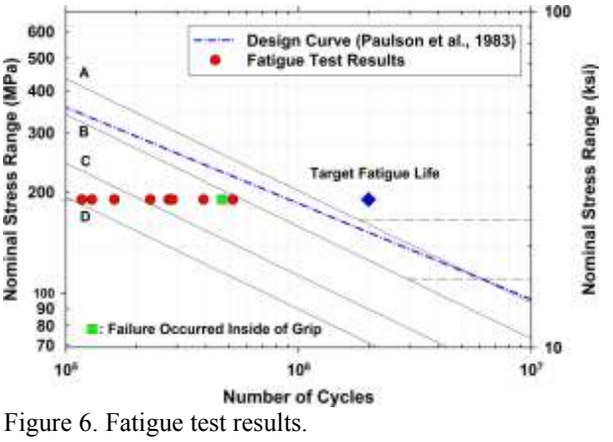


Figure 6. Fatigue test results.

To verify influence of section loss in fatigue performance, fatigue test results are plotted with respect to section loss in Figure 7. Comparison shows that specimens having larger section loss demonstrate less fatigue life, but distinct trend is not shown. Minimum and maximum fatigue lives exhibited by the specimens having section loss of 13.1% and 7.7%, respectively. Range of section loss of the specimens having fatigue lives less than 0.2 million cycles was from 13.1% to 33.2%. Therefore, little section loss could make large difference in fatigue life. It may be concluded that strands having large section loss definitely exhibit low fatigue life, whereas little section loss could exhibit low fatigue life as well.

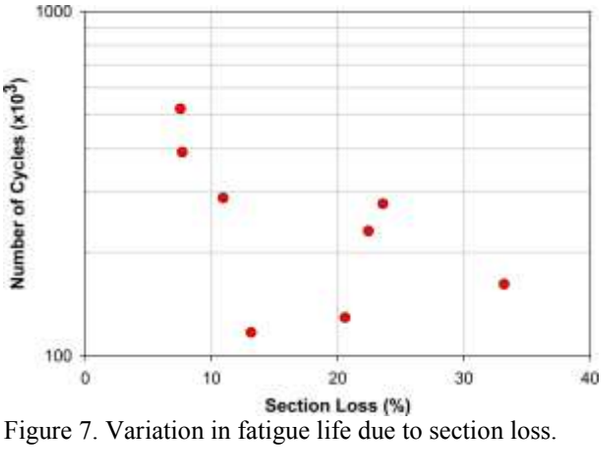


Figure 7. Variation in fatigue life due to section loss.

4 CONCLUSTIONS

The fatigue test results demonstrated that corroded strands exhibit low fatigue life and could not satisfy required fatigue resistance of two million stress cycles recommended by Eurocode. Irrespective to the section loss due to corrosion, fatigue life could significantly less once strand was corroded.

ACKNOWLEDGMENTS

This research was supported by a grant(18CTAP-B132914-02) from Technology Advancement Research Program(TARP) funded by Land, Infrastructure and Transport of Korean government.

REFERENCES

AASHTO. 2012. *AASHTO LRFD Bridge Design Specifications*. Washington D.C.

ASTM. 2016. *ASTM A1061-16 Test Method for Testing Multi-Wire Steel Prestressing Strand*. West Conshohocken, PA: ASTM International.

Eurocode. 1994. *EN 1992-1-1 Eurocode 2: Design of Concrete Structures – Part 1-1: General Rules and Rules for Buildings.*

Lee, J.H. 2015. *Prestressed Concrete – Strength Design and Limit State Design*. Paju, Korea: Dongmyungsa (in Korean).

Paulson, C., Frank, K.H., and Breen, J.E. 1983. A Fatigue Study of Prestressing Strand. *FHWA/TX-82/54+300-1*. Austin, TX: Texas State Department of Highways and Public Transportation.

MS06: Footbridges: Advances in vibration serviceability assessment

Organizers: C. Caprani, F. Tubino, K. Van Nimmen & F. Venuti

Maintenance, Safety, Risk, Management and Life-Cycle Performance of Bridges – Powers, Frangopol, Al-Mahaidi & Caprani (Eds)
© 2018 Taylor & Francis Group, London, ISBN 978-1-138-73045-8

Dynamic analysis of scissors-type of deployable pedestrian bridge under earthquake

Y. Chikahiro, S. Zenzai & S. Shigeru
Shinshu University, Nagano, Japan

I. Ario
Hiroshima University, Higahi-Hiroshima, Japan

ABSTRACT

In recent years, the world has seen several types of natural disasters that have caused many critical situations in the lives of people by damage of an infrastructure. It is important to rebuild the damaged traffic routes immediately in such serious situations in order to facilitate quick relief and restoration activities.

This paper presents a dynamic analysis of new type of emergency bridge, called Mobile Bridge, which can be quickly constructed in case of damage after a natural disaster. The concept of the bridge is based on the application of a scissors mechanism, which enables its rapid deployment. During the deployment phase, the bridge is supported only at one end resulting in cantilever boundary conditions. Once deployed, the bridge has two supports hence the deployed, second condition is the simply supported beam case, where the supports have horizontal and vertical displacement constraint. After finishing construction, the pedestrian bridge is set on the upper decks aligned at the line of top hinges. Up to now, the authors have constructed several types of the experimental Mobile Bridges for pedestrian and vehicle loading. In the case of deployable structures as well as the static analysis of different configurations of expansion, it is important to investigate dynamic behavior of the system. The high compliance and flexibility of the scissors-type bridge may influence the comfort and safety of users in case of heavy dynamic loads such as human induced impacts, wind gusts, or earthquakes.

The presented research deals with fundamental numerical results to clear dynamics of the Mobile Bridge based on the experimental pedestrian bridge. From the point of using the Mobile Bridge in disaster area, it is needed to clear dynamic behavior. Therefore numerical simulation included both eigenvalue and seismic response analysis with model validation. From these results, it was possible to estimate basic mechanical characteristics of dynamic properties of the bridge. The conducted research allows for better and safer design of the structure of the Mobile Bridge.

ACKNOWLEDGMENT

This research has been supported by Grant-in-Aid for Research Activity Start-up 16H06840 in 2016 - 2018 and Yamaguchi Scholarship Foundation in 2017 - 2018. The author wishes to thank my undergraduate students, Mr. Hayashi and Mr. Minami, for their continuous supports.

REFERENCES

Ario, I., Nakazawa, M., Tanaka, Y., Tanikura, I., and Ono, S., 2013. Development of a prototype deployable bridge based on origami skill, Automation in Construction, 32: 104-111.

Ario, I., Chikahiro, Y., and Tanaka, 2011. Y., Dynamic analysis for the prototype of a new type of Mobilebridge, Proc. of the 7th European Nonlinear Dynamics Conference (ENOC 2011).

Ario, I., Structure with the expanding and folding equipment as a patent (No.2006037668) registered in 2012, Japan, 2006.

Chikahiro, Y., Ario, I., Nakazawa, M., Ono, S., Holnicki-Szulc, J., Pawlowski, P., Graczykowski, C., and Watson, A., 2016. Experimental and numerical study of full-scale scissor type bridge, Automation in Construction, 71: 171-180.

Holnicki-Szulc, J. (Ed.), 2008, Smart Technologies for Safety Engineering, Wiley.

Hunt, G. W., and Ario, I., 2005. Twist buckling and the foldable cylinder: an exercise in origami. Int J Non Linear Mech, 40(6): 833-843.

Pinero, E. P., 1965, Three Dimensional Reticular Structure, United States Patent 3, 185, 164.

Maintenance, Safety, Risk, Management and Life-Cycle Performance of Bridges – Powers, Frangopol, Al-Mahaidi & Caprani (Eds)
© 2018 Taylor & Francis Group, London, ISBN 978-1-138-73045-8

A Dynamic System Identification of the Ha'penny Footbridge

R. Donnelly
Roughan & O'Donovan Innovative Solutions (ROD-IS), Dublin, Ireland

M. Nogal
Dept. Civil, Structural and Environmental Engineering, Trinity College Dublin, Ireland

P. Gorman
Dublin City Council, Dublin, Ireland

A.J. O'Connor
Dept. Civil, Structural and Environmental Engineering, Trinity College Dublin, Ireland

ABSTRACT: The Ha'penny Footbridge is a historic cast iron structure in Dublin City Centre and a well-known Irish landmark. The main objective of this research was to establish a comprehensive picture of the dynamic behaviour of the bridge. This information and the associated model could then be used in future structural health monitoring (SHM) and damage detection, with the aim to aid in the structure's preservation and prolong its serviceability. The methodology of this study began with the creation of a preliminary finite element (FE) model using the computational software MATLAB (The MathWorks Inc). This model was designed to assess the free-vibrational response of the structure in three dimensions from first principles, including its natural frequencies and mode shapes. The modes obtained from this preliminary analysis were then used to assist an operational modal analysis (OMA), carried out using strain gauges fitted to the structure. The results of this analysis were used in order to update and calibrate the FE model. The result of this research and experimentation was an accurate representation of the bridge within acceptable limits. The FE model developed using MATLAB was found to have improved accuracy when compared to a previous model created using a FE software package in 2001. The calculated damping ratios of the structure were found to be low and so the installation of a permanent SHM system was recommended. In addition, it was recommended that the structure be fitted with an increased number of strain gauges to allow for strain measurements to be gathered in multiple directions.

1 INTRODUCTION

1.1 *Introduction*

The continuous development of high-performance building materials has led to an increasingly common trend towards the design of lighter and more flexible bridge structures. This is especially true in the design of pedestrian bridges, which are typically more slender due to lower loading requirements and typically shorter spans. With this low stiffness and mass comes reduced natural frequencies and hence, a higher probability of resonant vibrations during service. Excessive vibrations can lead to serviceability failure, in that the bridge may be rendered unsuitable for use by the public, or in ultimate failure due to fatigue and related damage. A lack of understanding of the modal identity of pedestrian structures can result in serious consequences, as was seen in the excessive movement of the London Millennium Footbridge shortly after it's opening in 2000 (Dallard et al., 2001). This widely-publicised failure incited an increased interest in the study of lateral excitations and responses, where previous research had primarily been focused on vertical movement.

The need for a comprehensive understanding of dynamic behaviour is not only applicable to modern designs, but also to historic structures. This is especially true in the case of bridges, where increasing populations and associated changes in loading patterns are altering the operational excitation. Previous examples of dynamic investigations into historic structures can be found in Gentile and Gallino (2008) and Gentile and Saisi (2013). From these, it is clear that knowledge of the dynamic systems of these structures is essential to their preservation. From this literature, as well as studies carried out in Altunişik et al. (2011), Bayraktar et al. (2009), Barton et al. (2011) and Hu et al. (2012), it can be seen that the dynamic system identification (DSI) and establishment of SHM systems in structures may be powerful tools. These tools, often used in conjunction with FE models, can allow for the identification of areas of weakness and developing damage within the structure. Over time, this may lead to improved efficiency in the repair of the structure in question and may ultimately prevent collapse.

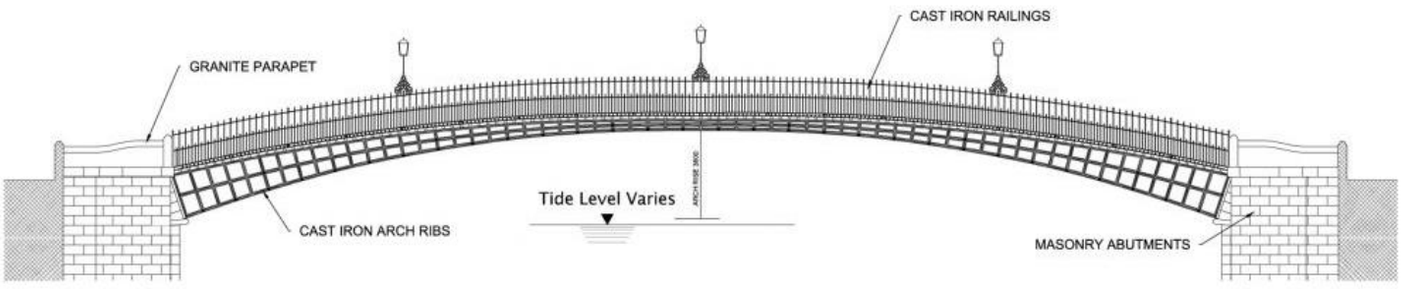


Figure 1. Side elevation of the Ha'penny Bridge (Dublin City Council, 2017a)

1.2 *The Ha'penny Bridge: History and Background*

The Ha'penny Bridge (officially known as the Liffey Bridge) is a landmark structure spanning the Liffey River and is one of the defining features of Dublin, Ireland. The footbridge was erected in 1816, currently making it over 200 years old. It is a cast iron bridge which was originally built as an alternative to a ferry which connected the North and South sides of the city. Its name is derived from the half-penny (ha'penny) toll which was required in order to cross. The bridge was designed by John Windsor with iron cast in the Coalbrookdale Foundry in England (Dublin City Council, 2017a). At the time of its opening, the bridge catered to a city of a much smaller size and had just 450 pedestrians crossing the bridge daily. In recent times, this has increased to an estimated average of 30,000 per day (Dublin City Council, 2017b). This exemplifies the level to of change in the amount and pattern of loading that the bridge has experienced within its lifetime.

The bridge has the form of an elliptical arch which spans 42.8m with a width of 3.6m. The arch has a 3.35m rise above high water at the centre-span. It was constructed in 6 individual sections, each separated by a cast iron diaphragm plate. The main arch structure of the bridge consists of three longitudinal ribs of cruciform section, one at each side of the bridge's width and one running along the centre-width. The ribs consist of three longitudinal chords with vertical members at intervals, creating a grid-like pattern. The three ribs are connected by a series of transverse and bracing members. The transverse members of the arch consist of cast iron tubes that contain tension rods which are believed to be of wrought iron. Figure 1 shows the geometry of the structure in elevation.

In the late 1990's, Dublin City Council (DCC) commissioned a complete renovation of the bridge from Mott MacDonald Consulting Engineers. This included a structural assessment, the renewal of existing bridge members and the replacement of certain members which were deemed beyond repair. In addition, the timber decking of the original design was replaced with stiffened steel and covered with an epoxy coating. Although there was some replacement of structural members, 98% of the original cast iron was re-used. The results of the structural investigation were published in (Mott McDonald Consulting Engineers, 2001) and the bridge was re-opened in December 2001.

The aforementioned structural investigation of the footbridge comprised of a theoretical dynamic analysis but did not include any experimental analysis to support it. This was also carried out before the completion of the renovation and so only considered the bridge structure as it existed previously. Additionally, there were a number of assumptions made about the geometry of the structure which may not necessarily hold true. For example, it was assumed that the bridge is completely straight in plan and is fully symmetrical about its longitudinal axis and its mid-span. These assumptions may be more likely in the event of a modern footbridge, however the age of the structure and the technology at the time of construction must be considered. Hence it was decided that these assumptions may not readily be made. It is also worth noting that the previous model took into account vertical displacements only, disregarding the fact that the bridge is free to move in three dimensions. The negative consequences of such assumptions were seen in events such as the excessive lateral movement of the London Millennium Bridge (Dallard et al., 2001) under pedestrian loading, as previously referenced. Overall, the consideration that this previous model may not be entirely reliable is one which must be explored.

2 METHODOLOGY

The methods used in this study consisted of the development of a preliminary FE model in MATLAB, followed by the use of this model's results to determine the optimum sensor locations on the bridge. The bridge was then instrumented before testing of the bridge response under ambient loading. The resulting response signals were processed and interpreted and finally the modal responses were used to calibrate and update the original MATLAB model.

2.1 *Finite Element Model*

The Ha'penny Bridge structure is a relatively complex arch structure, typical of cast iron bridges of its time. The structure consists of a large number of members oriented in the lateral, longitudinal, vertical and diagonal directions. Given the level of interactivity between members and the individual impact of each member on the stiffness properties of the bridge, it would be considered a vast oversimplification to model the structure as a single degree of freedom system. As the objective of this research was to provide an accurate representation of the bridge, it was necessary to discretise the structure into a multi-degree of freedom (MDOF) system allowing for free movement in three dimensions.

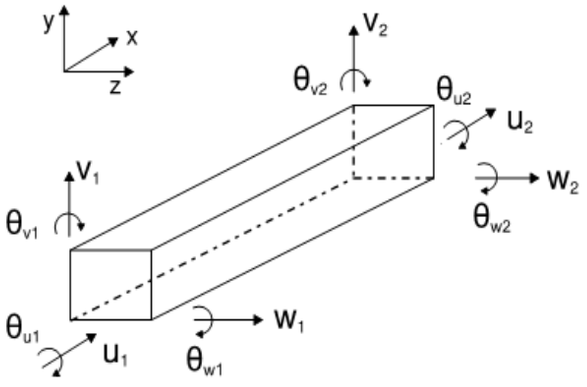


Figure 2. DOF of a space frame element

Keeping this in mind, the elements chosen for use in the model were space frame elements. Space frame elements may be considered as a combination of truss and beam elements which are capable of resisting forces in both the axial direction and directions perpendicular to the longitudinal axis of the bar (Quek and Liu, 2003). They are two-noded elements with six DOF at each node, three translational in the x, y and z directions, and three rotational about the x, y and z axes (Fig. 2). Hence each individual element has a total of twelve DOF before the introduction of boundary conditions. In this FE model, a single space frame element was used to represent each member of the structure.

The MATLAB program represented the structure as a MDOF system in free vibration. This was done using the equation of motion as shown in Equation 1 where *M*, *C* and *K* are the mass, damping and stiffness matrices of the system, *u* is the displacement and *F(t)* is a force vector at time *t*.

$$M\ddot{u} + C\dot{u} + Ku = F(t) \tag{1}$$

Assuming free vibration, it was possible to set the damping and applied forces to zero, giving Equation 2. Harmonic motion was then assumed giving Equation 3, where $q_n(t)$ is a vector of the modal coordinates for mode *n* at a time *t* and is a function of the natural circular frequency ω_n, and φ_n is the deflected shape. Hence Equations 2-3 can be simplified into Equation 4 which is known as the Characteristic Equation of the system and is a conventional eigenvalue problem.

$$M\ddot{u} + Ku = 0 \tag{2}$$

$$u(t) = q_n(t)\phi_n \tag{3}$$

$$(K - \omega_n^2 M)\phi_n = 0 \tag{4}$$

Solving this problem returns a set of eigenvalues, which are representative of the squares of the natural circular frequencies, and a set of eigenvectors which represent the mode shapes of the structure.

2.2 *Experimental Methods*

The chosen form of experimentation for this research was testing under ambient vibration. In this case, the ambient loading experienced by the bridge was predominantly due to pedestrian traffic. It was acknowledged that this form of loading would be the least disruptive to the general public and would also minimise the risk of damage to the structure. In addition, testing the bridge under operational conditions requires a lower amount of specialized equipment than in the case of free or forced vibration testing.

The chosen instrumentation for this operational modal analysis (OMA) was strain gauges. There are a number of reasons why these gauges were chosen. Firstly, the aesthetics of the bridge had to be considered. Given that this historic bridge is one which is frequently visited by tourists, the fitting of more bulky instruments such as accelerometers may be considered an eyesore. Strain gauges, on the other hand, are much smaller and more discrete instruments. The chosen gauges were FLA-5-11 gauges from TML. An additional consideration is the difference in cost between these gauges and other forms of instrumentation. They are a much cheaper alternative to accelerometers and require no calibration.

2.3 *Bridge Instrumentation and Testing*

The FE model was a necessary tool in determining appropriate locations for the strain gauges. A preliminary analysis of the structure using the FE model returned the mode shapes as shown in Figure 3. From these, it can be seen that the maximum displacement in modes 1 and 2 are at mid span, and for 3 and 4 are at the quarter spans. Hence instrumenting these areas would provide the most effective results.

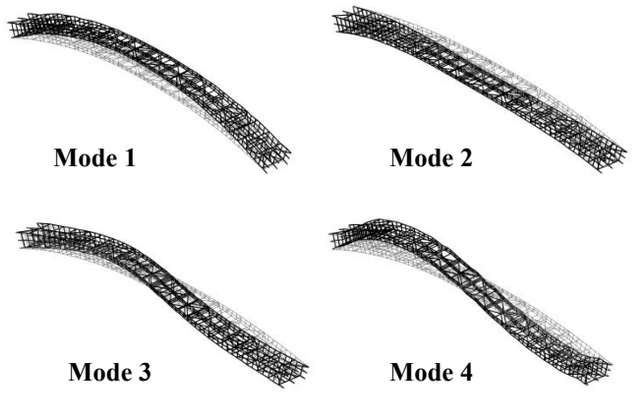


Figure 3. Mode shapes 1-4 from the preliminary MATLAB model – lighter colour indicates original shape

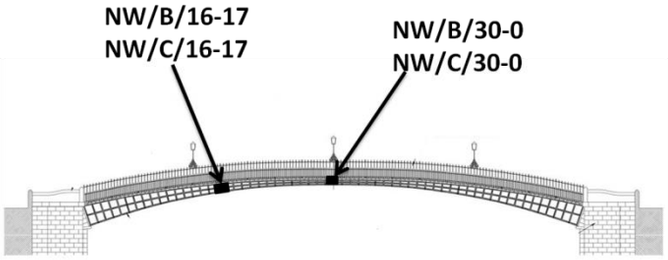


Figure 4. Western elevation of the footbridge with arrows indicating strain gauge locations (two gauges at each location). Modified from (Dublin City Council, 2017a)

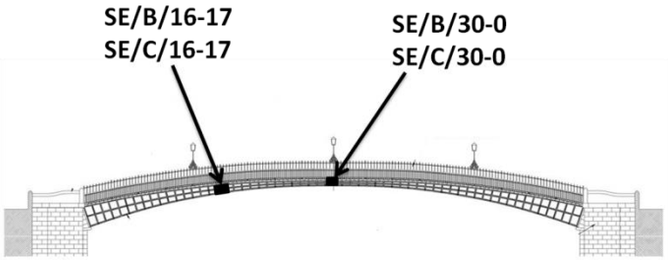


Figure 5. Eastern elevation of the footbridge with arrows indicating strain gauge locations (two gauges at each location). Modified from (Dublin City Council, 2017a)

The gauges were attached to the bridge at the Northern quarter span on the Western elevation, the Southern quarter span on the Eastern elevation, and at mid-span on both elevations. There were 8 sensors in total. They were oriented along the longitudinal axis and were attached to the bottom and middle chord members of the longitudinal arch ribs (Figs. 4-5).

The bridge was instrumented on the 14th March 2017. The gauges were attached to the top surface of the members. They were weatherproofed using buthyl rubber tape and sprayed with white paint to make them more aesthetically discrete. Testing occurred on the 27th March 2017. The test was carried out using a Vishay MicroMeasurements data logger with StrainSmart logging software (Micro Measurements). The loading applied to the structure consisted of the free and random movement of pedestrians over the bridge under normal conditions. The readings were taken over a 15 minute (900s) period at a sampling rate of 100Hz, resulting in a total of 900,000 test samples.

3 RESULTS

The resulting raw signals from the operational testing were obtained and recorded. Each sensor was named in accordance to a coordinate-based naming system developed for the purpose of this study. No data was read for the sensor SE/C/30-0 due to wiring issues during testing. However it was assumed that this member, which was the bottom chord member at mid-span on the Eastern elevation, had similar behavior to the middle chord member in the same area. This assumption was made based on the behavioural similarities seen between the middle and bottom chord sensors in all other locations.

Although the sensors were roughly zeroed before the recording of data, it was noticed that certain signals had their mean above or below zero. Also, evidence of noise and zero drift could clearly be seen in the raw signals. Thus it was necessary to apply a post-processing algorithm in order to reduce distortion and error caused by these issues. A Fast Fourier Transform (FFT) was also included in this algorithm and implemented in order to convert the signals from the time domain to the frequency domain. This process is summarized in the flow chart in Figure 6.

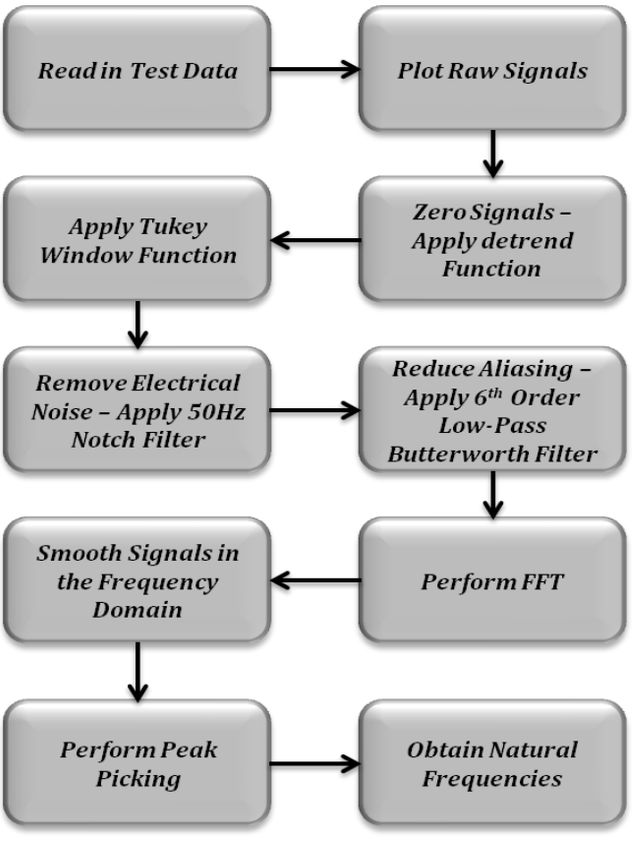


Figure 6. Post-processing procedure adopted for the raw input data signals

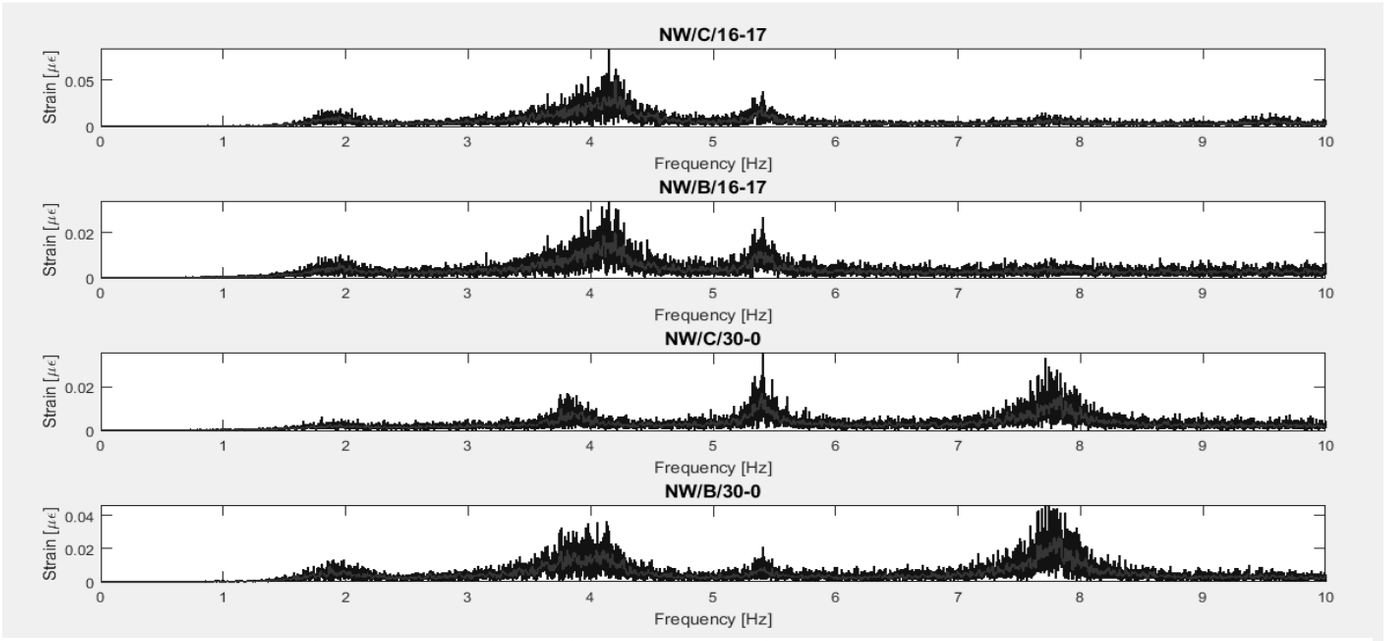


Figure 7. Frequency spectra from sensors on the North Western side of the bridge

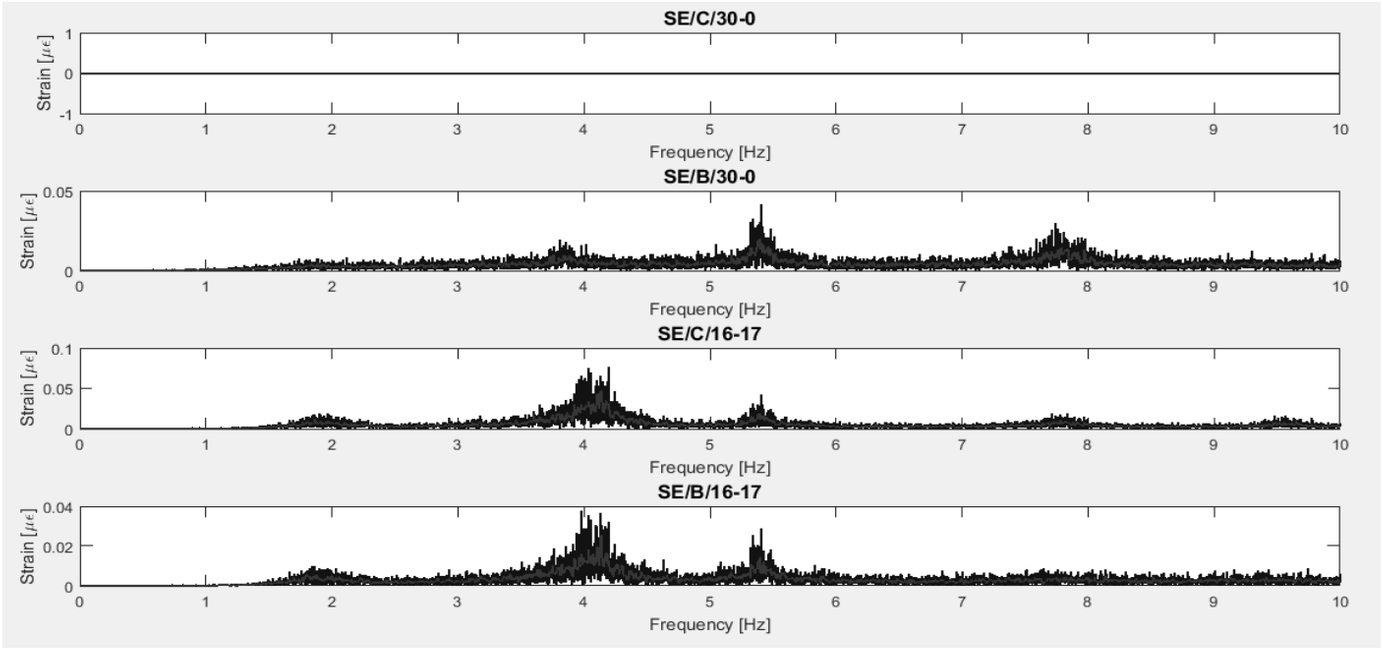


Figure 8. Frequency spectra from sensors on the South Eastern side of the bridge

Table 1. Comparison of experimental and MATLAB model frequencies

Mode	Experimental (Hz)	MATLAB (Hz)	Error (Hz)	Error (%)
1	1.92	4.5916	2.67	139.15
2	4.11	5.8503	1.74	42.34
3	5.41	8.5428	3.13	57.91
4	7.78	9.2503	1.47	18.90
		Average:	2.25	64.57

The values in Table 1 show quite a large discrepancy between the experimental frequencies and the frequencies obtained from the preliminary MATLAB model. The percentage error of 64.57% is high and must be reduced in the model calibration stage.

The damping ratios (ξ) of the bridge were calculated using the Half-Power Bandwidth method as shown in Equations 5-6. The results are shown in Table 2 (Donnelly, 2017).

$$D = \frac{D_{max}}{\sqrt{2}} \tag{5}$$

$$\xi = \frac{f_2 - f_1}{f_2 + f_1} \tag{6}$$

where D_{max} is the amplitude of the signal at a peak point (i.e. at a natural frequency of the signal) and $f_{1,2}$ are the frequencies at which a horizontal

line from the *D* value on the Y-axis would cross the peak.

Table 2. Damping ratios calculated from experimental data

Sensor No.	Damping Ratio Mode 1 (%)	Damping Ratio Mode 2 (%)	Damping Ratio Mode 3 (%)	Damping Ratio Mode 4 (%)
NW/C/16-17	0.23	0.17	0.03	-
NW/B/16-17	0.19	0.21	0.02	-
SE/C/16-17	0.21	0.13	0.05	-
SE/B/16-17	0.27	0.11	0.03	0.07
NW/C/30-0	-	0.22	0.04	0.02
NW/B/30-0	0.24	0.19	0.03	0.05
SE/C/30-0	N/A	N/A	N/A	N/A
SE/B/30-0	-	0.13	0.03	0.06
Average:	0.23%	0.17%	0.03%	0.05%

Damping ratios could not be calculated for some of the sensors as these modes did not appear in the frequency spectra of these gauges. This is possibly due to proximity to local minima. These damping ratios are very low and may be cause for concern regarding the health of the bridge. Typical damping ratios for metal footbridges sit at around 0.4% (Bachmann, 1995). Lower damping ratios imply that the structure will take longer to return to its undeformed state after vibration. This means that the bridge members are more susceptible to fatigue and related damage.

4 MODEL UPDATING

The results of the OMA as shown in the previous section imply that the natural frequencies of the MATLAB model need to be reduced significantly in order to represent the bridge structure more accurately. Basic knowledge of dynamic theory dictates that natural frequency is inversely proportional to mass and directly proportional to stiffness. Therefore, a reduction in natural frequency would come about through a decrease in stiffness and/or an increased structural mass. As there was a high level of uncertainty initially regarding the material properties of the cast iron used in the bridge, the Young's modulus (E) and the density (ρ) of the iron were considered the most significant sources of uncertainty in the model. Additional uncertainty lay in the definition of boundary conditions at connections. It was also considered that the original decision to neglect the non-structural members was a simplification that could lead to inaccuracy.

The original estimation for the E value of the material was 90GPa with an estimated ρ value of 7200 kg/m^3. The boundaries at connections were considered perfectly rigid in all restricted directions and the influence of non-structural elements (e.g. lights, railings, decking) was ignored. Thus, the calibration of the model involved the adaptation of the material and boundary parameters and the consideration of non-structural elements. The decided method for the consideration of the mass of the non-structural elements was through the introduction of an equivalent density. This density was calculated based on mass

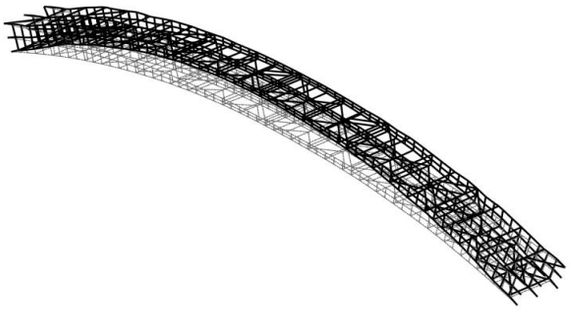


Figure 9. Mode Shape 1 - calibrated MATLAB model

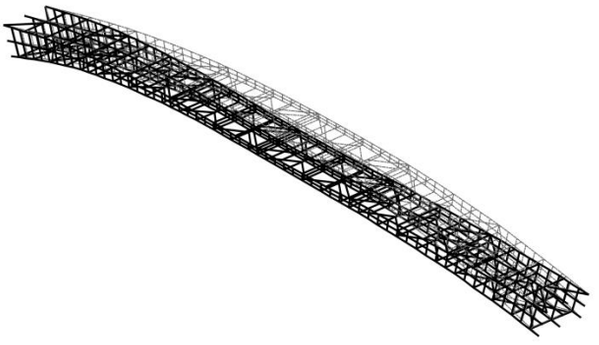


Figure 10. Mode Shape 2 - calibrated MATLAB model

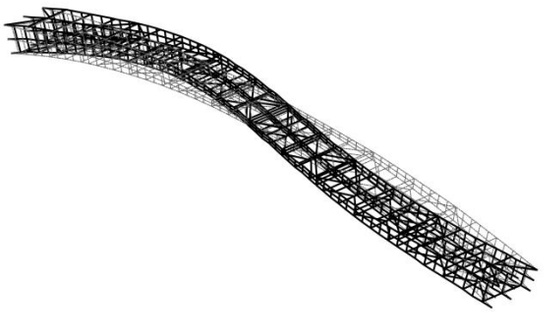


Figure 11. Mode Shape 3 - calibrated MATLAB model

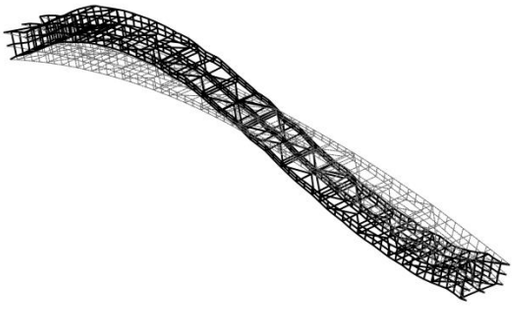


Figure 12. Mode Shape 4 - calibrated MATLAB model

estimations and was applied over each element in the model. Firstly, the total mass of the structural elements (m_{NS}) was roughly calculated using elevations and sections obtained from Dublin City Council. The total volume (v_S) and mass (m_S) of the structural elements was then calculated from the model and all of these parameters were combined in Equation 7 to find the equivalent density of the structure (ρ_{eq}).

$$\rho_{eq} = \frac{m_{NS}+m_S}{v_S} \quad (7)$$

Using information about the railings and deck geometries obtained in Mott McDonald Consulting Engineers (2001) and Dublin City Council (2017a), an estimated non-structural mass of $17x10^3$ kg was obtained (Donnelly, 2017). The total weight and volume of the structural members were found to be $44.4x10^3$ kg and $6m^3$, respectively, assuming a maximum cast iron density of 7400 kg/m^3 (Angus, 2013). This resulted in an equivalent density of 10,500 kg/m^3 to be applied to all structural members in the model. The E modulus was obtained with a criterion of minimum averaged error between the obtained and the observed frequencies of the first 4 vibration modes, resulting in 83 GPa, an appropriate reduction within the range stated in Angus (2013). Finally, previously-defined boundaries which were considered to be perfectly rigid pins were allowed some rotation to account for loosened bolts or connections which are not perfectly flush. Results from the updated model are shown in Figures 9-12 and Table 3 (Donnelly, 2017).

Table 3. Comparison of experimental (Exp.), updated model and 2001 model frequencies

Mode	Exp. (Hz)	MATLAB (Hz)	Error (Hz)	Error (%)	2001 Model (Hz)	Error (%)
1	1.92	3.64	1.72	89.58	3.194	66.35
2	4.11	4.64	0.53	12.90	3.385	-17.64
3	5.41	6.76	1.35	24.95	3.629	-32.92
4	7.78	7.33	-0.45	-5.78	-	-
		Average:	1.01	33.30		38.97

It can be seen in Table 3 that the average percentage error between the experimental and MATLAB frequencies was reduced from 64.57% to just 33.3%. The average total error was reduced from 2.25Hz to just 1.01Hz. The previous dynamic model of the bridge carried out in 2001 (Mott McDonald Consulting Engineers, 2001) had an average percentage error of approximately 38.97%. Thus it is clear that the updated MATLAB model is more accurate.

Another point worth noting is the difference in interval sizes between the modes in the MATLAB model and the 2001 model. The 2001 model shows very closely spaced modes of vibration, however the MATLAB model contains very distinct and separate modes. In this respect, it could be argued that the calibrated MATLAB model is significantly more accurate than the 2001 model, given that the results of experimentation on the bridge also show distinctly spaced modes of vibration.

5 CONCLUSION

5.1 *Conclusions*

The conclusions of this research may be summarised as in the bullet points below:

- The FE model developed in MATLAB was proven to be effective at estimating the natural frequencies of the Ha'penny Bridge structure within a reasonable error range.
- The updating of the FE model led to a decrease in the percentage error from 64.57% to 33.3% and a decrease in the average total error from 2.25Hz to 1.01Hz.
- The most significant error in the preliminary MATLAB model was in the first mode, where the actual value was 1.92 Hz. This unusually low frequency value could suggest damage in the bridge structure. Alternatively, this frequency could represent the frequency of the walking load as described in Bachmann (1995). This will be investigated through further study.
- The updated FE model was proven to have a lower average error than the previous model developed in 2001.
- The updated FE model was shown to better represent the frequency intervals between modes than the 2001 model.
- The use of strain gauges was found to be effective in obtaining the natural frequencies of the bridge.
- The evaluation of the mode shapes from the experimental data was considered inconclusive due to a high amount of uncertainty caused by the strain gauge placement along a single axis.
- The damping ratios of the structure were found to be very low and were significantly below average for a metal footbridge.

As outlined in the above points, the calibrated MATLAB model was shown to represent the dynamic bridge system in a more accurate way than the 2001 model. Knowledge of the correct modal frequencies, shapes and damping ratios, in conjunction with an accurate bridge model, can be essential in prolonging the service life of footbridges such as this one.

The previous model was created using a software package in an industry setting. The use of analysis software such as in this case is common within industry due to time constraints and practicality issues. However, the outcome of this study should serve as a warning as regards the level of accuracy of the results returned. This is especially true in the modeling of historic bridges, where often there was no consideration of dynamics during the structure's design stage. Therefore, it is common that recent models have no older point of comparison. Additionally, historic structures often have a high level of uncertainty associated with their material properties due to less accurate testing procedures and quality control issues at the time of construction, as well as due to degradation of materials over time. This leaves models at risk of significant errors unless calibrated against experimental data.

5.2 *Future Recommendations*

It is strongly suggested that further study should be carried out into the dynamic system of the Ha'penny Bridge in the future. In this future research, it is recommended that an increased amount of instrumentation be fitted to the bridge. This will allow for a fuller picture of the bridge's dynamic response to be obtained. If possible, it would be ideal to orient gauges along the three axes of the bridge (longitudinal, vertical and transverse), possibly through the use of rosette strain gauges. This would allow for the principal stresses in members to be calculated, as well as removing the ambiguity regarding mode shapes that was apparent in this study. The ability to confirm the mode shapes of the structure may serve to further validate the MATLAB model.

From a long-term perspective, it is recommended that a permanent SHM system is fitted to the bridge. The low damping ratios calculated in this study imply that the bridge has a lower capacity to prevent excessive oscillation than it should have. In addition, the significantly low frequency for the first mode could signify damage. The severity of these issues is heightened due to the age of the bridge and the brittle nature of cast iron. Further monitoring of the bridge may give more insight into practical damping measures which may be implemented in order to preserve the structure and maintain its serviceability for years to come. In addition, initial signs of failure or damage may be detected more quickly and effectively, allowing for repair and maintenance.

ACKNOWLEDGEMENT

This study was supported by Dublin City Council and the Department of Civil, Structural and Environmental Engineering in Trinity College Dublin.

REFERENCES

ALTUNIŞIK, A. C., BAYRAKTAR, A., SEVIM, B. & ÖZDEMIR, H. 2011. Experimental and analytical system identification of Eynel arch type steel highway bridge. *Journal of Constructional Steel Research,* 67**,** 1912-1921.

ANGUS, H. T. 2013. *Cast Iron: Physical and Engineering Properties*, Elsevier Science.

BACHMANN, H. 1995. *Vibration Problems in Structures: Practical Guidelines*, Springer Basel AG.

BARTON, E., MIDDLETON, C., KOO, K., CROCKER, L. & BROWNJOHN, J. 2011. Structural Finite Element Model Updating Using Vibration Tests and Modal Analysis for NPL footbridge – SHM demonstrator. *Journal of Physics: Conference Series,* 305**,** 1.

BAYRAKTAR, A., ALTUNIŞIK, A. C., SEVIM, B. & TÜRKER, T. 2009. Modal Testing, Finite-Element Model Updating, and Dynamic Analysis of an Arch Type Steel Footbridge. *Journal of Performance of Constructed Facilities,* 23**,** 81-89.

DALLARD, P., FITZPATRICK, T., FLINT, A., LOW, A., RIDSDILL SMITH, R., WILLFORD, M. & ROCHE, M. 2001. London Millennium Bridge: Pedestrian-Induced Lateral Vibration. *Journal of Bridge Engineering,* 6.

DONNELLY, R. 2017. *A Dynamic System Identification of the Ha'penny Footbridge.* MAI, Masters of Engineering, Trinity College Dublin.

DUBLIN CITY COUNCIL. 2017a. *Ha'penny Bridge: Design and Engineeering* [Online]. Available: http://www.bridgesofdublin.ie/bridges/hapenny-bridge/design-and-engineering [Accessed 2017 January].

DUBLIN CITY COUNCIL. 2017b. *Ha'penny Bridge: Overview* [Online]. Available: http://www.bridgesofdublin.ie/bridges/hapenny-bridge [Accessed January 2017].

GENTILE, C. & GALLINO, N. 2008. Ambient vibration testing and structural evaluation of an historic suspension footbridge. *Advances in Engineering Software,* 39**,** 356-366.

GENTILE, C. & SAISI, A. 2013. Operational modal testing of historic structures at different levels of excitation. *Construction and Building Materials,* 48**,** 1273-1285.

HU, W.-H., MOUTINHO, C., CAETANO, E., MAGALHÃES, F. & CUNHA, Á. 2012. Continuous dynamic monitoring of a lively footbridge for serviceability assessment and damage detection. *Mechanical Systems and Signal Processing,* 33**,** 38-55.

MICRO MEASUREMENTS StrainSmart Data Aquisition Software. Wendell, NC, USA: Vishay Precision Group,.

MOTT MCDONALD CONSULTING ENGINEERS 2001. Ha'Penny Bridge Structural Appraisal. Dublin, Ireland.

QUEK, S. S. & LIU, G. R. 2003. *Finite Element Method: A Practical Course*, Elsevier Science.

THE MATHWORKS INC MATLAB R2016b. R2016b ed. Natick, Massachusetts, USA.

Maintenance, Safety, Risk, Management and Life-Cycle Performance of Bridges – Powers, Frangopol, Al-Mahaidi & Caprani (Eds)
© 2018 Taylor & Francis Group, London, ISBN 978-1-138-73045-8

Parameter identification of a biodynamic walking model for human-structure interaction

A. Firus & J. Schneider & H. Berthold & M. Albinger
Institute of Structural Mechanics and Design
Technische Universität Darmstadt, Darmstadt, Germany

A. Seyfarth
Institute of Sport Science
Technische Universität Darmstadt, Darmstadt, Germany

ABSTRACT: To account for the human-structure interaction during walking on flexible structures, a pedestrian is typically represented by an equivalent single degree of freedom (SDOF) system moving over the structure at a constant speed together with an external force. The latter corresponds to the force exerted by a pedestrian when walking on a rigid structure while the SDOF system is responsible for modifying the force at the contact point in order to account for the human-structure-interaction (HSI). This contribution presents a novel method for experimental identification of the SDOF parameters (stiffness and damping), which is based on a combined analysis of biomechanical and structural measurements. All the investigations were performed on an experimental pedestrian bridge, which was instrumented with biomechanical force plates, a 3D motion capture system as well as several sensors for the acquisition of the structural responses. Since both structural and biomechanical responses were recorded simultaneously, an accurate comparison between the measurements and the results of the structural analysis is allowed.

1 INTRODUCTION

The human-structure interaction (HSI) effect usually occurs in case of walking on lightweight and slender structures, which are prone to an excessive level of vibration. However, the interaction is usually neglected by common methods for the numerical analysis of pedestrian induced vibrations, which typically consider the walking pedestrian as a time dependent load moving over the structure at a constant speed (Fig.1a). In many cases this simplified approach leads to an overestimation of the structural responses (Caprani and Ahmadi 2016, Živanović 2015, Van Nimmen et al. 2017). In order to improve the accuracy of structural simulations, several coupled human-structure systems were developed in the last decades. They represent the human body as a mechanical model with equivalent dynamic parameters, i.e. mass, stiffness and damping. The complexity of the models varies from a simplified representation of the pedestrian by its moving mass (Fig. 1b) towards more realistic assumptions such as a single degree of freedom (SDOF) system (Fig. 1c) or even bipedal energy based spring-mass-dampers systems (Qin et al. 2013, Fig. 1d). An extensive overview over different approaches for prediction of structural responses with consideration of the HSI is given by Shahabpoor et al. (2016).

One of the main issues of the common HSI models is represented by the lack of systematic experimental validation of the dynamic model parameters for pedestrians walking on flexible structures, which are likely to differ from the parameters determined during walking on a rigid surface (Živanović 2015). Silva and Pimentel (2011) and Toso et al. (2016) performed experimental studies on identification of stiffness and damping for an equivalent SDOF system of a walking pedestrian. These studies are based on the correlation between the acceleration of the human body at the waist level and the ground reaction forces (GRF) recorded during periodic activities. However, the GRF considered there are taken from literature or measured using force plates installed on a rigid structure.

This contribution proposes a novel method for the identification of human body dynamic parameters, which considers pedestrian locomotion on a flexible structure. The investigations were performed on an experimental pedestrian bridge instrumented with biomechanical force plates, a 3D motion capture system as well as several sensors for the acquisition of the structural responses. The synchronous measurement

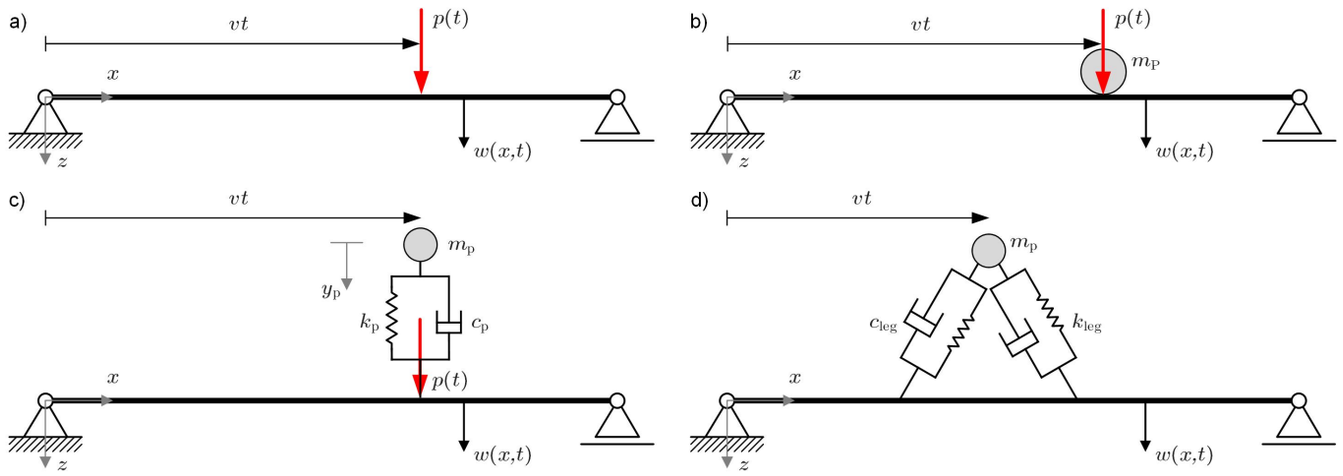


Figure 1: Mechanical models for prediction of pedestrian induced vibrations: a) moving force; b) moving mass; c) single degree of freedom system (SDOF); d) bipedal model

of both structural and biomechanical responses also allows an accurate comparison between the measurements and the structural analysis.

2 FORMULATION OF THE PROBLEM

2.1 *Background*

The vertical ground reaction force of a pedestrian walking on a rigid surface can be determined by means of the second Newton's law of motion as a sum of the inertial forces of all body segments (Racic et al. 2009):

$$p_{\mathrm{b}}(t) = \sum_{i=1}^{n_{\mathrm{s}}} m_i \cdot (\ddot{y}_{\mathrm{b},i}(t) + \mathrm{g}) \tag{1}$$

m_i denotes the mass and $\ddot{y}_{\mathrm{b},i}$ the acceleration (relative to the rigid surface) of the centre of mass (COM) of the i-th out of n_{s} body segments while the gravitational acceleration is depicted by the term g.

The contact force exerted by a pedestrian walking on a rigid floor is equal to the ground reaction force $p_{\mathrm{b}}(t)$ and is thus solely dependent on the body weight and step frequency of the pedestrian. In contrast to this, the contact force $p_{\mathrm{p}}(t)$ induced by a walking pedestrian in an oscillating structure is additionally affected by the interaction effects between the pedestrian and the structure. It can be expressed as a sum of the ground reaction force induced on the rigid ground $p_{\mathrm{b}}(t)$ and an interaction force term $p_{\mathrm{h}}(t)$, according to Equation 2:

$$p_{\mathrm{p}}(t) = p_{\mathrm{b}}(t) + p_{\mathrm{h}}(t) \tag{2}$$

It is to be mentioned that Equation 2 is valid only under the assumption that the walking behaviour of the pedestrian is not affected by vibrations of the underlying structure. In case of the walking on rigid structures it is assumed that $p_{\mathrm{h}}(t) = 0$, which leads to $p_{\mathrm{p}}(t) = p_{\mathrm{b}}(t)$.

Considering a human body consisting of n_{s} body segments, Equation 2 yields (Van Nimmen et al. 2016):

$$p_{\mathrm{p}}(t) = \underbrace{\sum_{i=1}^{n_{\mathrm{s}}} m_i \cdot (\ddot{y}_{\mathrm{b},i}(t) + \mathrm{g})}_{p_{\mathrm{b}}(t)} + \underbrace{\sum_{i=1}^{n_{\mathrm{s}}} m_i \cdot \ddot{y}_{\mathrm{h},i}(t)}_{p_{\mathrm{h}}(t)} \tag{3}$$

where

$$\ddot{y}_{\mathrm{h},i}(t) = \ddot{y}_{\mathrm{p},i}(t) - \ddot{y}_{\mathrm{b},i}(t) \tag{4}$$

describes the additional COM acceleration of the i-th body segment which occurs due to the interaction between the pedestrian and the structure, whereas $\ddot{y}_{\mathrm{p},i}(t)$ represents the total acceleration of the i-th body segment when walking on a flexible structure. Furthermore, the corresponding (interaction) COM displacement of the i-th body segment relative to the contact point on the flexible structure is defined as:

$$y_{\mathrm{rel},i}(t) = y_{\mathrm{h},i}(t) - w(t) \tag{5}$$

where $w(t)$ depicts the displacement of the structure at the contact point.

The numerical approach considered in this investigation describes the pedestrian by a SDOF model (Fig. 1c) system which crosses the structure together with an external force induced at the contact point between the SDOF system and the structure. The external force corresponds to the ground reaction force induced by a pedestrian while walking on a rigid structure ($p_{\mathrm{b}}(t)$ in Equation 2), while the SDOF system serves for modifying the force $p_{\mathrm{p}}(t)$ at the contact point in order to account for the HSI. This effect occurs due to the spring and damping forces generated by the relative movement between the mass m_{p} and the contact point, which are comprised by the term $p_{\mathrm{h}}(t)$ in Equation 2. As the SDOF comprises the whole body mass at a single point m_{p}, corresponding to the COM of the body, Equation 3 reads:

$$p_{\mathrm{p}}(t) = p_{\mathrm{b}}(t) + m_{\mathrm{p}} \cdot \ddot{y}_{\mathrm{h}}(t) \tag{6}$$

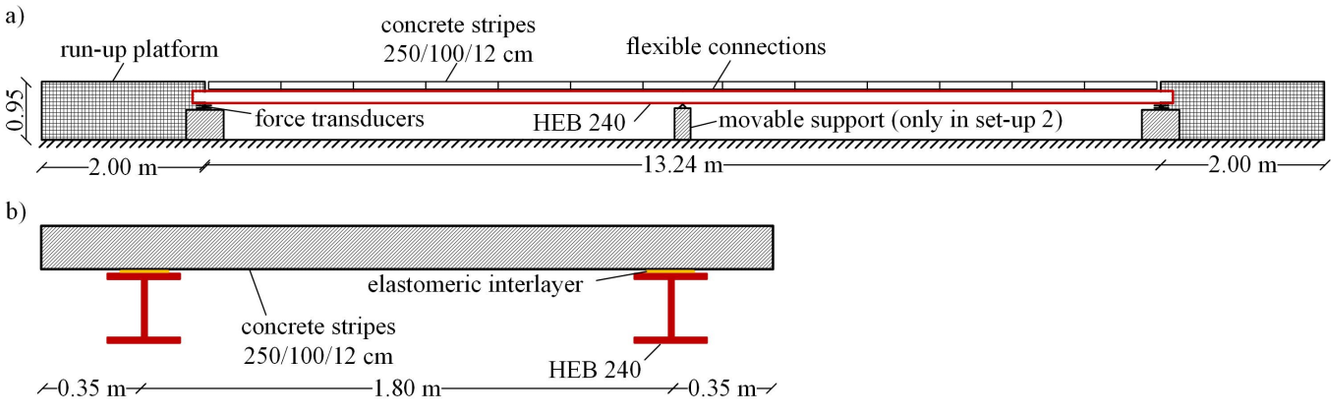


Figure 2: Experimental pedestrian bridge: a) side view; b) cross section

Expressing the equilibrium of the SDOF, Equation 6 can be written as:

$$p_{\mathrm{p}}(t) = p_{\mathrm{b}}(t) - k_{\mathrm{p}} \cdot y_{\mathrm{rel}}(t) - c_{\mathrm{p}} \cdot \dot{y}_{\mathrm{rel}}(t) \tag{7}$$

k_{p} and c_{p} represent the stiffness and the damping of the SDOF system. Their experimental identification is discussed in the following sections.

2.2 *Methodology*

In order to identify the unknown parameters k_{p} and c_{p} in Equation 7, the difference between the contact force of a pedestrian walking on a rigid structure and the corresponding contact force on a flexible structure is expressed as:

$$\Delta p(t) = p_{\mathrm{b}}(t) - p_{\mathrm{p}}(t) \tag{8}$$

$\Delta p(t)$ is considered to occur due to the interaction effects between the subject and the structure. Introducing Equation 8 in Equation 7, the following expression is obtained:

$$\Delta p(t) = k_{\mathrm{p}} \cdot y_{\mathrm{rel}}(t) + c_{\mathrm{p}} \cdot \dot{y}_{\mathrm{rel}}(t) \tag{9}$$

By time discretisation of Equation 9, the following Equation system is formulated (Lipfert et al. 2012):

$$\begin{bmatrix} \Delta p(t_1) \\ \Delta p(t_2) \\ \vdots \\ \Delta p(t_n) \end{bmatrix} = \begin{bmatrix} y_{\mathrm{rel}}(t_1) & \dot{y}_{\mathrm{rel}}(t_1) \\ y_{\mathrm{rel}}(t_2) & \dot{y}_{\mathrm{rel}}(t_2) \\ \vdots & \vdots \\ y_{\mathrm{rel}}(t_n) & \dot{y}_{\mathrm{rel}}(t_n) \end{bmatrix} \cdot \begin{bmatrix} k_{\mathrm{p}} \\ c_{\mathrm{p}} \end{bmatrix} \tag{10}$$

It can be solved using the unconstrained least-squares method in order to identify the unknown vector $[k_{\mathrm{p}} \quad c_{\mathrm{p}}]^{\mathrm{T}}$. However, $\Delta p(t_i)$, $y_{\mathrm{rel}}(t_i)$ and $\dot{y}_{\mathrm{rel}}(t_i)$ have to be determined through experimental investigations.

3 EXPERIMENTAL INVESTIGATIONS

3.1 *Experimental pedestrian bridge*

The experiments were carried out on an experimental footbridge (HUMVIB-Bridge), located on the campus of TU Darmstadt. The supporting structure consists of two longitudinal simply supported steel beams (steel type S235JR) with a span of 13.24 m and a cross section HEB 240 (Fig. 2). In order the keep the natural frequency in a range excitable by pedestrian walking, a contribution of the deck plate to the global stiffness of the system had to be avoided. Hence a deck plate consisting of 13 precast reinforced concrete stripes (250 x 100 x 12 cm) was installed. The concrete stripes only contribute to the structural dynamic behaviour as additional mass. Moreover, the use of concrete stripes reduces the uncertainties in numerical analysis, since the influences from the scattering of the concrete material parameters are also avoided. The gap between the stripes is 2 cm. It is small enough to secure a safe locomotion of the subjects (without tripping) but large enough to avoid a contribution of the concrete to the global stiffness of the structure. The concrete elements are deployed on the steel beams using a thin elastomeric interlayer (t=5 mm) in order to prevent slipping between the steel and concrete components.

The total mass of the experimental pedestrian bridge of 12 tons leads to a fundamental frequency of the structure of 2.03 Hz, confirmed also by experimental investigations. The corresponding modal damping ratio was identified to be 0.3 %.

Furthermore, an additional movable support was planned, in order to allow a flexibility of the structural system for further research topics, e.g. investigations of stiffer and higher frequent structures.

3.2 *Measurement set-up*

Since the solution of the least squares problem formulated in Equation 10 requires both information regarding the body kinematics and the structural behaviour, a combination of experimental methods for structural analysis and biomechanics is needed. The measurement set-up is shown in Figure 3. Moreover, the body kinematics and the forces induced at the contact point are required both for walking on a rigid and on a flexible structure. Therefore the investigations included the following structural configurations:

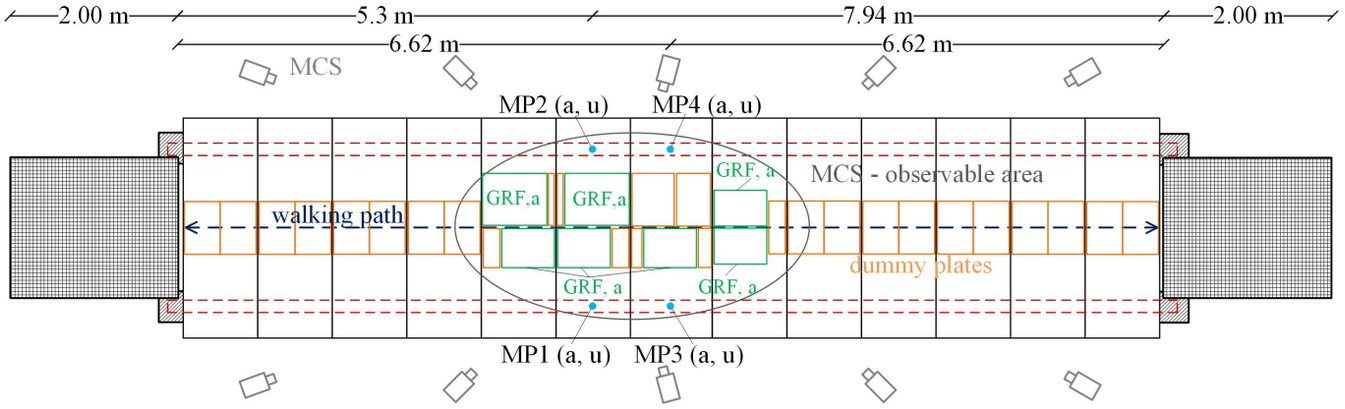


Figure 3: Measurement set-up

- set-up 1: simply supported beam, denoted in the following as ”flexible structure”;
- set-up 2: continuous beam, denoted in the following as the ”rigid structure”. In this configuration the additional movable support was installed at the midpoint, in the vicinity of the force plates.

So far, the investigation focused on analysing the scenario of single pedestrians walking over the structure. A total number of six subjects (four males and two females) aged 29.7 $\pm$ 8.4 years with a body mass of 71.6 $\pm$ 6.9 kg were investigated. Each of them performed eight trials in each structural configuration, whereas they were asked to walk over the bridge along the predefined walking path (s. Fig. 3) with a the prescribed frequency of 2 Hz (controlled by metronome beats).

The structural responses in vertical direction were recorded using 1D seismic accelerometers (PCB-TLD393B04) and linear variable displacement transducers (HBM 1-WA/50MM-L). The relevant locations for this investigation are shown in Figure 3. The only processing applied to the signals from the structural measurements is a low pass filter with a cut-off frequency of 35 Hz. The same frequency content was used as well in the numerical analysis.

The acquisition of the forces exerted by the walking pedestrians on the structure employed five force plates of type KISTLER 9260AA6 (600 x 500 x 50 mm) and two force plates KISTLER 9287CA (900 x 600 x 100 mm) with a mass of 8.6 and 25 kg, respectively (Kistler 2017). They were installed on the concrete stripes, around the midpoint of the bridge (Fig. 3) so that a number of up to four steps could be recorded during the trials. In order to level the walking path (due to different heights of the force plates), dummy plates were installed on all the other concrete elements along the walking path. This secures proper conditions for natural gait behaviour and reduces the tripping hazard of the subjects. It is to be noted, that the measurement accuracy of the force plates might be affected by vibrations of the structure they are installed on (Werkle et al. 2016). Therefore the force plate signals recorded during walking on the flexible structures have

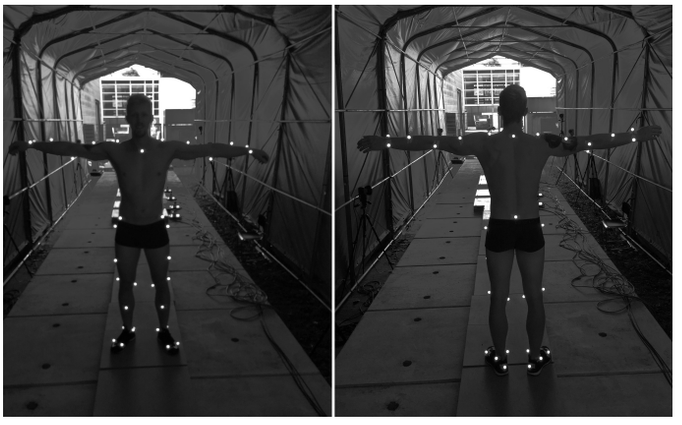


Figure 4: Typical marker instrumentation of a subject: front view and back view

to be processed by subtracting the inertial forces generated by the accelerations of the force plate mass. This leads to the necessity of acceleration measurement at the location point of each force plate. Furthermore it should be noted that the force plates present (in case of proper installation) natural frequencies of about 200 Hz (9260AA6) and 500 Hz (9287CA) (Kistler 2017). Therefore it is presumed that internal vibrations of the force plates and relative vibrations of the force plates with respect to the bridge surface can be excluded.

The human body kinematics was recorded using a *Qualisys*® motion capture system. It includes ten infrared cameras which focused on the location area of the seven force plates, in order to assure a proper correlation between the force signals and the body kinematics data. The time-dependent 3D position for a number of 41 reflective markers placed on the subject body (Fig. 4) was recorded in every trial at a high sampling rate. Additional markers were installed at the corners of the force plates in order to record the displacement $w(t)$ of the contact point. It should be noted that the infrared cameras are very sensitive to changes in light conditions. Hence the bridge, which is situated outside, had to be covered by a tent during the investigations (s. Fig. 4).

The kinematic data was processed using a low pass filter with a cut-off frequency of 12 Hz. An anthro-

pometric model was then used to calculate the COM (Winter 2009). The displacements of the COM in the rigid and flexible configuration ($y_{\mathrm{b}}(t_i)$ and $y_{\mathrm{p}}(t_i)$) were subsequently employed together with the displacement of the contact point $w(t_i)$ for determination of the matrix entries $y_{\mathrm{rel}}(t_i)$ in Equation 10 according to Equations 4 and 5. The COM velocities $\dot{y}_{\mathrm{rel}}(t_i)$ were calculated by numerical differentiation of the relative displacement vector.

4 RESULTS

4.1 *Experimental results*

In the following, the procedure of parameter identification will be illustrated by reference to the results of the first (male) subject, aged 47, with a body mass of 69 kg. For now, the four steps recorded will be analysed separately, whereas a "step" is defined in the following as a period from one minimum to the next minimum of the force resulting by superimposing the data from the left and right foot (Fig. 5).

The ground reaction force difference $\Delta p(t)$ has to be determined by subtracting the force signal recorded in the flexible configuration from the force time history recorded on the rigid structure (s. Equation 8). However, the two structural configurations were investigated independently and are thus not correlated with respect to their time vectors. In order to overcome this issue, a Fourier approximation in the phase angle form was computed according to Equation 11 for every step in each configuration as average from all the eight trials.

$$p(t) = G + \sum_{i=1}^{5} G \cdot \alpha_i \cdot \sin(2 \cdot \pi \cdot i \cdot f_{\mathrm{s}} \cdot t - \varphi_i) \quad (11)$$

Herein α_i and φ_i represent the Fourier coefficients and the corresponding phase shift of the i-th harmonic. f_{s} depicts the step frequency and G is the subject weight. The Fourier approximations were subsequently synchronised in time for each of the four steps.

Figure 5 shows typical Fourier approximations of the forces measured during the investigations on the stiff and on the flexible structure as well as the corresponding difference. The results shown were recorded for the first subject. The difference $\Delta p(t)$ is considered to occur due to the human structure interaction and has to be compensated within the structural analysis by the SDOF system. As expected, a general trend of higher GRF maxima in the rigid configuration could be noticed for all the subjects investigated. This effect arises presumably as a consequence of the interaction effects.

Due to the uncorrelated measurements in the rigid and flexible configuration, also the COM time histories had to be represented by equivalent Fourier series

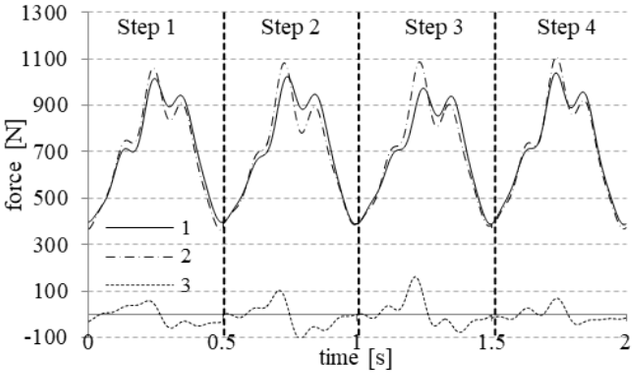


Figure 5: Fourier approximation of the GRF (subject 01): 1 - exerted by the subject on the flexible structure $p_{\mathrm{p}}(t)$, 2 - induced on the rigid structure $p_{\mathrm{b}}(t)$ and 3 - the corresponding difference $\Delta p(t)$

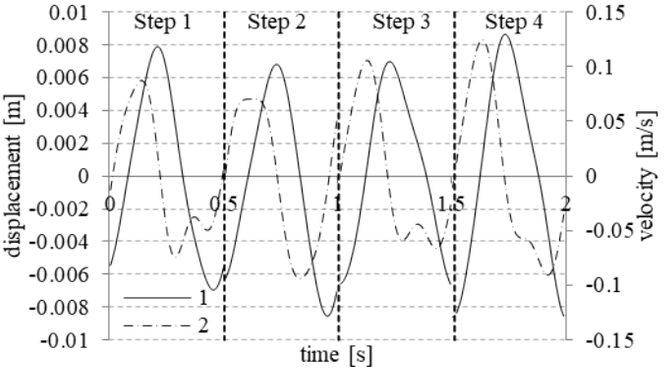


Figure 6: COM relative time histories used in the optimisation process for the subject 01: 1 - displacement $y_{\mathrm{rel}}(t)$, 2 - velocity $\dot{y}_{\mathrm{rel}}(t)$

(including five harmonics), as average from all the trials. Figure 6 illustrates exemplarily the relative displacement and relative velocity time histories ($y_{\mathrm{rel}}(t)$ and $\dot{y}_{\mathrm{rel}}(t)$) determined from measurements according to Equations 4 and 5 for the subject 01.

After introducing the contact force difference $\Delta p(t)$ (Fig. 5) and the COM relative motion quantities $y_{\mathrm{rel}}(t)$ and $\dot{y}_{\mathrm{rel}}(t)$ (Fig. 6) of subject 01 in Equation 10, the stiffness constants and damping coefficients shown in table 1 were determined by solving the unconstrained least squares problem. The results reveal a rather high intra subject variability. A statistical analysis over the four steps leads to average values of k_{p}=4001 N/m and c_{p}=358 Ns/m. The corresponding standard deviations amount to 1980 N/m and 200 Ns/m which represent about 50% of the average values.

It is to be mentioned that the optimisation was performed only in one step over the whole time window. Therefore it is expected that the reconstructed force difference using the parameters from table 1 and Equation 10 matches the measured time history only to a limited extent. This effect ist clearly illustrated

Table 1: Human body parameters of Subject 01:

Parameter	Step 1	Step 2	Step 3	Step 4
k_{p} [N/m]	4691	2425	6495	2392
c_{p} [Ns/m]	286	599	417	128

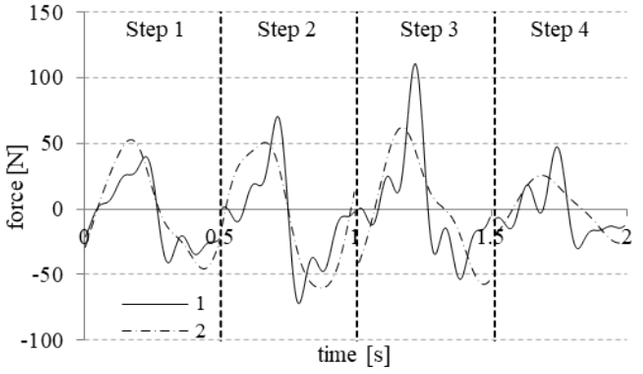


Figure 7: Ground reaction force difference (subject 01): 1 - measured, 2 - reconstructed by introduction of the optimised parameters k_p und c_p (table 1) in Equation 10

in Figure 7. An improvement of the method would be represented by determination of time dependent parameters (Firus et al. 2017).

4.2 *Structural analysis*

Since both structural and biomechanical responses were recorded simultaneously, it was possible to check the influence of the optimised parameters in the numerical model. The structure was modelled using a beam formulation in modal coordinates. The mechanical HSI model used within the investigation is represented in Figure 1c. It represents a SDOF system travelling over the bridge at a constant speed, together with a harminic force $p(t)$, which represents the forced induced by a pedestrian on a rigid structure, as measured in gait laboratories using force plates or instrumented treadmills (Racic et al. 2009). The SDOF system serves for modifying the contact force induced when walking on the flexible structure, in order to account for HSI. For a detailed presentation of the formulation of the coupled system human-bridge implemented within the present investigations, it is referred to Caprani and Ahmadi 2016. The equilibrium equations of motion were integrated using the time-stepping method of Newmark (Werkle 2008).

Figure 8 shows the acceleration time histories computed at the midspan of the structure for the subject 01 using the moving force (MF) and the interaction (SDOF) approaches. For the SDOF representation of the human body, the average parameters k_p=4001 N/m und c_p=358 Ns/m determined from table 1 were considered, while the force adopted in the MF model represents the average force (Fourier approximated) measured for subject 01 in the rigid configuration. In order to facilitate the comparison, the figure also includes a typical acceleration time history measured at midspan (MP4). Figure 8 reveals, as expected, that the moving force approach results in higher accelerations than the SDOF model. In this case, a difference of about 13% occured. It is obvious that the MF model significantly overestimates the measured result. The MF maximal acceleration of 1.35 m/s^2 lies about 16% above the average measured result of 1.16 m/s^2

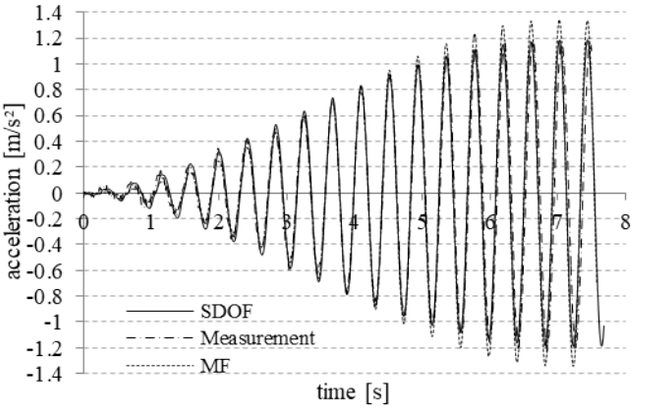


Figure 8: Measured and computed acceleration time histories at midspan of the bridge for a subject walking with a step frequency of 2 Hz

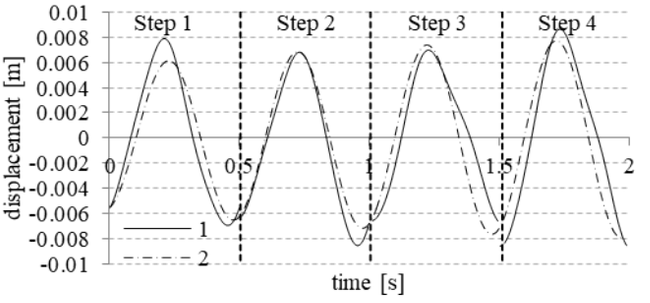


Figure 9: COM relative displacement time history $y_\mathrm{rel}(t)$ for subject 01: 1 - determined from measurements; 2 - computed using the SDOF approach

(from eight trials). However, the results of computations using the SDOF mechanical model generated a maximal acceleration of 1.19 m/s^2 and revealed thus a very good match with the measured result.

A further check of the results' quality was performed by comparing the computational relative displacement of m_p and the simulated force induced by the SDOF into the structure with the corresponding results determined from the measurements. Figure 9 and Figure 10 show satisfactory matches for both the order of magnitude and the time history trends between the computed quantities and the measured results. However, some remarkable differences can be noticed, especially in the case of the force comparison. They occur most likely due to the assumption of constant parameters k_p and c_p as average values from all the steps.

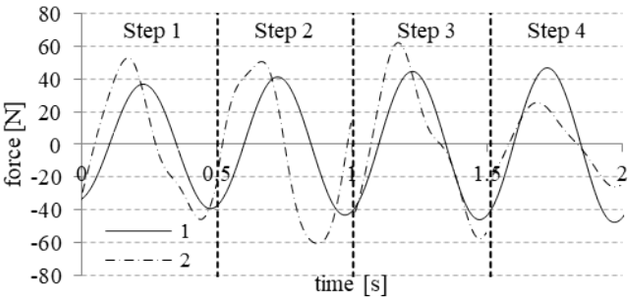


Figure 10: force time history exerted by the SDOF on the structure: 1 - computed using the SDOF approach and 2 - estimated using Equation 10 and the optimised parameters determined from measurements

Table 2: Stifness constants damping coefficients of the SDOF system determined for a pedestrian walking on a flexible structure

Parameter	Subject 01	Subject 02	Subject 03	Subject 04	Subject 05	Subject 06
k_p [N/m]	4001 $\pm$ 1980	4970 $\pm$ 1769	6436 $\pm$ 3302	13999 $\pm$ 2477	5732 $\pm$ 1479	7801 $\pm$ 2113
c_p [Ns/m]	358 $\pm$ 200	608 $\pm$ 286	108 $\pm$ 93	639 $\pm$ 577	289 $\pm$ 114	500 $\pm$ 201

The procedure described above was employed for the analysis of the data from all the six subjects investigated. The results are given in table 2.

Since no direct correlation between the values of the stiffness and damping coefficients to the step number (one to four) could be found, only the average values of the four steps and the corresponding standard deviations are included. Analysing the standard deviations of all the subjects, it is clear that the intra-subject scattering has a similar (rather high) level of magnitude as observed for the first subject. Considering the data from all the subjects, the average stiffness and damping are determined to 7157 $\pm$ 3592 N/m and 417 $\pm$ 204 Ns/m. They lead to natural frequencies of the SDOF system between 1 and 2 Hz. These values are situated at the lower bound of the parameter ranges given in the literature (Shahabpoor et al. 2016).

5 CONCLUSIONS

This work focuses on the experimental identification of the parameters of an SDOF system representing a pedestrian walking on a flexible structure. The SDOF can be used for consideration of human-structure interaction effects within the numerical analysis of pedestrian induced vibrations. A novel method for parameter identification was proposed. It is based on a combination of experimental methods for structural and biomechanical analysis and implies measurements both on a rigid and on a flexible structure. The investigations performed on six subjects revealed average values of 7157 $\pm$ 3592 N/m for the stiffness constant and 417 $\pm$ 204 Ns/m for the damping coefficient, based on four steps analysed for each of the eight trials per subject. These values lie at the lower bound of the ranges specified in the literature and lead to natural frequency of the human body between 1 and 2 Hz. The scattering of the results was found to be rather large (standard deviation around 50%) for both intra-subject and inter-subject analyses. So far, no clear correlation between the different steps could be found.

Furthermore, the authors would like to highlight the importance of the cooperation between civil engineering and sport science on this topic. This facilitates a better understanding of the adaptation mechanisms of the human body walking on flexible structures and can lead to significant improvements of the vibration serviceability guidelines, which should include reliable models for considering the human-structure interaction effects.

ACKNOWLEDGEMENTS

The scientific discussions on this topic with Katrien Van Nimmen and Peter Van Den Broeck are greatly acknowledged.

REFERENCES

Caprani, C. C. & E. Ahmadi (2016). Formulation of human-structure interaction system models for vertical vibration. *Journal of Sound and Vibration 377*, 347–366.

Firus, A., J. Schneider, A. Seyfarth, & C. Schuhmacher (2017). Investigation of the human-structure interaction on a full scale experimental footbridge. In *Proceedings of the 6th International Footbridge Conference (Footbridge2017)*, Berlin, Germany.

Kistler (2017). Product catalogue: Force plates and accessories. Biomechanics measuring systems for performance diagnostics, gait analysis, rehabilitation, and ergonomics. Winterthur, Switzerland.

Lipfert, S., M. Günther, D. Renjewksi, S. Grimmer, & A. Seyfarth (2012). A model-experiment comparison of system dynamics for human walking and running. *Journal of Theoretical Biology 292*, 11–17.

Qin, J. W., S. S. Law, Q. S. Yang, & N. Yang (2013). Pedestrian-bridge dynamic interaction, including human participation. *Journal of Sound and Vibration 332*, 1107–1124.

Racic, V., A. Pavic, & J. M. W. Brownjohn (2009). Experimental identification and analytical modelling of human walking forces: Literature review. *Journal of Sound and Vibration 326*, 1–49.

Shahabpoor, E., A. Pavic, & V. Racic (2016). Interaction between walking humans and structures in vertical direction: A literature review. *Shock and Vibration 2016*, 1–22.

Silva, F. T. & R. L. Pimentel (2011). Biodynamic walking model for vibration serviceability of footbridges in vertical direction. In *Proceedings of the8th International Conference on Structural Dynamics (EURODYN 2011)*, Leuven, Belgium.

Toso, M. A., H. M. Gomes, F. T. Da Silva, & R. L. Pimentel (2016). Experimentally fitted biodynamic models for pedestrian-structure interaction in walking situations. *Mechanical Systems and Signal Processing 72-73*, 590–606.

Van Nimmen, K., G. Lombaert, G. De Roeck, & P. Van den Broeck (2016). Human-induced vibration of footbridges: The effect of vertical human-structure interaction. In *Dynamics of Coupled Structures, Volume 4, Conference Proceedings of the Society for Experimental Mechanics Series*, pp. 299–307.

Van Nimmen, K., G. Lombaert, G. De Roeck, & P. Van den Broeck (2017). The impact of vertical human-structure interaction on the response of footbridges to pedestrian excitation. *Journal of Sound and Vibration 402*, 104–121.

Živanović, S. (2015). Modelling human actions on lightweight structures: Experimental and numerical developments. *MATEC Web of Conferences*.

Werkle, H. (2008). *Finite Elemente in der Baustatik* (3rd ed.). Wiesbaden, Germany: Vieweg.

Werkle, H., A. Firus, & W. Francke (2016). Einfluss personeninduzierter schwingungen auf die messgenauigkeit in ganglaboren. *Bauingenieur 90*, 110–119.

Winter, D. (2009). *Biomechanics and Motor Control of Human Movement* (4th ed.). New Jersey, USA: John Wiley Sons Inc.

Maintenance, Safety, Risk, Management and Life-Cycle Performance of Bridges – Powers, Frangopol, Al-Mahaidi & Caprani (Eds)
© 2018 Taylor & Francis Group, London, ISBN 978-1-138-73045-8

Robust vibration serviceability assessment of footbridges for crowd walking excitation

K. Lievens & P. Van den Broeck
Department of Civil Engineering, Technology Cluster Construction, Structural Mechanics and Building Materials Section
KU Leuven, Technology Campus Ghent, Belgium.

G. De Roeck & G. Lombaert
Department of Civil Engineering, Structural Mechanics Section
KU Leuven, Leuven, Belgium.

ABSTRACT: For slender footbridges, the dynamic response to human-induced loading needs to be verified in a vibration serviceability assessment. The assessment is commonly based on a simplified load model and relying on the nominal values of the modal parameters of the structure as predicted by a finite element model. Often, resonance with a single mode is considered and a reduction factor rates the risk for resonance with that mode. For a reliable response prediction, uncertainties in the modal parameters of the structure must be dealt with, however. If the vibration levels exceed a predefined comfort criterion, a Tuned Mass Damper (TMD) can be installed. In this contribution, a robust vibration serviceability assessment is proposed. Different levels of uncertainty are introduced to account for the effect of uncertainties in the modal parameters resulting in a multi-interval assessment. Realistic loading scenarios are implemented using detailed simulations considering variability of the pedestrian walking characteristics. The contribution of multiple modes is considered and the instantaneous peak acceleration is retained and tested to criteria for vibration comfort. The procedure is illustrated for a slender footbridge. First, the response is evaluated for different levels of uncertainty. Second, the procedure is applied in the design of a TMD by tuning its mass, stiffness and damping constants such that an effective reduction of the vibration levels is ensured. The advantage of the robust interval-based approach is that it allows understanding how the uncertainties in the modal parameters of the structure affect the response prediction. Besides, the method investigates the trade-off between the TMD parameters and its robustness against uncertainties in the modal parameters. The level of uncertainty can be determined based on a monitored or assumed range of variations of the modal parameters of the structure.

1 INTRODUCTION

Slender structures such as footbridges are often characterised by low natural frequencies that may lie in the range of human-induced loading. As these light structures are generally also lightly damped, they are sensitive to human-induced excitation. A vibration serviceability assessment is therefore required to evaluate the dynamic response of the footbridge to human-induced loading.

Frequently used procedures for the assessment have been presented by guidelines such as Sétra (2006) and HiVoSS (2008). For these simplified methods, the load induced by number of randomly distributed pedestrians N is translated to an equivalent load induced by N_{eq}, equally distributed and perfectly synchronised pedestrians. Resonance conditions between one mode of the structure and the first or second harmonic component of the walking load are considered. A reduction factor is included for frequencies which significantly deviate from the expected loading frequencies. However, for footbridges, multiple modes are often excited simultaneously all contributing to the response. Besides, more detailed load models also consider two other important aspects: human-human interaction (HHI) and human-structure interaction (HSI) (Venuti et al. 2016). HHI models describe the synchronisation among pedestrians. In general, for a higher pedestrian density, the synchronisation rate increases resulting in a decrease of the average walking velocity and average step frequency. The relation proposed by Weidmann (1993) is widely applied to link the pedestrian density and average walking speed. Recently, it was investigated that HSI con-

siderably affects the response as well. In vertical direction, the added damping due to the pedestrian bodies must be considered (Van Nimmen et al. 2016, Caprani and Ahmadi 2016, Salyards and Noss 2014). In (Van Nimmen et al. 2017), it was found that the effective damping due to the pedestrians is significantly higher than the modal damping of the empty structure.

As the vibration serviceability assessment strongly depends on a good knowledge of the modal parameters, it is recommended to account for the effect of uncertainties in that modal parameters. The natural frequency and modes can be calculated by a finite element model (FEM) while the modal damping can be estimated based on experience with similar structures such as the values proposed in Sétra (2006) and HiVoSS (2008). Relatively small variations of the nominal values of the modal parameters may lead to large discrepancies in the predicted response, however. In Van Nimmen et al. (2014), it was found that natural frequencies predicted by a detailed FEM of a structure may be up to 10% off from the actual measured values. Also large variations of the modal damping depending on the acceleration amplitude are reported in Avci (2016). Up to now, this uncertainty in the modal parameters of the structure is not accounted for in any of the conventional methods for the response prediction and evaluation of footbridges.

Therefore, this paper proposes an approach for the robust vibration serviceability assessment of footbridges. Both the effect of uncertainties in the modal parameters of the structure and the stochastic nature of the load are accounted for. Different levels of uncertainty are considered to account for the effect of uncertain modal parameters resulting in a multi-interval approach. Based on state-of-the-art load models such as Venuti et al. (2016), Li et al. (2010) and Van Nimmen et al. (2016), the stochastic nature of the load is considered by simulating multiple realistic walking scenarios accounting for variability of the walking characteristics of the pedestrians. HSI effects following Van Nimmen et al. (2017) and HHI effects according to Weidmann (1993) and Venuti and Bruno (2007) are accounted for. The robust assessment then consists of an evaluation of the range of calculated instantaneous peak response.

The outline of the paper is as follows. First, the strategy of the robust vibration serviceability assessment is presented (section 2). Second, in section 3, the procedure is applied to a case study where also a TMD design is discussed by solving an optimisation problem where constraints for vibration serviceability are imposed. Finally, in section 4, a number of conclusions are drawn summarising the advantages of the presented approach.

2 METHODOLOGY FOR ROBUST RESPONSE PREDICTION

In the robust vibration serviceability assessment, both uncertainties in the modal parameters of the structure and the stochastic nature of the loads are considered. The section is organised as follows. First, the methodology to deal with uncertainties in modal parameters is discussed. Second, a summary of the state-of-the-art load models is given. Third, it is given how to extract the instantaneous peak acceleration and to perform the multi-interval assessment.

2.1 *Uncertain modal parameters*

To deal with uncertainties in the natural frequency and modal damping of the structure, a multi-interval approach is proposed which allows assessing the sensitivity of the vibration serviceability assessment to a change in the modal parameters of the structure (Lievens et al. 2016). A multiplication factor β which is modelled as a convex fuzzy number is used to characterise the uncertainty and its value lies in an interval between its minimal value $\beta^{-}(\alpha)$ and maximal value $\beta^{+}(\alpha)$ depending on the value of the membership function (situated between 0 and 1) corresponding to different levels of uncertainty α. The boundaries of these intervals increase linearly for a higher level of uncertainty.

Here, β_{f_j} and β_{ξ_j} are defined to account for uncertainty in the nominal value of the natural frequency f_j and modal damping ξ_j, respectively, of mode j. The interval bounds for the multiplication factor of the natural frequency corresponds to 10% deviation on the nominal value of the natural frequency (Van Nimmen et al. 2014) for the largest level of uncertainty ($\alpha = 0$). The nominal values of the natural frequency correspond to the case with no uncertainty ($\alpha = 1$). Uncertainty in the modal damping is modelled similarly although in this case a wider range of 0.5 to 1.5 times the nominal value is considered. The membership functions of the multiplication factors are visualised in figure 1(a) for the uncertain natural frequency and in figure 1(b) for the uncertain modal damping. These intervals will be considered for the natural frequency and modal damping in all further analyses in the paper. Since these input parameters are modelled as fuzzy numbers, the output variable (response) is also a fuzzy number.

For structures where the contribution of multiple modes is considered, it is assumed that the uncertainties affect the natural frequency of all modes in an identical way ($\beta_{f_j} = \beta_f$). A similar approach is assumed for the modal damping ($\beta_{\xi_j} = \beta_\xi$). Therefore, the assumption is made that the same level of uncertainty α holds for both the natural frequency and modal damping simultaneously.

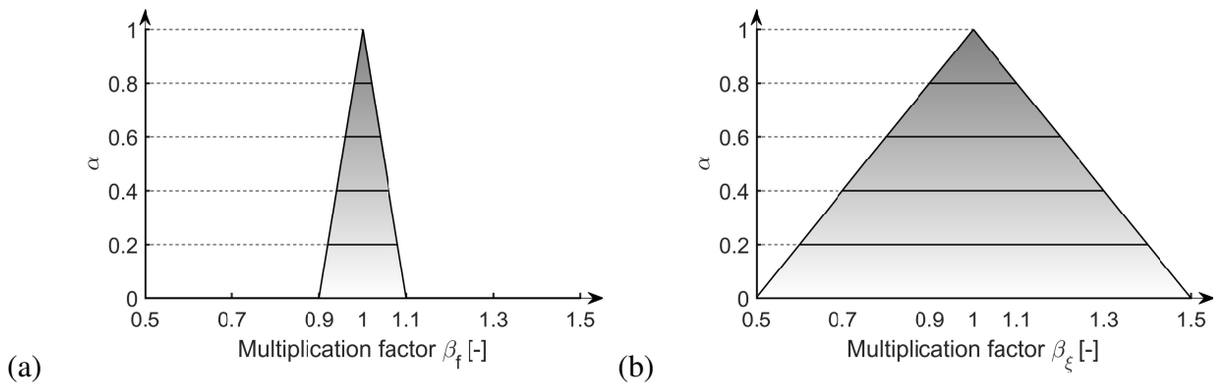


Figure 1: Multi-interval approach for the multiplication factor at different levels of uncertainty α for (a) natural frequency and (b) modal damping.

2.2 *Stochastic nature of human-induced loading*

The model considered in this paper is based on the advanced state-of-the-art load models in Venuti et al. (2016) and Van Nimmen et al. (2016). This section describes how these models are used, for both the single pedestrian walking force and the crowd-induced force model. It is also indicated how the HHI- and HSI-effects are implemented.

2.2.1 *Single pedestrian force*

The pedestrian's walking force of a single footstep is written as a summation of harmonic components as:

$$\frac{F(t)}{G} = \sum_{n=1}^{5} A_n(f_s)\sin(\frac{\pi n}{T_c}t) \quad \text{for} \quad 0 \leq t \leq T_c \qquad (1)$$

with $F(t)$ the force [N] of one single footstep at time t, G the weight of the pedestrian [N], $A_n(f_s)$ the Fourier coefficient of the n-th harmonic component of the generalised load model as a function of the step frequency f_s [Hz] and T_c [s] the contact period between foot and ground. The model given by Li et al. (2010) is used to calculate the walking force in vertical direction, specifying the values of $A_n(f_s)$. The contact time according to Li et al. is found as $T_c = T_s/0.76$ with $T_s = 1/f_s$. By considering a continuous sequence of forces alternatingly induced by left and right foot and respecting the contact time, the step-by-step force is derived.

2.2.2 *Crowd model and induced force*

To develop the model for a moving crowd, a large number of pedestrians must be considered which are each characterised by their trajectory, weight G, step frequency f_s and walking speed v_s. Here, a continuous uni-directional pedestrian flow is assumed. The walking paths of the individual pedestrians are straight lines in the longitudinal direction of the bridge. The weight $G = 700$ N of each pedestrian is equal for all pedestrians. Two important aspects must be considered: interaction among pedestrians and interaction between structure and pedestrians.

Multiple pedestrian densities are considered in the assessment, going from low densities (0.2 pers./m^2) to a high occupancy (1.5 pers./m^2). For densities higher than 0.7 pers./m^2, free movement of the pedestrians is restricted resulting in a decrease of the overall walking speed v_s. The relation between the pedestrian speed and density d [pers./m^2] is given in Weidmann (1993) and Venuti and Bruno (2007) as following:

$$v_s = \bar{v}_s \left(1 - \exp\left[-\gamma\left(\frac{1}{d} - \frac{1}{d_{\text{jam}}}\right)\right]\right) \qquad (2)$$

with $\bar{v}_s$ the average free walking speed, γ a fitting coefficient accounting for the travel purpose and d_{jam} the jam density, i.e. the maximal possible density at the structure corresponding to a null speed flow. d_{jam} generally ranges between 5 and 6 pers./m^2 (Venuti and Bruno 2007). Based on equation (2), the pedestrian speed v_s is found as a function of the density. An expression relating the average step frequency $\bar{f}_s$ of the pedestrians at a specific density and the walking speed v_s was derived from a large set of data from tests in the laboratory (Bertram and Ruina 2001) and is given by Venuti and Bruno (2007) as follows:

$$\bar{f}_s = 2.93v_s - 1.59v_s^2 + 0.35v_s^3 \qquad (3)$$

Five different pedestrian densities d are considered in this paper. The average walking speed and step frequency for the considered densities are shown in figure 2. Therefore, following parameters are used in eq. (2): an average free walking speed of $\bar{v}_s = 1.34$ m/s, the coefficient for travel purpose $\gamma = 1.913$ and the jam density $d_{\text{jam}} = 5.4$ pers./m^2 (Weidmann 1993).

The step frequencies of the pedestrians are sampled from a zero-truncated Gaussian distribution $f_s \sim \mathcal{N}(\mu_{f_s}, \sigma_{f_s})$ with μ_{f_s} the mean value and σ_{f_s} the standard deviation of the step frequency. In nominal conditions, μ_{f_s} equals the value as obtained from equation (3). The value for σ_{f_s} depends on the pedestrian density. For low densities (d <1 pers./m^2), 0.10 Hz is assumed in this paper for σ_{f_s} (Butz et al. 2008). For higher densities ($d \geq$1 pers./m^2), the free movement of the pedestrians is restricted resulting in a decrease of the average speed and mean step frequency

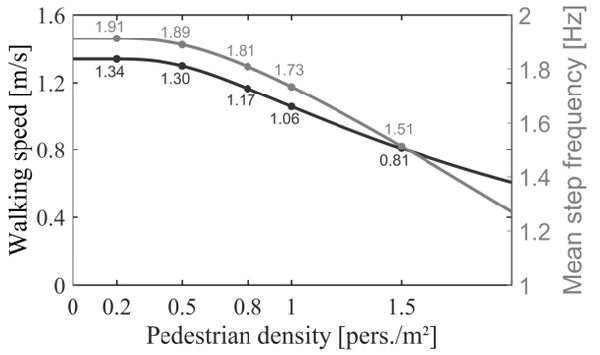


Figure 2: Relation between pedestrian density d and walking speed v_s [m/s] (dark) and between pedestrian density d and average step frequency $\bar{f}_s$ [Hz] (light).

$\bar{f}_s$. Furthermore, a higher level of synchronisation is found resulting in a decreased value of σ_{f_s} (0.05 Hz) (Butz et al. 2008). For all pedestrians, the same walking speed is considered, determined by the pedestrian density (equation (2) and figure 2). At each time step, the longitudinal position of each pedestrian on the footbridge is calculated based on the walking speed. Their lateral position is sampled from a uniform distribution covering the width of the bridge. In the simulations, the arrival times of the individual pedestrians are sampled from a Poisson distribution (Živanović 2012). The total modal load of the flow is then found as the superposition of the modal load of the individual pedestrians, respecting the arrival times. In figure 3, an example is given of the spatial distribution of the single step forces of a sample of walking pedestrians during an arbitrary time interval $[t_{i,k}, t_{i,k} + T_{c,k}]$ with $t_{i,k}$ the time of the i-th start point of one single footstep in the flow simulation of pedestrian k and $T_{c,k}$ the contact time of the footstep of the k-th pedestrian.

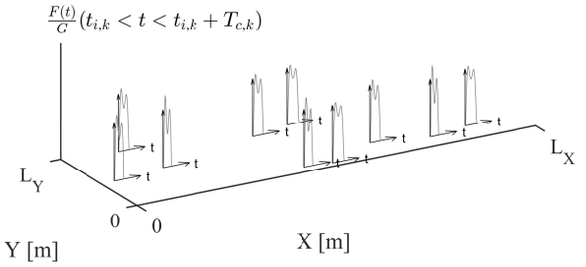


Figure 3: Spatial distribution of single step forces of randomly distributed pedestrians with different characteristics during a time interval $[t_{i,k}, t_{i,k} + T_{c,k}]$ with $t_{i,k}$ the time of the i-th start point of one single footstep in the simulation of pedestrian k and $T_{c,k}$ the contact time of the footstep of the k-th pedestrian.

No active interaction is assumed, implying that the internal driving forces of the pedestrians remain unaltered when walking on the vibrating footbridge. Then, the interaction force between the pedestrian and the footbridge is formulated as the sum of the ground reaction force on a rigid surface and a term resulting from the interaction between the footbridge and the human body as a mechanical system. Following the pseudo moving crowd model of Van Nimmen et al. (2017), the forces move step-by-step while the SDOFs, representing the human bodies, are distributed uniformly over the bridge deck on fixed positions. The parameters of the SDOFs match those of persons assuming a walking posture. To account for inter-subject variability of the human-body parameters, the natural frequency is sampled from $f_H = \mathcal{N}(3.25, 0.32)$ [Hz] and the damping from $\xi_H = \mathcal{N}(0.30, 0.05)$ [-] (Matsumoto and Griffin 1998, Matsumoto and Griffin 2003). The pseudo moving crowd model gives results which deviate at most 5% from a model where the SDOFs move with the loads for all densities of 0.2 pers./m^2 and higher since the model accounts for the actual spatial distribution of the pedestrians (Van Nimmen et al. 2017).

2.3 *Response calculation and evaluation*

The time history of the modal load of the entire flow is constructed as discussed in section 2.2.2 for each mode contributing to the response. Then, a discrete-time state-space model is used to compute the acceleration response of the generated flow. The instantaneous peak value of the bridge acceleration in a time interval with length T, is calculated to statistically characterise the response. The mean value $\mu_{\ddot{u}_{\max}(T)}$ and standard deviation $\sigma_{\ddot{u}_{\max}(T)}$ of the instantaneous peak response are calculated according to (Davenport 1964, Der Kiureghian 1980, Preumont 1985, Piccardo and Tubino 2012) based on the power spectral density (PSD) function of the acceleration time history. In Lievens et al. (2016), this methodology is verified for the prediction of human-induced vibrations. The length of the time window T is here set to twice the time a single pedestrian needs to cross the footbridge T_{cross} as proposed in (Živanović 2012, Association Française de Génie Civil, Sétra/AFGC 2006, Research Fund for Coal and Steel 2008) and the 95th percentile of the instantaneous peak value $\ddot{u}_{95}$ is calculated, here approximated as $\mu_{\ddot{u}_{\max}(T)} + 2\sigma_{\ddot{u}_{\max}(T)}$.

To account for variability on the average walking frequency, an interval for μ_{f_s} is defined as follows:

$$\mu_{f_s} \in [\bar{f}_s(d) - 0.1, \bar{f}_s(d) + 0.1] \tag{4}$$

The interval width of 0.2 Hz for μ_{f_s} is found by evaluating eq. (3) for almost all values of v_s assuming $\sigma_{v_s} = 0.2$ m/s (Živanović 2012). Continuous flows of pedestrians are then composed for each pedestrian density and for each value of μ_{f_s} in the interval as described before, with the following pedestrian characteristics: $f_s \sim \mathcal{N}(\mu_{f_s}, \sigma_{f_s})$ (see section 2.2.2).

The multi-interval analysis then consists of evaluating a range of calculated response. At each level α, the relevant statistical quantity of the response $\ddot{u}_{\max}(d, \alpha)$ for a density d then is expressed as:

$$\ddot{u}_{\max}(d, \alpha) = \max_{\beta_f(\alpha), \beta_\xi(\alpha), \mu_{f_s}(d)} (\ddot{u}_{95}) \tag{5}$$

Similarly, the minimal instantaneous peak value $\ddot{u}_{\min}(d, \alpha)$ is extracted obtaining a range for the instantaneous peak value at level α that can be compared to criteria for vibration comfort from Sétra (2006).

3 APPLICATION

3.1 *The Phénix footbridge*

The Phénix footbridge is a slender construction situated nearby the railway station of Charleroi (Belgium). The construction has a single span of 38.25 m and a width of 13.35 m and a wooden deck is constituted by the steel frame. A neoprene bearing at each corner supports the structure. A detailed description of the footbridge is given in Lievens et al. (2016). In figure 4, the modal parameters of the first three modes are summarised as calculated by the FEM. A modal damping ratio of 0.4% for each mode shape is assumed based on Sétra (2006) and HiVoSS (2008).

3.2 *Vibration serviceability assessment*

The response is calculated following the methodology from section 2. Simulations are performed for the different pedestrian densities considered in this paper accounting for variability on the average step frequency μ_{f_s} and for uncertainties in the modal characteristics as defined by multiple values of the multiplication factors β_f and β_ξ. The response is evaluated by calculating the mean value and standard deviation of the instantaneous peak value in a time window of $2 \times \frac{38.25 \text{ m}}{1.34 \text{ m/s}} \approx 57$ s. A fixed discretisation of 0.01 Hz is considered for the interval of the average step frequency (eq. (4)) while the intervals of the multiplication factors β_f and β_ξ were discretised with a fixed number of 21 uniformly distributed values.

Figure 5 shows the results of the vibration serviceability assessment for the Phénix footbridge as a function of the level of uncertainty in the modal parameters α for each pedestrian density. The overall maximum vertical response at the bridge deck is evaluated. The level $\alpha = 1$ represents the possible acceleration levels considering variability in the loading only while for higher levels of uncertainty, the minimal and maximal possible value of the instantaneous peak acceleration account for both variability in the loading and uncertain modal parameters. It is clearly illustrated in figure 5 how a wider range of uncertainties in the modal parameters leads to a larger interval of the instantaneous peak response.

The values of the instantaneous peak acceleration for $\alpha = 1$ and the average value of μ_{f_s} for each pedestrian density are indicated with cross points. The value of the calculated response remains rather constant for densities up to 1.0 pers./m^2 and strongly increases for the highest density.

The levels for vibration comfort according to Sétra (2006) are also indicated on figure 5: maximal, medium or minimal. At the level $\alpha = 1$, a medium level for vibration comfort is predicted for most of the pedestrian densities (0.2-1 pers./m^2) and a minimal level is predicted for the highest density. When the effect of uncertainty in the natural frequency and modal damping is considered, it is found that, for some values of the parameters, the level of comfort becomes minimal for all densities.

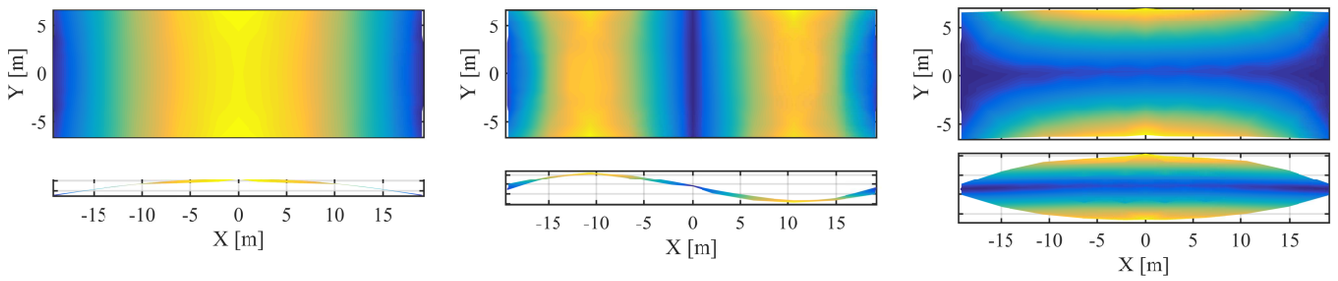
The reduction in the walking speed for increasing pedestrian density drives the values of the step frequency closer to the natural frequency of the first mode in this particular case. Then, resonance is more likely to occur. Especially, for the densities up to 1 pers./m^2, the effect of uncertainty is large since the risk for resonance is very small at nominal conditions of the flow. For a density of 1.5 pers./m^2, the risk for resonance with the first mode is already high in the nominal case. For a better understanding of the results from figure 5, information about the shifted value of the natural frequency and the average value of μ_{f_s} (figure 2) must be simultaneously considered.

To support this interpretation, the PSD function for accelerations is plotted for two pedestrian densities (0.2 and 1.5 pers./m^2) in figure 6 considering the nominal values of the modal parameters and the nominal conditions for the flow. For low pedestrian densities, the added mass of the pedestrians hardly affects the value of the natural frequency (1.65 Hz, first small peak). A second peak at ± 1.9 Hz represents the first harmonic component of the walking load. The rather small range of accelerations at nominal conditions (0.2 pers./m^2, figure 5) is due to the low risk for resonance between the natural frequency of 1.65 Hz and the possible values of f_s at that density. If the effect of uncertainties in the natural frequency is accounted for, the risk for resonance between the range of μ_{f_s} and the uncertain value of the natural frequency $\beta_f \times \pm 1.65$ Hz strongly increases. On the contrary, for high densities, the value of the natural frequency of the footbridge is significantly affected by the pedestrians and is close to the values of μ_{f_s} in the range 1.51 ± 0.1 Hz (first peak around ± 1.5 Hz). At nominal conditions, resonance is likely to occur between the decreased value of the natural frequency and values of μ_{f_s} in the range 1.51 ± 0.1 Hz. The effect of uncertainties in the natural frequency is rather small since at nominal conditions, the loading frequency could already coincide with the natural frequency (resonance conditions), resulting in a worst case situation. Other peaks in the PSD represent the higher harmonic components of the load or the contribution of other modes.

3.3 *TMD design and reassessment*

3.3.1 *TMD parameter tuning*

According to the results from figure 5, vibration comfort can not be guaranteed, and the installation of a TMD is opted to reduce the vibration levels. The



(a) mode 1 ($f_1 = 1.65$ Hz, $\xi_1 = 0.4$ %, $m_1 = 126.9$ ton)

(b) mode 2 ($f_2 = 5.22$ Hz, $\xi_2 = 0.4$ %, $m_2 = 100.2$ ton)

(c) mode 3 ($f_3 = 6.15$ Hz, $\xi_3 = 0.4$ %, $m_3 = 21.5$ ton)

Figure 4: Top and side view of the first three modes of the Phénix footbridge as calculated by the FEM: (a) 1st bending mode, (b) 2nd bending mode, (c) 1st torsional mode.

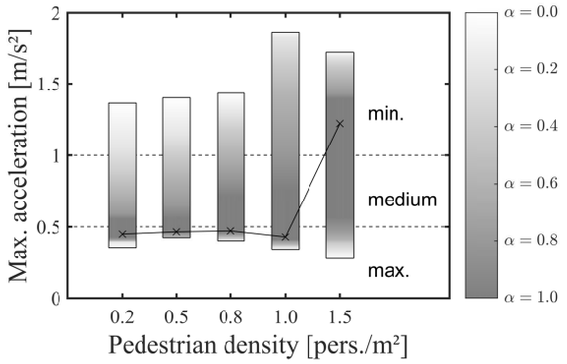


Figure 5: Robust vibration serviceability assessment for the Phénix footbridge: possible range of the instantaneous peak response accounting for variability of the load and for uncertain modal parameters of the structure, indicated by increasing levels of uncertainty in the natural frequency and modal damping (dark to light) and indication of the response in nominal situation (–×–). Comfort criteria according to Sétra (2006).

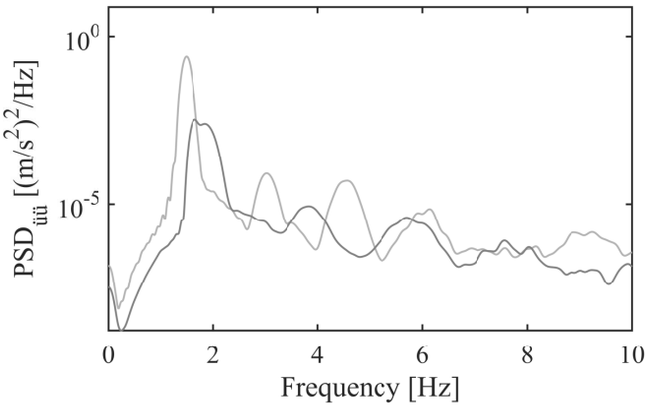


Figure 6: PSD of the acceleration response at mid span for $d = 0.2$ pers./m^2 (dark) and $d = 1.5$ pers./m^2 (light) with $\beta_f = 1$, $\beta_\xi = 1$ and $\mu_{f_s} = \bar{f}_s(d)$.

TMD mass m_{TMD}, stiffness k_{TMD} and damping c_{TMD} are tuned by solving an optimisation problem. The aim is to minimise the cost of the TMD while meeting vibration serviceability criteria. Therefore, the total mass of the TMD m_{TMD} is taken as a measure of its cost. Criteria for vibration serviceability are added as constraints to ensure an acceptable probability of exceeding a threshold for vibration comfort $\ddot{u}_{\text{comfort}}$. The TMD parameter tuning problem then is formulated as follows:

$$\begin{aligned} &\underset{m_{\text{TMD}},k_{\text{TMD}},c_{\text{TMD}}}{\text{minimise}} \quad m_{\text{TMD}} \\ &\text{subject to} \quad \mu_{\ddot{u}_{\max}(T)} + 2\sigma_{\ddot{u}_{\max}(T)} \leq \ddot{u}_{\text{comfort}} \\ &\qquad\qquad \forall\beta_f(\alpha), \forall\beta_\xi(\alpha), \forall\mu_{\text{fs}} \end{aligned} \tag{6}$$

In this case, the limit for vertical vibrations is $\ddot{u}_{\text{comfort}} = 1$ m/s^2 corresponding to a medium level of vibration comfort. The location of the TMD corresponds to the mid span of the footbridge at the antinode of mode 1. The working direction is vertical.

A non-linear constraint is implemented for all combinations of possible values of the mean step frequency of the flow μ_{f_s}, and all possible values in the intervals of the multiplication factor of the uncertain frequency β_f and modal damping β_ξ at the level α.

The proposed methodology allows to investigate the trade-off between the cost of the TMD and the level of robustness, i.e. for what deviations from the nominal values of the modal parameters vibration serviceability is still guaranteed. To illustrate the trade-off, the problem for the Phénix footbridge is solved twice. First, it is assumed that no information is available about variations or uncertainties in the modal parameters, for instance in design stage. In this case, the largest level of uncertainties in the modal parameters is considered ($\alpha = 0$). This allows estimating the TMD required when there is insufficient time for designing and installing the TMD based on measurements in between the construction of the bridge and before it is put into service. When measurements can be performed after construction, only seasonal variations of the modal parameters need to be accounted for. In this case, a higher α-level can be opted leading to a smaller TMD mass and a more cost-effective design. Here, the problem is solved for $\alpha = 0.6$. The trade-off thus encompasses the total cost, containing the cost for measurements and/or TMD units, and the timing of the design process.

The optimisation problem defined in eq. (6) is solved using a gradient based method with an interior-

point approach for handling the constraints (*fmincon* function in Matlab (The Mathworks, Inc. 2015)).

3.3.2 *Results and discussion*

The solution of the optimisation problem from equation (6) (TMD constants) for the two considered values of α is summarised in table 1. A lower TMD mass and damping are found for the design at a lower level of uncertainty ($\alpha = 0.6$). From the optimisation routine, it is found that the frequency of the TMD is close to the natural frequency of the first mode of the footbridge in the range between $\beta_f^-(\alpha) \times 1.65$ Hz and $\beta_f^+(\alpha) \times 1.65$ Hz, as was expected for the given position. In table 1, the values of the TMD parameters are also given in dimensionless terms considering the nominal values of the modal mass and natural frequency of the first mode. Besides, following parameters are also given: the TMD frequency $f_{\text{TMD}} = \frac{1}{2\pi}\sqrt{\frac{k_{\text{TMD}}}{m_{\text{TMD}}}}$, the mass ratio $\mu_{\text{TMD}} = \frac{m_{\text{TMD}}}{m_{j,\text{ver}}}$, frequency ratio $\rho_{\text{TMD}} = \frac{f_{\text{TMD}}}{f_j}$ and damping ratio $\xi_{\text{TMD}} = \frac{c_{\text{TMD}}}{4\pi m_{\text{TMD}} f_{\text{TMD}}}$ with j the number of the mode to which the TMD is tuned to (here $j = 1$) and $m_{j,\text{ver}}$ the corresponding modal mass considering the mass-normalised vertical modal displacement at the location of the TMD.

	$\alpha = 0.0$	$\alpha = 0.6$
m_{TMD} [kg]	1266.7	651.6
k_{TMD} [N/m]	126994.1	59917.4
c_{TMD} [Ns/m]	2025.2	796.1
f_{TMD} [Hz]	1.59	1.53
μ_{TMD} [%]	0.94	0.49
ρ_{TMD} [-]	0.96	0.92
ξ_{TMD} [%]	7.98	6.37

Table 1: Optimised values of the parameters of the TMD for the two considered values of the parameter α.

The entire vibration serviceability is now repeated for the footbridge with TMD, considering the optimised TMD parameters. The results of the analyses are summarised in figure 7. For all pedestrian densities, a strong reduction of the response is found compared to the results from figure 5. For a pedestrian density of 1 and 1.5 pers./m^2 and a TMD design at $\alpha = 0$, the maximal predicted acceleration equals 1 m/s^2, satisfying the design constraint (figure 7-left intervals). Similar, for the TMD designed for $\alpha = 0.6$, the maximal predicted acceleration equals 1 m/s^2 at the level $\alpha = 0.6$ (figure 7-right intervals). For higher levels of uncertainty, the medium comfort level is not met for all densities considered. For both designs, the constraint for vibration serviceability are only active for the pedestrian densities of 1 and 1.5 pers./m^2. The assessment considering nominal values ($\alpha = 1$) results in the smallest range of accelerations since only the effect of variability of the loading is present. That range is also visible in figure 7. For higher levels of uncertainty, a wider range of calculated vibration levels is found. An indication is also given for the peak response at nominal conditions.

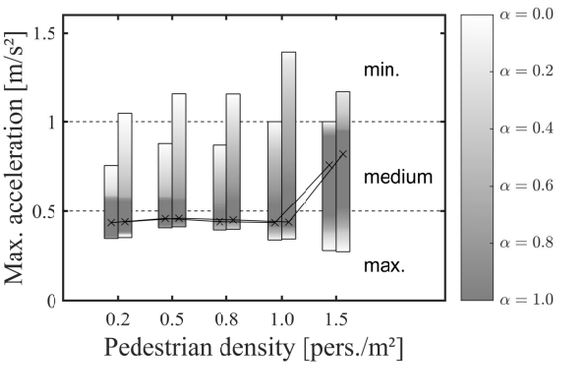


Figure 7: Robust vibration serviceability assessment for the Phénix footbridge equipped with TMD with parameters as summarised in table 1: TMD designed at (left) $\alpha = 0$, (right) $\alpha = 0.6$. Possible range of the instantaneous peak response accounting for variability in the load and for uncertain modal parameters of the structure, indicated by increasing levels of uncertainty in natural frequency and modal damping (dark to light) and indication of the response at nominal conditions (–×–). Comfort criteria according to Sétra (2006).

The power spectral density function of the acceleration response for the structure equipped with TMD is given in figure 8. Compared to the results from figure 6, the peak value of the PSD for $d = 1.5$ pers./m^2 has decreased while for $d = 0.2$ pers./m^2, the value remains constant. This means that the response for the higher density is more influenced by the TMD than for the lower pedestrian density.

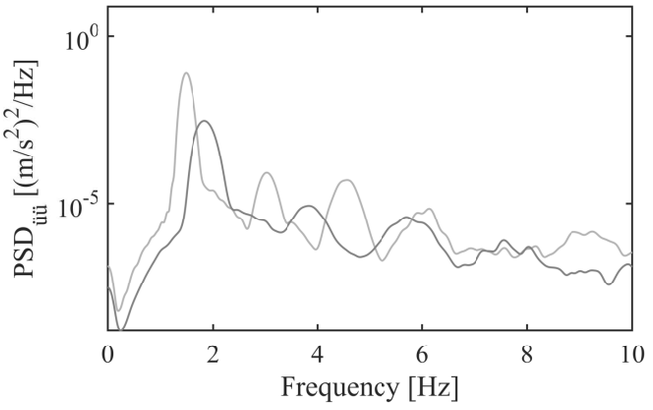


Figure 8: PSD of the acceleration response at mid span for $d = 0.2$ pers./m^2 (dark) and $d = 1.5$ pers./m^2 (light) with $\beta_f = 1$, $\beta_\xi = 1$ and $\mu_{f_s} = \bar{f}_s(d)$ for the footbridge with TMD tuned at $\alpha = 0.0$.

4 CONCLUSIONS

A strategy is proposed to account for the effect of uncertainties in the modal parameters of the structure and for variability of the loading in the vibration serviceability assessment of footbridges subject to human-induced loading. Therefore, different levels of uncertainty are introduced for the modal parameters leading to a multi-interval assessment. The width

of the intervals determines the robustness of the assessment resulting in a range for the calculated acceleration levels. An advanced load model which accounts for variability of the walking load is used by simulating continuous flows of pedestrians. Human-structure interaction effects are also accounted for.

The proposed multi-interval assessment is illustrated for the response prediction of the Phénix footbridge showing how the predicted vibration levels were affected by the effect of uncertainties. Next, the robust design of a TMD is considered. Its parameters are tuned by solving an optimisation problem minimising the total mass. Design constraints are added to satisfy criteria for vibration comfort. It is found that for a decreasing range of uncertainty in the modal parameters of the footbridge, the TMD mass required to satisfy the design constraints also decreases without violating the design constraints illustrating the trade-off between cost and robustness.

The proposed methodology has two advantages compared to other approaches. First, by accounting for variability in the walking load and for uncertainties in the modal parameters, a range of values for the instantaneous peak acceleration is found, rather than one single value, which is compared to a threshold for vibration comfort. Second, the sensitivity of the response and the TMD performance to the required degree of robustness (level of uncertainty) can be investigated. In that way, the multilevel approach allows to investigate the trade-off between the total cost of the TMD and the level of uncertainty.

5 ACKNOWLEDGEMENTS

The financial support for the research by the Agency for Innovation by Science and Technology in Flanders (IWT), recently transferred to the Research Foundation - Flanders (FWO), is gratefully acknowledged.

REFERENCES

Association Française de Génie Civil, Sétra/AFGC (2006). *Sétra: Evaluation du comportement vibratoire des passerelles piétonnes sous l'action des piétons*. Association Française de Génie Civil, Sétra/AFGC.

Avci, O. (2016). Amplitude-Dependent Damping in Vibration Serviceability: Case of a Laboratory Footbridge. *Journal of Architectural Engineering 22*(3), 04016005.

Bertram, J. E. A. & A. Ruina (2001). Multiple Walking Speed-frequency Relations are Predicted by Constrained Optimization. *Journal of Theoretical Biology 209*(4), 445–453.

Butz, C., M. Feldmann, C. Heinemeyer, G. Sedlacek, & et al. (2008). Advanced load models for synchronous pedestrian excitation and optimised design guidelines for steel footbridges (SYNPEX). Report, Research Fund for Coal and Steel.

Caprani, C. C. & E. Ahmadi (2016). Formulation of human–structure interaction system models for vertical vibration. *Journal of Sound and Vibration 377*, 346–367.

Davenport, A. G. (1964). Note on the distribution of the largest value of a random function with application to gust loading. In *ICE Proceedings*, Volume 28, pp. 187–196. Thomas Telford.

Der Kiureghian, A. (1980). Structural response to stationary excitation. *Journal of the Engineering Mechanics Division 106*(6), 1195–1213.

Li, Q., J. Fan, J. Nie, Q. Li, & Y. Chen (2010). Crowd-induced random vibration of footbridge and vibration control using multiple tuned mass dampers. *Journal of Sound and Vibration 329*(19), 4068–4092.

Lievens, K., G. Lombaert, G. De Roeck, & P. Van den Broeck (2016). Robust design of a TMD for the vibration serviceability of a footbridge. *Engineering Structures 123*, 408–418.

Lievens, K., K. Van Nimmen, G. Lombaert, G. De Roeck, & P. Van den Broeck (2016). Prediction of peak response values of structures with and without tmd subjected to random pedestrian flows. In *Journal of Physics: Conference Series*, Volume 744, pp. 012227. IOP Publishing.

Matsumoto, Y. & M. Griffin (1998). Dynamic response of the standing human body exposed to vertical vibration: influence of posture and vibration magnitude. *Journal of Sound and Vibration 212*(1), 85–107.

Matsumoto, Y. & M. J. Griffin (2003). Mathematical models for the apparent masses of standing subjects exposed to vertical whole-body vibration. *Journal of Sound and Vibration 260*, 431–451.

Piccardo, G. & F. Tubino (2012). Equivalent spectral model and maximum dynamic response for the serviceability analysis of footbridges. *Engineering Structures 40*, 445–456.

Preumont, A. (1985). On the peak factor of stationary Gaussian processes. *Journal of Sound and Vibration 100*(1), 15–34.

Research Fund for Coal and Steel (2008). *HiVoSS: Design of Footbridges*. Research Fund for Coal and Steel.

Salyards, K. A. & N. C. Noss (2014). Experimental evaluation of the influence of human-structure interaction for vibration serviceability. *Journal of Performance of Constructed Facilities 28*(3), 458–465.

The Mathworks, Inc. (2015). *MATLAB version 8.6.0 (R2015b)*. Natick, Massachusetts: The Mathworks, Inc.

Van Nimmen, K., G. Lombaert, G. De Roeck, & P. Van den Broeck (2014). Vibration serviceability of footbridges: Evaluation of the current codes of practice. *Engineering Structures 59*, 448–461.

Van Nimmen, K., G. Lombaert, G. De Roeck, & P. Van den Broeck (2016, February). Human-induced vibrations of footbridges: The effect of vertical human-structure interaction. In *Proceedings of the 34th International Modal Analysis Conference Series*, Orlando, FL.

Van Nimmen, K., G. Lombaert, G. De Roeck, & P. Van den Broeck (2017). The impact of vertical human-structure interaction on the response of footbridges to pedestrian excitation. *Journal of Sound and Vibration 402*, 104–121.

Van Nimmen, K., P. Verbeke, G. Lombaert, G. De Roeck, & P. Van den Broeck (2016). Numerical and experimental evaluation of the dynamic performance of a footbridge with tuned mass dampers. *Journal of Bridge Engineering 21*(8), 1–1.

Venuti, F. & L. Bruno (2007). An interpretative model of the pedestrian fundamental relation. *Comptes Rendus - Mecanique 335*(4), 194–200.

Venuti, F., V. Racic, & A. Corbetta (2016). Modelling framework for dynamic interaction between multiple pedestrians and vertical vibrations of footbridges. *Journal of Sound and Vibration 379*, 245–263.

Weidmann, U. (1993). *Transporttechnik der Fussgänger: Transporttechnische Eigenschaften des Fussgängerverkehrs (Literaturauswertung)*. ETH, IVT.

Živanović, S. (2012). Benchmark footbridge for vibration serviceability assessment under the vertical component of pedestrian load. *Journal of Structural Engineering 138*(10), 1193–1202.

Maintenance, Safety, Risk, Management and Life-Cycle Performance of Bridges – Powers, Frangopol, Al-Mahaidi & Caprani (Eds)
© 2018 Taylor & Francis Group, London, ISBN 978-1-138-73045-8

Model Updating of a GFRP footbridge using Tchebichef Moment Descriptors

J.W. Ngan, C. Caprani, Y. Bai
Department of Civil Engineering Monash University, Melbourne Australia

ABSTRACT: The Modal Assurance Criterion (MAC) is the most widely used indicator to correlate mode shapes. However, it is recognized that the single index nature of the MAC is insufficient to detect localized differences in mode shapes. Mode shapes of structures made from Glass fibre-reinforced polymer (GFRP) can exhibit localized features. Consequently, model updating process of GFRP structures may not be optimal with the MAC. This paper proposes a shape-descriptor–based model updating procedure using Tchebichef Moment Descriptors (TMDs) for improved model updating of GFRP structures. Shape descriptors are advantageous in describing mode shape features at a range of fidelities, and so are well suited for use in model updating procedures. The proposed model updating framework is implemented on a benchmark GFRP footbridge which exhibit localized differences in mode shapes. The method is validated using a simulated model updating of the footbridge. A combination of shape descriptors and natural frequencies for the updating objective yield the most improved numerical model. The updating results suggest that the proposed method is an improvement for model updating of GFRP structures.

1 INTRODUCTION

Finite element (FE) analysis is a powerful tool for numerical analysis of building structures. Due to modelling simplifications and uncertainties, discrepancies often arise between FE predicted results and experimental measurements. A process termed 'model updating' is therefore frequently carried out on FE models to improve accuracy of numerical predictions. In structural dynamics, mode shapes are generally used for model updating, along with frequencies. Mode shapes between numerical and experimental models are typically compared using correlation indicators.

The most widely used indicator is the modal assurance criterion (MAC). Since it was first presented by Allemang (1982), it has been used extensively to correlate mode shapes in model updating. The MAC indicates the degree of consistency between two mode shapes using values between 0 (indicates no correlation) and 1 (perfect correlation). The main advantage of the MAC is that it is a single number. However, a single number is unable to reveal extended information regarding differences between two mode shapes. Localized differences could be easily missed using the MAC.

In structural dynamics, the term 'mode localization' refers to vibration confinement, i.e. where the magnitude of a specific part of the free vibrational mode is large relative to the rest of the mode (Kim & Lee, 1998). To graphically illustrate the concept of localized mode shapes, the example of a plate disc from Wang, Mottershead & Mares (2009a) is shown in Figure 1. The first mode shapes of the plate with and without an added mass are given in Figure 1a and 1b respectively. From here one can observe that the mode shape ordinate opposite the location of the added mass is significantly larger than the remaining ordinates.

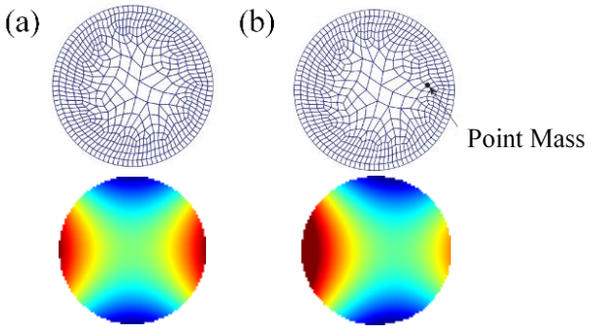


Figure 1. Localization of mode shape due to added mass in (b) compared with (a) (after (Wang, et al., 2009a)).

Structures made-wholly from glass fibre-reinforced polymer (GFRP) can exhibit localized mode shapes (Zivanovic, et al., 2014). Consequently, their behavior deviates from that idealized. This deviation can originate from (1) manufacture: randomness in GFRP material properties associated with the fibre-matrix built-up (Bank, 1993), and; (2) fabrication: the connection methods of GFRP structural members (either bolted or adhesive). Consequently, model updating of GFRP structures using the single number of the MAC may not be optimal. Indeed, as will be seen, this issue was found in the recently-constructed Monash GFRP Footbridge (Ngan, et al., 2016). Therefore, an alternative to the MAC is needed for model updating of GFRP structures.

Since mode shapes are images, they can be classified based on its features of the shape represented. To this end, descriptors or indices can be used to indicating resemblance of features in the mode shapes. These shape descriptors can then be used to compare

mode shapes, simply by correlating paired shape descriptors. Since there are generally more than one shape descriptor for a given mode shape, mode shapes can be correlated using two or more descriptor terms, unlike the single index of the MAC. Consequently, this approach can reveal significantly more information about mode shape differences for model updating. Application of shape descriptors in model updating has been pioneered by Wang, Mottershead and their team (Wang, Mottershead & Mares 2009a, b, Wang, Mottershead, Ihle, et al, 2011, Wang, Mottershead, Sebestian, et al, 2011, Wang, et al, 2013)

The presented work is a model updating framework based on Tchebichef moment descriptors (TMDs) that was previously studied by Wang et al (2011). In this study, the model updating framework is proposed for model updating of GFRP structures. The work demonstrates the benefits of using the finer sensitivity of shape descriptors on a laboratory GFRP footbridge. This paper informs on the effectiveness of the proposed framework for GFRP structures.

2 MODEL UPDATING FRAMEWORK

Model updating is an iterative method which uses the sensitivity of model responses to each parameter in order to optimize model parameters. The method has been well-described by Friswell and Mottershead (Frisswell & Mottershead, 1995). The presented framework uses Tchebichef shape features i.e. TMDs to correlate mode shapes for updating.

2.1 *Tchebichef moment descriptors*

TMDs are derived from Tchebichef polynomials that inherit orthogonal properties (El-ghazai, et al., 2009) (Mukundan , et al., 2001). This property yields orthogonal shape features, which are highly efficient and advantageous in classifying mode shape features (Wang, et al., 2011) (El-ghazai, et al., 2009). The nth discrete Tchebichef polynomial, $t_n(x)$ up to order of N is defined as (Mukundan , et al., 2001):

$$t_n(x) = (1-N)_n \, {}_3F_2(-n,-x,1+n;1,1-N;1) \tag{1}$$

where x is the discrete pixel position in the x direction of a quadrilateral image; ${}_3F_2$ is the generalized hypergeometric function given as:

$${}_3F_2(a_1,a_2,a_3;b_1,b_2;z) = \sum_{k=0}^{\infty} \frac{(a_1)_k (a_2)_k (a_3)_k}{(b_1)_k (b_2)_k} \frac{z^k}{k!} \tag{2}$$

where $(a)_k$ is the Pochhammer symbol or rising factorial, k defined as:

$$(a)_k = a(a+1)(a+2)\cdots(a+k-1) \tag{3}$$

The Tchebichef polynomials of Equation (1) requires scaling because the value of $t_n(x)$ grows as N^n (Mukundan , et al., 2001). Therefore, a scaled Tchebichef polynomial is defined as

$$\tilde{t}_n(x) = \frac{t_n(x)}{\beta(n,N)} \tag{4}$$

where $\beta(n,N)$ is the scaling constant independent of x with definition outlined in (Mukundan , et al., 2001). The two-dimensional TMDs of an intensity function of a mode shape image, $f(x,y)$ can be obtained as the product of two discrete Tchebichef polynomial given by:

$$T_{nm} = \sum_{x=0}^{N_x-1} \sum_{y=0}^{N_y-1} \tilde{t}_n(x) \tilde{t}_m(y) f(x,y) \tag{5}$$

where N_x and N_y are the total number of image pixel in the x and y dimensions of the image in which the scaled Tchebichef polynomials is calculated, and n and m denote the Tchebichef polynomials of the x and y dimension respectively.

2.2 *Sensitivity Analysis*

In each iterative updating step, the sensitivities of the ith FE model outputs (e.g. TMDs and natural frequencies) $\mathbf{R}$, to changes in the jth FE model parameters, $\mathbf{P}$ (e.g. mass density, stiffness), are computed. For consistency of units between different parameters and outputs, a normalized sensitivity matrix is considered. The increment of parameters and difference in outputs are divided by the initial parameter values and initial outputs respectively. The normalized sensitivity matrix $\mathbf{S}$ (of dimension $i \times j$) is calculated for iteration k as (Frisswell & Mottershead, 1995):

$$\mathbf{S}_k = \left[S_{ij} \right] = \left[R_{ii} \right]^{-1} \left| \frac{\delta \mathbf{R}_i}{\delta \mathbf{P}_j} \right| \left[P_{jj} \right] \tag{6}$$

where $\delta\mathbf{R}$ is the difference in measureable outputs of the FE model due to an increment in model parameters $\delta\mathbf{P}$, for response i, and parameter j. R_{ii} and P_{jj} are diagonal, square matrix holding the initial output and parameter values respectively.

The iterative model updating function is based on the sensitivity matrix, and is given as (Anon., 2015)

$$\theta_{k+1} = \theta_k + \left[S_k^T S_k \right]^{-1} S_k^T \left(\mathbf{R}_m - \mathbf{R}_k \right) \tag{7}$$

where $\boldsymbol{\theta}_k$ and $\boldsymbol{\theta}_{k+1}$ are vectors containing the FE model parameters of the current and next iteration steps; $\mathbf{R}_m$ is the measured (target) metric and $\mathbf{R}_k$ is the output metric from the current iterative step. The final parameters are found when the Euclidian norm difference of the output metrics between increments is sufficiently small (taken here as < 1%)

$$\varepsilon = \left\| \frac{(\mathbf{R}_m - \mathbf{R}_k)}{\mathbf{R}_k} \right\| \leq 0.01 \tag{8}$$

The metrics $\mathbf{R}_m$ and $\mathbf{R}_k$ contains the TMDs and natural frequencies of the experimental and FE model respectively.

3 TEST STRUCTURE

The Monash University pultruded GFRP Footbridge is 9 m long and 1.5 m wide. It was constructed in 2016 for the study of human-induced vibration. The results of experimental modal analyses and numerical modelling details are given in this section.

3.1 *Description of footbridge*

The deck of the footbridge is a sandwich panel made from pultruded GFRP box sections incorporated between two GFRP flat sheets as shown in Figure 2. The orthotropic deck is supported on two pultruded FRP I-beam girders, spanning about 8.8 m. All components in the footbridge are joined together using adhesive bonding to ensure full composite action. No bolted connections or steel components are used. Bi-directional fibre orientations for flat sheets, box section and I-beam girders were adopted to maximize strength and stiffness in both transverse and longitudinal directions (Figure 2). The footbridge has a mass per unit length of 92.56 kg/m.

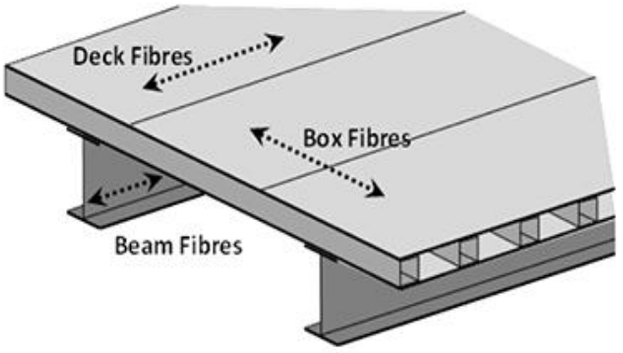


Figure 2. Fibre orientation of pultruded sections

3.2 *Experimental Modal Analysis*

Experimental modal analysis (EMA) was carried out to identify the modal properties of the footbridge. The footbridge was instrumented using 10 accelerometers (sensitivity of 10^4 mV/g) on measurement grids which are shown in Figure 3 and Figure 4.

The footbridge was excited using an electrodynamic APS 118 shaker (known as shaker test). The shaker was placed at the location shown in Figure 3 to ensure excitation of majority vibrational modes. Following this, a second EMA test was conducted using an impact hammer to excite the structure. A following roving hammer test was carried out by repeatedly hitting the hammer at each accelerometer position in Figure 4 while simultaneously acquiring responses. The acquired acceleration data was processed in MACEC (Reynders, et al., 2014), a well-known system identification program. Frequency response functions (FRFs) were obtained from the experimental data to extract natural frequencies and mode shapes of the footbridge.

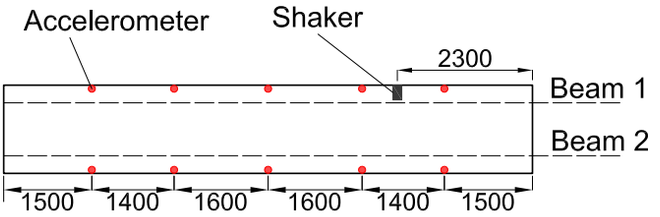


Figure 3. Measurement grid for shaker tests

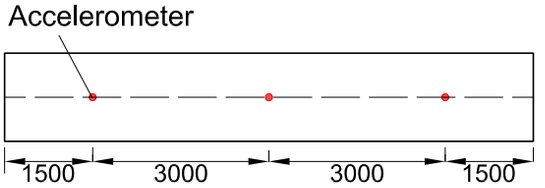


Figure 4. Measurement grid for impact hammer tests.

3.3 *Numerical Modelling*

An FE model of the footbridge was developed in LUSAS software. All components of the footbridge including flat panels, box sections, and bottom I-beam girders are modelled using 8-node quadrilateral shell elements (QTS8). This shell element has six degrees of freedom at each node: translation in nodal x, y, and z directions and also rotation about nodal x, y, and z axes.

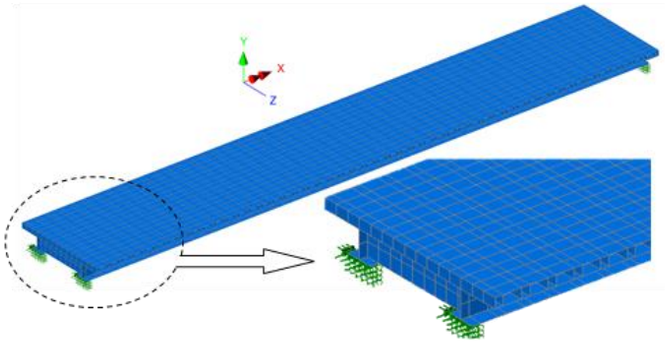


Figure 5. The 3-D FE model of the GFRP footbridge.

Orthotropic material properties for GFRP are incorporated in the FE model. The orthotropic shell elements in each respective component are orientated according to the fibre directions in the actual footbridge (Figure 2). Spring-supported boundary conditions are considered for the four load cells supporting each end of the I-beams. Left end supports are constrained in all three directions (x, y and z). At the right end, the support configuration allows free displacement in the longitudinal (x-axis) direction.

3.4 *Modal Results*

The modal properties identified from both shaker test and impact hammer test of the EMA are summarized in Table 1. Eigenvalue analysis is carried out to extract the modal properties i.e. natural frequencies and mode shapes of the first six modes of vibration from the FE model. The natural frequencies from the FE model and shaker test are summarized in Table 2, and the MAC values are given. The mode shapes from experimental and FE model are given in Figure 6 and Figure 7 respectively.

Table 1. Comparison between natural frequencies from shaker test and impact test.

	Natural Frequencies (Hz)		
Mode	Shaker Test	Hammer test	Difference (%)
1	5.86	6.17	5.3
2	10.02	-	-
3	18.14	19.60	8.1
4	20.60	-	-
5	25.60	-	-
6	37.54	38.30	2.0

Table 2. Summary of natural frequencies from shaker test and FE model.

	Experimental Shaker testing		FE model		
Mode	Nat. Freq.(Hz)	Damping ξ (%)	Nat. Freq. (Hz)	NFD[1] (%)	MAC
1	5.86	0.59	5.95	1.5	0.98
2	10.02	0.96	9.62	4.0	0.97
3	18.14	0.61	20.27	11.7	0.98
4	20.60	1.65	23.87	15.9	0.64
5	25.60	1.33	28.85	12.7	0.66
6	37.54	0.92	39.52	5.3	0.85

[1] Natural frequency difference

3.5 *Discussion*

From the results, it can be observed that the ordering of FE mode shapes is identical to the experimental mode shapes. This is expected since the footbridge is built to closely resemble the FE model; for example, with no additional railings and covers. Natural frequencies obtained from shaker tests are uniformly lower than from the hammer test.

The results suggest that the maximum displacements of the experimental mode shapes (shaded red in Figure 6) exhibit some localized features. Since the footbridge structure is globally symmetric, it is intuitive that the maximum displacement of the experimental mode shape should be symmetric. This is true in FE mode shapes (Figure 7). These observations are most likely explained by mass loading of the shaker. Since the shaker mass is relatively close to the mass of the footbridge (mass ratio of 1:17), it contributed mass to the vibrating system, possibly leading to the observed localization of the mode shape's peak.

To examine if the localized feature of mode shape is due to mass loading effect of the shaker, five experimental modal analyses were conducted. In each test, the shaker position was varied as shown in Figure 8. The first mode shape obtained for each test is overlaid in Figure 8. Shaker position 1 corresponds to the initial shaker position as given in Figure 3.

As can be seen in Figure 8, the peaks of most mode shapes (shaker positions 1 to 5) are localized, most notably towards the north edge of the footbridge. This feature, most notably for test positions 1 to 5, is most severe for positions 1 and 4. It is certainly likely that due to the bridge's light weight, the high relative mass of the shaker influences the vibrating system.

Interestingly, as the shaker is placed towards the south edge (location 5 and 6 in Figure 8) the localized effect reduces and eventually balances out at position 6. Seemingly, the shaker mass is balancing out some asymmetry of structural stiffness, since the mass of the overall system is constant for each test. Thus, it appears that there is a reduced longitudinal stiffness along the footbridge, most notably along beam 1 (Figure 3).

The MAC values for the modes of vibration are given in Table 2. As can be seen, the MAC for the first three modes suggest high consistency between the FE model and experimental results, with high MAC values (more than 0.9) despite the presence of the localized feature in mode shapes. This highlights the inability of the MAC to indicate the localized feature of mode shapes. As such, model updating procedures based on MAC would fail to capture the seeming reduced stiffness of beam 1, but would instead lead to a more global scaling that would improve MAC a little.

4 APPLICATION OF THE FRAMEWORK

The model updating framework outlined earlier is now carried out to improve the structural representation of the FE model, i.e. capture the reduced longitudinal stiffness and natural frequency prediction.

For the GFRP footbridge, accurate structural behavior representation from the FE model is needed for subsequent analysis, e.g. transient analysis. Furthermore, accurate representations of the first three modes of vibration are needed due to the characteristics of these natural frequencies to human walking. To give an example, the first natural frequency was found to coincide with the third harmonic of walking frequencies (Ngan, et al., 2016). Therefore, the model updating considers the dynamic properties of the first three modes of vibration. The mode shapes (TMDs) and natural frequencies are selected as the target output metrics of the updating process (i.e. $\mathbf{R}_m$ and $\mathbf{R}_k$ of Equation 7).

Two updating processes are conducted. (Denoted as Case 1 and Case 2). Each case considers different output metrics for updating. For Case 1 the updating only consider the mode shape's TMDs while Case 2 consider both TMDs and natural frequencies.

The model updating and TMD algorithm is carried out in MATLAB. A Visual Basic (VB) program was written to carry out inter-Object-Communication (COM) between MATLAB and the FE software, LUSAS. The key processes in this model updating are outlined in this section.

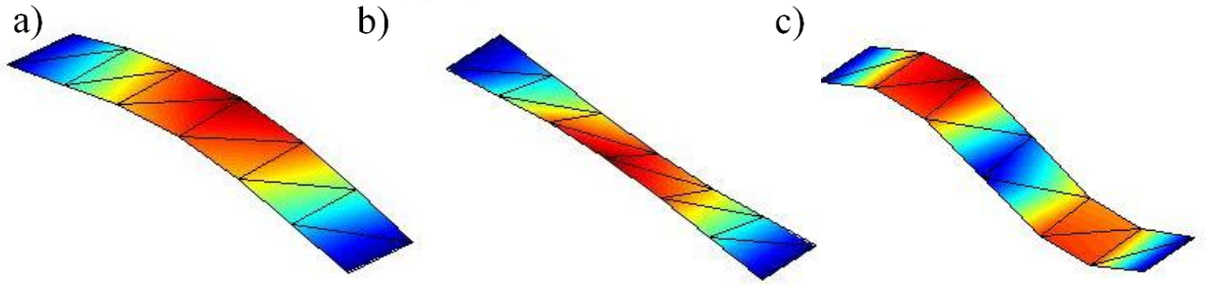


Figure 6. First three modes of vibration obtained from shaker test: (a) f = 5.86 Hz, (b) f = 10.02, (c) f = 18.14 Hz.

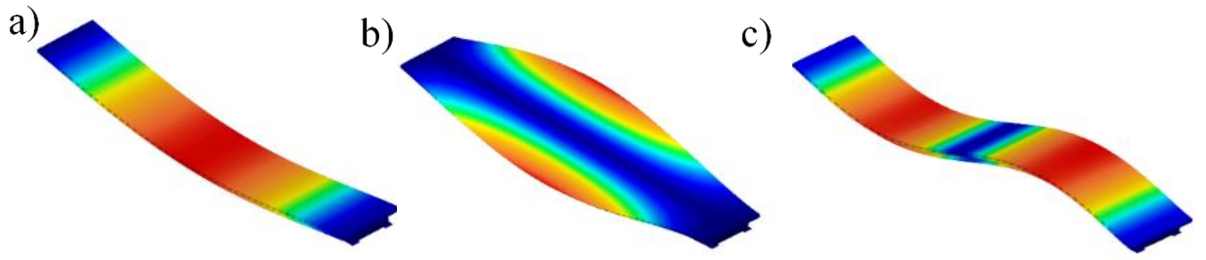


Figure 7. First three modes of vibration from FE model (a) f = 5.95 Hz, (b) f = 9.62 Hz, (c) f = 20.27 Hz.

4.1 *FE Model parameterization*

The results from the five experimental modal analyses suggest an imbalanced longitudinal stiffness that is balanced out by the mass loading of the shaker. Since the longitudinal stiffness is mainly contributed by the I-beam girders, the imbalanced stiffness must originate from properties related to the I-beams. Two possible explanations for this are: (1) poor bond quality between the I-beam girder and deck, resulting in a lack of composite action, or; (2) different material properties of the two longitudinal I-beams, perhaps due to different manufacturing runs of the sections. Both potential causes can be represented as a lowered elastic modulus for the affected beam; i.e. beam 1 in Figure 3.

To capture the effect of a differing elastic modulus of some of the GFRP components, the bridge is parameterized into three regions: the longitudinal elastic modulus of each I-beam (denoted as E_{beam1} and E_{beam2}), and the deck components (denoted as E_{deck}).

To correlate the shaker test results, the shaker mass is introduced in the FE model. A non-structural mass is implemented to represent the 52 kg shaker mass on the deck of the FE model similar to position 1 in Figure 8). The natural frequencies of the FE model after modelling of the shaker mass are summarized in Table 3 following the presentation of the updating results.

4.2 *Mode shape image interpolation*

In previous works (Wang, Mottershead, Ihle, et al 2011), full-field measurement of mode shapes are obtained through 3-D scanning vibrometers. Full-field measurements provide finer resolution of mode shape information compared to traditional spatially-discrete measurements from accelerometers. In turn, the use of TMDs on full-field mode shapes are more prevalent. Nevertheless, in this work only discrete measurements were taken at the grid points noted in Figure 3.

Due to the lack of full-field measurements, the full-field experimental mode shapes are interpolated from the discrete measurement points (accelerometers). This is conducted by first representing the pixels correspond to position of discrete measured points as the equivalent image intensity. Image intensity is represented by a greyscale with black (pixel value of 0) representing global minimum and white representing global maximum (pixel value of 1) of a mode shape. Then, the pixels of the remainder (un-measured region) of the mode shape image are obtained using spline interpolation of the discrete measured pixels, which preserves shape smoothness resulting in a continuous mode shape field. This is important for the comparison with FE mode shapes which are smooth continuous mode shapes generated from LUSAS.

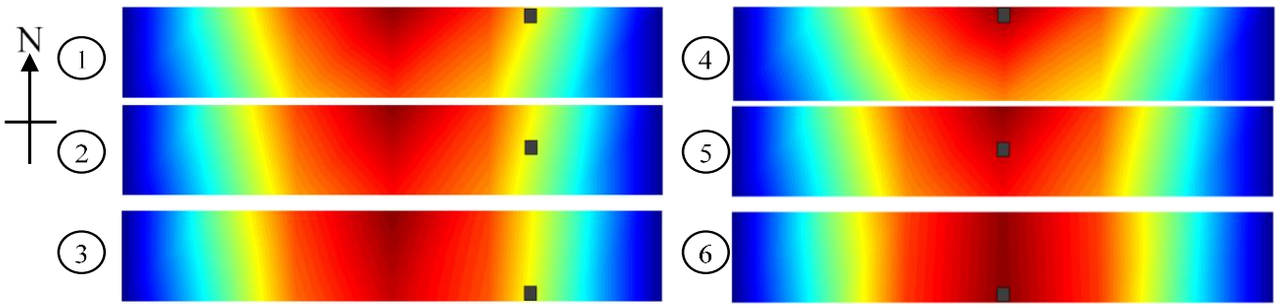


Figure 8. Top view of first vertical mode shape from EMA for each considered shaker position (Grey box denotes the shaker) (Not to scale). Position 1 was the initial shaker position.

4.3 *Tchebichef shape features of mode shapes*

To describe the features of mode shapes, top views of both FE and experimental mode shapes (similar to Figure 8) are obtained. These are then each decomposed into 30 Tchebichef moment descriptors. The first seven are shown in Figure 9

The TMD decomposition results, showing the magnitude of each TMD, for the first three FE mode shapes are given in Figure 10 as an example. As can be seen, several TMDs for each mode shape are significant. For example, mode 1 is predominantly the 6th Tchebichef feature (TMD 6 in Figure 9). More importantly, the localized feature of the modes can be detected through the TMDs, which is not possible using the MAC. Similar to Wang, Mottershead, Ihle, et al (2011), the dominant TMDs can be selected to perform model updating. In this study, the first six maximum TMDs are selected.

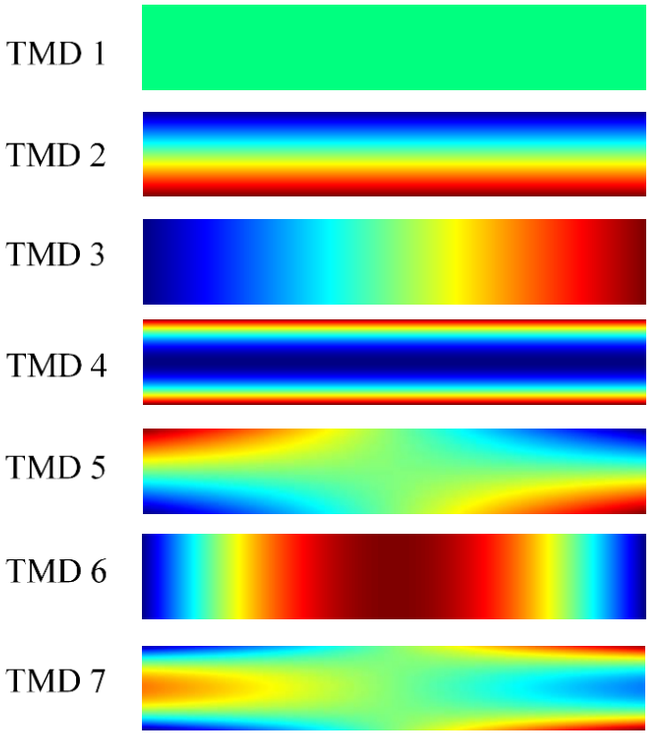


Figure 9. Example Tchebichef Moment Descriptors.

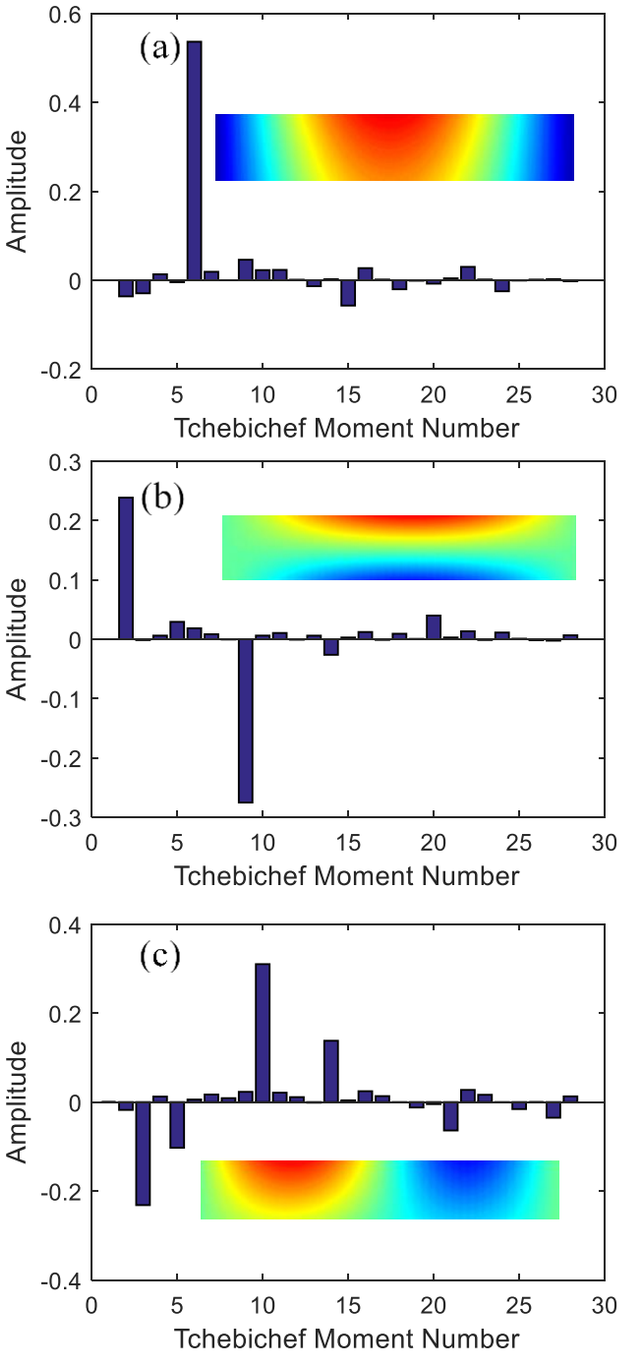


Figure 10. TMDs of FE mode shapes: a) first b) second and c) third mode.

It should be noted that the magnitudes of TMDs between experimental and FE mode shapes are different. This is because mode shapes are generated from different source, i.e. FE mode shapes from LUSAS

and the experimental mode shapes from MATLAB have different image intensity and size. To resolve this for comparison in model updating, the TMD amplitudes from each source are normalized (Wang, Mottershead, Ihle, et al 2011).

4.4 *Validation of framework*

To validate the model updating framework, a simulated model updating is conducted. The simulated updating aims to reproduce a known reduced stiffness by pre-defining a lowered elastic modulus for the model parameters. For this, a set of TMDs (similar to Figure 10) were obtained using values for parameters E_{beam1} and E_{beam2} as 15 GPa and 24 GPa respectively. The starting values of parameters E_{beam1} and E_{beam2} are 22 GPa and 24 GPa respectively. The parameter updating histories of the simulated updating is shown in Figure 11. It is observed that the parameter converges to the prescribed solutions within eight iterations. Consequently, the proposed model updating framework is verified as being applicable for the closely-related experimental specimen.

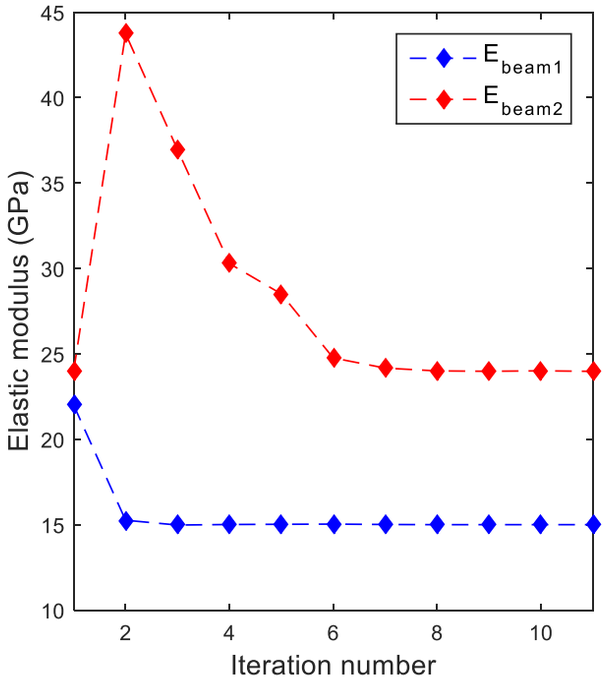


Figure 11. Model parameter updating history - simulated case.

5 RESULTS AND DISCUSSION

The results of the two model updating cases as mentioned previously are given. In both cases, the starting values for E_{beam1} and E_{beam2} are 22 GPa and 24 GPa respectively.

For Case 1 (using TMDs only), the parameter updating histories is shown in Figure 12. The parameters E_{beam1} and E_{beam2} converged to values of 20.3 GPa and 25.9 GPa respectively.

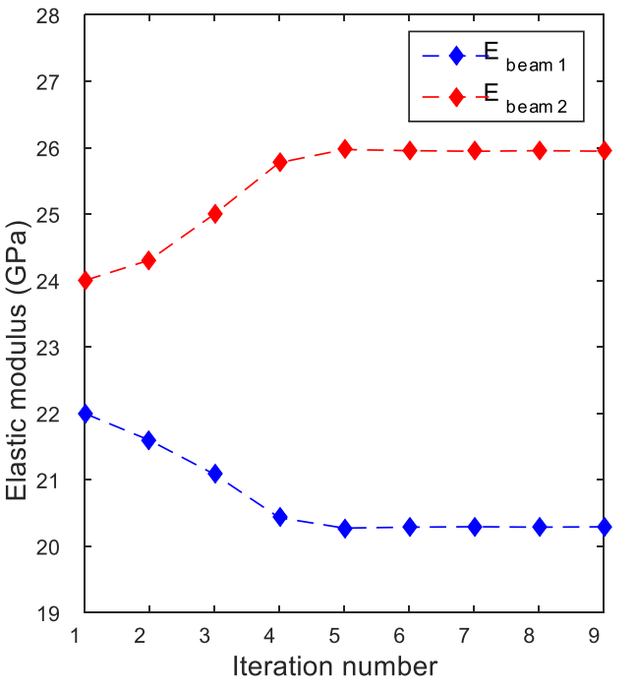


Figure 12. Parameter updating history of Case 1

For Case 2 (using both natural frequencies and TMDs), the parameter updating histories are shown in Figure 13. The values of parameters E_{beam1} and E_{beam2} converged to 30.6 GPa and 42.5 GPa respectively.

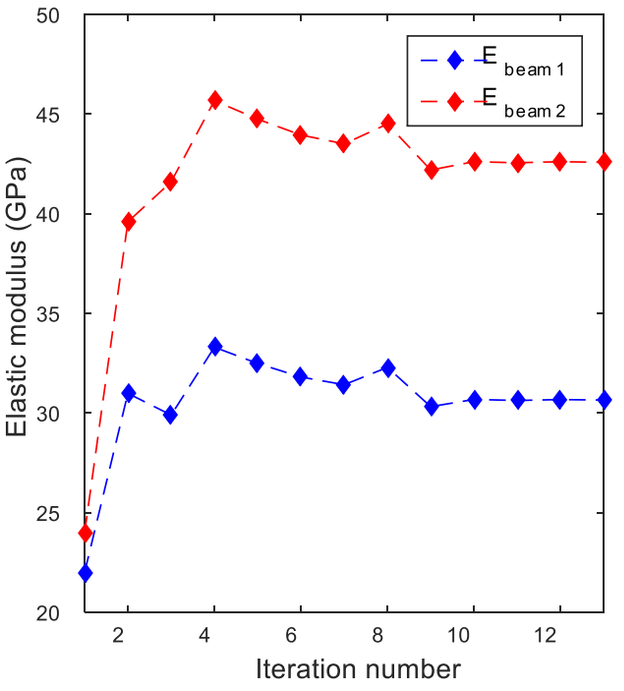


Figure 13. Parameter updating history of Case 2

5.1 *Comparison of Updated FE models*

The natural frequencies extracted from the updated models of both cases are summarized in Table 3. The results show that the updated model from Case 2 gives better natural frequency prediction than Case 1. This is intuitive since natural frequencies are included in the model updating objective. However, the changes in parameter values of Case 2 are physically

not meaningful. The variation of parameters E_{beam1} and E_{beam2} are too significant and are beyond physical range of GFRP material properties (i.e. ±20% from Ye, et al (1995)). This suggests possible modelling uncertainties in the FE model which are not considered in the model updating. Consequently, the values of parameters E_{beam1} and E_{beam2} are updated to physically non-meaningful values to compensate for natural frequencies objectives.

Table 3. Comparison of natural frequencies

		FE model	Updated FE model	
Mode	Experimental	Initial[1]	Case 1	Case 2
1	5.86	5.29	5.35	5.99
2	10.02	9.23	9.28	9.71
3	18.14	16.68	16.85	18.81
4	20.60	20.83	21.02	22.71
5	25.60	23.99	24.17	25.78

1: After shaker mass incorporated

Indeed, the results from Case 1 and 2 indicate a reduced longitudinal stiffness which can be caused by several factors such as imperfect bonding connection or GFRP material properties. Despite the exclusion of natural frequencies in Case 1, the model updating nonetheless improves the structural representation of the FE model.

6 CONCLUSION

This paper considers a model updating framework which correlates mode shape features using TMDs. The TMDs can discriminate shape features of the mode shapes, most notably localized shape features that is not possible using a traditional scalar indicator, i.e. the MAC. The experimental results of the GFRP footbridge suggest the existence of reduced stiffness of the I-beam girders. Consequently, this results in localized mode shapes in the footbridge. The proposed model updating framework is implemented to improve the natural frequency correlation and structural behavior representation of the FE model, i.e. reduced structural stiffness.

Full-field measurements give two-dimensional mode shape information at a fine resolution. As such, the TMDs from full-field mode shapes are more prevalent. However, in this study, approximated mode shapes are used in place of full-field measurements. A useful outcome of this work is that TMDs coupled with approximated mode shape measurements provide superior information to traditional scalar mode shape estimators (e.g. the MAC). The updating results show that the suggested model updating framework can update the FE models in a meaningful way using approximated mode shapes. Further work should be carried out to investigate the performance of the model updating framework on approximated mode shape against full-field measurements. Nonetheless, it is instructive that the updating results show the capability of the TMD-based model updating to be an improvement on traditional model updating processes for GFRP structures. As such, this form of model updating should find good use in examining GFRP structures in the field.

REFERENCES

Allemang, R. J. & Brown, D. L., 1982. *A correlation coefficient for modal vector analysis.* s.l., s.n., pp. 110-116.

Anon., 2015. *FEMtools theoretical Manual, Version 3.8.2.* Belgium: Dynamic Design Solutions, Lueven.

Anon., n.d. *LUSAS User Manual v15-2.0.* s.l.:s.n.

Bank, C. L., 1993. Fibre Reinforced Plastic (FRP) reinforcement for Concrete structures: Properties and application. pp. 56-86.

El-ghazai, A., Basir, O. & Belkasim, S., 2009. *Scale invariant of Radial Tchebichef Moment for Shape-based Image Retrival.* s.l., s.n.

Frisswell, M. I. & Mottershead, J. E., 1995. *Finite element model updating in structural dynamics.* Dordrecht: Kluwer Academics .

Kim, D. O. & Lee, I. W., 1998. A study on mode localization phenomena: Influences of the stiffness and the mass of the couper on mode localization. *Journal of Sound and Vibration ,* 216(1), pp. 53 - 73.

Mukundan , R., Ong, S. H. & Lee, P. A., 2001. Image analysis by Tchebichef moments. *IEEE Trans. Image Processing,* Volume 10, pp. 1357- 1364.

Ngan, J. W., Caprani, C. & Bai, Y., 2016. *Dynamic Performance Assessment of a Novel Pultruded Fibre Reinforced Polymer Footbridge.* s.l., s.n.

Reynders, E., Schevenels, M. & Roeck, G. D., 2014. *MACEC User's Manual.* s.l.:Report BWM.

Wang, W. Z. et al., 2011. Finite element model updating from full-field vibration measurements using digital image correlation. *Journal of sound and vibration,* 330(8), pp. 1599-1620.

Wang, W. Z., Mottershead, J. E. & Mares, C., 2009a. Mode shape recognition and finite element model updating using the Zernike Moment Descriptor. *Mechanical Systems and Signal Processing,* Volume 23, pp. 2099-2112.

Wang, W. Z., Mottershead, J. E. & Mares, C., 2009b. Vibration mode shape recognition using image processing. *Journal of Sound and Vibration,* 326(3-5), pp. 909-938.

Wang, W. Z. et al., 2013. *Model updatingusing Shape Descriptors from full-field images.* s.l., s.n., pp. 425-436.

Wang, W. Z., Mottershead, J. E., Sebestian, C. H. & Patterson, E. A., 2011. Shape features and finite element model updating from full-field strian data. *International journal of Solids and Structures,* 11(12), pp. 1644-1657.

Ye, B. S., Svenson, A. L. & Bank, L. C., 1995. Mass and volume fraction properties of pultruded glass fibre-reinforced composites. *Composites,* Volume 26, pp. 725-731.

Zivanovic, S., Feltrin, G., Mottram, J. T. & Brownjohn, J. W., 2014. *Vibration Performance of Bridges Made of Fibre Reinforced Polymer.* Orlando, USA, s.n.

Maintenance, Safety, Risk, Management and Life-Cycle Performance of Bridges – Powers, Frangopol, Al-Mahaidi & Caprani (Eds)
© 2018 Taylor & Francis Group, London, ISBN 978-1-138-73045-8

Vibration Serviceability Assessment of a Multi-Span Footbridge

J.W. Ngan, C. Caprani
Department of Civil engineering, Monash University, Melbourne Australia

A. de Lacy
WSP Australia Pty Limited

ABSTRACT: Footbridge designs are becoming ever more innovative and creative. This can result in footbridges with structural forms that are complicated and slender, and so potentially lively. Serviceability problems due to excessive vibrations have been reported in many recent footbridges. Further, current vibration serviceability approaches can be overly-conservative resulting in unattractive changes to designs. This paper evaluates the vibration serviceability of a multi-span footbridge (denoted as NB Bridge) using a novel approach. The NB Bridge is modelled as a 1-D beam model using finite elements (FE) method. This model is calibrated against a complete 3-D structural model of the bridge using model updating techniques. Moving loads are applied to the bridge model to simulate crossing of random (1) single pedestrian, and (2) pedestrian crowds. Vibration serviceability is evaluated using current guidelines, namely the European Guideline HiVoss (2008) and French Guideline Setra (2006), both of which are commonly applied in practice. This paper therefore illustrates this 1-D finite element beam modelling approach for vibration serviceability assessment of footbridges with similar complexity.

1 INTRODUCTION

1.1 *Background*

The advancement of engineering technology and greater understanding of construction materials have led to footbridges that are longer, lighter, and more aesthetically pleasing. Some of these footbridges can be quite slender, potentially leading to serviceability problems due to excessive vibrations. This usually occurs when the natural frequencies of the structure are within harmonic range of pedestrian pacing frequencies. Moreover, vibrations can be further amplified when large crowds crossing the structure are in sync with one another. Over the last decade or so, numerous vibration serviceability problems in footbridges have been reported, including some well-known cases such as the Millennium Bridge, London (Dallard, et al., 2001), the T-bridge, Japan (Fujino , et al., 1993) and the Pont du Solferino, Paris (Danbon & Grillaud, 2005). For most footbridges with vibration serviceability problems, pedestrian loads are usually the main source of loading leading to vibrations. Consequently, this has drawn much research attention on developing reliable techniques to better predict human-induced vibrations in footbridges.

To predict human-induced vibrations, dynamic forces of pedestrians can be modelled analytically as time-varying forces acting on footbridges (Živanović, et al., 2005). This state-of-the-practice approach has been commonly adopted and has received much research attention. Consequently, design guidelines and codes have also adopted the moving force approach to define design procedures (Caprani & Ahmadi, 2016). For example, this approach has been adopted in the European guideline HiVoss (2008) and French guideline Setra (2006). However, there is lack of moving force validation for different footbridge designs, particularly for new innovative footbridge designs. As a result, current guidelines may result in overly conservative vibration predictions. This may result in unattractive footbridge design changes or costly vibration control solutions to satisfy vibration serviceability needs. With increasing pressure for more aesthetically pleasing footbridges, the need to understand the applicability of the moving force approach for vibration serviceability of innovative footbridge designs is becoming increasingly important. However, works to update this knowledge are still limited. This is important for the vibration assessment of new footbridges, particularly for landmark bridges.

The work presented here evaluates the vibration serviceability of a proposed multi-span footbridge (denoted the NB Bridge) using a combined approach. The work is based on a finite element moving force modelling approach, and uses model updating to facilitate the use of a simple beam model of the structure. The work here is instructive for the performance of the current state-of-the-art on vibration serviceability for different footbridges and crowd considerations.

1.2 *The NB Bridge Structure*

The NB Bridge is a 270 m long cable-stayed footbridge (Figure 2). The superstructure of the bridge is a concrete-steel composite deck supported by steel girders on each side. The bridge has three spans: two cable-supported spans and a middle span between the mid-river piers. The longest cable-stayed span has a length of 126 m and is supported by 5 cables as shown in Figure 2a.The width of the bridge deck is 5 m and

widens at the middle span from 5 m to 15 m (Figure 2). The deck of the NB Bridge has a mass of 4150 kg/m for the narrower deck and 10240 kg/m for the wider deck. The calculated bending stiffness, *EI* of the composite section for the 5 m width deck is 1.248×10^{10} N m^2.

2 NUMERICAL MODELLING

2.1 *Basis*

The complex form of the NB Bridge (Figure 2) needs a three-dimensional (3-D) finite element model to accurately capture the global behavior, incorporating cable pre-stress and mast structure for example. This model is developed in commercial FE software, which does not have the capability to represent moving force crowd models. For this, an in-house 1-D beam model is used with the moving force crowd model. The key challenge then, is to replicate the dynamic behavior of the full 3-D model within the 1-D beam model. This challenge is met using model updating to match natural frequencies and mode shapes between the models by tuning key parameters of the 1-D beam model. By doing so, the complexity of the 3-D model is then inherent in the 1-D beam model.

It is acknowledge that some commercial FE software has the capability to export FE model properties into a general format which can be used by other FE software, avoiding the need for the model updating process. However, to date, the in-house 1-D beam model is yet to have the capability to utilize general formats of FE models from other software. Therefore, the aforementioned model updating approach is adopted in this study.

2.2 *3-D Finite Element Model*

Figure 1 shows the 3-D model of the NB Bridge. The deck is modelled using 1-D beam elements with end releases and offsets as appropriate to reflect the intended deck cross-sections. 2-D shell elements are considered across the deck to model the stiffness associated with the concrete deck. Mast structure is modelled using 1-D beam elements of tapering cross-sections. The cables are modelled as linear-elastic 1-D beam elements of equivalent axial stiffness anchored at both sides of the deck. The mass of the 3-D model reflects the self-weight, super-imposed dead loads, and a reduced live load equivalent to a pedestrian density of 0.5 ped/m^2.

2.3 *Initial 1-D Finite Element Beam Model*

In the in-house 1-D beam model, the deck of the NB Bridge is modelled using 141 Euler-Bernoulli beam elements which have Hermitian interpolation shape functions and two degrees-of-freedom per node (vertical translation and rotational about node). Nodes of the 1-D beam model are located at feature points (bridge points in Figure 2a). The element sizes are approximately 2 m, spaced evenly between the feature points. The mast piers (blue lines in Figure 2) of the NB Bridge are not considered in the 1-D beam model, but their effects are implicitly included by the model calibration. The beam model has lumped mass assumed. Equivalent beam properties (bending stiffness and mass) are implemented to define the mass and stiffness matrices of the beam elements.

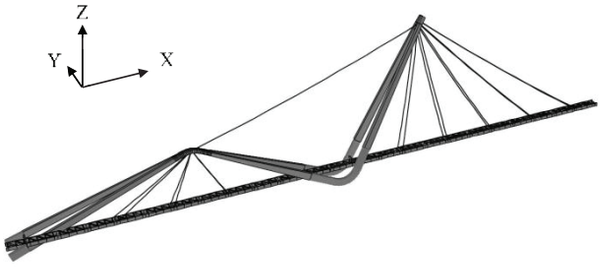


Figure 1. 3-D FE model of the NB Bridge.

The cable supports are modelled as additional vertical spring stiffness at corresponding vertical nodal degree-of-freedoms in the beam model (Figure 2). This additional stiffness is a representative surrogate to model the effect of the cables in the 1-D beam model. Modelling of cable support stiffness is initially taken as 1×10^6 N/m for all cables. The damping ratio of the NB Bridge is taken as 0.5% for the first two modes, this is based on bridge damping ratios reviewed by Heinemayer et al. (2009) for footbridges with similar complexity. Rayleigh damping is assumed thereafter to obtain the damping matrix.

2.4 *Single pedestrian Modelling*

Pedestrian induced forces are represented by the moving force model which is a periodic force represented by a Fourier series (Bachmann, et al., 1995):

$$G(t) = W \sum_{k=0}^{r} \eta_k \cos(2\pi k f_p + \varphi_k) \quad (1)$$

where $W = m_p g$, m_p is the mass of pedestrian, f_p is the pacing frequency, r is the number of harmonics, η_k and ϕ_k are the dynamic load factor (DLF) and phase angle respectively. Reasonably, it is assumed that the moving pedestrian force maintains contact with the beam surface throughout the crossing (i.e. continuous contact force). The number of harmonics, DLFs and phase properties varies between different authors.

This work considers Young's DLFs for up to four contributing harmonics (Young, 2001). The phase angle for each harmonic is taken as uniformly random in the interval 0 - 2π.

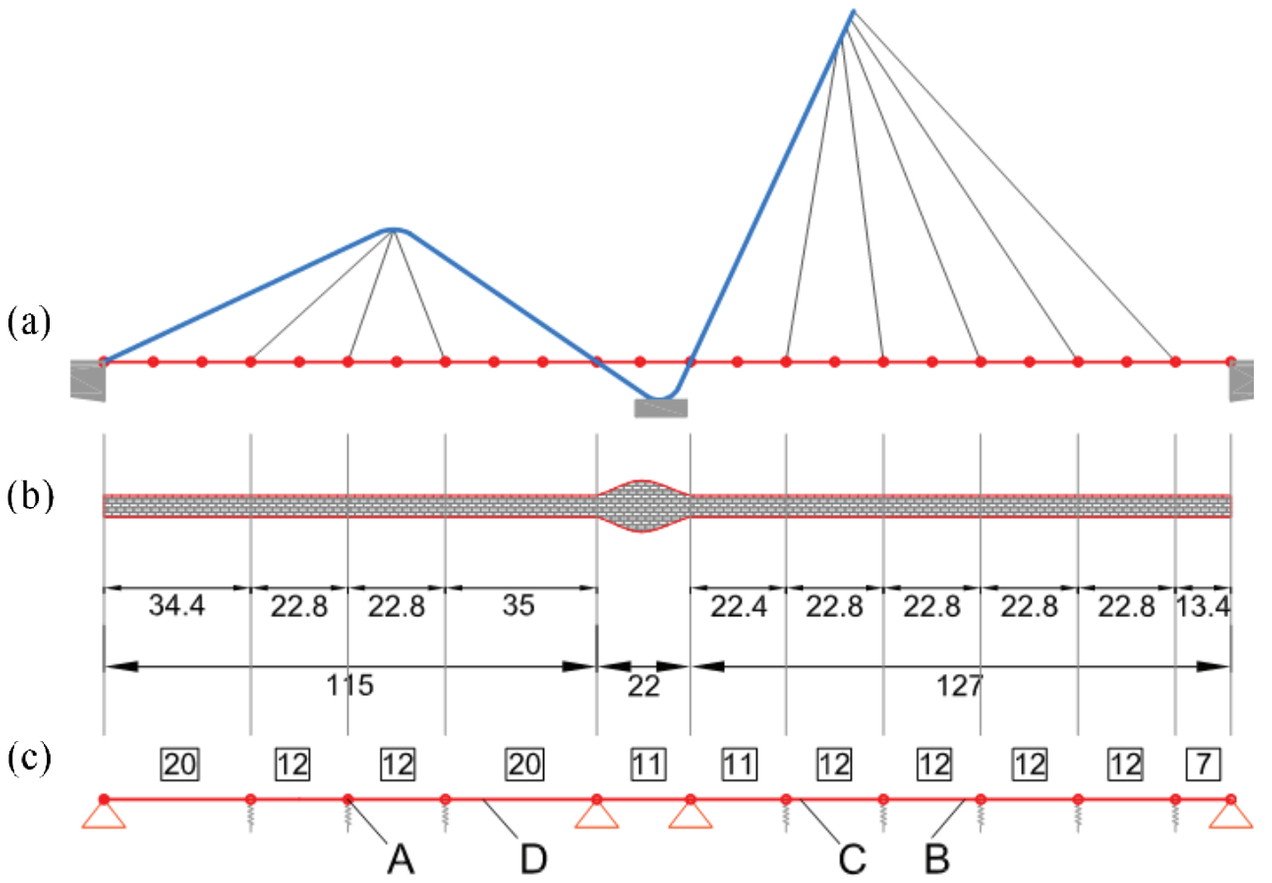


Figure 2. The NB Bridge: (a) elevation, showing points used for defining the mode shapes from the 3-D model (red dots); (b) plan view of deck, with key dimensions; (c) 1-D finite element beam model showing rigid supports and cable spring stiffness supports along with the number of Euler-Bernoulli elements used in each sub-section in boxes.

As a constant pedestrian velocity, v is assumed, the position of the moving pedestrian force at time t in Equation (1) is distributed to adjacent nodes of beam elements according to a global shape function. As will be required later, the global shape function is given with respect to velocity and time:

$$\mathbf{N}(vt) = \{0_{1\times4} \ldots \mathbf{N}^j(vt) \ldots 0_{1\times4}\} \tag{2}$$

where $\mathbf{N}^j$ is the Hermite shape function for the jth element for which the pedestrian force is located (Caprani & Ahmadi, 2016). When the pedestrian moves off the structure, this shape function becomes zero. The equations of motion are therefore written as:

$$\mathbf{M}\ddot{\mathbf{d}} + \mathbf{C}\dot{\mathbf{d}} + \mathbf{K}\mathbf{d} = \mathbf{N}^T(vt)G(t) \tag{3}$$

where $\mathbf{d}$, $\dot{\mathbf{d}}$ and $\ddot{\mathbf{d}}$ are the vectors of displacement, velocity, and acceleration; $\mathbf{M}$, $\mathbf{C}$, $\mathbf{K}$ are the mass, damping, and stiffness matrices of the beam model respectively. Transient solutions from equation (3) are obtained using Newmark-β integration.

In this work, random characteristics for pedestrians are generated using different distributions for pedestrian walking parameters. Pedestrian's pacing frequency, f_p is considered as normally distributed with mean and standard deviation of 1.96 Hz and 0.21 Hz respectively (within normal range of walking frequencies of 1.8 – 2.2 Hz (Živanović, et al., 2005)). The pedestrian mass, m_p is represented by a log-normal distribution with mean and standard deviation of 73.85 kg and 15.68 kg respectively (Portier, et al., 2007). The step length is taken to be normally distributed with mean and standard deviation of 0.66 m (Barela & Duarte, 2008) and 0.066 m (coefficient of variation of 10%) (Caprani, et al., 2012). Pedestrian velocity, v is obtained from the product of step length and pacing frequency.

Worth noting, is that the moving force model does not consider any mass or stiffness interaction between moving pedestrian and bridge structure (Živanović, et al., 2005; Caprani, et al., 2012).

2.5 *Crowd Modelling*

The forces on the NB Bridge due to a crowd at any point in time is taken as the superposition of individual pedestrian forces from Equation (1). The equation of motion of a crowd loading is simply an extension of Equation (2), considering the forces imparted by each pedestrian:

$$\mathbf{M}\ddot{\mathbf{d}} + \mathbf{C}\dot{\mathbf{d}} + \mathbf{K}\mathbf{d} = \sum_{i=1}^{n} \mathbf{N}_i^T(v_i t)G_i(t) \tag{4}$$

in which $\mathbf{N}_i(v_i t)$ is the global shape function vector calculated for the position of ith pedestrian at time t. Other variables are as defined previously.

The characteristics of each pedestrian in the crowd are generated as described previously. Different crowd densities have been considered in the literature (Bachmann & Ammann, 1987). A crowd density of 0.5 ped/m^2 (following Setra (2006)) is considered to represent a medium crowding scenario. The total number of pedestrians in the crowd is calculated by taking products of crowd density with crowd length and width. The crowd length and width are taken as 500 m and 5 m respectively, so that the bridge will be wholly covered for a time, even allowing for random walking speeds. This corresponds to 1250 pedestrians in total. An exponential distribution with mean of 0.56 m is used to describe the intervals of pedestrian arrival (Caprani, et al., 2012). The velocity of each pedestrian is determined from their individual step length and pacing frequencies. In this simulation, pedestrians with different velocities are free to overtake each other. Crowd synchronization effects (i.e. instances where two or more pedestrians have the same pacing frequency) is considered in the crowd modelling, similar to Colin & Ahmadi (2016). For this work, a synchronization level of 20% (following Fujino et al. (1993)) is considered for all crowd simulations, (i.e. at most 20% of pedestrian forces on the bridge model at any time instance will have their pacing frequencies be in-sync).

3 MODEL CALIBRATION PROCEDURE

As noted earlier, the dynamic properties of the NB Bridge from the 1-D beam model are calibrated against those obtained from a full three-dimensional finite element model of the NB Bridge (referred to as 3-D model). Specifically, the natural frequencies and mode shapes are matched to those of the 3-D model. For comparison of mode shapes, the mode shape vertical displacements from the 3-D model are extracted at positions along the centerline of the deck, identified as red points in Figure 2a. It is acknowledged that use of even a calibrated 1-D modelling app roach retains yet some approximations. Nevertheless, once a reasonably conservative serviceability criterion is adopted, the results are meaningful for a crowd vibration serviceability assessment.

3.1 *Initial dynamic properties*

Figure 3 shows the dynamic properties i.e. natural frequencies and mode shapes of the first four modes of vibration from the initial 1-D beam model and 3-D model with the mode shapes overlaid on each other. Interestingly the sequence of mode shapes are in good agreement with those of the 3-D model. However, large differences in natural frequencies are observed, with the 1-D beam model under-predicting the natural frequencies. Further, mode shape displacements are not well-correlated for some modes. The Modal Assurance Criterion (MAC) (Allemang & Brown, 1982) is calculated for the mode shapes and are summarized in Table 2 following the calibration procedure.

The large errors in dynamic properties from the initial 1-D model are expected of course, and due to the unknown spring stiffnesses required to match the effects of the cables, pre-stress, and mast behaviors. Initially, the uniform spring stiffness value (1×10^6 N/m) defined for all cable supports clearly needs to be updated to properly capture the 3-D model behavior.

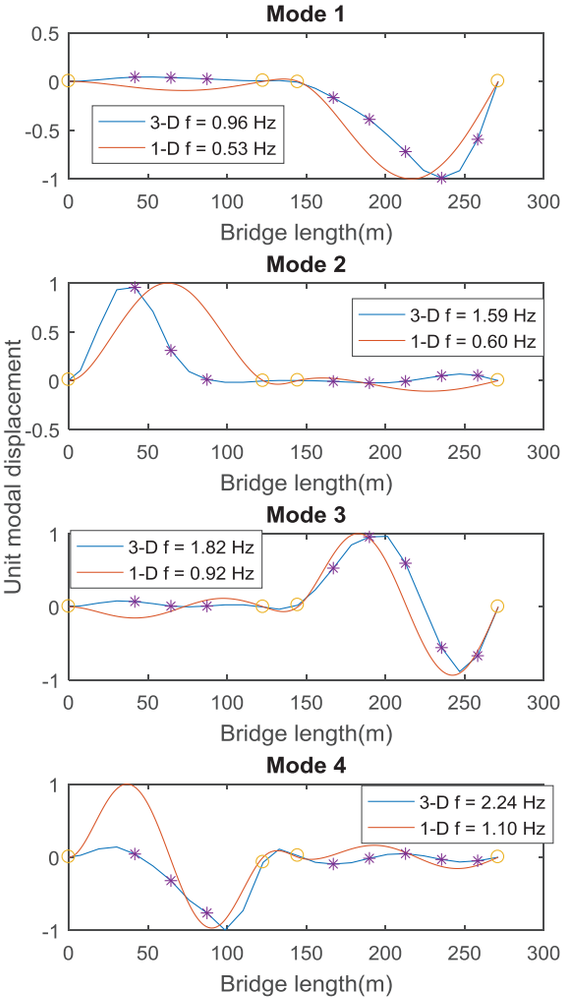


Figure 3. Comparison of modal properties from Initial 1-D beam model and 3-D beam model (* denote cable supports, o denote pier supports).

3.2 *Model updating*

The large difference between dynamic properties from both models are reconciled through finite element model updating (Frisswell & Mottershead, 1995). In structural dynamics, model updating is an iterative method which uses the sensitivity of model responses to each parameter to optimize model parameters until a good agreement of dynamic (modal) properties is achieved. Model updating procedures

have been well-described by Friswell and Mottershead (Frisswell & Mottershead, 1995) and can be found summarized in past papers (Živanović, et al., 2007). Therefore, details on model updating are not outlined in this paper.

In each iterative updating step, the sensitivities of the *i*th FE model outputs, **R**, to changes in the *j*th input parameters, **P** (e.g. mode shape, and natural frequencies), are computed. For consistency of units between different parameters and outputs, a normalized sensitivity matrix is considered. The normalized sensitivity matrix **S** (of dimension $i \times j$) is calculated for iteration k as (Frisswell & Mottershead, 1995):

$$\mathbf{S}_k = \left[S_{ij}\right] = \left[R_{ii}\right]^{-1} \left[\frac{\delta \mathbf{R}_i}{\delta \mathbf{P}_j}\right] \left[P_{jj}\right] \tag{5}$$

where $\delta\mathbf{R}$ is the difference in measureable outputs of the FE model due to an increment in model parameters $\delta\mathbf{P}$, for response i, and parameter j. R_{ii} and P_{jj} are diagonal, square matrix holding the initial output and parameter values respectively.

For this work, the 1-D beam model is updated using the dynamic properties of the first four modes of vibration. The dynamic properties i.e. natural frequencies and mode shapes (MAC) from the 3-D model are taken as the target properties for updating. The 8 cable spring stiffness in the 1-D beam model are selected to be optimize during the updating process.

3.3 *Updated dynamic properties*

The updated cable stiffness are given in Table 1. The modal properties of the updated 1-D beam model are given in Table 2, along with a comparison to those of the initial 1-D beam model and 3-D model.

Table 1. Spring stiffness parameter changes.

Cable	Initial ($\times 10^6$ N/m)	Updated ($\times 10^6$ N/m)
1	1	9.18
2	1	11.8
3	1	34.5
4	1	21.0
5	1	11.9
6	1	4.56
7	1	2.49
8	1	16.3

The results show that the updated 1-D beam model overall produce improved natural frequencies, in good agreement with the natural frequencies from the 3-D model. The MAC values improved significantly (> 0.9) from the initial model, showing that the updated 1-D beam model produces quite accurate mode shapes (compared to the 3-D model). From Figure 4, it is evident that the mode shapes are in far better agreement than the initial 1-D beam model. As such, the model updating procedure is demonstrated to be feasible for tuning a 1-D model to represent more complex 3-D behavior, at least in one direction, as is considered for this work (vertical).

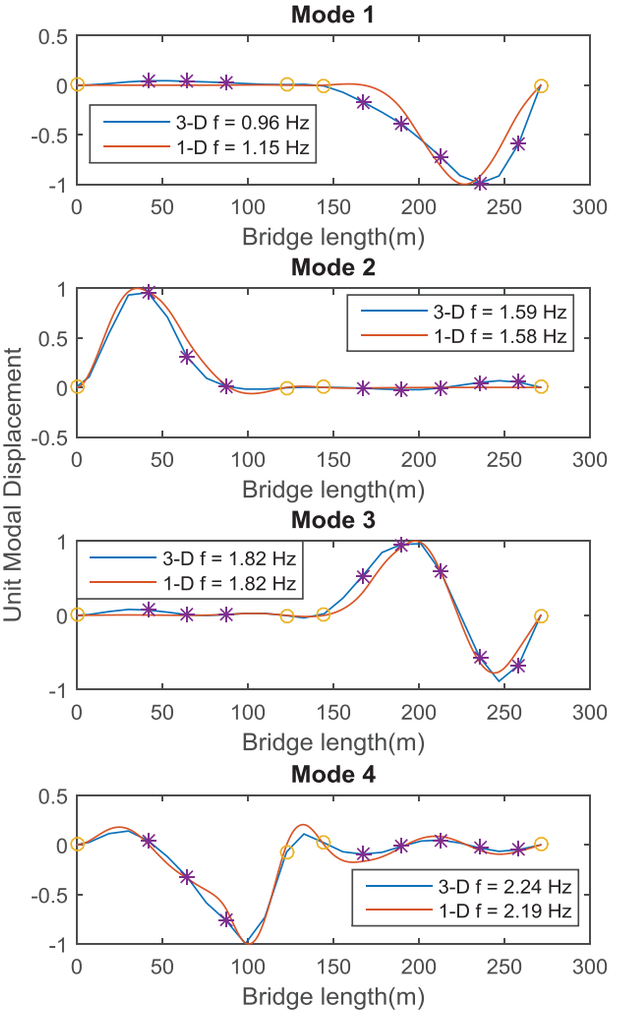


Figure 4. Comparison of modal properties from Updated 1-D beam model and 3-D beam model (* denote cable supports, o denote pier supports).

Table 2. Comparison of natural frequencies from models.

	3-D	Initial 1-D			Updated 1-D		
Mode	Hz	Hz	NFD %	MAC	Hz	NFD %	MAC
1	0.96	0.53	44.8	0.86	1.15	-19.8	0.96
2	1.59	0.60	62.2	0.49	1.58	0.6	0.99
3	1.82	0.92	49.5	0.79	1.82	0.0	0.96
4	2.24	1.10	50.9	0.48	2.19	2.2	0.95
5	2.31	1.71	26.0	0.86	2.25	2.6	0.94
6	2.71	1.98	26.9	0.84	2.50	7.7	0.96
7	3.20	2.86	10.6	0.93	3.45	-7.8	0.95
8	3.52	3.22	8.5	0.94	3.54	-0.5	0.93
9	4.49	4.32	3.8	0.81	4.63	-3.1	0.84
10	5.44	4.83	11.2	0.74	5.32	2.2	0.74

NFD%: Natural frequency difference.

From Table 2, the first updated natural frequency error is found to be outstanding (10% greater than all other natural frequency difference), suggesting that tuning vertical spring stiffnesses may be insufficient to match this natural frequency. This also suggest that

there are other parameters in the 3-D model that influences the first mode, which could not be considered in the 1-D beam model. Such parameters can be related to mast pier effect for example. Nevertheless, this error is justifiable since the first natural frequency is less likely to result significant resonance from pedestrians (i.e. not within range of walking frequencies).

4 VIBRATION SERVICEABILITY ASSESSMENT

Following the calibration process, the moving force analysis is performed on the updated 1-D beam model to obtain vibration responses due to single pedestrian and crowds, modelled as described earlier.

4.1 *Considered vibration responses*

Acceleration responses are the common measures for vibration responses. In this work, only the vertical acceleration responses is of interest. This is taken as the 1-s root-mean-squared (RMS) acceleration of the 1-D beam model. The metric for any particular scenario (single pedestrian or crowd) is taken as the maximum 1-s RMS value of that response over the duration of the scenario. Four locations of this response are considered, as given in Table 3.

The selection of output locations is justified as follows. Clearly, the accelerations at the mid-spans of the two cable spans are relevant (points A and B in Figure 2c). Two more points are considered also though. Several modes of vibration from the 1-D beam model, most notably modes 3 and 4 coincide with normal range of walking frequencies (1.8- 2.2 Hz). This suggests that pedestrian walking may have a significant resonance at these modes. Therefore, the locations of the maximum modal ordinates of modes 3 and 4 are also selected (C and D in Figure 2c).

Table 3. Considered vibration response locations.

Point	Description
A	Mid-span of left cable supported span
B	Mid-span of right cable supported span
C	Maximum modal displacement of mode 3
D	Maximum modal displacement of mode 4

4.2 *Evaluation of vibration serviceability*

Maximum acceleration limits are recommended in codes and design guidelines. The predicted vibration responses of the NB Bridge are evaluated against those of the European guideline HiVoss (2008) and French Setra (2006) guideline. For structures with first natural frequency less than 5 Hz, the acceleration limits for maximum and mean comfort level are 0.5 m/s^2 and 1 m/s^2 respectively.

4.3 *Random Single Pedestrian Response*

Figure 5 illustrates the acceleration time history at point A of the NB Bridge to a single pedestrian traversing the structure. A total of 1000 single pedestrian simulations are conducted using the random characteristics mentioned previously. The distributions of the 1000 maximum RMS responses for the four points of interest are given in Figure 7. The characteristic responses are defined as the 95 percentile value of the distributions and are also given in Figure 7.

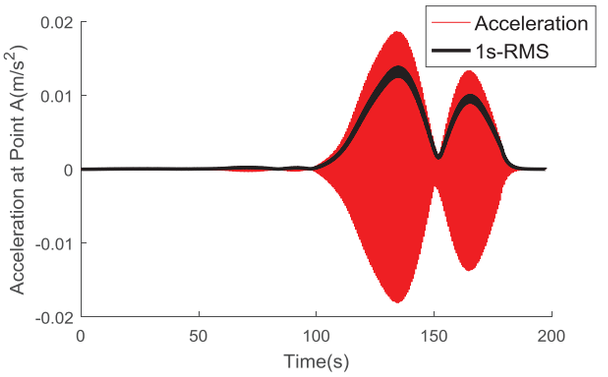


Figure 5. Acceleration time history and 1-s RMS at point A for bridge subjected to a single pedestrian.

4.4 *Random Crowd Loading Response*

A total of 100 crowd simulations are performed. Each of the 1250 pedestrians in a crowd are generated with random crowd characteristics. Figure 6 shows the acceleration time response history of the NB Bridge at Point A for a sample random crowd. The distributions of the 100 maximum RMS responses for all four points considered are also given in Figure 8. Also shown again are the 95 percentile values of the distribution, along with the mean and maximum comfort limits earlier.

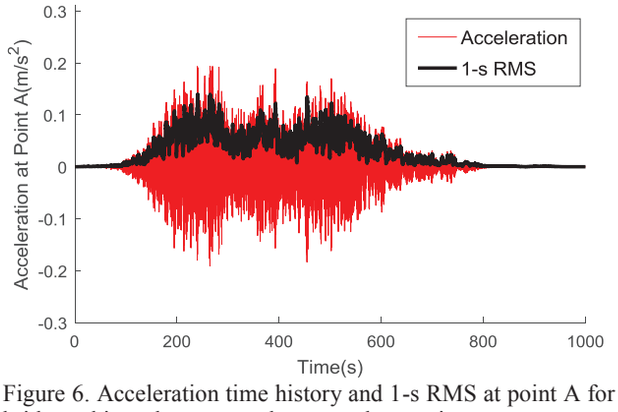


Figure 6. Acceleration time history and 1-s RMS at point A for bridge subjected to one random crowd scenario.

4.5 *Discussion*

From the preceding results, it is clear that for single pedestrians, the characteristic responses are well below the limit for maximum comfort. Of note, Point A

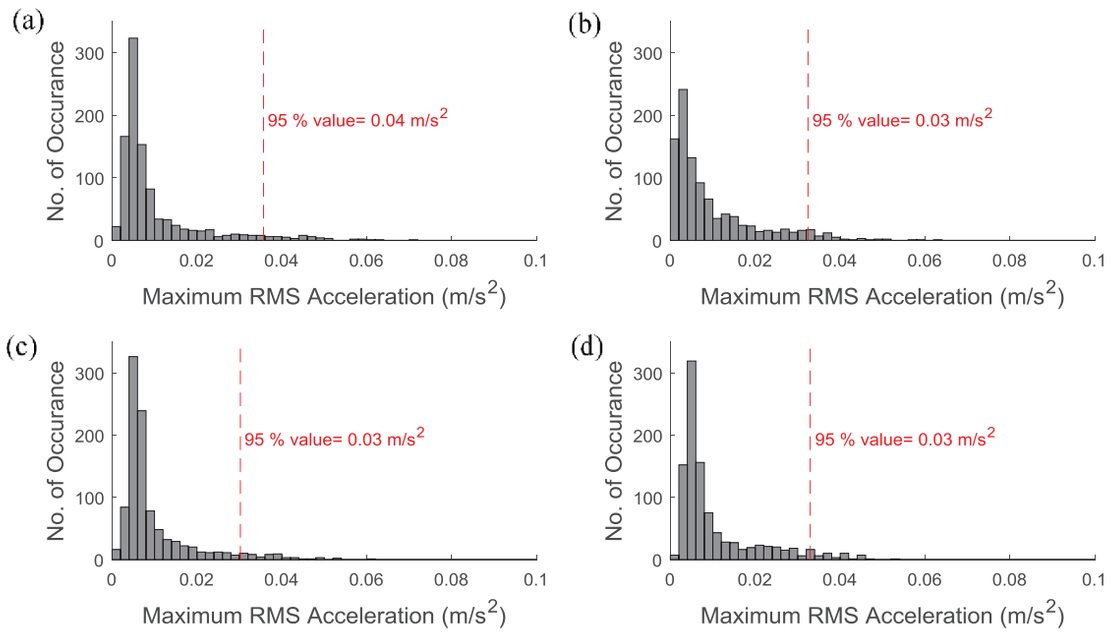


Figure 7. Histograms of 1-s RMS acceleration responses under random single pedestrians at: a) Point A; b) Point B; c) Point C, and; d) Point D.

has the highest characteristic response for single pedestrians. In contrast to the single pedestrian results, for the random crowds, Point B is found to have the highest response. It is interesting that the histogram of responses for Point B has two peaks (bi-modal distribution), suggesting that there exists a loading topology that offers a severe response. This seems to occur mainly when the maximum crowd density is located fully along the span, along with a maximum number of synchronized pedestrians. All single pedestrian responses are well below maximum comfort limit. Similarly, the characteristic crowd responses for points A and C. The critical responses occur for points B and D, with characteristic responses being between the maximum and mean comfort levels. Interesting one crowd response was above mean comfort level for Point B.

Notably, the critical response locations under crowd loading are not readily identified using the single pedestrian results (Point A), nor just by identifying the maximum span (Point B). Instead, the dynamic behavior (frequency of mode 4 leading to Point D) should also be considered when assessing likely critical response locations

5 SUMMARY & CONCLUSIONS

5.1 *Summary*

This work proposes a methodology to assess the vibration serviceability of a bridge with complex form using state-of-the-art crowd modelling. A calibrated 1-D modelling approach of the NB Bridge is considered to allow efficient simulations of pedestrian crowd crossings. The dynamic properties of the NB Bridge from the 1-D beam model are calibrated against those from a full 3-D model using model updating. Following the calibration, the simulations of pedestrian crossing are conducted using moving force models. Moving force model is applied onto the 1-D beam model to simulate random single pedestrians and random crowd loading. Maximum RMS acceleration responses along key locations of the NB Bridge are obtained. Histograms of these responses are established and the 95-percetile values found. These are compared with limits imposed by HiVoss and Setra guideline. Since all characteristic maximum RMS accelerations are well below the 1 m/s^2 limit imposed by HiVoss (2008) and Setra (2006), the footbridge is deemed acceptable in terms of vibration serviceability.

5.2 *Conclusions*

The approach presented here allows for improved vibration serviceability assessment of complex structural forms. Suitably accurate 1-D model representation of footbridges with complex structural forms can be obtained through calibration with detailed 3-D models using model updating. Such simpler 1-D models can then be used in a more advanced vibration serviceability assessment algorithm, as is done here. This work is therefore suitable for engineering practice to allow efficient modelling and vibration predictions of footbridges with similar complexity.

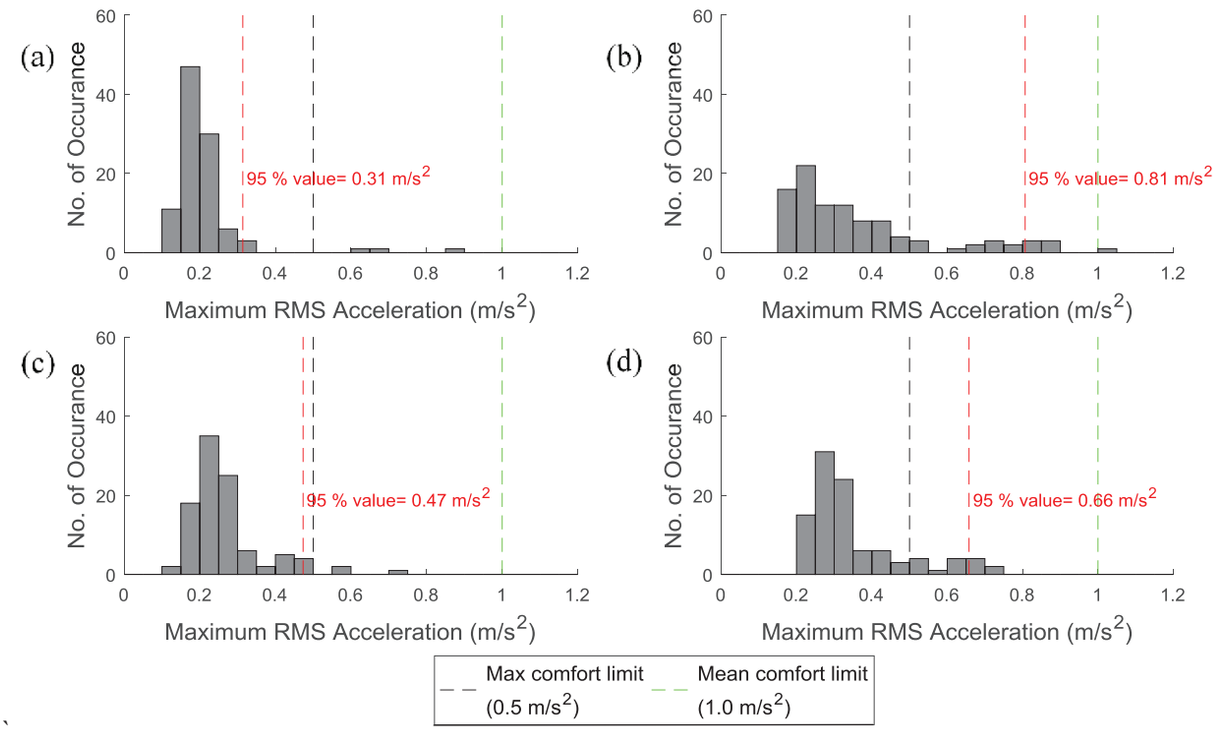


Figure 8. Histograms of 1-s RMS acceleration responses under random crowds at: a) Point A; b) Point B; c) Point C, and; d) Point D.

Although the method developed here uses advanced modelling of crowds and moving force presentation of the pedestrian imparted forces, it should be recalled that the present simulation does not consider the influences of mass damping and stiffness of humans on the overall bridge system dynamic properties. This leaves the possibility that the accelerations due to the simulated crowd could even be less. Nevertheless, it is possible, as suggested in Setra (2006), that the mass of the bridge model is adjusted to include the crowd, to represent these effects on the system's dynamic properties. However, conservatively, this approach is not taken here and the performance is yet found to be acceptable.

REFERENCES

Allemang, R. J. & Brown, D. L., 1982. *A correlation coefficient for modal vector analysis.* s.l., s.n., pp. 110-116.

Anon., 2008. *HiVoSS: Design of footbridges,* s.l.: Research Fund for Coal and Stee.

Anon., 2015. *FEMtools theoretical Manual, Version 3.8.2.* Belgium: Dynamic Design Solutions, Lueven.

Bachmann , H. & Ammann, W., 1987. *Vibrations in structures-induced by man and machine,* Zurich: IABSE, structural engineering document.

Bachmann, H., Pretlove , A. J. & Rainer , H., 1995. *Dynamic forces from rhythmical human body motions.* Birkhäuser, Basel,: s.n.

Barela , A. & Duarte, M., 2008. Biomechanical characteristics of elderly individuals walking on land and on water. *J of Electromyogr Kinesiol,* 18(3), pp. 446-54.

Caprani, C. & Ahmadi, E., 2016. Formulation of human-structure interation system models for vertical vibration. *Journal of Sound and Vibration,* Volume 377, pp. 346-367.

Caprani, C., Keogh, J., Archbold, P. & Fanning, P., 2012. Enhancement factors for the vertical response of footbridges subjected to stochastic crowd loading. *Computers and Structures,* Volume 102-103, pp. 87 - 96.

Dallard, P. et al., 2001. London millennium footbridge: Pedestrian-induced lateral vibration. *ASCE J Bridge Eng,* 6(6), p. 412.

Danbon, F. & Grillaud, G., 2005. *Dynamic Behaviour of a steel footbridge: characterization and modelling of the dynamic loading induced by a moving crowd on the Solferino footbridge in Paris.* s.l., s.n.

Frisswell, M. I. & Mottershead, J. E., 1995. *Finite element model updating in structural dynamics.* Dordrecht: Kluwer Academics .

Fujino , Y., Pacheco , B. M., Nakamura , S. & Warnitchai, P., 1993. Synchronization of human walking observed during lateral vibration of congested pedestrian bridge. *Earthquake Eng Struct Dynam,* 22(9), pp. 741-58.

Heinemayer, C. et al., 2009. Design of lightweight footbridges from human-induced vibrations. *Sedlacek G, Heinemeyer C, Butz C, Geradin M (Eds).*

Portier, K., Tolson, J. K. & Roberts, S. M., 2007. Body weight distribution for risk assessment. *Risk Anal ,* 27(1), pp. 11-26.

Setra, 2006. *Footbridges: Assessment of vibration behaviour of footbridges under pedestrian loading.* Paris: Technical guide, Service d'Etudes Techniques des Routes et Autoroutes.

Young, P., 2001. *Improved floor vibration prediction methodologies.* s.l.:ARUP vibration seminar .

Živanović, S., Pavic, A. & Reynolds, P., 2005. Vibration Serviceability of Footbridges under human-induced excitation: A literature review. *Journal of Sound and Vibration,* 279(1-2), pp. 1-74.

Živanović, S., Pavic, A. & Reynolds, P., 2007. Finite element modelling and updating of a lively footbridge: The complete process. *Journal of Sound and Vibration,* Volume 301, pp. 126-145.

Maintenance, Safety, Risk, Management and Life-Cycle Performance of Bridges – Powers, Frangopol, Al-Mahaidi & Caprani (Eds)
© 2018 Taylor & Francis Group, London, ISBN 978-1-138-73045-8

A study of pedestrian evacuation on bridge sidewalk by simulation method

Z.R. Jin, X. Ruan & Y. Li
Department of Bridge Engineering, Tongji University, Shanghai, China

ABSTRACT: Pedestrian evacuation has become an important issue of operation safety for bridges nowadays. In this paper, cellular automata are discussed and illustrated as the foundation for evacuation simulation. Floor field model, as a combination of updating rules, is then integrated into cellular automata for updating the position of each pedestrian. To consider the effect of coordinators in pedestrian flow, a state transition rule is proposed to account for the variation of pedestrian's moving strategy. By the model, evacuation time of different spans of bridges with various sidewalk widths is obtained through simulation, which indicates that a wider sidewalk is necessary for the longer bridge to further decrease the evacuation time. The effect of emergent blocking of the bridge on the evacuation time is also investigated. Furthermore, the position of coordinators is optimized to reduce the evacuation time to the maximum extent.

1 INSTRUCTION

Long bridges are usually designed specifically for the use of automobile passing or train passing, or both. However, sidewalks would be sometimes designed as well for maximizing the function of this structure. In most cases, given the safety concern, the sidewalk which enables the passing of pedestrian or non-motor vehicle is separated from the main motor vehicle lanes. This measure, in another aspect, may trigger the evacuation problems due to the fact that the sidewalk for evacuation is relatively narrow while the exit of the sidewalk is located at the very end of the bridge. In some scenarios, a sidewalk is also built as an auxiliary component for sightseeing. When the arches of a bridge are also accessible for the recreational purpose, e.g., Sydney Harbor Bridge (Fig 1), the issue of pedestrian evacuation becomes much more noteworthy. Hence, the safe evacuation for long bridges with sidewalk needs an inspection to evaluate whether a certain geometry layout of the sidewalk is appropriate for the pedestrian evacuation under some emergency.



a



b

Figure 1 (a) Full view of Sydney Harbor Bridge (Copyright belongs to Brian Giesen, from flickr); (b) Group of pedestrians climbing the arch of Sydney Harbor Bridge (Copyright belongs to ImageCup, from flickr)

Many methods have been proposed to address the problem of evacuation. At the micro level, models are established on the continuous or discrete basis. Herein, cellular automata (CA) functions in a spatial and temporal discrete system (Von Neumann & Burks 1966). When used for evacuation simulation,

it updates pedestrians' positions synchronously according to the local environment and the pre-defined local rules. Through the iteration of applying local rules to each cell, the flow of pedestrian is emulated. Based on CA model, several updating rules have been proposed in previous studies to tackle different aspects of evacuation problems. The floor field CA model is widely utilized to evaluate the evacuation behaviors for a variety of structure layouts. Many improvements have been made on floor field CA model to incorporate some certain scenarios where the pedestrians may behave distinctly from the common sense, e.g., group behavior(Lu et al. 2016) and evacuation from the fire(Zheng et al. 2011) or smoke(Yuan & Tan 2011). However, few applications of floor field CA model is adopted in the scenarios of the evacuation on bridge sidewalks, whose geometric feature are quite distinct due to long span but small width.

Thus, in this paper, the conventional floor field CA model is modified to fit for the evacuation simulation of the sidewalks in long span bridges. The evacuation time is compared among different widths of sidewalk for the given spans of bridges. Also, the adverse effect caused by the local blocking due to the emergency like fire or explosion is discussed on the basis of further simulation. Finally, to improve the efficiency of the evacuation process, two coordinators are allocated along the span of the bridge. Their influence is reflected based on the state transition rules of pedestrian, which is proposed for the first time. The optimal positions of coordinators are investigated on the premise of the evacuation time obtained from the simulation.

The rest of this paper is organized in the following pattern. The next section is aimed to present a brief introduction of the floor field CA model and the state transition rules for the consideration of coordinator's influence. The framework of simulation will be articulated in section 3. Then in section 4, the application of the modified floor field for the evaluation of sidewalk evacuation problem is conducted, and the foregoing topics are discussed based on the output of simulations. For conclusion, in section 5 the observations of this work are summarized, and the further applications of floor field CA for evaluation on the evacuation problem in bridge sidewalk are suggested.

2 THE MODIFIED FLOOR FIELD CA

2.1 *Physical environment of basic CA model*

In the basic CA model, the finite and continuous evacuation plane is divided into some cells with lattice of certain sizes. These cells have well-defined boundaries, and the states of this cells are finite. In the problem of evacuation simulation, each cell is occupied by obstacles, e.g., walls or barricades, by a pedestrian, or just empty. The information like each pedestrian's moving parameters and obstacle's occupation parameters is stored in the relevant cell, which serves as the input for the subsequent updating of pedestrians. In this work, Von Neumann neighborhood is adopted as Figure 2, where the current position of a pedestrian is at the center of the neighborhood. Under this constraint, the moving range of a pedestrian for a time step would be in the four directions, i.e. up, down, left and right. Pedestrians update their position synchronously at each time step, based on the beforehand defined local rules, its current state and the environment which is formed by the nearby pedestrians and the obstacles. During the updating process, the moving parameters of each pedestrian are transferred from the previous cell to the target cell as shown in Figure 3, which mimics the movement of the pedestrians in real time. In the relatively dense pedestrian flow, a typical spatial occupation of a pedestrian can be set as a square area whose side length is 0.5m . Therefore, the size of each cell is set to be 0.5m ×0.5m in this application, and each cell can only be occupied by a single pedestrian. At each time step, a pedestrian is required to move only one cell from the current position or stay still.

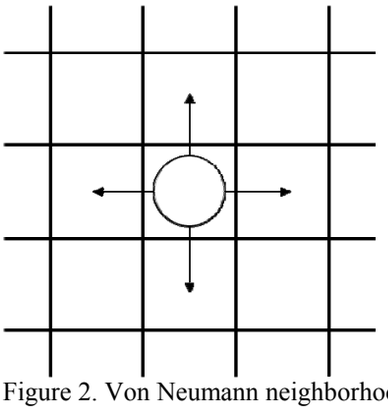


Figure 2. Von Neumann neighborhood

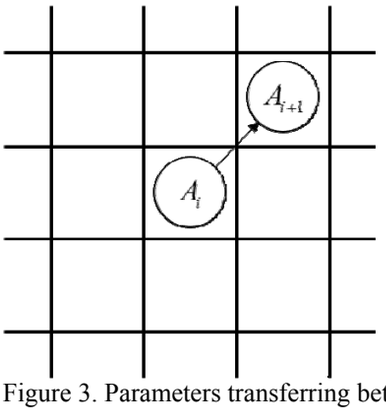


Figure 3. Parameters transferring between cells

2.2 *A detailed introduction of floor field CA model*

The floor field CA model is constructed at the micro level and the pedestrians are allowed to move in the neighborhood at each time step in accordance with the dynamic probability calculated by the pre-defined local rules. In the first place, the floor field CA was inspired by the chemotaxis phenomenon that commonly exists in nature(Kirchner & Schadschneider 2002). As a typical floor field CA model, two kinds of floor field are combined to present an interactive updating scheme that enables the variations of transition probability and further determines the movement of a pedestrian. The static field S and the dynamic field D will facilitate the pedestrians to be more likely to move in the direction where the field values are higher.

The static field S represents the pedestrian's ability to find the most favorable way to egress, which is determined by the shortest routine to get to the exit. The nearer one cell is to the exit, the more attractive this cell will be to a certain pedestrian, in terms of the evacuation process. The dynamic field D stands for pedestrian's behavior of following others when evacuating, the certain values of dynamic field D illustrate the virtual trace left by the pedestrian flow. In this sense, the chemotaxis phenomenon is correlated to show that people tend to follow the trace, i.e., the herding behavior.

The first proposed calculation method of static field S is based on the absolute distance to the exit(Kirchner & Schadschneider 2002). In applications of floor field CA to the evacuation simulations of long bridge sidewalks, the powers to the natural base are too large for practical calculation. To deal with it, the distance difference is adopted here to measure the attractiveness of the cells in the neighborhood, which is stated in the literature(Zheng et al. 2011). The static field S is constant throughout the entire evacuation process and is not influenced by the presence of any pedestrian. Conversely, the dynamic field D is time-dependent and will always change following the rules of diffusion and decay. At each time step, the dynamic field D of a cell from which a pedestrian moves out will increase by one. And the dynamic field D will decay with probability δ and diffuse with probability α to one of its neighboring cells(Kirchner & Schadschneider 2002). In addition to the original paper that proposed the floor field CA model, the inertial field is added later to take into account the fact that pedestrians are likely to keep their moving direction while evacuating(Nishinari et al. 2004).

In the Von Neumann neighborhood as depicted in Figure 1, the transition probability of the pedestrian is obtained through Equation 1 below:

$$p_{ij} = N \exp\left(k_S S_{ij}\right) \exp\left(k_D D_{ij}\right) p_I(i,j) I_{ij} \left(1 - n_{ij}\right) \xi_{ij} \qquad (1)$$

where

$$p_I(i,j) = \begin{cases} \exp(k_I) & \text{if } cell(i,j) \text{ accords with the direction} \\ 1 & else \end{cases}$$

$$n_{ij} = \begin{cases} 0 & \text{if } cell(i,j) \text{ is not occupied by another pedestrian} \\ 1 & \text{else} \end{cases}$$

$$\xi_{ij} = \begin{cases} 0 & \text{if } cell(i,j) \text{is forbidden by obstacles} \\ 1 & \text{else} \end{cases}$$

To make sure that the summation of transition probability equals to 1, the normalization item is added in as Equation 2:

$$N = \left[\sum \exp\left(k_S S_{ij}\right) \exp\left(k_D D_{ij}\right) p_I(i,j) \left(1 - n_{ij}\right) \xi_{ij}\right]^{-1} \qquad (2)$$

Where k_S, k_D and k_I are sensitivity parameters used to determine the weights of S_{ij}, D_{ij} and $P_I(i,j)$, respectively.

2.3 *Pedestrian contraction at a wide exit*

According to the observations of the previous studies of floor field CA model, it is noteworthy that the pedestrian will form an unusual array at the exit when the width of the exit is relatively large, which is a common situation in the bridge sidewalk. This phenomenon can not accord with what is happening in reality and is mainly attributed to the underlying updating rule that each pedestrian longs for the shortest path to egress. In this scenario, the pedestrian on both sides of the exit will always choose the side cells at the exit and crowd around it struggling to get out. This problem was noticed by (Nishinari et al. 2004) first, and he caught the inspiration from hydrodynamics to called this effect as the contraction. By merely weighting more the cells near the center of a wide exit owing to the contraction, the static field S is modified accordingly. After this modification, the status of crowding array on both sides of an exit is obviously mitigated. Whereas, the cells far from the center of exit are not fully utilized during evacuation. In this work, a discounting parameter is proposed to shrink the distance between the inner cells and the cells near the center of an exit while still incorporating the static field influence of the lateral cells of an exit. This process is explained by Equation 3:

$$L_D(i,j) = \beta L_O(i,j) \qquad (3)$$

where $L_O(i,j)$ is the original distance between the inner cells and the cells at the exit; β is the discount factor that equals to 1 for the exit cells farthest from the center and a certain value for the exit cell at the center. And for the cell in between, β changes linearly. Then $L_D(i,j)$ is adopted as the input for the static field S determination.

As described in Figure 4a and Figure 4b (the geometry of the evacuation space is only chosen for visualization concern), if $\beta = 0.8$ for the cell at the center of an exit, the previous crowding at both sides of the exits is remarkably downsized and a conventional phenomenon of arching emerges again, which means that the simulation is more realistic.

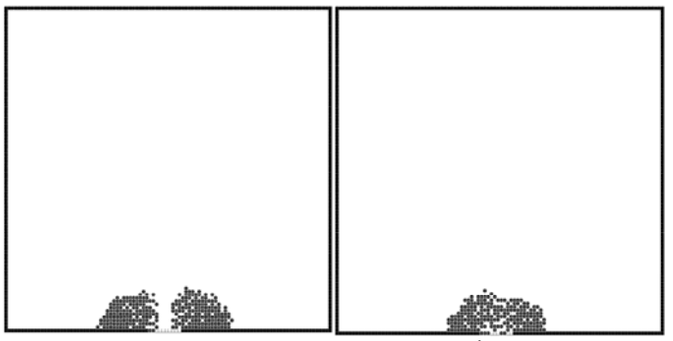


Figure 4 (a) Pedestrian distribution at the exit without considering contraction (b) Pedestrian distribution at the exit when $\beta = 0.8$

2.4 *Coordinator's influence and state transition*

As well known, when the width of a sidewalk is small and the evacuating path is long, the influence of the oscillation in pedestrian flow on the ultimate evacuation time will be obvious. If the pedestrian flow is kept more ordered, the evacuation time may me reduced to some extent. Since the dynamic field D represents the herding behavior of the pedestrians which leads to the deviation from the shortest path for evacuation, a large D will hinder the smooth process of evacuation. With this in mind, if a coordinator is allocated along the span in the process of evacuation, he is supposed to prevent the pedestrians getting into chaos, and mathematically, the dynamic field will get decreased within a certain range of the coordinator.

Here we set k_D in a range of [k_{Dmin}, k_{Dmax}], where the min value lessens the herding behavior of pedestrians and accordingly reduces the oscillation in pedestrian flow; the max value is the original k_D of all the inner cells, which will entail a high probability of oscillation. The variation of k_D is based on the relative distance between the cells and the coordinators, which is shown in Equation 4:

$$k_D = \begin{cases} k_{D\min} + \left(\dfrac{L_C}{L_E}\right)^2 \left(k_{D\max} - k_{D\min}\right) & L_C \le L_E \\ k_{D\max} & L_C > L_E \end{cases} \quad (4)$$

where L_C is the relative distance between a certain cell and its closest coordinator; L_E is the coordinator's effective range.

This variation of k_D ensures that a state transition of the pedestrian takes on around the coordinators. The variation pattern is illustrated in Figure 5. It is clear that when a pedestrian is close to a coordinator, the latter's influence decreases slowly. While when a pedestrian is getting far from the coordinator, the coordinator's influence for an ordered evacuation diminishes rapidly until k_D equals to the original value k_{Dmax}.

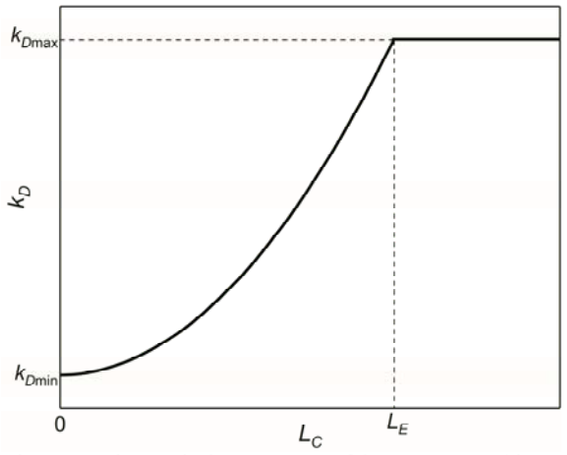


Figure 5 The variation pattern of k_D versus L_C (the state transition rule)

3 FRAMEWORK OF SIMULATION

The bridge sidewalks from which the pedestrians evacuate from is discretized into cells based on the aforementioned cell size. Initially, each cell would be either empty or occupied by the wall or a pedestrian at most. For each of the pedestrians, the next action could be moving to one of the neighboring cells or stay still following the transition probabilities calculated at each time step based on Equation 1 All of the pedestrians will choose their target cells for the next time step synchronously. Only one of the pedestrians will be randomly selected to move into the target cell while the other stay at current cells, in case that a confliction happens when several pedestrians share the same target cell.

The detailed framework for conducting an evacuation simulation on a long bridge sidewalk is elaborated as follows:

Step 1: Initialize a series of pedestrian and then populate them into the bridge sidewalk with random positions.

Step 2: Calculate the static field S of each cell with contraction effect considered. The static field S remains constant in the following simulation.

Step 3: Obtain the transition probabilities from Equation 1. Different values of k_D are derived from Equation 4 when the coordinator's influence is taken into account. Then the pedestrian will randomly de-

termine the target cells referring to the current transition probabilities.

Step 4: Deal with the conflict scenario if necessary.

Step 5: Update the dynamic field floor D for this time step according to the decay and diffusion rules mentioned before. The values of the dynamic field D at all the cells are initialized as zeros and are time-dependent throughout the simulation process.

Step 6: Iterate from Step 1 to Step 4 until all of the pedestrians have evacuated from the bridge sidewalk.

For the sake of a better visualization, an example of evacuation process simulated by the proposed model is present in Figure 6.

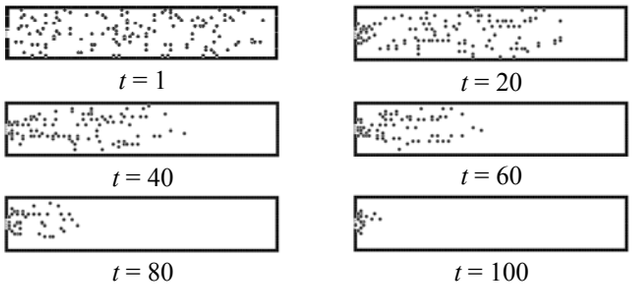


Figure 6 The evacuation process (unit: time step)

4 SIMULATION AND ANALYSIS

4.1 *Parameters setting*

The input parameters are list below for evacuation simulations using the floor field CA, and the disordered pedestrian flow is emulated by this combination of parameters(Kirchner & Schadschneider 2002): $k_S = 4$, $k_{Dmin} = 0$, $k_{Dmax} = 2$, $k_I = 0.2$, $\alpha = 0.3$, $\delta = 0.3$, $\beta = 0.8$, the cell size is 0.5m×0.5m.

4.2 *Influence of sidewalk width*

The width of a sidewalk is studied with respect to the appropriate width for a certain span of the bridge. The geometric layout of the bridge sidewalk is described in Figure 7. The bridge spans are 100, 300, 500, 700 and 900 (unit: m) while the widths of sidewalks are 1.0, 1.5, 2.0, 2.5 (units: m) in this comparative analysis. The practical layouts of bridge sidewalk in China have been consulted before the adoption of these widths. The number of pedestrians for each span of the bridges is calculated on the hypothesis that the people density is 0.6 (unit: person/m^2) when the width of the sidewalk is 2.0m. Thus, the initial pedestrian numbers are 120, 360, 600, 840 and 1080 (units: person) for the previously defined spans, respectively. In all, there are 20 groups of simulation scenarios and the evacuation time of each group is the average over 24 simulation runs.



Figure 7 The geometric layout of the bridge sidewalk

The evacuation time information of different sidewalk widths for a certain bridge span is illustrated in Figure 8. For the sake of comparison, the decrease percentages of evacuation time are calculated with the sidewalk width of 1m as the benchmark. Three different kinds of variation patterns can be discerned from Figure 8:

For the bridge sidewalk of 100m, the evacuation time decreases rapidly when the width of sidewalk begins to ramp up. However, a decline in decrease percentage is observed when the width reaches 2.5m. This is mainly due to the fact that a sidewalk width of 2.0m is enough for a smooth evacuation. Further increase in sidewalk width cannot improve the evacuation efficiency but may boost the probability of an oscillation since pedestrians may walk more freely than before. This oscillation may exert an adverse effect on the overall evacuation process.

For the bridge sidewalk of 300m and 500m, the evacuation time decreases with the increase in sidewalk width. And after the sidewalk width reaches 2.0, the evacuation time keeps stable approximately, which means that a width of 2.0m is proper for the evacuation of these volumes of pedestrians when the bridge spans are 300m and 500m.

For the bridge sidewalk of 700m and 900m, the evacuation time keeps decreasing along with the sidewalk getting wider. Even though the sidewalk width has arrived at 2.5m, there is still a potential that the evacuation time will be further decreased.

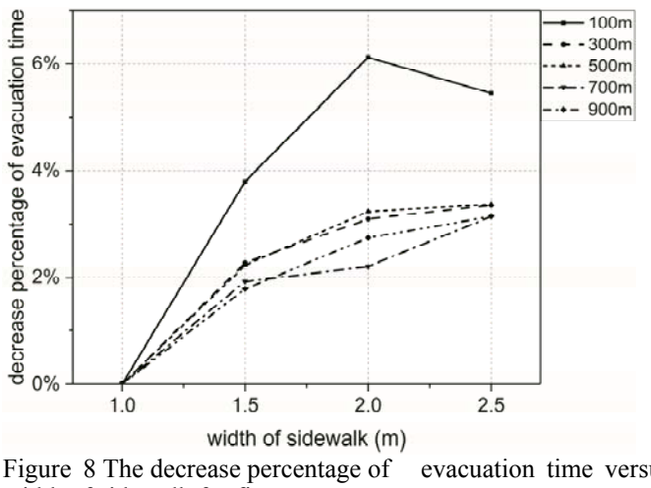


Figure 8 The decrease percentage of evacuation time versus width of sidewalk for five spans

4.3 *Influence of local blocking*

To investigate the outcome of emergency, e.g., fire and explosion, different blocking positions along the bridge span are set to evaluate the increase in evacuation time. The bridge span of 500m is chosen to be evacuation space. The blocking positions include one of the exits, 1/8, 1/4, 3/8 of the span, and the middle of the span, as depicted in Figure 9. The pedestrians on both sides of the blocking can not transverse to the other side. Accordingly, the static field S at each cell should be calculated based on the distance to its accessible exit.

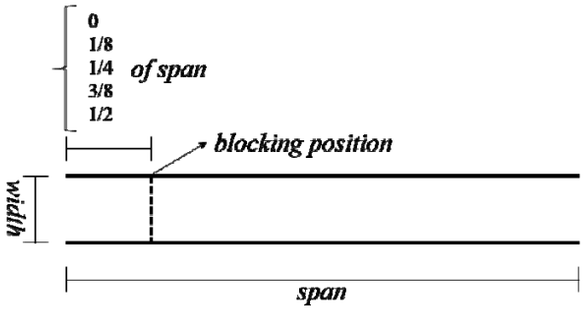


Figure 9 The blocking positions on the bridge sidewalk

The evacuation time information of different sidewalk widths for a certain blocking position is shown in Figure 10. And the evacuation benchmarks for each sidewalk width are the values of no-blocking scenarios for 500m span analyzed in Section 4.2. In Figure 10, the increase percentages of evacuation time are presented. It is straightforward that the variation of sidewalk width has little influence on the increase percentages of the evacuation time for the same blocking position. Nevertheless, the blocking caused by an emergency does increase the evacuation time to some extent, and increase percentage can accord well with the distance between the exit and the pedestrian farthest from it. This result confirms that under this people density and sidewalk width layouts, the overall evacuation time changes linearly with the distance that the farthest pedestrian is going to transverse to reach the exit.

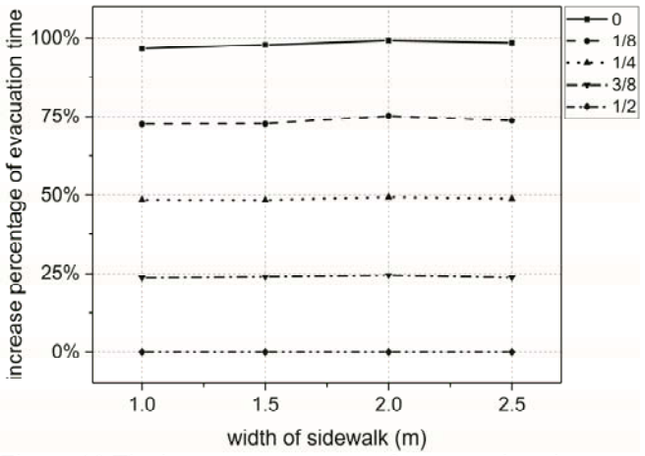


Figure 10 The increase percentage of evacuation time versus width of sidewalk for five blocking positions

4.4 *Influence of coordinators and the position optimization*

In this work, in a bid to improve the evacuation efficiency, the concept of coordinator is proposed to keep a certain range of bridge sidewalk more ordered than original state. The method of such intention is to decrease the values of k_D, as detailed previously. The positions of coordinators include one of the exit, 1/8, 1/4, 3/8 of the span, and the middle of the span, as depicted in Figure 11. In consideration of simplicity, only two coordinators are allocated symmetrically on both sides of the mid-span. (Except for the mid-span scenario, where only one coordinator is allocated.) The L_E is set as 100 (unit: cell) for all the scenarios. Based on the positions of coordinators and the value of L_E, if the span is less than 500m, there will be an overlap of effective range for different scenarios, making things too complicated for discerning the variation. Therefore, only bridge spans of 500m, 700m and 900m are discussed in this topic.

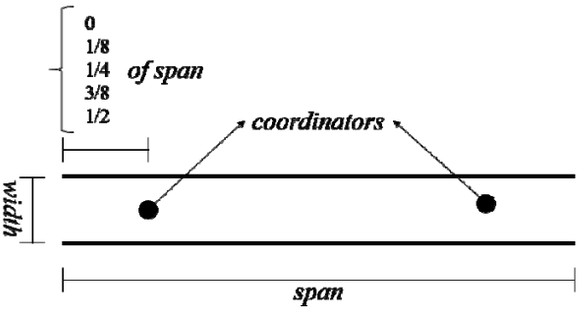


Figure 11 The positions of coordinators on the bridge sidewalk

The evacuation time information of different positions of coordinators for a certain bridge span is shown in Figure 12. The evacuation time without coordinators from Section 4.2 is chosen as the

benchmark for comparison. In Figure 12, the decrease percentages of evacuation time are presented. According to the data in Figure 7, when the bridge spans are 700m and 900m, the nearer coordinators are to the exit, the more evacuation time get decreased. Whereas, for bridge span of 500m, the 1/8 of the span is the optimal position for the allocation of coordinators. Moreover, the influence of the coordinators is more salient for the bridge span of 700m than that for the bridge span of 500m and 900m, when the coordinators are allocated at the same positions of the span.

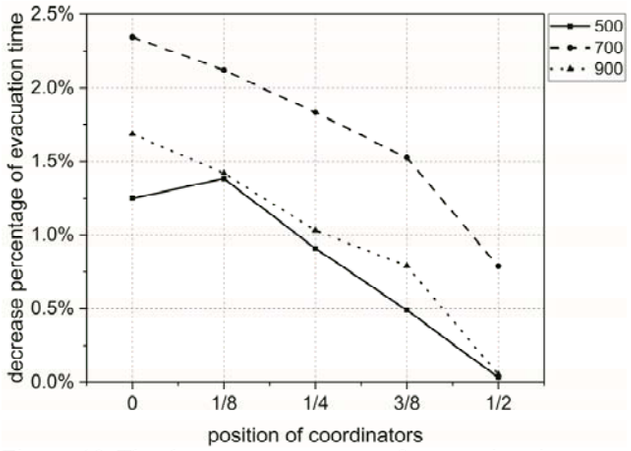


Figure 12 The decrease percentage of evacuation time versus position of coordinators for three spans

5 CONCLUSION

This paper introduces the floor field CA model to study the pedestrian evacuation bridge sidewalks. The floor field CA model is modified based on the geometric features of evacuation space: the method of the static field *S* calculation is chosen specifically for computational ease; the pedestrian contraction at the exit is modeled properly for a more realistic crowd simulation when the width of an exit is large. Furthermore, the concept of coordinators is proposed to enhance the evacuation efficiency, by introducing the state transition controlled by the values of k_D. On the basis of the previous simulations and discussions, the following conclusions are drawn:

- The widths of the bridge sidewalks do influence the overall evacuation time. And for fixed people density, the variations of evacuation time versus sidewalk widths show three distinct patterns among five spans of bridges. When the pedestrian flow is disordered for small span (100m), simply increasing width will not decrease the evacuation time monotonously. For large span (700m and 900m), the width of 2.5m can be further increased to get a higher evacuation efficiency.
- The variation of width of sidewalk has little influence on the evacuation time when some positions are blocked. And the evacuation time only depends linearly on the farthest distance between a pedestrian and the exit under the people density and sidewalk layout specified in the context.
- The coordinators allocated along the span do have a positive effect on the evacuation efficiency. Generally, the nearer the coordinators to the exit, the more obvious efficiency enhancement will be.

We do recognize that there still exist some limitations for a deep analysis of evacuation time on the bridge sidewalk in this work. The number of pedestrians for a certain bridge span is fixed for comparison ease. And the coordinator's effective range is not studied in a sensitivity analysis due to space limitation. For the further study, the people density can be changed to gain more insight into the variation patterns evacuation time. The coordinator's effective range should be discussed or calibrated against the in-situ test to obtain a more comprehensive understanding of its mechanism. In a nutshell, this work only provides a basic idea on the study of the width of long bridge sidewalk for evacuation's concern.

6 ACKNOWLEDGEMENT

This work is supported by National Nature Science Foundation of China [grant number 51478337], [grant number 51678435]; Fundamental Research Funds for the Central Universities in China, and the Peak Discipline Open Fund of Transportation Engineering of Tongji University (Grant No. 2016J012302).

7 REFERENCE

Kirchner, A. & Schadschneider, A. (2002) Simulation of evacuation processes using a bionics-inspired cellular automaton model for pedestrian dynamics. *Physica A: statistical mechanics and its applications,* 312**,** 260-276.

Lu, L., Chan, C.-Y., Wang, J. & Wang, W. (2016) A study of pedestrian group behaviors in crowd evacuation based on an extended floor field cellular automaton model. *Transportation Research Part C: Emerging Technologies*.

Nishinari, K., Kirchner, A., Namazi, A. & Schadschneider, A. (2004) Extended floor field CA model for evacuation dynamics. *IEICE Transactions on information and systems,* 87**,** 726-732.

Von Neumann, J. & Burks, A. W. (1966) Theory of self-reproducing automata. *IEEE Transactions on Neural Networks,* 5**,** 3-14.

Yuan, W. & Tan, K. H. (2011) A model for simulation of crowd behaviour in the evacuation from a smoke-filled compartment. *Physica A: Statistical mechanics and its applications,* 390**,** 4210-4218.

Zheng, Y., Jia, B., Li, X.-G. & Zhu, N. (2011) Evacuation dynamics with fire spreading based on cellular automaton. *Physica A: Statistical Mechanics and its Applications,* 390**,** 3147-3156.

Maintenance, Safety, Risk, Management and Life-Cycle Performance of Bridges – Powers, Frangopol, Al-Mahaidi & Caprani (Eds)
© 2018 Taylor & Francis Group, London, ISBN 978-1-138-73045-8

Uncertainty propagation in serviceability assessment of footbridges

F. Tubino, L. Pagnini & G. Piccardo
University of Genoa, Genoa, Italy

ABSTRACT: The paper deals with the propagation of uncertainties inherent to structural and loading parameters on the serviceability assessment of footbridges. Based on the equivalent spectral model, the standard deviation and maximum value of the footbridge acceleration are expressed as a function of the probability distribution of the step frequency and of the modal properties of the footbridge. The assessment of the propagation of uncertainties in the characterization of such parameters is carried out using the Taylor expansion method. The results are discussed and compared with conventional verifications, based on deterministic evaluations.

1 INTRODUCTION

Modern footbridges can be very sensitive to human-induced vibrations and their serviceability assessment is a central issue in their design. Recent guidelines provide straightforward procedures to deal with their serviceability analyses, based on simplified expressions of pedestrian-induced forces. Dealing with multi-person traffic, a uniformly distributed resonant equivalent load is commonly provided by guidelines and a deterministic estimate of the maximum acceleration is thus obtained, to be compared with suitable serviceability limits (e.g. SETRA 2006). The Equivalent Spectral Model is an alternative loading model that allows estimating the maximum footbridge acceleration as a function of the probabilistic distribution of step frequency (Piccardo & Tubino 2012). Assuming deterministic values for the structural dynamic parameters (modal mass, natural frequency and damping ratio) and for the loading parameters (dynamic loading factor, pedestrian weight and pedestrian step frequency distribution), a deterministic estimate of the maximum footbridge acceleration is obtained. Since, however, the estimate of several structural and loading parameters is uncertain, the serviceability assessment should consider this randomness.

This paper discusses the propagation of uncertainties in both the structural and the loading parameters on the serviceability assessment of footbridges. Based on the Taylor series expansion technique (e.g., Pagnini 2010), the uncertain parameters having large influence on the maximum acceleration are identified. The proposed procedure is then applied to a case study. Results are discussed and compared with conventional verifications, based on deterministic evaluations.

2 SERVICEABILITY ASSESSMENT OF FOOTBRIDGES

Vibration serviceability assessment of footbridges is commonly carried out through simplified procedures (SETRA 2006, ISO10137 2007, BSI 2008, HIVOSS 2009), based on equivalent loading for pedestrian groups modelled as a resonant harmonic load, whose amplitude is defined as a function of the expected pedestrian density. The equivalent loading expressions are based on numerical simulations of the forces exerted by pedestrian groups, modelling the single pedestrian loading as a moving harmonic with a frequency distribution according to a Gaussian function having a mean value coincident with the natural frequency of the footbridge.

The Equivalent Spectral Model (ESM, Piccardo & Tubino 2012) allows estimating the standard deviation of the footbridge acceleration and its maximum expected value as functions of the harmonic content of the loading and structural parameters characterizing the dynamic behavior of the structure. It is based on the following expression for the power spectral density function of the j-th modal force:

$$S_{F_j}(\omega) = \frac{N_p}{4}(\alpha_m G_m)^2 \, p_\Omega(\omega) \tag{1}$$

where N_p is the number of pedestrians, α_m and G_m are, respectively, the mean value of the dynamic

loading factor and of the weight of pedestrians, $p_\Omega(\omega)$ is the probability density function of the step frequency of pedestrians, assumed as normal:

$$p_\Omega(\omega) = \frac{1}{\sigma_\omega \sqrt{2\pi}} \exp\left[-\frac{(\omega - \omega_{pm})^2}{2\sigma_\omega^2} \right] \quad (2)$$

ω_{pm} and σ_ω being the mean value and the standard deviation of the step circular frequency, respectively.

Based on the ESM, the standard deviation of the footbridge acceleration in terms of the j-th modal principal coordinate p_j can be expressed as follows:

$$\sigma_{\ddot{p}_j} = \sqrt{\frac{\pi \omega_j}{4 M_j^2 \xi_j} S_{F_j}(\omega_j)} \quad (3)$$

where ω_j, M_j, ξ_j are, respectively, the footbridge natural circular frequency, the modal mass and the damping ratio of mode j.

The expected value of the maximum acceleration can be then estimated as follows:

$$\ddot{p}_{j\max} = g_{\ddot{p}_j} \sigma_{\ddot{p}_j} \quad (4)$$

where $g_{\ddot{p}_j}$ is the peak factor, which can be estimated according to the Davenport formulation (Tubino & Piccardo 2016) as:

$$g_{\ddot{p}_j} = \sqrt{2\ln\left(2\nu_{\ddot{p}_j}\tilde{T}\right)} + \frac{0.5772}{\sqrt{2\ln\left(2\nu_{\ddot{p}_j}\tilde{T}\right)}}$$
$$\nu_{\ddot{p}_j} = \frac{1}{2\pi} \quad \tilde{T} = N\frac{\omega_j L}{c_m} \quad N = 10 \quad (5)$$

L being the span length. In the following, a simplified assumption is made, and the mean walking velocity c_m (m/s) is assumed as proportional to the mean step frequency n_{pm} (Hz), as usual in practice (see, e.g., FIB 2005) being $n_{pm}=\omega_{pm}/2\pi$:

$$c_m\,(\mathrm{m/s}) = 0.9 n_{pm} \quad (6)$$

3 ANALYSIS OF UNCERTAINTIES

The estimate of footbridges' serviceability is affected by the uncertainty of the parameters characterizing both loading and structural properties.

In the following Sections, a synthetic bibliographic analysis of uncertainties affecting the characterization of pedestrian loading (Section 3.1) and structural modal properties (Section 3.2) is proposed.

3.1 *Pedestrian loading*

Pedestrian loading (Eq. (1)) is defined as a function of the number of pedestrians N_p, of the mean value of the dynamic loading factor α_m and pedestrians' weight G_m and of the parameters defining the probability distribution of the step frequency of pedestrians (i.e., mean value ω_{pm} and standard deviation σ_ω). The number of pedestrians N_p can be assumed as a deterministic design requirement, set by the owner of the structure taking into account its location. Dealing with the other loading parameters, the literature is not very rich in information about α_m and G_m, while a certain amount of data are available concerning the statistical distribution of the step frequency, commonly assumed as normal. Table 1 reports results of experimental data available in the literature dealing with the probability distribution of step frequencies, including mean value n_{pm}, standard deviation σ_{np} and coefficient of variation $V_{np}= \sigma_{np} /n_{pm}$. The number of persons N_p on which these values are determined is also reported.

Table 1. Pedestrian step frequency

Reference	N_p	n_{pm}	σ_{np}	V_{np}
Matsumoto et al. (1978)	505	2	0.173	0.09
Pachi & Ji (2005)	400	1.8	0.11	0.06
Sahnaci & Kasperski (2005)	251	1.82	0.12	0.07
Zivanovic et al. (2007)	1976	1.87	0.186	0.1
Ricciardelli et al. (2007)	116	1.84	0.172	0.09
Zivanovic et al. (2010)	38	1.95	0.15	0.08
Sahnaci & Kasperski (2011)	227	1.92	0.13	0.07
Niu et al. (2016)	94	1.77	0.15	0.08

3.2 *Structural properties of the footbridge*

The structural parameters affecting the dynamic response are the structural modal mass M_j, natural circular frequency ω_j and damping ratio ξ_j. The modal mass can be evaluated with a certain degree of accuracy. Fundamental frequency can be either estimated on the basis of experimental measurements on the structure investigated or by a finite element model, once the mass and the stiffness matrices are known. For some types of structures, the a priori estimate can be very uncertain (e.g., buildings for the presence of masonry and secondary elements). Concerning footbridges, estimates obtained from finite element models may be affected by limited errors due to the modelling of structural restrains and/or secondary elements, which can cause a discrepancy between the numerical prediction and the actual value. Zivanovic et al. (2006) and Van Nimmen et al. (2014, 2016) reported a discrepancy between measured natural frequencies and numerically predicted ones for a large number of footbridges (Table 2). Uncertainties might also arise from environmental effects (e.g., temperature variation). Possible variation of the natural frequency due to these actions has been reported, e.g., by Moser & Moaveni (2011), and by Hu, Caetano & Cunha (2013) (Table 3).

Table 2. Variation of footbridge natural frequency (measured vs FEM model) (Zivanovic et al. 2006, Van Nimmen et al. 2014, 2016).

Bridge	Exp	FEM
Podgorica	1.66	1.83
Eeklo	1.71	2.03
Wetteren	0.71	0.74
Ninove	2.97	2.93
Mechelen	3.75	3.70
Anderlecht	2.85	3.04
Knokke	1.55	1.67
Leuven	3.06	2.92
Brugge	1.64	1.86
Charleroi	1.66	1.65

Table 3. Variation of natural frequency of footbridges due to temperature effects (Moser & Moaveni 2011, Hu, Caetano & Cunha 2013).

Bridge	Mean (Hz)	Min (Hz)	Max (Hz)
Dowling Hall	4.68	4.61	4.81
FEUP Campus	0.979	0.906	1.056

Damping is one of the most uncertain quantity. It is the result of dissipation mechanisms involving the soil and foundation, the structure and the aerodynamics. It can be subjected to large variations according to the level of structural displacement and to the wind velocity. Reliable estimates can only be obtained from experimental measurements on the existing structure; however, the damping value may still be affected by uncertainties concerning the measurements and the technique adopted for its identification. Usually, recourse is made to empirical models calibrated on collections of measurements obtained on structures of similar typology. SETRA (2006) recommends assuming a value for first modal damping ratio according to the structural typology (Table 4).

Table 4. Damping ratio (SETRA 2006)

Type	ξ_1 (%)
Reinforced concrete	1.3
Pre-stressed concrete	1
Mixed	0.6
Steel	0.4
Timber	1

HIVOSS (2009) provides minimum and average values for damping ratio according to construction material (Table 5).

Table 5. Damping ratio (HIVOSS 2009)

Type	ξ_1 min (%)	ξ_1 average (%)
Reinforced concrete	0.8	1.3
Pre-stressed concrete	0.5	0.6
Composite steel concrete	0.3	0.6
Steel	0.2	0.4
Timber	1	1.5
Stress ribbon	0.7	1

Different values can be found in the literature concerning experimental measurements on real footbridges (e.g. Zivanovic et al 2006, Zivanovic et al 2010, Moser & Moaveni 2011, Hu, Caetano & Cunha 2013, Van Nimmen et al. 2014, 2016, Tubino et al. 2016). Table 6 summarizes some of the recent data available in the literature specifying the corresponding structural typology. It should be noticed that the experimental damping ratios of the fundamental mode of vibration reported in Table 6 are not always related to a vertical flexural mode; the scattering of values in Table 6 could also be related to the different nature of the fundamental modes.

Table 6. Experimental values of damping ratio.

Bridge	Type	ξ_1 (%)
Podgorica	Steel	0.26
Reykjavik City	Concrete	1.11
Dowling Hall	Steel	0.44
FEUP Campus	Stress ribbon	1.03
Eeklo	Steel	1.94
Wetteren	Steel	2.12
Ninove	Steel	1.18
Mechelen	Steel	1.08
Anderlecht	Steel	0.45
Knokke	Steel	0.14
Leuven	Steel	2.47
Brugge	Steel	0.24
Charleroi	Steel	0.41
De Gasperi	Steel	0.5
Serra	Steel	0.6

4 UNCERTAINTY PROPAGATION

Many procedures allow propagating the uncertainties (e.g., Kareem 1987, Solari 1996). In this paper, Taylor Series Expansion (TSE) is adopted. After recalling the analytical formulation (Section 4.1), in Section 4.2 TSE is applied to footbridge serviceability assessment.

4.1 *Analytical formulation*

Let R be a quantity representative of the response of a structural system. Let us consider an adequate model of the structural behavior which estimates the response R; it is a function of a set of parameters listed by a vector $\mathbf{x}=\{x_1, x_2,..x_n\}^T$. As the evaluation of these quantities is affected by uncertainties, the errors inherent their estimate propagate over R.

TSE expands the original function R around the mean value of $\mathbf{x}$, i.e. $\mathbf{x}_m=\{x_{1m}, x_{2m},..x_{nm}\}^T$:

$$R(\mathbf{x}) \simeq R(\mathbf{x}_m) + \sum_{i=1}^{n} (x_i - x_{mi}) \frac{\partial R}{\partial x_i}(\mathbf{x}_m) + ... \quad (7)$$

Applying statistical operators to Eq. (7), one obtains the mean value R_m and its variance σ^2_R as functions of the statistical moments of $\mathbf{x}$:

$$\begin{aligned} R_m &\simeq R(\mathbf{x}_m) \\ \sigma^2_R &\simeq \nabla^T R(\mathbf{x}_m) \mathbf{C}_X \nabla R(\mathbf{x}_m) \end{aligned} \quad (8)$$

where $\nabla R = \left\{ \frac{\partial R}{\partial x_1} \quad \frac{\partial R}{\partial x_2} \quad \cdots \quad \frac{\partial R}{\partial x_n} \right\}^{\mathrm{T}}$ stands for the gradient of R and $\mathbf{C_X}$ is the covariance matrix of $\mathbf{x}$.

When the covariance among different random parameters can be neglected (i.e. considering $\mathbf{C_X}$ as a diagonal matrix), the second Eq. (8) reduces to:

$$\sigma_R^2 \simeq \sum_{i=1}^{n} \left(\frac{\partial R}{\partial x_i}(\mathbf{x}_m) \right)^2 \sigma_{xi}^2 \tag{9}$$

Thus the coefficient of variation of the response quantity R, $V_R=\sigma_R/R_m$, may be expressed as follows:

$$V_R^2 \simeq \sum_{i=1}^{n} V_{Ri}^2; \quad V_{Ri} = c_{xi} V_{xi}, \quad c_{xi} = \frac{\partial R}{\partial x_i}(\mathbf{x}_m) \frac{x_{mi}}{R_m} \tag{10}$$

where V_{Ri} is the variation coefficient of R related to the sole uncertainty in the i-th parameter x_i; $V_{xi}=\sigma_{xi}/x_{mi}$ represents the variation coefficient of the random parameter x_i; c_{xi} are propagation coefficients defining the influence of the i-th uncertain parameter on the variation coefficient of R.

TSE is particularly suitable when $R(\mathbf{x})$ is described by an analytical model. In this case, the procedure can be implemented through symbolic calculation tools, giving rise to closed-form solutions. However, when $R(\mathbf{x})$ is a non-linear function and the uncertainties are very large, TSE evaluation loses precision.

4.2 *Application to footbridges' serviceability assessment*

Dealing with footbridge serviceability assessment, the response quantities of interest are the standard deviation of the modal acceleration and its maximum value (thus, $R=\sigma_{\ddot{p}j}$ or $R=\ddot{p}_{j\max}$). The vector of random parameters is defined as follows:

$$\mathbf{x} = \left\{ V_{\omega_p} \quad \alpha_m \quad G_m \quad \tilde{\omega}_j \quad \xi_j \quad M_j \right\}^T \tag{11}$$

where $\tilde{\omega}_j = \omega_j / \omega_{pm}$ and $V_{\omega p} = \sigma_\omega / \omega_{pm}$ is the coefficient of variation of ω_p.

Considering the standard deviation of the acceleration as the response quantity of interest, $R=\sigma_{\ddot{p}_j}$ and assuming that the random parameters are uncorrelated, the coefficient of variation of R may be expressed through Eq. (10). The propagation coefficients c_{xi} are given by:

$$\begin{aligned}
&c_{x1} = c_{V_{\omega p}} = -\frac{1}{2}\left[1 - \frac{1}{V_{\omega p}^2}\left(\tilde{\omega}_j^2 - 1 \right)^2 \right]\Bigg|_{\mathbf{x}_m}; \\
&c_{x2} = c_{\alpha m} = 1; \qquad c_{x3} = c_{Gm} = 1; \\
&c_{x4} = c_{\tilde{\omega}_j} = \frac{1}{2}\left[1 - \frac{1}{V_{\omega p}^2}\left(\tilde{\omega}_j^2 - \tilde{\omega}_j \right) \right]\Bigg|_{\mathbf{x}_m}; \\
&c_{x5} = c_{\xi_j} = -\frac{1}{2}; \qquad c_{x6} = c_{M_j} = -1
\end{aligned} \tag{12}$$

where $\bullet|_{\mathbf{x}_m}$ means quantities calculated in the mean values of the parameters.

Eq. (12) clearly shows that the propagation on $\sigma_{\ddot{p}_j}$ of the structural damping ratio, of the modal mass, of the dynamic loading factor and of pedestrian weight are independent on the other random parameters. The contributions related to the ratio between the footbridge natural frequency and the average pedestrian step frequency and to the coefficient of variation of pedestrian frequency are instead dependent on their mean values. Indicatively, when $\tilde{\omega}_j = 1$, $c_{\tilde{\omega}_j} = -c_{V\omega p} = 0.5$.

The maximum response $\ddot{p}_{j\max}$ is related to $\sigma_{\ddot{p}_j}$ through the peak coefficient which is only ruled by $\tilde{\omega}_j$ in the proposed formulation. Therefore, the related propagation coefficients are the ones listed in Eq. (12), except from the one related to $\tilde{\omega}_j$, referred to as $c'_{\tilde{\omega}j}$:

$$c'_{\tilde{\omega}j} = \frac{1}{\Upsilon}\left(\frac{\Upsilon - 1}{\Upsilon + 1} \right) + c_{\tilde{\omega}j}; \quad \Upsilon = 2\,ln\left(\frac{L}{4.5}\tilde{\omega}_j \right) \tag{13}$$

being $c_{\tilde{\omega}j}$ the value given by the second of Eqs. (12). In the usual values of L, $c'_{\tilde{\omega}j} \approx c_{\tilde{\omega}j}$.

5 APPLICATION TO A CASE STUDY

The proposed procedure is applied to a real footbridge in Milan (Figure 1) that was the object of extensive full-scale experiments carried out to assess the dynamic characteristics and the vibration level induced by pedestrians.

The structure is made by a steel depressed double hinged arc. The main span length is L = 60 m; ω_1 =13.6 rad/s and ξ_1 = 0.005 have been measured during the experimental tests. Moreover, the following nominal values can be assumed: M_1 = 51000 kg; G_m = 600 N, α_m = 0.4 (Tubino et al. 2016). From Table 1, it is assumed ω_{pm}=12.55 rad/s $V_{\omega p}$ =0.08. The analysis is carried out investigating the contribution of the first mode to the structural response, i.e. j=1.



Figure 1. Footbridge crossing Viale De Gasperi in Milan (Italy).

At first, a preliminary sensitivity analysis is carried out in order to detect the parameters mainly affecting footbridge serviceability (Section 5.1), then the propagation coefficients are analyzed (Section 5.2). Finally, uncertainty propagation is performed in Section 5.3, where results are also compared with conventional verifications.

5.1 *Preliminary sensitivity analysis*

Figure 2 reports a preliminary sensitivity analysis of the structural response carried out assuming N_p=50. The variation of $\sigma_{\ddot{p}_1}$ varying each investigated parameter around its nominal value is plotted. The diagrams highlight the prominent role of the quantity $\tilde{\omega}_1$, pointing out that possible differences between the actual value of the frequency ratio and the value assumed as nominal quantity give rise to large differences in the estimate of the structural response. Especially, it shows that possible overestimates of $\tilde{\omega}_1$, i.e. possible overestimates of the natural frequency of the footbridge and underestimates of the pedestrian loading frequency, lead to underestimate the structural response and therefore to non-conservative evaluations.

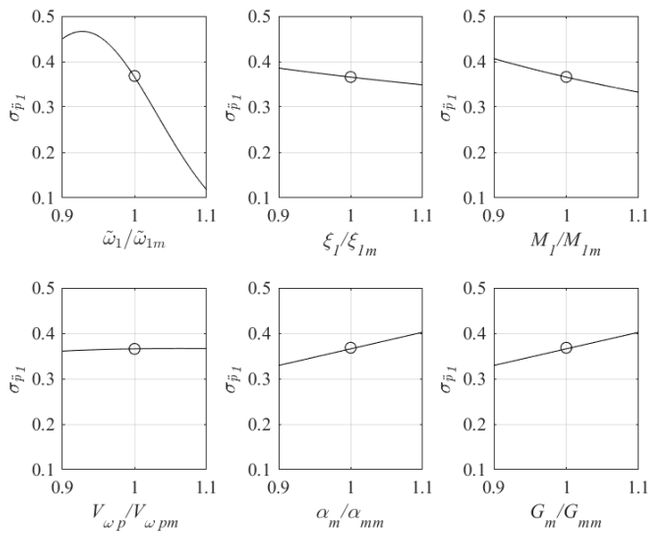


Figure 2. Response quantity $\sigma_{\ddot{p}_1}$ varying the input parameters. The circle indicates the estimate in the nominal value.

5.2 *Propagation coefficients*

Figure 3 plots the propagation coefficients in Eq. (12), solid line, and in Eq. (13), dashed line, as functions of $\tilde{\omega}_1$. The mean values of the parameters are assumed equal to the nominal value. Figure 4 shows a parametric diagram of $c_{\tilde{\omega}_1}$, $c'_{\tilde{\omega}_1}$ and $c_{V\omega p}$ for different values of $V_{\omega p}$. In both diagrams, the dashed vertical line indicates the nominal value of $\tilde{\omega}_1$.

Coherently with Figure 2, the diagrams show the prominent role of $\tilde{\omega}_1$, which is characterized by the largest propagation coefficient (in modulus) in the range of the nominal value of the parameters investigated, i.e. $\tilde{\omega}_1$=1.085, $V_{\omega p}$=0.08. It can also be noted that such coefficient becomes smaller than the others in resonant conditions, around $\tilde{\omega}_1$=1; it increases again for $\tilde{\omega}_1$<1. Especially, this trend is particularly marked when $V_{\omega p}$ is small, i.e. when the range of variation of the step frequency of the pedestrians is small.

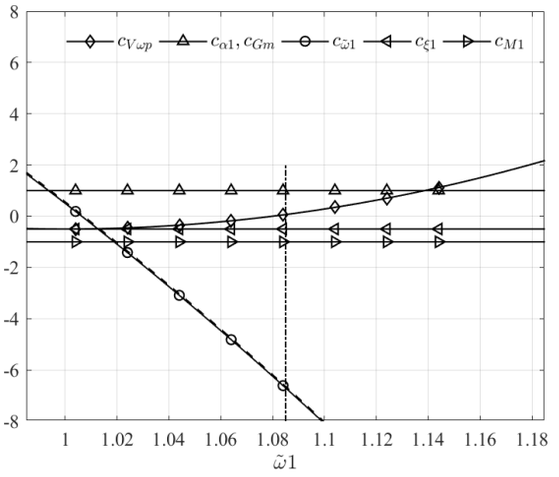


Figure 3. Propagation coefficients for the response quantity $\sigma_{\ddot{p}1}$ and $\ddot{p}_{1\max}$

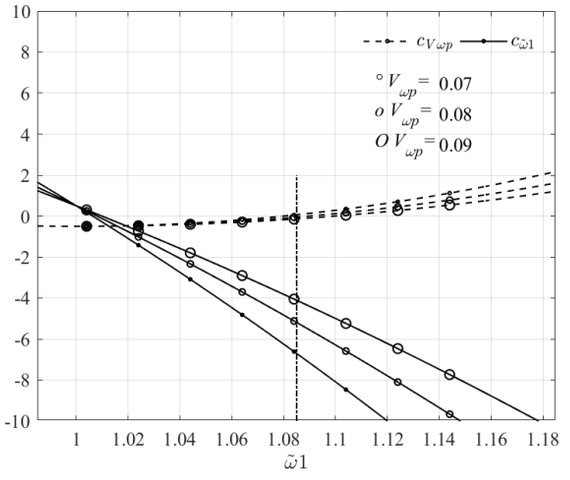


Figure 4. Variation of the propagation coefficients with $\tilde{\omega}_1$ and $V_{\omega p}$. The vertical line reports the mean value of $\tilde{\omega}_1$

5.3 *Uncertainty propagation analysis and comparison with conventional verifications*

The uncertainty propagation is carried out considering the actual scattering in the parameters in the application of the ESM described in Section 2. The mean value of the parameters is assumed equal to the nominal values. Concerning the pedestrian load parameters, the coefficient of variation of $V_{\omega p}$ is assumed 0.16 (see Table 1). Given the lack of information, the coefficient of variation for α_m and G_m is assumed 0.1. Concerning structural parameters, and taking into account the scattering related to both ω_1 and ω_{pm} (Table 1-3), the coefficient of variation of $\tilde{\omega}_1$ is assumed 0.1; the coefficient of variation of damping ratio ξ_1 is assumed 0.3; the coefficient of variation of the modal mass is assumed 0.05.

The propagation of uncertainties is carried out by Eq. (10) and Eq. (12) which account both for the role of each parameter in the analytical expression of the response and for the uncertainty inherent in the parameters. Table 7 summarizes the results obtained for the response quantity $\sigma_{\ddot{p}1}$; each row considers the related parameter as uncertain and assumes the nominal values of others. Results obtained on the peak value are essentially the same, being the values of the propagation coefficients c_{xi} almost coincident.

Table 7. Uncertainty propagation on the response standard deviation by TSE

x_i	V_{xi}	c_{xi}	V_{Ri}
$V_{\omega p}$	0.16	-0.065	0.09
α_m	0.1	1	0.1
G_m	0.1	1	0.1
$\tilde{\omega}_1$	0.1	-6.7	0.67
ξ_1	0.3	-0.5	0.15
M_1	0.05	-1	0.05

Values reported in Table 7 show that errors in the estimate of the involved frequencies, of the structure and the pedestrian loading, represent the main sources of uncertainties in the evaluation of the structural response. In this case, notwithstanding the prediction of this quantity is characterized by limited uncertainty, it affects the response evaluation according to a propagation factor larger than 5. Its prediction should require therefore a large effort in order to reduce errors in the prediction of the dynamic response.

Among the other structural parameters involved, it can be noted that the large scattering concerning damping evaluation is rather mitigated by the related propagation coefficient. The uncertainty in the modal mass is very small, however it propagates straight forward on the response.

Concerning the other dynamic loading parameters (coefficient of variation of the step frequency, average dynamic loading factor and average pedestrian weight), they all have comparable effect on the uncertainty of the response, providing a variation which is negligible if compared with the one provided by the uncertainty in the non-dimensional frequency characterization.

As a final remark, it should be noticed that the coefficient of variation of the response, taking into account the uncertainty in all the parameters (assumed as uncorrelated) is obtained applying Eq. (10) and it is given by $V_R = 0.71$.

A comparison with results provided by conventional verifications can be finally carried out.

SETRA (2006) provides the equivalent uniformly-distributed resonant loading per-unit-length:

$$f(t) = \frac{10.8\sqrt{\xi_j N_p}\,\alpha_m G_m \cos(\omega_j t)}{L} \tag{14}$$

Considering a sinusoidal mode shape, the modal load is given by:

$$F_j(t) = \frac{2\times 10.8\sqrt{\xi_j N_p}\,\alpha_m G_m \cos(\omega_j t)}{\pi} \tag{15}$$

The maximum acceleration $\ddot{p}^S_{j\max}$ provided by this standard loading condition is:

$$\ddot{p}^S_{j\max} = \frac{10.8\sqrt{\xi_j N_p}\,\alpha_m G_m}{\pi M_j \xi_j} \tag{16}$$

Table 8 reports the nominal values of the maximum footbridge acceleration obtained applying the ESM and the standard loading condition suggested by SETRA (2006). The number of pedestrians is assumed as N_p=50. A suitable interval of variation of the footbridge maximum acceleration provided by ESM taking into account the propagation of uncertainties is also reported ($R_m(1\pm V_R)$).

It can be noted that the conventional verification based on Eq. (16) provides a conservative estimate of the maximum footbridge acceleration if compared with the mean value provided by the equivalent spectral model, Eq. (4). However, taking into account for the randomness of the involved parameters, the response spread up to such an extent, so that results based on conventional evaluations turn out to be no longer representative of the actual response. Especially, within the range of variation obtained by the application of ESM, they can result non-conservative, providing unsafe evaluations.

Table 8. Comparison between conventional verification and uncertainty propagation results

	SETRA	ESM R_m	$R_m(1\pm V_R)$
$\ddot{p}_{j_{max}}$ (m/s^2)	1.61	1.45	0.42-2.48

6 CONCLUSIONS

In this paper, the propagation of uncertainties inherent to structural and loading parameters on the serviceability assessment of footbridges has been analyzed through the Taylor Series Expansion method. The joint analysis of the uncertainties of the loading parameters reported in the literature and of the propagation coefficients has allowed to identify the main parameters causing uncertainty in footbridges' serviceability assessment.

The application to a real case study has highlighted the determinant role of the frequency ratio (i.e. the ratio between the footbridge natural frequency and the mean pedestrian step frequency). Dealing with the specific case analyzed, it has been shown that conventional verifications based on equivalent uniformly distributed resonant load, are conservative with respect to estimates supplied by the Equivalent Spectral Model based on the nominal values of the

parameters. However, considering the large uncertainties inherent the estimate of the involved parameters, conventional estimates can lead to non-conservative evaluations.

It should be finally remarked that experimental measurements (Zivanovic 2012, Van Nimmen et al. 2014b) demonstrate that human-structure interaction could significantly affect human-induced vibrations of footbridges. This aspect, that has been neglected in the present paper, constitutes an additional source of uncertainty for the definition of the dynamic properties of the coupled pedestrians-footbridge system (Tubino 2018).

7 REFERENCES

BSI. 2008. UK National Annex to Eurocode 1: Actions on structures—Part 2: Traffic loads on bridges. NA to BS EN 1991-2:2003. British Standards Institution.

FIB. 2005. Guidelines for the design of footbridges. Lausanne: International Federation for Structural Concrete.

HIVOSS. 2009. Design of footbridges guideline. Human induced vibrations of steel structures, http://www.stb.rwth-aachen.de/projekte/2007/HIVOSS/download.php RFS2-CT-2007-00033.

Hu, W.H., Caetano, E., Cunha, A. Structural health monitoring of a stress-ribbon footbridge. Engineering Structures 2013; 57: 578-593.

ISO10137. 2007. Bases for design of structures – Serviceability of buildings and walkways against vibration. Geneva: International Organization for Standardization.

Kareem, A. 1987. Wind effects on structures: a probabilistic viewpoint. *Probabilistic Engineering Mechanics* 25: 166-200.

Matsumoto, Y., Nishioka, T., Shiojiri ,H,. Matsuzaki, K. 1978. Dynamic design of footbridges. *IABSE Proceedings* 17/78: 1-15.

Moser, P. & Moaveni, B. Environmental effects on the identified natural frequencies of the Dowling Hall Footbridge. Mechanical Systems and Signal Processing 2011; 25: 2336-2357.

Niu, S., Wang, C., Gao, S. 2016. A novel crowd random loads model for pedestrians walking on footbridge. *Arch. Applied Mech*. 86: 1369-1381.

Pachi, A. & Ji, T. 2005. Frequency and velocity of people walking. *The structural Engineer* 83: 36-40.

Pagnini, L. 2010. Reliability analysis of wind-excited structures. *Journal of Wind Engineering and Industrial Aerodynamics* 98: 1-9.

Piccardo, G. & Tubino, F. 2012. Equivalent spectral model and maximum dynamic response for the serviceability analysis of footbridges. *Engineering Structures* 40: 445-456.

Ricciardelli, F., Briatico, C., Ingolfsson, E.T., Georgakis, C.T. 2007. Experimental validation and calibration of pedestrian loading models for footbridges. In: *Proc. Experimental Vibration Analysis for Civil Engineering Structures EVACES 2007*: 219-225.

Sahnaci, C. & Kasperski, M. 2005. Random loads induced by walking. In: Soize C, Schuëller GI, editors. *Proc. VI European Conference on Structural Dynamics*, EURODYN 2005, Rotterdam. Millpress:441-446.

Sahnaci, C. & Kasperski, M. 2011. Simulation of random pedestrian flow. In: G. De Roeck, G. Degrande, G. Lombaert, G. Muller (eds.) *Proc. VIII European Conference on Structural Dynamics, EURODYN 2011*, Leuven, Belgium.

SETRA. 2006. Footbridges - Assessment of vibrational behaviour of footbridges under pedestrian loading. Paris: Technical Department for Transport, Roads and Bridges Engineering and Road Safety. Ministry of Transport and Infrastructure.

Solari, G. 1996. Evaluation and role of damping and period for the calculation of structural response under wind loads. *Journal of Wind Engineering and Industrial Aerodynamics* 59: 191-210.

Solari, G. 1997. Wind excited response of structures with uncertain parameters. *Probabilistic Engineering Mechanics* 12(2): 75-87.

Tubino, F. & Piccardo, G. 2016. Serviceability assessment of footbridges in unrestricted pedestrian traffic condition, *Structure and Infrastructure Engineering* 12(12): 1652-1662.

Tubino, F., Carassale, L., Piccardo, G. 2016. Human-induced vibrations on two lively footbridges in Milan, *Journal of Bridge Engineering* ASCE, 21(8).

Tubino, F. 2018. Probabilistic assessment of the dynamic interaction between multiple pedestrians and vertical vibrations of footbridges, *Journal of Sound and Vibration* 417: 80-96.

Van Nimmen, K., Lombaert, G., De Roeck, G., Van den Broeck, P. 2014. Vibration serviceability of footbridges: Evaluation of current codes of practice. *Engineering Structures* 59: 448-461.

Van Nimmen, K., Lombaert, G., Jonkers, I., De Roeck, G., Van den Broeck, P. 2014b. Characterisation of walking loads by 3D inertial motion tracking, *Journal of Sound and Vibration* 333: 5212-5226.

Van Nimmen, K., Verbeke, P., Lombaert, G., De Roeck, G., Van den Broeck, P. 2016. Numerical and experimental evaluation of the dynamic performance of a footbridge with tuned mass dampers. *Journal of Bridge Engineering ASCE* 21(8): C4016001.

Zivanovic, S., Pavic, A., Ingolfsson, E.T. 2010. Modeling spatially unrestricted pedestrian traffic on footbridges. *Journal of Structural Engineering ASCE* 136(10): 1296-1308.

Zivanovic, S., Pavic, A., Reynolds, P. 2006. Modal testing and FE tuning of a lively footbridge structure. *Engineering Structures*; 28: 857-868.

Zivanovic, S., Pavic, A., Reynolds, P. 2007. Probability-based prediction of multi-mode vibration response to walking excitation. *Engineering Structures* 29: 942-954.

Zivanovic, S. 2012. Benchmark footbridge for vibration serviceability assessment under the vertical component of pedestrian load, *Journal of Structural Engineering ASCE* 138(10): 1193-1202.

Maintenance, Safety, Risk, Management and Life-Cycle Performance of Bridges – Powers, Frangopol, Al-Mahaidi & Caprani (Eds)
© 2018 Taylor & Francis Group, London, ISBN 978-1-138-73045-8

Vision-based methodology for characterizing the flow of a high-density crowd

J. Van Hauwermeiren
KU Leuven, Department of Civil Engineering, TC Construction, Structural Mechanics and Building Materials, Ghent, Belgium

P. Van den Broeck & K. Van Nimmen
KU Leuven, Department of Civil Engineering, TC Construction, Structural Mechanics and Building Materials, Ghent, Belgium
KU Leuven, Department of Civil Engineering, Structural Mechanics Section, Leuven, Belgium

M. Vergauwen
KU Leuven, Department of Civil Engineering, TC Construction, Geomatics, Ghent, Belgium

ABSTRACT: The vibration serviceability assessment of footbridges exposed to high density crowds is often imperative for the design. Due to the lack of representative operational loading data, current models for crowd-induced loading remain unvalidated. This lack of data can partly be ascribed to the fact that the existing techniques to directly register human-induced loading are infeasible to apply for a high-density crowd. Instead, this contribution is taking a first step towards the indirect measurement of crowd-induced loading by identifying the individual walking trajectories of a high-density crowd from video footage. A unique case study of a footbridge exposed to real pedestrian traffic with a density of 1 person/m^2 is presented. Based on the collected video footage, the detection of each individual pedestrian in the crowd is obtained by employing an image segmentation algorithm. Next, each detection is associated to the corresponding track by using a motion-based prediction model. Subsequently, the obtained tracks are converted to world coordinates using two different setups: mono and stereo vision. The accuracy of the identified tracks is investigated. Finally, the flow characteristics are analyzed. The error propagation of measurement noise of the detection was observed to result in an accuracy in an order of magnitude of centimeters for the stereo-vision setup. Also, the error was found to be nearly constant for the entire bridge deck. In case of the single-view setup, the maximum error is higher than the stereo setup, especially for oblique viewing angles. A track obtained by mono-vision conversion has nearly the same accuracy as a track obtained by stereo vision provided that the true height of each pedestrian is accounted for. The identified mean walking velocity in the crowd is found to be in agreement with a widely-applied speed-density model in literature.

1 INTRODUCTION

As materials nowadays are ever stronger, structures become more slender and therefore more prone to dynamic excitation. In case a structure is designed for human occupants (e.g. grandstand, footbridges, ...), this trend is further stimulated by the relatively small service load. As a consequence the structural design of such structures is often governed by the vibration serviceability requirements. Although an accurate description of the human-induced load is indispensable to make a reliable prediction of the dynamic performance of a structure, designers are forced to rely on simplified force models. These models are based on unvalidated assumptions and neglect several important phenomena, such as the interaction between the crowd and the structure (Venuti and Bruno 2009). The main reason that current load models are unvalidated is the absence of well-documented full-scale operational loading data. However, this data is the only way forward for a further development of reliable load models that describe crowd-induced loading (Živanović 2012).

This absence can partly be ascribed to the fact that classical techniques to directly register human-induced loading are impractical to be applied for high-density crowds, involving a large number of participants. While these techniques have proven their

competence for laboratory or small-scale applications (Racic et al. 2010, Dang and Živanović 2015), upscaling these techniques is infeasible due to practical and/or economical reasons. Promising alternatives to register the crowd-induced loading are inverse force identification techniques (Van Nimmen et al. 2016), or indirect force characterizing techniques (Van Nimmen et al. 2014, Racic et al. 2010). The latter method characterizes the crowd-induced force by combining the 2D position of each pedestrian in the crowd with the participant's 3D body motion, more specifically the time-variant step frequency.

The pedestrians' trajectories can be obtained from video footage through the application of tracking algorithms on video footage of the pedestrians on the footbridge. The challenge of tracking people based on video frames has already received large attention in the literature. However, several challenges remain present, especially for high density crowds (Nguyen et al. 2016). The main developments in this domain are established within the context of video surveillance (Wang et al. 2014) or automotive safety applications (Gerónimo et al. 2010). Typically, these algorithms aim for a semantic understanding of the video footage. As a consequence, the conversion of the obtained tracks to world coordinates and, more importantly, the related accuracy of those world coordinates has not been investigated. This conversion and the quantification of the accuracy is indispensable for structural dynamical purposes.

This contribution presents a methodology to determine the trajectories of each pedestrian in a high density crowd on a footbridge, expressed in world coordinates. The methodology is illustrated by the application on a high-density crowd on a footbridge.

The outline of the paper is as follows. First, in Section 2 the footbridge structure is presented. Section 3 introduces the methodology for determining the pedestrians' tracks based on video footage, while Section 4 presents the methodology to convert the obtained tracks to world coordinates. In Section 5 the accuracy of the obtained tracks is analyzed and discussed. Section 6 presents the results of the applied methodology. Finally, Section 7 summarizes the main conclusions.

2 THE WAALSE KROOK SOUTH FOOTBRIDGE

The Waalse Krook South footbridge is a steel pedestrian and bicycle bridge with a single span of 23 m and a width of 6.8 m, designed by Couse & Goris architects in a collaboration with TV RCR Aranda Pigem Vilalta Architects (see also Figure 1). The bridge deck is composed of a two-way ribbed steel-concrete composite plate (2 cm steel, 12 cm concrete). The bridge deck is supported by two neoprene bearings on one side, and two steel columns on the other side.



Figure 1: The Waalse Krook South footbridge.

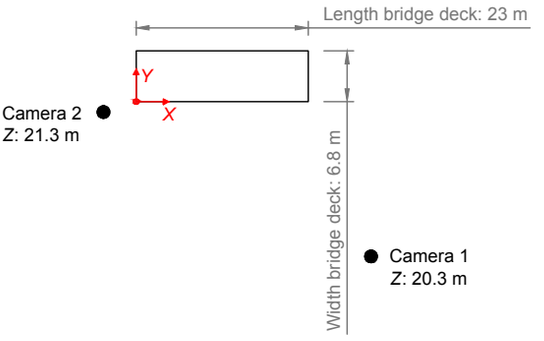


Figure 2: Schematic plan view of the bridge, camera positions and definition of the global axes X and Y. The axis Z coincides with the vertical direction.

2.1 *Camera setup*

Two stationary cameras are used to capture the motion of the pedestrians on the bridge deck. The position of camera 1 (outdoors, Nikon D3300) and camera 2 (indoors, Canon XA25) is given in Figure 2. The resolution of both cameras is 1920x1080p. The framerate is respectively 24 fps and 25 fps. A snapshot of the field of view of both cameras is shown in Figure 4. The area of the bridge deck in the snapshot of camera 1 is 5.11×10^5 pix^2 and for camera 2 is 5.04×10^5pix^2. This results respectively in an average ground sampling distance of 17.5 mm/pix and 17.4 mm/pix.

2.2 *Experimental program*

The experimental study considered 142 pedestrians walking on the bridge deck. This corresponds to a pedestrian density of approximately 1 persons/m^2. Prior to the experiment, the height and body mass of each participant was measured. The pedestrians were distributed over the entire bridge deck and were asked to walk at a self-selected speed. The total test duration was 10 minutes.

3 PEDESTRIAN DETECTION AND TRACKING

Determining the trajectories of each pedestrian in a crowd is a three-step process: (1) the detection of each pedestrian in each frame, (2) the association of each

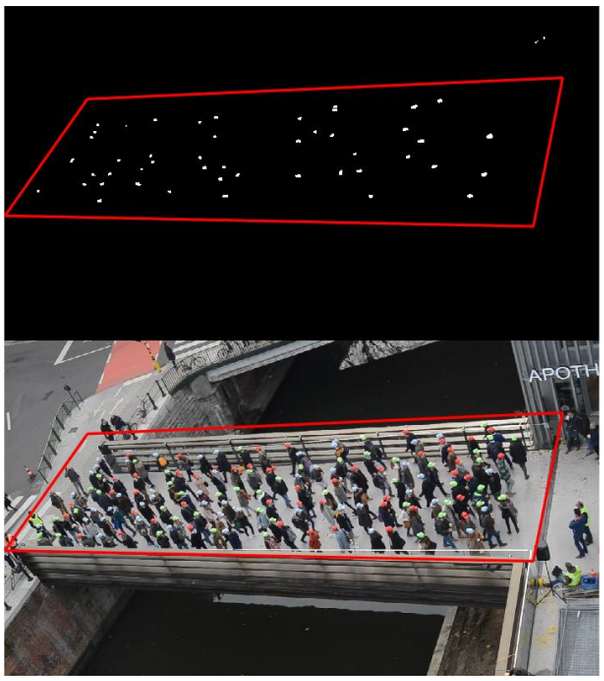


Figure 3: Example of a detection mask of blue colored hats on the bridge deck.

detection to its corresponding track and (3) the conversion of image coordinates to world coordinates.

The pedestrians can be tracked with one camera i.e. a mono-vision setup or multiple cameras i.e. a stereo-vision setup.

For the implementation of the methodology outlined in this section, various functions of the Computer Vision System Toolbox from Matlab R2016b™ are used (The MathWorks Inc. 2013).

3.1 *Detection*

Tracking a large number of pedestrians in video images requires stable, robust and scalable algorithms. Over time, many techniques have been developed for human detection in video footage. Typically, these techniques employ machine learning techniques (Girshick et al. 2014). The methods are effective for their intended purposes (e.g. video surveillance, face recognition etc.). However, for the detection of humans in large-density crowds the algorithms often become unstable due to the fact that parts of the body are occluded. Also, the computational cost of techniques based on machine learning is high.

In the present experimental study, a color segmenting technique is used. Each pedestrians was equipped with a colored hat in order to facilitate the detection. The method segments each pixel of the frame in two categories: detections of the colored hat of a pedestrian and the background. This approach has the main advantage that only the head of the pedestrian is detected, which enhances the accuracy of the obtained track. In addition, the robustness of the algorithm is not susceptible to occlusion of (parts of) the participant's body, provided that the viewing angle of the camera is not too oblique.

Three colors were used for the hats: red, blue and green. The colors were chosen in such a way that no overlap exists with the colors of the background in the RGB color-space. Next, 20 frames involving a varying illumination are used as training frames from which the pixels corresponding to the colored hats are selected. Mean and standard deviation of the resulting color vector are calculated. A 95% confidence volume in the RGB color-space is determined, assuming a multivariate normal distribution for each color vector. Subsequently, a detection mask is obtained for each frame by segmenting each pixel in the frame according to the obtained 95% confidence volumes of the colored hats. Finally, the detection of the hats is done by selecting the blob areas on the mask that exceed a user-defined area. In the present work, only blob areas larger than 12 pixels are retained. Other blob areas are considered as noise. An example of a detection mask is shown in Figure 3.

3.2 *Tracking*

Since there are several pedestrians, and thus multiple tracks, the data association problem is a multi-object tracking problem. A Kalman filter is used as a motion-based estimation model to predict the location of each pedestrian in the next frame. As a result of the relative high frame rate of the cameras, the frame-by-frame walking speed of the pedestrian only changes slightly. For this reason the motion model of the Kalman filter is configured with a constant velocity. The velocity in the motion model of the current frame is estimated as the average velocity of the past 5 frames. Both measurement and model noise are assumed to have a standard deviation of 3 pixels, invariant of the direction. The motivation for this assumption is given in Section 5.

The approach of using a Kalman filter has two advantages. First, the location of a track in the consecutive frame is estimated, which is subsequently used to determine the likelihood that a certain detection corresponds to a track. The association problem is solved by applying the James Munkres' variant of the Hungarian assignment algorithm (Munkres 1957). The second advantage of the Kalman filter is that an estimate can be made of a track's location when no measurement of that track is found in the next frame(s), e.g. due to occlusion. This allows to pick up a track when it becomes visible once more after several occluded frames.

4 CONVERSION FROM IMAGE COORDINATES TO WORLD COORDINATES

The identified tracks are obtained in one ore more image planes. However, further analysis is performed in world coordinates, so a conversion is required.

4.1 *Camera model*

The camera model that is used in the present work is the standard pinhole camera model. This section briefly discusses the used camera model. For a detailed description the reader is referred to (Hartley and Zisserman 2003).

The pinhole model describes the relation between world points $\mathbf{M} = [X, Y, Z, W]^{\mathrm{T}}$ and the image points $\mathbf{m} = [x, y, w]^{\mathrm{T}}$ in homogeneous coordinates. In case of Euclidean coordinates the last component i.e. W or w equals 1. The projection is described by equation (1) where $\simeq$ means "equal up to a non-zero scale factor":

$$\mathbf{m} \simeq \mathbf{PM} \tag{1}$$

$$\mathbf{m} \simeq \mathbf{K}[\mathbf{R}^T | -\mathbf{R}^T\mathbf{t}]\mathbf{M} \tag{2}$$

with $\mathbf{K}$ the matrix describing the intrinsic parameters of the camera:

$$\mathbf{K} = \begin{bmatrix} \alpha_{\mathrm{x}} & s & u_{\mathrm{x}} \\ 0 & \alpha_{\mathrm{y}} & u_{\mathrm{y}} \\ 0 & 0 & 1 \end{bmatrix} \tag{3}$$

with α_{x} and α_{y} the focal length, expressed in pixels, s the skew and u_{x} and u_{y} the location of the principal point, expressed in pixel coordinates. As digital cameras do not posses any skew, it holds that $s = 0$.

$\mathbf{R}$ and $\mathbf{t}$ are a 3×3 matrix and 3×1 vector describing the orientation and position of the camera in world coordinates respectively. The matrix $\mathbf{P}$ is a 3×4 matrix and is called the projection matrix.

Equation (1) is a linear equation and is an idealization of the actual projection mechanism of real-life cameras. The linear model does not capture radial or tangential distortion effects, typically present in such cameras.

As the influence of tangential distortion is usually much smaller than radial distortion, only the latter effect is taken into account. The effect is modeled with a polynomial function that describes the relation of the distorted and undistorted coordinates in the focal plane. As a consequence, the relation between the image point $\mathbf{m}$ and the world point $\mathbf{M}$ becomes non-linear and is denoted with by the vector function F:

$$\mathbf{m} = F(\mathbf{x}, \mathbf{M}) \tag{4}$$

With $\mathbf{x}$ being the camera parameter vector that contains all the relevant parameters of the camera model.

4.2 *Camera calibration*

The camera parameter vector $\mathbf{x}$ can be obtained by camera calibration. Several techniques exist for this calibration. In this work the methodology presented in (Triggs et al. 2000) is used. In this methodology the cameras are calibrated using correspondence points which were measured on the image planes (image coordinates) and on the bridge deck, the bridge railing and 1.7 m above the bridge deck (world coordinates). The 3D location of the world points was measured reflectorless with a total station, yielding accuracies of 2 mm + 2 ppm root mean square. Figure 4 shows the location of these correspondence points. The points are non-coplanar and scattered over the volume of the bridge deck, as this is the region of interest for the pedestrian detection.

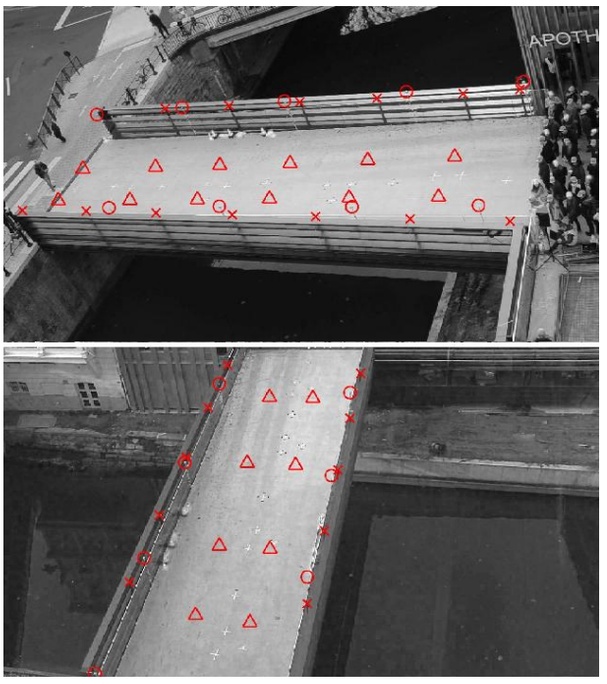


Figure 4: Snapshot of camera 1 (top) and camera 2 (bottom). Correspondence points used for calibration are situated on the bridge deck (△), the bridge railing (X) and on points 1.7m above the bridge deck (O).

For a given camera parameter vector $\mathbf{x}$ the reprojection error $\boldsymbol{\epsilon}$ is defined as $\boldsymbol{\epsilon} = \mathbf{m}_{\mathrm{c}} - \tilde{\mathbf{m}}_{\mathrm{c}}$, with $\mathbf{m}_c$ the image coordinates of the correspondence points and $\tilde{\mathbf{m}}_c$ the estimated image points obtained as $\tilde{\mathbf{m}} = F(\mathbf{x}, \mathbf{M})$.

The camera parameter vector $\mathbf{x}$ is estimated in such a way that the squared sum of the reprojection errors (i.e. $\boldsymbol{\epsilon}^{\mathrm{T}}\boldsymbol{\epsilon}$) is minimized. The calibration procedure yields camera parameter vectors for which the mean reprojection error is 0.60 pix and 0.91 pix for camera 1 and 2 respectively. This is considered to be sufficiently accurate for the envisaged purpose.

4.3 *Transformation of image coordinates to world coordinates*

In this paragraph two different approaches to retrieve 3D information about the pedestrians are discussed. First, the 3D position is determined using a multi-view setup. Second, the 3D position of the pedestrians is determined from a single view, using a planar homography.

4.3.1 *Retrieving the 3D position using stereo vision: triangulation*

When the projection matrices of both cameras $\mathbf{P}_1$ and $\mathbf{P}_2$ are known, the 3D information of a point $\mathbf{M}$ can be retrieved if the point is visible in both cameras i.e. $\mathbf{m}_1$ and $\mathbf{m}_2$.

The point $\mathbf{M}$ is the point for which the following holds:

$$\begin{cases} \mathbf{m}_1 &= \mathbf{P}_1\mathbf{M} \\ \mathbf{m}_2 &= \mathbf{P}_2\mathbf{M} \end{cases} \tag{5}$$

Since some measurement noise is always present, no exact solution for $\mathbf{M}$ exists. Therefore, $\mathbf{M}$ is found in such a way the the true reprojection error $\sum_{i=1}^{2} D(\mathbf{P}_\mathrm{i}\mathbf{M}, \mathbf{m}_i)$ is minimized. The practical procedure is described in (Moons et al. 2010).

4.3.2 *Retrieving the 3D position using single view geometry: homography*

Although 3D information is typically obtained from multiple 2D images, there are ways to obtain 3D information of points based on a single image. However, in this case one or more assumptions are to be made as a single view is mathematically insufficient to retrieve 3D information about an object.

In the present work a planar homography is used to obtain the 3D information about an object detected in a single frame. The homography describes the linear transformation of a 2D point. As such it can describe the transformation of a point in one plane to a corresponding point in another plane. In this case, the first plane is the (undistorted) image plane while the second plane π is defined as the horizontal plane 1.7m above the bridge deck.

It is assumed that the participants' heads coincide with the plane π. The consequences of this assumption will be investigated in paragraph 5.

The homography $\mathbf{H}_\pi$ is a 3×3 matrix and is defined as the relationship between the image coordinates $[x, y, w]^\mathrm{T}$ and the world coordinates $[X, Y, W]^\mathrm{T}$:

$$\mathbf{m}\begin{bmatrix} x \\ y \\ w \end{bmatrix} \simeq \mathbf{H}_\pi \begin{bmatrix} X \\ Y \\ W \end{bmatrix} = \begin{bmatrix} h_{11} & h_{12} & h_{13} \\ h_{21} & h_{22} & h_{23} \\ h_{31} & h_{32} & h_{33} \end{bmatrix} \begin{bmatrix} X \\ Y \\ W \end{bmatrix} \tag{6}$$

where the world coordinates are only expressed in terms of X and Y as the plane is horizontal.

The relationship between image coordinates and world coordinates is also described by equation (1). As it is assumed that each detection lies on the plane π, it holds that $Z = 1.7$m. This relation and equation (6) are substituted in equation (1). Rearranging yields the components of the homography matrix homography matrix $\mathbf{H}_\pi$.

Finally, the world coordinates $\mathbf{M}$ are calculated based on the detected image coordinates $\mathbf{m}$ by applying the inverse homography:

$$\begin{bmatrix} X \\ Y \\ W \end{bmatrix} \simeq \mathbf{H}_\pi^{-1}\mathbf{m} \tag{7}$$

5 ACCURACY OF THE IDENTIFIED TRACKS

In this paragraph the accuracy of the determined tracks is investigated. First, the measurement noise of the detection is discussed. Second, the accuracy of the stereo-vision setup is assessed. Third, the accuracy of the single-view setup is evaluated. Finally, a comparison is made between the tracks determined with the stereo and the mono-vision setup.

5.1 *Measurement noise of the detection*

Assume a certain participant in the test. The center of gravity of the colored hat on the image plan is denoted as $\mathbf{q} = [x_\mathrm{q}, y_\mathrm{q}]^\mathrm{T}$.

The measurement of this point is denoted as $\tilde{\mathbf{q}} = [\tilde{x}_\mathrm{q}, \tilde{y}_\mathrm{q}]^\mathrm{T}$.

It is assumed that the components of $\tilde{\mathbf{q}}$ are normally distributed around the components of the real center of gravity $\mathbf{q}$:

$$\tilde{x}_\mathrm{q} \sim \mathcal{N}(x_q, \sigma_{x_\mathrm{q}}^2) \tag{8}$$

$$\tilde{y}_\mathrm{q} \sim \mathcal{N}(y_q, \sigma_{y_\mathrm{q}}^2) \tag{9}$$

Furthermore it is assumed that the variation is the same in x and y direction (i.e. $\sigma_{x_\mathrm{q}} = \sigma_{y_\mathrm{q}}$) and that the measurement noise in both directions is independent. Hence, the joint probability density function (PDF) reads:

$$f_{\tilde{x}_\mathrm{q}\tilde{y}_\mathrm{q}}(x, y) = f_{\tilde{x}_\mathrm{q}}(x) f_{\tilde{y}_\mathrm{q}}(y) \tag{10}$$

The standard deviation $\sigma_{x_\mathrm{q}} = \sigma_{y_\mathrm{q}}$ is assumed to be 3 pixels. The border of the 95% confidence area of the corresponding joint PDF $f_{\tilde{x}_\mathrm{q}\tilde{y}_\mathrm{q}}$ is a circle with center $\mathbf{q}$ and a radius of 6 pixels. The 95% confidence area comprises the hat of the participant, see Figure 5.

The point in world coordinates which corresponds to the point(s) $\mathbf{q}$ is denoted as $\mathbf{Q} = [X_\mathrm{Q}, Y_\mathrm{Q}]^\mathrm{T}$. The world point which corresponds to the measured point(s) $\tilde{\mathbf{q}}$ has a probabilistic distribution as well and is denoted with $\tilde{\mathbf{Q}} = [\tilde{X}_\mathrm{Q}, \tilde{Y}_\mathrm{Q}]^\mathrm{T}$.

5.2 *Accuracy of the mono-vision setup*

In case $\mathbf{Q}_\pi$ is obtained by a single view, $\tilde{\mathbf{Q}}_\pi$ can be obtained by change of stochastic variables since the relation between $\mathbf{q}$ and $\mathbf{Q}_\pi$ is invertible. This relation is described by a planar homography and is given by equation (6). The point $\mathbf{Q}_\pi$ has the index π as it is



Figure 5: Detection of a person on the bridge deck. Dot: real center of gravity, $\mathbf{q} = [390\text{pix}, 370\text{pix}]^{\text{T}}$. Line: boundary of 95% confidence area of the measured center of gravity $\tilde{\mathbf{q}}$.

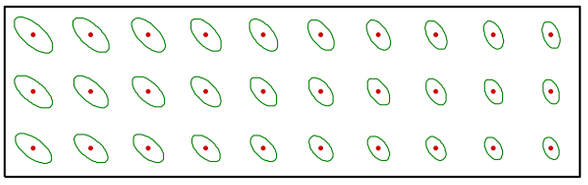


Figure 6: Boundaries of 95% confidence areas (lines) for different locations $\mathbf{Q}$ (dots) on the bridge deck. Confidence areas are rescaled with a factor 3 around the center of gravity of each confidence area.

assumed that this point lies on the plane π i.e. the assumption that was made when defining the homography $\mathbf{H}_\pi$. In this paragraph camera 1 is considered.

The components of an image coordinate $\mathbf{q}$ can be written as a functional of the coordinate $\mathbf{Q}_\pi$:

$$x_{\text{q}} = v_1(X_{\pi,\text{Q}}, Y_{\pi,\text{Q}}) \tag{11}$$

$$y_{\text{q}} = v_2(X_{\pi,\text{Q}}, Y_{\pi,\text{Q}}) \tag{12}$$

The joint PDF of $(\tilde{X}_{\pi,\text{Q}}, \tilde{Y}_{\pi,\text{Q}})$ is obtained through change of stochastic variables and is given by:

$$g_{\tilde{X}_\text{Q}\tilde{Y}_\text{Q}}(X_\pi, Y_\pi) = |J| f_{\tilde{x}_\text{q}\tilde{y}_\text{q}}\left[v_1(X_\pi, Y_\pi), v_2(X_\pi, Y_\pi)\right] \tag{13}$$

With J the Jacobian defined by:

$$J = \begin{bmatrix} \frac{\partial v_1(X_{\pi,Q}, Y_{\pi,Q})}{\partial X_\pi} & \frac{\partial v_1(X_{\pi,Q}, Y_{\pi,Q})}{\partial Y_\pi} \\ \frac{\partial v_2(X_{\pi,Q}, Y_{\pi,Q})}{\partial X_\pi} & \frac{\partial v_2(X_{\pi,Q}, Y_{\pi,Q})}{\partial Y_\pi} \end{bmatrix} \tag{14}$$

The 95% confidence area of $g_{\tilde{X}_{\pi,\text{Q}}\tilde{Y}_{\pi,\text{Q}}}$ is depicted in Figure 6 for different locations $\mathbf{Q}$ on the bridge deck.

Next, the maximum error e_{mono} is calculated as the maximum distance between the point if no error occurred (which corresponds in this case with the mean value $(X_{\pi,Q}, Y_{\pi,Q})$ and the boundary of the 95% confidence area. The maximum measurement error for every possible location $\mathbf{Q}$ on the bridge deck is shown in Figure 7.

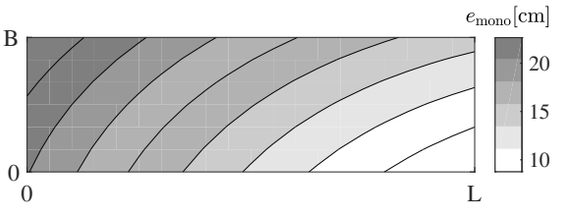


Figure 7: Maximum measurement error of a mono setup e_{mono} for every possible location of $\mathbf{Q}$ on the bridge deck.

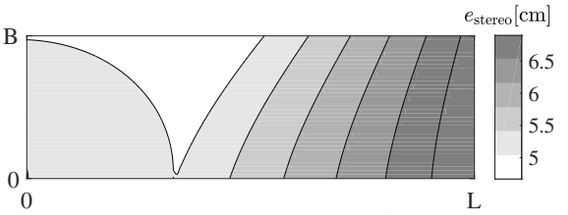


Figure 8: Maximum measurement error of a stereo setup e_{stereo} for every possible location of $\mathbf{Q}$ on the bridge deck.

The result shows that the maximum error as a result of the measurement error is 25 cm, in the North-West corner of the bridge deck. The lowest error is found in the South-East corner of the bridge deck. The error increases with the obliqueness of the viewing angle of the camera.

5.3 *Accuracy of the stereo-vision system*

Since the equations that describe the relation between the image points on two planes, $\mathbf{q}_1$ and $\mathbf{q}_2$, and the corresponding point in world coordinates $\mathbf{Q}$ are not invertible, a simplified approach is taken to evaluate the accuracy of the stereo-vision system.

A point $\mathbf{Q}$ is considered which lies on the bridge deck. The corresponding image coordinates of the different cameras $\mathbf{q}_1$ and $\mathbf{q}_2$ are calculated using equation (4). Next, one of the image points is translated by 6 pixels (the radius of the 95% confidence area of $\tilde{\mathbf{q}}$) in the $\pm x$ or $\pm y$ direction, i.e. 4 possible locations for the measured point $\tilde{\mathbf{q}}$ are considered. Then, the corresponding 3D location $\tilde{\mathbf{Q}}_i$ is obtained by using the procedure explained in paragraph 4.3.1, with one image point translated 6 pixels and one image point not shifted. This is done for both image points. Finally, the horizontal error $e_{\text{stereo},i}$ is defined as the horizontal distance between $\tilde{\mathbf{Q}}_i$ and $\mathbf{Q}$ and is calculated for all 8 possible combinations. The final error e_{stereo} is obtained as $\max_i(e_{\text{stereo},i})$.

Figure 8 depicts the maximum measurement noise for every possible location of $\mathbf{Q}$ on the bridge deck. From this figure it can be observed that the measurement error is low (order of magnitude 6 cm) and that the measurement error is nearly constant for every location of $\mathbf{Q}$ on the bridge deck.

5.4 *Comparison of mono versus stereo vision*

A comparison is made between the tracks determined by triangulation (stereo vision) and the tracks determined using a homography (mono vision) for 40

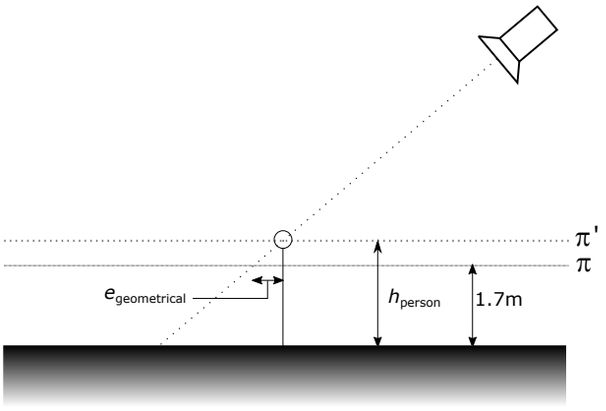


Figure 9: A geometrical error occurs when using a homography if a person's height is higher or lower than 1.7 m (i.e. the height of the reference plane π).

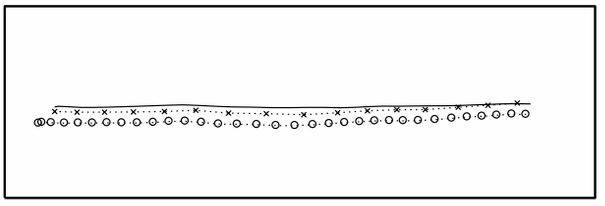


Figure 10: Part of a track of a person with a height of 1.55 m. Tracks calculated by triangulation (solid line), homography (dashed line with marker O) and homography with the reference plane translated to take into account the height of the person (dashed line with marker X). The relative horizontal distances of the dashed lines with respect to the solid line are rescaled with a factor 3.

pedestrians. The latter considers two different calculation methods: (1) the height is not explicitly taken into account (and assumed to be 1.7 m) and (2) the height of the pedestrian is taken into account by translating the plane π with a distance $(h_{\text{person}} - 1.7\text{m})$. The horizontal geometrical error increases as $|h_{\text{person}} - 1.7\text{m}|$ increases and as camera becomes more oblique, see also Figure 9 and 10.

The comparison considers pedestrians crossing the bridge a single time. The error for each frame is calculated as the difference in horizontal distance of the track using a homography relative to the track determined by triangulation. Next, the root mean square error (RMSE) is calculated for each track.

Figure 11 depicts the RMSE of the tracks determined by mono versus stereo vision. In this graph it can clearly be seen that the RMSE of the tracks increases with $|h_{\text{person}} - 1.7\text{m}|$ in case the height of the person is not taken into account, reaching RMSE values higher than 0.30 m. On the other hand, taking into consideration the height of the person results in an average RMSE of 0.04 m, independent of the person's height.

6 RESULTS OF THE VISION-BASED METHODOLOGY

Figure 12 shows a typical result of the obtained track of a pedestrian based on the vision-based methodology and its corresponding velocity. The figure shows

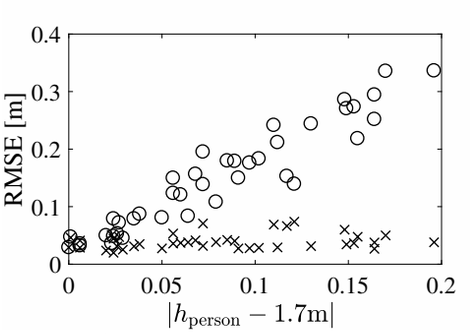


Figure 11: RMSE of tracks determined by using a homography relative to the tracks obtained by stereo conversion as a function of the quantity $|h_{\text{person}} - 1.7\text{m}|$: height of the pedestrian not taken into account (O) and height explicitly taken into account (X).

that the walking velocity varies over time, which is a result of the fact that (1) pedestrians have to deviate from a straight line to avoid collision with other pedestrians causing them to change route and speed and (2) the current case study involved lower speeds when turning on either side of the bridge due to local congestions.

The pedestrians turn in a zone of approximately 2 meter at the end of the bridge decks. These zones are indicated in gray in Figure 6. Since these parts of the track are an artificial situation, they are omitted in further analysis.

Figure 13 shows the distribution of the average walking velocities of the pedestrians during the test. The figure shows that the mean walking velocity is 0.96 m/s. The walking speed is also be predicted using an average speed-density relation, as proposed in (Weidmann 1993). Based on this relation, an average walking velocity of 1.05 m/s is predicted for a crowd density of 1 person/m^2. The comparison shows that the measured walking velocity is 9% lower than the predicted velocity. This may be ascribed tho the fact the predicted velocity in (Weidmann 1993) considers an unidirectional flow, whereas the real situation is bidirectional. In (Weidmann 1993) the reduction of speed is estimated to be about 4-9% in case of an equal flow in both directions. This estimate is in agreement with the observed mean velocity.

7 CONCLUSIONS

A methodology is presented to track the pedestrians in a high-density crowd based on camera footage. By taking the appropriate measures prior to the start of the experiment, the presented algorithm is capable to determine the trajectories of each pedestrian.

The effect of error propagation of measurement noise of the detections was investigated. In case of the stereo setup, the final error has an order of magnitude of 6 cm and is nearly constant over the bridge deck. In case of a mono-vision setup, the maximum error is 25 cm in the North-West corner of the bridge. The error increases as the obliqueness of the camera increases.

A mono-view conversion of the identified tracks is compared to a stereo view transformation. Using

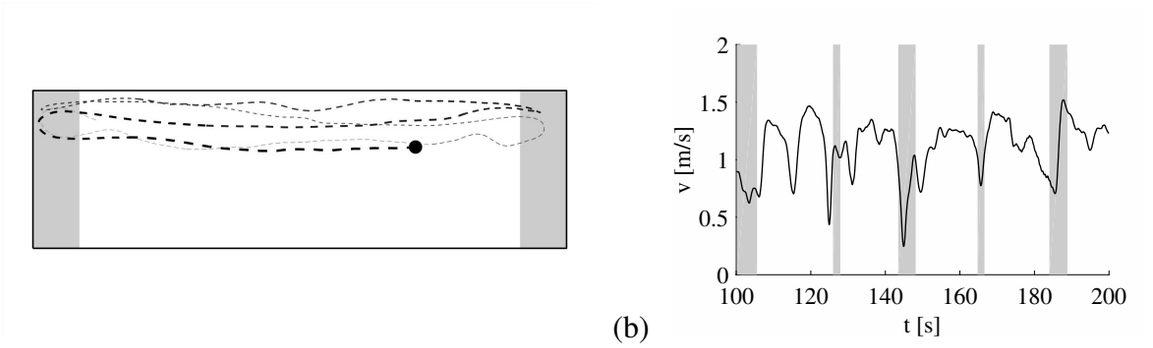


Figure 12: Example of the result of the vision-based methodology. (a) Trajectory of a pedestrian between 100s and 200s. The gray hue indicates the location on the bridge deck where the longitudinal component of the distance to the border is less than 2 m. (b) Corresponding velocity of the pedestrian. The gray background indicates the time slots when the longitudinal component of the distance of the pedestrian to the border is less than 2 m.

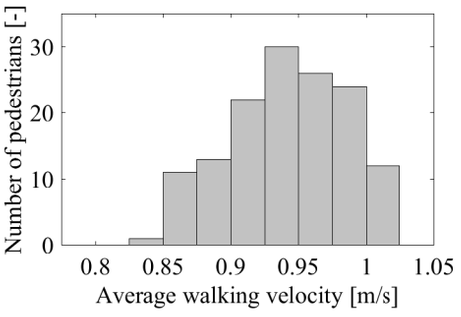


Figure 13: Distribution of the average walking velocities of the pedestrians during the test.

a homography yields RMSE's up till 0.35 m, especially for persons whose height is remarkably higher or lower than the height of the reference plane. By taking into account the height of the pedestrian, the RMSE can be mitigated to 0.04 m.

The proposed pedestrian-tracking methodology is applied to a case study with a high-density crowd of 1 person/m^2. A comparison of the measured mean walking velocity compared to the velocity predicted by a well-known speed-density model in literature, indicates that the measured velocity is in good agreement with the predicted velocity.

ACKNOWLEDGMENTS

The financial support of the Research Foundation Flanders (FWO) funding this research is gratefully acknowledged.

REFERENCES

Dang, H. V. & S. Živanović (2015). Experimental characterisation of walking locomotion on rigid level surfaces using motion capture system. *Engineering Structures 91*, 141–154.

Gerónimo, D., A. M. López, A. D. Sappa, & T. Graf (2010). Survey of pedestrian detection for advanced driver assistance systems. *IEEE Transactions on Pattern Analysis and Machine Intelligence 32*(7), 1239–1258.

Girshick, R., J. Donahue, T. Darrell, & J. Malik (2014). Rich feature hierarchies for accurate object detection and semantic segmentation. In *Proceedings of the IEEE Computer Society Conference on Computer Vision and Pattern Recognition*, pp. 580–587.

Hartley, R. & A. Zisserman (2003). *Multiple View Geometry in Computer Vision*, Volume 2.

Moons, T., L. V. Gool, & M. Vergauwen (2010). 3D Reconstruction from Multiple Images Part 1: Principles. *Foundations and Trends in Computer Graphics and Vision 4*(4), 287–404.

Munkres, J. (1957). Algorithms for the Assignment and Transportation Problems. *Journal of the Society for Industrial and Applied Mathematics 5*(1), 32–38.

Nguyen, D. T., W. Li, & P. O. Ogunbona (2016). Human detection from images and videos: A survey.

Racic, V., J. M. W. Brownjohn, & A. Pavic (2010). Reproduction and application of human bouncing and jumping forces from visual marker data. *Journal of Sound and Vibration 329*(16), 3397–3416.

The MathWorks Inc. (2013). Computer Vision System Toolbox. *(Mathworks) http://www.mathworks.com/products/computer-vision/*, http://www.mathworks.com/products/computer–vision/.

Triggs, B., P. F. P. McLauchlan, R. I. Hartley, & A. W. A. Fitzgibbon (2000). Bundle Adjustment: A Modern Synthesis. In *ICCV '99 Proceedings of the International Workshop on Vision Algorithms: Theory and Practice*, Volume 34099, pp. 298–372.

Van Nimmen, K., G. Lombaert, I. Jonkers, G. De Roeck, & P. Van Den Broeck (2014). Characterisation of walking loads by 3D inertial motion tracking. *Journal of Sound and Vibration 333*(20), 5212–5226.

Van Nimmen, K., K. Maes, P. Van Den Broeck, G. De Roeck, & G. Lombaert (2016). Inverse identification of pedestrian-induced loads. In *Proceedings of ISMA 2016 - International Conference on Noise and Vibration Engineering and USD2016 - International Conference on Uncertainty in Structural Dynamics*.

Venuti, F. & L. Bruno (2009). Crowd-structure interaction in lively footbridges under synchronous lateral excitation: A literature review.

Wang, X., M. Wang, & W. Li (2014). Scene-specific pedestrian detection for static video surveillance. *IEEE Transactions on Pattern Analysis and Machine Intelligence 36*(2), 361–374.

Weidmann, U. (1993). Transporttechnik der Fussgänger, Transporttechnische Eigenschaften des Fussgängerverkehrs (Literturauswertung). Technical Report 90.

Živanović, S. (2012). Benchmark Footbridge for Vibration Serviceability Assessment under the Vertical Component of Pedestrian Load. *Journal of Structural Engineering 138*(10), 1193–1202.

Maintenance, Safety, Risk, Management and Life-Cycle Performance of Bridges – Powers, Frangopol, Al-Mahaidi & Caprani (Eds)
© 2018 Taylor & Francis Group, London, ISBN 978-1-138-73045-8

Using full-scale observations to estimate the parameters governing human-structure interaction

K. Van Nimmen
KU Leuven, Department of Civil Engineering, Structural Mechanics, 3001 Leuven, Belgium
KU Leuven, Department of Civil Engineering, Technology Cluster Construction, Structural Mechanics B-9000 Ghent, Belgium

P. Van den Broeck
KU Leuven, Department of Civil Engineering, Technology Cluster Construction, Structural Mechanics B-9000 Ghent, Belgium

G. Lombaert
KU Leuven, Department of Civil Engineering, Structural Mechanics, 3001 Leuven, Belgium

ABSTRACT: The further development and improvement of prediction models for crowd-induced vibrations of footbridges requires detailed information on representative operational loading data. This paper uses an inverse method to estimate the parameters that govern human-structure interaction from the resulting structural response. The parameters of interest concern the dynamic characteristics of a single-degree-of-freedom (SDOF) system, applied to describe the mechanical interaction between the pedestrian and the structure. The parameter estimation procedure assumes that the dynamic behaviour of the emtpy structure and the distribution of step frequencies in the crowd are known. The dynamic characteristics of the SDOF model are estimated by minimizing the discrepancy between the observed and the simulated power spectral density of the structural response.
The proposed approach is applied to a real footbridge. First, the operational modal characteristics of the empty structure are identif ed and used to calibrate the f nite element model of the structure. Second, the structural response induced by a pedestrian density of 1 persons$/\mathrm{m}^2$ is observed. The corresponding non-resonant response is used to estimate the distribution of step frequencies in the crowd. Finally, the parameter estimation procedure is applied and a reasonable estimate of the dynamic characteristics of the SDOF model is obtained.

1 INTRODUCTION

Prone to human-induced vibrations, the dynamic performance of footbridges under crowd-induced loading is often imperative for the design. Although the force exerted by a pedestrian on a perfectly rigid laboratory f oor is well known (Racić et al. 2009), the mechanical interaction between the human body of the pedestrian and the supporting structure (human-structure interaction, HSI) is not (Georgakis and Ingólfsson 2014, Tubino and Piccardo 2016). However, the latter is expected to have a signif cant impact on the structural response to pedestrian excitation, in particular for high pedestrian densities (Kasperski 2014, Busca et al. 2014, Bocian et al. 2013, Pedersen 2015).

In the low-frequency range of interest for vibration serviceability (0-10 Hz), the dynamic behaviour of the human body in vertical direction for a person standing still, resembles that of a highly damped single-degree-of-freedom (SDOF) system for which the natural frequency ($2.7 < f_{\mathrm{H}} < 7.0$ Hz) and damping ratio ($20 < \xi_{\mathrm{H}} < 60$ %) largely depend on the body posture (Matsumoto and Griff n 1998, Matsumoto and Griff n 2003, Van Nimmen et al. 2017a). Based on these observations, the pedestrian excitation is often modeled as the superposition of the force exerted by a pedestrian on a rigid f oor and a mechanical interaction term which depends on the dynamic properties of both the human body and the footbridge (Alexander 2006, Van Nimmen et al. 2017a, Shahabpoor et al. 2016, Venuti et al. 2016). However, the SDOF system is an approximation of the human body of a pedestrian and these assumptions should be validated and its model parameters calibrated based on in-f eld observations involving walking persons (Van Nimmen et al. 2017a, Tubino and Piccardo 2016).

This contribution applies the parameter estimation

procedure proposed in (Van Nimmen et al. 2017b) to estimate the dynamic characteristics of the SDOF interaction model from the (measured) response of the supporting structure. The methodology assumes that the dynamic behaviour of the emtpy structure and the distribution of step frequencies in the crowd are known and uses the measured structural response induced by pedestrians as input. In the present contribution, this methodology is applied to a real footbridge. The dynamic behaviour of the empty footbridge is experimentally identif ed and applied to calibrate the f nite element model of the structure. Next, the structural response induced by a high pedestrian density is observed. The distribution of step frequencies in the crowd is derived from the corresponding non-resonant structural response. Finally, the parameter estimation procedure is applied to estimate the dynamic characteristics of the SDOF interaction model from the full-scale observations.

The outline of this paper is as follows. First, the coupled crowd-structure model is introduced (Section 2). Second, the parameter estimation problem is formulated (Section 3). Third, the approach is applied to full-scale data collected on a real footbridge (Section 4). The conclusions are summarized in Section 5.

2 COUPLED CROWD-STRUCTURE MODEL

Pedestrians in a crowd are active systems for which the walking behaviour is controlled by an internal driving term. The pedestrian and the supporting structure (e.g. the footbridge) are considered as two linear subsystems coupled at a single contact point. In this way, the contact force not only depends on the internal driving term of the pedestrian but also on the dynamic properties of both subsystems (Van Nimmen et al. 2017a, Shahabpoor et al. 2016).

A modally reduced system is derived from the linear dynamic f nite element (FE) model of the supporting structure. The governing equations of motion in modal coordinates read:

$$\ddot{\mathbf{z}}(t) + \mathbf{\Gamma}\dot{\mathbf{z}}(t) + \mathbf{\Omega}^2\mathbf{z}(t) = \mathbf{\Phi}^\top \mathbf{p}(t) = \mathbf{\Phi}^\top \mathbf{S}_\mathbf{p}(t)\mathbf{p}_\mathbf{p}(t) \quad (1)$$

with $\mathbf{z}(t) \in \mathbb{R}^{n_m}$ the modal coordinate vector, n_m the number of modes retained in the modally reduced system, $\Omega^2 \in \mathbb{R}^{n_m \times n_m}$ a diagonal matrix containing the square of the natural frequencies $\omega_j = 2\pi f_j$ in rad/s, $\Gamma \in \mathbb{R}^{n_m \times n_m}$ a diagonal matrix containing the terms $2\xi_j\omega_j$ with ξ_j $[-]$ the modal damping ratios, $\mathbf{\Phi} \in \mathbb{R}^{n_{\text{DOF}} \times n_m}$ a matrix which has the mass-normalised mode shapes $\boldsymbol{\phi}_j$ as columns, $\mathbf{\Phi}^\top\mathbf{p}(t)$ the modal projection of the external forces $\mathbf{p}(t) \in \mathbb{R}^{n_{\text{DOF}}}$ with n_{DOF} the number of degrees of freedom (DOF) of the FE model. The vector of the forces $\mathbf{p}(t)$ contains the contact force(s) between the bridge and the n_{H} pedestrian(s). For each pedestrian, the contact is reduced to a single point representing at the same time the left and the right foot. The time history of the n_{H} contact forces $p_{\text{p}}(t)$ are collected as rows in the force vector $\mathbf{p}_\mathbf{p}(t) \in \mathbb{R}^{n_{\text{H}}}$. Using the selection matrix $\mathbf{S}_\mathbf{p}(t) \in \mathbb{R}^{n_{\text{DOF}} \times n_{\text{H}}}$, the forces are transfered to the corresponding DOFs of the FE model of the structure.

At this point, the key assumption is made that the walking behaviour of the pedestrian is not affected by the vibrating surface, i.e. the internal driving term of the pedestrian is identical to the one in case of a rigid supporting system. Assuming a *f xed-driver term* allows the body motion and, hence, the contact force of a pedestrian $p_{\text{p}}(t)$, to be decomposed in a term resulting from the driving term $p_{\text{F}}(t)$ and a term resulting from the interaction between the pedestrian and the supporting structure $p_{\text{H}}(t)$:

$$p_{\text{p}}(t) = p_{\text{F}}(t) + p_{\text{H}}(t) \quad (2)$$

For a perfectly rigid f oor, thus without interaction ($p_{\text{H}}(t) = 0$), the contact force equals the ground reaction forces (GRFs) as registered by the force plates or an instrumented treadmill f xed to a rigid laboratory f oor ($p_{\text{p}}(t) = p_{\text{F}}(t)$) (Racić et al. 2009). When a large number of pedestrians is involved, these force terms are governed by (imperfectly known) parameters characterizing inter- and intra-person variabilities (Racić et al. 2009, Caprani et al. 2012). Given the fact that the focus is on the resulting structural response, a number of reasonable simplifying assumptions can be made. The comprehensive numerical analysis performed by Tubino et al. (Tubino and Piccardo 2016) shows that the statistical distribution of the walking speed and the pedestrian weight have a negligible inf uence on the dynamic response of the structure. Therefore, all pedestrians are assumed to have the same weight and walking speed v_s [m/s]. The latter is def ned in terms of the pedestrian density d [pedestrians/m^2] (Bruno and Venuti 2009). The walking trajectories are straight lines parallel to the longitudinal axis of the bridge deck. The arrival times are assumed to follow a Poisson distribution (Živanović 2012). The step frequencies are assumed to follow a Gaussian distribution ($f_s = \mathcal{N}(\mu_{f_s}, \sigma_{f_s})$ [Hz]) (Association Française de Génie Civil, Sétra/AFGC 2006). Together, the pedestrian's step frequency f_s and weight G characterise the vertical walking load $p_{\text{F}}(t)$, described in this study by a probabilistic single-person force model that accounts for intra-person variabilities (Živanović et al. 2007). This load model accounts for the f rst f ve main and intermediate harmonics of the walking load as well as for the narrow-band nature of the force around each (sub-)harmonic.

When the supporting structure is f exible, the contact force $p_{\text{p}}(t)$ in addition depends on the interaction between the two subsystems. The interaction term $p_{\text{H}}(t)$ in Eq. (2), can be further elaborated based on the mechanical properties of the SDOF system representing the human body (Matsumoto and Griff n 2003,

Van Nimmen et al. 2017a):

$$p_{\mathrm{p}}(t) = p_{\mathrm{F}}(t) - m_{\mathrm{H0}}\ddot{u}(t) + c_{\mathrm{H1}}\left[\dot{u}_{\mathrm{H1}}(t) - \dot{u}(t)\right] + k_{\mathrm{H1}}\left[u_{\mathrm{H1}}(t) - u(t)\right] \quad (3)$$

with m_{H1} the sprung mass, m_{H0} the unsprung mass, k_{H1} and c_{H1} the spring and damping element, $m_{\mathrm{H}} = m_{\mathrm{H1}} + m_{\mathrm{H0}}$ and $u_{\mathrm{H1}}(t)$ and $u(t)$ the displacements of the mass m_{H1} and the bridge at the contact point, respectively. The mechanical properties of the interaction model (m_{H0}, m_{H}, k_{H1} and c_{H1}) are assumed identical for all pedestrians.

3 PARAMETER ESTIMATION PROBLEM

The parameter estimation procedure detailed in this section, is borrowed from (Van Nimmen et al. 2017b).

The objective is to identify the parameters that determine the effect of HSI on the resulting structural response: the dynamic characteristics of the linear mechanical systems representing the pedestrians in the crowd. It is assumed that the structural response induced by the pedestrians and the dynamic behaviour of the emtpy structure are known. The former requires vibration measurements on the structure during operation. The latter can be predicted using a f nite element model or identif ed directly from experimental vibration data using system identif cation techniques (Peeters and De Roeck 1999, Reynders and De Roeck 2008). In addition to the dynamic behaviour of the empty structure and the HSI-effects, the structural response also depends on the total *f xed-driver term* induced by the crowd. To limit the number of variables in the parameter estimation problem, it is assumed that the following a-priori information on this *f xed-driver term* is available: the distribution of step frequencies ($f_s = \mathcal{N}(\mu_{f_s}, \sigma_{f_s})$ [Hz]). The latter can be derived from empirical relations (Bruno and Venuti 2009), e.g. as a function of the pedestrian density (see Section 2) and/or, preferably, be based on additional information collected in situ.

In (Van Nimmen et al. 2017b) it is shown that when a suff ciently long duration of the structural response induced by a certain pedestrian density is considered, the statistical effect of the remaining unknown stochastic parameters, i.e. the effect of the randomness in the f xed-driver term, on the PSD of the resulting structural response can be averaged out. The randomness of the f xed-driving term results from the arrival times and the intra-person variabilities (see Section 2). As these parameters are much more diff cult to identify experimentally, it is a great advantage to be able to average out their statistical effect.

Next, an optimisation problem is formulated where the objective function measures the difference between the PSD of the experimentally observed ($\tilde{\mathbf{G}}_{\ddot{u}}$) and the numerically simulated ($\mathbf{G}_{\ddot{u}}$) structural response within a frequency range def ned by a lower (ω_{l} [rad/s]) and upper bound (ω_{u} [rad/s]). For now, it is assumed that the structural response is observed in a single output location. The residuals are computed at discrete frequencies ω_k [rad/s]: $\omega_k = \omega_{\mathrm{l}} + k\Delta\omega$ for $k = 0, ..., N$, with $N + 1 = (\omega_{\mathrm{u}} - \omega_{\mathrm{l}})/\Delta\omega + 1$ the number of samples and $\Delta\omega$ the selected frequency resolution. The decision variables in this optimisation problem are the natural frequency f_{H1} and the modal damping ratio ξ_{H1} of the selected linear mechanical system (see Section 2). These parameters are assumed identical for the different persons on the structure and are subject to the following physical constraints: $f_{\mathrm{H1}} > 0$ and $\xi_{\mathrm{H1}} > 0$. The problem, subject to 2 inequality constraints, is formulated in standard form:



Figure 1: The Waalse Krook South footbridge.

$$\underset{f_{\mathrm{H1}},\, \xi_{\mathrm{H1}}}{\text{minimise}} \quad \frac{\| \tilde{\mathbf{G}}_{\ddot{u}} - \mathbf{G}_{\ddot{u}}(f_{\mathrm{H1}}, \xi_{\mathrm{H1}}) \|_2^2}{\| \tilde{\mathbf{G}}_{\ddot{u}} \|_2^2} \quad (4)$$

$$\text{subject to} \quad f_{\mathrm{H1}} > 0 \quad (5)$$

$$\xi_{\mathrm{H1}} > 0 \quad (6)$$

and can be categorised as a nonlinear programming problem due to the nature of the objective function (Nocedal and Wright 2006). The inequality constrained optimisation problem is solved using the lsqnonlin-solver (MATLAB (MATLAB 2015)) by means of the trust-region-ref ective algorithm.

Based on a numerical verif cation example, it is shown in (Van Nimmen et al. 2017b) that the above proposed methodology allows to estimate both the natural frequency and the modal damping ratio of the SDOF model. The results also suggest that as the structural response is predominantly sensitive to the natural frequency of the interaction model, the corresponding estimation uncertainty is low.

4 APPLICATION TO FULL-SCALE DATA

4.1 *Waalse Krook South Footbridge*

The Waalse Krook South footbridge is a steel pedestrian and bicycle bridge with a single span of 25 m and a width of 6 m, designed by Couse & Goris architects in a collaboration with TV RCR Aranda Pigem

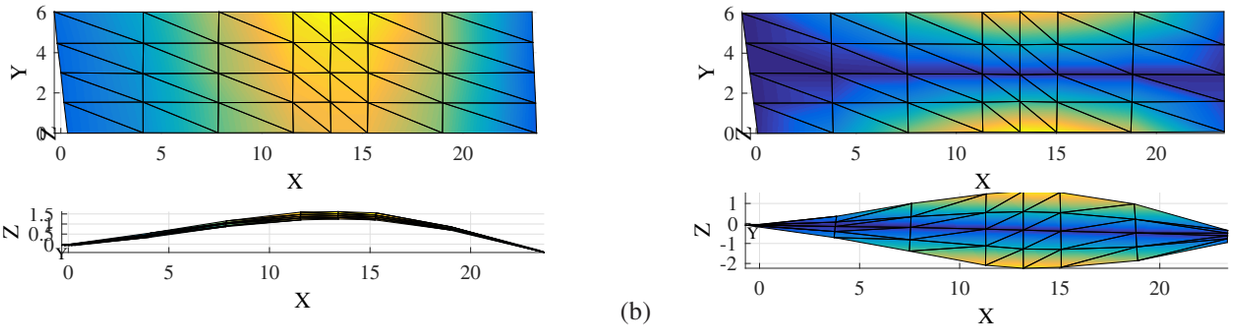


Figure 2: The operational modal parameters of the two modes identif ed for the empty footbridge: (a, left) 3.30Hz, 0.86% and (b, right) 4.14Hz, 0.25%.

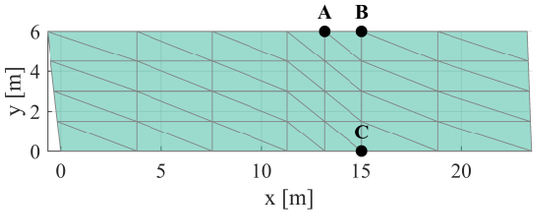


Figure 3: The measurement locations A, B and C on the bridge deck.

Vilalta Architects (Figure 1). The bridge deck is composed of a two-way ribbed steel-concrete composite plate. The bridge deck is supported by two neoprene bearings on one side, and two steel columns on the other side.

An operational modal analysis is performed for the empty footbridge. The vibration data was collected using tri-axial accelerometers (GeoSIG GMS-18) for a total of 40 grid-points. The output-only data have been processed using the reference-based covariance-driven stochastic subspace identif cation (SSI-cov) algorithm (Peeters and De Roeck 1999, Reynders and De Roeck 2008). Two modes with a frequency up to 5.5 Hz are identif ed (see Figure 2): a vertical bending mode and a torsional mode.

A detailed f nite element (FE) model is developed according to the architectural drawings using the FE software ANSYS. The FE model consists of Timoshenko beam elements for the supporting columns and the ribs of the bridge deck, and a regular mesh of 4-node shell elements (Mindlin-Reissner theory) for the steel-concrete composite bridge deck. By tuning the translational stiffness of the neoprene supports, an optimal agreement is obtained with the experimentally identif ed natural frequencies and mode shapes: for both modes, the relative frequency deviation is limited to 2% and the corresponding MAC-values are high (>0.95).

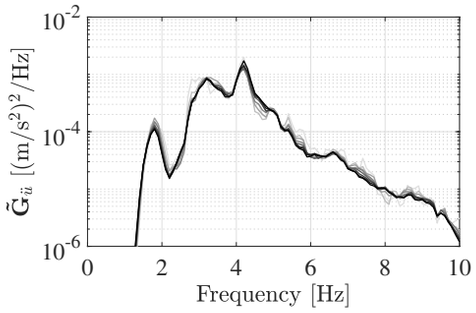
In the following, the numerical simulations are performed based on the experimentally identif ed natural frequencies and modal damping ratios, and the mass-normalized mode shapes of the calibrated FE model. All modes with a natural frequency below 20 Hz are taken into account. Unless stated otherwise, the simulated and measured structural response are both low-pass f ltered with a cut-off frequency of 10 Hz.

4.2 *Full-scale observations*

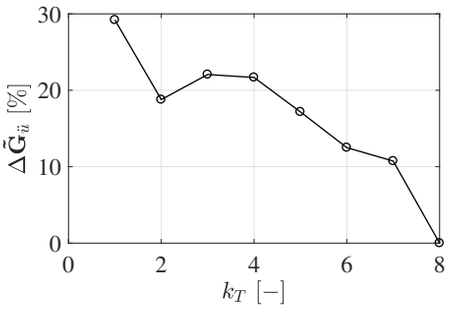
A full-scale measurement campaign was carried out considering a pedestrian density of 1 persons/m^2. Different types of human excitation were considered: (1) standing still (duration 5 minutes), (2) free walking (duration 10 minutes) and (3) synchronized walking whereby a metronome was used to aim for resonance between the second harmonic of the walking load and the fundamental or second natural frequency of the footbridge (duration 5 minutes). The short test durations were imposed by practical limitations. During these tests, the vertical structural response was registered at 3 locations on the bridge deck, corresponding to the anti-nodes of the f rst and second mode of the footbridge (f gures 2 and 3).

The test of interest in the present study involves free walking. Based on the preliminary data analysis, a time frame of 8 minutes ref ecting the stationary response of the structure, is selected. The structural response is low-pass f ltered with a cut-off frequency of 10 Hz. The PSD of the structural response is calculated considering $n_T = 8$ [-] consecutive time windows of length $T = 60$ s, with 50% overlap. In Figure 4 the convergence of the PSD is f rst analysed by evaluation for an increasing number k_T of consecutive time windows of length T. Analogously to the formulation of the objective function in Section 3, the convergence error ($\Delta \mathbf{G}_{\ddot{u},k_T}$) is def ned as the discrepancy between the PSD calculated considering k_T ($\mathbf{G}_{\ddot{u},k_T}$) and the total of $n_T = 8$ ($\mathbf{G}_{\ddot{u},n_T}$) consecutive time windows. This Figure 4 shows that as a result of the relative short measurement duration of 8 minutes, a convergence error of approximately 10% remains which, in turn, will inevitably result in an error on the results of the parameter estimation procedure.

The dominant contributions around 3.3 Hz and 4.1 Hz in Figure 5 show that the pedestrians mainly excite the fundamental and the second mode of the footbridge. In addition, the structural response is characterized by clear contributions around 1.8 Hz. These contributions ref ect the non-resonant excitation by the fundamental harmonic of the walking load. The aim is now to use this observation to derive information on the distribution of step frequencies in the crowd. To do so, the structural response is f rst low-pass f ltered with a cut-off frequency of 2.3 Hz such



(a)



(b)

Figure 4: (a) The PSD of the structural response induced by a pedestrian density $d = 1.0$ pedestrians/m^2 measured at the location A indicated in Figure 3 calculated for an increasing number k_T of consecutive time windows of length $T = 60$ s, for $k_T = 1$ (white) up to $k_T = 8$ (black) and (b) corresponding convergence error $\Delta\tilde{\mathbf{G}}_{\ddot{u}}$.

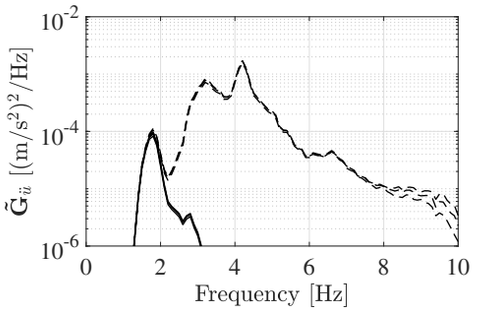


Figure 5: The PSD of the structural response induced by a pedestrian density $d = 1.0$ pedestrians/m^2 measured at the locations indicated in Figure 3: low-pass f ltered with a cut-off frequency of 10 Hz (dashed) and 2.3 Hz (solid).

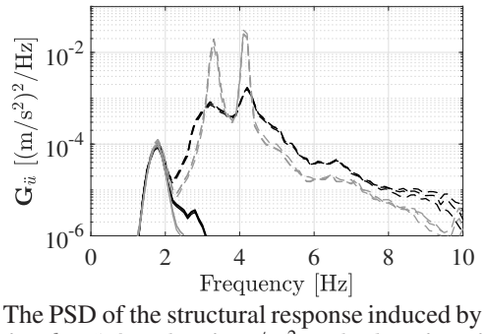


Figure 6: The PSD of the structural response induced by a pedestrian density $d = 1.0$ pedestrians/m^2 at the locations indicated in Figure 3: low-pass f ltered with a cut-off frequency of 10 Hz (dashed) and 2.3 Hz (solid), measured (black) and simulated without HSI (grey).

that the inf uence of the dynamic modes of the structure is minimised. Figure 5 shows that in this way, the contribution of the fundamental harmonic of the walking load to the PSD of the structural response is isolated and is in fact hardly inf uenced by the dynamic contribution of the modes of the footbridge. Second, it is in addition assumed that this contribution is not inf uenced by HSI, an assumption that is reasonable based on the observations made in (Van Nimmen et al. 2017a). Based on this assumption and by minimizing the difference between the PSD of the measured and simulated structural response low-pass-f ltered at 2.3 Hz, the following distribution of step frequencies in the crowd is f tted: $\mathcal{N}(1.68, 0.13)$ Hz. At this point, the simulations are performed without HSI, i.e. with $p_{\text{p}}(t) = p_{\text{F}}(t)$ (see also Section 2). Figure 6 shows that based on this f tted distribution of step frequencies, a good agreement is found between the PSD of the measured and simulated structural response for frequencies below 2.3 Hz. Figure 6 also shows that for frequencies higher than 2.3 Hz, and in particular for frequencies close to the fundamental and second natural frequency of the footbridge, signif cant differences are observed between the PSD of the measured and simulated structural response. It is reasonable to assume that these differences are largely due to HSI that is disregarded in these simulations.

4.3 *Parameter estimation*

Finally, the objective is to estimate the parameters governing HSI using the full-scale observations detailed in Section 4.2. To this end, the parameter estimation problem formulated in Section 3 is solved. The structural response is simulated using the coupled crowd-structure model introduced in Section 2. The dynamic behaviour of the structure (Section 4.1) and the PSD of the structural response and the distribution of step frequencies in the crowd (Section 4.2) are used as input. The following solution is obtained:

$$f_{\text{H1}} = 3.10\text{Hz}$$

$$\xi_{\text{H1}} = 0.25\% \tag{7}$$

Figure 7 shows that in this way a reasonable f t is obtained between the simulated and measured PSD of the structural response. The agreement has signif cantly improved around the contribution of the fundamental and second mode of the footbridge. These results corroborate recent f ndings in the literature (Shahabpoor et al. 2016, Van Nimmen et al. 2017a). Although the present application illustrates the potential of the proposed procedure, a considerable level of uncertainty remains due to (small) modelling errors and the limited duration of the experimental observations.

To illustrate the effect of HSI on the vibration serviceability for the Waalse Krook footbridge, Figure 8 shows a typical time history of the structural response simulated with and without HSI for a window of 8 minutes. This f gure illustrates that although the maximum vibration levels are in both cases below the limit for maximum vibration comfort (0.5 m/s^2 (Association Française de Génie Civil, Sétra/AFGC 2006)),

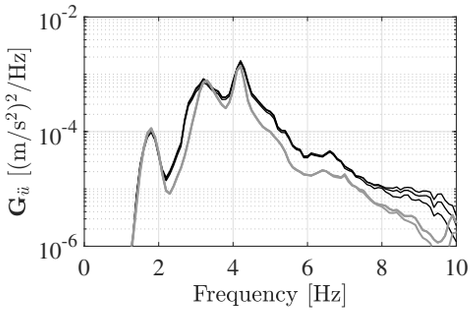


Figure 7: The PSD of the structural response induced by a pedestrian density $d = 1.0$ pedestrians$/\mathrm{m}^2$ at the locations indicated in Figure 3: measured (black) and simulated with HSI (grey).

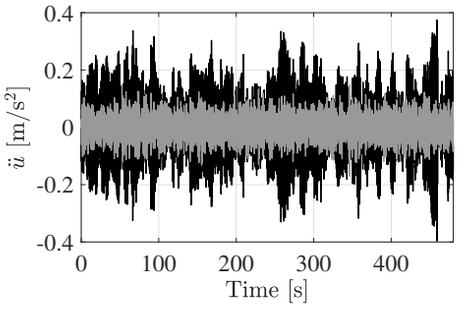


Figure 8: Typical time history of the acceleration levels at location A, simulated without (black) and with HSI (grey).

the maximum structural response is almost 3 times lower when HSI is accounted for.

5 CONCLUSIONS

In this contribution, an inverse method is applied to estimate the parameters that govern the effect of HSI from the measured response of the supporting structure. The parameters of interest concern the dynamic characteristics of a SDOF model, applied to describe the interaction between a linear mechanical system representing the human body (SDOF system) and the supporting structure. The parameter estimation procedure assumes that the dynamic behaviour of the empty structure and the distribution of step frequencies in the crowd are known. By minimizing a cost function that measures the discrepancy between the observed and the simulated PSD of the structural response, the dynamic characteristics of the considered SDOF interaction model are estimated.

The proposed approach is applied to a real footbridge. Full-scale testing involved (1) ambient excitation and (2) the excitation by a pedestrian density of 1 persons$/\mathrm{m}^2$. The ambient vibrations are applied to identify the operational modal characteristics of the empty structure and are subsequently applied to calibrate the f nite element model of the structure. Next, for the load case involving pedestrian excitation, the distribution of step frequencies in the crowd is estimated from the corresponding non-resonant structural response. Finally, the proposed parameter estimation procedure is applied and an estimate of 3.10 Hz and 0.25% is obtained for the natural frequency and damping ratio of the SDOF model, respectively. These results corroborate recent f ndings in the literature. Although the present application illustrates the potential of the proposed procedure, a considerable level of uncertainty remains due to (small) modelling errors and the limited duration of the experimental observations.

ACKNOWLEDGEMENTS

This research is funded by the Research Foundation Flanders (FWO). The f nancial support is gratefully acknowledged.

REFERENCES

Alexander, N. (2006). Theoretical treatment of crowd-structure interaction dynamics. *Proceedings of the Institution of Civil Engineers: Structures and Buildings 159*(6), 329–338.

Association Française de Génie Civil, Sétra/AFGC (2006). *Sétra: Evaluation du comportement vibratoire des passerelles piétonnes sous l'action des piétons (Assessment of vibrational behaviour of footbridges under pedestrian loading)*. Association Française de Génie Civil, Sétra/AFGC.

Bocian, M., J. H. G. Macdonald, & J. F. Burn (2013). Biomechanically-Inspired Modelling of Pedestrian-Induced Vertical Self-Excited Forces. *Journal of Bridge Engineering 18*, 1336–1346.

Bruno, L. & F. Venuti (2009). Crowd-structure interaction in footbridges: Modelling, application to real case-study and sensitivity analysis. *Journal of Sound and Vibration 323*, 475–493.

Busca, G., A. Cappellini, S. Manzoni, M. Tarabini, & M. Vanali (2014). Quantif cation of chances in modal parameters due to the presence of passive people on a slender structure. *Journal of Sound and Vibration 333*, 5641–5652.

Caprani, C. C., J. Keogh, P. Archbold, & P. Fanning (2012). Enhancement for the vertical response of footbridges subjected to stochastic crowd loading. *Computers and Structures 102-103*, 87–96.

Georgakis, C. T. & E. Ingólfsson (2014, July). Recent advances in our understanding of vertical and lateral footbridge vibrations. In *Proceedings of the 5th International Footbridge Conference*, London, UK.

Kasperski, M. (2014, June–July). Damping induced by pedestrians. In *Proceedings of the 8th International Conference on Structural Dynamics of EURODYN*, Porto, Portugal.

MATLAB (2015). *R2015b*. Natick, Massachusetts: The MathWorks Inc.

Matsumoto, Y. & M. J. Griff n (1998). Dynamic response of the standing human body exposed to vertical vibration: inf uence of posture and vibration magnitude. *Journal of Sound and Vibration 212*(1), 85–107.

Matsumoto, Y. & M. J. Griff n (2003). Mathematical models for the apparent masses of standing subjects exposed to vertical whole-body vibration. *Journal of Sound and Vibration 260*, 431–451.

Nocedal, J. & S. Wright (2006). *Numerical Optimization*. Springer Science+Business Media, Second edition.

Pedersen, L. (2015, January – February). Implications of interaction between humans and structures. In *Proceedings of IMAC 33, the International Modal Analysis Conference*, Orlando, Florida, US. Springer-Verlag.

Peeters, B. & G. De Roeck (1999). Reference-based stochastic subspace identif cation for output-only modal analysis. *Mechanical Systems and Signal Processing 13*(6), 855–878.

Racić, V., A. Pavić, & P. Reynolds (2009). Experimental identif cation and analytical modelling of walking forces: a literature review. *Journal of Sound and Vibration 326*, 1–49.

Reynders, E. & G. De Roeck (2008). Reference-based combined deterministic-stochastic subspace identif cation for experimental and operational modal analysis. *Mechanical Systems and Signal Processing 22*(3), 617–637.

Shahabpoor, E., A. Pavić, & V. Racić (2016). Identif cation of mass-spring-damper model of walking humans. *Structures 5*, 233–246.

Tubino, F. & G. Piccardo (2016). Serviceability assessment of footbridges in unrestricted pedestrian traff c conditions. *Structure and Infrastructure Engineering*.

Van Nimmen, K., G. Lombaert, G. De Roeck, & P. Van den Broeck (2017a). The impact of vertical human-structure interaction on the response of footbridges to pedestrian excitation. *Journal of Sound and Vibration 402*, 104–121.

Van Nimmen, K., P. Van den Broeck, & G. Lombaert (2017b, September). Inverse identif cation of the pedestrian characteristics governing human-structure interaction. In F. Vestroni, F. Romeo, and V. Gattulli (Eds.), *Proceedings of the 10th International Conference on Structural Dynamics, EURODYN 2017*, Rome, Italy, pp. 2889–2894.

Venuti, F., V. Racic, & A. Corbetta (2016). Modelling framework for dynamic interaction between multiple pedestrians and vertical vibrations of footbridges. *Journal of Sound and Vibration 379*, 245–263.

Živanović, S. (2012). Benchmark footbridge for vibration serviceability assessment under vertical component of pedestrian load. *Journal of Structural Engineering 138*, 1193–1202.

Živanović, S., A. Pavić, & P. Reynolds (2007). Probability-based prediction of multi-mode vibration response to walking excitation. *Engineering Structures 29*(6), 942–954.

Maintenance, Safety, Risk, Management and Life-Cycle Performance of Bridges – Powers, Frangopol, Al-Mahaidi & Caprani (Eds)
© 2018 Taylor & Francis Group, London, ISBN 978-1-138-73045-8

Comparison between structure- and crowd-based mitigation strategies on vibrating footbridges

F. Venuti
Department of Architecture and Design
Politecnico di Torino, Italy

A. Reggio
Department of Structural, Building and Geotechnical Engineering
Politecnico di Torino, Italy.

ABSTRACT: Due to their lightweight, slenderness and extremely low structural damping, footbridges may often be prone to vibrations under human-induced excitation. As a consequence, structural control devices, mainly TMDs, have been installed before or after the footbridge opening to mitigate excessive vibrations under pedestrian dynamic loading. The aim of this study is to explore an alternative approach towards the mitigation of human-induced vertical vibrations: instead of acting on the structure, the novel approach acts on the source of excitation, that is, the crowd flow. Bearing in mind the dependence of the step frequency on the walking velocity, which in turn depends on the crowd density, a strategy based on the modification of the crowd flow along the footbridge, through the proper location of obstacles on the deck, is proposed. The crowd-based strategy can be quickly implemented, either as a permanent (e.g., benches or light poles) or an emergency temporary measure (e.g., Jersey barriers), and is expected to be cheaper than structure-based alternatives. The study is carried out by means of numerical simulations. Crowd dynamics simulations are performed through the commercial software Mass Motion, which is based on a microscopic model of crowd dynamics. The generated pedestrian trajectories and velocities are then used to build the force signals, that are subsequently applied on a 1DOF structure model to calculate the vertical response. The effectiveness of the proposed crowd-based mitigation strategy is then evaluated on an ideal footbridge and finally compared with the one of a linear viscoelastic TMD, the latter designed to meet vertical vibration serviceability requirements.

1 INTRODUCTION

Footbridges are very often lightweight and slender structures with extremely low structural damping. For this reason, they are prone to vibrations under dynamic loadings, in particular under human-induced excitation. In the last fifteen years, an increasing number of cases has been reported where mitigation measures had to be installed before or after the footbridge opening to reduce excessive human-induced vibrations (e.g, Dallard et al. 2001, Dziuba et al. 2001, Caetano et al. 2010, Tubino et al. 2016).

Because increasing structural mass or stiffness implies high costs and undesired aesthetic impact, mitigation measures on footbridges generally consist in adding supplemental damping devices, such as viscous dampers (Dallard et al. 2001) and friction dampers (Law et al. 2004). A similar purpose can be accomplished by transferring most of the structural vibration energy to an attached Tuned Mass Damper (TMD), which, in its simplest form, is composed of an auxiliary mass-spring-dashpot passive system dissipating the energy away by vibrating out of phase with the structural motion (Housner et al. 1997). TMDs have been widely applied on real-life bridges for response control against wind-induced loads, primarily (Soong and Dargush 1997), yet successful applications on pedestrian bridges exist wherein TMD is used to mitigate either vertical or horizontal human-induced vibrations (Dallard et al. 2001, Dziuba et al. 2001, Brownjohn et al. 2004, Caetano et al. 2010). Unlike buildings, for which TMDs with high mass ratios are recently receiving considerable attention (De Angelis et al. 2012, Reggio and De Angelis 2015), technical reasons cause the TMD mass in bridges to be typically below few percent (1%-5%) of the structural mass. This limitation may possibly jeopardize in practice the effectivess of the control device as well as its robustness against detuning effects derived from structural nonlinearities or uncertainties.

An alternative approach to vibration mitigation on footbridges has been first suggested by Carroll et al. (2012) and subsequently investigated by Venuti and Bruno (2013) for the case of lateral vibrations due to Synchronous Lateral Excitation. According to this approach, the reduction of the structural response can be obtained by acting on the source of excitation, i.e. on the crowd flow, in analogy to what is done to reduce wind-induced vibrations on tall buildings (Kareem and Kijewski 1999) or long-span bridges (Sarwar and Ishihara 2010). Carroll et al. (2012) suggested the installation of temporary barriers along the footbridge path, while Venuti and Bruno (2013) investigated a strategy of crowd flow control based on the smooth widening/narrowing of the walkway width along the footbridge span. In both cases, the aim is to modify the distribution of the crowd density and, as a consequence, of the walking velocity and step frequency, i.e. modify the dynamic load exerted by the pedestrians. Both proposals require a modelling approach quite different from the one usually adopted and prescribed by codes and guidelines. In fact, the pedestrians are intelligent agents, whose behaviour is influenced by the interactions with the surrounding pedestrians and environment according to specific rules. Therefore, crowd models should be used to properly describe the pedestrian walking behaviour.

The aim of this study is to systematically explore the effectivess of crowd-based mitigation strategies on the reduction of footbridge vibrations. Specifically, the proposed strategy is based on the control of crowd flow by means of obstacles located along the footbridge span. In this paper, the very first results are presented in the case of footbridges crossed by unidirectional pedestrian traffic and with vertical vibrations. In order to emphasise similarities and differences with well established structural control strategies, comparisons with an optimally designed linear viscoelastic TMD are finally made.

The paper develops as follows. Section 2 presents the adopted modelling approach; Section 3 describes the benchmark footbridge adopted as case study; Section 4 is devoted to the design of crowd- and structure-based retrofitting measures; in Section 5 the results of the numerical simulations are illustrated and comparisons between the two mitigation strategies are discussed; in Section 6, conclusions and research perspectives are outlined.

2 MODELLING APPROACH

The study is carried out by means of numerical simulations and the following modelling assumptions are made:

a1. even though it is widely accepted that Human-Structure-Interaction (HSI) occurs when pedestrians walk on a flexible structure, there is still great uncertainty about how to model HSI (Shahabpoor et al. 2017). Therefore, HSI is neglected in this study. This choice is justified by two main reasons: on the one hand, this allows to better focus on the effects of the crowd flow on the structural response, without introducing further sources of uncertainty; on the other hand, modelling HSI still belongs to the research field, while codes and guidelines neglect its effects;

a2. the obstacles placed along the footbridge span to achieve the crowd flow control are modelled as purely geometrical constraints, not affecting the mass, stiffness and damping properties of the footbridge.

Figure 1 illustrates a scheme of the adopted modelling approach, whose details are provided below.

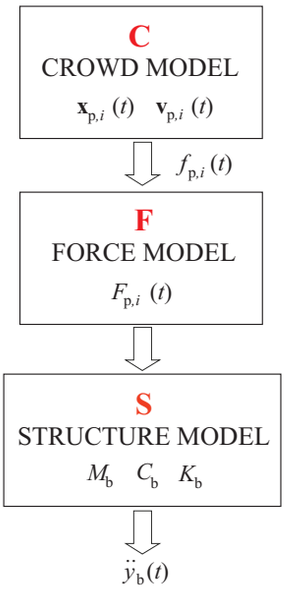


Figure 1: Scheme of the modelling approach

2.1 *Crowd model*

Simulations of crowd flow are performed through the commercial software Mass Motion v. 8.5 (Oasys Ltd. 2017), which is based on a microscopic model of crowd dynamics derived, as a modified version, from the Social Force Model first proposed by Helbing and Molnár (1995). In such a model, each individual pedestrian is described as an agent, whose goal is to reach her final destination walking at her desired velocity. Desired velocities v_{des} are randomly assigned to the pedestrians from a Normal distribution, with mean 1.34 m/s and standard deviation (std) 0.26 m/s (Buchmueller and Weidmann 2006). While walking, each agent is subjected to a set of forces that modify her desired velocity on the basis of the interaction with neighbouring pedestrians and the environment (walls, obstacles, etc.). The interested reader is referred to Helbing and Molnár (1995) and Oasys Ltd. (2017) for a detailed description of the mathematical and numerical framework.

Crowd flow simulations result in trajectory $\mathbf{x}_{\mathrm{p},i}(t) = [x_{\mathrm{p},,i}, z_{\mathrm{p},,i}]$ and velocity $\mathbf{v}_{\mathrm{p},i}(t) = [v_{x\mathrm{p},,i}, v_{z\mathrm{p},,i}]$ for each i-th pedestrian along time t, where x and z are the longitudinal and the transverse footbridge axis, respectively.

2.2 *Force model*

Trajectory $\mathbf{x}_{\mathrm{p},i}(t)$ and velocity $\mathbf{v}_{\mathrm{p},i}(t)$ are then used to build the moving time-varying force $F_{\mathrm{p},i}(t)$ exerted by the i-th pedestrian on the footbridge.

The continuous force model of Young (2001) is assumed as reference, where $F_{\mathrm{p},i}(t)$ is described by a sum of n Fourier harmonic components:

$$F_{\mathrm{p},i} = G_{\mathrm{p},i} + \sum_{j=1}^{n} G_{\mathrm{p},i}\, DLF_j \sin\left(2\pi j f_{\mathrm{p},i}\, t - \theta_j\right), \quad (1)$$

where: $G_{\mathrm{p},i} = m_{\mathrm{p},i}\, g$ is the pedestrian weight, being $m_{\mathrm{p},i}$ the pedestrian mass and g the gravity acceleration; $f_{\mathrm{p},i}$ is the pedestrian step frequency; DLF_j and θ_j are, respectively, the Dynamic Load Factor and phase shift of the j-th contributing harmonic.

With respect to the model of Young, here the pedestrian step frequency $f_{\mathrm{p},i}$ is not constant in time, being calculated as a function of the walking velocity $v_{\mathrm{p},i}(t)$ according to the relation proposed by Venuti and Bruno (2007):

$$f_{\mathrm{p},i}(t) = 2.93 v_{\mathrm{p},i}(t) - 1.59 v_{\mathrm{p},i}^2(t) + 0.35 v_{\mathrm{p},i}^3(t). \quad (2)$$

In this study, only the first contributing harmonic is considered in (1). Its DLF_1 is expressed as a function of $f_{\mathrm{p},i}$ (Young 2001), and this dependence causes DLF_1 to be time-variant as well:

$$DLF_1(t) = 0.41(f_{\mathrm{p},i}(t) - 0.95) \leq 0.56. \quad (3)$$

Note that the time-variant pedestrian characteristics are assumed to vary in time continuously and not on a step-by-step basis.

Mass $m_{\mathrm{p},i}$ is randomly assigned to each pedestrian from a Normal distribution with mean 75 kg and std 15 kg (Zivanovic 2012).

This model allows to account for both inter-subject and intra-subject variability of human load.

2.3 *Structure model*

The footbridge is modelled as a Single Degree of Freedom (SDOF) system, representing a structural vertical vibration mode of interest, whose dynamics is governed by the well-known equation of motion:

$$M_{\mathrm{b}}\ddot{y}_{\mathrm{b}} + C_{\mathrm{b}}\dot{y}_b + K_{\mathrm{b}} y_{\mathrm{b}} = F, \quad (4)$$

where $y_{\mathrm{b}}(t)$ is the displacement response at the antinode, the overdot indicating differentiation with respect to time t; M_{b}, C_{b} and K_{b} are the modal mass, damping and stiffness of the footbridge, respectively; $F(t) = \sum_{i=1}^{N} F_{\mathrm{p},i}(t)\, \Phi\left(x_{\mathrm{p},i}(t)\right)$ is the modal force, being N the number of pedestrians walking on the footbridge at time t, $\Phi(x)$ the unity-normalised modal shape of the structure. The contribution of the pedestrian modal mass is neglected according to assumption a1.

3 DESCRIPTION OF THE BENCHMARK FOOTBRIDGE

Numerical simulations are performed on a benchmark footbridge, whose dimensional and dynamic properties are summarised in Table 1 and Figure 2. A sinusoidal modal shape function $\Phi = \sin(\pi x/L)$ is assumed for the first vertical mode.

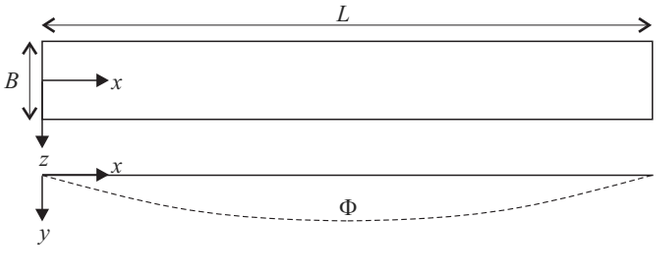


Figure 2: Schematic plan and side view of the footbridge

Table 1: Properties of the benchmark footbridge

L [m]	B [m]	m_{b} [kg/m]	f_{b} [Hz]	ζ_{b} [-]
100	3	1500	1.8	0.005

In order to set the pedestrian traffic condition (i.e. the incoming pedestrian density) that is likely to induce the highest acceleration response on the footbridge, a parametric study is carried out with Mass Motion (MM). Ten simulations of crowd dynamics are performed by increasing the incoming pedestrian density ρ in the range [0.1, 1] ped/m^2. In each simulation, N_{tot} pedestrians have been generated at the footbridge entrance over a time T. Arrival times in MM are randomly generated according to a uniform distribution. The time T is set equal to 10 times the average crossing time $T_1 = L/v_{\mathrm{m}}$, where v_{m} is the mean walking velocity, initially estimated as a function of the crowd density according to the Weidmann (W) fundamental law (Buchmueller and Weidmann 2006):

$$v_{\mathrm{m,W}} = 1.34\left\{1 - \exp\left[-1.913\left(\frac{1}{\rho} - \frac{1}{5.4}\right)\right]\right\}. \quad (5)$$

Hence, the total number of pedestrians N_{tot} that enter the footbridge is equal to $10\rho LB$.

For each simulation, both average density and velocity are calculated over a time period T_{full} corresponding to full occupancy of the footbridge. The latter has been derived by excluding the initial and final time periods corresponding to pedestrians populating and leaving the bridge, respectively. The lower

and upper boundaries of T_{full} have been determined as the first and last time instant when N_{m} pedestrians are on the footbridge, being $N_{\text{m}} = \rho LB$. Results are reported in Figure 3. Simulations of crowd dynamics were run twice, since the velocities obtained with MM are lower than those predicted through Eq. 5. Therefore, a second run was necessary to tune the time T in order to obtain the expected average density on the footbridge (white circles in Fig. 3). Figure 3 also plots the frequency ratio $f_{\text{r}} = f_{\text{p,m}}/f_{\text{b}}$, where the mean step frequency $f_{\text{p,m}}$ is obtained as a function of $v_{\text{m,MM}}$ through Eq. 2.

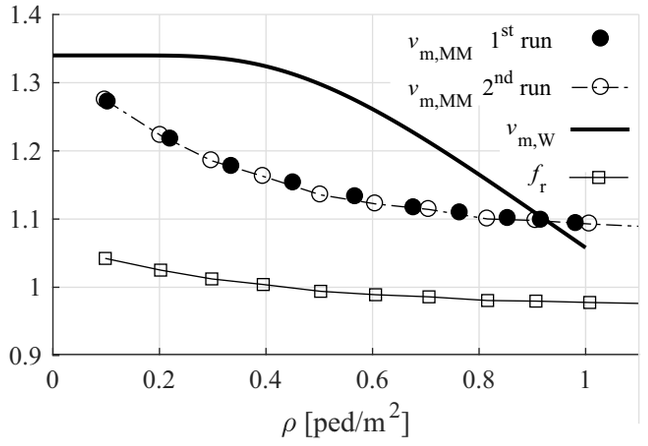


Figure 3: Mean walking velocity v_{m} [m/s] and dimensionless frequency ratio f_{r} vs ρ

The crowd density corresponding to the f_r value closest to unit, i.e. $\rho = 0.4$ ped/m^2, is selected as the worst case scenario for the following simulations.

4 DESIGN OF MITIGATION STRATEGIES

4.1 *Crowd-based strategies*

Crowd flow control strategies have been proposed in the fields of applied mathematics and transportation engineering. The control of the crowd flow, e.g., in evacuation scenarios, is often obtained by means of punctual obstacles, such as columns, located in strategic positions, in order to force the crowd flow to follow certain patterns and avoid the formation of jams or to ease the evacuation (Helbing et al. 2002, Helbing et al. 2005).

Taking inspiration from the above cited literature, the proposed strategy of crowd flow control is based on the location of obstacles along the footbridge path. The obstacles can be intended either as permanent (e.g., benches or light poles) or as emergency temporary measure (e.g., Jersey barriers). In the second case, they can be easily and quickly installed whenever the footbridge is expected to be crossed by a crowd density which could induce vibrations above the comfort limits.

Two different types of obstacle layout are investigated (Figure 4):

- obstacles located along the footbridge longitudinal axis in order to force lane separation (LS);
- obstacles located along the footbridge lateral edges in order to obtain bottlenecks (BN), i.e. local narrowing of the footbridge width.

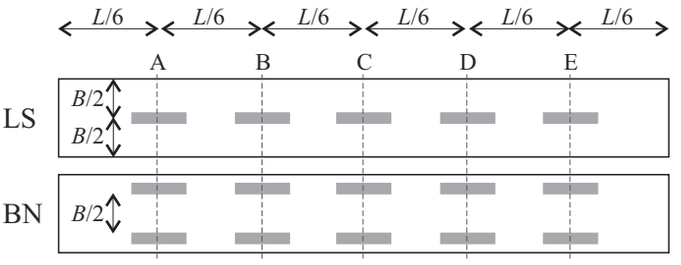


Figure 4: Scheme of the investigated obstacle layouts

Each obstacle have dimensions $l = L/10$ and $b = B/10$. Table 2 summarises the number of obstacles and their position for each investigated layout; layout 0 represents the uncontrolled configuration of the footbridge.

Table 2: List of the investigated obstacle layouts

Layout	Type	n°	Position
0	-	-	-
1	LS	1	C
2	LS	3	B-C-D
3	LS	5	A-B-C-D-E
4	LS	2	B-C
5	LS	2	B-D
6	BN	2	C
7	BN	6	B-C-D
8	BN	10	A-B-C-D-E
9	BN	6	A-C-E
10	BN	6	A-B-C

4.2 *Structure-based strategy*

To control the dynamic response of the footbridge in the first symmetric vertical mode, a linear viscoelastic TMD is considered to be installed where the relevant modal shape function $\Phi(x)$ attains its maximum, i.e., at the footbridge's mid-span.

Assuming the modal shape to be set to unity at the TMD location, $\Phi(L/2) = 1$, a generalised SDOF structure - TMD system (Figure 5) can be introduced, whose equations of motion are written as:

$$\ddot{y}_{\text{b}} + 2\zeta_{\text{b}}\omega_{\text{b}}\dot{y}_{\text{b}} + \omega_{\text{b}}^2 y_{\text{b}} = \frac{F}{M_{\text{b}}} + \frac{u}{M_{\text{b}}},$$

$$\mu\ddot{y}_{\text{d}} = -\frac{u}{M_{\text{b}}}, \tag{6}$$

$$\frac{u}{M_{\text{b}}} = 2\mu\zeta_{\text{d}}\alpha\omega_{\text{b}}(\dot{y}_{\text{d}} - \dot{y}_{\text{b}}) + \mu\alpha^2\omega_{\text{b}}^2(y_{\text{d}} - y_{\text{b}}).$$

In Equations 6, $y_{\mathrm{b}}(t)$ and $y_{\mathrm{d}}(t)$ are the vertical displacements of the footbridge's mid-span section and of the TMD, respectively; M_b is the modal mass of the footbridge; $F(t)$ is the modal input force acting on the footbridge, as defined in Section 2.3; $u(t)$ is the force exerted by the TMD on the mid-span section of the footbridge. Furthermore, the following parameters are defined: ω_{b} and ζ_{b} are the uncoupled modal frequency and damping ratio of the footbridge; $\zeta_{\mathrm{d}} = c_d/(2\sqrt{k_d\, m_d})$ is the uncoupled damping ratio of TMD; $\mu = m_{\mathrm{d}}/M_{\mathrm{b}}$ and $\alpha = \omega_{\mathrm{d}}/\omega_{\mathrm{b}}$ are the mass ratio and the frequency ratio of the generalised SDOF structure-TMD system, denoting with $\omega_{\mathrm{d}} = \sqrt{k_{\mathrm{d}}/m_{\mathrm{d}}}$ the uncoupled natural frequency of TMD.

Within the set of five parameters that govern the response of the generalised SDOF structure - TMD system, modal properties $\omega_{\mathrm{b}} = 11.31$ rad/s and $\zeta_{\mathrm{b}} = 0.005$ are known data of the footbridge (see Table 2), mass ratio $\mu = 0.01$ is set out as a customary value in pedestrian bridges, while frequency ratio α and damping ratio ζ_{d} are the design parameters of the TMD, to be determined on the basis of an optimisation criterion. Following Warburton (1982), who considered a random white noise force applied to the undamped SDOF structure and minimised the variance of its displacement response, the optimal values of the TMD design parameters are determined accordingly as:

$$\alpha_{\mathrm{opt}} = \frac{\sqrt{1+\frac{\mu}{2}}}{1+\mu} = 0.9926,$$
$$\zeta_{\mathrm{opt}} = \sqrt{\frac{\mu(1+\frac{3}{4}\mu)}{4(1+\frac{\mu}{2})(1+\mu)}} = 0.0498. \tag{7}$$

Regarding the applicability of Warburton parameters (7) to the case under consideration, it may be observed, on the one hand, that pedestrian traffic is not accurately represented by a white noise input; on the other hand, that the minimisation of the displacement response is not a suitable optimisation criterion when the design objective is to control the acceleration response. Recent numerical investigations conducted by Tubino and Piccardo (2015), however, have demonstrated that Warburton parameters lead to a control performance comparable to the one obtained by maximising, under normal unrestricted pedestrian traffic, the TMD efficiency in reducing the acceleration response.

5 RESULTS

This section presents the results of the computational simulations performed on the benchmark footbridge without and with mitigation measures. For each layout, the response was simulated 20 times and peak values of the acceleration were extracted from each time history and averaged across the 20 simulations.

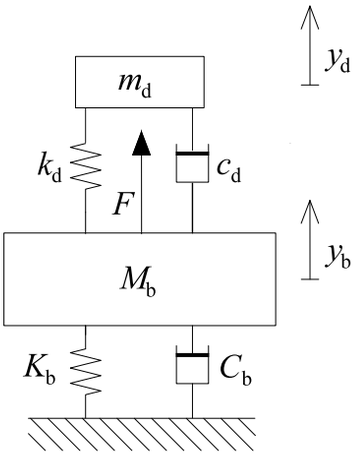


Figure 5: Mechanical model of the generalised SDOF structure - TMD system.

The statistical reliability was checked by calculating mean and std of the crowd density and walking velocity and peak acceleration on the footbridge during T_{full} and averaging their values over increasing number of simulations. The relative error in average estimation between successive simulations n and $n+1$ falls below 0.5 % for both statistics of crowd density and velocity and below 1 % for peak acceleration when $n > 15$.

5.1 *Footbridge uncontrolled response*

Figure 6 illustrates the time histories of the number of pedestrians/crowd density on the footbridge and of the acceleration response for one of the 20 simulations. The average peak acceleration $a_{\mathrm{peak},0}$ during the period of full occupancy equals 1.2 m/s^2. Therefore it exceeds the upper limit of minimum comfort (1 m/s^2) according to the Sétra/AFGC (2006) guideline by 20%.

Figure 7 plots the probability density function (PDF) of moduli v of actual velocity and v_{des} of desired velocity, as obtained with MM for one of the 20 simulations. It can be observed that the distribution of actual velocities follows a normal distribution with lower mean (1.15 m/s) and std (0.21 m/s) with respect to desired velocities. This is expected, since desired velocities correspond to unconstrained pedestrian behaviour (i.e., a pedestrian walking alone, that is, ρ=0), while, in the presence of a higher crowd density, mean walking velocity decreases and std decreases as well (Butz et al. 2008). Step frequencies, calculated as a function of walking velocities, also follow a normal distribution with mean 1.79 Hz and std 0.15 Hz.

5.2 *Footbridge controlled response*

The effectiveness of each mitigation measure is evaluated by calculating the ratio between the controlled and the uncontrolled average peak acceleration :

$$r_{a,j} = a_{\mathrm{peak},j}/a_{\mathrm{peak},0} \quad \text{for } j = 1, 3, \ldots, 11. \tag{8}$$

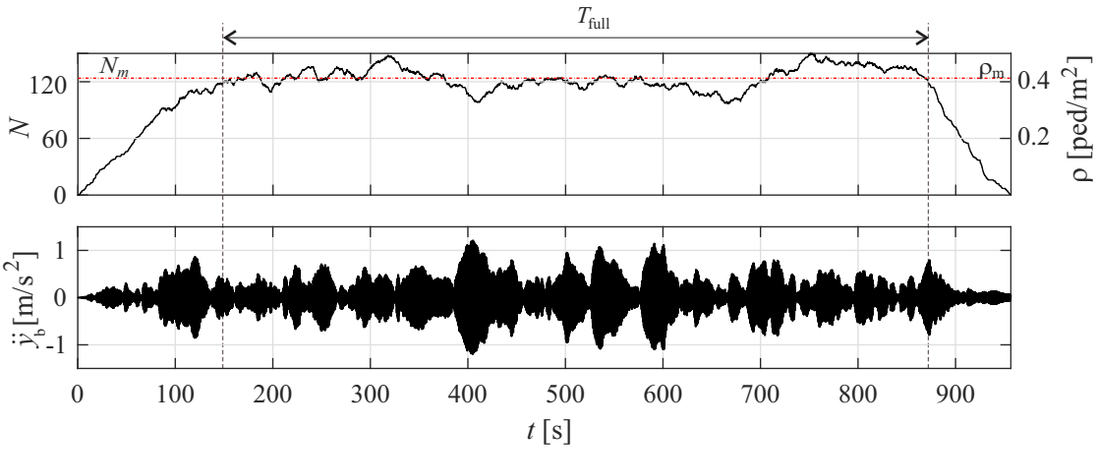


Figure 6: Example of time history of the number of pedestrians, pedestrian density and acceleration response

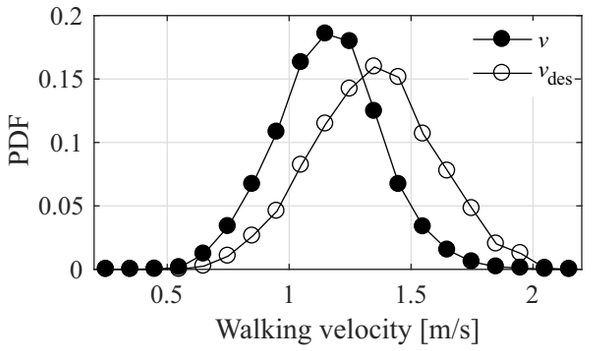


Figure 7: Example of PDF of actual and desired walking velocities

Figure 8 plots the obtained acceleration ratio for each mitigation layout. As a reference, the Sétra/AFGC (2006) upper limit of minimum comfort, normalised with respect to $a_{\text{peak},0}$, is reported as a dashed horizontal line.

Regarding the crowd-based mitigation strategies, BN layouts are, in general, more effective than the LS ones in reducing the peak acceleration response: maximum reduction amounts to 31% in BN layout 8, while it is limited to 11% in LS layout 2. This difference can be explained by looking at the distribution of crowd density, which is locally increased due to the obstacle placement. As a consequence of this density increase, the frequency ratio f_{r} decreases and moves away from the resonance condition (see Figure 3). Figure 9 illustrates the distribution of crowd density, averaged over T_{full}, for layout 0, LS layout 2 and BN layout 7: it becomes apparent that the density increase is much higher in the BN case, since the obstacle location causes a higher local reduction of the footbridge width.

Considering the structure-based mitigation strategy (layout 11), the optimised linear viscoelastic TMD is able to reduce the average peak acceleration by 60%. Even though the effectiveness of TMD in reducing the structural response is higher, it should be noted that the two mitigation strategies are not directly comparable. In fact, the TMD is designed according to an optimum criterion, which is not the case for the presented crowd-based mitigation strategy. Moreover, the two strategies have been compared from a quantitative point of view, but other factors should be considered when chosing the mitigation approach to be adopted. For instance, the crowd-based mitigation strategy presents some advantages, with respect to the structure-based counterpart: it can be adopted as temporary measure, since it can be quickly installed and removed; its design, installation and maintenance costs as expected to be lower; different obstacle layouts can be adopted on the basis of the traffic condition that is expected to cross the footbridge.

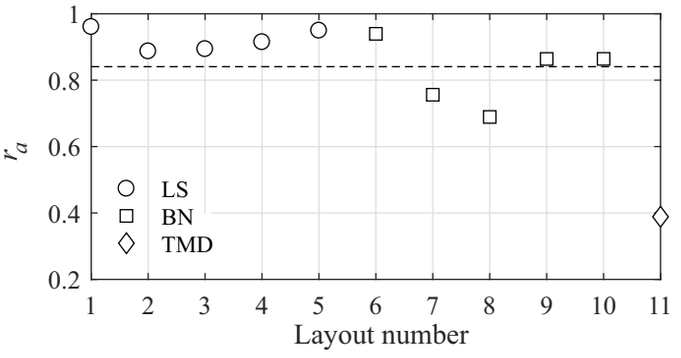


Figure 8: Peak acceleration ratio for each mitigation layout

6 CONCLUSIONS

In this paper, an alternative approach to the mitigation of human-induced vibrations on footbridges has been proposed. The approach is based on the crowd-flow control by means of obstacles located along the footbridge span. This strategy allows to act on the source of excitation instead of acting on the structure.

The proposed strategy has been applied to a benchmark footbridge crossed by unidirectional traffic and subject to uncomfortable vertical vibrations under human loading. Different layouts of obstacle placement have been investigated, in order to determine the most effective one in reducing the peak vertical acceleration. The maximum reduction, amounting to 31%, has

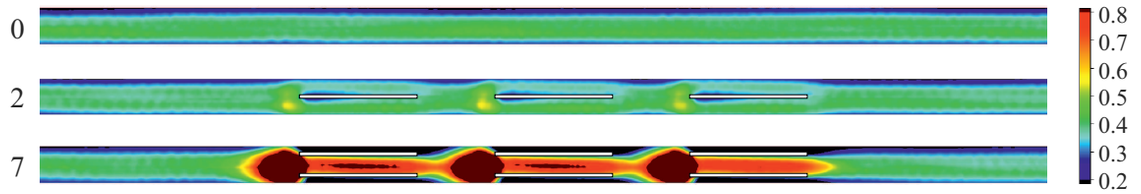


Figure 9: Example of crowd density distribution averaged over T_{full} for layouts 0, 2 and 7.

been obtained when the obstacles are placed to create local bottlenecks along the footbridge. The effect of locally reducing the footbridge width results, in fact, in a local increase of the crowd density and in a consequent, favourable shift of the pedestrian input frequency away from the resonance condition.

The control performance obtained through the proposed crowd-based mitigation strategy has been measured against the one achieved by way of a linear viscoelastic TMD, which is a structure-based mitigation strategy widespread, nowadays, in pedestrian bridges. Although the effectiveness of TMD seems to be higher, it has to be noted that a mere quantitative comparison in terms of control performance between the two mitigation strategies may be misleading, given their irreducible differences as to design, installation and maintenance costs. Moreover, the crowd-based mitigation strategy can be designed not only as a permanent solution (e.g., through the installation of benches or light poles) but, more interestingly, as an emergency temporary measure (e.g., through the placement of Jersey barriers). In both cases, the obstacle placement is supposed to slightly modify the footbridge dynamic properties.

The proposed crowd-based mitigation strategies, even if demonstrated only for a simple case study, could have good potential and is worth to be further investigated. A possible critical issue lies in the fact that the main effect of the obstacle placement is to locally increase the crowd density. If the incoming crowd density is quite high, this could lead to possible congestions, with consequent onset of panic conditions and increase in the time needed to cross the facility. Moreover, HSI should be taken into account to have a reliable estimate of the structural response. These aspects will be investigated in the next development of this study.

ACKNOWLEDGEMENTS

The authors wish to thank Oasys Ltd for having provided free licences of the software Mass Motion for academic use.

REFERENCES

Brownjohn, J., P. Fok, M. Roche, & P. Omenzetter (2004). Long span steel pedestrian bridge at Singapore Changi Airport - Part 2: crowd loading tests and vibration mitigation measures. *The Structural Engineer 82*(16), 21–27.

Buchmueller, S. & U. Weidmann (2006, October). Parameters of pedestrians, pedestrian traffic and walking facilities. Technical Report n. 132, ETH, Zürich.

Butz, C., M. Feldmann, C. Heinemeyer, G. Sedlacek, B. Chabrolin, A. Lemaire, M. Lukic, P. O. Martin, E. Caetano, A. Cunha, A. Goldack, A. Keil, & M. Schlaich (2008). Advanced load models for synchronous pedestrian excitation and optimised design guidelines for steel footbridges (SYNPEX). Technical Report RFS-CR 03019, Research Fund for Coal and Steel.

Caetano, E., A. Cunha, F. Magalhaes, & C. Moutinho (2010). Studies for controlling human-induced vibration of the Pedro e Inês footbridge, Portugal. Part 2: Implementation of tuned mass dampers. *Engineering Structures 32*, 1082–1091.

Carroll, S. P., J. S. Owen, & M. F. M. Hussein (2012). Modelling crowd-bridge dynamic interaction with a discretely defined crowd. *Journal of Sound and Vibration 331*, 2685–2709.

Dallard, P., T. Fitzpatrick, A. Flint, A. Law, R. M. Ridsdill Smith, M. Willford, & M. Roche (2001). The London Millennium Bridge: pedestrian-induced lateral vibration. *Journal of bridge Engineering 6*(6), 412–417.

De Angelis, M., S. Perno, & A. Reggio (2012). Dynamic response and optimal design of structures with large mass ratio TMD. *Earthquake Engineering and Structural Dynamics 41*, 41–60.

Dziuba, P., G. Grillaud, O. Flamand, S. Sanquier, & Y. Tetard (2001). La passerelle Solferino: comportement dynamique (Dynamic behaviour of the Solferino bridge). *Bulletin Ouvrages métalliques 1*, 34–57.

Helbing, D., L. Buzna, A. Johansson, & T. Werner (2005). Self-organized pedestrian crowd dynamics: Experiments, simulations and design solutions. *Transportation Science 39*, 1–24.

Helbing, D., I. J. Farkas, P. Molnar, & T. Vicsek (2002). Simulation of pedestrian crowds in normal and evacuation situations. In M. Schreckenberg and S. D. Sharma (Eds.), *Pedestrian and Evacuation Dynamics*, pp. 21–58. Berlin: Springer.

Helbing, D. & P. Molnár (1995). Social force model for pedestrian dynamics. *Physical Review E 51*(5), 4282–4286.

Housner, G., L. Bergman, T. Caughey, A. Chassiakos, R. Claus, S. Masri, R. Skelton, T. Soong, B. Spencer, & J. Yao (1997). Structural control: Past, present and future. *Journal of Engineering Mechanics 123*(9), 897–971.

Kareem, A. & T. Kijewski (1999). Mitigation of motions of tall buildings with specific examples of recent applications. *Wind and Structures 3*(2), 201–251.

Law, S. S., Z. M. Wu, & S. L. Chan (2004). Vibration control study of a suspension footbridge using hybrid slotted bolted connection elements. *Engineering Structures 26*, 107–116.

Oasys Ltd. (2017). *Mass Motion Help*. Oasys Ltd.

Reggio, A. & M. De Angelis (2015). Optimal energy-based seismic design of non-conventional Tuned Mass Damper (TMD) implemented via inter-story isolation. *Earthquake Engineering and Structural Dynamics 44*, 1623–1642.

Sarwar, M. W. & T. Ishihara (2010). Numerical study on suppression of vortex-induced vibrations of box girder bridge section by aerodynamic countermeasures. *Journal of Wind Engineering and Industrial Aerodynamics 98*, 701–711.

Sétra/AFGC (2006). *Passerelles piétonnes. Évaluation du comportement vibratoire sous l'action des piétons. (Footbridges. Assessment of vibrational behaviour of footbridges under pedestrian loading)*. Sétra/AFGC.

Shahabpoor, E., A. Pavic, V. Racic, & S. Zivanovic (2017). Effect of group walking traffic on dynamic properties of pedestrian structures. *Journal of Sound and Vibration 20*(207-225).

Soong, T. & G. Dargush (1997). *Passive Energy Dissipation Systems in Structural Engineering*. New York: Wiley.

Tubino, F., L. Carassale, & G. Piccardo (2016). Human-induced vibrations on two lively footbridges in Milan. *Journal of Bridge Engineering 21*(8), 1–10.

Tubino, F. & G. Piccardo (2015). Tuned mass damper optimization for the mitigation of human-induced vibrations of pedestrian bridges. *Meccanica 50*, 809–824.

Venuti, F. & L. Bruno (2007). An interpretative model of the pedestrian fundamental relation. *Comptes Rendus Mecanique 335*, 194–200.

Venuti, F. & L. Bruno (2013). Mitigation of human-induced lateral vibrations on footbridges through walkway shaping. *Engineering Structures 56*, 95–104.

Warburton, G. (1982). Optimum absorber parameters for various combinations of response and excitation parameters. *Earthquake Engineering and Structural Dynamics 10*, 381–401.

Young, P. (2001). Improved floor vibration prediction methodologies. In *Proceedings of Arup Vibration Seminar on Engineering for Structural Vibration - Current Developments in Research and Practice*, London, UK.

Zivanovic, S. (2012). Benchmark footbridge for vibration serviceability assessment under vertical component of pedestrian load. *ASCE Journal of Structural Engineering 138*(10), 1193–1202.

Maintenance, Safety, Risk, Management and Life-Cycle Performance of Bridges – Powers, Frangopol, Al-Mahaidi & Caprani (Eds)
© 2018 Taylor & Francis Group, London, ISBN 978-1-138-73045-8

Dynamic Study of Yangtze River Bridge at Chongqing-Lichuan Railway

K.J. Chen & Y.P. Zeng & *S.X. Chen*
China Railway ErYuan Engineering Group Co.Ltd, ChenDu, China

ABSTRACT: Hanjiatuo Yangtze River Bridge is a railway steel truss girder cable-stayed bridge with span arrangement of (81+135+432+135+81) m. As a double track railway bridge for mixed passenger and freight traffic, it is the largest bridge in the world with less weight relatively and it is easily affected by dynamic effects. In this paper, firstly, the restraint system between the pylons and girder is studied under the consideration of braking force and seismic response. For this long span structure, a control system consisting of a novel velocity based locking device with self-control panel and a viscous damper is presented to control the braking force-induced vibration and seismic response respectively. Then, a scaled steel truss girder section model is tested in the wind tunnel laboratory, with additional dynamic loads acting on the bridge including dynamic interactions from the vehicles. The vortex-induced vibration under low wind speed is discovered in the test, for which a segmented deflector is creatively proposed to suppress the vibration.

1 PROJECT OVERVIEW

Hanjiatuo Yangtze River Bridge is a steel truss cable-stayed bridge over the Yangtze River at Chongqing-Lichuan Railway, located at Fuling District, Chongqing Province, China. The bridge ranks among the longest cable-stayed bridges in the world in the year 2013, with the span of (81+135+432 +135+81) m.

It is a double-track railway bridge for mixed passenger and freight, with the train speed of 200 km/h. The spacing between two tracks is 4.4 m, and the designing load is CR-live loading.

2 PROTOTYPE

As shown in Figure 1, a semi-floating system is adopted in the main bridge, with pylon-pier fixed and pylon –girder detached.

Two parallel N-shape steel trusses are used for the girder, with a spacing of 18m. The height of the truss is 14m, and the panel length 13.5m. The steel box girder is chosen for upper and lower chords with the slab thickness of 50mm, and monolithic joint welding method is adopted. On top of the orthotropic steel bridge deck is the concrete ballast slab with the thickness of 15cm. The material for both the truss and deck is Steel Q3701qD.

The pylon is a single column shape in longitudinal direction and designed in vase pattern (fold line H shape) in transverse direction. The cross section of the pylon and cross-girder is hollow rectangular. Except for the lower cross-girder and upper pylon which are pre-stressed, other components reinforced concrete structure using C50 concrete. The height of P10 and P11 is 182.5m and 187.5m respectively.

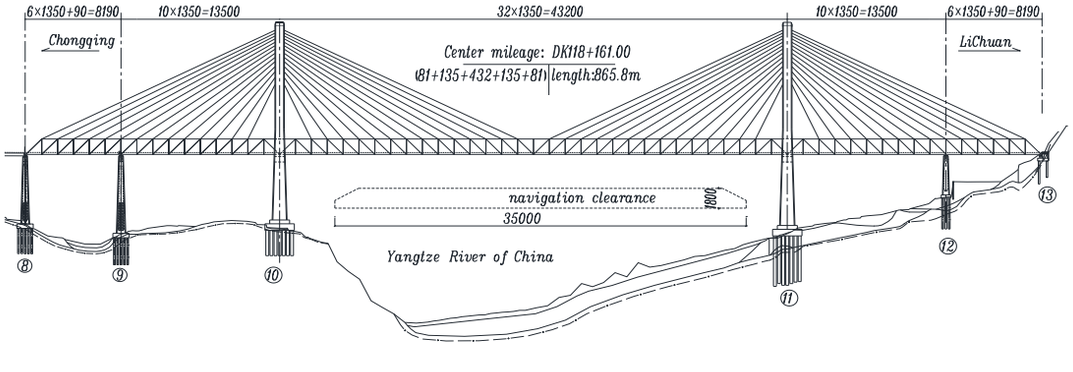


Figure 1. Overall layout of Hanjiatuo Yangtze River Bridge.

The 56 pairs of stay cables using galvanized high strength steel wire bundle constitute double parallel fan-shaped planes. The spacing of the cable on the pylon is 2.5~4m, and the spacing on the girder is 13.5m. In order to reduce the hinge effect at the anchoring point, the anchorage device at the girder side is designed to spherical hinge.

3 PYLON-GIRDER CONSTRAINT SYSTEM

For large span cable-stayed railway bridge, an appropriate pylon-girder constraint system should satisfy three demands: (1) the girder can slide and retract freely under temperature loading; (2) the pylon can restrain excessive movement of the girder under living and braking force to ensure the driving safety; (3) the system can reduce the seismic response, and guarantee the constraint system and structure not damaged as well, under earthquake striking.

Based on these demands, a semi-floating system is utilized instead of fixed bearing in longitudinal direction, leading the girder retracting freely under temperature loading. However, compared with highway cable-stayed bridge, the living load has a large effect on cable-stayed railway bridge, especially the braking force and traction force. Therefore, the braking/traction force should be well controlled as well as the seismic force. Considering the differences in aspects of quantity and property between these forces, a control system consisting of a novel velocity based locking device with self-control panel and a viscous damper is introduced to control the vehicle-induced vibration and seismic response respectively.

3.1 *Seismic force control*

The seismic force can be controlled by using hydraulic viscous damper which can increase the damping in the structure. So, the force transmission relationship between the pylon and girder is modified and the seismic response of the structure is reduced consequently. The constitutive relation of the hydraulic viscous damper is shown as follow:

$$F=CV^{\alpha} \tag{1}$$

Where, F denotes the damping force, C is the damping factor, V is the relative velocity of the damper, α represents the velocity index.

Based on Equation (1), theoretical resistance force of the damper is close to zero when the deformation is slow, such as temperature induced deformation, while the force is increasing under seismic force because of large relative velocity between the pylon and girder. In this circumstance, the longitudinal movement is restrained at the joint of pylon and girder by the dampers and the seismic response is also reduced.

Since the damping parameters have great influence on the restraint effect, a numerical model is built to analyze the seismic responses at different c andαvalue, and the main results are shown in Figure 2~5 (Chen 2010, 2011,2012).

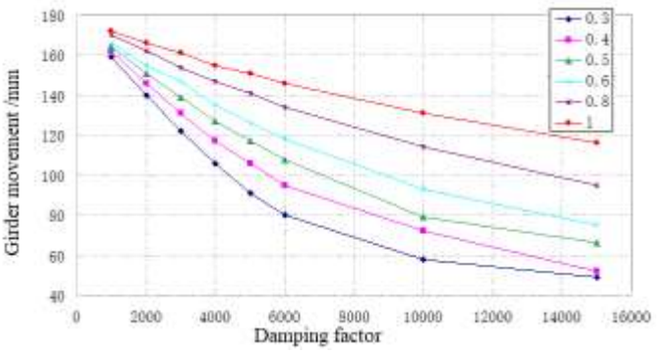


Figure 2. Effect of damping factor on girder movement.

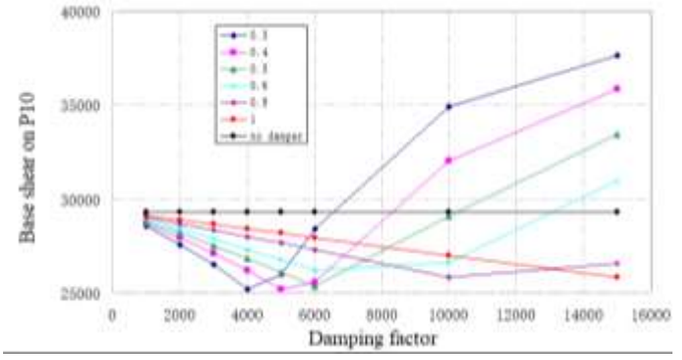


Figure 3. Effect of damping factor on base shear on P10.

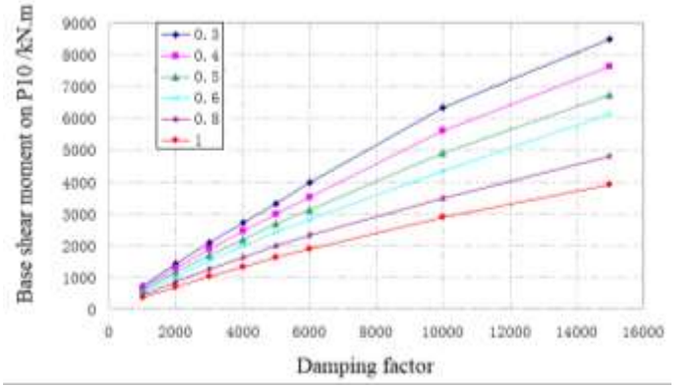


Figure 4. Effect of damping factor on base moment on P10.

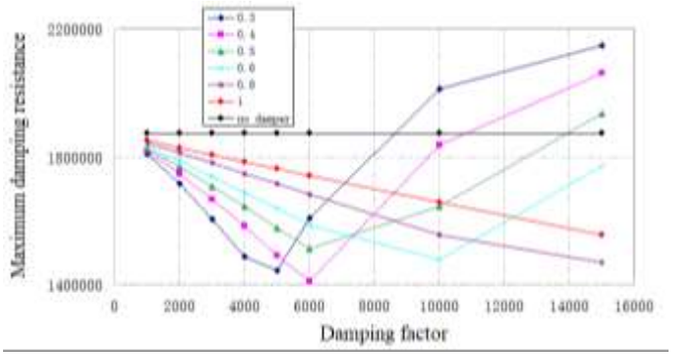


Figure 5. Effect of damping factor on the maximum resistant force in the damper.

It can be seen in Figure 2 that as C increases and α decreases, the beam displacement decreases, which means the damping effect is enhanced. But, for the economical viewpoint, the fabrication cost is increasing with the tonnage and stroke being improved. As for the base shear and moment, when C value is small, the damping effect is improved with α decreasing. However, when C becomes larger, an inflexion point arises.

Hence, for this bridge, the damping factor C is designed to be 4000KN(s/m) and α to be 0.4, which can result to reduction rate of 62.1%, 14.8% and 19.2% for displacement, base shear and base moment respectively.

3.2 *Braking force control*

Given that the braking force is much smaller compared with seismic force, the corresponding pylon-girder relative displacement and damping force is smaller according to Equation (1). So, the effectiveness of the damper is limited for the vibration response caused by braking and living forces. Therefore, a novel velocity locking device with self-control panel is proposed.

The velocity threshold for this device is 0.15mm/s, i.e. when the relative velocity surpasses 0.15mm/s, the locking device starts to work, acting as a rod with large stiffness between the pylon and girder. In this way, the braking force-induced vibration can be greatly controlled (see Figure 6). Under temperature loading, the relative displacement speed between the pylon and girder is lower than the threshold, hence the girder can still retract freely without thermal secondary force. Under seismic force, however, this device might be easily destroyed because of its large stiffness and low damping. In another hand, to pursue large designing strength, the cost will be raised and the moment and shear in the pylon will increase tremendously. Hence, a control panel is added on common locking device, i.e. when the earthquake induced force in the device is larger than 2300 KN, the locking device will deactivate and the damper starts to function. After the earthquake, the locking device can be reset allowing the traffic recovery.

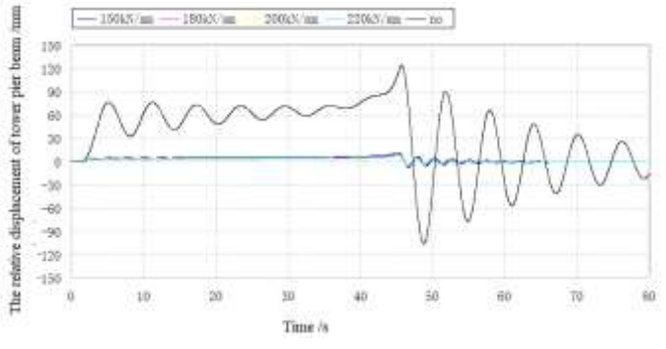


Figure 6. The controlling effect of locking device to girder displacement under barking force.

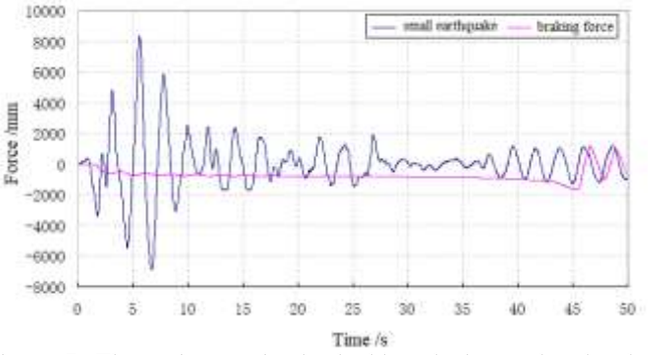


Figure 7. The resistance in the locking device under the designed earthquake and braking force (the blue curve corresponds to earthquake induced resistance).

4 KEY TECHNOLOGY FOR WIND RESISTANCE OF STEEL TRUSS GIRDER

In this part, the wind resistance performance is discussed in detail, including the vortex-induced vibration, buffeting and wind-rain induced vibration of the cables, through wind tunnel test, numerical modeling and theoretical analysis also. Herein, only the vortex-induced vibration is presented with the corresponding vibration control method.

4.1 *Wind tunnel test of section model*

In wind tunnel test, two models with geometric scale ratio of 1:45.77 and 1:19.74 are utilized with damping ratio about 0.43%. Angle values α=0°,+3°,-3°,+5°,-5°are tested on full-bridge state and construction state, and the results are compared afterwards.

It is noted that, at full-bridge state, the vertical vortex vibration occurs forα=-3° and -5°, especially forα=-5°the maximum vibration amplitude on one side reaching 110mm with wind speed of 13m/s. At the largest single-cantilever state, the vertical vortex vibration occurs forα=-3° and -5° again, and the maximum vibration amplitude on one side reaches 42mm with wind speed of 13.2m/s when α=-5°. For each incidence angle, there is no torsion vortex vibration at both full-bridge and construction states.

When the vertical damping ratio increases to 0.98%, there still appears obvious vertical vortex vibration, but the amplitude is decreasing. For α=-5°, the amplitude on one side is 49mm and the lock-in wind velocity region does not largely change.

The resistance in the locking deivce under the designed earthquake and braking force (the blue curve corresponds to earthquake induced resistance)



Figure 8. Section model in wind tunnel test.

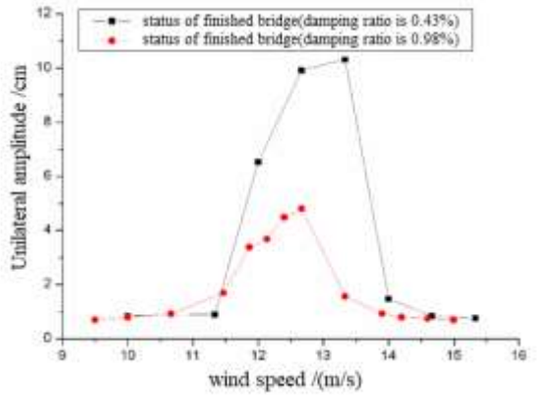


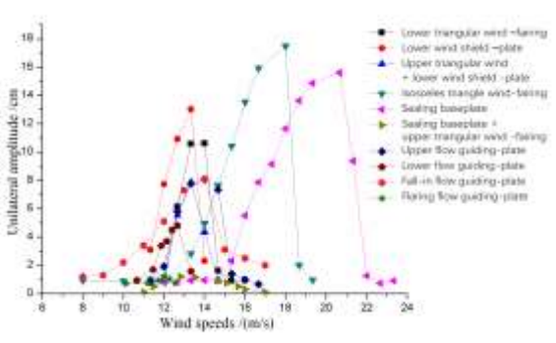
Figure 9. Vortex-excited vibration at full-bridge state (incidence angle α=-5°).

4.2 *Vortex-excited vibration control method*

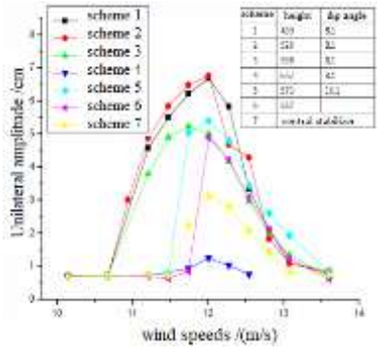
In order to control the vortex-excited vibration, experiments for ten models are conducted, which are (1)lower triangle wind fairing, (2) lower wind shields, (3) upper triangle wind fairing and lower wind shields, (4) isosceles triangle wind fairings, (5)sealing the bottom of girder, (6) sealing the bottom of girder and upper triangle wind faring, (7) upper baffle plate, (8) lower baffle plate, (9) introverted baffle plate, (10) external baffle plate.

Figure 10(a) shows the results for each controlling method in wind tunnel test. Amongst all the methods, No.6 and No.10 are the most effective, which can totally eliminate the vertical vortex-induced vibration. However, taking into account the aspects of fabrication, maintenance and structural details, method (10) is recommended.

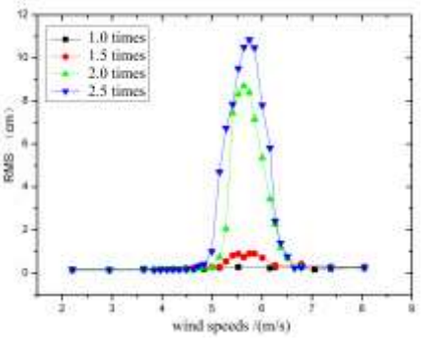
Based on the baffle plate method, other7 optimized plans are tested to discuss the influence of suspension point height and inclination angle of the deflector on vortex-induced vibration. The results are presented in Figure 10(b). It can be seen that Plan 4 is the most effective one with suspension height of 0.6m and inclination angle 5.5, and the amplitude of vortex-induced vibration is about 1.4cm.



(a) effect of each method



(b) optimization of hanging point and inclination angle



(c) optimization of segment distance

Figure 10. Research process of eliminating the vortex-induced vibration.

Theoretically speaking, for sectional baffle plate, the vortex frequencies are different between the adjacent girders, which will lead to the vibration reduction much easier. Therefore, segment distance is discussed. The results show in Figure 10(c) that, the most effective arrangement is the one with segment spacing equal the length of the plate. It can also be seen that, the elimination effect is decreasing obviously when the spacing is larger than 1.5 times the plate length. Thus, taking into account fabrication, material consumption and additional loading generally, the arrangement with spacing equal the plate length (see Figure 11) is adopted in the end.



Figure 11. Sectional baffle plates (before and after installation).

5 RESEARCH ON WIND-VEHICLE-BRIDGE COUPLED VIBRATION

Wind-vehicle-bridge coupled vibration system is a time-varying system under double stochastic excitation, i.e. rail roughness and fluctuating wind, includ-

ing bridge-vehicle interaction, wind-vehicle interaction and wind-bridge interaction. In this paper, wind tunnel test is first carried out to obtain the aerodynamic coefficients of vehicle (CRH2 train, full-load train and no-load train) and bridge, and also to obtain the flutter derivatives under different wind attack angles. Four loading cases are considered, i.e. no vehicle on the bridge, vehicle on the windward side, vehicle on leeward side and vehicles on both sides. For each loading case, six average wind speed values, e.g. 10m/s、15m/s、17m/s、20m/s、25m/s、30m/s, are utilized as subcases. The results show that, the vehicle-bridge aerodynamic interference is significant and therefore, it should be taken into account in vibration calculation.

In analytical study, the fluctuating wind field is simplified to transverse and longitudinal distributed 1D multi-variants random wind field, which is further simulated using spectral method along the bridge at uniformly-spaced distance. After extracting the aerodynamic data from wind tunnel test, the vibration of wind-vehicle-bridge coupled system is analyzed with CRH2 Train under three loading cases, i.e. vehicle on the windward side, vehicle on leeward side and vehicles on both sides. Subsequently, the response of the train and bridge is obtained (Chen 2011, Zhang 2012, Li 2013), and the results indicate that:

(1) For bridge structure: in each case, the deflection span ratio, acceleration and rotation angle of the bridge can all meet the requirements. The responses are increasing with the train speed and wind speed increasing, in transverse, longitudinal and rotational directions.

(2) For train: the dominant response is when the train is on the windward side or on both sides. The derailment coefficient and horizontal wheel force can meet safety requirements. The result shows that the response of the train increases as the train speed rises up, and the train acceleration will exceed the limit when the wind speed reaches high value. Hence, wind speed and train speed for one-train and double-train running should be controlled and the standard is illustrated in Table 1 and Table 2.

Table 1. Wind and train speed standard with one train running.

Average wind velocity (Va)	Instantaneous wind velocity (Vi)	Train velocity
Va≤17 m/s	Vi≤25 m/s	Designed train speed 200km/h
17<Va≤20 m/s	25<Vi≤30 m/s	≤110 km/h
Va＞20 m/s	Vi＞30 m/s	Close rail transit

Table 2. Wind and train speed standard with double-train running.

Average wind velocity (Va)	Instantaneous wind velocity (Vi)	Train velocity
Va≤15 m/s	Vi≤22 m/s	Designed train speed200km/h
15<Va≤17 m/s	22<Vi≤25 m/s	≤160 km/h
17<Va≤20 m/s	25<Vi≤30 m/s	≤90 km/h
Va＞20 m/s	Vi＞30 m/s	Close rail transit

6 CONCLUSIONS

Hanjiatuo Yangtze River Bridge at Chongqing-Lichuan Railway is a long span structure with notable dynamic effect. Based on this bridge, the study on the long span cable-stayed railway bridge is carried out, and several key technologies are proposed and solved. The bridge starts serving at the end of 2013 and works well in nearly 4 years of operating, which verifies the effect and reliability of the research results. The research results are of a great importance in contributing to the development and application of railway cable-stayed bridges in the future.

Acknowlegment

This research was supported by Ministry of Railways of the People's Republic of China under Grant No. 2009G004-D.

References

Chen S.X. & He X.Y. & Zeng Y.P. 2011. Research on Route of Yangtze River Bridge on Chongqing-Lichuan Railway. *Reports of Railway Location and Overall Design in Complex Mountainous Area, China Railway Book Concern*.

Chen, K.J. & Zeng, Y.P. & Chen, S.X. 2010. Design Instruction of Hanjiatuo Yangtze River Bridge on Chongqing-Lichuan Railway. *The shop drawing design instruction Finished by China Railway Eryuan Engineering Group CO.LTD*.

Chen, K.J. & Zeng, Y.P. & Chen, S.X. 2012 Overall Design of Hanjiatuo Yangtze River bridge in Chongqing-Lichuan railway. *Bridge Construction*, 5:31-40.

Zeng, Y.P. & Chen, K.J. & Chen, S.X. 2012. Study and Design of Low Retracting Ring Prestressed Cable-Tower Anchorage in Cable-Stayed Bridge. *Bridge Construction*, 5:42-49.

Chen, K.J. & Zeng, Y.P. & Chen, S.X. 2011 Study of Key Technology in Construction of Long Span Railway Cable-Stayed Bridge. *The Study Report Finished by China Railway Eryuan Engineering Group CO.LTD*.

Zeng, Y.P. & Chen, K.J. & Chen, S.X. 2013. Study and Fatigue Test of Double Integral Anchor Plates-Anchor Box Cable-Girder Anchorage. *Bridge Construction*, 6:21-28.

Zhang, Q. & Li, Y.L. & Deng J.T. 2012. Study of Influence of Truss Width on Train-Bridge Coupling Vibration of Long Span Railway Steel Truss Girder Cable-Stayed Bridge . *Bridge Construction*, 1:19-23.

Li, Y.L. & Xiang, H.Y. & Hou, G.Y. & Chen K.J. 2013. Aerodynamic characteristics of CRH2 train in combination of vehicle-bridge with cross wind action. *Actaaro dynamic asinica,* 5:579-582.

Gao, Z.Y. 2007. Overall Design of Wuhan Tianxingzhou Yangtze River Rail-cum-Road Bridge. *Bridge Construction*, 2:5-9.

Dan, D.F. & IMAI, K. 2004. Reliability of Long Span Bridges Based on Design Experience with the Honshu-Shikoku Bridges. *Journal of Constructional Steel Research*, 60 (3): 373-392

Maintenance, Safety, Risk, Management and Life-Cycle Performance of Bridges – Powers, Frangopol, Al-Mahaidi & Caprani (Eds)
© 2018 Taylor & Francis Group, London, ISBN 978-1-138-73045-8

FIR and IIR filtering and data driven stochastic subspace identification for the continuous dynamic modal parameter identification of cable stayed bridge

Inamullah Khan, Khurram Malik & Sarfraz Ali
NUST College of Civil Engineering, National University of Sciences and Technology, Risalpur, Pakistan.

Deshan Shan
Bridge Engineering Department, Civil Engineering School, Southwest Jiaotong University, Chengdu, Sichuan Province, China.

ABSTRACT: With the advancement in technology, the need for an effectual health monitoring of structures, specially the long span cable stayed bridges have increased the quest for a continuous monitoring of these cable stayed bridges so that, an accurate and reliable data is collected from these sophisticated instruments installed at these bridges and then analyzed in a very effective way. Therefore in this paper the FIR and IIR filter are introduce one by one, to the dynamic data obtained from real life cable stayed bridge. Then the reconstructed signal obtained after performing the filtering was used for the continuous modal parameters identification such as Frequency and Damping Ratio using the improved Data Driven Stochastic Subspace Identification (DATA-SSI). For this purpose the real life data has been collected form Sutong cable stayed Bridge, and the proposed technique was applied to this real life data. The results shows that the proposed method gives better results and the modal parameters obtained by this technique are more accurate and consistent and provides better representation of real life bridge health monitoring.

1 INTRODUCTION

In recent years bridge health monitoring is emerging as a new field and the monitoring campaigns of long span bridges are becoming more common day by day Wenzel (2009). In order to develop a more reliable and efficient monitoring system at these long span cable stayed bridges to continuously monitor its structural performances we need a noise free signal data, which is mostly required for a reliable data base for the accurate data analysis (Cross et al. 2013). Generally in cable stayed bridges the vibration responses are obtained using centralized data acquisition with wired sensors, however these wired sensors have proven to be difficult in case of dense deployment on large structures such as long span cable stayed bridges (Wu et al. 2013), with the advancement in technology these wired sensors are replaced by wireless sensors because the performance of these wireless sensors are better than the traditional wired sensors, Shi and Cattani (2012). Lynch and Loh (2006) reviewed almost 150 papers on wireless sensors for structure health monitoring. Also about the performance of wireless sensors the recent studies carried out by (Jang et al. 2010, Cho et al. 2010, Nitta at al. 2005, Gao at al. 2006, Rice and Spencer (2009), Tanner at al. 2003) shows very good performance of wireless sensors on large scale infrastructure such as cable stayed bridges. These wireless sensors then transmit the data to the central computer for further detail data analysis. The key challenge in transmitting these signals from the sensors to the central computer is the contamination of these signal with unwanted noise, which may cause the results obtained from these data analysis as false and misleading, thus creating false alarms for the structural safety and may distort the whole bridge monitoring system. Therefore some efficient and effective techniques are required to avoid these problems, for this purpose the introduction of filters such as FIR and IIR will be an effective approach to deal with such type of problem in order to extract the modal parameters such as Natural frequency, Damping ratio and Mode shape from the sensors data very efficiently and accurately, because it is very important for the assessment of structural performance and for the calibration of the analytical design methods (Cho et al. 2004).

Filtering and parameter estimation are closely related to each other, because in general the information is carried out in a number of signal parameter but in reality the observation collected from any structure in the form of signal contains noise by Arce (2005), therefore filtering the unrequired noise and accurate estimation of the modal parameter is becoming more and more important in recent years specially for the monitoring of long span cable stayed bridge, because the FIR and IIR are not use

before in modal parameter identification of long span cable stayed bridges. Therefore for the first time an attempt is made to introduce these filters in bridge health monitoring for better and accurate estimation of modal parameters such as Natural Frequency, Damping Ratio and Mode Shape.

Ambient excitation method specially in bridge engineering to identify the structural modal parameters in time or frequency domain is getting more and more importance. In order to extract these operational modal parameters a number of stochastic identification techniques have been developed in the past, but among them the stochastic subspace identification (SSI) is very effective and multivariate identification technique. The SSI algorithm is an advanced technique for performing operational modal parameter identification (Lin et al. 2013). SSI uses the ambient vibration response data to identify the system model by linear algebraic manipulations Shan and Li (2009). The SSI consist of two methods, i) Data Driven Stochastic subspace identification (DATA-SSI) and, ii) Covariance Driven Stochastic subspace identification (CO-SSI). The DATA-SSI method perform better than the CO-SSI because the identification starts directly from the raw time series, instead of using the covariance matrices, thus making the identification process more fast and effective and consumes less time in its processing as compare to the CO-SSI. Overschee and Moor (1996), (Bassville etal. 2007), (Weng et al. 2008), Bonyapinyo and Janesupasaeree (2010) studied the applications of DATA-SSI, but they directly identified the modal parameter and does not treat the data using any type of filter, thus the results obtained by them were not very accurate, because of the inclusion of noise in the data analysis. Therefore in this paper first data treatment has been done using filters such as FIR and IIR, then the DATA-SSI is adopted because of its inherent advantages of less computational time, stability and robustness (Bonyapinyo et al. 2006). Another major problem with DATA-SSI is, it's an offline method and can only be used for a fix batch of data, hence cannot be used in on online fashion, (Goethals et al. 2006) come up with sliding window technique, but it was proved not to be so effective, secondly it was not applied to some real life data for continuous modal parameter identification and also there were no discussion and information about the mode shape. Therefore some improvements are made in DATA-SSI in this paper, to identify the continuous modal parameter such as frequency, damping ratio and mode shape.

2 FILTERS

Filtering is the most commonly used technique in digital Signal Processing (DSP) Shenoi (2006), but to the knowledge of the Author it is never tried in bridge health monitoring. Filtering is the most commonly used technique in digital Signal Processing (DSP) Shenoi (2006), but to the knowledge of the Author it is never tried in bridge health monitoring. Therefore it is a first attempt to use these filters for signal processing from the dynamic data obtained from the accelerometers installed at a long span cable stayed bridge. The basic phenomenon of introducing filters in the dynamic analysis of cable stayed bridge is to remove the unwanted frequencies and the noise. In science and engineering noise is consider as the disturbance, especially the random noise and thus reduces the clarity of signals Wu and Huang (2005). As the collected data from the sensors $\mathrm{d(t)}$, consist of the true signal $\mathrm{s(t)}$ and noise $\mathrm{n(t)}$, hence it can be written as:

$$\mathrm{d(t)} = s(t) + n(t) \tag{1}$$

Since noise is obliquitous and depicts highly undesirable and dreaded part of any data, therefore most of the data analyst design some techniques to remove the unwanted noise and extract the true information from the true signals collected from the sensors data Wu and Huang (2005). In order to carry out the above process effectively FIR and IIR were introduced and then the filter designing of each of them were carried out to match our collected data, so that the dynamic modal parameter identification should be carried out effectively and efficiently and provides the true and accurate assessment of the long span cable stayed bridge.

2.1 Vibrations

The Finite Impulse Response (FIR) filters are linear discrete-time filters having high filter order, stable and characterized by their impulse responses. Therefore an impulse response can have either a finite or infinite duration. A finite impulse response $\mathrm{h(n)}$ having its non-zero values over a finite time interval and zero and even beyond that interval, thus its finite impulse response can be written as Lai (2003):

$$\mathrm{h(n)} = \{ h_0, h_1, h_2, \cdots, h_N, 0,0,0, \cdots \} \tag{2}$$

In addition it also contain non-zero values in the interval, $0 \leq \mathrm{n} \leq \mathrm{N}$. Thus it is referred as a FIR or system order N. Therefore an N^{th} order FIR filter has an impulse response with a length of $(\mathrm{N}+1)$ samples, where h_0, h_1 etc. are the filter coefficients, filter weights and filter tap coefficient. In case of FIR filter the output sequence is related to the input and the impulse response of the filter by convolution sum and can be expressed as Lai (2003).

$$y(n) = \sum_{m=0}^{M} x(m)\, h(n-m) \quad (3)$$

This equation shows the non-recursive nature of the FIR filter, because the output samples is only dependent on "N" input for N^{th} order filter, thus the summation on the right hand side is a convolution between x(n) and h(n), also called the impulse response of the filter. Since the discontinuity are more in frequency domain, therefore to cope up with the frequency response we need a window which tapper off smoothly rather than a rectangular window in order to reduce the ripple effect, therefore hamming window is selected in this paper, because its performs better as compare to the other rectangular window. Hamming window can be mathematically expressed as:

$$\omega(n) = 0.54 - 0.46\cos\left(\frac{2\pi n}{N-1}\right) \quad (4)$$

Where $n = 0,1,\ldots,N-1$ and the above equation defines the window samples as already shifted (indices from 0 to N−1).

2.2 IIR filters

Infinite Impulse Response (IIR) filter are having impulse responses that are infinite in the duration, thus it is opposite to the FIR filters. As IIR filters are recursive, therefore the relationship between input and output is expressed as:

$$y(n) = -\sum_{k=0}^{N} a(k)\, y(n-k) + \sum_{k=0}^{M} b(k)\, x(n-k) \quad (5)$$

Rearranging the above equation in linear difference equation form and can be rewritten as:

$$\sum_{k=0}^{N} a(k)\, y(n-k) = \sum_{k=0}^{M} b(k)\, x(n-k) \quad (6)$$

With $a(0) = 1$, we can write the above equation as:

$$\sum_{k=1}^{N} a(k)\, [z^{-k}\, y(n)] = \sum_{k=0}^{M} b(k)\, [z^{-k}\, x(n)] \quad (7)$$

Where z^{-1} is the unit delay function of one sample and can be expressed as: $z^{-k}\, x(n) = x(n-k)$

Thus a transfer function in the form of "z" can be expressed as:

$$H(z) = \frac{y(n)}{x(n)} = \frac{\sum_{k=0}^{M} b(k)\, z^{-k}}{\sum_{k=0}^{N} a(k)\, z^{-k}} \quad (8)$$

The ratio of the two polynomials can be expressed as:

$$H(z) = \frac{b(0)+b(1)z^{-1}+\cdots+b(M)z^{-M}}{1+a(1)z^{-1}+a(2)z^{-2}+\cdots+a(N)z^{-N}} \quad (9)$$

In this paper Butterworth function is used and its magnitude squared function for the nth order can be expressed as Lai (2003):

$$|H(\omega)|^2 = \frac{1}{1+C\omega^{2n}} \quad (10)$$

Where "C" is the constant which determine the transition of "ω" between pass band and the stop band to occurs. For normalized Butterworth filter, this point is at $\omega = 1$ and thus $C = 1$, therefore we also called it as cut off frequency. But the response at both $\omega = 0$ and $\omega = \infty$ are completely horizontal, thus we can say at such frequency the response is ideal.

3 DATA DRIVEN STOCHASTIC SUBSPACE IDENTIFICATION

3.1 Numerical modelling

The ambient excitation of a dynamic system of a bridge structure under classical formulation can be expressed as:

$$m\ddot{x}(t) + c\dot{x}(t) + kx(t) = fv(t) \quad (11)$$

Where “m” is the mass, “c” is the damping coefficient and “k” is the stiffness, $\ddot{x}(t)$, $\dot{x}(t)$ and $x(t)$ are the acceleration, speed and displacement vector at time instant t respectively. "f" is the input matrix of the force excitation and ν(t) is the input vector at time instant t.

Now considering the discrete form, DATA-SSI method performs the identification of the modal parameters using the state space model by the following equations:

$$x_{k+1} = A.x_k + \omega_k + 1 \quad , \quad y_k = C.x_k + \nu_k \quad (12)$$

Where $x_k$is the discrete time state vector at time instant k, y_k is a vector with the sampled outputs, A and C are the discrete state and output matrix respectively and ω_{k+1}, v_k are state noise and modelling in accuracies vectors respectively.

3.2 Data driven stochastic subspace identification algorithms

The data driven stochastic subspace identification (DATA-SSI) techniques utilizes Projection matrix created from the Hankel matrix as compare to the covariance driven stochastic subspace identification (CO-SSI). Secondly the calculation needs less memory due to the Projection method, even though this makes the principle of the method a little bit more complex, but still it is more efficient as compare to CO-SSI.

In case of DATA-SSI the number of block rows and columns in the Hankel matrix plays a very important role and thus the influence on the identification process is very prominent, the block columns

must be larger than the block rows, and the rows are generally multiplied with the number of sensors, so the column number of the Hankel matrix in case of DATA-SSI is larger as compare to COSSI method. The given Hankel matrix in case of DATA-SSI can be determined from the output data, computing the projection matrix of the row space of future into the row space of the past. In general using RQ decomposition on the Hankel matrix to calculate two projection matrices P_i, P_{i+1}, the Hankel matrix can be expressed as:

$$\text{Hankel} = \begin{bmatrix} y_0 & y_1 & y_2 & \cdots \\ y_1 & y_2 & y_3 & \cdots \\ y_2 & y_3 & y_4 & \cdots \\ \vdots & \vdots & \vdots & \ddots \end{bmatrix} = \begin{bmatrix} y_p \\ y_f \end{bmatrix} \tag{13}$$

After performing the RQ Decomposition, it can be written as:

$$\text{Hankel} = RQ = \begin{bmatrix} R_{11} & 0 & 0 & 0 \\ R_{21} & R_{22} & 0 & 0 \\ R_{31} & R_{32} & R_{33} & 0 \\ R_{41} & R_{42} & R_{43} & R_{44} \end{bmatrix} \begin{bmatrix} Q_{11} \\ Q_{12} \\ Q_{13} \\ Q_{14} \end{bmatrix} \tag{14}$$

$$P_i = \begin{bmatrix} R_{31} & R_{32} \\ R_{41} & R_{42} \end{bmatrix} \begin{bmatrix} Q_{11} \\ Q_{12} \end{bmatrix} \tag{15}$$

$$P_{i+1} = \begin{bmatrix} R_{41} & R_{42} & R_{43} \end{bmatrix} \begin{bmatrix} Q_{11} \\ Q_{12} \\ Q_{13} \end{bmatrix} \tag{16}$$

In order to get the observability matrix O_i. Singular value decomposition is performed on the projection matrix P_i to get:

$$P_i = USV^T = \begin{bmatrix} U_1 & U_2 \end{bmatrix} \begin{bmatrix} S_1 & 0 \\ 0 & S_2 = 0 \end{bmatrix} \begin{bmatrix} V_1^T \\ V_2^T \end{bmatrix} \tag{17}$$

$$P_i = O_i X_i = \begin{bmatrix} C \\ CA \\ \vdots \\ CA^{i-1} \end{bmatrix} \begin{bmatrix} x_i & x_{i+1} & \cdots & x_{i+j-1} \end{bmatrix} \tag{18}$$

$$O_i = U_1 S_1^{1/2} \tag{19}$$

Then eliminating the last block row of O_i in order to get O_{i+1}. Then we obtained the two Kalman Filtered states matrices x_i, x_{i+1}, based on the Kalman filtered state estimation, by using the observability matrices and the projection matrices.

$$x_i = O_i^{-1} P_i, \quad x_{i+1} = O_{i-1}^{-1} P_{i+1} \tag{20}$$

Hence the system matrix A can be written as follow:

$$A = x_{i+1} x_i^{-1} \tag{21}$$

Then using the last block row output data matrix $y_{i/li}$ and multiply the inverse Kalman filtered state matrix x_i to get the system matrix C and thus it can be written as:

$$C = y_{i/li} x_i^{-1} \tag{22}$$

Therefore the eigenvalue and the eigenvector can be obtained by eigenvalue decomposition on the system matrix A and can be written as:

$$A = \psi \Lambda \psi^{-1} \tag{23}$$

3.3 Modal parameter identification

After calculating these matrices the next step is to identify the modal parameters. The model parameters can be obtained by choose the suitable order, a suitable order of the system depends on the suitable date of the singular value decomposition on the projection matrix P_i in order to plot the singular value figure to decide the order. Then the diagonal matrix with n dimensions can be written as:

$$\Lambda = diag[\mu_i] \tag{24}$$

Where the matrix Λ is composed of the complex eigenvalue μ_i, and the relation between the eigenvalues of matrix A and systematic one is given as:

$$\lambda_i = \frac{\ln \mu_i}{\Delta t} \tag{25}$$

Where the eigenvalue of the system is λ_i, with sampling time interval of Δt. The relation between the systematic eigenvalues and λ_i and systematic intrinsic frequency ω_i and the systematic damping ratio ξ_i is given as:

$$\lambda_i, \overline{\lambda_i} = \xi_i \omega_i \pm j\omega_i \sqrt{1 - \xi_i^2} \tag{26}$$

Hence the frequency, the damping ratio and mode shape can be found from the equations given below:

$$f_i = \frac{\sqrt{|\lambda_i|}}{2\pi} \tag{27}$$

$$\zeta_i = \frac{-\lambda_i + \overline{\lambda_i}}{2\sqrt{\lambda_i \overline{\lambda_i}}} \tag{28}$$

$$\phi_i = C\psi_i \tag{29}$$

The schematic diagram of the whole process of the modal parameter identification is shown below:

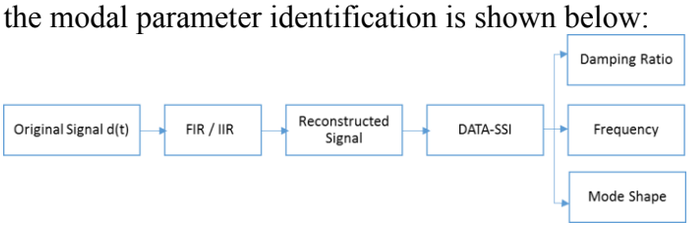


Figure 1. Modal parameters identification process

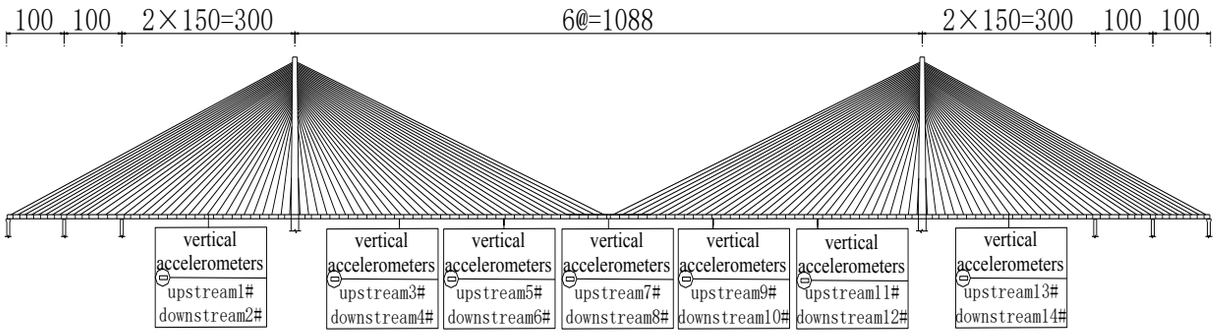


Figure 2. Layout of accelerometer on main girder (Unit:m)

3.4 Sliding window technique

Now giving a finite set of hankel matrix $\widehat{Y_0}$ ... $\widehat{Y_{2i}}$ and a finite dimensional estimate, then $\hat{O}$ for O can be found by SVD of $\hat{H}$, now it can be expressed as:

$$\hat{H} = \begin{bmatrix} \hat{Y}_0 & \hat{Y}_1 & \cdots & \hat{Y}_i \\ \hat{Y}_1 & \hat{Y}_2 & \cdots & \hat{Y}_{i+1} \\ \vdots & \vdots & \ddots & \vdots \\ \hat{Y}_i & \hat{Y}_{i+1} & \cdots & \hat{Y}_{2i} \end{bmatrix} \tag{30}$$

Generally DATA-SSI method process the data in one batch, hence it cannot be used as an online health monitoring technique, therefore a new method called sliding window technique is adopted to make the DATA-SSI a continuous online modal parameter identification process. For this purpose the new Hankel matrix must be adopted, which can be written as:

$$y_k^+ \equiv \begin{bmatrix} y_{k-i+1} \\ y_{k-i+2} \\ \cdots \\ y_k \end{bmatrix}, y_k^{-T} \equiv \begin{bmatrix} y_{k-i}^T & y_{k-i-1}^T & \cdots & y_{k-2i+1}^T \end{bmatrix} \tag{31}$$

Where y_k^+ and y_k^{-T} are the output measurements vectors and "i" is the number of block rows, therefore new Hankel matrix $\hat{H}$ can be written as:

$$\hat{H} = \frac{1}{p}\sum_{k=i}^{N} y_k^+ y_k^{-T} \tag{32}$$

Where k is ranging over the entire set of data and p is an optional normalization parameter and the length of the Hankel matrix is N. Finally the sliding window technique is applied to the already filter data. The new data is incorporated into $\hat{H}$ at the same rate as the old data is removed. Thus it can be expressed as:

$$\hat{H}_{N+1} = \hat{H}_N + y_{N+1-i}^+ (y_{N+1-i}^-)^T - y_i^+ y_i^{-T} \tag{33}$$

Where all the manipulations of $\hat{H}$ amount to update of the form

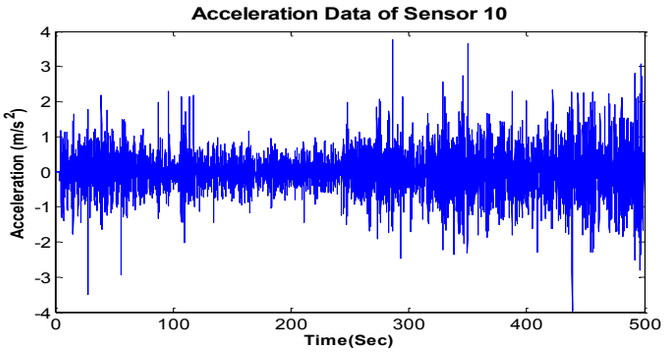
$$\hat{H}_{t+1} = \hat{H}_t + y_{t+1}^+ y_{t+1}^{-T} \tag{34}$$

4 RESULTS AND DISCUSSION

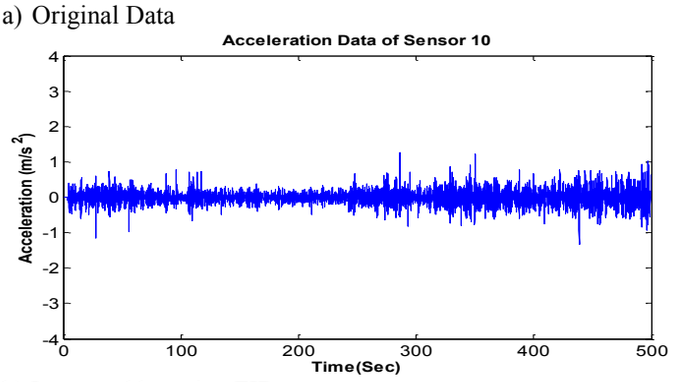
Sutong bridge is one of the longest spanning cable-stayed bridge is taken as a case study. It is located on Yangtze River and connecting the cities Suzhou and Nantong. The bridge is a seven span double pylon and double cable plane steel box girder cabled-stayed bridge having a main span of 1088m, the overall arrangement of span is 100+100+300+1088+300+100+100 = 2088m. In order to identify the modal parameters of Sutong bridge, the data collected from Sutong bridge was first filtered by using the FIR and IIR filters, then DATA-SSI algorithm is adopted based on MATLAB to get the required results.

4.1 FIR filtering of sutong bridge

In order to carry out the FIR filtering on the data collected from Sutong Bridge using MATLAB, each of the 14 sensors are filtered one by one, but due to space limitation only few of them are shown below:



a) Original Data



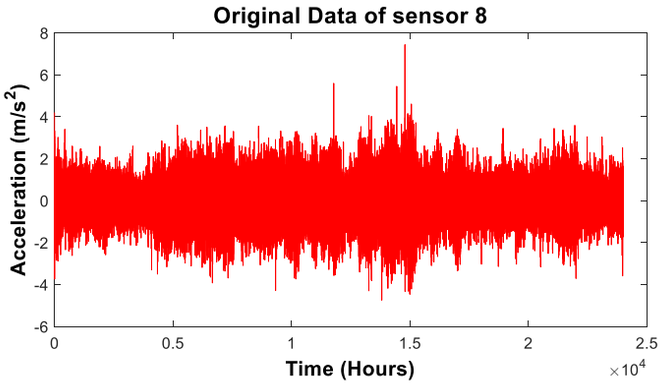
b) Improved by using FIR

Figure 3. FIR filtering of sensor # 10 data

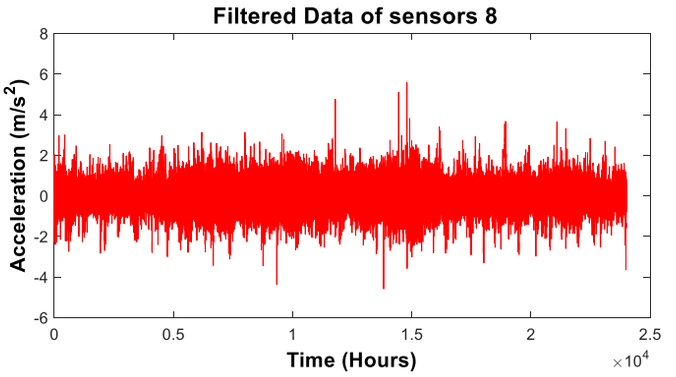
The results in Figure 3 shows that the filter works very effectively and the acceleration trend is very regular and compact after using the FIR filter as compare to without filtering the data. In Figure 3(a) it can be seen very clearly that the peaks are more pronounced as compare to the Figure 3(b), means that the filter works properly and have removed the unwanted noise very effectively and have made the data regular and compact.

4.2 IIR filtering of sutong bridge

Similarly in order to carry out the IIR filtering on the data collected from Sutong Bridge using MATLAB, each of the 14 sensors are filtered one by one, but due to space limitation only few of them are shown below:



a) Original Data



b) Improved by using IIR

Figure 4. IIR filtering of sensor # 8 data

The results in Figure 4 shows that the filter works very effectively. After using the FIR filter the acceleration trend is very regular and compact as compare to without using the IIR filter. Figure 4(a) depicts that the peaks are more pronounced as compare to the Figure 4(b), means that the filter works properly and have removed the unwanted noise very effectively and have made the data regular and compact.

4.3 Modal parameter identification of sutong bridge

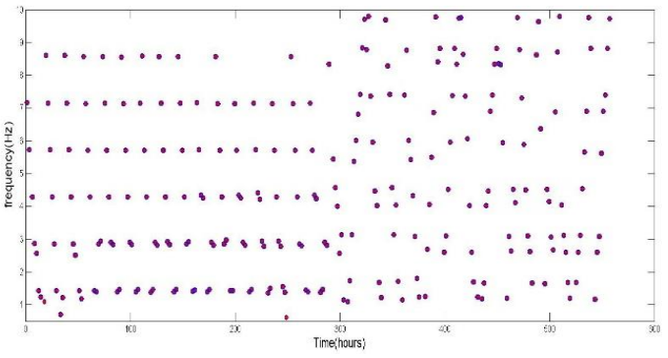
In order to identify the continuous modal parameters data was collected from Sutong bridge for a period of 1 month form 01-07-2011 to 31-07-2011. This was collected from 14 vertical accelerometer sensors installed at the bridge. The layout of the vertical accelerometer sensors are shown in Figure 2. The sensor details are shown in Table 1, whereas the sampling frequency is 20Hz. In our study we have only used the data obtained from the 14 vertical accelerometer sensors installed at the Sutong Bridge. The data was first processed by using the FIR and IIR filters one by one on the already collected data from the Sutong bridge, then the reconstructed signal obtained after performing the filtering is used to identify the modal parameters such as frequency and damping ratio using the DATA-SSI technique.

Table 1 Vertical accelerometer sensor's detail

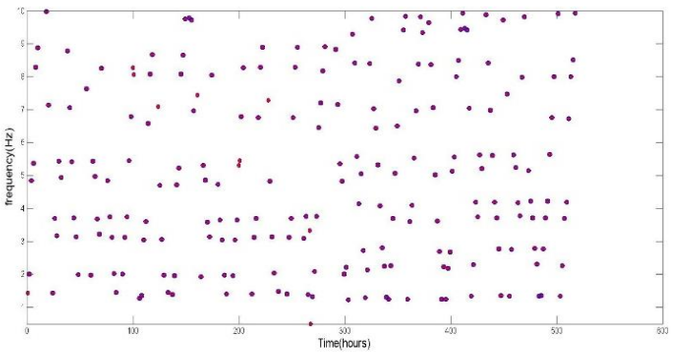
Vertical Accelerometer Numbering			
S/no	Vertical	S/no	Vertical
1	ZD020102	8	ZD050102
2	ZD020104	9	ZD050104
3	ZD030100	10	ZD050200
4	ZD030102	11	ZD050202
5	ZD030104	12	ZD050204
6	ZD030106	13	ZD070100
7	ZD050100	14	ZD070102

Figure 5 shows the frequency estimates obtained by using MATLAB. The frequency trend in Figure 5(b) as compare to Figure 5(a) is more compact and regular. The frequency band specially at frequency 1.5 to 2Hz, 3 to 3.7Hz and 4.7 to 5.4Hz is more pro-

nounced and compact and a regular trend can be seen from left to right in Figure 5(b), thus showing that the results obtained are very good after performing the FIR filtering, because after the introduction of filter the frequency trend become regular as can be seen clearly in Figure 5(b). It can also be deduced from the results obtained in Figure 5(b) that the vertical sensor's data is more robust in terms of vibration, because in cable stayed bridge the vibration are more, thus the results shows an accurate representation of the real life conditions. Figure 6 shows the Damping ratios obtained from the vertical sensors using MATLAB, with and without using the FIR filter, the results obtained shows that the damping ratio is not more than 0.1 to 0.6%. The Chinese specification for cable stayed bridge specified the maximum limits for damping ratio between 1%-2%. In our case the results obtained are within the limits, specially for the Figure 6(b) because it shows the real life representation of cable stayed bridge as compare to Figure 6(a), because in Figure 6(a) most of the damping ratios is around zero, which is not a true representation of cable stayed bridge, thus validates the proposed method.

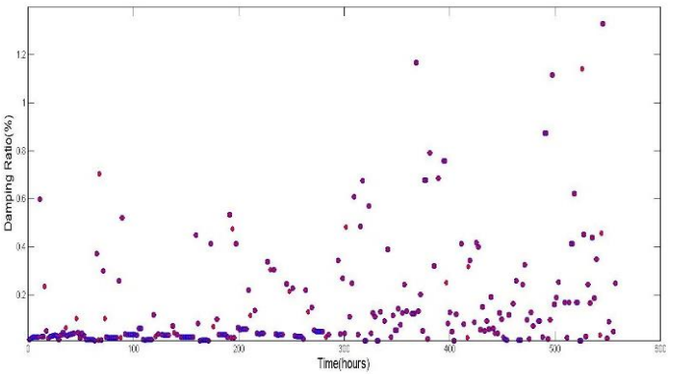


a) Original Data

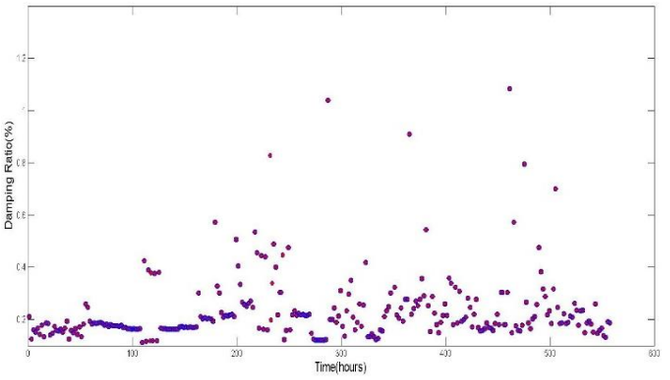


b) After using FIR filter

Figure 5. Frequency estimates before and after using the FIR filter



a) Original Data

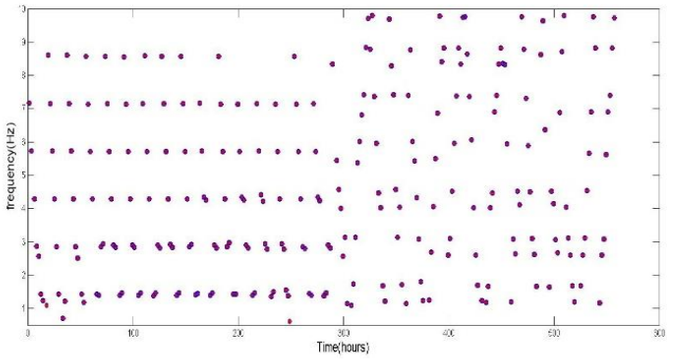


b) After using FIR filter

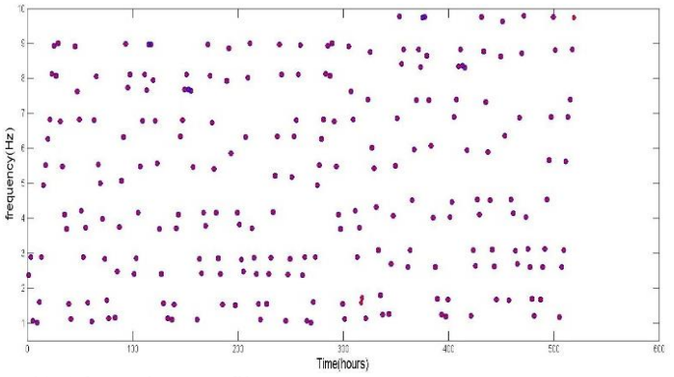
Figure 6. Damping estimates before and after using the FIR filter

Figure 7 shows the frequency estimates obtained by using MATLAB. The frequency trend in Figure 7(b) as compare to Figure 7(a) is more compact, regular and the extracted frequencies band from left to right is more regular. The frequency band specially at frequency 1 to 1.5Hz, 2.5 to 3Hz and 3.7 to 4Hz is more pronounced and compact and a regular trend can be seen from left to right in Figure 7(b), thus showing that the results obtained are very good after performing the IIR filtering, because after the introduction of filter the frequency trend become regular as can be seen clearly in Figure 7(b). It can also be deduced from the results obtained in Figure 7(b) that the vertical sensor's data is more robust in terms of vibration, because in cable stayed bridge the vibration are more, thus the results shows an accurate representation of the real life conditions. Figure 8 shows the Damping ratios obtained from the vertical sensors using MATLAB, with and without using the IIR filter, the results obtained shows that most of the damping ratio is between 0.1 to 0.3% and is not more than 1.2%. The Chinese specification for cable stayed bridge specified the maximum limits for damping ratio between 1%-2%. In our case the results obtained are within the limits, specially for the Figure 8(b) because it shows the real life representation of cable stayed bridge as compare to Figure 8(a), because in Figure 8(a) most of the

damping ratios is around zero, which is not a true representation of cable stayed bridge, thus validates the proposed method.

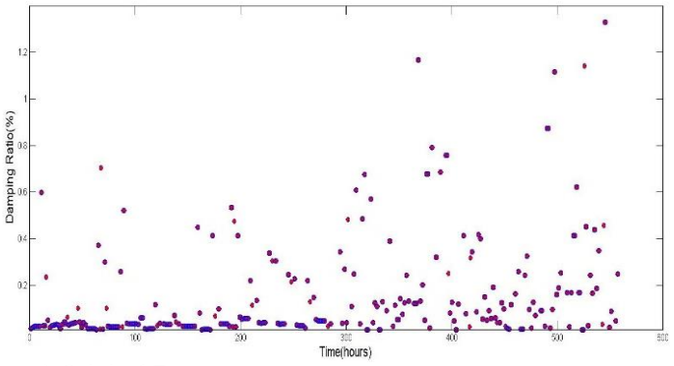


a) Original Data

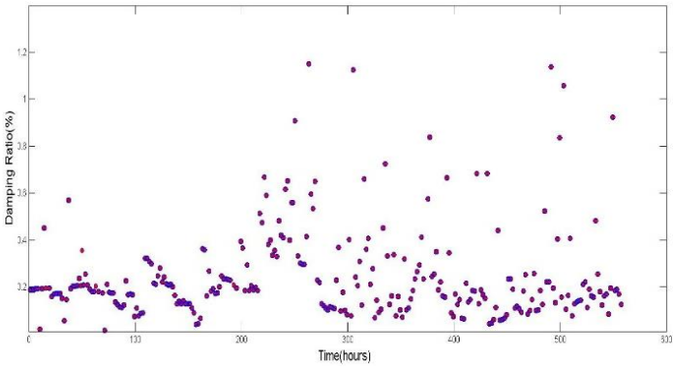


b) After using IIR filter

Figure 7. Frequency estimates before and after using the IIR filter



a) Original Data



b) After using IIR filter

Figure 8. Damping estimates before and after using the IIR filter

5 CONCLUSION

In this paper first the data is collected from Sutong bridge, a long span cable stayed bridge, then the data is filtered so that the noise and disturbance is removed from the data by using the FIR and IIR filters one by one. Then the reconstructed signal obtained after performing the filtering was used for the continuous modal parameter identification. Finally to get the continuous modal parameters DATA-SSI was engaged for the continuous modal parameter identification, because DATA-SSI is robust, accurate and consumes less time in data processing, with only problem of processing the data in one batch, hence sliding window technique was used to make it more suitable to be used for the continuous modal parameter identification. The above technique combines the advantages of two methods i.e. the filtering technique to remove the unwanted noise and secondly the continuous monitoring by employing the DATA-SSI. The modal parameters such as frequency and damping ratio obtained from the above used technique are very effective, robust and can provide more useful information about the real life bridge health monitoring.

REFERENCES

Arce, G. R. 2005. *Nonlinear Signal Processing: A Statistical Approach*. New Jersey: John Wiley & Sons, Inc. ISBN 0-471-67624-1.

Bassville, M., Benveniste, A., Goursat, M. & Mevel, L. 2007. In-flight vibration monitoring of aeronautical structures. *IEEE Control System Magazine*: 27–41.

Bonyapinyo, V. & Janesupasaeree, T. 2010. Data-driven stochastic subspace identification of flutter derivatives of bridge decks. *Journal of Wind Engineering and Industrial Aerodynamics* 98: 784–799.

Bonyapinyo, V., Lauhatanon, Y. & Lukkunaprasit, P. 2006. Nonlinear aerostatic stability analysis of suspension bridge. *Engineering Structures* 28(5): 793–803.

Cattani, C., Chen, S., & Aldashev, G. 2012. Information and modeling in complexity. *Mathematical Problems in Engineering*: Article ID 868413, 4 pages.

Chen, S., Huang, W., Cattani, C., & Altieri, G. 2012. Traffic dynamics on complex networks: a survey. *Mathematical Problems in Engineering*: Article ID 732698, 23 pages.

Cho, S., Yun, C., Lynch, J. P., Zimmerman, A., Spencer Jr, B. F. & Nagayama, T. 2004. Smart wireless sensor technology for structural health monitoring of civil structures. *Journal of Steel Structures* vol. 81: 267–275.

Cho, S., Jo, H. & Jang et al. 2010. Structural health monitoring of a cable-stayed bridge using wireless smart sensor technology: data analyses. *Smart Structures and Systems* vol. 6, no. 5-6: 461–480.

Cross, E. J., Koo, K. Y., Brownjohn, J. M. & Worden, K. 2013. Long-term monitoring and data analysis of the Tamar Bridge. *Mechanical Systems and Signal Processing* 35: 16-34.

Gao, Y., Spencer Jr. B. F., & Ruiz-Sandoval, M. 2006. Distributed computing strategy for structural health monitoring. *Structural Control and Health Monitoring* 13(1): 488–507.

Goethals, I., Mevel, L. & Moor, B. D. 2006. Recursive Output Only Subspace Identification for In flight Flutter Monitoring. *Belgian Federal Government*.

Jang, S., Jo, H. & Cho, S. et al. 2010. Structural health monitoring of a cable-stayed bridge using smart sensor technology: deployment and evaluation. *Smart Structures and Systems*, 6(5-6): 439–459.

Lai, E. 2003. *Practical Digital Signal Processing for Engineers and Technicians*. Elsevier Linacre House Jordan Hill: Oxford OX2 8DP 200 Wheeler Road, Burlington, MA 01803, ISBN 07506 57987.

Lynch, J. P. & Loh, K. J. 2006. A summary review of wireless sensors and sensor networks for structural health monitoring. *The Shock and Vibration Digest* 38 (2): 91–128.

Liu, Y. C., Loh, C. H. & Ni, Y. Q. 2013. Stochastic subspace identification for output-only modal analysis: application to super high-rise tower under abnormal loading condition. *Earthquake Engineering and Structural Dynamics* 42: 477–498.

Nitta, Y., Nagayama, T., Spencer Jr, B. F. & Nishitani, A. 2005). Rapid damage assessment for the structures utilizing smart sensor MICA2 MOTE. *Proceedings of the 5th International Workshop on Structural Health Monitoring*, Stanford, Calif, USA: 283–290.

Overschee, P. V. & Moor, B. D. 1996. *Subspace identification for linear systems: Theory – Implementation Applications*. Katholieke Universiteit Leuven, Belgium, Kluwer Academic Publishers, Boston/London/Dordrecht.

Rice, J. A. & Spencer Jr, B. F. 2009. Flexible smart sensor framework for autonomous full-scale structural health monitoring. *Newmark Structural Engineering Laboratory (NSEL)* Report Series no. 18, University of Illinois at Urbana-Champaign, Urbana, Ill, USA, http://hdl.handle.net/2142/13635.

Shan, D. S. & Li, Q. 2009. Modal parameter identification of girder bridge based on covariance based stochastic subspace algorithm. International conference on *Environmental Vibrations: Prediction, Monitoring and Evaluation*, Beijing.

Shenoi, B. A. 2006. *Introduction to digital signal processing and filter design*. Hoboken, New Jersey, John Wiley & Sons, Inc., ISBN-13 978-0-471-46482-2.

Shi, H., Wang, W., Kwok, N. M. & Chen, S. Y. 2012. Game Theory for Wireless Sensor Networks: A Survey. *Sensors* 12(7): 9055–9097.

Tanner, N. A., Wait, J. R., Farrar, C. R. & Sohn, H. 2003. Structural health monitoring using modular wireless sensors. *Journal of Intelligent Material Systems and Structures,* 14 (1): 43– 56.

Weng, J. H., Loh, C. H., Lynch, J. P., Linn, P. Y., Wang, Y. 2008. Output-Only Modal Identification of a Cable-Stayed Bridge Using Wireless Monitoring Systems. *Journal of Engineering Structures* 30(2): 1802–1830.

Wenzel, H. 2009. *Health Monitoring of Bridges*, John Wiley & Sons, Ltd. ISBN: 9780470031735.

Wu, N., Liu, C., Guo, Y. & Zhang, J. 2013. On-Board Computing for Structural Health Monitoring with Smart Wireless Sensors by Modal Identification Using Hilbert-Huang Transform. *Mathematical Problems in Engineering*, Article ID 509129, 9 pages.

Wu, Z. & Huang, N. E. 2005. Ensemble Empirical Mode Decomposition: a noise assisted data analysis method. *Advances in Adaptive Data Analysis* 1(1): 1-49.

MS07: Recent advances in bridge design and construction

Organizers: U. Attanayake & H. Aktan

Maintenance, Safety, Risk, Management and Life-Cycle Performance of Bridges – Powers, Frangopol, Al-Mahaidi & Caprani (Eds)
© 2018 Taylor & Francis Group, London, ISBN 978-1-138-73045-8

Deployable Mobile Bridge created from *ORIGAMI*

I. Ario
Department of Civil & Environmental Engineering
Hiroshima University, Higashihiroshima, Japan

S. Ono & I. Tanikura
Japan Construction Method and Machinery Research Institute, Fuji, Japan

Y. Chikahiro
Department of Water Environment & Civil Engineering
Shinshu University, Nagano, Japan

M. Nakazawa
Department of Civil & Environmental Engineering
Tohoku Gakuin University, Sendai, Japan

P. Pawlowski, C. Graczykowski & J. Holnicki-Szulc
Institute of Fundamental Technological Research, Polish Academy of Sciences, Warszawa, Poland

ABSTRACT: In the past, phenomenon of a bridge being washed away because of a typhoon, a heavy rain in the rainy season, a localised torrential rain, a tsunami and other floo disasters have been observed several times. Hence, new technology and science to restore bridges that have been washed away or damaged are facing an increasing demand. Using the latest technical developments in light structures, the post-buckling response of a thin cylindrical shell is reviewed herein similar to the concept of Origami. This engineering idea is very useful when applied to deployable bridge systems with a rapid construction method. The folding bridge design takes inspiration from the folding skills of Origami, where the scissors mechanism is understood and applied. This study presents a new type of bridge based on the folding idea of Origami and the multi-folding microstructure. The developed bridge system for providing relief after natural disasters is then reviewed by performing a field test in a real river.

1 INTRODUCTION

Globally, natural disasters come in many different forms, including earthquakes, floods tsunamis and landslides. Japan has a long history of devastating disasters, which killed thousands of people and severely devastated both the infrastructure of urbanised areas and transport links. The Great Hanshin Awaji earthquake occurred in 1995, destroying numerous buildings and civil engineering structures. In 2017, the region around Tohoku is still recovering from the 2011 earthquake and tsunami. Figure 1 shows several traffi infrastructures damaged by typhoons and earthquakes in Hokkaido, Tohoku and Kagoshima. Natural disasters can occur anywhere in the world and pose a threat to people in communities, where they will strike. A range of infrastructures will be damaged as an aftermath of a natural disaster. However, it is the rapid repair of any affected bridge or the installation of temporary bridges that is significantl beneficial Repairing all infrastructures is important, but very little improvement will be achieved if any bridge link is remains not passable. Having a bridge link allows for a two-way transport (e.g. evacuation and delivery of aid to local communities).

Urgency, risks, and hazards are present within disaster zones. If a prefabricated bridge is to be used as a temporary structure, it takes a significan time before it reaches a usable state (i.e. typically over a week). This will result in a delayed access of heavy machinery and emergency vehicles needed in a disaster zone to affected regions, consequently resulting to delayed recovery work. In other scenarios, where an emergency bridge is needed, necessary personnel (e.g. pro-



(a) Road collapsed by the Kumamoto earthquake.



(b) Bridge damaged by typhoon in Hokkaido.



(c) damaged bridge by typhoon in Hokkaido.



(d) fl wn bridge by typhoon in Kagoshima.

Figure 1: Bridges destroyed in Japan by natural disasters in 2016.

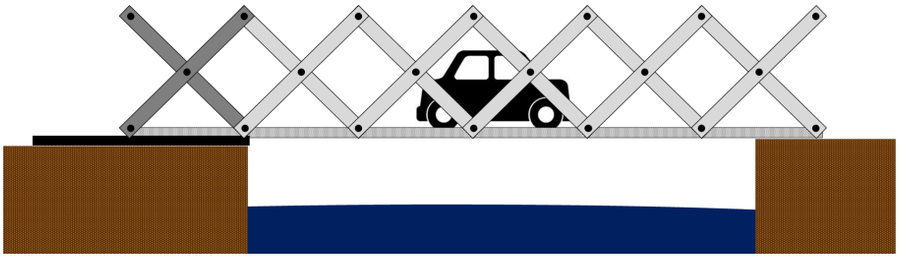


Figure 2: New concept of a scissor bridge based on Origami-folding idea.

fessional engineers) may not be available to construct them. Secondary hazards caused by localised damage would also possibly impede any rescue operations. These situations raise the important issue of selecting the critical activities to be performed in the immediate aftermath of a natural disaster.

In developing a deployable or folding bridge, the fundamental behaviour of the basic mechanisms for the buckling of a thin cylindrical shell under torsional loading must be considered and reviewed from a post-buckling perspective. Deflection are extensively considered in a large deflectio range to the point that the shell is allowed to fold to a fla two-dimensional form in a mechanism reminiscent of a deployable structure. Critical and initial post-buckling effects are explored herein through the concepts of energy minimisation and hidden symmetries. A truss element program is employed for comparison with the fina large-deflectio folded shape. As buckling develops, the mode shape must change to accommodate both the symmetry-breaking aspects of the predominately inward deflectio and the rotation of the peak and valley lines of the buckle pattern necessary to accommodate the geometry of the fina folded shape.

The concept behind the structure is inspired by two different forms of structural design techniques: Origami, which is the art of paper folding, and scissor mechanism, which is a principle using linked supports in a cross 'X'-shaped pattern as a basic unit in a structural system. The firs author thought that if a bridge can fold like the cellular post-buckling of Origami to be a beautiful pattern with a compact size, it would be very useful for the rapidly recovering bridge in Figure 2. A novel structural system that utilises both techniques is proposed herein specificall for constructing a bridge used to provide aid relief for displaced people in times of need and emergency situations. A scissor structure is employed using an Origami-inspired de-

ployment mechanics to create a foldable/deployable and movable bridge and show that constructing a bridge using a folding mechanism based on the academic science of Origami is useful. Hence, a deeper understanding of the essence of an 'Origami-inspired more useful industrial deployable bridge' is advisable.

In the fiel of bridge engineering, several studies have discussed the merits of modular bridges by Thomas and Sia (2013) and the use of lightweight materials (e.g. fibre-reinforce plastic) by Sedlacek (2003) or air tubes by Luchsinger (2004). These propositions allow for the rapid construction of bridges. However, various problems regarding the creation of large construction yards and the use of heavy industrial machinery remain. Any rescue technology should have a low level of complexity and a high degree of resilience to enable its deployment even by unqualifie personnel. Hence, we propose herein a new type of foldable and deployable bridge traded as the 'mobile bridge' (MB) (Japan patent no. 2006-037668 2012; PCT WO2015/193930A1 2015, including European patents). The MB can be quickly deployed and folded because of the scissor mechanism [1] that allows for a highly efficien construction and an easy transportation. The idea for this new bridge was based on the academic studies on post-buckling using the Origami fundamentals of Hunt and Ario (2005) and Pawlowski et al. (2013).

Previous studies (Ario et al., 2017; BBC News, 2015; Web exclusives on ASCE, 2015; Adachi et al., 2017; Chikahiro et al., 2017) evaluated the mechanism and the design concept of the MB through a numerical finit element analysis, followed by a fundamental static loading test using a small experimental bridge. The current research reviews the fiel testing of the latest MB in a real river and its fundamental experimental and numerical results using a full-scale experimental MB.

2 MB BASED ON ORIGAMI AND MULTI-FOLDING TECHNOLOGY

2.1 *Utilising the art of Origami in the fiel structural engineering*

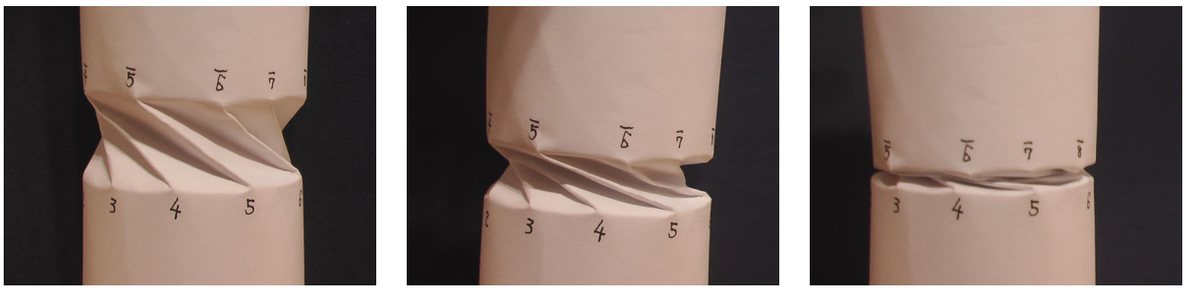
Buckling is recognized as one of the fundamental problems of elastic stability because of its signifi cance in the engineering design of, for example, a thin circular cylindrical shell under torsion and/or axial compression will experience a sudden reduction in stiffness at the onset of buckling. The two contrasting loading situations exhibit quite different characteristics of load/deflectio response as deformation continues into the large-deflectio range. While the former initially results in a highly unstable response followed by restabilization as it settles into a localized form of the well-known YOSHIMURA(1951) pattern (or, it is called "diamond pattern" deformation), the latter forms similar but oblique shapes which are capable of folding entirely in the axial direction without significan in-plane stretching. Figure 3 shows the development of these folds in a paper specimen twisted between two inner plastic mandrels. Following an initial buckling stage that involves both bending and membrane (in-plane) stretching, a pattern resembling an Origami type mechanism is generated. Such folding is prevented in the axially loaded problem which has YOSHIMURA pattern due to the significan stretching occurring at the restabilization stage. The framed core of the buckling pattern resembles a part of the pantographic-lift machine which is available to lift up and down a mechanically expanding/folding system along the vertical direction. Folding without stretching is undoubtedly of considerable interest in the fiel of deployable structures.

2.2 *Post-buckling problem using Origami techniques*

Cellular buckling of a cylinder made by origami, although extremely useful in engineering, is one of the worst issues in structural designing. The instability of a structure under a compressive stress such as buckling becomes an important problem. In the post-buckling theory, there is an opportunity in the cylindrical shell structure built using origami to study the compression buckling by which its symmetry is broken. As the cylinder is twisted, akin to a wet towel squeezed dry, periodic oblique wrinkles in the paper appear at buckling (it appears as a local periodic buckling pattern and this is a type of the multiple bifurcation buckling phenomenon called "cellular buckling"). In the world of Origami, this wrinkle pattern is called a Kresling-pattern, and was introduced by the French origami creator, Kresling(2001). An experiment relevant to this is the post-buckling experiment of the cylindrical shell structure of YAMAKI(1976).

The fundamental behaviour is generally not well understood. However the symmetry of the mode such as the number of waves and its angle of the wrinkles, and an angle variation, should be considered in determining the reason of folding (two or more compression buckling modes should appear in a multiple-singular point) of the energy equilibrium between the bending moment and the in-plane force in the test specimen. Hence, this problem would essentially become difficult The firs author worked thus nonlinear problem and observed deeply this phenomena by using this origami idea for the analysis comparison model, and applied it to the post-buckling theory of YAMAKI. The author fought desperately every day to determine the solution for the problem via geometric observation and reappearance calculation of the

[1] Although the upper and lower chords are the main elements that resist sectional forces in an ordinary truss bridge, the MB lacks chords but can be transported and constructed quickly using a scissor mechanism.



(a) (b) (c)

Figure 3: The foldable cylinder based on twist buckling of a paper roll in Hunt & Ario(2005).

method by which it was folded.

The firs author of this work discovered an important mechanism from the Kresling pattern according to which the truss was built, and its application to lightweight deployment structure has been proposed in this scientifi observation and approach. This was a turning point because most designers and engineers of structural engineering have to ensure that there is no occurrence of instability from buckling behaviour for a structure. However, we think that it is so useful to expand the deployable structure by using the minimum force based on the principle of the minimum energy with this initiated deformation of Kresling pattern in nature. So it is important to avoid buckling in structural design but it does become an aspect for the design of lighter deployable structures for space engineering if this Origami type buckling considered here becomes a useful mechanism when the folding lines from the deformed shell of Origami's post-buckling are considered. We realized that this idea is revolutionary using an engineering method from traditional Origami skills. We could obtain a new concept of engineering design by using Origami which adds to modern phenomenology. So, Origami engineering, can be considered a new construction concept. We believe that this method may become one of the solutions for many problems when solving with innovation and engineering values. This opportunity in the academic study became a turning point of research of Hunt & Ario(2005).

2.3 *Creation of Deployable Bridge based on Origami and Post-Buckling Theory*

In October 2004, the Chuetsu earthquake occurred in Niigata, Japan, following which we investigated the damaged infrastructures in the disaster zone. It is impossible for damaged infrastructure such as railway, bridges, and roads to be used at the time of a disaster. Thus, human efforts are required for the restoration tools to be involved quickly. However, these are very scarce. Moreover, the restoration technique in a distressed area, whether it is inside and/or outside the country, has to be repeatedly applied, and the necessity for a temporary bridge serving as a restoration tool has been realized. Joint research of the structural instability problem of the buckling theory of a multiple-folding micro-structure and the multiple singular points of the diamond truss model of a multilayered pantograph mechanism was conducted with a professor of Polish Academy of Sciences.

2.4 *Trigger of MB development*

The firs author found the deployable structure of the pantograph and a rapid restoration method, which is often used in the elastic expansion of a child's toy played, and related them to the problem of the previously discussed compression buckling. He envisaged an innovative possibility of utilizing the bridge and proposed that the deployable structure could be effectively used if a bridge could be folded similar to that of Origami creations. Although it seems similar to the accordion-like gate of a house, this expanding system in the construction site needs more stiffness in order to design a real bridge for transmitting structural loading. It is necessary for the minimum control force to expand and fold the whole mechanism. Our design is a new concept for the design of a bridge mechanism and selecting the most suitable structural members, using the principle of minimum energy of the post-buckling problem theory along with Origami folding skill and ideas. And we have two another approaches; one is based on the concept of the multiple folding microstructures theory and the other one is based on the concept of topological optimisation method using computing finit element method. Hence, it is realised that it is possible to build up the multi-folding type of bridge based on a principle of the minimum energy like the buckling pattern of Origami. Lightness and strength of the part are important parameters, and the dynamic equilibrium, structural stability, and appropriate structural form are essential considerations. The authors realistically chose the materials with a specifi tensile strength, equilibrium state of the stiffness, and structural stable conditions.

However, technical skill is required to apply the strategy which makes a primary member convergent. Although it is safe to improve the higher stiffness and the stronger bridge and reduce the number of the bridge parts, to ease the stress concentration in the bottom configuratio where the analysis and design



(a) carrying by a wagon



(b) expanding state



(c) expanding state



(d) on the service

Figure 4: Tests of foldable, movable and deployable bridge “Mobile bridge (MB0)” at November 2009.

are currently of a high-quality, we thought it was possible because of a specification Alternatively, when structural instability is well-controlled, it is possible to form the basis for the ability to fold a bridge effi ciently.

However, we have to firs understand the “Ori” (meaning folding) structure which is an unsolved academic problem, involving questions such as the method to fold and how to fold while maintaining the strength of the bridge. The mechanics of the classical post-buckling behaviour is in the territory of undeveloped dynamics in spite of the product called “Ori-Tatami” (it means multi-folding), which is a specialty of Japan. For a particular efficien collapse, The firs author has mathematically determined a multiple peculiar point (a rip of symmetry and multiple structural instability hide potentially). However, there is a high-risk in the case of a heavy construction such as a bridge structure that is sensibly usually evaded, but it is compound by the use of the structurally unstable pantograph mechanism and expanded the parts of the deck slab and the chord members from Origami idea. Thus, the whole system can be developed in terms of multiple structural stability by combining the most suitable and smart structural concept. The development structures are called “Deployable Structures” and often used in applications in the fiel of space engineering. But the deployable structure on the ground is influence by gravity, and its condition becomes generally more severe than in zero gravity space. I perceived that one could not generally understand that it was designed for such conditions, and the embodiment of the mechanical principle in the bridge was entrusted as a prototype shown in figur 4, while the construction was delegated to a manufacturing unit in Hiroshima university to conduct experiments in the limited budget. The manufacturing accuracy has also completed a prototype in the early stage in less than three months thanks to a highly skillful technical staff at Hiroshima University. This concept of a new bridge was created from Origami and it means people pray “Let us build up the peace in the world be like a bridge between countries or people.”

2.5 *Deployable structure*

The scissors mechanism in its most basic form consists of two linear elements joined at their centres by a pivot providing a hinge-connection. In the fully deployed state, the two members are in the shape of the character ‘X’, creating the deployed single scissor unit. This basic scissor unit is connected to the next unit by two hinges. The structure is deployable and has a large ratio of length change from the fully extended state to the folded state. In the non-deployed or compact state the structure can be easily transported or stored for future reuse. Pinero(1965), an architect from Spain, has presented the concept of a scissor type mechanism. He applied this idea to a deployable roof structure and obtained a patent in 1961. After this successful application, Zeigler(1976) and Escring(1989) focused on the geometric layout design of the scissor units and proposed deployable domes

using mechanisms. Recently, Hahawa & Saitoh et al.(2001) has analysed the strength and stability of scissor structures reinforced with a string system. Indeed, scissor type structures are being increasingly used in a wide range in the mechanical and space engineering field Glisic. Our current study for the MB plays an important role as an innovative product in the bridge engineering field The scissors mechanism enables the MB to be constructed and easily transported because of the compact preassembly configuration. These fundamental concepts of the design of the MB result in the following advantages:

1. The MB uses patented technologies (2012)& (2015) based on the scissors mechanism for deploying an emergency bridge system set within a modular design and incorporating deck-boards.

2. The MB is a compact transportable bridge system, *robotic bridge*, which is suitable for transportation on a car trailer or lorry.

3. The MB system has a completely novel design and offers extraordinary performance without requiring assembly of the block type using the trussed structures approach.

In addition, the MB can be deployed in a wide range of areas, not only during emergency situations, but also in normal operations. For example, many existing old bridges are in a poor technical state owing to improper maintenance or overloading. Smaller bridges are available to operate the scissors type of bridge using the MB, which is quick serving as a temporary bridge. This provides the advantage of movable bridges to act as a temporary bridge quickly and easily without interrupting traffi and increasing further damage to the existing bridge.

3 DESIGN OF MOBILE BRIDGE VER. 4.0

The MB has a scissor-like structure that is connected to the main structural members to form an 'X' shape; this enables expansion and contraction while retaining strength. The idea for this new bridge was developed from the academic studies on buckling based on Origami (Japanese traditional paper craft), which has attracted the attention of researchers in space engineering and other fields

The manufacturers developed MB version 4.0 (MB4.0) as a type of robotic bridge by improving its mobility and functionality and decreasing its weight. Therefore, MB4.0 has become more transportable and easier to set up at temporary construction sites without any foundation construction or crane operations. As a result, it is also less expensive.

MB4.0 is the fastest, largest, strongest, and lightest expanding scissoring bridge of the world. In addition, it is the fastest to set up. Because the bridge and its lanes are expanded simultaneously, the bridge is ready for use by traffi as soon as it is fully expanded. From the arrival of MB4.0 on site to its full expansion only takes approximately one hour. The actual extension time is only f ve minutes only. This is especially important for time-sensitive situations during a disaster.

The developers state that "from this testing of a new bridge concept, the next generation of bridge technology reaches a new stage in the fiel of bridge engineering. It is possible to use a real deployable and smart bridge with a scissors type bridge system using this structural theory."

3.1 *First test of MB4.0 for taking over a river*

We review the release of the firs test of the full-scale, novel scissors-like bridge structure MB4.0 Ario et al. (2017), Adachi et al. (2017), Chikahiro et al. (2017). The developers at the Institute of Engineering at the Hiroshima University conducted a fiel test in conditions resembling the real situations of bridge deployment. The test of the MB4.0 over a real river, called the Hongo river, demonstrated its capability for practical use on 24th April 2015 in Fukuyama, Japan. The width of the river was surveyed as about 17.1m and it was accessible before bridge construction.

During the test, MB4.0 arrived on one side of the river carried by a heavy trailer. This bridge system is equipped with an out-rigger system which enables the automatic removal from the transport trailer after connecting to a hydraulic pump. In the next step, the bridge, which is transported in the horizontal position, is rotated by 90° to the pre-deployment state. The expansion process can be easily controlled and it took only f ve minutes for the bridge to be fully deployed. The MB4.0 reached the other side of the Hongo river safely without any technical problems and was operated by a very limited technical crew, as shown in fig ure 5. The total time from the arrival of the MB4.0 on-site to its full expansion was approximately one hour. No work, including preparation of foundations for the other side of the river, was conducted during the test. The deployment of the bridge also did not involve the use of a crane or any other construction machine, which are typically involved in such situations. This is particularly important in time-sensitive situations characteristic of disasters.

In the current research, we developed the MB4.0 as a type of robotic bridge by improving its mobility and functionality and decreasing its weight. Thus, the MB4.0 has become more transportable and easier to set up at temporary construction sites without any foundation, construction, or heavy machine operations. As a result, it is also much more cost efficient The current model, the MB4.0, has a length of about 20 m and a height of 2 m, as listed in Table 1. The main structural members of the bridge are made of extruded aluminium alloy, while the frame of the hy-



(a) Expansion process of the MB4.0



(b) First test of the MB4.0

Figure 5: Tests of foldable, movable and deployable bridge "Mobile bridge^{TM}" at 24th March 2015.

Table 1: Configuration under a car loading for the MB4.0

Item	Details	Remarks
Length	3 m $\sim$ 20.8 m	6 units
Span	0 m $\sim$ 17. 3 m	5 units
Load for the deck	40 kN per a unit	For a car
Width	Outside: 2.5 m $\sim$ 3.0 m	Inside: 2 m
Height	Standing: 5 m	Carrying: 3.1 m, inside: 2 m
Weight	About 130 kN	-
Workers	2-3 persons	-
Expanding time	5-10 min.	-
Construction time	1 hour	-
Appear	Hiroshima	25th April 2013
Test place	Hongo river at Fukuyama	24th March 2015

draulic deployment system is constructed from steel SS400.

4 CONCLUSIONS

This study presents a new deployable and/or folding bridge design with a scissor structure based on post-buckling theory for a cylindrical shell using the Origami skill in the engineering field We applied the design to a full-scale MB4.0 with integrated lower deck boards and a fiel experiment related to crossing a real river in Japan. After demonstrating the structural safety of the bridge, we performed a fundamental numerical simulation and an experimental test to investigate the MB4.0 dynamics. The results lead to the following conclusions:

1. The development of a full-scale scissor-type bridge for three vehicles was successful, and its on-site usability was demonstrated based on the fiel experiment over a real river.

2. During the test, the constructing bridge was completed within 1 hour (the expanding bridge was taken for only 5 minutes) without any work performed on the foundations. Vehicles were then able to easily travel across it. The deployment was safely achieved with very little human involvement and without any problems such as those encountered in robot bridge.

3. This new bridge type has the fl xibility and improved mobility of a function; hence, it is a very useful emergency bridge without any foundation or construction.

Various numerical models were designed to provide the basis for the development of new methods for structural reinforcement and vibration suppression. The conducted research allows for a better and safer MB to be designed.

ACKNOWLEDGEMENT

This research has been supported by the Bilateral Programs between Japan Society for the Promotion of Science (JSPS) and Polish Academy of Sciences (PAN) in 2016 - 2018. The river's test of the finance had supported by the developmental grant from Minister of Economy, Trade and Industry in Japan in 2014 - 2015 to the collaborated companies: Hoshikei-kinzoku Industry Co., Ltd. and Sankyo Tateyama, lnc Sankyo Material Co., Ltd..

REFERENCES

Adachi, K., Ario, I., Chikahiro, Y. and Matsumoto, S.(2017), Scissoring origami inspired deployable bridge for a disaster, FootBridge 2017 Berlin.

Ario, I.(2012), Structure with the expanding and folding equipment as a patent (No.2006-037668) registered in Japan.

Ario, I., Nakazawa, M., Tanaka, Y., Tanikura, I. and Ono, S.(2013), Development of a prototype deployable bridge based on origami skill, Automation in Construction, Vol. 32, pp. 104-111. doi: 10.1016/j.autcon.2013.01.012

Ario, I.(2015), SCISSORS-TYPE RETRACTABLE STRUCTURE, Patent Publication Number: WO2015/193930A1.including registration of EP, Japan and China.

Ario, I., Chikahiro, Y., Tanikura, I., Ono, S., Nakazawa, M., Nakatani, S., Yamada, K., Nakamura, S., Tanaka, Y., Tsubaki, R., Matsumoto, S., and Adachi, K.(2016), Consider recovering method by mobile bridge how to install a disaster, Proc. of the 7th special symposium for reducing disaster, JSCE, at Kumamoto (in Japanese).

Ario, I., Hama, Y., Chikahiro, Y., Adachi, K., Watoson, A.(2017), Origami inspired deployable & movable bridge for disaster relief, FootBridge 2017 Berlin.

Chikahiro, Y., Ario, I., Nakazawa, M., Ono, S., Holnicki-Szulc, J., Pawlowski, P. and Graczykowski, C.(2014), An experimental study on the design method of a full-scale Mobile Bridge for a moving vehicle, The proceedings of 4th International Conference on Mobile, Adaptable and Rapidly Assembled Structures, Belgium, pp. 94-103.

Chikahiro, Y., Ario, I., Adachi, K., Shimizu, S., Pawlowski, P., Graczykowski, C., Holnicki-Szulc, J.(2017), Dynamic property of deployable emergency bridge using scissors mechanism, FootBridge 2017 Berlin.

Chikahiro, Y., Ario, I., Nakazawa, M., Ono, S., Holnicki-Szulc, J., Pawlowski, P., and Graczykowski, C. and Watson, A.(2016), Experimental and numerical study of full-scale scissor type bridge, Automation in Construction, Vol. 71, pp. 171-180.

Escrig, F.(1989), Design of Expandable Special Grids, IASS NIladrid, Vol. 4.

Engineers create emergency origami bridge, Science and Environment of BBC news 23 July 2015, http://www.bbc.com/news/science-environment-33625724

Glisic, B., Sigrid,A., and Peter, S.(2013), Structural analysis and validation of a smart pantograph mast concept, Computer - Aided Civil and Infrastructure Engineering, Vol. 28. Issue 9, pp. 651-665. doi: 10.1111/mice.12013

Hahawa, Y., Saitoh, M., Okada, A. and Miyasato, N.(2001), Basic Study on Structural Characteristics of String Scissors Structure, Part1 Proposal of String Scissors Structure and Possibility of PS Introduction, Summaries of technical papers of annual meeting Architectural Ins. of Japan.

Hunt, G.W. and Ario, I.(2005), Twist buckling and the foldable cylinder: an exercise in origami, Int. J. of Nonlinear Mechanics, 40(6), pp. 833-843.

Kresling B.(2002), Folded Tubes as Compared to Kikko (”Tortoise-Shell”) Bamboo, Origami3, Third International Meeting of Origami Science, Mathematics and Education (2001 Asilomar, California)(Thomas Hull, editor) AK Peters, Natick, Massachusetts, 197–207.

Luchsinger, R.H., Pedretti, A., Steingruber, P. and Pedretti, M.(2004), The new structural concept Tensairity: Basic principles, Progress in structural engineering, mechanics and computation, pp. 323-328.

Nakazawa, M. and Ario, I.(2012), Structural Characteristics of Scissors Type - Emergency Bridges, 5th Australian Small Bridges Conference, Australia.

New bridge unfolds in japan, The magazine of the american society of civil engineers, 18th August 2015, http://www.asce.org/magazine/20150818-new-bridge-unfolds-in-japan/

Pawlowski, P., Graczykowski, C., Holnicki-Szulc, J. and Ario, I.(2013), Smart, deployable skeletal structures for safety engineering, The proceedings of the 6th ECCOMAS Thematic Conference on Smart Structures and Materials, pp. 1-10.

Pinero, E.P.(1965), Three Dimensional Reticular Structure, United States Patent 3, 185, 164.

Sedlacek, G and Trumpf, H.(2003), Development of a lightweight emergency bridge, International Conference on High Performance Materials in Bridges, pp. 150-161.

Thomas, G.R. and Sia, B.J.(2013), A rapidly deployable bridge system, Structures Congress, pp. 656-667.

Yamaki, N.(1976), Experiments on the post-buckling behaviour of circular cylindrical shells under torsion, In: Budiansky, B. (ed), Buckling of Structures, IUTAM Symposium, June 1974, Cambridge, USA, Applied Mathematics and Mechanics, Springer-Verlag, 1976.

Yoshimura, Y.(1951), On the mechanism of buckling of a circular cylindrical shell under axial compression and bending, Reports of the Institute of Science and Technology of the University of Tokyo, 5(5).

Zeigler, T.R.(1976), Collapsible Self-supporting Structure, United States Patent 3, 968, 808.

Maintenance, Safety, Risk, Management and Life-Cycle Performance of Bridges – Powers, Frangopol, Al-Mahaidi & Caprani (Eds)
© 2018 Taylor & Francis Group, London, ISBN 978-1-138-73045-8

Rational decision-support system for selecting bridge construction alternatives

U. B. Attanayake & H.M. Aktan
Western Michigan University, Kalamazoo, Michigan, United States of America

ABSTRACT: The bridge rehabilitation/replacement with conventional construction (CC) methods impacts motorized and non-motorized traffic mobility for a duration that extends from months to years. Accelerated Bridge Construction (ABC) concepts and methods are developed to reduce mobility impact time. ABC methods include prefabricated bridge elements and systems (PBES), slide-in bridge construction (SIBC), and self-propelled modular transporter (SPMT) moves. At present, highway agency policies have been establish to require evaluating every bridge site's suitability for implementing ABC methods. Since the ABC is not the solution for every site, highway agencies are demanding a robust and rational process to be implemented during network level and project level scoping to identify the most preferable construction methods for selected sites. A hybrid multi-criteria decision-support model was developed and presented in this paper. The model was developed using the Analytical Hierarchy Process (AHP) and accommodates quantitative as well as qualitative parameters identified through literature synthesis including post-construction and lessons learned reports and years of ABC experience of the authors. The quantitative parameters are customized based on the region specific data as well as the site-specific data. However, the qualitative parameters are judged based on the experience/knowledge from experts. The model has the ability to include additional qualitative parameters, contingent to project manager's discretion. Further, the model incorporates a hybrid approach of integrating the region specific data, the site-specific data, and the experience/knowledge from experts to automatically perform AHP steps with reduced user input.

1 INTRODUCTION

When bridges are replaced using conventional construction (CC) methods, motorized and non-motorized traffic mobility is impacted for a duration that extends from months to years creating difficulties and safety issues to the stakeholders. Accelerated Bridge Construction (ABC) concepts and techniques are designed to reduce mobility impact time. ABC methods include prefabricated bridge elements and systems (PBES), slide-in bridge construction (SIBC), and self-propelled modular transporter (SPMT) moves. Since the ABC is not appropriate for every site, highway agencies need a robust and rational process to be implemented during network level and project level scoping to identify the optimal construction methods for selected sites. As an example, the Michigan Department of Transportation (MDOT) evaluates every bridge project during the scoping process for ABC potential. In 2013, Aktan and Attanayake (2013) developed a multi-criteria decision-support framework to comparatively assess conventional construction (CC) vs. ABC. The framework was customized for implementation in Michigan and supplemented with a guided software program titled *Michigan Accelerated Bridge Construction Decision-support (Mi-ABCD) tool*. The software was developed using Microsoft Excel and Visual Basic for Applications (VBA) scripts. In the 2013 version of Mi-ABCD, the ABC only encompasses prefabricated bridge elements and systems (PBES) construction.

Recent ABC technologies, such as slide-in bridge construction (SPMT) and self-propelled modular transporter (SIBC) moves, are being increasingly implemented throughout the U.S. In Michigan, SIBC was implemented in three pilot projects involving four bridge replacements. Aktan et al. (2014) and Aktan and Attanayake (2015) present details of two projects, US-131 over 3-Mile Road and M-50 over I-96. Ridvanoglu et al. (2017) presents details of the other project, M-100 over the Canadian National (CN) railroad. To address the need of assessing four bridge construction/replacement methods (CC, PBES,

SPMT, and SIBC) for a site, the decision-support framework developed by Aktan and Attanayake (2013) was extended. Aktan and Attanayake (2015) present the updated scoping framework and the associated guidelines for its implementation. Later, Aktan and Attanayke (2017) updated the software to comparatively assess all four bridge construction/replacement methods. This article presents an overview of the software features, data structure, output formats, and implementation recommendations.

2 MATHEMATICAL FRAMEWORK IMPLEMENTED IN THE TOOL

2.1 *Significance of AHP in Evaluating Bridge Construction Methods*

The Analytical Hierarchy Process (AHP) was developed by Saaty (1980) for comparing a set of decision alternatives. AHP involves representing the complex problem in terms of parameters, and establishing a hierarchy. In the hierarchy, the top level includes the objective, the middle level includes the parameters that affect the objective, and the bottom level includes the decision alternatives that can be implemented to achieve the objective. The parameters in the hierarchy are subjected to pair-wise comparisons using an ordinal scale between 1 and 9. Where 1 represents equal importance and 9 represents extreme diverging importance between parameters. The decision alternatives are evaluated with respect to each parameter by the pair-wise comparison process. The pair-wise comparisons develop the AHP matrices. The priority vectors for the matrices are calculated and subjected to AHP synthesis in order to obtain normalized priorities for the decision alternatives (Saaty 1980).

Each AHP matrix is a unit positive reciprocal matrix, where the diagonal elements are unity and the lower triangular elements are reciprocal of the corresponding upper triangular elements. In an ideal consistent matrix if $a_{ij} > a_{ik}$ for all j and k, i.e., if one row dominates another row, the priority of the i^{th} element is greater than the priority of the k^{th} element. The measure of inconsistency in the AHP pair-wise comparison matrix is represented by a consistency ratio (CR). A CR of 0.10 or less is considered acceptable for the pair-wise comparison matrices, and normalized column-row averaging method is implemented to calculate the normalized preference rating for the variables in the matrix. However, increased number of parameters in a pair-wise comparison matrix may lead to inconsistencies requiring repeating the pair-wise comparisons (Saaty, 1980). A theoretically sound approach to manage inconsistency in a pair-wise comparison matrix is to take large powers of the matrix that enables transforming the complex order among the matrix elements to a linear order (Saaty, 2001). This process is utilized in several computing algorithms to calculate the Eigenvectors of a matrix, such as Mathcad Hessenberg form coupled with QR Decomposition algorithm. The algorithm uses the procedure of balancing with an order of N^2 that substantially improves the accuracy of an inadequately balanced matrix (Press et al. 1992). Using such algorithms to calculate Eigenvector associated with principal Eigenvalue of a matrix, leads to normalized preferences for the variables in the matrix (Saaty, 2001). This approach is an improvement over the normalized column-row averaging method and eliminates the need for repeating the pair-wise comparisons.

AHP provides the ability to group the parameters into several levels, such as categorizing the parameters into major-parameters and associated sub-parameters. This categorization enables us to identify not only the optimal decision alternative, but also the major-parameters that highly influence the problem and the decision. Therefore, specific to evaluation of bridge construction methods, a 4-level hierarchy is typically established for the AHP such that the top level includes the objective, the second level includes the major-parameters, the third level includes the sub-parameters, and the bottom level includes the decision alternatives. The key part of the hierarchy consists of major-parameters, sub-parameters, and decision alternatives. For this specific case, the AHP pair-wise comparisons are performed between (1) major-parameters, (2) sub-parameters under respective major-parameter, and (3) decision alternatives and each sub-parameter. This process results in three sets of AHP matrices for calculating normalized preferences for the major-parameters and the decision alternatives.

2.2 *Hybrid Methodology*

A methodology was developed considering the limitations in the available decision-making models for bridge projects and lessons learned from past ABC projects, in order to accomplish the following objectives:

- Warrant the decision-making for bridge projects with site specific data.
- Eliminate the apprehension with pair-wise comparison of parameters and associated consistency control.
- Simplify users' input and enable incorporating user judgment based on their experience.

As shown in Figure 1, the qualitative as well as quantitative parameters are included, along with the hybrid AHP. The AHP hierarchy consists of major-parameters, sub-parameters, and decision alternatives. The quantitative parameters have numerical values either assigned or calculated during the project planning stages. The quantitative parameters are incorporated in the decision-making based on project specific data (i.e., site-specific data, traffic data, life-cycle cost data), and general data for a state or a region (i.e., common site characteristics and economic indicators). On the other hand, the qualitative parameters are incorporated in the decision-making based on preference from users. The preferences of users are termed as preference ratings on an ordinal scale. The methodology implements Ordinal Scale Ratings (OSRs) ranging from 1 to 9 to form AHP pair-wise comparison matrices; thus, eliminating the pair-wise comparison step. The OSRs provide a uniform measure for quantitative and qualitative parameters, and enable the decision makers to provide preference for qualitative parameters based on past project experiences. Incorporating OSRs rather than pair-wise comparisons, the AHP is described as "hybrid."

The methodology includes a process wherein the OSRs of the quantitative parameters are calculated based on project specific data, and general data for a state or region. The OSRs for quantitative parameters represent interval data, i.e., the OSRs from 1 to 9 are equally split into range of values for respective quantitative parameter. For the qualitative parameters, the judgments from users are obtained as preference ratings that represent the OSRs. In this case, the OSRs represent ordinal data, i.e., the difference between 8 and 9 OSRs is not necessarily the same as difference between 5 and 6 OSRs.

3 Mi-ABCD TOOL

3.1 *Sample Popup Menus and Datasheet*

The VBA's Graphical User Interface (GUI) forms are utilized to interact with the user. These forms are termed as *Pop-up Menus* (Figure 2a and b), and the Excel sheets that are customized for user input are termed as *Datasheets* (Figure 2c). The main features of the *pop-up menu* are to provide (1) Command buttons, (2) Dropdown menus, (3) Tabs, (4) Text fields, (5) Check boxes, and (6) an Additional information button ( ) (Figure 2-a and b). The most commonly used features are the *command buttons* and *dropdown menus*. The primary features of a *datasheet* are (1) Command buttons, (2) Dropdown menus, and (3) Data input fields.

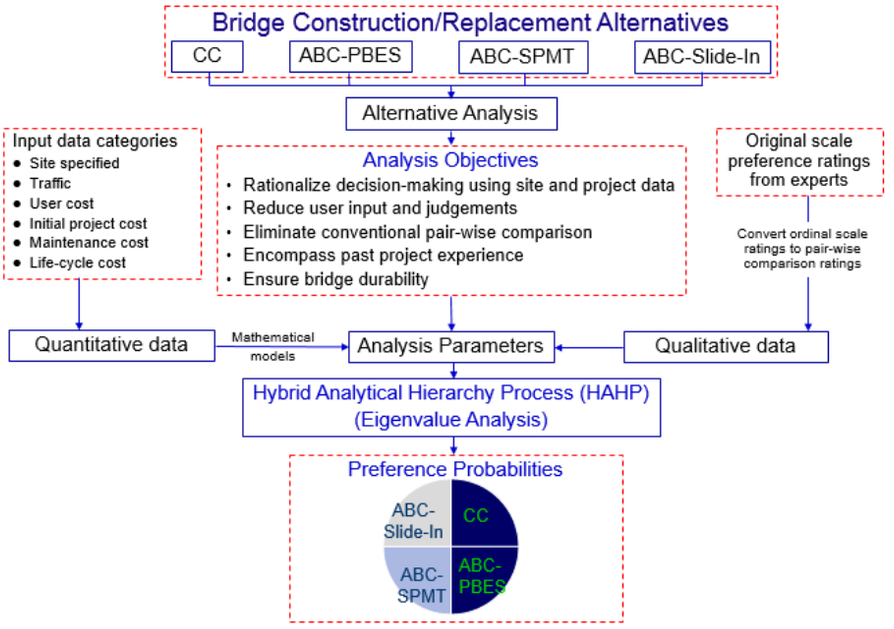


Figure 1: The methodology implemented in the decision-support tool

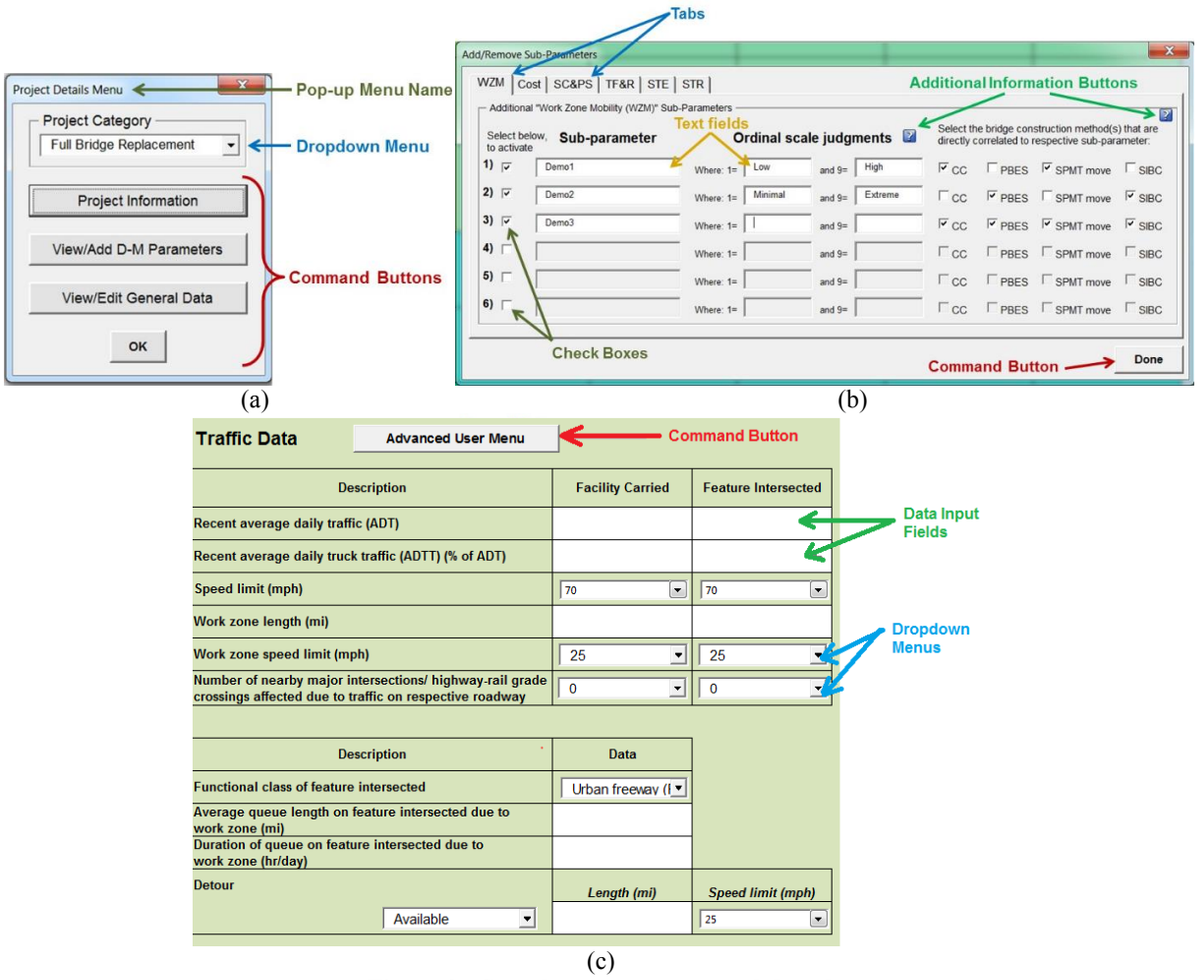


Figure 2: Sample popup menus and datasheet

3.2 *User Menus*

Data entry screens are for two types of users: (1) the *Advanced User* and (2) the *Basic User* (Figure 3a). The *Advanced User* is often a project manager who is familiar with the project specifics such as site-specific data, cost estimates, traffic data, and construction methodologies. The *Advanced User* enters and edits *Project Details, Site-Specific Data, Traffic Data, Life-Cycle Cost Data, and Preference Ratings*. Finally, the *Advanced User* also executes data analysis and view *Results*. The *Advanced User Menu* (Figure 3b) contains command buttons for entering and editing data, data analysis, and viewing results. In order to execute the analysis process, the *Advanced User* must complete all the steps before any *Basic User* is allowed.

The *Basic User* is generally on the project team, and enters the preference ratings for qualitative parameters based on their experience on recent bridge projects. The *Basic User* can view *Project Information,* enter *Preference Ratings,* execute data analysis, and view *Results* (Figure 3c). One of the advanced features in this software is that it allows the *Basic User* to describe reasoning in the text boxes on the *Preference Ratings* datasheet. The subsequent users can view the comments, but preference ratings of previous users are concealed.

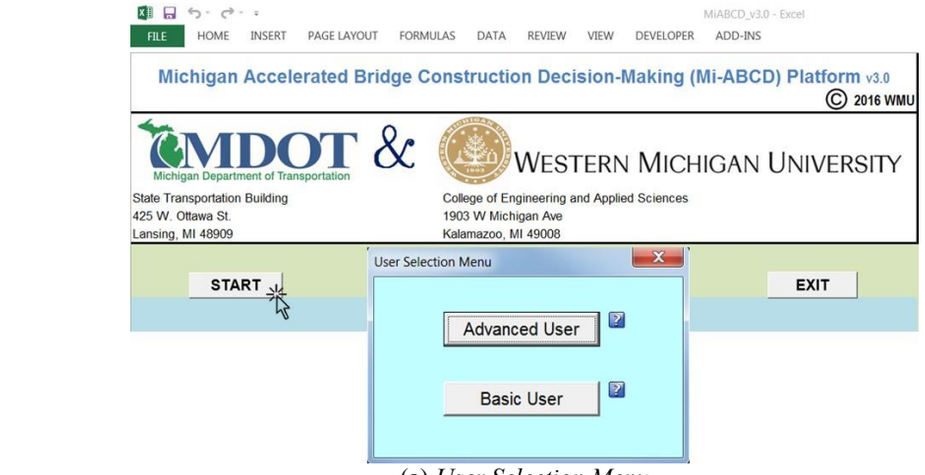
3.3 *Data Entry using the Advanced User Menu*

First, the *Advanced User* selects *Project Details* menu to access *Project Categor*y, *Project Information*, *View/Add D-M Parameters*, and *View/Edit General* data using *Project Details Menu* (Figure 3b). *Project Information* page allows specifying the *Evaluation options* and providing an image of the site and a description. The project description may include the project location, surrounding businesses and stakeholders, and any critical aspects that the project manager considers useful to the *Basic Users*. The *Evaluation options* includes the following:

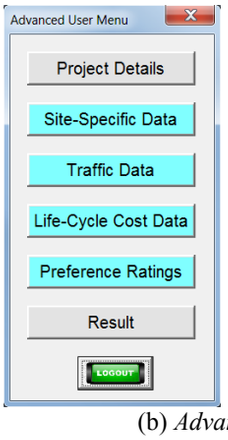
1) CC vs. PBES vs. SPMT move vs. SIBC
2) CC vs. PBES
3) PBES vs. SPMT move vs. SIBC
4) SPMT move vs. SIBC.

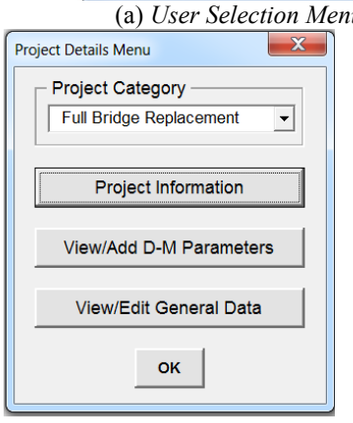
Note that the *Advanced User* selects the evaluation option based on the availability of staging area. For example, if staging area is unavailable for a project, evaluation options may be limited to CC vs. PBES. Next, the *Advanced User* can access *View/Add D-M*

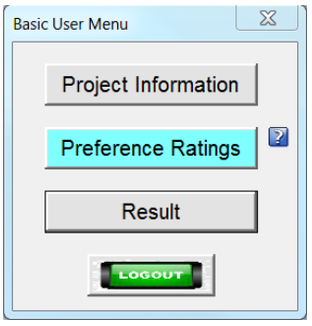
Parameters (Figure 3b), and review them or, if needed, add new parameters. The default decision-making parameters are grouped under major-parameters, sub-parameters, and secondary-level sub-parameters. Apart from the default sub-parameters, *Advanced User* can add up to six additional sub-parameters under each major parameter. Thus, a total of 36 (i.e., 6×6) additional sub-parameters can be incorporated in the decision-making process.



(a) *User Selection Menu*







(b) *Advanced User Menu* options (c) *Basic User Menu*

Figure 3: User menus

3.3.1 *General Data*

The *View/Edit General Data* command button opens the *General Data* datasheet. This datasheet includes a majority of the data needed for the workings of Mi-ABCD tool and the AHP evaluation of bridge construction methods (Aktan and Attanayake 2013; Aktan and Attanayake 2015). A majority of the data in the *General Data* datasheet will remain the same for a region and for a period of time. The *Advanced User* can modify the following data in the *General Data* datasheet. The following categories are included under the *General Data*:

1) County jobs multiplier.
2) Range for specialty equipment procuring distance.
3) Options for clustered bridge replacement projects.
4) Range for allowable ground bearing pressure.
5) Speed limit options.
6) Peak hour factors for roadway functional class.
7) Detour length.
8) User cost data.
9) Utility relocation cost.
10) Costs related to SPMT move.
11) Costs related to SIBC.
12) Correlation of decision-making parameters with bridge construction methods.

3.3.2 *Site-Specific Data*

The *Site-Specific Data* command button on the *Advanced User Menu* opens the *Site-Specific Data* datasheet. The data required for this datasheet is obtained from the layout of the project site, data from corridor planning process, and preliminary design of the proposed bridge.

3.3.3 *Traffic Data*

The *Traffic Data* command button on the *Advanced User Menu* opens the *Traffic Data* datasheet. Data from the corridor planning process and preliminary traffic study at the site are required for completing the datasheet.

3.3.4 *Cost Data*

The *Cost Data* command button on the *Advanced User Menu* opens the *Cost Data* datasheet. The data in this datasheet is related to the bridge construction methods. The project manager(s) needs to identify the cost estimates for the respective bridge construction method prior to entering the data. The following cost data categories are listed in the *Cost Data* datasheet:

1) The *cost of upgrading detour* is applicable only if the required detour duration is more than 14 days, and is added to the maintenance of traffic (MOT) cost.
2) The *specialty contractor cost for SIBC* is estimated based on the contractor availability and qualifications.
3) The *initial construction cost* deals with the cost of superstructure and substructure, excluding the maintenance of traffic cost, specialty contractor and equipment cost. .
4) The *repair activity cost* needs to include all of the costs associated with the repair of structure constructed using the respective bridge construction method.
5) The *average duration between the repair activities* data is not yet available for ABC projects. It is reasonable to assume that for ABC this duration is longer than CC. Accuracy of this estimate will improve once performance data of large number of ABC projects are available.
6) The *disposal cost or salvage value* for each bridge construction method is calculated considering the respective residual life of the structure with respect to life-cycle cost analysis period. Life expectancy of bridge with each construction method can be different. The life expectancy of the structure with CC is the basis for life-cycle cost analysis period. For service life expectancy greater that CC, *disposal cost or salvage value* will be negative.

3.3.5 *Preference Ratings*

The *Preference Ratings* command button on both the *Advanced User Menu* and the *Basic User Menu* opens the *Preference Ratings* datasheet. The qualitative judgments are assigned in the form of preference ratings on an ordinal scale of 1 to 9. Preference ratings are categorized into three groups: *Cost Preference Ratings*, *Site-Specific Preference Ratings*, and *Bridge Construction Method-Specific Ratings*. Under these three categories, a total of 35 ordinal scale ratings are provided by a user.

3.4 *Evaluation of Results*

The *Result* command on the *Advanced User Menu* or *Basic User Menu* displays the analysis results. The results are displayed in the following four formats:

1) Two pie charts showing the *Upper Bound Rating Result* and *Lower Bound Rating Result* of the bridge construction methods being evaluated (Figure 4 - top left). The pie charts show upper and lower bound ranges from the preference ratings of multiple users. With only one user the *Lower Bound Rating Result* will display equal value for the bridge construction methods.
2) A line chart showing the *Normalized preferences for major-parameters* from multiple users with different line types and colors representing each user (Figure 4 - top right).
3) A bar chart showing the *Normalized preferences for bridge construction methods* of multiple users (Figure 4 - bottom). Each bar is stacked with six different colors representing the contribution from six major-parameters: (i) Work Zone Mobility (WZM), (ii) Cost, (iii) Seasonal Constraints and Project Schedule (SC&PS), (iv) Technical Feasibility and Risk (TF&R), (v) Site Considerations (STE), and (vi) Structure Considerations (STR).

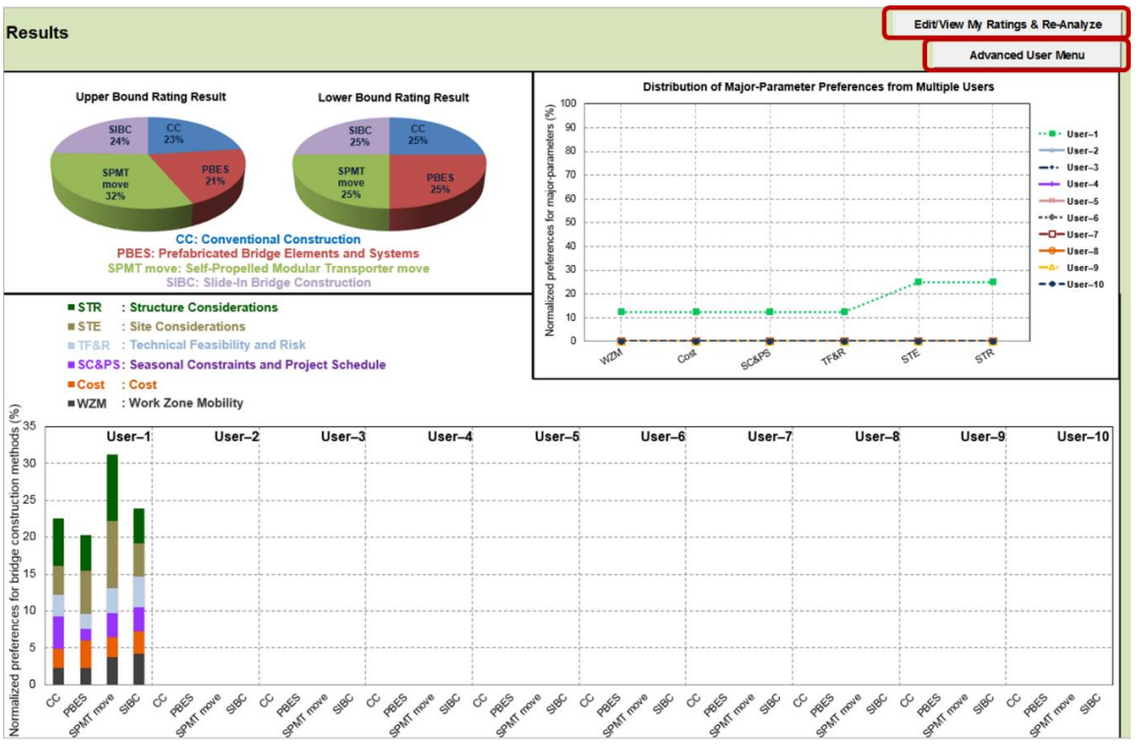


Figure 4: Results in chart format

4 SUMMARY, CONCLUSIONS, AND RECOMMENDATIONS

The policy statement developed by highway agencies requires the project selection to be based on the feasibility of ABC. If ABC is not justified for a project, a rationale is required. A multi-criteria decision-support framework to comparatively assess CC versus ABC, and a guided software program titled *Michigan Accelerated Bridge Construction Decision-support* (Mi-ABCD) tool were developed.

The specific conclusions related to the Mi-ABCD tool are as follows:

1. The tool is designed to evaluate CC, PBES, SPMT, and SIBC or any subset.
2. The tool incorporated a knowledge-base that consists of *General Data*. The general data does not require frequent changes and is extensively used during the computation process.
3. The *Advanced User* can display ratings from all the users and the associated comments. This allows the project team in a committee setting to review all the ratings and rationales provided by the users and deliberate over the results.
4. The *Advanced User* can *Remove All Ordinal Scale Ratings and Comments* and input a new set of ratings generated during the deliberation process to evaluate the results of the collective effort.
5. Project managers are expected to input best estimates for initial cost categories such as initial construction cost. In a future version, the cost data derived from completed projects can be incorporated into the knowledge-base as general data to minimize user input requirements.
6. Service life and maintenance frequency of bridges constructed using PBES, SIBC, or SPMT moves are estimated for life-cycle cost calculation. In a future version, the performance data needs to be incorporated into the knowledge-base as general data to minimize user input requirements.

4.1 *Recommended Mi-ABCD Tool Implementation Process*

1) For a particular project, the *Advanced User* first completes the datasheets for *Project Details, Site-Specific Data*, *Traffic Data*, and *Cost Data*. *Advanced User* can assign preference ratings, perform analysis, and view results.
2) To allow for *Basic User* data entry, the *Advanced User* must *Logout* and forward the saved file to the *Basic User*(s) sequentially for their entry of preference ratings and associated comments.
3) For the next *Basic User* to access the *Preference Ratings* datasheet as a "New User," the

current user must *Logout* after entering preference ratings, performing analysis, and viewing the results.

4) Finally, the *Advanced User* reviews the results using all the *Basic User* ratings, and deliberate at a meeting to develop the final decision on the construction method for the selected site. If needed, the *Advanced User* is privileged to *Delete All Ordinal Scale Ratings and Comments* and input a new set of ratings generated during the deliberation process to evaluate the results of the collective effort.

ACKNOWLEDGEMENTS

This project is funded by the Michigan Department of Transportation. The authors would like to acknowledge the support extended by Mr. David Juntunen, Mr. Corey Rogers, Mr. Mike Halloran, and the Research Advisory Panel (RAP) members for successful completion of the project. Authors acknowledge Abdul Wahed Mohammed's contribution in developing the software.

REFERENCES

Aktan, H. and Attanayake, U. 2017. "Research on Evaluation and Standardization of Accelerated Bridge Construction Techniques," MDOT RC-1618C, Report to the Michigan Department of Transportation, Lansing, MI.

Aktan, H. and Attanayake, U. 2015. "Research on Evaluation and Standardization of Accelerated Bridge Construction Techniques," MDOT RC-1618A, Report to the Michigan Department of Transportation, Lansing, MI.

Aktan, H., Attanayake, U., and Mohammed, A.W. 2014. Accelerated Bridge Construction and Structural Move Workshop, MDOT RC-1610, Michigan Department of Transportation, Lansing, MI.

Aktan, H., and Attanayake, U. 2013. "Improving Bridges with Prefabricated Precast Concrete Systems," MDOT RC-1602, Report to the Michigan Department of Transportation, Lansing, MI.

Ridvanoglu, O., Attanayake, U., and Aktan. H. 2017. "Monitoring during Lateral Bridge Slide," No. 17-03146, Transportation Research Record: Journal of the Transportation Research Board, Transportation Research Board of the National Academies, Washington, D.C.

Saaty, T. L. 1980. The Analytical Hierarchy Process, McGraw Hill, New York.

Saaty, T.L. 2001. "Decision-Making with the AHP: Why is the Principal Eigenvector Necessary?" Proc., 6th International Symposium on the Analytic Hierarchy Process (ISAHP), Berne, Switzerland.

Press, W.H., Teukolsky, S.A., Vetterling, W.T., and Flannery, B.P. 1992. Numerical Recipes in C – The Art of Scientific Computing, 2nd Ed., Cambridge University Press, New York.

Maintenance, Safety, Risk, Management and Life-Cycle Performance of Bridges – Powers, Frangopol, Al-Mahaidi & Caprani (Eds)
© 2018 Taylor & Francis Group, London, ISBN 978-1-138-73045-8

Standardizing Lateral Bridge Slide Design

U. B. Attanayake & H.M. Aktan
Western Michigan University, Kalamazoo, Michigan, United States of America

ABSTRACT: Accelerated Bridge Construction (ABC) methods such as prefabricated bridge elements and systems (PBES), slide-in bridge construction (SIBC), and self-propelled modular transporter (SPMT) moves are designed to reduce mobility impact time. In Michigan, USA, four bridges were replaced using SIBC, also described as the lateral slide. The Michigan projects, a large volume of lateral slide project documentation in the Federal Highway Administration (FHWA) repository, and resources available through state departments of transportation (DOTs) were reviewed and the successes, difficulties, and activities were documented and analyzed. Additionally, instrumentation and monitoring as well as refined finite element (FE) simulations of two slides completed in Michigan were performed to calculate structural effects of the slide and investigate the sources and effect of the difficulties. Design procedures, considerations, and limitations were formulated based on the findings from the completed projects and from FE simulation results. The final product of this work described in this article is a step-by-step process to standardize bridge slide activities and designs.

1 INTRODUCTION

Accelerated Bridge Construction (ABC) requires innovative planning, design, and materials to reduce onsite construction time with safety and cost efficiency constraints (Culmo 2011). ABC is implemented to reduce adverse mobility impacts of conventional construction (CC). Slide-In Bridge Construction (SIBC) is an ABC method where the new superstructure is constructed adjacent to the existing bridge on a temporary structure and moved in place with a sliding and an actuating system. SIBC provides opportunity to maintain traffic on the existing bridge during construction of a new superstructure parallel to the in-service bridge. After completion of the new superstructure, traffic can be shifted and maintained on the new superstructure while preparing the site and substructure at the final alignment. The new superstructure is moved into final alignment by a lateral slide. Typically, the maximum traffic impact duration during the SIBC is between 24 to 48 hours (SHRP2 2017).

Bridge slide operation requires additional activities compared to conventional construction. The additional activities include (i) a temporary structure designed and constructed to support a new superstructure during construction and lateral slide, (ii) a sliding system to provide interaction surfaces and a path during slide, and (iii) an actuating system to provide forces for initiating and maintaining bridge slide.

During the 2014-2015 period, three SIBC projects (the US-131 over 3 Mile Road, the M-50 over I-96 , and the M-100 over the CN railroad) were contracted and completed by the Michigan Department of Transportation (MDOT). These SIBC projects were monitored and activities, successes, and difficulties were documented and analyzed. Finite element (FE) simulations of the US-131 over 3 Mile Road and the M-100 over the CN railroad were performed to calculate structural and other effects of the slide to understand the sources and effects of the difficulties. Finding of SIBC monitoring and FE simulation activities are documented in Aktan and Attanayake 2017; Ridvanoglu et al. 2017; Mohammed et al. 2016; Aktan and Attanayake 2015; Aktan et al. 2015.

Twenty-eight (28) completed SIBC projects were reviewed, and data was compiled on SIBC components and design parameters, temporary structure design, sequence of operations, and constructability. Each SIBC implementation has been unique so far. Uncertainties include slide properties contributing to friction between surfaces, pushing and pulling force levels, and monitoring and controlling the force levels. The standardization purpose is to develop repeatable procedures for SIBC.

2 SLIDING SYSTEMS

A bridge sliding system, in most cases, consists of *Teflon* pads or rollers and an actuating system. Additional components are integrated into a slide mechanism to control the transverse and vertical movement of the superstructure.

2.1 *Sliding System Parameters and Design Considerations*

The weight of the superstructure and all the components and attachments above the sliding surface (W) act normal to the sliding surface. With the friction

coefficient of the sliding surface, weight controls the magnitude of the required sliding forces.

When neoprene pads *Teflon* and stainless steel shoes are used, bearing pressure (σ_B) is calculated as the ratio between vertical load at each sliding shoe and the contact area of a shoe. A uniform pressure distribution can be assumed for design. The number of shoes and the size of each shoe is based on the allowable pressure on the neoprene bearing pads. Typical values of interface pressure range from 0.5 ksi to 2 ksi (Aktan and Attanayake 2015).

Sliding system design requires static and kinetic friction assumption. Typical static friction values used in earlier projects range from 5% to 10% (Aktan and Attanayake 2015). Kinetic friction is a function of sliding velocity (v_s). The sliding velocity is not constant throughout the slide; however, a value needs to be assumed to estimate kinetic friction coefficient. In addition to the sliding velocity, kinetic friction is also a function of normal stress at the sliding surface (σ_B), *Teflon* composition, temporary sliding shoe surface roughness, surface treatment (lubrication applied at the interface), temperature, and the angle between the surface polishing of steel and the *Teflon* (Hwang et al. 1990). Even though a large number of parameters affect the kinetic friction coefficient, at least the bearing pressure and sliding velocity need to be considered in order to estimate a value. Kinetic friction estimates in earlier projects range from 3% to 5% (Aktan and Attanayake 2015).

Sliding force (S_F) is the sum of all frictional forces developed at the sliding surface. It is a function of weight and coefficient of friction. Since kinetic friction is a function of bearing pressure and velocity, sliding force is also a function of those parameters.

Sliding bearings are designed considering horizontal forces and vertical stress. Bearing deformation should be minimized. Deformations may change the contact area which, in turn, affects the bearing pressure, coefficient of friction, and consequently the sliding force. In order to accommodate the surface unevenness of the sliding girder, steel reinforced neoprene pads with *Teflon* should be used instead of a single *Teflon* layer. Dimpled *Teflon* is preferred to retain the lubricant on the sliding surface.

When rollers are used, manufacturer data sheets provide the maximum load capacity for their products. Based on the load capacity and the contact area, the maximum roller pressure (σ_R) can be calculated. The sliding track bearing capacity needs to be checked against the roller pressure. Hence, roller selection primarily depends on the allowable bearing capacity of the sliding track surface. This allows specifying the appropriate number of rollers to distribute the structure weight. The friction coefficient (μ) of typically used rollers for bridge slides is less than 5% (Aktan and Attanayake 2017). Static and kinetic friction coefficients are the same for rollers.

Vertical jacking is required when rollers or temporary *Teflon* pads are used. The number of jacking locations and the capacity of jacks are required. Generally, jacks are placed between each girder. Non-uniform load distribution due to deck overhang and safety barriers needs to be taken in to consideration. The superstructure needs to be analyzed under jacking loads to check the maximum stresses developed at the deck surface. Also, bearing stresses and the use of stiffeners at support locations need to be evaluated.

Transverse movement tolerance (t_T) defines allowable movement in a transverse direction. Tolerances are defined based on a specified sliding system and the project requirements. Movement in a transverse direction at the level defined by the tolerances will develop transverse forces (R_F) between transverse restraints and guides.

3 ACTUATING SYSTEM

A hydraulic operation system and hydraulic actuators are components of the actuating system that generates and delivers the required force to initiate and maintain a slide. Hydraulic operation system components include a reservoir, pump, and a hydraulic pressure control unit. Hydraulic cylinders and prestressing jacks are two available actuators utilized in many completed SIBC projects. Each actuator includes specific components and considerations to provide forces to initiate and maintain slide as well as to monitor movements.

Hydraulic fluid stored in the reservoir is pumped into the actuator during extension stroke and drained during a retraction. Pressure is monitored through a power control unit to control the displacement of the stroke. Pressure regulated and servo controlled units are available as pressure control systems. Pressure regulated units are capable of controlling hydraulic pressure manually (Searcy et al. 2012), whereas servo controlled systems monitor displacements through sensors and automatically calibrate applied pressure to adjust the movement (Anderson and Trankler 1991). Servo controlled systems can be used to maintain the bridge superstructure alignment because equal stroke is maintained between actuators by synchronizing measured displacements through the adjustment of actuating forces.

Hydraulic cylinders are primarily used for pushing the superstructure. Hydraulic cylinders with

pushing and pulling capabilities are very useful when the sliding structure needs to be retracted due to jamming or other reasons. Another alternative is the hydraulic prestressing jacks. A rod is connected to a superstructure and extended though the jack that is mounted against a stationary reaction frame. As the jack pulls the cable, the superstructure is moved towards the reaction frame. Also, a prestressing jack can be mounted against the sliding superstructure with one of the pulling rods connected to a reaction frame. This configuration allows pushing of the structure to the final alignment. The sliding operation is discrete, and the distance moved during each discrete event depends on the stroke length limitation.

3.1 *Design Considerations and Parameters*

The following is a list of parameters that need to be considered during the actuating system selection and design of the sliding operation:

- Actuating force (A_F) is the total force applied by an actuator to the superstructure. An actuating force that is slightly greater than the sliding force is adequate to maintain a slide because sliding can be initiated and maintained with low acceleration. The difference between an actuating force and a sliding force is defined as the net force (N_F).
- Actuator capacity (C) is the maximum force capacity. It should be larger than the estimated actuating force in order to compensate for the potential increase in sliding force. Capacities of actuators used in completed projects range from 30T to 110T.
- Actuator stroke length (S_L) defines the maximum length that a structure is pushed or pulled during each discrete slide event. Stroke length of actuators used in already implemented projects ranges from 2 in. to 48 in.
- Actuator jerk (j) is the rate of change of the acceleration and deceleration of the actuator (ramp up and ramp down durations). Sudden increases in acceleration result in greater reaction forces than sliding forces because of the dynamic response of the temporary structure.
- Reservoir volume and pump capacity of the hydraulic operation system should be sufficient to provide required sliding velocities and actuating forces.
- The connection between the hydraulic cylinder piston and the sliding track requires detailed design consideration. Connection points should be provided with tolerances to provide flexibility in attaching the cylinder to the sliding track. In addition, a swivel connection is most appropriate between the cylinder piston and the superstructure to prevent load transfer to the superstructure, except in the sliding direction.
- Prestressing jacks require a stationary reaction frame. A temporary structure can include the reaction frame, or part of the permanent substructure can be utilized as a reaction frame.

4 STANDARDIZING SIBC DESIGN

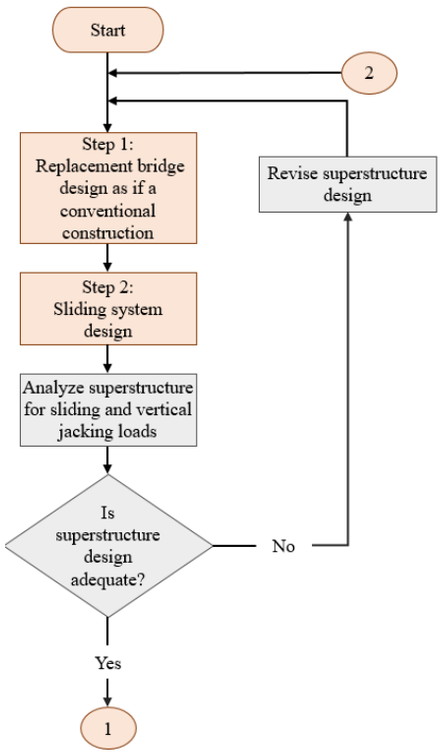
Design procedures, considerations, and limitations are formulated based on the findings from the reviewed and monitored projects as well as from FE simulations. A set of flowcharts depicting an overview and design of SIBC, a sliding system, and an actuating system were developed.

4.1 *Overview of SIBC Design*

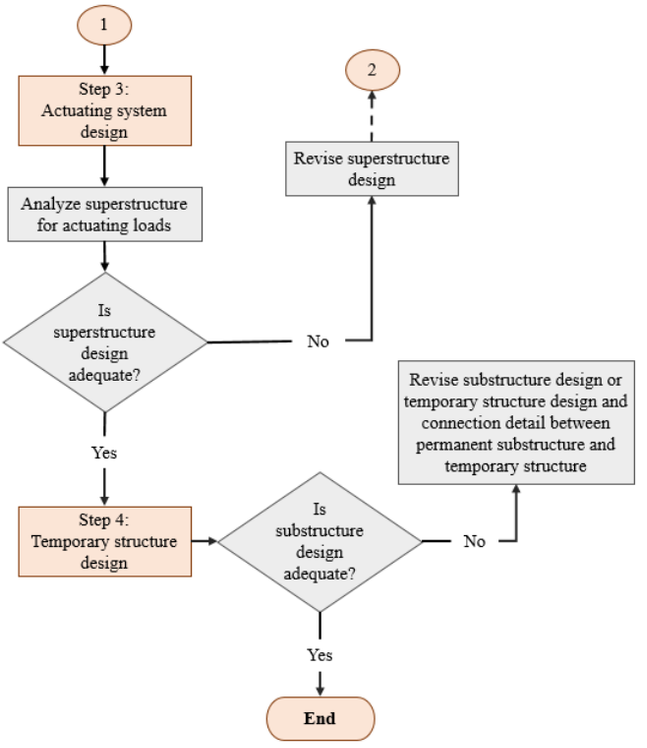
SIBC includes four primary design activities encompassing the design of the replacement bridge, sliding system, actuating system, and temporary structure (Figure 1). The process starts with the design of a replacement bridge as if the bridge will be constructed by conventional methods. At this stage, the loads from the bridge slide are not taken into consideration. Next, a sliding system is designed, and the superstructure design is checked against sliding loads and modified if necessary. The actuating system design is performed following the sliding system design. The superstructure is checked again for sliding loads. The final step is the temporary structure design under sliding loads.

4.1.1 *Sliding System Design Procedure*

The sliding system design process is depicted in Figure 2, Figure 3, and Figure 4. A typical sliding mechanism can be specified using either *Teflon* or rollers. Hence, the first step in a sliding system design is the selection of a slide mechanism. Based on past project experience and numerical simulation results, it is suggested to maintain a transverse movement tolerance of, at the most, 1 in. for *Teflon* and 0.1 in. for rollers. If *Teflon* is specified, the design process depicted in Figure 3 is followed. For rollers, the process shown in Figure 4 is followed.



(a) Step 1 and Step 2



(b) Step 3 and Step 4

Figure 1: An overview of SIBC design

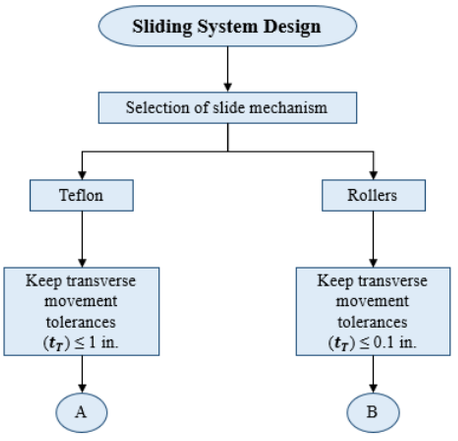


Figure 2: Sliding system design procedure

4.1.1.1 Design Procedure for a System with Sliding Shoes and Bearing Pads with *Teflon*

The design procedure is described in Figure 3. Weight of the superstructure is calculated after completing Design Step 1 in Figure 1. The number of sliding shoes and the size of a shoe are determined so that the bearing pressure on each shoe is maintained between 0.5 ksi and 2 ksi. Even though bearing pressure can be calculated based on the area under the sliding shoe, it can vary based on the changing contact area during slide. Contact area is affected by deformations of the sliding track because of the differential stiffness of the temporary structure. In previous projects, designers often used 1 ksi bearing pressure. As discussed in Aktan and Attanayake (2015), the friction coefficient decreases with increasing bearing pressure. However, for typical *Teflon* pads, the friction developed at the sliding surface with the above stated bearing pressure range is lower than the typical values used for a bridge slide design. Lubrication is often used to reduce friction between sliding surfaces. Hence, dimpled *Teflon* surfaces are recommended, as they can hold lubrication on the surface during slide.

The coefficient of friction is a function of sliding velocity. According to the data presented in Aktan and Attanayake (2015), for a velocity up to 0.1 in/s with a surface roughness of 2 micro inches and a bearing pressure range of 0.5 ksi to 2 ksi, the friction coefficient remains less than 5%. The maximum sliding velocities in the range of 0.07 in/s and 0.4 in/s have been recorded from past projects (Aktan and Attanayake 2015). When designing the sliding shoe and bearings, it is recommended to assume a reasonable sliding velocity using the data presented in Aktan and Attanayake (2015). The coefficient of friction is used for the sliding force calculation and bearing design. The breakaway friction coefficient for initiating the slide is the highest. Due to the lack of field data for quantification, 10% static and 5% kinetic friction coefficients are assumed. It is recommended to use these friction coefficients until more refined data is available from future implementations. Once the bearing pressure and the slid-

ing force is calculated, the sliding bearing is designed. If the bridge is moved on permanent bearings, the design needs to be evaluated against the permanent bearing design requirements based on the governing specifications. If the bridge is moved on temporary bearings, vertical jacking is required. It is recommended to specify the number of jacks, locations, and the capacity of each jack to minimize the differential movement of the bridge superstructure and thus, to minimize concrete cracking potential. Further, the superstructure design needs to be evaluated for the vertical jacking forces and deformation tolerances.

The typical practice is to construct the replacement bridge superstructure on sliding bearings and route traffic over the new superstructure on a temporary structure while preparing the site for bridge replacement. This requires checking the bearing design against the permanent bearing design requirements. Hence, irrespective of whether the bridge is to be moved on permanent bearings or not, the sliding bearing design needs to be evaluated against the permanent bearing design requirements.

4.1.1.2 Design Procedure for a Sliding System with Rollers

The primary steps of the design procedure are shown in Figure 4. The first step is to determine the number of roller assembly units needed for the slide. Here, each unit is referred to as an assembly because it consists of many rollers connected to form a chain of single rollers assembled with top and side plates. For multigirder bridges, the typical practice is to place one unit under each girder end. Once the number of units is decided, the next step is to calculate the load carried by each unit (P). Total weight of the bridge superstructure is acquired after completing Design Step 1, as shown in Figure 1. Knowing the total weight and bridge configuration, the load acting on each unit can be calculated. It is reasonable to assume that the load acting on each unit is equally distributed amongst the number of rollers in contact with the slide track. Only a limited number of discrete rollers in a chain is in contact with the slide track at a given position. The geometric dimension of roller units that can carry the load calculated in the previous step can be established using the technical specifications from the manufacturers/suppliers. A candidate roller assembly can then be selected based on the dimensions of the roller assembly and sliding track dimensions. Sliding track material properties required for calculations include the modulus of elasticity (E_T), Poisson's ratio (ν_T), and yield strength (fy_T). The next step in the design process is to acquire the design parameters from the technical specifications provided by the roller manufacturer. The design parameters are the number of rollers in contact with the track (n), radius of a single roller (R_R), contact length of a roller (L_R), and the elasticity modulus (E_R) and Poisson's ratio (ν_R) of the roller material.

The maximum normal stress (σ_{max}) acting on the sliding track can be calculated using the Hertz's formula (Eq. 1) (Hearn 1997). The current practice is to use an allowable stress design with a safety factor of 2. If the allowable stress limits are not satisfied, the designer has two options – select a roller assembly for reevaluation or increase the number of roller units selected to support the bridge superstructure. Once the allowable stress limits are satisfied, the sliding track deflection is calculated based on the support structure configuration and the loads. Rollers are installed just before the bridge slide and removed following the slide. As a result, vertical jacking is inevitable and requires calculating the number, location, and capacity of these jacks. In order to maintain superstructure alignment during slide and to control "racking", guide rollers need to be incorporated into the roller units located under the fascia girders. A coefficient of friction of 5% is used for the slide force calculation.

$$\sigma_{max} = 0.591\sqrt{\frac{P}{R_R L_R E'}} \qquad (1)$$

where,

$$E' = \frac{1-\upsilon_R^2}{E_R} + \frac{1-\upsilon_T^2}{E_T} \qquad (2)$$

When needed, the width of the roller contact area can be calculated using the following equation:

$$b = 2.152\sqrt{\frac{P\,E' R_R}{L_R}} \qquad (3)$$

Hertz's formula incorporates several simplified assumptions (Stachowiak and Batchelor 2014). Assuming a frictionless surface, the maximum shear stress (τ_{max}) is equal to one third of σ_{max} and is located at a distance of *0.393b* below the sliding surface of the track. When the bridge superstructure is supported on rollers, friction is present at the sliding tack surface reacting to the sliding or the tendency to slide. When friction is present and other assumptions are violated, the stress state becomes highly complicated. However, the stress calculated using Hertz's formula can still be used for design. As stated by Hearn (1997), the use of Hertz's formula is justified under static or very low rolling operations where failure normally arises as a result of excessive plastic flow which produces indentation to the surface.

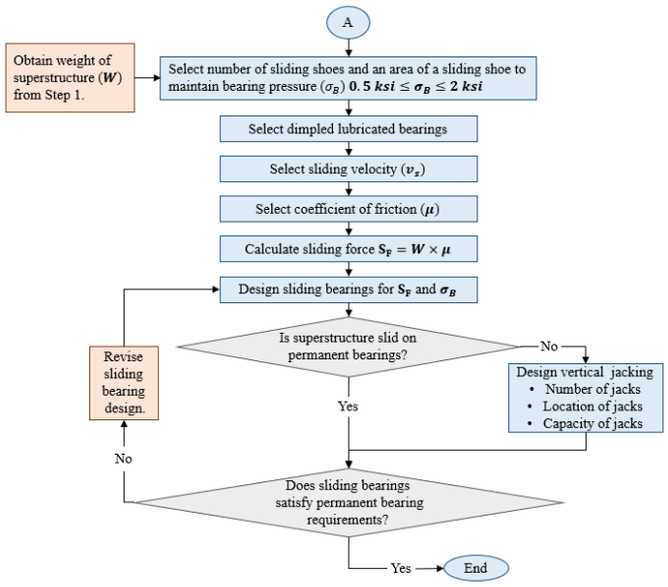


Figure 3: Sliding shoe and *Teflon* bearing pad design procedure

4.1.2 *Actuating System Design Procedure*

The design procedure is shown in Figure 5 and Figure 6. As the first step, a hydraulic operation system is specified. Actuating force capacity is a function of the sliding force and bridge superstructure acceleration and weight. Sliding force is calculated during the sliding system design. Superstructure weight has been previously calculated. Superstructure acceleration data is not widely available. Aktan and Attanayake (2017) recorded a maximum of 0.2%g acceleration in the sliding direction with the slide performed using rollers. Since the acceleration data for a slide using slide bearings has not been reported, the use of 0.2%g as peak superstructure acceleration is reasonable. In order to have adequate capacity to initiate the slide, the actuator needs to have 25% additional capacity in excess of the calculated required force. A maximum actuator capacity should be limited to 150% of the required capacity in order to have better control during a slide. Once the actuator force capacity is determined, the next step is to specify an appropriate stroke length. Different stroke lengths ranging from 2 in. to 48 in. have been used during completed slide projects. Having a short stroke length slows sliding operations due to frequent resets to the hydraulic actuator positions. Long strokes require additional alignment controls to reduce the potential for racking and jamming. Specifying a stroke length that is in between 20 in. and 40 in. is suggested. With limited slide monitoring and actuator control, it is suggested to specify a stroke length closer to the lower bound. With a longer stroke length, it is recommended to perform the slide using advanced slide monitoring systems such as servo controlled hydraulic actuators. Next, the hydraulic oil reservoir volume and pump capacity is specified based on the required force and stroke length. A sufficiently large hydraulic oil reservoir capacity needs to be maintained to control oil temperature.

Actuating the mechanism selection procedure is described in Figure 6. The use of a hydraulic actuator with pulling and pushing capabilities or a prestressing jack with pulling capability are the two alternatives suggested.

The hydraulic actuator requires having reactive and pushing connections at the sliding track and the superstructure, respectively. An actuator casing saddle with holes and pins, or ears, are two connection types used in many completed SIBC projects as reactive connections. It is important to provide a sufficient number of connection points with appropriate tolerances in both connection types to reduce delays while retracting the actuator at each slide cycle. A pushing connection is the connection between the actuator and superstructure where all the actuating loads are transferred to the superstructure. A swivel connection needs to be used for the pushing connection in order to assure load transfer alignment to the sliding direction.

A stationary reaction frame is needed when prestressing jacks are used for pulling or pushing a bridge. Depending on site conditions or the selected temporary and permanent structure types, temporary structure, permanent abutment wingwalls, backwalls, or even the superstructure itself can be used as a reaction frame. High strength steel tendons are used with prestressing jacks. Tendon elongation and relaxation need to be properly accounted for in order to minimize jerky movements and racking of the superstructure.

Servo controlled and pressure regulated mechanisms are available. It is strongly recommended to utilize a servo controlled mechanism to minimize the potential for jamming and superstructure racking due to the unequal friction on sliding surfaces. This is especially important with unguided sliding systems. The use of prestressing jacks creates additional risks because of tendon elongation and relaxation. Therefore, a servo controlled mechanism with synchronized and computerized monitoring and control capabilities is recommended.

5 SUMMARY, CONCLUSIONS, AND RECOMMENDATIONS

Standardized procedures for the design and component selection of lateral bridge slide activities are described. Flowcharts provided describe primary design considerations and compatible components for lateral bridge slide. The following conclusions are derived based on the developed standard procedures presented in this paper:

1. A replacement bridge can be designed as if it is to be constructed conventionally when SIBC is specified for the project. Even though SIBC will not require significant changes to the bridge design, the superstructure and substructure should be checked under SIBC loads.
2. A sliding system design includes a slide mechanism selection with options for *Teflon* with steel sliding shoes or rollers with sliding tracks. The design of the vertical jacking components is also included in a sliding system if temporary sliding bearings or rollers are used as a sliding mechanism. The use of *Teflon* requires the design of neoprene bearings with a *Teflon* surface and sliding shoes, while rollers are selected from manufactured products having the required capacity. Transverse movement tolerances, bearing pressure under sliding shoes, sliding velocity, coefficient of friction, and sliding force are estimated at this stage based on the specified and designed components.
3. Actuating system design includes a hydraulic operation system and an actuating mechanism selection including options of hydraulic actuators and prestressing jacks. A hydraulic operation system includes the design of stroke length, estimating actuating force and actuator capacity based on the sliding force calculated in the sliding system design, hydraulic pump reservoir volume, and pump capacity.
4. Hydraulic cylinders require reactive and pushing connections which may have a significant impact on slide quality and speed. On the other hand, prestressing jacks require a stationary reaction frame design.
5. Servo controlled and pressure regulated control mechanisms are available. Even though a force control mechanism can be specified with the hydraulic actuators, servo controlled pressure regulated control is strongly recommended to improve the quality of monitoring and to reduce the problems created from unequal friction at sliding tracks.

ACKNOWLEDGEMENTS

This project is funded by the Michigan Department of Transportation. The authors would like to acknowledge the support extended by Mr. David Juntunen, Mr. Corey Rogers, Mr. Mike Halloran, and the Research Advisory Panel (RAP) members for successful completion of the project.

REFERENCES

Aktan, H. and Attanayake, U. 2017. “Research on Evaluation and Standardization of Accelerated Bridge Construction Techniques,” *MDOT RC-1618C*, Report to the Michigan Department of Transportation, Lansing, MI, September.

Aktan, H. and Attanayake, U. 2015. “Research on Evaluation and Standardization of Accelerated Bridge Construction Techniques,” *MDOT RC-1618A*, Report to the Michigan Department of Transportation, Lansing, MI, September.

Aktan, H., and Attanayake, U., and Mohammed, A. W. 2015. “Michigan Department of Transportation Bridge Slide Showcase,” Report to the Michigan Department of Transportation, Lansing, MI, March.

Anderson, W. V. and Trenkler, F. 1991. “Continuous Bridge Slides Laterally into Final Position,” *International Association of Bridge and Structural Engineering Report (IABSE)*.

Culmo, M. P. 2011. Accelerated Bridge Construction- Experience in Design, Fabrication and Erection of Prefabricated Bridge Elements and Systems. FHWA, U.S. Department of Transportation.

Hearn, E.J. 1997. *Mechanics of Materials, Volume 2 - An Introduction to the Mechanics of Elastic and Plastic Deformation of Solids and Structural Materials* (3rd Edition), Butterworth-Heinemann, Waltham, MA 02451, USA.

Hwang J.S., Chang K.C., and Lee G.C. 1990. "Quasi-Static and Dynamic Sliding Characteristics of Teflon-Stainless Steel Interfaces." Journal of Structural Engineering, 2747-2762.

Mohammed, A. W., Attanayake, U. B., and Aktan, H. 2016. “Monitoring Substructure Deformations during Slide-in Bridge Construction," *ASCE Journal of Infrastructure Systems*, Vol. 23, No. 2.

Ridvanoglu, O., Attanayake, U., and Aktan. H. 2017. "Monitoring during Lateral Bridge Slide,” *Transportation Research Record: Journal of the Transportation Research Board*, No. 2630, Transportation Research Board of the National Academies, Washington, D.C., pp. pp. 23–32.

Searcy, A., Dobry, M., and Kolkman, L. 2012. West Mesquite Interchange at I-15, ASPIRE, Summer, 28-30.

SHRP 2. 2017. *Innovative Bridge Designs for Rapid Renewal: ABC Toolkit, SHRP 2,* Report No. S2-R04-RR-2. http://onlinepubs.trb.org/onlinepubs/shrp2/SHRP2prepubR04ABCToolkit.pdf . Accessed October 29, 2017.

Stachowiak, G. and Batchelor, A. 2014. Engineering Tribology, 4th Edition, Butterworth-Heinemann, 225 Wyman Street, Waltham, MA.

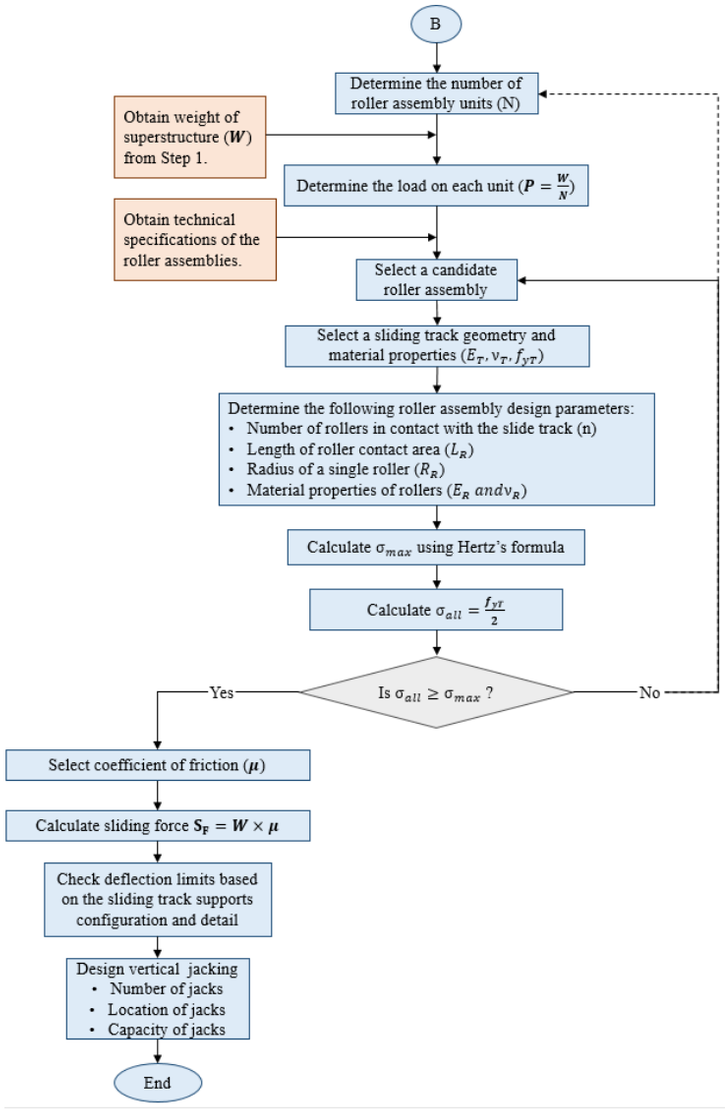


Figure 4: Design procedure for a sliding mechanism with rollers

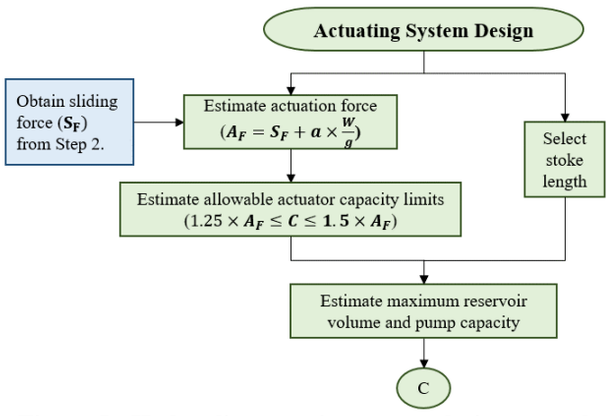


Figure 5: Hydraulic operation system design procedure

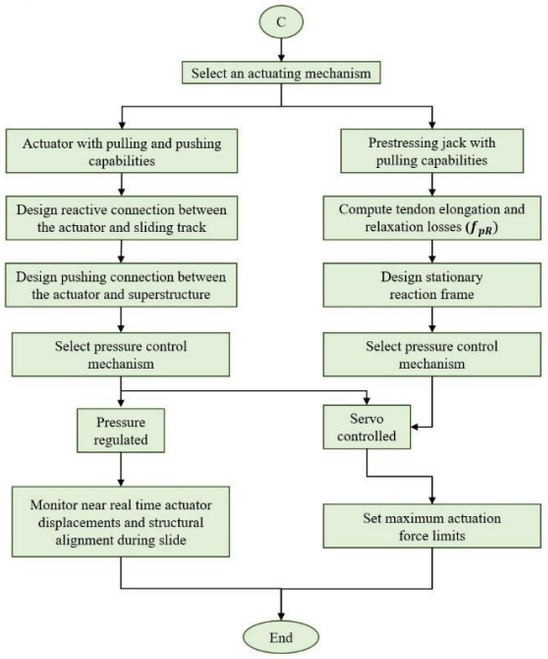


Figure 6: Actuating mechanism design procedure

Maintenance, Safety, Risk, Management and Life-Cycle Performance of Bridges – Powers, Frangopol, Al-Mahaidi & Caprani (Eds)
© 2018 Taylor & Francis Group, London, ISBN 978-1-138-73045-8

Accelerated Construction of Robust Bridges through Material and Detailing Innovations

B. Graybeal, Ph.D., P.E. & Z. Haber, Ph.D.
Federal Highway Administration, Washington D.C., United States of America
I. De la Varga, Ph.D. & R. Spragg, Ph.D.
SES Group & Associates, LLC, Washington D.C., United States of America

ABSTRACT: There is strong demand for construction innovations that facilitate rapid reconstruction of existing, degraded infrastructure. Robust solutions are needed so that infrastructure can uninterruptedly serve as the backbone of a modern economy. Given that the U.S. roadway network is largely built out, heavy demand focuses on in-service reconstruction with maintenance-free solutions. A significant advancement has been the push toward prefabrication of an ever-greater proportion of a bridge's structure, thus allowing for changes to the project critical path and increases in component quality. The move toward prefabrication has occurred concurrently with the move toward the use of advanced materials and detailing practices for the connections between prefabricated bridge components. The research conducted at the Turner-Fairbank Highway Research Center has been a key part of these advancements which are allowing higher quality bridges to be quickly constructed with the expectation of longer, uninterrupted service.

1 INTRODUCTION

Management of a bridge inventory inherently includes recognizing when major maintenance actions need to be taken and encouraging rehabilitation solutions that will deliver substantially improved performance. The fact that roadway networks commonly operate at capacity means that temporary restriction or removal of network nodes (i.e., bridges) can result in major impacts on the local and regional economy. Bridge owners need rehabilitation solutions that can be implemented in short timeframes and will provide robust performance for durations longer than can be achieved using common past construction practices. In essence, spending months to replace a bridge only to have it deteriorate within decades is not acceptable.

Bridge decks operate in an extremely aggressive environment. A common reinforced concrete bridge deck acts as both the plate that transmits loads into the structure and as the roof of the structure itself. A review of deck inspections of bridges across the USA demonstrates that the combined effect of environmental stressors and truck wheel loadings accelerates the degradation of the deck. Decks in regions with freezing temperatures, deicer application, and heavy traffic deteriorate faster. Those same roadways whose 24/7 service is ensured year round through heavy salt application are forced out of service too frequently for rehabilitation.

On the positive side, bridge decks often protect bridge superstructures and substructures leading to a situation where only the bridge deck needs to be replaced. This has led to the recognition that rapid redecking of bridges could provide major advantages to owners and users alike.

In the USA, bridge decks are commonly 20 to 24 cm thick and are reinforced by two orthogonal mats of 16 mm or 19 mm diameter reinforcing bars. Decks are commonly cast in place using conventional portland cement concrete.

The common construction methods of bridge decks pose a problem. The weather conditions for casting a large thin slab of concrete are rarely ideal, particularly when the construction schedule is constrained and opportunity for delay is limited. Any number of factors, including mix shrinkage tendency, consolidation, rate of water evaporation from the placed concrete, and superstructure restraint, can cause the deck to crack and thus expose reinforcing bars. The concrete itself may also be susceptible to environmental degradation, such as freeze-thaw distress, due to the mix design not sufficiently controlling the air content.

For these reasons and the fact that forming and casting a deck takes a significant amount of effort, there is a strong movement toward prefabrication of bridge decks. Precast concrete bridge decks have similar overall design as compared to conventionally constructed bridge decks, but they inherently require the creation of field-installed connections between

the precast pieces and from the precast pieces to the underlying superstructure elements. These connections need to perform at least as well as the precast components, lest the connections become the weak link necessitating further rehabilitation of the structure.

In the USA the use of precast bridge decks has been ongoing for decades. Early precast decks often relied on pretensioned deck panels that were post-tensioned together through unreinforced shear keys. This deck system was expected to perform well due to the compressive forces inherent in the deck; however, the complexity of the fabrication and construction proved to be a major challenge. The connections also sometimes underperformed, leading to deterioration of post-tensioning tendons and potential loss of precompression.

More recently there has been a trend toward the use of concrete deck panels with reinforced connections, such as shown in Figure 1 where the inset shows the overlapping hairpin bar reinforced connection. These types of precast decks generally do not require any pre- or post-tensioning, although pre-tensioning of the piece may be implemented to address excessive handling stresses. The factory cast concrete panels can be of high quality due to the tight controls that can be implemented in this fabrication environment. The primary challenge is with the complexity of the connections between the panels and from the panels to the girders. In order to create reinforced connections that transmit stresses from both mats of reinforcement between panels, the connection details have tended to become quite complex with sophisticated, expensive reinforcement details. Headed bars, hairpin bars, lacer bars, and even embedded steel sleeves have been used in an effort to reduce the size of traditional lap splice rebar connections. These solutions have often resulted in high costs for precast components and delayed construction operations when tolerances and fit-up issues arise in the field.

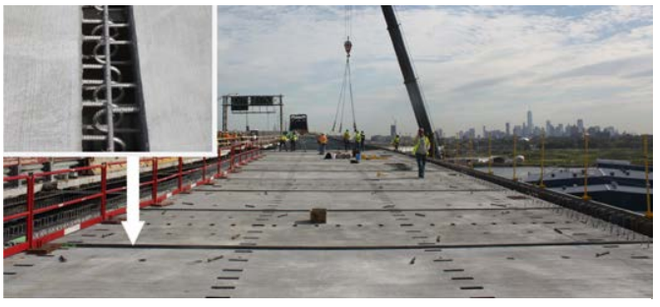


Figure 1. Precast deck panel installation on a bridge near New York City.

Also, the concept of inducing connection performance through reinforcement detailing without carefully considering the field-cast grout or concrete has sometimes led to the deployment of materials whose durability and resiliency pales compared to the precast components which compose the majority of the bridge deck area.

An emerging solution to these challenges is the use of advanced cementitious materials, including ultra-high performance concrete (UHPC). Over the past decade UHPC has proven to be a viable solution, having been deployed in field-cast connections between prefabricated components in nearly 200 bridges across the USA and Canada (Fig. 2). The enhanced mechanical and durability properties of UHPC allow for simpler connection details (Fig. 3), less expensive precast components, easier construction, and better overall system performance. Further discussion of key connection detail considerations and the advantages of using UHPC for these connections is provided in the following sections.



Figure 2. Bridges using UHPC in North America.



Figure 3. Simple, robust connection designed for use with UHPC.

2 DURABILITY OF MATERIALS

The durability of the materials used in a bridge deck is a foremost concern as it is central to ensuring overall system durability. Durability of cementitious composites is commonly measured in relation to the permeability of the material, based on the recognition that reduced permeation correlates with extended times prior to aggressors degrading the material.

The porosity and the degree of connectedness of the porosity will influence the permeability of the

cementitious material. One of the methods used to assess permeability is referred to as the Rapid Chloride Penetration Test (RCPT), which monitors the current flow through a 50 mm slice of concrete exposed to a NaCl solution (ASTM C1202). As the solution penetrates into the material, the current flow increases. The flow of current through the specimen is monitored for a period of six hours to determine a total amount of charged passed. This technique has been used to rank a wide range of cementitious materials for nearly the last three decades, and different performance classes have been established based upon the total charge passed over six hours, with the lower amount of charge corresponding to a less permeable, more durable material (Whiting 1981, ASTM C1202 2017).

Results from RCPT, shown in Fig. 4, indicate performance of the most common parent material used in prefabricated component bridge systems. The first of these materials is a concrete typical of that used in a precast facility. It is a concrete made with ordinary portland cement, a water-cement ratio of 0.35, and consists of 30 % paste, by volume. The other materials are examples of a commercial available cementitious grout and a UHPC that were mixed in accordance with manufacturer's requirements.

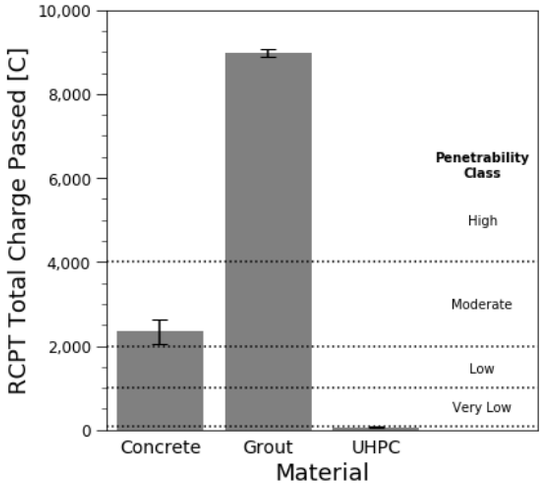


Figure 4. RCPT results indicating large penetration into the cementitious grouts and minimal penetration into UHPC.

The RCPT results (Fig. 4) indicate that the concrete as a low to moderate penetration and the UHPC has negligible penetration, while the grout material is highly penetrable. The superior performance of UHPC is attributed to the near elimination of capillary porosity and tortuous nature of the pore network (Graybeal and Tanesi 2007).

While the RCPT provides a somewhat qualitative estimate of the resistance to chloride penetration, more quantitative comparisons can be done by comparing chloride ion diffusion coefficients. This paper presents results of the apparent chloride ion diffusion coefficient determined from electrical resistivity as discussed in literature (Snyder 2001, Spragg et al. 2016). The apparent chloride ion diffusion coefficient (D) is inversely proportional to an estimated time to corrosion initiation, and can be used to quantify impacts on service life. Specifically, as the apparent diffusion coefficient decreases, the amount of time before corrosion begins increases. Values of D shown in Table 1 are similar to the results observed with RCPT, in that grout materials are more permeable than typical precast concrete and UHPC. These values can be used with life-cycle estimation equations, such as Fick's second law, which are detailed elsewhere (Weiss et al. 2017).

Table 1. Chloride ion diffusion coefficients (D) for typical materials used in precast systems.

Material	D [10^{-13} m^2/sec]
Concrete	180
Grout	500
UHPC	4

In addition to the penetration of chlorides, the ingress of water can lead to durability problems with cementitious materials. Most readily, is the expansion of water as it transitions from its fluid phase to its solid phase, i.e. water to ice. This can lead to stresses that build up and lead to cracking and scaling. The resistance to freeze thaw can be assessed using a ASTM C666 (2015), a method that subjects the materials to freeze/thaw cycles and monitors relative dynamic modulus. Dynamic modulus is a measure of stiffness, and as materials develop damage during freeze/thaw cycles the stiffness degrades and the material will break apart, ultimately demonstrating complete failure. The results are presented relative to the initial dynamic modulus which is measured before any freeze/thaw cycles are incurred (STP 169D, 2006). While not readily usable in service-life calculations, the performance in this test demonstrates resistance to freeze/thaw aggressors and provides relativistic performance between materials.

Figure 5 illustrates relative modulus degradation during freeze/thaw cycles for typical materials used in closure pours (Swenty and Graybeal 2013). The magnesium phosphate grout exhibited a very rapid loss in stiffness, suggesting that it would not perform well in a wet environment prone to freeze/thaw cycles. The other materials, a cementitious grout, an epoxy grout, and a UHPC, demonstrated a relative dynamic modulus of at least 90 %, even after 600 freeze/thaw cycles.

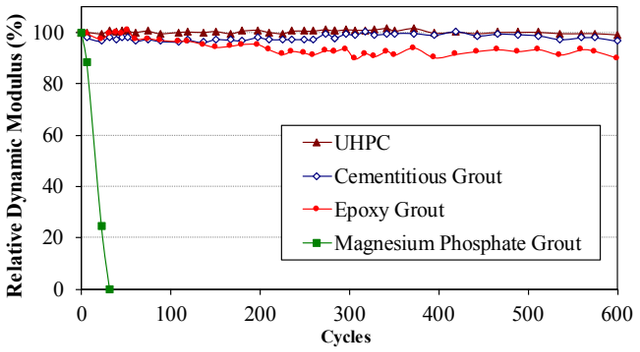


Figure 5. Freeze/thaw testing results of materials commonly used in closure pours. From Swenty and Graybeal (2013).

3 DIMENSIONAL STABILITY OF MATERIALS

A bridge deck is a restrained two-dimensional element. If the field-cast materials composing the bridge deck express dimensional instability, the expansion or contraction will be restrained by the rest of the system. Concretes and other portland cement-based materials naturally express shrinkage as they transform from a fresh state into a hardened state. Proper mix design can mitigate some shrinkage effects, as can proper curing of the concrete.

Shrinkage is a significant concern in the construction of conventional concrete bridge decks; often these decks will express regularly spaced shrinkage cracks within their first year in service. The use of precast deck panels eliminates these cracks, but raises the possibility of similarly detrimental cracks forming in the field cast connection filler should it express too much shrinkage as it cures. This is one of the primary reasons why bridge owners often require the use of non-shrink grouts in field cast deck level connections. In the USA, the common test method for qualifying these types of grouts is ASTM C1107 (2014). Unfortunately, experience has shown that grouts passing the C1107 thresholds can still exhibit significant shrinkage and their usage in precast system connections often results in shrinkage cracks within the grouts and at the interfaces with the precast pieces.

An extensive research study was performed by De la Varga et al. to evaluate the dimensional stability properties (i.e., expansion and shrinkage) of a set commercially-available grout-like materials (2015). It was observed that the test methods used for evaluating dimensional stability described in ASTM C1107 consider several parameters simultaneously (e.g., chemical expansion and shrinkage, autogenous and plastic shrinkage, etc.), thus providing a qualitative approach that is only useful for comparative purposes. The results showed that most of the grouts evaluated seemed to perform well in terms of dimensional stability when tested in accordance with ASTM C1107 (see Table 2). However, separate testing to specifically assess autogenous and drying deformations via ASTM C1698 (2014) and ASTM C157 (2017) demonstrated that ASTM C1107 is not necessarily an appropriate means to capture the full range of critical dimensional stability behaviors, especially for the most-commonly used non-shrink cementitious grouts (Figure 6). The amount of drying shrinkage shown in Figure 6 is starkly different from the results observed for these same materials according to ASTM C1107 as reported in Table 2.

Table 2. ASTM C1107 results indicating that many grouts can qualify as "non-shrink" by expressing minimal gross height change at specific time intervals.

	Average height change of hardened grout at a given age (%)*				
Grout	1 day	3 days	7 days	14 days	28 days
NSCG1**	-1.2	-1.2	-1.2	-1.2	-1.2
NSCG2	0.0	0.0	0.0	0.0	0.0
NSCG3	0.0	0.0	0.0	0.0	-0.1
NSCG4	0.0	0.0	0.0	0.0	0.0
UHPC	-0.4	-0.4	-0.4	-0.4	-0.4

* Maximum and minimum allowed by ASTM C1107 is 0.3 and 0.0 %, respectively.
** "NSCG" stands for Non-Shrink Cementitious Grout

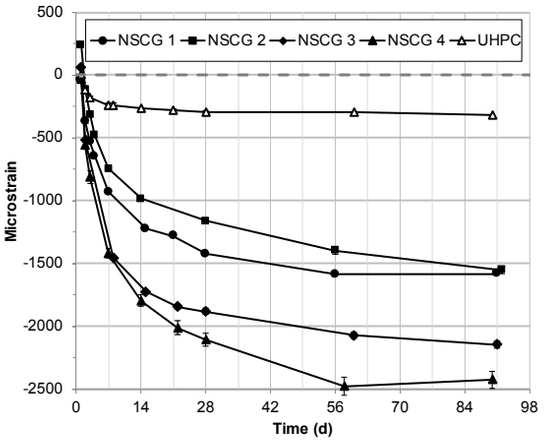


Figure 6. Drying deformations as a function of time. Adapted from (De la Varga and Graybeal 2015).

4 INTERFACE BOND

The use of prefabricated bridge decks includes acceptance of the fact that the deck will include multiple cold joints, two at each side of every connection. These interfaces must express good bond or else the deck will quickly experience stresses or shrinkage that will result in debonding, reflective cracking through any overlay, and leakage. Interface bond has two key elements: the tendency of the field cast material to bond and the tendency of the substrate to accept the bond. If both are present and appropriate then the bond at the interface may approach the tensile strength of the weaker of the two bonded materials.

Substrate bondability of concrete is driven by a combination of macrotexture and microtexture. A more "open" (or rougher) surface is preferred as this allows for interstitial spaces and a greatly increased surface area to which the field cast material can bond. Various techniques for roughening the concrete surface are commonly deployed, including hydro-demolition, scarification, sandblasting, and aggregate exposure using in-form retarders (ICRI Committee 310 2013), though some of these are not practical for precast component connections with extending connectors. Different degrees of roughness can be obtained depending on the technique selected; however, some of them are recognized to also cause some local damage to the concrete surface, thus affecting the bond performance. Figure 7 compares the bond strength of a cementitious grout and a UHPC when bonded to concrete substrates with different degrees of roughness. It is interesting to note that while increasing the surface roughness resulted in increased bond strengths for a cementitious grout, this was not the case for the UHPC material, where 90% of the bond strength achieved with a high roughness level could be obtained with a minimum (low) surface preparation.

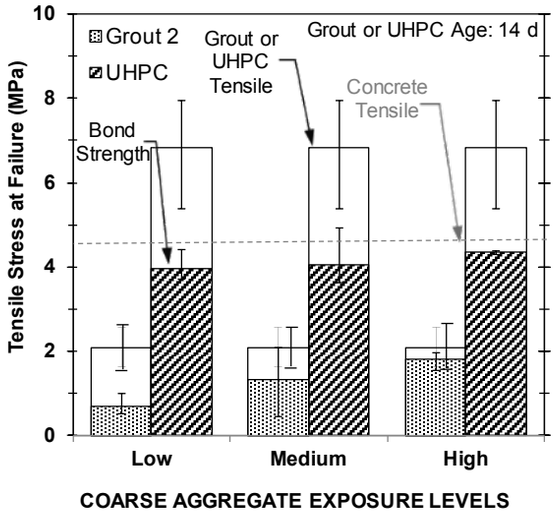


Figure 7. Tensile bond strength of a cementitious grout and an UHPC when different roughness levels are applied to the concrete slab (de la Varga et al. 2017a).

Field cast material bondability is driven by a combination of the rheological properties of the material and the material's tendency to create microscopic chemical bonds across the interface with the precast concrete substrate. Therefore, changes in the mixture design can purposely be made to provide the appropriate rheological and reactivity properties of the material.

Along the lines of favoring the proper reactivity of the field cast material, a low-cost strategy has been widely accepted in the concrete construction community: the provision of interface moisture at the concrete surface prior to the grout pour. Theoretically, when a fresh cementitious material is cast upon a dry concrete substrate the latter may demand mix water from the former. That is, water may be forced to migrate from the freshly-cast material to the dry substrate (Lukovic and Ye 2016). Migration of water could cause development of internal stresses at the interface and higher porosity in the field cast grout due to the loss of water required for hydration. Thus, water migration could be mitigated if additional moisture was present at the interface prior to placement of the fresh material (Bentz 2016). Extensive research has been carried out on this particular topic (Shearrer at al 2015, Beushausen 2015, Beushausen et al 2017). An example is provided in Figure 8, where the tensile bond strength of two cementitious grouts and a UHPC cast atop a concrete substrate with two different moisture conditions are compared. "SSD" corresponds to a moisture state known as "saturated surface dried".

Independent of the properties of the two materials being bonded, other means can be used in the field to guarantee a good bond. These include the use of bonding agents and ensuring the cleanliness of the precast concrete surface.

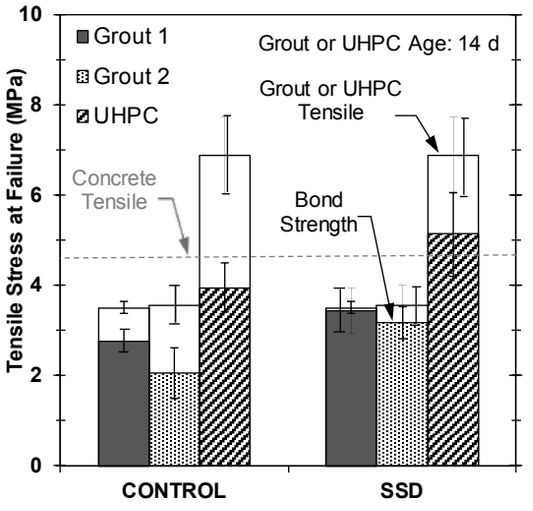


Figure 8. Effect of the substrate moisture condition on the tensile bond strength of two cementitious grouts and an UHPC (De la Varga et al. 2017b).

5 PERMEABILITY AT INTERFACE

The discussion of prefabricated bridge deck permeability is not complete without consideration of the permeability along the two dimensional bonded interfaces. Of specific concern is the vertical interface between the concrete of the precast element and the field-cast closure pour material. This vertical interface is exposed to chlorides from deicing operations and water, and the reaction products that create the chemical bond between the substrate and the field cast material may express different permeability than the parent materials. If the permeability is particularly large then these locations could be weak links in the durability of the system. Research investigating

this topic is currently underway with results anticipated in 2018.

6 REBAR DEVELOPMENT LENGTH

A key aspect of simplifying the detailing of deck level connection between precast components is recognizing that the field-cast material itself can affect the design. Common practice has always relied on overlapping and interlacing reinforcements to transfer forces, and smaller connections tended to become ever more heavily reinforced. Through the use of heavily fiber reinforced cementitious composites, it is possible to shift some of the stress transfer burden onto the field-cast material. The dense microreinforcement inherent in UHPC, along with the increased tensile capacity of the material, changes the tensile response of the material such that it can sustain tensile loads beyond cracking. Therefore, UHPC can provide significantly enhanced confinement around embedded reinforcements and can thus shorten the development length of these bars.

Extensive research conducted by Yuan and Graybeal (2014, 2015) and by Haber and Graybeal (2018) showed that bar sizes commonly used in bridge decks could develop the yield strength of the bar when embedded as little as eight bar diameters (d_b) into UHPC, assuming that sufficient cover concrete is provided. Key findings from these studies are discussed herein.

The bond strength between UHPC and embedded steel reinforcement was evaluated using the direct tension pull-out test set-up shown in Figure 10. This set-up was developed to simulate the tension-tension lap-splice configurations typically encountered in prefabricated bridge deck connections. Test specimens were created by casting UHPC strips atop a precast concrete slab. The precast slab had a series of protruding M25 Grade 420 bars which were centered along the length of the strips. Test bars were positioned to achieved the desired test parameters: embedment length (l_d), lap-splice length (l_s), clear spacing between bars (s), and clear cover (c). Other test variables included different commerially available UHPC-class materials, different reinforcement types and sizes, different fiber volume fractions (V_f), and different compressive strengths of UHPC.

Figure 11 depicts the relationship between the average peak bar stress in the bar prior to failure ($f_{s,max}$) and the embedment length for the three different reinforcing bar types, uncoated (Gr. 420), epoxy-coated (Gr. 420) and high-strength (Gr. 830); here, the clear cover, bar spacing, UHPC type and fiber volume (2%), and UHPC compressive strength were approximately constant. It can be observed that increasing the embedment length of a reinforcing bar increases the bar stress at bond failure and the relationship between the bar stress and the bonded length is nearly linear. This relationship is similar to that observed in normal-strength concrete, but is not typically observed in high-strength concretes. Thus, the observed linear relationship between bond strength and embedment length implies that the behavior attributed to traditional high-strength concretes may not be present in UHPC, potentially due to the enhanced pre- and post-cracking tensile response of the UHPC.

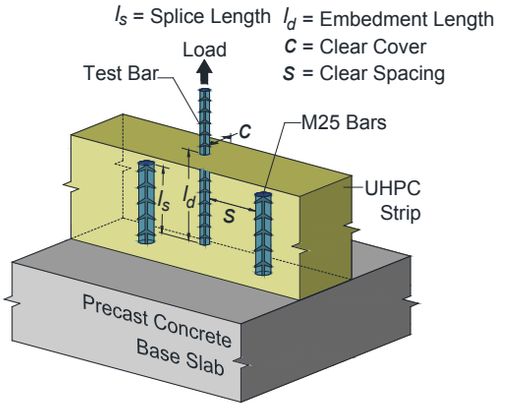


Figure 10. Direct tension pull-out set-up used for embedment length testing.

Other key findings were related to bar spacing and clear cover. As the bars spacing gets large, stress transfer from the loaded bars to the adjacent bars becomes less effective and more load must be carried by the UHPC thus reducing bond strength. On the other hand, when adjacent bars are in close proximity, load transfer also becomes less effective likely due reduced confinement of the bars by the UHPC. As it relates to side cover, bond strength between UHPC and embedded reinforcement tends to increase with increasing side cover; this is similar to conventional concrete.

An important question commonly posed by designers, related to bond of UHPC to reinforcement is "what is an approximate fiber volume fraction?" UHPC mix optimization can result in more efficient structural systems. Figure 12 depicts the relationship between the peak bar stress (normalized by the square root of the compressive strength of UHPC) and the fiber volume fraction when all other parameters are held approximately constant. The data reflects five different commercially available UHPC-class materials: U-A through U-E. This result indicates that increasing V_f results in enhanced confinement of the embedded bars when subjected to direct tension which increases bond strength. These results would also indicate that connections employing UHPCs with fiber volume fractions less that $V_f = 2\%$ may result in reduced ductility at the ultimate limit state.

In summary, the significant reduction in embedment length as compared to conventional cementitious materials leads to the opportunity to create small, simply reinforced connections with only ex-

tended bar stubs emanating from each adjoining precast deck panel. The data from the aforementioned studies was used to develop design guidance for bridge engineers and bridge owners interested in levering the innovative properties of UHPC to create simplified, yet robust connections. The design guidance is available in document published by FHWA (Graybeal 2014).

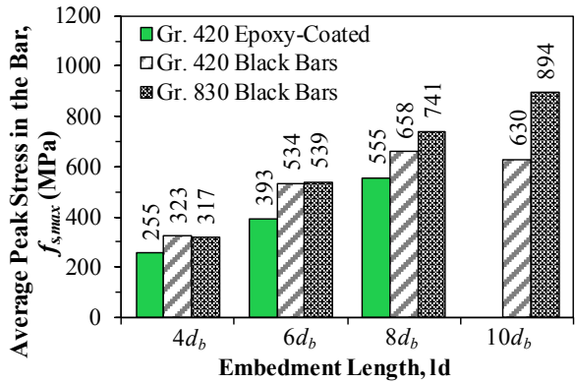


Figure 11. Peak stress in the embedded bar as a function of the bar embedment length.

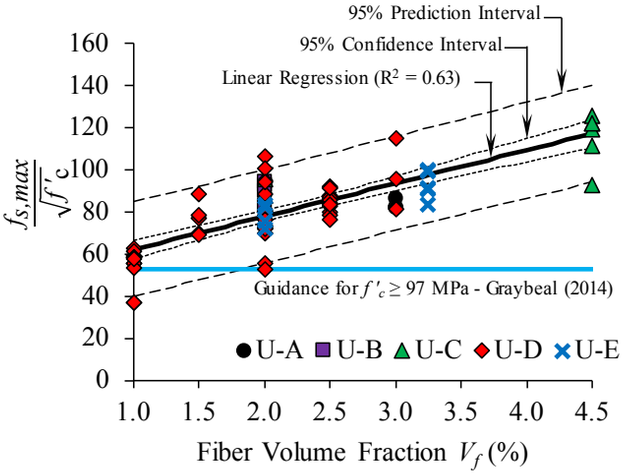


Figure 12. Relationship between peak bar stress and fiber content for $l_d = 8d_b$

7 SHEAR CONNECTIONS

The structural connection of precast deck panels to the underlying bridge girders is both critical to the structural performance of the bridge and complicated by the traditional need to have steel shear connectors passing between the girder and the deck. In order to ensure appropriate structural performance, structural design specifications define a maximum connector spacing. This spacing requirement often drives the detailing of the precast deck panel to include blockout through which the connectors will pass or be placed. The constructability challenges with this type of system are significant.

As with the deck level connections discussed previously, the use of heavily fiber reinforced cementitious composites can also allow for a redesign of these deck-to-girder connections. By using the rheological and mechanical properties of the field-cast material to the advantage of the connection, the configurations of the connectors on the girder and on the deck can be simplified. This allows the precast deck panel to be fabricated more cost effectively and it allows the field assembly of the deck panel to occur more easily.

Details such as those shown in Figure 13 have been tested and found to be capable of providing appropriate performance. Further information can be found in Graybeal (2012) and Haber et al. (2017).



Figure 13. UHPC deck-to-girder connection details for steel girder construction.

8 CONCLUSIONS

Bridge deck rehabilitation is a major part of any bridge management program. Having rehabilitation solutions that afford both better performance and a shortened construction timeframe is advantageous. Recent advancements in concrete, including the emergence of UHPC as a competent, practical material, has created new opportunities to address specific design and construction challenges.

There are many considerations that come into play when designing and detailing precast bridge decks. As discussed herein, consideration of critical material- and structural-scale parameters can lead to the development of innovative bridge construction solutions. The properties of UHPC address many of the shortcomings of traditional bridge decking and redecking operations. The overall process of using a prefabricated deck system addresses the timelines inherent in traditional cast-in-place deck construction and the commonly encountered issues with early age deck cracking. Precast deck panels, when designed for use with UHPC connections, can be easier to fabricate and easier to install than traditional deck panels. The UHPC connections offer greater durability and a system whose weak links have been addressed. As evidenced by the owners across the USA that are moving to demonstrate, integrate, then institutionalize UHPC connections technology into their bridge construction programs, this concept offers real advantages that address longstanding shortcomings in the bridge sector.

REFERENCES

ACI Committee 408. 2003. Bond and Development of Straight Reinforcing Bars in Tension. 408R–03.

ASTM C157. 2017. Standard Test Method for Length Change of Hardened Hydraulic-Cement Mortar and Concrete. ASTM International.

ASTM C666. 2015. Standard Test Method for Resistance of Concrete to Rapid Freezing and Thawing. ASTM International.

ASTM C1107. 2014. Standard Specification for Packaged Dry, Hydraulic-Cement Grout (Nonshrink). ASTM International

ASTM C1202. 2017. Standard Test Method for Electrical Indication of Concrete's Ability to Resist Chloride Ion Penetration, ASTM International.

ASTM C1698. 2014. Standard Test Method for Autogenous Strain of Cement Paste and Mortar. ASTM International.

Azizinamini, A., Stark, M., Toller, J.J., and Ghosh, S.K. 1993. Bond Performance of Reinforcing Bars Embedded in High-Strength Concrete. ACI Structural Journal, 90(5), pp. 554–561.

Bentz, D. P. 2016. 30 Years of Imaging and Modeling Building Materials at NBS/NIST: From PIXAR to MICROCHAR. Imaging of Construction Materials and Geomaterials, Paris, France.

Beushausen, H. 2015. The Influence of Precast Surface Moisture Condition on Overlay Bond Strength. Concrete Plant International.

Beushausen, H., Höhlig, B., Talotti, M. 2017. The influence of substrate moisture preparation on bond strength of concrete overlays and the microstructure of the OTZ. Cement and Concrete Research, 92.

De la Varga, I. and Graybeal, B.A. 2015. Dimensional Stability of Grout-Type Materials Used as Connections between Prefabricated Concrete Elements. Journal of Materials in Civil Engineering, 1107(9).

De la Varga, I., Haber Z.B., Graybeal, B.A. 2017a. Enhancing Shrinkage Properties and Bond Performance of Prefabricated Bridge Deck Connection Grouts: Material and Component Testing. Accepted by Journal of Materials in Civil Engineering.

De la Varga, I., Munoz, J.F., Bentz, D.P., Spragg R.P., Stutzman, P.E., Graybeal, B.A. 2017b. Grout-concrete interface bond performance: Effect of interface moisture on the tensile bond strength and grout microstructure. Submitted to Construction and Building Materials

Graybeal, B. A. 2014. Design and Construction of Field-Cast UHPC Connections. U.S. Federal Highway Administration, FHWA-HRT-14-084.

Graybeal, B. A. 2012. Ultra-High Performance Concrete Composite Connections for Precast Concrete Bridge Decks. U.S. Federal Highway Administration, FHWA-HRT-12-041. 110 pp.

Graybeal B., and Tanesi, J. 2007. Durability of an Ultrahigh-Performance Concrete. Journal of Materials in Civil Engineering, 19(10).

Haber, Z. B., and Graybeal, B. A. 2018. Lap-spliced Rebar Connections With UHPC Closures. ASCE Journal of Bridge Engineering. *Submitted.*

Haber, Z. B., Graybeal, B. A., Nakashoji, B, Fay, A. 2017. A New, Simplified Deck-to-Girder Composite Connections Using UHPC. Proceedings of the 2017 National Accelerated Bridge Construction Conference, Miami, FL, December 7-8. 10 pp.

ICRI Committee 310. 2013. Selecting and Specifying Concrete Surface Preparation for Sealers, Coatings, Polymer Overlays, and Concrete Repair. International Concrete Repair Institute, Guideline No. 310.2R-2013.

Lukovic, M. and Ye, G. 2016. Effect of moisture exchange on interface formation in the repair system studied by X-ray absorption. Materials (Basel), 9(1).

Shearrer, A.J., Riding, K.A., Peterman, R.J. 2015. Effects of Concrete Moisture on Polymer Overlay Bond Over New Concrete, K-TRAN: KSU-13-3.

Snyder, K.A. 2001. The relationship between the formation factor and the diffusion coefficient of porous materials saturated with concentrated electrolytes: theoretical and experimental considerations. Concrete Science and Engineering, 3(12).

Spragg, R., Qiao, C., Barrett, T.J., and Weiss, J. 2016. Assessing a concrete's resistance to chloride ion ingress using the formation factor, in Corrosion of Steel in Concrete Structures, A. Poursaee, Ed. London: Woodhead Publishing, 2016, pp. 211–238.

STP 169D. 2006. Significance of Tests and Properties of Concrete and Concrete-Making Materials, STP 169D. ASTM International.

Swenty, K., and Graybeal, B.A. 2013. Material Characterization of Field-Cast Connection Grouts. U.S. Federal Highway Administration, FHWA-HRT-13-041.

Whiting, D. 1981. Rapid determination of the chloride permeability of concrete. U.S. Federal Highway Administration, FHWA/RD-81/119.

Weiss, W.J., Spragg, R.P., Isgor, O.B., Ley, M.T., and Van Dam, T. 2017. Toward performance specifications for concrete: linking resistivity, RCPT and diffusion predictions using the formation factor for use in specifications. fib Symposium 2017.

Yuan, J., and Graybeal, B. 2015. Bond of Reinforcement in Ultra-High-Performance Concrete. ACI Structural Journal, 112(6).

Maintenance, Safety, Risk, Management and Life-Cycle Performance of Bridges – Powers, Frangopol, Al-Mahaidi & Caprani (Eds)
© 2018 Taylor & Francis Group, London, ISBN 978-1-138-73045-8

Bearing friction values for slide-in bridge construction

K. R. Johnson, S. Dorafshan, M. W. Halling, M. Maguire, P. J. Barr
Utah State University, Logan, Utah, USA

M. P. Culmo
CME Engineering, East Hartford, CT USA

ABSTRACT: Slide-In Bridge Construction (SIBC) has been used in Accelerated Bridge Construction (ABC) for the past decade. SIBC is carried out using bearing pads consisting of polytetrafluoroethylene (PTFE), and stainless and carbon steel surfaces.

Appropriate coefficients of friction (COFs) had not been determined for the use of SIBC in temporary applications. In this study, COF values in SIBC with variable surface roughness, lubrication type, and contact pressure were determined through experiments. Among three tested surfaces, the rough rolled stainless steel, as well as the carbon steel, produced COF values much higher than those resulting from the stainless ones with a #2B surface. Dry (no lubrication) and graphite lubrication resulted in high friction values, whereas the soap, grease, and oil had low friction values. Additionally, four different applied pressures were investigated. These experimental test results give additional insight into the application of sliding bearings in the field of slide-in bridge construction.

1 INTRODUCTION

1.1 *Sliding Bearings*

Bridges are vital elements of the United States transportation grid. With an average bridge age of 42 years, many bridges are on the verge of needing repairs or replacement (Infrastructure Card, 2017). Bridge construction can be time-consuming. Traffic delays and congestion that happen during construction impose extra cost on transportation agencies and passengers. According to Culmo (2011), Accelerated Bridge Construction (ABC) methods are defined as construction "that uses innovative planning, design, materials, and construction methods in a safe and cost-effective manner to reduce the onsite construction time that occurs when building new bridges or replacing and rehabilitating existing bridges." Using ABC methods reduces traffic impact and onsite construction time and increases the safety and construction quality. Common strategies in ABC are Prefabricated Bridge Elements and Systems (PBES), Geosynthetic-Reinforced Soil-integrated Bridge Systems (GRS-IBS), and Slide-In Bridge Construction (SIBC). ABC strategies are gaining popularity among state Departments of Transportation (DOTs). A survey in 2015 indicated that of the 31 states that responded to the survey, 16 have completed 6 or more ABC projects(Ofili, 2015).

One practical ABC method is Slide-In Bridge Construction (SIBC). The SIBC implementation guide states that using SIBC in a project to replace an existing bridge enhances the safety, reduces the construction time, reduces mobility impact, cuts project costs, and increases the quality of construction (FHWA 2013). The superstructure for the new bridge is constructed adjacent to the existing bridge so that during construction of the new bridge, the existing one can continue to be in service. The new bridge is built or assembled on top of tracks used to slide the structure into place once the existing one is removed. Typical bridge replacements can shut down traffic for anywhere from a couple of months to over a year. SIBC, on the other hand, generally allows the road to be open to traffic during the full construction period other than for a couple days or weeks.

The method used to slide the newly constructed bridge on the sliding track and into place typically uses sliding bridge bearings that have two flat sliding surfaces which have low coefficient of friction (COF) values when used together. The surfaces used for the sliding bearings include a polymer called Poly-Tetra-Fluoro-Ethylene (PTFE) and stainless or carbon steel. Use of PTFE and stainless steel interfaces in bridge bearings has been a common practice since around the 1960's, mainly for permanent use to allow movement due to prestress shortening,

shrinkage, creep, or seismic activities. These movements can also be caused by change in live loads, temperature, misalignments, and camber (Caltrans 1994). Using the bearings for SIBC is a short term use and has not been investigated nor specified before.

SIBC is an emerging area in the realm of bridge construction and transportation. Iowa DOT held a workshop to introduce ABC and SIBC to engineers (Iowa DOT, 2009). The Wisconsin DOT sponsored the University of Washington to conduct tests for determining COFs between several different stainless-steel finishes and a PTFE coated surface (Taylor and Stanton 2010). The purpose of this study was to provide the Wisconsin DOT with the results in a clear and straightforward way and to be implemented by the bureau of structures for bridge design. Since stainless steel polished to a #8 finish is more expensive and can be more difficult to obtain than other finishes, #2B rolled finish and rough as-rolled finish stainless steel was tested and then compared to the results of #8 polished stainless steel. The investigated parameters in determining COFs were surface finish, contact pressure, and sliding speed slide path. The COF for the #8 m irror finish increased as the slide path increased, whereas for the #2B rolled finish it stayed constant, and for the rough as-rolled finish it decreased. Based on the tests that were conducted, an equation was developed to help predict the friction coefficient as a function of the surface finish, the contact pressure, the sliding speed, and the slide path. After all of the tests were completed and the results were analyzed, it was determined that stainless steel with a #2B surface finish was an appropriate alternative to a #8 mirror finish in terms of COFs. The findings of this study were later inserted into the Wisconsin DOT bridge manual. This manual recognizes two slide-in methodologies using hydraulic rams as the bridge slides on a smooth surface and PTFE coated elastomeric bearing pads or using rollers instead of sliding pads and winches in place of a hydraulic ram (Wisconsin DOT, 2013).

The Strategic Highway Research Program 2 (SHRP2) has created an addendum for rapid bridge renewal called "ABC Toolkit on Lateral Slides". In this document, the applicability of using the SIBC, design considerations, and key components in implementation were discussed (SHRP2, 2013). FHWA published the guide for SIBC developed by Utah DOT and the Michael Baker Corporation (FHWA, 2013). The SIBC guide was designed to demonstrate the advantages of using SIBC and show how it can be implemented by state and local agencies (FHWA, 2013). One year after the manual publication, Michigan DOT initiated a workshop (Aktan et al. 2014). In the Michigan DOT workshop, static and dynamic COFs were discussed. In addition, the implementation of the COF values by Michigan DOT, in order to select required jacking hydraulics to move the bridge, was also explained.

2 TEST PARAMETERS

2.1 *Investigation*

The main goal of using bridge bearings in SIBC is to reduce the required force to push or pull a bridge across the slide track and into its final resting place. This force is governed by the amount of friction between the sliding surfaces which depends on several parameters. Similar to the study performed by Stanton, (2010), in this study, the following parameters were investigated to determine the surface COFs: surface roughness of the mating material which the PTFE slides on, lubrication used between PTFE and the mating surface (e.g. stainless steel), and contact pressure of the PTFE pads in contact with the mating surface.

2.2 *Surface Roughness*

Three mating surfaces were investigated in the laboratory testing. When using PTFE bearings for permanent bridge bearing applications, AASHTO specifies the mating surface to be stainless steel with a #8 mirror finish (AASHTO 2014). Although AASHTO recommends #8 mirror finish stainless for permanent bearing applications, for this study three mating surfaces were tested, namely, #2B stainless, #1 stainless, and hot rolled carbon steel surface. The resulting COF values for these surfaces are reported.

2.3 *Lubrication*

Four lubrications were investigated in the laboratory study. It is common practice to use lubrication in conjunction with dimpled PTFE pads to reduce the friction for PTFE sliding bearings. Small concave dimples are drilled out of the PTFE pads so that there is a place for the lubricant to be retained. Four lubricants were studied: common dish soap, grease, oil, and graphite. In addition, tests were also performed with no lubrication for reference (referred to as "dry" tests).

2.4 *Contact Pressure*

As the contact pressure between the PTFE and the mating surface increases, the COF decreases. Extensive testing was done for the NCHRP Report 432, High-Load Multi Rotational Bridge Bearings (NCHRP, 1999) where the researchers proposed that the COF decreases linearly as the contact pressure increases for pressures less than 21 MPa, and as the pressure increases into higher pressures the COF remains fairly constant. Considering this, the follow-

ing four pressures were investigated: 11 MPa, 21 MPa, 31 MPa, and 55 MPa.

3 TEST SETUP

3.1 *Laboratory Testing*

The tests were carried out in the System, Material, and Structural Health (SMASH) lab at Utah State University (USU). The testing was done during the winter months where the lab temperature was maintained at 15 °C to 18 °C.

3.2 *Test Setup*

The SMASH lab has a reaction frame to which the test setup was mounted. Figure 1 is a schematic drawing of the test setup. Two vertical rams were used to simulate the vertical load caused by the weight of a bridge by applying a load to a spreader beam, which pushed down and sandwiched the PTFE pads. Once this vertical load was applied, the horizontal actuator was used to slide the specimens back and forth with the only resistance being the friction between the PTFE pads and the mating surface. Load cells were placed between the vertical rams and the spreader beam to measure the vertical load for each ram. In order to prevent eccentric loading on the vertical rams or the load cells, spherical bearings were used. These were placed just under the load cells and on top of the spreader beam. Figure 2 shows the actual lab test setup. The horizontal actuator (shown on the right in this figure) is a servo hydraulic ram. This actuator has a built-in load cell to measure the horizontal load needed to slide the specimens. It also has built in sensors that measured the horizontal displacement, the speed, and the number of cycles continuously during the testing.

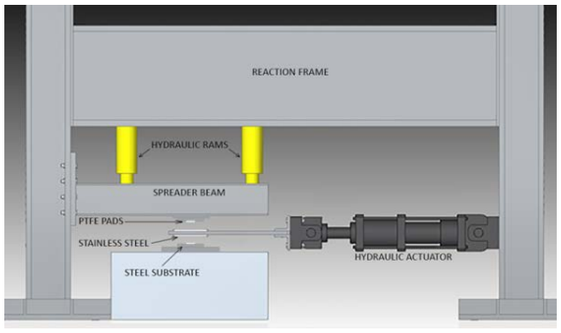


Figure 1. General test setup (schematic)

When using sliding bearings in a bridge slide, the PTFE bearing pads are placed on a track with the PTFE surface facing up. There is a mating surface slide shoe on the underside of the superstructure of the bridge that slides across the PTFE bearings. However, with the setup in the lab, two PTFE pads and two mating surface plates were used in order for the system to work properly and not have any extra resistance from the use of a roller or some other type of setup.



Figure 2. General test setup (actual)

Initially the plan was to attach the PTFE pads to the steel tongue and push them back and forth sliding along the stainless steel plates, which would create an eccentric loading on the pads as they slid from one end of the stroke to the other. To avoid this eccentricity, it was decided to keep the pads stationary by attaching them to the spreader beam above and the concrete block. Then, the mating surface plates were attached to both sides of the steel tongue and slid back and forth. Figure 3 shows how the mating surface plates and PTFE were attached and sandwiched together. The steel substrates, used to confine and hold the PTFE, were tack welded to the spreader beam and large plates below on the concrete block. The friction between the large steel plates and the concrete block was always higher than the friction between the PTFE pads and mating surface, which kept the base plate from sliding on top of the concrete block.



Figure 3. Test setup showing PTFE pads attached to steel substrates, and stainless steel sheets attached to steel tongue

4 TEST RESULTS

4.1 *Data Acquisition and Data Processing*

Two data acquisition units were used to collect the data. The MTS ram had its own system set up to it, and the two vertical rams were hooked up to a separate system. The vertical data acquisition only measured the vertical force for both vertical rams and time. The MTS data acquisition was set up to measure the horizontal forces, horizontal displacement, cycle count, and time at 100 samples per second.

The sliding speed was set to be constant at 254 mm/min. The ram was set to push the samples back and forth ± 25.4 mm, corresponding to a stroke of 51 mm. In order to produce a sliding speed, the MTS actuator was programed to run a ramp waveform instead of a s inewave or square wave. As the ram reached the end of the stroke, it switched directions and started moving the other way. When this change in direction happened, the force required to push the ram spiked higher due to the static friction. Figure 4 shows a graph of the horizontal force on the y-axis and displacement on the x-axis. This graph shows all 101 cycles for the test. The highest spike in force on the left hand side was the static friction for the first cycle. The force decreased suddenly after the first cycle, and then slowly continued to decrease as the cycles (or slide path) increased. It is easier to see the trend of the force decreasing over time when the cycles are spread out on a force versus time plot. Figure 5 shows the first 12 cycles of a test. The static friction was the highest on the first cycle, and then decreased slowly for each progressing cycle.

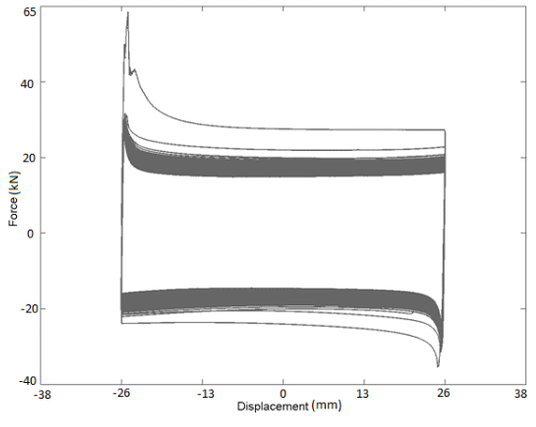


Figure 4 Typical graph of force versus displacement for all 101 cycles

COF is calculated using the following:

$$COF = F/(2 \times N) \quad (1)$$

where N is the normal force based on the contact pressure and F is the horizontal force and the two accounts for the two sliding surfaces in the test setup. When the COF is plotted, as shown in Figure 4, it looks much like the last plot of force vs time but with different values.

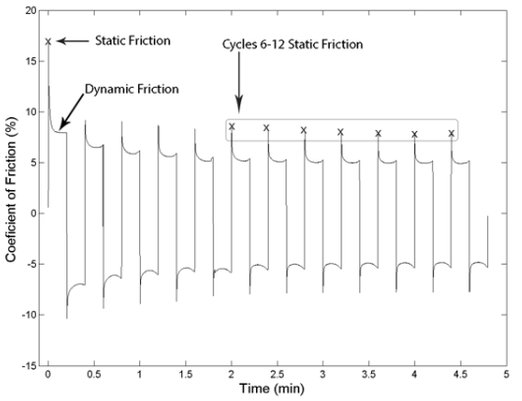


Figure 5 Typical plot of the coefficient of friction versus time (cycles 1-12)

The static friction is the amount of friction that keeps an object from moving. Dynamic friction is the friction present once the object is in motion. The dynamic friction is always lower than the static friction, therefore, the static friction values were critical and the focus of this study. In each test, COF values correspond to cycles one through 12, and cycle 101 was recorded.

After the testing was complete, the COF values were determined using equation (1). Table 1 shows the acronyms used in this paper to describe the performed tests.

Table 1 Acronyms used in test codes to identify parameters used for each test

Term	Description
2B	Stainless steel a #2B surface finish
RR	Stainless steel with a #1 surface finish, rough rolled (RR)
CS	Carbon steel
D	Dry test
Sp	Lubricant Soap
Grs	Lubricant Grease
Oil	Lubricant Oil
Gph	Lubricant Graphite

Static COF values for the performed tests are shown in Table 2. Note that not all the possible cases were tested.

Table 2 Static COF values (cycles: 1, mean of 6-12, and 101)

Roughness	**2B**			**RR**			**CS**		
Cycle	1	6-12	101	1	6-12	101	1	6-12	101
	11 MPa (contact pressure)								
D	-	-	-	14.12	6.53	5.85	-	-	-
Sp	5.66	2.28	2.84	24.25	6.99	4.05	18.35	7.63	4.63
Grs	5.15	0.99	1.55	4.20	2.81	3.26	6.86	4.30	3.81
Oil	4.04	1.05	1.49	16.07	5.92	3.10	20.15	6.22	4.32
	21 MPa (contact pressure)								
D	16.76	7.93	6.81	-	-	-	-	-	-
Sp	2.18	1.27	1.87	-	-	-	-	-	-
Grs	2.02	0.55	1.11	-	-	-	-	-	-
Oil	1.51	0.87	1.09	-	-	-	-	-	-
	31 MPa (contact pressure)								
D	12.1	4.90	4.75	4.10	2.47	2.33	-	-	-
Sp	2.45	1.20	1.57	5.02	3.97	3.49	7.05	3.27	2.01
Grs	1.06	0.46	0.81	4.11	2.28	2.92	2.75	1.73	1.72
Oil	2.75	0.77	0.79	5.99	2.60	1.47	6.85	3.19	1.86
Gph	9.49	9.67	6.12	-	-	-	-	-	-
	55 MPa (contact pressure)								
D	2.94	0.88	0.69	-	-	-	-	-	-
Sp	1.44	0.88	1.26	-	-	-	-	-	-
Grs	0.67	0.32	0.47	-	-	-	-	-	-
Oil	0.90	0.46	0.47	-	-	-	-	-	-

4.2 *Dry Tests*

Dry tests were performed using #2B and #1 stainless steel. No dry tests were performed on the carbon steel. Figure 6 shows typical dry tests that used the smaller #2B stainless steel sheets.



Figure 6. Dry test which used dimpled PTFE

4.3 *Soap*

A grocery store available dish soap was applied to both the PTFE pads and the stainless steel or steel plates. Dimpled PTFE pads were used for all of the soap tests. Figure 7 shows a typical picture of how much soap was applied to the PTFE and Stainless steel or steel.

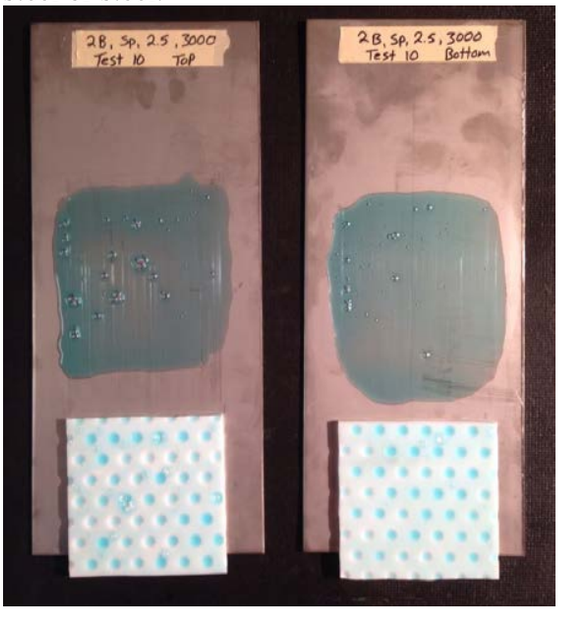


Figure 7 Typical soap test. Shows how much soap was applied to the sliding surfaces

4.4 *Grease*

Dimpled PTFE pads were used for all of the grease tests. A thick layer of grease was applied to the PTFE pads so that all of the dimples were filled and there was an even layer of grease on the pad. A layer of grease was also applied to the stainless steel

and carbon steel plates. Figure 8 shows the before and after picture for one of the grease tests. Even though the majority of the grease would get pushed off to the side, the sliding surfaces stayed lubricated throughout the tests.



Figure 8. Typical grease test. Grease was applied to PTFE pads and stainless steel or steel plates.

4.5 *Oil*

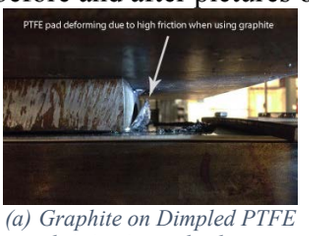
The type of oil used for the testing was 10W-40 automotive engine oil. An adequate layer of oil was applied to the specimens and the tests seemed to stay well lubricated throughout the testing. Figure 9 shows a typical oil test.



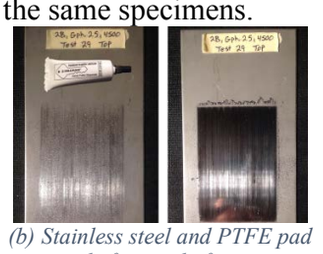
Figure 9. Typical Oil test. Shows oil on PTFE and stainless steel before testing

4.6 *Graphite*

For the graphite tests, standard tubes of powdered graphite were used. Both the PTFE and the stainless steel were coated with the graphite. Only two tests were done with graphite due to its poor performance as a lubricant. The first graphite test was performed using excessive amounts of graphite on the pad to compensate for losses and high COF values were observed. This led the PTFE pads to deform significantly (Figure 10a). It was suspected that there was too much graphite put on the test specimens and that using smooth PTFE instead of dimpled would possibly give better results. For the next graphite test that was performed, smooth PTFE pads were used instead of dimpled, and only a light even coating of graphite was applied to see whether COF values would decrease. Figure 10b is a picture of the stainless steel and PTFE pad used on top. This shows the before and after pictures of the same specimens.



(a) Graphite on Dimpled PTFE pad sitting in steel substrate



(b) Stainless steel and PTFE pad before and after

Figure 10. Graphite test

4.7 *Future Work*

Additional testing and analysis is recommended in order to more fully populate the expected friction values for various surfaces and lubricants. The effects of temperature are also of interest.

5 CONCLUSION

In this study, three parameters influencing the coefficient of friction (COF) for sliding bearings, which use PTFE-Steel sliding interfaces, were investigated. This research focused on testing the effects each of these parameters have when using PTFE sliding bearings for Slide-In-Bridge Construction (SIBC). The tested parameters were: (1) Surface Roughness, (2) Lubrication, and (3) Contact Pressure.

5.1 *Surface Roughness*

There were three surfaces roughness tested: stainless steel with a #2B surface roughness (2B), rough rolled stainless steel that has a #1 surface roughness (RR), and standard carbon steel (CS) which is readily available at construction sites. As expected, the #2B stainless steel resulted in lower COF values than the rough rolled stainless steel, followed by the carbon steel.

5.2 *Lubricants*

The lubrications that were tested were standard liquid dish soap, dielectric silicone grease (SAE-AS8660), automotive motor oil (10W-40 viscosity), powdered graphite, and dry tests. The dry tests and graphite tests had very high friction values, whereas

the soap, grease, and oil all resulted in low and comparable friction values.

5.3 *Contact Pressure*

It has been well documented by other researchers that as contact pressures increase, the COF values typically decrease when using PTFE bearing pads. The testing for this project produced results that agree with this pattern.

Acknowledgement

This work was sponsored in part by the American Association of State Highway and Transportation Officials in cooperation with the Federal Highway Administration and was conducted by the National Cooperative Highway Research Program, which is administered by the Transportation Research Board of the National Academies. The opinions and conclusions expressed or implied are those of the authors and not necessarily of the sponsoring programs.

This publication was supported in part by a subcontract from Rutgers University, Center for Advanced Infrastructure and Transportation (CAIT), under DTFH62-08-C-00005 from the U.S. Department of Transportation-Federal Highway Administration (USDOT-FHWA). Any opinions, findings, and conclusions or recommendations expressed in this publication are those of the author(s) and do not necessarily reflect the views of Rutgers University or those of the U.S. Department of Transportation-Federal Highway Administration.

The authors would also like to thank the D.S. Brown Company and R.J. Watson, Inc. for providing specimens for this testing.

REFERENCES

Caltrans (1994) *Memo to Designers 7-1*. California Department of Transportation.

NCHRP (1999). High-Load Multi-Rotational Bridge Bearings, NCHRP Report 432.

Wipf, T.J., Phares, B.M., Abendroth, R.A., Wood, D.L., Chang, B., and Abraham, S. (2004). *Monitoring of the Launched Girder Bridge over the Iowa River on US 20,* Iowa State University, Ames, IA, pp 100.

Ralls, M., Tang, B., Bhidé, S., Brecto, B., Calvert, E., Capers, H., Dorgan, D., Matsumoto, E., Napier, C., Nickas, W., Russell, H. (2005). *Prefabricated Bridge Elements and Systems in Japan and Europe.* Alexandria, Virginia, pp xii, 13.

FHWA (2007). *Manual on the Use of Self-Propelled Modular Transporters to Remove and Replace Bridges*, Project FHWA-HIF-07-022, U.S. Department of Transportation, Federal Highway Administration, Washington, D.C., pp 118.

LaViolette, M., Wipf, T., Lee, Y., Bigelow, J., Phares, B. (2007). *Bridge Construction Practices Using Incremental Launching,* Iowa State University (ISU), Ames, Iowa, pp 106.

Iowa DOT (2009). Iowa Department of Transportation Accelerated Bridge Construction Workshop: Workshop Report, Iowa Department of Transportation, Ames, IA, pp 87.

UDOT (2009). *Accelerated Bridge Construction SPMT Process Manual and Design Guide,* Utah Department of Transportation, Salt Lake City, Utah, pp 84.

Ardani, A. A., Lindsey, R., Mallela, J. (2010) *One-Weekend Job, Rapid Removal and Replacement of 4500 South Bridge in Salt Lake City, Utah.* Transportation Research Board, Utah.

Rosvall, E., Halling, M. (2010). Data Analysis of Utah's I-80 Bridges – For the Use in the Development of Accelerated Bridge Construction Standards. Utah State University, Logan, Utah, pp 90.

Rosvall, E., Halling, M., Lindsey, R. (2010) *Induced Stresses from Lifting and Moving Highway Bridges with Self-Propelled Modular Transporters.* Utah State University, Logan, Utah, pp 17-25.

Taylor, J.C., Stanton, J.F. (2010). *Friction Coefficients for Stainless Steel (PTFE) Teflon Bearings*, University of Washington, Seattle WA, Wisconsin Department of Transportation, Madison WI, Federal Highway Administration, Washington DC.

Culmo, M. (2011). Accelerated Bridge Construction – Experience in Design, Fabrication, and Erection of Prefabricated Bridge Elements and Systems, CME Associates, Inc., East Hartford, Connecticut, pp 347.

Kim, S., Holub, C., Elnashai, A. (2011) *Analytical Assessment of the Effect of Vertical Earthquake Motion on RC Bridge Piers.* American Society of Civil Engineers (ASCE), Vol. 137, pp 252-260.

FHWA (2013). *Slide-In Bridge Construction Implementation Guide*, Project: F-ST99 (232), U.S. Department of Transportation, Federal Highway Administration, Washington, D.C., pp 168.

Strategic Highway Research Program 2 (2013a). *ABC Standard Concepts: The Lateral Slide – Addendum to Innovative Bridge Designs for Rapid Renewal: ABC Toolkit,* SHRP2 Renewal Project R04, Publication Draft, Transportation Research Board, Washington D.C., pp 70.

Strategic Highway Research Program 2 (2013b). *Innovative Bridge Designs for Rapid Renewal: ABC Toolkit*, SHRP2 Report S2-R04-RR-2, Transportation Research Board, Washington D.C., pp 323.

Wisconsin DOT (2013). *WisDOT Bridge Manual,* CH 7-Accelerated Bridge Construction, Wisconsin Department of Transportation, Madison, USA.

Aktan, H., Attanayake, U., Mohammed, A. (2014). *Accelerated Bridge Construction and Structural Move – Workshop,* Western Michigan University, Kalamazoo, MI, pp 50. https://www.michigan.gov/documents/mdot/RC1610_Appendix_D-Part_I_464549_7.pdf.

AASHTO. (2014). *AASHTO LRFD Bridge Design Specifications*, Seventh Edition, American Association of State Highway and Transportation Official, Washington, DC.

Maintenance, Safety, Risk, Management and Life-Cycle Performance of Bridges – Powers, Frangopol, Al-Mahaidi & Caprani (Eds)
© 2018 Taylor & Francis Group, London, ISBN 978-1-138-73045-8

Dynamic Effects Caused by SPMT Bridge Transport

S. Dorafshan, M. Maguire, M. Halling, & P. Barr
Department of Civil and Environmental Engineering, Utah State University, Logan, Utah, USA
M. P. Culmo
CME Engineering, East Hartford, CT, USA

ABSTRACT: This paper studies the dynamic effects of Self Propelled Modular Transporter (SMPT) movement for the purposes of Accelerated Bridge Construction. First, accelerometers were attached to a SPMT and different motion cases were simulated in three loading conditions. For the out-of-plane direction, driving the SPMT over rough terrain provided the Peak Platform Acceleration (PPA) while start-and-stop motion was controlling for the in-plane direction. In the out-of-plane, accelerations were related to SPMT transport speed. The in-plane accelerations were not affected by the speed of the SPMT, but were affected by the ability of the operator to perform a smooth braking operation. Out-of-plane accelerations can be reduced by limiting the SPMT speed; however, in-plane accelerations may need to be reduced because some level of damage is likely acceptable to the falsework in a similar manner currently used for AASHTO LRFD earthquake design. The SPMT movement had a larger impact on the system as the total weight of the system decreased, both in out-of-plane and in-plane directions.

1 INRODUCTION

Bridges are vital elements of the United Stated transportation grid. With average age of 42 years, more bridges are on the verge of repair and replacement (Infrastructure Card, 2017). Bridge construction can be time-consuming so traffic delays and congestions that happen during the construction impose extra cost on the transportation agencies and passengers. According to Culmo (2011), Accelerated Bridge Construction (ABC) methods are defined as construction "that uses innovative planning, design, materials, and construction methods in a safe and cost-effective manner to reduce the onsite construction time that occurs when building new bridges or replacing and rehabilitating existing bridges." Using ABC methods reduces impact on mobility and onsite construction time, and increases the safety and construction quality. Common strategies in ABC are Prefabricated Bridge Elements and Systems (PBES), Geosynthetic-Reinforced Soil-integrated Bridge System (GRS-IBS), and Slide-In Bridge Construction (SIBC). ABC strategies are gaining popularity among state Departments of Transportation (DOT). A survey in 2015 indicated that 16 out of 31 states' that responded used ABC for 6 or more past projects(Ofili, 2015). ABC has five categories including structure placement methods which can be performed using Self Propelled Modular Transporters (SPMTs). According to the Federal Highway Administration, a SPMT is "a combination of multi-axle platforms operated through a state-of-the-art computer-controlled system that is capable of pivoting 360 degrees as needed to lift, carry, and set very large and heavy loads of many types" (FHWA, 2017). Using SPMTs reduces traffic disruption, speed-up the construction process, improves the quality of construction, and provide more options for constrictors (FHWA, 2007). SPMTs were introduced to the bridge industry in 2008 and are mainly used to transport superheavy bridges from a prefabrication site to their final position. Each SPMT module can be attached to the other modules for moving very large structures, forming a combination of multi-axle platforms operated by computer interface (Bellon 2017).

The bridge transportation process falls in the temporary works category which usually is performed and designed by contractors. SPMTs move at a walking speed, but the dynamic forces applied to the cargo during the transportation, especially in an emergency situation, can be an issue. Sudden stops, turns, and rotations can occur during transport and there is currently limited guidance for this in design. These dynamic forces are typically the responsibility of the contractor and the design engineer. To investigate the dynamic effects of SPMT movement to the bridge and falsework, the authors conducted a series of experiments.

2 EXPERIMENT

2.1 *Direction of Accelerations*

The maximum acceleration can happen in three directions in a 2-D plane, i.e. SPMT platform, longitudinal, transverse, and vertical. Therefore, to get the full acceleration field at any location on the platform, three accelerometers are required. On the other hand, the acceleration profile may change in different locations of the platform. Thus, three locations were instrumented, front and back on the platform, and middle on t he weights. Each accelerometer was mounted magnetically to measure one of three principle directions. Positive longitudinal is defined as the forward direction of the SPMT. Positive transverse is defined as perpendicular to the longitudinal direction on the platform plane, using the right hand rule with positive vertical defined as opposite of gravity (i.e. up). The direction of each sensor is shown in Table 1. The sensor placements and clusters are shown in Figure 1. Data acquisition system and sensors were made by Bridge Diagnostics Incorporated (BDI).

Table 1. Accelerometer's placement on the SPMT

Position	Accelerometer	Direction
	A2130	Longitudinal
Cluster 1	A2131	Transverse
	A2132	Vertical
	A2133	Longitudinal
Cluster 2	A2089	Transverse
	A2090	Vertical
	A1036	Longitudinal
Cluster 3	A1035	Transverse
	A2087	Vertical

2.2 *Load Cases*

During this experiment, the weights shown in Figure 2 were used to replicate the weight of a bridge superstructure. The vehicle was loaded with two stacks of crane counter weights: nine steel plates on one side and eight on t he other side. Each individual plate weighed 50 kN (Figure 2). Additionally, a steel platform on which the weights were placed weighed 150 kN, thus the total load on the SPMT was 10,000 kN. In the case shown in Figure 2, the SPMT carried 50% of its capacity which is referred to as the heavy load case. Four and five steel plates were removed from the SPMT to simulate medium load case. The medium load case was when the SPMT carried 5,000 kN or 25% of its capacity. After removing all steel weights, the total weight on the SPMT was only 150 kN which was 7.5% of its total capacity, which was called the light load case.

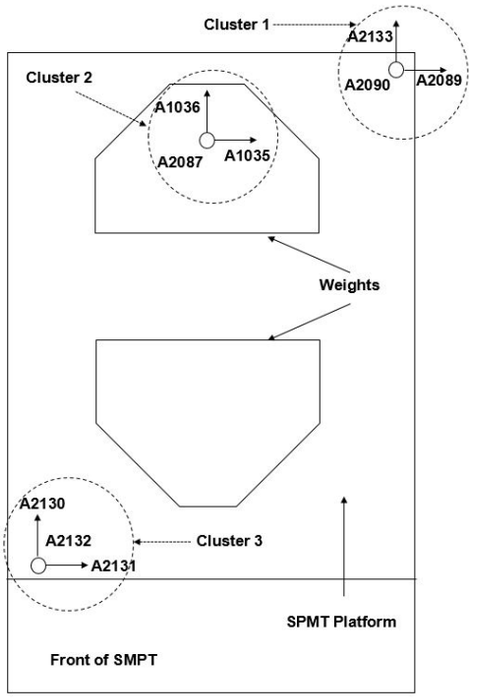


Figure 1 Schematic plan view of the sensor's placement



Figure 2. The steel weights on SPMT (heavy load case)

2.3 *Motion Cases*

The following scenarios, referred to as motion cases, were defined and investigated to cover all possible extreme events during the cargo transport:

- "Start and Stop" (SS): A sudden brake or a rapid take off can cause considerable longitudinal accelerations. This scenario is considered the most common event and can occur several times during one carriage, although typically not to the extreme.
- "Up and Down" (UD): Bouncing of the vehicle can cause significant acceleration in vertical direction. This may occur during raising or lowering of the cargo into place.

- "90 Degree Turn" (90): Turning while moving a bridge superstructure on the road can create both longitudinal and transverse accelerations.
- "Long Run" (LR): During a transport, it is possible to encounter uneven ground or the weight of the loaded SPMT can create uneven ground in poorly prepared roadbed. This motion case is characterized by a long run of road unevenness with locations of well and poorly compacted soil, causing significant vertical accelerations.
- "Rotation" (R): SPMTs can rotate 360 degrees causing accelerations in horizontal directions.

For each load case, defined in section 2.2, all the above motion cases where carried out. A schematic drawing of all performed tests is shown in Figure 3. As seen, in each load case, one UD, one R, one 90, two LRs, and four SSs were carried out. In addition, each SS motion case included three sudden start and stops.

2.4 *Peak Platform Accelerations*

After the test, the data was post-processed to obtain the Peak Platform Accelerations (PPA) in each direction and in each motion case. Table 2 shows the recorded PPAs in each direction for all clusters and load cases. In addition, the critical motion case in which a certain PPA was recorded was also identified. As the cargo weight decreased, the platform experienced greater accelerations. The maximum accelerations were similar between motion and load cases. The largest difference was observed in the transverse directions for the R motion which was likely affected by the evenness of the driving surface. The SS motion case was critical motion for the in-plane accelerations by imposing maximum accelerations in all sensors and all load cases. For transverse direction maximum accelerations occurred during the LR motion case for all load cases in three clusters expect in cluster 2 in medium load case. The SS motion case created the largest vertical accelerations as well, however it is unclear if they would be present in a series of linked SPMTs transporting a large bridge.

Figure 4 shows the time history graphs for critical cases identified in Table 2 in each cluster of sensors. As seen in the graphs, the longitudinal accelerations were considerably greater than transverse ones. The maximum longitudinal accelerations were also consistent with the SS motion case; therefore, the SS motion case can be used to represent the maximum in-plane accelerations. The SS motion was also the dominant motion case for the out-of-plane direction.

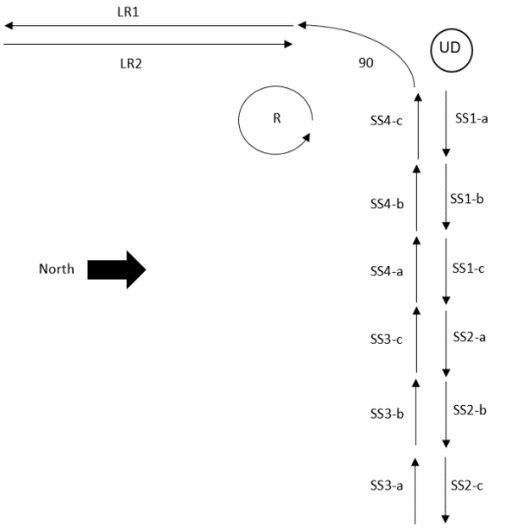
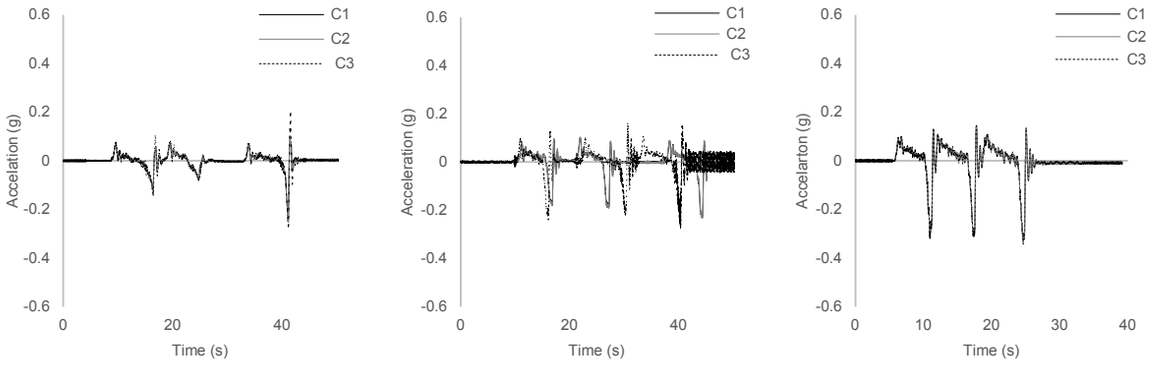


Figure 2 The schematic layout of the tests for each load case

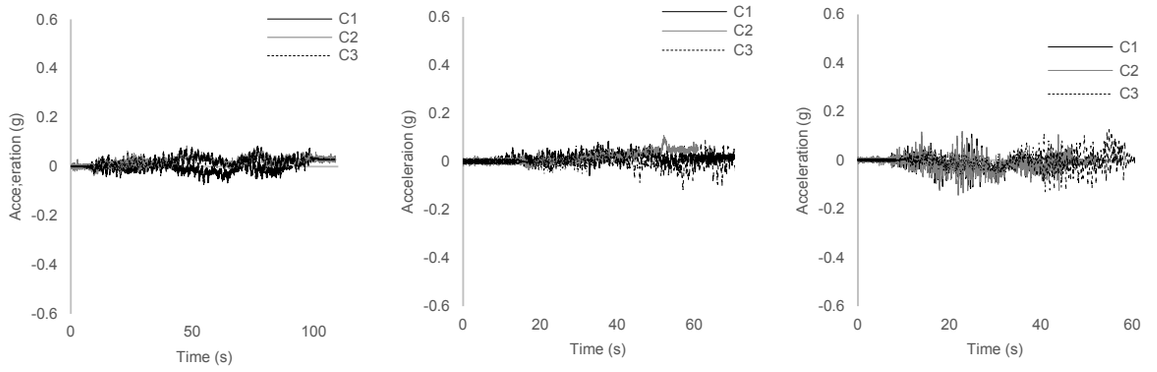
Maximum out-of-plane accelerations were considerably higher in the SS motion than any other. However, this is somewhat misleading because of the rotation of the platform during the starting and stopping maneuver. During a stop, vertical accelerations were generated by the rotation of the platform about some point between the center of the platform and the back axle, due to the heavy power pack attachment. During a large bridge move it was assumed that more than one SPMT will be linked, whether directly attached or through the attachment of the falsework and bridge assembly. By linking the SPMTs this rotation was assumed to be restrained significantly so only the in-plane readings from the Start and Stop Motion Case should be considered for design values. Maximum out-of-plane accelerations during the LR motion were caused by the velocity of the SPMT navigating uneven ground. For this reason, the out-of-plane accelerations from the LR motion were considered critical to design. Maximum longitudinal accelerations were significant in the LR motion, but rarely controlling simply based on the maximum measured accelerations. The maximum vertical accelerations during the LR motion is shown in Table 3. The time history graphs associated with the out-of-plane PPA is shown in Figure 5.

Table 2 Recorded PPAs in each direction for all clusters

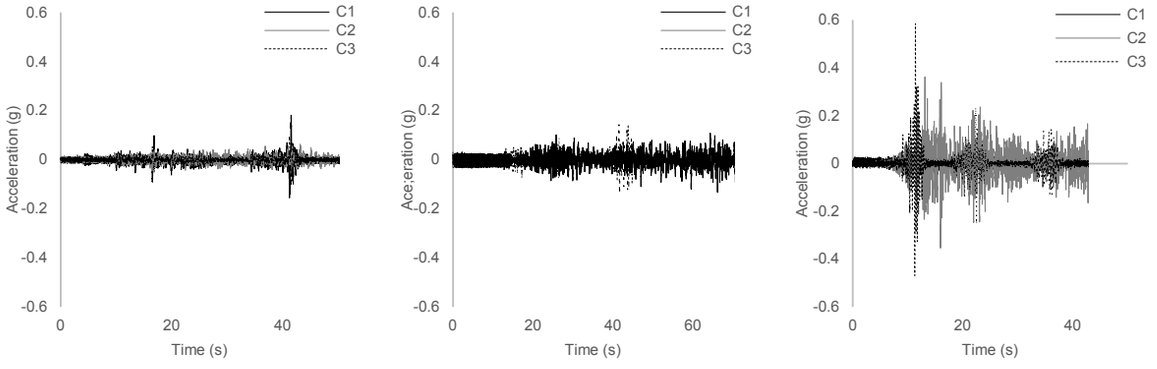
Cluster	Principle Direction	PPA (g)			Critical Motion		
		Heavy	Medium	Light	Heavy	Medium	Light
Cluster 1	Longitudinal	-0.25	-0.23	-0.33	SS	SS	SS
	Transverse	-0.07	0.08	-0.12	LR	LR	LR
	Vertical	0.18	0.11	-0.29	SS	LR	R
Cluster 2	Longitudinal	-0.25	-0.23	-0.34	SS	SS	SS
	Transverse	0.08	0.11	-0.14	LR	R	LR
	Vertical	-0.13	0.22	-0.57	SS	SS	SS
Cluster 3	Longitudinal	-0.27	-0.28	-0.34	SS	SS	SS
	Transverse	0.09	-0.12	-0.13	LR	LR	LR
	Vertical	-0.10	0.14	0.58	SS	SS	SS



(a) longitudinal-heavy *(b) longitudinal-medium* *(c) longitudinal-light*



(d) transverse-heavy *(e) transverse-medium* *(f) transverse-light*



(g) vertical-heavy *(h) vertical-medium* *(i) vertical-light*

Figure 3 Time history graphs of maximum accelerations during the tests

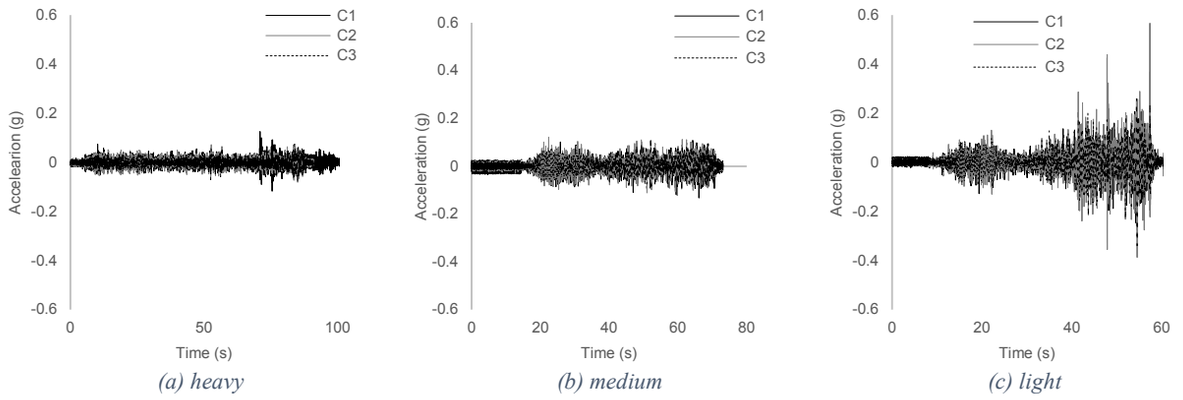


Figure 4 Time history graphs of the maximum vertical accelerations during the LR motion

Table 3 Maximum vertical accelerations recorded during LR motion

Cluster	Direction	PPA (g)		
		Heavy	Medium	Light
Cluster 1	Vertical	0.12	0.11	-0.24
Cluster 2	Vertical	-0.08	0.13	0.57
Cluster 3	Vertical	-0.07	0.12	-0.34

3 CONCLUSION

In this paper, the dynamic response of a loaded SPMT with 7.5%, 25, and 50% of its capacity was investigated during several common motion cases. It was found that traveling a long stretch of uneven ground was critical for the out-of-plane (vertical) direction (the Long Run) and rapid decelerations were critical for the in-plane (horizontal) direction (the Start and Stop). Transverse accelerations were found to not be critical for the in-plane direction. Increasing the payload of the SPMT decreased the measured accelerations significantly. Acceleration data was recorded from the platform in various locations during these motions.

The following conclusions can be made based on the testing and analysis of SPMT dynamic loads:

- Out-of-plane accelerations were controlled by the LR motion;
- Out-of-plane accelerations were related to SPMT transport speed;
- In-plane accelerations were controlled by the longitudinal direction of the SS motion.
- In-plane accelerations were not affected by the speed of the SPMT, but were affected by the ability of the operator to perform a braking operation;
- Transverse accelerations were considerably lower than the longitudinal accelerations, therefore longitudinal accelerations were considered the controlling case for the in-plane direction;
- Significant reductions in the PPA values were observed as payload increased. Contractors are recommended to use large loads, with respect to SMPT capacity, to reduce design forces;

ACKNOWLEDGEMENT

This work was sponsored in part by the American Association of State Highway and Transportation Officials in cooperation with the Federal Highway Administration and was conducted by the National Cooperative Highway Research Program, which is administered by the Transportation Research Board of the National Academies. The opinions and conclusions expressed or implied are those of the authors and not necessarily of the sponsoring programs.

This publication was supported in part by a subcontract from Rutgers University, Center for Advanced Infrastructure and Transportation (CAIT), under DTFH62-08-C-00005 from the U.S. Department of Transportation-Federal Highway Administration (USDOT-FHWA). Any opinions, findings, and conclusions or recommendations expressed in this publication are those of the author(s) and do not necessarily reflect the views of Rutgers University or those of the U.S. Department of Transportation-Federal Highway Administration.

REFERENCES

FHWA, (2007), Manual on U se of Self-Propelled Modular Transporters to Remove and Replace Bridges, Federal Highway Administration, https://www.fhwa.dot.gov/bridge/pubs/07022/hif07022.pdf.

Culmo, M. P. (2011). *Accelerated bridge construction-experience in design, fabrication and e rection of prefabricated bridge elements and systems* (No. FHWA-HIF-12-013). https://www.fhwa.dot.gov/bridge/abc/docs/abcmanual.pdf.

AASHTO. (2014). *AASHTO LRFD Bridge Design Specifications*, Seventh Edition, American Association of State Highway and Transportation Official, Washington, DC.

Infrastructure Card, (2017), https://www.infrastructurereportcard.org/cat-item/bridges/.

Ofili, Mike, "State of Accelerated Bridge Construction (ABC) in the United States" (2015). *University Honors Program Theses*. 118. http://digitalcommons.georgiasouthern.edu/honors-theses/118.

FHWA, (2017), https://www.fhwa.dot.gov/bridge/abc/spmts.cfm.

Bellon, W., Dorafshan, S., Maguire, M., Halling, M., & Barr, P., "Standardizing Accelerated Bridge Construction" (2017). *Research on C apitol Hill*. Paper 73. https://digitalcommons.usu.edu/roch/73

Maintenance, Safety, Risk, Management and Life-Cycle Performance of Bridges – Powers, Frangopol, Al-Mahaidi & Caprani (Eds)
© 2018 Taylor & Francis Group, London, ISBN 978-1-138-73045-8

Development of precast slab using ultra high strength fiber reinforced concrete for replacement on highway bridge

T.Kitamura, W.Zhao & I.Iwasaki
Taisei Corporation, Tokyo, Japan

M.Kishida & Y.Ishihara
Metropolitan Expressway Company Limited, Tokyo, Japan

I.Iwaki
Nihon University, Fukushima, Japan

ABSTRACT: The deteriorations of highway bridge concrete slabs constructed during the high economic growth period have become apparent. One of the efficient maintenance measures is to replace these slabs into new slabs. However, there is an obstacle that renewal work causes heavy traffic due to lane regulation for the replacing slabs. In addition, design standard has been revised due to increasing live load. Therefore, we need to develop new lighter slabs which has adequate strength for current standard, and develop efficient construction methods. From these reasons, in order to develop the precast panels using Ultra high strength fiber reinforced concrete (hereafter UFC) that are lighter than existing concrete slabs and the new connection system using perfobond strip shear connector between panels and steel girders, following several experiments were conducted. In this research, the behavior and durability of new panels and the connection systems were discussed.

1 INTRODUCTION

In Japan, a lot of infrastructures were drastically constructed from the high economic growth period of 1965. However, currently those constructions have been aging. In regard to the maintenance measures, replacement seemed to be an efficient measure instead of reinforcing and repairing structures. Particularly, bridge slabs have been simply deteriorating over time, in addition they have been suffering fatigue damage due to the repeated load caused by traffic of overload vehicles and increasing volumes. Therefore, the deterioration became apparent. In this research, we discussed a new slab replacement system for efficient renewal construction.

The age of most existing damaged slabs is over 40 years. Design standards of construction bridges have been revised by the change of the load regulation. The new slabs designed based on current standards are usually heavier and thicker than the existing slabs which are designed based on previous standards. If new replacing slabs are designed on current standards, the increase in weight of new superstructures causes reinforcement of substructures. Furthermore, traffic regulations during the replacing construction seems to cause heavy traffic congestion around the construction area. To overcome these problems, it is necessary to develop lightweight slabs in order to minimize effects on substructures and rapid replacement method in order to keep traffic safety and smooth. In this study, the structure of new precast panels and the new connections between panels and girders were developed. The behavior and durability of the new slab system were verified by experiments results.

2 THE STRUCTURE OF NEW PRECAST SLAB

A developed slab was designed for a single-span, 30 m long and 8.2 m wide, bridge as a replacement for an existing bridge at Tokyo Metropolitan Expressway. The type of superstructures was steel plate girders bridge, composed of three main girders with concrete slabs. Both existing slabs and new slabs were connected to the existing girders rigidly, and they behaved as composite girders.

The new structure was designed on the basis of Japanese Specification of Highway Bridges (Japan Road Association 2012) and UFC Guideline (Japan society of Civil Engineers 2004) (Fig. 1).

In order to make new slabs lighter, the ultra high strength fiber reinforced concrete (hereafter UFC) was used. The slabs had transverse and longitudinal ribs at the bottom of flat slabs. Pre-stressed concrete steel strands (hereafter PC strands) and pre-stressed concrete steel bars (hereafter PC bars) were also installed in those ribs.

UFC has compressive strengths of above 180 MPa, tensile strength of above 8 MPa, young modulus 50 N/mm^2. It contains 2% volume steel fiber reinforcement that is 15 mm long and no coarse aggregate. Its water-cementitious material ratio is less than 0.2.

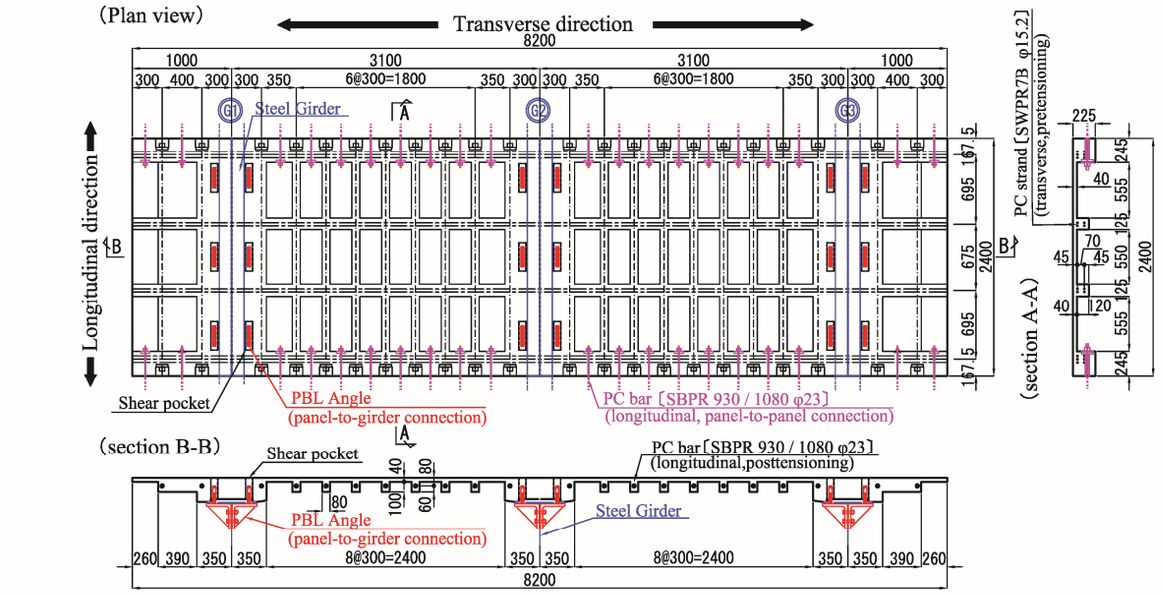


Fig. 1 dimensions of precast UFC panel

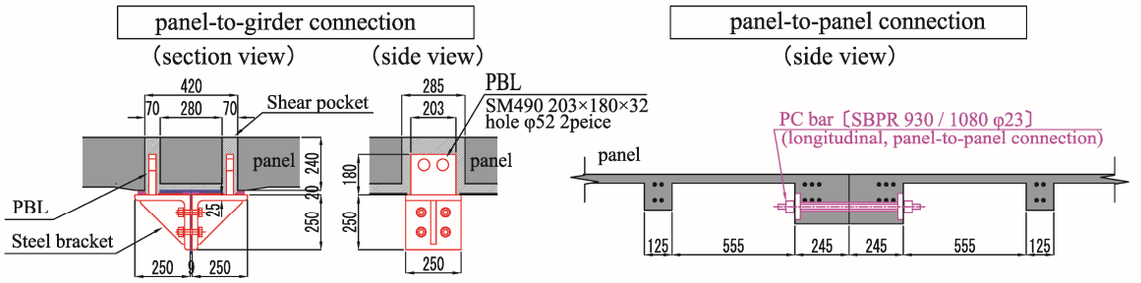


Fig. 2 detail of connections

The precast UFC panel was totally 225 mm thick and consisted of a 40 mm thick slab plates cast integrally with 120, 100 mm depth concrete ribs spanning in transverse, longitudinal direction in general section, respectively. In addition, the ribs were 185 mm depth at the part of panel-to-panel connection and panel-to-girder connection.

PC bars were SBPR 930/1080 (in Japanese Standards) (φ 23 mm), one PC bar was placed in every longitudinal rib and stressed by posttension method. PC strands was SWPR 7B (in Japanese Standards) (φ 15.2 mm), and 4 strands were placed in inner 2 ribs and 6 strands were placed in both outer ribs in transverse direction. All transverse PC strands were stressed by pretension method.

In actual construction, the precast UFC panels are fabricated by short line match casting method in precast concrete plants, shipped to jobsites, and placed on the girders. Then panel-to-panel and panel-to-girder connection are carried out (Fig. 2). The panel-to-panel connections are connected by tensioning with short PC bars (SBPR 930/1080φ, 23 mm).

In conventional method, the shear connectors of the panel-to-girder connections were set up on girders after removing the existing slabs. The method was not efficient in the point of rapid construction because a series of works was continuously conducted on girders, for example, cleaning the top flange of girder, welding studs on the flanges, installing new slabs. In order to accelerate these site work, the panel-to-girder connections using perfobond strip shear connector (hereafter PBL) was developed (Fig. 2). PBLs are combined with the fabricated steel brackets by welding (hereafter PBL angle). PBL angles are installed on the web of girders with bolts prior to setting panels. After setting panels, PBLs are placed in shear pockets of panels. The space in shear pockets and between panels and girders are quickly filled with shrinkage-compensating mortar as filling material. The new connection had no rebar in the hole of PBLs.

The depth of these UFC panels designed in this study was 144 mm in average, and the weight of the panels was lighter about 30% than precast conventional pre-stressed concrete slabs designed based on current specification.

3 PUSH-OUT TEST FOR THE PANEL-TO-GIRDER CONNECTION

3.1 *Objectives of test*

The new connection using PBL angles was applied to the panel-to-girder connection. Moreover, in Japan, the shear capacity of PBL was regulated except for the end-bearing effect (Japan society of Civil Engineers 2014). Thus, those experiments aimed to verify the shear capacity by the new connection and the effectiveness of concrete end bearing.

3.2 *Test variables and material properties*

Figure 3 shows the dimensions of the specimen. PBL had a thickness of 32 mm, a height of 180 mm, and a length of 203 mm. Shear pockets had a width of 70 mm, a height of 210 mm, and a length of 285 mm.

In order to assess the shear capacity by the new connection and the effectiveness of concrete end bearing, two test cases were conducted. One case (case 2: full resistance), the shear capacity was due to the full resistance including dowel action and end bearing. The other case (case 1: no end bearing), the shear capacity was due to all resistance except for end bearing. (Fig. 3).

For material properties of UFC, the compressive strength, tensile strength, splitting tensile strength, modulus of elasticity were determined with 100 × 200 mm cylinders. For the one of shrinkage-compensating mortar, the compressive strength was determined with 50 × 100 mm cylinders (Table 1).

Table 1. Material properties at time of test initiation

	UFC panel	Mortar
Compressive strength (N/mm^2)	218.0	63.2
Tensile strength (N/mm^2)	14.0	-
Splitting tensile strength (N/mm^2)	9.1	-
Modulus of elasticity (kN/mm^2)	53.0	-
		PBL
Yield strength (N/mm^2)		357
Tensile strength (N/mm^2)		533

3.3 *Test method*

Taking actual construction in a jobsite, panels and panel-to-girder connections were cast in horizontal position. After that, the two panels were put in vertical position, two girders were connected with splice plates and bolts.

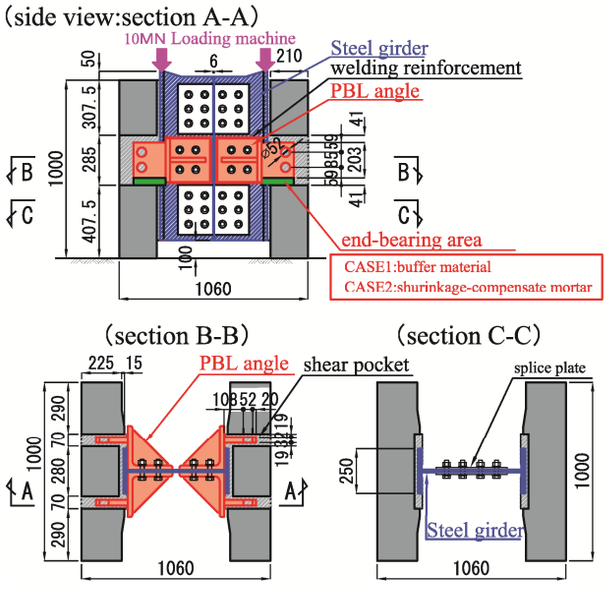


Fig. 3 the dimensions of specimen

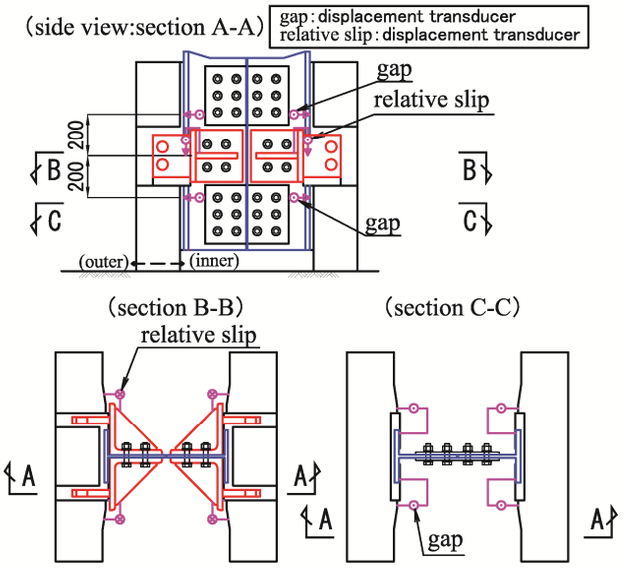


Fig. 4 the instruments

Loading method was as follows. The specimens were loaded cyclically by displacement control. This displacement presented the relative vertical slip between panels and PBL angles. The specimens were loaded and unload repeatedly every 0.2 mm until 1.0 mm, every 0.5 mm until 4.0 mm in the above relative slip. After the slip was over 4.0 mm, the specimens were loaded until failure.

The measurements of the tests were the value of load, the relative slip between girders and panels, and the horizontal gap of panels and girders (Fig. 4). The slips and the gaps were measured with displacement transducers.

3.4 *results*

The failure mode of the case 1, few cracks were observed on the surface of panels and pockets at the ultimate load. On the other hand, in the case 2, cracks were found out apparently. The two main cracks developed from the bottom edges of the PBL downward to expand a distance between each other.

Figure 5 shows shear force vs. relative slip between panels and girders. The slip presented the average value of 4 points. Y axis shows the shear force per a pair of PBLs, which was half magnitude of the load. For the target bridge, the equivalent of the design shear force owing to service load was 310 kN for a pair of PBLs. In contrast, the maximum shear forces measured were 668 kN (safety factor: 2.15) for case 1, 1281 kN (safety factor: 4.13) for case 2. In the case 1, the safety factor was less than that regulated by Japanese specification (Japan society of Civil Engineers 2014), which is more than 3.0.

In the case 1, the shear force increased initially with increasing slip. After the shear force reached a maximum (668 kN) at 1.43 mm of the slip, after that the shear force decreased gradually as the slip increased abruptly. Then, the shear force increased

gradually again and finally reached 553 kN at 10 mm of the slip. When the shear force was 310 kN that corresponds to the designed service state, no damage to the specimens was observed.

In order to ignore end bearing, buffer materials with a thickness of 41 mm were set under the PBLs in the pockets. Therefore, the bottom of PBLs did not reach the surface of pockets. So, dowel in the holes of PBLs resisted initially the shear force, and after cracks around dowel were generated, the resistance against sliding in the both interfaces of the crack maintained to resist partly the shear force.

On the other hand, in the case 2, when the shear force was 310 kN that corresponds to the designed service state, no damage to the specimens was observed same as case 1. Moreover, the shear force increased as the slip increased up to 10 mm of the slip. As shear force was increasing, PBL angle was also deforming. When the slip reached 10 mm, the deformation was very large and loading was stopped.

Figure 6 shows Shear force vs. horizontal gap between panel and girders. The gap presented each average of measurements of upper or lower side in the one side. In the both case, the gap of upper side was larger than that of lower side. It seemed that PBL angles were twisting inward.

According to several studies, when the types of experiments were conducted, the large rotation of slabs caused to make wrong estimate the shear capacity (Takahashi et al. 2015). Then, in the case 2, Figure 7 shows a picture of cutting surface in the side of PBL.

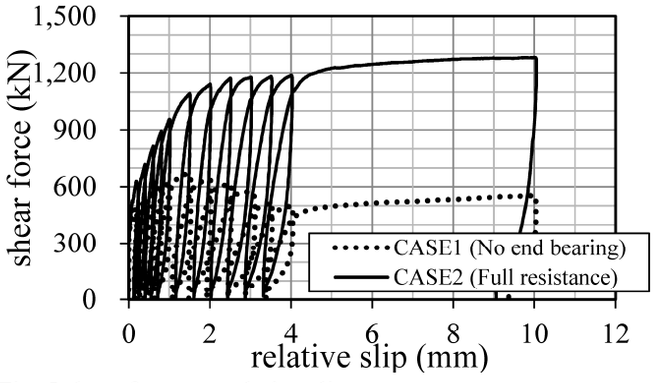


Fig. 5 shear force vs. relative slip

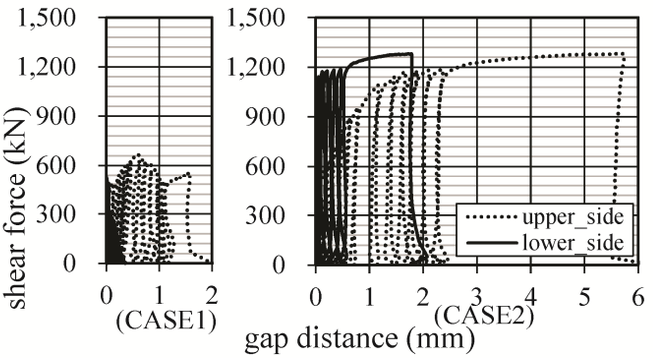


Fig. 6 Shear force vs. relative horizontal gap

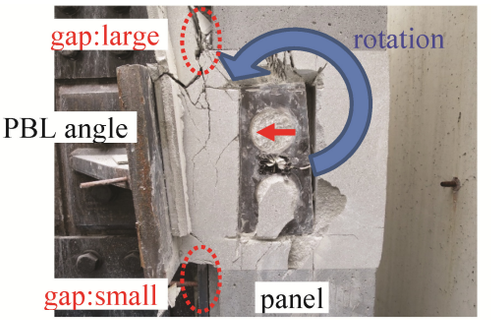


Fig. 7 cut section around PBL (case 2)

The upper hole in PBLs moved largely inside by rolling and the dowel in the hole was shear-fractured horizontally. However, the lower hole in PBL hardly moved, the dowel in the hole was not shear-fractured. In contrast, in the case 1, PBLs moved downward and the dowels in both holes were shear-fractured vertically. The panels remained nearly normal to the foundation in the both case. Judging from the above shear-fractured states of dowels, the deformation of PBL angles, and the states of panels, the results given by this experiment seems to be proper for the shear capacity.

3.5 *Comparison of test results and previous prediction*

In current specifications in Japan (Japan society of Civil Engineers 2014), concrete was used as filling material in pockets. Moreover, the proposed equation for shear capacity with PBL in Japan was based on the results of experiments without the effect of end bearing. Equation (1) was used when the hole of PBL was without a transverse rebar.

$$V_{psud} = 1.60 \cdot d^2 \cdot f'_{cd}/\gamma_b \qquad (1)$$

With $35\text{mm} \leqq d \leqq 90\text{mm}$, $12\text{mm} \leqq t \leqq 22\text{mm}$, $24\text{N/mm}^2 \leqq f'_{cd} \leqq 57\text{N/mm}^2$

where V_{psud} is the shear capacity at the hole (N), d is the diameter of the hole (mm), f'_{cd} is the compressive concrete strength (MPa), t is the thickness of the plate (mm), and γ_b is the member factor (=1.0).

According to Equation (1), the shear capacity of a pair of PBL was 1,094 kN.

On the other hand, there were many equations for shear capacity with PBL suggested by other researchers. For example, there were the equations suggested by Oguejiofor and Hosain (1994) and by Ahn et al. (2010). Most equations for shear capacity contained not only dowel action in the hole but also end-bearing effect. The equations were assumed that filling material in the shear pockets was concrete.

In this study, the new connection had twin PBLs. Then the results were compared with shear capacity that was calculated based on the equation for twin

PBLs suggested by Ahn et al. (2010). That was given by Equation following.

$$Q = 2.76h_{sc}t_{sc}f_{ck} + 1.06A_{tr}f_y + 3.32n\pi(d/2)\sqrt{f_{ck}} \quad (2)$$

where Q is the shear capacity at the shear connector (N), f_{ck} is the compressive concrete strength (MPa), A_{tr} is the area of the transverse rebar in the hole (mm^2), f_y is the yield strength of the transverse rebar (MPa), n is the number of holes, d is the diameter of the hole (mm), h_{sc} is the height of the plate (mm), and t_{sc} is the thickness of the plate (mm).

According to Equation (2), the shear capacity of a pair of PBL was 1,675 kN.

In Japan, PBLs were often used for connections between corrugated steel web and concrete slabs in pre-stressed concrete bridges. In this case, end bearing was not estimated because the steel plate of PBLs were continuous and there were no end-bearing zone. So end-bearing effect of PBL was not probably estimated for shear capacity. However, in terms of the new connections, since PBLs were set intermittently along girders, the end bearing seemed to be effective as other researchers suggested.

The shear capacity results (case 1), (case 2) obtained by experiments were compared to the shear capacity estimated by Equation (1), Equation (2), respectively.

The ratio of the experimental results to the estimated value were in the range of 0.6 to 0.8.

The causes of the shear-capacity reduction were probably not only that several parameters in the equation were out of the application range but also that shrinkage-compensating mortar used as a filling material, which had a few of aggregate interlock without coarse aggregate.

In each comparison, the differences between experimental results and estimated values were about 400 kN. If the main cause was lack of aggregate interlock, it was understood easily that the differences in the both case were almost same.

These results show that the end bearing acts effectively from the structure of the new connection. From the result of the case 2, the shear capacity of the new connection satisfies the safety factor regulated by above Japanese specification.

The connection proposed in this study should be expected the contribution of end-bearing effect of PBLs, and it should be expected that Japanese specification adopts that design. Moreover, for tight space between girders and panels, shrinkage-compensating mortar can be used effectively as a filling material. Therefore, it is necessary to investigate for the shear capacity of PBLs with shrinkage-compensating mortar.

4 FATIGUE DURABILITY TEST BY USING WHEEL RUNNING MACHINE

4.1 *objectives of test*

Bridge slabs was suffering the cyclic load of driving vehicles, and they were finally damaged by punching shear. Therefore, high fatigue durability was required for bridge slabs. In this study, in order to demonstrate the fatigue durability of the proposed precast UFC panels, fatigue durability test was conducted by using wheel running machine.

4.2 *Test variables and material properties*

The specimen consisted of two fabricated UFC precast blocks (2490 by 2800 by 225 mm, 1810 by 2800 by 225 mm). Their blocks were connected integrally by a line of transverse connection (Fig. 8).

The dimensions of specimens were based on the proposed UFC panel. The whole outer ribs which supported the specimen and connection area between two blocks were 225 mm thick. The inner area consisted of 40 mm thick slab cast integrally with 120 ,100 mm deep ribs spanning in transverse, longitudinal direction, respectively.

The amount of pre-stressing was determined based on the design of the precast UFC panel and introduced by posttension method.

Both blocks were fabricated by match casting method. After adhesive bonds are applied to their interfaces, which were connected at the next step, the blocks were placed facing each other. After that, they were pulled up each other and stressed by tensioning PC bar (SBPR 930/1080, (In Japanese Standard) φ 23mm) for the connection.

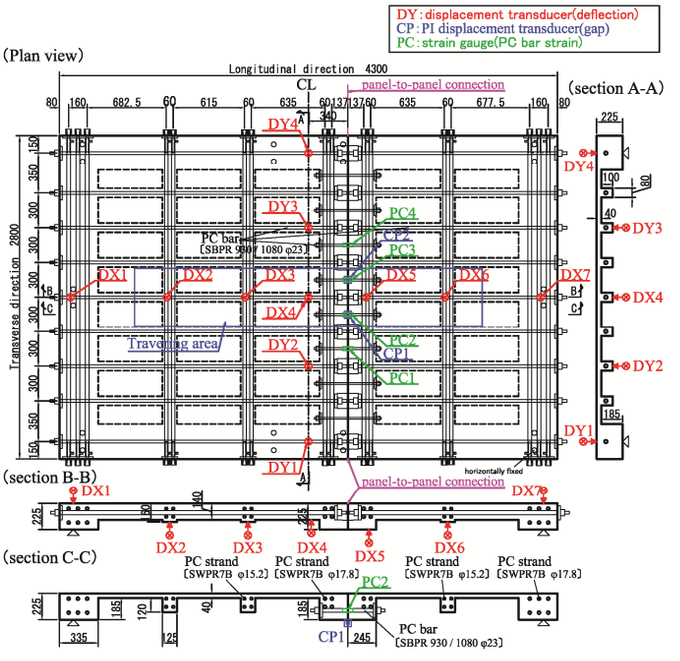


Fig. 8 the dimensions and measurements of specimen

For this experiment, the compressive strength, tensile strength, splitting tensile strength, modulus of elasticity were determined with 100 × 200 mm cylinders (Table 2).

Table 2. Material properties at time of test initiation

	UFC block	
Compressive strength (N/mm^2)	215.0	
Tensile strength (N/mm^2)	15.3	
Splitting tensile strength (N/mm^2)	11.7	
Modulus of elasticity (kN/mm^2)	52.1	
	PC strand	PC bar
Yield strength (N/mm^2)	1,027	1,795
Tensile strength (N/mm^2)	1,145	1,946

4.3 *test method*

The Wheel Running Machine had the steel wheel which was 320 mm wide and 750 mm in diameter, and the wheel was moved by crank mechanism and the traveling distance was 3,000 mm and 20 rpm (40 times loading per minute). the maximum load in vertical direction was 400 kN (Fig. 9).

Based on the loading program that conducted by Ministry of Land, Infrastructure and Transport in Japan (National institute for land and Infrastructure management 2002), fatigue durability test was performed for the specimen. In order to accelerate the loading experiment, the initial load was set as 157 kN, after that, the load was increased step by step. These loads were bigger than the live load (98 kN) specified for bridge design. Moreover, Static load test was conducted every 20,000 cycles. For static test, the loads at the stages were applied at the center of the specimen (Fig. 10).

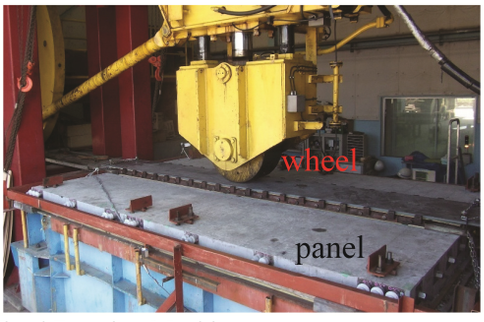


Fig. 9 Wheel Running Machine

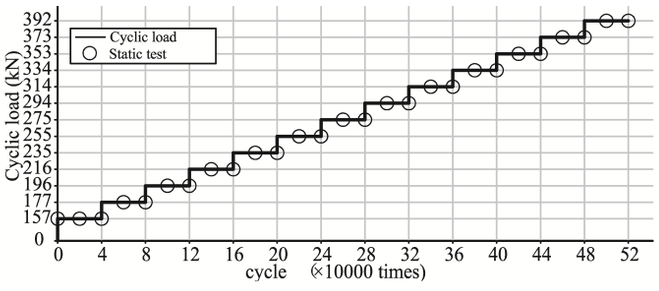


Fig. 10 cyclic program

The specimen was simply supported by pin with span length of 2,500 mm in longitudinal direction, and elastically supported by steel beam with span length of 3,900 mm in transverse direction.

The measurements of the test were the value of load, the vertical deflections in longitudinal and transverse direction, the horizontal gap, and the strain of PC bar for connection (Fig. 8). Vertical deflections, horizontal gaps, strains of the PC bar were measured with displacement transducers, PI displacement transducer, strain gauge, respectively.

4.4 *Results*

The development of cracking at the bottom of specimen was as follows. At 80,000 cycles of load (176.4 kN), cracks were found out at first at the bottom of two ribs in transverse direction. Next, with increasing cycles, cracks in the lower surface were gradually widening and propagating at transverse ribs, and then cracks were generating and developing in longitudinal ribs. Particularly, the range between DX2 (refer to Fig. 8) and DX3 was largely damaged. After that, at 447,500 cycles of load (372.8 kN), the vertical deflection at DX3 was developing drastically and the moving machine stopped owing to the limit of vertical deflection, which was set for 15 mm. Followed by, the state of upper and lower surface of the specimen was observed and it was determined that the specimen was critically damaged by punching shear.

After this loading test, all cracks were observed, and the specimen was cut in order to investigate the internal state (Fig. 11). In upper surface, the center point of the punching shear was about 850 mm away from the left side of specimen above the loading line and the cave-in on the upper surface was the range of 700 mm in diameter. In addition, several cracks were generated nearly horizontally in cut section of 40 mm thick slab. This was because the load was moving and shear cracks developed almost horizontally.

Figure 12 shows the distribution of deflections in two directions. These data of deflections were obtained by static load test. The distribution of vertical deflections in transverse direction had an approximately bilaterally symmetrical with respect to the center of the specimen. In contrast, in the similar distribution in longitudinal direction, the deflection of DX5 was slightly smaller than that of DX3 because the point of DX5 was located on the panel-to-panel connection, and transverse ribs close to DX5 have higher stiffness compared with the transverse rib close to DX3. Excluding that, until 400,000 cycles, the distribution had an approximately bilaterally-symmetrical with respect to the center of specimen, too. However, at 447,500 cycles, the deflection of DX2 developed drastically and became roughly

equivalent to that of DX4. This also indicated that punching shear failure was generated around DX2.

Figure 13 shows load vs. gap distance. The gap between precast panels increased slightly with increasing load. However, the gap was approximately 0.02 mm and very small even at the time of punching shear failure. Moreover, by unloading, that was almost closed again.

Figure 14 shows load vs. strain of PC bar. The strain of PC bar for connection remained nearly constant in spite of loading and unloading at all stages and hardly changed. Thus, though several cracks were generated around connection, pre-stressing effectively at interface until the failure and the function of the panel-to-panel connection seemed to be sufficient.

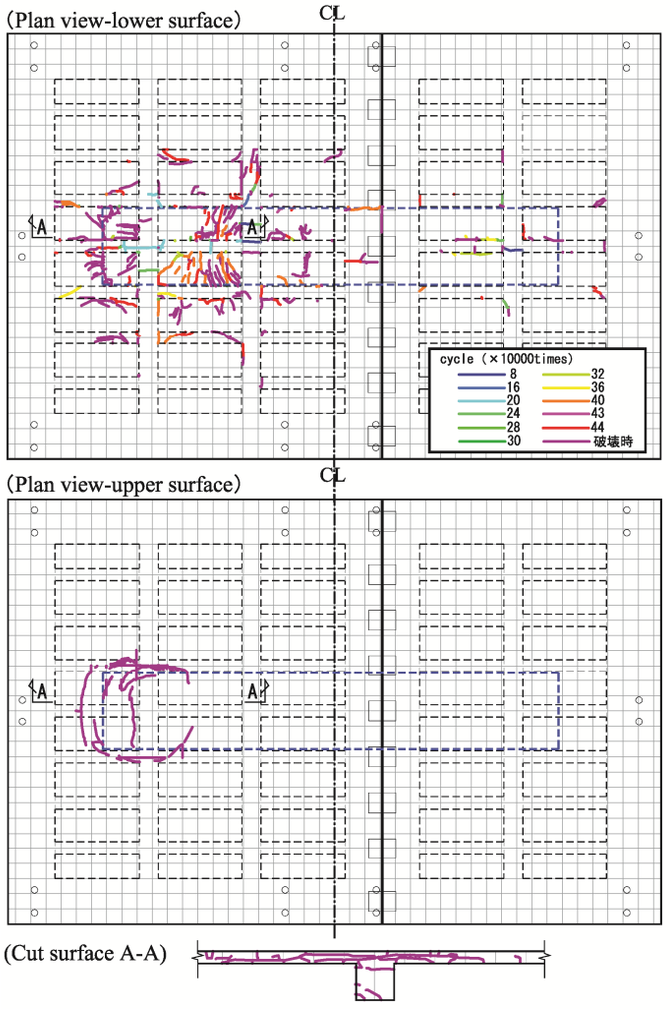


Fig. 11 observation of crack

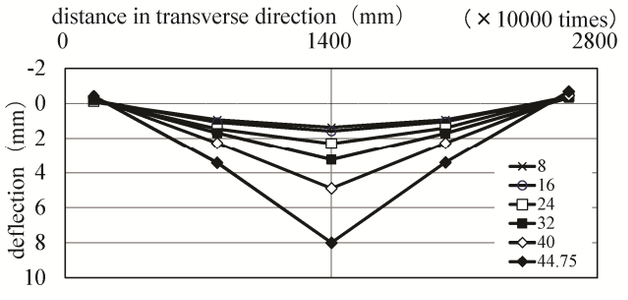


Fig. 12 distribution of deflection (1)

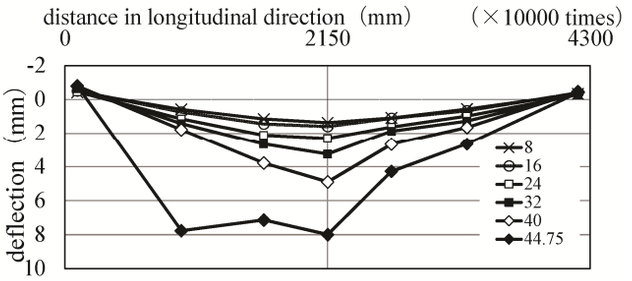


Fig. 12 distribution of deflection (2)

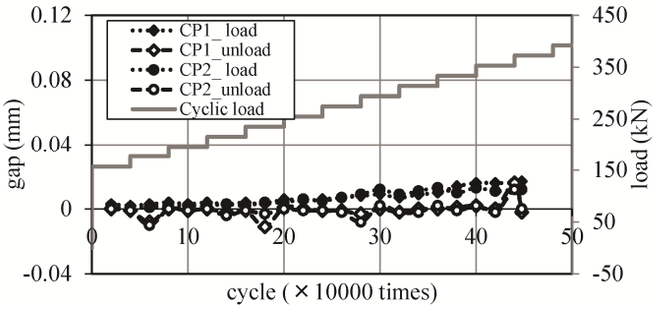


Fig. 13 load vs. gap distance

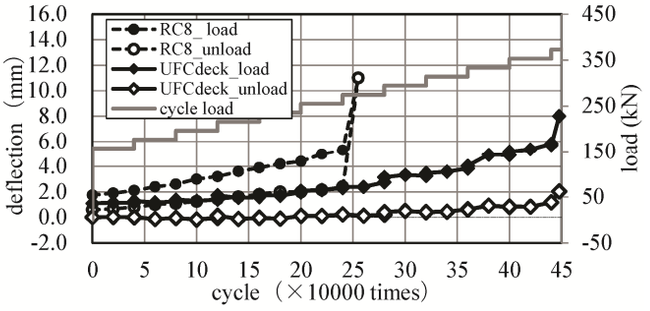


Fig. 14 load vs. strain of PC bar

4.5 *Fatigue durability*

It was recognized in Japan that bridge decks that designed on the basis of Specifications for highway bridge (Japan Road Association 1996) had commonly sufficient fatigue durability. For the typical specimen (hereafter RC8) designed based on the above specification, fatigue durability test was conducted by using wheel running machine. In this test, the same loading program was applied and RC8 was damaged due to punching shear failure. The results reported that the number of cyclic load was 255,600 (maximum load 274.7 kN). Figure 15 shows the change of vertical deflection at the center of specimen (DX4) compared with the result of RC8. The result demonstrated that the vertical deflections and the speed of increase in the deflection of UFC panel are much smaller than those of RC8. Though UFC slab is thin and has small cross-sectional shape due to structure with ribs compared with RC8 which was 250 mm thick and had a rectangular cross section, it is expressed that UFC panel has more fatigue durability than RC8.

Followed by, from the number of cyclic load at their failure, fatigue durability for each slab could be compared. For the comparison, their traveling cycles

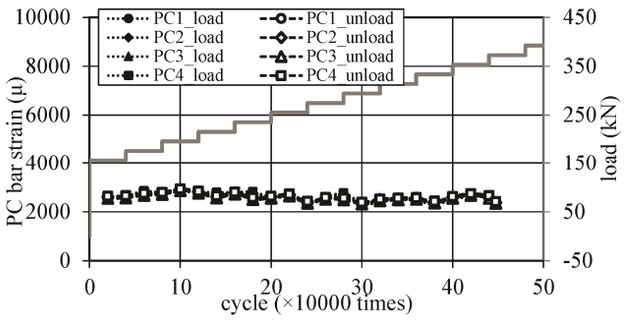


Fig. 15 deflection with experimental cycle

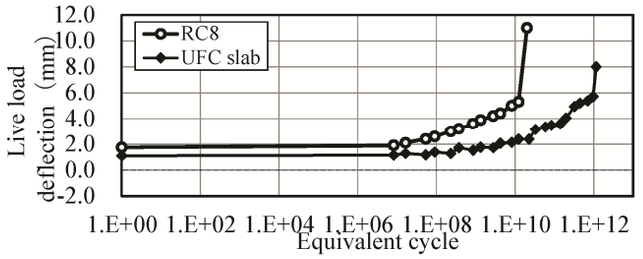


Fig. 16 deflection with equivalent cycle

were converted to equivalent cycles with regard to 98 kN load-level by using Miner's law (Matsui 1991) as,

$$N_{eq} = \sum (P_i/P_o)^m \cdot n_i \quad (3)$$

where, N_{eq} is an equivalent traveling cycle, P_o is the base referential load (98 kN), n_i is the traveling cycles with load P_i, and m is the inverse of the gradient of S-N curve (=12.76).

Figure 16 shows the vertical deflection vs. the equivalent traveling cycles. The punching shear failure of UFC panel occurred at 447.5 thousand cycles (113.9 billion equivalent cycles). By contrast, the punching shear failure of RC8 occurred at 255.6 thousand cycles (2.0 billion equivalent cycles).
Therefore, UFC panel has fatigue durability approximately 57 times as much as RC8.

5 CONCLUSION

5.1 *Push-out test for the panel-to-girder connection*

For the new panel-to-girder connection, two push-out tests were conducted on condition that filling material around shear connectors was shrinkage-compensating mortar. The test variables were whether or not buffer materials were installed under PBLs in the shear pocket of UFC panel.

From the results of the both case, for the shear capacity including end-bearing effect was larger than that without end-bearing effect. Moreover, the former and the latter were 4.13, 2.15 times as large as the shear force designed on service state, respectively. Since Japanese specification applied the shear resistance of PBL to the equation ignoring concrete end bearing and it was necessary that safety factor was more than 3.0, the latter was out of range. However, it is structurally clear that the end bearing of PBL in the new connection system acts efficiently from experimental result and the comparison with the shear resistance on the basis of the equation suggested by Ahn et al. (2010). As a result, the shear capacity of the new connection satisfies the safety factor regulated by Japanese specification (Japan society of Civil Engineers 2014).

If shrinkage-compensating mortar is used as filling material, the shear capacity decreases due to lack of aggregate interlock.

5.2 *Fatigue durability test by using wheel running machine*

In this study, fatigue durability test by using wheel running machine was conducted for the specimen with a transverse connection. The specimen was critically damaged by punching shear at 447,500 cycles of load (372.8 kN). Compared with RC8 which had commonly sufficient fatigue durability in Japan, the deflection at the center of specimen in this study was smaller than that of RC8. Moreover, these traveling cycle are converted to equivalent cycles with regard to 98 kN load-level. As a result, the precast UFC panel with transverse connection has fatigue durability approximately 57 times as much as RC8.

Thus, the precast UFC deck is efficient for replacement.

REFERENCES

Oguejiofor, E.C. & Hosain, M.U. 1994. A parametric study of perfobond rib shear connectors. Canadian Journal of Civil Engineering VOL.21: 614－625.

Ahn, J-H, Lee, C-G, Won, J-H, Kim, S-H. 2010. Shear resistance of the perfobond-rib shear connector depending on concrete strength and rib arrangement. Journal of Constructional Steel Research 66: 1295-1307.

Japan society of Civil Engineers (JSCE). 2004. Recommendations for design and Construction of Ultra High Strength Fiber Reinforced Concrete Structures (Draft).

Japan society of Civil Engineers (JSCE). 2014, Standard Specifications for Hybrid Structures: 74-78.

Japan Road Association. 1996. Design Specifications of highway bridge. Part Ⅱ Steel Bridges, Part Ⅲ Concrete Bridges.

Japan Road Association. 2012. Design Specifications of highway bridge. Part Ⅱ Steel Bridges, Part Ⅲ Concrete Bridges.

Matsui, S. 1991. Life time prediction of bridge. Japan Society of Civil Engineers Vol.30 No.6: 432-440.

National institute for land and Infrastructure management (NILIM). 2002. Experimental Study on the Fatigue durability of Highway Bridge slabs.

Takahashi, Y., Saito, S., Nakajima, A., Shima, H. 2015. Behavior of Headed Stud Shear Connectors in the push-out test with Simple Support and Lateral Restraint. Japan Society of Civil Engineers Vol.71 No.1: 113-127.

Maintenance, Safety, Risk, Management and Life-Cycle Performance of Bridges – Powers, Frangopol, Al-Mahaidi & Caprani (Eds)
© 2018 Taylor & Francis Group, London, ISBN 978-1-138-73045-8

An advanced technique for the analysis of box girder bridge superstructures

K. Kashefi
Arup, Adelaide, SA 5000

A. H. Sheikh
The University of Adelaide, Adelaide, SA 5005

ABSTRACT: An efficient modeling technique has been proposed to predict the behavior of thin-walled steel box-girders subjected to dynamic loading. In the proposed technique the general three-dimensional (3D) equations used for accurate representation of the structural deformation of these complex beam-like slender structures are decoupled into a two-dimensional (2D) cross-sectional problem and a one-dimensional (1D) beam problem through decomposition of the 3D strain field. The 2D cross-sectional problem is solved by a 2D finite element analysis considering in-plane as well as out-of-plane warping displacements of the beam section. The 1D beam problem is solved by a 1D beam finite element analysis and the results obtained are utilized to recover 3D stress, strain and displacement fields accurately. Numerical examples of thin walled box girders are solved using the proposed approach to show its performance. The comparison between the results obtained by the proposed method and detailed 3D finite element analyses highlights the accuracy as well as computational efficiency of the proposed method.

1 INTROUCTIONS

Box girder bridges are practically thin-walled beams having closed or combination of closed and open sections. The behavior of these structures under an arbitrary loading scenario is quite complex which is primarily due to the cross-sectional warping (out-of-plane warping) and the distortion of the sections (in-plane warping). A detailed 3D finite element (FE) analysis can predict the behavior of these structures accurately. However, considering the large number of elements and nodes involved with this approach it will require a large amount of computational resources which can be very expensive and not always available. Moreover, a significant amount of time and effort is required to create such detailed finite element models. This is inconvenient at, e.g., the preliminary design stage when the analysis is typically performed a large number of times while the design is being modified and improved.

The other extreme is to analyze these structures as one-dimensional beams. While this will make the analysis highly efficient computationally, models based on conventional beam theories such as Euler-Bernoulli hypothesis cannot predict the behavior of these structures accurately because they cannot capture the local deformations in the form of warping and other effects. For instance, Euler-Bernoulli beam theory does not consider the effect of shear deformation which is incorporated in Timoshenko's beam theory but this theory cannot capture the effect of warping deformations. Saint-Venant considered the effect of warping due to torsion which is absent in the above theories but this theory can only account for the unconstrained out-of-plane warping. The effects of shear deformations are still missing in the theory. An improved representation of the deformation of thin-walled beams is proposed by Vlasov (1961) to accommodate constrained warping (out-of-plane warping) but it cannot capture the distortion (in-plane warping) effects of the beam section (Dvorkin (1989)). A number of researchers (e.g. Bauld and Tzeng (1984), Chandra et. al. (1990), Lee (2005) and Sheikh and Thomsen (2008)) used Vlasov's theory and made some advancement. However, these theories require prior knowledge of the pattern of warping displacements which can change from one case to another. Subsequently, the effect of distortion in thin-walled box girders has been studied by few researchers (e.g. Razaqpur and Li (1991,1994) and Kermani and Waldron (1993)). These studies led to a better understanding of the behavior of thin-walled box girders which can have significant distortion. However, these techniques for modelling the distortion are based on ad-hoc assumptions and thus cannot be used in general cases.

In order to develop an accurate beam model for representing more realistic behavior of these structures, it is necessary to extract the exact potential

energy expression without any simplifying assumption that can eliminate important contributions. In this context, beam sectional analysis which was first proposed by Giavotto et al. (1983) and subsequently extended and employed by other researchers (e.g. Borri and Merlini (1986), Ghiringhelli and Mantegazza (1994) and Blasques (2014)) seems to be very attractive. In this approach, the complete 3D elasticity problem defining the actual behavior of beam-like structures is decomposed to a two-dimensional (2D) beam cross-sectional analysis and a one-dimensional (1D) beam analysis without any ad hoc assumptions. The method only assumes that the cross-sectional dimensions are small compared to the beam length which is true for medium to long-span bridge structures. The 2D beam sectional analysis is carried out using a 2D finite element discretization of the cross section where the effects of in- and out-of-plane warping deformations are considered. The 2D finite element analysis generates an accurate constitutive matrix (or stiffness matrix) of the beam cross-section which correctly accounts for the coupling between the different modes of deformation. This cross-section stiffness matrix is then used in the 1D beam analysis which can be carried out using a standard 1D beam finite element model. The cross section forces and moments obtained in the 1D beam analysis together with the warping solutions provided by 2D cross-sectional analysis, are used to obtain the warping displacements and finally to recover the detailed 3D stress and displacement fields in the cross section. The computational efficiency of this approach is remarkable in terms of the prediction of the 3D response of beam like structures.

In this paper, an efficient technique for obtaining the dynamic response of steel box girder bridges is developed where the cross-sectional analysis is based on an implementation of the theory given by Giavotto et al. (1983). Using the proposed method free vibration analysis as well as forced vibration analysis are investigated under time varying and instantaneous loads. The effect of damping is also incorporated following the concept of Raleigh damping (Clough (1975)). A computer code is developed to implement the 2D sectional analysis, 1D beam analysis as well as the recovery of the beam 3D response. Numerical examples of free and forced vibration response of box girder bridges are then solved by the proposed technique. The obtained results are compared with those obtained from the detailed 3D finite element analysis of these structures. The results highlight the accuracy and computational efficiency of the proposed method.

2 MATHEMATICAL FORMULATION

A brief overview of the methodology proposed by the authors is given in this section. For more detailed explanation on formulation refer to the other published work of the authors (Kashefi et al (2015)). The formulation is based on the assumption that the beam like structure has a slender geometry and does not have any abrupt variation of the cross-sectional geometry and material properties. Material remains linear elastic and the formulation considers small deformation theory.

2.1 *2D sectional analysis*

Figure 1 shows a typical beam like structure where the Cartesian coordinate axis (x-y-z) is used as the reference system which passes through the geometrical center of cross section. The displacement vector at an arbitrary point of a beam section $\{u\}$ can be divided into two components as

$$\{u\} = \{v\} + \{w\} \tag{1}$$

where $\{v\}$ is the displacement vector due to translations and rotations of the section without having any distortions and $\{w\}$ is due to the generalised 3D warping of the beam section. The first component of the displacement vector $\{v\}$ can be expressed in terms of translations $\{U\} = [U_x \quad U_y \quad U_z]^T$ and rotations $\{\theta\} = [\theta_x \quad \theta_y \quad \theta_z]^T$ of the section as

$$\{v\} = \begin{bmatrix} 1 & 0 & 0 & 0 & 0 & -y \\ 0 & 1 & 0 & 0 & 0 & x \\ 0 & 0 & 1 & y & -x & 0 \end{bmatrix} \begin{Bmatrix} \{U\} \\ \{\theta\} \end{Bmatrix} = [H]\{\Delta\}. \tag{2}$$

For the warping displacements, the beam section is discretized with 2D finite elements which help to express the displacements as

$$\{w\} = [N]\,\{d\} \tag{3}$$

where $\{d\}$ contains the nodal parameters of w_x, w_y and w_z and $[N]$ is their interpolation function.

The 3D stress-strain relationship is written as

$$\{\sigma\} = [D]\,\{\varepsilon\} \tag{4}$$

where the stress and strain vectors are arranged as $\{\sigma\} = [\sigma_x \quad \sigma_y \quad \tau_{xy} \quad \tau_{xz} \quad \tau_{yz} \quad \sigma_z]^T$ and $\{\varepsilon\} = [\varepsilon_x \quad \varepsilon_y \quad \gamma_{xy} \quad \gamma_{xz} \quad \gamma_{yz} \quad \varepsilon_z]^T$, respectively and $[D]$ is the corresponding constitutive matrix.

The stress resultants ($\{P\} = [\{F\}^T \quad \{M\}^T]^T$) at a section of the beam consist of three forces ($\{F\} = [F_x \quad F_y \quad F_z]^T$) and three moments ($\{M\} = [M_x \quad M_y \quad M_z]^T$) which are produced by the last three components of the stress vector $\{\tau\} = [\tau_{xz} \quad \tau_{yz} \quad \sigma_z]^T$ treated as tractions acting on the beam section having an area of A. These stress resultants can be obtained as

$$\{P\} = \int [H]^T \{\tau\} dA. \tag{5}$$

The strain vector can be now expressed in terms of derivatives of the displacements where the derivatives with respect to x and y (sectional coordinates) are separated from the derivatives with respect to z (axial coordinate) as

$$\{\varepsilon\} = [\partial_{xy}]\{u\} + [S]\{u\}_{,z} \tag{6}$$

Equations (1) to (3) are substituted in the above equation which leads to

$$\begin{aligned}\{\varepsilon\} = {} & [\partial_{xy}][H]\{\Delta\} + [S][H]\{\Delta\}_{,z} + \\ & [\partial_{xy}][N]\{d\} + [S][N]\{d\}_{,z}\end{aligned} . \tag{7}$$

As $[\partial_{xy}][H]$ in the above equation can be written as $[S][H][T]$ where $[T]$ is a 6x6 square matrix having all elements zero except $T(1,5) = -1$ and $T(2,4) = 1$, the strain vector can be rewritten as

$$\{\varepsilon\} = [S][H]\{\Psi\} + [B]\{d\} + [S][N]\{d\}_{,z} \tag{8}$$

where $\{\Psi\}$ is the sectional strain vector consisting of two shear strains, one axial strain, two curvatures and one torsional strain. The sectional strain vector can simply be expressed as

$$\{\Psi\} = [T]\{\Delta\} + \{\Delta\}_{,z} . \tag{9}$$

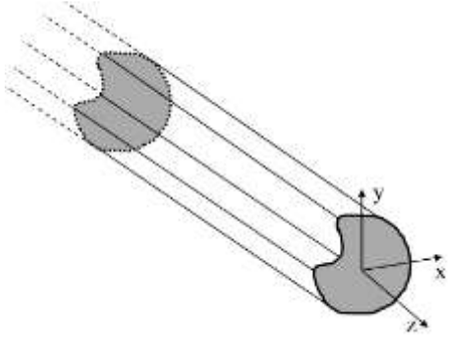


Figure 1. A typical beam like structure with reference coordinate system

2.2 *Equilibrium equations*

Now the virtual work principle ($\delta W_i = \delta W_e$) will be applied to get equilibrium equations of the beam section. For this purpose, a small element of the beam in the form of a small slice having a length of dz is taken. Assuming no variation of stresses and strains within the small length dz (along z), the internal virtual work can be written as

$$\delta W_i = dz \int \delta\{\varepsilon\}^T \{\sigma\} dA . \tag{10}$$

The external virtual work will be caused by the stresses or tractions $\{\tau\}$ acting on the two cross-sections of the slice and δW_e can be written as

$$\begin{aligned}\delta W_e = {} & \left[\int \delta\{u\}^T \{\tau\} dA + \frac{\partial}{\partial z}\left(\int \delta\{u\}^T \{\tau\} dA \right) dz \right]_{\text{at } (z+dz)} \\ & + \left[- \int \delta\{u\}^T \{\tau\} dA \right]_{\text{at } z} \\ = {} & \frac{\partial}{\partial z}\left(\int \delta\{u\}^T \{\tau\} dA \right) dz = dz\left(\int \delta\{u\}_{,z}^T \{\tau\} dA + \int \delta\{u\}^T \{\tau\}_{,z} dA \right)\end{aligned}$$

. (11)

So the final form of the virtual work can be written as

$$\int \delta\{u\}_{,z}^T \{\tau\} dA + \int \delta\{u\}^T \{\tau\}_{,z} dA = \int \delta\{\varepsilon\}^T \{\sigma\} dA \tag{12}$$

After substitution of Equations (1) to (5) and Equations. (8) to (9) in the above equation, the final form of equations will be:

$$\begin{aligned}& [A]\{d\}_{,zz} + \left([C] - [C]^T\right)\{d\}_{,z} + \\ & [E]\{\Psi\}_{,z} - [L]\{d\} - [M]\{\Psi\} = 0\end{aligned} \tag{13}$$

$$[E]^T \{d\}_{,z} + [M]^T \{d\} + [R]\{\Psi\} = \{P\} \tag{14}$$

where $[A] = \int [N]^T [S]^T [D][S][N] dA$,

$[C] = \int [N]^T [S]^T [D][B] dA$, $[E] = \int [N]^T [S]^T [D][S][H] dA$,

$[L] = \int [B]^T [D][B] dA$, $[M] = \int [B]^T [D][S][H] dA$,

$[R] = \int [H]^T [S]^T [D][S][H] dA$, $\{Q\} = \int [N]^T \{\tau\} dA$ and

$\{Q\}_{,z} = \int [N]^T \{\tau\}_{,z} dA$.

2.3 *Constraints*

It should be noted that the solution of above equations cannot be found unless suitable constraints are imposed. This is due to the use of $\{v\}$ (Equation (2)) in addition to $\{w\}$ (Equation (3)) to define the displacements of a point within the beam section. Actually, $\{w\}$ could be used to define the total displacement vector $\{u\}$ through the 2D finite element approximation but $\{w\}$ is used only for the warping displacements and $\{v\}$ is used in addition to define $\{u\}$. In the present case, the number of constraints is six as $\{v\}$ is defined in terms of $\{\Delta\}$ (Equation. (2)) which has six components. The constraints can be defined on the basis that the warping displacements should not contribute towards any translation or rotation of the beam section.

2.4 *Cross sectional stiffness and mass matrix*

Utilizing constraints in Equations (13) and (14) and the virtual work, the stiffness matrix of the beam section can be obtained as

$$[K_s]=[F_s]^{-1}=\left(\begin{bmatrix}[X_1]\\ [X_2]\\ [Y_1]\end{bmatrix}^T\begin{bmatrix}[L] & [C] & [M]\\ [C]^T & [A] & [E]\\ [M]^T & [E]^T & [R]\end{bmatrix}\begin{bmatrix}[X_1] & [X_2] & [Y_1]\end{bmatrix}\right)^{-1} \tag{15}$$

where $[X_1]$, $[X_2]$, $[Y_1]$ and $[Y_2]$ are linear operators that consist of constants (Kashefi et. al. (2015)).

This way the stiffness matrix of the section is defined accurately and can account for any geometrical and material coupling such as for composite structures.

Simliar to the cross-sectional stiffness matrix, we need to derive the cross-sectional mass matrix which will be utilised to derive the mass matrix of the beam elements. Using Equations. (1) and (2), the components of acceleration at a generic point of the section may be expressed as $\{\ddot{v}\}=\begin{bmatrix}\ddot{v}_x & \ddot{v}_y & \ddot{v}_z\end{bmatrix}^T=[H]\{\ddot{\Delta}\}$ where the effect of warping is neglected. Taking a slice of beam section of unit length (dz =1), the inertia forces of an element of small volume $dv = dxdy = dA$ (as dz =1) can be written using the above expression for the acceleration vector as $\{f^i\}=\rho dA\{\ddot{v}\}=\rho dA[H]\{\ddot{\Delta}\}$ where ρ is material density. Similar to Equation (5), the resultant inertial forces consist of three forces and three moments can be obtained by integrating the element inertia forces over the cross-sectional as follows.

$$\begin{aligned}\{F^i\}&=\int_A[H]^T\{f^i\}=\left(\int_A\rho[H]^T[H]dA\right)\{\ddot{\Delta}\}\\ &=[M_s]\{\ddot{\Delta}\}\end{aligned} \tag{16}$$

where $M_s=\begin{bmatrix}m & 0 & 0 & 0 & 0 & 0\\ 0 & m & 0 & 0 & 0 & 0\\ 0 & 0 & m & 0 & 0 & 0\\ 0 & 0 & 0 & I_{xx} & -I_{xy} & 0\\ 0 & 0 & 0 & -I_{xy} & I_{yy} & 0\\ 0 & 0 & 0 & 0 & 0 & I_{xx}+I_{yy}\end{bmatrix}$

In the above equation, m is the mass per unit length of the box girder whereas the other terms are corresponding to the different components of rotary inertia due to cross-sectional rotations which can be written as follows,

$$\begin{aligned}&m=\int_A\rho dA,\\ &I_{xx}=\int_A y^2\rho dA, I_{yy}=\int_A x^2\rho dA,\ I_{xy}=\int_A xy\rho dA\end{aligned} \tag{17}$$

2.5 *One dimensional dynamic analysis and three dimensional stress/strain recovery*

After calculating the sectional stiffness and mass matrix, the 1D beam finite element analysis needs to be carried out. A C^0 continuous displacement based isoparametric formulation is adopted for the derivation of these three-node elements considering bi-axial bending, bi-axial shear, torsion and axial deformations. According to isoparametric formulation, all the field variables are interpolated in terms of their nodal values in an identical manner. Sectional stiffness matrix $[K_s]$ (Equation (15)) is used to derive beam element stiffness matrix $[K_e]$ as

$$[K_e]=\int[B_z]^T[K_s][B_z]dz \tag{18}$$

In a similar manner, the mass matrix of an element can be derived and it can be expressed as

$$[M_e]=\int[N_z]^T[M_s][N_z]dz \tag{19}$$

The integrations found in Equations (18) and (19) are carried out numerically following the Gauss quadrature technique, where a full integration rule is applied and field consistent technique is used to stabilize the strain field.

The stiffness matrix and mass matrix for all elements are obtained and assembled together to form the global stiffness matrix [K_g] and mass matrix [M_g] of the structure.

In order to form the damping matrix [C_g] of the structure, Rayleigh technique (1896) is used which expresses the damping matrix in terms of stiffness and mass matrixes as

$$[C_g]=\alpha[M_g]+\beta[K_g] \tag{20}$$

where α and β are the Rayleigh constants, which are determined by solving the following simultaneous equations

$$\begin{Bmatrix}\alpha\\ \beta\end{Bmatrix}=2\frac{\omega_n\omega_m}{\omega_n^2-\omega_m^2}\begin{bmatrix}\omega_n & -\omega_m\\ -1 & 1\\ \hline \omega_n & \omega_m\end{bmatrix}\begin{Bmatrix}\xi_m\\ \xi_n\end{Bmatrix}. \tag{21}$$

In the above equation, ξ_m and ξ_n are the damping ratios corresponding to two modes of vibration (m and n) which can be obtained from experimental measurement (Thompson (2002)). ω_m and ω_n are the

corresponding frequencies of vibration which can be obtained from the free vibration analysis of the structure. Once the above matrixes and the global load vector $\{F_g(t)\}$ are obtained, the governing equation for free and forced vibration response of the structure can be expressed as the followings:

Undamped free vibration:

$$[K_g]\{\delta\}+[M_g]\{\ddot{\delta}\}=0 \tag{22}$$

Dynamic response:

$$[K_g]\{\delta\}+[C_g]\{\dot{\delta}\}+[M_g]\{\ddot{\delta}\}=\{F_g(t)\} \tag{23}$$

Equation (22) gives an eigenvalue problem which is solved by the simultaneous iteration technique of Corr and Jennings (1976) to calculate the natural frequencies of vibration, ω. The time integration method following Newmark beta (Bathe (2006)) is used to solve Equation (23) for the time history response of displacement, velocity and acceleration vectors.

Once the nodal displacement vector is obtained from the 1D finite element analysis, it can be utilized to evaluate the generalized strain vector $\{\Psi\}$, the cross section force and moment vectors, $\{P\}=[K_s]\{\Psi\}$, at any desirable section of the beam at any time (t). Based on $\{P\}$, the 3D displacements and stresses can be recovered using Equations (8) and (4).

3 NUMERICAL RESULTS AND DISCUSSION

A computer program is developed in FORTRAN to implement the proposed method for the static and dynamic (free and forced vibration) analysis of beams having different thin-walled cross-sections which are commonly found in bridge decks. The material properties used in the examples are that of steel with elastic modulus E = 200 GPa, Poisson ratio ν = 0.3 and the mass density ρ = 7948.89 kg/m^3.

3.1 *Single cell box girder-Cross sectional analysis*

A 20m long cantilever beam having a thin-walled cross-section as shown in Figure 2 is studied in this section.

For the sectional analysis, which is the initial step of static or dynamic response analyses, a 2D finite element analysis using eight-node quadratic isoparametric elements is carried out. The sectional analysis is carried out for different mesh sizes. Results show that a mesh consisting of 240 elements (corresponding to 3606 degrees of freedom (DOF)) is sufficient to have a converged solution. The non zero components of the sectional stiffness matrix predicted by the present approach are presented in Table 1, where K_{11} and K_{22} are transverse shear stiffness components corresponding to x and y axes, respectively, K_{33} is the extensional stiffness component, K_{44} and K_{55} are bending stiffness components corresponding to x and y axes, respectively, and K_{66} is torsional stiffness component. The sectional stiffness matrix is also calculated using the conventional beam theory and values are included in Table 1. A significant difference is observed between the values of transverse shear and torsional stiffness components of the thin-walled beam predicted by these two approaches. Moreover, the off-diagonal components of the cross-sectional stiffness matrix, which are due to shear-torsion and bending-extension couplings (K_{16} and K_{34}, respectively) cannot be captured by classical beam theories. The cross-sectional stiffness components evaluated by the proposed approach are the most accurate and this is verified by using these stiffness values in the 1D beam analysis for accurately predicting the static and dynamic responses of the girder.

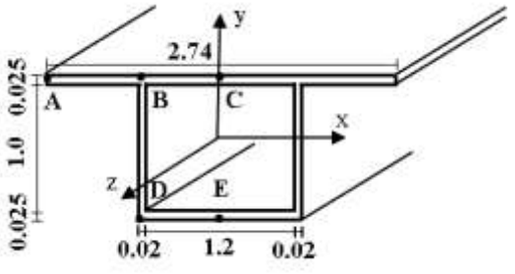


Figure 2: Single cell box girder beam (dimensions are in m)

Table 1. Cross section stiffness components for single box girder

Stiffness Components	Proposed Method	Conventional Beam Theory
$K11(N)$	6.068×10^9	(κGA)* 8.942×10^9
$K22(N)$	2.698×10^9	(κGA) 8.942×10^9
$K33(N)$	2.79×10^{10}	(EA) 2.79×10^{10}
$K44(N.m^2)$	5.376×10^9	(EIx) 5.449×10^9
$K55(N.m^2)$	1.237×10^{10}	(EIy) 1.234×10^{10}
$K66(N.m^2)$	2.437×10^9	(GJ)** 3.761×10^9
$K16(N)$	4.025×10^6	-
$K34(N)$	-2.674×10^4	-

* (κ) shear correction factor which is taken as 5/6 (Gere and Timoshenko (1990))

** GJ = (GJ)closed+(GJ)open= $\dfrac{4A^2G}{\oint ds/t}+G\sum\dfrac{st^3}{3}$ cf. (Megson (2012))

3.1.1 Dynamic response due to a suddenly applied load

In this section, the dynamic response of the girder under an instantaneously applied load ($F_y = -1.0\,kN$) at its free end is investigated. The element discretization and mesh details for the sectional analysis are the same as in the previous section. For the validation of the present results, the girder is also analyzed using the finite element software ABAQUS having 20-node quadratic hexahedral solid elements (C3D20). A total number of 12800 solid elements is used corresponding to 269760 Degrees of Freedom (DOF) (almost 75 times more than the DOF required in analysis of the same structure by the proposed approach) are used where the aspect ratio of an element is maintained as 1×2×2 (thickness× breadth ×length) in order to ensure a reliable and converged solution. Before undertaking the dynamic analysis of the girder using time integration method, the free vibration analysis of the structure is carried out by the proposed technique to obtain frequencies of vibration (ω_1 = 19.067 rad/s; ω_2 = 28.954 rad/s) which are required for the evaluation of damping ratios. In order to ensure that the frequency values calculated by the proposed method are accurate, these are also determined from a detailed 3D finite element analysis of the girder using ABAQUS (ω_1 = 19.108 rad/s; ω_2 = 28.90 rad/s) which shows a difference of less than 0.2%.

The forced vibration analysis of the girder is carried out using the proposed approach as well as a detailed 3D finite element (FE) model (ABAQUS) and the dynamic response of the structure is captured for a period of 1.2 sec. The time history diagrams for the deflection (u_y) at two points (A and E) on the free end cross section (Figure 2) obtained by the proposed method as well as the 3D FE analysis are presented in Figures 3-4. The time history responses for normal stress (σ_{zz}) at two points (A and D) obtained by the proposed method and 3D FE model are presented in Figures 5-6. As can be seen from these figures, the results predicted by the presented model are in very good agreement with those produced by the 3D FE analysis.

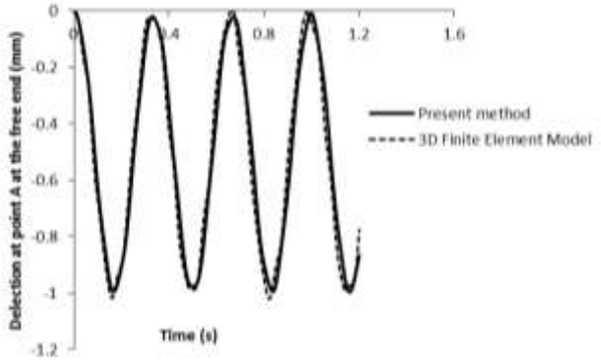


Figure 3. Time history of the deflection at point A (uy mm) of the free end section (Figure 2)

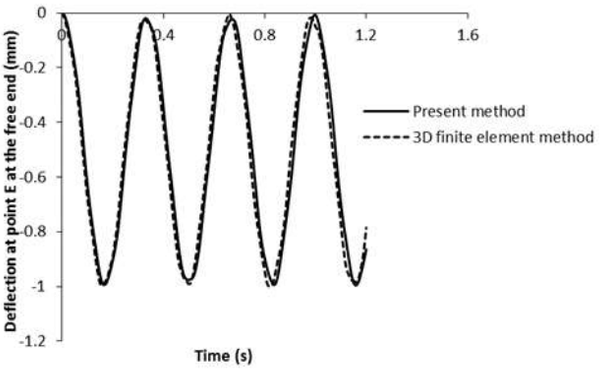


Figure 4. Time history of the deflection at point E (uy mm) of the free end section (Figure 2)

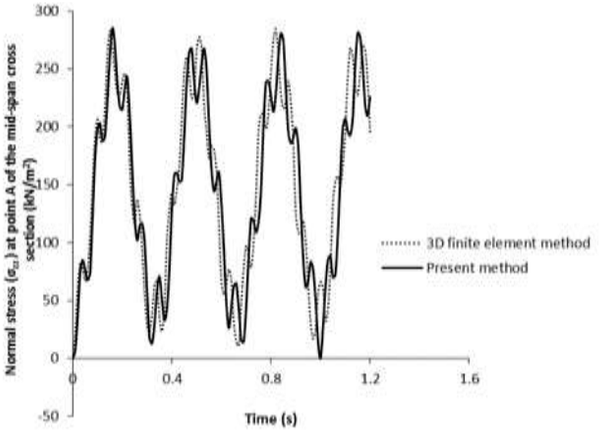


Figure 5. Time history of the normal stress (σzz kN/m2) at point A of the mid-span section (Figure 2)

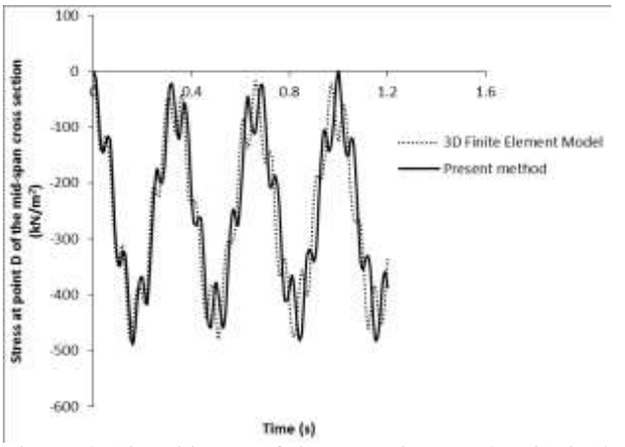


Figure 6. Time history of the normal stress (σ_{zz} kN/m2) at point D of the mid-span section (Figure 2)

As the effect of damping is not considered in the previous analysis, the structure is reanalyzed exactly in a similar manner taking damping ratio of 2% and 4% in order to show the effect of damping on the structural response. The time history diagrams for the deflection at point A on the free end section of this girder obtained from these two models are presented for a period of 2.5 sec in Figure 7. The amplitude of deflection is found to be reduced with the increase of damping ratios as expected.

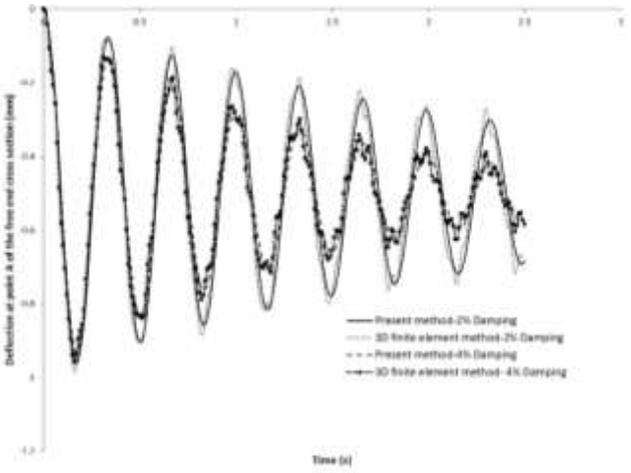


Figure 7. Time history of the deflection at point A (uy mm) of the free end section (Figure 2) considering damping

3.2 *Dynamic response of the two-cell box girder due to a time-varying load Two-cell box girder*

This section considers a 20 m long cantilever two-cell box girder as shown in Figure 8. The converged solution for cross-sectional analysis of this girder is obtained with 202 eight-node quadratic elements (DOF: 3021) .

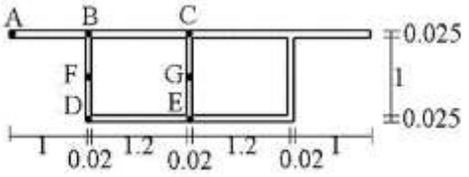


Figure 8-Two-cell box girder (dimensions are in m)

The dynamic response of this girder due to a time-varying load in the form of a triangular pulse (Figure 9) acting at the free end of the girder is predicted by the proposed method and the 3D FE analysis. For this purpose the 1D beam analysis of this girder is implemented using 15 three-node beam elements (DOF: 186). The 3D FE analysis is also performed for the validation of the present results using 20-node quadratic hexahedral solid elements (C3D20). A total number of 20800 solid elements (DOF = 435351; almost 145 times more than the DOF required for the proposed approach) are used where the aspect ratio of an element is maintained as 1×2×2. The time history for the deflection (u_y) at point A of the free end section is obtained using both 3D FE model and the present method. The results are plotted in Figure 10. The time histories for the normal stress (σ_{zz}) of points C and D at the mid-span section are illustrated in Figures 11-12 for both approaches. The results obtained by the present method are in very good agreement with those obtained by the 3D FE model.

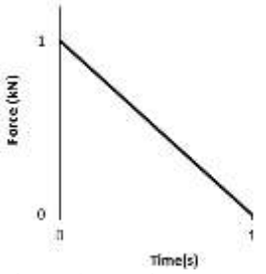


Figure 9: Load case 1 applied at the free-end

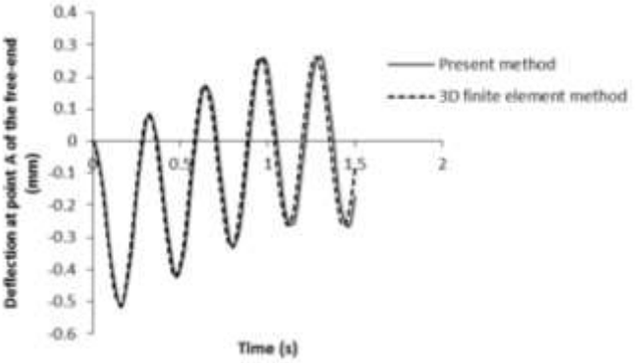


Figure 10: Time history of the deflection at point A (uy mm) of the free end section (Figure 8)

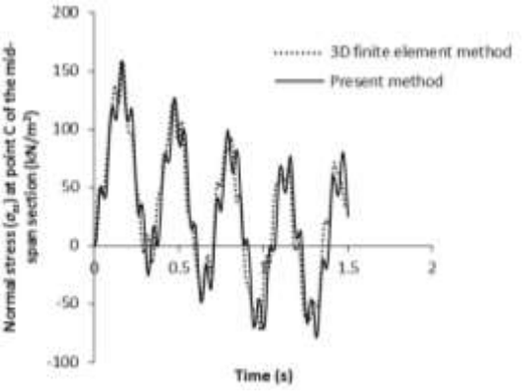


Figure 11: Time history of the normal stress (σzz kN/m2) at point C of the mid-span section (Figure 8)

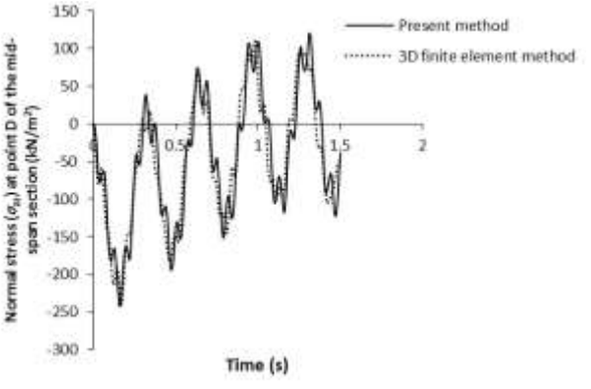


Figure 12- Time history of the normal stress (σzz kN/m2) at point D of the mid-span section (Figure 8)

4 CONCLUDING REMARKS

An innovative modelling technique is presented for dynamic analysis of thin-walled box girder bridge structures. The dynamic analysis includes free and forced vibration analyses under time varying and instantaneous loads. The capability of the proposed method is comparable to that of a detailed 3D FE model whereas the computational efficiency of the method is very high compared to 3D FE analysis (e.g. almost 150 times fewer DOFs). The method decomposes the full 3D equations defining the behaviour of any beam-like slender structure into a 2D cross-sectional problem and a 1D beam problem, which are solved by using a 2D plane FE model and 1D beam FE model, respectively. This decomposition actually helps the present approach to be computationally efficient. On the other hand, the accuracy of the solution is not affected as the method does not adopt any major assumptions unlike most of existing beam theories. From 2D analysis, a cross-sectional stiffness is obtained which can account for all of the geometrical couplings found in multi-cell bridge girders. Apart from the usual displacements due to translations and rotations of the section, the 2D sectional analysis also includes 3D warping displacements consisting of out-of-plane warping of the section as well as in-plane warping i.e., sectional distortion. This is while, it is very challenging to incorporate warping displacements properly in a beam theory. Once the cross-sectional stiffness matrix is evaluated using the 2D finite element analysis, it can be used in the 1D beam analysis for static, free vibration, forced vibration or any other type of structural analysis. Therefore, this method can provide a very useful analysis tool which can specifically be used in the preliminary design of these structures when the designer needs to understand the contribution of different parameters to the overall response of the structure.

In order to demonstrate the performance of the proposed method, numerical examples of thin-walled box girders have been solved and the results produced by this method have been compared with those generated from the detailed 3D FE analysis of these structures. The results produced by these two approaches are found to have very good correlations. Based on the above observation, the proposed method is highly recommended for the analysis and design of thin-walled box girder bridge structures.

5 REFERENCES

Abaqus Analysis User's Manual. Abaqus 6.12 /CAE documentation.

Bathe, K.-J. (2006), Finite element procedures. Klaus-Jurgen Bathe.

Bauld, N.R. and Tzeng L.S. (1983), A Vlasov theory for fiber-reinforced beams with thin-walled open cross sections. International Journal of Solids and Structures, 20(3): p. 277-297.

Blasques, J.P. (2014), Multi-material topology optimization of laminated composite beams with eigenfrequency constraints. Composite Structures. 111(0): p. 45-55.

Borri, M. and Merlini T. (1986), A large displacement formulation for anisotropic beam analysis. Meccanica, 21(1): p. 30-37.

Chandra, R., Stemple A., and Chopra I. (1990), Thin-walled composite beams under bending,torsion, and extensional load. AIAA Journal, 27(7): p. 619-626.

Clough, R.W. and Penzien J. (1975), *Dynamics of structures*.

Corr, R. and Jennings A. (1976), *A simultaneous iteration algorithm for symmetric eigenvalue problems.* International Journal for Numerical Methods in Engineering. **10**(3): p. 647-663.

Dvorkin, E.N., et al. (1989), A Vlasov beam element. Computers & Structures. 33(1): p. 187-196.

Ghiringhelli, G.L. and Mantegazza P. (1994), Linear, straight and untwisted anisotropic beam section properties from solid finite elements. Composites Engineering, 4(12): p. 1225-1239.

Giavotto, V., et al. (1983), Anisotropic Beam Theory and Applications. Computers and Structures. 16(1-4): p. 403-413.

Kashefi et. al. (2015), An efficient modelling approach based on a rigorous cross-sectional analysis for analysing box girder bridge superstructures, Advances in Structural Engineering, Vol. 19(3) 513–528.

Kermani, B. and Waldron P. (1993), Analysis of continuous box girder bridges including the effects of distortion. Computers & Structures. 47(3): p. 427-440.

Lee, J. (2005), Flexural analysis of thin-walled composite beams using shear-deformable beam theory. Composite Structures. 70(2): p. 212-222.

Megson, T.H.G.(2012), *Aircraft structures for engineering* students. Elsevier.

Prathap, G. and Babu C.R. (1986), *Field-consistent strain interpolations for the quadratic shear flexible beam element.* International journal for numerical methods in engineering. **23**(11): p. 1973-1984.

Rayleigh, J.W.S.B.(1896), The theory of sound. Vol. 2. Macmillan.

Razaqpur, A.G. and Li H. (1991), Thin-walled multicell box-girder finite element. Journal of Structural Engineering. 117(10): p. 2953-2971.

Razaqpur, A. and H. Li (1994), Refined analysis of curved thin-walled multicell box girders. Computers & structures. 53(1): p. 131-142.

Sheikh, A.H. and Thomsen O.T. (2008), An efficient beam element for the analysis of laminated composite beams of thin-walled open and closed cross sections. Composites Science and Technology. 68(10): p. 2273-2281.

Thompson, J.M.T. and Stewart H.B. (2002), *Nonlinear dynamics and chaos*. John Wiley & Sons.

Vlasov, V. (1961), Thin-walled elastic beams. Office of Technical Services, U.S. Department of Commerce,Washington 25. DC,'lT-61-I 1400.

Maintenance, Safety, Risk, Management and Life-Cycle Performance of Bridges – Powers, Frangopol, Al-Mahaidi & Caprani (Eds)
© 2018 Taylor & Francis Group, London, ISBN 978-1-138-73045-8

Construction simulation of cable-stayed bridges

J.A. Lozano -Galant
University of Castilla-La mancha, Ciudad Rea, Spain

D. XU
Tongji University, Shanghai, China

J. Turmo
Universitat Politècnica de Catalunya, BarcelonaTECH, Barcelona, Spain

ABSTRACT: In a staggered erected cable-stayed bridge made of concrete, time-dependent phenomena (such as creep or shrinkage) effects might play an important role in both its geometry and its stress state. In fact, because of these phenomena, stays will indeed lose force and higher bending moments will appear in the structure. To compensate these effects, one or two re-stressing operations are traditionally planned during the life time of long span cable- stayed bridges made of concrete. These re-stressing operations might be technologically challenging and always imply additional costs. To guarantee that allowable stresses and deflections are not exceeded during erection, a number of simulation methods are presented in the literature. Some of these methods, concretely those based on a backward simulation approach, fail addressing the effects of the time-dependent phenomena. To simulate these effects, methods based on the forward simulation approach are traditionally followed. Nevertheless, the main trade-off of these algorithms is that their computation is based on complex iterative processes that make simulation more time consuming. Furthermore, these methods are not able to avoid the need of additional re-stressing operations in service to prevent the effects of the time-dependent phenomena. To fill all these gaps, a new simulation algorithm, the Forward-Direct Algorithm (*FDA*), is formally presented in this paper to simulate the construction process of cable-stayed bridges including the time-dependent phenomena effects. This algorithm takes advantage of the unstressed length of the stays concept to carry out a computationally efficient simulation based on an innovative direct simulation approach. The major advantage of this algorithm is the fact that the prestressing operations during construction can be defined to avoid the need of additional re-tensioning operations in service. To illustrate the creep and shrinkage effects, the proposed algorithm is applied to a real cable-stayed bridge. This tool also can be used by the designer or the contractor for construction control of the strand by strand tensioning technique.

1 INTRODUCTION

Most cable-stayed footbridges are built on temporary supports (Menn 1986). In this erection method, the bridge superstructure is first erected on a set of temporary and permanent supports. Then, during the tensioning process of the stayed cables, the loads counterbalanced by the temporary supports are successively transmitted to the stay system. At the end of this tensioning process, a target geometry or stress state, known as the Objective Service Stage (*OSS*) (Hassan et al 2012) is achieved.

Cable-stayed bridges are extremely redundant and the effect of tensioning one cable has the effect of changing the stresses of the already installed cables. In order to achieve the *OSS* at the end of the construction process careful simulations are required. In fact, many researchers and practitioners have stated the importance of this simulation (Janjic et al. 2003). The traditional method to simulate the construction process of cable-stayed bridges is to start at the *OSS* and dismantle the structure. Several authors have proposed methods based on this "backward" approach both for the temporary supports (Lozano-Galant et al 2012a), and the cantilever erection method (Behin and Murray 1992, Wang et al. 2004). The primary challenge of this simulation is the difficulty to model any modification in the bridge design and/or in its tensioning strategy. To overcome these problems, a forward simulation, which follows the actual erection sequence on site was proposed for the temporary supports (Lozano-Galant et al 2012a) and the cantilever method (Wang et al 2004). Most of the simulation methods presented in the literature assume that any construction stage can be obtained by deactivating or activating group of elements, loads or boundary conditions from the following or the preceding construction stages. This hypothesis assumes that the construction process can be simulated by linear superposition of stages. Other works (Lozano-Galant et al. 2013) proposed a direct approach that avoided the need of this superposition of

stages. These procedures increased computational efficiency.

The main algorithms presented in the literature for the simulation of the temporary supports erection method are as follows: Backward Algorithm (BA) (Lozano-Galant et al. 2012a), Forward Algorithm (FA) (Lozano-Galant et al. 2012b) and Direct Algorithm (DA) (Lozano-Galant et al 2013). The main characteristics of each of these simulation methods are summarized in Table 1. This table includes the simulation direction (backwards, forwards or direct), the application or not of the superposition of stages principle (abbreviated in tale as Sup.), the use of a Local (LIP) or an Overall (OIP) Iterative Process, and if the simulation includes or not the effects of the Time-Dependent Phenomena (TDP).

Table 1. Characteristics of the simulation algorithms for the temporary supports erection method

Algorithms	Direction	Sup	LIP / OIP	TDP
BA	Backward	✔	✔ / ✘	✘
FA	Forward	✔	✔ / ✔	✘
DA	Direct	✘	✔ / ✘	✘

Analysis of Table 1 shows that any of the methods presented in the literature enables the simulation of the time-dependent phenomena. In order to fill this gap, this paper presents a method, the Forward Direct Algorithm, *FDA*, to simulate the construction process of cable-stayed bridges built on temporary supports including the effects of the time-dependent phenomena. This algorithm also enables the simulation of the stresses in the strand-by-strand tensioning technique. In the following section, the strand by strand tensioning technique is first described and then the simulation proposed by the *FDA* is summarized.

2 STRAND BY STRAND TENSIONING TECHNIQUE

Due to flexibility of cable-stayed bridges, the tension of individual strands of a stay cable does not remain constant as it varies during the stressing operation of each strand. To ensure the uniformity of forces in all strands of a stay cable at the end of the stressing operation, several patented methods might be used.

The stressing of multi-strand stay cable (Fig. 1.A) with a mono-strand jack might be carried by the following steps: (1) The first strand is fixed to one of the anchorages, and its other end is threaded into the other anchorage, and then cut and stressed to a calculated force, which takes into account the foreseen deformation of the structure. (2) The first strand is not yet wedged into the anchorage block, but wedged in a special single anchoring device provided with a load cell that gives a permanent reading of this force. (3) The second strand is then installed in a similar manner, cut and stressed. Then, the stressing is carried out with a mono-strand jack equipped with a load cell identical to the one indicating the force of the first strand. (4) As the second strand is stressed, the force of the first strand decreases, and the stressing operation is stopped when the readings of the two cells are identical. The second strand is then anchored in the permanent anchor block. At this point the first two strands are equally stressed. This process is carried out automatically by adequate software developed by the prestressing company. (5) The third strand is then installed and stressed until its force reaches the reading of the first strand (which decreases jointly with the force of the second strand). When the same forces are reached, the three strands are identically stressed.

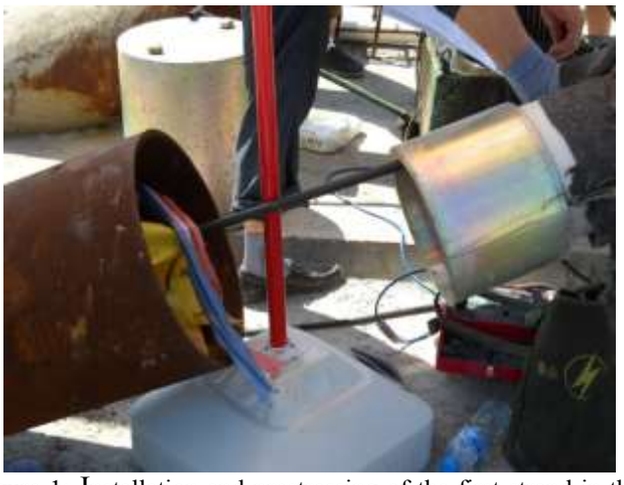


Figure 1: Installation and prestressing of the first strand in the strand by strand tensioning technique.

A linear approximation of the evolution of the strand forces in the strand-by strand tensioning process is presented in SETRA (2001). This analysis includes the stiffness of the structure into the stay cable-direction. The results of this approximation are close to the actual variation of tension on site for stay cables with a high number of strands.

3 SIMULATION OF THE CONSTRUCTION PROCESS

The simulation algorithms of cable-stayed bridges have to assure the achievement of the *OSS* by an adequate tensioning process. This process describes the tensioning operations to be introduced by the jack on site to transfer the load from the temporary supports to the stay cable system. The tensioning process plays an important role in the structural behavior of the structure both during construction and in service.

Usually stay cable system of cable-stayed bridges is prestressed on two tensioning operations. The

forces in the first operation are usually defined directly by the designer as a percentage, usually ranging between the 70% and 85%, of the prestressing forces in the *OSS*. Unfortunately, the calculation of the forces in the second prestressing operation is not straightforward, as it must take into account the effects of all the preceding and subsequent tensioning operations and time-dependent phenomena. In order to carry out this simulation, an algorithm, the Forward Direct Algorithm (*FDA*) is presented in this section. This procedure takes advantage of the unstressed length of the stays concept to avoid the need of an overall iterative process. Furthermore, the *FDA* enables the calculation of the stresses in the first strand obtained by the strand-by-strand tensioning technique.

In this section, the main hypotheses of the *FDA* are first explained in detail. Secondly, the unstressed length concept of the cables and its simulation in the *OSS* are described. Then, a procedure to include the effects of the time-depend phenomena into the strains in the OSS is presented. Finally, the simulation of the first and the last tensioning operations are summarized.

3.1 *Hypotheses*

The main hypotheses of the *FDA* are: (1) This algorithm is applied to the temporary supports erection method. (2) The simulation of the *FDA* is carried out according to the actual construction sequence (forward simulation). This modeling direction enables the simulation of the time-dependent phenomena effects. (3) The superposition of stages principle is used to simulate changes during construction in the structural system (e.g. placement of the stays), loads (e.g. stay prestressing) or boundary conditions. (4) A Local Iterative Process is used to simulate the lifting of the temporary supports produced by a tensioning operation or by the time-dependent phenomena effects. (5) Stay forces are simulated by imposed strains on the stays. (6) The *FDA* does not require separate models to calculate the evolution of stresses in the strands when the strand by strand tensioning technique is used. (7) The construction process is defined to achieve the *OSS*. (8) The simulation of the first prestressing operation differs from that of the last one. For this reason, each simulation is described separately in the following subsections. (9) The temporary supports are removed when the deck is lifted at its location. (10) At the end of the first tensioning operation all the loads are transferred to the stay system (in this way, during the last tensioning operation the structural system remains constant and without temporary supports). (11) To avoid the requirement of an overall iterative process, the prestressing of the last tensioning operation is based on the unstressed length concept. (12) The effects of the time-dependent phenomena (such as creep or shrinkage) are simulated by adding *Auxiliary Models* with amplified curvatures and axial strains in concrete elements. (13) To avoid excessive computation times, the increments of time in creep and shrinkage simulation vary from 1 to 360 days.

3.2 *Unstressed Length of the cables*

A length-based adjustment is sometimes used to introduce the tensioning of the stays on site. In this procedure the stays are made to accurately measure a so called unstressed or neutral length of a stay, L_0 (SETRA 2001). This is the length of a given cable when it has not axial stress or strain. This length is measured when the cable rests horizontally on a support that counterbalances the effects of its own self weight. L_0 is an intrinsic parameter that is independent of the conditions to which the stay is subjected on site.

This procedure is especially interesting for cable-stayed footbridges with prefabricated cables. In this case, the stay is then stressed on site from L_0 until its ends occupy the position of the anchorages in the deformed geometry, and the stressed length L_S is achieved. This is equivalent of introducing an imposed strain ε in the stay. With ΔL_n being the increment of length in the *nth* stay, the value of this strain can be calculated as presented in the following equation.

$$\varepsilon = \frac{\Delta L}{L_0} = \frac{L - L_s}{L_0} \tag{1}$$

According to (SETRA 2001) ε presents values close to -0.003. These parameters have been used to simulate the structural behaviour of cable-stayed bridges (see. e.g. (Janjic et. al 2001). In this paper, these strains are proposed to be used to simulate of the construction process of cable-stayed bridges. To do so, the *FDA* assumes that extending a L_0-length stay on site to get a given force F produces the same effect that shortening an L-length stay in the computer model to get such force. This is valid when the same stressed length L_S and the same axial force are obtained by both procedures. The shortening in the computer model might be simulated by mean of a unitary strain in the *OSS*, ε_{OSS}, which is related with the force F, the Young's Modulus of the cable material E, the cross sectional area of the stay A, L, L_0 and L_S by the following equation:

$$L_s = L_0 - \left(1 + \frac{F}{EA}\right) = L - \left(1 - \varepsilon_{OSS} + \frac{F}{EA}\right) \tag{2}$$

Using the strains ε_{OSS} enables a direct simulation of the construction process that does not require the application of the superposition of stages. Strains ε_{OSS} might be calculated by the procedure defined in the following section.

3.3 *Objective Service Stage (OSS)*

The *OSS* can be characterized by a set of stay forces. Some of the main criteria used to define these forces in the *OSS* are summarized in (Jorquera et al. 2016). Between these methods, is remarkable the Rigidly Continuous Beam Criterion (Lazar et al. 1972). In this method the stay forces are defined by projecting, into the stays direction, the vertical reaction of an equivalent continuous beam (in which the anchorages of the stay cables at the deck are replaced by supports).

Once defined the stay forces of all the stay cables in the *OSS*, they can be clustered into a vector $\{N_{OSS}\}$. These forces can be obtained by the sum of a passive, $\{N_P\}$, and an active state, $\{N_A\}$, as presented in Equation 4. The former vector includes the passive stay forces produced when the Target Load, *TL*, is applied into the structure and the latter one includes the effect of the prestressing of the stays.

$$\{N_{OSS}\} = \{N_P\} + \{N_A\} = \{N_P\} + [\Delta N]\{\varepsilon_{OSS}\} \quad (3)$$

The active state is simulated in the computer software by introducing imposed strains, ε_{OSS}, into the stays. The vector of imposed strains, $\{\varepsilon_{OSS}\}$, must be calculated taking into account the stiffness of all the structure. To do so, an Influence Matrix, $[\Delta N]$ that includes the effect in term of stay forces of the prestressing of every single stay in the rest of stays is required. The only unknown of Equation 4 is $\{\varepsilon_{OSS}\}$ and it can be directly defined by the following equation:

$$\{\varepsilon_{OSS}\} = [\Delta N]^{-1}(\{N_{OSS}\} - \{N_P\}) \quad (4)$$

in which $[\Delta N]^{-1}$ is the inverse of $[\Delta N]$.

3.4 *Including the time-dependent phenomena into the OSS*

Creep and shrinkage might play an important role in the structural behavior of concrete cable-stayed bridges. In fact, they change the stress state of the structure over time. Nevertheless, these phenomena are rarely included into the definition of the *OSS* due to a number of uncertainties (e.g. in the construction process).

In order to include time-dependent phenoemena effects $\{\varepsilon_{OSS}\}$ might be replaced by an alternative vector $\{\varepsilon_t\}$. This new vector can be used to simulate the construction process of cable-stayed bridges.

Assuming that every stay cable is prestressed in two operations, $\{\varepsilon_t\}$ includes the strains to be introduced into the last tensioning operation of each stay at their respective prestressing times. In those cases where the structural system is defined to remain invariable during the last tensioning operation, that is to say when all temporary supports are lifted in the first *N* tensioning operations, $\{\varepsilon_t\}$ can be calculated by modifying Equation (4) as follows:

$$\{\varepsilon_t\} = [\Delta N^{tT}]^{-1}(\{N_{OSS,tT}\} - \{N_{K-N,tT}\}) \quad (4)$$

in which $[\Delta N^{tT}]^{-1}$ is the inverse of an influence matrix in terms of increments of stay forces in the last tensioning operations, $\{N_{K-N,tT}\}$ is a vector that includes the stay cable forces after the first tensioning operations and $\{N_{OSS,tT}\}$ is the vector of target forces in the *OSS*.

A detail calculation of this equation can be found in Lozano-Galant et al. 2014 and Lozano-Galant and Turmo 2014.

3.5 *Simulation of the first tensioning operation*

The stay forces in the first tensioning operation assure that allowable stresses and deflections are not exceeded. In the *FDA*, these forces are defined to assure also the lifting of all the temporary supports. In this way, the structural scheme of the completed structure remains constant in the last tensioning operation.

The simulation of the first tensioning operation is summarized as follows: (1) The superstructure is staggered erected. (2) The effects of each stay prestressing are successively included. In this simulation, each stay prestressing is modeled by adding *Auxiliary Models*. The active forces of the stay cables are calculated to achieve the target force defined by the designer. (3) After each stay prestressing, the vertical reactions of the temporary supports are evaluated. If any temporary support is lifted, a Local Iterative Process is used to define an adequate structural system. A detailed explanation of this process can be found in (Lozano-Galant et al 2013).

3.6 *Simulation of the last tensioning operation*

The last tensioning operation assures the achievement of the *OSS*. The simulation of the stay prestressing is not as straightforward as in the case of the first tensioning operation. For this reason, in most of the algorithms based on a forward simulation, an Overall Iterative Process is required to assure the achievement of the *OSS* (see (Lozano-Galant et al. 2012b)). In this process, the deviations between the simulated model and the pursued state are successively corrected by updating certain parameters.

As in the case of the Direct Algorithm, *DA* (Lozano-Galant et al. 2013), the *FDA* uses the set of imposed strains at target time calculated in Equation (5) to avoid the need of the Overall Iterative Process and to include the effects of the time-dependent phenomena in the *OSS*.

4 EXAMPLE OF APPLICATION

To evaluate the proposed analysis, the *FDA* is applied in this section. First, the main characteristics of the cable-stayed bridge are described together with the tensioning process. Then, the obtained results are presented. To evaluate the creep and shrinkage effects throughout the Model-Code is used.

4.1 *Description*

The cable-stayed bridge is erected on 11 temporary supports placed every 15 m as described in Fig. 2.

The model of the structure includes a concrete pylon 55 m high, a 180 m long concrete deck and N=19 stay cables. Each stay cable is composed by 50 strands and they are arranged in a fan symmetric form and uniformly anchored every 9 m along the deck. The self-weight of the bridge deck, g_1, the dead load, g_2, and the Target Load, TL, are 135, 70.5 and 202.5 kN/m, respectively. In service, the structure includes a live load of 80 kN/m.

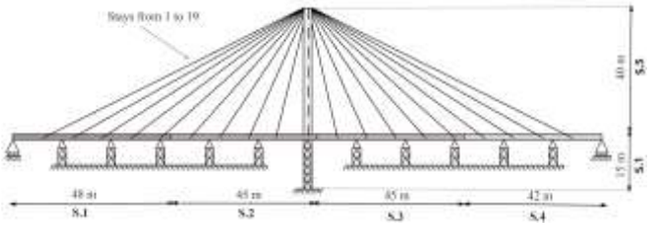


Figure 2: Geometry of the analysed cable-stayed bridge.

The superstructure is evolutionary erected by five construction stages (named from *S.1* to *S.5*). The length of the different segments of each of these stages are described in Fig. 2. The construction process is initiated at 28 days and each stage requires 12 days.

The *FEM* of the bridge consists of 360 elements for the deck, 110 for the pylon and 19 for the stay cables. The Area, A, Young's modulus, E, and the Inertia, I, of the different elements are summarized in Table 2.

The stay cables are prestressed in two operations. During the first prestressing operation, the stays are installed and prestressed to the 80% of their final force. These forces are presented in Figure 3.

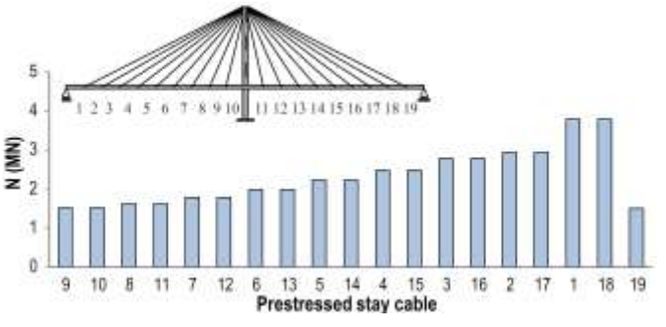


Figure 3. Axial forces in the first tensioning operation.

Table 2. Geometric properties of the bridge elements.

	A [m^2]	E [MPa	I [m^4]
Deck	5.4000	33500	4.2
Pylon	8.5400	33500	14.4
Stays	0.0072	195000	0.9

For the second prestressing operation the vector $\{\varepsilon_t\}$ is used. To include the effects of the time-dependent phenomena into this vector, the procedure described in Lozano-Galant et al. (2014) is used. The stays are prestressed from 88 to 107 days for the first tensioning operation and from 110 to 130 days for the second one. After both tensioning operations, the dead load (70.5 kN/m) is added.

The stay cables in the *OSS* are defined by the rigidly continuous beam criterion (Lazar and Nazmy 1972). The Target time, t_T, to achieve the *OSS* is defined at 130 days. Analyses were carried out until the age of 10000 days.

4.2 *Results*

In this section, the main results of the simulation by the *FDA* are summarized. Fig. 4 presents the axial forces at the second tensioning operation. This figure shows how the asymmetry of the construction process affects the tensioning process.

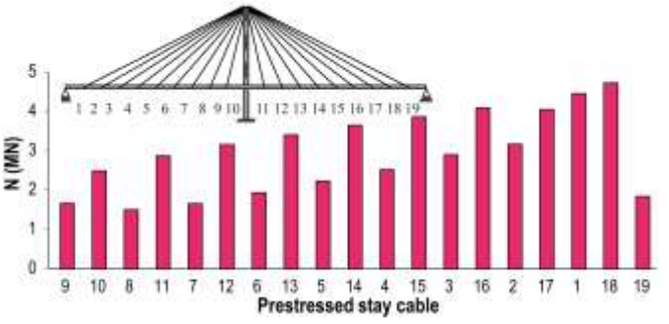


Figure 4: Axial forces in the second tensioning process.

The deck bending moments in the *OSS* (at 130 days) and at 10000 days are presented in Figure 5.

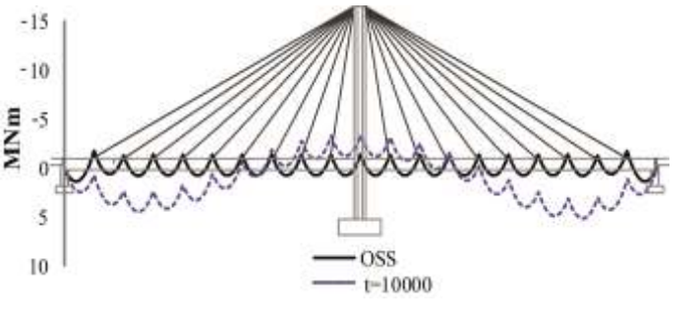


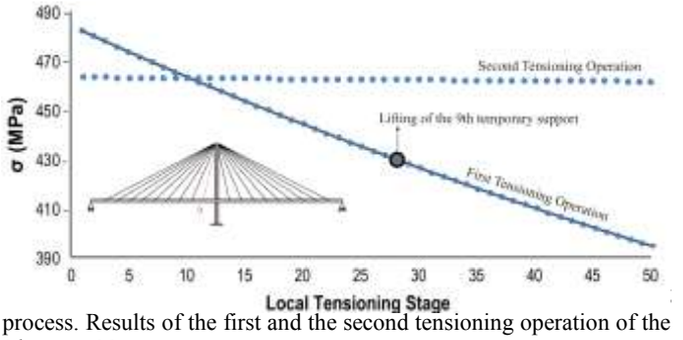
Figure 5: Bending moment diagrams at the end of the construction process at 130 and 10000 days.

The analysis of Figure 5 shows how the target behaviour is only achieved at certain time. The designer can choose what is more economical: using additional tensioning operations in service to correct these effects or avoiding these additional tensioning operations by taking into account these effects during the calculations done in the design process. If this last choice is done, stay forces can be incremented and deck and towers can be pre-cambered to mitigate the effects of the time-dependent phenomena.

With the *FDA*, the stresses in the strands of the stays can be easily calculated without the need of separate models, even when the strand-by-strand tensioning technique is used.

The fifty strands forming each stay are successively introduced into the structure and prestressed. The strain that is needed to achieve in the full stay the desired axial force is successively applied into each of the strands when placed to simulate its tensioning. In the model, when a new strand is introduced and prestressed the axial forces of all placed strands are modified. At the end of the stage, when all the strands are placed and prestressed all the forces in the strands are equal and the force of the stay matches the target value.

Fig. 6 shows the stress in the first strand of the *9th* stay in the first prestressing operation throughout the strand-by-strand tensioning technique. In this construction stage, the structural system consists of the set of the temporary and permanent supports. When the first strand is placed, a certain stress is obtained. Then, as new strands are successively introduced into the structure, the stress of the first placed strand is successively reduced. When all the strands have been placed and prestressed, the stress of the first strand is reduced 84.3 MPa respect to its value when first prestressed. This implies a prestressing loss of the first strand of 20.2%. When the *28th* strand is introduced and prestressed, highlighted in Fig.6, the axial force introduced into the stay is such that is able to unload the temporary support under the stay cable. Therefore, the structural system of the bridge changes as the unloaded temporary support is removed from the model. In the following stages, the stays will be re-stressed, using the strand-by-strand tensioning technique. In order to do so, the imposed strain in the strands when they were first prestressed is successively changed to the one that corresponds with the stage where the strands are being re-stressed.



process. Results of the first and the second tensioning operation of the 9th stay cable.

Fig 6 also shows the stress in the first re-stressed strand of the *9th* stay in the *35th* construction stage. As all the stays were placed and the temporary supports were unloaded and removed from the model in the preceding construction stages. This structural system remains constant throughout the re-stressing stage. When all the strands have been re-stressed, the stress of the first strand is reduced 1.70 MPa respect to its value when re-stressed. The increment of axial force along the re-stressed stage is 12.5 kN, which is the 5.2 % of that axial force introduced by the jack.

The comparison of the reduction percentages of the stress in the first strand obtained in the *1st* and the *35th* construction stages showed that lower reductions of stress were calculated when the stay is re-stressed. This can be explained by the fact that in the re-stressing stage the axial force introduced by the jack is lower as well the structural system of the bridge is stiffer as all the stays were placed in the preceding stages.

5 CONCLUSIONS

This paper presents the first algorithm, the Forward-Direct Algorithm (*FDA*), to include the effect of the time-dependent phenomena into the simulation of cable-stayed bridges built on temporary supports. This algorithm includes the following assumptions: (1) Forward simulation approach, (2) Application of the superposition of stages principle. (3) The Objective Service Stage (*OSS*) is defined in terms of axial forces in the stay cables to achieve the behavior of a continuous beam in the deck. (4) All temporary supports are removed before the last re-tensioning operation. (5) Stay cable forces are simulated by imposed strains.

The main innovation of the *FDA* consists of introducing the time-dependent phenomena effects into the unstressed length of the stays concept to calculate the prestressing strains to be introduced during the last re-tensioning operation. The application of the unstressed length concept has major advantages during the simulation (as the achievement of the *OSS* can be assured without any overall iterative process)

and during service (as time-dependent phenomena effects might be considered during erection).

To validate the results of the *FDA*, a cable-stayed bridge is analyzed. The results of this example showed the important role of time-dependent phenomena in cable-stayed bridges. A detailed analysis of the optimum time to define the *OSS* will be addressed in the future.

6 ACKNOWLEDGEMENTS

The authors are indebted to the Spanish Ministry of Economy and Competitiveness for the funding provided through the research project BIA2013-47290-R, BIA2017-86811-C2-1-R and BIA2017-86811-C2-2-R, funded with FEDER funds.

7 REFERENCES

Menn, C. 1986 Prestressed concrete bridges, Springer-Verlag, Zurich.

Hassan, M.M. Nassef, A.O. & El Damatty A.A 2012. Determination of optimum post-tensioning cable forces of cable-stayed bridges, *Engineering Structures*. 44: 248-259.

Janjic, D. Pircher, M. & Pircher, H. 2003 Optimization of Cable-Tensioning in Cable-stayed Bridges, *Journal of Bridge Engineering.* 8: 131-137.

Lozano-Galant, J. A. Payá-Zaforteza, I. Xu, D. & Turmo, J. 2012a. Analysis of the construction process of cable-stayed bridges built on temporary supports. *Engineering Structures*. 40; 95–106.

Behin, Z. & Murray, D. 1992 A Substructure-Frontal Technique for Cantilever Erection Analysis of Cable-Stayed Bridges, *Computers & Structures*, 42: 145-157.

Wang, P. H. Tang, T. & Zheng, H. 2004 Analysis of cable-stayed bridges during construction by cantilever method*, Computers & Structures*. 82: 329-346.

Lozano-Galant, J. A. Payá-Zaforteza, I. Xu, D. & Turmo, J. 2012b Forward Algorithm for the construction control of cable-stayed bridges built on temporary supports. *Engineering Structures.* 40: 119-130.

Lozano-Galant, J.A, XU, D. Payá-Zaforteza, I., & Turmo, J. 2013 Direct Simulation of the Tensioning Process of Cable-Stayed Bridges, *Computers & Structures*. 121: 64-75.

SETRA. 2001 *Recommandations de la Commission Interministrielle de la Precontrainte*. Service d'Etudes Techniques des Routes et Autoroutes, France.

Jorquera-Lucerga, J.J. Lozano-Galant, J.A. & Turmo, J. 2016 Structural behavior of non-symmetrical steel cable-stayed bridges, Steel and Composites Structures, 20, 447-468.

Lazar B.E., Troisky M.S. & Douglas M.C. 1972 Load analysis balancing of cable-stayed bridges. *Struct. Div ASCE* 1725–40.

Lozano-Galant, J.A, Ruiz-Ripoll, L, Payá-Zaforteza, I., & Turmo, J. 2014 Modification of the stress-state of cable-stayed bridge due to staggered erection of their superstructure, *Baltic Journal of the Road and Bridge Engineering*, 9(4): 241-250.

Lozano-Galant, J.A., & Turmo, J. 2014 Creep and shrinkage effects in service stresses of concrete cable-stayed bridges. *Computers and Concrete*. 13(4): 483-499, 2014

Maintenance, Safety, Risk, Management and Life-Cycle Performance of Bridges – Powers, Frangopol, Al-Mahaidi & Caprani (Eds)
© 2018 Taylor & Francis Group, London, ISBN 978-1-138-73045-8

Design of Pergola Structures for High Speed Rail Bridges

A.P. Ranasinghe
Jacobs Engineering, New York, USA
E.G. Honarvar
Jacobs Engineering, New York, USA

ABSTRACT:

Pergola structures also known as elevated slab structures are used in rail bridges where the rail alignment crosses over features such as roads and rail tracks at very large skews. These structures have become quite useful and popular in high speed rail projects where the track alignment is such that the avoidance of large skews is not possible. A pergola structure consists of two lines of several multi-span frames spanning the features crossed. In each multi-span continuous frame, standard precast pre-tensioned concrete (PC/PS) wide flange girders or for shorter spans PC/PS box girders placed in the transverse direction support a concrete deck slab that carries the guide way. The transverse girders are supported by two longitudinal reinforced concrete or post-tensioned edge beams. Each edge beam is supported by single columns through a pinned connection or a bearing. In this paper, the design requirements of track structure interaction analysis required in high speed rail structures are explained. Also steps taken to design the pergola structures in order to comply with the tight design criteria are discussed. Design details such as the edge beams, joints between pergola frames and transitions from pergola structures to other superstructure types are provided.

1 INRODUCTION

Pergola structures also known as elevated slab structures are used in rail bridges where the rail alignment crosses over features such as roads and rail tracks at very large skews. These structures have become quite useful and popular in high speed rail projects where the track alignment is such that the avoidance of large skews is not possible.

A pergola structure consists of two lines of several multi-span frames spanning the features crossed. In each multi-span continuous frame, standard precast pre-tensioned concrete (PC/PS) wide flange girders or for shorter spans PC/PS box girders placed in the transverse direction support a concrete deck slab that carries the guide way. The transverse PC/PS wide flange girders or PC/PS box girders are supported by two longitudinal reinforced concrete or post-tensioned edge beams. Each edge beam is supported by single columns through a pinned connection or a disk bearing.

In this paper, the design requirements of track structure interaction analysis required in high speed rail structures such as deflection, frequency, and acceleration are explained. Also steps taken to design the pergola structures in order to comply with the tight design criteria are discussed. Design details such as the edge beams, joints between pergola frames, transverse girder supports, and transitions from pergola structures to other superstructure types are provided. These design details provided can be quite useful in the construction, operation, and maintenance of Pergola Structures used in High Speed Rail Bridges.

Figure 1 shows a typical Pergola Structure with Box Girder Approach Structures.



Figure1. A Typical Pergola Structure with Box Girder Approach Structures

2 PERGOLA MODEL

The superstructure of pergola frames, including the deck and transverse PC/PS girders can be idealized in the FEM using a Grillage Model, as exhibited in Figure 2. In the Grillage Model, a grid of transverse and longitudinal beam elements characterizes the concrete deck slab. The columns and drilled shafts are modeled using beam elements placed at the center of gravity of these structural components.

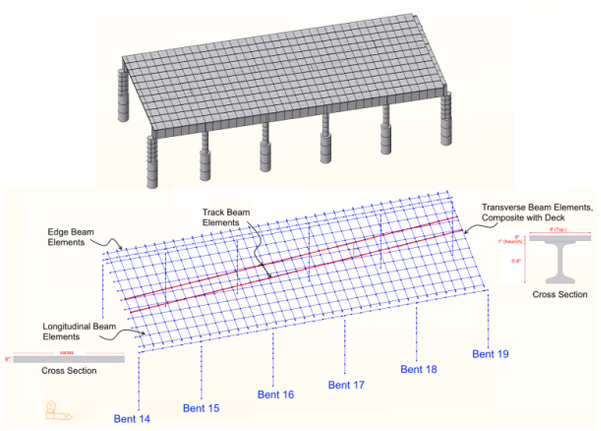


Figure 2. Finite Element Model of the Pergola Structure

The details of the Grillage Model are shown in Figure 2. In the transverse direction, the grillage members coincide with the centerlines of transverse PC/PS girders. The stiffness of transverse beam elements accounts for the composite action between the girder and deck. The deck slab behavior in the longitudinal direction is captured by placing longitudinal beam elements (cross beams) at appropriate spacing. The longitudinal beams are the same as the deck with zero weight.

In order to perform live load analysis, dummy beam elements with an infinitesimal stiffness and zero weight are employed to model track path along the bridge.

Soil-structure interaction was modeled using p-y curves along the drilled shafts.

3 TRACK STRUCTURE INTERACTION

Track Structure Interaction (TSI) Analysis is necessary to limit deformations and acceleration of Track Structure Interaction critical structures subjected to high-speed moving trains. To this end, the TSI analysis shall conform to the following design requirements: frequency analysis recommendations, track-serviceability limits, rail-structure interaction limits, and dynamic structural analysis limits.

3.1 *Frequency Analysis*

Using the Eigenvalue analysis in the FEM, the natural frequency of the primary modes of deformation of the Pergola Structure is determined. The calculated frequencies in the vertical, transverse, and torsional direction are compared to the corresponding values recommended by the design criteria to ensure well-proportioned structures and minimize resonance effects. For the pergola section, as the transverse span length is the dominant mode, the frequency limits were determined using the transverse span length.

3.2 *Track Serviceability Analysis*

The primary objective of the serviceability analysis is to limit track displacements due to structural deformations. The deformation limits are based on maintenance requirements, passenger comfort, and track safety standards. The vertical and transverse deflection limits are determined as a function of span length. However, the definition of the span length is unclear when a bridge frame consists of both transverse and longitudinal spans, as does the pergola section. Therefore, these limits are calculated for both of the minimum longitudinal and transverse span length of the pergola frames. Using the longitudinal span lengths result in the smaller defection limits compared to the limits calculated based on the transverse span lengths for the pergola frames. Since the deck is directly supported by the transverse girders, it is deemed more reasonable to define the deflection limits using the transverse span length rather than using the longitudinal span length.

In addition to vertical deflections, the rotation limits about transverse and longitudinal axis, relative vertical and transverse displacement at expansion joints, and the deck twist are checked.

3.3 *Rail Structure Interaction (RSI) Analysis*

Railway bridges and continuous welded rail constantly impart forces on each other due to their distinct responses to the applied loads. The structure loads, which are transferred to and from the rails through fasteners, increase the probability of rail fracture. Therefore, the values of relative displacements between two adjacent frames at expansion joints and rail axial stresses are evaluated using RSI analysis. The calculated values shall be lower than the limits specified by the design criteria to minimize the probability of rail fracture.

The RSI analysis will be performed using the Rail-Track Analysis Model available in the Midas Civil software, which is incorporated into the FEM described earlier. In RSI analysis, the specific construction method and construction sequence in addition to time-dependent deformations caused by prestressing, creep, and shrinkage will be considered.

The interaction between the rail on the bridge and the adjacent rail on the embankment is captured by ample rail extension to the embankments beyond the abutments. The rail extensions terminate at a perfectly plastic longitudinal spring supports. Force accumulation in this spring will be examined to validate the length of rail extension and must remain less than 39.7 kips typically.

The interaction between the rails and superstructure is represented by coupling springs along the length of the model (superstructure and embankment). Throughout the entirety of the FEM, springs representing the tie fasteners will be spaced at a maximum of 10 ft. Tie fastener spacing is assumed to be 27 in. across all project structures. Linear springs are used to account for the vertical and lateral stiffness, while bi-linear spring represents the longitudinal stiffness. The bi-linear longitudinal restraint accounts for force accumulation and displacement in the rail fasteners before rail slip occurs. Typical values for the longitudinal restraint is 1.37 kips per foot of track (unloaded) and 2.7 kips per foot of track (loaded) for non-ballasted track at the yield displacement of 0.02 in.

After completing the RSI analysis, if the relative displacement and axial stress limits given in the design criteria could not be met at the expansion joints, alternatives to connect and reinforce adjacent joint interfaces would be explored. As a commonly used alternative, longitudinal dowels or steel pipes may be used at the joint interfaces to reduce relative displacements and axial stresses, thereby satisfying RSI analysis requirements. The longitudinal dowels or steel pipes would allow for relative rotation about transverse axis and displacement in the longitudinal and vertical direction, but restrain the remaining degrees of freedom.

3.4 Dynamic Structural Analysis

Dynamic structural analysis is performed to assess the interaction between the bridge and all potential high speed rolling stock options and limit vertical deck acceleration. In particular, the occurrence of maximum dynamic amplification effects due to resonance is investigated by comparing the bridge's natural vertical frequency and the frequency of axle loading.

3.4.1 *Resonance and Cancellation Speeds*

The FEM is used to determine what vehicle speeds correspond to both resonance and vibration cancellation. If the resonance speed is close to the vehicle operating speed and substantial deflections occur, an alteration of the superstructure properties may be necessary.

3.4.2 *Determination of Vertical Impact Factor*

Using the dynamic analysis, dynamic live load vertical deflection, shear, and moment will be determined. The vertical impact factor imposed by the high-speed trainset is then calculated by comparing ratios of each dynamic load response with the corresponding static response. The maximum ratio will be the vertical impact factor used for the high-speed rail vehicle live load.

3.4.3 *Vertical Deck Acceleration*

The vertical deck acceleration limit is in place to ensure safety and passenger comfort. Typically for non-ballasted track bridges, the maximum deck acceleration is limited to 16.1 ft/s2(0.5g).

4 DESIGN ISSUS

4.1 *Design Issues Related to RSI*

Some of the step taken in order to comply with the tight design criteria for deflection, frequency, and acceleration to design the pergola structures are as follows:

4.1.1 *Reducing the Deflections*

The For high speed rail the live load deflection limit for passenger comfort and track maintenance is very stringent. The span to live load deflection ratio for this can be as high as 3500. The deflection can be reduced by using deeper girders and reducing the girder spacing. However, lighter girders are preferred as an increased superstructure mass can have an adverse effect on the natural frequency.

4.1.2 *Increasing the Natural Frequency*

The natural frequency can be increased by increasing the depth and the concrete strength of the girders.

4.1.3 *Reducing the Deck Acceleration*

The deck acceleration can be reduced by taking advantage of the composite action between the guideway and the deck. Figure 3 shows the guideway and the deck that will act together compositely.

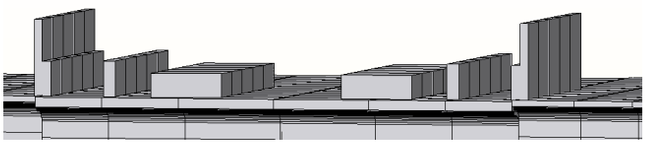


Figure 3. Typical Section of the Guideway and the Deck

4.2 *Other Design and Construction Issues*

Some design and construction issues are as follows:

4.2.1 *Edge Beam Support Condition*

In some pergola designs, the edge beam is supported on the pergola column directly. They are connected together with a small vertical steel I-beam. There are concerns however, that the concrete around the I-beam tends to crack over the years. The use of disk bearings placed on the pergola columns to support the edge beams is considered an expensive, yet a better solution. Figure 4 shows a disk bearing supporting an edge beam.

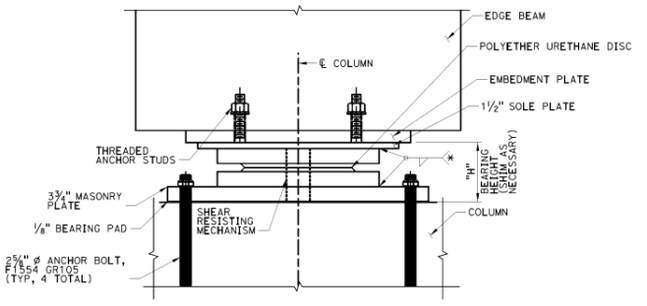


Figure 4. A Disk Bearing Supporting the Edge Beam

4.2.2 *Transverse Girder Connection to the Edge Beam*

Since the transverse girders are pre-stressed concrete girders, they are connected to the edge beams as simply supported. Figure 5 shows the typical interior girder elevation with the connection of the girder to the edge beam.

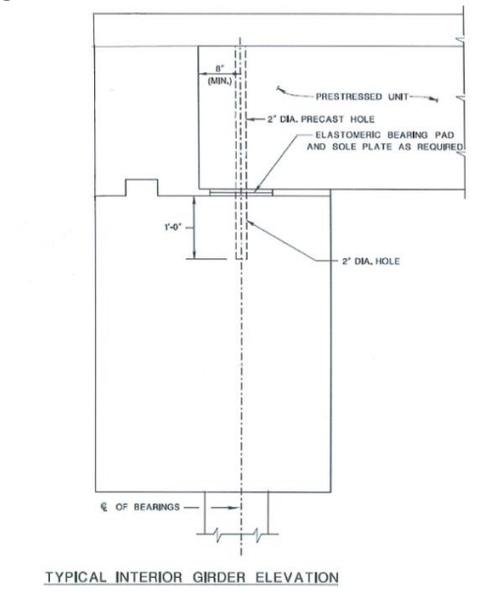


Figure 5. Girder Connection to the Edge Beam

4.2.3 *Joints between Pergola Frames*

The joints between the pergola frames should transfer no moments and should allow the pergola frames to move in the longitudinal direction independently. Figure 6 shows a pipe type connection and a link type connection. The pipe type connection is hard to build and cost effective but its long term performance is questionable. A link type connection is expensive but its long term performance is better than a pipe connection.

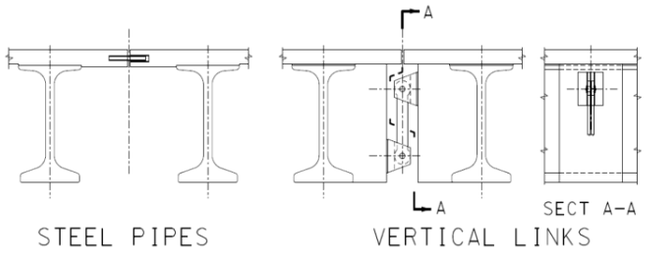


Figure 6. Connections between Pergola Frames

4.2.4 *Transition from Pergola Section to Approaches*

When there are right-of-way limitations, or utility conflicts the two edge beams of a pergola frame may not be of the same length. This often happens at the pergola frames near the approaches. In situations like this, if the approaches are box beams the box beam is cantilevered from the edge beam thus maintaining the continuity of the guideway. Figure 7 shows the transition of the pergola section to a box beam approach.

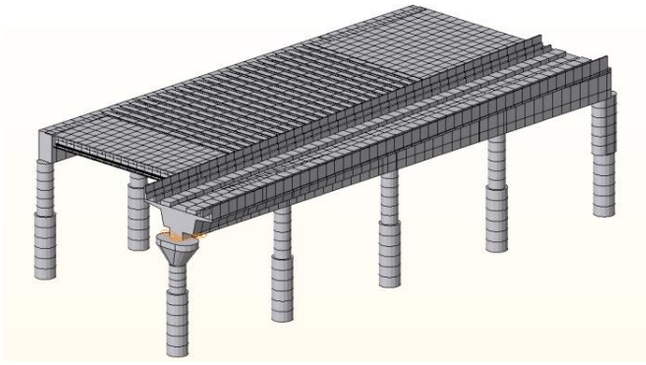


Figure 7. Transition from Pergola Section to Approaches

5. CONCLUSIONS

The methods suggested in this paper will help the designer to comply with the tight design criteria required for high speed rail bridges. Also, the additional design details provided will be very useful in the construction, operation, and maintenance of pergola structures used in high speed rail bridges.

6. REFERENCE

California High-Speed Train Project Design Criteria, February 2014, California High Speed Rail Authority, Selma, California, USA.

Maintenance, Safety, Risk, Management and Life-Cycle Performance of Bridges – Powers, Frangopol, Al-Mahaidi & Caprani (Eds)
© 2018 Taylor & Francis Group, London, ISBN 978-1-138-73045-8

How new performance based contracts add value in maintenance contracts

J. D. van der Walt
Assistant Lecturer, University of Canterbury, New Zealand

Dr. E. Scheepbouwer
Director Construction Management Programme, University of Canterbury, New Zealand

ABSTRACT: Public agencies in charge of maintaining highways and bridges walk a fine line between cost and quality. Recently the New Zealand Transport Agency (NZTA) has adopted many changes in their procurement methods to obtain greater value for money. The new Network Outcomes Contracts (NOC) have been set up to invest where needed and give more control to the agency. This research investigates how the use of the NOC contracts influenced the quality of the assets and whether this resulted in value creation or not. It is concluded that NOC contracts take a more long-term vision approach. However, some assets were arguably kept at too high level of service; a situation that allows present reduction in expenditure. In this paper, qualitative data have been used to identify lessons learned to date. This can assist agencies and contractors in their continued drive to improve outcome based contracts, creating value in the long term.

1 INTRODUCTION

As highway agencies are accountable to the public, delivering value has become an important issue politically. Maintenance regimes from highway agencies inevitably balance the cost of maintenance against the level of service. After years of operating performance based arrangements, the agency has opted for a change towards Network Outcome Contracts (NOC). Both contracts are applicable for the maintenance of highway assets (Zietlow, 2005). The former Performance-Specified Maintenance Contracts (PSMC) used a, '*best for asset'* approach. Contractors were reimbursed for performed work, but carried the majority of the risk. Over the years this approach has led to an increase in the level of service. Higher levels of service do not intrinsically translate to increased value, and recently the NZTA has opted to change towards an arrangement that focused more on providing value. Its goal was to decrease the cost while maintaining the quality of their assets. This paper discusses the differences between both methods with regards to the strategic goals of NZTA, how these goals are achieved and what concerns have been raised. Both PSMCs and NOCs will be discussed after which details on the new approach will be provided.

1.1 *Objective*

Aim: Investigate how the use of the NOCs influence the asset quality and whether this constitutes value creation over previous methods.

Scope:

- This will be a qualitative study as there is limited long term data available due to the recent implementation of NOCs.
- The focus is on experts in the industry who have had first-hand experience with NOCs.
- This study includes expert parties from client (transport agency), consultant, contractors and sub-contractors.

This study has been conducted in New Zealand, therefore is limited to the New Zealand context. However, the results can serve as an indication to other nations with similar contractual arrangements.

1.2 *Literature Review*

There are several business models that have been used in the past. The traditional equipment-based service model is centred on reimbursement of work and materials to meet standards. Cost of labour, equipment, maintenance and consultation for activities on highways and bridges were traditionally billed as a lump sum, once the activity was completed (Wheel, 2000).

Another approach is the cost-plus model. In this case a customer is provided with a detailed structure of prices for equipment, labour and consultation. Both parties agree on a fixed profit percentage to be added to the actual costs (Kim, Cohen, & Netessine, 2007).

Various types of performance-based contracts have been used for several decades in many European and Australasian countries (DeWitt et al., 2005). These contracts aim to refocus the industry, to measure performance instead of specification compliance (Mike Manion & Tighe, 2007).

Performance-specified maintenance contracting (PSMC) and its potential application to the international market has been extensively discussed by Gransberg et al. (Gransberg, Scheepbouwer, & Tighe, 2010). The traditional PSMC moves the focus from '*minimize cost*' to '*maximize value*'. The evolution of this produced the hybrid PSMC. This contract lets the owner hold control of the design contract, however allows the contractor to give significant input through Early Contractor Involvement (ECI) (Zietlow, 2004). This contract allows the contractor to offer alternatives that the design consultant can warrant (Porter, 2001).

Maintenance alliance contracts are normally reserved for the maintenance of large public works. Primarily, it is a way to share risks for major transport arteries on dedicated networks. Alliances have taken up many of the principles introduced by PSMC including working to deliver maximised value and ECI (Botha & Scheepbouwer, 2015; Scheepbouwer & Gransberg, 2014).

Outcome based contracts as a new business model has been increasingly discussed within the commercial and academic world (Ng, Ding, & Yip, 2013; Wirtz, Pistoia, Ullrich, & Göttel, 2016). The need for effective new business models are driven by three key components:

1) Value drivers are often an important factor for organizations. Therefore, when a change in value drivers is present, a need is created to change business model.
2) When value drivers are changed an organization's performance during this time is highly scrutinised to see if key outcomes are compromised.
3) Change in value drivers can result in partnerships changing, requiring new innovative agreements to be reached.

Outcome based contracts have evolved from these principles to focus on the holistic outcomes of assets rather than the resources required for a single asset (Lee & Barrett, 2003). Outcome Based contracts have the following goals:

1) Align both parties to the outcomes of a product or service.
2) Shift shared risk back to the client, increasing responsibility of the client.
3) A party that can attain best outcome results from both interior and exterior connections and collaborations, is more able to exceed expectations.(Ng et al., 2013)

Outcome based contracts draw from the classical approaches and trends seen in recent years. Moving the contractor closer to the client. Outcome based contracts also change the focus from *'value of asset'* to *'value of network'* perspective.

1.3 *Network Outcomes Contracts with Asset Management*

The introduction of NOCs was the conclusion of a process that was initiated by the need to find ways to reduce cost (a change in value drivers). The New Zealand Transport Agency undertook three years of investigation to meet this demand. NZTA identified multiple opportunities. Firstly, the NZTA identified that more work needs to be conducted by the agency instead of handing this off to an external supplier. This is particularly important in the fields of decision making and customer service. Secondly, move away from a risk adverse management culture therefore taking on more shared risk in the contract. This could result in reduced cost. Thirdly, introduce better methods to estimate Net Present Value as the current system was not applied consistently. Finally, investigate new methods to understand the risk of flat budgets limiting the amount of renewals undertaken. Following this investigation, the NZTA after considerable consultation introduced the NOC system to implement these changes (M. Manion, nd).

1.4 *Changes to Managing Assets*

At its core, the NOC is an outcome based contract and pursues a quality outcome. The NOC does not specify the methods of how the outcome is achieved, but does specify the performance measures to show that a quality outcome has been reached. Outcome based contracts have drawn from traditional performance based, alliances and hybrid contracts with a change of focus. The contractor retains the risk of the supply chain to build/maintain quality assets. The method of how the contractors establishes the cost for achieving a quality outcome is up to them (NZTA, 2015).

From the literature review and contract documents the following key elements will change in how assets are managed. Firstly, NOCs payment contain both measure and value and lump sum components. Secondly, the contractor is responsible for

managing the general condition of the asset, so that it remains serviceable and safe. The contractor must estimate the amount and type of repairs and approximate the cost of delivering them to the specified performance measures in the contract. Thirdly, the contractor must make provisions to achieve these performance measures in a lump sum component. Failing to provide the required level of performance will result in a financial penalty. However, suppliers who manage renewals investment below a target quantity are rewarded (M. Manion, nd; NZTA, 2015).

Like in previous methods, contactors are still able to seek variations to rates if quantities differ substantially from those listed in the schedule of prices. This is if they can sufficiently demonstrate a material effect from the quantity change. It is then up to the contractor to show that quantity has changed and that this has had a material effect, otherwise the rates as tendered remain for the increase of quantity (NZTA, 2015).

2 METHODOLOGY

The methodology of this research has consisted of gathering and analysing literature on the challenges faced and decisions made by NZTA. As well as this, an in-depth document study of the NOC has been completed to understand the methods and reasoning.

There is limited long-term maintenance data available on the NOC contracts due to their recent introduction, therefore this study instead will focus on a qualitative approach through structured interviews. Standardised questions were prepared which focused on key aspects of NOCs and the assessment of value. Interviews with representatives from the delivery teams, clients, contractors and other persons of interest were conducted. Results from these interviews have given insight on how the industry perceives the value of NOCs as well as insight into the operational character of the procurement system. Their expert opinion will form the basis of the results in this paper. This study surveyed from the sub categories in Table 1.

Table 1.Table showing subcategories of parties interviewed

	Client (Agency)	*Consultants*	*Contractor*	*Sub-contractor*
# of experts interviewed	3	3	3	2

3 RESULTS AND ANALYSIS

In this section, the opinions of the different parties will be stated. Each section contains a table that captures the opinions of the consulted experts with a continued discussion of the points. At the end of this section the results will be summarized.

3.1 *Client's Point of View*

The client's argument from the start has been around cost savings. From discussion with client representatives, NOC contracts aim to force contractors to be more effective in their management programs as the new contract will significantly limit maintenance funds. The contractor must offset this change with a smarter strategic maintenance strategy. The focus has been to prove value, as previous systems in place did not achieve the desired result. Before maintenance is allowed the contractor must comply with new more rigorous specifications to demonstrate value.

Table 2. Client, showing key factors that drive value and potential issues from the implementation of NOC in New Zealand.

Factors driving value for the Client (NZTA)	*Potential issues for the client (NZTA)*
• *Reduce cost* • *Results are more in line with desired outcomes* • *Increased co-operation* • *Drive strategic forward work planning* • *Sustainably of the industry is increased* • *Better understanding of customer behaviour* • *Performance measures drive quality* • *KPI and KRA show improvement* • *Upskill the industry* • *Industry adapting to holistic focus* • *Change in business model for the industry*	• Increased risk to the client • Require large increase in personnel • Potentially higher cost due to outsourcing and limited numbers of sub-contractors • Increased dissatisfaction from the public • Some performance measures are not realistic or effective in driving value and requires further work • Large amounts of resources required to implement NOCs • Communication with the public

The NZTA recognises that the implementation of the NOC will take time. Relevant staff and personnel must be retrained to work effectively with the new contract. Much effort has been put into establishing clarification of new terms in the contract.

An important part of the NOC is the inclusion of a clause specifying that a large proportion of work must be conducted by sub-contractors. This forces a substantial amount of funds back into the community and stimulates small business growth.

Large contractors are using their learnings from earlier contracts to minimise first year difficulties with NOC contracts. This shows the industry adapting to the new environment.

NOCs in South Canterbury, New Zealand show great improvement. They have moved from poor to outstanding due to more rigorous reporting and

communication. In general, the NZTA is reporting steady state or improvement in key areas.

NZTA reports that it has gained a better understanding of customer behaviour, and this has led to an improvement in efficiency. For example, more regular litter collection has been implemented outside of fast food restaurants. Another example includes more regularly cleaning graffiti from bridges. Both examples resulting in visually cleaner assets.

Looking ahead, NZTA representatives noted that NZTA is moving its focus from implementation to delivery and performance of the NOC contracts. This requires auditing that has not been well-established. Auditing this type of contract has presented several difficulties which they are working through currently.

3.2 *Contractors' Point of View*

Due to the decrease in funds and reduced control by the contractor, there is speculation within the construction industry that these changes will result in reduced level of service over time. Therefore, this could result in the inevitable rise of maintenance cost in the far future.

Severe weather events can result in the contractor losing a significant amount of income because of unexpected maintenance. This can put pressure on an already streamlined lump sum budget. With extreme weather events set to increase in the coming years this may not be a once off issue.

Meeting performance levels under extreme financial pressure is difficult. If contactors do not meet these levels of performance they are then also financially punished.

If certain assets are maintained to too high a standard, it can result in NPV issues for the rest of the network. Contactors must be careful in spending available funds as they are required to prove a network performance outcome.

Contractors speculated that some of the KPIs & KRAs require excessive resources which does not result in value. Contractors are pleased that NZTA has recognised this and are working on reforming the KRA & KPI framework.

All contracts agree that the NOC has put more pressure on their forward work program. They have been forced to innovate, especially to justify in terms of value. Contractors are forced to operate a much leaner program only conducting work that is absolutely necessary. An example of this is the heavy reliance on the ratio of defects over area to justify NPV.

To implement the new framework, the contract requires multiple parties to communicate from the NZTA. Previously contractors generally have had to deal with one point of call, instead now with the NOC framework, contractors are required to communicate with four and above personnel from the agency. Some contractors have indicated that this communication process is slowing performance and is not driving value.

Table 3. Contractor, showing key factors that drive value and potential issues from the implementation of NOC contracts in New Zealand.

Factors driving value for the primary Contractor	*Potential issues for the primary Contractor*
• *Decreased maintenance cost.* • *Longer contact period roughly 7 years. Allows for forward work planning and investment.* • *Larger area contracts* • *Increased in quality of work delivered* • *Requires the contractor to innovate to remain competitive* • *Potential gain if performance criteria are reached* • *Multiple parties are available from the NZTA when problem arise* • *Drives the industry forward as everyone is working for outcomes* • *Driver collaboration between client, consultant, contractor and sub-contractor* • *Drives sustainability of the industry* • *Drives better educational resources to train external industry*	• Reduced monetary value can appear as a potential loss of profit • Anxiety that less spending and less control by the contractor will result in a potential decreased level of service • Scope creep can become a real issue • Financial penalties if the contractor does not meet criteria • Events outside of the contractors control could significantly influence losses and gains • Lump sum portion of the bid requires extreme foresight, this can result in cost overruns and low margins • More communication is needed with different parties in the NZTA slowing progress and hindering performance • Contractors can be punished for keeping the asset in elevated condition. The rest of the network may be neglected • This might not be the best model for the public • Sub-contractors are, "hit and miss" in terms of quality and performance • Increased risk when using sub-contractors • Uncertainty of how handover will occur after the end date of the contract

Contractors must revolutionize the systems they use. Great efforts and resources are being invested into further development of techniques to preserve asset life for a low cost. An example of this is the 1st Signs approach to maintenance (M. Manion, nd).

Cooperation between the agency, contractor and subcontractor has become vital to success under the NOC contracts. The inclusion of a high proportion of subcontractors in the NOC has forced the principle contractor to increase H&S and environmental training to minimise risk.

3.3 *Consultants' Point of View*

Some consultants are expecting reduced quantity of work as NZTA is conducting much of the decision making and consumer service in house. NZTA has recently hired many new staff to support these contracts. Contractors have also taken a large proportion of the responsibility from the consultants.
Consultants, have been asked by contractors to develop methods and systems to support these new contracts.

There was a push from contractors to allow them to exclude consultants and allow much of the work to be completed in house. The NZTA disagreed as this would not provide value in terms of sustainability of the industry. Therefore consultant-contractor partnerships are still present, preserving some work for the consultant. The consultant has now moved to take up a supportive role for the primary contractor.

Table 4: Consultant, showing key factors that drive value and potential issues from the implementation of NOC in New Zealand.

Factors driving value for the Consultant	*Potential issues for the Consultant*
• *Consultant – contractor partnerships are still maintained* • *Higher standards of H&S, auditing and reporting* • *New need for engineering development and research* • *Quality work*	• Reduced decision-making work for the consultant • Loss of capability in the industry through consolidation • Increase of quality of work but a potential decrease of level of service

Consultants believe that there has been a loss of capability of the industry through consolidation caused by the formation of NOCs.

3.4 *Sub-contractors' Point of View*

The requirement of a high proportion of sub-contracted work in the NOC has led to the general unavailability of sub-contractors. This is particularly the case for local councils as the larger contracts offered by the primary contractor of the NOC are more appealing. This has led to councils struggling to find suitable sub-contractors to complete work. There has also been an increase in the average bid price due to the lack of competition in some cases. This could be a possible temporary side effect as more sub-contractors move into this space and restore competition. The sub-contractors reported that their business model has not changed under the new NOC contract, 'business as usual'.

Sub-contractors have reported that much more rigorous training is available to conduct work, especially in the areas of health and safety, environmental impact and forward work programming.

Table 5: Sub-contractors, showing key factors that drive value and potential issues from the implementation of NOC in New Zealand.

Factors driving value for the sub-contractor	*Potential issues for the sub-contractor*
• *Increased sub-contractor involvement* • *Increased amount of work given to sub-contractors* • *Increase training of sub-contractor staff* • *Possible gap in the industry for the formation of smaller contracting businesses* • *Higher standards of sub-contractor training* • *Taking on more diverse tasks*	• Sub-contractor's quality and standards and training differ greatly • Speciality sub-contractors could see number of jobs decrease • Lack of sub-contractor competition therefor increasing bid price for client

3.5 *Comparison and Discussion*

The introduction of the NOC contracts has been relatively well received by contractors, consultants and sub-contractors. It became clear that the previous contracting methods were not achieving the desired outcome for the NZTA. This need was driven originally by the financial crisis to reduce costs but has developed into a change that the industry needed. Over multiple years of consultation the NOC contract was introduced. Contractors and consultants felt that this contract has been long in the pipeline and they have had sufficient time to be consulted.
From the results, it was evident that NOC has clearly driven the industry in the direction that the agency wanted. This is evident by contractors reporting significant pressure on managing their forward work program with large oversight from the agency. Contractors have also felt the impact from the new value requirements. They have reported that it has become much more difficult to justify maintenance, driving value.

The NOC has introduced significant changes in communication and reporting. Results have shown that communication has driven value from the agency's point of view. However, contractors have insisted that communicating with multiple agency representatives have slowed down progress and is hindering value creation.

The consultants' view is that the primary contractor was previously not exposed to the agencies demands. Previously it was the consultant's job to act as an intermediary. With the NOC, the link between contractor and client has been narrowed exposing the contractor to more agency points of call.

Table 6. Comparison of opinions from the four affected parties: client, contractor, consultant and sub-contractor

NOC Driver (Client)	Principal Contractor	Consultant	Sub-contractor
Pervious method not producing ideal outcome	*Agree*	*Agree*	*Indifferent*
Need for change to NOC	*Agree*	*Agree*	*Agree*
Enhanced communication requirements drive value	*Does not agree, can slow down processes*	*Agree*	*Can slow down progress*
Performance measures leads to improved procedures and quality work	*Mostly*	*Mostly*	*Agree*
Reduce cost while maintaining current LoS	*Does not agree*	*Does not agree*	*Indifferent*
Enhance sustainability of the construction industry	*Agree, More training*	*Agree*	*Increase in the number of jobs*
Communicated changes with the public	*Does not agree, improvement needed*	*Does not agree, improvement needed*	*Indifferent*
Impact to business	*Large impact to procedures and business model*	*Loss of work*	*Increase of work*
NOC is an enhanced contracting method for the foreseeable future to boost value	*Agree, requires further review from Agency*	*Agree, requires further review from Agency*	*Agree*

The NOC has had the largest impact on the client and contractor, whereas the consultant and sub-contractor has felt less of its effects. The contractor has had to invest large amounts of resources into training and personnel to deal with the new terms of the NOC contact. This has also been the case for the agency. The consultant has moved to a supporting role and the sub-contractor has seen a significant increase in the amount of work as a direct result of the implemented NOCs.

The intention of the NOC to upskill and grow the larger construction industry appears to be working. The results from this paper suggest that the primary contractor is investing a significant amount of resources into the training of sub-contractors. The sub-contractors have reported that this training was improving their performance in key areas.

Some contractors are apprehensive that less spending and reduced control by the contractor will result in a decreased level of service compared to previous methods. It is the contactors' impression that NZTA has recognized this. Some contractors believe that changes in level of service due to NOC should have been better communicated with the public.

The intention of the agency was to decrease cost while maintaining quality. The implementation of strict performance measures was intended to achieve this. Some contractors and clients argue that this has resulted in an increased quality of work completed. However reduced funding could result in a decreased level of service provided to the public overall. There is speculation within the industry as to whether the current form of the NOC is of best value to the public.

Although the results of the paper show many potential issues, most parties interviewed agree that these issues can be mitigated or resolved with further implementation changes. NZTA has shown they are willing to listen to criticism and make changes. An example of this is where contractors criticised the current KPI and KRA framework used in the NOC. NZTA has responded and is currently re-evaluating the framework. All parties seem to agree that this change in procurement method is to the benefit of the client and will drive value.

4 CONCLUSIONS

Transport agencies are under increasing pressure to reduce cost and provide value for the taxpayer. In New Zealand, NZTA is under pressure from the Ministry of Transportation to reduce maintenance cost. However, maintaining assets is a balance of cost and quality. NZTA must find methods to retain quality in the face of cost savings. NZTA has introduced Network Outcome Contracts in a response to this pressure. These contracts fundamentally change how maintenance is completed in New Zealand. NZTA is taking onboard much of the decision-making process previously outsourced to consultants. The industry is optimistic about the implementation of NOCs. Overall affected parties agree that NOCs are the way forward for the industry. However, the industry is anxious that less spending and less control by the contractor will result in reduced levels of service over time. The industry also fears that possible short-term cost savings could result in long term cost. However, the industry agrees that with continued review the NOC will be a very successful framework for value driven maintenance compared to the previous method. This is echoed by the NZTA, where continuous auditing is now the main driver to improve the performance of these newly introduced contracts. The ideal outcome is a balance

between minimum investment in quality by the asset owners and minimum required repair needed by the maintaining party. As time goes on, an increasing amount of quantitative data will become available. Further research is required to ensure that value is continuously improved for the client and the taxpayer.

5 REFERENCES

Botha, P. S., & Scheepbouwer, E. (2015). Christchurch rebuild, New Zealand: Alliancing with a difference. *Proceedings of the Institution of Civil Engineers-Management, Procurement and Law, 168*(3), 121-129.

DeWitt, S., Yakowenko, G., Bohuslav, T., Ferguson, T., Hoelker, E., Molenaar, K., . . . Wagman, R. (2005). *Construction management practices in Canada and Europe No. FHWA-PL-05-010*.

Gransberg, D. D., Scheepbouwer, E., & Tighe, S. L. (2010). *Performance-Specified Maintenance Contracting—The New Zealand Approach to Pavement Preservation.* Paper presented at the First International Conference on Pavement Preservation, Newport Beach, California.

Kim, S.-H., Cohen, M. A., & Netessine, S. (2007). Performance contracting in after-sales service supply chains. *Management science, 53*(12), 1843-1858.

Lee, A., & Barrett, P. (2003). *Performance Based Building: first international state-of-the-art report*.

Manion, M. (nd). *1st Signs Approach to Maintenance Management* Paper presented at the Institute of Public Works Engineering Australia, IPWEA. https://www.ipwea.org/HigherLogic/System/DownloadDocumentFile.ashx?DocumentFileKey=8c302cdb-9166-4c6e-9a54-c394d9a3b6d6&forceDialog=0

Manion, M., & Tighe, S. (2007). Performance-specified maintenance contracts: adding value through improved safety performance. *Transportation Research Record: Journal of the Transportation Research Board*(1990), 72-79.

Ng, I. C., Ding, D. X., & Yip, N. (2013). Outcome-based contracts as new business model: The role of partnership and value-driven relational assets. *Industrial Marketing Management, 42*(5), 730-743.

NZTA. (2015). NOC Contract Clarifications. Retrieved from https://nzta.govt.nz/assets/Highways-Information-Portal/Technical-disciplines/Network-outcome-contracts/Clarifications

Porter, T. M. (2001). *Trends in the Procurement Models for Highway Maintenance.* Paper presented at the 80th Transportation Research Board Annual Meeting, Washington, DC.

Scheepbouwer, E., & Gransberg, D. D. (2014). *Comparative Analysis of New Zealand Alliance Contracting and US Project Delivery Models.* Paper presented at the Transportation Research Board 93rd Annual Meeting.

Wheel, A. (2000). Purchasing and supply chain management analysis, planning and practice: Thomson learning business press.

Wirtz, B. W., Pistoia, A., Ullrich, S., & Göttel, V. (2016). Business models: Origin, development and future research perspectives. *Long Range Planning, 49*(1), 36-54.

Zietlow, G. (2004). Implementing performance-based road management and maintenance contracts in developing countries-an instrument of German technical cooperation. *German Development Cooperation (GTZ), Eschborn, Germany*.

Zietlow, G. (2005). Cutting costs and improving quality through performance-based road management and maintenance contracts-the Latin American and OECD experiences. *Senior Road Executives Programme, Restructuring Road Management, German Development Cooperation, Birmingham*.

Maintenance, Safety, Risk, Management and Life-Cycle Performance of Bridges – Powers, Frangopol, Al-Mahaidi & Caprani (Eds)
© 2018 Taylor & Francis Group, London, ISBN 978-1-138-73045-8

Design method for scissors-type bridges

Y. Hama, I. Ario and K. Adachi
Department of Civil & Environmental Engineering
Hiroshima University, Higashihiroshima, Japan

ABSTRACT: Many natural disasters destroy infrastructure such as roads and bridges. It therefore becomes essential to restore them to serve as a refuge and help disaster victims. Several emergency bridges are often used for the restoration of these lifelines. We propose "Mobile Bridge" based on the concept of origami engineering as an emergency bridge that is smarter than existing emergency bridges. In this paper, the concept of influenc line diagrams into design of scissors structure is introduced for the firs time. This result revealed the basics of a design of SCI having the scissors structure that acted the moving load including a vehicle and a person. In addition, the rational reinforcement method of a bridge with a scissors structure and superiority is considered, as opposed to the double Warren truss structure that is used as a current emergency bridge and scissors structure.

1 INTRODUCTION

The damage and destruction to social infrastructure by natural disasters, such as earthquakes, floods landslides and tsunamis, are serious problems in disaster prevention for the inhabitants of a stricken area. In particular, many bridges were damaged by a typhoon No.10 in Hokkaido (shown in figur 1). There are assembling block type of temporal bridge (shown in figur 2(a)) to serve as lifelines after a disaster has occurred. However, they are not based on the design concept of an urgent bridge that can be used quickly to save lives at the stricken area. So we need to develop a new bridge of rescue type to survive victims. In other words, We have to consider how to rebuild damaged infrastructure and how to build a new type of rescue system which can be implemented quickly because time is very important when trying to save lives after an emergency. From a previous study on the optimization structure and deployable structure of bridges by Holnicki-Szulc et al. (2003) and Ario et al. (2006, 2010), we propose a new type of movable and deployable emergency bridge called Mobile Bridge (MB) (shown in figur 2(b)) by Ario et al. (2006) and Chikahiro et al. (2012). This bridge does not need assembling work because it is based on the scissors structure (SCI) consisting of the framework structure of the form 'X' by Ario (2013). A temporary bridge of the double Warren truss structure (DWT) exists in the typical assembling bridge. Two different bridges vary in a cross-linking process, but they become the structures that are apparently similar by equipping the reinforcing members in MB. Therefore, the firs purpose of this study is to confir whether the reinforced SCI can exhibit a greater proof stress than the DWT. The influenc line of the main posture used for the design of the bridge and design load are used for comparing the sectional force in both structures. The second purpose is to build the MB design method using the influenc line suitable for a moving load. As a design concept toward a bridge that is both lightweight and strong, we confir the superiority of MB, compared to a DWT, as the emergency bridge with an SCI.

2 ANALYSIS OF INFLUENCE LINES FOR LOADS

SCI is compared with DWT using each sectional force. The design methods for the sectional force of DWT and SCI are explained in the following paragraph.

2.1 *Influenc line analysis of DWT*

As a truss structure similar to SCI, a model of DWT is shown in figur 3 and explained. The form of DWT is similar to SCI. However, it is a different structural element in terms of structural mechanics. DWT consists only of axial forces (shown in figur 4). In contrast, SCI consists of an axial force, a shearing force, and bending moment. Because it is a statically indeterminate structure, its sectional force is calculated by using the nodal point method and the unit load method. In each nodal point of four corners and the





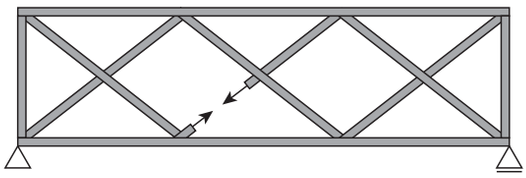
Figure 1: Collapsed bridges by natural disaster in Hokkaido (2016)



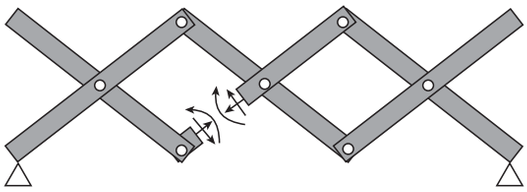
(a) Double Warren truss bridge



(b) Scissors type of bridge (MB2.0)



(c) Structural model of (DWT)



(d) Structural model of (SCI)

Figure 2: Double Warren truss (DWT) and scissors type of bridge (SCI)

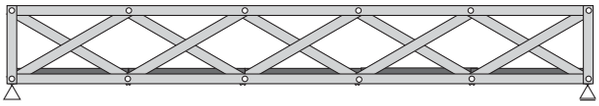


Figure 3: A bridge model of the Double Warren truss (DWT) (5 units)

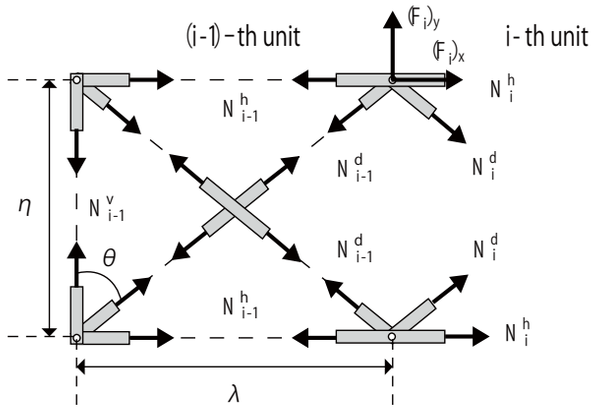


Figure 4: Sectional forces in an units of DWT

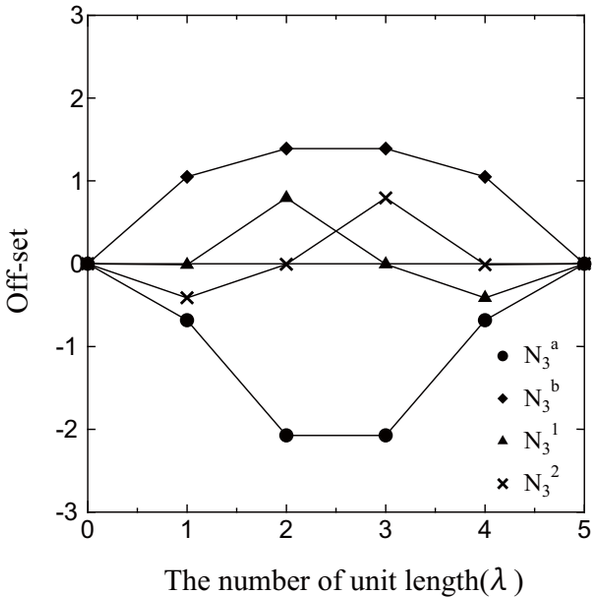


Figure 5: Influenc Line of axial force of 3rd unit (DWT)

pivot of each unit, the equilibrium equations are given by equations (1) and (2). In determining an influenc line, we take into account sectional forces when the unit load ($(F_i)_y = -1$) acts as nodal point external force as offset of influenc line. All influenc line diagrams of each sectional force are obtained by moving the unit load distance λ and repeating the calculation.

$$\begin{bmatrix} 1 & \cos\theta & 0 \\ 0 & \sin\theta & 1 \end{bmatrix} \begin{Bmatrix} N_i^v \\ N_i^j \\ N_i^h \end{Bmatrix} = - \begin{Bmatrix} \pm(F_i)_y \\ (F_i)_x \end{Bmatrix} \tag{1}$$

$$\begin{bmatrix} \cos\theta & \cos\theta & 0 & 0 \\ -\sin\theta & \sin\theta & -1 & 1 \end{bmatrix} \begin{Bmatrix} N_{i-1}^j \\ N_i^j \\ N_{i-1}^h \\ N_i^h \end{Bmatrix} = - \begin{Bmatrix} \pm(F_i)_y \\ (F_i)_x \end{Bmatrix} \tag{2}$$

Here, these letters have the following meanings: i, the number of units; v, vertical member; h, horizontal member; d, diagonal member; and F, nodal point external force. As an example, four influenc lines of the axial force of the members in the third unit of a DWT with f ve units are shown in figur 5. This fig ure shows that the maximum compression axial force occurs in the upper chord member and the maximum tension axial force occurs in the bottom chord member when a downward load acts.

2.2 *Influenc line analysis of SCI*

It is necessary for the nodal forces of the whole SCI structure to be calculated as the firs stage in calculating the sectional forces of SCI. The equilibrium equations of the nodal force and the condition equations of the combination region are given by equations (3) and (4).

$$L_d \boldsymbol{b}_i^L + R_d \boldsymbol{b}_i^R + \boldsymbol{b}_i^C = \boldsymbol{0} \tag{3}$$

$$\boldsymbol{b}_i^R + \boldsymbol{b}_{i+1}^L = \boldsymbol{P}_i \tag{4}$$

Here,

$$L_d = \begin{pmatrix} 1 & 0 & 1 & 0 \\ 0 & 1 & 0 & 1 \\ -\eta & \lambda & 0 & 0 \\ 0 & 0 & \eta & \lambda \end{pmatrix},$$

$$R_d = \begin{pmatrix} 1 & 0 & 1 & 0 \\ 0 & 1 & 0 & 1 \\ 0 & 0 & \eta & -\lambda \\ -\eta & -\lambda & 0 & 0 \end{pmatrix},$$

$$\boldsymbol{b}_i^* = \{(B_i^*)_x, (B_i^*)_y, (A_i^*)_x, (A_i^*)_y\}^{\mathrm{T}}, * = \{L, R\}$$

$$\boldsymbol{b}_i^C = \{(C_i)_x, (C_i)_y, 0, 0\}^{\mathrm{T}}$$

$$\boldsymbol{P}_i = \left\{(P_i^B)_x, (P_i^B)_y, (P_i^A)_x, (P_i^A)_y\right\}^{\mathrm{T}}$$

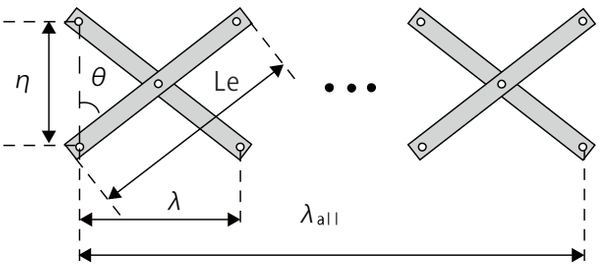


Figure 6: A bridge model of the scissors structure

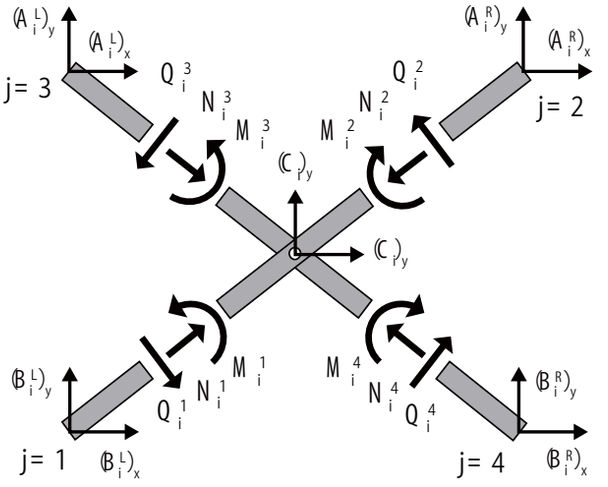


Figure 7: Sectional forces in an unit of SCI

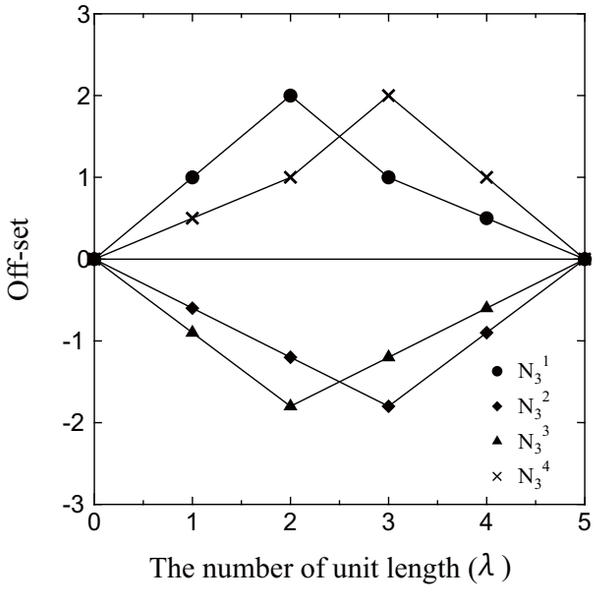
The definition of other letters are similar to DWT and are shown in figur 6. These formulas are derived from the equilibrium equations of nodal forces in the horizontal and vertical directions, as well as the bending moment around the centre point C in a scissors member. Overall, the nodal forces are calculated from equations (3) and (4). In the $i-$th scissors structure, the nodal forces and sectional forces are define as shown in figur 7. The sectional forces of the members such as the axial force, shear force and bending moment are calculated by coordinate transformation to the member direction using equations (5) - (7).

$$N_i^j = \pm(O_i^*)_x \sin\theta \pm (O_i^*)_y \cos\theta \tag{5}$$

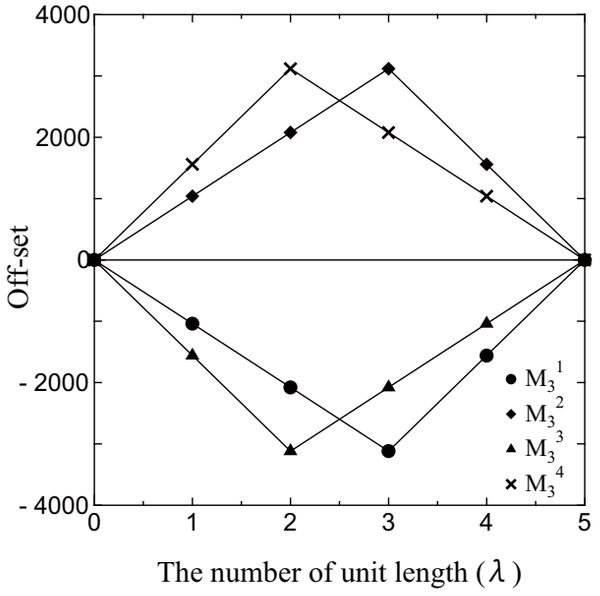
$$Q_i^j = \pm(O_i^*)_x \cos\theta \pm (O_i^*)_y \sin\theta \tag{6}$$

$$M_i^j = \{\pm(O_i^*)_x \cos\theta \pm (O_i^*)_y \sin\theta\}\,\chi, \quad 0 \le \chi \le L_e/2 \tag{7}$$

Here, these letters symbols have the following meanings. N, axial force; Q, shear force; M, bending moment; and O, representing A or B. The validity of this calculation method was already verifie by comparison with experiments of the a prototype and full-scale MB by Chikahiro et al.(2012) and Ario et al.(2014). The influenc lines are calculated by the acting of a unit load ($(P_i^B)_y = -1$), just as in a DWT. As an example, influenc lines of the axial force and bending moment of the members of the third unit in an SCI with f ve units simply supported are shown in figur



(a) Axial forces



(b) Bending moments

Figure 8: Influenc Line of sectional force of 3rd unit (SCI)

8 (L_e =6000mm, θ=60°). These figure show that a maximum sectional force occurs when a point load acts on the position at a distance 2λ or 3λ from the left supporting point. In addition, it is clear that bending moment, depending on the length of the member, is much higher than the axial force.

3 THE REINFORCEMENT METHOD OF SCI

The stiffness of SCI is low because of its high fl xibility. For this reason, it is necessary to raise the stiffness of the bridge by inserting a reinforcing member when the large load is assumed. If a number of the reinforcing members are required for larger loads, it is possible to set this because this is a module type that depends on the capacity of traffi loads. The sectional forces of reinforced SCI are calculated by the combination of the method introduced in a foregoing paragraph and the unit load method.

Table 1: Calculation conditions of SCI

Section	h400 × b60 × t19.7
height (mm)	400
width (mm)	600
thinness (mm)	19.7
length of main member(mm)	6000
length of reinforcing member(mm)	λ
material	SS400
Yonung's modulus (MPa)	206
specifi gravity	7.85
boundary condition	simple support

3.1 *Confirmatio of reinforcement effect*

The effect of the strut reinforcement of SCI has been examined since last year by Adachi et al.(2016). In this analysis, a rational reinforcement method is examined by the stress calculation of the real main posture design using the influenc line diagrams. For the purpose of reducing the maximum stress of SCI after expanding, some partial reinforcement patterns that changed place and the number of the horizontal reinforcing chord members that are equipped are made. The section of main member and reinforcing member are assumed to be a section like real MB with 400mm in height, 60mm in width and thinness 19.7mm. and only dead load is acted as the load conditions to compare. It then becomes clear that the member of the central unit of the whole SCI system has the maximum relationship stress. For this reason, the position of a reinforcing member is decided in the central unit of the model having f ve units. We pay attention to the maximum edge stress where a reinforcement effect was examined. The pattern having a lower horizontal member was confirme when few reinforcements were used. However, a large reduction in the maximum edge stress of the centre unit was confirme in a pattern having an upper horizontal member and both side horizontal members. For this reason, the stress-relaxation of the whole SCI is enabled by giving a similar reinforcement to the 2nd, 3rd, and 4th units, which produce maximum bending stresses. A pattern having three reinforing members is named pattern A and shown in figur 9. A pattern having six reinforcing members is named pattern B and shown in fig ure 10. The maximum edge stress is reduced by approximately 73% in the central unit, by approximately 72% in the 2nd and 4th units of pattern A, contrary to SCI which does not exhibit reinforcement by using reinforcing members. The maximum edge stress is reduced by approximately 97% in the central unit of pattern B, and by approximately 91% in 2nd and 4th units.

3.2 *Comparison between SCI and DWT*

In this section, We examine superiority of the SCI except the mobility by comparing the strength of DWT which are used as emergency bridge and SCI. We use

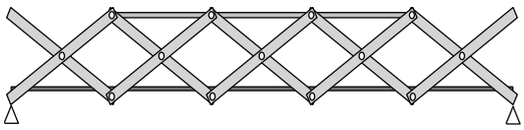


Figure 9: A reinforced model of SCI as a pattern A

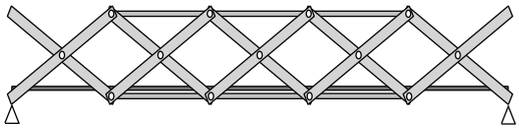


Figure 10: A reinforced model of SCI as a pattern B

the strength of the maximum distributed load strength per unit weight of the bridge as an index in comparing pattern A and pattern B with DWT. Live loads and dead loads are loaded like figure11 The maximum distributed load strength is equal to load when yielding or buckling occurs. The section of the DWT was decided so that its weight became almost same as that of reinforced SCI. The results of the comparison are given in table 2. It shows that both reinforcement patterns obtain the values that are bigger than DWT.

4 CONCLUSIONS

The main result of this structural analysis was the introduction of the concept of influenc line diagrams into the design of scissors structures for the firs time. This result revealed the basics of a design of SCI having the scissors structure that acted on a moving load, including both a vehicle and a person. Several points that were deduced by this analysis are summarized as follows.

1. Based on the equilibrium equations and the displacement conformity condition equations of the scissors structure, we developed the design method using the influenc line diagram for a live load design of SCI.

2. Using the program of the influenc lines, we analysed reinforcement methods and clarifie the rational reinforcement method.

3. As a comparison between the stresses of DWT and SCI, it was shown that SCI can have strength per unit weight that is bigger than DWT by reinforcement. In other words, SCI is effective structure and it is the more suitable as emergency bridge.

Table 2: Properties of SCI reinforced patterns and DWT

	Weight(kN)	Strength(kN/m^2)	index
Pattern A	58	21	0.36
Pattern B	78	57	0.73
DWT	65	10	0.15

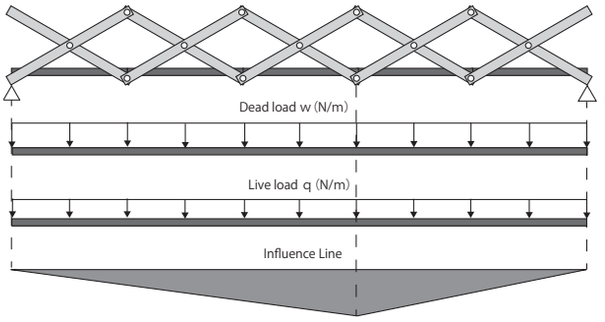


Figure 11: Section forces using the infuruence line under live and dead loading

ACKNOWLEDGEMENT

This research has been supported by the Bilateral Programs between Japan Society for the Promotion of Science (JSPS) and Polish Academy of Sciences (PAN) in 2016 - 2018.

REFERENCES

Ario and Watson, Structural Stability of Multi-Folding Structures with Contact Problem, Int. J. Non-Linear Mechanics, Vol. 324 (1-2), pp. 263-282.

Ario and Nakazawa, Nonlinear Dynamics behavior of Multi-Folding Microstructure Sys-tems based on Origami Skill, Int. J. Non-Linear Mechanics, Vol. 45(4), pp. 337-347, 2010.

Ario and Kim, Michell Problem for the Stiffness Formation of Structural Design in 3 Dimensional Space, Proc. of Optimizational Symposium in JSME, 7, pp. 179-184, 2006.

Ario, Structure with the expanding and fold-ing equipment as a patent (No.2006-037668) registered in 2012, Japan, 2006.

Ario, Nakazawa, Tanaka, Tanikura and Ono, DEVELOPMENT OF A PROTOTYPE DEPOYABLE BRIDGE BASED ON ORI-GAMI SKILL, Automation in Construction, Vol. 32, July 2013, 104-111.

Ario, Hama, Chikahiro, Adachi amd Watoson (2017), Origami inspired deployable and movable bridge for disaster relief, FootBridge 2017 Berlin.

Ario, Tanaka, Nakazawa, Furukawa, Chikahiro, Development of the prototype of a new emergency bridge based on the concept of optimized structure, J. Struct. Eng. 64A (2012) 1-12 (in Japanese).

Adachi, Ario, Chikahiro, SCISSORSING ORIGAMI INSPIRED DEPLOYABLE BRIDGE FOR A DISASTER, ASEA-SEC-3, 2016

Chikahiro and Ario, Dynamics Study for Design of Emergency Bridge with Scissors Structure, ICCEE, 2012

Chikahiro, Ario, Nakazawa, Ono, Holnicki-Szulc, Pawlowski and Graczykow-ski, n experimental study on the design meth-od of a full-scale Mobile Bridge for a moving vehicle, The proceedings of 4th International Conference on Mobile, Adaptable and Rapidly Assembled Structures 2014, pp. 94-103, http://dx. doi.org/10.2495/MAR140081 (Bel-gium, Conference).

Holnicki-Szulc, Pawlowski and Wiklo, High-performance impact absorbing materials - the concept design tools and applications, Smart Materials and Structures: Int. J. Non-Linear Me-chanics, pp. 461-467, 2003.

Hunt and Ario, Twist buckling and the foldable cylinder: an exercise in origami, Int. J. of Nonlinear Mechanics, Vol. 40(6), pp. 833-843., CD-ROM.,2005.

Lederman, You, Gliŝić, A novel deployable tied arch bridge, Journal of Engineering Structures, vol. 70 pp. 1-10, 2014

Nakazawa and Ario, Mechanical Property of Deployable Emergency Bridge Based on the Scissors Structures, Journal of safety problems, vol. 5 pp. 133-138 (in Japanese), 2010

Yang, Xu, Shen, Zhou, Xie, Energy absorption of thin-walled tubes with pre-folded origami patterns: Numerical simulation and experimental verificatio Journal of Thin-Walled Structures, vol. 103 pp. 33-44, 2016

MS08: Submerged floating tunnels and underwater tunnel: Design, safety and maintenance issues

Organizers: L. Martinelli, Y. Xiang & B. Faggiano

Maintenance, Safety, Risk, Management and Life-Cycle Performance of Bridges – Powers, Frangopol, Al-Mahaidi & Caprani (Eds)
© 2018 Taylor & Francis Group, London, ISBN 978-1-138-73045-8

Dynamic interaction with travelling vehicles in a submerged floating tunnel

M.G. Mulas & L. Martinelli
Departement of Civil and Environmental Engineering, Politecnico di Milano, Milano, Italy
G. Palamà
MS Candidate in Civil Engineering, Politecnico di Milano, Milano, Italy

ABSTRACT: The work aims to investigating the effect of vehicle-bridge interaction (VBI) on a Submerged Floating Tunnel (SFT), a novel type of bridge still at the feasibility study phase. The case study is a prototype SFT designed to cross the Messina's Strait, in Italy. Tethers guarantee the static equilibrium of the SFT subjected to Archimede's forces and, due to their length, behave in a non-linear way. The VBI coupled problem is solved through an uncoupled iterative procedure, where bridge and crossing vehicle are analyzed separately for the whole duration of the time history: the vehicle is subjected, on its wheels, to roughness and bridge motion and the bridge is subjected to vehicle's contact forces. The ANSYS code performs the non-linear analyses of the bridge, while a research code integrates the vehicle equation of motion and handles the data exchange between the two codes. The numerical procedure achieve convergence in a few iterations. Results show that the effect of crossing vehicle do not propagate on the tunnel, affecting only the nearby tethers.

1 INTRODUCTION

Natural dynamic excitations arising from earthquake, waves and currents affect the design of floating tunnels. At a lower level, the dynamic interaction tunnel-travelling vehicle is to be considered for fatigue and serviceability conditions. Due to transit of heavy vehicles, the tunnel response is coupled with that of the vehicle. The road roughness plays a role also.

The parametric oscillation of the anchoring tethers, induced by the motion of the tunnel, has been the subject of recurring studies. A suitable model for these oscillations is that of Mathieu's equation. A time-varying tension force arises in the anchoring system when dynamic loads, such as regular waves or possibly moving vehicles, act on the tunnel body. Sato et al. (2004) studied the possibility of the occurrence of unstable motions considering the arrangement of the mooring system lines, the effect of viscous damping, of quadratic damping and of external forces on the parametric excitation.

In a Mathieu type of instability, the growth of the oscillation amplitude is related to a parametric resonance in which the variation of the parameters must occur at twice the natural frequency of the system. This was verified, among others, in relation to submerged floating tunnels (SFTs), in (Sun 2011) where it was found that the displacement and velocity root mean square responses of tethers reach the peak if the circular frequency of the tube doubled that of tether. The authors pointed out, however, that owing to the damping force of water, the responses of the anchoring tethers decrease more rapidly compared with the tethers in air.

Parametric excitation of the tethers due to the wave motion has been more recently also studied in (Cantero et al. 2016), where the authors studied the frequent design situation of moored SFTs parametrically excited by long period waves. In this study, the authors included the contribution of multiple modes of vibration, and adopted the harmonic balance method to assess the amplitude of vibrations, arriving at discussing the validity of using stability charts for the design of mooring lines. A similar parametric excitation can be induced by moving vehicles inside the tunnel. The exciting force is due to the moving mass and weight of the vehicles and to their motion activated by both the motion of the tunnel and the asperities of the road.

Although less studied, a handful of works is available in the literature about this problem. The effect of moving loads on moored floating structures has been studied at different levels of detail e.g. by (Fleischer, and Park 2004, Tariverdilo et al. 2011, Zhang et al. 2016). Typically, several simplifying hypotheses are adopted in these studies, regarding both the structure and the way the moving vehicle is represented. In the

last study cited, as an example, the SFT was simplified as an elastically supported beam with springs and dampers at each end to represent the mooring system. According to the results of that numerical study, the vertical stiffness of the mooring system has a significant effect on suppressing the SFT displacements, and consideration should be given to the velocity and weight of vehicles during the design process of a SFT.

A similar, equally recent, study (Liang and Jiang 2016), adopted a simple model for the moving vehicle (the one-fourth vehicle model with two degrees of freedom: sprung mass and unsprung mass) while it retained an approximate modelling of the tunnel. This was simplified as an Euler-Bernoulli beam with two simple supported ends, while the anchoring system was modelled through spring elements to simulate the theters. For a 100 m long section, the influence of road roughness on traffic loads was studied within the finite element software ANSYS (Ansys 2017). Traffic was modelled as two approaching vehicles (speed 80 km/h, weight 20 kN) finding that it accounts for $1/10^{th}$ of the displacement due to 20m long waves having height 0.3 m, for a tunnel with positive buoyancy ratio 1.4 and 100 m depth of sea-bead. However, no details are given on how the roughness of the pavement was implemented in the ANSYS model or on the solution of the coupled vehicle-structure dynamic interaction problem.

The integration of the equations of motion of the coupled system composed of tunnel and moving vehicles, taking into account the roughness, poses computational problems connected to the time-varying nature of the structural matrices. One possible solution strategy relies on a forced uncoupling of the coupled equations, with a separate integration of the two systems (Feriani et al. 2008). At contact points, the bridge is subjected to the forces transmitted by the vehicle that, in turn, is subjected to an imposed motion at the wheels due to combined effect of roughness and bridge motion. An iteration process to restore equilibrium and compatibility at the system interface completes the uncoupled solution strategy. The iteration can be performed either within each single time step (STS) or on the whole time history (WTH) (Feriani et al. 2011). The two iterative procedures turned out to be equivalent, producing the same results (Maneo 2016).

The aim of this work is to analyze the vehicle-bridge interaction (VBI) for the SFT using the WTH procedure. The peculiar nature of the structure at study, subjected to hydrostatic and hydrodynamic forces, and characterized by a geometric non-linear behavior of the anchoring systems, requires the adoption of a sophisticated commercial code as ANSYS for a correct structural analysis. In this work the WTH procedure, derived for the case of structural linear behavior, is extended to a nonlinear system. The iterative procedure relies on ANSYS for the solution of the structural system and on an ad-hoc research code, named INTER, to integrate the equation of motion. Also, INTER handles the data exchange between the two systems and governs the iterative process.

The case study, a prototype tunnel crossing Messina' strait, is presented in Section 2. The vehicle and roughness model are described in Section 3. Section 4 presents the rationale for the derivation of the coupled equation of motion and the uncoupled solution strategy. Numerical results, in Section 5, show the positive performance of the iterative approach. Conclusions address the positive outcomes of this work and the need for further studies.

2 THE PROTOTYPE SUBMERGED FLOATING TUNNEL

The model structure to study the effects of vehicle-structure interaction is a design proposal devised for the Messina Strait crossing, in Italy. The crossing is 4680 m long and the maximum depth of the sea-bead is about 350 m. A side view of the tunnel is depicted in Figure 1.

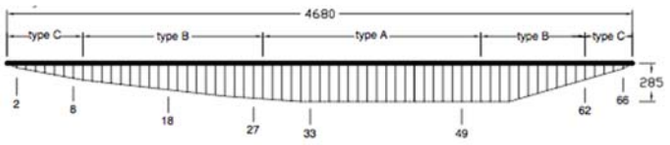


Figure 1. Lateral view of the SFT at study.

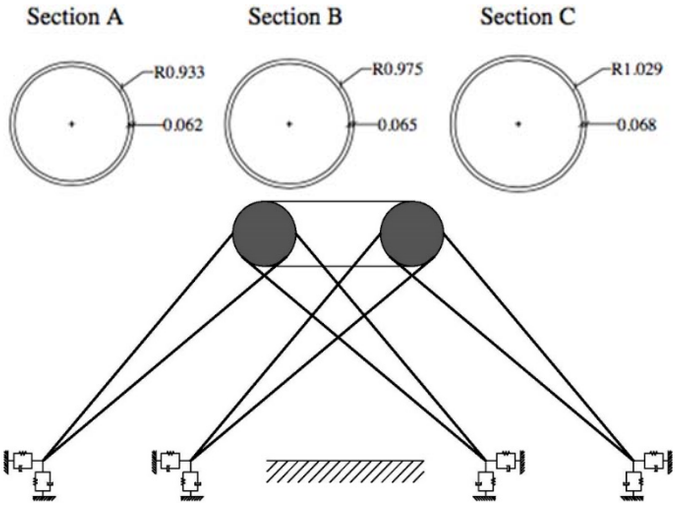


Figure 2. Cross-section of tunnels and tethers and tethers layout.

The general layout of the SFT comprises a double tube configuration with two straight independent tunnels located at a centreline distance of 40 m, connected at a distance of 480 m by escape routes introduced for safety reasons. The escape routes make the

tunnels behave as the chords of a Vierendeel beam in the horizontal plane and couple the response of the tubes due to their torsional stiffness, in the vertical plane. Further details on the design philosophy can be found in a companion paper (Perotti et al. 2018).

Each tube of the tunnel is independently anchored to the seabed (see Figure 2), replicating an anchoring scheme that demonstrated a good performance in previous studies (Shi 2013, Oregioni & Triaca 2016, Di Pilato et a. 2008) where the anchor bars were exploited in non-linear material behaviour range during strong earthquakes. Since the anchoring elements are hollow tubes, of different diameters and thickness along the length of the tunnel (see Figure 2), their buoyancy counteract their slenderness, contributing to achieve a straighter configuration in service, thus minimizing geometrical non-linear effects. Passive control devices are introduced at the tunnel-shore interfaces to limit the axial forces in the tunnel.

The first natural periods and frequencies, along with a classification of the modal shapes, are reported in Table 1 for the modes that involve mainly a global movement of the tunnels. Due to the coupling between the tunnels, also torsional modes are present. Local modes of the tethers are in the range between 0.185 and 0.324 Hz.

Mode	Type of mode	Freq. [Hz]	Period [s]
1	First Longitudinal vibration mode	0.157	6.369
2	Second Longitudinal vibration mode	0.337	2.967
3	First torsional vibration mode	0.443	2.257
4	Second torsional vibration mode	0.517	1.934
5	Third longitudinal vibration mode	0.534	1.872
6	First transversal vibration mode	0.559	1.789
7	First vertical vibration mode	0.561	1.782
8	Second vertical vibration mode	0.565	1.769
9	Second transversal vibration mode	0.565	1.769

Table 1. Global natural modes of the SFT under study.

3 MODELS ADOPTED

In the following the models for the vehicles and the road roughness are summarized. Among the possible models, a plane vehicle model is adopted (Green & Cebon 1994), consistently with the FE discretization of the tunnel. A 3D model could have been adopted as well. Many mathematical relations are proposed in the literature to describe the Power Spectral Density (PSD) of the roughness profile. This preliminary study adopts the one proposed by Eurocode 1. It must be underlined that the iterative procedure is not restricted to the models described here.

3.1 *Vehicle*

The 2D ½ vehicle model in Figure 3 has two axles, two contact points constrained to the road, and four degrees of freedom (dofs). The first two describe the vertical motion of the unsprung masses m_1 and m_2, the third is the vertical displacement of the body mass M and the fourth describes the pitch. The total mass adopted in the analyses is 40 t. The center of gravity *G* of the body mass M is located in the middle of the mass itself (a_1=a_2=1 m). The (damped) natural frequencies of the four modes are 1.59, 3.18, 23.89 and 23.91 Hz, respectively. The first mode is a "pitching" mode, the second one is a "surge" mode, with the three masses oscillating in phase.

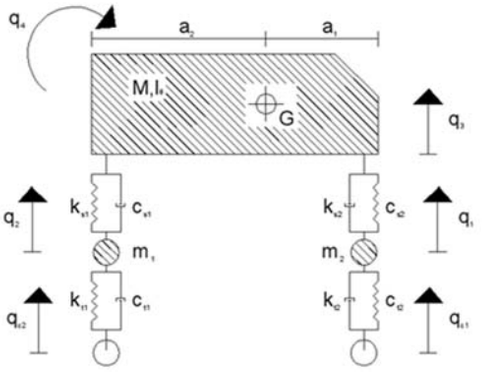


Figure 3. 2D Vehicle model from Green & Cebon (1994).

3.2 *Roughness*

The longitudinal roughness profile adopted in the analyses is generated by assigning random phases to amplitudes respecting the Power Spectral Density function defined in the Annex B of Eurocode1 (EN 1991-2. 2003). This power spectrum is defined by a straight line in a logarithmic plot, in accordance with ISO 8608:

$$\Phi(\Omega) = \Phi(\Omega_0)\left(\frac{\Omega}{\Omega_0}\right)^{-n} \quad (1)$$

In Eurocode 1, the parameters of the power spectrum were derived to describe different road quality scenarios. Pavements are subdivided in classes, from A to E, of descending quality. The class A pavements correspond to a newly paved highway, while a very good to good pavement belongs to class (A-B), the border between A and B. For this class, adopted for the tunnel roads, the reference cyclic frequency Ω_0 (rad m^{-1}) in Equation 1 is equal to 2. The value of the spectrum at the reference frequency. $\Phi(\Omega_0)$ (m^3 rad^{-1}) is 1. Finally, the parameter *n* is equal to 2.

4 EQUATION OF MOTION AND UNCOUPLED SOLUTION STRATEGY

The VBI coupled problem is solved by deriving the coupled equation of motion and subsequently devising an uncoupled iterative solution procedure. In this way bridge and crossing vehicle are analyzed separately: the vehicle is subjected, on its wheels, to roughness and bridge motion and the bridge is subjected to vehicle's contact forces.
The equations of motion are written under the following hypotheses:

- The vehicles travel at constant speed and along a straight line parallel to the tunnel axis;
- The horizontal motion of the vehicles is known and decoupled from the vertical one;
- The contact area between the generic tire of the vehicle and the road surface is reduced to a massless point;
- The contact between the wheel and the paving is perfect;
- Contact forces have only a vertical component.

Under the above assumptions and using the Lagrange's equations it is possible to define mathematically the problem of vehicle-structure interaction with a system of ordinary differential equations:

$$\frac{d}{dt}\left(\frac{\partial T}{\partial \dot{q}_k}\right)+\frac{\partial V}{\partial q_k}+\frac{\partial D}{\partial \dot{q}_k}=0 \qquad k=1,\ldots,n_{dof} \qquad (2)$$

In Equation (2), T is the total kinetic energy of the system composed of the tunnel and the crossing vehicles, V is the potential energy of the same system and D is the dissipation function that accounts for energy dissipation due to both the tunnel motion and the vehicle masses motion. The equation of motion obtained in this way describes the coupled behavior of the vehicle and of the structure.

The mass matrix of the coupled system is uncoupled, due to the assumption of massless contact points. The system of equations can be decoupled by moving to the right-hand side the terms coupling the motion of the structure and of the vehicles, as well as the time-dependent terms. In this way, coupling terms become, for each system, forcing terms.

The forcing term acting on the structure is a function of the static forces, of the floating forces and of three physically different terms:

- the first is given by the displacements and the velocities of the roughness profile, modified to include the static deflection of the bridge;
- the second depends on the displacements and the velocities of the contact points (in motion since the structure is in motion);
- the third is due to the motion of the vehicles.

The forcing term that acts on vehicles depends on the surface roughness, as well as on the displacements and the velocity of the contact points.

The separate equations of motion of the vehicles and of the tunnel cannot be solved independently, because the displacements of the structure contribute to the forcing term in the motion of the vehicles. Vice versa, the moving contact forces that the vehicles transmit excite the structure (Feriani et al. 2008). However, the two coupled systems can be resolved through an iterative procedure. In this work, the procedure named Whole Time History (WTH) is adopted. The general flow chart for the case at study is reported in Figure 4.

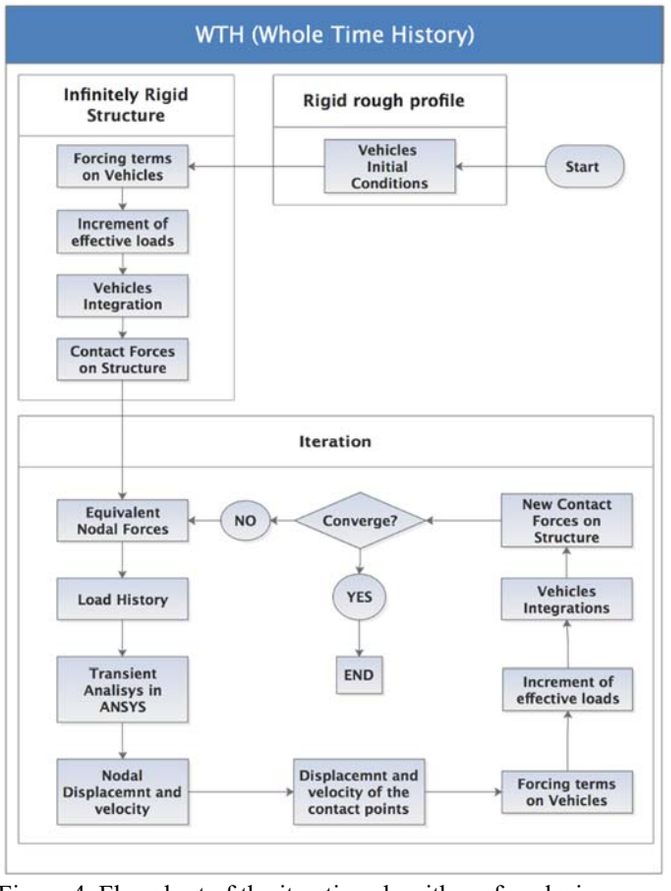


Figure 4. Flowchart of the iterative algorithm of analysis.

As the name suggests, the WTH procedure iterates throughout the entire time-history. First, the vehicles transit over a rigid roughness profile sufficiently long to eliminate the effect of their initial conditions of motion. Then, at each cycle, vehicles are repositioned at the beginning of the tunnel and the integration is repeated considering as forcing term the contact forces arising from the bridge motion obtained in the previous iteration. The ANSYS code performs the

non-linear analyses of the bridge, while the research code INTER integrates the vehicle and handles the data exchange with ANSYS.

At the first iteration, the vehicles moves on the structure that is considered as infinitely rigid. The INTER Code calculates the increase in the effective loads of the vehicles, which at this iteration depend only on the surface roughness or on initial disturbances such as bumps. Subsequently, INTER solves the equations of vehicle motion with the Newmark method (Newmark 1959) and calculates the contact forces to be transmitted to the bridge for each time step. Since contact points, in general, do not coincide with mesh nodes, contact forces are transformed into equivalent nodal loads (vertical forces and moments) on the tunnel model. Proper shape functions are used to this aim. On the tunnel, the equivalent nodal loads act only on the nodes directly loaded by the moving vehicle (named "useful nodes"). Thus, the code INTER generates a load history, including the entire tunnel crossing. transmits the load history to ANSYS which performs the transient analysis and transmits back to INTER the time history of the motion (vertical displacements, rotations and related first time derivatives) of the useful nodes. From these data, the INTER Code calculates (vertical) displacements and velocities of the contact points using the same shape functions previously adopted to compute nodal forces. Then, a new increment of the effective loads is computed, the equation of motion of the vehicles are integrated again and a new set of contact forces is determined.

The convergence criterion is written in terms of contact forces. For the i^{th} vehicle and at each time step k, the difference vector $\boldsymbol{R}$ is calculated between the value of the force at iteration j and that derived from the previous iteration. The mean square error, accounting for the N_t time steps of the whole time history, is normalized according to the weight of the vehicle along the whole integration domain:

$$err_i = \frac{1}{W_i}\sqrt{\frac{\sum_{k=1}^{N_t}\left(R_{i,k}^{j}\right)^2}{N_t}} \leq tol \qquad (3)$$

If the error in any vehicle wheel is less than a prefixed tolerance *tol*, the procedure ends, otherwise a new iteration is performed, transmitting to ANSYS the updated set of contact forces. On the base of the experience by the authors also in analyses considering up to 20 vehicles, the numerical procedure usually achieves convergence in a few iterations.

5 NUMERICAL ANALYSES

The procedure WTH and its implementation on the two codes, ANSYS and INTER, were validated by comparison with a closed form solution (Fryba 1972). A simply supported beam (15m long, cross-section 0.4×0.4m) is crossed by a moving load F=9.81kN traveling at 10, 20 and 30 m/s respectively. Figure 6 depicts the results in terms of time history of the vertical mid-span displacement for the case of 20 m/s. The agreement between numerical and closed form solution is excellent.

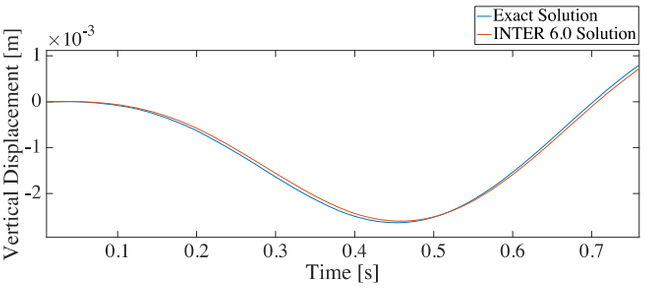


Figure 6. Test beam. Closed-form vs numerical solution, vertical mid-span displacement.

The results of the numerical analysis of a traffic induced vibrations on the SFT for the Messina Strait concern the traffic model depicted in Figure 6. This comprises two vehicles entering the two tunnels from opposite directions, and travelling with constant velocity of 20 m/s (72km/h). Two different roughness profiles are adopted for each tunnel. A bump at each tunnel entrance simulates the presence of the joints at the two ends. An integration time step of 0.1s is adopted, sufficient to integrate the tunnel, to maintain the time necessary for each analysis in 40 hours.

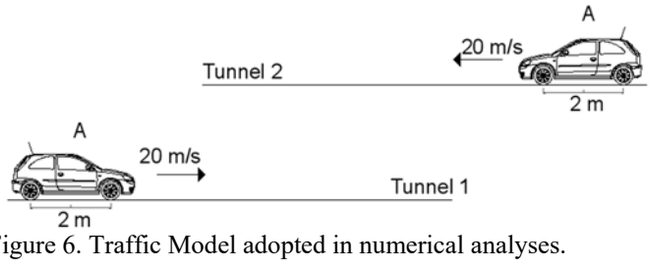


Figure 6. Traffic Model adopted in numerical analyses.

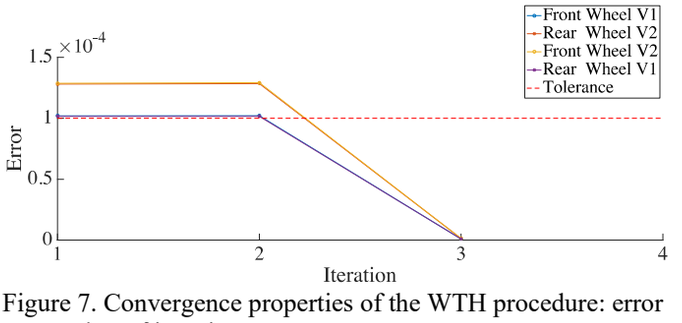


Figure 7. Convergence properties of the WTH procedure: error vs. number of iterations.

Figure 7 depicts the error measure in Equation 3 versus the number of iterations, for the front and rear

wheel of both vehicles. For the structure at study, only three iterations suffice to eliminate the error, and thus to enforce both equilibrium and compatibility throughout the entire time history between the structure and the vehicles in the VBI problem.

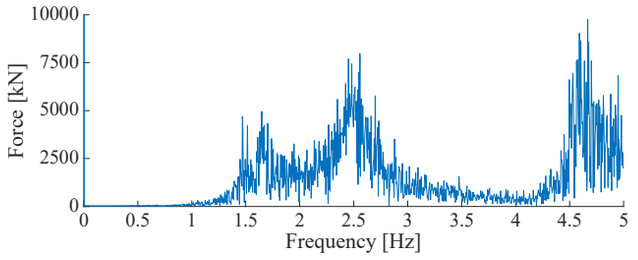


Figure 8. Contact force of front wheel - Vehicle 1: Fourier Spectrum

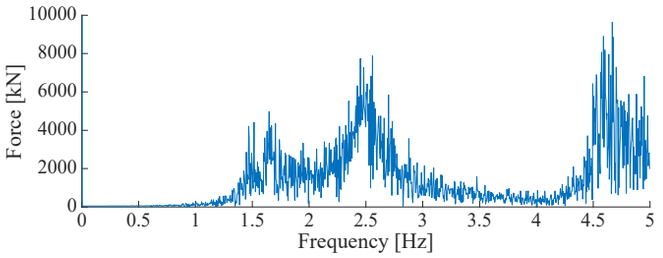


Figure 9. Contact force of rear wheel - Vehicle 1: Fourier Spectrum

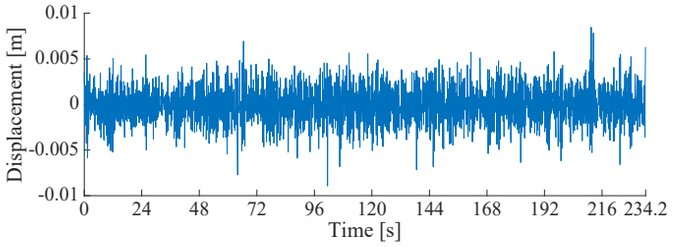


Figure 10. Vehicle 1, displacement of DOF#3: time history

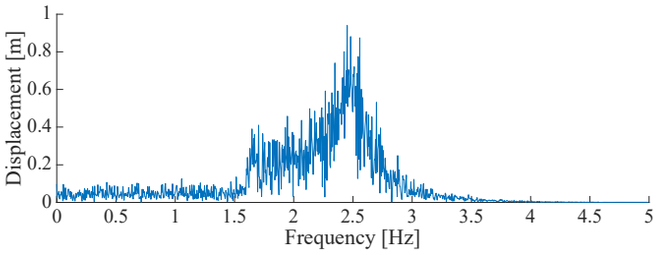


Figure 11. Vehicle 1, displacement of DOF#3: Fourier Spectrum

Figures 8 and 9 depict the frequency content of the contact forces for the front and rear wheel of Vehicle 1 respectively. The results for the two wheels are very close and similar to those of Vehicle 2. The wide frequency content of the force reflects the properties of the roughness profile adopted in the analysis. Figure 10 depicts the time history of the displacement of dof #3 in the vehicle model in Figure 3, corresponding to the vertical displacement of the mass M in the same figure. The smooth finishing of the road, and the small displacements of the structure lead to a limited motion of this mass, in the order of 5-8 mm.

Figure 11 shows the frequency content of the motion in Figure 10. The natural frequencies of the vehicle are 1.59, 3.18, 23.89 and 23.91 Hz respectively, while that of the structure are much lower (see Table 1). In Figures 8 and 9, and in Figure 11, the amplification of the response due to the resonance with the first mode of the vehicle, at 1.59 Hz, can be clearly appreciated, as well as resonances at 2.5 and 4.7 Hz, that are under further scrutiny to identify the structural modes, or the physical or numerical cause, they relates to. The resonance at 2.5 Hz is evident also in the vehicle response (Figure 10), while that at 4.7 Hz is evident only in the contact forces (Figures 8 and 9).

Finally, Figure 12 depicts the variation in the axial force in a reference tether (tether # 20, located 1908 m away from the tunnel end). As it can be appreciated, the variation due to a single vehicle is rather small, and is located around the time instant when the vehicle approaches the tether. A similar result is found for all the tethers. Thus, for this traffic model, the result shows that the effect of crossing vehicles do not propagate on the tunnel, and only affects the tethers nearby the vehicle position. This finding is consistent with the very small values of the vertical displacement of the tunnel, not reported here for the sake of brevity.

A small contribution, however, can be found at a previous time instant also. This corresponds to the instant when the vehicle travelling in the opposite direction overpasses the nearby transverse connection between the two tunnels. This finding highlights that traffic load will excite also torsional modes due to the tunnel and connection arrangements.

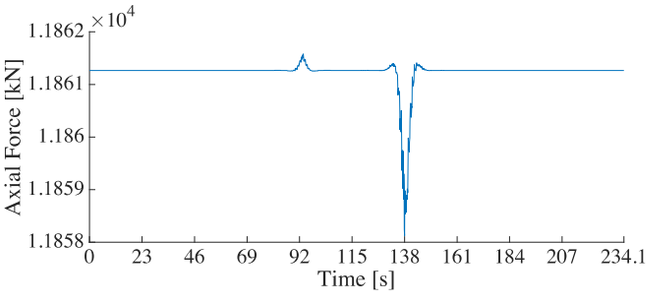


Figure 12. Axial force in tether n. 20, 1908 m away from the end of tunnel 2

6 CONCLUSIONS

This paper investigates the effect of VBI in a SFT proposal for the Messina Strait crossing, in Italy. The problem is tackled through the adoption of an uncoupled iterative solution strategy (WTH), based on the complete derivation of the coupled equation of motion.

In this work, the WTH procedure has been implemented in the research code INTER in such a way that the non-linear analysis of the structure relies on the commercial code ANSYS. A few tests on a simply supported beam validated the code implementation and the adoption of the procedure, by means of the comparison with a closed form solution. The extension to a nonlinear structure did not show any problem, apart from the need of a very high computing time. In fact, at each time step, ANSYS takes into account the geometric nonlinearities of tethers and iterates to find the equilibrium solution of the SFT. Thus, the solution strategy based on an uncoupled formulation of the equation of motion associated with an iteration process proved to be successfully, requiring a small number of iterations to achieve convergence with a very strict tolerance. It can be concluded that this work establishes a framework for investigating the most important aspects of VBI problem. Among these, we quote the vibration levels of the tunnel, which are of utmost importance for comfort and psychological acceptance of the SFT infrastructure, and the oscillations of the anchoring elements, important from the viewpoint of maintenance and durability.

From the computational point of view, further studies will concern the complete implementation of the iterative procedure, including also the vehicle model, with the mechanical APDL language of ANSYS. In addition, the adoption of the STS procedure that enforces equilibrium and compatibility at each time step could be investigated. Seen the heavy request of computing time, it would be interesting to analyze the effect of neglecting tethers nonlinearities on the outcome of the procedure.

The paper presents and discusses some preliminary results, concerning the transit of a single vehicle in each tunnel. Results show that the effect of crossing vehicles do not propagate on the tunnel, affecting the nearby tethers only. Undergoing studies show that the same situation holds for larger number of vehicles, when the spacing between two subsequent vehicles is of the order of 150-200 m, a reasonable value for safety reasons. The traffic effect on the motion of the tethers due to parametric excitation appears mild, but this aspect need to be further analyzed. In this respect, more severe load conditions can be considered, including crossing trains and the superposition with hydrodynamic loads due to waves and currents.

ACKNOWLEDGEMENTS

The partial financial contribution of MIUR (Italian Ministry of Higher Education) under grant PRIN 2015-2018, Project 2015TTJN95, “Identification and monitoring of complex structural systems”, is gratefully acknowledged.

7 REFERENCES

Sato, M. & Kanie, S. & Mikami, T. & Komuro, T. 2004. Fundamental study on the parametric excitation characteristics of Submerged Floating Tunnel. *Journal of applied mechanics*. Volume 7 (2004) Pages 31-38.

Sheng-nan Sun 2011. Parametric vibration of submerged floating tunnel tether under random excitation. *China Ocean Engineering*. June 2011.

Cantero, D. & Rønnquist, A. & Naess, A. 2016. Recent Studies of Parametrically Excited Mooring Cables for Submerged Floating Tunnels. *Procedia Engineering.* Volume 166, 2016, Pages 99-106.

Fleischer, D. & Park, S.K. 2004. Plan hydroelastic beam vibration due to uniformly moving one axle vehicle. *J. Sound Vib.* 273 (2004) 585–606.

Tariverdilo, S. & Mirzapour, J. & Shahmardani, M. & Shabani, R. & Gheyretmand, C. 2011. Vibration of submerged floating tunnels due to moving loads. *Applied Mathematical Modelling*. 35 (2011) 5413–5425.

Zhang, Y. & Dong, M-S & Ding, H. & Yang, L-C. 2016. Displacement response of submerged floating tunnel tube due to single moving load. *Procedia Engineering*. 166 (2016) 143–151, Proc. of 2nd International Symposium on Submerged Floating Tunnels and Underwater Tunnel Structures.

Liang, B. & Jiang B. Study on Composition and Simulation Analysis of Traffic Loads in Submerged Floating Tunnels. *Procedia Engineering*. 166 (2016) 180–189, Proc. of 2nd International Symposium on Submerged Floating Tunnels and Underwater Tunnel Structures.

ANSYS® Academic Research Mechanical, Release 18.1.

Feriani, A. & Mulas, M.G., & Lucchini, G. 2008. Vehicle-Bridge Interaction analysis: an uncoupled approach. In: *Proceedings of International Conference on Noise and Vibration ISMA 2008*, Editors P. Sas, M. De Munck, on CD-Rom, 609-624, Paper ID 142, Leuven, Belgium.

Feriani, A. & Mulas, M.G. & Poli, E. 2011. An uncoupled iterative approach for bridge-vehicle coupled systems. *In: Proceedings of the 8th International Conference on Structural Dynamics, EURODYN 2011*. Leuven, Belgio, 4-6 luglio 2011, European Association for Structural Dynamics.

Maneo, A. 2016. Procedure di integrazione iterative nell'analisi di interazione veicolo-struttura. *MS Thesis in Civil Engineering*. Politecnico di Milano, Italy (in Italian).

Perotti, F. & Foti, F. & Martinelli, L. & Tomasin, M. 2018. SFTs under dynamic loads: new design issues and numerical simulation, *Submitted for presentation at IABMAS 2018.*

Green, M. & Cebon, D. 1994. Dynamic response of highway bridges to heavy vehicle loads: theory and experimental validation. *Journal of Sound and Vibration*. 170(1), 51-78.

Newmark, N. M. 1959. A method of computation for structural dynamics. *Journal of Engineering Mechanics*, ASCE. 85 (EM3) 67-94.

EN 1991-2. 2003. Eurocode 1: Actions of structures. Part 2. Traffic loads on bridges, Annex B.

ISO 8608:1995 – Mechanical vibration – road surface profiles – reporting of measured data. British Standard, BS 7853, 1996.

Shi, C. 2013. Problems related to the seismic behaviour of submerged floating tunnel. *Phd Thesis. Politecnico di Milano (Italy)*.

Oregioni, M. & Triaca, S. 2016. Analisi e progetto di tunnel flottanti sullo Stretto di Messina. *Master Thesis, Politecnico di Milano (Italy)*, in Italian.

Di Pilato, M. & Perotti, F. & Fogazzi, P. 2008. 3D dynamic response of submerged floating tunnels under seismic and hydrodynamic excitation’, *Engineering Structures*, Volume 30, Issue 1, pp. 268-281, 2008.

Fryba, L. 1972. *Vibration of solids and structures under moving loads*. Noordhoff International Publishing, Groningen, 1972.

Maintenance, Safety, Risk, Management and Life-Cycle Performance of Bridges – Powers, Frangopol, Al-Mahaidi & Caprani (Eds)
© 2018 Taylor & Francis Group, London, ISBN 978-1-138-73045-8

Maximum stresses in mooring lines during parametric excitation

D. Cantero & A. Rønnquist
Norwegian University of Science and Technology NTNU, Trondheim, Norway

ABSTRACT: The ferry links crossing the fjords along the west coast of Norway are going to be replaced by fixed links. Among the proposed solutions is the construction of Submerged Floating Tunnels (SFT). A mooring system should be used to restrain the movements of these floating structures. Long period waves, such as swell waves, parametrically excite the system and might result in excessive vibrations in the cable. Relevant literature have extensively analyzed the lateral motions during parametric resonance. However, it is unclear how parametric excitation affects the stresses along the mooring line. The existing studies investigating the actual stresses developed during such violent situations are limited. Additional studies are deemed necessary for the safe design of this crucial element in SFT. Maximum tension and bending moments might vary in magnitude and location during parametric resonance. Thus, this paper investigates the maximum total stresses along the tether due to the combination of both spatial- and time-varying forces. The aim of this paper is to assess the necessity of using the stability charts for the design of mooring lines with respect to safe levels of cable stresses. This is achieved through the numerical analysis of a submerged cable model using Abaqus. Cable vibrations, forces and stresses are analyzed and compared for a range of amplitudes and frequencies of the support motions.

1 INTRODUCTION

As part of the E39 ferry-free project (Vegvesen 2012), the National Roads Authority (NRA) in Norway is planning to build floating suspension bridges and submerged floating tunnels. Because of their location (near the end of the fjords and next to the sea), they are exposed to sea states with wind waves and swell. In particular, swells have a long period and can last for several hours with effects that decrease linearly with water depth. Therefore, these constructions require mooring systems to hold them in place and to resist any imposed motion. Taut mooring systems made of steel tubes have been proposed, similar to those used in Tension-Leg Platforms (TLP) (Aage et al. 2000). These tension pipes or tethers have large dimensions and high pretension levels. The environmental loads on the bridge towers or the submerged tunnel lead to varying tension levels and imposed motions on the tether that define a parametrically excited system.

Under certain circumstances, parametric excitation leads to parametric resonance, which is an unstable situation that produces excessive lateral motions on the tether. For instance, under a harmonic imposed motion of the upper support with a frequency twice the fundamental frequency of the tether. That 2:1 frequency ratio is generally called the principal parametric resonance. Parametric excitation has been extensively studied before. In particular, when considering the particularities of submerged risers and immersed slender structures, good literature reviews on the instabilities of such structures can be found in (Franzini & Mazzilli 2015, Lei et al. 2013).

As indicated in (Cantero et al. 2017), the publications that have studied parametric excitation of cables mainly focus on lateral motion only, giving little or no attention to other load effects such as tension and bending moment values. For this reason, in (Cantero et al. 2017), the authors focus on the tension values reached during parametric excitation, concluding that additional dynamic effects on tension are very small. Now, this paper extends that thorough analysis to evaluate also the effects of parametric resonance on bending moments along the tether. This is achieved by numerical simulations with Abaqus (Abaqus 2011). In particular, some relevant case studies are investigated in detail. Maximum bending moments and tension values are compared by means of maximum sectional stress levels in terms of steel utilisation. Then multiple parametric studies are presented to evaluate the influence of different boundary conditions, excitation frequencies and excitation amplitudes.

2 NUMERICAL MODEL

The tether of a mooring system is modelled as a submerged beam and the wave-induced motion is represented as a sinusoidal imposed vertical displacement of the upper beam support. The beam is modelled considering rotational stiffness (k_r) at the ends. A schematic representation of the model is given in Figure 1. The model has been developed in ABAQUS (Abaqus 2011) using 40 beam elements (B21), including nonlinear geometric effects. The drag and added mass contributions of the hydrodynamic effect are included with the Morison equation. The beam, of total length L, is assumed to have an initial pretension T_0. The vertical motion of the upper support is prescribed to a harmonic motion with amplitude A and frequency f. Table 1 shows the additional model properties required and the particular values used in this study.

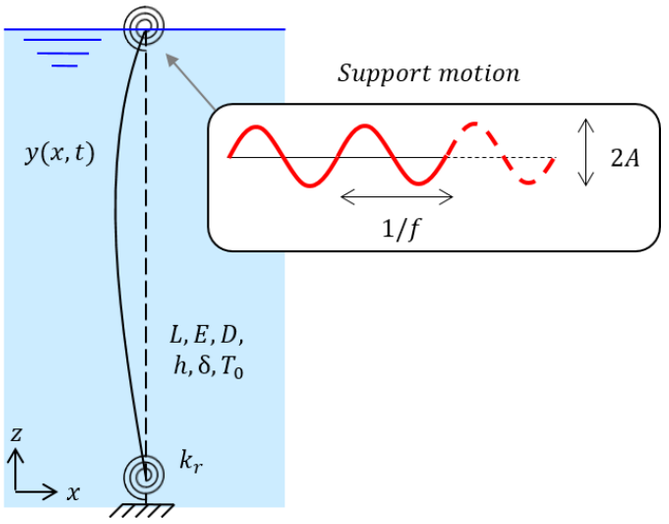


Figure 1. Sketch of tether and support motion

Table 1. Tether properties

Description	Symbol	Value	Unit
Length	L	400	m
Young's modulus	E	$2.1 \cdot 10^{11}$	N/m^2
Yield strength	R	$420 \cdot 10^6$	N/m^2
Diameter	D	1.119	m
Thickness	h	38	mm
Density	δ	7800	kg/m^3
Initial pretension	T_0	$18.5 \cdot 10^6$	N
Fundamental frequency	f_1	0.1299	Hz
2nd frequency	f_2	0.2648	Hz
3rd frequency	f_3	0.4096	Hz
Added mass coefficient	C_A	1	-
Drag coefficient	C_D	1.5	-

3 PARAMETRIC RESONANCE OF A DRY TETHER

This section investigates the response of a dry tether, i.e. without considering any hydrodynamic effects. The results highlight the importance of the instabilities produced by parametric excitation. In particular, the tether presented in Section 2, considering fixed rotational supports, is excited with an imposed support motion with twice the tether's fundamental frequency (2:1 frequency ratio). Figure 2a shows the time-history of the mid-span lateral displacements, featuring a maximum of 4.47 m, while the amplitude of the upper support motion is only 0.10 m. Similar beating-like behavior during parametric resonance have also been reported in (Lilien & Da Costa 1994), amongst others. However, other load effects have only rarely been investigated and additional analysis are required.

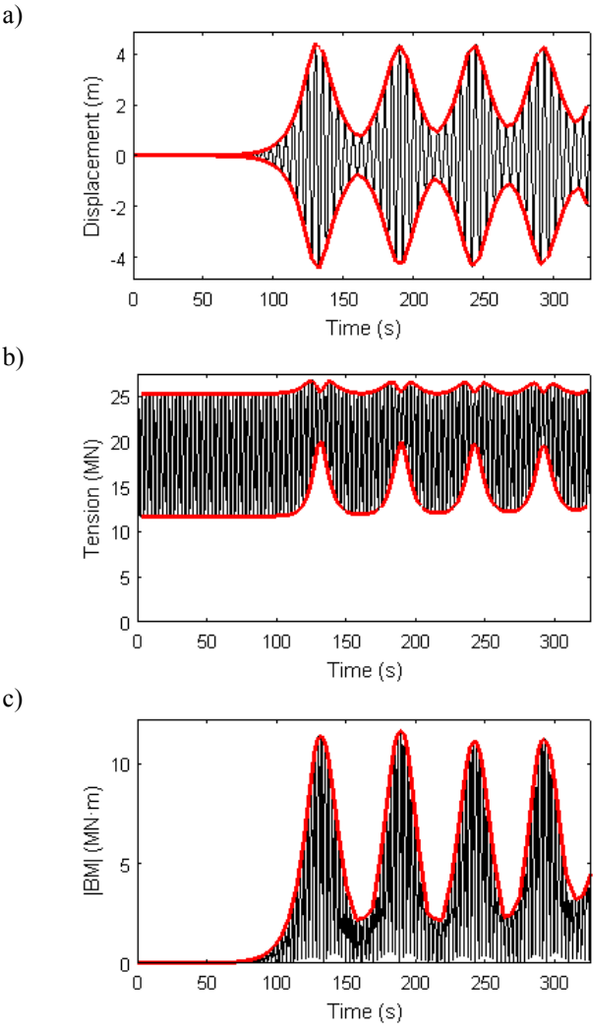


Figure 2. Tether responses under parametric resonance; a) Mid-span displacements; b) Mid-span tension values; c) Support Bending Moment in absolute value (Red lines = envelopes)

Figure 2b shows the time-history of the axial forces during parametric resonance. The tension values vary around the initial prestress tension and oscillate mainly because of the shortening and stretching of the tether length due to the imposed motion. The parametric resonance produces some small changes to the tension values. When larger lateral motions are observed (e.g. 130 s in Figure 2b), one can see an increase in tension values (both maximum and min-

imum) in Figure 2b. In any case, tension values never decrease and thus avoiding the risk of a temporarily slack tether. On the other hand, the maximum bending moment values on the tether clearly depend on the stability of the system as can be seen in Figure 2c. There is a clear increase in bending moment associated to an increase in the curvature of the deformed shape, which is directly related to the larger lateral motions observed during parametric resonance.

In order to compare both load effects, namely tension and bending moment, it is necessary to define them in terms of section stresses. Normalization of the maximum section stresses over steel's yield strength gives the utilisation of the material. Utilisation values greater than one indicate yielding of steel. When calculating utilisation values separately for each load effect, the total utilisation is the sum of all. Figure 3 shows the evolution in time of the utilisation for each load effect for the dry tether during parametric resonance. The results show that, while the tension utilisation remains approximately constant, the utilisation for bending moments varies significantly and is often greater than that of tension. Note that utilisation calculations are based on the envelopes of the load effects, shown in red in Figure 2.

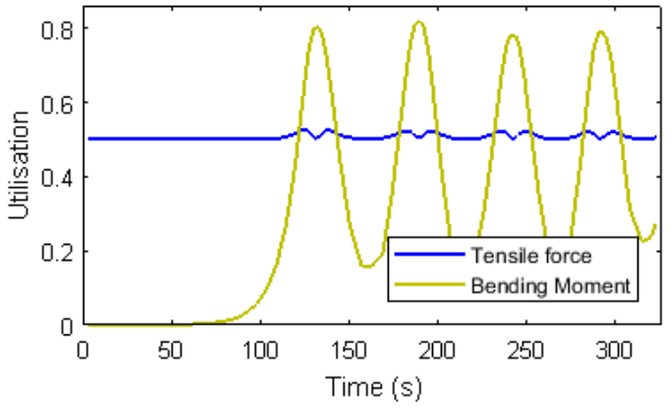


Figure 3. Utilisation of steel for a dry tether during parametric resonance

4 SUBMERGED TETHER

4.1 *Effect of hydrodynamic contribution*

Hydrodynamic effects, such as drag force and added mass, are the greatest contributors to the damping of the system. Parametric resonance of a submerged tether can still occur, but the stresses and responses differ significantly due to the higher energy dissipation. This becomes very clear when analyzing the same tether and support motion as in Section 3. Figure 4 shows the temporal evolution of the utilisation, now including the hydrodynamic effects. The utilisation for tensile forces remains practically constant and is of similar magnitude as for the dry tether case (Figure 3). Whereas the bending moment utilisation grows when the system arrives at the parametric instability, which occurs approximately after 140 s. However, the maximum bending moment values and so the associated maximum utilisation value is only a fraction of that observed in previous section. While the maximum bending moment utilisation for the dry case (Figure 3) is 0.82, for the submerged case it is barely 0.10. Therefore, these results confirm that the submerged tether can also become unstable after sufficiently long excitation period. However, the effects of parametric instability are considerably smaller when including the hydrodynamic effects.

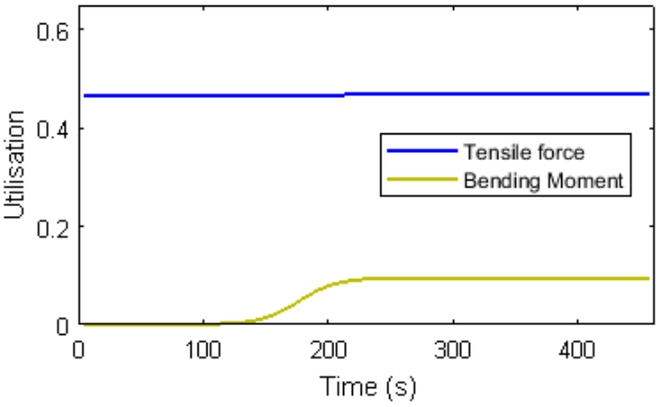


Figure 4. Utilisation of steel for a submerged tether during parametric resonance

4.2 *Effect of boundary condition*

The particular technological solution used to fasten the tether to the floating structure and to the seabed will determine the tether's behavior at those locations. In other words, boundary conditions of the tether are system dependent. When numerically modelling that system, it is very important to choose the correct properties of the boundary conditions. The possibilities range between free-to-rotate supports to fully restrained rotations. Therefore, this section investigates the effect of rotational stiffness (k_r) at the boundary conditions of the tether model. Figure 5 shows the fundamental frequency of the tether for various values of rotation stiffness. As expected, the stiffer the support, the higher the frequency.

Even though the frequencies change only slightly, the structural behavior changes significantly. This is particularly pronounced for bending moments. Figure 6 shows the bending moment diagram along the tether during parametric resonance. The tethers are excited with an imposed motion with a 2:1 frequency ratio. Because the tether's fundamental frequency varies (Figure 5), the excitation frequency is different depending on the rotational stiffness considered. Three particular rotational stiffness values are considered, which correspond to the cases marked with red dots in Figure 5. If the supports are free to rotate, the maximum bending moment is located at midspan and there is no moment at the supports (Fig-

ure 5a). However, as soon as the rotational stiffness increases more bending moments appear at the support (Figure 5b). If the rotations are fully restrained, the bending moment diagrams are dominated by the moments near the supports (Figure 5c). However, not only the location of the maximum is of interest, it is also important to note the difference in bending moment magnitudes for each case. While for the free-to-rotate case the maximum is 0.15 MN·m (Figure 5a), for the fully restrained rotation case the maximum bending moment is 1.35 MN·m (Figure 5c). For the considered tether and depending on the rotational stiffness, the maximum bending moment can be up to one order of magnitude greater.

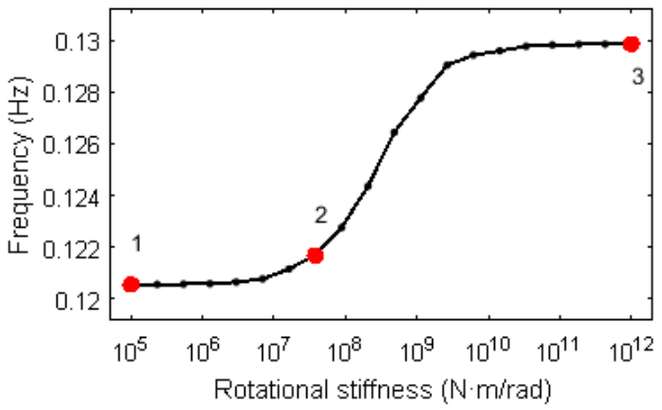


Figure 5. Tether's fundamental frequency for different rotational stiffness

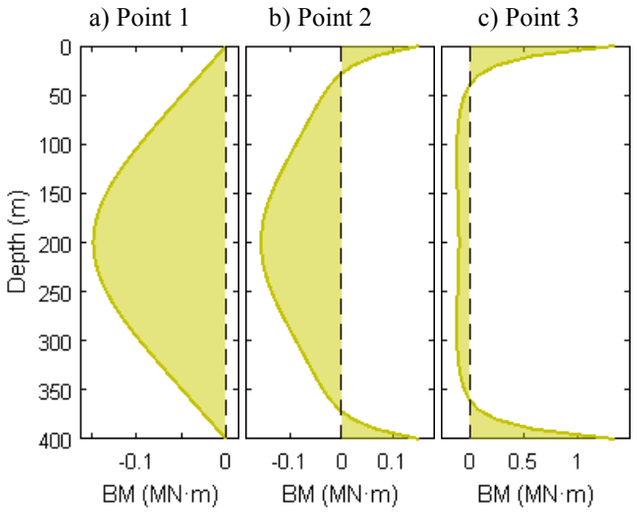


Figure 6. Bending moment diagram along the tether during parametric resonance for various rotation stiffness: a) Low stiffness (≡ free to rotate); b) Intermediate stiffness; c) High stiffness (≡ restrained rotations)

Figure 7 shows the corresponding maximum utilisation obtained during parametric resonance for each considered value of rotational stiffness. The utilisation due to tension is in practice constant, whereas for bending moment it is highest for the case with (effectively) fixed rotational supports. Therefore, to assume a high rotational stiffness is conservative and will give the highest (worst) utilisation values. A tether that allows for some rotation at the support can indeed become unstable by reaching parametric resonance, but the maximum stresses will be smaller than for the case with fully restrained rotations.

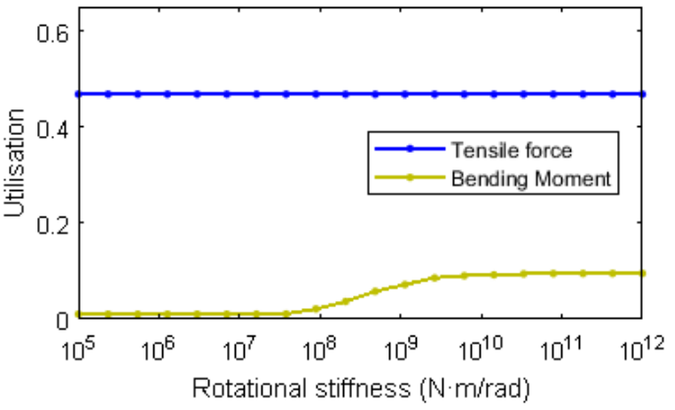


Figure 7. Maximum utilisation of steel for a submerged tether during parametric resonance for different rotational stiffness

4.3 *Support motion: Amplitude and frequency variation*

The imposed support motion, directly related to the wave loading, can vary in amplitude and frequency. It is common to represent the system's stability for any amplitude-frequency combination in graphical form using stability maps or Strutt diagrams. The limits between stable and unstable regions are delimited by the transition curves. The regions grouping all unstable solutions are often called instability tongues. Figure 8 shows the stability map for the tether under consideration in this study. To generate this figure, 1320 separate simulations were necessary, each considering 120 cycles of imposed motion. Each simulated case is represented with a dot in Figure 8. Small black docks indicate that the corresponding amplitude-frequency combination results in a stable response of the submerged tether. Whereas, large red dots indicate that the system is unstable, in other words, that it has reached parametric resonance.

Figure 8 also displays the theoretical transition curves based on the analytical expressions derived in (Cantero et al. 2017). This formulation gives the transition curves for a dry tether with internal damping. No analytical solution exist that includes hydrodynamic effects. For this reason, an internal damping of 10% is used to approximate the energy dissipation effects of the submerged case. This formulation provides a set of transition curves for each mode of vibration considered. Figure 8 shows as gray areas the instability tongues of the first three modes. The agreement between numerical and analytical results is acceptable.

This stability map shows that reasonably small amplitudes of support motions can lead to important unstable tether responses. Furthermore, the greater

the amplitude of the support motion is, the more frequencies there are that result in unstable motions.

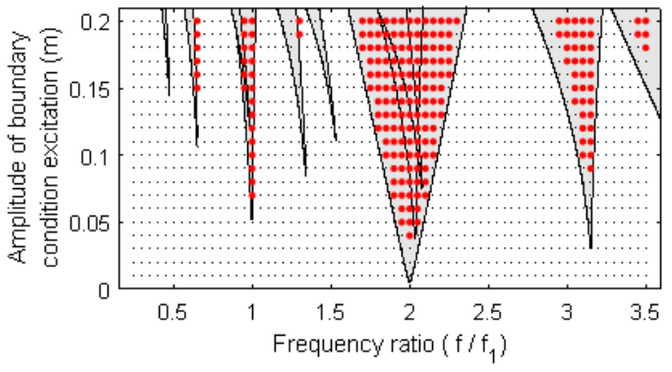


Figure 8. Stability map for submerged tether (stable = small black dot, unstable = large red dot) and theoretical instability tongues (see Appendix) associated to tether's 1st mode (Blue), 2nd mode (Green) and 3rd (Red) mode

As it is customary, the stability criteria to generate the Strutt diagram in Figure 8 is based on the values of lateral displacements of the tether. However, it is interesting to investigate the effect of the system's stability on other load effects for the same amplitude-frequency combinations. Figure 9 shows the maximum utilisation values due tension. It clearly shows a steady increase of the utilization with the amplitude of the support motion regardless of the particular excitation frequency. The effect of the system's stability is barely visible.

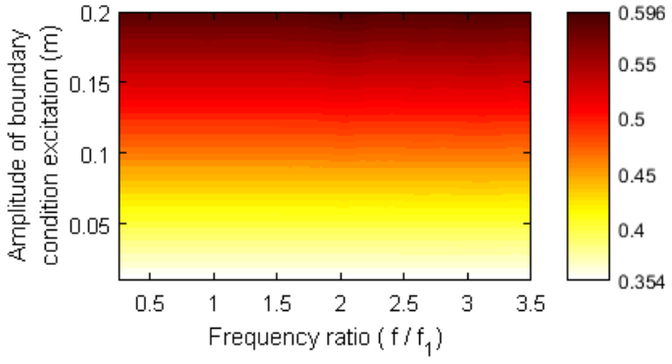


Figure 9. Maximum utilisation of steel due to tension

On the other hand, the maximum utilisation due to bending moments, shown in Figure 10, is strongly related to the stability of the system. The same instability tongues observed for lateral displacements (Figure 8) can be observed on the bending moment utilisation values (Figure 10). However, the magnitude of the utilisation values due to bending moment is rather small compared to those due to tension.

5 CONCLUSION

This document has investigated the effect of parametric excitation on the response of taut mooring lines. It extended existing studies in order to analyze other load effects that are generally not investigated. In particular, this study focused on maximum tension values and bending moments along the tether length. In order to compare both load effects, the results are expressed in terms of sectional stress values and normalized by the yield strength of the material, which gives the utilisation of steel. First, parametric resonance is investigated for the case of a dry tether. The instability produces significant dynamic effects that translate into large variations of bending moment utilisation. Then, the same tether is studied including the hydrodynamic effects. Larger energy dissipation mechanisms reduce the effect of parametric resonance. Tension utilisation is practically not influenced by the instability, whereas bending moments show only a moderate increase. Furthermore, the study of the influence of rotational stiffness at the supports has shown that the fully restrained rotational support leads to the highest stresses and is thus regarded as conservative. Finally, the analysis of multiple amplitude-frequency combinations for the support motion produced the stability diagram for the considered tether. With respect to the axial forces, the simulations confirm that the tension utilisation is practically independent of the systems stability and that it is directly proportional to the tethers elongation due to the imposed support motion. As for the bending moments, the system's stability clearly influences the results, obtaining larger utilisation values at the instability tongues. However, the magnitude of the utilisation values due to bending moment is rather small compared to those due to tension.

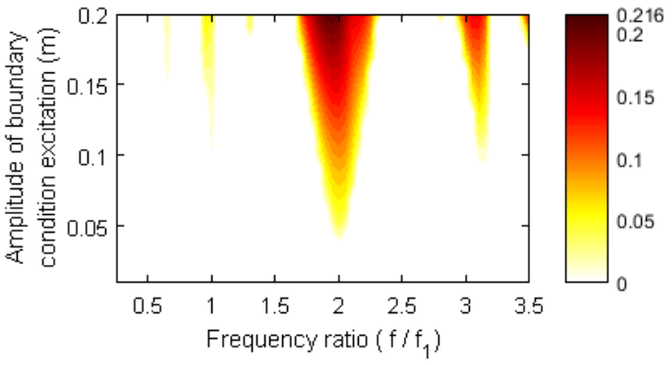


Figure 10. Maximum utilisation of steel due to bending moment

6 ACKNOWLEDGEMENTS

The research presented in this manuscript was possible thanks to the financial support of The Fjord Crossing research program for the Coastal Highway Route E39.

7 ACKNOWLEDGEMENTS

Aage, C., Bernitsas, M.M., Choi, H.S., Crudu, L., Incecik, A. & Murray, J.J. 2000. The Specialist Committee on Deep Water Mooring. Final report and recommendations to the 22nd ITTC. *International Towing Tank Conference*, Seoul, 2000.

Abaqus 2011. *Analysis User's Manual*. Dassault Systèmes, Providence.

Cantero, D., Rønnquist, A. & Naess, A. 2017. Tension during parametric excitation in submerged vertical taut tethers. Applied Ocean Research 65: 279-289.

Franzini, G.R. & Mazzilli, C.E.N. 2016. Non-linear reduced-order model for parametric excitation analysis of an immersed vertical slender rod. *International Journal of Non-Linear Mechanics* 80: 29–39.

Lei, S., Zhang, W., Lin, J., Yue, Q., Kennedy, D. & Williams, F.W. 2014. Frequency domain response of a parametrically excited riser under random wave forces. *Journal of Sound and Vibration* 333:485-498:

Lilien, J.L. & Da Costa, A.P. 1994. Vibration amplitudes caused by parametric excitation of cable stayed structures. Journal of Sound and Vibration 174: 69-90.

Vegvesen 2012. Ferjefri E39 English summary. http://www.vegvesen.no/vegprosjekter/ferjefriE39/English (accessed 14.11.17).

Maintenance, Safety, Risk, Management and Life-Cycle Performance of Bridges – Powers, Frangopol, Al-Mahaidi & Caprani (Eds)
© 2018 Taylor & Francis Group, London, ISBN 978-1-138-73045-8

Overview on the structural features of Submerged Floating Tunnels

B. Jiang & B. Liang
College of Civil Engineering, Chongqing Jiaotong University, Chongqing, P.R China
B. Faggiano, G. Iovane, F.M. Mazzolani
Department of Structures for Engineering and Architecture, University of Naples Federico II, Naples, Italy

ABSTRACT: With both the development in construction technology of offshore engineering and the ever growing demand for transportation to cross the waterways, submerged floating tunnel (SFT) attracts more and more attention. As an innovative structure, SFT represents much more advantages in comparison with the traditional structures in a long distance waterway crossing. The focus of this paper is to provide an overview of fundamental design aspects of SFT in the light of existing research and design reports. In particular, case studies adopting different cross-sections, various structural materials, support systems, structural connections, under diverse imposed loads, are presented. In addition to this, issues about the fabrication and erection processes, ventilation and evacuation plans are also summarized. The main aim behind the work presented herein is to provide a concise source of information to researchers working in this domain of engineering.

1 GENERAL BACKGROUND

The first idea of Submerged floating tunnels (SFT) dates back the beginning of 1900 (Hakkart, 1996) in Norway. An earliest milestone is the proposal for the Messina Strait Crossing (Italy), by Alan Grant in 1969 (A.N.C.E. 1971, Faggiano et al. 2001, Fig. 1). During time in Europe several opportunities of international cooperation on this subject have allowed a huge progress, starting from the earlier Forum of European National Highway Research Laboratories, involving the Norwegian Public Roads Administration with the Danish Road Institute and the Italian Company Ponte di Archimede S.p.A (FEHRL, 1996), up to the recent SIJLAB Sino-Italian joint laboratory, which consolidated the interest of China with the participation of the Institute of Mechanics of the Chinese Academy of Science to the joint venture linking the Italian Company Ponte di Archimede S.p.A, the University of Naples Federico II and the Polytechnic University of Milan, for the design of the first prototype of Submerged Floating tunnel (Mazzolani et al., 2008). The attention to SFTs is also testified by the dedicated international conference dedicated international conferences. The first one, namely "Submerged Floating Tunnels", was held in 1996 in Sandnes (Norway). Recently, in the last years, two international symposia on Archimedes bridges (ISAB2010) and on Submerged Floating Tunnels and Underwater Tunnel Structures (SUFTUS2016) were held in China, in Qiandao Lake and in Chongqing respectively.

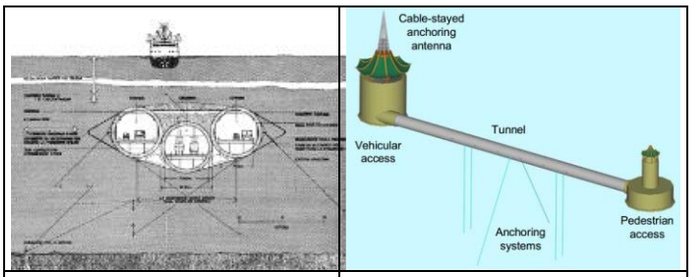


Figure 1. The Archimede bridge: a) Alan Grant, 1969; b) SIJLAB prototype, 2008. (Mazzolani et al. 2010)

Several feasibility studies have been carried out worldwide, the geographical distribution is shown in Figure 2. They are in Italy (Faggiano et al. 2001), in United States (Felch et al. 2001), in China, Jintang Strait (Mazzolani et al. 2002), Qiandao Lake (Mazzolani et al. 2008), Qiongzhou strait (Jiang et al. 2018), in Japan (Kanie, 2010), in Indonesia (Wahyuni et al. 2009), in South Korea (Seo et al. 2015) and in Mexico (Faggiano et al. 2016). The SFT idea has been also taken into consideration for Lugano Lake in Switzerland, the Gibraltar Strait and in Malta.

Based on existing projects, as well as research reports, this article summarizes the structural features of SFT and provides an overview of the main design issues. Specifically, the design options for cross section, materials, anchorages, structural connections

and loads are described. This overview provides pros and cons of the solutions adopted and therefore is a useful reference for future developments of the SFT.



Figure 2. Geographical map of SFT proposals worldwide

2 MAIN STRUCTURAL FEATURES

2.1 *Cross-section*

The cross section size and the internal arrangement of the SFT are determined by static and functional requirements, such as buoyancy ratio (such as buoyancy over weight ratio, BWR), strength and stiffness properties, water-tightening, size of infrastructures. Elongated (elliptical, polygonal) shapes guarantee the best behavior against hydrodynamic actions induced by waves and currents (Wang et al, 2007; Mandara et al, 2016), similarly to the case of emerged bridges that should resist the aerodynamic actions by wind (Fig. 3). The main features of cross-sections proposed in literature are summarized in Table 1.

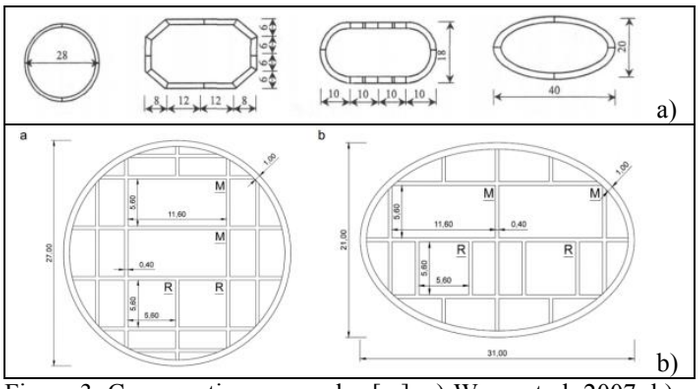
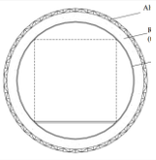
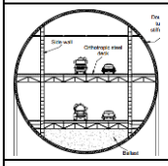
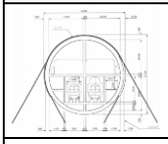
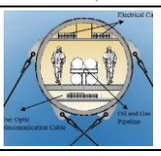
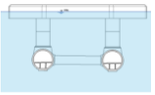
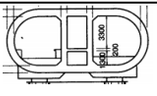


Figure 3. Cross sections examples [m]: a) Wang et al. 2007; b) Mandara et al. 2016

External walls of the tunnel must resist the hydrostatic pressure and eventual collisions from both internal and external sides, besides they should assure watertighting. In some cases a sandwich structure is proposed, where the external layer is a reticular spatial aluminum structure, conceived to absorb the impact by sinking objects and also to guarantee a high durability in the aggressive marine environment thanks to the peculiarity of the material aluminium.

Table 1. Cross-sections data sheet

Shape	Case study	Size	Function	Structural features
Single circular	Qiandao Lake, China (Mazzolani et al. 2008)			
		Φ: out 3.55m; in 2.50m	Motorway	"Sandwich" configuration exploiting good mechanical performance for each material.
	Messina Strait, Italy (Martire et al. 2009)			
		Φ: out 19.3m; in 18.6m	Motorway, Railway	Outer double steel tubes with stiffening ribs and inner steel walls and plates.
	Funka Bay, Japan (Kanie 2010)			
		Φ: 24m	Motorway, Railway	Upper layer for motorway and lower layer for railway, large BWR.
	Indonesia (Budiman et al. 2016)			
		Φ: 3-5m	Pedestrian way, Pipeline	Steel wall plate welded on circle frame and coated to prevent corrosion.
Multi circular	Sognefjord, Norway (Fjeld et al. 2012)			
		Φ: out 12.6m; in 11.0m	Motorway	Effective in resisting current loads and suppressing long-period resonance.
	Messina Strait, Italy (Alan Grant 1969)			
		Φ: out 12.3m; in 10.5m	Motorway, Railway	Compose of three single circles, outer steel shell to keep stable.
Rectangular	Oinaoshi, Japan (Kanie 2010)			
		Width: 5.7m; Height: 13.6m	Motorway, Pedestrian way	Include two-lane road with pedestrian walk, cross-section with fixed pile support.
	Baja California, Mexico (Faggiano *et al.* 2016)			
		Width: 32m; Height: 12m	Motorway	"Ad hoc" triangular shaped lateral steel wings for improving dynamic behavior.
Elliptical	South Sea of Korea, South Korea (Seo et al. 2015)			
		Width: 15.1m; Height: 13.5m	Railway	Suitable for accommodating railways and evacuation.
Oval	Osaka Bay, Japan (Sakurai 1996)			
		Width: 13.6m; Height: 6.2m	Railway	Double-track railway, central tunnel for ventilation and maintenance
Polygonal	Jintang Strait, China (Mazzolani et al. 2002)			
		Width: 27.9m; Height: 12.1m	Motorway	High residual buoyancy, inner cells designed for functional equipment and evacuation.

The appropriate strength and stiffness is then provided by the composite steel concrete circular structure.

In many cases, the tunnel is provided with perimetral cells, which can serve as either watertight compartments, protecting the transport lines from accidental partial flooding in case of out or inside collisions, or ballast compartments, for regulating the buoyancy ratio, or escape routes.

2.2 *Support system*

Four main types of support systems are taken into consideration, such as: free tunnel, column support, pontoons and tension leg, as shown in Figure 4 (Østlid 2010). The selection of support system depends on many factors, such as location, surroundings, destination of use, type of soil, water environment.

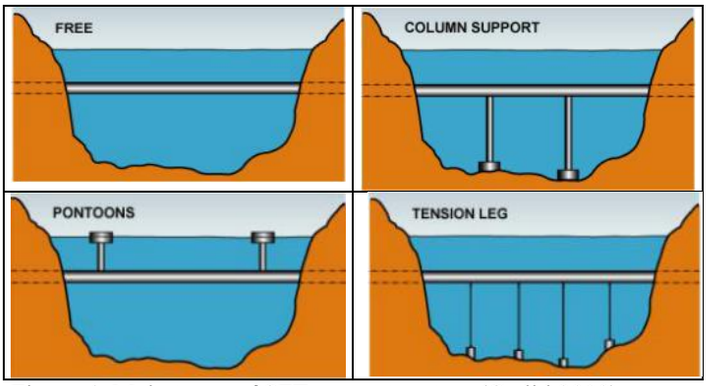
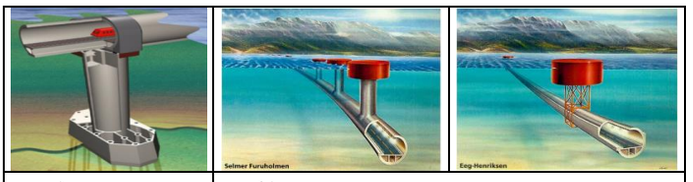


Figure 4. Main types of SFT support system (Østlid 2010)

Free system has no anchoring at all except at landfalls, it is independent of water depth. Obviously, the length of SFT with free support is limited.

Column support system could be employed for negative residual buoyancy (i.e. the buoyancy is lower than the self-weight). The water depth plays an important role in this case, it determining the piers height and therefore influencing the stability. Foundation of piers also specifically requires good geological condition of seabed, in order to keep pears in position (Fig. 5a, Haugerud et al. 2001).



a) b)

Figure 5. a) Column supports for Lugano Lake (Haugerud et al.2001); b) Pontoon for SFT proposal in Norway (Østlid 2010)

Pontoon system is independent of water depth, besides it is sensitive to wind, waves, currents and possible ships collision at the water surface (Fig. 5.b, Østlid 2010). Design should provide that the structure still survive in case of one pontoon lost. Furthermore, the pontoons must be placed for guaranteeing enough clearance for the navigation requirements.

Tension legs can be adopted for positive residual buoyancy (i.e. the buoyancy is greater than the self-weight). These are usually conceived as a series of cables groups, distributed along the tunnel axis with different configurations in the tunnel cross-section plane (Fig. 6, Yan et al. 2015).

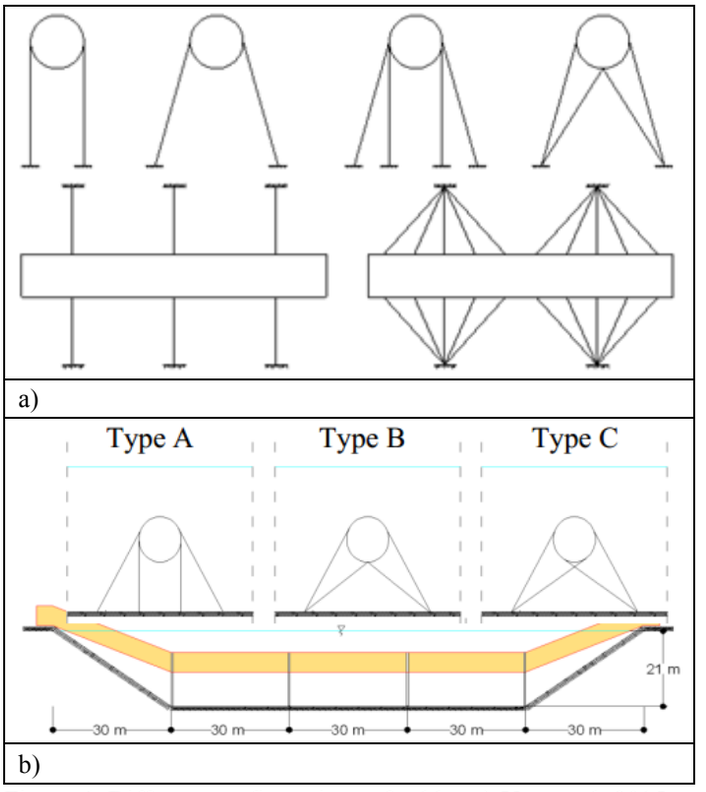


Figure 6. Different configurations of cables a) Yan et al. 2015, b) Wahyuni et al. 2009

Wahyuni et al. (2009) examined different configuration of anchoring cables, showed that Type C tension legs arrangement (Fig. 6b) has a better structural behavior in terms of stress and displacement, what has been also confirmed by Cifuentes et al. (2015) which carried out experimental test on small scale specimen equipped with both inclined and vertical mooring system (Fig. 7).

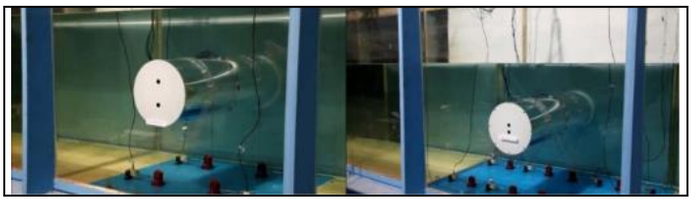


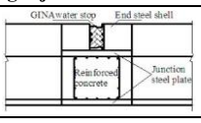
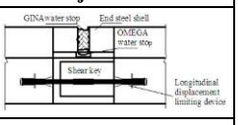
Figure 7. Experimental set up by Cifuentes et al. 2015

The effect of the anchorage configuration on the dynamic behavior of the STs has been investigated by Faggiano et al. (2001), Mazzolani et al. (2008), Martire et al. (2009, 2010, 2012). Specifically, Mooring cables behavior and modelling aspects are investigated by Cantero et al. (2016),

2.3 *Joints*

SFT is made up of pre-fabricated modules assembled in situ. The design of joints between inter-modules should conform to several requirements, such as water tightness, strength and stiffness, durability, workability, maintenance. They should guarantee the continuity between the module therefore they should realize full strength connections.
Zhang et al. (2010) discussed about two types of joints realizing a rigid and a flexible conditions. Main features are described in Table 2. However flexible joints, even though they are easier to realize and then less expensive, are not suitable.

Table 2. Features for rigid joint and flexible joint. (Zhang et al. 2010)

Features	**Rigid joint**	**Flexible joint**
Structural composition		
	End steel shell, GINA water stop, junction steel plate and reinforced concrete	End steel shell, GINA water stop, OMEGA water stop, shear key, longitudinal displacement limiting device
Construction	Long period and great difficulty	Convenient construction
Cost	Cheap	Expensive
Applicable position	End joint	Intermediate joint

The inter-modular joints for the Qiandao Lake SFT prototype (Mazzolani et al. 2010) are essentially bolted connections, designed for being set up and assembled when the modules are already submerged. At the external aluminum layer, a rubber ring crushed between the modules guarantees the water tightening of the connection. A sliding rubber ring is placed between steel and aluminum elements, in order to allow relative displacements due to thermal variations (Fig. 8).

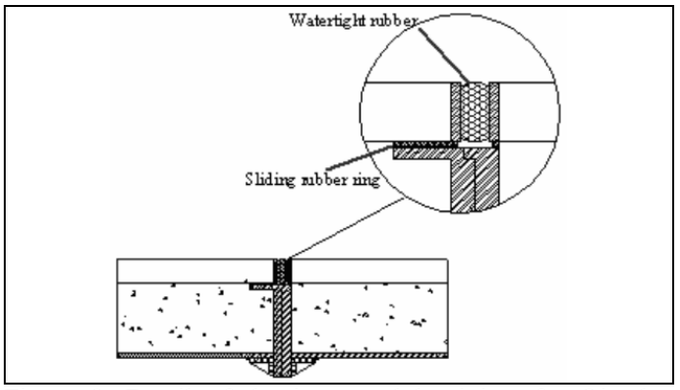


Figure 8. Detail of the inter-modular joints for Qiandao Lake SFT prototype (Mazzolani et al. 2010)

2.4 *Shore connections*

The connection of the SFT to the shore requires appropriate interface elements to couple the flexible tunnel in the water with the much more rigid shore infrastructure. This connection should be able to restrain tube movements, without any unsustainable increase in stresses. Furthermore, the connections must be watertight. A landfall tunnel realizes the transition between the SFT and the shore infrastructure. The latter can be either a tunnel bored in the ground or a special access structure, leading through ramps to the surface transportation ways.

This is the case for example of the SFT prototype for Qiandao Lake crossing in China (Mazzolani et al. 2007), which has the following features: at one end the access structure is conceived for allowing the vehicular and pedestrian access, it involves helicoidal ramp inside, at the other end only the pedestrian access is allowed. The access structures are completed by roofs, whose structural features are inspired to the Chinese traditional architecture (Fig. 9).

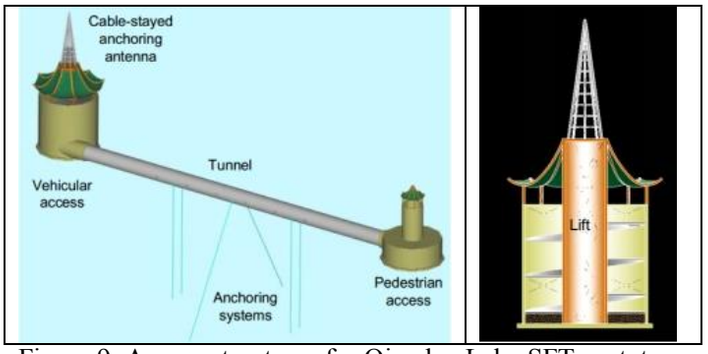


Figure 9. Access structures for Qiandao Lake SFT prototype (Mazzolani et al. 2007)

Another example is developed for the SFT proposal for crossing the Baja California in Mexico (Fig. 10). In this case, helicoidal ramps are provided at the tunnel ends at the shores with the purpose to reduce the length of tunnel, allowing a rapid connection to the surface transportation ways (Faggiano et al. 2016).

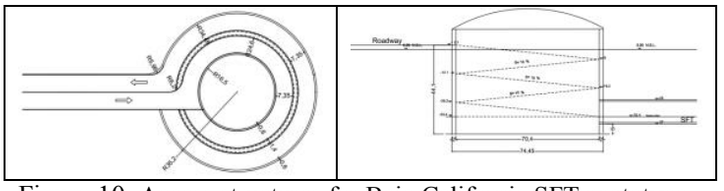


Figure 10. Access structures for Baja California SFT prototype (Faggiano et al. 2016)

2.5 *Material*

The selection of the materials applied for SFT must correspond to the planned structural and functional performances, taking account of several factors such as the resistance to the marine environment, fabrication, assembly and maintenance issues, time needed for the supply, cost and so on, further to strength and stiffness.

Suitable materials for the tunnel tube are steel, concrete, aluminum and rubber foam (Fehrl, 1996). Main related feature are reported in Table 3.

Suitable material for cables is steel for steel pipes or strands, but also synthetic fiber ropes, like CFRP (Lin et al, 2016), are proposed for application in marine environment. They should guarantee high tensile strength and resistance to corrosion and fatigue. Some features for different type of cables are reported in Table 4.

Table 3. Characteristics of different materials for the tunnel tube

Materials	Advantages	Disadvantages
Steel	Good mechanical properties; Good resistance to fatigue and abrasion; Good workability and weldability; Large strength-to-weight ratio.	Low resistance to corrosion; Low performance of welded connections with respect to fatigue Low resistance to fire.
Concrete	Good resistance to the corrosion in marine environment; Good resistance to abrasion; Good resistance to fire and high temperatures; Possibility to be cast to realize complex shapes; Low cost.	Negligible resistance to tensile stresses.
Aluminum alloys	Wide range of strength; Good workability; High resistance to marine corrosion; High resilience.	Poor resistance to fire; Low stiffness compared to steel; Low specific weight compared to steel; High cost.
Rubber foam	Extremely light weight Dissipation of the energy transmitted by external impacts	Poor resistance to fire and high temperature

Table 4. Characteristics of different types of cables for SFT (Lin et al. 2016)

Types	Advantages and characteristics	Defects
Steel pipe	Rigid rope Large bending stiffness, subjected to pressure	Heavy mass, small elasticity, worse workability, low tensile stiffness,
Steel strand or parallel steel strings	Flexible rope High tensile strength	Low resistance to corrosion and abrasion
Aramid strands	Light flexible rope Good resistance to corrosion and abrasion, low density	Low stiffness, low resistance to fatigue

3 LOADS

The "*permanent loads*" on a SFT are self-weight of the various structural and non-structural component, buoyancy and hydro-static pressure.

The buoyancy-weight ratio (BWR) is a key design parameter. It defines the relationship between self-weight and buoyancy of the structure. Common values range between 1.2-1.5, mediating the requirements of limiting design tensile stress and increasing the stiffness and stability of the cables. Hong et al. (2016) investigated the relationship between buoyancy-weight ratio (BWR), inclined mooring angle (IMA) and slack-taut performance (STP) under the wave actions (Fig. 11).

It is apparent from Figure 11 that the tether STP is sensitive to the both BWR and IMA of SFT. The effect by these two factors are coupled. For small IMA (close to 0), the slackening of cables is unabled to occur except for the small BWR. For large BWR a narrow range of IMA, around 10^{o}, can give rise to snap force, the snap IMA range becomes wider as BWR decreases. For BWR as small as 1.1, slackening always occurs.

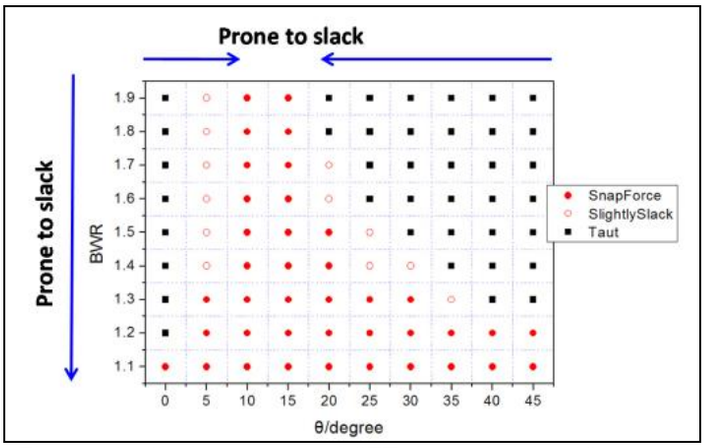


Figure 11. Slack-taut map of SFT (wave height: 12 m, and wave period: 15 s) (Hong et al. 2016)

The "*functional loads*" are associated with the passage of cars, trucks, trains and/or pedestrians, according to the destination of use of the SFT. Several studies have been carried out on the dynamic behavior of the tunnel under traffic loads (Tariverdilo et al, 2011; Dong et al, 2016), showing how an increase of the cable stiffness can lead to an improvement in the dynamic response of the tunnel system. According to the comparisons among different simulation methods, the moving vibration load is proved to be more appropriate for simulating the traffic load in SFT (Liang et al, 2017).

The "*accidental loads*" are related to emergency situations, such as fires, explosions, flood, infiltration, landslides, collisions (referring to floating object, boat wreck, submarines). Several studies have been carried out, testing the response under the action of fire loads (Ingason et al. 2013, Fig. 12.a) or explosions (Seo et al. 2013, Fig. 12.b) of the tunnel equipped with various safety systems. Figure 12.a presents the longitudinal ventilation system which is designed for SFT to create a longitudinal flow to prevent the smoke back-layering produced by the fire (Ingason et al. 2013). Figure 12.b shows the simulation of an explosion in a SFT through a simplified model of a simply supported beam with elastic springs subjected to impulse pressure.

The "*environmental loads*" are associated to currents, waves, tides, tsunamis, earthquakes, thermal variations, encrustations produced from underwater organisms. In particular, researches emphasize currents, waves and earthquake, which mainly affect the dynamic behavior of the SFT.

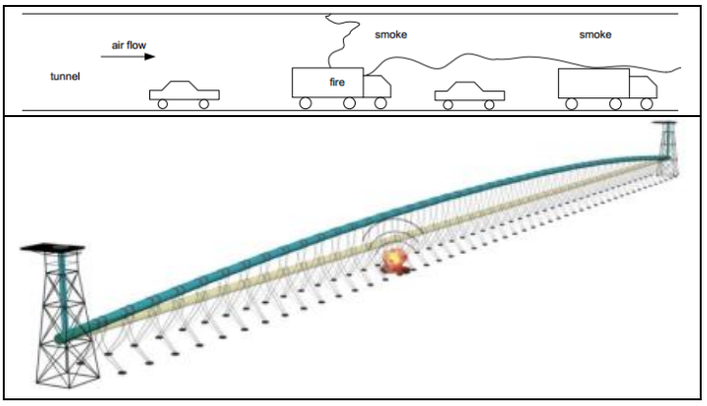


Figure 12. a) Fire ventilation in a tunnel with longitudinal ventilation (Ingason et al. 2013); b) SFT attacked by underwater explosion (Seo et al. 2013)

The tunnel being immersed in the water interacts with the water, both in static condition, through buoyancy, and in dynamic condition, it being affected by the surrounding water mass in movement, which give rise to an additional damping and inertia. Moreover vortex shedding can occur, at an extent depending on the shape of the cross section. The flow is unable to follow all along the surface of the structure, then it separates from the surface itself, creating a vortex which causes a local increase in rotational velocity. Higher flow velocity yields a reduction in dynamic pressure, which creates an attraction force by the vortex on the structure. The position of the separation point alternates between the top and bottom of the cylinder, and creates a vortex street, as illustrated in Figure 13 (Fjeld et al, 2012). Fluid-structure interaction for SFTs has been also recently investigated by Ge et al. (2010), Xiang and Zhang (2013) and Mandara et al. (2016).

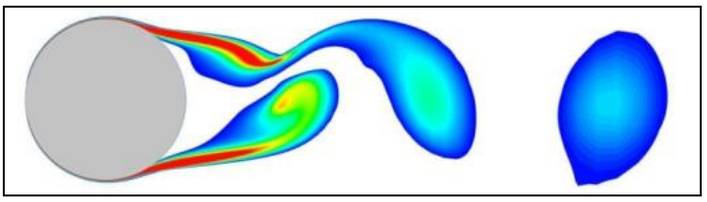
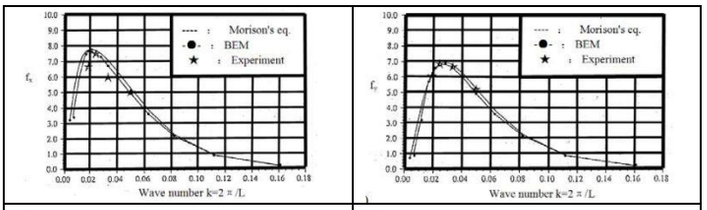


Figure 13. Vortex Street behind a circular cylinder (Fjeld et al. 2012)

With regards to the wave force model, Kunisu (2010) applied both the Boundary Element Method (BEM) and the Morison's equation Eq. (1), which estimate both drag and inertial forces, comparing the results with the experimental evidence.



a) b)

Figure 14. Estimation of wave force by different methods a) transverse and b) vertical directions (Kunisu 2010).

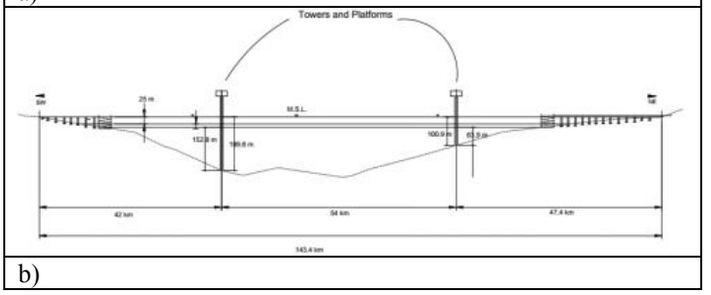
A satisfactory approximation is achieved. With regards to seism, SFTs seem to be particularly suitable in high seismicity zones, due to large transversal flexibility and to the beneficial effect of the water-structure interaction, giving rise to a reduction of the earthquake input energy on the tunnel. Deep studies on the seismic behavior of SFTs have being carried out in Italy by Di Pilato et al. (2008), Fogazzi and Perotti (2000), Martire et al. (2009, 2010, 2012), Martinelli et al (2011, 2016) aiming in all at characterizing the structural behaviour of SFTs during severe seismic events, estimating the performance of the different structural configurations, investigating the influence of the crossing length on the seismic response of SFTs, comparing the structural response to multisupport excitations, studying the characteristics of vertical ground motion propagation into water and its effects on the SFT seismic response.

4 VENTILATION AND EVACUATION

SFT is a closed structure and located underwater, hence lighting and ventilation are key issue, as well as the escape access for emergency in case of any accidents. For long structures, evacuation towers are set along the tunnel (Fig. 15), as proposed by Seo et al. (2015, Fig. 15a) and Faggiano et al. (2016, Fig. 15b).



a)



b)

Figure 15. Evacuation tower and platform for long SFT a) in South Korea (Seo et al. 2015), b) in Baja California, Mexico (Faggiano et al. 2016)

Towers are equipped with a top platform, for helicopter take-off and landing for facing emergency rescue, the towers are also designed for several services, including ventilation and tourism.

5 FABRICATION AND ERECTION

Indications to erection procedures can be found with reference to the SFT prototype in Qiandao Lake (Mazzolani et al. 2010), where all the construction phases including fabrication of the tunnel modular unit (Fig. 16) have been studied. To this specific concern, it is worth to note that the circular cross section has a sandwich structures. The internal steel tube and the external aluminum tube are preliminary realized, then they are used as a formwork for the concrete casting.

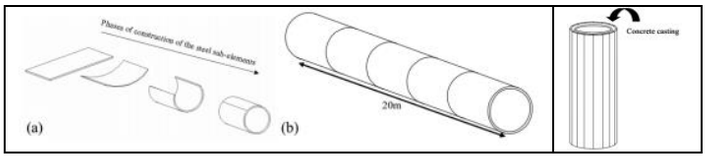


Figure 16. Fabrication of SFT modules (Mazzolani et al. 2010)

Fjeld et al. (2012) described the procedure of construction and installation in the feasibility study related to the Sognefjord crossing. The procedure mainly consist of the following steps: construction of elements, tow to assembly site, temporary mooring at assembly site, jointing of tunnel sections, landfalls, installation of SFT, installation of pontoons.

6 CONCLUSIVE REMARKS

In this paper, main structural features of SFT are briefly summarized with reference to existing researches. They are mainly related to cross-section, support systems, connections, materials, loads.

Also aspects like lighting, ventilation, evacuation, as well as the procedure of fabrication and erection are mentioned, they being very important for SFT design.

So far, the achievements of SFT are based on the theoretical studies, numerical simulation and experimental investigations. Nevertheless this structural type can benefit of the huge experience in the field of tunnels and off shore structures, from which SFT differentiates for the peculiar dynamic behavior. However to this concern some similarities can be found with aerial bridges.

Nowadays the state of knowledge is preparatory to the challenging realization of the first submerged floating tunnel.

REFERENCES

Budiman E., Wahyuni E., Raka I G.P., Suswanto B. 2016. Conceptual study of submarine pipeline using submerged floating tunnel. *Asian Research Publishing Network* 11(9):5842-5846.

Cantero, D., Rønnquist, A., Naess, A. 2016. Recent Studies of Parametrically Excited Mooring Cables for Submerged Floating Tunnels 2nd International Symposium on Submerged Floating Tunnels and Underwater Tunnel Structures, SUFTUS 2016; Chongqing; China; 16 December 2016, Procedia Engineering, Volume 166, 2016, Pages 99-106

Cifuentes C., Kim S., Kim M.H., Park W.S. 2015. Numerical simulation of the coupled dynamic response of a submerged floating tunnel with mooring lines in regular waves. *Ocean Systems Engineering* 5(2): 109-123.

Di Pilato, M., Perotti, F., Fogazzi, P. 2008. 3D dynamic response of submerged floating tunnels under seismic and hydrodynamic excitation. Engineering Structures, 30 (1), pp. 268-281.

Dong M., Zhang Y., Tang F., Yang L. 2016. Displacement response of submerged floating tunnel subjected to equidistant moving loads. *Chinese Journal of Applied Mechanics* 33(5):760-765.

Faggiano B., Mazzolani F.M., Landolfo R. 2001. Design and modeling aspects concerning the submerged floating tunnel: an application to the Messina Strait crossing. *Proceedings of the Fourth Symposium on Strait Crossings*, P.p. 511-520. Bergen, Norway.

Faggiano B., Panduro J., Rosas M.T.M., Mazzolani F.M. 2016. The conceptual design of a roadway SFT in Baja California, Mexico. 2nd International Symposium on Submerged Floating Tunnels and Underwater Tunnel Structures. *Procedia Engineer*ing 166:3-12.

Fehrl. 1996. Analysis of the submerged floating tunnel concept, *FEHRL (Forum of European National Highway Research Laboratories),* Transport Research Laboratory, *RG45 6AU, 1996.*Crowthorne, Berkshire.

Felch J., 2001. The Seattle-Bellevue Loop with still-water submerged floating tunnel. *Proceedings of the 4th Symposium on strait crossings*, Norway, Balkema, Rotterdam, P.p. 581-590.

Fjeld A., Søreide T. H., Haugerud S. A. 2012. Feasibility study for crossing the Sognefjord Submerged Floating Tunnel. *SFT design for crossing of Sognefjorden at Lavik*, Reinertsen Olav Olsen Group.

Fogazzi, P., Perotti, F. 2000. The dynamic response of seabed anchored floating tunnels under seismic excitation. Earthquake Engineering and Structural Dynamics, 29 (3), pp. 273-295.

Ge F., Lu W., Wu X., Hong Y., 2010. Fluid-structure interaction of submerged floating tunnel in wave field, Procedia Eng., 4, 263-271.

Haugerud S. A., Olsen T. O., Muttoni A.2001. The Lake Lugano Crossing-Technical Solutions, Swets & Zeitlinger B. V., Lisse, Netherlands, Strait Crossings 2001, P.p. 563-597.

Hong Y., Ge F., Lu W. 2016. On the two essential concepts for SFT: synergetic buoyancy-weight ratio and slack-taut map. *Procedia Engineering* 166:221-228.

Ingason H., Li Y., Brandt W., Wighus R. 2013. New challenges for the fire safety in submerged floating tunnels. Strait Crossings, 16-19. June, Bergen, Norway.

Jiang B., Liang B., Faggiano B., Iovane G., Mazzolani F. M. 2018. Feasibility Study on a Submerged Floating Tunnel for the Qiongzhou Strait in China. 9th International Conference on Bridge Maintenance, Safety and Management (IABMAS 2018). 9-13 July 2018, Melbourne Australia.

Kanie S. 2010. Feasibility studies on various SFT in Japan and their technological evaluation. *Procedia Engineering* 4:13-20.

Kunisu H. 2010. Evaluation of wave force acting on Submerged Floating Tunnels. *Procedia Engineering* 4:99-105.

Liang B., Jiang B. 2017. Study of simulation method for traffic load of Submerged Floating Tunnel (SFT), *Tunnel Construction* 37(10): 1232-1238.

Lin H., Xiang Y., Yang Y. 2016. Coupled vibration analysis of CFRP cable-tube system under parametric excitation in submerged floating tunnel. *Procedia Engineering* 166:45-52.

Mandara A., Russo E., Faggiano B., Mazzolani F.M. 2016. Analysis of fluid-structure interaction for a submerged floating tunnel. *Procedia Engineering* 166:397-404.

Martinelli, L., Barbella, G., Feriani, A. 2011. A numerical procedure for simulating the multi-support seismic response of submerged floating tunnels anchored by cables. Engineering Structures, 33 (10), pp. 2850-2860.

Martinelli L., Domaneschi M., Shi C. 2016. Submerged Floating Tunnels under Seismic Motion: Vibration Mitigation and Seaquake effects. *Procedia Engineering* 166:229-246.

Martire G., Faggiano B., Esposto M., Mazzolani F.M. 2009. The structural response of Submerged Floating Tunnel to multi support seismic excitations. Proceedings of the International Conference STESSA09, Seismic Behavior of Steel Structure in Seismic Areas, Philadelphia, USA, p. 19-26, Leiden: CRC-Press/Balkema.

Martire G., Faggiano B., Mazzolani F.M., Zollo A., Stabile T.A. 2010. Seismic analysis of a SFT solution for the Messina Strait crossing. *Procedia Engineering* 4:303-310.

Martire G., Faggiano B., Mazzolani F.M., Zollo A., Stabile T.A. 2012. A comprehensive study on the performance of Submerged Floating Tunnels during severe seismic events. Mazzolani & Herrera (eds), Stessa 2012:523-529. London: Taylor & Francis Group.

Mazzolani F.M., Landolfo R., Faggiano B. 2002. Submerged Floating Tunnel (Ponte DI Archimede) in the Jintang Strait. Analysis report. Naples, Federico II University.

Mazzolani F.M., Landolfo R., Faggiano B., Esposto M. 2007. A Submerged Floating Tunnel (Archimedes Bridge) prototype in the Qiandao Lake (PR of China): research development and basic design. Costruzioni Metalliche , Milan, Italy, Pp:45-63.

Mazzolani F.M., Landolfo R., Faggiano B., Esposto M., Perotti F., Barbella G. 2008. Structural analyses of the Submerged Floating Tunnel prototype in Qiandao Lake (P.R. of China). *Advanced in Structural Engineering* 11:439-454.

Mazzolani F.M., Faggiano B., Martire G. (2010). Design aspects of the AB prototipe in the Qiandao Lake. *Procedia Engineering* 4: 21-33.

Østlid H. 2010. When is SFT competitive? *Procedia Engineering* 4:3-11.

Sakurai S. 1996. Submerged floating tunnel proposed to connect Kansai, Kobe Airport. *Tunnelling and Underground Space Technology* 11(4):511-514.

Seo S., Sagong M., Son S. 2013. Global response of submerged floating tunnel against underwater explosion. Strait Crossings 2013, 16-19. June, Bergen, Norway.

Seo S., Mun H., Lee J., Kim J. 2015. Simplified analysis for estimation of the behavior of a submerged floating tunnel in waves and experimental verification. *Marine Structures* 44:142-158.

Tariverdilo S., Mirzapour J., Shahmardani M., Shabani R., Gheyretmand C. 2011. Vibration of submerged floating tunnels due to moving loads. *Applied Mathematical Modeling* 35(11):5143-5425.

Wahyuni E., Raka I G. P., Budiman E. 2009. Structural behavior of submerged floating tunnels with different cable configurations under environmental loading. *Dinamika TEKNIK SIPIL, Akreditasi BAN DIKTI* 110:212-215.

Yan H., Yang G., Yu J. 2015. The Lectotype Study on the Submerged Floating Tunnel. *Construction Technology* 44(7):113-116.

Zhang K., Xiang Y., Du Y. 2010. Research on tubular segment design of submerged floating tunnel, ISAB-2010, *Procedia Engineering* 4:199-205.

Zhang K., Xiang Y. 2013. Vortex-induced dynamic response analysis for the submerged floating tunnel system under the effect of currents. Journal of Waterway, Port, Coastal and Ocean Engineering, 139, 3, 183-189.

Maintenance, Safety, Risk, Management and Life-Cycle Performance of Bridges – Powers, Frangopol, Al-Mahaidi & Caprani (Eds)
© 2018 Taylor & Francis Group, London, ISBN 978-1-138-73045-8

Research on the Finite Element Analysis Method of the Bucket Foundation of Submerged Floating Tunnel

Jiajun Xiang, Xu Feng, Shilun Feng*
Institute of Civil Engineering, Tianjin University, Tianjin 300072, China
Jianbin Mao
China National Offshore Oil (China) Co., Ltd. Tianjin branch, Tianjin 300072, China

ABSTRACT: The anchor foundation of submerged floating tunnel has great influence on the safety and stability of the submerged floating tunnel. At present, there are few researches on the quantitative analysis method of anchor foundation of submerged floating tunnel. In this paper, a method of numerical simulation using ABAQUS finite element analysis software is put forward for the bucket anchor foundation of submerged floating tunnel. This method can conveniently and quantitatively analyze the uplift capacity of bucket anchor foundation of submerged floating tunnels in complicated geological and topographical conditions. Moreover, we compared the experimental data of entity model with the numerical simulation results to verify the feasibility of the finite element numerical simulation method.

1 MAIN TEXT

Submerged floating tunnel (SFT) is a new type of traffic across the water. It is characterized by not being buried under the river bed, nor on the river bed, but a closed structure suspended in the water.Due to the characteristics of the SFT, the anchorage foundation meeting the uplift requirements is the necessary guarantee for the safe passage of the SFT.

The length of the SFT is very long, and it spans a wide range of sea area, so that the geological terrain around the anchor foundation is very complex, and the soil environment of the anchor foundation is different. Therefore, an analytical method for quantitatively analysing the anchored foundations of the SFT plays an important role in the study of stability and safety of the anchored foundations of the SFT.

We have already made a study of the entity model experiment to the bucket foundation of the SFT. In this paper, we will establish the three-dimensional model by ABAQUS finite element analysis software according to the experiment of the entity model, and set up the soil parameters, for example, elastic modulus, Poisson's ratio, Moore -- Kulun plastic modulus and uplift load etc. to achieve quantitative analysis. Then the numerical simulation results are obtained by software analysis and calculation. In order to verify the feasibility of the finite element quantitative analysis method, the numerical simulation results are compared with the experimental results of the entity model. The text should fit exactly into the type area of 187 × 272 mm (7.36" × 10.71"). For correct settings of margins in the Page Setup dialog box (File menu) see Table 1.

2 BRIEF INTRODUCTION OF FINITE ELEMENT ANALYSIS SOFTWARE

The finite element analysis is mainly modeled by ABAQUS. ABAQUS is one of the most advanced large-scale finite element analysis software in the world, which has extensive simulation performance. It has numerous unit model, material model, analysis procedure and so on, so it can be used to analyze the various problems in various field, such as solid mechanics, rock mechanics and structural mechanics, especially to solve complicated problems and nonlinear problems. It is because of the excellent analytical ability and the reliability of analog complex systems of ABAQUS that it has been widely used in industry and research of various countries. The main advantages of ABAUS are as follow. First, it is powerful and convenient to use. In most simulations, even highly nonlinear problems, the user only needs to provide some engineering data, such as structural geometry, material properties, boundary conditions and load conditions. Second, nonlinear analysis is powerful. In nonlinear analysis, it can automatically select the corresponding load increment and convergence speed. It can not only select the appropriate parameters, but also adjust the

*Corresponding author. Tel.: +86-13902164874;
fax: +86-022-27405816.
E-mail address: shilunfeng@126.com(Shilun Feng)

parameters continuously to ensure the accurate solution in the analysis process. Third, it has a rich library of unit libraries and material models.

3 FINITE ELEMENT NUMERICAL SIMULATION

3.1 *The numerical mode*

We use ABAQUS to build the finite element model, which mainly includes the simulation of the bucket foundation and test soil. The bucket foundation is modeled on the 2# bucket in the previous model experiment, and the specific dimensions are given in Table1. The length of the test soil is about 6 times the diameter of the bucket foundation, and the depth is about 5 times the height of the bucket foundation. By trial calculation, such a region can basically eliminate the influence of the boundary effect on the calculation results.

Table1. The 2# bucket foundation size

Material	Characteristics of the bucket foundations			
	Mass /kg	Wall thickness /mm	Diameter /mm	Height /mm
Iron	3.77	3	220	220

In the process of modeling, we considered the following basic assumptions:

1. The test soil layer is shallow, so the simulated soil is not layered and adopts the same parameters;

2. The construction step is adopted to simulate the whole process of the experiment, which mainly considers the spatial displacement changes regardless of the time effect;

3. We will mainly simulate bucket foundation and test soil, and simplify simulation of the bucket foundations without consideration of detail changes. The force applied during the test is replaced by load, and no longer simulate other test instruments.

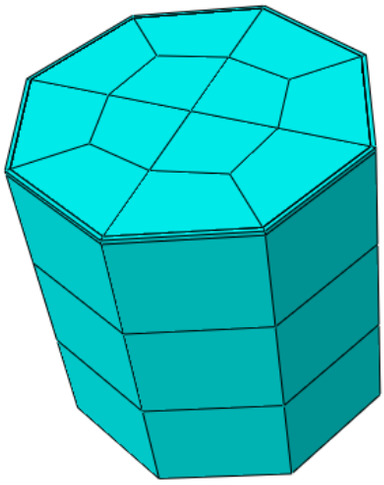
The overall model is modeled by taking the center of the bucket foundation as the coordinate origin and the deepest point of the soil layer as the Z axis 0 point. Both the bucket foundation and the test soil are modeled with a solid homogeneous model. The specific material parameters are shown below.

(1) Bucket foundation

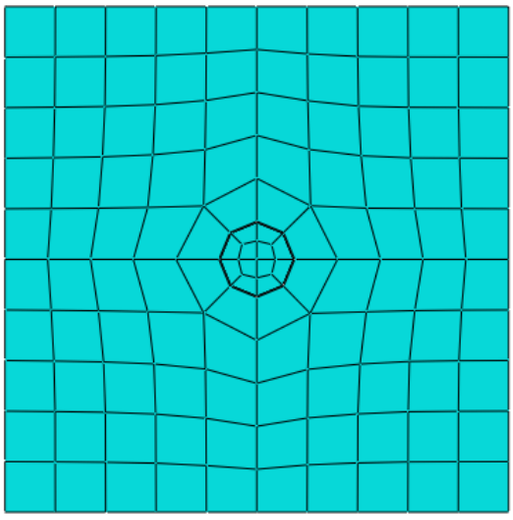
The diameter of the bucket foundation is 220mm, the barrel height is 220mm, and the barrel wall thickness is 3mm. A linear elastic constitutive model is adopted for the barrel structure. The density is 7850kg/m^3, and the elastic modulus are 2.5×10^4 MPa and Poisson's ratio is 0.26. The completed finite element model is shown in Figure 1.(a).

(2) Test soil

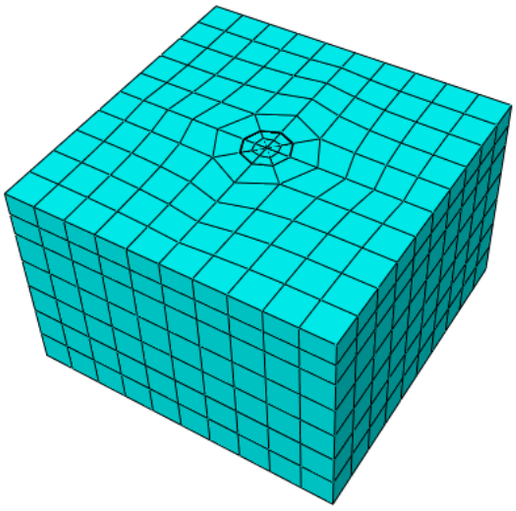
The basic dimensions of the test soil are: 1.5m long, 1.5m wide and 1m deep. The test soil type are cohesive soil and sandy soil. The density of cohesive soil is 1950kg/m^3, the elastic modulus is 58MPa, the Poisson's ratio is 0.42, the friction angle is 20°, and the cohesive force is 20kPa. And the density of sandy soil is 1050kg/m^3, the elastic modulus is 67.5MPa, the Poisson's ratio is 0.42, the friction angle is 25°, and the cohesive force is 0kPa. The complete finite element model is shown in Figure 1.(b)~Figure 1.(d).



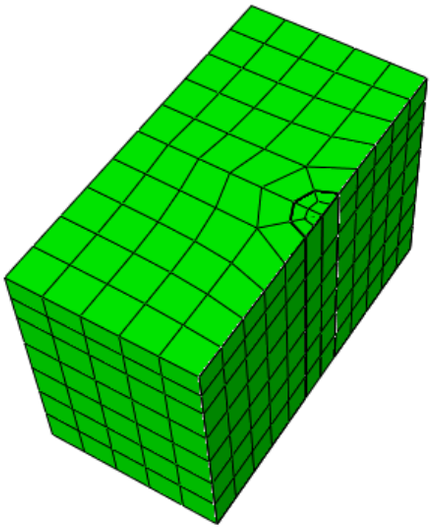
(a) bucket foundation;



(b) bucket foundation top view;



(c) bucket foundation isometric side view;



(d) bucket foundation profile;

Figure 1. finite element model: (a) bucket foundation; (b) top view; (c) isometric side view; (d) profile.

3.2 *Boundary conditions*

In the whole calculation model, the displacement boundary condition is adopted. The top surface of the whole model is a free boundary surface, the bottom surface is completely fixed to limit the displacement, and the plane displacement is restrained around.

The interaction between the bucket foundation and the soil is finite slip contact, and it's friction coefficient is 0.35.

3.3 *Model loading*

Model loading is mainly divided into two steps:

(1) Initial geostress balance

The geostress field is considered in terms of gravity stress field. First, the initial self-weight stress field is established. The test soil for static treatment, and the soil will sink under self-weight, so when the uplift process of the bucket foundation is simulated by finite element method, the initial geostress must be balanced in order to reach the initial state of natural soil layer. Therefore, the first stage of the numerical simulation is the geostress equilibrium stage. At this stage, ABAQUS will calculate the displacement field and stress field of the soil under the action of gravity, eliminate the settlement displacement and construct the initial geostress field.

(2) Uplift loading

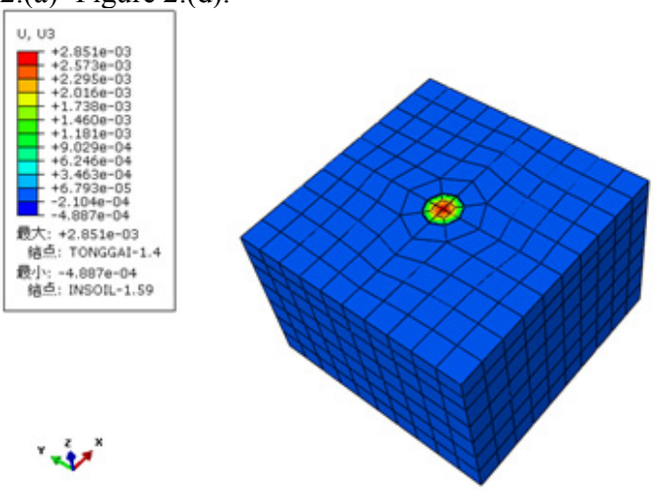
After removing the settlement displacement, the uplift load is applied to the bucket foundation with reference to the previous test loading force. First, the middle of the barrel is taken as the action point, and then the vertical concentrated force is applied at the action point. The loading force values of the test are shown in Table2.

Table2. Loading force

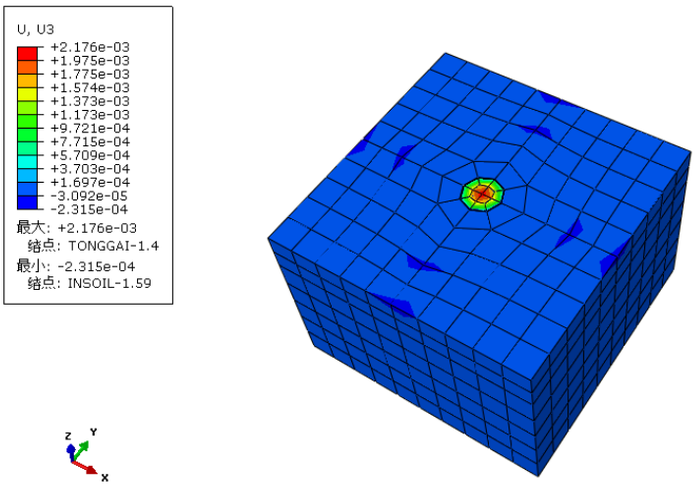
Test soil	Loading force	Action point
Cohesive soil	750	Center of barrel values
Sandy soil	500	Center of barrel values

3.4 *Result*

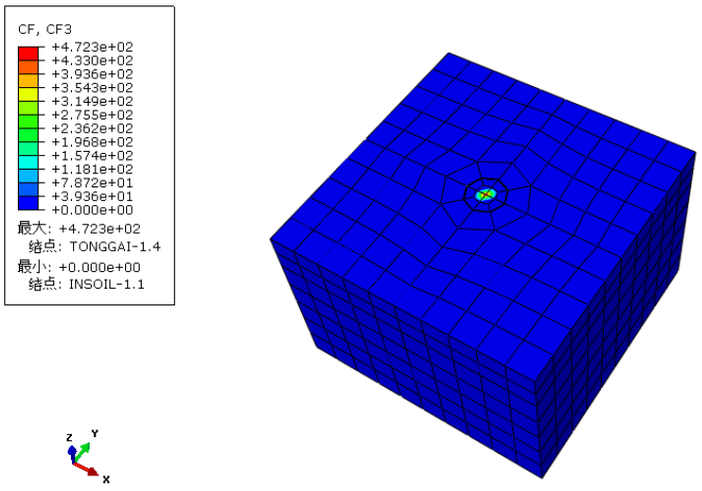
Through the software calculation, we can get the displacement contour and force— displacement curve after the model is loaded. The loading force is greater than the ultimate uplift capacity of the bucket foundation which we get from the previous test. So, as the loading force increase, when the loading force is greater than the ultimate uplift capacity of the bucket foundation, the bucket foundation will be pulled out, and a large shift will occur in the process of simulation, then the software calculation will diverge and eventually interrupt the calculation. Therefore, it can be considered that the force acting on the bucket foundation is the ultimate bearing capacity of the bucket foundation when the software calculation is interrupted. The displacement contour and the concentrated force contour of the 2# bucket foundation in the cohesive soil and sandy soil simulated test are shown in Figure 2.(a)~Figure 2.(d).



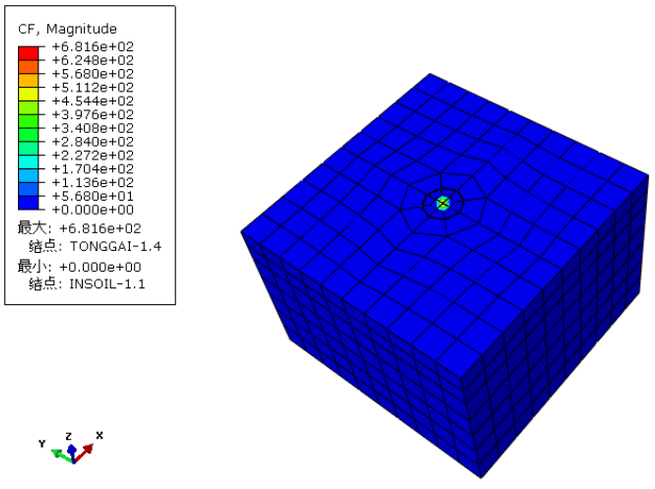
(a) The displacement contour of the cohesive soil;



(b) The displacement contour of the sandy soil;



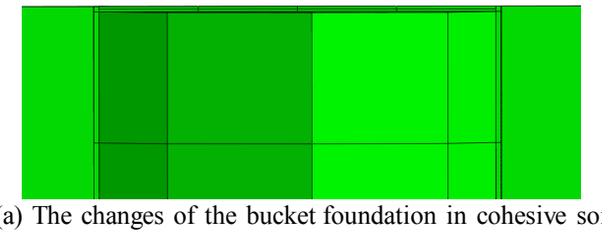
(c) The concentrated force contour of the cohesive soil;



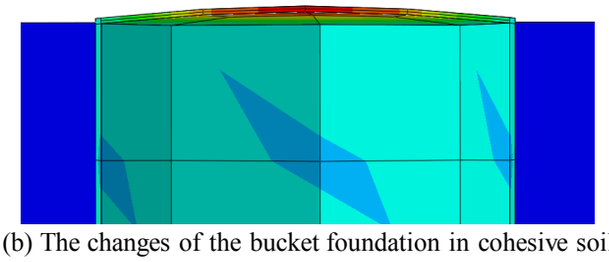
(d) The concentrated force contour of the sandy soil.

Figure 2. contour of simulation results: (a) The displacement contour of the cohesive soil; (b) The displacement contour of the sandy soil; (c) The concentrated force contour of the cohesive soil; (d) The concentrated force contour of the sandy soil.

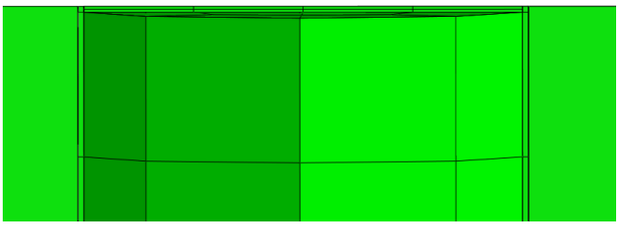
The bucket foundation will displace after loading, which is shown in Figure 3.(a)~Figure 3.(d).



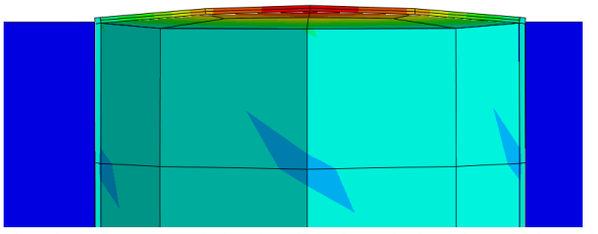
(a) The changes of the bucket foundation in cohesive soil: before loading;



(b) The changes of the bucket foundation in cohesive soil: after loading.



(c) The changes of the bucket foundation in sandy soil: before loading;



(d) The changes of the bucket foundation in sandy soil: after loading.

Figure 3. The changes of the bucket foundation in cohesive soil: (a) before loading; (b) after loading. The changes of the bucket foundation in sandy soil: (c) before loading; (d) after loading.

Through the software calculation and analysis, we also can get the force-displacement curve of the 2# bucket foundation in cohesive soil simulated test, which is shown in Figure 4~Figure 5.

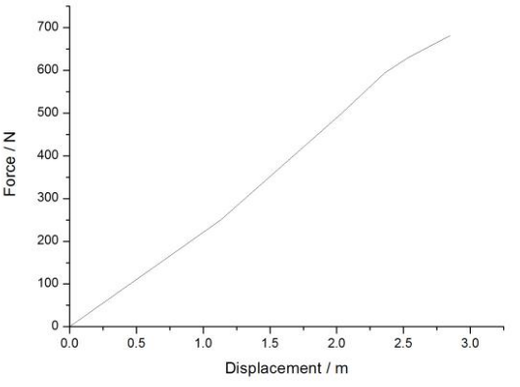


Figure 4. the force— displacement curve of 2# bucket foundation in cohesive soil simulated test

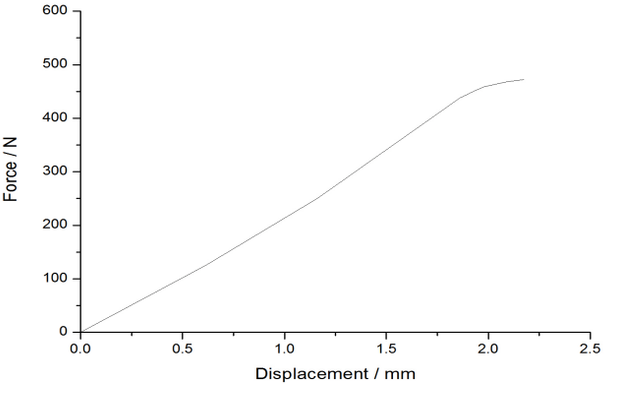


Figure 5. the force— displacement curve of 2# bucket foundation in sandy soil simulated test

4 RESULT COMPARISON

In the previous entity model experiments, we obtained the uplift load—displacement curve of the 2# bucket foundation in cohesive soil and sandy soil test shown in Figure 6~Figure 7.

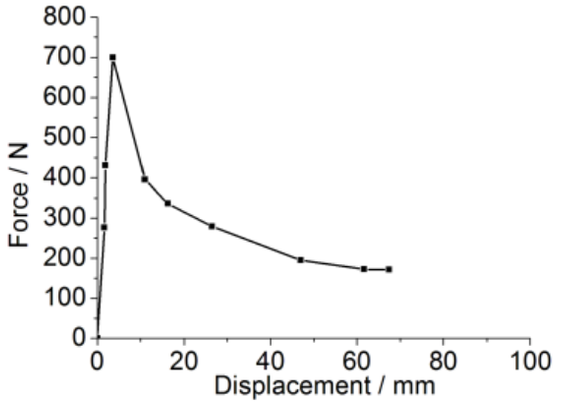


Figure 6. the uplift load—displacement curve of the 2# bucket foundation in the cohesive soil.

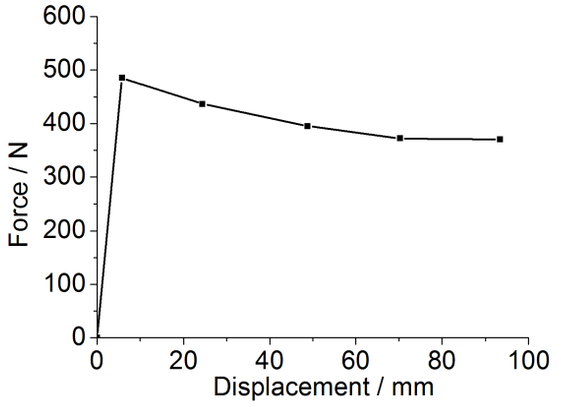


Figure 7. the uplift load—displacement curve of the 2# bucket foundation in the sandy soil.

Through the finite element software ABAQUS analysis, we got the results of numerical simulation. Compared the numerical simulation results with the previous experimental results, we got the contrast result given in Table3~ Table4.

Table3. Comparison of uplift test and numerical simulation of the bucket foundation in the cohesive soil.

Test cohesive soil	Uplift displacement s/mm	Uplift bearing capacity f/N
Model test	3.56	700.12
Numerical simulation	2.85	681.60
Error	-	2.65%

Table4. Comparison of uplift test and numerical simulation of the bucket foundation in the sandy soil.

Test cohesive soil	Uplift displacement s/mm	Uplift bearing capacity f/N
Model test	3.80	485.12
Numerical simulation	2.17	472.30
Error	-	2.64%

By comparing the data in the table, the error of the test result and the simulation result is below 3%, therefore, we believe that the numerical simulation method in this paper for calculating the uplift capacity of the bucket foundation is feasible.

5 CONCLUSIONS

In this paper, the numerical analysis of uplift capacity test of the bucket foundation is carried out. We use ABAQUS software to simulate the uplift test of the bucket foundation in the cohesive soil and the sandy soil. Finally, in the numerical simulation results, the force—displacement curve of the test is obtained, moreover, according to the curve, the ultimate uplift bearing capacity of the bucket foundation is also obtained. By comparing the numerical simulation results and the experimental results, it is proved that the proposed finite element method in this paper is feasible for quantitative analysis of ultimate uplift capacity of the bucket foundation.

6 ACKNOWLEDGMENTS

The research was financially supported by Ministry of Transport of the People's Republic of China (20130318740050), National Science Foundation of China(51379145), National Key Basic Research Program of China (2014CB046800) and National Science Foundation of China(51239008).

7 REFERENCES

AHRENS D. Submerged Floating Tunnels - a Concept Whose Time Has Arrived [J]. Tunneling and Underground Space Technology, 1997, 12 (4): 317-336.

Dyvik, R, Andersen, K.H. Model tests of gravity platform Ⅰ: Description [J]. Journal of Geotechcnical Engineering, 1989, 115 (11): 1532-1568.

Andersen, K.H, Dyvik, R. Model tests of gravity platform Ⅱ: Interpretation [J]. Journal of Geotechcnical Engineering, 1989, 115 (11): 1550-1568.

P.Fogazzi, F.Perotti, The dynamic response of seabed anchored floating tunnels under seismic excitation [J]. Earthquake Engng Struct. Dyn, 2000, 29: 273-295.

Jiajun Xiang, Xiaojian Pi, Shilun Feng, Chen Bian. Research on the Layout Plan of Tether-typed Submerged Floating Tunnel [J]. Procedia Engineering, 2016, 166: 69-75.

Xu Feng, Xiaojian Pi, Shilun Feng, Chen Bian. Research on the Uplift Bearing Capacity of Suction Caisson Foundation under Local Tensile Failure [J]. Procedia Engineering, 2016, 166: 61-68.

Hibbitt, Karlsson & Sorensen, Inc. ABAQUS/Sttandard User's Manual; ABAQUS/CAE User's Manual; ABAQUS Keyword Manual; ABAQUS QUS Theory Manual [M]. America: HKS, 2002.

ZHU Xiang-rong, WANG Jin-cang. Introduction to partly soil models in ABAQUS Software and their application to the geotechnical engineering [J]. Rock and Soil Mechnaics, 2004, 25 (2): 144-148.

Ma Yun-feng.Based on ABAQUS In-situ stress Balance of Geotechnical Engineering [J]. Science and Technology & Innovation, 2014, 8 (6): 61-64.

SI Hai-bao, CAI Zheng-yin.Development of static constitutive model library for soils based on ABAQUS [J]. Rock and Soil Mechnaics, 2011, 32 (2): 599-603.

DAI Ru-lin, LI Zhong-fang, WANG Jiao. Research on Initial Goe-Stress Balance Method Based on ABAQUS [J]. J Chongqing Technol Business Univ, 2012, 29 (9): 76-81.

Maintenance, Safety, Risk, Management and Life-Cycle Performance of Bridges – Powers, Frangopol, Al-Mahaidi & Caprani (Eds)
© 2018 Taylor & Francis Group, London, ISBN 978-1-138-73045-8

Feasibility Study on a Submerged Floating Tunnel for the Qiongzhou Strait in China

B. Jiang, B. Liang
College of Civil Engineering, Chongqing Jiaotong University, Chongqing, P.R. China
B. Faggiano, G. Iovane, F.M. Mazzolani
Department of Structures for Engineering and Architecture, University of Naples Federico II, Naples, Italy

ABSTRACT: Currently, one of the challenging tasks for the structural engineering is to construct a waterway crossing for the Qiongzhou Strait in the south of China. This project has also gained significant attention from researchers in academia. The study presented herein is centered on providing a feasible solution for accomplishing the above mentioned task. Initially, different alternative locations, judged on the basis of the environmental constraints, are studied. Then a comparison between various structural solutions, such as suspension bridge, submarine tunnel and SFT, presents the SFT as a suitable alternative for Qiongzhou Strait waterway crossing due to distinctive advantages, like, among others, shorter distance, lower cost, less impact on environment and navigation, etc. Based on the appropriate conception for cross sections, support systems, materials, joints and connection, a numerical FE model is developed by means of the software ANSYS/Fluent. The SFT structural behavior is analyzed under the influence of different environmental loading conditions, varying the wave heights and lengths, current velocities and water depths, which are typical in Qiongzhou Strait. The numerical results reveal that the proposed SFT solution performs safely even under extreme weather conditions.

1 INTRODUCTION

In the last two decades, several proposals for waterway crossing have been carried out in China due to the demand of traffic and the development of civil engineering technology, such as the crossings of Bohai Strait, Taiwan Strait and Qiongzhou Strait. Moreover, the successful experiences of waterway projects as Hangzhou Bay Bridge, Qingdao Jiaozhou Bay Submarine Tunnel, Xiamen Xiang'an Submarine Tunnel and Hong Kong-Zhuhai-Macau Bridge have greatly increased the enthusiasm and confidence to investing and realizing further projects.

In particular, the Qiongzhou Strait is located in the south of China, between Leizhou Peninsula and Hainan Island. Since 1980s, the local government started to investigate the feasibility for a Qiongzhou Strait waterway crossing and relevant research about this topic still keeps going even up to now. Tan et al. (2001) investigated the possibility to construct an undersea tunnel by means of the shield method, the investment estimation was made too. Mai et al. (2003) discussed the feasibility of a SFT in view of collecting a great amount of meteorological, hydrological, sea conditions and geological data and analyzing the present research situation. Li et al. (2009) studied the option of a cable-stayed submerged floating tunnel, whose feasibility was discussed from the aspects of construction technology, economic index and environmental protection. Yan et al. (2015) listed various layouts of tethers for the submerged floating tunnel and made a comparison of differences among the types and layouts respectively, then provided several proposals for SFT schemes. Wu et al. (2016) analyzed the advantages of SFT in the aspects of nature conservation, construction cost, operation risk with respect to other bridge solutions, also discussing the key technology problems for the selection of a SFT type.

In this article, at first the environmental conditions of Qiongzhou Strait are presented, with reference to the geological nature of the subsoil, weather and marine states. Possible alternatives of locations for crossing are discussed accordingly. Then the main characteristics of different type of structural solutions, like aerial bridges, submarine tunnel and submerged floating tunnel (SFT) are analyzed. As a result of the comparison, a central pattern has been judged as the most convenient for crossing the strait and the SFT solution as providing the best performances for the Qiongzhou Strait waterway crossing. Furthermore, a SFT proposal has been defined, by characterizing the main basic aspects. A FE numerical model has been then set up and hydrodynamic

analyses carried out for investigating the structural behavior.

2 SITE CONDITIONS IN QIONGZHOU STRAIT

2.1 *Geological and weather conditions*

The Qiongzhou Strait is one of the largest three straits in China. The length is about 80 km from east to west and the width ranges from 18 km to 35.5 km (29.5 km on average) from north to south. The seabed is generally wide and deep, with the water depth ranging from 80 m to 120 m along the central axis. In addition, scarps with a maximum height of 70m and a maximum slope angle of 22°-24° are located on the south and north shores (Tan et al. 2001).

Fractures are the major geological structure. The Qiongzhou Strait consists of several groups of fractures: the East-West fracture, the North-East fracture and the North-West fracture. The submarine strata are mainly sedimentary formed in the Tertiary and Quaternary Periods. The upper layer is filled with sludge, sandy clay or silt, while thick-bedded clay and silty sand are distributed on the bottom layer with thickness of hundreds meters.

According to statistics, about thirty-one earthquakes of magnitude above 4.75, from year of 1400 to 1995, have occurred in this area, among them ten ruinous earthquakes, nine of which are over 6.0 in magnitude. The most serious earthquake occurred in Qiongshan in the year of 1605 with a magnitude of 7.5. Two 6.1 magnitude earthquakes occurred in the Northern Gulf in December 1994 and January 1995, respectively. All of them are shallow earthquakes with the majority depth of focus ranging from 5 km to 20 km. All these indicate that the southeast coastal area tends to enter a period of active earthquakes. Besides, there is no records about volcano in this area.

The Qiongzhou Strait is located in a tropical area which is subject to the tropical monsoon climate. The average annual temperature is 24℃, the rainy season is from May to October and the average annual precipitation is more than 1500ml. Every year, the period from May to November is a typhoon season. Every year, in particular, there are more than 5 days in September when the wind force is stronger than Level 8 (Wind speed: 17.2-20.8 m/s). Besides, there are more than 24 days on average every year with dense fog.

2.2 *Location proposals*

According to careful investigations and evaluations, several proposals of locations for waterway crossing in Qiongzhou Strait are put forward by Yan et al. (2015) and Wu et al. (2016): the east line, the central line, and the west line, as shown in Figure 1.

The East Line is characterized by the complex topography, large water depth and high risk of earthquakes. Because the connection point of this line on Hainan Island is far away from Haikou, the capital city of Hainan Province, this line is inconsistent with the development requirements of this city. It would bring more disadvantages than advantages to Haikou and even the whole Hainan Island if constructed as proposed.

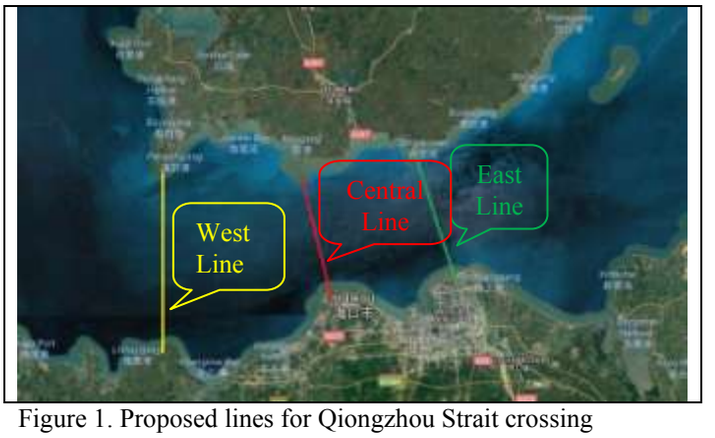


Figure 1. Proposed lines for Qiongzhou Strait crossing

The Central Line is a short waterway crossing distance, connected conveniently with the existing highways and railways at both shores. The main advantages of this line include low investment for the projects, shorter travel time, and low operation cost. Therefore, it can well meet the requirements of the city planning. However, the maximum water depth is 88 m.

The West Line, compared with the other lines, is characterized by a more flat seabed, with the maximum water depth equal to just 55 m, but the length of the waterway crossing is larger. It is farther away from the existing highways and railways at both shores, so the investment for the project would increase. In addition, this line has to avoid crossing the nature reserve located in this area, which may cause more obstacles in construction.

Among these three lines, the central line is the most appropriate location for the waterway crossing due to its shorter distance and better geological conditions compared with the others. Therefore the central line is selected in this article, as a consequence the studies hereafter are based on this location.

3 FEASIBILITY OF DIFFERENT CROSSING SOLUTIONS IN QIONGZHOU STRAIT

3.1 *General items*

The complexity of the design issues for traditional technological solutions, like either suspension and cable-stayed bridges or immersed and underground tunnels, increases as the distance to be covered grows up, so that the crossing of long span waterways can be, in many cases, very difficult and some-

times impossible for such traditional systems. The necessity to find alternative technical solutions rises. A Submerged Floating Tunnel (SFT) is an innovative underwater structure, applied for waterway crossing in particular case of long distances and has many features that make it advantageous compared to traditional structural types, allowing to solve some problems.

Hereafter main aspects for every bridge types are depicted and compared each other.

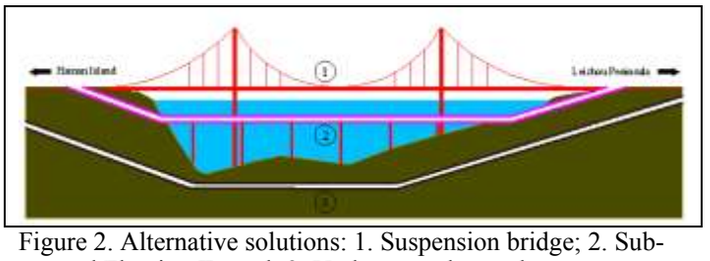


Figure 2. Alternative solutions: 1. Suspension bridge; 2. Submerged Floating Tunnel; 3. Underground tunnel

3.2 *Suspension and cable stayed bridges*

At present, the longest span of suspension bridges is found in the Akashi Bridge, whose main span reaches 1991 m. China has reached experience in construction of long-span bridges, such as the Zhoushan Xihoumen Bridge (1650 m, 2009), the Runyang Yangtze River Bridge (1490 m, 2005) and the Jiangyin Yangtze River Bridge (1385 m, 1999). The hydrological, meteorological, geological and navigational conditions of the Qiongzhou Strait are complicated and therefore it is difficult to construct a bridge in the large-depth zone. In the central line location aforementioned, the construction of a multiple spans bridge with a single span over 1000m could be feasible. By means of modern construction technology, the foundations and piers of long-span bridge can be constructed successful (Zhang, 2016). Compared with tunnels, the vehicles running on the bridge have undoubtedly much comfortable travel conditions, as lighting, ventilation, vision, and so on. As the same lower expense for the bridge operation are required, also for easier maintenance service. On the other hand, the central line is around 20km in length. If the bridge is designed with single spans of about 1000 m, about 20 piers and related foundations are needed, involving high cost. Conversely, the extension of the length of single spans gives rise to increasing height of the main tower of the bridge. For this reason, the design and construction of the foundation would become very hard.

Moreover, the Qiongzhou Strait is a busy sea crossing. For this reason, the piers of the bridge would impact on the ships navigation. In addition, the distance from the deck to the water surface would limit big ships from crossing the strait. Moreover, the tall main tower resulting from the long-span bridge would affect flights.

Because the bridge is directly exposed to the natural environment, the traffic would be affected largely by weather conditions. In case of strong wind, heavy fog, or other inclement weather situations, the safety of vehicles would be reduced inevitably, or what's worse, the traffic would be interrupted.

3.3 *Underground and immersed tunnels*

Over the past years, the world has seen great improvements in the technology of submarine tunnel design and construction. Several submarine tunnels have been completed in the past decades, such as the Seikan Tunnel (Japan, 1988) and the Channel Tunnel (Great Britain-France, 1994). In China, researchers have also obtained experiences from some subsea tunnel projects, such as the Xiamen Xiang'an Subsea Tunnel (2010) and the Qingdao Jiaozhou Bay Tunnel (2011). At present, the longest roadway immersed tunnel project is the Hong Kong-Zhuhai-Macao Bridge. The construction has been completed and the tunnel will be opened for public use before July 2018. Taking advantage of the design and construction experiences gained from China and foreign countries, an underground or immersed tunnel for crossing Qiongzhou Strait could be feasible. Compared with an aerial bridge, a submarine tunnel can assures the continuity of the vehicle travel, it being not influenced by the weather conditions. Moreover, it has far less impact in service on the environment. However, at the central pattern in the strait, the maximum water depth is around 85 m. Therefore, according to the construction experiences of existing submarine tunnels, the buried depth of such a submarine tunnel in this location would be over 100 meters. In order to meet the slope requirement, the submarine tunnel should be then extended to land with a very long distance. It is estimated that the minimum distance of the submarine tunnel would reach 30 km, what involve a high increment of the cost of construction.

A submarine tunnel needs to meet higher requirements for geological conditions. Due to some uncertainty factors that could exist in the construction it would result in large investment, high risks and a long construction period.

Due to the presence of fractures, landslide and water gushing accidents could almost inevitably occur during the construction and operation. Moreover in service, the cost on lighting, ventilation and maintenance would be higher than those of a bridge. As previously mentioned, the Qiongzhou Strait is located in a seismic region, so the subsea tunnel would suffer catastrophic damages in case of an earthquake. Once a disaster happens, the water flow into with high pressure through possible failures. As a consequence, the tunnel could never be repaired.

3.4 *Submerged Floating Tunnel (SFT)*

From Figure 2, it is evident that the length of the submerged floating tunnel is shorter as respect to subsea tunnel, the slope being reduced. Therefore the SFT has less influence on the surroundings. The lower length is of course also favourable for escapeing in case of accidents. The distance between the SFT and the water surface can guarantee the security of navigation. The unit cost of the SFT is constant, whereas the cost of the suspension bridge and the submarine tunnel increase rapidly as the span increases (Faggiano et al., 2010).

SFT is also a convenient solutions in seismic areas due to both the structural deformability and the damping effect of water, with a consequent reductions of the seismic effects.

So far, no SFT project has been constructed yet, even though several detailed studies have been carried out (Mazzolani et al. 2008, Jiang et al. 2017). In this case, the lack of specific construction experience is bridged by the consolidated experiences in the construction of subsea tunnels and off shore structures counterparts.

4 THE SFT PROPOSAL FOR QIONGZHOU STRAIT WATERWAY CROSSING

4.1 *General aspects*

Compared with a bridge or a submarine tunnel, SFT is the most suitable solution for the Qiongzhou Strait waterway crossing due to its distinctive advantages, such as, among others, shorter distance, lower cost, less impact on environment and navigation.

The Qiongzhou Strait is a busy shipping way. In order to satisfy the requirement of navigation space for big vessels and reduce the impact from the water surface wave, the clearance depth between the water surface and the submerged floating tunnel is proposed to be 30 m (Xiang et al. 2017).

Based on the geological condition of the central line and the navigation clearance requirement, the longitudinal profile for the proposed SFT is shown in Figure 3.

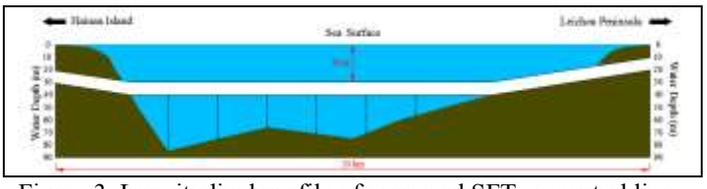


Figure 3. Longitudinal profile of proposed SFT on central line

4.2 *Cross-section*

The proposed reinforced concrete polygonal cross-section is illustrated in Figure 4.

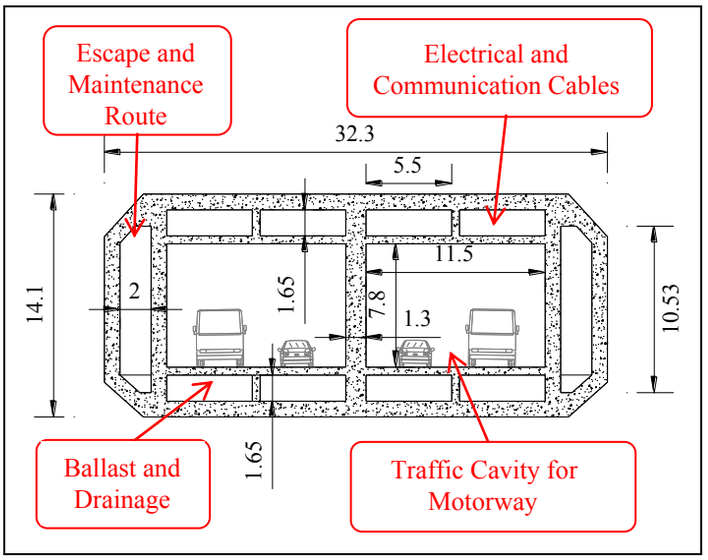


Figure 4. Proposed polygonal Cross-section [m]

For the Qiongzhou strait crossing, only the motorway traffic is considered. The elongated polygonal shape is selected joining a good performance in terms of hydrodynamic behavior, space exploitation, workability. As a counterbalance the streamlined external shape requires more accuracies and thus causes more difficulties to the construction technology.

The clearance space requirements for traffic lanes are defined according to the Code for Design of Road Tunnel (JTG D70-2004, in Chinese). Overall sizes are 14.1 x 32.3 m. Main walls have 1.0 m thickness (1.3 m the central wall), the other walls have 0.5 m thickness.

Reinforced concrete is widely used in maritime structures and particularly recommended when a large structural weight is required to stabilize the structure. It should provide the required structural strength and stiffness, as well as the weight needed to counteract the tunnel buoyancy.

4.3 *Support systems*

Among all the possible support systems of the SFT, free tunnel and pontoons are not suitable for the long distance and busy navigation in the Qiongzhou Strait. In addition, with the various fractures distributed at the seabed, column support is not an appropriate solution. Based on the geological condition of the Qiongzhou Strait, steel cable support is a reasonable alternative for the SFT, commonly proposed for several SFT prototypes (Wahyuni et al. 2009, Mazzolani et al. 2010, Seo et al. 2015, Faggiano et al. 2016).

In order to control the displacement induced by the environmental loads, either in the horizontal or vertical directions, the inclined configuration of four cables (0.3 m diameter) into a group is adopted, as shown in Figure 5.

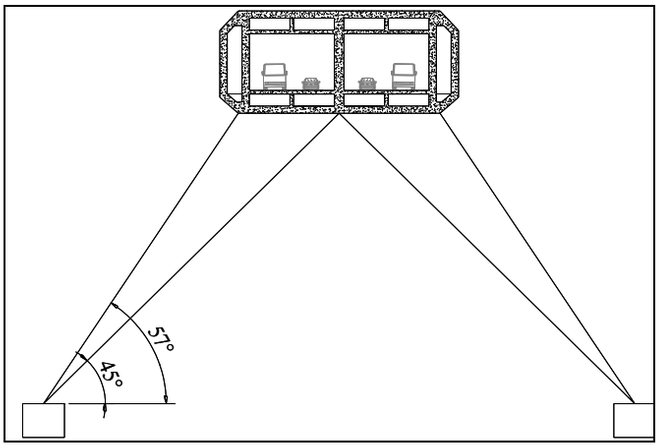


Figure 5. Proposed inclined configuration of cables

4.4 *Joints and connections*

The inter-module joints and the shore connections play a significant role in the whole SFT structure.

In general, the inter-module joints must guarantee the continuity of the structure. The SFT can be subjected to significant displacements and rotations in the longitudinal bending planes. In addition, the axial displacements are allowable at the terminal joints due to thermal variations and triaxial rotations (Martire, 2010). Therefore rigid joint are necessary. Also requirements of tightness, workability and durability should be satisfied.

The connection between the SFT and the shore involves appropriate interface transition elements to couple the flexible water tunnel with the rigid tunnel bored underground (Faggiano et al. 2016), also guaranteeing watertighting. In particular, the Qiongzhou Strait is located in seismic area, so the risk of submarine landslides needs additional attention.

Moreover, the longitudinal gradients of the bored tunnel should be opportunely fixed, taking account that the SFT should keep straight on the longitudinal direction and that the length of the bored tunnel is closely related to the cost of the entire project, therefore it should be limited as possible. The longitudinal gradients of a bored tunnel are proposed to range from 0.3% to 3%, according to the regulations specified in different codes, as shown in Table 1 (Zhang et al. 2013),

Table 1. Regulations for tunnel longitudinal gradients (Zhang et al. 2013)

Country	Code	Tunnel longitudinal gradient
P.R China	MOT. JTG D70-2004 Code for design of road tunnel	0.3%-3%, maximum 4% depending on traffic conditions
European Union	DIRECTIVE 2004/54/EC	> 5% normal, [3-5%] assistant measures > 3% no extra measures
USA	FHWA Road Tunnel	> 3%-4%
UK	Design code for Road and Bridge	> 6% depending on traffic and ventilation requirements
Norway	NPRA Motorway Tunnel	6%-8% normal
Sweden	VV Tunnel 2004	> 5% normal < 5% for short distance permitted by experts
The Netherlands	SATO	> 4% design speed 90 km/h > 3% design speed 120 km/h

5 NUMERICAL ANALYSIS

A Finite Element numerical model is implemented by means of the software ANSYS Workbench and Fluent in order to perform a preliminary rough evaluation of the structural performance of the SFT assumed against hydrodynamic loads. The model in fact represents just a short tube 100 m long. Therefore only displacement and rotation along the longitudinal direction Z are restrained at both ends of the tube. Spherical hinges have been assumed at both ends of the cables.

The model geometry is given in Figure 6. The material properties are given in Table 2.

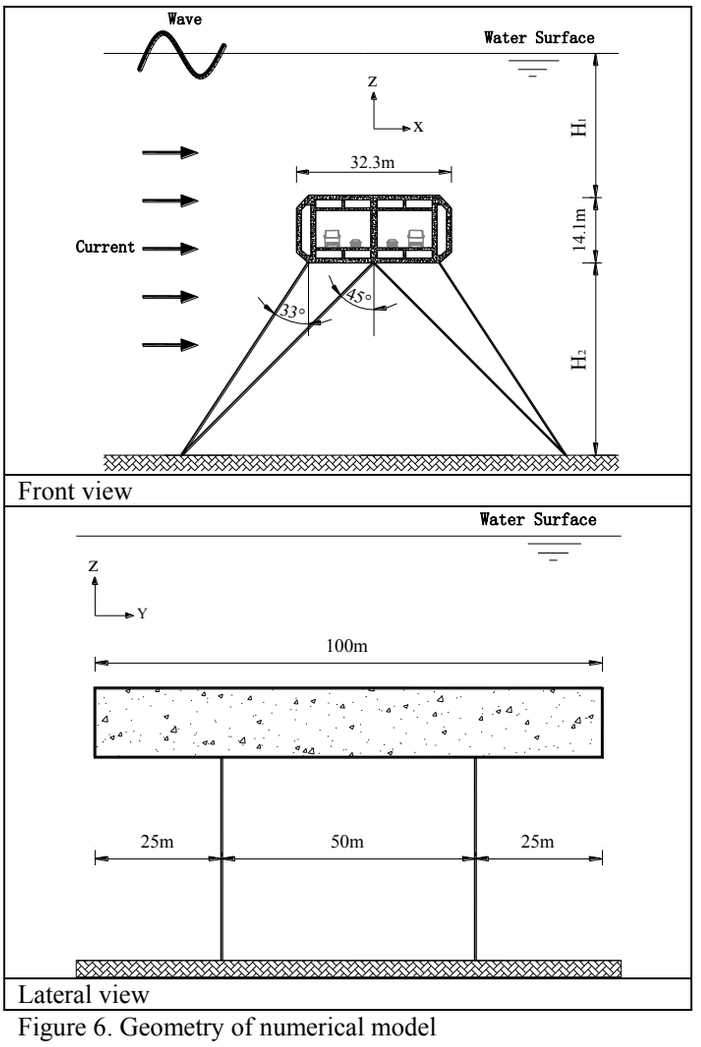


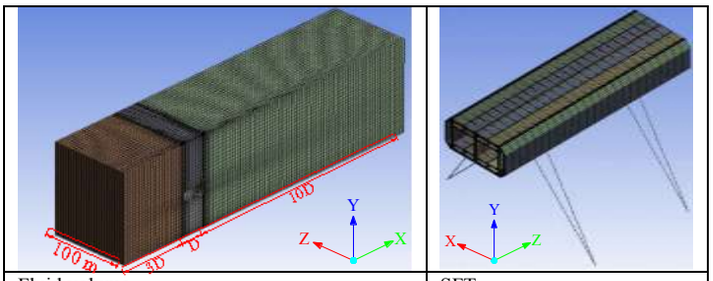
Figure 6. Geometry of numerical model

Table 2. Material properties

Properties	Materials	
	Concrete	Steel
Density	2500 Kg/m^3	7850 Kg/m^3
Elastic modules	32x10^3 MPa	201x10^3 MPa
Strength	35 MPa	1860 MPa

The fluid model is calculated first in Fluent, then the result data are transferred to ANSYS Workbench for Transient Structural Dynamic calculation. In order to reproduce the full turbulent phenomenon, the distance from the inlet upstream side has been assumed equal to 3D (D width of the polygonal section = 32.3 m), a distance of 10D has been set downstream the tunnel. The width along direction Z is set to 100 m, as the length of the tube. The depth of H_2 varies depending on the location of the proposed SFT. The hexahedron finite elements are applied for meshing the both the fluid and the tube, as shown in Figure 7. The cables are modeled as beam element.

For the sake of simplifying the calculation of the fluid model, the Airy wave and RNG viscous mode are applied for simulating the wave and turbulence, respectively, while the current is assumed as steady flow.



Fluid volume | SFT

Figure 7. Mesh scheme of numerical model

An appropriate mesh size for the model is very important for calculation accuracy. The mesh size of the fluid volume is 4.0 m. For the tube model, the mesh size ranges from 0.2 m to 4.0 m, depends on different zones due to its irregular shape, as shown in Figure 8.

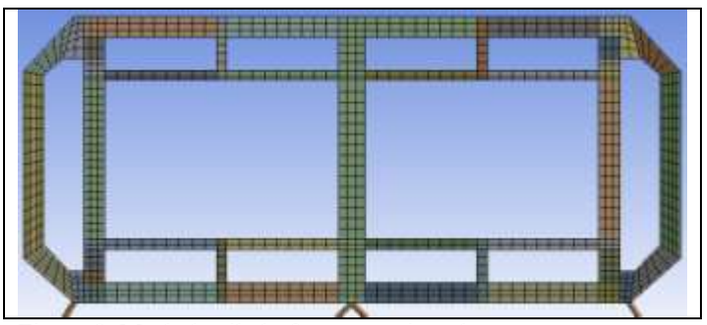


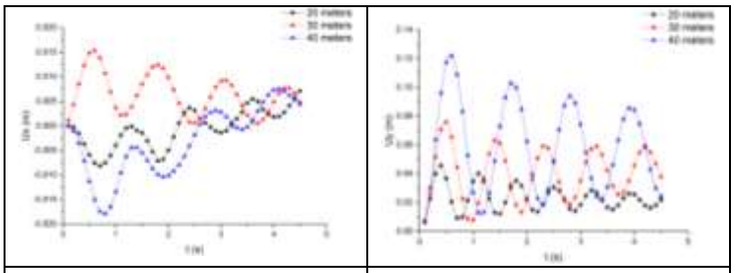
Figure 8. Mesh detailed of cross-section plane

Current, wave and traffic loads are considered in the model. Assumed parameters for current and wave loads as given in Table 3. Only motorway traffic loads are considered. According to the Chinese code (MOT. JTG D70-2004 Code for design of road tunnels), the traffic loads are defined as distributed loads of 10.1 kN/m^2 and arranged fully on the internal pavement.

Table 3. Analysis parameters assumed

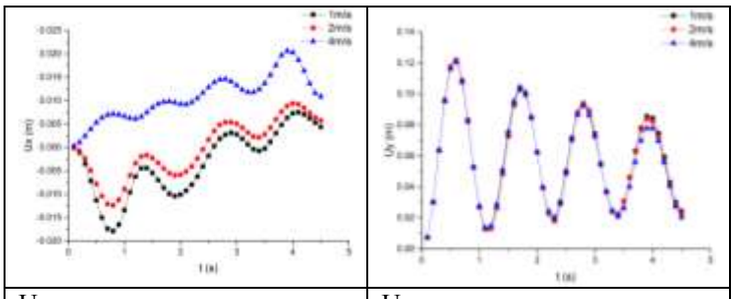
Water depth (Fig. 7)		
H_1= 30m	H_2= 40, 30, 20 m according to different geological seabed conditions	
Extreme wave	according to monitored data in Qiongzhou Strait	
Return period [years]	Height	Length
20	7m	115.11m
25	7.3m	119.45m
100	8.6	137.38
Current velocities	1.0 m/s, 2.0m/s, 4.0 m/s	

The U_x and U_y displacements at the tube mid-span are presented in Figures 9-11 with varying water depths, current velocities and waves. Because the limit speed of vehicle in the tunnel is 80 km/h, the figures only show the results within 4.5 s which equals to the time that the vehicle crossing the 100 m tube with limit speed.



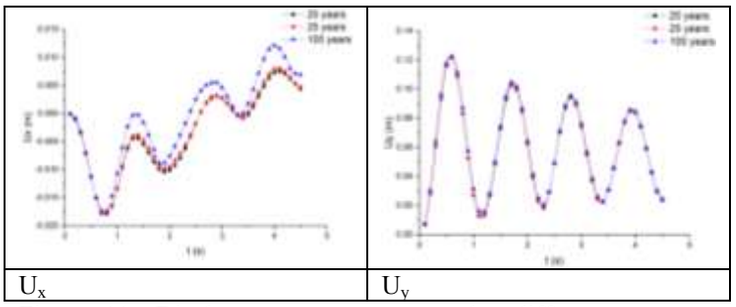
U_x | U_y

Figure 9. Displacement responses under different water depths H_2 (wave height: 7.0 m, current velocity: 1.0 m/s)



U_x | U_y

Figure 10. Displacement response under different current velocities (H_2:40 m, Wave height: 7.0 m)



U_x | U_y

Figure 11. Displacement responses under different waves (H_2:40 m, current velocity: 1.0 m/s)

In Figure 9, the maximum displacement values for H_2=40 m are U_x = 0.18 m, U_y = 0.12 m. The amplitudes of U_x and U_y are all reduced as far as H_2 depth decrease, as the wave effect is lower.

In Figure 10, for current velocity equal to 4.0 m/s, the maximum amplitude of U_x rises to 0.20 m. It is

apparent that the current velocity influences U_x, but it has a slight effect on U_y.

In Figure 11, the maximum displacement values are U_x = 0.18 m, U_y = 0.12 m. U_x and U_y don't have large changes while wave parameters change.

In general, the maximum U_x is 0.2 0m, the maximum U_y is 0.12 m. These displacement responses are acceptable relative to the size of structure. In addition, the maximum calculation stresses in the tunnel structure and cable are 18.52 MPa and 1025 MPa, respectively. They are all smaller than the defined strengths of materials in the model.

The results prove that the proposed SFT structure is safe even under extreme weather condition, whatever in the view of displacement and stress.

6 CONCLUSIVE REMARKS

This article presents the preliminary feasibility studies on a Submerged Floating Tunnel (SFT) for the Qiongzhou Strait waterway crossing.

Compared with proposed east line and west line for Qiongzhou Strait waterway crossing, the central line is an appropriate location because of its geological and weather conditions. On the other hand, the SFT is a better solution compared with bridge and submarine tunnel, due to its distinctive advantages, such as shorter distance, lower cost, less impact on the environment and navigation, etc.

A polygonal cross-section, the inclined cable support system, the rigid inter-module joints are selected for aforementioned aspects respectively.

By means of the Finite Element numerical software ANSYS Workbench and Fluent, the displacement responses at the SFT mid-span are analyzed, for different water depth, current velocity and wave parameters. The results reveal that the displacement response of proposed SFT is acceptable relative to the size of structure, even under extreme weather conditions. In addition, the calculation stresses in the tunnel structure and cables are all smaller than the strengths of related materials.

In conclusion, the SFT solution is feasible for Qiongzhou Strait waterway crossing according to the previous studies about location, design aspects and numerical analysis. This article aims to render the Qiongzhou Strait waterway crossing into reality. If the SFT solution is adopted by the decision maker for Qiongzhou Strait, it will be a revolutionary event of civil engineering in the world, and will also be considered the realization of a common dream of all SFT researchers.

7 REFERENCES

Faggiano B., Martire G., Mazzolani F.M. 2010. Cable supported immersed inversed bridge: a challenging proposal. *Procedia Engineering*, vol. 4, p. 283-291.

Faggiano B., Panduro J., Rosas M.T.M., Mazzolani F.M. 2016. The conceptual design of a roadway SFT in Baja California, Mexico. 2nd International Symposium on Submerged Floating Tunnels and Underwater Tunnel Structures. *Procedia Engineer*ing 166:3-12.

Li B., Yang J., Xiong J. 2009. Feasibility study on rope bridge style of submerged floating tunnel in Qiongzhou Strait. *China Water Transport*, 9(10):253-255.

Mai J., Guan B. 2003. A feasibility study on Qiongzhou Strait Submerged Floating Tunnel. *Journal of Railway Engineering Society*, 80 (4): 93-96.

Martire G. 2010. The development of Submerged Floating Tunnels as an innovative solution for waterway crossings, PhD Thesis in Construction Engineering, University of Naples "Federico II", Tutors: Prof. F.M. Mazzolani, B. Faggiano, Italy.

Mazzolani F. M., Landolfo R., Faggiano B., Esposto M., Perotti F., Barbella G. 2008. Structural analyses of Submerged Floating Tunnel prototype in Qiandao Lake (PR of China). *Advances in Structural Engineering*, 11(4): 923-938.

Mazzolani F. M., Faggiano B., Martire G. (2010). Design aspects of the AB prototipe in the Qiandao Lake. *Procedia Engineering* 4: 21-33.

Seo S., Mun H., Lee J., Kim J. 2015. Simplified analysis for estimation of the behavior of a submerged floating tunnel in waves and experimental verification. *Marine Structures* 44:142-158.

Tan Z., Wang M., Yang X. 2001. Construction technology of undersea tunnel and the feasibility of Qiongzhou strait tunnel .*Journal of Jiaozuo Institute of Technology (Natural Science)*, 20(4):286-291.

Wahyuni E., Raka I G. P., Budiman E. 2009. Structural behavior of submerged floating tunnels with different cable configurations under environmental loading. *Dinamika TEKNIK SIPIL, Akreditasi BAN DIKTI* 110:212-215.

Wu S., Chen X., Li Q., Cao G. 2016. Research on Type Selection of Submerged Floating Tunnel of Qiongzhou Strait. *Procedia Engineering*, 166:307-316.

Xiang Y., Chen Z., Yang Y. 2017. Research development of method and simulation for analyzing dynamic response of submerged floating tunnel. *China Journal of Highway and Transport*, 30(1):69-76.

Yan H., Yang G., Yu J. 2015. The Lectotype Study on the Submerged Floating Tunnel. *Construction Technology*, 44(7):113-116.

Zhang L. 2016. Main bridge project of the Hongkong-Zhuzhou-Macao Bridge. *Construction Mechanization* 26 (8): 12-16.

Zhang Z., Hu J., Liu H., Xu G. 2013. Study of the Maximum Longitudinal Gradient of Underwater Highway Tunnels. *Modern Tunneling Technology*, 50(4): 8-14.

Maintenance, Safety, Risk, Management and Life-Cycle Performance of Bridges – Powers, Frangopol, Al-Mahaidi & Caprani (Eds)
© 2018 Taylor & Francis Group, London, ISBN 978-1-138-73045-8

Research on Simulation of Traffic Loads in Submerged Floating Tunnel

B. Jiang
Chongqing Vocational Institute of Engineering, Chongqing, P.R China

S.Wu
Chongqing Vocational College of Public Transportation, Chongqing, P.R China

B. Liang, L. Chen
College of Civil Engineering, Chongqing Jiaotong University, Chongqing, P.R China

ABSTRACT: The situation of Submerged Floating Tunnel (SFT) subjected to various loads is complicated, it would be more complex if involving traffic loads. In order to find the appropriate method to simulate the traffic loads in SFT, the simulated formula of traffic loads is carried out in this paper. This formula borrows the experiences from the researches of traffic loads for roadway and railway, several influence factors are taken into account in the formula, such as static loads, road roughness, velocity of vehicle and external incentive loads. Then this paper investigates the characteristics of simulated traffic loads and the impacts on dynamic response of SFT structure due to different simulation of traffic loads. The results reveal that the simulation which proposed in this paper is more reasonable to calculate the traffic loads of SFT in a certain extent.

1 INSTRUCTIONS

Submerged Floating Tunnel (SFT) has several advantages, like shorter length, better economy, more friendly environment (Xiang et al. 2016), compared with other traditional waterway crossing structure (such as suspension bridge, tunnel, etc.) , which has attracted more and more academic and social attention in recent years. In the related researches of SFT, the internal traffic load must be taken into account as well as the reasonable form of traffic load simulation. Concerning the simulation method of SFT's internal traffic load, several related researches has been conducted already by the domestic and foreign scholars. Perotti et al. (2010) proposed that the simulation method of SFT can take references from the bridge traffic researches, because the SFT structure is similar to the closed underwater bridge and the studies of bridge traffic load is relatively mature. Martire (2010) used the constant uniform load to simulate the traffic load in SFT, according to the European standard (Env 1991-3, traffic loads on bridges) method in the study of bridge traffic load. Tariverdilo et al. (2011) simulated the traffic load in SFT as moving concentrated load along the tube longitudinal direction, on the basis of the simulation to study the dynamic response of SFT; Dong et al. (2016) simplified the traffic load in SFT as a series of equidistant and concentrated load, then studied the influence on SFT's dynamic response from the tension leg vertical stiffness, the value of traffic load and the vehicular gap; In the existing studies, the internal traffic load of SFT mainly simulated as uniform load or concentrated load, but the dynamic properties of traffic load are not fully considered.

In this paper, the traffic load of SFT is simulated as moving vibrant load, the fluctuation and periodicity of traffic load are considered, meanwhile considering the influence of the wave and current which belong to the external excitation loads. By means of the proposed traffic load simulation and numerical calculation, the variation law of traffic load is analyzed. In addition, the influence of different traffic load simulation methods on the vibration displacement response of SFT is also studied contrastively.

2 INFLUENCE FACTORS AND SIMULATION FORMULA OF TRAFFIC LOADS

2.1 *Simulated factors of traffic loads*

The traffic load is a random load, its motion and size vary randomly. In the existing studies of highway and railway traffic load, the traffic load is often simulated as vibrant load, therefore the traffic load of SFT is proposed as the moving vibrant load in this paper. The moving vibrant load is a kind of dynamic load with a certain frequency and amplitude, it can better reflect the dynamic characteristics of vehicles, it also can simulate the different traffic volumes and

different axle loads of vehicles by changing the vibration law.

In the aspect of railway traffic load research, Liang et al. (2006) propose that the railway traffic load could be simulated with an exciting force function, which corresponding to the vertical wheel rail force that appears mainly in the low frequency range (0.5-10Hz), the intermediate frequency range (30-60Hz) and the high frequency range (100-400Hz). The interaction force between wheel and rail is simulated by the excitation force which reflects irregularity, additional dynamic load and rail corrugation effect, it is shown in Equation 1.

$$F(t) = P_0 + P_1 \sin \omega_1 t + P_2 \sin \omega_2 t + P_3 \sin \omega_3 t \quad (1)$$

Where P_0 is the wheel static load, P_1, P2, P_3 are the amplitudes of the vibration load corresponding the vibration frequency of the rail ω_1, ω_2, ω_3 respectively.

$$P_i = M_0 a_i \omega_i^2 \quad (2)$$

Where M_0 is the unsprung mass, a_i is the height of the geometric irregularity corresponding to the different circular frequencies of vibration, it reflects the road condition. ω_i is the circular frequency of vibration.

$$\omega_i = 2\pi v_t / L_i \quad (3)$$

Where v_t is the velocity of train, L_i is the wavelength of geometric irregularity curve.

In the aspect of highway traffic load research, the simulation is simpler than railway traffic load. Zhang et al. (2001) used a simple force similar to the excitation form that can reflect its periodic characteristics and geometric irregularities to express vehicle loads approximately.

$$F(t) = P_0 + P \sin(\omega t) \quad (4)$$

Where P_0 is the wheel static load, P is the amplitude of vibrant load, only the traffic dynamic load, which caused by the road irregularity, is considered.

$$P = M_0 a \omega^2 \quad (5)$$

Where M_0 is the unsprung mass, a_i is the height of the geometric irregularity, it reflects the road condition. ω is the circular frequency of vibration.

$$\omega = 2\pi v_c / L \quad (6)$$

Where v_c is the velocity of vehicle, L is the wavelength of geometric curve.

According to the aforementioned simulation methods of railway and highway traffic load, it can be found that the simulated factors of traffic load mainly include: wheel static load, geometric irregularity of rail surface or road surface, velocity of vehicle, construction of vehicle (unsprung etc.).While studying the traffic load of SFT, the external excitation load (wave and current) should be considered except the above factors.

2.2 *Formula of traffic load*

On the basis of above analysis, the formula of moving vibrant load could been concluded for railway or roadway. In this paper, only the traffic of roadway is considered, the proposed formula of traffic load is given as Equation 7.

$$F(t) = P_0 + M_0 \cdot A_1 \cdot \omega_1^2 \cdot \sin(\omega_1 t) + M_0 \cdot A_2 \cdot \omega_2^2 \cdot \sin(\omega_2 t) \quad (7)$$

Where P_0 is the wheel static load, M_0 is the unsprung mass, A_1 is the road roughness, and it reflects the road condition. A_2 is the vertical vibration displacement of SFT structure caused by wave and current, it reflects the influence from external excitation load.

ω_1 is the circular frequency of vehicle vibration caused by road roughness:

$$\omega_1 = 2\pi v_c / L \quad (8)$$

Where v_c is the velocity of vehicle, L is the wavelength of geometric curve, equals to the length of vehicle.

ω_2 is the circular frequency of vehicle vibration induced by wave and current, it equals to the frequency induced by vortex vibration.

$$\omega_2 = \omega_s = 2\pi S_r v_f / D \quad (9)$$

Where Sr is the Strouhal number, usually equals to 0.2 (Qin et al. 2010). vf is the velocity of current. D is the section width of tube.

The simulation expression is based on the existing traffic load calculation formula, the particularity of the environment of SFT is considered, and the influence of external excitation load (wave and current action) is added.

3 NUMERICAL SIMULATION AND ANALYSIS

3.1 *Numerical model*

In view of the fact that there is no SFT project in the world, this paper refers to the existing design data and research results worldwide (Mazzolani et al. 2008, Kanie 2010, Seo et al. 2015, Faggiano et al. 2016), the proposed SFT model is built as shown in Figure 1.

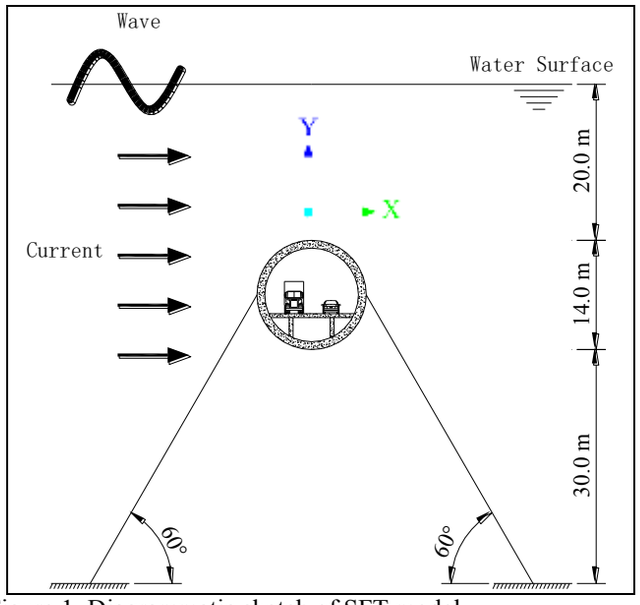


Figure 1. Diagrammatic sketch of SFT model

In this model, circular cross-section and inclined cable support system are selected for SFT. The circular cross-section consist of external shell and internal cavities, the upper cavity is designed for roadway traffic and the lower cavities are designed for ballast and functional equipment. In this paper, only one segment of the tunnel (100 m) is selected for calculation. There are two groups of inclined cables which arranged at the two ends of tunnel. The water depth is also assumed in Figure 1.

About the materials, the reinforced concrete and steel strand are adopted for tunnel and cables, respectively. The basic parameters for the model are given in Table 1.

Table 1. Fundamental parameters of SFT for numerical simulation

Properties	Unit	Value
Inner diameter of tube	m	12
External diameter of tube	m	14
Equivalent density of tube	kg/m^3	2500
Elastic modules of tube	GPa	32
Density of cable	kg/m^3	7850
Elastic modules of cable	GPa	201
Diameter of cable	m	0.3
Density of current	kg/m^3	1028

Based on aforementioned assumptions and parameters, another important factor BWR (Buoyance Weight Ratio) is calculated for 1.40.

As shown in Figure 1, current, wave and traffic loads are considered in the model. Current is assumed as steady flow, the velocity of current is defined for 1.0 m/s. Wave is assumed as airy linear wave, the properties of slight sea are adopted (Wave height: 1.0 m; Wave length: 13.0 m).

In order to study the differences of traffic load simulation method, three different types of traffic loads are selected: fixed distributed load, moving concentrated load and moving vibrant load. The fixed distributed load is arranged fully on the internal pavement, the moving concentrated load or moving vibrant load is assumed as distributed load applied in a small area. This area simulates the wheel of vehicle moving from one end to another end of tunnel. The parameters of traffic load is given in Table 2.

Table 2. Parameters of traffic load

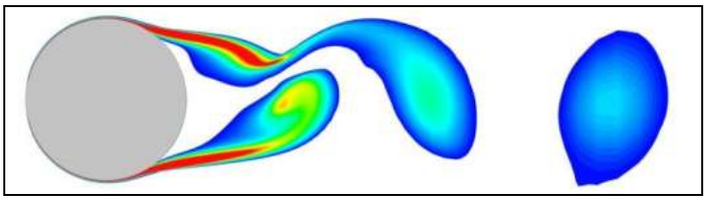
Parameters	Unit	Value
Static wheel load	kN	20
Unsprung mass	N · s^2/m	120
Length of vehicle	m	6
Road roughness	m	0.002
Velocity of vehicle	km/h	80

According to the China current highway tunnel design code MOT. JTG D70-2004 Code for design of road tunnel, the limit speed of vehicle in tunnel is 80 km/h, therefore the duration is 4.5s when the vehicle crossing the 100m tunnel. Only the results within 4.5s are presented.

The numerical simulation is implemented by means of the finite element analysis software ANSYS Workbench and Fluent. The fluid model with current and wave loads is calculated in Fluent at first, then the fluid result data could be transmitted directly to Workbench. The Transient Dynamic analysis is completed in Workbench. Finally, the dynamic response of tunnel structure can be obtained.

3.2 *Characteristics of traffic load*

Vortex shedding occurs because the flow is unable to follow along the surface of the structure and separates from the surface. This flow separation creates a vortex which causes a local increase in rotational velocity. Higher flow velocity yields a reduction in dynamic pressure, which creates an attraction force by the vortex on the structure. The position of the separation point alternates between the top and bottom of the cylinder, and creates a vortex street, as illustrated in Figure 2. (Fjeld et al, 2012)


Figure 2. Vortex Street behind a circular cylinder (Fjeld et al. 2012)

The transverse (Direction X) and vertical (Direction Y) displacements of tunnel structure induced by vortex should be calculated at first, in order to confirm the parameter A_2 in Equation 7. The point on mid-span is selected as the structural check point.

Only wave and current loads are considered in the first calculation, the traffic load is ignored. The results are shown in Figure 3.

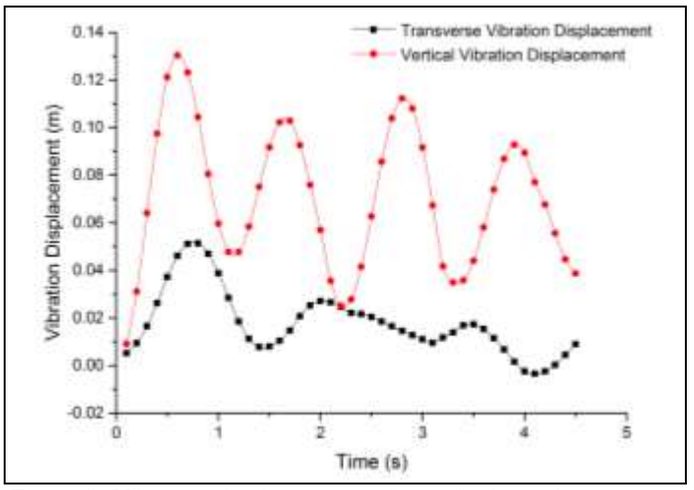


Figure 3. Vibration displacements of tunnel tube under wave and current loads

From the Figure 3, the amplitude of vertical vibration displacement is obviously larger and more regular than the transverse vibration displacement. Considering the aspect of safety, the maximum value (0.13 m) of the vertical vibration displacement is regarded as the influence value of the external excitation load A_2 (Equation 7) on the traffic load. The simulated traffic load as shown in Figure 4.

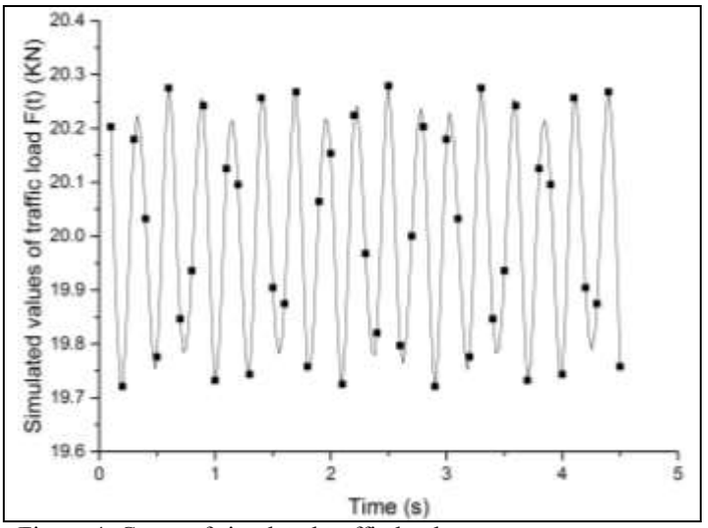


Figure 4. Curve of simulated traffic loads

From the Figure 4, the simulated value curve of traffic load has variable frequency and amplitude with time changes. It has a certain periodicity and this is consistent with the characteristics of the vibrant load. The wheel static load P_0 is 20 kN, therefore the simulated value curve fluctuates at 20kN. Moreover, the amplitude of the fluctuation curve deviates from the static load means the part of dynamic load in the traffic load, while the amplitude is larger, the proportion of dynamic load is greater.

3.3 *Comparative analysis of traffic load*

In order to study the rationality of traffic load simulation method, three different types of simulation methods are selected: fixed distributed load, moving concentrated load and moving vibrant load. Under the combined action of wave and current, the influence of different traffic load simulation methods on the vibration displacement response of SFT is compared and analyzed, and the change of vibration displacement in the mid-span of structure is observed as shown in Figure 5 and Figure 6.

The values of fixed distributed load and moving concentrated load are 20 kN, the moving load is calculated by using the previous simulation results, and the speed of moving load is 80 km/h. Because the traffic load is too small compare with wave and flow force, only the increment of vibration displacement is analyzed after adding different traffic loads, on the basis of the SFT structure without traffic load, as shown in Figure 5 and Figure 6.

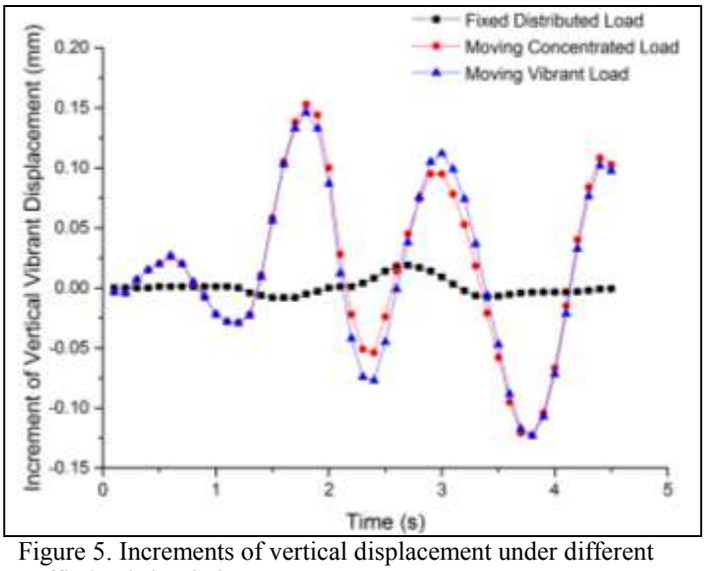


Figure 5. Increments of vertical displacement under different traffic load simulations

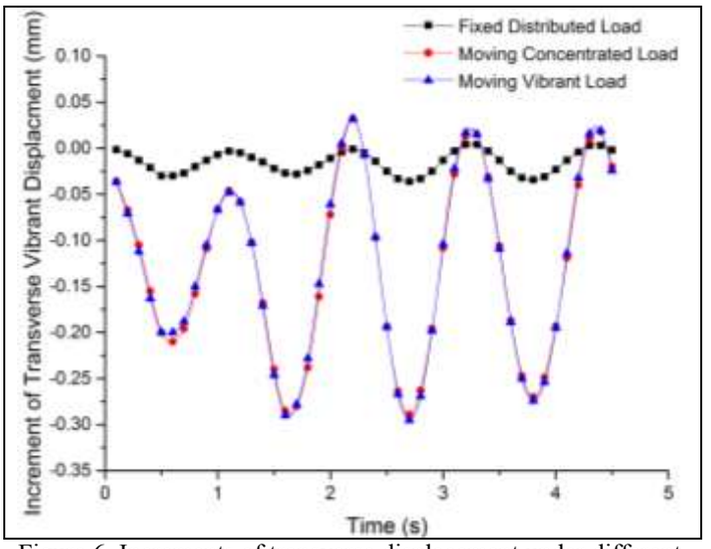


Figure 6. Increments of transverse displacement under different traffic load simulations

From Figure 5 and Figure 6, the increments of tunnel structural displacement under different simulation methods of traffic load are all slight. However, the amplitude of displacement variation of moving concentrated load and moving vibrant load is relatively larger than that of fixed distributed load.

The influence of the fixed distributed load on the vibration displacement of SFT is relatively slight, because it can be regarded as a part of dead load, equals to static load. The effects of moving concentrated load and moving vibrant load on the structural vibration displacement are very similar. The increments of longitudinal and transverse vibration displacement on mid-span appear relatively large regular fluctuation, as the traffic load moving from one end to opposite end. According to the foregoing analysis, moving vibrant load has additional dynamic load compare with moving concentrated load. The proportion of dynamic load is small in the moving vibrant load, hence the amplitude of vibration displacement is slightly larger in the calculation results of moving vibrant load. On the other hand, it also shows that moving vibrant load can real reflect the influence of dynamic load on structural vibration displacement response.

4 CONCLUSIONS

(1) The simulation method of traffic load in SFT should not only considers the factors such as wheel static load , road roughness, velocity of vehicle, but also the influence of the external excitation loads should be taken into account. The combined force of wave and current is the main component of external exciting load.

(2) The proposed simulation formula of moving vibrant load in SFT considers various influence factors. The traffic load is calculated with the volatility, in accordance with the characteristics of vibration load and traffic load.

(3) The influences of various simulation methods of traffic load on the structural vibration displacement response are different. The fixed distributed load equals to static load, has little effect. The effects of moving concentrated load and moving vibrant load are very similar, they all appear relatively large regular fluctuation on the mid-span. However, the moving vibrant load is more reasonable and realistic to reflect the influence of dynamic load on structural vibration displacement response.

(4) The numerical formulation and method are only evaluated by means of the numerical simulations in this paper, it should be evidenced by the experimental tests in the future studies.

5 REFERENCES

Dong M., Zhang Y., Tang F.,et al. 2016. Displacement response of submerged floating tunnel subjected to equidistant moving loads.*Chinese Journal of Applied Mechanics*, 33(5):760-765.

Faggiano B., Panduro J., Rosas M.T.M., Mazzolani F.M. 2016. The conceptual design of a roadway SFT in Baja California, Mexico. *Procedia Engineer*ing 166:3-12.

Fjeld A., Søreide T. H., Haugerud S. A. 2012. Feasibility study for crossing the Sognefjord Submerged Floating Tunnel. *SFT design for crossing of Sognefjorden at Lavik*, Reinertsen Olav Olsen Group.

Kanie S. 2010. Feasibility studies on various SFT in Japan and their technological evaluation. *Procedia Engineering* 4:13-20.

Liang B., Luo H., Sun C. 2006. Simulated study on vibration load of high speed railway. *Journal of the China railway Society*, 28(4):89-94.

Martire G. 2010. The development of Submerged Floating Tunnels as an innovative solution for waterway crossings. Doctoral thesis, University of Naples “Federico II”,Italy.

Mazzolani F. M., Landolfo R., Faggiano B., Esposto M., Perotti F., Barbella G. 2008. Structural analyses of Submerged Floating Tunnel prototype in Qiandao Lake (PR of China). *Advances in Structural Engineering*, 11(4): 923-938.

Perotti F., Barbella G., Pilato M.D. 2010. The dynamic behaviour of Archimede’s Bridges: Numerical simulation and design implications. *Procedia Engineering*, 4: 91-98.

Qin Y., Zhou X. 2010. Analysis on chaotic behavior of submerged floating tunnel under ocean currents effect. *Journal of the China Railway Society*, 32(4):146-150.

Seo S., Mun H., Lee J., Kim J. 2015. Simplified analysis for estimation of the behavior of a submerged floating tunnel in waves and experimental verification. *Marine Structures* 44:142-158.

Tariverdilo S., Mirzapour J., Shahmardani M., et al. 2011. Vibration of Submerged floating tunnels due to moving loads. *Applied Mathematical Modeling*, 35(11):5143-5425.

Xiang Y.,Yang Y. 2016. Challenge in design and construction of submerged floating tunnel and state-of-art. *Procedia Engineering*, 166: 53-60.

Zhang Y., Liang B. 2001. Dynamic response to subgrade of highway in geometric irregularity condition. *Journal of Lanzhou Railway University (Natural Science)*, 20(4):66-69.

Maintenance, Safety, Risk, Management and Life-Cycle Performance of Bridges – Powers, Frangopol, Al-Mahaidi & Caprani (Eds)
© 2018 Taylor & Francis Group, London, ISBN 978-1-138-73045-8

Submerged Floating Tunnels under Seismic and Seaquake Loadings

Luca Martinelli
Politecnico di Milano, Dep. of Civil and Environmental Engineering,
P.zza L. da Vinci 32, 20133 Milano, Italy

ABSTRACT: Submerged Floating Tunnels (SFTs), also named Archimedes Bridges, are a promising alternative to cross a water body. SFTs are normally designed with positive buoyancy, and are held floating underwater by a mooring system anchored at the seabed. In the case of an earthquake, SFTs will have to withstand both the effects of ground motion at the supports as well as the so-called "seaquake" loading. This last is due to the transmission through water of compressive waves originated by the seabed motion. The studies on seaquakes are contrasting with respect to the effects of the compressibility of the soil below the seabed. In this light, this paper extends the model for generating seaquake effects, set-up by the research group, by including this aspect. A first comparison of the loading due to seaquake with and without the presence of a compressible soil layer is carried out for a significant prototype structure.

1 INTRODUCTION

Submerged Floating Tunnels (SFTs), also named Archimedes Bridges, are a promising alternative to cross a water body, efficiently connecting the shores while having a very low impact on the landscape. SFTs lend themselves naturally to the crossing of large body of water due to inherent modularization of the structure, which allows to reach dimensions in plan of the order also of some kilometers.
Most of the SFTs design proposal have been drafted assuming the SFT is under positive buoyancy and is kept floating underwater by a mooring system, that is anchored to the seabed.

Depending on the type of mooring systems, SFTs can be restrained at several positions along their length (Fig. 1) and, in the case of an earthquake, will have to withstand both the effects of ground motion at the anchoring positions of the mooring system, and the so-called "seaquake" loading (Fig. 2).

This last loading term is due to the transmission through water of compression waves originated at the seabed due to the seabed motion, and works as a hydrodynamic pressure due to the compression waves. This phenomenon is important for SFTs since it can significantly contribute to the loading of the SFT main tunnel, of the anchor elements and the foundations.

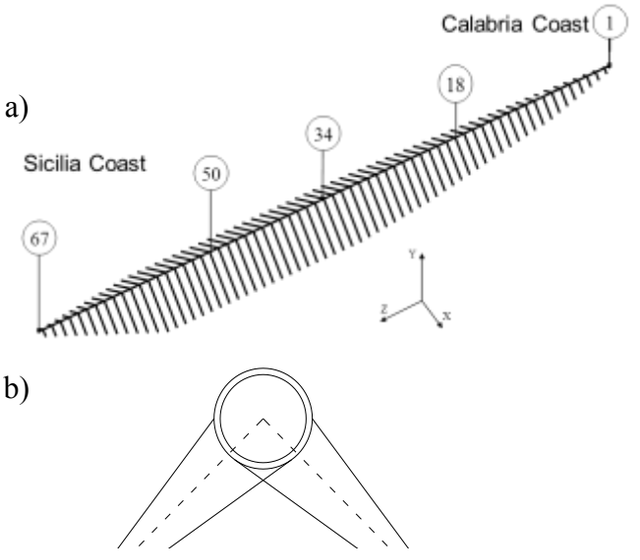


Figure 1. Scheme of the SFT proposed for the Messina Strait crossing (Italy); span 4680 m, maximum depth 350 m. (a) General view, (b) cross-section.

While the study on the dynamic response of SFTs subjected to environmental actions has made significant progress in the last years, seaquakes related research received less attention. Some studies on the effects of seaquakes, however, are nevertheless available in the literature, or their results can be of use also for SFTs (Crouse & Quilter 1991, Boore &, Smith 1999, Martire et al. 2010, Martinelli et al 2010,

2011, Shi et al. 2012, Shi & Martinelli 2013, Li et al. 2015, Lee et al. 2016), but are contrasting with respect to the effect of the compressibility of the last soil strata beneath the seabed on the motion of the water.

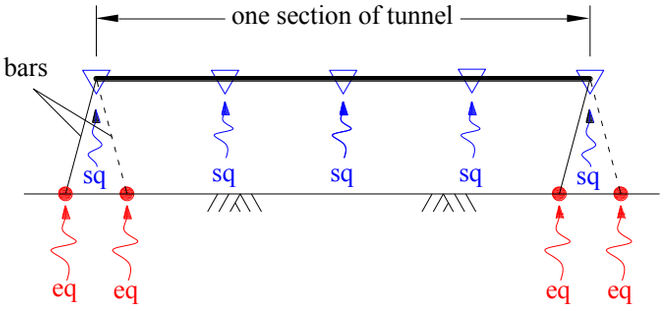


Figure 2. Schematics for a SFT under earthquake ("eq") and seaquake motion ("sq").

In this light, this paper extends the model for generating seaquake effects set-up by the research group (Martinelli et al 2010, 2011, Shi et al. 2012, Shi & Martinelli 2013) by including the compressibility of the last soil strata beneath the seabed and compares the theoretical result in the case of seabed corresponding to the bedrock to those when a flexible soil layer is interposed between the water and the bedrock.

The target structure for this exercise is the SFT in Figure 1, proposed for the Messina Strait crossing (Italy). This SFT spans 4680 m, has a maximum depth of the seabed of about 350 m while the tunnel of the SFT is located about 40 m below the surface.

2 FORCES ACTING ON SUBMERGED FLOATING TUNNELS DUE TO SEAQUAKES

The term seaquake denotes the transmission of compressive fluid waves from the sea bottom which moves under seismic conditions.

The detailed numerical simulation of the seaquake phenomenon involves complex studies related to wave propagation and fluid-structure interaction. Simplified approaches, appropriate at the design stage, rely on a representation of the seaquake loading on the tunnel by using the Morison equation (Equation 1), to represent the forces on a moving body in oscillatory fluid flow (Chakrabarti 1987):

$$f = \frac{1}{2} C_D \rho D |u - \dot{x}|(u - \dot{x}) + \\ + C_M \rho \frac{\pi}{4} D^2 (\dot{u} - \ddot{x}) + \rho \frac{\pi}{4} D^2 \ddot{x} \quad (1)$$

or, alternatively:

$$f = \frac{1}{2} C_D \rho D |u - \dot{x}|(u - \dot{x}) + \\ + C_A \rho \frac{\pi}{4} D^2 (\dot{u} - \ddot{x}) + \rho \frac{\pi}{4} D^2 \dot{u} \quad (2)$$

where C_D, C_M are the drag coefficient and inertia coefficient, respectively, C_A is the added mass coefficient, ρ is the water density, D is a relevant dimension in the cross-section (typically the cylinder's diameter), u, $\dot{u}$ are the instantaneous water particle velocity and acceleration (here the one of a water particle ideally located at the center of tunnel), $\dot{x}$, $\ddot{x}$ are structure velocity and acceleration, $u - \dot{x}$, $\dot{u} - \ddot{x}$ are the relative velocity and acceleration. Adoption of Morison equation is justified for the elements of a SFT on the base of the elements' characteristic dimensions and expected wavelength of the waves.

For the application of Equation 1, when seaquake effects are introduced, both the motion at the supports (denoted as "eq" in Fig.2) and the motion of water itself (denoted as "sq" in Fig.2) contribute to create the hydrodynamic pressure acting on the SFT's main tube and elements of the anchoring system.

A simplified model, which derives the motion of the water from a mono-dimensional wave propagation equation, has been adopted by the research group in previous works. This will be presented in the following.

3 SEAQUAKE INDUCED WATER VELOCITY AND ACCELERATION

When the ground below the seabed is excited by vertical seismic waves, as schematically depicted in Figure 2, it is possible to derive the vertical seaquake-induced motion of the water upon application of the linearized one-dimensional wave propagation equation, with the following assumptions and simplification (see Shi 2013 and also, e.g., Hamamoto 1995):

1. the hydrodynamic pressure due to the seaquake is associated with the water-transmitted seismic vibration from the sea bed to the floating structure, neglecting the scattered waves due the structure presence (i.e. the hydrodynamic pressure is related to incident waves);

2. the sea water is assumed as inviscid, incompressible and the velocity field is irrotational;

3. the water velocity (seaquake's velocity) at the seabed is the same as the vertical ground velocity (earthquake's velocity) at the same point;

4. the vertical ground motion of the water will be described in the frequency domain.

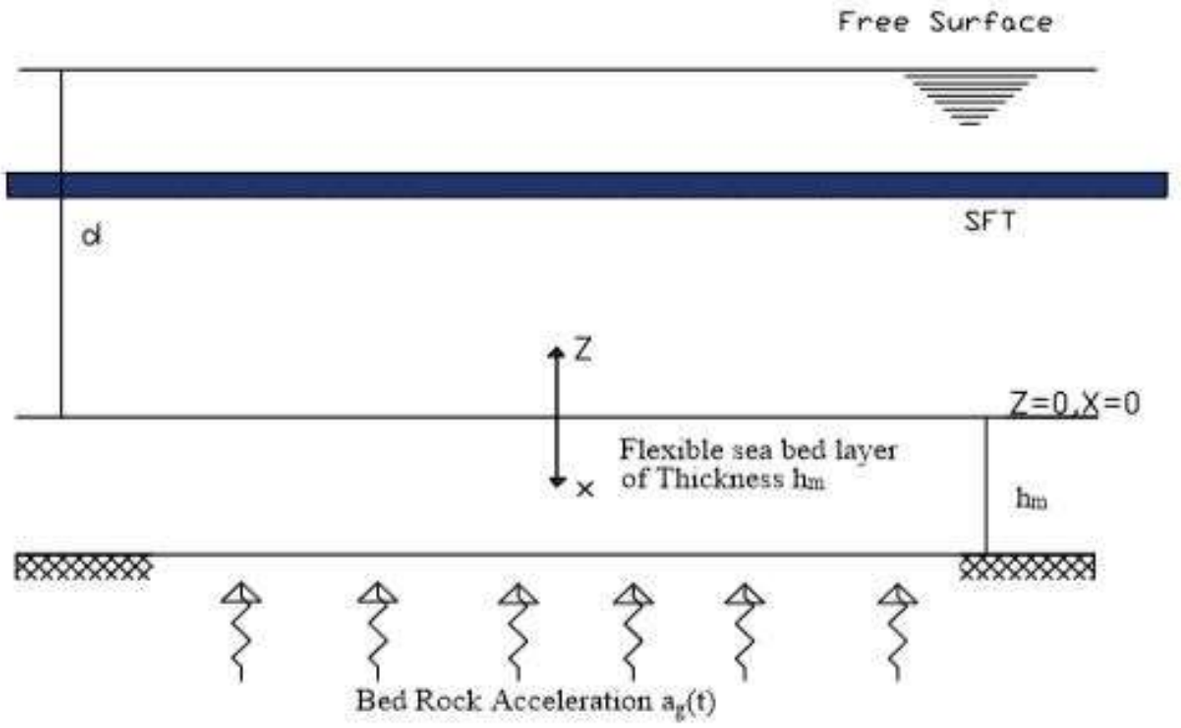


Figure 3. Schematics for definition of seaquake motion in water when a flexible soil layer is located between the water and the bedrock.

Thanks to the abovementioned hypotheses and simplification, the vertical component u of the water velocity (seaquake velocity) at a point in the water domain is given by the gradient of the scalar velocity potential function:

$$v = \nabla\phi = \frac{\partial\phi}{\partial z} \tag{3}$$

The velocity potential function, in turn, must satisfy the Helmholtz equation:

$$\nabla^2\phi = \frac{1}{c^2}\frac{\partial^2\phi}{\partial t^2} \tag{4}$$

where: ϕ is the velocity potential function of incident waves, ∇^2 is the Laplace operator and c is the acoustic wave velocity in water (herein assumed as 1560 m/s).

With reference to Figure 3, the boundary conditions for Equation 4 are the free surface and seabed one described in the following.

3.1 *Free surface boundary condition*

Assuming that the height of the waves, that will eventually ensue at the free surface, is small compared to the wavelength, a linearized free surface boundary condition can be adopted.

Including both the static requirement (pressure is constant across the free surface interface: $p = p_{atm}$, with p_{atm} the atmospheric pressure and p the pressure in water at the free surface) and the kinematic requirement (once a particle is on the free surface, it will remain there), this can be stated as:

$$\frac{\partial\phi}{\partial z} + \frac{1}{g}\frac{\partial^2\phi}{\partial t^2} = 0 \quad \text{at} \quad z = d \tag{5}$$

3.2 *Sea bed boundary condition*

The boundary condition at the seabed is that the motion of the water will follow there that of the ground:

$$\frac{\partial\phi}{\partial z} = \frac{\partial U_g(t)}{\partial t} \quad \text{at} \quad z = 0 \tag{6}$$

In Equation 6, g is the gravity acceleration, d the depth of the seabed, $U_g(t)$ the vertical ground displacement at the seabed ($x = 0$).

The seaquake acceleration can then be found as the derivative of the velocity:

$$\dot{v} = \frac{\partial v}{\partial t} \tag{7}$$

3.3 *Velocity Potential for seaquake*

With the previous assumptions and boundary conditions, assuming the motion at the seabed is harmonic with circular frequency ω and acceleration $a_g\, e^{i\omega t}$, the following holds:

$$\frac{d^2U_g(t)}{dt^2} = a_g e^{i\omega t} \tag{8}$$

and the velocity potential function takes the form (see Shi 2013, Hamamoto 1995):

$$\phi = \frac{cg\cos\left(\frac{(d-z)\omega}{c}\right)}{\omega\left(c\omega^3\cos\left(\frac{d\omega}{c}\right)+g\omega^2\sin\left(\frac{d\omega}{c}\right)\right)}a_g e^{i\omega t} + \\ -\frac{c^2\omega\sin\left(\frac{(d-z)\omega}{c}\right)}{\omega\left(c\omega^3\cos\left(\frac{d\omega}{c}\right)+g\omega^2\sin\left(\frac{d\omega}{c}\right)\right)}a_g e^{i\omega t} \tag{9}$$

4 DEDUCTION OF THE VELOCITY POTENTIAL FUNCTION FOR A SEAQUAKE AND FLEXIBLE SEABED

In the case of a flexible soil layer beneath the seabed, the vertical propagation of compression waves in the water is derived from the study of the linear viscoelastic system shown in Figure 3.

The system consists of a horizontal layer which extend to infinity in the horizontal direction and has the bedrock below. The layer is homogenous and isotropic and is characterized by the thickness, h_m, mass density, ρ_s, shear modulus, and damping factor, β.

The 1D wave propagation through the soil layer is the solution of the following Equation:

$$\frac{\partial^2 u}{\partial x^2} = \frac{1}{\alpha^2}\frac{\partial^2 u}{\partial t^2} \tag{10}$$

Where the velocity of propagation of the wave α, is: $\alpha = ((\lambda + 2\mu)/\rho_s\,)\text{^}(1/2)$, ρ_s is the density of the soil, μ and λ are the Lame's constants of the soil, defining its mechanical characteristics.

4.1 *Boundary conditions for the Seaquake wave equation*

In the following we will denote with u the ground displacement in the soil layer, with $a_s(t) = a_s\, e^{i\omega t}$ the bedrock acceleration, assumed as sinusoidal of circular frequency ω, with ρ_w the density of water, with ϕ the velocity potential function, with $E^* = (\lambda + 2\mu) + i\omega\,\eta$ the complex elasticity modulus for the soil layer, with $\eta = 2\beta\,(2\mu + \lambda)/\omega$ the viscosity constant of the soil layer, with β the damping ratio of the soil, and we will define k_s as:

$$k_s = \frac{\rho_s\omega^2}{E^*} \tag{11}$$

Taking into account the different positive directions shown in Figure 3 for the axes z and x, respectively used for describing the motion in the water and in the soil layer, the boundary conditions for Equation 10 can be listed as in the following.

4.1.1 *Compliance of ground layer and bedrock motion*

The compatibility of the ground motion with the one at the bedrock can be stated as:

$$a_s e^{i\omega t} + \frac{\partial^2 u}{\partial t^2} = 0 \quad at \quad x = h_m \tag{12}$$

where $a_s(t) = a_s\, e^{i\omega t}$ is the bedrock acceleration.

4.1.2 *Compliance of water and soil layer motion*

The compatibility of ground velocity with the water velocity can be stated as:

$$\frac{\partial u}{\partial t} + \frac{\partial \phi}{\partial z} = 0 \quad at \quad x = 0,\, z = 0 \tag{13}$$

where it has been accounted that the ground velocity is equal to the water velocity at the interface of water and soil layer, but the two have opposite positive directions.

4.1.3 *Equilibrium Equation at the interface of water and soil layer*

The equilibrium equation at the interface between water and the soil layer can be stated as:

$$\frac{\rho_s\left(\frac{\partial u}{\partial x}\right)\omega^2}{k_s{}^2}-\rho_w\frac{\partial\phi}{\partial t}=0\quad at\quad x=0,z=0 \tag{14}$$

where it has been accounted that the ground velocity and water velocity have opposite positive directions.

4.1.4 *Velocity Potential for water*

The solution of the PDE in Equation 10, with the listed boundary conditions, can be found in closed form in term of the velocity potential as:

$$\phi=\frac{-e^{i\omega t}2a_g e^{ik_s x}Mcg\cos\left(\frac{(d-z)\omega}{c}\right)}{Q}+ \\ -\frac{-e^{i\omega t}2a_g e^{ik_s x}Mc^2\omega\sin\left(\frac{(d-z)\omega}{c}\right)}{Q} \tag{15}$$

Where the constants Q, M, N, P are:

$$Q=\omega\left(N\omega\sin\left(\frac{d\omega}{c}\right)+P\cos\left(\frac{d\omega}{c}\right)\right)\cdot \\ \cdot\left(g\omega^2\sin\left(\frac{d\omega}{c}\right)+c\omega^3\cos\left(\frac{d\omega}{c}\right)\right) \tag{16}$$

$$M=g\rho_s\omega^2\sin\left(\frac{d\omega}{c}\right)+c\rho_s\omega^3\cos\left(\frac{d\omega}{c}\right) \tag{17}$$

$$N=\left(c^2k_s e^{2ik_s x}-c^2k_s\right)\rho_w+ \\ +\left(-ige^{2ik_s x}-ig\right)\rho_s \tag{18}$$

$$P=\left(-ice^{2ik_s x}-ic\right)\rho_s\omega^2+ \\ +\left(ck_s g-cgk_s e^{2ik_s x}\right)\rho_w \tag{19}$$

4.2 *Seaquake velocity and acceleration*

Once the Velocity Potential function is known, the water velocity can be obtained again by Equation 3 and form this, by derivation, the water acceleration.

5 COMPARISON OF RESULTS OF WATER VELOCITY WITH AND WITHOUT FLEXIBLE SOIL LAYER

In the following the results with and without the presence of a flexible soil layer will be presented in terms of transfer functions from known acceleration (typically the one at the bedrock) and velocity of the water at a selected depth (typically the depth of the tunnel).

The mechanical parameters for the soil layer have been taken from (Li et al. 2015) and are listed in Table 1. The depth of the water is compatible with the maximum one for the SFT in Figure 1 (325 m), the depth of the tunnel is 40 m below sea level. Water has no damping. The flexible soil layer is h = 30 m thick, the damping for the soil layer is 5% relative to the critical.

Table 1. Soil data for flexible soil layer.

Name	Type	l	m	ρ_s
		Pa	Pa	kg/m^3
G5	Soft Clay	1.6 x 10^7	1.4400 x 10^8	1600

The tunnel in Figure 1 had (Shi 2013) the first longitudinal vibration mode at 0.196 Hz, the second longitudinal mode at 0.391 Hz, the first transversal vibration mode at 0.580 Hz, the first vertical vibration mode at 0.580 Hz, the second transversal vibration mode 0.585 Hz, the second vertical vibration mode 0.585 Hz. The mooring system had the following natural frequencies of the local modes: first symmetric bending vibration mode 0.0616 Hz, first anti-symmetric bending vibration mode 0.0616 Hz, second bending vibration mode 0.1393 Hz, third bending vibration mode 0.2446 Hz. In the analyses, the range of frequencies up to 12 Hz will be studied.

The theoretical value of the resonance frequency of the water column is $f = c/4d$ = 1.2 Hz with c = 1560 m/s, while that of the soil layer is $f = V_p/4h$ = 2.76 Hz with V_p = 331.66 m/s.

Figure 4 reports the modulus of the transfer function from the acceleration at the seabed to water velocity at the tunnel position, this is practically the same as the modulus of transfer function from the bedrock acceleration to velocity of water at tunnel position without the flexible soil layer. Figure 5 depicts the modulus of the transfer function from bedrock acceleration to the water velocity at the depth of the tunnel, while Figure 6 that of transfer function from the bedrock acceleration to the water acceleration at the same location. Finally Figure 7 and 8 depicts the transfer function from the bedrock to the seabed respectively in the case of presence of the water layer and absence of the same (outcropping).

Figure 4 is characterized by the resonance peaks of the water layer, set at the odd multiples of the base resonance frequency of 1.2 Hz.

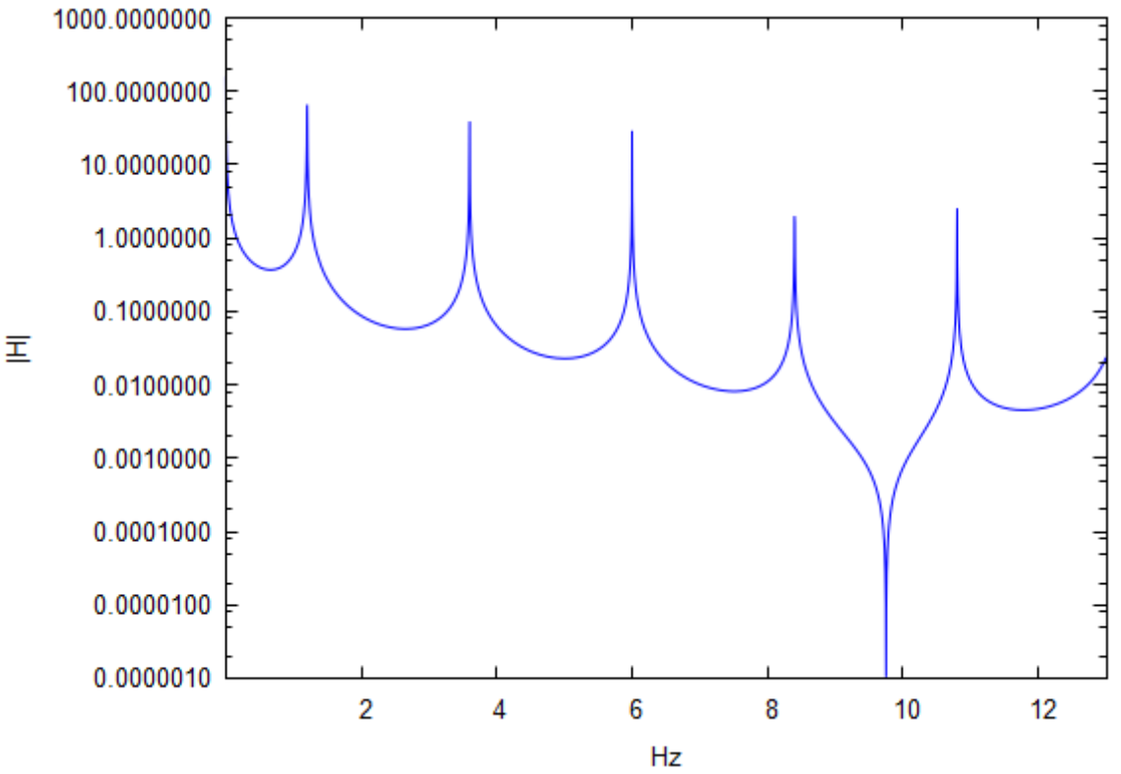


Figure 4. Modulus of the transfer function from the seabed acceleration to velocity of water at tunnel position

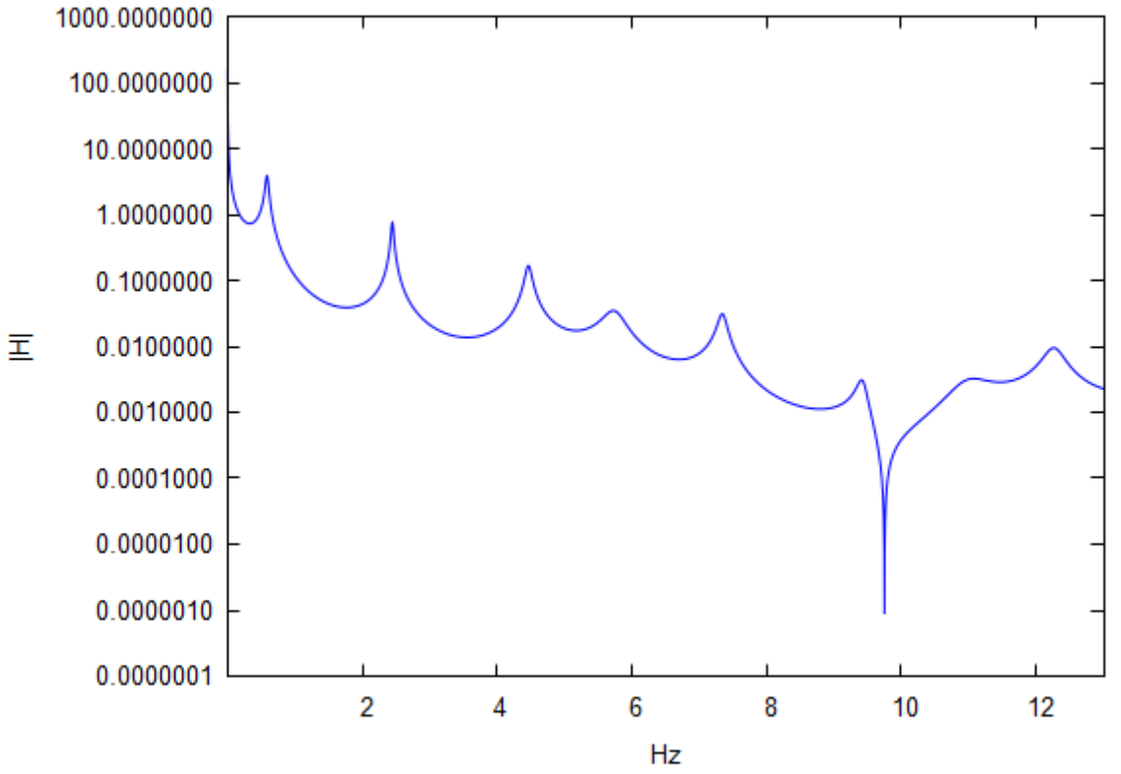


Figure 5. Modulus of the transfer function from bedrock acceleration to velocity of water at tunnel position.

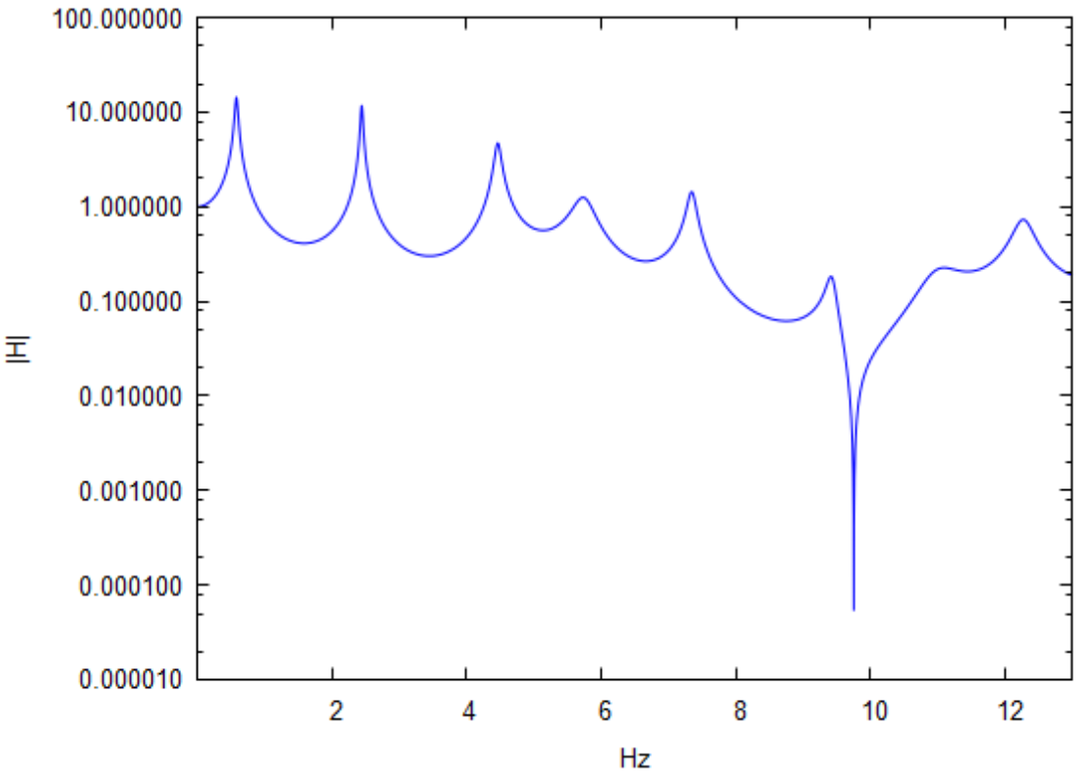


Figure 6. Modulus of the transfer function from bedrock acceleration to acceleration of water at tunnel position.

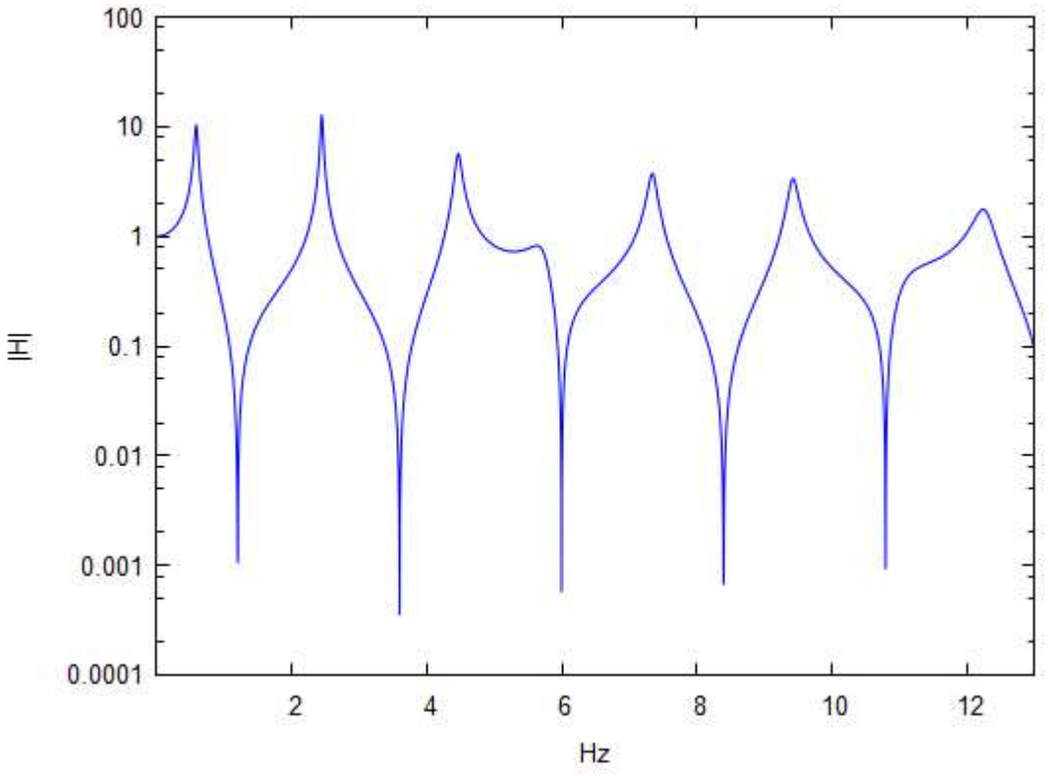


Figure 7. Modulus of the transfer function from bedrock acceleration to seabed acceleration.

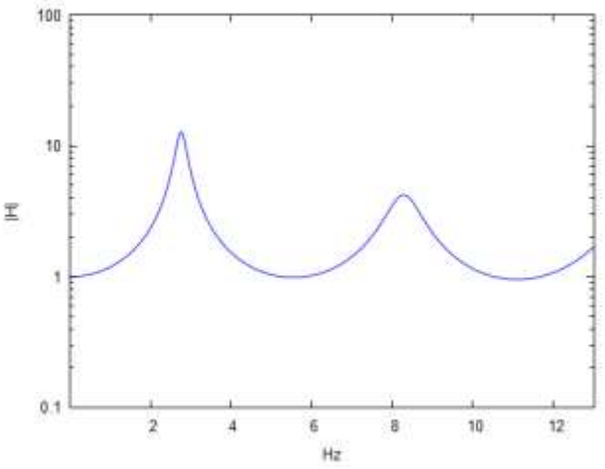


Figure 8. Modulus of the transfer function from bedrock acceleration to seabed acceleration when the water layer is not present, or very thin (0.1m).

By comparing Figure 5 to Figure 4 it is possible to appreciate the effect of the soil layer. This acts as a filter, that widens and reduces the resonance peaks, that get also shifted to lower frequencies. The de-amplification is more important for the higher harmonics of the base frequency.

By comparing instead Figure 7 and Figure 8 it is possible to appreciate the effect of the water layer on the seabed acceleration. In Figure 7 the peaks are at the odd multiples of 2.76 Hz, and while the water layer actually de-amplifies the ground motion at the frequencies of the odd multiples of 1.2 Hz, it amplifies the response at other frequencies (e.g. the peak below 1 Hz and the one in between 2 and 4 Hz).

6 CONCLUSIONS

In this initial work, the transfer function between the bedrock acceleration and the water velocity has been recomputed in closed form including the effect of a deformable soil layer. The effects of the water layer are of a de-amplification of the motion of the seabed at the resonance frequencies of the water layer, as it was also found by others authors, but contrary to what reported in several research works, an amplification effect has been found as well between each de-amplified frequency. The analysis of the effect of the soil layer in terms of the force given by Morison equation is ongoing.

7 REFERENCES

Crouse, C.B. & Quilter, J. 1991. Seismic hazard analysis and development of design spectra for Maul A platform. *In proc. of Pacific Conference on Earthquake Engineering*. New Zealand, Vol. 3, 137-148.

Boore, D.M. & Smith, C.E. 1999. Analysis of earthquake recordings obtained from the Seafloor Earthquake Measurement System (SEMS) instruments deployed off the coast of southern California. *Bulletin of the Seismological Society of America*. 89(1), 260-274.

Martire, G. & Faggiano, B. & Mazzolani, F.M. & Zollo, A. & Stabile, T.A. 2010. Seismic analysis of a SFT solution for the Messina Strait crossing. Special Issue Volume 4 (2010) ISAB-2010 Youshi Hong, Federico M. Mazzolani, Fuping Gao Eds., *Procedia Engineering* 4 (2010), 303–310. Available online at www.sciencedirect.com, 2010.

Jin Ho Lee & Sung Il Seo & Hyung Suk Mun 2016. Seismic behaviors of a floating submerged tunnel with a rectangular cross- section. *Ocean Engineering* 127 (2016), 32–47.

Dong, M.S. & Li, M. 2016. The dynamic responses of the of the submerged floating tunnel under seismic effect, Procedia Engineering 166 (2016) 152 – 159.

Inoue, Y. & Murai, M. & Noma, Y. & Aoki, T 2002. A Frequency and Time domain study on Response Analyses of Large Floating Structures due to Seaquakes. *In Proc. of the Twelfth (2002) International Offshore and Polar Engineering Conference*, Kitakyushu, Japan, May 26–31, 2002 ISBN 1-880653-58-3 (Set); ISSN 1098-6189 (Set).

Chao Li, Hong-Nan Li, Hong Hao, Kai-Ming Bi 2015. Simulation of seafloor seismic motions in southwest of Western Australia. *In Proc.of the Tenth Pacific Conference on Earthquake Engineering Building an Earthquake-Resilient Pacific* 6-8 November 2015, Sydney, Australia.

Chao Li & Hong Hao & Hongnan Li & Kaiming Bi 2015. Theoretical modelling and numerical simulation of seismic motions at seafloor. *Soil Dynamics and Earthquake Engineering,* 77(2015), 220–225.

Martinelli, L. & Barbella, G. & Feriani, A. 2010. Modeling of Qiandao Lake submerged floating tunnel subject to multi-support seismic input. Special Issue Volume 4 (2010) ISAB-2010 Youshi Hong, Federico M. Mazzolani, Fuping Gao Eds., *Procedia Engineering* 4 (2010), 311–318. Available online at www.sciencedirect.com, 2010.

Martinelli, L. & Barbella, G. & Feriani, A. 2011. A numerical procedure for simulating the multi-support seismic response of submerged floating tunnels anchored by cables. *Engineering Structures* 33 (2011), 2850-2860, doi:10.1016/j.engstruct.2011.06.009.(ISSN:0141-0296).

Shi, C. & Domaneschi, M. & Martinelli, L. 2012. Nonlinear Behaviors of Submerged Floating Tunnels under Seismic Excitation. *Applied Mechanics and Materials*. Vols. 226-228, (2012) 1124-1127, ISSN:1660-9336, DOI 10.4028/www.scientific.net/AMM.226-228.1124.

Shi, C & Martinelli, L. 2013. On the Generation of Seaquake velocity fields for Submerged Floating Tunnel structures. *Advanced Materials Research*, Vol. 690-693, (2013) 1172-1175, ISSN 1022-6680, DOI:10.4028/www.scientific.net/AMR.690-693.1172.

Chakrabarti, S.K. 1987, *Hydrodynamics of offshore structures*, Computational Mechanical Publication, Southampton Boston.

Hamamoto, T. 1995, Stochastic fluid-structure interaction of large circular floating islands during wind waves and seaquakes. *Probabilistic Engineering Mechanics*, 10, 209-224.

Shi, C. 2013. *Problems related to the seismic behaviour of Submerged Floating Tunnel*. PhD Thesis, Department of Structural Engineering, Politecnico di Milano (Italy).

Maintenance, Safety, Risk, Management and Life-Cycle Performance of Bridges – Powers, Frangopol, Al-Mahaidi & Caprani (Eds)
© 2018 Taylor & Francis Group, London, ISBN 978-1-138-73045-8

SFTs under dynamic loads: new design issues and numerical simulation

F. Perotti, F. Foti, L. Martinelli & M. Tomasin
Department of Civil and Environmental Engineering, Politecnico di Milano, Italy

ABSTRACT: In the paper some recent developments of the design trends in the field of seabed anchored Submerged Floating Tunnels are reviewed; the focus is on the implications on the anticipated dynamic behavior of the tunnel and on its numerical simulation. The design needs here considered are mainly of two types; the first is the necessity to cope with more stringent fire regulations. The second is the consideration of partial-flooding loading conditions, which was neglected in older designs according to the "no water ingress" principle. Both needs lead to the introduction, in the conceptual design, of the twin-tube solution, where two tunnels run parallel and are interconnected in order to allow fire escape. In addition, partial or total flooding of one of the two is considered, while the other can deliver sufficient buoyancy to avoid collapse. This evolution, along with the recent design activity performed within the E-39 Norwegian project, requires, in the writers' opinion, a review of the fundamental design choices, with a twofold purpose: first, to "classify" available options in view of coping with environmental loading scenarios (seismicity, wind waves, currents, naval and road/rail traffic, etc.) of different severity. Second, to discuss the various design configurations in view of the predictability of their structural behavior, especially under dynamic actions, this being a very delicate aspect for a never-built construction. Within this context, scope of the paper is to address the basic aspect of the SFT conceptual design along with the experimental and/or numerical procedures for simulating the dynamic behavior of the SFT under extreme environmental conditions. An example is finally given, illustrating some typical modelling options in relation to a SFT solution for the Messina Strait crossing, with particular reference to seismic response and seismic-induced hydrodynamic loading.

1 INTRODUCTION

Though a first realization is still missing, the Submerged Floating Tunnel is deemed to be a competitive option for crossing sea straits, fjords, alpine lakes and waterways in general (Ahrens 1996, Faggiano et al 2005, Østlid 2010, Ingerslev 2010). This is, first of all, for environmental reasons related to the small, or virtually zero, visual impact of the infrastructure and to the small occupation of surface land. Secondly, because among the various crossing solutions, the SFT should be the one less prone to interruption/limitation of its operability due to adverse weather conditions, this being of utmost importance when public transportation is involved.

On the contrary, adverse psychological reasons come from the novelty of the approach; in this light, a prototype installation was proposed some years ago within an international project (SIJLAB 2007). The prototype was intended as an icebreaker providing considerable insight into some design, construction and installation issues and acting as a real-size lab for some years, before becoming a mere tourism attraction. The prototype was thoroughly designed but never built, though remaining, in this writers' opinion, a necessary step towards the installation of the first "real" SFT.

After some years from SIJLAB it seems to be high time for reviewing some of the basic ideas and conceptual design options that were at the basis of the research activity performed in the late 90s and in the first decade of the new millennium, also in view of some emerging facts and situations; first of all, and on the "supply" side, the augmented capabilities of the scientific community to face complex physical experiments and numerical simulations. Secondly, by the "demand" point of view, the considerable pressure exerted by new initiatives; first of all, the E39 coastal highway project (NPRA 2011) involving the crossing of eight major fjords, today operated by ferries, and envisaging the adoption of a SFT for crossing the Bjørnafjord (NPRA 2014).

In this light some general considerations and remarks will be summarized in the present paper; the point of view will be unavoidably affected by two fundamental facts regarding the authors. The first is

their prevailing interest in matters related to structural dynamics, these being recognized as extremely important for the structural design of a SFT, but obviously sharing this importance with other aspects. The second is the "European" point of view on the topic, unavoidably biased by the two main drivers to the research performed, in the EC countries in the last decades (FEHRL 1996), i.e. the Messina Strait crossing in Italy and the already mentioned activity related to Norway projects. These can be regarded as paradigmatic cases; the Messina case due to the harshness of its environmental loading conditions for marine structures (earthquakes, tsunamis, wind waves, currents, naval traffic, etc.). In addition, for the absolute necessity to support a high speed railway, this resulting in rather strict performance criteria, also in terms of continuous operability.

Environmental loads are substantially less severe in Norwegian fjords, where seismic hazard is negligible and the sea conditions benefit from the shielding effect provided by the system of islands contouring the north coast. As an additional "relief", no railway track is anticipated to run parallel to E39. On the other hand, fjord conditions are often extreme in terms of sea depth, making the tunnel anchorage at the seabed unfeasible and pushing towards other design solutions (surface pontoons, …) which are outside the scope of this paper.

Under these premises, the following sections will be first devoted to review conceptual design criteria and basic options and then to summarize open issues related to testing, simulation and analysis supporting structural design of seabed anchored SFTs.

2 CONCEPTUAL DESIGN

2.1 *Tunnel and anchoring system*

The main features of the overall tunnel design will be here reviewed, with reference to the case of seabed anchored tunnels. The discussion doesn't pretend to be exhaustive, but rather to address aspects and criteria which has been investigated and/or debated within this research group.

2.1.1 *General arrangement*

The interconnected twin-tunnel arrangement (Figure 1) is the solution adopted in the most recent design proposals. In fact, it can satisfy two basic requirements: the first one is to provide safe escape in case of fires or other type of accidents occurring in one of the tunnels. The second is related to the "partial flooding" condition, which was not introduced in the earlier designs, but is considered in the most recent proposals; in such situation the flooded tunnel can benefit from the support of the other.

On structural grounds, connecting the two tunnels enhances their performance in terms of lateral stiffness, even though it makes the shore connection more complex; a possible solution, in this respect, could be to make the two tunnels come closer and merge when approaching the shore.

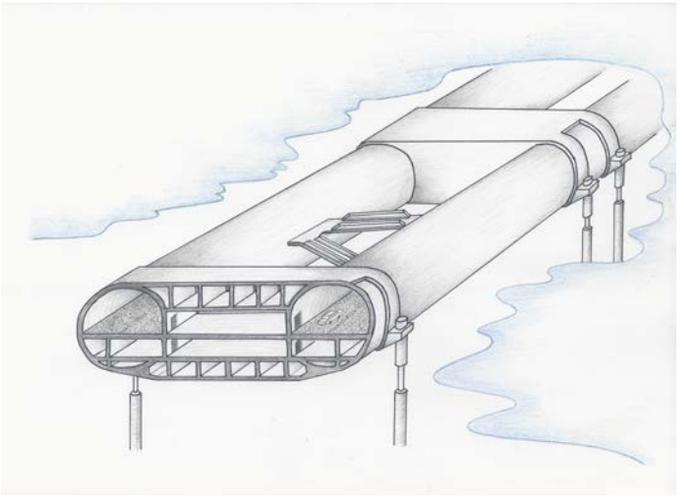


Figure 1. Twin-tunnel SFT

It can be noted that fire escape requirements result in what we could define as a "minimal" structural coupling between the tubes, with connection spacing up to 500 m. The type or "degree" of connection can obey to very different structural goals and criteria, also related to the strategy for seabed connection (see 2.1.3).

Finally, clearance above the tunnels is dictated by local regulations and ship traffic and by the benefits in term of reduction of wave loading; typical values are in the 20-30 m range.

2.1.2 *Plan layout*

The essential choice is here between a straight or curved tunnel. The second option obviously benefits of the arch effect resulting in largely increased stiffness; appears to be almost mandatory for long SFTs suspended to pontoons. For seabed anchored tunnels, the curved solution allows for vertical tethers layout.

On the other hand, coupling between axial and transverse behavior leads to a most problematic design of end connections. It can be regarded as non-advisable if strong seismic actions must be resisted and in all cases in which an anticipated variation of distance between the shores must be accommodated.

In the straight tunnel case, transverse stiffness can be provided by tethers inclined in the plane orthogonal to the tunnel axis. When longitudinal stiffness is considered, different options can be considered; the first is the adoption of double-inclination tethers. The second is to rely on the restraint offered by the tunnel end connections: here the introduction of dissipation devices should be carefully considered, in order to mitigate the dynamic behavior both in operation and in seismic conditions and to limit axial forces developing in the tunnel.

Within such context, the restraining system should be able to accommodate slow variations in the crossing length.

2.1.3 *Anchoring elements type and layout*

Two basic types of elements have been considered in SFT design; cables and tubular sections. The latter is deemed to be preferable for inclined long elements, since can benefit from buoyancy in order to avoid catenary effects, which unavoidably penalize serviceability performance.

For single-tube tunnels a typical layout of the anchor bars is the one in Figure 2, ensuring adequate lateral and torsional support

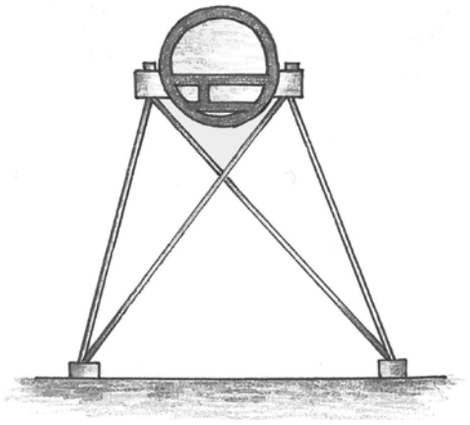


Figure 2. Typical layout of anchor bars for single-tube tunnels.

For a twin-tube system, the tethers arrangement is affected by the criterion adopted for connection between the tubes; for "densely" interconnected tunnels, an anchorage system can be introduced at all connections, so that the scheme of Figure 2 can be simply extended to the coupled tubes (Figure 3).

If the spacing between the connections is large, i.e. dictated only by fire escape requirements, each tube can be independently anchored to the seabed (Figure 4). A suitable plan layout must be devised, in this case, to avoid interference.

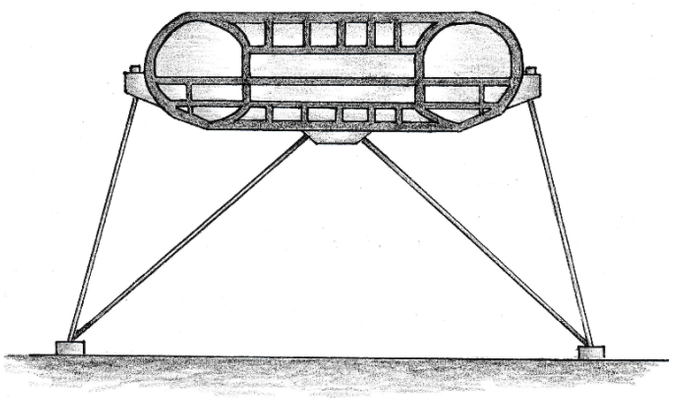


Figure 3. Layout of anchor bars for twin-tube systems with dense interconnection

When design criteria for tethers are to be established, a debated issue is whether they must be always tensioned in design conditions or they can go slack under extreme loading, typically under ULS seismic actions. It is in this writers' opinion that when severe design seismic loads are to be resisted very high buoyancy-to-weight (BtW) ratios are necessary to meet the first criterion, resulting in excessive tension loads on the foundation; on the other hand, it has been shown that in the Messina Strait case, the adoption of a BtW ratio of about 1.3 led to an acceptable dynamic response of the anchor bars, even though the "no compression" criterion was not satisfied (Fogazzi & Perotti 2000, Di Pilato et al 2008, Feriani et al 2008)).

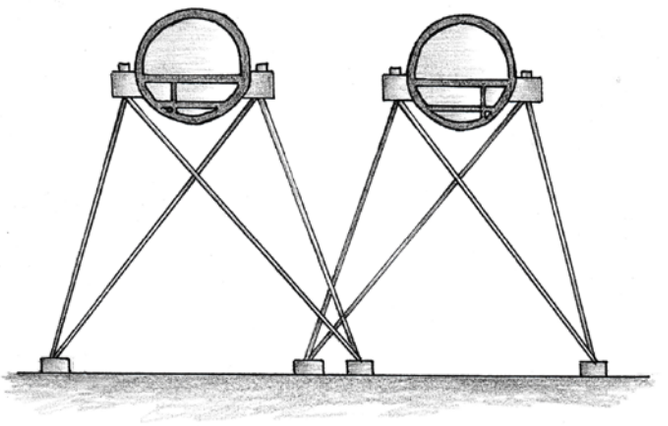


Figure 4. Layout of anchor bars for twin-tube systems with independent tethering

2.1.4 *Section shape and separation*

Circular hollow sections at a centerline distance of 30-40 m are currently proposed within the E39 project; this choice should be confirmed by studies regarding the hydrodynamic behavior, with special attention to galloping instability and to high-Reynolds regimes.

2.2 *Loading conditions*

Partial-flooding loading conditions have been introduced in recent proposals for SFTs, along with stricter fire-resistance provisions, thus resulting in the above quoted new design trends. Note that flooding is not necessarily related to sea water entering the tunnel, i.e. to loss of its integrity or tightness, but more likely to malfunctioning of internal water ballast systems.

Most loading conditions for SFTs are typical of tunnels, bridges and other road infrastructures. Some scenarios, however, are related to the particular location of the structure, such as the impact of sinking objects or the occurrence of an external explosion.

2.3 *Reparability*

The intrinsic modular structure of the SFT and its consequent stability in "incomplete" configuration should be exploited by considering, at the design stage, the possibility of replacing a damaged module. Note that the capacity of resisting partial flooding loading conditions and reparability are of utmost importance when issues regarding insurance policies for the infrastructure are considered.

3 ANALYSIS, TESTING AND SIMULATION

In this section some issues related to the experimental activity, both numerical and physical, supporting the SFT design process will be reviewed. Following a brief review of general modelling issues, the topics will be grouped according to the most relevant loading scenarios.

3.1 *General modelling issues*

As a general remark, it can be observed that the following considerations apply to loading conditions mostly involving "global" loading patterns (earthquakes, wind waves, current, traffic, etc).

3.1.1 *Structural modelling*

Based on the above consideration, structural modelling can be largely based on the introduction of beam elements for modelling the tunnels and to beam or cable elements for capturing the response of the tethering bars. A special attention must be devoted to the latter, whose dynamic behavior is prone to develop large transverse displacements, though essentially remaining within the small deformation range. In such conditions, the co-rotational formulation (Di Pilato et al 2008, Foti et al 2015, 2017), has proven to be effective for modelling the response of slender beams and cables; the formulation can incorporate refined material models (Foti 2016, Foti & Martinelli 2016, Foti et al 2016). These can capture important effects related to cable behavior, such as internal damping and fatigue behavior in zones of high curvature.

3.1.2 *Soil-structure interaction*

Simplified models, based upon the hypothesis of rigid mat foundations, can be applied to model the global structural behavior, both for the case of surface foundations and for pile groups. Piles have been often introduced in the design in order to resist tension forces developing in extreme conditions.

3.2 *Response to seismic actions*

Earthquake actions are transmitted to offshore structures of this type through two different mechanisms, either directly in terms of motion transmitted to the foundations or via hydrodynamic forces which develop due to the motion of the water surrounding the structure.

3.2.1 *General model for ground motion*

Given the structure size, the input ground motion must be defined also in terms of spatial variation; to this aim, stochastic models are available in the literature, usually defined in terms of direct and cross spectral densities. Starting from these models, artificial generation of time histories of free-field ground motion can be performed, characterizing the ground shaking at the seabed anchoring points and, more generally, along the tunnel axis.

3.2.2 *Ground-transmitted seismic excitation*

Based on the general ground motion model (see 3.2.1), the seismic excitation directly transmitted to the structure by the ground motion must take account of kinematic interaction. In this respect, effects due to the structure plan size must be introduced, to account for both the dimension of the foundation at a single anchoring section, and for the distance between the foundations (see Tomasin et al 2017).

3.2.3 *Water-transmitted seismic excitation*

Two different phenomena are relevant for a SFT. The first is the so called *seaquake* and is due to the vertical motion of the seabed under the tunnel; this motion is responsible for the transmission of vertically propagating compression waves. These waves interact with the tunnel by developing significant forces; to model these forces simplified approaches have been proposed, based on the free-field motion at the seabed, as specified by the general model (section 3.2.1) and on the solution of the 1D wave equation (see section 4.2).

A second hydrodynamic excitation mechanism can be due to *tsunami waves*. A wave of this type is originated where the fault rupture intersects the seabed; it propagates at a very high speed, with very long period and wavelength. Approaching the coast, the shoaling effects makes the wavelength and period become smaller and the height larger, often resulting in a dramatic run-up over the coast.

According to simple 2D models, the tsunami excitation doesn't appear to be critical for offshore structures, even though they are located on rather shallow waters. Special attention, however, should be devoted to structures under strong 3D effects. A typical situation is the one of a tsunami wave approaching the Messina Strait from South, thus undergoing the 3D effect due to the simultaneous reduction of the depth and width of the sea basin.

3.3 *Response to wave and current loading*

3.3.1 *Effect of wind waves*

Given the usual depth of a typical SFT, wind wave loading is often not deemed to be a critical issue among extreme environmental interactions.

Nevertheless, the topic has been addressed in many research works (see, for example Di Pilato et al 2008, Hong & Fe 2010) due to the severity of the wave scenario anticipated, as a typical example, in the Messina Strait and due to the consideration that the spectrum of large wind waves tends to match the frequency content of the transverse oscillations of long tethering elements.

To the aim of analyzing the effect of severe conditions, wave fields can be artificially simulated starting from a spectral density function describing the sea elevation at a point and a directional spreading function to account for the propagation of wave trains at different angles. Global wave kinematics can be derived based on the most suitable wave theory. Given the large wavelength of extreme waves, the Morison approach can be usually adopted to simulate wave-structure interaction. No linearization of the drag force has to be performed, since time domain step-by-step response must be performed anyway to represent geometrical non-linearity due to large oscillations of the tethers.

A similar approach can be adopted for extreme waves due to swells.

Different simulation criteria have to be introduced if wave loading need to be checked in serviceability conditions, along with traffic loading, for investigating fatigue and comfort issues. In such situation, given the small oscillation context linearized structural behavior can be assumed; on the other hand, for small waves diffraction effects cannot be neglected. The latter can be introduced as well via a linearized (potential) approach, resulting in frequency dependent hydrodynamic effects; accordingly, direct frequency domain analysis can be performed to evaluate the system response.

3.3.2 *Vortex induced vibration (VIV)*

The VIV issue is one of the most critical for the dynamic response of SFTs, especially in relation to fatigue effects. Two main problem arise; the first is that the transverse oscillations of long tethers can show natural frequencies of the order of the Strohual frequencies, so that lock-in conditions can occur.

The second problem lies in the values the of Reynolds numbers characterizing the current flow around both the tunnel and the tethering elements; these values are clearly outside the subcritical range, to which most of practical models and approaches refer. Note that, in this writers' opinion, global modelling of the SFT response to VIV excitation is necessary to capture coupling effects among VIV and other phenomena occurring at low frequencies, such as: transverse oscillations of tethering elements, longitudinal oscillations of the tunnel and structural response to long-period waves. On computational grounds, global modelling obviously requires simplified representation of the VIV phenomenon with special attention to lock-in behavior; the fluid oscillator model, in this respect, seems to represent the most suitable modelling tool. A question arises whether this approach, currently used in the subcritical regime, can be extended to the postcritical range.

VIV at high Reynolds numbers has recently received the attention of several research groups. In (Belloli et al 2015) the results of an extensive experimental campaign in the wind tunnel are shown and commented. High Reynolds numbers are here reached also exploiting surface roughness of a large diameter cylinder; both aerodynamic and aeroelastic tests are described. Even though the Reynolds number increase due to roughness cannot be precisely defined, the results clearly shown that VIV takes places as well in the postcritical range, showing similar features as detected in subcritical conditions. This allows for optimistic considerations about the possibility of adopting, and calibrating, fluid oscillator models for high Reynolds number VIV simulation.

3.4 *Response to traffic loads*

Dynamic behavior under vehicle-structure and train-structure interaction must be checked. Given the intrinsic time-dependent properties of the coupled vehicle-structure system, the simulation must be carried on by step-by-step analysis in the time domain; a promising option, in this respect, is represented by decoupled procures (see, for example Palamà 2017) in which the vehicle and structural system are separately integrated, and convergence is monitored on the global response. This allows for adopting different procedures for the two systems. In train-structure analysis, for example, non-linear effects in track-wheel interaction can be captured, though maintaining linearity in the response of the tunnel model.

3.5 *Response to accidents and intentional attacks*

Internal impacts, fires and explosions can be treated according to load models which are common in tunnel engineering. In setting simulation procedures and performance criteria, however, the location in water must be carefully taken into account.

A difficult situation arises when the case is considered of an external explosion, occurring in the water in proximity of the tunnel. The issue is new in tunnel engineering and simulation must face extremely complex phenomena. However, depth charges are sadly common in military operations against submarines, so that a vast literature on the topic is available and could be exploited if required.

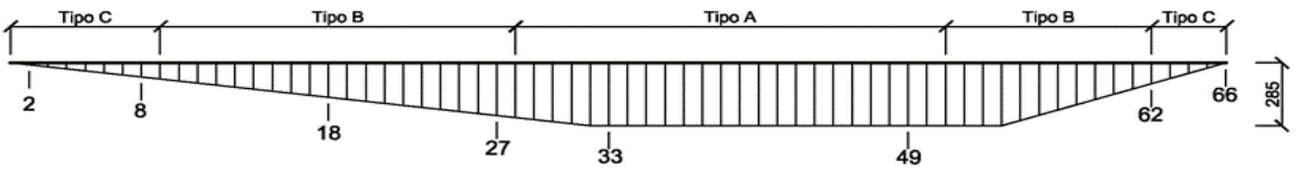


Figure 5. Side view of the model, showing the anchoring sections and the seabed profile, and organization of the mooring system (dimension in meters).

4 A CASE STUDY

A recent MS thesis supervised by one of the authors (Oregioni & Triaca 2016) deals with the Messina crossing and the seaquake effects.

4.1 *Description of the structure*

A general side view of the model, devised for the Messina crossing, is depicted in Figure 5. The model is based on one of the proposals for the crossing (see Bruschi et al 1990), modified in order to account for the more recent design trends.

In this light, a double tube configuration is addressed, in which escape routes connect the tunnels at a distance of about 500 m creating, on structural grounds, a Vierendeel beam acting in the horizoe. The anchoring system is of independent type, as shown in Figure 6, while the anchor bars show non-linear material behavior. Passive control devices are introduced at the tunnel-shore interfaces to limit both the axial forces in the tunnel and the longitudinal displacements in seismic conditions.

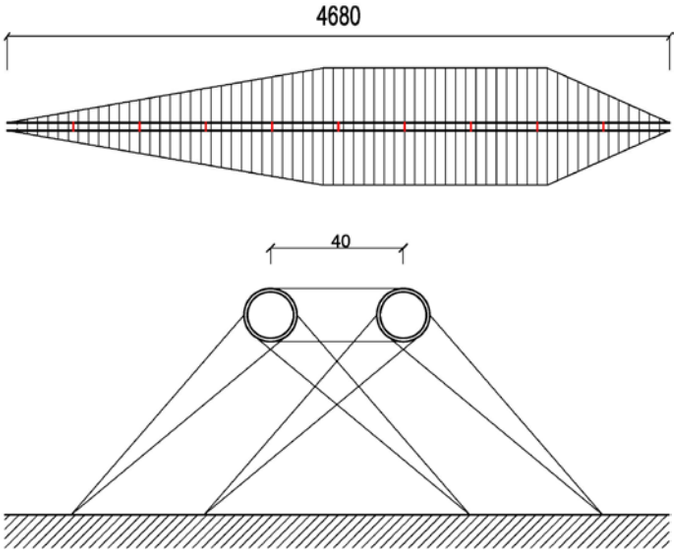


Figure 6. Top view of the model, showing the anchoring sections and the seabed profile, and organization of the mooring system (dimension in meters).

Each tube has a composite steel–concrete cross-section (Figure 7) and is assumed to behave elastically due to water tightness requirements. The anchor bars, which are assumed to have non-linear material behavior, are of three different sizes (Type A, B, C in Figure 5 and 7) depending on the seabed depth.

Since there is yet no specific normative on SFTs, appropriate rules from other fields have been adapted. In the case of the escape routes for fire or flooding, the distance has been set to 468 m to comply with EN 2004/54/CE, originally drafted for tunnels. This (paragraph 2.3.8) requires that the distance between emergency exit need to be less than 500m.

4.2 *Seaquake*

In the work (Oregioni & Triaca 2016), seaquake effects are introduced through the hydrodynamic pressure waves associated to the water motion due to the vertical oscillation of the seabed.

The water motion is assumed as that of a vibrating fluid column excited by the seismic motion of the seabed. It is computed in linearized form, at the depth of the SFT tunnel, from potential theory (Hamamoto 1995); the velocity potential is deduced from the wave equation (Shi & Martinelli, 2013) considering as boundary conditions the compatibility with the vertical seabed motion and the free surface condition.

Due to the non-linearity inherent to the SFTs behavior (both geometrical and mechanical), seaquake effects are accounted for in time domain. A realization of seismic vertical accelerations at the seabed according to the procedure in (Martinelli et al. 2010, 2011) is used to compute the vertical acceleration at the position of the nodes for which the seaquake related forces need to be computed. The force on the SFT elements due to the oscillatory flow caused by the seaquake is modeled adopting Morison's equation. The relative velocity of the SFT with respect to the water is used in computing drag forces.

Note that a more recent MS thesis work (Hemanth Kumar 2017), which is also the subject of the parallel paper (Martinelli 2018, submitted) was entirely devoted to seaquake modelling. Here the amplification effects on the water motion was studied

also considering a flexible soil layer interposed between the bedrock and the seabed.

4.3 *Main results*

The main results of the first study are that structural response under violent seismic actions is improved by admitting plasticization of the anchoring bars. These exceed the yield stress not only near the shores, where this was expected due to the "end effect" and to the smaller length of the bars, but also at a quarter and midspan. Seaquake shows a major effect on the response in the vertical plane. Longitudinal dissipation devices at the tunnel-shore interface are efficient in controlling the axial internal forces in the tunnels.

The problem of shear and bending moments developing in the tunnel close to the shore connections, anyway, deserves attention at the research and design level; different solutions pursuing a mitigation of the effects could be devised either by adopting a "denser" pattern for the anchoring system approaching the tunnel ends, or by introducing dissipation devices also in the vertical and lateral directions.

Finally, internal forces obtained in the case of three flooded compartments are higher than those due to seaquake and the asymmetry of the loading (one tube only is flooded) causes high torque actions. The most critical situation was found at the tunnels midspan.

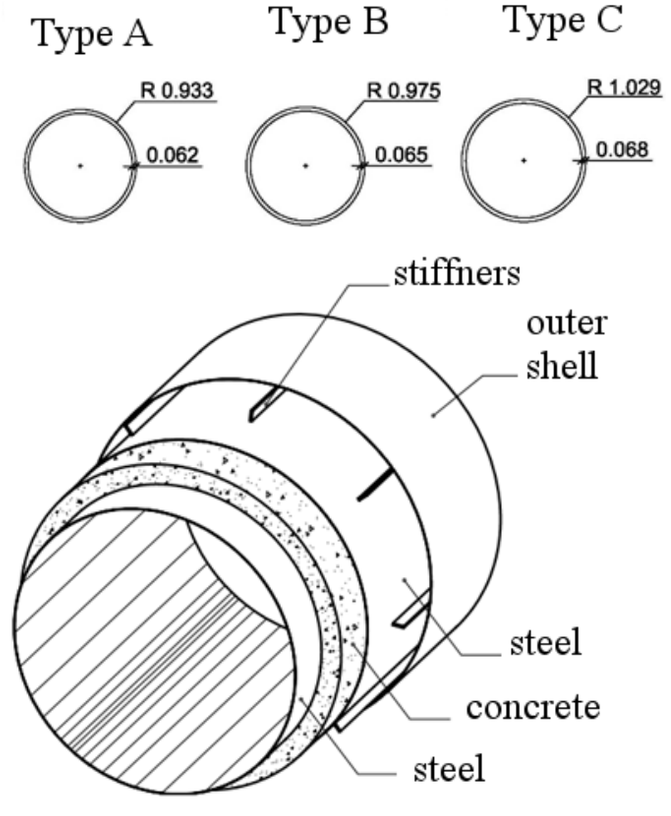


Figure 7. Type A, B, C of the anchoring bars cross-sections and composition of tubes cross-section (dimensions in meters).

5 CONCLUSIONS

In the paper, some general issues regarding the design and analysis of seabed anchored SFTs have been reviewed and discussed, trying to identify unresolved design issues and/or aspects of the SFT structural behavior needing a further research effort. Among these, and with reference to the twin-tunnel design solution, we can quote the following:

- end connection to the shores, especially in relation to seismic design,
- optimization of the distance between the connections,
- optimization of the distance between the tunnels,
- design for partial flooding conditions,
- replacement of damaged modules,
- 3D effects in tsunami loading of strait crossings,
- VIV modelling at high Reynolds numbers,
- train-SFT dynamic interaction,
- effect of an external explosion.

Finally, some recent activity performed by the research group has been summarized, focusing on the seismic behavior of twin-tube SFTs and on the seaquake excitation mechanism. Some results obtained in studying partial-flooding loading conditions are also commented.

REFERENCES

Ahrens, D. 1996. Submerged floating tunnels: a concept whose time has arrived, *Tunn. Undergr. Space Technol.* 11, 505-510.

Belloli, M., Giappino, S., Morganti, S., Muggiasca, S., Zasso, A. 2015. Vortex induced vibrations at high Reynolds numbers on circular cylinders, *Ocean Engineering* 94: 140-154.

Brancaleoni F., Castellani A., D'Asdia P. 1989. The response of submerged tunnels to their environment, *Engineering Structures*,11, 47-5.

Bruschi, R., Giardinieri, V., Marazza, R., & Merletti, T. 1990. Submerged buoyant anchored tunnels: tecnic solution for the fixed link across the Strait of Messina Italy *Proc. Of Strait Crossing,* Balkema, Rotterdam.

Fiorentino, A., Mazzolani, F.M., Perotti, F, et al (Italian Team of SIJLAB). 2007. *Design report of the Archimedes Bridge Prototype in Qiandao Lake (P.R. China)*.

Di Pilato, M., Perotti, F. & Fogazzi, P. 2008. 3D dynamic response of submerged floating tunnels under seismic and hydrodynamic excitation, *Engng. Struct.* 30(1): 268-281.

Di Pilato, M., Feriani, A. & Perotti, F. 2008. Numerical models for the dynamic response of submerged floating tunnels under seismic loading, *Earthquake Engng. Struct. Dyn.* 37:1203–1222.

Faggiano B., Landolfo R., Mazzolani F.M. 2005. The SFT: an innovative solution for waterway strait crossings. Proceedings of the IABSE Symposium "Structures and Extreme Events", Lisbon, Portugal, September 14-17.

Faggiano B., Landolfo R., Mazzolani F.M. 2001. Design and modelling aspects concerning the submerged floating tunnels: an application to the Messina Strait crossing". Proceedings of the 3rd International Conference on Strait

Crossings, Bergen, Norway, 1-5 September, Krokeborg ed., A.A. Balkema publishers, pp. 511-519.
FEHRL Report No 1996/2a, 1996. Analysis of the submerged floating tunnel concept". FEHRL (Forum of European National Highway Research Laboratories). Published by the Transport Research Laboratory, Crowthorne, Berkshire.
Fogazzi. P. & Perotti, F. 2000. The dynamic response of seabed anchored floating tunnels under seismic excitation. Earthq. Engng. Struct. Dyn. 29: 273-295.
Foti, F. 2016. A corotational finite element to model bending vibrations of metallic strands, In M. Papadrakakis et al. (eds.), *Proc. of the ECCOMAS Congress 2016, Crete, 5-10 June 2016*. Athens (Greece).
Foti, F. & Martinelli, L. 2016. Mechanical modeling of metallic strands subjected to tension, torsion and bending, *Int. J. Sol. Struct.* 91: 1–17.
Foti, F., Martinelli, L. & Perotti, F. 2015. Numerical integration of the equations of motion of structural systems undergoing large 3D rotations: dynamics of corotational slender beam elements. *Meccanica* 50: 751-765.
Foti, F., Martinelli, L., Perotti, F. 2017. A finite element approach for modelling galloping vibrations of iced suspended cables. *Procedia Engineering*. 199: 3127-3132.
Foti, F., Martinelli L. & Perotti, F. 2016. A new approach to the definition of self-damping for stranded cables, *Meccanica* 51: 2827-2845.
Hamamoto T. 1995. Stochastic fluid-structure interaction of large circular floating islands during wind waves and seaquakes, *Probabilistic engineering mechanics*, 10, 209-224
Hemanth Kumar G.H. 2017. The dynamic responses of submerged floating tunnel subjected to seaquake induced from flexible bed. MS thesis, Politecnico di Milano, Oct. 3 2017.
Ingerslev C. 2010. Immersed and Floating Tunnels, *Procedia Engineering,* 4, 51-59.
Martinelli L. 2018. Submerged Floating Tunnels under Seismic and Seaquake Loading, submitted for presentation at IABMAS 2018.
Martinelli L., Barbella G., Feriani A. 2011. A numerical procedure for simulating the multi-support seismic response of submerged floating tunnels anchored by cables. *Engineering Structures*, 33(10): 2850-2860.
Martinelli L., Barbella G., Feriani A. 2010. Modeling of Qiandao lake submerged floating tunnel subject to multi-support seismic input. *Procedia Engineering,* 4, 311-318.
Norwegian Public Roads Administration 2014. E39 fjord crossing project – Bjørnafjord - Data for the crossing and rørbru concept.
Norwegian Public Roads Administration 2011. *Project Overview - Coastal Highway Route E39*
Oregioni M. & Triaca S. 2016. Analisi e progetto di tunnel flottanti sullo Stratto di Messina, MS thesis, Politecnico di Milano, Dec 21 2016.
Østlid H. 2010 When is SFT competitive? *Procedia Engineering,* 4, 3-11.
Palamà, G. 2017. Procedura iterativa nell'analisi dell'interazione dinamica veicoli struttura: applicazione al tunnel flottante sullo stretto di Messina (in Italian). MS thesis, Politecnico di Milano, Dec 3 2017.
Shi C.X. & Martinelli, L. 2013. On the generation of seaquake velocity fields for submerged floating tunnel structures. *Advanced Materials Research* (690-693):1172-1175.
Tomasin M., Domaneschi M., Guerini C., Martinelli L., Perotti F. 2017 A comprehensive approach to small and large-scale effects of earthquake motion variability. *Comp. Struct.,* in press, (https://doi.org/10.1016/j.compstruc.2017.04.010)
Youshi Hong, Fei Ge 2010, Dynamic response and structural integrity of submerged floating tunnel due to hydrodynamic load and accidental load, *Proceeding Engineering*, 4, 35-50.

Maintenance, Safety, Risk, Management and Life-Cycle Performance of Bridges – Powers, Frangopol, Al-Mahaidi & Caprani (Eds)
© 2018 Taylor & Francis Group, London, ISBN 978-1-138-73045-8

An Experimental Study on Bending Behavior of Composite Hollow RC in Submerged Floating Tunnel (SFT)

J.H. Seo, D.H. Won &W.S. Park
Coastal Engineering Division, Korea Institute of Ocean Science and Technology, Bus

ABSTRACT: In case of a submerged floating tunnel (SFT), which is difficult to cast in-site underwater construction, it is modularized on land and then assembled them in the field. So, it is influential to investigate the structural performance of the joints between the modules. A concept of the steel composite hollow in SFT which stably maintains the joints has been proposed by applying prestressing method to resist various external loads. In this study, the bending behavior of module joints in a steel composite hollow tunnel was experimentally analyzed to evaluate the safety for the bending deformation which is dominant in SFT. Test results show that there is a difference at the module joint portion in the performance depending on whether or not the inner steel tube is connected. As a result, in the design of the module joint, depending on the purpose of SFT, it is possible to consider both methods which is allowing the ductility behavior of internal tube and controlling the tight connection. And, the failure criterion of the bending behavior of the module joint can be selected as the maximum load or deformation limit.

1 INSTRUCTION

1.1 *Outline of SFT*

SFT (Submerged Floating Tunnel) is a tunnel installed in the water and can be described as underwater bridges. There are various linking means for water-spanning structures; a general suspension bridge, an immersed tunnel, an underwater tunnel, and a SFT refers to an installed tunnel between a sea level and a seabed surface. It is commonly called Submerged Floating Tunnel (SFT), also called a suspended tunnel or Archimedes bridge. A SFT comes into the spotlight as an alternative technology for creating practical space with the introduction of eco-friendly concept.

The supporting methods of these SFTs are classified with to its own weight and buoyancy (Figure. 1). When the buoyancy is greater than the self-weight (W<B), there is a method of using a taut mooring system such as a tension leg. When the self-weight is larger than the buoyancy (W>B), either an additional buoyant pontoon or a way using the supporting piers on the seabed is used to equalize the total weight and buoyancy. And by corresponding the weight with buoyancy (W=B), there is also a way not to provide a separate support structure or mooring system.

These methods require the appropriate selection depending on each marine environment. Of the various marine environment, SFT can be useful in that it can directly connect the underground road network. That is it is feasible for a low slope since it has the lowest connecting section in comparison with other water-spanning structure types. In the intercontinental connection with deep water and long transversal distance, it means to secure economic feasibility.

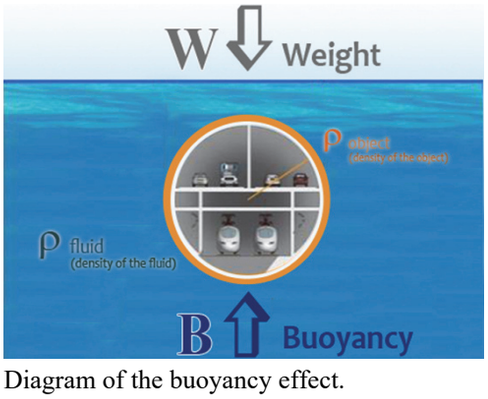


Figure 1 Diagram of the buoyancy effect.

Many countries have studied about SFT with these many advantages. Typical examples of research include Høgsfjord crossing in Norway, Messina Straits crossing in Italy, Lake Lugano crossing in Switzerland, and Northern Japan Exchange Axis, Funka Bay crossing connecting Hokkaido and Honshu in Japan, and in China, there is conducted a research in collaboration with Italy on the Archimedes Bridge Prototype in Qiandao Lake (Mazzolani et al., 2010; Park et al., 2012). Especially, in the Norwe-

gian coast, there are more than a thousand fjords with deep water and long transversal distance, and researches on SFT were conducted early on. As a part of the project "Coastal Highway Route E39", Norway's Public Roads Administration (NPRA) has an ambitious plan to solve the problem by building the world's first floating submerged tunnel system about 30 meters (100 ft) underwater beneath the Søgnefjord (Duan, 2014).

1.2 *Joint of composite hollow RC in SFT*

Since the SFT is difficult to cast in-site underwater construction, it is considered to be the most reasonable construction method using the module fabrication which move it from the coast to the field site using the ship. The joint structure that connects each module of the SFT must be capable to perform appropriate functions such as water tightness, transmission of force, flexibility, etc. while also reasonably performing the joining of each module.
This joint structure can be divided into a continuous joint that is tight connected each module according to the stiffness of the joint. And this joint structure not only applies to the connection between the SFT modules, but also refers to the module and the ventilating tower, and the connection with the ground as a final joint. Therefore, it is required to develop a new type module considering rapid construction, stability, and economical feasibility. This study focuses on the joint structure between the SFT modules.

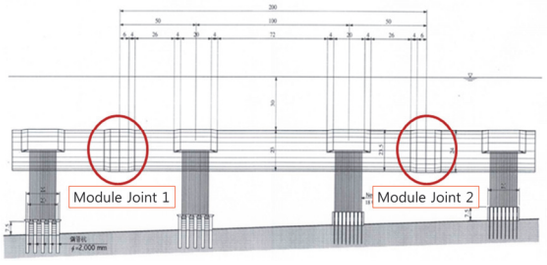


Figure 2 Side view of SFT

In case of Qiandao crossing in China, Funka Bay crossing in Japan, as well as the Busan-Geoje Fixed Links Immersed tunnel in Korea and Dutch immersion tunnel having the similar structures, the module joint methods to stably keep the concrete joints vulnerable to tensile are proposed as shown in Figure 2 and Figure 3. Fist of all, cross-section of SFT is applied steel composite hollow RC section under member. This section has inner tube, it has good ductility and strength (Han et al, 2008). In this research, this section applied SFT's section.
The joint of module composite hollow RC column need to solve connection method between concrete and steel tube, respectively. This connection method has been proposed. The connection of concrete has different connection method another module connection type which is arch post tension method because in-site construction is impossible. As shown Fig. 3, prestress tendon can be give initial stress in SFT. It is very good method for SFT. In this reason, this arch post-tension method is suggested. For connecting method of steel tube, high tension bolts are applied as shown Fig. 3. It already suggested method like as steel bridges design and construction method. Using a Gina profile and an Omega profile, they form the primary and secondary shield skirts, and provide prestressing with a coupler and a steel PC tendon (Mazzolani et al., 2010; Zhang, et al., 2010). And the empty space was applied by using mortar. Many countries have proposed various types of module joints for SFT, but none have actually been constructed yet.

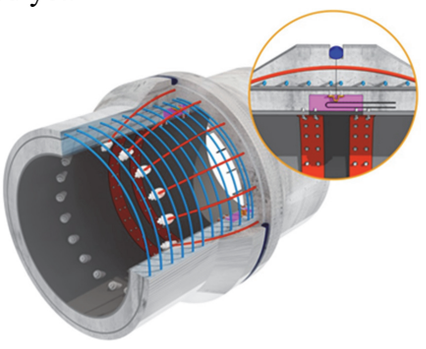

Figure 3. Module joint of composite hollow RC SFT.

Figure 3 shows the Gina and Omega profiles installing outer and inner respectively to completely block the water. In order to improve the structural stability of the module joint, it is necessary to connect the longitudinal steel rebar, the inner steel tube and the concrete. Therefore, the arched prestressing method is applied to bond the concrete with the longitudinal rebar. At this time, the thickness of the outside of cross section was increased to reduce the curvature and the stress concentration of the arched PC tendons introduced for tensile force. In additional, a rebar connection to improve the connection performance of the concrete was installed to be made up the intersection when both modules are jointed. The mortar is injected into this joint, and in case of the inner tube, it is installed through bolting or welding to enable complete joint.
The loads acting on the module joints in SFT (Figure 4) have various external loading conditions such as hydrostatic waves, seismic loads, especially, in case of an earthquake, the tensile force should be examined since the axial force is generated. The bending deformation expected to have a dominant influence among bending and torsion, axial tensile and compressive forces, this is an important factor for safety of SFT by generating tensile and compressive forces on tunnel walls. Therefore, it is required to design a joint in SFT that can be able to appropriately resist the horizontal and vertical shear force.
The module joint used in this study is based on the cross section of composite hollow in SFT proposed by Han et al. (2013). As shown in Figure 4, the tun-

nel length per module was set to 200 m and is assumed that it is moored by two mooring devices.

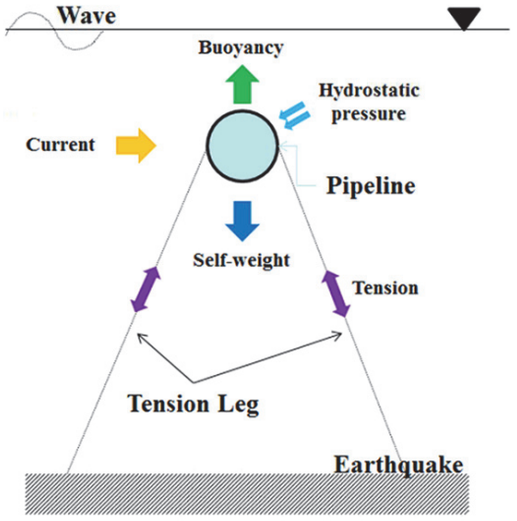


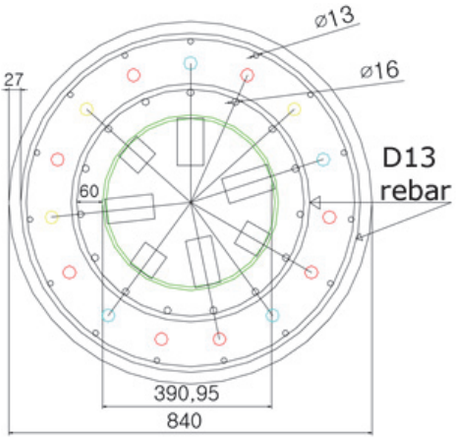
Figure 4. Various loads acting on the module.

This paper performed an experimental study for bending behavior of the module joint assuming that would be subjected to axial load. Test variable is connection type of inner steel tube. The main objective of this study is to evaluate the failure mode and bending behavior of the module joint of composite hollow RC in SFT using the proposed prestressing method.

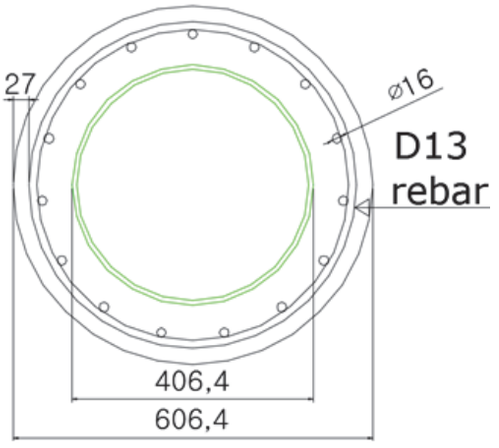
2 TEST PROGRAM

2.1 *Experimental Model*

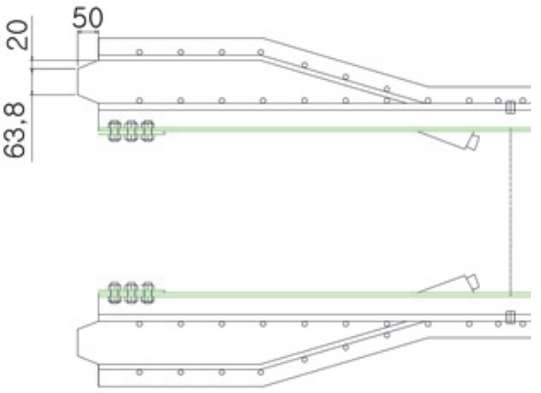
To verify the bending strength of joints between steel-composite hollow RC modules in SFT, Specimens were designed and manufactured as shown in Figure 5 and Figure 6. The total length (L) of the specimen is 7 m, connecting two modules of 3.5 m. Figure 5 shows design details of the test modules. This model is scale reduction model (1/100). This model designed by design code with the pre-stressed concrete. Variables studied in the test program are the presence or absence of the inner steel tube in PART A, and two specimens were manufactured for each connection type of inner steel tube. One specimen was bolted to an inner tube having 7.5 mm thickness (Figure 6), and another specimen was left unconnected and simulated with a hinged structure.



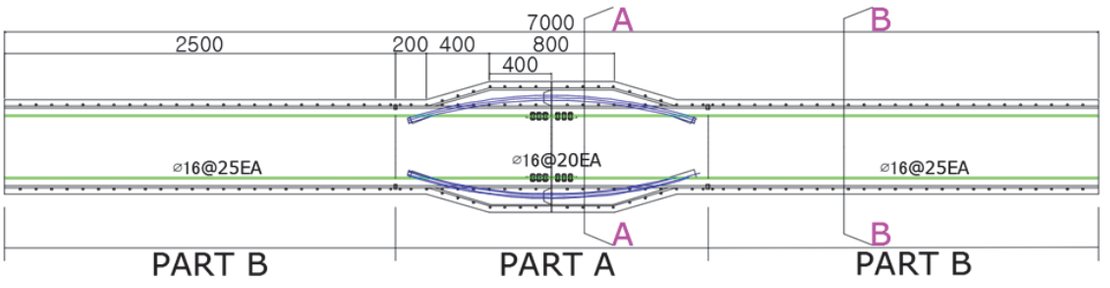
(a) Cross section A-A



(b) Cross section B-B

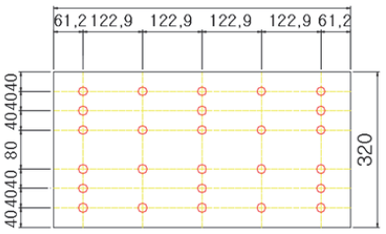


(c) Shear key of concrete

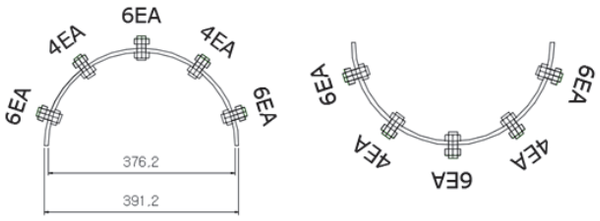


(d) Side view of specimen

Figure 5. Drawing of joint specimen (units: mm).



(a) Side view of connection plate



(b) Top plate (c) Bottom plate

Figure 6. High tension bolt for connection plate (units: mm)

Figure 7~8 show the production process of test specimens, which were fabricated by assembling the reinforcing bars to the molded specimens, attaching the gauges, pouring concrete into the tunnels and demolded. For specimen with bolting inner tube, at first, the inner steel tube was welded. Then the longitudinal steel bars were bonded using a coupler, then the lateral steel bars were bonded, and concrete was filled. After the two modular portions (PART B) were placed the concrete, post-tensioning was performed on the PART A which is the joint portion.



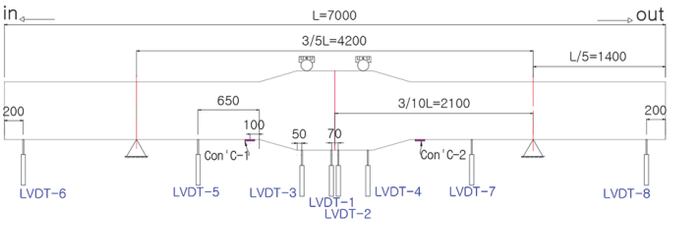
Figure 7. Molding and assembly.



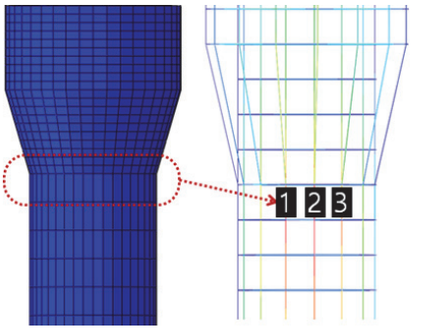
Figure 8. Pouring and demolding.

2.2 *Test Method*

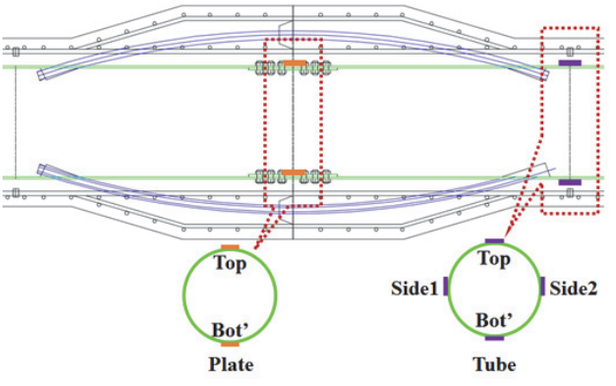
In order to evaluate the bending performance of the manufactured specimen, we refer to the bending strength test method of the pretensioned spun high strength concrete piles, F 4306 (KS, 1988). The deformation of specimen was investigated using four displacement gages (LVDTs) and twenty-four strain gage. To measure deflection, a displacement gages were installed at the lower part of the test specimen where four LVDTs #1 ~ #4 in front of PART, and other half LVDTs #5 ~ #8 were installed in front of the two modules on PART B (Figure 9(a)). And, to investigate the strain of steel reinforcement bars, the strain gauges were attached at the end of the welded section where the thickness was increased to reduce the stress concentration.



(a) Installation of LVDTs



(b) Strain gages for rebar



(c) Strain gages for inner tube



(d) Setting the specimen

Figure 9. LVDTs & strain gages (units: mm)

As shown in Figure 9(b), six strain gages were installed at longitudinal reinforcement bars with load-direction (Top-1, 2, 3) and opposite direction (Bottom-1, 2, 3). In addition, to investigate the bending behavior against axial tension and compression, the four gauges were set to the outside of inner tube in four directions (Tube Top, Tube Bottom, and Tube Side 1, 2) respectively. In the event of bolting case of the inner tube among the two specimens, there was the supplemental connecting steel plate at the center of the span, and two gauge were attached to the upper and lower parts and named Plate Top and Plate Bottom (Figure 9(c)). In addition, strain gauges (Con'C-1, Con'C-2) for measuring the concrete strain were similarly attached to the end of the tapered section of the joint in the opposite direction. Here, Con'C-1 means that it is installed in the inner direction (in) corresponding to the left side in Figure 9(a) and Con'C-2 indicates that of the opposite direction (out).

In this experiment, the displacement control method is applied by the loading control method using the actuator of 200 tonf. The test speed is shown in Figure 10, as the deformation amount of specimen increases, the joint speed is increased from 0.15 mm/s to 1 mm/s. The actuator is located at the center of the span where the joint part is placed. The acting load was based on the measurement value by the actuator.

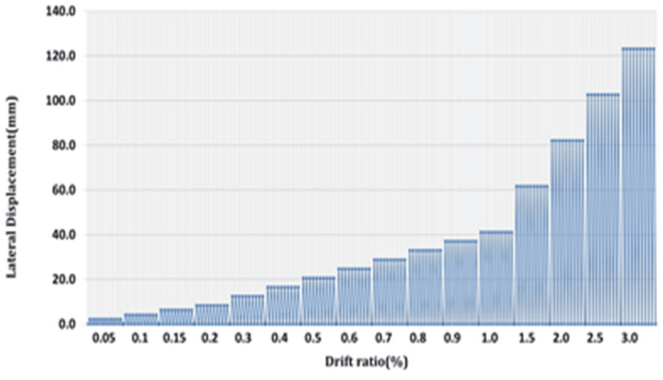


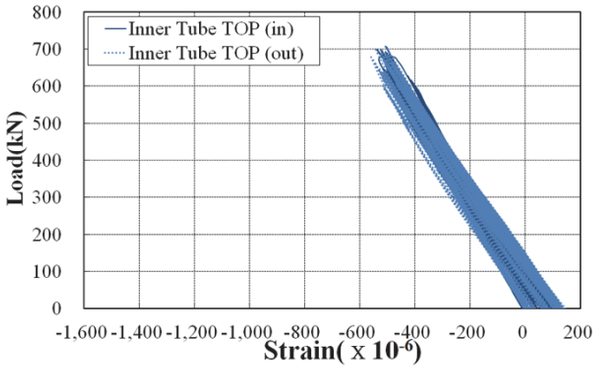
Figure 10. Half cycle low fatigue loading (10cycle/step).

3 BENDING BEHAVIOR OF MODULE JOINT

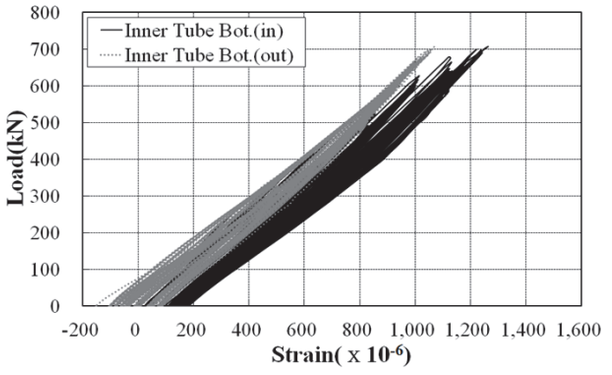
The cross section of the composite hollow in SFT does feature in which the longitudinal reinforcing steel and the inner tube are connected by the PC tendon, and the concrete surrounds the outer wall. In case of the acting load is applied on more than the performance of PC tendon with the prestressing, the inner tube is responsible for the safety of the structure. The safety criteria for evaluating the bending behavior of these modular joints depend on the application of the tunnel. There are two methods for ultimate strength calculation to determine the strength evaluation of the joint. One method is determining as the maximum load of the load-displacement curve, and another is determined as the deformation limit based on the deformation of the joint (Zhao, 2013). In this section, the bending behavior of module joints are analyzed and compared according to the presence or absence of the internal tube connection

3.1 *Test Result*

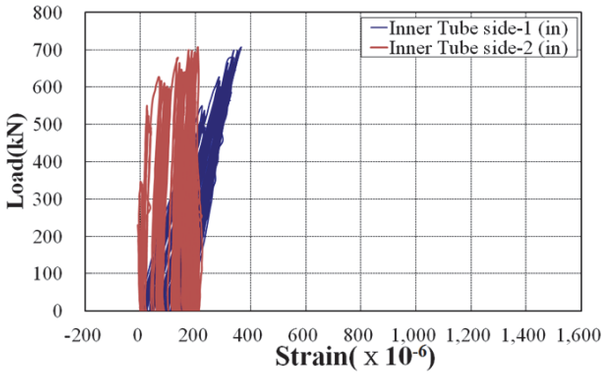
Figure 11 and Figure 12 show the results for the specimen which the inner tube is not connected. The strains obtained from the gauge (Tube Top, Bottom, Side 1, 2) attached to the inner tube (Figure 11) show that compressive force is generated at the upper part and tensile force is applied at the lower part as the loading rate increases, the bending behavior can be determined symmetrically without the torsional effect.



(a) Tube: Top



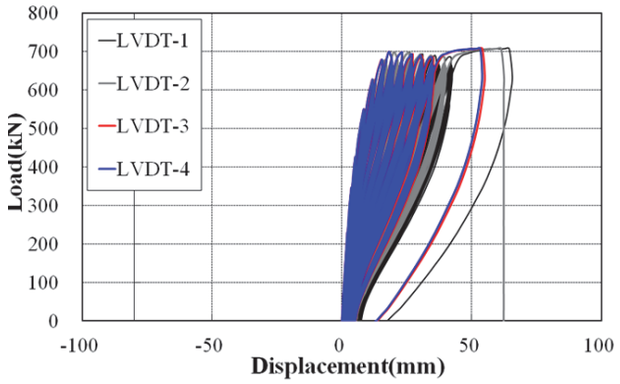
(b) Tube: Bottom



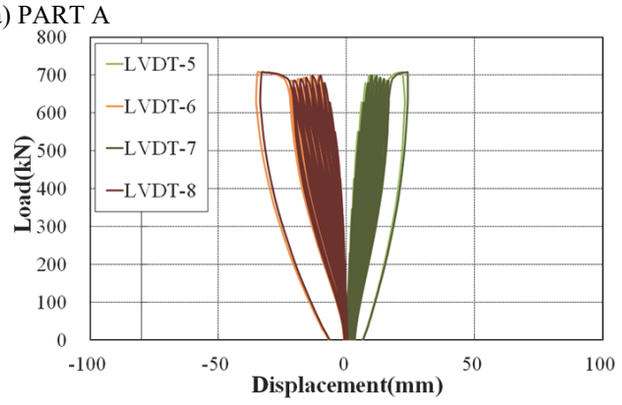
(c) Tube: Side

Figure 11. Strain curves of the specimen without inner tube connection.

Next, in the load displacement curve (Figure 12) of the specimen without inner tube connection, the maximum tensile displacement of about 60 mm occurred in the joints at PART A (LVDT 1 ~ 4), and the deformation of the close part to the center was larger. Also, it was confirmed that the maximum compressive displacement at PART B (LVDT 6, 8) was about 35 mm. It can be seen that the deformation of specimen which the inner tube is connected has larger bending deflection in both the tension and compression portion than that of without inner tube connection. It can be means that the resistance performance by the inner tube exhibits in the above section of acting load having the prestressing by the PC tendon in the tensile portion which is the opposite direction of loading.



(a) PART A



(b) PART B

Figure 12. Load-Displacement curves the specimen with connected inner tube

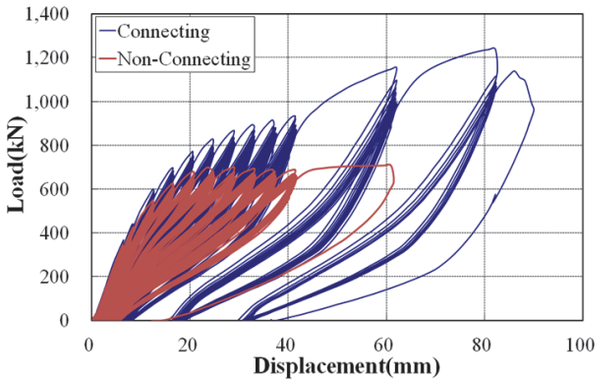


Figure 13. Comparison of performance of inner tube with the specimens.

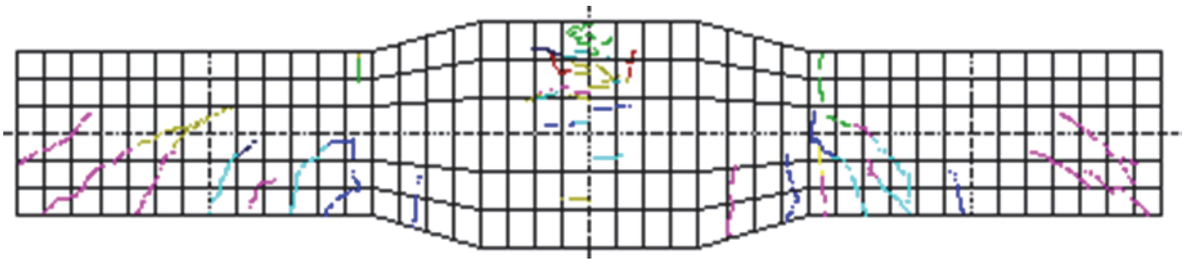
In order to compare the resistance performance by the inner tube, Figure 13 describes the load-displacement history curve. In case of the specimen (red solid line) without the inner connection, the maximum strength is 700 kN, whereas the specimen (blue solid line) with the inner connection by bolting has a maximum strength of 1,200 kN. It can be seen that the strength is relatively increased due to the connection performance of the inner steel tube.

In the event of the design method considering the seismic performance based on the ductility such as the railway bridge, it can be judged that the higher the extreme strength after the yielding, the better performance. In the case of a design method considering over the constant allowable displacement as the failure, the two specimens have similar performance because they show almost the same stiffness up to the displacement of 10 mm. Moreover, in the case of the unconnected specimen of the inner tube, the lower part of joint opened temporarily, but it was restored after the test by the PC tension, and the residual deformation was about 15 mm. Even if a failure of the module joint occurs in SFT, it is expected that the waterproof function operates normally by the internal omega profile due to itself ductile behavior. In the case of the specimen with inner tube connection, the lower part of joint was also widened temporarily, but it was restored after the loading by the PC tension, and the residual deformation was about 40 mm which has relatively less resilience than unconnected cases. It is considered that after yielding, the connected inner steel tube resists external force such as buckling, which has relatively less resilient than that of the not connected case.

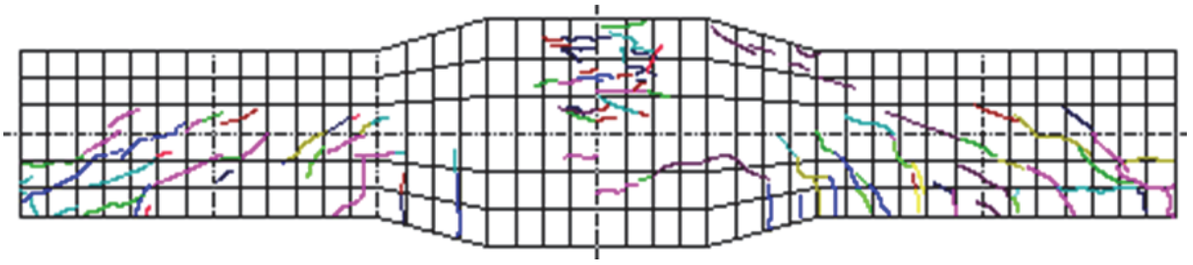
Experimental results show that the bending stiffness of the joints specimens is very similar according to presence and absence of the inner tube, but there was a difference in ultimate strength. Also, restoring force was decreased by connecting the inner tube. Therefore, when judging the performance of the module joint in SFT, it is reasonable to choose whether to calculate based on the maximum load in the load-displacement curve or the deformation limit of the joint with the purpose of the tunnel application.

3.2 *Comparison of Crack Patterns*

Figure 14 shows the cracking behavior of the specimens by acting load, and the cracks generated on the outer wall of the concrete with low tensile strength were observed by the bending moment. As the load increased, bending shear cracks began to occur at the end of the tapered section. Then, diagonal cracks was generated at the end of the beam. For PART A, the acting load portion, crushing characteristic occurred in the outer wall of the concrete while resisting the bending due to relatively large compression, and bending cracks occurred at the center of the tension portion in the opposite direction of the loading.



(a) Non-Connection (Front)



(b) Connection (Front)

Figure 14. Comparison of crack patterns.

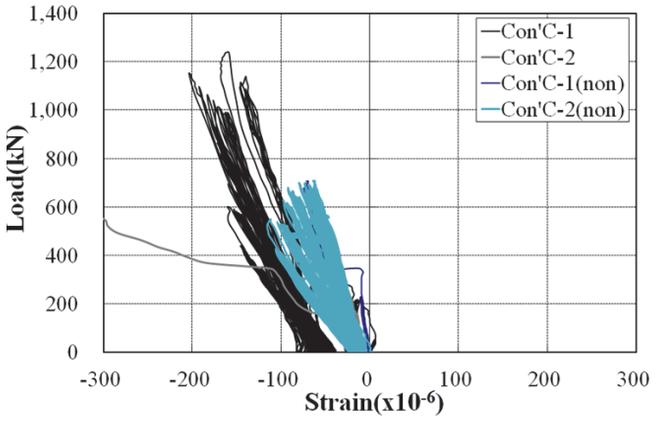


Figure 15. Concrete stains

In addition, it can be seen that cracks are more uniformly distributed over the entire cross section when the inner steel tube is connected. For the non-connection case having relatively smaller residual deformation observed the less cracks of 55% than in the connection case. It seems that the inner tube serves as a hinge in this structure. This can be exhibited on the concrete strain measured at the lower end of the tapered section (Figure 15). When the inner tube is connected, it shows a strain of 0.0002 at the maximum load, while it has a strain of about 0.0001 in case of without connection, which is measured up to about half. In this way, when the inner tube is connected, the bending moment is transmitted to the module portion (PART B) through the joint portion (PART A), and result in the wider cracks.

4 CONCLUSIONS

In this study, structural bending behavior of module joints with steel composite hollow RC in SFT applying prestressing method was studied experimentally. The performance of module joints in SFT was evaluated by experimenting with the connection of inner steel tube as the test variables which is responsible for safety when acting on the joints above the prestressing force. The main findings are summarized as follows,

(1) The bending stiffness of the module joints in SFT was very similar but there was a difference in strength. The maximum strength was increased from 700 kN to 1200 kN when the inner tube was connected, and the residual displacement was increased from 15 mm to 40 mm. However, this is superior to the maximum strength by connecting the inner tube, it is considered that the restoration force by PC tendon is reduced due to the deformation of the joint with bolting connection.

(2) Therefore, when designing the module joint, according to the application of SFT, it is possible to consider both the method which allowing the ductility behavior and tight controlling with bolting connection. In this case, it can be understood that a rational design is practicable by selecting criterion for judging the bending behavior performance of the module joint as either the maximum load or the deformation limit.

(3) Furthermore, considering the underwater environment, it is necessary to examine more various structural behaviors such as torsion which may affect the overall structure of the SFT. And the effects of deformation taking into account the foundation and the ground conditions should be fully examined.

ACKNOWLEDGEMENT

Funding: This work was supported by the National Research Foundation of Korea (NRF) grant funded by the Korea government (MSIT) (No. 2017R1A5A1014883).

REFERENCES

Duan, Yuxiang. 2014. Application of Suction Caissons to Submerged Floating Tunnel at Sognefjord in Norway. *Master thesis of Chalmers University of Technology*, Sweden.

Han, T. H., Lim, N. H., Han, S.Y., Park, J.S. & Kang, Y. J. 2008. Nonlinear Concrete Model for an Internally Confined Hollow Reinforced Concrete Column. Magazine of Concrete Re-search, 60(6), 429-40.

Han, T. H, Won, D. H, Han, S.H. & Park, W. S. 2013. Development and Performance Analysis of Steel-Concrete Composite Submerged Floating Tunnels. *Proceeding of Korean Soc. Hazard Mitig*. 11, 759-764 (in Korean).

KS (Korean Industrial Standard). 1988. Pretensioned Spun High Strength Concrete Piles. F 4306 (in Korean).

Mazzolani, F. M., Faggiano, B. & Martire, G. 2010. Design aspects of the AB prototype in the Qiandao Lake. *Procedia Engineering*, 4, 21-33.

NPRA (Norwegian Public Roads Administration). 2011. A feasibility study – How to cross the wide and deep Sognefjord.

Park, W.S., Han, S.H., Oh, M.H, Han, T.H & Ko, J.H. 2012. Technical trend on submerged floating tunnel. Korean Society of Civil Engineering, 60(8): 23-29 (in Korean).

Simulia, D. S. 2013. ABAQUS 6.13 User's Manual. *Dassault Systems*, Providence, RI.

Zhang, K., Xiang, Y., & Du, Y. 2010. Research on tubular segment design of submerged floating tunnel. *Procedia Engineering*, 4, 199-205.

Zhao, X. L. 2013. Static Design Procedure for Welded Hollow Section Joints - Recommendations. *IIW (International Institute of Welding) commission XV*, ISO/FDIS 14346:2012(E).

Maintenance, Safety, Risk, Management and Life-Cycle Performance of Bridges – Powers, Frangopol, Al-Mahaidi & Caprani (Eds)
© 2018 Taylor & Francis Group, London, ISBN 978-1-138-73045-8

A Novel Life-Cycle Based Management System for Disaster Mitigation of Bridges

Y.C. Sung
National Taipei University of Technology, Taipei, Taiwan
National Center for Research on Earthquake Engineering, Taipei, Taiwan
K.C. Chang
National Taiwan University, Taipei, Taiwan
C.C. Chen, C.C. Hsu., K.W. Chou & H.H. Hung
National Center for Research on Earthquake Engineering, Taipei, Taiwan

ABSTRACT: In the past few decades, more attention has been paid to the longevity of infrastructure. The long-term environmental factors such as chloride invasion and carbonation penetration detrimental to concrete make reinforcement corrosion and shorten the service time of bridge structures, giving a gradually decrease of structural performance. Based on our previous study, the relationship between structural performance and service time can be displayed and the time point for maintenance or retrofit when structural performance proceeds below threshold values can be predicted. This paper presents a novel life-cycle based bridge management system (BMS) with extendable structure. In the developed system, a novel technology is known as "Metadata" was adopted to integrate all the bridge inspection records and the evaluation results in the photos on-site. In other words, a single photo capable of storing all the information related to bridge status was created with superimposing the data layers. Therefore, different photos were taken at different time point just become a resume of bridge status. The time history of bridge status considering material deterioration is accordingly able to be recorded and evaluated qualitatively and quantitatively. As a result, the purpose of life-cycle-based bridge management can be fulfilled. This technology benefits data mining of inspection and evaluation, the decision making on necessary maintenance efforts for long-term problem of the deteriorated bridge can be done with ease. Also, to identify the seismic behavior of the bridges shortly after the strike of an earthquake, this system has to possess the capability of rapidly estimating the risk of bridge damages caused by an earthquake. By incorporating the analysis of earthquake attenuation relationships and fragility curves, rapid estimation of seismic risk analysis system was established. A seismic risk assessment system, which can instantly estimate and visually demonstrate the level of damage to bridges due to a specific seismic event and the corresponding economic loss due to the damage of bridges, was developed and also served as a reference for seismic retrofitting program of existing bridges. The achievements attained in this study can be helpful for earthquake mitigation strategy in the future.

1 INTRODUCTION

As the rising number of natural disasters reported worldwide, the government and the public have put more and more attention on the structural safety of infrastructures. The bridges have become the most crucial transportation infrastructure as a result of the high development of the economy in Taiwan, and therefore the structural safety of bridge is one of the primary concern in public issues. Taiwan has a sub-tropical climate, warm and wet environment makes material deterioration with easy and give a significant influence on the service time of bridges. Also, Taiwan is situated in a collision zone between the Philippine Sea and the Eurasian tectonic plates and therefore suffers from earthquakes frequently. Frequent earthquakes have inevitably caused significant damages to the existing bridges. The damages of the bridges due to earthquake not only lead to the loss of many innocent lives but also interfere with the rescue efforts, generating the countless amount of cost to the society and economy.

To achieve disaster mitigation, having an efficient BMS is very important to increase the resilience of the bridges after a disaster. This paper introduces the new development of life-cycle-based BMS in Taiwan. The developed system can deal with the problems of material deterioration, earthquake, and flood and so on. Moreover, benefits bridge authority doing decision-making on bridge maintenance.

According to the previous studies (Sung et al. 2010, 2011), the relationship between structural performance and service time can be displayed and the time point for maintenance or retrofit when structural performance proceeds below threshold values can be predicted. As a result, the time history of bridge status considering material deterioration is accordingly able to be recorded and evaluated qualitatively and

quantitatively. Then the purpose of life-cycle-based bridge management can be fulfilled. It is definite that the correct record of bridge inspection work helps engineers update condition of the bridge structure and would be valuable for structural safety evaluation. In the developed system, "Metadata" was adopted to integrate all the bridge inspection records and the evaluation results in the photos on-site. All the information of bridge status during the different period of life-cycle can be preserved, in other words, the whole resume of bridge status is possible to be established and fulfills life-cycle maintenance. The developed system can improve the efficiency and the quality of bridge inspection work. Therefore the evaluation of bridge safety can be obtained more comfortable and more accurate.

2 DEVELOPED MODULES OF BMS

2.1 *Framework of the system*

In general, a bridge life-cycle can be divided into four stages of plan, design, construction, and maintenance, respectively. Among which, the maintenance stage preserves the longest time of the total structural service time of a bridge. That is to say, doing the maintenance work on infrastructures plays a significant role to make sure the qualified structural safety performance and the satisfied service quality. Focused on the maintenance stage, the framework of the developed BMS includes three main technical parts with cooperated functionalities (Thompson, P. D. & Kerr, B. 1998). The first part is the modularization function that involves network-level, project-level, and element-level according to the different way of management and applications.

The second functional part of the BMS is the information database which stores bridge inspection data. The principle of design of this section is the customization functions. Moreover, the system design frame of this part focuses on Model, View, and Controller, respectively, and thus abbreviated by MVC. The Microsoft ASP.NET MVC design frame is capable of reducing the component coupling between each part of components in the system and raises system capability on extension flexibility. The tools used for the data processing are MySQL Database and CouchDB, which can substantiate the table-column object in the database with flexibility.

The third functional part of BMS is the module that applies expert system algorithms to evaluate and rate the condition of structures. This part accomplishes the design and implementation of the visual interface interacting with specialist knowledge, integration engine of expert algorithms, the analysis core of the Neural-aided expert system, the graphic user interface of expert system operation, and the management of a database for bridge inspection data. The structural evaluation of bridge deteriorations needs a professional judgment. Therefore an expert-like algorithm has been developed in the system. In general, the algorithms embedded in the BMS have to be reviewed and modified according to the back-feed information from field observation and senior engineers' determination. Also, the BMS also focuses on integrating extendable and modifiable modules to be available to the practical use. Figure 1 shows the framework of the developed system, the input layer of which includes inspection record, bridge inventory and the descriptions of the related regulations.

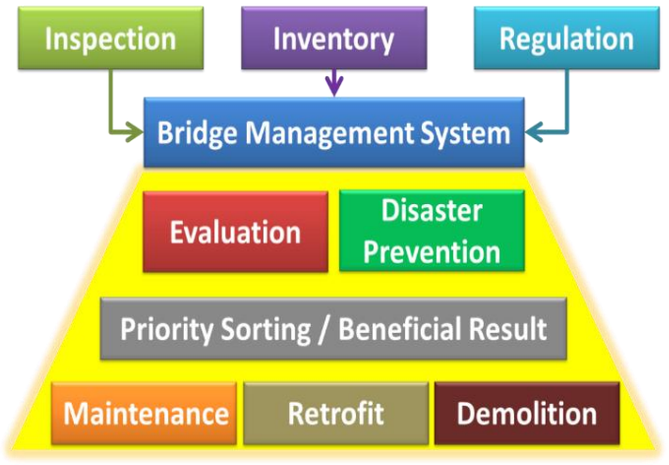


Figure 1. Framework of the developing BMS

In the proposed framework, the evaluation and disaster prevention modules are included as well in the system. The output layer provides bridge condition, priority sorting and the beneficial suggestions to authorities for making the optimal decisions. Figure 2 indicates the service bus which can be flexibly built to connect the other application functional modules.

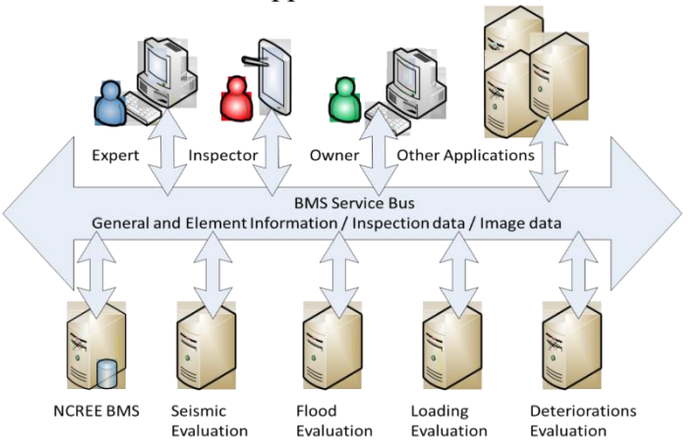


Figure 2. Service bus of the system

2.2 *Inspection module*

A flexible user-defined data frame of the database is proposed and constructed in the system, which allows the bridge engineers to keep the inspection easier and more efficient. An extended module was developed for having objective of simplifying field inspection

work by extracting representative items, building graphics operating interface and using intuitive and visual tools. To keep the raw data with less humanmade deviation, the core of this module aims at collecting the inspection data through the photos or illustrations but no evaluation by the inspectors.

The general information of a bridge includes bridge name, bridge location, date of inspection, design code used, load classification, date built, structural sections, structural length, number of spans, inspection records, and bridge structural descriptions available, as the essential data. They can be obtained either through review of design/construction drawings or the other technical documents and of course, can be investigated by site observation. The bridge components rating information is essential for following evaluation that includes traffic safety features, bridge deck condition, load bearing components, abutments, piers/bents or pile bents, superstructure, substructure, river channel protection, the approach slab and so on. It must be noticed that the purpose of BMS is to manage information about bridges and to assure their long-term serviceability for public use under owner's budgetary constraints. An inspection database is the core part of a BMS, which is built up of records obtained from maintenance activities.

Figure 3 shows the standard procedure of inspection work by using the developed system. First, the experienced inspectors must do the visual inspection and take the photos on site, second, the inspection photos will be upload to BMS database which with code-compatible evaluation module, and the evaluation can be performed by using the evaluation module. Final, the BMS can automatically export the inspection report for authority reviewing. Figure 4 shows the user-friendly visualization inspection system in developed system. The important information of the photos such as the location, the quantity message, crack length, crack width, and inspection date, etc. can be shown and the corresponding evaluation result can be determined automatically by the code-based evaluation module. All the inspectors have to do is to take the photos of damage but don't need to worry about what the bridge status should be evaluated. Just like the human health inspection process, this developed system separated functionality of inspection and evaluation. The advantage of this approach at least includes: (1) professional requirement of the inspector can be reasonably set up, too high-level qualification for senior engineers of design is unnecessarily applied to bridge inspection, (2) the humanmade deviation of evaluation result made by different inspectors is avoidable.

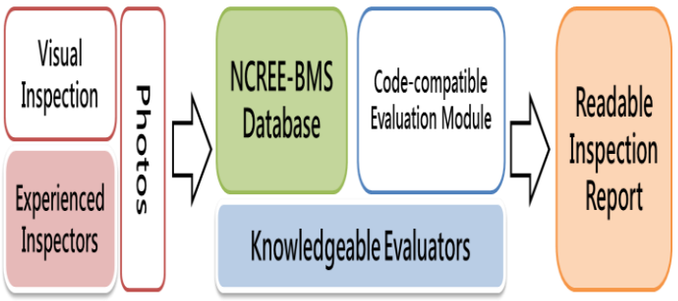


Figure 3. Procedure of inspection in developed BMS

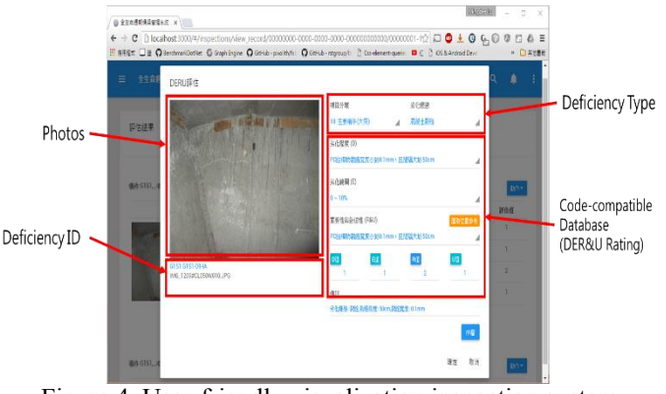


Figure 4. User-friendly visualization inspection system

2.3 *Disaster prevention modules*

In Taiwan, there are more than 25,000 existing bridges. A more significant part of them stride across the river and many bridges are reaching the old-age status. In addition to the material deterioration, earthquake and flood are two major types of disaster resulting in damage or failure to bridge structures. Based on the previous research work (Sung, Y.C. & Su, C.K. 2011), the neutralization (carbonation) and chloride-invasion into concrete usually result in material deterioration of reinforced concrete (RC) bridge and were adopted in the developed system. Figure 5 shows an estimation of possible time for reinforcement corrosion due to chloride-invasion of RC bridges along the coast. The seismic capacity of the deteriorated structure tends to degrade over time. By applying the method proposed, the plastic hinge properties of the neutralized or chlorided RC bridge column at different deterioration stages can be determined, and the decayed seismic capacity curves can be obtained through pushover analysis. As a result, the time-dependent fragility curves concerning some representative damage levels can be established, and the possible seismic loss can be expressed. Consequently, the seismic disaster prevention module can provide the failure probability of the bridge soon after an earthquake.

Furthermore, the BMS also connects the information with Taiwan Typhoon and Flood Research Institute (TTFRI) for scouring warning of the bridge. Figure 6 shows bridge scouring warning functionality in the flood disaster prevention module.

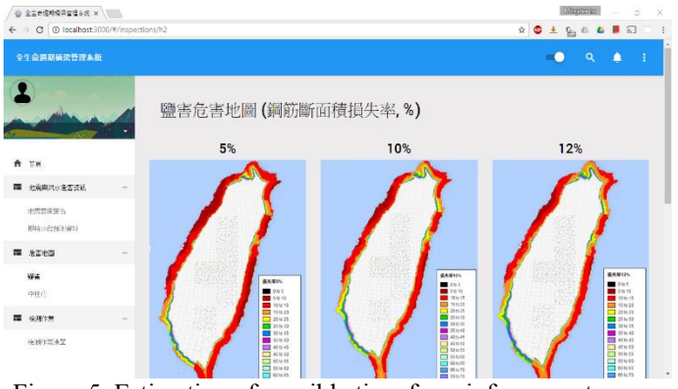


Figure 5. Estimation of possible time for reinforcement corrosion due to chloride-invasion of RC bridges along the coast

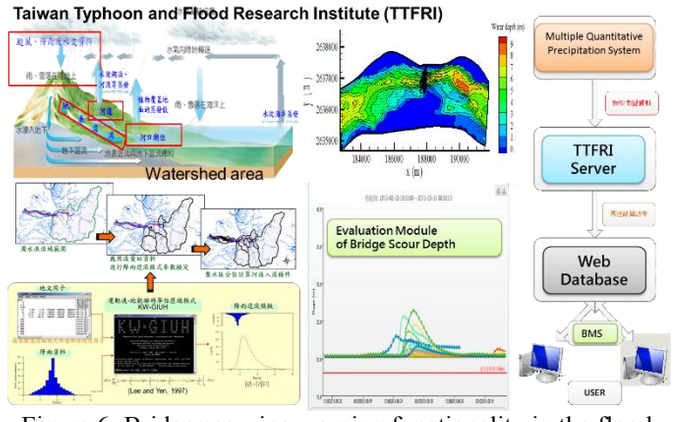


Figure 6. Bridge scouring warning functionality in the flood disaster prevention module

3 SIGNIFICANT FEATURES OF THE SYSTEM

3.1 *Seismic risk assessment module*

In the majority of cases when evaluating structures, fragility curves serve as the best indicator of the safety of a structure. A fragility curve represents the probability of a specific damage level for a particular type of structures under different levels of ground shaking. This information can be part of a disaster relief preparation plan for affected areas and a future reference when facing strong earthquakes to estimate the damages of the bridge as well as the lives and property loss.

As we know that an excellent seismic risk assessment system for the existing bridges should at least consist of four fundamental elements: (1) accurate simulation of earthquake, (2) sufficient database of seismic capacity of the bridges, (3) rapid evaluation of seismic loss and (4) visualized operation system. The first one deals with the nonlinear regressive analysis of attenuation law of peak ground acceleration (PGA). A relationship between PGA, seismic magnitude M and focus distance R is established to do the earthquake simulation. The second one relates to the seismic evaluation of many existing bridges through pushover analysis or time history analysis. From which, various structural damage statuses can be defined, and relevant statistical analysis can be done to obtain the fragility curves for seismic loss estimation. The third one concerns rapid calculation of probabilities with respect to various damage statuses under the situation of a specific earthquake. The cost, as well as time required for seismic repairing or retrofitting of the bridge, could be estimated instantly. The last one associates computer technology of software to exhibit visualization of the operation system. The objective-based technique is implemented to enhance the flexibility of system expanding.

Figure 7 presents the simulated earthquakes alongside the publicized earthquake records from the central weather bureau's (CWB). It shows that the simulated earthquake intensity maps obtained from this study and those released by CWB are quite similar. This result indicates that the nonlinear regression of attenuation law applied is satisfactory.

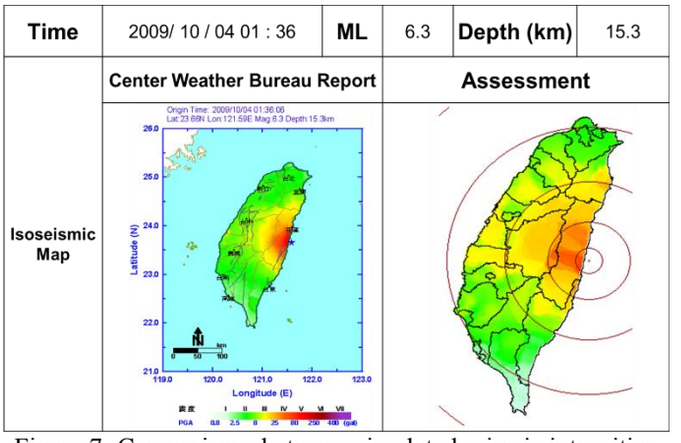


Figure 7. Comparisons between simulated seismic intensities and actual ones announced by CWB.

To establish a rapid seismic risk assessment system, the rapid estimation of expected damage of a structure under a specific earthquake event is crucial. The estimation can be accomplished by using the modified seismic evaluation method proposed (Sung, Y.C. et al. 2009.). However, due to the uncertainty in earthquake ground motion, and randomness of structure and soil properties, the estimation of expected damage is a probabilistic one. Figure 8 shows the estimated probabilities of different damage levels can be obtained immediately after an earthquake occurs as the PGA for each bridge site is known.

The fourth fundamental element of a good seismic risk assessment system for the existing bridges is a visualized operation system. It receives the input and command from the users while providing a window interface to present the results of the input values. The process management package is made up of some software components that includes an interface, window for the main program, data management components and file management components. Figure 9 shows the output the system displayed.

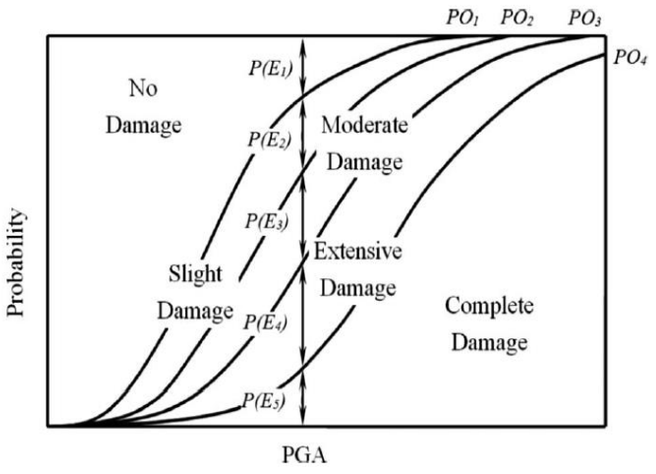


Figure 8. Fragility curves

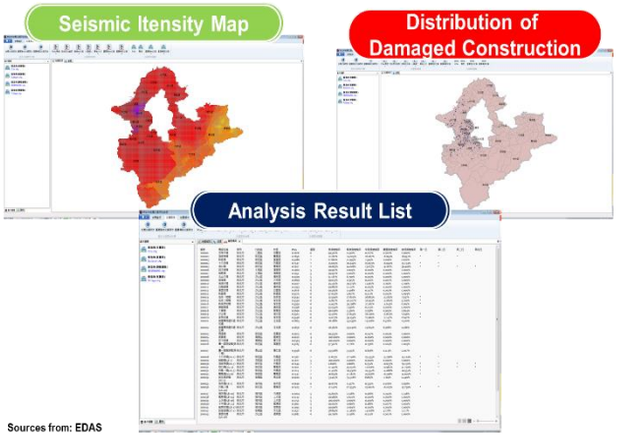


Figure 9. Output result of the seismic risk assessment

3.2 *Metadata technology application*

"Metadata" is a novel information technology which is applied and integrated with bridge inspection record photos on-site in the developing system of this study. The meaning of the terminology "Metadata" is data or information that provides information about other data, which puts the external field and inside office work of bridge inspection projects can be easily integrated with the high efficient division of labor by using such technologies.

Recently, the metadata has been extensively used to describe various data. For data of any type, metadata is the description of that data. To describe a digital photo with metadata often includes the brand of the camera creating this photo, exposure information (e.g., shutter speed), and descriptive keywords that could help one search this photo on a computer or the internet.

Metadata can be written outside or into a digital photo file. This study chose to write useful metadata into photos to facilitate the management of inspection photos whose number could be enormous. While a photo could contain all the required inspection results, all the inspection data we must manage is photos, no others. The management of inspection data becomes simple. Moreover, this choice of writing metadata into photos brings us the following advantages on bridge inspection.

First, users may classify, organize, or evaluate the metadata-embedded photos according to the preliminary inspection results contained in their metadata. In particular, the metadata embedded into a photo can be used to describe different deterioration patterns of a bridge part where the photo is taken. While capable of containing descriptive data, a photo could suffice to offer all inspection results without omission by itself. On the other hand, if metadata is enabled to describe cracks with geometric objects like points or polylines to record the crack distribution, such crack data may be depicted as a GIS (Geographic Information System) layer. Then this layer can be overlaid on or remove from the photo taken on the bridge part where those cracks are found (See Figure 10).

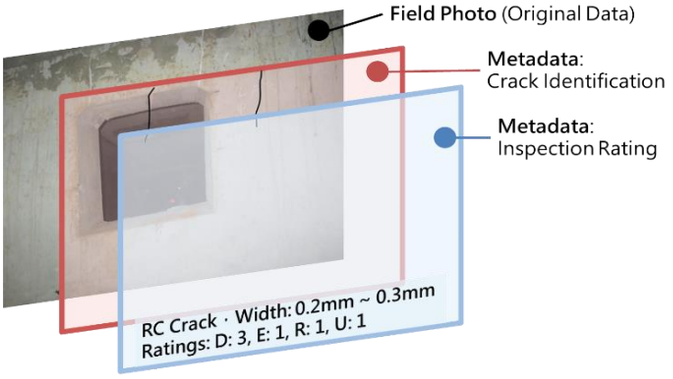


Figure 10. Depict metadata as GIS layers and overlay them on a photo

Operation Tool (OT), External Operation Tool (EOT), and Internal Operation Tool (IOT). The developed BMS offers Cloud Operation Tool (COT), a web application that helps the user upload inspection photos and then edit the metadata of those photos through its web interface. EOT is a mobile application (APP) that helps users write metadata into inspection photos on-site. Then they may upload these photos from their mobile devices to the developed BMS, or move these photos to their computers, then further process these photos using IOT shown in Figure 11.

IOT is a windows application that extends the functionalities of Windows Explorer. Working silently under Windows Explorer, this application identifies the inspection photos containing metadata, interprets and shows their metadata, and offers user interfaces for users to edit the metadata of a photo, upload photos, and even create reports that are supposed to use inspection photos.

Figure 12 shows that in addition to reading the metadata of photos, IOT can make the metadata as a grouping option for users to classify those photos in Windows Explorer. We can see three groups RP7, RP8, and RP12 there. Besides, Windows Explorer identifies each photo containing our metadata by sticking a graphical tag (an arrow-inside cloud) on the lower-left corner of that photo.

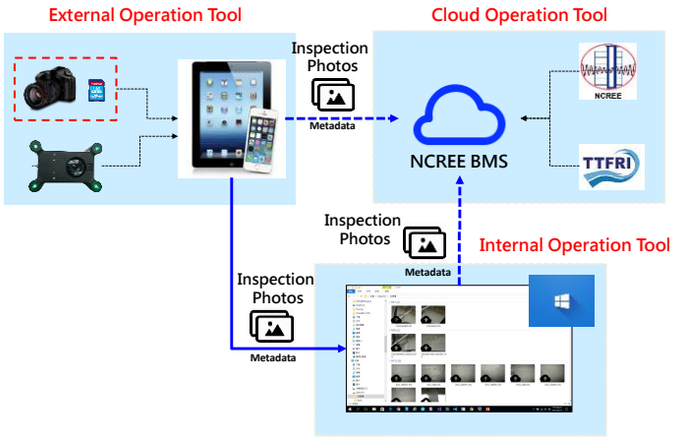


Figure 11. External, internal, and cloud operation tools to write metadata into inspection

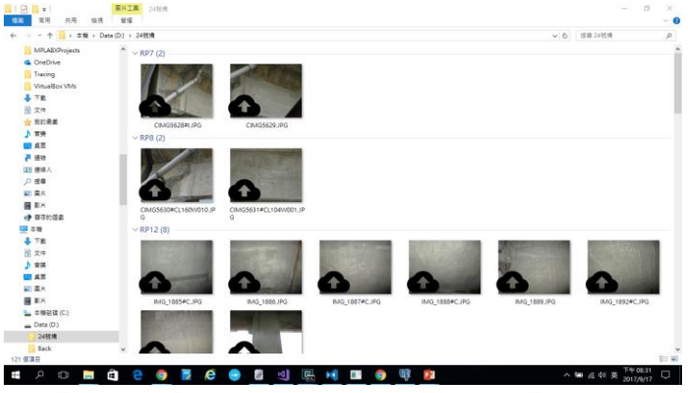


Figure 12. Photos are classified in Windows Explorer according to their metadata

In Figure 13, Windows Explorer shows the inspection results of photos including Ds, Es, Rs, and Us as well as those photos' the bridge names and element IDs. Figure 14 shows that IOT enables users to preview and edit a photo containing our metadata through a dialog that this tool offers in Windows Explorer. Figure 15 shows that we can select photos that containing our metadata of inspection and upload them at a time. It is worth to note that except for the uploading operation, all operations of IOT may be carried out off-line. While the user interface of a desktop application is often considered easier, smoother, and more efficient to operate than that of a web application, enabling users to conduct most of their work off-line makes IOT more effective than COT.

4 CONCLUSION AND REMARKS

In this paper, the developed framework of a life-cycle based bridge management system for bridge inspection and evaluation is introduced. One of the primary purposes of the developed BMS is to enhance the efficiency and the quality of bridge inspection work, to evaluate the capacity of bridge disaster resilience and to improve the exactitude of bridge information with code consistent result. The developed system provides the functionality of evaluating the time-variant structural capacity for bridge management and disaster prevention.

Two significant features of the system including seismic risk assessment and metadata benefit data mining of inspection and evaluation, the decision making on necessary maintenance efforts for seismic loss estimation and long-term problem of the deteriorated bridge. It is excepted that the achievements in this study could be helpful for disaster mitigation strategy in the future.

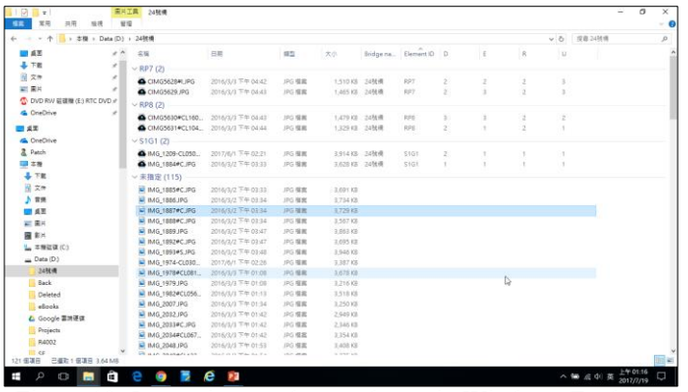


Figure 13. Inspection results are shown in Windows Explorer

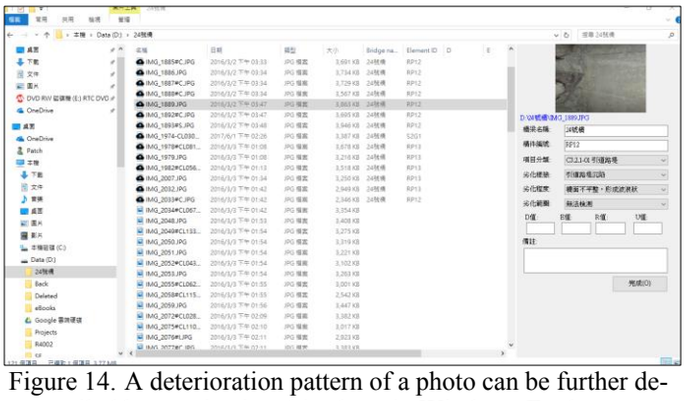


Figure 14. A deterioration pattern of a photo can be further detailed by previewing this photo in Windows Explorer

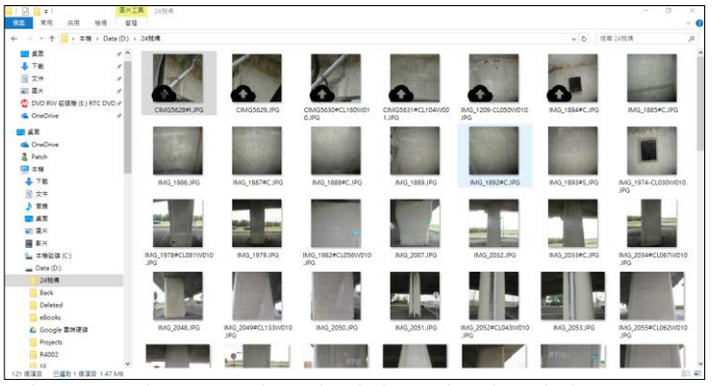


Figure 15. Photos may be uploaded at a time in Windows Explorer

5 REFERENCES

Sung, Y.C., Liao, W.I., Yen, W. Phillip, "Performance-Based Concept on Seismic Evaluation of The Existing Bridges," *Earthquake Engineering and Engineering Vibration*, Vol. 8, No. 1, 2009, 127-135

Sung, Y.C., Huang, C.H., Liu, K.Y., Wang, C.H., Su, C.K., and Chang, K.C., "Life-Cycle Evaluation on Deteriorated Structural Performance of Neutralized Reinforced Concrete Bridges," *Structure and Infrastructure Engineering,* Vol. 6, No. 6, 2010, 741-751

Sung, Y.C. & Su, C.K. 2011. Time-dependent seismic fragility curves on optimal retrofitting of neutralised reinforced concrete bridges. *Structure and Infrastructure Engineering,* Vol. 7, No. 10, October 2011, 797–805.

Sung, Y.C., Hsu, C.C., Hung, H.H. & Chung, Y.J. 2011. Seismic risk assessment system of existing bridges in Taiwan. *Structure and Infrastructure Engineering,* Vol. 9, No. 9, 2013, 903-917

Thompson, P. D. & Kerr, B. 1998. A New Bridge Management System for Ontario*, ITX Stanley Ltd.,* Canada.

MS09: Vibration-based structural health monitoring of bridges: Research and applications

Organizers: M.P. Limongelli, J.R. Casas & A. Cunha

Maintenance, Safety, Risk, Management and Life-Cycle Performance of Bridges – Powers, Frangopol, Al-Mahaidi & Caprani (Eds)
© 2018 Taylor & Francis Group, London, ISBN 978-1-138-73045-8

Monitoring Footbridges Using Wireless Mesh Networks

M. Domaneschi, C. Apostoliti & G.P. Cimellaro
Department of Structural, Geotechnical & Building Engineering, Politecnico di Torino, ITALY

B. Glisic & K. Kliewer
Department of Civil and Environmental Engineering, Princeton University, Princeton, NJ USA

ABSTRACT: This work deals with the identification of modal frequencies for an existing footbridge through an *output only* technique. The structure has a continuous curved girder and belongs to a frequently used structural system all around the world in urbanized areas. Consequently, the development of a suitable and effective monitoring is of paramount importance for guaranteeing continuous serviceability and safety. Long-gauge fiber optic strain sensors are installed along entire structure, including locations where local damages, or deteriorations, are expected. Besides, a wireless network monitoring system is under development to be applied in parallel to fiber optic one for a comprehensive assessment of the stiffer component (the main-span) of the bridge where only minor strains are registered by the fiber optic sensors.

1 INTRODUCTION

Structural condition and safety can be attained through structural health monitoring (SHM) activities. Frequently, they consist in the analysis of the structural response that consists in recorded variables (e.g. time histories) processed by numerical methods. SHM is declined in four main phases, from the damage assessment to the prediction of the structural remaining life. The intermediate phases are the localization and the quantification of damage.

SHM can be also associated to resilience for bridge structures to prepare for and adapt to incremental changes or damages. In particular, the time required to recover after a damaging event the original performance is the critical aspect to be investigated. Therefore, the capacity to assess damage presence, localization and intensity has occurred is obviously essential for developing resilient structures and communities.

A recently proposed technique, termed as *output-only*, employs the use of structural response variables for the assessment of the structural conditions. It means that the knowledge of the input forces in terms of intensity, distribution and time histories is not required. This inherent simplification is particularly attracting owing to the wide range of applicability. E.g. when operating without interrupting transportation networks is needed (Domaneschi et al. 2013, 2015, 2016, 2017; Sigurdardottir & Glišić 2015).

Despite the number of SHM methodologies and implementations, as the extensive literature in the field demonstrates, engineers and contractors rarely employ SHM on the structures they are designing and building. Indeed, also the most effective SHM methodologies are usually restricted to specific conditions (type of structure, loading conditions, etc). Such limitations could be overcome integrating different SHM schemes in a single solution so as to cover wider conditions. Furthermore, education in SHM could be developed in a wider sense including it within the most common university courses.

This paper deals with the assessment of the modal characteristics of the Streicker Bridge at the Princeton University Campus through an output-only method. The response data in terms of longitudinal strains and curvature are used. The monitoring system consists in a fiber optic sensor network embedded in the footbridge concrete elements. It is strain-monitoring oriented, and its configuration cannot be changed. The results are compared to previous outcomes from literature and restrictions in the performance of fiber optic monitoring systems are confirmed on the mid-span of the footbridge. It is justified by the high stiffness that characterizes the central element of the structure, developing strains of minor intensity.

To overcome such limits a network monitoring system is proposed. It consists in a number of wireless sensors that can perform within a network, by bridging the signals from one sensor to the next one, or being connected to a single wireless router. The proposed network system is dynamic-monitoring oriented, and it has a flexible application on different scenarios and geometrical arrangements on the structure.

The dynamic wireless sensors network and the embedded fiber optic system are complementary in nature and combined they can provide a wide range of information.

2 THE STRUCTURE

The Streicker footbridge was completed in 2010 at the Princeton University Campus overpassing Washington Road (Figure 1). It is 104 m long and consists in a central main-span supported by a steel arch and four lateral approaching legs. The deck is a post-tensioned high-performance concrete girder. Steel columns with "Y" shape support the lateral legs. More details on the structure can be found in (Sigurdardottir & Glišić 2015).

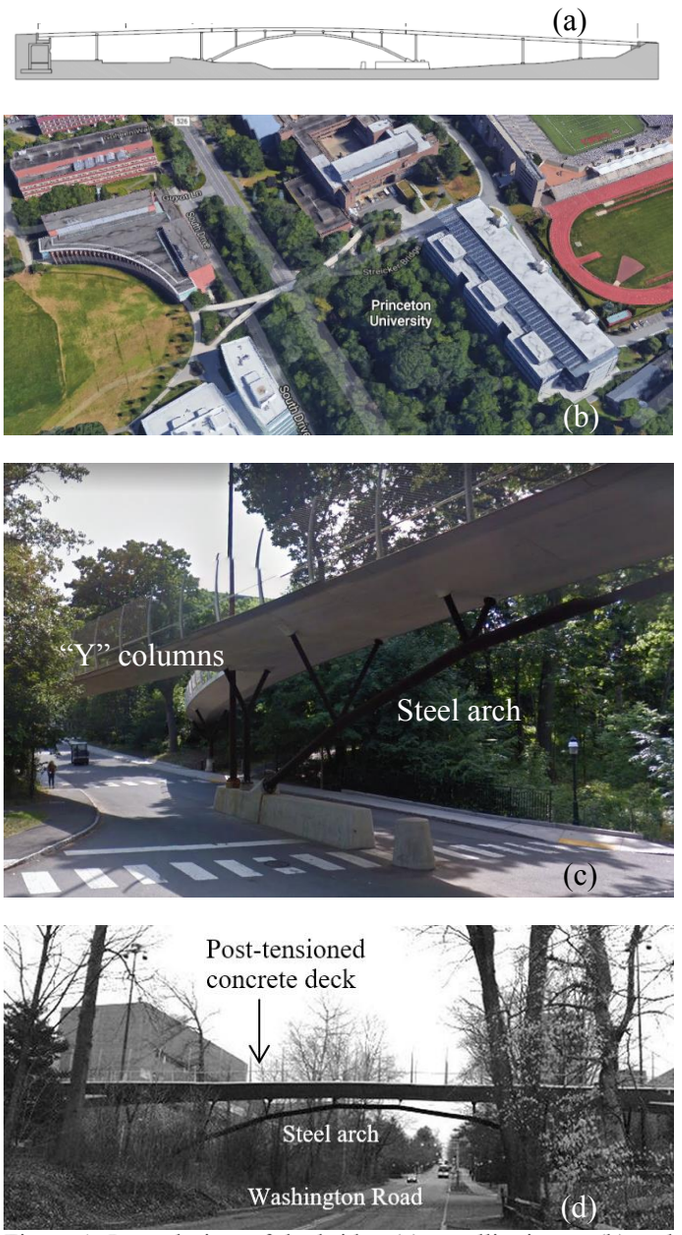


Figure 1. Lateral view of the bridge (a), satellite image (b) and detail of the supporting system (cd).

The four legs connect the bridge to the lateral bearings on the ground and the whole system results a slender varying cross section main girder. The original shape in the horizontal plane provides horizontal stability to the footbridge despite the intrinsic slenderness of the steel supporting columns. Vertical stability is provided also by the arch (Figure 1) in the central main-span and by the supporting columns under the legs. Cross section width increases from the midpoint of the main-span to the connections with the legs and then remains constant up to the ground bearings. The max deck depth is 0.6 m while the cross section diameter of the arch is 0.32 m.

3 THE STRAIN-MONITORING SYSTEM

Several SHM activities as detection of local damages and assessment of the dynamic characteristics of structures can be effectively performed by the use of long-gauge strain sensors. Among the others, fiber-optic sensors show a very high sensitivity and extend the monitored frequency range. Moreover, they have the advantage to allow implementations in aggressive environments where they have been proved unaffected by external perturbations (corrosion, electromagnetic interference, etc.).

The Streicker Bridge has been equipped with fiber optic sensors with the double aim of providing the structure of an effective monitoring system and also of profiting the University of an on-site laboratory for research and education on SHM. Both the purposes reflect the innovative visions of intelligent infrastructure and of dynamic educational facility.

Since the footbridge shows a fairly symmetric geometry, half of the main-span and the longest South-East leg only are equipped with the fiber optic sensors.

During the bridge construction, the sensors were embedded in the concrete deck using two different technologies. The first one is based on discrete fiber Bragg-grating (FBG) long-gauge strain and temperature sensors and the second one on distributed sensing employing Brillouin optical time domain analysis (BOTDA) for integrity monitoring. In the dynamic assessment of the present study only the first one is considered.

Discrete strain sensors can be classified as short- and long-gauge sensors with a length that spans e.g. from 0.01-0.1 m to 0.25–10 m respectively. The choice depends mainly by the material where they are embedded. For homogenous materials short ones can be suitable, instead for inhomogeneous materials long-gauge sensors give more benefits. Indeed, in the last case, long-gauge sensors allows to overcome local defects that introduce discontinuities in the mechanical material properties and consequently in the provided information concerning the local strain value.

The longitudinal strain in the bridge girder is the monitored parameter, while the derived one is the curvature (Domaneschi et al. 2017). This last is derived through parallel fiber optic sensors, one at the top and the other one at the bottom of the concrete deck cross section. Longitudinal strains are recorded

continuously with 250 Hz sampling frequency. The expected error in frequency is ± 0.06 Hz. In Sigurdardottir & Glišić (2015) additional details can be found.

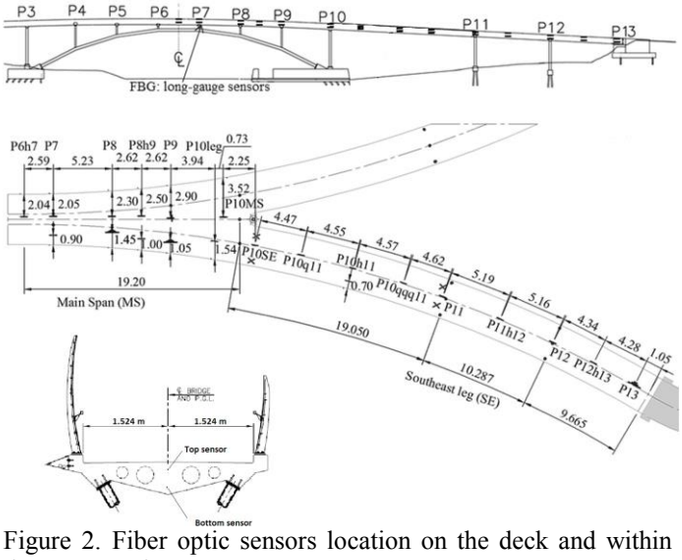


Figure 2. Fiber optic sensors location on the deck and within the cross section.

Figure 2 gives some details on the discrete sensors distribution on the bridge deck. Different topologies of the long-gauge FBG sensors are installed. The parallel one is only considered in this work and it consists of two FBG sensors parallel to the longitudinal axis of the deck aligned on the vertical symmetry axis. One sensor at the top and one at the bottom of the cross section. Parallel sensors capture axial strains in the cross section due to the internal normal force and bending moment. Bending moment in particular generates the girder curvature in the vertical plane. No significant shear or torsion forces are expected. Every long-gauge FBG sensor is temperature compensated (Sigurdardottir & Glišić 2015).

Bending moment M can be computed from curvature χ trough the strain data (ε_{top} , ε_{bottom}) and the structural characteristics (E, I respectively Young and inertia moduli).

$$\chi = (\varepsilon_{bottom} - \varepsilon_{top})/h \quad (1)$$

$$M = \chi EI \quad (2)$$

with h the vertical distance between the parallel sensors.

The monitoring system is distributed on the footbridge main-span on seven segments between columns P3–P10 (see Figure 2). Parallel sensors are at columns P7, P8, P9, and P10 and at two mid-spans between P6 and P7 (P6h7) and P8 and P9 4(P8h9). The South-East leg (three spans) is fixed to the main-span at one end and simply supported on the ground at the other end. The gauge length for the parallel sensors is fixed to 0.60 m.

4 LITERATURE REVIEW ON THE FOOTBRIDGE

The footbridge has been extensively tested in several experimental campaigns. Furthermore finite element (FE) simulations have been also performed with simple plane beam models. Therefore, literature data are available for comparison. In particular, the natural frequencies of the structure resulting from the experimental analyses are 3.11 Hz and 3.72 Hz. On the other hand, the natural frequencies evaluated using the FEM model were equal to 3.21 Hz and 3.77 Hz (Sigurdardottir & Glišić 2015). Vibration monitoring using a wireless MEMS accelerometer board is also reported in literature (Sabato 2015) and the modal frequencies are consistent with previous researches (3.08 Hz and 3.75 Hz). Records from 2010 tests – main-span.

The existing results from literature have been collected by employing specifically designed solicitation tests and quasi-static tests with heavy vehicles, group of pedestrians walking at specific frequencies or running peoples.

5 RESULTS

Two set of data are currently available for analysis, they were collected in 2010 and 2014. For both recorded sets of signals the input is unknown. The strains time histories from the parallel sensors are computed for obtaining the dynamic curvature in Equation (1) and the modal properties of the footbridge. It has been verified that curvature instead of strain vectors allows to halve the number of vectors to process without losing information (Domaneschi et al, 2017).

Collected curvature data have been processed in the frequency domain by computing power spectral density (PSD) through the *periodogram* function. The PSD of a stationary random process is, by definition, a real symmetric function mathematically related to the autocorrelation sequence by the discrete-time Fourier transform. The *periodogram* is an estimate of the PSD of a wide-sense stationary (weakly-stationary) random process, such as a finite-length segments of a signal.

5.1 *2010 tests – main-span*

All 2010 tests are performed on the main-span that resulted very stiff. So, a significantly low strain response from the embedded sensors results. Figure 3 reports a sample of records from sensors P6h7, P7 and P8. Perturbation or characteristic frequency contents cannot be identified.

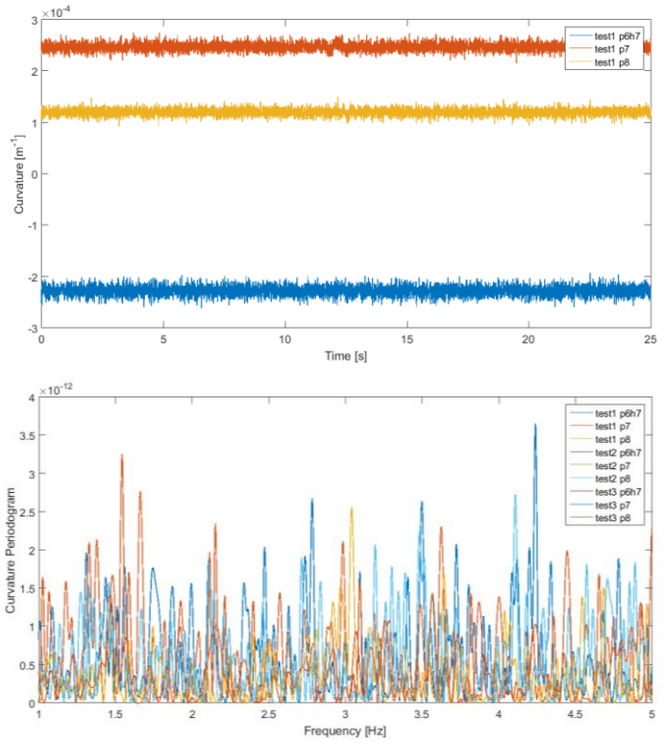


Figure 3. Sample of records (termed as set08 in the database, test 1-3) from sensors P6h7, P7 and P8.

5.2 *2014 tests – South-East leg*

Tests from 2014 are performed for extracting the legs characteristics. Thanks to the symmetry of the footbridge, the South-East leg of the bridge only is evaluated. The loading conditions are unknown but consist, as for 2010 tests, in pedestrians (groups of Campus students) that are walking and running randomly on the bridge at unknown frequencies.

Some additional explanations for explaining the acronyms for different sensors are the following ones: "P"=pier, Numbers=location of piers, "h"=halfway between sensors. So, P6h7 would stand for half way between pier 6 and pier 7, P10qqq11 for the 3rd quarter span (3/4th span) between pier 10 and pier 11, P10q11 for the 1st quarter span between pier 10 and pier 11. While, P7 means the sensors are located directly at pier 7.

Figure 4 depicts the processed results from the set termed as *DynamicPeaks1* in the database in both the time and the frequency domain. Some issues with the sensor system at P7 and P6h7 occur and data for those sensors are not available.

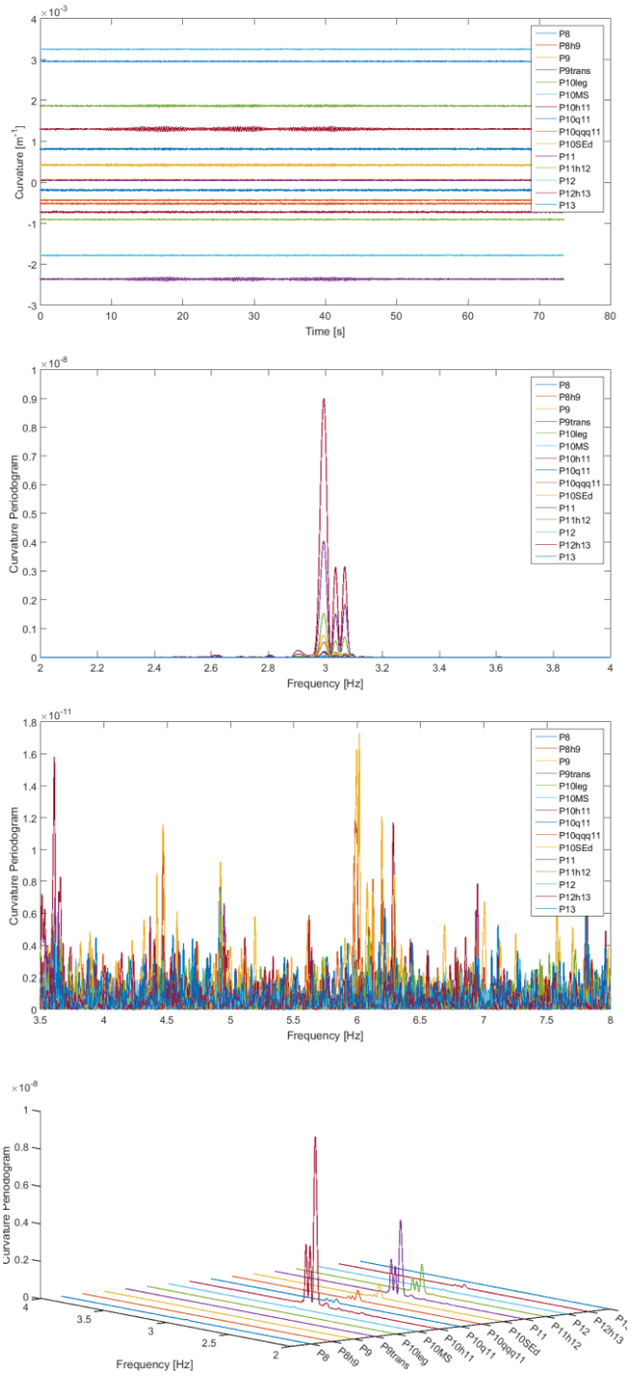


Figure 4. Processed results from the set termed as *DynamicPeaks1* in the database.

Figures from 5 to 10 reports the results in the frequency domain only for all the remaining data sets from 2014 tests. Figure 6 depicts also an overview of the time history records for *DynamicPeaks1* data set. The sensors between P10-P12 are characterized by the highest intensity responses.

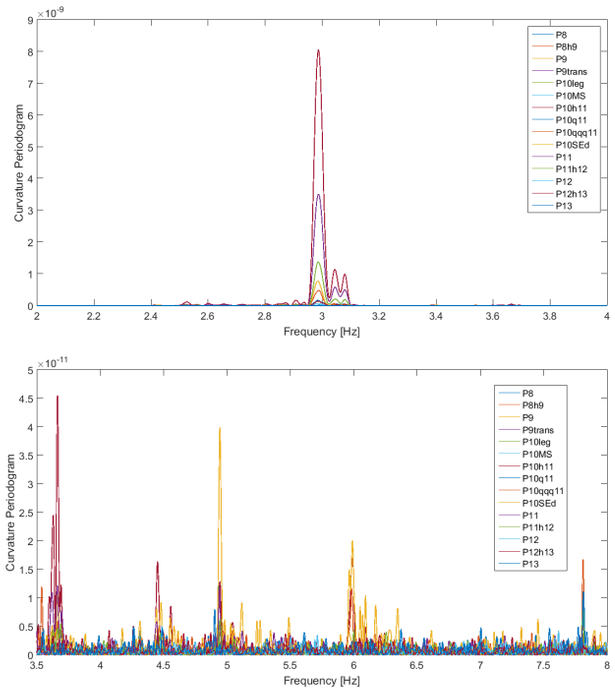


Figure 5. Processed results from the set termed as *DynamicPeaks2* in the database.

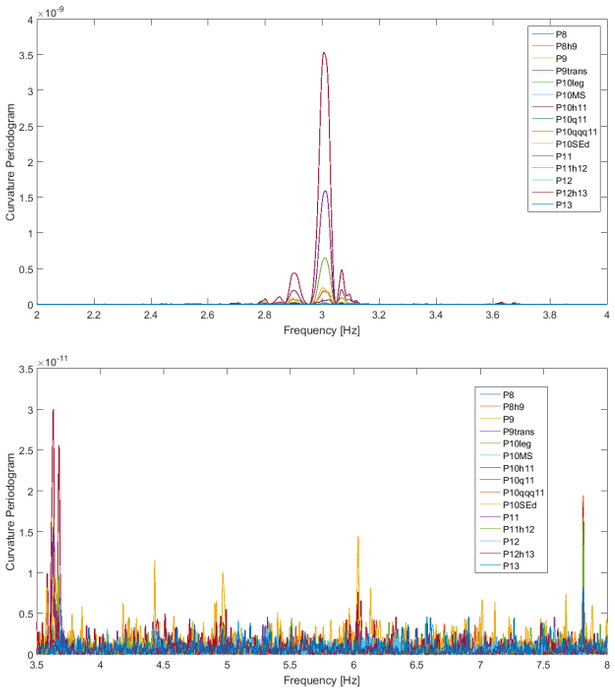


Figure 6. Processed results from the set termed as *DynamicPeaks3* in the database.

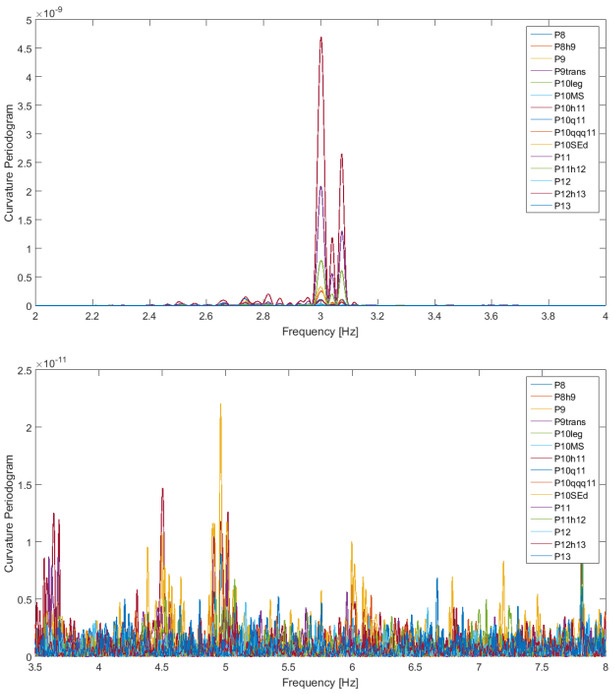


Figure 7. Processed results from the set termed as *DynamicPeaks4* in the database.

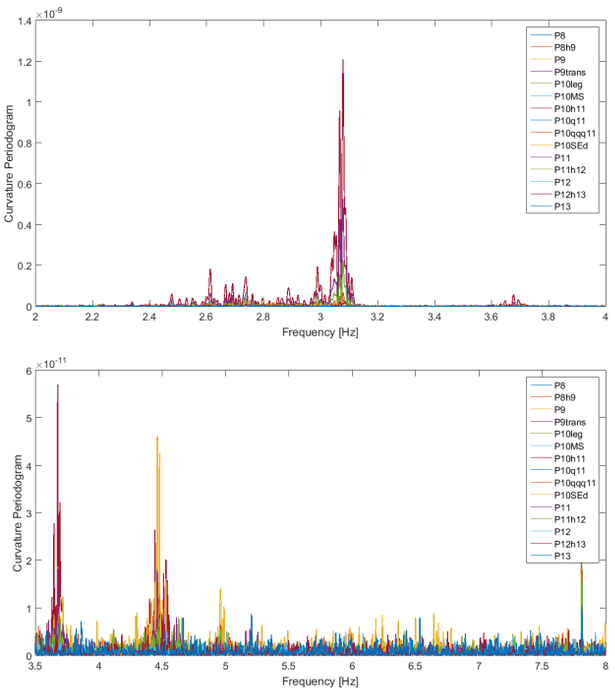


Figure 8. Processed results from the set termed as *RunningPeaks* in the database.

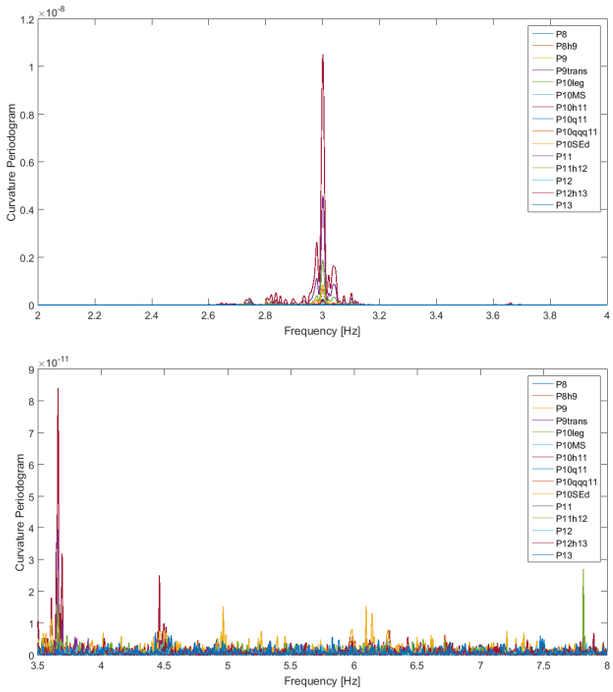
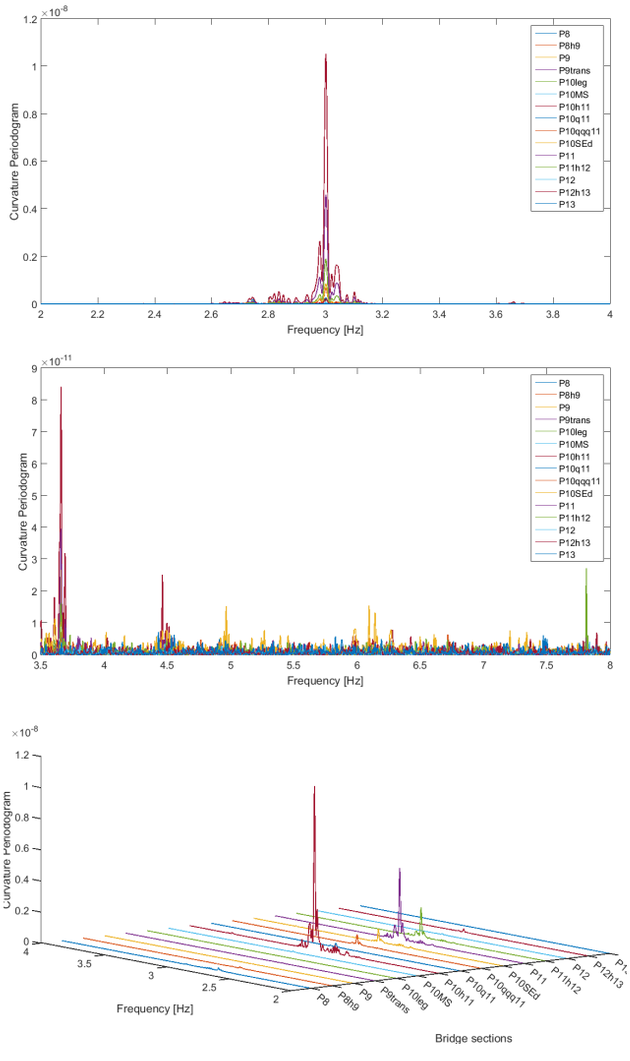


Figure 9. Processed results from the set termed as *DynamicPeaks41* in the database.



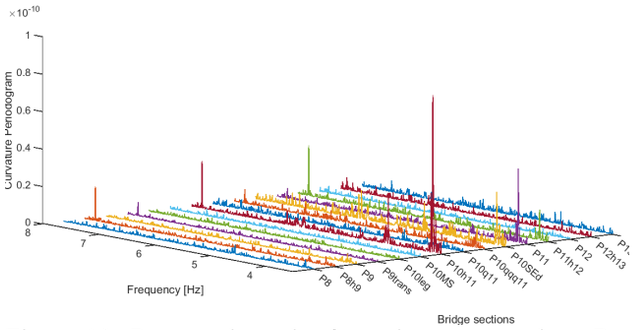


Figure 10. Processed results from the set termed as *DynamicPeaks42* in the database.

Table 1. Natural frequencies from 2014 tests (*DP=DynamicPeaks*, *RP=RunningPeaks*).

Signal	f_1[Hz]	f_2[Hz]	f_3[Hz]	f_4[Hz]	f_5[Hz]	f_6[Hz]
DP1	2.94	3.61	4.47	4.92	6.01	7.81
DP2	2.98	3.66	4.45	4.94	5.99	7.81
DP3	3.00	3.63	4.43	4.96	6.03	7.81
DP4	3.00	3.64	4.50	4.96	5.99	7.81
DP41	3.00	3.66	4.46	4.96	6.09	7.80
DP42	2.99	3.68	4.42	4.94	-	7.81
RP	3.08	3.67	4.46	4.96	-	7.81

From these results, the first amplification peak in the frequency domain is determined to be approximately 3 Hz for all of the experimental tests. This is a lower value with respect to those from literature in Table 1. Also, the second peak has lower values (approximately 3.6 Hz). The available results in the range [3.5 Hz, 8 Hz] highlight a third peak around 4.4 Hz, a fourth at 4.9, a fifth one at 6 Hz and last one at 7.8 Hz. Table 1 summarizes the results of the analyses from 2014 tests on the South-East leg of the footbridge for each recorded signal.

Owing to the location and topology of the embedded sensors, the recognized natural frequencies are reasonably associated to vertical flexural natural modes. Furthermore, comparable highlighted intensities in all data sets and the redundancy in the frequency values allow considering these outcomes accurate with satisfactory confidence.

The damping ratio of the first mode associated to 3 Hz natural frequency can be estimated by the applying the logarithmic decay formula at the sensor P10h11 and it is evaluated as 0.57%. This value, not reported by other research works in literature on the same footbridge, is compatible with others of similar slender structures (Shahabpoor et al., 2017; Van Nimmen et al, 2017).

6 THE PROPOSED DYNAMIC-MONITORING SYSTEM

A wireless monitoring system has been developed in parallel to the existing fiber optic elements to overcome the difficulties of the modal parameters identification on the main-span of the footbridge. Indeed,

the embedded strain sensors have registered only minor strains. The proposed solution comprises a wireless sensors network (WSN) for collecting inertial measurements. In detail, the network consists of 14 units, all synchronized together. Each unit is equipped with a three-axis accelerometer, a three-axis gyroscope, a magnetometer and a temperature sensor. The characteristics of each sensor in the sensing unit are detailed as follow:

- Ultralow noise density accelerometer ([20μg/√Hz]), range ±2/4/8g, resolution ≈4μg, 200 μA in measurement mode, drift 0.15 mg/°C.
- Low noise density gyroscope ([0.01deg/s/√Hz]), sensitivity scale factor 131 LSB/deg/s, full scale range 250 deg/s.
- The temperature sensor, resolution 0.25°, overall operating range [-40°,+125°], ultra-low power consumption 125nA@1Hz sample rate.
- Compass, sensitivity scale factor 0.6μT/LSB, full scale range ±4800μT.

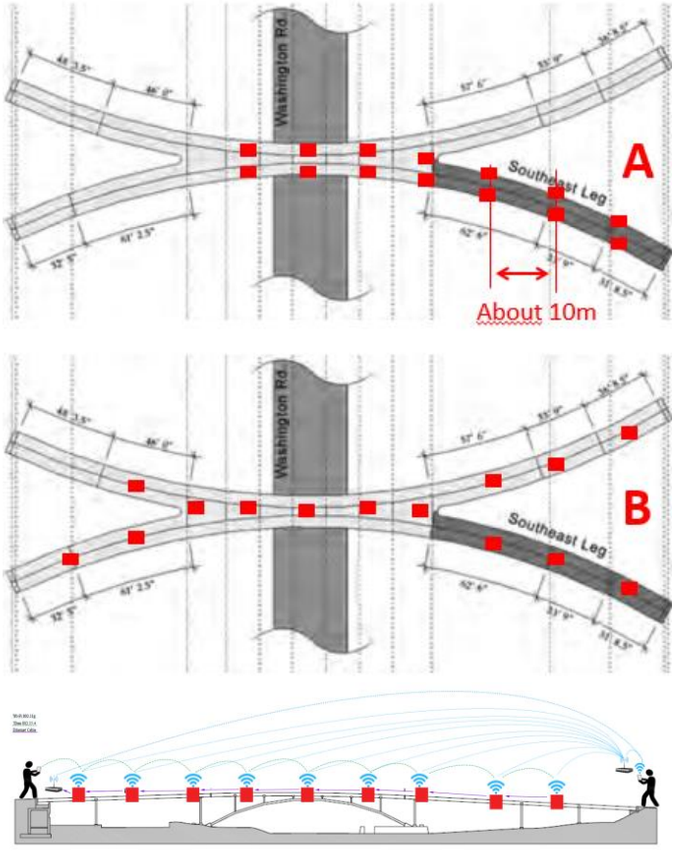


Figure 11. Proposed units distribution on the Streicker Bridge at the Princeton University Campus and the sensor network in different configurations.

The data are processed in real time through a custom architecture on an FPGA (Field Programmable Gate Array) and saved locally in a memory. Furthermore, they can be sent to the main control unit using the on-board Fiber Optics transceiver (up to 200km), over the air using Wi-Fi (IEEE802.11g) or ZigBee (IEEE802.15.4) standard.

The proposed WSN sets a new benchmark for inertial sensor performance with a power consumption for each unity of about 400μA, while the accelerometer noise performance is 11% better, gyro noise performance is 3% better and compass full scale range is over 4% better than competitive sensors.

The 14 units network can be arranged in different configurations on the bridge for confirming the outcomes from the fiber optic solution on the South-East leg and for collecting new information on the stiffer central span. In particular, Figure 11 reports two proposed units' distribution on the deck (A and B) and the WSN communication scheme. The first (A) evaluates the torsional modal components of the main-span and South-East leg through both the gyroscope records and two opposite vertical accelerations on the cross section. The evaluation of the complete structure is then performed through the second distribution (B), where the entire footbridge is covered by the WSN.

7 CONCLUSIONS

In this work, the modal characteristics of an existing footbridge on the Princeton University Campus in US are investigated. The investigation uses measurements collected by long-gauge fiber optic strain sensors embedded along the entire structure. Unknown pedestrian loading represents the external excitation. Therefore, the research can be ascribed within the *output-only* monitoring procedures.

The analysis firstly consider the time histories and the power spectral density of the distributed long-gauge dynamic curvature. For the South-East leg the dynamic characteristics are satisfactorily extracted and the damping ratio associated to the first identified mode is also computed. Comparison with literature results confirms the outcomes, even if slightly lower frequency values were noted. On the main-span, due to its high stiffness, the fiber optic sensors register only minor strains and characteristic modal properties cannot be identified.

In order to overcome such limitations, a wireless sensors network is proposed to integrate the embedded fiber optic system to provide a wide range of information.

The present investigation represents a first step toward the integration of the existing fiber optic system with a new wireless sensor network.

8 ACKNOWLEDGEMENTS

This material is based upon work supported by NSF GRFP Grant No. 1148900, NSF CMMI-1362723, and USDOT-RITA DTRT12-G-UTC16. Any opinions, findings, and conclusions or recommendations expressed herein are those of the authors and do not necessarily reflect the views of the funding agencies. Many thanks to HNTB, SMARTEC, Micron Optics,

and faculty, staff, and students of Princeton University.

The research leading to these results has also received funding from the European Research Council under the Grant Agreement n° ERC_IDEAL RESCUE_637842 of the project IDEAL RESCUE-Integrated Design and Control of Sustainable Communities during Emergencies and under the Grant Agreement n° ERC-PoC-2016_727261 of the Project IDEAL SENSOR-Integrated Smart Device for Emergency Management.

9 REFERENCES

Domaneschi, M., Limongelli, M.P. & Martinelli L. 2013. Vibration Based Damage Localization Using MEMS on a Suspension Bridge Model, *Smart Structures and Systems*, 12(6): 679-694.

Domaneschi, M., Limongelli, M.P. & Martinelli L. 2015. Damage detection and localization on a benchmark cable-stayed bridge, *Earthquakes and Structures*, 8(5): 1113-1126.

Domaneschi, M., Limongelli, M.P. & Martinelli L. 2016. Wind-Driven Damage Localization on a Suspension Bridge, *The Baltic Journal of Road and Bridge Engineering*, XI(1): 11-21.

Domaneschi, M., Sigurdardottir, D. & Glišić, B. 2017. Damage detection on output-only monitoring of dynamic curvature in composite decks, *Structural Monitoring and Maintenance*, 4(1): 1-15

Glišić, B. 2011. Influence of gauge length to accuracy of long-gauge sensors employed in monitoring of prismatic beams, *Measurement Science and Technology*, 22(3), art. no. 035206 (13pp).

Sabato, A. 2015. Pedestrian bridge vibration monitoring using a wireless MEMS accelerometer board, *IEEE 19th International Conference on Computer Supported Cooperative Work in Design (CSCWD)*, Calabria I.

Sigurdardottir, D. & Glišić, B. 2015. On-site validation of fiber-optic methods for structural health monitoring: Streicker Bridge, *J Civil Struct Health Monit*, 5: 529–549.

Shahabpoor, E., Pavic, A., Racic V. &, Zivanovic, S. 2017. Effect of group walking traffic on dynamic properties of pedestrian structures, *Journal of Sound and Vibration*, 387: 207–225.

Van Nimmen, K., Lombaert, G., De Roeck, G. & Van den Broeck, P. 2017. The impact of vertical human-structure interaction on the response of footbridges to pedestrian excitation, *Journal of Sound and Vibration*, 402: 104–121.

Maintenance, Safety, Risk, Management and Life-Cycle Performance of Bridges – Powers, Frangopol, Al-Mahaidi & Caprani (Eds)
© 2018 Taylor & Francis Group, London, ISBN 978-1-138-73045-8

Effectiveness damage characterization for different sensor settings: full scale case

J. Grandón
Lind Engineering, Chile

F. Cerda
Universidad de Concepción, Chile

ABSTRACT: Structural health monitoring aims at reducing and control risks associated to different damages levels in diverse structures, through the implementation of sensors and a signal processing and analysis. This work develops a methodology based on the modal analysis for estimate the number of sensors necessary to characterize a determined structural damage level in a specific bridge.

1 INTRODUCTION

1.1 *Work description*

This work uses an acceleration register from a forced vibration test of the Z 24 bridge, located in Switzerland, where different damage scenario were inflicted by progressive settlement levels in one pier of the bridge. Then, modal parameters are extracted by means of the frequency domain decomposition algorithm (FDD) and is applied to different damage identification and localization methodologies. Specifically, two methods for damage identification (modal frequencies and modal assurance criteria) and three for damage localization (Yuen function, modal shape curvature and coordinate modal assurance criteria). Finally, through a statistic criteria (Fisher information matrix optimization) different optimized sensor settings are obtained for this bridge, then an evaluation of the damage characterization effectiveness level is done by a function through a regression from an error function and the number of sensors to use is determined.

2 STUDY CASE AND FIELD EXPERIMENT

2.1 *Z-24 Bridge Switzerland*

The Z24 is a prestressed concrete bridge, with three sections, two lanes and a distance between abutments of 63.4 m. It is located in Canton Bern, Switzerland, and connects the towns of Koppigen and Utzenstorf.

In the structure, 17 accelerometers were arranged simultaneously (15 in the slab and two in the intervened stock) plus three used as reference points or PR that are fixed at all times.

The 17 accelerometers were grouped on the axes HH-1, HH-2, HH-3, in nine zones along the bridge called setups. Each setup has five accelerometers per axis and two more located in the strain.

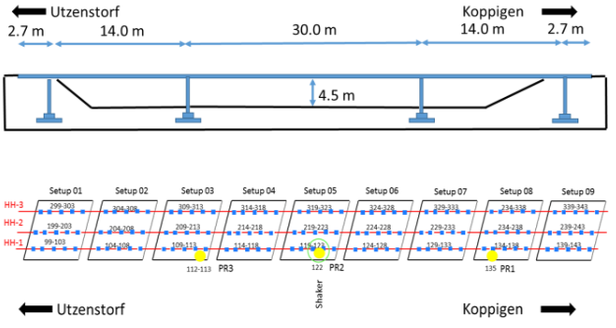


Figure 1. Z-24 Bridge

2.2 *Field test: forced vibration test*

The study case considered to generate different settlement conditions in the bridge on a real scale. Through an hydraulic system, damage scenarios were generated associated with different levels of progressive settlement (Kramer, Smet and de Roeck 2001).

The settlement was simulated by cutting the pier of the Koppigen area (axis 3). The dimensions of the three cuts are 0.4 m high, 1.1 m wide and 0.3 m thick.

The forced vibration test (FVT) used two sources of dynamic excitation capable of generating vibrations in different frequency bands. A large one located in the center, specifically at the reference point 2 (PR2) and a small one located at reference point 1 (PR1) to induce an excitation in the bridge in a cer-

tain frequency band, the excitation of both shakers ranged from 3 to 30 Hz.

The data collection at a rate of 100 Hz for 35 channels, was performed eight times (one for each damage condition) obtaining 8192 samples (Kramer, Smet and de Roeck 2001).

Table 1. Damage scenarios

Case	Date	Scenario
1	4/8/1998	First reference measurement
2	9/8/1998	Second reference measurement
3	10/8/1998	Settlement of 20 mm
4	12/8/1998	40 mm settlement
5	17/8/1998	80 mm settlement
6	18/8/1998	95 mm settlement
7	19/8/1998	Pier Inclination
8	20/8/1998	Third reference measure

3 THEORETICAL FRAMEWORK AND PROCEDURE

3.1 *Obtaining mode shapes: FDD*

The frequency domain decomposition (FDD) is a technique that allows modal parameters to be obtained without having knowledge of the input that affects the system. This technique is relatively similar to the classic approach where the modal parameters are estimated by simple peak picking. However, by decomposing the matrix of the spectral density function, the response spectrum can be separated into a set of systems of a degree of freedom, each corresponding to an individual mode.

With this decomposition technique, nearby modes can be identified with high accuracy even in the case of strong noise that contaminates the signal, and also the harmonic components of the response signal can be identified (Brinker et al., 2000).

3.2 *Damage identification: MAC*

The modal assurance criteria (MAC) is used as a measure to determine the level of correlation between the modes coming from the tests of a space without damage with a damaged space (Allemang y Brown, 1982).

3.3 *Damage localization: COMAC*

The coordinate modal assurance criteria (COMAC) is similar to the modal assurance criteria. The main difference is that this is a coordinate-by-coordinate comparison, so it delivers a vector of values that are associated to distances in the plane.

3.4 *Damage localization: Yuen Function*

The Yuen function provides another measure to quantify changes in a modal form. This function is defined on the length of a beam as a structure and is constructed from the mode vectors and the values of the modal frequencies of the system with and without damage.

3.5 *Damage localization: Modal Shape Curvature*

Another way to obtain spatial information of the damage in structures that work mainly to flexion is by calculating the derivatives of the modal forms. The derivative process has the effect of amplifying any discontinuity in the modal form caused by localized damage, which results in changes in the curvature of the element.

For a beam in which its modal forms can be approximated by measurements of discrete points equally spaced at a distance h over its length, the curvature of the modal form can be calculated using a central difference approach to the second derivative (Pandey y Biswas, 1991).

3.6 *Optimal positioning of sensors maximizing the Fisher information matrix.*

The maximization of the Fisher information matrix or covariance matrix is a criterion currently used in the SHM to position sensors along a given geometry (Meo and Zumpano, 2005) with the choice of strategic points that allow get as much information as possible from the dynamic response of the structure to achieve a modal recreation.

3.7 *COMEF*

The error matrix from the coordinate error function (COMEF), is used to determine the variation between an initial vector of reference ∅ ^ 1 vs the same eigenvector in an unknown time ∅ ^ 2.

The values of the normal vectors obtained from the modal reconstruction were used to verify the effectiveness in the configuration of sensors.

3.8 *Methodology*

To determine the degree of effectiveness or representativeness in the characterization of damage for different sensor configurations, the following procedure was carried out:

a) Modal shapes and frequencies were obtained.
b) Empirical normalization was applied.
c) Two criteria were applied for the identification of damage (modal frequencies and MAC) and three damage location criteria (the Yuen function, the modal curvature criterion and the COMAC).

d) Different configurations of sensors were estimated in order to characterize the damage by means of the Fisher information matrix maximization method, evaluating the level of effectiveness of this characterization through the COMEF error matrix.

This work used z axis data for obtain modal parameters. For that reason the modal forms obtained from that registers has vertical modes presents.

Using a basic finite element model, the basic vertical modes identified in this work are mode 1, 3 and 5. After that applying the FDD the vertical modes identified are same, 1, 3 and 5. So this work focus in these three modes.

In this work, we analyzed HH-1, HH2, and HH3-axes. The results from HH-3 axis were most accurate, most likely due to the influence of the excitation source for HH-1 and HH-2, all the results presented below correspond to those from this axis.

The data presented below in damage localization are for which the best results were obtained. In this case, all damage localization criterions show better results at mode 3.

4 RESULTS

4.1 *Modal shapes and frequencies*

The modal shapes obtained are presented below.

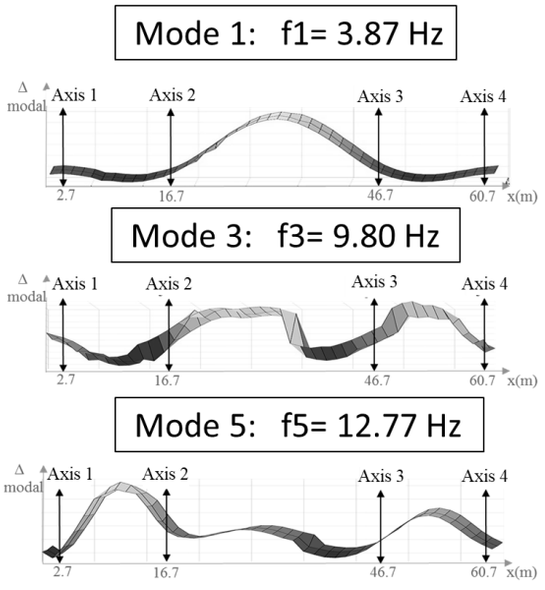


Figure 2. Modal forms

4.2 *Damage identification: frequencies*

From Figure 3, for the frequency of mode one, no considerable changes are observed throughout the different scenarios of measurement. This is a behavior is expected, since frequencies in low ranges are least affected by damage conditions.

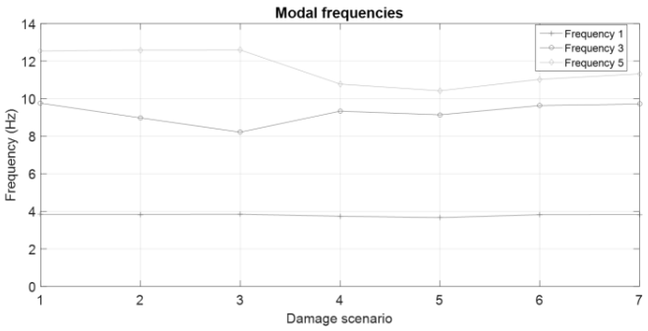


Figure 3. Modal frequencies

For the third natural frequency, there is a decrease from the scenario one (reference) to the scenario three (40 mm of settlement), which coincides with a progression of the damage on the bridge. In the scenario four, an increase in the frequency is observed, which is not expected as damage is increased, from a 40 mm settlement to 80 mm. For scenario five (90 mm of settlement), the frequency decreases again with respect to the previous scenario. For scenario six and seven (inclination of the pier and the third reference measurement) an increase in the value of the modal frequency was observed. The differences produced in scenario case number three and four are due to the fact that five days elapsed between one measurement and the other. So it could be possible the environmental conditions affected the system.

For the frequency of mode five, from the scenario one to three, it is not possible to see a clear reduction. For scenario four and five, a reduction in the value of the frequencies is observed. In scenarios six and seven a new increase of its value is observed. So it is not a consistent frequency decrease, as it would expect for the different damage increments.

4.3 *Damage identification: MAC*

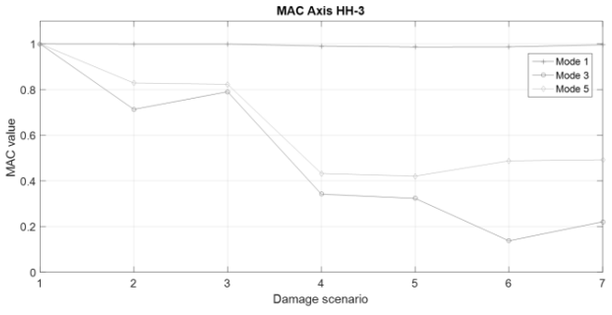


Figure 4. MAC values

From Figure 4, for mode one, it is observed that in all cases the MAC value is close to one. For mode three, there is a clear decrease trend in all cases where damage was simulated except for case number three. For mode five, a decreasing trend is observed except for case six, where there was a considerable approach to value one.

4.4 *Damage localization: COMAC*

The data presented below are for which the best results were obtained. In this case, all damage localization criterions show better results at mode 3.

The following Figure 5, 6 and 7 show the reference, undamaged mode shape on top, gray scale strips corresponding to the values obtained from the damage identification methodology, for each of the damage scenarios. At the bottom, there is a reference scheme of the bridge structure, to show the piers locations

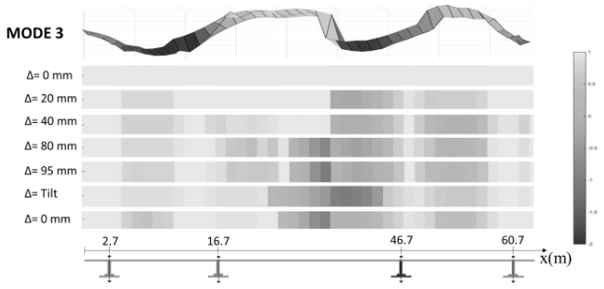


Figure 5. COMAC values

For scenario one (condition without damage, Δ = 0 mm) its length is light gray, since it is the base line for the modal comparison between the other states. For the condition of 20 mm of settlement small disturbances are evident around the second strain located in the area prior to 46.7 m and a small difference is observed for the area after 46.7 m. As the settlement conditions increase, the location of the damage and its magnitude also increase. For the inclination of the foundation, a considerable increase of the area after 46.7 m is observed. For the third reference measurement, it is observed that there is still damage, as the product of the different conditions previously imposed the bridge board suffered a cracking precisely in the areas where the COMAC indicated that there is damage.

4.5 *Damage localization: Yuen function*

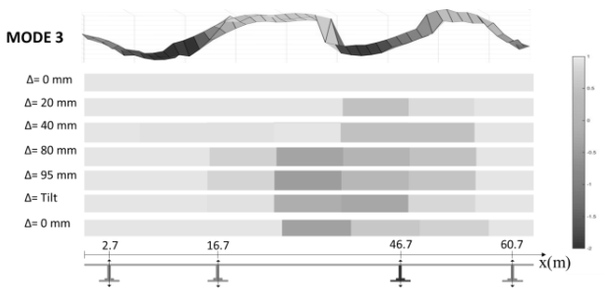


Figure 6. Yuen function values

There are two zones with damage, the largest in the area prior to 46.7 m and the other in the area after 46.7 m. However, in the area of 16.7 m and 2.7 m this criterion delivers damage, which does not agree with the documented.

4.6 *Damage localization: Modal Shape Curvature*

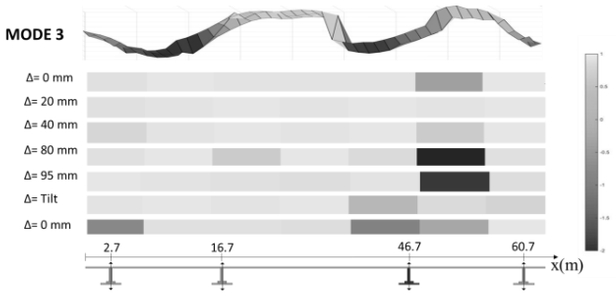


Figure 7. Modal Shape Curvature values

It is observed that it is not possible to detect a clear trend for all different cases.

4.7 *Sensor number and settings Fisher matrix*

Table 2 is presented with the different amounts of sensors used to obtain the different sensor configurations.

Table 2. Sensor number case

Case	Sensor Number
1	40
2	35
3	30
4	25
5	20
6	15
7	10
8	5

Figure 8 contains the different sensors settings for each case.

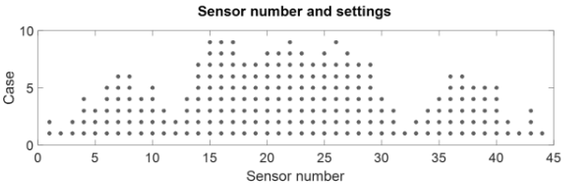


Figure 8. Sensor number and settings

It is observed that as the number of sensors decreases the trend indicates a high concentration in the center. That is interpreted as the need to have instrumented bridge areas that have greater span length.

4.8 *COMEF for different settings*

From Figure 9 and Figure 10 it is observed that as the number of sensors is greater, the error is smaller. Having an average error rate of 50% for the configu-

ration with 9 sensors, while an average error rate of 10% for the configuration with 30 sensors.

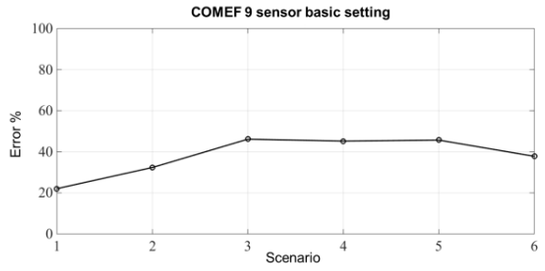


Figure 9. COMEF 9 sensor basic setting

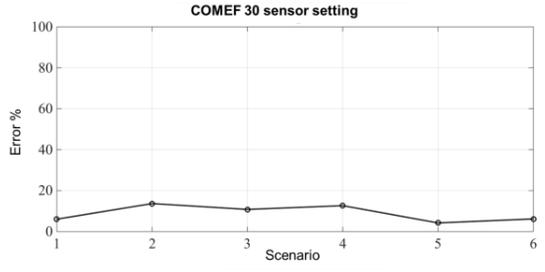


Figure 10. COMEF 30 sensor setting

4.9 *Damage characterization required level*

The previous results were stretched to obtain a relation between the desired damage characterization and the number of sensors to be used. For this purpose, the number of sensors used and the error percentage of the COMEF were compared, and an approximate function was obtained by means of a regression analysis.

The percentage of error of the COMEF is directly related to the level of representativeness or effectiveness in the characterization of the damage, which means, to a greater percentage of error, less number of sensors, therefore, a lower level of representativeness.

In the Figure 11it is presented the function that shows the level of effectiveness in the damage characterization. The function was calculated by means of an exponential adjustment with a confidence level of 95%, using three points to elaborate it.

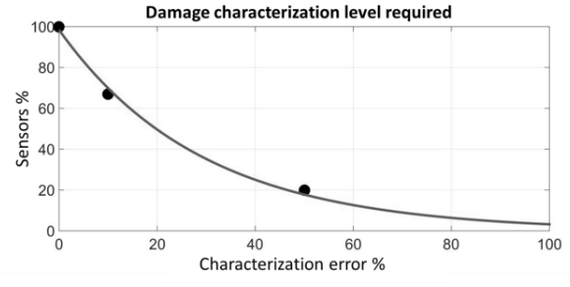


Figure 11. Damage characterization level required

It is observed that when passing the threshold of 10% of error (which is the one that was previously recommended) the percentage of error increases considerably, or in other words, the level of representativeness in the damage characterization decreases considerably.

It should be mentioned that product of the number of points that were used (three) the function resulting from the regression itself loses representativeness. However, the behavior of modal indicators is directly related to the number of sensors (as less quantity is available, less data volume is collected), corroborating the decreasing trend of the function that was obtained.

5 CONCLUSIONS

No positive results are obtained from damage detection techniques, since these criteria are too sensitive to environmental conditions and other variations that appear at the time of measurement.

The COMAC was the only damage location criterion that delivered the actual location of the damage along with its magnitude. The Yuen function and the modal curvature criterion did not give satisfactory results because, unlike COMAC, these two criteria come from mathematical approximations.

Product of the application of the location criteria it was observed that the damage suffered by a strain can be evidenced in the slab of the bridge, which is very useful considering that one of the main reasons of failure of the bridges in Chile has to do with scouring of the strains.

A valid function was determined, which allows entering as input the number of sensors to be used and delivering as output the level of representativeness in the damage characterization associated with that quantity, for this particular bridge.

The line of research in the future considers two points in particular:

1) The determination of a minimum number of sensors for this bridge, including economic, social aspects and also instrumentation.

2) Obtaining an instrumentation methodology to be applied in Chile, indicating the number of sensors needed for each specific bridge, minimum separation between them, position of the sensors with respect to the sources of excitation, choice of excitation source, etc.

6 REFERENCES

Allemang, R. J., Brown, D. L. (1982), "A Correlation Coefficient for Modal Vector Analysis," Proceedings, International Modal Analysis Conference, pp. 110-116.

Brincker, R., Zhang, L., y Andersen, P. (2001). Modal identification of output-only systems using
frequency domain decomposition. Smart materials and structures. 10(3). 441.

Catbas, F.; Aktan, A.; Allemang, R. & Brown, D. (1998) A Correlation Function for Spatial Locations of Scaled Mode

Shapes-(COMEF) Society for Experimental Mechanics, Inc, 16 th International Modal Analysis Conference, 2, 1550-1555.

Farrar C., Doebling S. y Nix D. (2001). Vibration-based structural damage identification. Phil. Trans. R. Soc. Lond. A 359, 131-149.

Farrar C. y Worden K. (2006) An introduction to structural health monitoring. Phil. Trans. R. Soc. A 365, 303–315.

Farrar, C. R., y Worden, K. (2013). Structural health monitoring: a machine learning perspective. John Wiley & Sons. Chichester.

Lieven, N. A. J. y Ewins, D. J. (1988) Spatial Correlation of Mode Shapes, The Coordinate Modal Assurane Criterion (COMAC) Proceedings, International Modal Analysis Conference, pp 690-695.

Maeck, J., & de Roeck, G. (2002). Description of Z24 Benchmark. Mechanical Systems and Signal Processing, 17. 127–131. Elsevier Science Ltd.

Mathworks (2014) MATLAB versión R2014b. www.mathworks.com.

Meo, M., y Zumpano, G. (2005). On the optimal sensor placement techniques for a bridge structure. Engineering Structures, 27(10). 1488-1497.

Pandey, A.K, Biswas, M. and Samman, M.M (1991) Damage detection from changes in curvature mode shapes. Journal of Sound and Vibration, 145(2), 321–332.

Yuen, M.M. (1985) A numerical study of the eigenparameters of a damaged cantilever. Journal of Sound and Vibration, 103, 301–310.

Maintenance, Safety, Risk, Management and Life-Cycle Performance of Bridges – Powers, Frangopol, Al-Mahaidi & Caprani (Eds)
© 2018 Taylor & Francis Group, London, ISBN 978-1-138-73045-8

Ambient vibration monitoring of a railway bridge for scour detection

C.W. Kim
Kyoto University, Kyoto, Japan
D. Kawabe, M. Kondo
West Japan Railway Company, Osaka, Japan

ABSTRACT: This study is intended to discuss a vibration-based scour monitoring of railway bridges under in-service condition. A long-term vibration monitoring was conducted on a railway bridge to investigate feasibility of the vibration-based scour monitoring in real-time. A high-precision three-axis wireless accelerometer was installed on the pier top to measure pier vibrations. Vibrations of bridge girders adjacent the observation pier were also monitored in order to clarify influences of bridge girder vibrations to pier vibrations. Both train-induced and ambient vibrations were investigated, and frequencies relevant to the pier were identified and adopted as a scour-sensitive feature. A Bayesian operational modal analysis in frequency domain was also applied to reduce the prediction error. Observations through this study showed that the pattern of the identified frequencies varied according to the water level as well as wind speed during the monitoring.

1 INTRODUCTION

The scour of railway bridges is one of the main causes of railway bridge failures during floods. How to provide a proper decision on the train operation control during heavy rain has been a keen technical issue for railway companies (Prendergast et al., 2013). West Japan Railway company operates more than 5000 km railways, for an example, and an improper decision to suspend operation due to floods leads to huge operating loss. The impact test on the bridge pier to identify changes in frequencies is a promising and conventional way of the scour detection (Abe *et al*. 2016). However, the impact test is a laborious and time-consuming method, and is inapplicable for the real time monitoring to make a proper decision on the train operation control during heavy rains. Therefore, the visual inspection during heavy rains has been adopted to make a decision for the operation control. An alternative way of the visual inspection as well as impact vibration test is utilizing ambient vibrations or microtremor although quality of the identified frequency information might be poorer than the impact test.

A real-time monitoring method focusing on bridge vibrations under operational conditions thus has been considered as an alternative method to the visual investigation for scour assessment during a flood. Since changes in structural integrity lead to changes in modal parameters such as natural frequencies, identification of modal parameters is the first step for the scour detection by means of vibration monitoring (Chang & Kim, 2016). Once sensors are installed and electric power is supplied in the observation bridge, the vibration monitoring guarantees highly frequent real-time scour inspection. The real-time vibration monitoring would help railway authorities to make a quick decision on resuming of train operation.

This study is intended to discuss a real-time scour detection focusing on changes in frequencies of a railway bridge pier that are identified from train-induced vibrations as well as microtremor. The accelerations of bridge girders connected to the target bridge pier are also examined to clarify influences of girder vibrations to the vibrations of the pier. For the real-time and long-term scour monitoring of the railway bridge, a wireless sensing device comprising a tri-axial accelerometer that can be remotely controlled was deployed on the top of the bridge pier.

Both stochastic subspace identification (SSI) (Overschee & Moor 1996) and Bayesian operational modal analysis (BAYOMA) (Au *et al*. 2013) are adopted to identify natural frequency of the bridge pier. The SSI is the adopted as a time-domain method

while the BAYOMA is adopted as a frequency-domain method. It is noteworthy that the Bayesian approach provides posterior probability distribution of the identified modal parameters and S/N ratio of modal responses, which is useful to assess reliability of observed data during flood. The influence of environmental factors such as water level, wind speed and passing train on identified pier frequencies is also investigated.

2 SYSTEM IDENTIFICATION

2.1 *Stochastic Subspace Identification*

In this study modal parameters of bridges in operational condition are identified utilizing the stochastic subspace identification (SSI) method that is a time domain method. The algorithm for the SSI is briefly described. Details about the SSI can be found in existing researches (*e.g.* Heylen *et al*. 1997, Overschee & Moor 1996).

The dynamic system of a structure is modeled by the state-space model as follows.

$$\mathbf{x}(k+1) = \mathbf{A}\mathbf{x}(k) + \mathbf{w}(k) \tag{1}$$

$$\mathbf{y}(k) = \mathbf{C}\mathbf{x}(k) + \mathbf{v}(k) \tag{2}$$

where $\mathbf{x}(k)$ and $\mathbf{y}(k)$ denote the state of structure and measurement at each time step k respectively. $\mathbf{w}(k)$ and $\mathbf{v}(k)$ denote the process noise and measurement noise vectors respectively, and are assumed to be stationary white noise.

System matrices **A** and **C** in Equations 1 and 2 which contain the modal information are estimated by means of the least squares method for the minimal prediction error of state $\mathbf{x}(k)$ given by the forward Kalman filter. The poles of the dynamical system provide modal properties of the dynamical system.

From the system matrices, we obtain the oblique projection matrix $\boldsymbol{O}_i$ that is estimated as following equation.

$$\boldsymbol{O}_i = \mathbf{Y}_\mathrm{f}\mathbf{Y}_\mathrm{p}^\mathrm{T}\left(\mathbf{Y}_\mathrm{p}\mathbf{Y}_\mathrm{p}^\mathrm{T}\right)^\dagger\mathbf{Y}_\mathrm{p} \tag{3}$$

where $(\cdot)^\dagger$ denotes the Moore-Penrose pseudo inverse matrix. $\mathbf{Y}_\mathrm{f}$ and $\mathbf{Y}_\mathrm{p}$ are block Hankel matrices of the future and past outputs respectively and defined as follows.

$$\mathbf{Y}_\mathrm{p} = \begin{bmatrix} \mathbf{y}(0) & \mathbf{y}(1) & \dots & \mathbf{y}(j-1) \\ \dots & \dots & \dots & \dots \\ \mathbf{y}(i-2) & \mathbf{y}(i-1) & \dots & \mathbf{y}(i+j-3) \\ \mathbf{y}(i-1) & \mathbf{y}(i) & \dots & \mathbf{y}(i+j-2) \end{bmatrix} \tag{4}$$

$$\mathbf{Y}_\mathrm{f} = \begin{bmatrix} \mathbf{y}(i) & \mathbf{y}(i+1) & \dots & \mathbf{y}(i+j-1) \\ \dots & \dots & \dots & \dots \\ \mathbf{y}(2i-2) & \mathbf{y}(2i-1) & \dots & \mathbf{y}(2i+j-3) \\ \mathbf{y}(2i-1) & \mathbf{y}(2i) & \dots & \mathbf{y}(2i+j-2) \end{bmatrix} \tag{5}$$

The singular value decomposition (SVD) is then applied to factorize $\boldsymbol{O}_i$ as

$$\boldsymbol{O}_i = \mathbf{U}\mathbf{S}\mathbf{V}^\mathbf{T} = (\mathbf{U_1}\mathbf{U_2})\begin{pmatrix}\mathbf{S_1} & \mathbf{0} \\ \mathbf{0} & \mathbf{S_2}\end{pmatrix}(\mathbf{V_1}\mathbf{V_2})^\mathbf{T} \simeq \mathbf{U_1}\mathbf{S_1}\mathbf{V_1^T} \tag{6}$$

where $\mathbf{U}$ and $\mathbf{V}$ are unitary matrices with the appropriate size and $\mathbf{S}$ is a diagonal matrix with non-negative elements. The diagonal elements of $\mathbf{S}$ are known as singular values of $\boldsymbol{O}_i$. Singular values in $\mathbf{S}$ are listed in descending order.

Therefore, the components in $\mathbf{U}_1\mathbf{S}_1\mathbf{V}_1{}^\mathrm{T}$ contain most of the information defining the elements in $\boldsymbol{O}_i$ and components in $\mathbf{U}_2\mathbf{S}_2\mathbf{V}_2{}^\mathrm{T}$ are regarded as trivial components. Theoretically, the optimal state sequence $\mathbf{X}_i = [\mathbf{x}(i)\ \mathbf{x}(i{+}1)\ \dots\ \mathbf{x}(i{+}j{-}1)]$ predicted by the Kalman filter in least square sense is obtained as follows.

$$\mathbf{X}_\mathrm{i} = \mathbf{S_1^{1/2}}\mathbf{V_1^T} \tag{7}$$

The significant components of orthogonal vectors in the state sequence can be extracted by applying SVD to $\boldsymbol{O}_i$, and the system matrices are obtainable from $\mathbf{X}_i$. The number of poles corresponds to the number of singular values determined in Equation 6. In other words, we can extract the significant modal components of the bridge from the measured acceleration data by the SVD.

2.2 *Bayesian Approach*

The identified frequencies and mode shapes of the bridge pier utilizing train-induced vibrations before flood can be collected, and the probability distribution of the collected frequencies are exploited as reference information. Therefore, it is possible to detect changes in stability of the bridge pier due to scour by comparing distributions of the identified frequencies before and after flood. However, a preliminary investigation on the target bridge, which is discussed in section 4, demonstrated that the identified frequencies by the SSI from a weak amplitude ambient vibration (microtremor) during the suspend operation due to the flood showed too large variations to be used in scour monitoring.

To cope with this technical problem, the Bayesian operational modal analysis (BAYOMA) (Au *et al*. 2013) as a Bayesian approach is adopted to identify natural frequencies of the bridge pier from microtremor during a flood. The Bayesian approach offers a powerful perspective for system identification that explicitly addresses uncertainty. It treats the modal identification as an inference problem where probability is used as a measure for the relative possibility of outcomes under a given model of the system and measured data. Another useful perspective of the BAYOMA is that it provides probability distribution of modal forces and power spectrum density (PSD) of prediction error.

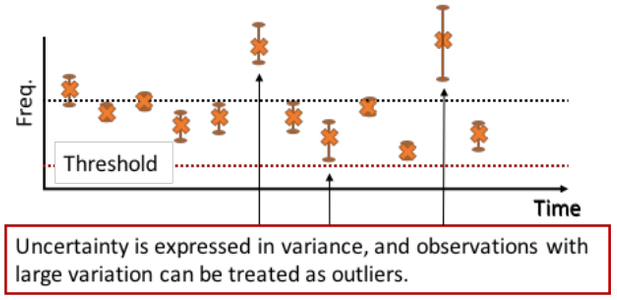


Figure 1. Identified frequencies by means of BAYOMA.

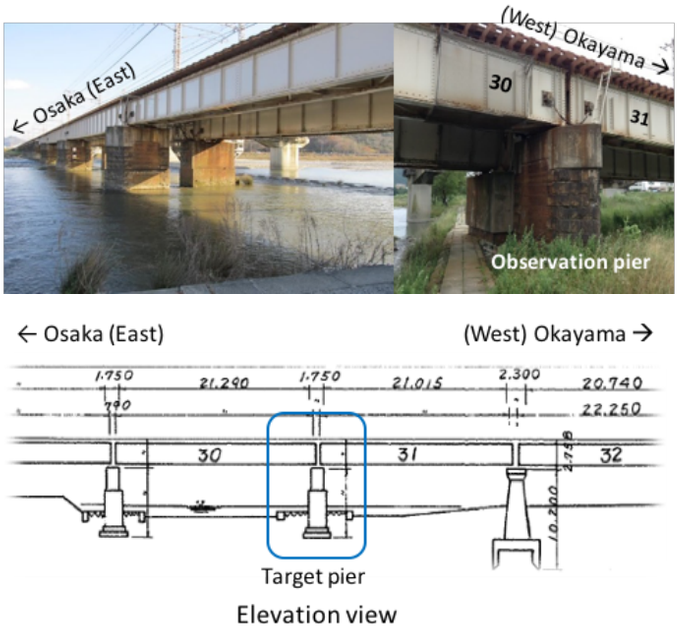


Figure 2. Photo and elevation view of the observation bridge and pier.

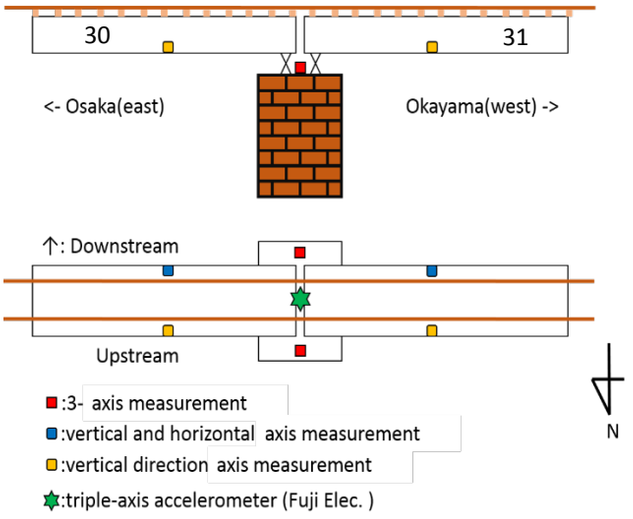


Figure 3. Sensor deployment map.

The coefficient of covariance (COV) and S/N ratio are adopted as indicator of uncertainty of identified values. Identified frequencies with low variance are selected utilizing the most probable value (MPV) which maximizes the posterior distribution in the Bayesian approach and the COV of the posterior distribution since the smaller the COV is, the smaller the uncertainty of the identified result is. Figure 1 shows the concept of mean and COV of identified frequencies by means of BAYOMA, and those with large variance can be treated as outliers.

The S/N ratio is the ratio of PSD of modal acceleration responses and PSD of prediction error, and a high S/N ratio can be interpreted as high-quality data comprising precise modal information of the bridge pier.

3 FIELD EXPERIMENT

The target bridge is commenced in 1890, and is located about 7 km far from the sea. It is a two-lane steel-girder railway bridge, and mass of the girder is around 30 t. Two lanes are connected at its superstructure, but two RC piers support each lane independently. The target bridge pier with a ship shape is located at the upstream, and train passes from the west to the east (see Figure 2).

Vibration modes of the bridge pier include rocking and sway modes of the pier and some modes are related to those of adjacent girders. Therefore, this study first estimates vibration modes of the bridge pier and adjacent girders by a network of cable accelerometers, and decides the target pier mode to be monitored for scour detection. It is noteworthy that the impact hammer test was conducted in 2011, and the rocking mode of the pier was identified as 15.93 Hz. Scour has not been occurred since then.

For practical applications, it is necessary to install sensors as few as possible to reduce monitoring cost. Therefore, one wireless sensor node, with an integrated tri-axial MEMS accelerometer (CPUKSNSS-00, Fuji Electric), was installed on the top of the bridge pier for the long-term and real-time scour monitoring. The wireless sensor enables us to control the sensor node remotely during floods. Sampling frequency was 200 Hz. The sensor deployment map is shown in Figure 3. An ultrasonic water level meter was also installed in the bridge.

On September 20 in 2016, typhoon no.16 was approached, and the water level was measured from 7:30 a.m. on September 20 to 16:00 a.m. on September 21. Figure 4a) shows the time history of the water level that denotes the distance between bottom flange of girder and the water surface, i.e. the higher the water level goes up, the smaller the measured value becomes. The water level starts to increase around 10:30 a.m. on September 20, and the peak water level of 1.8 m reached at 17:10 on September 20. The railway company has its own train operation criteria following water level, which are "Warning" at the water level of 2.5 m, "Reduce Speed" at the water level of 2.0 m and "Suspend Operation" at the water level of 1.5 m. The peak water level for the bridge was 1.8 m

that is between "Reduce Speed" and "Suspend Operation" levels. For information, time-history of wind speed (m/s) from 0:00 a.m. to 12:00 p.m. on September 20 is shown in Figure 4b) even though the observation point of wind was placed about 2 km distance from the target bridge.

4 SCOUR MONITORING

4.1 *Fundamental vibration modes*

This study first identified vibration characteristics from the train-induced vibrations measured for three days before flood utilizing the cabled sensors by means of the SSI. To extract stable structural modes from the stabilization diagram obtained in the SSI, this study determined a pre-selected frequency deviation tolerance as 0.25 Hz, 0.1 % as a pre-selected damping deviation tolerance, and 0.95 as a pre-selected lower bound of modal assurance criteria (MAC). It should be noted that the cable sensors were less sensitive to measure microtremor, and utilized only for measuring train-induced vibrations.

Figure 5 shows vibration modes relevant to the transverse mode of girders (4.8 Hz) and rocking motion of the pier (15.4 Hz) from the train-induced vibration. The identified dominant frequency of the bridge pier showed a smaller value than that of the impact test result, 15.9 Hz. However, considering additional mass by the passing train as well as bridge-train interaction (Chang *et.al.* 2014) it can be concluded that the frequency 15.4 Hz is relevant to the pier's rocking mode.

4.2 *Identified frequencies from microtremor*

The microtremor during the flood on September 20 was examined by means of the BAYOMA, and the identified frequencies from 14 Hz to 17 Hz were plotted in Figure 6 with PSD of the modal force, S/N ratio, wind speed and water level. The data length used in the identification was 1 minute. The horizontal axis shows a time scale in hour. The plots in Figure 6a) showed the mean and standard deviation of the identification frequencies. The coefficient of variation (COV) was estimated from the mean and standard deviation values to filter out outliers. In this study COV of 0.05 and S/N ratio of 2.5 were adopted as thresholds to remove outliers in the identified frequency. About 90 % of identified results were passed these filters. Those filtered results are plotted in Figure 7. During 0:00 to 9:00 a.m., when the wind speed and water level are low, identified frequencies and modal forces have scattered, and even the S/N ratio was low. On the other hand, during the period of strong wind from 9:00 a.m. to 15:00 p.m., modal forces and the S/N ratio are large, and identified frequencies showed less variation. In the period of the flood from 15:00 to 24:00, identified frequencies were clustered around 15.7 Hz.

Distributions of the frequency identified from microtremor during normal, strong wind, and flood conditions are summarized in Figure 8 in which mean values of the frequency under normal, strong wind and flood conditions were 15.9 Hz, 15.2 Hz and 15.7 Hz, respectively. There exists small difference between normal and flood condition. However, in comparing strong wind and flood conditions the mean frequency in the period of strong wind was 3.12% smaller than in flood period. Figure 9 shows the maximum PSD amplitude plot of the monitored accelerations, in which the PSD amplitude during the strong wind resulted in the most dominant.

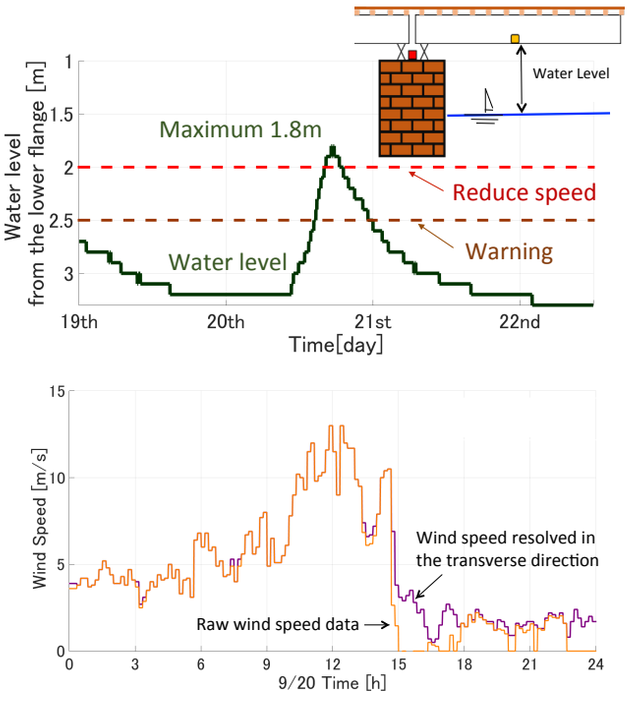


Figure 4. Water level and wind speed during typhoon no.16.

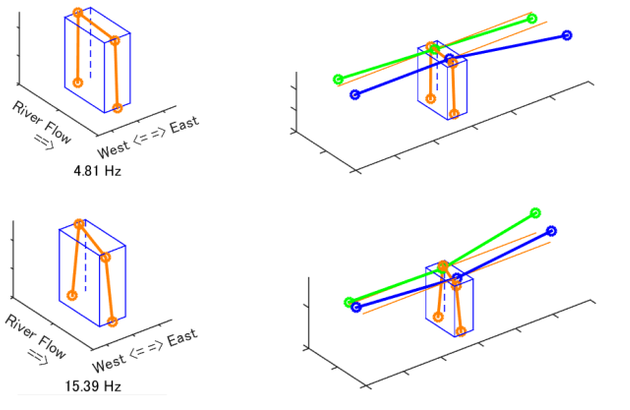


Figure 5. Identified mode shapes and dominant frequencies from the train-induced vibrations: a) near 5Hz for the transverse mode of girders, and b) near 15.9 Hz for rocking motion from the impact test.

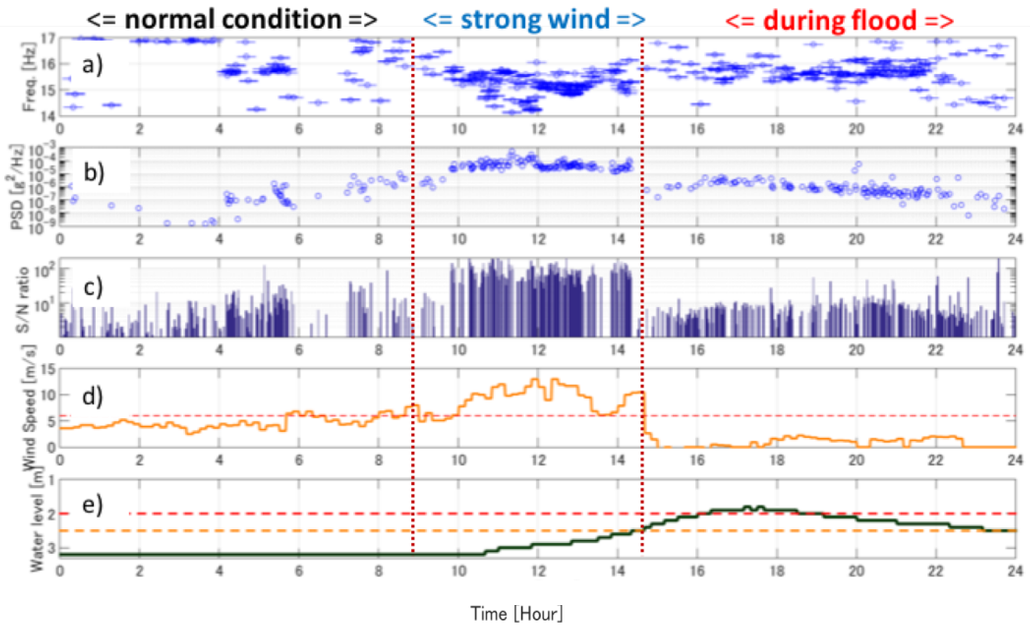


Figure 6. Bayesian approach: a) Identified frequencies; b) PSD of modal forces; c) S/N ratio; d) wind speed; and e) water level.

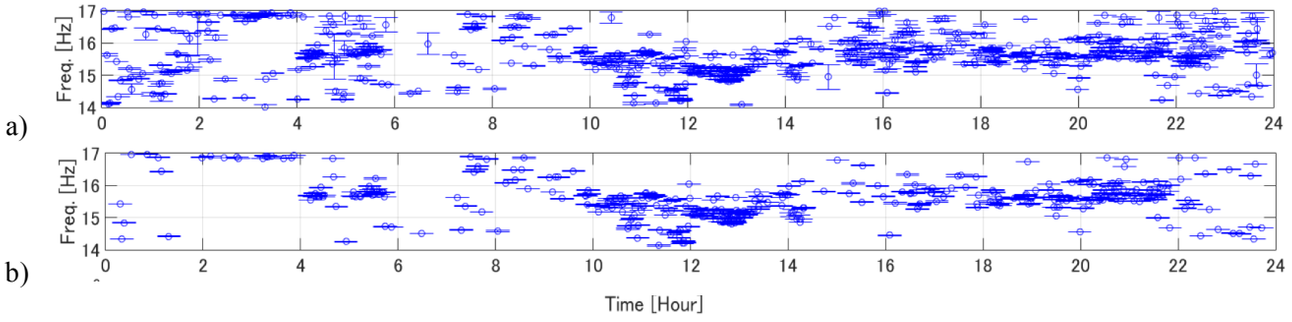


Figure 7. Bayesian approach (filtered identified frequencies): a) before being filtered; b) after being filtered.

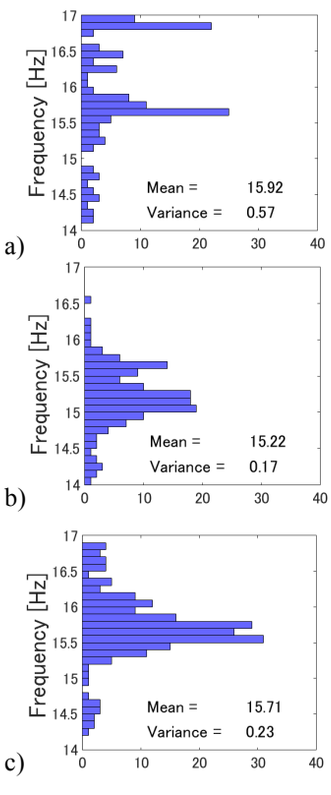


Figure 8. Identified frequency distribution: a) normal condition; b) strong wind condition; c) flood condition.

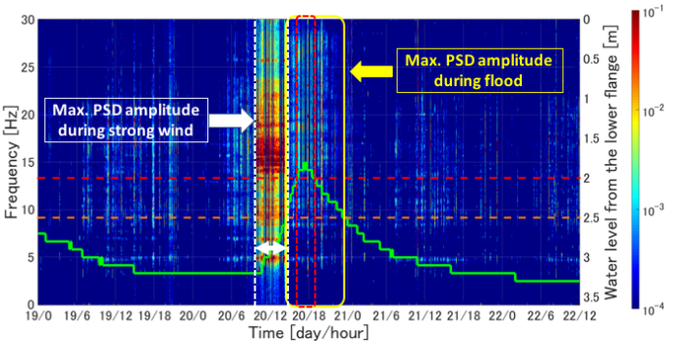


Figure 9. Maximum PSD amplitude.

Figure 10 shows the relationship between wind speed and amplitude of Fourier spectrum, which demonstrated the amplitude of Fourier spectrum drastically increased at wind speed of 6 m/s although the mechanism is not examined yet. It should be noted that there is no change in frequency during the flood, and can be concluded that low possibility of scour during high water level.

Distributions of identified frequencies before and after flood utilizing train-induced vibrations are shown in Figure 11, which demonstrates no notable changes in mean value and variance. It also demonstrates low possibility of scour due to the flood.

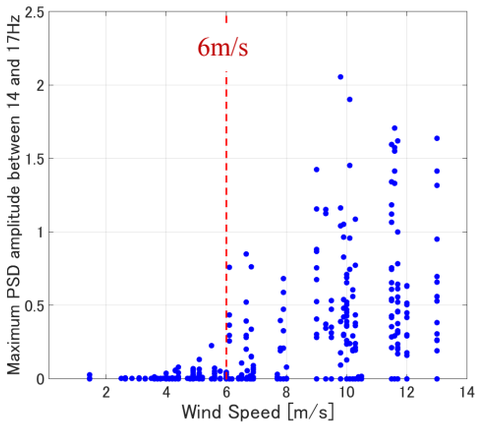


Figure 10. Relationship between wind speed and maximum amplitude of Fourier spectrum.

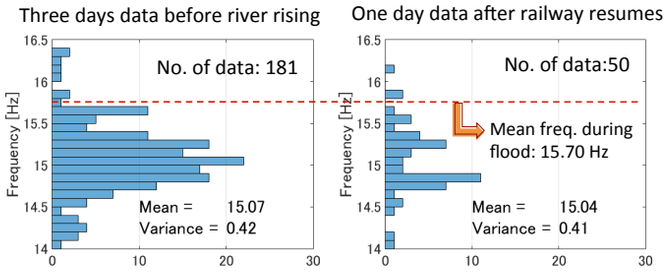


Figure 11. Distribution of natural frequency for one day after flood.

5 CONCLUSIONS

This study investigates a real-time scour assessment by means of vibration monitoring. The Bayesian approach and stochastic subspace identification are adopted for system identification. Influences of water level and wind speed were also examined. Observations from this study are summarized as follows:

The natural frequency of the bridge pier during a flood was identified in real-time, and there exists only a small difference between normal and flood conditions. However, comparing strong wind and flood conditions the mean frequency in the period of strong wind was smaller than that in flood period.

There was no notable change in frequency during the flood, and it can be concluded that low possibility of scour during high water level. Similar conclusion of low possibility of scour was derived from identified distribution before and after flood utilizing train induced vibrations.

REFERENCES

Abe, K, Natori, T, Kominato, Y, Sekiguchi, T, Yamano, A, Wang, L, 2016. Monitoring method of soundness of railway bridge by using sound diagnosis indices correlated with natural frequency, *J of JSCE*, Ser.A1, 72 (1):21-40. (in Japanese)

Au, SK, Zhang, FL, and Ni, YC, 2013, Bayesian Operational Modal Analysis: Theory, Computation, Practice, *Computers and Structures* 126: 3-14.

Chang, KC, Kim, CW, and Borjigin, 2014. Sudanna, Variability in Bridge Frequency Induced by a Parked Vehicle, *Smart Structures and Systems, An Int J.,* 13(5): 755-773.

Chang KC, and Kim CW, 2016, Modal-Parameter Identification and Vibration-based Detection of a Damaged Steel Truss Bridge*, Engineering Structures*, 122: 156-173.

Heylen, W, Lammens, S, and Sas, P, 1997, *Modal Analysis Theory and Testing*, K.U. Leuven.

Prendergast, LJ, Hester, D, Gavin, K, and O'Sullivan, JJ, 2013, An investigation of the changes in the natural frequency of a pile affected by scour, *J. of Sound and Vibration*, 332(25): 6685–6702.

Van Overschee, P, and De Moor, B, 1996. *Subspace Identification for Linear Systems*, Kluwer Academic Publishers.

System identification of a bridge by a sparse-like system matrix

T. Mimasu, Y. Goi & C.W. Kim
Department of Civil and Earth Resources Engineering, Kyoto University, Kyoto, Japan

ABSTRACT: Wireless sensors in structural health monitoring are useful to simplify deployment and to realize a remote control of deployed sensors. However, wireless sensors operate in significant constraint on power consumption. Reduction techniques of radio communications in sensor networks are useful to extend the battery life. This study is intended to a method to utilize sensor grouping so as to reduce amount of data by radio communications between sensors. The sensor grouping is decided by considering correlations between sensors, and then the original system matrix is reconstructed into a sparse-like system matrix by replacing components for the weakly correlated sensor in the system matrix with zero. To verify the validity of the proposed approach, the sensor grouping is examined by means of simulations and field experiments. Observations demonstrated feasibility of system identification utilizing the sparse-like system matrix.

1 INTRODUCTION

Maintaining and upgrading civil infrastructures including bridge structures are important technical issues in many countries. Structural health monitoring (SHM) utilizing vibration responses of structures has been developed as one of the effective techniques to evaluate bridge conditions (Deraemaeker et al. 2007). Moreover, various ways to identify parameters of structures are proposed such as FDD (e.g. Brincker et al. 2001), SSI (e.g. Overschee et al. 1991) and MAR (e.g. Kim et al. 2012).

In recent years, introduction of wireless sensors to SHM is expected because of simple deployment and remote control of sensors (Chae et al. 2012, Nagayama et al. 2010). Wireless sensors have been improved as wide range of potential applications. However, cabling of sensors is labor and cost consuming. That is a driving force of using wireless sensors in SHM. However, there are technical issues remained to be solved, such as extension of battery life, time synchronization among sensors, reduction of data loss during radio communication and so on. Especially, reduction of power consumption of wireless sensor networks is needed for health monitoring of bridges that require long service period. One way to reduce the total power consumption is to reduce or to optimize the radio communication between sensor nodes since the radio communication accounts for a major portion of total power consumption (Agarwal et al. 2005).

There are techniques to reduce the amount of data such as compressive sensing (CS). This study focuses on a sparse-like system matrix that converted from original system matrix. In general, when the amount of radio communication related to vibration data decreases, the quantity of information relevant to bridge's physical properties also decreases. However, if the system matrix can be reconstructed with sparse components that link to weakly correlated sensors and communication only between sensors of strong correlation is considered, we can reduce communication between sensors of weakly related.

This study is intended to reconstruct the system matrix with sparse components in system identification by replacing components for the weakly correlated sensor in the system matrix with zero. As a feasibility study, the sensor grouping is investigated by means of simulation and field experiment on real bridges.

2 METHODOLOGY

2.1 *Multivariate auto-regressive model*

The equation of motion for a bridge is described as

$$\boldsymbol{m}_b\ddot{\boldsymbol{z}}(t) + \boldsymbol{c}_b\dot{\boldsymbol{z}}(t) + \boldsymbol{k}_b\boldsymbol{z}(t) = \boldsymbol{p}\boldsymbol{f}(t) \quad (1)$$

where $\boldsymbol{m}_b$, $\boldsymbol{c}_b$, $\boldsymbol{k}_b \in \mathbf{R}^{n\times n}$ denote the mass, damping, and stiffness matrices of the bridge, respectively. n denotes the degree of freedom of the bridge model. $\boldsymbol{z}(t) \in \mathbf{R}^n$ and $\boldsymbol{f}(t) \in \mathbf{R}^r$ denote the displacement and external force vectors, respectively. $\boldsymbol{p} \in \mathbf{R}^{n\times r}$

denotes a load matrix that provides the location of action. If we consider ambient vibration, this equation can be rewritten into a multivariate autoregressive model (MAR) as follows.

$$\boldsymbol{y}_n = \sum_{i=1}^{p} \boldsymbol{A}_i \, \boldsymbol{y}_{n-i} + \boldsymbol{v}_n \tag{2}$$

where $\boldsymbol{y}_n$, $\boldsymbol{A}_i$ and $\boldsymbol{v}_n$ denote the time-series of the output at each sensor, i-th autoregressive coefficient matrix and error term, respectively. AR coefficient matrix can be estimated by the least squares method. Vibration characteristics of bridges, such as frequency, damping and mode shape, can be identified from the AR coefficient matrix (Kim et al. 2012). In other words, AR coefficient matrix comprises essential information of vibration characteristics of bridges.

2.2 *Criteria of correlation between sensors*

Spatial correlation between sensors is considered as a parameter for the sensor grouping. In this study, correlation between sensors can be evaluated by signal noise ratio and identified mode shapes.

The signal noise ratio (SNR) is a measure of signal strength relative to background noise, and usually measured in decibels (dB) as shown in Equation 3.

$$SNR = 10 \log_{10} \frac{\sum_{n=1}^{L} \tilde{y}_n^2}{\sum_{n=1}^{L} |y_n - \tilde{y}_n|^2} \tag{3}$$

where $\tilde{y}_n$ denotes the time-series of each sensor estimated from the system matrix. The larger the SNR is, the smaller the effect of noise becomes. Therefore, the SNR is used to evaluate the correlations between sensors installed on bridges.

In the system identification utilizing the MAR model, the AR coefficient matrix is estimated from vibration responses of all sensors on the bridge. If wireless sensors are used to measure vibrations, it should be avoided to collect all measured data in one place like a parent node as the volume of vibration data is extremely big. One way to solve this issue is to convert vibration data to AR coefficient in the multi-hop communication. If AR coefficients can be structured step by step utilizing vibration data from a small group of sensors, system identification can be efficiently conducted without collecting all the data in one place.

The contribution of each AR coefficient to system identification is not uniform, and coefficients with low contribution to the system identification are negligible. It can be regarded as zero in other words. Therefore, this study uses SNR to evaluate AR coefficients of weak contribution in the system identification. It noteworthy that the SNR-0based grouping was not enough to include torsional modes, and the sensors relevant to the torsional mode are included in the sensor grouping even though contribution is not so strong.

2.3 *Sensor grouping method*

2.3.1 *Concept of sensor grouping*

If correlations of components in AR coefficient matrix are weak, we can neglect contributions of relevant sensors by replacing the relevant AR component with zero, and the AR matrix can be reconstructed like a sparse-like matrix.

In other words, if we reconstruct the AR coefficient matrix by replacing the AR coefficient relevant to a sensor with zero and the predicted time series with the reconstructed AR matrix are different from the time series by the original AR matrix, then it can be concluded that the sensor cannot be neglected to keep same information with the original matrix. Vice versa is also true, and we can only consider sensors with strong contribution. This is the concept of sensors grouping proposed in this study.

Time-series can be also estimated from the reconstructed AR coefficient matrix. The SNR is thus adopted as an index to show contribution of sensors, which is calculated by utilizing the measured time-series and estimated time-series as shown in Equation 3. If the SNR after replacing AR coefficient of a sensor with zero led to lower value than the initial SNR estimated from the original AR coefficient matrix that includes all components, then contribution of the sensor is high and should be considered in the sensor grouping. In other words, if SNR shows a lower value once the component of the AR coefficient matrix of a sensor is replaced with zero, then it means that the sensor includes important information so as to show high SNR if considered, and thus the sensor should be considered in the sensor grouping.

2.3.2 *Method of reconstructing system matrix*

First, i-th autoregressive coefficient matrix $\boldsymbol{A}_i$ and the time-series of the output $\boldsymbol{y}_n$ are expressed as Equations 4 and 5, respectively.

$$\boldsymbol{A}_i = \begin{bmatrix} a_{1,1}^{(i)} & a_{1,2}^{(i)} & \cdots & a_{1,m}^{(i)} \\ a_{2,1}^{(i)} & a_{2,2}^{(i)} & \cdots & a_{2,m}^{(i)} \\ \vdots & \vdots & \ddots & \vdots \\ a_{m,1}^{(i)} & a_{m,2}^{(i)} & \cdots & a_{m,m}^{(i)} \end{bmatrix} \tag{4}$$

$$\boldsymbol{y}_n = [y_{1,1}^n \quad y_{2,1}^n \quad \cdots \quad y_{m,1}^n]^T \tag{5}$$

From the Equation 2, the output $y^n_{j,1}$ is reproduced by the sum of past output $\boldsymbol{y}^n_{j-i}$ multiplied by the AR coefficients. If the correlation between sensor j and sensor k is weaker than the other correlations, the contribution can be regarded as low. To estimate the AR coefficient assuming that there is no correlation between sensor j and k is essentially equivalent to replacing the AR coefficient $a_{j,k}$ with zero. An element

a)



b)

Figure 1. Bridge-A: a) photo; and b) elevation view.

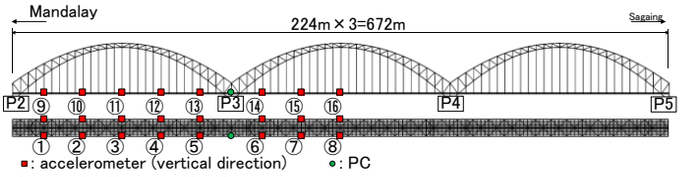


Figure 2. Sensor deployment.

of AR coefficient matrix in Equation 4 assumed to be zero is determined based on the correlation between the sensors as described in section 2.2, and the AR coefficient matrix is reconstructed as a sparse-like matrix according to the assumption. The least square method is used for estimating the AR coefficient matrix. Thus, if AR coefficient matrix is reconstructed based on the correlation between sensors in system identification, a sparse-like AR coefficient matrix can be formulated as Equation 6.

$$\widehat{\boldsymbol{A}}_i = \begin{bmatrix} \hat{a}_{1,1}^{(i)} & \hat{a}_{1,2}^{(i)} & \cdots & 0 & 0 \\ \hat{a}_{2,1}^{(i)} & \hat{a}_{2,2}^{(i)} & \cdots & 0 & 0 \\ 0 & \hat{a}_{3,2}^{(i)} & \cdots & \hat{a}_{3,m-1}^{(i)} & 0 \\ \vdots & \vdots & \ddots & \vdots & \vdots \\ 0 & \hat{a}_{m-2,2}^{(i)} & \cdots & \hat{a}_{m-2,m-1}^{(i)} & 0 \\ 0 & 0 & \cdots & \hat{a}_{m-1,m-1}^{(i)} & \hat{a}_{m-1,m}^{(i)} \\ 0 & 0 & \cdots & \hat{a}_{m,m-1}^{(i)} & \hat{a}_{m,m}^{(i)} \end{bmatrix} \quad (6)$$

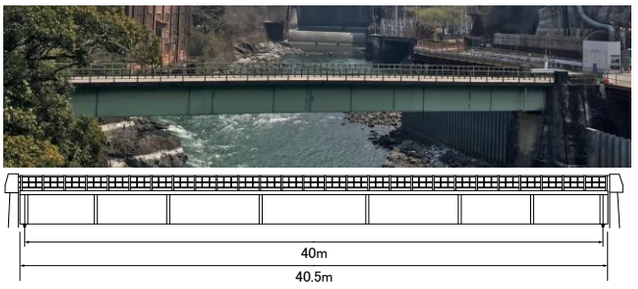
By estimating AR coefficients each time in sequence from vibration data of sensors necessary for AR coefficient estimation, it is possible to compress the amount of radio communication in wireless communication.

3 STRUCTURAL ANALYSIS

3.1 *Target bridges*

This study investigates two different bridge types: one is a long span steel arch bridge and another one is a simply supported steel girder bridge.

a)



b)

Figure 3. Bridge-B: a) photo; and b) elevation view.

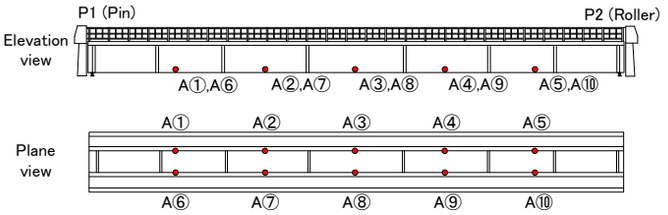


Figure 4. Sensor deployment.

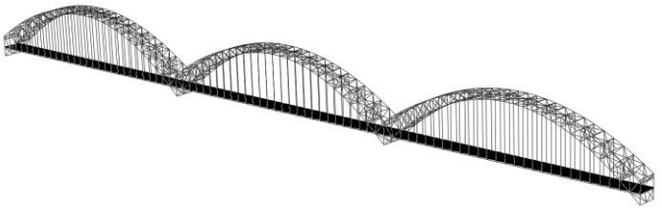


Figure 5. FE model of Bridge-A.

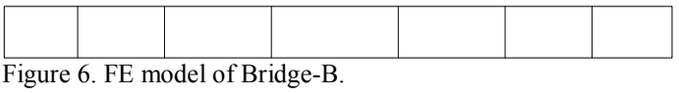


Figure 6. FE model of Bridge-B.

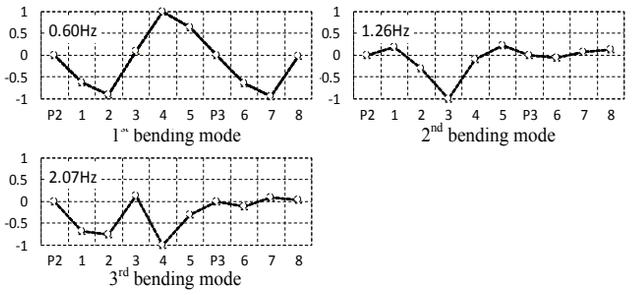
3.1.1 *Long span steel arch bridge*

The steel arch bridge comprises three spans of the through arch bridge and two spans of the through truss bridge (hereafter, Bridge-A) as shown in Figure 1. Total length and main span length is 1126m and 224m, respectively. Width is 16.6m. Observation position of the arch bridge is shown in Figure 2. 16 accelerometers were deployed on the bridge and also shown in Figure 2.

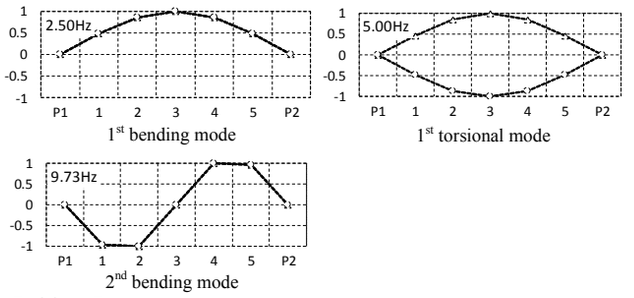
Ambient vibration responses of the bridge induced by passing vehicles were measured. Acceleration in vertical and horizontal directions were measured. However, this study discusses about the vertical responses.

3.1.2 *Steel plate girder bridge*

Another examined bridge is a simply supported steel girder bridge (hereafter, Bridge-B) that is shown in Figure 3. Total length and width are 40.5m and 4m, respectively. 10 accelerometers were installed on the bridge as shown in Figure 4. Forced vibration responses of the bridge induced by passing experimental vehicle were measured.

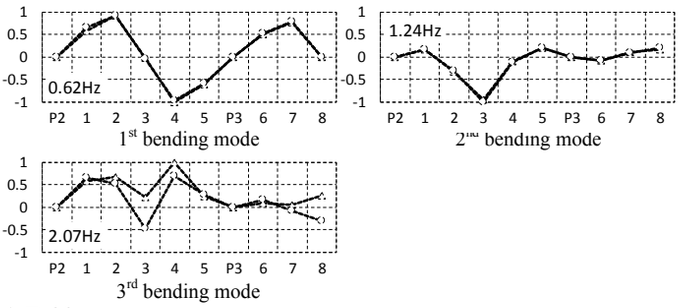


a) Bridge-A.

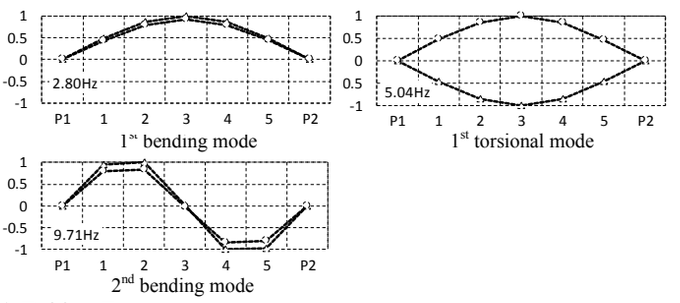


b) Bridge-B.

Figure 7. Results of the eigenvalue analysis.



a) Bridge-A.



b) Bridge-B.

Figure 8. Frequencies and mode shapes identified from simulated vibration responses.

3.2 *FE models*

Dynamic response analysis under a white noise input were conducted as a preliminary investigation by means of the finite element (FE) method. The model of Bridge-A, shown in Figure 5, is created based on the design documents. There are sidewalks on both side of the bridge, which are ignored in the model as the design document was unavailable. The model consists of RC deck, main girder, suspension member, arch girder, cross girder and cross beam. Total number of nodes in the FE model was 12553, that of elements was 13089. As the boundary condition, pin support was assumed at the P1, P2 and P4, and roller support was assumed at the P3.

The FE model for the Bridge-B shown in Figure 6 was modeled to a grid structure. Structural details considered in modeling were referred from the documents of periodic inspection and information obtained from the field experiments since the design documents of this bridge was not available. All elements of the bridge were modeled as beams. The RC deck and main girder was considered as the composite girder. Young's modulus of steel and RC deck was assumed to 210GPa and 21GPa, respectively. Total number of nodes in the FE model was 26, that of elements was 32. Pin supported at the P1 and roller supported at the P2 were adopted as boundary conditions.

3.3 *Eigenvalue analysis*

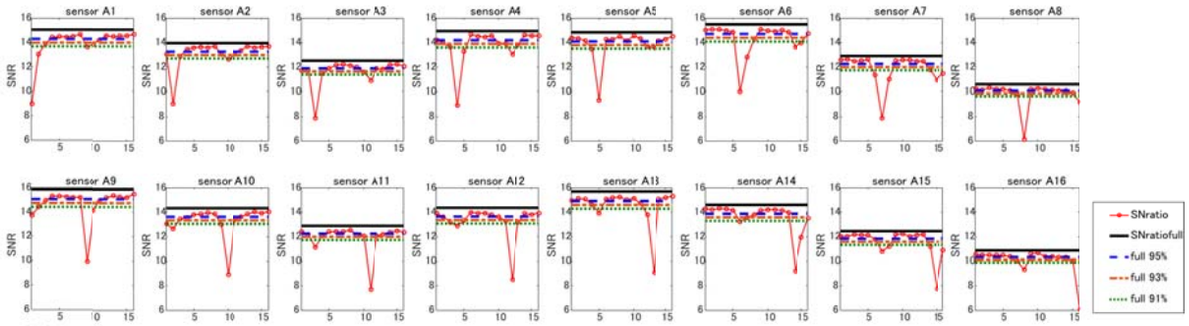
Results of eigenvalue analysis of each bridge are summarized in Figure 7 where mode shapes are in elevation view. In this paper unless otherwise specified, horizontal axis and vertical axis indicate the location of sensors and normalized value of mode vectors, respectively. For the location of sensors in the horizontal axis, numbers 1 to 8 correspond to A1 to A8 beneath - ○ - and those numbers beneath - △ - correspond to A9 to A16 in Bridge-A. For the Bridge-B, numbers 1 to 5 correspond to A1 to A5 beneath -○- and those numbers beneath -△- correspond to A6 to A10. The target modes are 1st bending mode, 2nd bending mode and 3rd bending mode for Bridge-A. Those target modes For Bridge-B are 1st bending mode, 1st torsional mode and 2nd bending mode.

3.4 *System identification*

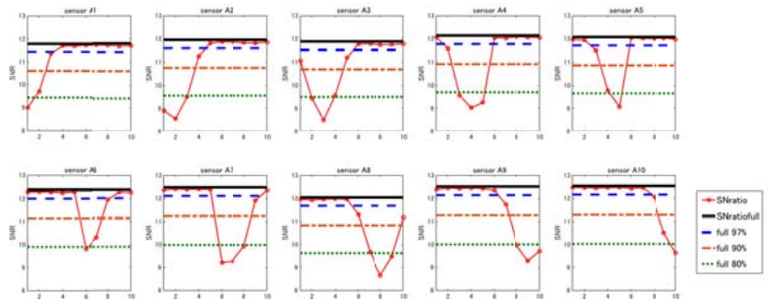
Dynamic response analysis of the bridges subjected to white noise inputs is conducted. Frequencies and mode shapes are identified by the MAR model from the simulated vibration responses, which are shown in Figure 8. For the Bridge-A, 1st bending and 2nd bending modes were comparable to those of eigenvalue analysis. Therefore, 1st bending and 2nd bending modes were considered to compare those results identified from the original system matrix and reconstructed system matrix. For the Bridge-B, three mode shapes were comparable to those of eigenvalue analysis.

3.5 *Applying the sensor group method*

Correlations between sensors are evaluated utilizing the simulation data. The SNR when the AR coefficient of each sensor is assumed to be zero is plotted in Figure 9. The description title on each graph indicates the target sensor. The horizontal axis shows the sensor number that is neglected in reconstructing the AR coefficient. The vertical axis indicates SNR when



a) Bridge-A.

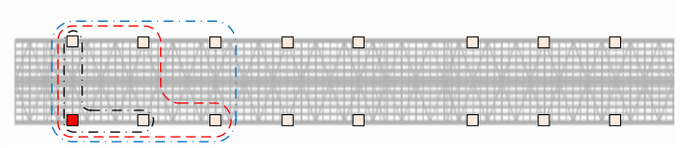


b) Bridge-B.

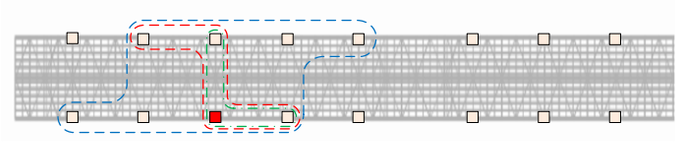
Figure 9. SN ratio of acceleration by reconstructing system matrix of multivariate AR model. (Horizontal axis: sensor to be neglected, Vertical axis: SNR)

the correlation between the target sensor and sensors to be neglected. For the Bridge-A, correlations between the target sensors and other sensors deployed along the same side were stronger than those between sensors deployed on the opposite side. In addition, the longer the length between sensors is, the weaker the correlation between the sensors becomes. For the Bridge-B, the same trends as Bridge-A were observed. The solid line indicate the SNR (SN ratio full) calculated utilizing the original AR coefficient matrix that considers correlation between all sensors. The broken line, dashed-dotted line and dotted line indicate the ratio to the SNR (SN ratio full), which are 95% (denoted to full 95%), 93% (denoted to full 93%) and 91% (denoted to full 91%) for the Bridge-A and 97% (denoted to full 97%), 90% (denoted to full 90%) and 80% denoted to full 80%) for the Bridge-B.

In this study, the threshold of SNR is artificially decided for each bridge, and sensor grouping is decided according to the threshold. In addition, the correlation that is necessary to correctly identify the mode shapes is also considered. For the Bridge-A, the correlation between sensors installed on the different span is unignorable since the SNR of sensors in the opposite girder resulted in lower SNR than the threshold. For the Bridge-B, the correlation between sensors installed on the different girders was negligible as SNR was not low even after replacing the component of the system with zero, but at least one sensor in the opposite girder should be considered so as to identify the torsional mode shape correctly. Examples of sensor grouping for each threshold are shown in Figure 10.

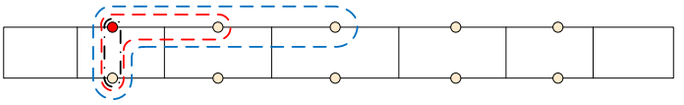


a-1) Sensor grouping for A1 sensor.

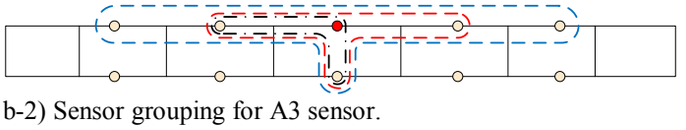


a-2) Sensor grouping for A3 sensor.

a) Bridge-A; solid line (threshold is 95%), dash line (threshold is 93%), dash-dotted line (threshold is 91%)



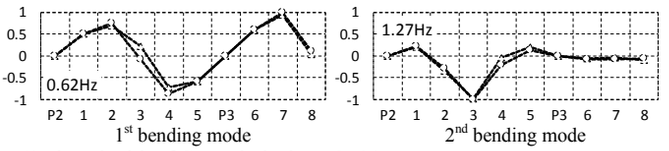
b-1) Sensor grouping for A1 sensor.



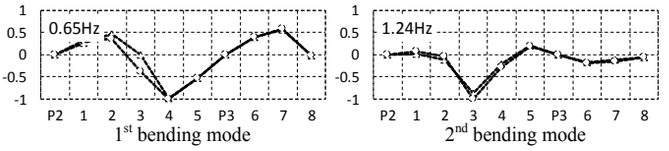
b-2) Sensor grouping for A3 sensor.

b) Bridge-B; solid line (threshold is 97%), dash line (threshold is 90%), dash-dotted line (threshold is 80%)

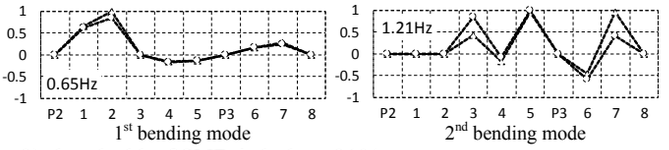
Figure 10. Examples of sensor grouping.



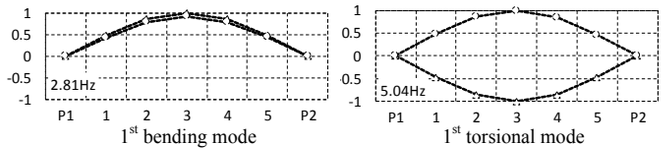
a-1) threshold of SNR is below 95%.

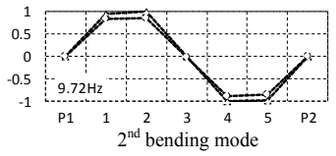


a-2) threshold of SNR is below 93%.

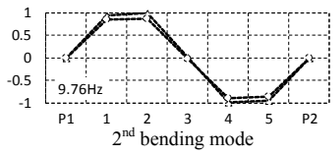


a-3) threshold of SNR is below 91%.

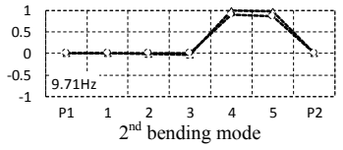




b-1) threshold of SNR is below 97%.

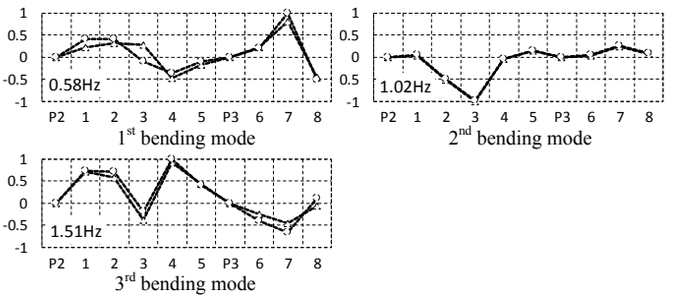


b-2) threshold of SNR is below 90%.

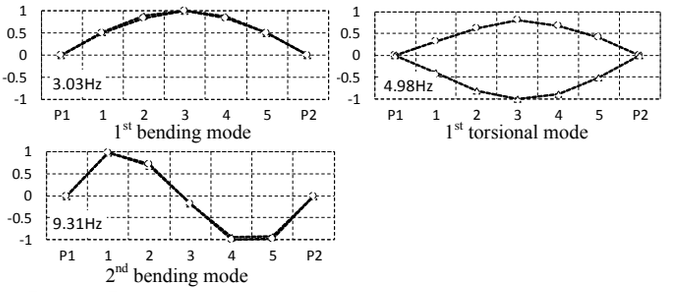


b-3) threshold of SNR is below 80%.

Figure 11. Identified natural frequencies and vibration modes by reconstructing system matrix; a) Bridge-A and b) Bridge-B.



a) Bridge-A.



b) Bridge-B.

Figure 12. Frequencies and mode shapes identified from measured vibration responses.

Table 1. Differences in frequencies and MAC values.

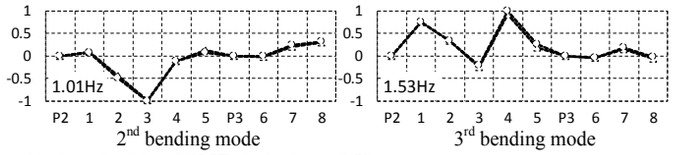
	Mode	SNR	Error of freq.	MAC
Bridge-A	1st bending	95%	0.00Hz	0.95
		93%	0.03Hz	0.89
		91%	0.03Hz	0.65
	2nd bending	95%	0.03Hz	0.91
		93%	0.00Hz	0.81
		91%	0.03Hz	0.04
Bridge-B	1st bending	97%	0.00Hz	0.99
		90%	N/A	N/A
		80%	N/A	N/A
	1st torsional	97%	0.00Hz	0.99
		90%	N/A	N/A
		80%	N/A	N/A
	2nd bending	97%	0.01Hz	1.00
		90%	0.05Hz	0.99
		80%	0.01Hz	0.67

Figure 11 shows frequencies and mode shapes identified from the AR coefficient matrix that is reconstructed based on the sensor grouping. Differences in frequencies and modal assurance criterion (MAC) between modes before and after reconstruction are summarized in Table 1. The MAC in Equation 7 is used to evaluate the correlation between two different mode vectors.

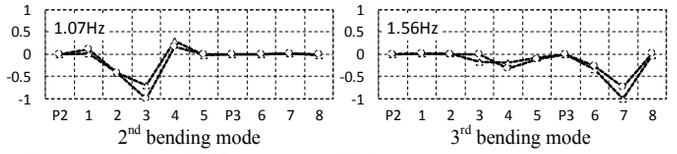
$$MAC_{ij} = \frac{(\Phi_i^T \Phi_j)^2}{(\Phi_i^T \Phi_i)(\Phi_j^T \Phi_j)} \quad (7)$$

where Φ_i, Φ_j are two mode vectors. The MAC value is bounded between 0 and 1, in which 1 indicates fully consistent mode shapes and however, 0 indicates inconsistency.

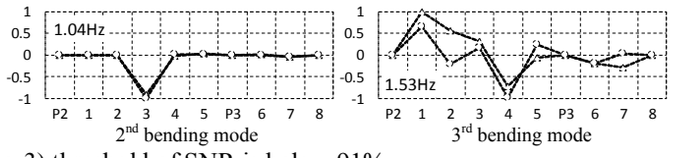
Table 1 shows that the difference in frequencies is up to 0.03Hz, and MAC for the 2nd bending mode is significantly small under the threshold of 91% for the Bridge-A. Under thresholds of 95% and 93%, the identified modes were comparable to the original modes. From the view point of reducing radio communications among sensors, it is better to select a sensor group with less sensors. Therefore, the sensor grouping under the threshold of 93% was selected. For the Bridge-B, 1st bending mode and 2nd bending mode were identified only under the threshold of 97%. Therefore, the sensor grouping under the threshold of 97% was considered. Although the frequency does not change so much, mode shapes were drastically changed.



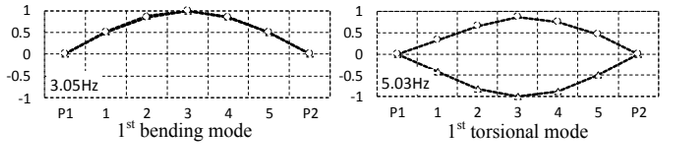
a-1) threshold of SNR is below 95%.

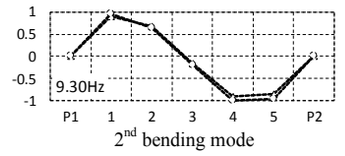


a-2) threshold of SNR is below 93%.

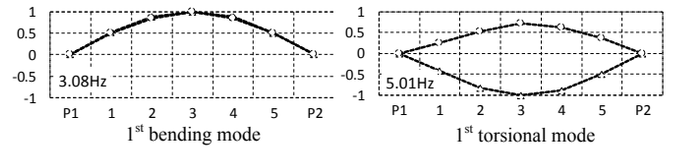


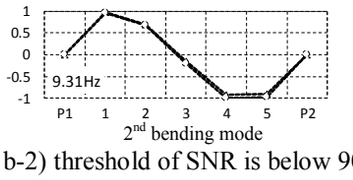
a-3) threshold of SNR is below 91%.



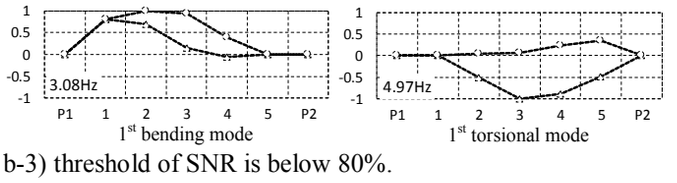


b-1) threshold of SNR is below 97%.





b-2) threshold of SNR is below 90%.



b-3) threshold of SNR is below 80%.

Figure 13. Identified natural frequencies and vibration modes by reconstructing system matrix; a) Bridge-A and b) Bridge-B.

4 SYSTEM IDENTIFICATION UTILIZING MEASURED DATA

4.1 *System identification*

Sampling rate of vibration measurement was 200Hz for both bridges. The lengths of vibration responses measured on Bridge-A and Bridge-B were 9000s and 10s, respectively. The frequencies and mode shapes identified from the measured vibration data by the MAR model are shown in Figure 12. Those mode shapes are comparable with those of eigenvalue analysis and identified from simulated responses. The comparison of frequencies identified from the simulated responses and the measured responses is summarized in Table 2, which shows that differences between simulation and experiment were from 7% to 27% for the Bridge-A, and from 2% to 7% for the Bridge-B. Insufficient information due to lack of design documents in FE modeling might be one reason for the difference.

Table 2. Comparison of frequencies identified from the simulated responses and measured responses.

	Mode	Frequency	
		Simulation	Experiment
Bridge-A	1st bending	0.62Hz	0.58Hz
	2nd bending	1.24Hz	1.02Hz
	3rd bending	2.07Hz	1.51Hz
Bridge-B	1st bending	2.80Hz	3.03Hz
	1st torsional	5.04Hz	4.95Hz
	2nd bending	9.71Hz	9.31Hz

Table 3. Differences in frequencies and MAC values.

	Mode	Threshold	Error of freq.	MAC
Bridge-A	2nd bending	95%	0.01Hz	0.95
		93%	0.05Hz	0.83
		91%	0.02Hz	0.72
	3rd bending	95%	0.01Hz	0.69
		93%	0.05Hz	0.04
		91%	0.02Hz	0.00
Bridge-B	1st bending	97%	0.01Hz	1.00
		90%	0.04Hz	1.00
		80%	0.05Hz	0.58
	1st torsional	97%	0.06Hz	0.99
		90%	0.03Hz	0.99
		80%	0.00Hz	0.70
	2nd bending	97%	0.01Hz	0.99
		90%	0.00Hz	1.00
		80%	N/A	N/A

4.2 *Correlation between installed sensors*

The SNR of vibration responses from the field experiment is estimated by using the same method discussed in Section 3 for simulation data. Correlations between sensors are almost same as those from simulated responses shown in Figure 9, and were omitted. Therefore, same sensor groupings as simulated responses are utilized to reconstruct the system matrix.

4.3 *System identification based on the reconstructed system matrix*

Frequencies and mode shapes identified from a sparse-like system matrix utilizing sensor groups are shown in Figure 13. The difference in frequencies and MAC values between before and after reconstruction are shown in Table 3. For the Bridge-A, the difference in frequencies is up to 0.05Hz. MAC value is large enough only when threshold is 95%. When thresholds are changed to 91% and 93%, the identified 3rd bending mode was not comparable with those from original AR coefficient matrix. Therefore, the sensor grouping was considered under threshold of 95% (see Figure 10 a) as examples of the sensor grouping). For the Bridge-B, 1st bending mode and 2nd bending mode are identified in all cases. Therefore, the sensor grouping under threshold of 90% was selected (see Figure 10 b) as examples of the sensor grouping).

5 CONCLUSION

This study investigates validity of system identification utilizing a sparse-like system matrix. Sensor grouping is examined by utilizing SNR which is an index indicating correlations between sensors. Dynamic response analysis is conducted by means of FE analysis as a preliminary investigation to decide the optimal sensor group. Field experiments are conducted to verify validity of the proposed method.

It is demonstrated that system identification utilizing a sparse-like system matrix based on the correlation between sensors is possible with a certain accuracy. The accuracy of system identification is significantly important for the sensor grouping. In addition, the accuracy of bridge model is also important to examine the optimal sensor group before sensors are installed on the bridges. Therefore, model updating of model parameter is needed. Future works will focus on feasibility study on actual wireless sensor networks, model updating and damage detection utilizing the sensor grouping.

REFERENCES

Agarwal, T., Schurgets, C. & Gupta, R. 2005. Dynamic power management using on demand paging for networked embedded systems, *Proceedings of the 10th Asia and South Pacific Design Automation Conference 2005*. 2: 755-759.

Brincker, R., Zhang, L. & Andersen, P. 2001. Modal identification of output-only systems using frequency domain decomposition, *Smart Materials and Structures*. 10(3): 441-445.

Chae, M.J., Yoo, H.S., Kim, J.Y. & Cho, M.Y. 2012. Development of a wireless sensors network system for suspension bridge health monitoring, *Automation in Construction*. 21: 237-252.

Deraemaeker, A., Reynders, E., Roeck, G.D. & Kullaa, J. 2008. Vibration-based structural health monitoring using output-only measurements under changing environment, *Mechanical System and Signal Processing*. 22(1): 34-56.

Kim, C.W., Kawatani, M. & Hao, J. 2012. Modal parameter identification of short span bridges under a moving vehicle by means of multivariate AR model, *Structure and Infrastructure Engineering*. 8(5): 459-472.

Nagayama, T., Moinzadeh, P., Mechitov, K., Ushita, M., Makihata, N., Leiri, M., Agha, G., Spencer, B.F., Fujino, Y. & Seo, J.W. 2010. Reliable multi-hop communication for structural health monitoring, *Smart Structures and Systems*. 6(5-6): 481-50.

Overschee, P.V. & Moor, B.D. 1991. Subspace algorithms for the stochastic identification problem, *Proceedings of 30th IEEE Conference on Decision and Control*. 2: 1321-1326.

Maintenance, Safety, Risk, Management and Life-Cycle Performance of Bridges – Powers, Frangopol, Al-Mahaidi & Caprani (Eds)
© 2018 Taylor & Francis Group, London, ISBN 978-1-138-73045-8

Obtaining full-field response for optimal sensor placement

J. Kullaa
Metropolia University of Applied Sciences, Helsinki, Finland

ABSTRACT: Optimal sensor placement (OSP) algorithms may require vibration measurements from all candidate sensor positions. A combination of experimental and numerical campaigns is proposed to obtain the full-field data. First, the response under typical excitation is measured with a redundant sensor network. Then, Bayesian virtual sensing is applied to estimate the full-field response that can be further used for OSP. Numerical simulations were performed for a structure subject to unknown random excitation. Noisy response was measured with an initial redundant sensor network, and the full-field response was estimated. Noise was added to the virtual sensors to mimic physical measurements. An OSP algorithm was applied using the virtual sensor data. The resulting optimal sensor network with a given number of sensors was compared to the initial sensor network with the same number of sensors.

1 INTRODUCTION

Structural monitoring and control utilize vibration measurements acquired by a sensor network. For a limited number of sensors, it is important to place them at optimal locations. A very common algorithm for optimal sensor placement (OSP) is the effective independence method (EFI) (Kammer 1991, 1992). The main advantage of EFI is that the optimal sensor positions can be selected using the analytical mode shape vectors only.

Optimal sensor placement depends on the application. For example, the objective may be system identification (Cherng 2003, Papadimitriou 2004, Papadimitriou & Lombaert 2012), model correlation (Yap & Zimmerman 2000), model updating (Reynier & Abou-Kandil 1999), control (Han & Lee 1999), damage detection (Worden & Burrows 2001, Yi & Li 2012, Flynn & Todd 2010), impact identification (Malardo & Aliabadi 2013), communication cost minimization (Krause et al. 2006), or response estimation (Kullaa 2017).

For some algorithms, measurement data are needed at all candidate degrees of freedom (DOFs) to make the decision for OSP. Due to the high number of candidate DOFs, measurements from all those locations can be difficult or even impossible. An alternative solution is to perform simulations using the finite element method. However, the excitation is often unknown, which makes the predicted response unreliable. Both the spatial distribution and the time history of the load are usually uncertain.

Both of the aforementioned disadvantages can be avoided with a combination of experimental and numerical campaigns. First, the response under typical ambient excitation is measured using a limited number of sensors. Then, virtual sensing is applied to estimate the full-field response that can be further used for OSP.

Virtual sensing (VS) techniques can be used to estimate the quantities of interest using the available measurements. Virtual sensing can be either analytical (model-based) or empirical (data-driven) (Lin et al. 2007).

Analytical virtual sensing techniques use information available from a limited set of physical sensors together with a finite element model to calculate an estimate of the quantity of interest. Analytical virtual sensing in structural dynamics has been studied e.g. in the following papers. Avitabile (2005) applied virtual sensing to correlation of analytical and experimental models using model expansion. Sestieri et al. (2013) estimated rotational DOFs from a limited set of measured translational DOFs. Hjelm et al. (2005) estimated stress histories from acceleration measurements. Iliopoulos et al. (2014) applied virtual sensing to fatigue assessment of wind turbines. Full-field dynamic stress/strain field was estimated from limited sets of measurement data by Pingle & Avitabile (2011) and Harvey et al. (2013). Papadimitriou et al. (2011) introduced a technique that uses Kalman filter to estimate power spectral density of strain anywhere in the structure for fatigue assessment. Eftekhar Azam et al. (2015) de-

veloped a dual Kalman filter for estimating the unknown input and states of a linear system. Maes et al. (2014) compared three different response estimation algorithms: a joint input-state estimation algorithm, a Kalman filter algorithm, and a modal interpolation algorithm. Kullaa (2016a) applied dynamic substructuring to virtual sensing.

Empirical virtual sensing can be used to replace a temporarily installed or failed sensor (Liu et al. 2009). Empirical virtual sensing has also been used for damage or sensor fault identification (Kullaa 2010, 2011). The accuracy of estimation can be increased by increasing the number of sensors in the network.

A combination of empirical and analytical virtual sensing was proposed by Kullaa (2016b) for a more accurate full-field response. This technique is also used in this study to generate measurement data for an iterative OSP algorithm. In order to mimic real measurements, a proper amount of noise is added to each virtual sensor.

The OSP procedure uses the data from the candidate virtual sensors. Due to variable excitation, modelling errors, and an iterative OSP algorithm, the resulting sensor network may be sub-optimal. Nevertheless, the proposed method is believed to work in practice and result in desired accuracy for engineering purposes.

This paper is organised as follows. Bayesian virtual sensing is described in Section 2. Optimal sensor placement is introduced in Section 3 using the selected objective function. In Section 4, numerical simulations are performed for a structure subject to unknown random excitation. An optimal sensor network with a given number of sensors is searched for and compared with the initial sensor network with the same number of sensors. Finally, concluding remarks are given in Section 5.

2 BAYESIAN VIRTUAL SENSING

Virtual sensing techniques estimate quantities of interest using the available physical sensors. Empirical virtual sensing is based on available historical measurements of the same quantity that is being estimated. In analytical virtual sensing, the quantity of interest is estimated using the available measurements and the system model.

2.1 *Bayesian empirical virtual sensing*

Empirical virtual sensing is based on the correlation between the measured quantities. Empirical virtual sensing uses regression techniques that can be implemented using different statistical methods, for example linear regression or neural network regression.

2.1.1 *Measurement model*

Consider a sensor network measuring p simultaneously sampled variables $\mathbf{y} = \mathbf{y}(t)$ at time instant t. Each measurement $\mathbf{y}$ includes independent measurement error $\mathbf{w} = \mathbf{w}(t)$:

$$\mathbf{y} = \mathbf{x}_m + \mathbf{w} \tag{1}$$

where $\mathbf{x}_m = \mathbf{x}_m(t)$ are the true values of the measured degrees of freedom. The objective is to find a less noisy estimate for the true values $\mathbf{x}_m$ utilizing the noisy measurements $\mathbf{y}$ from the sensor network.

2.1.2 *Bayes' rule*

A subset of the physical sensors is estimated by partitioning each observation into observed variables $\mathbf{v}$ and estimated variables $\mathbf{u}$ (typically a single sensor u). The partitioned variables are

$$\mathbf{y} = \begin{Bmatrix} \mathbf{y}_u \\ \mathbf{y}_v \end{Bmatrix},\ \mathbf{x}_m = \begin{Bmatrix} \mathbf{x}_{m,u} \\ \mathbf{x}_{m,v} \end{Bmatrix},\ \mathbf{w} = \begin{Bmatrix} \mathbf{w}_u \\ \mathbf{w}_v \end{Bmatrix} \tag{2}$$

Measurement error $\mathbf{w}$ is assumed to be zero mean, independent of $\mathbf{x}_m$, with a known covariance matrix

$$\boldsymbol{\Sigma}_w = E(\mathbf{w}\mathbf{w}^T) = \begin{bmatrix} \boldsymbol{\Sigma}_{w,uu} & \boldsymbol{\Sigma}_{w,uv} \\ \boldsymbol{\Sigma}_{w,vu} & \boldsymbol{\Sigma}_{w,vv} \end{bmatrix} \tag{3}$$

where $E(\cdot)$ denotes the expectation operator. From Bayes' rule,

$$\begin{aligned} p(\mathbf{x}_{m,u} \mid \mathbf{y}) &= p(\mathbf{x}_{m,u} \mid \mathbf{y}_u, \mathbf{y}_v) \\ &= \frac{p(\mathbf{y}_u \mid \mathbf{x}_{m,u}, \mathbf{y}_v) p(\mathbf{x}_{m,u} \mid \mathbf{y}_v)}{p(\mathbf{y}_u \mid \mathbf{y}_v)} \end{aligned} \tag{4}$$

The distributions in (4) can be evaluated as shown in the following.

2.1.3 *Likelihood*

Assuming Gaussian noise $\mathbf{w}$, the likelihood is obtained using Equation 1:

$$\begin{aligned} &p(\mathbf{y}_u \mid \mathbf{x}_{m,u}, \mathbf{y}_v) = p(\mathbf{y}_u \mid \mathbf{x}_{m,u}) = N(\mathbf{y}_u \mid \mathbf{x}_{m,u}, \boldsymbol{\Sigma}_{w,uu}) \\ &\propto \exp\left[-\frac{1}{2} (\mathbf{y}_u - \mathbf{x}_{m,u})^T \boldsymbol{\Sigma}_{w,uu}^{-1} (\mathbf{y}_u - \mathbf{x}_{m,u}) \right] \end{aligned} \tag{5}$$

2.1.4 *Evidence*

For simplicity but without loss of generality, assume zero-mean variables $\mathbf{y}$. The partitioned data covariance matrix $\boldsymbol{\Sigma}_y$ is

$$\boldsymbol{\Sigma}_y = E(\mathbf{y}\mathbf{y}^T) = \begin{bmatrix} \boldsymbol{\Sigma}_{y,uu} & \boldsymbol{\Sigma}_{y,uv} \\ \boldsymbol{\Sigma}_{y,vu} & \boldsymbol{\Sigma}_{y,vv} \end{bmatrix} \tag{6}$$

The precision matrix $\boldsymbol{\Gamma}_y$ is defined as the inverse of the covariance matrix $\boldsymbol{\Sigma}_y$ and is also written in partitioned form:

$$\boldsymbol{\Gamma}_y = \boldsymbol{\Sigma}_y^{-1} = \begin{bmatrix} \boldsymbol{\Gamma}_{y,uu} & \boldsymbol{\Gamma}_{y,uv} \\ \boldsymbol{\Gamma}_{y,vu} & \boldsymbol{\Gamma}_{y,vv} \end{bmatrix} \tag{7}$$

A linear minimum mean square error (LMMSE) estimate for $\mathbf{y}_u \mid \mathbf{y}_v$ is obtained by minimizing the mean-square error (MSE) and can be computed either using the covariance or precision matrix (Kullaa 2010, Bishop 2006). If each sensor signal is estimated in turn, the formulas based on the precision matrix result in a more efficient algorithm (Kullaa 2010). The evidence $p(\mathbf{y}_u \mid \mathbf{y}_v)$ is also Gaussian:

$$\begin{aligned} p(\mathbf{y}_u \mid \mathbf{y}_v) &= N(\mathbf{y}_u \mid \mathbf{K}\mathbf{y}_v, \boldsymbol{\Gamma}_{y,uu}^{-1}) \\ &\propto \exp\left[-\frac{1}{2} (\mathbf{y}_u - \mathbf{K}\mathbf{y}_v)^T \boldsymbol{\Gamma}_{y,uu} (\mathbf{y}_u - \mathbf{K}\mathbf{y}_v) \right] \end{aligned} \tag{8}$$

where $\mathbf{K} = -\boldsymbol{\Gamma}_{y,uu}^{-1} \boldsymbol{\Gamma}_{y,uv}$. Notice that the evidence is merely a normalizing factor, independent of $\mathbf{x}_{m,u}$.

2.1.5 *Prior*

The prior distribution $p(\mathbf{x}_{m,u} \mid \mathbf{y}_v)$ is obtained from the measurement model (1) by partitioning and conditioning:

$$p(\mathbf{y}_u \mid \mathbf{y}_v) = p(\mathbf{x}_{m,u} \mid \mathbf{y}_v) + p(\mathbf{w}_u) \tag{9}$$

from which the prior mean is

$$\begin{aligned} E(\mathbf{x}_{m,u} \mid \mathbf{y}_v) &= E(\mathbf{y}_u \mid \mathbf{y}_v) - E(\mathbf{w}_u) \\ &= E(\mathbf{y}_u \mid \mathbf{y}_v) = \mathbf{K}\mathbf{y}_v \end{aligned} \tag{10}$$

and the prior covariance is

$$\boldsymbol{\Sigma}_{\text{prior},uu} = \text{cov}(\mathbf{x}_{m,u} \mid \mathbf{y}_v) = \boldsymbol{\Gamma}_{y,uu}^{-1} - \boldsymbol{\Sigma}_{w,uu} \tag{11}$$

The prior distribution is also Gaussian:

$$\begin{aligned} p(\mathbf{x}_{m,u} \mid \mathbf{y}_v) &= N(\mathbf{x}_{m,u} \mid \mathbf{K}\mathbf{y}_v, \boldsymbol{\Sigma}_{\text{prior},uu}) \\ &\propto \exp\left[-\frac{1}{2} (\mathbf{x}_{m,u} - \mathbf{K}\mathbf{y}_v)^T \boldsymbol{\Sigma}_{\text{prior},uu}^{-1} (\mathbf{x}_{m,u} - \mathbf{K}\mathbf{y}_v) \right] \end{aligned} \tag{12}$$

2.1.6 *Posterior*

The posterior distribution (4) is obtained by some manipulation, resulting in a Gaussian distribution:

$$\begin{aligned} p(\mathbf{x}_{m,u} \mid \mathbf{y}) &= c_1 p(\mathbf{y}_u \mid \mathbf{x}_m) p(\mathbf{x}_{m,u} \mid \mathbf{y}_v) \\ &= c_2 \exp\left[-\frac{1}{2} (\mathbf{x}_{m,u} - \hat{\mathbf{x}}_{m,u})^T \boldsymbol{\Sigma}_{\text{post},uu}^{-1} (\mathbf{x}_{m,u} - \hat{\mathbf{x}}_{m,u}) \right] \end{aligned} \tag{13}$$

where c_1 and c_2 are constants and the posterior covariance $\boldsymbol{\Sigma}_{\text{post},uu}$ is

$$\boldsymbol{\Sigma}_{\text{post},uu} = \text{cov}(\mathbf{x}_{m,u} \mid \mathbf{y}) = (\boldsymbol{\Sigma}_{w,uu}^{-1} + \boldsymbol{\Sigma}_{\text{prior},uu}^{-1})^{-1} \tag{14}$$

and the posterior mean is

$$\hat{\mathbf{x}}_{m,u} = \boldsymbol{\Sigma}_{\text{post},uu} (\boldsymbol{\Sigma}_{w,uu}^{-1} \mathbf{y}_u + \boldsymbol{\Sigma}_{\text{prior},uu}^{-1} \mathbf{K}\mathbf{y}_v) = \mathbf{a}_u^T \mathbf{y} \tag{15}$$

where $\mathbf{a}_u^T$ is

$$\mathbf{a}_u^T = \begin{bmatrix} \boldsymbol{\Sigma}_{\text{post},uu} \boldsymbol{\Sigma}_{w,uu}^{-1} & \boldsymbol{\Sigma}_{\text{post},uu} \boldsymbol{\Sigma}_{\text{prior},uu}^{-1} \mathbf{K} \end{bmatrix} \tag{16}$$

Equation 15 shows that the posterior mean is a weighted sum of the measurements of all sensors in the network.

Notice that the MSE of the posterior (14) is always less than that of the measurement error, $\boldsymbol{\Sigma}_{w,uu}$. Therefore, the posterior mean is more accurate than the actual measurement.

Generally, the predicted DOFs **u** may include several variables. In the sequel, **u** is one-dimensional including one sensor only. For each sensor *u*, a corresponding row vector $\mathbf{a}_u^T$ is computed. All these vectors can be assembled in a coefficient matrix **A** to estimate all virtual sensors simultaneously:

$$\hat{\mathbf{x}}_m = \mathbf{A}\mathbf{y} \tag{17}$$

where each row *u* of matrix **A** represents the corresponding sensor.

A diagonal covariance matrix is assumed with variances (14) in the corresponding row *u*.

2.2 *Combined empirical and analytical virtual sensing*

Analytical virtual sensing uses a mathematical model of the system together with available measurements to estimate the quantity of interest. In combined virtual sensing, both empirical and analytical VS are used to obtain a more accurate estimate of the quantity of interest. First, empirical virtual sensing is applied to estimate a less noisy measurement. The empirical estimates will then be used in subsequent analytical VS.

In linear structural dynamics, the structural response can be written as a sum of modal contributions:

$$\mathbf{x}(t) = \sum_{i=1}^{N} \phi_i q_i(t) \approx \sum_{i=1}^{n} \phi_i q_i(t) = \boldsymbol{\Phi}\mathbf{q}(t) \tag{18}$$

where $\mathbf{x}(t)$ is the displacement response, N is the number of DOFs in the finite element model, $n << N$ is the selected number of active modes, $\boldsymbol{\Phi}$ is the truncated modal matrix consisting of the selected mode shapes ϕ_i as columns, and $\mathbf{q}(t)$ are the modal, or generalized coordinates.

The System Equivalent Reduction Expansion Process (SEREP) algorithm (Avitabile 2005) is briefly outlined. If $\mathbf{x}(t)$ is divided into measured and unmeasured DOFs, $\mathbf{x}_m(t)$ and $\mathbf{x}_e(t)$, respectively, the mode shape vectors are divided correspondingly:

$$\mathbf{x}(t) = \begin{Bmatrix} \mathbf{x}_m(t) \\ \mathbf{x}_e(t) \end{Bmatrix} = \begin{bmatrix} \boldsymbol{\Phi}_m \\ \boldsymbol{\Phi}_e \end{bmatrix} \mathbf{q}(t) \tag{19}$$

The upper equation reads

$$\mathbf{x}_m(t) = \boldsymbol{\Phi}_m \mathbf{q}(t) \tag{20}$$

The exact values $\mathbf{x}_m(t)$ are not known, but the posterior distribution is used instead.

$$\hat{\mathbf{x}}_m(t) = \mathbf{x}_m(t) + \mathbf{e}(t) \tag{21}$$

where $\hat{\mathbf{x}}_m(t)$ is given by (17) and $\mathbf{e}(t)$ is the posterior error with zero mean and diagonal covariance matrix $E(\mathbf{e}\mathbf{e}^T) = \text{diag}(\boldsymbol{\Sigma}_{\text{post},uu})$. Using Equation 20, Equation 21 becomes

$$\hat{\mathbf{x}}_m(t) = \boldsymbol{\Phi}_m \mathbf{q}(t) + \mathbf{e}(t) \tag{22}$$

with the weighted least squares (WLS) solution (Bar-Shalom 2001):

$$\hat{\mathbf{q}}(t) = (\boldsymbol{\Phi}_m^T \mathbf{W} \boldsymbol{\Phi}_m)^{-1} \boldsymbol{\Phi}_m^T \mathbf{W} \hat{\mathbf{x}}_m(t) \tag{23}$$

where the weighting matrix $\mathbf{W}$ is the inverse of $E(\mathbf{e}\mathbf{e}^T)$.

Once the estimate of $\mathbf{q}(t)$ is solved, any DOF can be computed from Equation 19:

$$\hat{\mathbf{x}}(t) = \boldsymbol{\Phi} \hat{\mathbf{q}}(t) \tag{24}$$

The error covariance of the WLS estimate of $\mathbf{q}(t)$ (23) is (Bar-Shalom 2001):

$$\boldsymbol{\Sigma}_{\mathbf{q}} = (\boldsymbol{\Phi}_m^T \mathbf{W} \boldsymbol{\Phi}_m)^{-1} \tag{25}$$

Notice that the model error in $\boldsymbol{\Phi}$ is ignored.

Finally, any DOF can be estimated using Equations 24, 23, and 17:

$$\begin{aligned} \hat{\mathbf{x}}(t) &= \boldsymbol{\Phi} \hat{\mathbf{q}}(t) \\ &= \boldsymbol{\Phi} (\boldsymbol{\Phi}_m^T \mathbf{W} \boldsymbol{\Phi}_m)^{-1} \boldsymbol{\Phi}_m^T \mathbf{W} \hat{\mathbf{x}}_m(t) \\ &= \boldsymbol{\Phi} (\boldsymbol{\Phi}_m^T \mathbf{W} \boldsymbol{\Phi}_m)^{-1} \boldsymbol{\Phi}_m^T \mathbf{W} \mathbf{A} \mathbf{y}(t) \\ &= \mathbf{H} \mathbf{y}(t) \end{aligned} \tag{26}$$

where

$$\mathbf{H} = \boldsymbol{\Phi} (\boldsymbol{\Phi}_m^T \mathbf{W} \boldsymbol{\Phi}_m)^{-1} \boldsymbol{\Phi}_m^T \mathbf{W} \mathbf{A} \tag{27}$$

The error variances of the virtual sensors are

$$\text{var}\left[\hat{\mathbf{x}}(t)\right] = \text{diag}(\boldsymbol{\Phi} \boldsymbol{\Sigma}_{\mathbf{q}} \boldsymbol{\Phi}^T) \tag{28}$$

The covariance matrix of the virtual full-field data is obtained as follows (assuming zero means):

$$\boldsymbol{\Sigma}_{\hat{x}} = E\left[\hat{\mathbf{x}}(t)\hat{\mathbf{x}}(t)^T\right] = \mathbf{H} E(\mathbf{y}\mathbf{y}^T) \mathbf{H}^T = \mathbf{H} \boldsymbol{\Sigma}_y \mathbf{H}^T \tag{29}$$

In order to produce virtual measurements, the noise characteristics should be the same as in the actual measurement chain. Therefore, a (diagonal) noise covariance matrix must be added to the covariance matrix of the virtual sensors (29):

$$\boldsymbol{\Sigma}_{\hat{y}} = \boldsymbol{\Sigma}_{\hat{x}} + \boldsymbol{\Sigma}_w \tag{30}$$

3 OPTIMAL SENSOR PLACEMENT

The objective is to estimate the full-field response for OSP. The procedure is depicted in Figure 1. The procedure consists of both experimental and numerical methods. The experiments are performed for the structure using a network with a limited number of sensors and the numerical analysis uses a finite element model resulting in the truncated modal matrix including all candidate DOFs. Notice that the excitation remains unknown.

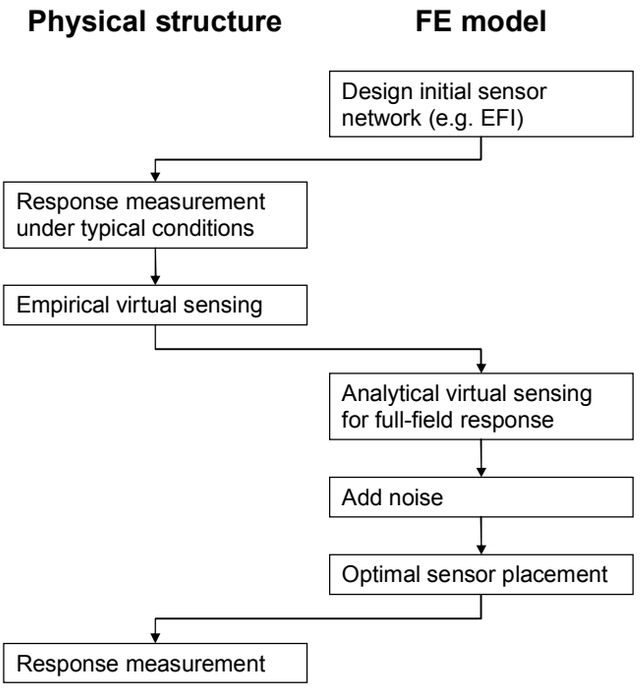


Figure 1. OSP procedure using both experimental and numerical methods.

First, an initial redundant sensor network is deployed. Response is measured under typical ambient excitation, because the excitation characteristics are expected to affect the optimal sensor placement.

Once the measurements are available, the full-field response is estimated as described in the previous section. An updated FE model is essential to produce accurate mode shapes in the desired frequency band. Independent Gaussian noise of full value is added to each virtual sensor to represent the measurement error in the actual measurement chain. The full-field response is used in the OSP algorithm like it was measured with physical sensors.

The proposed optimal sensor placement algorithm is an iterative procedure starting with an initial large sensor network including all candidate DOFs (backward sequential sensor placement, or BSSP). A single sensor is removed and the cost function is evaluated for the reduced sensor network. This is repeated for different sensor networks of the same number of sensors by removing each sensor in turn. Finally, the minimum cost is found, and the corresponding reduced sensor network is selected. The

process is repeated until the desired number of sensors or the required minimum accuracy is reached.

For the OSP algorithm in the following, the actual time histories are not needed, because the MSE and consequently the cost function can be evaluated from the covariance matrices and the modal matrix. The procedure is as follows.

1 Obtain the data covariance matrix of all candidate DOFs (30)
2 Do until stopping criterion (number of sensors or minimum accuracy)
3 For each sensor j, do
4 Remove sensor j
5 Update the covariance matrix (6) and compute the precision matrix (7). Store the diagonals of the precision matrix.
6 Compute the weighting matrix **W** in (23), which is the inverse of the diagonal posterior covariance matrix
7 Compute the error variance of all virtual sensors (Equation 28)
8 Evaluate the cost function (e.g. the maximum error variance)
9 Next j. Go to item 4
10 Find the removed sensor k corresponding to the minimum cost function
11 Remove sensor k permanently
12 Update data covariance matrix by removing the row and column corresponding to the removed sensor
13 Go to item 2

4 NUMERICAL STUDY

A structure for experimental data was not available for the present study. Therefore, experiments were replaced with numerical simulations. In order to make the study more realistic, two different FE models were used with intentional discrepancies between the two models. The first model represented the real structure (Fig. 2) while the second model was the actual FE model used for the full-field response estimation (Fig. 3).

The structure was a bridge deck with four longitudinal stiffeners. The length was 40 m and width 15 m. The deck was made of concrete with Young's modulus of E = 40 GPa, Poisson ratio of ν = 0.15, density of ρ = 2500 kg/m^3, and thickness of 250 mm. The steel stiffeners (E = 207 GPa, of ν = 0.30, ρ = 7850 kg/m^3) had a web with a thickness of t = 16 mm and a height of h = 1.4 m. The bottom flange had a thickness of t = 50 mm and a width of b = 700 mm.

In both models, the deck was modelled with shell elements. The stiffeners in the actual bridge were modelled with shell elements (Fig. 2). In the second model, they were modelled with beam elements and connected to the deck using rigid links (Fig. 3). The beam elements were assumed to be symmetrical I-profiles, which caused additional discrepancy compared to the real structure.

The ends of the beams were simply supported (the nodes of the bottom flanges in the first model and the beam nodes in the second model). Longitudinal displacements were fixed only at one end of the bridge. The corners of the deck were supported in lateral and vertical directions.

Two independent random loads were applied at nodes 774 and 872 in vertical direction (green squares in Fig. 2). Both excitation signals were low-pass filtered below 5.33 Hz. The standard deviation of either load was 100 N. The excitation was not measured.

Vertical accelerations were measured at 28 points shown in Figure 2. Same amount of noise was added to the signals, so that the mean signal-to-noise ratio was SNR = 21 dB.

Using the physically measured 28 accelerations, the empirical Bayesian virtual sensors were estimated. Then the full-field accelerations (all vertical DOFs of the bridge deck) were estimated using the truncated modal matrix from the finite element model of the bridge (Fig. 3). Full-value noise was added to all virtual sensors.

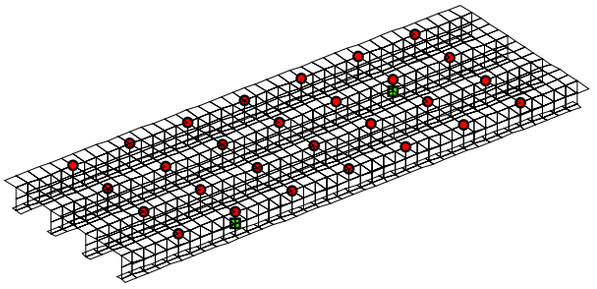


Figure 2. Finite element model representing the real structure. The initial 28 sensor positions are shown as red circles and the two excitation points as green squares.

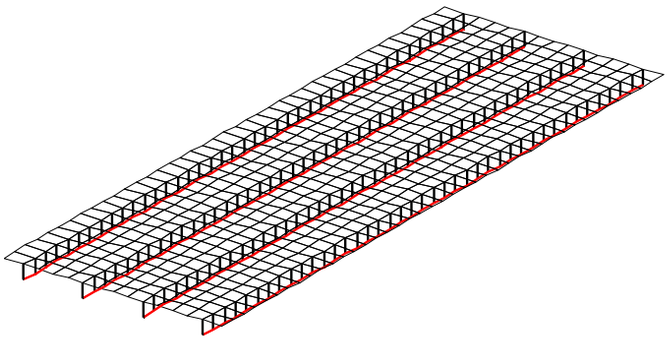


Figure 3. Finite element model of the bridge using shell and beam elements connected with rigid links.

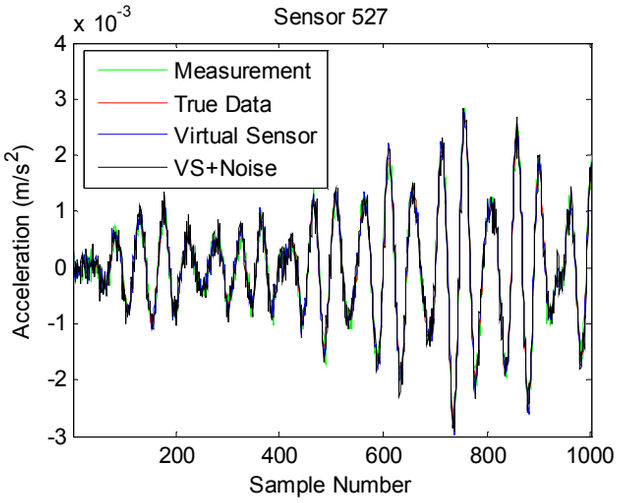


Figure 4. Time history of sensor 527. Red: true (noiseless) data. Blue: virtual sensor. Green: noisy measurement. Black: synthetic measurement (virtual sensor + noise).

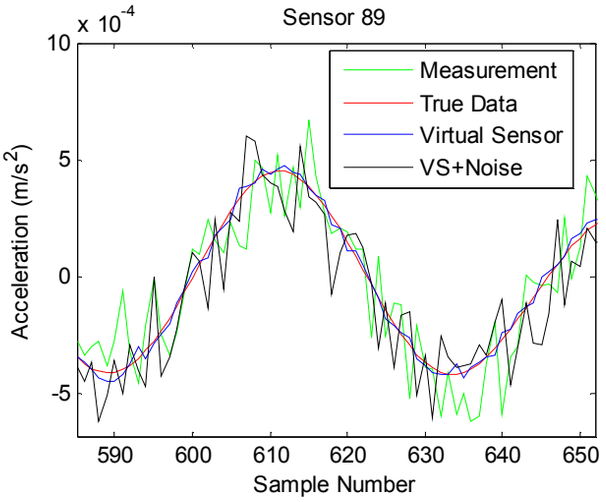


Figure 5. Detail of the time history of sensor 89. Red: true (noiseless) data. Blue: virtual sensor. Green: noisy measurement. Black: synthetic measurement (virtual sensor + noise).

A sample of virtual sensor 527 is plotted in Figure 4 and a detail of acceleration of virtual sensor 89 is shown Figure 5. The red curve is the noiseless true signal and green is the corresponding noisy measurement. The signals of the corresponding virtual sensors before and after noise addition are plotted in blue and black, respectively.

It can be seen that the virtual sensors closely corresponded to the actual signals and the noise levels in the actual and virtual sensors appear to be similar.

Once the full-field data were available, the next step was optimal sensor placement. In the present study, the objective was to minimize the error in the full-field response estimates using a minimum number of sensors. The cost function was the maximum standard deviation of the estimation error in the full-field virtual sensor data.

Starting with sensors at all 607 candidate positions (all vertical DOFs in the deck excluding the fixed DOFs) and removing one sensor in each round, the cost function was recorded and depicted in Figure 6. A comparison was made using the actual noisy measurements, and the corresponding cost function is shown in the same figure. The two data sets resulted in almost equal costs with a small number of sensors. In both cases, the cost function increased as the number of sensors was decreased, as expected.

Determining the number of sensors to be equal to 28, the optimal sensor positions are depicted in Figure 7 when using virtual sensors and in Figure 8 when using the actual measurements. The sensor positions were very similar in both cases. It can be seen that the sensors had a tendency to locate at six clusters. With this arrangement, the full-field data became most accurate.

A validation study was performed using a different realization of the random excitation. The excitation characteristics were the same. The standard deviations of the estimation errors of all virtual sensors were computed. Three sensor networks were analyzed: the two aforementioned optimal sensor networks and the initial equidistant network (Fig. 2). The errors are plotted in Figures 9–11 also showing the physical sensors. It can be seen that the optimal sensor placement was able to decrease the maximum error by almost 40% compared to the initial network with the same number of sensors. This demonstrates that designing the sensor positions can have an advantageous impact on the system performance.

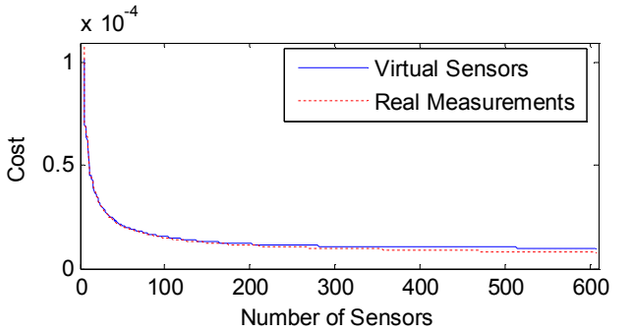


Figure 6. Cost function with different number of sensors using virtual sensors or real measurements.

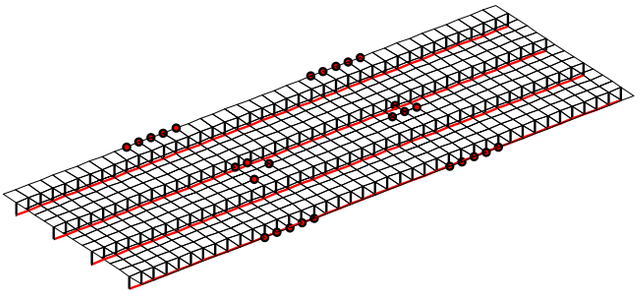


Figure 7. Optimal sensor positions for 28 sensors using synthetic data.

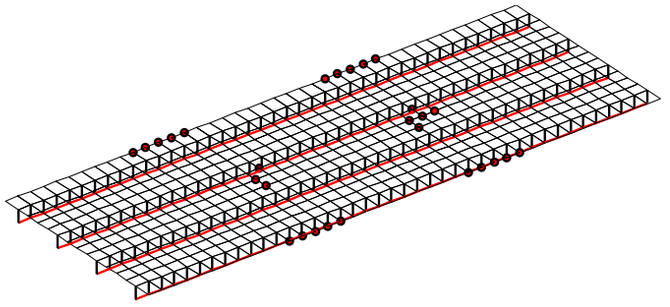


Figure 8. Optimal sensor positions for 28 sensors using real measurements.

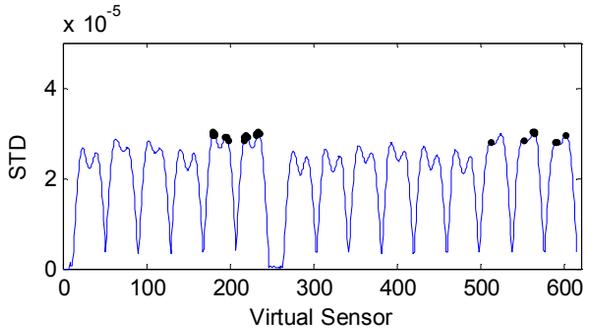


Figure 9. Standard deviations of the estimation errors in all virtual sensors using the sensor network in Figure 7 (shown with black dots) and a new realization of the excitation.

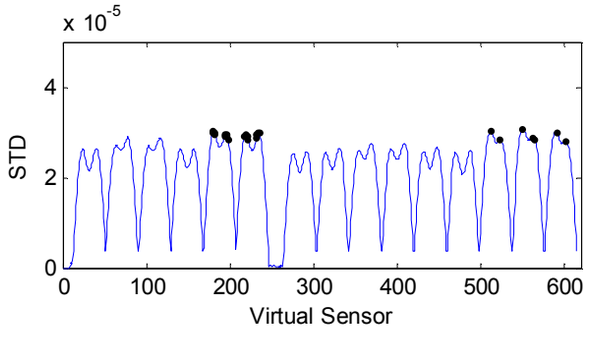


Figure 10. Standard deviations of the estimation errors in all virtual sensors using the sensor network in Figure 8 (shown with black dots) and a new realization of the excitation.

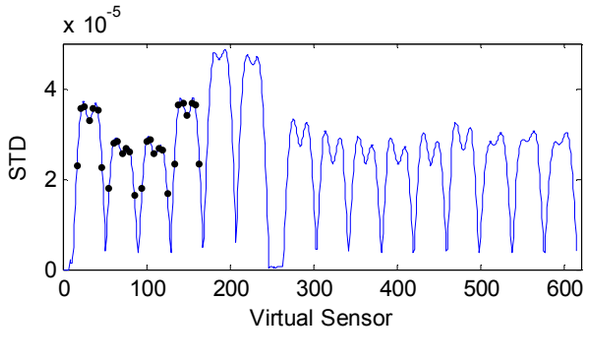


Figure 11. Standard deviations of the estimation errors in all virtual sensors using the initial sensor network in Figure 2 (shown with black dots) and a new realization of the excitation.

5 CONCLUSION

Optimal sensor placement was studied assuming algorithms that require sensor data from all candidate DOFs. Bayesian virtual sensing was applied to vibration measurements in order to obtain the full-field response data.

Because it is usually not possible to acquire measurements from all candidate positions, the response of the unmeasured DOFs has to be estimated. Simulating the response is another option, but since the excitation is unknown, the response may not be representative.

Full-field response data were estimated using Bayesian virtual sensing. The virtual sensors were less noisy than the corresponding hardware. Noise was added to all virtual sensors in order to simulate true measurements.

The finite element model must be accurate enough to represent the active mode shapes. Also, the number of sensors must be higher than the number of active modes to make the sensor network redundant.

Optimal sensor placement was studied for a bridge deck, in which the objective was to estimate the full-field response with desired accuracy. An iterative BSSP optimization algorithm was used, in which a single sensor was removed in each round from the initially fully occupied sensor network. The approach was to minimize the largest estimation error in the virtual sensors in each round.

In the proposed application, the actual time histories of the virtual sensors were not needed, because all necessary information was included in the statistical parameters. It should be noted, however, that the time histories could be computed whenever needed and the corresponding equations were derived.

In OSP, an engineering solution is often adequate. The sensor positions are sometimes guessed or located in an equidistant grid. The objective was to have a more sophisticated and cost-effective solution. Due to variable loading, there may not be an absolute optimum for the OSP problem. Nevertheless, data from a typical situation are preferred. In addition to loading, the finite element model includes modelling errors, the estimates of the sensor noise variances may be uncertain, and the BSSP algorithm may give a sub-optimal solution. Despite of these, it is believed that a good engineering solution can be found, which was also obtained in the numerical example. Experimental validation was left for a future study.

REFERENCES

Avitabile, P. 2005. Model Reduction and Model Expansion and Their Applications – Part 1: Theory. *Proceedings of IMAC-*

XXIII, A Conference & Exposition on Structural Dynamics. Society for Experimental Mechanics.

Bar-Shalom, Y., Li, X.-R. & Kirubarajan, T. 2001. *Estimation with applications to tracking and navigation.* Wiley.

Bishop, C.M. 2006. *Pattern recognition and machine learning*. Springer.

Cherng, A-P. 2003. Optimal sensor placement for modal parameter identification using signal subspace correlation techniques. *Mechanical Systems and Signal Processing* 17: 361–378.

Eftekhar Azam, S., Chatzi, E. & Papadimitriou, C. 2015. A dual Kalman filter approach for state estimation via output-only acceleration measurements. *Mechanical Systems and Signal Processing* 60–61: 866–886.

Flynn, E. & Todd, M.D. 2010. A Bayesian approach to optimal sensor placement for structural health monitoring with application to active sensing. *Mechanical Systems and Signal Processing* 24: 891–903.

Han, J-H. & Lee, I. 1999. Optimal placement of piezoelectric sensors and actuators for vibration control of a composite plate using genetic algorithms. *Smart Materials and Structures* 8: 257–267.

Harvey, E., Ruddock, J. & Avitabile, P. 2013. Comparison of full field strain distributions to predicted strain distributions from limited sets of measured data for SHM applications. *Tenth International Conference on Damage Assessment to Structures, Dublin, Ireland, July 2013*.

Hjelm, H.P., Brincker, R., Graugaard-Jensen, J. & Munch, K. 2005. Determination of stress histories in structures by natural input modal analysis. *Proceedings of IMAC-XXIII, A Conference & Exposition on Structural Dynamics. Society for Experimental Mechanics*.

Iliopoulos, A., Devriendt, C., Guillaume, P. & Van Hemelrijck, D. 2014. Continuous fatigue assessment of an offshore wind turbine using a limited number of vibration sensors. In V. Le Cam, L. Mevel, F. Schoefs (eds), *EWSHM - 7th European Workshop on Structural Health Monitoring, July 8–11, 2014, Nantes, France*: 772–779.

Kammer, D.C. 1991. Sensor placement for on-orbit modal identification and correlation of large space structures. *Journal of Guidance, Control, and Dynamics* 14: 251–259.

Kammer, D.C. 1992. Effects of noise on sensor placement for on-orbit modal identification of large space structures. *Journal of dynamic systems, measurements and control—Transactions of the ASCE* 114 (3): 436–443.

Krause, A., Guestrin, C., Gupta, A. & Kleinberg, J. 2006. Near-optimal sensor placements: maximizing information while minimizing communication cost. *Proceedings of the 5th International Conference on Information Processing in Sensor Networks (IPSN '06), New York, NY, USA, 2006*: 2–10.

Kullaa, J. 2010. Sensor validation using minimum mean square error estimation. *Mechanical Systems and Signal Processing* 24: 1444–1457.

Kullaa, J. 2011. Distinguishing between sensor fault, structural damage, and environmental or operational effects in structural health monitoring. Mechanical Systems and Signal Processing 25 (8), 2976–2989.

Kullaa, J. 2016a. Virtual sensing of structural vibrations using dynamic substructuring. *Mechanical Systems and Signal Processing* 79: 203–224.

Kullaa, J. 2016b. Combined empirical and analytical virtual sensing for full-field dynamic response estimation. In A. Güemes (ed.), *Proceedings of the 8th European Workshop on Structural Health Monitoring. Bilbao, Spain, July 5–8, 2016*.

Kullaa, J. 2017. Optimal sensor placement for virtual sensing of structural vibrations. Proceedings of the International Conference on Structural Engineering Dynamics (ICEDyn 2017). Maia, N.M.M., Neves, M.M., Sampaio, R.P.C. (eds.), Ericeira, Portugal, July 3–5, 2017.

Lin, B., Recke, B., Knudsen, J.K.H. & Jørgensen, S.B. 2007. A systematic approach for soft sensor development. *Computers and Chemical Engineering* 31: 419–425.

Liu, L., Kuo, S.M. & Zhou, M. 2009. Virtual sensing techniques and their applications. *Proceedings of the 2009 IEEE International Conference on Networking, Sensing and Control, Okayama, Japan, March 26–29, 2009*: 31–36.

Maes, K., De Roeck, G. & Lombaert, G. 2014. Response estimation in structural dynamics. In A. Cunha, E. Caetano, P. Ribeiro, & G. Müller (eds), *Proceedings of the 9th International Conference on Structural Dynamics, EURODYN 2014, Porto, Portugal, 30 June - 2 July 2014*: 2399–2406.

Mallardo, V. & Aliabadi, M.H. 2013. Optimal sensor placement for structural, damage and impact identification: a review. *Structural Durability & Health Monitoring* 9 (4): 287–323.

Papadimitriou, C. 2004. Optimal sensor placement methodology for parametric identification of structural systems. *Journal of Sound and Vibration* 278: 923–947.

Papadimitriou, C., Fritzen, C.-P., Kraemer, P. & Ntotsios, E. 2011. Fatigue predictions in entire body of metallic structures from a limited number of vibration sensors using Kalman filtering. *Structural Control and Health Monitoring* 18: 554–573.

Papadimitriou, C. & Lombaert, G. 2012. The effect of prediction error correlation on optimal sensor placement in structural dynamics. *Mechanical Systems and Signal Processing* 28: 105–127.

Pingle, P. & Avitabile, P. 2011. Full-field dynamic stress/strain from limited sets of measured data. *Sound and Vibration*, August 2011, 10–14.

Reynier, M. & Abou-Kandil, H. 1999. Sensors location for updating problems. *Mechanical Systems and Signal Processing* 13: 297–314.

Sestieri, A., D'Ambrogio, W., Brincker, R., Skafte, A. & Culla, A. 2013. Estimation of Rotational Degrees of Freedom by EMA and FEM Mode Shapes. In R. Allemang, J. De Clerck, C. Niezrecki & A. Wicks (eds), *Special Topics in Structural Dynamics, Volume 6, Proceedings of the 31st IMAC, A Conference on Structural Dynamics, 2013*: 355–365.

Worden, K. & Burrows, A.P. 2001. Optimal sensor placement for fault detection. *Engineering Structures* 23(8): 885–901.

Yap, K.C. & Zimmerman, D.C. 2000. Optimal sensor placement for dynamic model correlation. *Proceedings of the 18th International Modal Analysis Conference*: 607–612.

Yi, T-H. & Li, H-N. 2012. Methodology developments in sensor placement for health monitoring of civil infrastructures. *International Journal of Distributed Sensor Networks*: 1550–1329.

Maintenance, Safety, Risk, Management and Life-Cycle Performance of Bridges – Powers, Frangopol, Al-Mahaidi & Caprani (Eds)
© 2018 Taylor & Francis Group, London, ISBN 978-1-138-73045-8

Potential of Drive-By Inspection for Railway Bridges

A. H. Eslami-Khouzani & C. Caprani
Department of Civil Engineering
Monash University, Melbourne, Australia

ABSTRACT: Drive-by bridge inspection (DBBI) is a promising indirect monitoring approach due to its potential advantages over direct bridge monitoring. These advantages include economy and accessibility: one moving vehicle can monitor many bridges, with just a few sensors; and it is easier to instrument a vehicle than a bridge. As a result of these attractive features, it is gaining increased attention from researchers. However, most of the research done on DBBI has been conducted on highway bridges only. The application of the approach to railway bridges is not yet known. This paper will identify the challenges that are unique to the drive-by inspection of railway bridges. Firstly, the physics of vehicle-bridge interaction (VBI) and train-track-bridge interaction (TTBI) is described, as these are fundamental to DBBI. Then, a review of the research already done for DBBI on highway bridges is presented. From this, the problems facing DBBI are identified. Some of these problems may not exist for railway bridges, while there may be some further complicating issues not present for highway bridges. Therefore, these issues are assessed using the different physics of VBI and TTBI. From this, the potential of DBBI for railway bridges is considered, and the relevant research challenges identified.

1 INTRODUCTION

Bridges are critical transportation assets which require frequent monitoring. Similar to many developed countries, more than 40 percent of bridges in Australia are over 40 years old. In this time their loading conditions have changed due to increases in freight and traffic volume, and so they require ongoing inspection and maintenance (RMS 2012).

Routine inspection methods of bridges are based on visual inspections and non-destructive periodic testing which are time-consuming and inefficient (Quirk et al. 2017). However, other inspection methods can be used to overcome the problem. Indirect approaches for structural health monitoring of bridges have gained more attention because of their time- and cost-saving potential. For example, the direct monitoring of a bridge's vibration requires the installation of many sensors and other supporting equipment. Contrast this with an indirect monitoring approach in which a sensor-equipped moving vehicle can monitor all bridges it crosses. The potential of determining the vibration response of bridges using this indirect monitoring approach was first confirmed by Yang et al. (2004). This approach has become known as drive-by bridge inspection (DBBI).

Most of the research so far on DBBI concentrates on highway bridges. This is curious because railway bridges typically have a much higher vehicle to bridge mass ratio, compared to highway bridges. As such, trains are well-suited to DBBI due to the strong vibrations that can be imparted. In principle, such vibrations of the bridge can then be used to monitor the health of the bridge. Further, due to the regularity of trains on many rail lines, knowledge of the bridge behaviour can be built up over time, allowing changes to be more easily detected. Nevertheless, in spite of these synergies, there are other factors that may reduce its suitability.

This paper examines the potential of DBBI for railway bridges. Parameters and physics related to indirect bridge monitoring are presented. A review of DBBI for highway bridges is then given, including a discussion of the problems facing it. Finally, challenges of DBBI for rail bridges are stated, and its potential for railway bridges is examined.

2 PHYSICAL PARAMETERS OF DBBI

The physical parameters important for DBBI of the combined vehicle-bridge system are considered next. The effects of these parameters on DBBI will be assessed in section 4.

2.1 *Vehicle parameters*

A railway vehicle generally consists of a car body, secondary suspension system, bogie, primary suspen-

sion system and wheelsets. Two rigid wheels coupled by an axle is called a wheelset, and is connected to the bogie frame by the primary suspension. The bogie frame and the car body are connected by the secondary suspension. In contrast to railway vehicles, there is no bogie or secondary suspension system in highway vehicles.

2.1.1 *Vehicle-to-bridge mass ratio*

During a vehicle traverse, the vehicle adds mass to the system altering its dynamic properties. Depending on the relative size of the vehicle-to-bridge mass, the effect can range from small to large. Yang et al. (2013) and Chang et al. (2014) both studied this effect finding that larger vehicle/bridge mass ratio leads to larger changes in the vehicle-bridge system frequency compared to the bridge alone. Compared to highway bridges, train mass is generally heavier than highway vehicles. This can cause noticeable deviations in the vehicle-bridge system frequencies. Therefore, it is clearly necessary to consider the effect of mass in TTBI to incorporate frequency variations during the traverse.

2.1.2 *Axle spacing*

For both road and rail, axle spacing is important to the response when coupled with vehicle speed and bridge natural frequency. If the time period between the successive axles of a train passing a bridge is an integer multiple of the period of one of the bridge natural frequencies, then a resonant response will occur. Then, subsequent axles enter the bridge in phase with the vibration, exacerbating the amplitudes.

The fundamental difference between rail and road bridges is the existence of repeated regular loads with identical axle spacing in trains which can lead to resonant behaviour in bridges at certain speeds. Even various combination of vehicles in highway bridges do not generate such resonance to the same range of railway bridges since the distance between vehicles is random (Cantero et al. 2016).

This phenomenon is readily found using simulations, where the model parameters can be precisely controlled. However in practice, it is far more difficult to observe, since the parameters tend to vary, e.g. vehicle speeds, bridge frequency, etc.

2.1.3 *Vehicle suspension*

Vehicle suspensions add damping to the dynamic system, increasing energy loss, and so reduce vibrations. Yu and Chan (2004) studied the effect of vehicle suspension system on the dynamic behaviour of bridges. They considered three types of suspension systems: a rigid connection to simulate vehicles without suspension; spring connections to simulate the leaf-spring system, and; pre-compressed springs to simulate an alternative form of the suspension system. They find that the suspension systems make an obvious impact on both the dynamic characteristics of vehicles and bridge response. In particular, the fundamental frequency of vehicles is significantly changed with different suspension systems.

2.1.4 *Vehicle/bridge energy transmission*

Although energy transmission from the vehicle body to bridge structure plays a key role in VBI systems, only a few studies have focused on the mechanism of energy transmission. In one of them the author examined three different kinds of wheels to investigate the resolution of bridge dynamic responses including (a) inflatable wheels with a diameter of 300 mm and a width of 85 mm, (b) Solid Rubber wheels with a diameter of 300 mm and a width of 50 mm, and (c) Polyurethane wheels with the same diameter, but a width of 70 mm. The last one is basically a metal wheel surrounded by a thin layer of 10 mm polyurethane. Considering these three different cases, Yang et al. (2013) recognised that the most favourable wheel to extract the bridge dynamic characteristics is the polyurethane one since it has very small and even distributions of frequency amplitudes with the least interfere with bridge frequencies. Consequently, it can be inferred that the train wheels are even more favourable types to measure the dynamic properties of bridges since they are effectively rigid wheels with direct contact to the rail surface.

2.2 *Driving Surface*

A road surface or pavement is usually made of materials such as asphalt or concrete laid on a compacted base course. The International Standards Organisation (ISO) classifies the roughness of road profiles into A (very good), B (good), C (average), D (poor) and E (very poor) (ISO 1995). Obviously, the rougher a road, the more a vehicle bounces (or vibrates) on it. Road roughness is measured using a power spectral density (PSD) function.

For railways, the driving surface consists of rails, fasteners, sleepers and ballast. Track irregularities are deviations in track profile from ideal geometry. There are two types of irregularities: periodic such as railhead corrugation, cross-beam and sleeper effects; and random irregularities which is also described using a PSD function. These irregularities increase the vibration of bridges and trains (Frỳba 1996). In contrast to roads, long periods of low-temperature influence the dynamic properties of the ballast and track due to ice formation in the ballast and frost in the ground (Gonzales et al. 2013).

In railways, transition zones from embankments to rigid structures such as bridges, also influence track properties. There is currently insufficient experimental data on the behaviour of such sections (Coelho et al. 2009). On the other hand, turnouts (including switches and crosses) provide flexibility to train movements. At these locations, train-track dynamic

interaction is more complicated than typical tracks since large disturbances occur as the wheels are transferred across lines in the switch panel or when the wheels pass the gap between wing rail and nose rail in the crossing panel (Kassa and Nielsen 2009).

2.3 *Measurement precision*

2.3.1 *Physical parameters*

Because of the dynamic interaction between the vehicle and the bridge, sensors mounted on the vehicle measure the combined vehicle and the bridge response as it passes the bridge. Accurate knowledge of the vehicle dynamic behaviour allows the bridge response component to be identified by somehow filtering out the vehicle response. Hence the dynamic characteristics of the bridge can be identified, at least in principle. Of course, in practice, there are many sources of noise and error that affect the problem.

The parameters that influence the measurement precision of bridge dynamic characteristics by DBBI have been investigated in the research already done. Consistently it is found that lower vehicle speeds and a bigger vehicle-to-bridge mass ratio both increase accuracy (Chen and Xia 2009). Other researchers considered the effect of road profile and found better accuracy for a smooth road profile (Chang et al. 2010, Yang et al. 2012). It seems that increased vehicle response through any means—low damping, low mass, rough pavement—may dominate the bridge responses.

In an experimental study by Yang et al. (2013), the influence of volumes of existing random traffic flow was considered. A four-span continuous bridge with a length of 113 m and a width of 17 m was studied. Continuous traffic flow with the speed of over 50 km/h was defined as a large volume and the reverse as a small volume. In the former, the first five bridge frequencies could be identified with high precision, while in latter only the first bridge natural frequency was identified with enough accuracy.

2.3.2 *Data acquisition*

One fundamental issue of DBBI relates to frequency spectrum estimation. The duration, T, of the recording is $T = L/v$ where L is the bridge length, and v the vehicle velocity (assumed constant). Regardless of the sampling rate, the smallest possible frequency, Δf, that can be distinguished for a full period of the recorded time series is

$$\Delta f = \frac{1}{T} = \frac{v}{L}. \tag{1}$$

Consequently, changes in frequency smaller than this amount cannot be found in the frequency spectrum. The relationship between the discernible frequency changes, bridge length, and vehicle velocity are apparent: slower speeds and longer bridges are better for detection of smaller frequency changes.

A few studies examine the influence of sampling frequency on indirect bridge monitoring. First, Lin and Yang (2005) derived the first natural frequency of a bridge using a passing vehicle with a sampling rate of 100 Hz and a record time of 200 s, while Cerda et al. (2014) mention an effective sampling rate is about 1650 Hz for a low speed of 10 to 30 km/hr. Chae et al. (2012) find that a sampling frequency more than 100 Hz is required to obtain clear peaks in the frequency domain for vibration measurements. In another study, Bu et al. (2006) examined a vehicle with a speed of 20 m/s and four sampling rates: 100, 200, 500 and 1000 Hz and observed that the sampling variation has a small effect on the accuracy of bridge frequency identification at this speed. As can be seen, so far the research findings on sample rate for DBBI are consistent with the simple analysis of equation 1.

3 REVIEW OF DBBI FOR HIGHWAY BRIDGES

In recent years, new methods have been presented based on indirect bridge monitoring. At first, the idea was mainly about identifying the fundamental frequency of the bridge. More recent research attempts to consider the bridge damping and mode shapes. These methods will be introduced and reviewed in this section.

3.1 *Frequency-based methods*

The feasibility of obtaining bridge frequencies using indirect monitoring has been confirmed both theoretically and experimentally. Frequency domain approaches are most prevalent for identification of the bridge frequency.

In an experimental study, Lin and Yang (2005) used a 1.4 t commercial truck as a tractor and exciter of the bridge, and a 0.65 t one as a trailer and receiver of the bridge's dynamic properties. The tractor-trailer system moves on a 6-span curved bridge with 30 m span lengths comprised of six prestressed I girders. The bridge fundamental frequency was found with high precision for speeds lower than 40 km/h from the response spectrum of the moving vehicle. They also find the existence of ongoing traffic to be advantageous since it increases the vehicle response. To have clear peak responses in the frequency spectrum, they recommend determining the vehicle dynamic properties and using lower speeds with increasing pavement roughness increases. In a follow-on investigation, Yang and Chang (2009b) used empirical mode decomposition (EMD) to find frequencies for higher modes of bridges. The theory was verified with experimental studies and again confirmed that ongoing traffic improves identification.

Other studies have examined the effects of other physical parameters—such as speed, mass, and vehicle suspension—on the identification of bridge frequency.

Using scaled laboratory moving vehicle experiments, Toshinami et al. (2010) and Kim et al. (2011), focused on short span bridges to identify the bridge frequency. For different speeds, they found that the spectral resolution of vehicle response for higher speeds is not as clear as for lower speeds (see equation (1)). However, the responses have higher magnitude spectral peaks at the bridge frequency. They also found that damping changes could be determined from a vehicle acceleration spectra.

Using both theoretical studies and full-scale experiments, Siringoringo and Fujino (2012) examine the impact of vehicle frequency and driving velocity on bridge response. Firstly, from a range of vehicle configurations, they found that the bridge frequency can be obtained using vehicles with different mass and suspension systems since the bridge frequency remains untouched (although its spectral amplitude varies). Secondly, they examined the bridge frequency for various speeds from 10 to 40 km/h.They found that the bridge frequency for speeds less than 30 km/h can be extracted clearly (see equation (1)). A full-scale experiment was performed on a 59 m span with steel-box simply-supported girders to verify the findings. They mounted an accelerometer on a light commercial vehicle and found that, as expected, increasing the speed beyond 30 km/h reduces the accuracy of bridge frequency estimation. This is found to be due to both higher wheel bouncing and shorter measurement durations.

In identifying the bridge frequency from a VBI event, regard must be paid to the frequency shift that occurs under the added vehicle mass. Yang et al. (2013) show that for a larger and smaller natural frequency of bridge (or vehicle) in relation to the other sub-system, the frequency changes in a convex and concave form respectively. The maximum change happens at mid-span. However, if the vehicle/mass ratio is lower than 1% (which is typical for highway vehicles and bridges), the frequency variation can be disregarded. In an interesting experimental investigation, Chang et al. (2014) used a truck with a weight of 250 kN moving on a simply-supported 62 m-span box girder bridge to study the effect of a parked vehicle on the bridge frequency. The parked truck had an 8.2% mass and 2.231 frequency ratio to the bridge. A 2.6% reduction in bridge frequency was found when the truck was parked in the middle of the span. A follow-up laboratory experiment found a 9% reduction in the system frequency, showing agreement between laboratory and field experiments.

Because the success of bridge frequency identification is strongly dependent on the clarity of its spectral peak, researchers have examined various filtering methods to improve accuracy. Yang et al. (2013) examine a band-pass filter (BPF) and singular spectrum analysis (SSA) finding that the best filtering technique is a combination of both. Malekjafarian and O'Brien (2014) used the Frequency Domain Decomposition (FDD) method. Compared to the Fast Fourier Transform (FFT), they found that when the bridge and vehicle frequencies are close, the FDD method is superior to plain FFT. In a different approach, Li et al. (2014) tried to obtain bridge parameters using an optimization method, the Generalized Pattern Search Algorithm (GPSA). The bridge first natural frequency and stiffness were found with an error of 3.3% in the presence of 10% signal-to-noise ratio. Finally, in a recent laboratory experimental study, Kim et al. (2017) used a tractor-trailer system with two trailers. The heavy tractor acted as an exciter to the bridge, and the spectral responses of the two trailers were subtracted from one another to remove the effect of road roughness, allowing clear identification of the bridge frequency.

It is clear from the review that there remain some practical issues to address to improve the accuracy of bridge frequency identification. These questions can be summarized as:

1. How to eliminate the effect of road roughness on the vehicle response?
2. How to overcome the bridge frequency changing during a passing vehicle in a VBI?
3. Which filtering technique gives the most clarity of bridge frequency in the response spectrum?

Overall though, it can be seen that the feasibility of bridge frequency extraction from a passing vehicle is confirmed theoretically and experimentally.

3.2 *Damping-based methods*

Even for simple problems, damping estimation is complex (Williams and Salawu 1997), and so for DBBI the difficulty of accurately determining the bridge damping is compounded by the complexity of the dynamic system. However, a few studies have attempted to use DBBI to identify bridge damping. In the main, the approach taken is to identify use the magnitude of the spectral peak at the bridge frequency to estimate its damping.

In a theoretical study, McGetrick et al. (2009) investigated the bridge natural frequency and damping behaviour using an instrumented moving vehicle. With increasing bridge damping, they find the PSD magnitude of bridge frequency peaks decreases. This result was confirmed in a laboratory experimental study (McGetrick et al. 2010) for three damping cases. It was found that by measuring the acceleration of the moving vehicle, damping alterations can be detected from the response spectrum. This was also confirmed in a separate experimental study (Kim et al. 2014). Keenahan et al. (2013) also tried to monitor bridge damping variations as an early warning for triggering an inspection. They studied both Rayleigh and hysteresis damping models using a tractor-trailer vehicle, finding that changes in damping can be detected by subtracting the accelerations of one axle

from the other. For bridge damping identification, González et al. (2012) propose a 6-step method using measured axle accelerations to estimate the road profile under each axle and finding the optimum bridge damping ratio that yields a single road profile. The method is found reasonably insensitive to many parameters, including a pothole. However, it has not been confirmed in a field experiment.

3.3 *Mode shape-based methods*

Bridge mode shape extraction is particularly useful for calibrating numerical models (Zhang et al. 2012). (Yang et al. 2014) point out that in contrast to the problem of frequency resolution (see equation (1)), DBBI offers an excellent spatial resolution, since the vehicle contacts the full length of the bridge. Indeed, they show that the amplitude history of the bridge frequency component of the response spectrum is proportional to the corresponding mode shape. This is also noted in (Feng and Feng 2016).

Some studies try to derive the bridge mode shapes using multiple vehicles and reduce the effect of road roughness by subtracting signals of similar axles. Oshima et al. (2014) considered two heavy trucks located before and after four monitoring vehicles moving at a constant velocity. The theory comprises:

1. Estimating road roughness and bridge displacement based on vehicle acceleration and the relative displacement between the mass and road surface.
2. Obtaining bridge displacement by subtracting one vehicle displacement from another one.
3. Converting the obtained displacement to a fixed coordinate by interpolating mode shapes using polynomial functions.
4. Estimating mode shapes based on fixed location deformations obtained in step 3.

They validated the theory by a VBI numerical simulation. Malekjafarian and OBrien (2014) also realised that the road roughness can be eliminated by subtracting signals of similar axles. They modelled two successive axles moving over a bridge, then applied the Short Time Frequency Domain Decomposition (STFDD) method to estimate bridge mode shapes based on the acceleration response of the passing vehicle. It was shown that bridge mode shapes can be extracted by a truck towing two trailers. In a complementary study, They enhanced the STFDD method to obtain mode shapes with higher accuracy (OBrien and Malekjafarian 2016). Malekjafarian and OBrien (2017) proposed the use of a mechanical exciter mounted on a trailer axle to produce excitation frequencies near the bridge first natural frequency. This was done to make the bridge frequency peaks clearer in the response spectrum. With a better peak, the Hilbert Huang Transform was used to estimate mode shapes with high resolution. The model was validated using a numerical simulation at a speed of just 2 m/s, although the authors admit that this low speed may not make it practical. Recently, (Kong et al. 2017) used a truck and two trailers in a field test on a three 16.7 m-span prestressed bridge. They simulated the truck-trailer system with two numerical models finding that multi degree-of-freedom models provide better results compared to the field results.

4 THE DBBI CHALLENGE FOR RAILWAY BRIDGES

Table 1 summarizes the key parameters affecting DBBI for train and highway bridges. As shown in the previous sections, some are common between both bridge types, and are already solved so are unlikely to pose a problem for railways. However, railway bridge DBBI has some particular issues. In this section, the key parameters of TTBI are surveyed to identify potential problems facing DDBI implementation for railway bridges.

4.1 *Resonant behaviour in railways*

For DBBI, the significance of resonance is that it will enhance bridge vibration, potentially leading to clearer spectral peaks. Resonance may occur in railway bridges due to regular axle spacing at certain speeds as it has been explained in section 2.1.2. It can also happen due to a matching between track irregularity wavelength and bridge frequency. In spite of the potential for resonance, there exist sources of noise that will reduce its effects, such as wheel defects and sleeper settlements as the train passes (Arvidsson and Karoumi 2014).

4.2 *Non-linear behaviour of the bridge*

Non-linear behaviour of both bridge frequency and damping occurs because of the track-ballast interaction. A few studies have examined this and found that the bridge natural frequency tends to decrease with vibration amplitude while bridge damping tends to increase with a non-linear behaviour (Ülker-Kaustell and Karoumi 2013, Battini and Ülker-Kaustell 2011). In addition, frequency changes of ballasted railway bridges occur, caused by seasonal effects on the stiffness. Gonzales et al. (2013) studied this issue and found that the main reason is ground frost and frozen ballast which can increase the bridge natural frequency by about 35% during winter.

Compared to DBBI for highway bridges, the extended sources of non-linear behaviour in railway brides compounds the difficulty of accurate identification of bridge dynamic properties.

Table 1: Parameters affecting DBBI for highway and railway bridges showing positive (+) and negative (-) influences

DBBI Parameter	Highway bridges	Railway bridges	Reference
Speed limit	✓(-)	✓(-)	Lin and Yang (2005)
Number of vehicle passages	✓(-)	✓(+)	Lin and Yang (2005)
Initial vehicle/bridge acceleration amplitude	✓(-)	✓(-)	Yang and Chang (2009a)
Noise	✓(-)	✓(-)	Li et al. (2014)
Vehicle-bridge mass ratio	✓(-)	✓(+)	Liu et al. (2009)
Vehicle-bridge frequency ratio	✓(-)	✓(-)	Museros and Alarcón (2002)
Ongoing traffic	✓(+)		Yang and Chang (2009b)
Road roughness	✓(-)		Oshima et al. (2014)
Resonant behaviour		✓(-)	Arvidsson and Karoumi (2014)
Freeze and frost		✓(-)	Gonzales et al. (2013)
Bridge-ballast interaction		✓(-)	Ülker-Kaustell and Karoumi (2013)
Wheel-rail contact		✓(-)	Zhai et al. (2013)
Transition zones		✓(-)	Namura and Suzuki (2007)
Turnouts		✓(-)	Kassa and Nielsen (2009)
Track irregularities		✓(-)	Zhang et al. (2010)

4.3 *Wheel-rail contact*

Ordinarily, TTBI modelling assumes that the wheel and rail are always in contact (Xia and Zhang 2005). However, in truth the displacement of bridge and wheel may not be the same, and a more detailed assumptions could be taken into consideration to reflect the real contact behaviour. Two common types of wheel-rail interaction modelling are Hertz and Kalker creep contact theories for normal and lateral contacts, respectively. However, there are some problems with these approaches, and the real behaviour of wheel and rail cannot be completely simulated (Zhang et al. 2008).

For DBBI application, the wheel-rail contact will add noise to the response of the system, when compared to a numerical model assuming perfect contact. However, compared with highway bridge wheel-road contact, it is considered that wheel-rail contact will be less noisy, and so better for railway DBBI.

4.4 *Vehicle-bridge mass*

Increasing non-linear behaviour of railway bridges has been found as the mass ratio changes from 0.1 to 3 (proportion of an eight-passenger car with two locomotives to a 34 m span length bridge) (Liu et al. 2009). Bogie-bridge mass ratio was also found to have a higher effect on dynamic responses of the bridge, than car body-bridge or wheel-bridge mass ratio.

For DBBI, the increased mass ratio means that railway bridges offer the potential for more accurate bridge characteristics identification, compared to highway bridges.

4.5 *Transition zones and turnouts*

Two other parameters to consider which do not exist in highway bridges are transitions zones and turnouts. Transition zones between the slab and ballasted track, or between bridge and embankment are sections with sudden changes in vertical stiffness. A few studies done on transition zones and recognised that wheel-rail load and accelerations increase abruptly, although its effect on bridge response is not studied yet (Namura and Suzuki 2007). Moreover, some researchers tried to model the train-turnout interaction to measure the wheel-rail contact force precisely. However, its impact on bridge response is not investigated as well (Kassa and Nielsen 2009). For railway DBBI, these aspects are likely to complicate the identification of bridge properties in practice by adding sources of noise to the system that are difficult to model numerically.

4.6 *Track irregularities*

Track irregularity has a strong influence on the train accelerations. Unlike, highways, there are four main types of irregularities to be considered in tracks including gauge, cant (superelevation), alignment, and vertical profile (elevation). Majka and Hartnett (2009) investigated the effect of random track irregularities on bridge dynamic response using a train-bridge interaction model. They observed that the influence of track irregularities on bridge vertical response is insignificant. However, train response is sensitive to them. Similarly, Du Kim et al. (2009) found that the wavelength of rail irregularity has a great influence on car-body acceleration and the relative displacement of wheelsets, but has a negligible impact on bridge vertical displacement. Using a combined Precise Integration Method (PIM)-Pseudo-Excitation Method (PEM) approach, Zhang et al. (2010) found random track irregularities have a great influence on the vertical random vibration of the whole system and rotational random vibrations of the double-track bridges. In a comparative study, Gu et al. (2010) examined the process of deterministic irregularities against stochastic ones for track irregularities in elevation. They showed that vertical displacement and dynamic impact load caused by deterministic irregu-

larities are more considerable than random irregularities, and proved it in a case study (Gu and Franklin 2010). In some of the most recent studies, researchers tried to construct precise stochastic models of track irregularities to investigate its effect on wheel/rail contact force (Panunzio et al. 2017, Xu and Zhai 2017). However, the influence of these models on the bridge response has not studied yet.

For DBBI of railway bridges, track irregularity excites the vehicle, improving the magnitude of acceleration responses, but adds to the spectral noise.

5 CONCLUSIONS

The key findings for DBBI are:

1. Low speeds (< 40 km/h) are needed for adequate spectral resolution.
2. Bridge excitation is improved with a heavy vehicle or by the presence of ongoing traffic, and gives better spectral visibility of the bridge. This is an advantage for railway bridges since trains are heavier than highway vehicles.
3. Spectral clarity of the bridge decreases with noise, and there are comparable sources of noise in both road and rail bridges.
4. Driving surface roughness is a significant source of noise.

Aspects of DBBI unique to railway bridges are:

1. Resonant response happens due to passing successive axle loads at certain speeds.
2. Freezing of ballast and frosting the ground causes variations in bridge responses.
3. Non-linear bridge behaviour due to the ballast.
4. Track irregularities, Wheel-rail contact, and wheel defects add significant noise to the system, and are not easily characterized.
5. Transition zones and turnouts increase wheel-rail loads influence dynamic responses.

The effect of these parameters on DBBI is not yet known. Nevertheless, as can be seen from the literature, the potential of drive-by inspection using instrumented vehicles is comparable between railway and highway bridges. Since DBBI is maturing for highway bridges, it seems that it is also well-suited to rail bridges. However, there remain unique challenges to overcome for successful DBBI on railway bridges.

REFERENCES

Arvidsson, T. & R. Karoumi (2014). Train–bridge interaction–a review and discussion of key model parameters. *International Journal of Rail Transportation 2*(3), 147–186.

Battini, J.-M. & M. Ülker-Kaustell (2011). A simple finite element to consider the non-linear influence of the ballast on vibrations of railway bridges. *Engineering structures 33*(9), 2597–2602.

Bu, J., S. Law, & X. Zhu (2006). Innovative bridge condition assessment from dynamic response of a passing vehicle. *Journal of Engineering Mechanics 132*(12), 1372–1379.

Cantero, D., T. Arvidsson, E. OBrien, & R. Karoumi (2016). Train–track–bridge modelling and review of parameters. *Structure and Infrastructure Engineering 12*(9), 1051–1064.

Cerda, F., S. Chen, J. Bielak, J. H. Garrett, P. Rizzo, & J. Kovacevic (2014). Indirect structural health monitoring of a simplified laboratory-scale bridge model. *Smart Structures and Systems 13*(5), 849–868.

Chae, M., H. Yoo, J. Kim, & M. Cho (2012). Development of a wireless sensor network system for suspension bridge health monitoring. *Automation in Construction 21*, 237–252.

Chang, K., C. Kim, & S. Borjigin (2014). Variability in bridge frequency induced by a parked vehicle. In *Proceedings of the 4th KKCNN Symposium on Civil Engineering*, pp. 75–79.

Chang, K., F. Wu, & Y. Yang (2010). Effect of road surface roughness on indirect approach for measuring bridge frequencies from a passing vehicle. *Interaction and multiscale mechanics 3*(4), 299–308.

Chen, S. & H. Xia (2009). An identification method for fundamental frequency of bridge from dynamic responses due to passing vehicle. *Eng. Mech 26*, 88–94.

Coelho, B., J. Priest, P. Holscher, & W. Powrie (2009). Monitoring of transition zones in railways.

Du Kim, K., P. Warnitchai, et al. (2009). Dynamic analysis of three-dimensional bridge–high-speed train interactions using a wheel–rail contact model. *Engineering Structures 31*(12), 3090–3106.

Feng, D. & M. Q. Feng (2016). Output-only damage detection using vehicle-induced displacement response and mode shape curvature index. *Structural Control and Health Monitoring 23*(8), 1088–1107.

Frỳba, L. (1996). Dynamics of railway bridges. *T. Telford, London (UK)*.

Gonzales, I., M. Ülker-Kaustell, & R. Karoumi (2013). Seasonal effects on the stiffness properties of a ballasted railway bridge. *Engineering structures 57*, 63–72.

González, A., E. J. OBrien, & P. McGetrick (2012). Identification of damping in a bridge using a moving instrumented vehicle. *Journal of Sound and Vibration 331*(18), 4115–4131.

Gu, G. & F. Franklin (2010). Application of the structural articulation method to dynamic impact loading of railway bridges–a case study. *Vehicle system dynamics 48*(10), 1097–1113.

Gu, G., D. Lilley, & F. Franklin (2010). A structural articulation method for assessing railway bridges subject to dynamic impact loading from track irregularities. *Vehicle system dynamics 48*(10), 1077–1095.

ISO, S. (1995). 8608, mechanical vibration–road surfaces profiles–reporting of measured data. *International Organization for Standardization, Switzerland*.

Kassa, E. & J. C. Nielsen (2009). Dynamic train–turnout interaction in an extended frequency range using a detailed model of track dynamics. *Journal of sound and vibration 320*(4), 893–914.

Keenahan, J., E. OBrien, P. Mcgetrick, & A. Gonzalez (2013). The use of a dynamic truck-trailer drive-by system to monitor bridge damping. In *Structural Health Monitoring*, Volume 13, pp. 143–157.

Kim, C.-W., K.-C. Chang, P. J. McGetrick, S. Inoue, & S. Hasegawa (2017). Utilizing moving vehicles as sensors for bridge condition screeninga laboratory verification. *Sensors and Materials 29*(2), 153–163.

Kim, C.-W., R. Isemoto, P. McGetrick, M. Kawatani, & E. J. O'Brien (2014). Drive-by bridge inspection from three different approaches.

Kim, C.-W., R. Isemoto, T. Toshinami, M. Kawatani, P. Mcget-

rick, & E. OBrien (2011). Experimental investigation of drive-by bridge inspection. *SHMII-5 2011 - 5th International Conference on Structural Health Monitoring of Intelligent Infrastructure*.

Kong, X., C. Cai, L. Deng, & W. Zhang (2017). Using dynamic responses of moving vehicles to extract bridge modal properties of a field bridge. *Journal of Bridge Engineering 22*(6), 04017018.

Li, W.-m., Z.-h. Jiang, T.-l. Wang, & H.-p. Zhu (2014). Optimization method based on generalized pattern search algorithm to identify bridge parameters indirectly by a passing vehicle. *Journal of Sound and Vibration 333*(2), 364–380.

Lin, C. & Y. Yang (2005). Use of a passing vehicle to scan the fundamental bridge frequencies: An experimental verification. *Engineering Structures 27*(13), 1865–1878.

Liu, K., G. De Roeck, & G. Lombaert (2009). The effect of dynamic train–bridge interaction on the bridge response during a train passage. *Journal of sound and vibration 325*(1), 240–251.

Majka, M. & M. Hartnett (2009). Dynamic response of bridges to moving trains: A study on effects of random track irregularities and bridge skewness. *Computers & Structures 87*(19), 1233–1252.

Malekjafarian, A. & E. J. O'Brien (2014). Application of output-only modal method in monitoring of bridges using an instrumented vehicle. In *Civil Engineering Research in Ireland, Belfast, UK, 28-29 August, 2014*.

Malekjafarian, A. & E. J. OBrien (2014). Identification of bridge mode shapes using short time frequency domain decomposition of the responses measured in a passing vehicle. *Engineering Structures 81*, 386–397.

Malekjafarian, A. & E. J. OBrien (2017). On the use of a passing vehicle for the estimation of bridge mode shapes. *Journal of Sound and Vibration 397*, 77–91.

McGetrick, P., C.-W. Kim, & E. J. O'Brien (2010). Experimental investigation of the detection of bridge dynamic parameters using a moving vehicle. In *23rd KKCNN Symposium on Civil Engineering, Taipei, November 13-15, 2010*.

McGetrick, P. J., A. Gonzlez, & E. J. OBrien (2009). Theoretical investigation of the use of a moving vehicle to identify bridge dynamic parameters. *Insight-Non-Destructive Testing and Condition Monitoring 51*(8), 433–438.

Museros, P. & E. Alarcón (2002). An investigation on the importance of train-bridge interaction at resonance. In *Proceedings of the sixth conference on Computational structures technology*, pp. 335–336. Civil-Comp Press.

Namura, A. & T. Suzuki (2007). Evaluation of countermeasures against differential settlement at track transitions. *Quarterly Report of RTRI 48*(3), 176–182.

OBrien, E. J. & A. Malekjafarian (2016). A mode shape-based damage detection approach using laser measurement from a vehicle crossing a simply supported bridge. *Structural Control and Health Monitoring 23*(10), 1273–1286.

Oshima, Y., K. Yamamoto, & K. Sugiura (2014). Damage assessment of a bridge based on mode shapes estimated by responses of passing vehicles. *Smart Structures and Systems 13*(5), 731–753.

Panunzio, A. M., G. Puel, R. Cottereau, S. Simon, & X. Quost (2017). Construction of a stochastic model of track geometry irregularities and validation through experimental measurements of dynamic loading. *Vehicle System Dynamics 55*(3), 399–426.

Quirk, L., J. Matos, J. Murphy, & V. Pakrashi (2017). Visual inspection and bridge management. *Structure and Infrastructure Engineering*, 1–13.

RMS (2012). Annual report 2011-2012. *Roads and Maritime Services 2*, 24–30.

Siringoringo, D. & Y. Fujino (2012). Estimating bridge fundamental frequency from vibration response of instrumented passing vehicle: Analytical and experimental study. *Advances in Structural Engineering 15*, 417–433.

Toshinami, T., M. Kawatani, & C.-W. Kim (2010). Feasibility investigation for identifying bridge's fundamental frequencies from vehicle vibrations. *in Proceedings of the 5th International Conference on Bridge Maintenance, Safety and Management(IABMAS 10)*, 317–322.

Ülker-Kaustell, M. & R. Karoumi (2013). Influence of rate-independent hysteresis on the dynamic response of a railway bridge. *International Journal of Rail Transportation 1*(4), 237–257.

Williams, C. & O. Salawu (1997). Damping as a damage indication parameter. In *Proceedings of SPIE - The International Society for Optical Engineering*, pp. 1531–1536. The International Society for Optical Engineering.

Xia, H. & N. Zhang (2005). Dynamic analysis of railway bridge under high-speed trains. *Computers & Structures 83*(23), 1891–1901.

Xu, L. & W. Zhai (2017). Stochastic analysis model for vehicle-track coupled systems subject to earthquakes and track random irregularities. *Journal of Sound and Vibration 407*, 209–225.

Yang, Y. & K. Chang (2009a). Extracting the bridge frequencies indirectly from a passing vehicle: Parametric study. *Engineering Structures 31*(10), 2448–2459.

Yang, Y. & K. Chang (2009b). Extraction of bridge frequencies from the dynamic response of a passing vehicle enhanced by the emd technique. *Journal of sound and vibration 322*(4), 718–739.

Yang, Y., K. Chang, & Y. Li (2013). Filtering techniques for extracting bridge frequencies from a test vehicle moving over the bridge. *Engineering Structures 48*, 353–362.

Yang, Y., M. Cheng, & K. Chang (2013). Frequency variation in vehicle–bridge interaction systems. *International Journal of Structural Stability and Dynamics 13*(02), 1350019.

Yang, Y., Y. Li, & K. Chang (2012). Effect of road surface roughness on the response of a moving vehicle for identification of bridge frequencies. *Interaction and multiscale mechanics 5*(4), 347–368.

Yang, Y., Y. Li, & K. Chang (2014). Constructing the mode shapes of a bridge from a passing vehicle: a theoretical study. *Smart Structures and Systems 13*(5), 797–819.

Yang, Y.-B., W.-F. Chen, H.-W. Yu, & C. Chan (2013). Experimental study of a hand-drawn cart for measuring the bridge frequencies. *Engineering Structures 57*, 222–231.

Yang, Y.-B., C. Lin, & J. Yau (2004). Extracting bridge frequencies from the dynamic response of a passing vehicle. *Journal of Sound and Vibration 272*(3), 471–493.

Yu, L. & T. H. Chan (2004). Identification of multi-axle vehicle loads on bridges. *Journal of vibration and acoustics 126*(1), 17–26.

Zhai, W., H. Xia, C. Cai, M. Gao, X. Li, X. Guo, N. Zhang, & K. Wang (2013). High-speed train–track–bridge dynamic interactions–part i: theoretical model and numerical simulation. *International Journal of Rail Transportation 1*(1-2), 3–24.

Zhang, N., H. Xia, & W. Guo (2008). Vehicle–bridge interaction analysis under high-speed trains. *Journal of Sound and Vibration 309*(3), 407–425.

Zhang, Y., L. Wang, & Z. Xiang (2012). Damage detection by mode shape squares extracted from a passing vehicle. *Journal of Sound and Vibration 331*(2), 291–307.

Zhang, Z., J. Lin, Y. Zhang, W. P. Howson, & F. W. Williams (2010). Non-stationary random vibration analysis of three-dimensional train–bridge systems. *Vehicle system dynamics 48*(4), 457–480.

Maintenance, Safety, Risk, Management and Life-Cycle Performance of Bridges – Powers, Frangopol, Al-Mahaidi & Caprani (Eds)
© 2018 Taylor & Francis Group, London, ISBN 978-1-138-73045-8

The Interpolation Method for vibration based damage localization: influence of feature uncertainties

M.P. Limongelli
Politecnico di Milano, Department of Architecture, Piazza Leonardo da Vinci 32, 20133 Milano, Italy
Amin Fathi
Amirkabir University of Technology, 424 Hafez Ave, Tehran, Iran

ABSTRACT: Vibration-based methods for damage localizations often rely on a damage feature defined in terms of changes of modal or operational shapes. These methods allow detecting variations of the damage feature that can be ascribed to damage. Many of these methods are based on the detection of irregularities in the deformed shape of the structure. The accuracy of the methods proposed in literature is often verified on numerical models that, by their nature, cannot reproduce all the sources of uncertainties - environmental, operational, and experimental - that affect responses recorded of the structure. The availability of data recorded on real structures provides precious material for the verification of the real capabilities of the proposed damage identification algorithms. Due to several sources of uncertainty the values of the damage feature may undergo changes even in absence of any damage. This variability has to be properly accounted for in order to reduce the number of false or missing indications of damage. In this paper is investigated the influence of the uncertainties on the results provided by the Interpolation Method for damage localization. Specifically several different probabilistic models of the marginal probability of the damage feature are compared in order to verify select the one able to provide the highest accuracy in damage localization. The investigation is carried out with reference to the real case study of a prestressed concrete road bridge, the S101 Bridge in Austria. The bridge, built in the early 1960, is a typical example of a European highway bridge. Responses to ambient vibration have been recorded both in the undamaged and in several different damage scenarios artificially inflicted to the bridge. Damage was introduced by lowering one of the bridge piers and by cutting prestressing tendons of one beam of the bridge deck.

1 INTRODUCTION

The cost of maintaining bridge is a major part of the construction budget usually. Moreover if the inspection and monitoring system are not reliable, additional costs due to traffic delay will be added to the cost. Structural Health Monitoring (SHM) methods are one of the best tools for maintenance and inspection of structures that provide possibility of continuous inspection of the structure for damage detection in structural components. The general purpose of SHM is the rapid damage diagnosis of structure in order to ensure a proper safety level minimizing at the same time the maintenance costs. To achieve this goal the response of the structure has to be accurately recorded and robust algorithms for damage identification must be used to extract information from recorded data.

Non-destructive methods such as magnetic field methods, radiography, eddy-current methods, thermal field methods and acoustic or ultrasonic method are frequently used to inspect bridges. The main disadvantage of these techniques is that the location of damage must be known, why they are called a priori techniques. In the past few decades advances in sensors technology have significantly fostered the development of SHM methods and algorithms based on responses recorded by networks of sensors installed on the structure.

Vibration based methods are among the most effective tools for damage identification allowing to assess, at different levels of refinement, the structural health of structures equipped with a network of sensors. In reference Limongelli 2011 is presented the vibration-based Interpolation Method (IM) based on the detection of localized increases of curvature related to a reduction of stiffness.

This method has been extensively applied to the case of numerical models of bridges (Domaneschi et al, 2013 - Domaneschi et al, 2015) or using respons-

es recorded on a real bridge during a short monitoring carried out by impact tests (Limogelli et al 2014). An extended version of the IM has been proposed in reference (Limogelli et al 2017) based on a statistical modeling of the damage feature in the damaged configurations of the structure. The method was applied to the case of the prestressed bridge S101, artificially damaged with increasing levels of damage for research purposes (VCE, 2009; Sirigoringo et al., 2013). In reference (Limongelli et al, 2017) data recorded on the bridge in the several damaged configurations were used to check the capability of the proposed algorithm to localize damage.

Based on a previous applications of the IM on a multistory building (Limogelli et al 2014) a Lognormal probability distribution was assumed in (Limongelli et al, 2017) to model the damage feature in both the undamaged and the damaged configurations.

The validity of this assumption was not checked. Furthermore the statistical uncertainty connected with the limited amount of data available for a number of damaged configurations was not acknowledged. The damage localization algorithm was applied assuming as damage feature the Probability of Detection computed based on the conditional probability distribution. The latter, based on the available limited set of data data, was modelled as a lognormal distributions at all the instrumented locations.

In this paper, this statistical uncertainty will be accounted for by defining the damage feature as a function of the marginal probability distributions.

In the following of the paper the extended version of the Interpolation Method will be briefly outlined and the case study of the bridge S101 described. The second part of the paper reports the comparison of results related to different assumptions about the probability distribution of the damage feature.

The results provided by the IM depend on the choice of the threshold defined to select '*meaningful variations*' of the damage feature. This threshold is defined in terms of the accepted probability of the false alarm. An investigation on the sensitivity of results to this latter probability, for the different possible assumptions on the probability distributions of the damage feature is reported in the last part of the paper.

2 DAMAGE IDENTIFICATION

2.1. The Interpolation Error for damage localization

The Interpolation Method (IM) is based on the assumption of a beam-like behavior of the monitored structure and on the interpolation of the Operational Displacement Shapes (ODS) via a Cubic Spline function (Limongelli, 2011). Due to the so-called 'Gibbs phenomenon for splines' a localized discontinuity of curvature in the deformed shape of the structure causes strong oscillation of a cubic spline interpolating function at the location of the discontinuity. By defining the damage feature in terms of the interpolation error, an increase of this latter gives an indication of a variation of curvature therefore of a reduction of stiffness.

The method has been successfully applied for damage localization of bridges under seismic excitation or subjected to impact tests. In these cases the ODS can be computed form the Frequency Response Functions since the input is usually measured.

More details about these applications can be found in references (Limongelli, 2011; Domaneschi et al., 2014). When ambient vibrations or wind are used as a source of excitation, the input is unknown. In this case the Operational Deformed Shapes could still be estimated using on the Power Spectral Densities of the responses, assuming that the input is a white noise.

This assumption is widely applied in output only system identification (e.g. Brincker 2001, Peeters et al., 2001) and, even if it is not strictly verified over the entire frequency range, the PSDs give a good approximation of the deformed shape at different frequencies.

Under ambient vibrations the interpolation error can thus be defined as:

$$E(z,f_i)=\left[P_R(z,f_i)-P_S(z,f_i)\right] \quad (1)$$

being $P_R(z,f_i)$ and $P_S(z,f_i)$ the power spectral densities of the recorded (R) and interpolated (S) accelerations at location z and frequency f_i. 'Interpolated' means that are calculated from a cubic spline interpolation of the PDSs recorded at all the other instrumented locations.

In equation (1), the interpolation error depends on the considered ODS that is on the considered value of frequency. In order to characterize each location with a single error parameter, the norm of the error on the whole range of frequencies is considered:

$$E(z)=\sqrt{\sum_1^N E(z,f_i)^2} \quad (2)$$

The difference between the values of the interpolation error at a given location in two different configurations of the structure (reference and potentially damaged) or at two different moments of its life (beginning of monitoring and some-time afterward) should provide an indication about the existence of degradation at that location. Specifically an increase of the interpolation error should indicate the existence of an increase of curvature (decrease of stiffness) at the location where this variation occurs.

Due to several environmental (e.g. temperature or humidity) or operational (e.g. noise in recorded sensors, non-linear behavior of the structure, round off in signal processing) sources the values of the damage feature $E(z)$ may change even if there is no damage. In order to account for this, the statistical

variability of the interpolation error E has to be assessed. This issue will be addresses in the next section. Herein is reported the description of how the method is applied assuming known the statistical distributions of the damage feature in the undamaged and in the damaged configurations.

Herein we refer to damage as a stiffness loss at one section of the deck.

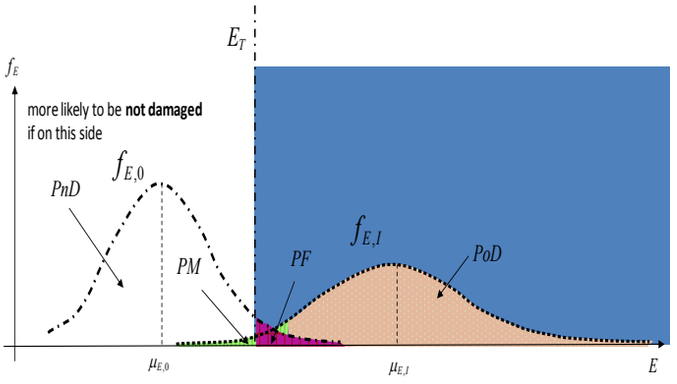


Figure 1. Distributions in the undamaged (J E,0) and in the inspection (*J E,I*) configurations

In Figure 1 the probability distribution of the interpolation error at one location z in the undamaged configuration $f_{E,0}$ is compared to the distribution in the inspection state $f_{E,I}$ assuming that the structure is damaged at z: damage induces a shift of the distribution toward a higher mean value of E.

In order to check the health of the structure, the distribution E_0 at each instrumented location z in the undamaged configuration has to be compared to the distribution E_I at the same location, calculated in the 'inspection phase'.

In order to compare the distributions pertaining to two different configurations, and also to select the locations where the highest variation of the damage feature occurs, will be utilized the Probability of Detection (PoD).

The PoD is the probability of damage being correctly denounced at location *z*, that is the probability that damage is denounced at *z* given the structure is damaged at z. The higher the PoD at location *z*, the higher the probability that location z is actually damaged.

In order to define this probability a threshold value has to be defined.

This PoD is given by the area under the probability distribution $f_{E,I}$ in the inspection (possibly damaged) phase, at the right of the threshold. For a given value of the threshold, the *PoD* at a given location increases with the severity of damage. Therefore the increase of the *PoD* at a given location will be assumed as an index of the increase of the severity of damage at that location.

Among all locations, the one corresponding to the highest value of the *PoD* will be assumed herein as the damaged one. The threshold E_T is defined herein in terms of the accepted probability of false alarm (PF) that is the probability that damage is denounced, given the structure is undamaged. This probability is given by the area under the probability distribution in the reference configuration $f_{E,0}$, at the right of the threshold.

The area under the distribution $f_{E,I}$, at the left of the threshold is the Probability of Missing alarm (PM) that is the probability that damage is not denounced, given damage exist at z.

The higher the threshold, the higher PM and the lower PF hence the choice of the threshold is always a tradeoff between the accepted probability of false and missing alarm.

In order avoid false alarms, a condition is imposed on the PoD based on the location of the mode of the damaged distribution with respect to the reference one. The mode of the distribution is the value corresponding to (one of) the maximum of the probability distribution

It is assumed that if the mode in the damaged configuration is higher with respect to the mode in the undamaged one, the location will be considered as 'damaged' and the corresponding PoD will be estimated as an index of the damage severity. If the mode is lower with respect to that in the undamaged configuration the location will be considered undamaged and the PoD will be assumed equal to zero.

2.2.Probabilistic model of the performance parameter

As described in the previous section, in order to account for the statistical variability of the damage feature its probability distribution has to be computed. This can be done using data recorded on the structure or using a numerical model. For the undamaged configuration the availability of recorded data is not an issue if a permanent monitoring system is installed on the structure.

For the damaged configurations of course this is not possible unless the structure is damaged and of course it would be never possible to dispose of responses corresponding to all the possible damage scenarios. The alternative could be a) the numerical modeling of the structure and of the possible damage scenarios or b) the probabilistic model of the damage feature.

The numerical modeling requires the model of the nonlinear behavior of the structure – for some type of structures this could be quite uncertain due to the many unknown involved in the problem – and of the environmental conditions – e.g. the temperature variation – that may alter the values of the damage feature irrespective of the damage state.

In some cases the numerical modeling could be not straightforward. The alternative probabilistic modeling presents other challenges but can possibly

exploit the knowledge of the structural behavior in the undamaged configuration.

The availability of data recorded on the S101 bridge provides an opportunity to check the modeling assumptions that could be made for a real case.

Specifically herein is reported an investigation relevant to the type of probability distribution that can be assumed for the damage feature in the damaged configurations. The aim is to verify the possibility to use the same distribution as in the undamaged configuration, just changing its parameters with the severity of damage.

In the next sections of the paper several different assumptions about the probability distribution of the Interpolation Error will be compared using data recorded on the S101 bridge to check the consistency of the assumption and the accuracy of results obtained.

3 THE CASE STUDY

3.1.The bridge S101

The S101 (see Figure 2) was a post-tensioned flyover of three spans for a total length of 56 m. In 2008 the bridge was demolished due to insufficient loading capacity and to allow the enlargement of underneath A1 Westautobahn. The bridge was supported on two couples of rectangular piers with a central span and the two side spans built in at the abutments. The structural cross section was a double webbed T-beams sustaining a slab with cross section of variable height with a minimum value of 20 centimeters at mid-span.

During the four days before its demolition, the Austrian bridge operator ASFINAG, owner of the bridge, allowed the execution of an experimental campaign of ambient vibration tests on artificially simulated damage scenarios. Ambient vibration tests were carried out between 10 and 13 December 2008. Progressive damage scenarios were artificially induced, simulating the settlement of a support by lowering one of the bridge piers and the loss of tension in the cables by progressively cutting a number of tendons.

A monitoring system, recording responses to ambient vibrations at several locations along the bridge deck in terms of accelerations, was installed by the Austrian company VCE, in order to provide a useful database for research purposes (VCE, 2009).

Responses of the bridge under the traffic in the underneath Westautobahn A1 were recorded by the network of three directional accelerometers throughout the three days of test.



Figure 2. The bridge S101: up) view; down) dimensions. From reference (VCE, 2009).

3.2.Simulated damage scenarios and network of sensors

The experimental campaign on the bridge can be divided into three phases corresponding to three different scenarios: 1) the initial (reference) configuration, 2) a support settlement, simulated through the cut of the north-western pier; 3) a loss of tension simulated by the cut of a number of tendons. In Table 1 is reported a summary of the sequence of tests on the several configurations of the bridge. More details of the tests sequence can be found in reference (VCE, 2009). In Phase 1 ambient vibrations were recorded in the undamaged configuration of the bridge.

In Phase 2, the pier was previously unloaded by applying a force on the bottom of the bridge slab with a hydraulic jack.

Table 1. Induced Damage scenarios

Scenario	Description of the scenario
U	Undamaged structure
A	Cut of the north-western column
B	First lowering the column (1cm)
C	Second lowering the column (2cm)
D	Third lowering the column (3cm)
E	Insertion of compensating plates
A_T	Column returned in original position
B_T	First tendon intersected
C_T	Second tendon intersected
D_T	Third tendon intersected
E_T	Fourth tendon partially intersected

Afterward the pier was cut at the base, near the foundation, and a slice of 10cm thickness was removed.

After the last reduction of pressure the pier underwent a total final settlement of 2.7cm. The lowering of the pier was carried out reducing the pressure in the jack in 3 steps. To simulate the repair of the pier, the initial configuration was restored by lifting the slab 6mm above the original level and inserting some compensating plates at the bottom of the pier. After the lifting, the closure of the cracks on the near pier was observed.

In Phase 3 the loss of tension in the cables was simulated by cutting an increasing number of tendons (see Table 1), in the same section of the deck corresponding to the pier previously cut (see Figure 2). During all the phases of test the bridge was instrumented with a dense network of sensors among which 15 tri-directional accelerometers along the bridge deck.

Due to the symmetry of the bridge, 14 sensors were deployed on the West side of the bridge to accurately capture its modal shapes and only one sensors (15) on the East side in order to differentiate torsional modes from flexural ones. The 15 sensors measured acceleration in the longitudinal, transversal and vertical directions, for a total of 45 signals for each test. In this paper only the results obtained by the analysis of the accelerations recorded in the vertical direction by the 14 sensors on the west side of the deck are reported. Accelerations were continuously sampled at 500 Hz during the three days of testing (10-13 December 2008). Data from each one of the damage scenarios (listed in Table1) were divided in several partial measurements corresponding to 5.5 minutes each.

4 DAMAGE IDENTIFICATION

The Interpolation Method outlined in section 2 has been applied to localize the several levels and types of induce damage based on the responses recorded by the network of 14 accelerometers installed on the west side of the bridge deck. For each response of 5.5 minutes duration (corresponding to 165.000 points at 500Hz sampling) the Power Spectral Density has been computed and used for the computation of the Interpolation Error according to equation (1). The entire set of data recorded throughout the three days of tests has been considered without any previous treatment or removal of portions of data.

4.1.Treatment of statistical uncertainties

Registration of responses of the bridge in the undamaged configuration was carried out for about 19 hours in the undamaged configuration (U) and for shorter times (between 1 and 5 hours) in the damaged configurations (A to E_T). Therefore, much more data are available for the reference configuration with respect to the damaged ones. Specifically, for the reference configuration, 152 samples of responses with duration 5.5 minutes are available while for the damaged configuration the total number of samples varies between 10 (for configuration E) to 85 (for configuration C_T). The distributions of the interpolation error obtained based on this sets of data are conditional to the particular considered sample that is to its mean and standard deviation: $f\left(E|\mu_E,\sigma_E\right)$. In reference (Limongelli et al., 2017) computations have been carried out with reference to the conditional probabilities $f\left(E|\mu_E,\sigma_E\right)$.

Herein the statistical uncertainty related to the limited number of samples will be taken into account by computing the marginal probability distribution $f\left(E\right)$ of the damage feature E through equation (3):

$$f\left(E\right)=\int_{-\infty}^{+\infty} f\left(E|\mu_E,\sigma_E\right)\cdot f\left(\mu_E\right)\cdot f\left(\sigma_E\right)d\mu_E d\sigma_E \qquad (3)$$

where μ_E and σ_E are the parameters of the probability distribution.

In order to retrieve the distributions $f\left(\mu_E\right)$ and $f\left(\sigma_E\right)$, a Monte Carlo simulation has been carried out assuming a normal shape of both distributions and generating a total number of 500 samples for each of the two distributions. Under these assumptions the integral in equation (3) has been numerically solved (Shampine, 2008) and a set of 150 samples of $f\left(E\right)$ has been generated.

Figure 3 reports the marginal distributions (based on log-normal distribution) of the undamaged and damaged scenarios U, E and D_T. computed from equation (3) assuming a lognormal distribution for the conditional probability $f\left(E|\mu_E,\sigma_E\right)$.

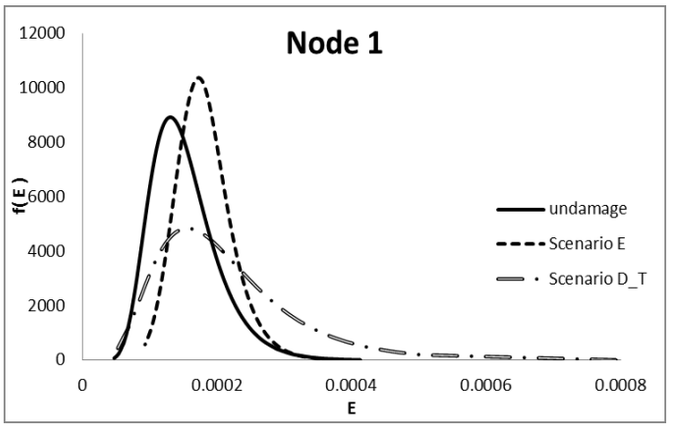
In order to choose the appropriate probability density function for the marginal probability $f\left(E\right)$, several assumptions have been tested: gamma, lognormal and normal distributions.

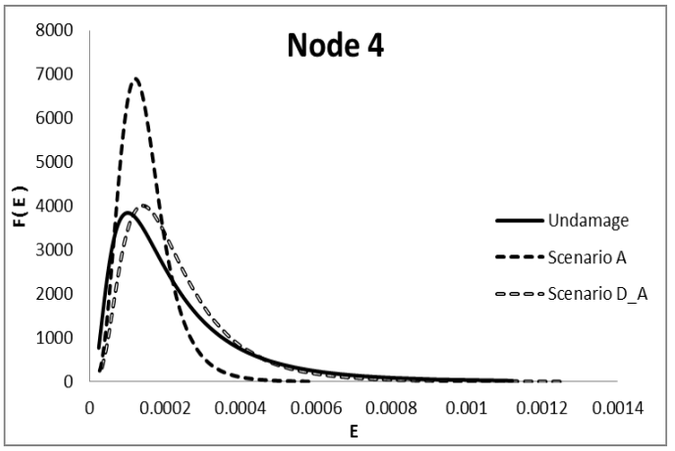
The Kolmogorov-Smirnov has been carried out for the distributions relevant to all locations in order to check their accuracy. The test is based on a statistic (Stat) defined as the largest difference between the theoretical and the empirical cumulative distribution function. The critical value (Δ) depends on the size of the sample and on the level of significance of the test (Faber, 2012).

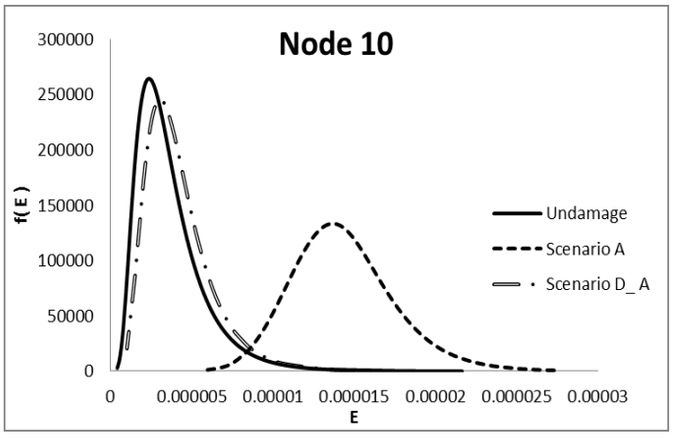
Based on these results the localization of damage has been performed assuming a lognormal model for the marginal probability $f\left(E\right)$. The Probability of Detection has been computed under this assumption and fixing the threshold in terms of a value of 1% for the accepted Probability of False alarm (PF).

Results (R) relevant to locations 11 and 12 are reported in Table 2 and show that for the modelling of $f\left(E\right)$ the log-normal and the gamma distributions have the highest accuracy with respect to all the oth-

ers. Similar results are obtained for the other sensors locations.







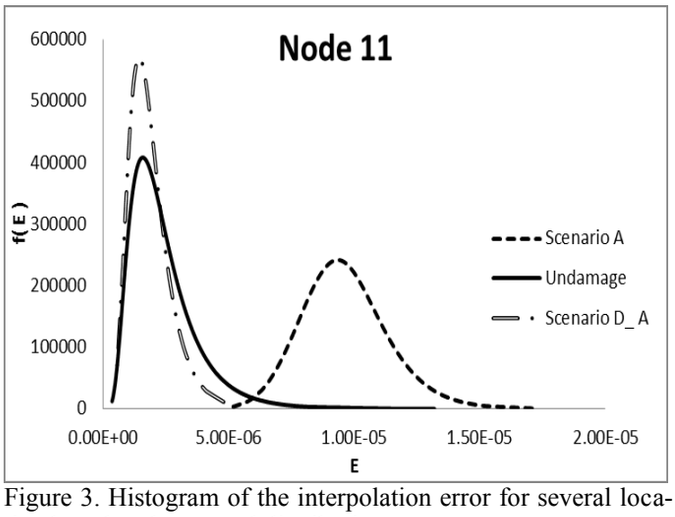


Figure 3. Histogram of the interpolation error for several location based on lognormal distribution

Table 2. Result of Kolmogorov-Smirnov test for nodes 11 and 12

		Log-normal		Gamma		Normal	
N	Δ	Stat	R	Stat	R	Stat	Res
11	0.072	0.025	**OK**	0.043	**OK**	0.092	**NO**
13	0.072	0.038	**OK**	0.058	**OK**	0.072	**NO**

4.2.Localization of damage

The location of the sensor number 11, is the closest to the lowered pier and to the beam section where the tendons were cut. This location is thus considered, for all scenarios, the damaged lone.

Figure 4 reports the values of the PoD at all the sensors locations (1 to 14) for scenarios A to E – corresponding to the lowering and following lifting of the pier.

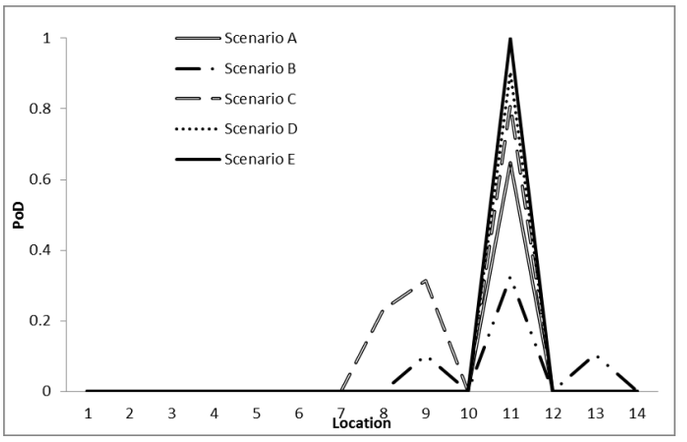


Figure 4. Probability of Detection based on the Log-normal distribution for $f(E)$ for damage scenarios A to E:

For all the scenarios related to the settlement of the pier (A to D) location 11 is correctly detected even if for the scenarios with the lowest amount of damage – A to C – some false alarms are present (see locations 8, 9, and 13). In scenario E the deck was lifted 6 cm over its original level. This certainly caused a variation of curvature even higher with respect to the one induced in scenario D by the lowering of the pier of 3cm. This is correctly detected by the method that finds the highest value of the PoD for scenario E.

The second damage scenario was induced by cutting a progressively increasing number of tendons at the top of one of the deck beams. This type of damage is not supposed to modify the stiffness of the structure thus no changes of the Operational Shapes were expected. This was actually confirmed by the results since no damage is detected for scenarios A_T to E_T.

5 INFLUENCE OF THE PROBABILISTIC MODEL

In this section will be investigated the influence

on the accuracy of damage localization, of the probabilistic model of the marginal probability $f(E)$.

Results similar to those reported in Figure 4 are obtained if the Gamma distribution is used to model the marginal probability $f(E)$.

In this second case the number of false alarms is slightly higher which is consistent with the lower quality of the fit indicated by the Kolmogorov-Smirnov test reported in section 4 (see Figure 5) .

The comparison of results obtained using different models for the marginal probability are reported Figure 6 for all the damage scenarios in terms of the PoD at location 11, the damaged one.

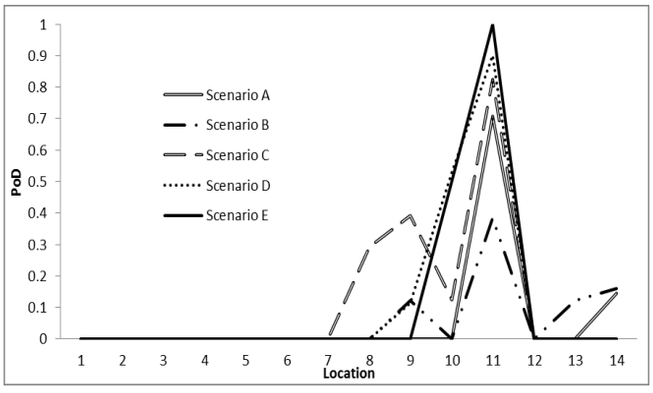


Figure 5. Probability of Detection based on the Gamma distribution for $f(E)$ for damage scenarios A to E:

At this location all the 3 models give reliable results indicating that the damage (represented by the PoD) increases starting from scenario B (1cm lowering of the pier) up to scenario E corresponding to the insertion of the compensating plates (lifting of 6cm over the original deck level).

As previously remarked the lifting of 6 cm over the original level certainly caused a variation of curvature even higher with respect to the one induced in scenario D by the lowering of the pier of 3cm. This is correctly detected by the method that finds the highest value of the PoD for scenario E. Starting from scenario A_T (the column is returned in its original position) and up to scenario E_T (the fourth tendon is partially cut) the PoD is always equal to zero, consistently with the expected behavior.

If other locations are considered the inaccuracy of the normal distribution with respect to the other two (lognormal and gamma) become more evident.

In Figure 7 are reported the values of the PoD at all the sensors locations for damage scenario E considering the three different probabilistic models. False alarms are found at locations 9 and 10 if the Normal distribution is used and a flase alarm is found at location 10 if the Gamma distribution is used. The most accurate results correspond the Lognormal model consistently with the results of the Kolmogorv-Smirnov test.

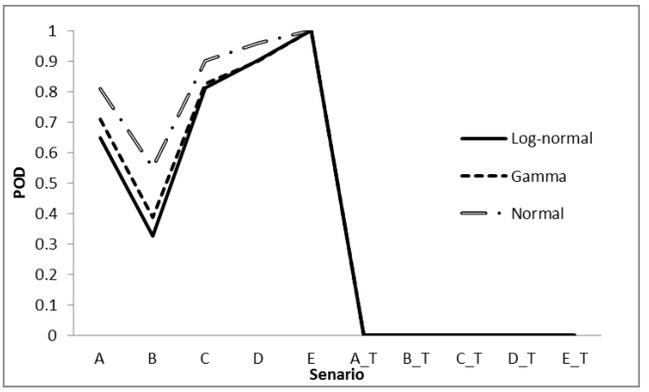


Figure 6. Probability of Detection at the damaged location for all the damage scenarios for location 11

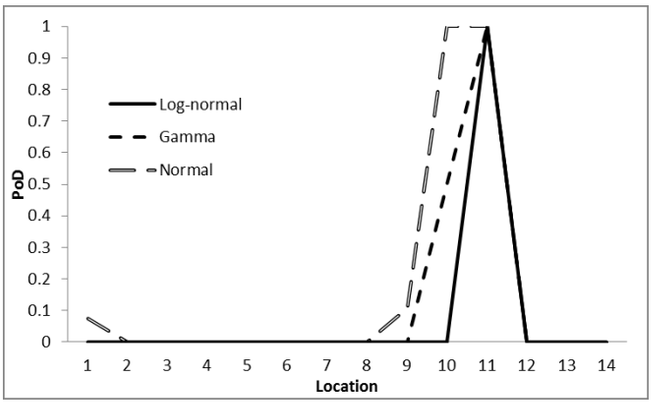


Figure 7. Comparison between the three probabilistic models for damage scenario E.

6 CONCLUSIONS

In this paper is investigated the influence of the probabilistic model of the marginal distribution of the Interpolation Error on the accuracy of damage localization.

Three distributions, Lognormal, Gamma and Normal have been considered and results compared in terms of the Probability of Detection. The latter is assumed as the damage feature.

The investigation has been carried out with reference to the case study of the S101m bridge for which data recorded in several damaged scenarios are available. The bridge was artificially damaged with several levels of severity and types of damage. The settlement of one pier and the loss of tension in the prestressing cables have been simulated by cutting respectively one of the piers and a number of tendons. Results show that the method is sensitive to the distribution chosen for the marginal probability. The Lognormal distribution - corresponding to the best-fit distribution according to Kolmogorov-Smirnov test – provides the most accurate results with the lowest number of false alarms with respect to the other tested distributions. The lognormal distribution corresponds to the best-fit both in the undamaged and in all the damaged distributions. This result is encouraging in the sense that, if confirmed

for other types of damage scenarios and structures, could enable to compute the distributions of the damage feature in the damaged configurations using the same probabilistic model of the undamaged configuration and changing the parameters based on the damage severity. As remarked, more investigations are needed to generalize this results and will be the object of further investigations together with the analyses of the sensitivity of results to the threshold value that is to the accepted probability of false alarm.

7 AKNOWLEDGEMENTS

The authors would like to thank the Vienna Consulting Engineers (VCE) company for providing the experimental data recorded during the tests on the S101 Bridge. The support of the Iranian ministry of science, research and technology (MSRT) to the stay of Amin Fathi at Politecnico di Milano is gratefully acknowledged.

8 REFERENCES

Brincker, R., Zhang, L., & Andersen, P. 2001. Modal identification of output-only systems using frequency domain decomposition. Smart materials and structures, 10(3), 441

Dilena, M., Limongelli, M. P., & Morassi, A. 2015. Damage localization in bridges via the FRF interpolation method. Mechanical Systems and Signal Processing, 52, 162-180.

Domaneschi, M., Limongelli, MP, & Martinelli, L. 2015. Damage detection and localization on a benchmark cable-stayed bridge. Earthquake and Structures , 8 , 1113-1126.

D omaneschi, M., Limongelli, M. P., & Martinelli, L. 2013. Multi-site damage localization in a suspension bridge via aftershock monitoring. Ingegneria Sismica, 3, 56-65.

Domaneschi, M., Limongelli, M. P., & Martinelli, L. 2013. Vibration based damage localization using MEMS on a suspension bridge model. Smart Structures and Systems, 12(6), 679-694.

Faber M.H. 2012. Statistics and Probability Theory. Springer Publishing Company, ISBN: 978-9400740556

Limongelli, M. P. 2014. Seismic health monitoring of an instrumented multistory building using the interpolation method. Earthquake Engineering & Structural Dynamics, 43(11), 1581-1602.

Limongelli, M. P., Tirone, M., & Surace, C. 2017,. Nondestructive monitoring of a prestressed bridge with a data-driven method. In Health Monitoring of Structural and Biological Systems 2017 (Vol. 10170, p. 1017033). International Society for Optics and Photonics.

Limongelli, M.P., 2011. The interpolation damage detection method for frames under seismic excitation. Journal of Sound and Vibration, 330. 5474–5489.

Peeters, B., & De Roeck, G. 2001. Stochastic system identification for operational modal analysis: a review. Journal of Dynamic Systems, Measurement, and Control, 123(4), 659-667.

Shampine, L. F. 2008. Matlab program for quadrature in 2D. Applied Mathematics and Computation, 202(1), 266-274.

Siringoringo, D. M., Fujino, Y., & Nagayama, T. 2011. Dynamic characteristics of an overpass bridge in a full-scale destructive test. Journal of Engineering Mechanics, 139(6), 691-701.

VCE. (2009). Vienna Consulting Engineers. “Progressive damage test S101. Flyover Reibersdorf”. Report nr. 08/2308.

Maintenance, Safety, Risk, Management and Life-Cycle Performance of Bridges – Powers, Frangopol, Al-Mahaidi & Caprani (Eds)
© 2018 Taylor & Francis Group, London, ISBN 978-1-138-73045-8

Uncertainties reduction on modal parameters estimation in existing bridges using ambient and free-vibration tests

N. De Conto, F. Lorenzoni, F. da Porto, C. Modena
Department of Civil, Architectural and Environmental Engineering, University of Padova, Italy

ABSTRACT: The correct estimation of modal parameters has an important role in ensuring the structural reliability of existing bridges. Operational modal analysis provides rather accurate extraction of natural frequency and mode shape but the corresponding damping estimates are subjected to higher uncertainties. This paper reports the results of ambient and free-vibration tests performed on four different typologies of road and railway bridges: steel trusses, multi-girder reinforced concrete, masonry and reinforced concrete arch bridges. In one case data acquired by a continuous structural health monitoring (SHM) system over a period of one year are available. In another case the passage of trains is exploited to perform free decays. Several frequency and time domain identification techniques are used to process AVT, whereas measured free decays are analyzed by the logarithmic decrement method applied to the autocorrelation functions of the signals. Outcomes are compared, evaluating the quality of modal damping estimates and results accuracy.

1 INTRODUCTION

The correct estimate of modal parameters has an important role in ensuring the structural reliability of existing bridges. Experimental modal analysis is very helpful to estimate modal parameters especially for: (i) existing structures, for which it is difficult to find information about the structure characteristics; (ii) new structures, after construction, to evaluate whether the modal parameters projected at the design stage are correct and in case to implement solutions to reduce vibrations.

In recent years, ambient vibration tests are becoming increasingly important because of their practical and economical side, comparing to force vibration test (Andersen et.al. 1999, Omenzetter et.al 2013). Furthermore, data are collected during the normal use of the structure and consequently the identified modal parameters are associated with realistic vibration levels. This technique provides very accurate estimate of natural frequency and mode shape but corresponding damping estimates present a significant scatter. The variability on modal parameters extraction can be due to several issues such as: (i) the length of time histories acquired; (ii) ambient noises or errors in signal acquisition; (iii) the type of data processing; (iv) the environmental condition during tests. To this, we must add factors influenced by the structural typology such as: the friction mechanisms between different structural parts or molecular mechanisms between building materials. An important role in the damping estimation is carried out by signal processing method. In particular, it has been observed (Magalhães et al. 2010, Brownjohn et al. 2010) that similar natural frequencies and modal shapes are obtained using different identification techniques and processing approaches for the same time history. Otherwise, largest discrepancies are observed in the modal damping ratios. It has been seen how methods in the frequencies domain, and particularly the Enhanced Frequency Domain Decomposition EFDD (Brinker et al. 2010), which is very easy to use and requires a low computational cost, gives a good result for damping ratio if a high coupling is not present between the modes. On the other hand, time domain methods, especially the COV-SSI (Peeters & De Roeck 1999), give good results, with shorter time series, especially in the flexibles structures with closely spaced modes.

In this research, four different typologies of road and railway bridges (steel trusses, multi-girder reinforced concrete, masonry and reinforced concrete arch bridges) were tested using ambient excitations. In one case data acquired by a continuous structural health monitoring (SHM) system (Caldon et al. 2014) over a period of one year are available. In another case the passage of trains is exploited to perform free decays (Huang et al. 1999, Ülker-Kaustell et al. 2011).

The data processing is based on several state of the art identification algorithms, in time and frequency domain (Ewins, 1984). The application of

various algorithms is relevant to increase the confidence on the obtained results and to evaluate their advantages and drawbacks.

2 CASE STUDIES

2.1 *Case Study I - Multi-girder reinforced concrete bridge*

Ponte Nuovo del Popolo bridge (Fig. 1) is located in the city center of Verona, on the Adige river. It is a three-span arched reinforced concrete bridge with an outer coating made of stone.



Figure 1. View of the Ponte Nuovo Bridge in Verona

The bridge has a total length of 90.5 meters. The central arch has a span of 33.42 meters, while the two lateral ones are 25.23 meters long. The overall width of the deck is 14.32 meters. The structure supports a two-lane roadway, one for each direction, and two sidewalks. The top of the deck slab, made of RC, has a design thickness equal to 18 cm. The static scheme consists of seven main girders and eleven cross beams in the transverse direction with stiffening function. The seven girders and the slab, because of the bad maintenance over the years, reveal severe damage in the middle of the spans due to water percolation. Girders and cross beams concrete is highly deteriorated, moldy and carbonated (Fig. 2).



Figure 2. Damaged elements of the Ponte Nuovo Bridge

A monitoring system has been installed in order to evaluate the general behavior of the structure for the damage detection. The system is composed by six uniaxial acceleration sensors (acceleration transducers) (Fig. 3), sixteen linear potentiometers (displacement transducers) and seven strain gauges for reading the deformations. The dynamic monitoring system is configured to record acceleration time series at fixed time intervals, every 12 hours. Each time history acquired by the system has a length of 20 minute with a sampling frequency of 100 Hz.

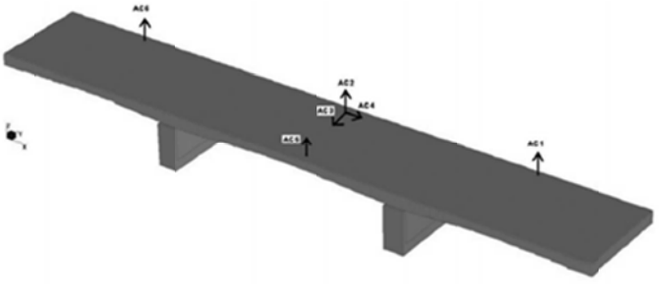


Figure 3. Sensor configuration of monitoring system of "Ponte Nuovo del Popolo" bridge

Thanks to the time histories acquired by the monitoring system, it was possible to evaluate how the type of data processing and the time length influence the estimation of the modal damping ratios. Two type of data processing have been considered: the EFDD and the SSI-UPC (Overschee & De Moor 1996). For each method, different parameters of the processing algorithms were considered as well as the length of time histories, varying between 3 and 20 minutes. In the case of the EFDD method, damping ratio estimates has a strong influence on time length and the number of points considered in the time segments used for the spectra calculation. This method was tested using 512, 1024 and 2048 points of the time segment. Figure 4, shows the results obtained with the EFDD method. It is possible to note that, if the number of point is not well chosen then the estimates can present high bias. For the analyzed case, there is a reduction in the damping estimation error if at least 1024 points and a minimum time length of 15 minutes are considered.

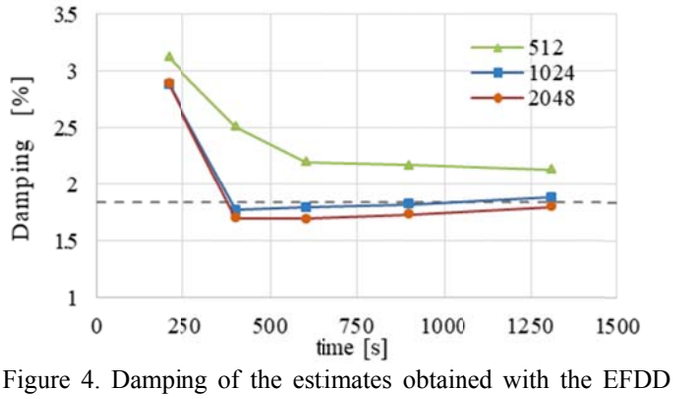


Figure 4. Damping of the estimates obtained with the EFDD method for the 1st modes using different algorithms parameters and different time lengths.

The parameter that has more relevant influence for the time domain method is the model order. The method was tested considering three different values of this parameter (80, 100, 150) and the same time length adopted in the previous method. Figure 5, presents results obtained by the SSI-UPC method. It

is clear that SSI method leads to good estimation using just 3 minutes of data and 150 point of the model order.

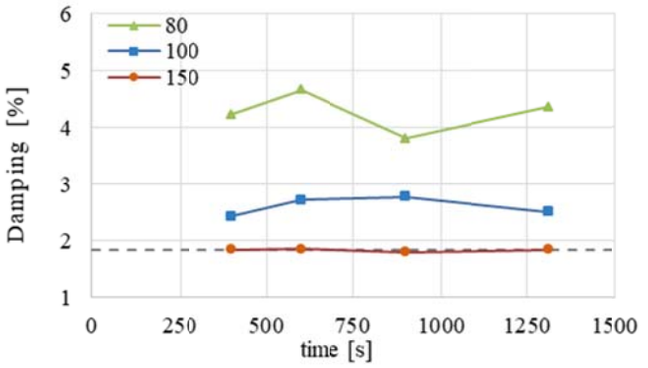


Figure 5. Damping of the estimates obtained with the SSI-UPC method for the 1st modes using different algorithms parameters and different time lengths.

The temporal evolution of the natural frequencies of the first seven vibration modes is presented in Figure 4. Each point of the graphs corresponds to a 12-hour average. The small blank spaces correspond to periods of system maintenance, for which no data is available. The high number of recordings acquired through the monitoring system allow to evaluate the presence of outliers and to evaluate dependencies of modal parameters with the environmental factors.

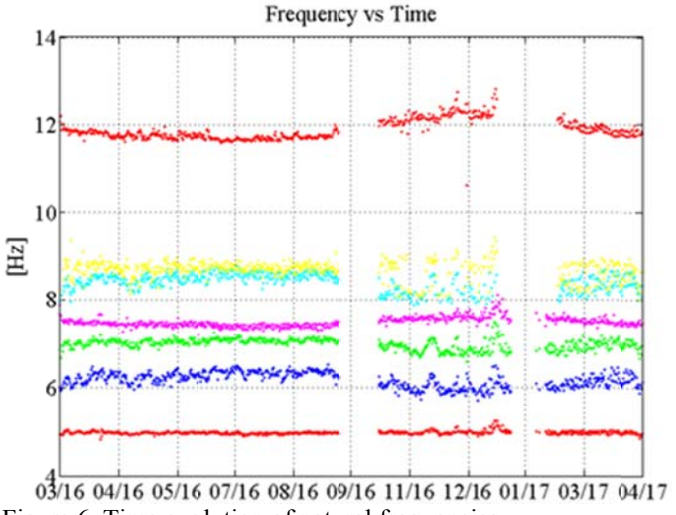


Figure 6. Time evolution of natural frequencies

Table 1. Modal Parameters

mode	$f_{[Min; Max]}$ [Hz]	f_{std} [Hz]	f_{CV} [%]	$\xi_{[Min; Max]}$ [%]	ξ_{std} [%]	ξ_{CV} [%]
1	[4.84 ; 5.24]	0.04	0.80	[0.60 ; 2.61]	0.30	22.72
2	[5.71 ; 6.53]	0.17	2.74	[0.81 ; 5.95]	0.68	15.81
3	[6.58 ; 7.50]	0.12	1.42	[1.08 ; 5.01]	0.65	19.36
4	[7.20 ; 8.12]	0.11	1.47	[0.43 ; 2.34]	0.36	25.17

The statistics of modal parameters extraction of the first four modes, are summarized in Table 1 where minimum, maximum, standard deviation and coefficient of variation (CV) of frequencies and damping values are presented. It is important to notice the significant difference between the standard deviation of frequency and damping ratio. Modal damping estimates present a higher scatter than the one observed in the natural frequencies, which is reflected in the CV.

2.2 *Case Study II – Steel bridges*

The Musile bridge (Fig. 7a) is located in Venice province along the railway line that connects Venice to Trieste. The steel trusses bridge was built in 1937 to cross Piave river.

It is composed by three spans of over 50m each. Every span is composed by double separate reticular structure equipped with diagonal roods and vertical supports that connect the two lower and upper beams. The structure is supported by masonry piers and abutments. Dynamic identification tests took place in September 2012.

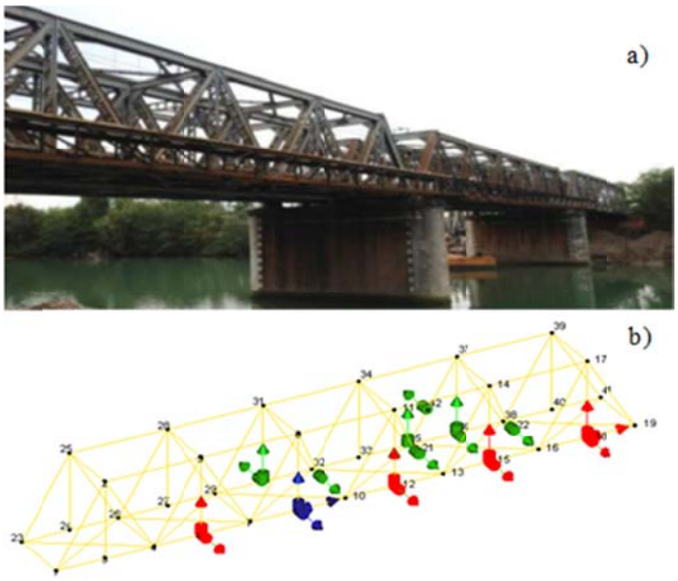


Figure 7. a) frontal view of the Musile bridge; b) sensor location and directions for all setups.

For the dynamic identification of the bridge 12 piezoelectric accelerometers were used, and placed in two different configurations (setups) for a total number of 11 measuring points in order to get the vibrations of the reticular trusses (Fig. 7b). The sensor records a signal of 1300 seconds long with a sampling frequency of 100 Hz. For both setup (Set1_MP and Set2_MP), during the acquisition time, a train passage was reordered. Modal parameters were extracted using time and frequency domain techniques. As a preliminary step the influence of the length of the time histories and the number of points considered in the time segments, used for the spectra calculation in the EFFD method, were evaluated. The time length of the output time series was modified from 350s to 660s. In the time series of 660s the passage of a train was recorded.

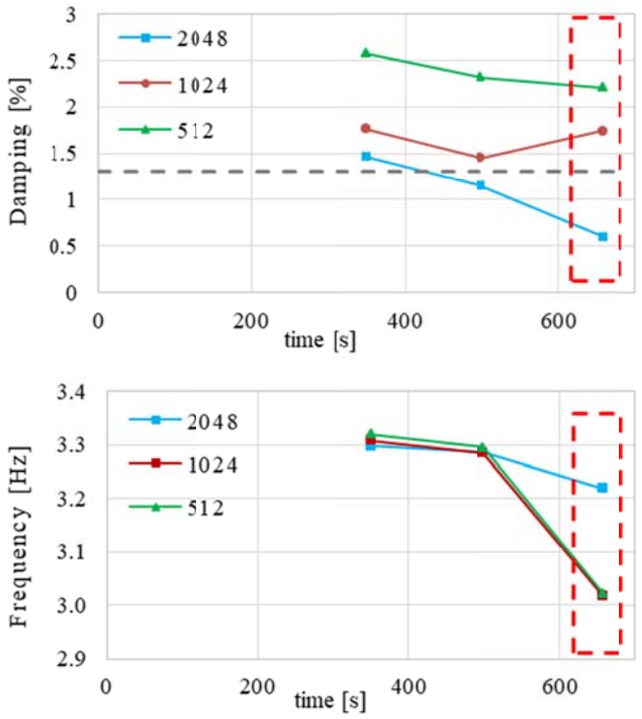


Figure 8. Damping and frequency obtained with the EFDD method for the 1 mode using different algorithms parameters and different time lengths.

Figure 8 shows the results. It is clear that, if in the recording of the time histories the hypothesis of white noise of the input are not satisfied (e.g. train transit, corresponding to the dashed rectangle in Figure 8) the estimates present several errors (both of frequency and damping). If trains are not considered (time length of 500s) the predicted outcomes with 1024 or 2048 points of the spectral density matrix converge to the same value.

For ambient vibration tests the modal parameters were estimated considering the time histories without the noise caused by train transits. Each time history was processed by the EFDD, SSI-COV and SSI-UPC methods. Thanks to the registration of the train passage, it was possible to perform a free vibration test (FVT). Natural frequencies and modal damping ratios of the bridge are identified by analyzing the free vibration response after the passage of a train. The methodology used to extract modal parameters consists of the following steps:

(i) isolate the part of the signal after the passage of the train (free decaying) and apply to the signal band-pass filters. Signal filtering is necessary to isolate contributions of the frequency of interest (Fig. 9a);

(ii) estimate the frequency applying the Fast Fourier Transform (FFT) algorithm;

(iii) calculate the autocorrelation function of the filtered signal of each accelerometer (Fig. 9b);

(iv) estimate the damping ratio applying the logarithmic decrement method to the autocorrelation function;

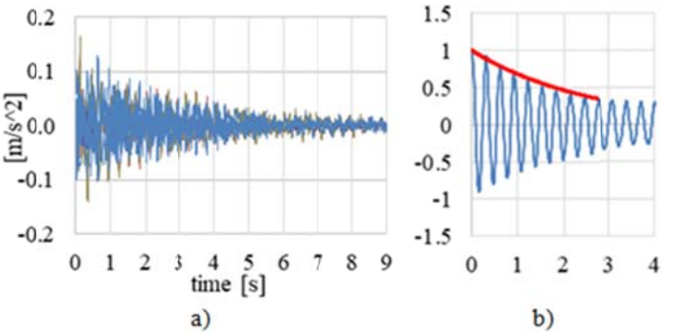


Figure 9. (a) Part of time history with free decays (b) Autocorrelation function for the time histories of one vertical accelerometers for the first setup.

Figure 10 summarizes the results of all used methodologies in term of frequency and modal damping ratio. The comparison between modal damping ratios, identified using FVT and ambient excitations, shows some differences. It is possible to note that the FVT allows to obtain excellent results, for frequencies and for damping, compared to ambient vibration test. This is due to the much higher level of vibrations. However, this type of methodology allows detecting just a few vibration modes. The estimated damping with AVT has higher standard deviation values with coefficients of variation of 70%.

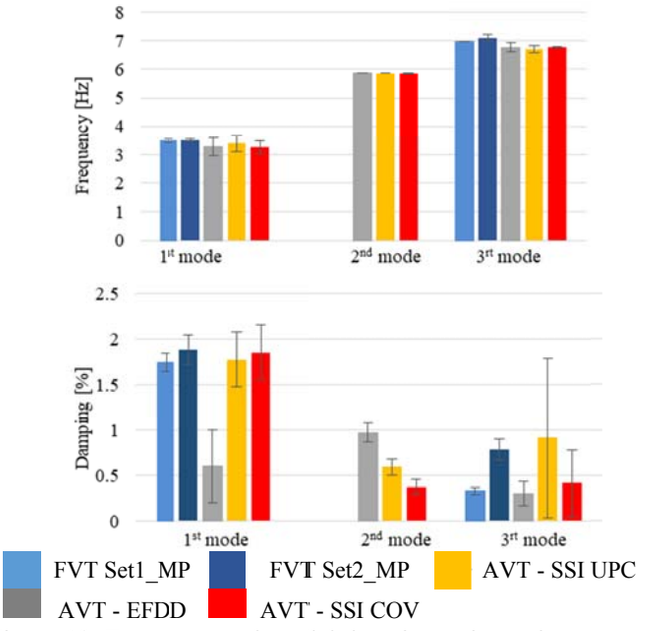


Figure 10. Frequency and modal damping ratios estimates provided the EFDD, SSI methods and free Vibration Technique.

2.3 *Case Study III – Masonry arch bridge*

The Gresal Bridge (Fig. 8) is located in the North-East of Italy, in Belluno province. It was built in the early XIX century and is currently used as a vehicular bridge. The structure is a three-span stone masonry arch bridge, with a total length of 67.40 m: the three spans are almost equal, the single arch clear length is about 15m; their shape is almost semi-circular with a radius of 7.39m, slightly increasing at the springers. The average thickness at the arch at

the key is 0.50m. The maximum height of the two piers is 12.75m and their section is rectangular.



Figure 11. View of the Gresal Bridge

During the month of March 2011, in collaboration with Veneto Strade S.p.A a dynamic identification test was carried out. To measure the response of the bridge eight piezoelectric accelerometers placed in three different configurations (setups) were used, one for every arch.

The structural response to ambient vibrations has been acquired for about eleven minutes with a sampling frequency of 100 Hz. During test execution, the bridge was not closed to traffic, which has been used as a natural load to excite the structure.

Time histories were processed with frequency (EFDD method) and time (SSI-UPC and SSI-COV method) domain methods. For the EFDD method it has been chosen to use a model with 2048 point and for the time domain method a model order n=170 for the SSI-UPC and n=100 for the SSI-COV. The bridge is rather massive and stiff and thus difficult to excite with ambient vibrations.

Figure 11 shows the results obtained in terms of natural frequencies and modal damping ratio. As expected, given the stiffness of the structure, high values of natural frequency are estimated. The results obtained with the three different methods are similar for the frequencies with low value of standard deviation (CV smaller than 3.5%). It was found a value of 4.96 Hz for the first mode, 8.29Hz for the second one and 10.41 Hz for the third one. Figure 13 shows the mode shapes for the first three vibration modes: the first one is a bending type in the transverse direction, the second one is a bending type in the longitudinal direction, while the third is torsional. Slight deviations are detected for damping but the predicted values have high level of standard deviations especially for the second and the third mode with CV greater than 100%.

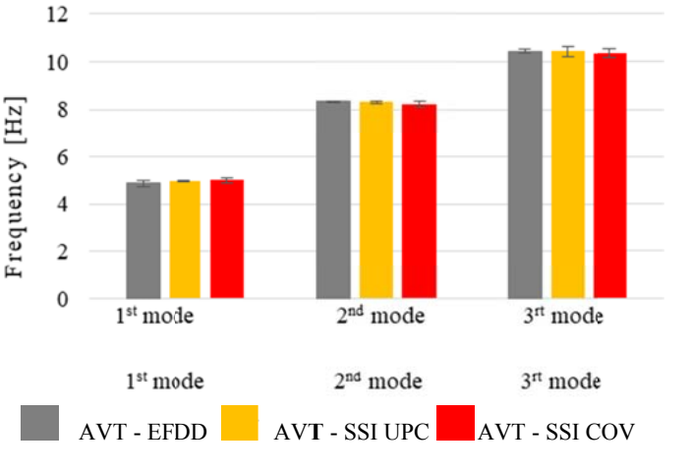


Figure 12. Frequency and modal damping ratios estimates provided the EFDD, SSI methods.

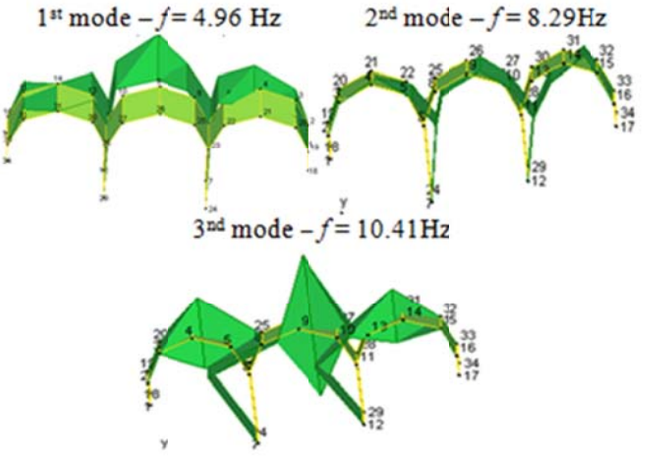


Figure 13. First three mode shapes for the Gresal Bridge.

2.4 *Case Study IV – Reinforced concrete arch bridges*

The bridge of St. Giustina is located in the Region of Trento (Italy) in front of the St. Giustina Dam. It is composed by a single arch span in reinforced concrete, with a total length of 68 m. The deck of the bridge is 9,00m wide for two traffic lanes and two sidewalks. The bridge is supported by two tapered arches (open spandrel arcs) linked together by several reinforced concrete beams. The height of the arch's section is 2,50m at the basis and 1,80m at the key. Along the length of the arch there are 16 vertical concrete columns that connect the arches with the slab, forming a rigid frame. All the columns are connected together with cross struts; the outer and higher columns are also transversally braced by X-shaped steel struts. The St. Giustina Bridge contains inside the concrete structure, the frame of the old steel bridge of St. Giustina erected in 1888. The old steel bridge was incorporated inside the new bridge in a reinforcement intervention in 1960.

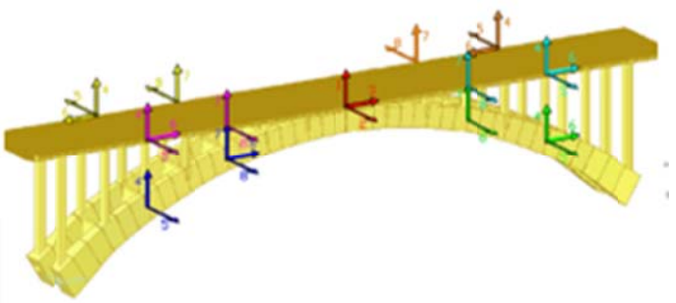


Figure 14. Sensor locations and directions of Santa Giustina Bridge.

In January 2010 ambient vibration tests were performed on the bridge to characterize its dynamic behavior. Tests lasted three day during which low temperatures were detected. Piezoelectric accelerometers with vertical axes were used to measure the bridge response. In order to obtain a good spatial resolution, eight different setups were used (Fig. 14). Three accelerometers were placed as reference sensors in the middle of the bridge and eight others were simultaneously moved to cover the entire area of the bridge. The structural response has been acquired for about eleven minutes with a sampling frequency of 100 Hz.

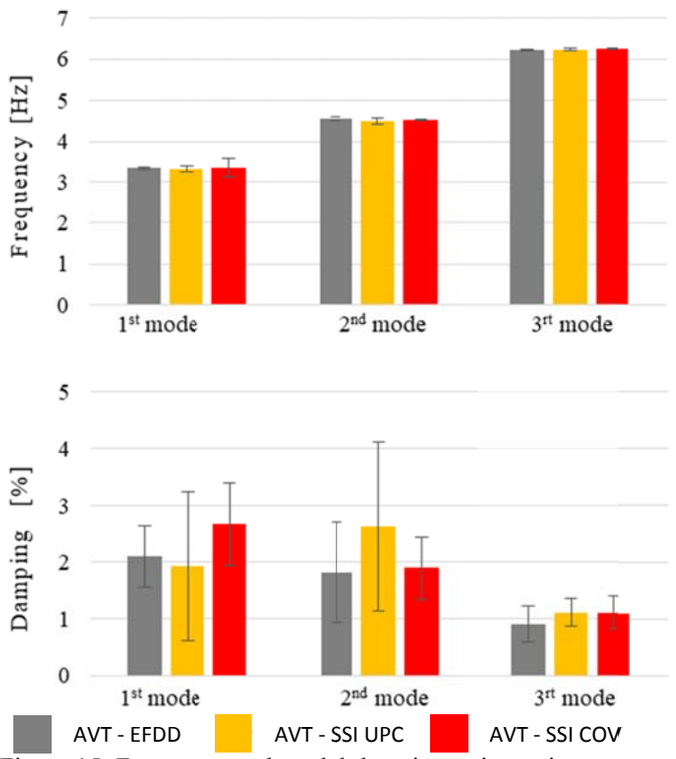


Figure 15. Frequency and modal damping ratios estimates provided the EFDD, SSI methods.

Time histories were processed with frequency (EFDD) and time (SSI-UPC and SSI-COV) domain methods. For the EFDD method it was chosen to use a model with 2048 point in the spectral analysis. A model order n=170 for the SSI-UPC and n=120 for the SSI-COV was considered sufficient for the correct definition of the signal. The results obtained with the three different methods are reported in Figure 15. The comparison between modal damping ratios identified using the three different identification algorithms shows some differences, especially for the first and second mode. However, all the values are within the interval of variation (defined by the standard deviation) presented for the AVT estimates.

3 COMPARISON OF THE RESULTS

In this paper, it has been analyzed the quality of estimates of the modal parameters. Table 2 shows the results for the four bridges analyzed. It is observed that every typology presents different behavior. For all structures, the algorithm used for the estimation of frequencies proved to be rather effective with low values of standard deviation (coefficient of variation CV from 0.3% to 8.5% for all modes). As expected, the modal damping estimate presents a much higher scatter with CV from 12% and 110% for the first two modes. In the end it is appropriate to compare the dynamic performance of the different structural typologies.

Steel bridges (ST) are very flexible and, as a consequence, easy to identify through ambient vibration tests. In the case of reticular steel bridges, due to symmetric geometry, just few sensors can get pretty accurate results. The principal modes (first transversal and second vertical) were identified using both time and frequency domain techniques that showed excellent results. AVT are not appropriate when the hypothesis of whiteness of the input are not satisfied (e.g. train transit). On the other hand, the passage of trains allows to perform FVT. In this case the results taken from the free decays are more accurate, because the noise influence is smaller (higher amplitudes).

Very susceptible to ambient vibration are also slender reinforced concrete arch (RCA) bridges. Indeed, like for the steel bridges, it was clearly simple to distinguish structural modes using basic techniques as PSD or FDD analysis because very clear and sharp peaks are identified. Despite these considerations, damping obtained has significant uncertainties with CV of standard deviation between 40% and 70%. This may be due to the use of relatively short time series (11 minute). Masonry arch (MA) bridge system identification encounters a challenging aspect. Damping estimates are characterized by the highest errors with a CV greater than 100%.

Multi-girder reinforced concrete (MGRC) bridges are rather easy to identify by ambient vibration tests. For the "Ponte Nuovo del Popolo" bridge a permanent SHM system was installed. Thanks to the available monitoring data over a period of one year it was possible to reduced drastically the uncertainties in the estimation of modal parameters (especially for damping ratios, resulting with a CV between 10% and 20%).

Table 2. Comparison of the frequency and damping ratio

	1st mode			2nd mode			3rd mode		
	f [Hz]	f_{std} [Hz]	f_{CV} [%]	f [Hz]	f_{std} [Hz]	f_{CV} [%]	f [Hz]	f_{std} [Hz]	f_{CV} [%]
ST*	3.42	0.29	8.5	5.89	0.01	0.2	6.88	0.02	0.2
MA*	4.96	0.16	3.3	8.29	0.14	1.7	10.41	0.30	2.9
RCA*	3.34	0.14	4.2	4.52	0.10	2.2	6.24	0.04	0.7
MGRC*	4.98	0.03	0.6	6.19	0.18	2.8	7.00	0.12	1.7

	1st mode			2nd mode			3rd mode		
	ξ [%]	ξ_{std} [%]	ξ_{CV} [%]	ξ [%]	ξ_{std} [%]	ξ_{CV} [%]	ξ [%]	ξ_{std} [%]	ξ_{CV} [%]
ST*	1.70	0.46	27	0.48	0.12	25	0.61	0.96	158
MA*	3.31	1.84	56	2.26	2.48	110	2.99	1.58	53
RCA*	2.26	1.60	71	2.01	1.60	80	1.05	0.48	46
MGRC*	1.32	0.27	20	4.38	0.54	12	3.38	0.61	18

*ST=steel trusses; MA=masonry arch; RCA=reinforced concrete arch; MGRC=multi-girder reinforced concrete

4 CONCLUSIONS

This paper reports the results of ambient and free vibration tests performed on different bridge typologies to extract modal parameters and quantify the uncertainties in damping ratio estimation. It was observed that the extraction of this parameters is influenced by the structural typology, the length of the acquired time histories, type and parameters of the modal analysis algorithm. For railway bridges, it was noted that the train passage could bring to an unprecise estimation of frequency and damping due to the non-stationarity of the input signal.

It is possible to state that the extraction of natural frequencies and mode shapes are rather easy to identify using ambient vibration tests. Damping ratio presents higher uncertainties especially for stiff bridges and when the acquired time histories are too short. A permanent SHM proved to be very useful to reduce uncertainties of the estimates

REFERENCES

Andersen, P., Brincker, R., Peeters, B., Roeck, G., Hermans, L., Krämer, C 1999. Comparison of System Identification Methods using Ambient Bridge Test. *Data Proceedings of the 17th International Modal Analysis Conference (IMAC)*, Kissimmee, Florida, USA.

Brinker, R., Ventura, C., Andersen, P. 2001, Damping estimation by frequency domain decomposition. *Data Proceedings of the 19th International Modal Analysis Conference (IMAC)*, Kissimmee, FL, USA.

Brownjohn, J.M.W., Magalhaes, F., Caetano, E., Cunha, A., 2010. Ambient vibration re-testing and operational modal analysis of the Humber Bridge. *Engineering Structures*, 32: 2003-2018.

Caldon, M., Islami, K., Lorenzoni, F., Modena, C. 2014 Integrated System for Continuous Dynamic Monitoring: ”Ponte Nuovo Del Popolo” Bridg. *7th European Workshop on Structural Health Monitoring.* La Cité, Nantes, France.

Ewins, D.J. 1984. Modal Testing: Theory and Practice, *Research Studies Press Ltd*., Letchworth, Hertfordshire, UK.

Huang, C. S., Yang Y.B., Lu, L.Y., Chen, H., 1999 Dynamic testing and system identification of a multi-span highway bridge. *Earthquake Engng. Struct. Dyn*. 28, 857-878.

Magalhaes, F., Cunha, A., Caetano, E., Brinker, R. 2010 Damping estimation using free decays and ambient vibration tests. *Mechanical Systems and Signal Processing, 24:*1274-1290.

Peeters, B. & De Roeck, G. 1999. Reference-based stochastic subspace identification for output-only modal analysis. *Mechanical Systems and Signal Processing*, 13(6): 855–878.

Omenzetter, P., Beskhyroun, S., Shabbir, F., Chen, G.W., Chen, X., Wang, S., Zha, A. 2013 Forced and ambient vibration testing of full scale bridges. *A report submitted to Earthquake Commission Research Foundation* (Project No. UNI/578).

Overschee, P. & De Moor, B. 1996: Subspace identification for linear systems – *Theory, Implementation, Applications. Kluwer academic Publishers*, ISBN 0-7923-9717-7.

Ülker-Kaustell, M., Karoumi, R., 2011 Application of the continuous wavelet transform on the free vibrations of a steel–concrete composite railway bridge. *Engineering Structures*, 33: 911-919.

Maintenance, Safety, Risk, Management and Life-Cycle Performance of Bridges – Powers, Frangopol, Al-Mahaidi & Caprani (Eds)
© 2018 Taylor & Francis Group, London, ISBN 978-1-138-73045-8

Monitoring of the Chillon viaduct after strengthening with UHPFRC

H. Martín-Sanz, V. Dertimanis, L.D Avendaño-Valencia & E. Chatzi
Department of Civil, Environmental and Geomatic Engineering (IBK)
ETH Zürich, Zürich, Switzerland

E. Brühwiler
Structural Maintenance and Safety Laboratory (MCS)
EPFL, Laussane, Switzerland.

ABSTRACT: Located at the shore of Geneva Lake, in Switzerland, the Chillon viaducts are two parallel structures consisted of post-tensioned concrete box girders, with a total length of 2 kilometers and 100m spans. Built in 1969, the bridges currently accommodate a traffic load of 50.000 vehicles per day, thereby holding a key role both in terms of historic value as well as socio-economic significance. Although several improvements have been carried out in the past two decades, recent inspections has demonstrated an alkali-aggregate reaction in the concrete deck slab reducing its strength. In order to strengthen the concrete deck and slow down further AAR, a layer of 40 mm of Ultra High Performance Fiber Reinforced cement-based Composite (UHPFRC) (incorporating rebars) was cast over the slabs, acting as a waterproof membrane and providing significant increase in resistance via the UHPFRC - RC composite action, in particular of the deck slab.
Two years after completing the works, a Structural Monitoring campaign was installed on the deck slab in one representative span, based on accelerometers, strain gauges, thermal and humidity sensors. This campaign seeks to reveal information on the behavior of UHPFRC-concrete composite systems, such as increase in stiffness, fatigue strength, durability and long-term performance. Consequently, the campaigns is expected to last for at least three years. A first insight of the analyzed results from the initial months of measurements is presented herein, along with future improvements or necessary changes on the deployment.

1 INTRODUCTION

The Chillon viaducts connect the Swiss region of Montreux and Villeneuve by means of two post tension concrete box girder structures, allocating a traffic load of 50.000 vehicles per day (Perret et al. 2014). With a length of 2 kilometers, divided in spans of 96, 98 and 104 m, these bridges along the shore of lake Leman stand not only as a critical item in the transport network, but also as a remarkable part of the cultural value of the region.

Since they were constructed in 1969, the bridges have been inspected and rehabilitated along the years, in order to maintain the safety levels in accordance with updated loads and codes. The last surveillance in 2014 revealed an Alkali-Silica Reaction (ASR) in an early stage, which motivated assessment of different solutions, both for strengthening the structure as well as diminishing the growing rate of the reaction. As established in Hobbs (1988), ARS is a combination of two phenomena: reactive aggregate and high humidity exposure. Currently, aggregates are selected carefully to avoid this type of issues, although for existing structures the only possible intervention involves minimizing the exposure of the section to water. Hence an ideal retrofitting method should serve as a waterproof membrane, while providing structural strength, as the ARS affects the concrete strength and its modulus of elasticity. In this context, an Ultra High Performance Fiber Reinforced cement-based Composite (UHPFRC) application on top of the existing deck was chosen as the most economical and convenient, based on numerous successful projects (Brühwiler & Denarié 2013, Martín-Sanz, Chatzi, & Brühwiler 2016). UHPFRC is characterized as an outstanding material for rehabilitation projects due to its exceptional mechanical and durability properties, low porosity and microcrak control. Furthermore, the works at each bridge were completed within a single month, rendering a short-term closure highly appreciated by the commuters (Bastien-Masse & Brühwiler 2015). Despite UHPFRC being used in past decades as a rehabilitation material, limited literature is available on the long term behavior for large scale projects.



Figure 1: View of Chillon viaducts at the shore of lake Geneva.

Taking into consideration the age of the bridges, the present structural damaged condition and the innovative solution used for their strengthening, a monitoring deployment was envisioned, aiming to render valuable information on the remaining lifespan of the viaducts. Structural Health Monitoring (SHM) techniques based on dynamic measurements are widely spread nowadays and can provide a non-invasive and convenient solution for bridge inspection and damage detection (Ko and Ni 2005, Brownjohn 2007). In this case, modal analysis will be combined with strain gauge measurements as well as temperature and humidity information, since it has been proven that the last two factors impose a variability in modal parameters, which can mask damage effects. Even though vibration-based methods have experienced a large improvement in recent years, with new sensors technologies and advances in automation, several drawbacks must still be overcome. Those shortcomings are related to a) lack of knowledge from the excitation source, as wind or traffic is usually not measured in Operation Modal Analysis (OMA), and b) the influence of environmental factors, as established by Peeters (2000). In order to assess the condition of the structures, these methods rely on changes on modal parameters, where a loss of stiffness indicates a possible damage scenario. Prediction of these events requires further analysis, since in reality, modal parameters are sensitive to several factors as well as deterioration. Starting by temperature effects, Kim, Park, & Lee (2007) observed that higher temperatures reduce modal frequencies, with more pronounced influence on flexural modes than on lateral ones. Watson & Rajapakse discovered that asphalt stiffness varies dramatically especially around the freezing point. Moreover, steel and concrete modules of elasticity are also considerably affected (Ubertini et al. 2017). However, further studies have shown that material properties are not the only factor that is altered. Taylor & Stanton (2010) echoed that friction coefficients for teflon bearings range between 3-5% at 25°C and 15% at -20 °C, and changes on support conditions shift the natural frequencies up to 50% (Alampalli 2000). Another modifying component pertains to the applied loads, including wind speed changes, which produce variations in structural dynamics (Cross et al. 2013), or heavy traffic in short span bridges, which varies structural mass and thus modal properties. In pursuance a method which differentiates ambient variability from damage, two main strategies have been followed: first, regression models, when the input is known and used to establish a relationship with the output (Wenzel 2009, Yuen and Kuok 2010) and second, pattern recognition methods, where imput is unknown and therefore Principle Component Analysis (PCA) is employed to obtain the representative components for the operational variations (Reynders & De Roeck 2014). Instead of PCA, AutoRegressive (AR) can be adopted, as demonstrated by Nandan and Singh (2011), or Polynomial Chaos Expansion (PCE) where the changes in environmental conditions can be described by stochastic propagation. In this paper, the latter will be applied following the works of Chatzi and Spiridonakos (Spiridonakos & Chatzi 2015; Spiridonakos, Chatzi, & Sudret 2016; Bogoevska, Spiridonakos, Chatzi, Dumova-Jovanoska, & Höffer 2017), where the method predicts the dynamic responses through meta-modelling. The structure of this paper is as follows: Firstly, the structural characteristics of the bridge are described, followed by a detailed explanation of monitoring implementation. Secondly, modal properties and strains are depicted, relating them with UHPFRC strengthening.The construction of a surrogate for the evolution of modal frequencies and strains, i.e., two quantities directly relating to the stiffness of the system, is described next, and finally concluding remarks are offered.

2 MONITORING DEPLOYMENT

2.1 *Structural description*

The viaducts of Chillon are two parallel structures with almost identical characteristics, constructed in the seventies by the same procedure. The box girder, comprising precast segments varying in height from

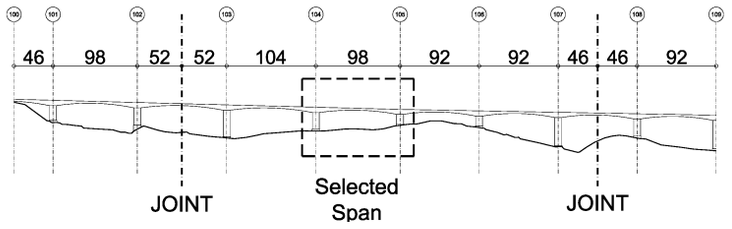


Figure 2: Selected monitored span.

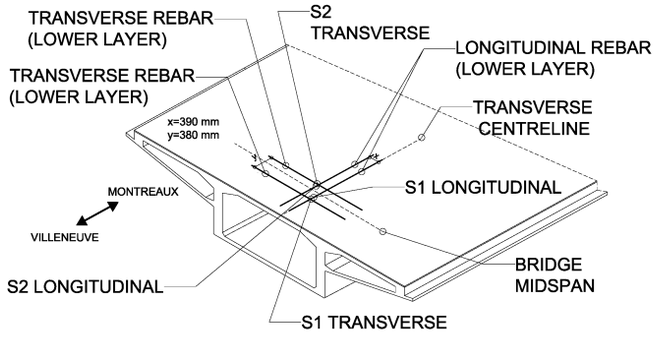


Figure 3: Bridge monitored sections and type of instrumentation.

5.2 to 2.2 m, was launched from the piers until midspan by means of a jacking frame and the interconnecting joints were concreted on site. Three different span lengths were included, in order to adjust the structure to the ground profile: 92, 98 or 104 m. The physical joints are located at the middle of the span, every five spans, creating a continuous deck over almost 500 m thanks to longitudinal prestress on the top section. In 2015, ARS was detected, leading to a strengthening campaign with UHPFRC. A layer of 40 mm with transverse reinforcement was applied, whereas on the supports, the thickness reached 50 mm to include additional longitudinal reinforcement up to 1/8 of the span. Eventually, the bottom zone of the supports was strengthened with conventional reinforced concrete.

2.2 *Monitoring deployment*

A primary objective of SHM lies in retrieving as much information as possible while using a limited number of sensors. In the case shown herein, it is not feasible to instrument both viaducts along the 2100 m they comprise. Therefore, a representative section is chosen, aiming to cover as many features as possible within the length of one span. The selected segment should gather the following characteristics: a) should be placed in the part of the viaduct closest to the lake (Viaduc du Lac), which is exposed to more wind and humidity, b) not be consecutive to the span with a cantilever joint, c) allow for a reasonable distance between power source and installation, d) maintain a straight profile to the extent possible. The span fulfilling the aforementioned requisites is number 5, with 98 m length and a non-symmetric shape (46m+52m) as depicted in Figure 2. The sensor placement is shown in Figures 4 and 5. In order to capture the mode shapes of the structure, eleven accelerometers built in ETH laboratory, are acquired by means of a GANTNER reading unit with 32 channels. Furthermore, three high precision accelerometers EPISENSOR type were used for a period of one month, in pursuance of a comparison between the custom and lower accuracy sensor and the higher precision (and higher cost) SED instrument. The latter were kindly offered by the Swiss Seismological Service institution for the purpose of this work. The environmental conditions were tracked by means of one humidity sensor and seven temperature sensors embedded in the concrete, located at the midspan of the bridge, on deck, walls and floor, to obtain a complete picture of temperature gradient inside the bridge. Finally, four strain gauges were installed as depicted in Figure 3, attached to the rebar. In order to limit the damage to the concrete structure to the absolute minimum, ground-penetrating radar techniques were deployed to display the reinforcement position and the cover concrete was locally removed. The cover is subsequently replaced again to ensure the protection of the steel. The latter sensors were connected to an HMB Data Acquisition System (DAQ), thus synchronization between both reading units (GANTNER and HBM) is required and relies on the PC clock to which they are connected. Datasets are stored every ten minutes, with a sampling frequency of 200Hz for the accelerometers, 100 Hz for the strains and 1Hz for environmental data.

3 MONITORING RESULTS

3.1 *Temperature and Humidity*

A common issue in SHM appears when part of the data is damaged or not completely recorded, due to power loss, program bugs or through the entry of dust particles inside the DAQs. In the case study shown herein, temperature, humidity and strains were missing over a period lasting 37 days (18th of March until 25th of May) and accelerations over 15 days (9th until 24th of May). In order to retrieve as much valid information as possible, humidity and temperature readings were collected from the nearest weather station, 8 kilometers from the viaducts at the same altitude. As the correlation between the bridge measurements and the station data results as adequate, the missing values were estimated by statistical methods. The procedure starts with first creating a Vector Autoregression (VAR) model, followed by the application of a Kalman filter, for the period where enough vibration data existed. The prediction provides accurate results, as observed in Figure 6, except at the point where vibration data is missing and therefore a jump on the expected trend is artificially created. Furthermore, despite the aforementioned correlation between variables, it is important to note the different behavior of each sensor depending on its location in the

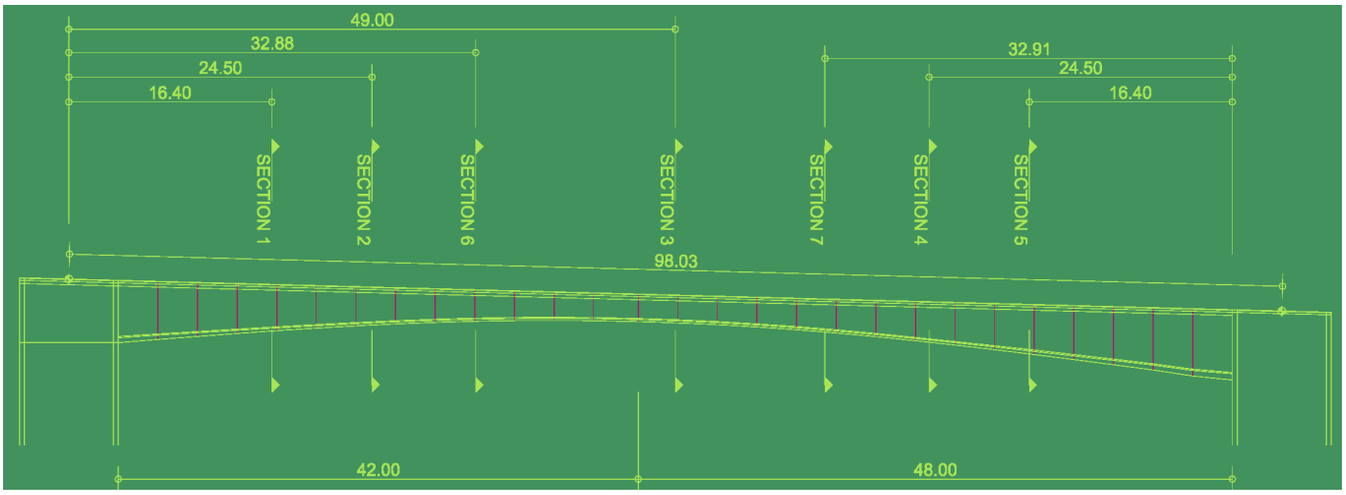


Figure 4: Viaduct instrumented segments

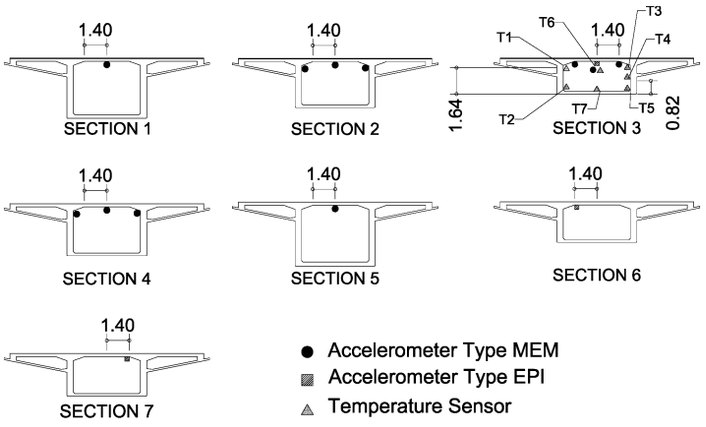


Figure 5: Sensor types and positions.

bridge. For example, sensors T6 and T7, positioned on the top and bottom deck respectively, present a trend very similar to the air temperature (with delay of four hours and a half, attributable to concrete thermal inertia), whereas sensors placed on the walls experience smoother temperature change with smaller amplitudes. Since the accelerometers are installed on the top deck, sensor T6 is taken as a reference for further analysis.

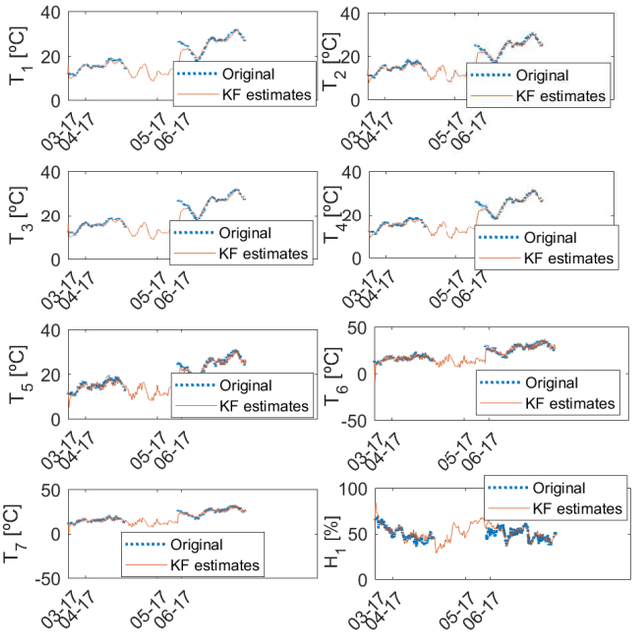


Figure 6: Estimated and original values from temperature and humidity sensors.

3.2 *Modal shapes and frequencies*

The reported period herein ranges from 24th of March to June 2017. In a previous campaign, a first evaluation of the acceleration data showed a low signal-to-noise ratio (SNR) due to grounding issues. This problem was remedied and, to confirm the validity of the data, three Episensors with high accuracy were installed and compared against the MEMs, revealing a good agreement between both systems (as observed in Figure 7). However, only the vertical channels are used for the analysis, ignoring at this stage the transverse ones, since the signal was not strong enough to obtain adequate results. The identification process to obtain the frequencies over time was achieved by contrasting several subspace methods, such as Stochastic Subspace Identification (SSI), Auto Regressive Ex-

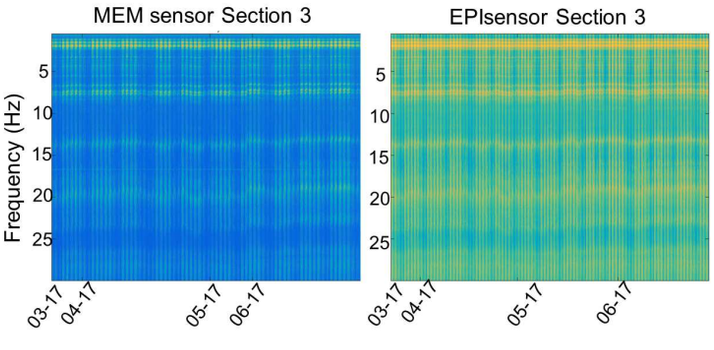


Figure 7: Frequencies over time from MEM sensor (left), Episensor (right).

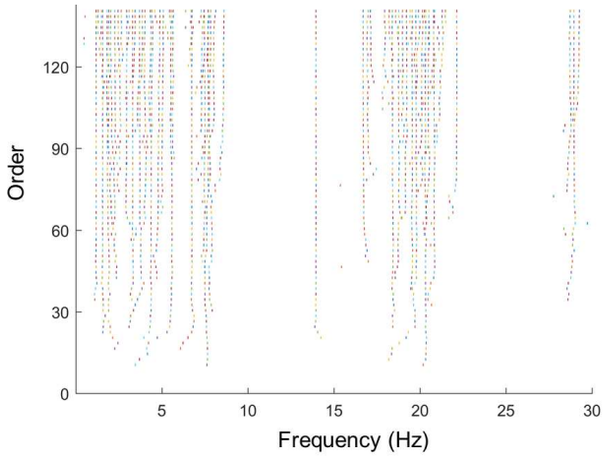


Figure 8: Stabilization diagram for reference setup.

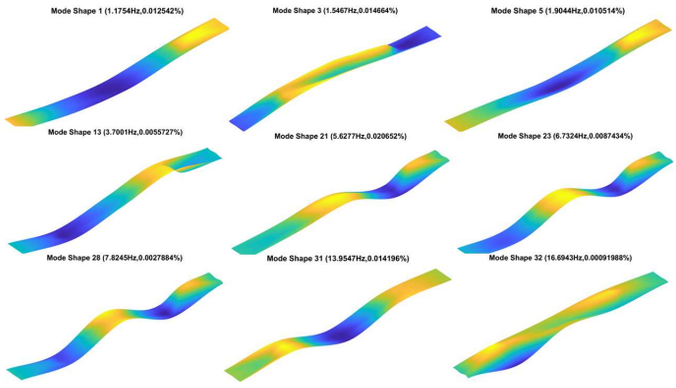


Figure 9: From top to bottom, left to right, modes 1, 3, 5, 13, 21, 23, 28 , 31 and 32.

ogenous model (ARX) and Eigensystem Realization Algorithm with Natural Excitation Technique (ERA NExT), using the built-in functions provided in MATLAB. Improved results were obtained with the latter, although a high order of the state space (120) was still required to capture more stable modes. Figure 8 depicts the need for model clustering, as a large number of modes appears in the range of 1 to 7 Hz and between 15 and 21 Hz. This process, based on Modal Assurance Criteria (MAC) and damping limited to 5% maximum, renders nine traceable modes along the three months of data. The identified modal shapes can be observed in Figure 9, along with frequency and damping in Table 1. Figures 10 and 11 present the evolution of the viaduct frequencies with respect to time and temperature during the analyzed period.

Table 1: Identified modes, damping and frequency.

	Frequency	Damping
Mode Number	Hz	%
Mode 1	1.175	0.012
Mode 3	1.547	0.015
Mode 5	1.904	0.011
Mode 13	3.700	0.006
Mode 21	5.628	0.021
Mode 23	6.732	0.009
Mode 28	7.824	0.003
Mode 31	13.954	0.014
Mode 32	16.694	0.001

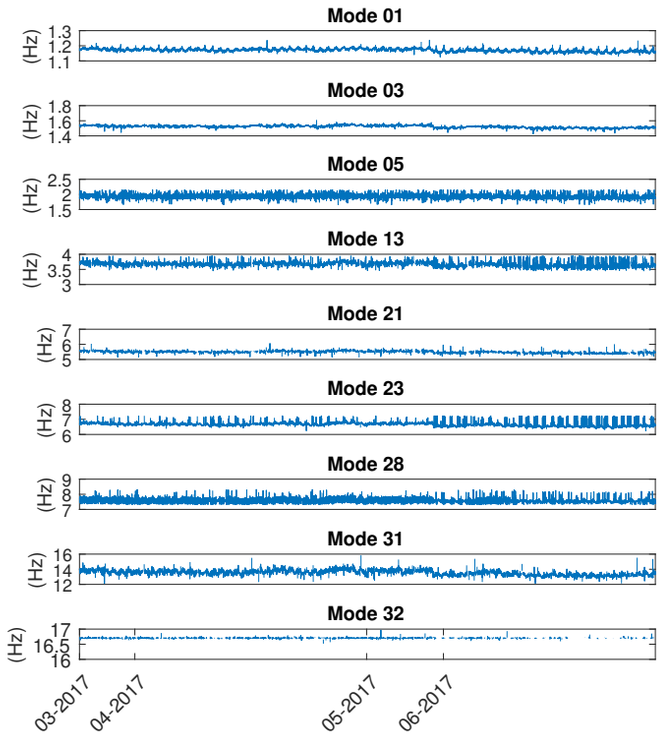


Figure 10: Frequencies evolution for the first nine modes over time.

4 MODAL UPDATE

As stated above, environmental changes can affect modal parameters and mask the effects of damage. In the case presented herein, a frequency shift can be observed due to temperature changes, more pronounced in modes 3, 21 and 31 than in the others, whereas variations in humidity bear a smaller impact. The field data indicates that the relationship between temperature and natural frequencies is inversely linear, decreasing the latter when the former rises. Although these results are in line with several examples found in the literature ((Cury, Cremona, & Dumoulin 2012), (Moser & Moaveni 2011)), a Finite Element Model has been developed, searching for validation of this results. To this end, the model tries first to match the conditions presented at the minimum temperature and then change the parameters most affected by the 30°C variation, to retrieve the final results. Following the work of Taylor & Stanton (2010), the bearing friction coefficient must be first reduced around 2,5% to account for an increase of temperature of 30°C. Secondly, the asphalt and concrete Elastic modulus were as well diminished, according to Lytton et al. (1993) and Fernando et al. (1993), respectively. Both references show a variance in the results depending on the type of aggregates, curing methods as well as applied loads, which render a range of values implemented on the FEM model through an iterative process. Finally, with regards to what UHPFRC is concerned, limited literature can be found on thermal dependent properties at environmental temperatures. In the BETON-FIB bulletin it was established that drying shrinkage is very low due mostly to the low poros-

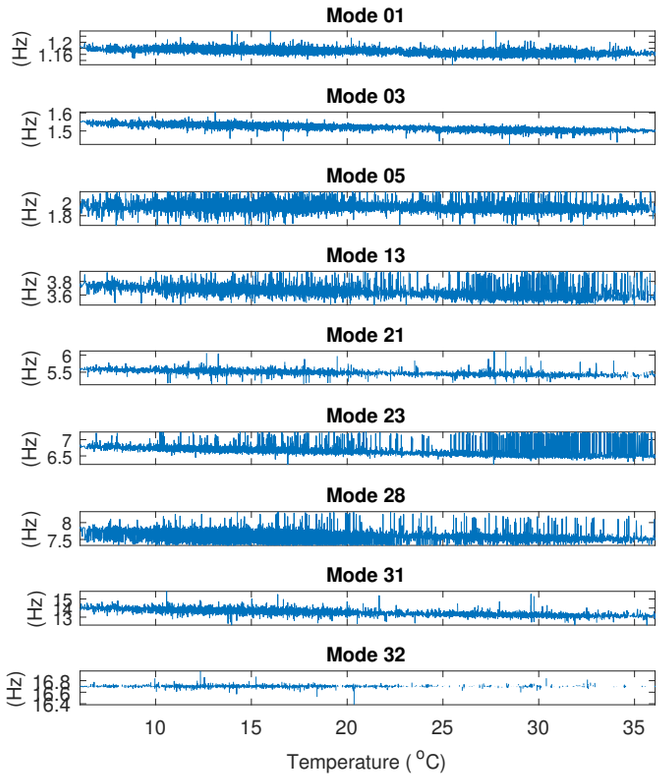


Figure 11: Frequencies evolution for the first nine modes over temperature.

ity of the material, whereas autogeneous shrinkage is large and may reach values higher than 1.2μm/mm. In terms of tensile creep, Garas, Kurtis, & Kahn (2012) demonstrated that microracking and porosity directly affect the behavior of this parameter, although heat treated UHPFRC shows a smaller compressive creep coefficient. Moreover, Dehn (2004) observed that hydrothermal reactions start to appear above 100 °C. With the aforementioned information in hand, and taking into consideration that the temperature variation reaches only 30°C, the E modulus of UHPFRC was left unchanged. At this point, it is important to note that the model exhibits a high sensitivity to friction coefficients at the bearings, noticed when the first matching process was performed. To this end, in the second round of model updating, the coefficient was changed only in a tight range in order to avoid fictitious results. Once a good agreement is achieved between the frequencies at maximum and minimum temperature for FE model and Chillon bridge, the bespoken parameters are modified following a linear law, obtaining Figure12 which can be compared to Figure11. The associated parameters for each temperature increment are displayed in Table 2. Although modes 5, 28 and 32 are not displayed, as the variation with temperature is almost imperceptible. Nevertheless, the remaining modes present a good agreement between FE model and reality, both at initial and final stage, proving the influence of environmental factors over the structure.

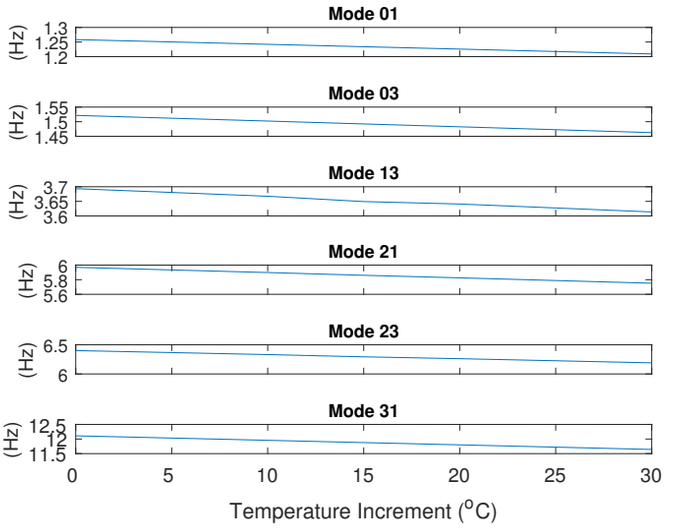


Figure 12: Frequencies evolution versus increment of temperature, obtained with FEM model.

5 STRUCTURAL IDENTIFICATION FRAMEWORK

The main goal of SHM is to predict damage or deterioration events at an early stage, by establishing certain operational characteristics that should remain constant if the structural safety is not in danger. As explained in the previous chapter, environmental conditions produce an effect on modal parameters which could conceal healthy states. Therefore, the framework presented herein, based on the works of Chatzi & Spiridonakos (2015), aims to describe dynamic characteristics varying with operational conditions by means of a statistical procedure based on PCE and Independent Component Analysis (ICA). The interested reader is referred to these sources for further details on the workings of these methods.

5.1 *Polynomial Chaos Expansion*

PCE permits to represent a random variable as a function of another random variable with a given distribution, as a polynomial expansion over multivariate products of polynomials that are orthonormal to that distribution. This method predicts the evolution of uncertainty in dynamical systems, which pertains to the case of SHM. Consider a system F conformed by several independent variables $\Xi_1 ... \Xi_N$, being N the number of variables. In the case explained herein those inputs will be the temperature and humidity, with a joint probability function (PDF) $p_\Xi(\zeta)$, while the output $Y = f(\Xi)$, with finite variance, will be also random and correspond to the structure frequencies. This output can be expressed as in Equation 1.

$$Y = f(\Xi) = \sum_{d(j)\in\mathbb{N}^N} \theta_j \phi_{d(j)}(\Xi) \tag{1}$$

being $\phi_{d(j)}$ the polynomial basis functions orthonormal to $p_\Xi(\zeta)$, d the multi-indices vector related to the multivariate polynomial basis and θ_j

Table 2: Parameter values for FE model at different temperatures.

	Friction(vert)	Friction(htal)	E mod. Asphalt	E mod. Concrete
ΔT	KN/m	KN/m	KN/m^2	KN/m^2
ΔT=5°C	2725000	217000	15000	35000000
ΔT=5°C	2713645	216096	14625	34504167
ΔT=10°C	2702291	215191	14250	34008333
ΔT=15°C	2690937	214287	13875	33512500
ΔT=20°C	2679583	213383	13500	33016666
ΔT=25°C	2668229	212479	13125	32520833
ΔT=30°C	2656875	211575	12750	32025000

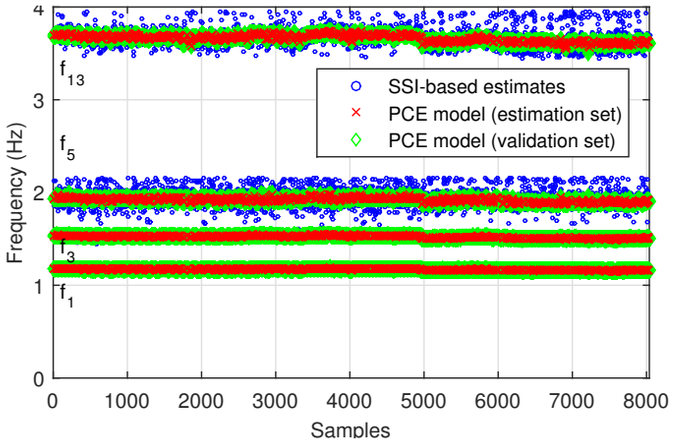


Figure 13: PCE natural frequencies estimates for modes 1, 3, 5 and 13, for both training and validation set versus SSI-based estimates.

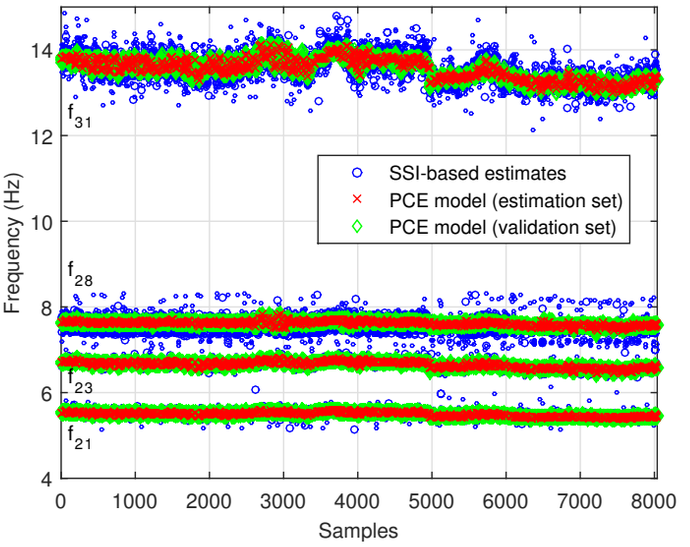


Figure 14: PCE natural frequencies estimates for modes 21, 23, 28 and 31, contrasting training and validation set with respect to SSI-based estimates.

the deterministic coefficients of projection, which are unknown. For a more detailed introduction to the method, the reader is referred to Blatman & Sudret. Nonetheless, a relevant characteristic of the approach should be noted: PCE relies on the independence of the inputs, which is not the case herein as temperature and humidity are directly correlated. To avoid this issue, Independent Component Analysis (ICA) is used, in particular the FastICA algorithm described in Hyvärinen & Oja (2000). Once these steps have been completed, the set of natural frequencies estimates is separated into training and validation sets. After discharging mode number 32 for not being stable enough, a total of 8543 samples is used out of 3000 constitute the training set.

5.2 *Results*

Figures 13 and 14 present the results for the training and validation sets, contrasted with the SSI- based frequency estimates. It may be observed that the method provides accurate predictions, even for mode 31 where the scatter is more pronounced. Nevertheless, damage prediction should be performed with a dataset comprising a longer time interval, where a full cycle of seasonal variations is present. This preliminary study shows that the method can be implemented for larger datasets, aiming to identify damage scenarios based on abnormal trends outside the estimated range. It should be mentioned that the process presented above was also performed for the strain values obtained from the four strain gauges installed on the bridge. However, the correlation between the environmental variables and the two longitudinal strain gauges, as well as for the two transverse, was discrepant and presented a value smaller than 0.75. In Figure15 the results from PCE analysis can be observed, showing that the method is not able to accurately capture the variations, in opposite to the previous example.

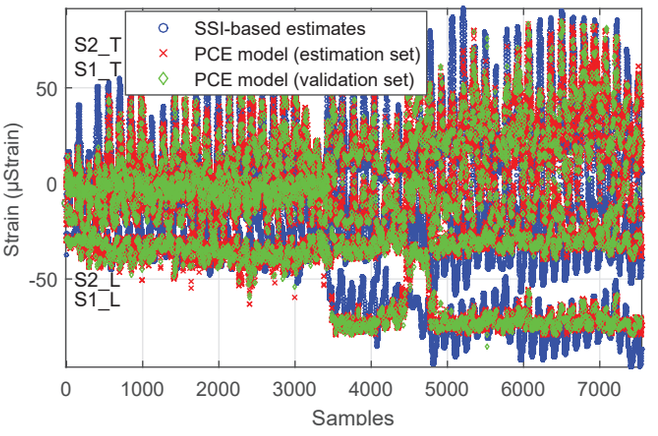


Figure 15: PCE strains estimates for the four strain gauges installed on the viaduct.

6 CONCLUSIONS

In this paper, the SHM deployement on Chillon viaduct is presented and the analysis of three months of data is explained. Natural freqquencies and damping is obtained through a SSI methodology , and contrasted with the environmental conditions, which are proven to constitute a relevant factor on modal analysis. Therefore, a physical model is implemented to validate the results obtained from the Subspace method, exhibiting a good agreement between them. Finally, a PCE methodology is applied in order to accurately describe the natural frequency fluctuations, achieving promising results for the current data. Further investigation should be conducted on the PCE outcome from strains and ambient data.

7 ACKNOWLEDGMENTS

The authors would like to acknowledge and gratefully thank the Swiss National Science Foundation (SNSF) within the context of project 154060 and the Swiss Seismological Service institution (SED).

REFERENCES

Alampalli, S. (2000). Effects of testing, analysis, damage, and environment on modal parameters. *Mechanical Systems and Signal Processing 14*(1), 63–74.

Bastien-Masse, M. & E. Brühwiler (2015). Strengthening the chillon viaducts deck slabs with reinforced uhpfrc. *IABSE conference- Structural Engineering: providing solutions to global challenges, Geneva*.

BETON-FIB, D. (2009). Structural concrete: textbook on behaviour, design and performance. *Bulletin 1*, 253–260.

Blatman, G. & B. Sudret (2010). An adaptive algorithm to build up sparse polynomial chaos expansions for stochastic finite element analysis. *Probabilistic Engineering Mechanics 25*(2), 183–197.

Bogoevska, S., M. Spiridonakos, E. Chatzi, E. Dumova-Jovanoska, & R. Höffer (2017). A data-driven diagnostic framework for wind turbine structures: A holistic approach. *Sensors 17*(4), 720.

Brühwiler, E. & E. Denarié (2013). Rehabilitation and strengthening of concrete structures using ultra-high performance fibre reinforced concrete. *Structural Engineering International*.

Brownjohn, J. M. (2007). Structural health monitoring of civil infrastructure. *Philosophical Transactions of the Royal Society of London A: Mathematical, Physical and Engineering Sciences 365*(1851), 589–622.

Chatzi, E. N. & M. D. Spiridonakos (2015). Structural identification and monitoring based on uncertain/limited information. In *MATEC Web of Conferences*, Volume 24. EDP Sciences.

Cross, E., K. Koo, J. Brownjohn, & K. Worden (2013). Long-term monitoring and data analysis of the tamar bridge. *Mechanical Systems and Signal Processing 35*(1), 16–34.

Cury, A., C. Cremona, & J. Dumoulin (2012). Long-term monitoring of a psc box girder bridge: operational modal analysis, data normalization and structural modification assessment. *Mechanical Systems and Signal Processing 33*, 13–37.

Dehn, F. (2004). Temperature behaviour of ultra high-performance concrete (uhpc)—a micro analytical reflect. In *First International Symposium on Ultra High Performance Concrete. Kassel, Germany*, pp. 731–742.

Garas, V., K. Kurtis, & L. Kahn (2012). Creep of uhpc in tension and compression: effect of thermal treatment. *Cement and Concrete Composites 34*(4), 493–502.

Hobbs, D. W. (1988). *Alkali-silica reaction in concrete*. Thomas Telford Publishing.

Hyvärinen, A. & E. Oja (2000). Independent component analysis: algorithms and applications. *Neural networks 13*(4), 411–430.

Kassir, M., K. Bandyopadhyay, & M. Reich (1993). Thermal degradation of concrete in the temperature range from ambient to 315 c (600 f).

Kim, J.-T., J.-H. Park, & B.-J. Lee (2007). Vibration-based damage monitoring in model plate-girder bridges under uncertain temperature conditions. *Engineering Structures 29*(7), 1354–1365.

Ko, J. & Y. Ni (2005). Technology developments in structural health monitoring of large-scale bridges. *Engineering structures 27*(12), 1715–1725.

Lytton, R. L., J. Uzan, E. G. Fernando, R. Roque, D. Hiltunen, & S. M. Stoffels (1993). *Development and validation of performance prediction models and specifications for asphalt binders and paving mixes*, Volume 357. Strategic Highway Research Program Washington, DC.

Martín-Sanz, H., E. Chatzi, & E. Brühwiler (2016). The use of ultra high performance fibre reinforced cement-based composites in rehabilitation projects: A review.

Moser, P. & B. Moaveni (2011). Environmental effects on the identified natural frequencies of the dowling hall footbridge. *Mechanical Systems and Signal Processing 25*(7), 2336–2357.

Nandan, H. & M. Singh (2011). A system identification based approach for estimating modal frequencies of bridges under environmental influence. *Civil Engineering Topics, Volume 4*, 273–284.

Peeters, B. (2000). System identification and damage detection in civil engeneering. *Katholieke Universiteit te Leuven*.

Perret, J., H. Mühlberg, P. P., & S. Cuennet (2014). Renforcement des viaducs de chillon. tracés, bulletin technique de la suisse romande. Technical report, Bulletin technique de la Suisse romande.

Reynders, E. & G. De Roeck (2014). Vibration-based damage identification: The z24 bridge benchmark. *Encyclopedia of Earthquake Engineering 482*, 1–8.

Spiridonakos, M. D. & E. N. Chatzi (2015). Data-driven polynomial chaos basis estimation.

Spiridonakos, M. D., E. N. Chatzi, & B. Sudret (2016). Polynomial chaos expansion models for the monitoring of structures under operational variability. *ASCE-ASME Journal of Risk and Uncertainty in Engineering Systems, Part A: Civil Engineering 2*(3), B4016003.

Taylor, J. C. & J. F. Stanton (2010). Friction coefficients for stainless steel/ptfe (teflon) bearings. Technical report, Wisconsin Department of Transportation.

Ubertini, F., G. Comanducci, N. Cavalagli, A. L. Pisello, A. L. Materazzi, & F. Cotana (2017). Environmental effects on natural frequencies of the san pietro bell tower in perugia, italy, and their removal for structural performance assessment. *Mechanical Systems and Signal Processing 82*, 307–322.

Watson, D. K. & R. Rajapakse (2000). Seasonal variation in material properties of a flexible pavement. *Canadian Journal of Civil Engineering 27*(1), 44–54.

Wenzel, H. (2009). The influence of environmental factors. *Encyclopedia of structural health monitoring*.

Yuen, K.-V. & S.-C. Kuok (2010). Ambient interference in long-term monitoring of buildings. *Engineering Structures 32*(8), 2379–2386.

Maintenance, Safety, Risk, Management and Life-Cycle Performance of Bridges – Powers, Frangopol, Al-Mahaidi & Caprani (Eds)
© 2018 Taylor & Francis Group, London, ISBN 978-1-138-73045-8

Development of Vibration-Based Parameters as Damage Sensitive Features for Bridge Structures

J.J. Moughty & J.R. Casas
Department of Civil and Environmental Engineering, Technical University of Catalonia (BarcelonaTech), Campus Nord, Calle Jordi Girona, 1-3, 08034, Catalonia, Spain

ABSTRACT: The process of damage identification in bridge structures traditionally involves the extraction of one or more of the numerous modal-based Damage Sensitive Features (DSFs) from vibration data obtained by direct sensor measurement. However the performance of these modal-based DSFs can suffer under changing environmental and operational conditions and are generally limited by their methodology, which assumes linear structural behaviour and signal stationarity. The present paper presents a detailed overview of the development of alternative DSFs derived from vibration characteristics, focusing on their conception, damage sensitivity evaluation and performance robustness assessment. Initially, selected vibration parameters are outlined to the reader before their damage sensitivity is determined on progressive damage test data obtained from a post-tensioned three-span bridge under ambient conditions using supervised machine learning techniques in conjunction with the Minimum Covariance Determinate (MCD) estimator to mitigate uncertainty surrounding sources of excitation. Secondly, the performance robustness of the vibration-based DSFs is assessed on highly non-stationary data obtained from a progressively damaged steel truss bridge subjected to vehicle excitation. Finally, a comparative evaluation of the vibration-based DSFs is made against modal-based DSFs performance from the literature.

1 INTRODUCTION

Although there are many damage detection methodologies available, there is still poor agreement on the optimal damage feature to use. A review of modal-based damage features in particular found that many may be over sensitive to external conditions, while others may be difficult to extract accurately in ambient conditions due to the low levels of input energy and presence of noise (Moughty & Casas, 2017a). Suitable damage features should be capable of being extracted consistently with ease, sensitive to damage and insensitive to external conditions. Furthermore, when planning the assessment of a bridge, the socio-economic value must also be factored, with more valuable structures deserving advanced assessment methods using multiple sensors and sensor types coupled with advanced analysis methodologies and bridge closures. However, the vast majority of bridge structures in the network are of lower socio-economic value and thus require a simple and effective methodology that is cost effective. The present study investigates the level of damage identification of four vibration parameters that can be extracted with ease and applied to both ambient and vehicle induced excitation responses without the need for bridge closures or additional input forces. The work presented herein advances previous work by Moughty & Casas (2017b) who assessed the damage sensitivity of a number of vibration parameters.

2 VIBRATION PARAMTERES

The selected vibration parameters used within the present study are explained in detail below:

Arias Intensity, defined by Arias (1970), is a vibration parameter used to describe an earthquake's energy over its total duration and is commonly used as an indicator of an earthquake's damage potential.

$$I_A = \frac{\pi}{2g} \cdot \int_0^\infty \ddot{x}(t)^2 \, dt \tag{1}$$

Destructive Potential Factor (DPF) is a variation of Arias Intensity, which was proposed by Araya & Saragoni (1984). It accounts for frequency characteristics in addition to vibration energy by including the variable υ_0, which is the number of zero crossings per unit of time.

$$P_D = \frac{\frac{\pi}{2g}.\int_0^{\infty} \ddot{x}(t)^2 \, dt}{{v_0}^2} \quad (2)$$

Distributed Vibration Intensity (DVI), first detailed herein, utilizes vibration intensity, which in simple harmonic motion context can be defined as $(I=a^2/f)$, where a is acceleration amplitude and f is frequency. The SI units of vibration intensity are mm^2/s^3, but its logarithmic power form of decibels (dB) is more commonly used. For the distributed variant employed in the present study, a Fourier transformation is applied to the acceleration response and the summation of the vibration intensity values is taken within a frequency range, denoted by (f_i) within the limits m-n in Equation 3. The frequency range should encompass the first few modes of vibration of the structure in question, in the present case the range is selected as $(m\text{-}n = 1Hz - 20Hz)$. In this way, Distributed Vibration Intensity may capture the damage sensitivity associated with energy and modal changes, while unwanted variation due to adjusting ambient conditions and frequency domain noise can be diminished over sufficient duration length, in addition to the application of Mahalanobis Squared Distance (MSD), as those variations are assumed to be Gaussian in nature.

$$DVI = \sum_{i=m}^{n} 10\log_{10}\left(\frac{{a_i}^2(f_i)}{f_i}/I_S\right) \quad \begin{matrix} for \;\; m \le f_i \le n \; (in\; Hz) \\ I_S = 10mm^2/s^3 \end{matrix} \quad (3)$$

Note that this parameter is assessed only in the ambient excitation case, as the vehicle-induced excitation test produces short, highly non-stationary responses that are deemed unsuitable for Fourier transformation.

Cumulative Absolute Displacement (CAD) is another novel vibration parameter that cumulatively sums a vibration signal, however in this case the acceleration signal is first transformed in displacements using integration and band-pass filtering to avoid drift.

$$CAD = \int_0^t |x(t)|dt \quad (4)$$

Note that this parameter is assessed only in the vehicle induced vibration case, as obtaining accurate displacements from long duration ambient induced accelerations is not feasible without additional known variables.

3 OUTLIER DETECTION METHODOLOGY

For the ambient condition test, the vibration parameters are assessed using Mahalanobis Squared-Distance (MSD), which is a common multivariate outlier detection algorithm that uses mean and covariance data to train and assess dataset continuity. MSD is determined as shown in Equation 5, where $\{X\}_\zeta$ is the potential outlier, $\{\bar{X}\}$ is the mean of the training data and $[\Sigma]$ is the covariance matrix of the training data.

$$D_\zeta = \left(\{\bar{X}\}_\zeta - \{X\}\right)^T [\Sigma]^{-1} \left(\{X\}_\zeta - \{\bar{X}\}\right) \quad (5)$$

In addition to the MSD, the Minimum Covariance Determinate (MCD) estimator is also employed to enhance robustness and reduce uncertainty regarding sources of ambient excitation by identifying and removing outliers from the training data prior to MSD. Although environmental conditions may remain relatively constant throughout the bridge test, the assumption of Gaussian distributed sources of ambient loading cannot be applied in some cases as one traffic lane under the bridge was still in operation throughout the test, in addition to feasible construction work nearby near-by. This leaves a case where the undamaged vibration data used to train the MSD may contain outliers itself due to passing traffic or construction vehicle activity, which is left included in the training data may negatively impact the subsequent test/damaged data results, particularly if the training data outliers are significantly dissimilar to the remaining data set. The MCD employed in the present study is the FAST MCD algorithm (Rousseeuw & Van Driessen, 1999), which removes erroneous data by first iteratively determining the subset of data whose covariance matrix has the lowest possible determinant to that of the total dataset. Once the MCD finds the data points that contribute most to abnormal variance compared to the remaining data, it returns newly updated mean and covariance values that can be used directly in the MSD.

4 TEST DATA

4.1 *Ambient Excitation - S101 Bridge*

The S101 Bridge was pre-stressed 3-span flyover near Vienna in Austria that had a main span of 32m and two 12m side spans. The deck cross-section was 7.2m wide double-webbed t-beam, whose webs had a width of 0.6 m. The height of the beam varied from 0.9 m in the mid-span to 1.7 m over the piers, as can be seen in Figure 1. In 2008, it was decided to replace the S101 Bridge due to insufficient carrying capacity and deteriorating structural condition being identified from visual inspection data.

A progressive damage test was conducted on the S101 Bridge across 3 days in 2008 though the completion of a number of sequential actions, which are presented in Table 1. Overall, the damage applied can be divided into two main stages; (1) simulated pier foundation settlement, (2) bridge deck stiffness loss through the severing of four pre-stressed tendons. During the test the bridge was closed to traffic, meaning that excitation was mainly ambient, although one traffic lane beneath the bridge was kept in use. As for environment sources of excitation, very

little temperature variation was observed throughout the test duration as sub-zero temperatures were kept within a 3 to 4 degree range due to persistent heavy cloud cover (VCE, 2009).

Vibration data was recorded by 13 accelerometers located on one side of the bridge deck, with a sample rate of 500Hz. Vibration recordings from the sensors did not cease throughout the progressive damage test. For the present study, the measured data was discretized into 66sec long segments of 33,000 samples.

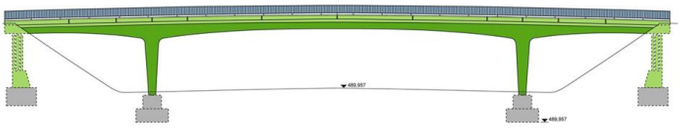


Figure 1. S101 Bridge longitudinal section

Table 1. Damage actions conducted on the S101 Bridge

Damage State	Description of Damage Actions
1	Undamaged
2	North-Western (NW) column cut through
3	First step of lowering bridge pier (1cm)
4	Second step of lowering bridge pier (2cm)
5	Third step of lowering bridge pier (3cm)
6	Compensating plates inserted & pier returned to original position
7	First pre-stressed tendon cut over NW pier
8	Second pre-stressed tendon cut over NW pier
9	Third pre-stressed tendon cut over NW pier
10	Forth pre-stressed tendon cut over NW pier

4.2 *Vehicle-Induced Excitation - Steel Truss Bridge*

The test data utilized within the present study has been obtained from a progressive damage test conducted on a Japanese bridge that was subjected to a moving vehicle excitation (Kim et al., 2013). The bridge in question was a simply-supported steel truss bridge that spanned 59.2m with a width of 3.6m and a max height of 8m. It was scheduled to be replaced in 2012, before which a progressive damage test was carried out while the bridge was closed to the public. Dynamic behavioral response was recorded from 8 uniaxial accelerometers, positioned as per Figure 2(b), with sample rates of 200Hz.

Table 2. Damage actions conducted on the Steel Truss Bridge

Damage State	Description of Damage Actions
1	Undamaged
2	Half cut in vertical member at mid-span
3	Full cut in vertical member at mid-span
4	Mid-span member reconnected
5	Full cut in vertical member at 5/8th span

The induced damage scenarios consist of severing vertical members of the truss structure in the locations presented in Figure 2(b). The progression of the damage states are described in Table 2 and presented in Figure 3. The damage actions began with the partial intersection of the mid-span vertical member (DMG1), before its full intersection was completed (DMG2). After which, the damaged member was reconnected (RCV) with a welded flange. Finally, the vertical member at 5/8th span was completed severed (DMG3).

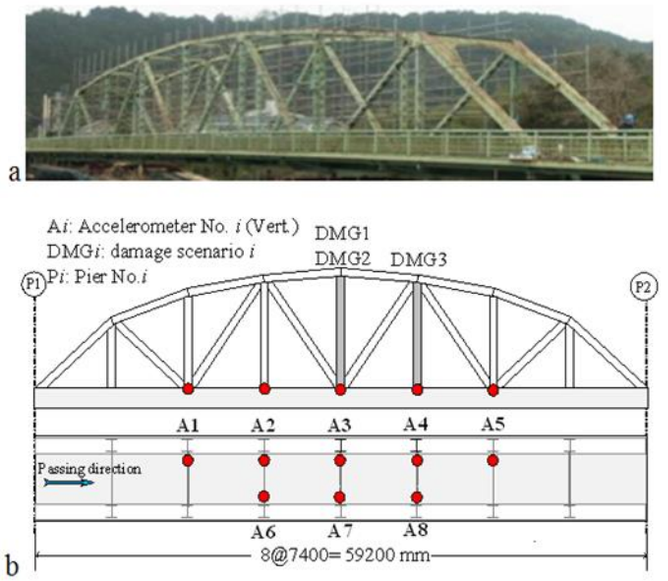


Figure 2. Steel truss bridge (a); Sensor & damage locations (b)

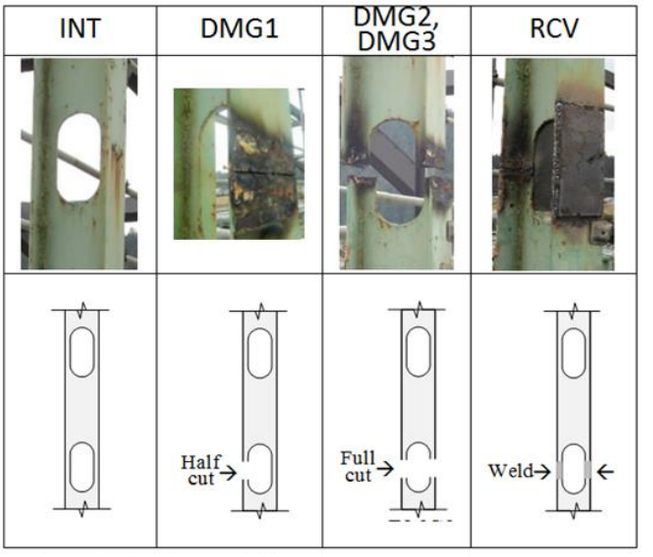


Figure 3. Steel truss bridge damage scenarios

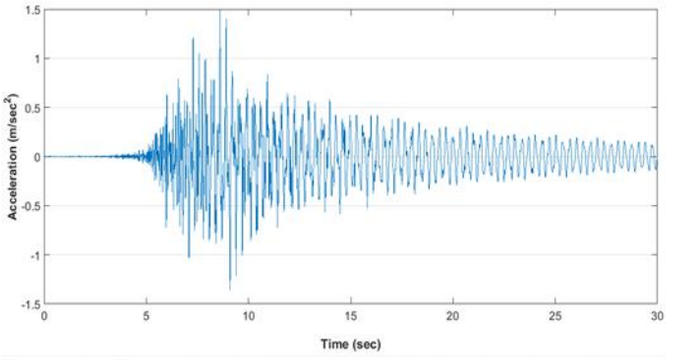


Figure 4. Example of vehicle induced vibration from the steel truss bridge (Sensor 3 – Undamaged Case)

For each damage scenario, a 21kN double-axle vehicle was driven across the bridge three times at approximately 40km/h to induce excitation. A sample time-history of acceleration response is presented in Figure 4. Note that no vehicle dynamics were obtained; however, the dynamic response of the bridge has been assessed in detail by Kim et al. (2014), who identified the first five vibration modes.

5 RESULTS

5.1 *Ambient Excitation - S101 Bridge*

The assessment of the chosen vibration parameters' damage identification ability under ambient conditions is conducted in two stages; (1) detection and (2) localization. There are three vibration parameters assessed herein; Arias Intensity (an energy-based parameter), Destructive Potential Factor (an energy-based parameter with empirical frequency denominator) and Vibration Intensity (an energy-based DSF with Fourier-based frequency denominator). The fourth vibration parameter, Cumulative Absolute Displacement, is not assessed under ambient conditions due to the difficulty of accurately obtaining displacements from ambient induced accelerations.
The MSD outlier detection algorithm is applied using 70% of the undamaged data to train, with 30% for validation and a threshold value of 95%. The MCD estimator is also applied to the training data to remove outliers that may be associated with unknown eternal sources of excitation.
For the first set of results for damage detection only, vibration parameters were extracted from thirteen sensor locations along one side of the bridge deck and were combined when input into the MSD outlier detection algorithm to increase damage sensitivity. For the second set of results for damage localization, the vibration parameters were not combined across sensors before MSD was applied, in this way the damage sensitivity is reduced, but possibility of damage localization is possible to assess.

Figure 5 to Figure 7 present the damage detection results of the vibration parameters; Arias Intensity, Destructive Potential Factor and Distributed Vibration Intensity, respectively. Both Arias Intensity and Destructive Potential Factor follow similar patterns, as is to be expected as both are measures of energy, however Destructive Potential Factor can deemed as more damage sensitive, particularly during the pier settlement test. In both cases the damage threshold is surpassed promptly as the pier is cut through, however the damage indicators return under the threshold sometime after the second pre-stressed tendon is severed. This may be explained by the fact that there was a duration of some hours between the second and third tendon cuts (night time) and temperature reduction and settling most likely occurred. Both parameters were able to sufficiently capture the sudden change in behavior exhibited by the bridge during the partial severing of the fourth pre-stressed tendon. It is worth noting that a visual inspection did not indicate any changes to have occurred between the third and fourth tendon cut.

In the case of the Distributed Vibration Intensity, the damage threshold is crossed promptly upon damage initiation and does not return throughout the remained of the test. Significant detail becomes visible via the Distributed Vibration Intensity, such as when the pier was fully cut through (~x=500); when the pier was returned to its original position (~x=1100); when a vibrating roller worked next to the bridge (~x=1300) and during the cutting of the final pre-stressed tendon.

In terms of damage localization capability of the three assessed features under ambient conditions, Figure 8 – Figure 10 present the results, where the vibration parameters of each sensor is assessed using MSD individually through time, revealing which sensor locations demonstrate the greatest damage sensitivity. The results are mixed, with Arias Intensity portraying false damage locations and failing to accurately locate the pier settlement, although it did signify damage at the correct location for during the third pre-stressed tendon cut, which coincided with cracking being observed at that time.

The Destructive Potential Factor and Distributed Vibration Intensity produced better results, although the Destructive Potential Factor highlighted damage in the center of the mid-span during pier settlement, while the Distributed Vibration Intensity correctly located the settlement and increasingly preferenced the same correct location for the pre-stressing loss.

5.2 *Vehicle-Induced Excitation - Steel Truss Bridge*

In this damage identification assessment there is the issue of controllability of each vehicle passage, as vehicle velocity and path can be difficult to consecutively replicate, therefore Sensor 1's Undamaged value is used as a fixed reference point for all of Sensor 1's subsequent damage states to account for some variation in vehicle passages. Additionally, the initial ambient bridge excitation level prior to vehicle passage was observed to fluctuate, which may impact the vibration parameters performance. To account for this, only passages with very low initial ambient bridge excitation are used.

Figure 11 to Figure 13 present the results of Arias Intensity, Destructive Potential Factor and Cumulative Absolute Displacement, respectively. Immediately, it can be seen that all vibration parameters can successfully detect and locate DMG 3 at Sensor 4, which is the most severe damage condition of the 3.

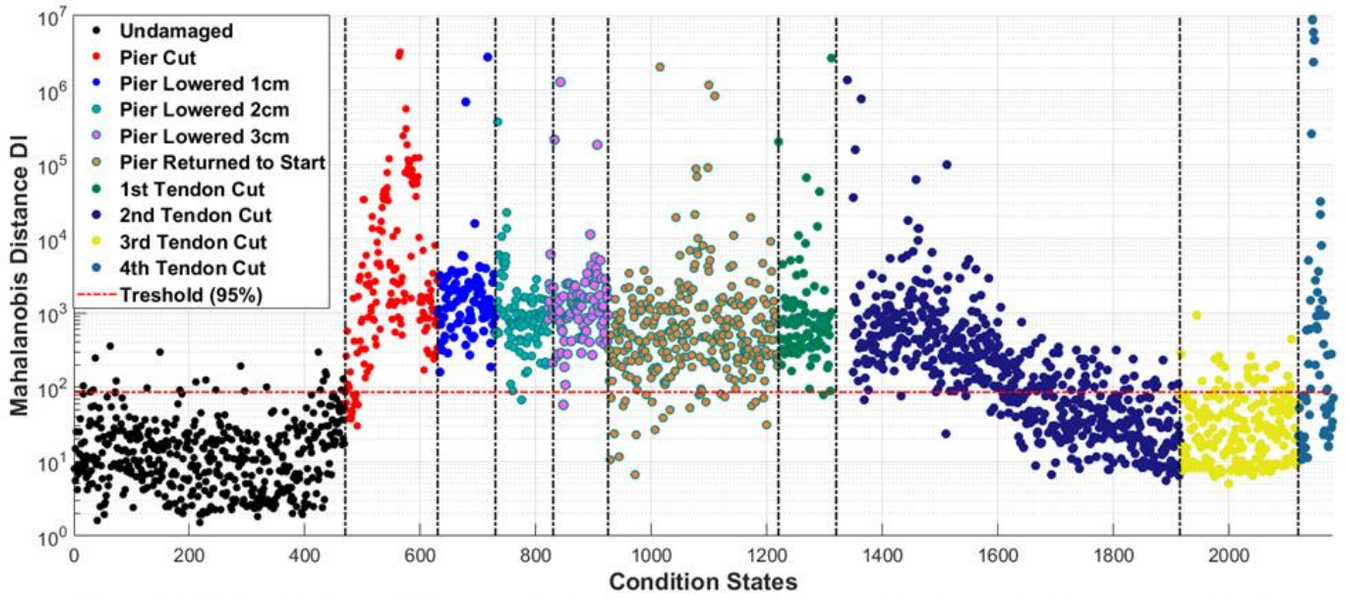


Figure 5. Mahalanobis Squared-Distance of Arias Intensity as a damage sensitive feature for 13 sensors combined

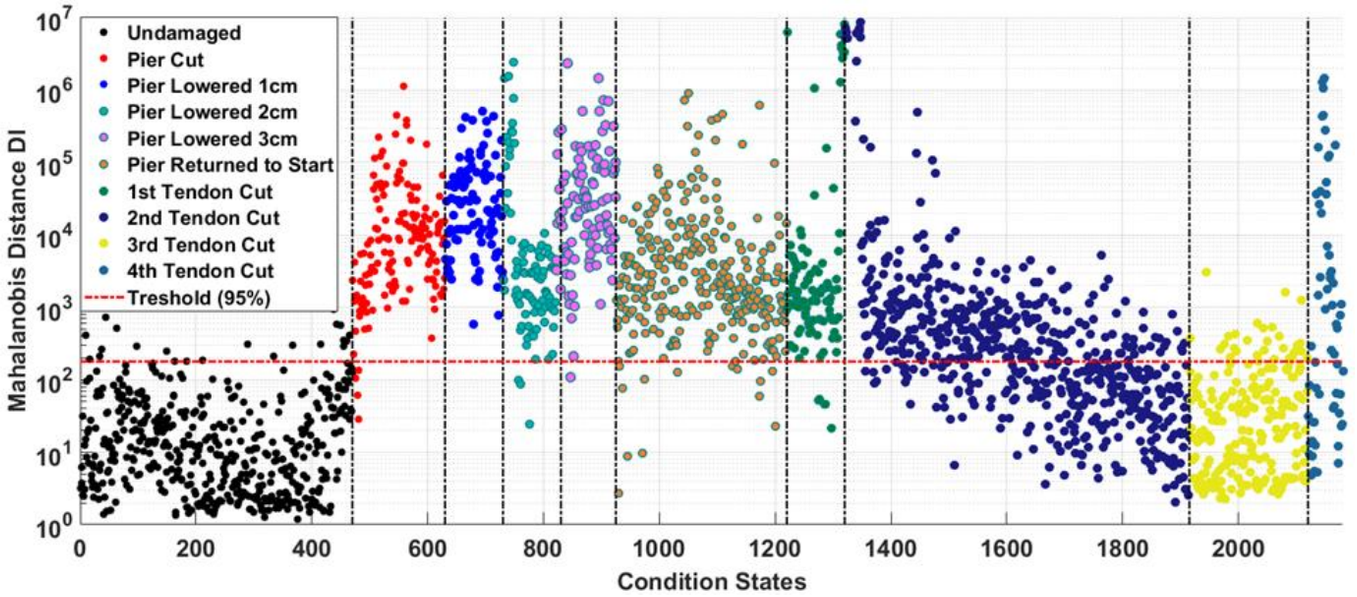


Figure 6. Mahalanobis Squared-Distance of Destructive Potential Factor as a damage sensitive feature for 13 sensors combined

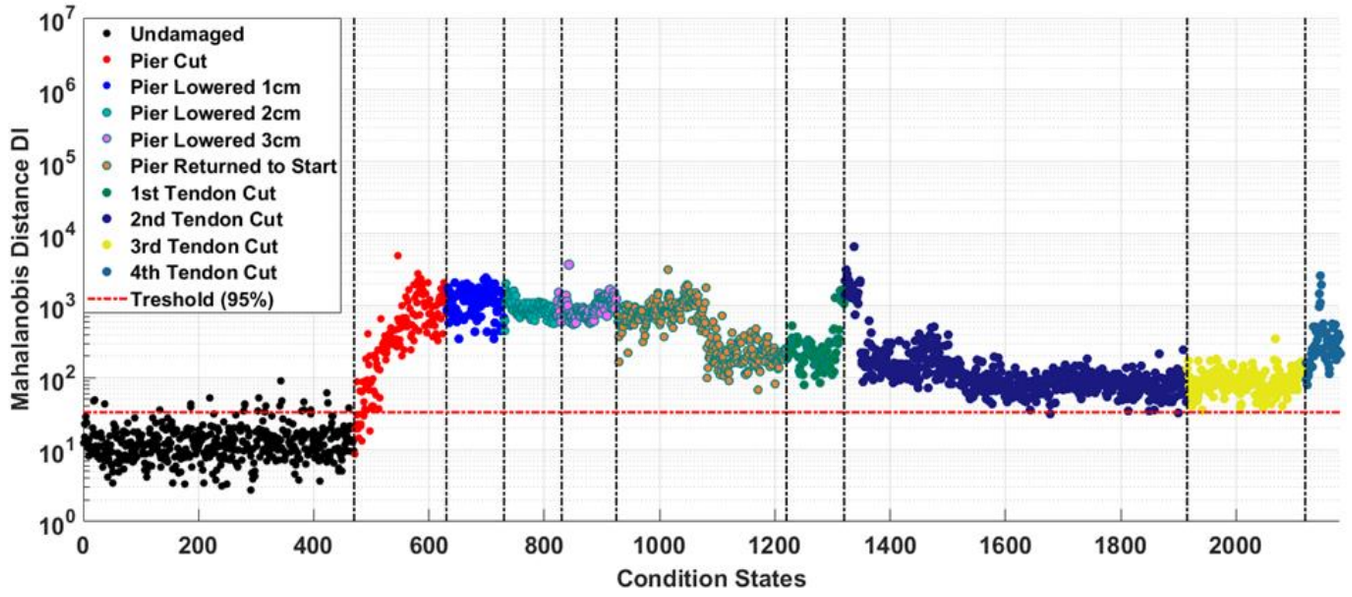


Figure 7. Mahalanobis Squared-Distance of Distributed Vibration Intensity as a damage sensitive feature for 13 sensors combined

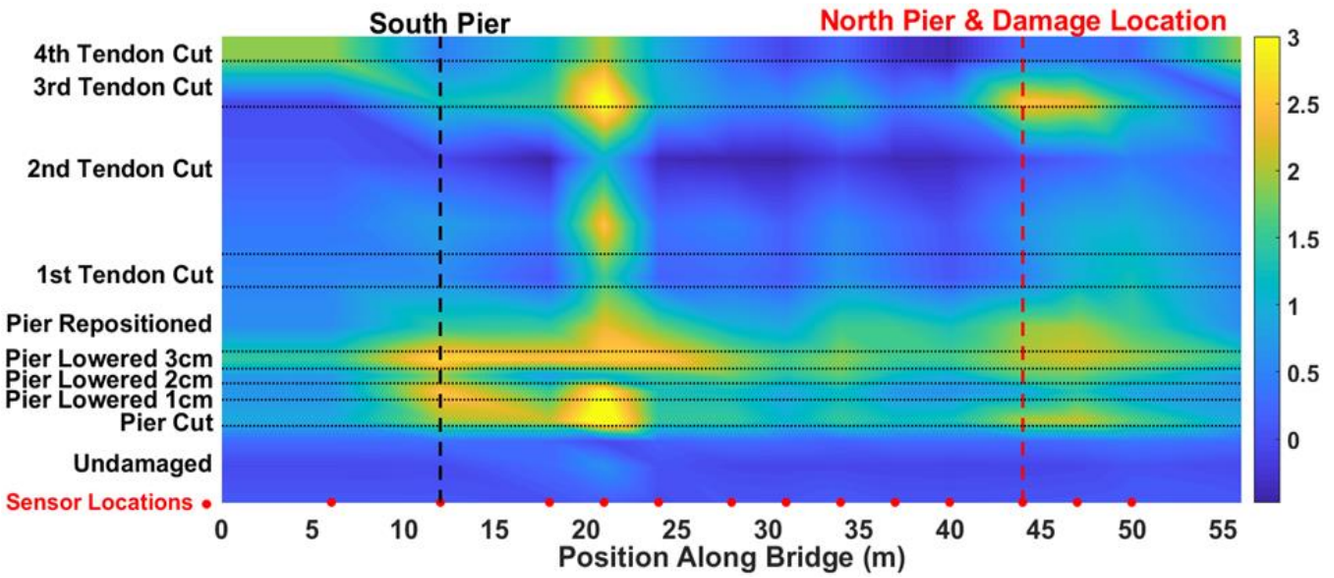


Figure 8. Mahalanobis Squared-Distance of Arias Intensity as a damage sensitive feature for 13 sensors individually

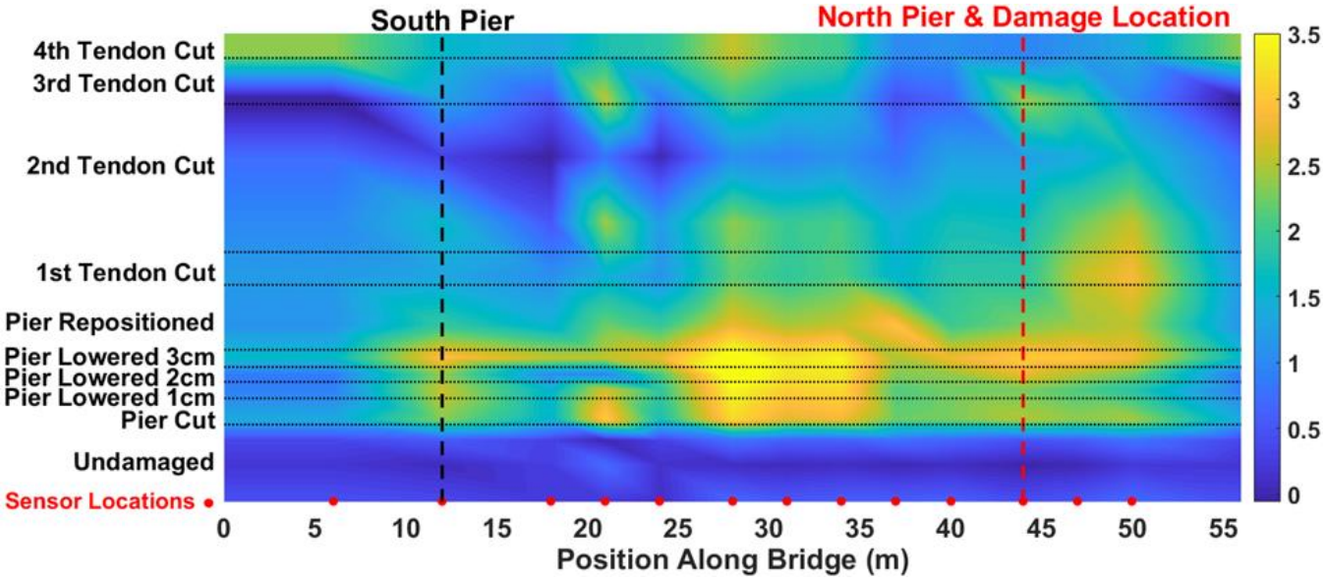


Figure 9. Mahalanobis Squared-Distance of Destructive Potential Factor as a damage sensitive feature for 13 sensors individually

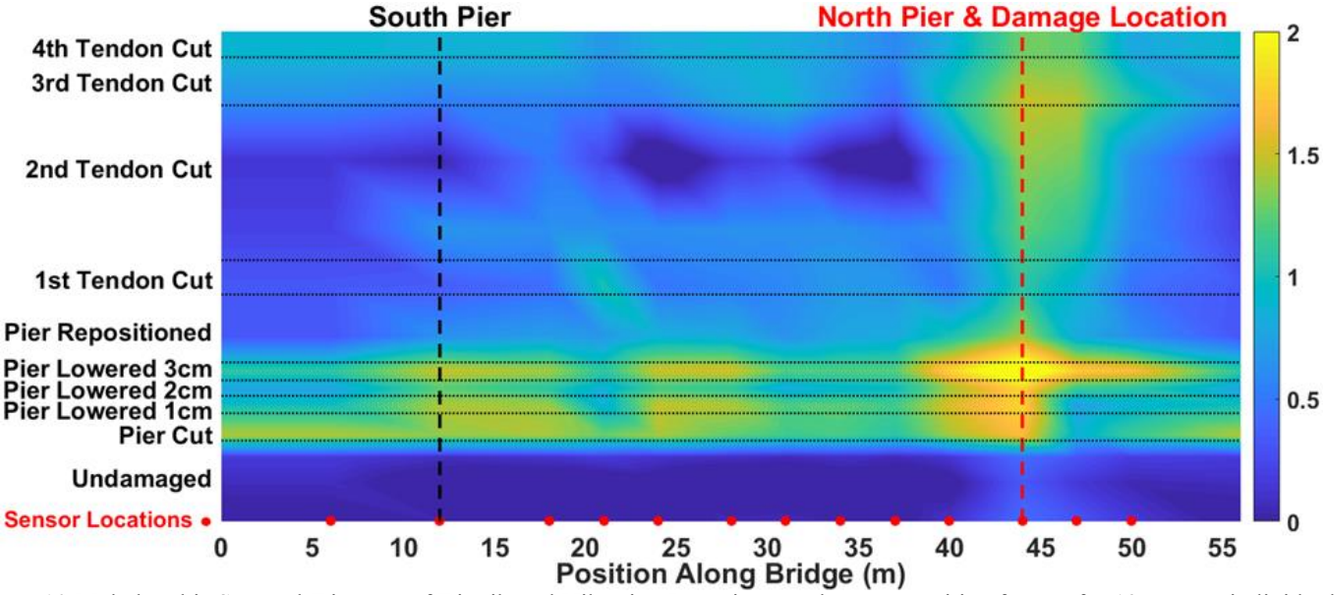


Figure 10 Mahalanobis Squared-Distance of Distributed Vibration Intensity as a damage sensitive feature for 13 sensors individually

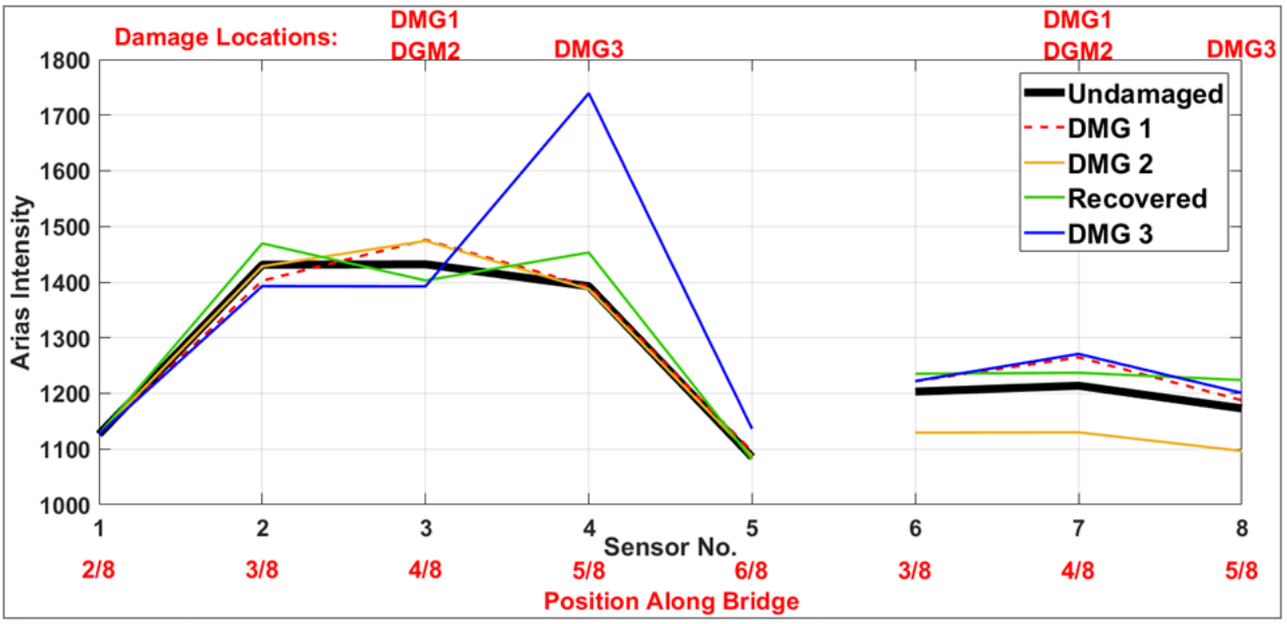


Figure 11. Arias Intensity across all sensors (Sensor 1 Undamaged used as a fixed reference point to account for variation in vehicle passages)

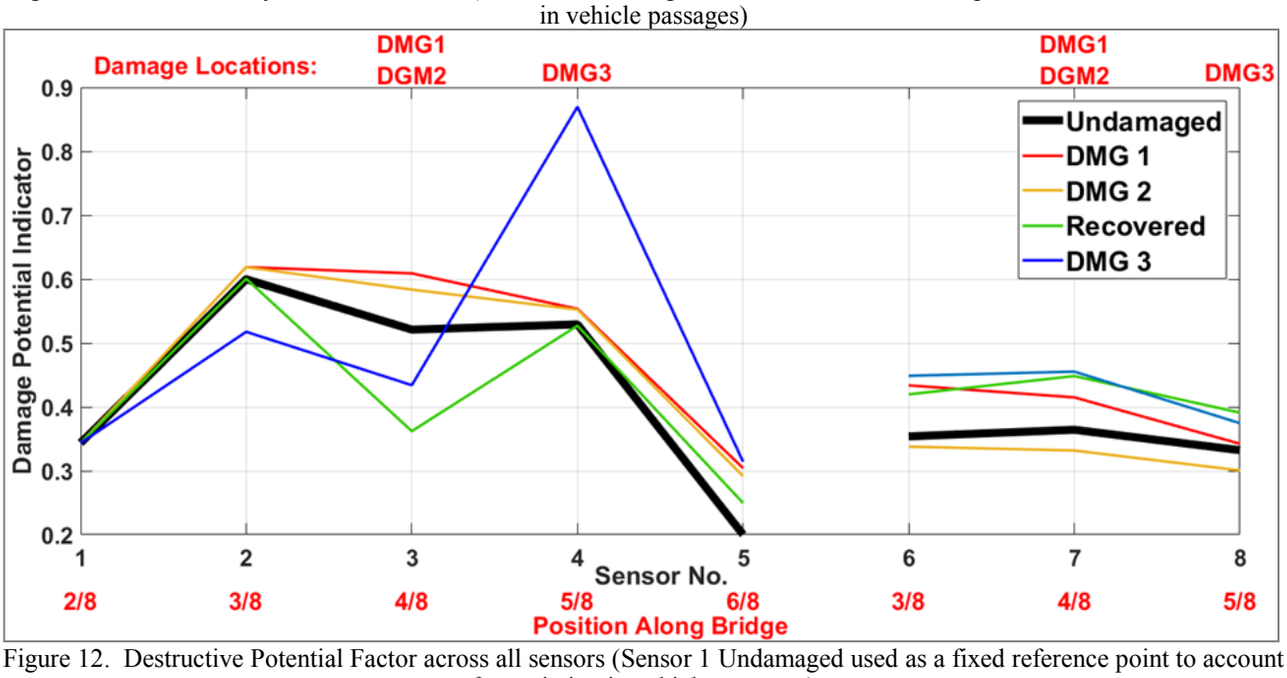


Figure 12. Destructive Potential Factor across all sensors (Sensor 1 Undamaged used as a fixed reference point to account for variation in vehicle passages)

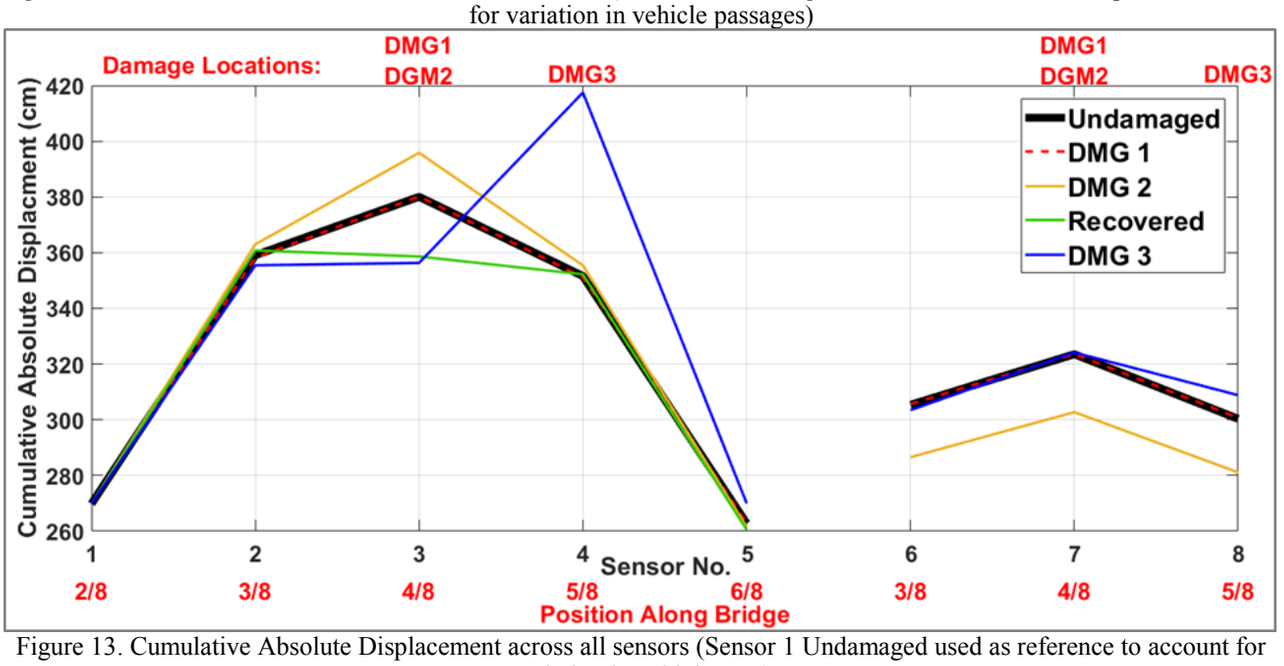


Figure 13. Cumulative Absolute Displacement across all sensors (Sensor 1 Undamaged used as reference to account for variation in vehicle runs)

The two damage conditions at the center span are also detected and located, although less pronounced. This is in line with Kim et al.´s (2014) findings using modal parameters. In the case of the recovered condition, all three vibration parameters show a reduction in damage, not only when compared to the previous two damage scenarios at that location, but also to the original undamaged case, signifying that the welded flange used to repair the center span actually enhanced its performance. This is again observed at Sensor 3 during DMG3.

For Sensors 6, 7 and 8, which are located on the opposite side of the bridge to the damage, results are less evident, save for the consistent trend of DMG2 portraying converse behavior to the opposite side of the bridge at Sensors 2, 3 and 4, which may indicate some compensating behavior or structural load redistribution through the truss elements.

6 DISCUSSION & CONCLUSIONS

To evaluate the damage identification capability of the assessed vibration parameters, results of from published works by VEC (2009) for the S101 Bridge and Kim et al. (2014) for the steel truss bridge are provided in Table 3 to Table 5 using modal frequencies, while Table 6 provides the percentage difference for the 3 vibration parameters assessed in the steel truss bridge assessment at the relevant damage locations.

Table 3. Modal frequency changes for the S101 Bridge pier settlement test under ambient excitation (VCE, 2009)

Mode	lowered 1cm	lowered 2cm	lowered 3cm
1st B. Mode	-2.2%	-3.2%	-10.6%
1st T. Mode	-4.6%	-6.7%	-14.4%
2nd B. Mode	-2.6%	-4.2%	-15.2%
2nd T. Mode	-12.3%	-18.8%	-24.3%
3rd B. Mode	+1.8%	+0.2%	-0.9%

Table 4. Modal frequency changes for the S101 Bridge for pre-stress failure test under ambient excitation (VCE, 2009)

Mode	1st Cut	2nd Cut	3rd Cut	4th Cut
1st B. Mode	-1.2%	-0.2%	-0.2%	-0.2%
1st T. Mode	-2.9%	-1.3%	-1.3%	-1.9%
2nd B. Mode	-1.2%	0.0%	0.0%	-0.2%
2nd T. Mode	-3.0%	-1.6%	-2.0%	-1.6%
3rd B. Mode	-3.4%	-1.3%	-0.6%	-1.3%

Table 5. Modal frequency changes for steel truss bridge damage test under vehicle induced excitation (Kim et al., 2014)

Mode	DMG1	DMG2	DMG3
1st B. Mode	+0.03%	-3.22%	-1.58%
2nd B. Mode	+0.16%	+0.09%	-5.51%
3rd B. Mode	X	-0.21%	-9.05%
4th B. Mode	+1.07%	+0.22%	-6.87%
5th B. Mode	+0.85%	+0.58%	-0.16%

Table 6. Vibration parameter changes from steel truss bridge damage test under vehicle induced excitation

Parameter	DMG1	DMG2	DMG3
Arias	+3.07%	+2.93%	+24.84%
DPF	+16.89%	+12.01%	+64.30%
CAD	+0.05%	+4.16%	+18.70%

Of the 3 vibration parameters assessed on the S101 Bridge under ambient excitation, the Distributed Vibration Intensity provided the greatest damage resolution per damage state and proved to be the best damage location indicator under ambient conditions. Due to the nature of the algorithm employed, an objective comparison with modal frequency changes from VCE (2009) is not possible, however from a subjective viewpoint, Distributed Vibration Intensity applied in this way seems to have performed more consistently.

Of the 3 vibration parameters assessed in the vehicle induced excitation test, the Cumulative Absolute Displacement produced results most in-line with reality by successfully detecting, locating each damage scenario with magnitudes equivalent to damage severity, indicating that it achieves up to Level 3 of the damage identification scale.

ACKNOWLEDGEMENTS

This project (http://trussitn.eu) has received funding from the EU's Horizon 2020 research and innovation programme under the Marie Skłodowska-Curie grant agreement No. 642453.
The authors would like to thank Prof. C.W. Kim of the Dept. of Civil and Earth Resources Engineering, Kyoto University, Kyoto, Japan for the generous sharing of the bridge data assessed within the present study.

REFERENCES

Araya, R. & Saragoni, R. 1984, Earthquake accelerogram destructiveness potential factor, Proceedings of the 8th World Conference of Earthquake Engineering, San Francisco, USA. vol. 2: pp 835–841.

Arias, A., 1970, A Measure of Earthquake Intensity, R.J. Hansen, ed. Seismic Design for Nuclear Power Plants, MIT Press, Cambridge, Massachusetts, pp. 438-483.

Kim, C.W., Chang, K.C., Kitauchi, S., McGetrick, P.J., Hashimoto, K. & Sugiura K., 2014., "Changes in modal parameters of a steel truss bridge due to artificial damage" Proceedings of the 11th Inter. Con. on Structural Safety and Reliability, ICOSSAR (pp. 3725-3732) New York

Moughty, J.J. & Casas, J.R. 2017a, A state of the art review of modal-based damage detection in bridges: development, challenges, and solutions. Applied Sciences 7(5): 510

Moughty, J.J. & Casas, J.R., 2017b, Performance assessment of vibration parameters as damage indicators for bridge structures under ambient excitation, 10th International Conference on Structural Dynamics, Rome, Italy, 10-13 Sept.

Rousseeuw, P.J. & Van Driessen, K., 1999, A fast algorithm for the minimum covariance determinant estimator, Technometrics 41(3) pp 212–223.

Vienna Consulting Engineers (VCE), 2009, Progressive Damage Test S101 Flyover Reibersdorf Report No. 08/2308. Vienna, Austria.

Maintenance, Safety, Risk, Management and Life-Cycle Performance of Bridges – Powers, Frangopol, Al-Mahaidi & Caprani (Eds)
© 2018 Taylor & Francis Group, London, ISBN 978-1-138-73045-8

A bespoke signal processing algorithm for operational modal testing of post-tensioned steel and concrete beams

D. Noble, M. Nogal & A.J. O'Connor,
Dept. of Civil, Structural & Environmental Engineering, Trinity College Dublin, Dublin 2, Ireland.

V. Pakrashi,
DSRL, School of Mechanical & Materials Engineering, UCD, Belfield, Dublin 4, Ireland.

ABSTRACT: The extraction of modal properties is a difficult task, especially when output-only data is measured. The accuracy of the estimation these modal properties is compromised by noisy signals, and signal filtering is required to suppress unwanted frequency content. Care is required to avoid over-filtering of the output data, which can eliminate valid structural frequency content. This paper describes the development of a bespoke signal processing algorithm to extract the modal properties of both simply supported post-tensioned (PT) steel and concrete sections. Dynamic impact testing was conducted on a series of different PT steel and concrete beams. Acceleration time-history data was recorded. This data was subsequently processed. The Fast Fourier Transform (FFT) was applied to the signal to convert into the frequency domain and a bespoke peak-picking algorithm was used to extract the natural frequencies of the beams. A comparison is made between the accuracy of the estimation of the modal properties for filtered and unfiltered data, and a sensitivity analysis of the filtering and peak picking parameters is conducted to determine the effect on the accuracy of the estimation of the modal parameters. The results show the effectiveness of the bespoke algorithm in increasing the accuracy of the estimation of the modal properties as opposed to the raw, unprocessed signals.

1 INTRODUCTION

Experimental modal analysis has been conducted on a series of steel and concrete beams in the lab (Noble *et al.*, 2015, 2016). The steel and concrete beams have been post-tensioned by treading a post-tensioning strand through their cross section and jacking the beam on a live end. A series of impact hammer strikes were applied to the tested structures, and the dynamic response of the structure was measured using an accelerometer. The output signal only was measured, no measurement signal was taken of the dynamic input signals therefore the experiments conducted are considered as output-only dynamic tests. These tests are becoming increasingly common, especially in the field of Operational Modal Analysis (OMA), in which the modal parameters of a structure are determined from the structures response to ambient vibration conditions. The modal properties are thus extracted from the Fourier Transform representations of the system output signals.

The testing was conducted in order to determine the existing relationship between post-tensioning force magnitude and modal properties of post-tensioned steel and concrete specimens, as there is significant disagreement between researchers in this field (Tse, Morse and Hinkle, 1978; Raju and Rao, 1986; Bartlett, 1987; Bažant and Cedolin, 1987; Bert, 1987; Saiidi, Douglas and Feng, 1994; Williams and Falati, 1999; Chan and Yung, 2000; Miyamoto *et al.*, 2000; Kim, 2004; Zhang and Li, 2007).

This paper outlines a bespoke signal processing algorithm, and subsequent bespoke peak-picking methodology applied to a series of impact response signals obtained from the dynamic testing described in full (Noble *et al.*, 2015, 2016). The paper is organized as follows; the fundamental theory behind digital signal processing is first introduced. The bespoke signal processing algorithm followed to filter the obtained signals is described in the following section. A detailed description of each of the steps of the signal processing algorithm and the effect of each signal filter on the raw data signal is subsequently described in the following sections. A curve smoothing function used to smooth both time and frequency domain representations is then described. The following section describes the peak-picking algorithm used to identify the natural frequencies of the structural system(s) tested. The cumulative effect of the filtering on the raw data is then outlined. The Inverse Fourier Transform is subsequently applied to the smoothed, normalized, filtered, frequency domain representation. Finally, conclusions based on the described filtering regime are drawn.

2 SIGNAL PROCESSING

The main assumption underlying all forms of modal analysis is that any dynamic response signal may be represented, in the time domain, as an infinite series of sinusoids, each with their own unique amplitude and frequency. The amplitudes are considered as the modal contribution of each mode of vibration to the overall dynamic signal, whereas the frequencies are defined as the natural vibration frequencies of the structural system, for the

corresponding mode shape of vibration. All other seemingly random portions of the vibration response are considered as a noise components of the system, and as such, asystematic.

2.1 *Noise*

Noise is any unwanted or seemingly random portions of the measured vibration response of the system. Quality assurance of the measured dynamic data is of utmost importance. The signals obtained should be of sufficient strength and clarity and free of excessive noise (Ewins, 2000). This unwanted frequency content is attenuated by appropriate use of signal processing and signal filtering that is outlined in detail in this paper.

2.2 *Aliasing*

Aliasing is an error associated with digital signal processing (DSP) in which the existence of very high frequency components in the signal are missed as the sampling rate is not large enough. It is not possible to determine any frequency greater than the Nyquist frequency, $\omega_{N_{yq}}$. The solution to this is to use an anti-aliasing filter. The anti-aliasing filter is a low pass, sharp cut-off filter. The type of filter implemented is usually a high order low pass Butterworth filter (Butterworth, 1930). Anti-aliasing filters are not automatically built-in to signal analysers and data collectors, and thus the signal must be post-processed.

2.3 *Leakage*

Leakage is a signal processing problem related to discrete signals and the definition of the Fourier Transform. The Fourier Transform is defined as an integral over the range of $(-\infty, +\infty)$. Leakage occurs due to the need to take only a finite length of time-history, coupled with the assumption of periodicity (Ewins, 2000). When the periodicity assumption is not valid and there is a discontinuity at the beginning or the end of the signal in the time domain, the resulting frequency spectrum does not indicate the original frequency. This frequency is actually not represented. Energy has `leaked' into a number of the spectral lines close to the true frequency and the spectrum is spread over several lines (Ewins, 2000). The effects of leakage were mitigated against throughout the course of this study by making use of *'zero padding'* (adding zeros before and after signal) which artificially removed the periodicity requirement. However, impact signals, experience minimal distortion due to leakage provided the signal is analysed over the appropriate region.

2.4 *Windowing*

Windowing involves the modification of the signal in the time domain in order to suppress the effects of unwanted frequency content and minimize the effects of leakage. Avitabile (Avitabile, 2001) warns that all windows distort data, as they distort the peak amplitude and appear to indicate more damping than actually exists. Avitabile (Avitabile, 2001) suggests in order to avoid the use of windows to continuously sample a periodic repetition of the data, or to completely observe the signal in one data sample. The latter is obtained by choosing impulse/impact excitation as the type of dynamic excitation, which was chosen as the form of input excitation for this study.

3 SIGNAL PROCESSING REGIME APPLIED TO OBTAINED SIGNALS

The following procedure was applied to the raw impact response signals obtained from the steel and concrete testing and presented in (Noble *et al.*, 2015, 2016);

1. The initial acceleration vs. time data obtained from the accelerometer attached to the steel or concrete beam following impact hammer strike was read in.
2. Initial *'zero padding'*, *'windowing'* and offset correction was applied to the obtained accelerometer data.
3. The initial data analysis was performed.
   - The Fast Fourier Transform (FFT) of the unfiltered initial acceleration-time data, as outlined above, was computed.
   - The peaks in the initial spectrum were computed using a bespoke peak picking algorithm – the peaks are the computed natural frequencies of the system.
4. The initial data was subsequently filtered. Following initial data analysis, the natural frequencies were unintelligible, thus the signal required to be filtered to remove excessive noise/frequency content corrupting the identification of the natural frequency. The *'zero padded'*, *'windowed'* and offset initial data was subsequently filtered as outlined below.
5. The following filtering was performed;
   - The *'zero-drift'* was removed by applying a low pass Butterworth filter to the data.
   - The signal was smoothed, first by removing electrical noise frequency content of 50Hz and all harmonics, and then by subsequently applying a smoothing function to remove excessive high-frequency noise in the signal.

- A high pass filter was applied to remove all low frequency noise components corrupting the signal.
- An anti-aliasing filter was applied to the data.

6. The data was then subsequently windowed again.
7. The FFT of the filtered acceleration-time data was then computed to convert the acceleration-time signal into the frequency domain.
8. The main peaks were then extracted from the frequency domain curve to determine the natural frequencies of the structural system.

Figure 1 outlines a flow chart describing the bespoke signal processing algorithm followed for the concrete beam specimens as outlined previously (Noble *et al.*, 2015, 2016).

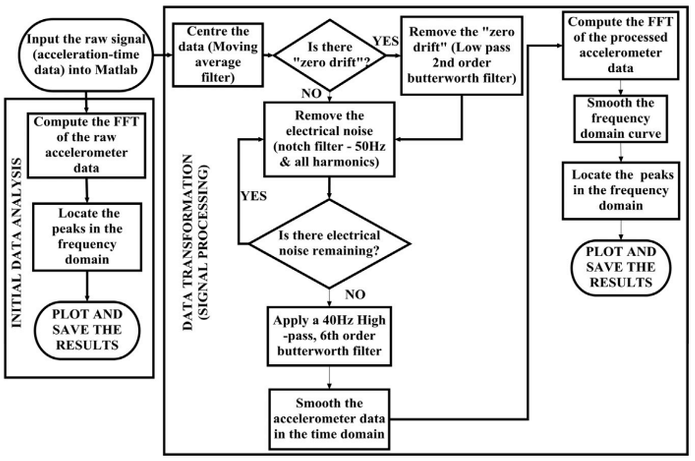


Figure 1. Signal processing flow chart as applied to the concrete beam tested (reproduced from (Noble *et al.*, 2016)*)*

In certain cases, the fundamental frequency may not be identifiable from the raw data signal, as evident for the signal represented in the time and frequency domains in Figure 2 and *Figure 3* respectively, and as outlined previously by (Noble *et al.*, 2016)

This paper identifies the need, in some instances for signal filtering and the removal of low and high frequency noise for the correct estimation of the fundamental frequencies of vibration.

3.1 *Initial 'zero-padding' and 'windowing'*

The initial data signal is characterized by the blue signal in Figure 2. The signal has an initial offset, as shown in Figure 2. The signal is initially processed by cutting an initial portion of the data in the time domain. The position of the maximum acceleration in the raw signal was identified, and the first 1/3 of the signal, from the initial acceleration to the maximum acceleration was removed, and thus the signal was 'windowed' in order to ignore/remove any frequency content in this portion of the signal. The remaining signal was then forced to begin at 0. The initial offset was removed by subtracting the initial offset from all parts of the signal. The red signal in Figure 2 is the result of preprocessing the blue signal by 'zero padding' and removing the initial offset.

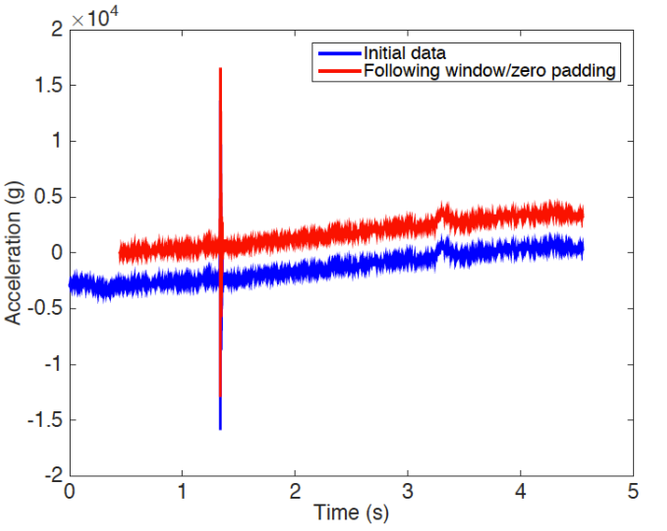


Figure 2. Raw output data collected (blue) and following windowing/zero padding (red) in the time domain

3.2 *Initial Data Analysis*

Figure 3 shows the initial frequency domain representation of the windowed data following initial processing (Figure 2). As shown in Figure 2, there is a very low frequency component in the signal, where the overall trend in the data is rising slightly from left to right. This is known as 'zero drift' and is an instrumentation error in the accelerometer. When the Fourier Transform is performed on the data, it assumes that all parts of the data/trends in the data are periodic, and that therefore the 'zero drift' is also a periodic component of the signal. As a result, the very low frequency content dominates the frequency domain representation of the signal, and thus the fundamental structural modes of vibration are not readily identifiable through peak-picking as they are drowned out by the dominance of the low frequency 'zero drift'.

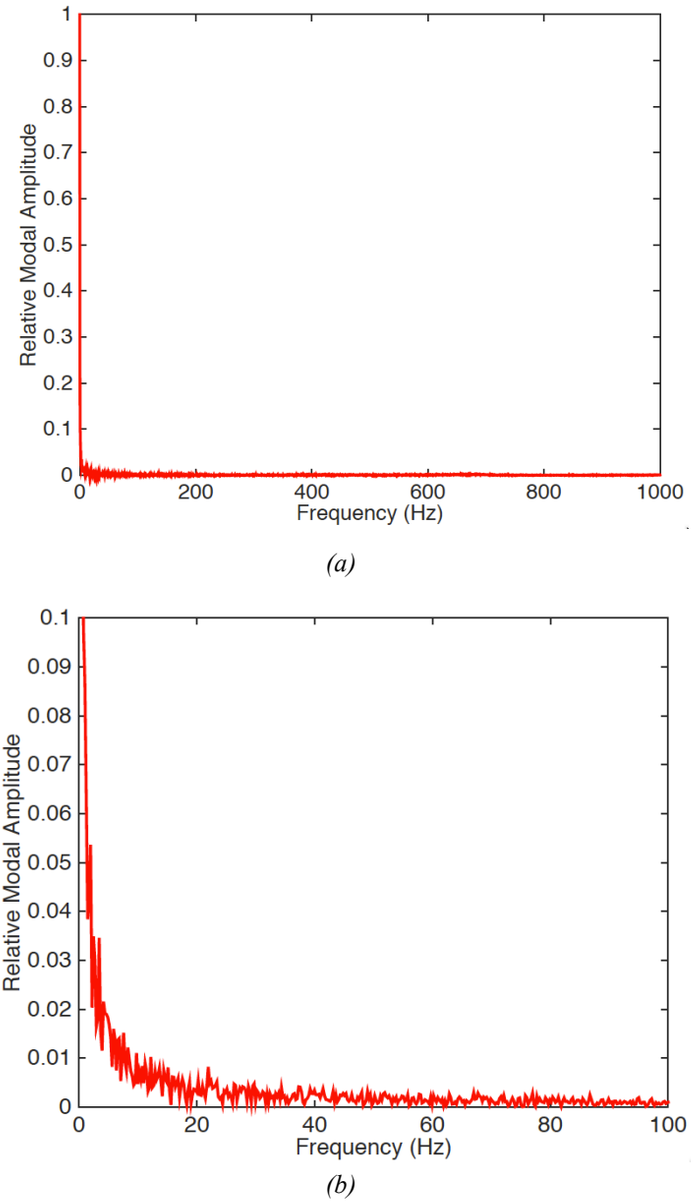


Figure 3. Frequency domain representation of the initial (raw) time domain data

3.3 *Moving Average Filter*

A moving average filter was applied to the initial data in order to remove the effects of some high frequency noise on the data signal. *Figure 4* shows both the time and frequency domain of the raw data signal following the implementation of a moving average filter. The blue data in both the time and frequency domain represents the unfiltered, raw initial data, while the red represents the data following the application of the moving average filter. The moving average filter is a standard technique in signal processing whereby the signal is smoothed by removing high-frequency, unwanted, line noise in order to uncover the fundamental structural frequencies. A moving average filter, of length N takes the average of every N consecutive samples in the signal, where N is the sample size. The filter itself has a delay of (N-1)/2, and this must be adjusted for in the filter. As outlined in *Figure 4*, the effect of the filter is to smooth the signal, removing unwanted high frequency noise.

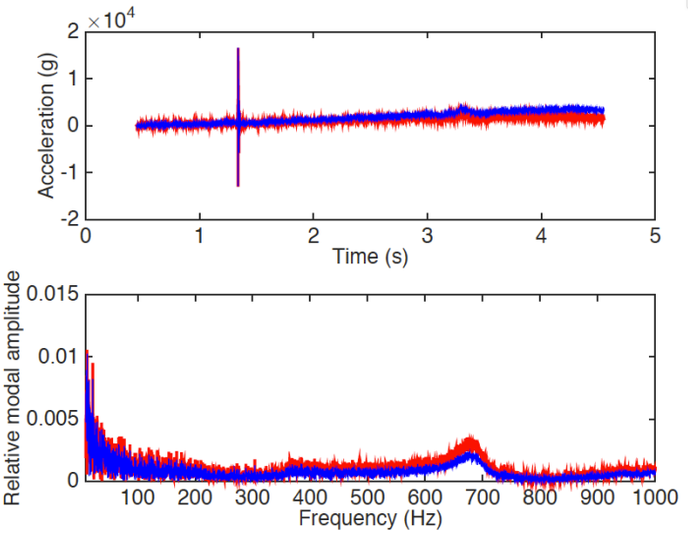


Figure 4. Time and frequency domain representation of raw data signal following application of moving average filter.

3.4 *Removing 'zero drift'*

As outlined in section 3.2, 'zero drift' is a low frequency noise component in the accelerometer signal due to an instrumentation error in the accelerometer, meaning that the signal oscillates about a non-zero or drifting datum. As outlined previously since the Fourier Transform assumes periodicity, this low frequency noise dominates the signal, thus making the structural vibration frequencies unintelligible. A low (2^{nd}) order, high-pass Butterworth filter, with a cutoff frequency of 0.1Hz was thus applied to the signal. This meant that low frequency components of the signal (<0.1Hz) were suppressed/attenuated, thus removing the very low frequency 'zero drift' from the data, and thus forcing the data to oscillate about the zero datum, as shown in *Figure 5*.

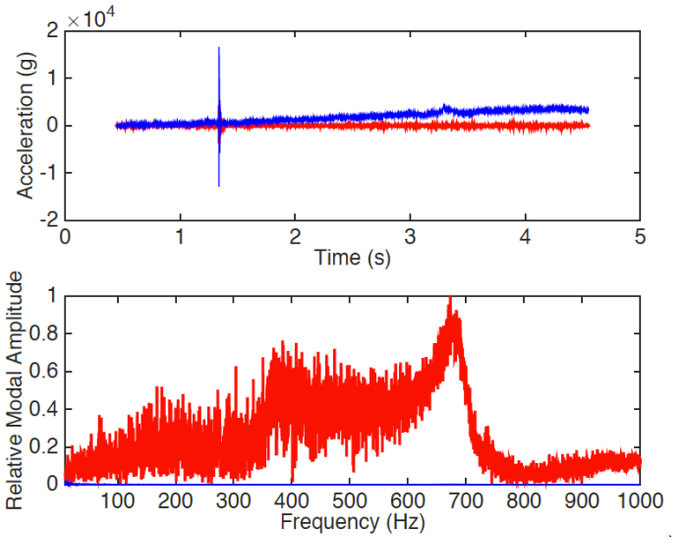


Figure 5. Time and frequency domain representations of raw data signal following removal of low frequency 'zero drift'.

3.5 *Smooth signal – remove electrical noise*

The main component of noise in the data is electrical noise. The sources of accelerometer noise can be broken down into the electrical noise from the circuitry that converts the mechanical vibration into a voltage signal that is thus correlated against a given acceleration, and the mechanical noise from the accelerometer itself. Ambient vibration of the system will also contaminate the pure structural signal. The A/C mains by which the accelerometer is powered has an alternating current with a frequency of 50Hz. This 50Hz signal, including all of its harmonics, is represented in the output data. This 50Hz electrical noise and its harmonics are filtered out by means of a 'notch' filter. A notch filter is a high order bandpass filter that removes specifically defined frequencies, while passing all other frequencies. *Figure 6* shows the result of applying a series of notch filters of 50Hz and its multiples to the data. The blue signal in *Figure 6* represents the raw signal, whereas the red signal represents the raw signal following removal of the electrical noise.

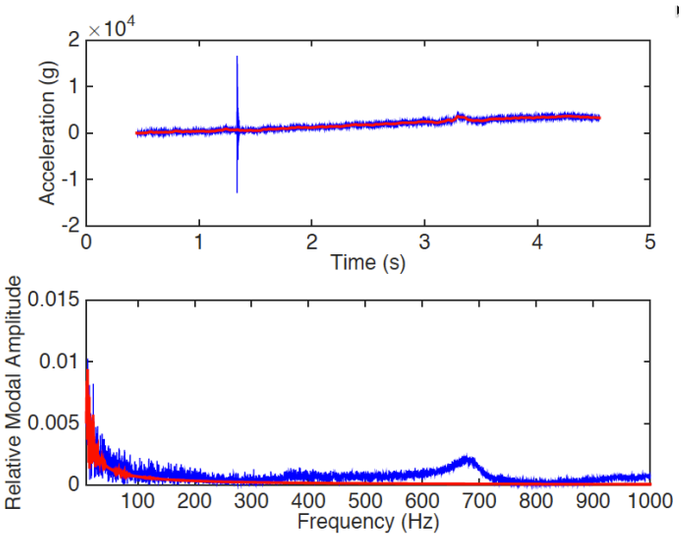


Figure 6. Time and frequency domain representation of raw signal before and after removal of electrical noise.

3.6 *High pass filter*

The fundamental bending frequency of the post-tensioned concrete beam sections tested was estimated to be 78Hz (Noble *et al.*, 2016). This estimation does not account for the effect of the mass of the jacks situated either end of the beam, tensioning the post-tensioning strand. The effect of the jacks should be to reduced the predicted frequency. The fundamental bending frequency, and subsequent harmonics were of interest in the testing conducted, thus a high pass filter was applied to the data in order to suppress the unwanted low frequency noise and to determine the fundamental bending frequencies via peak picking. *Figure 7* shows the time and frequency domain representation of the raw data signal following the application of the 40Hz high pass filter. The blue data represents the raw data signal, whereas the red signal represents the signal following application of the high order (8^{th} order) 40Hz high-pass filter. The frequency domain representation indicates the suppression of the frequency content of the signal <40Hz.

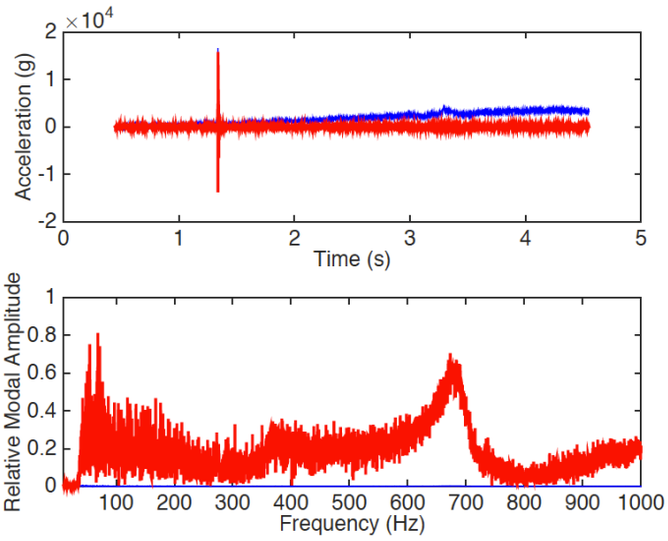


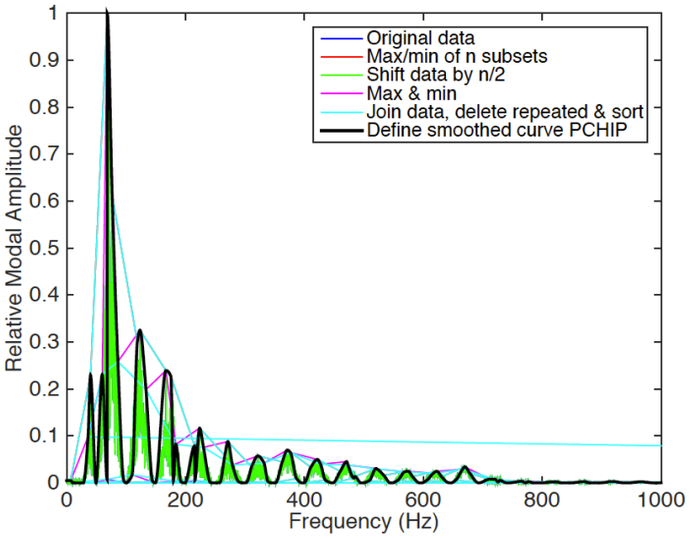
Figure 7. Time and frequency domain representation of raw data signal following application of 40Hz high pass filter.

3.7 *Curve smoothing function*

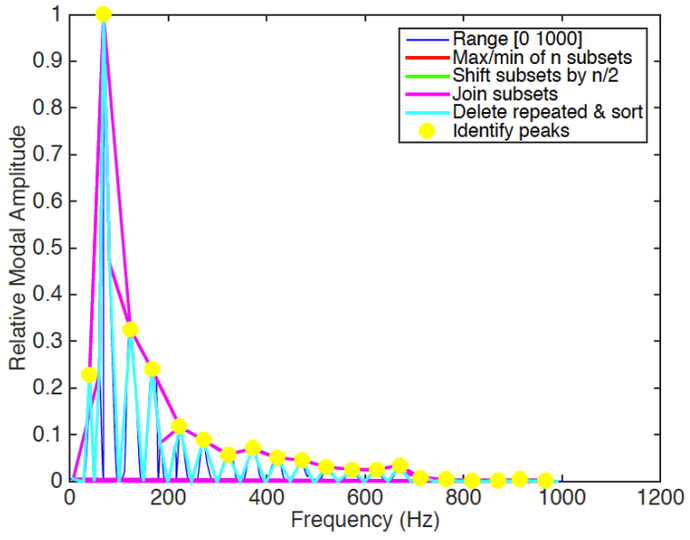
Figure 1 shows a flow chart outlining the series of different filters applied to the raw data. Following the application of each of the filters described previously, a frequency domain representation was obtained by which the fundamental structural vibration frequency could be obtained. In order to determine an estimation of the fundamental frequency, the frequency domain curve required smoothing. A smoothing algorithm was applied to the frequency domain data by identifying the most relevant points. With this aim, the data set is split into a series of n subsets. The smaller the value of n, the smother the final curve is. Then, the maximum and minimum values of the frequency domain representation of the data in each subset are calculated. In order to remove the effect of lag on the data, the data set is shifted by a value of $n/2$, and the new maximum and minimum values of the shifted subsets, calculated. In that way, the points identified during both rounds, which are up to $4n$ positions, represent the most relevant points of the frequency domain curve. Finally, a continuous curve is defined using a piecewise cubic Hermitic polynomial by interpolation within the identified points.

Figure 8(a) shows the performed steps of the curve smoothing function of the frequency domain

representation of a response signal. The blue curve shows the frequency domain representation of the filtered impact response signal in the range of interest of 0 to 1,000Hz. The red curve shows the definition of the maximum and minimum values in each of the defined subsets. The green curve shows the filtered impact signal shifted by n/2. The magenta curve shows the maximum and minimum values of the shifted subsets. The cyan curve shows the sorted data. Finally, the black curve shows the representation of the cubic interpolation function joining the maximum and minimum points in the subsets.



(a)



(b)

Figure 8. (a) Curve smoothing function of frequency domain representation of signal using piecewise cubic interpolation. (b) Peak-picking function of the smoothed frequency domain representation.

3.8 *Find the peaks in the frequency domain*

The peaks of the frequency domain representation of the signal, are, by definition, the natural frequencies of vibration of the structural system. The peaks are identified via a peak-picking algorithm. The peaks are identified using the *'findpeaks'* function in MATLAB (MATLAB, 2014). The function returns a vector with the local maxima and the corresponding index of the input signal vector. This index is then used to identify the corresponding frequency from the frequency vector. A local peak is a data point that is larger than its two neighboring points. The unsmoothed frequency domain representation produces too many local peaks to identify a fundamental frequency, therefore the frequency domain representation required smoothing. Figure 1 shows the steps involved in identifying the fundamental frequencies of the signal.

1. The smoothed frequency domain data was organized into column vectors and plotted (blue curve).
2. The data was filtered into the range of interest (0-1000Hz).
3. The filtered and smoothed frequency content was divided into a series of n subsets.
4. The maximum and minimum values of each subset was subsequently calculated (red curve).
5. The subset data was shifted by a value of n/2 (green curve).
6. The maxima and minima values of the shifted subsets were thus calculated and the values were joined (magenta curve).
7. The repeated values were deleted and the values were sorted (cyan curve).
8. The MATLAB (MATLAB, 2014) *'findpeaks'* function was thus used to identify the peaks in the smoothed frequency domain (yellow data points).

These peaks are identified as the fundamental frequencies of vibration. *Figure 8*(b) shows the steps of the function in graphical format. The fundamental frequency of vibration for the post-tensioned concrete beams tested was estimated to be 74Hz (Noble *et al.*, 2016). The fundamental frequency identified from peak-picking for the given signal was 69Hz. This represents a 7% error in estimation of the predicted fundamental frequency, however, the structural system tested included the mass of the jacks on either end of the beam (Noble *et al.*, 2016), and this is expected to reduce the expected frequency.

3.9 *Cumulative effect of filtering*

The subsequent sections describe the filters applied to the data in depth, and outline the effect of each individual filter on the raw data signal. *Figure 9* presents the time and frequency domain representations of the filtered signal following the

cumulative effects of the signal filtering as described in Figure 1 and subsequent sections.

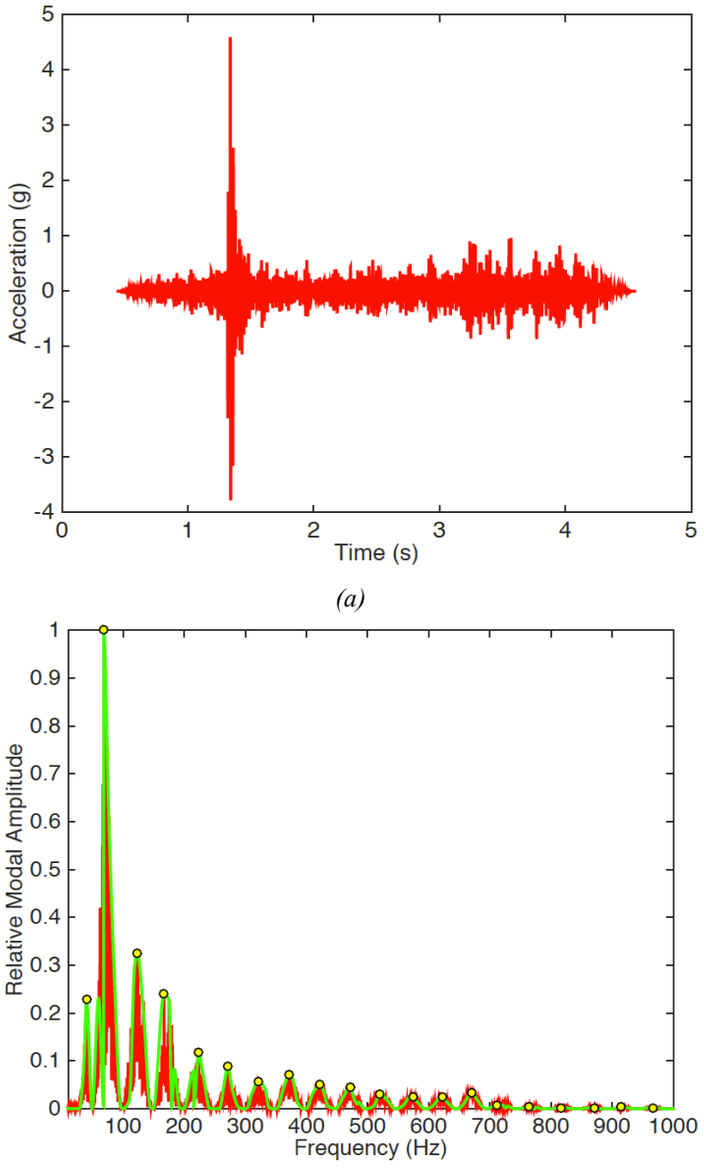


Figure 9. Time (a) and frequency (b) domain representation of filtered response signal

3.10 *Smoothed frequency domain curve*

Figure 10(a) shows the smoothed frequency domain representation of the output response signal. The Inverse Fourier Transform (IFT) was subsequently performed on the smoothed, normalized, frequency domain representation. The IFT transforms the signal from the frequency domain back into the time domain. Since the frequency domain representation has been normalized, the IFT does not represent the correct amplitude of vibration. This is not of interest however, as the frequency was the parameter of interest (Noble *et al.*, 2015, 2016).

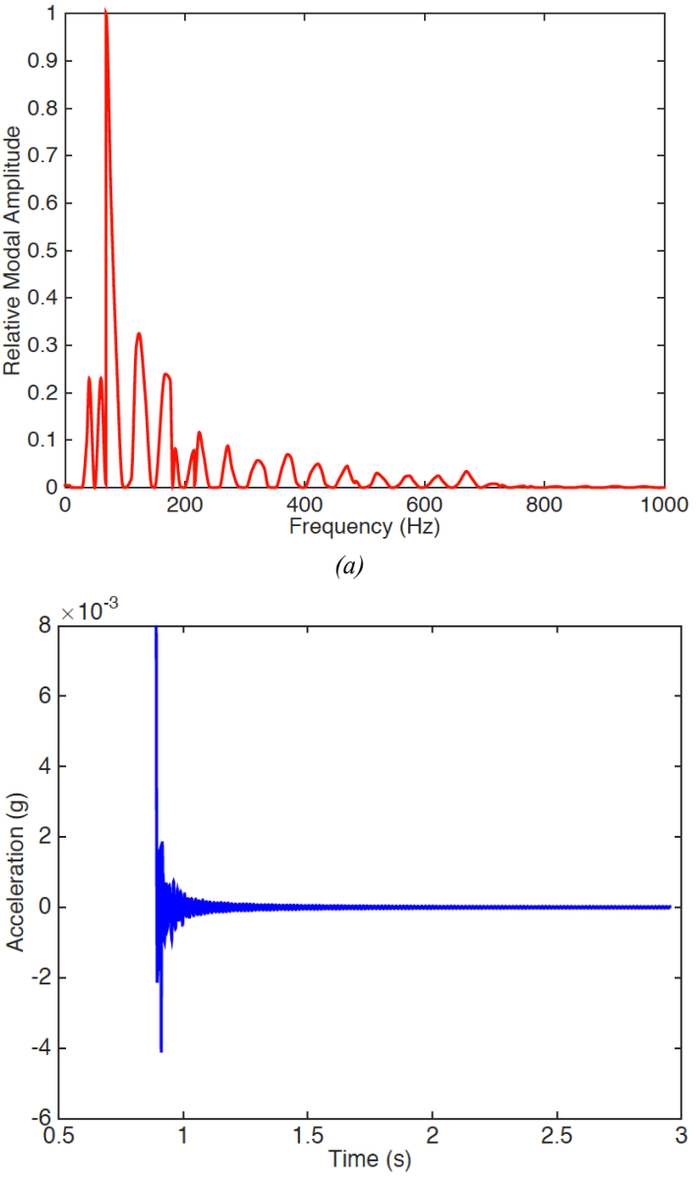


Figure 10. (a) Smoothed frequency domain representation of output response signal; (b) Inverse Fourier Transform (IFFT) of frequency domain representation of output response signal.

4 CONCLUSIONS

This paper outlined the importance and effect of signal filtering on raw acceleration response data for steel and concrete beams in order to identify the fundamental frequencies of vibration (Noble *et al.*, 2015, 2016). The paper outlines the difficulty in identifying the appropriate fundamental frequency using unfiltered accelerometer data. The effect of noise components is such as to distort the structural vibration signal, meaning that the main structural vibration frequencies may be unintelligible. The noise components may be removed through careful filtering. The filters applied to the accelerometer data, and described throughout the paper are; moving average filter, zero-drift filter, notch filter removing electrical noise, 40Hz high pass filter, and

an anti-aliasing filter. The most important filters in terms of identification of the natural frequencies are the zero drift and 40Hz high-pass filters, removing the dominant low-frequency noise components. The second most important filter in terms of structural frequency identification is the electrical notch filter, removing the electrical noise from the A/C circuitry in the accelerometer.

Care must be taken in signal filtering in order to avoid over-filtering. Over filtering of the signal leads to confirmation bias, furthermore, if care is not exercised, valid structural frequency content may be removed. The described signal processing regime allowed for the correct identification of the predicted fundamental frequencies of vibration for both steel and concrete sections as outlined previously (Noble *et al.*, 2015, 2016). Such an approach can be helpful for tracking frequency changes and real time monitoring and assessment of structural systems (Krishnan *et al.*, 2018).

5 ACKNOWLEDGEMENTS

The authors would like to gratefully acknowledge the financial support donated by the Irish Research Council (IRC) under its Embark initiative (Grant No. RS/2012/111). The authors would also like to sincerely thank Banagher Concrete, Heitons Steel, Roadstone Ireland, Fairyhouse Steel, and Freyssinet Ireland for their support in supplying testing materials throughout the duration of the project.

6 REFERENCES

Avitabile, P. (2001) 'Experimental Modal Analysis - A Simple Non-Mathematical Overview', *Sound and Vibration Magazine*, January.

Bartlett, F. (1987) 'Discussion of "Free Vibration Behavior of Prestressed Beams" by K. Kanaka Raju and G. Venkateswara Rao (February, 1986, Vol. 112, No. 2)', *Journal of Structural Engineering*, 113(9), pp. 2085–2087.

Bažant, Z. and Cedolin, L. (1987) 'Discussion of "Free Vibration Behavior of Prestressed Beams'' by K. Kanaka Raju and G. Venkateswara Rao (February, 1986, Vol. 112, No. 2)', *Journal of Structural Engineering*, 113(9), p. 2087.

Bert, C. (1987) 'Discussion of "Free Vibration Behavior of Prestressed Beams" by K. Kanaka Raju and G. Venkateswara Rao (February, 1986, Vol. 112, No. 2)', *Journal of Structural Engineering*, 113(9), pp. 2087–2088.

Butterworth, S. (1930) 'On the Theory of Filter Amplifiers', *Experimental Wireless & the Wireless Engineer*, 7, pp. 536–541.

Chan, T. H. T. and Yung, T. H. (2000) 'A theoretical study of force identification using prestressed concrete bridges', *Engineering Structures*, 22(11), pp. 1529–1537.

Ewins, D. J. (2000) *Modal testing: theory, practice, and application*. Research Studies Press (Mechanical engineering research studies: Engineering dynamics series).

Kim, J. (2004) 'Identification of prestress-loss in PSC beams using modal information', *Structural Engineering and Mechanics*, 17(3), pp. 467–482.

Krishnan, M., Bhowmik, B., Hazra, B. and Pakrashi, V. (2018) 'Real time damage detection using recursive principal components and time varying auto-regressive modeling', *Mechanical Systems and Signal Processing*. Academic Press, 101, pp. 549–574.

MATLAB (2014) *version 8.3.0 (R2014a)*. Natick, Massachusetts: The MathWorks Inc.

Miyamoto, A., Tei, K., Nakamura, H. and Bull, J. (2000) 'Behavior of Prestressed Beam Strengthened with External Tendons', *Journal of Structural Engineering*, 126(9), pp. 1033–1044.

Noble, D., Nogal, M., O'Connor, A. and Pakrashi, V. (2015) 'Dynamic impact testing on post-tensioned steel rectangular hollow sections; An investigation into the " compression-softening " effect', *Journal of Sound and Vibration*, 355, pp. 246–263.

Noble, D., Nogal, M., O'Connor, A. and Pakrashi, V. (2016) 'The effect of prestress force magnitude and eccentricity on the natural bending frequencies of uncracked prestressed concrete beams', *Journal of Sound and Vibration*, 365, pp. 22–44.

Raju, K. K. and Rao, G. V. (1986) 'Free Vibration Behavior of Prestressed Beams', *Journal of Structural Engineering*, 112(2), pp. 433–437.

Saiidi, M., Douglas, B. and Feng, S. (1994) 'Prestress Force Effect on Vibration Frequency of Concrete Bridges', *Journal of Structural Engineering*, 120(7), pp. 2233–2241.

Tse, F. S., Morse, I. E. and Hinkle, R. T. (1978) *Mechanical vibrations: theory and applications*. Allyn and Bacon (Allyn and Bacon series in mechanical engineering and applied mechanics).

Williams, M. S. and Falati, S. (1999) 'Modal testing of a post-tensioned concrete model floor slab', in *Proceedings of the International Modal Analysis Conference - IMAC*, pp. 14–20.

Zhang, Y. and Li, R. (2007) 'Natural Frequency of Full-Prestressed Concrete Beam', *Transactions of Tianjin University*, 13(5), pp. 354–359.

Maintenance, Safety, Risk, Management and Life-Cycle Performance of Bridges – Powers, Frangopol, Al-Mahaidi & Caprani (Eds)
© 2018 Taylor & Francis Group, London, ISBN 978-1-138-73045-8

The effect of local scour of a single pier on the vibration parameters of a multi-span bridge under seismic excitation

A. Anžlin
National Building and Civil Engineering Institute, Dimičeva ulica 12, 1000 Ljubljana, Slovenia

L.J. Prendergast & K. Gavin
Faculty of Civil Engineering and Geosciences, Delft University of Technology, Netherlands

M.P. Limongelli
Politecnico di Milano, Department of Architecture, Piazza Leonardo da Vinci 32, 20133 Milano, Italy

ABSTRACT

Several regions in Europe are prone to both seismic and scour hazards thus bridges can suffer from the joint actions of these two phenomena. The two types of hazards are actually independent as to the generation process but the loss of surrounding soil due to scour may significantly modify the dynamic parameters of the structure thus changing its response to a subsequent earthquake.

Permanent monitoring through vibration-based methods can be an effective support in bridge assessment procedures providing updated information about the structural state and performance. Information from the monitoring system allow both the prompt detection of a possible damage state after an extreme event and also support for long term assessment of the structural conditions.

For bridges under multiple hazard the possibility of using the same network of sensors for different hazards can increase the benefit/cost ratio related to the use of a monitoring system.

In this paper, some preliminary results of a numerical investigation carried out on the finite element model of a bridge under flood and seismic actions are reported. The numerical model of a multi-span bridge, developed using OpenSees, is subjected to a seismic base input considering several defined scour conditions. Scour has been modelled as the incremental increase in length of one of the piers and the effect of scour on the seismic response is investigated. The evolution of modal periods and of deck peak accelerations under seismic excitation have been studied in order to investigate the feasibility of these parameters as performance indicators able to detect the presence of scour in one piers for a bridge under seismic excitation. The first part of the paper reports a brief description of the main damage scenarios connected to scour and to seismic actions. The second part of the paper reports the results of a non-linear dynamic analyses of a scoured bridge under seismic input. Several scour depths have been considered in order to study the sensitivity of several vibration-based parameters to the intensity of the scouring.

1 INTRODUCTION

1.1 Bridge scour

Bridge scour is the term used to describe the removal of soil from around bridge foundations caused by adverse hydraulic action (Hamill 1999). There are three main forms of scour: general, contraction and local scour. General scour occurs naturally in river channels and is a fundamental behavior of evolving rivers. It involves the natural erosion and deposition behavior of a river channel that occurs due to changes in the hydraulic parameters governing channel form, for example flow rate or sediment supply (Forde et al. 1999; Federico et al. 2003). Contraction scour occurs due to the sudden increase in flow velocity at the location of a bridge caused by a narrowing of the river channel, as water is channeled between the sub-structural elements of a bridge (piers or abutments). The increased velocity has an associated increase in the shear stresses imposed on the streambed sediment. Once the threshold shear stress of a given bed material is surpassed, sediments are mobilized (Briaud et al. 1999). Finally, local scour occurs around individual piers or abutments due to their disruption of the local water-flow characteristics. The flow is channeled downward once it meets the obstruction, which can cause scour holes to develop on the upstream end of a pier due to the generation of horseshoe vortices. Furthermore, the flow separating at the sides of the pier causes wake vortices to form which can expand the scour hole around the pier (Heidarpour et al. 2010). Figure 1 shows a schematic of the scour process around a cylindrical pier-type object.

Scour is one of the leading causes of bridge failure worldwide (Briaud et al. 2001; Briaud et al. 2005; Melville & Coleman 2000; Wardhana & Hadipriono

2003). In the United States, bridge failure inventories claim that scour is either the leading factor or a major contributory factor to sudden bridge failure. For example, one study of 500 bridge failures that occurred between 1989 and 2000 in the United States claimed that 53% of the failures were attributed to flood-related mechanisms including scour (Wardhana & Hadipriono 2003). Another similar study from an earlier period specified scour as the primary cause of failure in 600 documented bridge failures (Shirole & Holt 1991). Scour represents a significant cost burden on infrastructure managers between preventative measures, inspections and associated repairs.

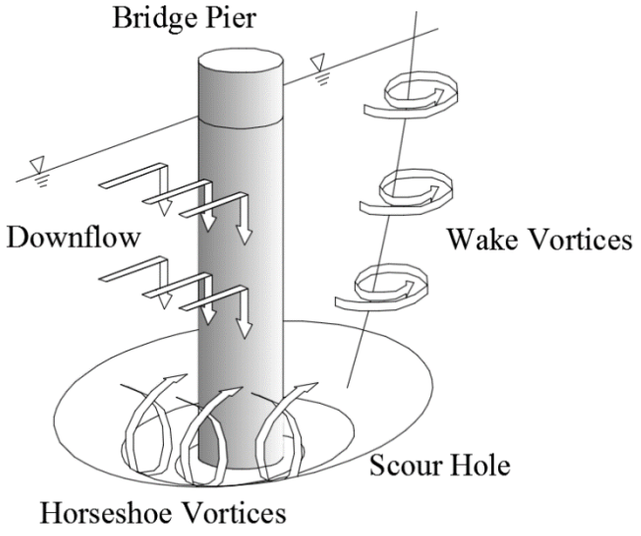


Figure 1: Schematic of local scour - modified from Prendergast & Gavin (2014)

Scour failures tend to occur quite suddenly and generally without much warning. For example, in North Dublin, Ireland in August 2009, a railway bridge on the main Dublin to Belfast rail line partially collapsed as a train passed overhead (Maddison 2012). Fortunately, there were no causalities in this particular incident, however the rail line was out of service for some time afterwards.

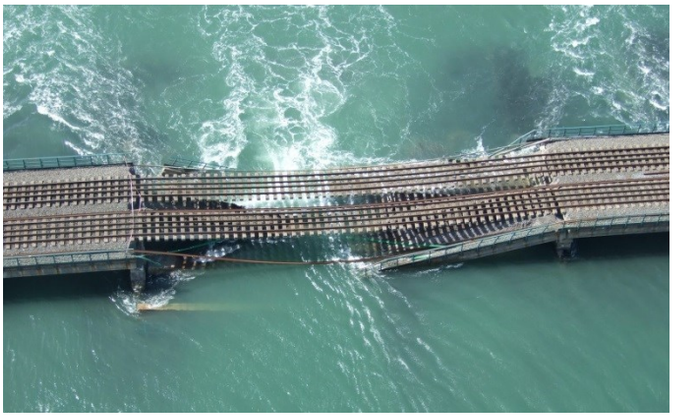


Figure 2: Collapsed Malahide Viaduct on Dublin-Belfast rail line (Maddison 2012)

Figure 2 shows a photo of the bridge after collapse. The bridge is located in a tidal estuary, and tidal scour was deemed to be the cause of collapse.

Monitoring of scour has become a topic of significant importance for asset managers. Scour monitoring was traditionally undertaken by visual means, whereby a diver would inspect the condition of a foundation at discrete periods. The main drawback of these methods is the subjectivity of the condition ratings, as well as the dangers of inspecting for scour during floods. For example, the primary focus of these inspections were to visually assess the magnitude of a scour hole, in terms of its depth, proximity to a foundation as well as any auxiliary impacts present (cracking or other evident damage). Moreover, scour holes tend to refill with sediment as flood waters subside making their detection by discrete visual means quite challenging. In response to the need for more reliable methods, several mechanical and electrical instruments have been developed to remotely monitor scour (Prendergast & Gavin 2014; Fisher et al. 2013). These instruments typically measure the depth of a scour hole near a foundation element with varying degrees of accuracy. A variety of methods exist that use physical sensors placed on or near the ground that move with changing bed level elevation (Hunt 2009; Briaud et al. 2011), or they rely on electromagnetic or sonic methods (Forde et al. 1999; Yu 2009; Nassif et al. 2002). One common drawback of the majority of these types of instruments is that they are typically incapable of assessing the *distress* experienced by the bridge due to the presence of scour at the foundations.

The need for more information on the condition of the structure due to scour has led to the evolution of the vibration-based scour monitoring field. Several authors have investigated how the dynamic response of bridges or specific bridge elements varies under scour, see (Briaud et al. 2011; Prendergast et al. 2016; Prendergast et al. 2017; Prendergast et al. 2013; Chen et al. 2014; Bao et al. 2017; Elsaid & Seracino 2014; Foti & Sabia 2011) among others. For example, Ju (2013) studied how the natural frequency of a bridge varied with scour incorporating fluid-structure interaction. Chen et al. (2014) present a case study of a vibration-based bridge scour detection scheme applied to a cable-stay bridge based on measuring ambient velocity changes. Prendergast et al. (2013) investigated how the natural frequency of a single pile varied as it was scoured, on a both a laboratory and field scale. Moreover, they put forward a numerical model capable of tracking the frequency change using site specific soil parameters. Prendergast et al. (2016; 2017) build on this method and investigate if scour can be detected and located using frequency measurements of an integral-type bridge structure.

The majority of these studies agree that the loss in stiffness due to scour can be traced using vibration

measurements, whereby the stiffness loss manifests itself as a change in modal properties (Doebling et al. 1996). This topic is receiving an increasing amount of interest in the literature in recent years.

1.2 Seismic actions on bridge performance

Collapse of bridges due to seismic actions may be the result of the application of old design codes that did not consider at all seismic design or did not apply capacity design principles. According to the capacity design principles, the design of the structures (or the upgrading for existing ones) has to be performed so as to enhance the energy dissipation capacity. This can be achieved avoiding brittle failures and allowing controlled energy dissipation.

The first goal is achieved designing the structure with a resistance with respect to brittle collapse mechanisms higher with respect to the resistance to ductile mechanisms. For example the resistance to shear failure has to be higher with respect to the resistance to bending failure and the resistance of the superstructure should be lower with respect to the resistance of the foundations. The second goal of controlled energy dissipation is pursued by allowing the formation of flexural plastic hinges in predefined (controlled) locations. This enables the development of stable collapse mechanisms and thus the dissipation a large amount of energy. For example in the case of a bridge this means that the structure is designed to allow the formation of flexural plastic hinges in as many piers as possible. On the other hand, such deformations are not allowed to occur in the deck and the foundations, which are designed assuming the maximum anticipated actions at the base of the piers.

The capacity design principles can be applied through proper detailing of critical regions (e.g. reduced spacing of the transversal steel bars in reinforced concrete structures, or reduced transversal sections in steel structures) and through design of the structural elements carried out based on the resistance with respect to brittle mechanisms and not based on the actions.

If capacity design is not applied, as is the case of most bridges built according to old design codes, brittle collapse mechanisms with very limited energy dissipation capacity are likely to occur.

Bridge piers usually represent one of the weak elements under seismic actions due to inadequate detailing (Anzlin et al. 2015) that limit their capacity to deform in the non-elastic range without sensible reductions of strength (ductility).

Another common bridge collapse mechanism is due to the collapse of the deck girders due to large relative displacements between pier columns. Collapse may occur at expansion joints due to compression or tension failures or – in case of simple supported girders - to the unseating of deck due to insufficient seat width (see Figure 5).

In simply supported span bridges the unseating of the bridge deck could be dually affected by scour due to the increased flexibility that increases the maximum potential displacement of the deck induced by seismic actions. In this paper, the effect of scour local to one of the piers on a multi-span bridge is investigated in terms of how it changes the seismic response of the bridge. This is investigated using numerical modelling, as discussed in the following section.

1.3. Seismic behavior of scoured bridges

The seismic response of a bridge depends on its dynamic characteristics that are strongly related to the stiffness of the piers. As remarked in section 1.1, scour causes a stiffness loss of the scoured pier due to the increase of clear length and this may sensibly affect the modal characteristics of the bridge. The increased flexibility in general, for bridges in stiff-medium soils – has a beneficial effect on the severity of the seismic action but at the same time leads to an increase of relative displacement that has a detrimental effect on other collapse mechanism linked for example to the unseating of the deck girders.

Furthermore the variation of the relative stiffness between piers induced by a single pier scouring induces a redistribution of the actions in the piers thus to a possible increase of the shear forces in non-scoured piers.

1.4. Monitoring of bridges under scour and seismic hazards

To date a number of bridges under seismic threat are monitored with permanent network of sensors. Despite the importance of the topic and the large number of bridges that may be under the combined hazard of scour and seismic actions, a limited number of studies have been devoted to this topic. The aim of this paper is to provide an insight to the behavior of a scoured bridge under seismic actions and to check the feasibility of simple vibration-based damage detection algorithms to detect damage induced by the joint hazard of scour and seismic action. Several data driven vibration-based algorithms of damage localization have been proposed in literature and can be used for the case of bridges under seismic excitation (Doebling et al. 1996, Limongelli 2010, 2011, 2014, Kim et al. 2002, Pandey et al. 1991, Ratcliffe 2000, Zhang et al 1998, among many others). In this preliminary study only the modal period and the peak acceleration have been used as indicators of a scouring condition in one of the bridge piers.In this paper, using numerical modelling the effect of scour local to one of the piers on a multi-span bridge is investigated in terms of how it changes the seismic re-

sponse of the bridge. The use of the variation of modal frequencies and of peak deck accelerations at the pier locations as indicators of scour in one pier is investigated with reference to several scenarios corresponding to increasing scour magnitudes.

2 FINITE-ELEMENT MODELLING

The effect of scour on the seismic response of a multi-span bridge is investigated numerically using OpenSees, an open source dynamic modeling software (MacKenna et al. 2016). Section 2.1 present the model used in this study, section 2.2 discusses how scour is modelled and section 2.3 presents how seismic motions are incorporated.

2.1 Multi-span bridge model in OpenSees

A six-span bridge supported by five I-shaped bridge columns (the cross-section is presented in Figure 3 and 4) was considered in this study. The deck of the structure was modelled as an elastic beam column with the geometrical characteristics representing a cross-section displayed in Figure 4. The abutments of the bridge were simplified into roller supports enabling the longitudinal movements of the bridge. The elastomeric bearings in the first and the last column were modelled with elastic springs whose stiffness was proportional to the shear modulus and the geometrical characteristic of the bearings.

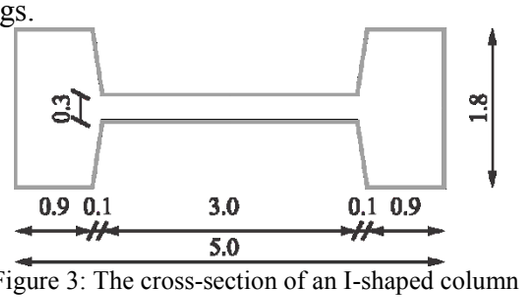


Figure 3: The cross-section of an I-shaped column

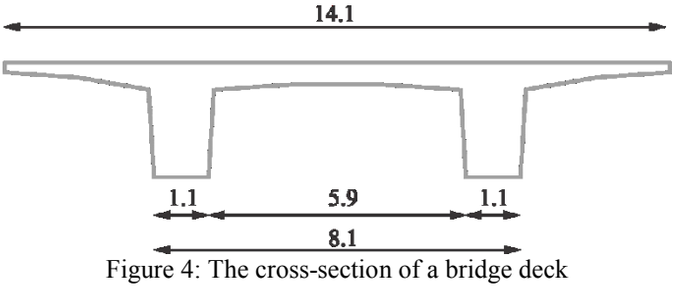


Figure 4: The cross-section of a bridge deck

2.2 Scour modeling

Local scour of one of the piers is modelled as an increase in the effective length. In total, 10m of scour is considered and only one pier is affected, pier 4 (see Figure 5). The scour depth is incremented in 2m increments and the seismic loading is applied for each scour condition in the perpendicular direction of the traffic (longitudinal direction).

2.3 Seismic modelling

OpenSees program platform (MacKenna et al. 2016) has been used for the modal and non-linear dynamic analysis of the bridge. The lumped plasticity model (Giberson 1969) was used for the modelling of a non-linear response of bridge columns. The characteristics of the non-linear spring located at the bottom of each column (see Figure 5) are based on the tri-linear idealization of the full moment-curvature analysis of a column cross-section. The material characteristic of discretized fibres of steel, unconfined and confined concrete are based on the recommendations of Eurocodes 8/2 (CEN 2005a) and 8/3 (CEN 2005b). The behavior of the non-linear spring was defined using Takeda hysteretic rules (Takeda et al. 1970) assuming the unloading stiffness factor to have a value of 0.5. The damping matrix was defined as a linear combination of the mass and initial stiffness matrices using a Rayleigh approach (Clough & Penzien 1993).

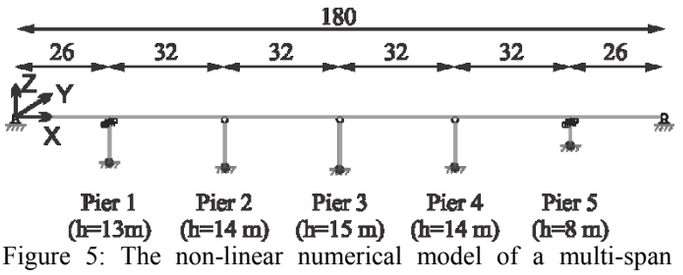


Figure 5: The non-linear numerical model of a multi-span bridge with springs located at the bottom of each pier.

3 ANALYSIS & RESULTS

In this section, the results of the analysis are presented. The model presented in the previous section is used to perform a modal study (section 3.1) and a seismic response analysis (section 3.2).

3.1 Modal analysis

The first two modal shapes obtained from the numerical model in OpenSees (by obtaining a solution of the Eigenproblem) (Clough & Penzien 1993) are shown in Figure 6 and 7 for both the no scour and full (10m) scour scenarios.
Mode 1 is a longitudinal mode (in the traffic direction) and mode 2 is a lateral bridge mode (perpendicular to the traffic direction). As expected, scour increases the global flexibility of the bridge, particularly in the transversal direction. The first two modal shape results due to a scour depth of 10m for the fourth pier (pier 4 in the numerical model) are shown in Figure 7. The comparison with the corresponding modal shapes relevant to the scenario without scouring points out the effect of the latter on these parameters. The asymmetry in the structure's stiffness before and after scour has shifted the modal displacement in the lateral direction towards the scoured pier. This is sensible as if we consider the

increased flexibility of the scoured pier, this should experience larger movements under a dynamic motion.

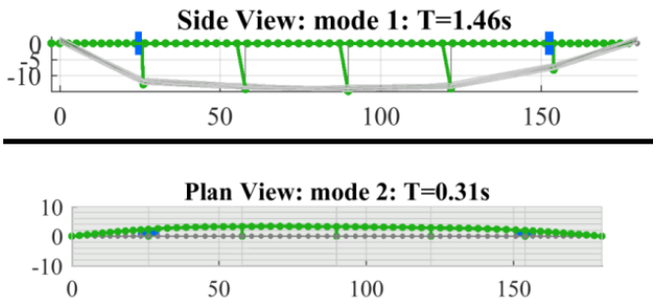


Figure 6: The 1st and 2nd mode shape of the bridge with no scouring

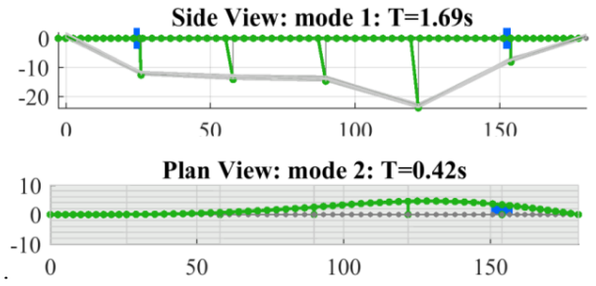


Figure 7: The 1st and 2nd mode shape of the bridge with 10 m scouring

The effect of different scouring depths (scour depth S between 0m and 10m) on the natural periods (first T_1 and second T_2) of the bridge is evident from the values reported in Table 1.

Table 1: 1st and 2nd modal periods (T_1 and T_2) of the bridge with different levels of scouring

Scour S [m]	**0**	**2**	**4**	**6**	**8**	**10**
T_1 [s]	1.46	1.54	1.6	1.64	1.67	1.69
T_2 [s]	0.31	0.34	0.37	0.39	0.41	0.42

Table 2: Variation of the 1st and 2nd modal periods of the bridge with different levels of scouring

Scour S [m]	**0**	**2**	**4**	**6**	**8**	**10**
$\Delta T_1/ T_1$ [%]	0.0	5.5	9.6	12.3	14.4	15.8
$\Delta T_2/ T_2$ [%]	0.0	9.7	19.4	25.8	32.3	35.5

As expected, both modal periods increase with the flexibility of the scoured pier. Scouring has a stronger effect on the second mode as shown in Table 2 by the percentage variations of the two modal periods with respect to the initial values: the percentage variation of the second mode is around twice or higher than the corresponding variation of the first one. This means that the effect of scouring on the dynamic response of this type of bridges is likely to be much higher in the transversal direction than in the direction of the traffic. For this reason in the following sections are reported the results of a dynamic analyses of the scoured bridge under a seismic input acting in the transversal direction - perpendicular to the traffic.

3.2 Seismic response under progressive scour of single pier

The response of the bridge under an applied seismic input is investigated for the range of scour depths presented in Table 1. A seismic motion with duration of approximately 40 seconds and scaled to peak ground acceleration (PGA) of approximately 1 m/s^2 is considered for the seismic analyses of the bridge. Figure 8 shows the time history of the scaled earthquake ground motion (Athens 1999 earthquake) used in this study and its response spectrum. The seismic excitation is applied in the lateral direction to the bridge (to excite mode 2), perpendicular to the traffic direction.

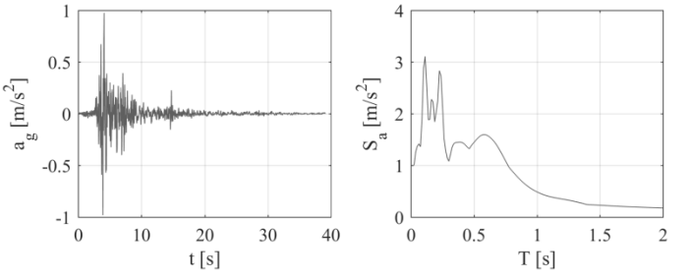


Figure 8: The earthquake ground motion record with peak ground acceleration of 1.0 m/s^2 considered for the lateral excitation of the bridge and the response spectra of the ground motion.

Responses to the applied ground motion in terms of absolute accelerations a, displacements u, and shear force F in the piers are shown in subsequent plots.

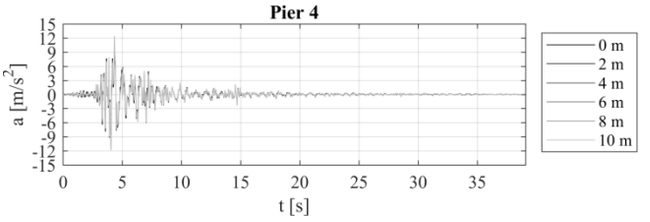


Figure 9: The time domain signal of the absolute acceleration a at the deck level of the Pier 4 for the bridge with no scour (S=0) and investigated levels of scouring (S=2, 4, 6, 8 and 10 m).

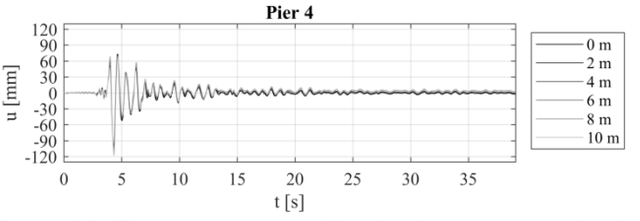


Figure 10: The time domain of the displacement u at the deck level of the pier 4 between the bridge with no sour (S=0) and investigated levels of scouring (S=2, 4, 6, 8 and 10 m).

Figure 9 shows the absolute acceleration measured at the deck level of the scoured column (Pier 4)

for scour depths ranging from 0m to 10m. The maximum (peak) acceleration increased under scour from 11.6 m/s^2 for 0m of scour to 12.4m/s^2 under 10m scour.

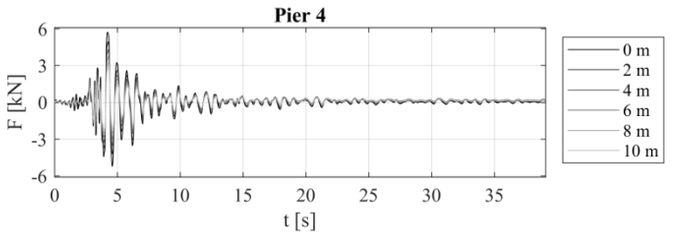


Figure 11: The time domain of the shear force F at the base level of the pier 4 between the bridge with no scour (s=0) and investigated levels of scouring (s=2, 4, 6, 8 and 10 m).

Figure 10 shows the displacement measured at the deck level above the scoured pier 4 for scour depths ranging from 0m to 10m under the applied seismic load (Figure 8). Figure 10 shows that some nonlinear plasticity is evident in the responses, particularly for larger scour depths.

The peak displacement observed at the deck level of the scoured pier 4 due to the applied seismic load increases from 0.1 m at the deck level for 0m of scour to 0.12 m for a scour depth of 10m affecting the pier. This is sensible as the increased flexibility of the scoured pier enables it to translate further under the applied excitation.

Finally, Figure 11 shows the absolute shear force calculated at the base of the scoured pier 4 due to the applied seismic load in Figure 8. The shear force is presented in kN. Scour depths are varied from 0m to 10m at pier 4 and the peak shear force calculated at the base of the pier decreases under scour from 5.72kN for the case where there is 0m scour to 2.92kN for the case where there is 10m scour at the pier.

Table 3: Maxima value of the shear in the piers Vp for different levels of scouring and maxima value of the total shear in the piers.

	Scour S [m]	**0**	**2**	**4**	**6**	**8**	**10**
F [kN]	Pier 1	1.56	1.56	1.52	1.52	1.52	1.52
	Pier 2	5.63	5.65	5.75	5.81	5.85	5.90
	Pier 3	5.76	5.77	5.89	5.90	5.91	5.90
	Pier 4	5.72	4.94	4.32	3.77	3.30	2.92
	Pier 5	1.01	1.03	1.02	1.03	1.04	1.04
F_T [kN]		19.7	18.9	18.5	18.0	17.6	17.3

Table 3 reports the absolute value of the maximum shear in each piers F and the total shear F_T in the piers. At the increase of the scour depth from S=2m to S=10m, the shear F decreases in Pier 4 (the scoured one) by almost 50% with respect to the initial value (un-scoured condition) and increases by values between 2% and 5% in the other piers. The scour is thus beneficial for the scoured pier but of course not for the other resisting elements where the effect of the increased flexibility of the bridge, leading to a reduction of the total shear in the piers F_T, is canceled by the redistribution of the internal actions induced by the change of stiffness ratios between piers.

As shown in Figure 12, with the increase of the scour depth, the normalized shear F/F_T (ratio between the shear force in the pier and sum of the forces in the piers) sensibly decreases in Pier 4 and increases (with a lower rate) in all the other piers. For example at the increase of the scour from S=2m to S=10m, the normalized shear F/F_T for pier 4 decreases from 29% to 17% and increases from about 29% to 34% for piers 2 and 3. The variation of shear forces in piers 1 and 2 due to scouring is much smaller due to the presence of the elastomeric bearings (the connection of the deck and the piers in the direction of seismic loading is not rigid) mon the tops of these piers.

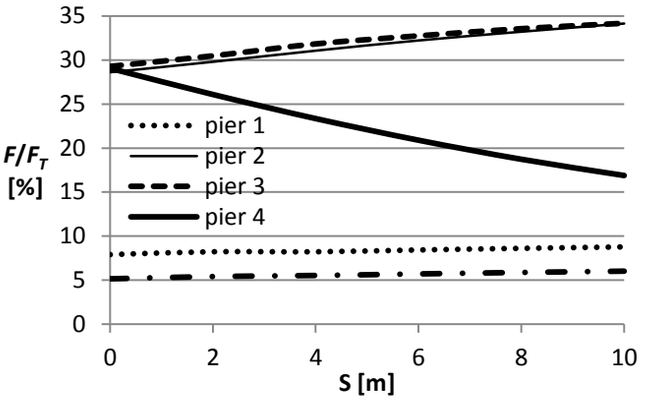


Figure 12: Maxima shear forces in the piers normalized to the total shear in the piers as a function or the scour depth

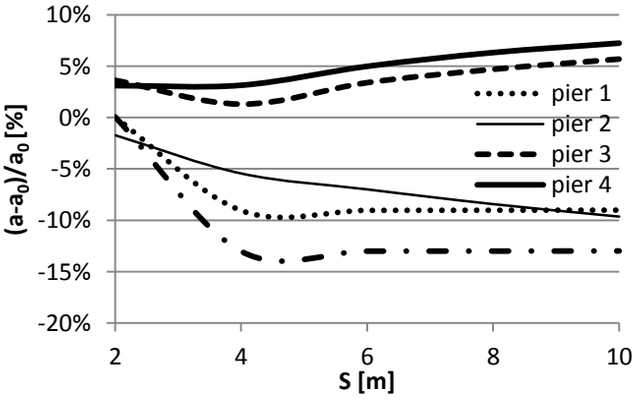


Figure 13: Variation of the maxima absolute acceleration normalized to the reference value a_0 as a function of scour depth

The percentage variation of the maximum absolute accelerations on the deck at the location of the piers are consistent with the variation of the second modal shape. At the increase of the scour depth, the acceleration increases in the scoured pier (pier 4) and in the pier nearby (pier 3) and decreases in the other piers as shown in Figure 13.

4 CONCLUSION

The effects of uncorrelated hazards, in the present case, scour occurrence and earthquakes is becoming a topic of increased interest. Though independent in their generation, the effect of an earthquake will vary depending on the scoured condition of the foundations. In this paper, the effect of local scour on the seismic response of a bridge was investigated briefly. A multi-span bridge was programmed using OpenSees and one of the piers was subjected to scour. Scour was modelled as the increase in the effective length of one of the piers with the remaining piers remaining unscoured. In total, 10m of scour was examined in increments of 2m. A seismic motion was applied to the bridge in the transverse direction (perpendicular to traffic) based on a modal study undertaken.

The effect of scour is to increase the peak displacement of the pier (at deck level), with a corresponding increase in the peak acceleration at the same level. The shear force at the base of the scoured column drastically decreases with scour, however this results in a redistributed higher shear being experienced by adjacent columns.

The increased flexibility of the bridge can be detected monitoring the increase of the modal period in the transversal direction, perpendicular to the traffic. The variations of the peak accelerations on the deck in the transversal direction show higher values at locations close to the scoured pier.

This paper presents preliminary results. Future research will investigate a more exhaustive set of parameters including multiple seismic records, various applied directions, variations in bridge properties and multiple scoured locations.

ACKNOWLEDGEMENTS

The authors wish to acknowledge COST Action TU1406 'Quality Inspection for Roadway Bridges – Standardization at a European Level' for enabling this collaboration.

REFERENCES

Anzlin, A., Fischinger, M. & Isakovic, T., 2015. Cyclic response of I-shaped bridge columns with substandard transverse reinforcement. Engineering Structures, 99, pp.642–652. Available at: http://www.sciencedirect.com/science/article/pii/S0141029615003582 [Accessed December 7, 2017].

Bao, T. et al., 2017. Critical insights for advanced bridge scour detection using the natural frequency. Journal of Sound and Vibration, 386, pp.116–133. Available at: http://dx.doi.org/10.1016/j.jsv.2016.06.039.

Briaud, J.L. et al., 2001. Erosion Function Apparatus for Scour Rate Predictions. Journal of Geotechnical and Geoenvironmental Engineering, pp.105–113.

Briaud, J.L. et al., 2011. Realtime monitoring of bridge scour using remote monitoring technology, Austin, TX. Available at: http://tti.tamu.edu/documents/0-6060-1.pdf.

Briaud, J.L. et al., 2005. SRICOS-EFA Method for Contraction Scour in Fine-Grained Soils. Journal of Geotechnical and Geoenvironmental Engineering, 131(10), pp.1283–1295.

Briaud, J.L., Ting, F. & Chen, H.C., 1999. SRICOS: Prediction of Scour Rate in Cohesive Soils at Bridge Piers. Journal of Geotechnical and Geoenvironmental Engineering, (April), pp.237–246.

CEN, 2005a. EN:1998-2:2005 - Eurocode 8: Design of structures for earthquake resistance - Part 2: Bridges,

CEN, 2005b. EN:1998-3:2005 - Eurocode 8: Design of structures for earthquake resistance - Part 3: Assessment and retrofit of buildings,

Chen, C.-C. et al., 2014. Scour evaluation for foundation of a cable-stayed bridge based on ambient vibration measurements of superstructure. NDT & E International, 66, pp.16–27. Available at: http://linkinghub.elsevier.com/retrieve/pii/S0963869514000589 [Accessed February 23, 2015].

Clough, R.W. & Penzien, J., 1993. Dynamics of structures,

Doebling, S. et al., 1996. Damage identification and health monitoring of structural and mechanical systems from changes in their vibration characteristics: a literature review, Los Alamos, New Mexico. Available at: http://www.osti.gov/energycitations/product.biblio.jsp?osti_id=249299 [Accessed May 8, 2012].

Elsaid, A. & Seracino, R., 2014. Rapid assessment of foundation scour using the dynamic features of bridge superstructure. Construction and Building Materials, 50, pp.42–49. Available at: http://linkinghub.elsevier.com/retrieve/pii/S095006181300809X [Accessed October 29, 2013].

Federico, F., Silvagni, G. & Volpi, F., 2003. Scour Vulnerability of River Bridge Piers. Journal of Geotechnical and Geoenvironmental Engineering, 129(10), pp.890–900.

Fisher, M. et al., 2013. An evaluation of scour measurement devices. Flow Measurement and Instrumentation, 33, pp.55–67. Available at: http://linkinghub.elsevier.com/retrieve/pii/S0955598613000666 [Accessed September 30, 2013].

Forde, M.C. et al., 1999. Radar measurement of bridge scour. NDT&E International, 32, pp.481–492.

Foti, S. & Sabia, D., 2011. Influence of Foundation Scour on the Dynamic Response of an Existing Bridge. Journal Of Bridge Engineering, 16(2), pp.295–304.

Giberson, M., 1969. Two nonlinear beams with definitions of ductility. Journal of the structural division. Available at: https://trid.trb.org/view.aspx?id=105529 [Accessed December 6, 2017].

Hamill, L., 1999. Bridge Hydraulics, London: E.& F.N. Spon.

Heidarpour, M., Afzalimehr, H. & Izadinia, E., 2010. Reduction of local scour around bridge pier groups using collars. International Journal of Sediment Research, 25(4), pp.411–422. Available at: http://linkinghub.elsevier.com/retrieve/pii/S1001627911600085 [Accessed January 23, 2012].

Hunt, B.E., 2009. NCHRP synthesis 396: Monitoring Scour Critical Bridges - A Synthesis of Highway Practice, Washington, DC.

Ju, S.H., 2013. Determination of scoured bridge natural frequencies with soil–structure interaction. Soil Dynamics and Earthquake Engineering, 55, pp.247–254. Available at: http://linkinghub.elsevier.com/retrieve/pii/S0267726113002017 [Accessed October 29, 2013].

Kim J.T., Stubbs N. (2002). "Improved damage identification method based on modal information" Journal of Sound and Vibration, 252 (2002), pp. 223-238.

Limongelli, M.P., (2010). Frequency Response Function Interpolation for Damage Detection under Changing Environment. Mechanical Systems and Signal Processing, 24(8), 2898-2913.

Limongelli, M.P., (2011). The interpolation damage detection method for frames under seismic excitation. Journal of Sound and Vibration, 330. 5474–5489.

Limongelli, M.P., (2014). Seismic health monitoring of an instrumented multistorey building using the Interpolation Method. Earthquake Engng. Struct. Dyn. doi: 10.1002/eqe.2411

MacKenna, F., Fenves, G.L. & Scott, M.H., 2016. Open System for Earthquake Engineering Simulation. Available at: http://opensees.berkely.edu.

Maddison, B., 2012. Scour failure of bridges. Proceedings of the ICE - Forensic Engineering, 165(FE1), pp.39–52.

Melville, B.W. & Coleman, S.E., 2000. Bridge scour, Highlands Ranch, CO: Water Resources Publications.

Nassif, H., Ertekin, A.O. & Davis, J., 2002. Evaluation of Bridge Scour Monitoring Methods, Trenton, NJ.

Pandey A.K., Biswas M., Samman M.M. (1991). "Damage detection from change in curvature mode shapes". Journal of Sound and Vibration, 145 (1991), pp. 321–332.

Prendergast, L.J. et al., 2013. An investigation of the changes in the natural frequency of a pile affected by scour. Journal of Sound and Vibration, 332(25), pp.6685–6702.

Prendergast, L.J. & Gavin, K., 2014. A review of bridge scour monitoring techniques. Journal of Rock Mechanics and Geotechnical Engineering, 6(2), pp.138–149.

Prendergast, L.J., Gavin, K. & Hester, D., 2017. Isolating the location of scour-induced stiffness loss in bridges using local modal behaviour. Journal of Civil Structural Health Monitoring. Available at: http://link.springer.com/10.1007/s13349-017-0238-3.

Prendergast, L.J., Hester, D. & Gavin, K., 2016. Determining the presence of scour around bridge foundations using vehicle-induced vibrations. Journal Of Bridge Engineering, 21(10).

Ratcliffe C.P., (2000). A frequency and curvature based experimental method for locating damage in structures. Transactions of the American Society of Mechanical Engineers. Journal of Vibration and Acoustics, 122: 324–329.

Shirole, A.M. & Holt, R.C., 1991. Planning for a comprehensive bridge safety assurance program. In Transport Research Record. Washington, DC: Transport Research Board, pp. 39–50.

Takeda, T., Sozen, M. & Mielsen, N., 1970. Reinforced concrete response to simulated earthquakes. Journal of the structural division.

Wardhana, K. & Hadipriono, F.C., 2003. Analysis of Recent Bridge Failures in the United States. Journal of Performance of Constructed Facilities, 17(3), pp.144–151.

Yu, X., 2009. Time Domain Reflectometry Automatic Bridge Scour Measurement System: Principles and Potentials. Structural Health Monitoring, 8(6), pp.463–476. Available at: http://shm.sagepub.com/cgi/doi/10.1177/1475921709340965 [Accessed September 22, 2013].

Zhang, Z., Aktan, A.E. (1998). Application of modal flexibility and its derivatives in structural identification. Research in Nondestructive Evalua*tion ,* 10*,* 43-61.

MS10: Corrosion and safety of existing concrete bridges

Organizers: M. Akiyama, D.M. Frangopol & H. Matsuzaki

Maintenance, Safety, Risk, Management and Life-Cycle Performance of Bridges – Powers, Frangopol, Al-Mahaidi & Caprani (Eds)
© 2018 Taylor & Francis Group, London, ISBN 978-1-138-73045-8

Effect of different steel weight loss distributions on the life-cycle reliability of PC girders

N. Nishiya, H. Fukushima, A. Sakurai & M. Akiyama
Waseda University, Tokyo, Japan

P. Bocchini & D. M. Frangopol
Lehigh University, Bethlehem, PA, USA

ABSTRACT: In this paper, the time-dependent reliability of PC girders in a marine environment is estimated considering the spatial variability of steel weight loss. Non-linear finite element (FE) analysis of aging PC girders is performed. Spatial variation of steel weight loss represented by uniform, Gaussian and non-Gaussian stochastic fields is included in the FE modelling. To obtain the relationship between input parameters and computational results from FE analysis, the response surface method is used for reducing the time required to repeat the structural analysis. The life-cycle reliability outcomes associated with three different models for the steel weight loss distribution are compared and discussed in an illustrative example.

1 INTRODUCTION

Steel corrosion in concrete structures due to chloride attack is one of the primary causes of deterioration. This results in cracking and spalling of concrete cover, loss of bonding strength between rebar and concrete, and shortening of service life. Life-cycle performance prediction of concrete structures plays an important role in the design of new concrete structures and in the decision making with respect to inspection, repair, strengthening, and demolition of existing concrete structures (Akiyama et al. 2010, 2012, 2014a, and 2017, Frangopol 2011, Frangopol et al. 2012, Yanweerasak et al. 2016).

Despite extensive research in this field, a number of issues still remain unclear. One of the main intricacies is the uncertainty associated with the physical parameters involved in the problem. Because of the presence of uncertainties, long-term structural performance must be predicted based on probabilistic methods and life-cycle reliability assessment methodologies should be established.

Spatial variability associated with material properties, geometry and environmental factors that affect the corrosion process of concrete structures has to be investigated further. Recently, a finite element (FE) analysis was used to evaluate the potential effects of corrosion damage on the structural performance of corroded RC beams (Shimomura et al. 2011), and its validation was verified by comparing the computed results to those of the test beams (Kallias & Rafiq 2010, Coronelli & Gambarova 2004). These studies focus on the damages as reductions in the effective material properties and geometry of the RC members, in which the effects of the corrosion were modeled by modifying the geometry of the steel and concrete elements and the constitutive laws of steel, concrete, and their bond interface. However, Coronelli and Gambarova (2004) reported that one of the primary challenges in the numerical simulation is the difficulty in quantifying the loss in the steel cross-section along the rebar length. In addition to the improved constitutive models, it is important to accurately estimate the location and level of the reinforcement corrosion in the FE analysis and adequately represent their damages as the input data into the FE models (Akiyama et al. 2014b). Therefore, the location and degree of the reinforcement corrosion must be adequately assessed if the performance of corroded RC structures is to be reliably predicted by the FE models.

The use of X-ray technology as a non-destructive method is a promising technique that avoids the aforementioned problems. Recently, Akiyama & Frangopol (2013) and Lim et al. (2016, 2017) have used the X-ray and digital image processing techniques to study and quantify the spatial variability in the steel weight losses along the corroded bars inside RC members. The advantages of this method are of considerable interest because (a) the evolution of the steel corrosion and its relationship with the corrosion cracking of the same corroded RC member can be studied at various points in time, and (b) a good accuracy of the estimated steel weight loss can be obtained. Moreover, these techniques can be used to derive the residual cross-sections of the corroded bar at various times and locations. Lim et al. (2016) reported the statistical information used for modeling

the spatial variability in the steel corrosion and incorporated with the probabilistic model to predict the long-term structural performance of corroded RC structures.

In this paper, based on the previous experimental results using X-ray (Lim et al. 2016, 2017), longitudinal steel weight loss over the PC girder is represented by one-dimensional Gaussian and non-Gaussian random fields, and uniform corrosion. Time-dependent failure probability of PC girder in a marine environment is estimated based on non-linear FE analysis with randomly distributed steel weight loss. The performance function to estimate the failure probability is defined by the comparison of the moment capacity at the yielding of steel and demand due to the self-weight and traffic load. To reduce the computational time of FE analysis, the response surface method (RSM) is included in the proposed life-cycle reliability formulation. In an illustrative example, fundamental insights on the spatial distribution associated with the steel weight loss are presented.

2 MODELING OF SPATIAL RANDOM FIELDS ASSOCIATED WITH THE STEEL WEIGHT LOSS IN CONCRETE STRUCTURES

2.1 *Spectral representation method*

The spectral representation method (SRM) is a versatile method in generating stochastic fields and processes (Shinozuka & Deodatis 1996). This method can be used within a Monte Carlo Simulation (MCS) to solve the stochastic problems in structural engineering. In this study, based on the formulations presented by Papakonstantiou & Shinozuka (2013), spatial variability associated with the steel weight loss in PC girders is represented by the one-dimensional Gaussian stochastic field:

$$f(t) = \sqrt{2}\sum_{j=1}^{N}\sqrt{2S_{f_0f_0}(\kappa_j)\Delta\kappa}\cos\left(\kappa_j t + \varphi_j\right)+\mu \quad (1)$$

where

$$\kappa_j = j\Delta\kappa \;;\; \Delta\kappa = \frac{\kappa_u}{N} \quad (2)$$

$$S_{f_0f_0}(\kappa_j) = \frac{\sigma^2 b}{2\sqrt{\pi}}\exp\left(-\frac{b^2\kappa_j^{\,2}}{4}\right) \quad (3)$$

φ_j= independent random phase angle distributed uniformly over the interval [0,2π], κ_u = upper cutoff wave number corresponding to the t axis in the space domain, μ = mean, and $S_{f_0f_0}$ = power spectral density function (PSDF). In this study, for all Gaussian random fields, the PSDF is given by Equation (3), where σ is the standard deviation and b is proportional to the correlation distance of the stochastic fields.

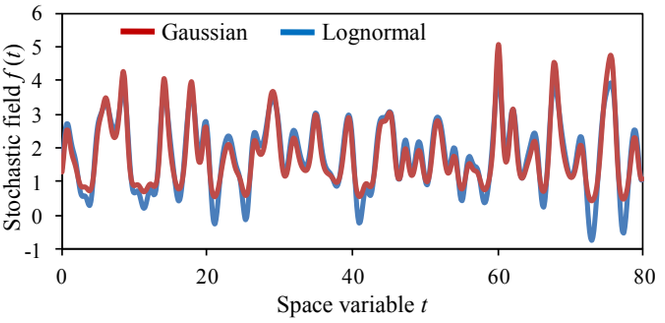


Figure 1 Comparison of Gaussian and lognormal stochastic fields assuming mean = 1.8, standard deviation = 1.0 and auto-correlation length parameter = 1.0

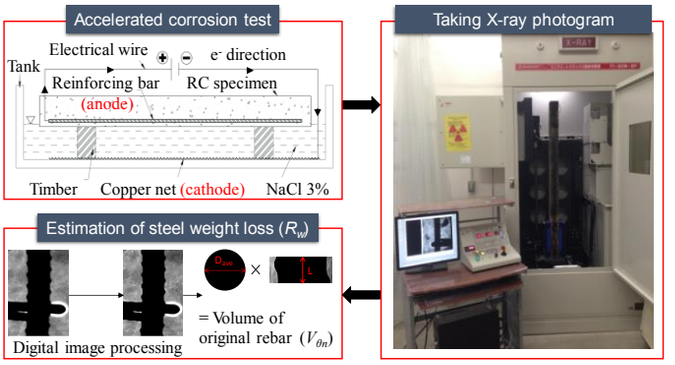


Figure 2 Procedure for estimating the steel weight loss in the corroded RC beam by X-ray and digital image processing

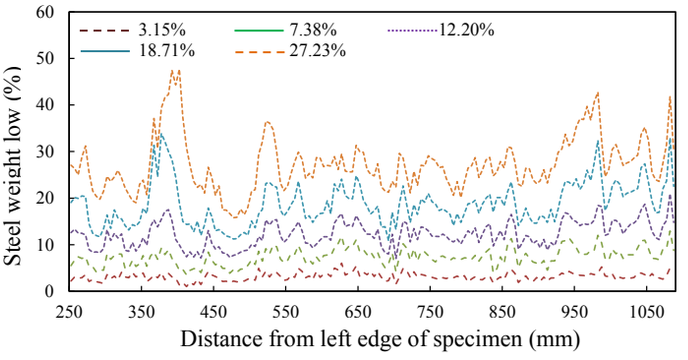


Figure 3 Example of relationship between steel weight losses along the length of the specimen

In addition, the Non-Gaussian stochastic field is simulated for the longitudinal steel weight loss according to the procedure presented by Shields et al. (2011).

Figure 1 shows an example of the one-dimensional Gaussian and lognormal stochastic fields.

2.2 *Spatial distribution associated with the steel weight loss in RC beam*

The parameters of the spatial distribution of the steel corrosion are calibrated based on the experimental results to visualize the steel corrosion distribution in RC specimens using X-ray techniques. These techniques have been applied to visualize the nonuniform steel corrosion distribution over the RC component.

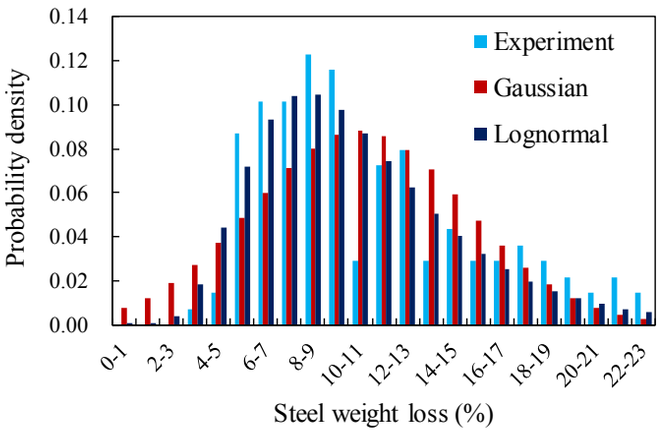


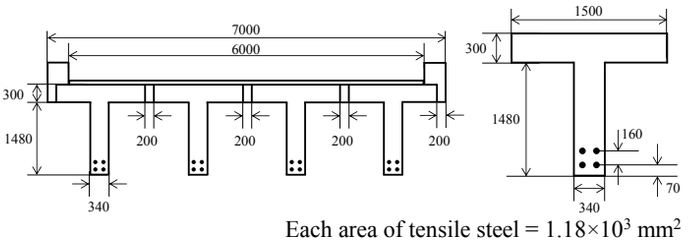
Figure 4 Probability density of steel weight loss

Figure 2 shows the procedure for estimating the steel weight loss of the corroded RC beam (Lim et al. 2016, 2017). The locations for taking X-ray image photograms of the RC beam corroded by electrical corrosion start from distances of 250 to 1090 mm with 14 times the 60 mm interval from the left side of the specimen. Figure 3 shows an example of the relationship between the distance from the left edge of a specimen and the local steel weight loss of the longitudinal rebar. The local steel weight loss was calculated by the volume of the sound rebar estimated by X-ray when $W_{xray,\,g}$ = 3.15%, 7.38%, 12.20%, 18.71%, and 27.23%, where $W_{xray,\,g}$ is the averaged steel weight loss of tensile rebar over the RC beam. Figure 4 shows the probability density of steel weight loss when the mean steel weight loss over the RC beam is 7.38%. It is confirmed that lognormal distribution has a better fit to the experimental data than Gaussian distribution. Therefore, a Non-Gaussian stochastic field is needed for the modeling of the spatial distribution associated with the steel weight loss.

In this paper, the spatial steel corrosion distribution based on experimental results shown in Figure 3 is used for estimating the parameters to reproduce the stochastic field independent of rebar diameter, water to cement ratio, concrete cover, and corrosion speed. Additional research is needed to investigate these effects on the statistics of the spatial variability of rebar corrosion. In addition, in this study, it is assumed that all longitudinal rebars have the same spatial variability of rebar corrosion. The corners in rectangular cross-sections can be more prone to corrosion. The spatial variability of steel corrosion in the transverse direction of RC components needs to be taken into consideration.

3 MODELING THE DETERIORATION OF PC GIRDERS DUE TO CHLORIDE ATTACK

Akiyama et al. (2010, 2012) proposed a probabilistic model for hazards associated with airborne chlorides by considering the spatiotemporal variation effects. The results of the hazard assessment associated with



Each area of tensile steel = 1.18×10^3 mm^2

Figure 5 Analyzed bridge girder (unit in mm)

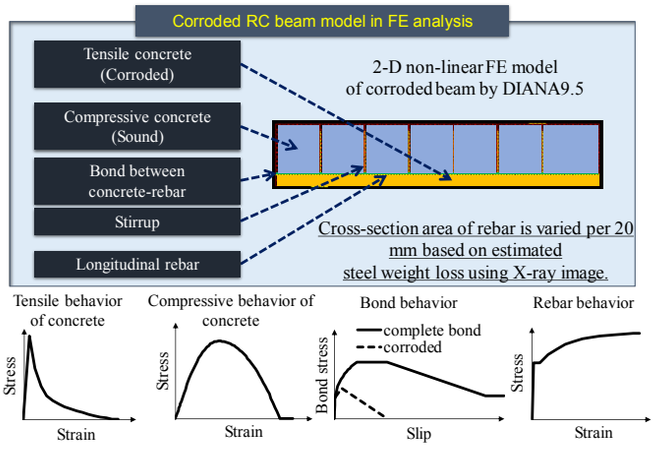


Figure 6 FE model and material constitutive model

airborne chlorides depend on the ratio of the sea wind, the wind speed at the analyzed location, and the distance from the coastline.

Using the hazards associated with airborne chloride, the steel weight loss MR_w (t) given the corrosion resulting from chlorides at time t is estimated using the following nine random variables.

x_1 : wind speed
x_2 : model uncertainty associated with attenuation of airborne chloride
x_3 : model uncertainty associated with relationship between airborne chloride and surface chloride concentration
x_4 : critical threshold chloride concentration at occurrence of steel corrosion
x_5 : model uncertainty associated with estimation by diffusion equation
x_6 : critical threshold of corrosion amount at crack initiation
x_7 : concrete cover
x_8 : steel corrosion rate before the occurrence of corrosion crack
x_9 : steel corrosion rate after the occurrence of corrosion crack

When representing the random fields, MR_w (t) is used as the mean in the Gaussian and non-Gaussian stochastic fields associated with the steel weight loss.

4 ILLUSTRATIVE EXAMPLE

4.1 *Description of PC girder and FE modeling*

Assuming that the PC bridge girder shown in Figure 5 has sufficient stirrups to prevent brittle failure, structural reliability associated with only flexural

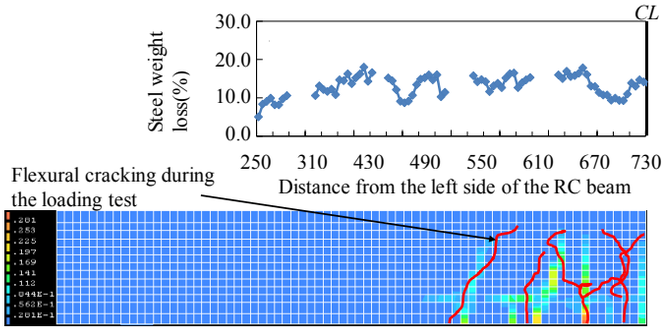


Figure 7 Comparison of contour of principal tensile strain, flexural cracking during the experiment and steel weight loss

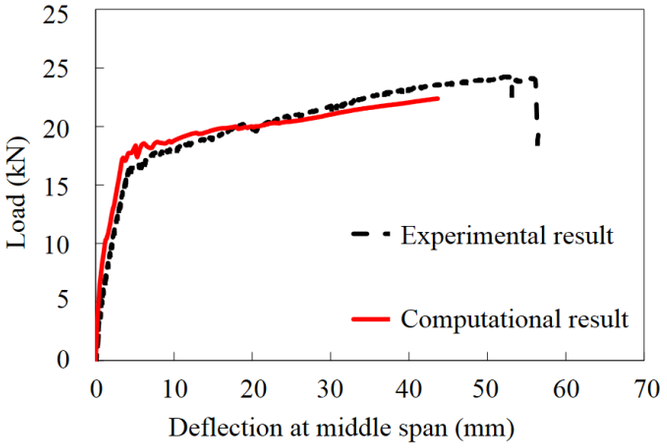


Figure 8 Comparison of computational and experimental results of the relationship between load and deflection

failure is estimated in this paper. Steel weight loss over the PC girder is represented by the discussed random field, simulated via SRM.

Based on the comparison of experimental and computational results, FE modeling of deteriorated concrete members has been investigated (Lim et al. 2016). Figure 6 shows the FE model and constitutive model of concrete in compression and tension, steel reinforcement, and bond stress-slip relationship. Based on the one-dimensional Gaussian and lognormal stochastic fields, the spatial variability associated with the reduced cross-sectional area of the rebar was modeled by varying the cross-sectional area in each steel truss element with a length of 20 mm (mid-point method). Since the expansion of the corrosion products caused the cracking and spalling of concrete, the concrete region that was damaged by corrosion exhibited a reduced performance compared to that of the undamaged concrete regions. The corrosion damage on the concrete cover was considered in the FE model by modifying the stress-strain relationship of the concrete, as suggested by Coronelli & Gambarova (2004). The residual bond stress-slip curve, as proposed by Kallias & Rafiq (2010), is used herein for the deteriorated steel concrete bond interface element, and the well-known bond stress-slip relation in CEB (1993) is used to model the perfect bond between steel and concrete.

It was confirmed that when the steel weight loss distribution in concrete members is obtained, the FE

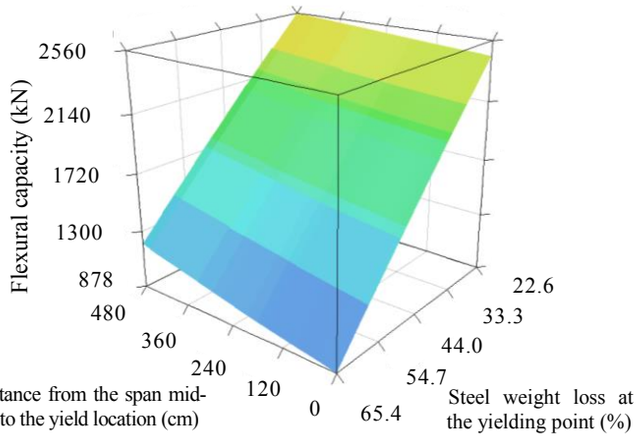


Figure 9 SRM used in the life-cycle reliability analysis

model could provide a better prediction of the flexural capacity of the corroded beams. Figure 7 shows the comparison of contour of the principal tensile strain obtained from the FE analysis, flexural cracking caused during the bending test, and steel weight loss. Figure 8 depicts the comparison of computational and experimental results of the relationship between load and deflection. Taking into consideration the actual steel weight loss of the corroded RC member, the FE model is in good agreement with the experimental results.

Using MCS with the FE analysis and SRM, life-cycle reliability of PC girders with randomly distributed steel weight loss can be estimated. However, the time required to repeat the FE analysis many times may be impractical. In this study, RSM is used to approximate the relation between the desired output of FE analysis and random variables (Okasha & Frangopol 2010, Liu et al. 2001, Frangopol et al. 2017). Figure 9 shows the RSM for obtaining the flexural capacity used in the life-cycle reliability analysis of PC girders.

4.2 *Estimation of moment due to the traffic load*

The critical flexural limit state for the PC girder is considered. Flexural resistance is compared with the bending moment due to dead and traffic loads. Following the computer simulation method of traffic load using the statistics of vehicles presented by Matsuzaki et al. (2010), the probabilistic density distribution of the bending moment is evaluated.

4.3 *Life-cycle reliability of PC girder*

The time-dependent failure probability of PC girder in a marine environment at the time $T = t$ after construction is estimated by

$$P_f(t) = \int_{0\%}^{100\%} \left\{ P\left(D_e > C_a \middle| MR_w = x\right) \cdot P\left(MR_w = x \middle| T = t\right) \right\} dx \quad (4)$$

where, $P\ (D_e > C_a \mid MR_w = x)$ is the conditional probability of exceedance of PC bridge girder capac-

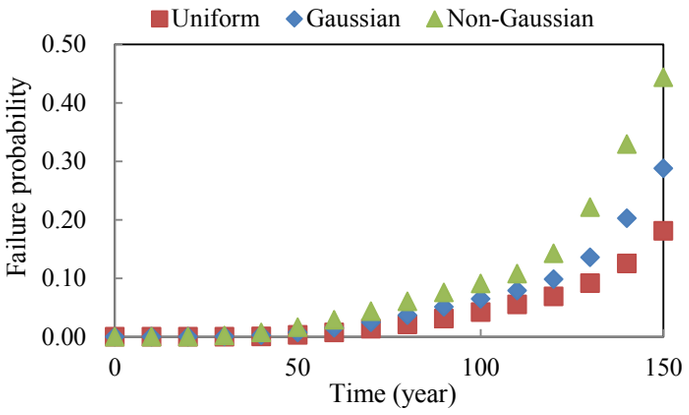


Figure 10 Time-dependent failure probability

ity C_a under traffic loading demand D_e, P ($MR_w = x|T = t$) is the conditional probability that MR_w is equal to x given $T=t$, and MR_w is the mean steel weight loss.

Figure 10 shows the effect of the different models of the steel weight loss distribution on the time-dependent failure probability of PC girder. Even if the global steel weight loss along the PC bridge girder is the same, the maximum local steel weight loss depends on the model of the spatial distribution. This result is in agreement with what found in other studies about non-uniform corrosion of steel beams (Christou & Bocchini 2014). The capacity C_a of a PC bridge girder assuming Gaussian and non-Gaussian stochastic fields simulated for the longitudinal steel weight loss could be smaller. Due to the tail difference between Gaussian and Non-Gaussian probability density functions, the failure probability assuming a non-Gaussian stochastic field is the largest as shown in Figure 10.

5 CONCLUSIONS

Life-cycle reliability of PC girder in a marine environment was estimated considering the spatial distribution of steel weight loss. RSM was included in the proposed life-cycle reliability formulations for improving the computational efficiency. Effect of the difference of modeling the steel corrosion distribution on the life-cycle reliability of PC girder was presented in the case study.

The results indicate that it is important to take into account the spatial variability of steel corrosion distributions.

ACKNOWLEDGMENTS

The authors would like to acknowledge Mr. Vasileios Christou for his help during the development of the random simulation algorithm.

REFERENCES

Akiyama, M., Frangopol, D. M., & Matsuzaki, H. 2014a. Reliability-based durability design and service life assessment of concrete structures in an aggressive environment. Chapter 1. In D.M. Frangopol & Y. Tsompanakis (Eds.), Maintenance and safety of aging infrastructure (pp. 1–26). London: CRC Press/Balkema, Taylor & Francis Group.

Akiyama M & Frangopol DM. 2014. Long-term seismic performance of RC structures in an aggressive environment: emphasis on bridge piers. *Structure and Infrastructure Engineering*, 10: 865-79.

Akiyama, M., Frangopol, D. M., & Suzuki, M. 2012. Integration of the effects of airborne chlorides into reliability-based durability design of reinforced concrete structures in a marine environment. *Structure and Infrastructure Engineering*, 8: 125-134.

Akiyama, M., Frangopol, D. M., & Yoshida, I. 2010. Time-dependent reliability analysis of existing RC structures in a marine environment using hazard associated with airborne chlorides. *Engineering Structures*, 32: 3768-3779.

Akiyama, M., Frangopol, D. M. & Takenaka, K. 2017. Reliability-based durability design and service life assessment of reinforced concrete deck slab of jetty structures, *Structure and Infrastructure Engineering*, 13: 468-477.

Akiyama, M. & Frangopol, D. M. 2013. Estimation of steel weight loss due to corrosion in RC members used on digital image processing of X-ray photogram. In: Strauss A, Frangopol DM, Bergmeister K, editors. Proceedings of the third international symposium on life-cycle civil engineering; life-cycle and sustainability of civil infrastructure systems. London: CRC Press/Balkema, Taylor & Francis Group plc; 1885-1891.

CEB. CEB-FIP model code 1990. Bulletin d'Information 213/214. Lausanne (Switzerland); 1993.

Christou, V. & Bocchini, P. 2014. An Efficient Methodology That Simulates a Multi-Dimensional Non-Gaussian Field to Evaluate the Effect of the Spatial Distribution of Corrosion in a Steel Beam. In Proceedings of the 2014 Structure Congress (G. Bell, M. A. Card eds.), ASCE, 1059-1069. DOI: 10.1061/9780784413357.094

Coronelli, D. & Gambarova, P. 2004. Structural assessment of corroded reinforced concrete beams: modelling guidelines. *Journal of Structural Engineering*, ASCE, 130: 1214-1224.

Kallias, A. N. & Rafiq, M.I. 2010. Finite element investigation of the structural response of corroded RC beams. *Engineering Structures*, 32:2984-2994.

Frangopol, D. M., Dong, Y. & Sabatino, S. 2017. Bridge life-cycle performance and cost: analysis, prediction, optimisation and decision-making, *Structure and Infrastructure Engineering*, 13: 1239-1257

Frangopol, D. M. 2011. Life-cycle performance, management, and optimization of structural safety under uncertainty: Accomplishments and challenges. *Structure and Infrastructure Engineering*, 7: 389–413.

Frangopol, D. M., Saydam, D., & Kim, S. (2012). Maintenance, management, life-cycle design and performance of structures and infrastructures: A brief review. *Structure and Infrastructure Engineering*, 8: 1-25.

Lim, S., Akiyama, M. & Frangopol, D.M. 2016. Assessment of the structural performance of corrosion-affected RC members based on experimental study and probabilistic modeling, *Engineering Structures*, 127: 189-205.

Lim, S., Akiyama, M., Frangopol, D.M. & Jiang, H. 2017. Experimental investigation of the spatial variability of the

steel weight loss and corrosion cracking of RC members: Novel X-ray and digital image processing techniques, *Structure and Infrastructure Engineering*, 13: 118-134.

Liu, D., Ghosn, M., Moses, F., and Neuenhoffer, A. 2001. Redundancy in Highway Bridge Substructures. National Cooperative Highway Research Program, NCHRP Report 458, Transportation Research Board, National Academy Press, Washington D.C.

Matsuzaki, H., Akiyama, M., Oki, F., Nakashima, K. & Suzuki, M. 2010. A method for structural reliability analysis of concrete beams under marine environment over lifetime and its application to pre-tensioned PC beams. Japan Society of Civil Engineers Journal E, 66: 147-165. (in Japanese)

Okasha, N.M., & Frangopol, D.M. 2010. Time-variant redundancy of structural systems. *Structure and Infrastructure Engineering*, 6: 279-301.

Papakonstantinou, K. G. & Shinozuka, M. 2013. Probabilistic model for steel corrosion in reinforced concrete structures of large dimensions considering crack effects. *Engineering Structures*, 57: 306-326.

Shields, M. D., Deodatis, G. & Bocchini, P. 2011. A simple and efficient methodology to approximate a general non-Gaussian stationary stochastic process by a translation process. *Probabilistic Engineering Mechanics*, 26(4): 511-519.

Shimomura, T., Saito, S., Takahashi, R., Shiba, A. 2011. Modelling and nonlinear FE analysis of deteriorated existing concrete structures based on inspection. In: Andrade C, Mancini G, editors. *Proceedings of the joint fib-RILEM workshop; modelling of corroding concrete structures*, Vol. 5. Dordrecht (Heidelberg, London, New York): Springer; 281-304 [RILEM book series].

Shinozuka, M. & Deodatis, G. 1996. Simulation of multidimensional Gaussian stochastic fields by spectral representation. *Applied Mechanics Reviews*, 49(1): 29-53.

Yanweerasak, T., Akiyama, M. & Frangopol, D.M. 2016. Updating the seismic reliability of existing RC structures in a marine environment by incorporating the spatial steel corrosion distribution: application to bridge piers, *Journal of Bridge Engineering*, ASCE, 21: 04016031-1-17.

Maintenance, Safety, Risk, Management and Life-Cycle Performance of Bridges – Powers, Frangopol, Al-Mahaidi & Caprani (Eds)
© 2018 Taylor & Francis Group, London, ISBN 978-1-138-73045-8

Optimum Strengthening Strategy for Deteriorating Reinforced Concrete Bridges

H. Baji & C.Q. Li
RMIT University, Melbourne, Australia

ABSTRACT: Corrosion of reinforcing steel in concrete is the one of the most predominant causes of deterioration in reinforced concrete (RC) bridges. This paper presents an optimal strengthening strategy for corrosion-affected RC bridges. By combining concepts of strengthening and maintenance optimization, an innovative strengthening strategy for structures strengthened by different methods such as FRP composites can be developed. Formulation of the proposed strategy is based on cost optimization. In this strategy, the optimum strengthening time and quantity of the strengthening material can be determined. Application of the proposed methodology is presented in a worked example for a corrosion-affected RC bridge girder strengthened with Fibre Reinforced Polymers (FRP) sheets. The paper concludes that the developed strategy can be a useful tool, which can assist asset managers in developing rehabilitation plan for deteriorated RC bridges under their management.
df

1 INTRODUCTION

Most of reinforced concrete (RC) structures are exposed to continuous deterioration from harsh environment such as exposure to chloride ions, carbon dioxide, sulphate dioxide, etc. This deterioration results in reduction of load carrying capacity leading to structures with service life shorter than the anticipated design life. For instance, in Australia, 30,000 bridges are approaching the end of their lifespan (Australian Local Government Association, 2013). Furthermore, these structures might become subjected to increasing demand during their operating lifetime. For instance, the demand for increasingly heavier truckloads is forcing bridge owners to upgrade the existing structures. One apparent solution to deal with deterioration and increasing demand is to replace the infrastructure. However, this is very costly if not impossible. The most viable and practical solution for maintaining safe operation of these structures is to restore and/or increase their capacity using strengthening schemes.

Due to their excellent mechanical and chemical properties, ease and efficiency of application and relatively low cost, strengthening using Fibre Reinforced Polymers (FRP) is emerging as an alternative to the traditional methods and is becoming an increasingly popular strengthening technique among researchers and practitioners worldwide. The effectiveness of FRP confinement in increasing the strength and structural performance is attributed to its ability to avoid or delay undesirable failure, such as, concrete crushing or longitudinal reinforcing bar buckling. FRP strengthening techniques have been used for flexural and shear strengthening of RC beams and slabs (Bonacci and Maalej, 2000, El Maaddawy et al., 2007, Capozucca, 2013, Al-Saidy et al., 2016, Xie and Hu, 2013) and strengthening of RC columns (Bae and Belarbi, 2009, El Maaddawy, 2008, Pantazopoulou et al., 2001, Wei et al., 2009). It has been shown that significant increase in strength and structural performance can be achieved using FRP strengthening.

There has been extensive research on methods of FRP strengthening for RC members. Nonetheless, strategies that determine the optimal required amount of FRP strengthening and more importantly the appropriate time to perform such an action have received less attention. Although various maintenance strategies in which optimum maintenance times are obtained can be found in the current literature (Akgül and Frangopol, 2005, Baji et al., 2017a, Barone et al., 2013, Mori and Ellingwood, 1994, Thoft-Christensen and Sorensen, 1987), in most of these strategies only the time of maintenance actions is optimized. In these studies, it

is assumed that after each maintenance action the structure is reinstated to its original condition without giving any details of how this is achieved. Furthermore, these strategies deal with repair of the structure rather than strengthening (Baji et al., 2017b).

In this paper, an optimal strengthening strategy for corrosion-affected RC bridges is presented. The optimal time for strengthening and amount of strengthening material are the output of the optimisation. Deterioration of strength is modelled as a stochastic process and the probability of structural failure is calculated using the first passage reliability method. In order to illustrate application of the proposed strategy, a numerical example of a corrosion-affected RC bridge girder strengthened with FRP composites is given.

2 METHODOLOGY

2.1 *Formulation of the strengthening strategy*

Due to corrosion, area of reinforcing steel is decreasing leading to strength loss, which in turns increases the probability of structural failure. In order to restore strength of structural RC members to an acceptable level, structural rehabilitation in terms of either repair or strengthening would be necessary. Nonetheless, strengthening of structural members does not stop the deterioration process, and even after repair or strengthening, the structure is still subject to deterioration. Major structural strengthening is generally a once in a lifetime action, which is intended to increase the structural strength so that it can meet the intended design service life. Therefore, service life of structure can be divided into pre and post-strengthening phases. Schematic strength degradation before and after strengthening is shown in Figure 1(a). In this figure, R_0 and R_a are the initial strength and the acceptable residual strength (beyond which structure is deemed to fail), respectively. From structural safety point of view, it is required to keep the probability of structural failure smaller than a predefined acceptable level for the whole service lifetime. The rationale for the proposed strategy is that, whilst keeping the probability of structural failure under control throughout its lifetime, the total expected cost, which is the sum of the expected cost of failure and cost of preventive strengthening action, is minimized. This concept is illustrated in Figures 1(b). p_f and p_a are the probability of failure and the acceptable probability of failure, respectively. As can be seen in Figure 1(b), the optimum repair time, t_p, is found in a way that before and after strengthening using FRP, the probability of failure, p_f, is less than the acceptable probability of failure, p_a. From this strengthening strategy, the optimal strengthening time and quantity of strengthening material can be determined.

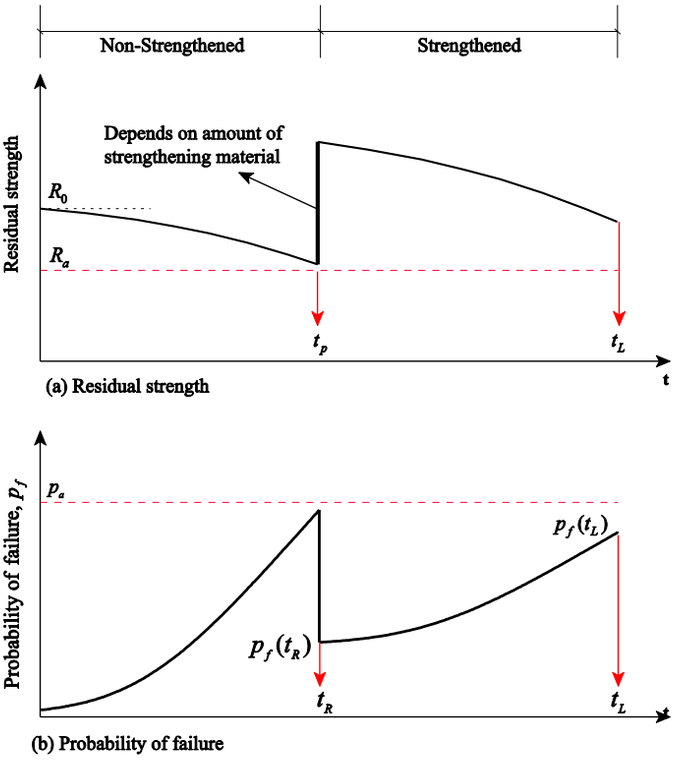


Figure 1. Degradation before and after strengthening

Referring to Figures 1(a and b), the optimum strengthening problem can then be mathematically formulated as follows,

$$\text{Minimize: } E(C_T) = E(C_R) + E(C_F) \quad (1a)$$

$$\text{Subject to: } p_f(t_R) \le p_a \,;\, p_f(t_L) \le p_a \quad (1b)$$

where, E denotes the expected value, t_R = strengthening time, t_L = predefined lifetime of the structure, C_T = total cost of maintenance, C_F = cost of failure and C_R = cost of repair and strengthening actions. Cost of repair includes cost of material required for strengthening, installation and indirect cost due to unavailability of the structure during repair. Cost of failure includes the direct cost of replacement as well as the indirect cost such as traffic delay. By having the unit cost of repair, c_r, and failure c_f, the cost terms in Equation 1a can be calculated as follows,

$$E(C_R) = c_r \quad (2a)$$

$$E(C_F) = c_f \left\{ E\left[N_F(0,t_R)\right] + E\left[N_F(t_R,t_L)\right] \right\} \quad (2b)$$

where $E[N_F]$ = expected number of failures. Using the annual discount rate all the costs are converted to the present cost. According to Equation 2b, the cost of failure is divided into two parts: before and after strengthening. These costs are two competing costs where by delaying the strengthening action time, t_R, the expected cost of

failure before strengthening increases, while the expected cost of failure after strengthening decreases. Combining these competing costs with the cost of strengthening action, results in the total expected cost for which a minimum point exists.

The design variables in the optimization problem defined in Equations 1a and 1b are the strengthening time, i.e., t_R and the amount of strengthening material, which determines the jump in the residual strength after strengthening [see Figure 1(a)]. The amount of strengthening also affects the expected number of failures after strengthening, i.e., $E[N_F(t_R, t_L)]$, in Equation 2b.

2.2 *Evaluation of expected number of failures*

The expected number of failures is a key factor in solving the proposed optimization problem. Assuming the structural system under ultimate strength as a renewable system, the renewal theory approach (Elsayed, 2012) can be used for calculating the expected number of failures. However, in the first passage probability method, the outcrossing rate, i.e., the rate at which the random process outcrosses a critical barrier or level can be used to evaluate the expected number of failures. The outcrossing rate can be interpreted as the expected number of failures per unit time (Ditlevsen and Madsen, 1996, Andrieu-Renaud et al., 2004). Having this rate, the probability of failure can also be calculated. This unique feature in the first passage probability method simplifies the optimization procedure, as by having only the outcrossing rate both the expected number of failures and the probability of failure can be determined.

For problems involving stochastic process of structural response, $S(t)$, the structural reliability depends on the time that is expected to elapse before the first occurrence of $S(t)$ outcrossing a critical level (the threshold) $R(t)$ sometime during a given time interval $[0, t]$. Under the assumption that the outcrossing events are independent, i.e., Poisson assumption, the outcrossing rate can be determined (Melchers, 1999). An analytical solution to Equation (5) has been derived in Firouzi et al. (2016) when $S(t)$ is a Gaussian process and the threshold $R(t)$ is deterministic. This is expressed as follows,

$$\nu_R^+ = \frac{\sigma_{\dot{S}|S}}{\sigma_S}\phi\left(\frac{R-\mu_S}{\sigma_S}\right)\times \left[\phi\left(\frac{R-\mu_{\dot{S}|S}}{\sigma_{\dot{S}|S}}\right)-\frac{\dot{R}-\mu_{\dot{S}|S}}{\sigma_{\dot{S}|S}}\Phi\left(\frac{\dot{R}-\mu_{\dot{S}|S}}{\sigma_{\dot{S}|S}}\right)\right] \quad (3)$$

where ν_R^+ is the outcrossing rate of the response process $S(t)$ relative to the threshold R, $\dot{R}$ is the slope of R with respect to time, $\dot{S}(t)$ is the time derivative process of $S(t)$. $\phi()$ and $\Phi()$ are standard normal density and cumulative distribution functions, respectively. μ and σ denote the mean and standard deviation, and "|" denotes the condition. For a given Gaussian stochastic process with mean function $\mu_S(t)$ and auto-covariance function $C_{SS}(t_i, t_j)$, all variables in Equation 3 can be determined (Papoulis and Pillai, 2002).

For stationary processes with deterministic barrier, the outcrossing event is a homogeneous Poisson process with a constant rate. In non-stationary random processes, on the other hand, the outcrossing event follows the non-homogeneous Poisson process with variable rate. The expected number of failures and the expected cost of failure considering the annual discount rate in the interval [0, t] are calculated by,

$$E\left[N_F(0,t)\right] = \int_0^t \upsilon_R^+(\tau)d\tau \quad (4a)$$

$$E\left[C_F(0,t)\right] = c_f\int_0^t \upsilon_R^+(\tau)\exp(-\gamma\tau)d\tau \quad (4b)$$

where γ = the annual discount rate. Equation 3 can be used for calculating the outcrossing rates.

2.3 *Evaluation of probability of failure*

The limit state can be formulated as follows,

$$G(R,S) = R(t) - S(t) \quad (5)$$

In the first passage probability method, the outcrossing events at which $G(R, S) < 0$ follow the Poisson distribution (homogeneous or non-homogeneous) with mean rate of υ_R^+. In the time-dependent reliability, the interest lies mainly in the time expected to elapse before the first outcrossing. The probability of the first occurrence of such an excursion is the probability of structural failure $p_f(t)$ during that time period. This is known as the "first passage probability" and under the assumption of Poisson processes it can be expressed as follows [e.g., Melchers (1999)],

$$p_f(t) = p_f(0) + \left[1-p_f(0)\right]\left(1-\exp(-\int_0^t \nu_R^+(\tau)d\tau)\right) \quad (6)$$

where $p_f(0)$ is the probability of structural failure at time $t = 0$. Since it is unlikely that the structural response exceeds a critical limit at the beginning of structural service, the probability of structural failure at $t = 0$ is zero, i.e., $p_f(0) = 0$.

3 APPLICATION

3.1 *Case study*

In order to illustrate application of the proposed strengthening strategy, a reinforced concrete bridge

girder is considered. The bridge is subjected to corrosion. In the considered strengthening scheme, an FRP strip is epoxy-bonded to the soffit of a degraded RC girder to enhance its bending capacity. It has been shown that by using this strengthening scheme, the ultimate flexural strength of RC sections can be enhanced by up to 100% of its original strength with considerable improvement in mitigating flexural cracks development (Saadatmanesh and Ehsani, 1990). It is assumed that the performed maintenance action does not affect level of steel corrosion rate, i.e., the rate of deterioration before and after the strengthening action is the same. However, after FRP strengthening, in addition to reduction in the reinforcement area, deterioration of the FRP material also contributes to strength degradation. In order to consider different environmental conditions, which govern amount of damage done to the reinforcement and consequently to the overall strength of RC girder, variety of corrosion rates represented by the corrosion current density ranging from 1.0-4.0 $\mu A/cm^2$ is considered.

For the purpose of illustration, height, h, and width, b, of 1000 mm and 400 mm are assumed for the RC beam girder, respectively. The width of the external FRP sheet attached to the soffit of the girder, b_f, and number of FRP layers are treated as the optimisation variables of strengthening strategy. The thickness of one layer FRP is 1.2 mm. Reinforcing steel bars with a 25 mm diameter with reinforcement percentage of 1% are embedded into RC girders with an average cover thickness of 100 mm, as is shown in Figure 2.

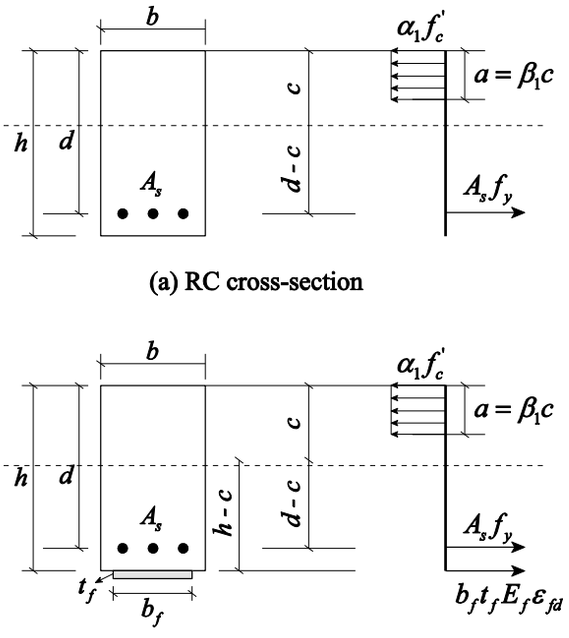


Figure 2. Geometry of RC girder cross-section

Preventive maintenance, which includes repair and strengthening in this study, is a maintenance action that only requires minimal repair as well as strengthening. It is generally known that the total cost associated with failure is greater than that associated with a preventive maintenance, i.e., the cost of maintaining a structural system before its failure is lower than the cost of maintaining it after failure (Elsayed, 2012). The failure and preventive costs of an RC structure include direct costs such as material, labour cost, and some other indirect cost, e.g., traffic delay cost in bridge structures. In this study, a sensitivity analysis by considering a range of c_f/c_r ratio is carried out. The strengthening strategy is designed for a 100 years lifetime. A discount rate, γ, of 2% is used in the optimisation.

The flexural failure of the cross-section is considered as the dominant failure mode. Therefore, the structural strength, R, is the flexural strength. Li (2003) suggested taking the limit of 70% of the original strength, i.e., $R_a = 0.70 \times R_0$ as the acceptable level of residual strength. This value is considered as a deterministic variable in this study. Therefore, the limit state used in the time-dependent reliability analysis can be formulated as follow,

$$G = 0.70R_0 - R(t) \tag{7}$$

where R_0 is the initial strength. With treatment, the residual strength, $R(t)$, is taken as the random process and the $0.70R_0$ is considered as the acceptable resistance. Formulation of the limit state in Equation 7 is similar to that shown in Equation 5. This problem mathematically represents a down crossing problem and its solution is the same as that of outcrossing, when the problem is looked at "upside-down". The acceptable probability of failure, p_a, is taken as 0.01.

3.2 *Strength degradation*

Strength of under-reinforced RC beam sections occurs due to crushing of concrete in the compressive side, i.e., when maximum compressive strain in this zone reaches the ultimate strain capacity of concrete, of the cross-section. At this state, the reinforcement has already yielded. The ultimate flexural strength of the cross-section, used as R in the limit state, can be evaluated as follows,

$$M_{u,RC} = A_s f_y \left(d - \frac{a_{RC}}{2} \right) \tag{8a}$$

$$a_{RC} = \frac{A_s f_y}{\alpha_1 \beta_1 f_c' b} \tag{8b}$$

where α_1 and β_1 = the equivalent rectangular stress block parameters, b = cross-section width, A_s = reinforcement area, f'_c = compressive strength of concrete and f_y = yield strength of reinforcing steel.

On the other hand, failure of an FRP-strengthened RC cross section is most likely to occur either by crushing of the concrete in the compression zone or by debonding of the FRP sheet from the RC girder. There are other possible failure modes such as concrete cover separation and plate end interfacial debonding (Ceci et al., 2012). However, here, it is assumed that the FRP reinforcement is anchored at its ends so that such failures do not occur. Debonding dominates when the strain at the interface of concrete and FRP reaches a limiting value, ε_{fd}, which is generally less than the ultimate strain in an FRP coupon determined from a direct tension test, ε_{fu}. The model chosen for this study is based on a fracture mechanics approach, which is adopted by the ACI 440.2 (2008) guidelines. In this model, the tensile strain at which debonding initiates can be calculated as,

$$\varepsilon_{fd} = 0.41\sqrt{\frac{f_c^{'}}{E_f t_f}} \le 0.90\varepsilon_{fu} \quad (9)$$

where E_f and t_f are the young's modulus and thickness of the FRP sheet and f'_c is the compressive strength of concrete. The ultimate flexural strength of RC cross-section strengthened with FRP sheet with width of b_f and thickness of t_f can be determined as follow,

$$M_{u,FRP} = A_s f_y\left(d - \frac{a_{FRP}}{2}\right) + b_f t_f E_f \varepsilon_{fd}\left(h - \frac{a_{FRP}}{2}\right) \quad (10a)$$

$$a_{FRP} = \frac{A_s f_y + b_f t_f E_f \varepsilon_{fd}}{\alpha_1 \beta_1 f_c^{'} b} \quad (10b)$$

Due to the corrosion process, the rebar area and consequently, the structural strength decrease over time. Because of material degradation, reinforcement area and mechanical properties of the FRP material deteriorate over time. Using material degradation models for physical corrosion and FRP properties available in the literature, the residual cross-sectional strength can be determined by employing standard concrete design codes [e.g., ACI 318 (2014)]. The remaining reinforcement area, A_{net}, can be calculated as follows,

$$A_{net}(t) = \left(1 - \frac{0.0232 i_{corr} t}{d_b}\right)^2 A_s \quad (11)$$

where d_b and A_s are the diameter and cross-sectional area of the original rebar. i_{corr} is the corrosion current density and t is time since corrosion initiation in years. Degradation model for mechanical properties of FRP material is taken from Karbhari and Abanilla (2007) study and can be expressed as follows,

$$\sigma_{fu,net}(t) = \left[1 - 0.0337\ln(365t)\right]\sigma_{fu} \quad (12a)$$

$$E_{f,net}(t) = \left[1 - 0.0042\ln(365t)\right]E_f \quad (12b)$$

where σ_{fu} and E_f are the original ultimate strength and modulus of elasticity of the FRP sheet and $\sigma_{fu,net}$ and $E_{f,net}$ are the remaining ultimate strength and modulus of elasticity.

Table 1 shows the probabilistic models for basic random variables used for finding statistics of the residual strength over time. The probabilistic models for section dimensions are from Nowak & Szerszen (2003) study. The probabilistic model for concrete compressive strength is based on Bartlett and MacGregor (1996) study. For yield strength of reinforcement, the model proposed by Bournoville et al. (2004) is used. For FRP mechanical properties, models from Atadero & Karbhari (2008) are used. In this table, δ shows the model error in evaluating the flexural strength of RC girder. The probabilistic model is taken from Baji et al. (2016) study. It is assumed that the model error for RC and FRP-strengthened cross-section is the same.

Table 1. Probabilistic models of basic variables

Variable	Nominal	Bias*	COV**	Distribution
b mm	400	1.00	0.02	Normal
d mm	900	1.00	0.04	Normal
f'_c MPa	32	1.20	0.18	Lognormal
A_s	$0.01bd$	1.00	0.02	Normal
f_y MPa	518	1.12	0.05	Beta
t_f mm	1.20	1.00	0.05	Lognormal
σ_{fu} MPa	887	1.17	0.15	Weibull
E_f GPa	64.9	1.00	0.20	Lognormal
δ	1.00	1.00	0.12	Lognormal
i_{corr}, $\mu A/cm^2$	1.0-4.0	0.50	0.58	Uniform

* Bias = Mean/Nominal

** COC = Coefficient of Variation

Using the Monte Carlo simulation technique, with 50,000 runs, statistics of the strength process, i.e., mean and standard deviation, are determined.

3.3 *Results*

If the remaining lifetime is longer than the specified service lifetime of the structure, no strengthening is required. Otherwise, strengthening is required. Based on the assumptions made for the considered case study, remaining lifetime of the RC girder considering the ultimate limit state shown in Equation 7 can be predicted.

Figure 3 shows the probability of failure over time considering different corrosion rates. The predicted lifetime is based on the acceptable

probability of 0.01. Considering the specified lifetime of 100 years, for all the assumed corrosion rates except the low corrosion rate (i_{corr} = 1.0 μA/cm^2) the remaining lifetime of the considered RC girder is less than the specified 100-year service life. Therefore, strengthening action within service life of the structure is not required.

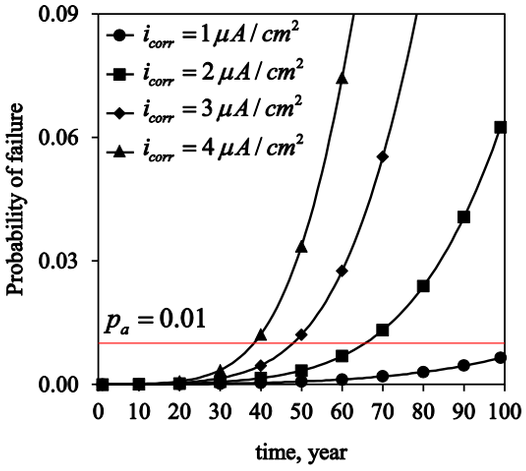


Figure 3. Probability of failure for different corrosion rates

In order to find the solution to the formulated optimized strengthening strategy, a generic computer code was programmed. The Genetic Algorithm method was used to minimize the cost function defined in Equations 1a, b. For the considered case study with i_{corr} = 2 μA/cm^2, c_f/c_r = 100 and γ = 0.02 the result of optimization is shown. Any strengthening action within this feasible time satisfies the two constrains shown in Equation 1b. As Figure 4(a) shows, after around 58 years, residual strength of the considered RC girder decreases to an unaccepted level, i.e., the probability of failure becomes less than the acceptable probability of failure, p_a, [see Fig. 4(b)]. By applying one layer of FRP with 135 mm width, the strength is restored [see Figure 4(a)]. The optimum time corresponds to minimum expected cost during the whole life of structure as is shown in Figure 4(c). Figure 4(b) shows that in the whole service life of the structure, probability of structural failure does not exceed the assumed acceptable level (0.01 in this example).

For higher deterioration rates, i.e., higher corrosion rates, in order to keep the structure in the safe region, more FRP layers are required. To investigate the effect of the corrosion rate represented as the corrosion current density i_{corr} on optimum strengthening time and number of required FRP layers, various values of the corrosion current density ranging from 2.0 to 4.0 μA/cm^2 corresponding to low-to-high corrosion intensities are examined. The result is shown in Figure 5. As is expected, for high corrosion rates, earlier strengthening action with higher number of FRP layers is required. Furthermore, with increasing the corrosion rate, the expected number of failures increases and, as such, the total expected cost goes up. Nonetheless, the optimum cost is in the same range, as for higher corrosion rates more FRP material is used.

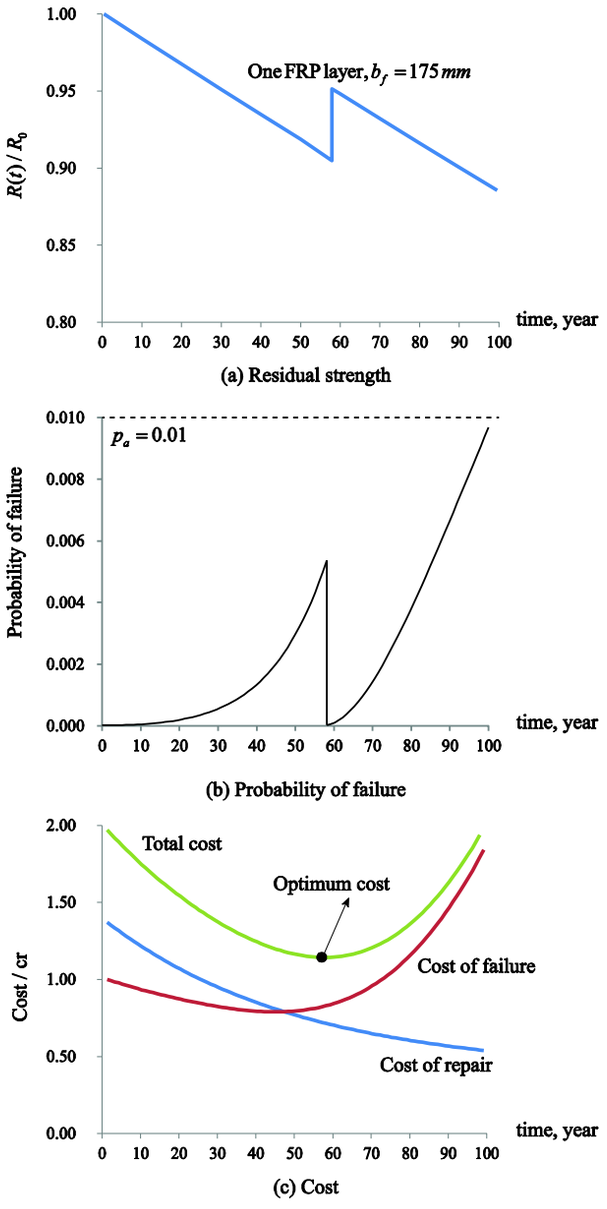


Figure 4. Optimum strengthening strategy for i_{corr} = 2 μA/cm^2

Figure 6 shows the influence of the unit cost of failure c_f on the optimal strengthening time, where the cost of failure ranges from $c_f = 50c_r$ to $200c_r$. In this case, the corrosion current density is 2 μA/cm^2 and the discount rate is assumed 2% in the calculations. It can be seen that the value of the optimal strengthening time decreases when the cost of failure goes up. In the case with a lower cost of failure, the optimal strengthening time can be delayed, and lower total cost is expected. Furthermore, for higher cost of failure more FRP material is required.

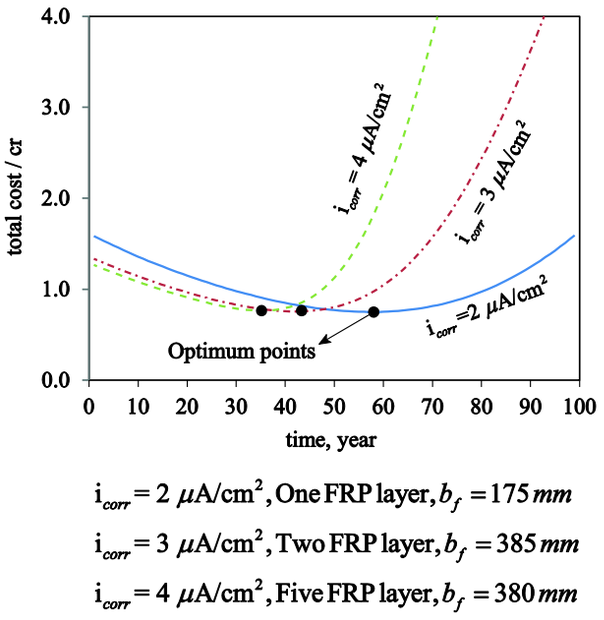


Figure 5. Effect of different corrosion rates

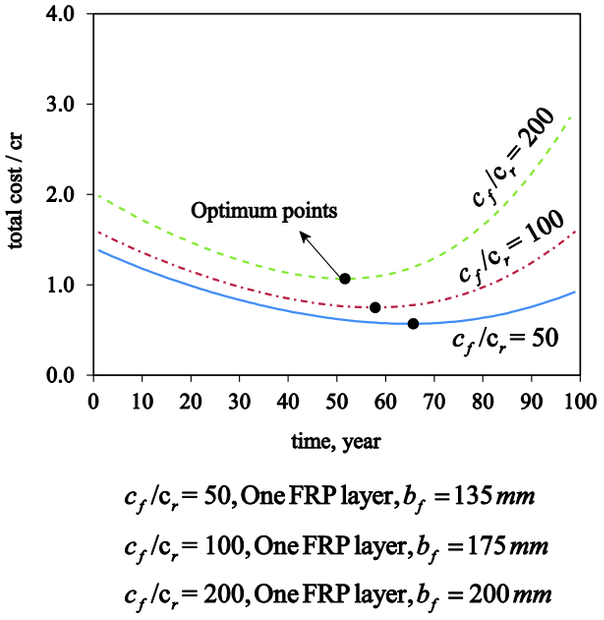


Figure 6. Effect of different costs of failure

In order to make an informative decision on strengthening of an RC structure with FRP composites, wide range of environmental and economic factors need to be considered. Outcome of the strengthening strategy should cover all the possible scenarios. Using results of the strengthening action and based on the available information at any time, decision makers can decide on the right strengthening strategy.

4 CONCLUSION

In this paper, a methodology for optimal strengthening strategy for RC bridges has been proposed. With this strategy, the optimum time for strengthening and required amount of strengthening in terms of number and width of FRP sheets can be optimized based on minimization of total expected cost. The developed strategy incorporates time-dependent reliability analysis in which the structural deterioration is modelled as a stochastic process and the probability of structural failure is calculated with advanced outcrossing method. An example of a corrosion-affected RC bridge girder strengthened with FRP composites is provided to illustrate the application of the developed strategy. It has been found in the paper that the proposed methodology can determine the optimum strengthening time and amount of FRP strengthening, i.e., number and width of required FRP layers efficiently. It has also been found that the deterioration rate represented by the corrosion current density and the cost of failure are the key factors in determining the number of required FRP layers. It can be concluded that the developed strategy can equip structural engineers and asset managers with a useful tool for effective strengthening of deteriorated structures in the management of vast asset of deteriorating bridges.

5 ACKNOWLEDGEMENT

Financial support from Metro Trains Melbourne, Australia and Australian Research Council under DP140101547, LP150100413 and DP170102211is gratefully acknowledged.

6 REFERENCES

ACI 318 2014. Building Code Requirements for Structural Concrete and Commentary. Farmington Hills, MI, USA: American Concrete Institute.

ACI 440 2008. Guide for the design and construction of externally bonded FRP systems for strengthening concrete structures. Farmington Hills, MI, USA American Concrete Institute.

Akgul, F. & Frangopol, D. 2005. Lifetime Performance Analysis of Existing Reinforced Concrete Bridges. I: Theory. *Journal of Infrastructure Systems* 11 (2): 122-128.

Al-Saidy, A., Saadatmanesh, H., El-Gamal, S., Al-JabriI, K. & Waris, B. 2016. Structural behavior of corroded RC beams with/without stirrups repaired with CFRP sheets. *Materials and Structures* 49 (9): 3733-3747.

Andrieu-Renaud, C., Sudret, B. & Lemaire, M. 2004. The PHI2 method: a way to compute time-variant reliability. *Reliability Engineering & System Safety* 84 (1): 75-86.

Atadero, R. A. & Karbhari, V. M. 2008. Calibration of resistance factors for reliability based design of externally-bonded FRP composites. Composites Part B: Engineering, 39 (4): 665-679.

Australian Local Government Association. 2013. *Bridges to a Stronger Future* [Online]. Available: http://apo.org.au/node/36517 [Accessed].

Bae, S. & Belrabi, A. 2009. Effects of Corrosion of Steel Reinforcement on RC Columns Wrapped with FRP Sheets.

Journal of Performance of Constructed Facilities, 23 (1): 20-31.

Baji, H., Ronagh, H. & Melchers, R. 2016. Reliability of ductility requirements in concrete design code. *Structural Safety* 62 (2016): 76-87.

Baji, H., Li, C.Q., Scicluna, S., & Dauth, J. 2017a. Risk-cost optimised maintencne strategy for tunnel structures. *Tunneling and Undergound Space Technology* 69 (2017): 72-84.

Baji, H., Yang, W. & Li, C.Q. 2017b. An Optimum Strenghening Strategy for Corrosion-Affected Reinforced Concrete Structures. *ACI Structural Journal* 114 (6): 1-12.

Barone, G., Frangopol, D. M. & Soliman, M. 2013. Optimization of life-cycle maintenance of deteriorating bridges with respect to expected annual system failure rate and expected cumulative cost. *Journal of Structural Engineering,* 140 (2): p.04013043.

Bartlett, F. M. & MacGregor, J. G. 1996. Statistical analysis of the compressive strength of concrete in structures. *ACI Materials Journal* 93 (1996): 158-168.

Bonacci, J. F. & Maalej, M. 2000. Externally bonded fiber-reinforced polymer for rehabilitation of corrosion damaged concrete beams. *ACI Structural Journal* 97 (5): 703-711.

Bournoville, M., Dahnke, J. & Darwin, D. 2004. Statistical analysis of the mechanical properties and weight of reinforcing bars. Lawrence, KS: University of Kansas Center of Research.

Capozucca, R. 2013. Assessment of CFRP strengthened RC beams through dynamic tests. *Composites Part B: Engineering* 46 (2013): 69-80.

Ceci, A. M., Casas, J. R. & Ghosn, M. 2012. Statistical analysis of existing models for flexural strengthening of concrete bridge beams using FRP sheets. *Construction and Building Materials* 27 (1): 490-520.

Ditlevsen, O. & Madsen, H. O. 1996. *Structural* reliability *methods*, Wiley New York.

El Maaddawy, T. 2008. Post-repair performance of eccentrically loaded RC columns wrapped with CFRP composites. *Cement and Concrete Composites* 30 (9): 822-830.

El Maaddawy, T., Soudki, K. & Topper, T. 2007. Performance evaluation of carbon fiber-reinforced polymer-repaired beams under corrosive environmental conditions. *ACI Structural Journal* 104 (1): 3-11.

Elsayed, E. A. 2012. *Reliability Engineering*, John Wiley & Sons.

Firouzi, A., Yang, W. & Li, C.Q. 2016. An efficient solution for calculation of upcrossing rate of non-stationary Gaussian process. *ASCE Journal of Engineering Mechanics* (Accepted paper).

Karbhari, V. M. & Abanilla, M. A. 2007. Design factors, reliability, and durability prediction of wet layup carbon/epoxy used in external strengthening. *Composites Part B-Engineering* 38 (1): 10-23.

Li, C.Q. 2003. Life cycle modeling of corrosion affected concrete structures-initiation. *ASCE Journal of Materials in Civil Engineering* 15 (6): 594-601.

Li, C.Q., Ian Mackie, R. & Lawanwisut, W. 2007. A Risk-Cost Optimized Maintenance Strategy for Corrosion-Affected Concrete Structures. *Computer-Aided Civil and Infrastructure Engineering* 22 (5): 335-346.

Melchers, R. E. 1999. *Structural reliability analysis and* prediction*,* New York, John Wiley & Sons.

Mori, Y. & Ellingwood, B. R. 1994. Maintaining reliability of concrete structures. II: Optimum inspection/repair. *Journal of Structural Engineering* 120 (3): 846-862.

Nowak, A. S. & Szerszen, M. M. 2003. Calibration of design code for buildings (ACI 318): Part 1- Statistical models for resistance. *ACI Structural Journal* 100 (3): 377-382.

Pantazopoulou, S., Bonacci, J., Sheikh, S., Thomas, M. & Hearn, N. 2001. Repair of Corrosion-Damaged Columns with FRP Wraps. *Journal of Composites for Construction* 5 (1): 3-11.

Papoulis, A. & Pillai, S. U. 2002. *Probability, random* variables*, and stochastic processes*, McGraw-Hill

Saadatmanesh, H. & Ehsani, M. 1990. Fiber composite plates can strengthen beams. *Concrete International* 12 (3): 65-71.

Thoft-Christensen, P. & Sorensen, J. D. 1987. Optimal strategy for inspection and repair of structural systems. *Civil Engineering Systems* 4 (2): 94-100.

Wei, H., Wu, Z., Guo, X. & YI, F. 2009. Experimental study on partially deteriorated strength concrete columns confined with CFRP. *Engineering Structures* 31 (1): 2495-2505.

Xie, J.-H. & Hu, R.-L. 2013. Experimental study on rehabilitation of corrosion-damaged reinforced concrete beams with carbon fiber reinforced polymer. *Construction and Building Materials* 38 (2013): 708-716.

Maintenance, Safety, Risk, Management and Life-Cycle Performance of Bridges – Powers, Frangopol, Al-Mahaidi & Caprani (Eds)
© 2018 Taylor & Francis Group, London, ISBN 978-1-138-73045-8

Strengthening of Reinforced Concrete Bridges by External Prestressing

L. H. B. Pinheiro, L. M. Trautwein & L. C. Almeida
University of Campinas - UNICAMP, FEC - SP, Brazil

ABSTRACT: The lack of maintenance along with the increase of the weight of (Brazilian) road vehicles require the strengthening of bridges in Brazil. Rehabilitation techniques and structural reinforcement can make this strengthening technically and financially viable. However, since there are no specific rules on how to carry out this type of analysis in Brazilian bridges, or procedures for the calculation of specific reinforcements, several methods are not considered while choosing the type of structural reinforcement, and neither the right efforts are taken for a proper assessment. This work studies the flexural reinforcement of structures in reinforced concrete by external prestressing, exposing advantages and disadvantages of its use and the characteristics of this reinforcement method. Finally, a calculation methodology is proposed employing a theoretical example of structural reinforcement of an old Brazilian bridge by external prestressing with the use of lubricated steel wire ropes, reinforced concrete deviators and anchor blocks. In order to base the calculation the rules of the bridge project were used to find the project efforts and the existing steel area. Based on the current standards and the bridge expansion project, new efforts were determined on the main beams. Considering these new efforts and the existing steel area, the necessary prestressing steel area was determined so that along with the existing passive steel rebars the bridge can withstands the new traffic conditions

1 INTRODUCTION

Due to market demands, freight vehicles often carry a very heavy weight, previously considered as rare or impossible for a single truck. The bridges over which these vehicles travel may be exposed to strains higher than those assumed in the original project, calculated in line with the standards of the period when the construction took place.

Old bridges were submitted to different types of forces and exposed to bad weather conditions which along with the lack of maintenance leads to the development of defects, which can corrode the reinforcement, wear out the concrete and cause various anomalies, reducing the strength of the bridge as well as its expected utility.

The greater amount of cars on the highways demand the expansion of the roads and also the bridges that are part of these roads.

The expansion of freight vehicles, the increase in weight of freight vehicles and the reduction of the original strength of the bridges, requires the reinforcement of their structure in order to increase their capacity to resist tensions and to safely support new working conditions.

Out of the various existing techniques of structural reinforcement, the prestressing of the main beams by external cables anchored to them can function as a competitive alternative taking account the implantation of the bridge in traffic, material savings and efficiency in increasing resistance.

2 OBJECTIVES

The objective of this work is to exemplify a methodology for the analysis of the structural reinforcement by external prestressing of a theoretical Brazilian bridge, calculated with old norms and assuming that there will be a need of amplification, besides the adequacy of the resistance for the design loads suggested in the current norms.

3 ADVANTAGES AND DISADVANTAGES

A single external cable system can be used to reinforce multiple stresses simultaneously, such as positive and negative bending moments and shear stresses, due to cable tilt and compression effect. Other advantages can be cited:

- Less amount of concrete used, since it eliminates the need to thicken the entire element;
- Reduction of formwork and shoring;
- Low weight added to existing structure;
- Less frictional prestress losses due to the use of lubricated steel wire ropes;
- Easy determination of the eccentricity between applied forces and the center of gravity, since the fixing of deviator and anchor blocks are at determined heights;
- The main beams can be reinforced with the bridge in traffic;
- It is not necessary to correct deformations before structural reinforcement;
- Possibility of maintenance and exchange of lubricated wire ropes;

• Better distribution of bending moments and shearing forces along the hyperstatic beams (SOUZA & RIPPER 1998);
• Decrease of deformations;
• In a bridge widening, this reinforcement may exempt the need for additional beams;
• Prestressing equipment are lightweight, making it easier to use at heights. (ALMEIDA 2001);

Even with so many advantageous features, some aspects must be observed when considering this type of structural reinforcement. Among them, we can highlight:
• Unconventional equipment and techniques, require specialized labor;
• Requires high corrosion protection especially on anchorages and deviators;
• The reinforcement is externally exposed, allowing impacts or fire action;
• Failure at one point ends up disabling the entire reinforcement cable;
• The difficulty in the execution of reinforced concrete anchor and deviator blocks, as well as drilling the existing beams might make this type of reinforcement unfeasible;
• The weight of the deviator and anchor blocks in concrete should be considered in the structural calculation;
• There may be a relevant second-order effect due to the eccentricity between the structural displacements and the non-adherent prestressing cable;
• The introduction of the prestressing force can be damaging to the low compressive strength concrete, especially at points of stress concentration (deflectors and anchorage);
• We need to calculate the hyperestatic prestressing efforts;

4 MAIN COMPONENTS OF THE SYSTEM

This technique consists of anchoring cables externally to the structure at its ends and then prestressing them, and there may be deviations in its trajectory by deviator blocks. The rectilinear cable with deviations is called polygonal, widely used for external prestressing, where the cables are free from contact with the structure, except for the anchorage and deviator regions, where they introduce forces of opposite direction to the requests, as shown in Figure 1.

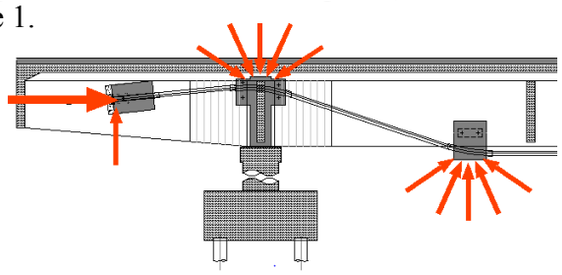


Figure 1. Forces from the external prestressing

Firstly, the elements for anchoring and diverting cables are installed. These anchors and deflectors may be metallic, as in Figure 2 or in reinforced concrete as shown in Figure 3, but cross girders and other elements of the structure can be used for this purpose.

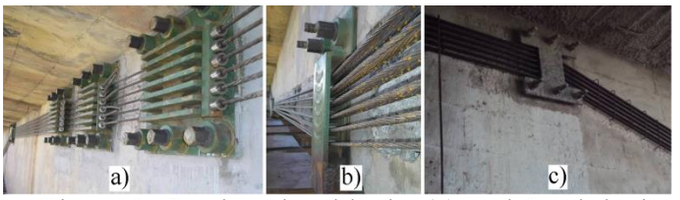


Figure 2. Steel anchor blocks (a) and Steel deviator blocks (b), (c).

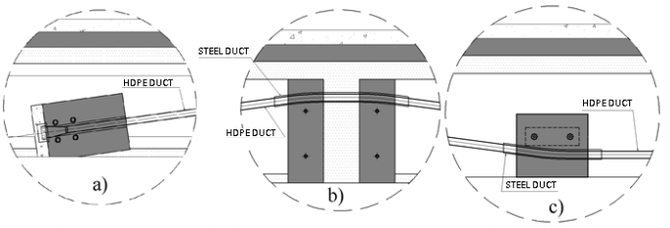


Figure 3. Reinforced concrete anchor blocks (a) and deviator blocks (b), (c).

Non-adherent prestressing cables consist of lubricated wire ropes coated by high-density polyethylene (HDPE). To increase the tensile strength, several of these may be joined within a duct, such as that of Figure 4, which is filled internally with epoxy resin or cement paste.

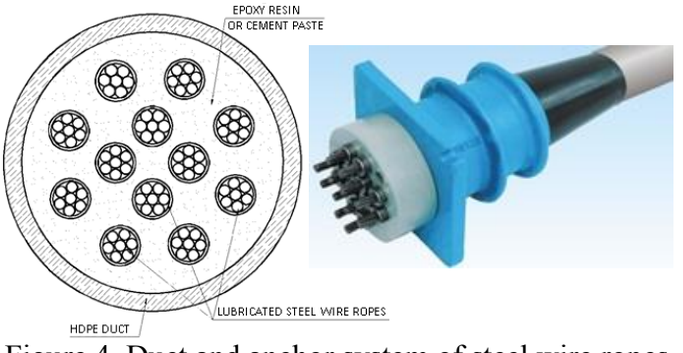


Figure 4. Duct and anchor system of steel wire ropes

This system, which is widely used in reinforcements by external prestressing, has several advantages such as protection against ultraviolet rays due to HDPE, against corrosion due to grease, possibility of replacing, controlling and maintaining internal cables during the life of the bridge.

5 THEORETICAL EXAMPLE

In order to exemplify this technique of flexural reinforcement of main beams, we will analyze a typical situation in which a bridge built in the late 1970s must be expanded, but we do not have its original design. After an inspection of the bridge we obtain the mechanical characteristics of the existing concrete as well as the geometry of the bridge.

Structural analysis is done with this information, based on the norms valid in design period, by calculating the forces for which the bridge was originally projected, then the reinforcement is calculated, ensuring that it withstands the forces of the enlarged bridge, which will be verified by the current norms.

5.1 *Bridge characteristics*

The fictitious bridge analyzed has span of 20 m, and longitudinal beams supported on the mesostructure. It is a typical structural system of this period (DNIT 2004) in two reinforced concrete girders and 5 cross girders.

The total width of the cross section is 10 m, 830 cm of traffic lanes. There is no protection between the lane and the sidewalks, only guardrails protect bridge cross section ends.

This bridge was designed to withstand the 360 kN of a vehicle with load, in line with the old NB-6 1960.

Figures 5 and 6 show the design of the original bridge.

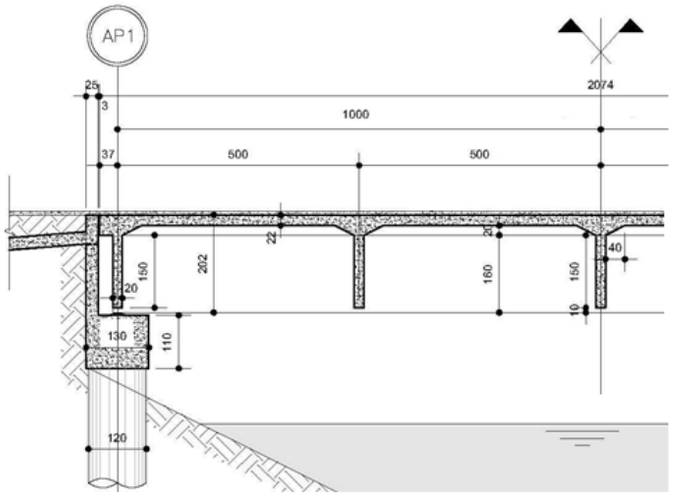


Figure 5. Longitudinal half elevation (dimensions in cm)

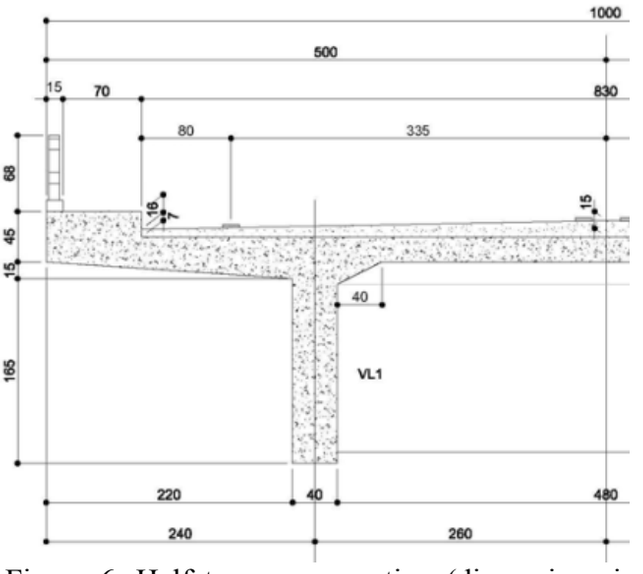


Figure 6. Half transverse section (dimensions in cm)

The enlarged bridge will have the characteristics of Figure 7, with 11,30 m of total width, being 10,50 m of traffic lane and must withstand the 450 kN of vehicle with load (NBR 7188, 2013).

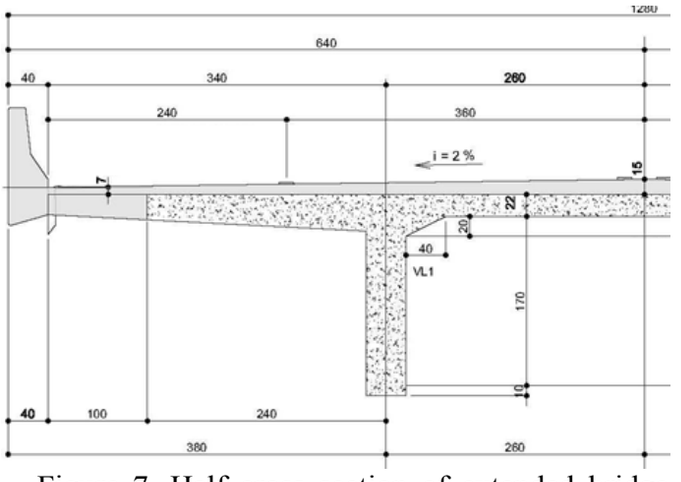


Figure 7. Half cross section of extended bridge (dimensions in cm)

5.2 *Structural analysis of the old bridge*

The original dead loads were determined by the geometry of the elements detailed by the bridge inspection, resulting in the forces of Figure 8

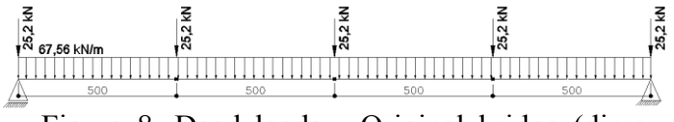


Figure 8. Dead loads - Original bridge (dimensions in cm)

For the vehicular live loads of the project, we used the old standard of bridges and road loads, NB-2 of 1961 and NB-6 of 1960, which considers the standard vehicle of 360 kN weight.

This vehicle and the distributed load is placed on the most unfavorable position for each girder, that results in the static load scheme of Figure 9 for the most requested beam (calculated by influence line on cross section).

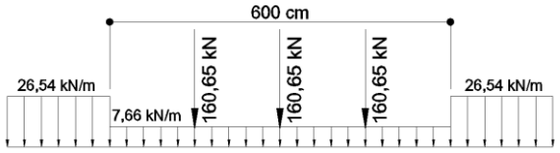


Figure 9. Vehicle live loads - Original bridge.

The previous loads resulted in the following bending moments, shown in Table 1:

Table 1. Project bending moments of the original bridge (M_0, units in kN.m).

Efforts	Partial values (S_k)	Final value (S_d)
M_{0G} (dead load)	3630,0	9262,4
M_{0Q} (vehicle live load)	2986,0	

With the values of Table 1, and characteristics of the existing bridge, according to the Brazilian concrete standard of the design period, NB-1 1978, the existing reinforcement was determined, resulting in 118 cm² AC- 50 steel.

5.3 *Structural analysis of the enlarged bridge*

For the new conditions of the bridge, extended and longer runway length, considerable efforts are expected to increase in the main beams.

Considering the external reinforcement solution with anchor and deviator blocks in reinforced concrete, these elements were arranged according to Figure 10 and their weights considered in the dead loads with the weight of the other elements, according to Figure 11.

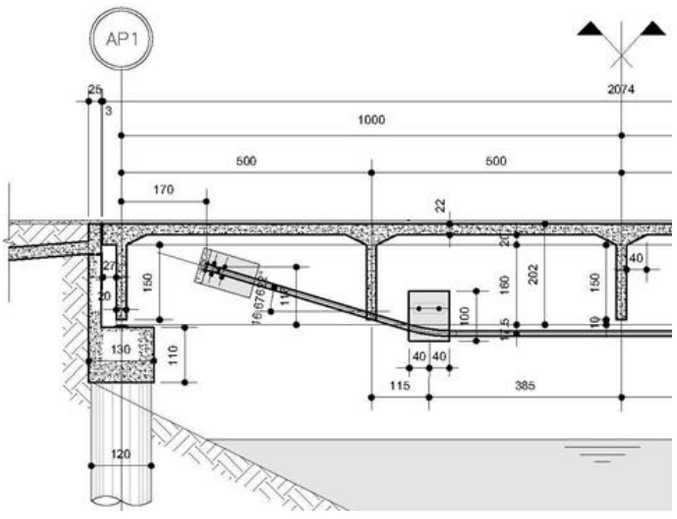


Figure 10. Prestressing system on longitudinal half elevation (dimensions in cm)

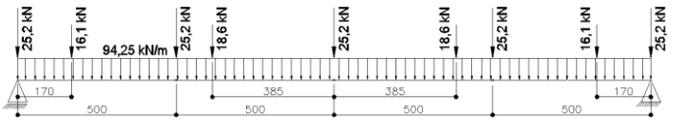


Figure 11. Dead loads - Enlarged bridge (dimensions in cm).

The corresponding Brazilian standard, NBR 7188 of 2013, was used to determine the final vehicle live loads, shown in Figure 12, for each main beam.

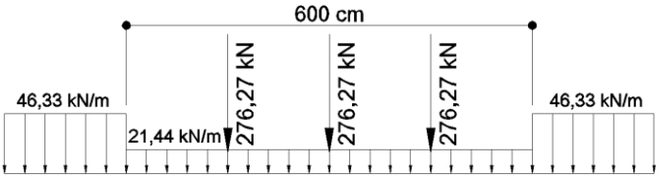


Figure 12. Vehicle live loads - Enlarged bridge.

For the calculation of the efforts, Brazilian multiplier coefficients were used, 1,35 for dead loads and 1,5 for live loads, resulting in the values shown in Table 2.

Table 2. Enlarged bridge bending moments (M_F, units in kN.m).

Efforts	Partial values (S_k)	Final value (S_d)
M_{FG} (dead load)	5106,25	14953,79
M_{FQ} (vehicle live load)	5373,5	

5.4 *Comparison of forces*

Table 3 shows an increase of about 60% of the efforts, an increase that must be resisted by the external prestressing system.

Table 3. Comparison of bending moments (M, units in kN.m).

Forces	S_k	S_d	ΔS_d
M_{0G}	3630,00	9262,40	5691,39 (61,4%)
M_{0Q}	2986,00		
M_{FG}	5106,25	14953,79	
M_{FQ}	5373,50		

5.5 *Reinforcement calculation*

As a result of updating of standards, some parameters taken into account changed, such as the resistant section considered, which was changed in relation to the flanges.

A steel pretension area is adopted to withstand increased stress. This steel is pulled to its limit (determined by the Brazilian standard of reinforced concrete), anchored eccentrically and with inclined geometry, that generates concentrated efforts at the points of deviation and anchorage.

In this case, the prestress steel area was determined to withstand the total value of the bending

moment request. From this total steel area, the existing steel portion was subtracted and this value was adjusted for commercial steel areas, resulting in two cables by girder, with 7 steel wire ropes of 12,7 mm of CP-190 RB steel (steel effective area = 13,82 cm²).

The concentrated forces, conferred by this initially adopted reinforcement, are represented in Figure 12.

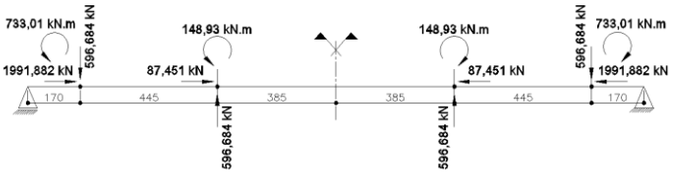


Figure 12. Equivalent loads by external prestressing

The forces explained in the previous figure generate bending moments of opposite direction to the vehicles live and dead loads, according to Figure 13.



Figure 13. Bending moments diagram from external prestressing.

The combination of these forces with those of the dead loads and the vehicle live loads constitute the new requesting effort. This value may be smaller than the initially acting force, because it also contains the inverse force, applied by the reinforcement.

The values of requesting moments are:

$M_{Dead\ loads} = 5106{,}25\ kN.m$;

$M_{Vehicle\ live\ loads} = 5373{,}5\ kN.m$;

$M_{External\ Prestressing} = -3537{,}18\ kN.m$;

Applying the Brazilian standards coefficients to these values, the final actuating bending moment value (M_{df}) is determined, resulting in:

$M_{df} = 11770{,}23\ kN.m$.

For the resistant section considered, with the existing passive steel area and active steel area calculated, the bending moment resistant M_{rd} = 13616 kN.m. This value is greater than the final acting bending moment M_{df}.

Once this condition is confirmed, the armature previously adopted is sufficient to withstand the increase of bending moments, being this armature constituted of two cables by girder, with 7 steel wire ropes of 12,7 mm of CP-190 RB steel.

If M_{rd} were smaller than M_{df}, it would be necessary to consider another larger area of prestressing steel, to recalculate the applied concentrated forces (equivalent loads), to recalculate the forces generated by it, determining the new bending moment, then calculating the resistant bending moment M_{rd} of the section with the new steel area until the condition $M_{rd} > M_{df}$ is satisfied.

6 CONCLUSION

For this theoretical case, the existing bridge with two cables by girder, with 7 steel wire ropes of 12,7 mm of CP-190 RB steel (steel effective area = 13,82 cm²) are sufficient to absorb the 61.4% increase of bending moments.

This reinforcement can be done without interrupting traffic on the bridge, probably with less inconvenience than a conventional situation of reinforcement by enveloping or by adding metal plates.

7 REFERENCES

SOUZA, V. C.; RIPPER, T. Patologia, recuperação e reforço de estruturas de concreto. São Paulo, Pini, 1998.

ALMEIDA T. G. M. Reforço de vigas de concreto armado por meio de cabos externos protendidos. University of São Paulo. São Carlos, 2001.

DNIT - Brazil's national transport infrastructure department. Manual de Inspeção de Pontes Rodoviárias. Road Research Institute. 2nd Ed. Rio de Janeiro, 2004.

ABNT - Brazilian Association of Technical Norms. NB-6 Carga Móvel em Pontes Rodoviárias. Rio de Janeiro, 1960.

ABNT - Brazilian Association of Technical Norms. NBR-7188, Road and pedestrian live load on bridges, viaducts, footbridges and other structures. Rio de Janeiro, 2013.

ABNT - Brazilian Association of Technical Norms. NB-2 Cálculo e execução de pontes em concreto armado. Rio de Janeiro, 1961.

ABNT - Brazilian Association of Technical Norms. NB-1 Projeto e execução de obras de concreto armado – Procedimento. Rio de Janeiro, 1978.

ABNT - Brazilian Association of Technical Norms. NBR-6118, Design of concrete structures – Procedure, 2014.

Maintenance, Safety, Risk, Management and Life-Cycle Performance of Bridges – Powers, Frangopol, Al-Mahaidi & Caprani (Eds)
© 2018 Taylor & Francis Group, London, ISBN 978-1-138-73045-8

Inhibiting corrosion of prestressed cables using an ultrasonic impregnation process

X. Hallopeau
Freyssinet International & Cie, Rueil-Malmaison, France

P. M. Dubois & D. Michaux
PMD-ATEAV Systems sprl, Ophain, Belgium

ABSTRACT: The civil engineering process stabilizes in the long term the corrosion of prestressed concrete cables. The process principal idea is to saturate the protective grout of the cables - irrespective of the cables condition - with an inhibiting solution conveyed by a vibrating ultrasonic power pump. The process is slightly intrusive. A map of the injection faults within the existing cement grout can be established. Additional cement grout can be injected where needed. The process was applied to a viaduct for the first time in 1994. The effectiveness of the treatment was assessed in 2012 when the entire viaduct was demolished. The process is regarded as a long-lasting and durable treatment.

1 INTRODUCTION

Often older types of construction were built with bonded prestressed cables. When cables become corroded, the treatment can be challenging in different ways. The cables are embedded within the inner concrete structure of the beam. They are barely accessible. Since they are threaded within a metallic sheath, no electrochemical protective process can be applied. Therefore, the authors imagined how to gain access another way. First an appropriate corrosion inhibitor saturates the existing protective cement grout, then additional cement grout is further injected where injection faults are discovered.
The rehabilitation process of prestressed cables was devised and applied in 1994 as a test case to a span of a five girder of the Lultzhausen viaduct, in the Grand Duchy of Luxembourg, close to the high head dam of Esch-sur-Sûre and crossing the lake of La Haute-Sûre. The bridge was constructed in 1960, each beam was prestressed by 11 cables (each with 12 wires of 7 mm diameter). Exposure to moisture was minimal (precipitation during 120 days) and the number of ice days are around 20 days between 1961 and 1990. The Belgian Scientific Center for Construction Engineering (Belgian Building Research Institute – BBRI) validated the process between 2000 and 2008. Many bridges have been treated since 1994: Rail bridge Duferco 1999 (Belgium), Huccorgne Viaduct 2004 (Belgium), Courrier Viaduct Highway E411 2008 (Belgium), Colmar-Berg Bridge 2008 (Grand Duchy of Luxembourg), Courcelles Viaduct on the Wallonia highway 2011 (Belgium), Bridges 118 and 211 on the Highway A7 close to Lyon 2014-2016 (France). A detailed communication was published in SETRA paper #59 of November 2008. Several communications were presented at the Structural Faults and Repair Congress in Edinburgh in June 2008, at the "Le Pont" Symposium in Toulouse in 2005 and 2008. Some results were also presented on the Huccorgne Viaduct build in 1968, cable type 12 wires of 7 mm diameter, subjected to de-icing salt, and treated in 2004. Some wires treated and non-treated were autopsied in 2014.

2 METHODOLOGY

2.1 *Principle*

The unique idea of the process is to take advantage of the energetic properties of ultrasonic waves in order to impregnate the existing cables and to permeate the surroundings with the inhibiting solution. The effect of ultrasound on the inhibiting solution is to build up a cavitational condition in vapour phase. The energy released by the cavitation effectively clears the pores in the grout at the site of the prestressed cable interface and the inhibiting solution has direct access to the prestressed steel to be protected. The open path is the same path that the corrosive agents (water, oxygen, chlorides) have used over the decades of the lifecycle of the structure. The main difference is that ultrasound makes it possible to cover the paths in a few hours. The cavitational condition in the vapour phase is generated by an al-

ternating ultrasonic power pump. It expands and contracts generating alternating overpressures and underpressures at an ultrasonic frequency of approximately 23000 Hz (Figure 1). Consequently, the impregnation of the cable surroundings by the inhibiting solution occurs under low pressure.



Figure 1. Impregnation of the inhibiting solution using the ultrasonic transducer after boring and installing the injection nozzles.

The selected inhibiting solution is a calcium nitrite solution whose effectiveness - with or without chlorides present - is proven by several studies and practical findings over thirty years, Schiebl et al. 2000. Calcium nitrite transforms permeable ferrous oxide into impermeable ferric oxide which restores the natural passivation coating of the steel embedded in sound concrete, causing no secondary effect to the steel behaviour. The calcium nitrite concentration was defined in excess to chloride content in a ratio of $[Cl^-]/[NO_2^-]$ equal to 0,7, Elsener et al. 2003.

2.2 *Experimental procedure*

The treatment consists of three stages:

- Stage #1: Installing the injectors
- Stage #2: Impregnating the corrosion inhibitor
- Stage #3: Filling the grout faults

During the treatment the progress of the inhibitor from one hole to the next is timed. A mapping of the migration timings is obtained revealing details about the quality of the grout filling or packing. The following mapping (Figure 2) provides the migration time of the inhibitor versus location of injection point with color code, for instance in yellow the migration time between 2 points of injection is around 15 min to 30 min indicating relative bad grout filling quality, and in black superior to 120 min indicating a compact grout.
This mapping quantifies and localises how serious the injection faults are visualized in Figure 3 for a Type 12 cable of 7 mm diameter.

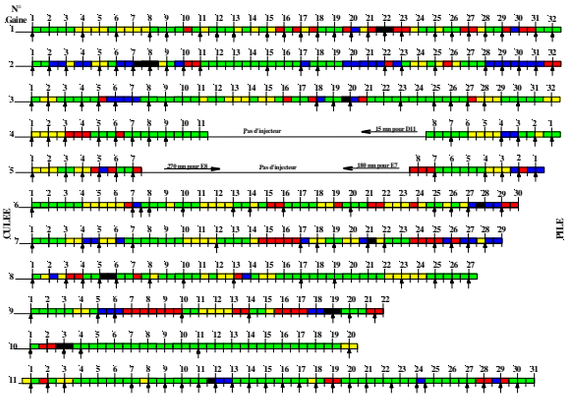


Figure 2. Mapping the migration times of the inhibiting solution. The arrows mark the injection points (11 treated cables in 1 beam).



Figure 3. Illustrates the injection faults (Cable type 12, diameter 7 mm).

After the injection of the inhibiting solution has been completed and based upon the mapping obtained earlier, the nozzles are reused to inject a very fluid Portland cement-based microgrout, In the case of a complete empty gap of long range within the injection site, grout is injected.

2.3 *Re*sults

2.3.1 *Case Lultzhausen viaduct*

The last and rare opportunity to validate the process occurred when the Lultzhausen viaduct was replaced, a decision made because of concerns about the stability of several beams in spans left untreated in 1994. The viaduct deck was demolished and replaced with a new deck in 2012. The span treated in 1994, Figures 4, merited a special soft demolishing procedure as illustrated in Figures 5.
Scaffolding supported the span which was then cut into sections. The cutting of the sections was visually inspected in detail. One section was selected to undergo tests in the lab. The test was completed in 2012. The findings of the analysis are commented on below.
Investigations performed in 1990 revealed that many cracks were present along the prestressed cable pathways with water leaks and lime deposit emanations.
Many cables were poorly or not injected, showing some advanced corroded condition, but still unbroken with no reduction in bearing capacity.



Figure 4. Locating the 1994 treated span of the Lultzhausen viaduct



Figure 5. Saw cutting demolition and test element.

Selection of the preserved beam section for analysis was conducted in order to keep sufficient longitudinal length of the treated prestressed cables as well as transverse prestressed cables left untreated in 1994. The beam of a little more than 30 m in length was sawn in approximately ten sections of more or less 3 m length, all inspected.

A test program on one representative cut, including six treated core samples (Figure 6) and two non-treated core samples, had been entrusted to the Laboratory of Construction Materials of the University of Liège, Belgium 2012. The test program included the following investigations:

- Macroscopic description
- Chloride content per cement weight by potentiometric titration
- SEM observation on polished section
- Semi-quantitative analysis of nitrite content by colorimetric method
- Cement content analysis
- XRD mineralogical identification



Figure 6. Core localization

The visual examination of the sawed cuttings indicates that the microgrout reinjection is in excellent condition (Figure 7). The interface front between the older grout (dark) and the reinjected grout (white) is clearly marked in the last picture.



Figure 7. Visual examination of the cuttings

The retreat of the threads, after the cutting, was almost the same for every cable. This finding confirms the excellent quality of the microgrout reinjection process. It was feared that the action of the nitrites might alter the adherence of the prestressed steel and older/newer grout interface. No such problem occurred and the ULS (Ultimate Limit State) was not modified. Therefore, we can conclude that the waterproof barrier between the prestressed steel and the outside environment was restored along the full cable length and that the input of newer corrosive agents was prevented (water, oxygen, chlorides). The chloride content measurements match to approximately 0.01 % chlorides with respect to the grout mass. Therefore, no significant pollution due to chloride had occurred. Those measurements are coherent with the fact that the work is in a protected area where in principle no salt is spread in winter.
Determining the nitrite content using the colorimetric method with test strips to the treated cables of the longitudinal prestressed and to the untreated cables of the transverse prestressed, shows beyond doubt that the process is effective and long-lasting (Figure 8). The visual examination showed that no further corrosion of the prestressed cables had resumed.
Even though the testing was not quantitative, it can be seen that after approximately 20 years, a significant amount of nitrites are still available in case new aggressive agents appear. The long-lasting effect of the treatment is thus practically unlimited.

2.3.2 *Case Huccorgne viaduct*

Most of the time the corrosion of prestressed cables is initiated by pollution involving chlorides.
In the presence of chlorides, the corrosion velocity and severity level becomes considerably worse even if the pH in the cables environment stays around 11 or 12. In principle a pH of 11 or 12 inhibits corrosion when no chlorides are present. A distinctive characteristic of the nitrites is to enable a corrosion inhibiting effect most notably effective when chlorides are present, provided that the quantity of nitrites is sufficiently available. The application of this process ensures this important point because the process soaks and saturates the environment surrounding the prestressed cables. It should be noted that the use of nitrites in concrete was developed back in the 1970s as inhibiting agents in marine environments.



Figure 8. Treated (left) and untreated (right) prestressed cables

A convincing example to mention is the test application in 2004 to the Huccorgne viaduct on the Wallonia highway in Belgium, applied to particularly damaged prestressed beams. Ten years later, 2014 inspection, the repaired area that may possibly show exemplary evidence of cracks does not present any cracking nor any sign that corrosion had resumed (Figures 9, 10 and 11). A detailed intrusive test assessment on autopsied wires confirms these findings: chemical analysis and SEM observations performed by the Laboratory of Construction Materials of the University of Liège in Belgium showed that the treated wire presented on its surface a thin layer of 20 microns of hydrated calcium aluminosilicate and iron, while the non-treated wire a 150 microns layer of iron oxide Fe_2O_3 and FeO(OH), and ferrous hydroxide $Fe(OH)_2$ demonstrated active corrosion.



Figure 9. Rehabilitation of the Huccorgne viaduct



Figure 10: Cable treated



Figure11: Cable non treated

3 CONCLUSION

The results demonstrate that the effectiveness and long-lasting effect of the process to stabilize the corrosion of the prestressed cables seems to be widely confirmed as a benefit from approximately 20 years experience even if only two treated works have so far been destructively investigated. The other works were inspected annually and no degradation were observed on treated beams. Therefore, we can regard this as a reliable process that takes its place beside other high technology processes like the cathodic protection of reinforced concrete and other electrochemical processes. It is important to note that the process does not require any maintenance phase and that it can be renewed or further completed if needed.

It is important to further highlight how the application process bears little impact to highway traffic since it is usually implemented from the inner side of the bridge structure. The process comes within the scope of durable development since it significantly extends the life of prestressed civil engineering structures endangered by corrosion.

4 REFERENCES

Bulletin du Centre des Techniques d'Ouvrages d'Art, SETRA n°59. 2008. 8-19.

Cailleux, E., Pollet, V., Dubois, P-M., Michaux, D. 2008, A new corrosion treatment for prestressed rebars: the direct injection of a corrosion inhibitor by an ultrasonic pump, Structural Fault and Repair, Edinburgh.

Centre Scientifique et Technique de la Construction (CSTC), Rapport DE 61079/bis. 2001. Rapport DE 61079/2. 2002. Rapport DE 61079/3. 2006.

Dubois, P-M. & Michaux, D., 2005. Procédé de stabilisation de la corrosion de câbles de précontrainte, Colloque Le Pont, Toulouse.

Elsener, B., Cigna, R. 2003. Mixed-in inhibitors, Corrosion of steel in reinforced concrete structures, COST Action 521, Final report. 41-51.

Gilles, P., Dubois, P-M., Michaux, D. 2008. Problématique des chlorures dans la postcontrainte - Exemple de traitement de la corrosion par le procédé PMD-ATEAV au viaduc de Courrière (Belgique), Colloque Le Pont, Toulouse.

Laboratoire des Matériaux de Construction de l'Université de Liège (ArGEnCo). 2012. Rapport GMC/12/027.

Schiebl, P., Dauberschmidt, C. 2000. Evaluation of calcium nitrite as corrosion inhibitor, sixth CANMET/ACI International conference on superplaticizers and other chemical admixtures in concrete. 105-119.

Maintenance, Safety, Risk, Management and Life-Cycle Performance of Bridges – Powers, Frangopol, Al-Mahaidi & Caprani (Eds)
© 2018 Taylor & Francis Group, London, ISBN 978-1-138-73045-8

Effects of current density on the spatial variability associated with steel corrosion and flexural behavior of corroded RC beams

S. Lim, H. Song, & M. Akiyama
Waseda University, Tokyo, Japan

D.M. Frangopol
Lehigh University, Bethlehem, PA, USA

ABSTRACT: Since structural performance of corroded RC members primarily depends on localized corrosion damages on their reinforcements, modelling the spatial steel corrosion is important for the long-term performance assessment of RC structures. To achieve this purpose, there is a need to study the time-variant spatial distribution of steel corrosion. The impressed current technique by means of applying current density has been widely used to investigate the effect of steel corrosion on the structural capacity deterioration. It was reported that current density has great influence on the propagation of average crack width, steel corrosion, and structural behavior of RC members. However, the study of the effect of current density on the spatial variability of corrosion and cracking is scarce. Therefore, the main objective of this paper is to study, using X-ray and digital image processing techniques, the effects of current density on the spatial steel corrosion and corrosion cracking of corroded RC beams.

1 INTRODUCTION

Chloride-induced corrosion is a dominant deteriorating mechanism of RC structures in marine environments. The distribution of corrosion on the steel reinforcements in RC structures due to chloride attack is not uniform; it varies along the length of structures due to several factors such as variability of steel and concrete properties, environmental exposure, and workmanship (Akiyama et al. 2016, Palsson et al. 2002). Since the structural performance of corroded RC members primarily depends on localized reinforcement corrosion, modelling the spatial variability associated with steel corrosion is important for their long-term structural performance assessment.

In order to model the spatial steel corrosion, it is necessary to study how the steel corrosion increases and changes at different corrosion stages (Kashina et al. 2013a,b, Alonso et al. 1998, Vidal et al., Zhang et al. 2014). Such a study requires a continuous monitoring method by a non-destructive method (e.g., Akiyama et al. 2013, Lim et al. 2016, and Lim et al. 2017). In previous studies, without considering the effect of applied current density, Lim et al. (2016, 2017) used X-ray and digital image processing techniques to investigate the effects of water-to-cement ratios and amount of stirrup reinforcement on the spatial variability of steel corrosion and structural performance of accelerated-corrosion RC beams.

However, several studies reported the significant effect of the current density on the corrosion cracks and flexural performance of RC members. El Maaddawy & Soudki (2003) reported that, at the same magnitude of corrosion, the crack width of RC prisms increases significantly with the increase in current densities from 200 to 500 $\mu A/cm^2$. Saifullah and Clark (1994) also found similar results in which crack width increases with the current density (150 to 4000 $\mu A/cm^2$). Mangat & Elgarf (1999) conducting an extensive study on 111 RC beams using different current densities (1000 $\mu A/cm^2$, 2000 $\mu A/cm^2$, 3000 $\mu A/cm^2$ and 4000 $\mu A/cm^2$) found that flexural load-deflection (P-δ) responses of accelerated-corrosion RC beams are more dependent on current density when the steel weight loss increases. They found that at a higher steel weight loss, the flexural load-deflection (P-δ) performance decreased substantially with the increase in the current densities from 1000 to 4000 $\mu A/cm^2$. However, at a lower steel weight loss, the same increase in current densities has marginal effect on the flexural capacity of RC beams. It can be noted that studies on the effects of current densities on the spatial variability of steel corrosion and cracking are scarce.

Therefore, the main objective of this paper is to study, using X-ray and digital image processing techniques, the effects of current density on the spatial variability associated with steel corrosion and corrosion cracking of RC beams.

2 EXPERIMENTAL PROGRAM

The detailed experimental program (e.g., quality of concrete materials and steel reinforcement, RC specimen fabrication, and experimental test) was reported in Lim et al. (2017). The main difference between the experimental program reported in this paper and that of Lim et al. (2017) is that the objective herein is to study the effects of different current densities on the spatial variability associated with steel corrosion of corroded RC beams. Therefore, only a brief review of the experimental program is described herein.

2.1 *Concrete mixing proportion and test specimens*

Two RC beams, I-1 and I-2, with a cross-section of 80 mm × 140 mm were made. Table 1 shows the mixing proportion of concrete of the RC beams, and Figure 1 illustrates the details of RC specimens. The two beams were reinforced with a longitudinal rebar having a diameter of 13 mm (1-DB13) and stirrups with a diameter of 6 mm and space of 100 mm (DB6@100) were provided in the shear spans.

Table 1. Mix proportion of concrete

Notation	Water	Cement	FA*	CA†	AE††
	Kg	Kg	Kg	Kg	ml
I-1 & I-2	181	362	754	961	2715

* Fine aggregate
† Coarse aggregate
†† Air entrained and water reducing agent

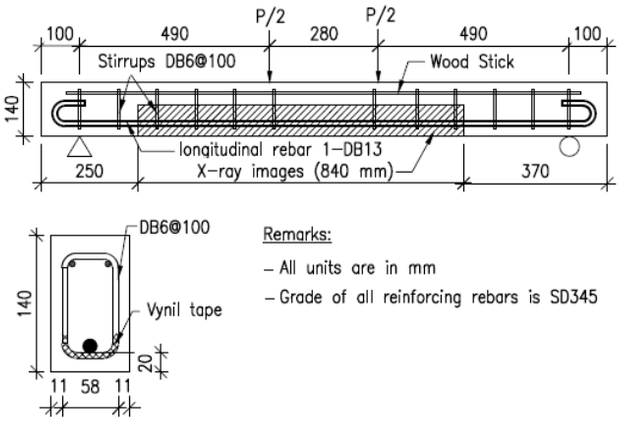


Figure 1. Details of the test specimen.

2.2 *Experimental procedure*

After the curing of the specimens for 28 days, the corrosion of the longitudinal bars was accelerated using the impressed current technique. Figure 2 shows the test setup of the accelerated corrosion test. The RC specimens were partially immersed into the solution containing 3% of NaCl. The steel reinforcement served as an anode, while a copper plate

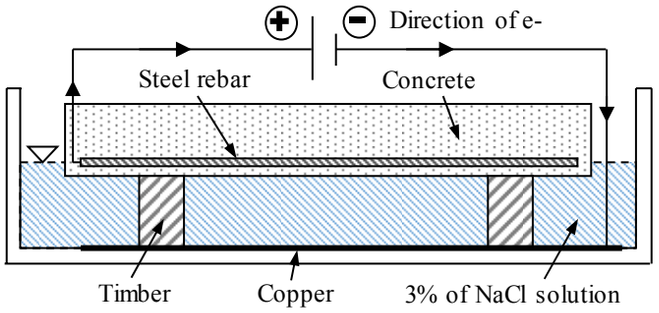


Figure 2. Test setup of the acceleration corrosion test.

served as a cathode. The current densities (I_{cor}) of 100 μA/cm^2 and 500 μA/cm^2 were used for accelerating corrosion of the longitudinal rebars of the beams I-1 and I-2, respectively. During the corrosion process, the corrosion test was halt at three different times so that the spatial variability of steel corrosion and corrosion crack can be assessed at each stage by means of X-ray imaging and digital image processing techniques (see more details in Lim et al. 2017).

At three different stages of corrosion before taking X-ray images, the photographs of corrosion crack that occurred at the bottom of the beam were taken. The locations for taking photographs are the same of the X-ray images (see Figure 1). The surface crack width was measured in 5 mm intervals along the bottom of the beam between the distance of 250 mm to 1090 mm from the left edge of the specimen.

Once before and several times during the corrosion process, X-ray radiography was performed on the undamaged and corroded RC beam to take photograms of the original and corroded rebars inside the concrete beams from 12 different viewing angles (i.e., $\theta_1 = 0°$, $\theta_2 = 30°$, $\theta_3 = 60°$, $\theta_4 = 90°$, $\theta_5 = 120°$, $\theta_6 = 150°$, $\theta_2 = 180°$, $\theta_8 = 210°$, $\theta_9 = 240°$, $\theta_{10} = 270°$, $\theta_{11} = 300°$ and $\theta_{12} = 330°$).

The local steel weight loss per 5 mm, *Rw*, was estimated along the rebar length using digital image processing of X-ray images from eight different viewing angles which can be expressed as:

$$Rw = \frac{1}{k}\sum \frac{W_{\theta_n} - W'_{\theta_n}}{W_{\theta_n}} \times 100 \quad (1)$$

where $W_{\theta n}$ and $W'_{\theta n}$ are the weights of original and corroded rebars at any viewing angle, respectively, the subscript θ_n indicates the viewing angles in which $n = \{1, 2, 4, 6, 7, 8, 10, 12\}$, and k is the number of viewing angles. At the end of the experimental program, the four-point beam bending test was performed as shown in Figure 1. The applied load and mid-span displacement were recorded. The beam was loaded until collapse by the crush of compressed concrete.

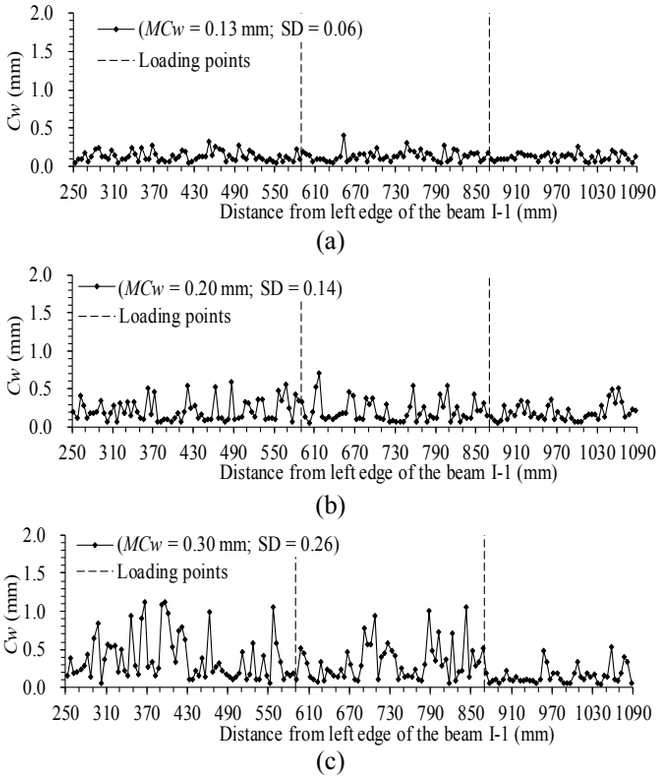


Figure 3 Spatial variability of surface crack width of beam I-1 at different average steel weight loss of (a) *MRw* = 2.13%, (b) *MRw* = 8.03%, (c) *MRw* =12.05%

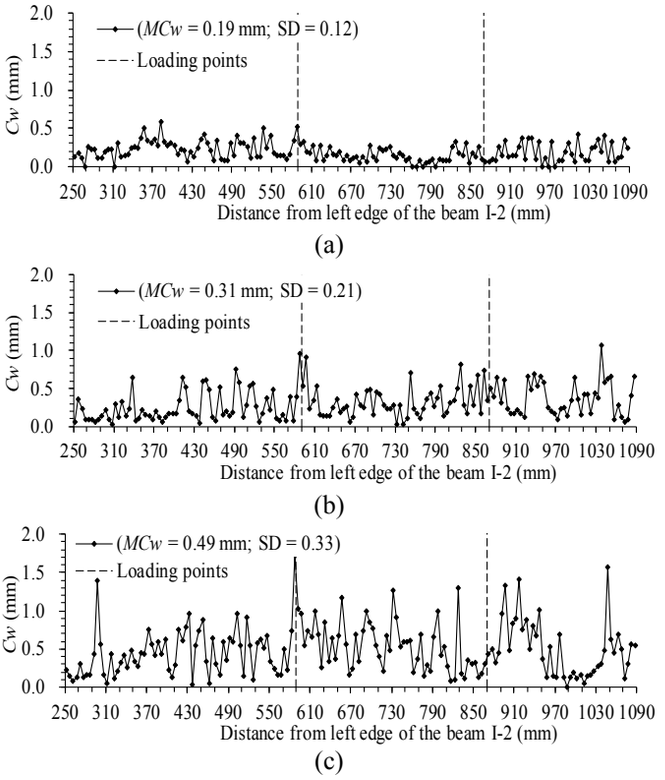


Figure 4 Spatial variability of surface crack width of beam I-2 at different average steel weight loss of (a) *MRw* = 3.05%, (b) *MRw* = 7.02%, (c) *MRw* =12.81%

3 EXPERIMENTAL RESULTS AND DISCUSSION

3.1 *Effect of current density on corrosion crack width*

It was observed in this experimental study that the longitudinal corrosion surface crack only occurs at the bottom of the beams due to the very thin concrete cover. Figures 3 (a), 3 (b), and 3 (c) illustrate the increase in spatial variability of surface crack width *Cw* over the length of beam I-1 at different degrees of corrosion or values of average steel weight loss, *MRw* = 2.13%, 8.03%, and 12.05%, respectively. Figures 4 (a), 4 (b), and 4 (c) show the increase in spatial variability of crack width over the length of beam I-2 at *MRw* = 3.05%, 7.02%, and 12.81%, respectively. For the two beams, it can be seen that the variability of their surface crack width increases with *MRw*. However, with a side-by-side comparison at approximately the same values of *MRw*, the variability of surface crack width of beam I-2, which was corroded using I_{cor} = 500 μA/cm^2, is always bigger than that of beam I-1, which was corroded using I_{cor} = 100 μA/cm^2.

Figure 5 shows the effect of current densities 100 μA/cm^2 and 500 μA/cm^2 on the increase in the average crack width at different values of *MRw* for beams I-1 and I-2, respectively. It can be seen that the corrosion crack width of beam I-2 (I_{cor} = 500 μA/cm^2) increases more quickly than the crack width of I-1 (I_{cor} = 100 μA/cm^2) at approximately the same average of steel weight loss.

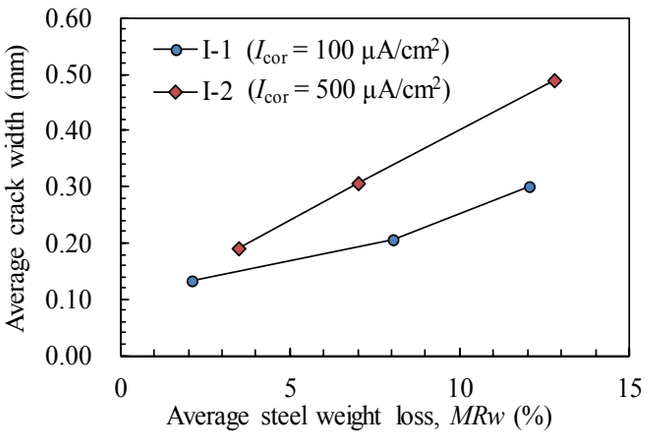


Figure 5 Growth of crack width of beams I-1 and I-2 at different average steel weight loss.

This experimental result indicates that corrosion crack width increases with the current density. Therefore, using the high level of current density to accelerate steel corrosion can lead to a faster expansion of corrosion product, higher internal pressure to the surrounding concrete, and eventually a larger crack width. Mangat and Elgarf (1999) also reported similar results in which the crack width of the corroded RC prisms increased significantly when the impressed current density was increased from 200 μA/cm^2 to 500 μA/cm^2.

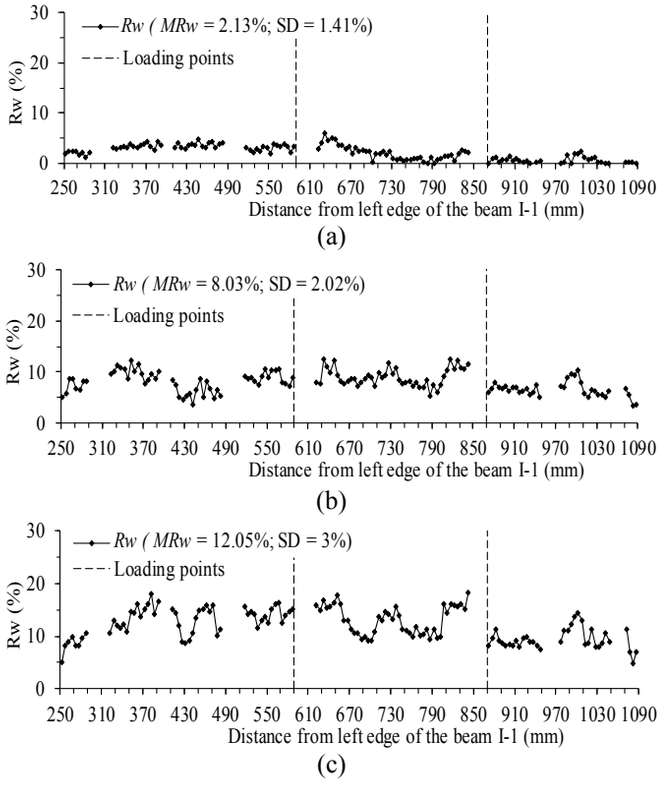


Figure 6 Spatial variability of steel weight loss of beam I-1 at different average steel weight loss of (a) *MRw* = 2.13%, (b) *MRw* = 8.03%, (c) *MRw* =12.05%

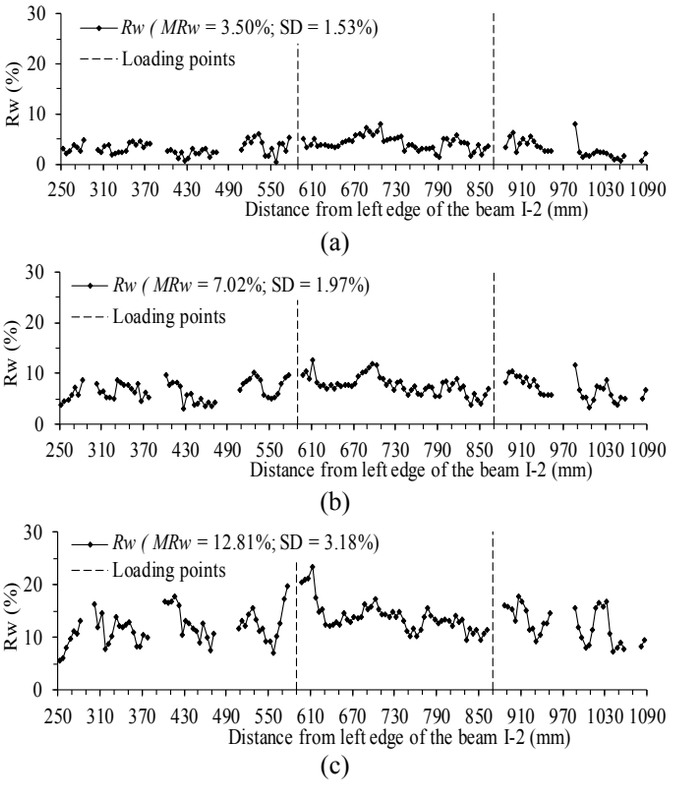


Figure 7 Spatial variability of steel weight loss of beam I-2 at different average steel weight loss of (a) *MRw* = 3.05%, (b) *MRw* = 7.02%, (c) *MRw* =12.81%

3.2 *Effect of current density on the spatial variability associated with steel corrosion*

Figures 6 and 7 depict the spatial variability associated with steel weight loss over the length of beams I-1 and I-2, respectively, at three different degrees of corrosion. Since it is very difficult to obtain exactly the same degree of corrosion, the spatial steel corrosions of the two beams are compared at approximately the same value of average steel weight loss, *MRw*. Generally, it can be seen that the distribution of corrosion is non-uniform over the length of each beam, and the variability in steel corrosion (as indicated by the standard deviation, SD) increases with the corrosion degree (as indicated by *MRw*).

Moreover, it is worth noting that the effect of current density on the spatial steel corrosion seems to be dependent on the degree of corrosion. At a small corrosion degree (*MRw* < 8%), the effect of current density on the spatial variability of steel corrosion is minor since there is no significant difference between the spatial variability of steel corrosion of both beams. However, at larger degree of corrosion of about *MRw* = 12.5%, the effect of large current density becomes more pronounced. In fact, the local maxima of steel weight loss for the beam I-2 at the location of 610 mm reaches approximately 23 % in comparison to the local maxima of steel weight loss of beam I-1 of only about *Rw* = 18%.

This experimental result suggests that as the degree of corrosion become larger, the large current density I_{cor} = 500 μA/cm^2 might induce larger local attack penetration or pitting corrosion than the small current density I_{cor} = 100 μA/cm^2. Therefore, for the experimental study of accelerated-corrosion RC members by means of impressed current technique, one shall limit the maximum current density which might provide corrosion rate similar to that occurring in the field (e.g., Andrade et al. 1989) since using large current density might result in larger pitting corrosion.

3.3 *Effect of current density on the load-deflection response*

The load-deflection curves of the beams I-1 and I-2 are plotted in Figure 8. As expected, the corroded beam I-2 with a large current density of 500 μA/cm^2 has lower flexural performance than the corroded

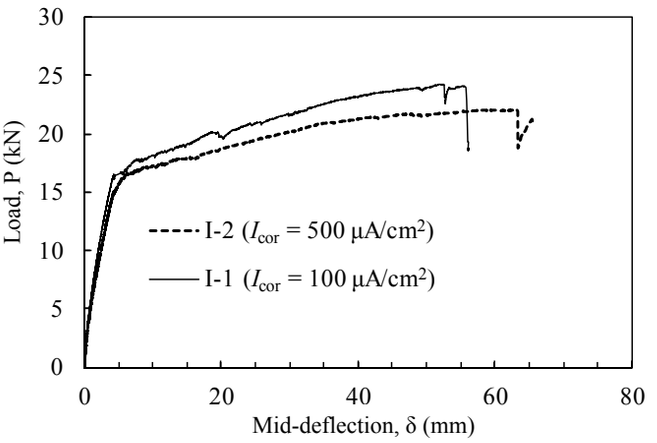


Figure 8 P-δ responses of corroded RC beams I-1 and I-2.

beam I-1 with a small current density of 100 μA/cm^2. The lower performance of the beam I-2 results from the fact that I-2 has larger crack widths and local steel weight loss in the maximum moment region than that of beam I-1 (see Figures 3 (c) and 4 (c), and Figures 6 (c) and 7 (c)).

4 CONCLUSIONS

In this paper, the effects of different current densities (100 μA/cm^2 versus 500 μA/cm^2) on the spatial variability associated with surface crack width and steel corrosion were investigated at different degrees of corrosion or values of average steel weight loss. Moreover, structural performance of RC beams corroded using the current density of 100 μA/cm^2 and 500 μA/cm^2 was investigated and discussed along with their spatial distribution of steel weight loss and corrosion cracking. Based on the experimental results reported, the main findings can be summarized as follows:

1. It was confirmed that the crack width of the accelerated-corrosion RC beams increased significantly with the increase in current density from 100 μA/cm^2 to 500 μA/cm^2. The reason might be attributed to the fact that the large current density induced larger steel corrosion in a shorter time than the small current density. This might lead to a faster expansion of corrosion product, higher internal pressure to the surrounding concrete, and thus a larger crack width.
2. Effects of current density on the spatial variability seems to be dependent on the degree of corrosion. As the degree of corrosion increases, the large current density might induce larger local attack penetration or pitting corrosion than that associated with the small current density.
3. Since the larger current density used increases the surface crack width significantly and can induce larger local pitting corrosion on the steel reinforcement, the use of larger current density results in lower flexural performance.

REFERENCES

Akiyama M., Frangopol D.M. & Takenaka K. 2017. Reliability-based durability design and service life assessment of reinforced concrete deck slab of jetty structures. *Structure and Infrastructure Engineering*, 13(4), 468–477.

Akiyama, M., & Frangopol, D.M., 2013. Estimation of steel-weight loss due to corrosion in RC members used on digital image processing of X-ray photogram. *Proceedings of the Third International Symposium on Life-Cycle Civil Engineering*, IALCCE2012, Vienna, Austria, October 3-6, 2012; in Life-Cycle and Sustainability of Civil Infrastructure Sytems, A. Strauss, D.M. Frangopol and K. Bergmeister eds., CRC Press/Balkema, Taylor & Francis Group plc, London, 389, and full paper on DVD, Taylor & Francis Group plc, London, 1885-1891.

Alonso, C., Rodriguez, J., & Diez, J.M. Factors controlling cracking of concrete affected by reinforcement corrosion. *Materials and Structures*, 1998, 31,435–441.

Andrade, C.; Alonso, M. C.; Gonzalez, J. A.; and Rodriguez, J.1989. Remaining Service Life of Corroding Structures. *IABSE Report 57/1, Durability of Structures*, pp. 259-364.

El Maaddawy T. A., & Soudki, K. A. 2003. Effectiveness of Impressed Current Technique to Simulate Corrosion of Steel Reinforcement in Concrete. *Journal of Materials in Civil Engineering*, 15(1), 41–47.

Kashani, M.M., Crewe, A.J., & Alexander, N.A. 2013a. Nonlinear stress–strain behaviour of corrosion-damaged reinforcing bars including inelastic buckling. *Engineering Structures*,48,417–429.

Kashani, M.M., Crewe, A.J., & Alexander, N.A. 2013b. Use of a 3D optical measurement technique for stochastic corrosion pattern analysis of reinforcing bars subjected to accelerated corrosion. *Corrosion Science*, 73, 208–221.

Lim, S., Akiyama, M., Frangopol, D.M., & Jiang, H. 2017. Experimental investigation of the spatial variability of the steel weight loss and corrosion cracking of RC members: Novel X-ray and digital image processing techniques. *Structure and Infrastructure Engineering*, 13, 118-134.

Lim, S., Akiyama, M., & Frangopol, D.M. 2016. Assessment of the structural performance of corrosion-affected RC members based on experimental study and probabilistic modeling. *Engineering Structures*, 127, 189-205.

Lim, S., Jian, H., Akiyama, M., & Frangopol, D. M. 2014. Experimental investigation on the relationship between the spatial variation of steel weight loss and the cracking width of RC member using X-ray photograms. In H. Furuta, D. M. Frangopol, and M. Akiyama (ed.), *Life-cycle of structural systems: design, assessment, maintenance and management*; Proceedings of fourth international symposium on life-cycle civil engineering, IALCCE2014, Tokyo, Japan, 16-19 November, 2014. CRC Press/Balkema, Taylor & Francis Group, London.

Mangat, P.S. & Elgarf M.S.E. 1999. Flexural Strength of Concrete Beams with Corroding Reinforcement. *ACI Structural Journal*, 96(1), 149–158.

Palsson, R. & Mirza, M. S. 2002. Mechanical response of corroded steel reinforcement of abandoned concrete bridge. *ACI Structural Journal*, 99(2), 157–162.

Saifullah, M., & Clark, L. A. 1994. Effects of corrosion rate on the bond strength of corroded reinforcement. *Corrosion and Corrosion Protection of Steel in Concrete*, Proceedings of International Conference held at the University of Sheffield, R. N. Swamy, ed., Sheffield Academic Press, 591-602.

Vidal, T., Castel, A., & Francois, R. Analyzing crack width to predict corrosion in reinforced concrete. *Cement and Concrete Research*, 2004, 34, 165–174.

Zhang, W., Zhou, B., Gu, X., & Dai, H. 2014. Probability distribution model for cross sectional area of corroded reinforcing steel bars. *ASCE Journal Material Civil Engineering*, 26(5):822–832.

Maintenance, Safety, Risk, Management and Life-Cycle Performance of Bridges – Powers, Frangopol, Al-Mahaidi & Caprani (Eds)
© 2018 Taylor & Francis Group, London, ISBN 978-1-138-73045-8

Seismic failure mode evaluation of bridges with deteriorated isolators

H. Matsuzaki, Y. Kubo, T. Tsumura & S. Unjoh
Tohoku University, Sendai, Japan

ABSTRACT: Isolated bridges are designed so that seismic energy is mainly dissipated at isolators. It is important that seismic safety and reparability of isolated bridges with deteriorated isolators are maintained as well as those with sound isolators. In this study, seismic failure modes of isolated bridges were evaluated considering uncertainties in the material and mechanical properties and aging deterioration of isolators. It was shown that response of isolated bridges is affected by deterioration of the lead core of the isolator and that failure probability of the isolator is mainly controlled by the rupture strain associated with deterioration of the rubber of the isolator.

1 INTRODUCTION

Reinforced concrete bridge columns with isolators subjected to the design ground motion are designed within limited nonlinear response to ensure that seismic energy is mainly dissipated at isolators. From view point of capacity design method, the yield strength of the isolator is set to be lower than that of the reinforced concrete column so that the isolator yields in advance under the design ground motion (Park & Otsuka (1999), Jangid (2007) and Zhang & Huo (2009)). However, lateral force of the isolator can increase due to the post-elastic stiffness under more severe ground motion. This increase in the lateral force of the isolator can result in rupture of the isolator or large nonlinear response displacement of the column. Once isolators are ruptured, several months will be needed to repair permanently, since isolators are designed for each bridge and manufactured after receiving an order. Thus it is necessary to consider strain hardening of the isolator to control seismic response in such a large shear strain range and enhance reparability of isolated bridges after seismic events.

Furthermore, decrease in rupture strain and increase in stiffness of isolators due to aging deterioration has been reported by Hayashi *et al.* (2014) and Shinohara & Hoshikuma (2015). It is important that seismic safety and reparability of isolated bridges with deteriorated isolators are maintained as well as those with sound isolators. Thus dynamic response characteristics of isolated bridges with deteriorated isolators should be investigated. Incremental dynamic analysis proposed by Vamvatsikos & Cornell (2002) is an essential and useful tool to investigate complex nonlinear dynamic response of isolated bridges. It is also noted that required capacity ratios between the isolator and the column to prevent rupture of isolators should be investigated considering effects of aging deterioration on the mechanical properties of isolators.

In this study, performance of isolated bridges will be investigated based on incremental dynamic analysis. Furthermore, effects of deterioration of isolators on the seismic failure modes of isolated bridges will be investigated based on fragility analysis.

2 TARGET BRIDGES AND ANALYTICAL CONDITIONS

2.1 *Target bridges*

Target bridges are reinforced concrete columns with 5 lead rubber bearings (LRB) at the top of a column on the stiff soil. Combinations of 2 types of reinforced concrete columns and 2 types of LRB were considered as shown in Table 1. These isolated bridges were designed based on the design specifications of highway bridges by Japan Road Association (2012) and the manual on bearings for highway bridges by Japan Road Association (2004). Mechanical properties of the isolators and the reinforced concrete columns are shown in Tables 2 and 3, respectively. Mechanical properties in Tables 2 and 3 are calculated using nominal values in the design. Bridges A (C) and B (D) have the same column, but rupture strength of the isolator of Bridge B (D) is higher than that of Bridge A (C).

Table 1. Dimensions of the target bridges

		Bridge A	Bridge B	Bridge C	Bridge D
Superstructure	Mass (ton)	600			
Isolator	Section (mm)	450×450	600×600	480×480	580×580
(LRB)	Total thickness of rubber (mm)	80	140	90	130
	Diameter (mm) and number of lead core	75×4	75×4	75×4	75×4
Column	Section (mm)	2600×2400		3000×2400	
	Height (mm)	10000		14000	
	Mass (ton)	260		352	
	Longitudinal reinforcement ratio (%)	1.41		2.87	
	Volumetric ratio of tie (%)	0.87		1.03	

Table 2. Mechanical properties of the isolators per column

Bridge	Yield strength (MN)	Yield stiffness (MN/m)	Strength at hardening initiation (MN)	Equivalent stiffness (MN/m)
A	0.870	51.4	2.00	14.1
B	0.870	66.0	3.58	13.7
C	0.870	55.8	2.28	14.0
D	0.870	65.2	3.34	13.8

Table 3. Mechanical properties of the reinforced concrete columns

Bridge	Yield strength (MN)	Yield displacement (mm)	Ultimate displacement (mm)
A, B	3.43	33.8	203
C, D	2.79	67.7	305

Table 4. Capacity ratios and equivalent natural periods

Bridge	R_{QY}	R_{QU}	T_{EQ} (s)
A	0.25	1.73	1.66
B	0.25	3.00	1.68
C	0.31	2.40	1.89
D	0.31	3.44	1.91

Table 5. Deterioration of isolators assumed in the analysis

Case	Stiffness ratio	Rupture strain ratio	Shear strength ratio of lead core
0 (Sound)	1.0	1.0	1.0
1	1.2	0.8	1.0
2	1.2	0.8	0.5

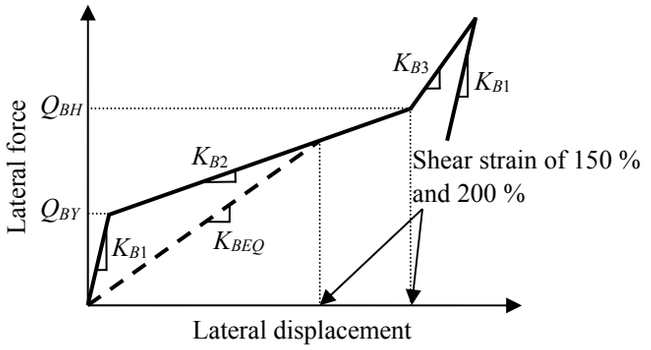


Figure 1. Lateral force-lateral displacement relationship of isolators

It is an advantage of using LRB that property of LRB can be easily controlled by the diameter of lead core and dimensions of rubber, which is associated with capacity ratios R_{QY} by Zhang & Huo (2009) and R_{QU} by Matsuzaki *et al.* (2017), respectively. The values of R_{QY}, R_{QU} and T_{EQ} in Table 4 were calculated using nominal values in the design based on Equations (1)-(3).

$$R_{QY} = Q_{BY} / Q_{CY} \tag{1}$$

$$R_{QU} = Q_{BR} / Q_{CU} \tag{2}$$

$$T_{EQ} = 2\pi \sqrt{(M_U + M_C)(1/K_{BEQ} + 1/K_{CY})} \tag{3}$$

where Q_{BY} is the yield strength of the isolator, Q_{CY} is the yield strength of the column, Q_{BR} is the rupture strength of the isolator and Q_{CU} is the ultimate strength of the column, M_U is the mass of superstructure, M_C is the mass of the column, K_{BEQ} is the equivalent stiffness of the isolator as shown in Figure 1 and K_{CY} is the yield stiffness of the column.

2.2 *Analytical model*

Mechanical properties of deteriorated isolators are modelled with reference to the experimental results of actual isolators reported by Hayashi *et al.* (2014). Three cases were considered as shown in Table 5. In Case 0, the isolator is sound. In Case 1, 20 % increment of stiffness and 20 % reduction of rupture strain associated with deterioration of rubber is assumed, but the lead core is sound. In Case 2, the lead core is also deteriorated in addition to deterioration of rubber in Case 1.

LRB was idealized based on a tri-linear model considering strain hardening of rubber as shown in Figure 1. The ratio of K_{B1} to K_{B2} was set as 6.5:1 based on Japan Road Association (2004) and the ratio of K_{BEQ} to K_{B3} was set as 1:2.59 based on Adachi (2002) in Figure 1. Skeleton and hysteresis of reinforced concrete columns were idealized based on bi-linear model and Takeda degrading stiffness model by Takeda *et al.* (1970), respectively. Thus the ultimate strength was idealized as same as the yield strength of the column. Dynamic response analysis

Table 6. Input ground motions

Earthquake	Recording station
1995 Kobe	Kobe (JMA), Inagawa (Hanshin Expressway), Shin-Kobe (KEPCO) and Kobe University
2003 Tokachi-oki	Shimizu (MLIT), Tsurui-Nishi (KiK-net), Tsurui-Higashi (KiK-net) and Taiki (KiK-net)
2004 Niigataken-Chuuetsu	Tookamachi (K-NET), Ojiya (K-NET) and Nagaoka (KiK-net)
2008 Iwate-Miyagi	Ichinoseki-Nishi (KiK-net) and Higashi-Naruse (KiK-net)
2011 Tohoku	Kaihoku bridge (MLIT) and Shin-Bansui bridge (MLIT)
2016 Kumamoto	Ichinomiya (K-NET), Ohzu (K-NET), Takamori (K-NET), Yabe (K-NET) and Kikuchi (KiK-net)

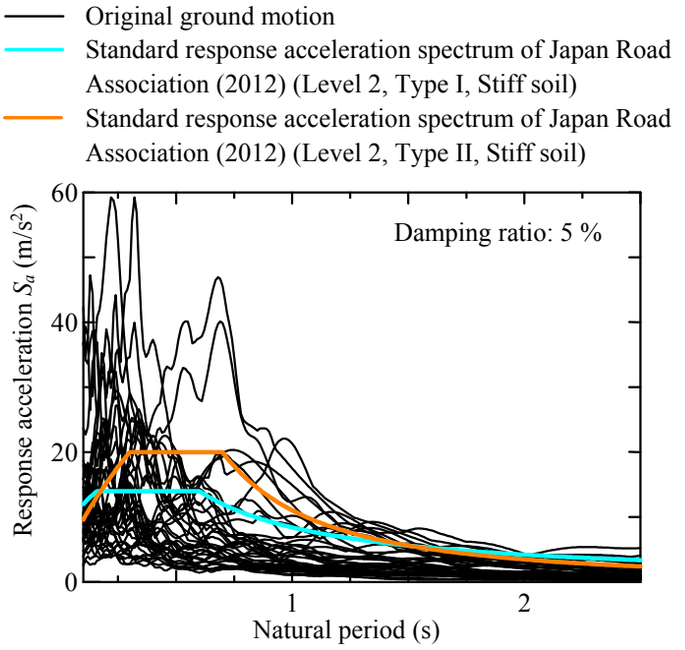


Figure 2. Response acceleration spectra of original ground motions

Table 7. Uncertain factors and coefficients multiplied by characteristic value

Uncertain factor		Distribution	Characteristic value	Coefficient	
				Mean	C.O.V
Superstructure	Mass	Normal	600 ton	1.05	0.05
Isolator	Yield strength	Normal	Listed in Table 2	1.13	0.18
	Stiffness	Normal	Listed in Table 2	1.00	0.07
	Rupture strain	Normal	250 %	1.34	0.11
Column	Compressive strength of concrete	Normal	23.5 N/mm^2	1.20	0.10
	Section area of steel bar	Normal	Nominal value	0.97	0.01
	Yield strength of steel bar	Normal	295 N/mm^2	1.20	0.07
	Young's modulus of steel bar	Normal	2.06×10^5 N/mm^2	0.97	0.01
	Mass	Normal	Listed in Table 1	1.05	0.05
	Ultimate displacement	Normal	Calculated based on JRA (2012)	1.062	0.181

was conducted by idealizing a reinforced concrete column with isolators as a 2 degree of freedom model. Rayleigh damping was assumed, in which the damping ratios of the column and the isolator were 2 % and 0 %, respectively.

2.3 *Input ground motions*

A total set of 40 lateral components of strong ground motions recorded in Japan were selected as shown in Table 6. Response acceleration spectra S_a calculated using 5 % damping ratio of these original ground motions are shown in Figure 2. Various types of ground motions in terms of response acceleration spectra were included in input ground motions.

2.4 *Uncertain factors and fragility analysis*

Uncertainties in the material and mechanical properties of isolated bridges were included in the analysis. Uncertain factors considered in the analysis are listed in Table 7 with coefficients multiplied by nominal values or calculated values. Statistical values are based on Adachi (2002) and Public Works Research Institute (2013).

Fragility analysis was conducted based on Monte Carlo simulation considering the uncertainties listed in Table 7. Number of trials in Monte Carlo simulation was set as 100,000. In fragility analysis, limit states associated with the lateral displacement of isolators and columns were considered. Threshold values are rupture strain for isolators and ultimate displacement δ_{ls3} for columns based on Japan Road Association (2012). If the response displacement exceeds the ultimate displacement of the column in advance, it is considered that the column is damaged. On the other hand, if response shear strain exceeds the rupture strain of the isolator in advance, it is considered that the isolator is damaged. If the isolator or the column of the bridge is damaged, it is considered that the bridge system is damaged.

Elastic response acceleration at the equivalent natural period S_a (T_{EQ}) was adopted as the intensity measure in the fragility analysis. As input ground motions in the fragility analysis, ground motions adjusted to the required S_a (T_{EQ}) by varying amplitude property was used without varying phase property.

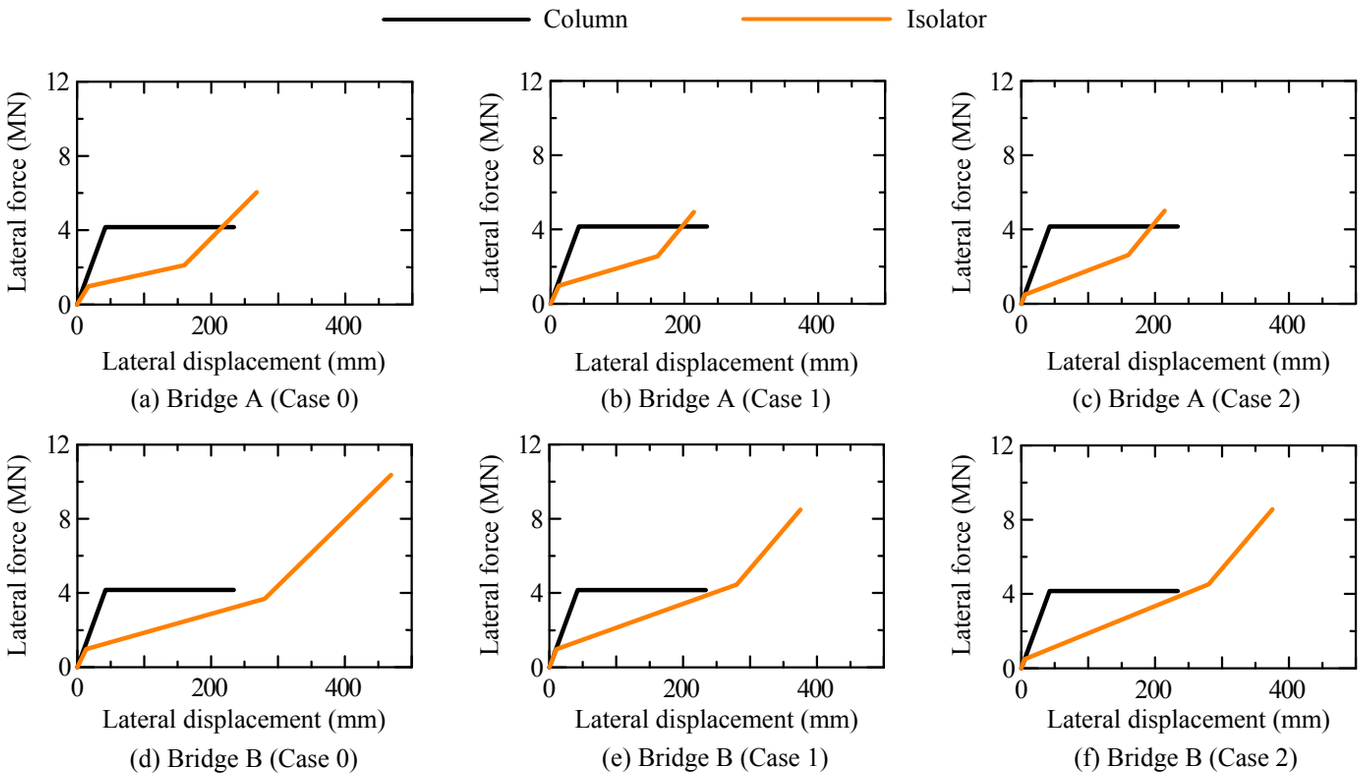


Figure 3. Skeletons of lateral force-lateral displacement relationship of the isolator and the column based on the mean values

3 FAILURE MODE OF BRIDGES WITH DETERIORATED ISOLATORS

3.1 *Skeletons of force-displacement relationship of the isolators and the columns*

Skeletons of lateral force-lateral displacement relationship of isolators and columns for Bridges A and B calculated based on the mean values listed in Table 7 are shown in Figure 3. Rupture strength of the isolator of Bridge B is much higher than that of Bridge A, and there is an adequate hierarchy between the rupture strength of the isolator and the ultimate strength of the column if the isolator is sound (Case 0) in Bridge B even if effects of the inertia force of the column evaluated by dynamic response analysis is considered.

However, if isolators are deteriorated, there is an insufficient hierarchy between the rupture strength of deteriorated isolators and the ultimate strength of the column, especially in Cases 1 and 2 of Bridge A. It is also noted that the yield strength of the isolator is degraded by deterioration of the lead core in Case 2.

3.2 *Performance of isolated bridges evaluated based on incremental dynamic analysis*

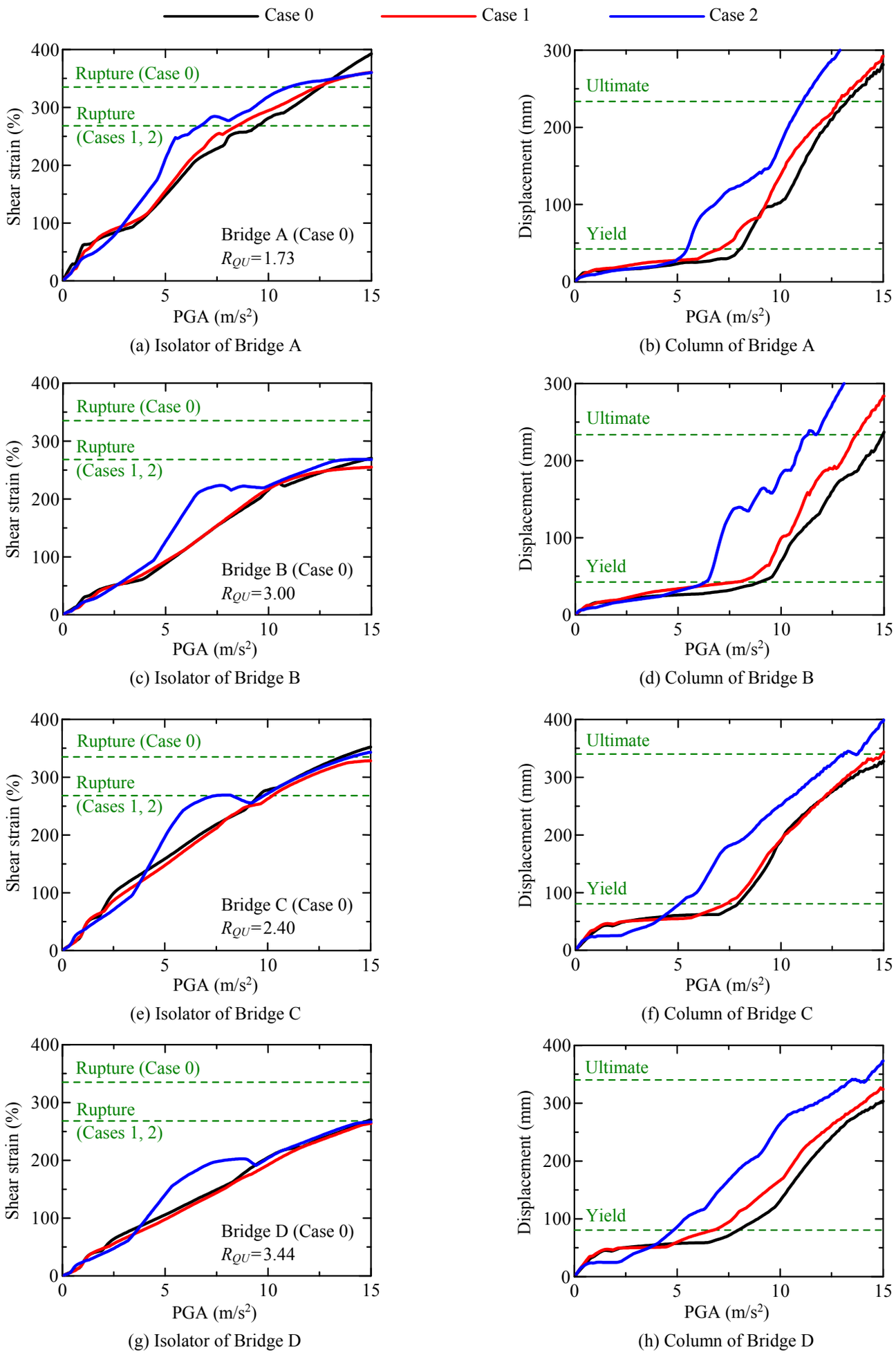
To investigate effects of deterioration of isolators on the seismic performance of isolated bridges, response of the target bridges subjected to NS component of JMA Kobe record during the 1995 Kobe earthquake was evaluated with different intensity by increasing amplitude of the ground motion. Peak ground acceleration of the original NS component of JMA Kobe record is 8.18 m/s^2. Dynamic response analysis was conducted using the mean values listed in Table 7.

Response of the isolators and columns of the target bridges are shown in Figure 4. Response shear strain of the isolator decreases if the capacity ratio R_{QU} increases as shown in Figure 4. This is because lateral force of the isolator is controlled by the lateral force and the inertia force of the column, and the maximum lateral force transferred by the column is the ultimate strength of the column. Thus safety margin for the isolator can be controlled by the capacity ratio R_{QU}.

Figure 4 shows that there is a little difference in the response of isolators between Cases 0 and 1. But it is noted that rupture strain of the isolator in Case 1 is reduced by 20 % compared to that in Case 0. If the lead core of isolators are also deteriorated, response shear strain of the isolator increases due to the reduction of energy absorption at the lead core especially after the column yields. This reduction of energy absorption mainly affects the increase in the response displacement of the columns as shown in Figure 4.

3.3 *Fragility curve*

Fragility curves of the target isolated bridges are shown in Figure 5. Failure members of Bridges A and C, which have low capacity ratio R_{QU}, can be not only the column but also the isolator even if the isolator is sound as shown in Figure 5 (a) and (g).



(a) Isolator of Bridge A

(b) Column of Bridge A

(c) Isolator of Bridge B

(d) Column of Bridge B

(e) Isolator of Bridge C

(f) Column of Bridge C

(g) Isolator of Bridge D

(h) Column of Bridge D

Figure 4. Response of isolators and columns evaluated based on incremental dynamic analysis using the mean values

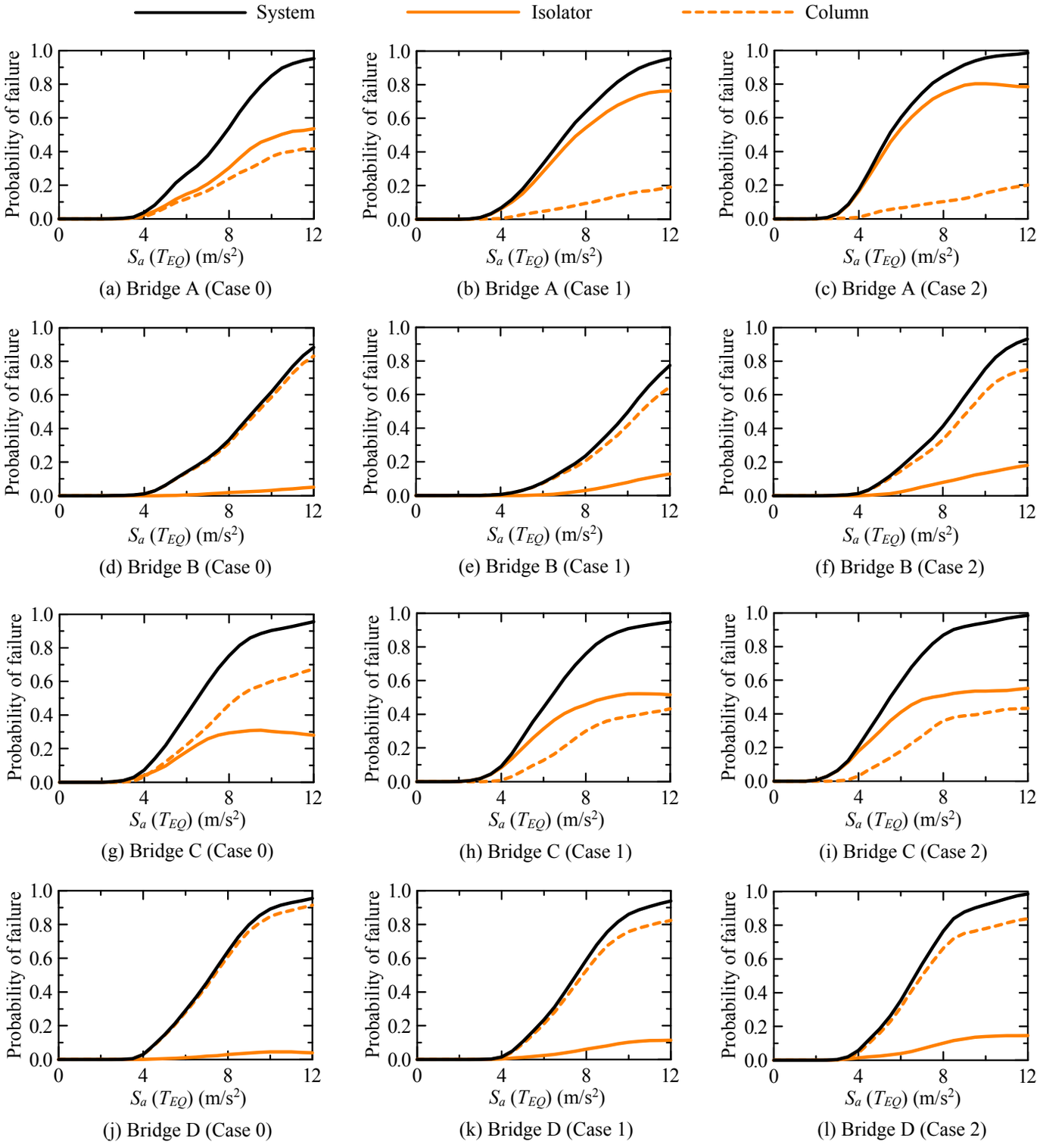


Figure 5. Fragility curves of the target bridges

This is because there is an insufficient margin for the isolator as shown in Figure 4 if capacity ratio R_{QU} is low. On the other hand, rupture of the isolator can be prevented if there is an adequate hierarchy between the rupture strength of the isolator and the ultimate strength of the column by settting an appropriate capacity ratio R_{QU}.

Probability of failure at the isolator in Cases 1 and 2 increases compared to that in Case 0 as shown in Figure 5. It is noted that the difference between fragility curves of Cases 1 and 2 are not significant, even though the lead core is sound in Case 1 and deteriorated in Case 2. This is because failure probability of the isolator is mainly controlled by the rupture strain associated with deterioration of the rubber as shown in Figure 3.

4 CONCLUSIONS

Failure modes of isolated bridges with deteriorated isolators were investigated based on incremental dynamic analysis and fragility analysis based on dynamic response analysis considering uncertainties in

the material and mechanical properties as well as strain hardening of isolators in large shear strain range. The following conclusions were drawn:

1) It is confirmed that safety margin for the isolator increases as the capacity ratio R_{QU} increases by incremental dynamic analysis. This is because the maximum lateral force transferred by the column is the ultimate strength of the column.
2) If the lead core of the isolator is sound, effects of deterioration of rubber on the response of the isolator and the column is not significant. However, response of the isolator and the column is affected by deterioration of the lead core of the isolator. This reduction of energy absorption mainly affects the increase in the response displacement of columns.
3) Failure probability of the isolator is mainly controlled by the rupture strain associated with deterioration of the rubber of the isolator.

ACKNOWLEDGEMENTS

This study was supported by JSPS KAKENHI Grant Number JP26420452. It is appreciated that strong ground motions were provided by K-NET and KiK-net of NIED, JMA, JAEE and NGA database of PEER.

REFERENCES

Adachi, Y. 2002. Reliability Analysis and Limit State Design Method of Isolated Bridges under Extreme Ground Motions. Doctoral Thesis, Kyoto University, Japan.

Hayashi, K., Adachi, Y., Komoto, K., Yatsumoto, H., Igarashi, A., Dang, J. and Higashide, T. 2014. Experimental Verification for Remaining Performance of Lead Rubber Bearings with Aging Deterioration. *Journal of JSCE* (A1) 70(4): I_1032-I_1042.

Jangid, R.S. 2007. Optimum lead-rubber isolation bearings for near-fault motions. *Engineering Structures* 29(10): 2503-2513.

Japan Road Association 2004. *Manual on bearings for Highway Bridges*. Tokyo: Maruzen.

Japan Road Association 2012. *Design Specifications of Highway Bridges V Seismic Design*. Tokyo: Maruzen.

Matsuzaki, H., Onodera, M., Tsumura, T. and Suzuki, M. 2017. Effects of Deterioration of Isolators on the Seismic Failure Modes of Isolated Bridges with Reinforced Concrete Columns. *Journal of Structural Engineering*, JSCE, 63A: 397-410.

Park, J.-G. and Otsuka, H. 1999. Optimal yield level of bilinear seismic isolation devices. *Earthquake Engineering and Structural Dynamics* 28(9): 941-955.

Public Works Research Institute 2013. *Technical Note of PWRI* 4262.

Shinohara, M. and Hoshikuma, J. 2015. Experimental Evaluation of Property of Lead Rubber Bearing Damaged due to Earthquake. *Journal of JSCE* (A1) 71(4): I_587-I_599.

Takeda, T., Sozen, M.A. and Nielsen, N.N. 1970. Reinforced concrete response to simulated earthquakes. *Journal of the Structural Division*, ASCE, 96(12): 2557-2573.

Vamvatsikos, D. and Cornell. C.A. 2002. Incremental Dynamic Analysis. *Earthquake Engineering and Structural Dynamics* 31(3): 491-514.

Zhang, J. and Huo, Y. 2009. Evaluating effectiveness and optimum design of isolation devices for highway bridges using the fragility function method. *Engineering Structures* 31(8): 1648-1660.

Maintenance, Safety, Risk, Management and Life-Cycle Performance of Bridges – Powers, Frangopol, Al-Mahaidi & Caprani (Eds)
© 2018 Taylor & Francis Group, London, ISBN 978-1-138-73045-8

Durability of reinforced concrete bridges in marine environments

R.E. Melchers & I.A. Chaves
The University of Newcastle, Newcastle, Australia

ABSTRACT: Achieving long-term durability for reinforced concrete structures particularly in marine environments remains a matter of much interest. Recent research findings based on observations from actual bridge performance and specially conducted long-term experiments for a wide variety of concretes indicate that chloride concentrations are involved only indirectly in initiating reinforcement corrosion and in serious active corrosion. For high quality concretes loss of concrete alkalinity (i.e. acid neutralizing capacity) as imparted by the cement content rather than direct corrosion attack of the steel reinforcement is the critical aspect. The rate of dissolution of calcium hydroxide, normally very low, is increased by chlorides and by greater internal surface area, such as in poor quality, porous, concretes. Only when the concrete pH drops below sufficiently will large-scale reinforcement corrosion be possible. However, cracking of concrete cover through to the reinforcing bars may cause accelerated localized loss of alkalinity, and thus severe very localized corrosion.

1 INTRODUCTION

Structural engineers rely heavily on prediction - for consequences and for their likelihood of occurrence. This requires good quality models, including for structural deterioration. The models should be robust, valid and defensible for extrapolation. Poor quality models, 'heuristics', 'expert systems', machine learning or similar 'models' not based on solid understanding of the processes involved in deterioration run the risk that predictions based on them will be problematic at best and 'hocus-pocus' at worst.

For reinforced concrete (RC) structures, including bridges, the most common concern is the long-term effect of exposure to marine conditions, principally corrosion of reinforcement caused by seawater (Richardson 2009; Gjorv 2009; Angst et al. 2012). Carbonation and alkali-aggregate reactions are of less concern (Parrott 1987). Often RC structures are given some degree of protection with impressed current systems, or more recently with sacrificial anodes, but these also deteriorate. Usually they require (often expensive) maintenance at least every 10-15 years. Thus, the question must be asked whether these protection or alternative systems are strictly necessary, since there is a considerable history of successful, durable RC structures, exposed, unprotected, to marine environments for long periods of time (e.g. Gjorv 2009; Melchers et al. 2009; Angst et al. 2012; Melchers & Chaves 2017a, 2107b).

A wealth of academic and largely theoretical literature exists about marine corrosion of RC structures but much of this does not appear to relate well to practical experience (Angst et al. 2009; Melchers & Chaves 2017a). Much conventional thinking is founded on the notions of chloride diffusion and the chloride 'threshold', the latter supposedly defining when damaging reinforcement corrosion becomes important (e.g. Richardson 2002; Gjorv 2009). This criterion increasingly has been questioned (e.g. Melchers & Li 2006; Angst et al. 2009) with the result that the current RC corrosion literature now refers to 'chloride-induced' corrosion, indicating that the effect of chlorides is not fully understood.

The next section reviews two bridges exposed to marine environments for which detailed observations were possible. Experiences for many other RC structures also are considered. These experiences are then compared with results and conclusions reported only recently for RC specimens in long-term laboratory exposure conditions.

2 RC BRIDGES IN MARINE EXPOSURES

2.1 *Long-term observation and investigation*

Corrosion of reinforcement in RC structures is a slow process, even in some of the most aggressive exposures. Controlled experimental studies usually are not feasible in conventional university or re-

search laboratory settings. An alternative is to use an 'archaeological' approach, in which existing older structures are examined, with interpretation of the observations based on reconstructions of the likely operational and environmental conditions.

Learning from actual operational experiences with real structures has the draw-backs that (1) usually there are only a few structures available for investigation, (2) they tend to be one-off so that investigation of causative parameters is difficult, and (3) typically they are not well-documented (or the documentation no longer exists or cannot be found). Nevertheless, several investigations along these lines have been described (e.g. Chitty et al. 2005; Melchers et al. 2009; Melchers 2015; Angst et al. 2012). Two Australian examples are given below.

2.2 *Hornibrook Highway Bridge (Brisbane)*

This was a 2.6 km long road bridge completed in 1935 (Melchers et al. 2017). Its RC substructure comprised 292 spans supported on RC headstocks, each supported on 3 precast, driven, RC piles (879 in total). Each pile typically was 380 x 460 mm in cross-section and reinforced with 4 round steel reinforcing bars of 32mm nominal diameter, with 60mm cover. The headstocks were cast-in-situ over the ends of the piles with reinforcement from the piles going into the headstocks. During the 1990s some concrete cracking and spalling of the headstocks was noted and confirmed by detailed surveys in 1998 and 2003. Subsequently its use was limited to pedestrian traffic. The bridge was almost completely demolished in 2011-2. At that time independent observations noted that there was considerable corrosion evident for the headstocks and the RC approach bridges but not for the RC piles. These showed almost no signs of reinforcement corrosion, such as longitudinal cracking, spalling of concrete cover and rust staining. This was the case in the splash zone, in the tidal zone (usually considered the most prone to reinforcement corrosion) and in the immersion zone.

Through good cooperation between the local highway agency, university researchers and, most importantly, the demolition contractor, more detailed investigations were then undertaken, as follows.

During demolition most piles were extracted vertically from the sand foundation material although some had to be cut off. They were then stored in the contractor's demolition yard where many were examined for visible signs of reinforcement corrosion. Randomly selected 2-3 m lengths of piles were transported to the university structural testing laboratory for more detailed examination. These were cored for compression strength testing and cut transversely for examination of the cross-sections. The concrete strength was very high (Table 1), as noted also in the earlier investigations. The concrete pH also was very high, at around pH 12 across more than 95% of the cross-sections. Close inspection showed no significant air-voids around the bars, and this was confirmed by removal of the longitudinal reinforcement from the concrete (Fig. 1). Both are remarkable since at the time of construction concrete compaction most likely was by hand rodding. Also, at the time of construction, adding water to the concrete mix for workability was not prohibited, although the importance of water-cement ratio was recognized. Further, it has been reported that Emmanuel Hornibrook, the bridge designer, was remarkably careful in the design and the construction of the bridge components and, when in doubt, insisted on adding more cement to the concrete (Melchers et al. 2017).

Table 1. Summary of properties of the concretes and corrosion.

Property	Units	
Concrete strength (cores)	MPa	66-76
Concrete cover (typical)	mm	60
Concrete chloride content at bars	kg/m^3	5 - 14
Concrete pH at reinforcing bars		~ 12
Apparent carbonation depth	mm	2-5



Figure 1. Concrete surface adjacent to a reinforcment bar in a randomly selected pile, showing no evidence of air voids or separation between the steel and the concrete.

One of the few locations were some minor reinforcement corrosion was observed on the laboratory-cut cross-sections, the pH local to that corrosion spot was around 7 despite the pH elsewhere on the cross-section being around 12.

Despite the apparently excellent condition of the nearly 900 RC piles overall, one case in particular must be considered. It is the case for which a transverse crack some 60% inward from one face of the pile was discovered (Melchers et al. 2017). When examined, the crack surface was found covered with a layer of watery-looking rust stain. The two reinforcement bars on what would have been the tension side were corroded right through. Each bar showed a conical end some way into the space left by the steel that had corroded away (Fig. 2). Other than very minor rust staining on the outside surface of the pile, there were no signs warning of reinforcement corrosion. Apart from the alarm this case should raise with practitioners, the immediate research question is 'what happened to the corroded steel?" The next question obviously is "why?".

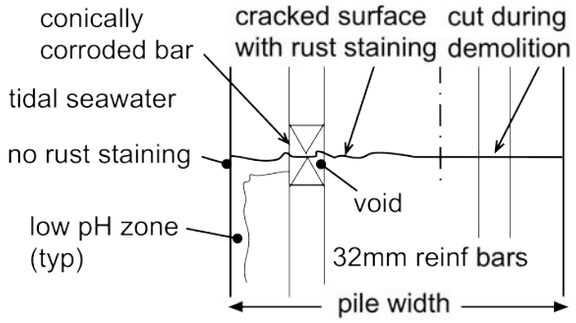


Figure 2. Schematic view of the highly localized reinforcement corrosion found in one of the piles of the Hornibrook bridge. The tidal seawater would remove the highly soluble ferrous chlorides generated by crevice corrosion in the void region.

2.3 *Sorell Causeway Bridge (Tasmania)*

This bridge, constructed in 1957, consisted of 34 simply-supported spans each 13 m long exposed to a marine environment. Each span comprised 14 precast, post-tensioned T beams connected together by transverse post-tensioning (Papé & Melchers 2011). Unlike subsequent post-tensioned bridges, the ducts, made using inflatable tubes, did not contain a steel duct liner. There were two tendons per beam, each consisting of 18 cold-drawn high-tensile wires of 5.1 mm diameter. The remaining space was pressure grouted with mortar. The concrete cover to the tendons in the stem of the T beams was around 25mm. The bridge was demolished in 2002 following observations of visible damage along the line of the profile of the lower tendon. This was the case only for the most exposed T beams.

Three of the beams were transported to the University of Newcastle for load-testing and detailed examination: one considered from visual examination to be the most damaged by tendon corrosion, a slightly damaged beam and a randomly selected, apparently undamaged, beam. The load tests have been described elsewhere, as have results of the detailed examinations (Papè & Melchers 2013). The beam in apparently good condition showed little or no evidence of corrosion of the tendons, such as concrete cracking, spalling or rust stains. For this beam phenolphthalein measurements on the concrete cross-sections showed much of the interior concrete still at pH>12.

The most damaged beam revealed severe corrosion of the prestressing strands, with the pattern of corrosion being worse at one side of the outer layers of strands, with some strands remaining as almost hemispherical in cross-section (Fig. 3). This beam also showed considerable rust staining in the area where most of the corrosion had occurred but only a small amount of deposited rusts, including black and green rusts (Papé & Melchers 2011). It was apparent that most of the metal that had corroded away was not present as corrosion product anywhere within or the outside surfaces of the beam. Some rust was found below the tendon in the region where the concrete T beam stem had split roughly vertically. There was remarkably little rust on the exterior of the T beam stem.

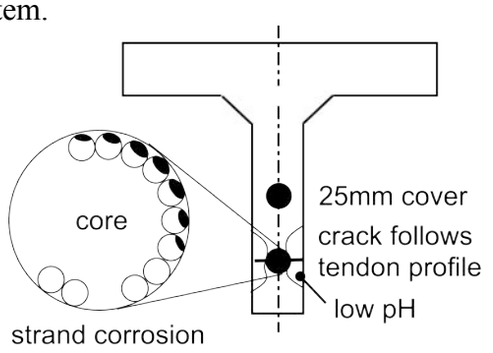


Figure 3. Schematic view of the cross-section of the most damaged T beam, showing corrosion damage of strands forming tendon, low pH regions and location of concrete cracking.

Breaking open the beam showed that much of each tendon duct was filled with grout but also that there were sizeable air-voids that interfaced with the strands of the tendon. Some also appeared to be located at or close to where significant strand corrosion was observed (Fig. 3). At these point the concrete pH was low (around 7-9), but overall the pH of the concrete cross-sections was quite high (>10-12) in most areas. It was postulated (Papé (2008) that the low pH was the result of carbonation. However, whether this is possible, in view of the existence of 25mm of concrete cover and the grout around the tendon, is an interesting question. For good quality concretes carbonation is known to penetrate only a few millimetres into the concrete (Parrott 1987).

2.4 *Other RC structures*

Summaries of experiences with the long-term behaviour of reinforced concrete structures exposed to marine environments or de-icing salts world-wide (Gjorv 2009), including many bridges (Melchers & Li 2009), show many cases with excellent long-term performance, usually associated with structures constructed with ‘good workmanship’ and with high quality, very low permeability concretes. Some of these have been reported in more detail, as summarized by Angst et al. (2012). There also are many cases of poor durability and severe corrosion problems associated with poor quality or undefined concretes. Careful analysis shows that in some cases the effects of other influences have not been properly considered. One example is road bridges without a bitumen wearing or riding course. Detailed rather than cursory observations showed that motor vehicles and lorries often cause physical damage to the concrete cover of the bridge deck and that corrosion damage then followed, rather than the damage being

the direct result of inward diffusion of chlorides from de-icing salts causing corrosion that then cracked the cover (e.g. Lukas 1985; Volkswein & Dorner 1986). Similarly, destruction of the concrete matrix protecting the steel may be caused by volume changes resulting from alkali-aggregate reactions, with corrosion then following (Jensen 1996; Richardson 2002; Gjorv 2009). Structural bending and shear actions also may cause deterioration of the concrete cover and thus long-term corrosion problems, even though cracks in concrete up to about 0.3mm usually are considered acceptable. However, the relevance of this criterion is questionable as it has its origins short duration in laboratory tests (Beeby 1978).

3 FROM FIELD OBSERVATIONS TO THEORY

The conventional model for the commencement and development of reinforcement corrosion as a function of exposure period is attributed to Tuuti (1982) although proposed earlier by Clear (1976) (Fig. 4). It presumes negligible corrosion before the initiation time t_i followed immediately by a high rate of damaging corrosion. A slight modification is allow more time for chloride diffusion after t_i before damaging corrosion starts (Weyers et al. 1997) including allowance for minor cracking of the concrete, such as caused by beam bending, which increases overall permeability (Francois & Arliguie, 1999).

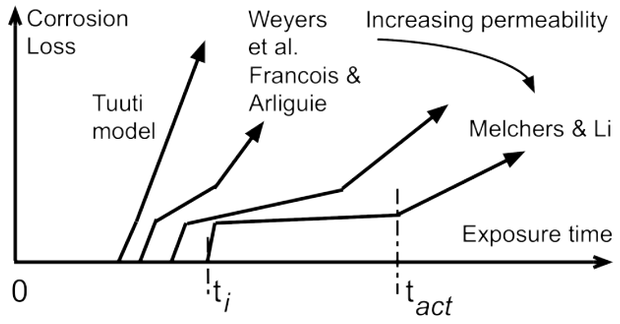


Figure 4. Integrated model for the initiation and development of reinforcement corrosion showing separation between initiation at t_i and start of active corrosion at t_{act}.

A more comprehensive, integrated model is shown in Figure 4. It is based on observations from field studies (Melchers & Li 2006). Unlike the earlier models and proposals, it distinguishes between the quality of the concrete. For dense, impermeable concretes it has serious, active corrosion commencing only at some later time t_{act}. This implies immediately that the mechanisms for the initiation differs from that for active corrosion (Melchers & Li 2006). It also was proposed that active corrosion after t_{act} is the result of loss of concrete alkalinity and in particular the loss of $Ca(OH)_2$ as accelerated by the presence of chlorides. This hypothesis is discussed further below.

The differentiation between t_i and t_{act} was used by Melchers & Li (2009) to review and analyse some 300 individual reinforced concrete structures, using information, of various levels, as reported in the literature and in various reports. This showed that for most structures there were considerable differences between the values of t_i and t_{act} (Fig. 5). Similar results, but with higher values of t_i and t_{act} were obtained for structures with (non-reactive) limestone and dolomite aggregates (Melchers & Li 2009). Independent support for the separation of t_i and t_{act} has been reported for long-term (25 year) laboratory exposures of pre-cracked beams (Yu et al. 2015).

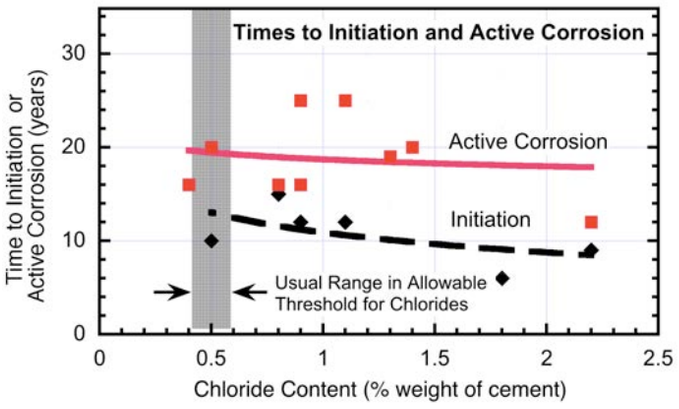


Figure 5. Trends for times to initiation (t_i) or active corrosion (t_{act}) as a function of concentration of chlorides estimated at the reinforcement. The typical range for acceptable chloride concentration threshold is shown.

An interesting feature of Fig. 5 is the relatively low influence of chlorides. This contrasts with many earlier laboratory test results that appear to show that chlorides much increase corrosion losses. However, almost invariably these tests were conducted using a simulated porewater solution under accelerated conditions such as through stirring the solution or using air bubbling. Evidently, these conditions do not properly represent those relevant inside actual concrete structures.

The low sensitivity to chlorides shown in Fig. 5 is unlikely to accidental or fortuitous. Firstly, it was observed also for realistic model reinforced concrete samples exposed for more than 10 years in a high humidity environment (Melchers & Chaves, 2017a). Secondly, it is consistent with corrosion theory and detailed investigations under laboratory conditions for corrosion mechanics, as summarized below.

For corrosion to be possible, it is necessary to satisfy the thermodynamic conditions for the chemical reactions involved. In electrochemistry these are summarized in the Pourbaix diagram (Jones, 1996). It shows that without an applied potential (such as often is applied in electrochemical tests), corrosion of ferrous iron in pure water can occur only for pH <

about 9 (Pourbaix 1970; Jones 1996; Chitty et al. 2005). The addition of chlorides to the solution can initiate pitting corrosion at (much) higher pH values, increasing with the chloride concentration (Pourbaix 1970). These conditions only indicate whether corrosion can occur, not how fast it will progress. The latter is important for infrastructure applications.

In severely corrosion damaged structures very considerable amounts of corrosion product typically are seen, and these are unlikely to be the result only of pitting corrosion. More general, overall corrosion is required. For this to be possible it is necessary for the high alkalinity ('acid-buffering capacity') of the concrete surrounding the steel bars to drop, to a pH of about 9 (Pourbaix 1970; Jones 1996). This also is consistent with field observations (Melchers et al. 2006; 2017). The time taken for the pH to reduce sufficiently will depend on (a) the initial 'alkalinity' (acid-neutralization capacity) of the concrete, (b) the rate of loss of alkalis from the concrete and possibly (c) the rate of 'carbonation'. The first is related to the cement content of the concrete but may be boosted by alkaline materials such as calcium carbonate, while the second and third depend on the rate of diffusion, leaching or dissolution of various species, including chlorides, oxygen, alkalis and, for carbonation, carbon dioxide. These rates depend, in turn, on the permeability of the concrete relative to each species. The alkali of most importance for significant reduction of pH is calcium hydroxide $Ca(OH)_2$ since it tends to maintain a pH of about 12.

The environment for corrosion inside most concretes can be characterized as 'wet and stagnant'. Water is required for corrosion to occur but it must be present at the steel-concrete interface and it must be available. There is evidence from corrosion in soils that moisture may be held in the pore structure and only when the moisture content is sufficiently high (but not too high to exclude oxygen) will corrosion occur (Gupta & Gupta 1979). The stagnant conditions also are important. Classic experiments (Heyn & Bauer 1908) showed that for mild steel immersed in weak stagnant, solutions of about pH=7 corrosion loss was very similar, for variety of dilute solutions of salts, including NaCl. This was explained many years later (Brasher 1967) as the result of stagnant solutions permitting the weak passive film formed on ferrous materials (*cf.* Evans 1960) to remain in place. This is increasingly less likely to occur as the water velocity increases. Carefully controlled laboratory exposure experiments by Mercer & Lumbard (1959) provide direct support - in near-stagnant conditions chlorides had almost no influence on the amount of corrosion. Unfortunately, many laboratory experiments using solutions have been conducted under non-stagnant conditions. Their validity for actual reinforced concrete structures is, therefore, questionable (*cf.* Poursaee & Hansen 2009).

4 TIME TO INITIATION

A long-term experiment, commenced in 2004, throws some light on initiation, as well as active corrosion (Melchers & Chaves 2017a) In the experiment a large number of concrete specimens each 40 x 40 x 160 mm long, with a 6 mm diameter smooth mild steel bar placed centrally in the longitudinal direction and made to a variety of water/cement and aggregate/cement ratios. All were made with the same aggregates. The specimens were cast in steel moulds of high dimensional accuracy and vibrated for an equal amount of time on the laboratory shaking table. They were then continuously exposed to a high humidity (>95% RH) 20˚C laboratory fog-room environment. The specimens were water saturated whenever inspected in the fog room. It is noted that this wet environment ensures carbonation as a cause of any corrosion can be discounted (Parrott 1987).

All except one series (series C) were made using standard commercial (blended) Portland (GP-type) cement, sourced at the same time from one manufacturer. Series C was made with sulphate-resistant cement. Further, except for one test series made with freshwater (series K) all specimens were made with Pacific Ocean seawater. This was done to obviate the time required for chloride ions to diffuse to the steel bar. Since the chloride concentration was high right from the time the specimens were made, initiation of reinforcement corrosion could be expected from first exposure.

One or two specimens from each set of specimens were withdrawn from the fog-room about every 12 months (Melchers & Chaves, 2017b) examined externally, and broken open to reveal the state of the steel bar and of the interior concrete. For the reference set (series B) this showed that after 2-3 years exposure some concrete mixes showed corrosion of the steel bar, but others did not. The latter were the concretes with higher strength, greater density and thus lower permeability. Also, series K showed no corrosion, both in the first few years and for the next 12 years (i.e. to date). Where corrosion was observed (in the B series) it was in the form of pitting or localized corrosion along the lower part of the reinforcing bar, that is, away from the casting direction and closest to the shaking table.

This pattern continued for the following years, with only moderate increases in corrosion observed for the denser concretes and more for the concretes of lower densities and thus greater permeability. After 12 years exposure the concretes with the highest aggregate cement ratios (i.e. lowest overall cement contents), and thus highest permeabilities, showed moderate corrosion all around the reinforcing bars, but still insufficient to cause longitudinal cracking along the bars. This pattern is consistent with Fig. 4.

Examination of the concrete at the concrete-steel interface showed the presence of air-voids, particu-

larly for the less dense concretes, predominantly along the lower part of the bars (i.e. away from the casting direction). Air-voids are known to leave less or none of the alkaline calcium hydroxide layer typically found around reinforcement bars and also have long been considered as involved with the localized or pitting corrosion of reinforcement (Verbeek 1975; Angst, et al. 2017). However a clear link between air-void location and pitting was not established. The present results do show such a connection from sections cut across the specimens (Fig. 6). Also, the higher propensity of air-voids and pitting along the lower parts of the bar is consistent with field experience and attributed to the degree of concrete compaction during construction (e.g. Nawy 2008).

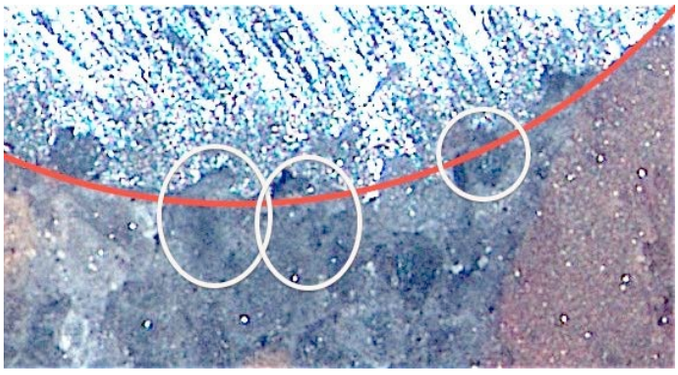


Figure 6. Part cross section of lower part of steel bar showing voids in concrete at interface and localized corrosion.

5 TIME TO ACTIVE CORROSION

The experiments outlined above also have thrown new light on the time to active corrosion, t_{act}. Already after the first few years it was observed that the specimens in series C, made with sulphate-resistant cement, showed a remarkable difference in the colour of the interior concrete. The lighter coloured region was greater for the more permeable concretes and increased with longer exposures. Closer examination of the specimens made with GP cement also showed a (much less obvious) colour difference (Fig. 7).

Analysis of the dark and of the light-coloured concretes revealed interesting differences. In brief, the light coloured concrete appeared permeable, was devoid of $Ca(OH)_2$, showed negligible carbonates and had a pH around 7-8. If it had reached the steel bar, the bar invariably was corroded to some degree. In contrast, the darker concrete was less obviously permeable, showed high concentrations of $Ca(OH)_2$ and high pH (10-12) (Melchers & Chaves, 2016).

The more open structure of the light-coloured concrete indicates loss of material (i.e. calcium hydroxide) and also greater permeability. Taken together, these observations support the proposition (Melchers & Li 2006) that active corrosion for high quality, dense, low permeability concretes is through the loss of calcium hydroxide and that this loss is by leaching from the outside inwards.

Importantly, it is well-known that loss of $Ca(OH)_2$ is governed by its rate of dissolution in water. It is very low for pure water (Sagues et al. 1997; Marinoni et al. 2008) but is accelerated by the presence of NaCl in proportion to its concentration (Johnson & Grove 1931). In this regard, it is noted that the surface area available for the dissolution process is greater for the more permeable concretes, consistent with the experimental observations.

By comparison, the K series made with fresh water showed much less penetration of a light coloured region, and thus a much lower rate of $Ca(OH)_2$ dissolution. For these concretes the pH at 12 years was still high.

Overall, the critical point is that the lighter outer zone of the specimen (Fig. 7) is the result of dissolution and leaching of $Ca(OH)_2$ from the specimen. When this zone eventually reaches the steel bar, the local pH will reduce to below about 9 and allow corrosion to proceed. It is clear from the experimental results that this can occur irrespective of the local concentration of NaCl.

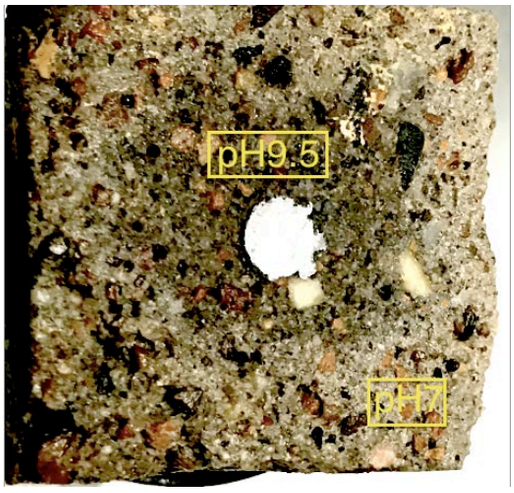


Figure 7. Concrete cross-section of a 12 year old specimen made with GP cement immediately after it was cut open, showing inner darker and outer lighter zones. Indicative spot pH values are shown.

INFLUENCE OF CONCRETE CRACKING

The experiments described above were for uncracked concrete specimens. However, concrete cracking is likely to affect both dissolution and leaching of $Ca(OH)_2$ from the concrete matrix, the latter mainly through reducing the effectiveness of the concrete cover and the alkalinity it holds. This is consistent with experimental results (Francois & Arliguie 1999) although not described in those terms. From short-term experimental results it was concluded that even if cracks penetrated to the rein-

forcement, the severity of any resulting corrosion was directly proportional only to crack width (e.g. Beeby 1978). This was attributed to the alkalinity of the concrete providing 'autogenous healing'. However, large-scale laboratory observations indicate that irrespective of width, transverse cracks penetrating to the reinforcement permit the commencement of corrosion at the crack base (Francois et al. 2012). This is consistent with the notion of loss of alkalinity, facilitated now by the presence of cracks. It is consistent with the severe localized corrosion for the Hornibrook bridge (Fig. 2) and for the Sorell bridge (Fig. 3). In the latter, it also explains the considerable presence of low pH concrete inside the beams, earlier noted as not easily explainable 'carbonation' (Papé 2008) but now explainable in terms of dissolution and leaching of $Ca(OH)_2$ from the concrete matrix. In both these cases, it is likely also that in the longer term corrosion under low oxygen conditions in the crevice corrosion conditions at the concrete-steel interface producing soluble ferrous chlorides also was involved (Wranglen 1974).

6 PRACTICAL IMPLICATIONS

From a practical perspective, the most important parameter to arise from the present work is t_{act}. It describes when serious corrosion can be expected to commence, irrespective of any previous, short-term initiation as indicted by the parameter t_i. In most practical structures, it is the case that once serious corrosion has commenced the lifetime of the structure has been seriously compromised. Certainly simulations can be carried out to ascertain the extra life (to t_L) possible after t_{act} has been reached, but the aim of design or rehabilitation should be to extend the time for t_{act} as long as possible, economically.

The second practical outcome from the present work is the clear indication that cracking, even hairline cracking, of the concrete, particularly transverse cracking through to or close to the reinforcement, such as might result from high bending stresses, can have a very detrimental effect. As noted, the research on which current design Code rules are based used short-term testing and did not allow development of the mechanisms exposed both by the field experience now available and as supported by the present longer-term experimental work and also seen in other recent experimental work (cf. Francois et al. 2012). It follows that design rules for cracking need to be revised, particularly for marine exposure conditions.

The third aspect to arise from the present work is that it reinforces the crucial role of concrete alkalinity. The importance of this has long been recognized as a key factor in maintaining passivity against corrosion of steel reinforcement. The recent experimental results for chloride induced corrosion reinforce this role since alkalinity dissolution is now seen to be critical in the development of conditions that permit commencement of active, serious corrosion of the reinforcement, including in chloride environments. Since high alkalinity conventionally is associated with high cement contents, the immediate inference is that longer durability can be achieved with higher cement content. However, opposing this are the increasing environmental and economic pressures to reduce cement contents in concretes. In this context, other ways of enhancing the alkalinity of concretes are of interest. One possibility is the use a relatively high proportion of low alkalinity aggregates such as limestone and non-reactive dolomites (Melchers & Li 2009). When these were used as aggregates they increased the time t_{act} to active corrosion. This observation is consistent with (anecdotal) experience, for example, in those parts of Europe (Lukas 1985) and in Florida (Lau et al. 2007) where the predominant aggregates are calcareous.

Finally, the overall mechanisms described herein differ from the conventional wisdom in some important ways. They give a role to chlorides that differs significantly from the conventional wisdom, and one that differentiates between initiation of reinforcement corrosion and its eventual serious, active, commencement. Overall, the mechanisms are consistent with fundamentals in corrosion science and, importantly, are consistent with practical experience and observations for high quality reinforced concrete structures. The present results also bring a degree of unity between carbonation-induced and chloride-induced corrosion. In both, it is the loss of protective alkalinity that permits eventual, active corrosion.

7 CONCLUSION

The work reported herein shows that the primary role of chlorides in so-called 'chloride-induced' corrosion of reinforcement lies in accelerating the solubility of the alkaline calcium hydroxide in the concrete matrix, including around the reinforcing bars and thereby eventually allowing depassivation of the steel reinforcement. Evidence was presented also that initiation is largely the result of air-voids at the concrete steel interface and therefore is controlled mainly by concrete mix design and by compaction of the concrete. This relates directly to an important part the usually poorly defined 'good workmanship' required for good concretes.

ACKNOWLEDGEMENTS

The authors acknowledge the support of the Australian Research Council and the Civil Engineering laboratories at the University of Newcastle.

REFERENCES

Angst U. M. and 15 others. 2017. The steel-concrete interface. *Materials and Structures*, 50(143): (24 pp.)

Angst, U.M., Elsener, B., Jamali, A. & Adey, B. 2012. Concrete cover cracking owing to reinforcement corrosion - theoretical considerations and practical experience. *Materials and Corrosion*, 63(12): 1069-1077.

Angst, U.M., Elsener, B., Larsen, C.K. & Vennesland, O. 2009. Critical chloride content in reinforced concrete – A review. *Cement and Concrete Research* 39: 1122-1138.

Beeby, A.W. (1978) Corrosion of reinforcing steel in concrete and its relation to cracking. *The Structural Engineer*, 56A(3) 77-80.

Brasher, Dora M. 1967. Stability of the oxide film on metals in relation to inhibition of corrosion. I. Mild steel in the presence of aggressive ions. *Brit. Corrosion J*. 2: 95-103.

Chitty, W.-J., Dillmann, P., L'Hostis V. and Lombard, C. 2005. Long-term corrosion resistance of metallic reinforcements in concrete - a study of corrosion mechanisms based on archaeological artefacts. *Corros. Sci.* 47: 1555-1581.

Clear, K.C. 1976. Time-to-corrosion for reinforcing steel in concrete slabs. V. 3: Performance after 830 daily salt applications, FHWA-RD-76-70, Washington: Federal Highway Administration, Apr., 64 pp.

Evans, U.R. 1960. *The corrosion and oxidation of metals: scientific principles and practical applications*, London: E. Arnold.

Francois, R. & Arliguie, G. 1999. Effect of microcracking and cracking on the development of corrosion in reinforced concrete members. *Mag. Concrete Res*. 51(2) 143-150.

Gjorv, O.E. 2009. *Durability design of concrete structures in severe environments*. London: Taylor & Francis.

Gupta K. & Gupta B.K. 1979. The critical soil moisture content in the underground corrosion of mild steel. *Corros. Sci.* 19: 171-178.

Heyn, E. and Bauer, O. 1908 Ueber den Angriff des Eisens durch Wasser und wässerige Losungen. *Stahl und Eisen*, 28(44): 1564-1573.

Jensen, V. 1996. Present experience with aggregate testing in Norway, (In) *Proc. 10th Inter. Conf. Alkali-Aggregate Reaction in Concrete*, Melbourne Australia. 133-142.

Johnston, J. & Grove, C. 1931. The solubility of calcium hydroxide in aqueous salt solutions. *J. Am. Chem. Soc.* 53 (11): 3976–3991.

Jones, D.A. 1996. *Principles and Prevention of Corrosion*. Second Edition. Upper Saddle River: Prentice-Hall.

Lau, K., Sagues, A.A., Yao, L. & Powers, R.G. 2007 Corrosion performance of concrete cylinder piles. *Corrosion*. 63(4): 366-378.

Lukas, W. 1985. Relationship between chloride content in concrete and corrosion in untensioned reinforcement on Austrian bridges and concrete road surfacings. *Betonwerk und Fertigteil-Technik*. 51(11): 730-734.

Marinoni, N., Pavese, A., Voltolini, M. & Merline, M. 2008. Long-term leaching test in concretes: An X-ray powder diffraction study. *Cement & Conc Comp*. 30: 700-705.

Melchers, R.E. 2015. Field experience and the long-term durability of reinforced concrete structures. *Proc. Second Intl. Conf. on Performance-based and Life-cycle Structural Engineering*. 9-12 Dec. Brisbane: Uni of Queensland.

Melchers, R.E. & Chaves, I.A. 2016. Long-term durability of reinforced concrete structures in marine environments. *Proc. Eurocor2016*, Montpellier, 11-15 Sept.

Melchers, R.E. & Chaves, I.A. 2017a. A comparative study of chlorides and longer-term reinforcement corrosion. *Materials and Corrosion.* 68(6): 613-621.

Melchers RE & Chaves, I.A. (2017b) Modelling durability of reinforced concrete structures, *Brian Cherry Int. Conc. Symp.* Melbourne: Aust. Corros. Assn.

Melchers, R.E. & Li, C.Q. 2006. Phenomenological modelling of corrosion loss of steel reinforcement in marine environments. *ACI Materials J.* 103(1): 25-32.

Melchers, R.E. & Li, C.Q. 2009. Reinforcement corrosion initiation and activation times in concrete structures exposed to severe marine environments. *Cem. Conc. Res.* 39: 1068-1076.

Melchers, R.E., Li, C.Q. & Davison, M.A. 2009 Observations and analysis of a 63-year old reinforced concrete promenade railing exposed to the North Sea. *Mag. Conc. Res.* 61(4): 233-243.

Melchers, R.E., Pape, T.M., Chaves, I.A. & Heywood, R. 2017. Long-term durability of reinforced concrete piles from the Hornibrook Highway bridge. *Aust J. Struct. Eng*. 18(1): 41-57.

Mercer, A.D. & Lumbard, E.A. 1995. Corrosion of mild steel in water. *British Corrosion J.* 30 (1): 43-55.

Nawy, E.G. 2008. *Concrete Construction Engineering Handbook*. Boca Raton: CRC Press. pp. 30-57.

Papé T.M. 2008. *Investigating the correlation between pre- and post-demolition assessments for precast, post-tensioned beams in service for 45 years*. PhD thesis, The University of Newcastle, Australia.

Papé T.M. & Melchers R.E. 2011. The Effects of Corrosion on 45-Year-Old Pre-stressed Concrete Bridge Beams. *Structure and Infrastructure Engineering* 7(1&2): 101-108.

Papè T.M. & Melchers R.E. 2013. Performance of 45-year-old corroded prestressed concrete beams. *Structures and Buildings, Proc. Inst. Civil Engs*. 166(10): 547-559.

Parrott, L.J. 1987. *A review of carbonation in reinforced concrete*, Building Research Establishment, Dept Env. UK.

Pourbaix, M. 1970. Significance of protection potential in pitting and intergranular corrosion. *Corrosion* 26(10): 431-438.

Poursaee, A. & Hansen, C.M. 2009. Potential pitfalls in assessing chloride-induced corrosion of steel in concrete. *Cement and Concrete Research* 39: 391-400.

Richardson, M.G. 2002. *Fundamentals of durable reinforced concrete*. London: SponPress.

Sagues, A.A., Moreno, E.I. & Andrade, C. 1997. Evolution of pH during in-situ leaching in small concrete cavities. *Cement and Concrete Research*. 27 (11): 1747-1759.

Tuuti, K. 1982. *Corrosion of steel in concrete*. Stockholm: Swedish Cement and Concrete Research Inst. Res. Rep. No. 4.

Verbeek, G.J. 1975. *Mechanisms of corrosion of steel in concrete*, Pub. SP-49, Farringham: Am. Conc. Inst. 21-38.

Volkswein, A. & Dorner, H. 1986. Untersuchungen zur Chloridkorrosion der Bewehrung von Autobahn-Brucken aus Stahl-oder Spannbeton, *Forschung Strassenbau und Strassenverkehrstechnik*, Heft 460, Bundesminister fur Verkehr, Abteilung Strassenbau, Bonn-Bad Godesberg, Germany.

Weyers, R.E. 1997. Corrosion service life model concrete structures, In *Repair and rehabilitation of reinforced concrete structures*. WF Silva-Araya, OT De Rincon and LP O'Neill (ed). Reston: ASCE. 105-119.

Wranglen G. 1974. Pitting and sulphide inclusions in steel, *Corros. Sci*. 14: 331-349.

Yu, Linwen, Francois, R., Vu Hiep Dang & Gagne R. 2015. Development of chloride-induced corrosion in pre-cracked RC beams under sustained loading: Effect of load-induced cracks, concrete cover, and exposure conditions. *Cem. Conc. Res.* 67: 246-258.

Maintenance, Safety, Risk, Management and Life-Cycle Performance of Bridges – Powers, Frangopol, Al-Mahaidi & Caprani (Eds)
© 2018 Taylor & Francis Group, London, ISBN 978-1-138-73045-8

Damage accumulation in aging highway bridges considering multiple earthquake events

B. Panchireddi, U. Yadav & J. Ghosh
Indian Institute of Technology Bombay, Mumbai, India

ABSTRACT: Aging highway bridges exposed to harsh environmental conditions and located in active seismic regions may reveal a cumulative increase in earthquake-induced damage along their service lives when compared to pristine structures. While environmental degradation mechanisms are typically continuous throughout the lifetime, earthquake shocks are intermittent that depend on the seismicity of the region. Among different aging mechanisms commonly observed in bridges, this study focuses on corrosion deterioration of critical bridge components such as bridge piers. A framework is proposed that simultaneously considers multiple earthquake occurrences and corrosion deterioration of bridge components in determining the damage accumulation. Along with the statistical uncertainty associated with corrosion deterioration and occasional main-shock occurrence, uncertainties stemming from material properties is also considered in this study. For a representative case-study bridge in California, an appreciable increase is observed in the cumulative damage index while considering the effects of corrosion deterioration as compared to pristine bridge structures.

1 INTRODUCTION

The health and prosperity of transportation infrastructure is critical for the growth of the nation. Highway bridges, which are the critical components of the transportation infrastructure are facing substantial structural problems. For example in United States, more than one in nine bridges are labeled as structurally deficient or functionally obsolete and moreover many bridges among them are at the end of their service life period (FHWA 2016). In India, investigations by Wakchaure & Jha (2011) revealed that total road network includes 70,934 km of National Highways. It is found that in about 14,500 bridges on the National Highways, 1713 bridges are in distressed condition that may require repair or rehabilitation and 2018 bridges to be old and weak that may require reconstruction.

Highway bridges are subjected to a multitude of stressors along their service life when exposed to the outside environment. Among such stressors, corrosion deterioration emerges as a primary mechanism that affects the performance of highway bridges (Vu & Stewart 2000). Bridges as well as any other structures in nature, deteriorate over time. Corrosion is a continuous process that deteriorates the bridge throughout its service life and is random in nature, often marked by significant level of uncertainty (Enright & Frangopol 1998, DuraCrete 2000, Choe et al. 2008). In recent times efforts have been made to include the corrosion in the performance prediction, design, construction and maintenance of the reinforced concrete (RC) structures.

Across the globe, many highway bridges are located in seismically active regions and are likely to experience continued exposure to earthquakes in the form of main shocks and aftershocks throughout their service life. Repeated earthquake loads lead to the damage accumulation in the bridge which may eventually cause a structural collapse if the threshold limiting capacity is exceeded. The prediction of the remaining life period of the partially deteriorated bridges is necessary for the optimum management of the bridge. The inherent weakening of the bridge structure after the first earthquake may finally lead to collapse of the structure for relatively lesser intensity subsequent earthquakes. Repeated seismic loads on the RC structures weakens the structures elements which may increase the cost of retrofitting and repair of the structure. The annual direct costs of repair of these bridges are estimated to be in billions. Hence the prediction of level of damage in an RC structure due to earthquake loads is utmost necessary. The critical step here is to choose an indicator which actually represents the cumulative damage of bridges under repeated seismic shocks. This study adopts Park and Ang damage index as it has consistency and good correlation with experimental test

data for buildings and bridges (Chai et al. 1994, Williams & Sexsmith 1997).

Even though the determination of damage accumulation after multiple earthquakes for RC structures is critical, very few studies have been reported in the literature. Lee et al. (2009) evaluated the effect of repeated earthquakes on RC bridge piers considering one real and one artificial earthquake loads. Investigations by Wen & Kang (2001a, b), Ghosh & Padgett (2010) and Sanchez-Silva et al. (2011) while calculating the seismic life-cycle analysis of pristine or deteriorating bridges assume that the bridges are completely repaired to pristine level before the occurrence of next earthquake. Kumar & Gardoni (2012) emphasized the importance of considering the occurrence of more than one damaging earthquake during the in seismic design. Abdelnaby & Elnashai (2014) reports that the structures subjected to series of seismic loads may occur as a result of significant reduction in the stiffness and strength properties of structural components. Nazari et al. (2015) and Zhai et al. (2014) focused on the quantification of the amount of damage accumulation in buildings. Ghosh et al. (2015) have investigated on the damage accumulation in bridges that are subjected to multiple earthquakes. However, the deterioration mechanism due to corrosion in conjunction with multiple earthquake occurrences is not considered in most of the above studies. The present study mainly focuses on the damage accumulation in bridges subjected to multiple main-shocks considering the effect of uniform corrosion deterioration in California region where the environmental condition is mostly marine.

The next section of the paper discusses the process of corrosion deterioration in RC structures and its ill-effects on bridge components.

2 CONTINUOUS DEGRADATION OF BRIDGE COMPONENTS DUE TO CORROSION

Corrosion is a natural process that may cause weakening of the structural components and lead to reduction in the load carrying capacity or even failure of the critical components of the structure (Kayser & Nowak 1987). In RC structures, corrosion process consists of two phases:- the corrosion initiation phase and the corrosion propagation phase (Liu & Weyers 1998).

2.1 *Corrosion initiation phase*

Chloride penetration in concrete causes the corrosion in RC structures as the protecting passivating layer around the steel is dissolved by the chloride ions. Corrosion initiates when the chloride concentration exceeds a critical threshold value around the steel reinforcement. For marine environmental conditions under chloride induced corrosion, this study adopts the initiation time (T_i) from DuraCrete (2000).

2.2 *Corrosion propagation phase*

In reinforced concrete structures, after the end of corrosion initiation phase, the propagation phase begins. Corrosion rate is an important parameter in determining the extent of deterioration (loss in reinforcing area, cover and core concrete strength etc.) and the resulting damage from corrosion. This study adopts the parametric equation for corrosion rate proposed by DuraCrete (2000) as a function of relative humidity, temperature and chloride content that clearly are the parameters influence by corrosion. More details can be found in DuraCrete (2000).

2.3 *Effects of corrosion on material properties*

The corrosion process not only reduces the area of reinforcing steel bars but may also lead to the loss of ductility of material that could possibly cause the brittle failure in concrete members (Coronelli & Gambarova 2004, Stewart 2009). Almusallam (2001) stated that even for a limited mass loss of steel (about 13%) makes its behavior more brittle. The formation of oxidized products due to corrosion leads the propagation of longitudinal cracks and spalling of the concrete cover. In addition to area loss of steel, other secondary effects considered in this paper are presented below.

2.3.1 *Effects of corrosion on concrete*

To estimate the residual capacity of the bridge that is affected by corrosion, the reduction in the properties of cover concrete strength has to be taken into account. This study adopts the reduced cover concrete strength due to micro-cracking from rust formation as proposed by Coronelli & Gambarova (2004) and Molina et al. (1993).

2.3.2 *Effects of corrosion on reinforcing steel*

Experiments conducted by Du et al. (2005) reveals that the residual strength of reinforcing steel depends on the residual area of the steel. It is obvious that the residual area of steel depends on the rate of corrosion. The residual strength of steel is given by

$$f(t) = \left(1.0 - 0.005\, Q_{corr}(t)\right) f_0 \tag{1}$$

where, f and f_0 are the yield or ultimate strengths of corroded and non-corroded reinforcing bars respectively, Q_{corr} is the amount of corrosion of reinforcement (%) which depends on the residual area of reinforcement and is given by

$$Q_{corr}(t) = \frac{A_{s0} - A_s(t)}{A_{s0}} \times 100 \tag{2}$$

where, $A_s(t)$ is the average cross-sectional area of the corroded reinforcement and A_{s0} is the initial cross-sectional area of non-corroded reinforcement.

The next section of the paper explains the determination of damage accumulation index in bridges subjected to multiple earthquakes with and without considering corrosion deterioration.

3 INTERMITTENT DAMAGE DUE TO EARTHQUAKES AND DAMAGE ACCUMULATION FRAMEWORK

Bridges located in moderate to high seismic zones are more likely to experience multiple earthquakes in the form of multiple main-shock events or mainshock-aftershock sequences. This study limits only to multiple mainshock events during the service life period of the bridge. The framework for prediction of damage index in the bridge due to multiple main-shocks for both pristine and corroded bridge conditions is detailed below.

3.1 *Predictive damage accumulation indices*

The Park & Ang (1985) damage index considers both the limit states such as: a) ductility or monotonic structural deformation, and b) dissipated hysteric energy. This index estimates the level of damage in reinforced concrete elements and structures that are subjected to cyclic loading as:

$$D = \frac{\mu_m}{\mu_u} + \beta \frac{E_h}{M_y \theta_y \mu_u} \tag{3}$$

where, D is the Park and Ang damage index, μ_m is the maximum ductility caused by the earthquake, μ_u is the ultimate ductility capacity under monotonic loading, E_h is the total dissipated hysteretic energy, M_y is the yield moment capacity, θ_y is the yield rotation angle, and β is a dimensionless constant usually assumed to be 0.05 for RC structures. The engineering demand parameters (*EDP*s) μ_m and E_h are directly correlated with the intensity of ground motion and the properties of the structure. For instance, Cornell et al. (2002) highlighted that the *EDP*s can be related to the intensity of ground motions using the equation given by

$$EDP = a(IM)^b \tag{4}$$

where, a and b are regression coefficients and IM is the peak intensity of seismic shocks. To represent linear regression model, the Equation 4 can be transformed into linear equation as

$$\ln(EDP) = \ln(a) + b\ln(IM) \tag{5}$$

For single shock events, the damage index D is expected to be linearly varying with IM as shown in the equation

$$\ln(D_1) = \alpha_1 + \beta_1 \ln(IM_1) \tag{6}$$

where, D_1 is the damage index after the first earthquake excitation, α_1 and β_1 are the regression coefficients and IM_1 is the ground motion intensity of the first earthquake shock.

However, when the corrosion deterioration is considered, the damage index after first shock depends on both the intensity of the earthquake, as well as the time along service life of degrading bridge structure when this first shock occurs. So, for the same single shock events, the damage accumulation index for corrosion case (say D_{1C}) is expected to be a linearly varying with IM and the time to first shock (t_1).

$$\ln(D_{1C}) = \alpha_{1C} + \beta_{1C} \ln(IM_1) + \gamma_{1C}\, t_1 \tag{7}$$

where, D_{1C} is the damage index after the first earthquake excitation considering corrosion, α_{1C}, β_{1C} and γ_{1C} are the regression coefficients, IM_1 is the ground motion intensity of the first earthquake shock and t_1 is the time to first shock.

Unlike single shock events, the damage index evaluation due to multiple earthquake shocks also depends on previous damage and hence the history of previous earthquake shocks. The total energy dissipated (E_h) due to multiple earthquakes will be cumulative (Equation 8) while the maximum ductility (μ_m) may have achieved during the most immediate seismic pulse or during any of the previous seismic pulses depending on the intensity of earthquake shocks (Equation 9).

$$E_h = E_{h1} + E_{h2} \tag{8}$$

The maximum curvature ductility is given by

$$\mu_m = \max(\mu_{m1}, \mu_{m2}) \tag{9}$$

where, E_{h1} and E_{h2} are the dissipated hysteretic energy after the first and second earthquake respectively, μ_{m1} and μ_{m2} are the corresponding maximum curvature ductilities due to first and second earthquakes.

The damage index in the structure increases with every shock as represented by the following equation

$$D_n > D_{n-1} > D_{n-2} > .... > D_2 > D_1 \tag{10}$$

where, D_n is the damage index of the structure after it has been exposed to n shocks. Consequently, the damage index after n earthquake shocks can be described as a multilinear regression model and is given as following (Ghosh et al. 2015).

$$\ln(D_n) = \alpha_n + \beta_n \ln(IM_n) + \gamma_n \ln(D_{n-1}) ... \\ ... + \delta_n \ln(IM_n)\ln(D_{n-1}) \tag{11}$$

where, D_n is the damage index after the n^{th} earthquake shock with ground motion intensity of IM_n. $D_{n\text{-}1}$ is the damage index after n-1 earthquake

shocks. The parameters α_n, β_n, γ_n and δ_n are the regression coefficients.

Consideration of corrosion deterioration in bridges located in seismic regions is expected to further contribute to damage accumulation. In other words, the damage accumulation in the corroding structure subjected to n earthquake shocks is likely to be greater than that of the damage accumulation for the same structure subjected n shocks in pristine condition (Equation 12).

$$D_{nC} > D_n \tag{12}$$

The index (D_{nC}) representing damage index of the corroded structure after it has been exposed to n shocks, can be expressed as the following equation

$$\ln(D_{nC}) = f\left[IM_n, D_{(n-1)C}, t\right] \tag{13}$$

where, $D_{(n\text{-}1)C}$ is the damage index after n-1 earthquake shocks considering corrosion deterioration and t is the time to n^{th} seismic shock. While some of the proposed functional forms for damage index calculation in corroding structures may be speculative, the adequacy of the models will be demonstrated later in the case-study example.

3.2 *Damage index exceedance probabilities: Lifetime main shock hazard*

As indicated earlier, the damage accumulation index is now a multi-dimensional parameter and can be expressed as a regression equation. The probability of exceeding different levels of damage given the structure is subjected to certain number of earthquakes is calculated. This probability expressed as $P[D>d \mid n\ shocks]$, can be evaluated using Monte Carlo trials. Based on the earthquake occurrence probabilities, first a large number of earthquake intensities are generated. The probability of exceeding a certain level of damage index is then computed using Equation 14.

$$P\left[D>d \mid n\,shocks\right] = \frac{1}{N_{MC}} \sum_i I\left[D_{ni} > d\right] \tag{14}$$

where N_{MC} is the total number of Monte Carlo simulations, D_{ni} is the accumulated damage index after n shocks for the i^{th} Monte Carlo simulation and I[.] is the indicator function which equals to 1 when I[.] is true and 0 if I[.] is false. The damage accumulation framework for deteriorating bridges and pristine bridge structures is demonstrated in the next section using a case-study example.

4 CASE STUDY

Given the potential of frequent earthquake events, this study demonstrates the proposed damage accumulation framework for a case-study bridge located in California. While several researchers have investigated the potential vulnerability of highway bridges (as-built or aging) in California (Mackie & Stojadinović 2001, Zhang & Huo 2009, Alipour et al. 2010), literature on damage accumulation due to repeated earthquake events and aging is negligible.

4.1 *Representative case-study bridge: Bridge attributes and numerical modelling*

Ramanathan (2012) has conducted extensive review of the different bridge types in California region and revealed that the highest percentage of overall bridge inventory are the multi-span continuous box-girder bridges. The current study considers a typical 2-span box-girder bridge with 3 cells. The layout of the adopted box-girder bridge is illustrated in the Figure 1. In this study single square column bents are adopted instead of rectangular columns without altering the typical crosssectional area for simplicity.

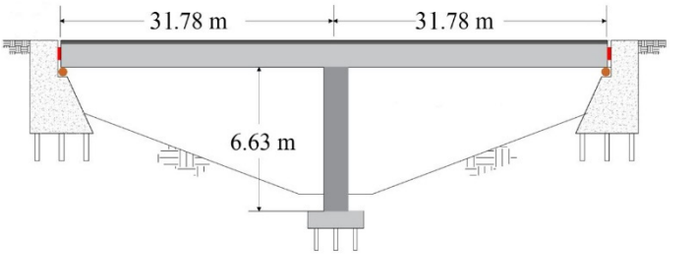


Figure 1. Layout of adopted two-span box-girder bridge

This study adopts the basic material properties such as concrete compressive strength (f_{ck}), yield strength of steel (f_y), bridge properties such as column height (H), span length (L) based on the extensive review of bridges conducted by Mangalathu et al. (2016) using in-house database obtained from Caltrans. The weight of the super structure is calculated to be 5200 kN for the case-study bridge. Since the present study limits to the modeling of the bridge column, the super-structure mass including the self-weight of the column is assumed to be represented as a lumped mass on the column. The column consists of 1.29 m × 1.29 m section and longitudinal steel reinforcement ratio of 2.25% of the cross-sectional area. The bridge column is modeled in OpenSees (Mazzoni et al. 2009) as a beam-column element using nonlinear *RCSection2d*. The concrete is modeled using *Concrete04* material and steel is modeled using *Hysteretic* material which is capable of considering the strength degradation during repeated load cycles. *RCSection2d* command allows area updating that is necessary to determine damage accumulation of aging highway bridges. However, material property updates are newly introduced in this paper as will be elaborated in the later section.

The probability distribution of parameters involved in determining the corrosion initiation time is adopted from Choe et al. (2008) and DuraCrete (2000). The average corrosion initiation time considering a cover depth of 38.1 mm (Choe et al. 2008)

for the case-study bridge is observed to be 10 years. Figure 2 and Figure 3 shows the variation of cover concrete strength and reinforcement area of steel with service life period along with the uncertainty band (mean ± standard deviation) that indicates the variability around the mean value.

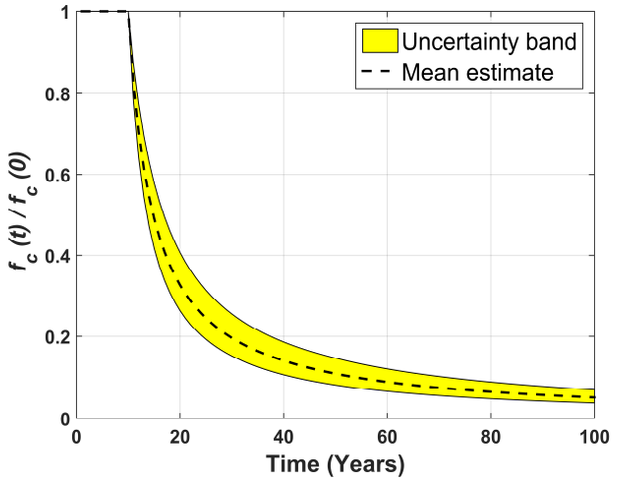


Figure 2. Variation of cover concrete strength with time

Figure 2 indicates that the cover concrete strength of the bridge column greatly affected by corrosion deterioration. There is a substantial concrete strength loss of about 90% in the exposure period of 100 years. Figure 3 reveals that the reinforcing area of steel reduces to about 75% of its original value after the exposure period of 100 years.

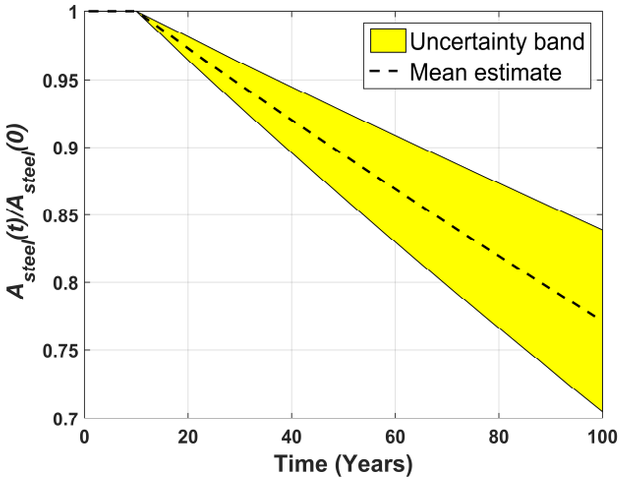


Figure 3. Variation of reinforcing area of steel with time

4.2 *Effect of corrosion deterioration on flexural capacity of case-study bridge column*

To determine the effect of corrosion deterioration on the flexural capacity of the bridge column, pushover analysis is performed on the pristine column and deteriorating column under uniform corrosion at 25, 50, 75 and 100 years of service life of the bridge. The moment and curvature values obtained through the analysis are recorded for all the cases.

Figure 4 shows the idealized moment-curvature plots along with the yield and ultimate points. It can be seen that the corrosion deterioration leads to the reduction in the yield moments which increases the curvature ductility of the structure. The Park and Ang damage index thereby increases indicating the impact of corrosion on flexural capacity of column. Compared to pristine bridge column, the yield moment of the steel has been reduced by 6.8%, 12.25%, 15.4% and 24.28% for the cases of uniform corrosion deterioration for 25, 50, 75 and 100 years respectively. From Figure 4 it can also be observed that the ultimate curvatures and ultimate moments being reduced with the exposure time period which clearly indicates that the corrosion deterioration effects the flexural capacity of bridge column.

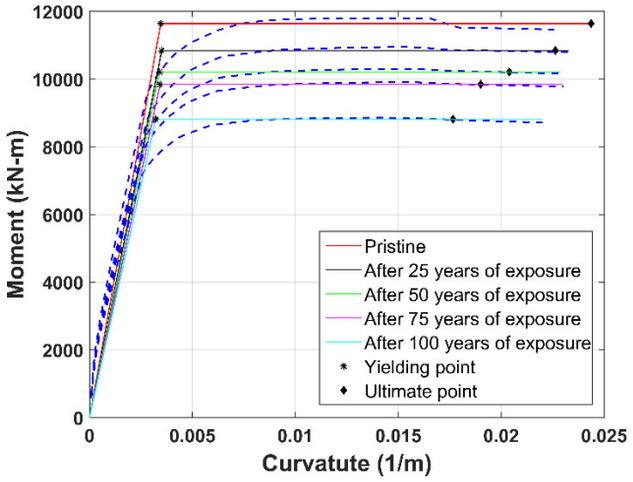


Figure 4. Pushover curves for the case-study bridge column in pristine condition and corrosion deterioration condition after 25, 50, 75 and 100 years of service life.

4.3 *Damage index measurements for single and multiple earthquakes*

The damage index measurement for the non-linear time history analysis of the bridge structures subjected to earthquake loads requires the estimation of maximum curvature ductility caused by the earthquake, the ultimate ductility capacity obtained from the pushover analysis and the dissipated hysteretic energy as explained earlier (Equation 3). Earthquake pulses from a suite of 100 ground motions develop by Gupta & Krawinkler (2000) and Krawinkler et al. (2003) for the California region are adopted for the present study. The peak ground accelerations (PGAs) of these ground motions range from 0.03-1.3 g and the duration varying from 28.7- 99.96 sec.

4.3.1 *Single earthquake scenario*

To quantify the damage index, the bridge column is subjected to single earthquake shock selected randomly from 100 available ground motions. The analysis was carried out for both the pristine and corroded bridge column conditions. Figure 5 pre-

sents the linear regression fit of the damage index with intensity of the single earthquake ground motion for a pristine bridge condition. The fitted linear regression equation is obtained as following

$$\ln\left(D_1\right) = 0.14 + 1.72\ln\left(PGA_1\right) \quad (15)$$

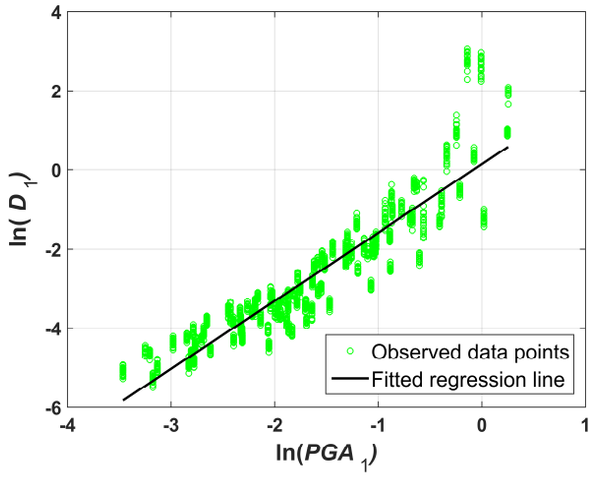


Figure 5. Linear regression model for predicting the damage index following a single shock occurrence for a pristine bridge

A good value of the coefficient of determination (R^2) of 0.84 and a relatively low estimate root mean squared error (*RMSE*) of 0.44 indicates that the model regression fit is adequate.

When the corrosion deterioration is considered, the damage index after the first shock (D_{1C}) depends also on time to first shock (t_1). Since the time when the earthquake occurs during the service life of the bridge is uncertain, a uniform distribution is assumed. Figure 6 shows the multi-linear variation of damage index for a corroded bridge subjected to a single shock. It can be clearly seen that for larger intensity earthquakes, the damage index at end of service time is very critical.

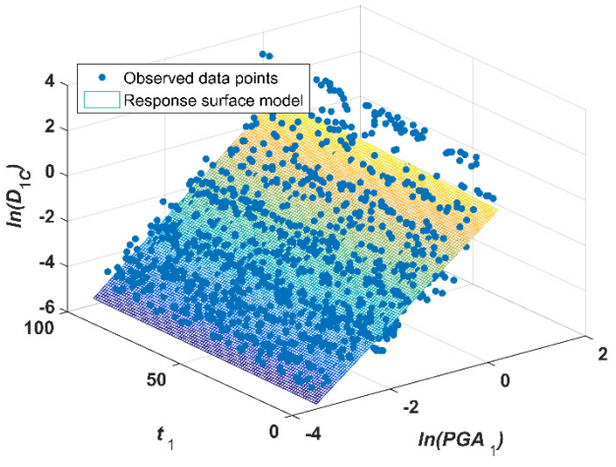


Figure 6. Multilinear regression model for predicting the damage index of a corroded bridge section subjected to single earthquake shock

The multilinear regression equation for D_{1C} in terms of PGA_1 and t_1 is given by

$$\ln\left(D_{1C}\right) = 0.18 + 1.76\ln\left(PGA_1\right) + 0.003t_1 \quad (16)$$

The regression equation has a coefficient of de termination (R^2) of 0.81 and a relatively low root mean squared error (*RMSE*) of 0.55 indicating the regression fit to be adequate.

4.3.2 *Multiple earthquake scenario*

Damage accumulation in bridges due to multiple shocks depends on the accumulation of damage in bridges due to previous earthquakes and the impact of ongoing corrosion deterioration. This study limits the number of earthquake shocks to two for damage accumulation comparison in pristine and deteriorating bridge structures. It should be noted that when the corrosion deterioration is considered, the material properties need to be updated before analyzing the response of the bridge subjected to second and subsequent earthquake shocks. Hence, the bridge column that is modeled using OpenSees should now be capable of updating the material properties of steel and concrete, area of steel and other parameters that are affected by corrosion while still maintaining the damaged or deformed structure shape after the previous earthquake. However, while the *RCSection2d* command is capable of updating the area of the steel whenever necessary, other parameters such as concrete and steel material properties that are likely to change due to corrosion deterioration also requires updating. Consequently, new material definitions for concrete and steel are added to the source code which have the same baseline properties as that of *Concret04* and *Hysteretic* material, but with additional capability of updating the parameters whenever necessary. This procedure is briefly explained in the following section.

4.3.2.1 *Modification of OpenSees source code*

Each material defined in OpenSees has a C++ code file (with a ".cpp" extension) and an associated header file (with ".h" extension). Similar in lines to the already existing *Concrete04* and *HystereticMaterial* files, this study added two new material files. These new materials were named *ConcreteUpdate* and *HystereticUpdate* and have no functional difference when compared with their non-updatable precursors. After reviewing the source files of already existing materials with updatable parameters it can be observed that the updation of parameters is possible only if the material class contains certain virtual functions of the class MovableObject defined in MovableObject.h. Additionally, every updatable parameter is identified by its parameterID. Consequently, three functions namely setParameter, updateParameter, activateParameter were identified and added to the new material classes in the header files and their definitions were stated externally in the .cpp files of the new materials. These functions were identified as critical components to implement

the parametric updating of the material properties. In order to create the user input for a material in OpenSees an OPS function is declared in the model builder files: TCLModelBuilderUniaxialMaterialCommand.cpp. The header file <OPS_Globals.h> and the input function definition is now added in the new material files respectively and all the parameters are initialized in the constructor. For a successful compilation of the source code with new materials, it is also necessary to modify the software development files namely material.vcxproj and material.vcxproj.filters. With all the above mentioned changes, this new source code of OpenSees was compiled successfully leading to a new OpenSees executable. This step ensures that in addition to the area of steel for a corroding and already damaged bridge, the material characteristics of steel and concrete can also be simultaneously updated. The dynamic analysis of the bridge subjected to the second earthquake followed by the first earthquake is conducted using the new updated OpenSees executable

4.3.2.2 *Damage index determination*

The multilinear regression equation for damage index calculation when the corrosion deterioration is not considered is as follows

$$\ln\left(D_2\right) = 0.07 + 0.14\ln\left(PGA_2\right) + 0.07\ln\left(D_1\right)\ldots \\ \ldots - 0.34\ln\left(PGA_2\right).\ln\left(D_1\right) \tag{17}$$

When the corrosion deterioration is considered the damage index after the second earthquake (D_{2C}) is not only a function of PGA_2 and D_{1C} but also the function of time to second shock (t_2). The multilinear regression equation is found to be

$$\ln\left(D_{2C}\right) = 0.36 + 0.27\ln\left(PGA_2\right) + 0.002t_2\ldots \\ \ldots + 0.11\ln\left(D_{1C}\right) - 0.32\ln\left(PGA_2\right).\ln\left(D_{1C}\right) \tag{18}$$

The above equations are fitted to have a minimum value of the coefficient of determination (R^2) of 0.80 and a relatively low estimate root mean squared error (*RMSE*) of 0.5 indicating that the model regression fits are satisfactory.

4.3.3 *Damage index exceedance probabilities for both corrosion and non-corrosion cases*

Figure 7 depicts the probability of exceedance of different levels of damage index as the column is subjected to two main shocks for both corrosion and non-corrosion cases using Equation 14. The figure reveals that the probability of structural damage increases with number of shocks. Additionally, irrespective of the number of shocks, the probability of failure is higher for the corrosion case as compared to that of a pristine structure. For instance, say at a damage index value of 0.5, the percentage difference between the damage exceedance probabilities for corrosion and non-corrosion cases are found to be 19% for the single shock scenario and 36% for the two-shock scenario. These results clearly indicate the necessity of considering aging mechanisms within a probabilistic framework while estimating the seismic performance of highway bridge structures.

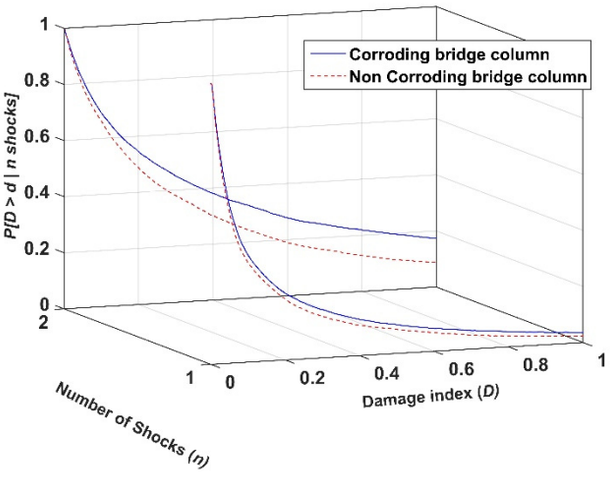


Figure 7. Probability of exceedance of different levels of damage index subjected to different number of earthquake shocks ($P[D > d \mid n\,shocks]$).

5 CONCLUSIONS AND FUTURE WORK

Bridges, which have a unique role in the transportation network and are more susceptible to corrosion deterioration due to which these bridges are turning to be structurally deficient and their number is increasing greatly. Also, bridges located in high seismic regions may experience continued exposure to earthquakes. Low intensity earthquakes may not directly collapse the structure but impart damage accumulation in it. The quantification of this damage considering the continuous effect of corrosion deterioration should be performed in order to assess the condition of the bridge. A damage accumulation framework for single and multiple earthquake scenarios for both pristine and corroded bridge condition is detailed in this study. The OpenSees source code for the concrete and steel materials are rewritten in such a way that they are capable of updating the parameters whenever necessary as the damage accumulation in the bridges for multiple earthquake events needs the material properties to be updated. An appreciable impact of corrosion deterioration on the damage accumulation index is observed through this study for the single earthquake events. For instance, say at a damage index value of 0.5, the percentage difference between the damage exceedance probabilities for corrosion and non-corrosion cases are found to be 19% for the single shock scenario and 36% for the two-shock scenario. A structure expected to be in moderate damage state that can be repaired to reuse may actually be in severe damage

condition that requires reconstruction when the effect of corrosion deterioration is considered.

The present study worked on damage accumulation in bridges considering multiple main-shocks events only. The effect of mainshock-aftershock sequences on the performance of corroded bridge structure could be a studied later. Seismic damage accumulation in highway bridges considering improved corrosion degradation models could be a future scope for study.

REFERENCES

Abdelnaby, A.E. and Elnashai, A.S., 2014. Performance of degrading reinforced concrete frame systems under the Tohoku and Christchurch earthquake sequences. *Journal of Earthquake Engineering*, *18*(7), pp.1009-1036.

Almusallam, A.A., 2001. Effect of degree of corrosion on the properties of reinforcing steel bars. *Construction and Building Materials*, *15*(8), pp.361-368.

Chai, Y.H., Priestley, M.N. and Seible, F., 1994. Analytical model for steel-jacketed RC circular bridge columns. Journal of Structural Engineering, 120(8), pp.2358-2376.

Choe, D.E., Gardoni, P., Rosowsky, D. and Haukaas, T., 2008. Probabilistic capacity models and seismic fragility estimates for RC columns subject to corrosion. *Reliability Engineering & System Safety*, *93*(3), pp.383-393.

Cornell, C.A., Jalayer, F., Hamburger, R.O. and Foutch, D.A., 2002. Probabilistic basis for 2000 SAC federal emergency management agency steel moment frame guidelines. *Journal of structural engineering*, *128*(4), pp.526-533.

Coronelli, D. and Gambarova, P., 2004. Structural assessment of corroded reinforced concrete beams: modeling guidelines. *Journal of Structural Engineering*, *130*(8), pp.1214-1224.

Du, Y.G., Clark, L.A. and Chan, A.H.C., 2005. Residual capacity of corroded reinforcing bars. *Magazine of Concrete Research*, *57*(3), pp.135-148.

DuraCrete, 2000. Probabilistic Performance Based Durability Design of Concrete Structures: Final technical report The European Union – Brite EuRam III.

Enright, M.P. and Frangopol, D.M., 1998. Probabilistic analysis of resistance degradation of reinforced concrete bridge beams under corrosion. *Engineering structures*, *20*(11), pp.960-971.

FHWA. (2016). "Federal Highway Administration NBI data." <https://www.fhwa.dot.gov/bridge/nbi/no10/yrblt16.cfm > (Oct. 11, 2017).

Ghosh, J and Padgett, J.E., 2010. Aging Considerations in the Development of Time-Dependent Seismic Fragility Curves. *Journal of Structural Engineering* 136(12):1497–1511.

Ghosh, J., Padgett, J.E. and Sánchez-Silva, M., 2015. Seismic damage accumulation in highway bridges in earthquake-prone regions. *Earthquake Spectra*, *31*(1), pp.115-135.

Gupta, A. and Krawinkler, H., 2000. Behavior of ductile SMRFs at various seismic hazard levels. *Journal of Structural Engineering*, *126*(1), pp.98-107.

Kayser, J.R. and Nowak, A.S., 1987. Evaluation of corroded steel bridges. In *Bridges and Transmission Line Structures* (pp. 35-46). ASCE.

Krawinkler, H., Medina, R. and Alavi, B., 2003. Seismic drift and ductility demands and their dependence on ground motions. *Engineering structures*, *25*(5), pp.637-653.

Kumar, R. and Gardoni, P., 2011. Modeling structural degradation of RC bridge columns subjected to earthquakes and their fragility estimates. *Journal of Structural Engineering*, *138*(1), pp.42-51.

Lee, D.H., Kim, D. and Lee, K., 2009. Analytical approach for the earthquake performance evaluation of repaired/retrofitted RC bridge piers using time-dependent element. *Nonlinear dynamics*, *56*(4), pp.463-482.

Liu, T. and Weyers, R.W., 1998. Modeling the dynamic corrosion process in chloride contaminated concrete structures. *Cement and Concrete Research*, *28*(3), pp.365-379.

Mangalathu, S., Jeon, J.S., Padgett, J.E. and DesRoches, R., 2016. ANCOVA-based grouping of bridge classes for seismic fragility assessment. *Engineering Structures*, *123*, pp.379-394.

Mazzoni, S. et al., 2009. OpenSees command language manual. University of California, Berkeley.

Molina, F.J., Alonso, C. and Andrade, C., 1993. Cover cracking as a function of rebar corrosion: part 2—numerical model. *Materials and structures*, *26*(9), pp.532-548.

Nazari, N., van de Lindt, J.W. and Li, Y., 2015. Quantifying changes in structural design needed to account for aftershock hazard. *Journal of Structural Engineering*, *141*(11), p.04015035.

Park, Y.J. and Ang, A.H.S., 1985. Mechanistic seismic damage model for reinforced concrete. *Journal of structural engineering*, *111*(4), pp.722-739.

Ramanathan, KN. 2012. Next Generation Seismic Fragility Curves for California Bridges Incorporating the Evolution in Seismic Design Philosophy. Georgia Institute of Technology.

Sanchez-Silva, M., Klutke, G.A. and Rosowsky, D.V., 2011. Life-cycle performance of structures subject to multiple deterioration mechanisms. *Structural Safety*, *33*(3), pp.206-217.

Stewart, M.G., 2009. Mechanical behaviour of pitting corrosion of flexural and shear reinforcement and its effect on structural reliability of corroding RC beams. *Structural safety*, *31*(1), pp.19-30.

Vu, K.A.T. and Stewart, M.G., 2000. Structural reliability of concrete bridges including improved chloride-induced corrosion models. *Structural safety*, *22*(4), pp.313-333.

Wakchaure, S.S. and Jha, K.N., 2011. Prioritization of bridges for maintenance planning using data envelopment analysis. *Construction Management and Economics*, *29*(9), pp.957-968.

Wen, Y.K. and Kang, Y.J., 2001a. Minimum building life-cycle cost design criteria. I: Methodology. *Journal of Structural Engineering*, *127*(3), pp.330-337.

Wen, Y.K. and Kang, Y.J., 2001b. Minimum building life-cycle cost design criteria. II: Applications. *Journal of Structural Engineering*, *127*(3), pp.338-346.

Williams, M.S. and Sexsmith, R.G., 1997. Seismic assessment of concrete bridges using inelastic damage analysis. *Engineering structures*, *19*(3), pp.208-216.

Zhai, C.H., Wen, W.P., Li, S., Chen, Z., Chang, Z. and Xie, L.L., 2014. The damage investigation of inelastic SDOF structure under the mainshock–aftershock sequence-type ground motions. *Soil Dynamics and Earthquake Engineering*, *59*, pp.30-41.

Maintenance, Safety, Risk, Management and Life-Cycle Performance of Bridges – Powers, Frangopol, Al-Mahaidi & Caprani (Eds)
© 2018 Taylor & Francis Group, London, ISBN 978-1-138-73045-8

Optimum lifetime inspection and maintenance planning for bridges considering utility

S. Sabatino
Department of Civil Engineering, University of Texas Arlington, Arlington, TX 76019, USA
D. M. Frangopol
Department of Civil and Environmental Engineering, Engineering Research Center for Advanced Technology for Large Structural Systems (ATLSS Center), Lehigh University, Bethlehem, PA 18015, USA

ABSTRACT: Highway bridges are constantly subjected to deterioration mechanisms that contribute to an overall decrease in structural resistance and increase in loads over their life-cycle. In order to ensure that the performance of bridges is maintained throughout their lifetime, cost efficient bridge intervention planning must be considered. An optimization procedure for life-cycle inspection and maintenance planning of highway bridges is proposed herein. The proposed approach considers three objectives: the minimization of life-cycle costs, the maximization of sustainability, and the minimization of the expected damage detection delay, all in a probabilistic, life-cycle context. Utility functions are used in order to consistently quantify and compare the three aforementioned objectives. Overall, the proposed approach can be used to establish optimum lifetime inspection and maintenance plans for highway bridges considering life-cycle costs, sustainability, and expected damage detection delay.

1 INTRODUCTION

The performance of deteriorating highway bridges can be quantified at the cross-section, component, or overall structural (system) level. Typically, performance assessment activities associated with the components rely on visual inspections results. Visual inspection results are usually employed to establish a condition rating index to measure the bridge's remaining load-carrying capacity. The conditions of bridges in the United States are rated using two different methods based on visual inspection (i.e., National Bridge Inventory (NBI) condition rating system and Pontis). Generally, bridge management systems characterize the performance of structural elements by discrete condition states which incorporate predefined degrees of damage (Hawk & Small 1998; Thompson *et al.* 1998). Based on the identified condition states, maintenance interventions may be prioritized among all inspected structural components.

As a result, it is advantageous to study the effect of inspections on the maintenance activities of a bridge. In order to ensure that the performance of deteriorating highway bridges is maintained throughout their lifetime, cost efficient bridge intervention planning must be considered. An optimization procedure for life-cycle inspection and maintenance planning of highway bridges is proposed herein. The proposed approach considers three objectives: the minimization of life-cycle costs, the maximization of sustainability, and the minimization of the expected damage detection delay, all in a probabilistic, life-cycle context. Utility functions are used in order to consistently quantify and compare the three objectives. The outputs of the proposed optimization procedure are optimal lifetime inspection and maintenance plans for a bridge (e.g., when to inspect and repair the bridge). Ultimately, this decision support tool can be employed to ensure that decision makers implement cost optimized decisions regarding inspection and maintenance associated with highway bridges.

2 SUSTAINABILITY ASSESSMENT

Within the context of life-cycle and structural engineering, two definitions of sustainability are typically considered when establishing sustainability metrics. The first representation of sustainability defines it as: "meeting the needs of the present without comprising the ability of future generations to meet their own needs" (Adams 2006). The second definition of sustainability is sometimes referred to as the "triple bottom line" because it emphasizes that economic, environmental, and social objectives must be simultaneously satisfied within a sustainable design or plan (Elkington 2004). Considering these definitions, it is important to measure the performance of highway bridges whose functionality is vital for economic and social purposes. Generally, sustainability should be quantified in terms of economic, social,

and environmental metrics, as indicated in Figure 1. In this section, the procedure for determining the sustainability associated with a particular lifetime maintenance plan using utility theory and the widely accepted definitions of sustainability is outlined.

The inclusions of societal and environmental impacts along with economic consequences effectively encompass the concept of sustainability within a robust risk analysis framework. Combining the economic, societal, and environmental, risk metrics allows decision makers to make informed decisions regarding the lifetime intervention planning by providing them with a complete picture of system performance (Sabatino *et al.* 2015, 2016). Generally, a structure is more sustainable if its life-cycle cost is relatively low. On the other hand, a structure is more sustainable if the energy, carbon dioxide emissions, and user delays arising from its maintenance are low. For highway bridges under repair, in general, the social metrics may include downtime and fatalities.

Utility theory is used herein in order to depict the relative desirability of lifetime intervention strategies (e.g., lifetime inspection and maintenance plans) to the decision maker. In general, utility is defined as a measure of value to the decision maker; utility theory provides a framework that can measure, combine, and consistently compare these relative values (Ang and Tang 1984, Sabatino *et al.* 2015, 2016). Multi-attribute utility theory can then be used to transfer the utility of each attribute involved in the performance assessment (e.g., economic, social, and environmental risks) into one utility value that effectively combines the effects of all risks investigated as shown in Figure 2. This flowchart shows the computation procedure for calculating a sustainability metric that is expressed as a multi-attribute utility value. In this procedure, u_i and k_i represent the utility function and associated weighting factor corresponding to the ith risk attribute.

The first step in the sustainability assessment is to evaluate the performance of a bridge considering the

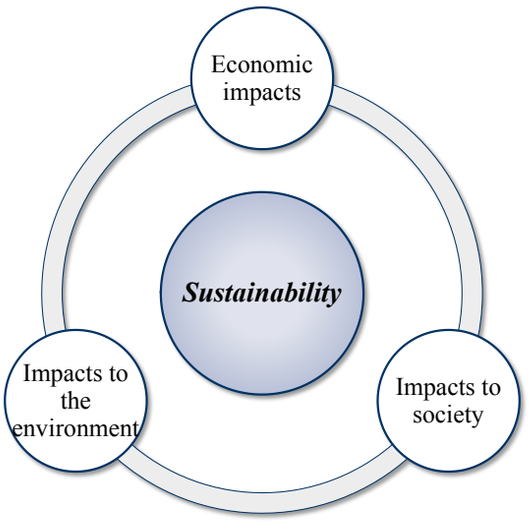


Figure 1. The three metrics of sustainability

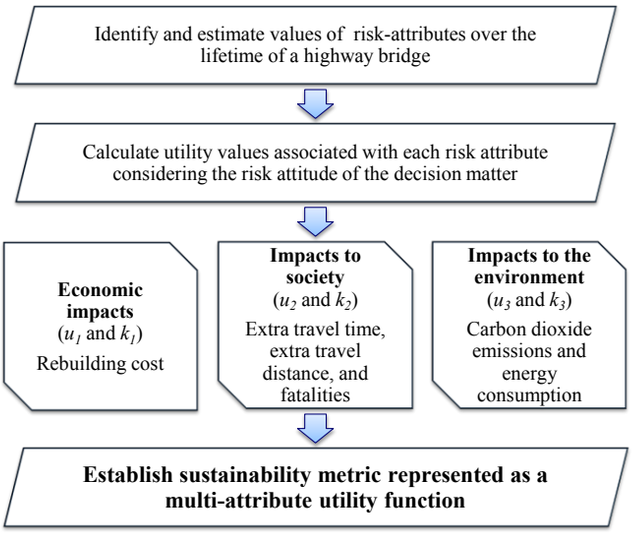


Figure 2. Procedure for calculating the multi-attribute utility value representative of sustainability

associated hazards. An increase in live loads and the effect of chloride contamination are the hazards considered herein for bridge superstructures. For the proposed decision support tool, the probability of system failure is considered as input information. The next step includes the risk assessment process. The risk attributes investigated herein include the rebuilding and repair costs, extra travel time and distance that drivers endure, fatalities that may occur, energy consumption, and carbon dioxide emissions.

After estimating the lifetime risks associated economic, environmental, and societal consequences of failure, the decision maker can assign utility values to the investigated attributes (e.g. risk attributes) associated with each alternative considering his/her risk attitude. Utility theory is applied in order to normalize each attribute value corresponding to solution alternatives (i.e., lifetime intervention plans) to a number between 0 and 1; this ensures that all attributes are directly comparable to each other. The formulation of the utility function corresponding to each attribute depends on the knowledge, preferential characteristics, and risk attitude of the decision maker. For the risk attributes analyzed, each of the corresponding utility functions may be formulated as monotonically decreasing functions. Considering an exponential formulation, the utility associated with a single attribute (e.g., economic, social, and environmental risks) can be expressed as (Ang and Tang 1984, Sabatino *et al.* 2015, 2016):

$$u_x = \frac{1}{1-\exp(-\gamma)}\left[1-\exp\left(-\gamma\frac{x_{\max}-x}{x_{\max}-x_{\min}}\right)\right] \quad (1)$$

where x is the mean of the attribute under investigation, x_{max} and x_{min} denote the maximum and minimum value of the attribute, respectively, and γ is the risk attitude of the decision maker. Note that $\gamma > 0$ indicates risk-aversion and $\gamma < 0$ denotes risk-acceptance.

A multi-attribute utility function that effectively represents all aspects of sustainability can then be obtained by combining the utility functions associated with each risk attribute. The multi-attribute utility function representative of sustainability of a highway bridge is (Sabatino *et al*. 2015)

$$u_s = k_1 u_1 + k_2 u_2 + k_3 u_3 \quad (2)$$

where k_1, k_2, and k_3 are the weighting factors corresponding to each sustainability metric, economic, social, and environmental attributes, respectively and u_1, u_2, and u_3 are the utility functions for the economic, social, and environmental attributes, respectively.

3 EXPECTED DAMAGE DETECTION DELAY ASSOCIATED WITH INSPECTION

Damage detection using particular inspection methods and the analysis and interpretation of inspection data are associated with significant uncertainties, including the randomness of damage occurrence and the imperfection of an inspection method. Because there are two events corresponding to an inspection results of "no damage" (i.e., no damage occurrence or damage occurs but is not detected), it is imperative to include the probability of detecting damage and the inspection quality within this probabilistic lifetime intervention planning framework (Mori & Ellingwood, 1994, Frangopol & Estes 1997, Enright & Frangopol 1999, Estes & Frangopol 2001, Onoufriou & Frangopol 2002). This section describes the procedure for calculating the expected damage detection delay associated with an inspection schedule. The procedure for calculating the expected damage detection delay associated with an inspection schedule is outlined in Figure 3.

The ability to detect damage depends upon the quality of inspection technique being employed, severity of damage, and number and timing of inspections. Considering the severity of the damage, the quality of inspection method can be quantified with a detectability function $P_{ins}(\delta)$. The detectability function represents the probability that a particular damage intensity, characterized by δ, is detected at time t (Frangopol *et al.* 1997).

$$P_{ins}(\delta) = \Phi\left(\frac{\delta - \delta_{0.5}}{\sigma_\delta}\right) \quad (3)$$

where $\Phi(\cdot)$ = standard normal cumulative distribution function, $\delta_{0.5}$ = damage intensity at which the inspection method has a 50% probability of detection, and σ_δ = standard deviation of the damage intensity $\delta_{0.5}$

Damage detection delay is defined as the duration between the point in time when a structure has been damaged and the instance in time when the damage is identified by inspection (Kim & Frangopol 2011,

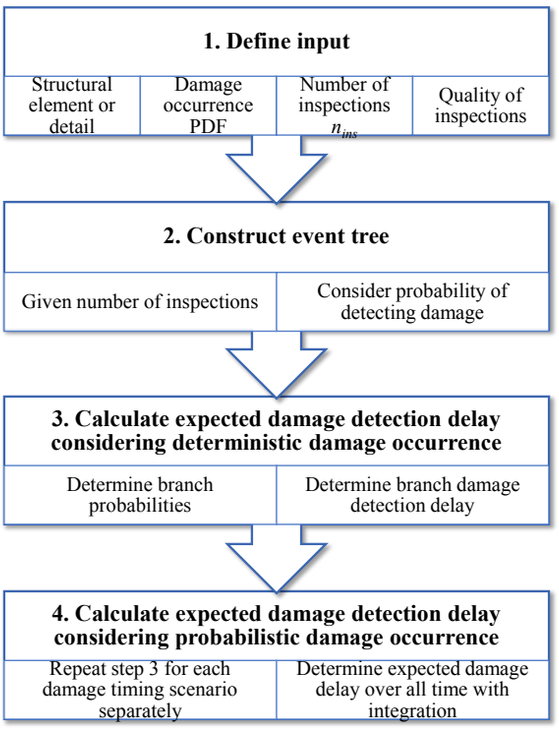


Figure 3. Procedure for calculating the expected damage delay associated with an inspection schedule

Kim *et al.* 2013, Sabatino & Frangopol 2017). The detection delay is calculated as

$$t_D = t_{ins} - t_d \quad (4)$$

where t_d = actual time that damage occurs and t_{ins} = time of inspection. Equation 4 assumes that the inspection method employed is perfect; however, inspections are imperfect and uncertainties in the detection of damage are present. In order to account for the probability of damage detection, an event tree model can be established considering b_n = 4 inspections, as shown in Figure 4. This event tree encompasses all the possible events associated with detection and no detection at every inspection. Using the event tree model in Figure 4 and the branch probabilities and associated damage detection delays listed in Table 1, the expected damage detection delay can be expressed as (Kim & Frangopol 2011):

$$E[t_D] = \sum_{i=1}^{b_n} \left(P_{b,i} \cdot t_{D,i}\right) \quad (5)$$

Where b is the number branches considered in the event tree, $P_{b,i}$ is the probability occurrence of branch i, and $t_{D,i}$ is the damage detection delay associated with branch i.

The damage detection delay is also affected by the uncertainty of damage occurrence and propagation, in addition to the uncertainty associated with the inspection method. If four inspections are used, damage occurrence between each inspection must be considered. For instance, damage can occur before the first inspection (case 1), between the first and second inspection (case 2), between the second and

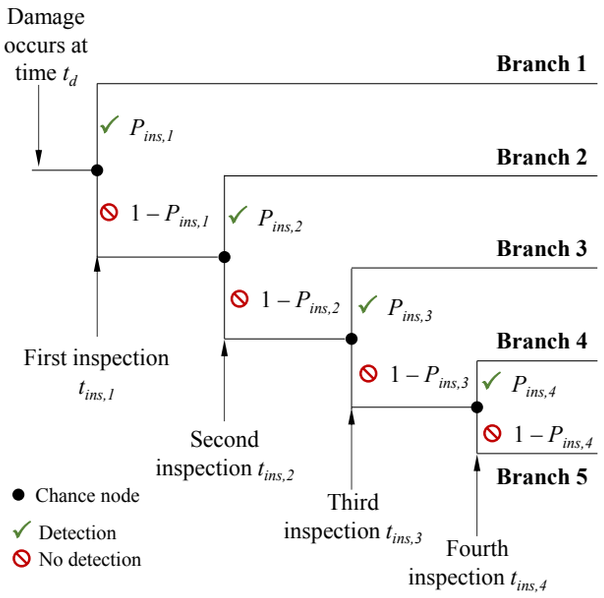


Figure 4. Decision tree for damage detection delay considering one element with four inspections

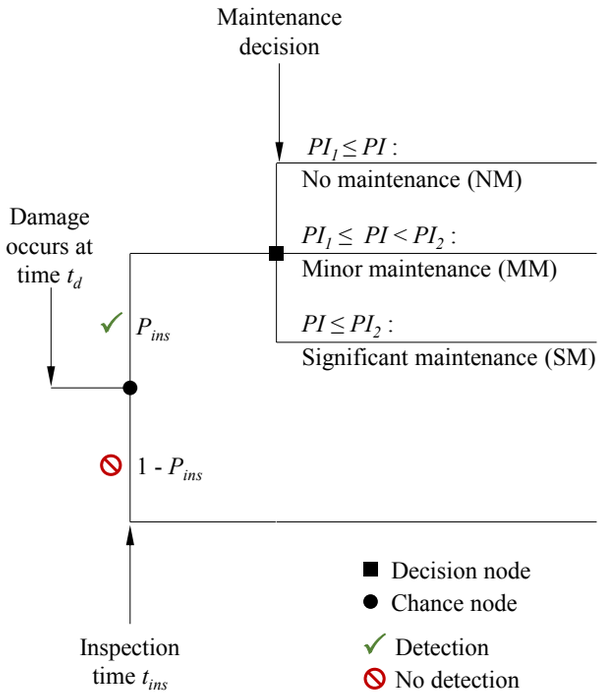


Figure 5. Decision tree for one inspection and maintenance of a structural element

third inspection (case 3), or between the third and fourth inspection (case 4). Considering these four cases when damage may occur and given the damage occurrence probability density function $f(t)$, the expected damage detection delay is (Kim & Frangopol 2011)

$$E[t_D] = \sum_{i=1}^{b_n} \left(\int_{t_{ins,\,i-1}}^{t_{ins,1}} \left(E[t_D]_{case,i} \cdot f(t) \right) dt \right) \quad (6)$$

Where $E[t_D]_{case,i}$ is the expected damage detection delay, when the damage occurs between the $(i-1)$th inspection and the ith inspection.

The interaction between inspection and maintenance plans are depicted in Figure 5. For each inspection detecting damage, a check is performed using a performance indicator PI and two prescribed threshold levels of this performance indicator, PI_1 and PI_2. If damage is detected and $PI \geq PI_1$, then no maintenance should be performed. However, if $PI_1 \leq PI < PI_2$ or $PI \leq PI_2$, then minor maintenance (e.g., preventative maintenance) or major maintenance (e.g., essential maintenance) should be implemented, respectively.

Once the expected damage detection is calculated for a particular lifetime inspection plan, then it may be converted to a utility value using Equation 1. This utility value u_d incorporates the risk-attitude of the decision maker to depict the relative value or attractiveness of using such an inspection plan.

Table 1. Event tree branch probability of occurrence and damage detection delay

Branch	Branch probability	Damage detection delay
1	$P_{ins,1}$	$t_{ins,1} - t_d$
2	$P_{ins,2}\ (1 - P_{ins,1})$	$t_{ins,2} - t_d$
3	$P_{ins,3}\ (1 - P_{ins,1})\ (1 - P_{ins,2})$	$t_{ins,3} - t_d$
4	$P_{ins,4}\ (1 - P_{ins,1})\ (1 - P_{ins,2})\ (1 - P_{ins,3})$	$t_{ins,4} - t_d$
5	$P_{ins,5}\ (1 - P_{ins,1})\ (1 - P_{ins,2})\ (1 - P_{ins,3})\ (1 - P_{ins,4})$	--

4 LIFE-CYCLE COST

One of the most critical metrics in the evaluation of bridge performance is life-cycle cost. The optimal allocation of resources can be achieved by minimizing the total cost while ensuring structural performance is always at a desired level. In the proposed decision support tool for bridge decision makers, the expected life-cycle cost considering lifetime interventions associated with a bridge structure can be expressed as

$$C_I = C_{ins} + C_{maint} \quad (7)$$

where C_{ins} is the expected cost of inspections and C_{maint} is the expected maintenance cost. Once the life-cycle cost of an intervention plan (e.g., inspections and maintenance actions) is calculated, the corresponding cost utility u_c may be determined considering Equation 1 and a maximum budget.

5 OPTIMAL LIFETIME INSPECTION AND MAINTENANCE PLANS FOR HIGHWAY BRIDGES

The lifetime intervention optimization formulation herein requires the computation of life-cycle performance indicators, specifically sustainability, ex-

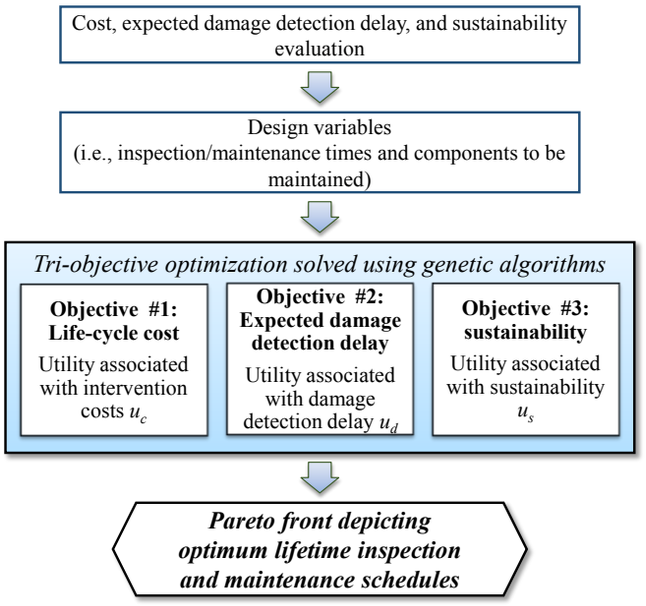


Figure 6. Flowchart describing the tri-objective optimization procedure

pected damage detection delay, and life-cycle cost. Given a maximum budget, a decision maker's risk attitude, and the number of inspections performed throughout the life-cycle, a decision maker could use the output of the proposed optimization procedure to ensure that the optimal intervention planning in terms of cost and performance is being implemented. A flowchart describing the methodology developed for this particular optimization problem is shown in Figure 6. The three objectives employed in this optimization are simultaneously maximized to achieve optimal intervention schedules.

The tri-optimization problem described herein can be solved using Genetic Algorithms with an adequate number of generations. The final result is a 3D Pareto front, depicting the simultaneous balance between utility associated with life cycle cost u_c, expected damage detection delay u_d, and sustainability u_s. Embedded within this Pareto front are lifetime intervention plans detailing when to perform inspections and maintenance throughout the life-cycle of a highway bridge. Bridge decision makers can use the three-dimensional Pareto front to make decisions based upon their budget or desired performance (e.g., sustainability or expected damage detection delay).

6 CONCLUSIONS

The proposed decision support tool allows for informed choices to be made regarding bridge inspection and maintenance interventions. Utilizing the established methodology, optimal lifetime inspection and maintenance plans are determined for highway bridges. All three objectives employed in the adopted optimization procedure are expressed in terms of utility, measured on a consistent scale from 0 to 1. Sustainability is calculated considering the risks associated with the economy, the environment, and society. Additionally, expected damage detection delay is determined considering the uncertainties that lie in inspection quality and damage detection. The total life-cycle cost is calculated as the cost of inspection and maintenance throughout the lifetime of a bridge. Overall, this decision support tool can be used to ensure that financial resources are being efficiently allocated to inspection and maintenance operations throughout the lifetime of highway bridges.

7 ACKNOWLEDGEMENTS

The support from (a) the National Science Foundation through grant CMMI-1537926, (b) the Commonwealth of Pennsylvania, Department of Community and Economic Development, through the Pennsylvania Infrastructure Technology Alliance (PITA), and (c) the U.S. Federal Highway Administration Cooperative Agreement Award DTFH61-07-H-00040 is gratefully acknowledged. The opinions and conclusions presented in this paper are those of the authors and do not necessarily reflect the views of the sponsoring organizations.

8 REFERENCES

Adams, W.M. 2006. *The future of sustainability: re-thinking environment and development in the twenty-first century*. Report of the IUCN Renowned Thinkers Meeting, 29–31.

Ang, A. H–S. & Tang, W.H. 1984. *Probability Concepts in Engineering Planning and Design,* Vol. II, Wiley, New York.

Elkington, J. 2004. *Enter the Triple Bottom Line*. Adrian Henriques and Julie Richardson (Eds.), The triple bottom line: does it all add up? Earthscan, Sterling, VA.

Enright M.P. & Frangopol D.M. 1999. Condition prediction of deteriorating concrete bridges using Bayesian updating. *Journal of Structural Engineering* 125(10): 1118–1125.

Estes A.C. & Frangopol D.M. 2001. Minimum expected cost-oriented optimal maintenance planning for deteriorating structures: application to concrete bridge decks. *Reliability Engineering & System Safety* 73(3): 281–291.

Frangopol D.M., Lin K.Y., & Estes A.C. 1997. Life-cycle cost design of deteriorating structures. *Journal of Structural Engineering* 123(10): 1390-1401.

Frangopol, D.M. & Estes, A.C. 1997. Lifetime bridge maintenance strategies based on system reliability. *Structural Engineering International* 7(3): 193-198.

Hawk, H. & Small, P. 1998. The BRIDGIT bridge management system. *Structural Engineering International* 8(4): 309-314

Kim, S. & Frangopol, D.M. 2011. Inspection and monitoring planning for RC structures based on minimization of expected damage detection delay. *Probabilistic Engineering Mechanics* 26: 308-320.

Kim, S., Frangopol, D.M., and Soliman, M. 2013. Generalized probabilistic framework for optimum inspection and maintenance planning. *Journal of Structural Engineering* 139(3): 435-447.

Mori Y & Ellingwood B.R. Maintaining reliability of concrete structures. I: role of inspection/repair. *Journal of Structural Engineering* 120(3): 824–45.

Onoufriou, T. & Frangopol, D.M. 2002. Reliability-based inspection optimization of complex structures: a brief retrospective. *Computers & Structures* 80(12): 1133-1144.

Sabatino, S., and Frangopol, D.M. 2017. Decision making framework for optimal SHM planning of ship structures considering availability and utility. *Ocean Engineering* 135: 194-206.

Sabatino, S., Frangopol, D.M., & Dong, Y. 2015. Sustainability-informed maintenance optimization of highway bridges considering multi-attribute utility and risk attitude. *Engineering Structures* 102: 310-321.

Sabatino, S., Frangopol, D.M., & Dong, Y. 2016. Life-cycle utility-informed maintenance planning based on lifetime functions: Optimal balancing of cost, failure consequences, and performance benefit. *Structure and Infrastructure Engineering* 12(7): 830-847.

Thompson, P.D., Small, E.P., Johnson, M., & Marshall, A.R. 1998. The Pontis bridge management system. *Structural Engineering International* 8(4): 303-308.

Maintenance, Safety, Risk, Management and Life-Cycle Performance of Bridges – Powers, Frangopol, Al-Mahaidi & Caprani (Eds)
© 2018 Taylor & Francis Group, London, ISBN 978-1-138-73045-8

FEM Approach to Appraise Bridges Affected by Alkali-Silica Reaction (ASR)

R.V. Gorga
MASc candidate – University of Ottawa, Ottawa, ON, Canada

L.F.M. Sanchez
Assistant Professor – University of Ottawa, Ottawa, ON, Canada

B. Martín-Pérez
Associate Professor – University of Ottawa, Ottawa, ON, Canada

M. Noël
Assistant Professor – University of Ottawa, Ottawa, ON, Canada

ABSTRACT: Modeling the expansion and damage generated by alkali-silica reaction (ASR) in reinforced concrete structures is quite complex, yet necessary to obtain accurate predictions of the structural responses of distressed concrete members. Several ASR models have been developed over the past decades to predict expansion and damage at the material (microscopic) or the structural (macroscopic) scales. However, those models tend to either neglect or overemphasize the critical physicochemical parameters of the reaction, which limits their applicability. Therefore, a new simple yet reliable finite element approach is proposed in order to fill this gap. It accounts for the most important parameters affecting ASR through an engineering approach, without the need for non-technical guesses or to "fit" model parameters. The proposed model is validated through the computational simulation of reinforced concrete specimens cast and monitored in the laboratory. An application example of a real ASR-affected bridge is also provided.

1 INTRODUCTION

Alkali aggregate reaction (AAR) is a concrete distress mechanism that results from a chemical reaction between the alkalis from the concrete pore solution and some mineral reactive phases from the aggregates used to make concrete. AAR is normally divided into two different mechanisms, so-called alkali-silica reaction (ASR) and alkali-carbonate reaction (ACR), ASR being by far the most commonly found around the world according to Fournier & Bérubé (2000).

The authors state that to develop ASR, three components are considered necessary1) aggregate containing reactive mineral phases, 2) high moisture content (normally assumed ≥ 85%) and 3) high alkali content. As by Saouma et al. (2015), the ASR mechanism is considered to be fairly well understood (at least in its major steps) and, its development can be described overall in four major stages. The first stage is defined as 'nucleation', where the reaction products start forming and filling surrounding aggregates, matrix voids and flaws. It is followed by a second step ('development') where significant expansion occurs with minor crack formation. Then, a third stage ('acceleration') takes place with the presence of important crack formation. Finally, the fourth and last stage is defined as 'deterioration' (which could also be called the deceleration phase), during which severe damage is found as well as a levelling off trend of ASR expansion, which might likely be caused by leaching (often found in laboratory testing) or by theoretical completion of the reactive mineral within the aggregates.

It is clear that ASR is a complex and non-linear mechanism, both physically and chemically, and even more so in the case of reinforced concrete structures where the influence of anisotropic confinement and stress states must be considered. Therefore, to accurately predict the structural implications of the reaction on concrete structures, an ASR expansion and damage model must be able to properly simulate both aspects.

2 ASR COMPUTATIONAL MODELS

Esposito (2016) classifies the existing ASR models in 4 different categories:

1- Models based on ion diffusion/reaction products, which describe the chemistry involved in great detail (micro-models). They take into consideration the dissolution and diffusion of alkali and silica ions as well as water availability. Examples of micro-models include those by Poyet et al. (2007) and Multon et al. (2009).
2- Models based on gel production, which describe the deterioration process at the aggregate level (micro-meso-models). They generally express the reaction kinetics as a function of the change in mass or volume of the gel and associate these variations to imposed strains or

pressure. Examples of micro-meso-models include those developed by Ulm et al. (2002), Grimal et al. (2008a, b) and Pignatelli et al. (2013).

3- Models based on internal pressure, which are capable of characterizing damage within the different constituents of the concrete (coarse aggregate, fine aggregate, cement paste, interfacial transition zone, etc.) by analyzing a representative elementary volume (meso-models). Examples of meso-models include those by Wu et al. (2014) and Esposito (2016).
4- Models based on concrete expansion, in which the effects and structural implications of the ASR expansion are modeled by imposing an expansive time-dependent strain to the concrete elements (macro-models). The strain is either based on phenomenological laws or on reaction kinetics laws of thermodynamics. Examples of macro-models include those developed by Charlwood (1994), Ulm et al. (2000) and Saouma & Perotti (2006).

Even though important progress has been accomplished in the field recently, most existing approaches either neglect or overemphasize the critical physico-chemical parameters of the reaction. This leads the models to become either incapable of assessing the distress mechanism properly, or too complex, requiring heavy computer programing/processing and, more importantly, the need to "fit" some of the variables with literature data or non-technical guesses. This fact, unfortunately, tends to make these models less useful and attractive in practice.

This work aims to develop a new simple yet reliable engineering-based finite element approach to assess damage in reinforced concrete structures affected by ASR. The macro-model (based on concrete expansion) intends to be a middle ground between the existing overcomplicated and oversimplified approaches. It is capable of technically accounting for the most important parameters influencing the chemical and physical aspects of the reaction, thus removing the need to "fit" certain (sometimes unmeasurable) parameters. Moreover, the model uses the widely used FE software Abaqus/CAE v.6.14 – Simulia (2014), making it easily accessible for the engineering community.

3 RESEARCH SIGNIFICANCE

Currently, according to Sanchez (2014) and Sanchez et al. (2015), some of the biggest challenges in civil engineering are:

1- How to detect the damage degree of an ASR-affected structure/structural member (i.e., diagnosis);
2- To understand the structural implication of the damage;
3- To establish an accurate correlation between ASR development, the losses in mechanical properties and durability of the affected material;
4- To assess the influence of confinement from internal reinforcement, boundary conditions and loading;
5- To understand the reaction`s potential to produce further damage (i.e., prognosis).

Such information is essential in selecting efficient remedial/rehabilitation strategies for existing structures in the field. This project aims to develop a practical and accurate FE model capable of predicting ASR future expansion and damage behaviour (prognosis) and structural implications in affected infrastructure.

4 IMPLEMENTATION

4.1 *Reinforced Concrete*

Abaqus offers several material models to represent non-linearity and damage in concrete. Three of the most well-known are smeared cracking, brittle damage and concrete damaged plasticity (CDP). Based on the mathematical implementation and customization options, it was determined that CDP was the model that better fit the needs of the current work.

CDP is based on the principle that the damage in quasi-brittle materials (i.e., concrete) can be defined by evaluating the dissipated fracture energy required to generate micro-cracks, as by Chaudhari & Chakrabarti (2012). According to Wahalathantri et al. (2011) and Bompa & Onet (2010), based on the CDP`s mathematical implementation and on the Drucker-Prager hyperbolic function, the material model is capable of representing the elastic and inelastic hydrostatic pressure-dependent behaviour of concrete under compression and tension. The main failure mechanisms are assumed to be either concrete crushing or tensile cracking. An idealized triaxial representation of a concrete failure surface, like the one used in the material model, is presented in Figure 1.

Lastly, the model is capable of qualitatively estimating the cracking intensity and orientation by evaluating the plastic strain. If an element or region passes the elastic limit, it starts developing plastic strain locally until global equilibrium is reached. As the load increases the plastic zone also increases, therefore simulating damage accumulation.

Reinforcement is usually modeled as either shared nodes, smeared reinforcement or through the use of constraints. For this work, the shared nodes approach was selected as the best option due to its simplicity and wide applicability.

The CDP material model was previously validated by modeling six beams tested by Vecchio and Shim (2004). On average, the proposed FE model overesti-

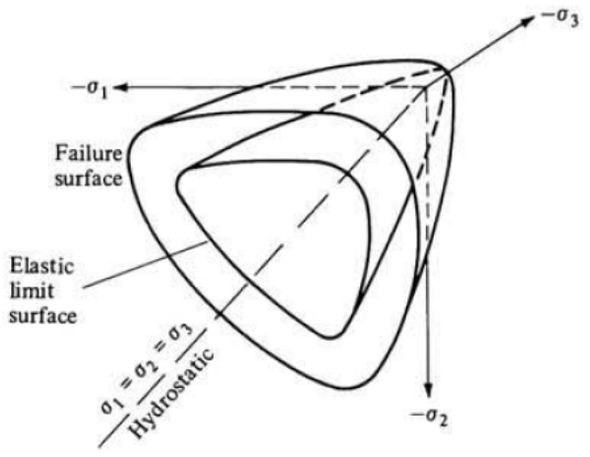


Figure 1. Schematic failure surface in three-dimensional stress space. Source: Chen (2007).

mated the ultimate load by 4% and underestimated the ultimate deflection at midspan by 11%, therefore proving its capability of accurately modeling undamaged reinforced concrete.

4.2 *ASR*

In order to assess the chemical aspects of the reaction, which can be understood as the reaction kinetics and expansion prediction over time, a physico-chemical analytical model was adopted. This model was previously developed at the Concrete Research Group (CRG) at the University of Ottawa and is able to describe the free evolution of the reaction over time based on Larive's equation, as by Larive (1997) and seven of the most important parameters of the reaction. Hence, the equation was found to be capable of describing the free expansion of the reaction over its lifespan only based on simple (and measurable) parameters as by Sanchez et al. (2016a).

Larive's equation (Equation 1) is a time dependent exponential function that represents the reaction phases previously described only three coefficients: τ_c characteristic time, τ_l latency time and ε^{∞} expansion at infinity, as illustrated in Figure 2.

$$\varepsilon(t) = \frac{1-e^{-\frac{t}{\tau_c}}}{1+e^{-\frac{(t-\tau_l)}{\tau_c}}} \times \varepsilon^{\infty} \qquad (1)$$

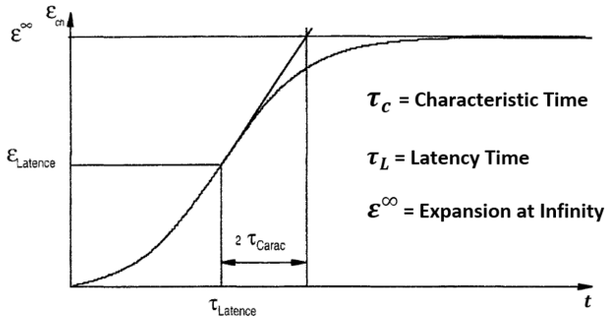


Figure 2. Larive's Equation. Source: Adapted from Larive (1997)

The seven parameters considered by the analytical equation are the type of reaction (ACR or ASR), aggregate type (coarse, fine or coarse and fine), aggregate reactivity (from negligible to very high damage degree based on Sanchez et al. 2016b), temperature, moisture (relative humidity), alkali content in the mix and exposure conditions. Moreover, the model is capable of assessing the variation of some parameters such as temperature and moisture content over time. This allows the development of expansion curves that simulate the real climatic conditions of the structure under evaluation.

Another consequence of ASR expansion that has to be accounted for is the mechanical properties deterioration, according to Sanchez et al. (2017). The ASR-affected mechanical properties that are considered are the compressive strength, the tensile strength and the modulus of elasticity, which are reduced over time as a function of the expansion level. This reduction is a direct consequence of the physical degradation (cracking) of the aggregate particles and cement paste. The model provides the reduction percentage of each parameter for each aggregate type at different expansion values and the parameters are assumed to vary linearly between the data points.

Therefore, the chemistry involved is computationally implemented in the model by imposing an equivalent ASR strain based on the free ASR expansion model. The curve obtained from this analytical approach can be understood as the input (reference) expansion curve for the model because it represents the free (i.e., unrestrained and unconfined) expansion over time expected to be observed.

The physical aspects of the reaction were assessed by taking into consideration the triaxial stress-state dependency of the expansion. Gautam et al. (2017) proposed a non-linear mathematical approach that states that the expansion due to ASR is reduced in the compressed direction and redistributed to the less stressed/unstressed directions. The expansion can be reduced to 34% or increased up to 232% of the reference expansion, depending on the stress state of the analyzed direction as well as the other two directions. It is important to note that the effect of tensile stresses on the reaction is not considered, therefore any regions that are not being compressed automatically have the expansion equal to the reference.

In order to implement the relationship developed by Gautam et al. (2017), an Abaqus user subroutine (USDFLD) was developed. As the reaction progresses, it is possible to state that the effect of confinement (due to the reinforcement, for example) and localized structural damage will influence the structure's stress state and, consequently, the local development of the reaction in terms of expansion and damage. Therefore, to take this into consideration, the subroutine was developed so that at every time increment, it updates the values of the expansion along

each principal direction in each finite element as a function of the current stress state.

In order to properly simulate the confinement effect as the expansion progresses, the steel reinforcing bars were modeled as beam elements instead of truss elements. The former tends to generate higher and more realistic confinement values because it presents both axial and transverse stiffness, while the latter presents only axial stiffness.

5 VALIDATION

Sanchez et al. (2016a) performed a push-off test to analyze the effect of ASR damage on the shear capacity reinforced concrete members. They designed, fabricated and tested S-shaped push-off specimens with different reinforcement ratios, damage degree levels and confinement configurations. The expansion of the unloaded specimens parallel to the main stirrups with 0.12% ± 0.01% final expansion was measured over time and was used as validation for the proposed ASR expansion FE model. The specimen taken as the reference was not reinforced. Figure 3 shows the specimen that was analyzed, which has two 400R steel 10M stirrups (total of 400 mm^2) crossing the shear plane and a reinforcement ratio (ρ) of 0.76%. All specimens were 650 mm high, 450 mm wide and 200 mm thick. The reactive aggregate used was the highly reactive New Mexico gravel combined with the non-reactive Laval sand. The concrete was 35 MPa, it had 4.63% of alkalis, and the specimens were stored at 38° C at 100% relative humidity. Lastly, leaching was noticed during the experiment, which likely led to a reduction of the final expansion expected for the specimen.

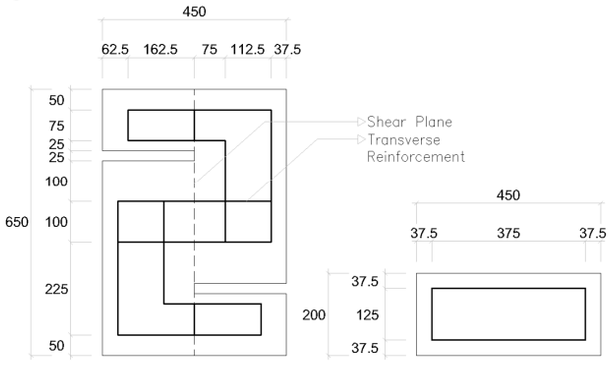


Figure 3. Push-off specimen design (dimensions in mm). Source: Adapted from Sanchez et al. (2016a).

A total of three analyses were performed in order to investigate the importance of accounting for the anisotropy of the reaction and the deterioration of the mechanical properties. The first analysis applied the anisotropic stress-state relationship and reduced the mechanical properties over time, therefore it is referred to as "anisotropic with damage" and it is the model`s standard. The second analysis is referred to as "anisotropic without damage" and it assumes that the reaction is anisotropic but ignores the deterioration of mechanical properties due to ASR development. The third analysis assumes that the reaction is isotropic and maintains the initial mechanical properties throughout the analysis, therefore titled "isotropic without damage".

According to Sanchez et al. (2017), the reduction in the modulus of elasticity was 5% at 0.05% expansion and 27.3% at 0.12% expansion for concrete mixtures cast with this aggregate. The tensile strength was reduced by 31.8% at 0.05% expansion and by 45.8% at 0.12% expansion. The compressive strength was slightly increased by 4.4% at 0.05% expansion and then reduced by 11.7% at 0.12% expansion. It is worth noting that the increase happened because the gain of compressive strength over time was larger than the reduction due to the deterioration of the material at 0.05% expansion. Otherwise, at 0.12% expansion the deterioration mechanisms already govern the overall behaviour, thus leading to a reduction of the compressive strength.

The expansion vs time curves reported by Sanchez et al. (2016a) and determined through the FE model for the specimens with no stirrups (0S) and 2 stirrups (2S) are plotted in Figures 4-5. Note that since the stress field of the no stirrups (0S) case is totally undisturbed, the FE results are exactly equal to the input free expansion curve obtained using the analytical model described in Section 4.2.

It is important to note that the expansion curve based on the analytical ASR model corresponding to the same mix, aggregate and conditions described by Sanchez et al. (2016a) provides a final expansion of 0.20%, which is much higher than the 0.125% measured in the test after 9 months. This is likely attributable to alkalis being lost in the early stages of the reaction (leaching), which is not accounted for in the expansion equation. Therefore, the strategy adopted was to reduce the alkali content available in the mix using one of the model`s coefficients to indirectly account for this phenomenon. It was determined that the best fit was for a reduction of 9.3% in the alkali content (from the original 4.63% to 4.20%).

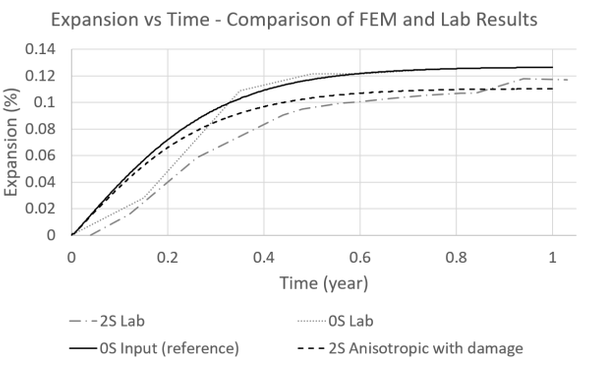


Figure 4. Expansion vs time curve – lab results and FEM results.

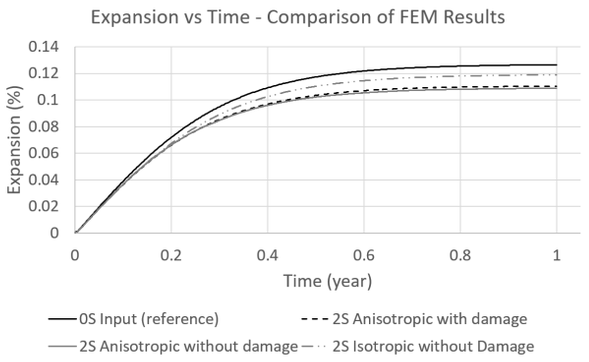


Figure 5. Expansion vs time curve – comparison of FEM results.

Both the values measured in the test and calculated through the FE model were extracted from the same location, approximately 2.5 cm below the main stirrups. This means that the curves represent the behaviour of the specimens' core and not the concrete cover.

The damage extent (plastic strain) is presented in Figure 6. The dark zones are assumed to be undamaged (uncracked) and the colored zones go from little damage extent (dark blue) to large damage extent (light blue).

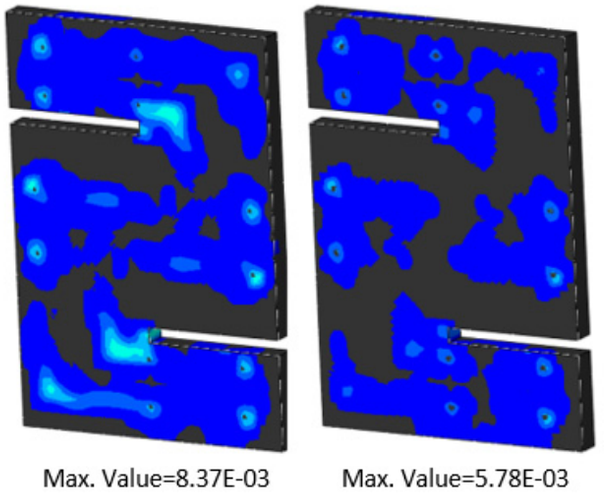


Figure 6. Push-off specimen's core (anisotropic with damage case on the left and anisotropic without damage on the right) – qualitative crack size and distribution (plastic strain)

Figures 7-8 display the stresses along the X direction for the 2S anisotropic with damage and 2S isotropic without damage cases, respectively. The grey zones are zones where tensile stresses govern. All other colored regions are governed by compressive stresses.

Lastly, the parameter entitled "field variable" along the X direction is presented in Figure 9. This parameter represents the reduction or increase of the expansion compared to the reference (free expansion input curve). If the value is equal to 1.0, the expansion is equal to the reference. However, if the parameter is

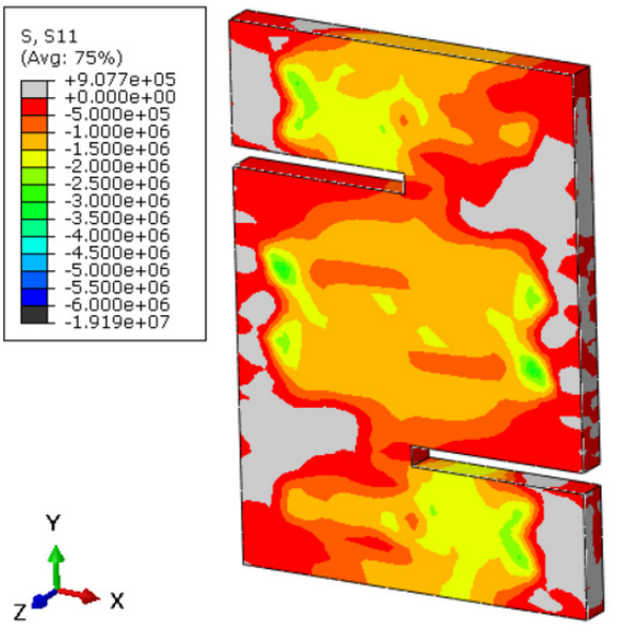


Figure 7. Push-off specimen's core (anisotropic with damage case) - stress field in the X direction.

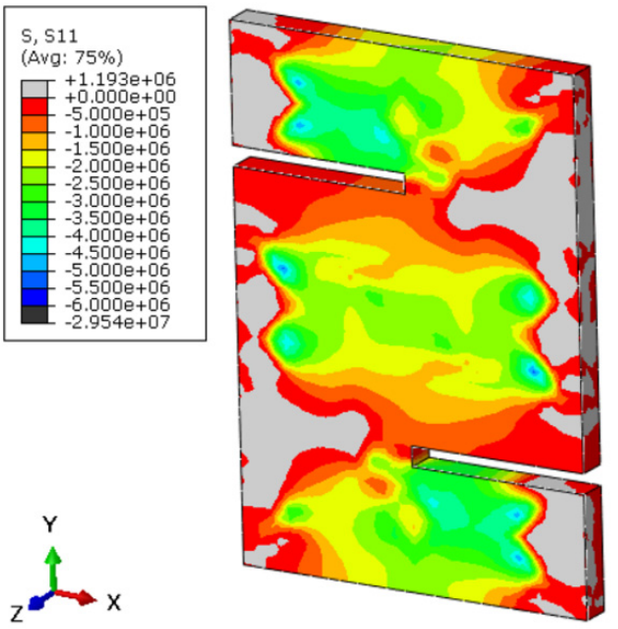


Figure 8. Push-off specimen's core (isotropic without damage case) - stress field in the X direction.

greater or smaller than 1.0, that value represents the percentage of the reference expansion that is being applied to the specific element. For example, if the region has a value of 0.6 it means that an expansion equal to 60% of the reference expansion will be applied there.

6 DISCUSSION OF RESULTS

From Figure 4, it is clear that the model for the no-stirrups case (0S input reference curve) represents the

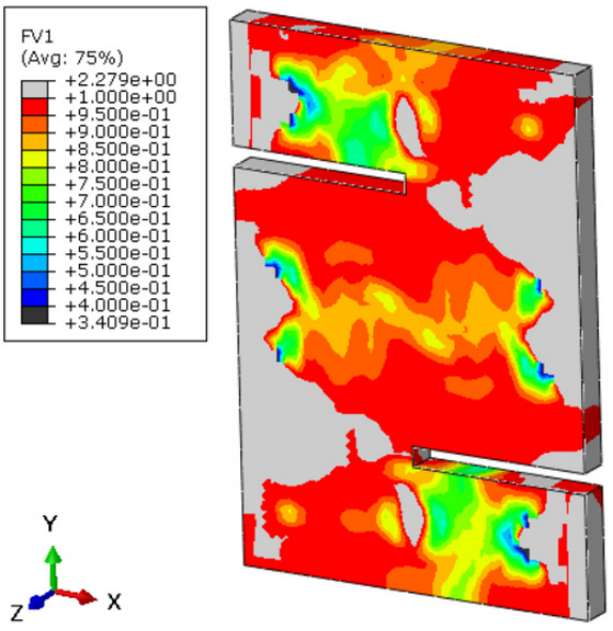


Figure 9. Push-off specimen's core (anisotropic with damage case) –field variable in the horizontal direction.

measured values well, except for the initial stages of expansion (between 0 and 0.30 years). This is very likely due to the fact that the analytical free expansion model does not take leaching into consideration.

As previously mentioned, the strategy adopted to indirectly take the effect of leaching into consideration was to reduce the coefficient that describes the alkali content available in the mix. However, having less alkalis available in the mix and losing alkalis over time (leaching) are two different phenomena chemically and physically speaking, which probably led to the observed inconsistency in the beginning of the reaction. This indicates that leaching has an effect not only on the final expansion (like the alkali content in the mix) but also on the reaction kinetics as it seems to increase the reaction's latency time (i.e., it seems to decrease the expansion in the early stages). Therefore, the analytical free expansion model could be improved to account for this phenomenon.

Likewise, the same initial behaviour for the 2-stirrups case is expected, wherein the calculated expansion is higher than the one measured in the tests, as shown in Figure 4. As predicted by Gautam et al. (2017) and verified by Sanchez et al (2016a), the expansion was reduced due to the reinforcement confinement effect in the concrete core, leading to a lower expansion vs time curve. The results illustrated in Figure 4 validate both the stress-strain relationship programmed through the user subroutine and the capability of the reinforced concrete model to simulate reinforcement confinement.

As shown in Figure 5, it is possible to state that reducing the mechanical properties (2S anisotropic with damage case) does not have a significant impact on the expansion of the specimen over time. The only difference observed in the curves was that the expansion keeps increasing very slowly when damage is considered, due to the widening of cracks as the values of the mechanical properties are reduced as a function of the expansion. On the other hand, when there is no damage and only the original mechanical properties are assumed, the expansion tends to reach a plateau without increasing further.

Even so, there are two significant consequences of reducing the mechanical properties in the model. As Figure 6 illustrates, the cracks are considerably larger (lighter blue areas) and the undamaged zone (dark region) is considerably smaller when the mechanical properties are reduced. Also, this reduction would impact the structural response of the specimen if loads were applied to the structure, likely leading to larger deformations. The only reason why this was not observed in the specimens is because the case analyzed was unloaded, which is not the case for most real structures in service.

Figures 7-8 clearly show that assuming isotropic expansion does not yield results as accurate as the anisotropic stress state-dependent relationship proposed by Gautam et al. (2017). Not only is the expansion over time further from the recorded lab data but also the isotropic case stresses are unrealistically high when compared to the anisotropic case. When isotropic expansion is assumed, the expansion keeps increasing regardless of the confinement, which leads to incoherent larger compressive stresses in the concrete and tensile stresses in the reinforcement. Thus, it is possible to state that the approach widely used in the past of simply imposing an equivalent isotropic expansive strain to the entire structure would not be capable of accurately simulating the structural implications of the reaction.

Lastly, it is important to emphasize that the largest reduction in expansion observed in Figure 9 happened where the compressive stresses are the largest, as predicted by Gautam et al. (2017). These regions basically include the regions where the reinforcement was passing through along the Z direction (small blue-green zones) and region between stirrups (central orange-yellow region).

7 APPLICATION EXAMPLE – ROBERT-BOURASSA/CHAREST OVERPASS

According to Sanchez et al., (2016b), the Robert-Bourassa/Charest (RBC) overpass was a highway bridge structure in Quebec, Canada, consisting of a deck supported by Y-shaped piers (Figure 10). It was built in 1966 using an alkali-silica reactive limestone aggregate, which led to the development of ASR over time. Especially over the last 3 decades, many signs of distress such as reinforcement corrosion and map cracking were spotted on the structure. Further analyses indicated that the map cracking was caused by

ASR and freeze-thawing cycles, which also aggravated the effect of corrosion. The extent of damage led to its demolition in 2010-2011; however, detailed evaluations (i.e., visual inspection, mechanical, microscopic and residual expansion assessment, displacement measurements, etc.) were performed and recorded before that took place.



Figure 10. RBC overpass (QC, Canada). Source: Sanchez et al. (2016b).

As an example of the applicability of the proposed model, it was implemented to analyze the pier of the RBC overpass. The plastic strain (cracking intensity) and the maximum absolute stresses (positive or negative) are presented in Figures 11-12, respectively.



Figure 11. RBC overpass pier – Cracking pattern comparison – RBC pier on the left and FE model on the right. Source: Sanchez et al. (2016b).

It is easy to see the resemblance of the cracking pattern between the FE model and the RBC pier in Figure 11. The largest crack is clearly at the bottom following the longitudinal reinforcement. However, damage on the laterals of the inferior region are noticeable, as well as where the arms connect and at the connection with the pier. Lastly, the cracks along the arms were not captured in the FE model, which implies that the model still needs adjustments to fully capture the behaviour of the concrete member.

Figure 12 shows that most of the pier is under compression, as expected. However, it is clear that the left

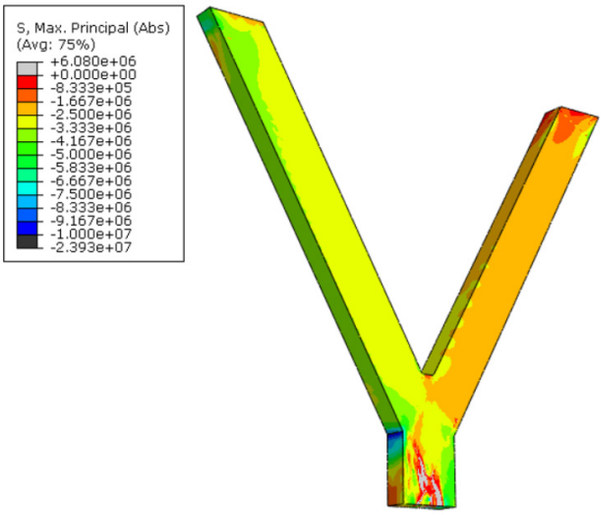


Figure 12. RBC overpass pier – Maximum absolute stresses in the concrete.

arm is under a greater compressive stress as a consequence of the dead load of the longer span. The only region under tension is at the bottom where large cracks are forming, according to Figure 11.

8 LIMITATIONS AND FUTURE RESARCH

Even though the presented results are very promising, there are still a number of aspects that must be further accounted for and evaluated to fully describe ASR-distress behaviour of real structures in the field. Some of the most important phenomena that should be accounted for to a certain degree in the reinforced concrete model are creep, shrinkage, concrete confinement effect and concrete/reinforcement bond, as well as freeze and thaw cycles, leaching and porosity in the ASR model. Moreover, aspects such as the effect of loading on the mechanical properties loss and on boundary conditions still have to be analyzed in greater depth.

Future work for the authors will be to further improve the FE analysis by comparing the results of the RBC overpass to measurements obtained from the technical inspections, and extending the analysis to predict structural response. Since the behaviour over time is being correctly modeled, the methodology can be applied to assess at what point in time the structure would reach a critical stage requiring rehabilitation or to be removed from service.

9 CONCLUSIONS

Based on the analysis and results presented, several conclusions can be made:

1- The CDP model in Abaqus was capable of accurately simulating the behaviour of ASR-affected reinforced concrete structures.

2- The analytical free expansion model predicted the ASR reaction well, except for the overestimation at the beginning, very likely because it does not account for leaching.
3- The anisotropic stress-strain relationship proposed by Gautam et al. (2017) yielded better results than the isotropic case.
4- The effect of reinforcement confinement on ASR expansion was observed and it described the experimental results well.
5- Accounting for degradation of mechanical properties did not noticeably affect the expansion over time for the unloaded specimens considered in this study, but it led to wider cracks and an overall larger damaged zone.
6- The proposed FE model was validated using experimental push-off test specimens tested by Sanchez et al. (2016a) and proved to be capable of accurately simulating ASR. Therefore, it can be used to evaluate real ASR-affected structures like the RBC overpass.

10 REFERENCES

Bompa, D. V., Onet, T. 2010. Identification of concrete damaged plasticity constitutive parameters. *The National Technical Scientific Conference – Modern Technologies for the 3rd Millenium.* Oradea, Romenia.

Charlwood, R. 1994. A review of alkali aggregate in hydro-electric plants and dams. *International Journal on Hydropower Dams*, 73–80.

Chaudhari, S. V., Chakrabarti, M. A. 2012. Modeling of concrete for nonlinear analysis using finite element code ABAQUS. *International Journal of Computer Applications* 44(7): 14-18.

Chen, W. F. (1st ed.) 2007. *Plasticity in Reinforced Concrete*. New York: McGraw-Hill.

Esposito, R. (1st ed.) 2016. *The deteriorating impact of alkali-silica reaction on concrete, expansion and mechanical properties*. Eschede: Ipskamp Drukkers.

Fournier B, Bérubé A. 2000. Alkali-aggregate reaction in concrete: a review of basic concepts and engineering implications. *Can. J. Civ. Eng*., vol. 27(2), pp.167–91.

Ferche, A. C., Panesar, D. K., Sheikh, S. A., Vecchio, F. J. 2017. Toward macro-modeling of alkali-silica reaction-affected structures. *ACI Structural Journal*, Title No. 114-S91.

Gautam, B. P., Panesar, D. K., Sheikh, S. A., Vecchio, F. J. 2017. Multiaxial expansion-stress relationship for alkali silica reaction-affected concrete. *ACI Materials Jounal*, Title No. 114-M17.

Grimal, E., Sellier, A., Le Pape, Y., & Bourdarot, E. 2008a. Creep, shrinkage, and anisotropic damage in alkali-aggregate reaction swelling mechanism-Part I: A constitutive model. *ACI Materials Journal*, 105: 227–235.

Grimal, E., Sellier, A., Le Pape, Y., & Bourdarot, E. 2008b. Creep, shrinkage, and anisotropic damage in alkali-aggregate reaction swelling-Part II: Identifications of model parameters and applications. *ACIMaterials Journal*, 105: 236–242.

Larive, C. 1997. Apports combinés de l'éxpérimentation et de la modélisation à la compréhension de l'alcali-réaction et de ses effets mécaniques, *Laboratoire Central des Ponts et Chaussées*, France.

Multon, S., Sellier, A., & Cyr, M. 2009. Chemo-mechanicalmodeling for prediction of alkali silica reaction (ASR) expansion. *Cement and Concrete Research*, 39: 490–500.

Pignatelli, R., Comi, C., Monteiro, P. 2013. A coupled mechanical and chemical damage model for concrete affected by alkali-silica reaction. *Cement and Concrete Research*, 53: 196–210.

Poyet, S., Sellier, A., Capra, B., Foray, G., Torrenti, J. M., Cognon, H., Bourdarot, E. 2007. Chemical modelling of alkali silica reaction: Influence of the reactive aggregate size distribution. *Materials and Structures*, 40: 229–239.

Saouma, V. E.; Martin, R. A.; Hariri-Ardebili, M. A.;Katayama, T. 2015. A mathematical model for the kinetics of the alkali-silica chemical reaction. *Cement and Concrete Research, 68*.

Saouma, V., Perotti, L. 2006. Constitutive model for alkali-aggregate reactions. *ACI Materials Journal*, 103: 194–202.

Sanchez L. F. M. 2014. Contribution to the assessment of damage in aging concrete infrastructures affected by alkali-aggregate reaction. *PhD thesis, Laval University, department of geology and geological engineering*, Quebec, Canada.

Sanchez, L. F. M., Fournier, B., Bastien, J., Mitchell, D., 2016a. Assessment of structures subjected to concrete degradation. *ASCET Report*, Quebec, Canada.

Sanchez L. F. M., Fournier B., Bastien, J., Mitchell, D., Noël, M., 2016b. Overall assessment of an ASR affected overpass "Robert-Bourassa/Charest" after nearly 50 years in service. 8th *International Conference on Bridge Maintenance, Safety and Management*, Foz do Iguaçu, Brazil.

Sanchez L. F. M., Fournier B., Jolin M., Duchesne J. 2015. Reliable quantification of AAR damage through assessment of the Damage Rating Index (DRI). *Cement and Concrete Research*, 67: 74–92.

Sanchez L. F. M., Fournier B., Jolin M., Mitchell D., Bastien, J., 2017. Overall assessment of Alkali-Aggregate Reaction (AAR) in concretes presenting different strengths and incorporating a wide range of reactive aggregate types and natures. *Cement and Concrete Research*, 93: 17-31.

Simulia Dassault Systèmes Corp. 2014. Abaqus/CAE - Complete Abaqus Environment - version 6.14. Providence, RI, USA.

Ulm, F. J., Petrson, M., Lemarchand, E. 2002. Is ASR-expansion caused by chemoporoplastic dilatation? *Computer Science and Engineering*, 4: 47–55.

Ulm, F. J., Coussy, O., Li, K., Larive, C. 2000. Thermo-chemo-mechanics of ASR expansion in concrete structures. *ASCE Journal of Engineering Mechanics*, 126: 233–242.

Vecchio, F. J., Shim, W. 2004. Experimental and analytical reexamination of classic concrete beam tests. ASCE Journal of Structural Engineering. 130(3): 460-469.

Wahalathantri, B. L., Thambiratnam, D. P., Chan, T. H. T., Fawzia, S. 2011. A material model for the flexural crack simulation in reinforced concrete elements using Abaqus. *International Conference on Engineering, Design and Developing the built environment for Sustainable Wellbeing*, 1: 260-264.

Wu, T., Temizer, I., Wriggers, P., 2014. Multiscale hydro-thermo-chemo-mechanical coupling: Application to alkali-silica reaction. *Computational Materials Science*, 84: 381-395.

Maintenance, Safety, Risk, Management and Life-Cycle Performance of Bridges – Powers, Frangopol, Al-Mahaidi & Caprani (Eds)
© 2018 Taylor & Francis Group, London, ISBN 978-1-138-73045-8

Techniques to Rehabilitate Bridge Columns Affected by Alkali-Silica Reaction (ASR)

L.F.M. Sanchez
Assistant professor, University of Ottawa
M. Noël
Assistant professor, University of Ottawa
V.A.A. Santos
Postdoctoral-fellow, University of Ottawa

Robert-Bourassa/Charest (RBC) overpass was a highway bridge structure (Quebec, Canada) that was built using an alkali-silica reactive limestone aggregate. Over nearly 5 decades, many signs of distress developed on the various structural members of the structure mainly due to alkali-silica reaction (ASR), freeze-thaw (FT) cycles, as well as steel corrosion. One of the major concerns regarding RBC structural long-term performance was related to the distress degree of the Y-shaped columns and thus a number of rehabilitation techniques including surface treatments (rigid coatings, silane/siloxane based products) and structural confinement (GFRP wrapping systems) were adopted to suppress further ASR-induced expansion and damage. In 2010/2011, prior to its demolition, several cores were extracted from the different members of RBC, which enabled the microscopic and mechanical characterization of damage from the various treated columns. This paper presents a comparison of the efficiency among the different rehabilitation techniques used to mitigate ASR in RBC columns. Results show that different damage degrees are found according to the group of columns; greater SDI and PDI and lower modulus of elasticity values were obtained from the North-West specimens, followed by the South-West/East cores. Microscopic analyses showed evidence of ASR and freeze and thaw mechanisms and marginal to moderate expansion & damage levels were obtained from the distinct columns assessed.

1 INTRODUCTION

1.1 *Alkali-silica reaction (ASR)*

Alkali-silica reaction (ASR), one of the most harmful distress mechanisms affecting concrete structures worldwide, is a chemical reaction between "unstable" silica mineral forms within the aggregates and the alkali hydroxides (Na, K – OH) dissolved in the concrete pore solution. ASR generates a secondary product, the so-called alkali-silica gel, that upon moisture uptake induces expansive pressures within the reacting aggregate material(s) and the adjacent cement paste, thus causing microcracking, reduction of material's properties (mechanical/durability) and, in some cases, functionality in the affected structure (Fournier & Bérubé, 2000).

Currently, one of the most significant challenges in dealing with aging damaged infrastructure is to establish the correlation between the distress "signatures" caused by a given damage mechanism (e.g., ASR), and the reductions in mechanical properties, physical integrity, durability and performance of the affected material, as well as their structural implications (Sanchez et al. 2015a). In this context, studies dealing with a multi-level evaluation proposed by Sanchez et al. (2017), suggest that both the *Stiffness Damage Test (SDT)* and the *Damage Rating Index (DRI)* (respectively mechanical and microscopic procedures) are able to provide a diagnostic evaluation of the "*actual damage degree*" of concrete affected by ASR. Although very promising, this multi-level approach was initially developed using laboratory (i.e., well controlled) samples and has barely been used for the condition assessment of aging infrastructure. Therefore, there was a need to further verify the efficiency and reliability of this approach for the evaluation of real damaged concrete structures.

1.2 *Robert-Bourassa/Charest Bridge*

The Robert-Bourassa/Charest (RBC) overpass was a highway bridge structure (Quebec, Canada) that was built in 1966 using an alkali-silica reactive limestone aggregate. The bridge was made of a deck resting on reinforced concrete Y-shaped columns, themselves supported by massive concrete foundations (Figure 1). No specific information is available on the concrete mix designs; however, technical reports indicate that the 28-day concrete design strengths were 24 MPa for the foundation blocks and 28 MPa for the columns and decks (ICAAR Visit Report, 2000).

Over the last three decades, many signs of distress developed on the various elements of the structure. This included extensive steel corrosion and concrete delamination/spalling at the level of the deck; map cracking, scaling, disaggregation and pop-outs affecting the massive concrete foundations due to ASR and freeze-thaw (FT) cycles; and concrete spalling and steel corrosion on the columns and foundations exposed to salt-water spray from traffic on the Robert-Bourassa highway (Bérubé et al. 2005).

One of the central concerns regarding RBC structural long-term performance was related to the distress degree of the Y-shaped columns, and thus a

number of rehabilitation techniques including surface treatments (rigid coatings, silane/siloxane based products) and structural confinement (GFRP wrapping systems) were adopted to suppress further ASR-induced expansion and damage. In 2010/2011, RCB was demolished, yet prior to its demolition, several cores were extracted from its structural members (bridge deck, columns and foundation blocks), which enabled the use of the multi-level assessment proposed by Sanchez et al. (2017) for the overall condition assessment of the bridge.



Figure 1. Robert-Bourassa/Charest overpass after nearly 50 years in service (Sanchez et al. 2016).

1.3 *Preliminary condition assessment results*

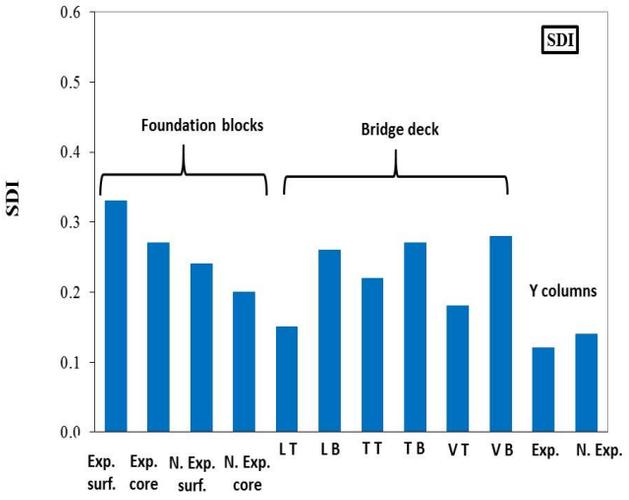
Sanchez et al. (2014, 2015a, 2015b, 2017) developed a multi-level approach for evaluating ASR-affected concrete. After analyzing a wide range of concrete strengths (25, 35 and 45 MPa) and more than ten different aggregate types, a chart of damage values was developed (Table 1). It is worth noting that this chart was created using laboratory samples under free-expansion conditions whereas expansion in real structures is constrained by reinforcement and boundary conditions, as well as triaxial stress states. Nevertheless, this chart might be used as "benchmark" and considered as the "worst scenario" for ASR-affected concrete.

Table 1. ASR damage multi-level assessment (Sanchez et al 2016)

ASR damage degree (%)	Reference expansion level (%)	Multi-level assessment	
		SDI	DRI
Negligible	0.00 – 0.03	0.06 – 0.16	100 - 155
Marginal	0.04 ± 0.01	0.11 – 0.25	210 - 400
Moderate	0.11 ± 0.01	0.15 – 0.31	330 - 500
High	0.20 ± 0.01	0.19 – 0.32	500 - 765
Very High	0.30 ± 0.01	0.22 – 0.36	600 – 925

Sanchez et al. (2016) applied the multi-level approach developed in the laboratory to assess different RBC members such as the bridge deck (BD), untreated columns (C) and foundation blocks (FB). Figures 2 and 3 demonstrate respectively the mechanical (i.e.) SDT and microscopic (i.e., DRI) results obtained while the condition assessment.

A) SDI: different reinforced concrete members



B) PDI: different reinforced concrete members

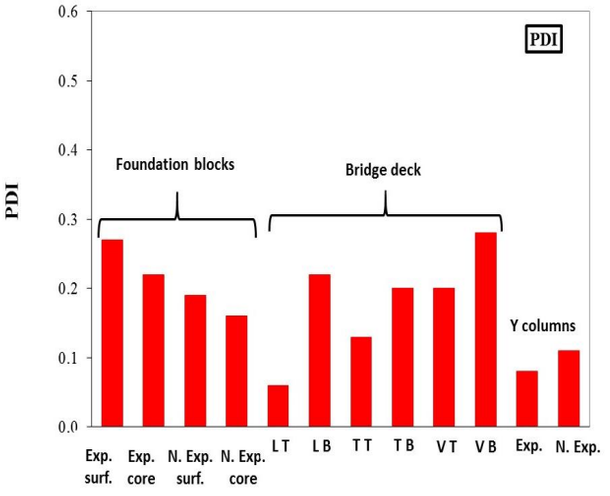


Figure 2. SDI and PDI for members of the RBC bridge (Sanchez et al. 2016).

Considering the mechanical and microscopic results, and comparing those with the benchmark provided in Table 1, it can be observed that the actual damage degree of the FB, BD and C could be classified as very high, high, and moderate, respectively, with "free expansion" values around 0.30%, 0.20% and 0.12%. These values suggested that the unconstrained concrete expansion in some members had actually surpassed the yielding threshold of the steel reinforcement (0.20%). Otherwise, no appraisal was performed on the columns previously treated with the different rehabilitation techniques illustrated in

1.2 and thus no assessment of their performance in stop/mitigating ASR-further expansion and damage was performed.

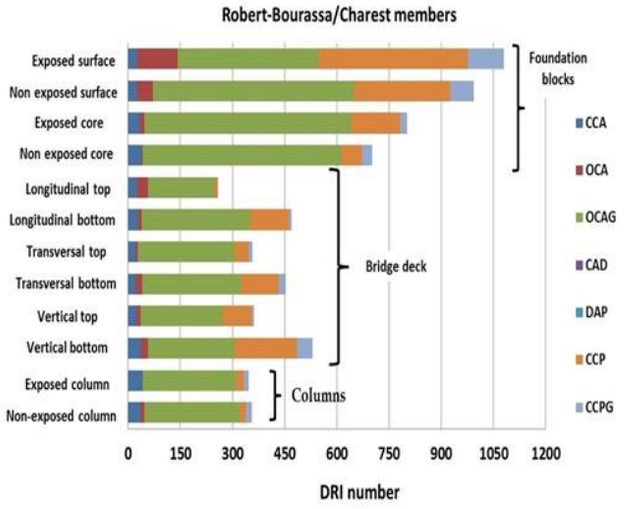
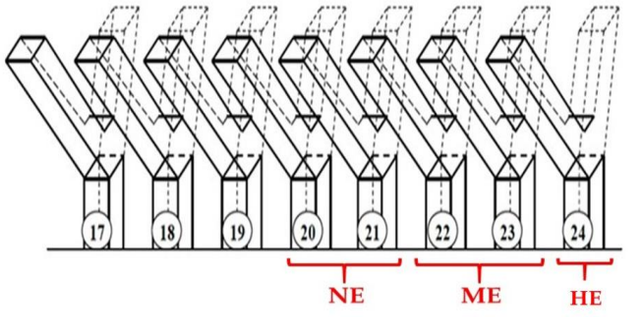


Figure 3. DRI numbers for members of the RBC bridge (Sanchez et al 2016).

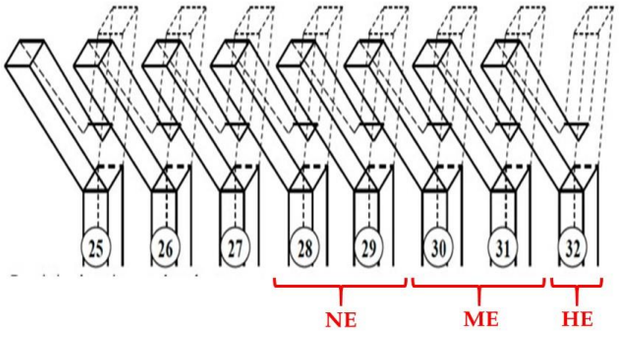
2 SCOPE OF THE WORK

This paper presents the test results of the condition assessment of cores extracted from 10 Y-shaped treated (T) & untreated (UN), highly exposed (HE), moderately exposed (ME) and non-exposed (NE) to the environment columns of RBC according to Figure 4 and Table 2. The objective of this work is to assess the influence of the exposure class and the different ASR mitigation actions used in the different RBC columns to control ASR further expansion and damage.

A) North-West group of columns



B) South-West group of columns



C) South-East group of columns

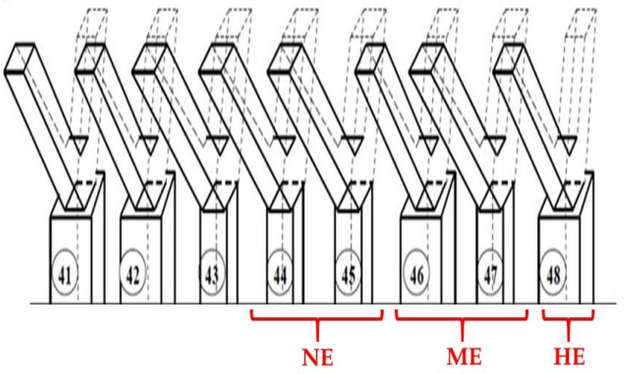


Figure 4. Identification of RBC treated columns: a) North-West group; b) South-West group and; c) South-East group.

Table 2. Number of cores extracted from the different RBC treated columns with their respective treatment techniques.

Colum number	Exposure class	Treatment	Test Samples		
			SDT	DRI	fc
17	HE	UN	3	2	3
22	ME	T; Waterproof sealant + Cementitious coating	3	2	3
23	ME	T; Waterproof sealant + Silane/siloxane sealants	3	2	3
24	HE	T; GFRP sheet	3	2	3
25	HE	T; Waterproof sealant	3	2	2
28	NE	T; Waterproof sealant	3	2	-
29	NE	T; Epoxy sealant	3	2	-
30	ME	T; Waterproof sealant + copolymer modified coating	2	2	-
32	HE	UN	3	2	2
42	NE	UN	2	2	2

3 MATERIALS AND METHODS

3.1 *Column's treatments and visual inspection*

In 2000, RBC columns were treated using different techniques to try to mitigate further expansion and damage caused by ASR and freeze and thaw coupling. A number of techniques were selected and applied on exposed and non-exposed members and bi-annual visual inspections were performed in the coming years. The description of the different products selected for use can be found hereafter.

- Waterproof polymer-modified sealant (WPMS): is a hand spray applied material to stop water leakage and/or moisture uptake into the structural member;
- Cementitious coating: is a protective coating applied to concrete members to prevent moisture uptake and improve the member's aesthetics;
- Silane/siloxane sealants: is a water repellent material which does not provide the member with a bar-

rier effect. Normally used to decrease the moisture uptake from the environment.
- GFRP sheet: high-performance carbon sheets are often used to reinforce distressed concrete structural members, prevent water leakage and also avoid moisture uptake;
- Epoxy coating: is a protective polymeric coating applied to concrete members to prevent moisture uptake;
- Copolymer modified coating: is a high-build copolymer modified coating formulated for use on concrete to avoid water leakage and moisture uptake.

The bi-annual visual inspections performed on the distinct RCB columns after the application of the above systems were not that conclusive. Over the years. Therefore, questions arose on their efficiency to mitigate ASR/freeze and thaw further induced expansion and damage. Moreover, the "initial" damage value of the different columns was never obtained prior to the application of the rehabilitation products, and thus visual comparison was found to be inaccurate. Otherwise, with RCB demolishment in 2010/2010, various cores were extracted from the different columns, which enabled the use of the multi-level assessment proposed by Sanchez et al. (2017) and thus the evaluation of the damage degrees attained in each of the different columns. A detailed visual inspection was also performed on all columns prior to the cores extraction.

3.2 *Laboratory test methods*

3.2.1 *Stiffness Damage Test (SDT)*

The Stiffness Damage Test (SDT) is used to quantify the damage degree of concrete affected by AAR (Sanchez et al. 2014, 2015a, 2015b). The method is based on cyclic loading (using 40% of the compressive strength of sound concrete with the same characteristics as the tested material. In this work, it was assumed 40% of the compressive strength of the least damaged column, i.e., column 32) of concrete samples (cylinders or cores). The full procedure is described in Sanchez et al. (2014, 2015a, 2015b) and the same parameters were adopted in this study. Using a controlled loading rate of 0.10 MPa/s, five cycles of loading/unloading were applied on each set of samples presented in Table 2. Each set comprised of three concrete cores extracted from the same column and with the same characteristics (i.e., environmental conditions and depth from surface).

3.2.2 *Damage Rating Index (DRI)*

The DRI is used to quantify the degree of damage in concrete affected by AAR through a semi-quantitative petrographic analysis (Grattan-Bellew & Mitchell, 2002; Powers & Shrimer, 2007). A microscopic analysis is performed with the use of a stereomicroscope (15-16x magnification) where damage features generally associated with ASR are counted within a 1 cm^2 area drawn on the surface of a polished concrete section. The number of counts corresponding to each type of petrographic feature is then multiplied by weighting factors to balance their relative importance in terms of the material's overall distress. Ideally, a surface of at least 200 cm^2 should be used, yet for comparative purposes, the final DRI value is normalized to a 100 cm^2 area (Grattan-Bellew & Mitchell, 2002). The procedure is fully described in Villeneuve & Fournier (2012) and the same parameters were used in this study. The analyses were performed on two companion samples of the cores tested using the SDT according to Table 2.

3.2.3 *Compressive strength*

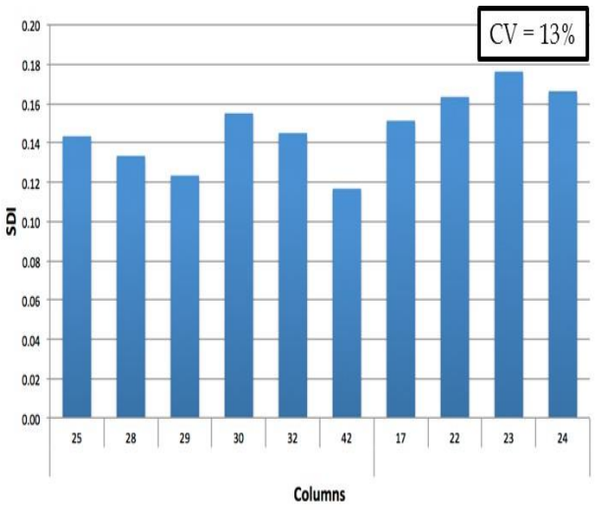
Although it has been shown that the compressive strength is less influenced by AAR and/or freeze and thaw when compared to other parameters such as tensile strength and modulus of elasticity (Sanchez et al. 2017), it was decided to carry out compressive strength tests on cores extracted from all the columns with two objectives: a) first, to determine the ultimate compressive capacity of the least damaged column so that 40% of that values might be used for stiffness damage testing and; b) to evaluate the structural implications (if any) of ASR and freeze and thaw damage over time of columns treated with different rehabilitation techniques.

4 RESULTS

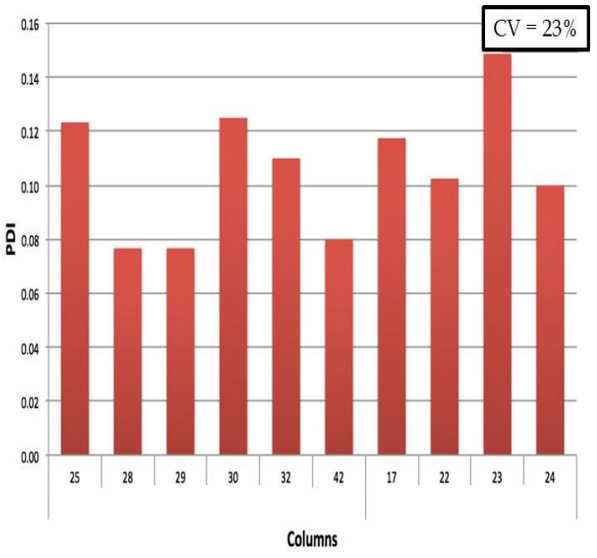
4.1 *Stiffness Damage Test (SDT)*

Figure 5 presents the results of three SDT output parameters as described by Sanchez (2014) and Sanchez at al. (2015c): A) the *Stiffness Damage Index (SDI)*, a measure of the dissipated energy caused by the closure of cracks under compression loading, B) the *Plastic Deformation Index (PDI)*, which quantifies the slipping across surfaces as the internal cracks close under compression loading and, C) the *Modulus of Elasticity (E)*, that corresponds to the average values obtained from the 2nd and 3rd cycles of stiffness damage testing.

A) SDI: for the different RBC columns



B) PDI: for the different RBC columns



B) Modulus of elasticity: for the different RBC columns

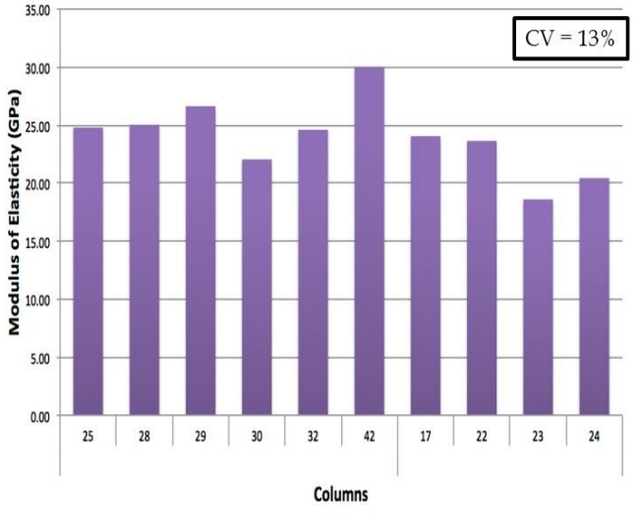


Figure 5. SDT obtained for the different columns of RBC: A) SDI and B) PDI and, C) Modulus of elasticity.

As seen in Figure 5, higher SDI and PDI values were obtained from the North-West specimens, followed by the South-West and South-East cores. Moreover, the untreated (UN) and highly exposed (HE) columns (i.e. 17, 32 and 42) did not necessarily present higher damage degree as it would be expected since one of the conditions for ASR development is the presence of high relative humidity (or moisture). The SDI values obtained from the above columns were 0.15, 0.14 and 0.12 while the PDI results were 0.12, 0.11 and 0.08 respectively.

The columns 22, 23 and 24 presented the highest SDI and PDI values amongst all members: 0.16, 0.18 and 0.17 and 0.10, 0.15 and 0.10, respectively. Those elements were treated and classified ME/HE as per Table 1. Columns 25 and 30 also presented relatively high values of SDI and PDI (0.14, 0.15 and 0.12 and 0.13 respectively). Those are treated and HE and ME columns. Finally, the members 28 and 29 showed the lowest SDI and PDI results, (with the exception of the SDI value of columns 42), being 0.13, 0.12 and 0.07 for both respectively. The latter are treated and non-exposed members.

Overall, the damage degree found in all the columns was considered marginal as per Table 1. Furthermore, the values obtained on the different UN or T columns were lower than the damage results found on the FB and BD cores.

The modulus of elasticity values obtained showed agreement with the SDI and PDI values; i.e. the higher SDI and PDI, the lower the modulus of elasticity. E results ranged from 30 GPa (i.e. column 42- non treated and HE and down to 17 GPa (column 23- treated and ME). Through a structural engineering perspective, some of the results obtained can be considered fairly low compared to the firstly adopted while the design of the bridge.

4.2 *Damage Rating Index (DRI)*

Figure 6 presents the semi-quantitative microscopic responses (i.e. DRI numbers) of all the columns samples. C and S represent core and surface of the columns cage, respectively. It is worth noting that the columns cover was disregarded in the analysis and surface here means nearby the transverse stirrups whereas core means exactly the center of the columns. All of the samples presented closed cracks within the aggregate particles (CCA), which as per Sanchez 2015b might be attributed to other phenomena than ASR (i.e. aggregate production- crushing, sieving and also weathering). However, open cracks with and without gel within the aggregate particles (OCA and OCAG, respectively) are indeed ASR damage features. Likewise, cracks in the cement paste with and without gel (CCP and CCPG) are also caused by ASR and are often found in latter and higher stages of the chemical reaction as per Sanchez et al 2015b.

As seen in Figure 6, most of DRI numbers are in the range between 200 and 400. According to Table

1, that represents a marginal damage degree, which is in agreement with the SDT results.

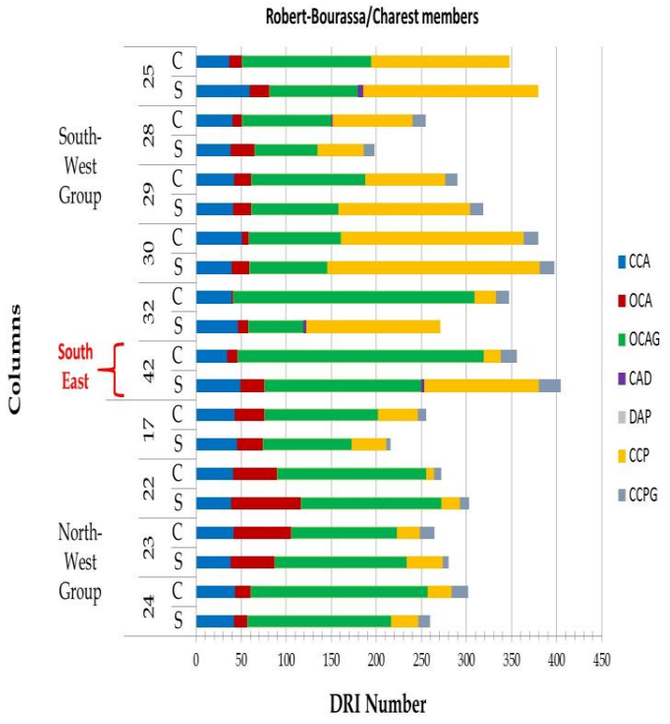


Figure 6. DRI numbers for RBC columns.

The DRI number from cores extracted from the North-West group ranged from 200 to 300. Very few differences were visualized from one core to another and from surface vs core specimens. The results obtained from the South-West/East columns were on average slightly higher. They ranged from 200 to 400. Highly and moderately exposed cores (column 25 and 30) normally presented more damage than NE columns (i.e. 28 and 29). Moreover, important amount of cracks in the cement paste were found when compared with the North-West group which shows that ASR development, although microscopic, was more pronounced on this group of columns. No significantly difference was found from specimens cored from the surface vs core of the columns.

Overall, the damage degree found in all the columns was considered marginal as per Table 1. Furthermore, the values obtained on the different UN or T columns were lower than the damage results found on the FB and BD cores.

4.3 *Compressive strength*

Figure 8 presents the compressive strength results of cores from the distinct columns. The results varied between 32 MPa (columns 23) and 42 MPa (column 32). Most of the samples still presented compressive strength greater than 35 MPa, although technical reports indicate that the 28-day concrete design adopted for the columns was strengths 28 MPa (ICAAR Visit Report, 2000). Therefore, even though microscopic and SDT analysis showed the presence of marginal to moderate ASR, the current damage features seem to still not influence the compressive strength of the affected materials, as state previously by a number of authors (Sanchez et al. 2017, Nixon, & Bollinghaus, 1985, Pleau et al., 1989)

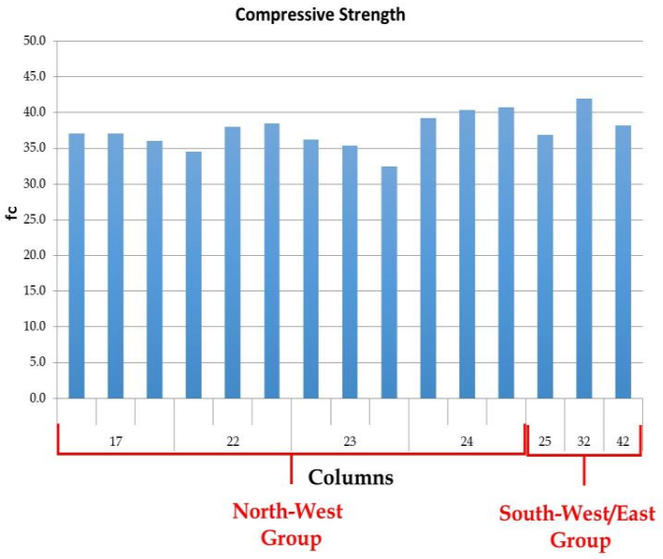


Figure 7. Compressive strength results for RBC columns.

5 DISCUSSION

5.1 *Thorough evaluation of RBC treated columns*

In Figures 5, 6 and 7, a number mechanical and microscopic parameters were evaluated with respect to the comprehensive damage definition proposed by Sanchez et al., 2017 as presented hereafter: a) mechanical properties loss, b) stiffness reduction and c) physical integrity loss. The results showed that the overall damaged found in the various treated and untreated columns of the North-West and South-West/East can be considered marginal as per Table 1. This was confirmed through the analysis of the DRI number and especially the DRI bar chart (Figure 7) where the low amount of cracks in the cement paste (i.e. orange bar) for the North-West columns indicates an initial ASR state while the higher amount of cement paste cracks in the South-West/East columns group might highlight a more advanced distress degree. However, analyzing thoroughly the South-West/East bar charts, it is clear that although the cement paste cracks are more pronounced on average, the cracks in the aggregate particles are less evident, which likely indicates the presence of other mechanisms than ASR leading or at least contributing to the deterioration process such as freezing and thawing.

Another interesting aspect regarding the overall damage of RBC columns is that very few difference was verified amongst the columns in terms of damage. It was anticipated at the beginning that more exposed columns (HE and ME) might present greater damage degree, which did not actually occurred.

This could be at least partially explained due to the compressive stresses found in the field which could have mitigated partially ASR development and thus decreasing the data scattering from the different columns. Likewise, it was not evident to differentiate the efficiency of the distinct treatments used in the columns since the results obtained were quite close to each other. The compressive stress state cited above could be an explanation and moreover the marginal damage degree of the elements does not contribute for the further understanding on the efficiency of the products.

Finally, through an engineering perspective, the compressive strength values obtained from the columns indicate that the elements present compressive values greater than expected which confirms the capacity of the bright to withstand the design loads. However, lower values of modulus of elasticity might indicate a potential issue with respect to the serviceability (i.e. deformation) of the structure. Visual inspections previously performed had clearly indicated the presence of important deflections of the bridge which now can be at least partially explained by the low modulus of elasticity found in some members.

5.2 *Assessment of the expansion attained to date due to ASR*

As previously mentioned, Sanchez et al. (2014, 217) developed a multi-level approach for evaluating ASR-affected concrete using laboratory samples under free-expansion conditions. Otherwise, it is clear that in concrete structures in the field, confinement effects caused by reinforcement, load configurations and boundary conditions will change the responses and deterioration process of the affected material. Anyway, the multi-level approach previously proposed might be used as "reference values" and considered as the "worst case scenario" of ASR-affected concrete. Furthermore, the beauty of using the multi-level approach is that it correlates with ASR expansion attained to date, and thus provides engineers in charge of affected structures with an idea about the current state of the chemical reaction and its potential for further development, which are essential information while the selection of rehabilitation techniques for damaged structures/structural components. Figure 9 presents the expansion values obtained from distinct columns.

The results show that the expansions attained by the different columns evaluated ranged from 0.05% to 0.11%, indicating a marginal to moderate damage degree on average. North-West columns group presented higher expansion levels than South-West/East group. No clear indication on the efficiency of the treatment could be obtained through this study (very likely due to the low damage states of the columns and the fact that the "0" values of damage – prior to the columns treatment - are not known), although for the majority of the columns, a more exposed condition generated a higher expansion level (e.g. columns 22, 23 and 24 when compared to 28 and 29). Moreover, comparing these results with the ones previously obtained from the FB and BD, it is clear that ASR-induced expansion and damage presented much lower values which indicates a much more sound state.

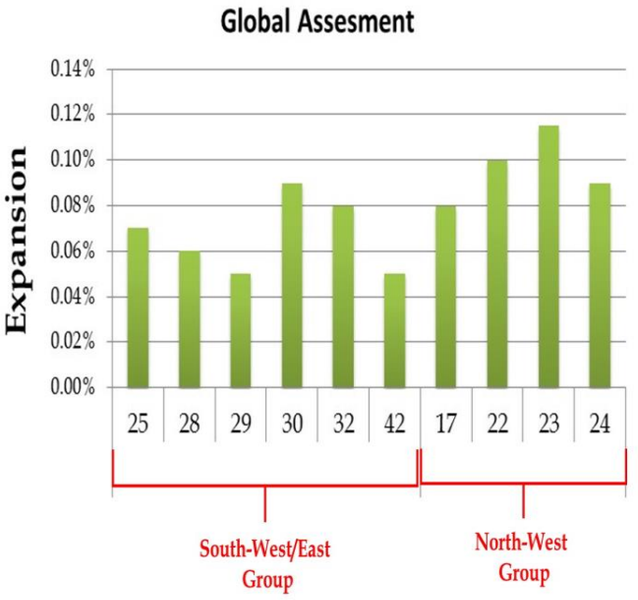


Figure 9. Potential expansion attained for the different RBC columns.

6 CONCLUSION

After performing an important experimental campaign, through the use of the multi-level assessment protocol proposed by Sanchez (2014), on cores extracted from distinct columns of a 50-year old bridge structure affected by ASR, one may conclude that:

- Different damage degrees are found according to the group of columns, greater SDI and PDI values were obtained from the North-West specimens, followed by the South-West/East cores;
- It was anticipated that columns untreated and exposed would present much greater damage compared to non-exposed and treated elements. However, the results did not clearly and significantly vary according to the exposure condition and treatment type of the column, although on average and for the majority of the columns, a more exposed condition generated a higher expansion and damage level.
- The damage degree obtained for the distinct columns was considered to be marginal to moderate as per Sanchez et al (2016, 2017, Table 1). This could likely explain why the different types of treatment could not be compared to each other with respect to their efficiency; i.e.

- The microscopic analysis performed through the DRI showed evidences that some of the columns might have suffered from other deterioration processes than ASR, especially freezing and thawing. According to the DRI charts, Sought-West columns group were likely more distressed due to freezing and thawing whereas North-West columns presented greater ASR distress features.
- The multi-level approach seems to work quite well since the vast majority of results obtained through the mechanical and microscopic tools were similar and complementary;
- Although the damage chart proposed by Sanchez (2014) was developed through the use of laboratory samples under free-expansion, it provides a link between the damage indices and the expansion potential of the affected material, which relates to the management and structural implications of ASR-affected aging infrastructure. In this work, the expansion levels obtained from the different columns ranged from 0.05% to 0.11%, which indicates the initial stages of ASR classified according to Table 1 as marginal to moderate levels.

7 REFERENCES

Bérubé, M.A.; Smaoui, N.; Fournier, B.; Bissonnette, B.; Durand, B. 2005. Evaluation of the expansion attained to date by concrete affected by ASR - Part III: Application to existing structures. Canadian Journal of Civil Engineering, 32, 463-479.

Fournier, B.; Bérubé, M. A. 2000. Alkali–aggregate reaction in concrete: a review of basic concepts and engineering implications. Canadian Journal of Civil Engineering, 27,167-191.

Grattan-Bellew, P. E., Mitchell, L. D. 2002. Quantitative Petrographic Analysis for Concrete. 8th Symposium on Alkali-Aggregate Reactivity in Concrete. Montréal, Canada.

ICAAR Visit Report. 2000. Report of the visit of structures affected by AAR in the Quebec City area. 11th International conference on alkali-aggregate reaction, Quebec, Canada.

Nixon, P.J.; Bollinghaus, R. The effect of alkali aggregate reaction on the tensile strength of concrete. Durability of Building Materials pp. 243-248, 1985.

Pleau, R.; Bérubé, M. A.; Pigeon, M.; Fournier, B.; Raphael, S. 1989. Mechanical Behavior of Concrete Affected by AAR. 8th ICAAR - International Conference on Alkali-Aggregate Reaction in Concrete. Kyoto, Japan, 1989.

Powers, L.; Shrimer, F. H. 2007. Quantification of ASR in concrete: an introduction to the Damage Rating Index. 29th International Conference on Cement Microscopy, May, Québec, Canada.

Sanchez, L.F.M., Fournier, B., Jolin M, Bastien, J. 2014. Evaluation of the Stiffness Damage Test (SDT) as a tool for assessing damage in concrete due to ASR: test loading and output responses for concretes incorporating fine or coarse reactive aggregates. Cement and Concrete Research, 56, 213-229.

Sanchez, L. F. M., Fournier, B., Jolin M, Bastien, J. 2015a. Evaluation of the Stiffness Damage Test (SDT) as a tool for assessing damage in concrete due to ASR: input parameters and variability of the test responses. Construction and Building Materials, 77, 20-32.

Sanchez, L. F. M., Fournier, B., Jolin M., Duchesne, J. 2015b. Reliable quantification of AAR damage through assessment of the damage rating index (DRI). Cement and Concrete Research, 67, 74-92.

Sanchez, L. F. M., Fournier, B., Bastien, J., Mitchell, D., and Noël, M. 2016. Overall Assessment of an ASR Affected Overpass "Robert-Bourassa/Charest" After Nearly 50 Years in Service. 8th International Conference on Bridge Maintenance, Safety and Management, June 26-30, Foz do Iguacu, Brazil.

Sanchez, L. F. M., Fournier, B., Jolin, M, Bastien, J., Mitchell, D. Overall assessment of alkali-aggregate reaction (AAR) in concretes presenting different strengths and incorporating a wide range of reactive aggregate types and natures. Cement and Concrete Research, vol. 93, 17-31, 2017.

Smaoui. N.; Bérubé. M.A.; Fournier. B.; Bissonnette. B. & Durand. B. Evaluation of the Expansion Attained to Date by Concrete Affected by ASR - Part I: Experimental Study. Canadian Journal of Civil Engineering. 2004, 31: 826-845.

Villeneuve, V., Fournier, B. 2012. Determination of the damage in concrete affected by ASR – the damage rating index (DRI). 14th ICAAR - International Conference on Alkali-Aggregate Reaction in Concrete (ICAAR), May, Austin, USA.

Maintenance, Safety, Risk, Management and Life-Cycle Performance of Bridges – Powers, Frangopol, Al-Mahaidi & Caprani (Eds)
© 2018 Taylor & Francis Group, London, ISBN 978-1-138-73045-8

Influence of Tendon Breaks on Structural Behavior of Concrete Beams

H. Kaneko & K. Suzuki
University of Fukui, Fukui, Japan

K. Amaya, K. Hamaoka & M. Hara
NIPPON PS Co,Ltd., Fukui, japan

M. Fukuda
West Nippon Expressway Company Limited, Osaka, Japan

E. Sasaki & P. Tuttipongsawat
Tokyo Institute of Technology, Tokyo, Japan

T. Kuroda & K. Takase
OMRON SOCIAL SOLUTIONS CO.,LTD, Tokyo, japan

Y. Ikawa
NEXCO-West Consultants Company Limited, Hiroshima, Japan

ABSTRACT: In recent years, breaks of Prestressed Concrete (PC) tendon have been reported. For the maintenance and management of PC structures, it is important to grasp the characteristics of PC structures that have tendon breaks. In this study, with the pre-tensioned PC beam specimens, analytical and experimental approaches are taken. The experimental results show that stress distribution locally changes near the breaking point, whereas the influence on the global behavior is small, when tendons break. If the tendon break occurs in the region where bending stresses are large, crack initiation is induced with reduction of the bending stiffness. Elastic waves resulting from the tendon break tend to propagate throughout the beam and can be captured by monitoring micro vibration of the beam surface. A natural frequency slightly decreased as the number of tendon break increased. In contrast, a damping ratio tends to increase with increasing the number of tendon break.

1 INTRODUCTION

The number of bridge construction has significantly increased in Japan since the late 1960s~1970s. Over decades, structural deterioration has progressed in these bridges. Among several damage cases in aging bridge structures, break of tendons in prestressed concrete (PC) beam is one of the serious damage cases that directly relates the loss of load carrying capacity. Actually, collapsing cases of a PC bridge due to the break of PC tendons have been reported. In order to secure the safety of PC structures, it is important to grasp the behavior of PC beams when PC tendons broken and also to accumulate the data that lead to develop a judgement method for the tendon break.

The objectives of this study are to reveal influence of tendon breaks on stress distribution and bending stiffness, and also to find a method to capture elastic waves generated by the tendon break. Moreover, natural vibration measurement is also performed to understand the change of natural frequency and structural damping. With the pre-tensioned PC beam specimens, FEM analysis is firstly performed to obtain the load-displacement relationship with a parameter of effective prestress level; then, bending experiments are done to evaluate the structural behavior with and without tendon breaks.

2 PRE-EXPERIMENT

2.1 *Finite Element Analysis (FEA)*

In order to grasp bending behavior and the crack initiation load, non-linear static Finite Element Analysis (FEA) is performed by ABAQUS/standard. Figure 1 illustrates the FEM model. The analytical model is created based on the rectangular section. 8-node cubic elements (C3D8) are employed to represent the concrete part, and 4-node 2D rebar elements are used to represent the PC tendon. The mesh size is 10 mm in the whole of the model. Initial stresses are given to the rebar elements to introduce stressing forces into the PC tendon. For the boundary condition, simply-supported condition is modeled. The distance between supports is set to 1900 mm. The loading is given by distributed loads in 200 mm range at the span center.

2.1.1 *Material property of PC tendon*

Table 1 shows the material property of PC tendon. The elastic modulus is 200,000 MPa, the Poisson's ratio is 0.3, and the density is 7850 kg/m^3. As shown in Figure 2, the elasto-plastic constitutive law is set with a yield stress of 1705 MPa, the tensile strength of 1927 MPa and the maximum strain of 0.11 based on JIS. The definition is a bilinear isotropic hardening rule, and the slope of which after the tensile strength is constant.

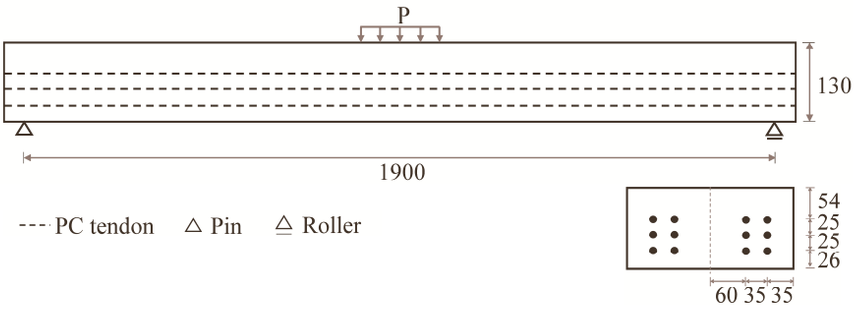


Figure 1. FEM model

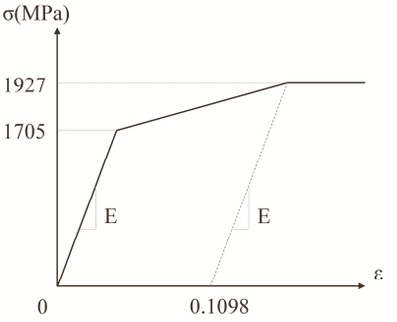


Figure 2. Constitutive law of PC tendon

Table1. Material property of PC sleeper

Name	Physical properties		Unit
Concrete	Elastic modulus	43000	MPa
	Poisson's ratio	0.2	
	Density	2500	kg/m^3
PC tendon	Elastic modulus	200000	MPa
	Poisson's ratio	0.3	
	Density	7850	kg/m^3
	Strength at 0.2% permanent elongation	1705	MPa
	Tensile strength	1927	MPa
	Maximum elongation	0.11	

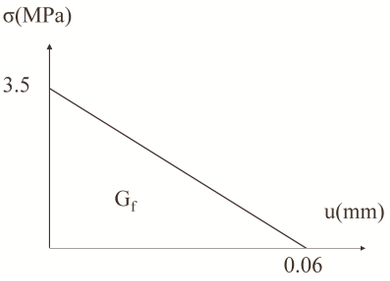


Figure 3. Stress after cracking

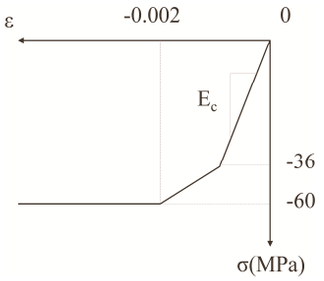


Figure 4. Stress-strain curve

2.1.2 *Material property of concrete*

Table 1 shows the material property of the concrete. The elastic modulus is 43,000 MPa, the Poisson's ratio is 0.2, and the density is 2500 kg/m^3. In regard to the elasto-plastic constitutive law of concrete, Concrete Damaged Plasticity Model is applied. The dilation angle is used 30 degrees. The yield surface applied in this study is the modified yield function developed by Lee and Fenves.

Figure 3 shows the energy curve on stress-deformation relations in the tensile condition after cracking in concrete. The tensile strength is determined f_{tk} = 3.53 N/mm^2 from the calculation Equation 1 by Japan Society of Civil Engineers (JSCE).

$$f_{tk} = 0.23 f_{ck}^{2/3} \quad (1)$$

where f_{ck} = compressive strength.

In order to avoid the problem of localization dependent on element size, the stress after cracking is defined by breaking energy. The value of breaking energy is G_f, which is determined G_f = 100 N/m from the calculation Equation 2 by JSCE.

$$G_f = 10\,(d_{max})^{1/3} \cdot f_{ck}^{1/3} \quad (2)$$

where d_{max} = maximum size of aggregate.

Figure 4 shows the stress-strain curve of concrete in the compressive condition. The compressive strength is 60 N/mm^2, and the ratio of the biaxial compressive strength to the uniaxial compressive strength is 1.16. The strain at compressive strength is 0.002 in accordance with the JSCE. In consideration of convergence of analysis, the stress-strain slope over the compressive strength is set to be zero so that the stress becomes constant in this region. Furthermore, the viscoelastic attenuation by Duvaut-Lions is given to the model.

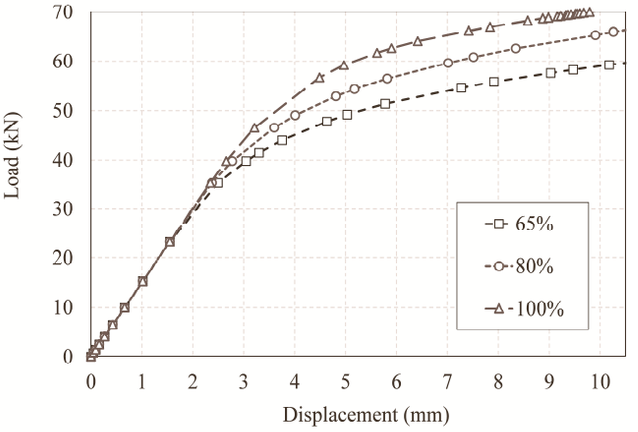


Figure 5. Analysis result

2.1.3 *Analysis procedure*

The analysis processes based on the load control method. The analysis step is divided into two steps. In the first step, introduction of prestress and loading of dead load are carried out, and in the second step, the distributed load is applied to upper surface of the center of the model. Parameters in analysis are introduction values of prestress level to take tendon's relaxation into account. Introduced prestress to the PC tendon are three levels of 100%, 80% and 65% of the initial prestress force.

2.1.4 *Analysis results*

Figure 5 shows the P-δ curve obtained from analysis. The displacement in the graph means the deflection of the lower surface of the beam at the span center. The displacement in Figure 5 indicates the P-δ data in the second step of the analysis. The displacements after the first step were 1.04 mm at prestress 100%, 0.82 mm at 80% and 0.64 mm at 65%, respectively.

No difference in the initial stiffness in each prestress level is seen until the loading load reaches 30 kN. A change of slope appears at 37 kN for prestress 65%, 44 kN for 80% and 50 kN for 100%, respectively. This study defines those load values as the crack initiation load. As the prestress value increases, the crack initiation load shows to go up. From this analysis results, the crack initiation load for the experiment is assumed as approximately 37 kN considering the prestress level was the minimum. The 90% of 37 kN, which is 34.2 kN, is used as the elastic limit that is the maximum load at which cracking does not occur.

2.2 *PC sleeper breaking test*

The experiment is conducted using three specimens which are two tendon break specimens and one healthy specimen. As a PC beam, PC sleepers used in railway are used. Considering the arrangement of PC tendons of the PC sleeper, the specimens are to be upside down. As a loading method, as shown in Figure 6, three points bending is applied (Fig. 6). A PC tendon is artificially cut at three sections of A-A', B-B', and C-C' with a disc grinder. The displacement and strain are measured in each section (Fig. 6). In addition, elastic waves are recorded at two points where are the span center and the span quarter.

2.2.1 *Test specimen*

Figure 6 shows dimensions of the specimen. Longitudinal length is 2000 mm and the cross section is 130 mm × 270 mm at the center. A stranded wire that consists of three wires with the diameter of 2.9 mm each is placed in the concrete as a PC tendon, which has initial tension of 31.8 kN. There are four tendons in a row, in total 3 rows and 12 tendons are in a specimen. For the purpose of cutting a tendon, targeted tendons in tendon break specimens are exposed by chipping the concrete at A-A', B-B' and C-C' sections.

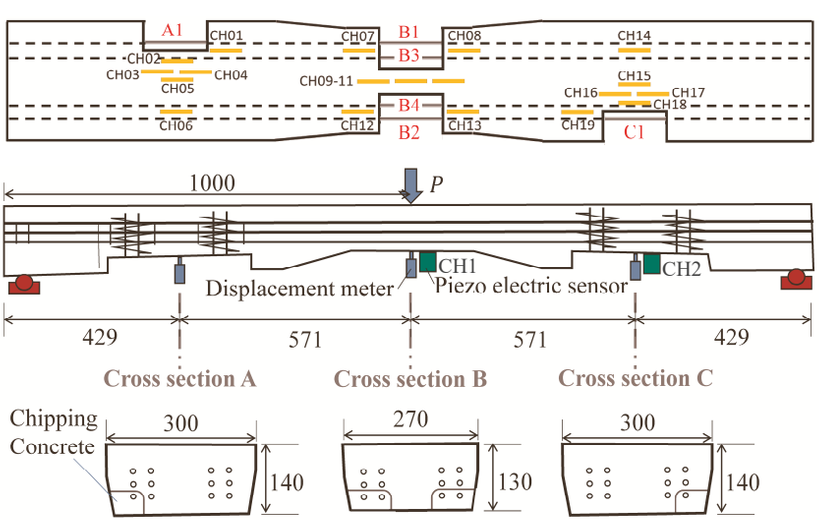


Figure 6. PC sleeper overview and measuring positions

2.2.2 *Measurement method*

19 strain gauges and 3 displacement meters are instrumented in each specimen. In addition, 2 piezo electric sensors are installed for those 2 tendon break specimens. Installed positions are shown in Figure 6. The strain gauge is attached to the lower surface of the concrete of the specimen. Attachment positions of 2 piezo electric sensors are near cross section B-B' and C-C'. The displacement and strain are measured in the vertical and longitudinal direction, respectively.

2.2.3 *Loading procedure*

Figure 7, 8 show the loading procedure. The load is increased to 34.2 kN; that is the elastic limit, determined by the FEM analysis, and then is decreased to 0 kN in each time. Upon loading, dead load ratios $k_1 = 0.5$ and $k_2 = 0.75$ are set as a ratio of the total load to assume a short span bridge and a long span bridge respectively.

In the healthy specimen, beam responses for bending without tendon break are grasped. As shown in Figure 7, loading and unloading are repeatedly given in the order of dead load assumed a short span bridge, dead load assumed a long span bridge, elastic limit load (34.2 kN), and 1.3 times the elastic limit load. Subsequently, the load is increased to the ultimate load.

The other 2 specimens are used to break the tendons and to evaluate the beam behavior to compare with the healthy one. As shown in Figure 8, the tendon is cut when the load is P_1 ($k_1 \times P_2$ or $k_2 \times P_2$) or P_2 (34.2 kN). Before and after cutting the tendon, one cycle of loading and unloading is carried out to grasp the influence of one tendon break on the beam behavior. The exposed PC tendon is artificially cut with a disc grinder in the order of A1, C1, B1, B3, and B2 under loaded condition. B4 tendon is cut by increase of load without the cut work of a disc grinder.

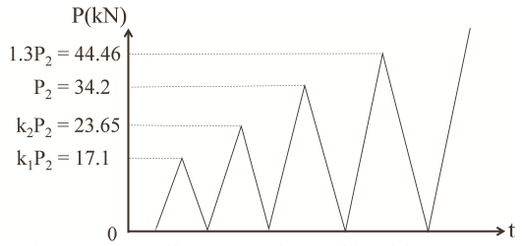


Figure 7. Loading procedure of healthy one

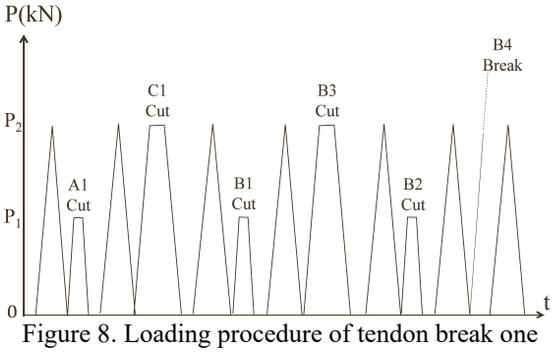


Figure 8. Loading procedure of tendon break one

3 FINDINGS OBTAINED FROM PRE-EXPERIMENT

(1) The validity of the analysis method
Prediction of crack initiation load and prior confirmation of beam behavior are carried out by FEA with a model based on the test specimen. The validity of this analysis method was confirmed because the experimental results were in good agreement with this analysis results of 80% prestress responses (Fig. 10). The assumed elastic limit 34.2 kN was somehow conservative.

(2) Effects of tendon breaks on bending behavior
Stress distribution locally changes near the breaking point, whereas the influence on the global behavior is small, when a tendon break (Fig. 11). If the tendon break occurs in the region where bending stresses are large, crack initiation is induced with reduction of the bending stiffness (Fig. 12).

(3) Possibility of capturing elastic wave for detection monitoring of PC beam break
Elastic waves resulting from the tendon break tend to propagate throughout the beam and can be captured by monitoring micro vibration of the beam surface. In addition, its wave velocity is approximately 3600 m/s (Fig. 13). This suggests that longitudinal waves are predominant in elastic waves due to the tendon break.

4 PC GIRDER RESPONSES DUE TO TENDON BREAK

4.1 *Finite Element Analysis (FEA)*

Before an experiment is carried out, a crack initiation load is analyzed using the FEM model validated in the pre-experiment. Table 2 shows the material property of the concrete and the PC tendon. Figure 14-16 show constitutive laws. Details of the analysis model are shown in Figure 17. The parameter of prestress levels consists of 100%, 80% and 60%. Figure 18 shows the analysis result. The result indicates that the crack initiation load is assumed to be 60 kN. Based on the conservative consideration, the maximum load in the elastic state determined as 54 kN which is 10% less than 60 kN.

Table2. Material property of PC girder

Name	Physical properties		Unit
Concrete	Elastic modulus	33200	MPa
	Poisson's ratio	0.2	
	Density	2370	kg/m^3
PC tendon	Elastic modulus	200000	MPa
	Poisson's ratio	0.3	
	Density	7850	kg/m^3
	Strength at 0.2% permanent elongation	1458	MPa
	Tensile strength	1715	MPa
	Maximum elongation	0.127	

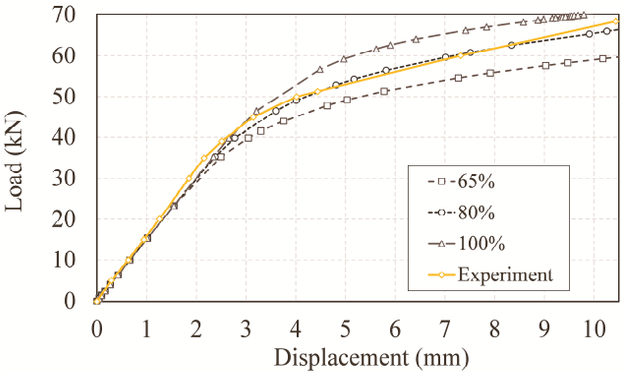


Figure 10. Comparison of experimental and analysis

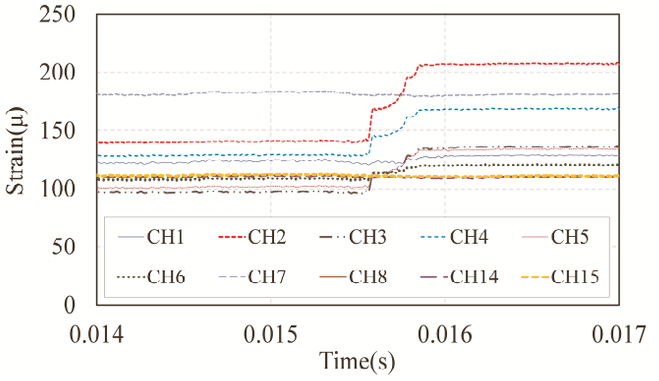


Figure 11. Strain at the time of PC break in cross section A

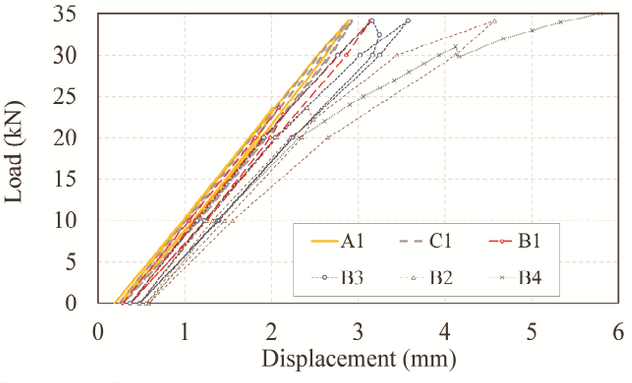


Figure 12. P-δ curve at each experimental phase

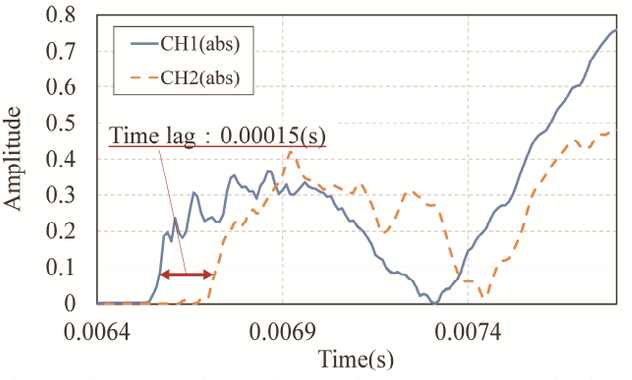


Figure 13. Captured waveforms when PC tendon B4 broke

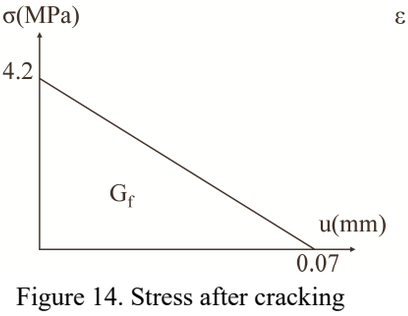


Figure 14. Stress after cracking

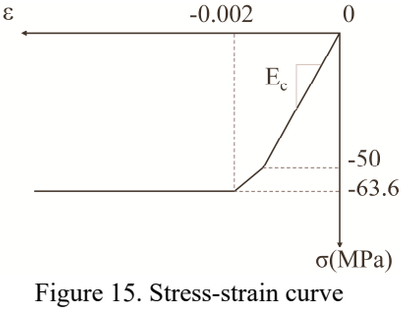


Figure 15. Stress-strain curve

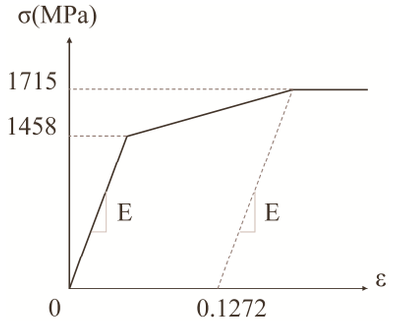


Figure 16. Constitutive law of PC tendon

Concrete	3D solid
PC tendon	Rebar
Pre-stress	1120 MPa (per piece)
Elements	373751
Element size	10 mm
Scale	Half
Loading method	Bending load

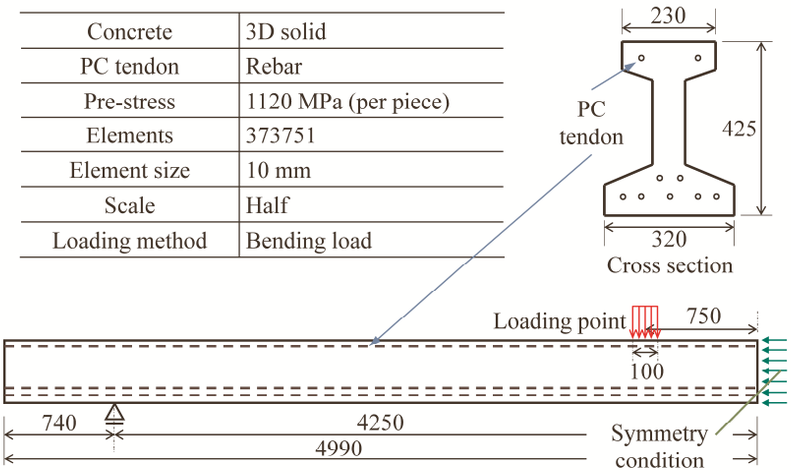


Figure 17. Overview of FEM model based on specimen

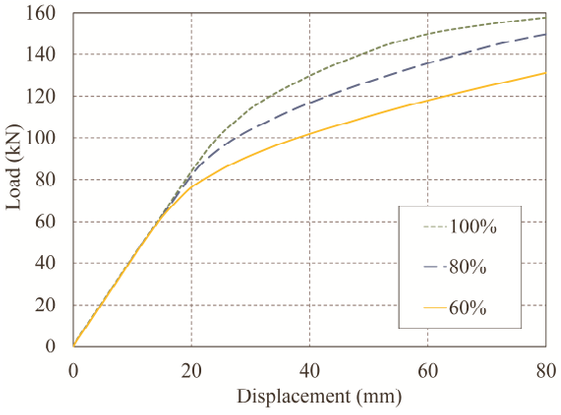
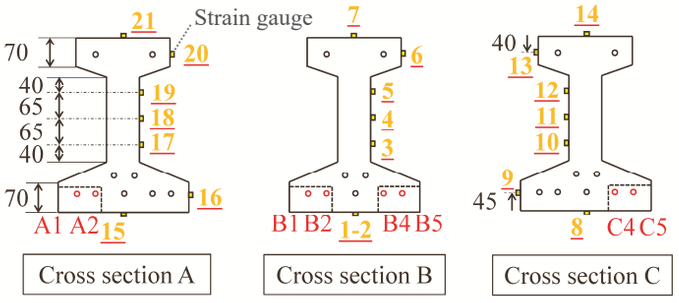


Figure 18. Analysis result



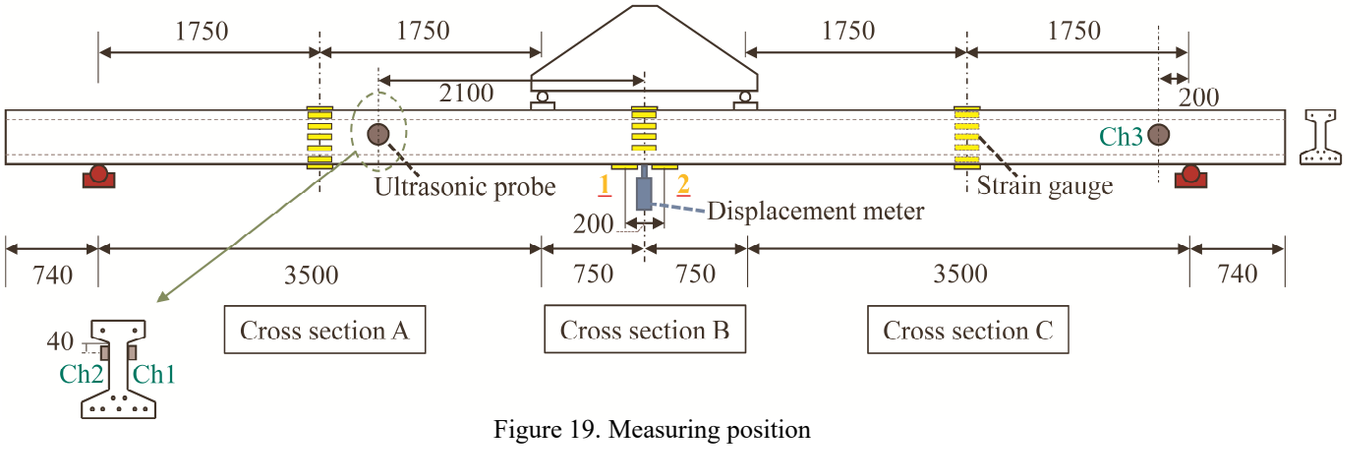


Figure 19. Measuring position

4.2 *Experimental overview*

Loading is given with four-point bending. Three cross sections A-A', B-B', and C-C' are allocated to the specimen as tendon break locations. In those sections, a part of the PC tendons is exposed in advance by chipping concrete. In each experimental phase, a PC tendon is artificially cut with a grinder to simulate actual break cases except the final phase. Regarding measurement, displacement, strain and elastic waves are measured at the position as shown in Figure 19. In addition, natural vibration measurement is performed every time when the PC tendon is cut.

4.2.1 *Test specimen*

Figure 20 shows the overview of the specimen used in the experiment. The body is pretension prestressed girder, the length of which is 9980 mm. The PC tendon is the PC steel stranded wire of 10.8 mm diameter. In total, 9 tendons are placed in the girder. 1128 MPa stress is given to each tendon. The girder specimen was used for more than 30 years in an actual bridge.

4.2.2 *Measurement method*

The apparatus of data acquisition is almost same as the case of pre-experiment; that is, displacement meters, strain gauges, ultrasonic probes as a piezoelectric sensor. Figure 19 shows the installation positions of those. The ultrasonic probe is a 50 kHz wideband vertical probe manufactured by JAPAN PROBE CO., LTD. The probes capture the elastic waves and the waves are logged as voltage. The data sampling rate for the strain and elastic wave data are 500 Hz and 2 kHz, respectively.

Type	Pre-tensioning
PC tendon	9 PC steel strands
Total length	9980 mm
Span length	8500 mm
Cross section	Refer to the figure







Actual appearance

Figure 20. Test specimen overview

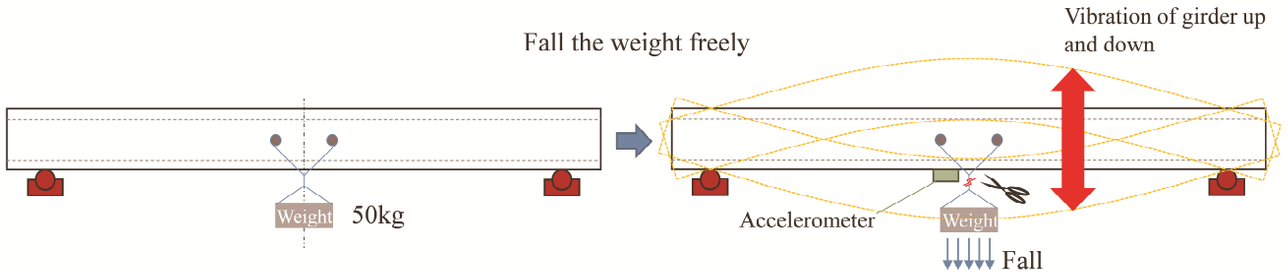


Figure 21. Natural vibration measurement method

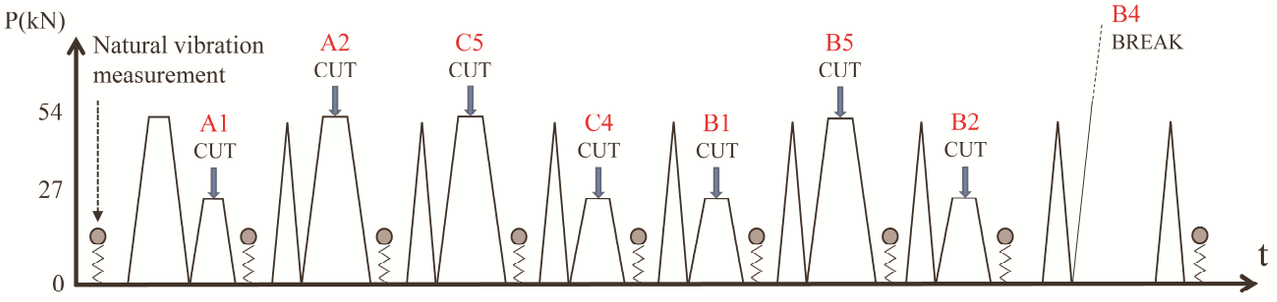


Figure 22. Loading procedure

4.2.3 *Natural vibration measurement*

In natural vibration measurement, free vibration is generated by releasing a 50 kgf-weight suspended from the specimen, and a damping vibration is recorded using an accelerometer installed on the lower surface of the specimen (Fig. 21). In this experiment, this is implemented every time when PC tendon is cut.

4.2.4 *Loading procedure*

Figure 22 shows the loading procedure. The experimental flow is similar to the pre-experiment. In the loading test, the dead load ratio to total load is set to 50% which is 27 kN.

As shown in Figure 22, the exposed PC tendon is artificially cut under loaded condition in the order of A1, A2, C5, C4, B1, B5, and B2. Finally, by increasing the load, PC tendon B4 is broken.

5 EXPERIMENTAL RESULTS

5.1 *P-δ curve*

Figure 23 shows the P-δ curve when PC tendon was cut. When the PC tendon was cut in cross sections A-A' and C-C', the P-δ curve plots no significant change compared with one of B-B'. In contrast, displacement significantly increases after the PC tendon breaks at B-B' where the level of bending moment is large. The influence of PC tendon break on the beam depends on the location. Tendon break may induce concrete breaking cracks if the break location has high stresses. Consequently, the bending rigidity and structural integrity would be reduced.

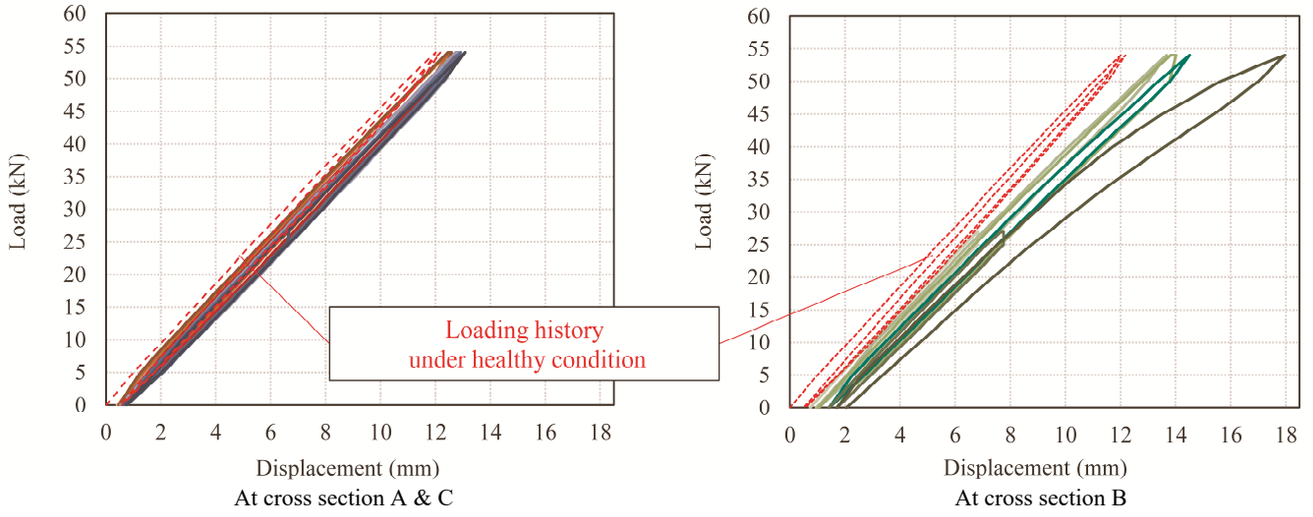


Figure 23. P-δ curve when PC tendon broke at each cross section

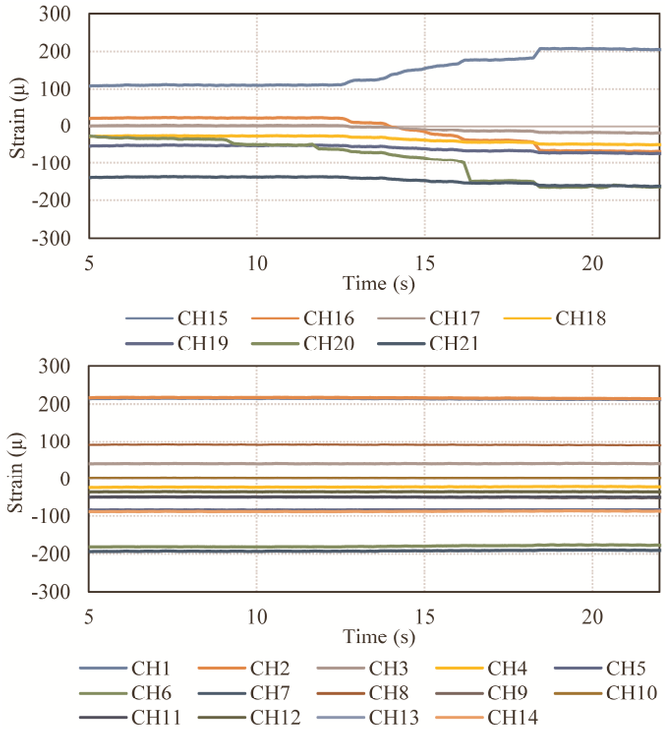


Figure 24. Strain at the time of break in section A

5.2 *Strain responses*

Figure 24 shows strain responses when the PC tendon was cut or had a break. Strain in section A-A' only change in the case that the PC tendon of cross section A-A' breaks. Strain at B-B' and C-C' is not influenced by the tendon cut at section A-A' at that time. Similar phenomenon occurs at section A-A' and B-B' when tendons are cut at section C-C'. Strain responses at the beam surface are not influenced by the tendon cut if the cut location is further than 570 mm. These experimental results also show that stress distribution locally changes in the cross section near the breaking point. The difference in behavior between Figure 11 and Figure 24 depends on the installation position of gauges. These responses mean that bending stress increased after the tendon break. Note that Figure 11 showed the response of lower surface of the specimen. CH 15-21 in Figure 24 showed strain level increased. The strain in compressive area changed to lower values, and the one in tensile area changed to higher values.

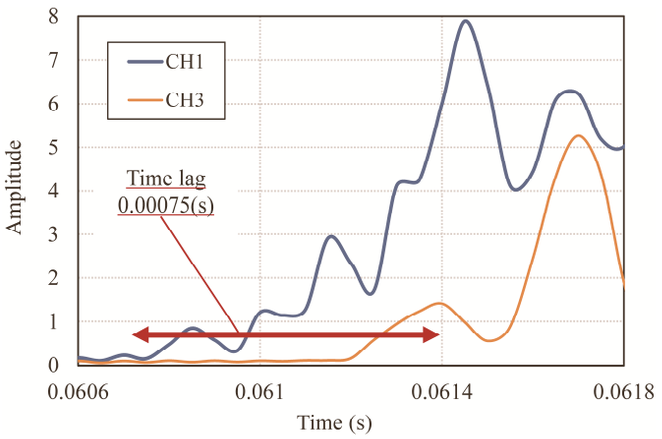


Figure 25. Captured waveform when PC tendon B4 broke

5.3 *Elastic wave*

Figure 25 shows the waveform obtained from the breakage of PC tendon B4 by loading. The time difference between the waves captured with ultrasonic probes CH1 and CH3 is calculated by a cross-correlation function. A wave velocity is calculated from that and it is approximately 2600 m/s. This result is different from the wave velocity obtained from the pre-experiment. Unlike the pre-experiment, it seems that the change in the wave caused by the propagation path has occurred because the position where the wave is caught was far from the breakage occurrence position. Moreover, the web thickness is thinner than that of the PC sleeper. It might be due to the change in the wave mode from longitudinal waves to surface waves immediately after the start of the wave propagation. The speed of surface waves is lower than that of longitudinal ones.

5.4 *Vibration characteristic*

5.4.1 *Data processing method*

The natural frequency in this paper is the dominant frequency obtained by fast Fourier transform of the experimental data.

The data gained in the experiment is processed in the following procedure regarding damping characteristics. First, the vibration waveform at the natural frequency in the vertical first order mode is extracted by applying a band pass filter around the natural frequency. Second, in order to obtain the accuracy damping vibration waveform, an autocorrelation function calculation is performed with data after the maximum amplitude of the extracted waveform. Third, the exponential attenuation curve is approximated by least square method using a maximal value of the acquired damping vibration waveform. Finally, the logarithmic decrement and damping ratio are obtained from Equation 3, 4 using the exponential attenuation curve.

$$\delta = \frac{1}{m} \cdot \ln \frac{a_n}{a_{n+m}} \tag{3}$$

where m = the number of cycles; and a_n = the amplitude of the nth wave.

$$\zeta = \frac{\delta}{2\pi} \tag{4}$$

5.4.2 *Natural frequency and damping ratio*

Figure 26 shows the processed data obtained from the experiment. A natural frequency slightly decreased as the number of PC tendon break increased. In contrast, a damping ratio tends to increase with increasing the number of PC tendon break. Both the natural frequency and the damping ratio are considerably changed at time 8th breaking of PC tendon, which result from the fracture of beam. A tendon break does not significantly affect the change of frequency characteristics unless all the PC tendons placed in the lowest rows break.

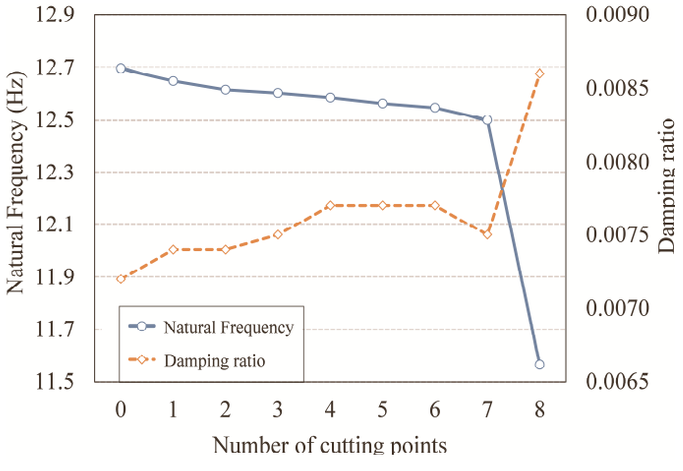


Figure 26. Damping characteristics

6 CONCLUSIONS

This paper described the structural behavior of PC beam in terms of tendon break. The structural responses were observed and evaluated by bending experiments using strain gauges, displacement meters and piezo electric sensors. The conclusions are summarized as follows.

(1) The bending behavior of the PC girder can be simulated by applying initial stresses to rebar elements, defining destructive energy to the concrete for tension behavior and perfect elasto-plasticity to the tendon.

(2) The stress distribution changes in the vicinity of the breaking point, whereas the influence on the global behavior is small, when tendons break. When tendon break occurs in the region where bending stresses are large, the bending stiffness reduces accompanied by crack inducing.

(3) Elastic waves caused by tendon break tend to propagate throughout the beam and can be captured by monitoring micro vibration of the beam surface.

(4) It is suspected that longitudinal waves are predominant in elastic waves resulting from the tendon break. However, it is necessary to consider the influence by the propagation path of the generated wave. Further work is needed to explore this effect.

(5) Frequency characteristics do not considerably change by tendon breaks except for the case that all the PC tendons placed in the lowest rows break. However, a natural frequency slightly decreases with increasing the number of PC tendon break. In contrast, a damping ratio trends to increase with increasing the number of that. In this experiment, results showed that the damping ratio increased by 20% when all tendons in the lowest part of PC related to the primary mode broke in addition to damage concrete.

7 REFFERENCE

ABAQUS. 2013. Abaqus 6.13 Analysis User's Guide, Dassault Systèmes.

Duvaut, G. & Lions, J. L. 1976. *Inequalities in Mechanics and Physics*. New York: Springer.

Japan Society of Civil Engineers. 2007. Standard Specification for Concrete Structures.

Lubliner, J., Oliver, J., Oller, S. & Oñate, E. 1989. A Plastic-Damage Model for Concrete, *International Journal of Solids and Structures*, Vol.25, no.3: 229–326.

Lee, J. & Fenves, G. L. 1998. Plastic-Damage Model for Cyclic Loading of Concrete Structures, *Journal of Engineering Mechanics* Vol. 124, No. 8: 892-900.

Railway Technical Research Institute. 2016. RTRI Report, No.30.

MS11: Special elements in bridge construction and practice

Organizer: M. Nasser Darwish

Maintenance, Safety, Risk, Management and Life-Cycle Performance of Bridges – Powers, Frangopol, Al-Mahaidi & Caprani (Eds)
© 2018 Taylor & Francis Group, London, ISBN 978-1-138-73045-8

Bridges Approach Slabs with Fibre Reinforced Polymers

M. Nasser Darwish, *F.ACI*
Faculty of Engineering, Alexandria Univ., Alexandria, Egypt

ABSTRACT:. Conventional steel reinforcing bars in concrete bridge approach slabs (BAS) are subject to high corrosion levels, and hence, fibre reinforced polymers (FRP) bars are their potential substitutes in aggressive environments, since they have higher resistance to aggressive exposures and corrosion. BAS seldom receive appropriate design considerations and are common sources of problems. Their behaviour is governed by soil-slab interaction, leading to varying relative stiffnesses which affect the straining actions especially under heavy loads, and where the moments are reduced with the reduction in rigidity. If neglected, this may lead to irrational designs. BAS are applications where the mechanical properties of FRP bars, i.e. high strength and low stiffness (rigidity), are suitable and advantageous. The BAS is designed as structurally reinforced with FRP bars adapting the principles of reinforced concrete strength design. FRP bars not only enhance strength but also durability. However, serviceability rather than strength requirements control the design. The inherent differences between FRP reinforced BAS and steel reinforced BAS are highlighted and some special considerations of BAS addressed.

1 INRODUCTION

Bridge concrete approach slab (BAS) are transition slabs laid on i mmediate approaches to a bridge generally with one end resting on wall/abutment. They are supposed to form gradual transition between concrete bridge slabs and adjacent concrete/asphalt pavements or embankments and to provide a smooth and structurally sound transition to the adjacent roadway pavement, and mitigate voids and excessive differential settlement between the bridge structure and the approach embankment. Conventional steel reinforcing bars in concrete bridge construction are often subject to high corrosion levels, hence, fibre reinforced polymers (FRP) bars are potential substitutes to steel reinforcement in aggressive environments. Similarly BAS with steel reinforcement suffer from high corrosion, in addition to other severe conditions, including loss of support, poor soil compaction, water ingress, drainage problems…etc.

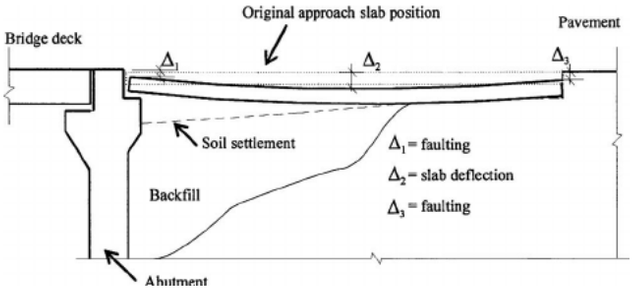


Figure 1. Sketch for bridge approach slabs (*internet BAS photo*)

There are several applications using FRP reinforcement in bridge construction mainly slab decks (eg. see ACI 440 2007), however, less in concrete pavements and slabs on grade (SOG) (ACI 325 2015, Choi et al. 2005, Darwish 2002, Walton et al. 2005), FRP dowels for transverse pavement joints (Shalaby et al. 2001) however, relatively fewer applications of FRP bars in BAS as standalone elements. The use of FR concrete in BAS (Caltrans 2008), and FP decks as replacement units for deteriorated BAS (Chai et al.) were reported.

FRP bars have higher resistance to aggressive exposures and corrosion, key aspects in determining the concrete cover to the reinforcement and tolerable crack widths, hence are potential substitutes to steel reinforcement in aggressive environments and potentially may extend service life. In addition, FRP bars are magnetically neutral (transparent), and hence can be used where electromagnetic neutrality is a requirement especially with the advent of the new smart/intelligent bridge and traffic systems and toll and loop detectors.

Although BAS are important structural elements however they seldom receive appropriate design considerations and are common sources of problems. They are supposed to be cast on uni form, well-compacted soils, and their end may be simply supported at the abutment or resting on a sl eeper slab/beam or just on the underlying grade, i.e. SOG. Adequate compaction under BAS is generally difficult in such restricted areas, and may not be fully achieved. Differential settlement mainly between the bridge end/abutment founded on a more unyielding foundation and the BAS founded on a soil/fill pro-

duces a "bump" in the roadway at the end of the bridge, i.e. sudden change in the slope grade of the BAS, rather than relative smooth transition between the bridge and approach pavement. This affects rideability and driving conditions, and may lead to further deterioration and cracking of the BAS with repetitive loads (Rajek, 2010), and BAS settlement constitutes a major problem (New Mexico Dept. of Transportation 2006).

In previous papers advanced concrete structural analyses of steel reinforced BAS was discussed (eg. Darwish 2016) and FRP reinforced SOG have been investigated (eg. Darwish 2002). In this paper FRP reinforced BAS are addressed and the inherent differences between BAS with FRP and those with steel bars highlighted. The BAS is considered as structurally reinforced with FRP bars adapting the principles of reinforced concrete design. FRP bars not only enhance strength but also durability. However, deflections rather than strength requirements control the design.

2 NUMERICAL IDEALIZATION

From a structural point of view for both cases of BAS: either reinforced with FRP or with steel bars, a typical BAS can be considered as supported on the bridge abutment at one end and on a sleeper slab/beam at its other end, or without the sleeper (Darwish 2016). The sleeper is supposed to reduce settlement and erosion due to water beneath the pavement. BAS can also be just SOG. BAS have been modeled as two way slabs assuming several boundary conditions (Rajek 2010, Thiagarajan et al. 2010) these range from:

- simply supported as a suspended bridge slab without accounting for the underlying soil support to account for any unexpected erosion beneath the slab or softening of soil underneath;
- SOG resting on one end on non-yielding supports, i.e. abutment, and with or without a sleeper slab/beam on the other end.
- SOG resting on the soil underneath.

Soil support underneath the slab can be modeled by using elastic springs (i.e. modulus of sub grade reaction proportional to the subgrade stiffness) although other soil representations (e.g. elastic half space) could be used. The underlying soil can be assumed with no voids (elastic springs over entire span); or with a percentage of voids due to washout or bad compaction (elastic springs over part of the span). Proposals to reinforce the underlying soil were suggested (Chen et al. 2016).

Several numerical idealizations have been adopted (see e.g. ACI325 2015, Darwish 2016). These include: linear Finite Element Method (FEM) and FE with partial soil support and idealizations with limited nonlinearities to model BAS. FEM with full material nonlinearities for SOG considering the concrete slab and reinforcement properties are few (Darwish et al. 1988, Laco et al. 2016). Analyses which consider both the reinforced concrete slab and underlying soil material nonlinearities are rare. Idealizations with material nonlinearities can help assess the actual factors of safety involved and help towards better design, as resulting displacements and loads provide bases for comparison with serviceability criteria derived from tests, practice and pertinent standards.

It has been shown (e.g. Darwish 2016) that assuming the BAS as simply supported beam over its entire length between the abutment and the sleeper, and neglecting the soil elastic support underneath the slab, produces high design moments leading to highly conservative and uneconomical designs. In turn, full soil support may be un-conservative, and the design as a SOG disregarding the abutments/supports seems to be conservative. Considering the far end of the BAS on a sleeper as non-yielding may lead to unconservative deflections. As expected accounting for elastic soil support produces smaller moments, and a reduction in slab thickness. Some design guidelines take into account the potential loss of soil support and void formation under the slab due to consolidation, poor drainage...etc. and provide for partial degree of support to the BAS, by using an effective span factor, less than the actual span e.g. sometimes considered about 0.70 of the suspended span. Several studies on the performance of approach slabs have been carried by researchers and transportation agencies (e.g. Thiagarajan, et al. 2010). As naturally expected the most conservative deflection practical idealized situation is for the case of a SOG, and for smaller values k, modulus of subgrade reaction, the differences increase, and cases approach each other for higher values of k (Darwish 2016).

BAS behaviour is governed by soil-slab interaction, leading to varying relative stiffnesses which affect the straining actions especially under heavy loads, and where the moments are reduced with the reduction in rigidity (Darwish et al. 1988, Losberg 1978). If neglected, this may lead to uneconomical thicknesses and irrational designs. Hence, BAS are applications where the mechanical properties of FRP bars, i.e. high strength and low stiffness (rigidity), are suitable and advantageous (Darwish 2002).

3 AIM & SCOPE

This paper aims at investigating the structural; design of BAS reinforced with FRP bars, based on treating the slab as a structural concrete SOG element applying the principles of reinforced concrete strength design and considering the reinforcement as structurally active to contribute to the load carrying capacity, similar to steel reinforced BAS. The beneficial characteristics of FRP bars in BAS are

utilized and the behaviour of FRP reinforced BAS reinforced are discussed. In addition, the differences between FRP and steel bars reinforcement in BAS are highlighted, and serviceability concerns discussed.

4 PROPERTIES OF FRP BARS

FRP bars are composed (ACI440 2007, Egyptian FRP Code 2005) of continuous high strength fibres embedded in a resin. Fibers are generally made with materials of relatively high modulus of elasticity and high ultimate strength, e.g. glass and carbon. Glass FRP (GFRP) bars are the least expensive among FRP bars. Nevertheless, they possess the lowest tensile strength, (f_{ult}), and modulus of elasticity, (E), in comparison to other FRP materials. In addition, glass fibers may be affected by the alkalinity inherent in the concrete if not properly protected by the surrounding resin matrix. Carbon fibers (CFRP) have high strength and stiffness; and low ultimate strain however may be more expensive than GFRP.

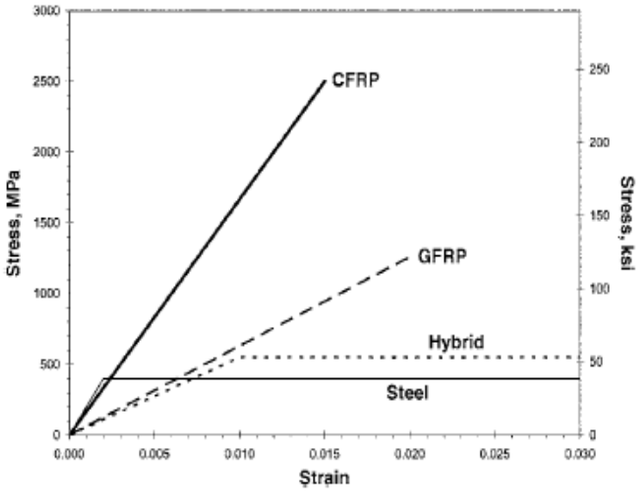


Figure 2. Typical stress-strain curves for FRP (ACI440 2007)

Other mixed breaded bars are available. Internal FRP bars are only considered here, and no ne ar surface mounted bars NSM, or FRP grid or grating systems discussed.

FRP bars are of anisotropic natures and may suffer from brittle fracture, and cannot generally be bent cold. Moreover, they suffer from lack of plastic behavior (i.e. are non duc tile), premature tendon rupture, low dowel resistance and have relatively poor shear strength in the transverse direction. The strength of FRP bars is time dependent and they may suffer creep rupture, hence limiting the sustained load, e.g. to 50-60% of the static short-term tensile strength, may be required. Besides, long-term strength characteristics for FRP bars need consideration (ACI 440 2007). FRP bars should also be checked for fatigue, serviceability criteria, cyclic, or sustained load combined with environmental effects, durability and long term performance. Improving the bond be tween FRP bars and the concrete enhances force transfer; increases the cracking moments; and reduces crack width. In flexural members reinforced with FRP bars, the tension stiffening effect (i.e. tension carried by the concrete between two cracked sections) is generally insignificant. There are inherent differences in behavior between steel and FRP bars. FRP bars have linear stress-strain diagram; and have higher tensile strength. However, their elastic moduli, (E), are generally lower than that of steel. Hence, FRP reinforced BAS will typically have larger deflections, larger crack widths, greater flexural strength, and less ductility behavior than those reinforced with steel bars. Consequently, deflection limits are an important parameter in design considerations. In addition, strength reduction factors or material resistance factors are generally lower than those for steel.

5 SOG WITH FRP BARS

Unlike steel, the elastic modulus of FRP is only slightly higher than that of concrete (especially for GFRP the modular ratio, $n=E_G/E_c$, is small (i.e., just above 1 f or high strength concrete) unlike that for steel, hence limited tensile stress can be transmitted from the concrete to the FRP bars, and most of the tensile load is absorbed by t he concrete. Generally when the tensile strength of the concrete is exceeded, cracks form and the cracking process continues until the cracks extend over most of the cross section and the neutral axis depth is much closer to the compressive end of the slab than in the case of steel. Hence, generally (Darwish 2002) i) a large portion of the cross section is subjected to tensile strains; ii) much larger curvatures and deflections are expected; iii) shear strength is reduced due to increased crack width and reduced size of the compression stress block; and iv) bond of FRP rods may be reduced. In addition, in FRP reinforced concrete flexural members, the transition from the uncracked section to the fully-cracked section may be more abrupt than when using conventional steel bars. However this is not the case for BAS due to presence of the underly-ing soil and membrane effects and, as such, transitions are gradual due to the soil elasticity. In addition, the cracking loads may be generally less than those calculated based on the section modulus of the transformed cross section due to the possible debonding of the FRP bars from the surrounding concrete.

The traditional “drag theory” used for calculating the required steel reinforcement for uniform temperature and shrinkage in BAS as SOG is not directly valid for FRP bars since they have different bond characteristics than steel bars and no plastic deformation. This equally applies to available guidelines for determining steel reinforcement for continuously reinforced concrete pavements and

minimum amount of steel reinforcement, e.g. the Yoder formula (Darwish 2002). The shrinkage and temperature effect of continuously reinforced concrete pavements CRCP reinforced with FRP have been studied and modifications to the formula were suggested (e.g. Choi et al 2005, Walton et al. 2005).

Generally modes of failure of flexural concrete elements reinforced by FRP bars include: i) shear failure of bars at a crack due to low dowel resistance; ii) flexural failures by rupturing of the reinforcement, however only for small amounts of reinforcement; iii) failure by slipping of the FRP bars due to loss of bond; and iv) crushing of the concrete in the compression region. However, in BAS, the membrane effects and the presence of the subgrade undermines the previous failures (Darwish 2002). FRP reinforced slabs will normally have wide cracking. The large depth and width of the cracks virtually diminishes shear resistance that could be provided along the crack/joint due to aggregate interlocking. Hence, the ability to transfer shear loads across joints (or cracks), and resistance to punching is less in BAS with FRP bars due to low dowel resistance of FRP bars and increased crack width. Estimating the load carrying capacity of and deflections of BAS are discussed hereafter.

The increase in crack width may not seriously affect FRP bars durability, however affects the durability of the concrete section and the ingress of aggressive factors and slab riding conditions. There is a decrease in GFRP durability with time, and its durability may be vulnerable on exposure to alkaline environment. Fire protection is generally not a serious issue in BAS with FRP bars since failures are not detrimental due to soil existence. Environmental reduction factors on FRP allowable stresses for the case of concrete section exposed to earth, should be applied (Egyptian FRP Code 2005) and long term performance assessed. The increase in strength with using FRP is modeartly effective in reducing the deflections and crack width realtive to steel reinforcement. The design of FRP reinforced SOG is generally governed by serviceability requirements rather than strength (New Mexico Dept. of Transportation 2006). Due to the lack of potential ductility plastic methods of analysis i.e. the yield line theory (as an upper bound solution), may not be totally valid for FRP reinforced concrete slabs. Besides, there may be a lack of moment redistribution in cases of FRP reinforced slabs thus requiring additional conditions when applying lower bound solutions (Darwish 2002).

6 STRUCTURAL DESIGN

From a structural concrete design point of view concrete FRP reinforced BAS can be treated similar to steel reinforced BAS (Darwish 2016), and regarded as typical SOG with special boundaries, subjected to heavy truck loads, along with other environmental loads. The conventional design of the SOG thickness is generally based on empirical methods or limited theory. These stemps from service load flexural concrete tensile stresses computed by elastic analysis with an allowance for shrinkage and temperature; or on practical guidelines. The basis is to design the slab as plain or very lightly reinforced concrete slabs relying on the flexural strength of the plain concrete (ACI 325 2015) which is completely disregarded in the design of most concrete structures (Losberg 1978). Reinforcement is generally placed to control the width of shrinkage and temperature cracks, and the amount of reinforcement is calculated by applying an arbitrary ratio to the gross concrete cross section area, based on temperature effects. The reinforcement used thus increases in direct proportion to the slab thickness, and its depth is arbitrary based on observed performance.

6.1 *Structurally Active BAS*

Structurally active reinforced concrete BAS are reinforced for structural action and designed assuming the slab to be cracked under wheel loads, and reinforcement provided and positioned according to concrete design requirements, i.e. to carry flexural and other tension forces and contribute to the load carrying capacity. The conventional "absence of crack" criterion will lead to a relatively thick slab. For the interior loading case, there is a prominent positive maximum moment (tension at the bottom of the slab) under the load in comparison with a small negative radial moment, Fig. 3.

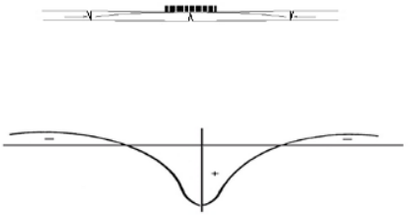


Figure 3. High positive & low negative moments under interior loading

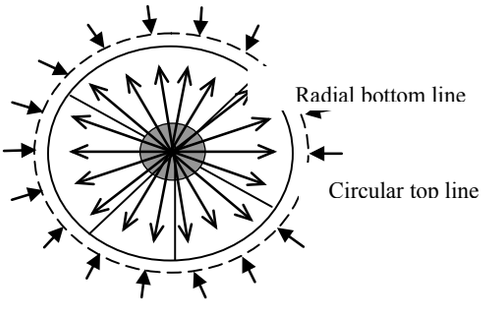


Figure 4. Bottom & top cracking lines (Losberg 1978)

The high positive moments from a co ncentrated load will require significant thickness, if tensile cracks are to be avoided. An aggravating situation is that the thicker and more rigid the slab is made, the higher the maximum moment will be (Darwish et al. 1988; Losberg 1978).

To apply the principles of reinforced concrete, the slab is designed to crack, and two way bottom reinforcement is provided to resist the tensile stresses caused by the positive peak moment, while the slab thickness is designed so that concrete in tension can resist the relatively low negative moment, Figure 3. Such design results in thinner slabs. This, in turn, will decrease the value of the positive moment peak, and the rigidity will further decrease as the bottom of the slab cracks.

7 BEHAVIOR OF ACTIVELY REINFORCED BAS

A typical behavior of a SOG under the interior loading case is linear prior to concrete bottom cracking, the effect of which is a reduction of the slab flexural rigidity. The occurrence of bottom cracking marks the start of the effectiveness of the reinforcement structural contribution. The deflection curves continue with no sharp jumps or kinks in the displacements corresponding to the occurrence of concrete cracking as all transitions are gradual and smooth, and continue even after concrete top cracking due to the soil elasticity (Darwish et al. 1988, Darwish 2002).

7.1 Design of Actively Reinforced BAS

The same principles for steel reinforced BAS (Darwish 2016) are applied for FRP reinforced BAS. A design envelope may be used for the estimation of the top cracking loads of actively reinforced SOG with bottom active reinforcement based of synthesis of nonlinear FE results. Details are found elsewhere (Darwish et al. 1988, Darwish 2002). It accounts for the reinforcement amount and position, concrete properties, and geometric section properties, besides load and soil characteristics. Only the interior loading case is mentioned here due to space limitations. The top cracking loads are related to the sum of positive and negative moment of resistances M^+, and M^-, respectively, and can be expressed as (Fig. 5):

$$(M^+ + M^-)/P = \psi\{a/l_{cracked}\} \qquad (1)$$

where:

M^+= positive ultimate moment, per unit width, provided by the bottom reinforcement= $A_s f_s (d - 0.50 a')$

A_s= area of bottom reinforcement,

f_s = stress in the bottom reinforcement at ultimate positive moment,

d= reinforcement effective depth,

a'= depth of equivalent concrete compressive rectangular stress block,

M^-= negative ultimate moment, per unit width, provided by top flexural concrete strength,

P= concrete top cracking load, P_{tc},

ψ= function relating $(M^+ + M^-)/P$ and a/1,

a= radius of loading area,

l= radius of relative stiffness, relates the slab stiffness to soil stiffness, (length)= $(D/k)^{0.25}$

D= flexural rigidity per unit width of the slab section, (force*length),

k= modulus of subgrade reaction,

l_{gross}= radius of relative stiffness, based on the gross section properties= $(D_{gross}/k)^{0.25}$,

D_{gross} = flexural rigidity per unit width of the gross section,

$l_{cracked}$= radius of relative stiffness, based on fully-cracked section properties, and

$D_{cracked}$ = flexural rigidity/ unit width of fully-cracked section.

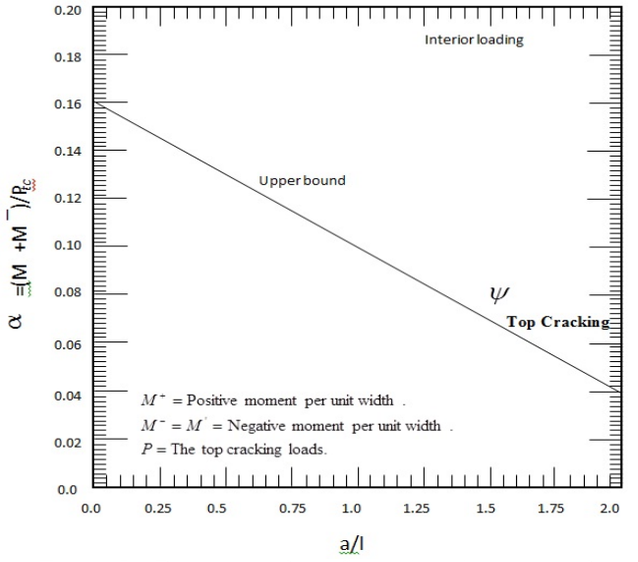


Figure 5. Design envelope for estimatiing top cracking loads (Darwish et al 1988)

The value a/1 is based on the fully cracked not the uncracked section properties.

7.2 Estimating Deflections

Estimating the deflections for FRP reinforced BAS with FRP is crucial regarding the serviceability criteria for loads higher than the cracking loads. Similar to deflections treatment in steel reinforced BAS, (Darwish 2016), coefficient η_1 (less than 1) is to be multiplied by t he deflection of the fully cracked slab based on elastic linear analysis, to estimate the typical deflections, for bottom reinforced slabs under interior loading. It is estimated by comparing deflections resulting from FE analysis at top cracking Δ' with those obtained under the same loads but applying linear elastic analysis of the fully cracked cross section, $\Delta_{cracked}$'.

The deflections for the fully cracked section are calculated at the center interior point, and represent the upper deflection limit. The lower bound for the slab deflection is the elastic deflection of the uncracked section. A typical value for the deflection coefficients at the top cracking load, η_1, is 0.60. For infinite slabs with predefined joints or cracks, with adequate load transfer, these coefficients seem to increase by approximately 20% (Darwish et al. 1988) more than for infinite slabs say 0.72. Similar approximate coefficients could be obtained for finite size slabs, following the same procedure. In essence the coefficients represents the effect of the contribution of other less stressed, less cracked sections to resist loads and decrease the overall deflection at a certain section. One can approximately estimate the slab deflections, in the nonlinear range, under external loads greater than the bottom cracking load, for infinite slabs with bottom reinforcement, under interior loading case, as follows:

-Calculate the bottom cracking load from linear analysis, P_{bc}, and the corresponding deflection, Δ_{bc}, based on the uncracked section properties. P_{bc} can be calculated from the elastic theory by equating the resulting moment M due to the load P, to the flexural cracking moment of the slab, $f_r\ h^2/6$. This may be expressed as (Darwish et al. 1988; Losberg 1978):

$$M = f_r (h^2/6) = P(1 + \upsilon) \{0.04901 - 0.07958 \ln (a/l) + - 0.0781 (a/l)^2 \} \quad (2)$$

for a/1*<1.0, where f_r is the concrete flexural tensile strength.

The deflection, Δ, for an infinite slab under interior loading, the deflection (e.g. Δ_{bc} at the bottom cracking load can be approximately expressed from elastic theory as:

$$\Delta_{bc} = \Delta = 0.03125 (4 - a/l) Pl^2/D \quad (3)$$

Estimate the top cracking load with the help of Fig. 5. Calculate the maximum deflection corresponding to that load, $\Delta'_{cracked}$, calculations based on the *fully cracked* cross section properties. The deflections can be calculated for a/l*=0, as:

$$\Delta'_{cracked} = \Delta = 0.125 Pl^2/D \quad (4)$$

- Using the displacement coefficient η_1 estimate the deflections at the top cracking load:

$\Delta'_{tc} = \Delta = \eta_1 \Delta'_{cracked}$

Δ' = Δ'_{tc} = deflection computed from FE, for the load causing top cracking

$\Delta'_{cracked}$ = deflection computed from elastic analysis for a fully cracked cross section, for the load causing top cracking ,

η_1 = coefficient for estimating deflection at top cracking load from the deflection of a fully cracked section, and

Such deflections and loads exclude the dead load effects .

-Estimate the deflection under the applied load assuming the deflection curve to be composed of linear segments. This can be expressed as

$$\Delta' = \Delta_{bc} + \{(\Delta_{tc} - \Delta_{bc}) (P - P_{bc}) / (P_{tc} - P_{bc})\} \quad (5)$$

where, P_{tc} and P_{bc} are the loads causing top and bottom cracking, respectively. Thus, the deflection, Δ at any load P could be calculated. The deflections under edge and corner loading conditions are generally larger than those under interior loading, and may control serviceability.

Since BAS are under reinforced sections, for steel bars, f_s is assumed equal to the yield stress, f_y. However, since FRP bars have linear stress-strain relationships up to rupture, the stress in the FRP reinforcement f_s, can be assumed to be approximately about 50% of its tensile strength due to time dependent effects and aggressive environment. In addition, the tensile strength of FRP bars cannot be fully utilized as it is accompanied by excessive deflections. The moment M^+ can be considered as a property of the section, its material, and reinforcement amount and position.

For an uncracked section, the gross moment of inertia, I_{gross}, for a plain concrete section does not practically differ from that of a reinforced concrete section. Therefore, the radius of relative stiffness, l_{gross}, is nearly the same for both sections, and the bottom cracking load; failure load, according to elastic analysis is practically the same regardless of the reinforcement amount, position and properties, in elastic analysis. In the design envelope the properties of the fully cracked section are used. The values of $l_{cracked}$ are smaller for FRP reinforced BAS than for steel reinforced BAS, as expected. Hence as can be depicted from the curve (Fig. 5) the top cracking loads for FRP reinforced BAS are higher than those for steel reinforced BAS, due to low elastic moduli of FRP bars. For small values of a/1 less than approximately 0.20, it is more likely that failure will be governed by punching shear rather than flexure, for either FRP or steel reinforcment.

8 SPECIAL CONSIDERATIONS

Prior to cracking BAS have the same behavior and practically the same bottom cracking loads regardless of the reinforcement type (FRP or steel) or amount (plain or reinforced), since linear analysis does not recognize the presence of the reinforcement or its effects in increasing the load carrying capacity. After cracking, FRP reinforced BAS exhibit greater reduction in stiffness than steel reinforced BAS and

hence have greater deflections. For slabs with FRP the top cracking loads are higher than for those with steel bars, as expected, due to the reduced stiffness of the FRP cracked slab, i.e. smaller $1_{cracked}$ value. However, this is accompanied by excessive deflections, Δ, that should be checked against serviceability and geotechnical limitations (Chen et al. 2016).

8.1 *Finite vs. Infinite BAS*

The nonlinear FE analysis for either SOG with FRP or with steel (Darwish 2016) is general and can account for all BAS sizes, infinite and finite, with any boundaries, and special conditions or loadings, however, this may be complex, hence simplified approaches may be needed. The presented approach referred to here was developed based on synthesizing data from FE results into simple charts for infinite SOG, however can be extended to finite size slabs. As expected, the most conservative deflection under a concentrated central load is the case of infinite SOG rather than finite ones, and for higher values of k, the differences in deflections decrease between the cases, and approach each other for higher k values-Coefficients greater than 1.0 can be developed to account for that (Darwish 2016). Hence for estimating the deflections for a BAS under bottom and top cracking loads, apply a coefficient (less than 1) when using $l_{cracked}$ for loads greater than the bottom cracking loads. In addition apply a coefficient (greater than 1.0) to account for finite size slabs (or slabs with predefined joints) relative to infinite size slabs. The effect of own weight, and edge loading should be considered. As superposition is not applicable in the nonlinear stages, hence for specific or special cases and combined loadings, full nonlinear finite element analysis may be resorted to.

8.2 Serviceability

For BAS serviceability criterion rather than strength generally controls the design. FRP bars are not subject to corrosion and the high corrosion resistance is independent of the cover thickness, hence conventional crack width limitations for that reason solely, are not applicable. Long term deflections of FRP reinforced concrete slabs should be considered, and there is need to limit GFRP bars strains under sustained loads due to potential failure from creep rupture and alkaline related deterioration. Temperature and shrinkage effects can be incorporated in the design procedure (e.g. Choi et al. 2005, Darwish et al. 1988). Practical tolerable crack widths were addressed (Choi et al 2005, Waldron et al. 2005). Designs of BAS based on settlement analysis have been reported (e.g. Seo et al. 2002, New Mexico Dept. of Transportation 2006). BAS should provide relative smooth transition between the bridge and approach pavement. However BAS typically experience uneven transition and differential settlement causing inconveniences and bumps adjacent to the bridge end piers and in the pavement at the bridge ends. Suggestions that a tolerable bump may have a slope or angular distortion of 1/200 for simply supported spans and for bump rating and indices were proposed (Seo et al. 2002). Some treat the bump at the end of the bridge as a standalone design issue with prevention as a design goal (New Mexico Dept of Transportation 2006).

9 CONCLUSIONS

Fibre reinforced polymers (FRP) bars are potential substitutes to steel reinforcement in concrete approach slabs (BAS). FRP are non metallic and possess magnetic transparency and unlike steel have higher resistance to aggressive exposures and corrosion, key aspects in determining the concrete cover to the reinforcement and tolerable crack widths. BAS behaviour is governed by soil-slab interaction, leading to varying relative stiffnesses which affect the straining actions under heavy loads, and where the moments are reduced with concrete cracking, and the decrease in flexural rigidity can significantly affect the stress distribution, reduce the maximum moments and increase deflections. If neglected, this may lead to uneconomical thicknesses and irrational designs. The mechanical properties of FRP bars, i.e. high strength and low stiffness (rigidity), are suitable and advantageous in BAS. The treatment of FRP reinforced BAS is similar to steel reinforced BAS, and both are reinforced SOG. The BAS is considered as structurally reinforced with FRP bars adapting the principles of reinforced concrete strength design, as employed for steel reinforced BAS. FRP bars not only enhance the strength but also durability. However, serviceability rather than strength requirements control the design. The inherent differences between BAS with FRP bars and those with steel are highlighted, and special features of FRP reinforced BAS addressed. Nonlinear concrete slab analysis can lead to utilizing beneficial material properties and to improved economical designs and full use of new materials, often disregarded in conventional analysis.

REFERENCES

ACI 440R 2007. Report on Fibre Reinforced Polymers, USA.

ACI 325.9R 2015. Guide to Construction of Concrete Pavements, USA.

Caltrans 2008. Use of Fibre Reinforced Concrete in Bridge Approach Slabs. *Report CA09-0632*, Univ. of California Berkley USA, Caltrans December.

Chai Y. & Chen T. Use of Fibre Polymer Decks as replacement Units for Deteriorated Approach Slabs,

www.dot.ca.gov/hq/esc/earthquake_engineering/workshop/Manuscripts.

Chen Q. & Abu Farsakh M. 2016. Mitigating the bridge end bump problem: A case study of a new approach system with geosynthetic reinforced soil foundation. *Geotextiles and Geomembranes, Vol. 44, Issue 1, February*

Choi J. & Chen R. 2005. Design of Continuously Reinforced Concrete Pavements using GFRP Rebars. *Publications no.FHWA-HRT-05-081*, West Virginia Univ., USA, October.

Darwish, M. & Nilson, A 1988. Structural Analysis and Design of Reinforced Concrete Slabs on Grade. *Report 88-7,* Department of Structural Engineering, Cornell Univ., New York, USA, August 1988, 371 p.

Darwish M. 2002. Design of Concrete Slabs on Grade Structurally Reinforced with FRP Bars, *Proceedings ACI International Conference, Mexico.*

Darwish M. 2016. Improved Structural Design of Reinforced Concrete Slabs on Grade. *Proceedings IABMAS 8th Conference, Brazil, June*.

Eddie D., Shalaby A. & Rizkalla S. 2001 GRFP Dowels for Concrete Pavements. *ACI Structural Journal March-April*.

Laco K & Borzovic V. 2016. Design of Approach Slabs of Road Bridges. *Solid State Phenomena, Vol. 249*.

Losberg, A. 1978. Pavements and Slabs on Grade with Structurally Active Reinforcement, *ACI Journal, Dec., pp. 647–657.*

National Housing and Building Research Council HBRC 2005. Egyptian FRP Code of Practice, Cairo, Egypt.

New Mexico Dept. of Transportation 2006. Settlement Issues Bridge Approach Slabs. *Report NM04MNT-02,* Univ. of New Mexico, December.

Rajek, G. 2010. Numerical Modeling of the Performance of Highway Bridge Approach Slabs. *Msc.Thesis*, Univ. of Wisconsin-Madison, USA.

Seo J., Ha H. & Briaud J. 2002. Investigation of Settlement of Bridge Approach Slabs expansion Joint Numerical Simulations and Model Tests. *Report 0-4147-2*, Texas A& M Univ., USA, December.

Thiagarajan, G. et al. 2010. Bridge Approach Slabs for Missouri DOT Looking at Alternatives and Cost Efficient Approaches. *Report, TRB 0915*, Missouri Dept.of Transportation, USA, December.

Walton S. & Bradberry T. 2005. Feasibility of a Concrete Pavement Continuously Reinforced by GFRP Bars. *Proceedings ConMet'05, Vancouver, Canada, August*.

internet/bridge approach slab photo/bridge joint/ www.research gate.net/www.suggestkeyword.com/Nov 2017

Maintenance, Safety, Risk, Management and Life-Cycle Performance of Bridges – Powers, Frangopol, Al-Mahaidi & Caprani (Eds)
© 2018 Taylor & Francis Group, London, ISBN 978-1-138-73045-8

Guidance on Defects in Hidden Bridge Components

T.M. Pape
AECOM, Brisbane, Australia
P. Burnton
Arup, Brisbane, Australia
J. Collins
Arup, Leeds, United Kingdom
D. Ashurst
Arup, West Midlands, United Kingdom
P. Sparkes
AECOM, Croydon, United Kingdom
J. Webb & C. Christodoulou,
AECOM, Birmingham, United Kingdom

ABSTRACT: Recent catastrophic or unexpected structural failures in road and rail bridges (such as Stewarton rail bridge, Ayrshire, De la Concorde bridge in Canada and more recently the Italian concrete bridge near Lecco) have, in part or full, been attributed to concealed deterioration or deficiencies in one or many components. Defects are usually identified in the course of regular visual inspections carried out by a competent inspector, making an assessment on the condition of the visible components, with reference to appropriate guidelines provided in standard inspection manuals. Hidden defects present unknown risks to the overall integrity of the structure if not identified and rectified.

In recognition of these risks, members of the Bridge Owner's Forum in the UK initiated a project to develop a guide that provides recommendations for identifying, inspecting, designing and maintaining bridges with hidden components. Recently published by CIRIA, Arup and AECOM have collaboratively developed this guide, which the current paper provides a summary of findings from the guide. Translated into an Australian context, key concepts are discussed, such as defects in typical hidden components, proposed risk assessment techniques for management, and recommendations for the development of more targeted inspection and maintenance regimes (that may include health monitoring techniques) to critical areas. The paper also provides various design and planning recommendations for consideration in the preliminary evaluation phase.

1 INTRODUCTION

Bridge owners, operators and engineers including designers, assessors and maintainers all play key roles in bridge management. A core component of a bridge management programme is on-site examinations by a competent bridge inspector. These inspections are central to recording bridge condition and are used by bridge owners to ensure defects are identified and rectified within reasonable timeframes as well as identifying larger maintenance works. When coupled with a refined numerical assessment of capacity, the risk posed by a bridge and / or individual components to threatening safety can be better defined. Generally, this works well in Australia: there are few serious failures. However, amongst other items the success of the process is sensitive to the quality of the access available during the inspection. If an inspection does not include all elements since, for example they are hidden and not easily examinable, the adverse effects can be significant or in the worst cases catastrophic.

High profile cases in recent years such as at Stewarton, de la Concorde, Hammersmith and Boston Manor have bought the importance of hidden defects in bridge components to the forefront of bridge owners' focus. Prompted by these and other cases, the Bridge Owner Forum (BOF) identified the need to define good practice when inspecting, identifying and maintaining hidden bridge components.

BOF approached the publisher CIRIA to produce a new guidance document covering these areas. In December 2014, CIRIA procured the joint services of AECOM and Arup to write this report, recently published as CIRIA Guide C764 "Hidden Defects in Bridges – Guidance for Detection and Management" (Collins et al, 2017). Guidance is given to:

- Define the component that may contain a defect. Common defect types are described.
- Inspection guidance on
- Identification and maintenance
- Design guidance

This paper provides a brief summary of guidance provided in C764. Whilst this guide was written for a UK and Ireland audience, this paper has been expanded to provide an Australian context to this issue. The paper discusses what a hidden defect is, some examples where hidden defects have been instrumental in catastrophic structural failures, an overview of current practices in identifying and managing such defects and components, and then outlining potential solutions in how to manage bridges with hidden components.

2 EXAMPLES OF HIDDEN DEFECTS

2.1 *Definition of a Hidden Defect*

The key driver in a bridge inspection is to identify components that have defects. Defects are defined broadly as a detrimental action to a bridge component that:

> "*risks the ability of the bridge to be defined as meeting service level and safe for use criteria*"
> (Highways Agency, 2007)

Defects can be formed or become apparent at any time in the structure's life. Six primary sources have been listed as principal sources of defects:

- Inadequate design
- Naturally occurring damage
- Accidental or deliberate damage
- Material deterioration
- Reduced functionality of component
- Other sources such as poor design detailing

Usually, most components are visible or accessible to inspect and assess its condition. A hidden component is an element that would not usually be visually inspected as part of a bridge inspection i.e. to within touching distance using normal inspection techniques such as visual techniques and hammer tapping. Its obscurement may be due to design, deterioration, functionality of the component, or simply that an element may not be accessible at the time of the inspection (e.g. submerged piles).

Unfortunately, in some cases the time a defect is found is once the component has failed. In the case where a component is hidden or not visible, this presents a significant risk, particularly if it is a structure-critical member.

It is also important to consider untypical hidden defects and untypical hidden components. This may include unusual or bespoke detailing, accidental inclusion of temporary works, or any form or structure (intentional or otherwise) that may lead to a detrimental condition (such as water retention), and thus a compromise in the structural integrity of a component or the overall structure itself. A hidden component can also be a one that no one knows exists, but may cause a defect that is detected by non-visual means.

2.2 *Case Studies*

Case studies were collected for the CIRIA report to provide useful background reading as well as give a practical context to this topic. A short summary of five case studies is given below, two of which are Australian examples, and the rest are those that became central to forming the new guidance of the CIRIA report.

2.2.1 *Stewarton Rail, United Kingdom*

In January 2009, a train derailed as it crossed the Stewarton Rail Bridge, leaking various heavy fuels into the local waterways. There were no injuries or fatalities however the bridge had collapsed completely (Figure 1). The ensuing investigation demonstrated that the predominant cause of the collapse was due to a shear failure in two of the three main girders. The failure was initiated due to significant section loss (some complete) in the web plates, which were buried under ballast.



Figure 1. The Stewarton Rail Bridge after collapse

Prior to the collapse, concerns had been raised on corrosion to visible areas of the bridge. It was also noted that at defined locations there were areas under ballast that may be prone to severe corrosion and lamination leading to loss of section. Following this urgent defect report, the bridge owner inspected the main girder to assess the issues raised, suggest actions and recommendations. The full extent of the corrosion in buried areas was not identified in this inspection and no recommendations were raised to repair the defect

2.2.2 *Del La Concorde Bridge, Canada*

In 2005 the suspended span of a highway bridge over a dual carriageway collapsed, killing five people. Brittle failure to a half-joint detail had occurred (Figure 2). Whilst there were a number of contributing factors including leaking expansion joints, the root cause of failure was identified as inadequately fixed reinforcement. Half joint reinforcement detailing offers little redundancy to such defects. This hidden defect was exacerbated by: high stress concentrations focussed at re-entrant corners; the debris and moisture trapping nature of the joint's re-entrant corner and the difficulty of accessing the bearing shelf for inspection or maintenance.



Figure 2. Failure of De la Concorde bridge

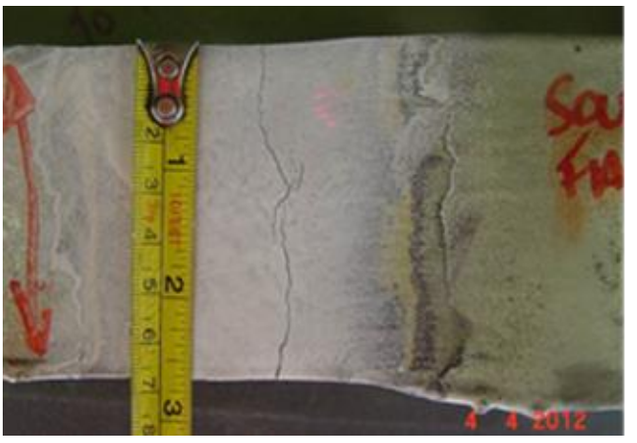


Figure 3. Crack in electro-slag weld, Boston Manor Viaduct

2.2.3 *Boston Manor Viaduct, UK*

The 1 km Boston Manor viaduct is in Brentford, West London (Wearne, 2014) (Nicholls, 2015) carrying the dual carriageway of the M4 motorway. Opened in 1965, its girders and trusses have over 600 electro-slag butt welds. Electro-slag welding is rarely encountered in bridgeworks: Boston Manor is thought to be the only electro-slag welded bridge on the UK trunk road network. Following concerns over the method's susceptibility to fatigue and brittle fracture, by the late 1970s the method was superseded.

As late as 2011's principal inspection, no cracks breaking through the surface of the paint system had been found. Aware of the historic issues of electro-slag welding, the Highways Agency (bridge owner) commissioned a numerical assessment of the welds. No issues were found. To verify the assessment, non-destructive testing (NDT) and material samples were taken in 2012. The rapid development of events was remarkable:

- Mid March 2012, start of NDT inspection.
- 22 March 2012, first crack in electro-slag weld identified.
- 23 March 2012, further cracks found and 17.5t emergency weight restriction imposed.
- 28 March 2012, increasing incidence of crack discovery: 7.5t emergency weight restriction imposed.

In total, 111 cracks were found in electro-slag welds (Figure 4). It was stated that the cracks would require remediating within a maximum of 250 weeks to avoid critical failures. A summer embargo on structural works was approaching around the London 2012 Olympic and Paralympic Games, during which all weight restrictions required removing. Work to remove cracks by grinding / burring started immediately. Just seven days before the embargo, the road was closed to all traffic due to the continued propagation of some cracks, meaning brittle fracture was a real possibility. The cracks were finally removed by burring under monitoring by thermal image detection. The bridge reopened 13 July 2012 to 7.5 tonne traffic

2.2.4 *Hornibrook Highway Bridge, Australia*

Located in an aggressive marine environment, the Hornibrook Highway Bridge was completed in 1935 as a privately commissioned construction project. It consisted of 294 spans, was 2684 m long and was the longest road viaduct across water in Australia when completed (Melchers et al. 2017). It was demolished in 2011 due to extensive deterioration in the timber superstructure and the reinforced concrete headstocks, however the majority of reinforced concrete piles were in remarkably good condition.

One exception to this was a pile that 'bent' whilst being extracted during the demolition process. Upon closer inspection, the cross-section of the pile showed that two of the four reinforcing bars was either completely or severely corroded, adjacent to rust staining along the failure plane. The remaining two bars were in good condition with no signs of deterioration. With the exception of a very fine transverse crack where the failure initiated, no rust staining or deterioration was observed on the external concrete surface.



Figure 4: Pile showing reinforcing bars in good and poor condition

2.3 *Bus Station Retaining Wall*

The bus station is partly set below ground level with secant pile walls in an arched form retaining the fill and roads as well as supporting the structural deck above the bus station. An unreinforced block wall acted as an architectural facing in front of the piled retaining wall. Inspectors noted that the block wall was often damp in one length of the wall. This observation was nearly a decade after the station had opened. Further investigations revealed that soil had been washed into the space between the piles and blockwall by groundwater. This in turn had caused a stormwater pipe to rupture and increase the water flow and hence rate at which soil was lost below the road. The block wall was acting as a retaining structure for which it was not designed, its curved shape providing the strength to prevent collapse. A large hole had formed below the adjacent road – the source of the material now in the void between pile and blockwork. Two potentially catastrophic hidden defects were identified; overloading and potential collapse of the block wall and formation of a large sinkhole in the road above.

Similar hidden sinkholes have been known to form in several situations including below the curved spill through surface protection at bridge abutments, at joints in stormwater culverts, and behind retaining walls, including bridge abutments, adjacent to rivers or stormwater channels.

3 CURRENT MANAGEMENT STRATEGIES

3.1 *Overview*

Responsibility for the management of bridge infrastructure rests with many different organisations and authorities worldwide. The management of their infrastructure is typically governed by a series of documents, guidelines, standards, specifications or technical notes. In some cases where organisations are small, have limited resources or are responsible for a small number of bridges in their network, these are often managed implicitly or on an individual basis. The following sections provide an overview of current bridge management practice in the UK and Australia in relation to hidden components.

3.2 *UK*

Typical bridge management practice for trunk roads is defined in the Design Manual for Roads and Bridges (e.g. BD 63 (Highways Agency, 2007)). For local roads, the document "Well Managed Highway Infrastructure – A Code of Practice" (UKRLG, 2016) is preferred. For the purposes of identification and mitigation of hidden defects, the approaches outlined in the two documents is similar. Bridge condition is recorded from a regime of inspections including general, principal, and special inspections. Inspections provide key information for all maintenance interventions, including decisions for monitoring or testing. However these guidance documents currently do not explicitly detail a regime for uncovering and inspecting hidden components for general or principal inspections.

The owner and maintainer of bridges on the British heavy rail network, Network Rail, operates inspections similar to the highways' authorities' inspections, conducting routine and detailed examinations of varying frequency and using a risk-based approach. Under this regime, it would not be usual practice to expose hidden components. Following the collapse of the Stewarton Bridge in 2009, Network Rail reviewed their inspection approach to incorporate hidden critical elements (HCE). This interesting, proactive work is detailed in the CIRIA guide and has resulted in intrusive inspection to approximately 4000 bridge spans. This has led to a programme of works, including bridge replacement and strengthening. HCE examination has now entered the regular cycle of bridge inspections.

In total, 111 cracks were found in electro-slag welds. It was stated that the cracks would require remediating within a maximum of 250 weeks to avoid critical failures. A summer embargo on structural works was approaching around the London 2012 Olympic and Paralympic Games, during which all weight restrictions required removing. Work to remove cracks by grinding / burring started immediately.

3.3 *Australia*

In Australia, a range of asset management documentation relating to bridges exists. From a high level perspective, Austroads provides several documents that presents collated information and best-practice summaries of bridge management practices in Australia. These guidance documents include:

- Guidelines for Bridge Management – Structure Information (AP-R252-04)
- Guide to Asset Management (currently being updated)
- Guide to Bridge Technology (currently being updated)

A deskstop study shows that all state road authorities have formal documentation that provide high-level asset management guidance for their infrastructure. In relation to bridges, various documents of varying levels of sophistication and depth exist to provide more specific guidance. Relating to the inspection of bridges, again most state road authorities have developed their own bridge or structure inspection manuals to govern the inspection requirements and outputs. Informal risk management regimes may also be in place for specific at-risk

components, such as halving joints or post-tensioned cables.

However it should be noted that only a handful of manuals specifically mention hidden components, and a lesser number to provide documented guidance for their management. With the exception of the Queensland Department of Transport and Main Roads (TMR), there are no publically available guidelines that provide risk management strategies for bridge managers/owners to identify, inspect and manage structure-critical components that are hidden or inaccessible. The following documents provide guidance on hidden defects:

- AS5100.8 (2017): Mentions the use techniques to inspect hidden areas in certain applications, such as timber bridge drilling or Ground Penetrating Radar for void detection. However guidance is minimal and provides no broader recommendations.
- Level 3 Inspection Criteria for Potentially Structurally Deficient Bridges" (TMR, 2016): identifies the "possibility of hidden distress" as a factor to be considered when assessing a bridge for an immediate risk to public safety.
- VicRoads Structure Inspection Manual (2014): some references made to hidden deterioration.
- Transport for NSW, Assets Standards Authority: released Technical Note TN 072 (2014) that identifies hidden structures, used by both road and rail authorities. They define hidden structures as "structures or components of a structure that are obscured in such a way that they are not readily visible" and state that "the examination of hidden structures is important to assure ongoing structural integrity". Some guidance is given to inspecting such components, but lacking in specifics.
- Structures Examination Engineering Manual (RailCorp, 2009): relates to the identification of defects that may be indicators of hidden components deterioration, such as "stain trails indicating hidden corrosion or working members"

In summary, there is currently minimal published guidance for bridge asset owners or managers to assist in identifying and developing strategies to manage hidden components and their defects. Risk management strategies dealing with items such as half-joints, hinges, post-tensioning cables or other special or low-redundancy hidden components are generally dealt with on a unique bridge or issue-specific case. Consideration should be given to this area, particularly relating to structural capacity.

4 PROPOSED MANAGEMENT STRATEGY

4.1 *Overview*

It is anticipated that the vast majority of bridge owners already have a bridge management approach from which the task of identifying at-risk structures can commence. Where a process does not already exist to do so, it is recommended that bridge owners mandate a new programme of managing hidden defects.

To formalise a process on how a bridge owner / operator / maintainer can manage the risks posed by hidden defects to their portfolio of bridges, the CIRIA report provides detailed guidance, largely based on the approach taken by Network Rail post-Stewarton. It is representative of a proactive approach.

An overarching risk management approach is recommended in the management of hidden defect in bridges. This is based on a process developed as part of the UK's bridge assessment processes (Highways Agency, 2015). A cyclical three stage process is recommended in the guide, which comprises the following steps:

- Understanding the risk features
- Implementing a targeted inspection regime
- Evaluation and implementation

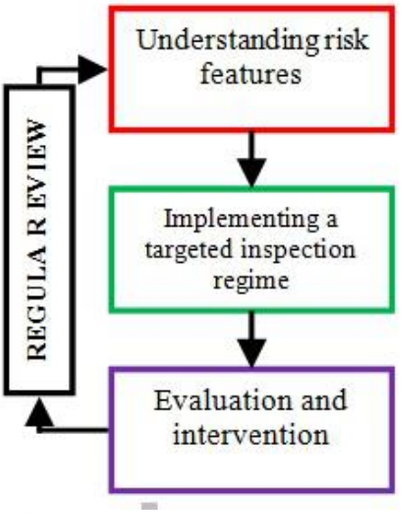


Figure 5: Simplified flow chart of suggested process for managing hidden defects

The process is shown in Figure 5 and is explored further in the following sections.

4.2 *Understanding the Risk Features*

This phase predominantly involves collating and reviewing existing information about a bridge in order to understand the criticality of a bridge and its components in isolation and as part of a network. It involves the following steps:

- Review of bridge inventory information
- Review of bridge componentry

– Identify component criticality to bridge.

It also involves the review of existing information pertaining to a bridge such as drawings, photographs, previous inspections and assessments, maintenance records, modification and construction records.

It is recognised that each bridge portfolio managed will be distinct, though there may be common features that can streamline management. Considerations towards structure redundancy, ductility, environmental conditions, bridge loading history and the impact of condition on the structural capacity of the bridge will be required in the overarching exercise of identifying and understanding risks associated with hidden defects.

An important aspect of this phase is to be asking "what is not recorded?" and "what cannot be seen", as this process can often lead to uncovering issues not previously explored that relate to hidden components.

Identification of critical components and the effect of their deterioration must be considered on a case-by-case basis by an experienced bridge engineer. Critical components may differ significantly between superficially similar bridges. Some examples of areas that may be more critical than others include:

– truss members where there is little or no structural redundancy
– half-joints
– post-tensioning st
– eel members in regions of high stress \main cables of suspension bridges.

The outcome of this process will be an understanding of which hidden components are present in the assets being managed and how critical their condition is to the safety of the structure. Bridges can then be prioritised based on their susceptibility to these defined defects. Note that this guide does not recommend a method for prioritisation, although this should be undertaken on a risk basis. It is recommended that prioritisation be undertaken by experienced bridge engineers.

The review from this phase will inform the second phase (i.e. the inspection regime) of this process.

4.3 *Targeted Inspection Regime*

Inspections are considered a core component of bridge management and are crucial to accurately determine risk. Hidden defects investigation could be either undertaken as a special/Level 3 inspection or worked into a current Level 2 inspection regime. The former should be considered where the risk of failure of a hidden component with significant consequences is likely to occur before the next inspection. This would be an interim measure until intervention works are undertaken. Where it is not possible to inspect all hidden components within the required cycle of Level 2 inspections those of greatest risk should be prioritized.

Thorough inspection is vital. The hidden defects inspector should actively search for and identify the likely cause of a defect. If the cause is not found or unclear, it is equally important that this is recorded for further investigation by others. The key distinction the CIRIA guide makes is for inspectors to ask "what can I not see?".

It is possible that an element that is in poor condition with widespread defects has no detrimental effect on the load carrying capacity of the structure. So, while recording condition is useful and important, there may be a disparity with what is of prime importance to the bridge owner, i.e. bridge capacity and management of risks posed to bridge users/third parties

4.4 *Evaluation and Intervention*

As in any bridge management regime, high quality inspections are only of value if they are accurately interpreted and remedial works enacted upon. This stage of bridge management is generally well recorded in existing guidance. Accurate interpretation may include consideration of how the identified condition of the hidden element effects bridge capacity: numerical assessment may be required. Then, if unacceptable risk remains, remedial works would follow that may include:

– Monitoring
– Load restrictions
– Further numerical assessment
– Component replacement
– Alternative load path provision
– Strengthening
– Bridge replacement
– Updating of emergency plans.

Residual risks should be highlighted and mitigated.

4.5 *Regular Review*

Risk posed by a hidden defect may change over time due to:

– Condition degradation
– Load changes
– Changes in load path
– Developments in structural understanding
– Cultural change in risk perception

It is hence vital that once the hidden defects programme is set up, it is regularly reviewed. This should include incorporation of intrusive works to

hidden areas as part of the established inspection regime.

4.6 *Final Comments*

Undertaking a hidden component inspection may require much pre-planning, intrusive works and disruption to bridge users.

Given the considerable efforts to facilitate the inspection, other works that could take advantage of this access could be considered.

If undertaken wholeheartedly, this is not a short exercise, however it does reduce the likelihood of unforeseen failures, such as those described in the case studies.

5 USE OF TECHNOLOGY

There is recent interest in use of technology, notably drones and photographic visual techniques to inspect areas of bridges that are difficult to access (McRobbie et al, 2014, Lovelace, 2015).

Where an area is difficult to access, initial inspection by drone may assist in identifying locations where thorough inspection is most needed. However, in general, inspection using technology should not be undertaken in place of principal inspections.

A rapidly developing area that may form an information source into the risk-based approach is Structural Health Monitoring (SHM). Bridge engineers have identified the potential for SHM to greatly assist in bridge management, and numerous existing bridges where hidden defects have been identified or are suspected have had SHM installed (Anderson et al, 2012). A SHM system:

- constantly samples instrumentation output during bridge operation, and possibly as early as during construction
- includes multiple structural components
- processes output to generate information that assists general bridge management
- allows access to historic data captured by SHM.

It is vital to understand that when retrofitting SHM, pre-existing damage is identified and recorded. Otherwise, only the rate of deterioration will be measured not an absolute measure of damage accrued.

6 DESIGN GUIDANCE

The above discussion outlines strategies for existing bridges. For new structures risks associated with hidden components and their defects can be mitigated at the design phase. This requires the designer to review the overall structure for areas where components may become hidden or difficult to inspect, understand the criticality of the hidden components, the processes that may result in defects at these hidden components and the opportunity to eliminate these hidden components. The review should also consider moisture traps or other mechanisms that may increase deterioration of a component.

The ultimate aim is to eliminate such components or issues, however this is not always be possible, for example piles will be in the ground and reinforcement embedded in concrete. Therefore, the designer should aim to provide a considered approach to mitigation of this risk. Other options is to allow for long-term monitoring strategies to be installed to either monitor the bridge (such as structural health monitoring, see Section 6 for further discussion) or to provide on-going mechanical support to eliminate the risk (e.g. dehumidification in post-tensioning applications or cathodic protection applications).

Beyond the specific guidance given in this section, the designer of a new bridge looking to avoid critical defects in hidden deck components is directed to Hendy and Iles (2015) and Soubry (2001).

7 CONCLUSIONS

Defective bridges may put the travelling public, those working on the bridge and third parties at risk. Where a defect is not known and if applicable, appropriate monitoring is not undertaken, the associated risk cannot be managed or mitigated appropriately. In severe cases this can lead to severe network disruptions and at worst, fatalities, as observed for the collapse of the Stewarton rail Bridge in Scotland in 2009. A brief review of current bridge management publications in the UK and Australia highlights the lack of guidance on managing bridges with hidden components.

Based on these failures and lack of guidance, CIRIA published C764 “Hidden Defects in Bridges – Guidance for Detection and Management”, which provides considerable detail on all the common bridge types and their possible hidden defects. Guidance is given to:

- Define the component that may contain a defect. Common defect types are described.
- Inspection guidance
- Identification and maintenance
- Design guidance

Similarly in Australia, such manuals and guidance have not been developed to account for uncovering, inspecting and managing hidden components and subsequent defects. With aging bridge stock ever more heavily used, effective management of hidden bridge components is going to increase in importance unless extensive actions are taken. Bridge owners, managers and inspectors are urged to consider this most important subject in their day-to-day work.

ACKNOWLEDGEMENTS

C764 was funded by Freyssinet, Welsh Government, ICE, Transport Scotland, Highways England, Transport Infrastructure Ireland, Network Rail, TransportNI, Environment Agency, Ramboll, Mouchel, Strainstall, Arup and AECOM. Report contents have been shaped by the project steering group including members from the sponsorship organisations. Permission to present report C764 from CIRIA is gratefully acknowledged.

REFERENCES

Austroads, 2004, "Guidelines for Bridge Management: Structure Information", Sydney (AP-252/04).

Austroads, (in publication), "Guide to Asset Management", Sydney

Austroads, 2009, "Guide to Bridge Technology", Sydney

Collins, J, Ashurst, D, Webb, J, Sparkes, P, Ghose, A, 2017, "Hidden defects in bridges - Guidance for detection and management", C764, CIRIA, London

Hendy, C.R. and Iles, D.C. (eds), 2015, Guidance notes on best practice in steel bridge construction, P185/5, sixth issue, Steel Bridge Group, The Steel Construction Institute, Ascot, UK (ISBN: 978-1-85942-196-3)

Highways Agency, 2007, "Inspection of highway structures", Design manual for roads and bridges. BD 63/07, The Stationary Office, London

Highways Agency, 2012, Interim Advice Note 171/12, Risk Based Principal Inspection Intervals, IAN 171/12 , Highways Agency, London

Lovelace, B., 2015, Unmanned aerial vehicle bridge inspection demonstration project, Final Report 2015-40, Minnesota Department of Transportation, USA

McRobbie, S, Wright, M.A. and Chan, A., 2014, "Can technology improve routine visual bridge inspections?" Proceedings of the ICE – Bridge Engineering, vol 168, 3, Institution of Civil Engineers, London, UK, pp 197–207

Melchers, R.E., Pape, T.M., Chaves, I.A. and Heywood, R.J., 2017, Long-term durability of reinforced concrete piles from the Hornibrook Highway Bridge. *Australian Journal of Structural Engineering*, May, pp.1-17.

Nicholls T, Armstrong C, El-Belbol S, Harrison J, Makinson N, Smith Da, 2015, "Repairs to electro-slab weld defects on M4 Boston Manor viaduct", Proc ICE Bridge Engineering Institution of Civil Engineers, London, Vol 168(3), pp259-272

RAIB, 2010, Derailment of a freight train near Stewarton, Ayrshire, Report 02/2010, Rail Accident Investigation Branch, Derby, UK

Soubry, M, 2001, Bridge detailing guide, C543, CIRIA, London, UK (ISBN: 978-0-86017-543-8) www.ciria.org

Standards Australia, 2017, Australian Bridge Design Code: Rehabilitation and Strengthening, AS 5100.8, Standards Australia, Sydney, Australia

Wearne C, Armstrong C, Nichols T, Harrison J, 201, "Collaboration in an emergency: repairing London's M4 Boston Manor viaduct", Proc. ICE Civil Engineering, Institution of Civil Engineers, London, Vol 167(1), pp33-39

Maintenance, Safety, Risk, Management and Life-Cycle Performance of Bridges – Powers, Frangopol, Al-Mahaidi & Caprani (Eds)
© 2018 Taylor & Francis Group, London, ISBN 978-1-138-73045-8

Captain Cook Bridge Bearing Replacement

W Mengel, P Adams, W Hansford, J Spathonis
Queensland Department of Transport and Main Road

ABSTRACT: The Captain Cook Bridge is the most trafficked bridge in Queensland. The original DU Glacier and stainless steel sliding plates failed and were replaced in 1996-97. Routine inspections in July 2016 found that the PTFE sheet had extruded from the sliding bearings on the bridge's two main suspended spans at its southern end. Bespoke bearing designs were implemented in February 2017.

This paper discusses the innovative bearing design changes, how the replacement bearing design evolved, the jacking of the suspended spans, traffic control and strategies to allow the new bearings to be installed. This paper discusses the bearing design changes and a new sliding material, *Orkot TXMM®*. This was the first trial of Orkot in a bridge bearing in Queensland. As this material has a high allowable compressive stress, it not expected to extrude under a substantial increase in traffic loading. As part of the design changes, a new lateral restraint was installed.

1 BACKGROUND

The Captain Cook Bridge crosses the Brisbane River and provides the main arterial feed into Brisbane's CBD from the southern suburbs and Gold Coast region. The bridge was opened to traffic in 1972, and is currently the most trafficked bridge in Queensland, with an annual average daily traffic of 135,000 vehicles.

Captain Cook Bridge contains two separate 550m long bridges, one for each four lane carriageway. The five span, twin cell, variable depth, post-tensioned precast box girder forms the superstructure for each bridge. There are two 34m long suspended spans in each bridge spanning the cantilevers between piers 1 and 2, and piers 3 and 4 respectively — refer to Figure 1. The bridges, each with a kerb-to-kerb width of 13.4m, share common substructure foundations.

The suspended spans are supported on three bearings at each end, with fixed hinged bearings at one end, and sliding knuckle bearings at the other end. The original sliding bearings contained stainless steel sheet and a DU-Glacier bearing material. Inspections discovered that the sliding material had failed and the stainless steel sheets were discharging. They were subsequently replaced in 1996-97 with thicker 6mm stainless steel plates and 4mm thick glass filled polytetrafluoroethylene (PTFE) sliding material (Fong 2000). After 20 years of service, routine inspections in July 2016 revealed the extrusion of the PTFE sheeting from the sliding bearings on the southern Suspended Spans B — refer to Figure 2.

With the frequency of heavy vehicles and hauling expected to increase with the commencement of major construction activities in the CBD and planned high-rise developments, immediate action was required to prevent further deterioration of the bearings and potential structural damage to the bridge.

This paper will briefly discuss the bearing failure but will primarily focus on the bearing design, maintenance and logistical activities to jack the suspended spans, remove the old bearings and install the replacement bearings. Others have addressed the bridge dynamics and bearing loads in more detail (Hourigan 2017).

At the same time as work was progressing on the replacement of the damaged bearings, the project team also had to address other critical work on three access ramps on the adjoining Riverside Expressway.

2 SLIDING BEARING CHARACTERISTICS

All of the original Captain Cook Bridge bearings were specially designed hence are unique to this structure. These bearings consisted of an upper stainless steel plate, and a sliding material forming a low friction sliding surface. The low friction sliding material was confined within a recess in the top of a knuckle. The fulcrum of the base plate is curved (760mm radius) to allow the knuckle to rotate over the base plate. This arrangement accommodates deck rotations and sliding due to live-load induced deflections and thermal expansion. The sliding friction creates an overturning moment, causing a rotation about the transverse axis. The bearing stresses are redistributed so that the centroid of pressure is eccentric to resist the overturning moment. This results in a non-uniform stress distribution across the knuckle. This bearing behaviour is summarised in Figure 3 and was considered in the design of the new knuckles.

It was previously concluded (Fong 2000) that the original 1970's bearings failed because of the DU-Glacier plates' inability to tolerate non-uniform bearing stresses. A number of factors could have con-

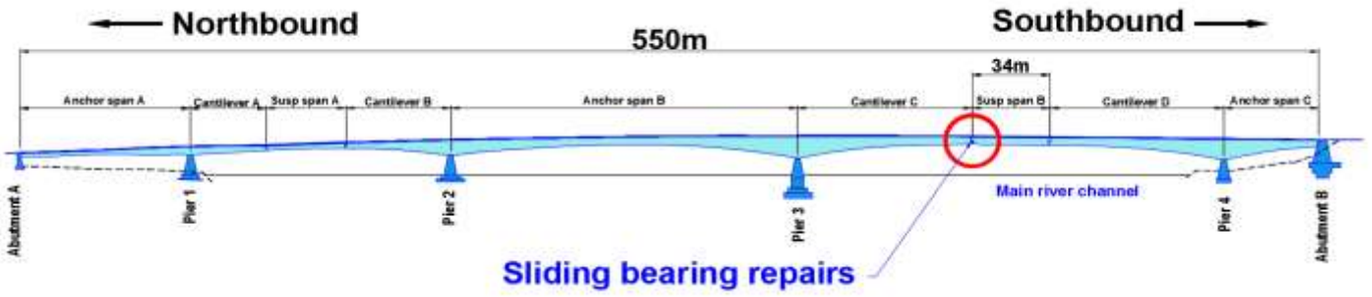


Figure 1 — Captain Cook Bridge – view looking downstream



Figure 2 — Extrusion of the PTFE bearing material

tributed to the current failure of the PTFE — refer to Figure 4. From a design perspective it is important that the PTFE is fully confined within a recess to prevent extrusion under high pressure. Factors that have influenced failure are:

2.1 Increased friction at the sliding interface due to contamination and wear of the PTFE and stainless steel plate– the seal disintegration may have contributed to this failure

2.2 High stress at the leading edge due to poor bearing geometry and high friction

2.3 Increased traffic loads and greater traffic density since last repairs

2.4 Inability of the bearings to adapt to lateral alignment changes due to transverse deck thermal movement and bearing wear

2.5 High leading edge stresses caused excess rotation and separation or very low pressure on the trailing edge allowing extrusion

2.6 Failure and degradation of the adhesive used to bond the PTFE to the knuckle.

Instrumentation installed around the bearing joints after failure and before replacement indicated a very lively bridge structure resulting in considerable knuckle rotation and sliding action. The aggregated sliding movement due to thermal expansion and contraction would be in the range of 1km over a 50 year period. However the sliding movement resulting from traffic weight induced deck deflection, including braking, is estimated to exceed 30km.

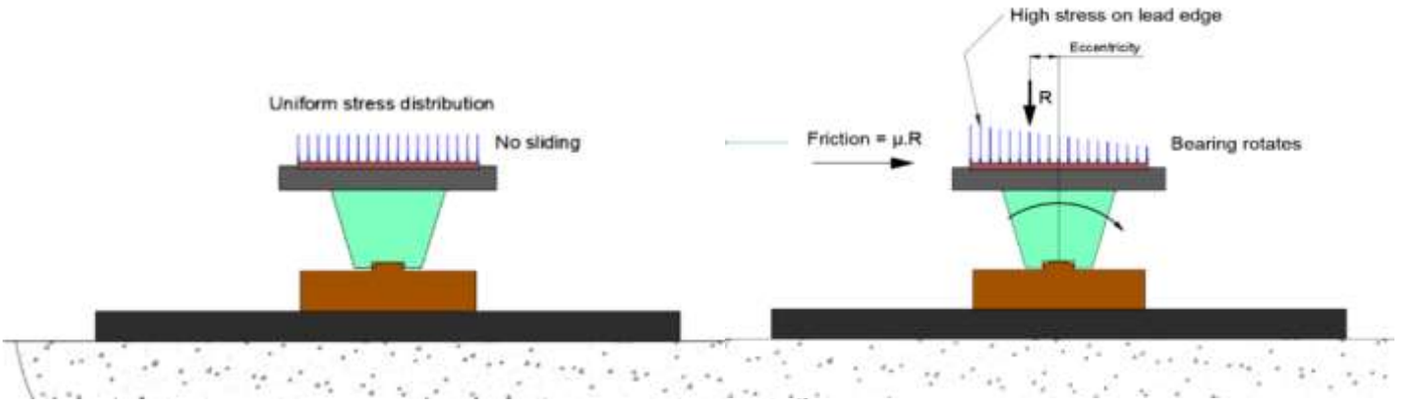


Figure 3 — Sliding knuckle static and dynamic characteristics

3 RECTIFICATION STRATEGY

The bearing rectification strategy had to be developed to allow the repair work for each structure to be completed in an 8 hour period without full traffic closure. A key objective was to minimise disruption to the traffic network into and out of the CBD.

The repair history showed that the two previous designs only lasted 20 years. Hence it would not be worthwhile duplicating what was already there as the PTFE had demonstrated that it extruded under the applied load conditions. The ideal solution would be to remove the existing bearing and replace it with an off-the-shelf spherical bearing. However due to the size of a spherical bearing, this would require removal of the bottom baseplate and grout. However, the tight time restraints and pressure to ensure that the work was carried out in the designated time, meant that the existing bearing base plate had to remain. A new design replacement knuckle required a similar configuration so that it could fit into the space available.

A mathematical analysis of the current rectangular bearing arrangement yielded the following relationship. (N.B. The formula for a circular bearing pad differs from a rectangular/square bearing pad)

$$(Peak\ stress)/(Uniform\ stress) = 1 + \mu.6.h/w$$

where μ equals the coefficient of friction (1)

Hence it can be seen that the stress amplification on the leading edge of the knuckle is influenced by the coefficient of friction and the rotating height to width *(h/w)* ratio — refer to Figure 3. A design was proposed whereby the geometry was improved considerably and a different sliding material was used. Two basic options for a suitable replacement were considered — a Maurer spherical bearing and Orkot TXMM® (Trelleborg 2014). The Maurer spherical bearing would not fit into the desired space unless significant additional work was carried out such as removal of the original baseplate and grout. Due to time constraints the project team decided that this was not an option. Also the EU approved sliding material patented by Maurer is not available as a separate component.



Figure 4 — Extruded PTFE from bearing

Because a timely decision had to be made to allow the detailed design to commence, the material selected for use was Orkot TXMM®. This material had not previously been used in this particular application in Queensland but is used extensively in critical applications within the marine industry. The Orkot family of products have been in use for over 60 years. It has very low frictional properties due to dispersed PTFE and MoS_2 and can be used without

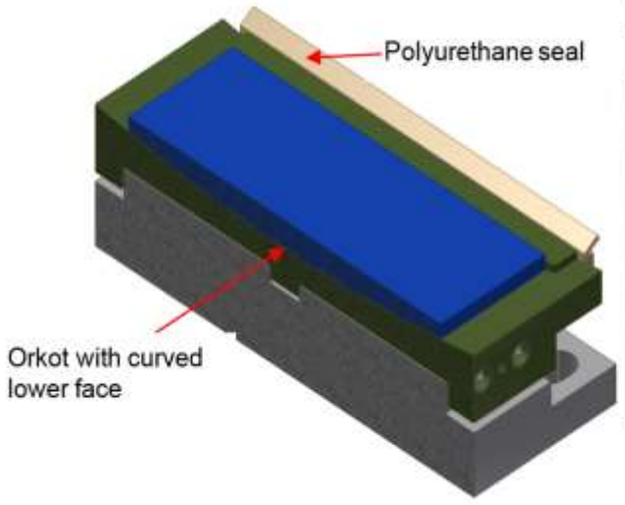


Figure 5 — Section through new knuckle

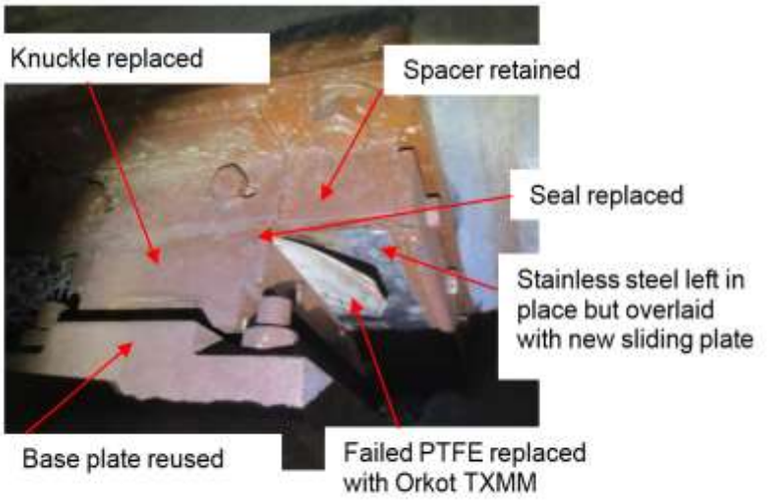


Figure 6 — What was replaced?

additional lubrication. It is superior to most other products on the market because of its high compressive strength of 280 MPa. Its high compressive strength is attributed to the laminated reinforced construction which prevents material flow under high compression forces. Other plastic materials can be used at high compressive loads but these materials must be fully confined on all sides with a small allowable running clearance (approx. 2mm). The Orkot manufacturer, Trelleborg, were very cooperative and supplied the required technical information to allow wear calculations to be performed. The design incorporated a high wear allowance. The Orkot material was manufactured to design specifications by Trelleborg in the United Kingdom.

A design was formulated which fulfilled the operational requirements. This design required that an existing thick spacer plate had to be removed and replaced with a thinner plate. The design team checked to see whether this was physically possible and found that some of these plates had been welded in place. The construction drawings did not show any welds! Because of the position of these welds, an alternative approach was required. It was thought that the welding may have been a fabrication error as not all plates had been welded.

Because of this issue, the design was further constrained. Further detailed investigation highlighted that the top and bottom halves of the current bearings may not be parallel. To counteract any misalignment, the bottom of the Orkot bearing had a machined radius so that the bearing material could self-align when installed. Ideally this radius should have been in the vicinity of 500mm but due to conflicting design requirements a radius of 1700mm was adopted. A number of different thickness stainless steel shims were on hand to pack below Orkot to compensate for different installed bearing heights. Figures 5, 6 & 7 show — a section through the new knuckle, what was replaced and the installed bearing.

The Captain Cook Bridge was designed in the late 1960's. The design was imperial and all fasteners were made with British Standard Whitworth (BSW) threads. Where necessary these BSW fasteners were interchanged with Grade 8.8 zinc plated Unified National Coarse (UNC) fasteners. When the bearings were manufactured in the early 1970's, the marking of hole positions would have been a manual process. There was a concern over the accuracy of the position of hole centres which had to be aligned with new components. To compensate for this, hole clearances in the new components were increased. Compressed air powered die grinders were available to enlarge holes where required (this was required in one instance). The compressed air was sourced from a compressor located on a truck on the bridge deck with associated lines fed through the expansion joint. The old bearings were measured under difficult conditions to ensure there was no gross variation in dimensions.

If the new bearings could not be installed for some unforeseen reason, the fall-back position was to remove the old knuckles, clean the PTFE recesses and install new PTFE replacement inserts. These PTFE inserts had already been sourced and cut to size and contained the same 25% glass. This would then allow the bridge to remain operational until any problems encountered could be resolved at a later date.

The original design allowed for the lateral restraining forces of each suspended span to be counteracted by the centre bearing whose lateral clearance dimensions were smaller than the two outer bearings. Because this lateral restraint design could be improved significantly and to remove this requirement from the revised bearing design, the project team decided to relocate the lateral restraint away from the centre bearing to one of the cells — refer to Figure 8. Irrespective of this decision, there is a requirement for a high vertical movement temporary lateral restraint to control the deck during jacking as the centre bearing (with its lateral restraint function) had to be removed. The new lateral restraint was fully adjustable so that running clearances could be set as well as the relative lateral position of the suspended span with respect to the cantilever. This new lateral restraint fulfilled two roles — a temporary restraint during jacking and a permanent restraint for normal operation.



Figure 7 – Installed replacement bearing before final lowering showing a strain gauge housing on the end of the knuckle

4 BEARING DESIGN SUMMARY

There were a number of design changes implemented (refer to Figure 6), all of which will contribute to longer bearing life, namely:

4.1 *Sliding material*

The traditional material used in applications such as this is PTFE. Because the PTFE with 25% glass failed previously this was replaced with Orkot TXMM®. The coefficient of friction of Orkot TXMM® is low and in combination with other mechanical properties led to the consideration that it will perform better in this situation than glass filled PTFE. Orkot contains dispersed PTFE, MoS_2 and the reinforced layers within Orkot provides the high load capacity. After considering a number of factors, it was decided that it was safe to use Orkot in a trial capacity and monitor its long-term performance.

4.2 *Sliding plate*

This is usually made from stainless steel because it is a relatively inexpensive material and is corrosion resistant. However it is soft and susceptible to abrasion and scratching. This was replaced with a ground and polished steel plate (grade K1042). The plate was coated with 50 µm of electroless nickel followed by 15µm combination of electroless nickel and PTFE. After electroplating the sliding plate was heat treated to achieve a high surface hardness. This surface treatment was selected because of its corrosion and scratch resistance and low coefficient of friction. The back of the plate was sand blasted and was retained in place with epoxy and screws.

4.3 *Knuckle material*

The previous knuckle was manufactured from mild steel. Because of the tighter dimensional design constraints this knuckle was more highly stressed than the previous design. The material selected was Bisalloy 80.

4.4 *Scraper seals*

The previous seals were made from rubber which was compressed against the stainless steel plate. This design failed as rubber has a relatedly short life span. Also as the rubber became worn, it lost is preload. This was replaced with a purpose made polyurethane seal (E93A hardness) which was deflected/sprung against the sliding plate to compensate for wear. Polyurethane is a very hard wearing material and has a long life expectancy in excess of 20 years. The seals can be easily replaced without disturbing the bearings.

4.5 *Greasing points*

Grease nipples were fitted to the new knuckles to allow the rocking area beneath the knuckle to be greased. The primary reason for this is to prevent moisture from entering this area and to prevent fretting corrosion which was present in the previous bearing design.

4.6 *Load monitoring*

Very late in the manufacturing process a decision was made to instrument the knuckles with strain gauges at both ends. A preferred solution would be to integrate a weighing system into the knuckle at the design stage. The new 'smart' bearing knuckles were calibrated prior to installation. The weighing system permitted monitoring during the installation works, and subsequently during service. However

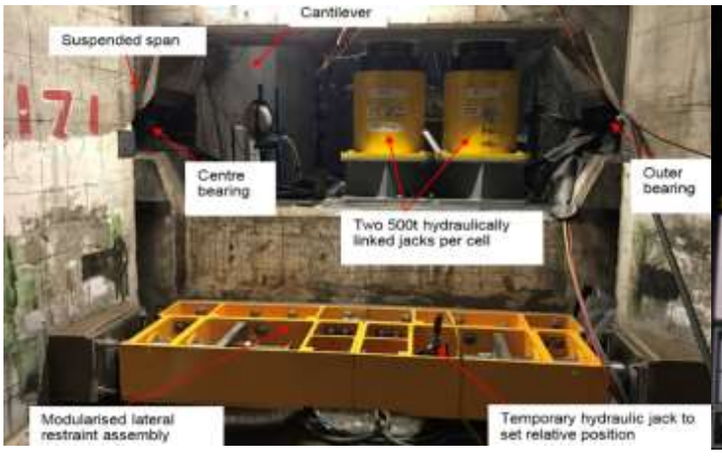


Figure 8 – View of lateral restraint and 500t jacks



Figure 9 – Jacking control console

because of their exposed position the strain gauges are susceptible to potential damage.

4.7 *Lateral restraint*

Removal of this function from the centre bearing reduced the side load and hence would increase the life at the knuckle/baseplate interface. It also fulfilled the lateral restraint role during jacking operations.

5 JACKING SYSTEM

The 800 tonne suspended span is supported on adjacent cantilever spans by halving joints with the cantilever spans providing the bottom diaphragm and the suspended span containing the top diaphragm. Four 500 tonne hydraulic jacks were used to jack the suspended span by approximately 27 mm – refer to Figures 8, 9, 10 & 11. Each 500t jack weighted 550kg. The hydraulic jacks are double acting with a lock ring incorporated on the outside of the main piston. The lock rings are manually adjusted as jacking progresses to ensure safety in the unlikely event of a hydraulic failure.

During bearing rectification works, the suspended span rested solely on these lock rings. The sizing of the hydraulic jacks is usually on the basis that the jack capacity should be more than twice the intended load to be lifted. In this case the total jack capacity was over four times the load. The sizing of these jacks was more about future-proofing the inventory of jacks.

At the base of each jack, a check valve and bypass valve is incorporated into the main lift circuit to protect against hydraulic circuit failure during lifting. However this check valve must be bypassed during lowering operations to allow the jack to retract.

The vertical movement of the jacks are controlled by a string potentiometer which produce 25 pulses per mm (Hansford 2011). Because the structure is heavily reinforced at the halving joint, it has a high transverse stiffness. Four independently controlled jacks could have been used however the loads in each jack would have varied widely because of the system tolerances. To overcome this, the hydraulic jacks were arranged in pairs. The load in each jack within a pair was identical. The computer system controlling the jacking operation was programed to control only two '1000t' jacks with the area of each '1000t' jack equal to twice the area of one 500t jack. The computer system automatically multiplies the programed jack area by the jacking pressure to display the jacking force of each jack pair.

The hydraulic hoses, air lines and control lines had previously been fed from inside the bridge through the expansion joint and attached to the outside of the bridge rails. The jack's hydraulic power unit, a 415 volt 3 phase diesel generator and an air compressor were mounted on a truck. At the commencement of repairs, this truck was moved into place and occupied one of the outside lanes. The hoses and lines tied to the outside of the bridge railing were quickly attached and jacking operations commenced with only minimal delays. In the days leading up to the jacking, a trial lift occurred where the bridge was raised by 1-2mm to generate full working pressure. The system integrity was verified and the hydraulic lines and jacks were checked for oil leaks.

Throughout the jacking operation, the deck crew were in constant mobile phone contact with the jacking crew inside the bridge. This allowed the deck crew to stop traffic during the raising and lowering of the suspended span. During jacking the deck crew would constantly check for potential binding of the finger joints.

6 OPERATIONAL ISSUES

The work inside the bridge cells was defined as a confined space. All personnel had to undergo the mandatory confined space training. The work space gases had to be constantly monitored as per regulations. All personnel had to undergo site specific

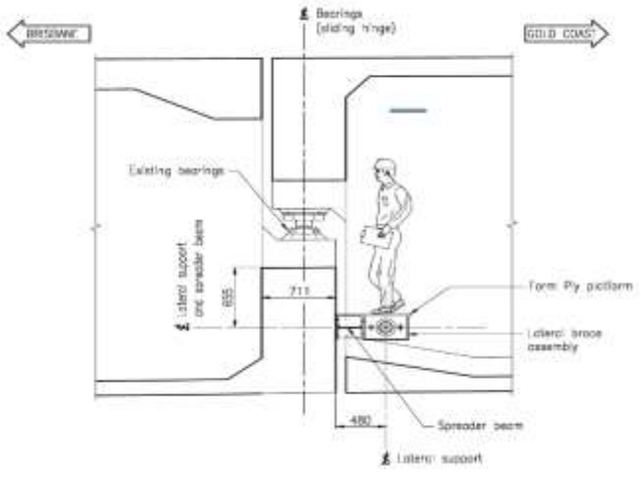


Figure 10 — Section through sliding hinge

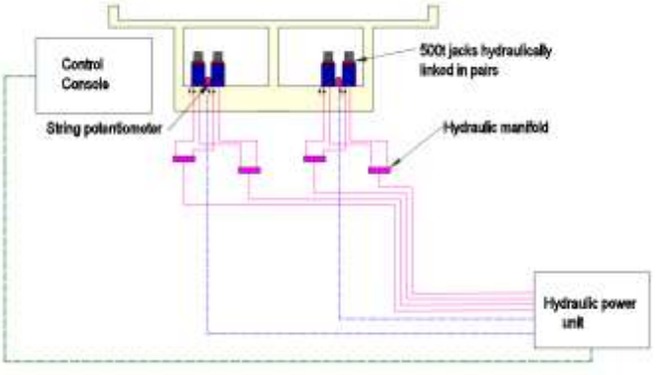


Figure 11 — Schematic of jacking system

safety induction training as well as prestart meetings.

All personnel working in close proximity to the hydraulic jacks and high pressure hydraulic lines were required to wear safety spectacles and protective gloves.

The January/February jacking times coincided with high summer temperatures. Although the work was performed at night, the concrete had not cooled down sufficiently and inside temperatures were still high. To improve the safety of working in the confined space, heavy plastic curtains were hung from the ceiling to cordon off a work area in each cell. Each work area was cooled by three portable self-contained air conditioning units. The hot air generated by the air conditioning units was removed by flexible ducts which led into the expansion joint gap. Although the temperature inside the cells was still high, potential heat stress was well managed. Bottles of cool water were available and mandatory work breaks outside the bridge were enforced.

7 PREPARATION ACTIVITIES

All activities that could be performed in advance were undertaken in the weeks leading up to the jacking. Where these activities included deck work this was carried out at night with single lane closures. The replacement bearings, lateral restraints, tools and material handling equipment were all purchased weeks before the deadline. The synchronised computer jacking system and cabling were repaired so that backup systems were available. Installation preparation activities included:

7.1 Erection of scaffolding to access the elevated entry door on the southern abutment

7.2 Cleaning of any vermin, dust and old equipment from inside the bridge

7.3 Erection of scaffolding inside the structure to allow horizontal access through the bridge cells

7.4 Installation of material handling conveyors

7.5 Installation of an electricity supply to the jacking point for lighting, air conditioning and power tools

7.6 Installation of steel spacers for the hydraulic jacks to transfer the jacking forces into the structure

7.7 Installation of four hydraulic jacks plus have a spare jack inside the bridge

7.8 Installation of all hydraulic hoses, air lines and jacking control lines with the outer ends tied to the outside of the bridge railings

7.9 Installation of the new lateral restraint

7.10 Removal of sections of the bridge deck railing over the expansion joint. This was replaced with a hinged section so that hand rails did not have to be removed on the jacking night

7.11 Ensure all required equipment, parts and tools were laid out on benches inside the bridge

7.12 Installation of air conditioners and hot air ducting

7.13 Undertake a trial jacking of the bridge to test the system for functionality and leaks

7.14 Days before the jacking, a full technical team briefing occurred inside the bridge at the workface describing the work, roles and responsibilities.

8 TRAFFIC CONSIDERATIONS

The dates of the two jacking operations were planned well in advance. The outbound structure was programmed to start at 8pm on Saturday 28 January continuing until 6am on Sunday 29 January 2017. This included a two hour contingency buffer. The inbound structure had similar jacking times on the Saturday 18 and Sunday 19 February 2017. The jacking times were planned not to coincide with major sporting events or entertainment events such as the *Adele* concerts which would generate large concentrated traffic flows.

Agencies such as Queensland Police Service and Brisbane City Council were advised of closure times. A decision was made not to broadly advertise the repairs as the project was to be treated as a normal maintenance activity. The police were engaged to assist traffic controllers in controlling traffic flow. During the repair period, only passenger vehicles and small single axle trucks (approx. 5t GVM) were permitted to cross the bridge. Large trucks had to bypass via alternate routes. The outside traffic lanes were channelled into the two centre lanes to ensure the load was distributed over the main box sections not the cantilevered wings. Additionally, the speed limit was reduced from 80km/h to 40km/h.

During the short period where the bridge was being jacked all traffic was stopped. After jacking had stopped and the jack's lock rings engaged, the low speed traffic was permitted to flow.

The jacking height was limited to 27mm. To prevent traffic running over the end of the expansion joint fingers, 25mm thick plywood sheets were temporarily nailed to the asphalt deck wearing surface.

9 CONCLUSIONS

After the bearing failures were discovered in July 2016, the following 6 months were occupied with the planning, design, manufacture and preparation prior to the installation of the replacement bearings. A number of components were changed to improve the life expectancy of the bearings. The changes included a new lateral restraint that was designed to replace the in-service operational lateral restraint, previously provided by the centre bearings. The design changes adopted and the attention to detail in the preparation work allowed the works to be completed well within the allocated timeframe.

Strain gauges were installed onto the new knuckles to allow the real-time, in-service monitoring of traffic and environmental loads.

Within one night, the bridge was jacked and bearing rectification works completed under live traffic. This resulted in minimum interference to one of the state's busiest transport routes.

The bearing rectification works were successfully completed on both suspended spans by February 2017. Regular inspections of the bearings will be undertaken in the future to monitor their performance and wear.

10 ACKNOWLEDGEMENTS

The authors would like to acknowledge the large collective efforts and spirit of cooperation of the numerous personnel associated with all phases of this project. Also acknowledged are the businesses who supplied, manufactured and tested the various components that were required for the project.

11 REFERENCES

Fong K, Pritchard R. 2000. *Refurbishment of Captain Cook Bridge Bearings*, Austroads Bridge Conference – Bridging the Millennia, Australia pp 317-333.

Hourigan M, Moua P, Fleet M, Heywood R, Spathonis J. 2017. *Rectification of Captain Cook Bridge Bearings,* Austroads Bridge Conference — Bridges: Connecting Communities, Melbourne Australia.

Trelleborg Sealing Solutions. 2014. *ORKOT Marine Bearings – Engineering Manual*, Trelleborg, Sweden.

Hansford W, Spathonis J. 2011. *Synchronised heavy lifting system for bridge structures,* Queensland Roads Edition No 10.

Maintenance, Safety, Risk, Management and Life-Cycle Performance of Bridges – Powers, Frangopol, Al-Mahaidi & Caprani (Eds)
© 2018 Taylor & Francis Group, London, ISBN 978-1-138-73045-8

Reliability Assessment of Reinforced Concrete Pylons Subjected to Biaxial Bending

Ji Hyeon Kim & Hae Sung Lee
Seoul National University, Seoul, Republic of Korea

ABSTRACT: This paper presents the reliability assessment of reinforced concrete pylons for cable-supported bridges subjected to biaxial bending moment. The load contour method is employed to determine the strength of reinforced concrete pylons under biaxial bending. The failure surface defined by the load contour method is utilized as the limit state function in the reliability analysis. The load parameter and the strength parameter such as the material and geometric properties are considered as random variables. The most probable failure point and reliability index are calculated by the Hasofer-Lind Rackwitz-Fiessler algorithm with the gradient projection method for the advanced first-order second-moment reliability method. The reliability analyses of the pylon for cable-supported bridges in Korea are performed for the surface exponents of 1 and 2. The effect of the surface exponents and the comparison of the reliability index for uniaxial bending to that for biaxial bending are discussed in detail.

1 INTRODUCTION

A robust reliability assessment method of reinforced concrete (RC) columns subjected to biaxial bending is proposed by Kim and Lee (2017). The proposed method is utilized to evaluate a reliability level of rectangular sections for short columns in the study. The proposed scheme certainly plays an important role for code calibration procedure, in which the reliability indices for various real sections should be evaluated to set a target reliability index. The reliability levels of RC pylons need to be estimated accurately to determine a proper a target reliability index of a wind load-governed limit state for cable-supported bridges.

As a cross-section of the pylons for cable-supported bridges is usually designed as a hollow section, the section properties for internal forces have to be estimated based on the effective flange width considering the shear lag or determined by rigorous analysis. However, most design codes (AASHTO, 2012; KMOLIT, 2016a; KMOLIT, 2016b) state that the full compression flange width effect is valid for the capacity of a cross-section at the strength limit state. The scope of this study is to estimate the reliability index of an RC pylon for the strength limit state, and thus, the entire cross-section is valid to evaluate the strength of RC pylons.

This paper adopts the reliability assessment method proposed by Kim and Lee (2017) in order to estimate reliability levels of RC pylons for cable-supported bridges subjected to biaxial bending. The failure surface defined in the load contour method is provided as the limit state function for the reliability analysis. The minimization problem defined by the advanced-first order second-moment reliability method (AFOSM) (Haldar and Mahadevan, 2000) is solved by using the Hasofer-Lind Rackwitz-Fiessler (HL-RF) algorithm with the gradient projection method (Liu and Der Kiureghain, 1991). The axial force (P) - bending moment (M) interaction diagram (PMID) of a pylon under uniaxial bending is interpolated by using the cubic spline method as presented in Kim et al. (2015). The PMIDs about the principal axes of the section are used in constructing the load contour. The sensitivities of the limit state function required in the HL-RF algorithm are calculated through the direct differentiation method.

The reliability indexes and most probable failure points (MPFPs) of the pylon for cable-supported bridges in Korea are calculated in case that the surface exponents of the load contour are 1 and 2. The effect of the surface exponents are investigated through the reliability analyses. The reliability index of RC pylons subjected to uniaxial bending is compared to the reliability index under biaxial bending. It is demonstrated that the reliability index of a pylon for biaxial bending may become significantly lower than that for uniaxial bending depending on the surface exponent.

2 RELIABILITY ASSESSMENT METHOD

2.1 *3-dimensional PMID*

Kim and Lee (2017) adopts the load contour method proposed by Bresler (1980) in order to define the PMID of an RC column subject to combined axial and biaxial bending moment in the 3-dimensional axial force (P)-moments (M_y, M_z) space.

$$\Phi(\mathbf{F},\mathbf{B}) = \Phi(P, M_z, M_y, \mathbf{B}) = 1 - \left(\frac{M_y}{\widetilde{M}_y(P)}\right)^{\alpha} - \left(\frac{M_z}{\widetilde{M}_z(P)}\right)^{\alpha} = 0 \quad (1)$$

where $\mathbf{F} = (P, M_y, M_z)^T$, $\mathbf{B}$ is the surface parameter vector of the PMID, and α is the surface exponent that is determined by the strength characteristic of a cross section. M_y and M_z represents the y-directional and z-directional moments, respectively. $\widetilde{M}_y(P)$ and $\widetilde{M}_z(P)$ are the ultimate moment capacities for a given P in pure bending about the y and z direction, respectively. The surface exponent, α, determines the feasible region of the load contours that present the PMID in $M_y - M_z$ plane. The α of 1 indicates the lower limit of the columns strength and describes a straight line connecting the $\widetilde{M}_y(P)$ and $\widetilde{M}_z(P)$. The α of 2 denotes the upper limit of the column strength and the load contours are drawn as the ellipse.

The PMIDs of the column subject to the y and z directional uniaxial bending moment are expressed in terms of the axial force, respectively, and are defined in the $P - M_y$ plane and the $P - M_z$ plane as follows:

$$\Phi_k(P, \widetilde{M}_k, \mathbf{B}_k) = 0 \quad \text{for} \quad k = y, z \quad (2)$$

The subscript k indicates the direction of the uniaxial bending moment hereafter.

The limit state of an RC column is defined by the PMID given in Eq. (1) and described as $\Phi(\mathbf{F}_q, \mathbf{B}) = 0$. That is, $\Phi(\mathbf{F}_q, \mathbf{B}) > 0$ and $\Phi(\mathbf{F}_q, \mathbf{B}) < 0$ represent the safe and failure states of the RC column, respectively. $\mathbf{F}_q$ denotes the internal force vector. The relations between the internal forces and the external loads are assumed to be linear, although each external load component may have nonlinear load effects on an RC column.

$$\mathbf{F}_{q,0} = \begin{pmatrix} P_q \\ M_{q,y} \\ M_{q,z} \end{pmatrix} = \mathbf{C}_0 \mathbf{q} \quad (3)$$

Here, $\mathbf{C}_0$ and $\mathbf{q}$ are the load effect matrix and load parameter vector, respectively. Each column of the load effect matrix is composed of the load effects calculated in the structural analysis for the nominal value of the corresponding load component. The load parameter vector represents the statistical properties of the load components. The nominal values of the load parameters are given as 1, and the mean value of each load parameter becomes the bias factor of the original load component. The statistical distribution and coefficient of variation (COV) of each load parameter follow those of the original load component.

The surface parameters are determined based on the strength parameters representing the material and geometric properties of a cross section. The strength parameters of an RC column are conveniently written in one vector

$$\mathbf{s} = (s_j) = (f_{ck}, f_y, E_s, A_{gt}, A_{s,1}, \ldots, A_{s,m}, y_{s,1}, \ldots, y_{s,m}, z_{s,1}, \ldots, z_{s,m})^T \quad (4)$$

where f_{ck}, f_y, E_s indicate the compressive strength of concrete, the yield strength of the reinforcing bar and the Young's modulus of the reinforcing bar, respectively, and are included in the material properties. m, A_{gt}, $A_{s,k}$, $y_{s,k}$, $z_{s,k}$ denote the number of reinforcing bars, the gross area of a cross section, the area and position of the k-th reinforcing bar in the y and z direction, respectively. he position of a reinforcing bar is the distance from the extreme compression fiber of the cross section to the center of the reinforcing bar. The geometric properties consist of the area and position of each reinforcing bar and the gross area of a cross section.

The PMID of $P - M_k$ plane is composed of infinite sampling points, which represent the ultimate strength combinations of RC Columns. Kim et al. (2015) suggested the analytic form of the PMID in $P - M_k$ plane by introducing a piecewise cubic polynomial functions (Kreyzig, 2006). The polynomial function, called as the cubic spline, is used to interpolate two adjacent points as a piecewise continuous and twice differentiable function.

2.2 *AFOSM*

The strength parameters of an RC column, the load parameters are considered to be random variables. All random variables are assumed to be statistically independent to each other in this study. For the compactness of forthcoming derivations, the random variables are written in one vector, $\mathbf{X} = (\mathbf{q}, \mathbf{s})^T$. In case that all random variables are normally distributed and statistically independent to each other, the reliability index and corresponding MPFP are evaluated by solving the following minimization problem through the AFOSM (Haldar and Mahadevan, 2000):

$$\min_{\overline{\mathbf{X}}} \beta^2 = \left\|\overline{\mathbf{X}}\right\|_2^2 \quad \text{subject to} \quad \overline{\Phi}(\overline{\mathbf{X}}) = 0 \quad (5)$$

where β and $\|\cdot\|_2$ denote the reliability index and the 2-norm of a vector, respectively, while the overbarred variables indicate standardized random variables and $\overline{\Phi}(\overline{\mathbf{X}}) = \Phi(\mathbf{X})$. Since the limit state function is nonlinear with respect to the random variables, the minimization problem given in Eq. (5) is solved iteratively by the HL-RF algorithm with the gradient projection method (Liu and Der Kiureghain,

1991). The Rackwitz-Fiessler method (Rackwitz and Fiessler, 1978) is adopted for nonnormal random variables to estimate the equivalent normal distribution.

The sensitivity of the PMID with respect to the random variables is required for iteration procedures of the HL-RF algorithm. The direct differentiation method is utilized to compute the sensitivity of the PMID. Detailed formulations of the sensitivity for the PMID with respect to the random variables are derived in references (Kim et al., 2015 and Kim and Lee, 2017).

3 APPLICATIONS TO RC PYLONS

The reliability analyses are performed for the design sections of RC pylons for two cable-stayed bridges and one suspension bridge: The Incheon Bridge (IB), Busan Harbor Bridge (BHB), Yi Sun-shin Bridge (YSB), and New-millennium Bridge (NMB). Since the load combination under a strong wind condition without the live load governs the failure of the pylons, the dead and wind load effects are considered in the analyses.

The general view of the three cable-supported bridges and the longitudinal wind direction (WD) are presented in Figure 1. WD1 indicates the longitudinal wind direction acting on the left pylon to the right pylon, and WD3 designates the opposite wind direction of WD1. The front view of the pylons for the cable-supported bridges is illustrated in Figure 2, and the transverse wind directions denoted as WD2 and WD4 are indicated with the arrows at the top of each pylon in the figure. The transverse wind load is applied to both columns of a pylon simultaneously. Each pylon consists of two symmetric columns, and

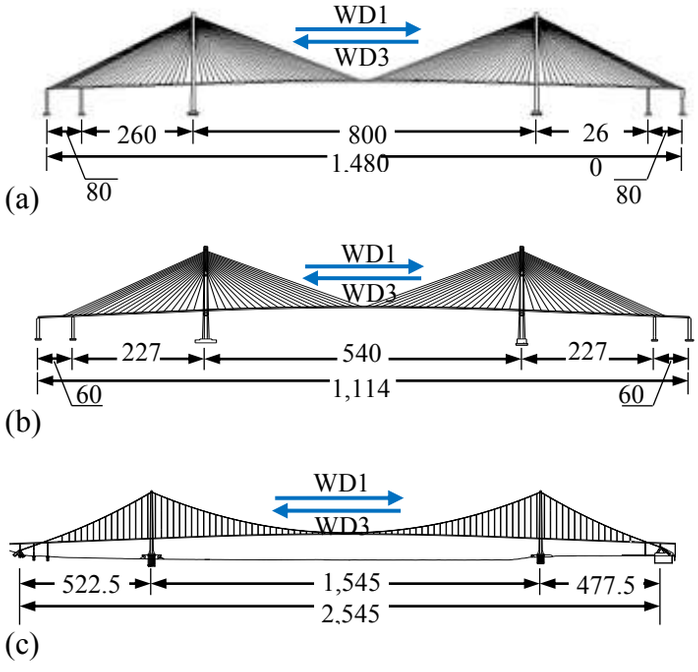


Figure 1. General view of cable-supported bridges and longitudinal wind direction: (a) IB; (b) BHB; (c) YSB (Unit: m)

the reliability analysis is conducted for the bottom section of the left column for a pylon marked with a dotted circle in Figure 2.

Figure 3 shows the geometry and arrangement of reinforcements of the cross-section at the bottom of the pylons. Since the member axis of each column of the pylons is inclined from the vertical line, the cross-sections shown in Figure 3 are projected to the plane perpendicular to the member axis and marked with a dotted line in Figure 2 for the reliability analysis. The inclined angle of the column and sectional properties of the bottom sections of the pylons are

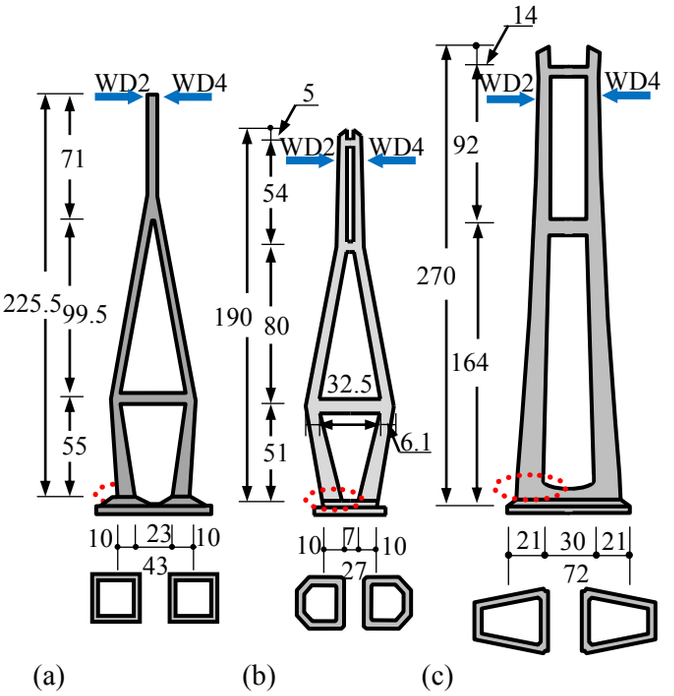


Figure 2. Front view of the pylon and transverse wind load direction: (a) IB; (b) BHB; (c) YSB (Unit: m)

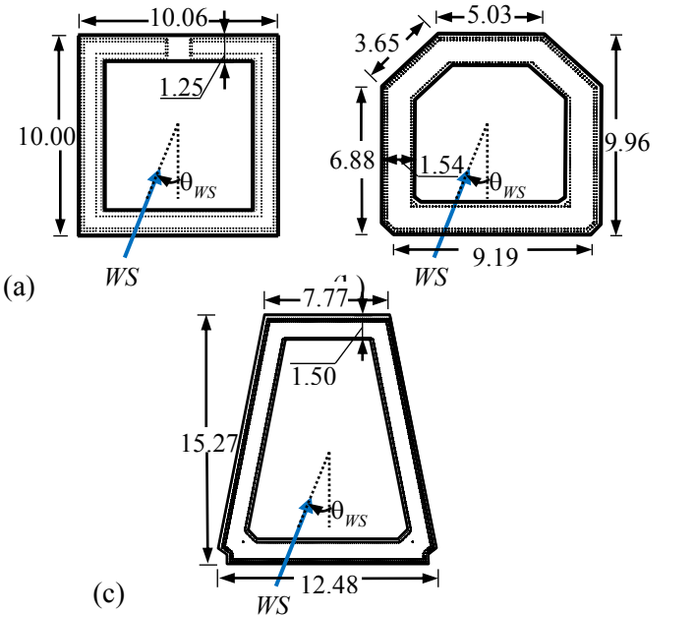


Figure 3. Geometry and rebar arrangement of the bottom section for the pylon: (a) IB; (b) BHB; (c) YSB (Unit: m)

summarized in Table 1. The nominal values of the compressive strength of concrete and the yield strength and Young's modulus of the reinforcements are also provided in the table. The reinforcement ratio of the cross-section where the lowest reliability index satisfies the target reliability index of 3.1 for $\lambda_{WS} = 1$, $\delta_{WS} = 0.3$ is quoted from Kim et al. (2017), and is summarized for the three bridges in the table.

The statistical parameters of the random variables are given in Table 2 and quoted from the previous works (Kim et al., 2015; Kim et al., 2017). DC_P, DC_G, DC_C, DW, and WS indicate the dead load due to the self-weights of the pylons, girders, cable members, wearing surfaces and utilities, and the wind load, respectively.

The load effects induced by each load parameters are calculated using a commercial program, and are presented in Tables 3 and 4 for the longitudinal and transverse directions, respectively. WD in parentheses refers to the wind load direction illustrated in Figures 1 and 2. The calculated load effects include a moment amplification effect in axial forces and bending moment due to the P-delta effect. In the tables, the compression depicts a positive sign. The positive bending moments in the longitudinal and transverse directions represent the clockwise action in Figure 1 and the counterclockwise action in Figure 2, respectively.

Table 1. Inclined angle of the pylons and sectional properties of the sections

Bridge	Inclined angle	A_{gt}	Rebar ratio	f_{ck}	f_y	E_s
	(°)	(m^2)	(%)	(MPa)	(MPa)	(GPa)
IB	6.18	36.16	1.84	45	400	
BHB	12.14	47.48	0.52	40	400	200
YSB	3.22	69.35	0.46	40	400	

Table 2. Statistical parameters of the random variables

Random variable		Nominal value	Bias factor	COV	Distribution type
Material properties	f_{ck}	40/45MPa	1.15/1.16	0.10/ 0.095	Lognormal
	f_y	400/500MPa	1.15/1.09	0.08/ 0.05	Lognormal
	E_s	200GPa	1.00	0.06	Lognormal
Geometric properties	$A_{s,avg}$	-	1.00	0.015	Normal
	$\eta_{s,avg}$	0.00	1.00	-	Normal
	A_{gt}	-	1.01	0.056	Normal
Load parameters	DC_P	1.00	1.05	0.10	Normal
	DC_G	1.00	1.03	0.08	Normal
	DC_C	1.00	1.00	0.06	Normal
	DW	1.00	1.00	0.25	Normal
	WS	1.00	1.00	0.30	Gumbel

Table 3. Load effect matrices in the longitudinal direction

Bridge	Load effect	Load effect matrix					
		DC_P	DC_G	DC_C	DW	WS (WD1)	WS (WD3)
IB	P_q(MN)	115.9	82.0		30.4	0.8	-0.8
	M_q(MN·m)	0.0	87.2		-81.9	375.9	375.9
BHB	P_q(MN)	124.3	96.0		17.8	6.0	-5.9
	Mq(MN·m)	0.0	-63.4		79.7	596.8	596.8
YSB	P_q(MN)	271.7	95.3	51.3	28.1	2.5	-2.5
	M_q(MN·m)	0.0	-798.5	1008.0	-209.0	653.0	653.8

Table 4. Load effect matrices in the transverse direction

Bridge	Load effect	Load effect matrix					
		DC_P	DC_G	DC_C	DW	WS (WD2)	WS (WD4)
IB	P_q(MN)	115.9	82.0		30.4	-59.1	36.1
	M_q(MN·m)	-118.7	-25.6		-23.6	800.7	-782.9
BHB	P_q(MN)	124.3	96.0		17.8	-29.6	29.7
	Mq(MN·m)	-124.3	-23.1		-2.7	535.9	-525.4
YSB	P_q(MN)	271.7	95.3	51.3	28.1	-112.5	65.2
	M_q(MN·m)	255.0	50.0	9.9	14.8	2023.0	-1304.1

The angle of attack of the wind load to the pylon, θ_{WS}, is indicated in Figure 3. The angle of $\theta_{WS} = 0°$, 90°, 180° and 270° correspond to WD1, WD2, WD3, and WD4, respectively. The angle of attack of the wind load varies from 0° to 360° while the nominal magnitude of the wind load is maintained constant. The effect of the surface exponent and the angle of attack on the results of the reliability analysis is investigated. For $\alpha = 2$, the reliability analysis is performed with an interval of 5° for the angle of attack of wind load. The interval for the angle of attack for $\alpha = 1$ is defined as 1° in order to clearly illustrate the discontinuity of the reliability indexes later on the figures.

The variations of the reliability indexes and the standard normal wind load at the failure point with the angle of attack for IB are presented in Figures 4 and 5, respectively. The variation patterns of the two figures are quite similar to each other, which implies that the wind load governs the failure of the pylon for the biaxial loads. The reliability levels of $\alpha = 2$ are higher than the target reliability level for all the angle of attack, which is exactly the same for the other bridges. The lowest reliability index of $\alpha = 1$ is calculated as 2.98 close to the WD2, which is 4% smaller than the target reliability index. Since the failure surface of the pylon is linearly interpolated in the case of $\alpha = 1$, the strength of the pylon for biaxial bending decreases sharply and results in a lower reliability level.

Figure 6 shows the nominal load effects and the failure points for IB with respect to $0^{\circ} \le \theta_{WS} \le 360^{\circ}$, which are marked with centered symbols every 5° or 1° in a counter-clockwise direction. The solid squares in the figure indicate the internal forces at ϕ = 0°, while the solid circles are associated with θ_{WS} = 90°, 180° and 270°.

The axial forces corresponding to each centered symbol are different, and the load effects are located on different M_Y-M_Z planes in 3D space. Since the dead and wind loads generate the bending moments in the opposite and same directions in WD2 and WD4, respectively, the position of a large circle constructed with black blank circles, which present the nominal load effects, is shifted above the axis of M_Y = 0. The results clearly show that the angles of attack for the failure points on the moment axes in Figure 6 exactly coincide with those where the discontinuities of α = 1 and are observed in Figures 4 and 5. The reliability index of the pylon is calculated for uniaxial bending corresponding to θ_{WS} = 0°, 90°, 180° and

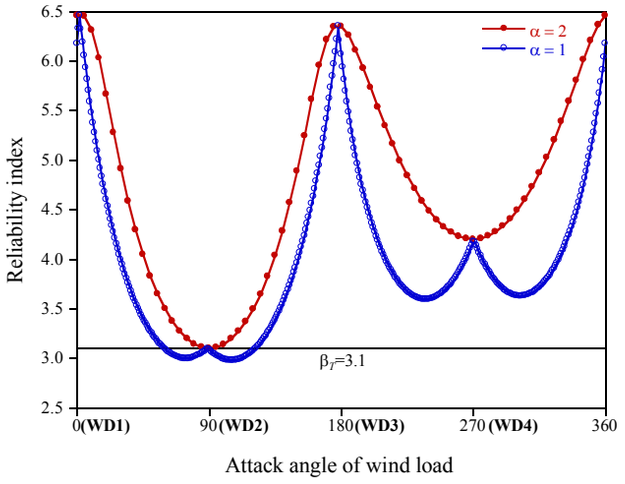


Figure 4. Reliability indexes of pylons for IB under biaxial bending

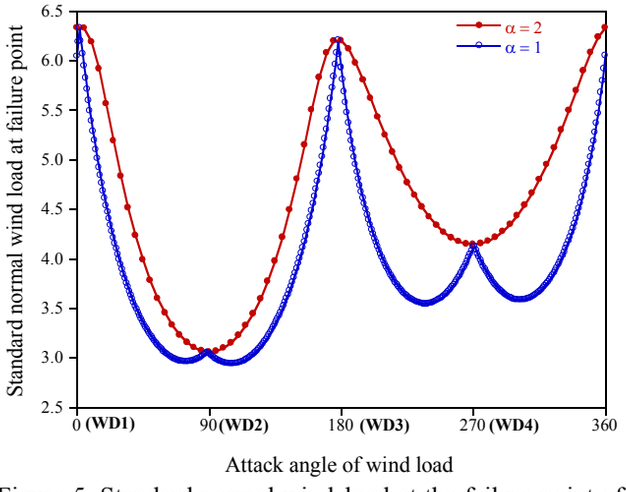


Figure 5. Standard normal wind load at the failure point of pylons for IB under biaxial bending

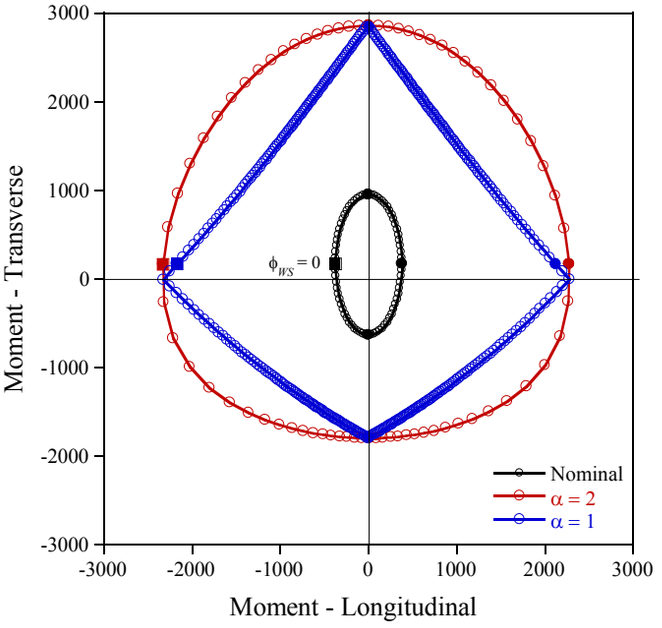


Figure 6. Nominal bending moments for IB

270° and is compared with that for biaxial bending in Table 5. The bending moments about the axis perpendicular to the wind load and the axial forces given in Tables 3 and 4 are considered for uniaxial bending. A slight difference in the reliability indexes between uniaxial bending and biaxial bending is caused by the biaxial moment due to the dead load.

Since the wind loads in WD2 and WD4 induce the tensile and compressive axial forces, respectively, the pylon under the load effects in WD4 exhibits a higher level of safety than that in WD2 even though the total nominal moment in WD4 is larger than that in WD2. This is because the moment capacity of a pylon decreases rapidly as the compressive axial force diminishes in the tensile failure region of the PMID. The longitudinal wind load yields a similar level of reliability indexes in WD1 and WD3. As in the transverse wind load case, the difference in the reliability indexes in WD2 and WD4 is caused by the opposite wind load effect on the axial forces of the pylons. However, the axial forces induced in the pylons by the longitudinal wind load are much smaller than those by the transverse wind load, which leads to a less significant difference in the reliability indexes between the two longitudinal

Table 5. Comparison of reliability indexes under uniaxial and biaxial bending for IB

Wind direction	Reliability index	
	Uniaxial bending	Biaxial bending (α = 2)
WD1	6.47	6.46
WD2	3.10	3.10
WD3	6.36	6.35
WD4	4.20	4.20

wind load cases in comparison to the transverse wind load case. The reliability index seems to be proportional to the distance between the nominal load effect and the failure point as shown in Figures 4 and 6. However, it should be noted that such a proportional relationship may not be valid according to the failure mode of a pylon depending on the load combination (Kim et al., 2015).

Figures 7 and 8 show the reliability indexes and the standard normal wind load at the failure point for BHB under biaxial bending, respectively. The comparison of reliability indexes for uniaxial and biaxial bending is presented in Table 6, and the nominal load effects and the failure points in M_y–M_z space are illustrated in Figure 9. The smallest reliability index is calculated in WD2 for both uniaxial bending and biaxial bending of $\alpha = 2$. However, the lowest reliability level of $\alpha = 1$ is calculated as 2.21 at $\theta_{WS} = 215°$, and the reliability indexes of $\alpha = 1$ decreases more rapidly in the range of $180^\circ \le \theta_{WS} \le 360^\circ$ than at $0^\circ \le \theta_{WS} \le 180^\circ$. The large biaxial moments are generated in the range of $180^\circ \le \theta_{WS} \le 360^\circ$ by the superposition of the bending moment in the longitudinal and transverse direction, and are very close to the failure surface of $\alpha = 1$. The combination of bending moments with a short distance to the failure surface yields a higher probability of failure.

The comparison of reliability indexes for uniaxial and biaxial bending is presented in Table 6. Since the ratio of bending moment due to the dead load to the wind load is apparently large in comparison with the other bridges (*vide* Tables 3 and 4), the failure points for biaxial bending exist within the quadrant and not on the axes. The reliability levels for uniaxial bending are a little bit higher than those for biaxial loads in WD1, WD3, and WD4 for $\alpha = 2$ as shown in Table 6.

The results of the reliability assessment for YSB are presented in Figures 10-12, and Tables 7. Discussions on the results of the YSB are similar to those of IB. For YSB the bending moments due to the dead and wind load are produced in the same

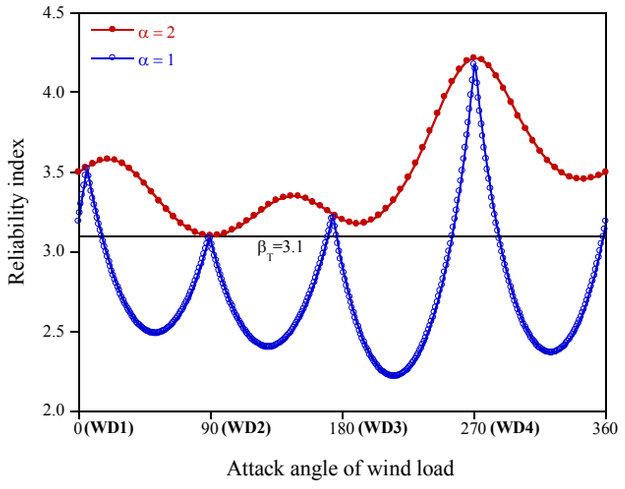


Figure 7. Reliability indexes of pylons for BHB under biaxial bending

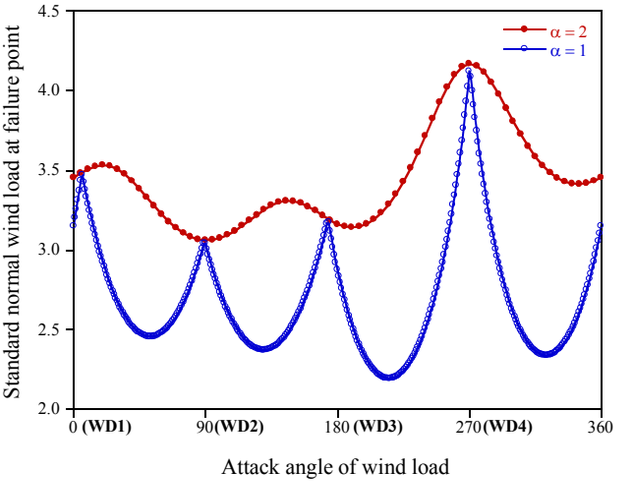


Figure 8. Standard normal wind load at the failure point for BHB under biaxial bending

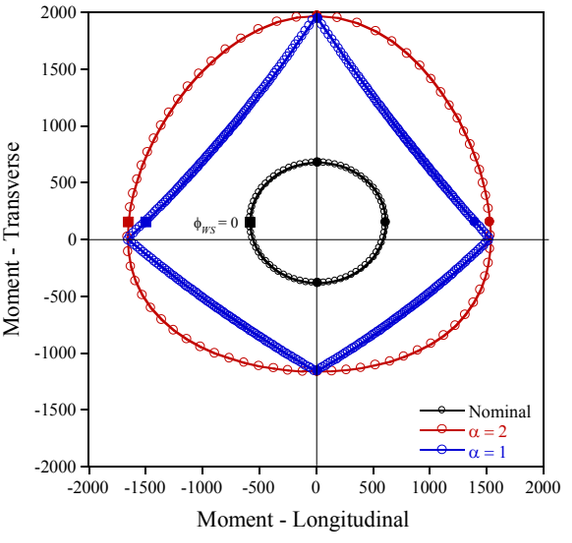


Figure 9. Standard normal wind load at the failure point for BHB under biaxial bending

Table 6. Comparison of reliability indexes under uniaxial and biaxial bending for BHB

Wind direction	Reliability index	
	Uniaxial bending	Biaxial bending ($\alpha = 2$)
WD1	3.51	3.50
WD2	3.10	3.10
WD3	3.21	3.20
WD4	4.27	4.22

transverse direction. Thus, the unions of the nominal load effects are positioned below the axis of $M_y = 0$ as shown in Figure 12. In the three bridges, the minimum reliability indexes for biaxial bending are lower than that for uniaxial bending by 4% to 28% and are summarized in Table 8. Therefore, even if a pylon secures a high reliability level for uniaxial bending, a significantly lower reliability level may result for biaxial bending, which depends on the surface exponent.

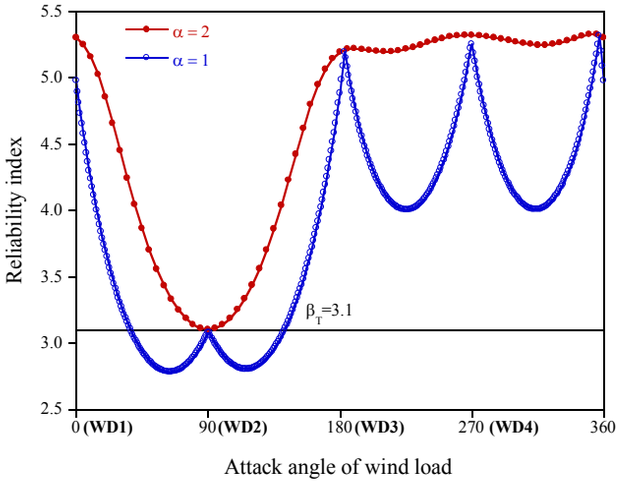


Figure 10. Reliability indexes of pylons for YSB under biaxial bending

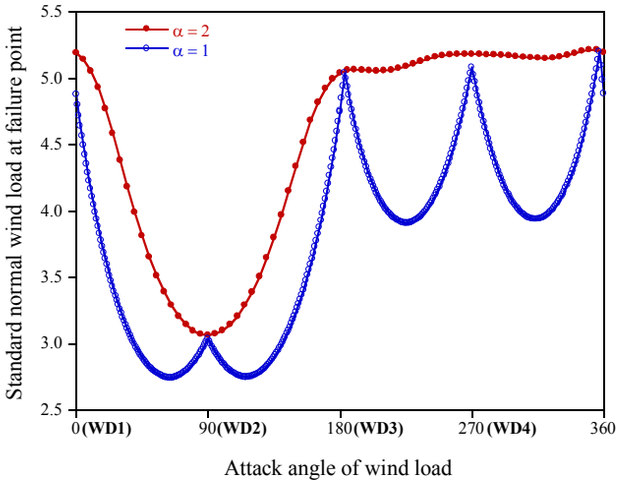


Figure 11. Standard normal wind load at the failure point for YSB under biaxial bending

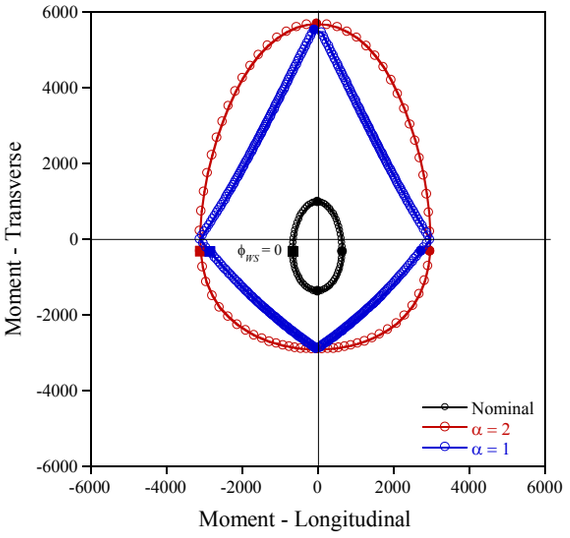


Figure 12. Nominal bending moments for YSB

Table 7. Comparison of reliability indexes under uniaxial and biaxial bending for YSB

Wind direction	Reliability index	
	Uniaxial bending	Biaxial bending (α = 2)
WD1	5.32	5.30
WD2	3.10	3.10
WD3	5.20	5.19
WD4	5.32	5.32

Table 8. Minimum reliability index of pylons of five bridges (α = 1)

Bridge	Angle of attack	Minimum reliability index	Difference with target reliability index
	(°)		(%)
IB	106	2.98	3.9
BHB	215	2.22	28.4
YSB	64	2.78	10.3

4 CONCLUSIONS

This paper presents the reliability assessment of RC pylons for three cable-supported bridges in Korea. The failure surface of RC pylons is defined by the load contour method. The load and strength parameters are considered as random variables. The reliability analysis is performed for the section of which the lowest reliability index secures a certain target reliability index. The surface exponents of the load contours are used as 1 and 2 in order to calculate the reliability index for the lower and upper limits of the strength.

The limit state of a pylon is mainly governed by the wind load. The reliability level for surface exponent of 1 is higher than the target reliability index of 3.1 for all angle of attack. The minimum reliability index under biaxial bending for surface exponent of 1 is reduced by 4-28% of the target reliability index. Since the reliability index for biaxial loads varies significantly with the surface exponent, most design codes specify the surface exponent as one in order to deduce conservative design. The precise surface exponent for a cross-section is required for more economical design.

ACKNOWLEDGEMENTS

This research was supported by a grant (17SCIP-B119964-02-000000) from the Ministry of Land, Transport and Maritime Affairs of the Korean government through the Korea Bridge Design & Engineering Research Center of Seoul National University.

REFERENCES

AASHTO (American Association of State Highway and Transportation Officials). 2014. *AASHTO LRFD Bridge Design Specifications*, Washington, DC.

Haldar, A., & Mahadevan, S. 2000. *Probability, Reliability and Statistical Methods in Engineering Design,* John Wiley & Sons, Inc., New York, 181-224.

Kim, J. H., Lee, S. H., Paik, I., and Lee, H. S. 2015. "Reliability assessment of reinforced concrete columns based on the P-M interaction diagram using AFOSM." *Struct. Safety*, 55, 70-79.

Kim, J. H., & Lee, H. S. 2017. "Reliability assessment of reinforced concrete columns subjected to biaxial bending using the load contour method." *Engineering Structures*, 150, 636-645.

Kim, J. H., Yoo, C-H., and Lee, H. S. 2017. "Evaluation of wind load factors of RC columns for wind load-governed limit stat in reliability-based design code." *Journal of Bridge Engineering, ASCE*, 22(9): 04017053.

KMOLIT (Korea Ministry of Land, Infrastructure and Transport). 2016a. *Korean Highway Bridge Design Code* (*Limit State Design*), KMOLIT, Seoul.

KMOLIT (Korea Ministry of Land, Infrastructure and Transport). 2016b. *Korean Highway Bridge Design Code (Limit State Design) – Cable Supported Bridges*, KMOLIT, Seoul.

Kreyszig, E. 2006. *Advanced Engineering Mathematics*, 9th ed., John Wiley & Sons, Inc.

Liu, P. L., and Der Kiureghian, A. 1991. Optimization algorithms for structural reliability. *Structural Safety*, 9, 161-177.

Rackwitz, R., & Fiessler, B. 1978. "Structural reliability under combined random load sequences." *Comput. Struct.*, 9(5), 489-494.

Maintenance, Safety, Risk, Management and Life-Cycle Performance of Bridges – Powers, Frangopol, Al-Mahaidi & Caprani (Eds)
© 2018 Taylor & Francis Group, London, ISBN 978-1-138-73045-8

Experimental research on shear behavior of rubber-ring perfobond connector

Y.Q. Liu, Y. Liu & F. Wang
Department of Bridge Engineering, Tongji University, Shanghai, China

ABSTRACT: To mitigate the shear concentration of partial holes in groups, perfobond connector with an easy-installed rubber ring was proposed. Then nine modified push-out tests including four specimens with one hole and five specimens with four holes were conducted to reveal the shear mechanism of the rubber-ring perfobond connector. The presence and thickness of rubber rings, the number of holes and the arrangement of rubber rings were investigated in the tests. The test results showed that the failure of perfobond connector consists of four stages, including the damage of bond, the shear failure of concrete dowel in the hole, the tension-shear yielding and the failure of perforated rebar. The yield slip of perfobond connector can be increased by 260% to 745% by employing the rubber ring, which was related to the thickness of rubber ring and the deformation ability of perforated rebar. The presence of rubber ring which decreased the area of concrete dowel reduced the shear capacity by 15%. The strain difference of steel plate in adjacent rows was reduced by placing the rubber rings on the first and the fourth rows, indicating rubber rings could be utilized to alleviate the non-uniform shear distribution. Finally, the existing formulas of shear capacity based on previous modified push-out tests were evaluated.

1 INSTRUCTION

Perfobond connectors have the advantages of simple structure, easy installation, and excellent shear behavior and fatigue performance. In recent years, the application of perfobond connectors has been increased in the composite bridges, such as the interface of composite girders, the joint of hybrid girders and pylons, the anchorage zone of composite pylons and the anchorage joints between suspenders and girders, etc. Perfobond connector ensures that load is transferred efficiently between steel and concrete components.

The shear behavior of perfobond connector was mainly studied by push-out tests. Yamadera et al. (1993) first proposed and carried out a modified push-out test. Then Wang et al. (2013) and Su et al. (2014, 2016) summarized the failure modes and the appropriate situations of different test methods. As perfobond connectors are increasingly employed in hybrid structures and anchorage joints, Zhang et al.(2007), Wang et al. (2014), He et al. (2016), Nakajima et al. (2016), Xiao et al. (2016) analyzed the effects of hole diameter, perforated rebar diameter, thickness of plate, concrete compressive strength and bond on the shear performance of perfobond connector by conducting modified push-out tests. Recently, scholars had begun to focus on the structural behavior of perfobond connectors arranged in multi rows and columns. Oguejiofor & Hosain (1994) suggested that increasing the number of holes can enlarge the shear strength of perfobond connector when the spacing between two adjacent holes is larger than 2.25 times hole diameter. Martins et al. (2010) and Vianna et al. (2013) carried out push-out tests respectively and found that the number of holes had only a small effect on the shear bearing capacity. Ahn et al. (2010) concluded that when the perfobond connectors were arranged in two columns, the average strength was 80% of the strength of a single connector.

In the hybrid structures joints and composite anchorage zones, some of the connections may have worked in the plastic stage, although the overall load does not reach the load carrying capacity of the structures. The shear of connectors is mainly related to the shear stiffness and the position in the group. Decreasing the initial shear stiffness or increasing the slip at the start of bearing shear can reduce the shear of connectors. Xu et al. (2014, 2016) decreased the initial shear stiffness of studs by using the rubber sleeves, which had a negligible effect on the shear capacity. Therefore, this paper presents a rubber ring used on perfobond connectors to increase the slip at the beginning of bearing shear. By setting the rubber rings to some of the holes in connector group, the shear of each hole may tend to be

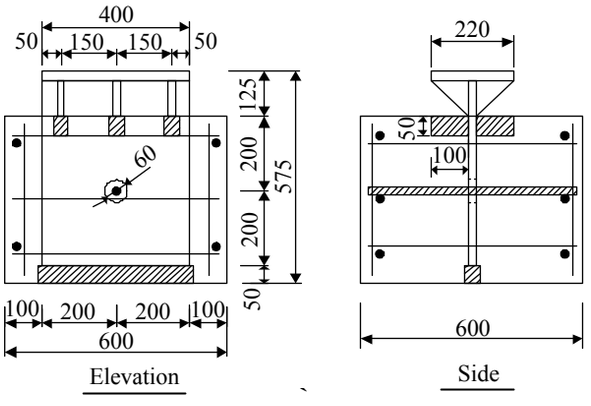
uniform, and the composite behavior of joints would be optimized.

In this paper, modified push-out tests including four specimens with one hole and five specimens with four holes were conducted to study the shear behavior of rubber-ring perfobond connectors. The parameters investigated were the presence and thickness of rubber rings, the number of holes and the rubber rings arrangement. The failure modes, load-slip curves, load-strain curves of steel plate and perforated rebar were analyzed and compared. The shear mechanism of rubber-ring perfobond connectors was discussed. Finally, the existing shear capacity formulas based on modified push-out tests were collected and evaluated in comparison with the test results.

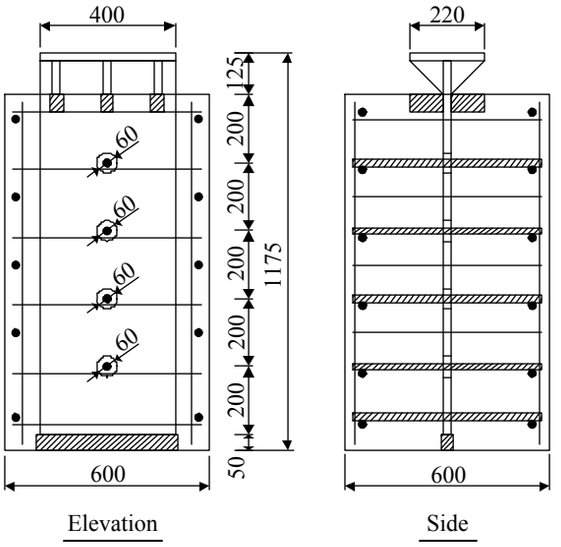
2 MODIFIED PUSH-OUT TEST

2.1 *Test specimens*

Fig 1 shows the configuration of specimens. To examine the influence of rubber ring parameters on the shear behavior, the irregular distribution of shear in the multi-hole specimens and the reasonable arrangement of the rubber rings in the joints, nine modified push-out test specimens were designed. The thickness of rubber ring of the four single-hole specimens was 0 mm, 2 mm, 4 mm, 6 mm, respectively. The position of rubber rings of the five multi-hole specimens was none, all the holes with the thickness of 4 mm, 1st and 4th hole with the thickness of 2 mm, 4mm and 6 mm, respectively. Detailed parameters are shown in Table 1.



(a) Single-hole specimens



(b) Multi-hole specimen

Figure 1. Specimen configuration.

Table 1. Parameters of specimens.

Specimen	d/mm	d_s/mm	n	t_r/mm	Position
PB	60	20	1	-	None
RPB-1	60	20	1	2	Hole
RPB-2	60	20	1	4	Hole
RPB-3	60	20	1	6	Hole
MPB-1	60	20	4	-	None
MPB-2	60	20	4	4	All holes
MPB-3	60	20	4	2	1st & 4th hole
MPB-4	60	20	4	4	1st & 4th hole
MPB-5	60	20	4	6	1st & 4th hole

The thickness and length of the steel plate were 20 mm and 400 mm. In the area between the top steel plate and the concrete block, stiffening ribs were provided to prevent the buckling of the steel plate during the loading process. 50 mm height of foams were mounted below the ribs to avoid the contact between the ribs and concrete block during loading. Similarly, 50 mm high wood blocks were placed at the bottom of the steel plates before pouring the concrete to remove the end pressure of steel plates. Since cohesive and frictional force existed in the actual structures, the specimens were not greased to reflect the real shear behavior of perfobond connectors in the joints.

2.2 *Rubber ring details*

A rubber ring including the inner ring and the wings on both sides of the steel plate was put forward to increase the slip of perfobond connector at the start of bearing shear. The outer diameter of the inner ring is the same as that of the hole, and the internal diameter is the outer diameter minus twice the thickness of the inner ring. The length and thickness of the wings are 10 mm and 4 mm, respectively, to

prevent the rubber rings from falling off during pouring concrete. The rubber rings with various thicknesses are shown in Fig 2.



Figure 2. Rubber rings with various thicknesses.

As the hardness of rubber rings is small, the installation only needs to compress the rubber ring into the hole manually, and then restore the geometry so that the outer surface of the ring and the hole wall contact. The installation process is simple and efficient.

2.3 *Material properties*

In the casting of concrete blocks, cubic and cylindrical specimens were fabricated to test the properties of concrete. The compressive strength of concrete cube f_{cu} and cylinder f_c was 52.1 MPa and 45.5 MPa, respectively. The cube splitting strength f_t was 4.6 MPa and the elastic modulus E_c was 40.6 GPa. The rubber employed in the test was natural rubber with the measured Shore hardness of 61 degrees. The tensile strength was 20.7 MPa, and the elongation at break was 549%.

The yield strength of the steel plate was 345 MPa. As the failure mode of specimens was the fracture of perforated rebar, the tensile tests of the fractured rebar of the single-hole specimens were conducted after demolishing the concrete blocks. The yield strength f_y and tensile strength f_u of each rebar are shown in Table 2.

Table 2. Rebar material properties.

Specimen	f_y /MPa	f_u /MPa
PB	438.3	562.3
RPB-1	413.8	560.7
RPB-2	470.7	581.6
RPB-3	508.0	617.9

2.4 *Test setup and instrumentation*

The specimens were loaded by using a servo hydraulic testing machine with a capacity of 20000 kN. The loading scheme referred to the Eurocode 4 (2005). Before the formal loading, five cyclic loading with the load range from 5% to 40% of the estimated ultimate strength were conducted since the load-slip curve had been stable after five cycles. Force control was utilized with the loading speed of 2 kN/s during the cyclic loading, while the formal loading used displacement control. Depending on the slip less or more than 3 mm, the loading speed was 0.2 mm/min or 0.5 mm/min. Lime cushion with the thickness of 2 mm was placed on the top and bottom of the specimens to avoid the emergence of a large eccentricity. Short rebars were welded to both sides of the steel plate and wrapped in foam to obtain the slip at the hole of perfobond connectors. The space below the short rebars was guaranteed to be not less than 50 mm. 2 and 8 LVDTs with a precision of 1/1000 mm were employed in single-hole and multi-hole specimens. The test setup and loading are shown in Fig 3.



Figure 3. Test setup and loading.

Strain gauges were mounted on the steel plate and perforated rebar to further explore the shear mechanism of rubber-ring perfobond connectors. Five strain gauges were vertically arranged on a horizontal section with a vertical distance of 60 mm from the center of the hole. The arrangement of steel plate strain gauges is shown in Fig 4.

Five strain gauges were arranged on each perforated rebar, including the upper and lower edges at the hole, the upper edge which was 40 mm from the center of the hole, the lateral sides which were 10 mm and 15 mm from the centerline, as shown in Fig 5. Wherein the strain gauges on the upper and lower edges were parallel to the longitudinal direction of rebar, while the strain gauges on the lateral sides were perpendicular to the axial direction.

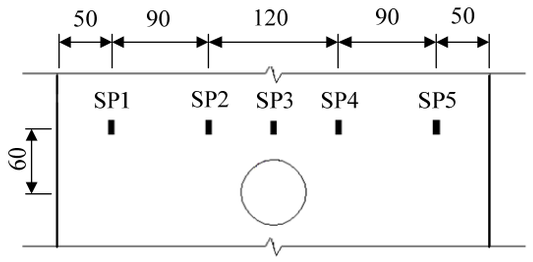


Figure 4. Strain gauges on steel plate. /mm

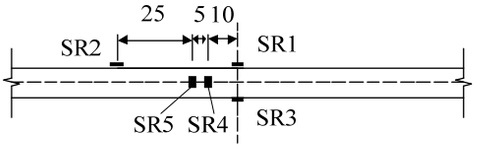


Figure 5. Strain gauges on perforated rebar. /mm

3 TEST RESULTS

3.1 *Failure modes*

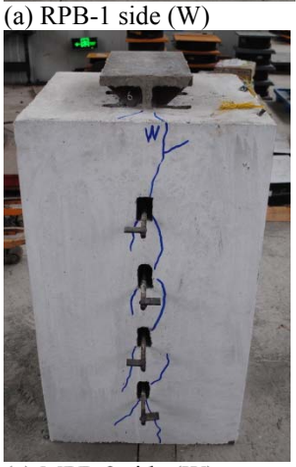
Fig 6 shows the crack distributions of concrete blocks. The crack sounds were heard when the specimens were loaded to about 70% bearing capacity, and the cracks appeared on both the top surface and the two lateral surfaces perpendicular to the steel plate. On the lateral surf aces parallel to the steel plate, no cracks were found in all the single-hole specimens, MPB-4 and MPB-5, while sim ilar vertical cracks appeared in MPB-1~3.



(a) RPB-1 side (W)



(b) RPB-1 top



(c) MPB-2 side (W)



(d) MPB-2 side (S)

Figure 6. Crack distributions on concrete blocks.

It could be seen from the shapes and distributions of cracks that the cracking was m ainly due to the failure of the bond between the steel plate and concrete. When the specim ens were loaded to the ultim ate bearing capacity, fracture sounds of perforated rebar were apparently heard.

Only the concrete at both ends along the length direction of the steel plate was cut to avoid breaking the actual shear planes. Then the concrete blocks were manually separated into two parts. Figure 7 shows the original shear plane for PB and RPB-2.



(a) PB shear plane



(b) RPB-2 shear plane

Figure 7. Shear planes of perfobond connectors.

As the slip increased, the concrete near the loading end was compacted, and the perforated rebar m oved toward the wall of the hole. The part close to the loading side of rubber ring was com pletely squashed. Both sides of the wings encountered large deformation and were sheared off. However, the lower part of the rubber ring rem ained intact and free from the concrete in the hole. The shear plane of the conventional perfobond connector was utterly vertical, while the shear plane of the rubber-ring perfobond connector form ed a sm all inclination with the steel plate surface. The rubber ring enlarged the span of the concrete dowel, resulting in a bending mode to some extent and the tensile cracking of the lower part of the concrete dowel. There were slip traces on the steel plate surface and concrete shear plane, indicating the existence of friction in the sliding process.

3.2 *Load-slip curves*

Fig 8 gives the load-slip curves of single-hole specimens, where the slip used the mean of the values measured by two LVDTs. The load-slip curve of the ordinary perfobond connector specimen PB included four stages. The initial phase of loading was a linear elastic stage with high stiffness, mainly relying on the bond between the steel plate and the concrete to resist the load. When the load increased to the cracking load V_c, the sounds of cracking were heard, which marked the end of the first stage. Followed by a rapid decline in bond, the load was mainly born by the concrete dowel and the perforated rebar, leading to reduced stiffness of the specimen. With the increase of slip, the shear failure of concrete dowel occurred, and the load reached the yield bearing capacity V_y. Although the concrete shear plane still retained the mechanical friction, the load in the third stage was mainly taken by the perforated rebar. As the slip grew, the load dropped to some extent. When the slip further increased, the shear plane of the perforated steel was in the strengthening stage, so that the load approximately linearly rose to the ultimate bearing capacity V_u. Then the perforated rebar was sheared off, and the load dropped sharply.

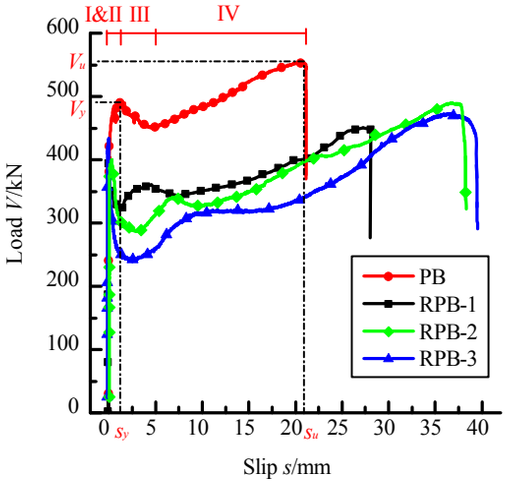


Figure 8. Load-slip curves of single-hole specimens.

There were some differences between the load-slip curves of rubber-ring perfobond connector specimens RPB-1~3 and that of PB. Table 3 summarized the test results. Due to the rubber ring, fewer loads were carried by the concrete dowel in the first stage. The cracking loads of the four single-hole specimens were close to each other, indicating that the load in the initial stage was mainly supported by the bond. The load dropped dramatically with the growth of slip after the damage of the bond. As the increase of the rubber thickness, the yield bearing capacity V_y and the yield slip s_y reduced and grew, respectively. The main reason was that setting rubber ring diminished the area of concrete dowel, while the small stiffness of rubber improved the slip capacity of perfobond connectors. The third and fourth stages of RPB-1~3 were similar to that of PB. The ultimate slip s_u increased with the thickness of rubber ring, but the improvement was not evident when the thickness was greater than 4 mm. That was because there were limits on the deformation capacity of perforated rebar.

Table 3. Test results.

Specimen	V_c /kN	V_y /kN	s_y /mm	V_u /kN	s_u /mm
PB	401.2	491.7	1.12	555.2	20.69
RPB-1	394.4	357.5	4.03	447.8	28.10
RPB-2	392.0	339.7	6.82	489.4	36.79
RPB-3	421.2	316.0	9.46	472.6	36.66
MPB-1	1336.4	1607.5	1.42	1839.8	19.08
MPB-2	1064.2	1091.1	6.50	1647.0	33.24
MPB-3	1093.3	1437.1	3.46	1789.5	24.11
MPB-4	1172.9	1401.3	5.10	1711.7	22.11
MPB-5	1193.0	1436.8	7.77	1739.7	26.64

Compared to the ordinary perfobond connector, the yield bearing capacity of rubber-ring perfobond connector decreased about 30%. Since the failure mode was the fracture of perforated rebar, the ultimate bearing capacity reduced by 15.4%. The difference between ultimate bearing capacity and yield bearing capacity was related to the properties of perforated rebar. The yield slip grew by 260% to 745%, which was determined by the thickness of the rubber ring.

Fig 9 shows the load-slip curves of multi-hole specimens, where the slip was the average of values measured by the LVDTs in the first row. The overall trend of the load-slip curve of MPB-1 was similar to that of PB, and MPB-2 which used rubber rings on all of the holes was identical to RPB-2. Each specimen contains four perforated rebars, resulting in several sounds of the fracture of rebars and the multi-step ladder in the failure stage curves.

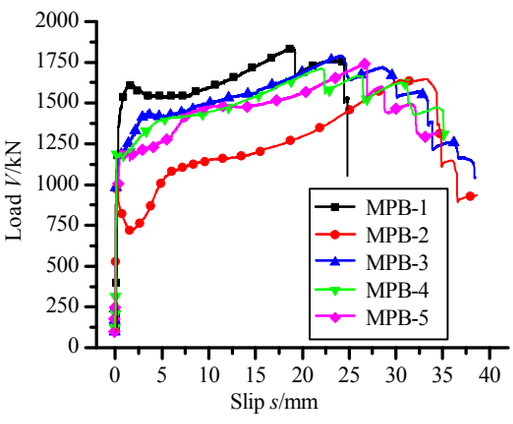


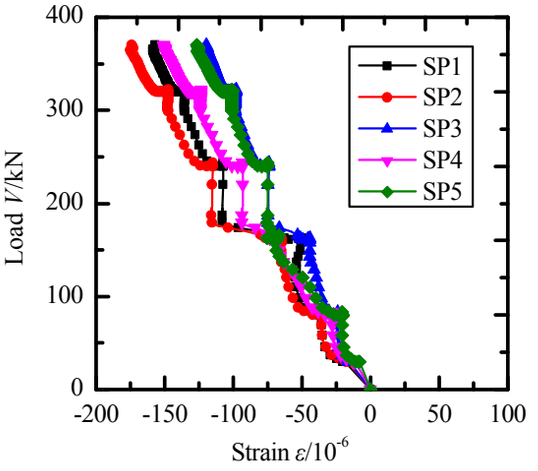
Figure 9. Load-slip curves of multi-hole specimens.

The rubber rings with different thicknesses were employed on the first and fourth holes in MPB-3~5. The cracking loads of these three specimens were close, which were less and larger than that of MPB-1 and MPB-2, respectively, indicating that concrete dowels were involved in carrying load at the first stage in the multi-hole specimens. As the middle concrete dowels could bear load when the bond was damaged, the load-slip curves of MPB-3~5 did not appear the sharp drop of load in that of RPB-1~3 and MPB-2. The larger thickness of the rubber made the more hysteresis of carrying shear of the hole, the smaller stiffness in the second stage and the higher yield slip. The yield bearing capacity and the ultimate bearing capacity of these three specimens were close, which were about 89% and 95% the yield and ultimate capacity of MPB-1, respectively because the area differences of the concrete dowel were relatively small and the failure mode was the fracture of perforated rebars. The ultimate slip of MPB-2 was greater than MPB-3~5 and MPB-1. The ultimate slip of MPB-4 was less than that of MPB-3, possibly due to the difference in material properties of individual perforated rebar.

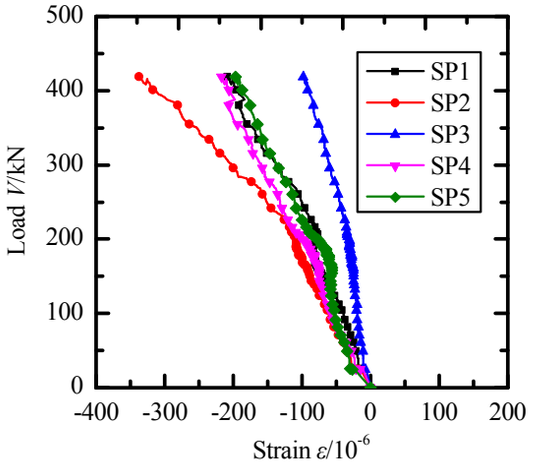
3.3 *Load-strain relationship of steel plate*

Fig 10 shows the load-strain relationships of each measuring point on the steel plate in PB and RPB-3. The full cross-section of the steel plate was compressed, and the vertical strain increased linearly with the growth of load. After the concrete block cracked, the slip increased rapidly resulting in the damage of most strain gauges. The measured strain of SP2 and SP4 whose horizontal distance from the center of the hole was 60 mm were relatively large, followed by SP1 and SP5. Due to the bond and friction, the vertical strain measured by SP3 which located in the centerline of the steel plate was minimal. The strain on both sides of the centerline was asymmetric.

The steel plate strain patterns in each row of the multi-hole specimens were similar to that of single-hole specimens. Fig 11 compares the steel plate load-strain relationship of each row between MPB-1 and MPB-3, where the strain took the average of SP2 and SP4. In the multi-hole specimens, the strain of the steel plate reduced gradually with the increase of the row number. Each curve was intercepted by the same load, and the horizontal distances of the adjacent intersections in the same specimen reflected the load magnitude between the adjacent holes. The steel plate strain of the first row in MPB-3 decreased by applying the rubber rings, and the horizontal distances of adjacent intersections were less than those of MPB-1, indicating that a reasonable arrangement of rubber rings could alleviate the local shear concentration.



(a) PB



(b) RPB-3

Figure 10. Load-strain relationships of single-hole specimens.

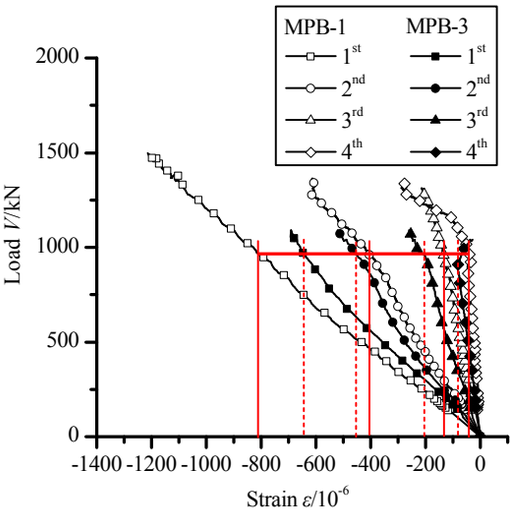
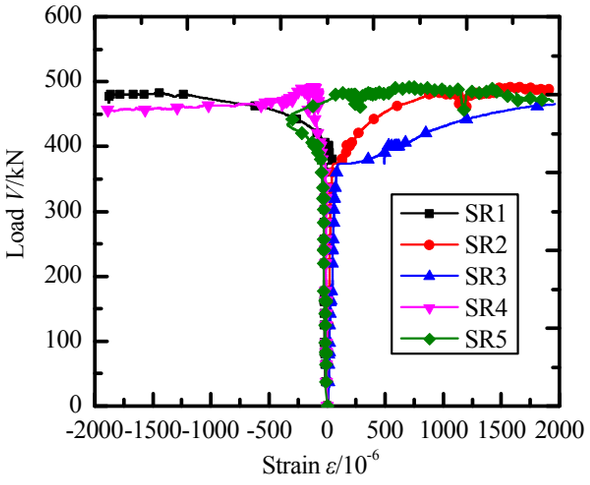


Figure 11. Comparison of load-strain relationships between multi-hole specimens.

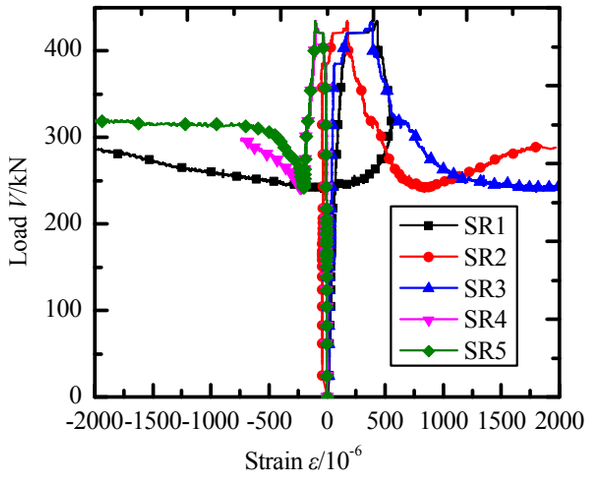
3.4 *Load-strain relationship of perforated rebars*

Fig 12 shows the load-strain relationships of perforated rebars. At the initial loading phase, the load was mainly resisted by bond and concrete dowel, re-

sulting in the small strain of perforated rebars. When the load reached the cracking load, the strain rose rapidly. The tensile strain of SR3 grew fastest. Then the compressive strain of SR1 and the tensile strain of SR2 increased, which showed the bending characteristics of perforated rebar. As the slip increased further, the strain of SR4 and SR5 rose. It was noted that SR4 was in compression while SR5 was in tension, indicating that the horizontal distance from the center of hole to the shear plane in PB was 10 mm to 15 mm. On the contrary, both SR4 and SR5 were in compression in RPB-3, indicating that the shear plane moved away from the centerline after setting the rubber ring.



(a) PB



(b) RPB-3

Figure 12. Load-strain relationships of perforated rebars.

4 EVALUATION OF SHEAR CAPACITY FORMULAS

4.1 *Existing formulas*

This paper collected the Formulas (1) to (5) of shear bearing capacity for perfobond connectors, which were based on the modified push-out test results.

Where A_c is the area of concrete dowel, A_s is the area of perforated rebar, A_{tr} and f_y' are the area and yield strength of transverse reinforcements, τ_b and A_b are the bond strength and contact area between the steel plate and concrete block, and t is the thickness of steel plate.

Zhang et al. (2007) proposed Formula (1) by regression of the test results of 31 specimens. The authors believed that the shear bearing capacity was mainly provided by the concrete dowel and perforated rebar. Tensile strength was chosen to calculate the shear bearing capacity. Wang et al. (2013) carried out the push out tests using horizontal loading, including 33 specimens and presented Formula (2) to calculate the shear bearing capacity. Where the coefficients α, β and δ are 0.9974, 0.1293 and 220 kN, respectively. The authors supposed that the transverse reinforcements had contributions to the bearing capacity, while the contributions of concrete dowel were ignorable. The bond was considered in the tests, but only the constant term δ was given in Formula (2).

$$V_u = 0.95\times(2A_cf_c)+0.94\times(2A_sf_u) \tag{1}$$

$$V_u = \alpha(2A_sf_u)+\beta(2A_{tr}f_y')+\delta \tag{2}$$

Wang et al. (2014) proposed Formula (3) based on three series of 24 groups of modified push-out test results, in which the shear bearing capacity was affected by the concrete dowel, perforated rebar and transverse reinforcements. Yield strength was used to consider the contributions of perforated rebar and transverse reinforcements. He et al. (2016) conducted 12 specimens of modified push-out tests to analyze the individual contribution of the bond, concrete dowel and perforated rebar. Then Formula (4) was put forward. Nakajima et al. (2016) studied the results of the 35 modified push-out test specimens and presented Formula (5). The authors believed that the shear bearing capacity was provided by the concrete dowel and perforated rebar, both of which were related to the thickness of steel plate.

$$V_u = 0.498A_c\sqrt{f_c}+0.255A_sf_y+0.065A_{tr}f_y' \tag{3}$$

$$\begin{cases} V_u = \tau_bA_b+1.06A_cf_{cu}+2.09A_sf_y \\ \tau_b = -0.022f_{cu}+0.306\sqrt{f_{cu}}-0.573 \end{cases} \tag{4}$$

$$\begin{cases} V_u = V_c+0.84d_sf_yd^{0.1}t^{0.8} \\ V_c = 0.15\alpha A_cf_c^{0.65}A_s^{0.43}t^{-0.5} \\ \alpha = 6.9d_s^{0.4}d^{-0.7} \end{cases} \tag{5}$$

4.2 *Comparison of formulas*

The calculated results by substituting the measured parameters in the experiments into Formula (1) to

(5) were compared with the ultimate bearing capacity obtained by the tests, as shown in Table 4. Although Formula (1) did not consider the bond, the overall error was minimal among the five equations. The reasons were that the contribution of concrete dowel was overestimated and tensile strength was used to consider the effect of perforated rebar. In Formula (2) and (3), different strengths of perforated rebar were used, and the difference of coefficients was substantial. The contribution of transverse reinforcements was taken into account in both equations, resulting in larger calculation results. Formula (5) was usable for a specific parameter range, which was not applicable when the diameter of perforated rebar was greater than 16 mm or the rebars and concrete with high strengths were employed.

Since Formula (4) took account of cohesive force, the calculation error of PB was small. The calculation errors of the specimens with rubber ring were about 20%. The possible reason was that the constraint effect of the steel plate on the concrete in the hole was significantly reduced, and the contribution of concrete dowel should be reduced in the shear capacity formula. On the other hand, the increase of slip capacity caused a decline in residual bond and friction. Therefore, the formula of the shear bearing capacity of rubber-ring perfobond connector needs to be further studied.

Table 4. Calculated results of each formula /kN.

Specimen	(1)	(2)	(3)	(4)	(5)	Test
PB	549	656	651	588	137	555.2
Error/%	-1	18	17	6	-75	
RPB-1	517	655	618	550	128	447.8
Error/%	15	46	38	23	-71	
RPB-2	500	668	651	569	142	489.4
Error/%	2	36	33	16	-71	
RPB-3	494	690	670	576	150	472.6
Error/%	5	46	42	22	-68	

5 CONCLUSION

The following conclusions could be drawn based on the investigations above.

(1) When the load reached the ultimate bearing capacity, the failure mode of both ordinary and rubber-ring perfobond connectors was the fracture of perforated rebar. The rubber ring enlarged the span of concrete dowel, resulting in the bending characteristic of concrete dowels.

(2) Compared to conventional perfobond connectors, the yield capacity of the rubber ring perfobond connector reduced by about 30% and the ultimate capacity decreased by 15.4%. The yield slip increased by 260%~745%, depending on the thickness of rubber rings.

(3) By applying the rubber rings, the strain differences of adjacent rows were diminished, indicating that a reasonable arrangement of rubber rings could alleviate the local shear concentration.

(4) The calculation errors of the shear capacity formula considering the contributions of the bond, concrete dowel and perforated rebar were small. The constraint effect of the steel plate on the concrete dowel was reduced by employing rubber rings.

6 REFERENCES

Yamadera N., Itoh N., Morikawa H. 1993. Design of the Tsurumi fairway bridge. *Bridge and Foundation Engineering*, 2(2), 23-32. (in Japanese)

Wang Z., Li Q., Zhao C. 2013. Ultimate shear resistance of perfobond rib shear connectors based on a modified push-out test. *Advances in Structural Engineering*, 16(4), 667-680.

Su Q., Wang W., Luan H. et al. 2014. Experimental research on bearing mechanism of perfobond rib shear connectors. *Journal of Constructional Steel Research*, 95, 22-31.

Su Q., Yang G., Bradford M. A. 2016. Bearing capacity of perfobond rib shear connectors in composite girder bridges. *Journal of Bridge Engineering*, 21(4), 06015009.

Zhang Q., Li Q., Tang L. 2007. Fracture mechanism and ultimate carrying capacity of shear connectors applied for steel-concrete joint segment of bridge pylon. *China Journal of Highway and Transport*, 20(1), 85-90. (in Chinese)

Wang W., Zhao C., Li, Q. et al. 2014. Study on load-slip characteristic curves of perfobond shear connectors in hybrid structures. *Journal of Advanced Concrete Technology*, 12(10), 413-424.

He, S., Fang, Z. et al. 2016. Experimental study on perfobond strip connector in steel–concrete joints of hybrid bridges. *Journal of Constructional Steel Research*, 118, 169-179.

Nakajima A. & Nguyen M. H. 2016. Strain behavior of penetrating rebar in perfobond strip and its evaluation of shear resistance. *Journal of JSCE*, 4(1), 1-18.

Xiao L., Li X., John Ma Z. 2016. Behavior of perforated shear connectors in steel - concrete composite joints of hybrid bridges. *Journal of Bridge Engineering*, 22(4), 04016135.

Oguejiofor E. C. & Hosain M. U. 1994. A parametric study of perfobond rib shear connectors. *Canadian Journal of Civil Engineering*, 21.4, 614-625.

Cândido-Martins J. P. S., Costa-Neves L. F., Vellasco P. C. G. da S. 2010. Experimental evaluation of the structural response of Perfobond shear connectors. *Engineering Structures*, 32(8): 1976-1985.

Vianna J. da C. et al. 2013. Experimental study of Perfobond shear connectors in composite construction. *Journal of Constructional Steel Research*, 81: 62-75.

Ahn J., Lee C., Won J. et al. 2010. Shear resistance of the perfobond-rib shear connector depending on concrete strength and rib arrangement. *Journal of Constructional Steel Research*, 66(10): 1295-1307.

Xu, X., Liu, Y., He, J. 2014. Study on mechanical behavior of rubber-sleeved studs for steel and concrete composite structures. *Construction and Building Materials*, 53, 533-546.

Xu, X. & Liu, Y. 2016. Analytical and numerical study of the shear stiffness of rubber-sleeved stud. *Journal of Constructional Steel Research*, 123, 68-78.

EUROCODE 4. EN 1994-1-1. 2005. Design of Composite Steel and Concrete Structures Part 1.1 General Rules and Rules for Buildings. CEN-European Committee for Standardization, Brussels.

Maintenance, Safety, Risk, Management and Life-Cycle Performance of Bridges – Powers, Frangopol, Al-Mahaidi & Caprani (Eds)
© 2018 Taylor & Francis Group, London, ISBN 978-1-138-73045-8

Effect of Hinge-Type Connections on the Lateral Cyclic Behavior of a Prestressed High-Strength Concrete Pile

B. Lim & J. W. Kang
Hongik University, Seoul, Republic of Korea
Y. J. Kim & H. Yoon
Korea Institute of Civil Engineering and Building Technology, Goyang, Republic of Korea

ABSTRACT: This paper presents the cyclic behavior of a prestressed high strength concrete (PHC) pile with hinge-type pile head connections designed for reducing the bending moment due to lateral loads. The PHC pile is a hollow cylindrical prestressed pile made by centrifugal compaction and is being increasingly used in the foundation of civil structures because of its good seismic performance and cost effectiveness. This study investigated the seismic performance of full-scale PHC piles with four head types. The pile specimens consist of a reference specimen with no pile cap, a hinge specimen with a pile cap on the head, a hinge specimen with a pile cap and reinforcing steel, and a hinge specimen with prestressing steel. The cyclic response of the four PHC pile specimens was obtained by quasi-static tests conducted with displacement-controlled lateral cyclic loadings. According to the test results, the PHC pile with a pile cap had the best lateral displacement capacity among the specimens. The other hinge specimens also showed good cyclic performance with only minor damages due to the reduced bending moment around the pile head, whereas the reference specimen with no pile cap exhibited severe damage. It was observed from hysteresis curves that the PHC pile with a pile cap had better bearing and energy dissipation capacities compared to the regular reinforced concrete pile. Design features of the PHC piles, experimental configuration, and the test results will be presented. The proposed head connections can be used to diminish the flexural damage of PHC piles due to ground motions.

1 INTRODUCTION

Prestressed High Strength Concrete (PHC) piles are characterized by excellent resistance to lateral and impact loads and large load carrying capacity owing to prestressing effect of tendons and high compressive strength of concrete. They are usually fabricated with a high strength concrete with the compressive strength of over 80 MPa, which is greater than the compressive strength of a regular prestressed concrete (PC) by at least 1.6 times. Thus, they have the advantages of less cracking due to hitting and high corrosion resistance (Aoshima *et al*., 2006). Furthermore, compared to PC piles, PHC piles allow the penetration of the hard middle layer and the implementation of long piles, and are usually cheaper than steel pipe piles (Hwang & Cho, 2005). Therefore, in the US and Europe, PHC piles are frequently used in deep foundation for bridges as well as for high-rise buildings.

Pile foundation must be designed to sufficiently endure vertical load and horizontal earth pressure, and effectively resist seismic load. Thus, the sufficient horizontal load bearing capacity of pile foundation is one of the key considerations for seismic design of structures. In fact, many earthquake damages due to insufficient horizontal load bearing capacity of piles have been reported across the world. On June 28, 1948, shear failure occurred on the independent footings of many buildings due to an earthquake of 6.8 magnitude in Fukui , Japan. In 1964, damages to pile foundations of various structures occurred due to liquefaction caused by the Niigata earthquake. Sugimura *et al*. (1981) evaluated the damages of existing piles due to the earthquake in Miyagi in 1978 and proposed a foundation design method to improve them. To investigate the causes of the damages of structures and pile foundations caused by an earthquake of 7.2 magnitude that occurred in KOBE, Japan in 1995, Mizuno *et al*. (1996) analyzed the damage patterns, soils, and environmental characteristics around the buildings and suggested an improvement of pile design. In 1989 in San Francisco, USA, the substructure and pile connections of the Oakland Bay Bridge were damaged seriously by an earthquake of 6.9 magnitude (Elgamal *et al*., 2008). To reduce these earthquake damages, it is critical to attain sufficient displacement ductility of piles. In particular, the design details of pile-footing connections have a large effect on the seismic performance of pile foundation because the cross-section

and stiffness of members change rapidly around the connection part. Depending on the method of reinforcing the connection of pile foundation, the stress concentration on the pile-footing connection can be mitigated in various patterns. Recently, active studies have been conducted to reinforce the connections of PHC pile and footing with infilled concrete and additional steel bars and to understand the horizontal behavior characteristics of pile systems. Larosche *et al*. (2014) performed an experiment to reinforce three connections of PHC piles and footings arranged in a row with infilled concrete, tie bars, and axial bars and apply the Joshua Tree seismic load which had occurred in California in 1992. Through this experiment, they evaluated the constrained stress of infilled concrete, the ductility of foundation, and the damages of piles, and proposed a footing design method. Bang *et al*. (2016) carried out a lateral loading experiment after arranging infilled concrete and reinforcing bars in the hollow parts of PHC piles and evaluated the bending moment, ductility, and energy dissipation capacity of pile connections. They also found that the behaviors of pile-footing connections depended on the insertion depth of piles, the number and location of longitudinal reinforcing bars. Yang *et al*. (2016) analyzed the load versus displacement curve, ductility and bearing capacity of piles according to the arrangement method of reinforcing bars in the connection between PHC piles and footings.

These reinforcement methods for the head of PHC files increase the bending stiffness of the footing connection, thus increasing the lateral displacement ductility of piles. However, this type of connection is expected to exhibit lower lateral displacement ductility than the connection of full hinge structure if the vertical load bearing capacity of a pile does not change. In this study, the pile head is made into a hinge structure by mounting a pile cap on the connection of PHC pile and footing. Then the increase in the lateral displacement ductility of pile and the decrease in the bending moment of the connection are evaluated. To this end, quasi-static lateral load tests were performed by producing a fully fixed specimen with no pile cap and with the pile-footing connection reinforced by infilled concrete, axial and lateral reinforcement bars, a full hinge specimen with a pile cap on the head pf PHC pile, a partial hinge specimen with the connection reinforced by axial and lateral reinforcement bars and with a pile cap on the pile head, and a partial hinge specimen with PC steel wires extended to the footing and with no infilled concrete.

This paper introduces the design characteristics of PHC pile connections and describes a quasi-static experiment method for evaluating the seismic performance of the connections. The seismic performance of PHC piles with the connection reinforced with a pile cap is presented by comparing the load versus displacement curves, fracture patterns, and energy dissipation capacity of the specimens to which four reinforcement methods have been applied.

2 PREPARATION OF SPECIMENS AND EXPERIMENTAL METHOD

2.1 *Preparation of the PHC pile specimens*

PHC piles generally have a hollow cross-section and are fabricated using a centrifugal force to produce concrete with uniform characteristics. To produce high-strength concrete with 80 MPa or higher compressive strength, silica powders, high-performing water reducing agent, and a special admixture are added (Aoshima *et al*., 2010).

The PHC pile specimens used in this study comprise high-strength concrete with 80 MPa or higher compressive strength and nine PC steel materials with a 9.2mm nominal diameter. Their diameter, thickness and length are 500 mm, 80 mm, and 3500 mm, respectively. Specimens were produced by classifying these PHC piles into four categories depending on the existence of pile cap and the internal reinforcement method of footing connections. Figure 1 shows the PHC pile specimens of these four types. Specimen A is a fully fixed specimen with no pile cap and with the pile-footing connection reinforced by infilled concrete, axial and lateral reinforcement bars. Specimen B is a full hinge specimen with a pile cap on the head pf PHC pile. Specimen C is a partial hinge specimen with the connection reinforced by axial and lateral reinforcement bars and with a pile cap on the pile head. Specimen D is a partial hinge specimen with PC steel wires extended to the footing and with no infilled concrete.

Specimens A, B, and C were fabricated in a length of 3.5 m by applying one cutting method, which cuts the concrete and PC steels together for 5m long PHC piles produced in a factory. Specimen D was fabricated with nine PC steel bars at the end of the 3.5m long PHC pile exposed for 500 mm. The design reference compressive strength of the footing concrete and the infilled concrete of the hollow part of PHC piles is 30 MPa. The reinforcement bar of the infilled concrete in the hollow part of pile is D19 deformed bar with a yield strength of 400 MPa.

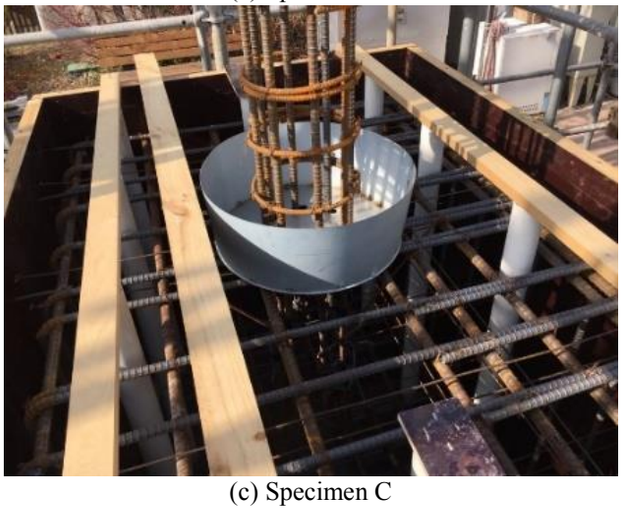
The pile cap mounted on the pile head of Specimens B, C and D have a crown diameter of 501 mm, a bottom diameter of 545 mm, a height of 201 mm, and a thickness of 1.2 mm. Figure 2 shows the dimensions of the pile cap.



(a) Specimen A



(b) Specimen B



(c) Specimen C

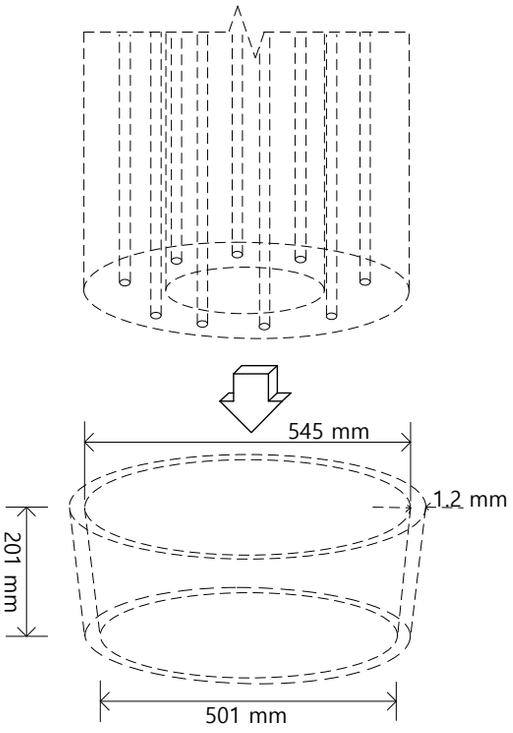


(d) Specimen D

Figure 1. PHC pile specimens prepared in this study.



(a) Pile cap mounting



(b) Pile cap dimensions

Figure 2. Pile cap mounted on the PHC pile head.

Table 1. Dimensions and material properties of the four PHC pile specimens.

Specimens	A		B		C		D	
	Pile	Footing	Pile	Footing	Pile	Footing	Pile	Footing
Dimension (mm)	Ø500-80	1500 × 2000	Ø500-80	1500 × 2000	Ø500-80	1500 × 2000	Ø500-80	1500 × 2000
Height (mm)	3500	1300	3500	1300	3500	1300	3500	1300
Prestressing bar	9-Ø9.2	-	9-Ø9.2	-	9-Ø9.2	-	9-Ø9.2	-
Longitudinal bar	8-D19	-	8-D19	-	8-D19	-	8-D19	-
Transverse rebar	D13@150	D13@150	-	-	D13@150	D13@150	-	-
Concrete strength (MPa)	80	30	80	30	80	30	80	30
Yield strength of longitudinal bar (MPa)	400	-	-	-	400	-	-	-

For all Specimens A to D, the PHC piles were inserted into the footing by a length of 100mm. The footing is a concrete block with a horizontal length of 1500 mm, a vertical length of 2000 mm, and a height of 1300 mm. The loading unit at the top is a concrete block with a horizontal length of 1500 mm, a vertical length of 1500 mm, and a height of 1200 mm. Eight D19 reinforcing bars were arranged in Specimen A and Specimen C for the reinforcement of infilled concrete. A laser riser was used to combine the footing top with the PHC piles accurately at right angle. Table 1 shows the dimensions of each specimen and the dynamic characteristics of materials. Figure 3 shows the schematics of the connections of the four PHC pile specimens.

2.2 *Quasi-static test*

To evaluate the seismic performance of the four PHC pile specimens with different connection details, a quasi-static test was conducted, which applied lateral load at the top end of the piles while applying an axial load. As shown in Figure 4, the piles were placed on the top of the footing and a loading concrete block was placed on the pile top. The long-term allowable axial load of 1400 kN was applied to the pile by an actuator in the axial direction and the pile was loaded laterally by an actuator supported on a reaction wall. The lateral actuator was connected to the loading unit of the pile at a height of 3000 mm above the pile bottom. The actuator applied the lateral load to the pile cyclically up to a displacement of 178.84 mm with a displacement control method that increases the lateral displacement in increments of 6.39 mm. Positive and negative loads were repeated in two cycles in each displacement step as shown in Figure 5.

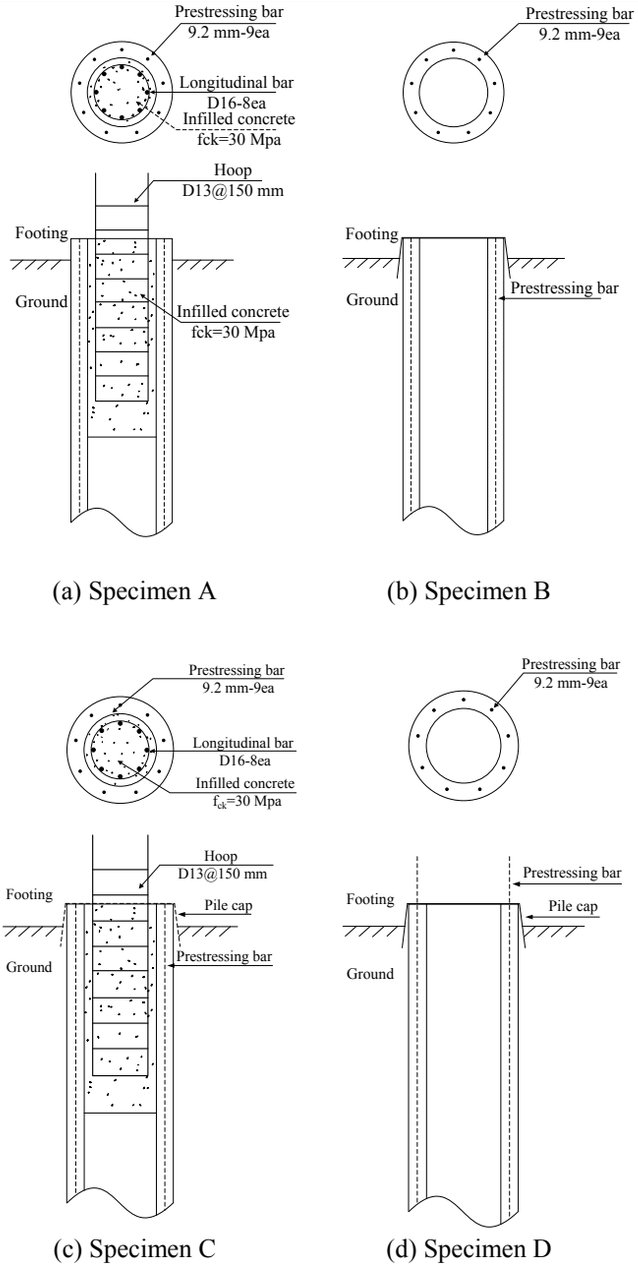


Figure 3. Schematics of the four PHC pile specimens.

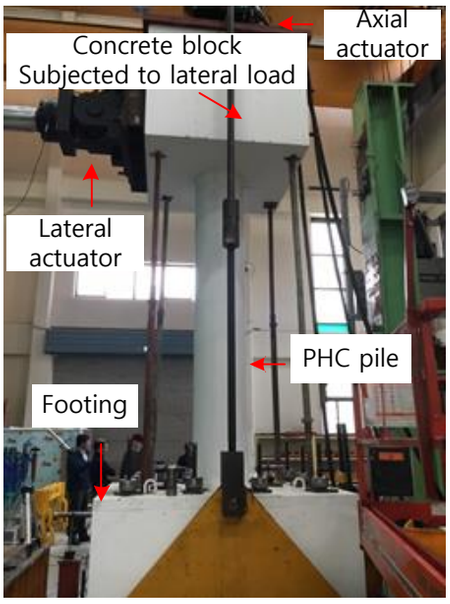


Figure 4. Quasi-static test setup with a PHC pile specimen.

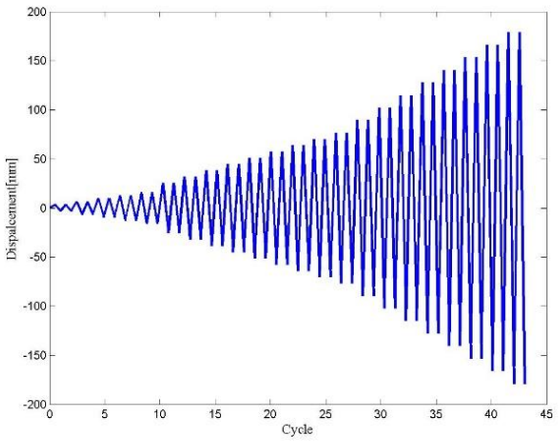


Figure 5. Cyclic loads for the quasi-static test.

3 TEST RESULTS AND DISCUSSION

3.1 *Fracture patterns of the PHC pile specimens*

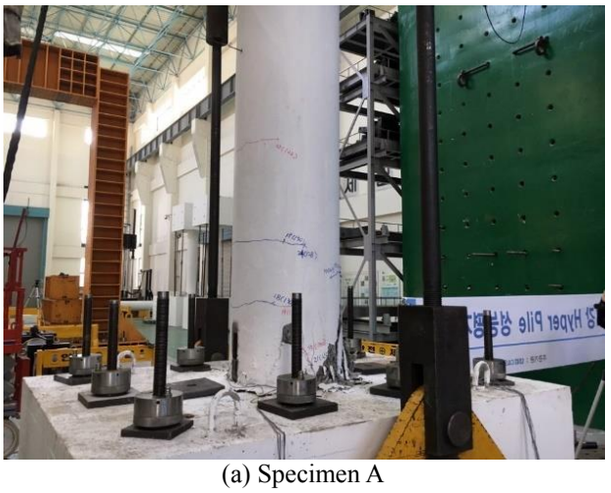
The quasi-static test was repeated until the four PHC pile specimens were fractured. Figure 6 shows the fracture patterns of these four PHC piles. In the case of Specimen A, initial flexural cracks were observed near the connection of PHC pile and footing at a lateral displacement of 44.72 mm. The flexural cracks progressed as the lateral displacement increased. Then longitudinal shear cracks occurred at a lateral displacement of 57.49 mm. As the lateral displacement of the specimen increased, the widths of flexural and longitudinal shear cracks increased. At a lateral displacement of 77.10 mm, the specimen reached its maximum load 135.77 kN, and the pile was fractured at a lateral displacement of 131.50 mm.

In the case of Specimen B whose connection to the footing is close to hinge, longitudinal cracks of the pile developed at a lateral displacement of 89.43 mm. There were no significant flexural cracks generated until then. Then it reached the maximum load of 98.98 kN at a lateral displacement of 149 mm.

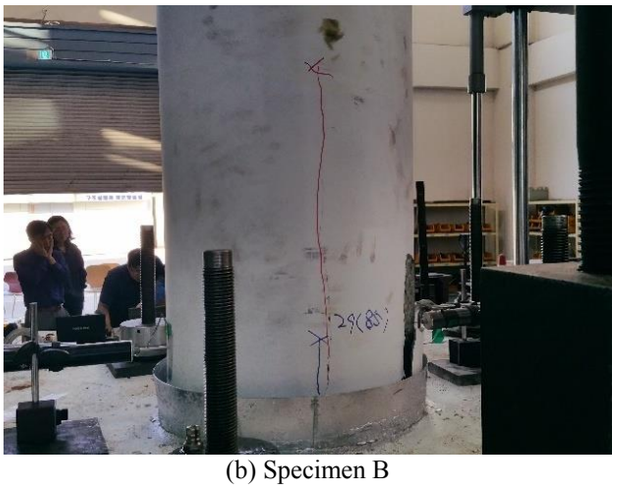
In the case of Specimen C whose connection is reinforced with infilled concrete and rebars, longitudinal shear crack occurred earlier than flexural cracks as in the case of Specimen B. The lateral displacement at the development of the longitudinal crack was 51.10 mm. The width of the longitudinal cracks increased as the lateral load increased and the length of cracks increased toward the pile top. The cover concrete was spalled at a lateral displacement of 106.84 mm. Then it reached the maximum load of 140 kN at a lateral displacement of 120.3 mm. After reaching the maximum load, the PHC pile was fractured at a lateral displacement of 140.54 mm.

In the case of Specimen D, no significant flexural bending and longitudinal shear cracks were generated unlike the other specimens, and the cover concrete was separated at a lateral displacement of 173.75 mm. The specimen reached the maximum load of 114.32 kN at a lateral displacement of 173.75 mm. The separation of concrete from the surface of the PHC pile specimens seems to have been caused by the concentration of stress along the cracks at the connection of PHC pile and footing.

The results of this test showed that the displacement of Specimen D was greater by 2.25 times, 1.17 times, and 1.24 times than those of Specimens A, B, and C, respectively at the maximum lateral load. In other words, the lateral displacement ductility was large in the order of Specimens D, B, C and A. The reason that the lateral displacement ductility values of specimens B, C, and D were larger than that of Specimen A is that the PHC pile connection using a pile cap proposed in this study increases the lateral flexibility of the PHC piles. Specimens B to D with a pile cap showed some cracks in the connections and the body of PHC piles, but their lateral load bearing capacity did not decrease much until the end of test compared to Specimen A.



(a) Specimen A



(b) Specimen B



(c) Specimen C



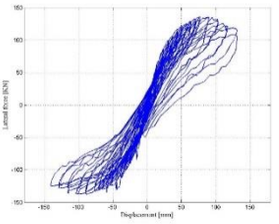
(d) Specimen D

Figure 6. Fracture patterns of the four PHC pile specimens.

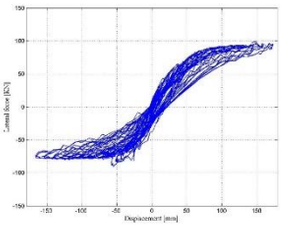
3.2 *Lateral load-displacement curves*

The yield load, peak load, and ultimate load of each specimen are shown in Table 2. Furthermore, the ductility ratio of each specimen was calculated by using the yield displacement and ultimate displacement at fracture.

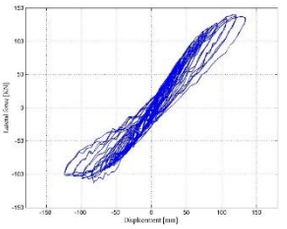
As shown in Table 2, ductility ratios of Specimens A, B, C, and D are 2.15, 5.55, 3.16, and 5.37, respectively. Specimen A has the lowest displacement ductility due to the connection with the infilled concrete reinforced with tie bars and axial bars. Therefore, its lateral flexibility is relatively small compared to others. Specimen C shows a greater displacement ductility compared to Specimen A because a pile cap was mounted between the footing and pile, which improved lateral flexibility.



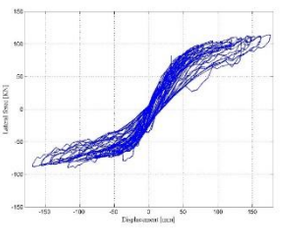
(a) Specimen A



(b) Specimen B



(c) Specimen C



(d) Specimen D

Figure 7. Hysteresis curves obtained from the quasi-static test of the four PHC pile specimens.

Table 2. Lateral load and displacement values at yielding, peak, and ultimate states of the four PHC pile specimens.

Specimens		A	B	C	D
Yielding state	P_y(kN)	125.13	58.59	68.88	68.36
	δ_y(mm)	57.40	30.30	41.25	32.35
Peak state	$P_{\max}$(kN)	135.77	98.98	140	114.32
	$\delta_{\max}$(mm)	77.1	149	120.3	173.75
Ultimate state	P_u(kN)	108.40	96.01	136.71	114.32
	δ_u(mm)	123.20	168.3	130.2	173.75
Ductility ratio	(δ_u/δ_y)	2.15	5.55	3.16	5.37

Specimen B shows a greater displacement ductility compared to Specimens A and C because the head was reinforced only with a pile cap with no tie bars and axial bars and the connection is close to a full hinge. Specimen D shows a similar displacement ductility as that of Specimen B because the PC steel wires do not greatly affect the bending stiffness of pile although the PC steel wires are extended from the pile to the footing.

3.3 *Viscous damping ratio*

The energy dissipation capacity is one of the items that should be considered to evaluate the seismic performance of structures. The dissipated energy of a structure can be expressed by an area surrounded by the load versus displacement curve. Figure 8 shows a schematic of the load versus displacement curve as well as the dissipated energy and maximum strain energy for a structure under cyclic loading.

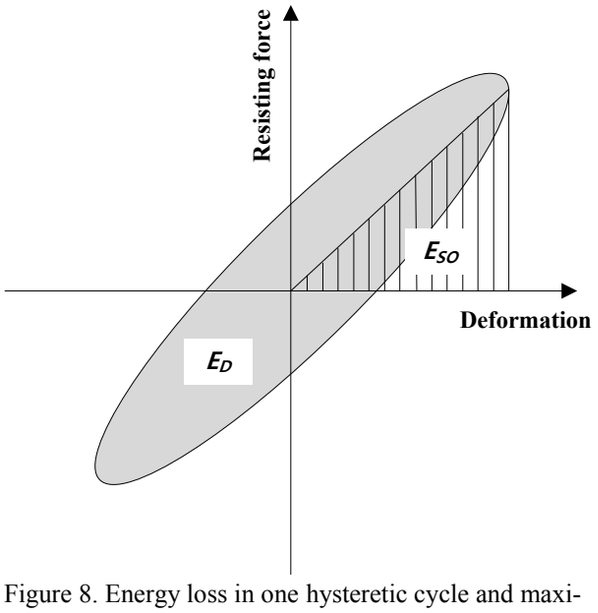


Figure 8. Energy loss in one hysteretic cycle and maximum strain energy.

In this figure, E_D denotes the dissipated energy in one cycle, and E_{So} denotes the maximum strain energy. The area ratio of E_D and E_{So} calculated through Equation (1) can be used to indicate the viscous damping ratio of specimens (Chopra, 2001).

$$\zeta = \frac{1}{4\pi}\frac{E_D}{E_{So}} \tag{1}$$

Figure 9 shows the viscous damping ratios of Specimens A to D calculated using Equation (1).

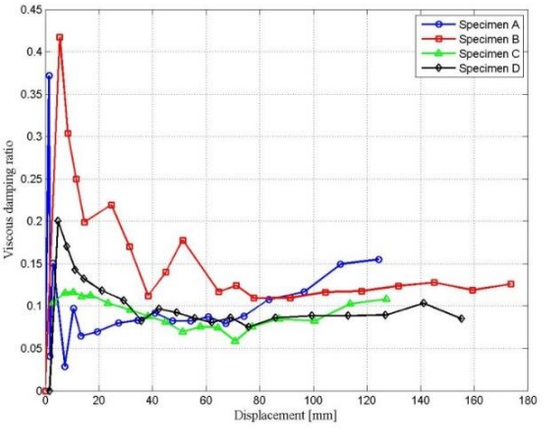


Figure 9. Viscous damping ratio of each specimen.

Among the specimens, B and D with large lateral displacement ductility showed large damping ratios in general. This is because Specimens B and D whose connection of PHC pile and footing is close to a full hinge have a larger energy dissipation capacity in lateral behaviors compared to Specimens A and C.

4 CONCLUSION

In this study, four types of PHC pile specimens were fabricated depending on the existence of pile cap and the internal reinforcement method of the footing connection. The load versus displacement curves recorded by applying repeated loads to the specimens were compared, and the fracture patterns and the viscous damping ratio of PHC piles were compared.
Specimens B and D exhibited larger displacements at the peak lateral load compared to Specimens A and

C. The descending order of ductility ratio of the specimens was B, D, C, and A. Furthermore, the comparison of viscous damping ratios of the specimens showed that Specimens B and D whose connections are close to a full hinge had a greater energy dissipation capacity than those of Specimens A and C. Based on these findings, applying the head reinforcement method of Specimens B and D to the PHC pile footing is expected to provide excellent seismic performance.

5 ACKNOWLEDGMENT

This research was supported by "A study on Design and Construction of High Performance Reinforced Concrete Pile". This work was also supported by the Korea Institute of Energy Technology Evaluation and Planning (KETEP) grant [No. 20151520100990] funded by the Ministry of Trade, Industry and Energy of the Republic of Korea.

6 REFERENCES

Aoshima, K., Shimada, H. & Komuro, T. 2006. Mechanical characteristics of pile head joint with improved simplified connection method for precast concrete piles. *J. Struct. Const. Eng* 71(607): 125-132.

Aoshima, K., Horii, Y. & Kobayashi, H., Adachi, T. 2010. Structural performance of improved simplified connection system at precast concrete pile head under high axial load. *J. Struct. Const. Eng* 75(653): 1271-1278.

Bang, J. W., Oh, S. J., Lee, S. S. & Kim, Y. Y. 2016. Pile-cap connection behavior dependent on the connecting method between PHC pile and footing. *Journal of the Korea Institute for Structural Maintenance and Inspection* 20(3): 25-32.

Chopra, A. K. 2001. *Dynamic of structures: theory and applications to earthquake engineering*, Prentice-Hall, Upper Saddle River, New Jersey: 99-105.

Elgamal, A., Yan, L., Yang, Z. & Conte, J. P. 2008. Three-dimensional seismic response of Humboldt Bay bridge-foundation-ground system. *J. Struct. Eng* 134(7): 1165-1176.

Hwang, Y. C. & Cho, C. H. 2005. Pile foundations in Korea. *Journal of the Korean Geotechnical Society* 21(2): 8-20.

Larosche, A., Cukrov, M., Sanders, D. & Ziehl, P. 2013. Prestressed pile to bent cap connections: Seismic performance of a full-scale three-pile specimen. *J. Bridge Eng* 19(3): 04013012.

Mizuno, H., Iiba, M. & Hirade, T. 1996. Pile damage during the 1995 Hygoken-Nanbu earthquake in Japan. *Proceedings of the 11th World conference on Earthquake Engineering* (vol. 977). Acapulo, Mexio:[sn].

Sugimura, Y. & H. Oh-oka. 1981. Report on the damage of precast prestressed concrete piles during the 1978 off-Miyagi prefecture earthquake. *Kenchiku KenKyu Shiryo*, BRI, 31

Yang, Z. & Wang, W. 2016. Experimental and numerical investigation on the behaviour of prestressed high strength concrete pile-to-pile cap connections. *KSCE Journal of Civil Engineering* 20(5): 1903-1912.

Maintenance, Safety, Risk, Management and Life-Cycle Performance of Bridges – Powers, Frangopol, Al-Mahaidi & Caprani (Eds)
© 2018 Taylor & Francis Group, London, ISBN 978-1-138-73045-8

Seismic vulnerability analysis of typical bearings for simply supported railway bridges

Guojing Yang
China Railway Eryuan Engineering Group Co., Ltd., Chengdu, China

Jun Dong
China Railway Eryuan Engineering Group Co., Ltd., Chengdu, China

D.S. Shan
Bridge Engineering Dept, Southwest JiaoTong University, ChenDu, China

ABSTRACT: Seismic damage had shown that bearing damage was common in the actual damage of bridge structures. It was considered as the weakest part of seismic performance in bridge structure system. Based on 32m-span simply-supported girder railway bridges in China, considering the mechanical characteristics of two kinds of typical bearings, a precise nonlinear dynamic analysis model was established. The bearing damage index based on the displacement failure criterion was put forward, and then the vulnerability curves of two kinds of bearings under different damage states were formed by traditional reliability probability analysis method. The seismic performance of two kinds of bearings was compared and evaluated from the viewpoint of vulnerability. The results show that the vulnerability of the two kinds of bearings under different damage states is obviously different under earthquake. When the pier is low, the double spherical aseismic bearing has a good isolation effect, which effectively reduces the failure probability of the bearing components under different damage conditions. However, with the pier height increasing, the isolation effect gradually decreases, which indicates that for simply-supported bridges with high piers, the seismic performance of bearings cannot be improved by using it.

1 INTRODUCTION

Earthquake is one of the most serious natural disasters that mankind face, for it brings huge casualties and economic losses. Railway as the lifeline of earthquake relief work, the seismic damage of railway bridges not only causes huge economic losses, but also leads to indirect economic losses, for the secondary disasters such as traffic disruption will retard the relief work and hinder the post-disaster reconstruction.

The lesson of railway bridges' seismic damage is profound, and railway bridges have been destroyed in varying degrees in all previous violent earthquakes. The investigation of seismic damage in recent years shows that the damage of bearings is one of the most common seismic damage of railway bridges. As an important component connecting the superstructure and substructure of bridge, the bearing mainly plays the role of transmitting the reaction force from the superstructure and bearing the horizontal deformation. The research has showed that the bearing damage is very common in actual seismic damage of bridge structure, and it belongs to the vulnerable part of bridge structure (Wu 2012). Other superstructure damage such as the collision of adjacent beams or the longitudinal and transverse displacement of bridge, appears mostly after the failure of bridge bearing. Once the deflection exceeds the allowable value of the movable bearing, the bridge is tilted or the bearing falls. According to statistics, the bearing anchors of at least 19 rail bridges are cut in Tangshan earthquake in July 28, 1976 (Wang 2013). Therefore, it is necessary to study the seismic vulnerability of bearings.

Different requirements for bridge isolation design leads to different type of bearings adopted, and different types of bearings exhibit different mechanical characteristics under the action of the earthquake. In this paper two types of typical bearing for railway bridges are selected, namely spherical bearing and double spherical aseismic bearing. Based on the analysis of bearing capacity, a precise nonlinear dynamic analysis model is established. The bearing damage index is put forward according to displacement failure criterion and the vulnerability curves of these two types of bearings under different damage states are formed by traditional reliability probability analysis method (Howard 2001). The seismic performance of the two types of bearings is evaluated from the point of vulnerability, which provides a reference for seismic design of similar bridges.

2 MECHANICAL MODEL OF TYPICAL BEARINGS

2.1 *Overview of bridges and typical bearings*

In this paper, the prestressed concrete simply supported bridge with a span of 32 meters, which are most widely used and distributed in China, is taken as the research object. The bearing vulnerability under the conditions of different pier heights from 10 to 50 meters is studied. Two-piece prefabricated post- tensioned T-beam is used in the superstructure of the simply supported girder bridge. The full length of the beam is 32.6m with the calculated span of 32m and height of 2.5m, and the width of bridge deck is 4.9m. The main girder adopts C50 concrete, and the column pier adopts C40 concrete. Two types of bearings are considered which are respectively spherical bearing and hyperboloid spherical isolation bearing. The schematic diagram of the structure is shown in Figure 1.

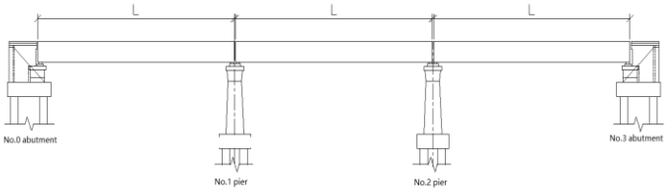


Figure 1. Diagrammatic sketch of calculation model of three-span simply supported girder bridge.

The spherical bearing is a kind of bearing developed on basis of pot rubber bearing. After years of development, its design theory, production and inspection technology have been mature. The advantages of the bearing lies in: ①the bearing parts are free of rubber material, so that the problems such as unmanageable rubber quality and rubber aging problem will not exist; ②the plane displacement and angle rotation of the bearing are provided by the sliding between plane friction pair and spherical friction pair, so the rotational resistance is smaller and the rotation is more flexible; ③the skateboard is made of the new sliding material which has high carrying capacity and good wear resistance, therefore it can effectively reduce the bearing size. Because of its unique advantages, it has been gradually applied to railway bridges.

The double spherical aseismic bearing is a new-type bearing formed on basis of the spherical bearing by using the large radius spherical friction pair instead of the plane friction pair and setting a shearing resistance device, whose structure is shown in Figure 2. Double spherical aseismic bearing works based on the friction pendulum principle. When the earthquake happens and the horizontal force exceeds a predetermined value, the shear pin and the safety screw of the limiter are cut and the horizontal limit constraint of the bearing is released, so the large radius spherical friction pair can slide freely horizontally. The earthquake energy is consumed gradually through that friction resistance and the structural period is prolonged, so the purpose of shock absorption and seismic resistance can be achieved. After the earthquake, the weight of the structure can form a restoring force that make the structure back to the original position.

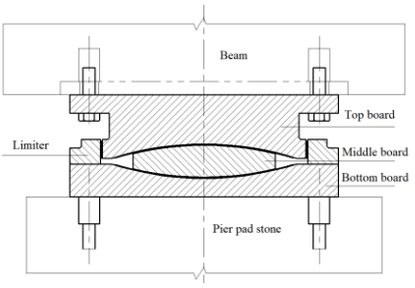
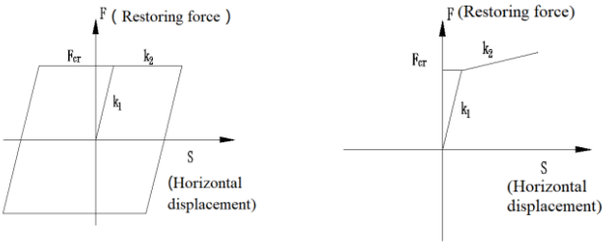


Figure 2. Structure of double spherical aseismic bearing.

2.2 *Mechanical Model of Bearing*

The horizontal stiffness of the bearing has great influence on the seismic response of the main structure of the bridge (Ye 2001) and longitudinal seismic wave input method is adopted to study the vulnerability of the bridge along the longitudinal direction, therefore, the mechanical properties of the bearing in the horizontal direction is mainly discussed in this paper.

In the conventional seismic response analysis, the restoring force-displacement models of the spherical bearing and the aseismic bearing are both bilinear. However, there are some differences between the two models, as is shown in Figure 3.



(a) Spherical bearing (b) double spherical aseismic bearing

Figure 3. Restoring force-displacement relationship of bearing.

The lateral force “F” is the horizontal seismic action of the bearing at a certain moment, and the lateral displacement "S" is the horizontal displacement of the bearing corresponding to the lateral force F at a certain moment. k_1 denotes the stiffness of the bearing before slipping, while k_2 denotes the stiffness of the bearing after slipping. F_{cr} means the horizontal sliding critical force of the bearing. The parameters comparison of the spherical bearing and the spherical aseismic bearing is shown in Table 1.

Table 1. Summary table of bearing parameters.

parameter	Spherical bearing	Double spherical aseismic bearing
F_{cr}	1.5e+05 (N)	3.0e+05 (N)
k_1	5.0e+06 (N/m)	1.0e+07 (N/m)
k_2	5.0e+01 (N/m)	1.7e+06 (N/m)

By comparing the parameters of the spherical bearing and double spherical aseismic bearing, it is found that the spherical aseismic bearing has a greater horizontal sliding critical force and pre-slip stiffness than the spherical bearing. The stiffness of the spherical bearing is almost zero after slipping, but the stiffness of the spherical aseismic bearing is still very large, which is about 0.17 times of the pre-slip stiffness.

2.3 *Establishment of Damage Index of Bearing*

To evaluate the vulnerability of bearings, the damage state of the structure must be determined and damage index should be quantified firstly. The research performed by Hwang, H, et al. (2001) has shown that the failure process of bridge structures can be described by 5 states, namely, undamaged, slight damage, Moderate damage, Extensive damage and complete destruction. There are many different criteria for determining the damage index of components. These criteria can be summarized as follows(Fan 1999): strength failure criterion, deformation failure criterion, energy failure criterion and deformation and energy double failure criterion. The damage degree of bearings is directly related to its deformation. In the general study, the deformation of bearings is used as an index to measure the damage degree. In this paper the maximum allowable displacement of 8160 spherical bearings and double spherical aseismic bearings at the longitudinal direction of the bridge is 30mm. The relationship between the damage degree and displacement of these two types of bearings is determined after referring to relevant data (Li 2012, Fan 2001), as is shown in Table 2. The displacement of 30mm, 45mm, 75mm and 150mm are taken as the demarcation points for slight damage, moderate damage, Extensive damage and complete destruction respectively.

Table 2. The relationship between the damage index and damage level of bearings for simply supported girder bridges.

Damage Level	Damage Index (mm)
Basically Undamaged	$D \leqslant 30$
Slight Damage	$30 < D \leqslant 45$
Moderate damage	$45 < D \leqslant 75$
Extensive damage	$75 < D \leqslant 150$
Complete Destruction	$D > 150$

3 STRUCTURE MODELING

3.1 *Calculation model*

The finite element analysis model of three-span simply supported girder bridge is established by using OpenSees software, and the nonlinear time history analysis of the structure is carried out. As the main girder remains in the elastic state under the earthquake load and the actual seismic damage investigation also shows that the main girder will not be destroyed, the main girder is simulated with elastic three-dimensional beam element. As the pier is to withstand enormous earthquake force, it is usually allowed to be into plastic state in seismic code, so that a plastic hinge will appear in the expected location of piers to prevent the other components from being destroyed by utilizing the rotational energy dissipation of the plastic hinge. Therefore, the piers are modeled by elastic-plastic fiber beam elements. Pile-soil interaction is simulated by the equivalent spring element. The stiffness of the spring is calculated by the *m* method according to the Specification (Yang 2015). The bearing is simulated by the bilinear hysteresis model.

3.2 *Ground motion input*

Ground motion input is the basis for the structural seismic response analysis. The differences between the seismic excitations have great influence on the seismic response of structures. The uncertainty of ground motion leads to the uncertainty of the seismic response of bridge structure, so it is very important to select suitable earthquake wave records for structural vulnerability analysis. Generally, earthquake waves can be categorized into two types: measured earthquake wave and artificial earthquake wave. Based on an overall consideration of various factors, the measured earthquake waves are chosen as input.

At present, the measured Wenchuan earthquake waves are relatively comprehensive, and can really reflect the Chinese geological condition. According to the site type of the actual bridge, considering the strength and the integrity of earthquake wave records, 80 earthquake waves are selected as the original ground motion input for the nonlinear dynamic analysis of the bridge. The response spectra of the 80 earthquake waves and the average response spectrum are shown in Figure 4.

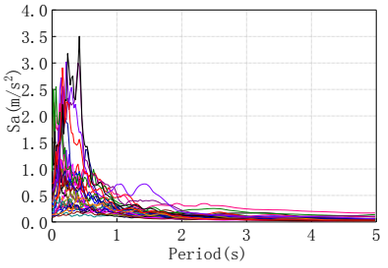


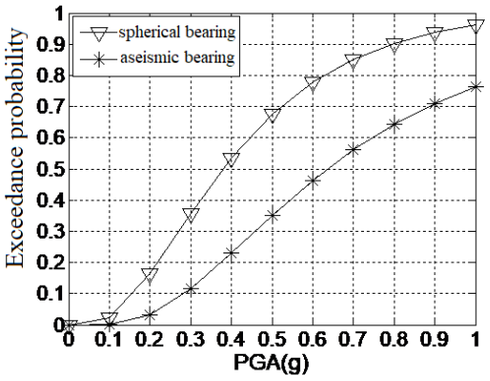
Figure 4. Acceleration response spectra of 80 ground motion records.

4 VULNERABILITY ANALYSIS OF BEARINGS

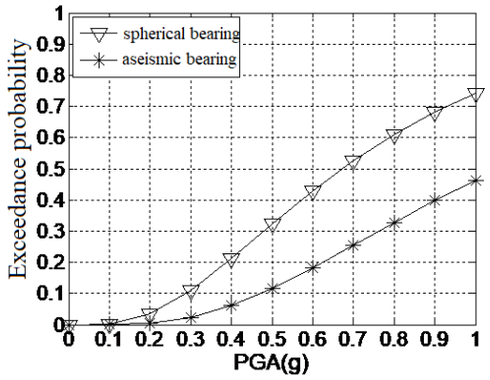
4.1 *Comparative analysis of vulnerability curves for two kinds of bearings*

In order to compare the seismic vulnerability of these two kinds of bearing components for 32m-span simply supported girder bridges with different pier height, the seismic vulnerability curves of the two kinds of bearings under different damage states are plotted in one graph, as shown in Figure 5 to Figure 9.

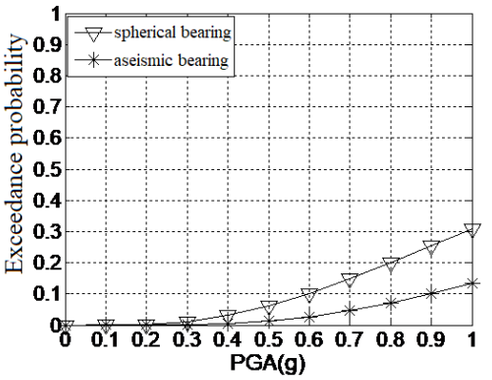
As can be seen from the above figures, (1) the seismic vulnerability of spherical bearing is larger than that of double spherical aseismic bearing under different damage states. (2) When the ground peak acceleration (PGA) is less than 0.1g, the vulnerability of the two kinds of bearings under Slight and Moderate damage states is very small. With the increase of seismic intensity (PGA), the seismic vulnerability of these two kinds of bearings increases and the deviation value of them also increases gradually. However, when the seismic intensity reaches a certain degree, the deviation value decreases gradually. (3) When the seismic intensity is 0.2g, the failure probability of the two kinds of bearings in the Extensive damage state begins to deviate. The failure probability of some simply supported girder bridge in the complete destruction state also begins to deviate, and the deviation value increases with the increase of seismic intensity index.



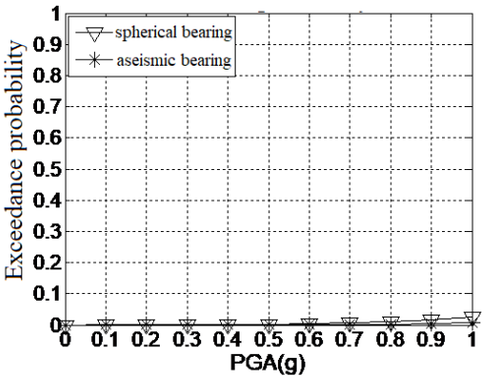
(a)Slight damage



(b) Moderate damage

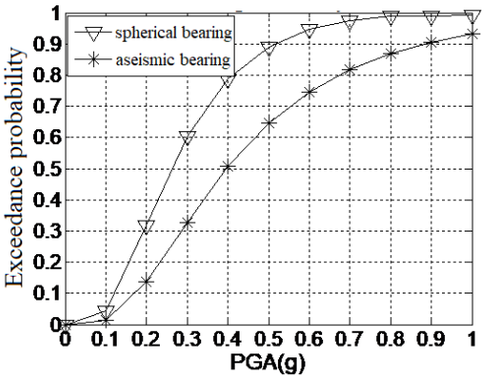


(c)Extensive damage

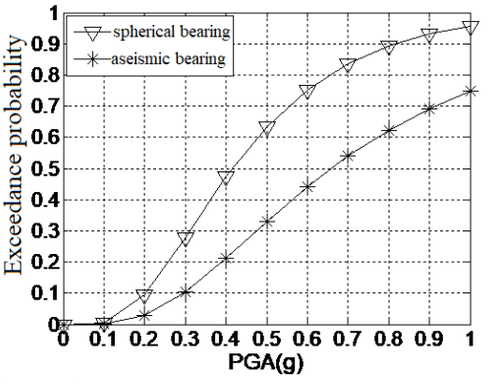


(d) Complete Destruction

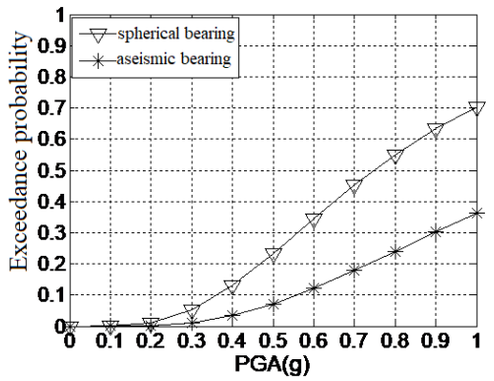
Figure 5. Comparison of Seismic Vulnerability Curves of Bearing with Pier Height of 10m.



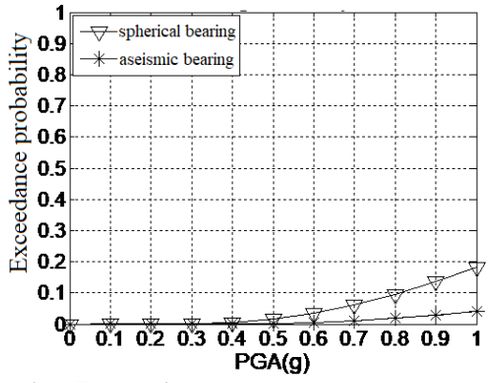
(a) Slight damage



(b) Moderate damage

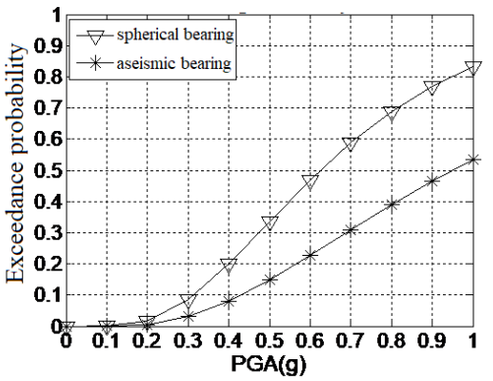


(c) Extensive damage

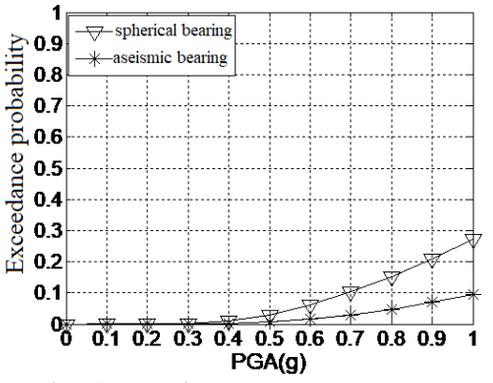


(d) Complete Destruction

Figure 6. Comparison of Seismic Vulnerability Curves of Bearing with Pier Height of 20m.

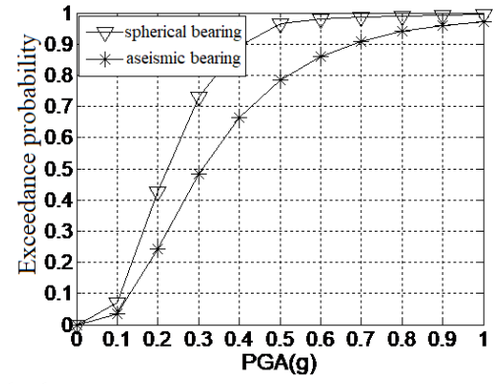


(c)Extensive damage

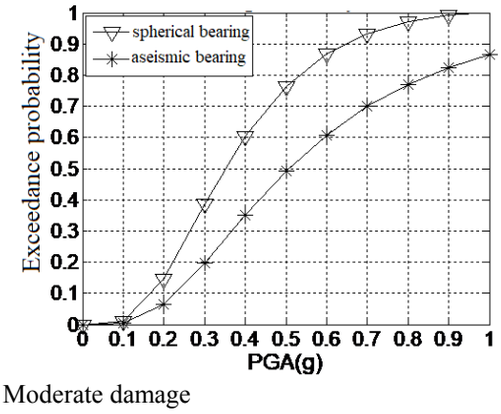


(d) Complete Destruction

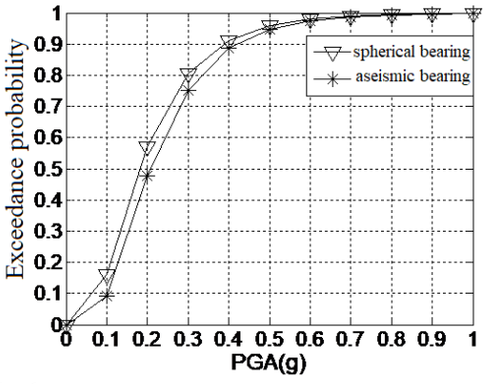
Figure 7. Comparison of Seismic Vulnerability Curves of Bearing with Pier Height of 30m.



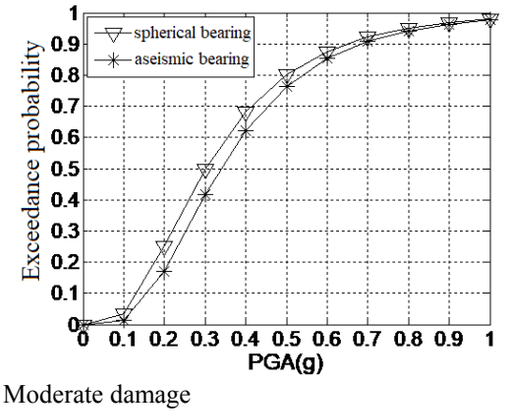
(a)Slight damage



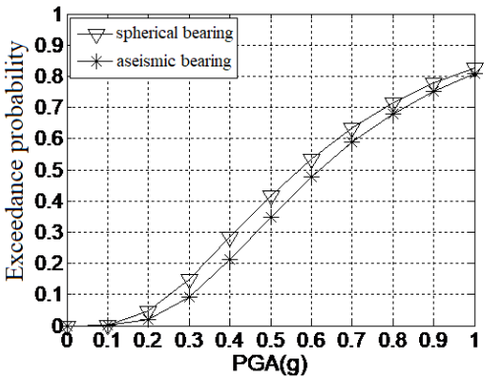
(b) Moderate damage



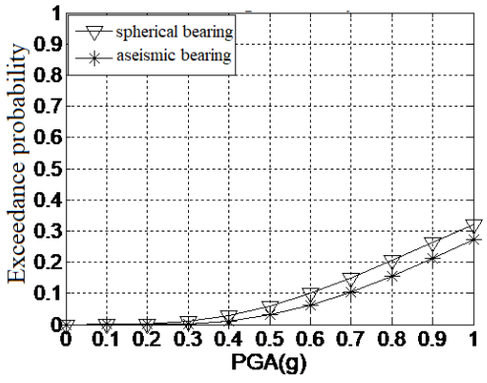
(a)Slight damage



(b) Moderate damage

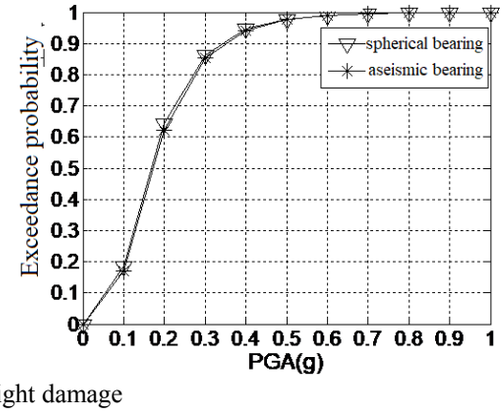


(c)Extensive damage

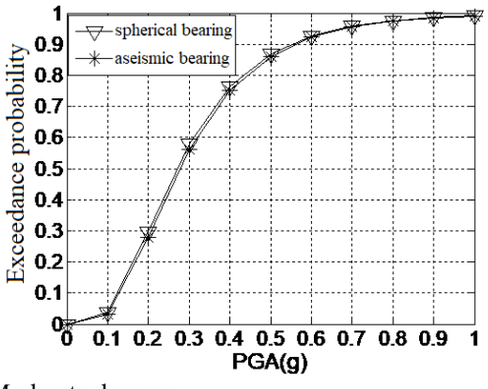


(d) Complete Destruction

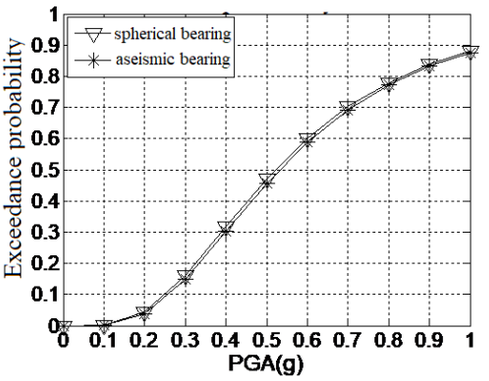
Figure 8. Comparison of Seismic Vulnerability Curves of Bearing with Pier Height of 40m.



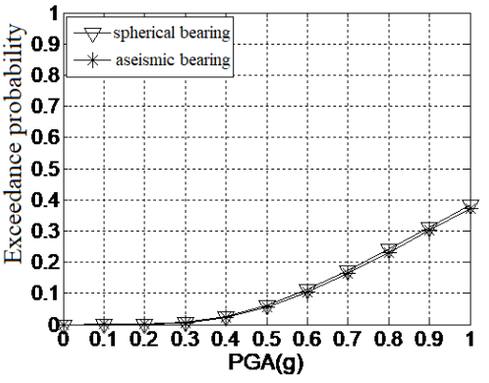
(a)Slight damage



(b) Moderate damage



(c)Extensive damage



(d) Complete Destruction

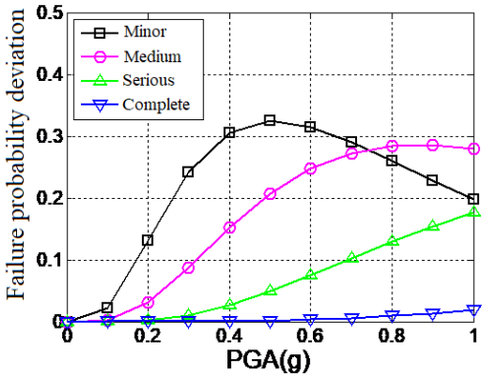
Figure 9. Comparison of Seismic Vulnerability Curves of Bearing with Pier Height of 50m.

4.2 *Analysis of Seismic Damage Probability Deviation for Two Kinds of Bearings*

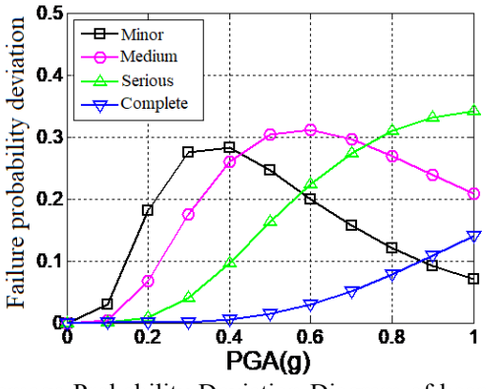
For further study on the failure probability deviation of these two kinds of bearings with different pier height, the trend that damage probability deviation changes with PGA for these two kinds of bearings is given, as is shown in Figure 10. In Figure 10, Slight, Moderate, Extensive, Complete stands for the Slight damage, Moderate damage, Extensive damage, complete destruction respectively.

As can be seen from Figure 10, (1) for all simply supported girder bridges with different pier height, the trend of failure probability deviations of the two kinds of bearings corresponding to Slight damage and Moderate damage state firstly increases and then decreases with the increase of PGA. (2) For simply supported girder bridges with different pier height, the damage probability deviation of bearings is inconsistent, and the range that the maximum deviation value occurs is also not the same. However, it can be seen that the damage probability deviation value decreases with the increase of the pier height, and the PGA corresponding to the maximum probability deviation value also gradually reduces. It indicates that with the pier height increasing, the effect of seismic mitigation and absorption of double spherical aseismic bearings is gradually decreasing. For example, under Slight damage condition, the maximum deviation value of damage probability of

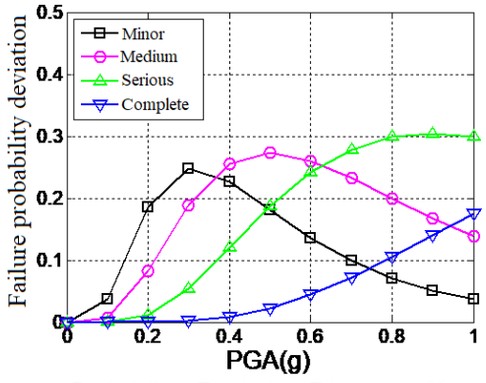
bearing is about 30% and the corresponding PGA is about 0.5g for the simply supported girder bridge with 10 meters pier height, while for the simply supported girder bridge with 40 meters pier height, the maximum deviation value of damage probability of bearing is about 10% and the corresponding PGA is about 0.2g. (3) For the simply supported girder bridge with 10m~30m pier height, the damage probability deviation value of bearing components increases with the increase of PGA. When the seismic intensity is 1.0g, the damage probability deviation value of bearing for all simply supported girder bridge with different pier height reaches maximum. However, for the simply supported girder bridge with 40m~50m pier height, the maximum deviation value of bearing appears when the seismic intensity is 0.9g, and the maximum value is 4.99% and 1.12% respectively.



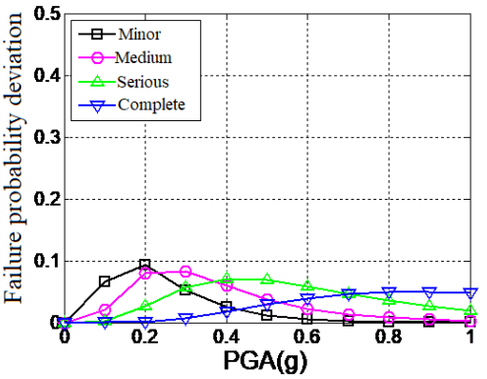
(a) Damage Probability Deviation Diagram of bearings with pier height of 10m



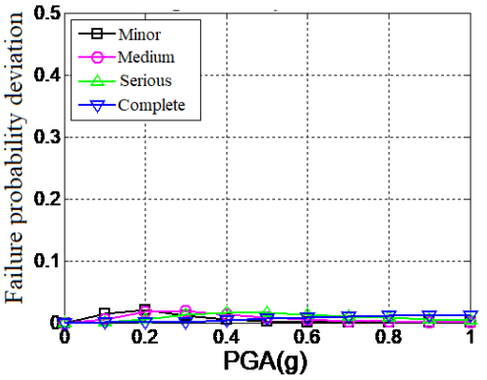
(b) Damage Probability Deviation Diagram of bearings with pier height of 20m



(c) Damage Probability Deviation Diagram of bearings with pier height of 30m



(d) Damage Probability Deviation Diagram of bearings with pier height of 40m



(e) Damage Probability Deviation Diagram of bearings with pier height of 50m

Figure 10. Damage Probability Deviation Diagram of Two Kinds of Bearings for Simply Supported Bridges with Different Pier Height.

5 CONCLUSION

In this paper, the seismic vulnerability analysis of two kinds of typical bearings is carried out by taking the 32m-span simply supported girder railway bridge as the study object and the law of the failure probability of the two kinds of bearings with different pier height is discussed. Through comparison and analysis, the main conclusions are obtained as follows:

Under the action of earthquake, the failure probability of different bearings for railway aseismic bridge under different damage states is obviously different. Taking bearing deformation as the damage index, the theoretical vulnerability curves of two typical bearings are calculated, which provides reference data for the seismic design and reinforcement of the substructure of similar bridges.

When the pier height is small, the double spherical aseismic bearing has a good effect of seismic isolation, and it can effectively reduce the failure probability of the bearings in different damage states. But with the increase of pier height, the effect of seismic isolation gradually weakened. It indicates that for the simply supported girder bridge with high pier height, the spherical aseismic bearing doesn't work well in improving the seismic performance of the bearing components.

6 REFERENCE

Wu, W.P. Li, L.F, Wang, L.H & Huang, J.M. 2012. Evaluation of seismic vulnerability of high-pier long-span bridge using incremental dynamic analysis. Journal of Earthquake engineering and engineering vibration 32(3) :117-123.

Wang, Yan. 2013. Research on Seismic Performance and Fragility of Isolated Railway Bridges. Zhejiang: Zhejiang University.

Howard, H. Liu, J.B. & Chiu Y.H. 2001. Seismic fragility analysis of highway bridges. Mid-America Earthquake Center Technical Report.

Ye, A.J. Hu, S.D. & Fan, L.C. 2001. Simulation of seismic behavior for bridge bearings. Journal of Tongji University 29(1): 6- 9.

Fan, L.C. & Zhuo, W.D. 1999. Seismic design for bridge. Beijing: China Communication Press.

Li, L.F. Wu, W.P. Huang, J.M. &Wang, L.H. 2012.Study on system vulnerability of medium span reinforced concrete continuous girder bridge under earthquake excitation. China Civil Engineering Journal 45(10): 152- 160.

Fan, L.C. &Wang, Z.Q. 2001. Seismic isolation design of bridge. Beijing: China communication press.

Yang, P.Yang G.J. & Zeng, Y.P. 2015.Analysis of seismic vulnerability and adaptation of simply-supported girder bridge on ChuanZang Railway. Journal of Railway Engineering society 12(207):51-57.

Maintenance, Safety, Risk, Management and Life-Cycle Performance of Bridges – Powers, Frangopol, Al-Mahaidi & Caprani (Eds)
© 2018 Taylor & Francis Group, London, ISBN 978-1-138-73045-8

Hanger replacement effect: experimental and numerical investigation on the Bosphorus Bridge

S. Bas
Department of Civil Engineering, Faculty of Engineering, Bartin University, Bartin, Turkey

N. M. Apaydin
Department of Structures, General Directorate of Turkish State Highways, Ankara, Turkey

A. Ilki
Department of Civil Engineering, Istanbul, Istanbul Technical University, Istanbul, Turkey

N. Catbas
Civil, Environmental and Construction Engineering Department, University of Central Florida, Florida, USA

ABSTRACT: As from its construction, the Bosphorus Bridge underwent various retrofitting and repairment studies. The most critical one is the replacement of the inclined hanger ropes with vertical hanger ropes. The project is recently completed; however, the response of the bridge with vertical hanger is not estimated due to the lack of Structural Health Monitoring data. In this study, the effects of the vertical hanger arrangement on the bridge's response are aimed to be determined by making experimental data and numerical analyses. For this objective, finite element model of the bridge with inclined and vertical hangers are developed. Considering the modal analysis results, comparative study is conducted to identify the hanger replacement effects on the bridge. The outcomes reveal that the frequencies of the vertical deck modes of the bridge are changed as 10-25 % in terms of frequency. Thus, stiffness of the bridge in vertical direction is obtained to increase.

1 INTRODUCTION

Suspension bridges are special civil infrastructures among the transportation systems including long-span viaducts, tube tunnels, underwater systems etc. One of the distinguished side of the suspension bridges is the strengthening, maintenance, management and structural safety challenges mostly related to the post construction of them. Therefore, an efficient way to track the structural changes in these bridges is of crucial issue. In addition, the monitoring of these large-scale structures has certain challenges varying from the limited time to interruption in their operational functions during testing. The most effective solution to these difficulties is newly adopted approach of Structural Identification (St-Id), which contains Structural Health Monitoring (SHM) system to detect the changes/anomalies in the large-scale civil infrastructures (Catbas, Kijewski-Correa & Aktan 2013, Catbas, Susoy & Frangopol 2008). The general definition of SHM system made by Catbas, Kijewski-Correa & Aktan (2013) and Aktan, Catbas, Grimmelsman & Tsikos (2000) is to reliably make operational and performance prediction of large-scale infrastructure systems. Certain research and case studies in the literature were conducted on the long-span bridges by (Frangopol 2011, Frangopol, Saydam & Kim 2012, Fujino & Siringoringo 2011, Wang, Tao, Li & Zhang 2016, Wong & Ni 2009)

The Bosphorus Bridge shown in Figure 1 is firstly decided to permanently monitor after the critical hanger rope breakage event in 2004. Before this event, the bridge was identified many times; however, these aims were achieved with portable monitoring in the study of (Tezcan, İpek, Petrovski, Paskalov & Durgunoglu 1975, Petrovski, Paskalov, Stojkovichet & Jurokoviski 1974, Brownjohn, Dumanoglu, Severn & Blakeborough 989, Erdik & Uckan 1988).



Figure 1. The Bosphorus Bridge.

These studies were basically focused on the verification of the developed FE model of the bridge with the recorded experimental data on the basis of the dynamic response properties. With regard to the studies conducted through permanent SHM system of the bridge (Bas, Apaydin & Celep 2016a, 2016b, Bas, Apaydin, Ilki & Catbas 2017, Apaydin (2010), Apaydin, Bas & Catbas 2015, Erdik & Apaydın 2007and Kosar (2002). These studies are made on the bridge with the inclined hanger arrangement. After

the most comprehensive rehabilitation project for the Bosphorus Bridge recently finished in 2016, the effects of the hanger replacement form from inclined to vertical on the dynamic properties of the bridge are not investigated yet. In this study, this investigation is carried out by making a comparative study. For this aim, the FE model of the bridge having inclined hangers is updated through the SHM data obtained during the extreme wind event. Similar efforts are made for the bridge with the inclined hangers but, due to no SHM data in very limited time to obtain experimental data, only FE model of the bridge with vertical hanger is established considering all provisions given in the rehabilitation project. Then, the changes in the modal characteristics of the both model are compared to identify the effects of the hanger replacement on structural response of the bridge.

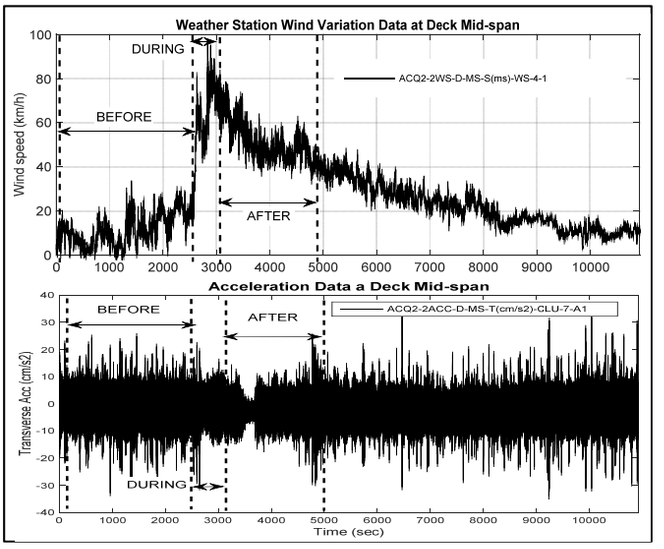


Figure 2. Wind speed variation and three time ranges: Before, During and After.

2 WIND VIBRATION CHARACTERISTICS OF THE BRIDGE USINH SHM DATA

2.1 *Extreme wind event*

Due to the location of Istanbul, strong winds is not usual for the bridges on the Bosphorus straits. However, the Bosphorus Bridge experienced a critical wind load in 2012, leading to larger displacement in transverse direction. During the event, wind speed reached from the average speed of 20 km/h to approximately 100 km/h within the short duration of 10 min. The variation of wind speed was recorded from the SHM system of the bridge. Figure 2 shows the sharp increase in wind speed obtained from weather station. According to site observations and bridge engineer's predictions, extreme wind load was forced the bridge to lateral direction. Data from the weather station sensors proved these statements. In Figure 3, wind speed was plot-ted against to wind directions in polar chart considering bridge's layout.

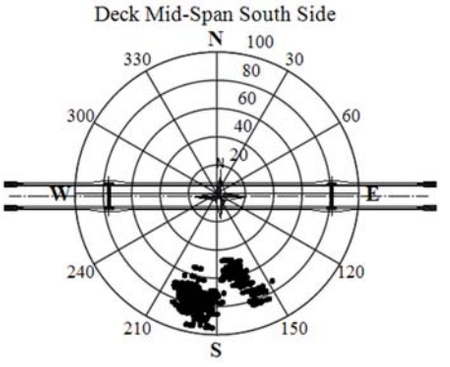


Figure 3. Wind speed-wind direction plot during the extreme wind event.

As shown in Figure 2, total wind duration is divided into three time ranges of Before, During and After. For model updating of the bridge, Before and After ranges are considered making utilizing structural identification (St-Id) approach. However, the bridge was in heavy traffic operation recording Before range data, which means to have higher noise content than After range. Thus, After range is regarded as ambient vibration data for modal characteristics identification of the bridge.

Developing bridge-based data analysis that includes filtering, averaging and windowing, the modal properties of the bridge are obtained utilizing fundamental FFT analysis as depicted in Figure 4. More details are also given in Table 1.

3 FE MODELS OF THE BRIDGE

In order to obtain more reliable outcomes, 3-D full-scale shell FE model of the Bosphorus Bridge with inclined hanger is established considering its as-built drawings given in (KGM 1973). General modeling considerations are given in Figure 5. All components of the bridge from towers, deck, portal beams and approach span are modeled with steel thin shell plate elements. The boundary conditions are considered as shown in Figure 5. Accordingly, 4121 points, 263 frame elements, 387 cable elements and 3996 shell elements are used for the Bosphorus Bridge with inclined and vertical hanger elements. The FE model of the bridge is demonstrated in Figure 6. Apart from the hanger replacement, the other retrofitting works including strengthening of the tower base section and damper placement on the expansion joints are also considered.

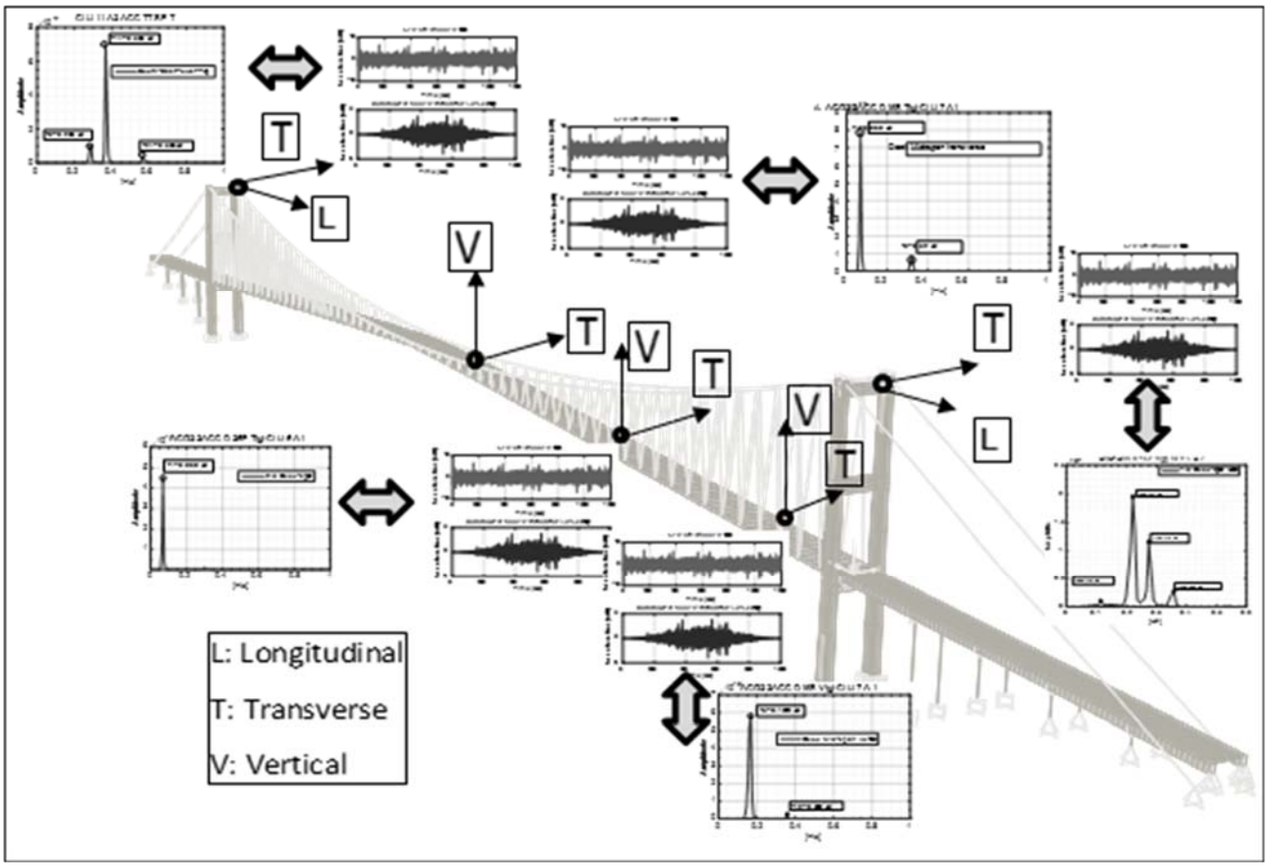


Figure 4. Structural identification of the Bosphorus Bridge from After range data.

Table 1. Dynamic vibration properties from experimental and FE model of the bridge with inclined hanger.

Mode Number	Mode Shape	Frequency/Period [Hz]/[s]					
		FEM		After		Change (%)	
		Period [s]	Freq. [Hz]	Period [s]	Freq. [Hz]	Period [s]	Freq. [Hz]
Mode-1	1st L_{sym}	13.090	0.076	12.766	0.078	2.538	-2.979
Mode-2	1st V_{asym}	7.220	0.139	8.065	0.124	-10.472	12.097
Mode-3	1st V_{sym}	6.481	0.154	6.250	0.160	3.696	-3.750
Mode-4	1st L_{asym}	5.020	0.199	4.967	0.201	1.069	-1.159
Mode-5	2nd V_{sym}	4.620	0.216	4.525	0.221	2.102	-2.262

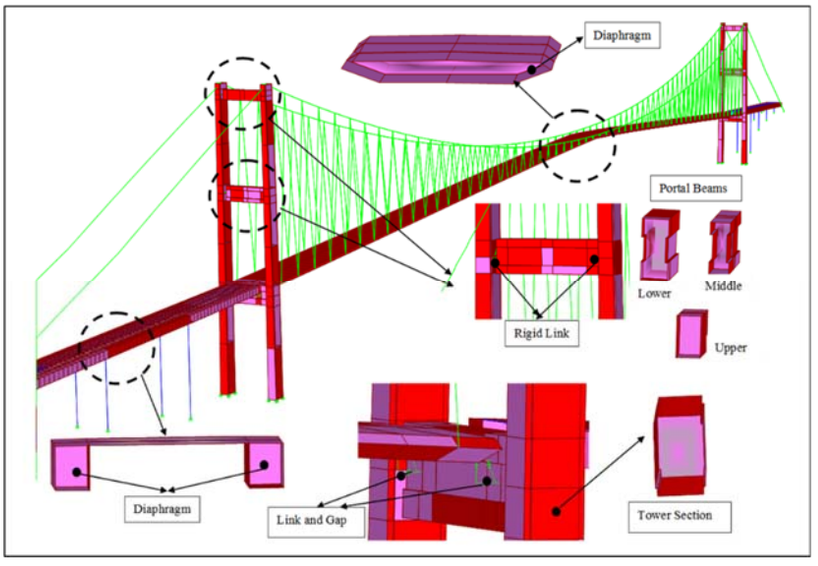


Figure 5. Considerations for FE modeling of the bridge.

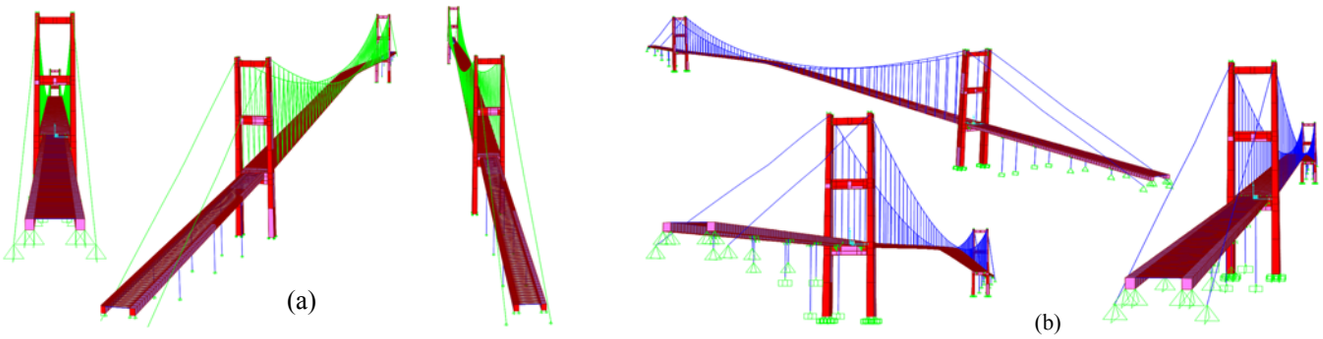


Figure 6. 3-D full-scale shell FE model of the bridge: (a) Inclined hanger (b) vertical hanger.

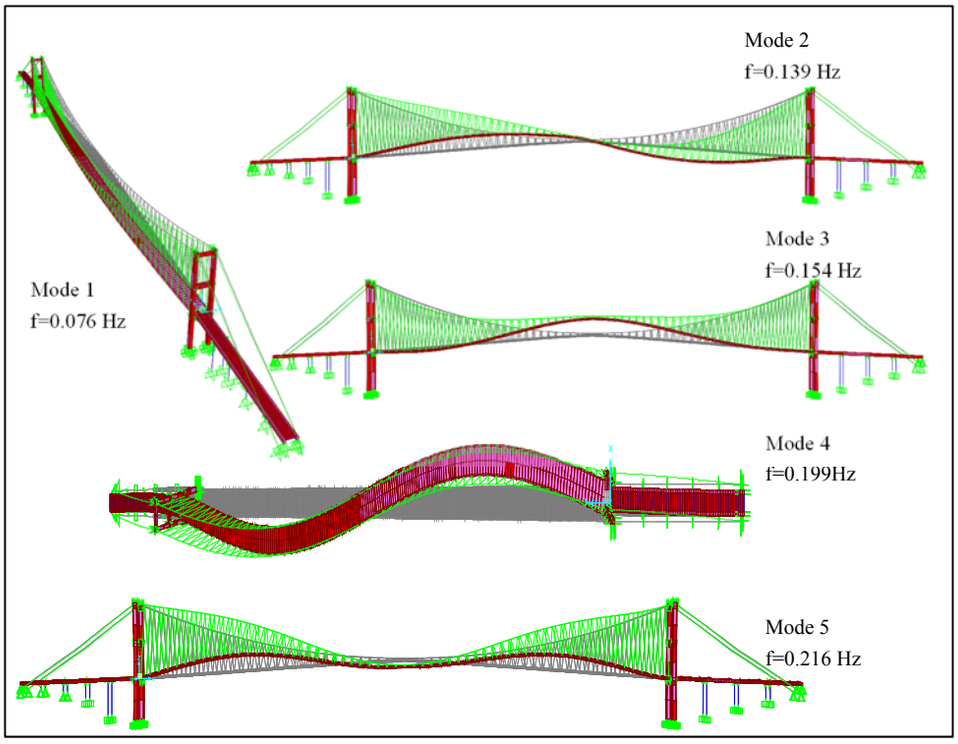


Figure 7. Mode shapes and corresponding frequencies of the bridge with inclined hangers.

Table 2. Comparison of the bridge with inclined hanger and vertical hanger.

Mode Number	Mode Shape	3-D Full-scale shell FE model					
		Inclined Hanger (IH)		Vertical Hanger (VH)		Change (%)	
		Period [s]	Freq. [Hz]	Period [s]	Freq. [Hz]	Period [s]	Freq. [Hz]
Mode-1	1st L_{sym}	13.090	0.076	13.120	0.076	0.229	0.000
Mode-2	1st V_{asym}	7.220	0.139	6.435	0.155	-10.873	11.511
Mode-3	1st V_{sym}	6.481	0.154	5.228	0.191	-19.333	24.026
Mode-4	1st L_{asym}	5.020	0.199	4.911	0.204	-2.171	2.513
Mode-5	2nd V_{sym}	4.620	0.216	4.183	0.239	-9.459	10.648

L_{sym}: Lateral symmetric; L_{asym}: Lateral asymmetric;V_{sym}:Vertical symmetric; V_{asym}:Vertical asymmetric

4 MODAL ANALYSIS AND MODEL UPDATING OF THE BRIDGE

The modal analysis of the FE model of the bridge with inclined hanger is first conducted and the results are given for the first five effective modes in Table 1. Besides, the first five modes and corresponding frequencies are depicted in Figure 7. Based on the percentage change in modal characteristics of the FE model of the bridge with inclined hanger, the FE model is resulted to be properly developed. Only difference in Mode-2 is seen to be high with percentage of 10 % in terms of modal period. These outcomes prove that the considerations for the established FE model are well determined and they are implemented reliably to the FE model of the bridge with vertical hanger.

5 EFFECTS OF THE HANGER REPLACEMENT ON THE DYNAMIC RESPONSE OF THE BRIDGE

Due to the lack of SHM data recorded from the bridge with vertical hanger in a very limited time as from the project completion date of 2016, the effects of the new hanger arrangement on the bridge response are identified with the developed FE model of the bridge with vertical hanger. For this aim, a comparative study is adopted and the results are given in Table 2. As expected, the frequencies and periods of the vertical modes of 1^{st} V_{asym}, 1^{st} V_{sym} and 2^{nd} V_{sym} are relatively changed. Based on modal frequencies, the bridge with vertical hanger has higher rigid vertical response than that with inclined hanger. In lateral modal vibration of the bridge, no variation is obtained. The reason for high rigidity in vertical direction is estimated to be direct connection of vertical hangers to the deck instead of vertical component of the inclined hanger. However, stress release is predicted in the deck of the bridge in longitudinal direction. Therefore, additional structural arrangement may be required. Besides, this study indicates that structural response of the bridge with vertical hanger will be changed under extreme events of earthquake, wind, traffic, marathon etc. due to the variation in the modal frequencies of the bridge. For instance, the frequency features of simulated earthquakes to be used for seismic analysis of the bridge should be adapted taking the new modal frequencies into account. Future work of the study is to verify these outcomes with SHM data and laboratory model of the bridge with vertical hanger.

6 CONCLUSION

In this study, the effects of vertical hanger arrangement on suspension bridges are obtained. For this aim, newly completed hanger replacement project for the Bosphorus Bridge is considered. The effects are specified with the comparative study on the modal properties of the bridge. First of all, wind vibration characteristics of the bridge with inclined hanger are determined dividing the SHM data into certain parts. These characteristics are then adopted for the modal validation of the 3-D full-scale FEM of the bridge. For this purpose, the FE models of the bridge with inclined and vertical hanger are established according to as-built project drawings. The FE model of the bridge with inclined hanger is updated with the SHM wind data; however, due to the lack of the SHM data for the bridge with inclined hanger, its FE model is not verified with experimental results. Therefore, the hanger replacement effects are investigated on the basis of the updated model with inclined and the model with vertical hanger. According to the comparative outcomes, the following points are obtained;

- As expected, the frequencies and periods of the vertical modes of 1^{st} Vasym, 1st Vsym and 2nd Vsym are relatively changed.
- On the basis of modal frequencies, the bridge with vertical hanger has higher rigid vertical response than that with inclined hanger.
- In lateral modal vibration of the bridge, no variation is obtained.
- The reason for high rigidity in vertical direction is estimated to be direct connection of vertical hangers to the deck instead of vertical component of the inclined hanger.
- Stress release is predicted in the deck of the bridge in longitudinal direction. Therefore, additional structural arrangement may be required.
- Structural response of the bridge with vertical hanger will be predicted to change under extreme events of earthquake, wind, traffic, marathon etc. due to the variation in the modal frequencies of the bridge.

7 REFERENCES

Aktan, A. E., Catbas, F. N., Grimmelsman, K. A. & Tsikos, C. J. 2000. Issues in Infrastructure Health Monitoring for Management. *Journal of Engineering Mechanics*, 126, 711-724.

Apaydin, N. M., Bas, S. & Catbas, F. N. 2015. Long-span bridges: behavior under operational and extreme wind loads. *Third International Conference on Smart Monitoring, Assessment and Rehabilitation of Civil Structures (SMAR2015)*. Antalya, Turkey.

Bas, S., Apaydin, N. M. & Celep, Z. 2016. Earthquake performance of the two approach viaducts of the Bosphorus suspension bridge. *Earthquakes and Structures*, 11, 387-406.

Bas, S., Apaydin, N. M. & Celep, Z. 2016. Free Vibration Analysis and Seismic Performance Assessment of Two Approach Viaducts of Bosphorus Suspension Bridge. In: Caner, A., Gülkan, P. & Mahmoud, K. (eds.) *Developments in International Bridge Engineering: Selected Papers from Istanbul Bridge Conference* 2014. Cham: Springer International Publishing.

Bas, S., Apaydin, N. M., Ilki, A. & Catbas, F. N. 2017. Structural health monitoring system of the long-span bridges in Turkey. *Structure and Infrastructure Engineering*, 1-20.

Brownjohn, J. M. W., Dumanoglu, A. A., Severn, R. T. & Blakeborough, A. 1989. Ambient vibration survey of the Bosporus suspension bridge. *Earthquake Engineering & Structural Dynamics*, 18, 263-283.

Catbas, F.N., Kijewski-Correa & Aktan, A.E. 2013. *Structural Identification of Constructed Systems-Approaches, Methods and Technologies for Effective Proactive of Structural Identification*. American Society of Civil Engineers (ASCE) Structural Engineering Institute (SEI).

Catbas, F. N., Susoy, M. & Frangopol, D. M. 2008. Structural health monitoring and reliability estimation: Long span truss bridge application with environmental monitoring data. *Engineering Structures*, 30, 2347-2359.

Erdik, M. & Uckan, E. 1988. *Ambient vibration survey of the Bogazici Suspension Bridge*. Department of Earthquake Engineering, Kandilli Observatory and Earthquake Research Institute, Bogazici University.

Erdik, M. & Apaydın, N. 2007. *Earthquake Response of Suspension Bridges*. In: Inan, E. & Kırış, A. (eds.) Vibration Problems ICOVP 2005. Dordrecht: Springer Netherlands.

Frangopol, D. M. 2011. Life-cycle performance, management, and optimisation of structural systems under uncertainty: accomplishments and challenges. *Structure and Infrastructure Engineering*, 7, 389-413.

Frangopol, D. M., Saydam, D. & Kim, S. 2012. Maintenance, management, life-cycle design and performance of structures and infrastructures: a brief review. *Structure and Infrastructure Engineering*, 8, 1-25.

Fujino, Y. & Siringoringo, D. M. 2011. Bridge monitoring in Japan: the needs and strategies. *Structure and Infrastructure Engineering*, 7, 597-611.

KGM 1973. *Record Book: the Bosphorus Bridge*. Ankara, Turkey: General Directorate of Turkish State Highways.

Kosar, U. 2002. *System Identification of the Bogazici Suspension Bridge*, PhD, Bogazici Univsity.

Memisoglu Apaydın, N. 2010. Earthquake performance assessment and retrofit investigations of two suspension bridges in Istanbul. *Soil Dynamics and Earthquake Engineering*, 30, 702-710.

Petrovski, J. P., Paskalov, T., Stojkovichet, A. & Jurokoviski, D. 1974. *Vibration studies of Istanbul Bogazici Suspension Bridge*. Sjopje, Yugoslavia: Institute of Earthquake Engineering and Engineering Seismology (IZIIS).

Tezcan, S. S., İpek, M., Petrovski, J., Paskalov, T. & Durgunoglu, T. Forced vibration survey of Istanbul Bogazici Bridge. *Proceedings of 5th ECEE Conference*, 1975 Istanbul, Turkey.

Wang, H., Tao, T., Li, A. & Zhang, Y. 2016. Structural health monitoring system for Sutong Cable-stayed Bridge. *Smart Structures and Systems*, 18, 317-334.

Wong, K. Y. & Ni, Y. Q. 2009. 12 - *Structural health monitoring of cable-supported bridges in Hong Kong*. Structural Health Monitoring of Civil Infrastructure Systems. Woodhead Publishing.

Maintenance, Safety, Risk, Management and Life-Cycle Performance of Bridges – Powers, Frangopol, Al-Mahaidi & Caprani (Eds)
© 2018 Taylor & Francis Group, London, ISBN 978-1-138-73045-8

Investigation of limit temperature span of continuous bridges considering track-bridge interaction

Y.H. Yan, D.J. Wu & Q. Li
Tongji University, Shanghai, China

ABSTRACT: This paper aims to study the limit span of continuous railway bridges without the setting of the rail expansion devices for continuous welded rail (CWR) on the bridges. The track-bridge interaction models are established for both three-span continuous bridges and continuous rigid frame bridges with different main spans. The additional stress of CWR on bridges and the relative displacement between the bridge and the rail are calculated under the effects of both train braking and temperature variation. The results show that the rail additional stress increases linearly with the increase of the temperature span. It is necessary to set up the rail expansion devices on three-span continuous bridges when the temperature span exceeds 220 m. The continuous rigid frame bridge can notably reduce the rail additional stress and thus a larger limit temperature span can be gained.

1 INTRODUCTION

For the continuous welded rail (CWR) on prestressed concrete railway bridges, the setting of the rail expansion devices can effectively reduce the interaction between the bridge and the rail, thus ensure the safety, stability and normal use of the track structure. The setting of rail expansion devices has its disadvantages at the same time, such as affecting the driving comfort, increasing the workload of maintenance and the construction cost (Esveld et al. 1995, Esveld 2001). Therefore, to determine the bridge span that it is necessary to set up the rail expansion joint has become a difficult problem for the design of the CWR on bridges.

The increase of span generally leads to the increasing of rail additional stresses and relative displacements between the bridge and the rail under the train braking and temperature variation (Railways, I. U. O. 2001). Many scholars have established the track-bridge interaction model of different structures by using finite element method, and the limit span of railway bridges to set up the rail expansion devices has been studied (W.S. Liu et al. 2013, Q.S. Wu et al. 2016). However, no unified conclusion has been reached so far.

To solve this problem, finite element models are established for track-bridge interaction analysis of both three-span continuous bridges and continuous rigid frame bridges with different span arrangement. Calculations are made on the additional stress of the CWR on bridges and the relative displacement between the bridge and the rail under both train braking and temperature variation. Finally investigation is conducted for the maximum temperature span of both continuous bridges and continuous rigid frame bridges without setting up the rail expansion devices.

2 COMPUTATIONAL MODELS

2.1 *Track-bridge interaction model*

Based on an actual railway bridge project, the track-bridge interaction models of three-span continuous bridges with span arrangements of 48m+64m+48m, 60m+100m+60m, 70m+125m+70m, 100m+160m+100m respectively are established. The main girder sections are box girders with single chest and room, which varies in height along the longitudinal direction. Fig. 1 presents the overall arrangement of continuous bridges, and the parameters of the concrete girders with different spans are listed in Table 1.

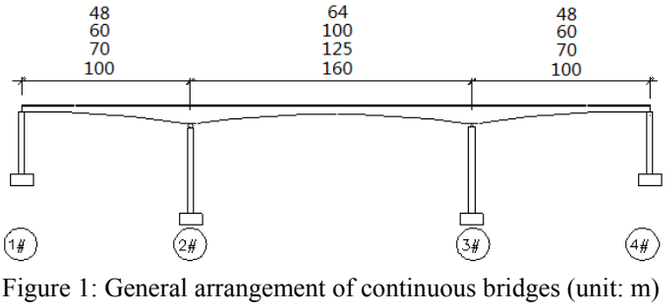


Figure 1: General arrangement of continuous bridges (unit: m)

Fig. 2 illustrates the finite element model for track-bridge interaction analysis. Beam elements were used to simulate the main girder, the rail and the rigid arms, linear spring elements were used to simulate the vertical, lateral and torsional rigidity of fasteners, and nonlinear spring elements were used to simulate the longitudinal resistance of the track. It is assumed that there is no rail expansion devices on the bridges.

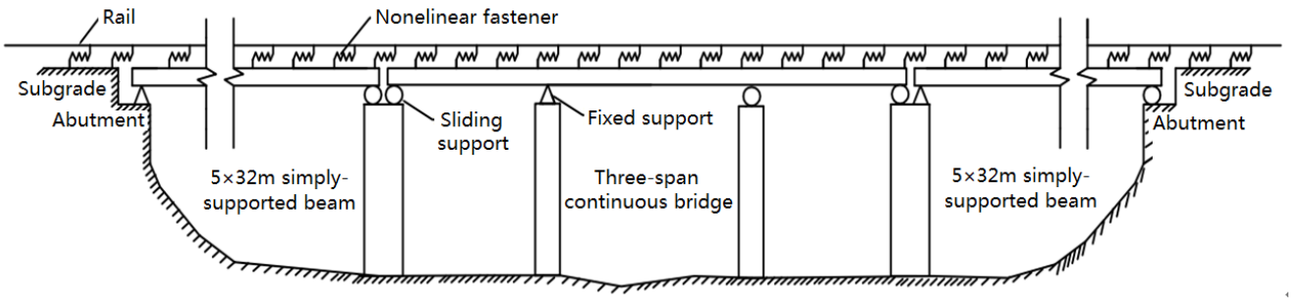


Figure 2: Track-bridge interaction model

Table 1: Parameters of concrete girder

Span arrangement (m)	Middle-span section		Support section	
	Area (m^2)	Height (m)	Area (m^2)	Height (m)
48-64-48	9.25	2.7	13.34	5.6
60-100-60	15.11	4.8	27.30	7.8
70-125-70	34.62	5.2	73.77	9.2
100-160-100	50.53	6.3	90.66	12.8

In order to take the adjacent structures into consideration, the simply supported beam and the subgrade on both sides of the continuous bridge are also modeled. Previous studies have shown that with the increase of span numbers, the maximum rail additional stress on the simply supported beam has largely converged when the span number reaches 5 (C.X. Yin 2000). And the length of the rail on the subgrade is set to 100m as recommended in the UIC code (Railways I. U. O. 2001). Therefore, the finite element model is considered as "100m subgrade + 5 ×32m simply supported beam + three-span continuous bridge+ 5×32m simply supported beam + 100m subgrade".

It is assumed that the horizontal force at the sliding bearing of simply supported beam is zero, and the horizontal force is borne only by the fixed bearing. The subgrade is assumed to be rigid and fixed. The longitudinal displacement at both ends of the rail is restrained to simulate the rail fastening-down zone. The longitudinal and vertical stiffness at the top of the pier is considered by linear springs at the corresponding positions. The model boundary conditions are shown in Fig. 3.

The type CHN60 rails and the type V fasteners are adopted in the design of CWR. The longitudinal resistance property of the track is determined according to China's "Code for design of railway continuous welded rail" (PRC, Ministry of Railways 2013), which considers two cases of both loaded and unloaded, as shown in Fig. 3.

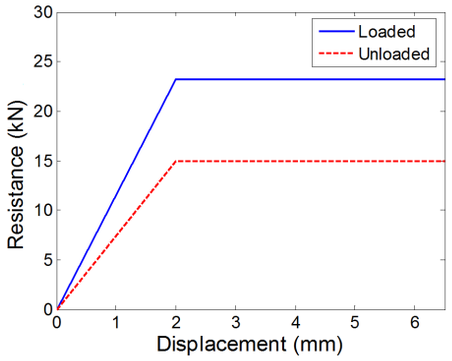


Figure 3: Longitudinal resistance relation curve

2.2 *Loads*

The analysis of the track-bridge interaction in railway bridges mainly includes the additional stress of CWR caused by train braking, temperature variation, deflection, etc (PRC, Ministry of Railways 2013). Among them, the additional stress of CWR caused by deflection are relatively small, so only train braking and temperature variation are considered in this paper.

2.2.1 *Train braking*

Scholars have done a lot of theoretical and experimental research on train braking (L. Lu et al. 2014). During the process of train braking, sliding and rolling frictions between the wheel and the rail are the main causes of braking force, which can be expressed as:

$$P_f = \mu mg \tag{1}$$

where P_f = train braking force, μ = wheel-rail friction coefficient, m = mass of the train.

The interaction between the rail and the bridge caused by train braking should be studied by dynamic methods, while many scholars have studied it by simply using static methods. It is found that the difference between the dynamic methods and the static methods is usually insignificant (Q.Y. Xu 2005). Therefore, the static methods are adopted in this paper.

The Chinese railway standard live loading are adopted in the calculation for vertical load of the trains (Fig. 4). The three-span continuous beam is fully loaded to simulate the train braking force. The wheel-rail adhesion coefficient is set to be 0.164.

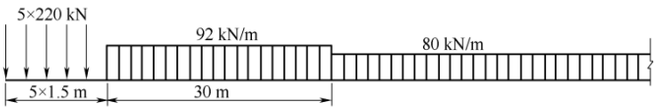


Figure 4: Computing graphs of China railway standard live loading

2.2.2 *Temperature variation*

According to China's "Code for design of railway continuous welded rail" (PRC, Ministry of Railways 2013) as shown in Table 2, the temperature difference between the concrete girder and the rail is set to 15℃ in this paper's calculation.

Table 2: Temperature difference of the beam

Beam type	Daily temperature difference of the ballasted track girders(℃)	Annual temperature difference of the ballastless track girders(℃)
Concrete girder	15℃	30℃
Steel girder	25℃	-

3 CALCULATION RESULTS

3.1 *Train braking*

Fig. 5 shows the distribution of the rail additional stress under different span arrangements. Table 3 lists the calculation results of the rail additional stress and the relative displacement between the bridge and the rail under train braking.

Table 3: The rail additional stress and the relative displacement between the bridge and the rail under train braking

Span arrangement of continuous bridges	Additional tensile stress (MPa)	Additional compressive stress (MPa)	Relative displacement between the bridge and the rail (mm)
48m-64m-48m	23.60	-20.88	2.43
60m-100m-60m	30.53	-27.61	3.41
70m-125m-70m	35.44	-33.65	4.26
100m-160m-100m	45.19	-41.36	6.21

As shown in Fig. 5, the rail additional tensile stress peaks at the left end of the three-span continuous bridge, while the rail additional compressive stress peaks at the right end of the continuous bridges with different span arrangements.

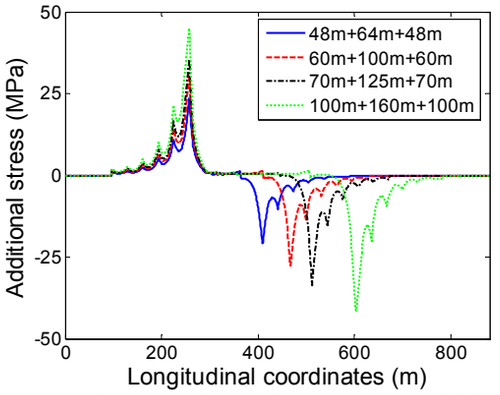


Figure 5: Distribution of the rail longitudinal additional stress under train braking

It can be noted from Fig. 5 that the distribution law of the rail additional stress under train braking with different span arrangements is basically the same. The additional stress at both ends of the three-span continuous bridge is larger compared with that in the middle section. The rail additional stress increases linearly with the increase of the span of the continuous bridge. When the length of the three-span continuous bridge is increased from 160m to 360m, the maximum value of the rail additional tensile stress under braking increases from 23.60MPa to 45.19MPa. And the relative displacement between the bridge and the rail increases from 2.43mm to 6.21mm.

3.2 *Temperature variation*

Fig. 6 presents the distribution of the rail longitudinal additional stress under different span arrangements when the temperature variation of the concrete girder is 15℃, and Table 4 lists the calculation results of the rail additional stress and the relative displacement between the bridge and the rail under temperature variation.

Similarly, the rail additional tensile stress peaks at the left end of the three-span continuous bridge, while the rail additional compressive stress peaks at the right end of the continuous bridges with different span arrangements.

Table 4. The rail stress and the relative displacement between the bridge and the rail under temperature variation

Span arrangement of continuous bridges	Additional tensile stress (MPa)	Additional compressive stress (MPa)	Relative displacement between the bridge and the rail (mm)
48m-64m-48m	30.20	-44.50	4.81
60m-100m-60m	30.54	-60.40	6.37
70m-125m-70m	30.61	-72.36	7.63
100m-160m-100m	30.78	-90.36	10.38

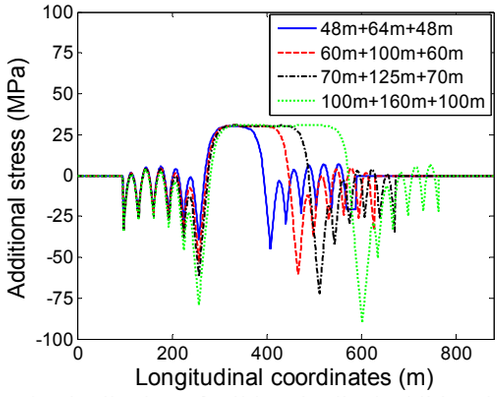


Figure 6: Distribution of rail longitudinal additional stress under temperature variation

It can be noted from Fig. 6 that for difference span arrangements, the distribution law of the rail additional stress under temperature variation is basically the same. Temperature variation induces the rail additional tensile stress on the continuous bridge, while induces the rail additional compressive stress on the adjacent simply supported beam. The rail additional compressive stress is larger at both ends of the simply supported beam, and is the largest at the end of the continuous bridge.

The rail additional compressive stress under temperature variation increases linearly with the increase of the span of the continuous bridge, while the increase of the rail additional tensile stress is not obvious. When the length of the three-span continuous bridge is increased from 160m to 360m, the maximum value of the rail additional compressive stress under temperature variation increases from 44.50MPa to 90.36MPa And the relative displacement between the bridge and the rail increases from 4.81mm to 10.38mm.

3.3 *Superposition of the effects of train braking and temperature variation*

It can be found from both Fig.5 and Fig. 6 that the rail additional stress peaks at the right end of the continuous bridge under both the train braking and the temperature variation, so the maximum rail additional stress can be obtained through the direct superposition of the train braking and the temperature variation.

It is found that the maximum value of the rail additional stress under both train braking and temperature variation is approximately linear with the temperature span of the continuous bridge (L.H. Cui et al. 2012). The temperature span refers to the distance between the fixed support and the most remote sliding support of continuous bridges. Fig. 7 illustrates the relationship curve between the rail additional stress and the temperature span.

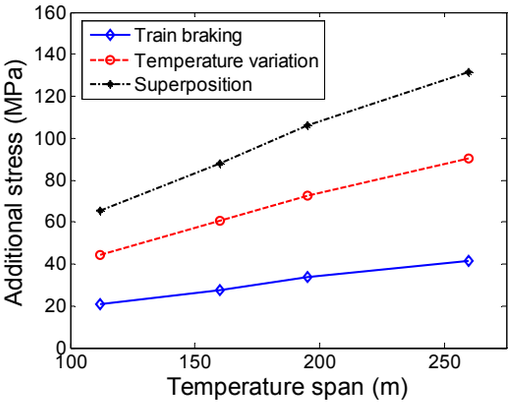


Figure 7: The change law of rail additional stress with temperature span of continuous bridges

It is found from Fig. 7 that the rail additional stress under both train braking and temperature variation increases linearly with the increase of temperature span of the continuous bridge.

According to China's "Code for design of railway continuous welded rail" (PRC, Ministry of Railways 2013), the rail stress should meet the following formula in the design of CWR:

$$\sigma_d + \sigma_t + \sigma_f + \sigma_z \le [\sigma] = \frac{\sigma_S}{k} \quad (2)$$

where σ_d = dynamic bending stress at the bottom of the rail, σ_t = maximum rail temperature stress, σ_f = larger value of the rail additional stress under both temperature variation and bending of the bridge, σ_z = rail additional stress under train braking, $[\sigma]$ = rail permissible stress.

The permissible stress of the ordinary rail is 351MPa, and the dynamic bending stress at the bottom of the rail is set to 150MPa. The temperature stress is approximately 85MPa (PRC, Ministry of Railways 2013) which is calculated from the rail temperature difference, so the residual permissible additional stress value is 351-150-85=116 MPa. In

the fitting formula of the rail stress obtained above, let:

$$y = 0.4501x + 15.981 = 116 \quad (3)$$

where x = temperature span of three-span continuous bridges (unit: m), y = rail additional stress (unit: MPa).

It can be solved that the value of x is 222.2, which means that it is necessary to set up the rail expansion devices on three-span continuous bridges when the temperature span exceeds 220 m. In general, the ratio of the side span to the middle span of the three-span continuous bridge is 0.4~0.6, so the limit range of the total length of the three-span continuous bridge is 310m~350m.

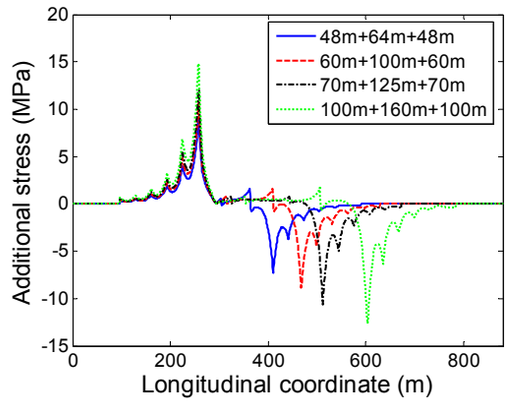
4 LIMIT SPAN OF THE CONTINUOUS RIGID FRAME BRIDGE

Due to its advantages of reasonable structure, convenient construction and smooth driving compared with the continuous bridge, the continuous rigid frame bridge has become one of the common bridge types of long-span bridges. For railway bridges, due to the large rigidity of continuous rigid frame bridges, the substructure will be allocated to greater stress in the track-bridge interaction. Therefore, the rail additional stress under load can be reduced, and thus the limit span of the beam bridge can be improved.

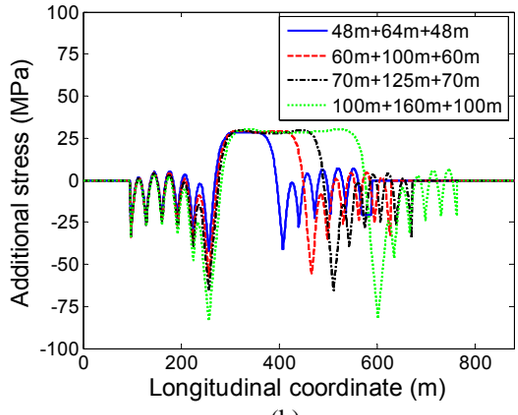
On the basis of finite element model of the three-span continuous bridges with different spans, the track-bridge interaction finite element model of three-span continuous rigid frame bridges is then established by changing the bearing constraint condition, in order to investigate the limit temperature span of continuous rigid frame bridges.

4.1 *Train braking and temperature variation*

The determination of train braking load and temperature variation is consistent with that of the above continuous bridges. Fig. 8 presents the distribution of the rail additional stress under both train braking and temperature variation independently.



(a)



(b)

Figure 8: Distribution of rail longitudinal additional stress under: (a) train braking; (b)temperature variation

It can be found from Fig. 8 that the distribution law of the rail additional stress on the continuous rigid frame bridge is consistent with that on the continuous bridge. The rail stress on the continuous rigid frame bridge is significantly reduced compared with that on the continuous bridge. The comparison of calculation results of these two different forms of bridge structure under both train braking and temperature variation is shown in Table 5.

It can be seen from Table 5 that there is little difference between the calculation results of these two different forms of bridge structure under temperature variation. However, the rail additional stress and the relative displacement between the bridge and the rail on the continuous rigid frame bridge are significantly reduced under train braking.

4.2 *Linear fitting results*

Similarly, the rail additional stress peaks at the right end of the continuous rigid frame bridge under both the train braking and the temperature variation, so the maximum rail additional stress can be obtained through the direct superposition. For the continuous rigid frame bridge, the rail additional stress is proportional to the length of the bridge, and the fitting curve is shown in Fig. 9.

Table 5: Comparison of calculation results between continuous bridges (CB) and continuous rigid frame bridges (CRFB)

Span arrangement	Train braking				Temperature variation			
	Additional compressive stress (MPa)		Relative displacement between the bridge and the rail (mm)		Additional compressive stress (MPa)		Relative displacement between the bridge and the rail (mm)	
	CB	CRFB	CB	CRFB	CB	CRFB	CB	CRFB
48-64-48	-20.88	-7.35	2.43	0.86	-44.50	-42.21	4.81	4.03
60-100-60	-27.61	-8.90	3.41	1.05	-60.40	-56.79	6.37	5.27
70-125-70	-33.65	-10.68	4.26	1.19	-72.36	-65.40	7.63	6.34
100-160-100	-41.36	-12.64	6.21	1.49	-90.36	-83.78	10.38	8.39

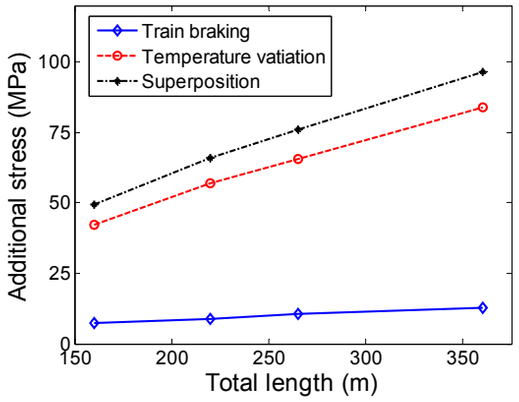


Figure 9: The change law of rail additional stress with bridge length of continuous rigid frame bridges

In the fitting formula of the rail stress obtained above, let:

$$y = 0.2322x + 13.633 = 116 \quad (4)$$

where x = total length of three-span continuous rigid frame bridges (unit: m), y = rail additional stress (unit: MPa).

It can be solved that the value of x is 440.9, which means that it is necessary to set up the rail expansion devices on three-span continuous rigid frame bridges when the total length exceeds 440 m.

It can be seen that the continuous rigid frame bridge can effectively reduce the rail additional stress, especially the rail additional stress under train braking. Based on track-bridge interaction, the limit length of the continuous rigid frame bridge can be raised from 310m~350m for the continuous bridge to 440m.

5 CONCLUSION

The track-bridge interaction of railway continuous bridges and continuous rigid frame bridges with different span arrangement is analyzed in this paper. The major conclusions can be drawn as follows:

(1) The rail additional stress at both ends of the three-span continuous bridge is larger compared with that in the middle section under train braking. The rail additional compressive stress reaches the peak values at the end of the continuous bridge under temperature variation.

(2) The rail additional stress and the relative displacement between the bridge and the rail increase linearly with the increase of the temperature span of continuous bridges.

(3) It is necessary to set up the rail expansion devices on three-span continuous bridges when the temperature span exceeds 220 m. The limit range of the total length of the three-span continuous bridge is 310m~350m.

(4) The continuous rigid frame bridge can effectively reduce the rail additional stress. The limit length of the continuous rigid frame bridge can reach 440m.

REFERENCE

C.X. Yin (2000) Dynamic analysis of railway bridge response to longitudinal braking force. *China Railway Science,* 21**,** 8-18.

Esveld, C. (2001) *Modern railway track*, MRT-Production.

Esveld, C., Delhez, R. C. M., Godart, P. & Mij, J. (1995) Avoidance of expansion joints in high-speed CWR track on long bridges. *Rail Engineering International*.

L.H. Cui, F.A. Guo & Z.G. Jiang (2012) Research on temperature span of ballastless track on large-span concrete bridge. *Journal of Railway Engineering Society,* 29**,** 11-13.

L. Lu & J.Z. Li (2014) Responses of long-span highway and railway cable-stayed bridge induced by train braking forces. *Structural Engineers***,** 47-53.

PRC, Ministry of Railways (2013) Code for design of railway continuous welded rail. Beijing, China Railway Publishing House.

Q.S. Wu, J.J. Ren & X.Y. Liu (2016) Research on the critical expansion length of large span continuous beam bridge for CRTS II slab track. *Journal of Railway Science and Engineering,* 13**,** 414-422.

Q.Y. Xu (2005) 3D finite element static and dynamic analysis of longitudinal additional forces of CWR on high speed railway bridges. Changsha, Central South University.

Railways, I. U. O. (2001) UIC Code 774-3 Track/bridge Interaction Recommendations for Calculations.

W.S. Liu, G.L. Dai & X.H. He. (2013) Sensitive factors research for track-bridge interaction of Long-span X-style steel-box arch bridge on high-speed railway. *Journal of Central South University,* 20**,** 3314-3323.

MS12: Bridge safety evaluation and risk assessment: Code requirements vs. practical considerations

Organizers: M. Liu & H. Nassif

Maintenance, Safety, Risk, Management and Life-Cycle Performance of Bridges – Powers, Frangopol, Al-Mahaidi & Caprani (Eds)
© 2018 Taylor & Francis Group, London, ISBN 978-1-138-73045-8

Code development for existing structures: influence of concrete strength statistics

B.L. Badimuena & S.M.C. Diniz
Federal University of Minas Gerais, Belo Horizonte, Brazil

ABSTRACT: Strengthening/ retrofitting of structures and infrastructures is a challenging and extremely relevant topic. One of the key tasks in the decision process over strengthening/ retrofitting or demolishing an existing infrastructure is its condition assessment and checking against expected performance rules, usually established in technical codes. However, the problem of performance evaluation of existing reinforced concrete structures is quite distinct from design of new ones. A question arises on the statistics of the concrete compressive strength to be used in the calibration of semi-probabilistic codes for existing structures. In this paper, Monte Carlo simulation is used in the determination of the probabilities of failure (and corresponding reliability indexes) associated to axially-loaded columns. Different scenarios are considered for the compound coefficient of variation, i.e. the one including statistical errors, size effects for the extracted cores, etc. The resulting safety levels for existing axially-loaded reinforced columns, assessed via ACI 562 Repair Code, are obtained and discussed.

1 INTRODUCTION

At present, strengthening/ retrofitting of structures and infrastructures is a challenging and extremely relevant topic. For instance, according to the 2013 ASCE Report Card for America's Infrastructure (ASCE 2013), one in nine of the US bridges are rated as structurally deficient, while the average age of the 607,380 bridges is close to 50 years. The Federal Highway Administration (FHWA) estimates that an annual investment of $20.5 billion is needed to eliminate the US bridge deficient backlog by 2028.

One of the key tasks in the decision process over strengthening/ retrofitting or demolishing an existing infrastructure is its condition assessment and checking against expected performance rules, usually established in technical codes. However, the problem of performance evaluation of existing structures is quite distinct from design of new ones. Design codes for new structures deal with uncertainties related to design and construction process; on the other hand, there is a change in the nature of such uncertainties, --from inherent to epistemic--, for a number of the variables affecting the existing structure performance.

In the case of reinforced concrete (RC) structures, concrete compressive strength is predicted from cylinder tests for a population of new structures, while in the case of an existing structure it is predicted from extracted cores of the actual structure. As such, a question arises on the statistics of the concrete compressive strength to be used in the calibration of semi-probabilistic codes related to existing structures.

In this paper, Monte Carlo simulation is used in the determination of the probabilities of failure (and corresponding reliability indexes) associated to axially-loaded RC columns. Different scenarios are considered for the compound coefficient of variation, i.e. the one including statistical errors, size effects for the extracted cores, etc. The resulting safety levels for existing axially-loaded RC columns, assessed via ACI 562 Repair Code (ACI 562 2013), are obtained and discussed.

2 EXISTING STRUCTURES VERSUS NEW STRUCTURES

The safety evaluation of existing structures is distinct from that related to the safety implementation in the design of new ones. While design codes for new structures allow for uncertainties in the design and construction processes, much of what was initially uncertain are no longer in the finished structure (Melchers 1999).

Nevertheless, even if existing structures undergo multiple investigations, some uncertainties in the main variables related to the structural performance will continue to exist. The determination of the actual values of various parameters (e.g. in situ concrete

compressive strengths, concrete modulus of elasticity, etc.) in the existing structure introduces uncertainty of its own. As such, similarly to the design of new structures, the current variability of the basic variables describing actions, properties of materials, geometry, and model errors related to existing structures must be taken into account. In this sense, realistic structural performance assessments can be established in probabilistic terms only.

A question of utmost importance is the definition of criteria for the assessment of the structural condition of a given structure. The following differences between the evaluation of new and existing structures must be taken into account in the assessment of structural performance (Diamantidis et al. 2012):

- Economic aspects – the additional costs necessary to increase the reliability of new structures are usually insignificant compared to those incurred for similar measures for existing structures;
- Social aspects - restrictions and relocations of users and the impact of loss of cultural values or inheritance do not influence the design of new structures;
- Principles of sustainable development - the reduction of waste and the recycling of materials are aspects that are much more significant in the case of the evaluation of existing structures.

In recognition to these differences between the assessment of structural performance of new and existing structures, new documents have been developed specifically for existing structures, while others are being revised in such a way to best address the problem of existing structures. For instance, while Chapter 27 in ACI 318 (ACI 318 2014) is dedicated to *Strength Evaluation of Existing Structures*, the ACI 562 Repair Code has been launched in 2013 specifically for existing RC structures. The 2020 fib-Model Code, an update of the current 2010 fib-Model Code (Féderation Internationale du Béton 2010) has been planned to be a single, merged structural code for new and existing structures.

3 EQUIVALENT CONCRETE COMPRESSIVE STRENGTH

Concrete compressive strength is an important variable in the design of RC structures. Based on semi-probabilistic design formats, current codes for design of RC structures deal with deterministic values in the design process in lieu of their random counterparts (Diniz 2008). In this way, the random variable "concrete compressive strength" is replaced by the "specified (or characteristic) concrete compressive strength", f'_c, in the limit states design of new structures.

The "specified concrete compressive strength", f'_c, is a well-established concept in the design of new structures and is based on a prescribed quantile in the corresponding probability density function (PDF) describing the random variable.

Considering that for the design of new structures the "specified concrete compressive strength" has fulfilled its function, the professionals are faced with the difficulty of defining an equivalent value for use in the equations of structural safety checks for the evaluation of existing RC structures. In defining an equivalent value, account shall be taken of the particularities of estimating the *in situ* concrete compressive strength. By introducing an "equivalent specified concrete compressive strength", the evaluation process resembles that of designing new structures to which the professionals are more accustomed, thus reducing the likelihood of errors related to the different verifications.

Although not an internationally agreed procedure, the "equivalent specified concrete compressive strength" has been adopted in a number of codes related to the evaluation of existing structures, e.g. ACI 562 (ACI 2013) and CAN/CSA S6-06 (CSA 2006). In the definition of the equivalent strength two issues must be dealt with: (i) the adjustment of strength results measured by cores; and (ii) the selection of appropriate quantiles to be used in the calibration of design codes for assessment of existing structures.

According to ACI 562 (ACI 2013), individual results are adjusted in such a way to take into account the most relevant influencing factors:

$$f_c = F_{l/d}\ F_{dia}\ F_{mc}\ F_d\ f_{core} \tag{1}$$

where $F_{l/d}$, F_{dia}, F_{mc}, F_d and f_{core} are the adjustment factors considering, the influence of the ratio height/diameter of the core, diameter, humidity and damage to the cores in the extraction procedure, and core strength, respectively. These coefficients are given in Table 9.1 of ACI 562. Statistical errors shall also be taken into account in the evaluation of the statistics of core strengths, considering the usual small numbers of cores extracted from the structure under investigation.

The criterion adopted by ACI 318 (ACI 2014) to define the specified concrete compressive strength, f'_c, considers that it corresponds to the tenth lower percentile of the compressive strength of the concrete obtained from cylinders tested at 28 days. In other words, the criterion adopted by ACI 318 stipulates that 1 in 10 test specimens will have a strength value lower than the specified strength.

According to ACI 214.4R (ACI 2010), several methods for converting in-place strength obtained from non-destructive tests to an equivalent value are based on a 10% quantile in the characterization of the *in situ* strength. However, a study by Bartlett & MacGregor (1996) has shown that in the finished structure, the specified strength represents approximately the 13% quantile for the *in situ* strength in the

case of walls and columns and approximately 23% for beams and slabs. The same study concluded that the value of the quantile associated with columns is more appropriate in the definition of an equivalent specified strength since column resistance is more sensitive to concrete compressive strength than beam or slab resistance. Therefore, any procedure that defines the specified strength for existing structures based on the 13% quantile of the *in situ* strength is more appropriate, while those assuming a 10% quantile is more conservative (ACI 214.4R 2010).

The procedure devised by Bartlett & MacGregor (1996) to specify the equivalent specified concrete compressive strength for existing structures considered the 13% quantile. Based on that procedure, ACI 562 (ACI 2013) and CAN/CSA S6-06 (CSA 2006) suggest Eq. 2 for the equivalent concrete compressive strength to be used in verification purposes of existing structures:

$$f'_{ceq} = 0.9 f_{cm} \left[1 - 1.28 \sqrt{\frac{(k_c V)^2}{n} + 0.0015} \right] \quad (2)$$

where f_{cm} is the mean resistance of cores, adjusted for size effects and humidity, V is the coefficient of variation of the cores strength, n is the number of extracted cores used in the estimation of the mean strength f_{cm} and k_c is a modification factor for the coefficient of variation of the cores strength, depending on the number of cores, given in Table 1.

Table 1. Modification factor for the coefficient of variation of cores strength (ACI 562 2013).

n	k_c
2	2.4
3	1.47
4	1.28
5	1.2
6	1.15
8	1.1
10	1.08
12	1.06
16	1.05
20	1.03
25 or more	1.02

4 RELIABILITY-BASES FOR RC EXISTING STRUCTURES

Among RC structural components, columns subjected to loads with small eccentricities are the most affected by concrete compressive strengths lower than those foreseen in the design process, or concrete variability superior to the reference value used in the calibration of the corresponding design code.

In addition, for the structural integrity of the structure, columns are those components whose local failure can lead to the overall failure of the structure. In this way, considering the importance of the concrete compressive strength in the column resistance and the importance of columns for structural integrity, the impact of actual concrete compressive strength on the reliability of existing RC columns shall be evaluated.

For the reliability assessment, --in addition to theoretical considerations related to the behavior of materials--, the relevant code recommendations are equally important and should be taken into account in the analysis. Relevant code recommendations considered in this work are those related to the behavior of the materials (concrete and steel), the determination of the load effects, and the procedure for estimation of the existing RC column resistance. To this end, ACI 562 (ACI 2013) and ACI 318 (ACI 2014) recommendations for axially-loaded RC columns are assumed herein.

4.1 *Performance function*

Considering the pertinent variables related to the problem at hand, the corresponding performance function used in the Monte Carlo Simulation (Ang & Tang 1990) procedure is given by:

$$M = \left[\alpha_c F_c \left(A_g - A_s \right) + F_y A_S \right] E_M - (G + Q) \quad (3)$$

where M is the safety margin, and the random variables F_c is concrete compressive strength, A_g is the area of the gross cross-section, F_y is the steel yield strength, G and Q are the dead and live loads acting on the column, respectively, and E_M represents the model error associated to column resistance estimation. The area of longitudinal steel, A_s, is taken as deterministic; the deterministic parameter α_c is taken as a function of the concrete grade. Further details are found in Badimuena (2016).

4.2 *Statistics of the load effects*

Figure 1 illustrates the procedure used in definition of the statistics of the load effects (mean dead load, μ_G, and mean live load, μ_Q), for the selected columns satisfying ACI 562 (ACI 2013) provisions.

In the computation of the design loads, S_d, from which the statistics of the acting loads may be defined, it is assumed that, design loads are equal to design column resistance, R_d, i.e. $S_d = R_d$ (Diniz & Frangopol 1997). Details about the structural configuration are given in the next section. For each assumed value of the mean concrete compressive strength, f_{cm}, the equivalent specified compressive strength is determined according to Eq. 2. In this study, two different values for the number of cores are assumed (three and eight); the corresponding k_c values are taken from Table 1.

In addition to the above information needed for the determination of the equivalent specified concrete compressive strength (n and k_c), Eq. 2 also calls for the coefficient of variation of cores strength. Therefore, two different values of the coefficient of variation, 5% and 10%, referred to herein as V_{master}, are considered (see Fig. 1). It is noted that the coefficient of variation associated to concrete compressive strength used in the calibration of ACI 318 for the design of new structures is 10% (Szerszen & Nowak 2003).

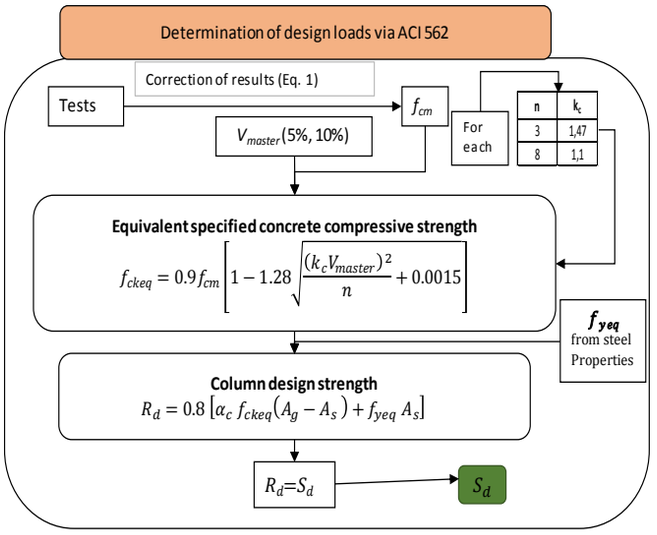


Figure 1 – Determination of design loads S_d according to ACI 562 (2013).

For a given RC column, based on the information presented in Galambos et al. (1982) for the dead load, G, and the live load, Q, and the corresponding design loads, S_d (as previously described), the complete statistics of these variables are defined. In this process, the ratio r between the mean dead load and mean live load is needed (see Fig. 2). In this study, the following values are assumed for this ratio: 0.5, 0.75, 1.0, 1.5, 2.0, 2.5, 3.0, 3.5, and 4.0.

4.3 *Statistics of material strengths*

Regarding the statistics of the random variable concrete compressive strength, F_c, for each value of the assumed mean strength, six different values of the corresponding coefficient of variation are considered. These values range from 5% to 17.5%; they have been selected in order to represent different scenarios for the variability of concrete strength in existing RC columns. The procedure for the generation of the PDF curves for the random variable concrete compressive strength, F_c, is summarized in Figure 3. For the random variable steel yield strength, F_y, PDF curves were generated according to ACI 562 recommendations and the statistics (bias factor and coefficient of variation) given in Galambos et al. (1982), as shown in Figure 4.

Each assumed value of the coefficient of variation of the cores strength, V, creates a resistance scenario for the analyzed column resulting in different PDF curve for the column resistance. The interaction between column resistance and corresponding load effects defines the reliability associated to each assumed scenario. As can be seen from Figure 5, the greater dispersion of the resistance curve the greater the probability of failure of the column.

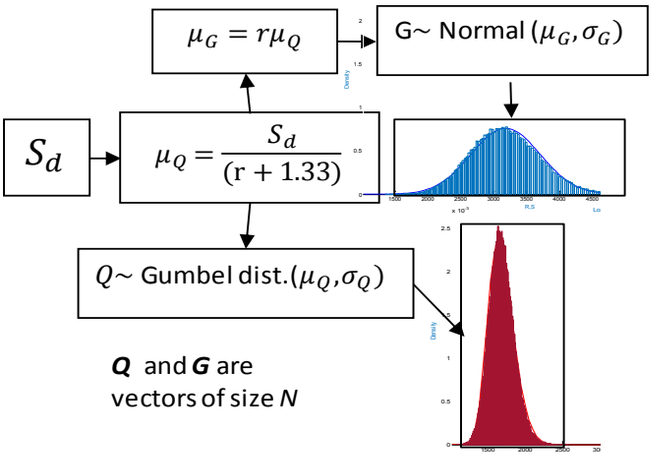


Figure 2 - Generation of the PDFs for the random variables dead load and live load acting on the column.

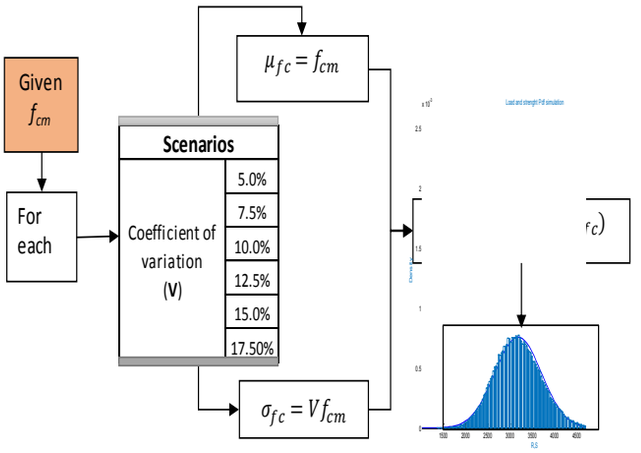


Figure 3 - Generation of the PDF for the random variable concrete compressive strength.

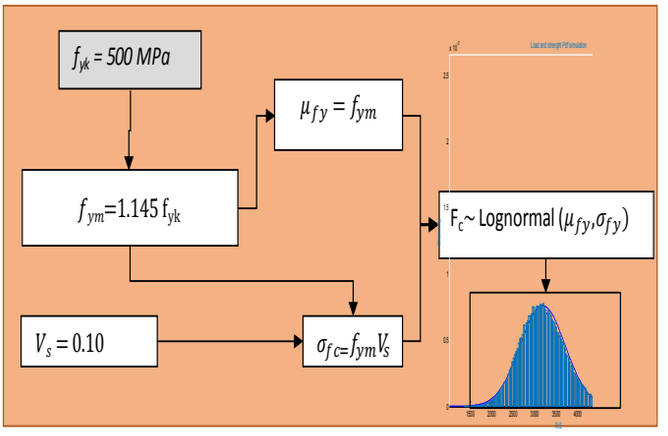
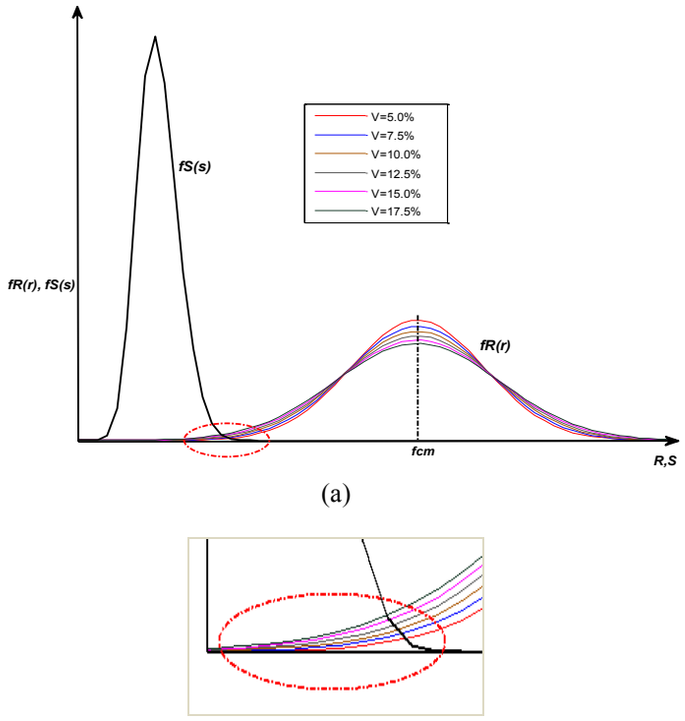


Figure 4 – Generation of the PDF for the random variable steel yield strength.



(a)

(b)

Figure 5 – (a) PDFs of column resistance, R, and load effects, S, for different values of the coefficient of variation of concrete compressive strengths; (b) details of the overlapped region.

5 DETAILS OF THE SELECTED COLUMNS

The selected columns correspond to two different cross-sections (rectangular, S1, and square, S2, see Fig. 6), four concrete compressive strengths (f_{cm} = 20, 30, 50 and 70 MPa), four longitudinal steel ratios (ρ_l = 1%, 2%, 3% and 4%). The characteristic steel yield strength is taken as 500 MPa for all columns. Details of the selected columns are presented in Table 2.

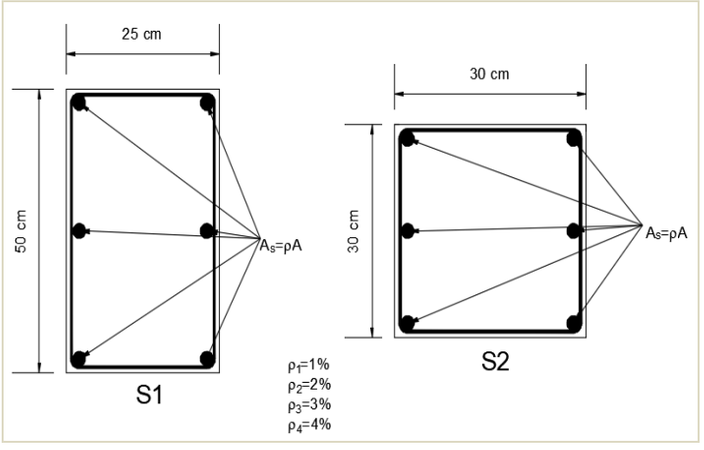


Figure 6 – Details of the columns cross-sections.

These columns were grouped in eight series (P1, P2, P3, P4, P5, P6, P7 and P8), each series representing a given cross-section and concrete compressive strength. For instance, series P4 correspond to S2 cross-section (square cross-section) and mean concrete compressive strength equal to 30 MPa. Each series contain four columns representing the four assumed longitudinal steel ratios. Additionally, for each combination of cross-section geometry, f_{cm}, and ρ_l (32 combinations), 9 load ratios are assumed (r = 0.5, 0.75, 1.0, 1.5, 2.0, 2.5, 3.0, 3.5, and 4.0). In total, 288 short axially-loaded columns have been selected for analysis.

Table 2. Details of the selected columns.

Column	Cross section	f_{cm} (MPa)	f_{yk} (MPa)	ρ_l	A_s (cm²)
P1	S1	20	500	1%	12.5
				2%	25
				3%	37.5
				4%	50
P2	S2	20	500	1%	9
				2%	18
				3%	27
				4%	36
P3	S1	30	500	1%	12.5
				2%	25
				3%	37.5
				4%	50
P4	S2	30	500	1%	9
				2%	18
				3%	27
				4%	36
P5	S1	50	500	1%	12.5
				2%	25
				3%	37.5
				4%	50
P6	S2	50	500	1%	9
				2%	18
				3%	27
				4%	36
P7	S1	70	500	1%	12.5
				2%	25
				3%	37.5
				4%	50
P8	S2	70	500	1%	9
				2%	18
				3%	27
				4%	36

6 RELIABILITY RESULTS

The reliability assessment was performed for the selected columns. As described in Section 4, it is assumed that the loads acting on the column follow ACI 562 (ACI 2013) recommendations. Eq. 2 used in the estimation of f'_{ceq} requires the coefficient of variation of the cores strength, V. As such, the information regarding the coefficient of variation used in the code calibration is needed. As presented in Section 4, two different values of V (V_1 = 5% and V_2 = 10%, referred to herein as V_{master}) are assumed. For each column, the assumed number of cores is taken

as 3 and 8, with the corresponding values of the coefficient k_c given in Table 1. This results in four different combinations of V_{master} and k_c, i.e. each of the 288 columns was checked for four combinations of V_{master} and k_c. Furthermore, while V_{master} represents the variability of the cores strength used in the calibration, the actual variability of the cores may differ from the values assumed in the calibration process. To account for the actual variability in the cores strength, the statistics of the column resistance are obtained considering 6 different values of the assumed measured strength obtained from cores (V = 5%, 7.5%, 10%, 12.5%, 15%, 17.5%).

Monte Carlo Simulation was used for the reliability assessment of each selected column for the ultimate limit state. The statistics of the basic variables used in this procedure are displayed in Table 3. Probabilities of failure (and corresponding reliability indexes) were computed for each column at a given scenario (V_{master}, k_c, and V). For each column in each scenario, a sample size of 10^6 is used in the simulation process. Considering the large volume of data that resulted from the investigation performed in this study, in what follows, only a few results are discussed and general results are highlighted.

Table 3. Statistics of the basic variables.

Mean	Coefficient of Variation	Type of distribution	Reference
Concrete Compressive Strength			
f_{cm}= 20, 30, 50, 70 MPa	5%, 7.5%, 10%, 12.5%, 15%, 17.5%	Lognormal	Assumed
Longitudinal Steel			
f_{ym} =572.5 MPa	10%	Lognormal	Assumed
Cross-Section Geometry			
B= 25 cm	2.2%	Normal	S1 (rectangular) JCSS (2001)
H=50 cm	2.8%	Normal	
B=30 cm	1.93%	Normal	S2 (square) JCSS (2001)
H= 30 cm	1.93%	Normal	
Model Error			
1.0	11%	Normal	Diniz & Frangopol (1997)
Dead Load			
See Figs.1 and 2	10%	Normal	Galambos et al. (1982)
Live Load			
See Figs.1 and 2	25%	Gumbel	Galambos et al. (1982)

Figures 7 and 8 present reliability indexes and probabilities of failure as a function of the load ratio r, respectively, for columns in series P3, and longitudinal steel ratio ρ_l= 1%. In these analyses, V_{master} = 0.05 and the number of cores is equal to 3. In these figures, for each group of bars corresponding to a given value of the load ratio, different results are obtained depending on the assumed variability of the measured strength obtained from cores. In Figure 7, two horizontal bars are shown as a reference. They correspond to the upper and lower values of the target reliability index (β_T, 3.8 and 3.1, respectively) suggested in the 2010 fib-Model Code (Féderation Internationale du Béton 2010).

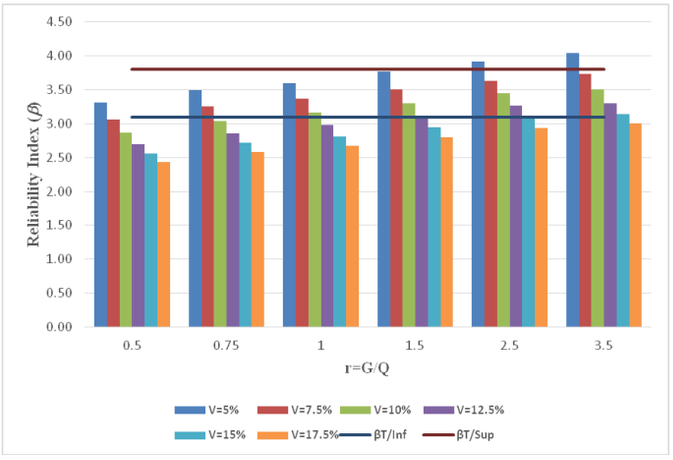


Figure 7 – Reliability indexes associated to columns in series P3, ρ_l= 1%, n = 3, and V_{master} = 0.05.

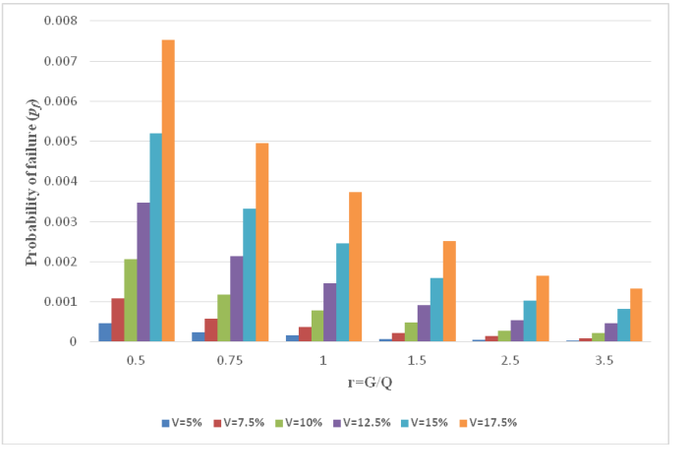


Figure 8 – Probabilities of failure associated to columns in series P3, ρ_l= 1%, n = 3, and V_{master} = 0.05.

It should be observed that reliability indexes can be easily obtained from the corresponding probabilities of failure. Additionally, in code calibration procedures, reliability indexes are frequently used as surrogate measures of the component reliability (e.g. Szerszen & Nowak 2003). However, it should be kept in mind that small differences in the range obtained for the reliability indexes translate in a much higher range in terms of probabilities of failure.

This is clearly seen by comparing the results displayed in Figures 7 and 8. For instance, when the load ratio, r, is equal to 0.5, the range in probabilities of failure is 7.5 x 10^{-3} - 4.6 x 10^{-4}, and the corresponding range in terms of reliability indexes is 2.43-3.31. In other words, while the highest probability of failure is about 16 times larger than the smallest probability of failure in the range, the highest reliability index is only 36% larger than the smallest reliability index in the range.

Figures 9 and 10 present reliability indexes and probabilities of failure as a function of the load ratio r, respectively, for columns in series P3, ρ_l= 1%, n = 3; however, V_{master} = 0.10. A comparison between Figures 7 and 9 (and Figures 8 and 10) shows a similar trend in both cases: (i) higher reliability levels are obtained as the load ratio increases, and (ii) decreased reliability as the concrete variability increases. It is also observed that an increase in the value of V_{master} used in the code calibration also increases the resulting reliability levels. This can be easily understood as a higher value of V_{master} translates into a lower equivalent concrete compressive strength, and consequently, more restrictive values of the loads that may act on the column.

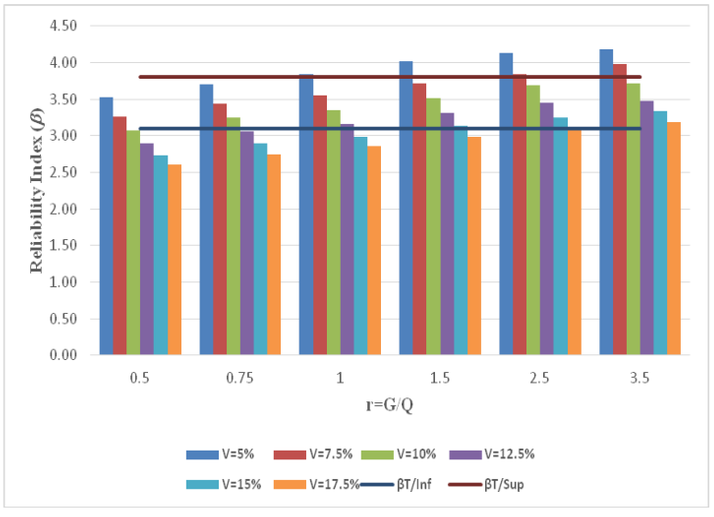


Figure 9 – Reliability indexes associated to columns in series P3, ρ_l= 1%, n = 3, and V_{master} = 0.10.

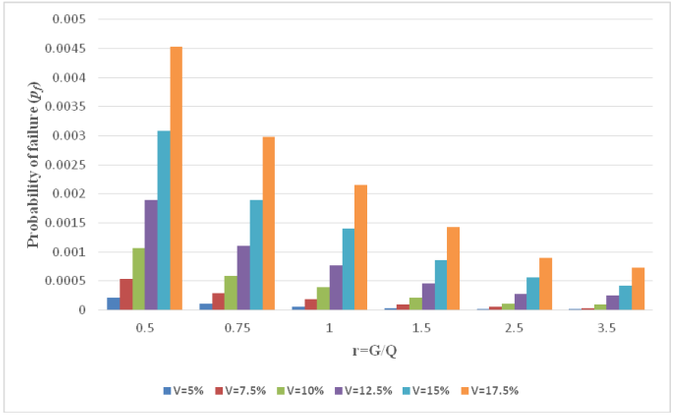
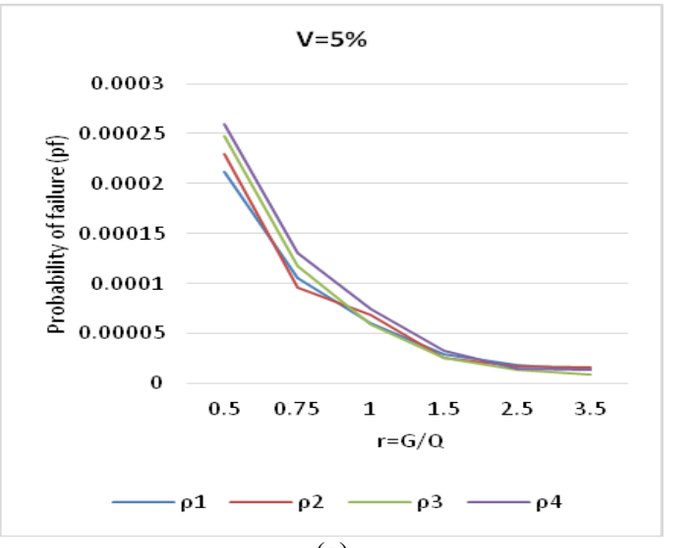
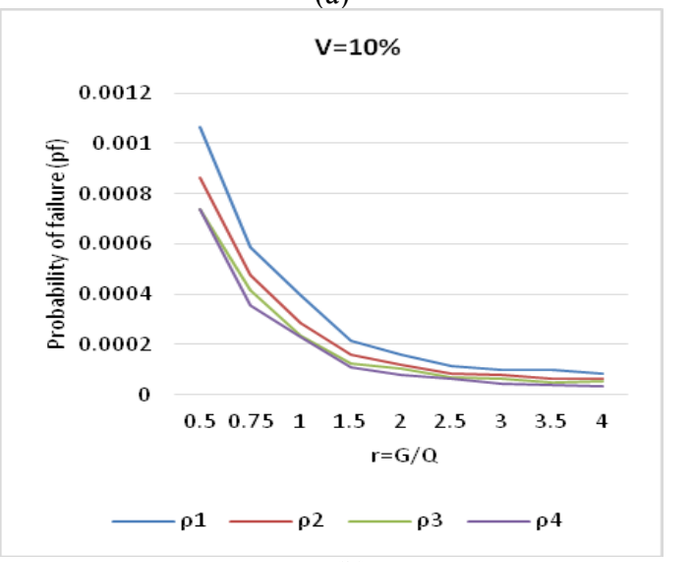


Figure 10 – Probabilities of failure associated to columns in series P3, ρ_l= 1%, n = 3, and V_{master} = 0.10.

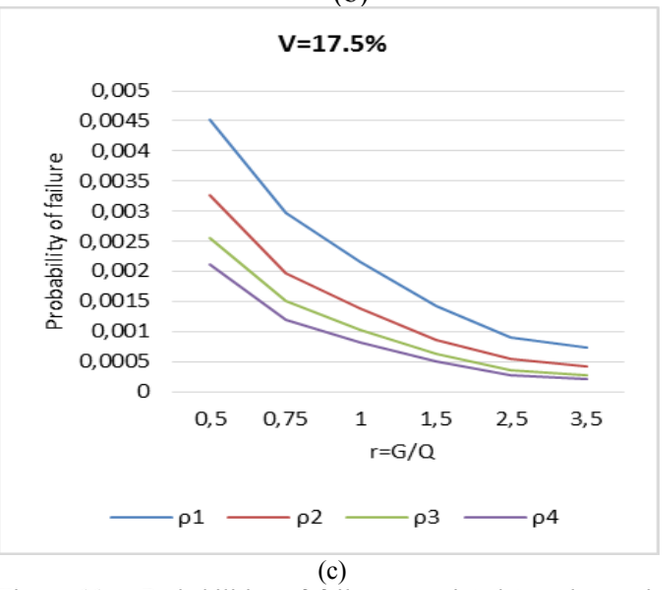
The effect of the longitudinal steel ratio on the column reliability is shown in Figure 11 (results presented in terms of the probability of failure).



(a)



(b)



(c)

Figure 11 – Probabilities of failure associated to columns in series P3, n = 3, and V_{master} = 0.10, for different values of the longitudinal steel ratio, ρ_l: (a) V= 0.05, (b) V= 0.10, (c) V= 0.175.

From Figure 11 it is seen that the influence of the amount of longitudinal steel is small for lower values of the coefficient of variation of the extracted concrete cores, V. However, this influence increases as this coefficient of variation increases, particularly for low values of the load ratio; see for instance Figure 11(c), which corresponds to V=17.5%.

7 SUMMARY AND CONCLUSIONS

In this study, the reliability levels associated to short, axially-loaded existing RC columns were assessed. These structural elements have been chosen since they represent the condition where the influence of the in situ concrete compressive strength would be the most relevant to the structural integrity.

It was considered that updated statistics are obtained for the in situ concrete compressive strength only. These updated statistics were obtained from information on strength of extracted cores adjusted for size effects and number of cores. The analysis corresponds to a snapshot of the safety margins at the time of the investigation; as such the time-dependent behavior of the materials involved, as often occurs in deterioration processes associated to RC structures, has not been taken into account.

Four different scenarios representing the combinations of V_{master} (used in the code calibration) and the number of cores were considered in the reliability assessment of 288 selected columns. Furthermore, for each column, 6 different values of the coefficient of variation of the extracted concrete cores, V, were assumed. Considering the large amount of data gathered in such analyses, only a few representative results were presented in the previous section.

It was observed that the coefficient of variation of the extracted concrete cores, V, has an important influence on the resulting reliability levels. This is particularly more evident when results are presented in terms of probabilities of failure. It is important to note that while for new structures the coefficient of variation of concrete compressive strength may vary in a small range, the coefficient of variation of the extracted concrete cores may fall within a much larger range.

Regarding the value of V_{master} used in the code calibration procedure, it was observed that an increase in such value increases the resulting reliability levels. It is observed that a higher value of V_{master} translates into a lower equivalent concrete compressive strength, and consequently, more restrictive values of the loads acting on the column and higher reliability levels.

Considering the range for the target reliability index suggested in the 2010 fib-Model Code (3.1-3.8), the resulting reliability levels violate such targets for a number of the selected columns in this study. This is particularly true for those columns representing a combination of smaller load ratios and higher coefficients of variation of the extracted concrete cores. Notwithstanding, it is important to note that there is still no consensus on target reliability levels for the assessment of existing structures.

Target reliability metrics for code calibration procedures of new structures are usually presented in terms of reliability indexes (e.g. Galambos et al. 1982, Szerszen & Nowak 2003). However, as highlighted in this study, small differences in the range of the reliability indexes translate in a much larger range in terms of probabilities of failure. Considering these significant differences, it is concluded that the assessment of important existing structures should be explicitly made in probabilistic terms.

8 REFERENCES

American Concrete Institute. 2014. *ACI 318: Building Code Requirements for Structural Concrete*. Farmington Hills.

American Concrete Institute. 2013. *ACI 562: Code Requirements for Evaluation, Repair, and Rehabilitation of Concrete Buildings*. Farmington Hills.

American Concrete Institute. 2010. *ACI 214.4R: Guide for Obtaining Cores and Interpreting Compressive Strength Results*. Farmington Hills.

ASCE 2013. *ASCE 2013 Report Card for America's Infrastructure*, American Society of Civil Engineers, www.infrastructurereportcard.org/bridges/

Ang, A.H-S. & Tang, W.H. 1990. *Probability Concepts in Engineering Planning and Design – Decision, Risk, and Reliability*, Vol. II.

Badimuena, B.L. 2016. *Avaliação da Confiabilidade de Estruturas Existentes: Influência da Resistência à Compressão do Concreto* (in Portuguese), M.Sc. Thesis, Federal University of Minas Gerais, Brazil, 219 p.

Bartlett, F.M. & MacGregor, J.G. 1996. Statistical Analysis of the Compressive Strength of Concrete in Structures. *ACI Materials Journal*, 93(2), pp. 158-168.

Canadian Standards Association – CSA. 2006. *CAN/CSA-S6: Canadian Highway Bridge Design Code*. Mississauga, Ontario.

Diamantidis, D., Holický, M., Sýkora, M., Marková, J., Vrouwenvelder, T., Tanner, P., Arteaga, A., Lara, C., Croce, P., Toprak, S. Senel, S.M., Inel, M. 2012. *Innovative methods for the assessment of existing structures*. Prague: Czech Technical University in Prague, Klokner Institute, 148 p.

Diniz, S.M.C. 2008. Structural Reliability: Rational Tools for Design Code Development. *Crossing Borders: 2008 Structures Congress*. Reston, EUA, ASCE.

Diniz, S.M.C. & Frangopol, D.M. 1997. Reliability Bases for High-Strength Concrete Columns, *Journal of Structural Engineering*, 123 (10), ASCE.

Féderation Internationale du Béton – CEB-FIP. 2011. *MC 2010: Model code 2010*. Lausanne.

Galambos, T., Ellingwood, B., MacGregor, J., Cornell, A. 1982. Probability based load criteria: assessment of current design practice. *Journal of Structural Division*, ASCE, pp.959-977.

Melchers, R. E. 1999. *Structural Reliability Analysis and Prediction*, John Wiley & Sons, 437 p.

Szerszen, M.M.; Nowak, A.S. 2003. Calibration of design code for buildings (ACI 318): Part 2- Reliability analysis and resistance factors. *ACI Structural Journal*, 100(3), pp. 383-391.

Maintenance, Safety, Risk, Management and Life-Cycle Performance of Bridges – Powers, Frangopol, Al-Mahaidi & Caprani (Eds)
© 2018 Taylor & Francis Group, London, ISBN 978-1-138-73045-8

Risk-based performance evaluation for concrete bridge deck repair

H. Huang & M. Liu
Relcon Infrastructure Management Inc., Denver, Colorado, USA

ABSTRACT: Repair of concrete decks has a significant impact on the total costs of a bridge repair and rehabilitation project. Therefore, it is important to establish a rational procedure and criteria for evaluating deck performance. This paper compares the evaluation procedures and performance criteria in the 2014 Canadian Highway Bridge Design Code with those in the Manual for Bridge Evaluation published by AASHTO in 2011. The fundamental differences between bridge design and evaluation have been identified, followed by a proposed evaluation procedure, where the risks related to the time-dependent uncertainties associated with concrete deterioration and the epistemic uncertainties in measurement and testing methods, including spatial variations, are considered. The proposed procedure is calibrated using a similar procedure for new structure design. More importantly, this paper emphasizes that new bridge design deals with group characteristics of future structures, while bridge evaluation addresses the status of individual elements in existing structures.

1 INTRODUCTION

Repair of concrete decks has a significant impact on the total costs of a bridge repair and rehabilitation (R&R) project. This is because a concrete deck is an important component in the structural system of a bridge, but it is also vulnerable to environmental attacks (*e.g.* extreme cold or hot weather, snows, winds and deicing salts) or increased heavy traffic loads. The amount of concrete materials in a bridge deck warrants an expensive construction for both new bridges and existing bridge R&R. Therefore, it is very important to establish a rational procedure and criteria for evaluating concrete bridge deck performance, particularly for bridge R&R projects.

1.1 *History of concrete bridge decks*

Before the 1920's, timber was used as decking for stone and steel bridges. By the 1930's, reinforced concrete was well established as a major building material. In March 1930, *Public Roads Magazine* published a paper of "computation of stresses in bridge slabs due to wheel loads" by Professor H.M. Westergaad of the University of Illinois as the foundation for modern design of concrete bridge decks. According to Item 107 from the 1994 National Bridge Inventory (NBI) published by Federal Highway Administration (FHWA) of the U.S. Department of Transportation, about 70% of the existing bridges in the U.S. have cast-in-place reinforced concrete decks, and about 90% of the total U.S. bridge deck areas are made of reinforced concrete.

1.2 *Functions of concrete bridge decks*

The primary function of a bridge deck is to deliver the reaction from vehicle tires to the bridge framing system that supports the deck. The additional functions of a concrete bridge deck include (a) proving a roadway to move; (b) distributing traffic loads to various supporting elements; (c) an important addition to the top flange of bridge girders behaving compositely with the framing members; (d) part of the stiffening system (*e.g.* horizontal diaphragms), particularly for torsion deformation; (e) acting as a slab structure when without a bridge framing system for a simple span bridge up to approximately 40 feet in length.

1.3 *Behavior of concrete bridge decks*

The responses of a concrete bridge deck subjected to wheel loads can be modeled as either a flexural member or a compression membrane having an "arching action". Making composite actions between the deck and the supporting floor system is a fundamental requirement for long-lasting concrete bridge deck construction. A lighter and composite bridge deck will provide economic and reliable solutions for both new bridge design and existing bridge R&R. Meanwhile, a concrete deck suffers wear, abrasion, and deterioration due to traffic contacts.

The steel reinforcement may also corrode. As a result, a concrete bridge deck usually contains a layer of special surface materials for better resisting traffic wear and abrasion, improving skid resistance and protecting the deck itself, while the steel reinforcement is often protected with epoxy-coating. For example, in Canada, the 90 mm (3.54 inches) asphalt layer with waterproofing system is used on top of concrete deck for protection.

1.4 *Causes of concrete deck deterioration*

There are many causes that are responsible for concrete deck deterioration. The most well-known cause is the deicing salts that dramatically increase the chloride-induced steel corrosion in a concrete deck. In fact, the root causes of concrete deck deterioration may be found in both design and construction, in addition to the operation phase of a bridge. For example, the concrete decks could be designed to be too thin or insufficient concrete cover over steel reinforcement. The supporting steel girders may be too limber, or more importantly, the concrete decks are not designed to composite with the steel girders. During the construction phase, the potential causes include, but are not limited to, dirty and reactive concrete aggregates, insufficient cement, too much water, excessive concrete placement temperature, incomplete consolidation, slow finishing, lack of uniform curing or concrete was too young when traffic was allowed. The poor design and lack of maintenance of deck drainage and expansion joints may also cause concrete deck deterioration.

1.5 *Performance evaluation of concrete decks*

The literature review on performance evaluation of concrete decks indicates that the relevant publications focus on two areas as the inspection techniques for condition assessment and the deterioration rates for remaining service life prediction. The current condition assessment is heavily relied on visual inspection at the top and bottom surfaces, particularly in the areas exposed to traffic or drainage. Although coring and/or nondestructive evaluation (NDE) may be used for condition assessment, if necessary, the current condition assessment on concrete bridge decks is considered to be subjective in nature. On the other hand, the deterioration rates of concrete bridge decks can be determined by either statistical modeling from bridge inventory database (*e.g.* the National Bridge Inventory, NBI) or time-dependent corrosion modeling with probabilistic initiation time, corrosion propagation rate or load models (Cady & Weyers 1984, Stewart & Rosowsky 1998, Oh et al. 2007). However, neither condition assessment nor determination of deterioration rates can provide the safety margin of an existing concrete deck due to lack of traffic loading information in the performance evaluation processes.

This paper compares the evaluation procedures and performance criteria for concrete bridge decks in the 2014 Canadian Highway Bridge Design Code (CSA Group 2014) with those in the Manual for Bridge Evaluation published by AASHTO in 2011. After then, the fundamental differences between a new bridge design and an evaluation of an existing bridge have been identified, followed by a proposed evaluation procedure, where the risks are related to the time-dependent aleatoric uncertainties associated with a stochastic process of concrete deterioration and the epistemic uncertainties in measurement and testing methods, including spatial variations.

2 BRIDGE EVALUATION CODES

The bridge evaluation code may be either a part of a design code for new structures (*e.g.* the *Canadian Highway Bridge Design Code* published in 2014) or a stand-alone manual such as the 2011 *AASHTO Manual for Bridge Evaluation*. In addition, the guidelines on condition surveys (*e.g.* the Ministry of Transportation Ontario (MTO)'s *Structural Rehabilitation Manual* published in 2007) are often used to perform field measurements.

2.1 *Canadian Highway Bridge Design Code*

Section 14 "Evaluation" of the 2014 *Canadian Highway Bridge Design Code* comprises the code requirements for evaluating an existing bridge in Canada, where the acceptable evaluation procedures include the ultimate limit states methods either using the load and resistance adjustment factors specified in Clauses 14.13 and 14.14 or the mean load method for the ultimate limit states specified in Clause 14.15.2.3. The load testing method specified in Clause 14.16 is also allowed for bridge evaluation. In addition, the serviceability limit states method shall be used in determining the load-carrying, stability, and load posting of masonry structures and bridges with excessive cracking, deformation, stress, or vibration. The other approved methods include the fatigue limit state specified in Clause 14.18.

The general bridge evaluation methodology in this Section requires (i) a condition inspection per Clause 14.6, (ii) determination of material strengths in accordance with Clause 14.7, and (iii) loads and load distribution in accordance with Clauses 14.8 to 14.11. The philosophy behind this general evaluation methodology is to maintain a consistent level of risk to human life for each element of the bridge (Allen 1992), in other words, the risks other than loss of a human life, such as the monetary loss of assets and the intangible loss of reputation, are not considered. The life safety criterion for the determi-

nation of the target reliability index (β) in bridge evaluation herein is related to the required evaluation level, expected warning of failure (*i.e.* brittle or ductile failure) and evaluation purpose (*i.e.* permit traffic or controlled vehicles). As a result, the β values ranges from 2.0 to 3.5 and the corresponding load factors and resistance adjustment factors are presented in Clauses 14.13 and 14.14, respectively.

For concrete bridge deck evaluation, a rapid method of evaluating the load carrying capacity is provided through Figures 14.4 and 14.5, based on NCHRP Report 292 (NCHRP 1987). The performance factor is set at 0.5 to ensure an adequate level of safety against a shear failure and intends to reflect the variations in the actual condition of the concrete deck. When the conditions specified for the rapid method are not satisfied, the resistance capacity of the concrete deck shall be determined per Section 8 of the 2014 *Canadian Highway Bridge Design Code* and expressed as an equivalent wheel load at the centerline of the span of the concrete deck. In addition, a resistance adjustment factor is introduced in Table 14.15 for all components that have no visible sign of defects or deterioration to fine-tune the resistance factors used in new bridge design. The bias coefficients and coefficients of variation (COV) of the resistance adjustment factors are presented in Table C14.6. The effects of defects and deterioration are discussed in Clause 14.14.3, where the uncertainties in determining the resistances of deteriorated or damaged materials at the critical member sections are recognized in general. However, no effort has been made to quantify these uncertainties.

2.2 *The Manual for Bridge Evaluation*

The Manual for Bridge Evaluation published by the American Associate of State Highway and Transportation Officials (AASHTO) serves as a standard and provides uniformity in bridge evaluation procedures and policies for the U.S. highway bridges. The first edition of *the Manual* was published in 2008 and the 2nd edition published in 2011 with 2011, 2013, 2014, 2015, and 2016 interim revisions (AASHTO 2011) is the current bridge evaluation code. *The Manual* replaces both the *Manual for Condition Evaluation of Bridges* and the *Guide Manual for Condition Evaluation and Load and Resistance Factor Rating (LRFR) of Highway Bridges* with any interim revisions before 2008 that were published by AASHTO. *The Manual* has been developed to assist Bridge Owners to meet the requirements in the National Bridge Inspection Standards (NBIS) with the eight sections, including (i) Introduction, (ii) Bridge Files (Records), (iii) Bridge Management Systems, (iv) Inspection, (v) Material Testing, (vi) Load Rating, (vii) Fatigue Evaluation of Steel Bridges and (viii) Nondestructive Load Testing, along with the nine illustrative examples in Appendix A. The load rating methods in Section 6 include the Load and Resistance Factor method, Load Factor method, and Allowable Stress method, and no preference is placed on any of these rating methods. Section 8 describes the field load test procedures for determining the live-load capacity of a bridge as well as for improving the confidence in the assumptions used in the analytical or computer modeling of the bridge.

For concrete deck evaluation, Section 6.1.5.1 states that the stringer-supported concrete decks and metal decks that are carrying normal traffic satisfactorily need not be routinely evaluated for load capacity. The bridge decks should be inspected regularly to verify satisfactory performance. This is because the primary structural action of concrete decks is not flexure, but internal arching or membrane action. There is significant reserve resistance capacity in concrete decks designed by the *AASHTO LRFD Bridge Design Specifications*, except for the heavily spalled and deteriorated concrete decks that may be required to check for punching shear under wheel loads. Nevertheless, Appendix A7 illustrates the procedure for reinforced concrete slab bridge design and legal load check, where the loads and resistance capacities are determined with Sections 4 and 5 of the LRFD design specifications, respectively. After then, the Rating Factor (RF) is calculated using the load-rating equations in Section 6A, considering the condition and system factors.

2.3 *Comparison of bridge design and evaluation*

It is clear that both Canadian and AASHTO bridge evaluation codes are based on the LRFD bridge design specifications. The target reliability index for bridge evaluation is generally smaller than that for bridge design, primarily due to economic considerations. The effects of the actual condition of a bridge component or system, including defects or deterioration, are taken into account with resistance adjustment factors in the Canadian evaluation code as well as condition and system factors in the *AASHTO Manual for Bridge Evaluation*. Similar assessment methodologies exist in other structural evaluation codes, specifications, regulations or guidelines worldwide. For instance, the UK Department of Transportation recommended implementation of bridge design codes with very few modifications for bridge evaluation (Micic et al. 1995). The American Concrete Institute (ACI) 318 *Building Code Requirements for Structural Concrete and Commentary* (ACI 318 2014) and ACI 562 *Code Requirements for Evaluation, Repair, and Rehabilitation of Concrete Buildings and Commentary* (ACI 562 2016) permit increasing the strength reduction

factor (*i.e.* phi-factor, ϕ) for assessment of existing concrete members from the design values as shown in Table 1 below. This has been justified by the improved reliability due to the use of accurate field-obtained material properties, actual in-place dimensions and well-understood methods of analysis. In fact, the increased ϕ values are directly caused by the reduced target reliability index (β).

The rest of this paper investigates the root causes of uncertainties (*i.e.* variations or deviations) in new concrete structures, including new concrete bridge decks, as well as the root causes of uncertainties in assessment of existing concrete structures. By comparing the characteristics of the uncertainties, the fundamental differences are identified, and the corresponding uncertainty treatments are suggested.

Table 1. Phi Factor ϕ in ACI 318-14 and ACI 562-16

Concrete Member	ACI 318 Design	ACI 562 Assessment	
Tension-controlled sections	0.9	1.0	1.0
Compression-controlled sections			
with spiral reinforcement	0.75	0.9	0.9
other reinforced members	0.65	0.8	0.8
Shear, torsion, interface shear	0.75	0.8	0.8
Bearing on concrete	0.65	0.8	0.8
Strut-and-tie models	0.75	N/A	0.8

3 ROOT CAUSES OF UNCERTAINTIES

In general, a phi-factor (ϕ) is used to account for the probability of understrength of a structural member due to variations of in-place material strengths and dimensions, effect of simplifying assumptions in the design equations among others (ACI 318 2014). The ϕ values also account for deviations of the actual strength from the nominal strength as well as the potential failure modes (*i.e.* brittle or ductile failure) and associated consequences of the failure (ASCE/SEI 7 2010). Therefore, a comprehensive understanding of the root causes represented by the phi-factor (ϕ) values is essential for the development of a rational evaluation procedure and performance criteria for existing structures.

3.1 *New concrete structures*

The phi-factors for new concrete structure design in ACI 318 were calibrated through a large database of construction material properties from North American industry including the Concrete Reinforcing Steel Institute, National Ready Mixed Concrete Association, Portland Cement Association, and Precast / Pre-stressed Concrete Institute (Nowak & Szerszen 2003). The root causes of uncertainties in new concrete structure design were identified as: (i) variations in construction material properties (*e.g.* compressive strength of concrete, yield strength of steel reinforcement, modulus of elasticity of concrete and steel reinforcement) during the producing and curing process; (ii) variation in component dimensions, locations of steel reinforcement, and moment of inertia, among other factors related to the fabrication process; and (iii) effects of simplifying assumptions in the design equations (*i.e.* professional factor). Thus, the resistance capacity R of a new concrete member is expressed as a product of the three factors M, F, and P as

$$R = Rn \times M \times F \times P \quad (1a)$$

$$R = \phi \times Rn \quad (1b)$$

$$\phi = M \times F \times P \quad (1c)$$

where Rn = nominal resistance, M = construction material properties parameter, F = fabrication factor, and P = professional factor. The statistical properties of M, F and P (*e.g.* the mean values m, the bias factors λ, and the coefficients of variation COV) were derived from either the large database mentioned above or previous studies documented in the available literature (Nowak & Szerszen 2003).

3.2 *Existing concrete structures*

Obviously, the uncertainties associated with the producing, curing and fabrication processes for new concrete members, represented by M and F, respectively, no longer exist in assessment of existing concrete members, but new uncertainties associated with the investigation procedure (dimension measurements and material properties tests) appear. The uncertainties represented by P will be the same only if the same simplifying assumptions are used in the design equations for assessment of existing concrete members, but the additional assessment equations associated with the measurement and testing process will add the new uncertainties. For example, Equation (6.4.3.1) of ACI 562-16 is a simplified expression to determine the equivalent specified concrete strength $f_{c,eq}$ from the core testing results as

$$f_{c,eq} = 0.9\,F_c\{1 - 1.28\sqrt{\frac{(k_c V)^2}{n}} + 0.0015\} \quad (2)$$

where F_c = average core strength as modified to account for the diameter, length to diameter ratio and moisture condition of the core per ASTM C42 procedures; k_c = modification factor per Table 6.4.3.1 of ACI 562-16; V = coefficient of variation of the core strengths; and n = number of cores tested. The corresponding uncertainties due to the assumptions in Equation (2) must be included in accurately determining ϕ for assessment of existing concrete members. In addition, Section 27.3.1.1 of ACI 318-14 requires "dimensions of members shall be established at critical sections". However, the critical sections of an existing concrete member vary for dif-

ferent load effects, such as moment, shear, and axial force, even if the load is identical and well known (*e.g.* a moving truck load on a concrete bridge for the potential failure mode of shear). In other words, the critical sections of an existing concrete member may not be identified before performing a field investigation. Thus, the uncertainties that the field investigation results may not represent the properties at the critical sections of an existing concrete member must also be included in accurately determining ϕ for assessment of existing concrete members. As a result, the resistance capacity R_e of an existing concrete member can be expressed as

$$R_e = Rn_e \times T_e \times P_e \times Cr_e \quad (3a)$$
$$R_e = \phi_e \times Rn_e \quad (3b)$$
$$\phi_e = T_e \times P_e \times Cr_e \quad (3c)$$

where Rn_e = nominal resistance of an existing concrete member, usually based on the average measurements from the field investigation or the nominal values in design codes, T_e = factor related to the field investigation procedures, including but not limited to construction-material property and dimension measurements, P_e = professional factor associated with an existing concrete member, and Cr_e = factor accounting for the fact that the field investigation results may not represent the properties at the critical sections of an existing concrete member. Obviously, the statistical properties of T_e, P_e and Cr_e should be completely different from those of M, F and P. However, only limited or no previous studies on T_e, P_e and Cr_e can be found in the available literature.

3.3 *Fundamental differences*

As stated above, the root causes of uncertainties in new concrete structure design and in assessment of existing concrete structures have been found to be completely different. More importantly, the characteristics of these uncertainties are compared in order to identify the fundamental differences represented by the corresponding phi-factors, which will result in the different uncertainty treatments suggested.

In decision-making theory, the characteristics of uncertainties can be categorized as either aleatory variability or epistemic uncertainty. The aleatory variability describes natural randomness and cannot be reduced by an increase in knowledge. It is very important to recognize that the aleatory variability represents the characteristics of a random process as a group, but not a property of individuals (*i.e.* each observation) in the group. On the other hand, the epistemic uncertainty is due to lack of knowledge or limited data, and may be eliminated with sufficient investigations. The epistemic uncertainty may be initially represented with the probability density function (PDF) as a prior distribution for Bayesian updating. The results of the Bayesian updating may be used for future performance prediction of an individual in the group.

Since M and F reflect the uncertainties in producing, curing, and fabricating new concrete members, M and F are the aleatory variability. This is because producing, curing, and fabricating new concrete members can be considered as a natural random process. P is an epistemic uncertainty as the uncertainties in P may be reduced or eliminated with sufficient investigations. Therefore, the phi-factor for new concrete structures represents a combination of the aleatory variability and the epistemic uncertainty. It should be noted that the phi-factor for new concrete structures is to account for the uncertainties in future structures. In other words, the resistance capacity of a future concrete structure does not exist at the time of design and construction. The actual resistance capacity of a future concrete structure will be different from the calculated one due to the natural randomness associated with the producing, curing, and fabrication processes. On the other hand, the actual resistance capacities at critical sections of an existing concrete structure exist at the time of assessment. The uncertainties in R_e are due to lack of knowledge (*i.e.* uncertainties associated with the investigation processes) or limited data. Although an investigation process itself can be considered as a natural randomness process, the aleatory variability associated with the investigation process only affects the associated results (*i.e.* our knowledge of the actual resistance capacities at critical sections), but does not affect the actual resistance capacities themselves. Therefore, all of T_e, P_e and Cr_e should be treated as the epistemic uncertainty. As a result, the fundamental differences between the phi-factors for new concrete-structure design and for assessment of existing concrete structures are found to be (i) the phi-factors for new concrete-structure design represent the group characteristics of a random process (*i.e.* a producing, curing, and fabrication process for new concrete members), and (ii) the phi-factors for assessment of existing concrete structures reflect the epistemic uncertainty that may be used for future performance prediction of an individual existing concrete member through Bayesian updating.

The uncertainty treatments for an aleatory variability are primarily dependent on the PDF for observations available, but the uncertainty treatments for the epistemic uncertainty may include but not be limited to: (i) Bayesian updating; (ii) the interval (minimum, mode, maximum) analysis from observations available or expert opinion elicitation (*i.e.* no additional information but the interval required); (iii) Dempster-Shafer evidence theory; (iv) fuzzy sets; (v) possibility theory; (vi) imprecise probability; (vii) logic trees with weights from subjective judgments; and (viii) adjustment factor approach. Furthermore, the uncertainty treatments for a combina-

tion of aleatory variability and epistemic uncertainty involve: (i) second-order probability; (ii) two-stage Monte Carlo simulations; and (iii) adjustment factor approach.

4 CODE CALIBRATION PROCEDURE

The values of the phi-factors for new concrete-structure design in ACI 318 were obtained from a rigorous design code calibration procedure (Szerszen & Nowak 2003), which includes the following five steps: (i) selection of the representative dimensions and reinforcement ratios for the structural concrete elements of interest; (ii) selection of the statistical models for loads and load combinations; (iii) selection of the resistance models; (iv) probability analysis using the component reliability index, β; and (v) determination of the values of the phi-factors for each of the design limit states, based on the calculated closeness to the predefined target reliability index, β_T. Ideally, a similar code calibration procedure should be applied to determine the values of the phi-factors for assessment of existing concrete members, where the general format of the limit state function is

$$g = R - Q \geq 0 \tag{4}$$

where g = safety margin; R = resistance capacity; and Q = demand in terms of load effect. When R and Q are treated as the random variables as shown in Figure 1, the probability of failure P_f is illustrated as the shaded area in Figure 2. The component reliability index β is calculated using the inverse standard normal distribution function Φ^{-1} as

$$\beta = -\Phi^{-1}(P_f) \tag{5}$$

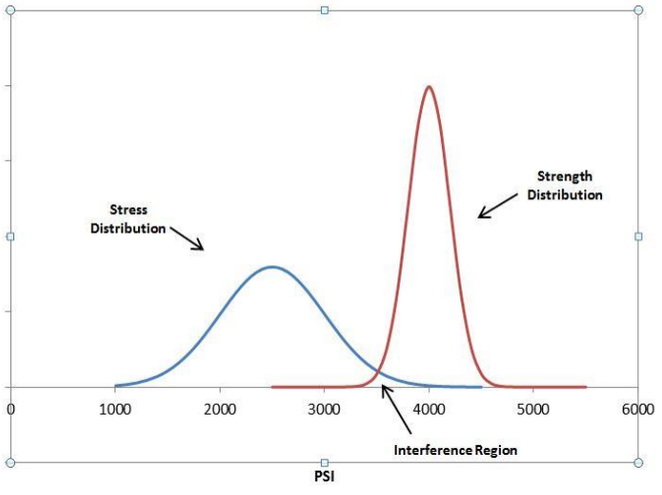


Figure 1: Random Variables R (Resistance) and Q (Demand)

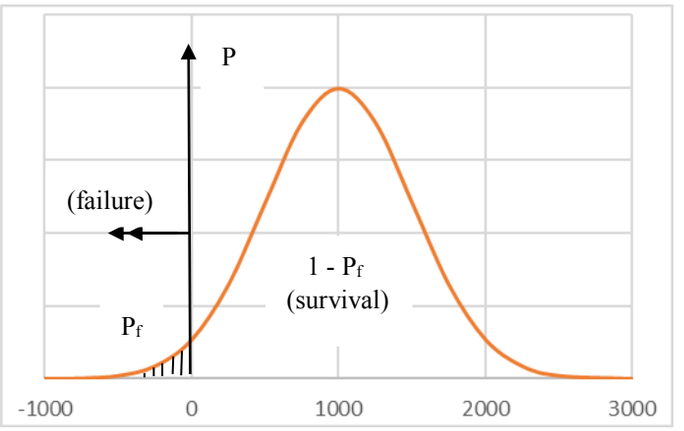


Figure 2: Probability of Failure P_f (the shaded area)

5 EXAMPLE

For each of the potential failure modes, R and Q for the different load combinations under consideration should be evaluated in order to accurately obtain the values of the phi-factors for assessment of existing concrete members. For example, for the potential failure mode of shear of a simply supported concrete beam, when the load combination only involves dead and live loads, the design equation can be expressed as

$$\phi_e R_{ne} = \gamma_D D_n + \gamma_L L_n \tag{6}$$

where γ_D and γ_L are the load factors for the dead and live loads, respectively. D_n and L_n are the nominal dead and live loads, respectively. The corresponding limit state equation is

$$g = R - Q = R - (D + L) = [(\gamma_D + \gamma_L (L_n / D_n))/ \phi_e] X_1 - X_2 - (L_n / D_n) X_3 \tag{7}$$

where the random variables X_1, X_2 and X_3 are R / R_{ne}, D / D_n and L / L_n, respectively.

Assuming the loading conditions for assessment of existing concrete members are identical to those for new concrete member design, ASCE/SEI 7-10 provides the statistical properties of the variables in Equation (7), as listed in Table 2. Thus, Equation (7) may be simplified as

$$g = 4.4 / \phi_e X_1 - X_2 - 2.0 X_3 \tag{8}$$

where the random variable X_1 in this case is a function of T_e , P_e and Cr_e that are related to the shear capacity of the concrete beam. The statistical properties of X_1 may be estimated as

$$\text{mean } X_1 = \text{mean } T_e \times \text{mean } P_e \times \text{mean } Cr_e \tag{9}$$

$$COVX_1 = (COVT_e^2 + COVP_e^2 + COVCr_e^2)^{1/2} \tag{10}$$

where the statistical properties of T_e , P_e and Cr_e (*i.e.* the mean values and COV) must be obtained from the Bayesian updating or other uncertainty treatments for epistemic uncertainty mentioned before.

Table 2: Statistical Properties of Variables in Equation (7) Based on ASCE/SEI 7-10

Variable	Value	Probability Distribution
γ_D	1.2	
γ_L	1.6	
L_n / D_n	2.0 (typical)	
X_2	Mean = 1.05 COV = 0.10	Normal
X_3	Mean = 1.00 COV = 0.25	Extreme Type I

It is emphasized herein that any statistical properties representing the group characteristics of a random process can only be used as a prior distribution for Bayesian updating in assessment of existing concrete members. Directly using the statistical properties representing the group characteristics in assessment of an individual existing concrete member may mislead the assessment outcomes. This is because the future performance of an individual existing concrete member can only be predicated by using the statistical properties updated from the field measurements that belong to the individual member. For example, the overall variability of in-place strengths that represents the group characteristics of a random process (*i.e.* a producing, curing and fabrication process for new concrete members) in Table 3.1 of ACI 214.4R-10 (ACI 214 2010) cannot be directly used without updating for assessment of an individual existing concrete member. Similarly, the within-test coefficients of variation in Section 7.1 of ACI 214.4R-10 and the repeatability in Section 3.2 of ACI 228.1R-03 (ACI 228 2003) must be updated for use in the assessment of an individual existing concrete member. These coefficients include, but not be limited to: 3.2% and 4.7% for the field coring tests by a single-operator and multi-laboratory operators, respectively, as shown in the precision statements of ASTM C42/C42M, 2.0% in ASTM C 597 for the ultrasonic pulse velocity measurement by one operator using different instruments or different operators using the same instrument, and 3.6% in ASTM C 873 for the three cast-in-place cylinders from the same batch.

As shown in Equations (9) and (10), the statistical properties of T_e, P_e and Cr_e are critical to determine the proper probability distribution of X_1. Thus, detailed studies of these statistical properties become necessary to correctly select the appropriate ϕ_e for various values of the target reliability index β_T. Advanced probability and statistical theories and techniques, such as propagation of uncertainty or error, autoregressive integrated moving average (ARIMA), and regression-Kriging, have a great potential in development of a rational procedure for the appropriate ϕ_e used in assessment of an individual existing concrete member. In absence of these detailed studies, the random variable X_1 is assumed herein to be a log-normal distribution with the mean value of 1.05 and the COV of 0.06. Table 3 summarizes the calculated probability of failure, P_f and corresponding reliability index β, through the 100,000 Monte Carlo simulations. The appropriate ϕ_e for the different values of the target reliability index β_T should be selected in accordance with the closest agreement between the calculated β and β_T. For example, if β_T is predefined as 2.5, ϕ_e should be 0.90. Similarly, ϕ_e should be 0.80, if β_T is assigned to be 3.0. Table 4 presents the sensitivity study results of X_1 (log-normal distribution) with different mean values and COV, where the calculated β is more sensitive to the changes of COV.

Table 3: Calculated Shear P_f under Dead and Live Loads

Assumed ϕ_e	0.80	0.85	0.90	0.95	1.00
Calculated P_f (%)	0.10	0.20	0.40	0.70	1.30
Reliability Index β	3.09	2.89	2.66	2.46	2.23

Table 4: Sensitivity Study Results of X_1

Assumed ϕ_e	0.80	0.85	0.90	0.95	1.00
Mean = 1.05, COV = 0.06	3.09	2.89	2.66	2.46	2.23
Mean = 1.05, COV = 0.15	2.66	2.46	2.26	2.06	1.84
Mean = 1.05, COV = 0.15	2.89	2.66	2.46	2.22	2.02

It should be pointed out that the Monte Carlo simulation results mentioned above are from only one load case of (1.2 Dead Load +1.6 Live Load), for purpose of illustration. The phi-factors for assessment of existing concrete members in Section 5.4 of ACI 562-16 and Section 27.3.2 of ACI 318-14 shall consider various load combinations as in ASCE/SEI 7-10. Thus, a rigorous code calibration process through multiple Monte Carlo simulations is required. Moreover, the assumption that the loading conditions for assessment of existing concrete members are identical to those for design of new concrete members needs to be validated, because the design life of a new concrete member is usually 50 years, but the remaining life of an existing concrete member may be much shorter than 50 years. More importantly, the load calibration process for new structures in ASCE/SEI 7-10 relies on the group characteristics of a random loading process, but the statistical properties of the loads applied to existing structures shall be updated to reflect the future loading prediction of an individual existing component. Finally, the target β_T for existing concrete members may be different from that for new concrete members because β_T is a function of various items (e.g. past structural behavior, engineering experiences, estimated construction costs and consequences of failure among others). β_T = 3.5 (*i.e.* $P_f \approx 0.023$ %) is

adopted for most of the components except for columns ($\beta_T = 4.0$) in new concrete structures, while the corresponding β_T for existing concrete structures is 2.5 (*i.e.* $P_f \approx 0.620$ %), primarily due to rehabilitation cost considerations.

6 CONCLUSIONS

This paper assessed the evaluation procedures and performance criteria for concrete bridge decks in both Canadian and AASHTO bridge evaluation codes, and determined that similar methodologies were adopted, where the bridge design specifications were modified with a reduced target reliability index, resistance adjustment factors, condition and system factors to represent the actual conditions of existing structures. Many other structural evaluation codes and specifications worldwide also implemented this approach. The further investigation on root causes of uncertainties in new concrete structure design and in assessment of existing concrete structures revealed that the phi-factors for new concrete structure design represented the group characteristics of a random process (*i.e.* producing, curing, and fabrication processes for new concrete members), whereas the phi-factors for assessment reflected the epistemic uncertainty that may be used for future performance prediction. The rigorous code calibration process through Monte Carlo simulations for assessment of existing structures was illustrated for only one load case (1.2 Dead Load +1.6 Live Load), where the statistical properties of the uncertainties in assessment of existing concrete structures (*i.e.* T_e, P_e and Cr_e) play a critical role for correctly selecting the appropriate ϕ_e for various values of the target reliability index β_T.

Although the routine load capacity evaluation is not required for concrete bridge decks, the statistical properties of T_e, Cr_e and P_e mentioned above may significantly affect the serviceability evaluation of the concrete decks. For example, the spatial and temporal variations of corrosion rates in a deteriorating reinforced concrete bridge deck were studied with structural health monitoring techniques (Marsh & Frangopol 2007). Furthermore, the field testing data indicated that the presence of heavy truck was an essential factor in the deterioration process of concrete decks (Szerszen & Nowak 2002). This is why the concrete spalling and potholes are often aligned with the traffic lanes. Therefore, the spatial variations on concrete bridge decks must be taken into account in the risk-based performance evaluation. This has been done in this paper by using an importance factor or a condition and system factor that is usually assigned to reflect actual conditions of the bridge decks. The advanced probability and statistical theories and techniques, such as propagation of error or uncertainty, autoregressive integrated moving average (ARIMA), and regression-Kriging, are expected to have a great potential in future development of such a rational procedure in safety assessment of existing concrete members.

REFERENCES

AASHTO 2011. *The manual for bridge evaluation*. Washington D.C: American Associate of State Highway and Transportation Officials.

ACI 214.4R 2010. *Guide for obtaining cores and interpreting compressive strength results*. Farmington Hills: American Concrete Institute.

ACI 228.1R 2003. *In-place methods for determination of strength of concrete*. Farmington Hills: American Concrete Institute.

ACI 318 2014. *Building code requirements for structural concrete and commentary*. Farmington Hills: American Concrete Institute.

ACI 562 2016. *Code requirements for evaluation, repair, and rehabilitation of concrete buildings and commentary*. Farmington Hills: American Concrete Institute (ACI).

Allen, D.E. 1992. Canadian highway bridge evaluation: reliability index. *Canadian J. Civil Engineering* 19: 987-991

ASCE/SEI-7 2010. *Minimum design loads for buildings and other structures*. Reston: American Society of Civil Engineers

Cady, P.D. & Weyers, R.E. 1984. Deterioration rates of concrete bridge decks. *J. Transportation Engineering* 110 (1): 34-44

CSA Group 2014. *Canadian highway bridge design code.* Canadian Standards Association

Marsh, P.S. & Frangopol, D.M. 2007. Lifetime multi-objective optimization of cost and spacing of corrosion rate sensors embedded in a deteriorating reinforced concrete bridge deck. *J. of Structural Engineering* 133(6): 777-787

Micic, T.V. Chryssanthopoulos, M.K. & Baker, M.J. 1995. Reliability analysis of highway bridge deck assessment. *Structural Safety* 17: 135-150

NCHRP 1987. *Report 292 strength evaluation of existing reinforced concrete bridges*. Washington DC: Transportation Research Board.

Nowak, A.S. & Szerszen, M.M. 2003. Calibration of design code for buildings (ACI 318): Part 1 – statistical models for resistance. *ACI Structural J.* 100(3): 377-382

Oh, B.H. Lew, Y. & Choi, Y.C. 2007. Realistic assessment for safety and service life of reinforced concrete decks in girder bridges. *J. of Bridge Engineering* 12(4): 410-418

Stewart, M.G. & Rosowsky, D.V. 1998. Time-dependent reliability of deteriorating reinforced concrete bridge decks. *Structural Safety* 20: 91-109

Szerszen, M.M. & Nowak, A.S. 2002. Deterioration scenarios for concrete deck slabs. In *Proc. 1st International Conference on Bridge Maintenance, Safety and Management*. Barcelona, Spain.

Szerszen, M.M. & Nowak, A.S. 2003. Calibration of design code for buildings (ACI 318): Part 2 – reliability analysis and resistance factors. *ACI Structural J.* 100(3): 383-391

Maintenance, Safety, Risk, Management and Life-Cycle Performance of Bridges – Powers, Frangopol, Al-Mahaidi & Caprani (Eds)
© 2018 Taylor & Francis Group, London, ISBN 978-1-138-73045-8

The Bridge Assessment Maze

Claire Jager
Principal Engineer, AECOM, Australia

Dr Torill Pape
Associate Director, AECOM, Australia

Dr Peter Shaw
Industry Director, AECOM, Australia

Dr Robert Heywood
Director, Heywood Engineering Solutions, Australia

ABSTRACT: Bridge assessments can often feel like a maze for asset owners with the wealth of information available internationally on approaches to determine the appropriate heavy vehicle access management strategy. Throughout the world, heavy vehicles are operating on bridges at levels that exceed the assessed load carrying capacities of the bridges determined using design based ("standard") assessment procedures. The cost of strengthening these bridges is unpalatable and the consequences of restricting access are unacceptable. Inspections of these bridges in most cases indicate they are performing satisfactorily leading one to question the plausibility of the assessments. The key to unlocking the bridge assessment maze is to understand the inherent assumptions that underpin every form of assessment. An appreciation of the nature and type of assumptions then leads to a more informed position regarding actual risks, which ultimately provides the avenue to developed targeted management strategies for individual bridges and on a network-wide basis.

This paper aims to provide some guidance through the bridge assessment maze to empower the asset owner or manager to understand the requirements and outputs of bridge assessments. The paper begins by providing the distinction between design and assessment and then outlines current bridge assessment processes in Australia and selected international jurisdictions. A comparison of assessment assumptions is then presented to demonstrate the variability in assessment results that can in turn impact on the required management strategy and investment. The findings provide justification for the development of further guidance on the practical and reliable assessment of bridges.

1 INTRODUCTION

Maintaining road network access is a critical enabler of the economy and social functionality of any city or region, of which bridges play an important role. In this context, asset owners and managers are faced with the challenge of managing aging bridges in a safe and risk informed manner whilst balancing productivity and access demands.

Asset owners and managers often rely on the engineering profession to help them understand the risks associated with the ongoing management of their structures including providing advice on bridge capacity and access management. However some advice being received is often conservative, indicating a bridge is supposedly unfit for purpose, despite visual evidence to the contrary. The ramifications of a conservative assessment are more likely to lead to strengthening recommendations or access restrictions/diversions, both of which are unpalatable and unnecessarily costly.

This 'plausibility gap' between theoretical assessments indicating bridge capacities are unsatisfactory and satisfactory past performance has been discussed previously (Heywood et al. 2017, Shave, 2003), and fuels the debate surrounding the actual load-carrying capacities of existing structures. Add to this the wealth of data, technology, codes and methodologies that are currently available in relation to assessing existing bridges, it is no wonder asset owners often feel like they are lost in a maze of conflicting information.

It is the intention of this paper to provide some guidance through this maze to empower the asset owner or manager to understand the requirements and outputs of bridge assessments. The paper begins by providing the distinction between design and assessment and then outlines current bridge assessment processes in Australia and selected international jurisdictions. The key to unlocking the bridge assessment maze is to understand the inherent assumptions that underpin every form of assessment, the concept of which is explored through a comparative exercise. An appreciation of the nature and type of assumptions leads to a more informed position regarding actual risks, which ultimately provides the avenue to develop targeted management strategies for individual bridges and on a network-wide basis. These concepts are discussed and explored in the closing sections of the paper.

2 BRIDGE ASSESSMENT PROCESS

2.1 *Overview*

When determining the assessed capacity of a structure it is imperative that the differences between design and assessment are understood. Design procedures are typically conservative by nature, reflecting the need to future-proof new structures for their intended service lives. In contrast, the main task of bridge assessments is to ensure that the structure or parts of the structure do not fail under loading (Rücker et al. 2006). Shave (2003) states that the 'assessment of existing structures is a complex problem that presents different challenges and demands different expertise from design. Fundamentally it requires a deeper understanding of structural theory and, in particular, recognition of the true way structures behave as the ultimate limit state is approached'. Many international codes recognized this by adopting a reliability-based and risk-informed approach to help resolve the often conflicting demands of asset preservation and maintaining operation access where disproportionate expenditure associated with design reliability is unacceptable (Heywood et al. 2017).

Structures are designed to incorporate an operating margin (shown in yellow/red in Figure 1) between the calculated capacity and ultimately failure of a structure to allow for uncertainties in the loading, materials, design process and construction. Therefore, when undertaking an assessment with increased knowledge of the structure, its behavior and the loads it supports, it can be inferred that a smaller operating margin can be accepted when compared with accepting a new structure into service.

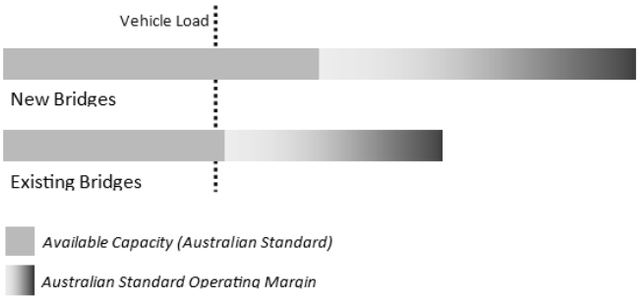


Figure 1: Operating Margins of new versus existing structure

The consequences of a conservative assessment methodology may include the unnecessary and costly strengthening or replacement of an asset. This conservatism arises from the adoption of design parameters for assessment and often leads to a 'plausibility gap' between unsatisfactory theoretical assessments and satisfactory past performance (Heywood et. al. 2017) that needs to be explained. One approach to understanding the plausibility gap is the adoption of realistic, bridge specific assumptions that reflect the actual loading, material strength and behavior of a structure. International assessment standards are addressing the 'plausibility gap', by adopting 'reliability-based' and 'risk-informed' assessment methods (ISO 13822:2015). Many international codes have applied these principles to help resolve the often conflicting demands of asset preservation and maintaining access in circumstances where 'disproportionate' expenditure associated with design reliability is unacceptable.

2.2 *Australian Assessment Approach*

Bridge evaluations within Australia are currently assessed in accordance with requirements set out in the Australian Standard suite (AS 5100); in particular Section 7 (AS5100.7) Assessment (Standards Australia 2017). Part 7 of AS 5100 was introduced in 2004 to rate existing bridges. However, its guidance was predominantly based on design principles, as confirmed by the commentary, which states in Clause C4: "Rating of bridges is based on the same principles and philosophy as the design of new bridges, as specified in AS 5100.1" (Heywood et al. 2014, Ng 2017). The Live Load Factor (LLF) stated for use when assessing a bridge is 2.0 compared with a LLF of 1.8 used when designing for SM1600 loading as specified in Part 2 of AS5100 Australia Standards 2017).

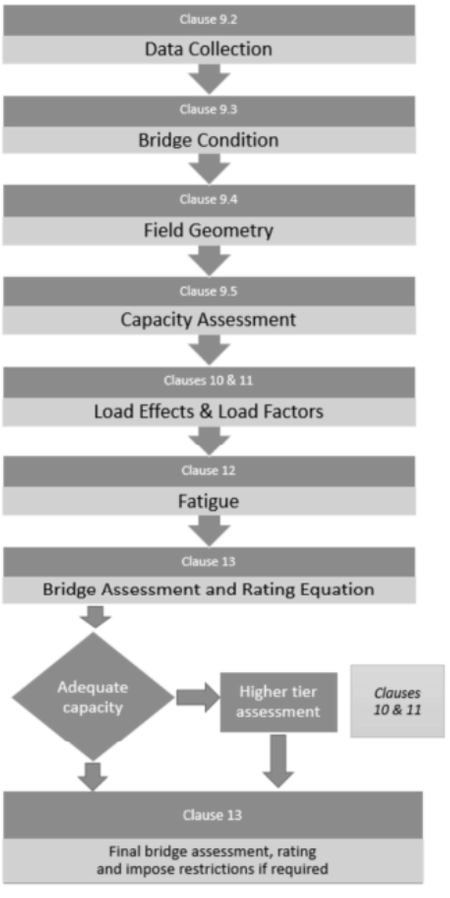
The recently revised version of AS5100.7 (2017) aligns with international practice by presenting a hierarchical framework of increasing complexity to enable optimized outcomes of assessments in accordance with the network access and safety requirements (Ng 2017). This framework is illustrated in Figure 2. Initially the assessment process is still largely based on design principles with capacity reduction factors and load factors in keeping with AS 5100.2 with some reductions being allowed when certain conditions are met (Australian Standards 2017). For example, reductions to the Dynamic Load Allowance (DLA) can be made where speeds are restricted or the measured road roughness is lower than the recommended threshold. Reductions in LLF are allowed when network specific vehicles, such as cranes or heavy load platforms, or if Intelligent Access Program (IAP) monitoring is installed on a vehicle. These modifications are shown in Table 1.

Figure 2, shows that if a structure is deemed to be operating at reduced margins, a higher tier assessment may be undertaken. AS5100.7 permits the use of advanced analysis methods, field testing (such as proof and dynamic load testing), structural health monitoring, and the use of other standards and codes (with approval from the relevant authority) (Standards Australia 2017). There is no specific guidance to Engineers or authorities as to the specific process or assumptions that should be incorporated as a part of a higher order assessment. The most recent ver-

sion of AS5100.7, while providing more advice on assessment of structures, still does not provide sufficient information to adress the 'plausibility' gap between theoretical assessments and in service behaviour that authorities are searching for. For example, there are currently no provisions in AS5100.7 (2017) to account for the remaining service lives of structures, reliability methods, target levels of reliability (β), site specific loading or the use of probabilistic methods in alignment with ISO 13822 and ISO2394:2015 (Ng 2017).

Type of load	Live load factor
Pedestrian, cyclist path and maintenance traffic loads	1.5
Traffic load (road traffic)	
(a) SM1600	1.8
(b) T44	2.0
(c) MS18	2.0
(d) H20-S16	2.0
(e) Semi-trailer, road train, B-double	2.0
(f) Road train and B-double with IAP and on-board mass weighing	1.8
(g) Crane	1.6
(h) Volumetric (livestock, liquid)	1.6
(i) Heavy load platform	1.5
Centrifugal forces (all road traffic)	1.8
Braking forces (all road traffic)	1.8
Traffic load (general rail freight traffic)	1.6
Traffic load (specific rail freight traffic)	1.4
Centrifugal and nosing forces (rail traffic)	1.6
Braking and traction forces (rail traffic)	1.6

Table 1 Traffic Load Factors for the Ultimate Limit State



(Standards Australia 2017)

Figure 2. Overview of AS 5100.7 (2017) existing bridge assessment procedure (Ng 2017)

2.3 *International Assessment Approach*

International assessment standards, such as ISO13822 'Basis for Design of Structures – Assessment of Existing Structures' (ISO 2010) and ISO 2394:2015 'General principles on reliability for structures' (ISO 2015), are addressing the 'plausibility gap', by adopting 'reliability-based' and 'risk-informed' assessment methods. While these standards are not bridge specific, they provide both practical and higher order guidance dedicated to structural assessment that are useful for bridge assessment in order to close the plausibility gap. ISO 13822 mandates that a plausibility check must be undertaken stating that 'discrepancies between the results of structural analysis (e.g. insufficient safety) and the real structural condition (e.g. no sign of distress or failure, satisfactory structural performance) shall be explained'. The standard provides some general guidelines for the assessment of existing structures with a focus on the principles of structural reliability and the consequence of failure. It acknowledges that assessment procedures for existing structures are vastly different to design code requirements for new structures, and that current design codes may provide insufficient knowledge to complete such an assessment in a thorough manner.

ISO 13822 (ISO 2010) provides an overview of a number of methods available to verify the reliability of a structure in terms of safety and serviceability. These include:

- Reliability assessment – takes into account the remaining working life of a structure, the reference period and changes to levels of service, and associated external changes.
- Target reliability level – accepted predetermined criteria to verify the safety and serviceability of a structure.
- Limit states concept – both ultimate and serviceability states are to be assessed, with consideration of the local and global structural effects and ductility.
- Plausibility check – to conduct a critical review of any discrepancies between the results of the analysis and the real-life condition of the structure.
- Assessment based on past performance.

Another standard that is relevant to the assessment of existing structures is ISO 2394:2015 General principles on reliability for structures (ISO 2015). This international standard constitutes a common basis for defining design rules relevant to the construction and in the use of the wide majority of buildings and civil engineering works, whatever the nature or combination of the material used.

ISO 2394:2015 (ISO 2015) constitutes a risk and reliability-informed foundation for decision making concerning the design and assessment of structures. It provides comprehensive guidance to the assessment of structures from both reliability and risk per-

spectives as well as traditional approaches. Its assessment approaches include (Cl 4.4):

- semi-probabilistic (lowest level)
- reliability-based
- risk-informed (highest level)

ISO 13822 (ISO 2010) and ISO 2394:2015 (ISO 2015) provide a framework for advancing bridge assessment in Australia. As discussed in Section 2.2, the new revision of AS5100 Part 7: Bridge Assessment (Standards Australia 2017) takes steps to differentiate between assessment and design. It also states that ISO 13822 (ISO 2010) "may be applied to show that a bridge is safe, provided the original physical and structural integrity of the component under consideration has not been significantly altered and similar traffic conditions have prevailed over the last 20 years (Cl 10.6.1)". This is a simplification of the provisions of ISO 13822 (ISO 2010) which include a number of additional criteria including condition and no changes to the conditions of loading occur.

The American Association of State Highway and Transportation Officials (AASHTO 2011, 2014) and Canadian Highway Bridge Design Code (CHBDC) address the disproportionally high cost of increasing safety of existing structures by adopting reduced target reliability indices compared to the design of new structures. Table 2 highlights the differences in the target reliability index and the reference period, reflected in changes in live load factor, between the design of new bridges and assessment of existing bridges.

Table 2 highlights some significant differences between assessment and design:

- The target reliability indices and the reference periods are smaller for assessment compared with design.
- The margins are smaller and greater care is required. As a consequence other refinements are considered such as ductility, redundancy and inspectability (Canada) and truck traffic volume (USA). The Canadian approach accepts lower margins for elements that are ductile, redundant and inspectable but penalises elements that are brittle, non-redundant and uninspectable. The result is load factors that are generally smaller but can be larger than design load factors. The AASHTO MBE (AASHTO 2011) code accounts for it through a reduction in the capacity reduction factor (ϕ).

In summary, the USA and Canada adopt different standards for accepting new bridges into service which are higher than the standards for removing bridges from service. This approach, which has been used in Canada since the 1980s, is consistent with the risk-informed approach of ISO 2394:2015 (ISO 2015). While the current revision of AS5100.7 has made a step in the right direction in acknowledging the difference between assessment and design, engineers and asset owners are looking for further guidance to explain the 'plausibility gap'. By providing engineers a framework in which to explore the 'plausibility gap' and develop an appreciation for the assumptions and associated risk it will enable asset owners to manage their networks in a more strategic and risk targeted manner.

Design or Assessment	*Reliability index (β)*	*Reference period*	*Load factors*	*Comments*
Canadian Highway Bridge Design Code – CSA S6-14 (12)				
Design	3.5	75 years	1.70	Design LL > 'as of right' traffic
Assessment	2 to 4	1 year	1.40 to 1.77	Depends on ductility, redundancy and inspectability
American Association of State Highway Transport Officials (AASHTO)				
Design	3.5	75 years	1.75	AASHTO LRFD Bridge Design Specification (13)
Assessment (Routine commercial traffic – Operational)	2.5	5 years	1.40 ADTT < 100 1.65 ADTT = 1000 1.80 ADTT > 5000	AASHTO Manual for Bridge Evaluation (MBE) (14)

Table 2 Differences between assessment and design: Canada and USA (Heywood et al 2017)

3 ASSESSMENT ASSUMPTIONS

3.1 *What is the capacity?*

An investigation was carried out by Collins (2015), where a thick slab beam was tested in shear to failure. Prior to undertaking the test, Collins invited 66 engineers from industry and universities to predict the failure load of the beam. A variety of codes were used by the participants and as can be seen in Figure 3, a vast range of answers were calculated from 300kN up to 4000kN. To put these shear capacities into perspective, the flexural capacity of the element was noted to be 2735kN. This leads the reader to question, which capacity is correct?

The beam failed at a load of 685kN. Based on the pre-test estimates provided, the majority of the predicted capacities were non-conservative as shown in blue shading in Figure 3. These results highlight that the assumptions used in an assessment are just as important to understand when making risk informed decisions as the result itself.

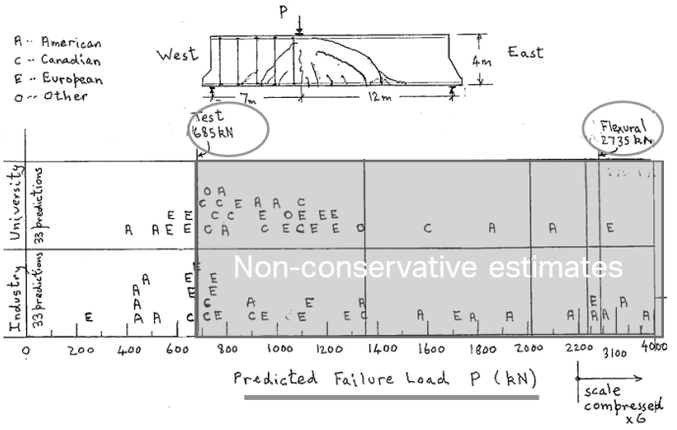


Figure 3: Load Failure Test Results (Collins 2015)

Without an appreciation of the assumptions by which a capacity of a structure is determined, asset owners cannot make informed decisions about the management of their structures.

To further illustrate the significance of assumptions, reviews of assessment outcomes have revealed a high degree of variability in results and a significant number of structures deemed as operating at reduced margins (Shaw et al 2014, Highways Agency 2003). The Queensland Department of Transport and Main Roads (TMR) undertook a review of over 500 bridge assessments and observed conservative and often erroneous results. The review determined that of the first 250 assessments, approximately 160 indicated that bridges were operating at reduced margins often contradicting the past performances of the structures. These low assessment results were due to conservative assumptions based on design practices and the use of inexperienced engineers leading to erroneous results (Shaw et al 2014).

A similar exercise was carried out by Parsons Brinckerhoff on behalf of the Highways Agency UK 10 years earlier (Shave 2003). A review of 294 bridge assessments was undertaken on structures deemed to be operating at reduced margins. The review analysed the reasons for the assessment failure and observed that the main contributing factors were:

- Increased loading
- Conservative analysis and assumptions
- Updates in standards/inappropriate use of standards
- Condition deterioration
- Design or construction errors

Both of these assessment reviews confirm that the assumptions used within an assessment are critical to the end result and that conservative design based assumptions can imply a structure is operating at reduced margins despite it still performing adequately. The results also imply that without a complete appreciation for the assumptions utilized within an assessment, the real risks cannot be understood and in turn managed.

To explore the impact of various assumptions and assessment approaches on assessment ratio, three investigations were undertaken:

- Code Comparison
- Assessment Methodologies
- Assessment Assumptions

3.1 *Limited Code Comparison*

In this section the shear capacity of prestressed concrete I girders are compared using the Canadian Highway Bridge Design Code and the 2004 and 2017 versions of the Australian Standard AS5100.

As discussed in Section 2.3, the CHBDC is one of the international standards that clearly differentiates between assessment and design parameters. It allows for a modification of the LLF based on the Reliability Index (β) and reference period. As shown in Table 3 this often results in a LLF less than that for design. However depending on the ductility, redundancy and inspectability of the element, it can result in an increase. Some of the other key differentiating assessment parameters between the Australian Standards and the CHBDC include:

- Material Factors – rather than use capacity reduction factors, material factors are applied to each individual material depending on the reliability of their properties.
- Dynamic Load Allowance – varies with relation to span. For spans <10m DLA = 0.4. For larger spans the DLA can be reduced up to 0.25.
- Special consideration for higher risk elements – provisions are included for higher risk elements (ductility, low redundancy, uninspectable) by increasing the LLF.

The above commentary by no means highlights all of the points of difference between the three codes. However, the abovementioned factors were used to compare the assessment of shear in pre-

stressed concrete I-girders using the three codes as shown in Table 3.

Table 3 Parameters for Prestressed Concrete I-Girders

Standard	LLF	DLA	Consideration of High Risk Elements	Method
AS5100.7 (2004)	2.0	0.4	No	Empirical
AS5100.7 (2017)	1.8	0.3	No	MCFT
CHBDC	1.8	0.25	Yes	MCFT

Note: MCFT = Modified Compression Field Theory

The following Rating Factor (RF) in accordance with the definition in AS5100.7 (2017) was used in the comparison:

$$RF = \frac{\text{Available bridge capacity for live load effects}}{\text{Live load effects nominated rating vehicle}}$$

Figure 4 illustrates the comparison between the Rating Factors for a particular prestressed concrete I girder superstructure when assessed using the three codes. The difference between the two Australian Standards highlights the difference between the truss analogy and Modified Compression Field Theory (MCFT) methodologies. Despite the differences in approach both indicate the bridge is operating at reduced margins.

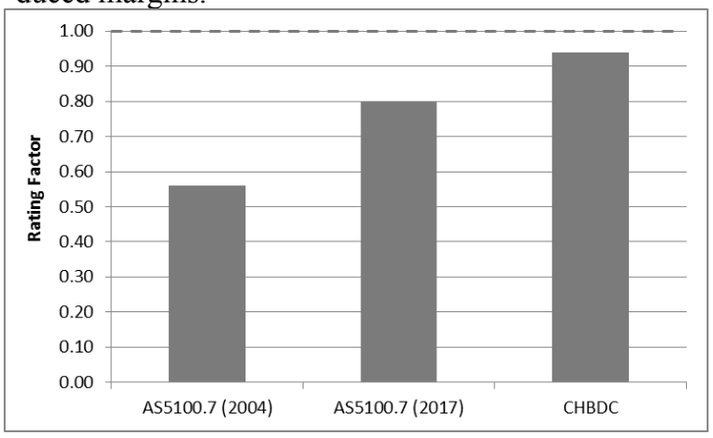


Figure 4 Rating Factor Comparison Prestressed Concrete I Girder Superstructure

The CHBDC is also based on Modified Compression Field Theory; however the capacity calculation is based on material factors compared with capacity reduction factors in the Australian Standards. This results in an increase of approximately 15% in the Rating Factor. The assessed structure showed no signs of overstress in the girders. The results indicate that there can be a significant variation in assessments when utilizing varying standards leading authority's to question their validity and which one is correct, if any. While all of the Rating Factors indicate the bridge is operating at reduced margins, the magnitude of the margin will influence the management strategy reinforcing the importance of understanding the assumptions behind an assessment.

This issue is not isolated to Australia with similar issues identified in USA (French 2010) and Germany (Teworte et al 2015). Moua et al (2017) investigated the impacts of assessment assumptions on the calculation of shear capacities of PSC-G bridges and concluded that the use of design based parameters was conservative for bridge assessments and that the use of higher order assessment methods was required to align with the in situ performances of the structures.

3.2 *Comparison of assessment methodologies*

The assessment of reinforced concrete deck slabs also tends to produce assessment results that are vastly different from the in service performances of structures. An investigation was undertaken to determine the variation in Rating Factor when various assessment methodologies and assumptions were used.

Three assessment methodologies/assumptions as applied to a bridge superstructure with a reinforced concrete slab deck with composite reinforced concrete kerbs, were investigated: elastic analysis; yield line analysis; and yield line analysis (including composite kerb). The comparison of the Rating Factors is shown in Figure 5.

The results indicate that if an elastic analysis approach to assessment is taken, the structure would be deemed to be operating at reduced margins (RF<1). The Highways Agency (2003) released a report stating that elastic analysis of concrete deck slabs can often lead to an inadequate assessment results. Concrete slabs have the ability to redistribute moments significantly prior to the formation of a failure mechanism and therefore an elastic analysis is rarely sufficient to prove that a slab is deficient in flexure.

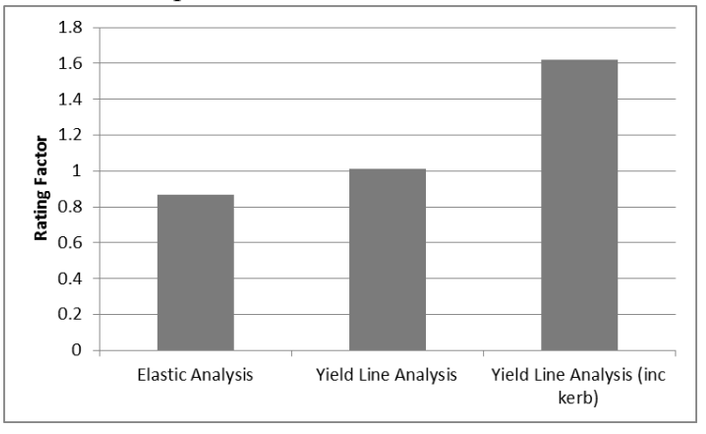


Figure 5 Rating Factor Comparison for Reinforced Concrete Deck Slabs

The yield line analysis indicated that the structure had adequate capacity – just. Whereas if the composite kerb was included, the results indicate the structure has sufficient reserve. The Highways Agency Report (2003) makes recommendations on an appropriate analysis methodology for reinforced concrete deck slabs. These results further build the case that the assumptions and risks associated with assessments must be understood in order to strategically and effectively manage structures on a network.

3.3 *Network Application*

An investigation of a group of 84 bridges was undertaken to compare the effects of assessment assumptions, and in turn investment decisions, across a network of structures. The sample of structures included bridges with prestressed concrete I girder and deck unit superstructures, and a variety of reinforced concrete substructures including portal frames and single columns. All assessed structures were deemed to be functioning satisfactorily based on their past performances under various different traffic scenarios.

The bridges were assessed at both Inventory and Operational Levels (Heywood et al 2017). At an Inventory Level, which is largely based on design parameters, 66 bridges had Rating Factors less than 1. When reassessed using Operational Parameters that reflected the existing life of the structure, condition, actual traffic loads and material properties and any higher risk elements, only 21 structures were deemed to be inadequate with RF <1.

The results once again reflect the importance of understanding the risks associated with the assumptions utilized in bridge assessments. Assessments based on parameters that better reflect the behavior of structures can provide a rational, risk-informed approach for the management of structures that have been deemed to have insufficient margins in accordance with Inventory Level assessments. Operational Assessments assist in explaining the plausibility gap between theoretical assessments and the in-service performance of structures. The use of operational bridge assessments can be used to inform investment and asset management prioritization. A Structure Management Plan should be put in place for operational structures to ensure the assumptions on which the assessment was based continue to align with the operation of the bridge.

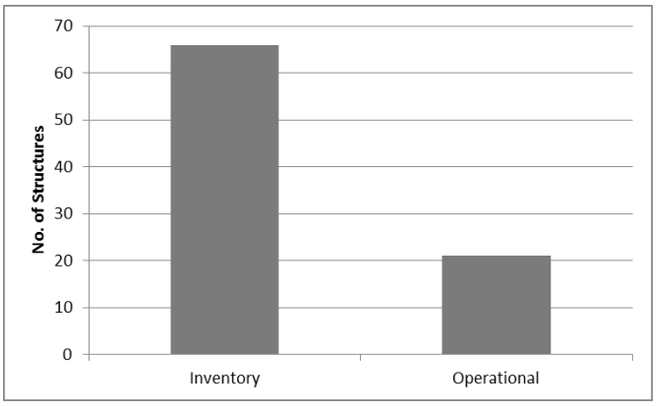


Figure 6 Number of Bridges with Rating Factors <1.0

4 DISCUSSION

The investigations outlined in Section 3 highlight the large variability in bridge assessment results based on the assumptions and methodologies underpinning assessments. Without an appreciation of these assumptions, it can leave asset owners questioning which assessments should be utilized for their management strategies. If conservative design assumptions or methodologies are applied, they can indicate that a significant number of structures are operating at reduced margins which don't correlate with the in-situ behavior of the structures, leading to a plausibility gap. International standards address this issue by applying a framework that allows assessors to include bridge specific assumptions that are based on observed bridge behavior and properties such as material strength. While the Australian Standard enables higher order assessments to be undertaken, there is no specific guidance to engineers or authorities as to the specific process or assumptions that should be incorporated.

It should be noted that higher order assessment does not necessarily indicate the need for refined assessment methods such as Finite Element Analysis (FEA). The investigations presented in Section 3 were undertaken without incorporating refined computer analyses. Assumptions that reflect the actual behaviors of the structures were used in the assessments. Where required, structural health monitoring or material testing can be undertaken to confirm these assumptions. While the use of FEA can be useful in certain circumstances and may indicate additional capacity, in simple elements such as a cantilever headstocks, no matter how refined the model, sufficient increase in operating margin will not be achieved if insufficient reinforcement has been provided in the original design.

When considering a framework for bridge assessments there are opportunities to learn from international experience and practice. Key items for consideration and further investigation include:

– A hierarchical, risk informed approach

- The adoption of a reliability-based assessment methodology
- Incorporation/guidance on the use of operational factors to reflect the actual behaviour of structures. This could include the use of material testing, actual vehicles based on Weigh In Motion (WIM)/Intelligent Access Program (IAP) data
- Consideration of higher risk factors including:
  - Redundancy
  - Inspectability
  - Ductility
- Guidance on appropriate factors to be used for infrequent vehicle assessments with increased control

Organisations, such as Austroads, have undertaken projects to investigate the various methodologies and processes adopted internationally for bridge assessments (Ng 2017). To ensure the ongoing credibility of the engineering profession more guidance is required to ensure bridge assessments results provide asset owners with a true appreciation of the risks associated with the ongoing management of their structures and networks. It is recommended that a supplementary guide be developed to complement AS5100.7.

5 CONCLUSION

Asset owners need to understand and, if necessary, refine the assumptions underpinning a capacity assessment of a structure. Assumptions which reflect actual, in-service behavior of a structure are more likely to result in realistic assessments than higher level analytical models such as Finite Element Analysis. By understanding the assumptions underpinning assessments, asset managers can make risk informed decisions when preparing their asset management strategies.

6 REFERENCES

AASHTO, 2014, "AASHTO LRFD Bridge Design Specification", 7th Edition, American Association of State Highway Transportation Officials, Washington DC.

AASHTO, 2011, "The Manual for Bridge Evaluation", 2nd Edition, American Association of State Highway Transportation Officials, Washington DC.

Austroads, 2016, Bridge assessment for High Productivity Freight Vehicle Access: Guidelines on Processes and Procedures, No. AP-R532-16, Austroads, Sydney, Australia

CAN/CSA S6-14, 2014, "Canadian Highway Bridge Design Code", Canadian Standards Association, Mississauga, ON, Canada

Collins, M.P., Bentz, E.C., Quach, P.T. and Proestos, G.T., 2015. The challenge of predicting the shear strength of very thick slabs. Concrete International, 37(11), pp.29-37.

French, C., "Discrepancies in Shear Strength of Prestressed Beams with Different Specifications", Minnesota Department of Transportation, January, 2010, pp 3-4.

Heywood, RJ, Shaw P, Mitchell J, Jager C, "Operational and Inventory Management of Bridges", 10th Austroads Bridge Conference, Melbourne, Victoria, 2017

Heywood, RJ, Shaw P, Pritchard, R, 2014, "Assessment Ratios for Evaluating Access by Heavy Vehicles to the Bridge Network", 9th Austroads Bridge Conference, Sydney, New South Wales, 2014

International Standard, ISO 2394: 2015, "General principles on reliability for structures"

Moua, P, Tsang J, Heywood R, Shaw P, "Shear in Prestressed Concrete I-girder Bridges", Austroads 2017 Melbourned

Ng A, Rooke A, Pape T, " Austroads Project TP1952 – Higher order assessments for existing bridges", Austroads, 2017 Melbourne

Rücker, W., Hille, F. and Rohrmann, R., 2006, Guideline for the assessment of existing structures, SAMCO Final Report.

Shave, J, 2003, A review of bridge assessment failures on motorway and trunk road network, Final Project Report, December, Highways Agency, Dorking, UK.

Shaw P, Pritchard R, Heywood R, "Bridge Analysis – Are We Data Managers or Engineers?", 9th Austroads Bridge Conference, Sydney, New South Wales, 2014

Standards Australia, 2004, "Bridge design Part 7: Rating of existing bridges", AS 5100.7

Standards Australia, 2017, "Bridge design Part 7: Bridge Assessment", AS 5100.7

Standards Australia, AS 5100.7 Supp 1–2006, "Bridge design Part 7: Rating of existing bridges – Commentary (Supplement to AS 5100.7–2004)"

Standards Australia, AS ISO 13822-2015, Basis of design of structures – assessment of existing structures (ISO 13822:2001, MOD), Sydney

Teworte, F. Herbrand, M. et al., "Structural Assessment of Concrete Bridges in Germany – Shear Resistance under Static and Fatigue Loading", Structural Engineering International, April, 2015

Maintenance, Safety, Risk, Management and Life-Cycle Performance of Bridges –
Powers, Frangopol, Al-Mahaidi & Caprani (Eds)
© 2018 Taylor & Francis Group, London, ISBN 978-1-138-73045-8

Bridge Risk Management: Credibility Gaps

P.S. McCarten
Queensland, Australia

ABSTRACT: Bridge asset managers are constantly facing significant challenges with aging bridge stocks, budget constraints and increased pressure from public scrutiny. The industry recognizes there are many technical and economic challenges associated with engineering and managing infrastructure systems. The reality that constructed systems perform differently than envisioned at planning, design, construction and operation phases in conjunction with the limited knowledge of constructed system behavior at different times and under different demand scenarios requires the Bridge Manager to apply a systematic risk based approach to developing maintenance, rehabilitation and replacement programmes.

In order to make good asset management decisions a Bridge Manager needs to:

- Understand the bridge management regime
- Have the knowledge and skills to challenge the code based design standards
- Have the ability to follow a systematic approach to investigating complex system problems
- Have the skills to identify the data (field and analytical) scope, extent and quality required to make informed decisions

For Bridge Asset Management Preservation Programmes to be adopted they must be recognized and accepted as credible by both the asset owner (Road Controlling Authority, RCA) and funding agency. A credibility gap occurs when there is a difference in expectation between the Bridge Manager and the approving agencies (in this Preservation Programme case the RCA and funding agency). Credibility gaps can occur in many aspects of bridge management and involve groups other than the RCA and funding agency, for example the freight industry and public community.

This paper provides an overview of bridge risk management and common credibility gaps and hence reinforces the need for good bridge asset management decision making. The recognition that bridge failures are continuing and with the average bridge age at failure being less than the normal design service life shows improvement in risk decision making is necessary.

1 INTRODUCTION

Bridge Managers have access to multiple tools to assist developing preservation and improvement programmes within a Road Controlling Authority (RCA) network. Bridge inventory and inspection data from both visual and special monitoring (e.g. structural health monitoring SHM) programmes is used with the analytical tools to develop maintenance, rehabilitation and replacement programmes to optimize network asset performance within the available budget. The analytical tools are also used in prioritizing network assets for more detailed assessments when the risks are determined to be significant – but what methods are used to quantify these risks?

Bridges under the responsibility of an RCA are generally public assets with budgets based on public monies. Bush et al (2011) recognized that while efficient application of current knowledge and learning is being achieved it may not be an effective use of effort and resources. Should sub-optimal outcomes result then it is contended there would be an adverse impact on the value of the public infrastructure. New Zealand Office of the Auditor General (NZOAG) and US Government Accountability Office (USGAO) audits confirm concerns in public spending identifying that:

- Bridge asset managers should move away from a maintenance and condition centric viewpoint to align with operational and strategic targets (USGAO 2008)
- Bridge engineers should deal with performance needs of an asset and provide the community with choices surrounding performance criteria (NZOAG 2004 and 2010)

- Bridge asset managers should move toward an advanced asset management approach

Advanced asset management is a process consisting of predictive modeling, risk management and optimized decision making to develop the required life cycle treatment options and long term funding predictions with clear links to delivered projects and strategic targets. Bush et al (2011) highlighted the importance of collecting complete, comprehensive and reliable data to define and report the linkage between bridge management and the wider strategic vision to ensure a sustainable and economic network is achieved.

McCarten (2012, 2014 and 2016) respectively set out the basic risk requirements, set out a performance measure regime which could be used to report the broader network performance and showed how more reliable performance measures could be achieved through a three level hierarchy of data collection, with:

Level 1 – qualitative

Level 2 – quantitative (based on as-built records)

Level 3 – quantitative (based on in-service performance records)

This paper focuses on risk but considers it in the wider context of the bridge management regime. The quality of the bridge risk decision making is also considered by making observations on 'credibility gaps' which suggest improvement may be required for Bridge Managers to maintain their role as trusted advisers to the RCA and wider community. This paper supplements the outcomes reported in the previous McCarten (2012, 2014 and 2016) papers.

2 BACKGROUND & DEFINITIONS

In order to understand bridge risk decision making it is necessary to understand the regime in which the risks are to be quantified and communicated. Most societies today have a degree of litigation, that is the tendency to take legal action to settle disputes. In litigious societies those making the risk decisions will be held accountable for their decisions. It is recognized those decisions will tend to be 'defensive' because the decision makers will be afraid of the cost, both monetary and reputational, if there is any possibility the decision taken could be inaccurate. Business sectors which consider they may be disadvantaged by bridge asset management decision making, e.g. the freight sector may consider decisions to downgrade a bridge load carrying capacity significantly and adversely impact their operations, and may pursue their right to challenge the decision making.

Bridge Managers and Bridge Engineers operating in a litigious regime will recognize the need for using high quality information, utilizing industry best practice and recognized assessment techniques to make the quality decisions expected by the RCA, industry and wider community.

Credibility is the quality of being 'trusted and believed' and relies on attributes of trustworthiness, reliability, dependability and integrity. Bridge Managers and Bridge Engineers must be credible to undertake their role as an adviser to the RCA.

A 'Credibility Gap' is defined as the apparent difference between what is said or promised by a representative of the government, large corporation or RCA and what happens or what is true. While the term first came into use in the 1960's and 70's with journalism, political and public discourse and was usually associated with skepticism about politicians it is now gaining wider use and is recognized in engineering and infrastructure management.

While it is clearly desirable to minimise the possibility of generating Credibility Gaps this paper will show that this outcome is unlikely for all gaps and Bridge Managers must manage them. Credibility Gaps will generally occur when the 'normal' bridge management and bridge engineering practices do not give the outcome expected by the RCA, industry and community.

This paper reviews bridge management systems and practices to identify likely and typical Credibility Gaps and provides suggestions for managing them.

3 MANAGING INFRASTRUCTURE SYSTEMS

Aktan et al (2013) have provided a comprehensive summary paper on managing complex engineering infrastructure systems. Civil engineering is a unique discipline as it is based on constructed systems while other engineering disciplines deal with manufactured products. Constructed systems are distinct in the way they are planned, financed, designed constructed and operated – especially with the uncertainties of as-built properties, loading, response and predicting changes in performance due to site specific conditions and environmental factors. The reality of how constructed systems actually perform can be significantly different from that envisioned by the designers, constructors and operators. It is recognized that each constructed system may perform differently at different sites even though the system is of a standard design.

The basic form for engineering and management of infrastructure systems is illustrated in Table 1 below.

Table 1: Performance Limit States, Hazard Event Exceedance Probability in the remaining Service Life (EP in SL), Criteria and Management

Limit State	EP in SL (%)	Performance Criteria	Lifecycle Asset Management
Utility & Functionality	100	Operational efficiency, safety & security; Robust and	Operational Management

		predictable lifecycle revenue stream	
Serviceability & Durability	>96	Effective and economical inspection, maintenance, repair & rehabilitation during lifecycle	Maintenance Management
Life Safety & Stability of Failure	20 - 60	Assurance of life safety, quick recovery of normal operations following a hazard (days-months)	Multi-hazards Risk Management
Safety at Conditional Limit States	<5	Minimise casualties, Protect escape routes, evacuation, search and rescue needs, Economic recovery (years)	Disaster response, Planning and Emergency Management

Table 1 shows the need to link the remaining service life EP for the limit state hazard events, the performance criteria for each limit state and the need for asset management throughout the lifecycle to ensure the performance requirements are met. It then becomes the responsibility of the Bridge Management team to either manage each bridge with compliance to the general Performance Limit States scheduled in Table 1 or to those specified by the RCA.

Bridge Managers are usually allowed the opportunity to adopt their own management strategy to achieve the specified performance requirements. While a wide range of management approaches can be adopted they are usually bounded by the following extreme strategies,

(a) Reactive approach to bridge management

(b) Proactive approach to bridge management

In many cases the RCA requirements will be set for a Bridge Management program which fixes the Bridge Inspection program and hence the use of the above strategies will be limited to either bridges requiring monitoring/special inspections or bridges identified with defects.

4 BRIDGE RISK MANAGEMENT

McCarten (2012) provided a comprehensive summary of bridge risk and risk assessment techniques from the basic definition with

- Likelihood considered to be the chance of something happening, often related to probability
- Consequence being the outcome of an event affecting objectives

The summary reinforced the need to implement risk management planning to obtain quality and extensive information on the fundamental issues:

- What can happen, how and why – by identifying the range of hazardous effects and the associated range of impacts on the structure response
- The possible consequences (in terms of impacts on objectives) and the factors influencing them
- The likelihood of the consequences and understanding what may affect the likelihood
- The effectiveness of controls in modifying the consequences or their likelihood
- The acceptability of the risk or the need for mitigation

Bridge management decision making is commonly based on using cost benefit analysis but this technique does not necessarily give high transparency for the risk decisions made.

The wider engineering industry has recognized the need to have transparency in risk decision making and provide guidance on industry and community acceptability. While there is still ongoing discussion and debate on the form and standards for risk management the representation given in Figure 1 below shows that generally accepted and in use.

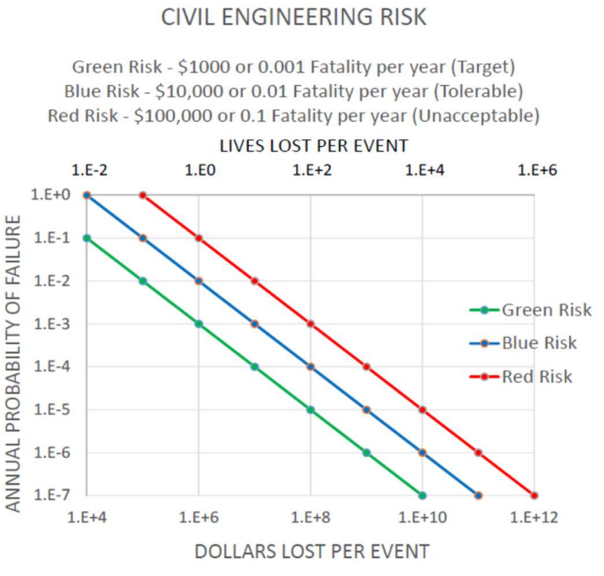


Figure 1. Civil Engineering Risk

Figure 1 has evolved from various studies including the following:

- the USACE to define acceptable risk for dam safety
- Baecher and Christian (2003) into geotechnical engineering risk
- Briaud et al (2013) into bridge scour risk

These studies have shown the risk representation and standards can be applied to various fields of civil engineering, but should they be applied to bridge management? This paper considers and reviews this proposition.

Figure 1 shows the generalized form for defining Civil Engineering Risk standards, recording target or acceptable [Green line], tolerable [Blue line] and unacceptable [Red line] risk standards. Figure 1 presents likelihood using 'Annual Probability of Failure' and consequences both in terms of 'Lives Lost per Event' and 'Dollars Lost per Event'.

While Figure 1 is used in this paper for discussion purposes for the application to a particular RCA calibration would be required, including:

- Adjusting the 'Dollars Lost per Event' to reflect the relevant currency
- Provide a method for adjusting the currency with time to ensure ongoing relevancy, and
- Calibrating the 'currency/life lost' ratio to meet jurisdiction requirements

Although Figure 1 has wide acceptance the presentation can be rationalized to take into account bridge management commonality and better fit bridge management decision making. Bridge hazards can be considered as likely, possible and extreme and relating these to repair, rehabilitation and replacement strategies is considered desirable. In this paper a well-managed bridge strategy will acknowledge extreme consequences (e.g. loss of life) are possible but this should not control basic decision making. More in-depth options analysis decision making would need to consider these consequences. The "Dollars Lost per Event" is the parameter that typically controls basic bridge decision making. In this paper it is assumed the bridge team is able to define and determine all direct costs associated with any repair/rehabilitation/replacement bridge strategy.

Over the last 20 years there has been significant research into methods and data requirements for determining the costs of bridge failure and the work of Wong et al (2005) provides a comprehensive summary of the direct and indirect costs that need to be determined. Wong et al (2005) developed methods for determining the cost consequences of both element and system failures for bridges, recognizing the differences between these bridge failure types, and identified there were deficiencies in the available information. The costs to be determined can be scheduled as below:

Direct Costs
- Bridge replacement (system failure)
- Bridge repair/rehabilitation (element failure)
- Access, traffic management and bridge removal (system failure)

Indirect Costs
- Traffic delay and diversion (element or system failure) during the bridge work
- Casualties (fatalities and injuries)
- Other costs, e.g. public enquiry/litigation, cost of reassessments of similar structures in the network (system failure), adverse public opinion and loss of morale

In this study it is necessary to determine the ratio of Total Cost/Direct Cost (TC/DC) for each event, recognizing the difference between an element failure and system failure event types, and irrespective of whether the event is planned (under a repair/rehabilitation/replacement program) or not. Wong et al (2005) investigated 9 case studies of bridges, with different materials, located in urban settings with relatively high levels of network redundancy (with many alternate routes available), bridges positioned over rail or road, and carrying relatively high traffic volumes (greater than 20,000 vpd along the road corridors). Based on the direct and indirect assumptions made in this study the Wong et al (2005) information suggests the following typical TC/DC ratios:

- Element failure 4.5 and 11.4
- Structural failure 41.5 and 49.8

Bridges in rural settings are typically located in a network with low level redundancy (low number of alternative routes), over waterways and carry relatively low traffic volumes and are expected to have significantly different TC/DC ratios. The Works Consultancy Services (1990) report determined actual direct costs of a bridge failure and assessed the indirect costs using the jurisdiction analysis method. Based on the assumptions in this study the Works Consultancy Services (1990) information provides a TC/DC ratio of 2.4 for the system failure. The bridge that failed was located adjacent to a small rural town (5,245 population) with limited network redundancy (the diversion cost was a significant proportion of the actual costs), the bridge was over water, bridge failure required temporary facility for utilities and pedestrian access (additional actual costs), and, the traffic volume carried on the bridge was low 3,217 vpd.

From the cases presented above there are clearly significant differences in the TC/DC ratio with these explained by the comments above. In this study the focus is bridge management decision making and it is considered both appropriate and realistic to use "lower bound" TC/DC ratios. The following TC/DC ratios have been adopted for the "lower bound"

- Element failure 2.5
- Structural failure 2.5

In adopting these TC/DC values it needs to be recognized the Direct Costs include all those necessary to complete the repair/rehabilitation/replacement, including:

- Actual physical works of the repair/rehabilitation/replacement
- Access works, including scaffolding, etc
- Temporary traffic management works, including diversion or shifting traffic routes through staged construction
- Temporary works removal, including diversions and the old bridge removal should a bridge replacement be required

It is also necessary to recognize that bridge management decisions involve financial expenditure and hence requires consideration of the 'true jurisdiction cost' of the indirect costs. In this study a sensitivity approach is taken to represent the jurisdiction perspective with an "upper bound" for decision making being TD/DC = 1.5. Based on this assessment the 'business as usual' tolerable risk guidance is given in Table 2 assuming the likely, possible and extreme bridge hazards have annual exceedance probabilities (AEP) of ≥ 20%, 3% and ≤ 0.5% respectively.

Table 2: Bridge Management Decision Making – Business as Usual
(Tolerable Risk $10,000 – Blue line)

Hazard	AEP (%)	"Dollars per Event" - Direct Cost	
		Maximum "Upper bound"	Element or System Failure "Lower bound"
Likely	≥ 20	$33,300	$20,000
Possible	3	$222,200	$130,000
Extreme	≤ 0.5	$1,333,300	$800,000

5 BRIDGE MANAGEMENT CREDIBILITY GAPS

The general definition of a Credibility Gap is presented above but in application to bridge management three different forms are identified. The forms are associated with different aspects of bridge management and are dependent on the 'degree of transparency' and 'level of communication' undertaken by the RCA or relevant stakeholder, e.g. funding agency. The three forms are given below:

1. Credibility Gap 1: Acceptance of the bridge maintenance or investment program. This gap is usually characterized by 'interest groups' within the community advising the investment program does not align with their expectations. Management of Credibility Gap 1 is focused on communications and consultation to ensure outcome expectations are better aligned
2. Credibility Gap 2: RCA bridge planning does not align with current practice. This gap is usually characterized by 'industry stakeholders'. An example of this gap is heavy haulage route planning where RCA information on route selection and strengthening requirements is based on theoretical analysis but industry practice based on actual usage suggests different outcomes, refer to Heywood (2016). Additional data collection, analysis and review, possibly with independent verification may be required to close the gap
3. Credibility Gap 3: RCA risk decision making does not align with government or community expectations. Three sub-types of Credibility Gap 3 occur with these defined by:
    a. Expected (Planned): 'Business As Usual' (BAU) bridge risk management. Bridge Manager and Bridge Management Team are required to know the assets, know the environment and associated hazards and manage the bridges accordingly. It is assumed the bridge service life is 100 years and hazards with 50% probability of occurrence in the service life (i.e. a 0.5% AEP of occurrence or 200 year return period event) should be managed
    b. Unexpected (Unplanned): Extreme event risk management. It is necessary to define the bounds of the BAU risk management to know whether the risks are extreme or not, and those used in this paper are given above
    c. Varying (Policy dependent): This Credibility Gap is essentially a subtype (a) but with uncertainty in assessing either the hazard or consequences and hence risk is poorly defined. Examples include lack of understanding the environment (e.g. seismic hazards (fault location and fault movement magnitude and likelihood) in some countries are not fully mapped and defined) or scientific evidence of hazards is not fully available (e.g. climate change). This reinforces the need for the Bridge Manager and Management Team to know the bounds of the BAU risks

Credibility demands are increasing with increasing traffic and freight demands and higher performance expectations. The case studies and discussions given

below focus on Credibility Gap 3 Sub-type (a) BAU bridge risk management.

6 CASE STUDIES

Four case studies are presented below providing different perspectives of bridge risk and failure issues before summarizing observations and detailed evaluations.

6.1 *General bridge failure analysis (2003)*

Wardhana and Hadipriono (2003) undertook analysis of over 500 bridge failures that occurred between 1989 and 2000 in the United States. The study found the failures related to design, detailing, construction, maintenance, materials and external event categories. The average bridge failure rate was 42 bridges per year and the average age at bridge failure was 52.5 years, with the range of ages from 1 year (during construction) to 157 years. The most frequent causes of bridge failure were attributed to floods and collisions, with floods (including scour) representing 53% of all failures. Bridge overload and lateral impact forces, from trucks, barges/ships and trains) constituted 20% of all bridge failures. The study reported that the design process was vulnerable to discontinuity or loss of the original design concepts. The mistakes, errors and omissions in the design process and the need for the bridge management team to be fully aware of the design concepts was emphasized. The study analysed the bridge type and bridge material to determine the numbers of failures of each. While the analysis did show that steel beam/girder and steel truss bridges constituted over 50% of all the bridge failures the study did not relate the numbers of bridge failures to the total numbers of each bridge type in the sample network studied nor relate the bridge failure category to the bridge type to determine the true vulnerability of each bridge and material type. The study recommended categorizing the failures as enabling (design or maintenance process), triggering (external event) and procedural (or management related) and suggested data for each should be collected and included into existing or new databases for future analysis. The study found that 11% of bridge failures were attributed to enabling causes with 85% to triggering causes. Further analysis showed 8% of the failures were maintenance related. The study reinforced the need for Bridge Managers to understand the triggering risks.

6.2 *General bridge failure performance (2014)*

Cook (2014) undertook analysis of over 100 bridge failures that occurred between 1987 and 2011 on a sample of New York State Department of Transportation bridges in the United States. The study followed the general method used by Wardhana and Hadipriono (2003) in respect to cause categorization but used the sample size to determine annual probability of failure estimates. The study also assessed conditional probabilities of collapse rates with consideration of the features used for the constructed bridges. The average bridge failure rate of 1/4,700 for the sample was verified by analyzing a further 6 samples before extrapolating to predict a total United States collapse rate of 128 bridges/years (95% confidence interval of between 87 and 222). The most frequent cause of bridge failure was attributed to floods and collisions, with floods (including scour) representing 52% of all failures. Bridge overload and lateral impact forces, from trucks) constituted over 30% of all bridge failures. The study recognized the sample may indicate failure trends specific to practices used in the sample region. The hydraulic data was analysed to check sub-category failure rates but the lack of clarity in the data limited this, it was considered that up to 80% of the hydraulic failures may be attributed to scour. The study found no significant reduction in collapse rate with enhancement of bridge design regulations. Although bridge age was a significant factor in maintenance and condition failures it was not significant in external event or triggered failures. Figure 2 below shows the distribution of bridge failures by age for the sample population.

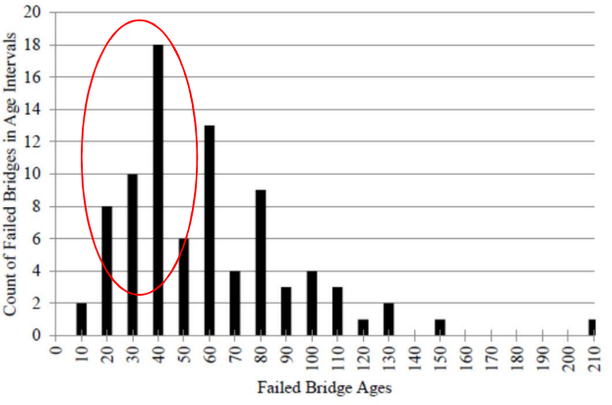


Figure 2. Distribution of bridge failures by age.

The average failure age is 54.8 years with a median of 50.5 years. The recognition that half the bridge failures have an age of less than 50 years, that hydraulic failures are common (with an average failure age of 47.9 years) and that the flood events that caused the failures are typically within the design standard range suggests there is room for improvement. It was noted that insufficient failure data was available to test the benefits of implementing under water inspections. The study report determined that by reducing the hydraulic failures by approximately 50% could reduce the annual total bridge failure rate by almost 30% and it is observed by addressing the failures highlighted in Figure 2 could improve the failure distribution and

the average bridge age at failure. The study concluded that more detailed information was required, on both causes and consequences, for future failure analysis and this requires a more robust data collection system that should be regulated or mandated at a federal level.

6.3 *Wairoa Bridge failure (1988)*

During Cyclone Bola (March 1988) the 56year old Wairoa Bridge failed with 6 of the 12 spans being washed away. The bridge provided SH2 access through the rural town of Wairoa (population 5,245) carrying traffic (AADT 3,217 vpd), pedestrians and the town main utilities. The replacement bridge was opened in December 1989 and a study of the failure costs was reported in Works Consultancy Services (1990). The costs took into account the initial 31km detour (March to June 1988) and the subsequent 12km detour in place through to bridge opening. While the new bridge direct costs amounted to $6.9M, other infrastructure costs (including both direct and consequential) amounted to $3.4M and when the additional road user costs were assessed the total cost of the bridge failure amounted to $18M. There was no loss of life associated with this bridge failure. The consequential costs were determined to be approximately 2.4 times the direct infrastructure costs. Hydraulic studies undertaken as part of the bridge replacement design showed the flow discharge experienced during the flood approximated 3% AEP event while the storm was assessed at a 1% AEP event. Even without correcting the dollars for time plotting these historic dollars and event probability range on Figure 1 shows the bridge failure falls beyond the 'unacceptable' red line. The bridge management industry needs to review this type of event to determine appropriate guidelines for managing the associated risks.

6.4 *Minneapolis I-35W Bridge failure (2007)*

In August 2007 the Minneapolis I-35W Mississippi River Bridge failed completely under peak hour traffic. The bridge (Wikipedia 2017) provided direct access to downtown Minneapolis, the University of Minnesota, area businesses and north suburban destinations for more than 140,000 vehicles per day. The bridge failure resulted in 13 deaths and 145 injuries and in any risk measure this is considered 'unacceptable'. The additional transportation costs associated with the failure due to detours (time and travel costs) were determined to approximate $400,000 per day and total $220M before bridge replacement, no cost has been put on the loss of human life. The economic impact of the bridge failure was estimated at $113,000 per day or $60M before bridge replacement. The replacement bridge cost was $234M. The technical review of the failure determined under sized gusset plates and renovations that reduced bridge strength and added extra bridge loading caused the failure. From ongoing inspection and rating the bridge was known to be structurally deficient. While the author is not aware of any failure probability assessment it clearly failed in the 40year service life and could be given a 0.5% to 3% AEP range. Plotting this event on Figure 1 clearly shows the event was 'unacceptable'. Due to the high profile of this failure the bridge management was put under close scrutiny and the duty of care and ethics of the team challenged and the litigation cases were substantial. The bridge management industry needs to review the decision making for this type of event to determine guidelines for managing the associated risks.

7 DISCUSSION

Bridge Managers need to show accountability and governance for the network bridge stock. In order to achieve this outcome informed decision making is required in all aspects of bridge management. Transparent and appropriate investigation, analysis and option assessment provides accountability for the processes. Credibility for the outcomes is tested when they are communicated to others. The paper has presented three types of credibility gap that may need to be managed. The Type One and Two credibility gaps can generally be addressed through comprehensive and transparent technical and communication processes. Type three, risk management, credibility gaps are starting to be recognized as the industry and community are being informed on the performance expected. Currently there are only a limited number of jurisdictions maintaining records of bridge failures and the standards for acceptable bridge risk management have not yet been set. Through the case studies of bridge failures and consideration of the Civil Engineering Risk the following potential credibility gap issues were identified:

1. Failure likelihood has been reported as 1/4,700 bridges, but should this be 1/6,000 or 1/10,000 to reflect the consequential costs to the community?
2. Failures typically occur during the bridge service life
3. Average bridge age considering all failures is 54.8 years, well below the design service life
4. Average bridge age for hydraulic failures is 47.9 years, well below the design service life
5. Specific bridge collapse failures show the consequential costs are significant and by most community measures are 'unacceptable', this is supported when the events are

plotted on the industry wide Civil Engineering Risk profile, Figure 1

6. There should be an industry agreed definition of bridge failure
7. Improvement in failure reporting and analysis is required to ensure informed decisions are made from the 'lessons learned'

It is recognized that managed bridge repair, rehabilitation and replacement limits the consequential costs and hence results in more acceptable bridge risk management. Examination of the bridge failure age distribution shows there is significant benefit in 'lessons learned' from the young bridge failures. Comparisons made to the industry developed Civil Engineering Risk profiles made in this study show it can provide a transparent basis for bridge management and the 'tolerable cost bounds' given in Table 2 could be used in decision making. It is recognized that should a bridge collapse occur then the event will most likely be 'unacceptable' and hence it is considered the RCA should encourage bridge managers to use a proactive preventive approach for bridge risk management to minimize the potential for extreme failures.

In order to manage the 'unacceptability' and consequences of extreme failures RCA's should be prepared. It is considered necessary for RCA's to have preparedness and emergency planning in place, with this involving ready access to temporary bridging facilities, trained and prepared recovery teams and emergency funding to manage the events. This study also reinforces the need to have high quality recording systems and emphasizes the seamless integration between bridge design and management teams.

8 CONCLUSIONS

It is concluded there is significant potential for credibility gaps in bridge risk management. To meet funding agency and community requirements for transparency and accountability it is suggested the industry wide Civil Engineering Risk be accepted for bridge management and the 'tolerable risk' profile be adopted for business as usual decision making. It is recognized that should bridge collapses occur the consequences will most likely be beyond the 'unacceptable risk' profile. To ensure credibility the RCA should encourage proactive preventive bridge management strategies be followed and preparedness and emergency planning be implemented. Jurisdictions must implement and maintain bridge failure reporting and regularly review and report on 'lessons learned'. Increasing traffic and freight demands on the road network in conjunction with increased expectations of performance reinforce the need for ongoing improvement in bridge risk management.

9 DISCLAIMER

The observations in this paper are those of the author and are presented to advance the topic in practice.

10 REFERENCES

Aktan, A.E., Moon, F. L., and Lowdermilk, D. S,. 2013. Engineering and Management of Infrastructure Systems. Presented to the 6th International Conference on Structural Health Monitoring of Intelligent Infrastructure, Hong Kong.

Baecher, G. B. and Christian, J. T. 2003. Reliability and statistics in geotechnical engineering, Wiley, New York.

Briaud, J-L., Gardoni, P. and Yau, C. 2013. Statistical, Risk, and Reliability Analyses of Bridge Scour. Journal of Geotechnical and Geoenvironmental Engineering, ASCE, ISSN 1090-0241/04013011(10).

Bush, S., Omenzetter, P., Henning, T. and McCarten, P.S., 2011. A Risk and Criticality based approach to Bridge Performance data collection and monitoring. Structure and Infrastructure Engineering, Special Edition: Asset Management, Taylor & Francis, UK.

Cook, W. 2014. Bridge Failure Rates, Consequences, and Predictive Trends. PhD dissertation, Utah State University, Logan Utah USA.

Heywood, R. 2016. Bridge assessment: An international perspective. Proceedings from the Engineering Technology Forum, Department of Transport and Main Roads, Queensland, Australia.

McCarten, P. S., 2012. Bridge Risk Management: Back to basics. Proceedings of IABMAS'12 Conference, Stresa, Italy.

McCarten, P. S., 2014. Bridge performance measures: A fresh perspective. Proceedings of IABMAS'14 Conference, Shanghai, China.

McCarten, P. S., 2016. Bridge Performance Measures: Robustness- Redundancy. Proceedings of IABMAS'16 Conference, Iguazu Falls, Brazil.

New Zealand Office of the Auditor General, 2004. Report of the Controller and Auditor General on Local Government: Results of the 2002/03 audits Part 2 Other Issues arising 2002/03. Wellington, New Zealand.

New Zealand Office of the Auditor General, 2010. New Zealand Transport Agency: Information and Planning for Maintenance and Renewing the State Highway Network. Wellington, New Zealand.

United States Government Accountability Office, 2008. Highway Bridge Program: Clearer Goals and Performance Measures Needed for a More Focused and Sustainable Program. GAO-081127T, Washington D. C., USA.

Wardhana, K., and Hadipriono, F. C. 2003. Analysis of Recent Bridge Failures in the United States. Journal of Performance of Constructed Facilities, ASCE Vol. 17, No. 3, August, 2003.

Wikipedia. 2017. I-35W Mississippi River Bridge. https//en.wikipedia.org/wiki/I-35W_Mississippi_River_Bridges

Wong, S.M., Onof, C.J., and Hobbs, R.E. 2005. Models for evaluating the costs of bridge failure. Proceedings of the Institution of Civil Engineers, Bridge Engineering 158, 117-128, ISSN 1478-4637.

Works Consultancy Services. 1990. Wairoa Bridge Failure: Assessment of Total Costs. Transit New Zealand, Wellington, New Zealand.

Maintenance, Safety, Risk, Management and Life-Cycle Performance of Bridges – Powers, Frangopol, Al-Mahaidi & Caprani (Eds)
© 2018 Taylor & Francis Group, London, ISBN 978-1-138-73045-8

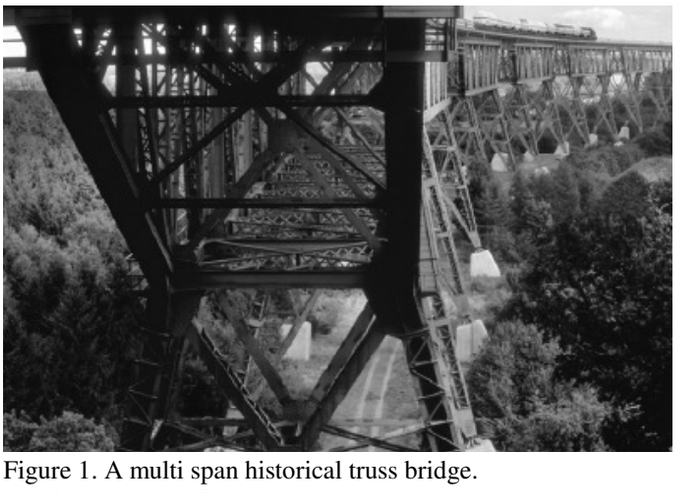
Codes and standard issues in assessing existing bridges

R. Pavan E. Siviero
AP&P srl, Italy

ABSTRACT: The assessment of existing structures adopting a specific code or standard is a technical procedure that is provided only in some nation. The possibility of harmonizing these type of procedure is needed in Europe, together with a completely new plan of infrastructural renewal. In this study new insight on this theme are provided, together with some code proposal for the new Eurocode era.

1 INTRODUCTION

Many existing bridges all over the world were not designed for the high service loads and the increased number of load cycles that they are exposed to today. Some bridges will have to be either strengthened or replaced in the next decades. Advancing their age, bridges could be subjected to a large variety of not designed actions or could also be not accurately maintained, leading to a particular state in which they need particular care and attention, in order to remain in service. Moreover, existing structures were not exempted from serious failures and engineers had regularly to suffer setbacks.
These setbacks contributed in many cases, however, to research and advancements in better understanding structural behavior and developing new theories (Kuhn et al. 2010). In these cases, the assessment procedures are needed.
The assessment of an existing structure aims at producing evidence that it will function safely over a specified residual service life. It is mainly based on the results of assessing hazards and load effects to be anticipated in the future, and of assessing material properties and geometry taking into account the present state of the structure (JCSS 2001). Guidelines for existing structures exist in a large number of countries. Thereby many countries have presented documents for particular categories of structures. In Canada, Germany, the Netherlands, Switzerland, UK and USA such guidelines have been prepared at a detailed level. In any assessment, the problem of fixing risk acceptance criteria is difficult since it must be compatible to codes for new structures (limit state analysis, safety factor format, etc.), and with national determined parameters (generally partial safety factor values) (Kuhn et al. 2010).


Figure 1. A multi span historical truss bridge.

As far as specific code and standards are not available, technical guide or pre-standard documents should be used. Moreover, procedures coming from evidenced based or field related experience, are quite extensively used also by bridge and infrastructures owner. Basing on past studies and research, a simplified approach has been developed by the author and applied in recent investigations of existing bridges. This approach is reported in the following paragraphs.

2 ASSESSMENT

2.1 *Ist level assessment*

The preliminary evaluation is the first level of investigation aiming at removing existing doubts about the safety of existing structures, adopting fairly simple methods and identifying critical parts or members in the structure. In order to identify critical members, it is necessary to carry out an intensive study of the available original design documents, along with a visual inspection of the structure and a photographic survey. The inspection procedure is of-

ten coded by infrastructural agencies manuals and procedures; however, at least the following points must be checked:

• The bridge construction is conforming to the original drawings and/or differences between as-built and drawings.

• Bridge modification during service (rehabilitation, strengthening, changes in the static system, etc.).

• Presence of any visual evidence of degradation (damaged expansion joints, supports, corrosion, cracks, vibration or loose rivets, collision, lack of structural members etc.).

Moreover, if available, inspection and maintenance reports can be used, and reference should be made to the evaluation report. The preliminary evaluation should include codes and recommendations analysis procedure where available, and conservative assumptions where information is lacking or doubtful. In this way, critical construction details can be identified.

2.2 *IInd level assessment*

The aim of the detailed investigation is to update the information obtained in other analysis by carrying out a refined assessment, especially for those members for which adequate safety was not confirmed by preliminary evaluation. At this stage a specialized consultant should assist. In this phase a FEM numeric model of the entire structure is developed. Based on the current code provisions, the structure should be recalculated and verification tables should report whether the structural members are safe or not. Concerning specific issues, such as the fatigue and seismic behavior of the bridge, detailed code provisions should be referred to. From this step-level investigation, non-destructive testing (NDT) could be used in order to characterize the basic material properties of the structure. The final report of the investigation should establish whether the structure is verified against specific issues and has sufficient static strength against actual loadings.

2.3 *IIIrd level assessment*

In case of key structures that have major consequences in terms of risks or costs related to a decision, a team of experts is needed in order to carefully check the conclusions and proposals reached in the last phase. Discussions and further assessments using specific tools can also be carried out to help reach decisions. At this level, on-site testing could be adopted in order to provide the dynamic identification of the structure, as reported in the following example.

2.4 *IVth level assessment*

This advanced level of investigation should be reserved for recurrent bridges along infrastructural nets, in which a rational procedure of analysis and intervention could help in determining if retrofitting interventions could be adopted, or if rational dismantling large scale operations are required. The procedure is based on a detailed survey of the existing bridge, a FEM analysis, a code verification procedure, NDT diffused sampling, and, based on these data on real scale testing of one case study structure, aims to determine the global static and cyclic behavior of the bridge. In specific cases, on-site dynamic identification could be performed. Concerning the fatigue assessment, in this case a LEFM investigation is required. Concerning seismic analysis, non-linear analysis is required. Specific material testing analysis should be performed dealing with the case analyzed. The advanced testing result should report on the various analysis performed, and should clearly state verification results indicating the specific retrofit needed for recurrent interventions. An advanced testing operation is reported in the following section, dealing with a recurrent existing bridge type in service along the railway lines.

2.5 *Assessment case studies*

As reported in the aforementioned step level classification, various stages of analysis could be adopted by bridge owners or managing agencies. Some examples have been developed by the author and could be found in detail in Pipinato (2016) the assessment of a new bridge is presented in order to evaluate different typologies of construction alternatives to gain different lifetime; while in Pipinato (2014) the assessment and rehabilitation of steel railway bridges using fiber-reinforced polymer (FRP) composites in the particular situation of the rehabilitation of metallic civil infrastructure using fiber reinforced polymer (FRP) composites is evaluated. The residual life of historic riveted steel bridges could be also assessed with an analytical approach or introducing an orthotropic steel deck design to extend the lifetime of plate and box girder bridge and viaducts, as explained in Pipinato et al. 2014 and in Pipinato (2014a). And however steel bridge exhibited in the past a wide amount of problems not evidenced in other bridges (Pipinato 2014b), for this particular type of structure a variety of technologies to repair and retrofit are available: this is the case reported for the fracture propagation and life cycle design of girders (Pipinato 2014c), or for advanced solutions of the corrosion protection (Pipinato 2014d). For network of bridges, however, an integrated solution has been presented in order to understand what is the possibility of prioritizing the bridge retrofit (Pipinato 2013a). A particular asset of bridges in

which the lifecycle assessment should be performed from the design stage is the case of long span bridges, where the traffic is represented also from exceptional moving loads and the consequent fatigue expected lifetime could fail in less than ten years from the construction stage if a correct detailing is not perceived (Pipinato 2013b-2013c-2010d); similar issues comes also from the original construction alternative choses, as demonstrated in Pipinato et al. 2012a. The particular case of fatigue sensitive materials of course is more recurrent in steel bridges where retrofit and assessment alternatives are in part applied (Pipinato 2012b), in part not well investigated, as is the case of coupled damages (seismic and fatigue, Pipinato 2012a,b, Pipinato et al. 2012c,d,e,f, Pipinato et al. 2011c,d). Wherever there is the possibility to investigate with full scale tests existing bridges, e.g. where managing agencies are interested to know the structural behavior of recurrent structures along their network, this could be an interesting occasion to understand how materials decay could influence the static and fatigue behavior of bridges: this is the case both of railway (Pipinato et al. 2011a,b, Pipinato 2011, Pipinato 2010b, Pipinato et al. 2010a,b,c,e Pipinato 2010, Pipinato et al. 2009, 2008a,b, Pipinato et al. 2007) and roadways (Pipinato 2010a). A particular and further subset is represented by monumental and large bridge structures (Pipinato and Modena 2010): in this case, a long and time-consuming but useful procedure should be performed, by evaluating al the assessment steps described before, in order to understand in detail the aforementioned problems that could influence the final retrofit design decision.

3 ESTIMATION OF KNOWLEDGE LEVEL AND CONFIDENCE FACTOR

The application of the aforementioned assessment procedures, lead to consequences in the structural analysis of the structure. Generally, as much information and tests have been performed onto the bridge, as much knowledge has been accumulated onto the structure, leading to more accurate data on the structural properties of materials, and on the structural behavior of the bridge itself. On the basis of this, a knowledge level listing could be drafted out, and consequently the so-called confidence factors could be applied, in a very similar procedure to the Italian existing standard for the assessment of existing buildings (Ministerial Decree, 2008).

3.1 *KL1-Knowledge level 1*

Geometry: the geometry of the structure is known or from a survey or from original drawings. In the latter case a visual survey is required to confirm the documentation. Collected data should be sufficient for developing a linear analysis.

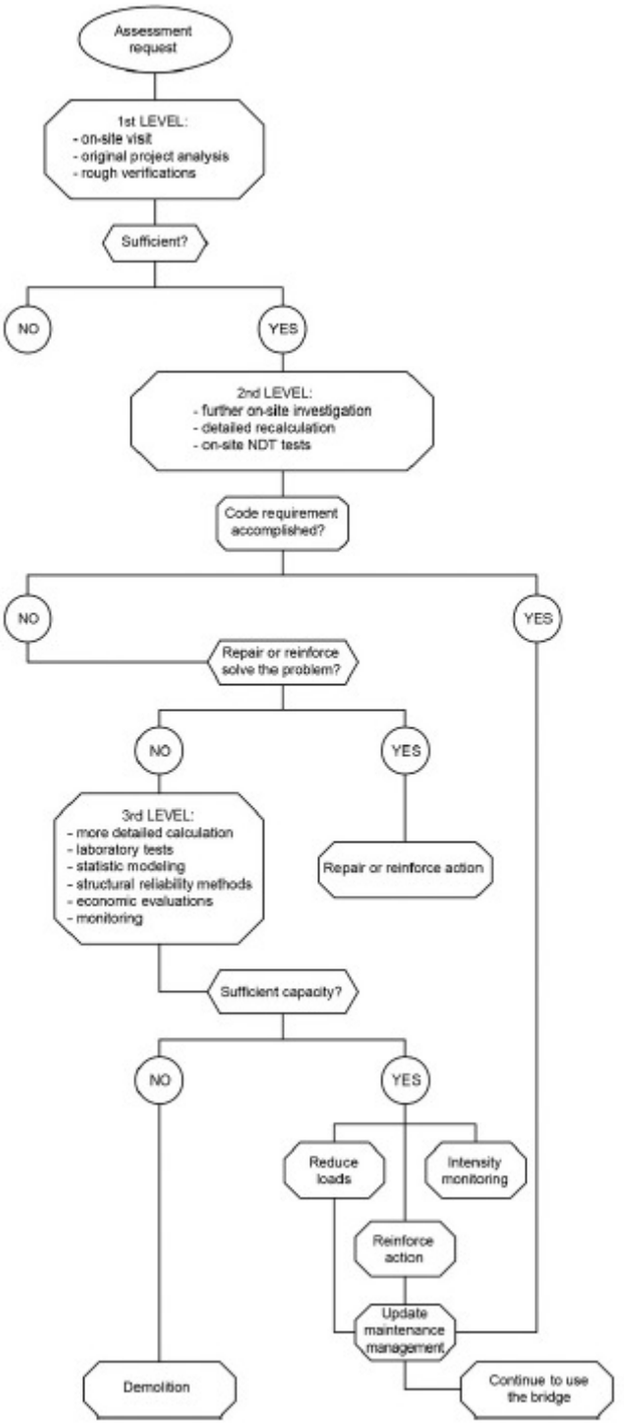


Figure 2. Step level assessment.

Structural details: details are not available from drawings and are designed according the practice of the construction age. A limited in situ verification is requested. Local resistance verification are required.
Materials property: material properties are not available, neither from the original documents, nor from original tests. Usual values of the practice are adopted, validated from limited in-situ tests.
Structural analysis type: The safety assessment in the case of limited knowledge is usually performed by static and dynamic linear analysis methods.

3.2 *KL2-Knowledge level 2*

Geometry: the geometry of the structure is known or from a survey or from original construction drawings. In the latter case a visual survey is required to confirm the documentation. Collected data should be sufficient for developing a linear or a non-linear analysis.
Structural details: details are available from original drawings or from not original construction documents. In this last situation, a limited verification of common details is performed. Local resistance verification are performed.
Materials property: material properties are available, from the original documents, or from original tests. Extensive in situ tests are performed to validate the original data whereas they are available from design and not from tests.
Structural analysis type: The safety assessment in the case of limited knowledge is usually performed by static and dynamic linear or non-linear analysis methods.

3.3 *KL3-Knowledge level 3*

Geometry: the geometry of the structure is known or from a survey or from original drawings. In the latter case a visual survey is required to confirm the documentation. Collected data should be sufficient for developing a linear or a non-linear analysis.
Structural details: details are available from original drawings or from original construction documents. Available data enable the implementation of a complete linear FEM model, performing local resistance verification, or the implementation of a non-linear model.
Materials property: material properties are available, from the original documents, or from original tests, or from an extensive in situ testing program. In the first case, limited in situ tests are developed to confirm the historical values; if the values obtained are minor than the original, an extensive in situ program is settled and performed. Available data enable the implementation of a complete linear FEM model, performing local resistance verification, or the implementation of a non-linear model.
Structural analysis type: The safety assessment in the case of limited knowledge is usually performed by static and dynamic linear or non-linear analysis methods.

3.4 *Confidence factors*

The confidence factor range should be calibrated according to the engineering knowledge level of the structure. Suggested values are in the following range:
- Confidence factor α: 1.30-1.35
- Confidence factor β: 1.20-1.25
- Confidence factor γ: 1.00-1.10

Although this procedure is suggested, it remains on the engineering choice of the structural engineer to establish the use of the confidence factor of the corresponding knowledge level, or in alternative, to use a lower confidence factor, when doubts arise from calculation. The confidence factor (CF) is considered a partial safety factor to be applied to the design strength in order to take into account for the lack of knowledge when analyzing existing structures:
$Fd = fm / (CF * \gamma m)$.

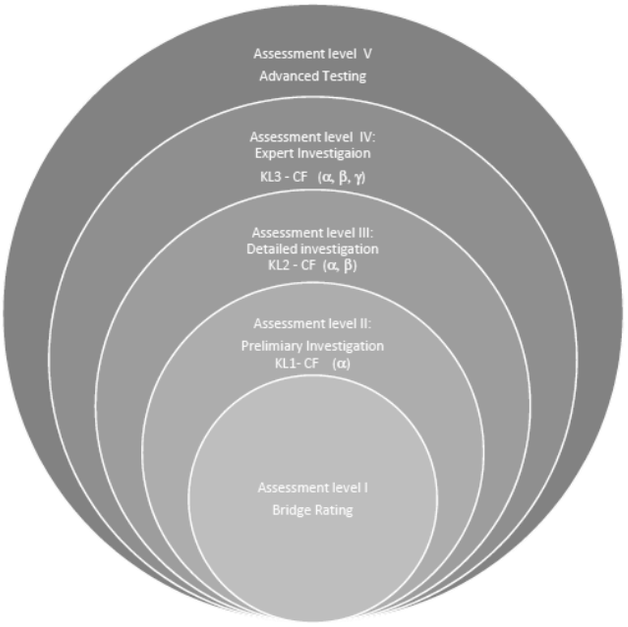


Figure 3. Step level assessment vs. knowledge level.

4 BRIDGE RATING

4.1 *United States of America*

The AASHTO LRFR Guide Manual is the first bridge load rating method in the United States to be based on modern principles of structural reliability and limit states design. The essential ingredients of a reliability-based design and evaluation include probabilistic models of the structural resistance and loads and a method for analyzing the reliabilities (or, conversely, the limit state probabilities) that are relevant to each bridge limit state. Such methods and tools have been applied to developing the AASHTO LRFD Specifications and the LRFR Guide Manual and are expected to be relevant also to improve rating methods for other countries. Details are available in the archival literature (Nowak, 1999; Moses, 2001).

4.2 *Australia*

Section 7 of the Austrian Bridge Design Standard provides rating guidelines with a commentary. The concept of rating is based on the limit state design philosophy and both serviceability and ultimate limit

states are considered. The ultimate action is defined as an action that has a 5% probability of being exceeded during the design life, which represents an average return interval of 2000 years; while the survivability action is defined as one having 5% probability being exceeded per year, corresponding to a return interval of 20 years.

4.3 *United Kingdom*

Document BD 21/01, Assessment of Highway Bridges and Structures, adopts a limit state format with appropriate partial safety factors for condition evaluation of most highway bridges except for cast iron bridges and masonry arch bridges. It is stipulated that bridges built after 1965 should normally be evaluated for serviceability as well as for the ultimate limit states; bridges constructed before 1965 do not need to be assessed for service limit states. Requirements for fatigue endurance however are not included in the standard and the reason stated is that the past stress history of each structure, which could profoundly influence fatigue limit checking, cannot generally be determined to the accuracy level required for assessment.

4.4 *Canada*

The GBSM (2012) is a reference document dedicated in particular for railway bridges. However, it shows a clear and easy procedure for the bridge analysis.

5 CONCLUSION

The assessment of existing structures adopting a specific code or standard is a technical procedure that is provided only in some nation. The possibility of harmonizing these type of procedure is needed in Europe, together with a completely new plan of infrastructural renewal. From the analysis of the documents presented, a review of existing assessment approaches and states rating practices have revealed a number of research issues that must be addressed for existing bridges evaluations (GDT 2009):

- -The bridge may contain archaic structural materials. Design documentation may be missing.
- -Material strengths in situ may be vastly different from the standardized or nominal values assumed in design. On the one hand, concrete strength can increase by as much as 150% beyond the 28-day standard basis due to continued hydration; on the other hand, the strength can deteriorate due to aggressive environmental attack from physical or chemical mechanisms. Failure to consider best estimates of strength and the time-dependent nature of the structural strength and stiffness invariably will lead to an erroneous estimate of in situ strength.
- - Analytical approaches to bridge evaluation usually (but not always) yield a conservative measure of actual load-carrying capacities [Bakht and Jaeger, 1990]. This conservatism is the result of assumptions made in the analysis regarding load sharing, composite action, support conditions and nonlinear behavior, in addition to differences in material strengths noted above.
- - Discrepancies among the different approved rating methods were noted. These discrepancies were confirmed by preliminary rating calculations performed on bridges. The reasons for these differences must be completely understood and addressed in developing new guidelines or codes.
- - Satisfactory bridge performance over a period of years of service provides additional information not available at the design stage. This information should be taken into account in designing in-service inspection programs and in making decisions regarding upgrading and rehabilitation.
- - Current condition assessment relies heavily on visual inspection. More quantitative models of structural deterioration have been developed but have yet to be incorporated in condition assessment procedures.
- - A test load must be a significant fraction of the expected maximum live load for the proof test to be informative and to lower subsequent risk.If the test load is increased to an informative level, the probability of damaging the bridge during the load test increases as well. This tradeoff between information gained and likelihood of damage must be part of the decision to load-test a bridge rather than relying on other rating methods.
- - Uncertainties in loads and resistances at the design stage are reflected in the safety factors (or load and resistance factors). At the evaluation stage, uncertainties can be either greater (e.g., due to deterioration) or less (measured properties; successful load test). These uncertainties must be identified and analyzed.

6 ACKNOWLEDGMENTS

This research was supported by the European Union, represented by the European Commission—Directorate General for Research and Innovation, Research Fund for Coal & Steel (RFCS) program, under grant agreement no. RFSR-CT-2015-00025. This funding is gratefully acknowledged.

7 REFERENCES

GDT (2009). Condition Assessment Of Existing Bridge Structures. GDOT Project No. RP05 – 01. Report Of Task 1 – Appraisal Of State-Of-The-Art Of Bridge Condition Assessment. By Naiyu Wang, Bruce R. Ellingwood, Abdul-Hamid

Zureick, Curtis O'Malley, Georgia Institute Of Technology School Of Civil And Environmental Engineering.

GBSM (2012). Guideline for Bridge Safety Management. Rail Safety, Canada Transport.

Ministerial Decree (2008). Norme Tecniche per le Costruzioni DM 14/01/2008, e Circolare esplicativa 617/2009, Ministero delle Infrastrutture, Roma

Nowak, A. S. (1999). "Calibration of LRFD Bridge Design Code." NCHRP Report 368, Transportation Research Board, National Research Council, Washington D.C.

Moses, F., (2001). "Calibration of Load Factors for LRFR Bridge Evaluation." NCHRP Report 405, Transportation Research Board, National Research Council, Washington D.C.

Kühn B., M. Lukić, A. Nussbaumer, H.-P. Günther, R. Helmerich, S. Herion, M.H. Kolstein, S. Walbridge, B. Androic, O. Dijkstra, Ö. Bucak (2010). Assessment of Existing Steel Structures: Recommendations for Estimation of Remaining Fatigue Life. Joint Report Prepared under the JRC – ECCS cooperation agreement for the evolution of Eurocode 3 (programme of CEN / TC 250).

JCSS (2001). Probabilistic Assessment of Existing Structures, Joint Committee on Structural Safety, 2001.

Pritchard B. (1992). Bridge Design for Economy and Durability – Concepts for new, strengthened and replacement bridges. London: Thomas Telford Service Ltd.

Pipinato, A. (2016). Structural analysis and design of a multispan network arch bridge. Proceedings of the Institution of Civil Engineers: Bridge Engineering, 169 (1), pp. 54-66. DOI: 10.1680/jbren.14.00013

Pipinato, A. (2014). Assessment and rehabilitation of steel railway bridges using fibre-reinforced polymer (FRP) composites. Rehabilitation of Metallic Civil Infrastructure Using Fiber Reinforced Polymer (FRP) Composites: Types Properties and Testing Methods, pp. 373-405. DOI: 10.1533/9780857096654.4.373

Pipinato, A., Pellegrino, C., Modena, C. (2014). Residual life of historic riveted steel bridges: An analytical approach. Proceedings of the Institution of Civil Engineers: Bridge Engineering, 167 (1), pp. 17-32. Cited 9 times. DOI: 10.1680/bren.11.00014

Pipinato, A. (2014a). Orthotropic steel deck design to extend the lifetime of plate and box girder bridge and viaducts. Bridge Maintenance, Safety, Management and Life Extension - Proceedings of the 7th International Conference of Bridge Maintenance, Safety and Management, IABMAS 2014, pp. 1329-1336.

Pipinato, A. (2014b). Steel bridges: Codes, design specifications and construction issues. Bridge Maintenance, Safety, Management and Life Extension - Proceedings of the 7th International Conference of Bridge Maintenance, Safety and Management, IABMAS 2014, pp. 1891-1898.

Pipinato, A. (2014c). Longitudinal web stiffening in steel girders: Fracture propagation and life cycle design
(2014) Bridge Maintenance, Safety, Management and Life Extension - Proceedings of the 7th International Conference of Bridge Maintenance, Safety and Management, IABMAS 2014, pp. 1886-1890.

Pipinato, A. (2014d). Steel bridge coatings and corrosion protection. Bridge Maintenance, Safety, anagement and Life Extension - Proceedings of the 7th International Conference of Bridge Maintenance, Safety and Management, IABMAS 2014, pp. 1899-1905.

Pipinato, A. (2013a). Retrofit procedures of bridge networks against seismic actions in Italy. Durability of Bridge Structures, pp. 215-228.

Pipinato, A. (2013b). Moving load and fatigue analysis of a long span high speed railway bridge.Advanced Materials Research, 629, pp. 403-408.

Pipinato, A. (2013c). Moving loads bridge response: Structural analysis and eurocode provisions (2013) Advanced Materials Research, 629, pp. 409-417. 10.4028/www.scientific.net/AMR.629.409

Pipinato, A., Pellegrino, C., Modena, C. (2012a). Structural Analysis of the Cantilever Construction Process in Cable-Stayed Bridges (2012) Periodica Polytechnica: Civil Engineering, 56 (2), pp. 141-166. DOI: 10.3311/pp.ci.2012-2.02

Pipinato, A., Pellegrino, C., Modena, C. (2012b). Fatigue behaviour of steel bridge joints strenghtened with FRP laminates. Modern Applied Science, 6 (10), pp. 1-15. DOI: 10.5539/mas.v6n10p1

Pipinato, A., Pellegrino, C., Modena, C. (2012c). Coupled damage in assessing the lifetime of bridge and viaducts. Life-Cycle and Sustainability of Civil Infrastructure Systems - Proceedings of the 3rd International Symposium on Life-Cycle Civil Engineering, IALCCE 2012, pp. 2292-2297.

Pipinato, A. (2012a). Coupled safety assessment of cable stay bridges. Modern Applied Science, 6 (7). DOI: 10.5539/mas.v6n7p64

Pipinato, A., Pellegrino, C., Modena, C. (2012d). Assessment procedure and rehabilitation criteria for the riveted railway Adige Bridge (2012) Structure and Infrastructure Engineering, 8 (8), pp. 747-764. Cited 21 times. DOI: 10.1080/15732479.2010.481674

Pipinato, A. (2012b). Assessment procedures and strengthening of an existing metal bridge. (2012) Bridge Maintenance, Safety, Management, Resilience and Sustainability - Proceedings of the Sixth International Conference on Bridge Maintenance, Safety and Management, pp. 3651-3655.

Pipinato, A., Pellegrino, C., Modena, C. (2012e). Life cycle assessment of existing steel bridges considering corrosion and fatigue coupled problems. Bridge Maintenance, Safety, Management, Resilience and Sustainability - Proceedings of the Sixth International Conference on Bridge Maintenance, Safety and Management, pp. 1003-1007.

Pipinato, A., Pellegrino, C., Fregno, G., Modena, C. (2012f). Influence of fatigue on cable arrangement in cable-stayed bridges. International Journal of Steel Structures, 12 (1), pp. 107-123. DOI: 10.1007/s13296-012-1010-5

Pipinato, A., Molinari, M., Pellegrino, C., Bursi, O.S., Modena, C. (2011a). Fatigue tests on riveted steel elements taken from a railway bridge (2011) Structure and Infrastructure Engineering, 7 (12), pp. 907-920. DOI: 10.1080/15732470903099776

Pellegrino, C., Pipinato, A., Modena, C. (2011b). A simplified management procedure for bridge network maintenance. Structure and Infrastructure Engineering, 7 (5), pp. 341-351. DOI: 10.1080/15732470802659084

Pipinato, A. (2011). Assessment of existing bridges: Safety and security issues [Problemi di sicurezza nelle valutazioni strutturali di ponti esistenti] (2011) Ingegneria Ferroviaria, 66 (4), pp. 355-371.

Pipinato, A., Pellegrino, C., Modena, C. (2011c). Fatigue assessment of highway steel bridges in presence of seismic loading (2011) Engineering Structures, 33 (1), pp. 202-209. DOI: 10.1016/j.engstruct.2010.10.008

Pipinato, A., Pellegrino, C., Modena, C. (2011d). Correlation between fatigue effects and seismic actions in highway steel bridges (2011) Proceedings of the 8th International Conference on Structural Dynamics, EURODYN 2011, pp. 1118-1123.

Pipinato, A. (2010a). Structural analysis and fatigue life assessment of the Paderno Arch Bridge. Bridge Maintenance, Safety, Management and Life-Cycle Optimization - Proceedings of the 5th International Conference on Bridge Maintenance, Safety and Management, pp. 3480-3484.

Pipinato, A. (2010b) Structural analysis and fatigue life assessment of the Paderno Arch Bridge Bridge Maintenance, Safety, Management and Life-Cycle Optimization - Proceedings of the 5th International Conference on Bridge Maintenance, Safety and Management, pp. 3486-3490.

Pipinato, A., Pellegrino, C., Modena, C. (2010a) Residual service life of existing railway bridges Bridge Maintenance, Safety, Management and Life-Cycle Optimization - Proceedings of the 5th International Conference on Bridge Maintenance, Safety and Management, pp. 1444-1452.

Pipinato, A., Pellegrino, C., Modena, C. (2010b) Structural analysis of historical metal bridges in Italy Advanced Materials Research, 133-134, pp. 525-530. DOI: 10.4028/www.scientific.net/AMR.133-134.525

Pipinato, A., Pellegrino, C., Modena, C. (2010c). Residual service life of existing railway bridges Bridge Maintenance, Safety, Management and Life-Cycle Optimization - Proceedings of the 5th International Conference on Bridge Maintenance, Safety and Management, pp. 1455-1462.

Pipinato, A., Modena, C. (2010). Structural analysis and fatigue reliability assessment of the paderno bridge (2010) Practice Periodical on Structural Design and Construction, 15 (2), pp. 109-124. DOI: 10.1061/(ASCE)SC.1943-5576.0000037

Pipinato, A. (2010). Step level procedure for remaining fatigue life evaluation of one railway bridge. Baltic Journal of Road and Bridge Engineering, 5 (1), pp. 28-37. DOI: 10.3846/bjrbe.2010.04

Pellegrino, C., Pipinato, A., Freno, G., Modena, C. (2010d). Arranging geometric configuration of cable-stayed bridges taking fatigue into account (2010) Large Structures and Infrastructures for Environmentally Constrained and Urbanised Areas, pp. 692-693.

Pipinato, A., Gueli, M., Pellegrino, C., Modena, C. (2010e). Innovative methods for railway steel bridge remaining life estimation (2010) Large Structures and Infrastructures for Environmentally Constrained and Urbanised Areas, pp. 384-385.

Pipinato, A., Pellegrino, C., Bursi, O.S., Modena, C. (2009). High-cycle fatigue behavior of riveted connections for railway metal bridges. Journal of Constructional Steel Research, 65 (12), pp. 2167-2175. DOI: 10.1016/j.jcsr.2009.06.019

Pipinato, A., Pellegrino, C., Modena, C. (2008a). Evaluation of fatigue strength of one riveted historical railway bridge. Bridge Maintenance, Safety, Management, Health Monitoring and Informatics - Proceedings of the 4th International Conference on Bridge Maintenance, Safety and Management, pp. 283-290. DOI: 10.1201/9781439828434.ch148

Pipinato, A., Pellegrino, C., Modena, C. (2008b). Scheduled maintenance actions and residual life evaluation of railway infrastructures for metallic structure bridges [Interventi di manutenzione programmata e valutazione della vita residua delle infrastrutture ferroviarie da ponte a struttura metallica]. Ingegneria Ferroviaria, 63 (2), pp. 125-134.

Pipinato, A., Pellegrino, C., Modena, C. (2007). Static load tests on a historical steel railway bridge (2007) Proceedings of the 9th International Conference on Steel, Space and Composite Structures, pp. 217-224.

Maintenance, Safety, Risk, Management and Life-Cycle Performance of Bridges – Powers, Frangopol, Al-Mahaidi & Caprani (Eds)
© 2018 Taylor & Francis Group, London, ISBN 978-1-138-73045-8

Horizontal Interface Shear Requirements for Precast Prestressed Concrete Bridge Beams with Slender Webs in Beam and Slab Bridge Constructions

M. Slevin
Banagher Precast Concrete, Queen Street, Banagher, Co. Offaly, Ireland
& Trinity College Dublin, College Green, Dublin 2, Ireland

A.J. O'Connor
Department of Civil, Structural and Environmental Engineering
Trinity College Dublin, College Green, Dublin 2, Ireland.

ABSTRACT: All over the world precast prestressed concrete bridge beams are commonly used in small to medium sized highway and railway bridges, i.e. 20-50m spans. The majority of these bridges are built using I and U shaped precast prestressed concrete bridge girders with slender webs. When combined with a cast insitu deck slab they form a composite section that must be capable of resisting the horizontal shearing forces developed at the interface between the two elements. Interface shear requirements are generally more onerous than vertical shear when determining reinforcement ratios and this has become quite a contentious issue for bridge engineers in recent years with differing clauses in the design codes. This paper presents work which will form part of a PhD research project examining the performance of 6nr 3.3m long beams dynamically and statically tested using a four point loading set-up with varying reinforcement ratios crossing the interface. The interface roughness and concrete strength will not vary as the parameters chosen are synonymous with bridge construction. The study will also investigate the appropriateness for setting the cohesion factor c equal to zero for fatigue and dynamic verifications as per clause 6.2.5(105) of Eurocode 2 Part 2(2005). The aim of the research is to propose a minimum interface shear reinforcement equation for incorporation into Eurocode 2 Part 1-1(2004). It is recognised that a minimum percentage of reinforcement is required across the interface to prevent interfacial slip and brittle failure at loss of adhesion. Eurocode 2 Part 1-1(2004) does not presently include a minimum requirement.

1 INTRODUCTION

The research project examines the performance of 6nr 3.3m long prestressed concrete T-beams cyclically and statically loaded using a four point loading test similar to the research carried out by Kovach(2008). These beams are reinforced with prestressing strands, as the majority of bridge beams are prestressed. 3nr beams have 1nr 8mm stirrup crossing the interface and 3nr beams have no stirrups crossing the interface. The interface roughness and concrete strength does not vary as standard bridge practice in Ireland and the United Kingdom use a very rough surface finish and a C57/70 bridge beam mix with a C40/50 insitu top slab mix. The finish on the cast against concrete surface is a very important factor in calculating the interface shear strength. Eurocode 2 Part 1-1(2004) and the CEB-FIP Model Code(2010) classify the different applicable types of finishes into four categories, very smooth (cast against a steel or timber form), smooth (left as cast), rough (exposing the aggregate or raking the concrete) and very rough (shear key or indented concrete surface). Depending on the finish of the cast against concrete the two parameters, friction (μ) and cohesion (c) are then calculated. For the prestressed T-beams a very rough finish was used, this is an average of 3mm roughness when measured using a sand patch test. In terms of fatigue, the reasoning behind setting c equal to zero is to do with on-site issues such as dust, dirt and possibly laitance on the interface which is not cleaned off prior to the deck being cast. A more onerous reason behind setting the cohesion factor c equal to zero is the possibility of a breakdown of the interface over time as it is subjected to repeated loading and unloading during the lifetime of a bridge (120 years). The result of which amounts to an increase in interface shear reinforcement of approximately 20%. Since the introduction of the Eurocodes designers have been using the coefficient of cohesion based on clause 6.2.5 of Eurocode



Figure 1: Interface Reinforcement Close To Beam Ends Showing a Rough Surface Finish (Source Banagher Precast Concrete)

2 Part 1-1(2004) and using their own views on clause 6.2.5(105) of Eurocode 2 Part 2(2005) as there is not enough information in the code specifically for precast prestressed bridge beams with cast on deck slabs. Section 6.8 of Eurocode 2 Part 2(2005) states that a fatigue verification is generally not necessary for prestressed steel in regions where under the frequent combinations of actions compressive stresses occur at the extreme concrete fibres. The national annex to Eurocode 2 Part 2(2005) also contains a clause that if the slab acts compositely with the supporting beams or webs then the structural element does not require a fatigue verification. For the majority of bridge structures this is the case and thus can omit the designer from having to carry out a fatigue check. For a typical two span highway overbridge of twenty five meters per span the interface shear links when designed using the provisions of (Eurocode 2 Part 1-1(2004)) can be at less than 100mm centres, the width of the interface can be as short as 250mm so placing concrete in and around these links is quite difficult(see figure 1) let alone trying to achieve a very rough surface finish. The codes always specify a maximum stirrup spacing but a minimum stirrup spacing should also be considered. From industry experience 100mm is manageable anything less is extremely cumbersome in order to produce a high quality finished product.

2 RESEARCH OBJECTIVES

Two major objectives have been defined for this research study:

1. Carry out a the state of the art review on interface shear, particularly regarding static and dynamic loading and a comparison with other recognised bridge design standards.

2. Propose a minimum interface shear reinforcement requirement for Eurocode 2 Part 1-1(2004) based on the testing undertaken. It is recognised that a minimum percentage of reinforcement is required across the interface to prevent interfacial slip and brittle failure at loss of adhesion. Eurocode 2 Part 1-1(2004) does not presently include a minimum requirement. The proposal will involve a review of the main bridge design standards along with experimental testing as part of the project. Recent bridge projects in Ireland and the United Kingdom have used the CEB-FIP Model Code(2010) recommendations for minimum interface shear reinforcement.

3 PREVIOUS RESEARCH

3.1 *Shear Friction Theory*

The shear friction theory is used in all of the major bridge design codes, i.e. BS5400-4(1990), Eurocode 2 Part 1-1(2004), CEB-FIP Model Code(2010), ACI 318-14(2014) and AASHTO LRFD-BDS(2007) for designing the reinforcement required to cross the longitudinal interface between concrete members cast at different times. In this case a precast prestressed concrete bridge beam with a cast insitu top slab. Figure 2 shows a rectangular concrete block with a cracked interface which has also slipped, this is known as the saw-tooth model and was initially developed around 1960 to predict the longitudinal shear strength of concrete interfaces with the following four parameters considered:

1. Compressive strength of the weakest concrete
2. Normal stress at the interface
3. Shear reinforcement crossing the interface
4. Roughness of the interface substrate

Birkeland and Birkeland(1966) stated that the external shearing loads tend to produce a slippage of the member along an axis, usually at an interface. This slippage is resisted by friction resulting from the external clamping force. If reinforcement is present along the interface this reinforcement will provide an external clamping force on the concrete. This reinforcement has to be anchored on both sides of the interface for it to be effective. The reinforcement then becomes stressed in tension as a direct result of the slippage of the concrete, known as dowel action, this tension provides an external clamping force on the concrete resulting in compression across the interface and the shear stresses being transferred by shear friction.

The literature review identified several milestones of the shear friction theory from 1960 to the present date which are summarized in Table 1.

3.2 *Minimum Interface Reinforcement*

Currently Eurocode 2 Part 1-1(2004) does not have a provision for calculating the minimum percent-

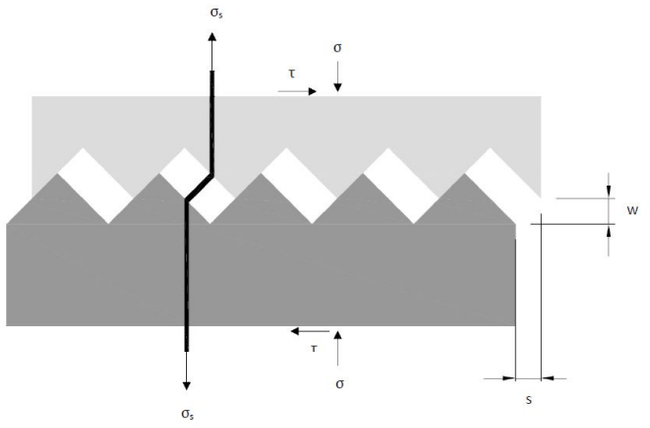


Figure 2: Shear Friction Theory

age of interface reinforcement required. BS5400-4(1990) and CEB-FIP Model Code(2010) have provisions for which the majority of bridge designers use. Hughes(1987) carried out several phases of testing to challenge the provisions of (BS5400-4(1990)). He came to the conclusion that they were conservative but should still be adhered to. Randl(2013) came up with an equation after performing extensive testing which was adopted in the latest version of the CEB-FIP Model Code(2010). Table 2 identifies the differences in the design codes in relation to the minimum percentage of interface reinforcement. It is clear further testing is required on this topic.

3.3 *Dynamic or Fatigue Verifications*

The general consensus amongst bridge designers is that clause 6.2.5(105) of Eurocode 2 Part 2(2005) is not required for short span highway and railway bridges. Reducing the coefficient of cohesion c to zero increases the amount of shear reinforcement crossing the interface to unmanageable levels. Figure 1 shows the end of a precast prestressed W beam with 12mm links at 100mm centres using a c value of 0.4 as per clause 6.2.5(2) of (Eurocode 2 Part 1-1(2004)). This is a very high ratio of stirrups, reducing c to zero would mean 12mm links at 80mm centres, an increase of 20%. Reducing c to zero also results in the design shear resistance of the interface without stirrups being equal to zero when designing to Exp(6.25) of Eurocode 2 Part 1-1(2004) or Exp(7.3-50) of CEB-FIP Model Code(2010), suggesting that the longitudinal shear stress capacity for concrete at the interface is neglected. According to Randl(2013) the shear resistance of concrete interfaces subjected to fatigue loading has not been investigated in a comprehensive way. Randl(2013) states that the most important thing to consider is will there be a crack along the interface. If the shear resistance of the interface is greater than the shear stress acting on it then the answer is unlikely and there is no requirement for shear reinforcement according to CEB-FIP Model Code(2010) and Eurocode 2 Part 1-1(2004). Chung and Chung(1976) were one of the first to carry out dynamic testing in 1976. They concluded that fatigue failure of the interface joint is not probable if the repeated load is not more than 55% of the ultimate static load or if the horizontal shear stress at the interface does not exceed $2.75N/mm^2$. Hughes(1987) carried out small scale push off tests, small scale RC T-beams and large scale precast prestressed M-beams in 1987 using both static and cyclical loading. He concluded that service stresses in bridgeworks tended to be $2.0N/mm^2$ and

Table 1: Shear Friction Theory Milestone Equations

Author	Equation	Note
Birkeland and Birkeland(1966)	$v_u = \mu\rho f_y$	Original Equation
Mattock and Hawkins(1972)	$v_u = 1.38 + 0.8(\rho f_y + \sigma_n)$	Contribution of Cohesion
Loov(1978)	$\frac{v_u}{f_c} = k\sqrt{\frac{\rho f_y + \sigma_n}{f_c}}$	Concrete Strength Added
Walraven et al.(1987)Walraven, Frenay, and Pruijssers	$v_u = C1(\rho f_y)^{c2}$	Based on Spherical Model
Randl(1997)	$v_u = cf_c^{\frac{1}{3}} + \mu(\rho k f_y + \sigma_n) + \alpha\rho\sqrt{f_y f_c}$	Cohesion, Friction and Dowel Action all considered

where;
v_u = ultimate longitudinal shear stress at the interface
μ = is the coefficent of friction
ρ = the reinforcement ratio
f_y = reinforcement yield strength
σ_n = is the (lowest expected) compressive stress resulting from an eventual normal force acting on the interface
f_c = concrete compressive strength
k = 0.5 for composite construction and 0.6 for monolithic construction
$C_1 = 0.822 f_c^{0.406}$
$C_2 = 0.159 f_c^{0.303}$
c = is the cohesion factor
α = parameter to allow for dowel action

Table 2: Minimum Interface Reinforcement Equations

Author	Equation
Hughes(1987)	$0.15\%bh$
BS5400-4(1990)	$0.15\%bh$
Eurocode 2 Part 1-1(2004)	No provision
CEB-FIP Model Code(2010)	$0.2\frac{f_{ctm}}{f_{yk}} \geq 0.001$
Randl(2013)	$0.2\frac{f_{ctm}}{f_{yk}} \geq 0.001$
ACI 318-14(2014)	Maximum of $0.062\sqrt{f'_c}\frac{b_w s}{f_y}$ and $0.35\frac{b_w s}{f_y}$

that the cracking stresses of $3.0N/mm^2$, $2.5N/mm^2$ and $2.0N/mm^2$ for monolithic, roughened and rough as cast surfaces respectively proved that the interfaces would remain uncracked at service loads. Loov and Patnaik(1994) carried out tests on RC T-beams in 1994 the results of which proved that the stirrups are typically unstressed and ineffective until the horizontal shear stress exceeded 2.0MPa.This indicates the strength of an interface without stirrups. They did confirm that the stirrups became relatively effective when the shear stress reached 3MPa.

4 EXPERIMENTAL STUDY

4.1 *Specimens*

Each beam had a top flange width of 550mm and depth of 100mm. The web was 300mm deep and 150mm wide. The beams were 3300mm long with an effective span of 3050mm. The slab did not cover the entire length of beam, this was based on previous research by Loov and Patnaik(1994). They cited an issue with cracks forming between the support of the beam and the interface at a distance equal to the effective depth of the web section. The slab at the end of the beam provides restraint against interface slip and to correct this the authors suggested reducing the slab length to allow for the horizontal shear failure. The beams were overly reinforced for bending with 4Nr 12.9mm prestressing strands and overly reinforced for vertical shear with 10mm links at 200mm centres. 3Nr 10mm lacer bars ran longitudinally in the top slab. The beams were designed to fail in interface shear only.

The beams were split into two series, comprising of three beams each. A control beam was also manufactured in order to obtain its ultimate strength. Test series 1 beams had no reinforcement crossing the interface. Test series 2 beams had an 8mm stirrup at 400mm centres (0.15% bh = minimum steel as per (BS5400-4(1990))) crossing the interface to represent minimum interface reinforcement.

The varying parameters were the level of load and the ratio of reinforcing stirrups crossing the interface. The beams were poured with C57/70 grade concrete and the top slabs cast twenty eight days later with C40/50 grade concrete. The beams had a very rough surface finish in accordance with (Eurocode 2 Part 1-1(2004)) Section 6.2.5 (2).

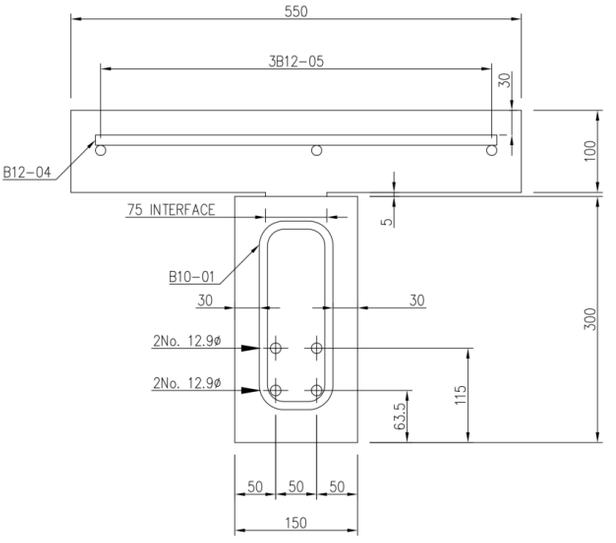


Figure 3: Prestressed TB1 Section

4.2 *Testing instrumentation*

Once the beams were positioned in the testing frame the instrumentation was installed. The instrumentation consisted of a hydraulic load cell and pump, two linear variable displacement transducers (LVDT's), four strain gauges attached to the outside face of the slab (SG1,2,3&4), two horizontal(SG8&9) and two vertical slip gauges(SG6&7). The instrumentation layout can be seen in figure 5 and is based on the work carried out by (Kovach(2008)).

4.3 *Cyclic Loading Procedure*

The beams were loaded with 16,800 cycles of load, the load cycle itself ranged between 150kN and 250kN as the ultimate strength of the beams was found to be in the region of 350kN and for fatigue purposes fatigue load model 1(FLM1) as per (Eurocode 1 Part 2(2002)) was used which corresponds to 70% of the ultimate load(LM1). The number of cycles was taken from Eurocode 1 Part 2(2002), it can

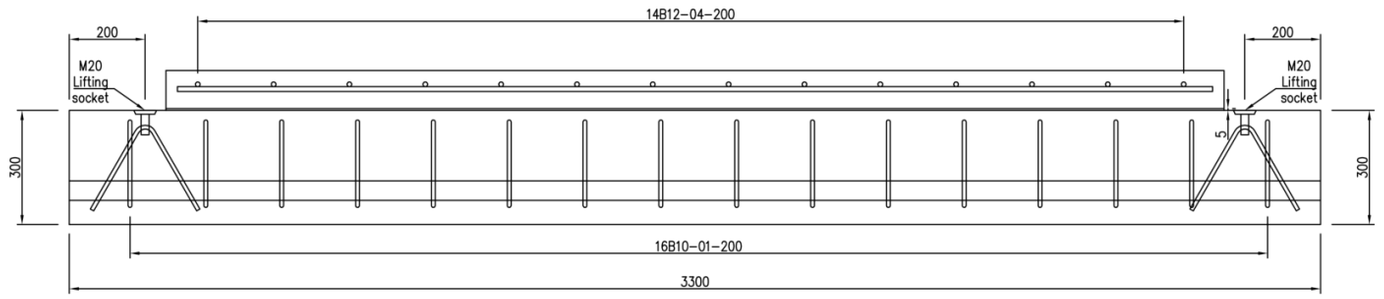


Figure 4: Prestressed TB1 Elevation

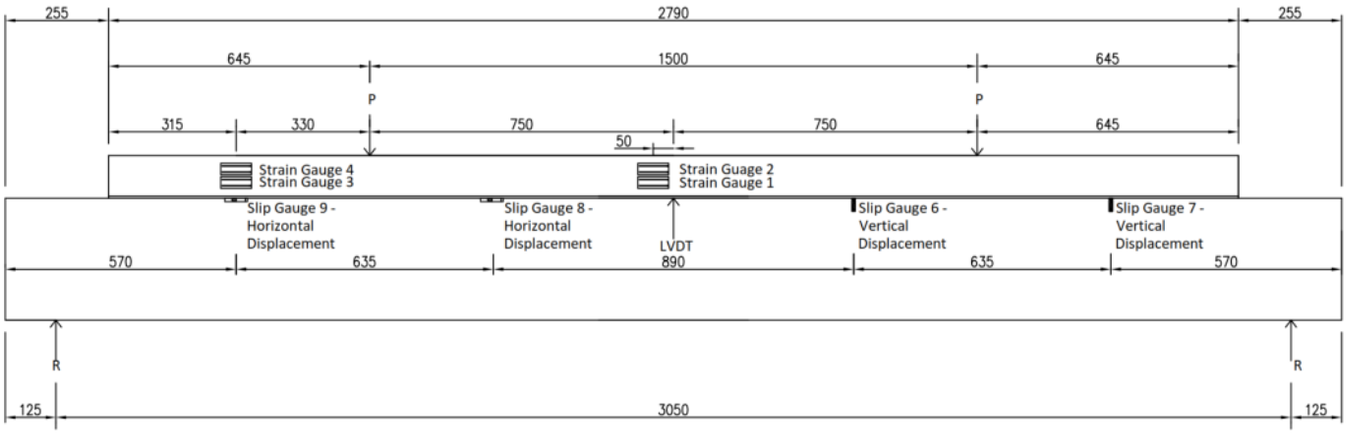


Figure 5: Phase 2 Instrumentation

be shown that two million commercial vehicles will cross the slow lane of a motorway bridge per year which equates to two hundred and forty million commercial vehicles during its lifespan. LM1 represents a vehicle weighing 600kN with four 150kN point loads dispersed through 400mm wide contact lengths. The test beams have 550mm wide top slabs and therefore can take half of a LM1 vehicle. From Table NA5 of Eurocode 1 Part 2(2002) the heaviest vehicle to use the bridge crosses it ten times per million crossings. The closest vehicle in weight to a LM1 vehicle crosses it seventy times per million crossings or 16,800 times during the life of a bridge. Clause 6.8.7 of Eurocode 2 Part 2(2005) states that Miners rule should be used to calculate the total number of cycles required. Using a minimum stress of 0.5MPa and a maximum stress of 4MPa the number of cycles was calculated at approximately 500,000 which is not practical for a laboratory test as it would take over 400 hours to perform.

4.4 *Test procedure*

The concrete beams were placed on a spreader beam which had 150mm wide x 250mm long x 50mm thick solid steel bearing pads to act as supports at the end of the 3.3m long concrete beam giving an effective span of 3.050m. The two point loads were applied using a steel spreader beam again fixed with 150mm wide x 250mm long x 50mm thick solid steel pads 900mm from the end of the concrete beam. The test setup can be seen in figure 5 and figure 6. All of the beams were subject to dynamic and static tests. The first beam that was tested was the control beam, PTB1-4 to see what the ultimate breaking load capacity was.



Figure 6: Phase 2 Test Set up Photo

5 EXPERIMENTAL RESULTS

5.1 *PTB1-1*

PTB1-1 was cyclically tested over three days prior to the static test. The cyclic test was ran from approximately 10am to 5pm and stopped when the lab was unoccupied over night. Following the cyclic test a visual inspection of the beam was carried out and the beam was found to be structurally sound, there were no signs of vertical shear or flexural cracks. The interface was uncracked even though gauge 9 read -0.71mm at maximum load during the cyclic test. This was put down to a faulty gauge as gauge 8 read -0.04mm and the vertical displacement gauges read 0.09mm and 0.01mm. It was unclear as to how a reading of 0.71mm was recorded. Therefore the gauges were all reset to zero for the static test. The beam was loaded in increments of 50kN with the test paused for inspection. There was no movement on any sensors until a load of 100kN was recorded. After 300kN all sensors were now giving values with sensor 7 the highest at 0.11mm. Noise was heard from the beam and the interface was starting to delaminate. The load was held for 5 minutes and sensors 8 and 9 were increasing but not rapidly. The load was increased and at 343kN delamination of the interface occurred. The horizontal slip gauges went from -0.09mm and -0.2mm to -1.09mm and -1.76mm respectively.

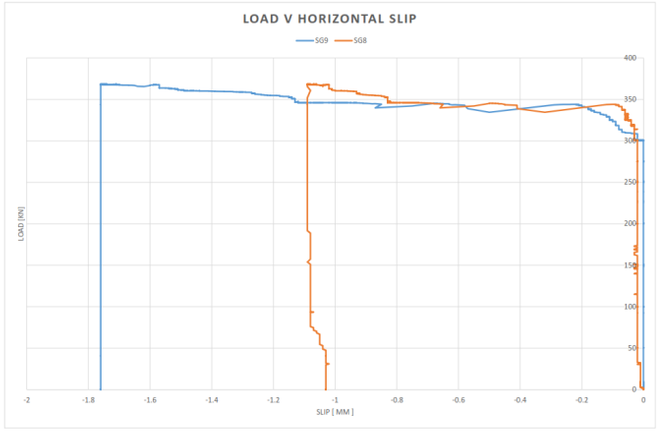


Figure 7: PTB1-1 Load v Slip

5.2 *PTB1-2*

PTB1-2 was statically loaded following a successful dynamic test. At 150kN all sensors started to signal movement albeit very slight. At 300kN vertical gauge 6 and horizontal gauge 9 both read 0.1mm and were steadily increasing. There were several vertical shear cracks clearly visible. These were the standard vertical shear crack running from load point to support. All of these cracks were on the right hand side of the beam where gauge 6 was located. At 317kN there were quite a lot of vertical shear cracks, with some in excess of 0.25mm. Gauge 6 was reading a vertical displacement of 0.9mm which was extremely large and showed delamination had occured. The beam was now carrying all of the load and the vertical shear cracks were excessive. All of the other gauges never read values greater than 0.1mm. It shows the brittle nature of an unreinforced interface where local delamination can materialise. The test was stopped at this stage as delamination had occurred and a failure of the prestressed beam was of no relevance to this study.



Figure 8: PTB1-2 Cracking at 300kN

5.3 *PTB1-3*

PTB1-3 was cyclically loaded for 16878nr cycles of load. The beam did not delaminate and was statically tested to failure. At 325kN gauge 7 started to steadily increase from 0.25mm upwards to 0.4mm whilst the load was held. Gauge 6 was holding well at 0.4mm and all of a sudden gauge 8 the horizontal slip gauge close to the midspan gave and went from 0.02mm to 0.82mm and at the same time gauge 6 went from 0.4mm to 0.69mm. The load was let off and the test stopped. Once delamination occurred at 325kN the beam acted alone and took the weight of the slab and all of the live load, vertical shear cracks opened up right away and were well in excess of 0.3mm. PTB1-1 failed at 343kN, PTB1-2 at 317kN and now PTB1-3 at 325kN. All failures were similar and consistant with each other which was very positive considering only 3nr beams were tested.

5.4 *PTB2-1*

PTB2-1 was statically tested after 16890 cycles of load were carried out. At 250kN the effect of the stirrups was already quite noticeable as the beam was considerably more stiff and composite as could be seen in the gauges. At 325kN the load was held and further visual inspections took place, slip gauge 9 reached -0.13mm and vertical shear cracks appeared on the beam. These cracks measured 0.1mm. Strain



Figure 9: PTB2-1 Cracks Underneath the Beam

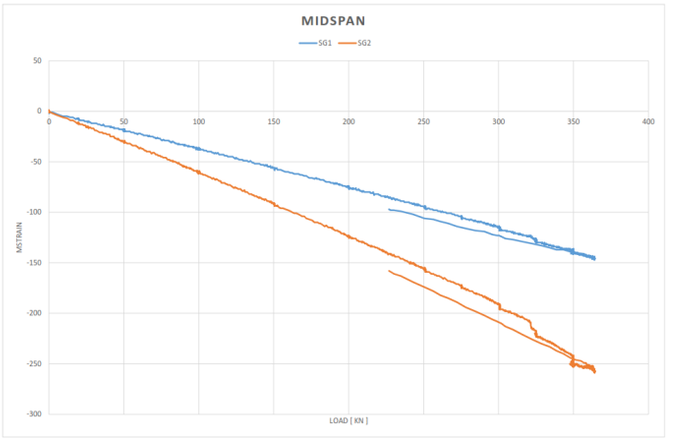


Figure 10: PTB2-1 End Strain

gauges 3 and 4 gave a slight spike and this represented the cracks occurring. The load was increased to 350kN which was not possible with series one beams. The load was held and the interface was still well intact apart from gauge 9 which had slipped to -0.23mm with more and more vertical shear cracks appearing. The load was held and the interface did not move any further. Flexural cracks were now also starting to appear. The cracks were now well in excess of 0.25mm and travelled under the beam and across the soffit as can be seen in figure 9. The load was increased to 364kN and held for 5minutes. This was the maximum load that the test rig was able to produce. The interface slipped again to -0.28mm as per gauge 9 but held well and did not increase any more under this load. Finally the load was withdrawn slowly and gauge 9 reverted back to -0.09mm. The effect of the stirrups, even though they only consisted of 1nr leg of 8mm bar at 400mm centres was quite impressive to see. Failure here was not an interface failure but a vertical shear and flexural one.

5.5 *PTB2-2*

PTB2-2 was statically tested after 17300 cycles of load were carried out, with no delamination of the interface. At 340kN the load was held and visual inspections took place, slip gauge 7 had moved approximately 0.1mm from the start of the test and vertical shear cracks appeared on the beam which represented a non composite member and a delamination of the interface even though visually it was not clear. These cracks measured in excess of 0.1mm. The load was increased to 365kN and held, the interface was still intact apart from gauges 7 and 9 which were slipping gradually. Gauge 7 had moved 0.2mm and gauge 9 0.3mm approximately so not much movement when compared to series one tests. The load was held for 5 minutes and the interface did not move any further.

5.6 *PTB2-3*

PTB2-3 was statically tested after 17708 cycles of load were carried out on the beam. At 325kN the load was held and visual inspections took place, slip gauge 7 had moved to 0.17mm and cracks were now visible on the beam. The flexural cracks near the midspan were 0.1mm and the vertical shear cracks at the beam end were 0.2mm. The load was increased to 365kN, the vertical cracking was now very excessive and spread down and under the web of the beam. The crack was in the order of 2mm. A prestressed beam failure was not wanted and so the test was stopped with a vertical shear and flexural failure cited. The interfaces of PTB2-1 at 364kN, PTB2-2 at 365kN and PTB2-3 at 365kN were still very much intact when the test was stopped. All failures were similar and consistant as per test series 1 beams.

6 CONCLUSIONS AND RECOMMENDATIONS

6.1 *Code Provisions:*

The test results prove that the provisions of the current bridge design codes are conservative and safe.

6.2 *Surface Preparation:*

Precast concrete manufacturers cast bridge beams internally and externally during all seasons. Trying to achieve a surface finish with high strength flowable concrete is extremely difficult. The method used in the experiments has been tested by Banagher Precast Concrete and works very well. In summary the beams are poured and finished. They are left rough as cast and after approximately 30 minutes the finishing foremen dash the tops with 8mm aggregate and clamp it into the concrete with a roughening tool. The beams are then covered and cured. When the beams are removed from the manufacturing line they are power washed and any loose aggregate is cleaned away. This method achieves an average roughness of 3mm which corresponds to a very rough surface as per (CEB-FIP Model Code(2010)).

6.3 *Minimum Links:*

At present there is no minimum interface links provision in (Eurocode 2 Part 1-1(2004)). Engineers are using the minimum provisions of (BS5400-4(1990)) and (CEB-FIP Model Code(2010)) for bridge beam

Table 3: Average Factor of Safety

Beam Type	Design Capacity	Stress @ 1st Interface Crack	Factor of Safety
PTB1-1	0.65	8.39	12.91
PTB1-2	0.65	7.76	11.93
PTB1-3	0.65	7.95	12.23
PTB2-1	1.17	7.95	6.80
PTB2-2	1.17	8.32	7.11
PTB2-3	1.17	7.95	6.80
Note: Units of Strength and Stress both in MPa			

Table 4: Summary of Results

Type	Beam Age	Slab Age	Beam Str.	Slab Str.	Int. Links	Design Cap.	1^{st} crack stress	SR
PTB1-1	148	119	77.02	77.22	None	0.65	8.39	3.58
PTB1-2	168	139	77.02	77.22	None	0.65	7.76	3.24
PTB1-3	174	145	77.02	77.22	None	0.65	7.95	3.32
PTB2-1	188	159	77.02	77.22	1B8-400	1.17	7.95	3.49
PTB2-2	160	131	77.02	77.22	1B8-400	1.17	8.32	3.36
PTB2-3	178	149	77.02	77.22	1B8-400	1.17	7.95	3.20
Note: Age in days, Str. = Strength, Units of Strength in MPa, Int. = Interface, Cap. = Capacity. Units of Stress in MPa, SR = Surface roughness, Units of Surface roughness in mm								

designs. The testing carried out proves that these provisions are safe and can be used in practice. Prestressed bridge beams will always contain stirrups crossing the interface for vertical shear requirements. Once the surface is rough and stirrups are present no additional interface stirrups need be provided. This is the view of the panel of experts involved in writing the new version of (Eurocode 2 Part 1-1(2004))

6.4 *Dynamic or Fatigue Verifications:*

There were no interface cracks until an average shear stress of 8.03MPa. Comparing this to the design resistance for an unreinforced joint of 0.65MPa shows the merit of this research and proves that not enough testing has been carried out to validate the overly conservative approach of reducing c to zero for fatigue verifications. In reality all bridges are dynamically loaded as they are used by vehicular traffic. To reduce c to zero results in an uneconomical design. Further laboratory testing should be sought to disprove clause 6.2.5(105) of Eurocode 2 Part 2(2005).

REFERENCES

Bridge Design Specification AASHTO LRFD-BDS. Bridge design specifications. *American Association of State Highway and Transportation Officials, Washington, DC, USA*, 2007.

American Concrete Institution Building Code ACI 318-14. Building code requirements for structural concrete (aci 318-14) and commentary. American Concrete Institute, 2014. ISBN 0870312642.

Philip W Birkeland and Halvard W Birkeland. Connections in precast concrete construction. In *Journal Proceedings*, volume 63, pages 345–368, 1966. ISBN 0002-8061.

British Standards Institution BS5400-4. Code of practice for design of concrete bridges. *British Standards Institution, London*, 1990.

The fib Model Code for Concrete Structures CEB-FIP Model Code. Model code 2010final draft, vol. 1, 2010.

HW Chung and TY Chung. Prestressed concrete composite beams under repeated loading. In *ACI Journal Proceedings*, volume 73. ACI, 1976. ISBN 0002-8061.

EN 1991-2 Eurocode 1 Part 2. *Actions on structures: Traffic loads on bridges*. Brussels, 2002.

EN 1992-1-1 Eurocode 2 Part 1-1. *Design of Concrete Structures: General Rules and Rules for Buildings*. British Standards Institution, 2004. ISBN 0580451917.

EN 1992-2 Eurocode 2 Part 2. Design of concrete structurespart 2: Concrete bridges design and detailing rules, 2005.

G Hughes. Longitudinal shear in composite concrete bridge beams. *Part*, 2:97, 1987.

Jonathon D Kovach. Horizontal shear capacity of composite concrete beams without interface ties. 2008.

RE Loov. Design of precast connections. In *a seminar organized by Compa International Pte, Ltd*, 1978.

Robert E Loov and Anil K Patnaik. Horizontal shear strength of composite concrete beams with a rough interface. *PCI Journal*, 39(1), 1994. ISSN 0887-9672.

Alan H Mattock and Neil Middleton Hawkins. Shear transfer in reinforced concrete-recent research. *PRECAST/PRESTRESSED CONCRETE INSTITUTE. JOURNAL*, 17(2), 1972. ISSN 0887-9672.

Norbert Randl. Untersuchungen zur kraftbertragung zwischen alt-und neubeton bei unterschiedlichen fugenrauhigkeite. 1997.

Norbert Randl. Design recommendations for interface shear transfer in fib model code 2010. *Structural Concrete*, 14(3): 230–241, 2013. ISSN 1751-7648.

Joost Walraven, Jerome Frenay, and Arjan Pruijssers. Influence of concrete strength and load history on the shear friction capacity of concrete members. *PCI journal*, 32(1):66–84, 1987.

Maintenance, Safety, Risk, Management and Life-Cycle Performance of Bridges – Powers, Frangopol, Al-Mahaidi & Caprani (Eds)
© 2018 Taylor & Francis Group, London, ISBN 978-1-138-73045-8

Bridge Safety Assessment for Strength II Limit State in AASHTO LRFD Specifications

Hani Nassif & Peng Lou
Rutgers, The State University of New Jersey, Piscataway, New Jersey, United States
Paul Truban
New Jersey Department of Transportation, Trenton, New Jersey, United States

ABSTRACT: The AASHTO LRFD Bridge Design Specifications (AASHTO 2016) defines Strength II limit state for various agencies to consider the load combination relating to the use of bridges in the United States by owner-specified special design permit vehicles, evaluation permit vehicles, or both. However, the code calibration process, initially performed in 1994, was applied only to the Strength I Limit State (Nowak 1999). Additionally, the configuration and characteristics of permit vehicles vary from state to state. This study presents the comparison of load effects among design permit vehicles from different agencies. Then the design permit vehicle of New Jersey Department of Transportation (NJDOT) is assessed using five years of permit vehicle records. In comparison with the current AASHTO live load factor of 1.35, the averages of the bias ratios at the 75-year level are found to be 1.31, 1.23, and 1.16 for the positive moment, shear, and negative moment, respectively.

1 INSTRUCTIONS

1.1 *Background*

Overweight vehicles are commonly considered to affect both the structural safety and deterioration of bridge structures. AASHTO LRFD Bridge Design Specifications (AASHTO 2016) defines Strength II Limit State with a load factor of 1.35 for agencies to consider the load combination relating to the use of bridges by owner-specified special design vehicles, evaluation permit vehicles, or both. However, this limit state has never been calibrated. In the United States, Nowak (*1993,1994*) initiated the development of truck live load models based on truck survey data collected in Ontario in 1975. The results constituted the major development of live load models for Strength I limit state. In addition, although same live load factor of 1.35 for Strength II Limit State is currently used, the configurations of design permit vehicles vary from state to state. Therefore, the factored design load for Strength II Limit State varies from state to state.

1.2 *Objectives*

The design permit vehicle from each state usually represents the local permit vehicles. This study aims at assess NJDOT Design Permit Vehicle. A total of 208,487 Permit vehicle registration records from 2010 to 2015 were provided by NJDOT. Load extrapolation was performed in order to get the extreme 75-year loads.

2 PERMIT VEHICLES FROM VARIOUS AGENCIES

Figure 1 shows the ratios of load effect caused by NJDOT Design Permit Vehicle and HL93. The load effects include maximum positive moment in simply supported beam (Simple Span Moment), maximum shear force in simply supported beam (Simple Span Shear), and maximum negative moment in two equal span continuous beams (Continuous Negative Moment). The ratios of Simple Span Moment and Simple Span Shear are around 1.5 for different span lengths between 20 *ft* and 200 *ft*. For Continuous Negative Moment, the ratio is consistently under 1.5 except for 40 *ft* span, which is 1.7. Figure 2 shows the design or evaluation permit vehicles currently used by agencies including New Jersey, Pennsylvania, New York State, Wisconsin, and California. It is important to note that Wisconsin *(2017)* and Virginia *(2016)* do not have the requirement of Strength II Limit State during the design while they do require the evaluation of the permit load rating if permit vehicles is requested to operating on a bridge. On the other hand, the states, such as New Jersey *(2016)* and New York State *(2016)* not only require the Strength II Limit State but also require considering the design permit vehicles in the service limit states.

Some state DOTs developed their design permit vehicle based on the envelope of load effects created by issued routine permit vehicles. However, this does not share the same philosophy of reliability-based LRFD design. Figure 3 shows the design load effects of different design permit vehicles comparing to NJDOT Design Permit Vehicle in terms of Simple Span Moment, Simple Span Shear, and Continuous Negative Moment. Based on Figure 2 and Figure 3, Pennsylvania and New Jersey has similar design permit vehicles and therefore the design load effects created are close. California Design Permit Vehicle has lower design load for short spans and higher design load for long spans comparing to NJDOT. Due to the different configuration of design permit vehicles, the design live load varies significantly among the agencies.

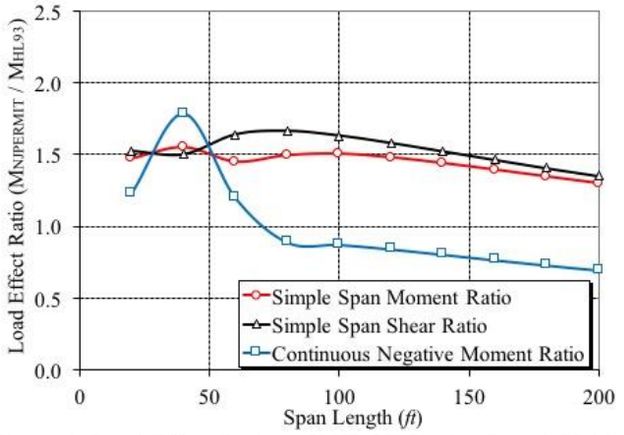
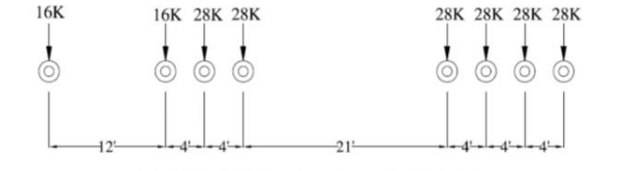
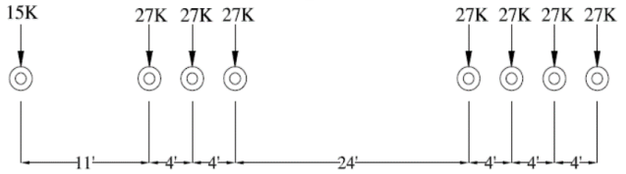


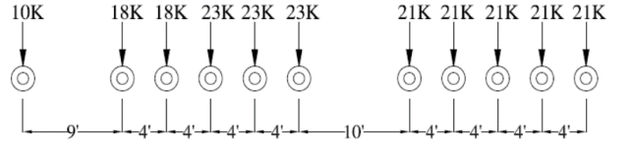
Figure 1. Load Effect Ratios of NJDOT Design Permit Vehicle and HL93



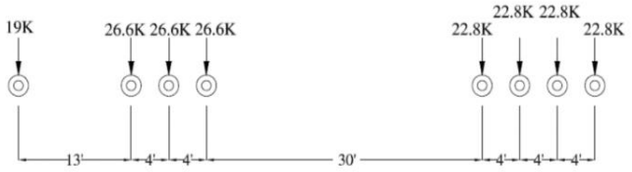
(*a*) NJDOT Design Permit Vehicle



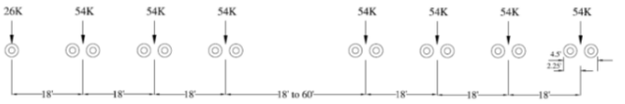
(*b*) Pennsylvania Design Permit Vehicle, P-82



(*c*) NYSDOT Design Permit Vehicle

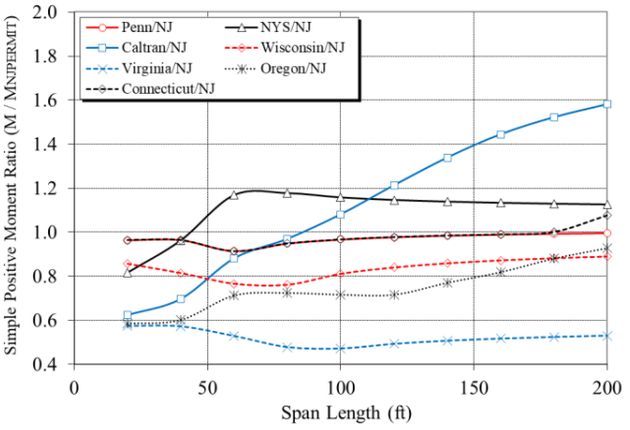


(*d*) Wisconsin Permit Vehicle, Wis-SPV

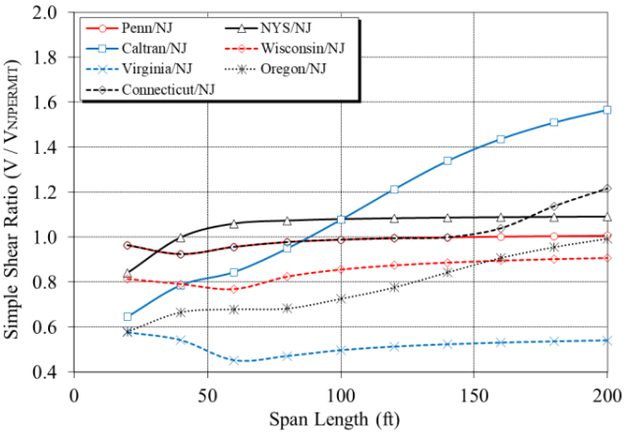


(*e*) California Design Permit Vehicle, P15

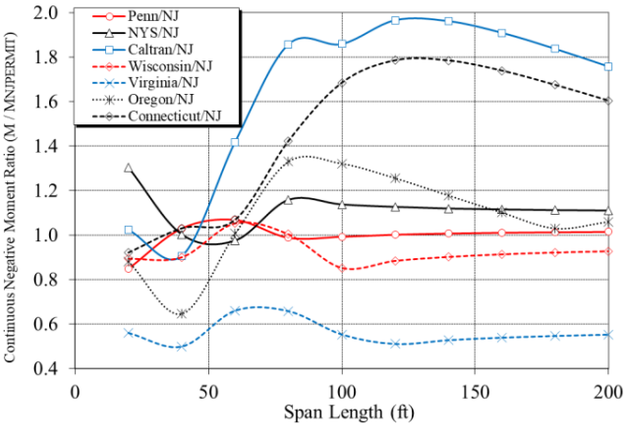
Figure 2. Permit Vehicles from Various Agencies in US



(*a*) Simple Span Moment



(b) Simple Span Shear



(c) Continuous Negative Moment

Figure 3. Load Effects of Permit Vehicles from Various Agencies in US

3 DATA PROCESSING AND LOAD EXTRAPOLATION

3.1 *Statistics of permit vehicle records*

Figure 4 shows the permits issued by NJDOT for each month from September 2010 to July 2015. In

general, the average annual increase for the number of permits is 7.66%. Figure 5 shows the distribution of permit vehicle records based on the number of axles. The majority of permit vehicle records, about 94.1% of total records, are five, six, seven, and eight axles vehicles. Figure 6 shows the Cumulative Density Distribution (CDD) of the Gross Vehicle Weight (GVW) plotted in Normal Probability Paper (NPP) along with the approximated Generalized Extreme Value (GEV) distributions. The GEV distribution is found to be the best fit with the location parameter $\mu = 105.4$, scale parameter $\sigma = 21.28$, and shape parameter $\xi = 0.04526$. This indicates this can be best described as a type II extreme value distribution, also known as Fréchet distribution.

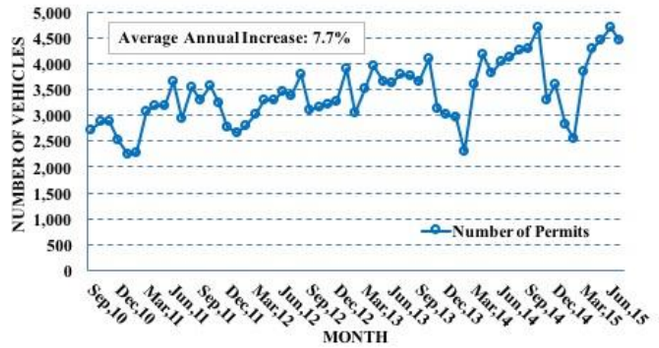


Figure 4. Permits Issued by NJDOT from 2010 to 2015

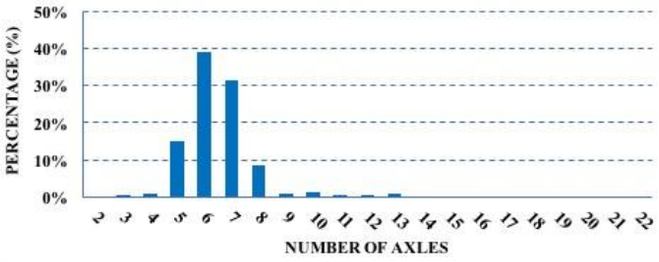


Figure 5. Number of Axles for Permit Vehicles

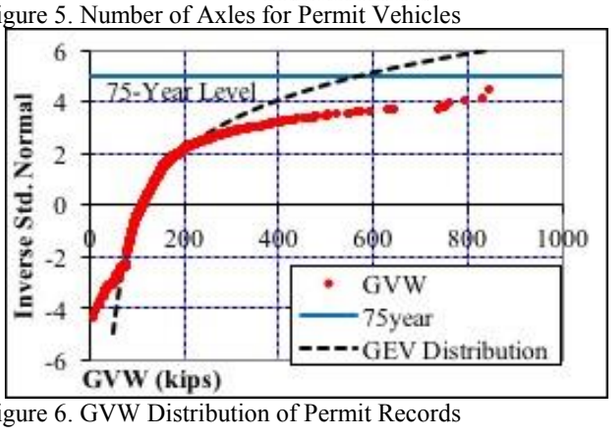
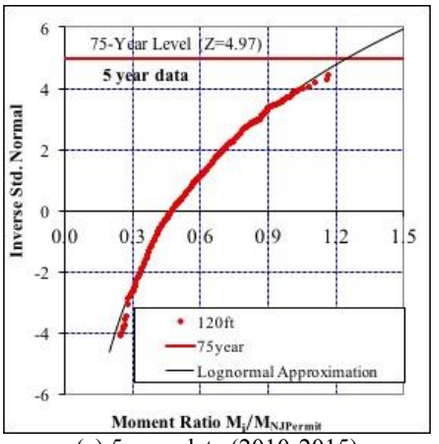


Figure 6. GVW Distribution of Permit Records

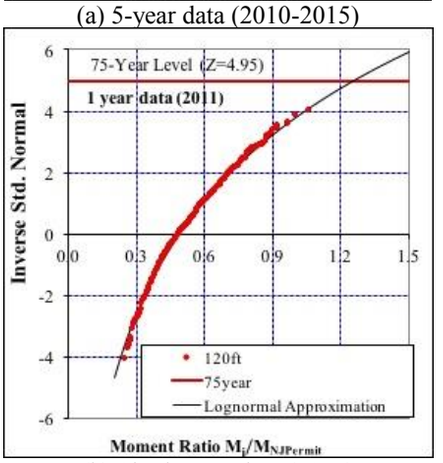
3.2 *Live load effects and load extrapolation*

The first step is to use Federal Bridge Formula to exclude the oversize vehicles from the database. In addition, there are about 0.25% of the records (516 records) that are heavier than 250 kips. These vehicles can be regarded as superload loads, which are distinguished from routine permits. However, when developing the design permit vehicles, one should not penalize all bridges for few extremely heavy superloads, which in some cases might even not be operated on the bridge network. Therefore, as the second step, only permit vehicles that are below 250 *kips* are considered for the load extrapolations. Then a total of 202,033 permit vehicle records are used to obtain the bias ratios, the load effects created by permit vehicle records over the load effect by NJDOT Design Permit Vehicle, of Simple Span Moment, Simple Span Shear, Continuous Negative Moment for span lengths ranging from 20 *ft* to 200 *ft*. For the load extrapolation method, lognormal approximation is used to predict the future 75-year maximum loads. This is different from GVW distribution, which is best described as type II extreme value distribution. The lognormal approximation method calculates the characteristic parameters of the lognormal distribution and plotted the distribution along with the bias ratios in NPP. This approach is found to be consistent, stable, and less sensitive to extreme loads. The coefficient of determination (R^2) is higher than 0.97 in every case.

Figure 7 shows an example of load extrapolation for Simple Span Moment of 120 *ft* span length using five-year data and single year data. It can be seen that the lognormal approximation fit the entire data very well. In addition, the extrapolated results are very close using either five-year data and single year data. This means the extrapolation method is effective and consistent over time.



(a) 5-year data (2010-2015)

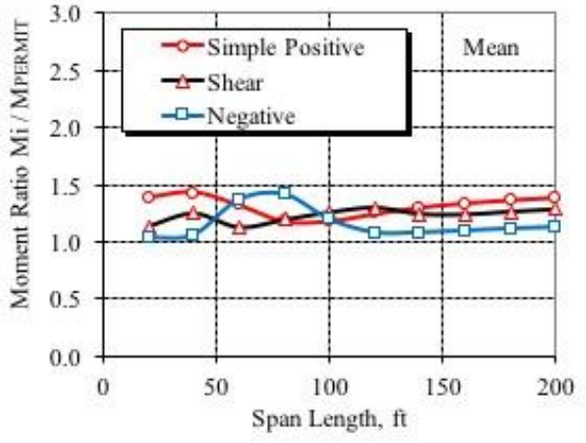


(b) Single year data (2011)

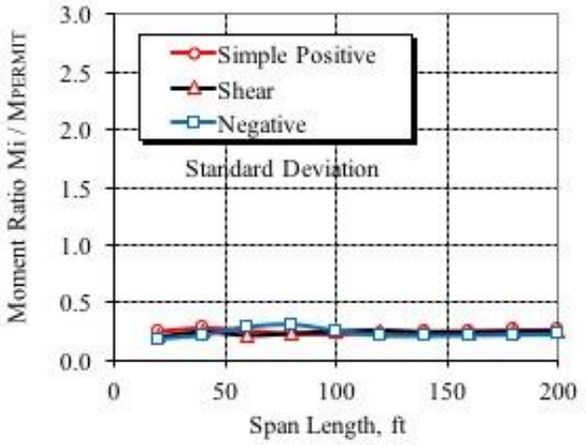
Figure 7. Load effect extrapolation (120 *ft* Simple Span Moment)

4 STATISTICAL PARAMETERS FOR THE STRENGTH II LIMIT STATE IN AASHTO LRFD

Figure 8 gives the mean and standard deviation of bias ratios for the predicted 75-year maximum loads for different span lengths. For New Jersey design permit vehicle, the means and standard deviation (STD) of bias ratio are consistent for different span lengths. This means the current NJDOT Design Permit Vehicle represent the local permit loads well and there is no need to change the configuration of the design permit vehicle. If the load extrapolation results in inconsistent over different span lengths, a new configuration should be proposed to represent the permit load better. The average value of the bias ratios at 75-year level is 1.31, 1.23, and 1.16 for the Simple Span Moment, Simple Span Shear, and Continuous Negative Moment, respectively. Considering the current live load factor, 1.35 for design permit load, in Strength II limit state, NJDOT Design Permit Vehicles gives close bias ratios based on the results. In addition, it is found that the coefficient of variations (CoV), which is about 20%, is higher than previous calibration works.



(*a*) Mean of Maximum 75-year load



(*b*) Standard Deviation of Maximum 75-year Load

Figure 8. Bias Ratio of predicted 75-year maximum loads to NJDOT Design Permit Vehicles

5 CONCLUSIONS

This study presents a study of the validation of Design Permit Vehicle for NJDOT Structural Design Manual. Permit vehicle registration records are used to perform live load extrapolation. The average value of bias ratio at 75-year level are found to be 1.31, 1.23, and 1.16 for Simple Span Moment, Simple Span Shear, and Continuous Negative Moment, respectively. The results are within the current live load factor, 1.35, for Strength II limit state.

6 PREFERENCES

- *AASHTO LRFD Bridge Design Specifications for Highway Bridges,* 7th ed. AASHTO, Washington, D.C., 2016.
- NJDOT. (2016). Design manual for Bridge & Structures, 6th ed. NJDOT, Trenton.
- NYSDOT. (2016). *NYSDOT LRFD Bridge Design Specifications*.
- Nowak, A. S. (1993). Live load model for highway bridges. *Structural safety*, *13*(1-2), 53-66.
- Nowak, A. S., Nassif, H., & DeFrain, L. (1993). Effect of truck loads on bridges. *Journal of transportation engineering*, *119*(6), 853-867.
- Nowak, A. S. (1994). Load model for bridge design code. *Canadian Journal of Civil Engineering*, *21*(1), 36-49.
- Nowak, A. S. (1999). *Calibration of LRFD bridge design code* (No. Project C12-33 FY'88-'92).
- Pennsylvania DOT. (2015). *Part 4 Structure Design Manual, April 2015 Edition*. Pennsylvania Department of Transportation.
- Virginia DOT. (2016). *Load Rating and Posing of Structures (Bridge and Culverts), December 2016*. Virginia Department of Transportation.
- WisDOT. (2017). *WisDOT Bridge Manual*. Wisconsin Department of Transportation.

Maintenance, Safety, Risk, Management and Life-Cycle Performance of Bridges – Powers, Frangopol, Al-Mahaidi & Caprani (Eds)
© 2018 Taylor & Francis Group, London, ISBN 978-1-138-73045-8

Large skewed bridge for high speed trains. Northwest of Spain

C. Jurado (Ph. D., M. Sc., B. Sc., MBA)
Polytechnic University of Madrid, (Spain) / Ingecal Ingenieros, S. L., Madrid, Spain.

ABSTRACT: During the years 2008 to 2010 it has been constructed in Spain the new railway line of high velocity trains, which will connect Valladolid with the northwest of Spain.

One of the first phases comprises the connection of provinces Valladolid and León with a train of 220 km/h of speed. The section Río Cea-Bercianos del Real Camino with 10.5 Km of length comprises 5 great viaducts from 36 to 442 meters with an inversion of 22 million Euros and it will cross the provinces of Valladolid and León in direction to Galicia on the Northwest of Spain.

The present paper exposes the project and construction of one of the most singular viaducts in this phase which crosses above the existing motorway M-31, with a very acute angle of 20º. The solution has been a skew bridge called in Spanish terminology "in pergola" with a length of 153 m.

1 THE SPANISH INFRAESTRUCTURE PLAN 2000-2020

Spain has undertaken with the assistance of European funds a tremendous effort to overcame its deficiencies in transport and infrastructures. From the end of eighties until the mid of the nineties, it has took with Germany the first place in the European Union (EU) in the percentage of Gross Domestic Product (GDP) allocated to investment in transport infrastructures.

From the threshold of 0.5-0.6% of GDP in the mid-eighties it has gone to values of around 1.7-1.8% in the last years (figure 1).

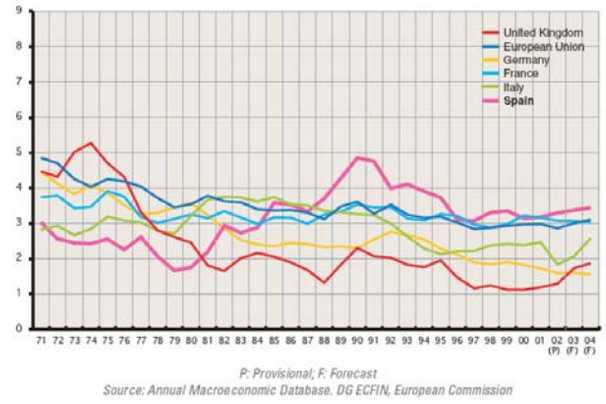


Figure 1. Trends in Public Investment by countries in EU (%GDP)

The Spanish Infrastructure Plan 2000-2020 projects to connect all the provinces with the centre of Spain with high velocity trains. The cost of the Plan will be about 114.2 thousand million Euros. The finance will be public and private. By the year 2020 all the capital of province will be connected by train with less than four and a half hours from Madrid, in the centre of Spain (figure 2).



Figure 2. Spanish Infrastructure Plan 2000-2020

In the year 2020 the 90 % of population of Spain will be to less than 50 km from a new station of high velocity railway net, so in the year 2020 the net of high velocity trains will be in Spain 10.000 kilometers.

2 INTRODUCTION

During the years 2008 to 2011 it has been constructed in Spain the new railway line of high velocity

trains (HVT) that will connect Valladolid with León in the northwest of Spain (figure 3).

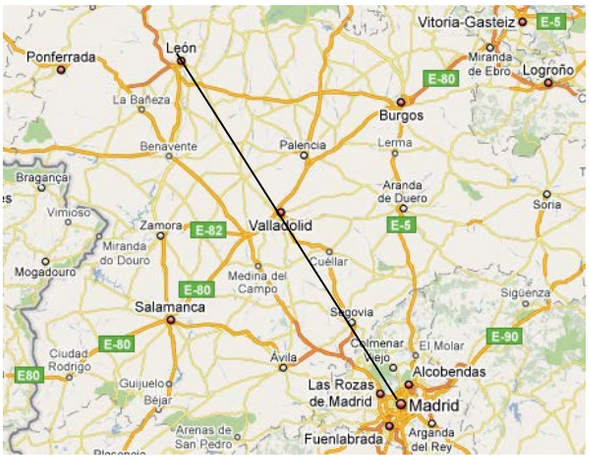


Figure 3. New railway line Madrid-Valladolid-León

This part of the Spanish Infrastructure Plan will cost 200 millions of Euros with a length about 183 kilometers. The speed will be about 220 kilometres per hour, but the railway platform is prepared to reach 350 kilometres per hour.

The connection between Palencia and Leon comprises 122.20 km and in the middle of it is the phase of Río Cea-Bercianos del Real Camino with a length of 10.5 kilometers (figure 4)

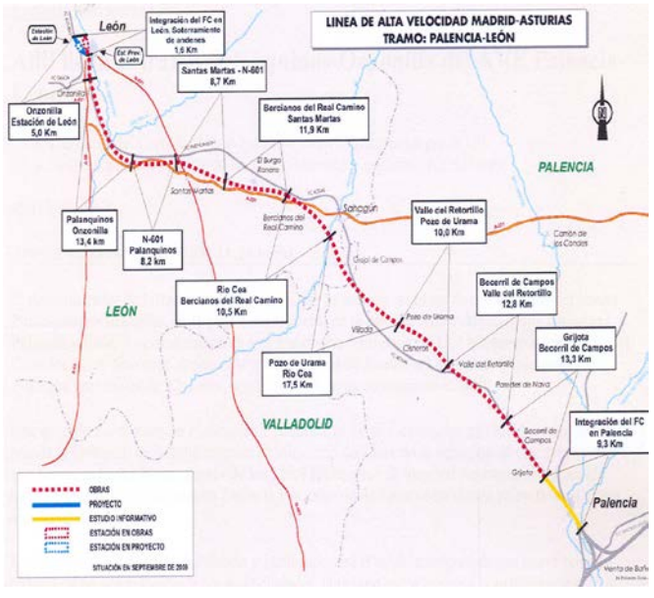


Figure 4. New line of High Velocity Trains. Section between Palencia and León (122,20 km)

The present paper exposes the project and construction of one of the most singular bridge in the section of Río Cea - Bercianos del Real Camino, from Palencia to León, which crosses over the existing motorway M-31. The solution of the bridge has been made a skew viaduct called "in pergola" with a length of 153 m and with a width of 14.5 m.

3 THE PROJECT

The phase Río Cea-Bercianos del Real Camino, passes near Sahagún's municipal area and the total length of platform of high speed reaches 10.5 km.

The work begins, approximately to 3 km to the south of the population of Sahagún, in the P. K. 55+100 of the informative study (300+000 P.K. of the project of construction), following with direction Northwest with a length of 10.501,635 m, up to the P. K. 65+587 of the informative study and to 0.6 km to the north of the population of Bercianos of Real Camino.

Between the kilometre point of 300+000 and the 310+500 which is the total length of the section it has been projected five great viaducts from 36 m to 442 meters and six bridges over the line of high velocity trains, to maintain the permeability for people and animals.

In the table 1 there is a resume of the five great viaducts in this phase Río Cea-Bercianos del Real Camino.

Table 1. The five viaducts included in the section of HVT Río Cea-Bercianos del Real Camino

Designation	P.K. BEGINING	P.K. END	TOTAL LENGTH (m)	STPANS DISTRIBUTIONS (m)
Viaduct over Cea river	300+072	300+188	116.00	35.50–45.00–35.50
Viaduct over Valle stream	300+861	300+897	36.00	36.00
Viaduct over Santiago road	306+501	306+943	442.00	32.00+3x41.00+50.00+5x 41.00 + 32.00
Viaduct over Coso stream	308+824	308+976	152.00	34.00–2x42.0–34.00
Pergola over A-231 motorway	308+980	309+133	153.00	76.50 + 76.50

The most singular viaduct between the five last ones in the fifth called "Pergola over the A-231 motorway" with a length of 153 meters (figure 5)

The project of the viaduct was made by the author of this paper, with a three-dimensional model of finite elements using the program SAP2000N, that it includes all the parts of the structure, such as: foundations made with piles (4,500 m of piles), mat foundations tying the piles, pillars, and the superstructure comprising a prestressed concrete slab, and the complete abutments.

The model of finite elements made consists of 8,806 nodes, 6,366 FRAME elements and 2,326 SHELL elements and the number of hypothesis studied was 1,306 with static and dynamic situations.

In view of the great obliquity of the crossing of the new railway line of high speed over the existing motorway A-231 which connect the provinces León and Burgos, with a very acute angle of 20 º, turns out to be necessary the disposition of retaining walls of great length in the zone of the acute angles North in the abutment E-1 (side Palencia), and South in the abutment E-2 (side León).

The deck is solved by means of a lightened slab of constant height of prestressed concrete, with a height in the axis of the deck of 1.52 meters and 1.0 meters in the edges.

The pillars of the viaduct have circular form, with diameters of 0.9 and 1.1 meters. Their heights are approximately equal and around of 6 meters.

The abutment 1 (low P. K.) is very singular and it is determined by the presence of the Viaduct over Coso stream immediately before, so it was necessary to arrange a unique abutment for the two structures, that allow in one side to dispose the support of the Viaduct over Coso stream and on the other side the support of the Pergola (figure 6)

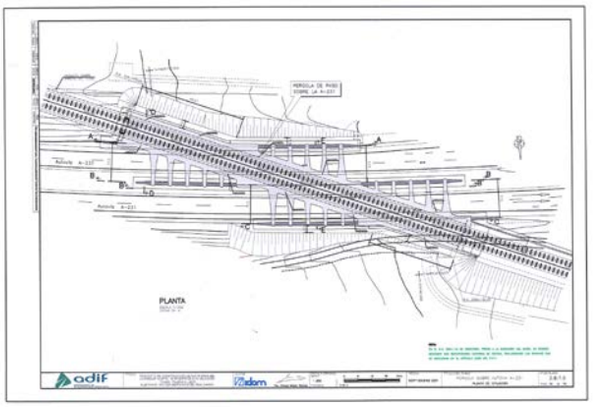


Figure 6. Pergola over A-231 motorway

The Abutment 2 is conventional with walls of containment of lands to avoid inundating the motorway A-231 (figure 7)

The foundation is deep trying to look for the rocky stratum. The abutments are founded by means of piles of 1.0 and 1.2 meters of diameter, whereas the intermediate pillars need piles of 1.0 and 1.5 meters of diameter. In the abutments where are the prestressed nerves of the deck, the foundation is solved by means of piles of 1.0 meter of diameter.

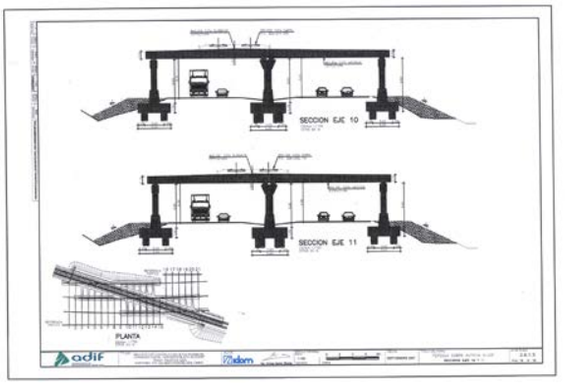


Figure 7. Transversal section of the Pergola viaduct

The soil under the structure is constituted by the next layers:

- Anthropic landfills with a maximum of 4.00 meters (called QXP).
- Tertiary sediments until the depth investigated of 30 meters, composed by:
  - Clay and slightly sandy clay (called TMA1)
  - Clayey lime (called TMA2)
  - Sand and limed sand (called TMA3)

So the foundation of the Pergola must be deep with piles of 1.20, 1.50 and 1.80 meters of diameter, which must be fixed at least 6 diameters in the materials with consistency or compacity hard and very hard.

In the figure 8 it must be seen the geological section of the soil in the transversal direction to the Pergola.

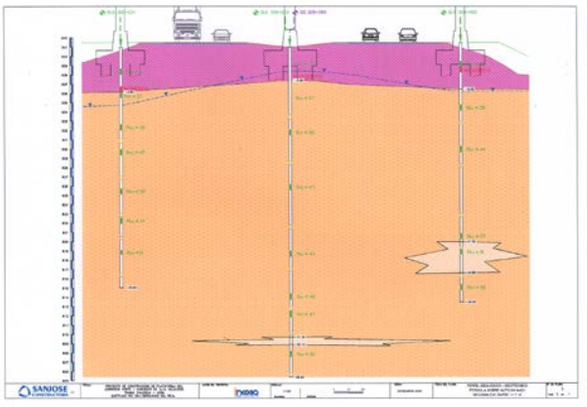


Figure 8. Geological transversal section to the Pergola viaduct

For the project of the pergola on the highway A-231 there has been generated an integral three-dimensional model that includes all the elements of the superstructure and of the infrastructure, such as:

- 16 piles of 1.00 m of diameter and 20 m of length in abutment E-1
- 48 piles of 1.20 m of diameter and 22 m of length in abutment E-1
- 24 piles of 1.00 m of diameter and 20 m of length in central pillar
- 16 piles of 1.50 m of diameter and 20 m of length in central pillar
- 16 piles of 1.00 m of diameter and 20 m of length in abutment E-2

- 48 piles of 1.20 m of diameter and 22 m of length in abutment E-2
- Slabs of foundations
- Abutments
- Prestressed deck, etc.

All of this constituted a complete three dimensional model of the whole structure that comprises 8,806 nodes, 6,366 FRAME elements and 2,326 SHELL elements (figures 9 and 10).

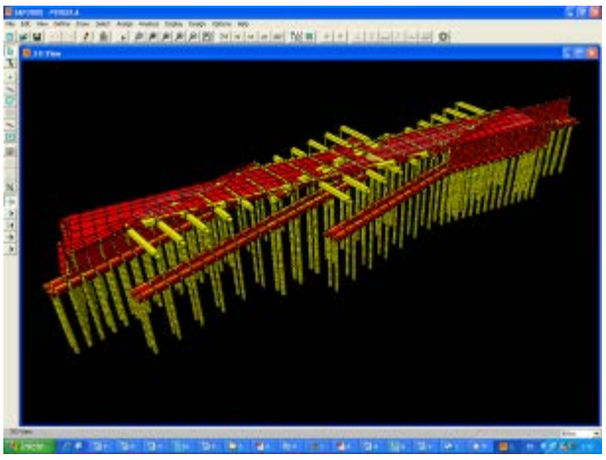


Figure 9. Three Dimensional Finite Element Model of the Pergola from the NE

This model permits to obtain all the responses of the Pergola such as moments, shears, axial forces, etc. in all the elements (figure 11).

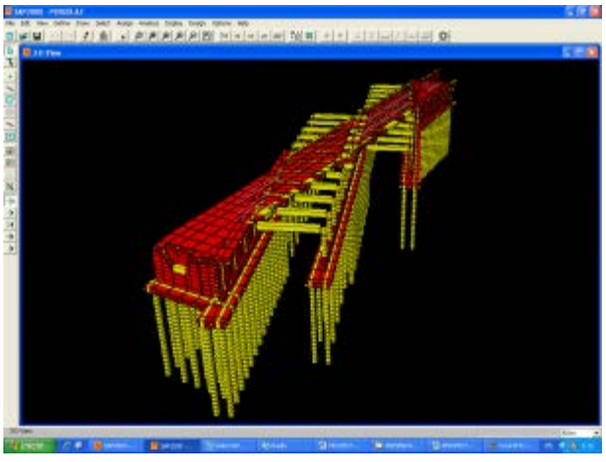


Figure 11. Transversal flexural moments in SHELL elements

4 CONSTRUCTION OF THE STRUCTURE

The structure is now under construction and the process of this was:

- First construction of piles.
- Second making the walls and the pillars (figure 12).
- Third the abutments (figure 13).
- Four the upper slab, etc.

In order to construct the prestressed upper slab it was necessary to cut one of the senses (two lanes) of the highway and to deviate the traffic temporarily for the other sense (two lanes), in order to scaffold one of the parts of the viaduct without any risk for the traffic, and to prestress the slab of the deck (figure 13)



Figure 12. Construction of central pillars (September 2009)



Figure 13. First phase of deviation of highway A-231 (November 2009)

5 CONCLUSIONS

As a conclusion it was projected a very singular Pergola viaduct by means of a three dimensional model of finite elements, which comprises all the parts of the infrastructure and the superstructure taking in consideration all static and dynamic loads by means of 1,306 with static and dynamic load combinations. The viaduct was finished in 2010.

6 REFERENCES

Euro code 1.1**.** *Bases of project and actions in structures.*

Euro code 2. *Project of structures of reinforced concrete.*

Euro code 3. *Project of structures of steel*.

Jiménez Salas, J.A. *Geotecnia y Cimientos*. Ed. Rueda.

Jiménez Montoya, P., García Meseguer, A., Morán Cabré, F. *Hormigón armado*. 14th Edition. Ed. Gustavo Gili.

MOPU. *Spanish rules relative to the actions to consider in the project of railway bridges. IAPF-2007*

Ministry of Public Works**.** *Norm of seismic construction: General part and Building Construction.* NCSE-O2.

Maintenance, Safety, Risk, Management and Life-Cycle Performance of Bridges – Powers, Frangopol, Al-Mahaidi & Caprani (Eds)
© 2018 Taylor & Francis Group, London, ISBN 978-1-138-73045-8

Repair and Retrofitting of Bridges – Present and Future

Harminder Singh
Associate Technical Director. Arcadis Australia Pty Ltd., Australia

ABSTRACT: Bridges are being constructed around the world and are increasing the number of assets to be maintained in the future. Since the Roman Empire to Victorian Era, the bridges are being constructed of timber, stone, masonry to the modern era of constructing the bridge with Glass-Fiber Reinforced Plastic materials. From stone masonry to concrete and steel, the bridge of each material type has different durability level, maintenance issues, repair and retrofitting requirements.

The modern bridges being constructed are more durable and lower life cycle cost. Now the focus is more on the environmental aggressivity in which the structure is being constructed and take adequate preventive measures at the design stage. The old structures before the 1980s have a lot of repair and retrofitting requirements. With the increasing load of traffic and the requirement to accommodate more number of lanes per bridge, it is a challenge for bridge engineers to check the structure to the lowest factor of safety, thus avoiding the widening of bridges in some cases and contributing to the long-term sustainability.

To overcome the challenges for the optimum use of bridges, the paper suggests the way forward for inspection, monitoring and asset management. With the BIM becoming more popular, it has also discussed about the requirement of single database of bridge assets where all the inspections, current and new assets information can be centrally located. The requirements for the assessment and repair of structures is discussed and the way forward for 3D printing for repair of concrete bridges. The paper also discusses about the various standards available for bridge maintenance in different countries. In the end, the critical discussion is presented about the future of bridges and repair requirements and the latest materials available to explore for use in structures to avoid major repair and maintenance in the future.

1 CONDITION AND ASSESSMENT OF BRIDGES

1.1 *Deterioration of Bridges*

There are different reasons for deterioration of structures and depending upon the location there are different factors lead to degradation of structures. In the coastal regions, the main reason of deterioration is saline environment where the air borne salts affects both the steel and concrete structures. For structures in high earthquake zones, the main attention is on designing the structures that can sustain in the high ground movement forces. Although the structures are designed for these transient forces but still in high intensity earthquakes, the structures have some cracking or minor damage that can lead to change in stress distribution and initiate the deterioration. The main reasons for deterioration of structures are:

a) Environmental aggressivity
b) Change in traffic need and live loads
c) Physical damage due to vehicle overloading and collision
d) Scouring, settlement, ship impact and earthquake
e) Steel structures – fatigue loading and corrosion
f) Substandard construction
g) Stray Currents
h) Fire

With the increase of traffic demand, every major road and bridges across the world requires to be widened or la ne rearrangement required to cater for the future traffic requirements. This requires the widening of bridges or some of the pedestrian path removed to accommodate new lane arrangement and change the load distribution in the structures. The impact of widening is more on skew and curved bridges where the load distribution changes quite significantly. With the special vehicles are to be accommodated on the bridges that have much heavier axle lo ads than the previously designed live loading so the fatigue check for residual life should help in understanding whether the bridge will be suitable for future demand.

The focus now is more on designing the structures that can sustain in the various impact situations either from rail, vehicles, ships etc. This requires the structures to design for higher collision loads in advance to cater for possible collision situation. But during the actual impact the force transferred to the structures could be higher than the designed forces that impacts the foundation. Post collision, the checking of bridge suitability to open for traffic, the foundation of the structure is often overlooked for any possible effects. In the other events like scouring of foundations, it is

important to check the foundations for excess scoring beyond the design requirements. The collapse of Malahide Viaduct, Ireland in 2009 (Figure 1) provides an example where the scouring lead to the collapse one of the bridge span when the commuter trains were few seconds away from the viaduct.

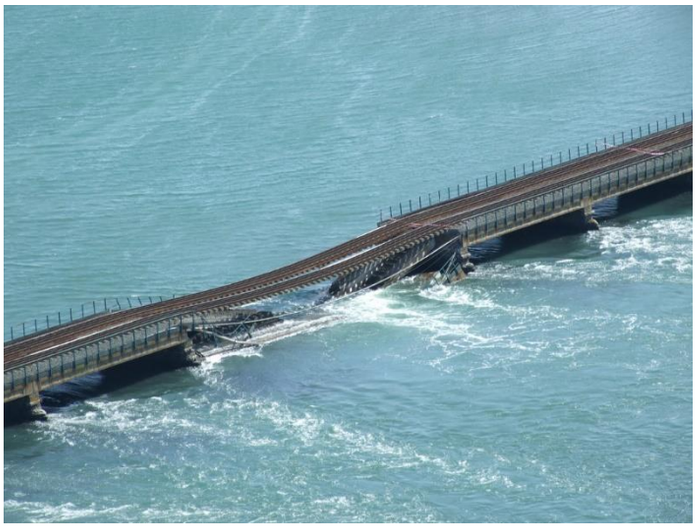


Figure 1 Lessons to be Learnt from Malahide Viaduct

The design of structures in the earthquake environment requires a careful detailing for the required ductility of the structural members. The 1995 Great Hanshin earthquake where the Hansin Expressway (Figure 2) collapsed due to low ductility of the substructure. Now the more focus is on the design that helped the structure to behave more elastically during the earthquakes.

The recent fire event of Greenfell Tower in London reminds the requirement for use of fire proof materials for bridges as well. With the more architects and urban designers involved in planning of bridges so the trend now is more towards amalgamating the structures to the surrounding environment by giving an eye-catching experience rather than 'concrete' view experience. It is to check that the cladding and some of the materials being used on shared path bridges are fire proof and these types of events can be avoided in the infrastructure sector.

1.2 *Bridge Inspection*

1.2.1 *Current Practice*

It is a normal practice worldwide to undertake the general inspection of structures every 2 years and detailed inspection within touching distance every 5 years. This frequency of inspection can be increased in case during the previous inspection the structure is found in bad condition or of significant importance. With the reducing budget of different local authorities, there is an impact on the spending for inspection and condition monitoring. The delayed inspections can further delay the repair of the structures significantly and sometimes become the reason of failure. The current practice of physical inspection of bridges helps in deciding the condition rating of different bridge components that can be used in the load rating and strengthening design (if required). However, the current system does not provide the comparison of all the available information based on the previous and current photographs and inspection reports.



Figure 2 Limited Ductility Lead to Collapse of Hanshin Expressway

1.2.2 *Latest Inspection Techniques*

With the advancement of technology, the inspection with drones has a huge opportunity for the future. In some of the sectors like high rise buildings this technology has already being used but it is still in the budding stage. The drone inspection is especially useful for bridges over creeks and rivers depending on the span of the bridge where a lot of temporary works are required for detailed inspection that can save the cost of temporary works. The bridge over railways are a very big candidate for drone inspection where the

small windows of access during rail closure can be used for inspecting the bridge quickly. The close images can be taken with the drones while maintaining the required gap from the structure. It is expected that the drone inspection can help in reducing the requirement of detailed. The little change can help in saving budgets for local authorities and can be used for the bridge maintenance works.



Figure 3 Drones are Huge Contributor for Inspection

1.3 *Early Detection System*

For medium to long span bridges and the bridges of significant importance, it is more prudent to monitor the structures remotely than inspecting at regular intervals. It helps in providing the real-time information of the structural behavior and gives an advanced warning if the distress is beyond the safe limits. The monitoring of concrete bridges could involve checking the vibrations, stress and strain levels with sensors at prominent locations along the structures. The data can be fed remotely into the centrally located database where the outputs can be generated in real time and can provide advance warnings.

The structures in the high earthquake zone also requires as real-time monitoring so that in any event of exceedance of movement that can lead to distress in structure, the traffic can be slowed down or stopped completely. Also, it will help in pinpointing the distress location and understanding the repair or refurbishment requirements.

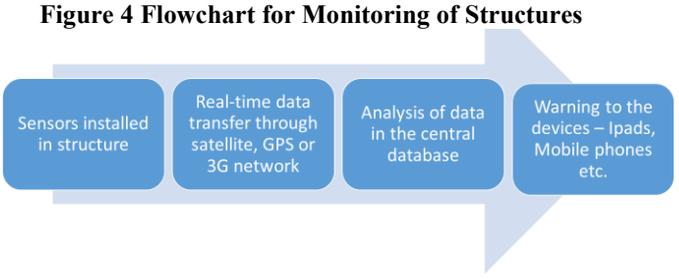
As a cheaper alternative, Moire tell tales by Bill Harvey Associates can be installed for checking any movement and cracking in structures. They have an accuracy of 0.1mm tell tales and images can be taken by drones from the distance and any movement can be checked from images later. With the drones, there is no need to access every tell t ales physically and drones can be helpful to record the data.

.

1.4 *Monitoring System*

Now with the architects involved in the planning of bridges it is a trend to provide more longer and slender structures where the serviceability could be a major concern. It is more prudent to install the sensors permanently for the life time monitoring of structures. For the normal situation, the system will be neutral and in case of any distress it can provide immediate warning to asset owner about the possible problem. These days the advanced system can provide the alerts on the mobile phones or IPad to several people in the monitoring team. If there is a frequent warning or significant warning the emergency inspection or mitigation can be planned. With this system, most of the bridges would not require frequent inspections. The savings from remote inspections can used for installing this system on other bridges. Most of the bridges have major defects in the superstructures. The sensors can be installed at the strategic locations along the span that follows the process shown in Figure 4 and hierarchy of bridge monitoring for future is as per Figure 5.

Figure 4 Flowchart for Monitoring of Structures



Digital Image Correlation is a 3D, full-field, non-contact optical technique to measure contour, deformation, vibration and strain on almost any material. The technique can be used for many tests including tensile, torsion, bending and combined loading for both static and dynamics applications. The method can be applied from very small (micro) to large testing areas – and the results are readily comparable with FEA results or strain gauges. The possibility of use of this technique in bridges should be explored further.

1.5 *Bridge Management System*

One of the point author advocate the use of asset management system where the real-time database of structural assets can be maintained for structures. The real-time monitoring system as discussed before can be connected to the asset management system that can provide real time alerts. The physical inspection data and photographs can be directly fed into the system where the automatic inspection reports can be generated that can save a lot of time and budgets to use for other automation activities.

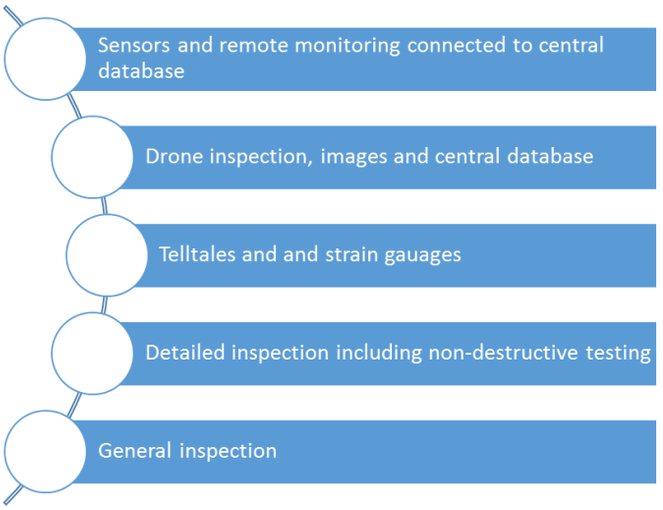


Figure 5 Proposed Hierarchy for Monitoring of Structures

The inspection data from drones can be fed into the system that can become the single source of all information. With the BIM becoming a norm for current and future projects, it is a challenge to the bring the existing assets in the BIM environment and its integration with the asset management system. To make the single source of all information, the existing assets can be digitized using drones and the 3D models can be used for asset tagging, tagging of inspection photos, recording and comparing defects and finally if there is any upgradation or widening required the same model can be used for providing the existing structural information. The as-built drawings and information of each bridge can be digitized and tagged to the model. Initially the cost will be high however at a later date the cost will offset by less manual data management, no data loss and less frequent inspections with higher confidence level in the available information. Drones can take 3D pictures, connect to the central system and compare with the previously inspected photographs. Any difference between previous and current photographs can help in identifying the possible distress where the mitigation can be planned.

2 ASSESSMENT OF BRIDGES

2.1 *Current Practice and Way Forward*

It is a normal practice to undertake the need based approach for bridge assessments. The requirements of bridge assessment could trigger by anything like due to change in traffic demand and other transient effects. The new vehicle load can significantly impact the structure that can deteriorate the condition of bridges. The assessment can also be due to widening of bridges where the study is required to check the existing structure for new distribution of forces. The main reasons that bridges require an assessment are:

a) Significant deterioration of structure due to age and other reasons
b) Increase in vehicle loading that require re-assessment of bridges in the network
c) Assessment of structure after significant natural event like earthquake, cyclone etc.
d) Accidental event – road or rail collision, ship collision etc.
e) Widening of existing structure

In most of the assessments it is found that there is significant reserve capacity in structural members that can eliminate the strengthening requirements. With the proposed real time monitoring system, the structures can be checked quickly under controlled conditions for new vehicle loading. The system can help in reducing the requirements of detailed assessment or improve the confidence level. For some of the initial sample bridges, the site results can be compared with assessment results to gain confidence and later the system can be solely used for checking the bridge suitability for increase in traffic demand.

2.2 *International Standards*

There are many standards available worldwide that provides a useful information for assessment and strengthening of structures.

European Standard EN 1504 has 10 parts that covers the complete lifecycle of structures from protection and repair of reinforced concrete. The standard also includes the test methods for material properties, specification for the key repair materials, including coatings, mortars, bonding agents and injection materials.

BA 32/90 is one of the UK standard for bridge assessment and repair of concrete structures that is in use for a long period. With the implementation of Eurocodes few years ago, this standard is still being used in conjunction with EN1504 and provides a useful initial information about bridge inspection and repair. The standard also covers the requirement of principal and special inspection.

ACI 562-16 is the latest standard available from American Concrete Institute which is now integrated with the ACI 318 requirements. The standard helps in understanding and identifying the unsafe structures and strengthening requirements. It is a performance based standard that provides the flexibility in the assessment and repair design process and identifies the

provisions to improve performance of the repaired structures.

3 REPAIR AND RETROFITTING

3.1 *Repair Requirements*

It has been rather disappointing to find out that only 75% of repairs survive 5 years. 25% of repairs survive 10 years and only 5% survive 25 years. There is a lot of research work undertaken on the repair of structures that bring out several products from different companies for improving the long-term durability of repairs. It is found that the failure of expansion joint and bearings are one of the significant reasons for deterioration of bridges. Now the integral bridges are more common for small to medium span structures that eliminates the maintenance requirements. The inspection of integral structures is much easier than the previous structures with bearings that have smaller parts and difficult to access for inspection.

The maintenance work of bridges has the following influence and constraints

a) Financial constraints and funds availability
b) Technical knowledge and knowledgeable staff
c) Number of assets and their importance to the public
d) Capability to organise effective quality assurance measures
e) Management methods

Serviceability failure can sometimes lead to deterioration of structures that includes cracking, spalling, shrinkage and deflection. This can happen due to poor workmanship, use of poor material, improper cover, concrete placement and other reasons. The serviceability is now a part of the design of structures and more focus is on the durability. These days with the scarcity of land more projects are being delivered in the brownfield sites where there is potential presence of a hazardous substance, pollutant, or contaminants. The environmental aggressivity is being checked in the design stage and appropriate steps are being taken in the design by providing adequate protection to structures.

3.2 *Decision for Repair and Retrofitting*

For a typical bridge in the urban environment or on a freeway there is limited opportunity to repair or replace the structure as the disturbance to the community is significantly high and thus limit the options to upgrade the structure. There are several reasons for repair of bridges discussed in the previous sections. It is also important to understand whether the residual life of structure is sufficient that warrant the decision making of whether the structure should be repaired or replaced. The typical example of collapse of 35W Bridge (Figure 6) in Minneapolis, USA where the existing bridge was even substandard for construction loads. The bridge was also rated as fracture critical, meaning that the failure of just one vital component could cause the whole bridge to collapse.

The conventional system in practice is to undertake the load rating and provide the residual capacity of different components of the bridge. The detailed inspection of the bridge that also includes the destructive and non-destructive investigations provides the condition assessment that help in selecting the factors based on the condition assessment. The inspection on site can provide the useful information about the level of strengthening requirements.

The condition factor and load rating help in decision making for strengthening. The process of decision for maintenance works generally follows the process as per Figure 7.



Figure 6 Collapse of 35W Bridge in Minneapolis, USA

During assessment and strengthening the serviceability and fatigue requirements should also be checked that later in the life of structure could become a main governing criterion for deterioration of concrete structures. However, this practice still provides a suc-

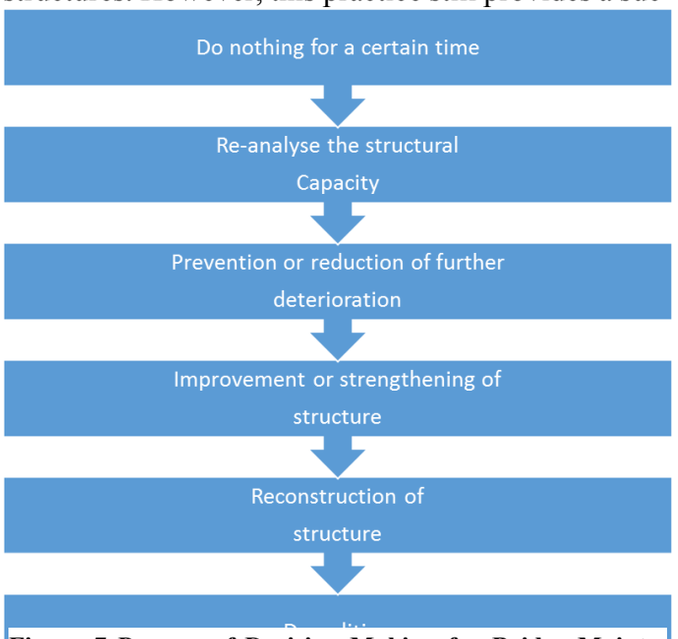


Figure 7 Process of Decision Making for Bridge Maintenance

cessful outcome and the bridges strengthened with this method have successfully delivered the right outcome.

Other factors that could affect the decision making for repair of bridges are:

a) Residual life
b) Serviceability requirements
c) Fatigue requirements
d) Further deterioration possibilities after repair
e) Foundation condition
f) Future demand of bridge use
g) Exceptional forces – like earthquake, change in weather

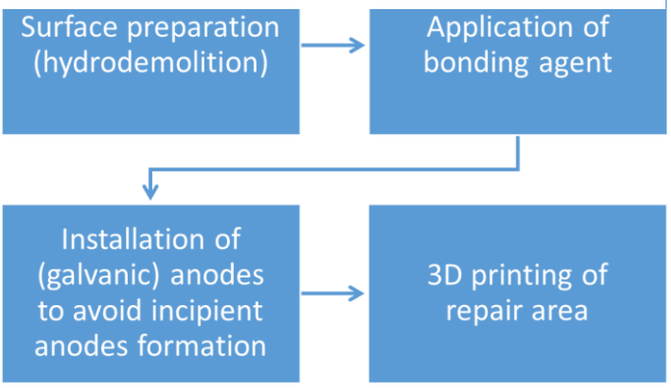
3.3 *3D Printing for Concrete Structures*

3D printing of structures is getting popular across the world and recently the 3D printed bridge for cyclists was completed in the Netherlands. The main benefit of 3D printed material is that the optimum material can be used in different parts of the structure thus avoiding the need of prismatic shapes where the same section is continued to the support because of the formwork simplicity and making simple shapes.

The similar 3D printing can be used for the repair and rehabilitation of structures. The suitability of this process depends upon the substrate strength. As the material is deposit in the required shape so there will be careful surface preparation required alongwith the bonding agent for adhesion of new material with the substrate. With the use of 3D printing for repair there is no formwork required and the repairs can be completed quickly without significant temporary works. With the smaller nozzles, the material can be deposited around the reinforcement that avoids the shadow formation which is commonly a problem with sprayed concrete. The flowchart for repair and strengthening with 3D printing is in Figure 8.

With the bigger nozzles, the 3D printing can also be used for strengthening of structures. The flexible fibers like polypropylene can be used to reduce shrinkage and increase the strength. The ready-mix materials available these days has a quick gain in strength that can help in open the structure for traffic sooner. The addition of micro fiber reinforcement can help in improving the tensile strength of concrete and avoiding additional reinforcement in some cases. The material can be made more workable by adding superplasticizer and retarder so there is blockage of nozzles during 3D printing.

Figure 8 Process of Repair/Strengthening with 3D Printing



4 DURABLE MATERIALS FOR CONSTRUCTION

While planning for the maintenance of existing structures it is also important to make the future structures more durable so they require less maintenance and improve the service life. With the new research available it is the time to incorporate these new materials in greater use.

4.1 *Self-Healing Concrete*

Materials are now developed to a level that the durability of the structures has increased significantly. In the concrete structures, there is a discussion going on for the use of self-healing concrete. The self-healing concrete can repair its own crack work based on the bacteria that can survive in green and hardened concrete for more than 200 years. They get activate when the water or moisture enter cracks and they start producing limestone the can close the gaps within

concrete. It is expected the crack upto 0.8mm can be repaired with the self-healing bacteria.

4.2 *Ultra-High Performance Concrete*

Ultra-High Performance Concrete (UHPC) with compressive strength ranges between 120 to 150 MPa is being encouraged to use across the world. The UHPC includes fine sand, silica fume, ground quartz, high range water reducer, an accelerator, steel fibers, and water. The Australian Standards already allow to use concrete grade upto 100 MPa however it is still not in the range of UHPC. With the use of fiber reinforced concrete the normal concrete can reach upto to the ultra-high strength.

4.3 *Fiber Reinforced Polymer Composites*

Fibre-reinforced polymer (FRP) is a composite material made of a polymer matrix reinforced with fibers. FRP composites have been included in new construction and rehabilitation of structures through its use as reinforcement in concrete, bridge decks, modular structures, formwork, and external reinforcement for strengthening and seismic upgrade. The applicability of FRP reinforcements to concrete structures as a substitute for steel bars or prestressing tendons has been actively studied. FRP reinforcements offer several advantages such as corrosion resistance, high tensile strength, lightweight and ease of handling. The most serious problems with FRP reinforcements are the lack of plastic behavior and the very low shear strength in the transverse direction. The AS5100.8 provides the guidelines for strengthening of bridge structures using FRP composites.

4.4 *Weathering Steel*

Other innovative material quite common but seldom used in Australia is Weathering Steel. It is becoming common in the Europe to use this material because of the benefit of low maintenance and low life cycle cost. Although the initial cost is slightly high but considering the cost of initial protective coating and maintenance cost for 20 years this comes out cheaper than the conventional steel. Also, there is a significant focus on the urban designs so these bridges built with weathering steel (although provides an ugly appearance and feels like the bridge is crumbling) can be covered with urban cladding panels of any shapes and sizes.

4.5 *High Strength Steel*

The Australian Standards and other international standards now allow the steel grade up to 700MPa that help in reducing the amount of steel required for the structure. The high strength steel can be combined with UHPC discussed above where the high strength of concrete can help in balancing the internal forces in the section. Another option is to prestress the deck or steel section that can help in improving the overall resistance of the section.

5 FUTURE OF BRIDGES AND REPAIR REQUIREMENTS

There is an indiscriminate mining across the world for construction and there is already a shortage of construction materials and alternative ways are being invented to use different materials. Sand, which is a basic ingredient of concrete found shortage and number of middle eastern countries are buying sand from overseas. The abundant sand available in the deserts cannot be used because of it quality and suitability. There is 40bn tons of sand and gravel is used per year all around the world.

The onus is on the engineers to consider sustainability as part of their design. There is a great demand to reduce the section sizes of structures that helps in reducing the overall self-weight and foundation sizes. There is a need to use innovative materials, high strength materials as discussed in the section above that can help in contributing to sustainability.

Recently the world first modular glass fiber reinforced plastic footbridge was installed in the UK. The bridge design with name of 'Pedesta' is developed by Arup alongwith the Mabey Bridge. The modular bridge is expected to be of particular interest to the rail industry, providing a safer alternative for quick installation.

With the more durable materials and strict quality control in place for the new structures, the need of repairs is expected to reduce in the future. The integral structures are becoming more popular that is helping in eliminating the maintenance requirements.

The bridges constructed in the 20th century are still a challenge by maintaining them well can help in and avoiding the reconstruction and attaining sustainability in the long term. These bridges are the main point of attention for planning, maintenance and prolonging the service life. In most of the cases and especially the arch structure can sustain more than 100 years of design life.

BIM is expected to be an integral part of the asset management system where the existing structures model can be used for asset tagging and other purposes. The planning for inspection, repair and upgradation can be planned from the single system and can become a common data environment for all type of works. The early detection system and monitoring system as discussed before can be linked with this asset management system, plan inspection with drones and connect to real time monitoring of the structures. So the future lies in how to maintain and prolong the life of existing structures, remote monitoring of structures, construction of the new structures sustainably using minimum materials.

6 CONCLUSIONS

There are a number of new materials available that has already helped in improving the construction quality but still the challenge lies with an open question about how to manage the existing structures. It is expected that the remote monitoring and drones will become integral part of asset management system and existing available system can be digitized and fed into the management system which can become a single source of all current and new assets. The BIM process will become a part of larger asset management system. There is a need to use less and high strength materials that contribute to the sustainable future.

7 ACKNOWLEDGEMENT

The author would like to thanks his family for their support while writing this technical paper. The author would also like to thank the Arcadis Civil Structures team for their motivation to write this paper.

8 REFERENCES

[1] IRISH INDEPENDENT. Packed Train Seconds from Disaster in Bridge Collapse - https://www.independent.ie/irish-news/packed-train-seconds-from-disaster-in-bridge-collapse-26560282.html

[2] BILL HARVEY ASSOCIATES. Monitoring movements in difficult to Access Locations - http://www.moiretelltales.com /applications/monitoring-movement-in-difficult-to-access-locations.html

[3] HARVEY, Bill. 2009 Monitoring and Measuring Historic Masonry Structures, 3rd Australasian Engineering Heritage Conference 2009

[4] EN 1504 All Parts Products and systems for the protection and repair of concrete structures. Definitions, requirements, quality control and evaluation of conformity.

[5] BA 35/90 Inspection and Repair of Concrete Highway Structures

[6] ACI 562-16 Code Requirements for Assessment, Repair, and Rehabilitation of Existing Concrete Structures and Commentary

[7] BUILDING RESEARCH ESTABLISHMENT. A Thematic Network on Performance Based http://projects.bre.co.uk/ conrepnet/pdf/newsletter4.pdf

[8] NATIONAL PUBLIC RADIO US. 10 Years After Bridge Collapse, America Is Still Crumbling. http://www.npr.org/2017/08/01/540669701/10-years-after-bridge-collapse-america-is-still-crumbling

[9] Full-scale 3D printed concrete bicycle bridge destined for Gemert, Netherlands is underway. http://www.3ders.org/articles/20170907- massive-3d-printed-bicycle-bridge-is-delivered-to-gemert-netherlands-by-truck.html

[10] GUARDIAN. World's first 3D-printed bridge opens to cyclists in Netherlands. https://www.theguardian.com/technology/2017/oct/18/world-first-3d-printed-bridge-cyclists-netherlands#img-1

[11] GUARDIAN. The self-healing concrete that can fix its own cracks. https://www.theguardian.com/sustainable-business/2015/jun/29/the-self-healing-concrete-that-can-fix-its-own-cracks

[12] ALTEMOSE, Patrick. Ultra High Performance Concrete : The Savior of American Infrastructure

[13] TIMES OF INDIA. Why Even Arab Nations are Buying Sand. https://timesofindia.indiatimes.com /world/middle-east/why-even-arab-nations-are-buying-sand/articleshow/60492513.cms?intenttarget=no

Maintenance, Safety, Risk, Management and Life-Cycle Performance of Bridges – Powers, Frangopol, Al-Mahaidi & Caprani (Eds)
© 2018 Taylor & Francis Group, London, ISBN 978-1-138-73045-8

Displacement Coefficient Method for Bridge subjected to Pulse-Like Ground Motions

K.Y. Liu
National Cheng Kung University, Associate Professor, Tainan, Taiwan

S. T. Wang
National Chiao Tung University, Graduated Student, Hsinchu, Taiwan

C. C. Hwang
National Cheng Kung University, Undergraduate Student, Tainan, Taiwan

C. H. Kuo
National Center for Research on Earthquake Engineering, Researcher, Taipei, Taiwan

ABSTRACT: This paper proposes the displacement coefficient, R_d, for bridge column subjected to near-fault earthquake. R_d is defined as a ratio between ultimate displacement and elastic displacement. 142 pulse-like ground motions are utilized to perform the nonlinear time history analysis with constant ductility from 1 to 6. This study investigates the R_d in four aspects, including (1) signal processing method, (2) orientation of the velocity, (3) hysteretic models, and (4) number of the ground motions. The analytical results are compared with the regulations specified in AASHTO 2011. For a structure with typical displacement ductility of 4, compared to the analytical results, the R_d in AASHTO 2011 is overestimated within the period of 0.5 second, and underestimated between 0.5 and 4 second. Therefore, the revised formulation of R_d is proposed, which could be suitable for the bridge considering the near-fault effect in Taiwan.

1 INTRODUCTION

1.1 *Background*

Taiwan is located at the boundary between the Philippine Sea Plate and Eurasian Plate. The present converging rate is around 80 mm per year (Yu et al. 2001). In this convergence, the Philippine Sea Plate lies beneath to the north of Taiwan, while the Eurasian Plate in southern Taiwan is hidden under the Philippine Sea Plate toward east of mainland. Such a complicated activities of the plate caused the frequent earthquakes and orogeny in Taiwan. In addition, those activities also caused numerous active faults. According to the latest distribution map of active fault announced by Central Geological Survey in 2012, there are 20 Type 1 active faults and 13 Type 2 active faults, both of which have been activated in the past 10,000 and 100,000 years, respectively. These faults lie on the north-eastern and south-western direction, and most of the faults are reverse fault, while some faults are strike-slip fault along the eastern and western direction. The Shanchiao fault near the Taipei city in Taiwan is located in the tensile stress zone, which is a normal fault.

On September 21, 1999, a devastating earthquake with 7.3 magnitude on the Richter scale is called Chi-Chi earthquake. Chi-Chi earthquake caused different levels of damages to thousands of bridges in the central of Taiwan. Approximately 20 percent of the bridges suffered different damage levels, and 26 bridges were considered severe damage. It has been confirmed that due to the fault crossing or ground surface rupture near the bridge site, the superstructures were fallen from the collapsed piers in nine bridges, including Shi Wei bridge, Dong Fong bridge, Pi Fong bridge, Chang Gung bridge, Wu Xi bridge, Ming Chu bridge, Tong Tou Bridge, Long Men Bridge, and Li Yu Bridge along the Chelungpu fault.

Taiwan is a narrow island, so the numbers of people live near the near-fault region within 10 kilometers are accounted for 8.6 million. Any earthquake like the Chi-Chi earthquake occur again will induce another disaster. Therefore, it is necessary to initiate research works on near-fault earthquake and its impact to the infrastructure.

1.2 *Research Process*

Figure 1 illustrates the procedure of this study. There are seven steps, from selection of input ground motions as the first step to the proposed formula of R_d in the final step. The details of each step will be explained in the following sections. Section 2 is characteristics of near-fault ground motion. Section 3 is the signal processing of the time history. Section 4 is engineering parameters. Section 5 is analysis method. Section 6 is analytical results. Section 7 is proposed formula of R_d.

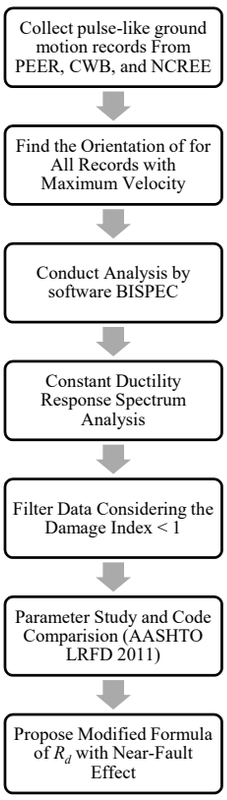


Figure 1: The procedure of research

2 CHARACTERISTICS OF NEAR-FAULT GROUND MOTION

When the fault was moving, the area closing to the ruptured fault was named near-fault area. It could be observed that there were some special characteristics for strong ground motion in the near-fault area. Thus, in seismic engineering, it was given a specific name called "Near-Fault Ground Motion".

2.1 *Peak of High-Strength Ground Motion and Acceleration response spectrum*

The seismic energy would dissipate during the process that seismic waves were traveling along the route of itself, and peak of ground motions and spectral accelerations would also degrade since that process. However, the ground motions which were near the fault provided a limit route to make the seismic energy to dissipate. As a result, the ground motions near the fault had higher peak value of ground motion, and acceleration response spectrum with different period than far-filed fault.

2.2 *Special Acceleration response spectrum in space distribution*

Near-fault ground motions had the characteristics including hanging wall effect and rupture directivity effect. Both of these characteristics caused the special difference of acceleration response spectrum in the space distribution comparing with the far-filed earthquake.

2.3 *Hanging Wall Effect*

The definition of hanging wall effect is that there are two stations located at both side of the inclined fault where are on the hanging wall and footwall position respectively. And the distance from the rupture surface are the same. When the fault was moving, it could be recorded the larger value of the ground motion on the station located in the hanging wall. The reason is that the station on the hanging wall position situated the radiative direction of seismic waves when the fault was moving. Therefore, it can sustain more strong seismic waves in this position.

2.4 *Rupture Directivity Effect*

The S wave superposed along the rupture direction of fault and caused the energy of seismic waves gradually increase along with the development of rupture of fault. This phenomenon was named rupture directivity effect. By the practical information and related predictable model could realize that the major reason to make the area of local low-frequency in acceleration response spectrum become larger, the larger earthquake magnitude is, and the smaller the frequency of the response spectrum amplification is. Since the accumulation of energy in the process when fault was rupturing hence the amplification along the rupture line of fault was positively correlated to the distance from station to epicenter (Spudich et al. 2014).

2.5 *Characteristics of Special Displacement of Ground Motion and Ground Velocity Time History*

2.5.1 *Permanent Ground Displacement*

The strong magnitude earthquakes caused by the activities of fault usually followed deformation of ground. Therefore, it produced the permanent ground motion in the areas where were near the fault. Even though there were no the situations that fault ruptured to the surface of the ground in the small magnitude, it could always observe the same deformation of ground for the same earthquakes in the areas where was near the epicenter.

2.5.2 *Velocity Pulse*

According to the results of rupture directivity effect and permanent ground displacement, it could be found there were some velocity time histories along with velocity pulses of single frequency and velocity pulses single direction recorded by several stations near the fault (Mavroeidis & Papageorgiou. 2003). These pulses would cause the low-frequency acceleration response spectrum to amplify, and these special velocity time histories would also lead to the increment of demand for nonlinear structural seismic design.

3 SIGNAL PROCESSING OF THE TIME HISTORY

This study collected the ground acceleration records from the Central Weather Bureau (CWB) in Taiwan, Pacific Earthquake Engineering Research Center (PEER), and National Center for Research on Earthquake Engineering (NCREE) in Taiwan to conduct nonlinear dynamic time-history analysis.

3.1 *The Central Weather Bureau in Taiwan (CWB)*

CWB set up hundreds of strong motion stations in Taiwan since 1991 and it has collected a lot of ground motion records. Most of the data belong to far-field records, where the near-fault data was primary collected from the Chi-Chi earthquake. The raw data are recorded by the strong motion stations and released by CWB after converting to an ASCII format. However, the acceleration time history downloaded from the CWB are without correction and the baseline usually drifts dramatically after the integration to velocity and displacement.

3.2 *The Pacific Earthquake Engineering Research Center (PEER Center)*

Chou et al. (2008) described the processing procedure of PEER strong motion database. Except for the baseline correction, PEER Center removed the instrumental response. In addition, a cosine taper was also adopted to revise the acceleration to zero in the start and the end of the acceleration to make the accelerations more smoothly in the two ends. However, in the processing procedure, PEER Center used a causal butterworth band-pass filter to the time history. This filter eliminated the permanent displacement for the seismic records.

3.3 *National Center for Research on Earthquake Engineering in Taiwan (NCREE)*

The processing procedure for NCREE mainly had two stages. Firstly, they used the re-mean to make baseline correction. The original acceleration records usually have small shifts in baseline, so the shift needed to be deducted and the baseline shift is the mean value of the first several seconds of pre-event noise before P-wave arrival. Second, the data collected from NCREE used the two points method (Iwan et al. 1985) to perform re-trend. The process was to remove the shifting of the baseline. During the earthquake, the seismograph might tilt when it met a strong shake. Therefore, in the acceleration time history, during the period of the strong shake, a box-like signal was mixed. An inclined line can be seen in the integrated velocity time history, and a least square method was used to find the slope of this inclined line between selected points. Then, the slope was corrected and the inclined line was back to the datum line. This way can reserve the permanent displacement.

4 ENGINEERING DESIGN PARAMETERS

Figure 2 shows the lateral force and lateral displacement relationship of one linear elastic system and one elastic perfect plastic system.
These two systems can be related by three engineering design parameters. R represents the force reduction factor. R_d is the displacement amplification factor, and C_y is the yielding strength factor. R, R_d, and C_y can be presented as function of displacement ductility, μ. μ is the ratio of the maximum displacement and yield displacement in elastic perfect plastic system. When μ is increasing, the plastic deformation of the structure would become more obvious. In this study, the major engineering parameter discussed is the displacement amplification factor R_d with respect to the constant value of displacement ductility μ.

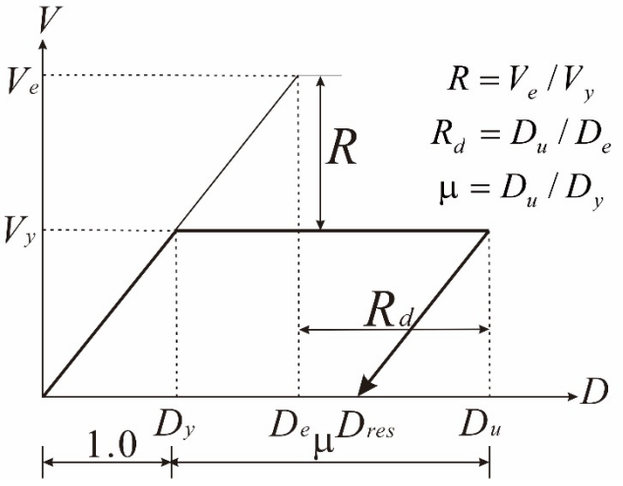


Figure 2: Force – Displacement Relationship

4.1 *Hysteretic Model*

4.1.1 *Elastic Perfect Plastic Model (EPP Model)*

Elastic Perfect Plastic Model (EPP model) is showed in Figure 3. EPP model is suitable for steel structure with an apparent yielding strength, and the corresponded hysteresis loop is well saturated. It is assumed the ratio of post yielding stiffness to elastic stiffness is zero.

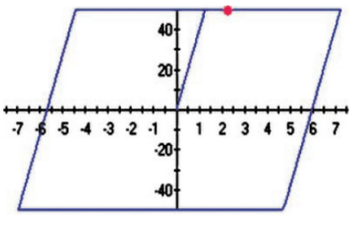


Figure 3: EPP Model

4.1.2 *Modified Clough Model (MC Model)*

Figure 4 shows a typical hysteresis loop for Modified Clough Model (MC Model). For a new design bridge column, it is expected to have a ductile failure. This

model is capable of describing the hysteresis behavior of reinforced concrete column member with sufficient lateral reinforcement. Obviously, the ratio of post yielding stiffness to elastic stiffness is zero for both EPP and MC models in this study for the reason of simplicity.

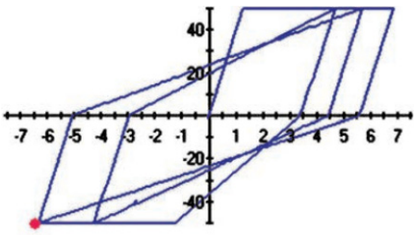


Figure 4: Modified Clough Model (MC model)

4.2 *Displacement Magnification Coefficient, R_d*

R_d is a ratio of displacement to measure the gap between ultimate displacement of a nonlinear system and elastic displacement of a linear system with same structural period. R_d is used to estimate the ultimate displacement by introducing a factor to amplify the displacement obtained from a linear elastic system. The definition of R_d can also be found in FEMA-440 (ATC 2005), FEMA-P695 (ATC 2009), and AASHTO Guide Specifications for LRFD Seismic Bridge Design (AASHTO 2011). In this study, only the regulations in AASHTO for bridge are discussed. The formulas in AASHTO are shown as follows:

$$R_d = \begin{cases} \left(1-\frac{1}{\mu_D}\right)\frac{T^*}{T}+\frac{1}{\mu_D} \geq 1.0 & \frac{T^*}{T} > 1.0 \\ 1 & \frac{T^*}{T} \leq 1.0 \end{cases} \quad (1)$$

in which

$$T^* = 1.25T_S \quad (2)$$

$$T_S = \frac{S_{D1}}{S_{DS}} \quad (3)$$

S_{D1} = Spectral response acceleration parameter at a period of 1 sec

S_{DS} = Spectral response acceleration parameter at short periods

According to the hypothesis that elastic system and elastic-perfect-plastic system have the same displacement, but it is not valid for short-period structures which may have an inelastic behavior. As a result, it can use R_d to adjust the elastic displacement for short-period structures. The formula for R_d defined that R_d is > 1 when the period of structures, T, is less than the characteristic ground motion period, T^*. The character μ_D in AASHTO is the same as μ in this study. There are different μ_D for various seismic design categories, SDC, in AASHTO. For bridges in strong earthquake region, μ_D may be taken as 6 for maximum local member displacement demand.

5 ANALYSIS METHOD

This study utilized BISPEC (Hachem 2013) to conduct nonlinear time-history analysis for a single degree of freedom (SDOF) system. The SDOF system is assumed to be an important bridge and located at a site which is near the Chelungpu fault in Taiwan. The analysis results are presented by constant displacement ductility μ to establish the relationship between structural period, T, and R_d. The structural period was from 0 to 10 sec, and the ductility μ was in a range of 1 to 6.

5.1 *Selections of Pulse-Like Time Histories*

This study collected pulse-like time histories from Strong Ground Motion Database of PEER with different types of faults, such as strike slip, normal, and reverse faults. The total number of records selected is 142. In order to reduce number of time histories, 39 records in the event of Chi-Chi earthquake were reserved. Eventually, 31 records applied to this study because those records are duplicated records for the comparison purpose used by NCREE to verify the signal processing process.

It could also be found the major fault type in Chi-Chi earthquake is reverse fault. Based on the code requirement, it is required to use seven ground motions for nonlinear time history analysis. Therefore, seven stations with tremendous velocity pulse are further selected, such as TCU052, TCU063, TCU065, TCU068, TCU075, TCU102, and CHY101, respectively. The raw data without signal processing of these seven stations can also be downloaded from CWB of Taiwan.

5.2 *Orientation of Maximum Velocity*

In general, the ground accelerations can be measured by accelerometer in two perpendicular horizontal directions and one vertical direction. However, it is not guaranteed that the signal with maximal velocity can be just recorded in the earthquake event. There is a need to reproduce a combined signal from two horizontal components corresponding to the velocity records at an angle to achieve the maximal velocity. For all 142 records, the specific angle has been found. Therefore, not only two individual horizontal components but also the combined component which contains the orientation of maximum velocity can be applied to the following constant spectrum analysis.

5.3 *Response spectrum*

As mentioned, PEER, CWB, and NCREE used the different methods to perform signal processing. CWB and NCREE reserved permanent displacement of the ground surface, but PEER eliminated the permanent displacement. Although the scope of this study is to focus the structural period within 10 sec, it is needed to investigate the permanent displacement by conducting the response spectrum analysis to acquire the average value of the 7 major records. Meanwhile, the difference in acceleration and velocity response spectrum within the period of 50 second were also compared by using records selected from PEER, CWB, and NCREE, respectively.

5.4 *Damage Index*

According to Bozorgnia and Vitelmo (2002), if the damage index (DI) is of 0, the system presents an elastic response. However, if DI is greater than 1, the system is about to be collapsed. Therefore, the structural response should be further examined whether the corresponding value of DI is greater than 1.0. Once DI is larger than 1.0, the system at a specified displacement ductility is failed. In this case, the results can't be included to be averaged with other results in same condition.

5.5 *Code Comparison*

It is expected that the analysis process is very time-consuming due to large amount of cases. The total number of the cases to be analyzed is about 511,200 by multiplying 142 motions, 3 signal processing methods, 2 hysteresis models, 6 displacement ductility, and 100 intervals of the period. As a result, some important parameters should be determined to reduce the number of cases. The analytical results will be discussed in four different aspects: (1) signal processing methods, (2) orientations of the records, (3) hysteretic models, and (4) numbers of records, respectively. In the end, the analytical results under these four criterions would be also compared with the current design requirements from AASHTO, so that to find the difference between analytical results and code values.

6 ANALYTICAL RESULTS

When dealing with the data in the following sections from 6.1 to 6.3, 7 records form PEER with the event of Chi-Chi earthquake will be selected to perform the analysis to obtain the global trend of R_d, But the suitable number of ground motions still need to be investigated in section 6.4. Moreover, for those 7 records, the orientation is in the east-west direction because the acceleration records have more notable pulse-like signal in this direction than in the north-south direction. In addition, the EPP model, as a standard model, is adopted to conduct the analysis for the comparison purpose.

6.1 *Signal Processing Methods*

Figure 5 indicates the acceleration response spectrum, velocity response spectrum, and displacement response spectrum by using the data from PEER, CWB, and NCREE, respectively. It can be observed the acceleration response spectrum and velocity response spectrum displayed duplicated results. But, a notable difference can be found on the displacement response spectrum when the structural period exceeds 10 sec, and it became more obvious between 30 and 50 sec. As a result, it is assumed the permanent displacement should be considered, and the signal should be specially processed to preserve the long duration component for the structure with long period, such as 10 sec. Otherwise, for conventional structure with the period less than 10 sec, there is no need to make special signal processing to include the permanent displacement in the spectrum analysis.

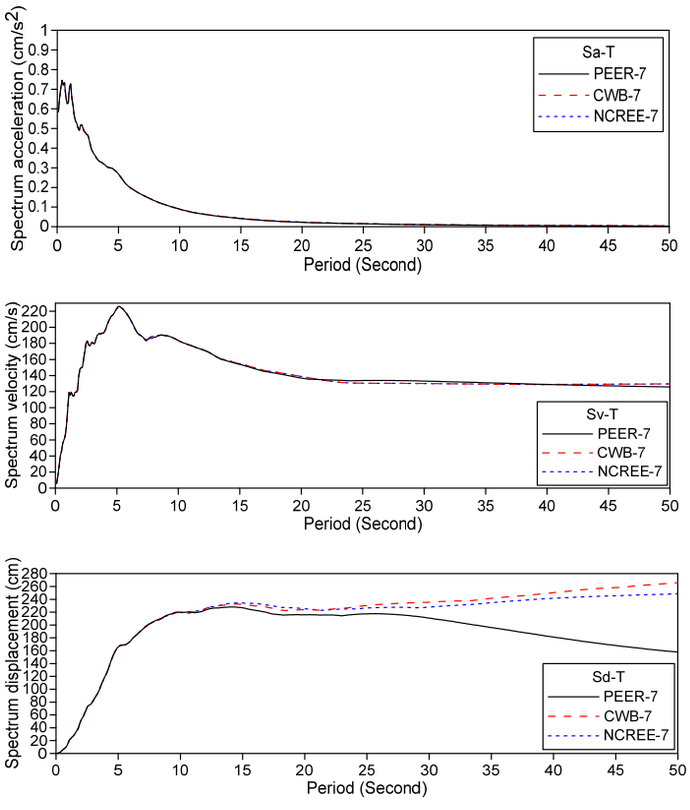


Figure 5: Spectrum analysis analyzed by data from three research institutions

Figure 6 shows the results of R_d analyzed by data given from CWB, PEER, and NCREE. In general, the analysis results for PEER, NCREE, and CWB are similar when μ is increased from 2 to 6. When μ is 2, and the period is within 0.5 sec, the R_d given by the code is close to 5. However, the analysis result just reaches 1.5. After the period of 5 sec, both code value and analysis result have almost same values. For μ is changed from 3 to 6, the code value is about two times

of the analysis result within the period of 0.5 sec It indicates the ultimate displacement of the structure may be overestimated based on the code regulations, particularly for structure with short period to obtain a conservative value of ultimate displacement. On the other hand, for the case with larger μ and the period is between 1 and 4 sec, the analysis result became slightly higher than the code requirement. It was more apparent when μ is increased from 4 to 6. Besides, the analysis results of R_d are smaller than the code values after the period of 4 sec for all cases with different μ.

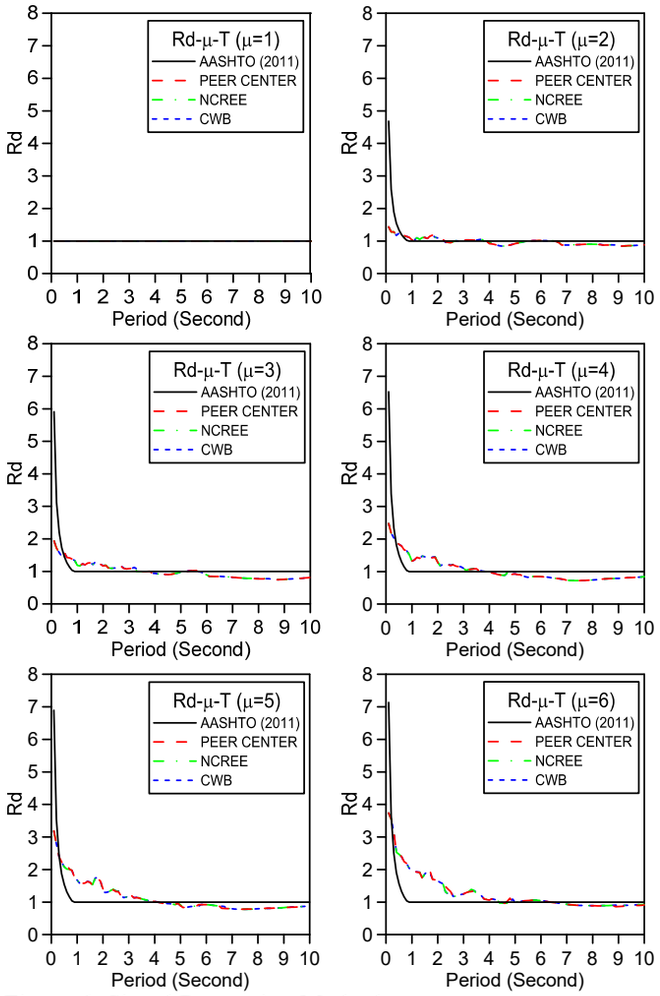


Figure 6: Signal Processing Methods

6.2 *Orientations of the Maximum Velocity*

Figure 7 shows the results of R_d analyzed by data with respect to west-eastern, north-southern, and maximum velocity direction. Overall, within the period of 0.5 sec, the values of R_d from AASHTO are double or triple than the analysis results if μ is in the range from 2 to 6. Though the trend of analytical results is similar, the results with maximum velocity direction is still slightly larger than the data with other two directions. The major difference between code requirement and analytical results can be found in the range of 0.5 to 4 sec. Before 4 sec, the analysis results exceed the code value; on the contrary, after 4 sec, the analysis results are gradually less than the code value. It is more obviously for the results with μ from 4 to 6. Besides, the analysis result are mildly fluctuated in the case of north-southern direction if μ is 5, and it becames more distinct if μ of 6 can be expected.

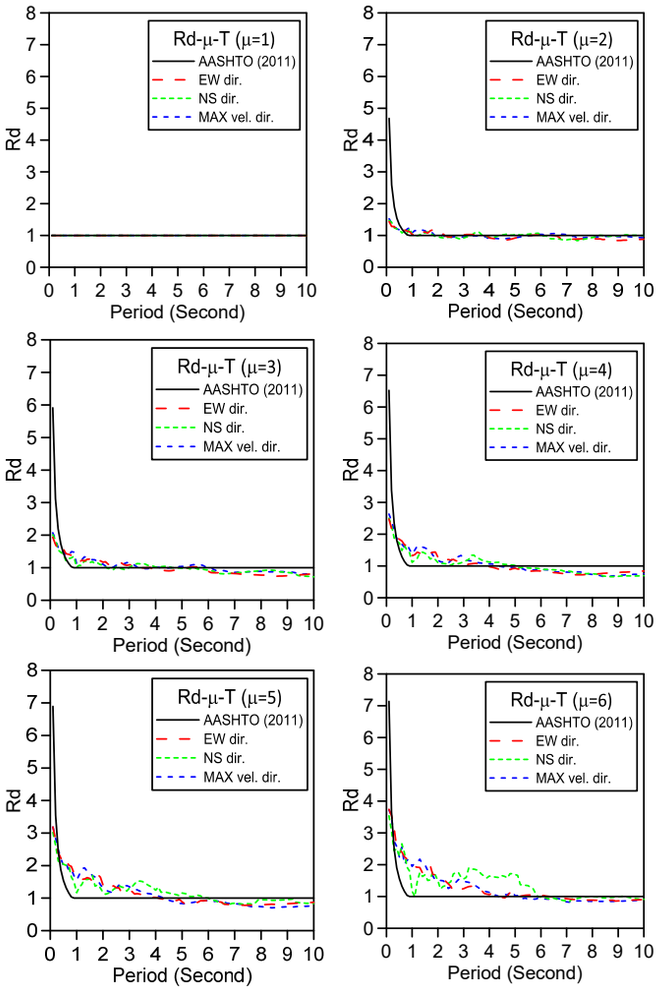
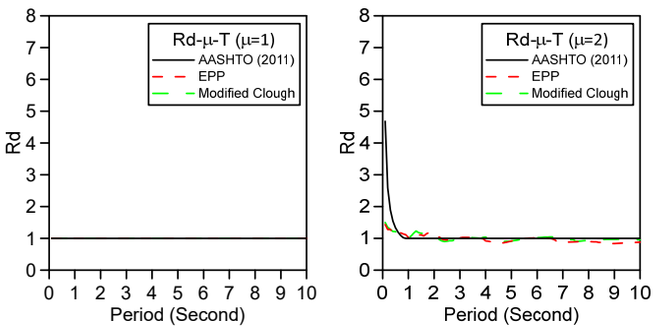


Figure 7: Orientations of the Records

6.3 *Hysteretic Models*

Figure 8 illustrates the results of R_d analyzed by data based on two kinds of hysteretic models. The results showed no obviously difference between these two models when μ is changed from 2 to 6. And the entire trend of the analysis results is quietly similar to the results mentioned above, such as the signal procession methods and orientations of the records.



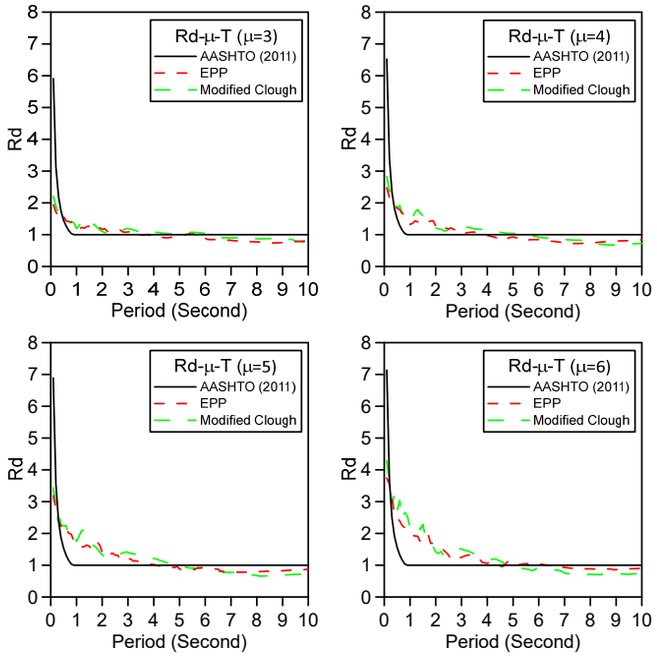
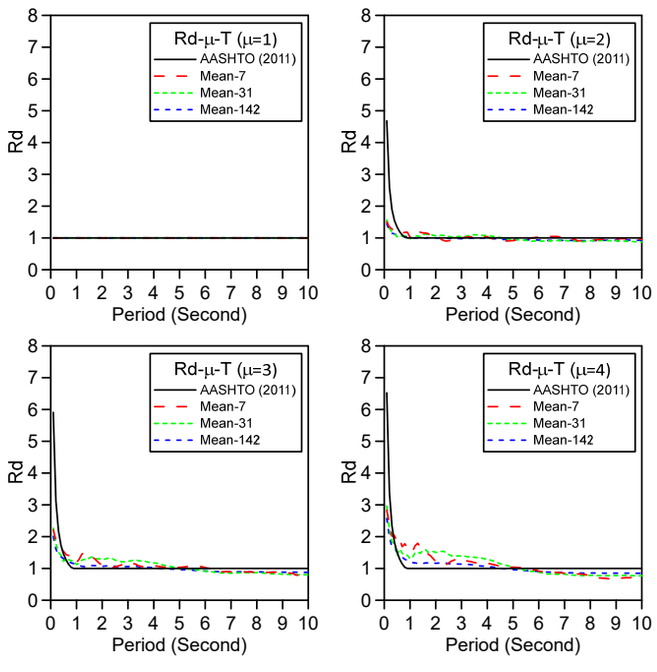


Figure 8: Hysteretic Models

6.4 *Numbers of Ground Motions*

Figure 9 indicates the results of R_d with respect to the three different numbers of ground motions: 7, 31, and 142 sets. Basically, when μ is increased from 2 to 6, the overall trend of the analytical results is very similar to the data mentioned from section 6.1 to 6.4. The code requirement gives higher value of R_d in short period than the one obtained from nonlinear time history analysis. Periods at 0.5 sec and 5 sec are two typical periods. It can be found, the analytical results are higher than the code value if the period is between 0.5 and 5 sec. After 5 sec, the analytical results are smaller than the code value as 1. In addition, results resulted from the average of 31 ground motions dominate the response as an envelope curve, if the structural period is located in the range of 1.5 sec to 5 sec.



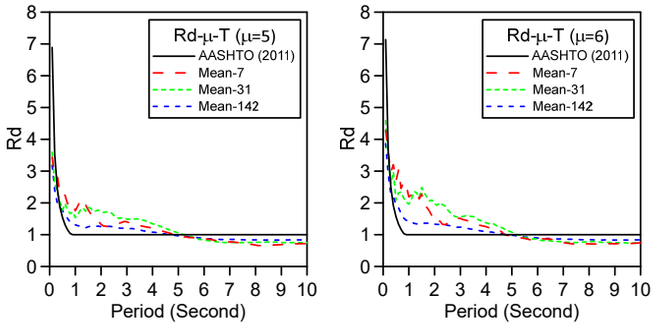


Figure 9: Numbers of Records

7 PROPOSED FORMULA OF R_d

Based on the previous discussions, in order to obtain the modified formula of R_d, the structural responses were determined by the following requirements. Total of seven pulse-like ground accelerations records in Chi-Chi earthquake were selected from PEER directly, and the time history records were adjusted to follow the orientation of maximum velocity. The Modified Clough model was applied to simulate the response of RC bridge column.

In the process of finding the proposed formula, this study referred to Miranda (2000) introducing the exponential relation in the nonlinear regression analysis. Unfortunately, the analytical results in medium and long period of this study can't be successfully described by the expression of exponential formula. Finally, the formula for structural subjected to near-fault earthquake are proposed in Eq. 2. Figure 10 illustrates the comparisons between the proposed formula and the analytical results, as well as the values obtained by AASHTO. The proposed formula can be divided into three segments according to the corner period T_0^M. Within $1.2T_0^M$, the proposed R_d has a linear inverse relation with period but is proportional to ductility. For the transition segment between $1.2T_0^M$ and $7.5T_0^M$, the proposed R_d is gradually decreased until reaching a constant of 1.0 at period of $7.5T_0^M$.

$$R_d = \begin{cases} 0.5+0.03\mu\left(10+\dfrac{1}{T}\right) & T<1.2T_0^M \\ 0.4\times\left[(0.3-0.2\mu)T+(1+\mu)\right] & 1.2T_0^M \le T \le 7.5T_0^M \\ 1 & T \ge 7.5T_0^M \end{cases} \quad (2)$$

in which

$$T_0^M = \frac{S_{M1}}{S_{MS}}$$

S_{M1} = Spectral response acceleration parameter at a period of 1 sec adjusted for site class effects

S_{MS} = Spectral response acceleration parameter at short periods adjusted for site class effects

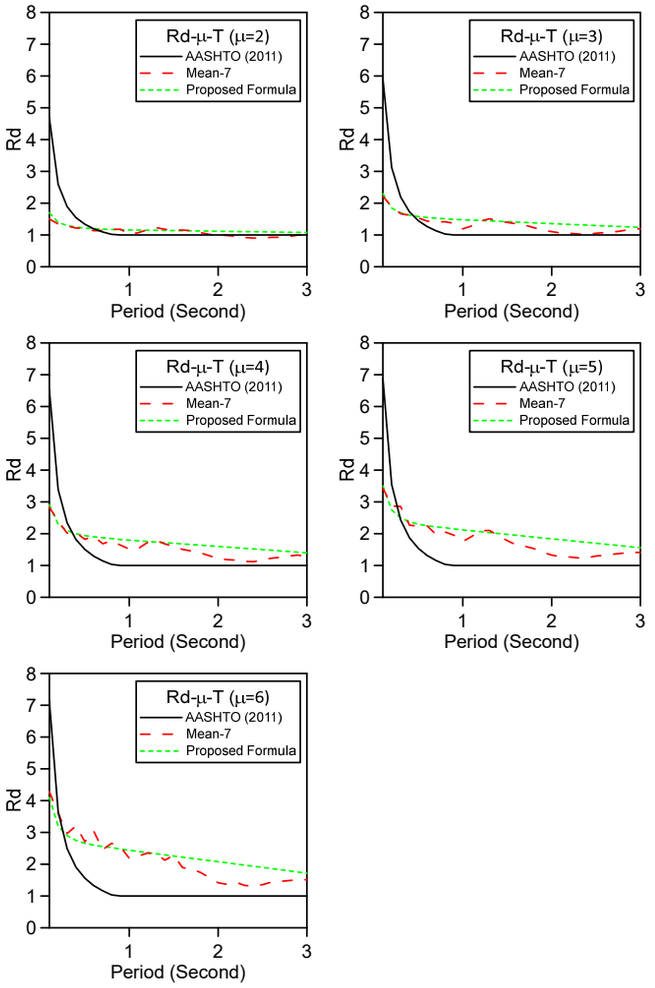


Figure. 10: Results of Proposed Formula

8 CONCLUSIONS

This study is a preliminary research on the issue of displacement-based performance assessment for bridge considering the near-fault effect. Major contribution is to propose the modified formula of displacement amplification factor R_d and structural period T within 3 second as well as constant displacement ductility μ from 1 to 6. The near-fault effect is considered by selecting the ground acceleration records with pulse-like signals from PEER. The nonlinear time history analytical results were presented to compare the displacement amplification factor suggested by AASHTO. It is found the analytical results gave a relative smaller displacement demand if the structure period is shorter around 0.5 sec, but have higher expected displacement for structural period is in the range of 0.5 and 5 sec. Consequently, the modified formula was proposed in this study and has a good agreement with the analytical results. In practical use, the engineers can easily carry out the performance check by multiplying the R_d and elastic response as a displacement demand, and compare it to the displacement capacity. Further research is therefore needed to address the R_d due to far-field earthquake to compare the difference.

REFERENCES

AASHTO. 2011. AASHTO Guide Specifications for LRFD Seismic Bridge Design. Washington D.C: American Association of State Highway and Transportation Officials. 2nd Edition. ISBN: 978-1-56051-521-0

Bozorgnia, Yousef & Vitelmo Bertero 2002. Improved Damage Parameters for Post-Earthquake. Los Angeles: Proceedings of SMIP02 Seminar on Utilization of Strong-Motion Data: 61 - 82.

Chiou, B., Darragh, R., Gregor, N. & Silva, W. 2008. NGA Project Strong Motion Database. Earthq. Spectra, Vol. 24, No. 1: 23-44.

FAMA & ATC. 2005. Quantification of Building Seismic Performance Factors. Report No. FEMA 440 & ATC-55, Redwood city: Applied Technology Council (ATC) & Washington D.C: Federal Emergenfy Management Agency (FEMA)

FAMA & ATC. 2009. Improvement of Nonlinear Static Seismic Analysis Procedures. Report No. FEMA P695 Redwood city: Applied Technology Council (ATC) & Washington D.C: Federal Emergenfy Management Agency

Hachem, M. M. 2012. BISPEC: Interactive Software for the Computation of Unidirectional and Bidirectional Nonlinear Earthquake Spectra. Nashville, Tennessee: Structures Congress 2004

Iwan, W. D., Moser, M. A., & Peng, C.Y. 1985. Some Bbservations on Strong-Motion Earthquake Measurement Using a Digital Accelerograph. California: Bull. Seismol. Soc. Am. Vol. 75, No. 5: 1225-1246.

K. S. Liu, T. C. Shin & Y. B. Tsai 1999. A Free-Field Strong Motion Network in Taiwan: TSMIP. TAO, Vol. 10, No. 2: 377-396.

Mavroeidis, G. P. & Papageorgiou, A. S. 2003. A Mathematical Representation of Near-Fault Ground Motions. Bull. Seismol. Soc. Am. Vol. 93, No. 3: 1099-1131

Miranda, E. 2000. Inelastic Displacement Ratios for Displacement-Based Earthquake Resistant Design. Auckland, NZ: 12WCEE 2000: 1096.

Ministry of transportation and communications R.O.C. 2009. Seismic Design Specification for Highway Bridge. Ministry of transportation and communications R.O.C. (in Chinese)

S. B. Yu, L. C. Kuo, Y. J. Hsu, H. H. Su, C. C. Liu, C. S. Hou, J. F. Lee, T. C. Lai, C. C. Liu, C. L. Liu, T. F. Tseng, C. S. Tsai, & T. C. Shin. 2001. Preseismic Deformation and Coseismic Displacements Associated with the 1999 Chi-Chi, Taiwan, Earthquake. Bull. Seismol. Soc. Am. vol. 91, No. 5: 995-1012

Spudich, P., Rowshandel, B., Shahi, S. K., Baker, J. W., & Chiou, B. S. J. 2014. Comparison of NGA-West2 Directivity Models. Earthquake Spectra, Vol. 30, No. 3: 1199–1221

Maintenance, Safety, Risk, Management and Life-Cycle Performance of Bridges – Powers, Frangopol, Al-Mahaidi & Caprani (Eds)
© 2018 Taylor & Francis Group, London, ISBN 978-1-138-73045-8

The Condition of Padang's Bridges after 2009 Earthquake Disaster

Masrilayanti, Ruddy Kurniawan, Nidiasari & Nurhamidah
Andalas University, Padang, Indonesia

ABSTRACT: The city of Padang, the capital of West Sumatra, Indonesia, has many of bridges, but it seems that the government is not paying attention to the data archieve of the bridges in a proper way. Yet, archiving is very important since doing in a good way will give positive benefits to the societies. In 2009, Padang was hit by a massive earthquake that caused so much structural damage to infrastructure, including bridges. After almost ten years of the earthquake, bridges condition in Padang were analyzed by using two methods, BMS 1993 (Indonesian Provisions) and FHWA (USA). This paper describes the condition of the bridges in Padang City after 8 years of the 7,9 Richter Scale shocking earthquake so that it can be determined whether it needs to give retrofitting or not to the bridges by priority scale. Three main bridges in Padang City were screening and analyzed using FHWA, namely Simpang Haru Bridge; Kuranji Bridge; and Marapalam Bridge. The results show that although by visually assessment with BMS Standard the condition of the bridges are good enough, using FHWA procedure finds that Marapalam Bridge has the highest priority to be retrofitted.

1 INTRODUCTION

1.1 *Padang as the risk region of disaster*

Padang is known as the capital city of West Sumatera, Indonesia. It lies on Sumatra 's west coast and has a beautiful scenery cause this province has hills, beach, valleys and lots of rivers. Padang consists of eleven districts, and every districts has their own characteristics and vulnerable cases of disasters.

Almost all of disaster types for tropical country are available in this city, such as earthquake, lanslides, or floods. Padang has a long history of earthquakes. This city stands under a dangerous two plates, namely Indo-Australian and Eurosian Plate. In addition, Padang region also has lots of volcanoes so that it can induce earthqukes as well.

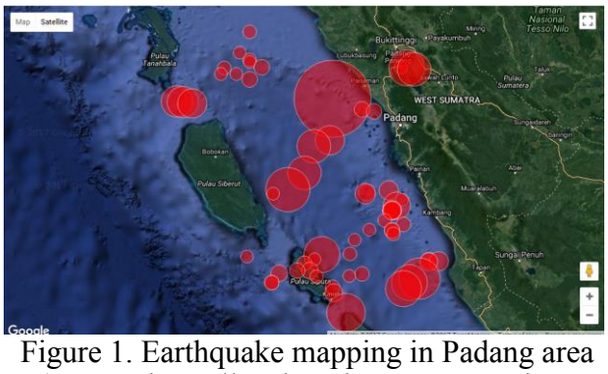


Figure 1. Earthquake mapping in Padang area (source: https://earthquake-report.com/)

In 2009, Padang was hit by a huge 7,6 RS earthquake. That earthquake caused many people lost, lots of houses and building collapse, and thousand of people death. Local government stated that around 130.000 house were severe damage, 60.000 houses were moderately damage and about 70.000 houses were slightly damage. In addition, bridges and road also had damage. However, since the epicentrum was about 70 km under the sea, the tsunami did not occur after the earthquake.

1.2 *System of Bridges Archiev*

There are three types of street or highway in Indonesia, namely; National Highway, Provincial Highway and Regional Highway. National Highway is a street built by the government to connect provinces. Provincial street is a street which located in a province to connect cities in a province, whereas regional street is a street or road which connecting districts within the city.

1.3 *Highway classification in Indonesia*

There are three types of street or highway in Indonesia, namely; National Highway, Provincial Highway and Regional Highway. National Highway is a street built by the government to connect provinces. Provincial street is a street which located in a province to connect cities in a province, whereas

regional street is a street or road which connecting districts within the city.

1.4 *Purpose of the research*

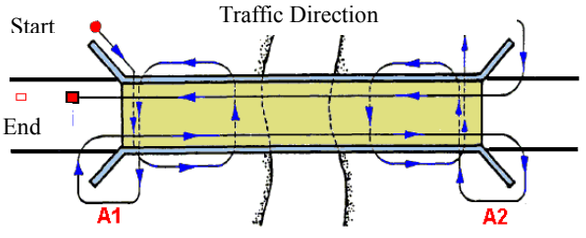
Research purposes are to obtain the condition of the bridges around Padang City by using BMS Standard, and to have the information of the bridges regarding their urgency to retrofitting. Retrofit should be conducted by a properly method. Caterino et al (2014) stated that the requirements of strengthening arises not only from deficiencies of the primary elements but also from the insufficiency of structural elements.

Thus, repairing activities of the bridges will focuses to the bridge's rank under its very condition. It is hoped that some arguments that the bridges retrofitting has been based on location priority will not happen anymore.

2 RESEARCH METHODOLOGY

The methodology of the research is mainly visual survey and analysing by using BMS Standard and FHWA-HRT-06-032 2006.For BMS Standard, about 236 bridges have been surveyed and marked by using BMS Standard. Then several bridges among them were analyzed by using FHWA procedure to get the information relating to their priority of retrofit.

Visual survey has been done by searching the overall condition of the bridge. Terms to be surveyed are: surface, pavement, piers, abutment, girder, truss, seating, plants or grass which are on the bridge's elements. Procedure to conduct the survey can be seen from the figure below.



A1 = Abutment 1
A2 = Abutment 2

Figure 2. Survey direction

For analysing by using FHWA Standard, the rank of the bridges can be obtained. The rank of the bridges aims to conduct the priority of the bridges to be retrofitted. The rank comes after evaluating the bridges by considering the screening proccess, asses the vulnerability of the bridges, and performance level of the bridges under earthquake. Out put will be 0 to 100, which informs that higher the rank, more vulnerable is the bridge.

3 BRIDGES SAFETY CONDITION AFTER HUGE EARTHQUAKE

3.1 *BMS Standard*

BMS stands for Bridges Management System and was released by Indonesian Government in 1993 in order to obtain a positive evaluation and maintenance of the bridges in Indonesia. BMS standard has 6 level of bridge's condition as can be seen in the table below:

Table 1. The marking value of BMS Standard

Condition	Meaning
0	The bridge is still new and no remarkable damages
1	Very little damages are found and not give any effects to the structures of the bridge
2	There are a few damages and it needs to be observed in the future of time
3	There are some damages and likely to be more serious in 12 months
4	There are serious damages and need to be fixed immediately
5	The bridge cannot be used anymore

Source: BMS Standard, 1993, Indonesia

The mark 0 to 5 are obtained by accumulating the evaluation marks of the bridge in several element conditions, those are: strength of the structure element, the damage of the elemen, the effects of the damages, and the function of the element.

After analyzing the bridge under BMS standard, the results is that commonly the condition of the bridges is good as can be seen from the graph below.

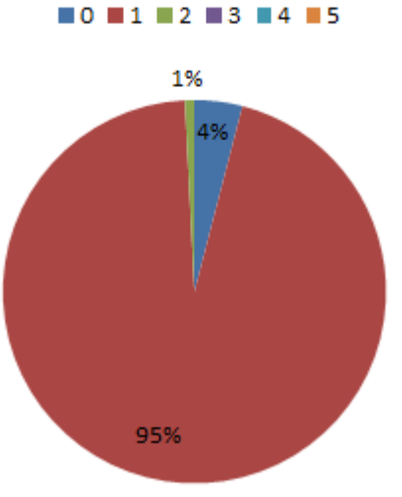


Figure 3. The distribution of BMS Standard marks on the bridges in Padang City (source: own research result)

3.2 *FHWA Standard*

FHWA stands for Federal Highway Administration and its tasks are to analyze, maintenane and arrange the evaluation of highway and its structures in USA. For this study, the regulation used are FHWA-HRT-06-032 2006 Part 1 which focuses on subject to bridge and its substructure. It evaluates the condition of the bridges by analyzing the seismic retrofit category (SRC) of the structures. The purpose of this evaluation is to obtain the bridge rank which defines how urgent the bridge to be retrofitted in order to overcome the earthquake or other disaster in the future.

To define the seismic retrofit category, it needs to find the anticipated service life (ASL) of the bridge. Anticipated service life is the remain age of the structure by reducing its age now to the year when it has been built.

There are three kinds of ASL relating to anticipated service life as can be seen in the table below:

Tabel 2. Categories of Anticipated Service Life

Service life category	**Anticipated service life**
ASL 1	0 - 10 yrs
ASL 2	11-40 yrs
ASL 3	> 40 yrs

Source: FHWA-HRT-06-032

Performance level is the performance of the bridge to overcome earthquake. Performance level can be obtained by considering the importance of the bridge's function, ASL value, and the kinds of ground moving due to earthquake. Classification of performance level can be seen in the table below.

Table 3. Classification of Performance Level

EARTHQUAKE GROUND MOTION	BRIDGE IMPORTANCE And SERVICE LIFE CATEGORY					
	Standard			**Essential**		
	ASL 1	**ASL 2**	**ASL 3**	**ASL 1**	**ASL 2**	**ASL 3**
Lower Level Ground Motion 50% probability of exceedance in 75 years; return period is about 100 years.	PL0	PL3	PL3	PL0	PL3	PL3
Upper Level Ground Motion 7% probability of exceedance in 75 years; return period is about 1000 years.	PL0	PL1	PL1	PL0	PL1	PL2

Source: FHWA-HRT-06-032

After obtaining the value of performance level, the earthquake dangerous level should be analysing by considering the intensity of ground vibration on the rock and its amplification on the soil layers above. There are several categories of this level as written in the table below.

Table 4. Hazard Level regarding the intensity of ground vibration.

HAZARD LEVEL	$S_{D1} = F_v S_1$	$S_{DS} = F_a S_s$
I	$S_{D1} \leq 0,15$	$S_{DS} \leq 0,15$
II	$0,15 < S_{D1} \leq 0,25$	$0,15 < S_{DS} \leq 0,35$
III	$0,25 < S_{D1} \leq 0,40$	$0,35 < S_{DS} \leq 0,60$
IV	$0,40 < S_{D1}$	$0,60 < S_{DS}$

Source: FHWA-HRT-06-032

Other terms that should be considered are vulnerability rating, seismic hazard rating and then bridge rank.

Vulnerability can be obtained by visual analyzing of the bridge. Bridge should be observed visually by evaluating its column, abutment, and liquifaction factors.

The values of FHWA range for bridges' rank lies between 0 to 100. 100 value means the condition of the bridge is urgent and need to be retrofitted as soon as possible. 0 value means that the bridge is not urgent and do not need to be repaired.

4 BRIDGES SAFETY FOR MITIGATION OF DISASTER

Three bridges are analyzed using BMS 1993 and FHWA namely Simpang Haru, Kuranji, and Marapalam Bridge. The first is located in Andalas Distric, the second is in Kuranji District, and the third is in East Padang District.

4.1 *Simpang Haru Bridge (Bridge I)*

Simpang Haru Bridge is a two spans precast concrete bridge and has been used by the people in the city for more than 25 years. The bridge is arranged in two single spans and the total length is

60 meters. The condition of the bridge overal is good, only has some cracks on the trotoar, plants on around the abutments and piers.

This bridge has been renovated in 2010 after the huge earthquake came hit Padang City. It suffered a quite critical damage due to the earthquake however it does not cause the bridge to collapse.

From the picture it can be seen that overal condition of the bridge is good. A small grass plant is on the piers of the bridge. The main girder is fine, however it needs to re-paint the bridge in order to get good aesthetic.



Figure 4. Simpang Haru Bridge (source: own research collection)

Thus by using BMS standard analysing, it can be said that the bridge is under condition 1. It means the bridge is safe and comfort for traffic and people.

Meanwhile, evaluation using FHWA results in 19,8. The value arrives from the condition of the bridge which is still good except of the plants around it. The bridge was built in 1992 and has routine maintenance from the local government. However, the urgency of the bridge is quite high since it lies on a crowded population area.The value 19,8 means that this bridge is not having high priority for retrofitting.

4.2 *Kuranji Bridge (Bridge II)*

The second bridge Kuranji bridge is a composite bridge and built in around 1992. The bridge is aranged in a continous two spans. BMS standard resumes that the bridge is also in condition 1. The photograph of the bridge can be seen in the figure below.



Figure 5. Kuranji Bridge (source: own research collection)

From the figure it can be described the overall condition of the bridge. Things to be considered are the condition of the pier foot, as due to the people activity around it, scouring could be a serious problem in the future. However, the bridge is just having an annualy maintenance from the local government such as painting, reinforcement, and re-surface. Thus it reform the bridge in a positive way.

For the second analysis (FHWA procedure), the value is 6,04. It comes from the condition of the bridge is quite good, no critical damages on the bridge, the age of service is 25 years old. Meanwhile, the urgency of the bridge is essential, which means the bridge is high urgent to be used for the population. The bridge also has a regular maintenance so that its condition is fair enough.

4.3 *Marapalam Bridge (Bridge III)*



Figure 6. Marapalam Bridge (source: own research collection)

The last bridge to be analyzed is Marapalam Bridge, located in East Padang District. It is a three spans prestressed bridge, and was built in 1995. Analyzed with BMS 1993, the mark of the bridge is 2 which means the bridge needs to be considered evaluated in 12 months ahead. However, no important damage can be visualized. The bridge also has a routine yearly maintenance such as painting, surface checking, and abutments. Only some cracking at the

abutment and some wild plants or grass are seen around the piers cap and the abutment as can be seen from the Figure 7.

Second analysis describes a different result because it gives mark as 66,4 rank of the bridge. It means this bridge has the highest priority among the three bridges. Visually BMS survey decides this bridge has nothing to be seriously afraid of relating to bridge performance, however analysis with FHWA regulation resumes on the contrary.

The problem with this bridge is that this structure does not have bearing on its support. The main girder is putting down directly to the seating as can be seen from the figure below. For FHWA analysis, bearing has a potential effect in calculating the bridge's rank. How bearing is used play an important role in assessing the performance of the bridge under earthquake load. If the bearing used is vulnerable to the earthquake load, the value of bridge's vulnerable is also high.



Figure 7. Plants and cracking on the Marapalam Bridge (source: own research collection)

From the Figure 8 below, it can be seen that main girder is directly attached to the support of the bridge. This condition could yield structure to have a great displacement when earthquake attacks. Thus, after analyzing the bridge, the result says that this bridge has the highest priority to be retrofitted among the three bridges.



Figure 8. The condition of Marapalam Bridge support (source: own research collection)

5 CONCLUSION

Analyzing the bridges under Bridge Management System (Indonesian provision), gives a positive results that mainly the bridges are in good conditions. The range is also small from 0 – 5 which means cannot implify the urgency of the bridges to be retrofitting in properly priority.

Meanwhile, using USA regulation to analyze the bridge relating its priority to have retrofitting, gives a clearer consideration. The range is far from 0 to 100, thus the bridges can be evaluated in a more specific mark.

From the three bridges assesments, the results are saying that Bridge III (Marapalam Bridge) is getting the highest mark, that is 2. Meanwhile Bridge I and II have the same mark in 1 condition. So it needs more asessment to choose which one of these two bridges should have a more priority to be retrofitting.

On the other hand, FHWA regulation gives the highest bridge rank to Bridge III since it has 66,04 point. It concludes that Bridge III should have the first priority to be repaired or retrofitting. Bridge I is the second and the last priority goes to Bridge II.

6 AKNOWLEDGEMENT

The authors wish to express their gratitude to Kemenristekdikti, (Indonesian Ministry of High Education and Research Department) for the precious financial support so that this research could be conducted, as stated in Research Project No: 059/SP2H/LT/DRPM/IV/2017.

7 REFERENCES

BMS 1993, Departemen Pekerjaan Umum

BPS Padang, 2014, *Indikator Kesejahteraan Rakyat Kota Padang*, BPS Kota Padang

Caterino, Nicola et al (2014), Damage Analysis and Seismic Retrofitting of Continuous Prestressed Reinforced Concrete Bridge, *Case Study in Structural Engineering* 2, 9-15.

FHWA, 2006, *Seismic Retrofitting Manual for Highway Structures: Part 1 – Bridges (Fhwa-HRT-06-032)*.

https://earthquake-report.com/

MS13: Advanced computational and experimental techniques for extreme load performance of bridges

Organizers: J. Hashemi, R. Al-Mahaidi & D.M. Frangopol

Maintenance, Safety, Risk, Management and Life-Cycle Performance of Bridges – Powers, Frangopol, Al-Mahaidi & Caprani (Eds)
© 2018 Taylor & Francis Group, London, ISBN 978-1-138-73045-8

Advanced Nonlinear Finite Element Modelling of Reinforced Concrete Bridge Piers

E.P.G. Bruun, A. Kuan, G.T. Proestos, E.C. Bentz, & M.P. Collins
Department of Civil Engineering, University of Toronto
Toronto, Ontario, Canada

ABSTRACT: Severe cracking was observed on the flexural tension face of a reinforced concrete hammerhead bridge pier cap. Determining the cause and severity of the damage was complicated by the geometry of the piers, which influenced the strut-and-tie mechanism. A tapered end cap raised questions about the development of the tension reinforcement in the chord, while a hexagonal pier column meant that the effective area of the compressive strut was uncertain. Depending on the assumptions made, widely different estimates of the ultimate capacity were reached by traditional calculation methods. Therefore, to accurately assess the safety of the bridge piers, a series of analyses were performed using VecTor2 – a nonlinear finite element analysis program (NLFEA) developed at the University of Toronto. A parametric study was conducted by varying the effective width of the piers and the amount of reinforcement engaged, and the factored strength of the pier was obtained using a novel procedure. This paper concludes that using 2-D NLFEA in a discerning manner allows engineers to understand complex 3-D situations.

1 INTRODUCTION

1.1 *Background*

Despite the development of simple and powerful tools to assess the strength of reinforced concrete structures, hidden complexity often makes determining the strength of even a simple structure a nontrivial task. Consider the following structure shown in Figure 1, which is a typical pier supporting a multi-span bridge in Canada. A recent inspection noted the presence of several vertical, and some diagonal, cracks, and it was concluded that strength of the pier needed to be determined to evaluate the overall safety of the structure. At a first glance, the structure appears to be a straightforward cantilever, suitable for a 2-D analysis using a strut-and-tie model. Looking more closely, the geometry of the pier complicates matters considerably through the section. The width of the bearing pad suggests that shear lag effects may be significant; when combined with the taper on the hammerhead and supporting column, it is not clear how much of the concrete section is effectively utilized. It is also not clear if all of the flexural reinforcement can be utilized, due to the anchorage detailing of the various layers of steel, as well as the aforementioned shear lag effects. When considering all of these factors, using simple code-based procedures is difficult.

Nonlinear finite element analysis (NLFEA) is a powerful tool for understanding overall structural behaviour given various geometric and material complexities. Specifically in the case of reinforced concrete, NLFEA allows engineers to consider effects such as post-cracking concrete tensile stresses, compression softening, bar development and crack slip among other things.

While NLFEA is appropriate for predicting the actual strength of a structure, it may also be necessary to verify that a structure has adequate capacity within a Load and Resistance Factor Design (LRFD) framework. For example, this may be needed when performing a code-based evaluation of an existing structure. However, it is problematic trying to assign a representative resistance factor to the predicted strength from an NLFEA output, since the associated resistance factors for concrete and steel are different, and guidelines for doing this currently do not exist.

Using the hammerhead pier structure as a case study, this paper describes a procedure for simplifying the complex geometry and evaluating the strength of these piers using VecTor2, a 2-D NLFEA program developed at the University of Toronto, which uses the Disturbed Stress Field Model (DSFM) (Vecchio 2000) as its theoretical foundation. A method is then described to obtain the factored strength of the pier for evaluation using an LRFD framework.

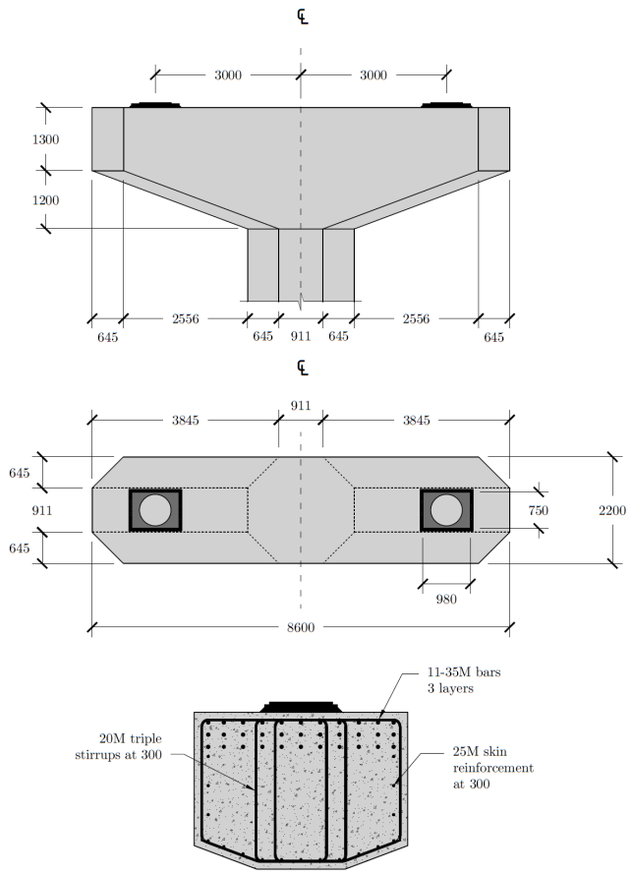


Figure 1. Elevation (top), Plan (middle) and Cross Section (bottom) of full hammerhead pier

1.2 *Description of Nonlinear Finite Element Analysis Methodology*

An analysis of the bridge pier was performed using a VecTor2, a 2-D finite element analysis program which is based on the DSFM. The DSFM, an advanced reinforced concrete material model based on the Modified Compression Field Theory (Vecchio 1986), is a smeared rotating-crack model which is formulated to consider tension stiffening, compression softening, and crack slip (Vecchio 2000). As the DSFM is capable of predicting the complete load-deformation behaviour of reinforced concrete elements, the full response of the hammerhead piers can be obtained from a VecTor2 model. Equally useful is the ability to calculate important parameters at any load level, such as the stresses and strains in the concrete and steel, crack patterns, crack widths and crack slips. Various other numerical models are implemented to complement the DSFM and allow for additional effects to be considered, such as tension softening, bond slip amongst others. VecTor2 uses 4-node rectangular elements for reinforced concrete materials, and 2-node truss elements for discrete steel reinforcement.

While a 3-D nonlinear finite element analysis based on the DSFM is possible to perform, it is a challenging task because a compatible preprocessor and postprocessor do not currently exist. In addition, the prohibitively large computational time needed to perform a full 3-D analysis currently makes nonlinear 3-D analysis of such a large structure impractical. Thus, a 2-D approach was used instead. To account for the aforementioned 3-D effects, a parametric study was performed to understand the sensitivity of the structural behaviour to varying model parameters. The key variables investigated were the effective section width and effective quantity of longitudinal reinforcement.

2 MODELLING PARAMETERS

The following subsections will outline the input parameters for the models created for this study. Conservative assumptions were made if precise information was not available.

2.1 *Model Mesh*

Due to symmetry, only half of the pier cap was modelled, using the centreline of the column as the vertical boundary. Figure 2 shows the schematic breakdown of the VecTor2 mesh used in the analysis, where the regions are described as follows:

Region A: The column base, which is further subdivided to represent the varying width as a result of the column taper. This region remains the same throughout all of the various VecTor2 models, as the column is not being directly investigated. The modelling assumptions for the column are discussed further in Section 3.1.

Region B: The connection point of the cantilever, which is further subdivided to allow for the out-of-plane width of the cantilever to be adjusted. A key part of this study (Sec. 4.2) is investigating how the effective width of the cantilever influences the capacity of the pier.

Region C: The cantilever portion of the pier cap with a constant thickness throughout. This region is also adjusted to account for the effective width of the pier (Sec. 4.2).

Region D: The end portion of the pier cap cantilever with a constant thickness of 911 mm. This region remains the same throughout all of the various VecTor2 models, which is a conservative assumption based on the minimum thickness of the column at its connection to the cantilever. The reasoning for this decision is discussed further in Section 3.3.

Region E: The baseplate spreading the applied load into the structure, with dimensions based on the assumptions discussed in Section 3.4.

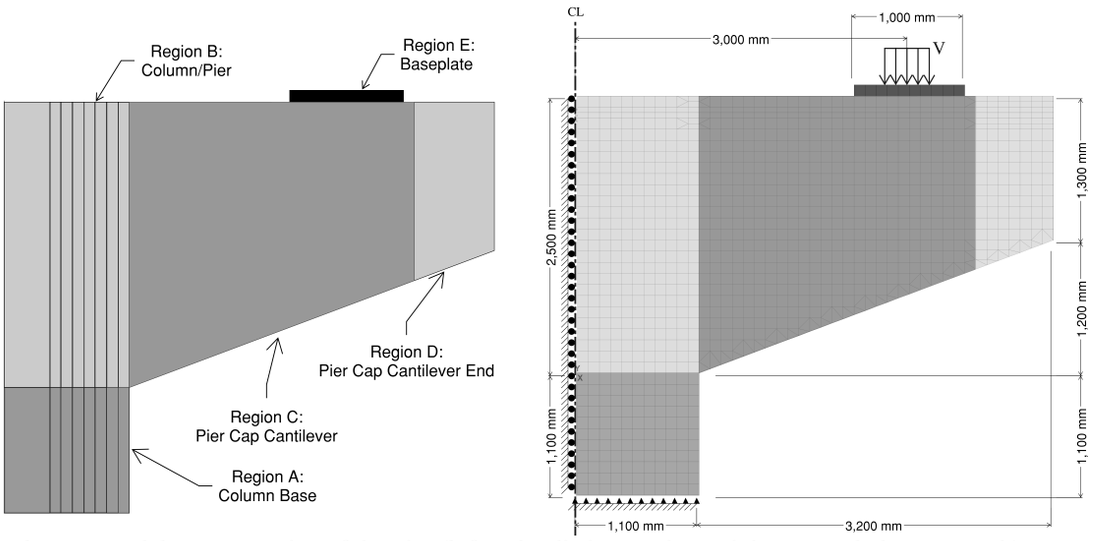


Figure 2. Finite element model representative of the pier (left = the distinct regions, right = actual element mesh)

To realistically represent the flow of forces in the structure, a portion of the pier column was also modelled (1100 x 1100 mm stub), with the horizontal boundary representing the base of the stub. Rollers were placed along the vertical boundary to allow for the development of horizontal reactions (moment couples) along this face, and pins along the horizontal boundary to represent the transfer of the applied shear force into the column. A summary of these boundary conditions is shown in Figure 3

Since VecTor2 makes use of relatively simple linear isometric elements, the element size was chosen to be 100 mm x 100 mm (XY-plane) in order to get a fine enough strain profile describing the structural behaviour through the depth of the pier. The irregular geometry of the column was modelled using elements of varying individual thickness (into the page).

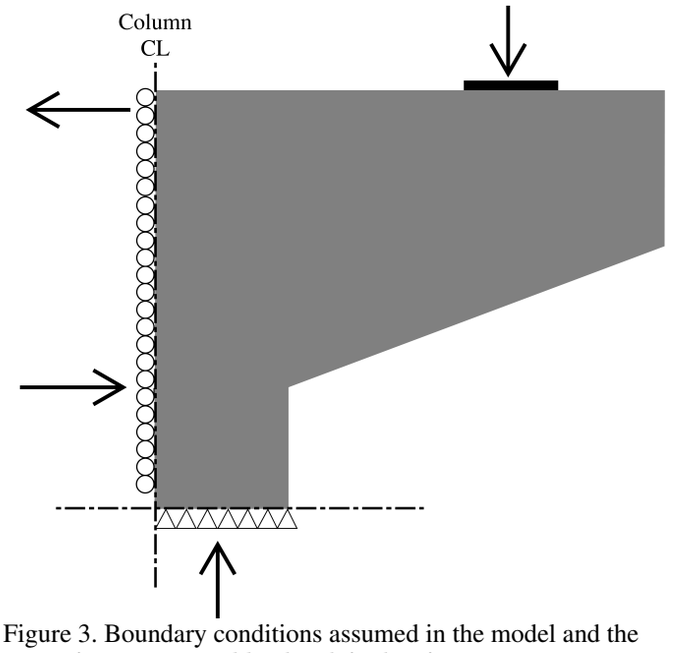


Figure 3. Boundary conditions assumed in the model and the approximate structural load path in the pier

2.2 *Material Properties*

The material properties were chosen according to the to design specifications, with $f'_c = 35$ MPa and $f_y = 400$ MPa. The Hognestad parabola was used to model the pre-peak stress-strain behaviour of the concrete, and a bilinear model was used for the steel.

2.3 *Steel Reinforcement*

The main flexural tension reinforcement was modelled as three layers of discrete elements across the top of the pier cap. To investigate the effect of varying levels of effective reinforcement on the capacity of the pier cap, the quantity of steel per layer ranged from 7000 $\frac{mm^2}{layer}$ (7 – 35M) to 11000 $\frac{mm^2}{layer}$ (11 – 35M).

Skin reinforcement and stirrups were distributed over the pier by averaging the steel over the concrete material in the region.

It was found that including the beneficial effects of the compression reinforcement did not lead to significant changes in the load-deformation behaviour of the piers. Thus, the analyses were performed without including discrete compression reinforcement in the finite element model.

2.4 *Applied Loading*

The bridge loading on the pier was distributed over a 500 mm width onto a 1000 mm wide base plate representative of the bearing details discussed in Section 3.4. In the analysis, the total load was incremented by 200 kN per load stage until ultimate failure.

3 IMPORTANT FINITE MODELLING ASSUMPTIONS

To account for the complexities caused by the geometry of the hammerhead piers, the following modifications were made to the 2-D model in order to capture the effects of the real 3-D structure.

3.1 *Pier Column Taper*

As shown in Figure 4, the tapered edges of the pier column were represented as discrete steps with a width of 100 mm (to match the typical element mesh size). Each step represented a 200 mm decrease in the overall width, although the final step was set to 911 mm to match the real minimum end width.

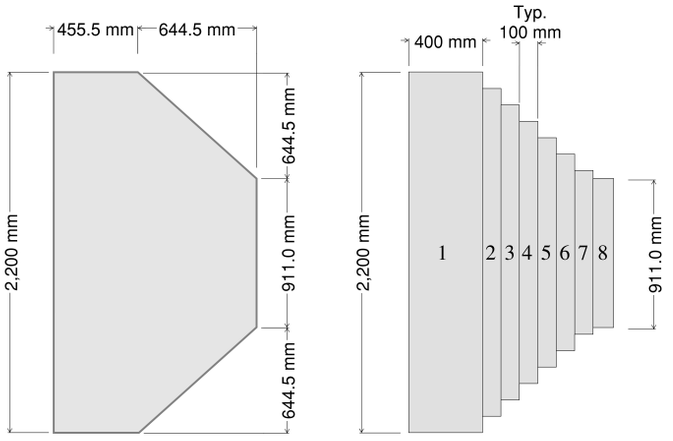


Figure 4. Cross-section of the pier half-column (left = as-built, right = model approximation)

The reinforcement in the pier column was represented as smeared throughout the slices, based on the resulting ρ_s from the as-built reinforcement as shown in Figure 5.

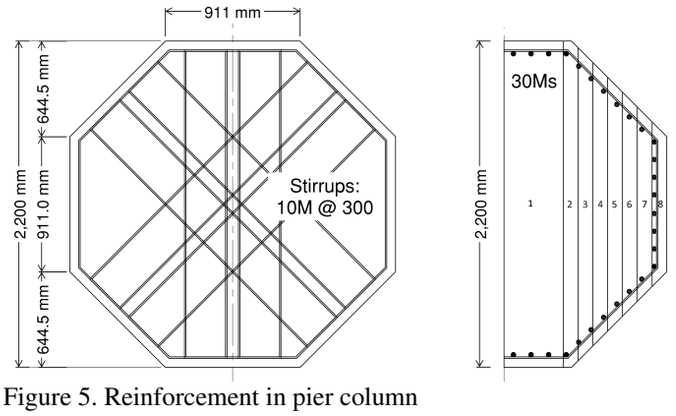


Figure 5. Reinforcement in pier column

3.2 *Pier Cap Chamfers*

As shown Figure 6, The cross-section of the pier cap cantilever was simplified to a rectangle, omitting the slight chamfer at the bottom edges and cap ends. The structural impact of this simplification was deemed minimal with respect to other parameters, such as out-of-plane effective width of the compressive strut or effective quantity of longitudinal steel.

3.3 *Pier Cap Ends*

In all the models the tapered portion at the end of the pier cap was omitted leaving only the minimum 911 mm constant width section (Fig. 7). This is a conservative but valid assumption since the region is not critical for the load carrying S&T mechanism, while the effect that this region has on the anchorage of the bars is handled explicitly when considering the development lengths of the reinforcement bars (Sec. 3.5). The variable W_{eff} refers to the effective width of the pier cap set as a parameter in the various models.

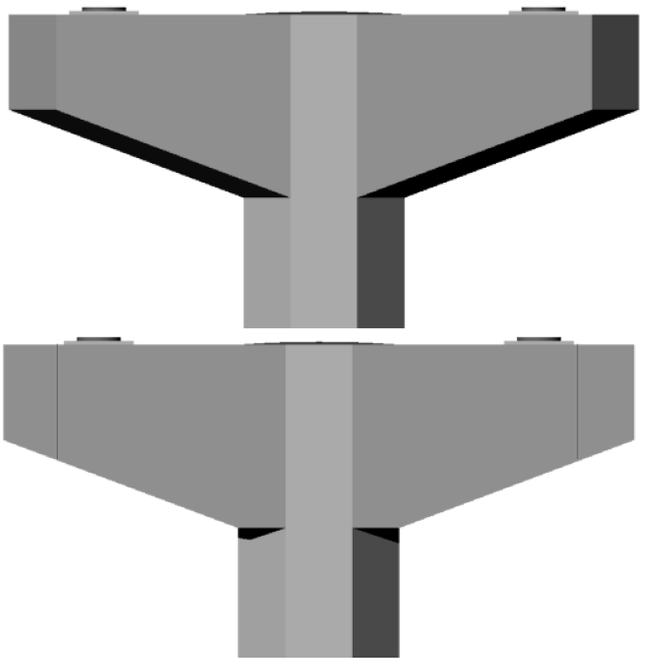


Figure 6. As-built (top) and simplified (bottom) pier cap profile. Note the uniform hammerhead thickness.

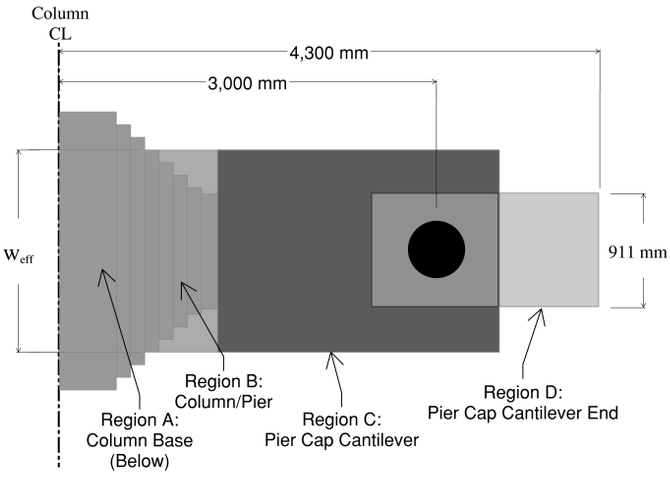


Figure 7. Plan view of pier cap showing simplified end portion

3.4 *Applied Load Bearing Area*

The pot bearing base plate is listed as 980 x 750 mm, with the bearing area further increased by 50 mm of grout at 45 degrees between the bottom of the plate and the top of the pier cap. The load is transferred through the pot plate, which has a diameter of 650 mm. As a conservative simplification, the base plate is modelled as stiff 1000 mm x 850 mm area, with the load distributed over a 500 mm width (Fig. 8).

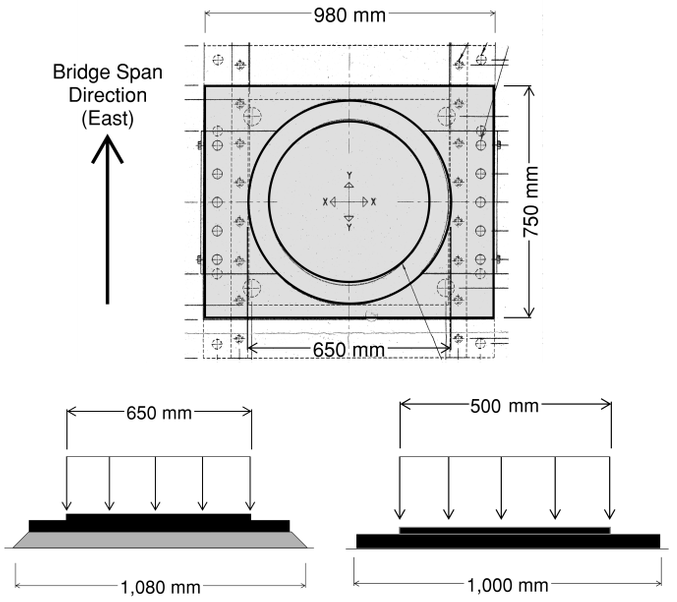


Figure 8. Plan view of pot bearing (top), with the actual (bottom left) and modelled (bottom right) loaded areas

3.5 *Reinforcement Bar Anchorage*

The longitudinal reinforcement in the pier cap was made up of mostly straight deformed bars, only the middle five bars had standard hooks at the end. While the taper at the pier ends was not modelled explicitly, its effect on the development of individual longitudinal bars was accounted for using the methodology described in this section. For example, since the outer bars were cut off closer to the column centreline due to the taper, their full development also occurred closer to the column and past the center of the applied load (Fig. 9) - ideally all the bars in an S&T chord should be detailed so that full development is achieved before this point.

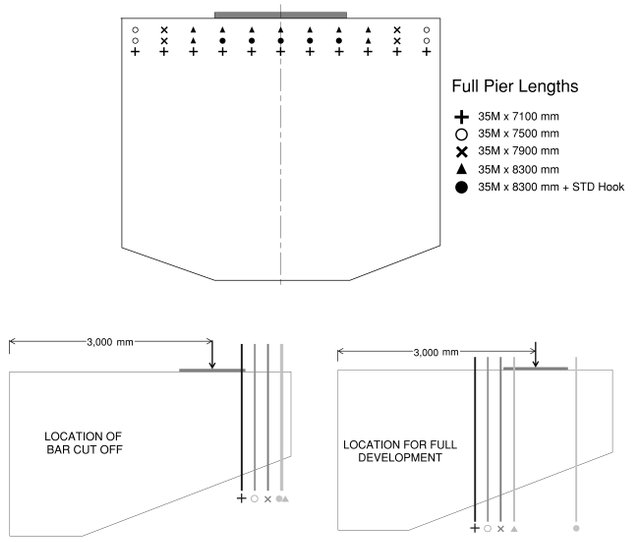


Figure 9. Cross-section of pier cap showing the 35M bars (top), where the cutoff points (bottom left) and full development points (bottom right) are shown for each type of bar

The axial force capacity of the top chord, accounting for incomplete anchorage, was then determined along the length of the cantilever. This capacity was compared to the demand in the longitudinal reinforcement from a sample VecTor2 model (in this case $W_{\text{eff}} = 1,200\,\text{mm}$, $A_s = 11,000\,\text{mm}^2$/layer) at around the peak load stages (Fig. 10). The anchorage was found to be adequate (i.e. capacity $>$ demand), especially when considering that the loads recorded in this model were significantly higher than the actual applied loads on the structure.

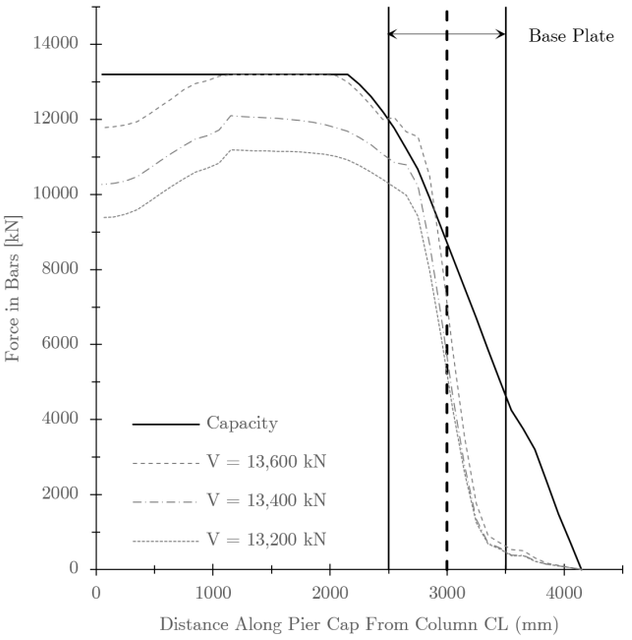


Figure 10. Demand on longitudinal tension reinforcement at applied loads ($W_{\text{eff}} = 1200\,mm$, $A_s = 11000\,\text{mm}^2$/layer)

4 ANALYSIS RESULTS

4.1 *Establishing the Parametric Study*

A total of 40 analyses were performed to obtain a comprehensive understanding of the behaviour of the hammerhead pier. The effective width of the structure was varied between 911 mm, the width of the thinnest section of the pier, up to the full width of 2200 mm (Fig. 12). Similarly, the quantity of steel included in the numerical model varied from a minimum of 7-35M bars per layer to the actual 11-35M bars per layer. This was done to account for the ambiguity in the number of bars that would be engaged by a load bearing area smaller than the full width of the pier.

4.2 *Results of Parametric Study*

Figure 11 compiles the results of all 40 analyses, with the ultimate nominal shear capacity being shown for the various widths and reinforcement quantities. It is apparent from the two plots that increasing the section thickness and quantity of reinforcement leads to gains

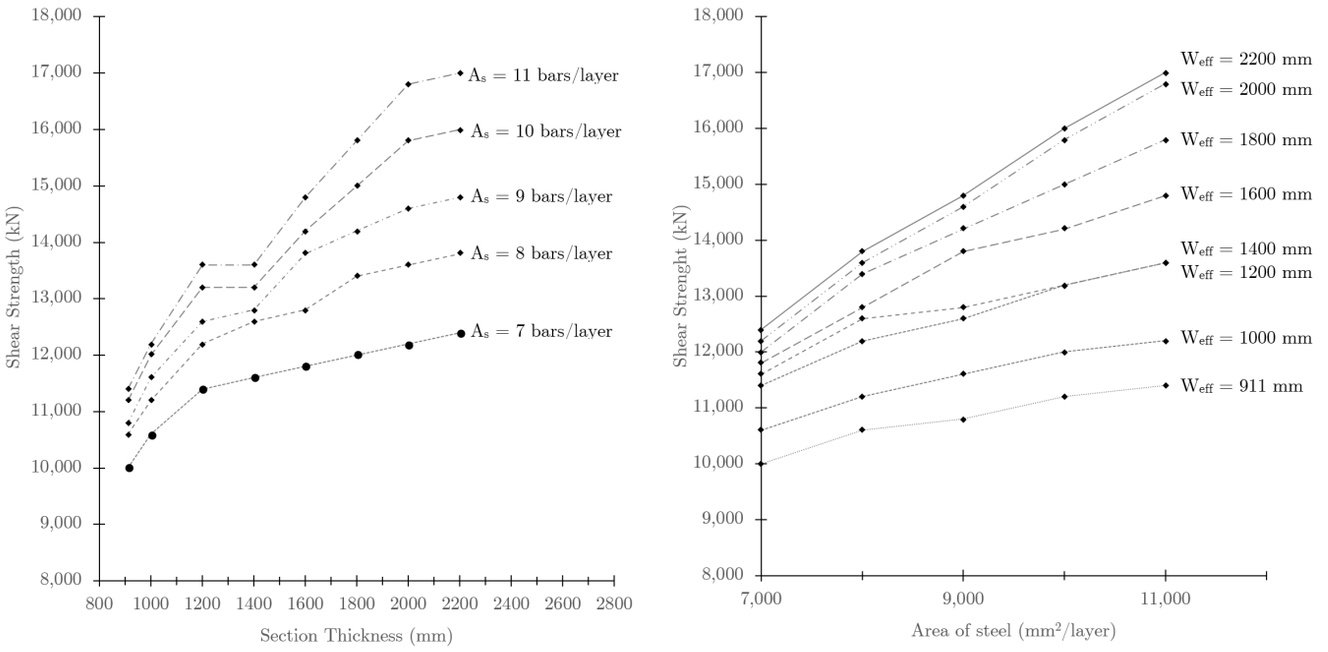


Figure 11. Influence of section thickness (left) and quantity of reinforcement (right) on ultimate capacity of pier

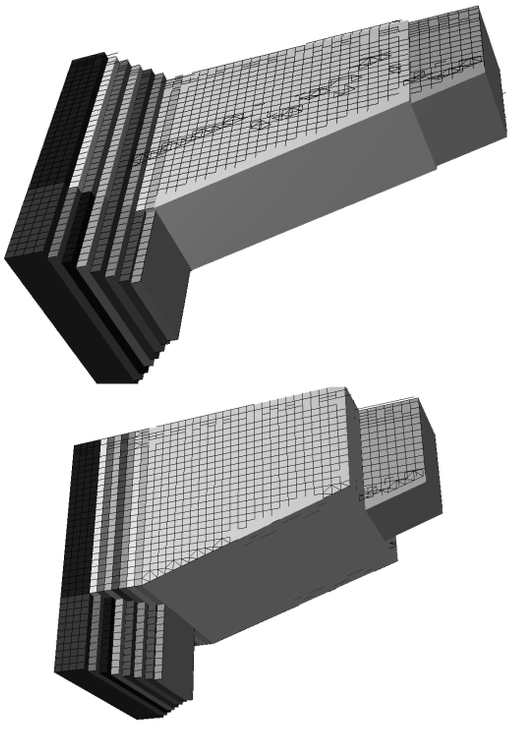


Figure 12. Effective width of pier cap varied from 911 mm (top) to 2200 mm (bottom)

in strength. Broadly speaking, increasing the thickness of the pier as well as the amount of steel led to proportionate gains in capacity. Generally, increasing the quantity of steel tended to provide larger gains in ultimate strength than increases in the thickness of the cross sectional area, which suggest that the amount of steel plays a major role in determining the strength of the structure. This was more pronounced in the analyses of the thicker sections, which benefited more than the thinner sections from additional steel in the tension chord.

5 DISCUSSION

5.1 *Failure Modes*

As VecTor2 is able to predict the complete load-deformation behaviour of the hammerhead pier structure, the failure mode can be understood by analyzing the element stresses and strains at failure. Figure 13 shows how the progression of failure events occurs as the effective section width is increased while maintaining the same amount of steel. If the effective section width is very thin relative to the quantity of reinforcement, then crushing of the concrete at the base of the pier occurs prior to yielding of the longitudinal steel. This can be seen in Figure 14. As the section gets larger, this pattern of events reverses and the steel yields followed by crushing causing failure.

5.2 *Integration of Results with an LRFD Framework*

Per the requirements of the National Building Code of Canada (Canadian Commission on Building and Fire Codes 2015), the factored strength of the structure must exceed the demands of the applied factored loads. The factored shear strength of the pier is thus obtained using the expression:

$$V_r = \phi_c V_c + \phi_s V_s \geq V_f$$

Where $\phi_c = 0.75$ and $\phi_s = 0.90$ are the strength reduction factors for concrete and steel accordingly (S6 Code Committee 2014). While this expression is straightforward for use with simplified design expressions, it is difficult to obtain the factored strength if the analysis is performed using NLFEA. Simply reducing the concrete cylinder strength and the steel

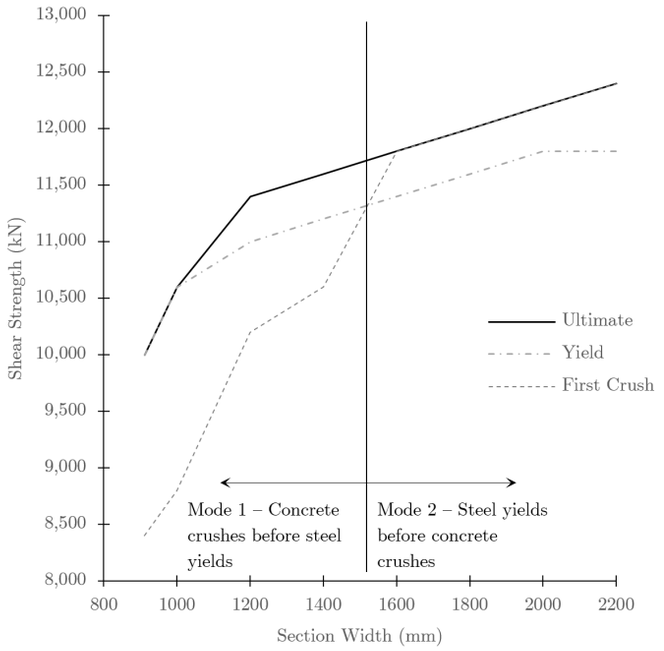


Figure 13. Influence of section width on shear strength. $A_s = 7000\,mm^2$ per layer)

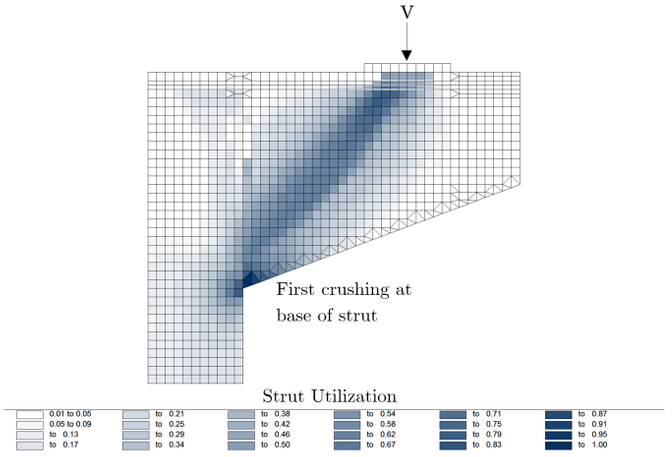


Figure 14. Crushing at the base of the pier

yield strength in the model by the corresponding resistance factors is not appropriate, as doing so would result in fundamentally changing the failure mechanism of the structure.

The approach taken in this study draws inspiration from the the ACI 318-14 code's provisions for flexural design (ACI Committee 318 2014). According to these provisions, the ultimate strain in the longitudinal reinforcement can be checked at failure to classify the failure mechanism. For tensile strains greater than 0.005, the failure is said to be governed by the tension failure of the longitudinal reinforcement. Conversely, strains less than 0.005 are a mixed failure mode where the crushing of the concrete has an influence on the ultimate factored flexural capacity. When applied to the VecTor2 analysis, the maximum strain in the flexural reinforcement was checked to determine whether the failure was clearly governed by yielding of the steel. An appropriate resistance factor obtained from the Canadian Highway Bridge Code was then applied (S6 Code Committee 2014). If the capacity of the analyzed structure is clearly governed by the behaviour of the steel, multiplying the ultimate load by the steel resistance factor of 0.90 is an appropriate way to obtain the factored strength. If crushing played a role, then the factored strength was obtained by multiplying the peak load by the concrete resistance factor of 0.75.

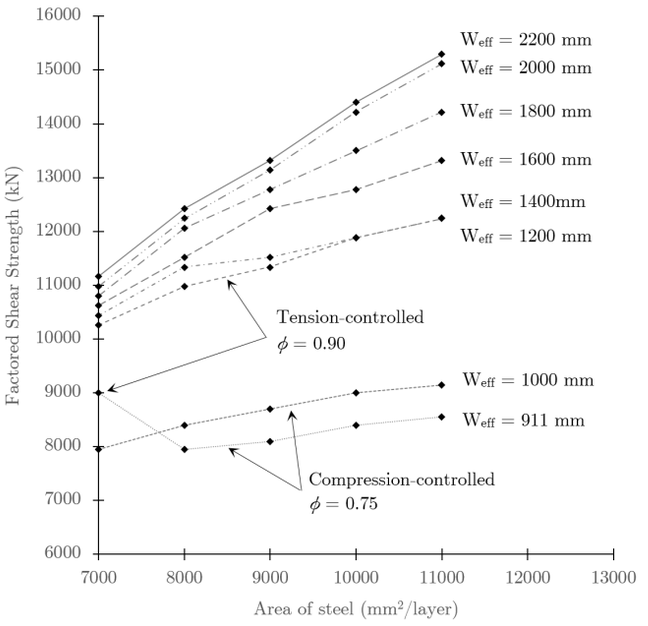


Figure 15. Factored shear strength of the pier

$$V_r = \begin{cases} \phi_s V_{ult} & \text{if } \varepsilon_s \geq 0.005 \text{ at failure} \\ \phi_c V_{ult} & \text{otherwise} \end{cases}$$

It should be noted that this analysis procedure is conservative for mixed failure modes where crushing occurs shortly after yielding, since the resistance factor used is either 0.75 or 0.90. Realistically, there should be a smooth transition where mixed failure modes which are controlled by both tension and compression are treated using a blended resistance factor which lies somewhere between 0.75 and 0.90.

Figure 15 shows the factored strength of the piers following an interpretation of the analysis results. In almost all cases, the ultimate strength is governed by yielding of the flexural reinforcement, with the exception of the thinnest possible section width (911 mm) or just slightly larger (1000 mm). The transition from tension-governed to compression-governed failure modes makes the spread of possible factored strengths particularly large, with the most conservative estimates of the factored strength being almost half the value of the most optimistic case, where all of the reinforcement and the full width of the pier are effective. When assessing the actual piers in question, it was determined that even with the most conservative assumptions, the structure was able to carry the required design loads.

5.3 *Crack Pattern Comparison*

As the purpose of the numerical modelling was to verify the safety of the cracked hammerhead pier, the crack pattern predicted by VecTor2 was compared against those seen in the actual piers. Figure 16 shows the predicted crack pattern of a typical analysis when the structure is carrying 50% of its maximum capacity, as well as a representative load-displacement plot which characterized almost all of the analyses. While the pier is heavily cracked, with predicted crack widths of up to 1.5 mm, it is quite far away from failing. All of the analyses performed predicted that the load causing first cracking was a small fraction of the ultimate strength, and well below the predicted service loads.

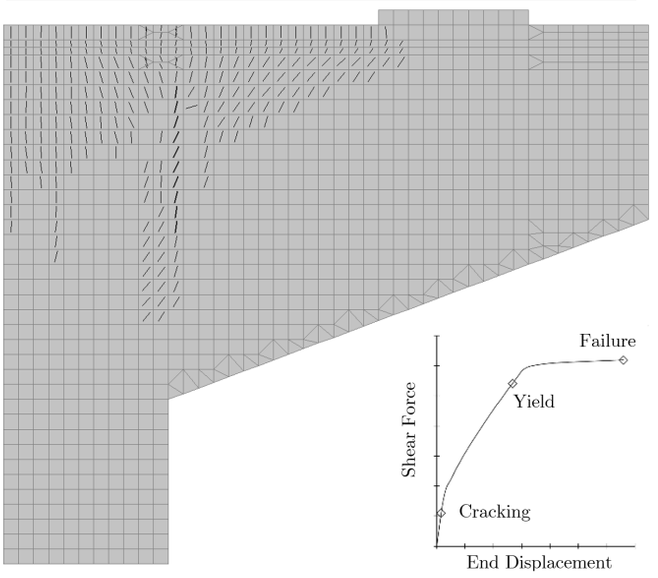


Figure 16. Typical crack pattern at 50% of member capacity

6 CONCLUSION

Nonlinear finite element analysis is a key part part of the modern structural engineer's toolbox when conducting an assessment of an existing structure which may be in distress. As shown from this case study of a cracked hammerhead bridge pier structure, the behaviour of seemingly simple structures can be complicated by subtle geometric features. In situations such as these, it is appropriate to turn to NLFEA to better understand the fundamental behaviour of these structures.

VecTor2, a 2-D NLFEA program based on the DSFM, was used to assess the piers. An extensive parametric study was performed to account for possible 3-D effects in the structure. The variables explored were the effective section width of the piers and the quantity of longitudinal reinforcement used, and the their effect on the piers' strength and failure mode were examined.

A simple procedure for using these NLFEA results within a LRFD framework was proposed, which assigns a representative resistance factor to the member's capacity by considering the strain in the longitudinal reinforcement at failure. While this method was used to obtain the factored strength for an existing structure, it is general enough to be used for designing new structures.

While a comprehensive 3-D nonlinear analysis to analyze reinforced concrete structures remains impractical for everyday use, the methodology discussed in this paper hopefully provides the practising engineer with a stronger foundation on which they can exercise their judgment when evaluating existing structures.

REFERENCES

ACI Committee 318 (2014). *318-14: Building Code Requirements for Structural Concrete and Commentary*. Farmington Hills, MI: American Concrete Institute.

Canadian Commission on Building and Fire Codes (2015). *National Building Code of Canada*. Ottawa,ON: National Research Council Canada.

S6 Code Committee (2014). *Canadian Highway Bridge Design Code*. Mississauga,ON: Canadian Standards Association Group.

Vecchio, Frank J., C. M. P. (1986). The modified compression field theory for reinforced concrete elements subjected to shear. *ACI Structural Journal V.83, No. 1*, 219–231.

Vecchio, F. J. (2000). Disturbed stress field model for reinforced concrete: Formulation. *Journal of Structural Engineering 126 (9)*, 1070–1077.

Maintenance, Safety, Risk, Management and Life-Cycle Performance of Bridges – Powers, Frangopol, Al-Mahaidi & Caprani (Eds)
© 2018 Taylor & Francis Group, London, ISBN 978-1-138-73045-8

Seismic analysis of a stone masonry arch railway bridge

C. Costa [a) b)], A. Arêde [a)] & R. Silva [a)]
[a)] *CONSTRUCT-LESE, Faculty of Engineering (FEUP), University of Porto, 4200-465 Porto, Portugal*
[b)] *Engineering Department, Polytechnic Institute of Tomar, 2300-313 Tomar, Portugal*

ABSTRACT: This paper focuses on the dynamic analysis of a stone masonry railway bridge under seismic loading. The simulation of the bridge structural behaviour is based on a 3D finite element model which includes the bridge components like piers, arches, spandrel walls, infill and foundations as well as the track components that are the rails, sleepers and ballast, both modelled using homogenous elements and elastic materials. Synthetic series of acceleration are used to represent the action of 5 earthquakes based on EC8. The structural modelling allowed to represent the bridge linear response in face of seismic actions aiming to evaluate the evolution of the dynamic effects in terms of deformations and stresses indicating an overall good behaviour.

1 INSTRUCTION

Arch bridges represent the most common typology of bridges in the European network of railway infrastructures, according to the survey carried out by the railway owners, representing 41% of the total inventoried bridges (Olofsson *et al.*, 2007). From these, 35% are over 100 years old, 62% have arch spans shorter than 10 m, 5% have spans larger than 40 m and 33% are made of stone (Bell, 2004).

The representativeness of this bridge typology and the increasing demands on weight and speed loads has been concerning the scientific community and the bridge owners to enhance the structural assessment of these bridges and to improve itself their condition state.

The assessment of the structural response and vulnerability to earthquakes is therefore of major importance to implement adequate management plans to guaranty the safety conditions of these bridges in the case of a seismic event.

The structural system of railway stone arch bridges is composed by the principal components, namely arches, spandrels and piers, formed in structural masonry, usually with regular (and large) stone blocks and (thin) mortared joints. Between the spandrels and above the arches, infill material is placed, usually also made up of stone and mortar (mixed with cement) but using stone blocks smaller and less regular those of the main components; this ends up as a more mortared material leading to an infill material similar to a poor concrete, as it is the case of Côa bridge according to documents of the bridge design (REFER, 1944).

The structural behaviour of stone masonry arch bridges is mainly controlled by the strength mechanisms and interaction between structural elements, as well as the mechanical behaviour of constituent materials; all these issues contribute for load transmission due to weight and traffic, foundation settlements and for the response to vibrations induced from traffic and earthquakes.

Regarding the global structural response under the most common loading (self-weight and traffic) two main mechanisms are activated according to the distinct bridge behaviour in the longitudinal and transverse directions (Gilbert, 1993). Under heavy loading, likely to approach failure conditions, the former is characterized by arch hinge mechanisms (see Figure 1a) resulting from transmission of vertical loads across the infill; the latter, mainly influenced by the interaction between infill, spandrels and arches, the bridge structural behaviour, is related with the transmission of horizontal pressures and the way how they are reacted namely characterized by out of plane mechanisms on the spandrels (see Figure 1b) and/or longitudinal cracking in the arch (Costa *et al.*, 2018).

During an earthquake, the development of the arch hinge mechanisms (joint opening by tensile failure) may came aggravated by additional vertical impulses due to the seismic action on the bridge, causing the collapse of the bridge as it seems to be the case of the bridge under river Claro shown Figure 2, due to Chile earthquake in 2010.

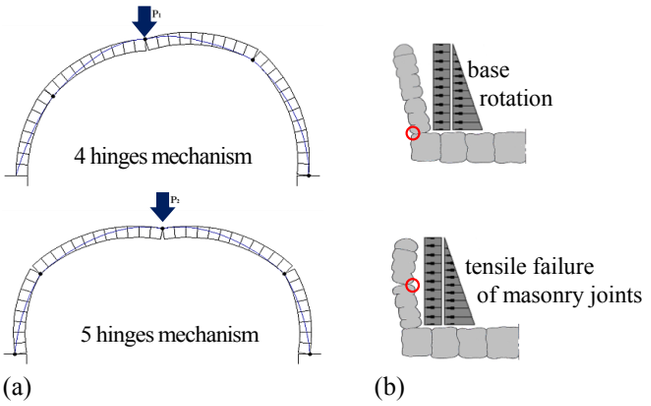


Figure 1. Failure modes: (a) arch hinge mechanisms and (b) out of plane of the spandrels.

In the transverse direction of the bridge, the out of plane mechanisms on the spandrels (rotation and sliding with joint opening by tension failure, shear failure or lack of equilibrium) may be aggravated by additional horizontal impulses, leading to the bridge collapse as the case shown in Figure 3 due to Umbria-Marche earthquake, Italy, in 1997.



Figure 2. Bridge collapse due to Chile earthquake in 2010 (http://revistaepoca.globo.com/Revista/Epoca/foto/0,,36940564,00.jpg).



Figure 3. Bridge collapse due to Umbria-Marche earthquake in 1997 (Resemini & Lagomarsino, 2004).

The bridge failure mechanisms due to dynamic effects of the seismic action depend on the characteristics of the earthquake and foundation soil, as well on the dynamic characteristics of the bridge (vibration modes, frequencies and damping) and the capacity of the structure to resist cyclic loading (particularly dependent with the limited capacity of masonry to resist cyclic loads, when not confined and the with degradation of the stiffness characteristics of the masonry filler as deformation increases).

The bridge vertical and longitudinal vibration modes are likely to influence the dynamic amplification on the arch mechanisms due to the effect of the vertical component of the seismic action while the bridge transversal vibration modes are expected to influence the dynamic amplification in the transverse mechanisms due to the horizontal component of the seismic action.

2 CASE STUDY

The analysis of the structural behaviour of the Côa bridge under the railway traffic loading was the focus of a previous study which resorted to test techniques and numerical models that also allow the study of the bridge under dynamic actions. Because it is a large structure, the analysis involved a great complexity associated with the characterization of the constituent materials and the geometry of the bridge itself. The dynamic characterization of the structure was also carried out based on modal identification by performing ambient vibration tests on the bridge, briefly referred to in this paper. Taking benefit of the already updated structural model of the Côa bridge, a seismic analysis of the bridge was carried out to evaluate its structural response and vulnerability to earthquakes. The main results of this analysis are presented and discussed in this paper, seeking to find out to which extent the effects of seismic action affect or condition the structural bridge behaviour.

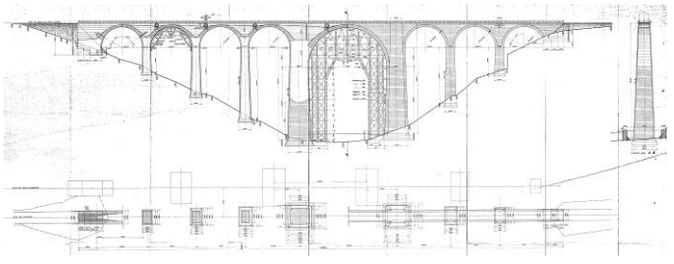
The Côa bridge, illustrated in Figure 4, was built in granite stone masonry in the late 1940s to replace an existing steel bridge over the Côa river in Beira Alta line of the Portuguese railways (REFER, 1944).



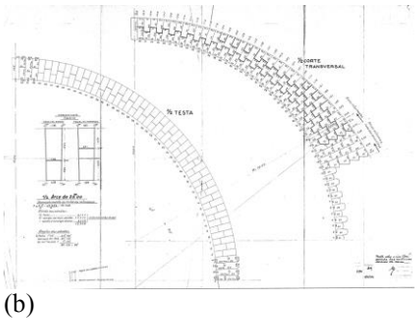
Figure 4. Côa bridge (at the right side) and piers and abutments of the replaced bridge.

The total length of the bridge is approximately 238 m, with 4.8 m width and supports one single-track. The bridge is formed by eight arches, one with a span of 38 m and the others with 20 m, which are supported onto seven piers and two abutments. The maximum height difference between the foundation and the pavement is approximately 56 m. The bridge also features thickness variation with height and also on the piers in the longitudinal direction. Figure 5 shows some drawing details of the bridge design.

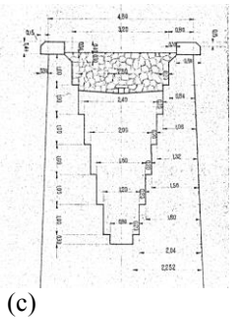
The arches consist of several ring segments with variable thickness. The foundations and external layer of the piers are made of regular stone masonry and the interior zone is filled with masonry consisting of irregular stones mixed with cement and mortar (called infill masonry). In the two highest piers, which support the larger arch span, the interior zone has distinct materials: from the foundation up to 18 m height it is made of regular stone masonry blocks, while the remaining zone consists of infill masonry.



(a)



(b)



(c)

Figure 5. Côa bridge design drawings: (a) elevation, (b) arch detail and (b) cross section (REFER, 1944).

The arches and piers support two spandrel walls with variable cross section composed of regular stone masonry. The backfill enclosed between them and the upper surface of the arches consists in infill masonry at the lower zone while the upper zone consists in dry stone material seated on a waterproof membrane with 9 cm thick. The railway track is formed by bi-block sleepers and UIC60 rails resting on about 50 cm thick ballast layer, placed above the backfill and delimited by sidewalks also in granite stone. At each side of the bridge there exist parapets made of puddled iron.

3 BRIDGE NUMERICAL MODEL

3.1 *FE model*

For the numerical modelling of Côa bridge a three-dimensional model based on the finite element method was developed in CASTEM software (CEA, 2011). This model, which FE mesh is shown in Figure 6, corresponds to an existing calibrated model already used to perform dynamic analysis under railway loadings resorting to ANSYS software (Jorge *et al.*, 2016). Common operations of output-input of FE meshes were carried out between software to perform subsequent analyses.

The arches, piers, spandrel walls, backfills, foundations, ballast and sleepers are modelled by tetrahedral finite elements. The rails are modelled by beam finite elements.

The boundary conditions were established using rigid supports to fix the node displacements at the foundations' base.

The mechanical properties of bridge materials are shown in Table 1.

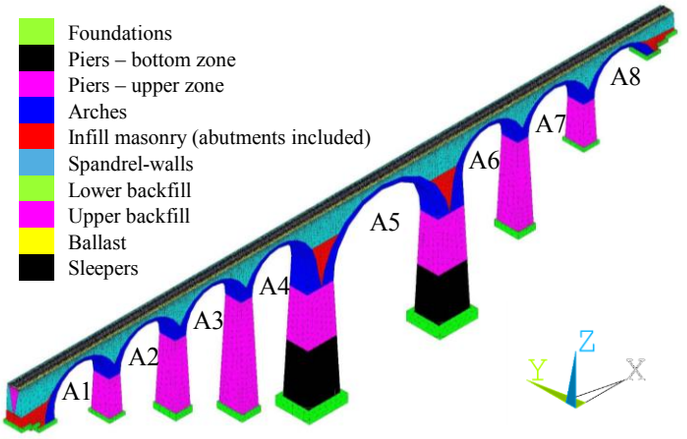


Figure 6. FE numerical model of Côa bridge.

Table 1. Mechanical properties of the calibrated materials.

Element material	Elastic modulus	Unit weight
	GPa	kN/m^3
Regular masonry	18.33	24.25
Infill masonry	13.49	24.25
Lower backfill	3.45	21.25
Upper backfill	0.34	19.60
Ballast	0.15	20.00
Sleepers	36.00	28.35
Rail	210.00	77.00

The elastic material properties and boundary conditions were adjusted to obtain numerically the dynamic characteristics measured in-situ. The assigned material properties were also based on bridge design data and on observations resulting from visual inspections on the bridge, as well as on the results obtained from material testing performed in other stone masonry structures (Arêde *et al.*, 2017 and Costa *et al.*, 2015).

3.2 *Modal analysis*

Figure 7 shows the values of the first ten natural frequencies and corresponding mode shapes. The modes 1 to 4, 6, 7, mainly involve movements of the bridge in the transversal direction. The other modes are refereed to movements in the vertical and longitudinal directions.

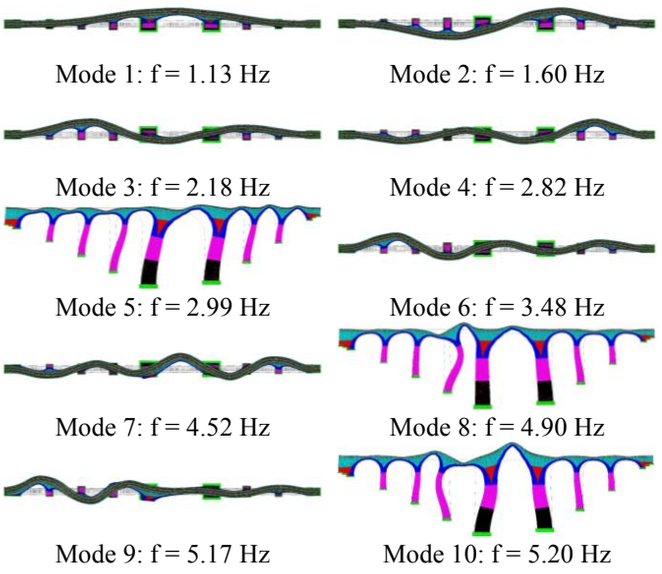


Figure 7. Numerical frequencies and mode shapes of the calibrated Côa bridge model.

3.3 *Model calibration*

The numerical model calibration was based on the bridge experimental modal properties, identified from measurements obtained in ambient vibration tests through the application of the Enhanced Frequency Domain Decomposition method, available at ARTEMIS (2009) software.

Figure 8 illustrates the configurations of the seven identified modes, including the average values of frequencies and damping coefficients. The analysis of the figure allows identifying modes associated to the transversal bending of the deck with very good definition. A detailed description of the bridge modal identification can be found in Jorge *et al.*, (2016).

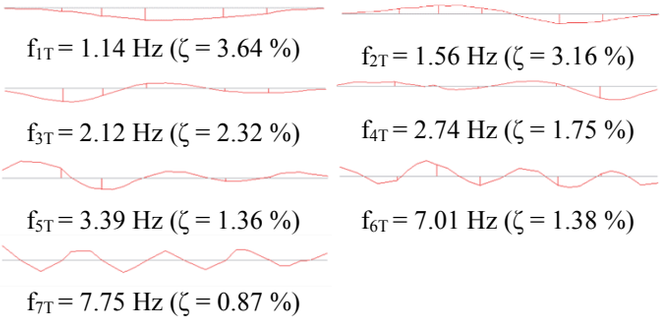


Figure 8. Experimental modal configurations for Côa bridge.

A sensitivity analysis and an optimization process using the modal pairing criterion based on modal assurance criterion (MAC) proposed by Allemang (2003), allowed to identify deviations between experimental and numerical values below 5% for all frequencies and all MAC values are higher than 0.90 (Jorge *et al.*, 2016).

4 SEISMIC ANALYSIS OF THE BRIDGE

4.1 *Methodology*

Due to the size of the structure a simplified methodology of analysis was adopted by considering the dynamic bridge response in the elastic regime. For material like masonry this is not the most suitable option, particularly if safety assessment is the focus. However, the present study mainly aims at obtaining response parameter estimates that allow understanding the structural behaviour trends when seismic action is included, rather than achieving very accurate response simulations.

The seismic analysis of the bridge was performed by integrating the dynamic equilibrium equations in the time domain, using the Newmark method implemented in the CAST3M software (CEA, 2011), under the seismic action simulated by artificial time series of ground accelerations as described in the next section. The Rayleigh damping matrix was adopted, based on the values of the two first calibrated frequencies. The integration time step was taken as 0.02 s, which was found appropriate and compatible with time series resolution.

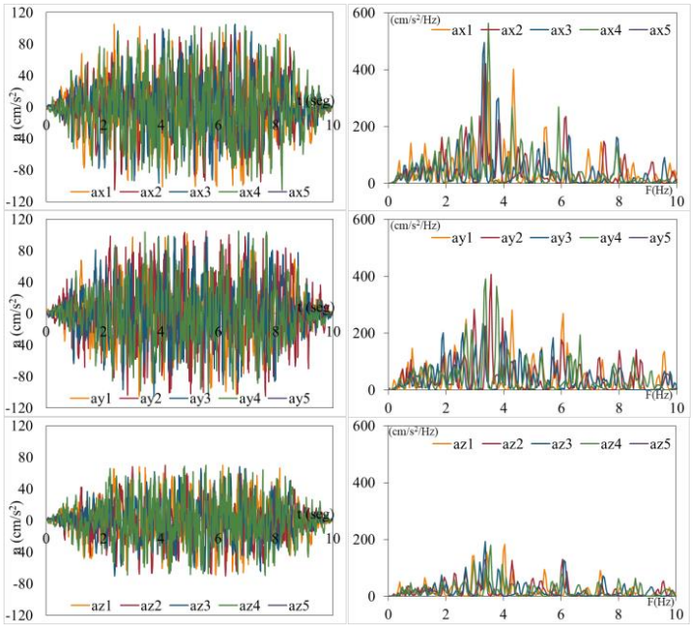
4.2 *Seismic action*

The seismic action was characterized by synthetic accelerograms (see Figure 9), artificially generated to match the response spectrum defined according to Eurocode 8 (NP EN1998-1, 2010) and the respective National Application annex. Figure 9 shows the 15 (5x3) time series of accelerations and the corresponding power spectral density plots.

The seismic load represents an earthquake of moderate magnitude at a small focal length and duration of 10 seconds, commonly referred as a near-field earthquake (EC8-NA type 2 seismic action). Seismicity was considered adequate for the bridge location (seismic zone 2.4) with soil class A (rock) and design peak-ground acceleration (PGA) of 0.1g, defined with an importance factor of 1 consistent with a bridge case of importance class II and a return period of 475 years.

It should also be noted that, the acceleration time series correspond to the design value of the seismic action PGA (NP EN1998-1, 2010), for which the corresponding effects do not have to be further fac-

tored by any safety factor in the context of combinations with other actions.



(a) (b)

Figure 9. Synthetic accelerograms in longitudinal, transverse and vertical directions: (a) time series and (b) spectral power densities.

5 RESULTS AND DISCUSSION

5.1 *Bridge response under the dead load*

The results of the linear static calculation, corresponding to the bridge behaviour under dead loads, are shown in Figure 10 in terms of the deformed configuration. The corresponding maximum values of the longitudinal-x, transverse-y and vertical-z displacements are summarized in Table 2. The results of the maximum and minimum principal stresses in each mesh zone are also included.

Regarding the maximum (absolute) values of the displacements and the principal stresses in the area of the arches and piers, it was verified, as expected, that they occur essentially in the arch 5 (the central on) and adjacent piers 4 and 5; these maximum values are also summarized in Table 3. The arch vertical displacement corresponds to about 1/6800 of the span and the horizontal displacements of piers are negligible (around 1/49000 of its height).

It is noted that the maximum tensile values in the arches' masonry are compatible with current values of tensile strength of the stone, although not necessarily the same for the masonry assemblage; on the other hand, the maximum compressions in the masonry have values usual in this type of stone masonry structures, well below the respective compressive strength. It is noteworthy that in the bridge design documents a reference to 57.85 MPa was found for the compression strength obtained on samples of granite stone used in the bridge (REFER, 1946).

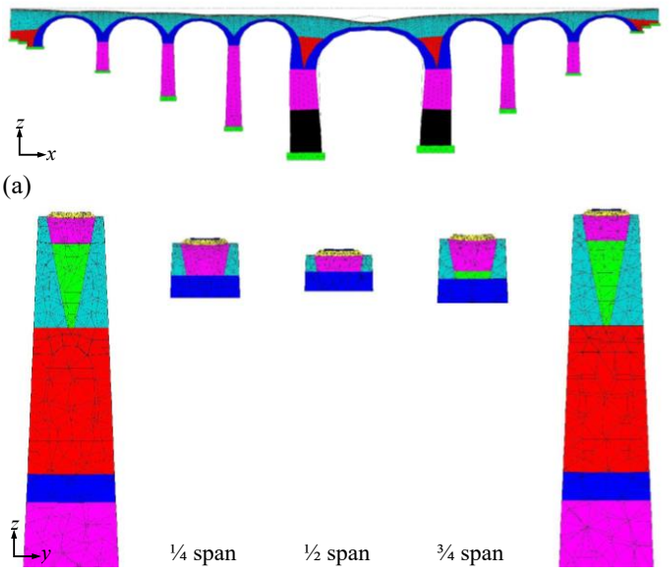


Figure 10. Bridge deformation due to its weight: (a) elevation and (b) transverse sections.

Table 2. Global results of the linear response of the bridge under the self-weight: Principal stresses and displacements.

Mesh zone	σ_1^+ MPa	σ_3^- MPa	*dx* mm	*dy* mm	*dz* mm
Foundations	0.24	-1.19	-0.06	0.04	-0.17
Piers bottom zone	0.07	**-2.00**	-0.62	0.06	-1.31
Piers upper zone	0.08	-1.41	**-1.14**	**0.06**	-2.30
Arches	**0.53**	-1.48	-1.13	0.06	**-5.56**
Infill masonry	0.30	-0.70	-1.10	0.04	-3.24
Spandrel	0.43	-1.44	-0.60	0.04	-5.56
Lower backfill	0.08	-0.12	-0.43	0.02	-4.73
Upper backfill	0.03	-0.06	-0.60	0.03	-5.58
Ballast	0.07	-0.12	-0.61	0.06	**-5.58**
Sleepers	**1.88**	**-3.10**	-0.56	0.02	-5.58

Table 3. Results of the linear response of the bridge under the self-weight in the piers 4 and 5 and arch 5: Principal stresses and displacements.

Mesh zone		σ_1^+ MPa	σ_3^- MPa	*dx* mm	*dy* mm	*dz* mm
Piers	1	0.02	-0.91	0.05	-0.04	0.72
upper zone	2	0.03	-1.03	-0.09	-0.04	-1.37
	3	0.02	-1.10	-0.08	0.05	-2.10
	4	0.06	**-1.41**	**-1.14**	0.06	**-2.30**
	5	**0.08**	-1.40	1.04	**0.06**	-2.14
	6	0.03	-1.02	0.04	0.05	-1.66
	7	0.03	-0.96	0.07	0.04	-0.78
Arch	1	0.17	-0.76	0.27	-0.03	-1.09
	2	0.14	-0.82	0.25	-0.03	-1.65
	3	0.20	-0.86	0.22	0.03	-2.50
	4	0.11	-0.78	**-1.13**	0.04	-2.56
	5	**0.53**	**-1.48**	-1.10	**0.06**	**-5.56**
	6	0.16	-0.79	1.03	0.04	-2.32
	7	0.26	-0.86	-0.22	0.03	-1.98
	8	0.39	-1.37	-0.21	0.03	-1.06

5.2 *Bridge response under the self-weight and the seismic action*

The maximum values of the linear dynamic bridge response under seismic action and self-weight are summarized in Table 4 for each bridge element in terms of the maximum effects of the five earthquakes considered in the analysis (in line 2 for each element). The values in Table 4 also refer the results of the bridge response considering the load case of the bridge dead load (in line 1 for each element).

In order to obtain final values, ultimate limit state combinations were considered according to the Eurocodes, for which the loading combinations included in Table 4 are as follows: $S_G = G_k$ (line 1); $S_E = G_k + E_d$ (line 2); where G_k represents the characteristic values of effects of the dead load while E_d corresponds to the design (absolute maximum) values of the earthquake effects. According to the previously mentioned, these values correspond directly to the results of the application of the accelerograms considered in the analysis. Table 4 also includes (in line 3 for each element) the ratio Δ (absolute value) of values obtained from the seismic analysis to those obtained only with the dead load.

Table 4. Result variations due to seismic action (maximum of the 5 earthquakes): Principal stresses and displacements.

Mesh Zone	*Load case*	σ_1^+ MPa	σ_3^- MPa	*dx* mm	*dy* mm	*dz* mm
Foundations	S_G	0.24	-1.19	-0.06	0.04	-0.70
	S_E	1.00	-2.68	0.13	0.10	-0.30
	Δ	*4.11*	*2.26*	*2.26*	*2.80*	*1.82*
Piers bottom zone	S_G	0.07	-2.00	-0.62	0.06	-1.31
	S_E	2.21	-5.26	-2.93	4.16	-3.23
	Δ	***32.93***	*2.64*	*4.72*	*70.59*	*2.46*
Piers upper zone	S_G	0.08	-1.41	-1.14	0.06	-2.30
	S_E	1.67	-4.00	9.60	15.23	-5.65
	Δ	*20.86*	*2.83*	*8.40*	*241.68*	*2.46*
Arches	S_G	0.53	-1.48	-1.13	0.06	-5.56
	S_E	6.55	-6.79	9.87	38.42	-8.87
	Δ	*12.33*	*4.59*	*8.76*	*698.53*	*1.59*
Infill masonry	G_k	0.30	-0.70	-1.10	0.04	-3.24
	S_E	1.33	-1.58	-9.18	28.86	-6.73
	Δ	*4.40*	*2.27*	*8.34*	*759.37*	*2.08*
Spandrels	S_G	0.43	-1.44	-0.60	0.04	-5.55
	S_E	3.71	-3.52	10.15	39.90	-8.83
	Δ	*8.70*	*2.44*	*16.78*	*1108.19*	*1.59*
Lower backfill	S_G	0.08	-0.12	-0.43	0.02	-4.73
	S_E	0.63	-0.64	9.50	36.93	-8.34
	Δ	*7.58*	***5.21***	*21.99*	*1943.58*	*1.76*
Upper backfill	S_G	0.03	-0.06	-0.60	0.03	-5.58
	S_E	0.11	-0.12	10.03	39.92	-8.23
	Δ	*3.29*	*1.93*	*16.64*	*1173.97*	*1.47*

Considering the results of the linear seismic analysis ($S_E = G_k + E_d$), for the peak values of the principal stresses, with respect to the results obtained with the dead load case ($S_G = G_k$), it is clear that the influence of the seismic action assumes relative significance, with a maximum increase ratio of 32.93 and 5.21, respectively for the maximum principal stresses (tension) in the piers upper zone and the minimum principal stresses (compression) of the lower backfill.

The large increase in the maximum principal stresses (tension), particularly in the arch zones where the maximum positive value of the principal stress was obtained, evidences the need to adopt a nonlinear material modelling for masonry, since, as fragile material, the capacity of the masonry to accommodate tensile stresses is limited. Nevertheless the maximum values of tension are confined to a restricted area as shown in Figure 11, where the distribution of maximum values of principal stresses are shown in the arch zone, for load cases with earthquakes 3 and 2, in Figure 11a and b, respectively.

The minimum values of the negative principal stresses (compression) are also located in the arch zone, which are still compatible with the usual values found for the masonry strength.

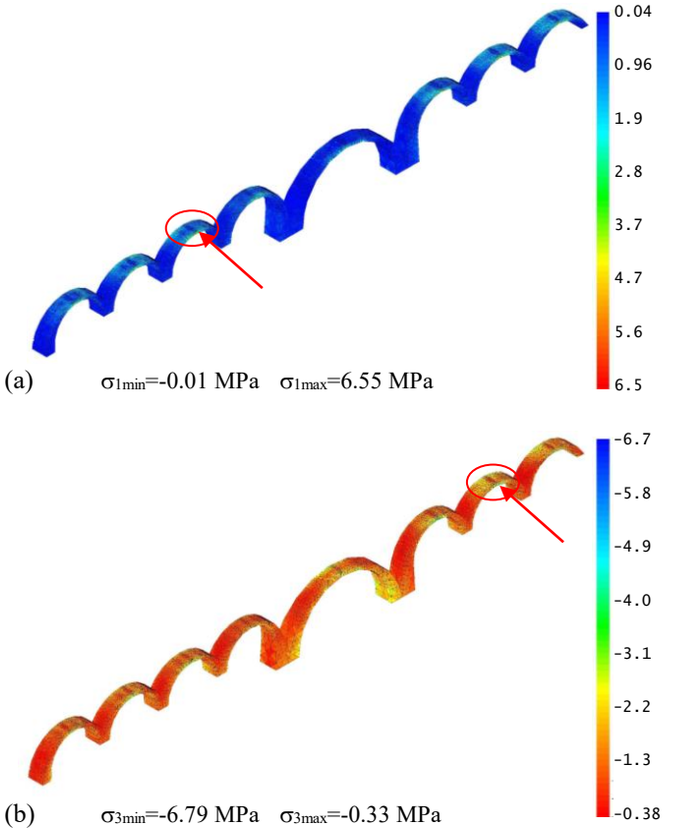
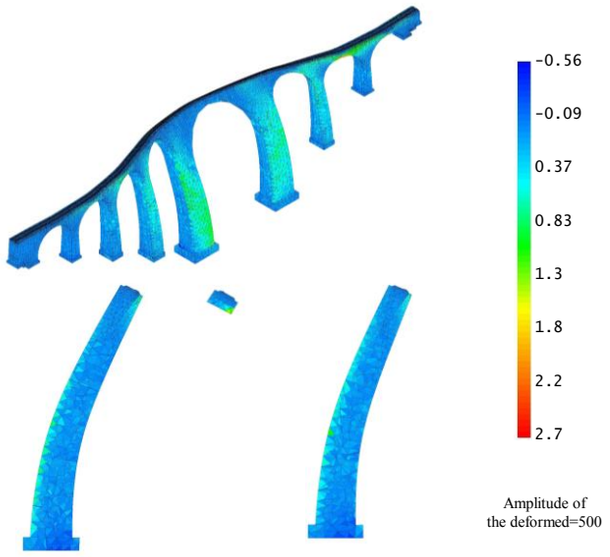


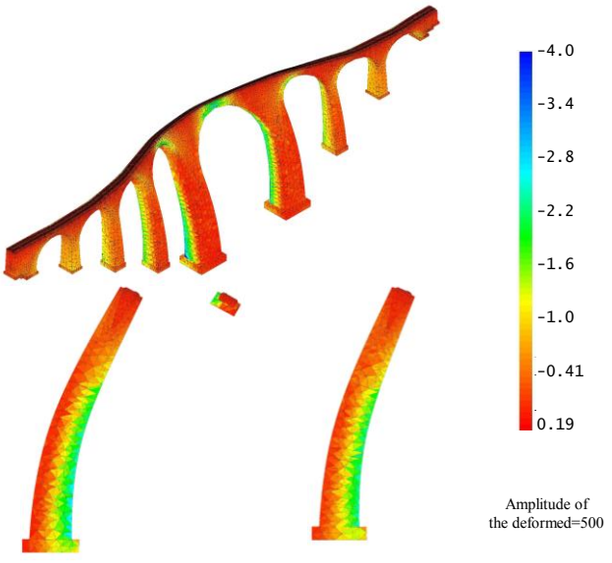
Figure 11. Principal stresses in the arch zone for the combination $G_k + E_d$: a) maximum and b) minimum.

The distributions of the maximum and minimum principal stresses in the deformed configuration of the bridge are shown in Figure 12 for the load case $G_k + E_d$. The figure includes a 3D view and three transverse sections through the ½ span of the principal arch 5 and the adjacent piers 4 and 5. The plots correspond to the step of analysis when the maximum transversal displacement in the principal arch (arch 5) is found considering the earthquake 4.

With respect to displacements, as expected, the influence of seismic action is very significant in the horizontal directions, particularly in the transverse one (*dy*) as shown in Table 4 by the increment ratios up to +241.68 in the transverse displacements of elements located in the bridge upper zone (piers upper zone, arches, backfill and spandrels). Lower increase is found in the vertical displacements.



(a) σ_{1min}=-0.58 MPa σ_{1max}=2 MPa



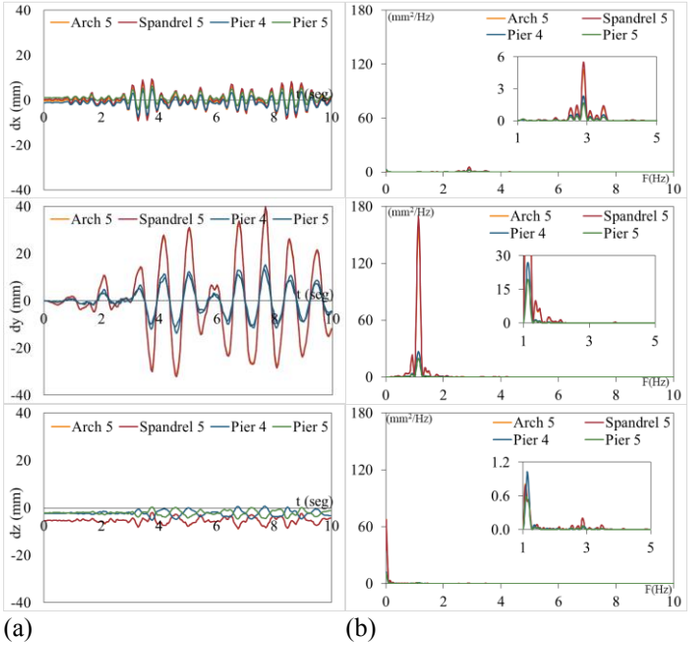
(b) σ_{3min}=-4.01 MPa σ_{3max}=0.22 MPa

Figure 12. Principal stresses plots in the deformed configuration of the bridge for the combination of seismic action and self-weight: a) maximum and b) minimum.

However, despite these high relative increments, the absolute values of bridge displacements are rather modest. In fact, it is noteworthy that the maximum vertical displacement for the seismic action (with self-weight) recorded in the arch 5 and is only 8.87 mm, which corresponds to about 1/4280 of that arch span. Also, the maximum absolute values of the transverse and longitudinal displacements are, respectively, 38.42 mm and 9.87 mm (corresponding to 1/1350 and 1/5670 of the bridge height), which are values clearly acceptable for an arch with 38 m span and bridge piers with 56 m total height.

The displacements' evolutions in arch 5, adjacent piers 4 and 5 and spandrel 5 in the nodes where the maximum (extreme) absolute values were found, for the action of earthquake 4 plus the bridge self-weight, are plotted in Figure 13a. The corresponding power spectral densities are shown in Figure 13b.

The analysis of the peaks shown in the plots of power spectral densities relative to displacements in Figure 13b allows verifying that the corresponding frequencies in x- and y-direction are coherent with frequencies of the bridge vibration modes involving the maximum modal amplitudes in the same direction (where 1.13 Hz is the first transverse mode frequency and 2.99 Hz corresponds to the first longitudinal mode). Although not perceptible in Figure 13b, for the z-direction a peak is also found near the frequency of the 1st vertical mode (f_{1V}=4.9 Hz) but the peaks with higher energy are found for frequencies near to 1.13 Hz and 2.99 Hz, thus indicating a correlation with the amplitude of vertical components in 1st transversal and 1st longitudinal modes of the bridge.



(a) (b)

Figure 13. Displacements of the principal arch and adjacent spandrels and piers in nodes with extreme values: (a) time history responses and (b) spectral power densities.

6 CONCLUSIONS

The structural response of the bridge indicates an overall good behaviour in face of seismic actions. In fact, the values found attest to the stiffness and strength capacity of the structure, with maximum longitudinal, transversal and vertical displacements (*dx*, *dy*, *dz*) in the zone of the principal arch of about 10, 40 and 10 mm, respectively, for which *dx* and *dy* correspond to about 1/5200 and 1/1300 of the bridge

height and *dz* corresponds to 1/3800 of the principal arch span. Moreover the masonry stresses obtained in the compression domain are compatible with the material strength and the maximum tensile stresses are observed in a small restricted area.

The analysis of the bridge displacements' time histories and their spectral power densities also allowed verifying, for transverse and longitudinal displacements, the proximity between the frequency values of the power spectral density peaks and those of the bridge vibration modes with higher amplitudes in the same directions (f_{1T}=1.13 Hz and f_{1L}=2.99 Hz); for the vertical displacements, the peaks are also found for frequency values close to the first longitudinal and transverse modes' frequencies, rather than to the first vertical mode. This fact is coherent with the higher aggravation of effects of seismic action in longitudinal and transverse directions (when compared with the effects of the dead load), indicating higher amplification effects in the horizontal directions than in the vertical one. Those results are also in agreement with the higher acceleration values that characterize the accelerograms in longitudinal and transverse directions than the vertical ones.

Finally it should be noted that the model used at the local level, may not be able to fully translate actual behaviour. In fact, by considering elastic materials there are some phenomena that are not represented in the used model and that can condition the obtained results, among which the most important are the aspects related to the non-linearity of the masonry behaviour in the tension domain and the degradation of the connections between masonry blocks due to the cyclic loads' action. In this context, it may be necessary to modify and adapt the used material constitutive models to ensure that seismic actions may or may not affect the local behaviour, particularly of the arches. Therefore as future developments for this study it is expected to use more adequate constitutive nonlinear models which should also allow taking in account other modelling conditions representing more severe scenarios of seismic events and bridge vulnerability.

Despite the adopted modelling shortcomings, still useful indications were obtained concerning the impact of seismic action in this kind of structures, namely concerning the locations and order of magnitude of stress and displacements aggravations likely to occur in the bridge structure.

AKNOWLEDGEMENTS

Part of this work reports to research financially supported by Project POCI-01-0145-FEDER-007457—CONSTRUCT—Institute of R&D in Structures and Construction, funded by FEDER funds through COMPETE2020—Programa Operacional Competitividade e Internacionalização (POCI) and by national funds through Fundação para a Ciência e a Tecnologia (FCT). It also includes research supported by the FCT project PTDC/ECM-EST_1691/2012 – Experimental and Numerical Characterization of Structural Behaviour of Stone Masonry Arch Bridges under Railway Traffic Loading, Application to Existing Portuguese Bridges. The authors thank Rui Calçada, Diogo Ribeiro and Pedro Jorge from FEUP, for collaboration in the tests and model calibration.

REFERENCES

Allemang, R. 2003. The modal assurance criterion - twenty years of use and abuse. Sound and Vibration, 37, 14-21.

ANSYS, I. ANSYS® Academic Research, Release 15.0, Help System.

Arêde, A., Costa, C., Gomes, A. T., Menezes, J.; Silva, R., Morais, M. & Gonçalves, R. 2017. Experimental characterization of the mechanical behaviour of components and materials of stone masonry railway bridges. Construction and Building Materials, 153, 663–681. doi: 10.1016/j.conbuildmat.2017.07.069

ARTeMIS 2009. ARTeMIS Extractor Pro - Academic Licence, Aalborg, Denmark.

Bell, B. 2004. European Railway Bridge Demography. WP1-02-T-040601-F-Deliverable D 1.2. Sweden, Sustainable Bridges - Assessment for Future Traffic Demands and Longer Lives, Project co-funded by the European Commission within the Sixth Framework Programme. www.sustainablebridges.net/main.php/D1.2-WP1-02-T-040531-F_Public.pdf?fileitem=22708836

CEA 2011. Presentation et utilization de Cast3M by E. Le Fichoux, Commissariat à l'Énergie Atomique. www-cast3m.cea.fr.

Costa, C., Arêde, A. & Costa, A. 2018. Strengthening of masonry bridges. In: Strengthening and Retrofitting of Existing Structures. Costa, A., Arêde, A. & Varum, H. (Eds.), Building Pathology and Rehabilitation, 9, 217-247. Springer, Singapore. doi: 10.1007/978-981-10-5858-5_10

Costa, C., Arêde, A., Costa, A., Caetano, E., Cunha, A. & Magalhães, F. 2015. Updating numerical models of masonry arch bridges by operational modal analysis, International Journal of Architectural Heritage, V. 9, p. 760-774. doi: 10.1080/15583058.2013.850557.

Gilbert, M. 1993. The Behaviour of Masonry Arch Bridges Containing Defects, PhD-Thesis, University of Manchester.

Jorge, P., Ribeiro, D., Costa, C., Arêde, A. & Calçada, R. 2016. Train-bridge dynamic interaction on a stone masonry railway bridge. IABMAS'16, Foz do Iguaçu, Brazil.

NP EN1998-1 2010. Eurocode 8: Design of structures for earthquake resistance, Part 1 + NAD, Brussels, Belgium, European Committee for Standardization (CEN).

Olofsson, I., Elfgren, L., Bell, B., Paulsson, B., Niederleithinger, E., Jensen, J., Feltrin, G., Täljsten, B., Cremona, C., Kiviluoma, R. & Bien, J. 2007. Assessment of European railway bridges for future traffic demands and longer lives – EC project "Sustainable Bridges". Structure and Infrastructure Engineering, 1 93-100

REFER, EPE. 1944. Substituição da ponte do Côa. Projecto de execução, Lisboa. (in Portuguese)

REFER, EPE. 1946. Processo de correspondência da obra da ponte do Côa, Lisboa. (in Portuguese)

Resemini, S. & Lagomarsino, S. 2004. Sulla vulnerabilita seismic di ponti ad arco in muratura, XI Congresso Nazionale "L'ingegneria sismica in Italia", Genova.

Maintenance, Safety, Risk, Management and Life-Cycle Performance of Bridges – Powers, Frangopol, Al-Mahaidi & Caprani (Eds)
© 2018 Taylor & Francis Group, London, ISBN 978-1-138-73045-8

Numerical assessment of composite bridges subjected to Wildland Urban Interface (WUI) fires

A.P. Dissanayake, S. Setunge, S. venkatesan
School of engineering, RMIT University, Victoria, Australia
K.A.M. Moinuddin & D. Sutherland
Centre for Environmental Safety and Risk Engineering, Victoria University, Victoria, Australia

ABSTRACT: Rapid expansion of urbanization has led to the increased vulnerability of infrastructures to bushfires and wildfires. Australian, bridge inspection manuals recommend a level 3 type of investigation as a post-bushfire bridge evaluation. Fire/structure interactions are dependent on fuel quantity, geometry, fuel characteristics, ambient conditions and structural characteristics. Given the scant research on wildland urban interface (WUI) fire, this research presents a numerical modeling approach of WUI fire with Fire Dynamic Simulation (FDS) software, utilizing the parallel computing facility. A domain size of 56m length 10m wide and 25m height with a uniform 200mm mesh resolution, that includes different fuel geometries and a bridge structure, were modeled in the analysis. The maximum temperature of the 12mm thick steel web and concrete bottom surface are around 350C and 115C respectively. Initial results show that there is no considerable strength degradation nor concrete cracking nor spalling. However, some dehydration of the concrete and reduction of Young's modulus in steel by 25% was observed. However, the strength degradation of steel up to 400C is limited. Further research is recommended to assess the cumulative effects on a structure when exposed to recurrent WUI fire events.

1 INTRODUCTION

Australia is one of the most bushfire-prone countries in the world. Annually, 'disaster-level' bushfires cost Australia an average of $77 million(*Total cost of bushfire* 2004). Total natural disasters cost in Australia is expected to increase from $9 billion to $33 billion by the year 2050 according to the Australian Business Round table for Disaster Resilience. Researchers have shown the potential influence of climate change on to the more severe and longer fire seasons around the globe (Flannigan, Mike et al. 2013). A warmer world means longer fire seasons and more drier fuels (Flannigan, M, Wotton & Marshall 2016). Meanwhile, the rapid urban sprawl and population decentralization in recent decades that have increased the size of the wildland urban interface (WUI) resulting more communities and infrastructures vulnerable to bush and wild fires (Massada et al. 2009).

Especially the bridges in bushfire prone areas can be exposed to extreme fire conditions depending on the availability of quantity, type and condition of vegetative fuel and the ambient conditions. Timber bridges are the most vulnerable form of structures in the face of a bushfire. Even though no bridge failure has been recorded in other types of bridges most of the bridge inspection manuals in Australia usually recommend a level 3 types of investigation on bridges as a post bushfire bridge evaluation process (Vicroads 2014).

There is a lack of research to understand the different fire exposure levels of bridges located in a WUI. This research paper presents the results of few case studies of an ongoing work designed to assess the thermo-mechanical performance of existing composite steel girder bridges exposed to most rational fire events covering a range of fuel and environmental conditions. Research results can help to predict the isolated and cumulative effects on a structure when exposed to recurrent WUI fire events in the future.

2 RESEARCH METHODOLOGY

This research is designed to understand the extreme effects that can be expected on to a bridge structure subjected to WUI fires given different environmental and fuel conditions. Numerical simulation of the WUI fire is accomplished using Fire Dynamic Simulator (FDS) software. FDS is a computational fluid dynamics (CFD) model of fire-driven fluid flow. FDS is capable of simulating interactions among atmosphere, fuel, and fire. 56m long and 10m wide and 25m high domain that contains different fuel geometries and a bridge structure is simulated. A 10m length portion of

a 25m long and 11.5m wide composite steel plate girder bridge with 5 numbers of girders is modeled to represent a typical bridge structure. Temperature development of the structure is monitored using Adiabatic Surface Temperature (AST) computing devices attached to various locations of the bridge. The thermal analysis is carried out using general purpose finite element software ABAQUS. The aim is to understand the effect of fuel characteristics and environmental factors that can potentially change the fire behavior on to the thermal response of the bridge. The fuel materials of WUI fires can be broadly categorized in to two groups: fine fuel (material less than approximately 5 mm diameter) and coarse fuel (larger material). This study is limited to the modeling of fine fuel in both ground and elevated forms. Future investigation will be extended towards coarser fuel to complete the spectrum of fuel grading.

3 WUI FIRE CHARACTERISTICS

Vegetative fuels and fires in a wildland setting can be categorized as surface, or crown types. Fallen twigs, leaves, barks, branches, grasses, and shrubs less than 1.8m tall are the examples of surface fires(Mell et al. 2007). The fires in elevated vegetation in trees are referred to as crown fires.

The fire-fuel interaction in a WUI involves gas generation by solid fuel pyrolysis, the subsequent combustion of the fuel gases, and the resulting heat flux back to the solid fuel, driving continued pyrolysis and fire spread along the fuel bed.

Fire danger ratings have been established to indicate the vulnerability and the severity of potential grass and wildland fires depending on atmosphere conditions. Increased fire danger rating levels, such as the McArthur (Noble, Gill & Bary 1980) are associated with fire weather conditions such as high temperatures, high curing (drying of vegetation) rate, low relative humidity (RH) values and in particular high wind conditions. For burning vegetation that contains moisture increases its ignition time and decreases the rate of flame spread. The stronger wind forces the hot fire plume closer to the downwind fuel bed, increasing both the radiative and convective heat fluxes. This process leading to a faster fire spread in higher winds (Mell et al. 2007).

Fireline intensity, defined as the heat release rate (HRR in kW) of the fire front divided by the effective length across the spreading direction. The HRR is the most important input for conducting CFD simulations of fire (Moinuddin, KA et al. 2011). Therefore, the fireline intensity (kW/m) is one of the most important factors that decide the fire-structure interaction in a WUI setting. Fireline intensity has a strong correlation with the fuel availability and the rate of spread of the fire (Cruz et al. 2015). Higher fuel load (ton/ha) normally results in higher fireline intensity and consequently has greater impact on a structure. This research looks in to effects of wind speed and fuel loading in WUI settings in terms of three case studies.

4 MODELLING OF FIRE DYNAMIC IN WUI

Both wildland and WUI fires are very difficult to study with full-scale repeatable experiments in the field due to their expense, safety implications, and variations in atmosphere, terrain, and fuel conditions. As an alternative to this problem, practical predictions of wildland fire spread have been accomplished through "operational" mathematical models based on empirical correlations for wildland fuels. They fail, however, when the fire spreads to the built environment where the empirical correlations may no longer apply (Evans, Rehm & McPherson 2003).

Fires where strong fire-atmosphere interactions occur, such as crown fires, routinely strain the credibility of the empirical fire spread models (Mell et al. 2007). Moreover, there are many fire behavior problems, of increasing relevance, that are outside the scope of empirical and semi-empirical models. This paper describes the development of a three-dimensional, fully-transient, physics based, computer simulation approach for modeling fire spread through surface and elevated fuels in a WUI.

Although the NIST's FDS tool was initially developed to study building fires, its use is extended to study WUI fire problems. The FDS model has the capacity to utilize data including the local topography, infrastructures, ignition and burning characteristics of vegetative fuels, and meteorological conditions to provide a time dependent simulation of fire spread in a WUI setting. FDS is a computational fluid dynamics (CFD) model of fire-driven fluid flow. It includes sub models for fluid flow, combustion, heat transfer, and thermal degradation of the vegetative fuel. The combustion is modeled by a 'mixed-is-burnt' fast chemistry model. Turbulence is treated with large-eddy simulation (LES) approach. The simulation results in a three-dimensional, time-dependent, prediction of fire behavior. Both convective and radiative heat transfer between the gas phase and the vegetation is accounted.

4.1 *Parallel computing*

Characterizing the wildfire dynamics and its impact on structures requires observation and modeling accounting for a very wide range of length scales ranging from fine scales representing fine fuels to scales of importance in the WUI in the problem by rational means of aggregation. So, the computational cost is very high. To solve a system of large equations a feasible high-performance computing facility is often required.

In FDS the parallel MPI (Message-Passing Interface) implementation is designed for running on distributed memory systems, e.g. a computer cluster. MPI is used to execute FDS as a parallel job on a distributed memory system in terms of mesh dividence. During this research, a high Performance Computing (HPC) system Spartan operated by Research Platform Services (ResPlat) at The University of Melbourne is used in conjunction with the MPI version available in FDS (Melbourne 2017).

4.2 *Fuel characteristics*

4.2.1 *Surface fuel*

Table 1. Vegetation parameters for grass

Parameter	Value
Vegetation bulk density	2.5 kg/m3
Vegetation height	1.0m
Vegetation moisture content	6.3%
Vegetation Surface to Volume Ratio (SVR)	9770m-1
Vegetation element density	440kg/m3
Maximum Mass loss rate	0.4 kg/s
Vegetation Drag Coefficient	0.125
Emissivity	0.9
Air temperature	35 $°C$



Figure 1. Typical grass land with around 2.4kg/m2(Johnson 2002)



Figure 2. Appearance of grass with 5 to 15% moisture content and 80% to100% cured (Johnson 2002)

A significant variation of the fuel characteristics can be expected over a land scape scale; however, this study idealizes the problem to a uniform fuel bed. Table 1 summarizes the fuel parameters used to represent the grassland. Many of these input parameters can be considered to be in which a large variation would not be expected among different kinds of grass, such as the heat of combustion of the fuel, char fraction, element density, and emissivity. For other properties are considerably based on the environmental conditions or specific plot of land.

For vegetative fuels, the surface-area-to-volume (SAV) ratio is an important parameter that measures the available fuel surface area for heat and mass transfer and production of combustible vapors (Bartoli et al. 2011; Beer 1993). Representative value of SAV ratios of grass used in the analysis is based on the grass species, *Eriachne burkittii* (kerosene grass) that is reported by Cheney (Cheney, Gould & Catchpole 1993)

Grass curing is another important parameter that is a measurement of grass 'greenness' and is related to the percentage of dead grass in a land. Curing is dependent on seasonal conditions such as rain, temperature and is also dependent on plant species and land type. As grasses cure, moisture content decreases. Grassland fire danger rating index (GFDI) Mark 3 stipulates fuel moisture is a function of curing, air temperature and relative humidity (Cruz et al. 2014). Plant moisture acts as a heat sink and thus influences fire behavior by increasing the specific heat required for the fuel to combust (Johnson 2002). As plant moisture decreases, fire intensity, potential ignitability and fire spread rate. [13,15,20-22]. Figure 1 and Figure 2 provides a visual estimation on the grass fuel load, curing and fuel moisture condition that is used for the present. In FDS, fuel moisture, air temperature and relative humidity are provided as input variables.

Note that an emissivity of 0.9 is characteristic of wildland vegetation (Evans, Rehm & McPherson 2003) (P.G Jarvis 1976) so the assumption that a fuel element is a perfect absorber is reasonable.

A linear degradation model is used to model the pyrolysis process of grass (Morvan & Dupuy 2004).

4.2.2 *Elevated fuel*

Table 2. Thermo-physical parameters used to model the elevated vegetation

Parameter	Moisture	Vegetation	Char
Thermal conductivity (W/m.K)	2.0	2.0	2.0
Specific heat (kJ/kg.K)	4.148	1.2	1.2

Density (kg/m3)	1000	514	300
Reference temperature (C)	100	200	350
Reference rate	0.002	0.0005	0.0002
Heating rate (C/min)	1.6	1.6	1.6
Heat of reaction (kJ/kg)	2500	418	418

Table 3. Fuel grading used for the elevated vegetation modelling

Parameter	Value
Foliage	
Diameter	0.5mm
Length	50mm
Bulk density	2.0 kg/m3
Small round wood	
Diameter	1mm
Length	100mm
Bulk density	0.4kg/m3
Medium round wood	
Diameter	2mm
Length	100mm
Bulk density	0.3kg/m3
Large round wood	
Diameter	3mm
Length	100mm
Bulk density	0.5kg/m3

Understanding the processes involved in transition from surface to crown fires, and assessing fire risk in the wildland–urban interface (WUI) is very important. A basic building block of elevated fuel is a single tree. There are only fewer published data on thermo-physical properties of elevated vegetation when compared to grasslands. Among the few, the Douglas fir tree experiments reported by NIST laboratory provides valuable information on material properties that can be used for numerical modelling. During the current work the information published in the NIST experiment (Mell et al. 2009) is taken as the basis for defining the fuel properties. In FDS, Lagrangian particles can be used to represent vegetation as sub grid scale objects in the analysis. A "simplified" Arrhenius degradation model is used to model the pyrolysis of the tree vegetation. The solid fuel is assumed to be comprised of 87.7% vegetation and 12.3% moisture. The incident heat flux first evaporates the moisture component of the fuel and then during the pyrolysis process, reaction produces 74% pyrolysate and 26% of solid residue char. The pyrolysate ($C_{3.4}H_{6.2}O_{2.5}$) starts the combustion process when sufficiently mixed with free oxygen in the atmosphere and produces CO2, CO, H_2O and soot. Table 2 summarizes the thermo-physical parameters of each constituent used in the analysis. Fuel present in Douglas fir trees can be graded in to different length scales and these are modeled by modifying the properties of the fuel particles. Table 3 summarizes the geometric properties of four types of fuel gradings which constitute a tree: small, medium and large round wood in the modeled as small cylinders.

4.3 *Atmospheric conditions*

4.3.1 *Domain BCs*

The inlet of the domain is simulated with an atmospheric wind profile. The right and left-hand sides of the domain are simulated as periodic boundary conditions while other boundaries except the ground, which is a no slip surface, are kept open at a constant pressure. As a result the simulated domain becomes just one segment of an infinite number of identical segments (Linn et al. 2012).

At the inflow boundary for the duration of the simulation, the dependence of the ambient wind with height above the ground, z, is defined to follow a power law (Figure 3). At the same time magnitude of the cross-wind velocity is assumed to remains zero.

$$u = u_0 \left(\frac{z}{z_0}\right)^p \quad (1)$$

A typical atmospheric wind profile can be represented of the form equation 1. It should be noted that z_0 is not at the ground, rather some height where the reference wind speed u_0 is measured, like an elevated weather station. It is assumed that the ground is located at $z = 0$ (McGrattan et al. 2013)

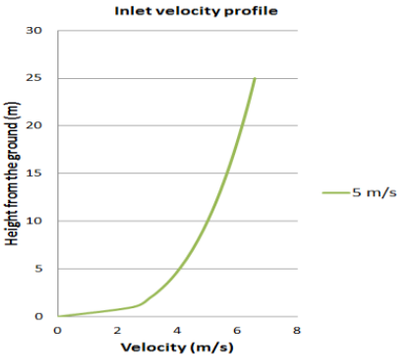


Figure 3:Inlet wind velocity profile, 5m/s, measured at 10m from the ground

4.4 *Adiabatic Surface Temperature (AST)*

Adiabatic surface temperature is a practical tool to express the thermal exposure of a surface to fire. The concept of AST was introduced by Wickström et al. in 2007 (Wickström, Duthinh & McGrattan 2007). AST is the temperature of a hypothetical perfect insulator exposed to the same heating (fire) conditions as of the real surface and that can be used for transferring data from fire models to thermo-mechanical models. Utilizing the AST helps to reduce the data flow in to the structural models by eliminating the dependency of the surface temperature on the net heat flux.

5 HEAT TRANSFER ANALYSIS

Heat transfer mechanism from the fire zone to boundaries of the girder is mainly through convection and radiation, while conduction is the main mechanism for heat transmission within the bridge assembly. For thermal analysis, temperature dependent thermal properties for steel, namely conductivity, specific heat and thermal expansion, were provided as input into ABAQUS. These properties are defined according to the Euro code 2 and 3 (EN 1993, 2004).

The heat transfer analysis of the steel girder is carried out using 8-nodes quadratic heat transfer brick elements available in ABAQUS, DC3D8, (Systèmes 2013). This element is well suited for the discretization of the structural domain and subsequent three-dimensional, steady state or transient thermal analysis of the system.

5.1 *Material properties*

The thermal and mechanical properties of structural steel and concrete are assumed to vary with temperature in accordance with Eurocode 2 and 3 (EN 1993, 2004). A material constitutive model recommended by Eurocode 3 is used to represent elevated temperature steel stress strain behavior in the model validation step. The degradation of the yield strength and Young's modulus at the elevated temperature is also taken as per the Eurocodes.

5.2 *Heat transfer model validation*

The general thermo-mechanical analysis procedure used in the investigation was validated by applying the similar procedure to model a reliable experimental results produced by Wainman and Kirby (1988) on a composite steel beam exposed to an ISO 835 standard fire (Figure 4). To represent the condition inside the furnace, during the heat tranfer analysis, coefficient of thermal radiation of 0.7 and convective heat transfer coefficient of 25kW/m^2 are used in the analysis.

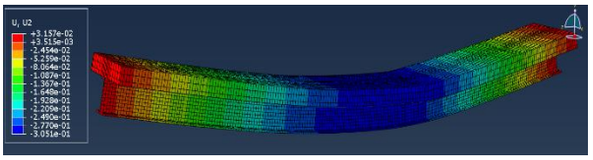


Figure 4: Vertical displacement response of the FE model of the composite steel beam

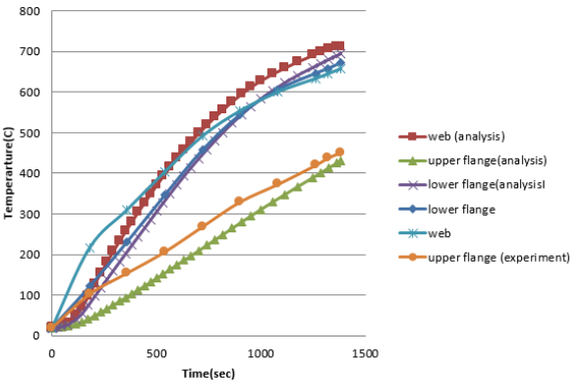


Figure 5.Temperature development of the selected points of the system, comparison of FE and test results.

Figure 5 and Figure 6 show the comparisons of predicted steel temperatures and the mid span deflection with that of measured in the fire test respectively. Measured temperature development of various location of the structural system and mid-span vertical deflection of the composite beam exposed to the ISO 834 fire are seen to be in close agreement with the FE predictions throughout the fire period. Overall, predicted temperature from the analysis is well comparable with measured data from the test.

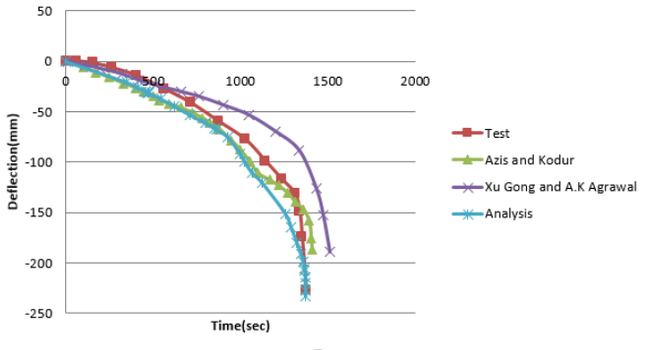


Figure 6. Mid span deflection response compared with experimental and other available numerical results in literature

6 RESULTS AND DISCUSSION

Model 1

Bridge structure is placed 32m away from the inlet boundary at the left-hand side. The grass strip starts 6m away from the away from the left side boundary. This allows the fire front to approach a quasi-steady heat release rate and rate of spread before reaching the bridge.

The wind velocity 10m above the ground is taken as 2m/s in this model, representing fairly mild conditions. Mesh size of the domain is maintained as a uniform 200mm spacing. As it was found that 250mm grid is sufficient to get grid-converged simulation (Moinuddin, KAM, Sutherland, D, Mell, W. 2017). The wind speeds used in the analysis is such that the fire-atmosphere interaction resulted a plume dominated fire. A predominantly vertical velocity field and a vertical flame and soot distribution can be seen in Figure 7 and Figure 8 respectively. The average fire spreading rate, estimated from visual representation of moving isosurfaces of HRR in Figure 9, is ≅ 0.3m/s within the entire domain.

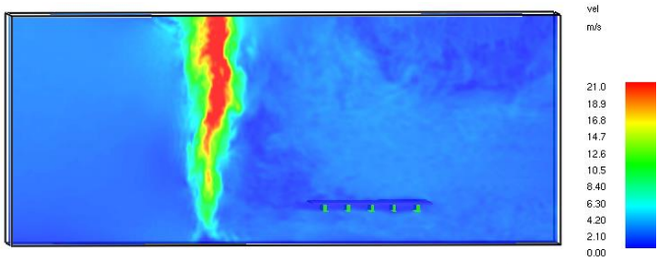


Figure 7. Wind velocity on the middle plane of the domain including the dominant fire plume.

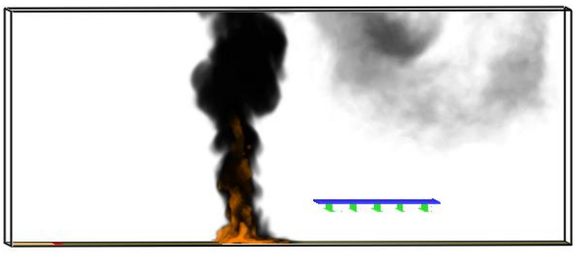


Figure 8.Fire plume and soot generation

After initializing the fire, the fireline intensity approaches a more or less a steady state value around 8000kW/m. Once the fire front enters under the bridge, initially plume dominated fire starts to bend as a result of the overhead physical obstruction. This increases the radiation energy transferred to the fuel bed in front of the fire front which in turn results an intensive burning and increased fireline intensity.

The adiabatic surface temperature of the structure was measured at the bottom surface of the concrete, mid height of the web and the flange bottom of each girder. A total of sixty-six AST measuring devices are used to monitor the bridge surface temperature. The average temperature development of each component is calculated using the results. Maximum AST reaches the value of 1200C (

Figure 10). Peak temperature resident time is very short and is about 30S.

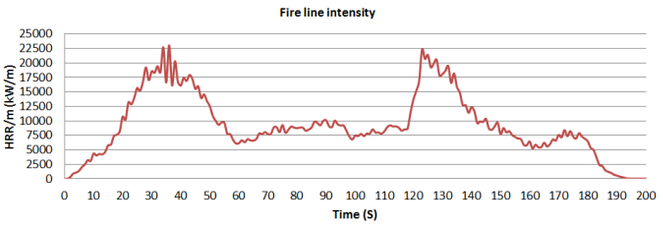


Figure 9. fireline intensity (hrr/unit length)

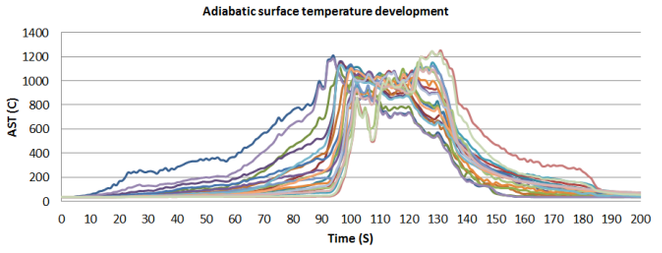


Figure 10. Adiabatic surface temperature development of the structure

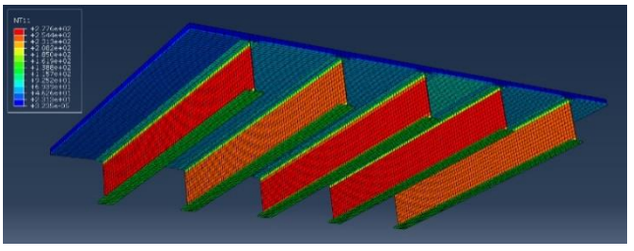


Figure 11. Temperature development of the heat transfer model in Abaqus FEM

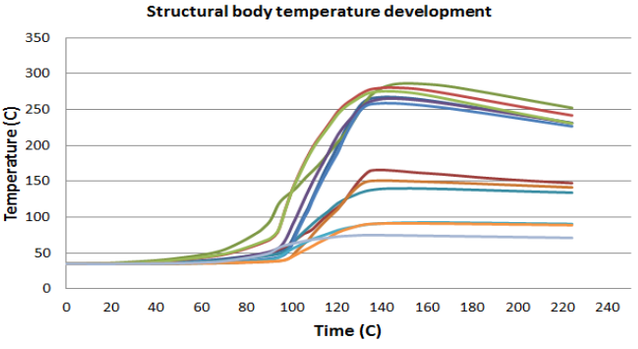


Figure 12. Body temperature development of the system

The temperature development of the structure can be grouped in to 3 categories. Relatively lesser thickness of the web results a highest temperature development that reaches around 300C. The bottom flange temperature development is around 150C. The concrete bottom surface temperature barely reaches 100C.

Model 2

In general, simulations of wild fires require models for both the fire-fuel interaction and the fire-atmosphere interaction. Second model is developed to understand the influence of wind speed on to the fire atmosphere and structure interaction. Cheney et al. (1993) has noted that the wind directly influencing fire spread is the net wind at the flame zone, not the wind measured remote from the fire. Wind speed of the model 1 is parametrically changed to achieve the model 2. The wind speed increased to 5m/s altered the fire-atmosphere interaction from a more plume dominated fire to a wind dominated (also known as boundary-layer mode) fire (Figure 13).

The higher wind forces both the flame and the hot fire plume closer to the downwind fuel bed (Figure 14), increasing both the radiative and convective heat fluxes. vapors at a rate dependent on the incident heat flux from the flame. The flame grows as the combustible vapors burn, which then creates a feedback mechanism for fire spread as the flame preheats additional unburned fuel ahead of the flame. As this process continues, the flame front progresses towards the unburned fuel. This is the process leading to a faster fire spread in stronger winds. For both wind speeds, radiation is the dominant heat transfer mechanism. The average rate of fire spread is increased to ≅ 0.6m/s. That in turn results a less residence time under the bridge even though the fireline intensity is increased (Figure 15) compared to the low wind speed case. As a result, even if the adiabatic surface temperature reaches to 1200C it results only lesser temperature development on the structure (Figure 16). The highest temperature 200C is recorded in the web of the structure. The concrete bottom surface temperature stays well below 100C (Figure 17).

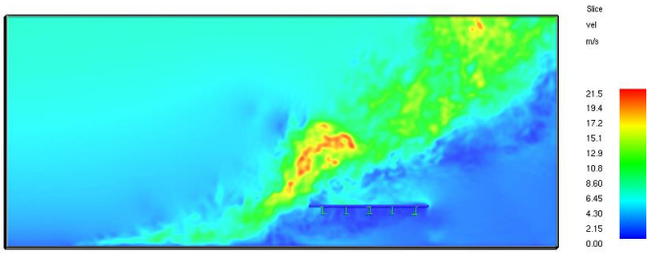


Figure 13. Velocity distribution of the domain (middle plane)

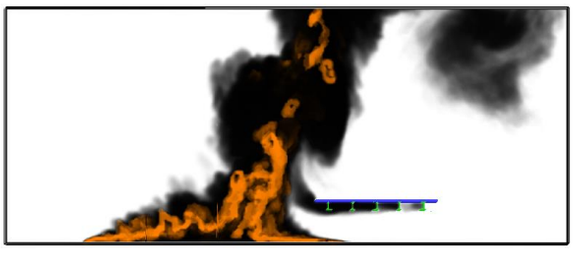


Figure 14. fire plume and soot generation

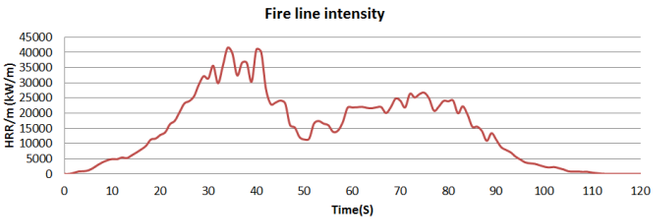


Figure 15. Fireline intensity (hrr/unit length)

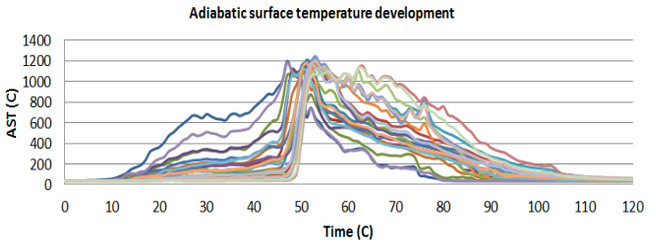


Figure 16. Adiabatic surface temperature development of the structure.

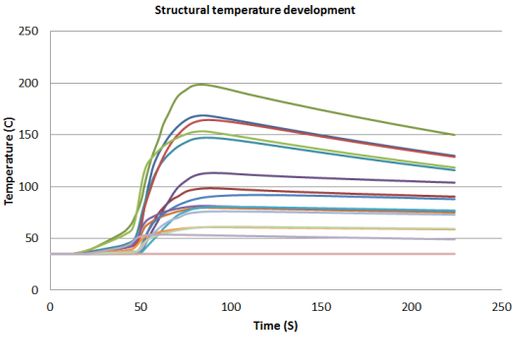


Figure 17. Body temperature development of the structure

Model 3

It has been identified that fires spreading in elevated vegetation are often more intense than fires spreading through surface vegetation such as grasslands(Mell et al. 2009; Miyanishi 2001). As a result, they are more difficult to suppress, produce higher heat fluxes and smoke. Such wildland fires can pose a serious threat to wildland–urban interface communities.

Model 3 is developed to understand the bridge-fire interaction where there is more elevated fuel load presents in the vicinity (Figure 18).

The domain size and the position of the structure is kept the same as the model 1 and 2. However the line of ignition was brought 11 m away from the bridge to reduce the computational cost. Five number of 4 m height and 2.0m diameter conical shape tress are introduced to the domain in two rows with 3 in front row. Wind is taken as 2m/s. Table 2 and Table 3 summarise the thermo-physical properties and the fuel gradings used to represent the elevated fuel.

The presence of more fuel in the vertical form has increased the fireline intensity from 8000kw/m to a maximum of 30000kW/m close to the bridge (Figure 20). Relatively low wind velocity give rise to a nearly vertical flame front (Figure 19). The average fire front progress rate is on average is the same as the Model 1(≅ 0.3m/s). The adiabatic surface temperature reached 1400C in some parts of the bridge (Figure 21). Introduction of the elevated vegetation along with the surface fuel increased the amount of fuel present around the structure. This has caused more than 50C temperature rise of the web when compared to Model 1.

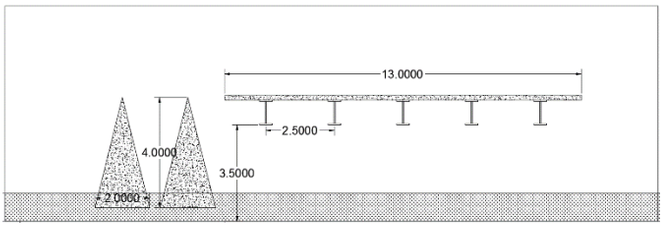


Figure 18. Distribution of surface and elevated vegetation fuel around the structure

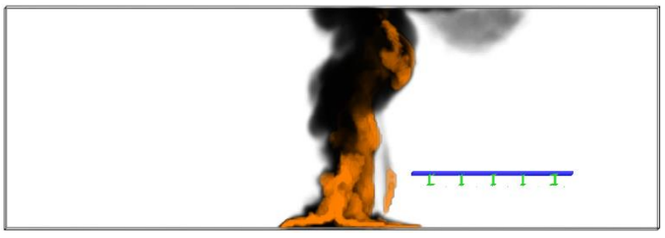


Figure 19. Fire plume and soot generation

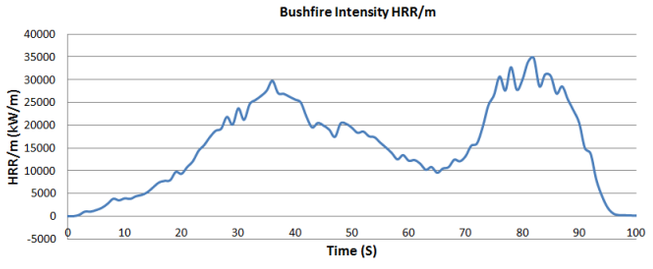


Figure 20. Fireline intensity (hrr/unit length)

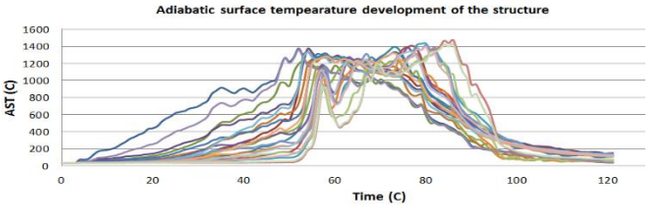


Figure 21. Adiabatic surface temperature development of the structure

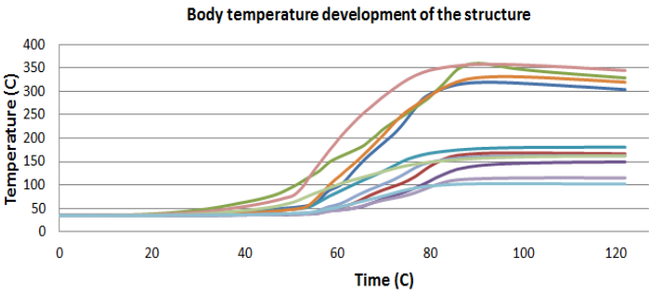


Figure 22. Body temperature development of the structure

7 CONCLUSION

Fire-structure interaction on a bridge located at a wildland urban interface is investigated in the form of three case studies. Temperature development of the various elements of the bridge system is taken as the primary output. The maximum temperature that is experienced by a structural element is used predict the degradation of the material strength parameters and possibility of the cracking of concrete.

Fireline intensity and the rate of spread are the most influential factors that affect the structural temperature development. Lower wind velocity in the domain tends to support a plume driven fire front with low intensity and slow progress. This type of fire tends to create higher temperature development of the structure due to the increased residence time of the flame front. In contrast, higher background wind velocity results a high intensity fires with a high rate of spread, however, such fires cause lower temperature development of the structure because of the lower residence time of the fire under the bridge. The presence of elevated fuel around the structure causes the highest temperature development (observed in these simulations) in the structure compared to the surface only fuel conditions.

Initial analysis results show the temperature developments of the structural components could not lead to a residual strength degradation of steel nor the cracking nor spalling of the concrete (Arioz 2007). This is mainly due to the less flame residence time that did not allow the temperature to build within the structure. However, the presence of elevated vegetation increases the risk significantly. The steel Young's modulus value decreased by 25% while the strength degradation of steel up to 400C is limited (BS 2005). Further parametric studies are needed to draw clear conclusions. Parametric studies are necessary to identify further critical fuel geometries around a bridge. These research results will in future help to predict the isolated and cumulative effects on a structure when exposed to recurrent WUI fire events.

Acknowledgement

The authors are grateful for the financial support received from the Australian government APA scholarship and the Bushfire and Natural Hazard CRC top up scholarship.

We thank the administrators of the Spartan HPC at the University of Melbourne for computing services and support.

REFERENCES

Arioz, O 2007, 'Effects of elevated temperatures on properties of concrete', *Fire Safety Journal*, vol. 42, no. 8, pp. 516-22.

Bartoli, P, Simeoni, A, Biteau, H, Torero, JL & Santoni, P-A 2011, 'Determination of the main parameters influencing forest fuel combustion dynamics', *Fire Safety Journal*, vol. 46, no. 1, pp. 27-33.

Beer, T 1993, 'The speed of a fire front and its dependence on wind-speed', *International Journal of Wildland Fire*, vol. 3, no. 4, pp. 193-202.

BS, E 2005, 'EN 1993-1-2 (2005) Eurocode 3: Design of steel structures - Part 1-2 :General rules- Structural fire design'.

Cheney, N, Gould, J & Catchpole, W 1993, 'The influence of fuel, weather and fire shape variables on fire-spread in grasslands', *International Journal of Wildland Fire*, vol. 3, no. 1, pp. 31-44.

Cruz, MG, Gould, JS, Alexander, ME, Sullivan, AL, McCaw, WL & Matthews, S 2015, *A guide to rate of fire spread models for Australian vegetation*, Australasian Fire and Emergency Service Authorities Council Limited and Commonwealth Scientific and Industrial Research Organisation.

Cruz, MG, Sullivan, AL, Leonard, R, Malkin, S, Matthews, S, Gould, JS, McCaw, WL & Alexander, ME 2014, 'Fire behaviour knowledge in Australia: a synthesis of disciplinary and stakeholder knowledge on fire spread prediction capability and application'.

EN, B 1993, *1-2: 2005,"Eurocode 3: Design of steel structures*, Part 1-2.

---- 2004, '1-2: 2004 Eurocode 2: Design of concrete structures-Part 1-2: General rules-Structural fire design', *European Standards, London*.

Evans, D, Rehm, R & McPherson, E 2003, 'Physics-based modelling of wildland–urban intermix fires', paper presented to Proceedings 3rd international wildland fire conference.

Flannigan, M, Cantin, AS, De Groot, WJ, Wotton, M, Newbery, A & Gowman, LM 2013, 'Global wildland fire season severity in the 21st century', *Forest Ecology and Management*, vol. 294, pp. 54-61.

Flannigan, M, Wotton, M & Marshall, G 2016, 'Climate Change and Wildland Fire Intensity', paper presented to AGU Fall Meeting Abstracts.

Johnson, A 2002, *North Australian Grassland Fuel Guide: Sturt Plateau & Victoria River District, NT*, Tropical Savannas CRC.

Linn, R, Canfield, J, Cunningham, P, Edminster, C, Dupuy, J-L & Pimont, F 2012, 'Using periodic line fires to gain a new perspective on multi-dimensional aspects of forward fire spread', *Agricultural and Forest Meteorology*, vol. 157, pp. 60-76.

Massada, AB, Radeloff, VC, Stewart, SI & Hawbaker, TJ 2009, 'Wildfire risk in the wildland–urban interface: a simulation study in northwestern Wisconsin', *Forest Ecology and Management*, vol. 258, no. 9, pp. 1990-9.

McGrattan, K, Hostikka, S, McDermott, R, Floyd, J, Weinschenk, C & Overholt, K 2013, 'Fire dynamics simulator user's guide', *NIST special publication*, vol. 1019, p. 6thEdition.

Melbourne, Uo 2017, *Spartan HPC-Cloud Hybrid: Delivering Performance and Flexibility*. https://doi.org/10.4225/49/58ead90dceaaa.

Mell, W, Jenkins, MA, Gould, J & Cheney, P 2007, 'A physics-based approach to modelling grassland fires', *International Journal of Wildland Fire*, vol. 16, no. 1, pp. 1-22.

Mell, W, Maranghides, A, McDermott, R & Manzello, SL 2009, 'Numerical simulation and experiments of burning douglas fir trees', *Combustion and Flame*, vol. 156, no. 10, pp. 2023-41.

Miyanishi, K 2001, *Forest Fires: Behavior and Ecological Effects*, Academic Press.

Moinuddin, KA, Al-Menhali, JS, Prasannan, K & Thomas, IR 2011, 'Rise in structural steel temperatures during ISO 9705 room fires', *Fire Safety Journal*, vol. 46, no. 8, pp. 480-96.

Moinuddin, KAM, Sutherland, D, Mell, W. 2017, 'Parametric Study of Grassfire using a Physics Based Model', *International Journal of Wildland Fire (submitted)*.

Morvan, D & Dupuy, J 2004, 'Modeling the propagation of a wildfire through a Mediterranean shrub using a multiphase formulation', *Combustion and Flame*, vol. 138, no. 3, pp. 199-210.

Noble, I, Gill, A & Bary, G 1980, 'McArthur's fire-danger meters expressed as equations', *Austral Ecology*, vol. 5, no. 2, pp. 201-3.

P.G Jarvis, GBJ, J.J. Lansberg 1976, *Vegetation and the atmosphere. Volume 2. Case studies : PP 172-240 (Chapter 7. Coniferous Frest)*, Academic Press.

Systèmes, D 2013, 'ABAQUS User's & Theory Manuals—Release 6.14'.

Total cost of bushfire, 2004, Australian Government of Criminalogy, <http://www.aic.gov.au/publications/current%20series/bfab/1-20/bfab002.html>.

Vicroads 2014, *Road structure inspection manual*.

Wainman, D & Kirby, B 1988, *Compendium of UK standard fire test data: Unprotected structural steel*, British Steel Corporation, Swinden Laboratories.

Wickström, U, Duthinh, D & McGrattan, KB 2007, 'Adiabatic surface temperature for calculating heat transfer to fire exposed structures', paper presented to Proceedings of the Eleventh International Interflam Conference. Interscience Communications, London.

Maintenance, Safety, Risk, Management and Life-Cycle Performance of Bridges – Powers, Frangopol, Al-Mahaidi & Caprani (Eds)
© 2018 Taylor & Francis Group, London, ISBN 978-1-138-73045-8

Joint irregularity in the seismic behavior of highway bridges

M.C. Gómez-Soberón, A. E. Gómez-Benítez & R. J. Aguirre-Eligio
Materials Department, Universidad Autónoma Metropolitana, Ciudad de México, México

ABSTRACT: Taking into account previous studies of bridges with irregularity in the superstructure or in the substructure, new models have been generated with irregularity in both systems. The group of studied bridges presented degrees of curvature between 0 and 180 °, each 30 °, and ratios of the extreme to the central span length of 1:0.25, 1:0.50, 1:0.75, 1:1.25, 1:1.50, 1:1.75 and 1:2.00. The irregularity, considering both systems, is analyzed by changing the length of an extreme or central pier in percentages of ± 0.25%, 0.50% and 0.75%. Models with joint irregularity have been analyzed elastically using a database of 53 accelerograms registered in the most seismic hazardous zone of Mexico. Dynamic analyses were developed to evaluate the maximum responses obtained with the elastic analyses, mainly in displacements or mechanical elements, grouped by statistical quartiles. The quartiles obtained with different irregular configurations only in the superstructure, were compared with those found for different irregular joint configurations. Recommendations were generated for bridges with joint irregularity.

1 INTRODUCTION

The superstructure of a bridge is considered irregular if it has curvature or if it is skewed; also if it presents changes of stiffness in elements in the spans. On the other hand, the irregularity of the substructure of a bridge is defined when there are variations in length, or differences in resistances or stiffness in their piers (Gómez & Salas, 2012).

During a bridge design process, its regular or irregular condition is generally determined to define the simplified method of analysis to use, which helps to model the structural behavior as close as possible to reality. The AASTHO (2012) regulation suggests unimodal, multimodal and step-by-step methods of analysis, depending on the importance and regularity of the structure and the seismic zone. In addition, it sets limit values such as ratios of curvature or stiffness between adjacent spans and between piers of the same bent or adjacent bents. This classification only considers to group bridges as regular and irregular. The recommendations of AASTHO (2010) emphasize that the maximum relationships can occur between the rigidities of the piers and girders. Simple and similar classifications are made in other design codes, such as Caltrans or Eurocode. Therefore, it is necessary to evaluate the influence of certain irregularity conditions in the seismic behavior of bridges, to propose recommendations for their analysis, design, inspection and maintenance.

Several studies have been developed concerning the analysis of the response of irregular bridges subjected to seismic load, with single irregularity, either in the superstructure or in the substructure. In recent studies about irregularity of the substructure (e.g. Tehrani & Mitchel, 2010; Isakovic & Fischinger, 2000 and Kappos *et al*., 2005), different irregularity conditions presented different influence on the seismic behavior of the bridges. In the case of columns with irregular substructures, there are significant variations in the demand of deformation of them, concentration of shear forces in short elements, variation of the demands of ductility and greater participation in higher modes, as Moehle & Eberhard (2000); Kappos *et al*. (2005) and Isakovic & Fischinger (2008). Experimental studies show that the energy absorbed by an irregular bridge is concentrated in the shorter piers (Tehrani & Mitchell, 2010). This cause, in some cases, systems with insufficient levels of security, as Calvi *et al*. demonstrated (Tehrani & Mitchell, 2010).

Nowadays, curved bridges are becoming more common, but they have a complex distribution of compressive and torsional stresses, which generates large demands on all their components. There are several studies that have analyzed the behavior of curved bridges, such as Seo & Linzell (2013), which

show that these structures are more susceptible to seismic load than straight bridges.

Gómez & Salas (2012) analyzed bridges with irregular substructure, while Gómez & Pérez (2013) studied bridges with irregularity in the superstructure. In these last two works, the analyses were based on the same type of viaduct regular bridge, with three or four spans and single piles per bent. This present work continues these previous studies, combining models with irregular superstructure with those with irregular substructure to form models with joint irregularity. This study intends to verify how much the vulnerability of structures with joint irregularity changes.

2 ANALYSIS MODELS

2.1 *Regular models*

The bridge model used to represent the regular structure is the same used by Gómez & Salas (2012) and Gómez & Pérez (2013). The structure has four or five spans of 50 m each, with three single piers by bent of 14 m high. The superstructure consists of an unicellular box section with a roadway of 14 m and a height of 2.3 m. The piers have a box section of 1.4 m by 4 m of external transverse dimensions. Figure 1 shows the general dimensions of the bridges and the transverse dimensions of girders and piers.

In the previous studies, different forms of connection between girders and piers were analyzed, but as these authors demonstrated (Gómez & Salas, 2012; Gómez & Pérez, 2013) for the obtained results there is no difference between one and the another option. Therefore, only continuous bridges are analyzed in this work, with a unique girder and releasing the longitudinal moment between girder and piers.

2.2 *Irregular bridge models*

Based on the model of Figure 1, irregularity models were constructed in the superstructure and substructure. The models with irregularities in the superstructure have curvatures between 0º and 180º, every 30º, or present changes in the relationship between the extreme span length with respect to the length of central span in ratios of 1:0.25; 1:0.50; 1:0.75; 1:1.25; 1:1.50; 1:1.75 and 1:2.00. The models with irregularity in the substructure have extreme or central piers with lengths of ±0.25, 0.50 and 0.75 the original length of the elements.

The models with joint irregularity were formed taking the models with irregularity in the superstructure and inserting the substructure conditions of irregularity. Figure 2 shows schemes of curved bridges, with changes in the length of the extreme spans and with changes in the length of a central pier (the change of the length of an extreme pier was also studied). Consequently, the models with joint irregularity are a combination of the models shown in Figure 2.

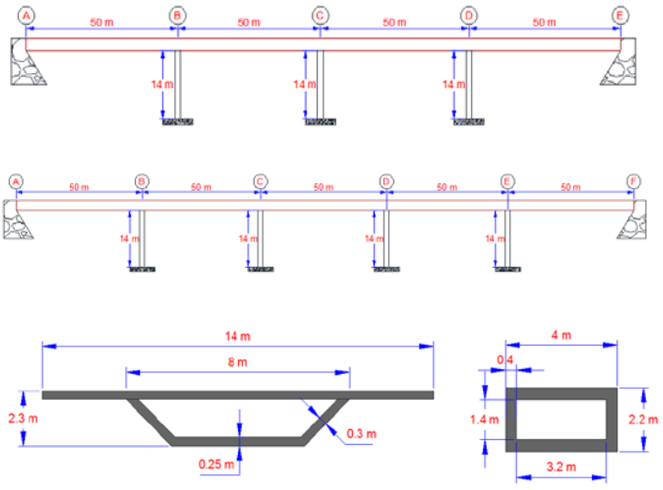


Figure 1. General regular bridge dimensions and elements transverse dimension.

3 SEISMIC LOAD

Regular and irregular structures were subjected to seismic load characteristic of one of the most hazardous seismic zone in Mexico (BMSF, 2000). For this, 53 three-component accelerograms were selected (although only the two horizontal components were applied), obtained in the Mexican States of Colima, Michoacán and Guerrero. The selection of accelerograms was based on the earthquake magnitudes or on the maximum soil displacements, velocities or accelerations.

Figure 3 shows the response spectrums for the greater horizontal component of the 53 accelerograms, considering 5% of critical damping. As it is observed in this figure, most of the records have peak spectral coordinate in periods lesser than 0.5 s, although the earthquake database has important diversity.

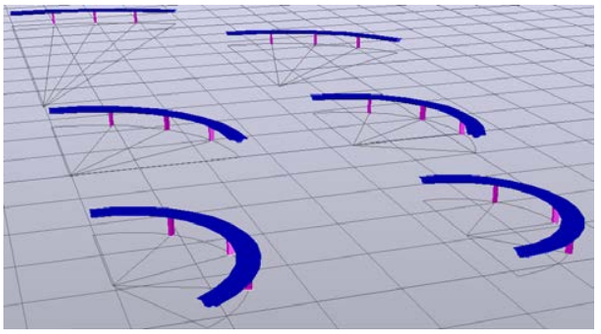
Greater horizontal component of the records is applied in the transverse direction of bridges, to produce the most unfavorable condition. The vertical component has not been considered; however some works show that it could be important for certain combinations of the dynamic properties of structure and soils, e.g. bridges located near the epicenter of an earthquake.

4 SUBSYSTEM ELASTIC RESPONSE

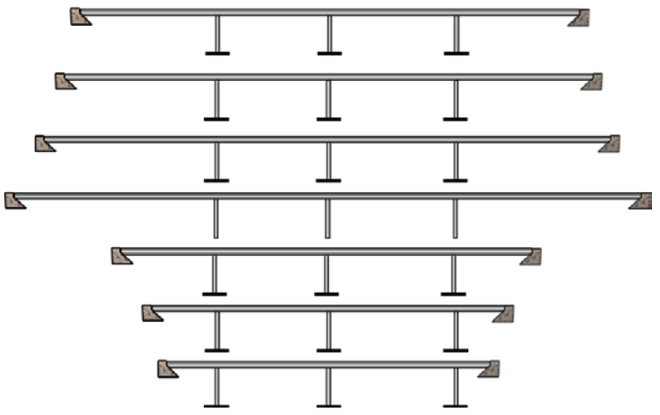
4.1 *Substructure irregularity*

The bridge models with superstructure or substructure irregular conditions were subjected to the 53 ac-

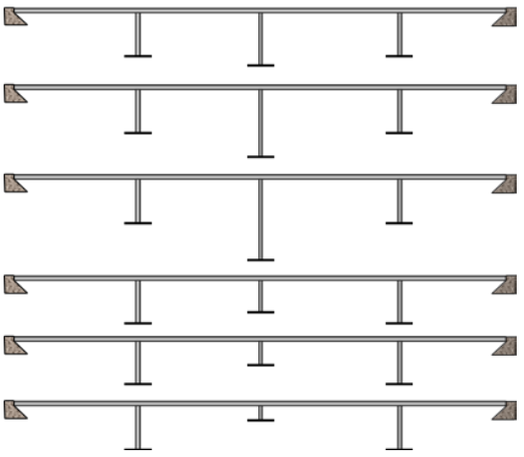
celerograms and elastic responses were captured, obtaining the maximum displacements and mechanical elements, although only the results of the maximum transverse displacements are discussed here, specifically in node C of Figure 1, in the structure elevation scheme.



a) Curved



b) Superstructure girder irregularity

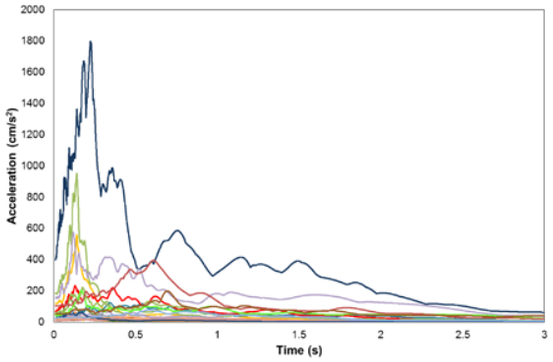


c) Substructure irregularity, central pier modification

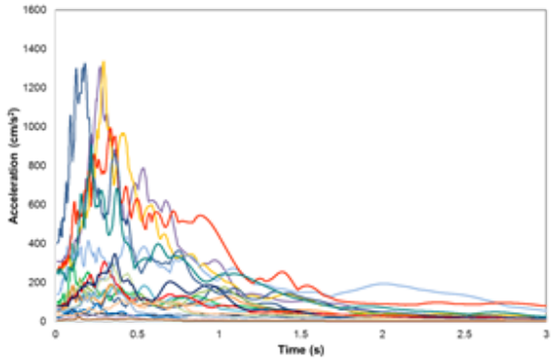
Figure 2. Schemes of bridges with single irregularity, in superstructure system (a and b) and substructure system

Elastic analyzes were performed with SAP 2000 program. In the studied models, the effect of soil-structure interaction was not considered, so the piers of the bridges are embedded in the base. In addition, elastic springs with transverse and rotational stiffness were used to simulate abutments and bearings.

Maximum displacements are used to define the normalized differences, between regular and irregular responses, as it is shown in equation 1. The normalized difference is organized from minor to the greater, in order to determine the statistical quartiles (25%, 50%, 75% and 100% of the values), with which the tendencies of variation for different irregular conditions of bridges are determined.



a) Colima and Guerrero states spectrums



b) Michoacán state spectrums

Figure 3. Elastic spectrums for the Colima and Guerrero (a) and Michoacan (b) states.

$$D_n = \frac{R_{IR} - R_R}{R_R} \quad (1)$$

where R_{IR} and R_R are irregular and regular responses, respectively.

For models with irregular substructure, the authors (Gómez & Salas, 2012) compared their dynamic properties, finding that the first two modal forms are similar, therefore it was defined that the changes in the responses were mainly associated with the irregularity variations themselves. Figure 4 shows the normalized differences of the maximum transverse displacements of the central node for the studied bridges, when the length of the central column is changed. In this figure, and in others of this work,

the horizontal axis represents the values of the normalized difference, indicating each line the changes for every substructure irregular condition; lines indicators represent each of the four quartiles. Figure 4 shows that the increase of the central column length produces more variation than the decrease of it. That is, the range of the normalized differences is greater when the length of the central pier is larger than that of the adjacent column, compared when this length is smaller. Thus, when the length of the central pier is less than 75% of the adjacent pier, the changes of the normalized differences are similar for all accelerograms; but when the length of the central pier is 75% larger than the adjacent pier, the normalized differences are greater.

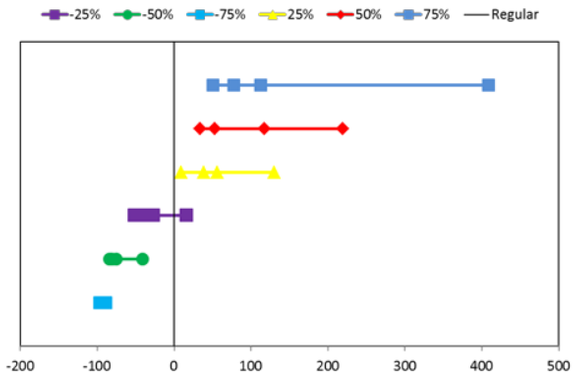


Figure 4. Normalized differences for bridges when the length of the central pier is changed.

Figure 5 shows the normalized differences in the maximum transverse displacements when the length of an extreme pier is changed. As it is observed, the trends are similar to those commented for Figure 4. However, when the central pier length is changed, more variations are recorded than when the length of the extreme pier is modified. For example, when the length of the central pier changes 75% (Figure 4), the normalized differences in the transverse displacement are similar to the values obtained from the normalized differences when the length of the extreme pier is changed only by 25% (Figure 5). From Figures 4 and 5 it is possible to conclude that a bridge is more vulnerable when the central pier has variation in its length, compared to structures that have piers close to the abutments, with the same variations.

4.2 *Superstructure irregularity*

The bridge models were subjected to the same seismic load and again the normalized differences of the transverse maximum displacements were obtained (Gómez & Pérez, 2013). Figure 6 shows the normalized differences organized by quartiles for the curved models. It is observed that, for greater change in the angle of curvature of the bridge, the results show greater dispersion up to 90º, and less dispersion for larger angles.

Figure 7 shows the normalized differences by quartiles for models where the length of the extreme span is changed. In this figure, it is observed that the greater the change in the length of the extreme piers, in relation to the length of the other spans, the greater dispersion in the normalized differences. Also, there is greater dispersion when the length is reduced than when it increases. Thus, it can be affirmed that bridges with extreme spans greater than the centrals, are more vulnerable.

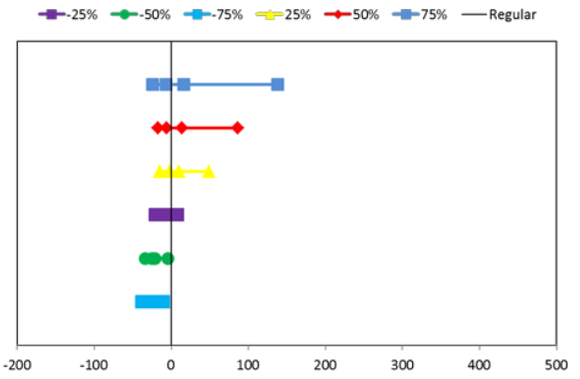


Figure 5. Normalized differences for bridges when the length of the extreme pier is changed.

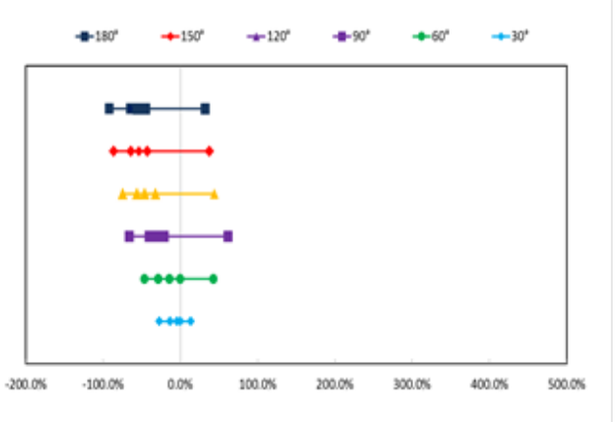


Figure 6. Normalized differences for curved bridges.

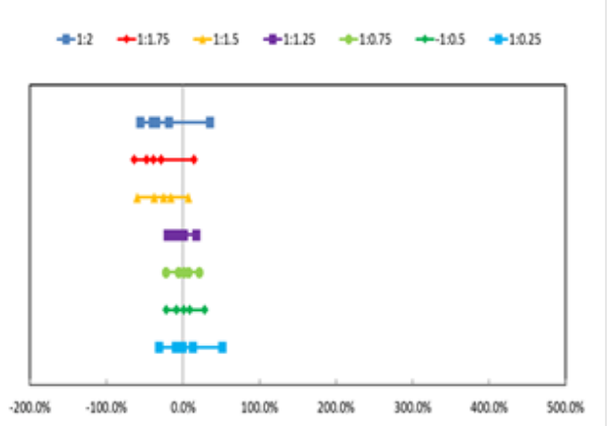


Figure 7. Normalized differences for bridge where the extreme span length is modified.

5 JOINT IRREGULARITY

For superstructure irregularity models were modified changing the lengths of the central pier and an extreme pier in percentages of ± 25%, 50% and 75%. In these models, elastic analyses were performed with the 53 accelerograms of Figure 3, and the normalized differences of the transverse maximum displacements were obtained with equation 1, they are also organized in quartiles. Figures 8 to 13 show the normalized differences of the maximum displacements of models with degrees of curvature of 30º, 60º, 90º, 120º, 150º and 180º, respectively, and with changes in the length of an extreme pier. For models with degrees of curvature of 120º or greater (Figures 11 to 13) minimal variation is observed when the irregularity of the substructure is included; while for bridges with lower degrees of curvature greater dispersions occur when the length of the extreme pier changes, especially for the case of bridges with a 30º curvature (Figure 8), which is the most common case of real curved bridges.

For bridges with changes in the length of the extreme spans and with changes in the length of the piers, the quartiles of the normalized differences were also determined. Figures 14 to 20 show the normalized bridge differences with changes in the ratio of the end-to-center span length from 1:2.0, 1:1.75, 1:1.50, 1:1.25, 1:0.75, 1:0.50 and 1:0.25, respectively. In these figures, and in the analyses where extreme pier is modified, it is observed that greater dispersions are generated in the models with joint irregularity when the length of the central pier is modified, compared to the dispersions obtained when the length of the extreme pier is modified. Also, greater dispersions occur when the length of the piers grows.

In general, a smaller length of the extreme spans, greater negative values of the normalized difference are obtained. So, the response of regular models is greater than that of irregular ones, although there is greater dispersion; and, therefore lower prediction and greater vulnerability. The variation of the fourth quartile is still not linear as it is assumed in many preliminary inspection methods and as it was found in models with irregularity only in one subsystem.

Comparing joint irregularity models with those with irregularity only in one subsystem, it is observed that in general there are greater dispersions in the first models, making the bridges with joint irregularity more no favorable and more vulnerable. When the length of the extreme pier is changed, this is less evident than when the length of the central pier is changed.

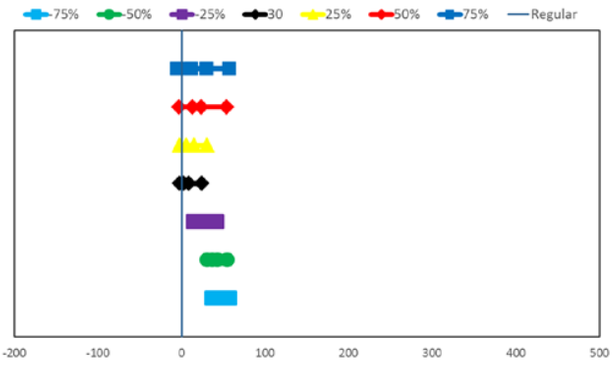


Figure 8. Normalized differences for 30° curved bridge where the central pier length is modified

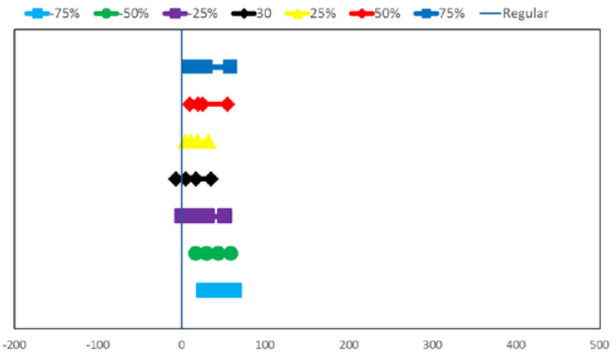


Figure 9. Normalized differences for 60° curved bridge where the central pier length is modified.

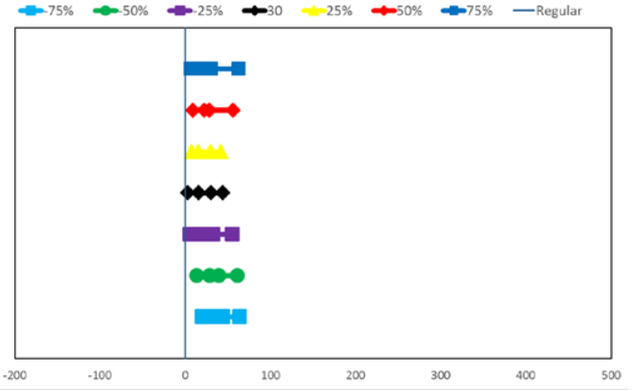


Figure 10. Normalized differences for 90° curved bridge where the central pier length is modified.

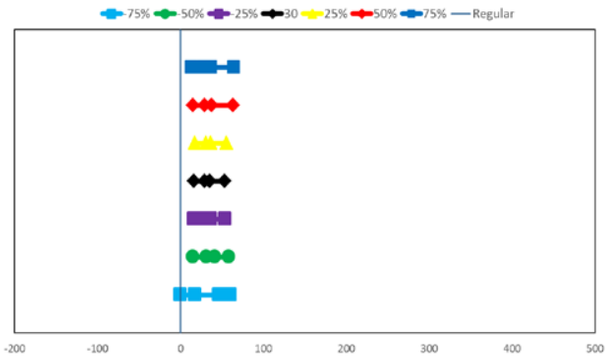


Figure 11. Normalized differences for 120° curved bridge where the central pier length is modified.

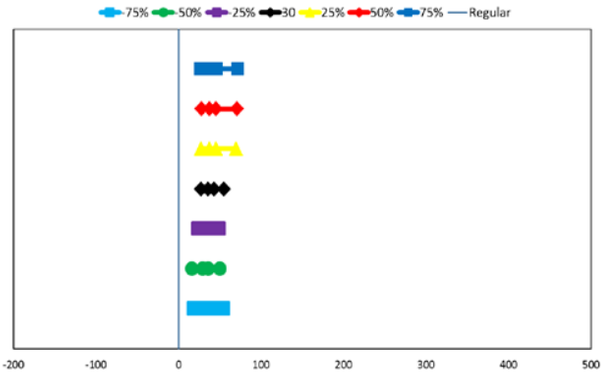


Figure 12. Normalized differences for 150° curved bridge where the central pier length is modified.

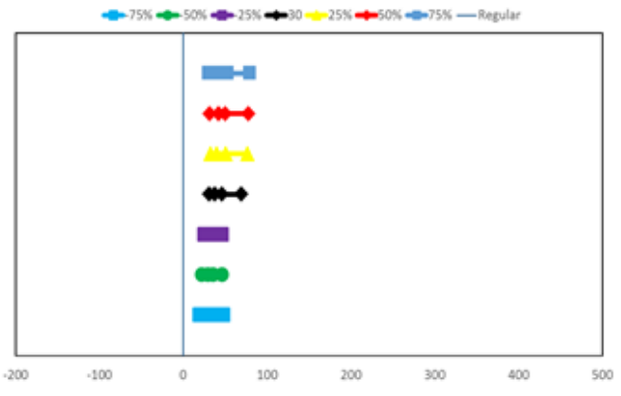


Figure 13. Normalized differences for bridge where the extreme span length is modified.

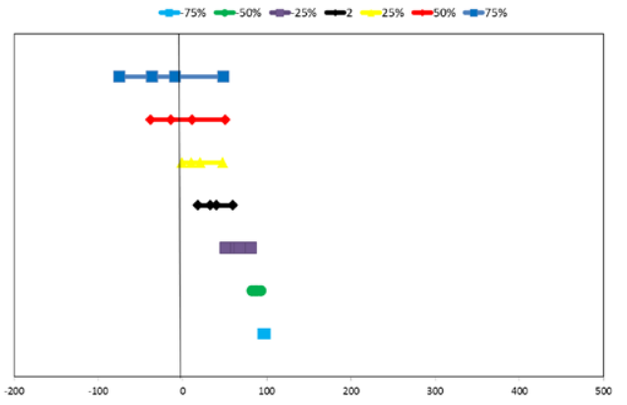


Figure 14. Normalized differences for bridge where the extreme span length is modified in relation 1:2.00 and change the central pier length.

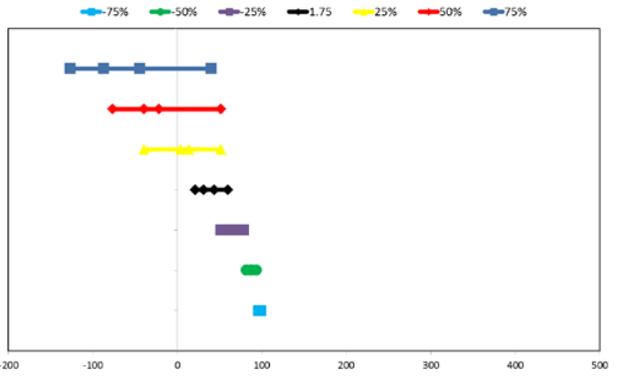


Figure 15. Normalized differences for bridge where the extreme span length is modified in relation 1:1.75 and change the central pier length

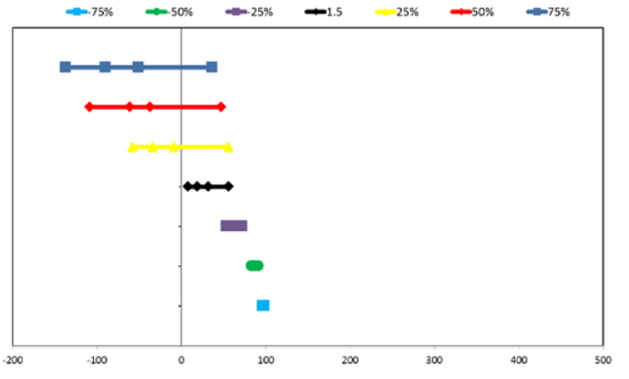


Figure 16. Normalized differences for bridge where the extreme span length is modified in relation 1:1.50 and change the central pier length.

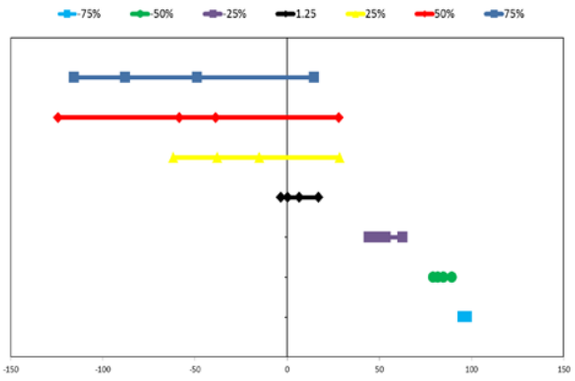


Figure 17. Normalized differences for bridge where the extreme span length is modified in relation 1:1.25 and change the central pier length.

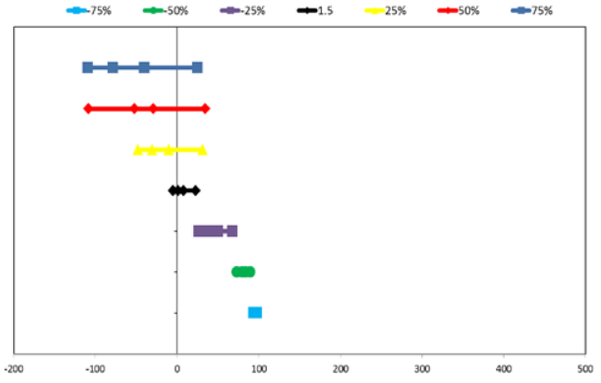


Figure 18. Normalized differences for bridge where the extreme span length is modified in relation 1:0.75 and change the central pier length

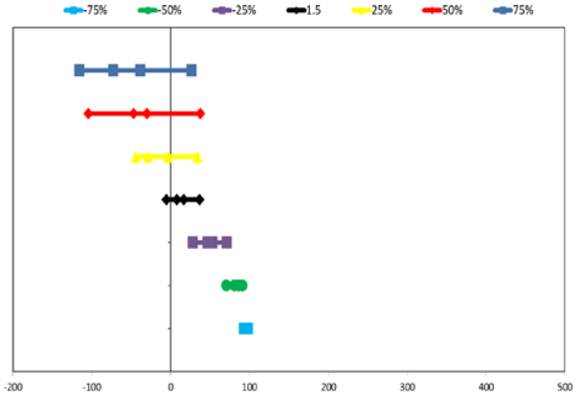


Figure 19. Normalized differences for bridge where the extreme span length is modified in relation 1:0.50 and change the central pier length

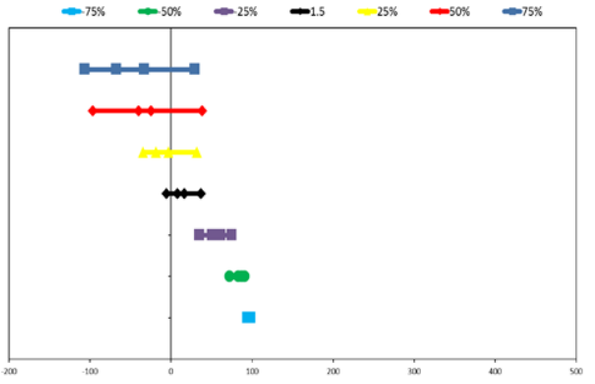


Figure 20. Normalized differences for bridge where the extreme span length is modified in relation 1:0.25 and change the central pier length

6 CONCLUSIONS

Although bridges have been studied with irregularity in their superstructure or substructure, parametric studies of bridges with joint irregularity have not been studied. That is the reason why this work analyzed bridges that show irregularity in both superstructure, considering curved systems (between 30º and 180º, every 30º) and with variation in the length of the extreme gaps (in ratios of 1:0.25, 1:0.50, 1:0.75, 1:1.25, 1:1.50, 1:1.75 and 1:2.00 with respect to the original length) and substructure, varying the length of some piers in percentages of ± 25%, 50% and 75%. For these models, elastic analyzes with a database of 53 earthquakes registered in the Mexican States of Colima, Michoacán and Guerrero were developed. From the results of analysis, the normalized differences between the responses of regular and irregular models, of the transverse maximum displacements are determined and grouped by quartiles to show trends of variation for each degree of irregularity.

From the results, it is observed that for curved bridges, the modification of the length of a pier generates greater dispersions if the structure has small angles of curvature, especially 30º. F or angles of curvature greater than 90º, no s ignificant variations are observed when the length of the piers is changed, compared when only the irregularity of the superstructure is considered.

For the models that have variations in the length of the extreme spans, in relation to the length of the central spans, when the length of one pier is modified (originally all equal), greater dispersions are generated. The ranges of the normalized differences are greater when the length of the central pier is changed than when this dimension varies in the extreme pier, as it occurs in the analysis of bridges

with irregularity only in the substructure. There is greater dispersion in the normalized differences as the length of the extreme span decreases, with respect to the initial length. In addition, there are greater dispersions when the length of the central pier is increased than when it is smaller than the original one. Not significant changes are observed when the length of the extreme piers changes.

As in the case of bridges with irregularity only in the substructure or only in the superstructure, in bridges with joint irregularity it is shown that the relation between the percentage of change of the length of piers and the variation of the normalized difference is not linear as it is assumed in all methods of preliminary inspection.

7 REFERENCES

AASTHO 2007. *AASTHIO LRFD Bridge Design Specifications*. American Association of State Highway and Transportation Officials.

AASTHO 2012. *AASTHO Guide Specifications for LRFD Seismic Bridge Design*. American Association of State Highway and Transportation Officials.

BMSF 2000. *Mexican Database of Strong Earthquakes*. Sociedad Mexicana de Ingeniería Sísmica.

Gómez-Soberón, C. & Salas, D. 2012. Parametric study of bridges with substructure irregular conditions, *IABMAS 6th Conference on Bridge Maintenance, Safety and Management*, Paper 1242.

Isakovic, T. & Fischinger, M. 2000. Regularity indices for bridge structures. *12th World Conference on Earthquake Engineering*. Paper 1725, Nueva Zelanda.

Isakovic, T. & Fischinger, M. 2008. Push-over analysis of two-span multicolumn bent RC bridge, experimentally tested on three shake tables. *Proceedings, 14th World Conference on Earthquake Engineering*, Paper 14_05_020106, Beijing, China.

Kappos, A. J., Parakeva, R. S. & Sextos, A. G. 2005. Modal pushover analysis as a means for the seismic assessment of bridges structures. *Proceedings, 4th European Workshop on seismic behavior of irregular and complex structures*, Paper 49, Greece.

Moehle, J. P. & Eberhard, M. O. 2000. *Bridge Engineering Handbook*. W. Chen & Duan L. (eds).

Gómez, C & Pérez, E.. 2013. Structural irregular effect on seismic bridge behavior. Paper ES363-794. Proceedings *International Conference on Earthquakes and Structures* (ICEAS13 ASEM13. Korea.

SAP-16 2010. *Integrated solutions for structural analyses and design*. Computers and structures , Inc.

Seo, J., Linzell, D. (2013). Use of response surface metamodels to generate system level fragilities for existing curved steel bridges. *Engineering Structures*, 52:642-653. http://dx.doi.org/10.1016/j.engstruct.2013.03.023.

Tehrani, P. & Michell, D. 2010. Seismic behavior and analysis of irregulares bridges with different column heights. *CEISCE, Seminar*, Quebec, Canada.

Maintenance, Safety, Risk, Management and Life-Cycle Performance of Bridges – Powers, Frangopol, Al-Mahaidi & Caprani (Eds)
© 2018 Taylor & Francis Group, London, ISBN 978-1-138-73045-8

Linking seismic resilience into sustainability assessment of limited-ductility RC bridges

A. Y. Al-Attraqchi, M. J. Hashemi, R. Al-Mahaidi & P. Rajeev
Department of Civil and Construction Engineering, Swinburne University of Technology, Melbourne, VIC 3122, Australia

ABSTRACT: Sustainability addresses the environmental, economic, and social impacts distributed over the life of a structure. However, in sustainability assessment of a structure, often ordinary events such as normal operation or maintenance actions due to ageing effects are considered and the resilience of the structure to devastating disasters that emphasizes on structural performance and recovery under extreme events is often ignored. Recent experience from natural and man-made hazards, however, highlights that extreme events, particularly earthquake, could affect with a large magnitude, the environmental, economic, and social aspects of our built environment. This study aims to systematically integrate the seismic-resilience into the sustainability assessment of a limited-ductility RC bridge. Sustainability metrics include repair cost, downtime, and environmental impacts and they are computed by consecutive hazard, structural response, damage, and loss analyses in accordance with the performance-based earthquake engineering (PBEE) methodology. Multi-axis substructure testing (MAST) system at Swinburne was used to realistically capture the three-dimensional response of the column, from elastic range to collapse. The data collected from the experiments were then used evaluate the damage-states of the column and quantify the associated seismic-repair sustainability metrics.

1 INTRODUCTION

1.1 *Sustainability*

Sustainability is defined as a set of economic, environmental and social conditions, in which all of society has the capacity and opportunity to maintain and improve its quality of life indefinitely, without degrading the quantity, quality or the availability of natural, economic and social resources (ASCE, 2013). Accordingly, sustainable development of structures aims to achieve a reasonable balance between the environmental, economic and social impacts distributed over the life-cycle of a structure (Willard, 2002). In sustainability studies, however, only the 'ordinary' events such as construction, normal operations, maintenance actions due to ageing effects and deconstruction are considered and the resilience of the structure that emphasizes on the impact of structural performance and recovery under 'extreme' events are often ignored (Bocchini et al., 2014). This could be due to the fact that ordinary events will certainly occur, while extreme events may be rare or never occur during the service life of a structure. However, worldwide experience from recent natural and man-made hazards, have shown that poor structural performance could lead to significantly high environmental, economic and social impacts, which highlights that the goals of sustainability cannot be achieved without considering the resilience of structures (Bocchini et al., 2014, Frangopol and Soliman, 2016, Rodriguez-Nikl, 2015, Asprone and Manfredi, 2015). Particularly, earthquake is a hazard with severe long-term consequences on civil structures that ranges from direct and indirect economic losses due to repair or reconstruction; to social effects such as disruption of structures functionality; and environmental impacts such as energy consumption and carbon dioxide emissions due to subsequent repair/replacement, among others (Gencturk et al., 2016, Hossain and Gencturk, 2014, Dong et al., 2013). Therefore, there is a need for a unified framework, in which structural resilience to extreme events, especially seismic hazard, is integrated into sustainability assessments.

This study aims to systematically integrate seismic-resilience into sustainability assessment of a reinforced concrete (RC) bridge. The quantification of sustainability metrics is applied only to the bridge piers, which is the focus of this paper. Sustainability metrics were computed by successive completion of the hazard, structural response, damage and loss analyses in accordance with the performance-based earthquake engineering (PBEE) methodology (Moehle and Deierlein, 2004). Performance of bridges is therefore integral to the evaluation of

transportation network performance under high intensity earthquake scenarios. Also, Multi-axis substructure testing (MAST) was used to realistically capture the three-dimensional response of the columns, from linear-elastic range to collapse. The data collected from the experiments were then used to probabilistically evaluate the damage-states of the column and quantify the associated seismic-repair sustainability metrics.

1.2 *PBEE framework*

The performance-based assessment framework established by the Pacific Earthquake Engineering Research Center (PEER) is used to assess the seismic vulnerability of the bridge structure. The framework performance assessment is divided into four analysis phases, which are seismic hazard analysis, response analysis, damage analysis, and loss analysis. The product of each analysis is then integrated using a total probability theorem.

The PBEE procedures require the prediction of the seismic capacity of structures which is then compared to the local seismic demand. It produces an interface of the expected level of damage for a given level of ground shaking. In order to estimate the structural response under seismic loads, Vamvatsikos and Cornell (2002) proposed a computational-based methodology called incremental dynamic analysis (IDA). The IDA method gives a clear relationship between the seismic capacity and demand. It involves performing nonlinear dynamic analyses of the structure under a suite of ground motion records, each is incrementally scaled to several intensity measure (IM) levels. The structure is pushed all the way from elastic to inelastic and to the final global dynamic instability (collapse). The IDA curves relate the seismological intensity measures (IM), such as peak ground acceleration (PGA) to the response quantities in terms of the engineering demand parameters (EDP), such as the maximum deflection or drift of the structure. Another common method used is the multiple strip analysis (MSA) method (Jalayer and Cornell, 2009), which is used to quantify the distribution of the structural response, EDP, over a range of earthquake shaking intensities, IM. The final results are quantitatively modelled and then integrated into a probabilistic risk analysis procedure in a suitable format to be integrated with a seismic hazard curve in order to calculate mean annual frequency of exceeding a certain capacity damage limit-state.

1.3 *Multi-Axis Substructure Testing*

Multi-Axis Substructure Testing system in the Smart Structures Laboratory at Swinburne provides a powerful tool for investigating the effects of earthquakes, hurricanes, and other extreme loading events on large structural components using hybrid simulation testing (Hashemi et al., 2015). A sophisticated 6-DOF control system is used utilizing eight high-capacity hydraulic actuators that enable application of complex multi-directional deformation or loading schemes to structural components. The system can be used for performing quasi-static test or hybrid simulations.

Evolved from pseudo-dynamic testing (Nakashima, 2001, Mahin and Shing, 1985), hybrid simulation is a versatile and economically viable experimental technique to evaluate the dynamic performance of large civil structures (Nakashima et al., 1992). According to a report developed by the US earthquake engineering community in 2010, hybrid simulation capabilities are a major emphasis of the next generation of earthquake engineering research (Dyke et al., 2010).

The bridge model is calibrated based on experimental multi-axis results of a limited ductility reinforced concrete column that was tested under cyclic quasi-static procedure.

2 PBEE METHODOLOGY

2.1 *Quantification of seismic hazard*

The first step of the performance-assessment framework is to quantify the seismic hazard at the site. This is usually done using the probabilistic seismic hazard analysis (PSHA), which was first proposed by Cornell (1968). The method considers the earthquake sources, the distance to the fault, uncertainties in earthquake size, location and ground motion intensity and using a total probability theorem to quantify the probabilistically distribution of the shaking intensity of the site. By using the results of the PSHA, ground motions can be selected to represent the seismic hazard at the site. However, in this study, PSHA has not been performed, instead a suite of 44 (two records from 22 earthquakes) ground motions were chosen based on the ATC63 project by FEMA (FEMA, 2009). The selected ground motions originate from severe seismic events of ranging in magnitude between 6.5 and 7.6 and closest distance to the fault rupture larger than 10km. Thus, only strike–slip and reverse sources are considered. Table 1. lists the details of the ground motions.

Table 1. List of ground motion details

ID	Name	Recording station	Year	M	PGA_{dir-1} (g)	PGA_{dir-2} (g)
12011	Northridge	Beverly Hills - Mulhol	1994	6.7	0.416	0.516
12012	Northridge	Canyon Country-WLC	1994	6.7	0.410	0.482
12041	Duzce, Turkey	Bolu	1999	7.1	0.728	0.822
12052	Hector Mine	Hector	1999	7.1	0.266	0.337
12061	Imperial Valley	Delta	1979	6.5	0.238	0.351
12062	Imperial Valley	El Centro Array #11	1979	6.5	0.364	0.380
12071	Kobe, Japan	Nishi-Akashi	1995	6.9	0.509	0.503
12072	Kobe, Japan	Shin-Osaka	1995	6.9	0.243	0.212
12081	Kocaeli, Turkey	Duzce	1999	7.5	0.312	0.358
12082	Kocaeli, Turkey	Arcelik	1999	7.5	0.219	0.150
12091	Landers	Yermo Fire Station	1992	7.3	0.245	0.152
12092	Landers	Coolwater	1992	7.3	0.283	0.417
12101	Loma Prieta	Capitola	1989	6.9	0.529	0.443
12102	Loma Prieta	Gilroy Array #3	1989	6.9	0.555	0.367
12111	Manjil, Iran	Abbar	1990	7.4	0.515	0.496
12121	Superstition Hills	El Centro Imp. Co.	1987	6.5	0.358	0.258
12122	Superstition Hills	Poe Road (temp)	1987	6.5	0.446	0.300
12132	Cape Mendocino	Rio Dell Overpass	1992	7.0	0.385	0.549
12141	Chi-Chi, Taiwan	CHY101	1999	7.6	0.353	0.440
12142	Chi-Chi, Taiwan	TCU045	1999	7.6	0.474	0.512
12151	San Fernando	LA - Hollywood Stor	1971	6.6	0.210	0.174
12171	Friuli, Italy	Tolmezzo	1976	6.5	0.351	0.315

2.2 *Response analysis*

Nonlinear dynamic response analysis is used to quantify statistical distribution of the structural response for different ground motions at increasing intensities. Incremental dynamic analysis (IDA) and multiple stripe analysis (MSA) are used for studying the structural response. The maximum drift value at each intensity measure is recorded to generate the IDA plots. By employing MSA, the mean of the lognormal drift values and the lognormal standard deviation are calculated at each stripe. These discrete data points are then fitted by a power-law model as shown in Eq. 1a and 1b.

$$\mu_{EDP|IM} = a(IM)^b \quad (1a)$$

$$\beta_{\ln EDP|IM} = c(IM)^d \quad (1a)$$

where $\mu_{EDP|IM}$ is the mean of the EDP and $\beta_{lnEDP|IM}$ is the lognormal standard deviation.

Multi-Axis Substructure Testing system was previously used as an advanced testing technique for studying the behaviors of a reinforced concrete column under quasi-static testing (Hashemi et al., 2017). The experimental results validate the collapse behavior of the columns in the numerical model.

2.3 *Damage states*

Damage states (DS) are defined based on the damage levels corresponding to the repairs necessary to bring the facility back to original state. They could be based on the structural or non-structural components damages due to the engineering demand parameter. Components are combined into performance groups that are affected in a similar manner by the EDP. In this study, only one performance group is used that corresponds to the damage of the columns. A sufficient number of damage states should be defined for each group to describe the range of possible damages at different levels of structural response.

The damage threshold limit states are obtained from the pushover curve as recommended by (Gencturk, 2011). In this study, the three limit states are the initial yielding drift, the drift corresponding to ultimate strength, and the collapse drift point. Further, uncertainties in the capacity to account for modelling errors and variation in material properties of these limit states are approximated by applying a 0.35 lognormal standard deviation to each limit state (Gencturk, 2011). The probability of being in a damage state given EDP is calculated from the limit states fragility curves based on Eq. 2. Next, the probability of being in a damage state given IM is calculated on Eq. 3.

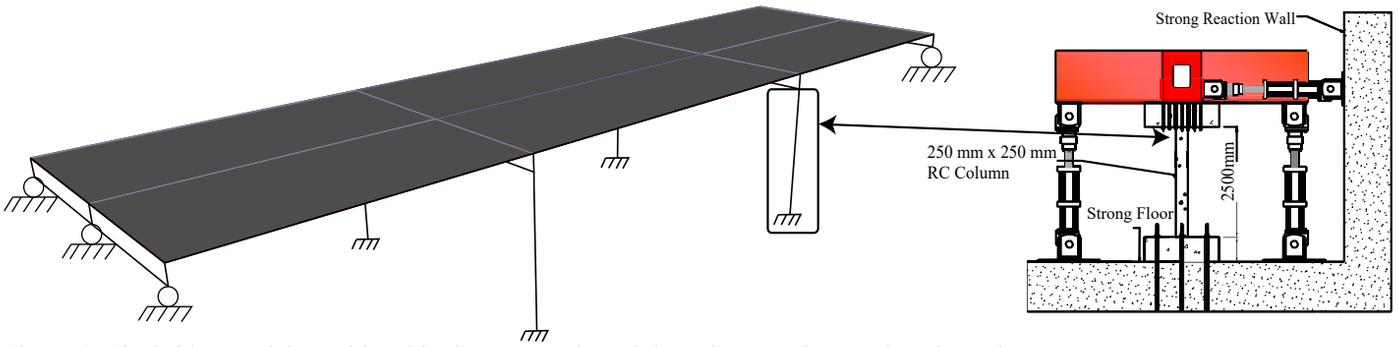


Figure 1. The bridge model considered in the case study and the column under quasi static testing.

$$P_{DS_i|EDP} = \left\{ \begin{array}{c} 1 - F_{DS_1}(EDP) \\ F_{DS_i}(EDP) - F_{DS_{i+1}}(EDP) \\ F_{DS_n}(EDP) \end{array} \right\} \text{for } 2 \le i < n \quad (2)$$

where F_{DS} is the fragility curve of exceeding EDP of a damage state, $P_{DS|EDP}$ is the probability of being in a certain damage state given EDP, and n is the number of the damage states.

$$P_{DS|IM} = \int_0^\infty P_{DS|EDP} f_{EDP|IM} \, dEDP \quad (3)$$

where $P_{DS|IM}$ is the probability of being in a certain damage state given IM, and $f_{EDP|IM}$ is the probability density function of EDP given IM, which is computed based on the IDA curves.

2.4 *Loss analysis*

The decision variable (DV) is the final step of the PBEE methodology. In this study, it is used to represent the economic, social, or environmental variables. There are many ways of expressing the losses as discussed in detail in (Moehle and Deierlein, 2004), in this paper the losses are defined as a constant value. A decision variable is defined for each damage state and the variable value given IM is based on Eq. 4.

$$\mu_{L_R|IM,NC} = \sum_{DS} \int_0^\infty \mu_{L_R|DS} P_{DS|EDP} f_{EDP|IM} \, dEDP \quad (4)$$

where $\mu_{LR|DS}$ is the mean loss DV corresponding to the DS and $\mu_{LR|IM,NC}$ is the mean of repair losses given IM and conditioned on no collapse.

A common approach is to split the equation into collapse case and non-collapse cases. By assuming mutually exclusive and collectively exhaustive events of collapse and no collapse, the mean of total seismic losses of the structure conditioned on the seismic intensity measure IM is described by Eq. (5).

$$\mu_{L_T|IM} = \mu_{L_{NC}|IM,NC}(1 - P_{C|IM}) - \mu_{L_C|C} P_{C|IM} \quad (5)$$

where $\mu_{LNC,IM}$ is the is the mean loss DV given IM for the non-collapse damage states, $\mu_{LC|C}$ is the mean collapse loss given collapse (note that the collapse loss is independent from IM), $P_{C|IM}$ is the collapse probability given IM.

The loss assessment converts the DSs to their consequent DVs. In this paper, four DVs are used, including the repair cost (related to economic aspect), downtime (related to social aspect), energy consumption and carbon dioxide emissions (related to environmental aspect).

3 BRIDGE CASE STUDY

3.1 *Model*

This bridge has three spans that are 10, 15 and 10 m long, for a total structure length of 35 m. It has integral bents with two columns per bent having a clear height of 5 m. The bridge is chosen to represent an average typical three-span bridge. The finite element model is developed using OpenSees (McKenna, 2011). The superstructure components are aggregated into one deck component and they are modeled as elastic elements. The bents are modeled using displacement based elements.

The columns were modelled using beam-with-hinges elements, of which the nonlinear behavior is assumed to occur within a finite length at both ends based on distributed plasticity. The plasticity model follows a peak-ordinated hysteresis response based on the Modified Ibarra-Medina-Krawinkler (IMK) (Ibarra et al., 2005) deterioration model of flexural behavior. The columns are calibrated based on previous quasi-static cyclic experimental results on a half scale specimen (Hashemi et al., 2017). The test was conducted by applying a constant axial load equal to 8% of the column's ultimate load carrying capacity, followed by imposing bidirectional lateral deformation reversals in displacement control that follows the hexagonal orbital pattern suggested in

FEMA 461 (Agency, 2007). This plasticity model was chosen because it is capable of capturing the important modes of deterioration that participate in side-sway collapse of RC structures. Explicit modelling of beam-column joints and bar-slip effects are not included since they are considered not necessary for performing collapse modelling of RC frames, according to FEMA-P695 (FEMA, 2009).

There are several methods for modelling the abutments. The first is just by modelling them as rollers, which is acceptable for multiple bridge spans since the effect of the abutments is minimum. In this paper, rollers are used to focus on the columns behavior as they resist the lateral forces. Other methods include considering the abutment-soil interaction and modelling it as a combination of linear springs based on material parameters recommended by Caltrans seismic design criteria guidelines (Caltrans, 2013).

3.2 *Results and discussion*

Dynamic time history inelastic analyses were carried out for the 44 selected earthquake records using OpenSees (McKenna, 2011). Prior to performing the IDA, pushover and cyclic analyses were conducted to check the static capacity of the structure and to determine the damage limit states, Figure. 2 shows the pushover and cyclic curves for a single column. The damage states were defined based on drift values corresponding to the yield point of the pushover curve, the pushover ultimate strength value, which are 1.0%,2.5%, respectively. As for collapse, it was defined based on the drift value corresponding to 5% drop in strength of the first cycle envelope, which corresponds to a drift of 5.0%. The two damage states are summarized in Table 2.

Table 2. Definition of damage states and the repair activities

States	Drift	Description	Repair Activity
DS0, no damage	< 1.0%	No/slight damage due to hairline cracks	No repair
DS1, NC	> 1.0% < 2.5%	Small flexural cracks Longitudinal rebar yielding	Epoxy injection to open cracks Repair/replacement of damaged cover concrete
DS2, NC	> 2.5%	Longitudinal rebar buckling Longitudinal rebar fracture Crushing of core concrete	Concrete removal and placement Epoxy injection of any cracks wider than 0.3mm Reinstatement of damaged concrete with a suitable repair mortar Wrapping of the column with CFRP

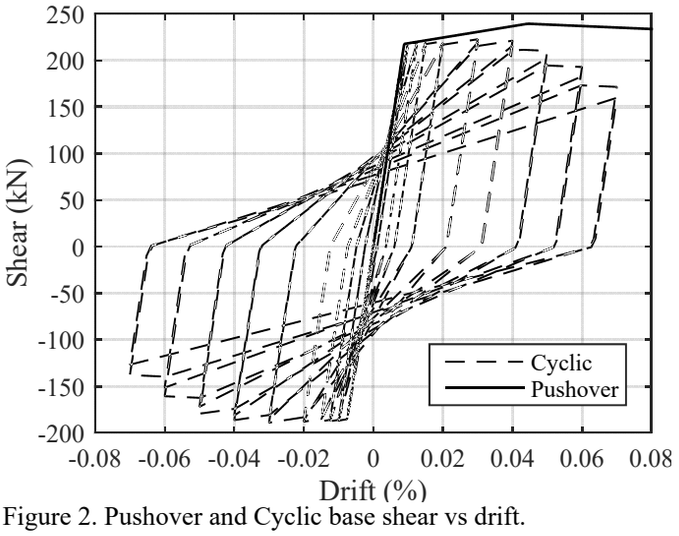


Figure 2. Pushover and Cyclic base shear vs drift.

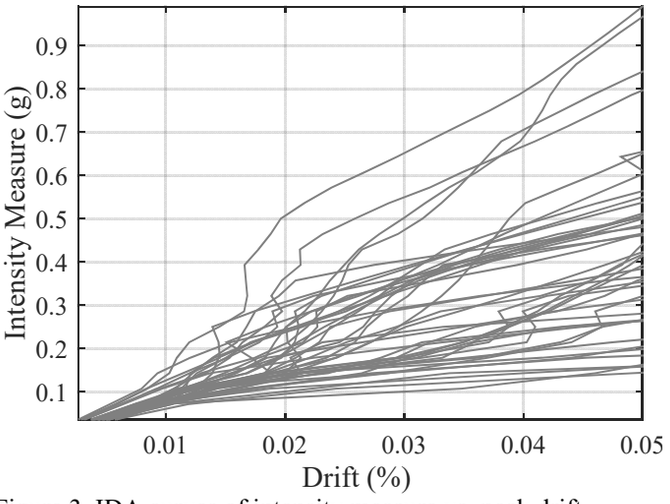


Figure 3. IDA curves of intensity measure vs. peak drift.

The data obtained from the IDA computations generate the IDA curves, as shown in Figure. 3. The IDA data are first processed from the beginning to the IM level where 50% (22 ground motions) of the data points are still available. Then, the median and standard deviations are fitted to generate a continuum of fragilities over the whole range of IM. Also, the global collapse probability is calculated from the IDA plots based on the 5% drift criteria, as shown in Figure 4. The area under the plot is collapse and area above the plot is no collapse. Fragility curves for damage states are shown in Figure 5. To illustrate the information contained in the fragility curves, consider the following example. If the drift value equals 2%, the conditional probability that a column is considered to have experienced minor damage or worse is 97.5%, to have a major damage or worse is 25.7%. Therefore, by the mathematics of set theory the probability of being in DS0 (no damage), DS1, and DS2 is 2.5%, 71.8% and 25.7%, respectively, as explained in Eq. 2.

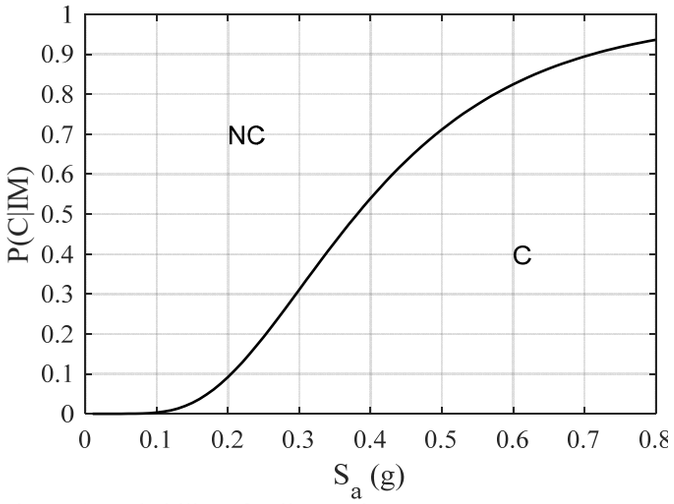


Figure 4. Probability of collapse given IM.

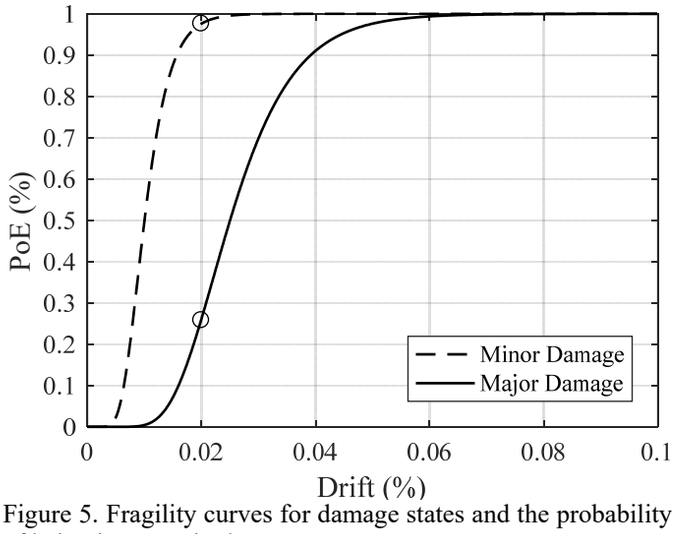


Figure 5. Fragility curves for damage states and the probability of being in a certain damage state.

By using Eq. 3, the probability of exceeding a damage state given the intensity measure was computed and it was used for the calculations of the loss decision variables in the next stage.

Finally, the expected losses for the structural repairs of the four decision variables for each damage state are summarized in Table 3. The mean structural repairs are based on the probability of exceeding the corresponding damage states (DS1 and DS2) given IM conditioned on no collapse.

Figure 6 shows the expected economic loses conditioned on seismic intensity. Economic viability is usually the main factor which governs the choice of repair type, as cost is usually the main driving force in any project. In order to quantify the cost of each repair activity, cost estimates were assumed, however ideally, they should be based on real estimates if available. The use of FRP for repair and rehabilitation of earthquake-damage structures can be considered as a cost-effective and time-saving alternative to replacement. It has been demonstrated that CFRP repairs can be used to rehabilitate an earthquake damaged RC column and return it to its initial collapse resistance capacity (Hashemi et al., 2016).

Figure 7 shows the expected social loses conditioned on seismic intensity. Social impacts deal with the consequences of the seismic repairs on the bridge functionality. The seismic repairs may cause disruption to public and reduced bridge capacity. Therefore, the repair downtime was considered as the social impact. Downtime is defined as the period between the occurrence of a seismic event and the completion of repair efforts and resuming operation. The repair downtime has two components, namely, the 'repair time', which is the time needed for the repair process and the 'mobilization time', which is defined as the time lag between the seismic event and the beginning of repair process. Unlike the repair, mobilization time could vary as it depends on activities such as inspection, damage assessment, consultations with professional engineers, financing, etc. (Mitrani-Reiser, 2007).

For the case study column in DS_2, the mobilization of one week was expected for site inspection, non-destructive testing, ordering materials, etc. Also, it was estimated that one day should be sufficient to complete the repair of the column. For the collapse state, a mobilization time of 30 days was allowed for the planning of reconstruction, which included: site inspection, preparation of a design and rectification procedure, engaging a contractor, ordering materials, etc. Similarly, the downtime for the other DSs was quantified as shown in Table 3.

Environmental impact assessment evaluates the repair activities in terms of the inflow (resource consumption) and outflow (hazardous effects of emissions) that influences the eco-system and human health. In this study the energy consumption and carbon dioxide (CO_2) emissions were considered as the input-output flow of the seismic repair in terms of the environmental impacts.

The energy consumption associated in the production and fabrication of repair materials such as repair mortar, FRP and epoxy is referred to as the material embodied energy in MJ/kg and are presented in Table 3 for the various materials used in the repair, based on data from Mara et al. (2014).

The total carbon emissions in $kgCO_2/kg$ for the respective materials used in this study are presented in Table 3 based on Mara et al. (2014). Figure 8 and Figure 9 show the environmental losses due to energy consumption and carbon emissions, respectively, conditioned on the seismic intensity.

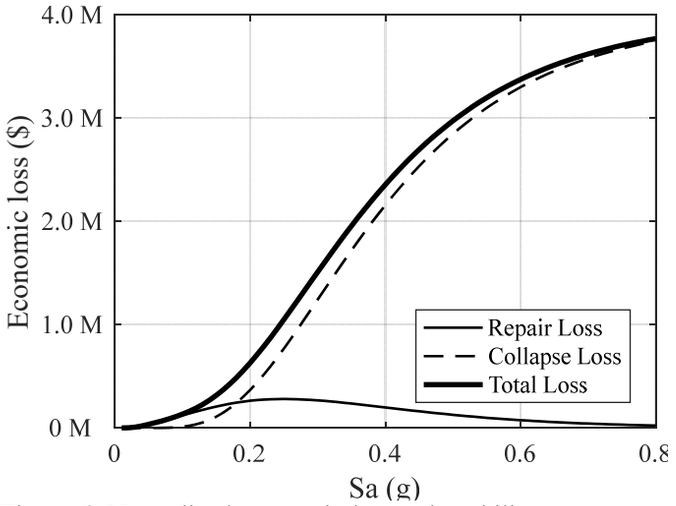


Figure 6. Normalized economic loss vulnerability curves conditioned on seismic intensity.

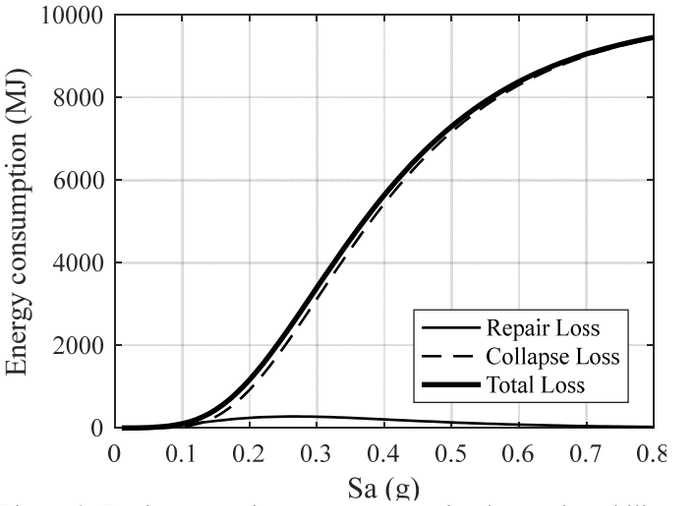


Figure 8. Environmental energy consumption loss vulnerability curves conditioned on seismic intensity.

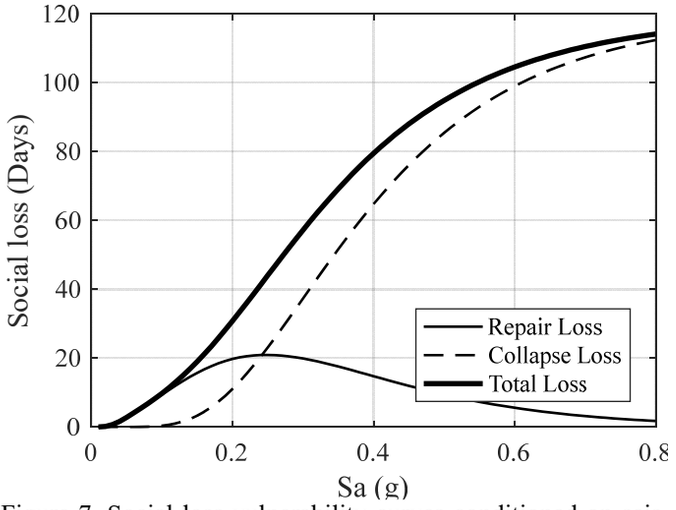


Figure 7. Social loss vulnerability curves conditioned on seismic intensity.

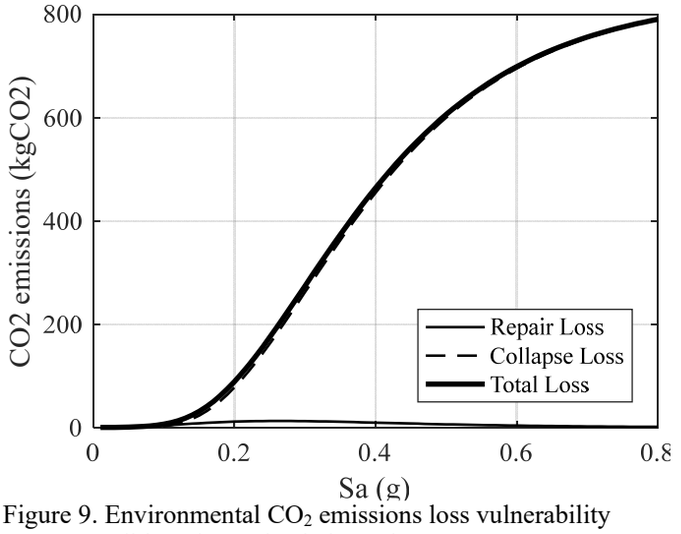


Figure 9. Environmental CO_2 emissions loss vulnerability curves conditioned on seismic intensity.

Table 3. Risk -based sustainability assessment of seismic repair

Damage States	**Economical**		**Social**		**Environmental**	
	Repair	Cost ($)	Repair Downtime		Energy consumption of repair materials (MJ)	CO_2 emissions of repair materials ($kgCO_2$)
			Repair Time (days)	Mobilization Time (days)		
DS_0		0	0	0	0.0	0.0
DS_1	Epoxy	100,000	1	7	19.2	1.8
DS_2	Concrete Epoxy CFRP	500,000	7	30	537.4	23.8
Collapse	Reconstruction	4,000,000	90	30	10067.8	842.7

4 CONCLUSION

A unified framework for sustainability assessment of structures is presented. This framework adopted the PBEE methodology to incorporate seismic-resilience into life-cycle sustainability assessment for RC bridges. Three out of the PBEE modules are presented, namely, structural response analysis, damage assessment, and loss assessment due to economic, social, and environmental factors. It is possible to incorporate the sustainability assessment in the design procedures to anticipate the cost, environmental and social impacts in the use phase of the structure so that it can be reduced by adopting a more resilient design. This can reinforce the necessity of incorporating structural damage and loss assessment in sustainability quantification procedure for seismic regions.

ACKNOWLEDGEMENTS

The first author would like to gratefully acknowledge the Australian Government for granting him the Research Training Program Scholarship (RTPS). The authors would like to acknowledge the support of Prof. John Wilson and the contribution of PhD students Scott Menegon and Yassamin Al-Ogaidi and the personnel of the Smart Structures Laboratory at Swinburne University of Technology.

REFERENCES

AGENCY, F. E. M. (2007) Interim Testing Protocols for Determining the Seismic Performance Characteristics of Structural and Nonstructural Components. Federal Emergency Management Agency Washington, DC.

ASCE (2013) Policy Statement 418 - The Role of the Civil Engineer in Sustainable Development. The American Society of Civil Engineers (ASCE).

ASPRONE, D. & MANFREDI, G. (2015) Linking disaster resilience and urban sustainability: a glocal approach for future cities. *Disasters,* 39**,** S96-S111.

BOCCHINI, P., FRANGOPOL, D. M., UMMENHOFER, T. & ZINKE, T. (2014) Resilience and Sustainability of Civil Infrastructure: Toward a Unified Approach. *Journal of Infrastructure Systems,* 20.

CALTRANS (2013) Seismic design criteria version 1.7. Sacramento, CA.

CORNELL, C. A. (1968) Engineering seismic risk analysis. *Bulletin of the seismological society of America,* 58**,** 1583-1606.

DONG, Y., FRANGOPOL, D. M. & SAYDAM, D. (2013) Time-variant sustainability assessment of seismically vulnerable bridges subjected to multiple hazards. *Earthquake Engineering & Structural Dynamics,* 42**,** 1451-1467.

DYKE, S., STOJADINOVIC, B., ARDUINO, P., GARLOCK, M., LUCO, N., RAMIREZ, J. & YIM, S. (2010) 2020 vision for earthquake engineering research: Report on an openspace technology workshop on the future of earthquake engineering.

FEMA, P. (2009) 695. Quantification of Building Seismic Performance Factors. *Federal Emergency Management Agency*.

FRANGOPOL, D. M. & SOLIMAN, M. (2016) Life-cycle of structural systems: recent achievements and future directions. *Structure and Infrastructure Engineering,* 12**,** 1-20.

GENCTURK, B., HOSSAIN, K. & LAHOURPOUR, S. (2016) Life cycle sustainability assessment of RC buildings in seismic regions. *Engineering Structures,* 110**,** 347-362.

GENCTURK, B. E. (2011) *Multi-objective optimal seismic design of buildings using advanced engineering materials*, University of Illinois at Urbana-Champaign.

HASHEMI, M., TSANG, H., AL-OGAIDI, Y., WILSON, J. & AL-MAHAIDI, R. (2017) Collapse Assessment of Reinforced Concrete Building Columns through Multi-Axis Hybrid Simulation. *ACI Structural Journal,* 114**,** 437.

HASHEMI, M. J., AL-MAHAIDI, R., KALFAT, R. & BURNETT, G. (2015) Development and validation of multi-axis substructure testing system for full-scale experiments. *Australian Journal of Structural Engineering,* 16**,** 302-315.

HASHEMI, M. J., AL-OGAIDI, Y., AL-MAHAIDI, R., KALFAT, R., TSANG, H.-H. & WILSON, J. L. (2016) Application of Hybrid Simulation for Collapse Assessment of Post-Earthquake CFRP-Repaired RC Columns. *Journal of Structural Engineering,* 143**,** 04016149.

HOSSAIN, K. & GENCTURK, B. (2014) Life-Cycle Environmental Impact Assessment of Reinforced Concrete Buildings Subjected to Natural Hazards. *Journal of Architectural Engineering***,** A4014001.

IBARRA, L. F., MEDINA, R. A. & KRAWINKLER, H. (2005) Hysteretic models that incorporate strength and stiffness deterioration. *Earthquake engineering & structural dynamics,* 34**,** 1489-1511.

JALAYER, F. & CORNELL, C. (2009) Alternative non-linear demand estimation methods for probability-based seismic assessments. *Earthquake Engineering & Structural Dynamics,* 38**,** 951-972.

MAHIN, S. A. & SHING, P.-S. B. (1985) Pseudodynamic method for seismic testing. *Journal of Structural Engineering,* 111**,** 1482-1503.

MARA, V., HAGHANI, R. & HARRYSON, P. (2014) Bridge decks of fibre reinforced polymer (FRP): a sustainable solution. *Construction and Building Materials,* 50**,** 190-199.

MCKENNA, F. (2011) OpenSees: a framework for earthquake engineering simulation. *Computing in Science & Engineering,* 13**,** 58-66.

MITRANI-REISER, J. (2007) An ounce of prevention: probabilistic loss estimation for performance-based earthquake engineering. California Institute of Technology, Pasadena, California, U.S.

MOEHLE, J. & DEIERLEIN, G. G. (2004) A framework methodology for performance-based earthquake engineering. *13th world conference on earthquake engineering.* Vancouver, British Columbia, Canada.

NAKASHIMA, M. (2001) Development, potential, and limitations of real–time online (pseudo–dynamic) testing. *Philosophical Transactions of the Royal Society of London A: Mathematical, Physical and Engineering Sciences,* 359**,** 1851-1867.

NAKASHIMA, M., KATO, H. & TAKAOKA, E. (1992) Development of real-time pseudo dynamic testing. *Earthquake Engineering & Structural Dynamics,* 21**,** 79-92.

RODRIGUEZ-NIKL, T. (2015) Linking disaster resilience and sustainability. *Civil Engineering and Environmental Systems,* 32**,** 157-169.

VAMVATSIKOS, D. & CORNELL, C. A. (2002) Incremental dynamic analysis. *Earthquake Engineering & Structural Dynamics,* 31**,** 491-514.

WILLARD, B. (2002) *The Sustainability Advantage,* Gabriola Island, British Columbia, Canada, New Society Publishers.

Maintenance, Safety, Risk, Management and Life-Cycle Performance of Bridges – Powers, Frangopol, Al-Mahaidi & Caprani (Eds)
© 2018 Taylor & Francis Group, London, ISBN 978-1-138-73045-8

Study on Impact Behavior of Piers Subjected to Vehicle Collisions

R. W. Li & D. Y. Zhou
Research Institute of Structural Engineering and Disaster Reduction College of Civil Engineering, Tongji University, Shanghai, China

ABSTRACT: Vehicle collision with reinforced concrete (RC) pier is one of the leading causes of viaduct failures. Therefore, impact behaviors of RC pier are of significant importance for viaducts safety. However, previous experimental impact studies were concentrated on impact behaviors of RC beam, few experimental studies on impact behaviors of RC pier was conducted. In this paper, a series of impact tests were conducted to study the reinforcement ratio and impact velocity effects on the impact behaviors. The impact test results showed that a high reinforcement ratio led to a high impact resistance that reducing the total displacement, residual displacement and energy absorption capacity, and a high impact velocity increased the total displacement, peak impact force and energy absorption capacity. Difference between the impact behaviors and the corresponding static behaviors was discussed, the results of which showed that the failure modes were both shear failure while the crack patterns were different.

1 INTRODUCTION

Reinforcement concrete (RC) piers have been widely used all over the world. These RC piers are under the threat of vehicle collisions, which makes bridges under high risk of collapse. A statistic investigation (Harik et al. 1990) showed that 15% of viaduct failures were caused by truck collisions in the period of 1951-1998. A similar study (Cook 2014) showed that 19.6% of viaduct failures were due to vehicle collisions over a 25-year period. These viaduct failures were mainly triggered by pier failure subjected to vehicle collisions. Because of high peak effect and short impact duration of impact loading, the pier failure induced by vehicle collision is distinguished from that by earthquake ground excitation. Therefore, much attention was directed to impact behaviors of the RC pier to ensure bridge safety in practice.

Most previous experimental studies on the RC pier were focused on their seismic performance, but only a few experimental studies on their impact behaviors were conducted. Many researchers conducted the traditional falling weight impact tests of RC beam to simulate the impact process of RC pier under vehicle collision. For example, studies carried out by Kulkarni & Shah (1999), Kishi et al. (2002) and Saatci & Vecchio (2009) reported the t the high strain rate effect on impact response of RC beams, the impact behavior of RC beams without stirrups and the shear mechanisms effect on impact behaviors of RC beams, respectively. Additionally, other researchers (Sukontasukkul & Mindess 2003, Cotsovos et al. 2008, Fujikake et al. 2009, Bhatti et al. 2009, Shakir et al. 2016) also conducted falling weight impact tests to study the impact behaviors of different beam. It is found that conclusions and finding obtained from these studies may not be directly used to RC piers since the failure modes and boundary conditions between these two structural members are different. Therefore, it is required to conduct horizontal impact tests on the RC pier to study its impact behaviors and failure mode, which is critical for establishment of design method for the RC pier under impact loading.

In this paper, a series of horizontal impact tests were carried out to investigate the impact behaviors and failure mode of RC piers. Moreover, the reinforcement ratio and the impact velocity effects on the impact behaviors were analyzed. Besides, post-impact damage of the RC pier and difference between impact test results and the corresponding static test results were also discussed.

2 TEST PROGRAM

2.1 *Test specimens*

Figure 1 showed the schematic view of five specimens, with four impact test specimens and a static one. All the tested specimens were 1500 mm in height with a rectangular cross section of 240 mm × 300 mm.

Table 1. Reinforcement and stirrup arrangement of each specimen

Test method	Specimen number	Reinforcement ratio (Diameter of reinforcement) mm	Stirrup ratio (Diameter of stirrup) mm
Static loading	BP-1	1.4% (8 D12)	5.6‰ (D6 @100)
Impact loading	BP-2	1.4% (8 D12)	5.6‰ (D6 @100)
	BP-3	3.1% (8 D18)	5.6‰ (D6 @100)
	BP-4	4.7% (8 D22)	5.6‰ (D6 @100)
	BP-5	1.4% (8 D12)	5.6‰ (D6 @100)

Cube compressive strength of concrete was 42 MPa. Three reinforcement ratios were employed as 1.4% (8D12), 3.1% (8D18) and 4.7% (8D22). Stirrup ratio was 5.6‰ (D6@100). The yield strengths of the rebars, i.e. D12, D18 and D6 were 484 MPa, 495 MPa and 519 MPa, respectively. The detailed information of rebars arrangement were illustrated in Figure 1.

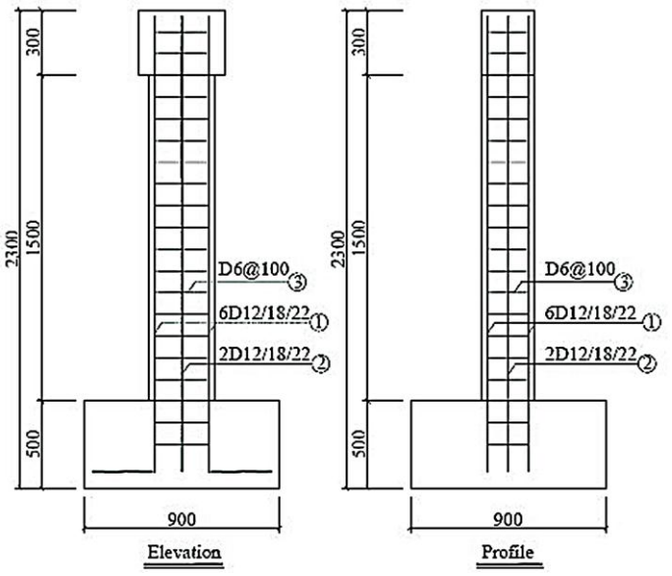


Figure 1. Schematic view of the tested specimens (unit: mm)

2.2 *Preparation of specimens*

For the static test, an MTS actuator was used to load specimen BP-1. Distance between the impact point and the bottom of specimen BP-1was set as 400 mm. The top of the specimen was designed to prevent the horizontal displacement and rotation, and the bottom was fixed on the floor. For the impact test, a simplified impact vehicle that was made of Chinese mild steel (Q235) with a mass of 1580 kg was used to load the specimens, which was shown in Figure 2. Velocity of the vehicle ranged from 0 m/s to 9 m/s. The impact point and boundary condition of each impacted specimen were the same as those of the static test.

Horizontal displacement at the impact point in the static test and the impact test were measured by displacement sensors. Contact force between the vehicle and the specimen in the impact test was measured by a dynamic load cell. The displacement at the impact point and impact force data were collected by a data acquisition system.

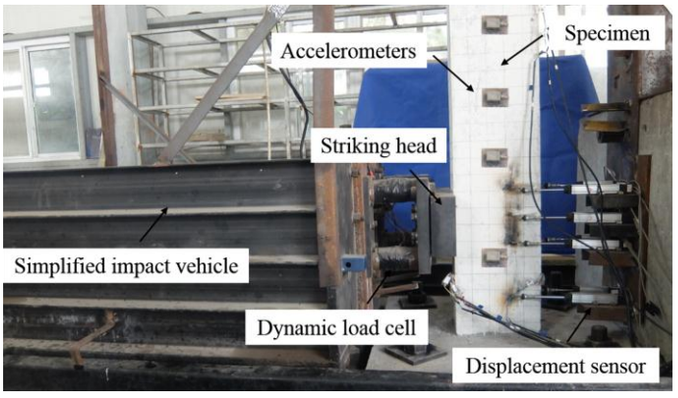


Figure 2. Schematic view of impact test

3 STATIC TEST RESULTS

3.1 *Failure mode*

Figure 3 showed that specimen BP-1 exhibited the shear failure with a principal diagonal shear crack. The principal diagonal shear crack initiated at the impact point and propagated downward with an angle of approximately 45 degrees. Moreover, it is found that several relative small diagonal cracks were respectively generated from the impact point downward and upward with angles ranging from 15 degrees and 45 degrees. Consequently, the final crack pattern of specimen BP-1 was ladder-shaped (see Figure 3).

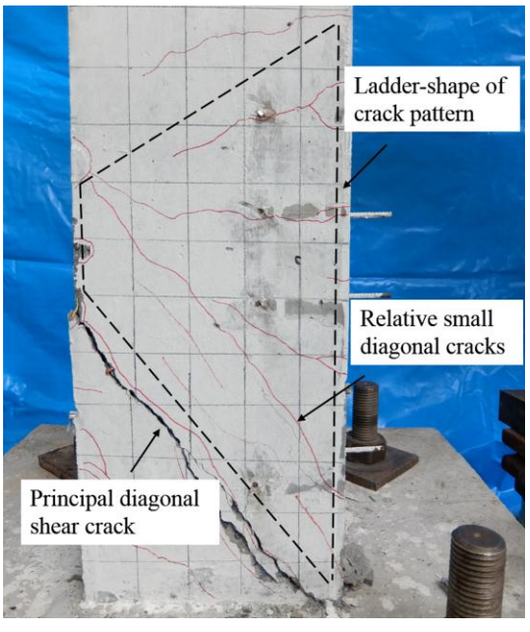


Figure 3. Failure mode of specimen BP-1

Table 2. Experimental results of the tested specimens

Test method	Specimen number	Impact velocity	Maximum force	Maximum displacement	Energy dissipation capacity	Failure mode
		m/s	kN	mm	kJ	
Static loading	BP-1	-	340	16.9	3.3	
Impact loading	BP-2	4.0	723	32.9	9.7	
	BP-3	4.0	703	25.9	8.9	Shear
	BP-4	4.0	705	21.3	7.8	
	BP-5	4.4	942	30.3	11.2	

3.2 *Load-displacement curve*

Figure 4 showed the load-displacement curve of the specimen BP-1 obtained from the static test. As illustrated in Figure 4, the maximum static force was 340 kN and the maximum horizontal static displacement at the impact point was 16.9 mm, and Both of which were listed in Table 2. Table 2 also presented the energy absorption capacity enveloped by the load-displacement curve of the static results, which was 3.3 kJ.

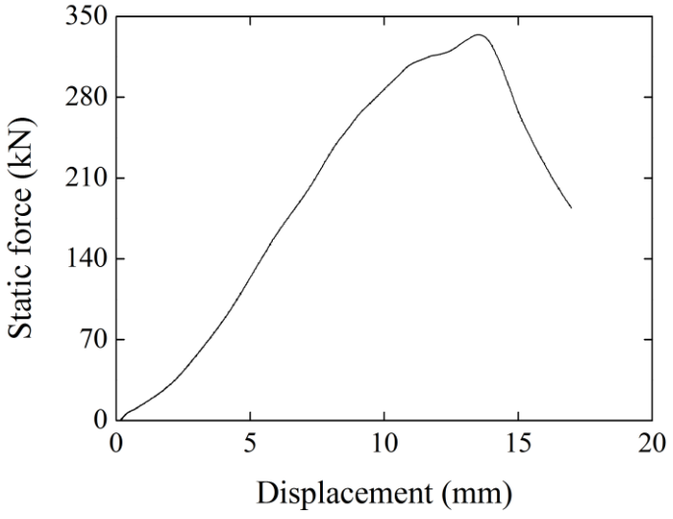
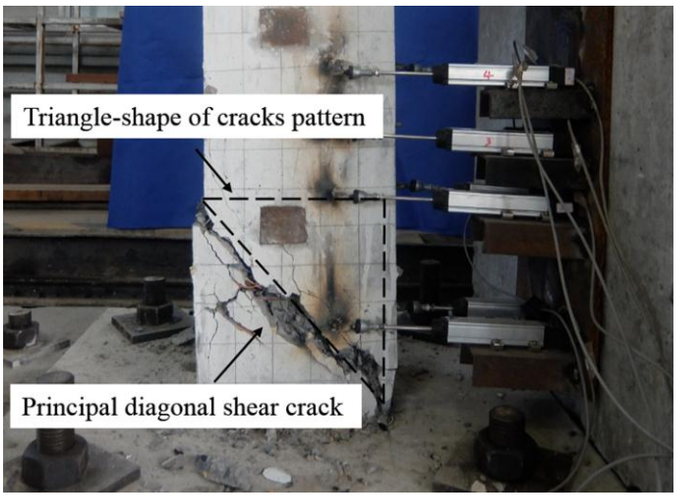


Figure 4. Load-displacement curve of specimen BP-1

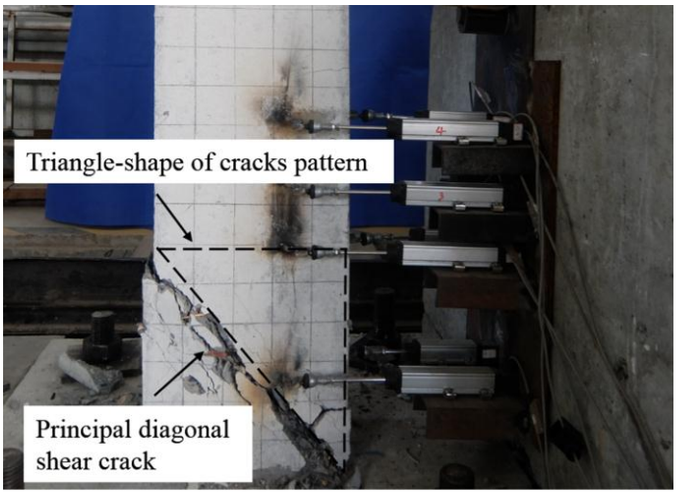
4 IMPACT TEST RESULTS

4.1 *Failure mode*

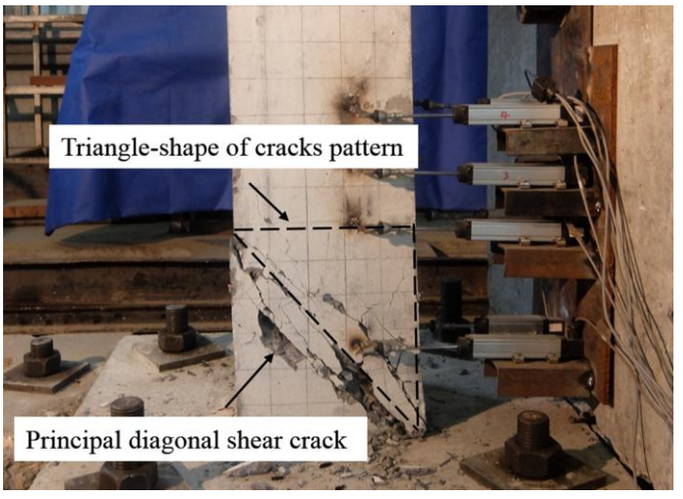
Figure 5 showed failure mode of each impacted specimen. As illustrated in Figure 5, all the impacted specimens failed in the shear pattern with a principal diagonal shear crack at the impact point. It is found that all the specimen sections were penetrated by the principal diagonal shear crack along an angle of approximately 45 degrees. Besides, there was no obvious diagonal cracks parallel to the principal diagonal shear crack appearing close to the impact point and the bottom of the specimen. Consequently, the final crack pattern of each impacted specimen was triangle-shaped (see Figure 5).



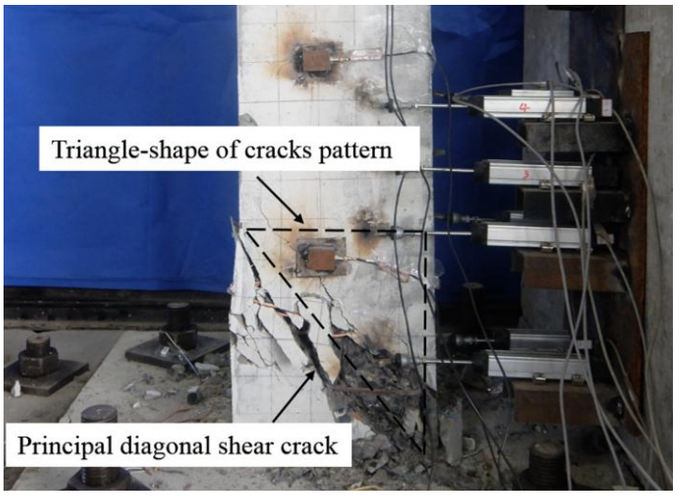
(a) Failure mode of specimen BP-2



(b) Failure mode of specimen BP-3



(c) Failure mode of specimen BP-4



(d) Failure mode of specimen BP-5

Figure 5. Failure mode of each impacted specimen

4.2 *Displacement time history*

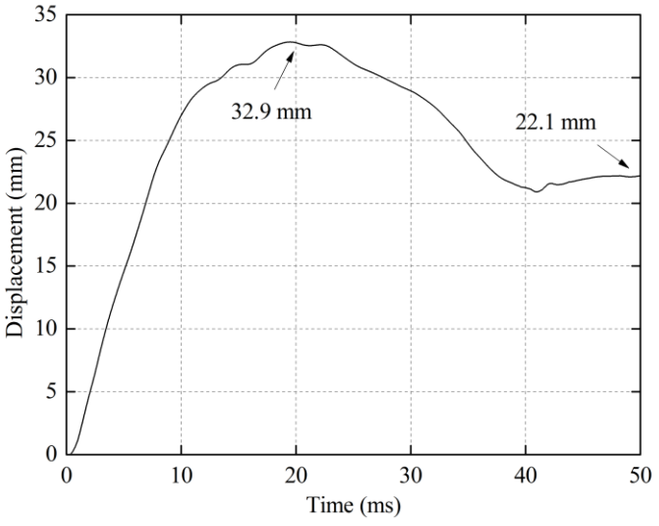
Figure 6 showed the displacement time history of each impacted specimen, and Table 2 presented the corresponding maximum values. As illustrated in Figure 6, it can be seen that a high reinforcement ratio improved impact resistance of the RC pier that reducing the total and residual displacement at the impact point. Comparing specimen BP-2 to BP-3 and BP-4, the maximum displacement was respectively reduced by 21% and 35%, and the residual displacement was respectively reduced by 32% and 52% as the reinforcement ratio increased from 1.4% to 3.1% and 4.7%. This is mainly owing to the improved RC pier stiffness with the high reinforcement ratio. Figure 6 also revealed that the total displacement increased with the increase of impact velocity. Comparing BP-3 to BP-5, the maximum displacement for an impact velocity of 4.0 m/s was 25.9 mm, and it increased by 17% (30.3 mm) for an impact velocity of 4.4 m/s. Additionally, it is found that ratio of the residual displacement to the total displacement increased from 50% to 65% as the impact velocity increased from 4.0 to 4.4 m/s. It can be explained that a higher impulse corresponding to a higher impact velocity can trigger more severe damage and plastic deformation of the RC pier and further result in a higher ratio of the residual displacement to the total displacement.

4.3 *Impact force time history*

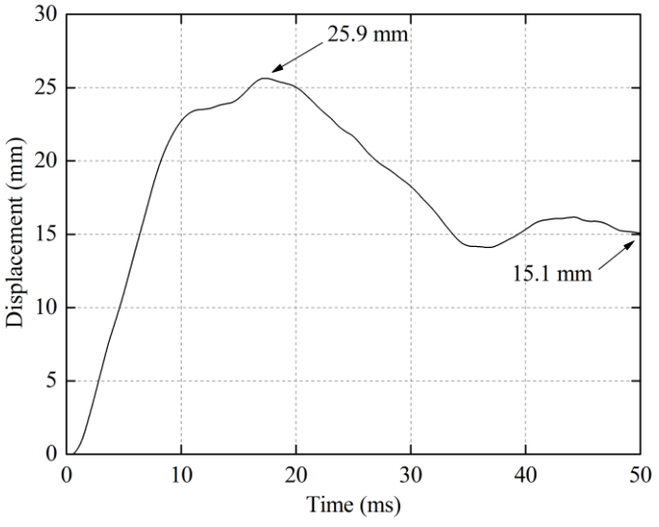
Figure 7 showed the impact force time history of each specimen, and Table 2 presented the corresponding peak values. It is found that the impact force time history can be divided into two phases. In the first phase, the impact force sharply increased to the peak value. This phase was defined from the zero of time to the end of the peak. This sudden increase occurred to obtain local acceleration of the impacted specimen, which was caused by vehicle collision. Duration of this phase was almost the same in all the impact tests, i.e. time ≤ 1.5 ms. In the second phase, the impact force gradually attenuated from the peak to zero. This phase finished with the complete failure of the impacted specimen. Duration of this phase was also almost the same in all the impact tests, i.e. time ≤ 28.5 ms.

As illustrated in Figure 7, it can be seen that the peak impact force was independent of the reinforcement ratio. The peak impact force was almost 700 kN when the reinforcement ratio increased from 1.4% to 3.1% and 4.7%. This is because the contact stiffness between the impact vehicle and the RC pier was unchanged, as a result of the constant value.

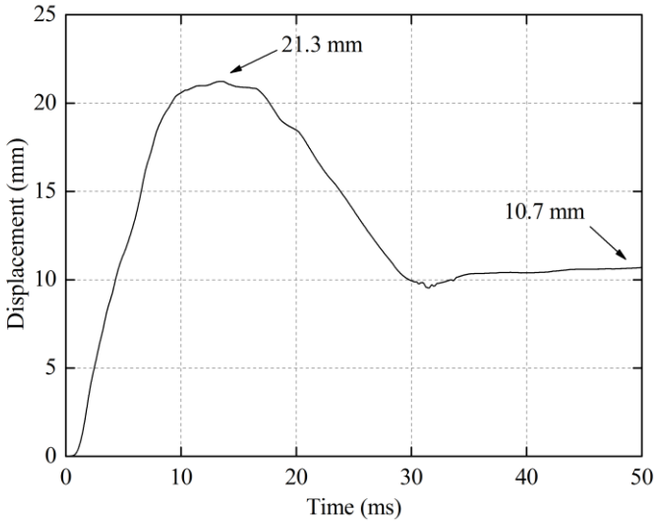
Compared BP-4 to BP-5, it is found that the peak impact force increased with the increase of the impact velocity. The peak impact force for an impact velocity of 4.0 m/s was 704 kN, and it was increased by 34% (942 kN) for an impact velocity of 4.4 m/s. This is because that a higher impulse induced by a greater impact velocity can lead to a larger peak impact force.



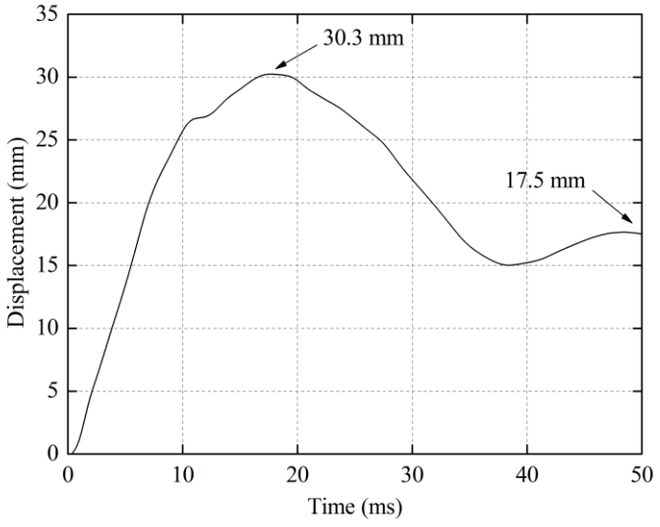
(a) Displacement time history of specimen BP-2



(b) Displacement time history of specimen BP-3



(c) Displacement time history of specimen BP-4



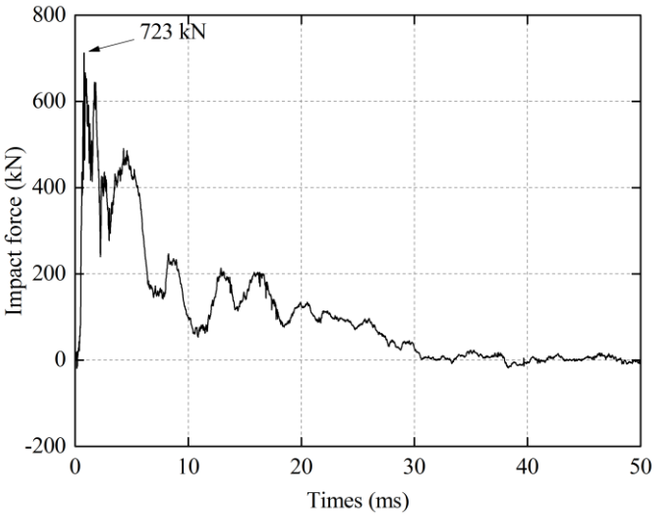
(d) Displacement time history of specimen BP-5

Figure 6. Displacement time history of each impacted specimen

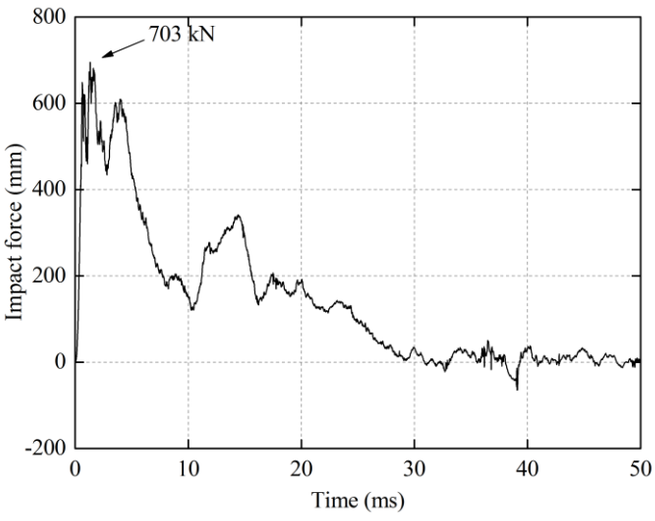
4.4 *Energy absorption capacity*

Figure 8 showed the load-displacement curve of each impacted specimen, and Table 2 listed the corresponding energy absorption capacities. Comparing BP-2 to BP-3 and BP-4, it can be seen that the energy absorption capacity was significantly affected by the reinforcement ratio. The energy absorption capacity was respectively reduced by 8 % and 12% as the reinforcement ratio respectively increased from 1.4% to 3.1% and 4.7%. It can be explained by the fact that the total displacement was reduced by the increased reinforcement ratio and the improved specimen stiffness that leading to a low energy absorption capacity.

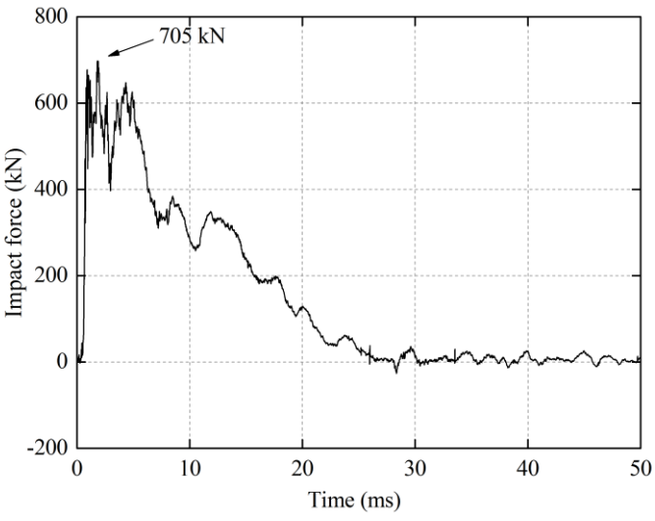
As illustrated in Figure 8 (c) and (d), it is found that the energy absorption capacity increased with the increase of the impact velocity. The energy absorption capacity increased by 26% for the reinforcement ratio of 3.1% as the impact velocity increased from 4.0 to 4.4 m/s. This is because a greater total displacement and impact force were induced by a higher impact velocity, as a result of a greater energy absorption capacity.



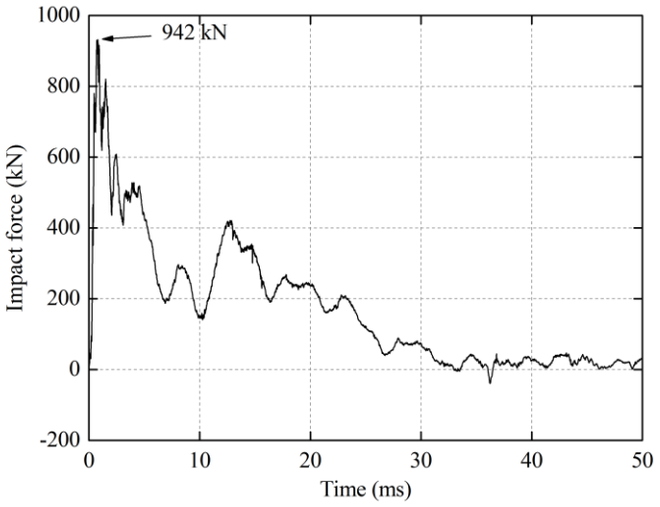
(a) Impact force time history of specimen BP-2



(b) Impact force time history of specimen BP-3



(c) Impact force time history of specimen BP-4



(d) Impact force time history of specimen BP-5

Figure 7. Impact force time history of each impacted specimen

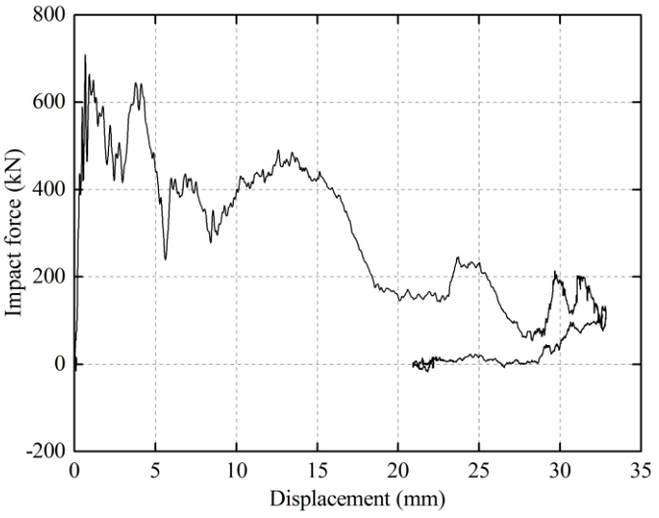
4.5 *Post-impact damage*

Figure 5 also showed the post-impact damage of each impacted specimen. In all the impact tests, the specimen reached the failure condition with the residual resistance provided by the reinforcements. As illustrated in Figure 5, it is found that the damage decreased with the increase of the reinforcement ratio. In BP-2 case, the principal diagonal crack was characterized with broken concrete, fractured stirrups and a large width at the impact point. In BP-3 and BP-4 cases, width of the principal diagonal crack was reduced. This is because that the residual resistance of the specimen was improved by a higher reinforcement ratio.

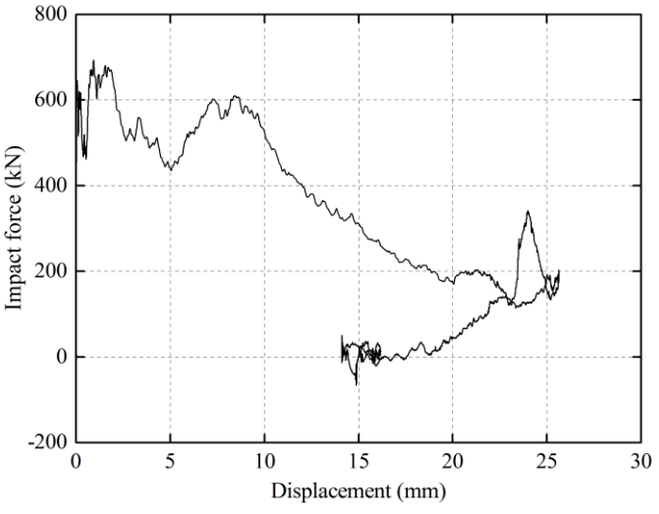
Compared to BP-3, it can be seen that the crack width of BP-5 became wider, more concrete spalled and stirrups were fractured. It can be explained by the fact that a greater amount of kinetic energy induced by a greater impact velocity of the vehicle was transferred into internal energy of the specimen, as a result of a more severe damage.

4.6 *Discussion*

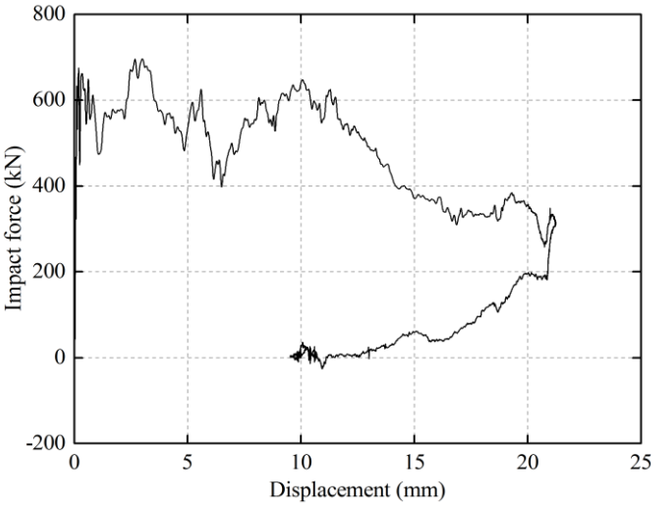
According to the above analysis, crack patterns varied between the static test results and the impact ones, although all the specimens exhibited the typical shear failure mode. Crack pattern of the static results was ladder-shaped, while those of the impact results were triangle-shaped. Moreover, several small diagonal cracks were observed close to the loading point in the static results, while there is no similar diagonal cracks appearing in the impact results. This is because that there is enough time for the high stresses in the rebars to transfer into the neighboring concrete and rebars after the formation of the principal diagonal shear crack in the static test, resulting in several small diagonal cracks forming close to the loading point. However, the impacted specimens had no enough time to respond to the rapid change of the impact loading, so that the high stress was mainly concentrated at the impact point.



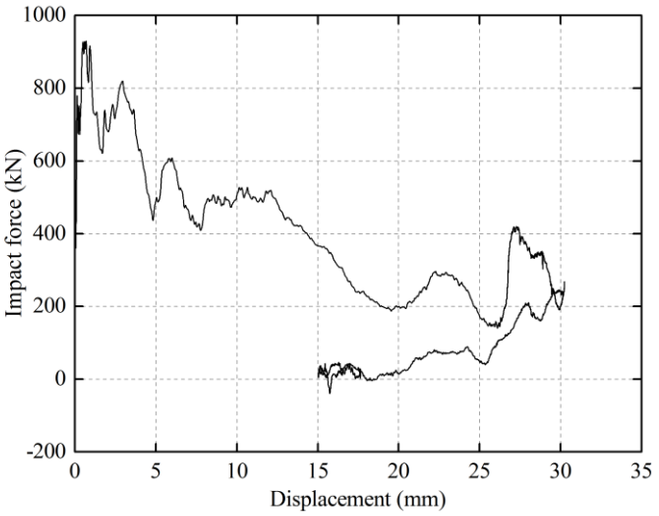
(a) Load-displacement curve of specimen BP-2



(b) Load-displacement curve of specimen BP-3



(c) Load-displacement curve of specimen BP-4



(d) Load-displacement curve of specimen BP-5

Figure 8. Load-displacement curve of each impacted specimen

5 CONCLUSIONS

In this paper, four impact tests were conducted to study the reinforcement ratio and the impact velocity on effects the impact behavior of RC pier. A static test on the same RC pier was also conducted to compare with the corresponding impact test results. Main conclusions were summarized as follows:

(1) The impact test results showed that a high reinforcement ratio enhanced the impact resistance that reducing the total and residual displacements and energy absorption capacity. The maximum displacement was respectively reduced by 21% and 35%, and the residual displacement was respectively reduced by 32% and 52% as the reinforcement ratio increased from 1.4% to 3.1% and 4.7%. The energy absorption capacity was also respectively reduced by 8% and 12%.

(2) The impact test results showed that the impact force and the total displacement increased with the increase of the impact velocity. The peak impact force and the maximum displacement respectively increased by 34% and 17% as the impact velocity increased from 4.0 to 4.4 m/s, and meanwhile the ratio of residual displacement to total displacement increased from 50% to 65%. Besides, the energy absorption capacity increased by 26% for the reinforcement ratios of 3.1% when the impact velocity increased from 4.0 to 4.4 m/s.

(3) In all the impact tests, the post-impact condition revealed a shear-type damage characterized by the principle diagonal crack starting from the impact point to the bottom of the specimen. The damage was reduced by increasing the reinforcement ratio and increased by increasing the impact velocity.

(4) Comparison between the static test results and the corresponding impact test results showed that the failure modes of RC piers under both static loading and impact loading were shear failure, while the crack patterns were different. The crack pattern of the former was ladder-shaped, while the latter was triangle-shaped.

REFERENCES

Bhatti, A.Q., Kishi, N. & Mikami, H. 2010. An applicability of dynamic response analysis of shear-failure type RC beams with lightweight aggregate concrete under falling-weight impact loading. *Materials & Structures* 44(1): 221-231.

Cook, W. 2014. *Bridge failure rates, consequences, and predictive trends*. PhD Thesis, Utah state University, United States.

Cotsovos, D.M., Stathopoulos, N.D. & Zeris, C.A. 2008. Behavior of RC Beams subjected to high rates of concentrated loading. *Journal of Structural Engineering* 134(12): 1839-1851.

Fujikake, K., Li, B. & Soeun, S. 2009. Impact response of reinforced concrete beam and its analytical evaluation. *Journal of Structural Engineering* 135(8): 938-950.

Harik, I.E., Shaaban, A.M., Gesund, H., Valli, G.Y.S. & Wang, S.T. 1990. United States bridge failures, 1951-1988. *Journal of Performance of Constructed Facilities* 4(4): 272-277.

Kishi, N., Mikami, H., Matsuoka, K.G. & Ando, T. 2002. Impact behavior of shear-failure-type RC beams without shear rebar. *International Journal of Impact Engineering* 27(9): 955-968.

Kulkarni, S.M. & Shah, S.P. 1999. Response of reinforced concrete beams at high strain rates. *Aci Structural Journal* 95(6): 705-715.

Saatci, S. & Vecchio, F.J. 2009. Effects of shear mechanisms on impact behavior of reinforced concrete beams. *Aci Structural Journal* 106(1): 78-86.

Shakir, A.S., Guan, Z.W. & Jones, S.W. 2016. Lateral impact response of the concrete filled steel tube columns with and without CFRP strengthening. *Engineering Structures* 116: 148-162.

Sukontasukkul, P. & Mindess, S. 2003. The shear fracture of concrete under impact loading using end confined beams. *Materials & Structures* 36(6): 372-378.

Maintenance, Safety, Risk, Management and Life-Cycle Performance of Bridges – Powers, Frangopol, Al-Mahaidi & Caprani (Eds)
© 2018 Taylor & Francis Group, London, ISBN 978-1-138-73045-8

Fragility analysis of non-ductile RC bridges subjected to extreme hydrodynamic forces

I. M. I. Qeshta
Civil and Infrastructure Engineering, School of Engineering, RMIT University, Melbourne, VIC 3000, Australia.

M. J. Hashemi
Department of Civil and Construction Engineering, Swinburne University of Technology, Melbourne, VIC 3122, Australia.

R.J. Gravina & S. Setunge
Civil and Infrastructure Engineering, School of Engineering, RMIT University, Melbourne, VIC 3000, Australia.

ABSTRACT: Existing reinforced concrete bridges are not typically designed to sustain the significant hydrodynamic forces resulting from river floods, tsunamis and hurricane waves. Particularly, there is an urgent need on vulnerability assessment and risk mitigation techniques for non-ductile bridges. For this purpose, a method for developing fragility functions is proposed in this research that relies on the nonlinear static analysis to estimate the global damage of bridge structures. The fragility functions consider the uncertainties both in the capacity in the form of material properties and the demand in the form of drag coefficient, and examine the ability of inundation depth, flow velocity and momentum flux to provide a reliable indication of the damage experienced by a non-ductile four-span bridge. The results showed that the velocity plays an important role as an intensity measure in the fragility analysis of non-ductile bridge structures.

1 INTRODUCTION

The damage of bridges during natural hazards leads to significant economic and social losses due to their vital role in emergency evacuation and post-disaster recovery (Mosqueda et al., 2007). Flood hazards such as tsunamis and wave surges have been reported among the major causes of bridge collapse in the United States (Wardhana and Hadipriono, 2003). In addition, the significant damage of bridges during hurricane Katrina in 2005 and Queensland floods in 2011 and 2012 has raised concerns on the resilience of existing bridges (Padgett et al., 2008, Pritchard, 2013). Current bridge design guidelines and retrofit strategies are not sufficient to withstand the extreme flood forces. In general, bridge response and failure mechanisms vary widely depending on the deck type, super- and sub-structure connectivity and applied forces. Ataei and Padgett (2012, 2015) and Ataei et al. (2010) investigated the unseating failure of simply supported decks under storm surges. The researchers reported that the bridge displacements and wave forces are among the most important parameters to be considered in vulnerability assessment. Salem et al. (2014) modelled the deck unseating failure of a bridge damaged by Tohoku tsunami in 2011 using applied element method. The researchers reported that the amount of trapped air plays significant role in the damage of bridge. Furthermore, Ataei and Padgett (2013) extended their investigation to include mapping the global response of bridge with the individual elements capacities in bridges with strong connection between deck and substructure.

Probabilistic modelling provides a practical tool to estimate the failure of bridges within an inventory given an intensity measure. The use of fragility functions for floods was first introduced by Koshimura et al. (2009a) using statistical models of field data. However, empirical fragilities have a number of drawbacks. The two main drawbacks are that they are specific to particular structures and/or area, and they suffer from lack of accuracy due to their dependency on visual observations (Koshimura et al., 2009b, Suppasri et al., 2011, Dias et al., 2009). Si-

hombing and Torbol (2015) estimated fragility curves by calculating the hydrodynamic forces through simulated tsunami waves. However, such method is computationally expensive considering the large number of models needed for fragility curve as well as it is limited to tsunami waves characteristics. This initiates the need for more practical schemes for fragility estimates that can capture the complete structural response of structures and do not require large computational cost.

Analytical models that adopt simplified patterns of flood load have recently been proposed (Attary et al., 2016, Petrone et al., 2017). The structure is usually subjected to incremental lateral static loads until failure in a process called "pushover", which is commonly used in earthquake engineering. It provides an indication of the capacity and demands of structures such as drifts, plastic deformations and element forces. Pushover analysis assumes that the structure undergoes the same mode shape throughout its dynamic time-history (Krawinkler, 1996). Several studies have been recently reported on the use of pushover analysis for generating fragility functions of building structures subjected to tsunami forces. The studies by Macabuag and Rossetto (2014) and Macabuag et al. (2014) showed that the load distribution has a significant effect on the pushover curve of the structure. The researchers also recommended further investigation of the application of tsunami in the post-peak stage and the use of a real-time history forces (Macabuag et al., 2014). This work was later extended by Petrone et al. (2017) to examine different discretization methods for tsunami applied loads. The study showed two main findings: first, tsunami loads should be discretized into constant number of point loads, and the variable height load-controlled pushover is more accurate in terms of the prediction of drift demands (Petrone et al., 2017).

Flow depth has been the most commonly adopted intensity measure in empirical fragility curves, as it is easy to measure in post-disaster field surveys. However, other parameters have also been reported to contribute to the magnitude of flood forces, such as flow velocity, momentum flux and acceleration (Nanayakkara and Dias, 2016, González et al., 2009, Løvholt et al., 2014). This implies that the use of flow depth as the only intensity measure can lead to a scatter in fragility data. In addition, most flood forces are directly related to the flow depth and velocity (ASCE, 2013, Attary et al., 2016). The use of momentum flux (hu^2) has recently been proposed as an intensity measure that combines both flow velocity and inundation depth (Park et al., 2014). In theory, the momentum flux has a linear relationship with the hydrodynamic forces, and hence, it can provide better correlation with the magnitude of force combining two intensity measures. However, the recent study by Attary et al. (2016) revealed that the accuracy of momentum flux can be affected by the magnitude and location of resultant force of the uniformly distributed tsunami load. Hence, an intensity measure called the kinematic moment of momentum flux was introduced to consider the effect of inundation depth on the force, which showed less scatter compared to other intensity measures (Attary et al., 2016). Moreover, Nanayakkara and Dias (2016) represented the tsunami force as a pressure distribution, in which the velocity was considered as a function of the flow depth.

However, limited research has been documented on the use of probabilistic risk assessment models for bridges subjected to significant hydrodynamic forces. Bridge structures have different topologies and modes of failure compared to other frame structures. Hence, the recently proposed fragility functions cannot be considered a reliable basis for assessing the vulnerability of bridges in flood-prone regions. The aim of this paper is to provide a preliminary study on the generation of fragility functions of reinforced concrete bridge subjected to flood hydrodynamic loads. The work presented in this paper examines the reliability of static nonlinear pushover analysis methods in risk assessment of non-ductile reinforced concrete bridges. In addition, the use of different intensity measures, i.e. flow velocity and momentum flux is studied. This research paves the way towards the implementation of practical analytical methods on the vulnerability assessment of bridges susceptible to collapse under extreme forces.

2 BRIDGE STRUCTURAL MODEL

A typical four-span reinforced concrete box-girder bridge is selected from the study by Li (2008). The bridge has an overall span length of 120 m and width of 8 m. Figure 1 shows the overall view of the bridge and the main details. As can be seen from the figure, the substructure consists of three main piers of equal height of 11 m, and two abutments of 1 m height. The box girder superstructure height is 1 m. The overall diameter of piers and concrete cover thickness are 1.2 and 0.08 m, respectively. The bridge three-dimensional (3D) model was developed using the Open System for Earthquake Engineering Simulation (OpenSees) (Mazzoni et al., 2006). The superstructure was represented by line elements located at its centroid. The elements had equal lengths of 7.5 m divided by nodes, while piers were modelled using twenty equal elements of 0.5 m length. The abutments and superstructure portion of piers height were modelled using a single element. Rigid elements were used for the superstructure centroid elements since the deck remains elastic throughout all loading phases of bridge.

The piers were modelled using displacement-based nonlinear beam column elements with four integration points to provide accurate distributed plasticity model. Single rigid elements were used for the abutments and superstructure portion of piers. The geometrical transformation was performed in the model using linear method for the superstructure elements. The P-Delta transformation was used for piers to capture the reduced capacity resulting from the additional bending moment induced on piers by the gravity loads at large displacements. The bridge was assumed to be fixed to the ground floor at all piers, while the abutments were allowed to move in the z-direction together with the elastic elements of piers.

The cross-section of elements of concrete was modeled using fiber approach, while layer approach was used for modelling the steel reinforcement. The concrete uniaxial stress-strain relationships were modelled using zero tensile strength Kent-Scott-Park and Karsan-Jirsa approaches (Karsan and Jirsa, 1969). The effect of confinement provided by the steel stirrups was considered in defining the materials properties of core concrete. The unconfined and confined concrete mean (μ) compressive strengths are 32 and 35 MPa, respectively. Both confined and unconfined concrete material models have an elastic modulus of 26 GPa. The steel spirals have a diameter of 0.02 m and were assumed to have a pitch of 0.5 m. The piers were reinforced with 20 longitudinal steel bars with a diameter of 0.03 m. The steel reinforcement was modelled using hysteretic model with mean elastic modulus of 208 GPa. The mean yield and ultimate strengths of steel were 500 and 530 MPa, respectively.

The torsional stiffness of piers was kept significantly large to prevent any premature torsional failure. The bridge masses are mainly contributed by the superstructure, whereas piers masses were found to be only 2.5% of the total bridge mass, and were, hence, neglected. The masses were distributed over the span nodes based on tributary elements. The fundamental period of vibration of the bridge was about 0.75 s. The gravity loads were calculated from the superstructure self-weight and other permanent objects on the bridge, and they were distributed along the bridge span nodes.

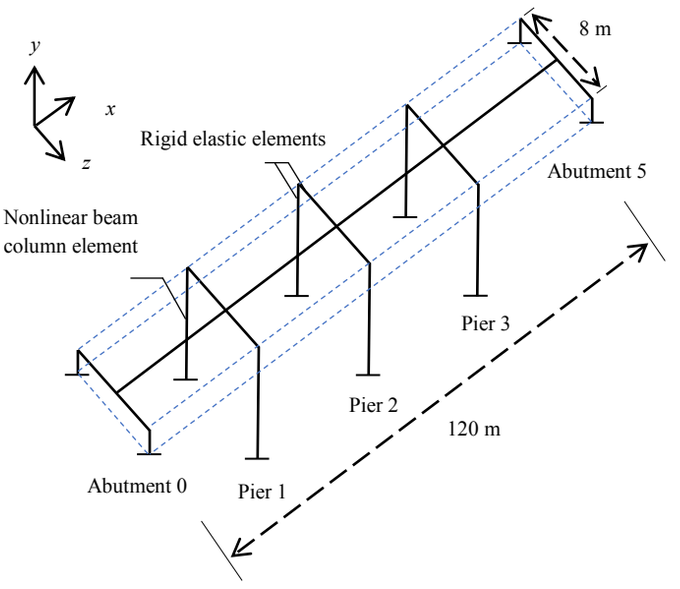


Figure 1. Bridge model main details.

3 FLOOD LOADING

River floods or tsunamis usually occur in the form of surging surface that does not have wave heights like the coastal hurricane storm surges. This eliminates any possible contribution from the wave height to the force. Thus, the forces that result from the flow are summarized as follows: hydrodynamic forces, hydrostatic forces, impulsive impact forces, buoyant forces and debris impact forces.

The hydrodynamic forces are the drag forces developed through the interaction between the structure and moving water. The hydrostatic forces generally occur due to the imbalance of hydrostatic pressure in both sides of bridge due to the accumulation of debris at one side, which results in different water depths (Zevenbergen et al., 2012). Impulsive impact force results from the air pockets that generate at the moment the water hits the structure (Douglass et al., 2006), and it is often expressed as 1.5 times the magnitude of hydrodynamic force (Ramsden, 1996). Buoyant forces form due to the displaced water by the bridge deck, and it can be significant if the air is entrapped between girders (Robertson et al., 2007). Debris impact forces usually depend on the moving objects that hit the structure, and vary widely depending on the type and amount of debris in the flood.

In this research, only the hydrodynamic forces are considered, as they dominate the tsunami and flood forces, and they can be estimated using the following equation:

$$F = 0.5 C_d \rho u^2 h b \quad (1)$$

where, C_d is the drag coefficient, ρ is the flood water density (1200 kg/m^3), u is the flow velocity, h is the

flow depth and b is the width or diameter of pier. Several patterns have been proposed for the distribution of flood forces on vertical objects. This ranges between triangular, trapezoidal and uniform patterns (Macabuag and Rossetto, 2014, Macabuag et al., 2014, Petrone et al., 2017). For simplicity, uniform pattern is used in this research as shown in Figure 2. The other distribution patterns will be investigated in future research.

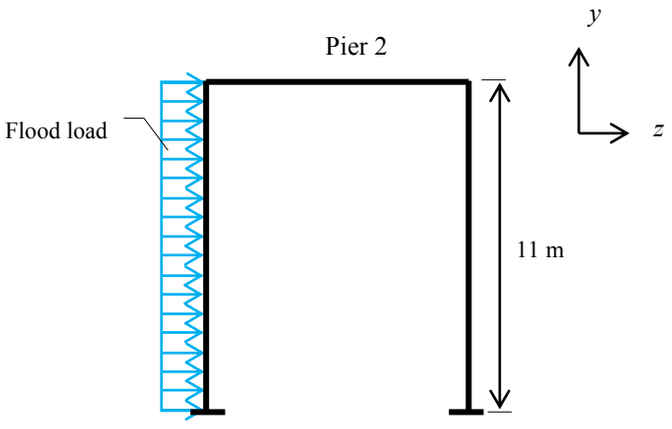


Figure 2. Distribution of flood load on bridge piers at full inundation.

4 FRAGILITY ANALYSIS

4.1 *Uncertainty of capacity and demand parameters*

The response of bridge subjected to flood load is sensitive to several parameters, either in flood forces or structural model. In this research, the concrete compressive and steel yield strengths follow a lognormal distribution with a standard deviation (v) of 0.4 and 0.3, respectively. The higher standard deviation of concrete is attributed to the large variability of its constituent materials properties. The flood density and steel and concrete elastic moduli were assumed to be deterministic. Table 1 summarizes all demand and capacity parameters used in the analysis. Uniform distribution was adopted for the drag coefficients with a range of values between 1.25 and 1.75 for circular columns or piers (ASCE, 2013).

Table 1. Capacity and demand parameters

Variable	**Type of distribution**	**Parameter used in distribution**
Concrete compressive strength, f_c'	Lognormal	v = 0.4, μ = 32 MPa
Concrete elastic modulus, E_c	Deterministic	-
Steel yield strength, f_y	Lognormal	v = 0.3, μ = 500 MPa
Steel elastic modulus, E_s	Deterministic	-
Drag coefficient, C_d	Uniform	Range = 1.25 to 1.75
Flood water density, ρ	Deterministic	-

4.2 *Methodology for development of fragility curves*

The adopted method for developing preliminary fragility functions for bridge is shown in Figure 3. The uncertainty in the structure parameters is first considered by generating random variables of f_c' and f_y. Ten random variables were generated using Latin Hypercube Sampling (LHS), giving a total of 100 structural models. The capacity curves from the model with mean values of f_c' and f_y is then obtained. Figure 4 shows the capacity curve obtained from the mean f_c' and f_y. The drift ratios are used as the engineering demand parameters (EDPs) for damage assessment, since the structure is subjected to lateral loads. In addition, it is assumed that the structure undergoes severe damage after exceeding the ultimate strength. As can be seen in Figure 4, the drift ratio corresponding to the peak strength of the mean capacity curve was found to be 0.0057 (at 10731 kN), and it is taken as the limit state of the fragility function. Although in reinforced concrete design the member is assumed to have structurally failed when it exceeds its ultimate strength (Nawy, 2000), such assumption does not give a clear indication on the amount of damage that the bridge experiences in the post-yield stage. However, for the sake of illustration of the methodology of fragility functions, this assumption is adopted in this research. Future research will address the use of different damage states of the structure, where more realistic time-history loads are applied in the inelastic deformation phase. The velocity was selected to have a maximum value of 10 m/s, and it was incremented by 0.5 m/s. The flood forces at the full inundation depth and 20 ranges of velocities are then computed with the ten random variables of C_d, which gives a total of 200 forces. A Froude number (Fr) limit is set to 2.0 in order to remove the unrealistic combinations of inundation depth and velocity (Foytong et al., 2013, Foytong et al., 2015). The drift ratios corresponding to the calculated flood forces are obtained and compared against the limit state. The cumulative probability of the drift ratios that exceed the limit state is finally obtained at each intensity measure.

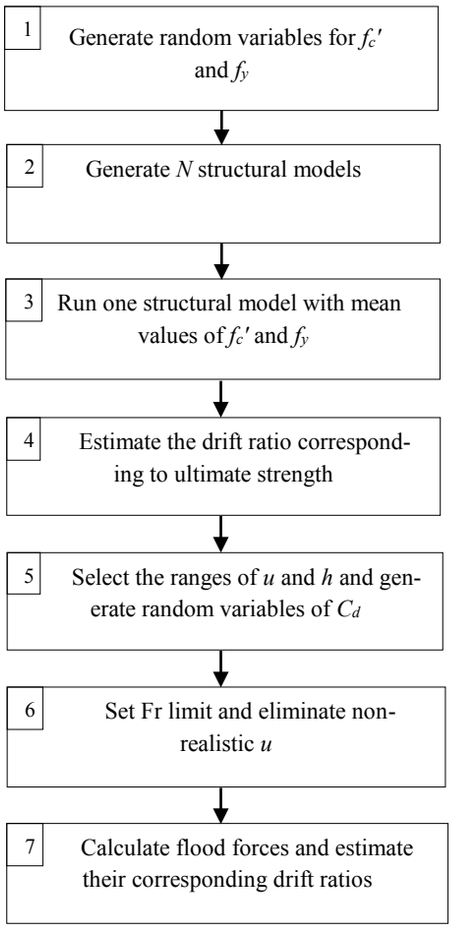


Figure 3. Methodology adopted for developing fragility functions for bridges under flood forces.

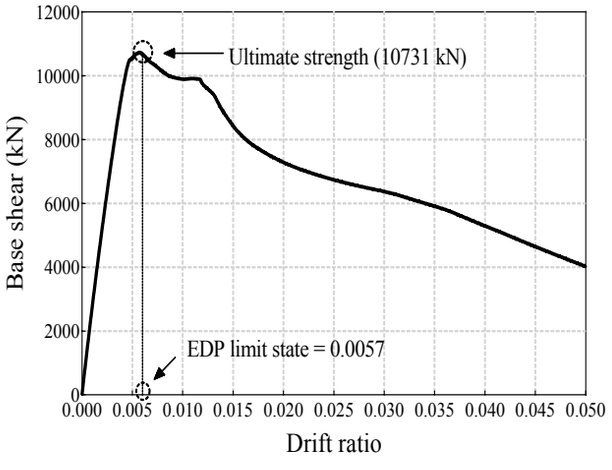


Figure 4. Capacity curve of the structural model from mean f_c' and f_y.

5 RESULTS AND DISCUSSIONS

The fragility curves were developed by adopting the method discussed in the previous section. Figure 5 shows the fragility of the reinforced concrete bridge at all velocity levels and full inundation. The figure shows that the transition zone representing the damage in bridge starts at velocity value of 4 m/s. The bridge had a high probability of collapse (up to 0.9) at velocity of 10 m/s, which corresponds to Fr value of 0.96. This shows that reinforced concrete bridges can be susceptible to collapse at relatively low Froude numbers compared to the threshold value of 2.0 given from past tsunami and flood events. In addition, Figure 5 indicates that velocity, as an intensity measure, has significant effect on the scatter of the fragility results. Such effect is ignored in most of the currently published fragility curves that adopt the inundation depth as the only intensity measure. For example, with the increase in inundation depth during tsunami or flood, at every single inundation and with the current range of velocities, the bridge exhibits different probabilities of failure.

As discussed earlier in this paper, the scatter of cumulative probability resulting from different intensity measures can be reduced by introducing intensity measures that combine both the velocity and inundation depth. As an example, Figure 6 presents the fragility curve using momentum flux (hu^2). In this method, one intensity measure is usually incremented while the other is implicitly increased through incrementing the momentum flux. As can be seen in Figure 6, the transition zone starts earlier compared to Figure 5, which highlights the significance of incorporating the inundation depth for providing better prediction of the bridge damage. However, the data provided in Figure 6 cannot be used to draw clear conclusions as they are extracted from only one depth. Hence, future research will provide further investigation of the effect of using methods that combine both intensity measures on the accuracy of fragility functions.

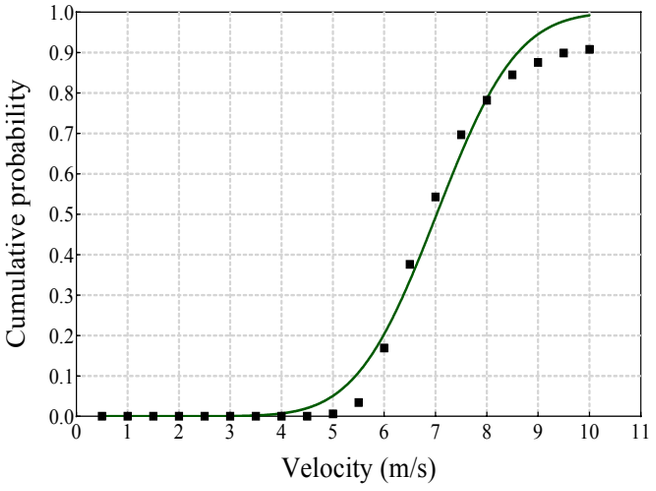


Figure 5. Cumulative damage probability for bridge, with velocity as the intensity measure.

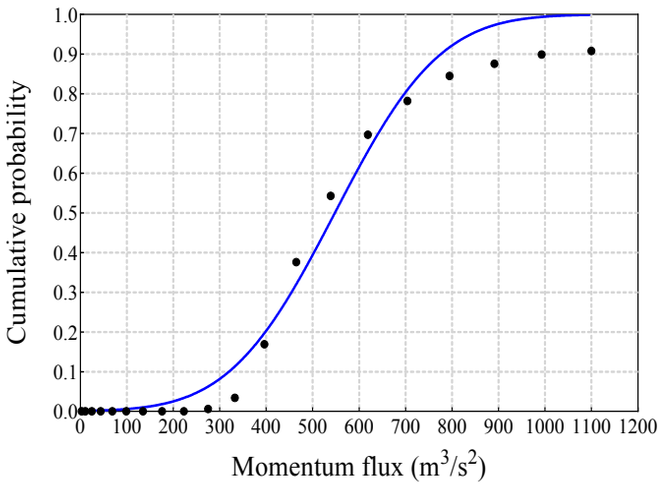


Figure 6. Cumulative damage probability for bridge, with momentum flux (hu^2) as the intensity measure.

6 CONCLUSIONS

This research proposes the first methodology to develop analytical fragility curves for bridges subjected to tsunamis and floods. To illustrate this method, a reinforced concrete box-girder bridge, which suffers from lack of ductility, was modelled and subjected to hydrodynamic load. The method addresses the global lateral deformation of bridge through nonlinear static pushover analysis. The piers drift ratios were taken as the engineering demand parameters for assessing the damage of bridge. The probability of exceeding the limit, taken as the drift corresponding to the ultimate mean strength, was estimated for all flood scenarios. The two commonly used intensity measures, i.e. inundation depth and velocity were also addressed. The fragility functions of bridge at different velocities were developed at the full inundation depth. In addition, the use of momentum flux as a combination between the two common intensity measures was discussed. The method presented in this research enables fast scanning of the vulnerability of bridges in flood-prone areas. Future research will focus on integrating this method with complex failure modes that involve the superstructure, which was simplified as a rigid elastic element in this study. Further investigations are also needed on the different methods for application of loads as well as more realistic time-history flood loads.

7 ACKNOWLEDGEMENTS

The significant help from Ali Y. Al-Attraqchi (Department of Civil and Construction Engineering, Swinburne University of Technology) with OpenSees simulations is gratefully acknowledged. Also, specials thanks to Professor Riadh Al-Mahaidi (Department of Civil and Construction Engineering, Swinburne University of Technology) for his support towards this research. The financial support towards this research provided to the first author for his doctoral study by RMIT University, Australia in the form of RMIT PhD International Scholarship is gratefully acknowledged.

8 REFERENCES

ASCE 2013. Minimum design loads for buildings and other structures. *ASCE/SEI 7-10.* Reston, VA: American Society of Civil Engineers.

ATAEI, N. & PADGETT, J. E. 2012. Probabilistic modeling of bridge deck unseating during hurricane events. *Journal of Bridge Engineering,* 18**,** 275-286.

ATAEI, N. & PADGETT, J. E. 2013. Limit state capacities for global performance assessment of bridges exposed to hurricane surge and wave. *Structural Safety,* 41**,** 73-81.

ATAEI, N. & PADGETT, J. E. 2015. Influential fluid–structure interaction modelling parameters on the response of bridges vulnerable to coastal storms. *Structure and Infrastructure Engineering,* 11**,** 321-333.

ATAEI, N., STEARNS, M. & PADGETT, J. 2010. Response sensitivity for probabilistic damage assessment of coastal bridges under surge and wave loading. *Transportation Research Record: Journal of the Transportation Research Board***,** 93-101.

ATTARY, N., VAN DE LINDT, J. W., UNNIKRISHNAN, V. U., BARBOSA, A. R. & COX, D. T. 2016. Methodology for development of physics-based tsunami fragilities. *Journal of Structural Engineering,* 143**,** 04016223.

DIAS, W., YAPA, H. & PEIRIS, L. 2009. Tsunami vulnerability functions from field surveys and Monte Carlo simulation. *Civil Engineering and Environmental Systems,* 26**,** 181-194.

DOUGLASS, S. L., CHEN, Q., OLSEN, J., EDGE, B. & BROWN, D. 2006. Wave forces on bridge decks. *Coastal Transportation Engineering Research and Education Center, Univ. of South Alabama, Mobile, Ala*.

FOYTONG, P., RUANGRASSAMEE, A. & LUKKUNAPRASIT, P. 2013. Correlation analysis of a reinforced-concrete building under tsunami load pattern and effect of masonry infill walls on tsunami load resistance. *The IES Journal Part A: Civil & Structural Engineering,* 6**,** 173-184.

FOYTONG, P., RUANGRASSAMEE, A., LUKKUNAPRASIT, P. & THANASISATHIT, N. 2015. Behaviours of reinforced-concrete building under tsunami loading. *The IES Journal Part A: Civil & Structural Engineering,* 8**,** 101-110.

GONZÁLEZ, F., GEIST, E. L., JAFFE, B., KÂNOĞLU, U., MOFJELD, H., SYNOLAKIS, C., TITOV, V. V., ARCAS, D., BELLOMO, D. & CARLTON, D. 2009. Probabilistic tsunami hazard assessment at seaside, Oregon, for near-and far-field seismic sources. *Journal of Geophysical Research: Oceans,* 114.

KARSAN, I. D. & JIRSA, J. O. 1969. Behavior of concrete under compressive loadings. *Journal of the Structural Division*.

KOSHIMURA, S., NAMEGAYA, Y. & YANAGISAWA, H. 2009a. Tsunami Fragility—A New Measure to Identify Tsunami Damage—. *Journal of Disaster Research***,** 479-488.

KOSHIMURA, S., OIE, T., YANAGISAWA, H. & IMAMURA, F. 2009b. Developing fragility functions for tsunami damage estimation using numerical model and post-tsunami data from Banda Aceh, Indonesia. *Coastal Engineering Journal,* 51**,** 243-273.

KRAWINKLER, H. Pushover analysis: why, how, when, and when not to use it. Proceedings of the 65th Annual Convention of the Structural Engineers Association of California, 1996.

LI, B. 2008. Seismic performance of hybrid fiber reinforced polymer-concrete pier frame systems. *FIU Electronic Theses and Dissertations***,** 195.

LØVHOLT, F., SETIADI, N. J., BIRKMANN, J., HARBITZ, C. B., BACH, C., FERNANDO, N., KAISER, G. & NADIM, F. 2014. Tsunami risk reduction–are we better prepared today than in 2004? *International journal of disaster risk reduction,* 10**,** 127-142.

MACABUAG, J. & ROSSETTO, T. Towards the development of a method for generating analytical tsunami fragility functions. 2nd European conference on earthquake engineering and seismology, 2014.

MACABUAG, J., ROSSETTO, T. & LLOYD, T. Structural analysis for the generation of analytical tsunami fragility functions. 10th Int. Conf. on Urban Earthquake Engineering, 2014.

MAZZONI, S., MCKENNA, F., SCOTT, M. H. & FENVES, G. L. 2006. The Open System for Earthquake Engineering Simulation (OpenSEES) User Command-Language Manual.

MOSQUEDA, G., PORTER, K. A., O'CONNOR, J. & MCANANY, P. 2007. Damage to engineered buildings and bridges in the wake of Hurricane Katrina. *Forensic Engineering (2007)*.

NANAYAKKARA, K. & DIAS, W. 2016. Fragility curves for structures under tsunami loading. *Natural Hazards,* 80**,** 471-486.

NAWY, E. 2000. *Reinforced concrete: A fundamental approach*.

PADGETT, J., DESROCHES, R., NIELSON, B., YASHINSKY, M., KWON, O.-S., BURDETTE, N. & TAVERA, E. 2008. Bridge damage and repair costs from Hurricane Katrina. *Journal of Bridge Engineering,* 13**,** 6-14.

PARK, H., WIEBE, D. M., COX, D. T. & COX, K. 2014. Tsunami inundation modeling: Sensitivity of velocity and momentum flux to bottom friction with application to building damage at Seaside, Oregon. *Coastal Engineering Proceedings,* 1**,** 1.

PETRONE, C., ROSSETTO, T. & GODA, K. 2017. Fragility assessment of a RC structure under tsunami actions via nonlinear static and dynamic analyses. *Engineering Structures,* 136**,** 36-53.

PRITCHARD, R. 2013. 2011 to 2012 Queensland floods and cyclone events: Lessons learnt for bridge transport infrastructure. *Australian Journal of Structural Engineering,* 14**,** 167-176.

RAMSDEN, J. D. 1996. Forces on a vertical wall due to long waves, bores, and dry-bed surges. *Journal of waterway, port, coastal, and ocean engineering,* 122**,** 134-141.

ROBERTSON, I. N., RIGGS, H. R., YIM, S. C. & YOUNG, Y. L. 2007. Lessons from Hurricane Katrina storm surge on bridges and buildings. *Journal of Waterway, Port, Coastal, and Ocean Engineering,* 133**,** 463-483.

SALEM, H., MOHSSEN, S., KOSA, K. & HOSODA, A. 2014. Collapse analysis of Utatsu Ohashi Bridge damaged by Tohuku Tsunami using applied element method. *Journal of Advanced Concrete Technology,* 12**,** 388-402.

SIHOMBING, F. & TORBOL, M. Large scale smooth particle hydrodynamics model for analytical fragility curves of a building subject to tsunami. World Congress ASEME, 2015.

SUPPASRI, A., KOSHIMURA, S. & IMAMURA, F. 2011. Developing tsunami fragility curves based on the satellite remote sensing and the numerical modeling of the 2004 Indian Ocean tsunami in Thailand. *Natural Hazards and Earth System Sciences,* 11**,** 173.

WARDHANA, K. & HADIPRIONO, F. C. 2003. Analysis of recent bridge failures in the United States. *Journal of performance of constructed facilities,* 17**,** 144-150.

ZEVENBERGEN, L., ARNESON, L., HUNT, J. & MILLER, A. C. 2012. Hydraulic design of safe bridges. *Report No. FHWA-HIF-12-018 HDS 7, Federal Highway Administration.* Washington, D.C.

Maintenance, Safety, Risk, Management and Life-Cycle Performance of Bridges – Powers, Frangopol, Al-Mahaidi & Caprani (Eds)
© 2018 Taylor & Francis Group, London, ISBN 978-1-138-73045-8

Dynamic response of an isolated bridge under basic pulse-type ground motions

M.H. Tsai & Z.Y. Jiang
Department of Civil Engineering, National University of Science and Technology, Pingtung County, Taiwan

ABSTRACT: Parametric studies on the dynamic response of a typical isolated bridge under three pulse-type ground motions were carried out in this study. The analysis results indicated that similar peak structural responses were induced under the three pulse motions. The peak isolator displacement could be effectively reduced as the stiffness ratio lied between 0.2 and 0.3. Seismic response of the isolated bridge under twenty pulse-like near-field and ten far-field earthquake records were compared with the pulse response. The analysis results indicated that for the considered range of the post-yield stiffness ratio, the mean-plus-one standard deviation response under the near-field seismic motions with scaled pulse period varied from 70% to 82% of that under the one-cycle Type-A pulse motions. Hence, the one-cycle Type-A pulse can be used as a pseudo-near field ground motion for the extreme seismic demand under pulse-like near-field earthquakes.

1 INTRODUCTION

From several major seismic events in the past decades, it is known that near-field (NF) earthquakes usually contain long-period pulses in the ground motions. The 1999 Taiwan Chi-Chi earthquake revealed that a major characteristic of the NF ground motions is the pulse-like velocity waves, which may be more destructive than their peak ground accelerations (PGA) for some structures (Makris & Chang 1998, Loh 1999). Chopra & Chintanapakdee (2001) compared the spectral characteristics of single degree-of-freedom (SDOF) systems under NF and far-field (FF) ground motions and indicated that the former may induce a larger strength demand with the same ductility factor. Since seismically isolated structures usually feature the lengthened structural period, they may be more vulnerable than non-isolated structures under the NF ground motions. Shen *et al*. (2004) combined a recorded seismic ground motion with different pulse functions to evaluate the effect of NF earthquakes on a seismically isolated bridge. Dicleli (2006) conducted a comprehensive numerical study to investigate the influence of characteristic strength and post-yield stiffness ratio of lead-rubber bearings (LRBs), PGA, pulse period, and cycle number of pulse motions on the NF seismic responses of an isolated bridge model. They indicated that the isolated bridge had larger dynamic response as the pulse period was approximate to the isolation period. Larger post-yield stiffness and characteristic strength of LRBs were suggested to reduce the displacement demand under NF ground motions. Jangid (2007) proposed a force function to find the optimum yield strength for LRBs of seismically isolated buildings under NF earthquakes. A yield strength ratio of 0.10~0.15 was suggested in the study. NF and FF seismic story drifts of two building models isolated with LRBs of varied post-yield stiffness ratio, isolation period, and characteristic strength were compared by Providakis (2008). Karalar *et al*. (2012) conducted sensitivity analysis and nonlinear time-history analysis to develop parametric equations for obtaining the optimum characteristic strength and post-yield stiffness of LRBs for isolated bridges located in NF regions.

The unique characteristic of the pulse-like NF ground motions implies that they may be represented with simplified or equivalent pulse functions. Several equivalent pulse functions were proposed to produce the approximate structural response under the pulse-like NF ground motions. Makris & Chang (2000) investigated the consistency between some recorded NF ground motions and three proposed pulse-type functions featuring different ground movement mechanisms. Eight simple pulse functions characterizing the effects of either the fling step or forward directivity were proposed by Xu & Xie (2006) to evaluate the relationships between pulse amplitudes and period for different pulses. He & Agrawal (2008) proposed an analytical velocity pulse model observed from NF ground motions for systematic design and assessment of seismic protective systems. Amiri *et al* (2008) used three pulse-type models to simulate the NF earthquake records

and the structural responses of three multi-story steel buildings under the pulse-type motions and the actual NF ones were compared. Sehhati *et al*. (2011) investigated the effects of NF ground motions on three different multi-story shear buildings and evaluated whether the simplified pulses are capable of representing the NF effects. Their analysis results revealed that the pulse-like ground motions may induce larger ductility demand and dispersion in structural response. Meanwhile, the proposed equivalent pulse model could capture the NF seismic response as the ratio of the pulse period to the fundamental structural period was in the range between 0.5 and 2.5.

From the literature review, it can be assured that the post-yield stiffness of the isolators is a key parameter in the NF seismic response because it is directly related to the extent of resonance between the isolated bridges and the pulse-like ground motions. Due to the uncertainties in the fault-rupture mechanism, the seismic demands of the pulse-like NF ground motions can vary significantly with earthquake events and are not easy to precisely predict. It could be more efficient in practical design of the isolated bridges against the NF seismic excitations if the maximum seismic demands can be roughly estimated by using some simple or equivalent pulse functions. Therefore, the peak dynamic responses of a typical isolated bridge subjected to pulse-type ground motions and twenty pulse-like NF seismic excitations were compared in this study. A bridge model was constructed to simulate the seismic response of the isolated bridge located in southern Taiwan and then used to carry out a parametric study for the peak dynamic response of the isolated bridge under three basic pulse motions proposed by Makris & Chang (1998). They may be regarded as the simplest pulses among those proposed simplified or equivalent pulse functions and thus easier for engineering applications. Moreover, the seismic responses of the bridge model with isolators of different post-yield stiffness ratios under twenty pulse-like NF and ten FF earthquake records were obtained. They were used to verify the effect of the post-yield stiffness ratio on the structural response and evaluate the validity of the pulse motions for the probable peak dynamic demand on the isolated bridge under pulse-like NF seismic motions.

2 BRIEF REVIEW OF THE ISOLATED BRIDGE

The isolated bridge is located at the Formosa Freeway in the Gia-Yi area of southern Taiwan. It is a three-span continuous bridge, as shown in Figure 1. Two LRBs were installed on each column bent and PTFE coated RBs were used at the abutments. The LRBs on the column bents can move in both the longitudinal and transverse direction, while the transverse movement of the RBs is restricted by shear keys at the abutments. This bridge was designed in 1990s. At that time, the design PGA was 0.33g and an important factor of 1.35 was used. This means that the designed PGA is approximate to 0.45g. The design displacement of the LRBs is 12.5 cm and the resulting equivalent damping is 18%. Also, it has an effective period of 2.04 sec in the longitudinal direction and 0.85 sec in the transverse direction due to the end restraints. The design dead load and live load for each LRB is 9006 kN (918 tf) and 1608 kN (164 tf), respectively. The design seismic force is 1348 kN (137 tf). Hence, the LRBs have effective stiffness equal to 10791 kN/m (1100 tf/m) and an energy dissipation capacity of 175.6 kN-m (18 tf-m).



Figure 1 The typical isolated bridge

3 NUMERICAL MODELING OF THE ISOLATED BRIDGE

After the construction of the bridge, the Central Weather Bureau (CWB) of Taiwan installed twenty-four accelerometers on the bridge to monitor the seismic response. In 1999, around one month after the Chi-Chi earthquake, an earthquake with a magnitude of 6.4 hit the Gia-Yi area. A finite element model for the bridge was constructed by using the SAP2000 program to simulate the bi-directional seismic response of the isolated bridge under the Gia-Yi earthquake. The superstructure, which is composed of continuously varied-depth box girders, and the bridge piers were modeled as beam-column elements. Total weight of the superstructure is about 42438 kN, including the live load. The LRBs on the pier tops were simulated by isolator elements, which exhibit bilinear hysteretic behavior in the horizontal directions and linear elastic behavior in the vertical direction. The RBs at the abutment were modeled by the frictional sliding type isolators with an initial lateral stiffness equal to that of the rubber layers and zero after slippage occurs. The coefficient of friction was assumed as 0.06 for the PTFE sliding surface.

In order to determine the bilinear parameters for the isolator elements, the elastic stiffness, yield strength, and post-yield stiffness were determined from the cyclic loading test results of the LRBs, as shown in Figure 2. With the characteristic strength, cyclic energy dissipation, and maximum displacement directly obtained from the test results, the associated yield displacement, elastic and post-yield stiffness, and yield strength were calculated. Since

the bearing displacement under the Gia-Yi earthquake was small, the parameters of the smallest test displacement were used in the simulation. However, very poor simulation results were obtained. Because the LRB was tested at a very low frequency, it was believed that the rate effect could play a role in the bearing parameters.

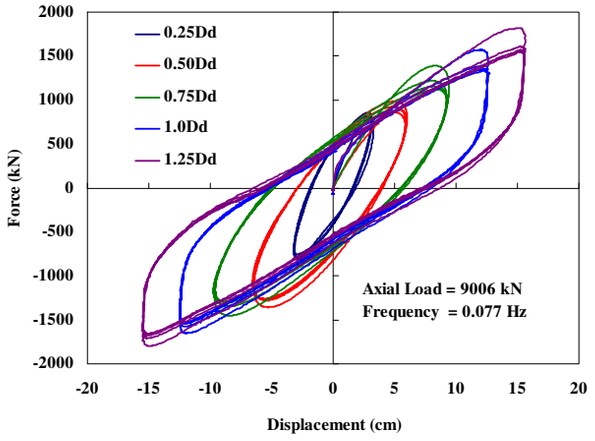


Figure 2. Cyclic loading tests of the LRBs

After several trial-and-error tuning, a better simulation result was obtained as shown in Figures 3a and b. Under the bi-directional excitation, longitudinal response had a better simulation result. The final determined parameters revealed that a high post-yield stiffness ratio was necessary for the simulation. The root-mean-square error of the acceleration time histories is 11.8% and 15.8% for the longitudinal and transverse response simulation, respectively. Since the isolated bridge was partially restrained in the transverse direction, this study was focused on its longitudinal dynamic response under pulse-type ground motions.

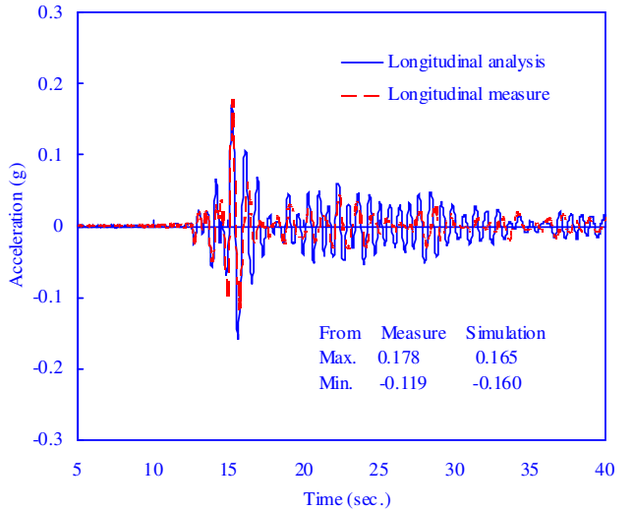


Figure 3a. The longitudinal simulation result

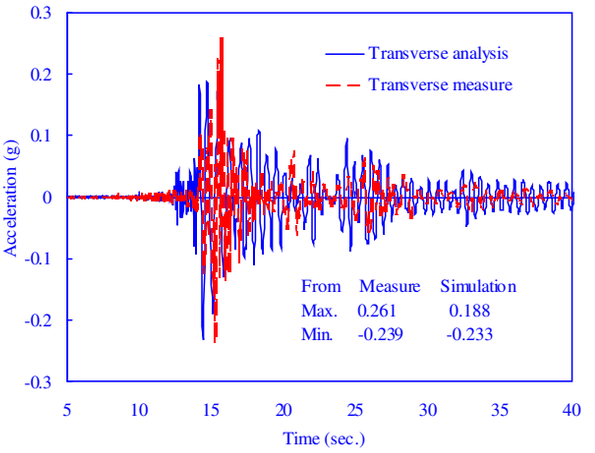


Figure 3b. The transverse simulation result

4 PEAK RESPONSE UNDER PULSE GROUND MOTIONS

The three basic types of pulse ground motions used in this study are the Type-A, Type-B, and Type-Cn functions proposed by Makris & Chang (1998). Their pulse ground accelerations are respectively expressed as

$$\ddot{u}_A(t) = \frac{\pi V_p}{T_p}\sin(\frac{2\pi t}{T_p}) = A_p \sin(\omega_p t), \quad 0 \le t \le T_p \qquad (1)$$

$$\ddot{u}_B(t) = \frac{2\pi V_p}{T_p}\cos(\frac{2\pi t}{T_p}) = B_p \cos(\omega_p t), \quad 0 \le t \le T_p \qquad (2)$$

$$\ddot{u}_C(t) = \frac{2\pi V_p}{T_p}\cos(\frac{2\pi t}{T_p} + \varphi) = C_p \cos(\omega_p t + \varphi), 0 \le t \le cT_p \qquad (3)$$

In the above expressions, A_p, B_p, and C_p are the corresponding PGA and T_p is the pulse period. Also, V_p is approximated to the peak ground velocity (PGV) and $\omega_p = 2\pi / T_p$. $c = (n + 1/2 - \varphi/\pi)$, is the multiplier of pulse duration for Type-Cn and n represents the cycle number. The Type-A, Type-B, and Type-Cn pulses represent fling-step ground motions, ground motions with forward directivity, and cyclic pulse ground motions, respectively.

Nonlinear time-history analyses of the isolated bridge model under the three pulse motions with a PGA of 0.5g were carried out. The pulse period T_p was varied from 0.5 to 14 seconds and three different numbers of cycles, namely one, two, and four, were considered. Different stiffness ratios, α, ranging from 0.05 to 0.5 were used in the parametric study to evaluate its influence on the pulse response. A period ratio defined as T_p / T_d, where T_d is the isolation period calculated with the post-yield stiffness of the LRBs, is introduced for the following discussion of analysis results. The peak acceleration and displacement at the deck center were collected to evaluate the effects of the period ratio, pulse type, cycle number, and post-yield stiffness ratio on the

dynamic response of the isolated bridge. Figures 4a-d show the peak structural acceleration and displacement responses with stiffness ratios of 0.05 and 0.45 under the 1-cycle pulse motions. The corresponding response under the scaled 0.5g Gia-Yi earthquake is also included in the figures for comparison. It is seen that the structural response was significantly enlarged under the pulse motions. Although the three types of pulse were proposed for different mechanisms of ground movement, they appear to have similar peak responses, especially near the resonant region of $T_p/T_d = 1.0$. As the stiffness ratio decreased from 0.45 to 0.05, it is observed that the acceleration response was moderately reduced, while the displacement response was significantly increased.

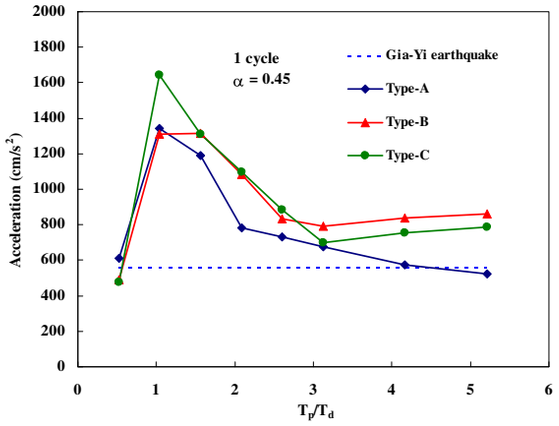


Figure 4a. Comparison of peak accelerations (α=0.45)

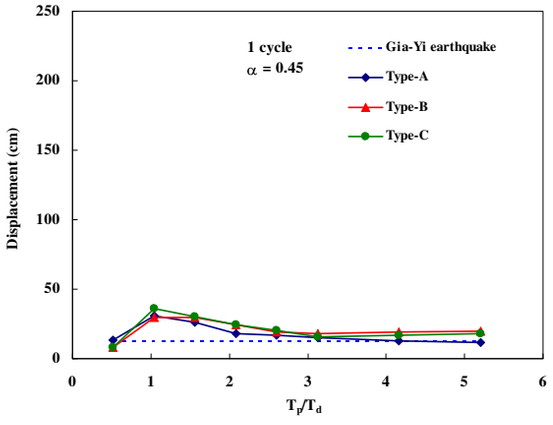


Figure 4b. Comparison of peak displacements (α=0.45)

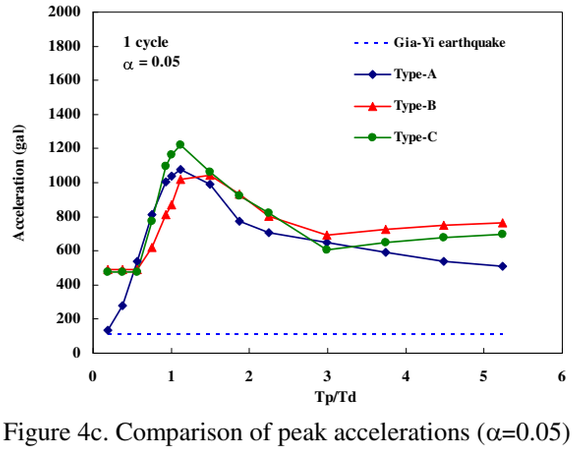


Figure 4c. Comparison of peak accelerations (α=0.05)

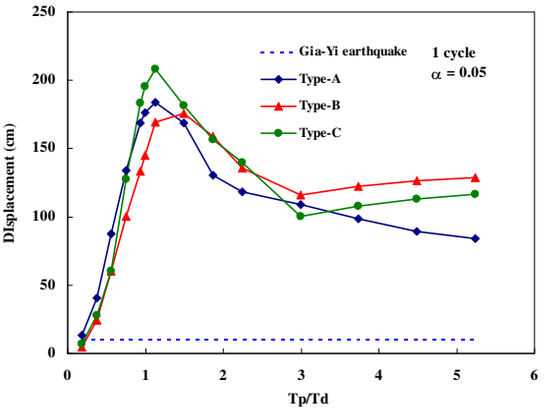


Figure 4d. Comparison of peak displacements (α=0.05)

In fact, irrespective of the stiffness ratio, the consistency of the peak structural response under the three pulse motions increases with the cycle number. Since the Type-Cn pulse is the one inducing the largest demand, it is used for the remaining discussion in this section. Figures 5a and b present the effect of period ratio and cycle number on the structural response. It is seen that the maximum response occurs in the resonant region where the period ratio is approximate to 1.0. The cycle number only takes effect at the resonant region. The resonant region approximately ranges from $T_p/T_d = 0.75$ to $T_p/T_d = 1.5$.

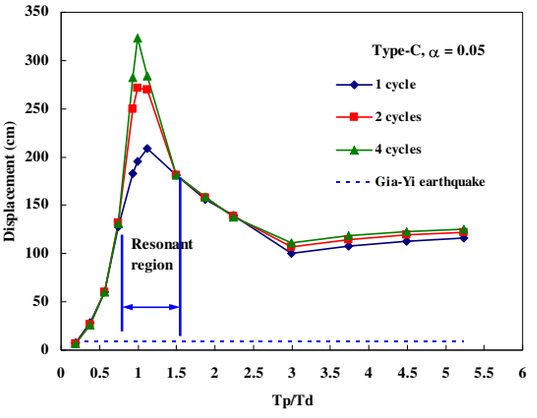


Figure 5a. Effect of period ratio and cycle number on peak displacements (α=0.05)

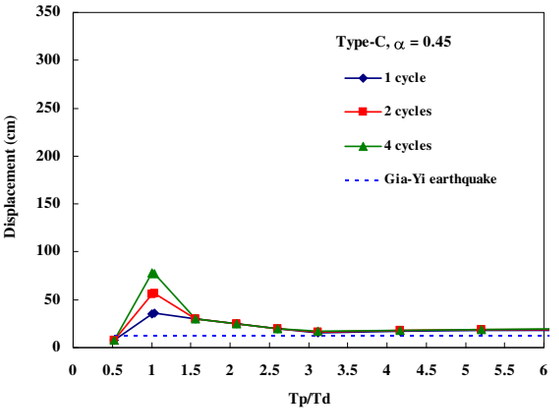


Figure 5b. Effect of period ratio and cycle number on peak accelerations (α=0.45)

The benefit of increasing post-yield stiffness ratio of the LRBs can be more pronounced as shown in Figures 6a and b. The figures show the variation of the peak deck acceleration and displacement with the post-yield stiffness ratio for the Type-Cn pulse motions. It can be seen that the displacement was effectively reduced as the stiffness ratio increased from 5% to 25%. When the stiffness ratio increases even further, the benefit to the displacement reduction becomes marginal. However, the acceleration response may generally increase with the stiffness ratio as expected. Even though, it is interesting to note that the increase in peak acceleration is less significant under the one-cycle pulse motions than under the multi-cycle pulse motions. Similar results were obtained for the Type-A and Type-B pulse motions, which are not shown herein.

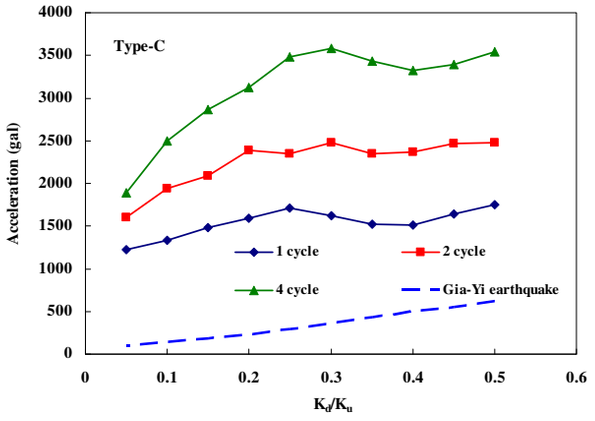


Figure 6a. Variation of the peak deck acceleration with the post-yield stiffness ratio

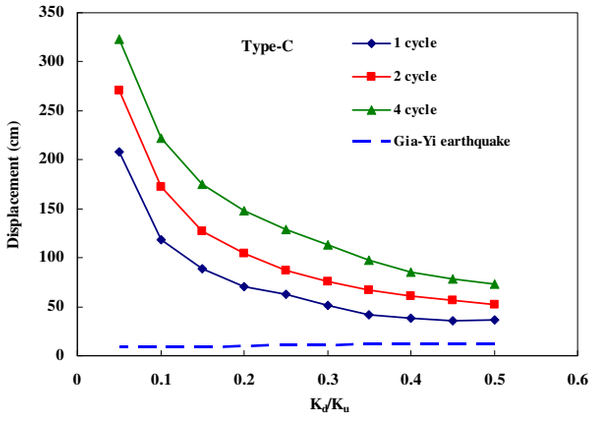


Figure 6b. Variation of the peak deck displacement with the post-yield stiffness ratio

5 PEAK RESPONSE UNDER NEAR-FIELD AND FAR-FIELD SEISMIC GROUND MOTIONS

From the analysis results of the isolated bridge under the pulse ground motions, it is known that the peak displacement could be significantly reduced and the peak acceleration moderately increased as the stiffness ratio of the LRBs was increased from low to medium values. The peak response occurs at a period ratio in the vicinity of 1.0. Also, they may increase moderately with the cycle number of the pulse ground motions. In order to understand the consistency between the pulse and seismic response of the isolated bridge, twenty pulse-like NF earthquake records were selected from the studies of Avsar & Özdemir (2013) and Baker (2007) for the seismic response analysis of the isolated bridge. Ten FF seismic ground motions were also selected from Avsar & Özdemir (2013) for comparison. All the seismic records were scaled to have a constant PGA of 0.5 g. Figures 7a and b show the 5%-damped individual and average response spectra of the NF and FF seismic records, respectively. It is observed from the figures that the NF ground motions have larger spectrum values than the FF ones in the medium-to-long period range. Hence, larger seismic response under the NF ground motions can be expected for the isolated bridge.

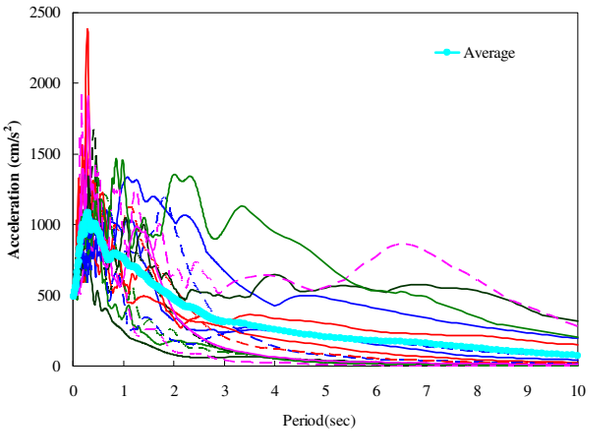


Figure 7a. The 5%-damped individual and average response spectra of the NF seismic records

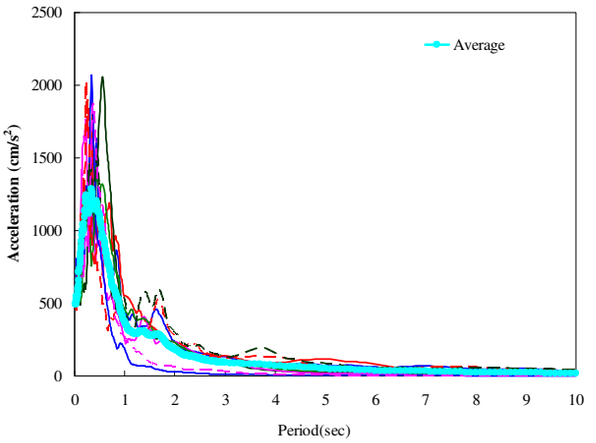


Figure 7b. The 5%-damped individual and average response spectra of the FF seismic records

Figures 8 and 9 present the peak structural response of the isolated bridge model with varied post-yield stiffness ratio under the pulse-like NF and FF seismic records, respectively. The mean (μ), mean-plus-one standard deviation (μ + σ), and mean-minus-one standard deviation (μ - σ) of the struc-

tural response are also indicated in the figures. It is apparent that the NF earthquakes induced significantly larger response than the FF ones. In general, the mean displacement and acceleration responses under the NF earthquakes are around 2~3 times of that under the FF earthquakes. It is interesting to note that the effect of increasing the post-yield stiffness ratio on the displacement response is more significant for the NF than the FF earthquakes, as shown in Figures 8a and 9a. As the ratio was increased from 0.10 to 0.25, the reduction in the mean displacement response was 30% for the NF earthquakes but only about 18% for the FF ones. Meanwhile, the amplification in the mean acceleration response was about 57% for both the NF and FF earthquakes in this range, as shown in Figures 8b and 9b. Variations of the mean and the mean-plus-one standard deviation curves show that the reduction in displacement and amplification in acceleration response are moderate as the stiffness ratio is larger than 0.25. A tradeoff between the displacement reduction and acceleration amplification should be determined if the LRBs are the only energy dissipation device against the NF earthquakes.

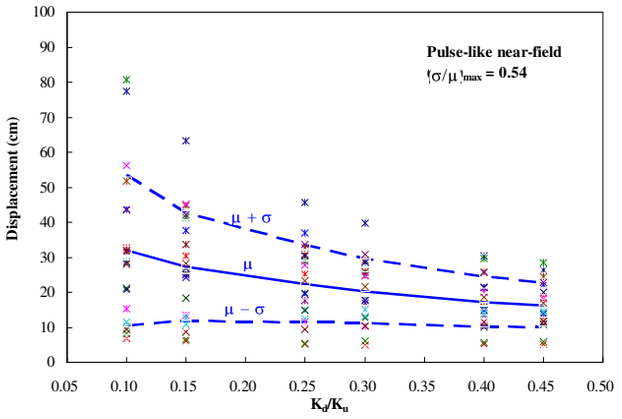


Figure 8a. Peak displacement response under the NF seismic records

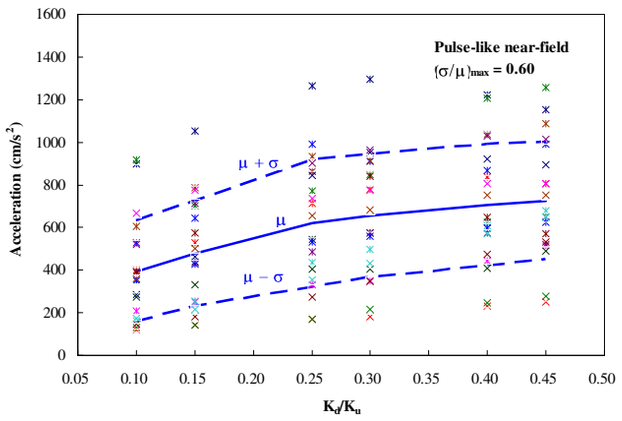


Figure 8b. Peak acceleration response under the NF seismic records

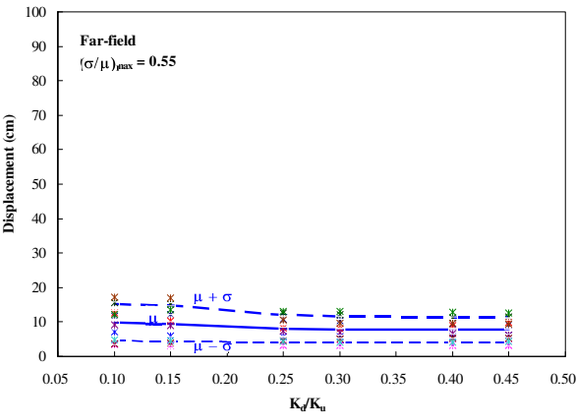


Figure 9a. Peak displacement response under the FF seismic records

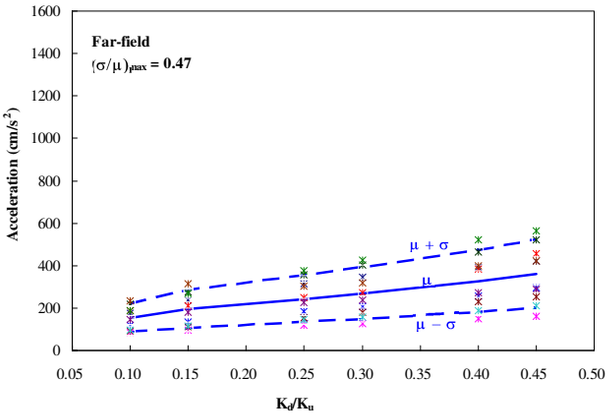


Figure 9b. Peak acceleration response under the FF seismic records

In a previous section, the influence of the period ratio on the peak structural response of the isolated bridge with LRBs of various post-yield stiffness ratios were investigated for the three pulse ground motions. It was shown that the peak response occurs as the isolation period is close to the pulse period. In order to understand if similar conclusion could be made for the pulse-like NF ground motions, the pulse period of the twenty NF ground motions were scaled to each specified pulse period and nonlinear time history analysis was conducted for the isolated bridge model with LRBs of different post-yield stiffness ratios. However, the peak displacement response under the NF ground motions with scaled pulse periods generally increases with the period ratio for each stiffness ratio, as shown in Figures 10a-d. The main reason for this apparent difference in the variation trend is that the pulse ground motions contain only a single frequency, while the NF seismic excitations have a wider range of frequency contents. Hence, even though the pulse period is away from the isolation period, there are still remaining seismic waves with periods close to the isolation period (Bake 2007). Nevertheless, increase in the peak displacement with the pulse period becomes moderate as the period ratio is larger than 2.0.

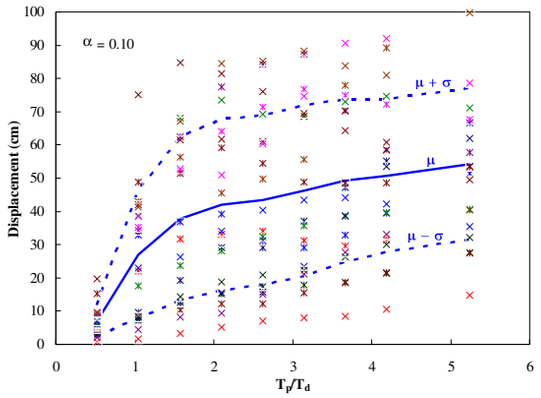


Figure 10a. Peak displacement response under the NF ground motions with scaled pulse periods (α= 0.10)

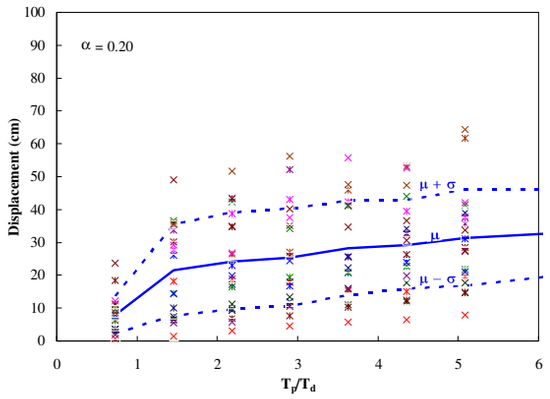


Figure 10b. Peak displacement response under the NF ground motions with scaled pulse periods (α= 0.20)

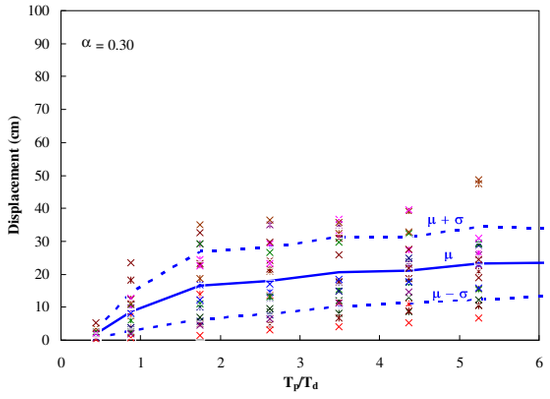


Figure 10c. Peak displacement response under the NF ground motions with scaled pulse periods (α= 0.30)

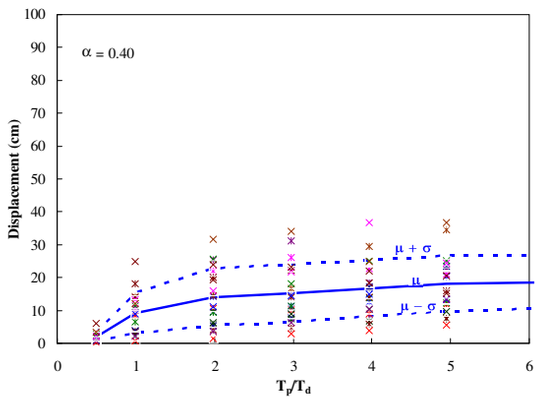


Figure 10d. Peak displacement response under the NF ground motions with scaled pulse periods (α= 0.40)

At last, figures 11a and b present the variation of the mean-plus-one standard deviation response of the peak displacement and acceleration with the post-yield stiffness ratio of LRBs, respectively, under the NF seismic motions with scaled pulse periods. It is seen that the increase of peak structural response gradually reduces with the increased pulse period. The corresponding response curves of the isolated bridge model under one-cycle excitations of the three pulse motions are also included in the figures. Apparently, the one-cycle pulse response is larger than the mean-plus-one standard deviation response under the pulse NF seismic excitations. The latter response generally varies from 70% to 82% of the pulse response under the one-cycle Type-A motions in the considered range of post-yield stiffness ratio. This implies that the one-cycle Type-A pulse may be an appropriate ground motion for the extreme seismic demand under pulse-like NF earthquakes. Because of its simple mathematical expressions, the peak structural response of an isolated bridge under the one-cycle Type-A ground motion with pulse period equal to the isolation period can be easily obtained.

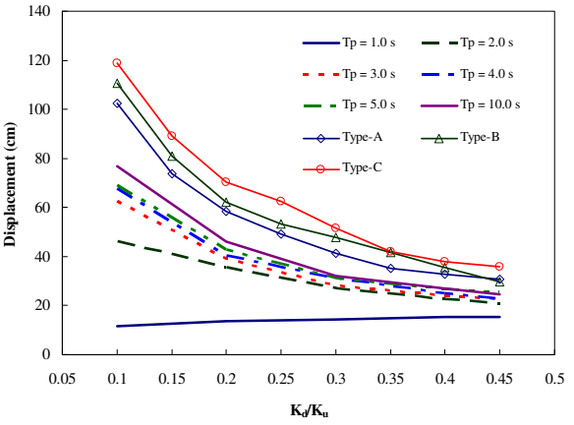


Figure 11a. Variation of the mean-plus-one standard deviation of peak displacement with the post-yield stiffness ratio of LRBs

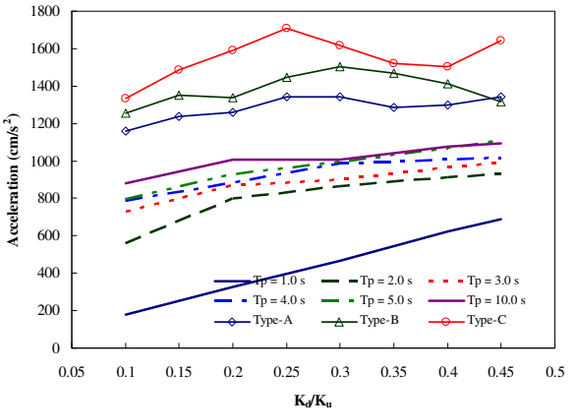


Figure 11b. Variation of the mean-plus-one standard deviation of peak acceleration with the post-yield stiffness ratio of LRBs

6 CONCLUSIONS

A typical seismically isolated bridge model with LRBs was constructed and verified with measured acceleration time histories under an earthquake event. Dynamic responses of the isolated bridge model under three types of pulse ground motion with various pulse periods and cycle numbers were investigated. The analysis results revealed that the three pulse motions have similar structural demands, especially as the cycle number increases. The pulse response depends on the pulse-to-isolation period ratio T_p/T_d. Peak displacement and acceleration response occur around the period ratio of 1.0. From the peak structural responses of the isolated bridge model with LRBs of various post-yield stiffness ratios, it was realized that the peak displacement decreases with increased stiffness ratio. However, an opposite trend was induced for the peak acceleration. Even though, it was observed that an optimal stiffness ratio exists in the range between 0.2 and 0.3 for reducing the peak displacement response.

In order to evaluate the consistency between the pulse and seismic structural response, twenty pulse-like NF and ten FF earthquake records were used for the seismic response analysis of the isolated bridge. The analysis results indicated that the effect of increasing the post-yield stiffness ratio on the displacement response is more significant for the NF than the FF earthquakes. Variations of the mean and the mean-plus-one standard deviation curves show that the reduction in displacement and amplification in acceleration response are moderate as the stiffness ratio is larger than 0.25. Moreover, seismic response of the isolated bridge model with LRBs of varied post-yield stiffness ratio under the twenty NF ground motions with scaled pulse periods was obtained. Different from the variations under the pulse motions, the peak displacement response under the NF ground motions with scaled pulse periods generally increases with the period ratio. Nevertheless, the increase in the peak displacement with the pulse period becomes moderate as the period ratio is larger than 2.0. A comparison between the structural response under the pulse-like NF and the one-cycle Type-A pulse ground motions revealed that the mean-plus-one standard deviation response of the former varied from 70% to 82% of the latter for the considered range of the post-yield stiffness ratio. This implies that the one-cycle Type-A pulse could be used as an appropriate ground motion to estimate the extreme seismic demand of the isolated bridge with LRBs under pulse-like NF earthquakes.

REFERENCES

Amiri, J.V., Davoodi, M.R., & Sahafi, A. 2008. Simulation of near-fault ground motions with equivalent pulses & compare their effects on MRF structures. In *The 14th World Conference on Earthquake Engineering, Beijing, October 12-17*, China.

Avsar, O. & Ozdemir, G. 2013. Response of seismic-isolated bridges in relation to intensity measures of ordinary and pulselike ground motions. *Journal of Bridge Engineering* 18(3): 250-260.

Baker, J.W. 2007. Quantitative classification of near-fault ground motions using wavelet analysis. *Bulletin of Seismological Society of America* 97(5): 1486-1501.

Chopra, A.K. & Chintanapakdee, C. 2001. Comparing response of SDF systems to near-fault and far-fault earthquake motions in the context of spectral regions. *Earthquake Engineering and Structural Dynamics* 30: 1769-1789.

Dicleli, M. 2006. Performance of seismic-isolated bridges in relation to near-fault ground-motion and isolator characteristics. *Earthquake Spectra* 22(4): 887-907.

He, W.L. & Agrawal, A.K. 2008. An analytical model of ground motion pulses for the design and assessment of smart protective systems. *Journal of Structural Engineering* 134(7): 1177-1188.

Jangid, R.S. 2007. "Optimum lead-rubber isolation bearings for near-fault motions," *Engineering Structures* 29: 2503-2513.

Karalar, M., Padgett, J.E., & Dicleli, M. 2012. Parametric analysis of optimum isolator properties for bridges susceptible to near-fault ground motions. *Engineering Structures* 40: 276-287.

Loh, C.S. 1999. "Interpretation of Structural Damage in 921 Chi-Chi Earthquake." In *International Workshop on 921 Chi-Chi Earthquake Reconnaissance, Taichung, December 14-17*, Taiwan.

Makris, N. & Chang, S.P. 1998. *Effect of Damping Mechanisms on the Response of Seismically Isolated Structures*. Report No. PEER-98/06, Pacific Earthquake Engineering Research Center, College of Engineering, University of California, Berkeley.

Makris, N. & Chang, S.P. 2000. Response of damped oscillators to cycloidal pulse. *Journal of Engineering Mechanics* 126(2): 123-131.

Providakis, C.P. 2008. Effect of LRB isolators and supplemental viscous dampers on seismic isolated buildings under near-fault excitations. *Engineering Structures* 30: 1187-1198.

Sehhati, R., Rodriguez-Marek, A., Elgawady, M., & Cofer, W.F. 2011. Effects of near-fault ground motions and equivalent pulses on multi-story structures. *Engineering Structures* 33: 767-779.

Shen, J., Tsai, M.H., Chang, K.C., & Lee, G.C. 2004. Performance of A Seismically Isolated Bridge under Near-Fault Earthquake Ground Motions. *Journal of Structural Engineering* 130(6): 861-868.

Xu, L. & Xie, L. 2006. Simplified ground motion pulses in the near-fault region. In *Proceeding of the 4th International Conference on Earthquake Engineering, Taipei, October 12-13,* Taiwan.

Maintenance, Safety, Risk, Management and Life-Cycle Performance of Bridges – Powers, Frangopol, Al-Mahaidi & Caprani (Eds)
© 2018 Taylor & Francis Group, London, ISBN 978-1-138-73045-8

Research on Seismic Performance of Self-Compacting Concrete Bridge Columns

Zhiqiang Wang, Hongliang Duan, Hongyi Wei, Jieli Yang & Xianfeng Sun
Tongji University, Shanghai, China

ABSTRACT: Using self-compacting concrete to cast the bridge pier can improve the placeability of the concrete, reduce the labor costs, and achieve convenient green construction. Due to there is relatively lack of the research on mechanical behavior of self-compacting concrete columns and little design criterion or manual can be followed, self-compacting concrete is used less in actual bridge engineering in China. The quasi-static tests of self-compacting concrete bridge columns were performed to study the seismic performance in this paper. Based on practical engineering background, two specimens of concrete bridge column, with self-compacting concrete (SCC) and normally-vibrated concrete (NVC), were conducted in 1:3 scale ratio. The main objective of this research is to evaluate the influences of concrete material on the seismic performance of bridge columns. The failure modes, ultimate strength, hysteresis loops, skeleton curves, ductility and residual displacement of columns are presented and analyzed. The quasi-static test results show that, compared with normally-vibrated concrete column, the displacement ductility and energy dissipation capacity of self-compacting concrete column is insufficient. For the failure mode, plastic hinge is formed at the bottom of normally-vibrated concrete column. The height of plastic region is about 30~50cm for normally-vibrated concrete column. The self-compacting concrete column shows similar damage form; the height of plastic region is about 20cm. Nevertheless, due to poor bonding performance of self-compacting concrete, the stripping between longitudinal reinforcements, stirrups and concrete is discovered.

1 INTRODUCTION

Among the high-performance materials which are actively developed and popularized in the construction industry in the world, self-compacting concrete can be used to improve the concrete workability, reduce the labor cost and realize the convenient green construction. Many scholars have studied the compressive performance of SCC columns, and different factors that influence the static and compressive mechanical behaviors of SCC columns are discussed [1~4]. Nevertheless, the research on the seismic performance of self-compacting concrete is merely a few from researchers abroad, and the domestic research is close to the blank. Furthermore, the seismic performance of self-compacting concrete members is studied in building industry initially [5~6]. Due to the lack of research on mechanical properties of self-compacting concrete columns and the design criteria that can be followed, the application of self-compacting concrete in bridge construction is limited, and it is mainly confined to the concrete filled into steel pipe in concrete-filled steel tubular arch bridges. In order to use self-compacting concrete piers in seismic regions, it is necessary to develop the experimental study on the piers with self-compacting concrete, and to investigate the seismic performance and damage mechanism of self-compacting concrete piers, thereafter providing reliable basic research results.

2 EXPERIMENTAL PROGRAM

2.1 *Test specimens*

Two cast-in-place column specimens are designed in this paper. The specimen 2# is a cast-in-place self-compacting reinforced concrete column, which is used to study the seismic performance and damage mechanism of bridge piers. Specimen #1 is the cast-in-place (CIP) reinforced concrete column, which is designed as the benchmark.

The columns of specimens are 3.2m in height with the rectangular cross-section of 0.5m×0.53m. The footing of dimension 1.6m×1.6m×0.6m, is used to anchor the specimen to the strong floor of the lab. The dimension of the column cap is

0.9m×0.5m×0.4m. The effective loading height is 3.4m. The shear span ratio of the specimen is 6.42. Figure1 shows the geometric sizes of the two columns.

The materials used are C40 concrete, hot-rolled plain bar with nominal yield strength of 235MPa (HPB235), the concrete of the 1# specimen is normally-vibrated concrete, and the 2# specimen is self-compacting concrete.

The longitudinal reinforcements of specimen consist of ten 20mm-diameter hot-rolled ribbed bars (HRB400) and fourteen 8mm-diameter supplementary plain bars(HPB235). The nominal yield strength of hot-rolled ribbed bar and hot-rolled plain bar is 400MPa and 235MPa respectively. Detailed reinforcement arrangement is shown in Figure 2.

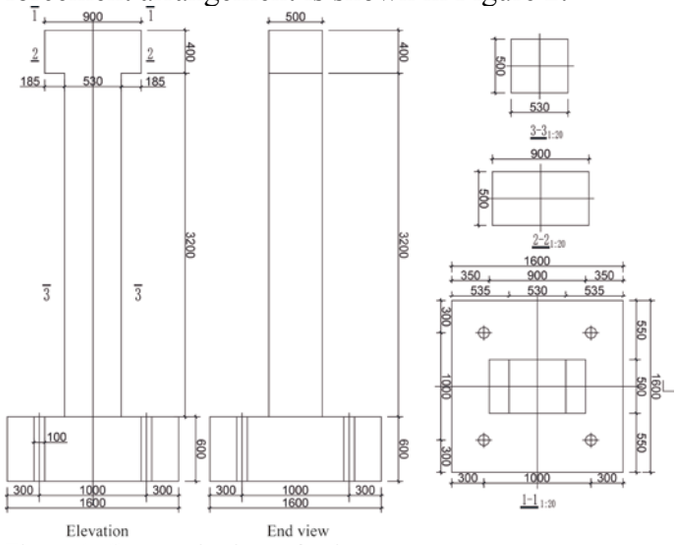


Figure 1. Geometric sizes of columns.

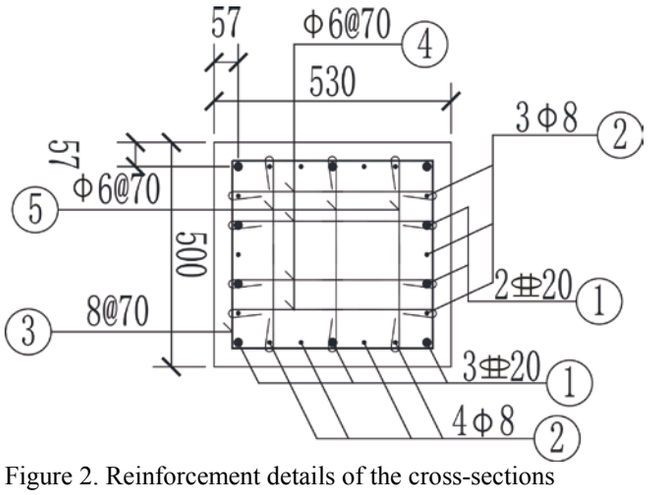
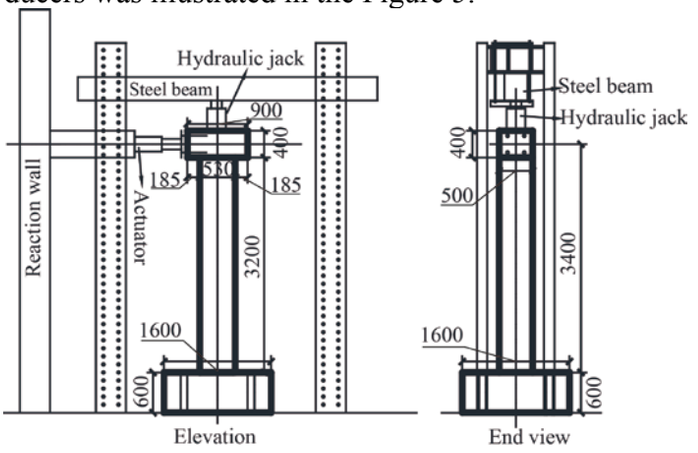


Figure 2. Reinforcement details of the cross-sections

2.2 *Loading and measurements*

The quasi-static cyclic loading experiment was conducted under displacement control. Figure 3 illustrates the test set-up for the cyclic loading test. Both the two specimens were subjected to a combination of axial load provided by a vertical actuator and repeated lateral loads applied by a hydraulic actuator mounted on the reaction wall. The displacement-controlled test was conducted on the basis of applied deformation levels, as shown in Figure 4, which were initiated by 2mm, and subsequently increased to 5mm, 10mm, 15mm, 20mm, 25mm, 30mm, 40mm, 60mm, and were finalized at failure. The maximum stroke of the actuator was ±250mm and each displacement was applied twice.

Global behavior of the specimens was estimated by measuring lateral displacements through displacement transducers and lateral force by a load cell of the actuator. The distribution of displacement transducers was illustrated in the Figure 5.



(a) Schematic diagram of test devices (unit: mm)



(b) Test specimen

Figure 3. Test setup

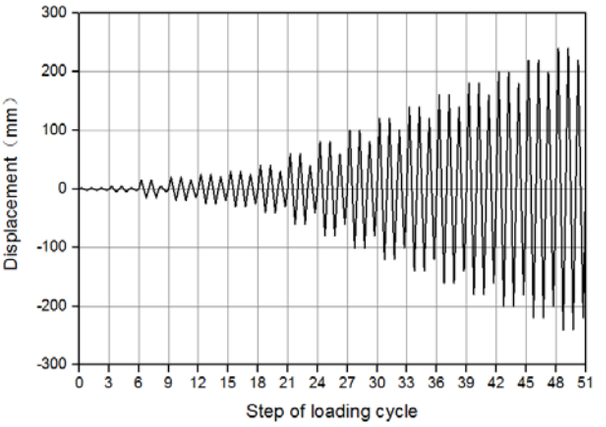


Figure 4. Loading procedure.

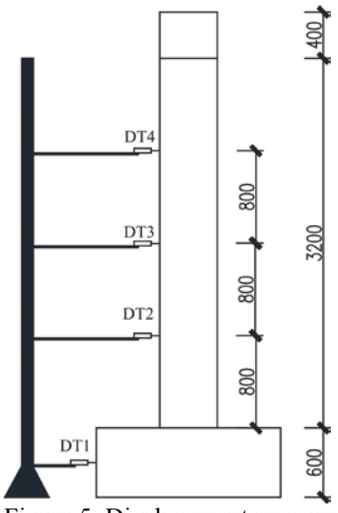


Figure 5. Displacement measurement.

3 TEST RESULTS

3.1 *Specimen damage and failure*

The performance level of bridge can be divided into five stages [7], which includes I: cracking, II: yielding, III: initiation of local mechanism, IV: full development of local mechanism, and V: strength degradation.

According to the above five stages, damage state and performance level of the two specimens are described as follows:

Level I initiated at the time when the column top displacement of 1# specimen and 2# specimen was 5mm and 10mm respectively. The hair-like cracks began to emerge, but they closed up after unloading.

The damage Level II was achieved when the top displacement of the 1# specimen and the 2# specimen pier reached 25mm and 20mm respectively. Corresponding to the 1# specimen, there were many bending cracks along the column, and a number of cracks extended to the side faces. The crack spacing was relatively uniform, about 15~20mm, the crack width was of 0.04~0.28mm.The crack width at the bottom of column was around 1mm. Crack still closed up after unloading. The measured value of the crack spacing in the 2# specimen was 20mm, and the width was 0.04~0.30mm.

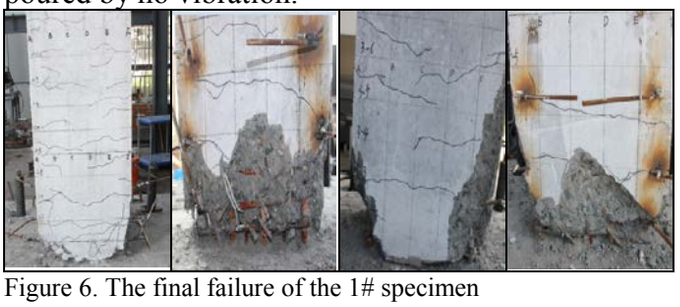
When the top displacement of 1# specimen and 2# specimen pier was 60mm and 80mm respectively, the piers reached the level III. At this time, corresponding to the 1# specimen, columns arose series of flexural cracks and diagonal cracks. The width of the fracture was 0.1~0.8mm, and multiple horizontal cracks closed up through cross section under the positive and negative load. The crack width of the column bottom was of 5~9mm, with a trend of column foot concrete to shed. The 2# specimen damage was similar to the situation. The crack width along the column was 0.1~0.42mm, with 3mm cracks at the bottom.

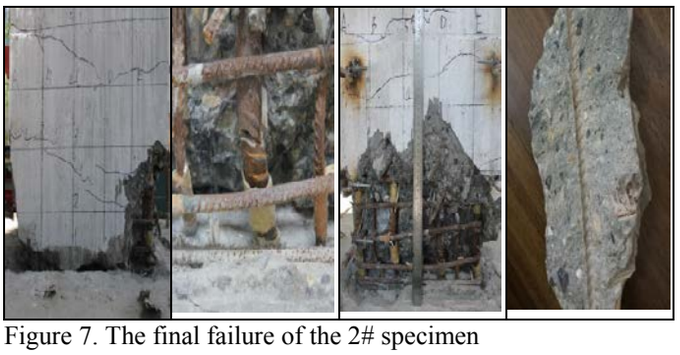
Level IV was when the corresponding loading displacement of the 1# specimen was 120mm, the concrete cracks of 1# specimen were staggered at a height of 15cm from the top surface of footing. In the course of the 10cm height above the platform, the concrete protective cover was peeled off and had a tendency to continue to flake. The crack width at the bottom of the column exceeded 10 mm. When the loading displacement reached 100mm, the 2# specimen was damaged as above. The concrete protective cover was peeled off at a height of 15cm from the footing. The crack width was more than 10mm.

When 1# specimen's load displacement achieved 160mm, the specimen carrying capacity reduced to 85% of the maximum load, reaching the level V of strength degradation. A large amount of concrete around the bottom fell out, and the width of the crack at the bottom measured about 20 mm. For the 2# specimen, the specimen carrying capacity reduced to 85% or less of the maximum load at the stage of 140mm displacement.

The final failure of the 1# specimen was shown in Figure 6. It can be observed that the destruction area was mainly concentrated in the column bottom. The height of plastic region was about 30~50mm. The longitudinal reinforcements buckled (one of the bars was fractured), and the stirrups bulged outward.

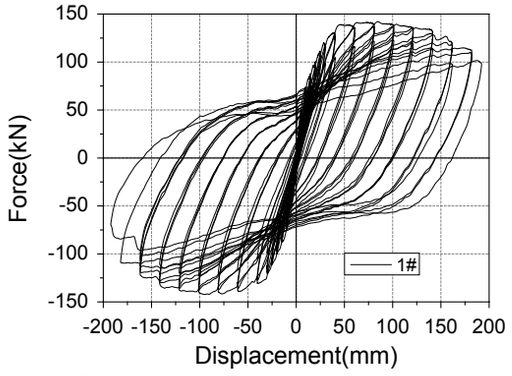
As shown in Figure 7, the 2# specimen was damaged in the same way with the height of plastic region about 20mm. Additionally, from the shed flake of the concrete protective cover, it could be observed that column longitudinal reinforcements and stirrups had complete separation interface to self-compacting concrete, providing inferior bonding performance. It might result from the self-compacting concrete poured by no vibration.


Figure 6. The final failure of the 1# specimen

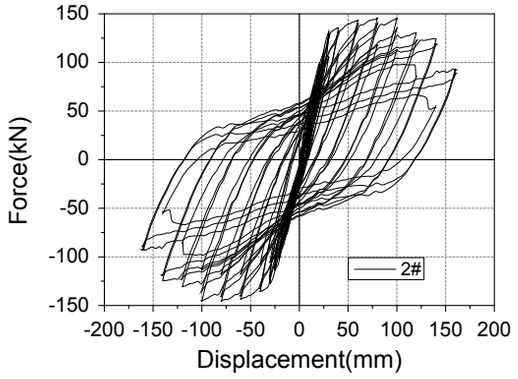

Figure 7. The final failure of the 2# specimen

3.2 *Evaluation of experimental results*

3.2.1 *Hysteresis curve*



(a) 1# Specimen



(b) 2# Specimen

Figure 8. Load-displacement relationship

The load-displacement relation of all specimens (Figure 8) reveals that the two specimens were in the elastic stage under the lower load. With the increase of the loading displacement level, the nonlinear phenomena such as the cracking of the concrete and the yield of the steel were gradually occurring. The hysteresis loop enlarged, and energy consumption increased. In general, both specimens showed flexible failure. Compared to the self-compacting concrete column, the ordinary vibrated concrete column had relatively plump hysteresis loops and slow intensity degradation throughout the test.

3.2.2 *Skeleton curves*

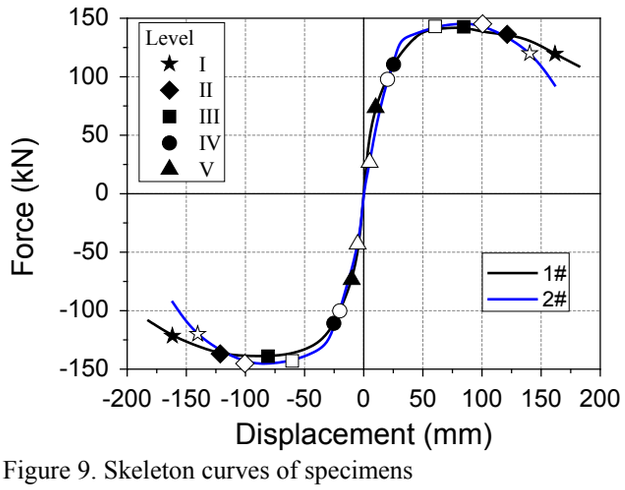


Figure 9. Skeleton curves of specimens

The skeleton curves of the two specimens is similar. In the early stage of loading, compared with the ordinary vibrated concrete specimen, the self-compacting concrete specimen was the earlier to crack and the stiffness was relatively small. When the displacement was loaded up to 80mm, both of the columns reached the ultimate carrying capacity. Then the carrying capacity began to decline. The ordinary vibrated concrete pier showed a gentler strength attenuation and a relatively good ductility.

3.2.3 *Drift*

The strength of the 1# specimen reduced to below 85% at 160mm loading, corresponding to the drift ratio of 4.71%. The strength of the 2# specimen decreased to 85% under 140mm loading with 4.12% drift ratio.

3.2.4 *Ductility*

The ductile coefficient calculated by the general yield bending moment method is shown in the table 1 below. On the whole, the self-compacting concrete column had relatively worse ductility compared to ordinary vibrated concrete pier.

Table 1. Ductility of the specimens

	Spec. #1	Spec. #2
Δ_y (mm)	21.7	25.2
Δ_u (mm)	158.7	140.6
μ	7.3	5.6

3.2.5 *Residual displacement*

The residual displacement at different load levels for all specimens is shown in Figure10. The specimen's relationship curve of the residual displacement was very close. At the initial loading, the specimen remained elastic as a whole. After unloading the specimen can be restored to the initial state and the residual deformation was close to zero. With the increase of the loading displacement, the specimen damage occurred and the residual deformation increases gradually.

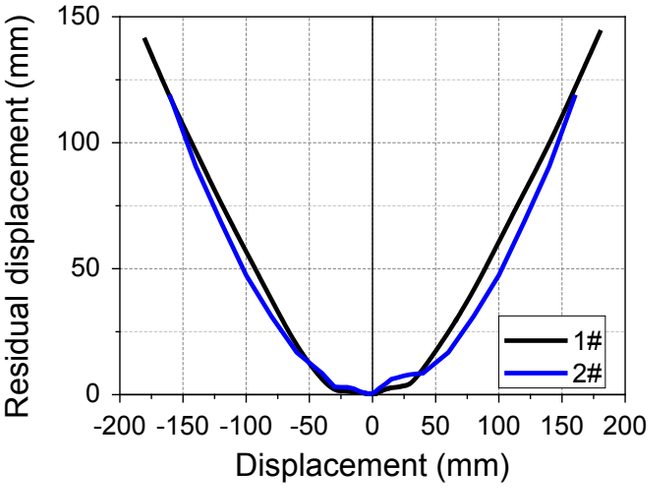


Figure 10. Residual displacement of specimens

4 CONCLUSIONS

In order to research on Seismic Performance of Self-Compacting Concrete Bridge Columns, a quasi-static cyclic loading experiment was conducted. Based on the results, the following conclusions can be drawn:

When the top displacement of the 1# and 2# specimen reached 160mm and 140mm respectively, the specimen carrying capacity reduced to 85% or less of the maximum load.

The failure of the two specimens was shown as flexible damage. Destruction mainly concentrated in the bottom of the column. A large number of concrete protective cover peeled off and core concrete crushed. Longitudinal reinforcements buckled and stirrups bulged outward. The height of plastic region of the 1# specimen was about 30-50mm. Correspondingly, the one of the 2# self-compacting concrete column was about 20mm.

The bonding performance of the self-compacting concrete was inferior. The stripping between longitudinal reinforcements, stirrups and concrete is discovered.

Comparison of hysteresis curve and skeleton curve, the normally-vibrated concrete column had relatively plump hysteresis loops and slow intensity degradation throughout the test.

The self-compacting concrete column had relatively worse ductility compared to normally-vibrated concrete column.

The residual displacement of the self-compacting concrete column and normally-vibrated concrete column was basically similar.

ACKNOWLEDGEMENTS

Financial support for this study was provided in part by the National Science Foundation of China under Award No. 51778470and 51378386, and by Science and Technology Commission of Shanghai Municipality under Award No. 13231200800.

PREFERENCES

Khayat K H, Trembley S & Paultre P.1999. Structural response of self-consolidating concrete columns. *Skarendahl A, Petersson O, First international RILEM symposium on self-compacting concrete*: 291–305.

Patrick Paultre & Kamal Khayat. 2005. Structural performance of self-consolidating concrete used in confined concrete columns. *ACI Structural Journal* 102(4): 560-568.

Angotti F, Galano L, Giordano S & Vignoli A. 2005. Assessment of structural performance of SCC and HSC little size slender columns via experimental tests. *Proceedings of first international symposium on design, performance and use of self-consolidating concrete*.

P. Srilakshmi & M. V. Seshagirirao. 2012. Comparison of different stress-strain models for confined self-compacting concrete (scc) under axial compression. I*nternational Journal of Advances in Engineering & Technology* 5(1):185-193.

H. Okamura, K. Maekawa & T. Mishima. 2005. Performance Based Design for Self-Compacting Structural High-Strength Concrete. *ACI Materials Journal*.

Mohanmmad Soleymani Ashtian & Rajesh P. 2014. Seismic Performance of High-Strength Self-Compacting Concrete in Reinforced Concrete Beam-Column Joints. *J. Struct. Eng*:140(5):21-27.

Hose, Y. D. & Seible, F. 1999. Performance evaluation database for concrete bridge components and systems under simulated seismic loads. *Pacific Earthquake Engineering Research Center, Berkeley, CA.*

Tiantian Li.2013. Research on Structural Details and Seismic Performance of Urban Viaduct Precast Segmental Concrete Column. *Shanghai：Tongji University*.

Hongliang Duan. 2017. Research on Mechanical Behavior of Self-Compacting Concrete Columns. S*hanghai：Tongji University.*

Maintenance, Safety, Risk, Management and Life-Cycle Performance of Bridges – Powers, Frangopol, Al-Mahaidi & Caprani (Eds)
© 2018 Taylor & Francis Group, London, ISBN 978-1-138-73045-8

Seismic Fragility of High-Speed Railway Bridge with High Pier

J. Dong
China Railway ErYuan Engineering Group Co.Ltd, ChenDu, China
D.S. Shan
Bridge Engineering Dept, Southwest JiaoTong University, ChenDu, China
G.J. Yang & Y.P. Zeng
China Railway ErYuan Engineering Group Co.Ltd, ChenDu, China

ABSTRACT: In order to evaluate the seismic performance of typical continuous rigid railway bridge with high pier under the action of near fault ground motion in western China, the vulnerability analysis of this type of bridge is carried out by using kernel density estimation method (KDE method). Considering the uncertainty of ground motions and bridge parameters, a model sample database is generated. The seismic response of the bridge is obtained based on the time-history analysis of the model sample database on the OpenSees platform. A bridge vulnerability analysis method based on KDE is proposed, in which the curvature ductility ratio and relative displacement are respectively considered as pier and bearing damage indexes. The longitudinal and transverse vulnerability curves of the structure are calculated and then the vulnerability distribution characteristics of the pier is studied deeply by this method. The results show that the failure probability of bearing is the highest among all the bridge members. It is also observed that the damage is mainly concentrated on the top and bottom of high pier under strong near fault ground motions. Further more, the established vulnerability curves can be used to evaluate the seismic performance of long span bridges with high pier, as well as to provide the basis for seismic risk assessment, seismic damage diagnosis and retrofit policy in transport system.

1 INTRODUCTION

In recent years, with the rapid development of traffic network in the west of China, a large number of railway lines have emerged in the western region. To cross the complex terrain, high mountains and deep valley areas, long span bridges with high pier are widely used, among which the multi-span continuous rigid frame railway bridge with high pier is more common. The increase of the pier height and span brings many technical problems about seismic design for railway bridges in this area. At the same time, the seismic activity in the western region of China is frequent in recent years, which makes the bridge operation safety being seriously challenged.

Since the beginning of 21st century, with the basic framework of probabilistic method for seismic design and evaluation based on performance put forward by the Pacific Earthquake Engineering Research (Mackie 2005), the seismic vulnerability curve has gradually become an important mean to evaluate the seismic performance of structures. At present, the study of seismic vulnerability has been deepened into various fields of traffic lifeline engineering. Bridge is an important hub of traffic lifeline system, therefore it is the key object of seismic vulnerability research.

Seismic vulnerability analysis methods generally include empirical method, test analysis method, and theoretical analysis method (Dong 2016). In recent years, due to the lack of real bridge seismic data in many areas, the theoretical vulnerability analysis of bridge has been more widely and deeply studied by scholars in various countries. Danusa (2012) conducted seismic vulnerability analysis for five common types of bridges in Quebec, Canada. Siqueira et al. (2014) made a design for strengthening and repairing a three-span continuous girder bridge in Quebec, Canada and established the seismic vulnerability curves of the bridge before and after the reinforcement. Noori et al. (2015) carried out the vulnerability analysis of the typical simple supported girder highway bridge in the central and eastern area of the United States, and studied the influence of the parameters (including the longitudinal inclination angle and the pier height) on the vulnerability of the bridge. Mosleh et al. (2016) established a probabilistic seismic demand model for a 32 meter-span simply supported girder bridge built in Iran in the 1990s and studied the seismic performance of the bridge under near fault and far field earthquakes. However, most of the above vulnerability analysis research work is aiming at the common regular bridges (such as simply supported bridge, medium and small span continuous girder bridge) and single bridge component (such as piers, bearings, etc.). For the western region of China, the vulnerability research for the railway long span

rigid frame and continuous girder bridge with high pier is few.

Based on this, the typical irregular rigid frame bridge in western China is taken as the study object in this paper. Considering the uncertainty of ground motion and bridge structure parameters and using the KDE based bridge vulnerability analysis method (Dong 2016), the vulnerability curve of the bridge structure is established and the seismic vulnerability character of the bridge structure is analyzed. And then the seismic performance of the typical railway bridge structure is evaluated, which provides the basis for the seismic design and post-earthquake damage identification of the bridge.

2 KERNEL DENSITY ESTIMATION BASED BRIDGE SEISMIC VULNERABILITY ANALYSIS METHOD

Seismic vulnerability refers to the probability that the damage degree of structures exceeds the specific damage state under the action of a certain intensity of earthquake (Nielson 2005). The calculation formula of seismic vulnerability probability for bridge components is as follows (Chen 2012):

$$P_f(IM,C)=P[\ D\geq C\ |IM\ ] \tag{1}$$

Where C represents the seismic response demand value of bridge components; D represents the capacity of bridge components to resist the seismic action; IM represents the ground motion intensity value; P_f (IM,C) indicates the probability that bridge components reach a specific damage state under the effect of earthquake with the intensity value of IM.

Carrying the conditional probability density function $f_{D|IM}$ of the seismic capacity of bridge components into the formula (1), then the vulnerability probability formula can be written as:

$$P_f(a,C)=P[D\geq C|IM=a]=\int_C^{+\infty} f_D(c|IM=a)dc \tag{2}$$

According to the theory of probability and statistics, the calculation formula of probability density function for seismic capacity of bridge components is:

$$f_D(c|IM=a)=\frac{f_{D,IM}(c,a)}{f_{IM}(a)} \tag{3}$$

Where $f_{D,IM}(\cdot)$ is the joint probability density distribution function of seismic capacity and ground motion intensity. The $f_{IM}(\cdot)$ is the edge distribution function of IM. Other symbols mean the same as above. If $f_{D,IM}$ $(\cdot)$ and $f_{IM}(\cdot)$ are known, the damage probability of bridge components can be calculated by using the formula (2), thus the seismic vulnerability curve of bridges can be established.

In order to establish the vulnerability curve of bridge components, taking N sets $\{(IM_i,D_i),\ i=1,\cdots,N\}$ of earthquake intensity data and the maximum response data obtained by time history analysis as the basis, the calculation formulas of the joint probability density function and edge distribution function of bridge structures are derived by introducing the kernel density estimation method (Rosenblatt 1956).

Firstly, the single parameter case for the random variable X is discussed, assuming that the X variable has n sample points $\{x_1,\cdots,x_n\}$. As can be seen from the definition of kernel density estimation, the kernel density estimate for the probability density distribution function is:

$$\hat{f}_h(x)=\frac{1}{nh}\sum_{i=1}^{n}K(\frac{x-x_i}{h}) \tag{4}$$

Where h represents the bandwidth parameters and $K(\cdot)$ represents the kernel function. The current commonly used kernel functions are uniform kernel function and Gaussian kernel function which can be seen for detailed function forms (Duong 2004). The results show that when the calculated sample points are sufficient, the accuracy of the evaluation results will not be affected no matter what type of the function is chosen. Therefore, the Gauss kernel function is used as the kernel function in this paper, namely $K(x)=\varphi(x)=\exp(-x^2/2)/\sqrt{2\pi}$. Carrying it into the last equation gives:

$$\hat{f}_h(x)=\frac{1}{nh}\sum_{i=1}^{n}\varphi(\frac{x-x_i}{h}) \tag{5}$$

Wand and Jones (1995) have discovered that the optimal bandwidth parameter of the formula (5) is $h^*\approx 1.059\sigma\cdot n^{-0.2}$, where σ is the standard deviation of X. The results show that the value of h will directly affect the correctness of the evaluation results. The seismic edge distribution function with the intensity of IM can be evaluated by using the formula (5), i.e., $\hat{f}_{IM}(a)$ is estimated by the intensity of N sets $\{IM_i,i=1,\cdots,n\}$ of ground motion records.

$$\hat{f}_{IM}(a)=\frac{1}{nh_{IM}}\sum_{i=1}^{n}\varphi\left(\frac{a-IM_i}{h_{IM}}\right) \tag{6}$$

The following discussion is about the multivariate random variables $\boldsymbol{X}\in \mathrm{R}^d$. D represents the dimension. If the n variables $\boldsymbol{X}=\{\boldsymbol{x}_1,\cdots,\boldsymbol{x}_n\}$ are known, the variables $\boldsymbol{x}_i(i=1,2\ldots,n)$ are independent of each other and there are m sample points in each variable $\boldsymbol{x}_i$, then the kernel density is estimated as follows:

$$\hat{f}_X(x)=\frac{1}{n|\boldsymbol{H}|^{1/2}}\sum_{i=1}^{n}K\left(\boldsymbol{H}^{-1/2}(x-x_i)\right) \tag{7}$$

Where $\boldsymbol{H}$ denotes the bandwidth matrix and belongs to the symmetric positive definite matrix. $|\boldsymbol{H}|$ denotes the determinant of the $\boldsymbol{H}$ matrix.

By introducing the standard normal kernel function of the multivariate parameter variable into Eq. (7), the kernel density estimation is solved as follows:

$$\hat{f}_{\boldsymbol{X}}(x)=\frac{1}{n|\boldsymbol{H}|^{1/2}}\sum_{i=1}^{n}\frac{1}{(2\pi)^{d/2}}\times\exp\left[-\frac{1}{2}(x-x_i)^{T}\boldsymbol{H}^{-1}(x-x_i)\right] \quad (8)$$

Where $(\cdot)^{\mathrm{T}}$ denotes the transpose of the matrix. Research carried out by Duong (2004) found that for the multivariate parameter variables, the complete type bandwidth matrix, which can be calculated using the smooth cross estimation method (Duong 2005), is usually used to estimate the kernel density when the correlation between the variables is unknown. Then, the time history analysis for the bridge under the action of n groups of earthquakes is carried out, and then the maximum dynamic response and the ground motion intensity $\{(IM_i, D_i),\ i=1,\cdots,n\}$ are extracted. The joint probability density function of the bridge component can be calculated by using the formula (8):

$$\hat{f}_{D,IM}(c,a)=\frac{1}{2\pi n|\boldsymbol{H}|^{1/2}}\sum_{i=1}^{n}\exp\left[-\frac{1}{2}\begin{pmatrix}c-D_i\\ a-IM_i\end{pmatrix}^{T}\boldsymbol{H}^{-1}\begin{pmatrix}c-D_i\\ a-IM_i\end{pmatrix}\right] \quad (9)$$

The formula (9) and (6) are substituted into the formula (3) to calculate the probability density function $f_D(c|IM=a)$ of the seismic capacity of bridge components. Next the integration is performed for solving the formula (2). Finally, the seismic vulnerability probability of the bridge members is:

$$P_f(a,C)=P[D\geq C|IM=a]=\int_{C}^{+\infty}f_D(c|IM=a)dc$$
$$=\frac{h_{IM}}{2\pi|\boldsymbol{H}|^{1/2}}\frac{\int_{C}^{+\infty}\sum_{i=1}^{n}\exp\left[-\frac{1}{2}\begin{pmatrix}c-D_i\\ a-IM_i\end{pmatrix}^{T}\boldsymbol{H}^{-1}\begin{pmatrix}c-D_i\\ a-IM_i\end{pmatrix}\right]dc}{\sum_{i=1}^{n}\varphi\left(\frac{a-IM_i}{h_{IM}}\right)} \quad (10)$$

The seismic damage probability of bridge components can be calculated by adopting formula 10, and then the bridge vulnerability curve can be established.

3 ENGINEERING EXAMPLES

3.1 *Engineering overview and finite element simulation*

The typical high-speed railway long span irregular rigid frame bridge with high pier in western China is selected as the research object in this paper. The span of the main bridge is arranged as 101m + 192m + 101m. The superstructure of the bridge is prestressed concrete box girder with variable cross-section, and the beam adopts C55 concrete. The height of the beam ranges from 6.9m to 13.2m and the width of the beam is 10.3m. The design value of the second stage dead load of bridge deck is 95kN/m. All piers of the bridge adopt rectangular hollow sections. The 2# pier of 74m height and 3# pier of 78m are rigid piers, and the 4# pier of 58m height is the cantilever pier. The longitudinal movable bearing at 0# abutment adopts spherical bearing whose type is TJGZ-LX-Q9000-ZX-e150-0.2g, while the longitudinal movable bearing at 3# side pier adopts spherical bearing whose type is TJGZ-LX-Q9000-ZX-e100-0.2g. The layout of the whole bridge is shown in Figure 1.

The finite element model of the full bridge is established by OpenSees software. The superstructure is simulated by beam element, considering the dead weight, the second stage dead load and the train load. The pier is modeled by fiber element, to which the constitutive models of steel and concrete are assigned. The concrete uses the Kent-Park constitutive model (Kent 1971). The value of constitutive model for ordinary concrete is based on Code for design of concrete structures (GB50010-2010), and the value of constitutive model for constrained concrete is calculated by Mander model (Mander 1988). The constitutive model of steel is determined by Giuffré-Menegotto-Pinto model (Menegotto 1973). The bearing is modeled with a bilinear spring element, and the abutment is modeled with a built-in zero length element with the material characteristics given in OpenSees. The effective stiffness and passive earth pressure of the bridge are solved according to California Department of Transportation, Caltrans Seismic design criteria. Six spring elements are used for equivalent simulation of bridge pile foundation. The full bridge calculation model is established by OpenSees Software.

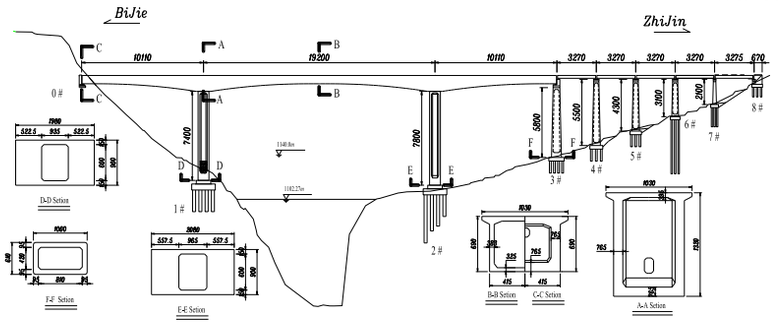


Figure 1. Schematic diagram of full-bridge layout (Unit: cm).

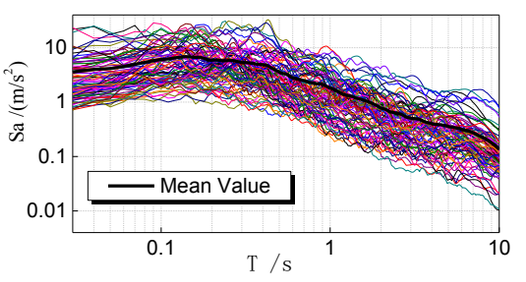


Figure 2. diagram of response spectrum characteristic.

3.2 *The uncertainty of ground motion*

As the bridge is located in Sichuan area, the measured ground motions of this area should be used for the time history analysis as far as possible to ensure that the calculated results are in accord with the actual engineering. Therefore, the measured ground motion records of Wenchuan earthquake in 2008 is chosen for the seismic vulnerability analysis in this paper. Based on the comprehensive consideration of the ground motion intensity and the integrity of measured data, 100 ground motion records from 40 observation stations in Sichuan province are selected. Figure 2 shows the acceleration response spectra and the mean spectra for each ground motion. Amplitude modulation of 100 ground motions is carried out, and then 10 PGA grades from 0.1g to 1.0g are obtained with the amplitude modulation step of 0.1g. Finally, 1000 sets of seismic analysis samples are generated.

3.3 *The uncertainty of bridge model parameters*

Because the structure is always affected by various factors (such as raw materials, construction technology, external disturbance and so on) in the construction process, randomness exists in the material property, component mechanical behavior and load effect. The above factors will affect the seismic performance of bridge structure itself, therefore, the uncertainty of above factors should be considered when conducting the vulnerability analysis. Pan (2007), Tavares (2012) and Mehdizadeh (2014) have studied the key parameters that affect the seismic performance of bridges, including the strength of steel and concrete, concrete density, the second stage dead load and bearing friction coefficient. According to the characteristics of the bridge in this paper, combining with the above scholars' research results, the key parameters and their distribution characteristic values considered in model bridge are given in Table 1. Parameter samples of the bridge model are generated by using Latin hypercube sampling method on the key parameters in Table 1, and then the analysis sample library of the bridge is formed. In view of the calculation scale and the selected sampling method, 1000 tests are used to generate 1000 bridge model samples in this paper.

Table 1. Uncertain parameters of model bridge and their distribution.

model parameter	Distribution type	mean value	variation coefficient
peak strength of C40 core concrete/MPa	Normal distribution	36.8	0.15
peak strength of C35 core concrete/MPa	Normal distribution	34.3	0.18
Steel yield stress/MPa	Normal distribution	400	0.06
Concrete density/ $Kg \cdot m^{-3}$	uniform distribution	2500	0.2
Steel hardening ratio	Lognormal distribution	0.02	0.25
Second stage dead load/$(kN \cdot m^{-1})$	Normal distribution	95	0.03
friction factor of bearing	Lognormal distribution	0.02	0.30

3.4 *Damage index of bridge structures*

In this paper, the long span rigid frame continuous girder bridge with high pier and is taken as the research object. The piers are very high and the height difference of the piers is very obvious (the maximum height difference reached 50.05m). In order to establish the vulnerability curve of long-span irregular bridge with high pier, it is necessary to make clear the damage index for the vulnerable parts of bridge. However, the selection and calculation method for reasonable damage indexes have been studied by Dong (2016) according to the characteristics of long span continuous rigid frame bridge with high pier. Based on the above literature, the cross section curvature is chosen as the damage index for the pier, and the relative displacement of bearing is chosen as the damage index for the spherical bearing. The specific damage index calculation method is described by Dong (2016). Due to the limited space, Table 2 only gives the calculation results of damage indexes in longitudinal direction.

Table 2. Uncertain parameters of model bridge and their distribution.

Damage state	position of section curvature/m^{-1}					Bearing member relative displacement/*mm*	
	1# pier bottom	1# pier top	2# pier bottom	2# pier top	3# pier bottom	0#abutment bearing	3#pier bearing
Slight damage	0.000405	0.000185	0.000400	0.000178	0.000460	150	100
Moderate damage	0.000468	0.000311	0.000462	0.000307	0.000545	300	200
Extensive damage	0.001280	0.001190	0.001270	0.001160	0.001480	600	400
Complete damage	0.003980	0.003830	0.003965	0.003821	0.004470	900	600

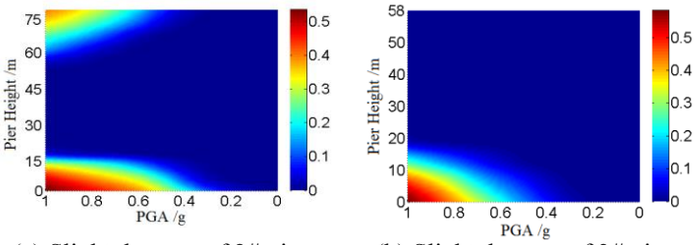
3.5 *Seismic vulnerability analysis of bridge structures*

3.5.1 *Seismic vulnerability analysis of the whole pier*

In order to study the vulnerability distribution of the whole pier, the vulnerability nephogram is used for analysis by referring to the method proposed in literature (Dong 2016). Namely using formula (8) to calculate the vulnerability curves of each element of the pier, and the vulnerability nephogram of the whole pier is plotted based on these curves. The vulnerability nephogram of each pier under longitudinal and transverse seismic action are shown in Figure 3 and Figure 4.

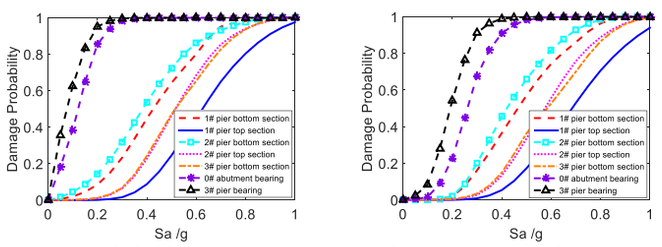
Based on the analysis of Figure 3, it can be seen that under the action of longitudinal earthquake, the bottom area of 3# pier is most likely to be slightly damaged. With the increase of PGA, the damage area extends from the bottom of the pier to the top gradually. The bottom and the top of 1# and 2# pier are easy to be damaged, and the damage area gradually develops from the two ends to the center with the increase of PGA. Therefore, the vulnerability of the pier at the bottom section and the top section should be focused on when conducting the seismic vulnerability analysis for railway irregular continuous rigid frame bridges.

It can be seen from Figure 4, under the action of transverse earthquake, the seismic damage is easy to occur in the bottom area of 1#~3# pier. Therefore, when the horizontal seismic vulnerability is conducted, the vulnerability of the bottom section of the pier should be paid attention. The above analysis results are consistent with the actual seismic damage.



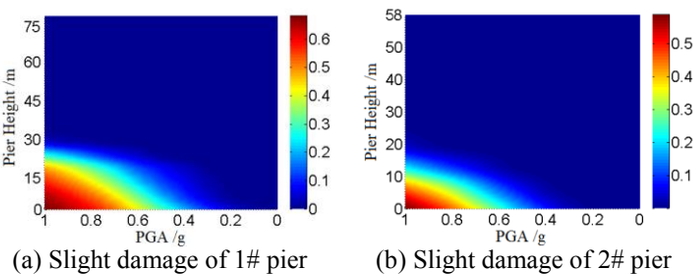
(a) Slight damage of 2# pier (b) Slight damage of 3# pier

Figure 3. Vulnerability nephogram of piers under the longitudinal earthquake.



(a)Slight damage (b) Moderate damage (c) Extensive damage (d) Complete damage

（1） the results of longitudinal direction



(a) Slight damage of 1# pier (b) Slight damage of 2# pier

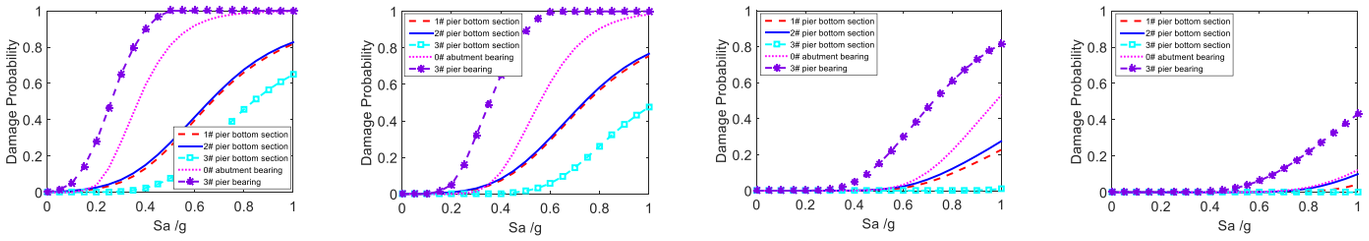
Figure 4. Vulnerability nephogram of piers under the transverse earthquake.

3.5.2 *Vulnerability analysis of each dangerous part of the bridge*

Based on the results of Section 3.5.1 and the actual damage, it is shown that for the long span continuous rigid frame bridge, the rigid piers (the bottom and top area) and the bearing are the most vulnerable components of the bridge. Seismic damage of the side pier is relatively small, and the seismic damage is mainly concentrated in the bottom of the pier. Therefore, when conducting the seismic vulnerability analysis for each dangerous component, the vulnerability of the parts such as the top and bottom section of 1#~2# pier, the bottom section of 3# pier, the bearing of 0# abutment and the bearing of 4# pier is the focus in this paper.

Using the KDE based seismic vulnerability analysis method proposed in this paper, the seismic vulnerability curve of bridge components can be generated. In this paper, the longitudinal and transverse seismic vulnerability curves of the bridge are established, and the strength index Sa are selected as the strength index of ground motion.

Figure 5 shows the longitudinal and transverse seismic vulnerability curves of each vulnerable part. It can be seen from the figure that the vulnerability curve of each part has similar shape and the damage probability increases with the increase of Sa. Under the action of earthquake, the bearing of 4# pier is the most vulnerable, followed by the bearing of 0 # abutment. And the last one is the bottom section of 1# pier. Using these generated vulnerability curves, the damage probability of each vulnerable part under the action of ground motion with different intensity can be evaluated, which can provide guidance for the seismic design optimization, bridge reinforcement scheme design, bridge reinforcement priority evaluation and economic loss evaluation after earthquake.



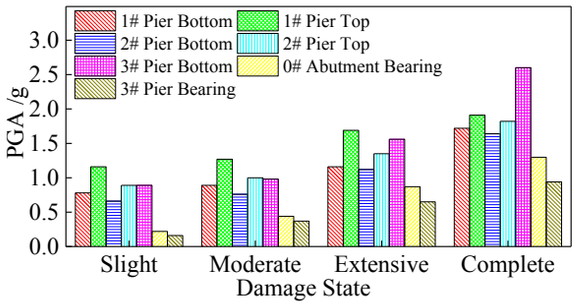
(a)Slight damage (b) Moderate damage (c)Extensive damage (d) Complete damage

（2） the results of transverse direction

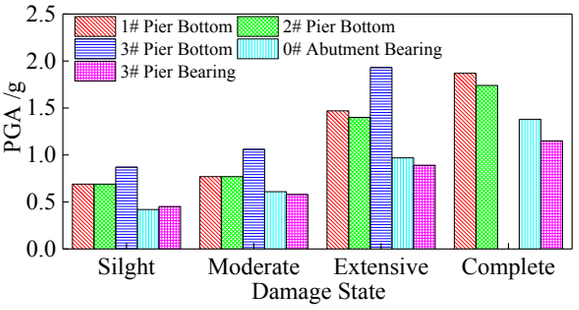
Figure. 5 Seismic vulnerability curves of different vulnerable positions.

3.5.3 *Comparative vulnerability analysis for each vulnerable component*

In order to reflect the seismic vulnerability of each component visually, the histogram of PGA median value for each vulnerable component corresponding to four damage states is given in figure 6. (If the median value of PGA is larger than 3.0g, the probability of seismic damage is very small and the graph is not plotted.)



(a) the result of longitudinal direction



(b) the results of transverse direction

Figure 6. Comparison of the median values of PGA for typical bridge members.

It can be seen from Figure 6, for the long span railway bridge with high pier, the bearing is the most vulnerable parts of the bridge and rigid piers are more prone to be damaged than other cantilever piers. The seismic vulnerability law of each component of irregular long span rigid frame bridge with high pier is more complicated compared to that of regular bridges. The geometrical irregularities, high order modes and other factors of the structure lead to the irregularities of the seismic response of piers, which makes the obvious difference in vulnerability of each pier. And the vulnerability distribution of each component has some differences in different damage states, while the seismic vulnerability distribution of each component for regular bridges has a certain law (Dong 2016 and Siqueira 2014). The uncertainty in the vulnerability distribution of long span continuous rigid frame bridge with high pier and the existence of a plenty of similar bridges in the western region both contribute to the seismic vulnerability research of typical railway continuous rigid frame bridges.

4 CONCLUSIONS

In this paper, the seismic vulnerability of the typical high-pier and long span continuous rigid frame railway bridges is analyzed by using vulnerability analysis method based on KDE. The main conclusions are as follows:

The characteristics that the damage probability of each element of piers varies with the peak acceleration value can be expressed intuitively by the vulnerability nephogram. In addition, the vulnerability nephogram can reveal the damage evolution process and the failure probability of the whole pier and reflect the vulnerability of the whole pier intuitively. Therefore, it is recommended to analyze the vulnerability of the whole pier by using the vulnerability nephogram.

The result of longitudinal seismic vulnerability of each dangerous component shows that for the pier members, they have a good seismic performance under the action of the design earthquake. The rigid pier is more prone to be damaged than the cantilever pier under the action of the earthquake with the same intensity. For the bearings, under the action of the design earthquake, the bearing members are prone to be damaged slightly and moderately, but hardly seriously or completely. In addition, by comparing the vulnerability of each component, it is found that the bearing is more prone to be damaged than the pier, which indicates that the bearing is the most vulnerable part among the bridges' dangerous components.

The result of transverse seismic vulnerability of each dangerous component shows that under the action of the design earthquake, almost all the piers and bearings will hardly be destroyed completely, and they have certain seismic performance. By comparing

the vulnerability of each component, it is found that the bearing is still the most vulnerable part.

References

Johnson, H.L. 1965. Artistic development in autistic children. *Child Development* 65(1): 13-16.

Mackie, K. & Stojadinovic, B. 2005. Fragility Basis for California Highway Overpass Bridge Seismic Decision Making. *Pacific Earthquake Engineering Research Center. Berkeley, CA: University of California*.

Dong, J. 2016. Fragility Analysis of Railway Long Span Rigid Frame - Continuous Combination System Bridge With High Pier Subjected To Near-Fault Ground Motion. *Chendu, SouthWest Jiaotong university*.

Danusa, H.T. & Padgett, J. & Paultre, P. 2012. Fragility curves of typical as-built highway bridges in eastern Canada. *Engineering Structures*, 40(1):107-118.

Siqueira, G.H. & Tavares, D.H. & Paultre, P. 2014. Seismic Fragility of A Highway Bridge in Quebec Retrofitted with Natural Rubber Isolators. *Ibracon Structures and Materials Journal*, 7(4):534-547.

Noori, H.Z. & Amiri, G.G. & Nekooei, M. & Zakeri, B. 2015. Seismic Fragility Assessment of Skewed MSSS-I Girder Concrete Bridges with Unequal Height Columns. *Journal of Earthquake and Tsunami*, 10(1):1-16.

Mosleh, A. & Razzaghi, M.S. & Jara, J. & Varum, H. 2016. Seismic Fragility Analysis of Typical Pre-1990 Bridges Due To Near- And Far-Field Ground Motions. *International Journal of Advanced Structural Engineering*, 8(1):1-9.

Nielson, B.G. 2005. Analytical Fragility Curves for Highway Bridges in Moderate Seismic Zones. *Atlanta: GA Georgia Institute of Technology*.

Chen, L.B. 2012. Seismic Vulnerability Analysis for Highway Bridges in Wenchuan Region. *Chengdu: School of Civil Engineering, Southwest Jiaotong University*.

Rosenblatt, M. 1956. Remarks on Some Non-Parametric Estimates of a Density Function. *Annuals of Mathematical Statistics*, 27(3):832-837.

Duong, T. 2004. Bandwidth selectors for multivariate kernel density estimation. *School of mathematics and Statistics, University of Western Australia*.

Wand, M. & Jones, M.C. 1995. Kernel Smoothing. *Chapman and Hall*.

Duong, T. & Hazelton, M.L. 2005. Cross-Validation Bandwidth Matrices for Multivariate Kernel Density Estimation. *Scandinavian Journal of Statistics*, 32(3):485-506.

Kent, D.C. & Park, R. 1971. Flexural members with confined concrete. *Journal of The Structural Division*, 97(7):1969-1990.

Ministry of Housing and Urban-Rural Development of the People's Republic of China. 2010. GB 50010-2010 Code for design of concrete structures. *Beijing: China Construction Industry Press*.

Mander, J.B. & Priestley, M.J. & Park, R. 1988. Theoretical Stress-Strain Model for Confined Concrete. *Journal of Structural Engineering*, 114(8):1804-1826.

Menegotto, M. & Pinto, P. 1973. Method of Analysis for Cyclically Loaded RC Plane Frames Including Changes in Geometry and Non-elastic Behavior of Elements under Combined Normal Force and Bending. *IABSE Proceedings. Lisbon*, 15-22.

California Department of Transportation, Caltrans Seismic design criteria, 2010. Version1.6. Division of structures, Sacramenton. *California: California Department of Transportation*.

Pan, Y. & Agrawal, A.K. & Ghosn, M. 2007. Seismic Fragility of Continuous Steel Highway Bridges in New York State. *Journal of Bridge Engineering*, 12(6):689-699.

Tavares, D.H. & Padgett, J.E. & Paultre, P. 2012. Fragility Curves of Typical as-Built Highway Bridges in Eastern Canada. *Engineering Structures*, 40:107-118.

Mehdizadeh, M. 2014. Uncertainty Treatment in Performance Based Seismic Assessment of Typical Bridge Classes in United States. *Orlando, Florida, the University of Central Florida*.

Maintenance, Safety, Risk, Management and Life-Cycle Performance of Bridges – Powers, Frangopol, Al-Mahaidi & Caprani (Eds)
© 2018 Taylor & Francis Group, London, ISBN 978-1-138-73045-8

Research on the influence law of central buckle on long-span suspension bridge's dynamic and seismic performance

L.P. Liu, Y. Liu & Y. Li
School of Transportation Science and Technology, Harbin Institute of Technology, Harbin, China. 150090

ABSTRACT: Based on an actual bridge project, three suspension bridge models with different kinds of central buckle were established on Finite Element Analysis model. The influence rule of central buckles on the long-span suspension bridge's dynamic and seismic performance was conducted by modal analysis and dynamic time history analysis. In terms of bridge's dynamic performance, it is found that the central buckle increases the overall stiffness of suspension bridge, impacts on the antisymmetric vibration mode significantly, and restrains longitudinal floating modes effectively. Besides, the rigid central buckle can make main cable's vibration modes in advanced. In the aspects of bridge's longitudinal seismic performance, the central buckles reduce the main girder longitudinal displacement and increase both main girder and main cable in the middle of span's internal force with these effects of the rigid central buckle increasing. The results also show that the central buckles make little influence on the displacement and internal force of bridge's other section. In the transverse direction, only the set of rigid central buckle increases the main girder's mid-span shear force, and doesn't influence on the displacement and internal force of the other parts. The research can provide some useful suggestions and references for the similar long-span suspension bridge structures' design.

1 INTRODUCTIONS

Setting central buckle at mid-span reasonably is an effective measure to improve rigidity of suspension bridge. Menkveld (2001) and Gimsing (2011) have analyzed the influence of central buckle on the New Tacoma Bridge. Since 1950s, central buckle has developed many derived forms. Viola (2005) has summarized them into three following kinds, 1) rigid buckle: jointing girder with main cable in a relatively fixed connection form at mid-span, such as triangular truss. 2)flexible buckle: establishing longitudinal restraints between girder and cable at mid-span with one or more pairs of inclined suspenders. 3)connecting girder and cable directly at mid-span.

Peng and Shao (2013) have deduced the differential vibrational equation of continuous suspension bridge with central buckle. The result shows that frequency of antisymmetric torsional mode is increased owing to the main cable's antisymmetric additional cable force near the central buckle. Wang et al. (2006a, 2006b) have drawn the following conclusions through studying on the dynamic performance of suspension bridge. Compared with short suspenders, setting central buckle results in improving structural stiffness. And the frequencies of vibration modes are increased in different degrees especially the modes of cable vibrating. Zou et al. (2009) have drawn the following conclusions through research on the effect of central buckle on the dynamic performance of three-tower ground-anchored suspension bridge. Firstly, the 1st vertical bending vibration mode is affected significantly. And some other vertical bending vibration modes are also affected fairly significantly. Secondly, due to the setting of central buckle, frequency of the antisymmetric torsional mode is increased obviously, lateral bending vibration frequencies are also increased, and mode of cable vibration is delayed. Thirdly, impact of central buckle on antisymmetric lateral bending vibration modes in single span is greater than that on symmetric vibration modes. By analyzing the effect of central buckle on dynamic performance of self-anchored suspension bridge, Li and Wang (2013) have concluded that bridge structure's displacement and internal force are affected slightly in elastic stage, whereas they are restrained greatly in elastroplastic stage. Zheng et al. (2009) have studied the influence of central buckle on long-span suspension bridge's deflection distributing law under live loading by Virtual Beam Method. It is the difference of longitudinal displacement constraints of central buckles on main cable that leads to the difference of deflection envelopes. Yang et al. (2008) have concluded that

difference from traditional two-tower suspension ones, the design of three-tower suspension bridges with central buckle may face many problems including the too high structural stress, the complexity of construction, connection and design. Structural responses of self-anchored suspension bridge with central buckle subjected to moving loads and effect of central buckle on overall stiffness of suspension bridges are also researched by Song et al. (2010). Wang (2013) has studied the central buckle's impact on the driving comfort and the vehicle-bridge coupled vibration. Ding (2002), Waisman (2011) and Ivana (2012) have analyzed the role of flexible central buckle and its long-term dynamics.

Setting central buckles in suspension bridges is a two-edged sword. The vibration periods of structure are reduced, so vibrational displacement of structure under excitations is decreased and the bending effect of vibrating short suspenders is mitigated. While some members get increased internal force demanding larger sectional design size. It increases the amount of materials consumption and structural weight. Structure's safety and reliability should be ensured through accurate static and dynamic analysis when central buckle is applied on long-span suspension bridge.

Model characteristics and time-history analysis of a suspension bridge over Yangtze River is conducted. The influence law of different forms of central buckle on seismic performance of long-span suspension bridge are discussed.

2 STRUCTURE AND MODEL

2.1 *Project overview*

The single-span suspension bridge adopts a simply supported structure system with two hinges. It is a fully enclosed, two-way and six-lane expressway bridge with 1490m main span and 470m side span. Seismic fortification intensity of the structural site is 7 degrees. Main cable is made of parallel galvanized high-strength steel wires whose cross-sectional area is 0.5155m^2. In completion state, theoretical design sag of main cable is 149.605m, rise span ratio is 1/9.96 and center distance of the two cables is 34.3m. Longitudinal horizontal distance of suspenders is 16.1m (the ones nearby towers is 20.5m away from the center line of bridge tower). As shown in Figure1, rigid central buckle is installed in the middle of main span to connect girder and main cable rigidly. The central buckle is a triangular truss whose vertical and inclined members are welded by wide-flange beams. And the upper and lower parts of the truss are connected by high-strength bolt group during the installation process. The main beam is closed flat steel box girder, 36.3m wide (comprising wind nozzle configuration) and 3m high. In the tower position, the main beam is supported on sliding bearing set on the crossbeam of tower. Gravity anchorage is adopted.

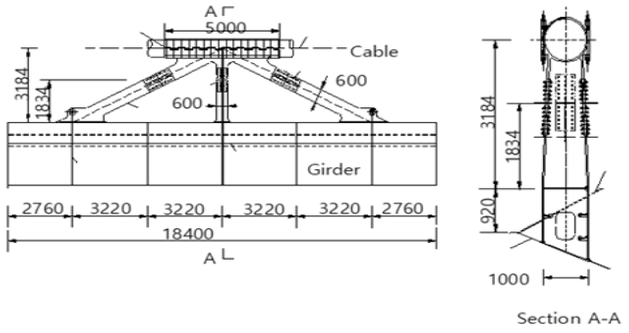


Figure 1. Diagram of the rigid central buckle (/mm)

2.2 *Modeling*

Finite element model of the bridge structure is established according to bridge design parameters by ANSYS Software. And girders are taken as spine beam model. They are simulated by 3D asymmetric variable section elastic beam element BEAM44. While main tower is simulated by 3D elastic beam element BEAM4, and main cable and suspender are simulated by 3D tension-only spar element LINK10.

The actual deck system is a closed all-welded flat streamlined steel box girder, while single-girder spine beam is used to simulate it. And the girder's stiffness and mass are satisfied. Stiffening girder is discreted as beam elements between two suspenders. Girder and suspenders are connected by massless rigid arm. Beam elements' rigidity is equal to stiffening girder's one, while beam elements' density is used to the equivalent one.

Simulation of cable system: main cable discretized according to the lifting points of suspenders is simulated by 3D spar element LINK10. Under competition state, main cable's initial strain is considered as element initial strain. And stiffness owning to gravity is also taken into account. Similarly, suspender is simulated by LINK10 and elements' initial strain is also considered. For mid-span rigid central buckle, diagonal and vertical bars are taken BEAM44 to simulate. For flexible central buckle, LINK10 is adopted.

Simulation of bridge tower: the suspension bridge's main tower consists of pillar and beam and is mainly subjected to axial compression under constant load. Main tower is simulated by beam element BEAM4 and the initial strain is taken into account.

Simulation of boundary condition: the subordinative relationship exists between the lower beam's displacement of main tower and the girder's translations in the bridge's transverse and vertical direction, and rotation in the longitudinal direction. The other three degrees of freedom, including one rotation and

two translations are not bounded. Two ends of main cables are treated as consolidation. Two main towers and the ground are consolidated.

Dimensional finite element model is established as shown in Figure 2.

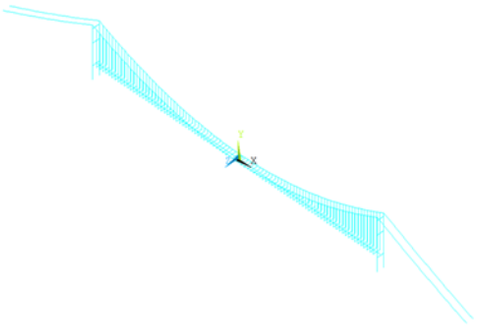


Figure 2. Three-dimensional finite element model of the suspension bridge

3 STRUCTURAL MODAL ANALYSIS WITH DIFFERENT FORMS OF CENTRAL BUCKLE

3.1 *Dynamic characteristic of suspension bridge ınstalled rigid central buckle*

The first 200 orders natural frequencies and mode shapes of this suspension bridge installed rigid central buckle are solved using Method of Block Lanczos. The first 20 orders natural vibration characteristic parameters are listed in Table 1.

Table 1. First 20 order vibration characteristics of the suspension bridge with rigid central buckle

Order	Frequency/Hz	Mode
1	0.04902	Symmetric lateral bending
2	0.08830	Antisymmetric vertical bending
3	0.12309	Antisymmetric lateral bending
4	0.12468	Symmetric vertical bending
5	0.17091	Symmetric vertical bending
6	0.18760	Antisymmetric vertical bending
7	0.21966	Cable's vibration
8	0.21974	Cable's vibration
9	0.22458	Cable's vibration
10	0.22560	Cable's vibration
11	0.23747	Symmetric lateral bending
12	0.24021	Symmetric vertical bending
13	0.24397	Symmetric torsion
14	0.25706	Side cable's vibration
15	0.25844	Side cable's vibration
16	0.26349	Side cable's vibration
17	0.26538	Side cable's vibration
18	0.26538	Side cable's vibration
19	0.27199	Antisymmetric torsion
20	0.27710	Side cable's vibration

3.2 *Dynamic characteristic of suspension bridge installed flexible central buckle*

The first 200 orders natural frequencies and mode shapes of this suspension bridge installed flexible central buckle are calculated in the same way. The first 20 orders natural vibration characteristic parameters are listed in Table 2.

Table 2. First 20 order vibration characteristics of the suspension bridge with flexible central buckle

Order	Frequency/Hz	Mode
1	0.04875	Symmetric lateral bending
2	0.08814	Antisymmetric vertical bendin
3	0.12183	Antisymmetric lateral bending
4	0.12467	Symmetric vertical bending
5	0.17090	Symmetric vertical bending
6	0.18758	Antisymmetric vertical bendin
7	0.21188	Cable's vibration
8	0.21974	Cable's vibration
9	0.22270	Cable's vibration
10	0.22458	Cable's vibration
11	0.23737	Symmetric lateral bending
12	0.24019	Symmetric vertical bending
13	0.24134	Symmetric torsion
14	0.25706	Side cable's vibration
15	0.25818	Side cable's vibration
16	0.26216	Side cable's vibration
17	0.26538	Side cable's vibration
18	0.26538	Side cable's vibration
19	0.26941	Antisymmetric torsion
20	0.27710	Side cable's vibration

3.3 *Dynamics behavior of suspension bridge without central buckle*

We can get the first 200 order vibration frequency and vibration mode of the suspension bridge without central buckle with the same method. Vibration characteristics of the suspension bridge's the first 20 order are listed in table 3.

Table 3. First 20 order vibration characteristics of the suspension bridge without central buckle

Order	Frequency/Hz	Mode

1	0.04874	Symmetric lateral bending
2	0.08327	Antisymmetric vertical bending & longitudinal Floating
3	0.11192	Antisymmetric lateral bending
4	0.12467	Symmetric vertical bending
5	0.12741	Longitudinal floating
6	0.17090	Symmetric vertical bending
7	0.18783	Antisymmetric vertical bending
8	0.21188	Cable's vibration
9	0.21974	Cable's vibration
10	0.22270	Cable's vibration
11	0.22455	Cable's vibration
12	0.23736	Symmetric lateral bending
13	0.24019	Symmetric vertical bending
14	0.24134	Symmetric torsion
15	0.24239	Antisymmetric torsion
16	0.25707	Side cable's vibration
17	0.25818	Side cable's vibration
18	0.26538	Side cable's vibration
19	0.26538	Side cable's vibration
20	0.26690	Side cable's vibration

We can draw some laws from the suspension bridge's dynamics behavior listed in tables 1-3.

(1) After installed the central buckle, the structural stiffness of the suspension bridge is increased, the value of stiffness and frequency of the flexibility model is less than the increase in rigid one.

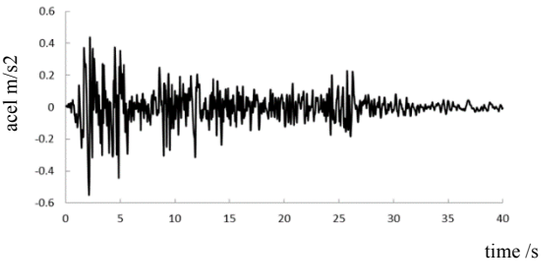
(2) Both the flexible central buckle and the rigid one have much more influence on the antisymmetric vibrating modes than on the symmetric ones, and both can restrain the longitudinal vibrating mode of suspension bridge.

(3) The setting of the rigid central buckle reduces the order of vibrating modes with the cable's vibration, makes the modes emerging in lower frequency. But the effect of flexible central buckle isn't so obvious.

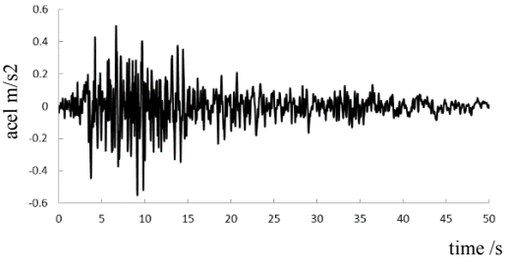
4 DIFFERENT CENTRAL BUCKLES INFLUENCE ON SEISMIC PERFORMANCE

4.1 *Seismic wave data*

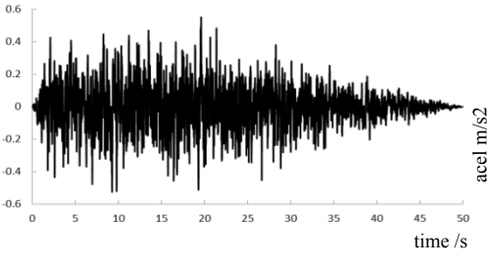
According to the site condition, two natural seismic waves and one artificial wave are used as inputting excitation. The three time-history-acceleration curves are showed in Figure 3.



a) El-Centro seismic acceleration time history



b) Taft seismic acceleration time history



c) Artificial seismic acceleration time history

Figure 3. Curves of seismic acceleration time history

The seismic precautionary intensity of the zone is 7 degrees on the Richter Scale. And design parameter of ground motion is 0.15g. The peak acceleration value of the seismic wave is adjusted to 0.55m/s^2 when performing the structure's seismic time-history response analysis under frequent earthquake action.

4.2 *Structural response under earthquake action in longitudinal direction*

Under earthquake action in longitudinal direction, the suspension bridge's structural responses with different modes of central buckle are conducted. The structural modes include bridge structures with rigid buckle, flexible one and none. Table 4 and 5 summarize the information of different central buckle's influence on structure.

Table 4. Longitudinal displacement of suspension bridges with different forms of central buckle

Section	Wave	Suspenders	Flexible	Rigid
Mid-point of girder	El-Centro	0.067	0.054	0.052
	Taft	0.067	0.072	0.029
	Artificial	0.311	0.075	0.047
End of girder	El-Centro	0.067	0.058	0.062
	Taft	0.067	0.076	0.037
	Artificial	0.314	0.081	0.053
Mid-point of	El-Centro	0.037	0.026	0.045

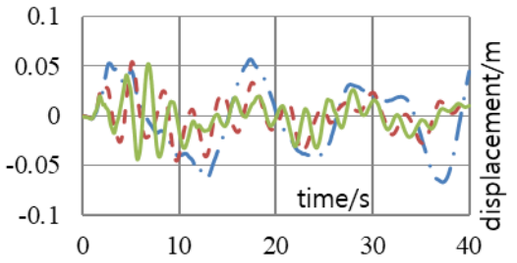
main cable	Taft	0.037	0.032	0.026
	Artificial	0.071	0.038	0.043
Top end of north tower	El-Centro	0.023	0.017	0.023
	Taft	0.024	0.023	0.018
	Artificial	0.042	0.037	0.027
Top end of south tower	El-Centro	0.026	0.020	0.029
	Taft	0.025	0.023	0.019
	Artificial	0.036	0.036	0.025

Table 5. Structural internal force of suspension bridges with different forms of central buckle

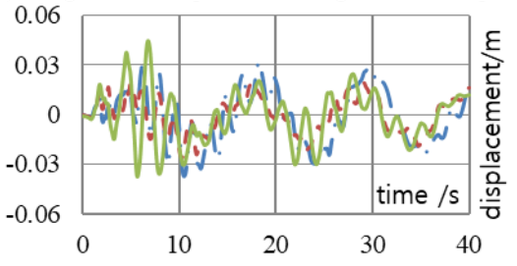
Section	Internal force	Wave	Suspenders	Flexible	Rigid
Mid-point of girder	Shear force/kN	El-Centro	1032	1868	4758
	Shear force/kN	Taft	1027	1871	3397
	Shear force/kN	Artificial	1040	2804	4276
	Moment/kN.m	El-Centro	250	6979	12359
	Moment/kN.m	Taft	258	7668	8327
	Moment/kN.m	Artificial	723	9308	10797
Bottom of north tower	Shear force/kN	El-Centro	4598	4492	3124
	Shear force/kN	Taft	4343	3872	4861
	Shear force/kN	Artificial	6771	6421	4607
	Moment/kN.m	El-Centro	244585	217243	152424
	Moment/kN.m	Taft	222386	218929	196221
	Moment/kN.m	Artificial	414033	364877	229442
Bottom of south tower	Shear force/kN	El-Centro	4630	4530	3093
	Shear force/kN	Taft	4373	3901	4826
	Shear force/kN	Artificial	6729	6401	4650
	Moment/kN.m	El-Centro	253028	226107	161116
	Moment/kN.m	Taft	230675	210454	187786
	Moment/kN.m	Artificial	405082	357139	230080
Mid-point of main cable	Stress/MPa	El-Centro	521	524	528
	Stress/MPa	Taft	521	525	526
	Stress/MPa	Artificial	522	525	528

Under the earthquake action of El-Centro seismic wave, time-displacement and time-force curves with different forms of central buckle are plotted in Figure 4.

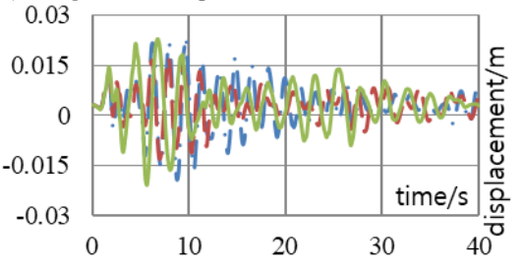
Some conclusions can be drawn from the above results, 1) the girder's longitudinal displacement decreased after installation central buckles. Among them, the rigid ones' impact is the most. But they have less effect on the longitudinal displacement of main cables and towers. 2) Longitudinal internal forces of girders and main cables increase obviously. As previous case, the rigid central buckle has the biggest influence.



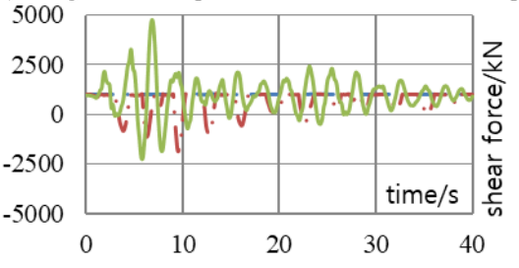
a) Longitudinal displacement of girder at mid-point



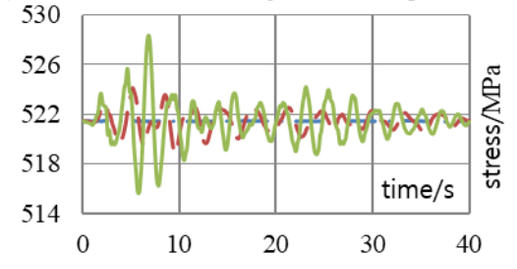
b) Longitudinal displacement of main cable at mid-point



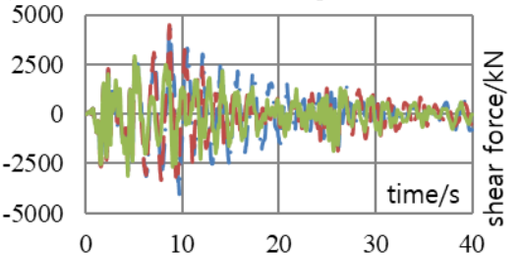
c) Longitudinal displacement of north tower at top end



d) Vertical shear force of girder at mid-point



e) Stress of main cable at mid-point



f) Longitudinal shear force of north tower at bottom end

Figure 4. Time-displacement/force curves with different forms of central buckle

(Suspender — · — · —; Slender — — — ; Rigid ———)

4.3 *Structural response under earthquake action in transverse direction*

Under earthquake action in transverse direction, the suspension bridge structural response with different mode of central buckle is conducted. Table 6 and 7 summarize the information of different central buckle's influence on structure.

Table 6 Transverse displacement of suspension bridges with different forms of central buckle

Section	Wave	Suspenders	Flexible	Rigid
Mid-point of girder	El-Centro	0.411	0.411	0.383
	Taft	0.100	0.100	0.098
	Artificial	0.236	0.236	0.212
End of girder	El-Centro	0.016	0.016	0.016
	Taft	0.013	0.013	0.013
	Artificial	0.018	0.018	0.020
Mid-point of main cable	El-Centro	0.374	0.374	0.378
	Taft	0.106	0.106	0.097
	Artificial	0.195	0.195	0.206
Top end of north tower	El-Centro	0.057	0.057	0.062
	Taft	0.052	0.052	0.055
	Artificial	0.095	0.095	0.102
Top end of south tower	El-Centro	0.057	0.057	0.062
	Taft	0.052	0.052	0.055
	Artificial	0.095	0.095	0.102

Table 7 Structural internal force of suspension bridges with different forms of central buckle

Section	Internal force	Wave	Suspenders	Flexible	Rigid
Mid-point of girder	Shear force/kN	El-Centro	35	78	195
	Shear force/kN	Taft	25	25	150
	Shear force/kN	Artificial	28	2499	203
	Moment/kN.m	El-Centro	91328	90952	81470
	Moment/kN.m	Taft	72094	71792	58431
	Moment/kN.m	Artificial	160424	159948	141110
Bottom end of north tower	Shear force/kN	El-Centro	5656	5657	5599
	Shear force/kN	Taft	4666	4666	4664
	Shear force/kN	Artificial	6553	6554	6985
	Moment/kN.m	El-Centro	146077	146081	143989
	Moment/kN.m	Taft	109856	109854	110477
	Moment/kN.m	Artificial	160123	160151	172409
Bottom end of south tower	Shear force/kN	El-Centro	5656	5657	5599
	Shear force/kN	Taft	4666	4666	4664
	Shear force/kN	Artificial	6553	6553	6985
	Moment/kN.m	El-Centro	146077	146081	143990
	Moment/kN.m	Taft	109856	109855	110477
	Moment/kN.m	Artificial	160123	160127	172408
Midpoint of main cable	Stress/MPa	El-Centro	522	522	522
	Stress/MPa	Taft	522	522	522
	Stress/MPa	Artificial	522	522	522

Some conclusions can be drawn from the above results, the transverse shear force increases much with the bigger rigid central buckle. But the flexible central buckle has the less affect.

5 CONCLUSION

The paper analyses the behavior of suspension bridge with three different central buckles, and some conclusions can be drawn.

1)The structural rigidity of suspension bridge can achieve increment by installing central buckle. In which, the rigid one has the most noticeable effect. The structural frequency increases obviously. The rigid central buckle has a great influence on the anti-symmetric torsional vibration mode of long-span suspension bridge, which can effectively restrain the longitudinal floating vibration mode. At the same time, it makes the vibration mode of the main cable in advance.

2)Under earthquake, the setting of the rigid central buckle makes the longitudinal displacement of the girder decreasing, and its mid-span force increasing. But the flexible central buckle has less influence on the tower's force. While in the transverse direction, the rigid one only caused the shear force in the middle span of the girder increasing. And it has less influence on other section's internal force and displacement.

6 REFERENCES

Ding Z. 2002. On nonlinear oscillations in a suspension bridge system. Transactions of the American Mathematical Society, Volume 354(1):265-274.

Gimsing N. J., Georgakis C. T. 2011, Cable supported bridges: concept and design, John Wiley & Sons, 8-15.

Ivana Bochicchio, Claudio Giorgi and Elena Vuk 2012. Long-term dynamics of the coupled suspension bridge system. Mathematical Models & Methods in Applied Sciences, Volume 22(9): 199-218.

Li Y. H. and Wang. C. 2013. Influence of central buckle on self-anchored suspension bridge under uniform seismic excitation. Journal of Highway and Transportation Research and Development, 7: 223-225.

Menkveld K, Pence W. O. 2001. Tacoma Narrows Bridge. Physics Teacher, 25(4): 45.

Peng W. H., Shao X. D. 2013. Analysis of free torsional vibration of suspension bridges with center ties. China Journal of Highway and Transport, 26(5): 76-87.

Song H., et al 2010. Influence analysis of central buckle in suspension bridge on different suspension systems. Engineering Sciences, Volume 12(7): 22-28.

Viola J. M., Syed S & Clenance J. 2005. The New Tacoma Narrows Suspension Bridge: construction support and engineering. Proceedings of the 2005 Structures Congress and the 2005 Forensic Engineering Symposium, 1-12.

Waisman H., Montoya A. & Betti R. et al. 2011. Load transfer and recovery length in parallel wires of suspension bridge cables. Journal of Engineering Mechanics, Volume137(4): 227-237.

Wang D., Chen C.M. & Liu Y. 2013. Central buckle influence research on dynamical characteristics of suspension bridge. Applied Mechanics & Materials, 405-408.

Wang H., et al. 2006a. Influence of central buckle on dynamic behavior of long-span suspension bridge. China Journal of Highway and Transport, Volume 19(6):49-53.

Wang H., Li A. Q., Zhao D. et al. 2006b. FE analysis and experimental study on local stress of steel box girder of Runyang suspension bridge. Journal of Harbin Institute of Technology, 38(7):1062-1064.

Yang J., et al. 2008. Overall design and structural type selection of three-tower and two-span suspension bridge of Taizhou Changjiang River highway bridge. Bridge Construction, No. 1: 37-40.

Zheng K. F., Xu R. D. and Li H. G. 2009. Detailed calculation method for influence of central cable band on live load deflection of suspension bridge. World Bridges, No. 2: 51-53.

Zou K. G., Wang H. & Liang S. T. 2009. Influences of central buckles on dynamic behaviors of triple-tower suspension bridge. Journal of Architecture and Civil Engineering, 26(4): 49-53.

MS14: Steel bridge rehabilitation

Organizer: M. Sakano

Maintenance, Safety, Risk, Management and Life-Cycle Performance of Bridges – Powers, Frangopol, Al-Mahaidi & Caprani (Eds)
© 2018 Taylor & Francis Group, London, ISBN 978-1-138-73045-8

AYALA BRIDGE, retrofitting of an historic steel bridge in Manilla (Philippines)

Vanessa BUCHIN-ROULIE, Nicolas KACZKOWSKI, Alexandre GROS, Fabien TESSON
Freyssinet International, Rueil-Malmaison, France

ABSTRACT: Ayala Bridge, in the center of Manilla, is a steel arch bridge built in the 1950s. It is comprised of 2 simply supported steel bridges constructed with 3 trusses connected together. The bridge has to be retrofitted for conformity to new codes (traffic and seismic). The retrofitting solution designed by Freyssinet was chosen because of its economy when considering both deck and foundations: it consists of minimizing the current seismic loads on piers and abutments, to get them lower than actual loads seen in the past under historic seismic and typhoon. Longitudinally, the 2 decks are linked together and extended with beams and new piles: the overall structure is working as a frame. Transversally, some seismic devices are placed. The overall steel structure is then strengthened using additional steel profiling and prestressing. Major parts of the work has been done with no traffic interruption at all.

1 INTRODUCTION

Ayala Bridge is one of the major bridges located in the center of Manilla (Philippines) over Pasig River. As a strategic axis (20 000 vehicles per day), its closure needed to be reduced to a minimum. It is comprised of 2 independent steel arch bridge of 61,6 meters (south span) and 73,8 meters (north span), constructed with 3 trusses connected together [Figure 1]. Transversally, the deck is composed of a concrete slab supported by stringers beams. The deck of 25,9 meters width supports 4 traffic lanes each of 3,05 meters and 2 sidewalks.

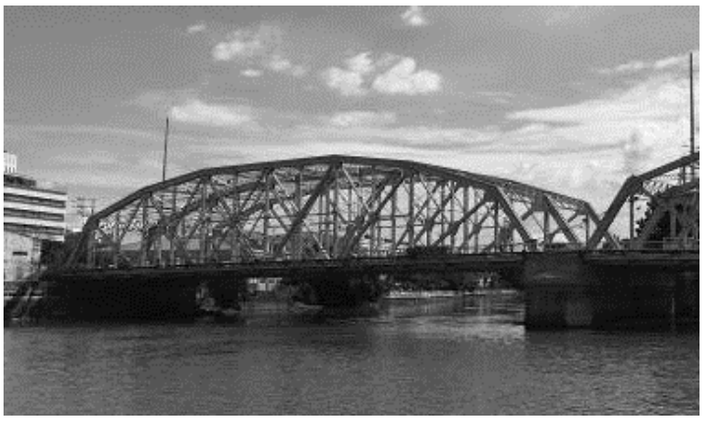


Figure 1. Global view of Ayala Bridge

Each bridge is fixed on piers and free on the abutments longitudinally, and fixed on piers and abutments transversally. The bearings are located under each arch.

The buried part of the concrete pier and abutment is about 2/3 of the total height. Piers and abutments are placed on driven timber piles.

In 2009, the bridge was declared as a historic legacy and landmark by the National Historical Institute, and consequently, should be preserved for posterity.

Rehabilitation and retrofitting of Ayala Bridge should be done in accordance with AASHTO 2002 regarding traffic loads including seismic action.

2 SURVEY AND INVESTIGATIONS

A full diagnosis of the present state of the bridge was done prior to any design work. The aim was to determine the current condition of the structure (steel trusses, bearings, deck, concrete structure), get essentials data to complete the design (confirmation of as built sections), and to check assumptions taken at tender stage regarding the soil capacity.

At this stage, a global geometry inspection of the steel structure are done with a 3D laser scanning technology in order to get the current configuration of trusses members and connecting nodes (with rivets and gusset plates).

For the assessment of inherent material properties and existing conditions, the steel materials are tested

in order to define its grade, strength, weldability, corrosion state and residual thickness. Regarding the concrete, carbonation and chloride content are defined as well as the location of rebar and its diameter. Compressive strength with samples and concrete homogeneity with ultrasonic pulse velocity are also measured to evaluate the quality of the existing material.

Soil investigation consists of cone penetration tests to evaluate the soil bearing capacity. Friction sleeve and vane tests are used to determine soil cohesive strength. CTP piezocone test is added to measure the pore water pressures to aid checking the risk of liquefaction.

Various laboratory investigation with samplings have been done to determine density, sieve analysis, Attenberg's limits and organic content.

The conclusion of tests done on the superstructure is that the steel structure and concrete deck are relatively well preserved, except in some areas located under the deck concrete structure that are extremely corroded. On the other hand, soil characteristics appeared to be poor compared to assumptions taken at tender stage. The retrofitting solution needed then to be adapted to real soil capacity.

If the investigation is correct regarding the substructure and superstructure, a huge risk existing on the wooden pile capacity is identified.

3 DESIGN OF THE RETROFITTING SOLUTION

3.1 *Re-design of the actual bridge*

In order to mitigate the lack of information regarding the wooden piles, the bridge was re-designed with the highest earthquake or typhoon felt since 1950.

The analysis of the existing bridge using FE model with software SAP 2000 allowed us to define the maximum reactions on piers and abutments under traffic loads given by the code used at construction time and existing earthquake or typhon felt since 1950. The stability of piers and abutment were then checked using Plaxis software taking into account soil and structure interaction [Figure 2]: different soil layers are modelized in order to obtain the maximum efforts in the piles. Wooden piles demand were then checked, with seismic action already felt since 1950 and compared to their capacity.

Due to a significant increase of the seismic action to conform to the AASHTO 2002 code, it was not possible to keep the bridge in its actual configuration (overloading of pier foundation and abutment would require significant strengthening). A new solution had, therefore, to be developed by Freyssinet.

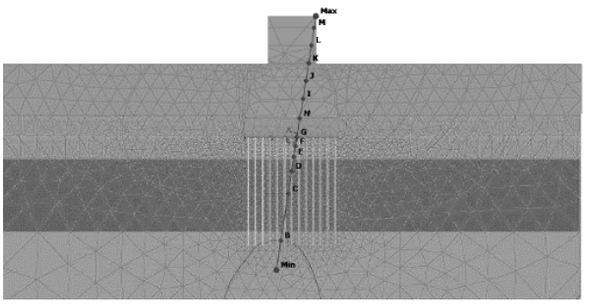


Figure 2. FE model of piers with soil-structure interaction

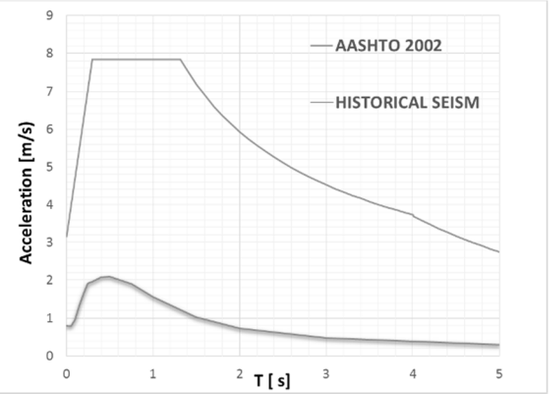


Figure 3. Comparison of AASHTO design spectrum and historic seism spectrum previously experienced by the bridge

3.2 *Seismic retrofitting*

The global behaviour of the bridge is critical for the existing foundations. The chosen retrofitting solution aims at minimizing the loads on the piers and foundations, calculated with current seismic codes, to reduce them to lower than the actual loads seen in the past on the structure under historic seismic or typhoon conditions.

Longitudinally, the two concrete decks are connected together with a continuity slab and extended using ground concrete beams, approach slabs and additional piles [Figure 4]. Indeed, the major longitudinal seismic effect is an axial load. The existing pier and abutments are self-stable when they are surrounded by soil but become unstable under an additional horizontal longitudinal seismic effort. The approaches on ground beams (length 25 meters) and 2 meter diameter pile (length 20m) will support the longitudinal seismic actions. Besides this, in order to minimize the effect on the pier and abutments, the bridge is placed on isolators. The overall structure is then working as a frame, with small impact on the actual foundations. Particular attention was paid to connection of the ground beam to the abutment and to the new piles.

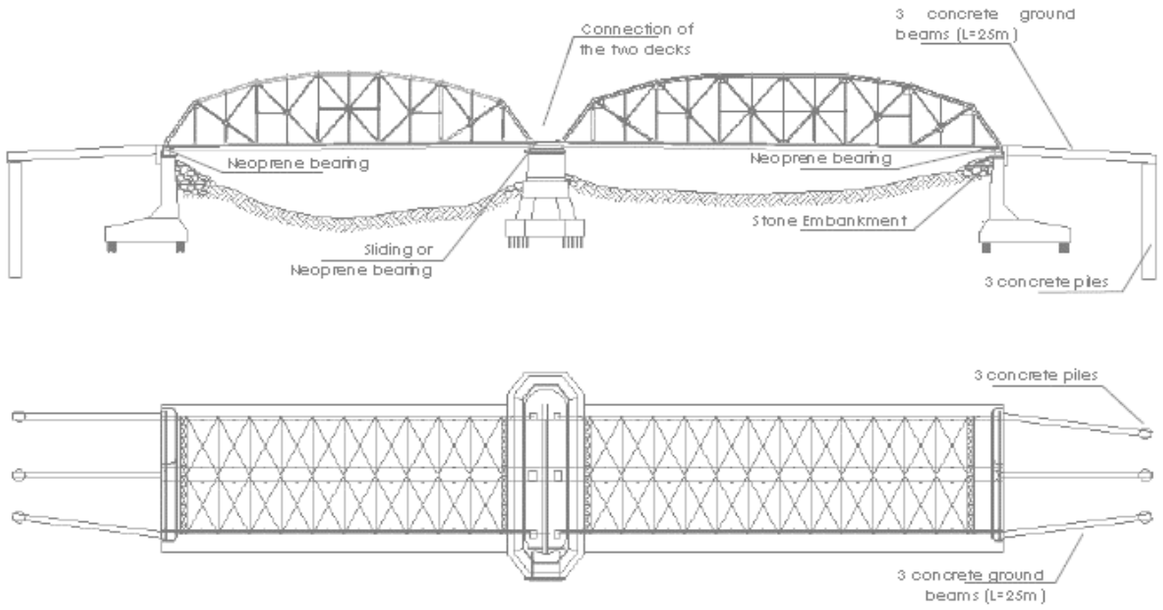


Figure 4. Global view of Ayala Bridge

Transversally, Fluid Viscous Dampers (FVD) are used simultaneously with isolators or High Damper Rubber Bearings (HDRB) to dissipate energy. Lateral stability under service loads is insured thanks to stop fuses [Figure 5]. These seismic devices are used to increase the overall damping and to ensure integrity of the bridge during and after an earthquake. They have low resistance to slow displacement (thermal variation) and become active during seismic motion [Figure 6]. In case of Ayala Bridge, FVD was chosen in order to comply with the past maximum loads seen by the pier [table1]. The overall seismic protection system was designed iteratively.

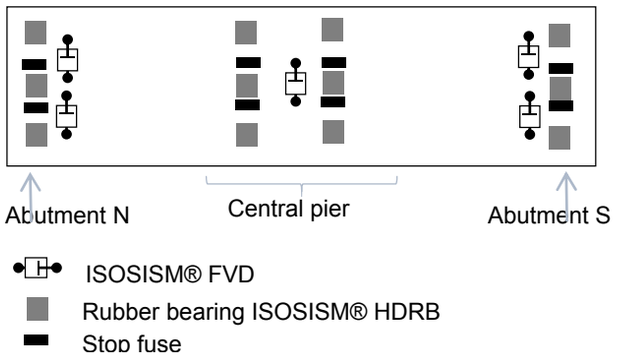


Figure 5. Layout of the bridge for transversal retrofitting

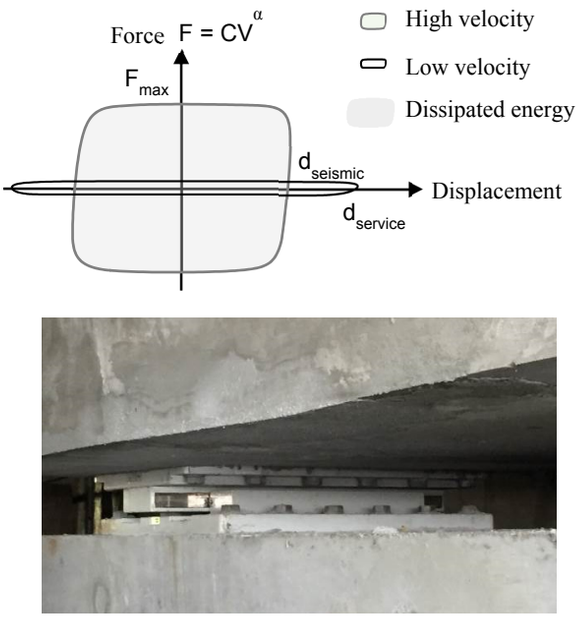


Figure 6. Fluid Viscous Dampers: Behaviour law and picture of FVD installed on pier

Table 1. Comparison of horizontal transversal effort on foundations

Fy	**South abutment [kN]**	**Central pier [kN]**	**North abutment [kN]**
Existing bridge	4063	13884	5125
Already seen typhoon/seism	3656	3656	3656
Retrofitted bridge	3200	2550	3150

Substructures are not completely embedded in the ground (around 2/3 of their height is embedded). Due to high seismic action at ground level and despite reduced longitudinal horizontal efforts, the abutments appear to be unstable whereas the pier remains stable. Considering that buried Substructure are self-stable under earthquake, the retrofitting solution consists, for the north abutment, in placing additional stone revetments on the embankment in front of the abutment [Figure 7]. This solution could not be applied to the south abutment, due to the depth of the river bed. Indeed, the stone embankment would have defined a slope that would have had an impact on the ship channel. To ensure stability of south abutment, 18 soil nails each of 25 meters long (capacity 800 kN) were required to be placed along the abutment [Figure 8].



Figure 7. Embankment for north abutment



Figure 8. Soil nails dispatched along north abutment

3.3 *Concept of the bridge strengthening*

The whole structure was checked using a 3D model on SAP 2000. All steel profiles were checked according to AASHTO 2002 code. This strengthening solution was chosen due to its economy in terms of work and materials.

The strengthening solution consists of adding a T profile welded on the top chord and on top of the transverse beam (to mitigate transversal effects) [Figure 9 and Figure 10].

Specific top nodes of the steel truss have been detailed to provide a proper connection between top chord and the top transverse strengthening members by taking into account the existing riveted gusset plates [Figure 11].

The bottom chord was strengthened by adding a straight centrally mounted prestressing cable placed inside the profile of each truss in order to balance extra-tension.

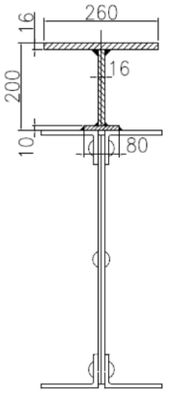


Figure 9. T profile welded on transverse beam

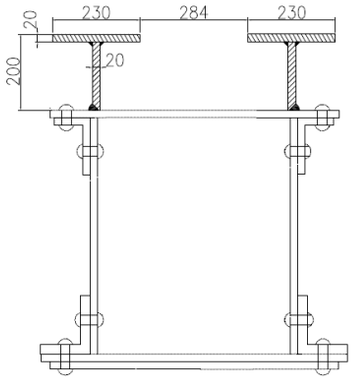


Figure 10. T profiles welded on top chord

The longitudinal rebars placed in the existing concrete slab appeared to be discontinuous at each crossbeam. In order to ensure the global function of the concrete slab during transversal seismic event, it was necessary to recreate this continuity by pouring a new slab (connected to the old one) on the top of the existing one. Finally, the full steel structure was sandblasted, restored locally as required to protect using a long-term corrosion protection system [Figure 12].



Figure 11. Example of node strengthening



Figure 12. View of the top chord being protected

4 JACKING OF THE BRIDGE

The bridge had to be jacked up of 70 cm in order to respect the required clearance regulation. The jacking was done prior to the retrofitting works, using a portal frame placed at each arch extremity with associated strand jacks [Figure 13. The connection of the cable to the deck structure was made with bespoke designed lugs fixed to the bearing pin [Figure 14]. The whole span was lifted simultaneously. After jacking, the approaches were adapted to suit the new bridge elevation.

Only jacking operations were done with traffic interruption. All other operations were done with full traffic or limited traffic (2 lanes instead of 4) on the bridge.



Figure 13 Bridge during jacking operation

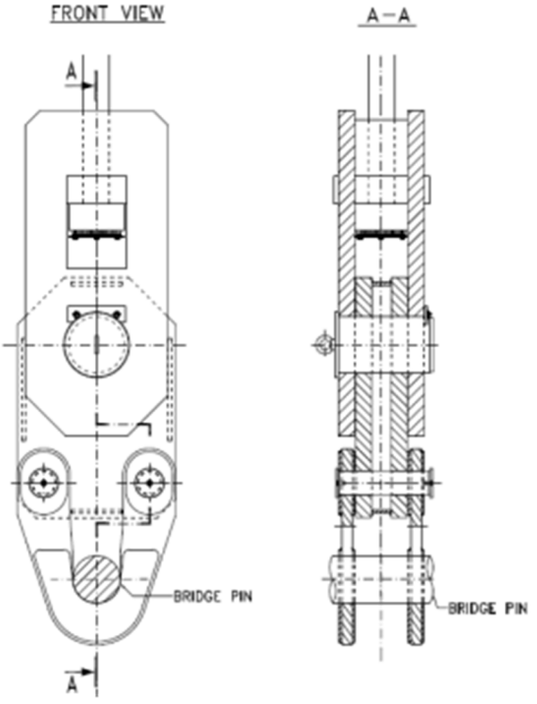


Figure 14 Lifting lugs

5 CONCLUSION

In this paper, we present an innovative solution designed and applied by Freyssinet on the Ayala Bridge in Manilla (Philippines). The technical solution consisted of reducing the load to the foundations using dampers and isolators (transversally) and an extended structure to support seismic loading (longitudinally).

One of the key elements for success in such project has been the need for the preliminary inspection to be as exhaustive as possible. Finally, this paper is presented to enable the reader to develop a full and comprehensive understanding of the different problems to be solved when considering any number of given/ chosen repair techniques.

Maintenance, Safety, Risk, Management and Life-Cycle Performance of Bridges – Powers, Frangopol, Al-Mahaidi & Caprani (Eds)
© 2018 Taylor & Francis Group, London, ISBN 978-1-138-73045-8

Orthotropic steel bridge deck study with UHPFRC cold composite overlay

L. Duan, T. O. N. Houankpo & C. S. Wang
Engineering Research Center for Large Highway Structure Safety of Ministry of Education, Chang'an University, Xi'an, China

E. Brühwiler
Laboratory MCS, École Polytechnique Fédérale de Lausanne (EPFL), Lausanne, Switzerland

ABSTRACT: This paper propose that steel bridge deck reinforced by UHPFRC (ultra-high performance fiber reinforced concrete) overlay on deck plate with cold composite design method. Sustainable and reliable composite design between steel plate and UHPFRC is a significant factor to ensure expected structural performance of steel and UHPFRC composite element. Test and numerical analysis were carried out to study behavior of steel bridge deck with UHPFRC composite overlay adopting cold connecting, including casting UHPFRC layer directly on steel plate, adopting gluing stub, and gluing corrugated steel plate connector, respectively. In experimental study, series of UHPFRC and steel deck plate composite specimens were fabricated and tested considering different composite ways. It was analyzed the stress state and the relative displacement between UHPFRC layer and steel deck plate. Results from test study indicate cold connecting corrugated steel plate connector was an optimal composite design method. Calibrated by test result, FE model was established for steel bridge deck with UHPFRC composite layer. It was analyzed the interface behavior between UHPFRC and steel deck plate, and also the stress reduction level of fatigue details in steel bridge deck. Learn from FE analysis study, UHPFRC composite overlay design method could improve local rigidity obviously and also reduce stress range at typical fatigue detail in steel bridge deck.

1 INTRODUCTION

Orthotropic steel bridge deck was characterized with large capacity, low dead load, fast factory prefabrication, etc. Thus, it was applied in lots of large span bridges, especially cable stayed bridge and suspension bridge. During the long-term service stage, if without efficient and in-time maintenance strategies, the structural performance of bridges would degrade due to couple action of increasing vehicle loads, environmental corrosion, material performance degeneration, occasional overloading problem, or other unpredictable factors, which reduce existing service life and threaten bridge safety obviously. Learn from engineering experience, problems of fatigue cracking and overlay durability on steel deck plate are two typical problems found in orthotropic steel bridge deck.

For fatigue problems in steel bridge deck, several researchers have been carried out fatigue tests for orthotropic steel deck in order to study the fatigue performance at different fatigue details and the welding methods (Tsakopoulos & Fisher 2005, Wang et al. 2012, Wang et al. 2016). Fatigue cracking has generally been found at four typical fatigue-sensitive regions in orthotropic steel bridge deck due to low stiffness, welding defect, residual stress and so on, especially in heavy traffic lanes (Connor & Fisher 2012, Wang et al. 2012). Fatigue cracks at deck plate are the most severe ones in typical fatigues, because the deck has a large deflection under wheel load to produce large transverse bending moments. With increasing knowledge for orthotropic steel bridge deck, the thickness of deck plate is increasing from 12mm in early design to 20mm in complicated detail nowadays in design. However, it is not an economical way to achieve rigidity by increasing deck plate thickness.

The durability problem of overlay on steel deck plate was caused by increasing traffic intensity influenced directly above and complicated environmental effector. There are typical three kinds of overlay for steel bridge deck, including traditional mastic asphalt, thin epoxy resin surfacing impregnated with granules and reinforce high performance concrete (RHPC) layer. The thicker mastic asphalt overlay has relative greater stiffness or rigidity than the epoxy resin overlay. The fatigue cracks in deck plate have been detected in orthotropic steel bridge structure either with a thick asphaltic surfacing or with a thin epoxy layer. Compared with mastic asphalt overlay, RHPC layer has greater stiffness without increasing dead load. Learn from engineering experiences, typical overlay damages include overlay fatigue cracking, local failure, track, delam-

ination, etc. Compared with overlay performance in concrete bridge, overlay in steel bridge have a relatively short service life, since they usually carry great local deflection and is vulnerable to fatigue cracking and local failure (Walter et al. 2007). For example, it was found pavement damage and fatigue cracks in steel bridge deck for Van Brienenoord Bridge in the Netherlands (Jong, 2007); there was obvious pavement local damage of Mafang Bridge in China, because of less rigidity, heavy vehicle volume and vehicle amount (Li et al., 2015).

In order to improve structural performance and extend service life, researchers have devoted to study improved design methods and effective reinforcement methods for orthotropic steel bridge decks. For example, several reinforcement methods were proposed and studied, like applying gusset plate, using high performance concrete overlay layer, special types of asphalt concrete, gluing hard wood beams, filling troughs with polyurethane, bonding second steel plate and so on (Kolstein 2007, De Jong 2007).

Ultra high performance fiber reinforced concrete (UHPFRC) shows relatively high compressive strength, high tensile strength, high compactness and good workability (Makita & Brühwiler 2014). It was encouraged the method of applying UHPFRC layer on steel deck plate by cold connecting (epoxy bonding) shear connector. In this method, a composite layer of UHPFRC increases the rigidity and leads to wider distribution of concentrated wheel loads, leading to a significant decrease in fatigue relevant stresses and local deformation. Instead of welding connectors on deck plate, cold bonding connectors can avoid new fatigue vulnerable detail introduced in welding process. Thus, the method realize an UPPFRC-steel bridge deck composite system, which can enhance pavement performance and improve the local rigidity.

The interface behavior between the UHPFRC layer and the steel deck plate was an important factor to achieve effective UHPFRC-steel bridge deck composite system (Duan et al. 2015). This paper focus on sustainable and reliable composite design study between steel deck plate and UHPFRC. Both test study and numerical analysis were carried out to explore interface behavior and effective shear connector designs. In experimental study, UHPFRC and steel deck plate composite specimens were fabricated and tested considering different composite ways, including without shear connector design and gluing corrugated steel plate shear connector. Calibrated by test result, FE model was established for orthotropic steel bridge deck model with UHPFRC composite layer in Abaqus software. It was analyzed the interface behavior between UHPFRC and steel deck plate, and the stress reduction level at fatigue details in steel bridge deck.

2 RESEARCH BACKGROUND

Effective composite design between UHPFRC overlay and deck plate can ensures overall load carrying behavior of UHPFRC – orthotropic steel bridge deck composite system, thus improving pavement performance and reducing stress range at fatigue sensitive detail of orthotropic steel bridge deck. Several researchers have devote to overlay composite design with orthotropic steel bridge deck. Generally, this composite design can be achieved by welding shear connectors, like stubs, curved rebars, L or T shape steel plates, welded steel mesh or steel plate with holes (PBL). Since new fatigue detail will be introduced during fabrication stage when adopting the traditional welding for connectors, it is explored to glue connectors with epoxy resin. The study at Adhesion Institute at the Delft University of Technology was focused on three possibilities: prefab overlay glued on steel deck by a wet two-component epoxy paste adhesive; casting on a wet two-component epoxy paste adhesive; placing overlay in a dry two-component epoxy paste adhesive with shaked in aggregates (Buitelaar & Braam 2004).

Shao focused on reactive power concrete (RPC) material exploration and RPC overlay design on steel bridge deck, in order to reduce stress at fatigue sensitive details of orthotropic steel deck. Learn from series of experimental and numerical results, the thin RPC pavement can effectively eliminate the risk of fatigue cracking in steel deck (Shao et al., 2012). The compact reinforced reactive powder concrete (CRRPC) was explored and applied to strength deteriorated asphalt overlays and to strengthen orthotropic steel deck (OSD) bridges, and the FE analyses and fatigue tests had found that the thin CRRPC layer reduced the vehicle-induced stresses in the steel bridge deck significantly (Cao et al. 2015).

By using the FE analysis, Walter (Walter et al. 2007) had modeled the connection between the overlay (cement concrete) and underlying steel deck by using an 8-node interface element available in DIANA software, together with a user-supplied constitutive model. Based on force-slip relationship and in order to study the interface between concrete and steel beam, springs elements had been used by Lin to simulate the shear stud connector between the concrete and steel beam (Lin et al., 2013). Experimental tests and numerical analysis had been concluded by Dieng (Dieng et al., 2013). In order to model the interface behavior between the UHPFRC overlay and steel deck in orthotropic steel deck bridge, he used the Coulomb's law and Coulomb's friction model developed in MSC. Marc (MSC. Marc Volume A, 2005).

3 EXPERIMENTAL STUDY

3.1 *Test program*

Experimental study is conducted for UHPFRC and steel deck plate composite beams considering different composite effects, in order to study the composite structural behavior and find out optimal composite design method. In this paper, two simple supported specimens with loading (F) at mid-span were designed to study the bending behavior of specimens. The loading device is shown in Figure 1.

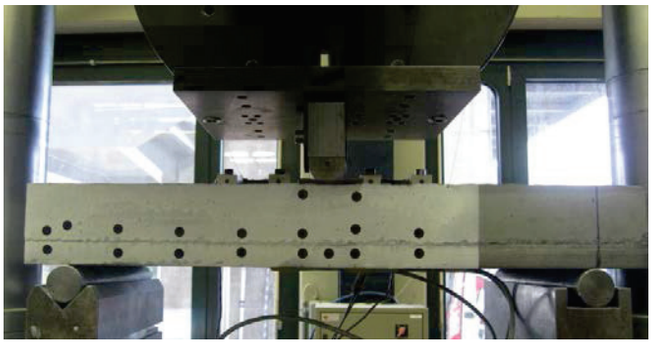


Figure 1. Applied load setup.

The span length of specimens were 420mm, and the width were 200mm. The thickness of steel plate was 20mm and the thickness of UHPFRC layer was 40mm. For specimen 1, the top surface of steel plate cleaned and shot blasted, epoxy is brushed on entire span length and aggregate is put on this epoxy interface, and then UHPFRC layer was cast. For specimen 2, after shot blasting steel plate, epoxy is brushed on entire span length, two connectors are glued at each half span, and then UHPFRC layer was cast. Figure 2 shows corrugated steel plate shear connectors glued on steel plate, which were fabricated by 4mm steel plate.

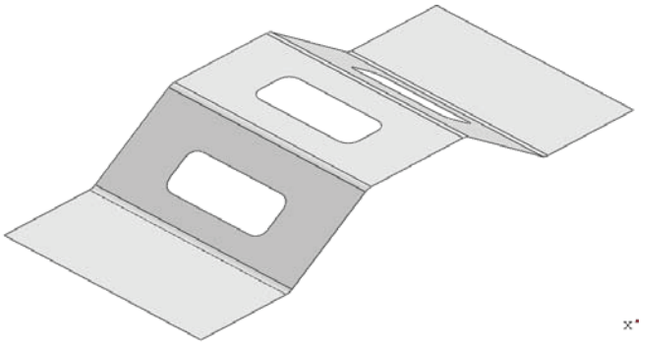


Figure 2. Corrugated steel plate shear connector.

3.2 *Test result analysis*

Specimens 1 and 2 have the same geometrical dimension, but different composite effect. The bending behaviors were described by force and steel strain at mid-span relationship, shown in Figure 3. Learn from Figure 3, at initial loading stage, specimen 1 has an early capacity reduction, which is caused by stably development of delamination between UHPFRC and steel under relatively weak composite design. The ultimate capacity of specimen 1 is controlled by interface composite effect. For specimen 2, there is a hardening stage, since greater shear resistance is supplied by composite interface by glued connectors. Thus, composite design effect, especially before steel plate yielding, is a significant factor to enhance structural rigidity.

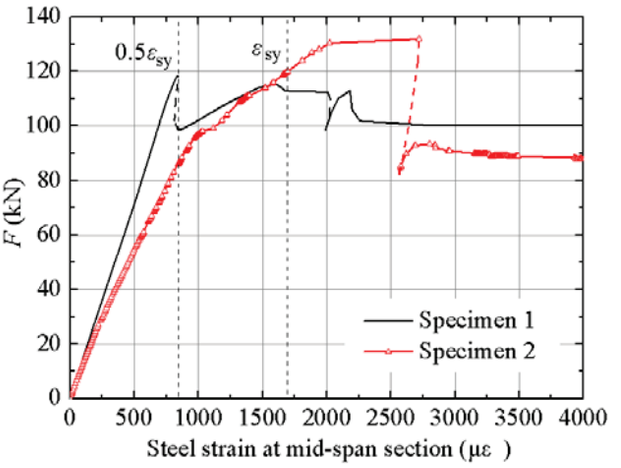


Figure 3. Force and steel strain curves.

In order to describe interface effect between UHPFRC layer and steel plate, relative displacement between UHPFRC and steel flange is measured at one end of specimens during loading procedure. Figure 4 shows force and relative displacement at one end of specimen. Learn from Figure 4, specimens 1 with epoxy gluing interface have greater rigidity improvement, which supplies even shear resistance along all span length. The relative displacement between two layers is always about zero before ultimate capacity. The ultimate capacity of specimen 1 is controlled by interface composite effect. For specimen 2, there is a bi-liner force and relative displacement curve before steel plate yielding. Before tensile elastic limit strength of UHPFRC, specimen 2 has no relative displacement, since specimen 2 with two connectors has sufficient shear resistance. When loading beyond tensile elastic limit strength of UHPFRC flange, there is a stable relative displacement increase in specimen 2. As steel plate is yielding, deflection in specimen 2 are increasing nonlinearly, which accelerates interface failure. Then the ultimate capacity is controlled by composite interface failure, like connector glue area sudden failure. After failure of connector glue surface, there

is a drop of capacity for specimen 2, and then specimens turn into a platform stage.

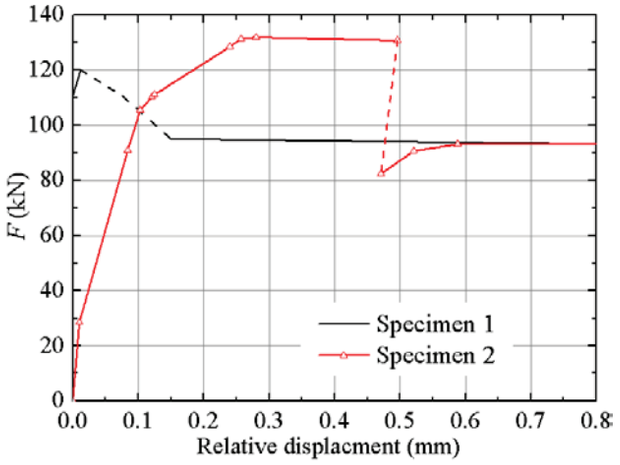


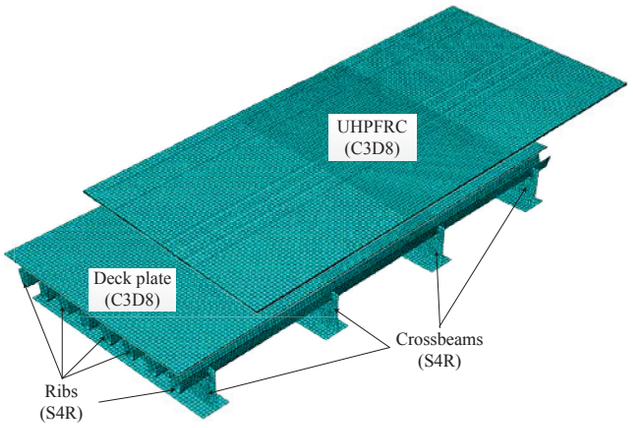
Figure 4. Force and relative displacement curves.

For specimen 1 and 2, the bending procedure can be described by four stages. Firstly, mid-span section is in elastic until attaining compressive strength of UHPFRC. The relative displacement is almost zero in this stage. Secondly, the mid-span section gradually turns into partial elastic until steel plate yielding. After steel plate yielding, the displacement grows quickly with force increasing slowly. Thirdly, as strain increasing obviously, crack is propagating through thickness of UHPFRC flange quickly, reducing effective section area. As crack propagating in UHPFRC flange, interface cracking is also quickly developed. Fourthly, the specimen attains ultimate capacity, which is controlled by interface delamination or resistance of mid-span section. After ultimate capacity, plastic hinge is formed at mid-span region and specimen turns into a platform stage.

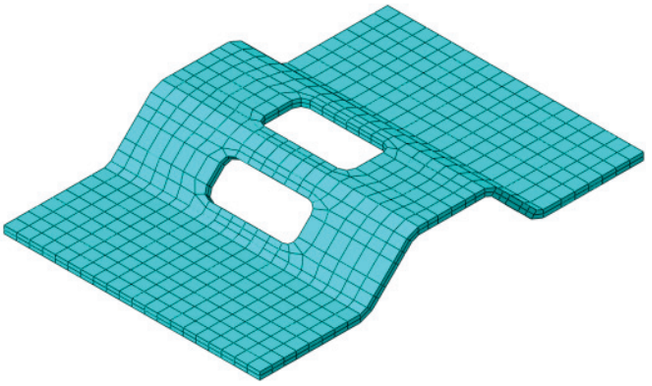
4 FINTE ELEMENT ANALYSIS

4.1 *Model establishment*

Typical full scale orthotropic steel deck model was selected from a suspension bridge for numerical analysis. The FE model consists of a UHPFRC layer, deck plate, longitudinal ribs, and cross beams. The FE model was 10.2 m long, 4.8 m width and 0.972 m high, shown in Figure 5. The thicknesses of deck plate, longitudinal rib and cross beam were 16 mm, 8 mm, and 10 mm, respectively. The dimension of longitudinal rib is 300mm (width) × 280mm (height) × 8mm (thickness). The FE model contains 8 longitudinal ribs with center distance of 600 mm. In longitudinal direction, the model has three spans of 3.0 m +3.0 m + 3.0 m. The thickness of UHPFRC layer above deck plate was 40 mm. Two kinds of composition effects between UHPFRC layer and deck plate were considered, including no shear connector and epoxy bonded with corrugated steel plate shear connector. The bonded corrugated steel plate connector had been modeled on the orthotropic steel deck bridge. In the FE model, 4 mm corrugated steel plate connector (shown in Fig. 5(b)) and 2 mm epoxy adhesive were taken into account in order to be uniform with experimental studies.



(a) Steel bridge deck segment with UHPFRC overlay.



(b) Simulation of corrugated steel plate connector.

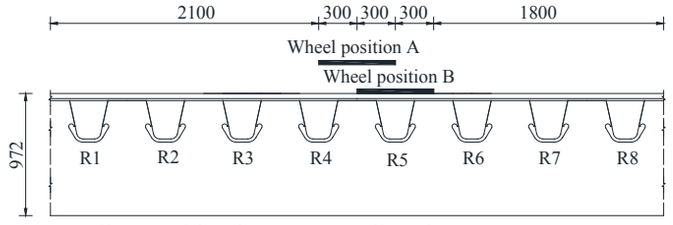
Figure 5. Establish of FE models.

In sofeware of Abaqus, Figure 5(a) shows the meshing of the different elements, such as solid elements eight-node brick elements with reduced integration (C3D8R) were used for the UHPFRC layer and deck plate, and four-node doubly curved shell element with reduced integration (S4R) was used for the crossbeams and ribs.

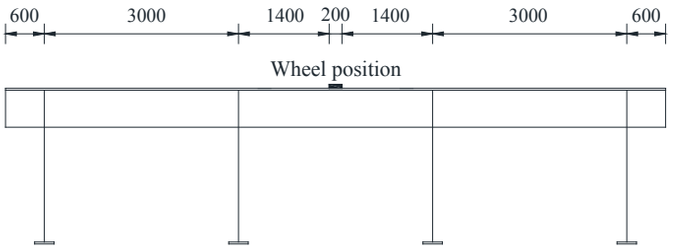
In this model, steel grade of Q345q (with nominal yield strength of 345MPa) was used for steel bridge deck. For steel grade of Q345q, the Young's modulus of Q345q is 206GPa, the Poisson's coefficient is 0.3, and the ultimate tensile stress is 424.35MPa. Both compressive and tensile properties of UHPFRC were considered in FE analysis. The compressive yield strength of UHPFRC was 128MPa, and the Young's modulus was 50GPa. The elastic tensile strength of UHPFRC was 6.8 MPa, and the Young's modulus was 50GPa. The ultimate tensile strength of UHPFRC was 9.3MPa. The

Young's modulus of the epoxy resin is 12.3 GPa and the Poisson coefficient is 0.34.

One wheel tire contact area (600× 200mm) for fatigue vehicle type 3 was adopted for static loading, according to the " Specification for Design of Highway Steel Bridge" (JTG D64-2015) in China. The loading position is shown in Figure 6. The deck plate supported on several longitudinal ribs had similar behavior with continuous beam under wheel loads. In Figure 6(a), two loading positions (position A and position B) for wheel loading were considered to achieve maximum position moment and negative moment, respectively. In Figure 6(b), wheel loads were located at mid-span section of middle span length.



(a) Loading position in transvers direction.



(b) Loading position in longitudinal direction.

Figure 6. Loading positions (unit: mm).

4.2 *Interface simulation*

The bonded interface behavior between corrugated steel plate shear connectors and steel plate UHPFRC was modeled by the friction method described by contact friction finite elements of Abaqus library (Houankpo, 2016). The kinematic method used in simulation consists to define the contact without penetration and friction conditions at the different nodes. This method using the Mohr-Coulomb's friction law allowed approaching the real behavior of the interface. According to the Figure 7, forces and relative displacements allowed to express the contact variables behavior at the nodes. The normal displacements with corresponding forces components (Un, N) and tangent displacements with corresponding forces component (Ut, T) can used to explain the conditions of contact friction.

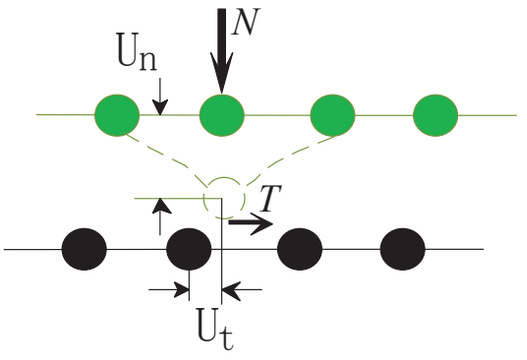


Figure 7. Contact variable in Coulomb's friction law.

The contact without penetration condition can be expressed as:

$$\left(U_n \geq 0 \ \textit{and} \ N \geq 0\right) \Rightarrow U_n N = 0 \tag{1}$$

The friction condition is:

$$\left(U_t > 0 \Rightarrow -\overline{T} = \mu \overline{D}\right) \text{or} \ \left(U_t > 0 \Rightarrow -\overline{T} < \mu \overline{D}\right) \tag{2}$$

where $\mu = \frac{T}{N}$ is the friction coefficient and $\overline{D} = \frac{\overline{U_t}}{\left|\overline{U_t}\right|}$.

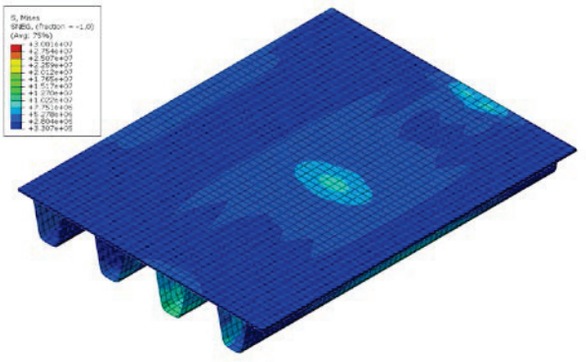
4.3 *Results analysis*

4.3.1 *Local stiffness analysis*

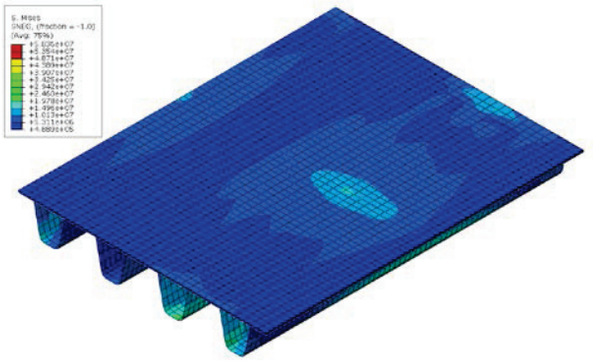
Learn from analysis results for the two models, deflections of deck plate were compared for local stiffness analysis, and the stresses at typical fatigue sensitive details were also compared. For the loading case A (shown in Fig. 6(a)), the deflection at bottom of deck plate between rib 4 and rib 5 were 0.49mm and 0.02mm for FE models with and without connector, respectively. The local stiffness of the deck plate increase 92% when adopting corrugated steel plate shear connector (cold bonding shear connector). The interface shear stresses under loading position were 6.8MPa and 2.33MPa. The shear stress at bottom of UHPFRC layer had been decreased about 66% because of contribution from composite design. The stresses at rib to deck plate detail were 98.89MPa and 43.53MPa for models with and without composite design (shown in Fig. 8(a)).

For the loading case B, the deflection at bottom of deck plate under rib 5 were 0.59mm and 0.14mm for FE models with and without connector, respectively. It can be noted that the stiffness of the pavement-deck plate system with bonded formed steel plate had been improved about 86.31%. The deflection at

the bottom of the rib5 had improved 50.3% if adopting composite effect. The stresses at rib to deck plate detail were 56.2MPa and 9MPa for models with and without composite design (shown in Fig. 8(b)). The normal stresses calculated at the free edge of crossbeam were 92.72 MPa and 52.27 MPa respectively, which contribute a lot to stop fatigue crack initiation and propagation.



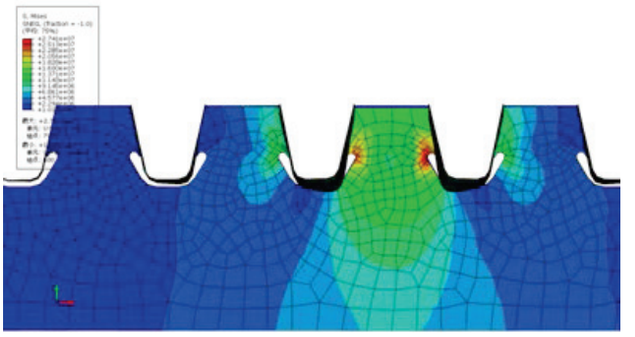
(a) Loading postion A.



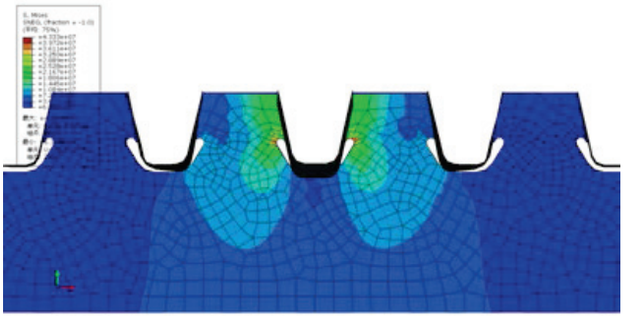
(b) Loading postion B.

Figure 8. Stress at rib to deck details.

For the FE model without shear connector, the calculated maximal stresses at free edge cutout of crossbeam were 36.68 MPa under loading position A and 43.33MPa under loading position B. Figure 9 shows stress distributions at free edge cutout of crossbeam for models for the FE model with colding bonding shear connector. These stresses value at free edge cutout of crossbeam had been reduced 26.40% and 30.76% respectively for the loading case A and B, respectively.



(a) Loading case A.

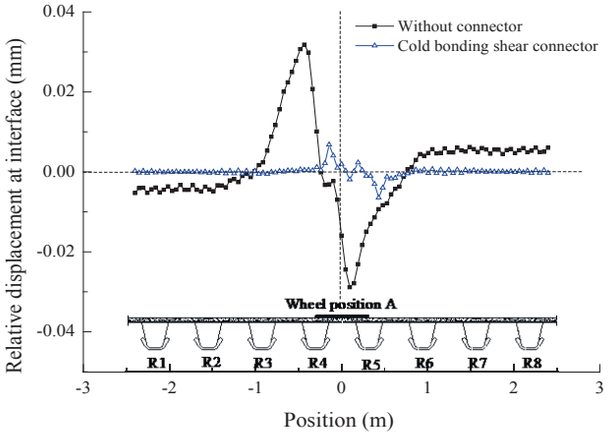


(b) Loading postion B.

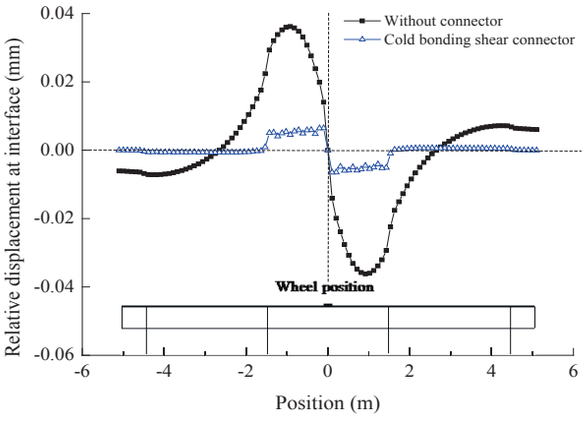
Figure 9. Stress at cut-out rib to crossbeam details.

4.3.2 *Relative displacement analysis*

Under loading position A, the relative displacement between UHPFRC layer and steel deck plate was analyzed. As shows in the Figure 10(a), the relative displacements were anti-symmetrically distributed along the transverse direction of cross section. For FE model without shear connector design, the maximal relative displacement was 0.36 mm around the wheel attaching surface, which this maximal relative displacement for FE with cold bonding shear connector was 0.06 mm. This difference of relative displacement would be more obvious with loading level increase. Figure 10(b) shows that the relative displacements distribution along the longitudinal direction. Learn from Figure 10(b), this relative displacement distributions between UHPFRC layer and steel bridge deck plate were also anti-symmetrically with the wheel loading position. The cold bonding shear connector had improved the composite action for UHPFRC layer and steel bridge deck system effectively by limiting relative displacement at interface.

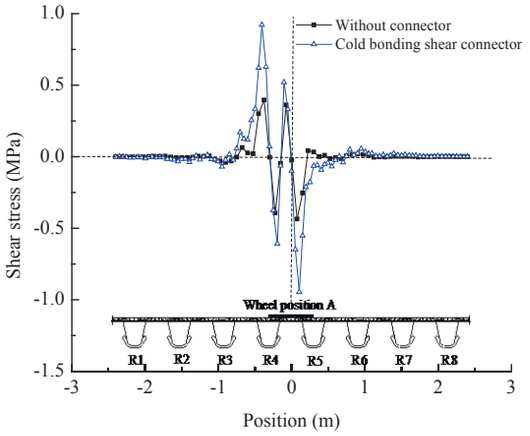


(a) Transversal direction.

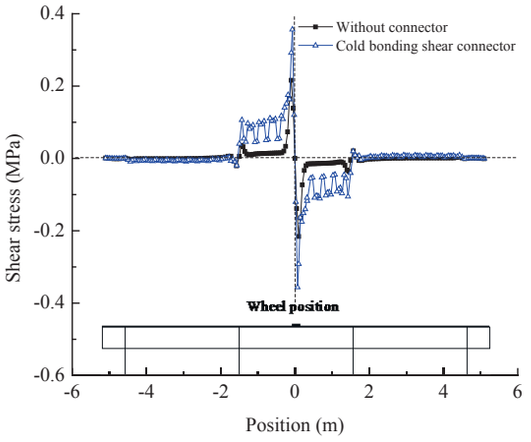


(b) Longitudinal direction.

Figure 10. Relative displacement at the interface of UHPFRC layer and steel deck plate under loading position A.



(a) Transversal direction.



(b) Longitudinal direction.

Figure 11. Shear stresses at the interface of UHPFRC layer and steel deck plate.

The shear stress at the interface between UHPFRC layer and steel deck plate was comparatively analyzed under the loading position A, shown in Figure 11. Learn from Figure 11(a), the interface shear stresses were anti-symmetrically distributed along the transverse direction of cross section. For FE model without shear connector, the maximal shear stress was 0.44 MPa around the wheel attaching surface, which maximal shear stress for model with cold bonding shear connector was 0.91 MPa. This difference of shear stress would be more obvious as loading level increase. Figure 11(b) shows the shear stress distribution along the longitudinal direction. FE analysis results revealed that the cold bonding connectors had a maximum shear stress of 0.36 MPa under the wheel attaching surface. It can be concluded that the cold bonding shear connector can ensure the composite action of the UHPFRC-steel bridge deck system by enhanced its shear resistance of the interface.

5 CONCLUSIONS

This paper is focused on orthotropic steel bridge deck composite with UHPFRC layer by cold bonding shear connector. Bending tests were conducted for steel and UHPFRC composite beams with different composite design ways, including epoxy gluing UHPFRC layer and bonding corrugated steel plate shear connectors.

(1) Learn from test study, composite design between steel and UHPFRC is an important factor affecting structural rigidity. Cold bonding corrugated steel plate shear connectors adopted in test study was proved to be an efficient composite design method.

(2) Finite element model was established by software of Abqus for two orthotropic steel bridge deck model with UHPFRC layer, considering no shear connector and cold bonding shear connector respectively. Learn from comparative analysis results, steel bridge deck and UHPFRC layer composite system can improve load rigidity of steel bridge deck and decrease stress level at typical fatigue details, which proved the effective composite ways of bonding corrugated steel plate shear connectors

6 ACKNOWLEDGEMENT

The authors gratefully acknowledge the financial support provided by National Natural Science Foundation of China (Grant 51578073, 51078039), the Major State Basic Research Development program of China (973 Program) Subprogram (Grant 2015CB057703), General Financial Grant from the China Postdoctoral Science Foundation (Grant No.2014M560738)), Construction and Technical Program of Ministry of Transport (Grant No.2014318223030) and the special Fund for Basic Scientific Research of Central Colleges of the P.R. China, Chang'an University (310821153401 and 310821153314).

7 PREFERENCES

Buitelaar, P., and Braam, C.R., 2004. Reinforced high performance concrete overlay system for steel bridges. 5th International CROW-workshop on fundamental modelling of the design and performance of concrete overlays 1&2 April 2004. Turkey: Istanbul.

Cao, J., Shao, X., Zhang, Z., and Zhao, H., 2015. Retrofit of an orthotropic steel deck with compact reinforced reactive powder concrete. Struct. Infrastruct. Eng. 12(3): 411–429.

Connor, R., Fisher J. W., et al., 2012. Manual for design, construction and maintenance of orthotropic steel deck bridges.

De Jong, F. B. P., 2007. Renovation techniques for fatigue cracked orthotropic steel bridge decks. The Netherlands: Delft University of Technology.

Dieng, L., Marchand, P., Gomes, F., Tessier, C., and Toutlemonde, F., 2013. Use of UHPFRC overlay to reduce stresses in orthotropic steel decks. Journal of Constructional Steel Research. 89: 30 - 41.

Duan, L., Noukpo Houankpo, T.O., Dong, P., Wang, C. S. and Brühwiler, E., 2015. UHPFRC Strengthening method for existing bridges. IABSE Conference Structural Engineering: Providing Solutions to Global Challenges September 23-25, Switzerland: Geneva.

Houankpo, T. N. O., 2016. Study of mechanical performance of UHPFRC used as pavement of composite steel bridge deck. China: Chang'an University.

JTJ D64-2015. Specification for Design of Highway Steel Bridges. 2015.Kolstein, M. H., 2007. Fatigue classification of welded joints in orthotropic steel bridge decks. The Netherlands: Delft University of Technology.

Li, W., Shao, X., Fang, H., and Zhang Z., 2015. Experimental study on flexural behavior of steel-UHPC composite slabs. China Civil Engineering Journal 48(11):93-102. (Chinese)

Lin, W., and Yoda, T., 2013. Experimental and numerical study on mechanical behavior of composite girders under hogging moment. Advanced Steel Construction. 9(4): 309-333.

Makita, T., and Brühwiler, E., 2014. Tensile fatigue behavior of Ultra-High Performance Fibre Reinforced Concrete (UHPFRC). Mater . Struct. 47(3): 475-491.

Shao, X., Cao, J., Yi, D., Chen, B., and Huang, Z., 2012. Research on basic performance of composite bridge deck system with orthotropic steel deck and thin RPC layer. China Journal of Highway and Transport. 25(2): 39-45.

Software M. Marc Volume A: Theory and User Information. USA: MSC Software; 2005.

Tsakopoulos, P. A., and Fisher, J. W., 2005. Full-scale fatigue tests of steel orthotropic deck panel for the Bronx-Whitestone Bridge rehabilitation. Bridge Structures 1(1): 55-66.

Wang, C.S., and Fu, B.N., 2012. Full-scale fatigue test of orthotropic steel deck, Seventh International Conference on Advances in Steel Structures; Proc. intern. symp., 16-19 April 2012. Nanjing, China.

Walter, R., Olesen, J. F., Stang, H., and Vajrum, T., 2007. Analysis of an orthotropic deck stiffened with a cement-based overlay. Journal of Bridge Engineering, ASCE, 12(3):65-77.

Wang, C. S., Zhai, M. S., Houankpo, T. N. O, and Tang, Y. M., 2016. Cold maintenance technique and assessment method for orthotropic steel bridge deck. China Journal of Highway and Transport. 29(8): 50-58.

Maintenance, Safety, Risk, Management and Life-Cycle Performance of Bridges – Powers, Frangopol, Al-Mahaidi & Caprani (Eds)
© 2018 Taylor & Francis Group, London, ISBN 978-1-138-73045-8

Effect of Diaphragms on the Exterior Girders during Bridge Construction

F. Hraib, L. Hui, R. Hindi
Department of Civil Engineering
Saint Louis University, St. Louis, MO, United States

ABSTRACT: During the construction of bridges, both live and dead loads play a critical role in the safety of the construction and the future serviceability of the bridges. Loads from screed machine and the fresh concrete weight can cause deflection of the overhang and excessive exterior girders rotation. The bridge permanent diaphragms keep the girders stable during construction, and they can potentially reduce the rotation as long as they are spaced properly. The main purpose of this study is to examine the effect of the spacing between diaphragms on the rotation of the exterior girder. Finite Element models were developed using SAP2000 software to simulate bridges with different diaphragms spacing. The results show that reducing the distance between diaphragms by 40% can decrease the rotation of the exterior girders by more than 60%. It also shows that the location of the screed machine along the span is very crucial.

1 INTRODUCTION

Construction of bridge superstructures is a very critical stage that if it is not carefully taken into consideration with the corresponding construction loads, many issues and deficiencies can occur during construction and the service life of the bridge may reduce. The lack of attention to loads and details during construction might result in significant instability of the structure and even failures of the bridges (Helwig and Yura 2012).

The overhang part of the deck slab is usually defined as the horizontal distance between the center line of the exterior girder and the edge of the bridge deck. The purpose of the overhang is to outspread the deck slab in the transverse direction which increases the deck's width without adding more girders. During construction, the overhang is subjected to loads from the fresh concrete weight, the screed machine weight, construction live loads and the weight of form work (Ashiquzzaman et al. 2016). The overhang formwork is often supported using steel brackets that rest on the web of the exterior girder, which creates torsion moments on the exterior girders as shown in Figure 1. These moments can lead to vertical deflection of the overhang and rotation of the exterior girder during construction (Clifton and Bayrak 2008). Hence, as the concrete is not hardened yet, and because of the deflection of the overhang formwork, a non-uniform deck slab thickness is expected in the transverse direction after the concrete is hardened. Also, as the steel brackets rest on the exterior girder, the girder can be subjected to excessive rotation and local buckling that may lead to reduction in the girders resistance and poor rideability in the future (Ashiquzzaman et al. 2017; Clifton and Bayrak 2008; Fasl 2008).

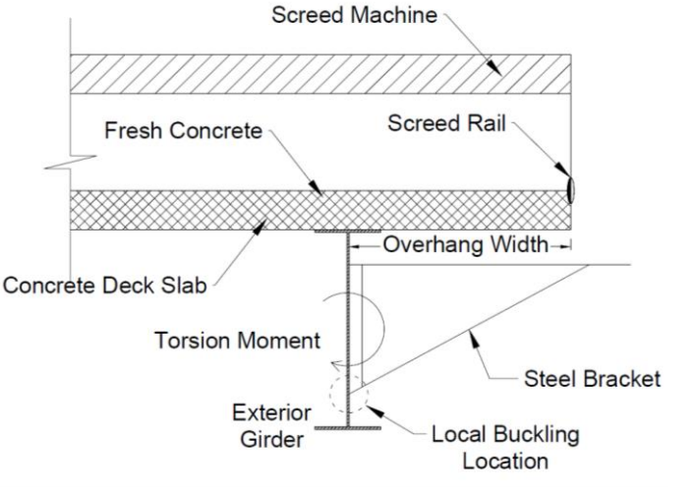


Figure 1. Overhang Definition and Exterior Girder Torsion Moment.

Permanent transverse bracing systems, represented by diaphragms or cross-frames, are designed to resist lateral forces during the service life of the bridge and assure stability of girders during construction. They also can resist the torsion moments in exterior girders from loads during the construction. However, these systems are not designed for loads during construction, and contractors tend to add temporary bracing systems to reduce the rotation of exterior girder. Common temporary bracing systems used now a days are timber blocks, diagonal and transverse ties and temporary cross-frames (Ashiquzzaman et al. 2016). The rotation of exterior girder is highly dependent on the geometry and the structural properties of the bridge superstructure (Ito et al. 2002; Schilling 1988).

The main purpose of this study is to examine the effect of the spacing between the bracing members on the rotation of the exterior girder. Finite Element models were developed using SAP2000 software to simulate bridges with different diaphragms spacing. The location of screed machine loads along the span of the bridge is examined as well to understand its effect on the girders rotation during construction. The study is concerned only with multiple span non-skewed steel girder bridges with steel diaphragms.

2 REFERENCE BRIDGE AND FE MODEL

In order to study the effect of diaphragms spacing, a reference bridge is selected as a benchmark. A three span field instrumented bridge was chosen for this study. Figure 2 shows the plan view of the reference bridge with its geometrical properties. It shows that the bridge superstructure consists of three W30x124 steel girders along three spans of 15.16 m (49`- 9``), 24.5 m (80`- 4``) and 15.16 m (49`- 9``). The girders spacing is 2.13 m (7 ft) with an overhang width of 94 cm (37 in) on each side. The original bridge is skewed by 3.8 degrees, but the skewness can be neglected in this study as it is very small and out of the scope of the research.

The diaphragms locations and spacing are also shown in Figure 2. C12x25 sections are used as diaphragms at all required locations in the reference bridge. The bridge is subjected to the fresh concrete load and the screed machine loads because they have the most effect on the rotation of the exterior girder. The weight of the concrete is taken based on the thickness of the deck slab that equals to 20 cm (8 in). On the other hand, the screed machine weight is distributed through 4 wheels on each overhang. The wheels weigh 340 Kg (750 lbs) each, and spaced at 61 cm (24 in), 122 cm (48 in) and 61 cm (24 in) from each other.

Finite Element (FE) models were developed using SAP2000 to simulate all bridges in this study. The FE model used has been verified with the field experimental results during construction (Ashiquzzaman et al. 2016). Figure 3 shows the finite element model of the reference bridge with the FE elements used for each corresponding member of the bridge's superstructure. Thick shell elements were used for both the girders and diaphragms while frame elements were used to model the steel brackets. The fresh concrete weight on the overhang part of the slab was simulated as point loads at the middle of each steel bracket, while the concrete in the internal bays is transferred to the edges of girder flanges as point loads along the span of the bridge. Finally, the screed machine loads were represented by point loads moving along a steel rail modeled using frame elements resting at the edge of the deck overhang. The rotation values are recorded at the middle of the web of the exterior girder along the span of the bridge for all models used in this study to assure consistent comparison of the results.

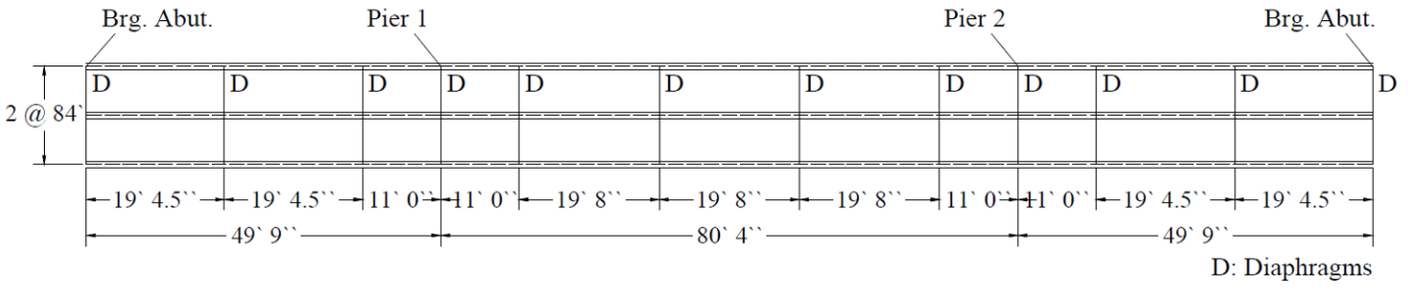


Figure 2. Reference Bridge Geometry.

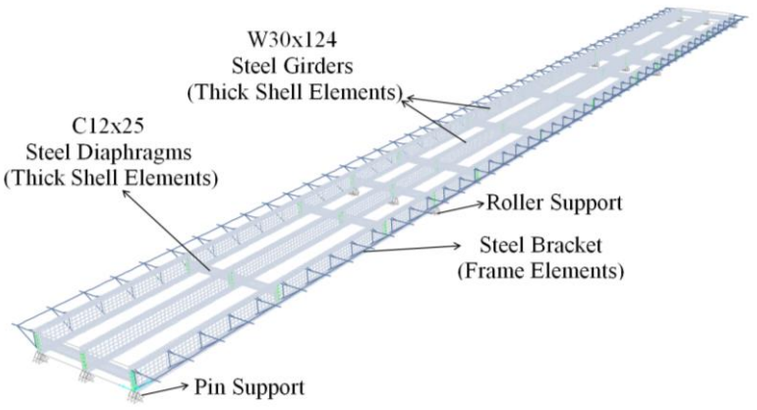


Figure 3. Finite Element Modeling.

3 DIAPHRAGMS SPACING EFFECT

In order to examine the effect of diaphragms spacing on the rotation of exterior girders, the number of diaphragms in the second span of the bridge has been ranged between 2, 4, 6 and 8. Only even number of diaphragms has been chosen in order to keep the middle of the span free in rotation, where it is expected to get the maximum rotation. The diaphragm spacing is then changed in the first and the second span in correspondence with the changes in the middle span. The diaphragms section was kept the same (C12x25) throughout the study in order to compare the results consistently. Figure 4 shows the diaphragms positioning and spacing for each case.

Figure 5 shows the rotation values at the middle and 1/3 of the second span for each case. The results show that increasing the number of diaphragms, which corresponds with reducing the diaphragms spacing, leads to significant reduction in the rotation of exterior girder. Increasing the number of diaphragms from 2 to 4, which parallels with diaphragm spacing of 8.2 m (26`- 10``) and 5 m (16`- 4``), respectively, reduces the rotation of exterior girder at the middle of the span by more than 60%.

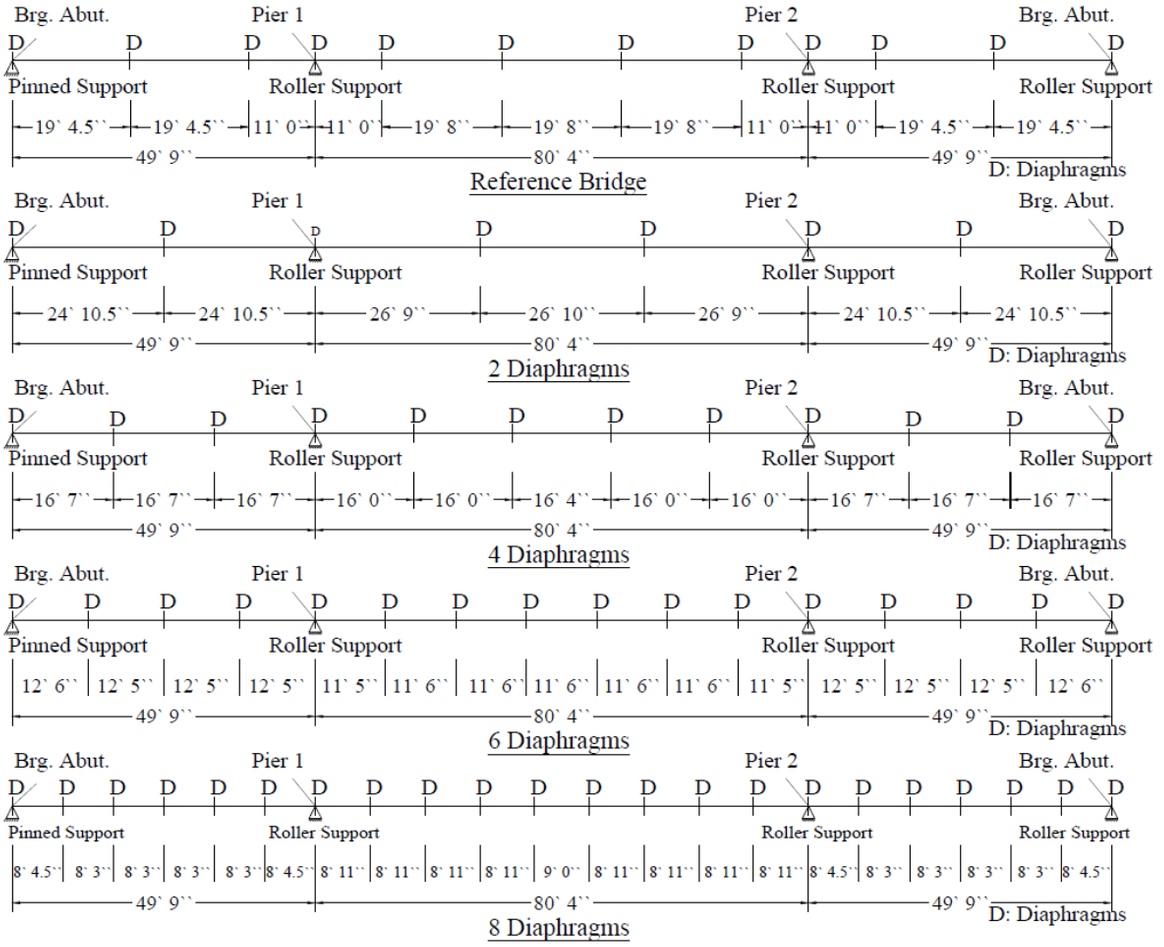


Figure 4. Diaphragms Positioning and Spacing.

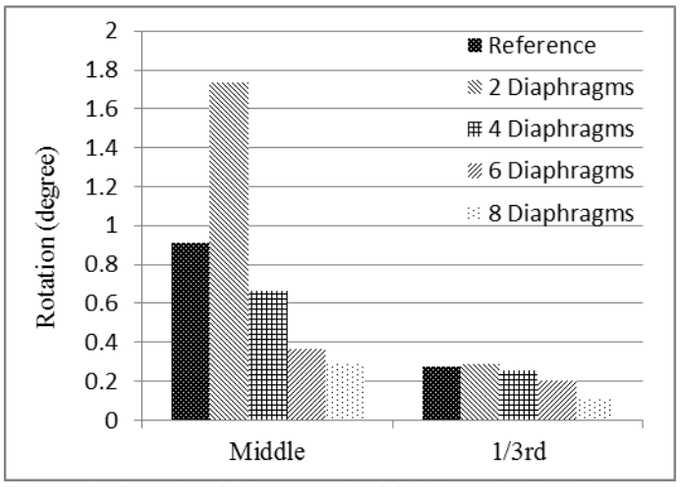


Figure 5. Rotation Values at the Middle and 1/3 of Second Span.

As Illinois Department of Transportation (IDOT) suggests that the maximum vertical deflection in the overhang during construction should not exceed 3/16 inches (IDOT 2012), the rotation of the exterior girder in the bridge in this study is limited to 0.29 degrees (0.005 rad). However, the rotation did not drop below IDOT limit until reducing the diaphragms spacing to 2.74 m (9 ft) by using eight diaphragms at the middle span. This confirms that the ratio between the unbraced length (B) and the diaphragm depth (D) is a very significant indicator (Ashiquzzaman et al. 2016). When B/D ratio dropped to below 4 in this specific bridge, the unbraced length changed to 2.74 m (9 ft), and as a result the rotation decreased to 0.29 degrees (0.005 rad).

The number of diaphragms at the second span of the reference bridge is four, with a maximum diaphragms spacing of 6 m (19`- 8``). However, compared to the bridge with 4 diaphragms at the second span, equally spaced at 5 m (16`- 4``), Figure 6 shows that even with the same number of diaphragms along the span, the maximum rotation is reduced by 27% just by rearranging the diaphragms locations in the reference bridge. This is because repositioning the diaphragms resulted in consistent and smaller diaphragms spacing along the span length.

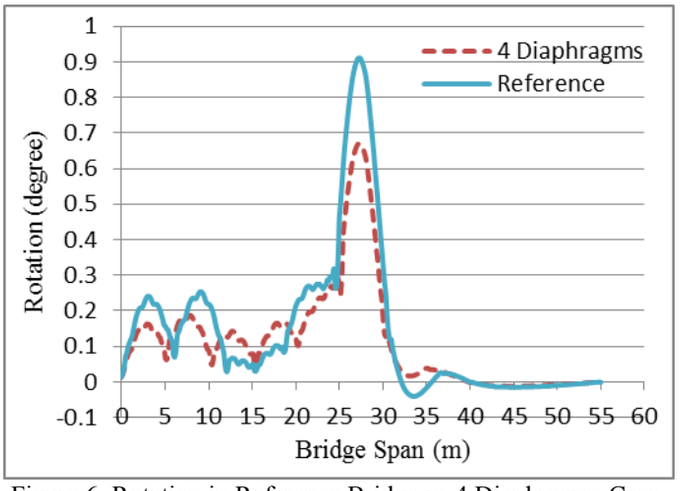


Figure 6. Rotation in Reference Bridge vs 4 Diaphragms Case.

4 SCREED MACHINE POSITION EFFECT

During the construction, the screed machine moves along the span of the bridge in order to finish the deck slab concrete surface. In this study, the machine loads and the corresponding concrete load has been simulated to move along the span of the reference bridge. The loading starts at Pier 1 and ends at the middle of the second span, where the loads were moved in the longitudinal direction of the bridge with 0.6 m (2 ft) step as shown in Figure 7.

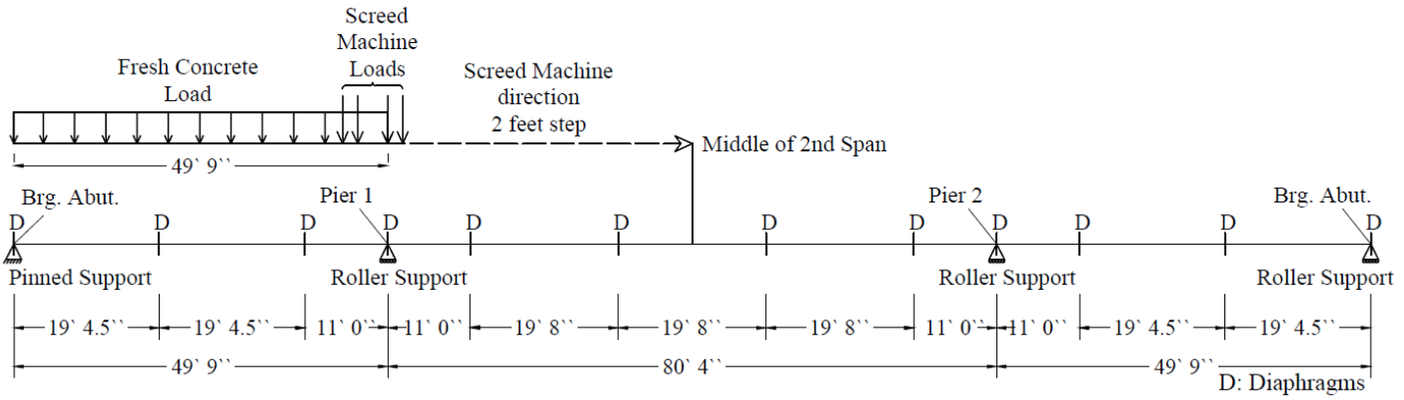


Figure 7. Screed Machine Movement along the Second Span

Figure 8 shows the rotation values in the exterior girder at the middle of the second span versus the location of the screed machine load. The results show a significant increase in the rotation when the load is exactly at the middle of the span. This is because the middle of the span is free to rotate and the screed machine locates exactly at half distance between 2 diaphragms that resist the rotation. It also can be noted that rotation starts to peaks up when the screed machine reaches the second diaphragm where the girder is free to rotate after that location. On the other hand, the results show that along the second span, the rotation of the exterior girder follows a pattern complies with influence line concept. The exterior girder is braced laterally by the diaphragms. Therefore, the girder can be looked at as a continuous beam supported by diaphragms and subjected to torsion moments along its span. Hence, as shown in Figure 8, rotation values alternate between negative and positive until reaching the maximum at the loading location at the middle of the span, this agrees with the influence line theory.

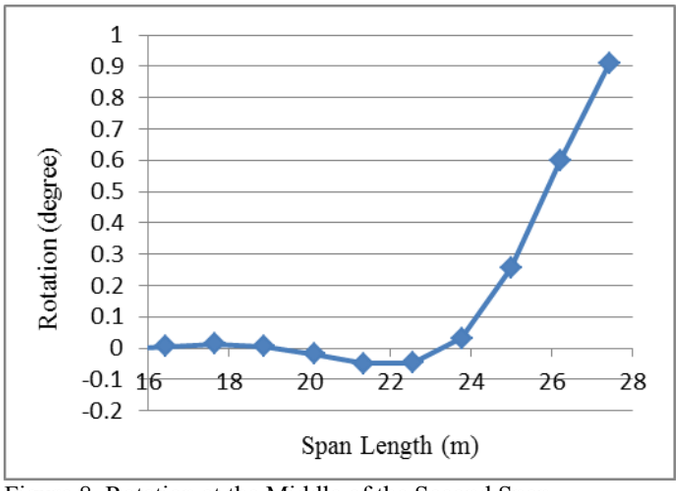


Figure 8. Rotation at the Middle of the Second Span.

Rotation values are also recorded along the second span of the bridge at the same location of the screed machine load with 0.6 m (2 ft) step, as shown in Figure 9. It is clear that the rotation peaks up when the load is located between 2 diaphragms, while it reaches minimum values when the load is close to the lateral support system members, the diaphragms. The results also show that between Pier 1 and the first diaphragm, the maximum rotation recorder is 0.245 degree (0.00427 rad), while between the first and second diaphragm it reaches 0.088 degree (0.01534) rad, and finally at the middle of the span it reaches 0.091 degree (0.01586 rad). This proves that the distance between the diaphragms is the critical factor in exterior girder rotation. When the distance between diaphragms is relatively small, the rotation value is low. The girder segment between Pier 1 and the first diaphragm in the second span of the bridge is 3.35 m (11`- 0``). The maximum rotation recorder at this segment is 70% lower than the maximum in the second segment where the distance between diaphragms is 6 m (19`- 8``). Therefore, it can be conclude that the rotation is very dependent on the location of the screed machine load and the distance between the lateral support system members represented by diaphragms in this study.

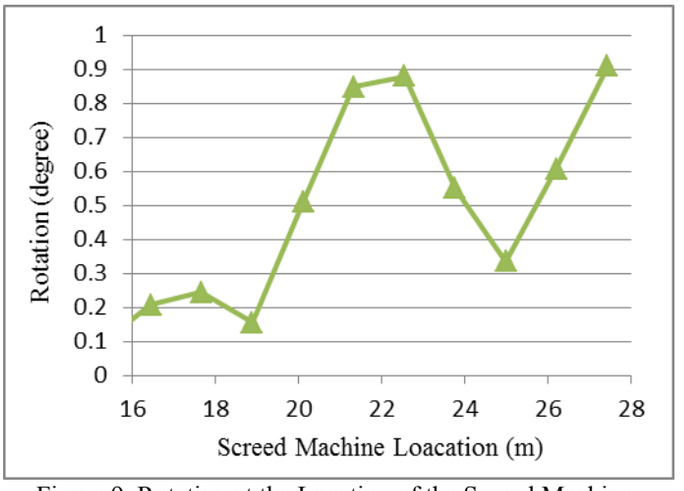


Figure 9. Rotation at the Location of the Screed Machine.

5 SUMMARY AND CONCLUSION

This research focused on understanding the effect of the transverse bracing system spacing, represented by diaphragms, on the rotation of the exterior girders. Finite element models of different bridges have been developed using SAP2000 and the rotations were recorded for each case at the exterior girders and then compared to each other. After analyzing the results the following conclusions can be drawn:

- Diaphragms spacing is a critical parameter in bridge geometry that affects the rotation of exterior girder during construction significantly. Where reducing the spacing between diaphragms by 40% led to more than 60% reduction in rotation.
- The location of the screed machine along the bridge is crucial. The maximum rotation value between two diaphragms is recorded at the load location when the load is at half distance between the diaphragms.
- The rotation of the exterior girder complies with the influence line theory, where the diaphragms act like lateral supports for the continuously braced beam (the exterior girder).

6 ACKNOWLEDGEMENT

This publication is based on the results of ICT-R27-179, Effectiveness of Exterior Beam Rotation Prevention Systems for Bridge Deck Construction - Phase II. ICT-R27-179 was conducted in cooperation with the Illinois Center for Transportation; the Illi-

nois Department of Transportation, Office of Program Development; and the US Department of Transportation, Federal Highway Administration.

7 REFERENCE

Ashiquzzaman, M., Calvo, C. M., Hui, L., Ibrahim, A., Lindquist, W., and Hindi, R. (2017). "Effectiveness of different bracing systems to prevent exterior girder rotation during bridge deck construction." *Engineering Structures*, 142, 272-289.

Ashiquzzaman, M., Hui, L., Ibrahim, A., Lindquist, W., Thomson, M., and Hindi, R. "Effect of Inconsistent Diaphragms on Exterior Girder Rotation During Overhang Deck Construction." *Proc., Structures*, Elsevier, 25-34.

Ashiquzzaman, M., Hui, L., Schmeltz, J., Merino, C., Bozkurt, B., Ahmed, I., Lindquist, W., and Hindi, R. (2016). "Effectiveness of Exterior Beam Rotation Prevention Systems for Bridge Deck Construction." Illinois Center for Transportation/Illinois Department of Transportation.

Clifton, S., and Bayrak, O. (2008). "Bridge Deck Overhang Construction. Report no." IAC 88-5DD1A003-2, Texas Department of Transportation, Austin, Texas.

Fasl, J. D. (2008). "The influence of overhang construction on girder design." University of Texas at Austin.

Helwig, T., and Yura, J. (2012). "Steel bridge design handbook: Bracing system design."

IDOT (2012). "Bridge Manual. Springfield, Illinois, USA: Illinois Department of Transportation.".

Ito, M., Karatani, E., and Komuro, Y. (2002). "Moment-inelastic rotation behavior of longitudinally stiffened beams." *Journal of Bridge Engineering*, 7(4), 223-228.

Schilling, C. G. (1988). "Moment-rotation tests of steel bridge girders." *Journal of Structural Engineering*, 114(1), 134-149.

Maintenance, Safety, Risk, Management and Life-Cycle Performance of Bridges – Powers, Frangopol, Al-Mahaidi & Caprani (Eds)
© 2018 Taylor & Francis Group, London, ISBN 978-1-138-73045-8

Inspection of Bingo Bridge by using high-sensitivity magnetic nondestructive testing

T. Ishikawa
Dept. of Civil, Environmental and Applied System Engineering, Kansai University, Osaka, Japan

Y. Kuramitsu
Dept. of Management, Nara Prefectural Office, Nara, Japan

H. Furuta
Faculty of informatics, Kansai University, Osaka, Japan

K. Tsukada
Graduate school of natural science and technology, Okayama University, Okayama, Japan

ABSTRACT: In Bingo Bridge which is the suspended bridge in Nara Prefecture, fracture of hanger rod was found in 2015. Furthermore, in this bridge, the surface corrosion of main cable and stiffening girders were also observed. This bridge was closed to traffic until all the hanger rods replaced to the hanger ropes. Therefore, to inspect the corrosion of main cable and the stiffening truss during the road closure, the high sensitivity magnetic nondestructive testing was applied. Additionally, one of the purpose of this research is to investigate the application of high sensitivity magnetic nondestructive testing on site.

1 INTRODUCTION

In Bingo Bridge which is the suspended bridge, fracture of hanger rod and fatigue crack on screw part of hanger rod were observed in 2015. Since these serious damages were found, this bridge was closed to traffic. Furthermore, in this bridge, the surface corrosion of main cable and stiffening truss was also observed.
In this study, inspection of corrosion of cable and stiffening girders was carried out by applying the high sensitivity magnetic nondestructive testing during the road closure. Additionally, one of the purposes of this research is to investigate the application of high sensitivity magnetic nondestructive testing on site.


Figure 1 Bingo Bridge


Figure 2 Fracture of hanger rod

2 BINGO BRIDGE

Figure 1 shows the Bingo Bridge in National Root 425 in Nara Prefecture. This bridge was built in 1963. In this bridge, the maximum vehicle weight for service is limited to 59kN or less. The length and width of road of this bridge are 163m and 4.5m, respectively. As shown in Figure 1, Bingo Bridge is the suspended bridge with stiffening truss.
The fracture of hanger rod and fatigue crack on screw part of hanger rod were found in 2015, as shown in Figures 2 and 3. They were located near the center of the bridge. One of the reasons of fatigue damage is assumed that the cyclic bending moment was introduced in the hanger rods by the



Figure 3 Location of damaged hanger rods

sticking of hinges. Damaged hanger rods were immediately replaced the new hanger rods. However, this bridge was closed until the all hanger rods were replaced to the hanger ropes. Figure 5 shows the replaced hanger rope in Bingo Bridge.

3 HIGH-SENSITIVITY MAGNETIC NONDESTRUCTIVE TESTING

3.1 *ELECT-SAM*

As generally know, the Eddy-current Testing or Electromagnetic Testing (E.T) is widely used as a nondestructive testing for detection of surface flaws. However, the E.T cannot be applied to detection of inner fatigue crack or inner corrosion of steel structures. Extremely Low-Frequency Eddy Current Testing with Spectrum Analysis of Magnetic field (ELECT-SAM) was developed for detection of inner corrosion of steel structures (Tsukada et al. 2016). Figure 5 shows the system of ELECT-SAM. This nondestructive testing system can detect inner corrosion at extremely low frequency by employing a magnetic probe using an anisotropic magnetic resistance (AMR) sensor with the sensitivity of $1\ \mathrm{nT}/\sqrt{\mathrm{Hz}}$. In this system, to estimate the plate thickness, the calibrated equations obtained by magnetic spectrum analysis of each material are prepared.

3.2 *USAC-MFL*

As above mentioned, the conventional E.T is difficult to inspect the inner cracks in steel structures because of its high permeability as well as owing to the variations in it. UnSaturated AC Magnetic Flux Leakage testing (USAC-MFL) was developed for detection of inner crack in thick steel plate and detection of inner defects of steel structures (Tsukada et al. 2017). The measurement system of USAC-MFL is shown in Figure 6.

4 INSPECTION OF INNER CORROSION ON UPPER CHORD IN STIFFENING TRUSS

By using ELECT-SAM, the thickness measurement of the upper chord in stiffening truss was carried out with measuring frequency of 1Hz or 10Hz. Figure 7 shows the situation of thickness measurement by ELECT-SAM. The locations of the thickness measurement are the points A to N in Figure 8 on the upper surface of upper chord. In this bridge, the two materials of JIS-SS400 and JIS-SM490 are used in upper chord. The guaranteed yield stresses of JIS-400 and JIS-SM490 are 245N/mm^2 and 325N/mm^2, respectively.



Figure 4 New hanger rope

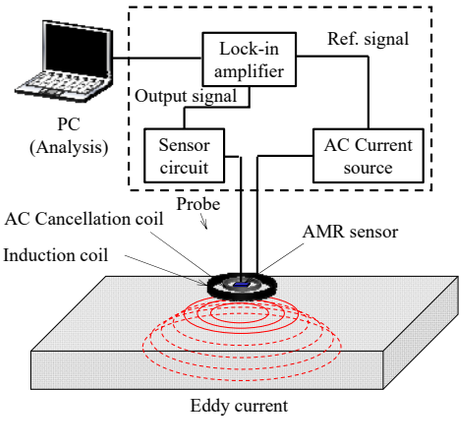


Figure 5 System of ELECT-SAM

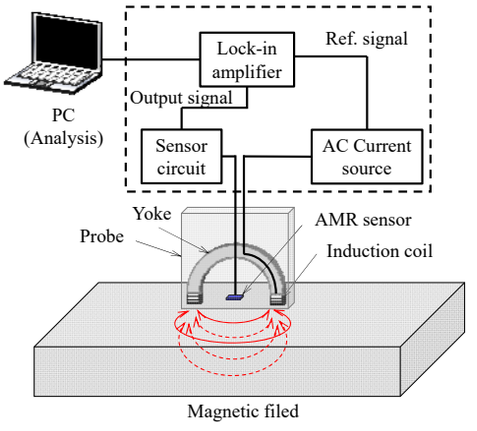


Figure 6 System of USAC-MFL

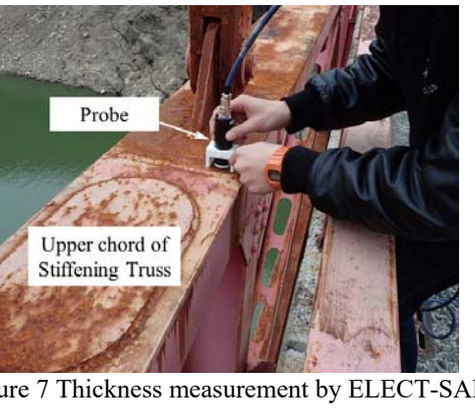


Figure 7 Thickness measurement by ELECT-SAM

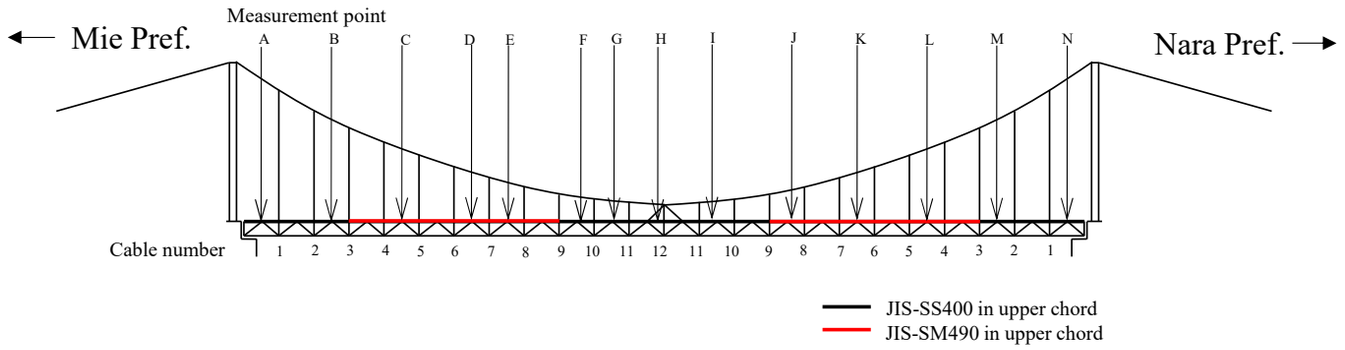


Figure 8 Location of thickness measured in Bing Bridge

Table 1. Measured thickness of top flange in upper chord (mm)

	A	B	C	D	E	F	G	H	I	J	K	L	M	N
Measured thickness	7.83	7.91	7.71	8.71	7.62	8.53	8.72	8.82	7.73	7.47	8.21	7.30	8.31	7.78
Thickness measured by U.T	9.17	9.37	9.80	10.2	10.0	9.28	9.08	9.76	8.73	9.66	9.74	9.21	9.63	9.64

Measured thickness of top flange in upper chord is listed in Table 1. As mentioned in Section 3.1, since the equations for JIS-SM400 and JIS-SM490 given by spectrum analysis are different in ELECT-SAM, each equation was applied to the each material on the upper chord in stiffening truss.

As listed in Table 1, measured thicknesses by ELECT-SAM are 7mm to 9mm. Design thickness of the upper chord in stiffening truss is the 9mm and measured thickness by ultrasonic testing (U.T) is also 9mm to 10mm. Therefore, it is presumed the measured thicknesses by ELECT-SAM are slightly thinner than the actual thickness. It is because the components of materials used in Bingo Bridge might not be completely same as that used in the calibrated new materials. However, the tendency of thickness distribution measured by ELECT-SAM is as same as that measured by U.T. Therefore, ELECT-SAM can be used for the detection and screening of thickness reduction by corrosion attack.

5 INSPECTION OF DETERIORATION IN MAIN CABLE

By using USAC-MFL, the inspection of corrosion in the main cable near the anchorage was carried out. Figure 9 shows the situation of inspection using USAC-MFL. For the line scanning of surface corrosion observed area, the probe for USAC-MFL was moved about 500mm by hand with measuring (measuring frequency of 11Hz). Measured intensity change vs. scanning time diagram was shown in Figure 10. When the corrosion or fracture of the cable are occurred, the intensity change measured by ELECT-SAM changes. As can be seen in Figure 10, difference of the peaks of intensity change is small. Therefore, it was presumed that the any corrosion or fracture inner the main cable was not occurred in the cable near the anchorage.

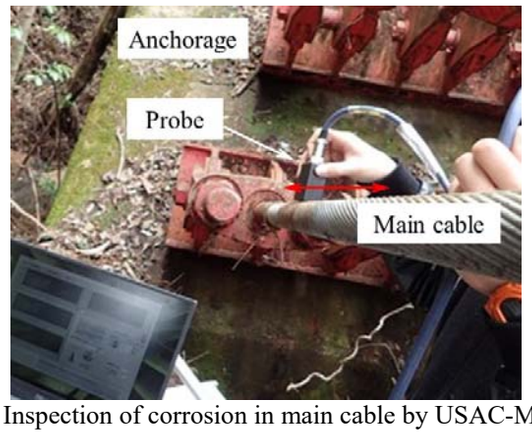


Figure 9 Inspection of corrosion in main cable by USAC-MFL

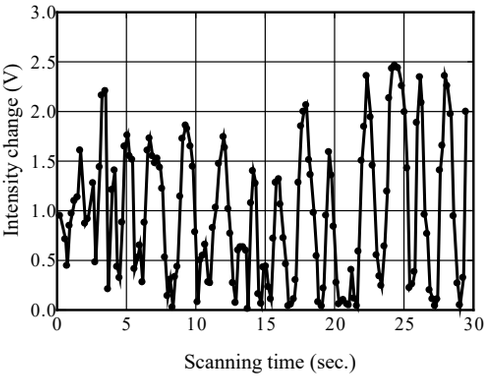


Figure 10 Intensity change vs. scanning time measured in main cable by using USAC-MFL

6 INSPECTION OF DEFECT IN HANGER RODS

The damaged hanger rods has temporarily replaced to the new rod shown in Figure 11 for repair work on Bingo Bridge. After that the all hanger rods have been replaced by the hanger ropes. As shown in Figure 12, the surface flaws were observed in one old hanger rod by magnetic testing (M.T). However, it decided that the surface flaws in Figure 12 is not a fatigue crack, because the crack direction is cor-

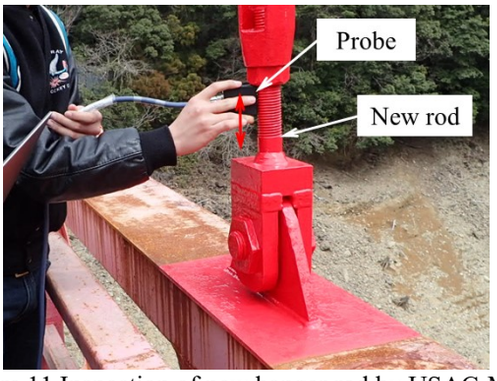


Figure 11 Inspection of new hanger rod by USAC-MFL

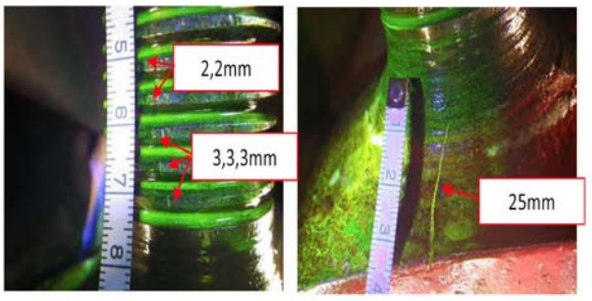
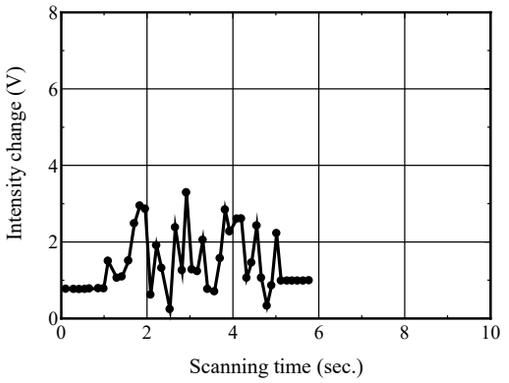
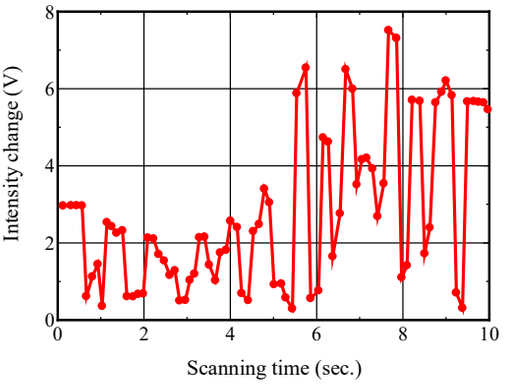


Figure 12 Measured flaws by M.T

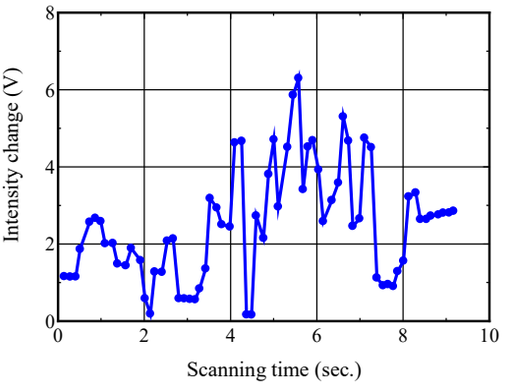
responding to the axial force direction in hanger rod. Therefore, the surface flaws observed rod, intact old rod and temporarily exchanged new rod were measured by using USAC-MFL. For the line scanning, the probe for USAC-MFL was moved between turnbuckle and hinge by hand with measuring (measuring frequency of 92Hz). Measured results are shown in intensity change vs. scanning time diagram in Figure 13. Since the material used in the new rod is different as that in original rods. Furthermore, new rod was fabricated by welding between hinge and rod parts. Therefore, the peak value of intensity change of new hanger rod is different from the old hanger rods. Meanwhile, the intensity change of the surface flaws observed old rod shows the same tendency as that of the intact old rod. Therefore, from the inspection by using USAC-MFL, it was presumed that the surface flaw measured in old rod is not a fatigue crack.



(a) New rod



(b) Surface flaws observed rod



(c) Intact old rod

Figure 13 Intensity change vs. scanning time measured in rod by using USAC-MFL

7 CONCLUSIONS

In this study, the inspection of the main cable, stiffening girder and hanger rods in Bingo Bridge was carried out by applying the high sensitivity magnetic nondestructive testing during the road closure. In the measured parts in this bridge, the serious defects have not detected. Furthermore, it was proved that the ELECT-SAM and USAC-MFL can be applied to the inspection of existing bridge.

ACKNOWLEDGEMENTS

The work was supported by the Council for Science, Technology and Innovation and Cross-ministerial Strategic Innovation Promotion Program (SIP), Infrastructure Maintenance, Renovation, and Management.

REFERENCES

Tsukada, K., Haga, Y., Morita, K., Song, N., Sakai, K., Kiwa T. and Cheng, W. 2016. Detection of Inner Corrosion of Steel Construction Using Magnetic Resistance Sensor and Magnetic Spectroscopy Analysis, IEEE Transactions on magnetics, Vol. 52, No. 7.

Tsukada, K., Majima, Y., Nakamura, Y. Yasugi, T., Song, N., Sakai, K. and Kiwa T. 2017. Detection of Inner Cracks in Thick Steel Plates Using Unsaturated AC Magnetic Flux Leakage Testing with a Magnetic Resistance Gradiometer, IEEE Transactions on magnetics, Vol. 53, No. 11.

Maintenance, Safety, Risk, Management and Life-Cycle Performance of Bridges – Powers, Frangopol, Al-Mahaidi & Caprani (Eds)
© 2018 Taylor & Francis Group, London, ISBN 978-1-138-73045-8

Theoretical analysis of CFRP bonding repair method using low-elasticity adhesive at the plate end

Kazuki Komon
Kyobashi Bridge Co. Ltd., Osaka, Japan

Toshiyuki Ishikawa
Associate Professor, Dept. of Civil, Environmental and Applied System Engineering, Kansai University, Osaka, Japan

Hiroyuki Suzuki
Professor, Meisei University, Tokyo, Japan

Yoshimichi Fujii
Professor, Kanazawa Institute of Technology, Ishikawa, Japan

Hironori Namaki
Dr. Eng., Kyobashi Bridge Co. Ltd., Osaka, Japan

ABSTRACT: Carbon fiber reinforced polymer, CFRP, is starting to be used for the repair and strengthening of steel members. However, debonding of CFRP plate is one of the concerns of this repair method. Therefore, some reduction techniques of stress concentration at the adhesive and were proposed. In this paper, the authors focused on the reduction technique of stress concentration at the adhesive end by using low elasticity adhesive at the plate end. By solving the differential equations regarding the axial force of steel plate and shear force of CFRP plate of CFRP bonded steel plate used low-elasticity adhesive at the plate ends, the characteristics on the shear and normal stresses in the adhesives are clarified. Furthermore, analytical results were verified by the FE analysis of CFRP bonded steel plates.

1 INTRODUCTION

Carbon fiber reinforced polymer, CFRP, is started to be used for the repair method against corrosion damage to steel bridges (Miller et al. 2001, Moy et al. 2007 and Tamai et al. 2005). CFRP plates are expected to be used as repair materials for steel members because the strength of CFRP is higher than that of steel and the weight of CFRP is lighter than that of steel. However, the brittle debonding of the CFRP plate is the most concern for CFRP bonding repair.

So far, for brittle debonding of the CFRP plate, the several methods such as the mechanical fastener at the end of the CFRP plate, the taper at the end of the CFRP plate, the step bonding of the CFRP plates, and the low elasticity adhesive at the end of the CFRP plate have been proposed. Several studies using low elasticity to the CFRP plate ends have been carried out (Coleman 1966, Fitton et al. 2005 and Ishikawa et al. 2008). However, the peel stress in adhesive layer did not investigate for the low-elasticity adhesive at the plate ends of CFRP bonded steel plate under axial loading. In the previous study, it was clarified that the high shear stress as well as high peel stress in the adhesive layer at the ends of CFRP effect for debonding of the CFRP plates. Therefore, some criteria for prevention of debonding the CFRP need both shear and peel stresses at adhesive ends.

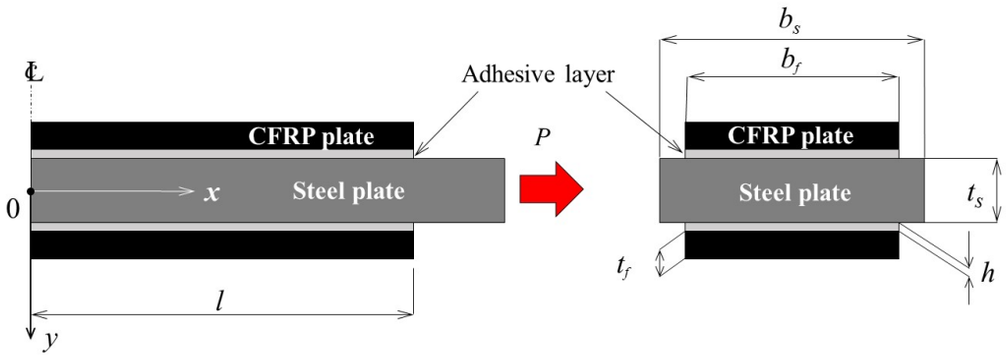
Therefore, it is necessary to evaluate the peel stress introduced in the adhesive layer even though the low-elasticity adhesive used at the ends of the CFRP plate.

In this research, by using the differential equations of CFRP bonded steel plate with low-elasticity adhesive at the ends of the CFRP plate, the shear and peel stresses introduced in the adhesive ends of the CFRP plate bonded steel plate under axial loading is derived.

2 THEORETICAL ANALYSIS OF CFRP BONDED STEEL PLATE WITH TWO KINDS OF ADHESIVES

2.1 *General solution of differential equations of CFRP plate bonded steel plates under axial loading*

For the steel plate with the CFRP plates bonded symmetrically to the upper and lower surfaces shown in Figure 1, the sectional forces acting on a differential segment are shown in Figure 2. For the theoretical analysis, the followings were assumed: (1) materials are all linearly elastic, (2) the shear and normal



(a) Side view (b) Cross section

Figure 1. CFRP plates bonded steel plate.

stresses in the adhesive layer are constant through the thickness, (3) the axial force and bending moment in the adhesive layer are negligible because the low Young's modulus of the adhesive.

From the equilibrium of the axial force in the differential segment of steel plate, the second order differential equation on the axial force in the steel plate $N_s(x)$ is given by the following equation (Ishikawa et al. 2013).

$$\frac{d^2N_s(x)}{dx^2} - c^2N_s(x) = -c^2\xi_0 P \tag{1}$$

where,

$$c = \sqrt{\frac{b_f G_e}{h} \cdot \frac{2}{1-\xi_0} \cdot \frac{1}{E_s A_s}} \tag{2}$$

$$\xi_0 = \frac{1}{1 + 2E_f A_f / (E_s A_s)} \tag{3}$$

E_s : Young's modulus of the steel plate,
E_f : Young's modulus of the CFRP plate,
A_s : sectional area of the steel plate,
A_f : sectional area of the CFRP plate,
G_e : shear modulus of the adhesive,
h : thickness of the adhesive,
b_f : width of the CFRP plate,
P : axial loading on the steel plate,
x : distance from the center of the CFRP plate (Figure 1(a)).

The general solution of Eq. (1) is given by the following equation.

$$N_s(x) = A_1 \cosh(cx) + A_2 \sinh(cx) + \xi_0 P \tag{4}$$

where,

A_1 and A_2: undetermined coefficients relevant to the axial force in the steel plate.

The relation between the shear stress in the adhesive $\tau(x)$ and the axial force in the steel plate $N_s(x)$ is given by the following equation.

$$\tau(x) = \frac{1}{2b_f}\frac{dN_s(x)}{dx} \tag{5}$$

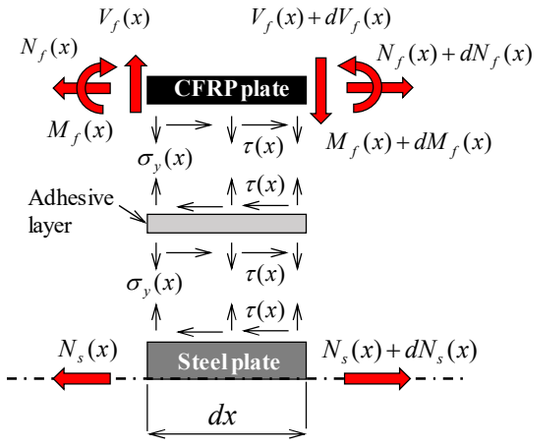


Figure 2. The sectional forces in a differential segment.

On the other hand, the fourth order differential equation for the shear force of the CFRP plate $V_f(x)$ is given by the equilibrium of the sectional forces in the differential segment of the CFRP plate (Ishikawa et al. 2013).

$$\frac{d^4V_f(x)}{dx^4} + 4\omega^4 V_f(x) = \omega^4 t_f \frac{dN_s(x)}{dx} \tag{6}$$

where,

$$\omega = \sqrt[4]{\frac{b_f E_e}{4h} \cdot \frac{1}{E_f I_f}} \tag{7}$$

E_e : Young's modulus of the adhesive,
t_f : thickness of the CFRP plate,
I_f : the moment of inertia of the CFRP plate.

The general solution of the shear force in CFRP plate, $V_f(x)$, is given by the following equation.

$$\begin{aligned} V_f(x) = {} & B_1\mathrm{CH}(\omega x)\mathrm{S}(\omega x) + B_2\mathrm{SH}(\omega x)\mathrm{C}(\omega x) \\ & + B_3\mathrm{CH}(\omega x)C(\omega x) + B_4\mathrm{SH}(\omega x)S(\omega x) \\ & + W\{A_1\mathrm{SH}(cx) + A_2\mathrm{CH}(cx)\} \end{aligned} \tag{8}$$

where,

$$W = \frac{ct_f}{4 + (c/\omega)^4} \tag{9}$$

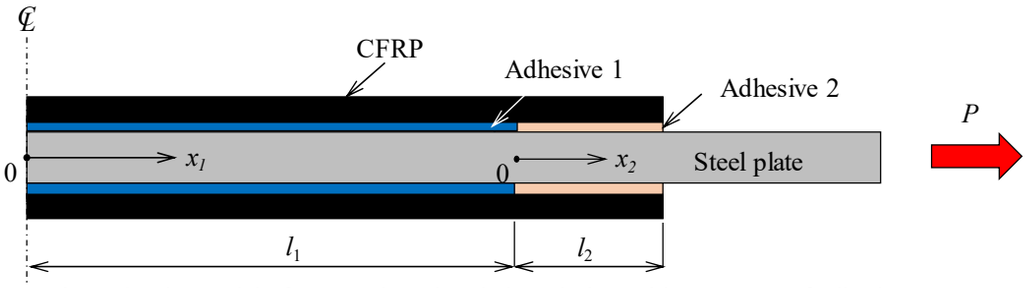


Figure 3. The model of CFRP plates bonded steel plate with two types of adhesives.

B_1, B_2, B_3, B_4 : Undetermined constant relevant to the shear force in the CFRP plate,

C(·) and S(·) : cos(·) and sin(·),

CH(·) and SH(·) : cosh(·) and sinh(·).

The peel stress introduced in the adhesive, $\sigma_y(x)$, is given by the following equation.

$$\sigma_y(x) = -\frac{1}{b_f}\frac{dV_f(x)}{dx} \tag{10}$$

The bending moment introduced in the CFRP plate, $M_f(x)$, is given by the following equation (Ishikawa et al. 2013).

$$M_f(x) = -\frac{1}{4\omega^4}\cdot\frac{dV_f(x)}{dx} \tag{11}$$

2.2 *Theoretical solution of CFRP plates bonded steel plate with two types of adhesives under axial loading*

In this study, differential equation of CFRP plates bonded steel plate with two types of adhesives under axial loading, as shown in Figure 3, is theoretically solved. The general solutions of axial forces in steel plate are given by the following equation. Note that, the boundary conditions at the center of CFRP plates, which are the symmetrical condition, are already applied in the following solutions.

$$N_s(x_1) = A_{11}\cosh(c_1x_1) + \xi_0 P \tag{12}$$

$$N_s(x_2) = A_{21}\cosh(c_2x_2) + A_{22}\sinh(c_2x_2) + \xi_0 P \tag{13}$$

where,

$$c_1 = \sqrt{\frac{b_f G_{e1}}{h}\cdot\frac{2}{1-\xi_0}\cdot\frac{1}{E_sA_s}} \tag{14}$$

$$c_2 = \sqrt{\frac{b_f G_{e2}}{h}\cdot\frac{2}{1-\xi_0}\cdot\frac{1}{E_sA_s}} \tag{15}$$

x_1 and x_2 : The distance from the center of the adhesive 1 and the distance from the boundary between the adhesives 1 and 2,

G_{e1} and G_{e2} : shear modulus of elasticity of adhesives 1 and 2,

A_{11}, A_{21} and A_{22} : Undetermined coefficient.

At the boundary between the adhesives 1 and 2 ($x_1=l_1$, $x_2=0$), the boundary conditions of $N_s(x_1=l_1)=N_s(x_2=0)$ and $\tau(x_1=l_1)h/G_{e1}=\tau(x_2=0)h/G_{e2}$ were applied. Furthermore, by applying the boundary condition of $N_s(x_2=l_2)=P$, undetermined coefficients, A_{11}, A_{21} and A_{22}, are respectively given by the following equations.

$$A_{11} = \frac{(1-\xi_0)P}{n\mathrm{SH}(c_1l_1)\mathrm{SH}(c_2l_2) + \mathrm{CH}(c_1l_1)\mathrm{CH}(c_2l_2)} \tag{16}$$

$$A_{21} = \frac{(1-\xi_0)\mathrm{CH}(c_1l_1)P}{n\mathrm{SH}(c_1l_1)\mathrm{SH}(c_2l_2) + \mathrm{CH}(c_1l_1)\mathrm{CH}(c_2l_2)} \tag{17}$$

$$A_{22} = \frac{n(1-\xi_0)S\mathrm{H}(c_1l_1)P}{n\mathrm{SH}(c_1l_1)\mathrm{SH}(c_2l_2) + \mathrm{CH}(c_1l_1)\mathrm{CH}(c_2l_2)} \tag{18}$$

where,

$$n = c_2/c_1 = \sqrt{G_{e2}/G_{e1}} \tag{19}$$

l_1 and l_2 : the ranges of adhesive 1 and 2, as shown in Figure 3.

On the other hand, the general solutions of the shear force of CFRP plates with two types of adhesives are given by the following equation. Note that, the boundary conditions at the center of CFRP plates, which are the symmetrical condition, are already applied in the following solutions.

$$V_f(x_1) = B_{11}\mathrm{CH}(\omega_1x_1)\mathrm{S}(\omega_1x_1) + B_{12}\mathrm{SH}(\omega_1x_1)\mathrm{C}(\omega_1x_1) + W_1A_{11}\mathrm{SH}(c_1x_1) \tag{20}$$

$$V_f(x_2) = B_{21}\mathrm{CH}(\omega_2x_2)\mathrm{S}(\omega_2x_2) + B_{22}\mathrm{SH}(\omega_2x_2)\mathrm{C}(\omega_2x_2) + B_{23}\mathrm{CH}(\omega_2x_2)C(\omega_2x_2) + B_{24}\mathrm{SH}(\omega_2x_2)S(\omega_2x_2) + W_2\{A_{21}\mathrm{SH}(c_2x_2) + A_{22}\mathrm{CH}(c_2x_2)\} \tag{21}$$

where,

$$W_1 = \frac{c_1t_f}{4+(c_1/\omega_1)^4} \tag{22}$$

$$W_2 = \frac{c_2t_f}{4+(c_2/\omega_2)^4} \tag{23}$$

$$\omega_1 = \sqrt[4]{\frac{b_fE_{e1}}{4h}\cdot\frac{1}{E_fI_f}} \tag{24}$$

$$\omega_2 = \sqrt[4]{\frac{b_f E_{e2}}{4h} \cdot \frac{1}{E_f I_f}} \tag{25}$$

E_{e1} and E_{e2} : Young's modulus of adhesives 1 and 2,

B_{11}, B_{12}, B_{21}, B_{22}, B_{23} and B_{24} : Undetermined coefficients.

Applying the boundary conditions of $V_f(x_1=l_1)= V_f(x_2=0)$, $M_f(x_1=l_1)=M_f(x_2=0)$, $M_f'(x_1=l_1)/E_fI_f = M_f'(x_2=0)/E_fI_f$, $\sigma_y(x_1=l_1)h/E_{e1}= \sigma_y(x_2=0)h/E_{e2}$, $V_f(x_2=l_2)=0$ and $M_f(x_2= l_2)=0$, the undetermined coefficients, B_{11}, B_{12}, B_{21}, B_{22}, B_{23} and B_{24}, are given.

$$\mathbf{B} = C^{-1}\mathbf{k} \tag{26}$$

where,

$$\mathbf{B} = \begin{pmatrix} B_{11} & B_{12} & B_{21} & B_{22} & B_{23} & B_{24} \end{pmatrix}^T \tag{27}$$

$$C = \begin{pmatrix} \mathbf{C_1} & \mathbf{C_2} & \mathbf{C_3} & \mathbf{C_4} & \mathbf{C_5} & \mathbf{C_6} \end{pmatrix} \tag{28}$$

$$\mathbf{C_1} = \begin{pmatrix} 0 \\ 0 \\ \mathrm{CH}(\omega_1 l_1)\mathrm{S}(\omega_1 l_1) \\ \{\mathrm{CH}(\omega_1 l_1)\mathrm{C}(\omega_1 l_1) + \mathrm{SH}(\omega_1 l_1)\mathrm{S}(\omega_1 l_1)\}/E_{e1} \\ \mathrm{SH}(\omega_1 l_1)\mathrm{C}(\omega_1 l_1)/(2\omega_1^2) \\ \{\mathrm{CH}(\omega_1 l_1)\mathrm{C}(\omega_1 l_1) - \mathrm{SH}(\omega_1 l_1)\mathrm{S}(\omega_1 l_1)\}/(2\omega_1) \end{pmatrix} \tag{29}$$

$$\mathbf{C_2} = \begin{pmatrix} 0 \\ - \\ \mathrm{SH}(\omega_1 l_1)C(\omega_1 l_1) \\ \{\mathrm{CH}(\omega_1 l_1)\mathrm{C}(\omega_1 l_1) - \mathrm{SH}(\omega_1 l_1)\mathrm{S}(\omega_1 l_1)\}/E_{e1} \\ -\mathrm{CH}(\omega_1 l_1)\mathrm{S}(\omega_1 l_1)/(2\omega_1^2) \\ -\{\mathrm{CH}(\omega_1 l_1)\mathrm{C}(\omega_1 l_1) + \mathrm{SH}(\omega_1 l_1)\mathrm{S}(\omega_1 l_1)\}/(2\omega_1) \end{pmatrix} \tag{30}$$

$$\mathbf{C_3} = \begin{pmatrix} \mathrm{CH}(\omega_2 l_2)\mathrm{S}(\omega_2 l_2) \\ 2\omega_2^3\{\mathrm{CH}(\omega_2 l_2)\mathrm{C}(\omega_2 l_2) - \mathrm{SH}(\omega_2 l_2)\mathrm{S}(\omega_2 l_2)\} \\ 0 \\ -\omega_2/E_{e2} \\ 0 \\ -1/(2\omega_2) \end{pmatrix} \tag{31}$$

$$\mathbf{C_4} = \begin{pmatrix} \mathrm{SH}(\omega_2 l_2)\mathrm{C}(\omega_2 l_2) \\ -2\omega_2^3\{\mathrm{CH}(\omega_2 l_2)\mathrm{C}(\omega_2 l_2) + \mathrm{SH}(\omega_2 l_2)\mathrm{S}(\omega_2 l_2)\} \\ 0 \\ -\omega_2/E_{e2} \\ 0 \\ 1/(2\omega_2) \end{pmatrix} \tag{32}$$

$$\mathbf{C_5} = \begin{pmatrix} \mathrm{CH}(\omega_2 l_2)\mathrm{C}(\omega_2 l_2) \\ -2\omega_2^3\{\mathrm{CH}(\omega_2 l_2)\mathrm{S}(\omega_2 l_2) + \mathrm{SH}(\omega_2 l_2)\mathrm{C}(\omega_2 l_2)\} \\ -1 \\ 0 \\ 0 \\ 0 \end{pmatrix} \tag{33}$$

$$\mathbf{C_6} = \begin{pmatrix} \mathrm{SH}(\omega_2 l_2)\mathrm{S}(\omega_2 l_2) \\ 2\omega_2^3\{\mathrm{SH}(\omega_2 l_2)\mathrm{C}(\omega_2 l_2) - \mathrm{CH}(\omega_2 l_2)\mathrm{S}(\omega_2 l_2)\} \\ 0 \\ 0 \\ -1/(2\omega_2^2) \\ 0 \end{pmatrix} \tag{34}$$

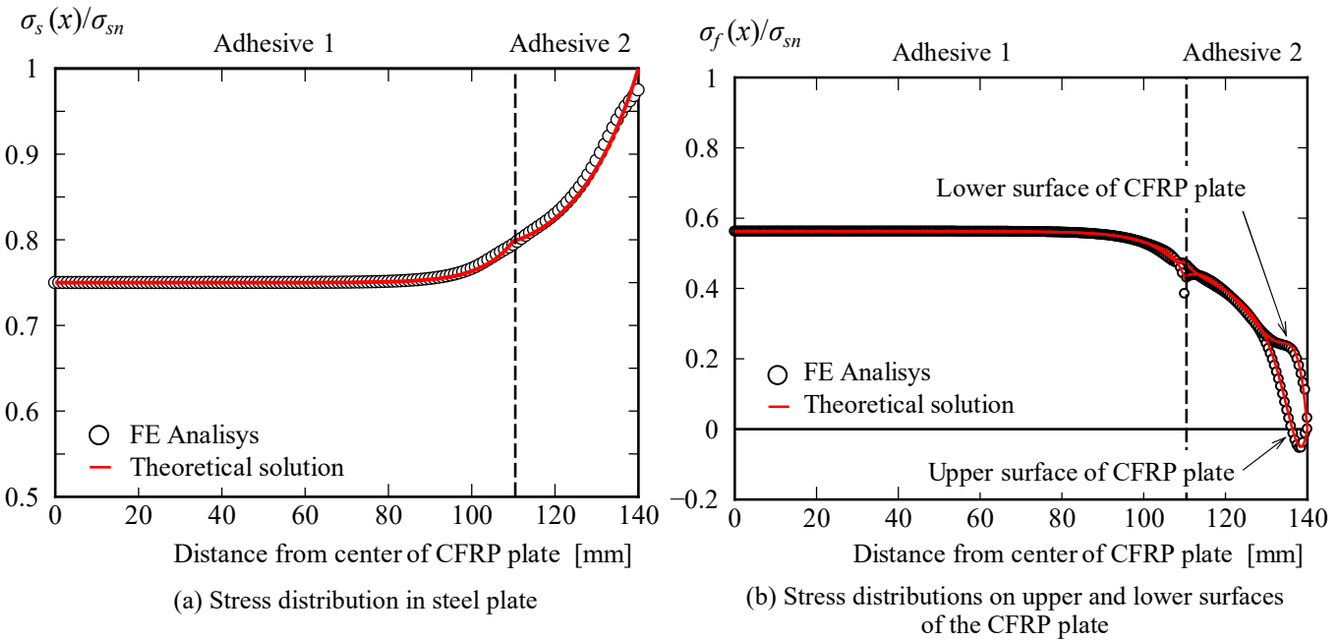
$$\mathbf{k} = \begin{pmatrix} -\mathrm{W}_2\{A_{21}\mathrm{SH}(c_2 l_2) + A_{22}\mathrm{CH}(c_2 l_2)\} \\ -c_2^3\mathrm{W}_2\{A_{21}\mathrm{SH}(c_2 l_2) + A_{22}\mathrm{CH}(c_2 l_2)\} \\ -\mathrm{W}_1 A_{11}\mathrm{SH}(c_1 l_1) + \mathrm{W}_2 A_{22} \\ -c_1\mathrm{W}_1 A_{11}\mathrm{CH}(c_1 l_1)/E_{e1} + c_2\mathrm{W}_2 A_{21}/E_{e2} \\ -c_1^2\mathrm{W}_1 A_{11}\mathrm{SH}(c_1 l_1)/(4\omega_1^4) + c_2^2\mathrm{W}_2 A_{22}/(4\omega_2^4) \\ -c_1^3\mathrm{W}_1 A_{11}\mathrm{CH}(c_1 l_1)/(4\omega_1^4) + c_2^3\mathrm{W}_2 A_{21}/(4\omega_2^4) \end{pmatrix} \tag{35}$$

Table 1 Dimensions and material properties

(a) Steel plate	
b_s x t_s [mm]	50×9
E_s [kN/mm^2]	200
(b) CFRP plate	
b_f x t_f [mm]	50×2
E_f [kN/mm^2]	150
Half-length of CFRP plate, l [mm]	100
(c) Adhesive 1	
h [mm]	0.5
l_1[mm]	110
E_{e1}[kN/mm^2]	2.0
G_{e1}[kN/mm^2]	0.741
(d) Adhesive 2	
h [mm]	0.5
l_2[mm]	30
E_{e2}[kN/mm^2]	0.5
G_{e2}[kN/mm^2]	0.185

3 COMPARISON OF THE ORETICAL SOLUTION AND FINITE ELEMENT ANALYSIS

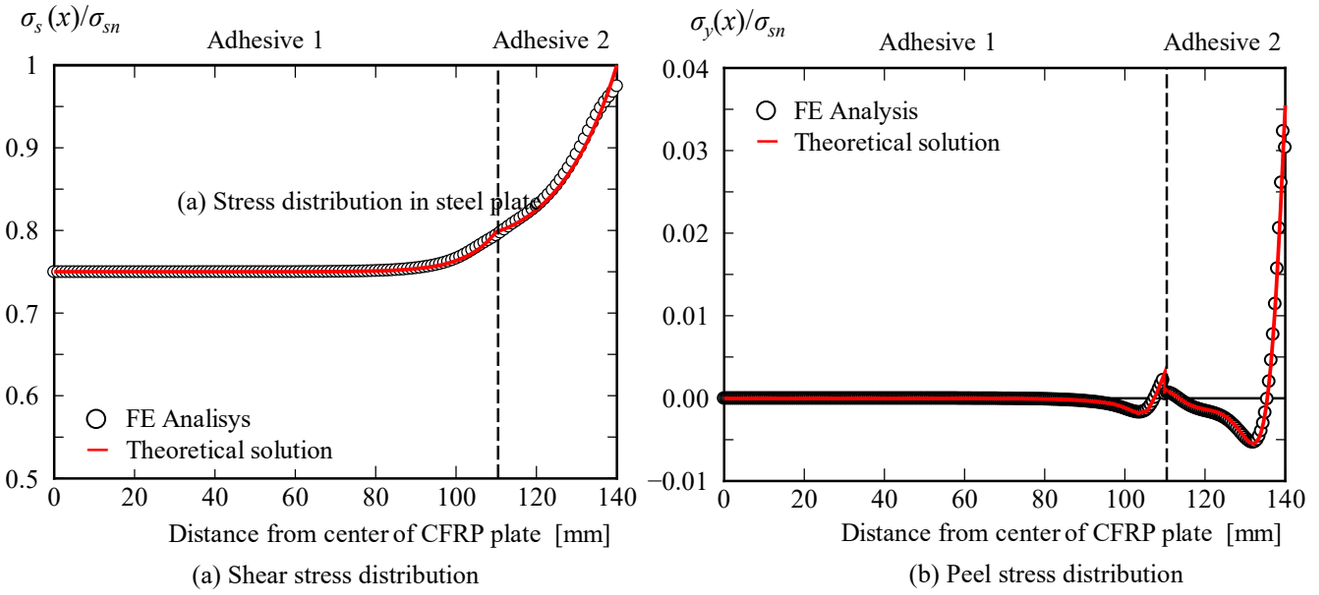
To verify the theoretical solution, Finite Element analyses of CFRP plates bonded steel plate with two types of adhesives under axial loading are carried out. Table 1 shows the dimensions and materials of steel plate, CFRP plate and adhesives for FE analyses. For FE analyses, MARC 2012 was used with plane stress condition. The element size of the adhesive was 0.1mm x 0.1mm.



(a) Stress distribution in steel plate

(b) Stress distributions on upper and lower surfaces of the CFRP plate

Figure 4. The stress distributions of CFRP plates bonded steel plate with two types of adhesives under axial loading



(a) Shear stress distribution

(b) Peel stress distribution

Figure 5. Stress distributions in the adhesive layer in CFRP plates bonded steel plate with two types of adhesives under axial loading

Figure 4 shows the stress distributions of the steel plate and the CFRP plate given by the theoretical solutions and FE analyses. In this figure, each stress is normalized by the nominal stress of σ_{sn} ($=P/A_s$). In Figure 4(a), the stress distribution in steel plate at the center of the plate thickness is shown. Since the stress distribution is not constant within the steel plate thickness in the FE analysis, the valued of $\sigma_s(x)/\sigma_{sn}$ given by FE analysis is not corresponding to 1 at x=140mm where the CFRP end. However, the stress distribution calculated by the theoretical solution shows the almost same as that given by the FE analysis.

As shown in Figure 4(b), since a bending moment is generated near the end of the CFRP plate, the stress distributions on upper and lower surfaces of the CFRP plate are different near the end of the CFRP plate. As can be seen from Figure 4(b), the stress distributions on the CFRP plate given by the theoretical solution and the FE analysis show almost the same distribution.

Figure 5 shows the distribution of shear and peel stresses in the adhesive layer given by the theoretical solutions and FE analyses. In this figure, the shear and the peel stresses are also normalized by σ_{sn}. The stress distributions in the center of the adhesion thickness obtained the FE analyses are shown in Figure 5.

As can be seen from Figure 5, the shear and peel stress distributions in adhesive layer given by the theoretical solutions are almost corresponding to the results of the FE analyses. In addition, the gaps of shear and peel stresses at the boundary between adhesive 1 and 2 can be also given by the theoretical solutions.

4 CONCLUSIONS

In this study, as the fundamental study of using low elasticity adhesive at the end of the CFRP plate, the theoretical solution of the stress in the CFRP plates bonded steel plate with two types of adhesives under the axial loading was given. Then, the theoretical solution was verified by using FE analysis result. It was shown that the stress distributions in CFRP plate bonded steel plate with two types of adhesives under axial loading were almost corresponding to the results of FE analysis.

REFERENCES

Coleman, R. 1966. Variable-Adhesive Bonded Joints, *Applied Polymer Symposia*, No.3, pp.99-108.

Fitton, M.D. and Broughton, J.G. 2005. Variable modulus adhesives: an approach to optimized joint performance, *International Journal of Adhesion & Adhesives*, Vol.25, pp.329-336.

Ishikawa, T., Okura, I., Nishida, T., Yokota, S. and Saito, M. 2008. Reduction of peeling shear stress by use of low elasticity adhesive near the adhesion end of CFRP plate, *Japan Society of Civil Engineers Structural Engineering Proceedings*, Vol.54A, pp.842-849.

Ishikawa, T., Miyashita, T. and Vigh, L.G. 2013. High Accuracy Solution of Stress Generated on CFRP Plate Adhesive Steel Plate Subjected to Uniaxial Tension, *Japan Society of Civil Engineers Proceedings A1 (Structure / Earthquake engineering)*, Vol.69, no.1, pp.89-100.

Miller, T.C., Chajes, M.J., Mertz, D.R. and Hastings, J.N. 2001. Strengthening of a steel bridge girder using CFRP plates, *Journal of Bridge Engineering*, ASCE, Vol.6, pp.514-522.

Moy, S.S.J. and Bloodworth, A.G. 2007. Strengthening a steel bridge with CFRP composites, *Structures & Buildings*, Vol.160, Issue SB2, pp.81-93.

Tamai, H., Takamatsu, T., Hattori, A., Haitani, T. and Sakuraba, M. 2005. Rehabilitation of secondary beam in chemical plant frame using carbon fiber reinforced plastic plate, *Journal of Construction Steel*, JSSC, Vol.13, pp.545-552.

Täljsten, B., Hansen, C.S. and Schmidt, W.J. 2009. Strengthening of old metallic structures in fatigue with prestressed and non-prestressed CFRP laminates, *Construction and Building Materials*, Vol.23, Issue 4, pp.1665-1677.

Maintenance, Safety, Risk, Management and Life-Cycle Performance of Bridges – Powers, Frangopol, Al-Mahaidi & Caprani (Eds)
© 2018 Taylor & Francis Group, London, ISBN 978-1-138-73045-8

Fatigue strength and improvement effect of the center stay rod

Shinya KAWANO
Honshu-Shikoku Bridge Expressway, Kobe-shi, Hyogo, Japan

Shoji OGO
Honshu-Shikoku Bridge Expressway, Kobe-shi, Hyogo, Japan

Atsuhiro OKUMURA
Honshu-Shikoku Bridge Expressway, Kobe-shi, Hyogo, Japan

Yoshiaki MIZOKAMI
Honshu-Shikoku Bridge Expressway, Kobe-shi, Hyogo, Japan

Masahiro SAKANO
Kansai University, Suita-shi, Osaka, Japan

ABSTRACT: Center stay is installed to control a relative displacement between a girder and a cable, to restrict the inclination of short suspenders around the center of a span, and to prevent bending fatigue of the suspender. A center stay was designed so that the rod section breaks with 60% (equivalent of an earthquake whose return period is 25 years) of tension force during an earthquake. However, two rods under force lower than the designed tension broke at a mounting screw section, not at the section with the minimum cross sectional area of the rod, which is the assumed failure point. This paper discusses the detailed survey of a fracture surface observation to confirm damage factors, estimation of the level of fatigue damage by measuring a stress frequency on a real bridge, a method to improve fatigue durability, and the result of a fatigue test of improved rod with which improved fatigue durability is expected.

1. INTRODUCTION

The Honshu-Shikoku Bridges, which connect Honshu and Shikoku with three routes, consist of ten suspension bridges including the Akashi-Kaikyo Bridge, the world's longest suspension bridge, five cable-stayed bridges, one truss bridge, and one arch bridge. Among these long-span bridges, center stays are installed on suspension bridges to control a relative displacement between a girder and a cable.

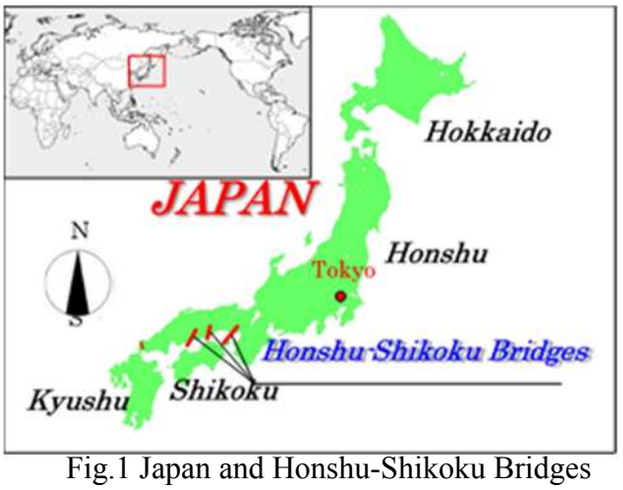


Fig.1 Japan and Honshu-Shikoku Bridges

A damage that differs from the one expected during the design phase occurred to a bridge. This study estimated the causes of the damage, and examined an improvement method. This paper reports the result of this study.

(1) Target bridge

The bridge, which is the subject of this study, is a three span, two hinge suspension bridge with the main span of 600 m. It has an asymmetric geometry with the main towers of varying heights (Fig. 2). Flat hexagonal shaped box girders are used and, as for the form of the bridge in service, the number of lanes changes from the four to two (south side) on the bridge. As a result, the live load is deviated to the south side (Photo1).

(2) Structure of the center stay

The center stay of this bridge is installed to prevent additional stress, such as bending, from occurring on a suspender rope by controlling a relative

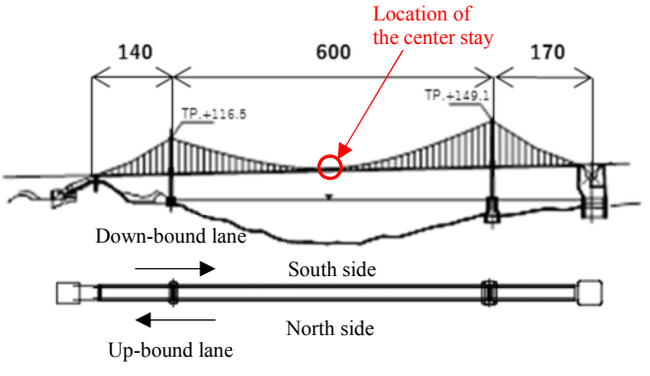


Fig.2 General view of the target bridge

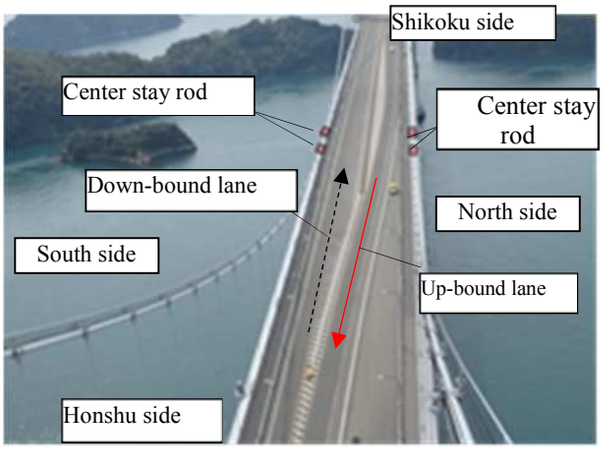


Photo.1 Lanes of the bridge

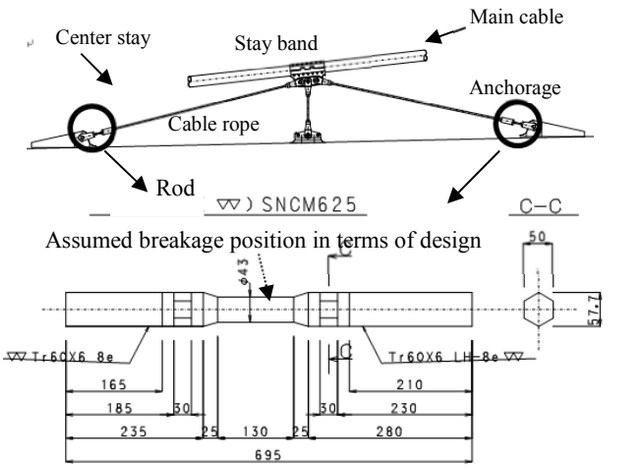


Fig.3 Outline of center stay

displacement between the girder and the main cable in longitudinal direction during a small-scale earthquake.

The center stay is positioned in the center of the main span. It consists of stay band, a stay rod (hereinafter called “rod”), and anchorages as shown in Fig.3 and Photo.2. The total of four center stays are installed on the bridge, two for the up-bound lane side and two for the down-bound lane side. The rod was designed to be broken at the section with the minimum cross sectional area in the center during a large-scale earthquake. These rods was actually broken almost as designed load when the Geiyo earthquake (M 6.7) occurred in March 24, 2001 as shown in Photo3.[1)]

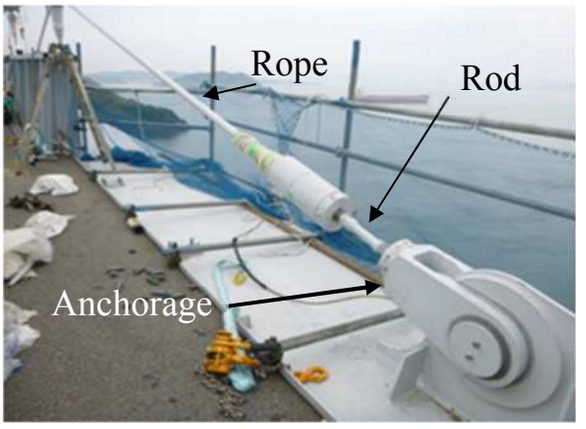


Photo.2 Center stay

Since the rod was designed to break with 60% tension force of the earthquake load, it can be dismounted as it is joined to the socket on the rope side and the anchor pin with screws to facilitate replacing a rod. As for the rod, Tr60 is used for screws, and its length is 695 mm. The material of the rod is SNCM625 (nickel-chrome-molybdenum steel).

During the inspection in 2014, breakage of the rods which were installed to down-bound lane, was found out even no large-scale earthquake occurred.

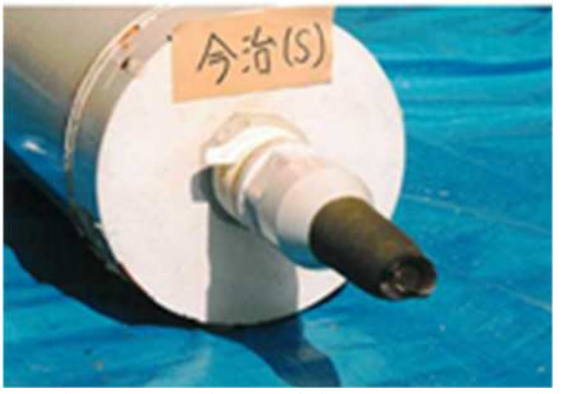


Photo.3 Breakage of the center stay rod caused by the Geiyo earthquake in 2001

2. CONDITIONS OF DAMAGE

The position of the breakage is the thread root at the first screw thread where the rod is engaged with the socket coupler on the rope side. (Photo.4)

The existing rods were replaced because they were broken when the Geiyo earthquake occurred in March 2001. It is relatively new rod as it is about 13 years old. The assumed position of the breakage is the minimum cross sectional area in the center of the rod as shown in Fig. 3, which is a different position of the broken rods this time.

3. INSPECTION OF CAUSE OF DAMAGE

In order to identify the causes of this damage, material characteristics were verified by a chemical composition analysis to conduct a macro-observation of the breakage surface, a micro-observation by SEM (Scanning Electron Microscope), and to investigate the presence of defects of the material. To confirm the condition of the occurrence of live-load stress on the rod, 72 hours continuous stress measurement was conducted on the target bridge. The chemical

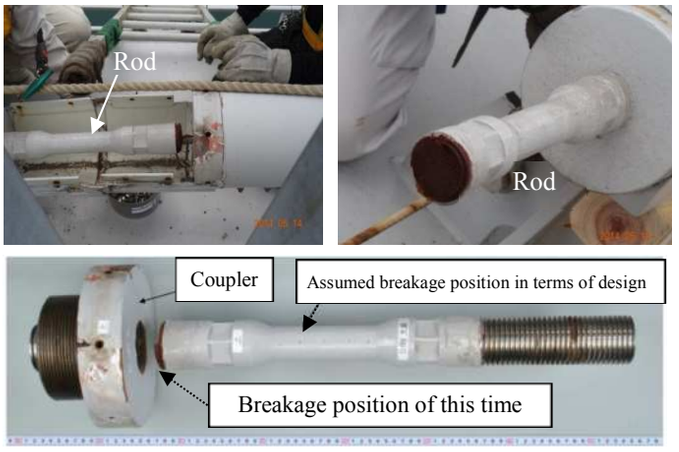


Photo.4 Condition of break in the rod

composition analysis included the rods of the up-bound lane where no damage was found.

(1) Observation of the breakage surface

a) Result of the macro-observation of the fracture

The result of the macro-observation of the fracture after descaling is shown in Fig.4(a).

Distinctive beachmark was found on the fatigue fracture of the two broken rods; therefore, it is assumed that fracture developed due to a repetitive stress.

The final breakage part is identified on the top of any section. When the transmission direction was assumed from the pattern of the beachmark, the starting point of the breakage was believed to be on the lower side.

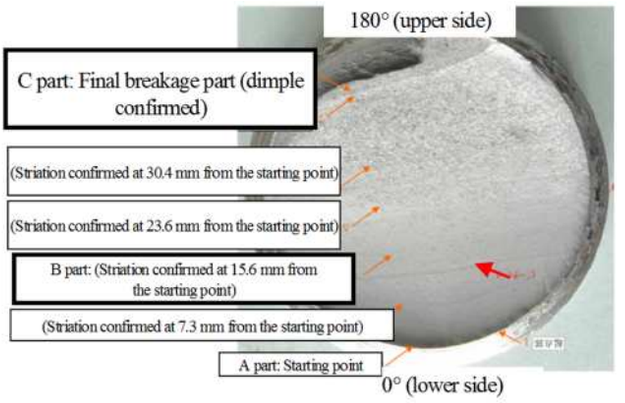
b) The result of micro-observation of fracture by SEM

The trace of occurrence of crack caused by defects and the corrosion was not found from the condition of the fracture in the neighborhood of the starting point. Distinctive striation (a striped pattern) was identified on the fatigue fracture as shown in Fig. 4 (b). And, on the top side that is assumed to be the final breakage part, a significant dimple (a hallow pattern) was identified on the ductile fracture as shown in Fig. 4 (c).

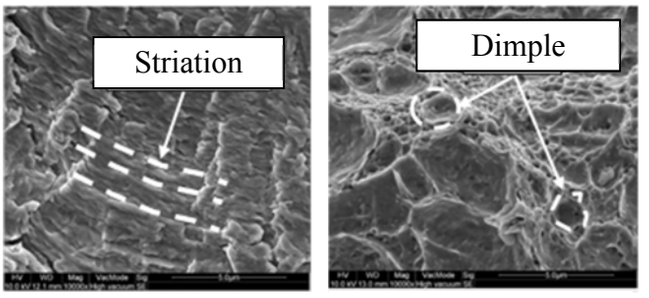
According to the results of the macro-observation and the cross-sectional observation with micro-observation by SEM, no defects including corrosion and fine cracks were identified.

(2) Chemical composition analysis of material

When the result of chemical component analysis was compared with specification values of SNCM625 listed in JIS G 4053 Low-alloyed steels for machine structural use, the all components were satisfied the criteria. In addition, the result matches with the test result during manufacturing, no significant deterioration is found. As a result, it was determined that the material had no problem.



(a) Result of macro-observation



(b) SEM image of B part (c) SEM image of C part

Fig.4 Appearance of breakage surface and the result of SEM observation

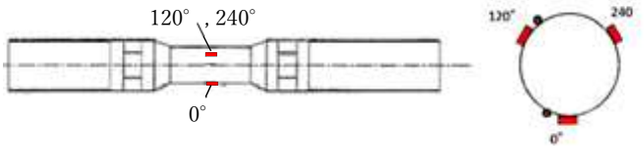


Fig.5 Positions to mount a strain gauge

(3) Other investigations

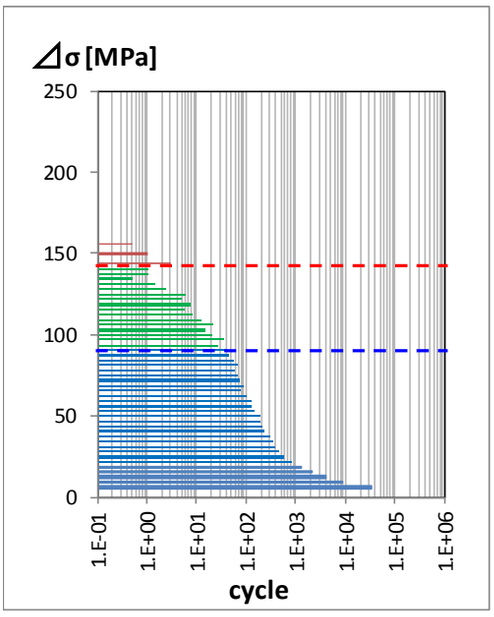
Apart from (1) and (2), although a structure observation, a Vickers hardness test, a liquid penetrant test of the rod screw, and a magnetic-particle test were carried out after etching, neither confirmed abnormality.

From the above mentioned results, it was confirmed that the assumed damage was led to following reason the assumed damage. A crack by repetitive stress gradually developed starting from the thread root so that the decreased cross section cannot bear with a pulling force. As a result, the breakage become large gradually.

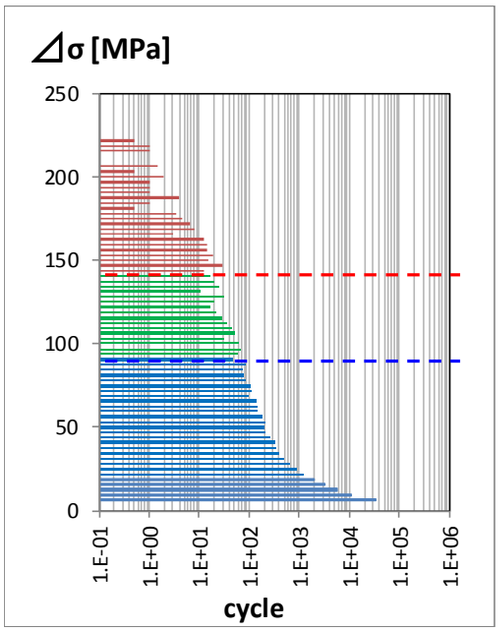
(4) Stress frequency measurement

To confirm the condition of the occurrence of live-load stress on the rod, 72 hours continuous stress measurement was conducted on the target bridge.

All four rods on the up-bound and down-bound lanes were measured. Fig.5 shows the positions to put a strain gauge. The gauges were installed at



(a)Up-bound lane
(end point side)
Unbroken rod



(b)Down-bound lane
(end point side)
Broken rod

Fig.6 Result of analysis of frequency

three locations (0° (the lower side), 120°, 240°) of the small diameter part of the center of the rod after recovering since it cannot be directly installed on the thread part on the breakage position.

Fig.6 shows the result of the stress frequency analysis of the measurement result which was converted from strain gauge of 0° to cross section area of thread root by FEM result as described next section. The strength ranges of 0° was larger than 120°, 240°. In addition, the strength ranges of down bound lane was larger than up bound lane.

4. FEM ANALYSIS

(1) Identification of stress concentration

FEM analysis was conducted to identify the stress concentration of the thread root.

a) Modelling

Fig.7 shows a model diagram. The rod and coupler were modelled by using two-dimensionally axisymmetric models to conduct the FEM analysis using ABAQUS, a general-purpose analysis code.

When making the model, the number of remaining screw threads of the coupler was set to three in order to similar the actual structure to reproduce the condition of damaged rod. The thread root R, where crack occurred, was set to 0.3 mm that was measured from a macro photograph of the cross section of the broken rod.

b) Result of the analysis

Fig.8 shows the maximum principal stress contour when tensile load to the axis direction was applied. The stress concentration was identified from the thread root R located in the first raw from the engaged part that is assumed as the starting point of the fatigue crack.

(2) Examination on structure that takes fatigue measures

The structure of rod for the fatigue measures was examined. And, the effect of measures was confirmed by the FEM analysis.

a) Examining measures

The following methods were considered for structural measures to improve the fatigue strength:

[1] A method to reduce stress by increasing the diameter of the thread part.

[2] A method to reduce the stress concentration of the thread root R that was the starting point of the crack.

With the method [1], substantial changes in structure, such as improved socket and anchor pin coupler, were required when increasing the cross sectional area to increase the diameter of the thread part.

On the other hand, with the method [2], change in the thread root R was required. The method [2] is seemed to be comparatively easy to take as it only involves the rod; and substantial structural change is not required. Therefore, the structure of rod for the fatigue was examined with method [2].

b) Modelling

The following two cases were analyzed by FEM analysis. The thread root R of a FEM analysis model

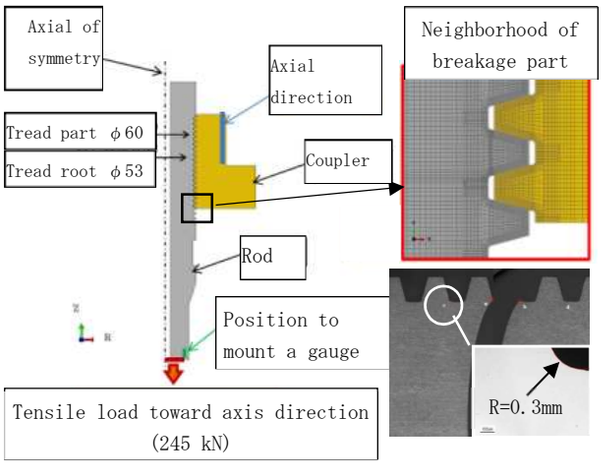


Fig.7 FEM analysis model diagram

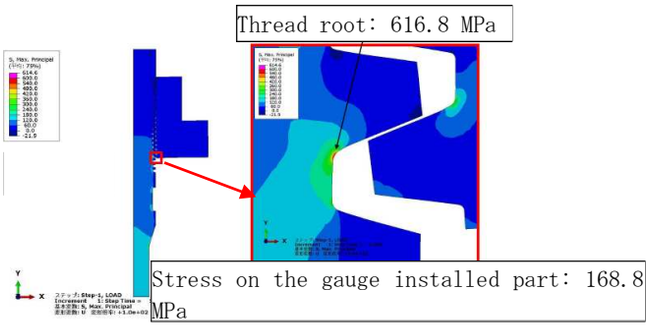


Fig.8 Result of the analysis (figure of the maximum principal stress contour)

Table1 Relation between radius and stress of the thread root R

R(mm)	Stress on the gauge mounted part (MPa)	Stress of the thread root (MPa)
0.3	168.8	616.8
0.5		521.3
0.7		464.7

for calculating stress concentration were set to 0.5 mm and 0.7 mm.

c) Result of analysis

Table 1 shows the relation between radius and stress of the thread root R. In the result of the analysis, reduction of the stress concentration by the increasing the thread root R was confirmed. As a result, the structure of the thread root R of 0.7mm that was decided the structure of rod for the fatigue measures.

5. FATIGUE TEST

With the results obtained in the previous chapters, improved fatigue durability of a rod can be expected by increasing the thread root R. The fatigue durability of rods was examined by the fatigue test using the manufactured real size test pieces.

(1) Test pieces

Fig.9 and Table 2 show the general drawing, materials, etc., of test pieces that are tested this time. There are three types of test pieces. The existing rod is an actual rod that was not broken at the time of 2014 and had been used for 13 years in the up-bound lane of the actual bridge. The two types of new rods were manufactured, one has the same shape as the existing rod with the thread root R of 0.3mm, and the other has the improved radius of 0.7mm.

The steel of existing rod is SNCM625. But the steel of the new rods are SNCM630. Since the tensile strength of steel used for the new rod is higher than that of the existing rod due to procurement reasons, as for the new rod, the tensile strength of the small diameter part was made the same as that of the existing rod by reducing the diameter of the small diameter part of the rod part.

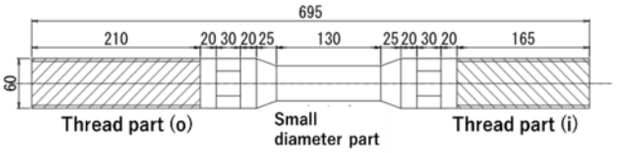
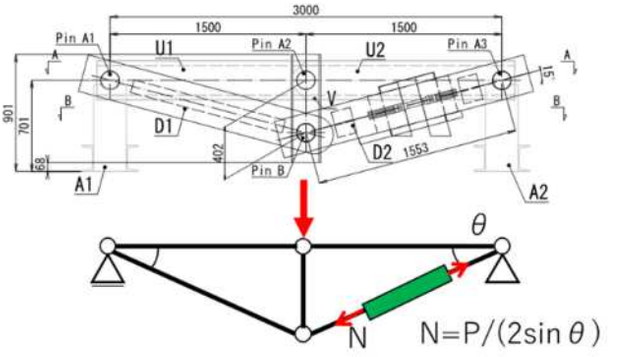


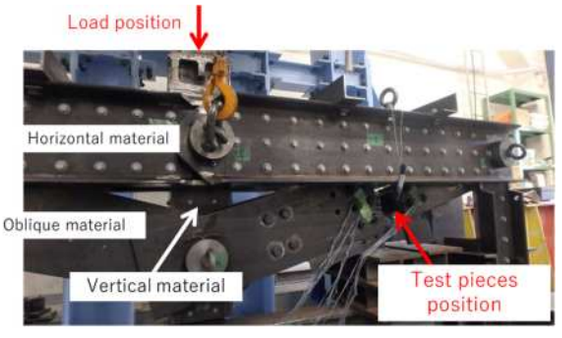
Fig.9 General drawing of test piece

Table.2 List of specifications of test pieces

Test pieces	Steel	Nunber of test pieces	Diameter(mm)	
			Small diameter part	Thread part
Existing rod	SNCM625	1	42.2	Max : 53.0 Min : 60.0
New rod(R0.3)	SNCM630	3	39.9	
New rod(R0.7)	SNCM630	3	39.9	



(a) Loading frame (general drawing)



(b) Loading frame (photo)

Fig.10 Fatigue test loading frame

There are one test piece for the existing rod and three each for the new rods. Fatigue test was conducted using the total of seven test pieces.

(2) Method of fatigue test

Fig.10 shows a loading frame. The loading frame is constructed so that loads can be transmitted to the test piece installed on a diagonal member by applying loads to vertical material. Fig.11 shows the positions to mount a strain gauge. In the small diameter part, single axis gauges with the length of 5 mm are installed at intervals of 90° for measuring nominal stress. In the neighborhood of thread part, single axis gauges with the length of 1 mm are installed at intervals of either 45° or 60° for detecting the occurrence of cracking.

For setting the applying load, the load range ΔP = 130 kN (P = 20-150 kN) is set according to the maximum stress range of the small diameter part obtained from the 72-hour stress frequency measurement at the actual bridge shown in Fig. 12 to allow the maximum stress range of 200 MPa to act at the small diameter part. A repetition frequency is set to 3 Hz.

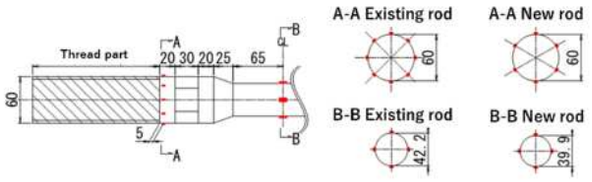


Fig.11 Positions to mount a strain gauge

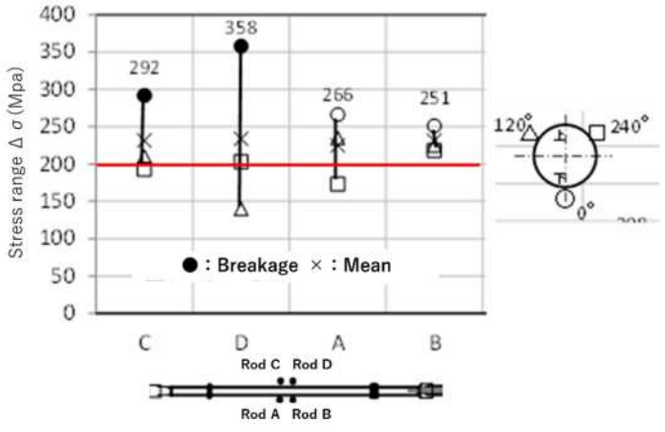


Fig.12 Stress range from 72-hour stress frequency measurement at a actual bridge

(3) Result of fatigue test

Typical results for each test piece are discussed in this section. Photo.5 shows the existing rod after the test. With the existing rod, breakage occurred at the thread part after load was applied 520,000 cycles. The position of breakage is the thread root of the first screw thread engaged with the anchoring body. And, by the breakage surface, to breakage is assumed an arc-like crack occurred in between 0 degree and 90 degrees. Therefore, fatigue breakage occurred at the actual bridge is believed to be reproduced.

Photo.6 shows the new rod (R0.3) after the test. With the new rod (R0.3), breakage occurred at threaded part after load was applied 1,620,000 cycles. The position of breakage is the thread root of the first screw thread engaged with the anchoring body, which is similar to that of the existing rod. And, by the breakage surface, to breakage is assumed an arc-like crack occurred in about 180 degrees.

Photo.7 shows the new rod (R0.7) after the test. With the new rod (R0.7), crack did not occur by the load range ΔP = 130 kN. Therefore, the load range ΔP = 260 kN (P = 20-280 kN) was set. In the result, breakage occurred at threaded part after load was applied 410,000 cycles. The position of breakage is the thread root of the first screw thread engaged with the anchoring body, which is similar to the other rods. And, by the breakage surface, to breakage is assumed an arc-like crack occurred in about 180 degrees.

A fatigue test is conducted on all seven test pieces. Fig.13 shows the result of fatigue test, together with fatigue design curves of cables and high-tensile bolts (K1-K5) that receive direct stress. The vertical axis indicates a stress measured at the small diameter part that is converted into the cross section of the thread root.

From Fig. 13, the existing rod has a shorter fatigue life than the new rod (R0.3). The existing rod is assumed had damage in actual bridge. And, in new rods (R0.3), it is assumed that there is a fatigue limit in 93MPa. In new rods (R0.7), it is assumed that there is a fatigue limit in 144MPa. Therefore, fatigue limit was increased to 1.5times by the changing the fatigue

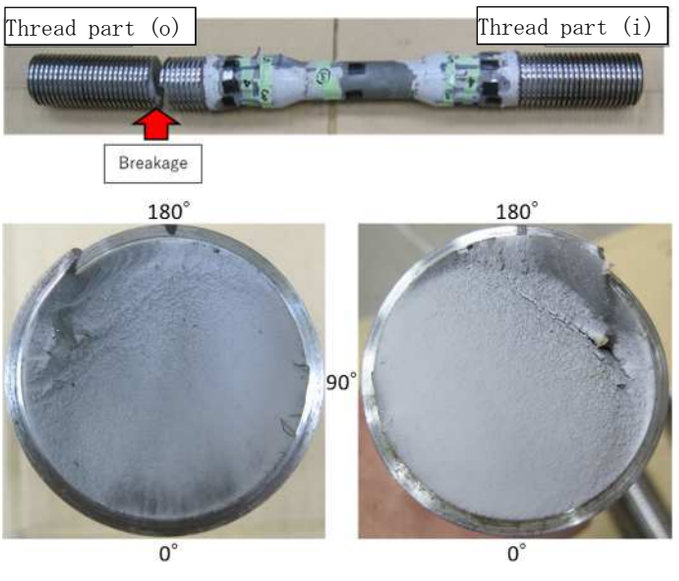


Photo.5 Existing rod after the test

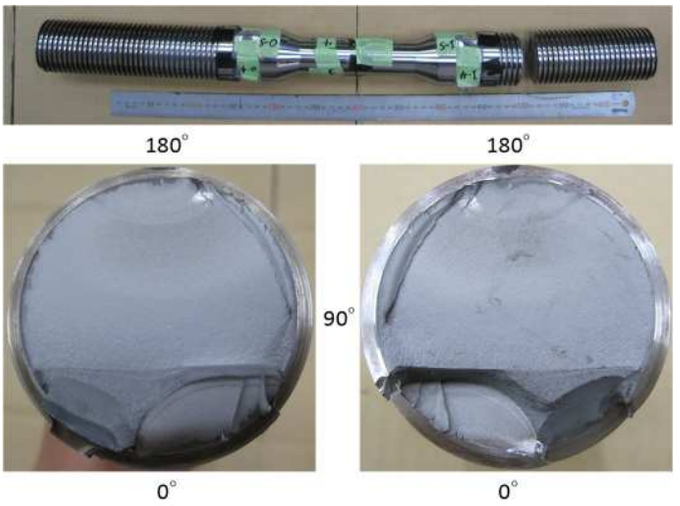


Photo.6 New rod (R0.3) after the test

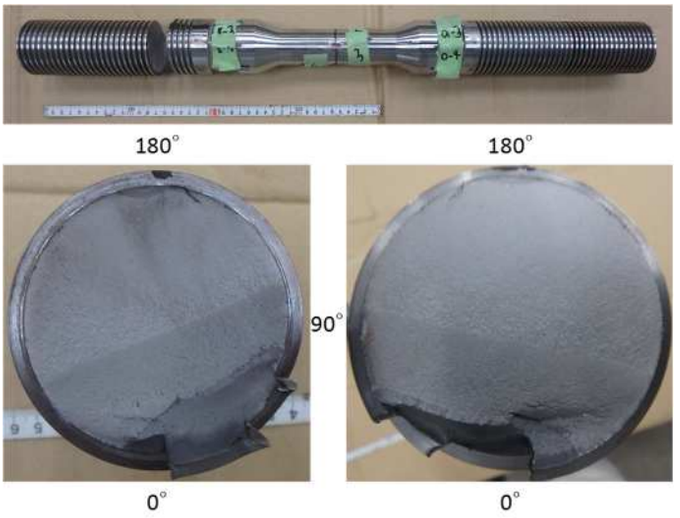


Photo.7 New rod (R0.7) after the test

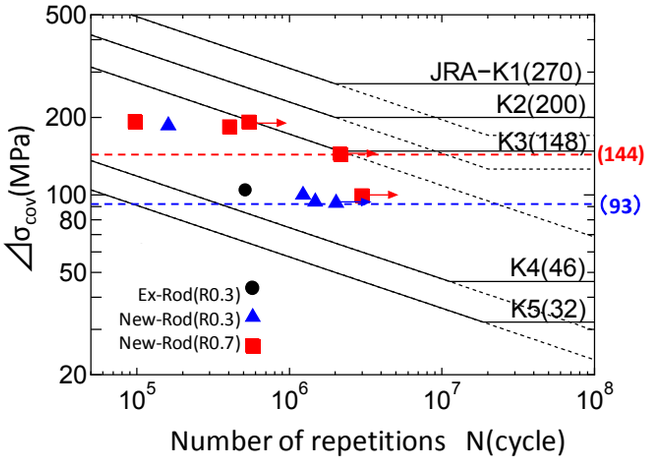


Fig.13 Summary of the result of fatigue tests

limit from 93MPa to 144MPa. Therefore, the fatigue strength is improved by changing the thread root R from 0.3mm to 0.7mm.

Meanwhile, it was confirmed that the fatigue life of one of the new rod (R0.3) and one of the new rod (R0.7) are reversed. According to the hearing investigation of the manufacturer, about ±0.1 mm of error occurs as manufacturing accuracy of the thread root R. In the future, a detailed investigation is required by measuring the thread root R of test pieces.

6. CONCLUSION

In this study, the following knowledge was obtained by conducting an investigation for the causes of breakage on the center stay rod and an actual size fatigue test:

• Inspection of cause of damage

(1)No defects, such as a problem with materials and a crack at the starting point, were found from the broken rod.

(2) In the result of observation of the breakage surface, fatigue crack occurred from lower-side.

(3)The cause of the breakage is a fatigue damage caused on the thread root of the first screw thread on the coupler side of the rod.

(4)The target bridge is in a state where vehicles lean to the down-bound lane. As a result, the stress range of the down-bound lane where the rod was broken becomes large.

(5)Fatigue damage may occur in a short time according to the 72-hour stress frequency measurement.

• Result of fatigue test

(1) Fatigue cracks were initiated at the thread root, and propagated in arc shapes, then finally broke the rod, similarly in the actual structure.

(2)The fatigue limit increased to 1.5times by changing the radius of the thread root from 0.3mm to 0.7mm.

According to the above mentioned result, the improved center stay rod was applied to the actual bridge. However, it is difficult to inspect the rod, since the rod is covered. Therefore, new inspection method that can detect a crack of the thread part without opening cover will be developed.

References

1) Kazuhiko FURUYA, Hiroshi ISOE, Hiroaki HOASHI, Shigeru HIRANO; Verification to the breakage of center stay rod of the first Kurushimakaikyo bridge and field observation in the Geiyo earthquake; Steel Construction Engineering; Vol. 10, No. 39; September 2003.

2) Japan Road Association; Manual of fatigue design for steel highway bridges; 2002.(in Japanese)

Maintenance, Safety, Risk, Management and Life-Cycle Performance of Bridges – Powers, Frangopol, Al-Mahaidi & Caprani (Eds)
© 2018 Taylor & Francis Group, London, ISBN 978-1-138-73045-8

Repair of corroded steel plate girders with ultra-high performance concrete

K.F. McMullen & A.E. Zaghi
University of Connecticut, Storrs, CT, United States of America
M.P. Culmo
CME Associates, Inc., Mansfield, CT, United States of America

ABSTRACT: As the world's bridge infrastructure ages, there is a growing need to develop new, innovative repair and maintenance methods to rehabilitate these critical structures. Corrosion damage of steel bridges is a prevalent problem especially beneath leaking deck expansion joints. Implementation of conventional repair methods is expensive and disruptive to traffic. The University of Connecticut is developing a novel repair method by encasing corrosion damaged sections with ultra-high performance concrete (UHPC) to restore bearing and shear capacity lost due to severe reduction of the plate thickness. This paper will present preliminary finite element analysis results and the design of a series of large-scale experiments conducted on full-scale corroded plate girders with the UHPC repair. The UHPC repairs have been designed to restore the as-built capacity of the girders. The goal of the study is to demonstrate the versatility and structural effectiveness of the UHPC repair.

1 INTRODUCTION

Throughout the world, corrosion damage of civil structures is a prevalent problem. National Association of Corrosion Engineers (NACE) International released a report estimating that US$2.5 trillion is spent globally on corrosion accounting for 3.4% of the global Gross Domestic Product (Koch et al., 2016). In the United States (US), the Federal Highway Administration (FHWA) estimates that approximately US$273 billion is spent annually on corrosion maintenance and a total of US$8.3 billion is spend solely on the repair and replacement of highway bridges (Koch et al., 2002).



Figure 1. Corrosion damage of steel bridge girders

One of the superstructures types that is susceptible to corrosion damage are steel girder bridges. Over half of the structurally deficient bridges in the US utilize a steel superstructure (FHWA, 2016). In the northern US, highway bridges are exposed to heavy amounts of precipitation, ice, and de-icing chlorides used for snow and ice control on the roads (Shi et al., 2009). The combination of moisture and chlorides expedites the corrosion of steel material (Albrecht and Hall Jr, 2003). The location which experiences the heaviest corrosion is directly beneath leaking bridge deck expansion joints. Girder ends, bearings, abutments, and piers beneath the expansion joints are the structural components that are most commonly effected (Kayser and Nowak, 1989, Usukura et al., 2013, Van de Lindt and Pei, 2006). Figure 1 shows corrosion damage of steel girder ends including web buckling due to section loss.

A recent study cited the lifespan of bridge deck expansion joints to be between 5-20 years (Chang and Lee, 2001). Once the expansion joints begin to fail, runoff and chlorides begin to leak on the girder ends below from the road above. The ends of steel girders transfer large bearing and shear forces from the girder to the bridge bearing. Several research projects have documented the effect of corrosion damage on the load carrying capacity of steel girders including both small-scale and full-scale experimental and analytical testing (Liu et al., 2011, Yamaguchi and Akagi, 2013, Ahn et al., 2013a, Khurram et al., 2014a, 2014b). The results show that when this critical section of the girder experiences section loss due to corrosion, the bearing and shear capacity of the girder are reduced.

The repair method to rehabilitate this type of corrosion at the end of steel girders is standardized for

many US Departments of Transportations (DOTs). The traditional method is to 1) jack up the superstructure to remove load from the girder end, 2) remove the corroded portion of steel, 3) weld or bolt new steel plates to the girder, and 4) lower the beams back on the bearing (FLDOT, 2011, Rossow, 2003 , Wipf et al., 2003, WisDOT, 2015). An example of the conventional repair method is shown in Figure 2. This method is expensive, time consuming, and difficult to construct. A sizable portion of the construction cost is due to jacking of the bridge and abatement and surface treatment of the corroded steel before the repair can be implemented.



Figure 2. Conventional repair for corroded steel bridge girders

Research is being conducted by many institutions to develop a new repair method for steel girder with corrosion damage. Ahn et al. (2013b) and Miyashita et al. (2015) are investigating the potential to apply CFRP sheets over corrosion damage. Ogami et al (2015) has developed a repair which envelopes the corroded area in an epoxy resin. However, these projects have yet to be accepted as a conventional repair method. This leaves a need for the development of a new, more cost-effective repair design.

In collaboration with the Connecticut Department of Transportation and the United States Federal Highway Administration, the University of Connecticut is developing a novel repair method for corroded steel girder ends by encasing the corrosion damage with ultra-high performance concrete (UHPC). UHPC is a flowable concrete material which includes significant quantities of high strength steel fibers. UHPC can achieve very high compressive and tensile strengths resulting in a material that can be facetiously described as "liquid steel." This repair will decrease construction costs, construction time, and traffic interruptions while providing a structurally efficient restoration of the girder capacity.

2 UHPC REPAIR METHODOLOGY

The repair method developed at the University of Connecticut encases the corrosion damage girder end in UHPC. Headed shear connectors, typically used for composite decks, are welded to the intact, uncorroded portions of the web, flanges, and stiffeners of the girder beyond the corrosion zone. UHPC is then cast, encasing the shear connectors and the corrosion damage, creating a structural column or panel at the end of the girder to carry the load demands on the girder. The composite action between the welded shear connectors and the UHPC panel allows the forces to bypass the corroded portion of the web. Bearing and shear forces carried by the girder are transferred from the web through the shear connectors to the UHPC panel.

UHPC was chosen as the desired repair material because of several advantages it has over conventional concrete and structural steel (Russell and Graybeal, 2013). The main advantages which benefit this repair design are the high early strength, high tensile strength, superior fatigue resistance, exceptional durability, and increased flowability. UHPC has the ability to achieve strengths as high as 80 MPa in as little as 12 hrs which would allow for minimal lane closures and traffic delays during construction. UHPC also has a high tensile strength due to the inclusion of steel fibers in the mix which can bridge cracks in the concrete reducing the need for additional reinforcement and performing the performance of the repair under bending moments. UHPC has proven fatigue performance under a large number of loading cycles improving the design life of the repair. The durability of the UHPC will also lead to a longer service life because it is far more impermeable than regular concrete. The flowability of UHPC provides several constructability advantages allowing the concrete to be poured or pumped to encase complex geometries or tight configurations.

The repair may be applied to the bridge while it is in-service and under traffic reducing traffic disruptions and lane closures. Being able to implement the repair in situ will remove the need for jacking of the superstructure by allowing the repair to be installed under load. The simplicity of construction will also reduce construction durations and improve work-zone safety.

3 PREVIOUS RESEARCH STUDIES

The University of Connecticut and the Connecticut Department of Transportation have been conducting extensive research on the constructability and structural performance of the UHPC steel girder end repairs. Phase 1 of the research project focused on design of the repair, extensive finite element modeling, and a proof-of-concept experimental study. This phase of the research study concluded in 2015.

The finite element research explored a broad range of repair configurations and geometries for both rolled girders and plate girders of varying sizes. The results showed that the repair configuration may be

adjusted based on the number of shear connectors, the layout of the connectors, and the geometry of the UHPC panel. Several geometries that were tested included a full-height end panel, a half-height end panel, a full-height bearing column with continued half-height end panel, a full-height bearing column only, and a half-height bearing column only. From the results of the finite modeling, it was apparent that the configuration and geometry were critical in determining the structural behavior and transfer of forces of the composite repair. Extensive results of the finite element studies are described in previous publications (Zmetra, 2015, Esmaili Zaghi et al., 2015, Zmetra et al., 2017a).

A proof-of-concept experimental study was conducted on half-scale, W21x55, 4.25 m long, rolled steel girders to demonstrate the global performance of the repair. Three girders were tested: an undamaged, damaged, and repaired girder. Both the damage and repaired girders had artificial corrosion damage introduced by removing 70% of the web and 40% of the flange. The repaired girder had a partial height UHPC repair applied with shear connectors welded to the undamaged portions of the web and bottom flange of the girder. The girders were tested using a large scale 3-point bend test set up. The results showed that a 70% reduction of the web thickness reduced the bearing capacity of the corroded girder by 76%. After the UHPC repair was applied, the bearing capacity of the repaired girder exceeded that of an undamaged girder shifting the failure mode to flexural yielding. The additional of the UHPC repair reduced the bearing strain demand on the repaired girder by 21 times compared to the undamaged girder. Overall, the results of the experimental study demonstrated the ability of the repair to restore full bearing and shear capacity of a corroded steel girder. Full results of the experimental study have been documented (Zmetra, 2015, Esmaili Zaghi et al., 2015, Zmetra et al., 2017b).

Recently, the Connecticut Department of Transportation and the University of Connecticut have engaged in the design of a field repair for a candidate bridge in Connecticut using the UHPC repair methodology. A design process has been developed to determine demands, design capacities, and necessary design checks for the structural repair design. The results of the design of the UHPC repair for this case study bridge have been documented by McMullen et al. (2017).

4 DESIGN OF EXPERIMENTS

A total of four full-scale plate girder will be experimentally tested to evaluate the structural performance and constructability of the UHPC repair. One of the girders will have corrosion damage with no repair as a baseline, and three of the girders will have three different UHPC repair configurations. The results of the study will be examined for 1) ease of construction including complexities and potential concerns for field application, 2) effect of vibrations during curing to simulate live load traffic during UHPC curing, and 3) structural performance of the different repair types.

4.1 *Test Specimens*

After reviewing several inspection reports, many of the bridges that have experienced heavy corrosion damage of the girder ends are welded plate girders constructed 50-60 yrs ago. To determine accurate sizes and dimensions of the plate girders constructed during this period, design drawings for a number of plate girder bridges in Connecticut were reviewed.

The primary advantage of welded plate girders over rolled girders is the flexibility in the size and dimensions of the members. Therefore, the goal of the design of the experimental plate girder specimens was to accurately represent a large number of diverse designs. After reviewing the drawings, it was found that for a large variety of plate girder designs the ratio of girder depth (D) to web thickness (t_w) and the ratio of stiffener spacing (d_0) to web depth (D) were consistent. Of the bridges reviewed, the average D/t_w ratio was 144 and the average d_0/D ratio was 0.74.

The final design of the plate girder was completed based on the original design of a 54-year-old bridge in East Hartford, CT. The web depth was 1.32 m with a web thickness of 9.5 mm and a stiffener spacing of 1.02 m. These dimensions correspond to a D/t_w ratio of 139 and a d_0/D ratio of 0.77, which was deemed as representative for typical plate girders. For the plate girder specimens, the bottom flange was designed to have a thickness of 25.4 mm and the top flange a larger thickness of 38.1 mm to improve the lateral torsional buckling stability of the specimens due to the lack of a composite deck during testing. The bearing stiffener had a thickness of 12.7 mm and the web stiffener had a thickness of 9.5 mm.



Figure 3. Full-scale plate girder end panel

For experimental testing, the girders will each be tested over a 5.28 m long span. To simplify construction and testing of each of the specimens, a splice connection was incorporated to separate the girder into a baseline section and a test section. The splice connection was placed directly after the end panel of the girder, since the end panel is the critical portion of the girder which is experiencing heavy corrosion damage. The splice connection was designed with a capacity equal to that of the full plastic shear capacity of the end panel of the test specimen. The baseline section of the girder included additional, closer spaced stiffeners as well as two sets of stiffeners directly beneath the point of loading to prevent any damage during testing. Figure 3 shows the plate girder specimen end panel.

The plate girder specimens were fabricated by a professional steel fabricator to ensure that all four specimens were comparable with similar dimensions.

4.2 *Corrosion Damage*

To accurately capture the extent and pattern of typical corrosion damage, inspection reports from over thirty bridges in Connecticut were examined. The bridges chosen had either a plate girder or rolled beam steel superstructure. Each of these bridges varied by span length, traffic volume, overall width, and several other factors. There was a good balance of bridges with extreme damage and structurally deficient ratings and non-deficient bridges with corrosion damage. After an in-depth review of the inspection reports, it was confirmed that there was a common pattern of heavy corrosion damage at the end of girders beneath expansion joints.

Of the bridges reviewed, the length, width, and depth of the corrosion damage varied significantly from surface rust to full perforations of the steel at isolated locations. Although corrosion damage is highly non-uniform and unpredictable, through review of the inspection reports several consistencies were found including the radial shape of the corrosion damage. Heavy corrosion damage is typically limited to the bottom 125 mm of the girder, and corrosion often extends past the end of the bearing towards mid-span.

One of the primary goals of simulating the corrosion damage to the girders was to preserve the non-uniform nature of typical corrosion damage. In previous research studies, corrosion damage has been modeled as a uniform section loss of equal thickness and height and is typically introduced by removing material with a milling machine (Ahn et al., 2013a, 2013b, Khurram et al., 2014a, 2014b). However, this is not representative of the corrosion found on bridges in the field. A non-uniform corrosion pattern was introduced to each of the girders through sandblasting and metal grinding. Another advantage of this method was that it preserved the condition of the end panel. Previous research projects (including the UHPC repair proof of concept project) simulated corrosion by removing a portion of the girder end, milling of the removed portion to simulate corrosion loss, and then welding the portion back into the girder. This introduces an added complexity due to modeling of the experiment because the girder consists of two separate pieces welded together which is not typically the condition found in the field.

Based on the inspection reports that were evaluated, only two limitations were used for introducing the corrosion damage: 1) the corrosion damage did not extend to a height greater than 125 mm, and 2) the corrosion damage extended at least 50 mm past the end of the bearing. To simulate the most extreme case of corrosion damage of steel girders, a target section loss of 70% of the web thickness and 50% of the bearing stiffeners was targeted (however, this was not a limitation). During implementation of the corrosion damage simulation, 100% section loss and full perforations were achieved in isolated locations. Detailed pictures of the corrosion damage of one of the plate girders is shown in Figure 4.



Figure 4. Corrosion damage applied to the plate girders

4.3 *UHPC Repair*

The goal of this research project was to evaluate the performance of repair configurations that would most likely be chosen by engineers for typical corrosion damaged bridges. Based on the Phase 1 and preliminary Phase 2 finite element analysis results, it was determined that repair of the bearing column is critical for rehabilitation of the bearing and shear capacity of the girder. The bearing column consists of the end portion of the web and the bearing stiffeners. This portion of the girder carries bearing and shear forces from the girder directly to the bearing.

Under severe corrosion damage, the local web buckling of the web plate and the bearing stiffener is the primary failure mode when corrosion is isolated to the girder end. If extreme corrosion extends farther past the bearing into the web end panel, then repair engineers may consider extending the UHPC repair panel into the entire end panel. In extreme cases, where the corrosion damage intercepts the tension field of the web plate, the shear capacity of the end panel may be reduced significantly.

Since heavy corrosion rarely extends far past the bearing towards mid-span, the experimental repair

geometries chosen for this research were predominantly for repair of the bearing column. Two of the girders will utilize a full-height UHPC repair column and one will have a partial-height UHPC repair column. This will provide experimental evidences for the effectiveness of the repair and enables engineers to choose the optimal repair design by minimizing the repaired volume of UHPC. For the design of the UHPC repairs, previous research has found that the number of shear connectors included is the controlling factor for the capacity of the repair (McMullen et al., 2017). Push-out tests were performed on shear connectors welded to a thin web. The individual capacity of a shear connector may be used to determine the capacity of the UHPC repair based on the number of connectors used. The target capacity for the experimental tests was the as-built bearing and shear capacity of the girders.

For this repair, 12.7-mm diameter headed shear connectors were chosen for the large-scale specimens. The results of the push-out tests found the ultimate shear capacity of a single stud to be 59.7 kN. The calculated bearing and shear capacities of the undamaged girder specimen were 1800 kN and 1600 kN, respectively. To restore the shear capacity to the girder a minimum number of 27 shear connectors are needed.

Each of the three repaired girders has 28 connectors welded to both sides of the web. The connectors should be welded to the uncorroded portion of the web. The pattern of the full- and partial-height repairs are shown in Figure 5. A standard Connecticut deck haunch is cast at the end of the girder and a diaphragm channel shape is welded to the bearing stiffener to simulate the typical geometry of the girder end found in real designs. These constraints will influence the constructability of the repair as far as access and forming around complex geometries.



Figure 5. Plate girder specimens before UHPC repairs (connector layout): a) full-height column; b) partial-height column

The UHPC used for the experimental tests will be two different mixes developed by Lafarge Holcim: Ductal JS1000 and Ductal JS1212. Ductal JS1000 is a general, fiber reinforced UHPC mix which can gain a strength of 83 MPa in four days. Ductal JS1212 is a high early strength mix that can achieve a compressive strength of 83 MPa in as little as 12 hours and sets in about two hours.

The first repaired girder will be a full-height column repair with JS1000. The goal of this repaired girder is to investigate the effect of vibrations at early strength of a UHPC repair with a long curing time. This will be done to evaluate if the repair can be implemented with minimal lane closure, and traffic can be restored soon after casting.

The second repaired girder will be a tall column repair with JS1212. This girder will test the ability to cast the repair and allow the UHPC to set and gain strength in a single construction shift allowing for full traffic load to be reestablished with minimal effect on the structural performance of the repair.

The third repaired girder will be a partial height column repair with JS1212. This girder will compare the differences between a taller column with a larger volume of UHPC and a smaller column with connectors welded closer to the corroded section. A partial height repair will also reduce the complexity of having to form around diaphragm connections and the deck haunch.

4.4 *Test Setup*

The previous experimental research on the repair design was conducted on half-scale rolled steel girders. To test full-scale plate girders, the test setup required substantial upgrades. The test setup consists of a large-scale three-point bend test of the plate girders. The load will be applied at $^{3}/_{10}$ the span of the girder closer to the test end panel. The location of the loading was chosen to induce large shear and bearing forces in the test end panel. The load will be applied with a hydraulic load ram. For the previous test, a 2,200 kN hydraulic load ram was used, however to test full-scale plate girders a 4,400 kN load ram was obtained.

The existing load frame had to be modified to support the plate girder specimens. Three additional spread beams were added to the load frame to engage all four columns that are tied in to the strong floor. The load ram will be mounted to the center of the load frame and the load will be applied to the top flange of the girder directly after the splice connection between the test end and the permanent end. The load ram is indicated with a red arrow in Figure 6.

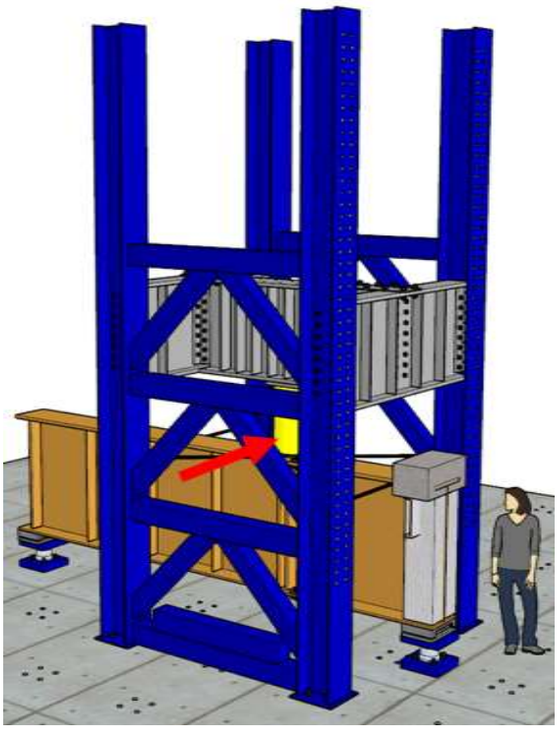


Figure 6. 3D rendition of the experimental test setup

The girder will be supported by two sliding Disktron bridge bearings manufactured by RJ Watson. Lateral support chains will be used to brace the top flange to simulate the lateral stability provided to the girder by a concrete deck.

Over 100 channels of data will be collected during each test. The instrumentation that will be used for the test include two five-degree of freedom load cells beneath each bearing, pressure transducers attached to the hydraulic load ram, strain gauges installed on the web and the flanges, shear studs, and on the UHPC panels, and string and rod displacement transducers. Digital Image Correlation will be used to map the strain distribution at the end panel.

A 3D rendering of the entire experimental test setup is shown in Figure 6.

5 FINITE ELEMENT ANALYSIS

Preliminary finite element models were developed to estimate the expected performance of the specimens. The finite element models were developed in a general-purpose finite element program, LS-Dyna. LS-Dyna was chosen because of its rigorous solving capabilities that enable refined analysis of the models including developing custom material models and capturing geometric nonlinearities.

The goal of developing these models was to evaluate the expected forces and failure modes of each test. This was done to: verify that the test setup was adequately designed to support the full capacity of the girders, ensure that the test specimens were designed correctly and that failure happens at the end panel, and obtain the level of web section reduction needed to introduce a notable reduction in the capacity of the damaged specimens. The models may be used to study different repair configurations and design parameters to finalize the design for each of the experimental plate girder specimens.

The first two models that were created and analyzed were an as-built, uncorroded plate girder and a corroded plate girder with the target section loss assigned to the web and stiffeners. Each of the models included bearings at either end of the girder which allowed for rotation in both the x- and y-direction, a load ram saddle used to apply the loading to the top flange of the girder, and lateral restraints to prevent rotation or lateral torsional buckling of the top flange. Figure 7 shows the full finite element model with all components included.

The steel plate girders including the web, flanges, and stiffeners were modeled using four-node, two-dimensional, shell elements. The bearings and load ram were modeled using eight-node, three-dimensional solid elements. The shell elements were fully integrated and were computationally less expensive compared to solid elements. Yet, they are able to capture the complex stress fields and failure modes, including web buckling, web crippling, and tension field formation. The shell elements also included five integration points through the thickness of the element and warping stiffness control. The lateral restraints were boundary conditions restricting movement of the top flange in the x- and y-directions at eight different points.

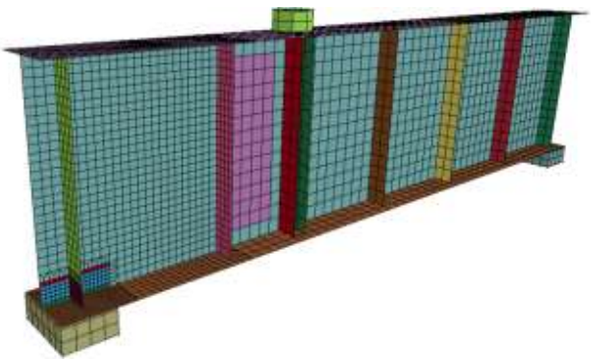


Figure 7. Finite element model of the entire analytical setup

For the preliminary finite element models, the corrosion damage was introduced to the model as a uniform section loss of the web and stiffeners. The corrosion damage applied to the web was 380 mm long and 125 mm tall with 33% (3.175 mm) of the thickness remaining. The corrosion damage applied to the stiffener was the same height as on the web and the full width of the stiffener with 50% (6.35 mm) of the thickness remaining. For the finalized models, 3D scanned geometry of the corrosion damage will be imported into the model to accurately model the non-uniform corrosion of the specimens.

The finite element models of the repaired girders required the addition of two different components: the shear studs and the UHPC panel. The shear connectors were modeled using spotwelds. Spotwelds are a definition in LS-Dyna typically used to model bolted or spot weld connections. Spot welds were used to model the shear connectors because they can capture the observed failure mode of studs embedded in UHPC that was found during the experimental push-out tests. The spot welds may be assigned to any location on the girder and have a contact assignment between the web of the girder and the UHPC panel to provide a secure stud connection. The material model of the spotweld elements was defined to model the load-slip behavior of shear studs captured from the experimental push-out tests. The details about the stud behavior is presented by McMullen et al. (2017) and Zmetra et al. (2017a). The UHPC panel was also modeled as a constant stress solid element. The UHPC material model was adopted from previous research. This model captures the nonlinear behavior of high-strength concrete in tension and compression.

A displacement control loading was applied to the girders. The load ram saddle was used to displace the top flange of the girder using a triangular acceleration profile. The results of each of the models were compared based on the deflection of the bottom flange directly beneath the point of loading and the bearing reaction force at the test end of the girder.

6 RESULTS OF FINITE ELEMENT MODELING

The first finite model that was developed for the intact plate girder. Under initial simulated loading, the girder behaved elastically as a tension field formed in the end panel. The simulated failure mode of the intact plate girder was web buckling of the end panel. This occurred under a load of 2980 kN corresponding to a bearing load of 2060 kN and a vertical deflection of 6.2 mm. The web buckling observed in the end panel was a ductile failure were the intact beam was able to continue to carry approximately 80% of the maximum load applied.

The next model was the damaged plate girder with section loss applied to simulate corrosion damage. Reducing the cross section area of the web and stiffener plates at the bearing induced localized buckling of these plates. The damaged plate girder failed under a load of 1446 kN corresponding to a bearing force of 996 kN and a vertical deflection of 3 mm. Applying a 66% section loss to the web and a 50% section loss to the stiffeners reduced the capacity of the plate girder by approximately 52%.

Next, different repair configurations were simulated to finalize the UHPC geometry, number of connectors, and layout of connectors for the experimental studies. It was concluded that 28 shear studs are needed to restore the bearing and shear capacity of the intact girder. The number of studs required by the finite element models also agrees with the design checks proposed by McMullen et al. (2017). The two UHPC geometries chosen for the repairs were a partial-height column and a full-height column. The partial-height column was 668 mm tall with four independent 152 mm by 152 mm columns as shown in Figure 8. The tall column repair was 1220 mm tall with four independent 152 mm by 152 mm columns as shown in Figure 8. The connectors were placed in a staggered pattern as shown in Figure 5.

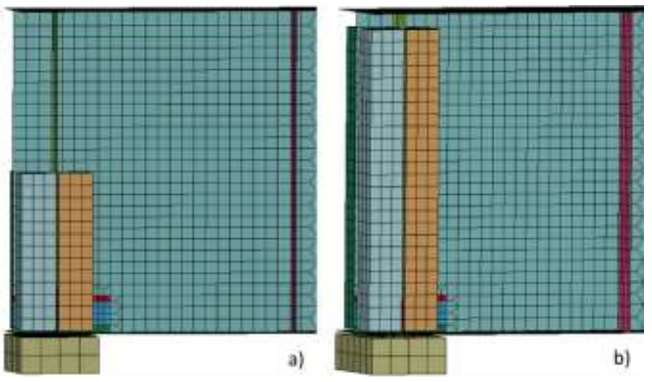


Figure 8. UHPC repair geometries: a) partial height repair; b) tall repair

The finite element simulations show that the partial height UHPC repair fails due to buckling of the end panel web similar to that of the intact plate girder. Failure of the partial height repair occurred under a load of 3220 kN corresponding to a bearing load of 2230 kN and a vertical deflection of 6 mm. The partial height UHPC repair increase the capacity of the plate girder 8% over the capacity of the intact plate girder maintaining the ductile failure mode.

The full-height UHPC repair column also failed due to web buckling of the end panel under a bearing force of 2360 kN and a vertical deflection of 6.76 mm. The tall repair column increased the capacity of the plate girder 15% over the as-built plate girder capacity. The additional capacity provided to the girder by the full-height UHPC repair is because the UHPC repair intercepts the tension field in the end panel providing added buckling support to the web.

The deformed shape and stress distribution of each of the analytical plate girder models is shown in Figure 8. Figure 9 shows the force-displacement relationship for each of the four analytical models.

After the plate girders are scanned and experimentally tested, the finite element models will be updated and refined to capture the conditions of the experimental test. The methodology for the development of the finite element models is described in detail by Zmetra et al. (2017a).

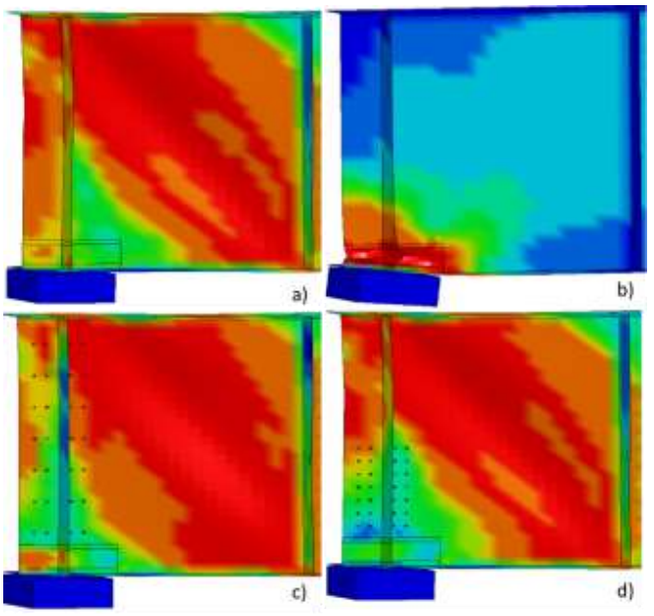


Figure 9. Plate girder finite element model deformed shapes: a) intact; b) corrosion damaged; c) tall repair column; d) partial height repair column

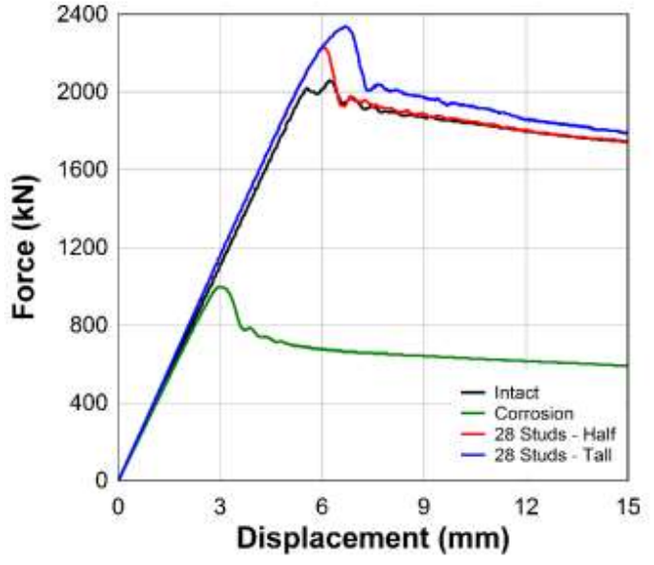


Figure 10. Analytical Force vs. Displacement results from the finite element models of the intact, corroded, and repaired plate girders.

7 CONCLUSION

The experimental and analytical research completed by the University of Connecticut and the Connecticut Department of Transportation has the potential to provide bridge owners with a new, cost-effective repair for corroded steel bridge girders. The novel repair method presented encases corrosion damage of steel bridge girders with UHPC mechanically attached by headed shear studs welded to the web of the girder. The preliminary finite element results demonstrated the adaptability of the repair to allow engineers to use different configurations and geometries to repair girders with complex structures. Both repair geometries presented increased the capacity of the plate girder over that of the as-built, uncorroded plate girder.

The results of the proposed full-scale experiments will validate the repair concept and show that this repair may be implemented in place of the conventional repair methods typically used. Using this repair may be more efficiency than the conventional repair improving constructability, minimizing project costs, preventing excessive traffic disruptions, and improving long-term durability of the repair.

8 ACKNOWLEDGEMENTS

The research presented in this paper was funded by the Connecticut Department of Transportation and the Federal Highway Administration Contract number SPR-2295. The authors would like to thank the ConnDOT for their support and advice through the course of the project especially Rabih Barakat, Timothy Fields, Anne-Marie McDonnell, Mary Baker, Brad Overturf, and Richard Hanley. The Connecticut Transportation Institute is thanked for managing the project and funds. The authors would like to thank our industry sponsors, especially Infra-Metals, United Steel, Lafarge Holcim, and RJ Watson. The support of Dr. Kay Wille, Dr. Kevin Zmetra, Dominic Kruszewski, and Alexandra Hain is also greatly appreciated.

9 REFERENCES

AHN, J.-H., KAINUMA, S., YASUO, F. & TAKEHIRO, I. 2013a. Repair Method and Residual Bearing Strength Evaluation of a Locally Corroded Plate Girder at Support. *Engineering Failure Analysis,* 33**,** 398-418.

AHN, J.-H., KIM, I.-T., KAINUMA, S. & LEE, M.-J. 2013b. Residual Shear Strength of Steel Plate Girder due to Web Local Corrosion. *Journal of Constructional Steel Research,* 89**,** 198-212.

ALBRECHT, P. & HALL JR, T. T. 2003. Atmospheric Corrosion Resistance of Structural Steels. *Journal of Materials in Civil Engineering,* 15**,** 2-24.

CHANG, L. M. & LEE, Y.-J. 2001. Evaluation and Policy for Bridge Deck Expansion Joints. Indiana Department of Transportation and Federal Highway Administration. Purdue University. SPR-2198.

ESMAILI ZAGHI, A., WILLE, K., ZMETRA, K. & MCMULLEN, K. 2015. Repair of Steel Beam/Girder Ends with Ultra High Strength Concrete. Connecticut Department of Transportation. University of Connecticut. SPR-2282. Phase I.

FHWA 2016. Bridges By Structure Type. Washington, DC.: National Bridge Inventory. Federal Highway Administration.

FLDOT 2011. Bridge Maintenance and Repair Handbook. *Steel Beam & Girder Repair.* Florida Department of Transportation. 4.6, 78-83.

KAYSER, J. R. & NOWAK, A. S. 1989. Capacity Loss Due to Corrosion in Steel-Girder Bridges. *Journal of Structural Engineering,* 115**,** 1525-1537.

KHURRAM, N., SASAKI, E., KATSUCHI, H. & YAMADA, H. 2014b. Experimental and Numerical Evaluation of Bearing Capacity of Steel Plate Girder Affected by End Panel Corrosion. *International Journal of Steel Structures,* 14**,** 659-676.

KHURRAM, N., SASAKI, E., KIHIRA, H., KATSUCHI, H. & YAMADA, H. 2014a. Analytical Demonstrations to Assess Residual Bearing Capacities of Steel Plate Girder Ends with Stiffeners Damaged by Corrosion. *Structure and Infrastructure Engineering,* 10**,** 69-79.

KOCH, G., VARNEY, J., THOMPSON, N., MOGHISSI, O., GOULD, M. & PAYER, J. 2016. International Measures of Prevention, Application, and Economics of Corrosion Technologies Study. *NACE International IMPACT Report*.

KOCH, G. H., BRONGERS, M. P., THOMPSON, N. G., VIRMANI, Y. P. & PAYER, J. H. 2002. Corrosion Cost and Preventive Strategies in the United States. Federal Highway Association & CC Technologies Laboratories, Inc. NACE International. FHWA-RD-01-156.

LIU, C., MIYASHITA, T. & NAGAI, M. 2011. Analytical Study on Shear Capacity of Steel I-Girders with Local Corrosion Nearby Supports. *Procedia Engineering,* 14**,** 2276-2284.

MCMULLEN, K., KRUSZEWSKI, D., ESMAILI ZAGHI, A. & WILLE, K. A Novel Repair Method For Steel Girders with Corrosion Damage Utilizing UHPC. International Bridge Conference, 2017 National Harbor, MD. Engineers' Society of Western Pennsylvania.

MIYASHITA, T., WAKABAYASHI, D., HIDEKUMA, Y., KOBAYASHI, A., OKUYAMA, Y., KOIDE, N., HORIMOTO, W. & NAGAI, M. Repair Method for Corroded Steel Girder Ends using CFRP Sheet. IABSE-JSCE Conference on Advances in Bridge Engineering, 2015. International Association for Bridge and Structural Engineering, 1-7.

OGAMI, H., FUJII, K., YAMADA, T. & IWASHAKI, H. 2015. Renovation of Corroded Girder End in Plate Girder Bridge with Resin and Rebars. *Implementing Innovative Ideas in Structural Engineering and Project Management.* ISEC Press.

ROSSOW, M. 2003 FHWA Bridge Maintenance: Superstructure. Federal Highway Association: Continuing Education and Development, Inc.

RUSSELL, H. & GRAYBEAL, B. 2013. Ultra-High Performance Concrete: A State-of-the-Art Report for the Bridge Community. McLean, VA. FHWA-HRT-13-060: Federal Highway Administration.

SHI, X., FAY, L., YANG, Z., NGUYEN, T. A. & LIU, Y. 2009. Corrosion of Deicers to Metals in Transportation Infrastructure: Introduction and Recent Developments. *Corrosion reviews,* 27**,** 23-52.

USUKURA, M., YAMAGUCHI, T., SUZUKI, Y. & MITSUGI, Y. Strength Evaluation for a Corroded Damaged Steel Girder End Considering its Collapse Mechanism. Proceedings of the Thirteenth East Asia-Pacific Conference on Structural Engineering and Construction (EASEC-13), 2013.

VAN DE LINDT, J. & PEI, S. 2006. Buckling Reliability of Deteriorating Steel Beam Ends. *Electronic Journal of Structural Engineering***,** 1-7.

WIPF, T. J., FANOUS, F. S., KLAIBER, F. W. & EAPEN, A. S. 2003. Evaluation of Appropriate Maintenance, Repair, and Rehabilitation Methods for Iowa Bridges. Iowa Department of Transportation. Iowa State University. Project TR-429.

WISDOT 2015. Bridge Manual: Ch. 40 - Bridge Rehabilitation. *Superstructure Inspection.* Wisconsin Department of Transportation. 40.14, 24-26.

YAMAGUCHI, E. & AKAGI, T. Degradation of Load-Carrying Capacity of Steel I-Girder End due to Corrosion. Proceedings of the Thirteenth East Asia-Pacific Conference on Structural Engineering and Construction (EASEC-13), 2013.

ZMETRA, K. 2015. *Repair of Corrosion Damaged Steel Bridge Girder Ends By Encasement in Ultra-High Performance Concrete.* Ph.D., University of Connecticut

ZMETRA, K., HAIN, A., ZAGHI, A. E. & WILLE, K. 2017a. Finite Element Analysis and Experimental Comparison for Repair of Corrosion Damaged Steel Girder Ends Using Ultra-High Performance Concrete Encasement. Washington, DC.: Transportation Research Board 96th Annual Meeting.

ZMETRA, K. M., MCMULLEN, K. F., ZAGHI, A. E. & WILLE, K. 2017b. Experimental Study of UHPC Repair for Corrosion-Damaged Steel Girder Ends. *Journal of Bridge Engineering,* 22**,** 04017037.

Maintenance, Safety, Risk, Management and Life-Cycle Performance of Bridges – Powers, Frangopol, Al-Mahaidi & Caprani (Eds)
© 2018 Taylor & Francis Group, London, ISBN 978-1-138-73045-8

Retrofitting method against fatigue cracking of web gap plates

C. Sakamoto
Kansai University, Osaka, Japan

M. Sakano
Kansai University, Osaka, Japan

H. Konishi
Japan Bridge Association, Osaka, Japan

M. Koyama
Ministry of Land, Infrastructure and Transport, Himeji, Japan

ABSTRACT: Lots of fatigue crackings were reported at the upper end of vertical stiffeners connected to sway bracings and web gap plates under RC slab in steel highway girder bridges. In this study, we investigate fatigue cracking behavior, and propose a retrofitting method against fatigue cracking at the upper end of web gap plates under RC slab. In this method, TRS (Thread Rolling Screw) is used to attach angle steel to upper flange, and HTB (High Tension Bolt) is used to connect angle steels to web gap plate. The effectiveness of the method is investigated through fatigue tests using a beam specimen with the web gap detail of the same size as the actual bridge under alternative loading using two actuators. As a result, the method can reduce the local stress concentration at crack initiation points to about 50~60 %, and can extend fatigue crack initiation life more than 2~6 times and fatigue crack propagation life more than 100 times after grinding away fatigue cracks.

1 INTORODUCTION

Lots of fatigue crackings were reported at the upper end of vertical stiffeners connected to sway bracings and web gap plates under RC slab in steel highway girder bridges (Japan Road Association 1997, Hanshin Expressway Technology Center 2012). Several countermeasures were proposed against those crackings, such as steel plate reinforcement between the upper flange and the vertical stiffener using high tension bolts after breaking RC slab, or re-welding. However, the work of breaking RC slab requires traffic lane closing, and re-welding may cause re-cracking. Whereas, the semicircular cutting method for web gap plate to reduce stress concentration at the weldment were proposed, but cracks may be propagated when short cracks have been already initiated. In this study, we investigate fatigue cracking behavior, and propose a retrofitting method against fatigue cracking at the upper end of web gap plates under RC slab. In this method, TRS is used to attach angle steel to upper flange, and HTB is used to connect angle steels to web gap plate.

The effectiveness of the method is investigated through fatigue tests using a beam specimen with the web gap detail of the same size as the actual bridge under alternative loading using two actuators.

2 EXPERIMENTAL PROCEDURES

2.1 *Specimen*

Figure 1 shows configurations and dimensions of the specimen, and location of strain gages. The depth and space of main girders are smaller than those of the actual bridge (Ichinose 2017), because of capacity of fatigue testing facility. But upper flange and web gap plates are of the same size as the actual bridge. The specimen has three main girders, which reproduce the alternative stress in the top of the middle girder when vehicles run on driving lane and passing lane alternatively. The specimen is made of JIS-SM490YA, SM490YB and SM400 steels, which are of the same grade as the actual bridge. The upper flange and upper end of vertical stiffener are welded with a 2mm gap by CO2 gas shield welding.

The specimen has 4 test parts with or without retrofitting methods as follows, A, B: No retrofitting method; C, D: Angle steel retrofitting method using TRS.

The effectiveness of these two types of retrofitting methods is investigated by comparing fatigue behaviour of these 4 test parts.

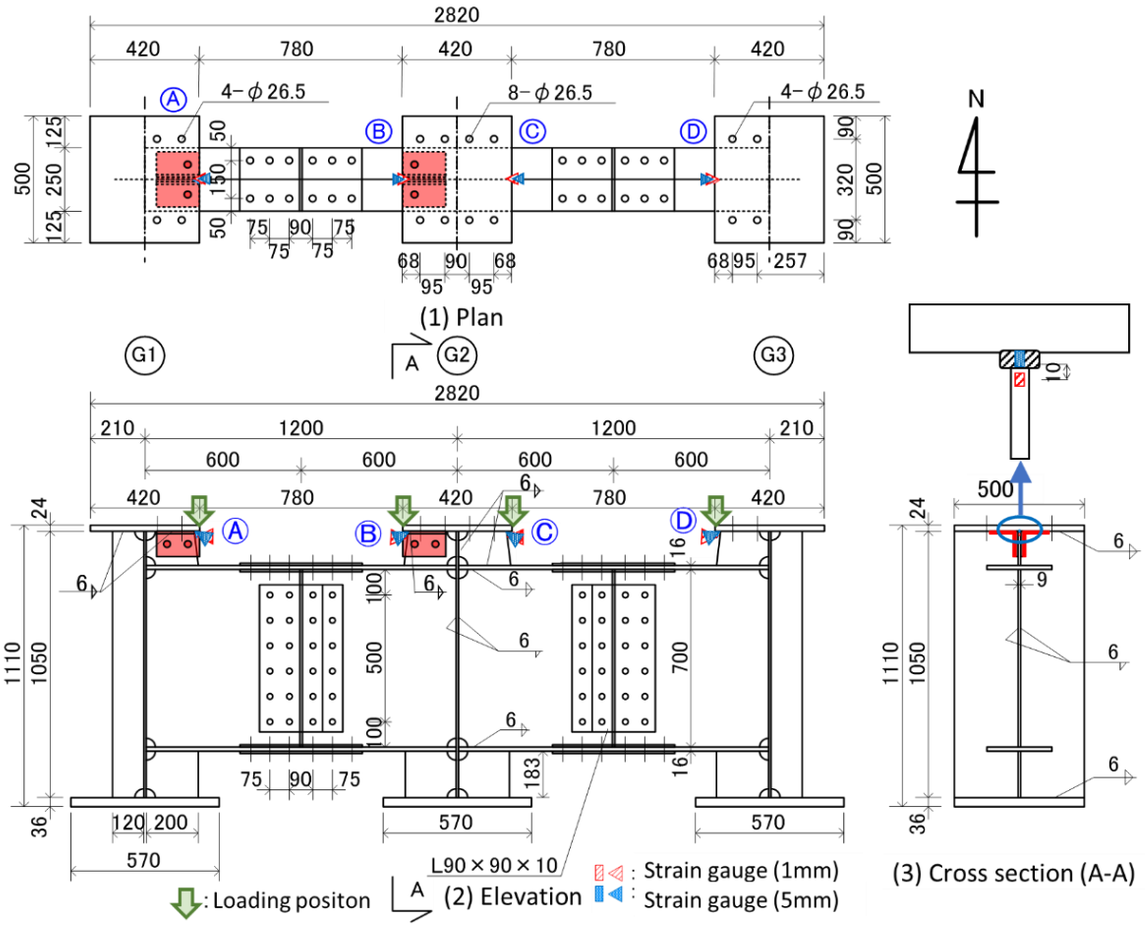


Figure 1. Configurations and dimensions of specimen

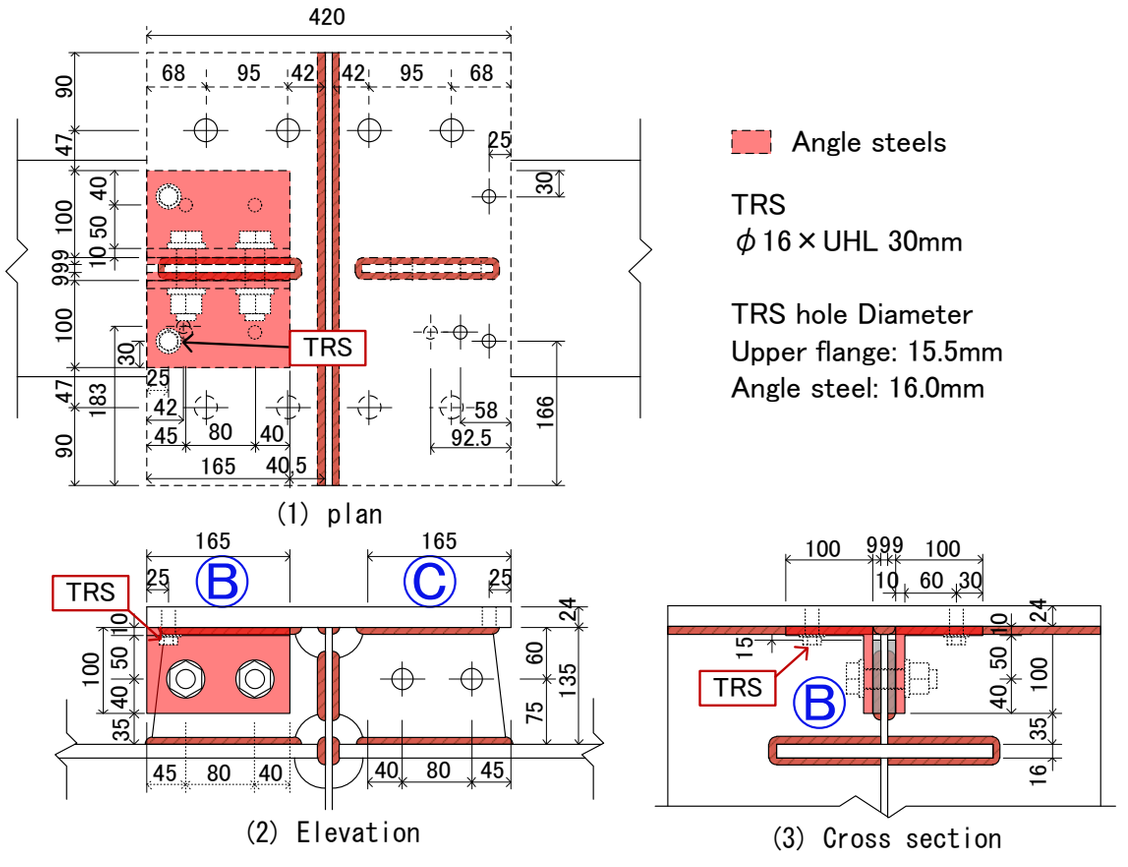
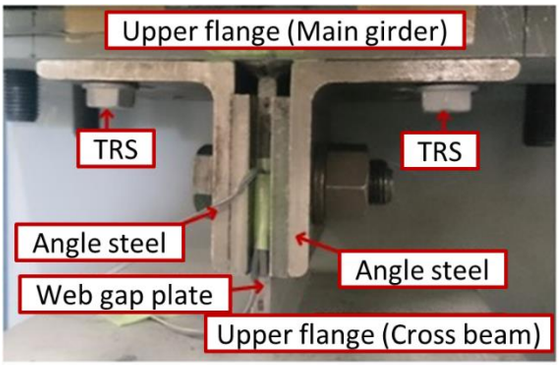
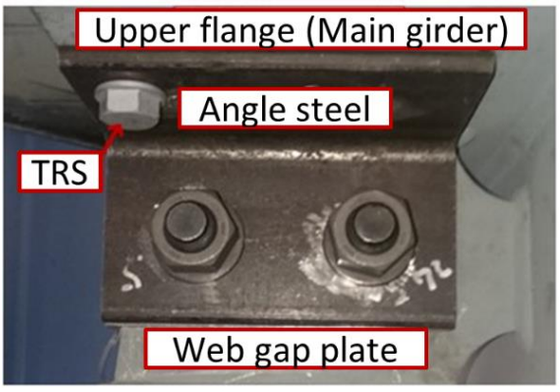


Figure 2. Retrofitting Details



(a) Cross section



(b) Elevation

Figure 3. Angle steel method using TRS

2.2 *Retrofitting method*

Figure 2 shows retrofitting details, and Figure 3 shows appearance of angle steel reinforcement using TRS. This method reduces the local stress concentration at the upper end of vertical stiffener by distributing the load to angle steel.

2.3 *Static loading test procedures*

Figure 4 shows the loading method and Figure 5 shows loading wave form. The static loading test was conducted using two actuators to reproduce the simultaneously and alternatively stress in the middle girder when vehicles pass on the driving lane and passing lane simultaneously and alternatively. Load range was 120kN (Pmax=140kN, Pmin=20kN).

In static loading test and fatigue test, two types of uniaxial strain gages were used. 1mm long strain gages were pasted on the plate side surface 10mm below the weld toe, in order to measure the local stress. Whereas 5mm long strain gages were pasted on the bead surface, in order to monitor initiation and propagation behavior of root cracks.

2.4 *Fatigue test procedures*

The fatigue test was conducted using two actuators under alternative loading to reproduce the alternative stress in the middle girder when vehicles run on the driving lane and passing lane alternatively. Loading frequency was 3-4Hz.

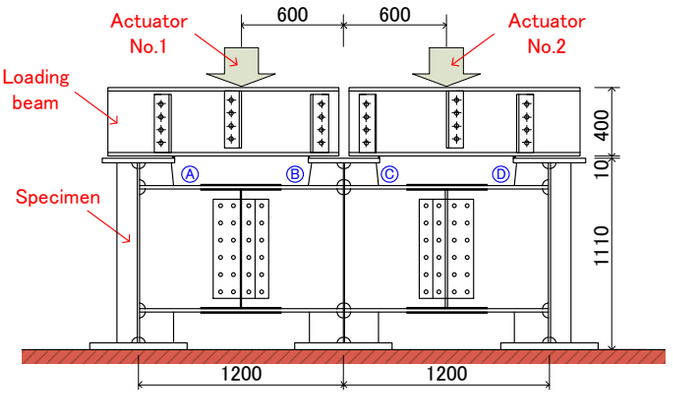


Figure 4. Loading Method

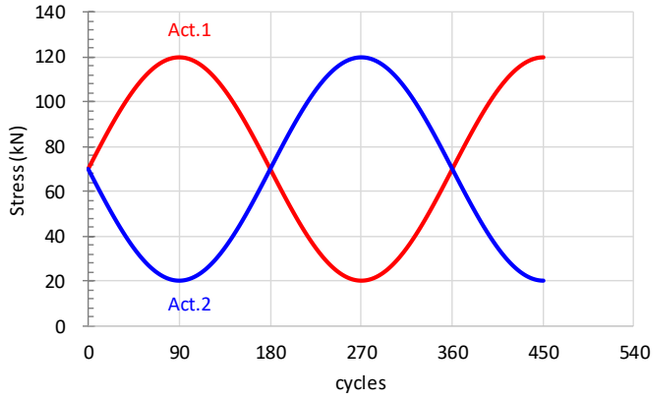


Figure 5. Loading wave form

Table 1. Fatigue test steps

Step	Test part	A	B	C	D
1	Purpose	Preventive measure		Recreating crack	
	Measure	TRS		None	
2	Purpose	Recreating crack		Post cracking measure	
	Measure	None		Grainding crack tips + TRS	

Table 1 gives fatigue test steps.

(1) Step1: In the test part A and B, purpose is to investigate the effectiveness of angle steel reinforcement using TRS. In the test parts C and D, purpose is to recreate cracks without measure.

(2) Step2: In the test part A and B, purpose is recreating cracks without measures. In the test parts C and D, purpose is to investigate the effectiveness of post cracking measure. Angle steel reinforcement using TRS was applied after grinding away crack tips.

Magnetic Particle Testing (MT) was used to detect toe cracks and to measure the crack length. Strain gages pasted on the bead surface were used to monitor initiation and propagation behaviour of root cracks.

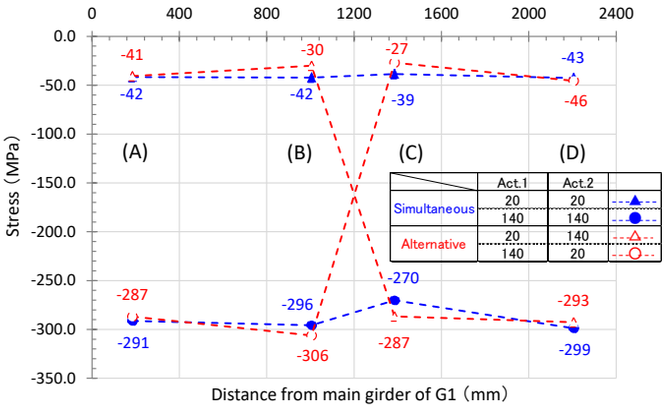


Figure 6. Stress Distributions under Simultaneous Loading and Alternative Loading

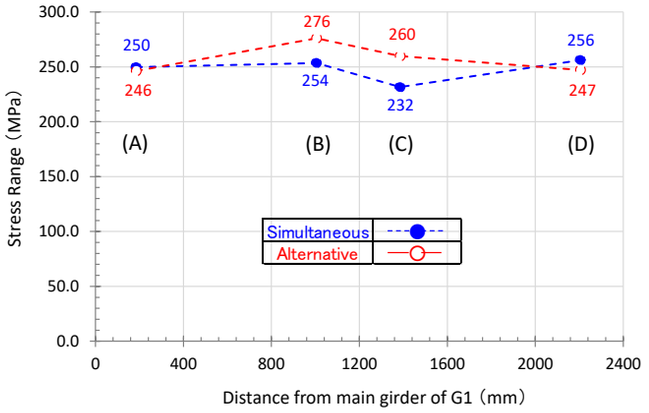


Figure 7. Stress Rage Distributions under Simultaneous Loading and Alternative Loading

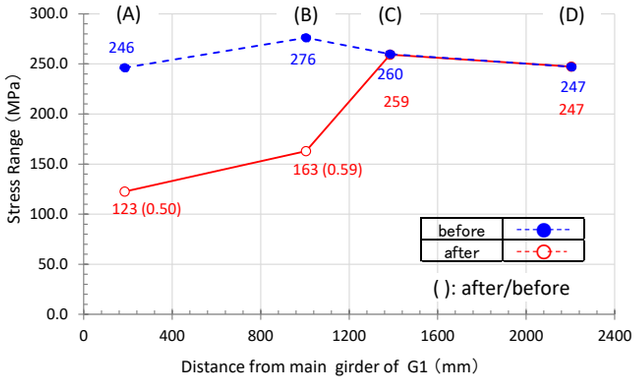


Figure 8. Stress Range Distributions Before and After Retrofitting

3 EXPERIMENTAL RESULTS

3.1 *Static loading test results*

Figures 6 and 7 shows the stress and stress range distributions under simultaneous loading and alternative loading. The stress range in middle girder (B and C) under alternative loading method increases about 10% of that under simultaneous loading. Alternative loading can reproduce the alternative stress at the upper end of web gap plates in the middle girder when vehicles run on the driving lane and passing lane alternatively.

Table 2. Fatigue test results

test part	measure	fatigue life (Mcycles)			crack length (mm)	
		Ns	Nd (R)	Nd (T)	initiate	last
A	preventive	>500	>500	>500	–	–
	none	80	540	110	8 (8)	13 (64)
B	preventive	>500	>500	>500	–	–
	none	>750	–	140	4	8
C	none	110	290	190	13 (4)	20 (155)
	post cracking	>750	>750	>750	–	20 (157)
D	none	>500	–	230	7	12
	post cracking	>750	>750	>750	–	2

toe (root)

Figure 8 shows the stress range distributions before and after retrofitting. Angle steel reinforcement using TRS can reduce the local stress concentration to about 50-60% of that before reinforcement.

3.2 *Fatigue test results*

Table 2 gives fatigue test results. Ns is the root crack initiation life defined as the number of loading cycles when the strain changes irreversibly. Nd(R) is the root crack detection life defined as the number of loading cycles when root cracks appears on the bead surface. Nd(T) is the toe crack detection life defined as the number of loading cycles when toe cracks are detected at the weld toe.

Figure 9 shows the relationship between strain and the number of loading cycles and Figure 10 shows the relationship between crack length and the number of loading cycles. Table 3 shows retrofit effectiveness

(1) Step1

a) Recreating crack (Test Part C, D)

In test part C, strain changes irreversibly after N=1.1Mcycles loading without retrofitting method. Therefore Ns can be estimated at 1.1Mcycles. When N=1.9Mcycles, toe cracks detected (Nd(T)=1.9Mcycles), and N=2.9Mcycles, root crack appeared on the bead surface (Nd(R)=2.9Mcycles) as shown in Figure 11. As shown Figure 10, toe crack is hardly propagated, but root crack propagated rapidly after it appeared on the bead surface.

In test part D, When N=2.3Mcycles, toe cracks detected as shown in Figure 12 (Nd(T)=2.3Mcycles).

b) Preventive measure (Test Parts A, B)

In test parts A, B, strain changes very little comparing with test parts C, D, and no fatigue cracks were detected after 5.0Mcycles loading. Angle steel reinforcement using TRS can prevent fatigue cracking and extend fatigue crack initiation life more than 2.2 (5.0Mcycles / 2.3Mcycles) ~ 4.5 (5.0Mcycles / 1.1Mcycles) times as shown Table 3.

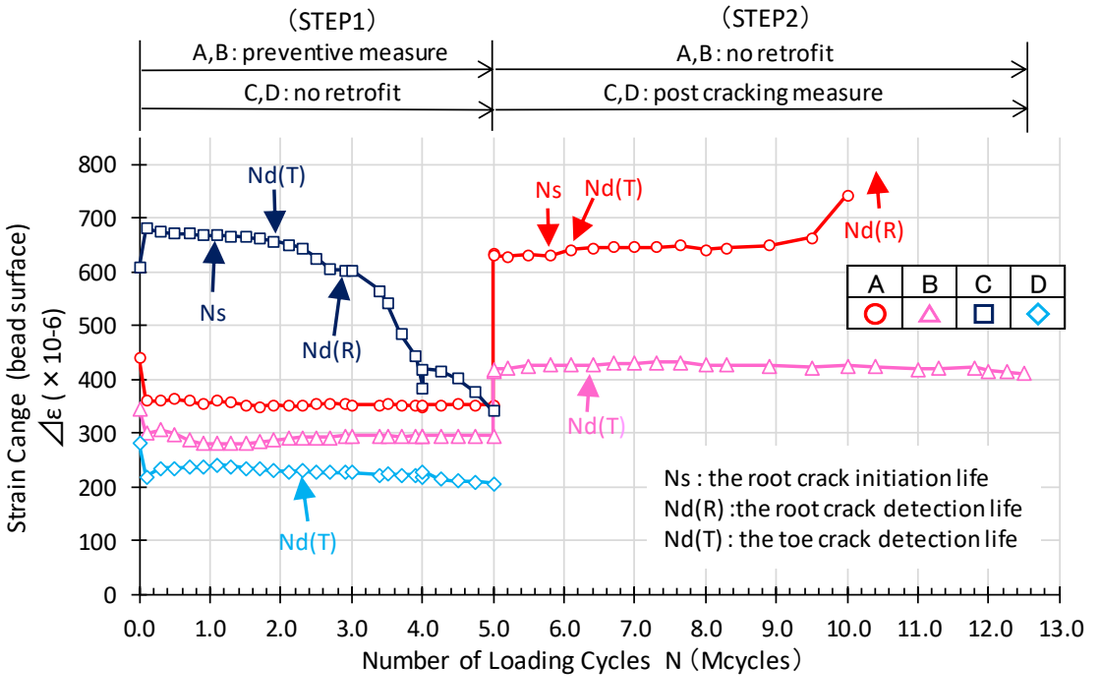


Figure 9. Relationship between strain and the number of loading cycles

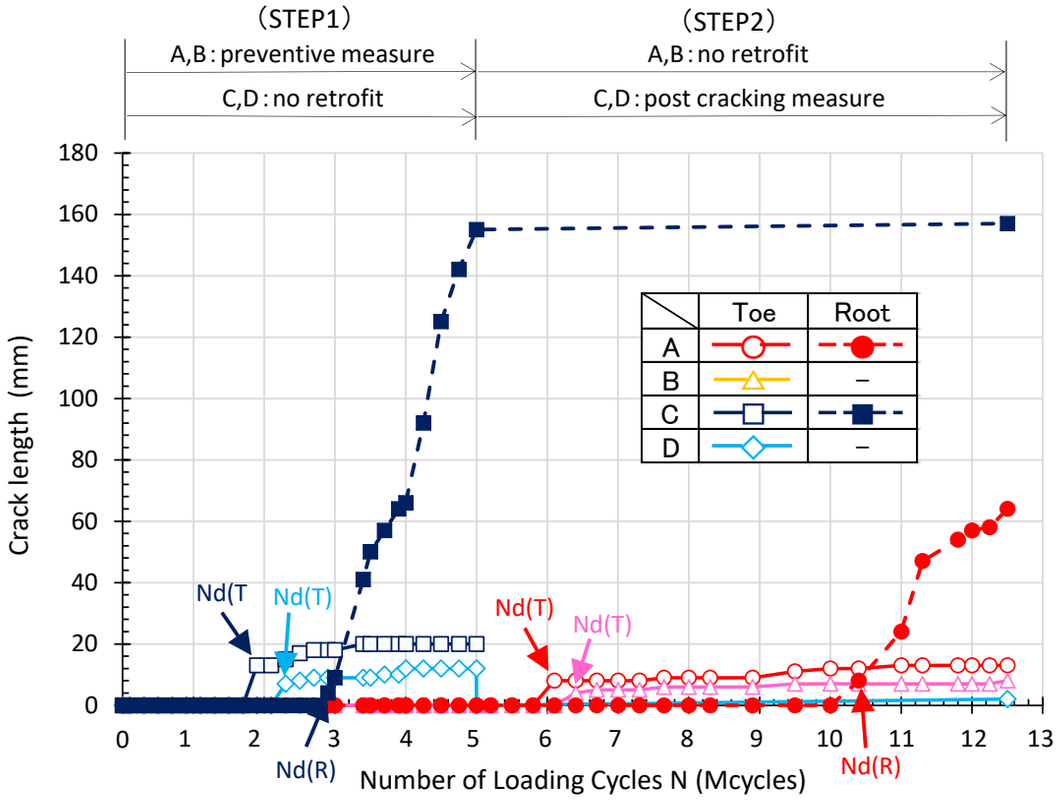
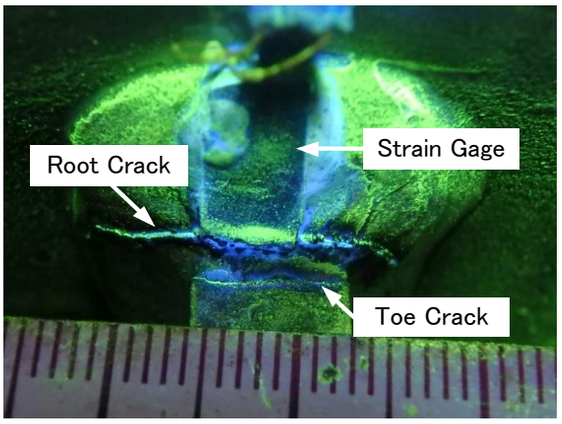


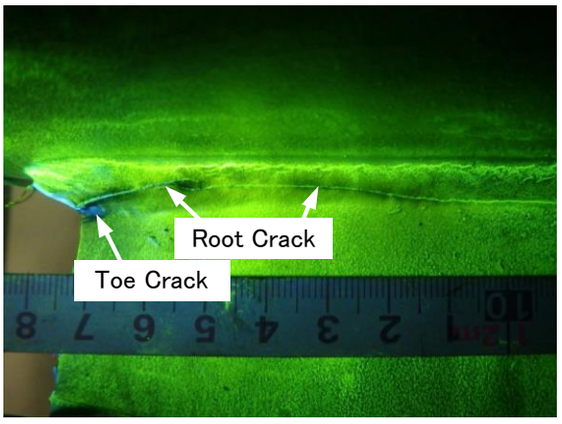
Figure 10. Relationship between crack length and the number of loading cycles

Table 3. Retrofit Effectiveness

test part	fatigue life		fatigue crack initiation life		crack growth rate		crack propagation life
	STEP1	STEP2	AB/C,D(①)	①/②	STEP1	STEP2	①/②
A	>500	80	–	>6.3times	–	–	–
B		140	–	>3.6times	–	–	–
C	110	>750	>4.5times	–	13mm/ 25Mcycles	2mm/ 750Mcycles	200times
D	230		>2.2times	–	7mm/ 20Mcycles	2mm/ 750Mcycles	130times



(a) Side view



(b) Face view

Figure 11. Propagated Toe Crack and Root Crack, Test Part C, N=5.0Mcycles

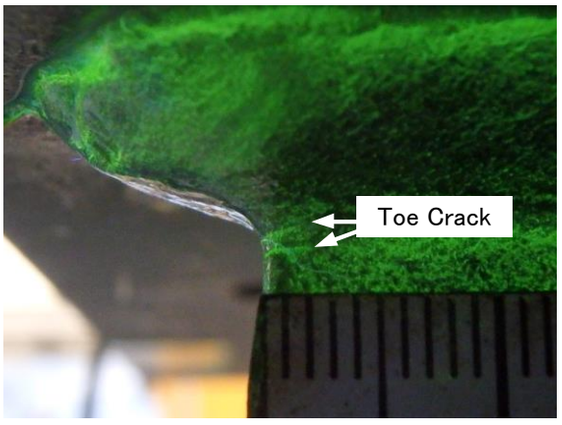


Figure 12. Propagated Toe Crack, Test Part D, N=5.0Mcycles

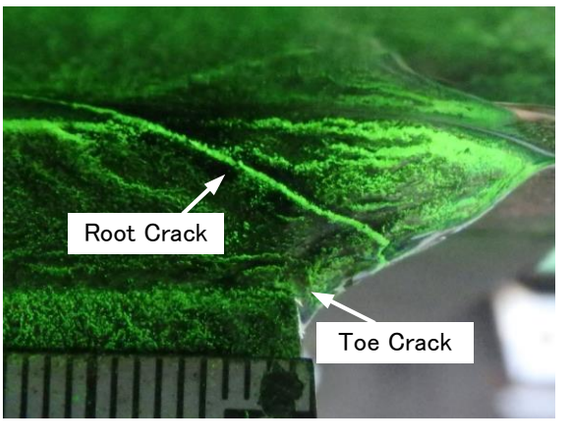


Figure 13. Propagated Toe Crack, Test Part A, N=7.5Mcycles

(2) Step2

a) Recreating crack (Test Parts A, B)

In test part A, strain changes after 0.8Mcycles loading. Therefore Ns can be estimated at 0.8Mcycles. When N=1.1Mcycles, toe cracks detected (Nd(T)=1.1Mcycles) and, when N=5.4Mcycles, root cracks appeared on the bead surface as shown in Figure 13 (Nd(R)=5.4Mcycles).

In test part D, when N=1.4Mcycles, root cracks appeared on the bead surface as shown in Figure 14 (Nd(R)=1.4Mcycles).

Angle steel reinforcement using TRS can prevent fatigue cracking and extend fatigue crack initiation life more than 3.6 (5.0Mcycles / 1.4Mcycles) ~ 6.3 (5.0Mcycles / 0.8Mcycles) times as shown Table 3.

b) Post cracking measure (Test Part C, D)

In test part C, crack tips were ground away by a bar grinder as shown Figure 15. After 7.5Mcycle loading, new root cracks with the length of 2mm was initiated from root tips as shown Figure 16. The retrofitting method can extend fatigue crack propagation life more than 200 (2mm/7.5Mcycles / 13mm/2.5Mcycles) times.

In test part D, crack tips were ground away by a bar grinder as shown Figure 17. After 7.5Mcycle loading, new toe crack with the length of 2mm was initiated as shown in Figure 18. The retrofitting method can extend fatigue crack propagation life more than 130 (2mm/7.5Mcycles / 7mm/20Mcycles) times.

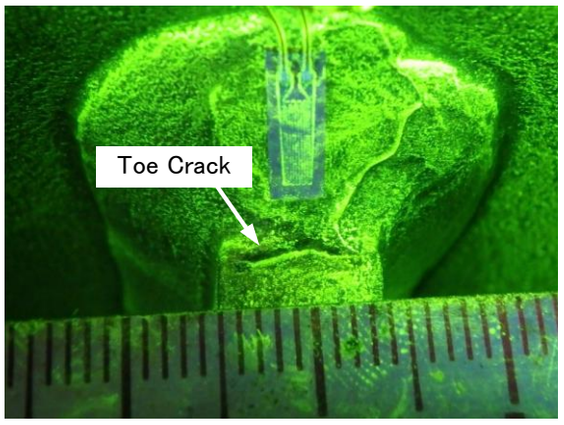


Figure 14. Propagated Toe Crack,
Test Part B, N=7.5Mcycles

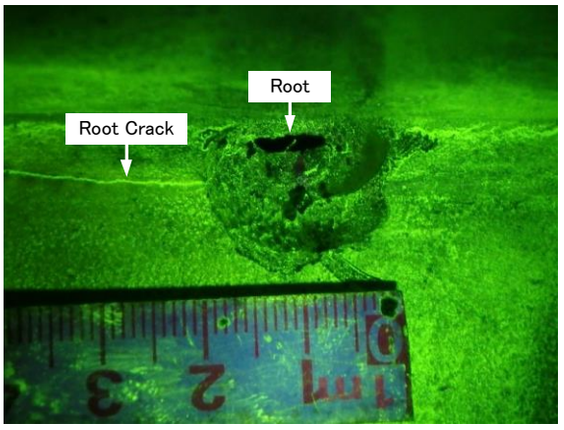


Figure 15. Grinding away crack tips,
Test Part C, N=5.0Mcycles

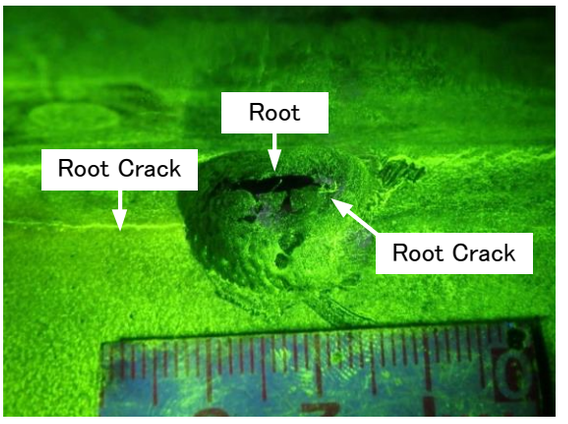


Figure 16. After post cracking measure,
Test Part C, N=7.5Mcycles

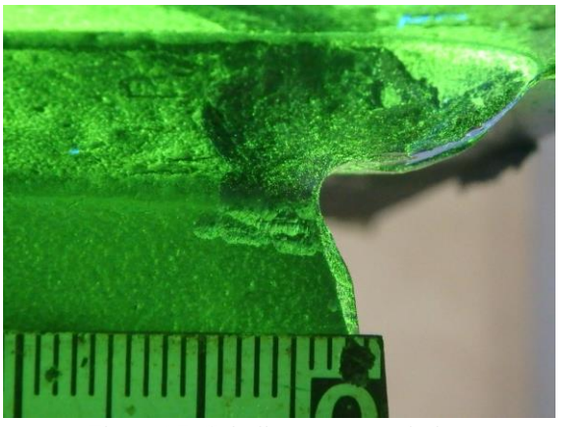


Figure 17. Grinding away crack tips,
Test Part D, N=5.0Mcycles

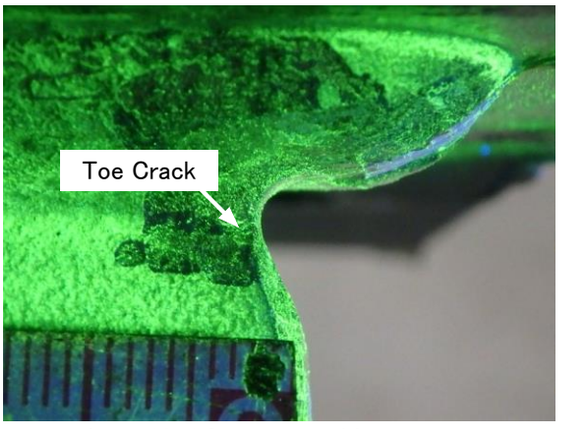


Figure 18. After post cracking measure,
Test Part D, N=7.5Mcycles

4 SUMMARY

The main conclusions obtained through this study are as follows,

(1) Alternative loading can reproduce the alternative stress at the upper end of web gap plate in the middle girder when vehicles run on the driving lane and passing lane alternatively.
(2) Angle steel reinforcement using TRS, can reduce the local stress concentration at the crack initiation point to about 50~60% of that before reinforcement.
(3) Without the retrofitting method, root crack is initiated after 0.8 to 1.1Mcycles loading and toe cracks are detected after 1.1 to 2.3Mcycles loading.
(4) As a preventive measure, the method can prevent fatigue cracking and extend fatigue crack initiation life more than 2.2~6.3 times.
(5) As a post cracking measure, angle steel reinforcement using TRS after grinding away crack tips can extend fatigue crack propagation life more than 100 times of that without the reinforcement.

5 PREFERENCES

Japan Road Association 1997. Fatigue of Steel Bridge

Hanshin Expressway Technology Center 2012. Fatigue Prevention of Steel Bridge in Hanshin Expressway (Three Revised Edition)

Kawashima, N., Fukuda, M., Morino, M., Sakano, M. 2008. Fatigue Strength Improvement for Cross Beam for Load Distribution in a Composite Plate Girder Bridge, *Proceedings of constructional steel, Vol.16, pp.471-478, 2008.11.*

Suzuki, H. 2015. Experimental Study on Strength of Joints Connected with Thread Forming Screws, *Journal of Structural Engineering Vol.61A, pp.614-626, 2015.3.*

Sakamoto, C., Sakano, M., Konishi, H., Koyama, M., 2017. Experimental Study on Retrofitting Method against Fatigue Cracking at the Upper End of Vertical Stiffener, *EUROSTEEL 2017, Copenhagen, Denmark*

Ichinose L. H., Koyama, M., Sakano, M., 2017. Fatigue prevention retrofit for connections of main girder to transverse beam or sway bracing in steel bridge, *EUROSTEEL 2017, Copenhagen, Denmark*

Mizokami, Y., Kamata, M., Kishi, Y., Sakano, M., 2017. A study on Repair Method using TRS for Fatigue Cracks in Orthotropic Steel Deck, *EUROSTEEL 2017, Copenhagen, Denmark*

Sakamoto, C., Sakano, M., Konishi, H., Koyama, M., 2017. Fatigue Behavior at the Upper End of Wep Gap Plate Under RC Slab, *ISSS 2017, Korea, Jeju*

Maintenance, Safety, Risk, Management and Life-Cycle Performance of Bridges – Powers, Frangopol, Al-Mahaidi & Caprani (Eds)
© 2018 Taylor & Francis Group, London, ISBN 978-1-138-73045-8

Adhesive and Bolting Reinforcement for Distortion-induced Fatigue of Steel Bridges

Y.Z. Wang, B. Cui, Q. Wang, L. Duan, C. S. Wang
Engineering Research Center for Large Highway Structure Safety of Ministry of Education, College of Highways, Chang'an University, Xi'an, China

ABSTRACT: Fatigue cracks in web gaps of steel girder bridges have serious effect on the fatigue life of bridges. This study is aimed at evaluating the effectiveness of adhesive and bolting single steel angle reinforcement technique, which means the stiffener is bolted with the steel angle and the flange plate is connected with the steel angle by structural adhesive. Full-scale fatigue tests were carried out to analyze the fatigue performance of weld toe details in the web gap region. Test results show that the stiffness of web gap region increase, and the out-of-plane distortion and the stress of the end of the web-to-stiffener weld toe and the web-to-flange weld toe decrease sharply after reinforcement, and fatigue cracks did not extend. The adhesive and bolting single steel angle reinforcement technique can effectively control distortion-induced fatigue cracking in web gaps of steel girder bridges without disruption to the concrete deck.

1 INTRODUCTION

In the multi-girder steel bridges, diaphragms or cross-bracing are connected with main girder by vertical stiffeners, which distribute loads transversely. In order to make construction much easier and avoid failures of fatigue details at vertical stiffener and tension flange welds, vertical stiffeners near tension flanges of the girder are cut short usually (Khalil et al. 1998). Therefore, several-centimeter web gaps are left between the vertical stiffener and the tension flange. Under the actions of the vehicle loads, the deflections of adjacent main girders are different, resulting in notable out-of-plane deformation at the web gap region, as shown in Figure 1. Approximately 90% of fatigue cracks in steel bridges were caused by out-of-plane distortion or secondary stresses at fatigue details (Connor and Fisher 2006), and the fatigue damage of the web gap in steel bridges is a typical fatigue problem induced by out-of-plane distortion.

Many studies have been carried out to investigate the reinforcement performance of the out-of-plane distortion-induced fatigue details at web gaps by field tests, finite element analysis, and experimental studies. Increasing the web gap length or connecting vertical stiffener with tensile flange can effectively reduce the stress concentration at web gaps (Fisher et al. 1990). Several alternatives were proved to be effective in reducing distortion-induced strains and stresses in the web gap region, such as connecting a plate between the stiffener and the top flange, and loosening of bolts connecting the cross-bracing to the stiffener (Shifferaw et al. 2013). Andrea proposed increasing the thickness of web gaps by bolting a steel angle to the flange and the web, and this method could increase the stiffness of web gaps and effectively reduced deformation and stress in web gap area (Andrea et al. 2001). Bolting angles with plate and stop-holes reinforcement methods were all effective in preventing the distortion of the web gap region, which drastically reduced the stress demands at the critical points. Slot repair was also used to repair the fatigue details, but results showed that this method had introduced higher magnitude fatigue stress in web gaps, which was believed to be the cause of crack re-initiation and propagation found in many repaired details (Zhao et al. 2007). The method of adhesive-bonded angles was effective to the cracks which did not propagate far away from web gaps and did not propagate perpendicularly to the direction of in-plane stress. In addition, this method was easy to operate on site, and also enhanced the fatigue performance of the detail. However, the risk induced by the adhesive failure due to the effect of the environment should be taken into account (Hu et al. 2006).

This paper carried out full-scale fatigue tests to investigate the effectiveness of the adhesive and bolting steel angle reinforcement, which means the stiffener is bolted with the steel angle and the flange

plate is connected with the steel angle by structural adhesive. Fatigue tests of a full-scale specimen was carried out to analyze the change of the out-of-plane distortion of web gap and the stresses of weld toe details of the end of the web-to-stiffener weld toe and the web-to-flange weld toe with the cyclic loading. The test results show that the stiffness of web gap region increase, and the out-of-plane deformation and the stress of the end of the web-to-stiffener weld toe and the web-to-flange weld toe decrease sharply after reinforcement, and fatigue cracks did not propagate. The adhesive and bolting single steel angle reinforcement technique can effectively control distortion-induced fatigue cracking in web gaps of steel girder bridges without disruption to the concrete deck. Adhesive and bolting reinforcement technique dose not introduce secondary stress into the fatigue sensitive details, and the process of the reinforcement has no negative influence of the fatigue sensitive details of web gaps. Compared with adhesive single steel angle reinforcement technique, the adhesive and bolting reinforcement technique avoid the falling of the steel angle when the structural adhesive failed because of external environment.

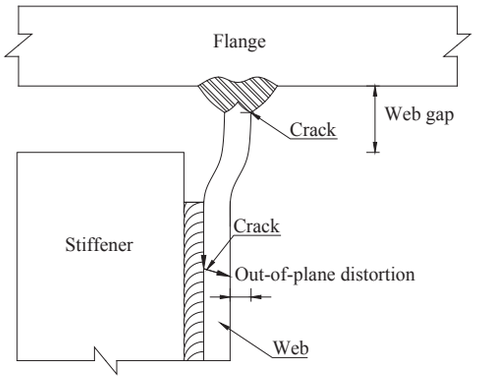
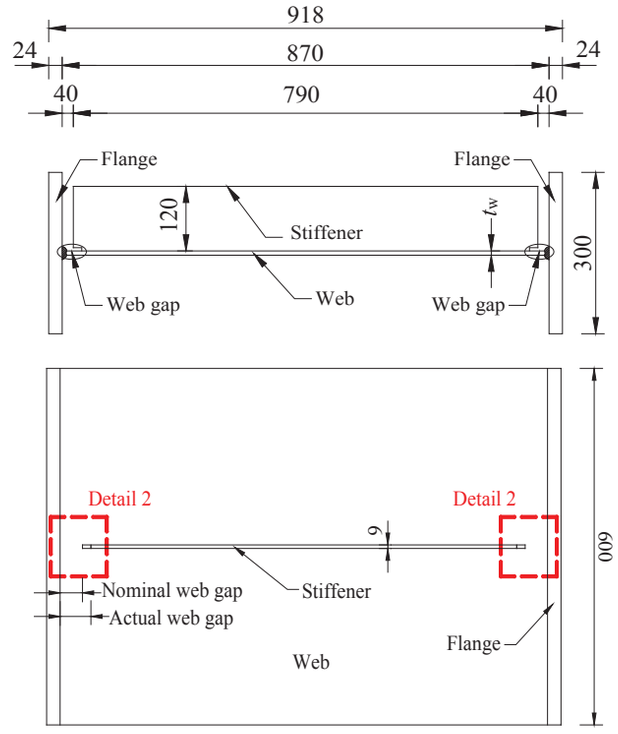


Figure 1. Out-of-plane distortion at web gaps

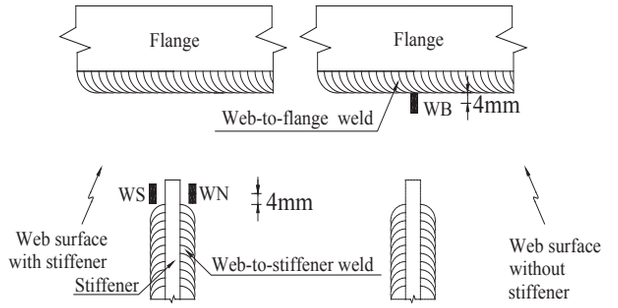
2 FATIGUE TEST PROGRAM

2.1 *Test Program*

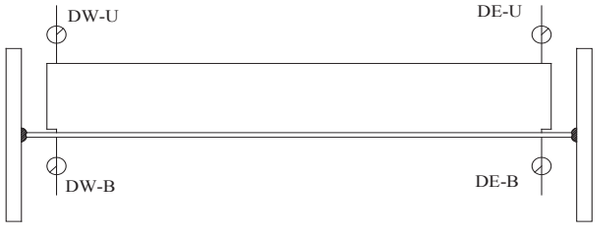
The full-scale specimen was I-shaped steel girders, comprised of flange, web and stiffener. The specimen was fabricated by steel grade of Q345qC with normal yield stress of 345MPa, in which q represents steel used in bridges and C means toughness level. The dimensions of the test specimen was determined to reflect the actual fatigue performance of web gaps effectively. Finite element analytical study results indicated that the length of the specimen had negligible effect on out-of-plane distortion and stress state of web gaps (Wang & Cheng 2010). Thus, 600mm long full-scale specimen was adopted, considering fixing and loading condition as well as fatigue test effectiveness. Figure 2 shows the dimensions of the specimen as well as the displacement and strain gauges arrangement. The dimensions of flange, web and vertical stiffener are 600mm × 300mm × 24mm, 870mm × 600mm×8mm, and 790mm × 120mm × 6mm respectively. The nominal web gap is 40mm and the actual web gap is 55mm. Strain gauges were arranged at web gap detail according finite element analysis results.



(a) Specimen dimensions



(b) Locations of strain gages



(c) Locations of dial indicators

Figure 2. Test Specimen (Unit: mm)

A 100kN capacity MTS servo hydraulic actuator is adopted to apply cyclic load (Fig. 3). Eight bolt holes with diameter of 24mm were drilled on two flanges separately, and four bolt holes with diameter

of 24mm were drilled on vertical stiffeners. Cyclic loads were applied by the hydraulic actuator to the stiffener, which simulates the actual acting lateral forces on the stiffener in steel girder bridge (Wang et al. 2014a, b, c). The cyclic load was directly applied on the top flange of the loading beam, and the loading beam was attached to a pair of angles, through which pulling on the vertical stiffener. The flanges were bolted to the fixing device. Consequently, the cyclic loads acted on the connection of vertical stiffener and the steel angles, causing the out-of-plane distortion in web gaps.

The load range of the specimen was determined according to the out-of-plane distortion between 0.2mm and 0.4mm. Then, loading frequency was determined according to the stability of the whole loading setups. Static tests were performed every 100,000 cycles during the process of cyclic loading, in order to record the crack length, out-of-plane distortion, and stress levels. The displacement of out-of-plane distortion and stresses of the test specimen in web gaps were monitored with a dynamic data acquisition system during the fatigue tests. This fatigue loading stopped when the propagation of fatigue cracks affected the stability of test setup.

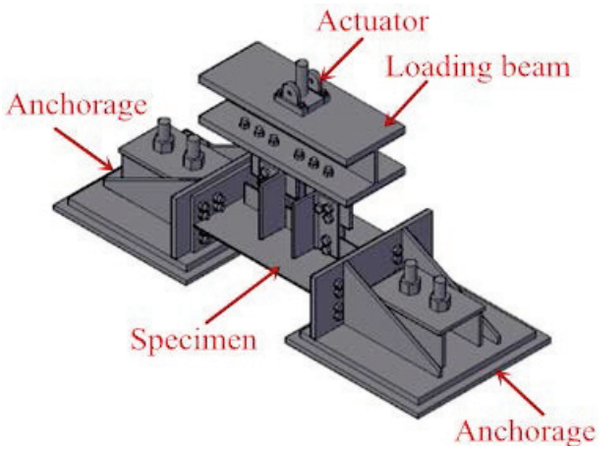


Figure 3. Loading equipment of fatigue test

2.2 *Adhesive and Bolting Steel angle Reinforcement Procedure*

Adhesive and bolting steel angle reinforcement used the mix-linked steel angle that one leg is bolted with the stiffener and the other leg is adhesive with the flange. Compared with the bolting steel angle reinforcement, this method does not need to remove the local part of the concrete deck where out-of-plane distortion induced-fatigue cracks initiate from the top flange at the web gap region. In addition, compared with the adhesive steel angle reinforcement, adhesive and bolting steel angle reinforcement avoids the falling of the steel angle, which is dangerous to the pedestrian and vehicles. Full scale fatigue tests were carried out to verify the feasibility and the practicability of the adhesive and bolting steel angle reinforcement.



(a) Nap the steel angle



(b) Nap steel girder surface



(c) Bolt the steel angle and the stiffener



(d) Finish reinforcement

Figure 4. Flowchart of reinforcement

The procedure of adhesive and bolting steel angle reinforcement is a combination of the two reinforcement methods (Fig. 4). The side which uses the adhesive is processed as the adhesive steel angle reinforcement, and the other side is processed as the bolting steel angle reinforcement. The first step is to drill holes at the specimen and the reinforcement steel angle. Then, the position of the bonding steel angle at the specimen and the steel angle were napped to increase the bonding performance of the structure adhesive. After mixing the structure adhesive, the steel angle was bonded with the flange of the specimen. The next step is bolting the steel angle with the stiffener. Finally, the reinforced specimen was installed in the test setups.

3 FATIGUE TEST RESULTS

Before the reinforcement, fatigue tests were carried out on the specimen for fatigue pre-cracking. Table 1 shows the number of cycles and the cyclic loading range before and after the reinforcement of the specimen. The finite element analysis of the actual bridges indicated that after the reinforcement of the fatigue details where fatigue cracks initiated in the web gap region, the magnitude of the load that the cross-bracing transmitted to the vertical stiffeners at the web increased due to the improvement of the local stiffness of the web gap. Therefore, the cyclic loading range after the reinforcement is larger than that before the reinforcement.

Table 1. Fatigue test results

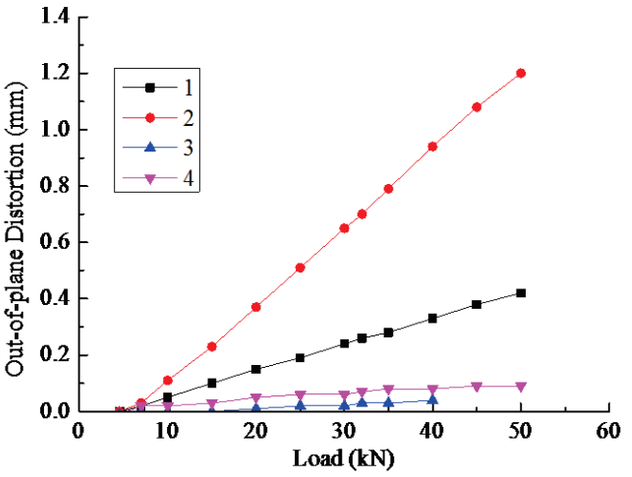
Specimen	Number of cycles before reinforcement	Loading range before reinforcement	Total Number of cycles	Loading range after reinforcement
	$\times 10^6$	kN	$\times 10^6$	kN
1	10.62	7-32	12.81	7-37/7-47

The loading cycles of specimen 1 after reinforcement was 2.19 million. In the former 1.6 million cycles, the loading range was 7-37kN. And the loading range was 7-47kN after 1.60 million cycles. After the reinforcement, the existing fatigue cracks at the web gap stopped propagating, and no new crack was observed at the reinforcement steel angle and the web gap region.

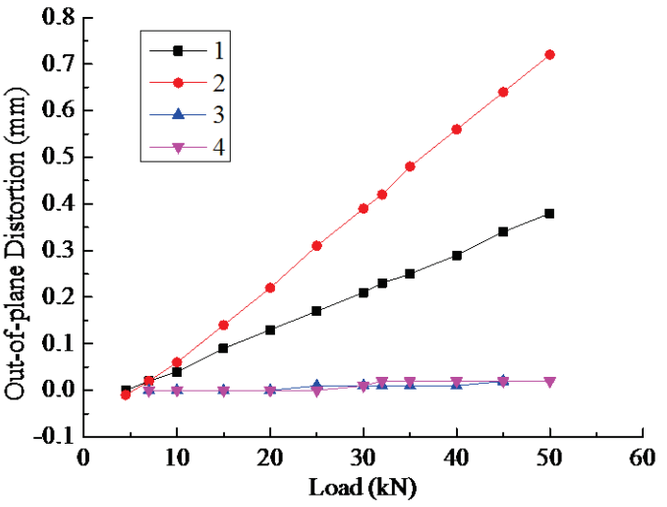
4 OUT-OF-PLANE DISTORTION ANALYSIS

4.1 *Out-of-plane Distortion-Load*

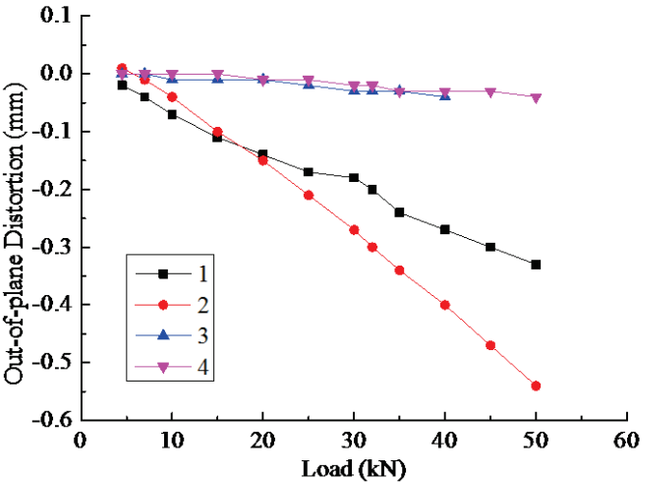
Figure 5 shows the out-of-plane distortion of four dial indicators of the specimen under the action of different load. Curve 1 shows the out-of-plane distortion measured in the static test before cyclic loading, so as to study of the fatigue mechanics of the web gap. And at that time the number of loading cycle is 0. Curve 2 shows the out-of-plane distortion measured in the static test after fatigue pre-cracking process and before the reinforcement. Curve 3 shows the out-of-plane distortion measured in the static test after the reinforcement before the cyclic loading. Curve 4 shows the out-of-plane distortion measured in the static test for the last time at the end of the reinforcement test.



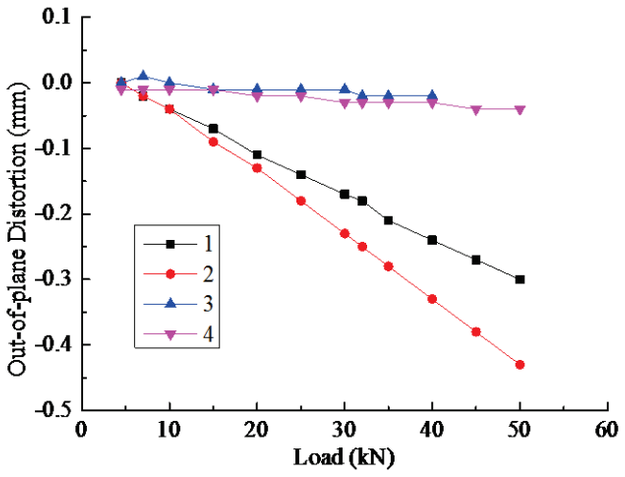
(a) DW-U



(b) DE-U



(c) DW-B



(d) DE-B

Figure 5. Out-of-plane distortion-load

With the number of the cycles increasing, fatigue cracks initiated and propagated at the web gaps, and the out-of-plane distortion of the web gap increased. After the reinforcement, the out-of-plane distortion of the web gap significantly decreased, and the increasing speed of the out-of-plane distortion is close to that of the specimen with no fatigue damage. At the end of the fatigue test, the out-of-plane distortion at web gap was far less than that of the specimen after the fatigue cracks occurred, which indicated that the adhesive and bolting single angle reinforcement was effective to decrease the out-of-plane distortion, thus improving the anti-fatigue property of the fatigue details at the web gaps.

4.2 *Out-of-plane Distortion-Number of Cycles*

During the process of the fatigue tests, the dial indicators DW-B、DE-B、DW-U and DE-U shown in Figure 2 monitored the out-of-plane distortion range at the web gap region. Figure 6 shows the specific out-of-plane distortion curves before and after the reinforcement.

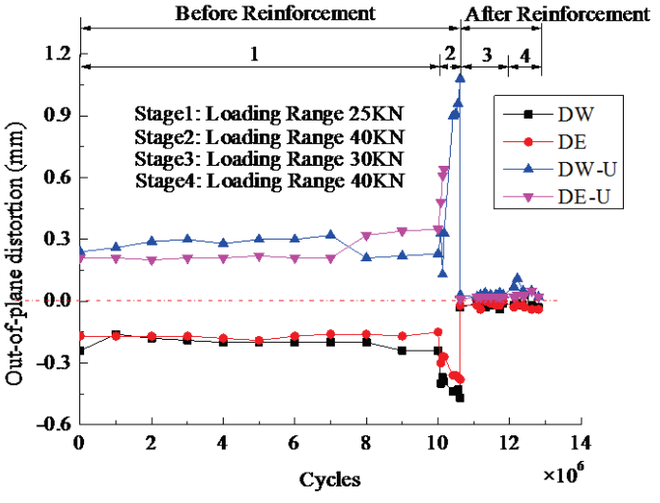


Figure 6. Out-of-plane distortion-number of cycles

Before and after the reinforcement of the specimen, the change of out-of-plane distortion range at the web gaps was recorded in Table 2 in detail. The out-of-plane distortion ①, ②, ③ and ④ in the Table 2 are corresponding to the curve 1, 2, 3 and 4 mentioned above respectively.

Table 2. Comparing of out-of-plane distortion

Dial indicator	Out-of-plane distortion				
	①	②	③	④	③/②
	mm	mm	mm	mm	
DW-B	-0.18	-0.5	-0.03	-0.03	6.0%
DE-B	-0.18	-0.8	-0.02	-0.04	2.5%
DW-U	0.26	1.13	0.03	0.02	2.7%
DE-U	0.23	0.68	0.01	0.02	1.5%

According to Figure 6 and Table 2, the out-of-plane distortion range of the web gap after the reinforcement decreased to 1.5%～6.0% of that before the reinforcement. The reduction of the out-of-plane distortion range indicated that this reinforcement method effectively improved the stiffness and the fatigue performance of the web gap.

5 STRESS ANALYSIS

The stresses at the web-to-stiffener weld toes and the web-to-flange weld toes at the web gap region were measured during the fatigue tests before and after the reinforcement, and could then be used to evaluate the fatigue strength of such details.

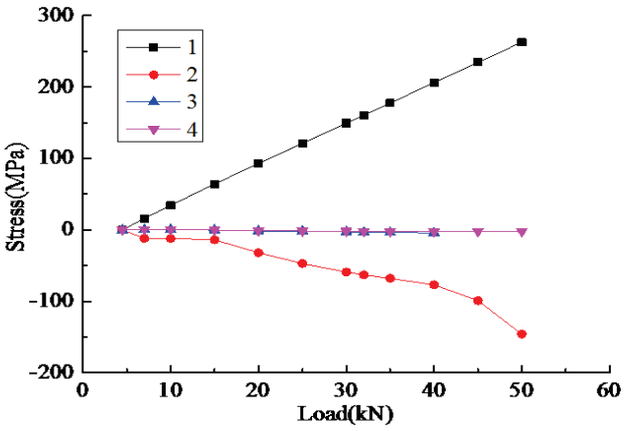
5.1 *Stress-Load Analysis*

5.1.1 *Stress of Web-to-stiffener Weld Toe-Load*

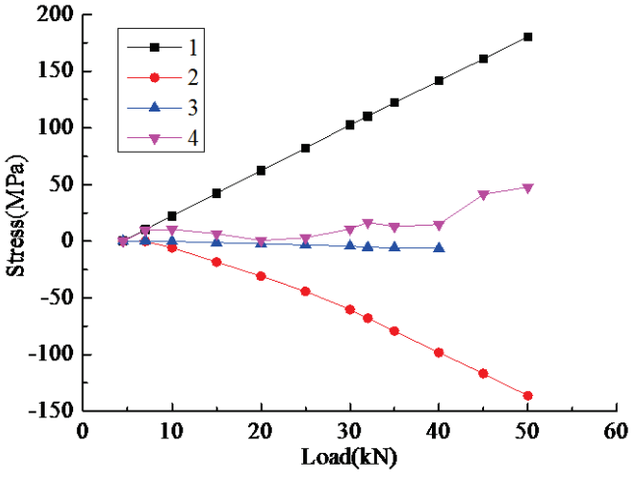
Figure 7 shows the stresses of three measuring points of the web-to-stiffener weld toe of the specimen under the action of different load. Curve 1 shows the stress of the web-to-stiffener weld toe measured in the static test before cyclic loading, so as to study of the fatigue mechanics of the web gap. And at that time the number of loading cycle is 0. Curve 2 shows the stress of the web-to-stiffener weld toe measured in the static test after fatigue precracking process and before the reinforcement. Curve 3 shows the stress of the web-to-stiffener weld toe measured in the static test after the reinforcement before the cyclic loading. Curve 4 shows the stress of the web-to-stiffener weld toe measured in the static test for the last time at the end of the reinforcement test.

Comparison of the stresses of curve 2 and curve 3 indicated that the adhesive and bolting steel angle reinforcement decreased the stress of the web-to-stiffener weld toe to a large degree. A conclusion can be draw by comparing curve 3 with curve 4 that at the end of the cyclic loading after the reinforce-

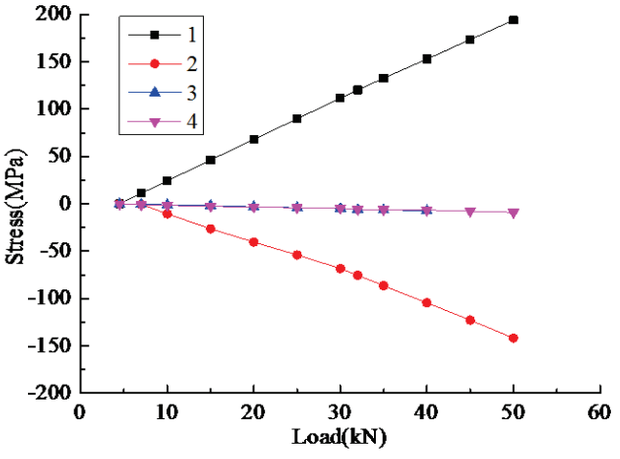
ment, the stress of the web-to-stiffener weld toe hardly changed from that at the beginning of the test, which indicated that there was no fatigue damage accumulated at the web gap after the reinforcement, and also indicated the effectiveness of this adhesive and bolting steel angle reinforcement method.



(a) Measuring point WS



(b) Measuring point ES

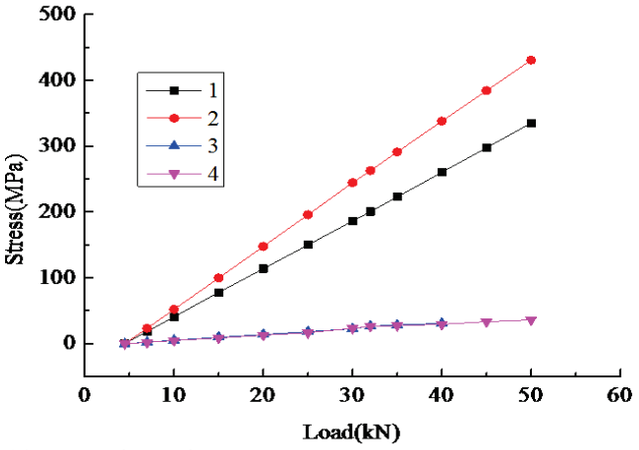


(c) Measuring point EN

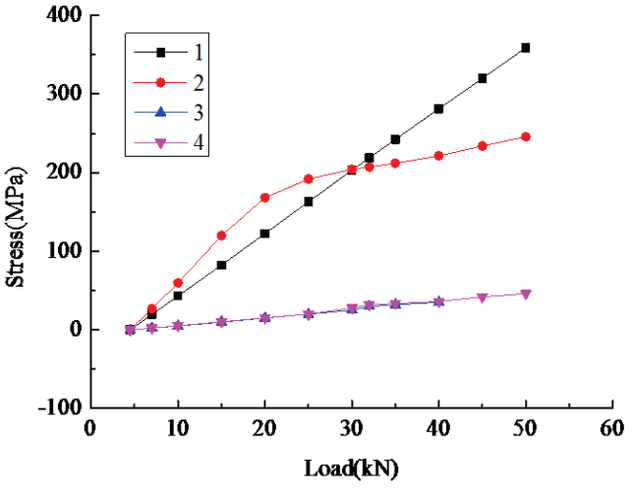
Figure 7. Stress of web-to-stiffener weld toe-load

5.1.2 *Stress of Web-to-flange Weld Toe-Load*

Figure 8 shows the stresses of two measuring points of the web-to-flange weld toe of the specimen under the action of different load. The stages that curve 1, 2, 3, 4 corresponding to are the same with the curves of stress of web-to-stiffener weld toe.



(a) Measuring point WB



(b) Measuring point EB

Figure 8. Stress of Web-to-flange Weld Toe-Load

As shown in the Figure 8, curve 2 indicated that the stress of the cracked details at the web-to-flange weld toe decreased to a lower level. Comparing curve 2 and curve 3, as for the cracking and non-cracking web-to-flange weld toe, the stresses of the web-to-flange weld toe were close to zero after reinforcement. Comparing curve 3 with curve 4, the stresses of the web-to-flange weld toe was also close to zero at the end of cyclic loading after reinforcement, which indicated that there was no fatigue damage accumulated at the retrofit web gap, and also indicated the effectiveness of the adhesive and bolting steel angle reinforcement.

5.2 *Stress-Number of Cycles Analysis*

5.2.1 *Stress of Web-to-stiffener Weld Toe-Number of Cycles*

Figure 9 shows the measurements of the web-to-stiffener weld toes for the specimen. The measured stresses at the end of the web-to-stiffener weld toe

before and after the reinforcement indicated that the adhesive and bolting single angle reinforcement decreased the stress of the web-to-stiffener weld toe to a large degree. After the reinforcement, the stresses of the web-to-stiffener weld toes hardly changed, indicating that there was no fatigue damage accumulated at the web gap after the reinforcement.

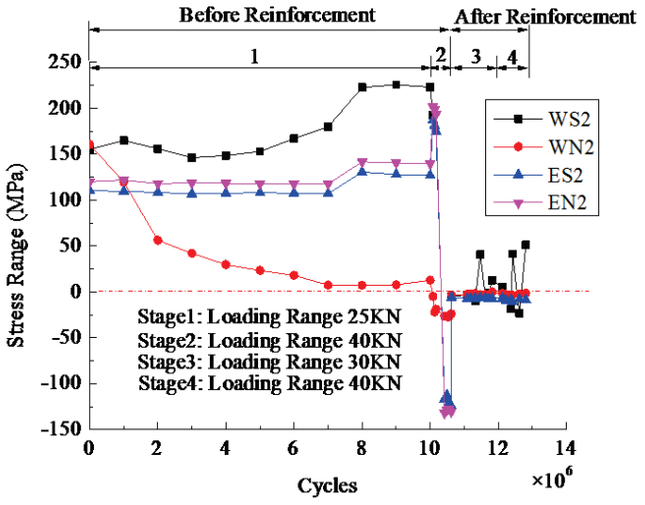


Figure 9. Stresses of web-to-stiffener weld toes

5.2.2 *Stress of Web-to-flange Weld Toe-Number of Cycles*

Figure 10 shows the measurements of the web-to-flange weld toes for the specimen. The stresses of the web-to-flange weld toes decreased to a lower level and close to zero after reinforcement, which indicated that there was no fatigue damage accumulated in the web gap region.

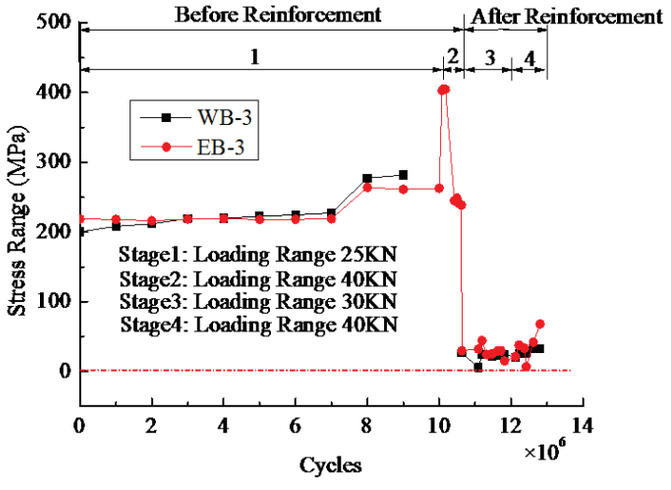


Figure 10. Stresses of web-to-flange weld toes

Before and after the reinforcement of the specimen, the stress ranges of the web-to- stiffener weld toe and the web-to-flange weld toe were recorded in Table 3 in detail. The stress range ①, ②, ③ and ④ in the Table 3 are corresponding to the curve 1, 2, 3 and 4 mentioned above respectively.

According to Table 3, the stress range of the web gap after the reinforcement decreased to 2.7%～14.8% of that before the reinforcement. After the reinforcement, the stresses of the web-to-stiffener weld toes as well as the web-to-flange weld toes reduced below 30MPa after reinforcement. Therefore, the adhesive and bolting steel angle reinforcement significantly improved the stiffness of the web gap region, reduced the stresses of the fatigue details.

Table 3. Comparing of stresses of web-to-stiffener weld toes and web-to-flange weld toes

Measuring point		Stress range ① MPa	② MPa	③ MPa	④ MPa	③/①
Web-to-stiffener weld toe	WS	150	-20	-4	-1	2.7%
	ES	102	-117	-5	51	4.9%
	EN	111	-123	-6	-8	4.8%
Web-to-flange weld toe	WB-3	187	261	27	33	5.4%
	EB-3	203	234	30	68	14.8%

6 CONCLUSIONS

Full-scale fatigue tests were carried out to investigate the availability, feasibility and practicability of the adhesive and bolting steel angle reinforcement. Based on the experimental study results, the following conclusions may be drawn:

(1) Adhesive and bolting steel angle reinforcement does not need to remove the concrete deck plate, and introduce little damage to the original structure.

(2) Adhesive and bolting steel angle reinforcement improves the stiffness of the web gap region. After the reinforcement, the out-of-plane distortion at the web gap region was reduced, and the stresses of the web-to-stiffener weld toe and the web-to-flange weld toe was decreased.

(3) After the web gap region was reinforced by the adhesive and bolting steel angle, the existing fatigue cracks at the web gap stopped propagating and there was no new crack initiating at the steel angle and the web gap.

(4) Compared with the hot reinforcement method, the adhesive and bolting steel angle reinforcement will not introduce the second stress into the fatigue details in the web gap region. The reinforcement process has no negative influence on the fatigue sensitive details in the web gap region.

(5) Adhesive and bolting steel angle reinforcement method has good safety, due to the steel angle will not fall when the structure adhesive fail because of the effect of the environment.

7 ACKNOWLEDGEMENT

The authors gratefully acknowledge the financial su pport provided by National Natural Science Foundat

ion of China (Grant 51578073, 51078039), the Major State Basic Research Development program of China (973 Program) Subprogram (Grant 2015CB057703), and the Special Fund for Basic Scientific Research of Central Colleges of the P.R. China, Chang'an University (Grants 10821153501, 310821153401 and 310821153314).

8 REFERENCES

Andrea, M. D. et al. 2001. *Behaviour and Rehabilitation of Distortion–Induced Fatigue Cracks in Bridge Girders*. Edmonton: University of Alberta.

Connor, R. J. & Fisher, J. W. 2006. Identifying effective and ineffective retrofits for distortion fatigue cracking in steel bridges using field instrumentation. *Journal of Bridge Engineering* 11(6): 745-752.

Fisher, J. W. et al. 1990. *Distortion-Induced Fatigue Cracking in Steel Bridges*. Washington D.C.: Transportation Research Board.

Hu, Y. Y. et al. 2006. *Use of Adhesives to Retrofit Out-of-Plane Distortion-Induced Fatigue Cracks.* Minneapolis: University of Minnesota.

Khalil, A. et al. 1998. Retrofit solution for out-of-plane distortion of X-type diaphragm bridges. *Transportation Conference, Ames, 19-20 August 1998*. Ames.

Shifferaw, Y. & Fanous, F. S. 2013. Field testing and finite element analysis of steel bridge retrofits for distortion-induced fatigue. *Engineering Structures* 49 (2013): 385-395.

Wang, C. S. et al. 2014a. Performance-based retrofitting methods for distortion-induced fatigue in steel girder bridges, *Proceeding of The 7th International Conference on Bridge Maintenance, Safety and Management*. London: Taylor & Francis.

Wang. C. S. et al. 2014b. Out-of-plane distortion fatigue test loading setups of vertical stiffener and flange web gap. CN: 201420361457.0.

Wang. C. S. et al. 2014c. Cold reinforcement structure for out-of-plane distortion fatigue in steel bridges. CN: 201420360073.7.

Wang, C. S. & Cheng, F. 2010. Out-of-plane distortional fatigue stress analysis at web gaps of steel bridges. *Journal of Architecture and Civil Engineering* 27(1): 65-72.

Zhao, Y. & Roddis, W. M. K. 2007. Fatigue behaviour and retrofit investigation of distortion-induced web gap cracking. *Journal of Bridge Engineering* 12(6): 735-745.

Maintenance, Safety, Risk, Management and Life-Cycle Performance of Bridges – Powers, Frangopol, Al-Mahaidi & Caprani (Eds)
© 2018 Taylor & Francis Group, London, ISBN 978-1-138-73045-8

Vibration Study of Train Passing Bridge with Small Radius and Reverse Curve

Y.M. Song
Shanghai University of Engineering Science, Shanghai, China
D.J. Wu & J. Zhang
Tongji University, Shanghai, China

ABSTRACT: In this paper, the vibration study for a newly-built curved railway bridge with small radius and reverse curve was performed. The motion equations of the train passing a bridge were established in moving coordinate systems, where coordinate transformation was used to build the geometric relationship between the train and the bridge. Wheel-rail interaction was simulated based on the modified Kalker linear creep theory. 20 field vibration tests for different operating conditions of the passing train were conducted, followed by the analyses on vibration responses of the test bridge, including characteristics such as natural frequency, acceleration, velocity and displacement. The operating performance for the train passing this small radius reverse curve bridge was evaluated according to the codes, and reasonable suggestions are proposed accordingly. Comparisons are presented between the theoretical analysis and the test results for the key dynamic characteristics, and the reasonable dynamic stiffness for such bridges is discussed.

1 INTRODUCTION

The vibration studies of train passing bridges have attracted much attention for more than one and half centuries. In recent years, due to the application of high-performance materials and the advances in high-speed and heavy-load railways, more slender bridges have been built worldwide, and the vehicle-induced vibration is much more crucial to the performance of such bridges (Au et al., 2001).

The analytical methods for vehicle-induced vibration on bridges are rather meaningful for parameter and mechanism studies (Fryba, 2013), while the finite element (FE) method is more applicable to bridges with complex geometries and components. The numerical models can be optimized and validated by field tests. The natural frequencies, modal damping ratio and mass of the bridge can be used to calibrate the bridge model (Zambrano et al., 2008), while the dynamic tests such as free field vibrations and track responses can be employed to evaluate the reliability of the model (Antolín et al., 2013). In recent years, more focuses were attached on the optimization of calculation efficiency and modelling accuracy. Zambrano et al. (2008) proposed a time-saving method by simplifying both the numerical model and the calculation method. Antolín et al. (2013) considered the nonlinear wheel–rail contact model, and significantly smaller force responses were obtained using this more realistic method due to the incorporation of frictional slip conditions.

In contrast to the extensive studies focusing on the straight bridges, only a few studies were conducted for the dynamic responses of horizontally curved bridges subjected to passing trains. Galdos et al. (1993) analyzed the dynamic responses of a horizontally curved box bridge using the step-by-step direct integration method. A numerical program was developed by Shan (1999) to analyze the dynamic responses of both the curved bridge and the vehicle under various speed. Yang et al. (2001) presented an analytic approach for a horizontal curved beam subjected to both the vertical and the horizontal moving loads. Focusing on the coupled vibration of the train passing the small radius curved bridge. Song et al. (2013) studied the wheel-rail contact force and creep force by considering non-jump and jump cases based on the Hertz's theory of elastic contact and Kalker's creep theory of wheel-rail interaction.

In this paper, the vibration responses of the train passing a bridge with small radius and reverse curve are studied. The transformation matrix between the global coordinate system and the local coordinate system considering curve super-elevation angle was derived, and the differential equations of vehicle-bridge coupled vibration were established by using the mode superposition method. The finite element method was also employed to build the numerical model for the test bridge. Field tests were conducted

on the test bridge and the results were compared to the preliminary theoretical analyses. Given the observed discrepancy, the possible reasons are discussed and the useful suggestions for dynamic stiffness are proposed.

2 COUPLING VIBRATION THEORY FOR THE TRAIN PASSING A CURVED BRIDGE

2.1 *Differential Equations of Motion*

The differential equations of motion for train passing a curved bridge are established as:

$$\begin{aligned}&[M_{\mathrm{v}}]\{\ddot{x}_{\mathrm{v}}\}+[C_{\mathrm{v}}]\{\dot{x}_{\mathrm{v}}\}+[K_{\mathrm{v}}]\{x_{\mathrm{v}}\}\\&=\{F_{\mathrm{vn}}\}+\{F_{\mathrm{vc}}\}+\{F_{\mathrm{ve}}\}+\{F_{\mathrm{va}}\}\end{aligned}\tag{1}$$

where $[M_{\mathrm{v}}]$ is the mass matrix of vehicles, $[C_{\mathrm{v}}]$ is the damping matrix of vehicles, $[K_{\mathrm{v}}]$ is the stiffness matrix of vehicles, $\{x_{\mathrm{v}}\}$ is the vehicle displacement vector, $\{\dot{x}_{\mathrm{v}}\}$ is the vehicle velocity vector, $\{\ddot{x}_{\mathrm{v}}\}$ is the vehicle acceleration vector. $\{F_{\mathrm{vn}}\}$ is the internal force vector including non-proportional damping force and other nonlinear internal force, $\{F_{\mathrm{vc}}\}$ is the wheel rail excitation force vector, $\{F_{\mathrm{ve}}\}$ is the centrifugal force and super high component vector, $\{F_{\mathrm{va}}\}$ is the additional inertia force and inertia moment while train curving bridge.

Modal superposition method is used to solve the equations of motion. The relationship between physical coordinates and modal coordinates for the Nth mode is as follows:

$$\{x_{\mathrm{v}}\}_N=[F_{\mathrm{v}}]_N\{q_{\mathrm{v}}\}_N\tag{2}$$

where $[F_{\mathrm{v}}]_N$ are normalized feature vectors. The train motion equation in modal coordinates is as follows:

$$\{\ddot{q}_{\mathrm{v}}\}+2[x_{\mathrm{v}}][w_{\mathrm{v}}]\{\dot{q}_{\mathrm{v}}\}+[w_{\mathrm{v}}^2]\{q_{\mathrm{v}}\}=[F_{\mathrm{v}}]^T[f_{\mathrm{v}}]\tag{3}$$

where $\{q\}$ is the modal coordinate of vehicle or bridge, $[x]$ is the modal damping matrix, $[w^2]$ is the circular frequency matrix, $[F_{\mathrm{v}}]^T$ is the normalizing modal matrix, $\{f\}$ are the vectors of external forces and pseudo internal forces.

2.2 *Moving Coordinate System and Coordinate Transformation*

The coupling relationship of wheel-rail-bridge can be determined by means of moving coordinate system and coordinate transformation when train passing the curved bridge. Each wheel moving coordinate system was established according to the right-hand rule as shown in Figure 1. Its origin is along the track center line, the coordinate x is along tangent direction of the curve, the coordinate y is in the upward vertical plane of the rail, and the coordinate z is along normal direction of curve.

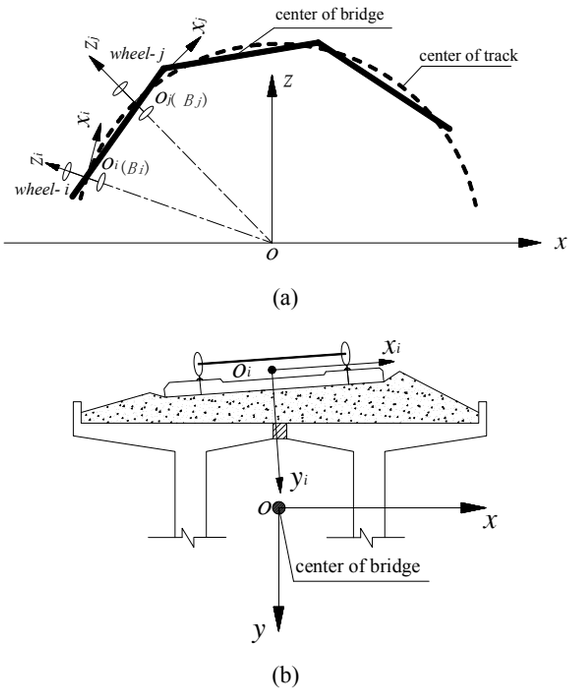


Figure 1. Moving coordinate of vehicle-curved bridge system: (a) horizontal plane, (b) vertical plane.

Assume that train moves forward at constant speed v and the mileage is S_i at time t, the coordinates (x_{Oi}, y_{Oi}, z_{Oi}) in the global coordinate system $oxyz$ can be obtained according to the mileage S_i. In the meantime, the angle α_{i} between tangent of curve and ox axis, the curvature R_{i}, and the angle of super-elevation γ_{i} could all be easily obtained. Therefore, the moving coordinates systems $o_{\mathrm{i}}x_{\mathrm{i}}y_{\mathrm{i}}z_{\mathrm{i}}$ and $o_{\mathrm{j}}x_{\mathrm{j}}y_{\mathrm{j}}z_{\mathrm{j}}$ are determined. In addition, assume that B_i (x_{Bi}, y_{Bi}, z_{Bi}) is a finite element node of bridge's center line, when node B_i coincides with the point of intersection that track center line projects on bridge's center line, the n-order vibration mode displacement vector of node B_i can be transformed into the coordinate system $o_{\mathrm{i}}x_{\mathrm{i}}y_{\mathrm{i}}z_{\mathrm{i}}$, that is:

$$\{\phi\}_{\mathrm{i,B}}=[\lambda]\{\phi\}\tag{4}$$

where $\{\square\}_{\mathrm{i,B}}$ is the vibration mode displacement vector in moving coordinate system, $\{\square\}$ is the vibration mode displacement vector in the global coordinate system, $[\lambda]$ is the coordinate transformation matrix. $[\lambda]$ is as follows by deduction:

$$\begin{cases}[\lambda]=\begin{bmatrix}\lambda_1 & 0\\ 0 & \lambda_1\end{bmatrix}\\ [\lambda_1]=\begin{bmatrix}\cos\alpha_{\mathrm{i}} & 0 & \sin\alpha_{\mathrm{i}}\\ -\sin\alpha_{\mathrm{i}}\sin\gamma_{\mathrm{i}} & \cos\gamma_{\mathrm{i}} & \cos\alpha_{\mathrm{i}}\sin\gamma_{\mathrm{i}}\\ -\sin\alpha_{\mathrm{i}}\cos\gamma_{\mathrm{i}} & -\sin\gamma_{\mathrm{i}} & \cos\alpha_{\mathrm{i}}\cos\gamma_{\mathrm{i}}\end{bmatrix}\end{cases}\tag{5}$$

The connection between the center of the bridge and the center of the track can be assumed to be rigid, so the vibration mode displacement vector in

moving coordinate system (that is $\{f\}_{\mathrm{i,B}}$) needs to be transformed into track center line by means of rigid arm constraint equations as follows:

$$\{\phi\}_{\mathrm{i}}=\begin{bmatrix}1&0&0&0&0&0\\0&1&0&z_{\mathrm{i,B}}&0&0\\0&0&1&-y_{\mathrm{i,B}}&0&0\\0&0&0&1&0&0\\0&0&0&0&1&0\\0&0&0&0&0&1\end{bmatrix}\{\phi\}_{\mathrm{i,B}} \tag{6}$$

where $\{f\}_{\mathrm{i}}$ denotes the vibration mode displacement vector in track center line, ($x_{\mathrm{i,B}}$, $y_{\mathrm{i,B}}$, $z_{\mathrm{i,B}}$) is coordinate value of node B_i in the moving coordinate.

If node B_i doesn't coincide with the point of intersection that track centerline projects on bridge's center line, any node's vibration displacement vector of bridge on the track center line can be determined by means of spline interpolation between two coincidence points.

2.3 *Wheel-Rail Contact Force*

Based on the wheel-rail creep theory of vehicle passing straight lines, the calculation of wheel-rail creep rate while vehicle passing curved bridges can adopt formulas as follows (Zhai, 2007):

$$\begin{cases}\xi_{1\mathrm{j}}'=\xi_{1\mathrm{j}}+(-1)^j\left[-b+\gamma_j\sin(\delta_j)\cos(\psi_{ws})\right]\cdot R_i & \text{(a)}\\ \xi_{2\mathrm{j}}'=\xi_{2\mathrm{j}} & \text{(b)}\\ \xi_{3\mathrm{j}}'=\xi_{3\mathrm{j}}+(-1)^j\cos(\delta_j)\cdot R_i & \text{(c)}\end{cases} \tag{8}$$

where $\xi_{1\mathrm{j}}$, $\xi_{2\mathrm{j}}$ and $\xi_{3\mathrm{j}}$ are respectively the longitudinal creep rate, lateral creep rate and spin creep rate while vehicle passing straight lines, $\xi_{1\mathrm{j}}'$, $\xi_{2\mathrm{j}}'$ and $\xi_{3\mathrm{j}}'$ are respectively the longitudinal creep rate, lateral creep rate and spin creep rate when vehicle passing curved lines, δ_{j} is the contact angle between wheel and rail, R_{i} is the curvature.

Creep coefficient is determined by the geometric relationship between wheel and rail, and is minorly affected by the curve. Hence, we can deal with it according to vehicle passing straight lines only considering the lateral displacement of wheel relative to track centerline.

According to Kalker's linear theory, the wheel rail creep contact force can be expressed as follows (Zhai, 2007):

$$\begin{cases}T_{x\mathrm{j}}=-f_{11}\xi_{1\mathrm{j}}'\\ T_{z\mathrm{j}}=-f_{22}\xi_{2\mathrm{j}}'+f_{23}\xi_{3\mathrm{j}}'\\ M_{\mathrm{j}}=-f_{23}\xi_{2\mathrm{j}}'-f_{33}\xi_{3\mathrm{j}}'\end{cases} \tag{9}$$

Where $\{f_{\mathrm{ij}}\}$ is the creep coefficient, T_{x} and T_{z} are longitudinal and lateral creep forces of wheel and rail, M_{j} is the rotating creep moment.

2.4 *Generalized Force for the Moving Train*

(1) Treatment of the first suspension force and the second suspension force

In theory, the first and the second suspension force should be transformed into the moving coordinate system when motion equations of vehicle are established. In fact, it is unnecessary to be transformed because of the small offset of bogie coordinate system, for example, cos(lr) almost equals to 1.0 even if the smallest radius is 350m.

(2) Centrifugal force and super-elevation component force

Assume that a wheel have the curvature of R_{i} and angle of super-elevation γ_{i} in its position, the centrifugal force and super-elevation component force in moving coordinate system can be obtained as follows (Xia and Zhang, 2005)

$$\begin{cases}C_{\mathrm{wi}}=-m_{\mathrm{wi}}R_{\mathrm{i}}v^2\\ H_{\mathrm{wi}}=m_{\mathrm{wi}}g\sin\gamma_i\\ V_{\mathrm{wi}}=m_{\mathrm{wi}}g(1-\cos\gamma_i)\end{cases} \tag{10}$$

where m_{wi} is the mass of wheel, C_{wi} is the centrifugal force along the direction of $o_{\mathrm{i}}z_{\mathrm{i}}$, H_{wi} is the super-elevation component force along the direction of $o_{\mathrm{i}}z_{\mathrm{i}}$, V_{wi} is the super-elevation component force along the direction of $o_{\mathrm{i}}y_{\mathrm{i}}$.

Take the average of n curvature and angle of super-elevation for each wheel approximately, the centrifugal force and super-elevation component force will be obtained as follows

$$\begin{cases}C_{\mathrm{b,c}}=-m_{\mathrm{b,c}}\left(\dfrac{1}{n}\sum_{i=1}^{n}R_i\right)v^2\\ H_{\mathrm{b,c}}=m_{\mathrm{b,c}}g\sin\left(\dfrac{1}{n}\sum_{i=1}^{n}\gamma_i\right)\\ V_{\mathrm{b,c}}=m_{\mathrm{b,c}}g\left[1-\cos\left(\dfrac{1}{n}\sum_{i=1}^{n}\gamma_i\right)\right]\end{cases} \tag{11}$$

where b denotes bogie, c denotes car body.

2.5 *Numerical analysis and field test*

Numerical analysis was conducted using VBC 2.0, which is a professional program for the analysis of vehicle-bridge coupled vibration developed by Tongji University. The motion equations are solved based on modal coordinate. In this paper, modal analysis was completed by commercial software ANSYS.

Some representative piers are taken as examples to analyze the dynamic response, such as No. 19 on the curved line. The time-history curve of pier top

lateral amplitude is shown in Figure 2 and the dynamic response of vehicle's lateral acceleration is shown in Figure 3 while freight train passing at the speed of 40 km/h.

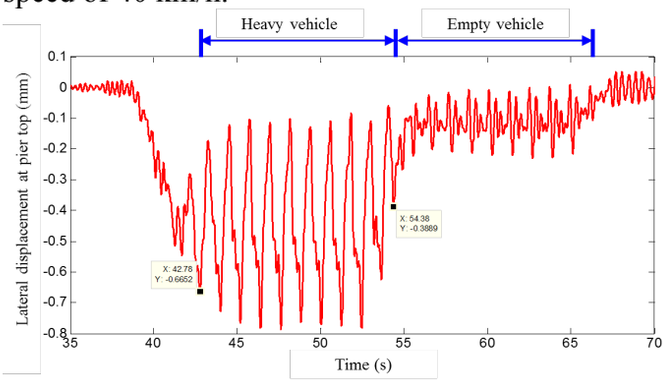


Figure 2. Time-history of lateral displacement at the top of the pier.

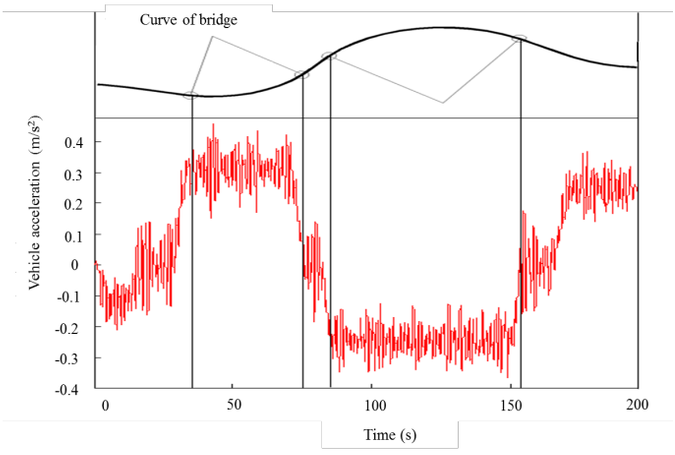


Figure 3. Time-history for the vehicle lateral acceleration.

3 TEST OBJECTIVES AND METHODS

3.1 *Overview of the Test Bridge*

The S-shaped curved bridge under test has a total length of 1728.91m. The reverse curve has a radius of 350m, which does not conform to the Section 3.4.5 of the Fundamental Code for Design on Railway Bridge and Culvert (2005). According to the preliminary analytical study and numerical simulation performed in the previous sections, three bridge spans with relatively higher piers between Pier No.45~55 were selected in this dynamic load test. The three spans are detailed as follows:

(1) *Intermediate straight bridge span*, namely 20m simply supported beam bridge span of piers No.45~46 on intermediate straight line (pier height at 11.75m).

(2) *Curved continuous rigid frame bridge span*, namely (20+26+20) m continuous rigid frame bridge span of piers No.50~53 on circular curve with radius R=350 m (pier height at 9.9m~11.3m).

(3) *Circular curve bridge span*, namely 20m simply supported beam bridge span of piers No.54~55 on circular curve with radius R=350 m (pier height at 10.75m). Picture of the testing bridge span is shown in Figure 4.



Figure 4. The curved bridge under test.

3.2 *Objectives and Methods*

According to vibration characteristics of theoretic analysis, the main objectives of the test includes:

(1) Evaluating the operation performance of the train passing the curved bridge with small radius and reverse curve.

(2) Comparing the theoretical analyses with the test results regarding the dynamic characteristics of the bridge under test.

(3) Evaluating the reasonable running speed of freight train passing the test bridge.

20 vibration tests are conducted given different loading and operating information of the passing train. The marshalling of the passing train includes the heavy train, the empty train and the empty heavy train. The test speed was set within the range of 20~40*km*/*h*. The transverse and vertical vibration characteristics of both the piers and the beams were monitored during the test.

3.2.1 *Layout of the Test*

The vibration velocity sensors and transverse displacement gauges were applied in the test with emphasis on the mid-span, where the maximum vibration responses are expected to occur based on preliminary analyses. The transverse vibration sensors were arranged at the top and bottom of Pier No.45. It should be noted that the pier bottom test point was 1.0 m above the top of the pier cap as the bearing platform was covered underground. The layout of the test points on the straight bridge is illustrated in Figure 5.

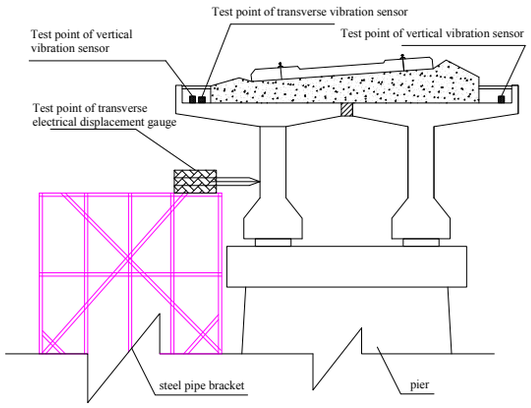


Figure 5. Arrangement of the test points at mid-span.

3.2.2 *Test Data Collecting and Processing*

As the raw data collected could include environmental vibration and instrument noise, further filtering processes are performed.

(1) Velocity Signal Filtering

The frequency spectrum of the velocity signal is analyzed using the Fast Fourier Transformation (FFT). As only the low-frequency responses of the bridge structure are of interest, low frequency signals less than 0.2Hz and high frequency signals greater than 20Hz were removed by filtering to eliminate the possible environmental and instrumental noises as well as the local vibration responses. Given the time history of the velocity signal at any test point, the time history of the displacement and acceleration could be obtained by integrating and differentiating along the time, respectively.

(2) Displacement Signal Filtering

The main difference of vibration characteristics between straight and curved bridges is that the center point of the amplitude shifts to the outside direction of the curve.

Electrical displacement gauges were used to monitor the transverse amplitudes and displacements of the bridge structure. The wavelet de-noising method was used to filter displacement signals. It was found in that the lateral displacement of the beam induced by centrifugal force was also filtered out when the method of velocity signal filtering was adopted. The time history of the displacement and the associated frequency spectra of an example test point is plotted in Figures 6 and 7.

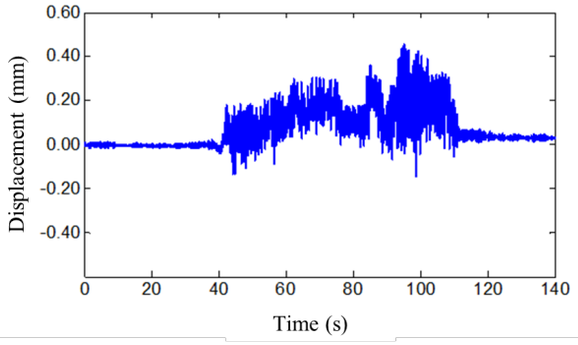


Figure 6. Time history curve for the lateral displacement at the top of Pier 55.

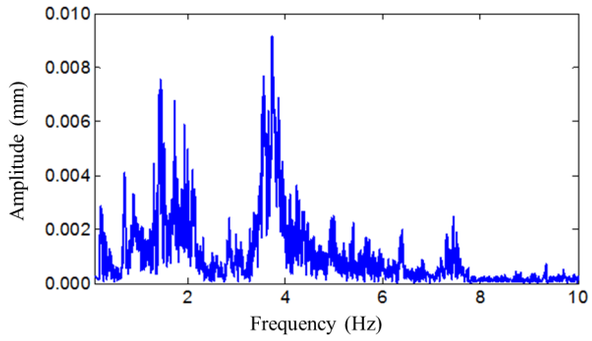


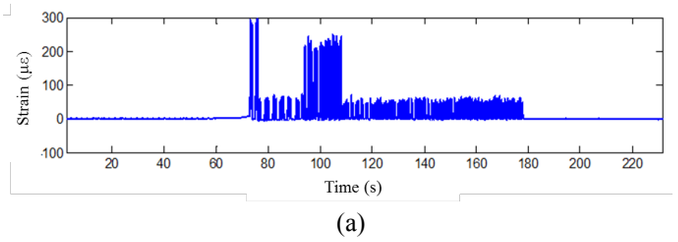
Figure 7. Frequency spectrogram for the lateral displacement at the top of Pier 55.

(3) Calculation of Train Speed and Axle Load

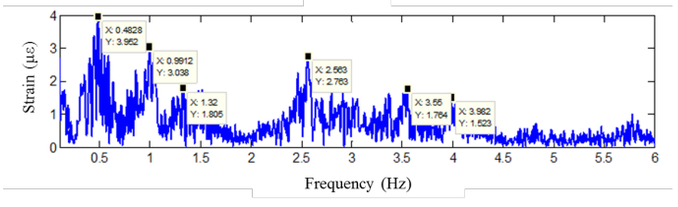
Train speed and marshalling information can be obtained by analyzing the strains of the steel rails. The time history of the strains and their associated spectra are shown in Figure 8. L is the length of the train between the two-wheel sets at head and tail, and the time of the two-wheel sets passing each test point is t_1 and t_2. The average speed of train can be computed as follows:

$$v=L/(t_2-t_1) \tag{12}$$

Simultaneously, the actual axle load of each freight train carriage can be calculated using the strain ratio between locomotive and vehicle.



(a)



(b)

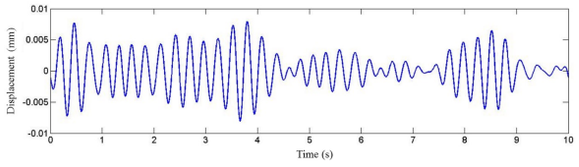
Figure 8. Dynamic responses of rail strains: (a) time history curve, (b) spectrogram.

4 BRIDGE VIBRATION CHARACTERISTICS ANALYSIS

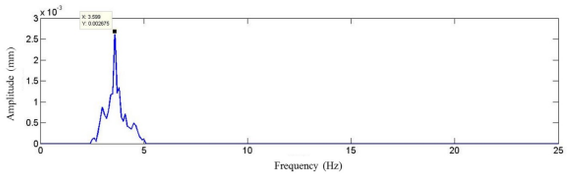
4.1 *Transverse Natural Vibration Frequency*

The residual vibration method was adopted in the tests because the train speed was relative slow and the transverse vibration responses of bridge mainly consist of low frequency signals. For example, Figure 9 shows the 10-second residual vibration history obtained by processing the data from the electrical displacement gauges on Pier No.54. It can be seen from the spectra that the 1st transverse vibration frequency of the pier is around 3.6*Hz*.

The average values of three representative groups of measured data are taken as the decision values of the tests, which are then compared against the normal allowance values in the Chinese Code for Rating Existing Railway Bridge (2004), as shown in Table 1. It can be seen that the transverse natural vibration frequencies of the representative bridge spans meet the requirements of the normal limited values of the code (2004). Reasonable stiffness of the pier-beam-system and foundation is also observed.



(a)



(b)

Figure 9. Residual vibration at pier top: (a) time history curve, (b) spectrogram.

Table 1. Frequency of transverse natural vibration of each bridge span.

Type	Intermediate Straight Beam		Curved Rigid Frame Beam		Circular Curved Beam	
	Pier Top	Mid. of Span	Pier Top	Bridge Span	Pier Top	Bridge Span
Average Value	2.87	2.77	3.57	3.50	3.60	3.60
Allowable Value	2.47		2.33		2.66	

4.2 *Vibration Acceleration*

4.2.1 *Transverse Vibration Acceleration*

It is required that the transverse acceleration of the bridge should be less than 1.4m/s^2 when only the modal contribution in the frequency range of 20*Hz* is considered per the Rating code (2004). The maximum transverse acceleration of pier and mid-span are presented in Table 2. The maximum transverse vibration acceleration occurred at mid-span of curved simply supported beam, which is 0.325 m/s^2 and less than the limited value. The transverse acceleration of pier and mid-span on curve was greater than that on straight line. The transverse acceleration of mid-span was greater than that of the top of the pier.

Table 2. The maximum transverse acceleration (m/s^2).

Test Point		Transverse Acceleration	Limit Value
Pier Top	No.45#	0.072	1.4
	No.51#	0.102	
	No.54#	0.130	
Mid Span	Intermediate Straight Beam	0.110	
	Curved Rigid Frame beam	0.325	
	Circular Curved Beam	0.220	

4.2.2 *Vertical Vibration Acceleration*

By reference to EURO-CODE, it is regulated in the Code for Design of High Speed Railway (2015) that the vertical acceleration should be less than 3.5m/s^2. The mid-span maximum vertical vibration accelerations of each test span are shown in Table 3. The maximum vertical vibration acceleration occurs at mid span of curved simply supported beam, and it is 0.463 m/s^2 and less than the limited value. The mid span vertical acceleration of curved simply supported beam is greater than that of the straight simply supported beam. The mid span vertical acceleration of curved continuous rigid frame beam is less than that of simply supported beam.

Table 3. The Maximum Vertical Acceleration (m/s^2).

Test Point		Vertical Acceleration	Limit Value
Mid Span	Intermediate Straight Beam	0.433	3.5
	Curved Rigid Frame Beam	0.419	
	Circular Curved Beam	0.463	

4.3 *Vibration Amplitude and Displacement*

4.3.1 *Transverse Amplitude*

As regulated in the Rating code (2004), when the heavy train speed is less than 80*km/h*, the maximum transverse amplitude of mid-span for the pre-stressed concrete beams should not exceed the following value:

$$A_{\max} \le \frac{L}{7.0B}(mm) \tag{13}$$

where, L is the calculated span of the bridge, and B is the center distance of the beam.

The maximum transverse amplitude at the top of the high pier with the pile foundation should not exceed the following limit:

$$A_{\max} \le \frac{(H+\Delta h)^2}{100B} + 0.2(mm) \tag{14}$$

where, B is the average width of the pier in the transverse direction, H is the overall height of the pier (from the top of the pier to the bottom of bearing platform), and Δh is the modified height considering characteristics of foundation soil, which is 1.0 considering the geological condition of this bridge.

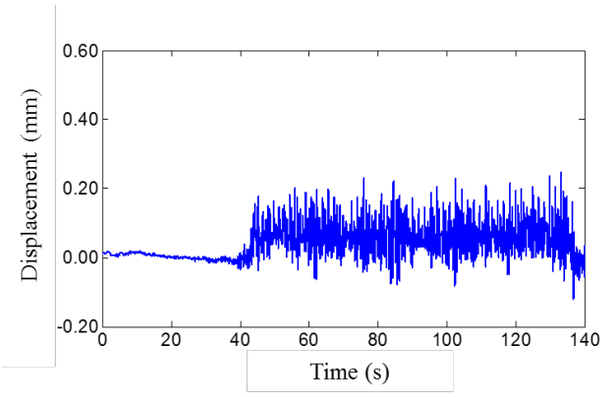
The comparisons of the transverse amplitudes between the measured values and the allowable values are shown in Table 4. The peak values of the measured amplitudes of the mid-span in each test span and those at the top of the piers are both less than the allowable values, which meets the safety requirements of train passing.

Table 4. Comparison of Transverse Amplitude Between Measured and Allowable Values (*mm*).

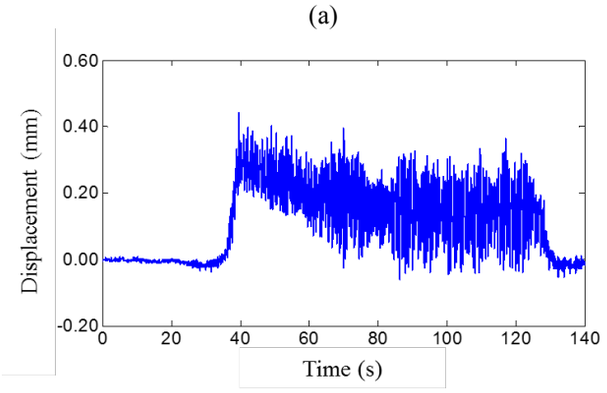
Bridge Span	Mid-span Measured Value	Allowable Value	Pier Top Measured Value	Allowable Value
Intermediate Straight Beam	0.35	0.68	0.17	0.72
Curved Rigid Frame Beam	0.36	0.76	0.22	0.71
Circular Curve Beam	0.22	0.68	0.16	0.65

4.3.2 *Transverse Displacement*

According to the Code for Design of High Speed Railway (2015), the limited safety value of the transverse amplitude at the mid-span is L/9000 for pre-stressed concrete beams. The limited safety value for the test bridge spans are computed as 2.2*mm* for the straight span and 2.9*mm* for the curved span, respectively. The time history of the transverse displacements at the mid-spans are shown in Figure 10 for the straight and the curved simply supported beam, respectively. The maximum transverse displacement of each mid-span is detailed in Table 5.



(a)



(b)

Figure 10. Time history curves of transverse displacement: (a) straight beam, (b) curved beam.

The maximum transverse displacement at each mid-span is far less than the limited value, and the transverse displacement of the curved simply supported beam is greater than that of the intermediate straight one. The reason could be that span have the tendency to shift to the outside of the curve under the action of centrifugal force. The transverse displacement of intermediate straight-line bridge is also shift to the same side irrespective of train driving direction. A possible explanation could be that intermediate straight-line bridge is subject to the smaller centrifugal force and some eccentricity exists between the center line and shear center of the test bridge.

Table 5. Maximum Transverse Displacement (*mm*).

Span	Intermediate Straight beam	Circular Curve beam
Measured Displacement	0.49	0.46
Allowable Value	2.20	2.20

5 REVISING OF CALCULATION MODEL

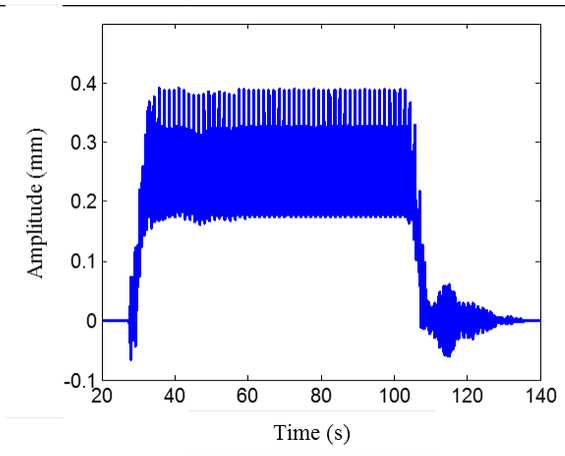
The finite element model of the test bridge is built in ANSYS. The transverse natural vibration frequency of bridge is calculated. According to the Guidelines for Seismic Design of Highway Bridges (2008), ***m***

method was adopted to calculate the foundation dynamic stiffness in the calculation model, and the dynamic stiffness of the pile was obtained as 3 times of the static stiffness.

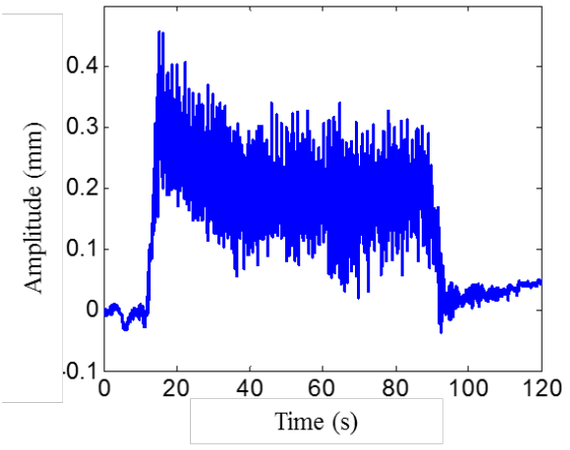
The preliminary result shows that the transverse natural vibration frequency obtained from the measured results didn't fit well with that of the numerical calculation results from the model. Therefore, the model was revised to correct the foundation dynamic stiffness according to measured values in Table 1. Assuming the static stiffness is K with ***m*** method, the actual dynamic stiffness can be obtained by inverse calculations performed in Table 6. Then the transverse natural vibration frequency was recalculated according to the revised calculation model. In Figure 11, the time history of the transverse vibration displacement obtained from the revised model and the measured data are compared and much better fit is observed.

Table 6. Comparison of dynamic stiffness and transverse natural vibration frequency.

Beam Type	Pier Bottom stiffness	Transverse Natural Vibration Frequency (*Hz*) Numerical Calculation	Measured Value
Intermediate Straight Beam	K	1.223	2.87
	$3K$	1.591	
	$8K$	2.885	
	Consolidation	4.824	
Circular Curve Beam	K	1.355	3.60
	$3K$	2.593	
	$12K$	3.607	
	Consolidation	5.233	



(a)



(b)

Figure 11. Comparison of transverse vibration displacement time history curves: (a) numerical simulation by revising calculation model, (b) measured results.

6 CONCLUSIONS

Based on both the theoretical and experimental analyses, it could be concluded that:

(1) The method of moving coordinate systems and coordinate transformation was used to establish the geometric relationship between the train and the bridge, and the wheel-rail contact force was simulated based on modified Kalker's linear creep theory.

(2) The main difference of vibration characteristics between the straight and curved bridge is that the center point of the vibration amplitude shifts to the outside curve.

(3) The main vibration characteristics of the test bridge under the operating train meet the requirements of serviceability and safety specified in the code, including multiple measures such as lateral acceleration, vertical acceleration, transversal amplitude and displacement.

(4) The dynamic stiffness of the foundation is much greater than the static stiffness in this study, indicating that the ***m*** method might not be a good approach, and further study is still needed.

7 ACKNOWLEDGMENTS

The authors are grateful for the financial support received from the National Natural Science Foundation of China (Grant No. 51478258).

REFERENCES

ANTOLÍN, P., ZHANG, N., GOICOLEA, J. M., XIA, H., ASTIZ, M. Á. & OLIVA, J. (2013) Consideration of nonlinear wheel–rail contact forces for dynamic vehicle–bridge interaction in high-speed railways. *Journal of Sound & Vibration,* 332**,** 1231-1251.

AU, F. T. K., CHENG, Y. S. & CHEUNG, Y. K. (2001) Vibration analysis of bridges under moving vehicles and trains: an overview. *Progress in Structural Engineering & Materials,* 3**,** 299–304.

FRYBA, L. (2013) *Vibration of solids and structures under moving loads*, Springer Science & Business Media.

GALDOS, N. H., SCHELLING, D. R. & SAHIN, M. A. (1993) Methodology for Impact Factor of Horizontally Curved Box Bridges. *Journal of Structural Engineering,* 119**,** 1917-1934.

MINISTRY OF COMMUNICATIONS OF THE PEOPLE'S REPUBLIC OF CHINA (2008) Guidelines for Seismic Design of Highway Bridges. Beijing, China, China Communications Press.

MINISTRY OF RAILWAYS OF THE PEOPLE'S REPUBLIC OF CHINA (2004) Code for rating existing railway bridge. Beijing, China, Railway Publishing House.

MINISTRY OF RAILWAYS OF THE PEOPLE'S REPUBLIC OF CHINA (2005) Fundamental code for design on railway bridge and culvert. Beijing, China, China Railway Publishing House.

NATIONAL RAILWAY BUREAU OF THE PEOPLE'S REPUBLIC OF CHINA (2015) Code for Design of High Speed Railway. Beijing, China, Railway Publishing House.

SHAN, D. S. (1999) Curved-Girder Bridges and Vehicles Coupled Vibration Analysis and Design Study of the Long-Span Curved-Girder Bridges in High-Speed Railway. Southwest Jiaotong University.

SONG, Y. M., WU, D. J. & LI, Q. (2013) Coupling Vibration Analysis of Train Curving Multi-Span Bridges on Small Radius Curve. *Chinese Quarterly of Mechanics,* 34**,** 240-245.

XIA, H. & ZHANG, N. (2005) *Dynamic interaction of vehicles and structures,* Beijing, China, Science Compress.

YANG, Y. B., WU, C. M. & YAU, J. D. (2001) Dynamic response of a horizontally curved beam subjected to vertical and horizontal moving loads. *Journal of Sound & Vibration,* 242**,** 519-537.

ZAMBRANO, A., RAUCI, M. & MALANGONE, P. (2008) Vehicle-structure interaction to analyse the primary dynamic aspects of railway bridges. *Structure & Infrastructure Engineering,* 4**,** 107-121.

ZHAI, W. M. (2007) *Vehicle-track coupling dynamics,* Beijing, China, Science Publishing House.

Maintenance, Safety, Risk, Management and Life-Cycle Performance of Bridges – Powers, Frangopol, Al-Mahaidi & Caprani (Eds)
© 2018 Taylor & Francis Group, London, ISBN 978-1-138-73045-8

Repairing a sinking bridge over Guadalquivir river

C. Jurado (Ph. D.,m Sc., B. Sc., MBA)
Polytechnic University of Madrid / Ingecal Ingenieros, S. L., Madrid, Spain

ABSTRACT: The bridge over Guadalquivir river, near Alcalá del Rio in Seville (Spain), that has nine spans of 30 m each, with a total length of 270 m, has suffer in the past a sinking of 14 cm and 6 cm on two of the central piers located in the centre of the river. The superstructure is isostatic and the foundation is constituted by two circular pier-piles of 1.50 m of diameter. Among different solutions the best technically and economically selected, was to use Jet Grouting injections

1 INTRODUCTION

The Spanish Administration has carried out in the past the construction of the Road Variant of Alcalá del Rio, which includes a bridge over the Guadalquivir River with nine isostatic spans, whose geometric definition is described later.

The mentioned structure consists of nine spans equal of 30.00m each one, which sums up a total length of 270.00m The deck comprises 10.00m of pavement plus two sidewalks of 1.00m, totaling a width of 12.00m

The bridge was designed with deep foundation in all its supports, due to the existing soft ground in the zone.
The foundation of the bridge is constituted by two circular pier-piles of 1.50 m of diameter for any support of the bridge and 25 m of length in the case of piers. In the piers, the piles has 2 m embedded in gravels and 12 m (8 diameters) in blue marls; the remaining 11 m corresponds to the exempt part of the pier, with the lowest 2 m corresponding to the average water depth of the Guadalquivir River in the above mentioned zone.

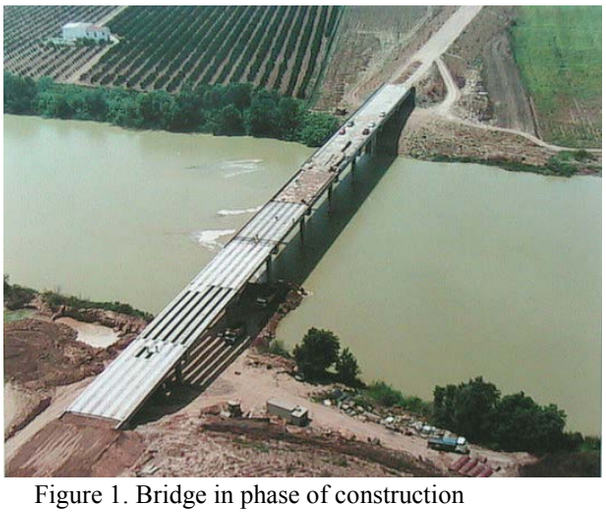


Figure 1. Bridge in phase of construction



Figure 2. Finished bridge

2 DETECTED PATHOLOGY

In the first week of the opening of bridge (in April), it was observed a vertical angle in the metal vehicles barriers and in the handrails of the bridge that was indicating the possibility of a descent of the deck, at the level of the piers P-4 and P-5 in the center of the river (Figure 3).

It was decided to verify the level of the mentioned piers by topography, observing average settlements in piers P-4 and P-5 of 13.9 and 5.4 cm. respectively. Due to this it was decided to carry out a following-up of the settlements by means of topography fixed bases of leveling on both sides of the bridge.

From the day 4th of April until 17th of May, it was observed that both abutments and the rest of the piers did not have suffer any settlement, but the piers P-4 and P-5 continued descending, reaching the average settlements

of 14.6 and 6.0 cm, respectively. The settlement of both pillars of each pier were similar.

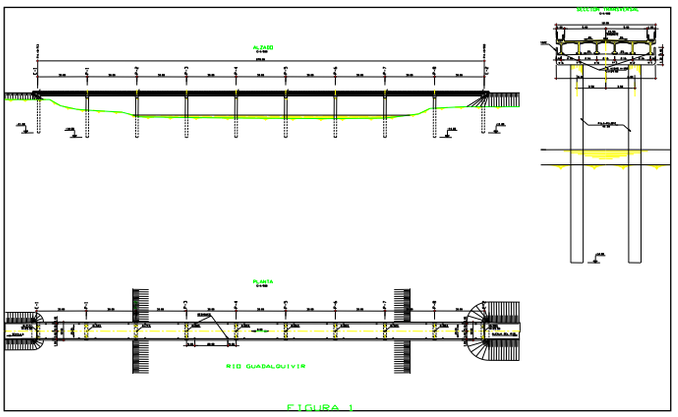


Figure 3. General drawings of the bridge

3 ACTIONS ON THE PIER-PILE

It was decided to review the project of the bridge verifying the validity of this. The actions over the pier-piles were calculated considering mainly the following loads:

- Dead loads.
- Live loads due to a uniform load of 0.40 Ton/m^2 and to a truck load of 60 T on, according to the Spanish Code of Bridges, considering different positions of it.

The maximum characteristic axial load that the piers transmitted to the ground (supposing that both pillars were working equally), without considering the action of the wind and the earthquake, it turned out to be of 503.02 Ton, for each pile. In case of performance of wind and earthquake the maximum and minimal loads were:

$Q_{máx}$: 554.22 Ton.
$Q_{mín}$: 451.82 Ton.

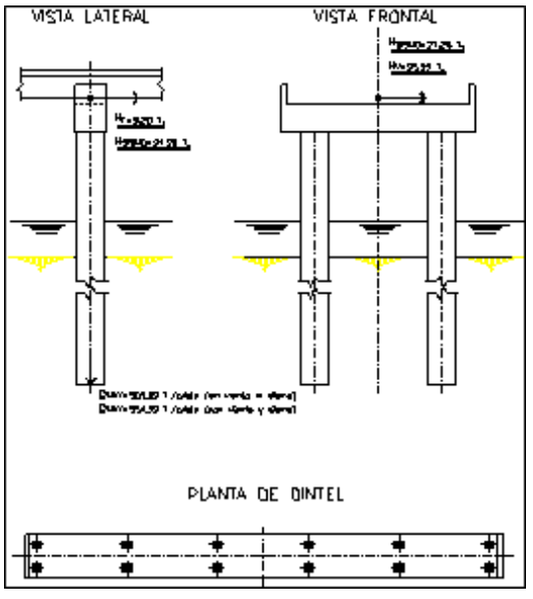


Figure 4. Actions on a pier-pile

Table 1

CP(T)	66.82	79.02	79.02	79.02	79.02	66.82
+	+	+	+	+	+	+
S.C.V.(T)	20.16	25.92	79.27	79.27	25.92	20.16
TOTAL(T	86.98	104.94	158.29	158.29	104.94	86.98

*C.P.DECK= 700.42 T.
*C.P.LINTEL= 72.00 T.
*C.P.PIER–PILES= 233.62 T

TOTAL=1,006.04 T.=503.02 T/pile

During the project of the bridge, a Geotechnical Campaign of soil recognition had been realized, consisting of soil borings, that indicated the existence of one alluvial of several meters of thickness and below it, the Mioceno substrate of marls of unlimited thickness. None of the borings were made under the piers P-4 and P-5. The alluvial was proved to be with a medium compacity and the marl with a compression resistance of q_u = 6.3 kp/cm^2. Inside the soil borings, there were realized S.P.T. tests, turning out to be with an average value of N_{SPT} =62.

With these values the ultimate load capacity for pile was turning out to be:

$$Q_h = Q_p + Q_f = A_p \cdot r_p + A_f \cdot r_f \quad (1)$$

A_p, A_f = Cross section and perimeter of pile
r_p, r_f = unitary ground resistance of tip compression and on lateral friction

$$q_u = 6.3 \text{ k}_p/\text{cm}^2 = 63 \text{Ton/m}^2 \quad (2)$$

In the project it has been adopted:

$$r_p = 5\, q_u = 315 \text{ Ton/m}^2 \qquad r_f = 0.25\, q_u = 15.75 \text{ Ton/m}^2 \quad (3)$$

The ultimate load of pile collapse, despising the collaboration of the resistance of shaft friction of the gravels it turned out to be:

$$Q_h = 1.766 \text{ x} 315 + 56.52 \cdot 15.75 = 1446 \text{ Ton} \quad (4)$$

The safety coefficient for the maximum load of service without magnifying was:

$$F = \frac{Q_h}{N_{\max}} = \frac{1446 Ton}{503 Ton} = 2.88 \quad (5)$$

Which was considered to be acceptable in the project. This coefficient of safety, if it was considered the existence of the earthquake and the transverse wind, was diminishing to F = 2.51 in the most loaded pier, value that also was considered sufficient.

4 RECOGNITIONS REALIZED AND RESULT OBTAINED

In view of the detected pathology it was decided the accomplishment of one additional field campaign of recognition, consisting of two mechanical rotatory soil borings, on the basis of the following hypotheses:

4.1 *Hypothesis*

Due to the similar settlement in the couples of pier-piles of each one of the pillars P-4 and P-5, an hypothesis was made that the marl could not be homogeneous, containing some soft nodules under the tip of the pile or some cavities.

There was discarded the imperfection or bad execution of the pile and especially on the tip, because it seemed to be strange that 4 piles and besides contiguous were badly executed. By the control taken during the construction heterogeneities were discarded also along the pillar.

4.2 *Realized recognition*

The recognition consisted of the execution of two mechanical rotatory soil borings, one between the two pillars of the pier P-4 and other one between those of the pier P-5.

The soil borings were executed on a boat since the piers P-4 and P-5 are located in the center of the river.

In situ standard penetrations test (S.P.T.) were made every 2.00 m of vertical distance in each boring, and recovery of soil-samples for laboratory tests.

4.3 *Result obtained*

The profiles of soil obtained were the following ones:

Table 2

BORING	PIER	MOUTH ELEV.	DEPTH (m)	TIPE OF SOIL
S-1	P-4	-1.98	From 0 to 0.25 m From 0.25 to 2.25m From 2.25 to 28.50m	Lime Gravel Blue Marl
S-2	P-5	-1.93	From 0 to 1.30 From 1.30 to 21.30	Fine Gravel Blue Marl

No hollows or soft zones were detected below the tip of the piles; nevertheless, the recognition put of manifest a consistency of the marl smaller that were awaited.

In effect, the Geotechnical recognition realised in the project indicated that the marl had one N_{SPT} = 62 and one resistance to compression of at least 6.3 kg/cm^2.

The S.P.T. test realized in the last recognition, had registered a N_{SPT} number even the half, along the pile and under the tip.

The average number N_{SPT} it turned out to be of 36 (on S-1) and of 35 (on S-2). All these values lower to N=62 obtained during the project recognition, carried out in the zones of abutments were up to 20 to 23 meters of depth, and there were not obtained number N_{SPT} of 60 or superior.

Applying the relation that proposes the bibliography between the S.P.T. test and the resistance of compression of q_u = N/7.5, it were obtained compression values as low as q_u=21/7.5=2.8 kg/cm^2, very far away from the value of 6.3 kg/cm^2 considered in the initial Geotechnical report during the project.

The tests to simple compression performed on samples gave low values, between 3.40 and 4.91 kg/cm^2, in the first 12 meters, except a value of 10.08 kg/cm^2. Major values of 6 kg/cm^2 were found below 16 m of depth, corresponding to values of N_{SPT} superiors to 50.

As conclusion the following points were indicated:

a) It was not confirmed the existence of large soft zones of soil or caves below the tip of the piles.
b) Nevertheless, it was putting of manifest that in the first 16 recognised meters, the marl had much less consistency than the awaited one in the project.
c) Due to the minor geomechanic resistance of the soil, it was decided to verify the safety coefficients of the piers P-4 and P-5, with new geomechanic parameters.
d) In the new calculations made, it was supposed that the resistance to simple compression along the pile and in the tip was of 5 kg/cm^2, that is equivalent to one number of N_{SPT} = 38 (q_u = 38/7.5 = 5 kg/cm^2). This directed to the conclusion that the piles were working near to the plastic limit of the surrounding soil and it was necessary to reinforce the foundation of the bridge.

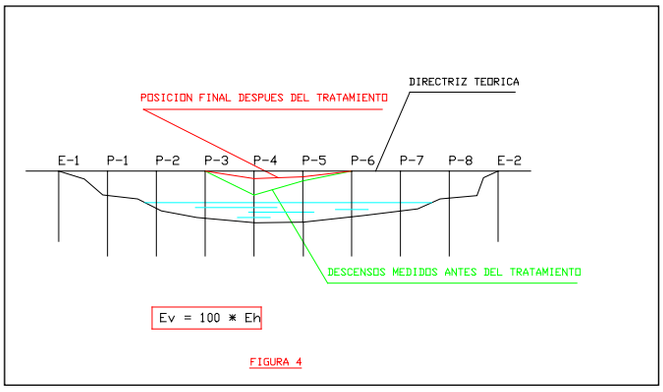


Figure 5. Lifting of piles P-4 and P-5

5 ADOPTED SOLUTION

An economic analysis for three possible solutions was made, obtaining that the best solution was to use Jet Grouting, with the minor cost and the minor problems of accomplishment and at the same time, it could be obtain a reduction in the settlements of piers P-4 and P-5. This solution consisted of the execution of 18 columns of Jet Grouting of injection distributed concentrically with the piles, nine vertical to a distance of the pile of 0,50-1,00 m and the other nine o a distance of the pile of 2,00 m and inclined approximately 6,5 º degrees (figure 6).

The injection would produce a column of soil-cement of approximately 40-50 cm. of diameter, consolidating and refilling the zones of the marls that surround the column.

The columns of Jet Grouting were executed alternatively, so that between 2 adjacent columns executed in the same day, there was at least 1,50 m, or 24 hours of consolidated cement of the adjacent columns, to the injection that was executed in this moment. The object of this gap in space and time was to avoid the possible fluidity of an important area during the injection of the mortar, and that could give place to an unforeseeable increase of the settlements. Also, during the execution of the treatment the traffic was not interrupted, though it was stopped in the lane that was over the pier-pile in treatment in every case and in the other lane the velocity of traffic was reduced.

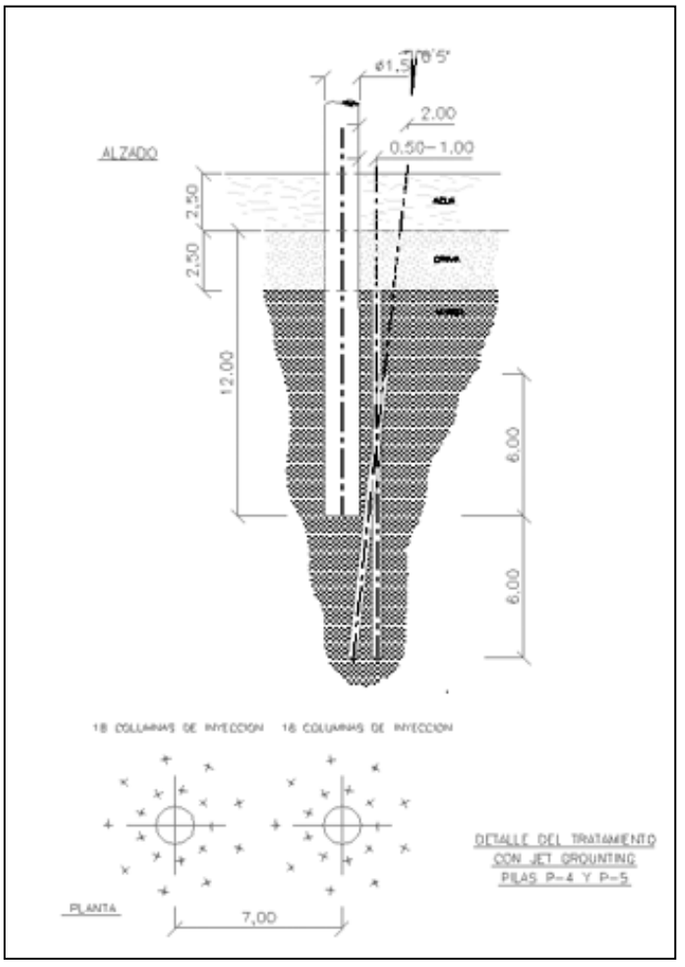


Figure 6. Scheme of jet grouting

The worst moment of the procedure was when one injection was executed. Therefore, it was recommended to make frequent controls of levelling of the affected piers, controlling the raising of the pier and also reducing the speed of the vehicles on t he bridge to avoid important dynamic loads. With the effective treatment, it was corrected the settlement of the piers P-4 and P-5 obtaining a rising of the twin pillars of approximately 10 cm as maximum.

INITIALSEAT	AL SEAT
P-4: 14.6 cm.	4.6 cm.
P-5: 6.0 cm.	3.5 cm.

The work was carried out during the months of June and July of this year.

6 REFERENCES

Bowles, J.E. 1996. Foundation Analysis and Design, Mc Graw-Hill Inc.

Jiménez Salas, J. A. 1980. Geotecnia and Cimientos (I, II and III) Madrid, Ed. Rueda

Xanthakos, P.P. Bridge Strengthening and Rehabilitation. Prentice Hall

MS15: Bridge loading – measurement and modelling

Organizers: C. Caprani, A. Nowak, E.J. O'Brien & X. Ruan

Maintenance, Safety, Risk, Management and Life-Cycle Performance of Bridges – Powers, Frangopol, Al-Mahaidi & Caprani (Eds)
© 2018 Taylor & Francis Group, London, ISBN 978-1-138-73045-8

Traffic load patterning on long span bridges

D. Guo & C. Caprani
Monash University, Melbourne, Australia

ABSTRACT: For highway bridges, current live load models typically replicate the effects of real traffic streams at a certain return period. Most standards stipulate that the worst load effect should be considered, obtained by patterning the live load on the adverse portion of the influence lines only. Certainly, this is a worst-case scenario, but real traffic does not pattern in this manner. This paper examines design standards' approach to load patterning against the behaviour of real traffic. Traffic microsimulation is adopted on a generic 1200 m bridge. We consider the possible road topologies that might give rise to design standard loading patterns. The results show that real traffic cannot achieve the code-inferred traffic pattern. The load effect results are extrapolated to represent assessment and design return periods. A possible road topology is put forward, and it can be the prototype of a new method to assess the load effect.

1 INTRODUCTION

1.1 *Background*

Long span bridges are critical pieces of infrastructure, and it is vital to construct and maintain them as economically as possible. The traffic load model for bridge design and assessment is designed to simulate the extreme load effect (LE) of actual vehicle traffic on the bridge. Normally, the standard requires engineers to pattern the live loads for the most critical case, which means to apply the maximum load on the adverse part of the influence lines (IL), while maintaining the load on the beneficial part at the minimum value (the live load is zero). For instance, the Australian load model SM1600 (Standards Australia 2017) requires that the uniformly distributed load (UDL) component is continuously or discontinuously applied to produce the most adverse effect. Similarly, the Eurocode (2003) load model LM1 requires that the UDL is applied only in the unfavourable parts of the influence surface. AASHTO (2007) also requires patterning the UDL of HL-93 to produce the extreme force effects. The same method and statement have been followed by many other national standards.

The inherent problem of the traditional (or current) load model method is that it is a combination of extremes: it combines extreme load values and extreme load topology. The possibility of this combination of extreme loads and arrangements has not been studied in detail (as will be seen later). As a result, bridge engineering practice follows a worst-case scenario approach that combines extreme (lifetime) load levels in an extreme (lifetime) traffic topology. Because of the formation of the truck platoon and other traffic phenomena, the traffic loading is obviously not perfectly evenly distributed, so it is reasonable to see some load patterning. But a more reasonable basis is needed to estimate the traffic behaviour effect in a long span bridge life cycle.

There can be significant implications when using the current load patterning approach for designing a new bridge. For example, the newly opened (2017) Queensferry Crossing of the Firth of Forth, Scotland. It is a multi-span cable-stayed bridge. The total length is 2700 metres with two main spans of 650 meters (Kite et al., 2011). In the design, the Eurocode load model is used, and the design live load patterning causes a significant moment in the centre tower. As a result, cables are overlapped to reduce the bending moment of the middle tower.

Of course, traffic load patterning does not only affect the new design but also have a great impact on the existing long-span bridge. For example, around 25% of the long-span bridges in North America reach the 75-year design lives and only 63% long-span bridges are in good condition (Maria et al., 2017). It is estimated that the maintenance of bridges in The United States has reached US$123 billion (ASCE, 2017). Obviously, if using a more accurate live load model to assess the status of the existing bridge, a lot of cases may be found to be safe, which can help save a lot of maintenance or repair costs.

1.2 *Traffic Loading on Long Span Bridges*

The traffic load of long-span bridges is governed by high volume traffic, usually congestion. A lot of research work on this topic is based on mixed vehicles and fixed vehicles gaps (Ivy et al., 1954, Buckland, 1981, Ditlevsen and Madsen, 1994, Nowak et al., 2010, Caprani et al., 2012). Such work assumed that cars and trucks were at the smallest bumper distance, and the weight data came from the on-site surveys or weigh-in-motion (WIM). However, WIM data is captured from the free flow traffic as the sensor is inaccurate in the congested traffic. (OBrien et al., 2015). Therefore, these measurements cannot be used directly for long span bridge loading. Another noticeable feature of the traffic is that the vehicle compositions can be quite different across lanes. For example, car drivers tend to change lanes to catch up with slow-moving trucks, which leads the truck ratio on the slower lane exceeding the average. This phenomenon is more serious in traffic congestion, often forming a long truck platoon on a local road. (Carey et al., 2017). Therefore, it can be unrealistic to directly use a survey or WIM data. To overcome this challenge, some researchers used videos of congested traffic (Ricketts and Page, 1997, Nowak et al., 2010, OBrien et al., 2012). Many observations can be obtained from the video, such as typical traffic jam scenario, but it is difficult to obtain accurate quantitative data.

The recent way to overcome the WIM problem is to use traffic micro-simulation to create congested traffic from free-flow traffic measurements. In introducing the intelligent driver model (IDM), Treiber et al. (2000) used the traffic microsimulation to recreate the congested traffic load patterns which have been observed. They introduced the bottleneck strength and discussed the relationship between it and various congestion types (or congestion modes). Caprani and OBrien (2008) first used this microsimulation method to estimate the bridge traffic loads. Later, Caprani et al. (2016) verify the bottleneck strength and congestion types. They use microsimulation to analyse the LE of multi-lane traffic. Contrary to the general view, they found that the full stop traffic was not the worst-case scenario on the bridge. It is the slow-moving traffic which produces the highest lifetime loading. The reason is that there are more opportunities for vehicles arrangements on the road.

There is not too much work done on the patterned traffic loading. Zhou et al. (2015) considered the patterned traffic LEs of multi-span bridge by using the above-mentioned traffic micro-simulation method. In the study, the beneficial part of the IL is ignored. It is found that the LE of the pattern traffic can reach 8 times the normal traffic on the bridge, which shows that the current standard is conservative. In spite of this, most engineers would suggest that the patterned traffic is to replicate the case of traffic accidents, and other cases interrupting the normal traffic.

Recently, Lipari et al. (2017) proposed an integrated approach to determine lifetime levels of traffic loading, considering the probability of occurrence of traffic incidents and incorporating the level of interruption to traffic flow (or 'bottleneck strength'). In doing so, they use traffic microsimulation to determine the traffic topology and estimate the resulting LE. This method shows that traffic micro-simulation is a suitable tool to analyse the hypothesized traffic events and their topologies. Therefore, this method is adopted in this study.

1.3 *Contribution*

This paper assesses the potential of observing patterned traffic topology for theorized traffic activities by using traffic microsimulation, as stipulated by design and assessment codes. The study demonstrates a practical topology that comes as close as conceivable to duplicating the conventional code-referred design. This could be a prototype of the load patterning method and it could have a noteworthy advantage in the plan of new bridges, however most likely in the assessment of existing bridges, where the expenses of extra strength are huge.

2 TRAFFIC MICROSIMULATION

Microsimulation models consist of vehicle-following models and lane-changing models to simulate the vehicle movements on the road. It is powerful and convenient to record the position, direction, speed, axle arrangement, and other features of one single vehicle at any time, making it very useful for bridge loading studies. In recent years, Microsimulation models have been widely used in traffic analysis with different levels of accuracy (Orosz et al., 2010). However, it is quite important to deal with the calibration and validation process, as the data is simulated, to ensure its validity (Treiber et al., 2000). Ten microsimulation models (including IDM) are compared by Brockfeld et al. (2004) and they found it is almost impossible to calibrate results to within 10% variance. The common range of differences is 14 to 16% and the performances of various models are quite similar.

2.1 *IDM & MOBIL Models*

Treiber et al. (2000) developed an Intelligent Driver Model (IDM) which is a car-following model. The model is collision-free with several parameters to control single vehicle driving behaviour in one lane. Many research studies adopted IDM to simulate traffic. The results from IDM simulation can match the

observed actual traffic scenarios quite well and, therefore, it is suitable to use for actual traffic analysis (Treiber et al., 2000, Kesting and Treiber, 2008, Helbing et al., 2009, Chen et al., 2010, Caprani, 2012).

In the IDM, the acceleration of one single vehicle is given by:

$$\frac{dv}{dt} = a\left[1 - \left(\frac{v(t)}{v_0}\right)^4 - \left(\frac{s^*(t)}{s(t)}\right)^2\right] \quad (1)$$

where a is the maximum acceleration; $v(t)$ is the speed of at time t; v_0 is the desired speed; $s(t)$ is the gap between the current vehicle to the front vehicle at time t; and $s^*(t)$ is the minimum desired gap at time t, given by:

$$s^*(t) = s_0 + Tv(t) + \frac{v(t)\Delta v(t)}{2\sqrt{ab}} \quad (2)$$

where s_0 is the minimum gap distance from the current vehicle to the front vehicle; T is the safe time headway; $\Delta v(t)$ is the speed difference between the current vehicle and front vehicle, and b is the comfortable deceleration.

Later on, a lane-changing model called Minimising Overall Braking Induced by Lane changes (MOBIL) was introduced by Kesting et al. (2007). Symmetric (US) or asymmetric (EU) passing rules both can be implemented. In MOBIL, a vehicle will change lane if there is a sufficient acceleration advantage to be gained:

$$\bar{a}_c - a_c > \Delta a_{th} + p\left[\left(a_n - \bar{a}_n\right) + \left(a_o - \bar{a}_o\right)\right] \quad (3)$$

where Δa_{th} is the acceleration threshold and $a(t)$ is the acceleration at time t, which is calculated by Equation 1. The subscript indicates the vehicle: old follower (o), new follower (n) and current vehicle (c) and the bar identifies the situation after a hypothetical lane-changing. The politeness actor, p, controls how much consideration a driver gives to the impact of the lane change on surrounding vehicles' accelerations.

2.2 *SIMBA and Parameters*

Commercial software using traffic microsimulation excludes bridge LE calculation. Consequently, since 2006, Caprani et al. (2012) developed a software program called Simulation for Bridge Assessment (SIMBA). SIMBA uses IDM and MOBIL for vehicle movements, coupled with LE calculation based on ILs at each time step of the simulation. Table 1 shows the model input parameters. They were used in some parts of past works since they have been shown to replicate genuine traffic behaviour quite well (Treiber et al., 2000, Kesting and Treiber, 2008, Caprani et al., 2012, OBrien et al., 2015).

Table 1. IDM and MOBIL parameters.

Parameters	Car	Truck
Safe time headway, T (s)	1.6	1.6
Maximum acceleration, a (m/s^2)	0.73	0.73
Comfortable deceleration, b (m/s^2)	1.67	1.67
Minimum jam distance, s_0 (m)	2	2
Elastic jam distance, s_1 (m)	0	0
Desired velocity, v_0 (km/h)	120±20%	80±20%
Acceleration exponent, Δ	4	4
Lane change politeness factor, p	0.2	0.2
Outside lane bias factor, ΔA_{bias}	0	0
Lane change threshold, ΔA_{th} (m/s^2)	0.4	0.4
Maximum safe deceleration, B_{safe} (m/s^2)	4	4

2.3 *Congestion Types and Bridge Loading*

Interestingly, traffic conditions are not a binary choice between free-flow traffic (FT) and congested flow traffic. Rather, traffic conditions occur over a range, with various forms of congested traffic, such as triggered stop-and-go waves (SGW or TSG), oscillating congested traffic (OCT), and the most severe – homogenous congested traffic (HCT). The difference between demand and capacity, named the bottleneck strength, mostly controls the occurrence of these traffic types. Usually, the higher the bottleneck strength, the lower road capacity at that road section. Treiber et al. (2000) visually illustrated the relationship between the bottleneck strength and different congestion types using a phase diagram. In the paper, the bottleneck strength ΔQ (or the dynamic capacity difference) is the local decrease of the traffic capacity:

$$\Delta Q = Q_{out} - Q'_{out} \quad (4)$$

where Q_{out} is the maximum dynamic road capacity on the (hypothetically) free road and Q'_{out} is the maximum dynamic road capacity with the bottleneck in place.

Bottleneck strength can be presented locally either by specifically decreasing the desired speed v_0 or by increasing the safe time headway T. Both can diminish the road capacity but the latter is more effective (Treiber et al., 2000) and so is used here.

Caprani et al. (2012) and OBrien et al. (2015) studied different types of congestion and their influence on long-span bridge traffic LE. The densest type of traffic, HCT, is that intended to be replicated by bridge live load models. However, since it is a continuous traffic flow, it does not have a natural pattern.

On the contrary, SGW has both dense and free flow regions, and of course, these regions may coincide with adverse and beneficial parts of IL, leading to severe load conditions. Figure 1 illustrates this case. However, no previous studies on this point are known. This paper discussed the LE of SGW and from it develops a traffic load patterning prototype.



Figure 1. An illustrative example of stop-and-go waves. The rectangles represent moving vehicles on the bridge.

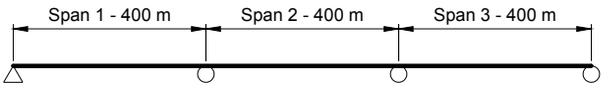


Figure 2. The elevation view of a generic 1200 m bridge.

3 THE TRAFFIC LOAD PATTERNING PHENOMENON

3.1 *Hypothesis*

In this section, we study the phenomenon of traffic load modelling and explain some rules about its real behaviour and code implicit behaviour. To do this, a hypothetical bridge is considered, with an IL that is sensitive to patterned load:

- Study 1: Firstly, we examine whether the natural patterning of traffic has a significant impact on bridge loading. This is done by generating different types of congestion on the bridge and examining the resulting LEs.
- Study 2: Second, by cropping the ILs, we apply code-referred traffic patterns, completely ignore the traffic flows of beneficial parts of ILs, and check the resulting LE.
- Study 3: Finally, we examine whether it is possible to simulate the code-referred traffic patterns through some critical incidents occurring in traffic flows without modifying the ILs. For these hypothetical critical traffic scenarios, we determine the resulting LEs.

A lot of information is gained by a comparison of the LEs from the above studies. However, before examining the results of these studies, the details of the studies are described.

3.2 *Basis of the Studies*

A generic bridge is used for the studies (Figure 2). This geometry can represent some existing bridges, such as The Millau Viaduct (204 + 6 × 342 + 204), Charilaos Trikoupis Bridge (286 + 3 × 560 + 286), and Brooklyn Bridge (283 + 487 + 283). The two traffic directions on the bridge are considered as independent, and so only one direction is considered.

For general bridges, the LE of a hypothetical IL, which is sensitive to load patterning, is considered (Figure 3). Both maximum and minimum values of the LE are studied. The study of the complete IL is used to show the load effect of actual traffic flow (Figure 3a). The code-implied traffic flow considers the worst-case maximum LE by cropping the beneficial region of IL (Figure 3b), and similarly for the worst-case minimum LE (Figure 3c).

The same input traffic data set is used throughout the work to avoid the irrelevant variable affecting the result. Since these studies are only relative comparisons, not to quantify the actual value of loading, this is acceptable. The traffic characteristics simulation data is obtained from A6 highway, near Auxerre in France. These data are important because they form the basis for Eurocode load models (Bruls et al., 1996). The traffic used in this work is randomly generated using Monte Carlo simulation (Jacob and Labry, 2002, Caprani, 2005). In Auxerre data, there is no recording of ordinary cars, but the study manually inserted them (Caprani, 2013, Caprani et al., 2016). The traffic flow is set to 1500 veh/h/lane and the truck percentage as 16% (Lipari, 2013). Additionally, an 80:20% distribution of trucks between lanes is set (Fwa and Li, 1995, Caprani et al., 2016).

For each study, 100-hours of congestion data is generated. Considering 1 hour of congestion per day, 100 hours of congestion is equivalent to 100 days for the bridge. While recording the value of LE, the total amount of load on each span is also recorded. In each simulated hour, the maximum LE is reserved for further analysis, regarded as the largest block (or "block maximum"). Of course, congestion doesn't happen immediately at the beginning of the simulation but takes time to build up on the virtual road. Hence the LEs for the first hour of the simulation are discarded. Following extreme value theory (Castillo, 2012), the generalised extreme value (GEV) distribution is used to fit the block maximum data of LE.

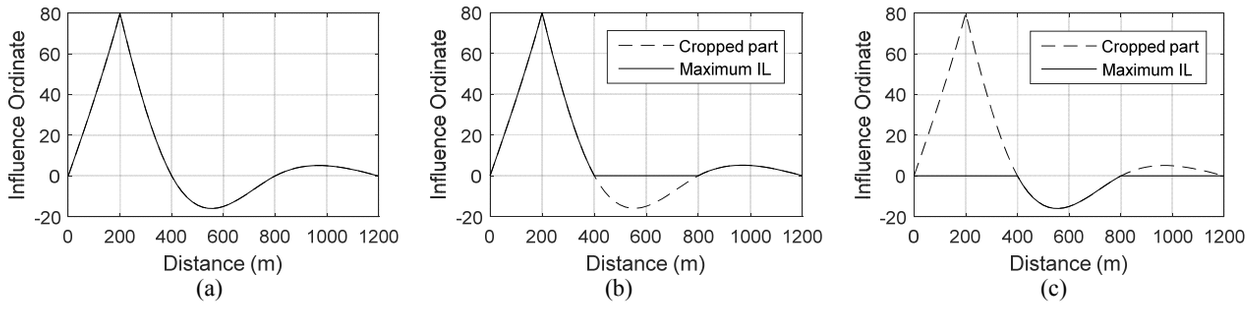


Figure 3. Influence lines of a generic 1200 m bridge for traffic patterning: (a) complete; (b) maximum and (c) minimum

3.3 *Study 1: The relationships between bottleneck and time headway (natural traffic).*

OBrien et al. (2015) and Caprani et al. (2016) respectively consider single and multi-lane LEs caused by different forms of traffic. However, the ILs used in these works are insensitive to load patterning. In fact, little work has been done in the literature to analyse the impact of different forms of traffic congestion on ILs with multiple lobes: those ILs with alternating positive and negative regions that are sensitive to load patterning. To solve this problem, a series of congestion types are generated by the layout settings in Figure 4 with the considered generic bridge and the hypothetical IL. Figure 5 shows the relationship between the locally-modified safe time headway parameter and resulting bottleneck strength which serves as a proxy for the type of congestion, based on the above layout. The results are close to those found in the previous papers (Treiber et al., 2000, Caprani et al., 2012, OBrien et al., 2015, Caprani et al., 2016).

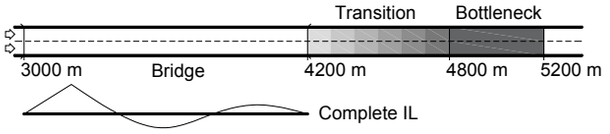


Figure 4. The simulation layout for Study 1.

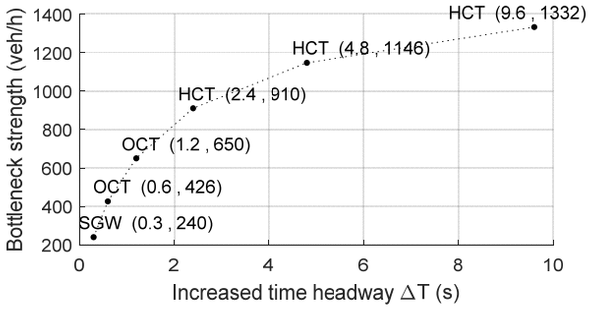


Figure 5. Congestion types and the relationship between time headway ΔT and bottleneck strength ΔQ. The number in the bracket is the coordinate of each dot point.

For each bottleneck strength considered, the maximum and minimum LE are extrapolated using the extreme values described previously. The results are shown in Figure 6. It can be expected that for the maximum LE, the free flow traffic is the least onerous form of traffic, and congestion traffic types give higher LE. However, there is a "saddle" in the graph. The light bottleneck ΔQ = 240 veh/h and strong bottleneck ΔQ = 1332 veh/h both trigger high LEs. These correspond to SGW and HCT congestion respectively. The fact that stop-and-go-wave traffic gives high LEs indicates that the natural 'pressure waves' in traffic do cause onerous LEs for patterning-sensitive ILs. Furthermore, the LE caused by second strongest bottleneck ΔQ = 1146 veh/h is similar to that of the strongest bottleneck ΔQ = 1332 veh/h, but the simulation time is much shorter. Moreover, vehicles in the bottleneck ΔQ = 1332 veh/h are only run at 3 km/h, which is unrealistic. Consequently, the bottleneck of ΔQ = 1146 veh/h is chosen for further study.

Figure 6 shows that for the minimum LE, the SGW bottleneck ΔQ = 240 veh/h produces minimum values. This further proves that the natural variation of traffic is important to pattern sensitive ILs. The critical bottleneck of ΔQ = 240 veh/h is used.

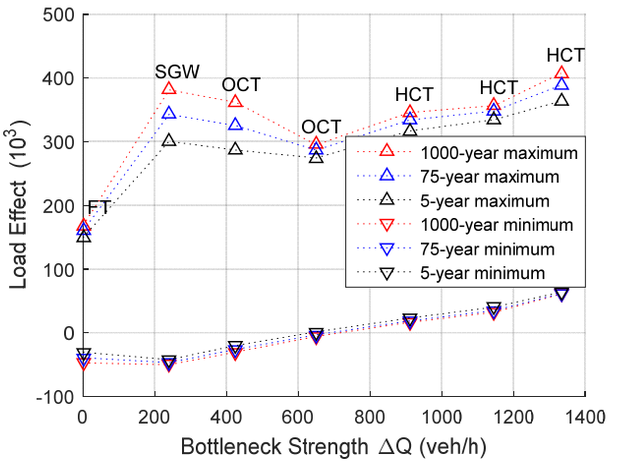


Figure 6. The relationship between middle bottleneck strength ΔQ and extrapolated LE in Study 1.

A useful visual representation of the traffic state is a spatio-temporal space mean speed (ST-SMS) plot (Treiber and Kesting, 2013). For the two critical types of traffic identified above, ΔQ = 240 veh/h and 1146 veh/h, ST-SMS plots are shown in Figure 7.

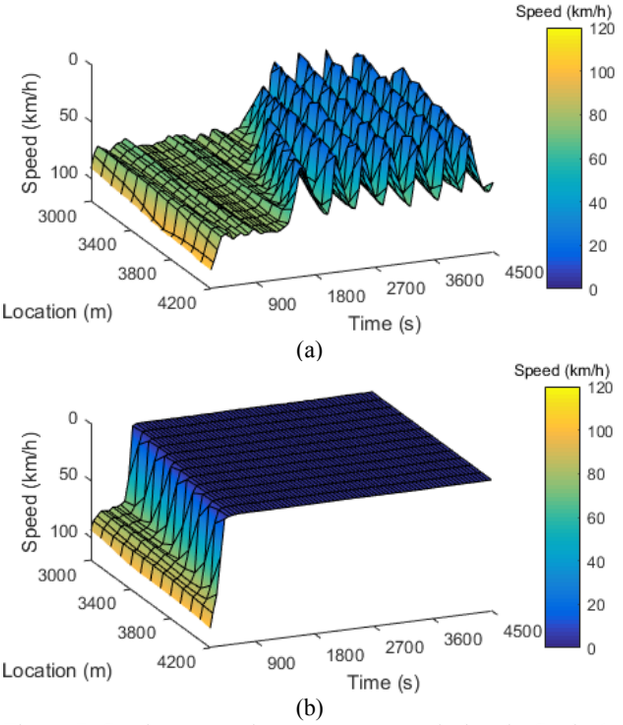


Figure 7. Spatio-temporal space mean speed plots in Study 1. (a) is ΔQ = 240 veh/h and (b) is ΔQ = 1146 veh/h traffic.

The difference in behaviour of the SGW and HCT forms of congestion is clear, and it is also clear that the pressure waves of the SGW are responsible for the high negative (minimum) LE observed. Of course, these findings are intuitively obvious, but the methods employed here allow them to be quantified, and allow further analysis of the less intuitive results.

3.4 *Study 2: Comparison between the real LE and load patterned LE (patterned traffic).*

In this study, the implications of typical code requirements to pattern live load are examined. The layout is shown in Figure 8. For the traffic stream simulated, as described earlier, this is effected by cropping the ILs. From the results of Study 1, the bottleneck strengths ΔQ = 1146 veh/h is used to cause HCT traffic in Study 2, which generates the maximum loading on the adverse or beneficial parts, leading to the maximum and minimum LEs.

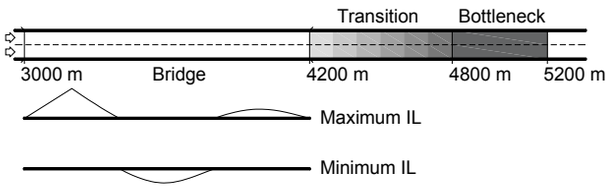


Figure 8. The simulation layout for Study 2.

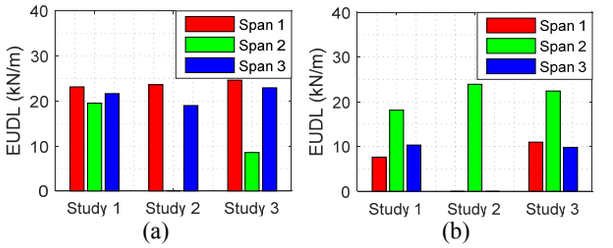


Figure 9. 1000-year extrapolated EUDL arrangement of a generic 1200 m bridge. (a) for maximum load effect and (b) for minimum load effect.

The results are expressed as a ratio to those of Study 1, for the bottleneck considered, and given in Table 2. The coincident total loads on each span are also extrapolated and converted to an equivalent uniformly distributed load (EUDL), and these are shown in Figure 9. For the maximum LE of 1000 years, the patterned traffic is 24.2% higher than that of the actual flow. The reason for this is evident from the EUDLs in Figure 9: Because the congestion traffic states of the characteristic LEs are the same (A small amount of variation is caused by extrapolation), the difference of 24.2% arises from the beneficial effect brought by the load in span 2. For the minimum LE of 1000 years, the difference becomes quite considerable at 124.4% of the LE for real traffic. Two aspects are different for this case: the critical traffic is stop-and-go waves (ΔQ = 240 veh/h), and the ratio of the beneficial and adverse areas of the IL is different.

In general, the conservatism in load modelling is significant, at least for this bridge and for IL.

Table 2. Load effects of a generic 1200 m bridge, expressed as a ratio of the 1000-year actual traffic results in Study 1.

Load effect	T_R*	Study 1	Study 2	Study 3
Maximum	5	93.8%	114.3%	107.2%
	75	97.6%	120.1%	113.0%
	1000	100.0%	124.2%	117.2%
Minimum	5	84.1%	205.6%	130.7%
	75	93.5%	216.7%	141.3%
	1000	100.0%	224.4%	148.0%

*T_R is the return period (years).

3.5 *Study 3: Cause of the critical case load patterning (manually controlled traffic)*

In this study, we examine the possibility that the traffic is actually modelled in a code-implied manner. To do this, we assume that two traffic accidents occur simultaneously at the critical positions of the IL, leading to the worst case maximum and minimum LE values. Figure 10 shows the hypothesized road layout for the worst-case scenario in maximum and minimum. The road topology is rather unrealistic, but in this study, we are only concerned about whether the patterned traffic is at all possible.

The additional bottleneck (No. 2) on the bridge is found to interact with the first bottleneck, limiting the throughput of vehicles in total. Therefore, several trial bottleneck strengths for the additional region are conducted. Again, the purpose is to have the minimum traffic density in the beneficial part of IL, while making the unfavourable part of the maximum density. But if the bottleneck is too small, there will be too many vehicles in the middle span (the two bottlenecks merge into one bottleneck). If it's too large, full congestion on the Span 3 will take longer to occur. In short, there is a trade-off between the vehicle density and congestion formation time. The results indicate that an empirical bottleneck strength of ΔQ = 1073 veh/h at the second incident location is suitable.

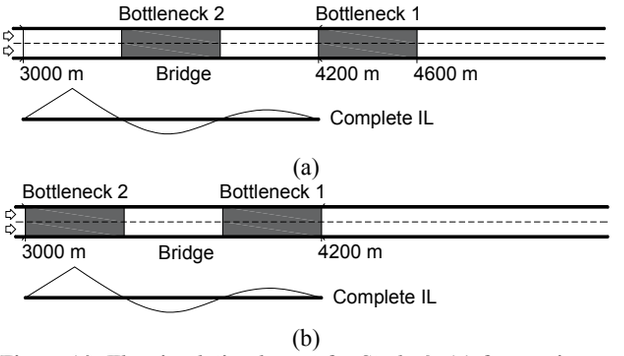


Figure 10. The simulation layout for Study 3. (a) for maximum load effect, and; (b) for minimum load effect.

In general, spatio-temporal density (ST-Density) plots show the vehicle numbers on the road sections. Figuratively speaking, the code-implied ST-Density plot would have a maximum density on the adverse regions and zero traffic density on the beneficial regions (Figure 11). This is considered as the target load patterned traffic densities. Corresponding to the target ST-Density plot, Figure 12 shows the actual ST-Density obtained in the simulation when road layout is simulated in Figure 10a. It can be seen that the road layout produces quite a similar result to the target, with a large number of the vehicles occupying the unfavourable parts. However, there are two points to note: (a) Because the vehicles can travel at high speed, the lowest density in the beneficial region occurs as traffic builds up at the second incident; (b) once the second incident has caused a high-density backlog of vehicles, a non-zero density of vehicles exists in the beneficial portion of the IL. Interestingly, for this optimised bottleneck setup (ΔQ_1 = 1073 veh/h and ΔQ_2 = 1146 veh/h), the beneficial region has a mean speed around 80 veh/km, which is near that of free-flow traffic. The result for the minimum follows the same logic and is listed in Table 2.

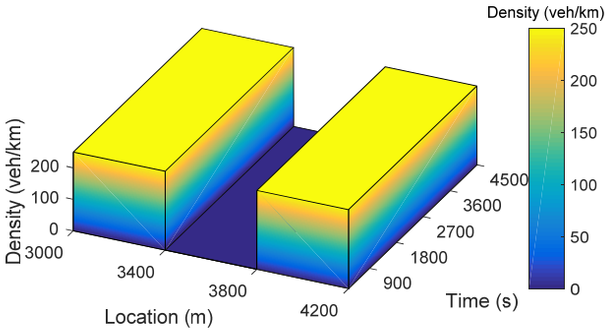


Figure 11. Spatio-temporal density plot for the target load pattern.

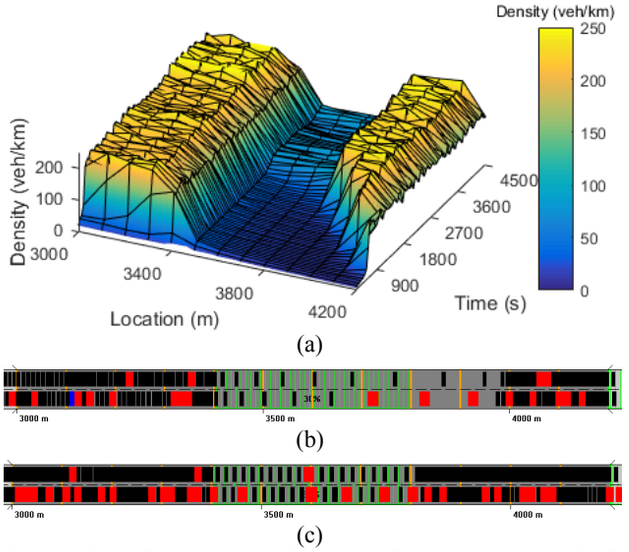


Figure 12. (a) Spatio-temporal density plot with maximum load effect. (b) is the traffic flow at time 1000 s in (a). (c) is the traffic flow at time 3000 s in (a). Note that the black boxes are cars and red boxes are trucks in SIMBA program.

This study suggests that it is possible to approach code-implied traffic patterning. However, multiple aspects must converge to make this possible: incidents must occur at the right place, and at a very specific set of inter-related bottleneck strengths. For normal traffic situations, the joint probability of these events is negligible. Finally, and importantly, in spite of the worst-case scenario approach, the results also show that it is impossible to have no traffic load on the beneficial parts of the IL. Obviously, a more rational approach to load patterning is needed.

4 RECOMMENDATION & CONCLUSION

Current codes and standards use a conservative load patterning approach to determine the design or assessment live load arrangement on the bridge. It only considers the worst-case scenario theoretically but ignores the probabilities of occurrence. The previously considered worst-case scenario is fully congested traffic (or HCT), however, SGW sometimes can be critical.

In this paper, a generic bridge is analysed with traffic microsimulation. It also considers a critical road topology with LE estimation. Three studies have shown that the traditional method is conservative: the LE is up to 1.24 times higher than that of any possible real traffic. It is also shown that it is impossible for traffic streams to pattern as per codes. A new load patterning method is needed for improved design and assessment of long-span bridges.

REFERENCES

AASHTO 2007. Bridge Design Specifications, Si Units. Washington DC: American Association of State Highway and Transportation Officials.

ASCE 2017. ASCE 2017 Report Card for America's Infrastructure.

BROCKFELD, E., KÜHNE, R. & WAGNER, P. 2004. Calibration and validation of microscopic traffic flow models. *Transportation Research Record: Journal of the Transportation Research Board*, 62-70.

BRULS, A., CROCE, P. & SANPAOLESI, L. 1996. ENV1991 - part 3: traffic loads on bridges: calibration of road load models for road bridges. *IABSE reports,* 74.

BUCKLAND, P. G. 1981. Recommended design loads for bridges. *Journal of the Structural Division,* 107.

CAPRANI, C. 2013. *Traffic Microsimulation for Bridge Loading Assessment and Management*.

CAPRANI, C. & OBRIEN, E. The governing form of traffic for highway bridge loading. 2008.

CAPRANI, C. C. 2005. Probalistic analysis of highway bridge traffic loading.

CAPRANI, C. C. 2012. Calibration of a Congestion Load Model for Highway Bridges Using Traffic Microsimulation. *Structural Engineering International,* 22, 342-348.

CAPRANI, C. C., LIPARI, A. & OBRIEN, E. J. 2012. Load effect of multi-lane traffic simulations on long-span bridges. *Bridge Maintenance, Safety, Management, Resilience and Sustainability*. CRC Press.

CAPRANI, C. C., OBRIEN, E. J. & LIPARI, A. 2016. Long-span bridge traffic loading based on multi-lane traffic micro-simulation. *Engineering Structures,* 115**,** 207-219.
CAREY, C., CAPRANI, C. C. & ENRIGHT, B. 2017. A pseudo-microsimulation approach for modelling congested traffic loading on long-span bridges. *Structure and Infrastructure Engineering***,** 1-14.
CASTILLO, E. 2012. *Extreme value theory in engineering*, Elsevier.
CEN 2003. EN 1991-2:2003 Eurocode 1: Actions on Structures *Part 2: Traffic Loads on Bridges*. Brussels: European Committee for Standardization.
CHEN, C., LI, L., HU, J. & GENG, C. Calibration of MITSIM and IDM car-following model based on NGSIM trajectory datasets. Vehicular Electronics and Safety (ICVES), 2010 IEEE International Conference on, 2010. IEEE, 48-53.
DITLEVSEN, O. & MADSEN, H. O. 1994. Stochastic vehicle-queue-load model for large bridges. *Journal of engineering mechanics,* 120**,** 1829-1847.
FWA, T. F. & LI, S. 1995. Estimation of Lane Distribution of Truck Traffic for Pavement Design. *Journal of Transportation Engineering-Asce,* 121**,** 241-248.
HELBING, D., TREIBER, M., KESTING, A. & SCHÖNHOF, M. 2009. Theoretical vs. empirical classification and prediction of congested traffic states. *The European Physical Journal B-Condensed Matter and Complex Systems,* 69**,** 583-598.
IVY, R., LIN, T., MITCHELL, S., RAAB, N., RICHEY, V. & SCHEFFEY, C. 1954. Live loading for long-span highway bridges. *American Society of Civil Engineers Transactions*.
JACOB, B. & LABRY, D. Evaluation of the effects of heavy vehicles on bridges fatigue. Proceedings 7th International Symposium on Heavy Vehicle Weights & Dimensions, 2002.
KESTING, A. & TREIBER, M. 2008. Calibrating car-following models by using trajectory data: Methodological study. *Transportation Research Record: Journal of the Transportation Research Board***,** 148-156.
KESTING, A., TREIBER, M. & HELBING, D. 2007. General Lane-Changing Model MOBIL for Car-Following Models. *Transportation Research Record: Journal of the Transportation Research Board,* 1999**,** 86-94.
KITE, S., HUSSAIN, N. & CARTER, M. 2011. Forth Replacement Crossing – Scotland, UK. *Procedia Engineering,* 14**,** 1480-1484.
LIPARI, A. 2013. *Micro-simulation modelling of traffic loading on long-span bridges.* University College Dublin.
LIPARI, A., CAPRANI, C. C. & OBRIEN, E. J. 2017. A methodology for calculating congested traffic characteristic loading on long-span bridges using site-specific data. *Computers & Structures,* 190**,** 1-12.
MARIA, J. D., CAPRANI, C. C. & GUO, D. 2017. Long span bridges – current age & design life – a global survey.
NOWAK, A. S., LUTOMIRSKA, M. & SHEIKH IBRAHIM, F. 2010. The development of live load for long span bridges. *Bridge Structures,* 6**,** 73-79.
OBRIEN, E. J., HAYRAPETOVA, A. & WALSH, C. 2012. The use of micro-simulation for congested traffic load modeling of medium- and long-span bridges. *Structure and Infrastructure Engineering,* 8**,** 269-276.
OBRIEN, E. J., LIPARI, A. & CAPRANI, C. C. 2015. Micro-simulation of single-lane traffic to identify critical loading conditions for long-span bridges. *Engineering Structures,* 94**,** 137-148.
OROSZ, G., WILSON, R. E. & STÉPÁN, G. 2010. Traffic jams: dynamics and control. *Philosophical Transactions of the Royal Society A: Mathematical, Physical and Engineering Sciences,* 368**,** 4455-4479.
RICKETTS, N. & PAGE, J. 1997. Traffic data for highway bridge loading. *TRL REPORT 251*.
STANDARDS AUSTRALIA 2017. AS 5100.2:2017 Bridge design. *Design loads.* Standards Australia.
TREIBER, M., HENNECKE, A. & HELBING, D. 2000. Congested traffic states in empirical observations and microscopic simulations. *Physical Review E.*
TREIBER, M. & KESTING, A. 2013. *Traffic flow dynamics*.
ZHOU, J., RUAN, X. & CAPRANI, C. C. 2015. Characteristic of traffic loading response for multi span large bridge. *In:* MAGALHAES, P. P. A. F. (ed.). CRC Press.

Maintenance, Safety, Risk, Management and Life-Cycle Performance of Bridges – Powers, Frangopol, Al-Mahaidi & Caprani (Eds)
© 2018 Taylor & Francis Group, London, ISBN 978-1-138-73045-8

Traffic and wind simulation for extreme loads on long-span bridges

A.A. Hayrapetova & A.J. O'Connor
Roughan and O'Donovan Innovation Solutions, Dublin, Ireland
J.D. Sørensen & H.S. Toft
Department of Civil Engineering, Aalborg University, Aalborg, Denmark

ABSTRACT: Long span bridges are repeatedly subjected to the simultaneous presence of multiple vehicles and predominantly vulnerable to wind induced effects. This paper presents an advanced traffic-wind modelling approach that extends and improves the load prediction capabilities within both the above mentioned load categories dependent on the given site-specific traffic and wind conditions. The traffic load on a bridge is modelled using a random mixing process for trucks and cars in each lane, where each vehicle is modelled individually with driver behavior parameters assigned randomly. The wind load on a bridge is divided into erratic components the modelling of which is based on the spectral tensor method. A general framework for analyzing for the combined effect of extreme traffic and associated wind loading in ultimate limit state analysis is developed and studied for a cable-stayed bridge.

1 INTRODUCTION

The design of long span structures such as cable-stayed and suspension bridges are subjected to many uncertainties due to stochastic wind actions and traffic mix/growth factors, detailed consideration of which are outside the scope of the current codes of practice. The European code for bridge design (Eurocode 1, EN 1991) provides a set of comprehensive methods for traffic and wind load representation on bridges having length and height not exceeding 200m. Based on the calculation of the most severe characteristic load effects, the Eurocode simplified load models may lead to conservative results for the longer structures. However, more accurate assessment loading can result in the retention of existing bridges for longer lives and opens up the prospect of designing longer spans.

The method proposed in this paper aims to contribute to the development of the lifetime performance evaluation of long span bridges through the application of accurate load modelling, such as traffic micro-simulation considered with instantaneous simulation of wind components. In the micro-simulation approach, traffic on a bridge is presented as a multi-vehicle system where each vehicle has its own set of geometrical characteristics and driver-behavioural preferences. The wind modelling is based on the spectral tensor representation method (Mann 1998) which leads to a more natural and more direct representation of the three-dimensional wind turbulent velocity field. Combined simulation stochastically and dynamically models discrete vehicle movements and wind fluctuations as a function of time and space within a system of a road-bridge network.

In the interaction mechanism between traffic and wind actions, there are local changes in aerodynamic forces due to the traffic presence on the bridge, which changes the shape of the structure exposed to wind. This effect increases when the dimension ratios between the traffic and bridge increase, e.g., when the traffic is congested.

The present study addresses extreme loading arising only from the governing traffic conditions and associated wind.

2 SIMULATION OF TRAFFIC LOADS AND THEIR EFFECTS

The "micro-simulation on parallel computers" software package Paramics (www.sias.ie) was selected as a traffic simulator in this study. It includes an advanced microscopic car-following model and inclusion of intelligent traffic system, which governs the movement of individual vehicles on the road network. Each vehicle is moved through the network according to its physical characteristics (i.e. vehicle size), the fundamental rules of motion (i.e.

time/velocity/distance) and rules of driver behavior (i.e. car-following rules and lane-changing). The driver behavior is controlled by a set of parameters combining driver constrains (e.g. driver's desired speed, awareness and aggressiveness, road speed limit, incident) and limitations based on vehicle type and kinematics (maximum speed and acceleration/deceleration capability). The mathematical model of the movement of driver-vehicle units in the system is based on the psycho-physical theory (Weidemann 1974, Fritzche 1994).

2.1 *Traffic analytical representation*

2.1.1 *Description of traffic regimes*

The simulations were performed for three distinct traffic regimes incorporating the vehicle velocity and density (Kerner, 2004):

1) $\rho_t^1 > 60$ *vehicle/km/lane,* $v_t^2 \leq 10$*km/hr*: Congested traffic flow where the average speed and the flow rate are nearly synchronised in different road lanes and remain 'stationary' during a relatively long time interval;
2) $20 < \rho_t \leq 60$ *vehicle/km/lane,* $10\text{km/hr} < v_t \leq 50\text{km/hr}$: Transition traffic flow of medium density where there is a difference in vehicle speeds across different lanes on a multi-lane road;
3) $0 < \rho_t \leq 20$ *vehicle/km/lane,* $v_t > 50$*km/hr*: Free-flowing where due to low traffic density lane changes are uninhibited and vehicles are fully free to change lane and to pass.

2.1.2 *Simulation of macro-components of traffic*

In the simulation, time is divided into a sequence of ½ second steps. For every iteration or time-step, three fundamental processes are carried out: (1) release vehicle, (2) set speed and (3) move forward. The vehicle release algorithm uses a number generated from a negative binomial distribution given by $P(n) = q(1\text{-}q)^{n-1}$ where $P(n)$ is the probability of $T_R = n$ and q is the probability of a vehicle being released in any one second. The general principle used within the speed-setting algorithm is that a number of constrains such as the target speed of the driver-vehicle unit, the speed of the vehicle in front, the car following model etc. are defined and an acceleration value is calculated for each constraint. The lowest of all the acceleration values, which may be negative, i.e., a deceleration, is then applied to the current speed to determine the speed of the vehicle in the next time-step. At each time step (Δt) in the simulation, each driver-vehicle unit is moved forward along its road a distance $d_t = v_t \Delta t$, where v_t is the current speed of the vehicle.

2.1.3 *Simulation of micro-components of traffic*

Driver behavior. A driver-vehicle (referred as to a Driver-Vehicle Unit (*DVU*)) response to its environment is described in the model by two parameters, driver's target headway (*h)* and reaction time *(r)*. The target headway is the bumper-to-bumper time gap that drivers try to achieve when following other vehicles in traffic. The reaction time is the lag in time between a change of speed of the preceding vehicle and the following vehicle's reaction to that change. In order to maintain safe operation, the drivers' headway needs to be at least as great as their reaction time.

Driver behaviour in the model is performed to reproduce micro- features of traffic under aggressive, rational and conservative patterns of driver behaviour. High aggressiveness would cause drivers to adopt lesser headways when following each other in the same lane or changing to a target lane. To determine the behaviour type the driver belongs to, a probabilistic model that is based on target headway *(h)* and reaction time *(r)* is used. The distribution, mean value and the coefficient of variation (COV) of the input values for the variables (*h)* and (*r)* are assumed according to inter-vehicle gap and reaction time in seconds, which are typical for drivers' behaviour in the real world and were determined using empirical observation data from earlier studies (Paramics 2002). Thus, for an "aggressive" pattern of behaviour, the mean values of h = 0.6sec and r = 0.4sec, which lead to dangerous driver behaviour in jams, are used. h = 1sec and r = 1sec in moderately dense traffic are dominant and assumed as "rational" behaviour. Finally, h = 2sec and r = 2sec are identified with safety conscious drivers, i.e., "conservative" pattern of behaviour. Heterogeneity across drivers is captured through the (*h)* and (*r)* variables sampled from the Normal statistical distribution that is not skewed to a particular direction of more aggressive or more conservative driver behaviour. Demonstrative scenarios are defined in Table 1 to cover the distinctive load combinations of the stochastic traffic.

Lane changing and overtaking. Variables *(h)* and *(r)* drawn from a statistical distribution and randomly allocated to the vehicles affect propensity to change lane. Lane changing in the model is done using gap-acceptance and gap availability policy. Considering traffic in both the current and the target lane (Figure 1): for a DVU_0 moving at a constant speed, a gap must exist both in front (lead) and behind (lag) the position it would occupy that is at least as large

[1] ρ_t – traffic flow density
[2] v_t – traffic flow average speed

as the target headway for that DVU_0. If there is a speed difference between the two lanes, this expression is extended to take into account the time it would take for the DVU_0 to attain the speed of the DVU_1 it would follow in the target lane. A vehicle will adjust its acceleration to find an acceptable gap. At all times the target range of lanes is adjusted subject to the behaviour parameters associated with the *DVU*: more aggressive drivers accept a smaller gap to force their way in. If no such gap is found, a vehicle will remain in its lane. Vehicles in the target lane DVU_2 may reduce to allow a 'courtesy let in'.

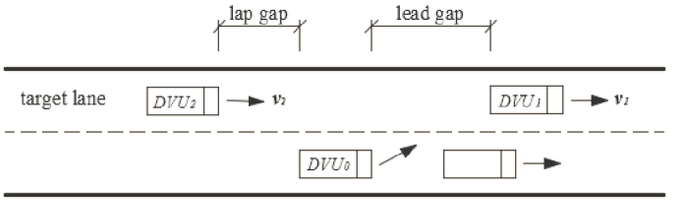


Figure 1. Gap acceptance model.

Table 1. Statistic of random driver behaviour variables.

Traffic regime	Driver behaviour	Statistical distribution	Target headway, *h (sec)*		Reaction Time, *r (sec)*	
			Mean	COV	Mean	COV
congested	aggressive	Normal	0.6	0.2 – 0.3	0.4	0.1 – 0.2
transition	rational	Normal	1.0	0.5 - 1.0	1.0	0.5 - 1.0
free-flowing	conservative	Normal	2.0	1.0 - 2.0	2.0	1.0 - 2.0

2.2 *Traffic load modelling*

The methodology used to derive traffic load models for long span bridges combines traffic microsimulation with bridge finite element analysis. Vehicle weights measured, e.g. from a Weigh-in-Motion station, are used to add statistically representative weights. For each vehicle type the measured histogram of gross vehicle weight is fitted to a bimodal Gaussian statistical distribution (O'Connor et al. 2001). Monte Carlo simulation is then used to generate weight data appropriate to the histogram.

The dynamic effect is modeled by multiplying each simulated static load from the vehicle by a normally generated random factor ϕ_{dyn} determined as (DRD 2004, O'Connor & Enevoldsen 2009):

$$\phi_{dyn} = [1 + N(41.5/W_{veh}\,; 41.5/W_{veh}\,)] \quad (1)$$

where W_{veh} (kN) = total vehicle weight.

In conditional passage of traffic at speeds v_t below 10km/h the dynamic supplement is negligible. Therefore, the following rules were adopted:

$$if\ v_t \le 10,\ \phi_{dyn} = 1$$
$$if\ v_t > 10, 1 < \phi_{dyn} \le 2 \quad (2)$$

2.3 *Model uncertainties*

The factors involved in the assessment of the traffic loads contain uncertainties. The distribution, mean and COV of the model uncertainties for vehicle loads can be introduced into the simulation as suggested in Table 2 (DRD, 2004).

Table 2. Statistical characterization of model uncertainty related to the traffic loads.

Traffic Regime	Distribution	Mean	COV
congested	Normal	1.0	0.2
transition	Normal	1.0	0.15
free-flowing	Normal	1.0	0.1

3 SIMULATION OF WIND LOADS AND THEIR EFFECTS

The wind field model for atmospheric surface layer turbulence developed by Mann was selected as a wind simulator in this study (Mann 1998). The basis of Mann's model is an application of rapid distortion theory implying a linearization of the Navier-Stokes equation, combined with the modelling of eddy lifetimes. The method is based on a model of the spectral tensor for atmospheric surface-layer turbulence at high wind speeds and can simulate three-dimensional fields of wind velocity fluctuations.

The tensor model has been successfully checked and calibrated with data from different atmospheric experiments which have been carried out with the purpose of estimating wind loads on large suspension bridges and wind turbines (Mann 1994).

3.1 *Wind analytical representation*

In the analysis of the wind characteristics, the wind field velocities over horizontal terrain is decomposed into the components of random processes consisting of (1) a constant mean wind speed V_m in the mean wind direction and (2) zero-mean turbulent $u_{x,y,z}(t)$ – along-wind, $v_{x,y,z}(t)$ – across-wind horizontal and $w_{x,y,z}(t)$ – across-wind vertical components fluctuating in space and time. Hence, the wind speed in the mean direction can be assumed as (ESDU 2001):

$$V_{x,y,z}(t) = [V_m + u_{x,y,z}(t), v_{x,y,z}(t), w_{x,y,z}(t)] \quad (3)$$

where V_m depends on the height variation of the wind and can be estimated over a selected time duration T of ten minutes or one hour averages of the basic wind speed irrespective of wind direction and time of year.

3.1.1 *Modelling of mean wind speed*

The long-term mean wind speed can be determined from a database of values recorded at or near the bridge site. The probability distribution function which normally fits the wind data satisfactorily is given by a Weibull PDF (e.g. Tuller & Brett 1984, Edwards & Hurst 2001) expressed as:

$$P(V_m) = 1 - exp[-{}^1\!/_2\,(V_m/\alpha)^k] \quad (5)$$

where k and α are shape and scale parameters, respectively.

The extreme mean wind speed to be used when the wind load effect is dominant is often assumed to follow a Gumbel distribution for the maxima (e.g. Gross et al. 1994, Carta et al. 2009). In an ultimate limit state analysis the extreme loading to be assessed may result from actions including extreme mean wind speeds with a recurrence period of 50 years and extreme wind speed gusts (EN 1991-1-4:2004).

The variation of the mean wind velocity with height over terrain of homogeneous roughness is assumed to be described by the logarithmic profile law (EN 1991-1-4:2004):

$$V_m(z) = k_r(z/z0)v_b, \quad z_{min} \le z \le z_{max} \quad (6)$$

where $k_r = 0.19(z_0/z_{0II})^{0.07}$ = terrain roughness factor depending on the roughness length z_0; z_{0II} = 0.05m for terrain category II; z_{min} = minimum height defined in Table 4.1 of EN 1991-2:2003; z_{max} = 200m; v_b = basic wind velocity.

3.1.2 *Modelling of wind velocity turbulence*

The stochastic field of wind velocity turbulence can be represented in terms of a discrete Fourier series (Mann 1998):

$$u_i(\boldsymbol{x}) = \sum_{\boldsymbol{\kappa}} e^{-i\boldsymbol{\kappa x}}\, C_{ij}(\boldsymbol{\kappa}) n_j(\boldsymbol{\kappa}) \quad (7)$$

where $u_i = i_{th}$ component of the turbulent velocity; $\boldsymbol{x} = (x, y, z)$ vector of spatial coordinates; $\sum_{\boldsymbol{\kappa}}$ = sum over all $\boldsymbol{\kappa}$ = three-dimensional wave vector with components $\kappa_i = m2\pi/L_i$, integer $m = -N_i/2, \ldots, N_i/2$ and L_i = length of the simulated wind field in the i direction; $n_j(\boldsymbol{\kappa})$ = independent Gaussian stochastic complex variables with unit variance; and $C_{ij}(\boldsymbol{\kappa})$ = coefficient matrix (Equation 8).

$$C_{ij}(\boldsymbol{\kappa}) = \frac{(2\pi)^{3/2}}{V(B)^{1/2}} A_{ij}(\boldsymbol{\kappa}) = (\Delta\kappa_1 \Delta\kappa_2 \Delta\kappa_3)^{1/2} A_{ij}(\boldsymbol{\kappa}) \quad (8)$$

where $\Delta\kappa_i = 2\pi/L_i$; $A_{ij} = \sqrt{\Phi_{ij}}$ with Φ_{ij} = spectral velocity tensor (Equation 9).

$$\Phi_{ij}(\boldsymbol{\kappa}) = \frac{\langle dZ_i^*(\boldsymbol{\kappa}) dZ_j(\boldsymbol{\kappa})\rangle}{d\kappa_1 d\kappa_2 d\kappa_3} \quad (9)$$

The corresponding cross-spectra and coherence functions are defined as:

$$\chi_{ij}(\kappa_1, \Delta y, \Delta z) = \iint_{-\infty}^{\infty} \Phi_{ij}(\kappa) e^{-i(\kappa_2 \Delta y + \kappa_3 \Delta y)} d\kappa_2 d\kappa_3 \quad (10)$$

$$coh_{ij}(\kappa_1, \Delta y, \Delta x) = \frac{|\chi_{ij}(\kappa_1, \Delta y, \Delta z)|^2}{F_i(\kappa_1) F_j(\kappa_1)} \quad (11)$$

The implementation of the Mann's model includes the following three steps:

(1) evaluation of the coefficient $C_{ij}(\kappa)$ by Equation 8;
(2) simulation of the Gaussian variable $n_j(\kappa)$;
(3) calculation of $u_i(x)$ from Equation 7 by Fast Fourier transform.

3.2 *Wind load modelling*

To apply the simulated wind velocities to the bridge model, they first have to be transformed into force components. The general expression of wind forces per unit length can be given by the following formulas (EN 1991-1-4:2004):

$$\begin{aligned} F_x(t) &= {}^1\!/_2\, \rho\, V_x(t)^2\, C_x\, (c_s c_d)_x\, d_{tot}\, L\, J_w \\ F_z(t) &= {}^1\!/_2\, \rho\, V_z(t)^2\, C_z\, (c_s c_d)_z\, b\, L\, J_w \\ M_y(t) &= {}^1\!/_2\, \rho\, V_y(t)^2\, C_y\, (c_s c_d)_y\, b^2\, L\, J_w \end{aligned} \quad (12)$$

where ρ = air mass density; $V(t)$ = wind instantaneous velocity, Equation 3; C = wind load factor; $c_s c_d$ = structural factor; L = length; d_{tot} = reference depth; b = width, J_w = factor taking into account the model uncertainties (see Section 3.3).

For a bridge structure the parameter which varies during the service life with and without traffic, is the reference depth d_{tot} (Figure 2) of exposure on wind action transversely to the deck (EN 1991-1-4:2004):

$$\begin{aligned} d_{tot} &= d + d_1 \quad && without\ traffic \\ d_{tot} &= d + d^* && with\ traffic \end{aligned} \quad (13)$$

where d = bridge depth; d_1 = parapet/barrier depth; d^* = 2m and 4m from the level of the carriageway, independently of the location of the vertical traffic loads on road and railway bridges, respectively.

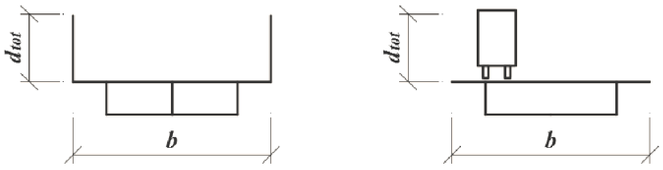


Figure 2. Reference depth.

The methodology used in this study to derive the wind pressure effects of passing vehicles is combined with the traffic micro-simulation model described in Section 2. For this reason, the traffic streams from the 'snapshot' files generated during the micro-simulation are used to calculate d_{tot} for each specified time step interval.

3.3 *Model uncertainties*

The wind model uncertainty J_w (Equation 12) includes the uncertainty of the parameters describing the model scale disagreement (model-size/full-size) and the wind climate. The distribution, mean and COV of the wind forces can be expressed as suggested in Table 3 (SAKO 1999).

Table 3. Statistic of random variables involved in the assessment of the wind loading.

Variable	Distribution	Mean	COV
model scale uncertainty	Lognormal	1.0	0.1
wind climate uncertainty	Lognormal	1.0	0.1

4 ANALYSIS FLOWCHART

The methodology developed in this paper combines three computer-aided techniques: traffic micro-simulation, Mann's model of wind simulation and bridge finite element (FE) analysis. In the first two steps, micro-simulation is used to predict multi-lane traffic and multi-component wind actions on the bridge. In the third step, FE structural analysis is used to compute the response of the bridge structure under the traffic and wind loads predicted in the first two steps. A communication interface program (CIP) is developed to link the three techniques with supplementary features and to compile the input and output data. The application of the theory outlined above is illustrated in the following sections.

5 NUMERICAL EXAMPLE

5.1 *Definition of long span cable-stayed bridge*

The bridge considered in this study is a cable-stayed concrete box girder with spans arrangement of 69.3m-130m-204m-204m-130-70m (Figure 3). It supports the cables by means of three concrete U-shape towers. There are 9 pairs of stay cables on either side of the tower with angle varying from 95 to 115 degrees. The deck of the bridge is 15.9m wide, with a single cell prestressed concrete box at constant depth of 3.5m. The bridge model considered for the analysis of the structure uses 3D frame FE with linear material and geometrical properties.

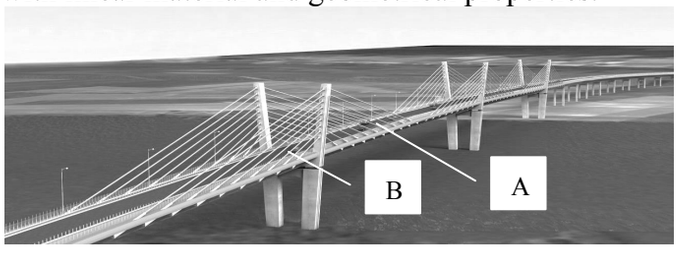


Figure 3. Bridge computer model visualization in isometric view: A – section at mid-span, B – section at support.

5.2 *Traffic load time-series simulation*

The road network has been modelled as a linear corridor adjacent to the bridge of length L = 809m with the approaching roadway at each end of the bridge equal to 5km. It was constructed with details of lanes, types and mix of vehicles and their characteristics.

Three regimes of traffic with assigned driver preferences defined in Section 2, Table 1, were artificially generated from the Auxerre traffic data (A6 motorway, France) on three lanes assuming 10% trucks for each lane. This condition is based on the philosophy of the Eurocode load model development and is by 1-step more severe than the condition measured in Auxerre (O'Connor et al. 2001, Sedlacek 2008).

The input traffic data assigned to scenarios are summarized in Tables 4 and 5. Clearly, the 'behaviour' of traffic at any particular instant is determined by the various conditions prevailing at that instant and these conditions are constantly changing. It is desirable therefore to relate traffic response to the periodic traffic flow without major changes in flow rate within the period. For that reason, the daily traffic volume was subdivided into 12 time periods of 2 hours duration.

Periodic simulation runs of the representative traffic of 1-year duration were executed for the selected bridge. Traffic load streams were obtained from the 'snapshot' files at 1-second intervals. Simulated patterns with the assigned vehicle weights, Table 5, were applied to the bridge model and its responses calculated, Figure 4. The bridge model itself is represented through the IS for longitudinal moments at mid-span (A) and support (B) of the main girder, Figure 3.

Table 4. Input data for traffic scenarios simulation

Variable	Symbol / Unit	Value
Bridge length	L_b *(m)*	809
Road length	L_r *(m)*	5000+L_b+5000
Road speed limit	v_{max} *(km/h)*	100
Number of lanes	N_l	3
Lane width	W_l *(m)*	3
Vehicle configuration	-	Table 5
Weight of vehicles	W_{veh} *(kN)*	Table 5
Percentage of trucks	-	10%
Target headway	*h (s)*	Table 1
Target reaction time	*r (s)*	Table 1
Vehicle desired speed	v_d* *(km/h)*	v_{d_car}=100, v_{d_truc}=75
Max acceleration rate	*a* (m/sec^2)	a_{car}=2.50, a_{truck}=1.40
Max deceleration rate	*d* (m/sec^2)	a_{car}=4.50, a_{truck}=3.70

*v_d – desired speed the driver wants to maintain after considering the road speed limit and the effect of surrounding traffic.

Table 5. Vehicle characteristics

Vehicle Type		Number of axles	Length (m)	Width (m)	Height (m)	Relative frequency (%)	Vehicle weight (kN) unloaded mean	unloaded SD	loaded mean	loaded SD
-	car	-	5.25	1.8	1.4	-	-	-	-	-
Type 1		2	7.5	2.5	4.0	10.6	70	35	190	30
Type 2		3	7.5	2.5	4.0	61.8	115	45	255	40
Type 3		5	14.5	2.5	4.0	25.2	225	60	435	75
Type 4		6	9.5	2.5	4.0	2.4	245	70	450	65

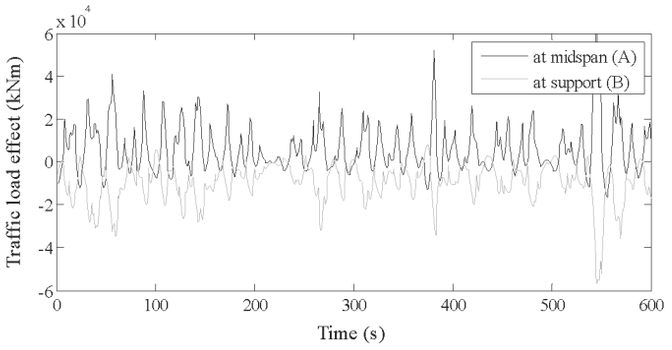


Figure 4. 10-minute simulation of longitudinal bending moment histories at mid-span (A) and support (B) of the bridge.

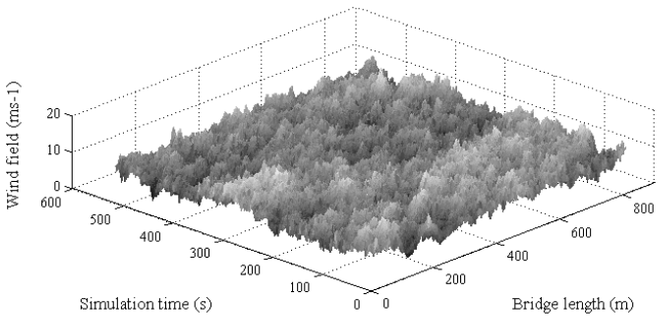


Figure 5. 10-min simulation of wind field on the main girder of the bridge in transverse direction.

5.3 *Wind load time-series simulation*

The wind climate at a given bridge site was characterised by the Weibull PDF of 10-minute wind speed averages V_m. For each value of V_m the Mann's simulator generated an estimate of the correlated along-wind *u(t)* and across-wind components *v(t)* and *w(t)* using spectral tensor function of Equation 7. Figure 5 demonstrates a 10-min simulation of along-wind field in x-direction parallel to the deck width and perpendicular to the span at positions horizontally aligned with 1m-separation.

Simulations of the random wind of 1-year duration were executed for the selected bridge. The input data assigned to the wind model are summarized in Table 6. The wind forces from the mixture of wind components, were calculated according to Equation 12 and applied to the bridge model and its responses calculated (as described in Section 4), Figure 6.

For the transverse wind pressure effects of the passing vehicles, the values of the depth d_{tot} (Equation 13) were obtained from the traffic snapshots at each time step of simulation. Figure 7 shows the distributions of d_{tot} averages for two regimes of simulated traffic compared to the corresponding Eurocode values.

Table 6. Input data assumed for wind simulation.

Parameter	Symbol / Unit / Description	Value
Mean wind speed	Weibull distribution:	
	shape factor	2
	scale factor *(m/s)*	10
Height of structure	*z (m)*	15
Terrain roughness	z_0*(m)*	0.05

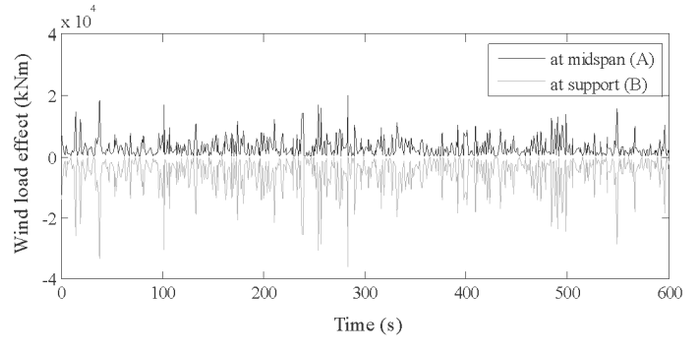


Figure 6. Transverse bending moment histories calculated from along-wind speed components in x-direction under passing congested traffic.

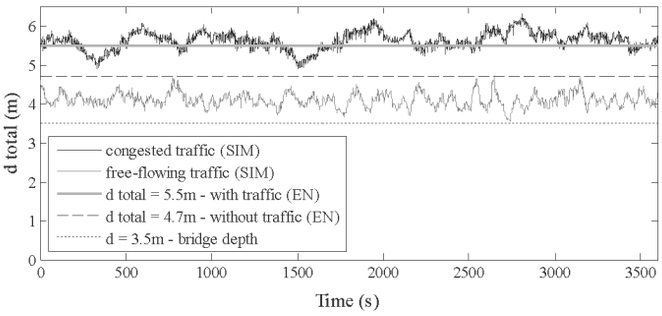


Figure 7. The distribution of the depth d_{tot} averages obtained from different regimes of traffic micro-simulations (SIM – simulated, EN – Eurocode value).

5.4 *Extreme traffic load and accompanying wind load for extreme analysis*

The statistical analysis of data in this study is based on the samples of maximum traffic load effects combined with associated wind in the vertical direction. The largest traffic and associated wind bending moments at critical locations A and B of the bridge deck were selected per hour from the parent popula-

tion of empirical traffic and wind load effects simulated for a 1-year period. Which PDF fits the data best depends on different conditions and the statistical parameters (e.g., size of random sample) are of importance. Since in the current work, the bending moment is obtained from the sum of effects generated from a large number of independent loads from the random vehicle weights, it is to be expected from the central limit theorem that the instantaneous bending moment is normally distributed. Assuming the hourly maximum of the bending moments to be Normal distribution, the extreme value *CDF* and *PDF* can be approximated as:

$$F_x(x) = F^n(x) = \Phi^n[(x-\mu)/\sigma] \quad (14)$$

$$f_x(x) = nF^{n-1}(x)f(x) \quad (15)$$

for some equivalent number n of independent Gaussian random variables in the sample, where Φ is the standardized normal distribution function and μ, σ are the mean and standard deviation, respectively, of the Gaussian random variables. With Δt time step in seconds, each of these bending moment maxima is the maximum of a sample of $3600/\Delta t$ mutually dependent Gaussian random variables. If the traffic speed is v_t, all vehicles within the length of the bridge L_b = 809m are replaced with $L_b/(v_t\Delta t)$ simulation steps. Therefore, there are at least $\frac{\lceil 3600/\Delta t \rceil}{\lceil L_b/(v_t\Delta t)\rceil} = 4v_t$ independent Gaussian variables in each set of moment maxima, which can be assumed to be distributed according to the *CDF* and *PDF,* defined by Equation 14, 15.

Figure 8 illustrates the estimated extreme value distributions (EVDs) fitted well to the data that line up approximately along a straight line. The EVDs have been used to calculate the characteristic moment due to traffic and wind, i.e. the expected value of maximum moment. This is repeated for return periods of 10 to 1000 years.

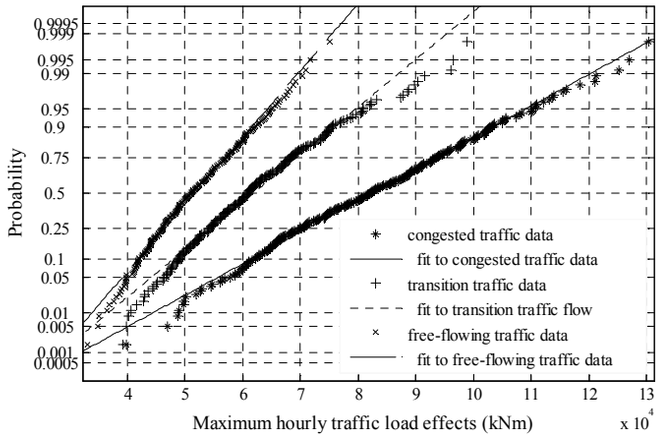


Figure 8. Mid-span moment distribution on probability plot

The extrapolated results are summarised in Table 7 where extreme traffic is combined with associated wind. The results show the peaks of longitudinal bending moments for congestion when the traffic is stationary, $v_t \leq$ 10km/h, and dynamic effect from traffic is ignored, ϕ_{dyn} = 1. The latter corresponds to platoons of trucks and cars travelling bumper-to-bumper. Clearly the lower moments for free-flowing and transition traffic result from the relatively bigger distances between the vehicles and thus simultaneously reduces the presence of loads on the bridge.

Table 7. Combined traffic and wind load effects simulated at mid-span (A) and support (B) of the bridge deck.

Traffic flow regime with associated wind	(a) Longitudinal moments (kNm)		(b) Transverse moments (kNm)	
	mid-span	support	mid-span	support
Free-flowing traffic	168527	177461	6285	-9175
Traffic in transition	200794	211630	8519	-10486
Congested traffic	230410	243993	8896	-11796
Without traffic	-	-	5983	-8738

5.5 *Comparison of results with Eurocode load models*

The simulated characteristic values are compared with the corresponding values for bending moments calculated in accordance with Eurocode 1. EN1991-2:2003 live load model 1 (LM1), consisting of concentrated and uniformly distributed loads, was used to represent the traffic load effect for general verification. The carriageway on the bridge deck was divided into notional lanes according to the formula for $w \geq 6$: $N = int(w/3)$, where w = 9m is the carriageway width. Taking three notional lanes, moments of *257640*kNm and *-296231*kNm were calculated for mid-span and support, respectively.

A simplified formula proposed in EN1991-1:2004 was used for the evaluation of the wind force:

$$F_W = {}^1/_2\ \rho\ v_b^2\ C\ A_{ref}\ C_s C_d \quad (16)$$

where ρ = density of air, v_b = basic wind speed, C = wind load factor, $CsCd$ = structural factor, $A_{ref} = bL$ and $d_{tot}L$ = vertical and transverse reference area.

In this case, the wind forces are the exact values: F_{Wvert} = *9077kN,* F_{Wtrans} = *5366kN* (without traffic), F_{Wtrans} = *6280kN* (with traffic).

The combination rules for variable actions utilised by EN1990 Annex A2 is:

$$E_d = \gamma_{QT} Q_T + \psi_{0W}\gamma_W Q_W \quad (17)$$

where Q_T and Q_W = characteristic values of the leading traffic action and accompanying wind action, respectively, γ_{QT} and γ_W = partial factors for traffic and wind accounting for model uncertainties and dimensional variations, and ψ_{0W} = wind combination

value. The methodology given in EN1990 has been further used to estimate the combined wind and traffic actions. Using the extreme value Normal distribution for time-dependent traffic and wind gives ψ_{0W} = 0.45. Although this value is lower than the value of 0.6 used in EN1990 Annex A1, it was decided to use 0.6 to achieve consistency with the EN1990.

Table 8 summarises the moments at mid-span (A) and support (B) calculated using Equation 17. Irrespective of the conservative assumptions made for the case study the difference is ≈ 25% between the Eurocode LM1 characteristic values and the corresponding simulated values. While the results will vary according to the assumptions made for site-specific situations, the outcome reflects the current code's conservatism for excessive loaded lengths.

Table 8. Comparison of characteristic values for longitudinal bending moment.

Load combination	(a) Simulated value (kNm)		(b) Eurocode value (kNm)	
	mid-span	support	mid-span	support
Traffic only	213617	-226211	257640	-296231
Traffic + wind	230410	-243993	277792	-332505

6 CONCLUSION

This paper proposes the use of advanced micro-simulation procedures in determining characteristic effects of stochastic traffic and wind loads on long-span bridges. The procedures are introduced as a tool for an extensive modelling of bridge-traffic-wind loading conditions derived from the real data when long-run simulation processes are required. The general aspects of the technique are outlined and demonstrated with reference to a specific case. Wind events in 3D turbulent fields are implemented in Mann's turbulence generator including the correlated response of all wind velocity components. Traffic events are generated using a micro-simulation approach as a multi-vehicle system where each vehicle has its own set of geometrical characteristics and driver-behavioral preferences. In the interaction mechanism between traffic and wind actions, the transverse wind pressure on the passing vehicles is obtained through the measurements of the reference depths d_{tot} of exposure from the snapshots of traffic at each time step of micro-simulation.

7 ACKNOWLEDGMENTS

The research leading to these results has received funding from the EU's Sevens Framework Programme (FP7/2007-2013) under the Marie Curie, Industry and Academia Partnerships and Pathways (IAPP) call, Grant agreement no. 286276.

8 REFERENCES

Carta, J.A., Ramírez, P., Velázquez, S. 2009. A reviewof wind speed probability distributions used in wind energy analysis. *Renew. Sustain. Energy Rev*. 13, 933-955.

Danish Road Directorate, DRD. 2004. Reliability-based classification of the load carrying capacity of existing bridges. *Report 291*.

Edwards, P.J., Hurst, R.B. 2001. Level-crossing statistics of the horizontal wind speed in the planetary surface boundary layer. *Chaos*, 11, 611-618.

EN 1990:2002 Eurocode – Basis of structural design.

EN 1991-2:2003 Eurocode 1: Action on structures – Part 2: Traffic loads on bridges.

EN 1991-1-4:2004 Eurocode 1: Actions on structures – General actions – Part 1-4: Wind actions.

ESDU. 2001. Characteristics of Atmospheric Turbulence Near the Ground, Part II: Single Point Data for Strong Winds.

Fritzsche, H.T. 1994. A model for traffic simulation. *Traffic Engineering and Control,* 35 (5), 317–321.

Gross, J., Heckert, A., Lechner, J. and Simiu, E. 1994. Novel Extreme Value Estimation Procedures: Application of Extreme Wind Data. *Extreme Value Theory and Applications*. Boston.

Kerner, B.S. 2004. Three-phase traffic theory and highway capacity. Physica A 333: 379-440.

Mann, J. 1998. Wind field simulation. *Prob.Engng.Mech*. Vol. 13, No. 4, pp 269-282.

Mann, J. 1994. Models in Micrometeorology. *Risø National Laboratory*, Roskilde, Denmark

O'Connor, A., Jacob, B., O'Brien, E., & Prat, M. 2001. Report of Current Studies Performed on Normal Load Model of EC1-Traffic Loads on Bridges, 5(4), RFGC, *Hermes Science Publications*: 411-434.

O'Connor, A. & Enevoldsen, I. 2008. Probability based assessment of an existing prestressed post-tensioned concrete bridge. *Engineering Structures*: 30, 1408 - 1416.

Paramics. 2002. Reference Manual. SIAS.

SAKO; Joint Committee of NKB and INSTA-B. 1999. Basis of design of structures. Proposal for modification of partial safety factors in Eurocodes. *NKB Committee and Work Reports*. 1990:01 E.

Sedlacek, G., Merzenich, G., Paschen, M., Bruls, A., Sanpaolesi, L., Croce, P., Calgaro, J.A., Pratt, M., Jacob, M., Leendertz, v. de Boer, Vrouwenfelder, A., Hanswille, G. 2008. Background document to EN 1991 – Part 2 – Traffic loads for road bridges – and consequences for the design. *JRC Scientific and Technical Report*, First Edition.

Tuller, S., Brett, A. 1984. The characteristics of wind velocity that favour the fitting of a Weibull distribution in wind speed analysis. *J.Appl.Meteorol*, 23, 124-134.

Weidemann, R. 1974. Simulation des Straßenverkehrsflusses. Institut für Verkehrswesen. *Universität Karlsruhe Schriftenreihe des IfV*, Vol. 8.

Maintenance, Safety, Risk, Management and Life-Cycle Performance of Bridges – Powers, Frangopol, Al-Mahaidi & Caprani (Eds)
© 2018 Taylor & Francis Group, London, ISBN 978-1-138-73045-8

Developing a new bridge live load model for South Africa

P.F. van der Spuy & R. Lenner
Stellenbosch University, South Africa

ABSTRACT: South Africa's bridge design code, TMH7, was first introduced in 1981. The code was found to be unconservative for narrow and short span bridges and revisions were issued in 1988. In 1991 it was proposed to increase the axle load by 25 % to 180 kN, but the code was not amended. In 1996 the legal limits for GVW and axle loads in South Africa were increased, but TMH7 loading was not updated. One year of WIM data was used to calculate hogging and sagging moments as well as shear forces for span lengths up to 50 m. The forces and axle weights were extrapolated normally to a return period of 975.3 years. The extrapolation resulted in a characteristic axle weight of 170 kN which was applied as a double axle. The extrapolated load effects and the tandem axle were used to calculate a characteristic distributed load of 15 kPa.

1 INTRODUCTION

South Africa's bridge design code, TMH7, was first introduced in 1981 and is based on the CEB-FIP Model Code of 1978 as well as BS5400 and the National Building Code of Canada. With time it was found that the code has various deficiencies, especially for narrow and short span bridges.

Revisions to the code were issued in 1988, but Oosthuizen et al. (1991) showed that the code still underestimated bending moments for spans between 4 m and 9 m as well as shear forces on span lengths below 23 m. A proposal was made to increase the axle load in lane 1 from 144 kN to 180 kN, but this amendment was never made. In 1996 the South African Department of Transport increased the legal gross vehicle weight and axle loads on South African roads, but no study was performed to determine the impact of this on the bridge loading code. The current load model is widely regarded as cumbersome to apply and various different applications thereof exist in industry.

When deriving the code in 1978, Liebenberg noted that a probabilistic study of extreme truck events was not viable due to a lack of statistical information at the time (Anderson 2006). Since then a substantial amount of WIM data has become available in South Africa.

WIM data was used to derive an improved live load model for bridge design in South Africa. This model is both up to date and simple to apply.

2 TMH7 LOAD MODELS

2.1 *NA loading*

NA loading is considered as normal traffic loading and consists of a distributed component (Figure 1) and an axle load in each lane. A dynamic allowance is included according to the Swiss formula (CSRA 1981).

The distributed component of NA loading, Q_{dist}, is 36 kN/m for the first 36 m loaded length and then reduces according to Equation 1.

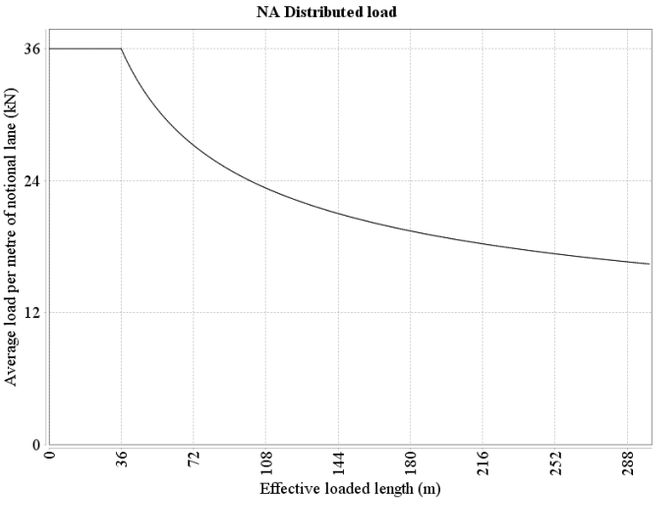


Figure 1. NA distributed load.

$$Q_{dist} = \frac{180}{\sqrt{L}} + 6 \quad (1)$$

where L = total aggregate loaded length.

The axle load component of NA loading, Q_{axle}, is given by Equation 2 in kN.

$$Q_{axle} = 144/\sqrt{n} \quad (2)$$

where n = the number of the notional lane in which the axle load occurs. The axle load therefore decreases as the number of loaded notional lanes increases.

2.2 *NB loading*

Nominal NB loading is a unit loading representing a single abnormally heavy vehicle. Thirty six units of NB loading are typically applied and referred to as NB36. This corresponds to a wheel load of 90 kN, an axle weight of 360 kN and a total weight of 1440 kN. The NB load configuration is shown in Figure 2.

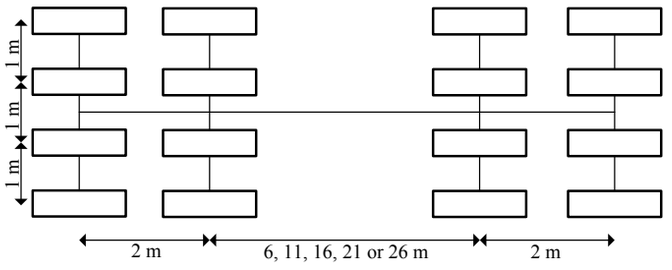


Figure 2. NB load configuration.

Only one NB vehicle is allowed on a bridge at a time without any other traffic loading acting in conjunction. No allowance is made for impact.

2.3 *NC loading*

Nominal NC loading is a loading representing multi-wheeled trailer combinations with controlled hydraulic suspension and steering intended to transport very heavy indivisible payloads. The applied loading is 30 kPa with a configuration as shown in Figure 3.

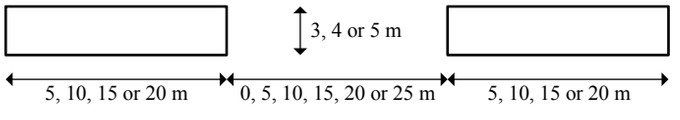


Figure 3. NC load configuration.

NC vehicles shall move along the centre line of a bridge only with an allowance of 1 m either side for moving offline. No allowance is made for impact.

3 REFERENCE TO EUROCODE

South African building and bridge design codes have historically been based on the British codes which have since been superseded by the Eurocodes (Van der Spuy 2014). Many of the building design codes in South Africa incorporate parts of the Eurocode or have adopted the Eurocode entirely. In this study the configuration of Load Model 1 of EN1991-2 (CEN 2003) was adopted as a preliminary measure, but different values were calculated for the axle and distributed loads.

4 WIM DATA

4.1 *Data source*

National Route 3 between Johannesburg and Durban is considered to be the heaviest freight route in South Africa (Lenner et al. 2017) and for this reason a station along this route was used for this study. The Roosboom WIM station has been measuring since November 2000 and the data from this station is considered to be of good quality (de Wet 2010a). One year (2016) of data was used as recommended by Sivakumar et al. (2008). This station measures traffic in the slow lanes in both directions.

4.2 *Traffic composition*

The number of vehicles in the year of data was 859 896. Figure 4 shows the distribution of vehicle types indicating that six and seven axle vehicles dominate the GVW tail.

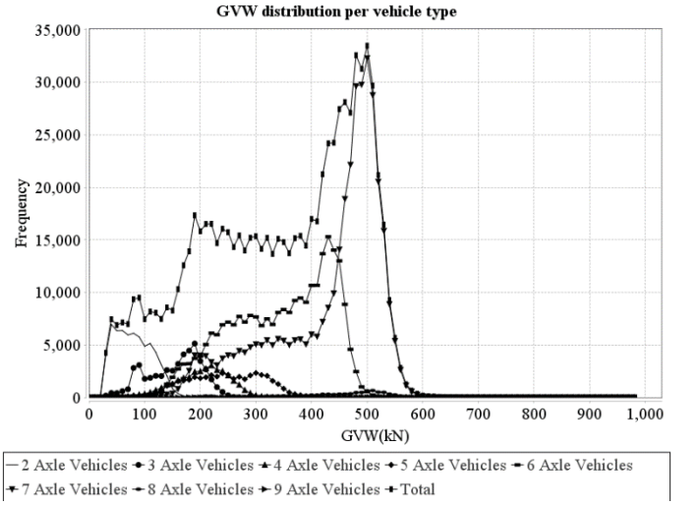


Figure 4. Vehicle type distribution.

Lenner et al. (2017) showed that, when compared to data from Auxerre measured in 1986, the South African axle loads are lower than those in Europe, but the GVW is higher. This serves as motivation not to adopt the Eurocode directly, but to calculate country specific axle and distributed loads for Load Model 1. The data from Auxerre, France, is the data that was

used to derive the Eurocode load models (Enright & OBrien 2012, Sedlacek et al. 2008, Zhou 2013, Zhou et al. 2012).

4.3 *Cleaning*

Slavik developed a technique called Golem (unpublished) to specifically address sources of WIM error for South African data. Golem rejects any vehicle that meets the following criteria:

- Travelling at less than 5 km/h or more than 150 km/h
- Truck length less than 4 m or longer than 26 m
- Fewer than two axles
- GVW less than 3.5 t
- Individual axle weight exceeding 16 t
- Axle spacing shorter than 0.53 m or longer than 10 m

Number of vehicle records removed by this screening is 33 855.

4.4 *Calibration*

De Wet (2010a,b) developed the Truck Tractor (TT) method which is a post-calibration procedure to correct the magnitude of recorded axle loads retrospectively. The application of this method results in a k-factor which is multiplied by all axle weights to suppress the systematic WIM error. The method has been accepted by the South African National Roads Agency Limited (SANRAL) and was applied in this study as a way to calibrate the data.

5 METHODOLOGY

5.1 *Span lengths investigated*

Short to medium span lengths between 5 m and 50 m were investigated based on the assumption that free flowing traffic governs for these span lengths (Caprani & OBrien 2010). Span lengths within this range cover the majority of bridges in South Africa.

5.2 *Creation of vehicle convoy*

Daily convoys of axles were created from the WIM file using axle distances as well as time stamps and speeds to determine inter-vehicle gaps. The time stamp resolution from the Roosboom station is 0.01 s which is preferable (Enright 2010).

5.3 *Calculation of load effects*

The load effects that were investigated are sagging moments and shear forces in single span structures and hogging moments in two span structures (Caprani 2005, Enright & OBrien 2012, Lenner 2014, Lenner et al. 2014). The daily convoys were passed over varying span lengths for the different load effects while recording the daily maximum values for each. The increment distance for the convoys was implemented as 0.444 m which corresponds to a time step of 0.02 s at 80 km/h.

5.4 *Return period*

A 5 % probability of exceedance in 50 years was used in this study, similar to the Eurocode (CEN 2003). This relates to a return period of 975.3 years (Enright 2010).

5.5 *Extrapolation*

With WIM data not being available for the full return period extrapolation techniques were applied. Only the upper tail of a parent distribution contributes significantly to the extrapolated value at the return period (Bailey 1996, Zhou 2013, Zhou et al. 2012) and therefore only the upper $2\sqrt{n}$ of daily maximum values were of interest for this study. To extrapolate to the return period a straight line was fitted to the upper $2\sqrt{n}$ of data points on Gaussian probability paper (Kozikowski 2009, Nowak 1993 1994, Nowak & Hong 1991). In South Africa heavy vehicles are allowed to travel on weekends and holidays and therefore for a return period of 975.3 years and 365 days per year the corresponding value on the vertical axis is 4.540. The Gaussian assumption was made in this study as it is the method that was used in the derivation of the AASHTO code (Nowak 1993) and the Eurocode (Sedlacek et al. 2008).

6 RESULTS

6.1 *Extrapolated load effects*

Daily maximum load effects were plotted on Gaussian probability paper and extrapolated to the return period. Hogging moments are shown in Figure 5, sagging moments in Figure 6 and shear forces in Figure 7. Table 1 gives a summary of the load effect values.

Table 1. Summary of extrapolated load effects.

Span length	Hogging	Sagging	Shear
m	kNm	kNm	kN
5	264	378	340
10	820	1258	528
15	1664	2234	626
20	2318	3535	740
25	2474	4865	826
30	2973	6127	888
35	3523	7451	937
40	4140	8877	975
45	5547	10331	1002
50	6864	11759	1018

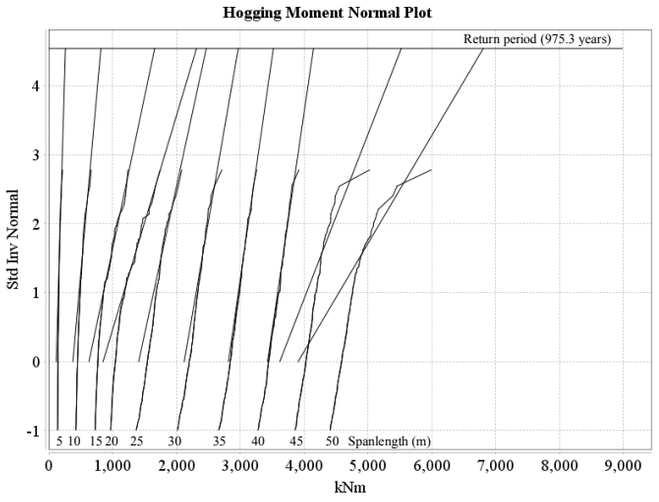


Figure 5. Extrapolated hogging moments.

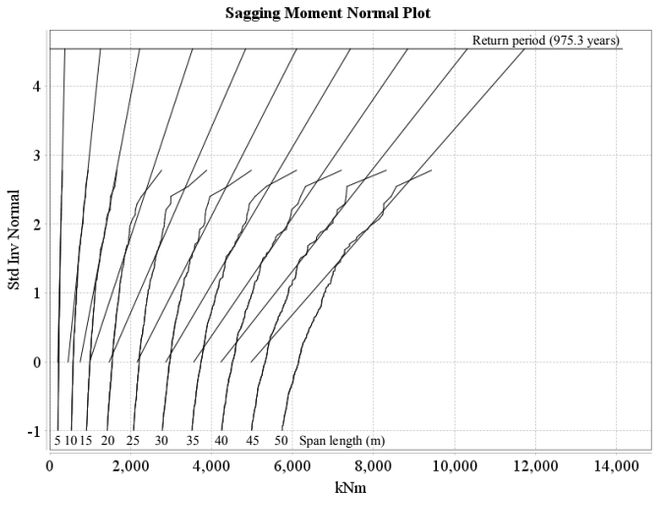


Figure 6. Extrapolated sagging moments.

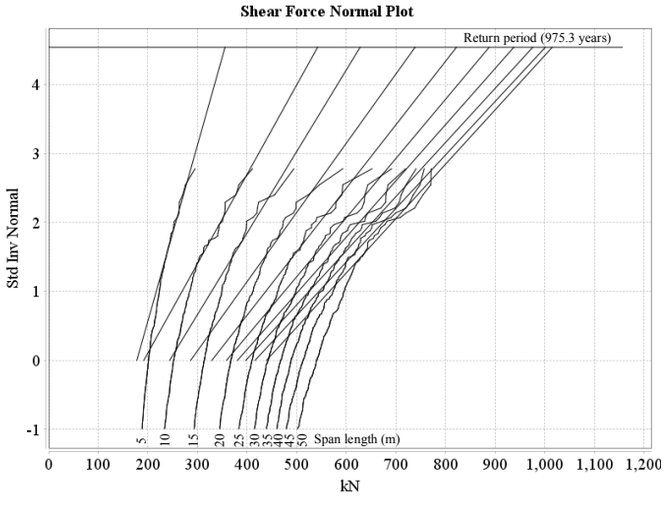


Figure 7. Extrapolated shear forces.

It is clear that for medium to longer span lengths the tails of the load effects do not strictly plot as straight lines on Gaussian probability paper. This is an indication that the Gaussian approximation to the distribution of the load effect tails should be revisited in subsequent research.

6.2 *Extrapolated axle weight*

Daily maximum axle weights were extrapolated as per Sedlacek et al. (2008) who used a half-normal distribution. Once again the upper $2\sqrt{n}$ of daily maximum values were fitted with a straight line on Gaussian probability paper. This resulted in a characteristic axle weight of 170 kN. The extrapolation of the axle weights is shown in Figure 8. From Figure 8 it can be seen that the tail of the axle weights plots as a straight line on Gaussian probability paper, indicating that axle weights closely resemble Gaussian behavior.

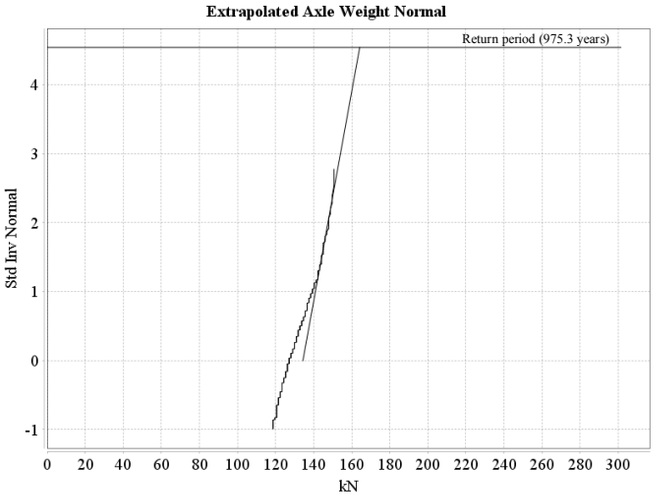


Figure 8. Extrapolated axle weights.

6.3 *Calculation of distributed loads*

The extrapolated axle weight of 170 kN was applied to the different span lengths as a double axle at 1.2 m spacing, similar to the Eurocode (CEN 2003). To reproduce the extrapolated load effects from Table 1, a distributed load was calculated which acts in conjunction with the double axle. The distributed load is shown in Figure 9 for different load effects and span lengths.

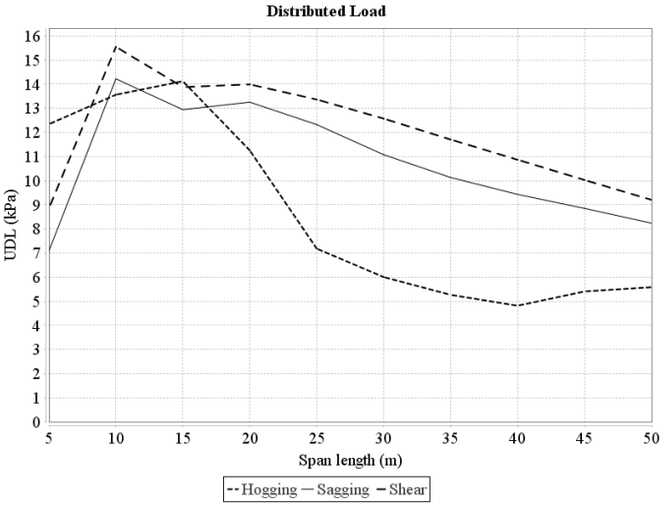


Figure 9. Distributed loads.

It can be seen that the hogging moment load effect for a 10 m span length produces the largest distributed load of approximately 15 kPa. The distributed load decreases with an increase in span length, creating the possibility of distributed load reduction with increasing span length. The proposed load model configuration is shown in Figure 10.

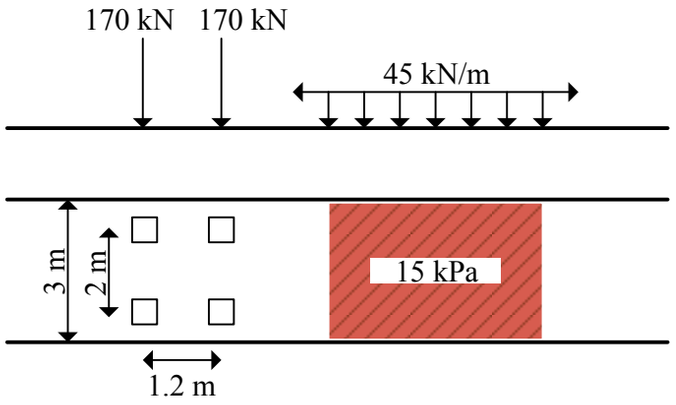


Figure 10. Proposed load model.

7 CONCLUSIONS

A preliminary traffic load model for single lane traffic has been derived for bridge design in South Africa. One year of data from the Roosboom WIM station was used to calculate daily maximum hogging moments, sagging moments and shear forces for span lengths up to 50 m. These forces were extrapolated on Gaussian probability paper to a return period of 975.3 years.

The resulting load model is a double axle of 170 kN each, spaced at 1.2 m apart with a distributed load of 15 kPa, shown in Figure 10. When compared to the Eurocode the load model has a lower axle load (300 kN for Eurocode), but a larger distributed load (9 kPa in the Eurocode) (CEN 2003).

This load model is limited to characteristic values and does not incorporate multiple lane presence or dynamic amplification as these will be addressed in future research.

When comparing this new load model to TMH7 NA loading, with dynamic effects removed, the deficiencies are clear. Figure 11 shows that TMH7 NA loading is under conservative for span lengths up to 22.5 m in hogging. Figure 12 shows deficiencies in sagging moments for span lengths up to 40 m. Figure 13 shows deficiencies in TMH7 for all span lengths in shear.

These deficiencies confirm the work performed in 1991 by Oosthuizen et al. and shows that it is vital to adopt a new live load model for bridge design in South Africa.

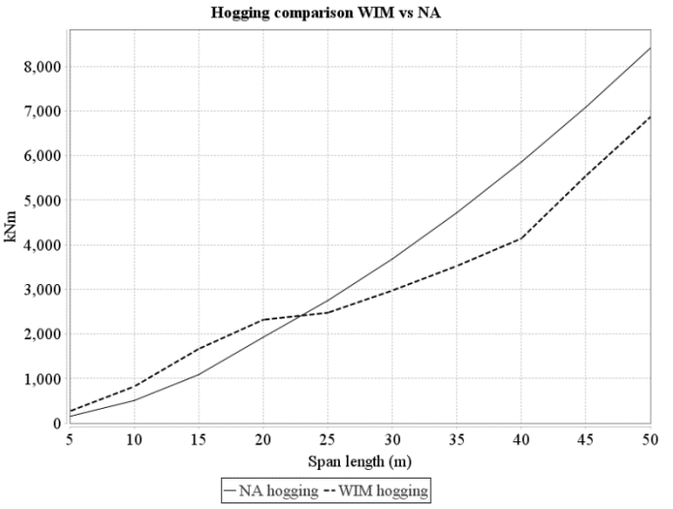


Figure 11. TMH7 vs WIM hogging comparison.

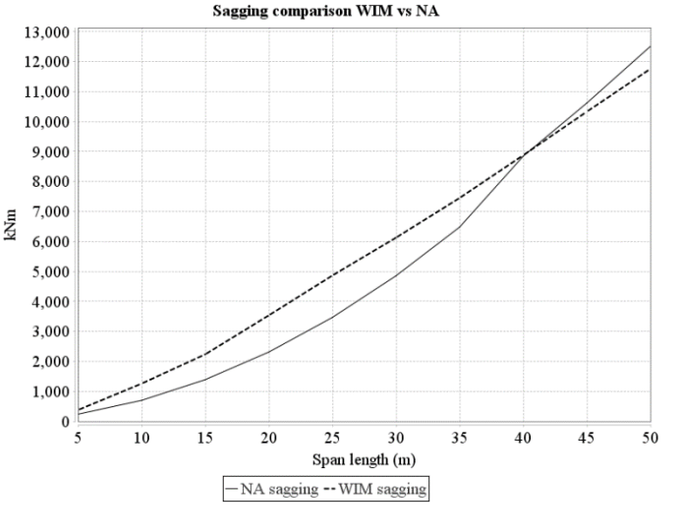


Figure 12. TMH7 vs WIM sagging comparison.

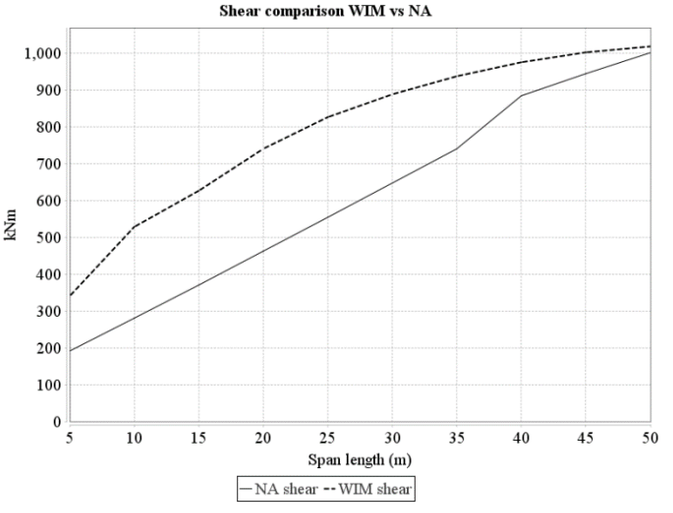


Figure 13. TMH7 vs WIM shear comparison.

REFERENCES

Anderson, J.R.B. 2006. Review of South African Live Load Models for Traffic Loading on Bridge and Culvert Structures Using WIM Data. MScEng Dissertation. University of Cape Town.

Bailey, S.F. 1996. Basic Principles and Load Models for the Structural Safety Evaluation of Existing Road Bridges. Doctoral Dissertation. EPFL.

Caprani, C.C. 2005. Probabilistic Analysis of Highway Bridge Traffic Loading. Doctoral Dissertation University College Dublin.

Caprani, C.C. & OBrien, E.J. 2010. Estimating Extreme Highway Bridge Traffic Load Effects, in: *Safety, Reliability and Risk of Structures, Infrastructures and Engineering Systems : Proceedings of the Tenth International Conference on Structural Safety and Reliability (ICOSSAR2009)*, Osaka, Japan. pp. 3053–3060.

CEN, 2003. EN1991-2: Traffic loads on bridges. Brussels.

Committee of State Road Authorities, 1981. TMH7 Parts 1 and 2: Code of Practice for the Design of Highway Bridges and Culverts in South Africa.

de Wet, D.P.G. 2010a. Post-Calibration and Quality Management of Weigh-in-Motion Traffic Data. Master of Science in Engineering Dissertation, Stellenbosch University.

de Wet, D.P.G. 2010b. WIM Calibration and Data Quality Management. *J. South African Inst. Civ. Eng.* 52: 70–76.

Enright, B. 2010. Simulation of Traffic Loading on Highway Bridges. Doctoral Dissertation. University College Dublin.

Enright, B. & OBrien, E.J. 2012. Monte Carlo Simulation of Extreme Traffic Loading on Short and Medium Span Bridges. *Struct. Infrastruct. Eng.* 9: 1267–1282.

Kozikowski, M. 2009. WIM Based Live Load Model for Bridge Reliability. Doctoral Dissertation. University of Nebraska.

Lenner, R. 2014. Safety Concept and Partial Factors for Military Assessment of Existing Concrete Bridges. Doctoral Dissertation. Universitat der Bundeswehr Munchen.

Lenner, R., de Wet, D.P.G., Viljoen, C. 2017. Bridge Loading and Traffic Characteristics in South Africa. *J. South African Inst. Civ. Eng.* Accepted for publication.

Lenner, R., Keuser, M., Sykora, M. 2014. Safety Concept and Partial Factors for Bridge Assessment under Military Loading. *Adv. Mil. Technol.* 9: 5-20

Nowak, A.S. 1994. Load Model for Bridge Design Code. *Can. J. Civ. Eng.* 21: 36–49.

Nowak, A.S. 1993. Load model for highway bridges. *Struct. Saf.* 13: 53–66.

Nowak, A.S., Hong, Y. 1991. Bridge Live-Load Models. *J. Struct. Eng.* 117: 2757–2767.

Oosthuizen, A.P.C., Meintjies, C.J., Trumpelmann, V., Peters, D., Ullmann, K.K.A.B., Oppermann, G.H.P. 1991. TMH7 Part 2: Traffic Loading (1991) Proposed Substitution of Section 2.6. Cape Town.

Sedlacek, G., Merzenich, G., Paschen, M., Bruls, A., Sanpaolesi, L., Croce, P., Calgaro, J.A., Pratt, M. 2008. Background document to EN 1991- Part 2 - Traffic loads for road bridges - and consequences for the design. JRC Scientific and Technical Reports.

Sivakumar, B., Moses, F., Ghosn, M. 2008. Protocols for Collecting and Using Traffic Data in Bridge Design Prepared for NCHRP. Paramus.

Van der Spuy, P.F. 2014. A Comparative Study Between the South African and European Bridge Design Codes for Bending and Shear. Master of Engineering Dissertation. University of Cape Town.

Zhou, X.Y. 2013. Statistical Analysis of Traffic Loads and Traffic Load Effects on Bridges. Doctoral Dissertation. Universite Paris Est.

Zhou, X.Y., Schmidt, F., Jacob, B. 2012. Extrapolation of Traffic Data for Development of Traffic Load Models: Assessment of Methods Used During Background Works of the Eurocode, in: *Bridge Maintenance, Safety, Management, Resilience and Sustainability - Proceedings of the Sixth International Conference on Bridge Maintenance, Safety and Management.* pp. 1503–1509.

Maintenance, Safety, Risk, Management and Life-Cycle Performance of Bridges – Powers, Frangopol, Al-Mahaidi & Caprani (Eds)
© 2018 Taylor & Francis Group, London, ISBN 978-1-138-73045-8

Using Images to Estimate Traffic Loading on Long-Span Bridges

F. Daize
Ecole Nationale des Travaux Publics de l'Etat, Lyon, France

E.A. Micu, E. J. O'Brien & A Malekjafarian
School of Civil Engineering, University College Dublin, Newstead Building, Dublin 4, Ireland

ABSTRACT: This paper presents the idea of correlating vehicle lengths extracted from images with weights from Weigh-in-motion (WIM) data. The purpose of this is the estimation of traffic loading on long-span bridges. WIM data from a motorway in Poland containing four months of records, is used to develop the length-weight correlation. As WIM data may contain some errors, a cleaning algorithm is applied to create a reliable database. Monte Carlo simulation is used to show the correlation. A sample of random traffic is simulated and a bootstrapping method is used to verify the correlation approach.

1 INTRODUCTION

The safety of a bridge can be precisely evaluated if the loading and resistance to loading are known. While the resistance has been well investigated in the literature (Attard and Stewart, 1998), (Darmawan and Stewart, 2007), (Pines and Aktan, 2002), (Stewart, 2001), (Stewart and Val, 1999), loading has not received the same attention, particularly in the case of long span bridges. Traffic loading is difficult to predict since it is highly variable and site specific. Clearly the values of load effects (bending moments, shear forces etc.) need to be lower than the values of resistance to ensure that the bridge is safe.

The governing case for long span bridges is known to be congested traffic conditions (Getachew, 2003), (Hwang et al., 2012), (Lutomirska, 2009), (Nowak et al., 2010), (Sedlacek et al., 2008). In this case, traffic loading represents a particular challenge due to lack of information about the inter-vehicle gaps and the car-truck mix. Weigh-in-motion (WIM) technology is the established method for obtaining the vehicle weights (Moses, 1979), (Carey et al., 2017). However, WIM technologies work well only for free-flowing traffic (OBrien et al., 2012). Thus, gathering the weight information of congested traffic is infeasible. Furthermore, WIM methods often only record trucks and provide little or no data about the cars and gaps between cars and trucks.

There have been many studies about traffic loading (Buckland et al., 1978), (Buckland, 1991), (Hayrapetova et al., 2012), (OBrien et al., 2012), but inter-vehicles gaps in congested situations, have not been well investigated. Several researchers use microsimulation to model congested situations (Caprani and OBrien, 2008), (Caprani, 2010), (Caprani, 2012), (Enright et al., 2013), (Treiber et al., 2000). A constant value for the gaps has been considered in other works (Getachew, 2003), (Hwang et al., 2012), (Lutomirska, 2009), (Paeglitis and Freimanis, 2016). Micu et al. (Micu et al., 2016) propose image analysis technique for surveying congested traffic. They show that this approach can provide valuable information about the congested traffic such as vehicle class, length, and inter-vehicle gaps. These parameters can be used in assessing the traffic loading on long span bridges, but the weights of the vehicles cannot be estimated directly from the images.

This paper proposes the correlation of lengths extracted from the images with weights from available WIM data. This means that the lengths extracted from the images are used to infer the vehicle weights. The correlation is constructed using Monte Carlo. This method effectively fits a function to the histogram of the data. For instance, for each extracted length, the authors generate a 'typical' weight using Monte Carlo simulation. The proposed method is used to simulate the vehicle weights from the vehicle lengths available at a Polish WIM site. The simulated weights are compared to the measured weights to assess the reliability of the proposed method. The method is also verified by simulating new traffic using a bootstrapping method. The results show that the vehicle weights can be inferred from the lengths with acceptable accuracy for the purposes of estimating extreme bridge traffic loading.

2 LENGTH-WEIGHT CORRELATION

2.1 *WIM Data*

2.1.1 *Raw data*

WIM data used in this paper is obtained from a WIM system installed on the A4 (E40) motorway with two lanes in one direction at Wroclaw, Poland. This WIM system uses piezo-quartz sensors embedded in the pavement to measure the properties of the passing vehicles. The data measured includes each vehicle's detailed information such as timestamp, wheelbase, total length, speed, vehicle type (car or truck), total weight (GVW), the number of axles, axle spacing, single axle weights, etc. Measurements represent 1,048,546 vehicles on both lanes (fast and slow lane) with 24 % of trucks registered from the period between 1st January and 27th April, 2008. Two sub-datasets are extracted from the database. The first sub-dataset is called WIM1 and the second one is WIM2 in this paper. Each sub-dataset contains 100,000 vehicles recorded on both lanes.

2.1.2 *Filtering rules*

The accuracy of the raw WIM data can be checked using different criteria (Enright, 2010). Some of them are used here to filter the raw data by removing the vehicle records that may contain errors. The vehicles are also classified as cars and trucks to properly discard the errors. First, the vehicles which have no information recorded are removed from the data. After this simple filter, 99,827 vehicles are left in WIM1. The general and specific rules that are then applied to the WIM1 data, are detailed in Table 1. The filtering rules are not applied to WIM2.

Table 1. Filtering criteria to identify records with likely errors.

General criteria	
No. of axles	< 2
Individual axle spacing	> 20 m
Individual axle weight	> 20 t
Wheelbase	> 30 m
GVW	> 100 t
Speed	< 60 km/h or > 120 km/h
Total length	< Wheelbase
Criteria specific to cars	
GVW	< 800 kg
Total length	< 2 m or > 8 m
Criteria specific to trucks	
GVW	< 1000 kg
Total length	< 2 m
Specific criteria	
Total length	= 23 m
GVW	= 920 kg

Many vehicles are recorded having the same length of 23 m but with very different values of weights ranging from the lowest to the highest value. As this might be due to a measurement error, they are removed from the database. Less than 0.1 % of the vehicles are removed at this stage.

Many vehicles are also recorded with the exact same weight of 920 kg but with values of length ranging from 0 m to 20 m. Unlike the 23 m long vehicles, the 920 kg vehicles constitute about 15 % of the whole data. As these vehicles create a very high local density around 920 kg which may cause some issues in the proposed correlation method, they are also discarded from the database. Finally, 82,883 vehicles are left in WIM1 after the filtering process.

Table 2. Evaluation of the loss after filtering.

Vehicle type	Percentage before filtering (99,827)	Percentage after filtering (82,883)	Waste among this graph	Waste among all vehicles
Cars in the slow lane	36.2%	32.7%	25.0%	9.0%
Cars in the fast lane	39.9%	38.5%	19.6%	7.8%
Trucks in the slow lane	22.3%	26.9%	0.4%	0.1%
Trucks in the fast lane	1.6%	1.9%	2.2%	< 0.1%
All the vehicles	100%	100%	17.0%	17.0%

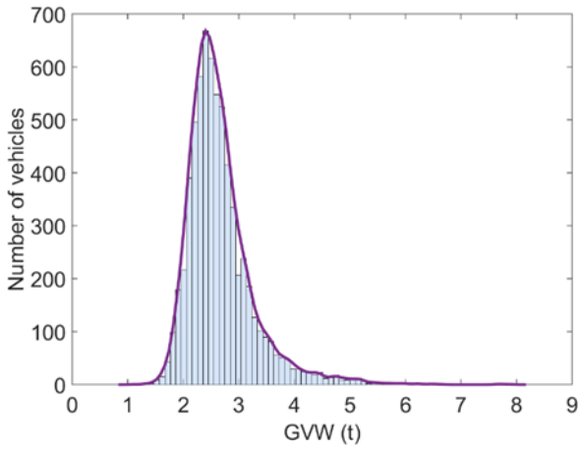
Table 2 gives details of the percentages of vehicles filtered from the database. It shows that the discarding process mostly removes cars rather than trucks. This may because WIM systems are designed to weigh trucks and little priority is given to the weighing of cars.

2.2 *Kernel density estimation*

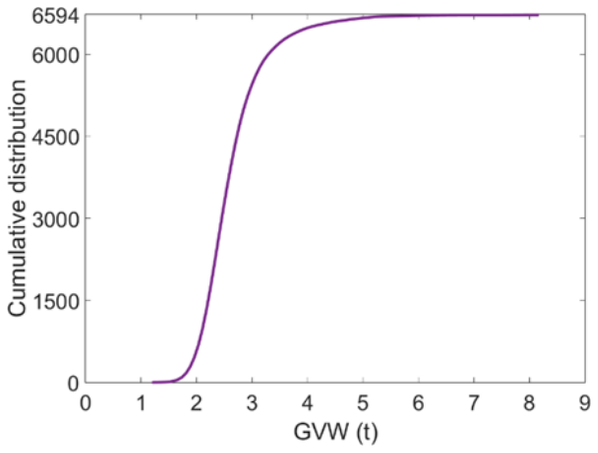
Due to the different distribution of vehicles in the two lanes, the WIM2 data is divided into slow and fast lane data. Using the total length of the vehicles, the WIM2 data is split into 100 slices with the same width for each lane. The lengths of vehicles in each slice are in a specified range. The number of vehicles is different from a slice to another and some slices may be empty.

The numbers of vehicles with given (weight interval, length) combinations are plotted as a histogram. A Normal Kernel density distribution (Jones and Kappenman, 1992) is fitted to the histogram for each slice. Figure 1(a) presents the histogram of the weights in slice 10 for the WIM2 data recorded in the slow lane. It contains vehicles with length ranging between 4.10 m and 4.30 m. It can be seen that most of these relatively short vehicles weigh 2 to 4 tonnes but these are exceptions. A Kernel density distribution fitted to the histogram is also shown. This process is repeated for all slices which results

in a Kernel density distribution for each slice in WIM2. A cumulative distribution function (CDF) is then defined for each Kernel density distribution to represent the probability of different vehicle weights in each slice. Figure 1(b) shows the cumulative distribution function of the data shown in Figure 1(a).



(a)

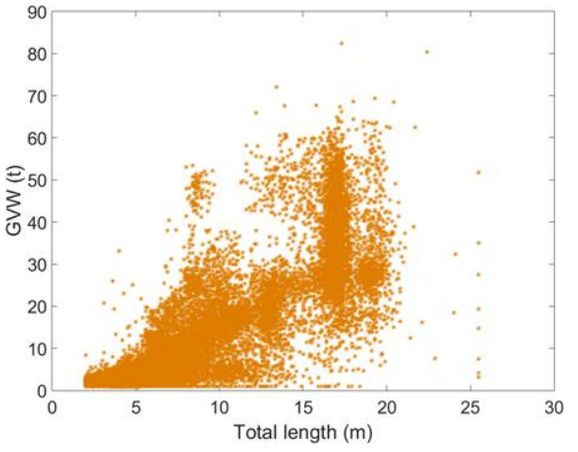


(b)

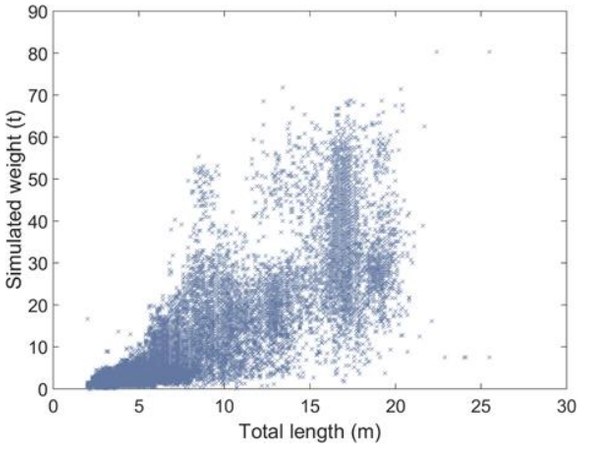
Figure 1. Distribution of the data in slice 10 of WIM2; (a) histogram of the vehicle weights and the kernel density fitted distribution; (b) the Kernel fit cumulative distribution of the vehicle weights.

2.3 *Weight simulation*

It is assumed that only lengths of the vehicles in WIM1 are available. This would be the case if the lengths were found from an analysis of vehicle images. In this section, the weights of the vehicles in WIM1 are generated using a Monte Carlo simulation using the length/weight relationship obtained from WIM2. Regarding the length of each vehicle in WIM1, it belongs to a slice in WIM2 data. Using standard bootstrapping (Taylor, 1989), a number between 0 and the maximum value of the cumulative distribution of that slice, is randomly generated. That number corresponds to a weight in the CDF plot of the slice. This weight is the assumed weight of the vehicle in WIM1. A similar procedure is repeated for all the vehicles in WIM1 to infer their weights from their lengths. The length-weight correlation of the WIM1 data is shown in Figure 2 - the recorded and simulated data are shown in Figures 2(a) and 2(b), respectively. It can be seen that the simulated data is a reasonable match with the recorded data.



(a)



(b)

Figure 2. Length-weight correlation: a) Recorded WIM1; b) Simulated weights for lengths in WIM1.

Figure 3 presents the density of vehicles versus weights for the simulated weights and recorded WIM1 data in slice 10 for both lanes. Both distributions display the same number of vehicles. As can be observed, the simulated weight data matches the recorded WIM1 data very well.

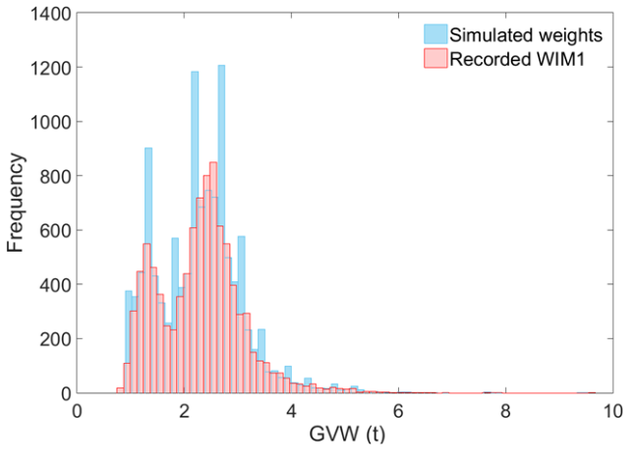


Figure 3. Histogram of recorded WIM1 and of simulated weight data.

2.4 *Comparison of simulations*

Bootstrapping is used in this section, to resample the data for the verification of the correlation approach. A new traffic is generated using bootstrapping only from the WIM1. This traffic includes the lengths of 82,883 vehicles for the fast and slow lane. Then, the correlation method proposed in Section 2.3, is used to simulate the weights of those vehicles. As a result, a new traffic including 82,883 vehicle lengths is generated using the bootstrapping method which is called "simulated traffic". The histogram of the simulated traffic in the slow lane, is compared to the recorded data in Figure 4. Both samples contain 51,455 vehicles. It is shown that the simulated traffic has a very similar histogram to the recorded data.

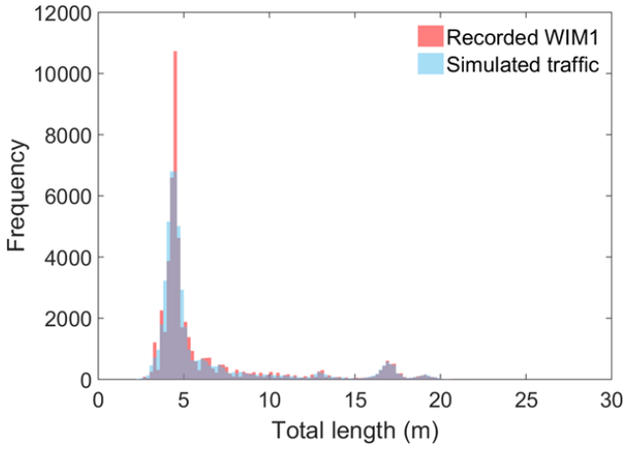
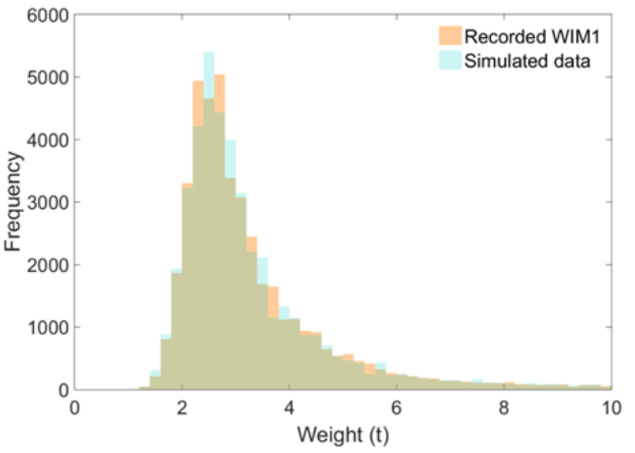


Figure 4. Histogram of recorded WIM1 data and of simulated traffic.

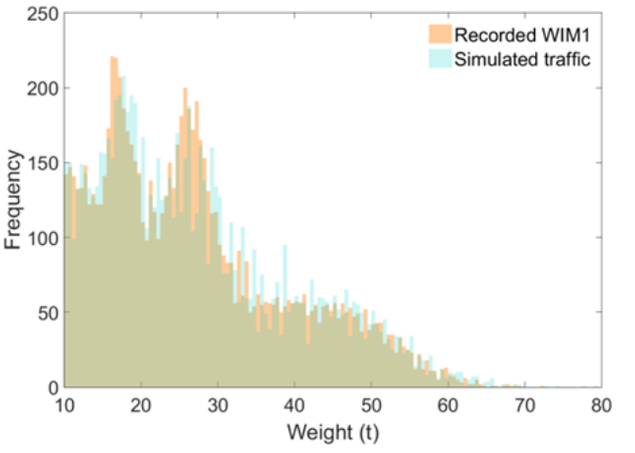
The weights of the vehicles in the new traffic data are simulated using the correlation method explained in Section 2.3.

2.5 *Results and discussion*

Figures 5 show the histogram of the frequency versus weights for the recorded WIM1 data and simulated traffic data at different scales. Figures 5(a) and (b) show the results for the weights from 0 to 10 tonnes which are evaluated every 200 kg and 10 to 80 tonnes which are evaluated every 50 kg, respectively. Figure 5 (b) is enlarged for better illustration due to the relatively low frequency of heavy vehicles.



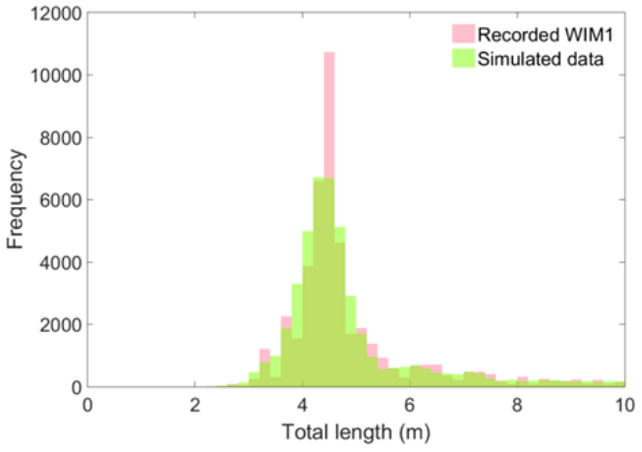
(a)



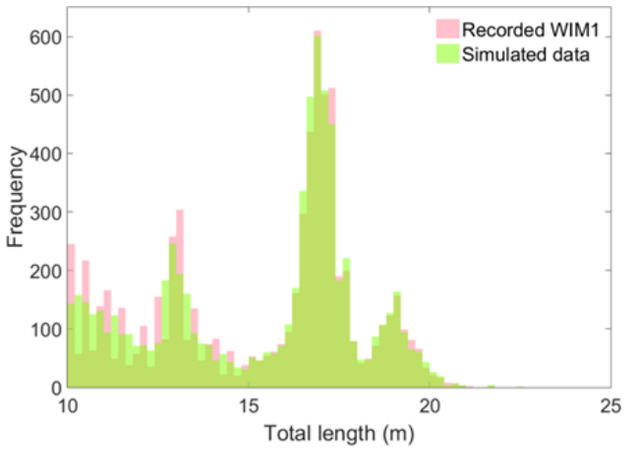
(b)

Figure 5: Bootstrapping results - weights: (a) weights from 0 to 10 t evaluated every 200 kg; (b) weights from 10 to 80 t evaluated every 50 kg.

The distribution of the lengths is illustrated in Figure 6. In this case, the lengths are evaluated every 20 cm. Figures 6(a) and (b) show the results from 0 to 10 metres and 10 to 25 metres, respectively. It can be seen in Figures 5 and 6 that the simulated traffic matches the recorded WIM1 data well. Most significantly, the trend of simulated traffic follows closely the trend of the recorded data.



(a)



(b)

Figure 6: Bootstrapping results - lengths evaluated every 20 cm: (a) Lengths from 0 to 10 m; (b) Lengths from 0 to 25 m.

The correlation between lengths and weights for the recorded slow lane WIM1 data and for the simulated traffic is illustrated in Figure 7. It can be observed that the simulated data is well correlated with the recorded data.

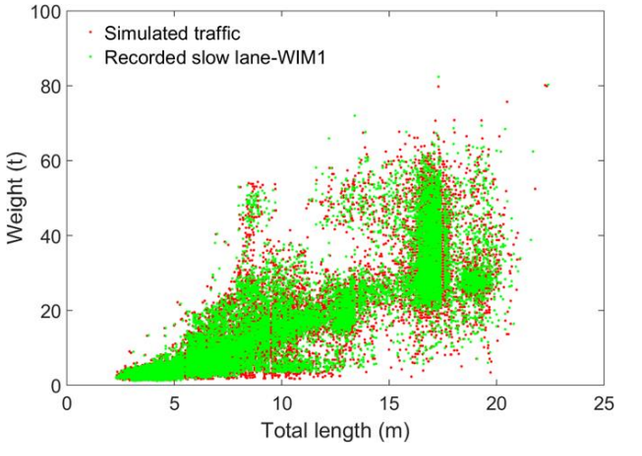


Figure 7: Bootstrapping results - correlation between length and weight.

3 CONCLUSION

This paper examines the possibility of correlating lengths extracted from images with weights from WIM data. Two datasets, WIM1 and WIM2 are used to test the correlation. A set of filtering criteria is used to reduce the possible errors of WIM measurements. The weights of the vehicles from WIM1 are simulated using their lengths. The simulated data are compared to the recorded data and show an acceptable accuracy. Random traffic is generated by bootstrapping. Bootstrapping is also used here to demonstrate the consistency of the Monte Carlo simulation. Appropriately, simulated vehicles have a higher probability of being generated in slices with a greater number of vehicles and will not be generated in slices with no vehicles. The results confirm that the proposed correlation method has good potential to be used for the estimation of the traffic loading on long-span bridges.

ACKNOWLEDGEMENT

The authors would like to thank Science Foundation Ireland for their support of this research under the US/Ireland programme. The authors also gratefully acknowledge the FP7 Samaris Project for providing Weigh-in-Motion data used in this research.

REFERENCES

ATTARD, M. M. & STEWART, M. G. (1998) A two parameter stress block for high-strength concrete. *Aci Structural Journal,* 95**,** 305-317.

BUCKLAND, P. G. (1991) North-American and British Long-Span Bridge Loads. *Journal of Structural Engineering-Asce,* 117**,** 2972-2987.

BUCKLAND, P. G., MCBRYDE, J. P., NAVIN, F. P. & ZIDEK, J. V. (1978) Traffic loading of long span bridges. *Bridge Engineering* 2.

CAPRANI, C. (2010) Using microsimulation to estimate highway bridge traffic load. *Proc. 5th Intl. Conf. on Bridge Maintenance, Safety and Management.*

CAPRANI, C. C. (2012) Calibration of a Congestion Load Model for Highway Bridges Using Traffic Microsimulation. *Structural Engineering International,* 22**,** 342-348.

CAPRANI, C. C. & OBRIEN, E. J. (2008) The governing form of traffic for highway bridge loading. IN E. CANNON, R. W. A. P. F. (Ed. *Proceedings of 4th Symposium on Bridge and Infrastructure Research in Ireland.* Galway, National University of Ireland.

CAREY, C., OBRIEN, E. J., MALEKJAFARIAN, A., LYDON, M. & TAYLOR, S. (2017) Direct field measurement of the dynamic amplification in a bridge. *Mechanical Systems and Signal Processing,* 85**,** 601-609.

DARMAWAN, M. S. & STEWART, M. G. (2007) Spatial time-dependent reliability analysis of corroding pretensioned prestressed concrete bridge girders. *Structural Safety,* 29**,** 16-31.

ENRIGHT, B. (2010) Simulation of traffic loading on highway bridges. *School of Architecture, Landscape and Civil Engineering.* Ireland, University College Dublin.

ENRIGHT, B., CAREY, C. & CAPRANI, C. C. (2013) Microsimulation Evaluation of Eurocode Load Model for American Long-Span Bridges. *Journal of Bridge Engineering,* 18**,** 1252-1260.

GETACHEW, A. (2003) Traffic load effects on bridges, statistical analysis of collected and Monte Carlo simulated vehicle data. *Structural Engineering.* Stockholm, Sweden, Royal Institute of Technology.

HAYRAPETOVA, A. A., O'CONNOR, A. J. & OBRIEN, E. J. (2012) Traffic Load Models for Long Span Bridges. *Bridge Maintenance, Safety, Management, Resilience & Sustainability.* Stresa, Italy, Taylor & Francis Group.

HWANG, E. S., LEE, K. T. & KIM, D. Y. (2012) Modeling of truck traffic for long span bridges. *Bridge Maintenance, Safety, Management, Resilience and Sustainability***,** 1100-1107.

JONES, M. C. & KAPPENMAN, R. F. (1992) On a Class of Kernel Density Estimate Bandwidth Selectors. *Scandinavian Journal of Statistics,* 19**,** 337-349.

LUTOMIRSKA, M. (2009) Live load models for long span bridges. *Civil Engineering.* Lincoln, Nebraska, University of Nebraska.

MICU, E. A., OBRIEN, E. J. & SEVILLANO, E. (2016) Application of image processing to the analysis of congested traffic. IN GOGGIND, J. (Ed. *Proceedings of Civil Engineering Research in Ireland.* Galway.

MOSES, F. (1979) Weigh-in-Motion System Using Instrumented Bridges. *Transportation Engineering Journal of Asce,* 105**,** 233-249.

NOWAK, A. S., LUTOMIRSKA, M. & SHEIKH IBRAHIM, F. I. (2010) The development of live load for long span bridges. *Bridge Structures,* 6**,** 73-79.

OBRIEN, E. J., HAYRAPETOVA, A. & WALSH, C. (2012) The use of micro-simulation for congested traffic load modeling of medium- and long-span bridges. *Structure and Infrastructure Engineering,* 8**,** 269-276.

PAEGLITIS, A. & FREIMANIS, A. (2016) Comparision of Constant-Span and Influence Line Methods for Long-Span Bridge Load Calculations. *Baltic Journal of Road and Bridge Engineering,* 11**,** 84-91.

PINES, D. & AKTAN, A. E. (2002) Status of structural health monitoring of long-span bridges in the United States. *Structural Engineering and materials,* 4**,** 372-380.

SEDLACEK, G., MERZENICH, G., PASCHEN, M., BRULS, A., SANPAOLESI, L., CROCE, P., CALGARO, J. A., PRATT, M., JACOB, M. L., V. DE BOER, VROUWENFELDER, A. & HANSWILLE, G. (2008) Background document to EN 1991-Part 2-Traffic loads for road bridges-and consequences for the design. *JRC—European Commission.*

STEWART, M. G. (2001) Reliability-based assessment of ageing bridges using risk ranking and life cycle cost decision analyses. *Reliability Engineering & System Safety,* 74**,** 263-273.

STEWART, M. G. & VAL, D. V. (1999) Role of load history in reliability-based decision analysis of aging bridges. *Journal of Structural Engineering-Asce,* 125**,** 776-783.

TAYLOR, C. C. (1989) Bootstrap choice of the smoothing parameter in kernel density estimation. *Biometrika,* 76**,** 705-712.

TREIBER, M., HENNECKE, A. & HELBING, D. (2000) Microscopic simulation of congested traffic. IN HELBING, D., HERRMANN, H. J., SCHRECKENBERG, M. & WOLF, D. E. (Eds.) *Traffic and granular flow'99.* 1 ed., Springer Berlin Heidelberg.

Maintenance, Safety, Risk, Management and Life-Cycle Performance of Bridges – Powers, Frangopol, Al-Mahaidi & Caprani (Eds)
© 2018 Taylor & Francis Group, London, ISBN 978-1-138-73045-8

Long span bridges – current age & design life – a global survey

J. De Maria
Undergraduate, Civil Engineering, Monash University, Australia
C. Caprani
Supervisor, Department of Civil Engineering, Monash University, Australia
D. Guo
Co-supervisor, Postgrad, Civil Engineering, Monash University, Australia

ABSTRACT: To identify the in common problems, future needs, and reveal the relationship between the age, design life, and status of long span bridges on an international scale, a global long span bridge survey was conducted and database constructed. From which, the details of location, construction and status per bridge were broken down and analysed to identify any potential relationships, or correlations, between the numerous categories of information recorded for each long span bridge. Analysis concluded that age and bridge type selection of most long span bridges within the North American region has resulted in rare achievement of design life objectives. The global long span bridge database is searchable, organisable, available in several formats, and is a strong foundation for further expansion and detail.

1 INTRODUCTION

1.1 *Background*

Bridges have been constructed to establish direct means of communication and transportation between populations for thousands of years. As construction and engineering technology has progressed, so has the size and number of bridges across the globe. Within the last century there has been unprecedented infrastructure growth, resulting in the construction of bridges that push the limits of their materials and engineering design.

Long span bridges account for only a small percentile of the total number of bridges in use around the globe. However, it is undeniable that these bridges, on a scale of their own, provide vital connections, across; mountains, valleys, bays, rivers, oceans and lakes, that are essential to the daily operation of cities and countries across the globe.

1.2 *Project objective*

Long span bridges, though vital to many communities, lack representation within a searchable, manipulatable and analysable construct. Due to the internet, information regarding long spans bridges is freely available, to an extent, however, this information is yet to be collected and presented in a meaningful and useful format.

Therefore, this project aimed to conduct a comprehensive survey of long span bridges from across the globe, and with the data collected construct a global long span bridge database. The database was then used to help identify in common problems experienced by long span bridges, and help identify the future needs for long span bridge design and construction.

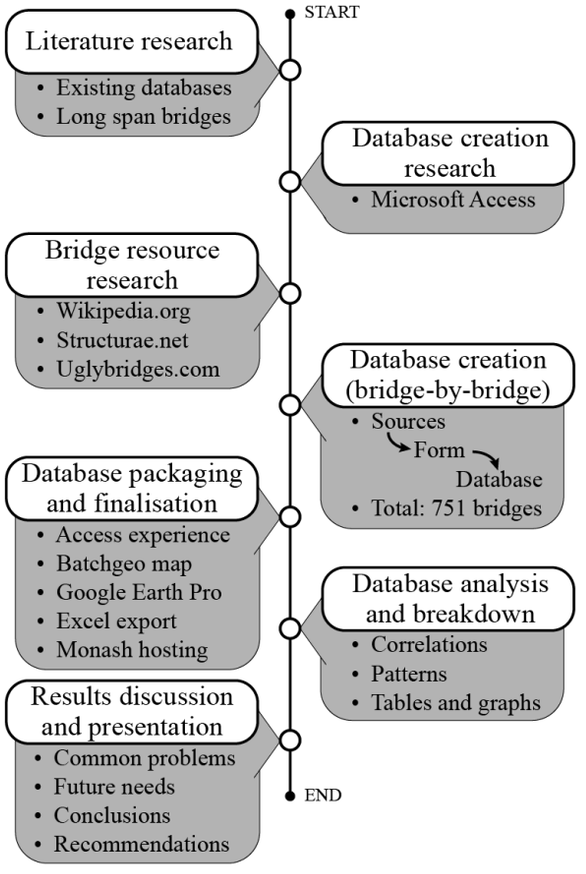


Figure 1. Methodology used to complete the global long span bridge database, database analysis and results discussion

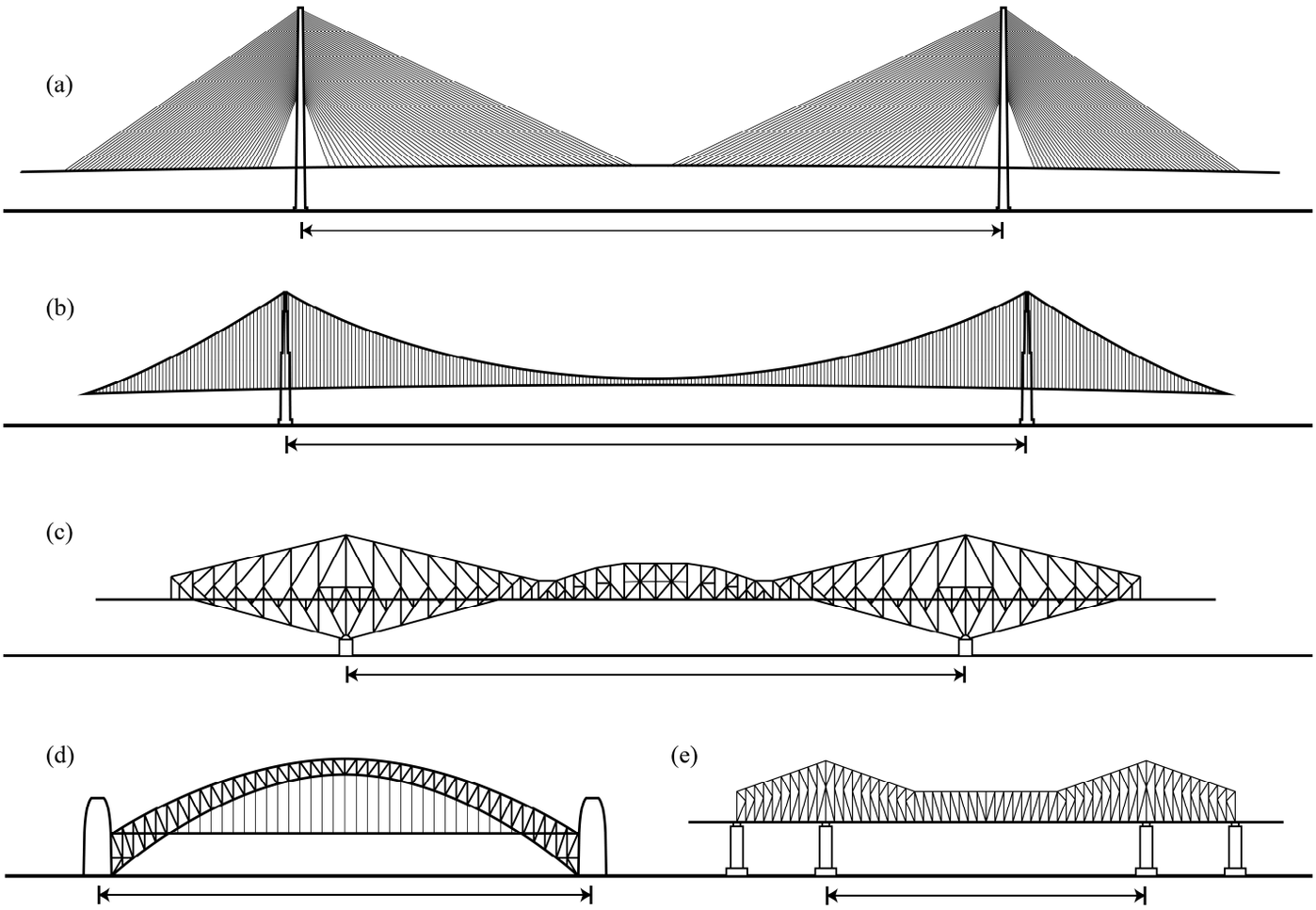


Figure 2. Span dimensions per bridge type used during survey. (a) cable stayed (b) suspension (c) cantilever (d) arch (e) truss (De Maria, 2017)(Original)

2 DEFINITIONS AND ASSUMPTIONS

2.1 *Global survey*

The survey of long span bridges was as globally extensive as available resources and time allowed. The survey included bridges from a total of 81 countries, which were assigned to one of seven global regions, either; Africa, Asia, Europe, Latin America/Caribbean, Middle East, North America, or Oceania. However, the information freely and easily available for each region or country varied greatly. At a minimum, details regarding location and construction were obtained. North America proved to be the most accessible region, largely due to the National Bridge Inventory being freely available online.

2.2 *Span*

'Span' is a term that may be interpreted to relate to different dimensions of a bridge structure. For this project, and in most interpretations, 'span' is defined as the distance between to ground supports (pylons) of a bridge structure. For this survey, the maximum (longest) span of each bridge structure is its qualification for being a 'long span' bridge, and should not be confused with the overall length of the bridge. See Figure 1 for diagrams clearly defining the 'span' dimension for each bridge type included in the survey and database.

2.3 *Long span*

The term 'Long Span' also needed to be defined in relation to the survey and database. For this project the term 'Long Span' was considered a flexible and relative term, meaning; that there was no set length to be greater than, and that it was relative to the bridge type.

However, it was also determined that, there is a point where the mechanics and effort required to span a given distance becomes so common place that it is no longer irregular, or special. Box girder bridges, usually associated with 'short span', or more common span lengths, can span up to approximately 150 metres. Therefore, to eliminate technology associated with smaller spans, a target was set to obtain details on all bridges across the globe with a main span greater than approximately 150 metres. (Hewson, 2003)

2.4 *Design life*

The concept and definition of 'Design Life', across the various international standards varies slightly from standard to standard, and is closely related with the concept of 'Service Life'. What follows are the definitions of Design Life, and Service Life, from three major international bridge and construction standards. The American Association of State Highway and Transportation Officials Load Resistance Factor Design (AASHTO LRFD), the Eurocode (EN 1990.2002), and the Australian Standard for Bridge Design (AS5100.1-2004).

2.4.1 *AASHTO LRFD Design Life*

Design Life – *"period of time on which the statistical derivation of transient loads is based"*

Service Life – *"the period of time that the bridge is expected to be in operation"*

2.4.2 *EN 1990.2002 Design Life*

Design Working Life – *"assumed period for which a structure or part of it is to be used for its intended purpose with anticipated maintenance but without major repair being necessary"*

Reference Period – *"chosen period of time that is used as a basis for assessing statistically variable actions, and possibly for accidental actions"*

2.4.3 *AS5100.1-2004 Design Life*

Design Life – *"the period assumed in design for which a structure or structural element is required to perform its intended purpose without replacement or major structural repairs"*

Service Life – *"a period over which a structure element is expected to perform its function without major maintenance or structural repair"*

2.4.4 *Database Design Life*

The definition for Design Life accepted and utilised for the survey, database and this report, matches the definitions of; Service Life from the AASHTO LRFD, Design Working Life from EN 1990.2002, and Design Life from AS5100.0-2004.

To be clear, for the survey, database and this report, the definition of Design Life used was - *the period of time assumed in design for which a structure is expected to be in operation with anticipated maintenance but without major repair or unanticipated structural rehabilitation.*

3 *THE GLOBAL LONG SPAN BRIDGE DATABASE*

This section is intended to thoroughly explain the method used, and the components of the global long span bridge database created, to aid readers in understanding the database, or to assist in extending this database, or creating their own database.

3.1 *Program utilised*

To log the details procured per bridge from surveying various internet sources, the computer program Microsoft Access® was utilised. Access is classified as a database management system (DBMS) and was suited to the task at hand due to the programs extensive data input, organisation, exportation, and interfacing features.

3.1.1 *Long span bridge form*

Critical to the completion of the global long span bridge database was the ability to design a 'form'



Figure 3. Global positions of all long span bridges included within the database.
(Locations traced from Batchgeo map, using database coordinates, then composited onto a simplified global map)

within Access to assist in logging the details per bridge. The form is pictured below as Figure 4.

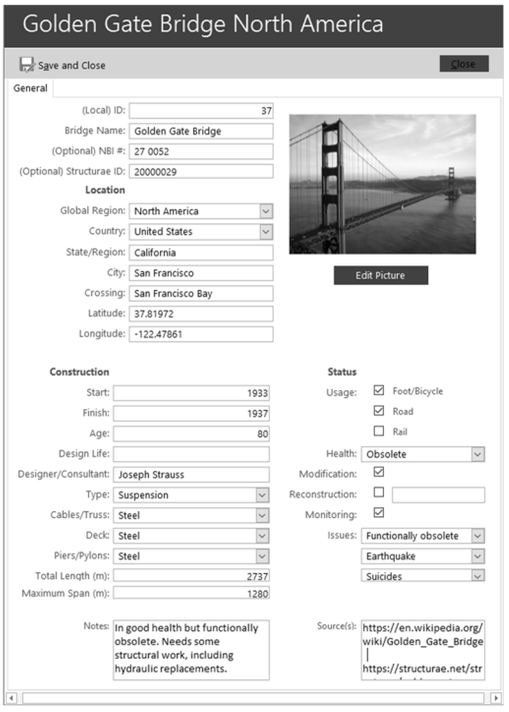


Figure 4. Access form created to log and edit bridge details per bridge surveyed for the database.

3.2 *Database entries*

Data entries per bridge were summarised under three sub categories; Location, Construction and Status. Other entries were present on the form to assist with administration and organisation of the database. The components within each category were as follows. Most entry fields are self-explanatory; however, several require some clarification.

Location
- Global Region
- Country
- State/Region
- City
- Crossing
- Latitude & Longitude

Construction
- Construction Start and Finish (year)
- Age
- Design Life
- Designer/Consultant
- Type
- Material, by;
    - Cable/Truss
    - Deck
    - Pier/Pylon
- Dimensions:
    - Total Length (m)
    - Maximum Span (m)

Status
- Usage;
    - Foot/Bicycle,
    - Road, or
    - Rail
- Health;
    - Good
    - Obsolete
    - Deficient
- Modification
- Reconstruction (with year)
- Monitoring
- Issues (abbreviated. Max 3 issues)

Other
- Database ID (internal)
- Bridge Name
- NBI Number (USA only)
- Structurae ID
- Image
- Notes
- Sources

3.2.1 *Construction type*

Bridge type was restricted to one of five bridge type classifications; Arch, Cable Stayed, Cantilever, Suspension, or Truss. Nearly all bridges surveyed were clearly identifiable with at least one of the classifications. If the structure was a combination of more than one type of bridge then the most dominant classification or the classification of the main span was used, and the other classification(s) were included in the Notes entry field.

3.2.2 *Construction material*

Bridge material was separated into three entry fields; Cable/Truss, Deck, and Pier/Pylon, to allow for improved detail of which structural elements are what material in multi material bridges.

3.2.3 *Bridge health status*

Bridge health was restricted to three possible responses; Good, Obsolete, and Deficient, and was adopted from the National Bridge Inventory (USA). Good defines a bridge structure that does not require any immediate rehabilitation, outside of the regular maintenance schedule, and is functionally suitable for its objective. Obsolete defines a bridge that is structurally sound, and in no need of unanticipated rehabilitation, but is no longer suitable or adequate for its objective. And, Deficient defines a bridge structure that is in need of urgent structural rehabilitation, and should, either; have vehicle load restrictions, or be closed from traffic entirely, depending upon the severity of the structural issues. A bridge within the inventory both obsolete and deficient is classified as deficient only. (Federal Highway Administration, 2016)

3.3 *Database sources*

The required details of each long span bridge surveyed were gathered from several online resources, including;

- Wikipedia.org
- Structurae.net
- Highestbridges.com
- Bridgehunter.com
- Uglybridges.com
    - USA only, uses the NBI
- Designer fact sheets/documents

Due to the National Bridge Inventory being freely available, bridges within the United States contain the most detailed and accurate entries.

All sources used, except for Uglybridges.com, were community, or crowd, collaborative efforts, and therefore the quality and accuracy of details varied greatly. To ensure bridges entered into the database were detailed as accurately as possible, the location, span, materials and usage were confirmed, when available, with satellite imagery (Google Maps), street view imagery (Google Street View), and with photographs available online.

3.4 *Database availability*

At the time of writing the Global Long Span Bridge Database exists in several forms. The database remains in its original form as an Access Database file, complete with imagery, a searchable list and organisable tables. From the Access database, it has been exported to Microsoft Excel, where the entries have been broken down and analysed. From Excel, the database, has also, been exported to a private Batchgeo.com map, where all bridges within the database are presented on a global map, with all database detailing (except imagery), which is filterable, and searchable. From Batchgeo.com the database was exported to a Google Earth (.kml) file, again, with all database detailing.

As will be stated, and explained further, in the conclusion of this report, the Global Long Span Bridge Database at present time of writing is considered to be a solid foundation for further refinement, expansion, detail and scope.

It is expected that the latest version of the database will be made available for research, or continuation, via the Monash University Civil Engineering faculty.

4 DATABASE ANALYSIS AND DISCUSSION

4.1 *Database composition*

Before diving deep into analysis and discussion about the age, status, design life, in common problems, and future needs of the long span bridges, it is important to have an understanding of the distribution of both the location and bridge structure type of the long span bridges included within the database. Table 1 below displays the contribution of long span bridges from each defined global region, as well as the number of individual countries that contributed and the country within with the leading contribution. It is of no surprise that the United States makes the largest contribution of long span bridges. Surprisingly, Norway, was the largest contributor from the European theatre, and whilst not unexpected, it is still very impressive, the contribution China has made, mostly within the last two decades.

Table 1. Number of bridges and countries per region.

Global region	Number of bridges	Number of countries	Major contributing country
North America	266	2	United States (245)
Asia	206	18	China (98)
Europe	199	29	Norway (51)
Latin America.	31	12	Brazil (11)
Oceania	18	2	Australia (16)
Middle East	16	7	Turkey (7)
Africa	15	11	None
Total	751	81	United States (245)

Table 2 below displays the database composition of the different bridge types, defined within the database, per region and in total. Of particular interest, the only region to make significant use of the truss and, closely related, cantilever, bridge structures for long spans is North America (United States). Also of note is the heavy use of cable stayed bridges within the Asia region. These two points of interest, are of importance, and will be recalled later in an analysis and discussion around the health and status of the long span bridges of different types.

Table 2. Number of bridges per bridge type, by region.

Global region	Bridge structure type				
	Arch	Cable stayed	Cantilever	Suspension	Truss
North America	47	29	67	51	72
Asia	39	87	9	64	7
Europe	30	70	42	48	9
Latin America.	3	15	6	7	
Oceania	3	5	8	2	
Middle East	5	5		6	
Africa	5	4	1	5	
Type total	132	215	133	183	88

Figure 5 below shows the distribution of long span bridge construction per global region over the last two centuries. There are several time spans of interest to note from the figure. Firstly, a dramatic increase during the 1930s within North America to combat the Great Depression as part of the Public Works Administration act (Public Works Administration, 1939), which is immediately followed by a reduction of construction during WWII and then the subsequent increase in North America and Europe immediately after. Second period of interest is the infrastructure construction boom within the Asian theatre, in line with, and most likely due to their recent economic boom. In contrast the North American region rate of construction has been declining since peaking in the 1960s.

4.2 *Age and design life*

The concept of 'Design Life' was defined in relation to this project and database in Section 2.4.4 of this report, and was determined, from various international construction standards, to be one of three time periods. From the AASHTO LRFD 2012 for the United States and North American region, the minimum design life for a permanent bridge structure was 75 years. From the Australian Standards AS5100.1 the design life is specified as 100 years, which is also the minimum design life specified in the base Eurocode, EN 1990, and the Chinese Standards. The British Standards BS EN 1990, and many other country specific adaptations of the Eurocode, specify a design life for bridge structures of 120 years.

Using the details logged per bridge regarding age, the number of long span bridges that exist beyond each of the three design lives was determined, and has been summarised in Table 3 below.

Table 3. Number and percentage of bridges beyond design life

Global region	Number and percentage of bridge beyond:					
	>75 years		>100 years		>120 years	
North America	65	24.4%	10	3.8%	3	1.1%
Asia	1	0.5%	0	0.0%	0	0.0%
Europe	20	10.1%	11	5.5%	9	4.5%
Latin America.	4	12.9%	3	9.7%	1	3.2%
Oceania	4	22.2%	0	0.0%	0	0.0%
Middle East	0	0.0%	0	0.0%	0	0.0%
Africa	4	26.7%	2	13.3%	0	0.0%
Global (total)	98	13.0%	26	3.5%	13	1.7%

However, it should be acknowledged that, the obtained design life values are from current editions of bridge design standards, and should only be applied to bridges constructed after the standards date of issue. Design life values from previous editions may have been greater, or lower, than current values, or the concept may not have been in consideration at all. At the time of writing this report, copies of superseded specifications have not been obtained, nor information regarding their inclusion or specification on design life.

Therefore, for the purposes of this analysis and discussion, current design life specifications have been applied and considered for all bridges.

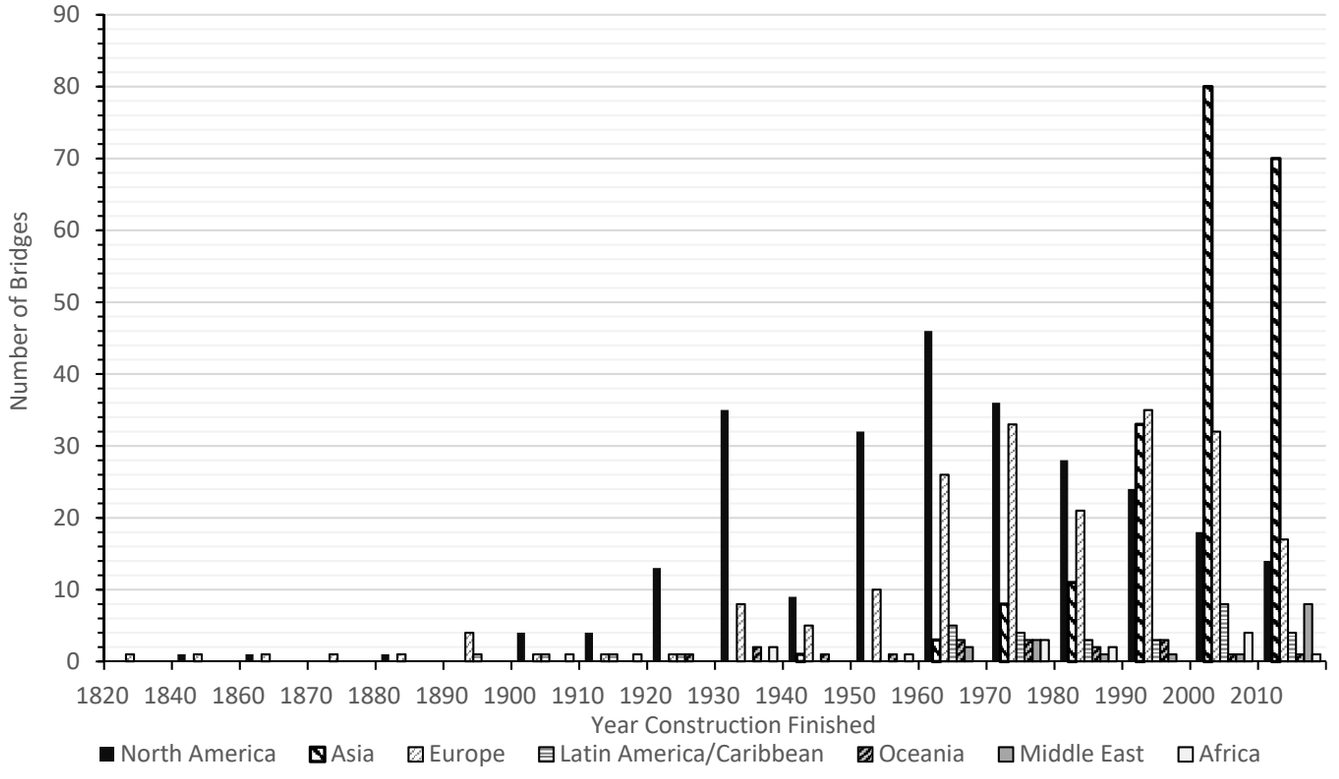


Figure 5. Number of bridges constructed per decade categorised by global region.

Figure 6 below displays the distribution of bridge age within the database entries using 5-year brackets and the three major global regions (for graph clarity). The bridges built during the dramatic construction rate increase during the 1950s and 1960s, in North America and Europe, are approaching the 75-year design life, whilst long span bridges built prior to WWII have passed the 75-year life, and will be approaching 100-years within the next two decades.

4.2.1 *Design Life and Rehabilitation*

Using recorded information of whether bridges underwent major repair, or unanticipated structural rehabilitation, an indication of how many bridges that have achieved target design life can be obtained.

This has been calculated as the number, and percentage, of bridges exceeding design life, that were rehabilitated prior to design life targets, and is summarised above right as Table 4. It is clearly apparent that for the majority of bridges that have exceeded target design life periods, structural rehabilitation has already been performed, and thus target design life, in accordance with the current definition, was not achieved. Only 8% of North American bridges, 5% of bridges in Europe, and collectively 12% of the global total, beyond the AASHTO LRFD specified design life of 75-years, were not structurally rehabilitated prior to reaching the 75 years of age.

Table 4. Number and percentage of bridges exceeding design life, that were rehabilitated prior to design life target

Global region	Bridges rehabilitated prior to design life: (% of bridges exceeding design life)					
	<75 years		<100 years		<120 years	
North America	60	92%	10	100%	3	100%
Asia	1	100%	0		0	
Europe	19	95%	10	91%	9	100%
Latin America.	0		2	67%	1	100%
Oceania	4	100%	0		0	
Middle East	0		0		0	
Africa	2	50%	1	50%	0	
Global (total)	86	88%	23	88%	13	100%

* bridges without rehabilitation dates were assumed rehabilitated prior to design life target

4.3 *Status and common problems*

Using information regarding; global region, bridge type, bridge health status, and bridge rehabilitation data, correlations can be drawn and conclusions made upon the status of the long span bridges around the globe, and the common problems that affect them.

Table 5, on the following page, summarises the health classification per global region as the percentage of bridges within each region. It is important to note that the National Bridge Inventory provided extensive information regarding the health and status of long span bridges located within the United States, which has likely affected results. However, given the fact that the United States contains the oldest collection of long span bridges, the

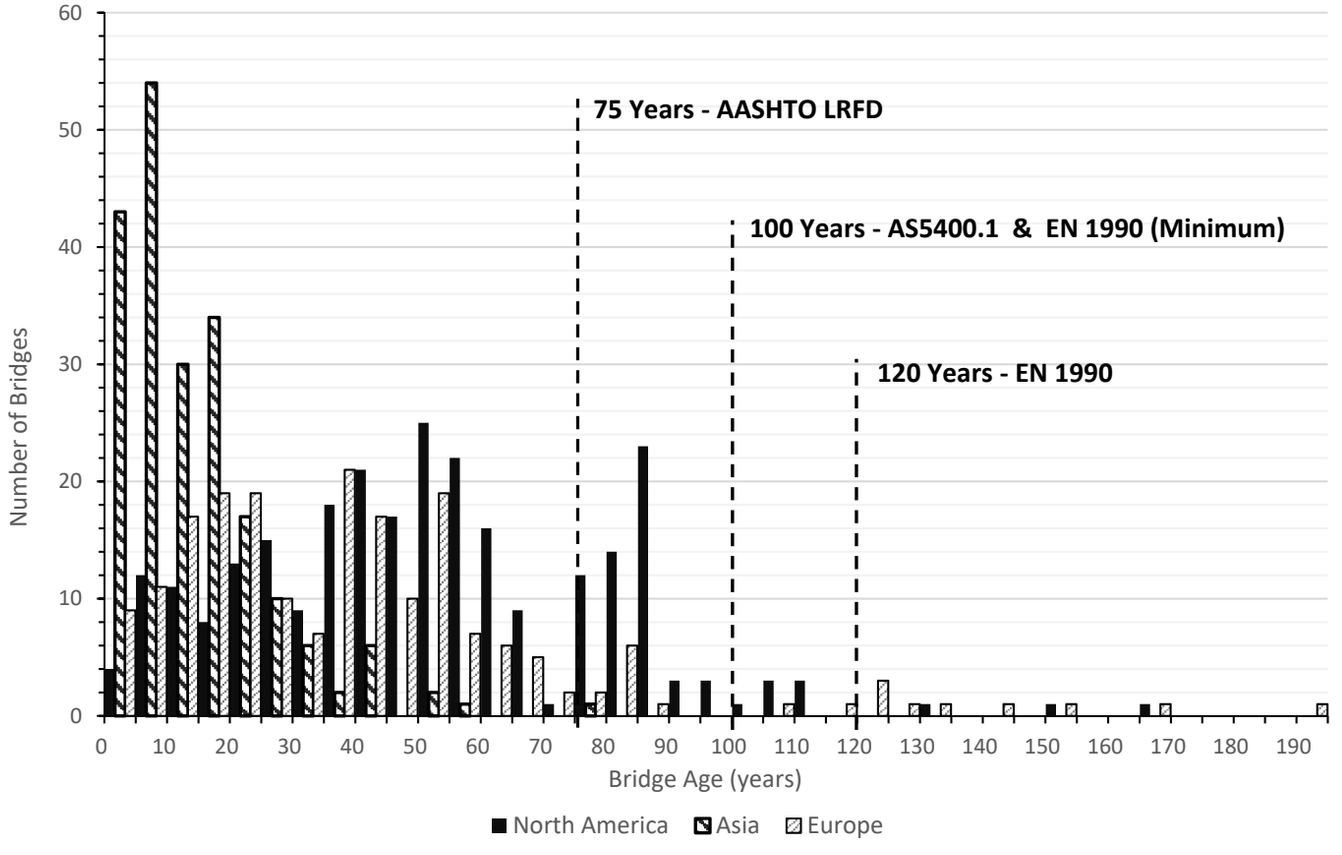


Figure 6. Number of bridges constructed per 5-year age bracket compared to design life.

indication from Table 5 that the North American region contains the highest percentage of structurally deficient bridges is not surprising.

Table 5. Bridge health classification per global region.

Global region	Percentage of global region total:		
	Good	Deficient	Obsolete
North America	63.2%	9.4%	27.4%
Asia	99.0%	0.5%	0.5%
Europe	95.0%	1.5%	3.5%
Latin America.	90.3%	3.2%	6.5%
Oceania	100.0%	0.0%	0.0%
Middle East	100.0%	0.0%	0.0%
Africa	100.0%	0.0%	0.0%
Global (total)	85.0%	4.0%	11.1%

The American Society of Civil Engineers has been publishing yearly Infrastructure Report Cards for the United States for several years now, and recorded that 9.4% of all bridges within the United States were classified as structurally deficient, which closely matches the determined percentage of structural deficient long span bridges within the North American region of this database. However, the latest Infrastructure Report Card reported that only 13.6% of United States bridges were classified functionally obsolete, while 27.4% of North American long span bridges within the database were classified as functionally obsolete. (ASCE, 2017)

A possible reason for the high rate of obsolete classifications amongst long span bridges within the United States is that long span bridges have a higher tendency to be placed along critical transportation routes, and the United States over reliance upon road vehicles for transportation does not assist the traffic capacity requirements of the long span bridge.

Figure 7 below, and Table 6 above right, display information regarding the structural rehabilitation and global region location of long span bridges. Figure 7 displays bridges per decade of construction that have been rehabilitated, which if viewed alongside Figure 5, in Section 4.2 of this report, and Table 6 below gives clear justification as to why the region rehabilitation percentage, of 62.4%, for North America is so high. Majority of bridges rehabilitated originate from the same time period in which North America's long span bridge construction peaks.

Table 6. Percentage bridges rehabilitated per global region.

Global region	Percentage of global region total	
	Only regular maintenance	Rehabilitated (reconstruction)
North America	37.6%	62.4%
Asia	92.7%	7.3%
Europe	58.3%	41.7%
Latin America.	67.7%	32.3%
Oceania	61.1%	38.9%
Middle East	87.5%	12.5%
Africa	46.7%	53.3%
Global (total)	61.3%	38.8%

If bridge type is now taken into consideration with both Table 7, bridge health classification per bridge type totals, and Table 8, bridge rehabilitation percentage per bridge type totals (both tables on the following page), further justification as to why the North American region has the highest percentage of structurally deficient long span bridges becomes apparent. Table 7 displays that the truss bridge type is the bridge type with the highest percentage of structurally deficient bridges, and cantilever being the second highest. Likewise, Table 8 displays that the truss and cantilever bridge types are the bridge types with the highest percentage of structural rehabilitation.

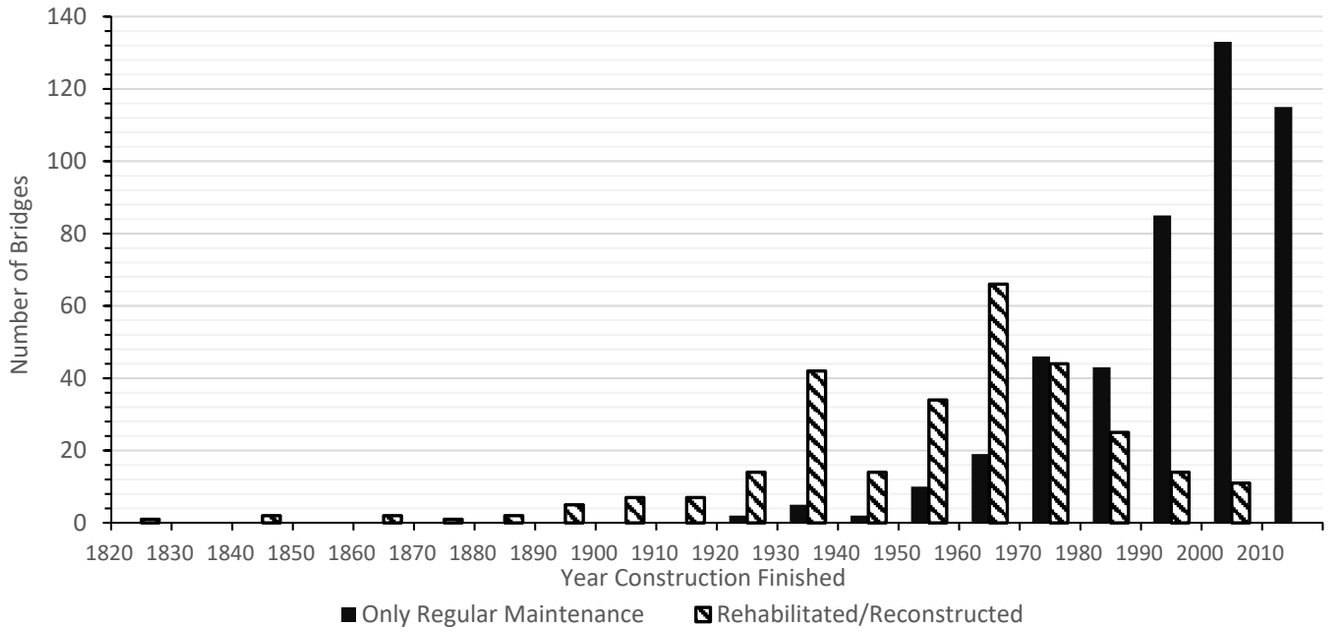


Figure 7. Number of bridges constructed per decade that have been rehabilitated.

Table 7. Bridge health classification per bridge type.

Global region	Percentage of bridge type total		
	Good	Deficient	Obsolete
Arch	87.9%	3.0%	9.1%
Cable Stayed	99.5%	0.0%	0.5%
Cantilever	81.2%	6.0%	12.8%
Suspensions	77.6%	4.4%	18.0%
Truss	65.9%	11.4%	22.7%

Table 8. Bridge rehabilitation per bridge type.

Global region	Percentage of bridge type total	
	Only regular maintenance	Rehabilitated (reconstruction)
Arch	58.3%	41.7%
Cable Stayed	81.9%	18.1%
Cantilever	52.6%	47.4%
Suspensions	57.4%	42.6%
Truss	36.4%	63.6%

Therefore, as the North American region is the region with the highest number of cantilever and truss bridge types, it is understandable that the region has the highest percentage of structurally deficient and rehabilitated long span bridges.

And, from Figure 8 below an indication as to why it is that truss and cantilever long span bridges have the highest percentage of deficiency and rehabilitation is given.

From Figure 8, it can be seen that, the percentage of bridge types affected by corrosion, wearing, capacity and overloading are highest for cantilever and truss long span bridges.

These results are in line with findings that were published in a 2011 ASCE journal performance review of all bridge types and bridges within the United States, using the U.S bridge inventory (NBI). It was concluded that truss bridges have the lowest condition performance, and in general it was concluded that the average bridge life till major rehabilitation was 63% of the objective 75-year design life. (Farhey, 2011)

If truss, cantilever and arch types are removed from the health classification and rehabilitation calculations per region, it is expected that the percentage of deficient North American bridges (Table 5) and percentage of rehabilitated North American bridges (Table 6) will decrease. This proves to be true, although, possibly for alternative reasons. If only cable stayed and suspension bridges are considered, percentage deficient and percentage rehabilitated bridges in the North American region fall to 6.3% and 56.3%, respectively, closer to the international results. However, in Table 9 the percentage of each bridge type number total per 10-year age bracket is summarised, and it can be seen that the truss bridge type is, collectively, the oldest bridge type, with an average age of approximately 52 years, with cantilever and suspension close behind.

Table 9. Percentage of bridge type totals per

Age (years)	Bridge structure type				
	Arch	Cable stayed	Cantilever	Suspension	Truss
0-9	21.2%	35.3%	6.8%	18.0%	4.5%
10-19	19.7%	29.3%	10.5%	14.8%	3.4%
20-29	6.1%	19.5%	12.0%	8.7%	10.2%
30-39	7.6%	9.8%	13.5%	5.5%	12.5%
40-49	8.3%	4.2%	21.1%	10.9%	18.2%
50-59	15.2%	1.4%	15.8%	14.8%	15.9%
60-69	6.1%	0.5%	5.3%	5.5%	12.5%
70-79	2.3%	0.0%	3.8%	3.3%	6.8%
80-89	10.6%	0.0%	6.8%	8.2%	10.2%
90-99	0.0%	0.0%	0.8%	2.7%	2.3%
Average age per type	38	17	45	46	52

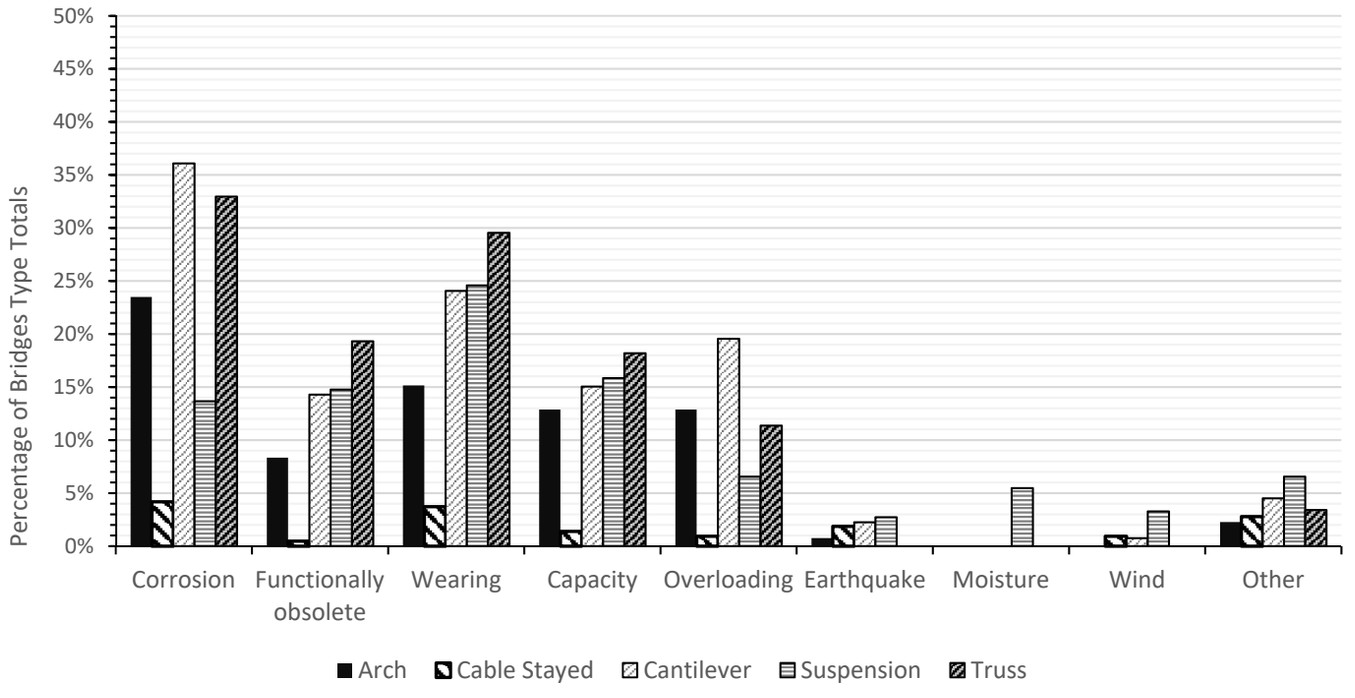


Figure 8. Percentage of bridge type totals affected by structural and environmental issues

5 FUTURE NEEDS, REVIEW AND RECOMMENDATIONS

5.1 *Future needs of long span bridges*

The present conditions within United States can be used to understand the future requirements of long span bridges around the globe. Except for China and Norway, most countries and individual managing bodies, do not have an infrastructure comparable to the United States, however, the treatment and monitoring of ageing bridges is comparable no matter the number of bridges. The ASCE estimated, in their most recent infrastructure report for the United States that the nation's backlog of bridge rehabilitation requires $123 billion (USD) to clear. (ASCE, 2017) Though this amount is for all bridges, regardless of span length, within the United States, it is still a warning as to the cost of neglect to bridge structures.

Closures on any bridge are disruptive and costly to both the managing body and the surrounding population. This cost is amplified for vital connections, which are often provided by long span bridges. Therefore, it is essential that future long span bridges are designed with the expectation of regular and unexpected maintenance, and that they are designed towards ease of accessibility and upgradeability.

For the ageing, long span bridges within North America, an effective replacement method for severely deficient, obsolete or outdated bridges needs to be devised. The ongoing maintenance costs of the high number of truss, cantilever and arch bridges within the United States can surely be mitigated by commencing their replacement with modern and more durable bridge technologies.

The average age of cable stayed structures is very low in comparison to the other bridge types, though so far the health and rehabilitation rate have been promising. Moving forward cables stayed bridges need to be closely monitored and documented, particularly within the Asian theatre.

Also after conducting this survey and database creation, it should be noted that higher standards in archiving of bridge information needs to be achieved, and if possible publicised. The NBI for the United States was an invaluable resource during this project, and so it is encouraged that other regions and countries around the globe share similar bridge inventory information. With more information, a deeper, more accurate, and meaningful analysis can be conducted, especially outside the United Sates.

5.2 *Database review and recommendations*

The database constructed for this investigation into long span bridges from across the globe has established a strong foundation, and it is recommended that the database be expanded in the future. However, expansion in terms of the quantity of bridges within the database should not be priority, instead, the database detail and scope of information per bridge needs to be improved. There is potential for far deeper and meaningful analysis in regards to the performance of long span bridges. It is recommended that details added include; side span lengths, number of spans, construction cost, maintenance costs, construction technique, traffic information, and design loading. Also, demolished long span structures, were omitted from the survey and should be added to the database.

6 CONCLUSION

The survey conducted and the subsequent database constructed were essential to the breakdown and analysis of long span bridges from around the globe. Whilst analysis has been completed, and valid points drawn regarding the age, design life and status of long span bridge structures, there is a need for more outside the United Sates. It can be concluded that the database created and used is a good foundation for further detail and expansion.

The concept of design life creates an interesting discussion about the expectations of how long a bridge should exist and how well it should perform. Till recently bridge construction has been doing the best we can with what is available, however, with recent strides towards sustainability, achieving the definition of design life is looking more promising than the last half century performance of long span bridge structures.

7 REFERENCES

American Association of State Highway and Transportation Officials. (2012). *AASHTO LRFD Bridge.* Washington: American Association of State Highway and Transportation Officials.

ASCE. (2017). *2017 Infrastructure Report Card: Bridges.* Retrieved from Infrastructure Report Card: http://www.infrastructurereportcard.org/cat-item/bridges/

Euorpean Committee for Standardization. (2004). *Eurocode - Basis of structural design.* Brussels: Euorpean Committee for Standardization.

Farhey, D. N. (2011). *Operational Structural Performances of Bridge Types.* Reston: American Society of Civil Engineers.

Federal Highway Administration. (2016, December 31). *Bridges and Structures: Frequently Requested NBI Information.* Retrieved from Federal Highway Administration: https://www.fhwa.dot.gov/bridge/britab.cfm

Hewson, N. R. (2003). *Prestressed concrete bridges: design and construction.* Cornwall: Thomas Telford Limited.

Kratky, R. J. (2004). *Assessment of Performance of Vital Long-Span Bridges in the United States.* Reston: American Society of Civil Engineers.

Public Works Administration. (1939). *America builds: The record of PWA.* Washington: U.S. Government Printing Office.

Standards Australia. (2004). *AS5400.1-2004 Bridge design.* Sydney: Standards Australia.

Maintenance, Safety, Risk, Management and Life-Cycle Performance of Bridges – Powers, Frangopol, Al-Mahaidi & Caprani (Eds)
© 2018 Taylor & Francis Group, London, ISBN 978-1-138-73045-8

A New Method to Understanding Loading and Traffic characteristics of Traffic flow

X.J. Wang, & X. Ruan
Department of Bridge Engineering, Tongji University, Shanghai 200092

ABSTRACT: This paper offers a damage identification and structural effect evaluation thought based on health monitoring system for large-scale bridge structures. By analyzing the sensitivity of response to traffic load, the concept and building method of categorized traffic are introduced, which categorizes the traffic into light class and heavy class on statistical periods, and the loading response of heavy class in the evaluation of structural response is prioritized. This concept of categorized traffic can be seen as a new understanding method for traffic flow loading and traffic characteristics. And it provides a new perspective to measure the traffic with different dimensions, which can bring convenience to bridge structure assessment. Then parameter characteristics and relativity of categorized traffic are counted to set the parameters and building forms of response evaluation model of categorized traffic. This paper endeavors to transfer the target of the system evaluation from safety to performance based on the practical application of the system and aims to improve the monitoring sensibility and propose new insight for its development via real-time corresponding between response data and load data over a synchronized period.

1 INTRODUCTION

In order to ensure safety, stability and durability of bridge structure, the health monitoring system is increasingly applied in large-scale bridges. While the introduction of new theories such as neural network algorithm and pattern recognition has made the theoretical system of health monitoring more mature, (S.T. Yang, 2008) there are still many problems to be solved. (X. Ai, 2009) First, the monitoring indicator lacks a reasonable plan, and there is no universal design methods and steps to follow; Second, it's without commonality because different bridges often have different health monitoring programs; Third, the health monitoring system lacks an unified and standardized evaluation criteria for bridge structure performance. (X.T. Jin, 2013) At present, there exists numerous monitoring indicators of the health monitoring system, which are divided into two categories: External load information and bridge response information. Most existing monitoring and early warning systems only study the response information and use their allowable values to judge whether the structure is safe or not. This kind of evaluation system is simple but flawed, mainly reflected in two aspects： First, the load and response data can not be used at the same time and the factors of structural performance can not be considered; Second, the sensitivity to structural changes is poor. By this kind of system, researchers can only measure greater damage but not nip in the bud. Therefore, a monitoring system that monitors the normal state of the structure to replace the monitoring system that monitors the safety state of the structure is in need. In this paper, the concept of 'normal state' for structure safety is presented. The concept is proposed to distinguish the differences between minor damage of structure and greater impairment that affecting structural safety and to raise the level of monitoring from safeguarding structural safety to maintaining normal structural performance. To achieve such monitoring objectives, it is inevitable to make good use of load and response monitoring data in the same period to realize the correspondence between load data and response data at the statistical level. Therefore, it can provide new ideas for structural health monitoring in daily life by using the load information of a certain period to determine whether the corresponding period of response information is reasonable.

In order to study the correspondence between load information and response information, the appropriate load form must be selected first. Among the loads that affect the structural response, the traffic load is the most influential and the most random one. Through the study (see Section 2.1), it

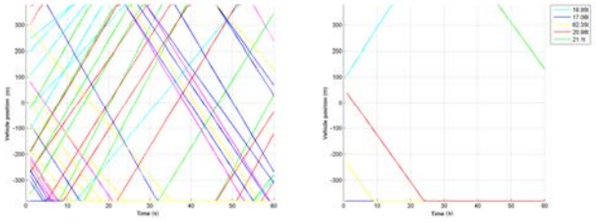
is found that the traffic flow of heavier vehicles has much greater impact on the structural response than that of lighter vehicles. Therefore, by analyzing the sensitivity of response to traffic load, the concept of categorized traffic are introduced, which categorizes the traffic into light class and heavy class on statistical periods. On the one hand, the categorized traffic method facilitates the streamlining of traffic flow data, on the other hand, with focuses on the heavy class of traffic flow in the study of the correlation between load and response, it can greatly increase the efficiency of analysis. Meanwhile, the introduction of this concept lays the foundation for the establishment of the normal state which takes the characteristics of heavy class as the main reference. On the basis of the above, the division standard of categorized traffic is studied, the selection of the representative parameters of categorized traffic and its characteristics is discussed, and the correlation of parameters between heavy class and light class is further explored.

2 A NEW METHOD TO UNDERSTANDING THE TRAFFIC LOAD

For the assessment of bridge structure performance, the vehicle load is the most critical load type mong the load data monitored by the health monitoring system. Among the many characteristics of vehicle loads, weight characteristic has the most influence on the response is the. Therefore, the study of the correlation between load and response should focus on the impact of weight of traffic flow.

2.1 *The concept of categorized traffic*

The influence of weight factor of vehicle load in the structural response is studied by the following data simulation. The vehicle situation of a six-lane freeway within a minute is shown in Figure 1, Figure (a) shows the time chart of all vehicles passing the survey section. The slope of the line represents the speed of the vehicle. The positive slope means that the driving direction of the vehicle is the positive direction of the bridge, and negative slope means the opposite. Similarly, Figure(b) shows the time chart of vehicles over 15 tons. There are five vehicles that meet this condition, they are located on the 1st, 5th and 6th lanes.



(a) *(b)*

Figure 1: Six-lane freeway traffic flow on a bridge within a minute

Fig. 2 to Fig. 3 describe time histories of the traffic flow above for two kinds of response and their corresponding influence lines on a cable-stayed bridge. The time chart and influence line of displacement in the middle of bridge are depicted in the Fig. 2. It can be seen that the load-sensitive section of mid-span displacement effect is within 400m in the middle of the bridge. A large peak of displacement response appears in about 3sseconds, and a small peak appears in about 50 seconds. For the rest of the time the response level is relatively small. Similar observations can be drawn by looking another response. To sum up, there are three vehicles in the sensitive sections of displacement response during the whole measuring period. Two of them are traveling in sensitive sections within the first 10 seconds, they are located in the middle of the bridge at about 3seconds, the total weight of them is 38 tons. Another one enters the sensitive section around 55 seconds, it weights 21 tons. By the comparison of these results, it is not difficult to find that the peak of response is associated with the heavy vehicles above 15t. And the light vehicles have a lesser impact on response.

To sum up, since the contribution of heavy vehicles to the response is much greater than that of light vehicles, analyzing the traffic information of heavy vehicles is the key to studying the correlation between vehicle load and response. Due to the small number of heavy vehicles , the separation of heavy vehicles from traffic can greatly reduce the amount of data and improve the efficiency of monitoring and analysis. Therefore, by studying the vehicle characteristics of different vehicle weight in the traffic flow and comparing the parameter characteristics differents of the lighter vehicle (the light class) and the heavier vehicle (the heavy class) this paper promotes a reasonable category method of categorized traffic.

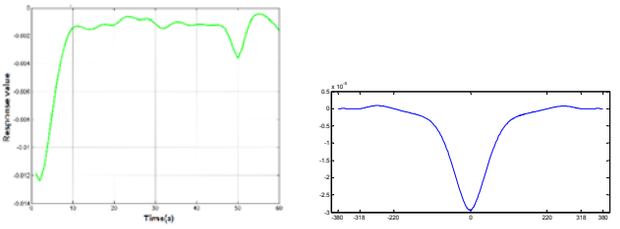


Figure 2: Time chart and Influence Line of Mid - span Displacement Response of a Cable - Stayed Bridge

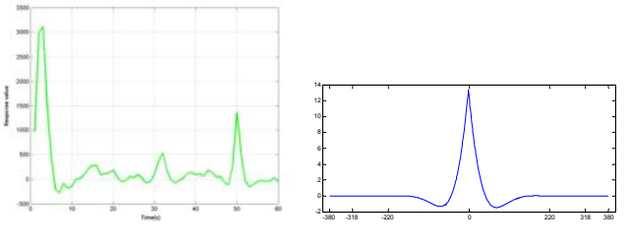


Figure 3: Time chart and Influence Line of Mid - span Moments Response of a Cable - Stayed Bridge

2.2 *Sensitivity Analysis and Determination of Statistical Interval*

In the process of building the categorized traffic, the statistical interval of the traffic flow parameters must be discussed first. Due to the traffic flow and load characteristics should to be considered in the response evaluation, the selection of parameter statistical interval should be based on the two characteristics above; Next, on the basis of determining the statistical interval, the division standard of categorized traffic should to be discussed.

For long-span bridges, due to the large longitudinal load length, the number of vehicles that can be deployed in the area of influence lines is large. The structural response is greatly affected by the overall load of the fleet and is relatively less affected by the axle load of a single vehicle. In the study of vehicle load, the traffic flow characteristics should be calculated during a period of time. The vehicle load characteristics should be analyzed from the traffic flow perspective, not from the perspective of the vehicle, so the appropriate statistical time interval should be chosen.

In the establishment of the traffic statistics model for traffic flow parameters such as flow, density, speed, load concentration and so on, the statistical interval should be firstly determined. The determination of the statistical interval is very important. It directly affects the shape of the traffic flow curve. This effect is more pronounced in the vicinity of the traffic capacity and in the crowded area. (Lloydsbach W. 1998) According to the general experience, when the statistical interval is lengthened, the discreteness of the measured point distribution decreases. At this time, an appropriate interval can be found so that the measured data can form a smooth and continuous curve. When the statistical interval is smaller than the optimal interval, the impact of single vehicle and other random factors can be significant. In previous studies at home and abroad, 15 minutes was usually used as the statistical interval for analyzing traffic flow statistical models, and 15 minutes was also the most commonly used statistical interval for calibrating the traffic flow model. (S. Chen, 2004) In addition, the recommended statistical interval in HCM over the years is also 15 minutes.

At the same time, the statistical interval also has an important influence on the parameters of the traffic flow considering the load characteristics in this paper, and it directly affects the statistical validity of the load concentration. Due to the consideration of vehicle load, traffic flow characteristics have changed significantly, and the statistical interval needs to be re-determined. Similarly, if the statistical interval is too large, the load concentration can hardly reflect the evolution of traffic flow in a short period of time and the stochastic characteristics of the basic parameters are reduced. If the statistical interval is small, the randomness and variability of various traffic parameters are too large, and the noise impact is serious. Therefore, the appropriate statistical interval should be able to eliminate the impact of random noise and to ensure the stability of the characteristics of traffic flow. And at the same time, the real traffic flow characteristics can be reflected to the greatest extent. The research on road capacity shows that the minimum statistical interval of traffic flow is the shortest time to ensure the stability of traffic flow. NRC considers that the statistical interval of 15 minutes can meet the requirements well. If the ratio of the statistical results of other interval to 15min is relatively small, it is considered that the statistical interval also reflects the traffic flow characteristics. Given the above, the statistic interval of 15 minutes is the best choice.

It showed, by example, if the statistical interval of 15 minutes is appropriate for the analysis of the load flow. One-month traffic data of a four-lane expressway of a certain section is selected, with the average traffic volume varying from 20 to 200. The hourly volume of traffic data varies significantly in a day. The traffic flow data is analyzed according to different statistical intervals, and the relationship between the variation of traffic volume and statistical interval is obtained and plotted in Fig. 4.

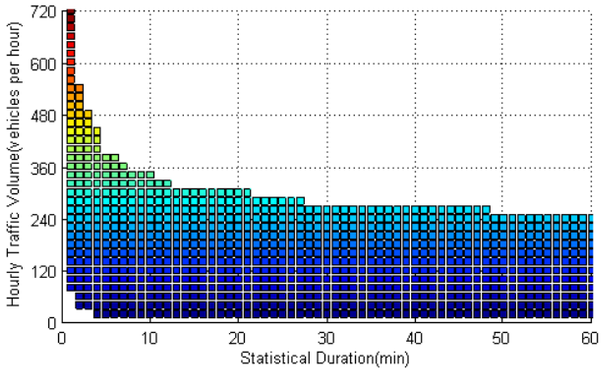


Figure 4: Relationship between statistical interval and traffic volume variability

Figure 4 reflects the relationship between traffic volume variability and statistical interval. Within the statistical interval of 13 minutes, the variability of traffic volume is very large. Some sections of statistical arguments have data, and some sections have no data, which reflects the randomness of traffic statistics and is distorted with the actual situation When the statistical interval exceeds 13min, the variation of traffic volume is basically stable, and the changes of statistical parameters need to be further investigated.

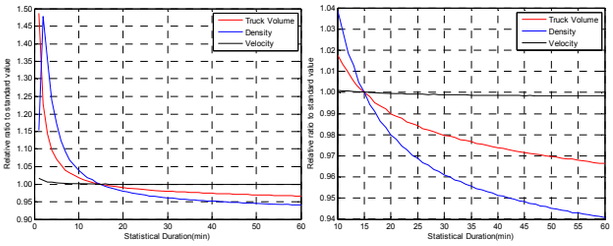


Figure 5: Performance of statistical interval and it's Partial enlargement

Select 15min as the standard statistical interval, and then compare traffic statistics obtained in other statistical intervals. The ratios of traffic statistics of other intervals to that of standard interval are drawn in Figure 5. Obviously, the result of deviation between the standard interval and the statistical interval higher than 15 min is basically within 5%. Therefore, in the subsequent calculation and analysis, the statistical interval of 15m in can meet the statistical requirements. 15min is also the basic statistical interval for data statistics in the traffic area.

Data statistic intervals higher than 60 min are widely regarded as inadequate to describe traffic behavior and characteristics under local traffic peak, so the relevant statistical calculations are also distorted. So the statistical interval of 15 minutes is also suitable for the analysis of traffic flow that incorporated load characteristics.

2.3 *Determination of categorized traffic standards*

The study about traffic flow and load characteristics above shows that the load level to a large extent affected the traffic flow characteristics. Considering that the effects of light vehicles below 20t on the response are not significant, the study of response should focus on the characteristics of the heavy class of traffic flow. In the process of forming a categorized traffic, the criteria for dividing the traffic flow should be uniformly selected according to the division standard of heavy truck mixed rate. Within a certain period of time particles (15min), select 20t as the limit of the heavy and light class. [In the 'Implementation on vehicles Overload management throughout the country' published by China's Ministry of Communications, China's Ministry of Public Security and five other ministries at 2004, the limit of overload traffic is prescribed. The standard of two-axle , three-axle, four-axle, five-axle and six-axle vehicles are 20t, 30t, 40t, 50t and 55t respectively. At the same time, according to the related survey results of freeway traffic load, the weight of the third type of vehicles (large buses and two-axle trucks) is about 8 ~ 16 t, and that of the fourth type of vehicles (triaxial large vans) is over 18t. Incorporating the above mentioned two points, within a certain period of time particles (15min), 20t can be selected as the limit of the heavy and light class.] Vehicles larger than 20t are grouped into the heavy class of traffic flow and less than 20t are classified as light class. The analysis of the characteristics of the traffic flow is based on the above conclusion.

In summary, this section presents a traffic classification method based on load characteristics of traffic. In a certain period of time particles, traffic flow is divided into light class and heavy class according to the vehicle load. The criteria of categorized traffic and the size of the time particle (Statistical interval) are determined, which lays the foundation for establishing a vehicle load model for response evaluation.

3 TRAFFIC LOAD AND FLOW PARAMETERS ANALYSIS BASED ON THE NEW METHOD

In the field of traffic the dynamic evolution law of traffic flow can be clarified by of traffic parameters, which is based on traffic engineering. By this method , for a vehicle-loaded bridge, a number of traffic and load parameters can be used to determine the "load flow" acting on the bridge, so as to assess its load response. In which the most crucial point is to analyze the correlation between traffic flow and load parameters by building a dynamic traffic flow model.

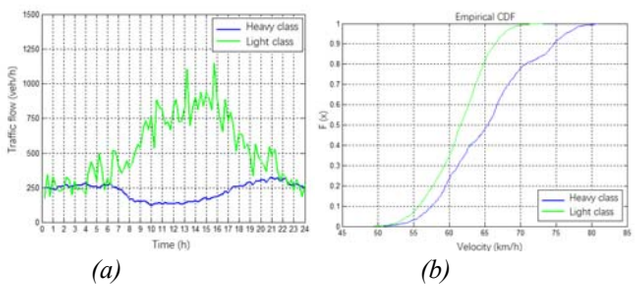
At the traffic level it forms a converged traffic flow by flow-dense statistics and loading. Considering the traffic load, these characteristics of the traffic flow occur essential changes. When considering the traffic flow of the load, the load parameters are combined or related to the relationship of vehicle density, average speed and other parameters. Due to the high randomness of the vehicle load (firstly, the type of vehicle is random , their appearance and axle type are different ; secondly, the load of the same type of vehicle is random , the load is irrelevant). It is difficult to take account of some parameters into the traffic flow. This problem can be solved by the above-mentioned method of categorized traffic. The establishment of categorized traffic greatly weakens the trouble to assimilated traffic caused by the random ness of the vehicle load.

3.1 *Parameter analysis of categorized traffic*

In the traditional traffic engineering , the parameters that characterize the characteristics of the traffic flow include flow, density and speed. In the range of the load flow, the parameters that characterize the traffic flow characteristics include load concentration and vehicle weight of 0.9 times the bifurcation value. The following analysis of categorized traffic is based on the above five parameters.

By analyzing the changes of categorized traffic flow and speed accumulation in one day, we can get Figure 6. As shown in Figure 6 (a), heavy traffic flow is more stable at any time in one day, which is about 250veh / h, during 8 am and 7pm, it appears a slight decline; On the contrary, light class traffic daily flow increased first and then decreased in the above period, the peak flow of which can be up to 1000veh / h, and during the rest time it is stable, which is around 250veh / h. For light class traffic fluctuations we can make a speculation as follows: during 8 am and 7pm, the Traffic flow is larger than that at any other time. During this period, most of the vehicles are small household vehicles and two-axle vans, the weight of the bicycle is lighter relatively. Although the traffic flow is relatively lower during the rest time, the mix-in ratio of trucks approaching the weigh t limit of the light class increases. Therefore, it is speculated that the load concentration levels in the two periods shouldn't differ significantly. The speculation above need to be verified later. If the speculation is consistent with the statistical value, combined with the characteristics that the light class vehicle has less influence on the response, the light class vehicle traffic flow can be simplified into the single parameter of the average load concentration at each moment when building the load model of the evaluation response, As a load model of "base frequency" of traffic flow load, the degree of convergence would be evaluated with the characteristics of heavy class traffic.

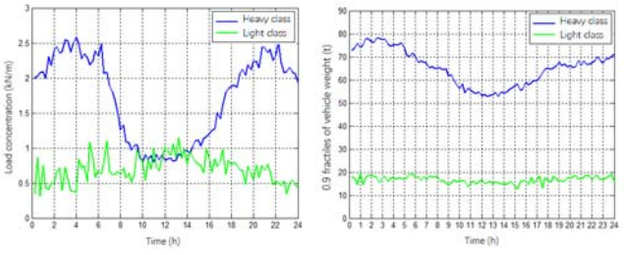
Accoding to Figure 6 (a), the speed distribution range of heavy class traffic is less than that of the light class, consistent with the above analysis results. It is known that the weight of vehicles would affect the speed: the heavier the weight, the slower the speed. So for the light class traffic it can be inferred that: during the daytime, the vehicle speed is faster and the load level is lower; in contrast, at night the speed is slower and the load level is higher. The inference supports the above speculation that the light class traffic has a relatively stable load concentration level at any time, and provides a basis for the assumption that the light class traffic flow takes only a single load concentration as a model parameter.



(a) *(b)*

Figure 6: The flow diversification and the cumulative speed distribution of categorized traffic in one day

For the categorized traffic, by analyzing its load characteristics, load concentration and the 0.9 times the quantile value changes of vehicle weight in a day, we can get Figure 7. As shown in Figure 7(a), the load intensity of heavy class traffic changes in a large range, which reaches the minimum value (about 0.9kn/m) during 8 am and 4 pm and reaches the maximum value (about 2.5kn/m) at night. The less load intensity during the daytime can attribute to less traffic. The load intensity of light class traffic in one day is more evenly distributed (about 0.7kn / m), which confirms the previous inference. Therefore, when building the load model for evaluating response, the light class traffic can be simplified as a single parameter of the average load concentration at each moment to form a load model with light class traffic load concentration as the "fundamental frequency" of the traffic load. According to Figure 7(b), the distribution tendency of 0.9-fold quantile value of heavy class is consistent with that of load concentration distribution, both of which are lower during daytime and larger at night. However, since the upper limit of light class division is 20t and the meaning of 0.9-fold quantile value is to determine the upper limit of traffic load, the 0.9-fold quantile value of light class does not get any time characteristic.



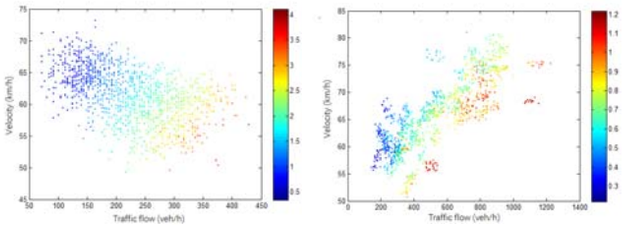
(a) *(b)*

Figure 7: The distribution of load concentration and the 0.9-fold quantile value for categorized traffic weight in one day

3.2 *Parameter correlation of categorized traffic*

Based on a comprehensive analysis of the correlation of the traffic flow, speed and load concentration, we can get Figure 8. According to the fuzzy boundaries of the relevance cloud graph in Figure 8, There is no obvious correlation between the three groups. The heavy class load concentration is evenly distributed with some linear combination between traffic flow and speed. And the correlation is obvious for the heavy class traffic, due to the linear correlation between the three parameters. If the flow rate-velocity matrix interval can be formed, the level of the load concentration between adjacent intervals is uniform and continuous. Therefore, it exits continuity in the response distribution between adjacent sections, which helps to build the load model to evaluate the structural response. Figure 9 shows the correlation between various parameters of

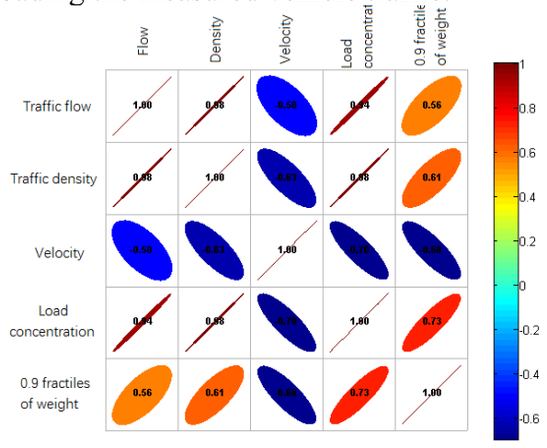
categorized traffic, heavy class shows in Figure (a) and light class in Figure (b).



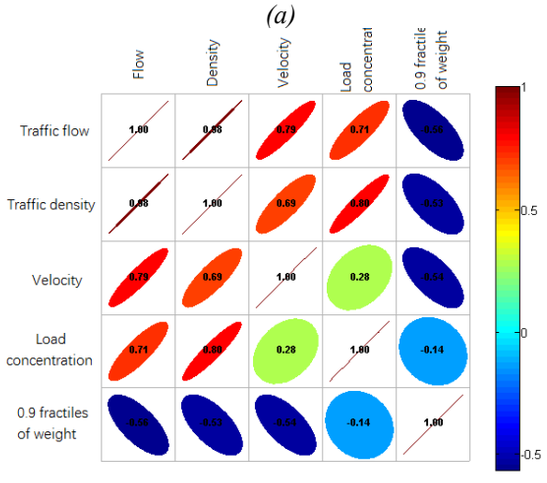
(a) *(b)*

Figure 8: Relationship between loading concentration, flow and velocity of categorized traffic

In summary, the light class traffic flow can be simplified into a single parameter of average load concentration at each moment when forming the load model of evaluation response. A load model with light class load concentration as the "base frequency" of traffic flow load can be built, and the response of heavy class traffic flow characteristics can be evaluated. Besides, for heavy class traffic, the method of dividing the two parameters into intervals can be applied when building the load model. The change of load concentration in different flow and velocity intervals would be counted, and the range of bridge response would be determined according to the influence line. In addition, the response of loaded bridge would be evaluated and corrected by loading the measured vehicle traffic.



(a)



(b)

Figure 9: The visual relevance between different parameters

4 CONCLUSION

To sum up, the existing monitoring methods mainly focuses on ensuring the safety performance of the structure, bud it can not find the daily performance changes in the structure. As a result, it can not give the opinion of repair in the structural damage development. In this paper, a kind of bridge health monitoring method based on normal state is proposed. This normal state method can make full use of load information and response information to exert timeliness and diversity of health monitoring system. On this basis, the influence of the load characteristics of traffic flow on the structure response is studied, and the concept of categorized traffic is proposed. The conclusions are as follows:

(1) Since the contribution of heavy vehicles to the response is much greater than that of light vehicles, analyzing the traffic information of heavy vehicles is the key to studying the correlation between vehicle load and response. Due to the small number of heavy vehicles, the separation of heavy vehicles from traffic can greatly reduce the amount of data and improve the efficiency of monitoring and analysis. Considering this, traffic flow is divided into light class and heavy class according to the vehicle load.

(2) 15 minutes is chosen as the statistical interval for analyzing traffic flow, because it is able to eliminate the impact of random noise and to ensure the stability of the characteristics of traffic flow.

(3) In summary, the light class traffic flow can be simplified into a single parameter of average load concentration at each moment when forming the load model of evaluation response. A load model with light class load concentration as the "base frequency" of traffic flow load can be built, and the response of heavy class traffic flow characteristics can be evaluated. Besides, for heavy class traffic, the method of dividing the two parameters into intervals can be applied when building the load model. The change of load concentration in different flow and velocity intervals would be counted, and the range of bridge response would be determined according to the influence line. In addition, the response of loaded bridge would be evaluated and corrected by loading the measured vehicle traffic.

ACKNOWLEDGEMENT

Research presented in this paper is sponsored by National Nature Science Foundation of China (No.51478337), which is gratefully acknowledged.

REFERENCES

S.T. Yang. (2008). Study on Acquisition and transmission system of health monitoring data for distributed bridge and

its key technology. *D. University of Electronic Science and Technology of China.*

X. Ai. (2009). Software design of the workstation in structural health monitoring system based on Wireless Sensor Networks. *J. Laboratory science. (01):181-183.*

X.T. Jin. (201 3). Research and desigh of bridge health monitoring general-purpose data acquisition system. *D. Wuhan University of Technology.*

Lloydsbach W. (1998). Introduction of Traffic Flow Theory. *G. Beijing University of Technology Press.*

S. Chen. (2004). Study on Practical Relationship Model of Urban Road Traffic Flow Velocity and Volume. *D. Southeast University*

Implementation on vehicles Overload management throughout the country. (2004). *S. China's Ministry of Communications, China's Ministry of Public Security.*

Maintenance, Safety, Risk, Management and Life-Cycle Performance of Bridges – Powers, Frangopol, Al-Mahaidi & Caprani (Eds)
© 2018 Taylor & Francis Group, London, ISBN 978-1-138-73045-8

Bridge Live Load Models in U.S. and Europe

Anjan Ramesh Babu
Graduate Research Assistant, Dept. of Civil Engineering, Auburn University, Auburn, AL, USA

Andrzej S. Nowak
Professor, Dept. of Civil Engineering, Auburn University, Auburn, AL, USA

Eugene J. O'Brien
Professor, School of Civil Engineering, University College Dublin, Dublin, Ireland

ABSTRACT: Overloaded vehicular traffic on bridges can cause premature damage such as fatigue cracking and accelerated aging and it can consequently reduce the service life. It is also an important part of any assessment of bridge safety at the ultimate limit state. Available Weigh-In-Motion (WIM) data provides an excellent source to study the effect of traffic loads on bridge structures. The objective of this study is to compare various types of traffic load and their effects on bridges in the United States and Europe. The database considered in this study includes WIM measurements from 20 U.S. states with 92 million records and 5 European countries (Poland, Netherlands, Czech Republic, Slovenia and Slovakia) with 2 million vehicles. The raw data is filtered to eliminate systematic errors and other questionable records. The filtering criteria used to process WIM data in the U.S. and Europe are compared.

1 INTRODUCTION

The prescience of traffic loads on bridges and understanding the trends of increasing traffic load is essential to maximize the lives of existing aging infrastructure and to design new bridges. Knowledge of current service level truck traffic helps in existing bridge evaluation and testing as well as bridge maintenance. ASCE's recently released 2017 annual report card grades American infrastructure with a D+ which means it is in poor, at-risk condition. Bridges are a significant part of transport infrastructure, and American bridges were graded C+. This means that they are in mediocre condition and need attention. In the United States (U.S.), the design service life of a bridge is 75 years as specified by AASTHO LRFD (Nowak 1999, AASHTO LRFD 2016). In Europe, the default service life of bridges is 100 years as dictated by the Eurocode although some variation is allowed in the National Annexes.

In this study, vehicular traffic loads and their load effects on bridges are compared across several states in the U.S. and a range of countries in Europe. Load effects, such as moments and shears, are dependent on trucks' axle configurations and distributions of load on each axle rather than just the overall weight of the vehicle (GVW). In this study, Weigh-In-Motion (WIM) data from 45 WIM stations, spatially distributed across 20 states in the U.S. (consisting of 92 million records) and 5 WIM stations in 5 countries across Europe (Poland, Netherlands, Czech Republic, Slovenia and Slovakia) (consisting of 2 million records) are aggregated and studied. The filtering criteria seek to filter rational data without eliminating unlikely axle configurations. Filtering criteria used in the U.S. and Europe are compared. Sorting criteria to sort regular truck traffic are also presented. The results are plotted on probability paper in the form of cumulative distribution functions (CDF's). From each plot, the mean and standard deviation can be easily read. Matlab routines are developed to filter raw data and for analysis purposes.

2 WIM DATABASE

The WIM database considered in this study is one of the most extensive databases available, collected from 45 WIM stations in the United States and 5 WIM stations in Europe. Out of 45 WIM stations, 13 are obtained from Alabama Department of Transportation (ALDOT), 14 from the NCHRP 12-76 (Sivakumar *et al.* 2011) project and 18 from FHWA under special pavement studies (SPSs). Out of 13 locations obtained from ALDOT, data for 2009 to 2014 was obtained first from ALDOT and later data for 2006 to 2008 was gathered from the authors of the ALDOT sponsored project – 'Development of Alabama traffic factors for use in mechanistic-empirical pavement design' (Turochy *et al.* 2015).

Records from the countries in Europe were obtained through the European 6th Framework research project, *ARCHES* and were previously used in other

studies (Enright and OBrien 2011, OBrien and Enright 2013). It is to be noted that the European data obtained were previously filtered, and more detail on the filtering procedures are given in the online report (Enright and OBrien 2011). From the data collected for each location, information about location, date, and time of collection, Gross vehicle weight (GVW), vehicle class, no. of axles, axle spacing, and individual axle loads were obtained for each vehicle recorded. Table 1 and Table 2 show in detail the information about vehicles obtained at each location.

Table 1. Details of WIM stations in Europe.

Country	WIM station	Year	Number of days	Number of records
Poland	Wroclaw	2008	87	176,758
Netherlands	Woerden	2005	77	578,573
Czech Republic	Sedlice	2007-2008	148	540,945
Slovenia	Vransko	2006	39	127,064
Slovakia	Branisko	2005-2006	290	528,198
				1,951,538

3 WIM FILTERING

In the analysis of WIM-based live load, the quality of the data is perhaps more important than the quantity of data. The first step in the analysis of WIM-based live loads is to scrub the data. The error in data recording caused by formatting, inaccurate calibration of sensors, erroneous post-processing, vehicles changing lanes, and other errors are to be filtered out. Also, by doing a general observation of the data, incorrect vehicle records can be seen. The type of sensors at each WIM site and the date last calibrated also contribute to better quality assurance.

Past studies about WIM have shown various reasons for WIM data filtering (Flinner 2004, Traffic Monitoring Guide 2016). NCHRP 12-76 developed some of the filtering criteria based on researcher experience and logical judgment. The SHRP 2 report (Kulicki *et al.* 2015) also used some of these filtering criteria. For the analysis of the data in this paper, filtering is used to reduce error and provide quality data. Sorting criteria are used to sort out regular truck traffic from a pool of WIM collected quality data.

The filtering process is applied to all the WIM data. A GVW threshold limit of 90 kN (20 kips) is used because it was observed that there was a lot of light traffic data that creates less damage on bridges and decreases the processing time. To have uniformity in the filtering, the criteria shown in Table 3 are applied to both data sets, from the two continents. Filtered results are shown in Table 1 and Table 2. The comparison of filtering criteria (Table 3) was made to understand explicitly the criteria's used by most researchers in the United States and Europe.

4 COMPARISION OF FILTERING CRITERIA IN U.S. AND EUROPE

Table 3 summarizes and compares the filtering criterias that are used in retaining the qualitative WIM data and further used for live load analysis. The filtering procedure used in this study is consistent with NCHRP 12-76 and in the study used in European WIM data (Enright and OBrien 2011). However, there is a variation in the threshold limits used; this variation is because of the interpretation of the different researchers and the nature of truck axle configurations in the United States and Europe.

5 DATA ANALYSIS

The quality data of the regular truck traffic after application of the filtering and sorting criteria are plotted on probability paper. GVW and load effects (moment ratio and shear ratio) for all data are combined. The data are plotted on probability paper to show the variability of the loads in each state and country considered in this study.

5.1 *Gross vehicle weight*

The GVW of WIM data for all the stations are plotted on probability paper to compare and see the differences between traffic loads on highways. The cumulative distribution functions (CDF's) of GVW for all locations are shown in Figure 1. It is observed that the mean (0.5 on the Y-axis) varies from 125 kN (28 kips) to 275 kN (62 kips). Variability in the distributions is seen to increase in the top 20% or so of the data (0.8 on the Y-axis), and greater variation in the top 1 % (0.99 on the Y-axis). In general, no single country or state stands out from the others in its traffic distribution. However, compared to all the data in this study, the European countries have heavier traffic loads. The Netherlands has the top 1% of heaviest loads compared to other data. Information on construction and interpretation of the normal probability paper plots can be found in probability textbooks, e.g. Nowak & Collins (2013).

Table 2. Details of WIM stations in the U.S.

State	WIM station	Year	Number of days	Records
Alabama	911 Alex City	2006-2008; 2013-2014	1590	2,181,188
	915 Sunflower	2006-2008; 2010-2015	1650	1,668,558
	918 Bucksville	2006-2008; 2013-2016	1200	9,454,026
	931 Athens	2006-2008; 2009-2011;2014	1170	9,133,511
	933 Muscle Shoals	2006-2008; 2009-2014	1410	5,061,730
	934 Sumiton	2006-2008; 2013-2014	1560	3,361,605
	942 Pine Level	2006-2008; 2013-2014	1530	3,249,384
	960 Whatley	2006-2008; 2013-2014	1530	1,435,591
	961 Mobile	2006-2008; 2013-2014	1500	5,171,572
	963 Grand Bay	2006-2008; 2013-2014	1500	6,574,376
	964 Ozark	2006-2008; 2009-2014	1380	3,767,670
	965 Shorter	2006-2008; 2013-2014	1320	6,562,102
Arizona	SPS-1	2008	365	35,572
	SPS-2	2008	365	1,430,461
Arkansas	SPS-2	2008	365	1,675,349
California	Lodi (Site 003)	2006-2007	304	837,667
	Antelope EB (Site 003)	2006-2007	258	943,147
	Antelope WB (Site 003)	2006-2007	256	651,090
	LA 710 SB (Site 059)	2006-2007	365	4,092,484
	LA 710 NB (Site 060)	2006-2007	333	4,661,287
	Bowman (Site 072)	2006-2007	134	3,298,499
Colorado	SPS -2	2008	365	343,603
Delaware	SPS-1	2008	365	201,677
Florida	US-29 (Site 9916)	2005	354	1,641,480
	I-95 (Site 9919)	2005	349	2,112,518
	I-10 (Site 9936)	2005	354	389,164
Illinois	SPS-6	2008	365	854,075
Indiana	SPS-6	2008	214	185,267
Kansas	SPS-2	2008	365	477,922
Louisiana	SPS-1	2008	365	85,702
Maine	SPS-5	2008	365	164,389
Maryland	SPS-5	2008	365	183,576
Minnesota	SPS-5	2008	365	55,572
Mississippi	I-10 (Site 3015)	2006	337	1,965,022
	I-55 (Site 2606)	2006	268	1,232,223
	I-55 (Site 4506)	2006	349	1,333,268
	US-49 (Site 6104)	2006	359	1,225,138
	US-61 (Site 7900)	2006	319	159,299
New Mexico	SPS-1	2008	245	117,102
	SPS-5	2008	245	608,280
Pennsylvania	SPS-6	2008	365	1,495,741
Tennessee	SPS-6	2008	365	1,622,320
Virginia	SPS-1	2008	365	259,190
Wisconsin	SPS-1	2008	365	226,943
				92,638,916

Table 3. Comparison of filtering criteria

Criteria	In this paper	In NCHRP 12-76	In Enright and O'Brien 2011
GVW	< 90 kN	< 54 kN	< 36 kN
axle weight	<9 kN & >312 kN	Same	> 400 kN
total length	< 2.2 m & > 36 m	> 36 m	N/A
steer axle spacing	< 1.5 m	< 1.5 m	N/A
axle spacing	< 1 m	< 1 m	< 0.4 m
speed	< 16 km/h & > 160 km/h	< 16 km/h & > 160 km/h	< 20 km/h & > 120 km/h
GVW	± 10% the sum of axle weights	± 10% the sum of axle weights	± 0.45 kN of sum of axle weights
FHWA class	< 3 & > 14	< 3 & > 14	N/A
sum of axle spacing	> wheel base by 0.3 m	> length of truck	> length of truck
axles	N/A	< 3	N/A
steer axle weight	N/A	< 27 kN & > 112 kN	N/A

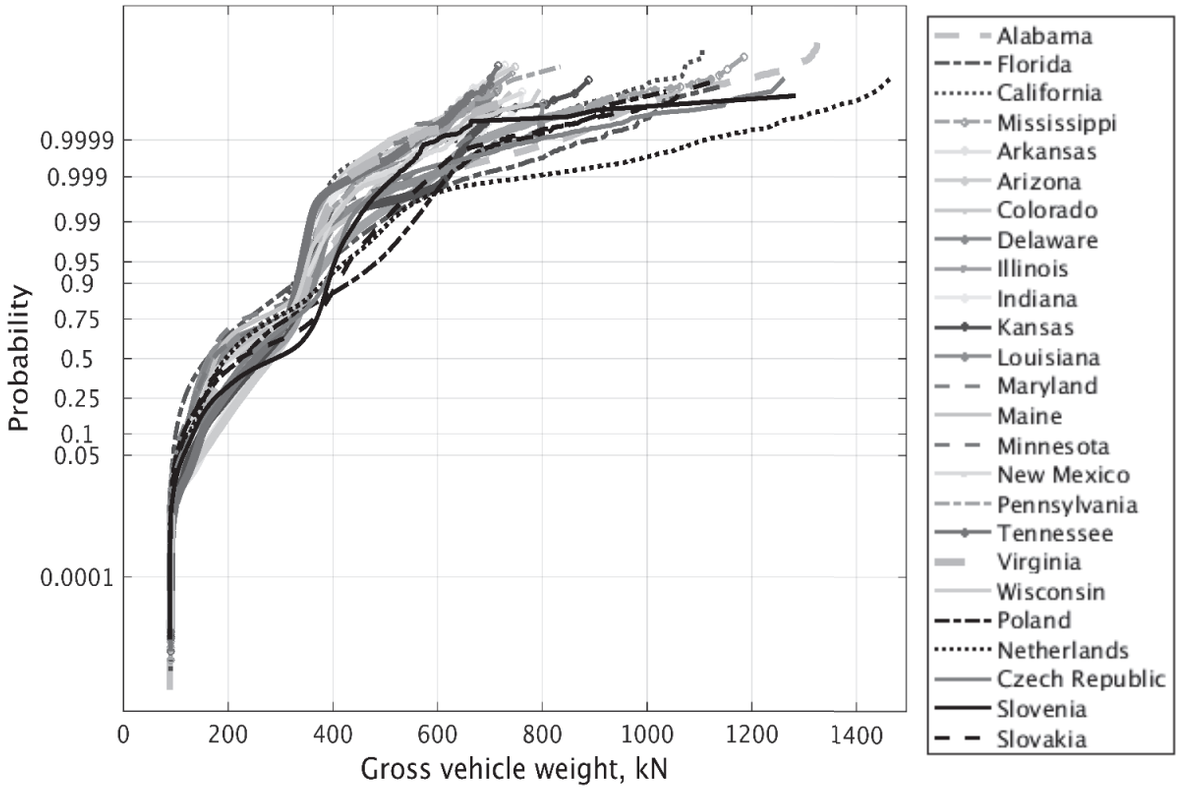


Figure 1. CDF's of GVW for all WIM stations

5.2 *Live load moments and shear forces*

The service life of the bridge is greatly affected by heavy vehicles loads and the resulting stresses on the bridge structure. It is, in fact, the load effects, such as moments and shear forces, that cause damage rather than gross vehicle weights (GVW). However, every state and country has a set of legal load limits to restrict the weights of vehicles and permits are required for those vehicles with loads above the legal limit. By using these regulations moments and shear forces can be controlled by imposing limits on load and axle configurations. To study this effect, the vehicles in the WIM data are run over the influence lines on bridges to obtain the maximum moments and shear forces over simply supported spans ranging from 9 m to 60 m. Each vehicle in this study is run over the influence line, and the resulting load effects were calculated using a MATLAB routine. Spans of 9 m, 18 m, 27 m, 36 m and 60 m are considered. For better interpretation, each calculated traffic load effect was divided by the corresponding effect found using the

current AASHTO design live load model used in the U.S. (HL-93).

In the probability paper plots shown for respective spans ranging from 9 m to 60 m in Figure 2 to Figure 6, the CDF curves for the top 20 % of heaviest vehicles in Poland and Netherlands are similar to the GVW plot. The extreme values of moment ratio are for the 18 m span (Figure 3). The mean values of a moment ratio range from 0.25 to 0.55 in the 9 m span, 0.22 to 0.6 in the 18 m span, 0.25 to 0.6 in the 27 m span, 0.25 to 0.56 in the 36 m span and 0.2 to 0.45 in the 60 m span. They are reasonably similar through the full range of spans.

Shear forces in the form of shear ratios are shown on probability paper plots for respective spans ranging from 9 m to 60 m in Figure 7 to Figure 11. The extreme values of shear ratios are for the 60 m span (Figure 11). Also, the Mississippi, Arkansas, and Florida states in the U.S. have greater shear load effects compared to the European countries. The trend in shear ratios are not similar to that for moment ratios. Shear ratios vary as the span length increases. This is evident in probability paper plots for shear ratios for the 9 m span (Figure 7) to 60 m spans (Figure 11). The mean values of shear ratio range from 0.3 to 0.6 in the 9 m span, 0.33 to 0.68 in the 18 m span, 0.25 to 0.7 in the 27 m span, 0.25 to 0.75 in the 36 m span and 0.2 to 0.8 in the 60 m span. As for moment ratios, they are reasonably similar for the full range of spans.

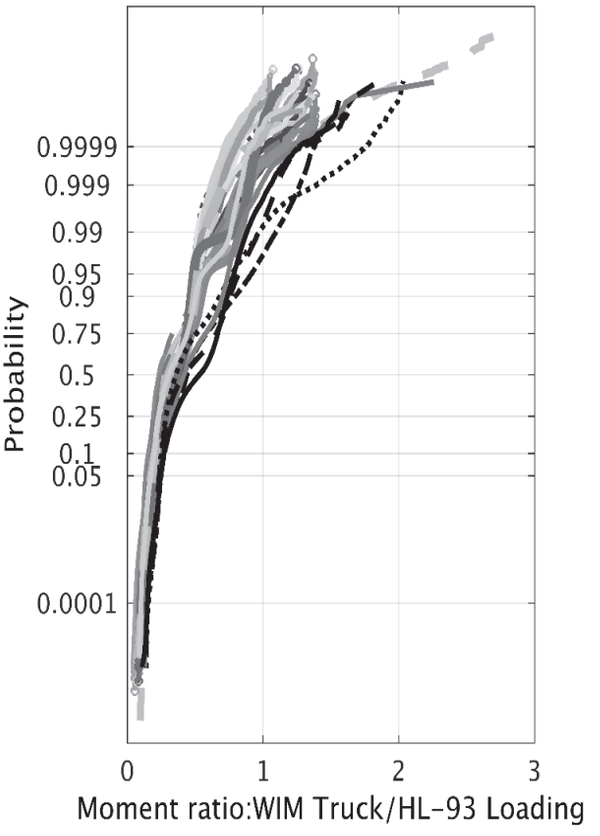


Figure 3. CDF's of moment ratio for 18 m span for all WIM stations

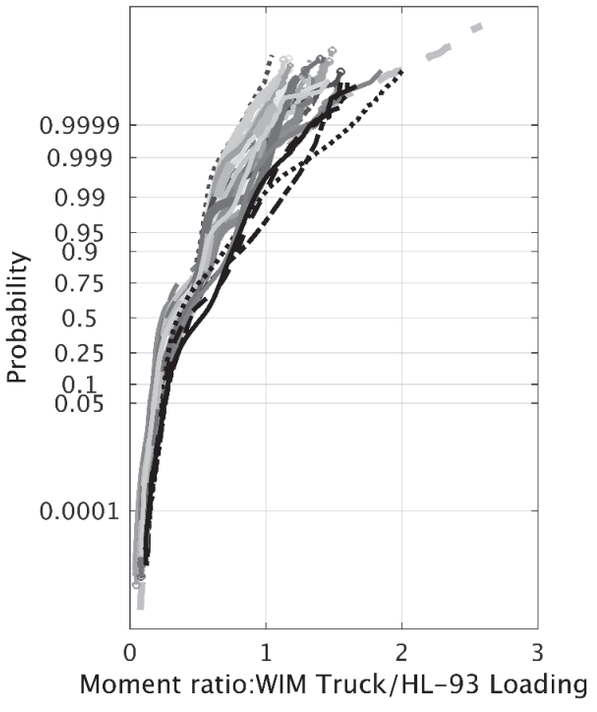


Figure 2. CDF's of moment ratio for 9 m span for all WIM stations

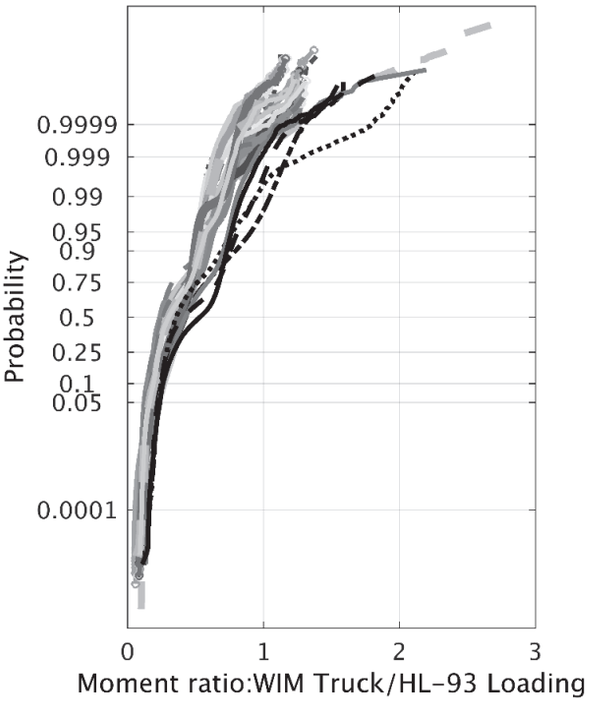


Figure 4. CDF's of moment ratio for 27 m span for all WIM stations

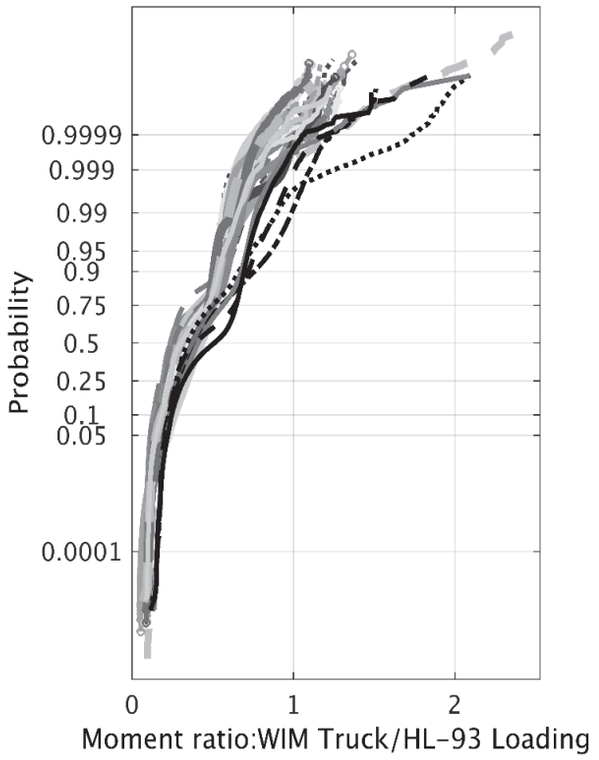


Figure 5. CDF's of moment ratio for 36 m span for all WIM stations

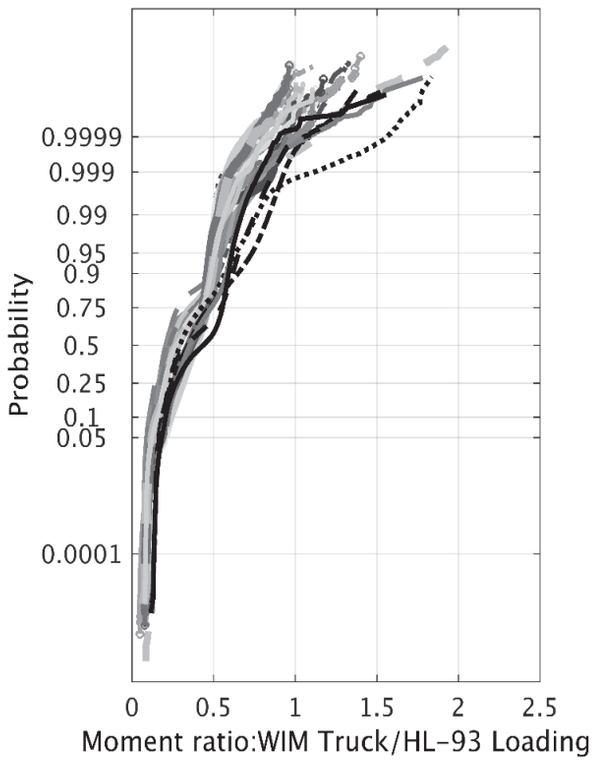


Figure 6. CDF's of moment ratio for 60 m span for all WIM stations

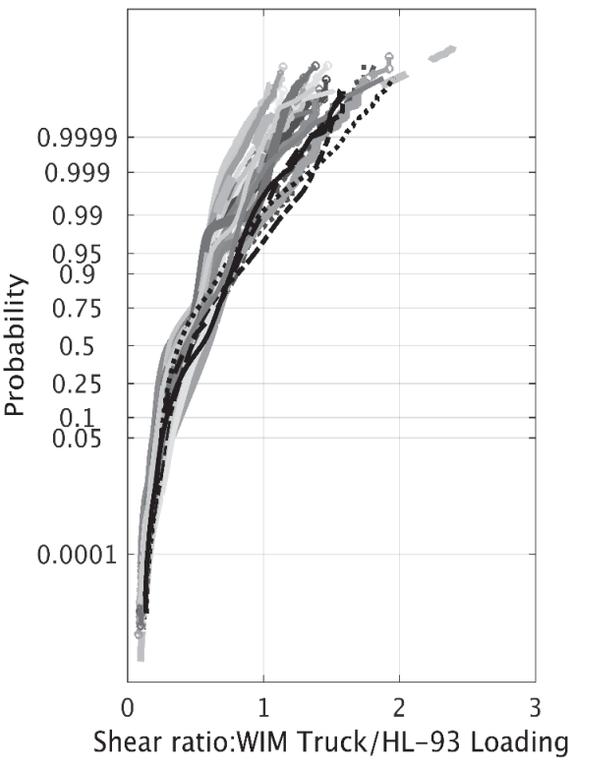


Figure 7. CDF's of shear ratio for 9 m span for all WIM stations

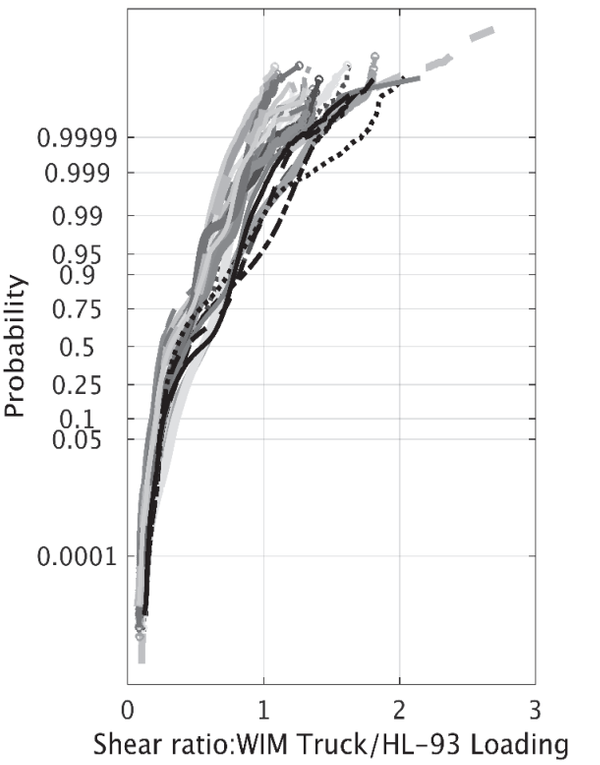


Figure 8. CDF's of shear ratio for 18 m span for all WIM stations

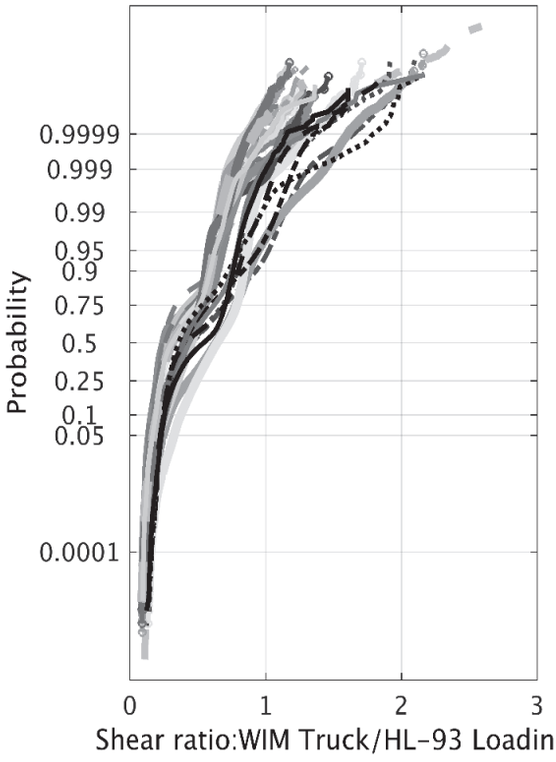


Figure 9. CDF's of shear ratio for 27 m span for all WIM stations

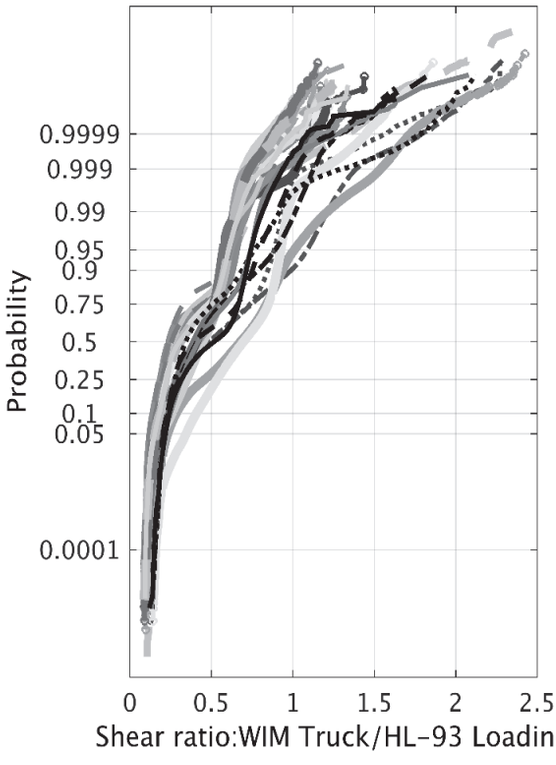


Figure 10. CDF's of shear ratio for 36 m span for all WIM stations

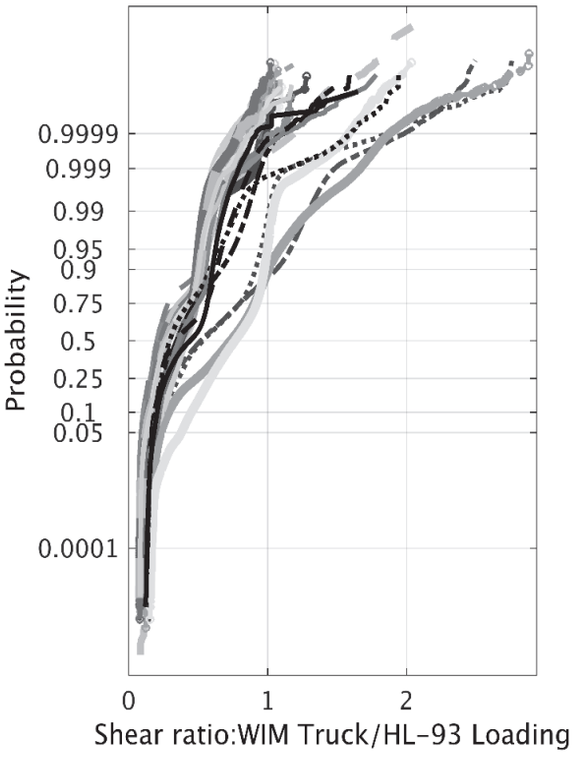


Figure 11. CDF's of shear ratio for 60 m span for all WIM stations

6 CONCLUSIONS

The extensive database used in this study included 92 million records from the U.S. and 2 million records from Europe. All the vehicular traffic was analyzed, and results are plotted on probability paper. Below are the conclusions from this study:

- Loads and load effects in Europe tend to be higher compared to the U.S.
- There is no single location that stands out for both higher loads and load effects.
- Load effects such as bending moment and shear force are more sensitive to short spans than longer spans.
- The filtering criteria used by the researchers in the two continents are similar. In Europe, additional filtering criteria based on ghost axles and split axles are used as photographic evidence was available. It is hard to present criteria that are definitive as traffic loads and WIM technologies/software are different in some sites and vary between continents.

The filtering criteria for inconsistent data and erroneous data eliminate a reasonable amount of data. Quality control methods should be adopted in each WIM location so that maximum benefits are obtained from the investment. Not only is this economical, but

higher quality data helps in providing a more accurate prediction of vehicular traffic.

7 REFERENCE

AASHTO LRFD Bridge Design Specifications, Customary U.S. Units, 7th Edition, with 2015 and 2016 Interim Revisions | AASHTO Bookstore

Enright, B. and OBrien, E.J., 2011. *Cleaning weigh-in-motion data: techniques and recommendations*. Dublin Institute of Technology, University College Dublin. http://www.is-wim.org/

Flinner, M., 2004. *Traffic data edit procedures pooled fund study: traffic data quality 'TDQ': final report*. Washington, D.C.: U.S. Dept. of Transportation, Federal Highway Administration, Office of Highway Policy Information.

Kulicki, J.M., Wasser, W.G., Mertz, D.R., and Nowak, A.S., 2015. *Bridges for Service Life Beyond 100 Years: Service Limit State Design*. SHRP 2 Renewal Project R19B, Transportation Research Board, Washington, DC.

Nowak A. S. and Collins K.R. 2013. *Reliability of Structures.* McGraw-Hill, New York.

Nowak, A.S., 1999. *Calibration of lrfd bridge design code. NCHRP Report* 368. National Cooperative Highway Research Program (NCHRP), Washington, DC.

OBrien, E.J. and Enright, B., 2013. *Using Weigh-in-Motion Data to Determine Aggressiveness of Traffic for Bridge Loading*. Journal of Bridge Engineering, 18 (3), 232–239.

Sivakumar, B., Ghosn, M., and Moses, F., 2011. *Protocols for collecting and using traffic data in bridge design*. NCHRP Project 12-76, National Cooperative Highway Research Program (NCHRP), Washington, DC.

Traffic Monitoring Guide, 2016. Federal Highway Administration.

Turochy, R.E., Timm, D.H., and Mai, D., 2015. *Development of Alabama Traffic Factors for use in Mechanistic-Empirical Pavement Design*. Transportation Research Board, Washington, DC. https://trid.trb.org/view.aspx?id=1372297

Maintenance, Safety, Risk, Management and Life-Cycle Performance of Bridges – Powers, Frangopol, Al-Mahaidi & Caprani (Eds)
© 2018 Taylor & Francis Group, London, ISBN 978-1-138-73045-8

Bridge Network Planning for Heavy Vehicles in Queensland

T.M. Pape, P. Shaw, C. Doherty, G. Danicic, A. Robertson
AECOM, Brisbane, Australia

D. Wilson
Queensland Department of Transport and Main Roads, Brisbane, Australia

ABSTRACT: The Queensland Department of Transport and Main Roads (TMR) is responsible for managing approximately 3000 bridges on its road network. Of these, approximately 2200 bridges are on the heavy vehicle network supporting freight movement and the Queensland economy. As the asset manager, TMR is responsible for ensuring that its assets are managed safely and cost-effectively and that heavy vehicle access is permitted where possible to support a vibrant economy. Since 2012, TMR has been assessing the structural capacities and associated risks of TMR's bridges on the defined heavy vehicle road network, which has included developing an understanding and quantification of the current structural capacities of all bridges. Out of this program, TMR, in conjunction with AECOM, has developed a rapid network operation assessment tool suitable for heavy vehicle scenario analyses. Building on this knowledge, TMR are reviewing heavy vehicle network plans for current and future demands to identify network capacity constraints and opportunities for TMR owned or managed bridge structures. This paper discusses the tools and methodology used to investigate heavy vehicle access to the network and presents the findings.

1 INTRODUCTION

Australia's economy is facilitated by freight movements and supports a diverse range of industries and sectors from commodities, import/export services, machinery and other manufacturing goods, agricultural applications, and general consumer and retail requirements (BITRE 2014). To enable this, road infrastructure plays a significant role.

The importance of freight transportation to the economy and wider community is recognized and supported by governments nationwide, and they therefore provide appropriate planning, policy development, funding, construction and management of supporting infrastructure to facilitate ongoing access for the freight community (Austroads, 2014). BITRE (2011) note that the freight task has increased eight-fold over the past five decades, and is predicted to continue growing.

On that basis, there has been renewed focus on enabling High Productivity Freight Vehicles (HPFV) increasing levels of network access. Various sources state direct benefits such as safety, productivity, fuel and environmental savings and indirect benefits such as lowering community freight exposure and slightly lower infrastructure maintenance costs (Austroads, 2014). This has been facilitated by the development of the Performance-Based Standard (PBS) scheme, which was formally adopted by the National Transport Commission (NTC) in 2011 as an alternative heavy vehicle regulatory scheme and is administered by the National Heavy Vehicle Regulator (NHVR). It seeks to match the right vehicles to the right tasks and networks, whilst encouraging innovation in vehicle design to achieve higher productivity, safety and minimize infrastructure impacts (NTC 2007, 2008).

Under the Heavy Vehicle National Law (HVNL), road network access is governed by road managers. Network road access is generally classified into two key types of heavy vehicle classes, namely (Hitchins and Ritzinger, 2016):

- General Access Vehicles: have unrestricted access to the public road network unless otherwise signposted
- Restricted Access Vehicles: can only access certain parts of the network in accordance with Notice or permit requirements

For the PBS scheme, a series of access levels has been established that cater for the various vehicle performance levels (Levels 1-4). Additional sub-levels were developed for PBS levels 2-4 to translate vehicle combination length requirements in gazettals prepared to incorporate PBS vehicles on existing networks (Class "A" and "B") (Hitchins & Ritzinger, 2016). These levels are governed by mass and vehicle length limits respectively, with a maximum gross mass of 50 t presently limiting General Access vehi-

Table 1. Summary of Network Access Requirements under PBS Scheme (NTC, 2008)

PBS Level	Example Vehicle	Network access by vehicle length (L) (m)		Mass Restrictions for Bridge Access (i.e. Bridge Access Formulae) (M = mass, L = length)	
		Class A	Class B	M ≤ 42.5 t	M ≥ 42.5 t
1	Semi-trailer General Access	< 20 (general access, gross mass limit = 50 t)		M ≤ 3L+12.5	M ≤ L+32.5
2	B-double, Truck and Dog	≤ 26	26< L≤ 30	M ≤ 3L+12.5	M ≤ 1.5L +29.5
3	A-double, Double Road Trains	≤ 36.5	36.5< L≤ 42	M ≤ 3L + 12.5	
4	B-triple, A-triple Triple Road Trains	≤ 53.5	53.5< L≤ 60		

cles. Table 1 maps the various PBS levels to network vehicles currently permitted network access.

In order for PBS vehicles to be granted unrestricted general network access, they are required to comply with a number of regulatory and standard requirements in keeping with these PBS levels which broadly take into account vehicle performance, safety, and infrastructure damage control (NTC 2007, 2008). The latter point relates predominantly to pavement and bridge infrastructure.

For bridges, additional access requirements have been implemented, which are outlined in Table 2. As a minimum, a vehicle is deemed to be Tier-1 compliant and be granted access to bridges if the vehicle specification complies with the axle spacing/mass schedule formulae, which are outlined in Table 1. These rules also apply for distances and masses between axle groups. An additional rule for B-doubles for clear spacing between axle groups is required.

Where vehicles do not comply with the Tier 1 conditions, the vehicle is then assessed against Tier 2 conditions, and failing that, Tier 3 conditions which requires a bridge-specific assessment by the asset owner. There is an implied understanding that with increasing tier levels, that increasing access is granted to heavy vehicles (Austroads, 2016).

Table 2. Requirements for bridge access under PBS Scheme (NTC, 2008)

Tier	Description	Requirements
1	*General access or Restricted access*	Access granted if compliant with axle spacing/mass schedule formulae
2	*Special access*	Load effects less than existing network vehicle
3	*Specific link access*	Approval by owner of bridge (detailed, bridge-specific assessment)

There are times where network upgrades are sought to obtain additional productivity gains, namely due to commercial, economic or community drivers. Where this occurs, consideration is required in relation to the impacts on the network as a whole. In particular, the impacts of such upgrades can be significant on bridges located on the network. As bridges are often known to be the cause of network access constraints (Austroads 2016), knowledge of these constraints can inform future planning requirements and inform funding allocation. It is therefore desirable to understand the capability of a bridge network for its current level of access and the capacity of the network to cater for future increases to meet productivity expectations.

The Queensland Department of Transport and Main Roads (TMR) is responsible for managing approximately 3000 bridges on its road network. Of these, approximately 2200 bridges are on the heavy vehicle network supporting freight movement and the Queensland economy. As the asset manager, it is TMR's responsibility to ensure that its assets are managed safely and cost-effectively and that heavy vehicle access is permitted where possible to support a vibrant economy. Since 2012, TMR has been assessing the structural capacities and associated risks of TMR's bridges on the defined heavy vehicle road network, which has included developing an understanding and quantification of the current structural capacities of all bridges. Out of this program, TMR, in conjunction with AECOM, developed a rapid network operation assessment tool suitable for heavy vehicle scenario analyses.

Building on this knowledge, TMR are reviewing heavy vehicle network plans for current and future demands to identify network capacity constraints and opportunities for TMR owned or managed bridge structures. This knowledge can then be used for investment planning for potential bridge renewals or upgrades, as well as confirming what action would be required to support the increased level of access to facilitate freight productivity. TMR were interested in exploring the Tier 1 PBS compliance requirements that defines vehicle access for a bridge network as a baseline.

2 OBJECTIVES

This paper discusses the tools and methodology used to investigate current and future bridge network access (general and unrestricted) for heavy vehicles that comply with current requirements for the TMR network. More specifically, the following objectives were identified.

- To identify and review network-critical bridges for various heavy vehicle configurations for current and proposed network route changes/upgrades.
- To identify and discuss key bridge restrictions and differences between current and proposed network route designations.
- To explore variations in network access for different PBS vehicles that comply with the Tier 1- axle mass and spacing schedule formulae for bridge access (known herein as Tier 1-compliant PBS vehicles).
- To explore any variations between the PBS levels and classes.
- To test the assumptions that underpins the PBS Tier 1 axle mass and spacing schedule formulae.

3 ASSESSMENT PARAMETERS

3.1 *Vehicle Development*

A suite of vehicles was developed to explore the different objectives of the project. Vehicles were divided into different groups according to type and functionality. The key areas for review were:

- Multi-Combination Vehicles (MCV) currently permitted unrestricted network access (compliant with Heavy Vehicle National Law (HVNL) requirements)
- PBS vehicles compliant with the Tier 1 axle spacing and mass schedule formulae (NTC 2007, 2008)
- A-double vehicles, with variations on axle groupings, spacing and configurations which are PBS Level 2B compliant.

Vehicles were defined by axle loads and axle spacings. "Gamed" vehicles were created alongside realistic vehicles aimed to maximise load effects while remaining compliant to the respective guide-line/ notice. For PBS vehicles, the axle loads were limited by the Tier 1formulae as specified Table 1 and GML axle group load levels as defined by HVNL. Figure 1 illustrates the spread of the designed PBS vehicles in each level. In total 35 vehicles were assessed across all PBS levels.

3.2 *Network and Bridge Selection*

Assessments were conducted on all bridges on the TMR freight and general access networks where the bridge information was available. Current and proposed PBS levels were also included. Table 3 gives an overview of the assessed bridge types.

Table 3. Summary of TMR's general access and freight route bridge stock

	Route Type			
	General Access	B-double	Road Train	Total
Simply Supported	581	1330	669	2580
Continuous	86	71	33	190
Timber	197	32	75	304
Excluded	16	4	1	21
Total	880	1437	778	3095

3.3 *Bridge Assessment Tool (NOAD)*

The assessment was carried out using TMR's Network Operational (bridge) Assessment Database (NOAD) and associated application (NOADapp) – which is similar to TMR's permit assessment tool with additional functionality for network application. It includes capacity assessments for all continuous and timber bridges on the TMR's road freight network and a significant proportion of the General Access network. The primary output of NOAD is TMR's accepted load rating factor, Equivalency Ra-

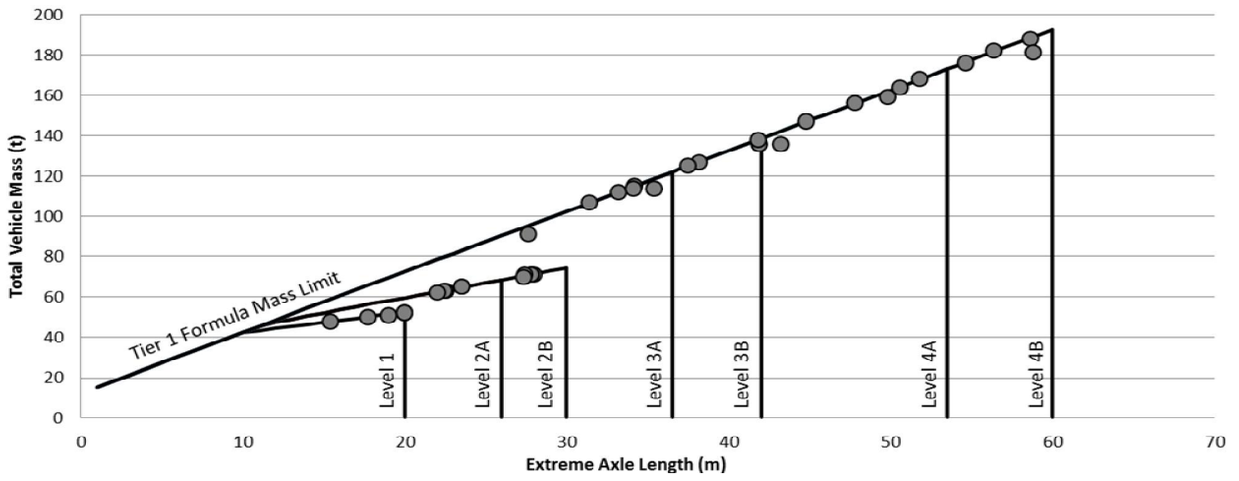


Figure 1. Graphical representation of PBS vehicle mass limits with designed PBS vehicles plotted

tio Traffic (ERT). The 95% confidence intervals ERTlo and ERTup are also computed, the mean of which is referred to as ERTnom. ERT values are calculated for all bridge structural components including superstructure and substructure. The formulation of ERT is given in Equation 1. (Heywood et al., 2014)

$$ERT = \frac{Available\ capacity\ for\ live\ load\ effects}{Live\ load\ applied\ by\ assessed\ vehicles} \quad (1)$$

NOAD produces a number of secondary outputs which allow for deeper investigation of specific bridges and vehicles impacts. These include:

- Critical position of vehicle on bridge
- Critical component of bridge (Superstructure/ Substructure)
- Combined live load factor and dynamic load allowance required for ERT = 1 (Risk Profile)
- Unfactored load effect comparison to the as-of right network vehicle (Useful for benchmarking and Tier 2 assessments)

NOAD is able to assess TMR's entire network for a given vehicle in approximately 1minute. Functionality was added to allow multiple vehicles to be run consecutively and results automatically recorded to a database. The assessment process now runs almost complete autonomously, greatly reducing the time taken for network assessments.

3.4 *Bridge Network Review*

PBS vehicles were assessed at an inventory level with the live loading factors in accordance with AS5100.7. At the completion of all vehicle runs, results were collated and tabulated. The assessment criteria used to review access for each vehicle to the bridge net-work is set out in Table 4.

Table 4. Assessment criteria

Outcome	Description
Accept $ERT_{lo}>1$	Bridge has sufficient capacity for access of the assessed vehicle
Review1 $ERT_{lo}<1$ $ERT_{nom}>1$	Bridge access requires review Permission for access will require certain conditions to be met (e.g. on-board mass monitoring)
Review2 $ERT_{nom}<1$ $ERT_{up}>1$	Bridge access is not permitted unless specific measures justify access. This may include: - Route specific requirements - Isolated bridge restriction in an otherwise accessible route - Intervention/investment Acceptance for access will require: - structure management plans - access controls - acceptance of shortening of asset life and associated risks
Reject ERTup<1	Bridge does not have sufficient capacity for access by the assessed vehicle

Results were collated in terms of their individual assessment criteria, based on either the number of Rejects (least conservative) or the number of non-accepts (Review 1, Review 2 and Rejects), which is the most conservative approach representing a 95% confidence level of access. The latter approach was more in keeping with TMR's high-level future planning objectives, and has been accepted herein. For detailed planning, investment and decision making, TMR may use a position between these two extremes consistent with the decision parameters in Table 4. Note that these assessments do not account for a 'past-performance' check based on current network access (e.g. road train and B-double routes), and are based purely on the capacities of the bridges to support the vehicles assessed.

Results were methodically reviewed, noting any trends and impacts due to vehicle type, bridge-specific issues, and changes in access due to proposed network upgrades. To explore route-specific changes, results were filtered and compared with existing and proposed network access levels. A list of deficient structures was identified for each route giving visibility of the impact different vehicle types have on the network.

4 RESULTS

4.1 *Overview*

Results were collated for all vehicles and bridges in a database allowing for a number of investigations to be conducted. The entire network was assessed for each bridge's designated network vehicle for a specific route (Route MCV) to give a baseline measurement of the network's performance. Comparisons between PBS vehicle at each access level and the TMR Guideline Vehicles were made using the number of Non-Accept bridges A review of the current and proposed PBS routes was presented as well as a comparison of different vehicle types, specifically A-doubles, B-doubles and Truck and Dogs.

4.2 *Current freight network*

One method for assessing network performance is to assess each structure for its Route MCV. Some routes allow Higher Mass Limit (HML) vehicles which are captured in the Route MCV's axle group loads.

Table 5 shows the typical Route MCV vehicle for each route type. Figure 2 illustrates the impact of the Route MCV and TMR assessment vehicles across the whole network and provides a baseline risk profile for assessing other vehicle impacts. It is important to reiterate that a non-accept criteria was used which does not represent a management strate-

gy for the existing network, but rather gives a forward looking planning perspective.

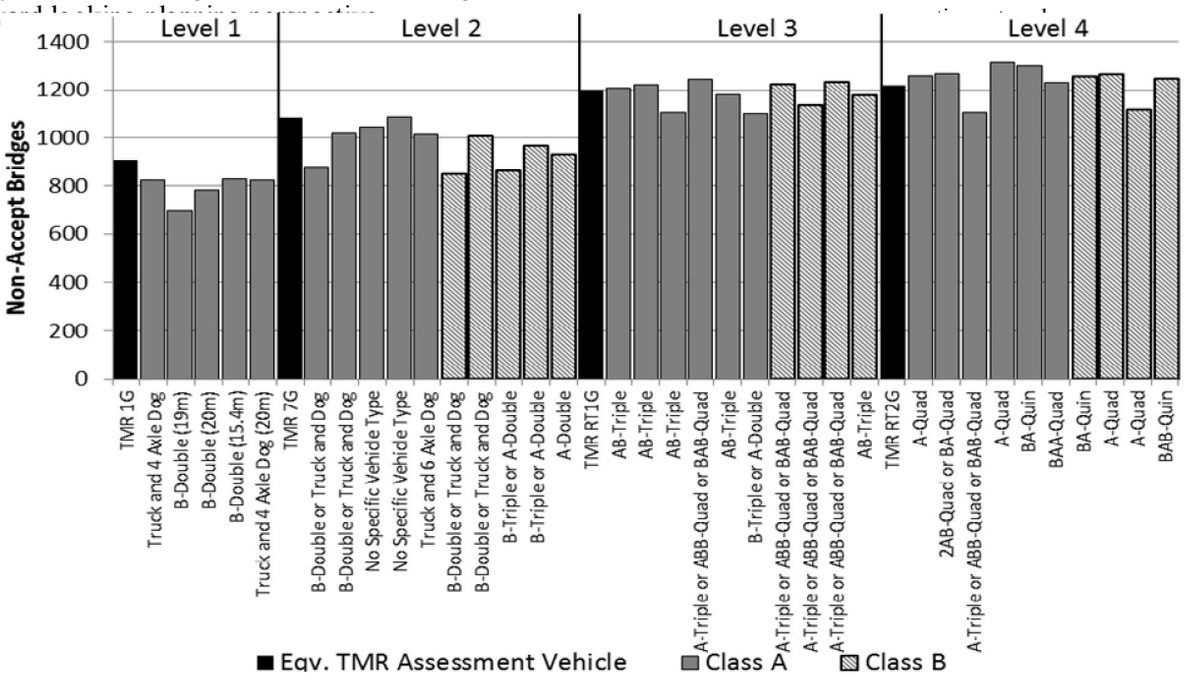


Figure 2. PBS vehicles assessment results across entire network

Table 5. Route MCVs by route type

Route Type	Route MCV
General Access	1G (GML), 1H (HML)
B-double	7G (GML), 7H (HML)
Road Train 1	RT1G(13) (GML), RT1H(13) (HML)
Road Train 2	RT2G(13) (GML), RT2H(13) (HML)

4.3 *PBS Vehicles*

To review the impact of introducing PBS vehicles on the bridge network, the number of non-accept structures was recorded for each PBS vehicle (Figure 3) and compared to the accepted guideline vehicles at GML loading. Generally at higher PBS levels, the impact to the bridge network is higher with some exceptions as discussed later.

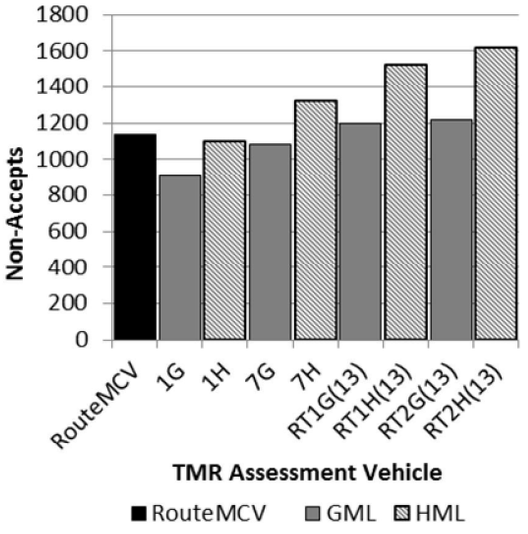


Figure 3. Impact of TMR Assessment Vehicles

Figure 4 provides a count of the critical bridge elements when assessed at each PBS level. It was noted that a structure may have multiple non-accept elements and this is captured. The assessed PBS level includes all sub level vehicle as all levels are compliant to the higher levels (e.g. Assessed PBS level 2B includes vehicles from level 2A and 1).

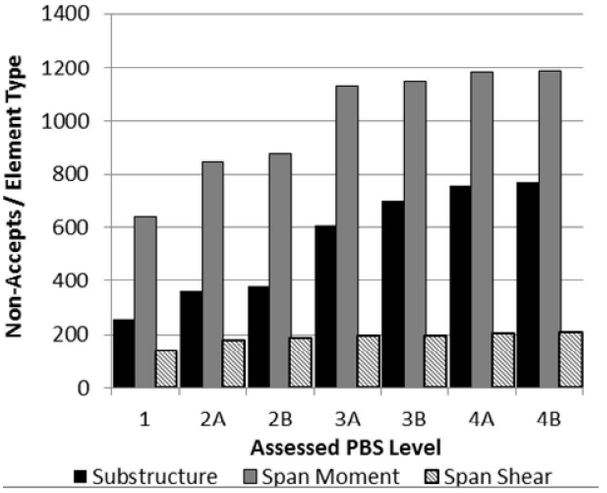


Figure 4. Distribution of non-accepts by critical element

It was found that the Tier 1 formulae may not be appropriate for limiting access consistently across the network. Bridges limited by shear capacity in their superstructure are impacted more by increased load intensity rather than vehicle length. This is in contrast to long span or continuous bridges and bridges limited by pier capacity, where longer vehicles result in

higher load effects with similar load intensities. Short span bridges were not affected by longer vehicles.

PBS Levels 1 and 2 generally produced results less than that of the equivalent TMR assessment vehicles. Levels 3 and 4 PBS vehicles were found to potentially exceed the TMR assessment road trains. B-Class vehicles typically performed better than the equivalent level A-Class vehicles. This was likely due to the design of the B-Class vehicles where it was difficult to add extra axle groups without exceeding the Tier 1 formulae mass limit.

The B-double results highlighted the sensitivity of the network to small changes in vehicle length and axle positions. The shortest B-double assessed was 15.4m and produced the largest number of non-accepts in its group. The 19m B-double, while heavier, produced the least number of rejects in the group. This sensitivity is attributed to the large number of short span bridges on the network, where a larger portion of the shorter vehicle could load bridges. Truck and dog configurations were found to perform slightly worse than the B-doubles.

A-double and A-Triple vehicles typically produced lower number of non-accepts then the equivalent B-double and B-Triple vehicles. This was attributed to the A-double and A-Triple vehicles having lower load intensity then the B Equivalents, possessing an extra axle group and longer overall length. However, the length requirements resulted in the shorter A-double vehicles assessing as PBS Level 2B, whereas B-doubles can run on the Level 2A network.

Timber bridges were found to not always trigger access restraints. Typically they have short spans and were less sensitive to vehicle length, and thus if assessed "Accept" for Level 1 and 2 vehicles, were assessed "Accept" for longer Level 3 and 4 vehicles. Likewise long span and continuous bridges were more commonly assessed as "Non-accept" in the higher Levels 3 and 4.

As part of the study, the sensitivity of the critical vehicle position and critical element due to axle configurations was investigated. It was found that small changes to axle configurations could greatly impact the critical element of the structure. The selection of test vehicles must be varied enough to capture this effect. This remains a risk of this study, that the critical compliant vehicle for each bridge was not found.

TMR currently specifies a number of routes with an existing PBS level and proposed PBS level. Figure 5 shows the impact of the created PBS vehicles on the existing PBS routes and compares it to the Route MCV assessment for that route. Note that no routes currently allow access for 4B PBS vehicles.

It was found that when looking at the existing PBS network only, the PBS vehicles on all levels have similar or less impact than the Route MCV.

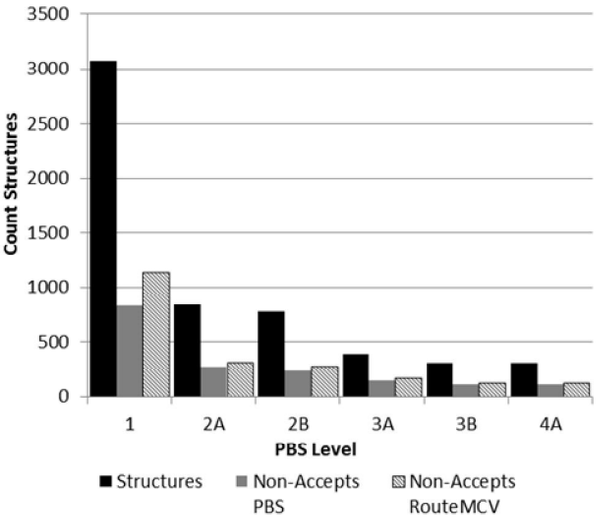


Figure 5. Existing PBS network performance

DISCUSSION

The results have highlighted a number of key observations in relation to TMR's bridge network for the vehicles assessed. These includes

- The variation in access noted across the different vehicles within each PBS level
- The majority of PBS Level 1 and 2 vehicles assess well against the Route MCV with similar access noted. Access results for Level 3 and 4 vehicles were variable and some vehicles exceeded the current network vehicle used to benchmark performance.
- The mass intensity of the vehicle type was found to be more significant than the length of the vehicle (as distinguished by Class "B" vehicles), however identifying an appropriate Class "B" vehicle to assess against the network was found to be difficult.
- The A-double and A-triple variants were found to result in slightly greater bridge access in comparison to B-double and B-triple variants
- The assessed PBS level of a bridge did not always comply with the current or proposed PBS level for a network route.

In addition to these observations, there are also more fundamental questions that have been raised. For Tier 1 compliant vehicles to gain unrestricted access to bridges on a PBS network, the vehicle must comply with the axle spacing/mass schedule formulae, with no further review required from the bridge owner.

As noted in Section 1, TMR have recently been through a process to identify bridges on the freight route that are currently operating at margins less than those recommended by the Australian Standards. These are predominantly structures that were designed for superseded design classes, have higher-

risk failure mechanisms, have condition issues or are insufficient for the loads currently accessing the network. In order to facilitate network access, TMR has maintained access for a number of network specific vehicles (the Route MCV), acknowledging the risks associated with this operation and developing appropriate structure management plans to cater for this. For new vehicles requesting general network access, this is granted where the load effects of this vehicle are less than those of the network vehicle.

From a planning perspective, understanding these risks inform future capital expenditure works (such as strengthening) which may be required to maintain or increase network access for productivity gains.

Risks remain, however, in the use of the Tier 1 bridge access formula. These concerns are not new and have previously been noted in two recent Austroads reports (Austroads 2014, 2016). The origin of the "Bridge Formulae" lies in the publication of the axle spacing/mass schedules to simplify access assessments in a day where computers were not extensively used (Austroads 2014). The schedules were developed from maximum span bending moment using pre-1976 bridge design codes (MS-18 design class). It did not account for shear considerations or substructure components, and made assumptions that access would not be granted to those bridges designed prior to the MS-18 design regime. Austroads also goes on to state that many of the conditions and assumptions on the use of the formulae have been omitted from the current PBS guidelines when assessing bridges. There are also concerns on the rigour of the formulae given the original method was borne out of working stress methodology and is currently being used in a Limit States assessment environment. A more detailed account of these considerations has been discussed previously (Shaw et al. 2017).

Additional considerations in this area include:

- Vehicle access dispensations for HML loading surrounding road friendly suspension
- Planning processes associated with proposed route upgrades for PBS levels
- The permit access regime for single trip and period permits, particularly for load-carrying combination vehicles such as HLPs and low loaders.

To date, very little work has been done to address these concerns which is confirmed by the current work and highlights that additional research is required. Echoing Recommendation 1.01 in the Austroads Report AP-R532-16, the Tier 1 bridge assessment methodology should be reviewed to "eliminate these uncertainties and inconsistencies to provide more robust, consistent and reliable Tier 1 Bridge Assessments". This in turn will lead to greater confidence in network assessments and appropriate risk management strategies when reviewing network operations for current and future access.

5 CONCLUSION

A study has been carried out on TMR's bridge network for PBS vehicles to explore opportunities for improved productivity and identify network-critical bridges that will impact on current and proposed network access. A number of realistic and "gamed" assessment vehicles were developed to comply with the PBS Tier 1 access requirements, which are reliant on axle mass and spacing schedules, for each level (1 – 4) and class (A and B). The bridge network was assessed for access using TMR's Network Operational (bridge) Assessment Database (NOAD), using a set of pre-defined assessment criteria. The assessment included structural capacity outputs for superstructure and substructure components, as well as continuous and timber bridges.

On a network level, results have highlighted the degree of variability within a PBS level that exists between different vehicle types, with axle configuration found to be most influential. Longer and heavier vehicles as defined by PBS Levels 3 and 4 were noted to be more critical for bridges with longer spans or that were continuous. PBS vehicles with A-type couplings were found to produce marginally better assessment results than vehicles with B-type couplings due to the longer draw-bar and additional axle group. A significant proportion of the network was flagged for non-access due to structural deficiencies in substructure or continuous components.

More broadly, the results lead to questions regarding the plausibility of the current PBS Tier 1 vehicle assessment regime which does not account for the assumptions that the original axle spacing mass schedules were based on. It is recommended that bridge access conditions be reviewed for the PBS scheme.

REFERENCES

Austroads 2014. *Quantifying the benefits of high productivity vehicles,* No. AP-R465-14, Austroads, Sydney, Australia.

Austroads 2016. Bridge assessment for High Productivity Freight Vehicle Access: Guidelines on Processes and Procedures, No. AP-R532-16, Austroads, Sydney, Australia

Bureau of Infrastructure, Transport and Regional Economics (BITRE) 2014. Freightline 1, Australia freight transport overview, BITRE, Canberra Australia

Bureau of Infrastructure, Transport and Regional Economics (BITRE) 2011. Truck productivity: sources, trends and future prospects, Report 123, Canberra, Australia

Dudgeon and Findlay 2016. High Productivity Vehicle Costs and Selected Freight Policy Implications, in Proceedings of 'Australasian Transport Research Forum', 6 – 18 November 2016, Melbourne, Australia

Heywood, R.J., Shaw P., Mitchell J., Jager C. 2017. "Operational and Inventory Management of Bridges", 10th Austroads Bridge Conference, Melbourne, Victoria

Heywood, R.J., Shaw, P., Pritchard, R. 2014. "Assessment Ratios for Evaluating Access by Heavy Vehicles to the Bridge Network", In *Austroads Bridge Conference, 9th, 2014, Sydney, New South Wales, Australia*.

Hitchins, D. and Ritzinger, A. 2016. Size does matter: but when is big too big? [vehicle design]. In *Australian Institute of Traffic Planning and Management (AITPM) National Conference, 2016, Sydney, Australia*.

NTC 2007. Performance-Based Standards Scheme – Network Classification Guidelines

NTC 2008. Performance-Based Standards Scheme – the Standards and Vehicle Assessment Rules

NTC 2016. Increasing heavy vehicle volumetric load capacity without increasing mass limits, Discussion paper.
Available at:
http://www.ntc.gov.au/Media/Reports/(6805FC2D-66DC-4B1C-C715-E034D3817C51).pdf

NTC 2017. Assessing the effectiveness of the PBS Scheme, Discussion paper, August, Available at: https://www.ntc.gov.au/Media/Reports/ (EE70D6AE-0895-3CE0-C3C4-AEE88C7138F).pdf

Ritzinger, A., Haldane, M. and ELISCHER, M. 2012. Productivity gains through expansion of performance based standards network in Queensland. In *12th Heavy Vehicle Transport Technology Conference*

Shaw, P., Heywood, R., Mitchell, J. and Wilson, D. 2017. Management of Heavy Vehicle Access to Bridges. In *Austroads Bridge Conference, 10th, 2017, Melbourne, Victoria, Australia*.

Maintenance, Safety, Risk, Management and Life-Cycle Performance of Bridges – Powers, Frangopol, Al-Mahaidi & Caprani (Eds)
© 2018 Taylor & Francis Group, London, ISBN 978-1-138-73045-8

Strength evaluation of prestressed concrete bridges by dynamic load testing

E.S. Hernandez & J.J. Myers
Department of Civil, Architectural and Environmental Engineering, Missouri University of Science and Technology, Rolla, Missouri, USA

ABSTRACT: The load rating of a bridge can be obtained by means of field load testing. The dynamic load allowance or impact factor is one of the parameters used to establish a bridge's flexural capacity during the rating evaluation process. The focus of this study centered on comparing Bridge A7957's dynamic load allowance obtained by experimental and analytical methods proposed in three different design and evaluation codes. To attain this goal, Bridge A7957 was instrumented with accelerometers at different locations. For different dynamic tests, the spans' response was measured with the accelerometers and a laser vibrometer. The dynamic load allowance was obtained experimentally and analytically using current design and evaluation codes. The impact factors obtained analytically resulted in larger values compared to the experimental results. This difference might have repercussions in the strength evaluation results of bridge structures.

1 INTRODUCTION

Field testing has largely confirmed reserves of strength capacity in existing bridges despite their age and existing condition. The sources that explain these differences might be diverse and may be attributed to field parameters that are not considered during the design or strength evaluation process of a bridge structure. The impact factor (IM) or dynamic load allowance (DLA) is a parameter that can be verified by means of a dynamic load test (Cai & Shahawy 2003, AASHTO 2010). Most design codes consider the dynamic load effects, by increasing the magnitude of the static live load applied to a bridge structure in some fraction. An accurate estimation of the DLA yields safe and rational load ratings of existing bridge structures. However, the complex nature of the factors affecting the DLA makes it difficult to estimate its value during the design and strength evaluation of a bridge (Barker & Pucket 2013).

The main objective of this study was to obtain the dynamic load allowance of Bridge A7957 by analytical and experimental methods to compare differences that may arise when both approaches are employed in bridge design and evaluation. To achieve this goal, the dynamic response of Bridge A7957's exterior spans was recorded with accelerometers and a laser vibrometer. The dynamic load allowance (or impact factor) was estimated using the analytical provisions proposed by the Ontario Highway Bridge Design Code (OHBDC) (OMTC 1983), the American Association of State Highway and Transportation Officials (AASHTO) Standard Specifications (AASHTO 1992), and the AASHTO LRFD Bridge Design Specifications (AASHTO 2012). The experimental DLA was estimated by comparing the measured dynamic and static responses of the bridge structure. The following sections detail the instrumentation plan and the static and dynamic tests conducted on Bridge A7957 to estimate its experimental dynamic load allowance before the structure was open in service.

2 ANALYTICAL AND EXPERIMENTAL DYNAMIC LOAD ALLOWANCE

Design codes have traditionally proposed analytical expressions to estimate the dynamic load allowance of a bridge structure as a function of the span length or the fundamental frequency of a bridge. In 1983, the Ontario Highway Bridge Design Code (OHBDC) presented an approach that allows to estimate the DLA in terms of the fundamental frequency of the bridge structure as Figure 1 illustrates. The AASHTO Standard Specifications (AASHTO 1992) recommend an expression to estimate the impact factor in terms of the span length, L, as presented in Equation 1:

$$IM = \frac{15.24}{L + 38} \leq 0.30 \quad (1)$$

In 1994, the AASHTO LRFD Bridge Design Specifications (AASHTO 2012) replaced the term *impact factor* used in the AASHTO Standard Specifications (AASHTO 1992) with the term *dynamic load allowance*. A DLA value independent of the span length was adopted as equal to 0.33 (33% of the static live load) for bridge components other than the deck.

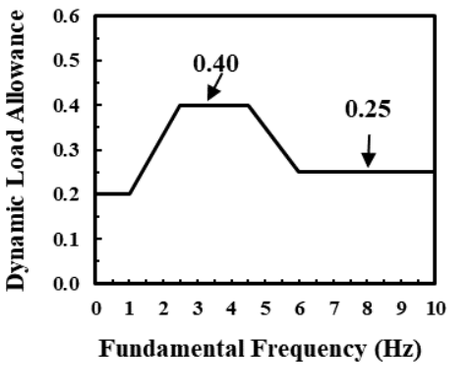


Figure 1. Dynamic load allowance vs. fundamental frequency (OMTC 1983, Paultre et al. 1992).

Several experimental definitions of the DLA have been reported in literature (Bakht & Pinjarkar 1989). As presented by Deng et al. (2015), the DLA is commonly defined as the ratio of the maximum dynamic and static responses regardless of whether the two maximum responses occur simultaneously. Equation 1 allows to calculate the DLA according to this definition.

$$DLA = \frac{R_{dyn} - R_{sta}}{R_{sta}} \quad (1)$$

where DLA = dynamic load allowance; R_{dyn} = maximum dynamic response; and R_{sta} = maximum static response. The estimation of the static response can be obtained by: (1) conducting a quasi-static test where vehicles move across the bridge at a low speed between 5–16 km/h; (2) filtering the measured dynamic response with a low-pass filter to eliminate the dynamic components of the signal; and (3) using finite element models (FEM) to calculate the static response when the vehicle weight and loading position are known (Paultre et al. 1992, Deng et al. 2015). In this study, the first and third options were selected and compared to estimate Bridge A7957's DLA.

3 BRIDGE DESCRIPTION

Bridge A7957, built along Highway 50 in Osage County, Missouri, is a three-span, continuous, precast-prestressed (PC/PS) concrete bridge with a 30-degree skew angle (Figs. 2-3), and excellent road surface condition. Each span has PC/PS concrete Nebraska University 53 (NU53) girders (Hernandez & Myers 2015a, Hernandez & Myers 2016a). The first span's girders are 30.48 m long and fabricated with conventional concrete (CC), defined by the Missouri Department of Transportation (MoDOT) as a Class A mixture, with a compressive strength of 55.2 MPa. The second span's girders are 36.58 m long and cast with high-strength self-consolidating concrete (HS-SCC) of 68.9 MPa. Girders in the third span are 30.48 m long and employed normal-strength self-consolidating concrete (NS-SCC) with a nominal compressive strength of 55.2 MPa. The cast-in-place (CIP) deck was built with a 25% fly ash replacement of a portland cement mixture with design compressive strength of 27.6 MPa. The PC/PS concrete panels, with a target compressive strength of 55.2 MPa, span between the girders' top flange underneath the CIP deck in the transverse direction (Fig. 2b). The superstructure is supported by two abutments and two intermediate bents (Fig. 2a) with target compressive strength of 20.7 MPa. The second intermediate bent and abutments were cast with a concrete mixture that used a 20% fly ash replacement of portland cement and a nominal compressive strength of 20.7 MPa. The third intermediate bent was built using high-volume fly ash concrete (HVFAC) with a 50% fly ash replacement of portland cement and a specified compressive strength of 20.7 MPa.

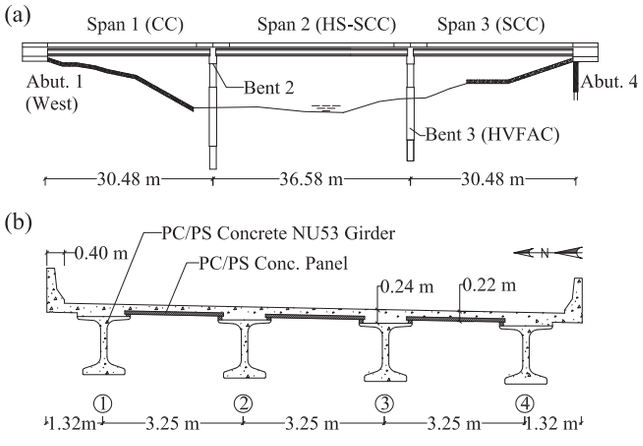


Figure 2. Bridge A7957. (a) elevation; (b) cross-section.

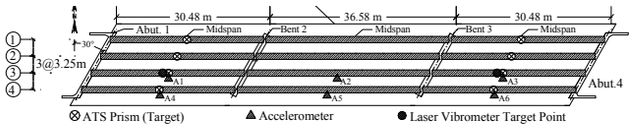


Figure 3. Bridge A7957 plan view and instrumentation layout.

4 FIELD TEST EQUIPMENT

The instrumentation was designed to collect: (1) the static vertical deflection at midspan of girders 1–4

(spans 1 and 3); (2) the dynamic deflection at midspan of girder 3 (spans 1 and 3); and (3) girder 3 and 4's vertical acceleration at midspan locations (Fig. 3). The details about the sensors employed and their installation are described next.

4.1 *Accelerometers*

Six accelerometers were deployed on the bridge superstructure to record the vertical acceleration at midspan sections of PC/PS concrete girders 3 and 4 (Figure 3). Figures 3-4a show details of the measurement instruments mounted to the girders' bottom flange (only at midspan sections).

4.2 *Automated total station (ATS)*

An automated total station (ATS), Leica TCA 2003, was used to estimate the girders' deflection during the static test conducted on the first and third spans. The ATS recorded the coordinates of targets (prisms) placed at the exterior-span girders' bottom flange (at midspan sections), as illustrated in Figures 3-4. The ATS has an accuracy of 1 mm ± 1 ppm (distance measurements) and 0.5 arc-seconds (angular measurements). The accuracy of the ATS has been reported as 0.1 mm in vertical deflection measurements (Merkle & Myers 2004).

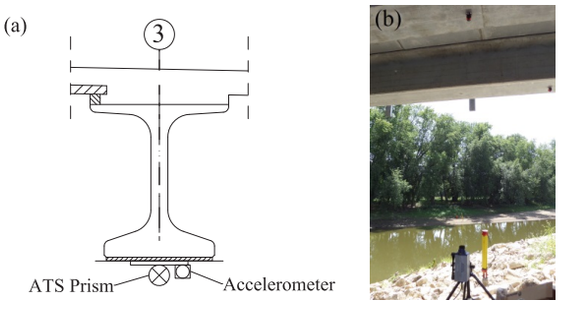


Figure 4. Girder 3's instrumentation. (a) ATS prism and accelerometer. (b) Remote sensing vibrometer (RSV-150).

4.3 *Remote sensing vibrometer*

The remote sensor vibrometer (RSV-150), shown in Figure 4b, was employed to record the dynamic bridge response (vertical deflection) of the exterior spans' girder 3 (at midspan). The RSV-150 has a bandwidth up to 2 MHz for nondestructive test (NDT) measurements and can detect the vibration and displacement of distant structures. The accuracy of the RSV-150 to record the dynamic response of a point is ± 0.025mm.

5 FIELD TEST PROCEDURE

Static and dynamic tests were conducted on Bridge A7957. The following subsections depict the test procedure and load configurations planned to obtain the maximum static and dynamic responses of the bridge superstructure.

5.1 *Static test*

Static load tests were performed on the exterior spans of the bridge. A MoDOT H20 dump truck was utilized to obtain the maximum static response of the bridge superstructure. Quasi-static tests were conducted by passing the truck at a crawl speed of 16 km/h. Figure 5 shows the average truck's dimensions and weight. Figure 6 illustrates the load configuration applied to spans 1 and 3 during the static tests 1and 2.

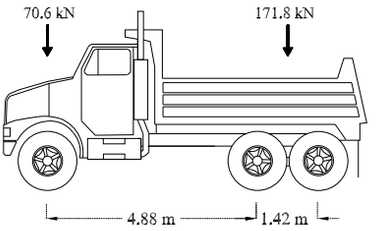


Figure 5. MoDOT H20 dump truck (average dimensions).

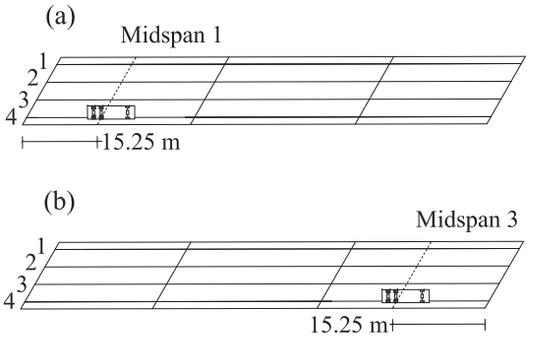


Figure 6. Static test configurations. (a) Static test 1 (span 1). (b) Static test 2 (span 3).

5.2 *Dynamic test*

Speeds varying from 16 km/h to 96.6 km/h were used during the dynamic load tests. For each test, the truck speed was increased at a rate of 16 km/h until the maximum speed of 96 km/h was attained. The maximum dynamic and static responses were compared to estimate the experimental dynamic load allowance. Experimental data was recorded with the RSV-150 at a sampling rate of 120 Hz. The truck was driven over the south side of the bridge (along the west–east and east–west directions), separated 0.60 m from the safety barrier's edge.

6 FINITE ELEMENT MODELING

The commercial finite element software ABAQUS (Simulia 2012) was employed to create 3D, linear,

finite-element simulations of Bridge A7957 for each of the load stops described in Figure 6. The bridge's geometry was created from construction documents and was modeled with solid elements (Fig. 7). The finite element models simulated the bridge's geometry considering the primary members (CIP RC deck and PC/PS concrete girders) and secondary members (RC safety barriers and diaphragms). Each bridge component material was assumed to be linear elastic for the level of load applied during the tests. The modulus of elasticity (MOE) of the different bridge components was obtained by averaging the results of MOE tests conducted on companion specimens the same day of the tests. Table 1 lists the modulus of elasticity of the different bridge component that were used to create the finite element simulations as reported by Hernandez & Myers (2015b) and Hernandez & Myers (2016b). Two different sets of MOE values were used as the FEM input, depending on whether the load stop was conducted in April or August of 2014. Experimental deflection values reported by Hernandez & Myers (2016c) were utilized to calibrate the finite element models and to reproduce a geometry that could predict the bridge's response with a reasonable level of accuracy. The trucks' positions over the slab deck and distances between the trucks' axles were simulated as recorded for each load configuration. Concentrated forces were applied at the location of the trucks' wheels to simulate the axle's weight values reported by MoDOT personnel.

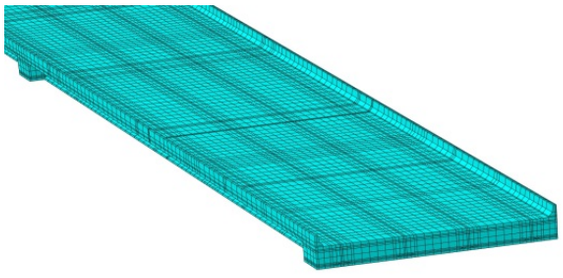


Figure 7. Bridge A7957's finite element model geometry.

Table 1. Bridge Components' MOE.

Bridge Component	April Test (GPa)	August Test (GPa)
Span 1's Girders	38.80	41.20
Span 2's Girders	39.30	42.25
Span 3's Girders	38.70	39.99
Safety Barriers	35.51	33.78
CIP Deck, Diaphragms	31.03	31.03

7 LOAD TEST RESULTS

The vertical static deflection measured at midspan locations of the end spans 1 and 3's girders are shown in Figure 8. Although both exterior spans have the same geometry (Fig. 2) and were subjected to the same truck load, a 5% difference was observed between the deflection responses recorded at midspan 1 and 3. The difference might be attributed to: first, a slight variation on the application of the truck load on each span; second, the accuracy of the ATS might have affected the experimental values due to the low level of load applied during the test. This difference may be corrected in future tests by taking caution regarding the location of truck loads and the level of load used during the test. The level of load applied needs to be relatively high so that the error of ATS measurements is kept low during data recording. In addition, Girder 3's static deflection at midspan (Fig. 8) was compared to the quasi-static (filtered) response recorded with the RSV-150 when the truck passed over the bridge at a crawl speed of 16 km/h and the static deflection value obtained with the FEM simulations. These comparisons were conducted to verify if the quasi-static deflection recorded with the RSV-150 was representative of the bridge's static response and could be used to estimate the dynamic load allowance.

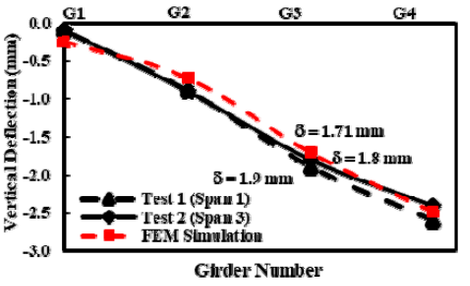


Figure 8. Vertical static deflection (girders' midspan).

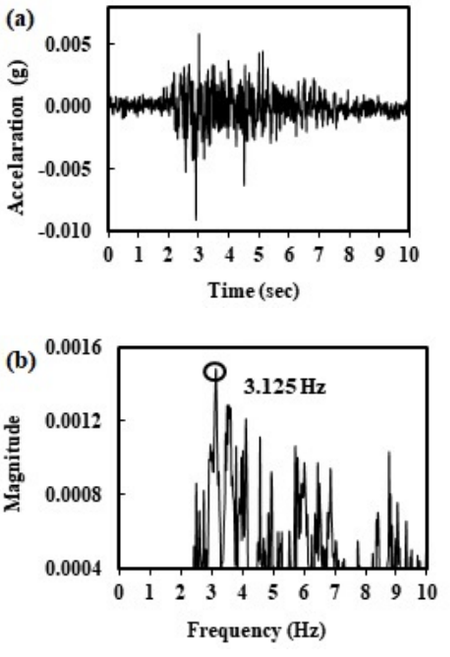


Figure 9. Dynamic response. (a) Measured acceleration. (b) Natural frequency extracted through FFT.

Figure 9a presents the acceleration response collected with sensor A1 (Fig. 3) deployed at girder 3's midspan. This acceleration data was recorded when the truck was driven from west to east at 96 km/h. Figure 9b presents the fundamental frequency estimated from Fast Fourier Transformation (FFT) applied to the recorded acceleration data shown in Figure 9a. The fundamental frequency of the bridge corresponded to a value of 3.125 Hz. Using the approach proposed by the OMTC (1983), this fundamental frequency yields a dynamic load allowance value of 0.40 according to Figure 1. Figure 10 shows that the quasi-static deflection recorded with RSV-150 was very close to the static deflection collected with the ATS (1.77 mm vs. 1.80 mm) and the value obtained from FEM simulations (1.77 mm vs. 1.71 mm) shown in Figure 8. Consequently, the filtered quasi-static response of the spans was assumed to be the maximum static deflection of girder 3's midspan and was employed to estimate the exterior spans' DLA for the different truck speeds employed during the dynamic test.

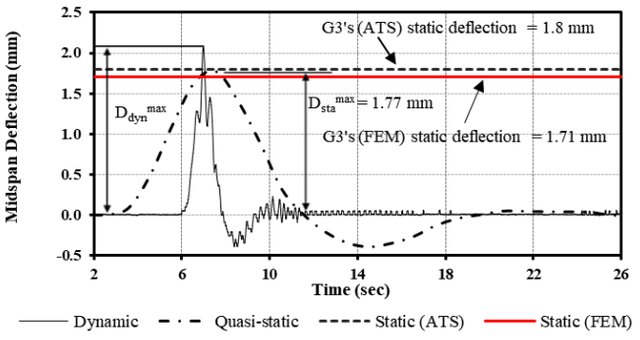


Figure 10. Maximum static and dynamic vertical deflection.

In addition, Figure 10 presents the maximum dynamic deflection (2.08 mm) measured with the RSV-150 when the truck speed was 96 km/h. The experimental DLA was estimated with Equation 3.

$$DLA^{\exp} = \frac{D_{dyn}^{\max} - D_{sta}^{\max}}{D_{sta}^{\max}} \quad (3)$$

where DLA^{exp} = experimental dynamic load allowance; D_{dyn}^{max} = maximum dynamic (measured) vertical deflection (mm); and D_{sta}^{max} = maximum static deflection obtained from passing the test truck at a crawl speed (mm). Table 2 lists shows in row 1 the trucks used to pass the truck over the bridge during the test. The bridge's maximum dynamic and static deflection recorded for the different speeds during the dynamic tests are presented in rows 2 and 3, respectively. In addition, the experimental values of the DLA corresponding to different truck speeds are presented in row 4. The maximum experimental DLA value was 0.175 corresponding to a truck speed of 96 km/h. The values of the experimental dynamic amplification factor, DAF^{exp}, are presented in row 5 and were estimated using Equation 4:

$$DAF^{\exp} = (1 + DLA^{\exp}) \quad (4)$$

Table 2. Experimental and analytical dynamic load allowance.

Speed (km/h)	16	32	48	64	80	96
D_{dyn}^{max} (mm)	1.77	1.79	1.79	1.77	2.03	2.08
D_{sta}^{max} (mm)	1.77	1.77	1.77	1.77	1.77	1.77
DLA^{exp}	0.000	0.010	0.010	0.000	0.150	0.175
DAF^{exp}	1.000	1.010	1.010	1.000	1.150	1.175
DLA*	0.40	0.40	0.40	0.40	0.40	0.40
IM** (spans 1 & 3)	0.222	0.222	0.222	0.222	0.222	0.222
IM** (span 2)	0.204	0.204	0.204	0.204	0.204	0.204
DLA*	0.33	0.33	0.33	0.33	0.33	0.33

Values were estimated according to: * Ontario Highway Bridge Design Specification (OMTC 1983); ** AASHTO Standard Specifications (AASHTO 1992); and *** AASHTO LRFD Bridge Design Specifications (AASHTO 2012).

The DLA estimated as a function of the bridge's fundamental frequency proposed by the OHBDC (OMTC 1983) is presented in row 6. The impact factor obtained with the AASHTO Standard Specifications (AASHTO 1992) and the DLA obtained using the AASHTO LRFD Bridge Design Specifications (AASHTO 2012) are listed in rows 7 through 9. By comparing the maximum experimental DLA to the values obtained using these design specifications (OMTC 1983, AASHTO 1992, AASHTO 2012), it was determined that the analytical methods provided more conservative values compared to the experimental approach. This variation may have different sources and may directly affect the strength evaluation result or load rating of an existing bridge obtained by the analytical methods proposed in current evaluation codes.

8 CONCLUSIONS

The dynamic load allowance of Bridge A7957 was successfully obtained from field measurements and by using three design specifications (OMTC 1983, AASHTO 1992, AASHTO 2012). The DLA obtained with the design specifications resulted in larger values compared to the values obtained experimentally. This disparity might be attributed to the presence of in-situ factors not considered by the theoretical methods proposed in current design and evaluation codes. More importantly, the variation between the experimental and analytical DLA values may have repercussions in the rating factor of exist-

ing bridge structures. Further research is needed to understand the source of these variations.

ACKNOWLEDGEMENTS

The authors gratefully acknowledge the financial support provided by the Missouri Department of Transportation (MoDOT) and the National University Transportation Center (NUTC) at Missouri University of Science and Technology (Missouri S&T). The authors would like to thank the System and Process Assessment Research Lab (SPAR) at Missouri University of Science and Technology for allowing the use of the Remote Sensor Vibrometer (RSV-150) during the load tests.

REFERENCES

American Association of State Highway and Transportation Officials (1992). *AASHTO Standard Specifications for Highway Bridges*, Washington, DC.

American Association of State Highway and Transportation Officials (2010). *The manual for bridge evaluation (2nd Edition) with 2011, 2013, 2014 and 2015 interim revisions*, Washington, DC.

American Association of State Highway and Transportation Officials (2012). *AASHTO LRFD Bridge Design Specifications, U.S. Customary Units (6th Edition)*, Washington, DC.

Bakht, B. & Pinjarkar, S. G. (1989). Dynamic testing of highway bridges. A review. *Transportation Research Record 1223, Transportation Research Board, Washington, D.C.* 93-100.

Barker, R. M. & Pucket, J. A. (2013) *Design of highway bridges: An LRFD approach,* Hoboken, N.J. USA, John Wiley & Sons.

Cai, C. & Shahawy, M. (2003). Understanding Capacity Rating of Bridges from Load Tests. *Practice Periodical on Structural Design and Construction* (8): 209-216.

Deng, L., Yu, Y., Zou, Q. & Cai, C. S. (2015). State-of-the-art review of dynamic impact factors of highway bridges. *J. Bridge Eng.*

Hernandez, E. S. & Myers, J. J. (2015a). Use of self-consolidating concrete and high volume fly ash concrete in Missouri bridge A7957. *ACI SP 304–6* 85-100.

Hernandez, E. S. & Myers, J. J. (2015b). Use of Self-consolidating Concrete and High Volume Fly Ash Concrete in Missouri Bridge A7957. *Sustainable Performance of Concrete Bridges and Elements Subjected to Aggressive Environments: Monitoring, Evaluation and Rehabilitation* (SP 304): 85-100.

Hernandez, E. S. & Myers, J. J. (2016a) Field Load Test and Girder Distribution Factors of Missouri Bridge A7957. *2016 PCI Convention and National Bridge Conference.* Nashville, TN.

Hernandez, E. S. & Myers, J. J. (2016b) Initial in-service response and lateral load distribution of a prestressed self-consolidating concrete bridge using field load tests. IN BAKKER, J., FRANGOPOL, D. M. & VAN BREUGEL, K. (Eds.) *5th International Symposium on Life-Cycle Civil Engineering (IALCCE 2016).* Delf, The Netherlands, CRC Press / Balkema - Taylor & Francis Group.

Hernandez, E. S. & Myers, J. J. (2016c) Monitoring the Initial Structural Performance of a Prestressed Self-Consolidating Concrete Bridge. IN RILEM (Ed. *8th International RILEM Symposium on Self-Compacting Concrete (SCC2016).* Washington, DC.

Merkle, W. J. & Myers, J. J. (2004) Use of the Total Station for Load Testing of Retrofitted Bridges with Limited Access. IN LIU, S. C. (Ed. *Smart Structures and Materials 2004 - Sensors and Smart Structures Technologies for Civil, Mechanical, and Aerospace Systems.* San Diego, CA.

Ontario Ministry of Transportation and Communications (OMTC) (1983). *Ontario Highway Bridge Design Code (2nd Edition)*, Downsview, ON, Canada.

Paultre, P., Chaallal, O. & Proulx, J. (1992). Bridge dynamics and dynamic amplification factors: A review of analytical and experimental findings. *Can. J. Civ. Eng* (19): 260-278.

Simulia (2012) Abaqus Analysis User's Manual. Version 6.12 ed. Providence, RI. USA, Dassault Systèmes Simulia Corp.

Maintenance, Safety, Risk, Management and Life-Cycle Performance of Bridges – Powers, Frangopol, Al-Mahaidi & Caprani (Eds)
© 2018 Taylor & Francis Group, London, ISBN 978-1-138-73045-8

Limiting exterior girder rotation during construction for non-skewed bridges

L. Hui, F. Hraib, R. Hindi
Department of Civil Engineering
Saint Louis University, St. Louis, MO, United States

ABSTRACT: The construction of bridge deck often introduces torsional moments acting on the exterior girder. To resist these torsional moments and limit the maximum exterior girder rotation, diaphragms are commonly used as transverse bracing system. However, the unbraced lengths of diaphragms are typically not designed for torsional moments introduced by construction loads, which may lead to excessive rotation on bridge exterior girders during bridge deck construction and cause many safety and maintenance issues. In this study, a parametric study was conducted to evaluate the significance of different parameters. Around three thousand finite element models were built to find the relation between the rotation and the ratio of the unbraced length (B) to girder depth (D). Then a simple method, which combines primary curves of B/D ratio in term of rotation and tables of section modification coefficients, was developed for engineers to easily determine the maximum allowable B/D ratio.

1 INTRODUCTION

The bridge decks are generally designed past over the exterior girder to increase the width of decks without increasing the required number of girders. As shown in Figure 1, the construction of deck overhang on steel bridge girders is most often finished with the usage of overhang brackets (Idaho Department of Transportation., 2008). Generally, deck overhang brackets are placed between 0.9 m and 1.2 m along the exterior girder to support the construction loads coming from fresh concrete, screed machine, and other construction live loads. In most cases, these loads on the overhang brackets can result in torsional moments acting on the exterior girders and may lead to exterior girder rotation that is not usually considered in the design of bridges (Yang, 2009).

The maximum rotation of exterior girder can be expected to occur near the midspan section (Ashiquzzaman et al., 2016). In this case, the fresh concrete is placed from the abutment, or the pier of the bridge to the middle of the span, as well as the screed machine is located in the center of the span. As shown in Figure 2, the torsional moments are mainly caused by the loads from fresh concrete and screed machine acting on the overhang bracket. The fresh concrete in the interior bay also affects the total torsional moments, but relatively small due to the fact that the hanger bolts are not able to transfer moment to the girder system.



Figure 1 Overhang bracket used during bridge deck construction

To resist the torsional moments introduced by construction loads, diaphragms are commonly used during bridge design and construction as transverse bracing system. However, the unbraced lengths of the diaphragms are typically designed to resist the lateral loads during service stage, without considering torsional moments introduced by construction loads. This may lead to excessive rotations on the exterior girder of the bridge during bridge deck construction, which can cause bridge failure resulting from global and local instabilities during deck construction (Fasl, 2008). Also, some potential maintenance issues such as thin deck and reduced concrete cover may occur that can lead to long-term corrosion and cracking in the deck.

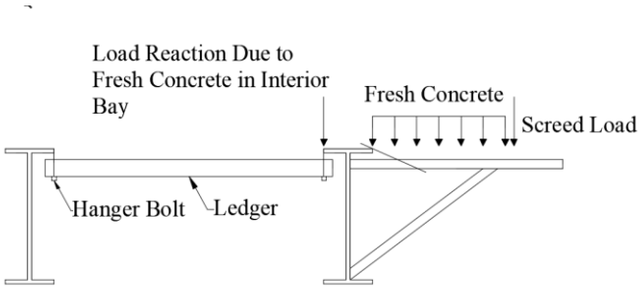


Figure 2 Construction loads during bridge deck placement

A parametric study was conducted in this study to evaluate the effects of girder section, span length, girder spacing, overhang width, number of girders, unbraced length and diaphragm section. The results indicate that the maximum exterior girder rotation is mainly affected by girder section, overhang width, and unbraced length. Based on the results of the parametric study, around three thousand finite element models were created using automatic finite element modeling program developed in this study. By conducting regression analysis, a simple method to determine the maximum allowable ratio of the unbraced length (B) to girder depth (D) was developed. This method uses the combination of primary curves and section modification coefficients to find the maximum B/D ratio based on the required rotation value and specific bridge geometry.

2 PARAMETRIC STUDY

2.1 *Finite Element Modeling*

A parametric study using Finite Element Method was conducted to evaluate the effects of bridge geometry. Seven parameters, including girder section, girder spacing, overhang width, number of girders, unbraced length and diaphragm section, are considered as having most possibilities to affect the exterior girder rotation. Table 1 shows the selected parameters and their ranges of values.

Table 1 Parameters for evaluating effect of span length

Parameters	Range
Girder Section	Wide Flange Section
Span Length (m)	9 to 23
Girder Spacing (m)	1.8 to 3
Overhang Width (m)	0.53 to 1.22
Number of Girders	3 to 6
Unbraced Length (m)	3 to 7.6
Diaphragm Section	W14X53 to W14X90

Finite element models were developed in Sap2000 to conduct the parameter analysis. As shown in Figure 3, thick wall shell elements were used for the bridge girders and diaphragms to include the distortion and warping effects of the girder. The steel overhang brackets were modeled using frame elements to support the loads from fresh concrete and screed machine. In order to simulate the bridge under the maximum rotation, the fresh concrete loads were distributed from the beginning of the span to the middle, while the wheel loads of screed machine were located in the center of the span.

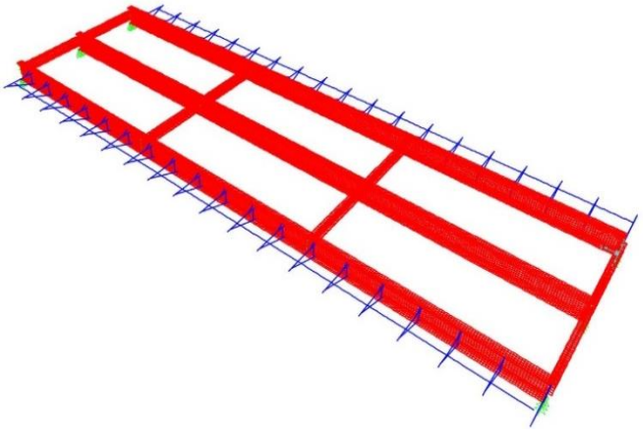


Figure 3 Finite Element Model for Parametric Study

2.2 *Analysis results*

2.2.1 *Effect of girder section*

To evaluate the effect of girder section, six wide flange beam sections, including W27X84, W30X90, W33X118, W36X135, W40X149 and W44X230 from AISC shape database, was chosen to conduct the parametric analysis. As shown in Figure 4, the rotations of exterior girders vary significantly from section to section. When the girder dimensions change, the torsional constant, which affects the abilities of girders to resist torsional moments, also changes correspondingly. In general, the normal weight of the girder can be a convenient indicator to approximately evaluate the ability for the girder to resist the torsional moment.

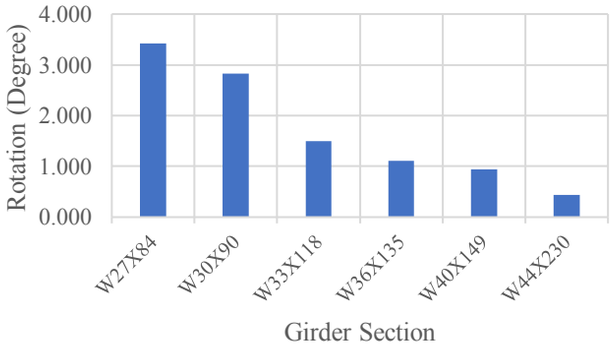


Figure 4 Effect of girder section on exterior girder rotation

2.2.2 *Effect of span length*

The effect of span length was evaluated based on W30X124 wide flange beam section since it is commonly used in bridge design. According to the AASHTO LRFD Bridge Design Specifications, the minimum girder depth is specified as 0.033 of the span length. Therefore, the maximum span length can be taken as 30 times of girder depth, which is around 23 m for W30 section. In order to study the effect of span length on exterior girder rotation, the span lengths were selected from 9 m to 23 m.

Since the diaphragms usually provide strong constraint in between bridge supports to prevent the girder rotation at diaphragm location, the span length has very limited effect on the exterior girder rotation. The finite element results indicate that when the span length changes from 9 m to 23 m, the rotation only changes by about 1% (shown in Figure 5).

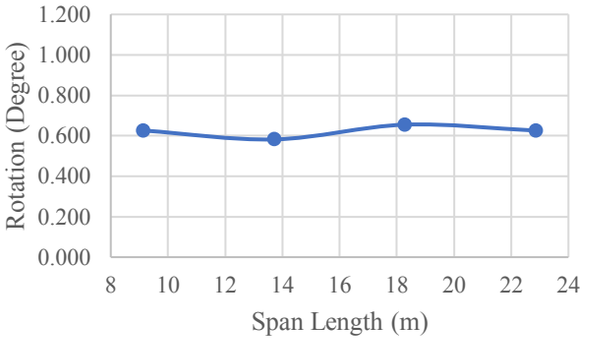


Figure 5 Effect of span length on exterior girder rotation

2.2.3 *Effect of Girder spacing*

During bridge design, a wider girder spacing is generally used when deflection limits do not control the design without considering the effect on girder rotation (Raymond A. Hartle, 2003). In this section, the girder spacing is selected varying from 1.8 m to 3 m, which covers most cases in bridge design.

The results show that the girder spacing does not have much effect on exterior girder rotation during bridge deck construction. As shown in Figure 6, the rotation reduces by only 6% when the girder spacing increases from 1.8 m to 3 m. The reason is that the temporary formwork system for bridge deck placement is typically designed using hanger bolts to connect ledger to the top flange of the girder (Dayton Superior., 2007), which are unable to transfer torsional moments to the girder system.

2.2.4 *Effect of overhang width*

The overhang width is typically designed based on the common rule of thumb that makes the overhang approximately 0.35 to 0.5 times of girder spacing (US Department of Transportation, 2012). Therefore, the overhang widths have been ranged from 0.53 m to 1.22 m to satisfy the design requirements and cover most cases in practice.

A wider overhang often results in an increasing torsional moment which leads to higher chances for the exterior girder rotation to exceed the limit value. Figure 7 shows that when the overhang widths increase from 0.53 m to 1.22 m, the rotations on the exterior girder increase by 175% correspondingly. This suggests that the overhang width has a significant effect on exterior girder rotation since it changes the total torsional moments acting on the exterior girder.

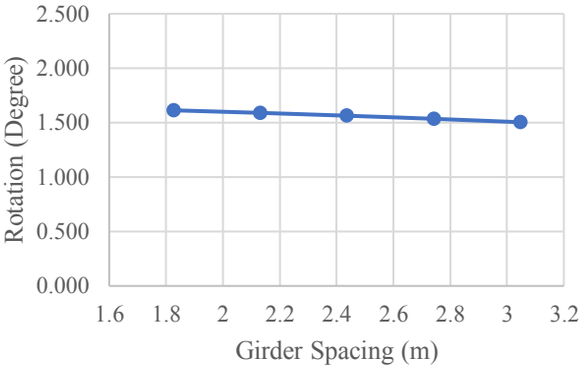


Figure 6 Effect of girder spacing on exterior girder rotation

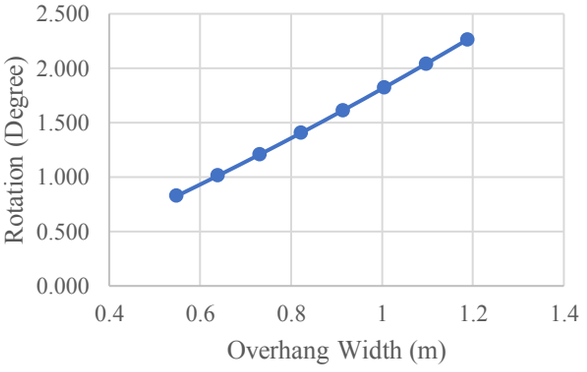


Figure 7 Effect of overhang width

2.2.5 *Effect of number of girders*

The effect of the number of girders has been evaluated using finite element analysis for four bridges with three, four, five and six girders, respectively. The results indicate that the number of girders has not much effect on the exterior girder rotation. As shown in Figure 8, for the bridge with six girders, the rotation only increases by 5% compared with the bridge with three girders.

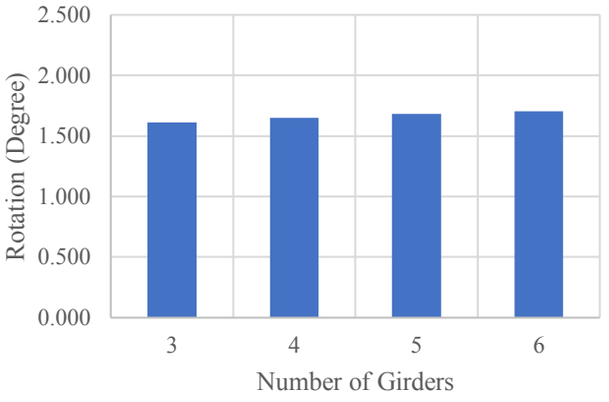


Figure 8 Effect of number of girders

2.2.6 *Effect of Unbraced length*

The unbraced length represents the distance between the braced points along the bridge longitudinal direction to resist the bulking or distortion under considered loads (Haaijer et al., 1982). However, the unbraced length is often designed according to the loads under the service stage, which often result in large unbraced lengths that are not able to limit the exterior girder rotation to the requirements during bridge deck construction. In order to analysis the effect of unbraced length, the maximum unbraced length was taken 7.6 m based on AASHTO specification, while the minimum was 3.0 m.

Figure 9 shows the unbraced length has a significant effect on exterior girder rotation. As the unbraced length increases from 3 m to 7.6 m, the rotation increases by 400%.

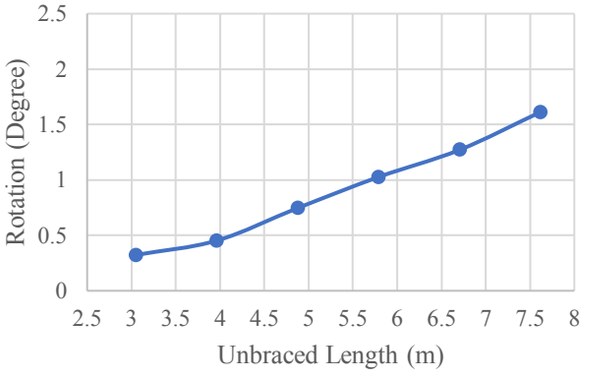


Figure 9 Effect of Unbraced Length

2.2.7 *Effect of diaphragm section*

In order to analyze the effect of diaphragm section, six different diaphragm sections are chosen: W14X53, W14X61, W14X68, W14X74, W14X82, W14X90. The girder section, which is W30X124, is constant during the whole analysis. The results show that the diaphragm section has very limited effect on the exterior girder rotation. As shown in Figure 10, the rotation values keep around 1.6 degree for all diaphragm sections. The maximum difference is only 2%.

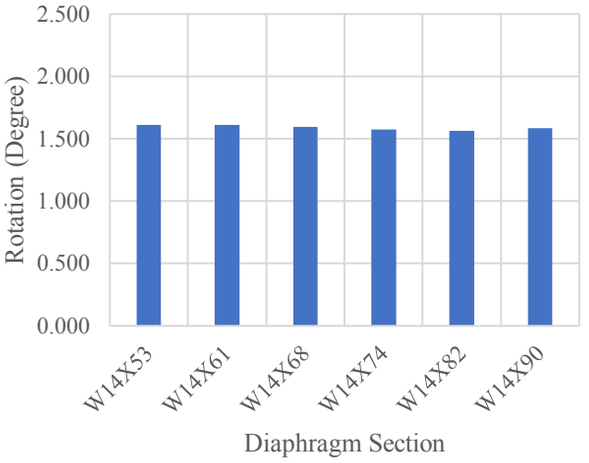


Figure 10 Effect of diaphragm sections

3 ALLOWABLE B/D RATIO

3.1 *Analysis procedures*

According to the parametric study, girder section, overhang length and unbraced length have the most significant effect on exterior girder rotation. The other four parameters including span length, girder spacing number of girder and diaphragm section have limited effects and can be ignored. Also, the previous study indicates that the ratio of the unbraced length (B) to girder depth (D) can be an effective indicator for analyzing the exterior girder rotation (Ashiquzzaman et al., 2016). Therefore, B/D ratios are used as the target values for the evaluation based on the rotation limit of the exterior girder.

To analyze the relations between B/D ratio and other parameters, about three thousand finite element models were built for all the wide flange girder sections from AISC section database. An automatic finite element modeling computer program using MATLAB and SAP2000 was developed to reduce the time consuming for modeling and analysis.

Figure 11 shows the analysis procedures based on this computer program. The pre-processing and post-processing is finished using MATLAB, while the finite element analysis is conducted in SAP2000. The program creates the information for nodes, elements, materials, sections and boundary conditions based on the bridge geometry and then generate the SAP2000 input file. The input file is imported to SAP2000 and finite element analysis is processed using SAP2000 API functions. Then the results are collected by MATLAB for the regression analysis.

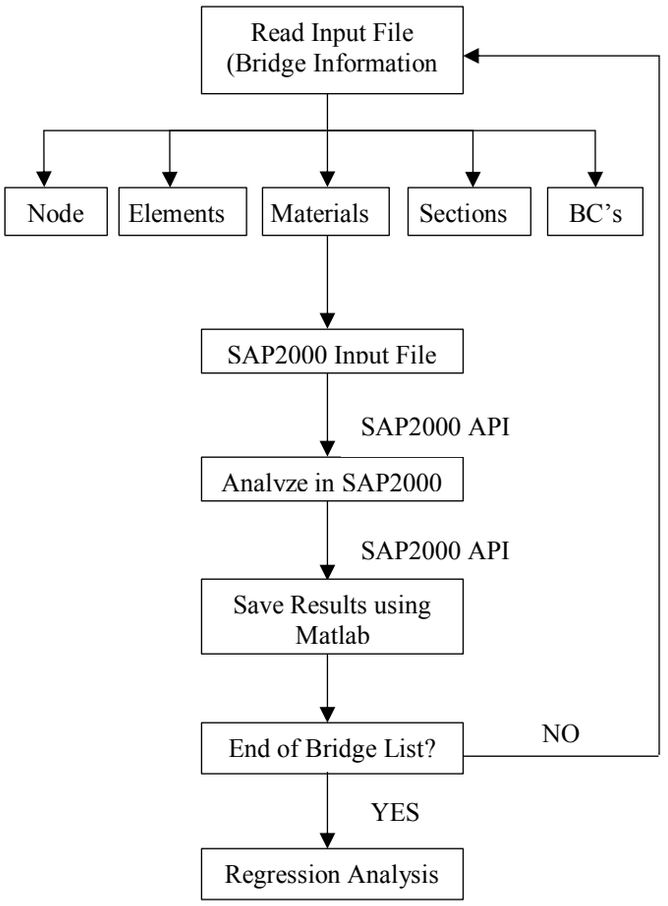


Figure 11 Automatic modeling program using MATLAB and SAP2000

3.2 *Results*

Several primary curves regarding the rotation limit of exterior girder and B/D ratio were developed for wide flange section. For the purpose of including the effect of girder sections and overhang length, section modification coefficients were also developed. Figure 12 shows a primary curve for W30 sections. The B/D ratio increases in corresponding with the increase of rotation limit, which means a larger unbraced length can be used when the bridge has a larger rotation limit. Table 2 shows the section modification coefficients that represent the effects of girder sections and overhang length. The interpolation method can be used to determine the coefficient for the overhang width not listed in Table 2.

Therefore, once the limit of the exterior girder rotation is known, the maximum allowable B/D ratio can be easily determined based on the Equation (1).

$$Ratio = B \times C \quad (1)$$

Where Ratio = Maximum allowable B/D ratio; B = B/D ratio from primary curve; C = Section modification coefficient.

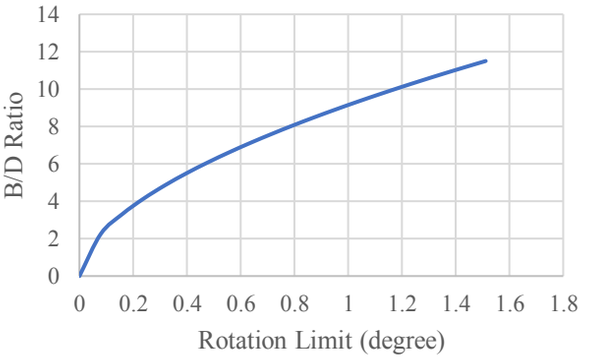


Figure 12 Primary Curve for W30 Section

Table 2 Section Modification Coefficient for W30 Section

Girder Section	Overhang Width (m)						
	0.46	0.61	0.76	0.91	1.07	1.22	1.37
W30X90	1.61	1.14	0.87	0.69	0.56	0.47	0.39
W30X99	1.75	1.25	0.96	0.76	0.62	0.52	0.44
W30X108	1.87	1.34	1.02	0.81	0.66	0.55	0.46
W30X116	2.00	1.41	1.07	0.85	0.69	0.57	0.48
W30X124	2.12	1.49	1.12	0.88	0.71	0.59	0.49
W30X132	2.23	1.57	1.18	0.93	0.75	0.62	0.52
W30X148	2.52	1.74	1.29	1.00	0.80	0.66	0.55
W30X173	3.79	2.41	1.67	1.22	0.92	0.71	0.55
W30X191	4.18	2.66	1.85	1.35	1.02	0.79	0.62
W30X211	4.66	2.97	2.06	1.51	1.15	0.89	0.70
W30X235	5.34	3.33	2.29	1.67	1.26	0.98	0.77
W30X261	6.02	3.76	2.58	1.89	1.44	1.12	0.90
W30X292	7.03	4.29	2.91	2.11	1.61	1.26	1.01
W30X326	8.21	4.90	3.29	2.38	1.81	1.43	1.16
W30X357	9.51	5.52	3.64	2.61	1.98	1.57	1.29

3.3 *Example*

A bridge located in the state of Illinois has basic design information shown in Table 3. The Illinois Department of Transportation recommends 4.8 mm as the maximum overhang deflection in the vertical direction. Thus, the maximum rotation limit can be determined as 0.3 degree for the bridges with an overhang width of 0.91 m.

Table 3 Basic design information for example bridge

Parameter	Value
Span Length (m)	183 + 296 + 183
Girder Section	W30X124
Overhang Width (m)	0.91
Girder Spacing (m)	1.83
Number of Girders	3
Diaphragm Section	W14X53

According to the Figure 12 and Table 2, it is convenient to find that the B/D ratio is 4.6 from the

primary curve, while the section modification coefficient is 0.881 for W30X124 section. Using Equation (1), the maximum allowable B/D can be determined as following:

$$Ratio = B \times C = 4.6 \times 0.881 = 4.05 \quad (2)$$

Therefore, the maximum allowable B/D ratio can be determined as 4.05, which also means the maximum unbraced length is 3.1 m.

4 CONCLUSION

Based on the parametric study and analysis for allowable B/D ratios, the following statements can be concluded:

- The girder section, overhang width and unbraced length have significant effects on exterior girder rotation. The other parameters have very limited effects and can be ignored.
- The allowable B/D ratio increases while the rotation limit increases.
- The allowable B/D ratio can be easily determined without complex calculations based on the method developed in this study.

5 ACKNOWLEDGEMENT

This publication is based on the results of ICT-R27-179, Effectiveness of Exterior Beam Rotation Prevention Systems for Bridge Deck Construction - Phase II. ICT-R27-179 was conducted in cooperation with the Illinois Center for Transportation; the Illinois Department of Transportation, Office of Program Development; and the US Department of Transportation, Federal Highway Administration.

6 REFERENCES

ASHIQUZZAMAN, M., HUI, L., SCHMELTZ, J., MERINO, C., BOZKURT, B., AHMED, I., LINDQUIST, W. & HINDI, R. 2016. Effectiveness of Exterior Beam Rotation Prevention Systems for Bridge Deck Construction. Illinois Center for Transportation/Illinois Department of Transportation.

DAYTON SUPERIOR. 2007. Bridge Deck Handbook.

FASL, J. D. 2008. The influence of overhang construction on girder design.

HAAIJER, G., GARRETT JR, J. & KLIPPSTEIN, K. 1982. Effective lengths for laterally unbraced compression flanges of continuous beams near intermediate supports.

IDAHO DEPARTMENT OF TRANSPORTATION. 2008. Load Resistance Factor Design (LRFD) Bridge Manual.

RAYMOND A. HARTLE, P. E., KENNETH E. WILSON, P.E., S.E., WILLIAM A. AMRHEIN, P.E., S.E., SCOTT D. ZANG, P.E., JUSTIN W. BOUSCHER, E.I.T., LAURA E. VOLLE, E.I.T. 2003. LRFD Design Example for Steel Girder Superstructure Bridge with Commentary.

US DEPARTMENT OF TRANSPORTATION, F. H. A. 2012. Steel Bridge Design Handbook.

YANG, S. 2009. Impact of overhang construction on girder design. United States, North America.

Maintenance, Safety, Risk, Management and Life-Cycle Performance of Bridges – Powers, Frangopol, Al-Mahaidi & Caprani (Eds)
© 2018 Taylor & Francis Group, London, ISBN 978-1-138-73045-8

Impacts of Specialized Hauling Vehicles on the Texas Bridge Network

José Weissmann
University of Texas at San Antonio, USA
Angela J. Weissmann
University of Texas at San Antonio, USA

ABSTRACT: The Federal Highway Administration (FHWA), by a memorandum dated November 15, 2013, requires a state to certify that it either does not permit operation of Specialized Hauling Vehicles (SHV) or conducts bridge force effects load rating analyses using the standard American Association of State Highway and Transportation Officials (AASHTO) HS20 or HL93 loads and applicable SHV load configurations. Texas does allow operation of SHVs, although the number and range of actual gross vehicle weights, axle weights, axle configurations, and spacing was previously unknown. AASHTO has adopted one SHV Notional Load Rating (NRL) configuration for screening purposes and four SHV bridge load rating configurations (SU4, SU5, SU6 and SU7) which are now incorporated in the Manual for Bridge Evaluation (MBE). However, due to the specific types of SHVs this project found operating within Texas, it may be necessary to supplement the AASHTO SHV load configurations with SHV configurations unique to Texas to ensure accurate bridge load rating practices. This paper discusses the network level bending moment analysis that screened the approximately 32,000 Texas bridges for impacts of the actual SHV configurations found operating in Texas, determined candidates for posting and calculated an initial posting load for the selected bridges.

1 INTRODUCTION

A single-unit truck is designed such that the engine, driver compartment and the cargo are carried on the same truck chassis. A Specialized Hauling Vehicle (SHV) is a modified single-unit truck with 4 to 7 axles. The SHV is modified by adding from 1 to 4 liftable axles that can be raised once the cargo is delivered or, when loaded, to make steering through an intersection easier (although the potential for overturning might be increased). SHVs may be designed as dump trucks, construction trucks, ready mix trucks, solid waste trucks and other types. Figure 1 depicts and example of a 5 axle SHV dump truck.

The Federal Highway Administration (FHWA) by a memo dated November 15, 2013 (FHWA,2013), requires a state to certify that it either does not permit operation of Specialized Hauling Vehicles (SHV), or conducts bridge force effects load rating analyses using the standard American Association of State Highway and Transportation Officials (AASHTO) HS20 and HL93 loads and applicable SHV loads based on five configurations that are now incorporated in the Manual for Bridge Evaluation (MBE) (AASHTO, 2011). These recommendations and regulations are in anticipation of significant impacts on short span bridges for the five proposed SHV rating configurations documented in the MBE. Bending moment ratios higher than one based on operating rating loads for a particular bridge may lead to bridge capacity limitations and possible posting needs. Depending on the SHV configuration, live load moment ratios, calculated using the operating rating for the bridge as a basis, may be of the order of 1.2 leading to increase of 20% to the live load stresses.

The FHWA memo also establishes a short deadline – December 31, 2017 – for the evaluation of bridges with spans shorter than 200ft. Analysis of a current version of the Texas bridge inspection data base for the on- and off-system roads shows that this encompasses about 21,000 on-system bridges and 11,000 off-system bridges. On-system bridges are managed directly by TxDOT whereas off-system bridges are managed by municipalities and counties. About 25% of on-system bridges have load ratings that make them sensitive to SHVs. About 54% of the off-system bridges have low ratings that make them vulnerable to SHV operations.

This paper summarizes the network level analysis that screened the bridges that are candidates for posting and calculates an initial posting load for these screened bridges.

Extensive road side surveys and visits to different quarries and truck operators using static scale measurements determined axle loads and spacing for 11

standard 4 to 7 axle SHVs operating in Texas. The 4 AASHTO configurations were also analyzed.

Figure 1 illustrates the six axle SHV configuration dump truck identified by the field research. Several four, five, six and seven axle SHVs were also identified and had their load patterns characterized for this study.



Figure 1. Six Axle SHV Dump Truck.

2 METHODOLOGY

When a load rating analysis shows that a bridge does not have sufficient load capacity for the SHVs identified by the surveys or for the ones specified by AASHTO, the bridge must be posted for load. Posting signs must conform to the Manual on Uniform Traffic Control Devices (MUTCD). The MUTCD has only one sign (R12-5) that depicts silhouettes of trucks for load posting; these silhouettes represent the three standard legal vehicles. The MUTCD does not allow any other truck silhouettes to be used on signs, so there will be no new silhouettes depicting the SHVs on a posting sign. This makes sense, considering that there is a safety issue of having truck drivers attempting to count the number of axles depicted on a sign while traveling at highway speeds.

Several states are in the process of developing bridge posting signs for regulating SHV operations. Sign designs developed by Virginia, Oregon, Ohio, Delaware, and Kentucky DOTs that provide weight limits for SHVs have one thing in common: they tie an allowable Gross Vehicle Weight (GVW) to the number of axles in the Single Unit (SU) truck. Oregon DOT has been active on this issue and has several recommendations for SHV posting signs.

The posting sign depicted in Figure 2 is intended to be used without any other posting signs when a bridge has sufficient capacity for routine commercial traffic and permit loads, but does not have sufficient capacity for the different SHV configurations.

The methodology discussed later in this paper takes into consideration these proposed signing approaches and is directed at calculating a GVW limit for the different SHV axle configurations.



Figure 2. Oregon DOT SHV Posting Sign for Bridges Posted for SHVs Only.

The recommended posting analysis for Texas' on and off-system bridges is based on moment ratios calculated for every on and off-system bridge statewide. The denominator of these moment ratios is always the bending moment induced by the operating rating load recorded in PonTex/BRINSAP – this is the National Bridge Inventory (NBI) (FHWA,1995) version of the Texas bridge database. The numerator is the moment induced by each SHV configuration analyzed in this study, and by the SU/SHV configurations proposed by AASHTO. These are described in an FHWA memo dated November 15, 2013, and are also included in the latest AASHTO bridge load rating recommendations summarized in the MBE. The AASHTO SHVs must also receive a comprehensive analysis of impacts and associated posting requirements.

The analyses of the six- and seven-axle configurations together with the six and seven axle configurations defined by AASHTO are used to illustrate the bridge rating analysis methodology.

The first step of the analysis consists in running the MOANSTR (Weissmann et al., 2002). network bridge analysis program to calculate moment ratios for the SHV configurations under consideration. The MOANSTR program's core is a finite differences routine that calculates live load moment envelopes generated by the studied SHV configurations and PonTex/BRINSAP operating rating loads. The MOANSTR routine incorporates previous research by Matlock (Matlock et al., 1968) and others (Ibsen, 1987, Weissmann & Harrison, 1992 and Weismann et al., 2002). MOANSTR calculates moment envelopes and identifies the maximum live load bending moments (positive and negative) induced by the SHV configuration and the operating rating load for all on- and off-system bridges statewide. For the posting analysis, these moment ratios are calculated based on

the operating rating load recorded in PonTex. This assumes that the TxDOT Bridge Division uses the operating rating as a limit when it comes to bridge posting decisions.

3 CALCULATIONS

SAS computer code was written to compare the proposed rating GVW for all these configurations taking into account any existing possible GVW limitations already recorded in PonTex bridge database under the variables "Loading Restriction" and "Load Restriction in Thousands of Pounds." Variable values 3 and 9 for item "Loading Restriction" are of particular interest for the posting analysis, since they represent bridges that are already posted for GVW. Existing postings need to be compared with the SHV calculated postings to check if they may control the GVW posting. There are 492 off-system bridges and 48 on-system bridges with a code of 3 or 9 for item "Loading Restriction" in PonTex (September 2016 version).

A specific off-system bridge (Structure ID=121020AA2241001) is used to illustrate the computerized calculations performed for all on- and off-systems bridges statewide. Figure 3 shows the GIS map of this bridge location. Figure 4 depicts the street view from Google Maps and part of the bridge data block. This bridge is located in Harris County with a structure length of 75 ft and three simply supported spans of 25 ft each. This bridge is already posted for GVW, as may be observed in Figure 4, with a limit of 36 tons. The operating rating recorded in PonTex for this bridge is also 36 tons represented by a HS load configuration.



Figure 3. GIS Snapshot of Off-System Bridge 121020AA2241001.

Table 1 summarizes the computerized calculations to determine the posting load for bridge 121020AA2241001, for the 6- and 7-axle configurations identified by the field work, and for the theoretical AASHTO SHV configurations. This process was repeated thousands of times by the computerized routines developed during this project for every on- and off-system bridge in Texas.



0000_StructureID	7 Fac Carried	41 1 Load Type	41 2 Load 1000 lb	latitude	longitude
121020AA2241001	HOLLAND AVE	9	72	29.7593	-95.2337

Figure 4. C Street View and Basic Information for Off-System Bridge 121020AA2241001.

The calculations summarized in Table 1 resulted in moment ratios exceeding operating rating for the 6 and 7 axle AASHTO SHV configurations and for the 6 axle SHV configuration identified in this project. The 7-axle SHV configuration did not induce moments above operating rating on this bridge, so these calculations were not included in Table 1.

Recommended posting tons for the 6- and 7-axle configurations were then calculated using the following approach: GVW for each configuration should be capped to operating rating moment values. In other words, the GVW limit for a given configuration is calculated by dividing the GVW for the configuration by the operating rating moment ratio so as to reduce the GVW for the SHV configuration to operating rating levels.

For example, the recommended posting GVW for the AASHTO SU6 vehicle for this particular bridge is calculated by dividing the GVW of the AASHTO SU6 vehicle, which is 34.75 tons, by 1.199, the moment ratio. This resulted in the recommended 29 tons GVW posting for the AASHTO SU6 vehicle.

The same process was implemented for the 6-axle SHV. Dividing this truck's 37.29 tons of GVW by the operating rating moment ratio for this load, which is 1.243, results in a recommended posting load of 30 tons. Therefore, the recommended load that should appear on the bridge posting sign for the 6 axle single unit truck should be the lowest value of 29 tons, controlled by the AASHTO SU6 configuration. Note that 29 tons is also lower than the existing posting for this bridge (36 tons GVW is recorded in PonTex).

The same procedure was followed for the only 7-axle configuration exceeding operating rating, the AASHTO SU7. The recommended posting load for the 7 axle single unit truck for this bridge should be 32 tons. This value is the AASHTO SU7 GVW

(38.75 tons) divided by its moment ratio 1.221. This is the controlling load for the 7-axle SHV posting and it is determined by the AASHTO SU7 configuration.

Table 1. Rating Calculations for Off-System Bridge 121020AA2241001

Six Axle SHV	Moment ratio AASHTO SU6	1.199
	Recommended Posting tons AASHTO SU6	29
	Moment ratio X-XXX-OO 6-axle dump truck	1.243
	Recommended posting X-XXX-OO-6-axle dump truck	30
	Item 41.2 Pontex tons	36
	Lowest tons	29
	Governing Rating Load	SU6 AASHTO
Seven Axle SHV	Moment Ratio AASHTO SU7	1.221
	Recommended Posting tons AASHTO SU7	31.7
	Moment Ratio X-XXX-OO-X 7-axle dump truck	N/A
	Recommended Posting tons CTR 7 axle SHV	N/A
	Item 41.2 Pontex tons	36
	Lowest tons	31.7
	Governing Rating Load	SU7 AASHTO

The limits for the 4 and 5 axle SHVs were calculated in an analogous manner. Table 2 shows the full summary of the results for this specific bridge. Table 2 also includes some of the data field values, variable names and definitions. A Microsoft Access data base was developed, summarizing the calculations for all on- and off-system bridges that presented bending moment ratios above one as previously discussed. The on-system data table of recommended SHV postings encompasses 1,956 bridge records whereas the off-system table encompasses 6,081 bridge records. The Access data set contains all the necessary information to identify a specific bridge in the system including its geographic coordinates, thus enabling an easy display of the results using a geo referenced computerized environment such as ArcMap.

Table 2. Recommended Posting Tons for Off-System Bridge 121020AA2241001

SHV Type	Variable Definition	Data Set Variable	Data Set Value
4 Axle	Recommended SHV GVW Posting (tons)	PostedTons4	25.1
4 Axle	Controlling Rating Load	RatingLoad4	Garbage_x_x_oo_4postedtons
4 Axle	Bending Moment Ratio for Rating Load	Garbage_x_x_oo_4ratio	1.274
5 Axle	Recommended SHV Posting	PostedTons5	27.9
5 Axle	Controlling Rating Load	RatingLoad5	AASHTOSU5postedtons
5 Axle	Bending Moment Ratio for Rating Load	AASHTOSU5ratio	1.112
6 Axle	Recommended SHV Posting	PostedTons6	29
6 Axle	Controlling Rating Load	RatingLoad6	AASHTOSU6postedtons
6 Axle	Bending Moment Ratio for Rating Load	AASHTOSU6ratio	1.199
7 Axle	Recommended SHV Posting	PostedTons7	31.7
7 Axle	Controlling Rating Load	RatingLoad7	AASHTOSU7postedtons
7 Axle	Bending Moment Ratio for Rating Load	AASHTOSU7ratio	1.221

The Access data tables containing calculations of recommended posting loads for the four, five, six and seven-axle configurations for both on- and off-system bridges are also available in GIS map format. The data items summarized in Table 2 and those for the bridge posting calculation example are included in the GIS data block for all the on- and off-system bridges statewide.

Figure 5 shows a snapshot of the GIS system developed for this project. It highlights the data block for an off-system bridge in the outskirts of Kerrville, Kerr County – Structure ID 151330G00020001. This particular bridge is located 0.13 miles SW of SH16 and the recommended posted load for the six axle SHV is controlled by the AASHTO SU6 configuration and limited to 31.9 tons, which should be rounded to 32 tons for the posting sign. The bending moment ratios for the AASHTO SU6 and the 6 axle dump truck configurations are respectively 1.09 and 1.13, or 9% and 13% above the operating load recorded as an HS load with 36 tons of GVW. This bridge is not currently posted. The recommended posting load for the four-axle SHV is 28.6 tons, which should be rounded to 29 tons. The 4 axle posting load is controlled by the garbage truck characterized during the field survey. For the 5-axle SHV configurations, the recommended posting load for this specific bridge is 32.4 tons and it is being controlled by the garbage truck characterized during the field survey.

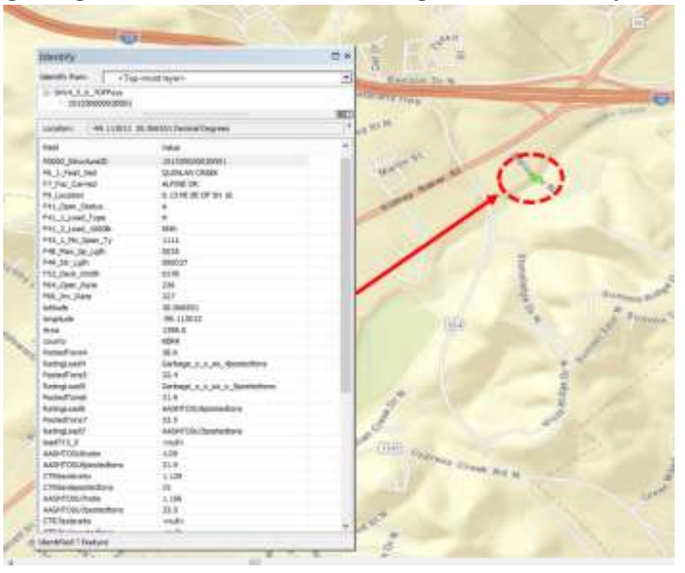


Figure 5. GIS System Summarizing Bridge Recommended Postings Statewide.

4 CONCLUSIONS AND RECOMMENDATIONS

The computerized data sets for on- and off-system bridges discussed in this paper should be used to prioritize bridges for detailed posting analysis on a bridge by bridge basis, and subsequent implementation of adequate SHV posting signs. The computerized tools developed in this project provide an invaluable management tool for the TxDOT Bridge Division. They should be implemented in a timely manner in order to meet the tight deadlines for the review of bridge posting policies for SHVs established by the FHWA memo dated November 15, 2013.

One possible way of streamlining the task of evaluating thousands of bridges for posting could be by grouping these bridges in blocks segmented by the bending moment ratios available in the Access database generated by this project, then evaluating the

posting for the highest moment ratios statewide first. In addition, criteria to prioritize bridges for posting based on risk should be developed. Risk attributes could be identified that measure the strategic importance of a given bridge, such as traffic volume and composition, and availability of detours.

SHVs are primarily short haul vehicles used on local activities that require equipment to haul solid waste (garbage trucks), granular materials (dump trucks) and concrete (concrete drum trucks) and thus are expected to operate in specific urbanized areas of the State of Texas. These specific urbanized areas and associated road networks and bridges should be identified and used as one of prioritization criteria for posting bridges impacted by SHVs.

The potential magnitude of the SHV impacts in Texas is particularly critical for the off-system bridges that are managed by counties and municipalities. While about 2,000 of the approximately 21,000 on-system bridges will experience live load bending moments induced by SHV configurations that supersede the operating rating moments, a significantly higher percentage of the off-system bridges is affected. About 6,000 of the 11,000 off-system bridges will experience live load bending moments induced by SHV configurations that supersede the operating rating moments. This reflects the average age of the off-system bridge system, which is older than the on-system age. Due to their age, many Texas off-system bridges were designed for lower design loads such as H loads and do not have the load capacity to support SHV operations. This lower original load capacity may also have been reduced by deterioration due to the bridge age.

5 REFERENCES

AASHTO, 2011. "Manual of Bridge Evaluation, 2nd Edition".

FHWA, Federal Highway Administration memo on "Load Rating of Specialized Hauling Vehicles", https://www.fhwa.dot.gov/bridge/loadrating/131115.cfm, November 15, 2013.

Imbsen, R.A. and R.A. Schomber. Simplified Bridge Load Rating Methodology Using the National Bridge Inventory File, Arizona Department of Transportation, August 1987.

Matlock, H., T. P. Taylor, A Computer Program to Analyze Beam-Columns Under Movable Loads, Research Report 56-4, Center for Highway Research, University of Texas at Austin, June 1968.

Recording and Coding Guide for the Structure Inventory and Appraisal of the Nation's Bridges, Report No. FHWA–PD-96-001, Federal Highway Administration, http://www.fhwa.dot.gov/bridge/mtguide.pdf, 1995.

Weissmann, J., and R. Harrison, "The Impact of Turnpike Doubles and Triple 28s on the Rural Interstate Bridge Network," Transportation Research Record 1319, TRB, National Research Council, 1992.

Weissmann J., R. Harrison and M. Diaz, A Computerized Model to Evaluate the Impacts of Truck Size and Weight Changes on Bridges, First International Conference on Bridge Maintenance, Safety and Management, IABMAS 2002, Barcelona, 14-27, July, 2002

Maintenance, Safety, Risk, Management and Life-Cycle Performance of Bridges – Powers, Frangopol, Al-Mahaidi & Caprani (Eds)
© 2018 Taylor & Francis Group, London, ISBN 978-1-138-73045-8

Impact of quantity of weigh-in-motion data on load effects on bridges

A. Žnidarič, M. Kreslin & J. Kalin
Slovenian National Building and Civil Engineering Institute, Ljubljana, Slovenia

G. Turk
University of Ljubljana, Faculty of Civil and Geodetic Engineering, Ljubljana, Slovenia

ABSTRACT: Quantity of weigh-in-motion (WIM) data influences the results of bridge (and pavement) load modelling. However, no clear recommendations existed about how many vehicle records are needed for reliable prediction of load effects. Impact of quantity of WIM data on the results of bridge traffic load modelling was studied using three WIM dataset that contained almost one million heavy vehicle records. The main goals of the study were to investigate (a) variation of the bridge load modelling results as a function of WIM data sample size, and (b) how much data is needed for the results to converge. The datasets were quality-checked, which included visual validation of all heaviest vehicles. Vehicles with more than seven axles were eliminated to minimise the influence of random special transports. Convolution method was used as an efficient traffic load modelling tool to generate a multitude of different outcomes. Paper describes the approach taken and results from three locations with different traffic densities. Results for bending moments and shear forces are presented as a function of bridge span (5, 15, 25, 35 and 45 m) and size of data sample, which varies from 10 000 vehicles to the full dataset. Paper concludes with recommendations about the required number of WIM records for reliable bridge load effect modelling.

1 INTRODUCTION

Modelling of load effects (bending moments and shear forces) caused by heavy traffic is a standard procedure to evaluate the effects of heavy traffic on bridges. The results of modelling greatly depend on quality and quantity of axle load information that is in most cases collected by weigh-in-motion (WIM) systems. Unfortunately, no clear recommendations exist about how much WIM data is needed for reliable prediction of load effects. The only criteria, based on engineering judgment, are given in the European specifications for WIM (COST 323, 2002), where it is suggested that:

- accuracy of WIM data for bridge traffic load modelling shall be of at least class C(15), meaning that errors of roughly 95 % of gross weights shall be within ±15 %, and axle loads within ±20 % of the static values, and that
- as many vehicle records as possible (but at least 100 000) shall be used.

The purpose of work was to investigate influence of number of WIM vehicle records on the results of bridge traffic load effect modelling and to set some recommendations for the future work. In other words, the study investigated:

- variability of the traffic load effects calculated from equally sized WIM subsets, and
- how quickly the calculated load effects converge and how much data is needed to provide stable and reliable results.

2 WIM DATA SOURCES

All data in the study was collected at three different sites using a bridge weigh-in-motion (B-WIM) system.

2.1 *Bridge WIM*

Bridge-WIM or B-WIM refers to a specific method that uses an instrumented bridge or culvert to weigh the heavy vehicles while they cross the structure. B-WIM systems provide equivalent set of vehicle parameters (axle loads, gross weight, axle spacing, velocity, vehicle category…) as the more established pavement WIM systems, but also have some specific advantages (Žnidarič et al., 2016):

- The instrumentation is completely portable and can be moved from a bridge to another. Unlike the pavement WIM systems, portable installations

provide similar quality of results as the permanent ones.
- Accuracy of results is generally high, especially on smooth pavements. Installations are possible on rougher or rutted surfaces, where pavement WIM installations would not even be considered.
- In most installations all sensors are mounted underneath the bridge deck. Consequently, installation and maintenance activities do not interrupt the traffic. This is advantageous for sites where cutting into the pavement is not allowed, when installation of a pavement based system is not feasible due to heavy traffic or if permits for road closures are difficult to obtain.
- Collected strains records can be used to generate bridge related indicators (influence lines, dynamic amplification factors, girder factors), in order to optimise structural assessment (ARCHES, 2009; Žnidarič & Lavrič, 2010).

The obvious weakness of B-WIM is that a suitable bridge is needed to install the system. Furthermore, while instrumenting common slab or beam-and-slab bridges is straightforward, setting-up a less common structure requires substantial knowledge about bridges. A typical installation of an underpass under a four-lane highway is shown in Figure 1. The sensors in the middle row are used for weighing, while the separate pairs of sensors, one per lane, are used to determine vehicle velocities.

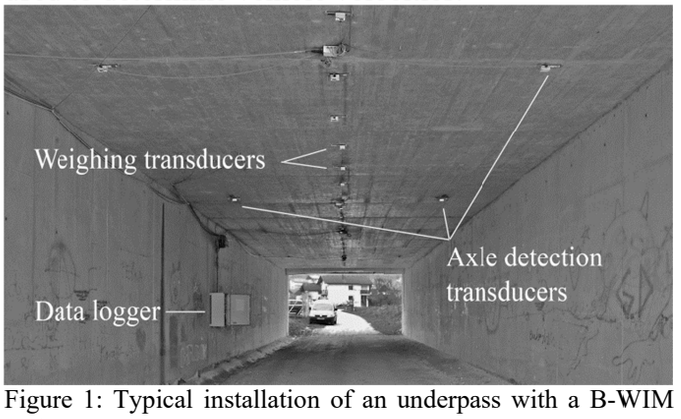


Figure 1: Typical installation of an underpass with a B-WIM system

2.2 *Data sets*

The primary source of data, denoted as Dataset 1, contained 793 799 or almost two years of vehicle-by-vehicle records collected on a low-volume motorway. It was complemented by Datasets 2 and 3 from the busiest motorway in Slovenia, containing 147 525 and 106 872 vehicle records resp. All three datasets were temperature and velocity calibrated (Žnidarič et al., 2016). In the final stage, all vehicles within the top 10^{th} quantile with respect of their gross weight and axle loads were visually checked with dedicated software, to provide the highest possible quality of the data (Žnidarič, 2017), without any abnormally heavy axle loads that might appear in the measured data as a result of misdetected axles. This software visually compares the measured and the calculated strain responses, which, with the help of the photos, allows to either approve the result, or to reweigh the vehicle after adding or deleting the misdetected axles.

3 CONVOLUTION METHOD

The convolution method is an established technique for modelling of bridge traffic load effects. It is computationally less demanding than the full simulations. Moses and Verma (1987) and Žnidarič (2017) have also shown that the convolution can give similar results to Monte Carlo simulation, if the assumption of independent traffic in the two lanes is valid. Good matches between results were obtained with convolution and other more sophisticated traffic load modelling methods in the ARCHES project (2009). In Slovenia, the convolution method, similar to the one proposed by Moses & Verma (1987), has been used for over 20 years (Žnidarič & Moses, 1997; Žnidarič, 2010).

It shall be noted that for bridge traffic load modelling applications, the WIM systems must not only provide information about axle configurations and loads of each vehicle, but also time stamps of individual vehicles at a resolution of at least one hundredth of a second, to allow accurate modelling of inter-vehicle spacings. These are required to properly simulate the extreme loading events (Žnidarič et al., 2015).

3.1 *Calculation of load effects*

As the first step, the quality-approved vehicle records, containing information about their individual axle loads and spacings, are converted into load effects (bending and hogging moments, shear forces) by using the influence lines, either theoretical or experimental. The predicted *static* load effect, Q_S, moment or force, is determined as:

$$Q_S = \sum_{i=1}^{N} AL_i I(x_i) \quad (1)$$

where AL_i is load of axle i, N is number of axles of the vehicle and I_i is the value of the influence line due to axle i at location x. The Q_S values of all vehicles are combined into histograms of static load effects, separately for each traffic lane. In most cases, tail modelling or smoothing is used to extend the results beyond the measured values.

The convolution method assumes that the highest load effect is achieved when two vehicles from independent traffic flows in each traffic lane are placed side by side on a bridge at the place of maxi-

mum effect, which is defined as a loading event. In Europe, such an approach can be justified on well over 90 % of bridges (SAMARIS D19, 2006; Žnidarič et al., 2011) which influence lines are shorter than 30 m. On these bridges, due to the length of common heavy vehicles which does not exceed 15 m, the critical event happens due to *one* vehicle in each of the two traffic lanes.

Assuming that the distributions of the load effects for both lanes are independent, which can be justified for opposing traffic, but taken with reserve for traffic in the same direction, the probability mass function (PMF) for a combined event, with vehicles meeting each other, can be expressed as:

$$\mathrm{f_Z(z)} = \sum_{\mathrm{k=-\infty}}^{\infty} \mathrm{f_X(k)\, f_Y(z-k)} \tag{2}$$

where f_X and f_Y are the probability mass functions of load effects from two adjacent lanes, and f_Z is the new probability mass function of the load effects for multiple-presence events composed of vehicles from both lanes of traffic. X and Y are random variables representing load effects for lanes 1 and 2, respectively, whereas Z is a random variable representing load effect for a multiple-presence event. If f_X and f_Y are divided into m bins, then the length of f_Z will be equal to $2m - 1$ bins (MathWorks, 2013).

The probability function $f_Z(z)$ includes all possible combinations of vehicles from lanes 1 and 2, including the highly unlikely multiple presences of the heaviest vehicles on both lanes.

3.2 *Probability distribution of extremes*

Many engineering applications require predictions of future conditions, typically the highest possible (likely) loading and the lowest bearing capacity. This inevitably requires extrapolation from the available data (Ang & Tang, 2006).

If Z is the initial random variable, in this case the convoluted load effect, with known initial distribution function $F_Z(z)$, then we can divide the sample space Z into N_T observation periods, where each sample will be a subset of observations ($z_1, z_2, \ldots, z_N$). Since every observed value is unpredictable prior to being actually observed, we can describe the maximum value Z_N of the sample of size N_T as:

$$\mathrm{Z_N} = \max_{1 \le i \le N_T} \mathrm{Z_i} \tag{3}$$

The largest value of the sample size N_T taken from population Z is also a random variable whose distribution can be derived from that of the initial variate Z. If Z_N is less than some value z, then all other sample random variables must also be less than w. If we assume that $Z_1, Z_2, \ldots, Z_N$ are independent and identically distributed as the initial variate Z:

$$\mathrm{F_{Z_1}(z) = F_{Z_2}(z) = \cdots = F_{Z_N}(z) = F_Z(z)} \tag{4}$$

then the distribution function for Z_N is

$$\begin{aligned} \mathrm{F_{Z_1}(z)} &= \mathrm{P(Z_N \le z)} \\ &= \mathrm{P(Z_1 \le z, Z_2 \le z, \ldots, Z_N \le z)} \\ &= \mathrm{\left(F_Z(z)\right)^{N_T}} \end{aligned} \tag{5}$$

N_T is defined as:

$$N_T = N_{ADT}\, N_D\, N_P\, \alpha \tag{6}$$

where N_{ADT} is the measured or average daily number of heavy vehicles, N_D is number of days in a year, typically taken as 250 working days, and N_P is the period that the load effects are forecasted to, expressed in years. Parameter α defines the probability of exceedance of load effect. It is either taken as the mean or median value or is calculated to correspond to a specific return period (Žnidarič, 2017). In traffic load modelling words, if we:

- have a measured dataset of load effects from N_T days of traffic and
- assume that the distribution is stationary (if drastic changes happen, measurements shall be repeated),

we can approximate the maximum expected load effect by raising the measured distribution F_Z to the power of N_T.

The adopted procedure is demonstrated with the highest quality, visually cleaned dataset 1. 25-m long generic simply supported influence line was used to generate the bending moments and shear forces for all 793 799 vehicles. Then the load effects were converted into histograms. Fifty bins were used over the entire data range, meaning that the bin sizes were not constant, but were adjusted according to the size of data subsets. Calculations of load effects were performed separately for the slow and for the fast lane. Results were convoluted and raised on the power of N_T. In this case, the 75-year return period was considered, which corresponds to α equal to 0.6346. No traffic increase was accounted for (Leahy et al., 2016), as it has no effect on demonstration of influence of quantity of data on bridge traffic load modelling.

3.3 *Example*

Individual steps of this procedure are shown in Figure 2, from the individual lane PDFs ((a) and (b)), convoluted PDF (c), with tail detail (d), convoluted CDF on powers of N_T , corresponding to 10, 20 and 75-year return periods (e).

For comparison, the Figure 2 (f) compares the maximum daily bending moments on the Gumbel proba-

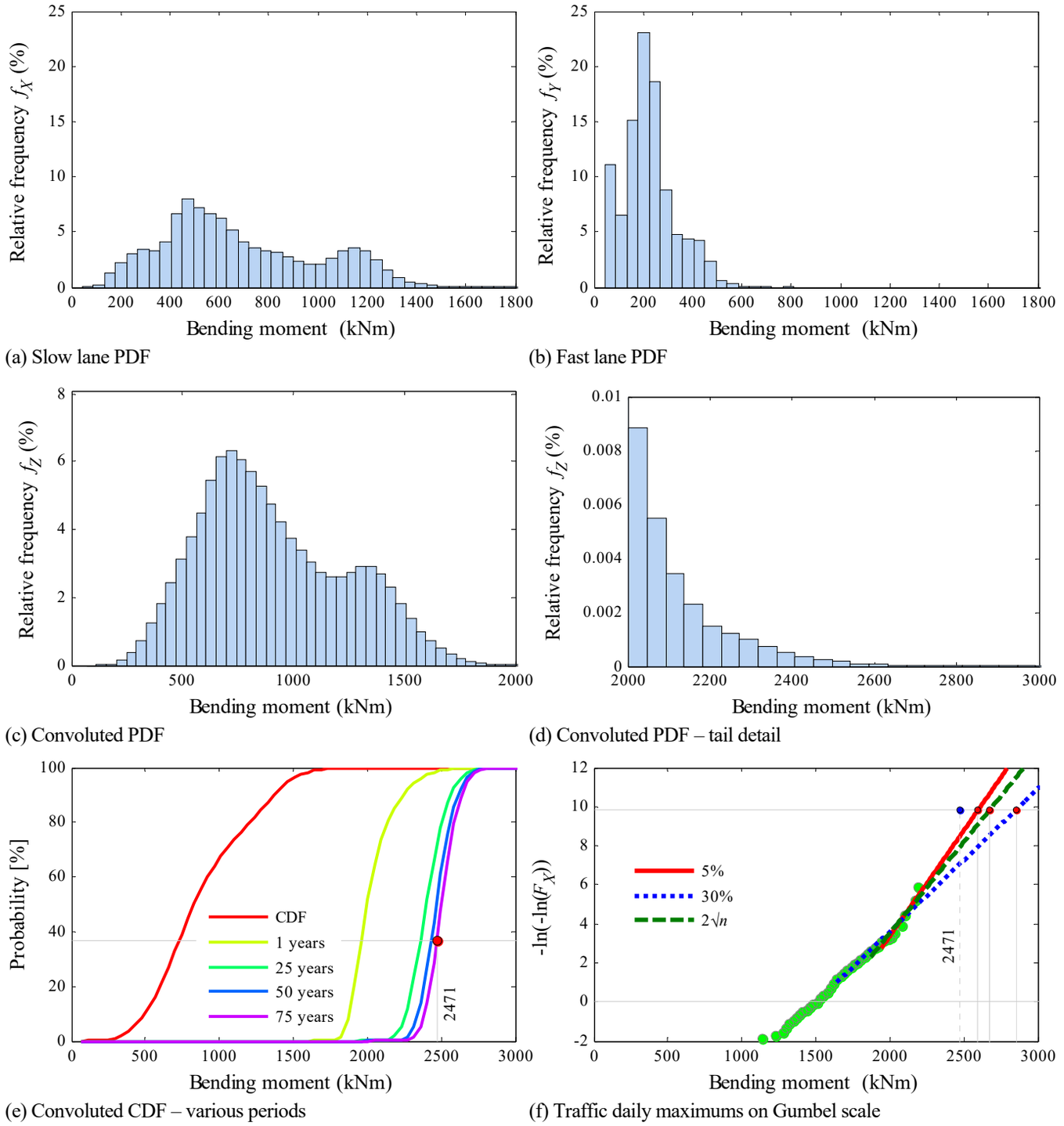


Figure 2: Dataset 1: steps of convolution procedures, all data, 50 bins, 75-year return period

bility plot, using three different number of data from the tail for extrapolation: top 5%, top 30% and top $2\sqrt{n}$ results, where n is the size of data sample (Castillo, 1988). This diagram compares the 75-year return period bending moment, calculated with convolution, with three extrapolated daily maximum values based on different number of points in the tail.

4 INFLUENCE OF QUANTITY OF WIM DATA

In the next step the dataset 1 was divided into subsets of various lengths. The shortest individual ones comprised 15 days of data and 17 250 vehicles each. Figure 3 displays all 46 subsets of 75-year return period results. Only the complete days, with all 24 hours of traffic, were considered. Each subset started at midnight, immediately after the previous subset ended. In all subsequent examples, moderate Gaussian kernel smoothing was applied (Žnidarič, 2017), to soften the tails with sparse data, particularly in the shorter subsets. Figure 3 also displays the mean value and the ±1 standard deviation (sigma) curves. From there the mean value of 2471 kNm and coefficient of variation of 5.5 % are established.

Evident is the wide variability of the results, caused by insufficient number of vehicles and by in-

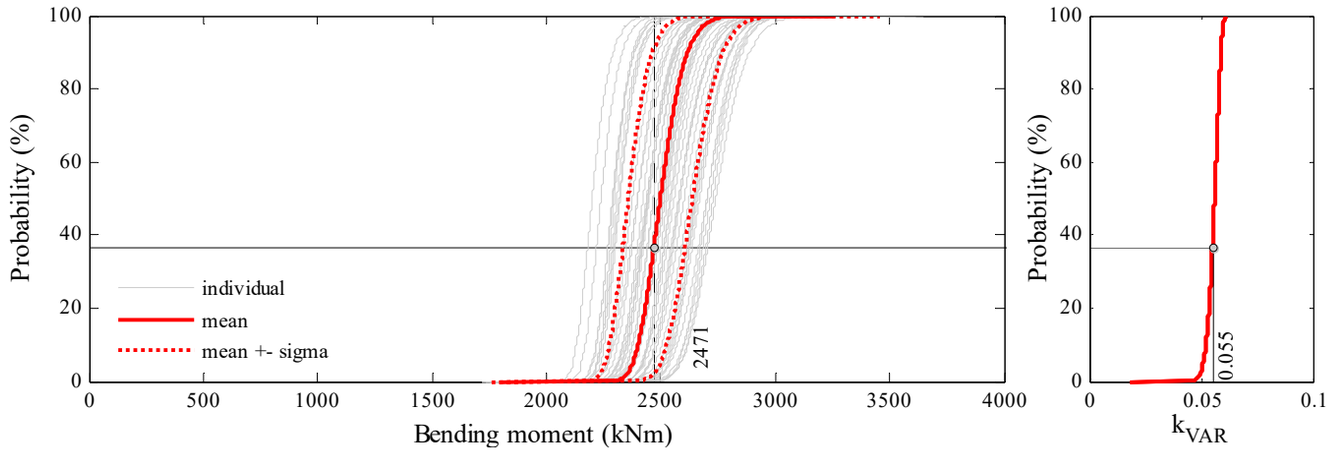


Figure 3: Bending moments for 2-week data slots – mean value and standard deviation

consistent number of exceptionally heavy vehicles in these short individual subsets.

The procedure was repeated for nine different measurements periods: 2 weeks, 1, 2, 3, 4 and 6 months, 1 year, 1 year and a half and for all 696 days. With more data, the mean value of the characteristic load effect starts to increase and at certain point reaches the level of the results of the largest dataset. This is summarised in Figure 4 that displays the mean bending moments and their coefficients of variations as a function of days of data in the subsets. To compare the results with those from Datasets 2 and 3, with different number of heavy vehicles per day, the procedure was rerun with datasets organised not in days but in number of vehicles. Data sets containing 20-, 50-, 75-, 150-, 250-, 400- and all 794-thousands of vehicles were generated. As expected, the graphs in Figure 5 resemble those from the previous figure.

Finally, the procedure was repeated for five different lengths of influence lines. Resulting bending moments and shear forces at bridge entrance, for all five spans and the first two datasets are presented in Figures 6 and 7. All results are normalised to the end

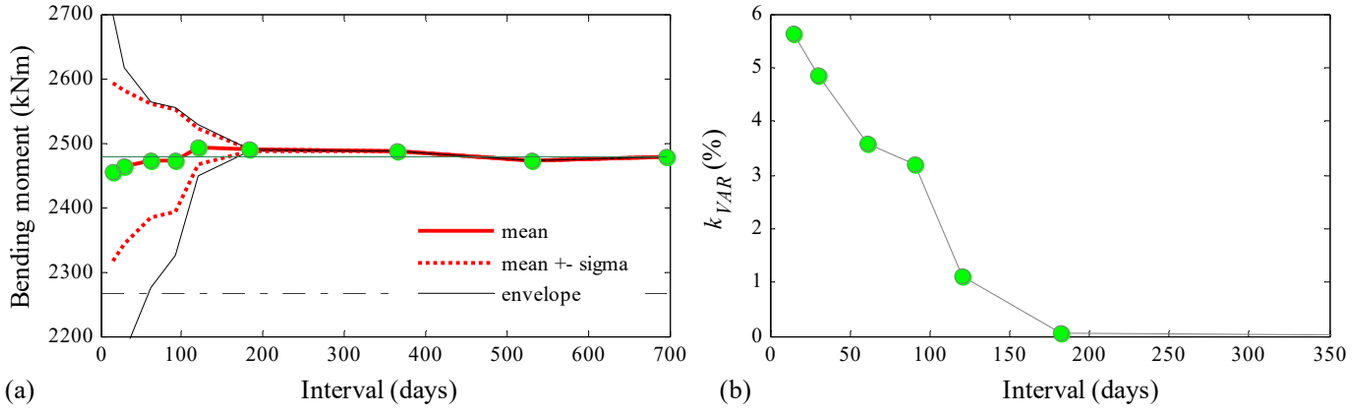


Figure 4: Dataset 1: Influence of the duration of measurements on 75-year return period bending moments, (a) mean values and (b) coefficients of variation

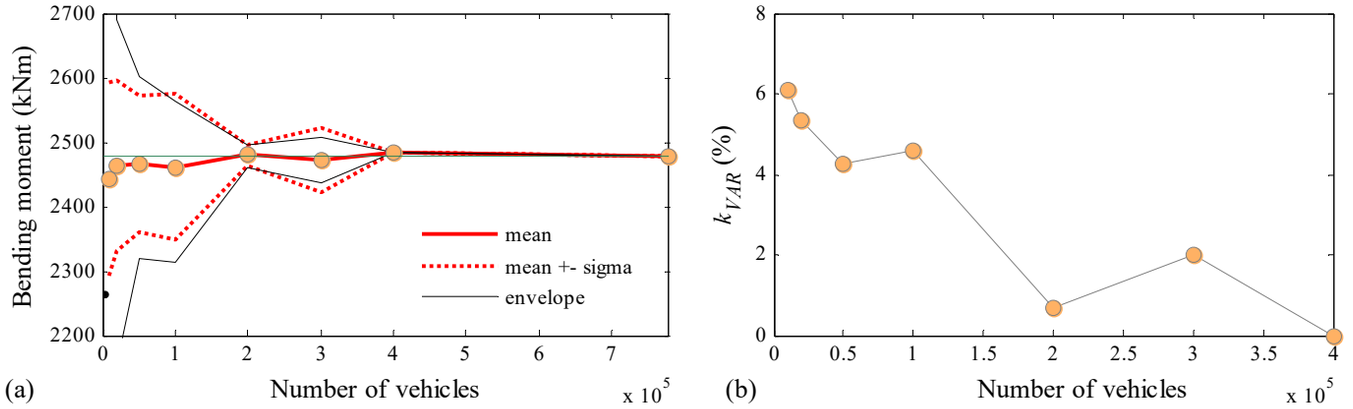


Figure 5: Dataset 1: Influence of number of vehicles on 75-year return period bending moments: (a) mean values and (b) coefficients of variation

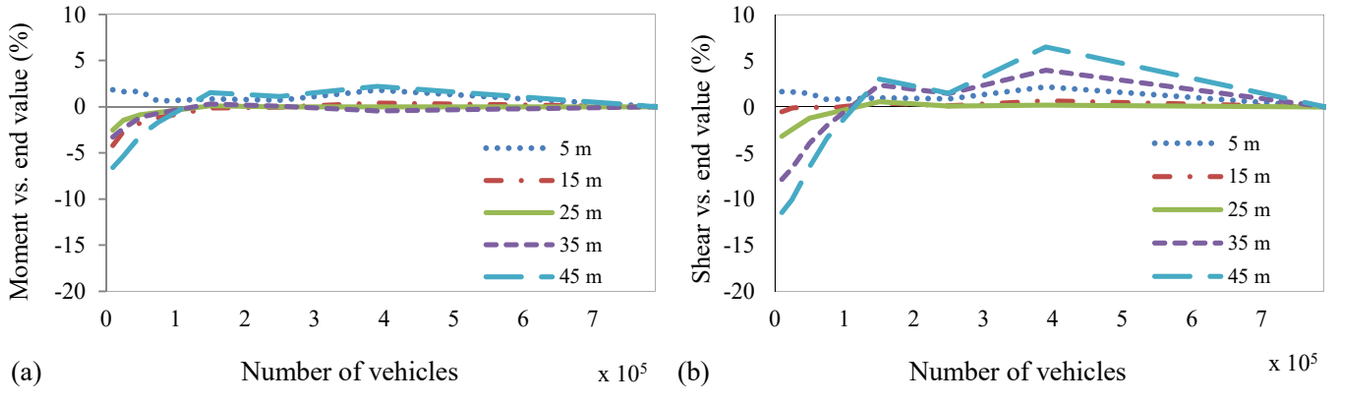


Figure 6: Dataset 1: Influence of number of vehicles on 75-year return period load effect, for various spans: (a) bending moments and (b) shear at bridge entrance

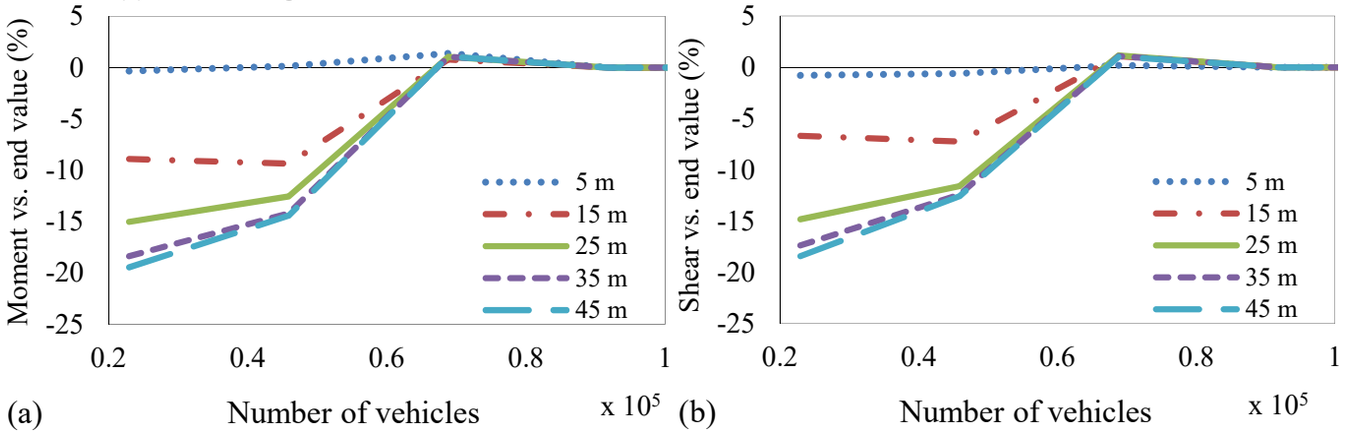


Figure 7: Dataset 2: Influence of number of vehicles on 75-year return period load effect, for various spans: (a) bending moments and (b) shear at bridge entrance

values compiled from the largest datasets that provide the most reliable reference for the specific sites.

4.1 *Results*

Table 1 summarises the attained differences, in %, with respect to the end values, for all three datasets, for five spans and for various sizes of subsets. Figure 8 summarises all differences (errors) for bending moments and shear forces from Table 1.

The clear conclusion for the three sites is that having more than 100,000 vehicles will, regardless of the span length, provide stable results that vary insignificantly with more data. Results may be underestimated for up to 5 % if the datasets contain between 50,000 to 100,000 vehicles. Datasets with less data provide unpredictable, in most cases severely underestimated results. By far the most consistent are results for the 5 m span, which error never exceeds the ±2 % interval, which might suggest, after verification with more datasets, that for very short bridges less data might be sufficient.

4.2 *Discussion*

The following can be concluded in relation to the impact of the quantity of data on modelled characteristic load effects on bridges:

– The three datasets are fundamentally different. The first one was collected on a motorway with low-volume traffic, but contains nearly 800 000 vehicles accumulated over almost two years. The other two datasets contain data from another high-volume motorway. Both measurements were considerably shorter and the datasets contain only 13 % to 18 % of vehicles from the dataset 1. In addition, the dataset 2 was acquired almost 10 years ago, with an older generation of B-WIM software, while the other two datasets are from years 2013 to 2016.
– To eliminate the effect of sparse extremely heavy vehicles, those with more than seven axles were treated as escorted special vehicles and were not considered in data modelling.

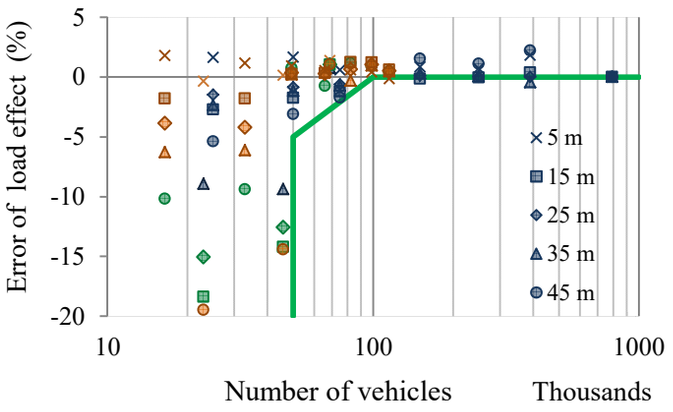


Figure 8: Errors of bending moments and shear forces as a function of size of the samples, 3 datasets, 5 spans

Table 1: Influence of the size of data subsets – the differences with respect to the end values containing all available data

		Bending moments - difference vs. end value (%)					Shear forces - difference vs. end value (%)				
	Vehicles	5 m	15 m	25 m	35 m	45 m	5 m	15 m	25 m	35 m	45 m
VA0028	25000	1.64	-2.71	-1.48	-2.36	-5.38	1.65	-0.09	-2.44	-6.61	-10.01
	50000	1.67	-1.73	-0.86	-1.14	-3.11	1.48	0.03	-1.20	-3.92	-6.49
	75000	0.60	-1.18	-0.61	-0.73	-1.71	0.80	-0.16	-0.75	-2.00	-3.38
	150000	0.84	-0.16	0.11	0.29	1.52	1.00	0.45	0.58	2.39	3.04
	250000	0.72	-0.04	0.01	0.07	1.13	0.90	0.12	0.10	1.45	1.50
	390000	1.82	0.39	0.01	-0.45	2.20	2.18	0.69	0.21	3.99	6.52
	793799	0.00	0.00	0.00	0.00	0.00	0.00	0.00	0.00	0.00	0.00
VA0072	22960	-0.36	-8.91	-15.06	-18.38	-19.48	-0.80	-6.70	-14.84	-17.41	-18.47
	45920	0.14	-9.36	-12.57	-14.22	-14.42	-0.62	-7.27	-11.62	-12.46	-12.62
	68880	1.36	0.77	1.03	1.04	1.06	0.16	1.09	1.13	1.07	1.04
	101680	0.00	0.00	0.00	0.00	0.00	0.00	0.00	0.00	0.00	0.00
VA0468	16450	1.79	-1.80	-3.86	-6.27	-10.19	1.52	-1.10	-4.78	-9.06	-15.00
	32900	1.18	-1.81	-4.20	-6.11	-9.40	1.26	-1.70	-5.00	-8.81	-13.54
	49350	0.93	0.24	0.36	0.21	0.74	1.11	0.99	0.01	0.95	-2.31
	65800	0.53	0.33	0.26	0.43	-0.76	0.58	0.21	-0.31	-1.38	-4.05
	82250	0.58	1.24	0.64	-0.29	1.16	0.86	1.27	1.29	1.36	1.39
	98700	0.40	1.21	1.03	0.99	0.94	0.52	1.32	1.24	1.02	1.00
	115150	-0.14	0.62	0.51	0.49	0.45	-0.10	0.63	0.63	0.49	0.53
	131600	0.00	0.00	0.00	0.00	0.00	0.00	0.00	0.00	0.00	0.00

- On all three sites the most reliable, visually inspected results were used. The subsets with less than 50 000 vehicles generated lover values of load effects, with higher coefficients of variations. This means that the load effects from smaller subsets, based on shorter measurements, are less reliable and can generate results which can be either greatly underestimated or even overestimated, if some extremely heavy vehicles had been captured in that specific timeslot.
- The above seems not to be valid for the shortest 5 m span, where the bending moments and shear forces at the bridge entrance do not change for more than ±2 %, regardless of the size of the subsets. The most probable reason is that the extreme axle loads on shorter vehicles (4-axle rigid trucks) are common and can be captured regularly, even in smaller subsets of WIM data. The longer vehicles with extreme gross weights (cranes and low-loaders that carry bulky loads), which affect longer spans, are on the other hand less common and are captured only during longer measurements.
- For all other spans, and in all six cases (bending moments and shear forces on three locations), the mean load effects reached the 'accurate' end values at around 50,000 to 100,000 vehicles. At those instants, the coefficients of variation typically dropped below 3 %.
- Based on the three sets of WIM data (more would strengthen the conclusion) it can be recommended that bridge traffic load modelling should be based on at least 100,000 vehicles.
- Datasets with at least 50,000 vehicles may give usable, but less conservative outcomes, with higher uncertainties that need to be evaluated and accounted for in the results.
- A convergence test, using the above approach with varying size of the datasets, is a useful tool to test how the results depend on the number of vehicles in the database.

5 CONCLUSIONS

Parametric studies were performed to give an answer about how much weigh-in-motion data is needed for reliable calculation of load effects on bridges. For this purposes, three sets of WIM data have been prepared. The first one was collected over a period of almost two years on a low-volume motorway. The other two measurements lasted only 31 and 57 days resp., but have been collecting data on the busiest motorway in Slovenia, with three to four times more traffic than in the first case.

On all three sites, the most reliable, visually inspected datasets were used as a reference to test the impact of the quantity of data on the modelled load effects. The procedure was repeated with subsets of data containing different number of vehicles. The goal was to assess how quickly the results, as a function of the subset size, converge to the 'accurate' results, which were calculated from the maximum available size of the sample.

The results of the analysis confirm the existing recommendations, which were based on engineering judgement, that at least 100 000 vehicle records are needed for reliable forecast of load effects on bridges. Datasets between 50 000 and 100 000 vehicles are acceptable, but the results will likely be underestimated for up to 5%, with higher coefficient of variation. The datasets with less than 50,000 vehicles will either considerably underestimate or overestimate thee load effects, depending on the extremely heavy vehicles that have or have not been captured in the specific subset.

The exception was the shortest 5 m span, where the bending moments and shear forces at the bridge entrance did not change for more than ± 2 %, regardless of the size of the subsets. The explanation is that the very heavy axle loads on the shorter rigid vehicles (3- and 4-axle trucks) are captured regularly, even in smaller subsets of WIM data. The extremely heavy longer vehicles that affect longer spans, are on the other hand less common and are captured randomly.

It is evident that using a few more long-lasting datasets would be beneficial. Nevertheless, the results give some clear indications about quantity of weigh-in-motion data needed to reliably model the traffic load effects on bridges.

6 REFERENCES

Ang, A. H. & Tang, W. H., 2006. *Probability Concepts in Engineering Planning and Design.* 2nd ed. Somerset: Wiley.

ARCHES D08, 2009. *Recommendations on bridge traffic load monitoring,* Brussels: European Commission.

Castillo, E., 1988. *Extreme Value Theory in Engineering.* New York: Academic Press.

COST 323, 2002. *Weigh-in-Motion of Road Vehicles: Final Report of the COST 323 Action. Jacob, B., OBrien, E.J., Jehaes, S. (Eds.),* Paris: LCPC.

Leahy, C., OBrien, E. J. & O'Connor, A., 2016. *Considering Traffic Growth in Characteristic Bridge Load Effect Calculations.* Foz do Iguazu, Taylor & Francis Group, London, pp. 230-236.

MathWorks, 2013. *MATLAB, http://www.mathworks.com/products/matlab/.* [Online].

Moses, F. & Verma, P., 1987. *Load Capacity Evaluation of Existing Bridges,* Washington D.C.: National Cooperative Highway Research Program (NCHRP) - Report No. 301.

SAMARIS D19, 2006. *State of the art report on assesment of structures in selected EEA and CE countries.* http://www.fehrl.org/?m=32&id_directory=355 ed. Ljubljana: ZAG.

Žnidarič, A., 2010. *The method for determining and controlling capacity of state road bridges, Report P 901/09-670-1, in Slovene,* Ljubljana: ZAG.

Žnidarič, A., 2017. *Influence of number and quality of weigh-in-motion data on evaluation of load effects on bridges, Doctoral dissertation.* Ljubljana: University of Ljubljana.

Žnidarič, A., Kalin, J. & Kreslin, M., 2016. *Recent advances in Bridge WIM technology.* Foz do Iguasu, IABMAS.

Žnidarič, A. et al., 2015. *Guidelines on collecting WIM data and forecasting of traffic load effects on bridges, Re-Gen D3.1 report,* Dublin: NRA Ireland.

Žnidarič, A. & Moses, F., 1997. *Structural Safety of Existing Road Bridges.* Kyoto, McGraw Hill, pp. 1843-1850.

Žnidarič, A., Pakrashi, V., OBrien, E. J. & O'Connor, A., 2011. A review of road structure data in six European countries. *Proceedings of the Institution of Civil Engineers - Urban design and planning,* 164(4), pp. 225-232.

MS16: Bridge monitoring: Techniques and results regarding bridge condition and loading

Organizers: E.O.L. Lantsoght & D.A. Hordijk

Maintenance, Safety, Risk, Management and Life-Cycle Performance of Bridges – Powers, Frangopol, Al-Mahaidi & Caprani (Eds)
© 2018 Taylor & Francis Group, London, ISBN 978-1-138-73045-8

Structural health monitoring and serviceability assessment of bridges in Romania

C. C. Comisu
Department of Bridges, Faculty of Civil Engineering, Technical University "G h. Asachi" of Iasi, Iasi, Romania

M. C. Scutaru
Department of Civil and Industrial Engineering, Faculty of Civil Engineering, Technical University "Gh. Asachi" of Iasi, Iasi, Romania

N. Țăranu
Department of Civil and Industrial Engineering, Faculty of Civil Engineering, Technical University "Gh. Asachi" of Iasi, Iasi, Romania

G. Boacă
Department of Bridges, Faculty of Civil Engineering, Technical University "G h. Asachi" of Iasi, Iasi, Romania

ABSTRACT: The main scope of the research is to develop an integrated health monitoring system to improve serviceability assessment of bridges in Romania. The system must integrate the actual practice mainly based on visual inspections and combines the response of different reliable sensors, installed on the structure to monitor the damage progress, with enhanced realistic deterioration models. The system was developed to cover the parameters for the most important deterioration mechanisms: reinforcement corrosion, concrete carbonation and the changes in the structures behavior.

The use of permanent monitoring systems has several advantages:
- A more reliable prediction of the damage progress
- Traffic interference is reduced
- An input for defining maintenance and repair strategies
- The costs of access to the structure and resources for inspection and testing are reduced
- Structural elements with difficult access are easily monitored
- An evaluation of the need for further inspection and testing

1 INTRODUCTION

In 2017 in Romania five people died every day due to traffic accidents, finding an increase in their number from year to year. This must stop in no time establishing himself adopting a strategy that will lead primarily to remove the causes that favors road accidents. There are multiple causes: poor technical state of bridges and roads, failure to traffic rules, vehicle built to modern highway traffic regime, but obliged, without alternative, to circulate on infrastructure in its great majority built in the 1980s.

In accordance with the studies and researches realized in the last years, especially regarding the bridges exploited from the network of the national roads it is revealed the fact that the majority of these bridges is at the limit between the satisfactory state and the unsatisfactory one. From the data gathered as a result of the studies undertaken in Romania on a sample of approx. 1000 of bridges, it has been concluded that over 90% from the total number of bridges had major degradations.

The observations made over the technical state of the bridges from the network of national roads in Romania, have pointed to the necessity to applies an modern program of health monitoring system in order to allows the application of a system identification and damage detection, the optimization to planning process of the necessary works with beneficial implications regarding the management, the allocation of the financial resources and thus, an efficient system to administration of the patrimony of bridges.

The current methods of service-life prediction in Romania are based especially on visual inspections having a pronounced subjective character to carry out the condition assessment. These methods present a series of major disadvantages:

1) The low precision in indicating the moment of apparition of the evolution stage and of the achievement of the critical manifestation level of the structural degradation processes

2) The high costs in order to ensure the access of the surveillance staff in those parts of the structure of bridges

3) The long interval of time necessary between inspections and the adoption of the intervention decision in the case of signalization of the manifestation on the structure of major degradations that can severely affect the security and the functionality of the bridge

In order to ensure the viability of the state of bridges, Faculty of Civil Engineering and Building Services of the "Gheorghe Asachi" Technical University from Iasi has developed a research program with the main scope to develop a SHM system for durability assessment (Comisu et al. 2006). The system

must interface and integrate the actual practice mainly based on visual inspections and combine the response of a number of different reliable sensors, installed on the structure to monitor the severity of a structural damage, with enhanced realistic deterioration models. The SHM system is based on a network of sensors developed to cover the most important deterioration mechanisms: corrosion of reinforcement in bridges, carbonation of concrete, freeze-thaw cycles, alkali-silica reaction and mechanical damage, as well as the changes in the structures behavior and safety, static deformation, strains, crack widths and vibrations.

2 OBJECTIVES AND SCOPE

The program of health monitoring system of bridges network in Romania has the following objectives:

1) Improving the durability requests of bridge structures through the application of an integrated permanent and active monitoring system of the transportation substructure from Romania

2) The program of health monitoring system of bridges network must cover the most important deterioration mechanisms: corrosion of reinforcement in bridges, carbonation of concrete, freeze-thaw cycles, alkali-silica reaction and mechanical damage, as well as the changes in the structures behavior and safety: static deformation, strains; crack widths and vibrations (frequencies, amplitudes, accelerations and vibration modes)

3) The identification of the most relevant degradation processes and mechanisms, specific to the structure of the bridges

4) The projection of an active integrated monitoring system of bridges network in Romania. The experimental research program consists of the testing in lab and in situ, in order to calibrate, some specific sensors within the scope of monitoring the degradation mechanisms through corrosion, carbonation, critical displacements and deformations, vibrations (frequencies and amplitudes)

5) The projection of a data acquisition and transmission system to a central monitoring unity. The experimental program deals with the calibration, in lab and in situ, of the data acquisition and transmission system at the Faculty of Civil Engineering and Building Services within the "Gheorghe Asachi" Technical University from Iaşi

6) The projection of a data processing and analysis system. It will be created a soft dedicated to the processing and analysis of the acquired data. The experimental program consists of the calibration in a lab and in situ of the processing and analysis system of the data acquired in situ

7) The integration of the information obtained within the surveillance and revision works by a technical authorized staff (this system is being applied at the moment) with the data acquired from the sensors deposited on the monitored structure (the new proposed monitoring system). The validation of the integrated continuous monitoring system of the transportation substructure, and especially of the bridges structure

8) The possibility to adopt a decision in time. The dynamic testing process, of identification of the dynamic characteristics, of the 3D calculation model calibration, of comparison with the values calculated in the previous phase, and of starting the warning protocol, must develop in a precise and rapid succession. The decision of launching the warning and protection protocol of the bridge must be a precise, clear and detached process from any shade of human subjectivism

9) The optimized administration of the transportation substructure. The access from time to the data base, to a calibrated 3D calculation model, enables the diagnosis in time of the technical condition of the section from the transportation substructure, and especially of the specific bridge. The calculation model enables the identification of the degradation type, the position of the degradation on the structure, the severity of the process, so that it can be established precisely:

- The duration in which the bridge can still be exploited in the established security and comfort of the traffic conditions
- The type of the necessary reparation works (the material consumption, manual labor, machines
- The rational repartition of the financial resources

10) Turning efficient the flux of necessary information in order to adopt in time the decisions to effectuate the reparation and consolidation works, to optimize the maintenance and financial resources allocation strategies necessary in the field of transportation substructure

11) The application of an integrated active monitoring and structural identification system will offer in time a complete and precise picture of the technical condition of the transportation substructure, thus realizing an efficient work instrument in the management process

12) The extrapolation of the results achieved at national and international level (through internet, participation to conferences and profile symposiums, initiation of national and international collaboration programs) by correlating and systemizing the data achieved in the field of the bridges in synthesis works and application instructions for all the engineering constructions (tunnels, railways, roads, industrial and profile constructions)

3 ACTIVE HEALTH MINITORING SYSTEM

The bridges network in Romania will be equipped with a system of sensors which will permanently determine their technical condition, indicating the temperature, the humidity and implicitly the moment of the apparition of the white frost, the PH and also the corrosion state of the metal fitting and of the concrete, the condition of crack, of deformation, displacement and vibrations (frequent and amplitudes). This information will be transmitted through a wireless system to a center zone of monitoring, where they will be centralized, registered, processed, and analyzed with the help of dedicated software to this scope. The information regarding the temperature, the humidity, the apparition of the white frost, the PH, the degree of corrosion, the degree of cracking, the degree of deformation, the displacements and vibrations, will be visualized in a direct and continuous manner, in a real time and on monitors placed in the center zone monitoring, which will be placed at the beginning in a research lab from the Faculty of Civil Engineering and Building Services from Iaşi, the technical assistance will be ensured on the entire duration of the exploitation by the research collectives consisting of teachers, the students, those from the master and the doctoral candidate will be directly involved in this research program. The software used in order to analyze the monitored information will be equipped with a decisional protocol that will break out a warning signal in the moment in which the values of the monitored parameters will surpass a critical level established by the alert (Sousa et. al., 2016).

In order to be able to identify the critical line of alert and to make the warning signal, especially in the case of the bridges, the software has to have stocked in his memory for each parameter monitored the mathematic model of the specific degradation model and also the possibility to identify in a real time the progressive stage in which the degradation process manifests at the structural level. Within this scope, there has to be effectuated separately for each degradation process, theoretical and experimental studies that will be able to identify a correspondent mathematic model, the evolutionary manifestation process on the structure and the critical alert levels, and who's surpassing to displace the active monitoring protocol, of protecting by the application of the maintenance and/or reparations works of the degraded structure.

1) The active monitoring of the temperature parameters and the humidity allow the identification in a real time of the apparition moment of the fog and of the white frost on the road section or on the monitored bridge. The active monitoring of the process enables the fact that immediately after reaching the critical alert level, the protective protocol of the structure is tripped. In case of fog and white frost on the highway sections, the consequences are very severe, with numerous victims and very important material losses, so the protection protocol has to start in time and consists of releasing visual and sound signals in order to reduce the driving speed, to increase the distance between the vehicles, to direct quickly the police and SMURD towards the specific sector, to deviate the circulation towards local deviation variants, to put into function the bridges, a heating system installed in the dale that will remove the white frost from the bridge

2) The active monitoring of the PH enables the identification of the starting moment of the process of carbonating the concrete and also of structural fission followed by the corrosion of the resistance metal fitting. The active monitoring of the process allows that immediately after achieving the critical level of alert, a structure protection protocol starts, that can consist, according to the seriousness of the degradation process, of the preventive application of some current maintenance works, special reparation works that will ensure the structural protection by removing the degradation process from the structure

3) The active monitoring of the displacement condition enables the identification of the moment in which, under the action of the current duties from the traffic, or after the production of a special event (earthquake, floods followed by the erosion of the substructures, the modification of the route or of the bed trellis of the course bed crossed, accidents through hitting the construction materials, too heavy transportations, massive landslips, terrorists attacks, etc.) the arrow of the structure exceeds the admissible value (critical level of alert), and thus there is the danger of surpassing the capacity of the structure and of losing the structural stability, followed by the collapse of the bridge and thus In the case in which it is built on a highway, it will produce very severe consequences with numerous victims and important material losses. The active monitoring of the process of the displacement condition of a bridge built on a highway enables the application of a protection and administration crisis protocol, by directing rapidly the police and SMURD teams towards the affected sector, an imposition protocol of the restrictions regarding the speed and the weight, followed by the deviation of the circulation towards other routes.

The active monitoring processes of the temperature parameters and humidity, of the pH and of the displacement conditions, is permanently developed on the level of transportation substructure, following that on the monitors placed in the center regional of monitoring, the surveillance staff will be enabled to visualize these parameters continuously. The process of monitoring enables the starting, in the moment of surpassing, the critical alert levels, in time the active protection protocol of the monitored section.

Trough comparison with the permanent and continuous monitoring process of the parameters of

temperature, humidity, pH and arrows, the monitoring of the vibration parameters is applied periodically (frequencies, amplitudes and specific forms of vibrations) in an interval of maximum one year, and compulsory, after the production of some special events (earthquakes, floods followed by the erosion of the substructures, modification of the route or of the bed trellis of the crossed course bed, accidents caused by the percussion of the constructive elements, too heavy transportations, massive landslips, terrorists attacks, etc.) and consists of the dynamic testing of the bridge with the help of a series of apparatus of dynamic exercise, acquisition, processing and analysis (fig. 1), installed in a mobile lab which will be displaced periodically in the location of the bridge (Sousa et.al., 2013, Khoo et.al., 2004).

Monitoring the vibration parameters will be applied at the beginning of the bridge's exploitation, being considered as dynamic testing at T_0 time, and deals with the covering of the following 3 standard stages:

1) Exercising the bridge with an electrodynamics vibrator or through impact produced with the help of a special hammer

2) Identification of the dynamic characteristics (values and special vectors, amortization characteristics) with the help of electronic equipment used for data acquisition and of a calculation program dedicated to the modal analysis

3) Calibration of the 3D calculation model is realized in time and consists of a comparison between the dynamic characteristics obtained by testing dynamically the bridge, and the dynamic characteristics of a 3D calculation model of the tested bridge built with the help of a dedicated calculation program based on the finitely element method

The instruction process will be realized in the Bridge Tests Lab, one time only, on the occasion of the first modal testing, at the T_0 time, of the specific bridge. The calibration process deals with the modification in successive stages of the theoretical dynamic characteristic values, of the 3D model, until theses will coincide with those experimentally obtained, in situ, and considering that at the T_0 time the bridge presents a very good technical condition, and having a total index $I_{ST} > 80$ points.

The 3D calculation model thus calibrated at the T_0 time is stocked in the data base of the specific bridge, as a *"dynamic stamp"* of the bridge, at the T_0 time that will enable the *"dynamic identification"* of the specific structure.

Periodically, at an interval of maximum one year, and compulsory after the production of a series of special events (earthquakes, floods followed by the erosion of the substructures, accidents caused by the percussion of the constructive elements, too heavy transportations, massive landslips, terrorists attacks, etc.) the cycle consisting of 3 standard stages will repeat: exercising, identification of the dynamic characteristics and calibration of the model. All the subsequent calibrations of the 3D calculation model socked in the data base, will be made in successive steps, at T_i time and will consist of the modification both of the mechanical characteristics of the materials (because of the rheological processes of contraction and slow flowing of the concrete, relaxation and corrosion of the metal fitting, carbonation of the concrete) and of the modification of the structural geometrical characteristics (as an effect of the propagation of a fissure process, displacement, deformation or vibration of the structure) in relation with the calculation calibrated model from the previous test stage, at the Ti-1 time (Haritos et al., 2004).

The monitoring process continues in successive steps on the entire duration of exploitation of the bridge until, as a result of the modal analysis effectuated at a T_Z time, modifications with significant values of the dynamic characteristics will be identified, situation in which an active monitoring process will start, process which consist of the following stages:

1) The starting of a warning protocol produced by a modification with significant values of the dynamic "stamp" of the bridge and which indicates the presence on the monitored bridge of a structural degradation process

2) The identification of the type of degradation, its position on the structure and the degree of development of the degradation process, the place on the structure where it manifests and its seriousness is realized by calibrating the 3D calculation model stocked in the data base. The process bears the name of "structural identification" of the bridge

3) The starting of the protection protocol which consists of imposing a reduction of the speed and of the weight, of increasing the distance between vehicles, of closing certain circulation lines, of directing the firemen, the police, and of the SMURD teams towards the monitored bridge, and finishing with forbidding the circulation on the bridge and complete and precise indication of the duration of closure, of the possible deviation routes.

4 INTEGRATION OF THE PROCESS OF MONITORING AND IDENTIFICATION SYSTEM

After the calibration and the implementation of the active monitoring system and of the structural identification system in dynamic regime, at the level of the road section and according to the financial resources allocated and of the priority offered in the strategic plan of development at the national level, the integration process follows directed to two strategic axes of action:

At the knowledge extraction and decision-making supported by the SHM data stage, the following steps are covered (Fig. 1):

Step 1. Monitoring of the chemical parameters enables the identification of the appearance moment of the process of carbonating the concrete followed by the corrosion of the steel reinforcing roads (Swartz and al. 2009, Jang and al. 2002)

Step 2. Monitoring of the bridges enables the identification of the moment in which, under the action of the traffic, or after the production of a catastrophic event (earthquake, floods followed by the erosion of the substructures, terrorist's attacks, etc.), the deformation state of the bridge exceeds the admissible value, and achieves a critical level of alert

Step 3. By comparing with the permanent and continuous monitoring process of the physical and chemical parameters and structural deformations of bridge, the monitoring of the dynamic parameters is applied periodically (frequencies, amplitudes and specific forms of vibrations) in an interval of maximum one year and compulsory, after the production of some catastrophic events (earthquakes, floods followed by the erosion of the substructures, accidents caused by the percussion of the constructive elements, heavy transportations, terrorists attacks etc.)

Step 4. Each the dynamic testing of the bridge performed in situ is followed in the laboratory by a process of recalibration of 3D model of each bridge. If monitoring of the dynamic characteristics to the T_i step does not identify significant changes in the dynamic mark of the bridge from the T_{i-1} step, then the technical condition of the bridge is diagnosed as being "adequate"

Step 5. Monitoring process continues in successive steps on the entire duration of exploitation of the bridge until, as a result of the structural monitoring of the bridge, in T_z step, will be identified modifications with significant values of the dynamic characteristics in relation with the dynamic mark of the bridge from the T_{z-1} step (Karbhari and al. 2009)

The use of permanent monitoring systems has several advantages once the system is installed:

- A more reliable prediction of the progress of damage as a function both of the measured parameters and of the application of realistic deterioration models, as well as a better understanding of individual deterioration mechanisms and their interaction
- Traffic interference is reduced
- An input for defining maintenance and repair strategies (time and extent) as a function of the actual and foreseeable levels of deterioration
- The costs of access to the structure and resources for inspection and testing are reduced
- Structural elements with difficult access are easily monitored
- An evaluation of the need for further inspection and testing

5 CASE STUDY

The suspended bridge over an arm of the Danube River, has a length of 360 m, with three openings of 60+240+60 m (fig. 2). The bridge ensures the passage of light vehicles with a weight of up to 3.5 tons, on a single lane, with traffic light. The superstructure of bridge is hybrid, consisting of two sections of 70 m precompressed concrete panel and a 220 m metallic panel on the central opening.

They were executed precision measurements in 38 characteristic points, 19 upstream and 19 downstream, with a Leica Sprinter 150M digital level with a precision of 1.5 mm per 1 km measured. The topographical landmarks were installed on both sides of the bridge, both downstream and upstream. On the bridge abutment, two sections were measured to determine possible rotations. On the marginal openings, measurements were made in the bearing points and in the middle of the opening. On the central opening, were made measurements from the joining of the metal plate to the concrete one and continued from each third cable to the middle of the bridge.

5.1 *Precise level measurement*

Measurements were made of precision levelling in characteristic measuring points.

The points are fitted on both sides of the bridge from both downstream and upstream towards.

Abutments were measured on two sections to determine the possible rotations. The marginal openings were made measurements of end points and mid-span.

Were measured 38 points, 19 sections (19 upstream and 19 downstream).

5.2 *Dynamic characteristics of the suspended bridge*

To measure the dynamic characteristics of the suspended bridge, the Pulse model 3560B with the 7540A frame has been used, with 5 input channels and 1 output channel. The maximum measurement frequency is 25.6 kHz. To identify the values and eigenvectors, 6 piezoelectric accelerometers, model 4507B-002 Delta Tron, were mounted on each opening of the bridge.

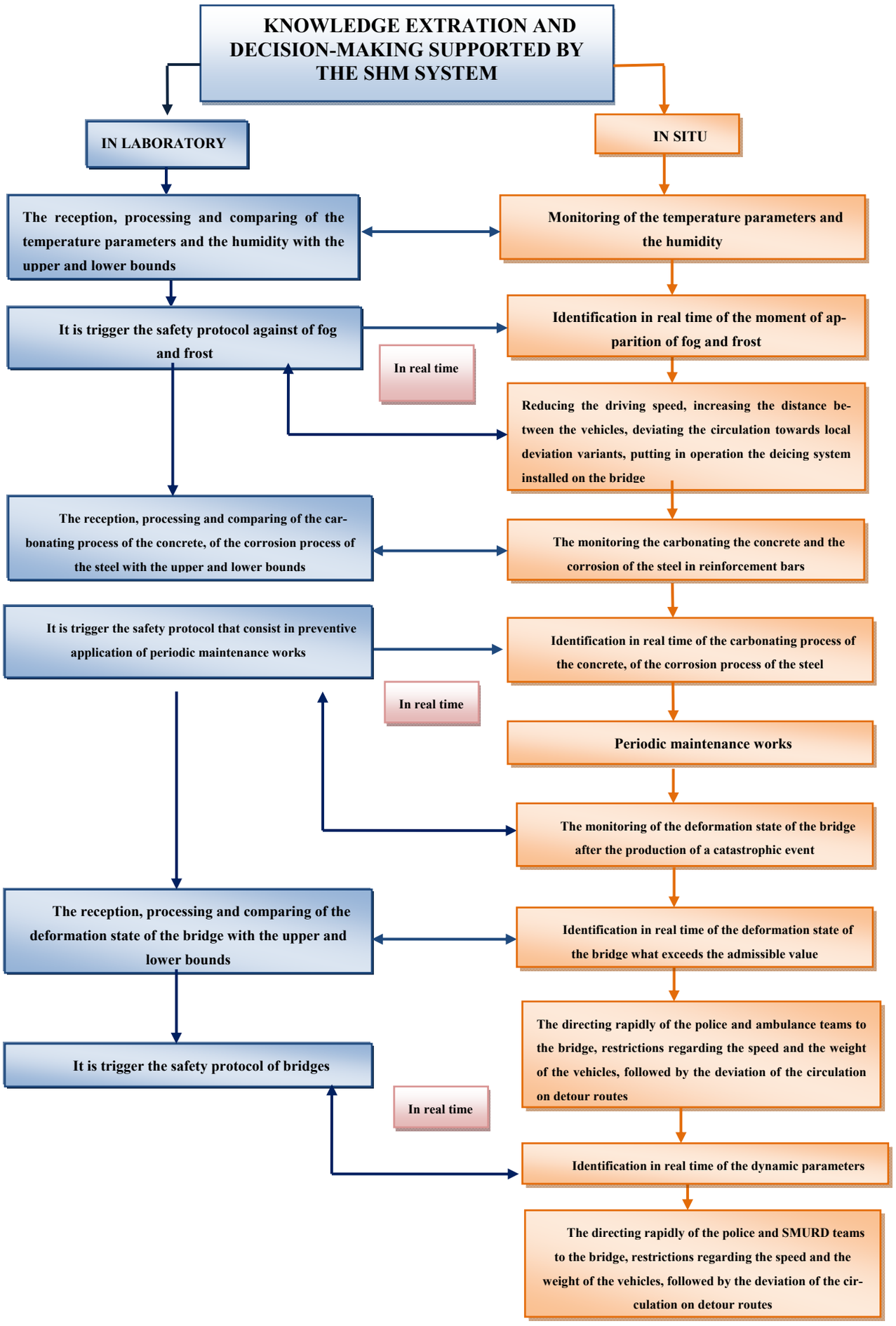


Fig. 1 – Knowledge extraction and decision-making supported by the SHM System

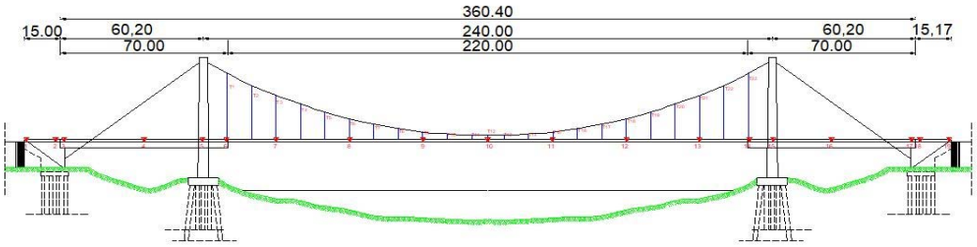


Fig. 2. Longitudinal lengths

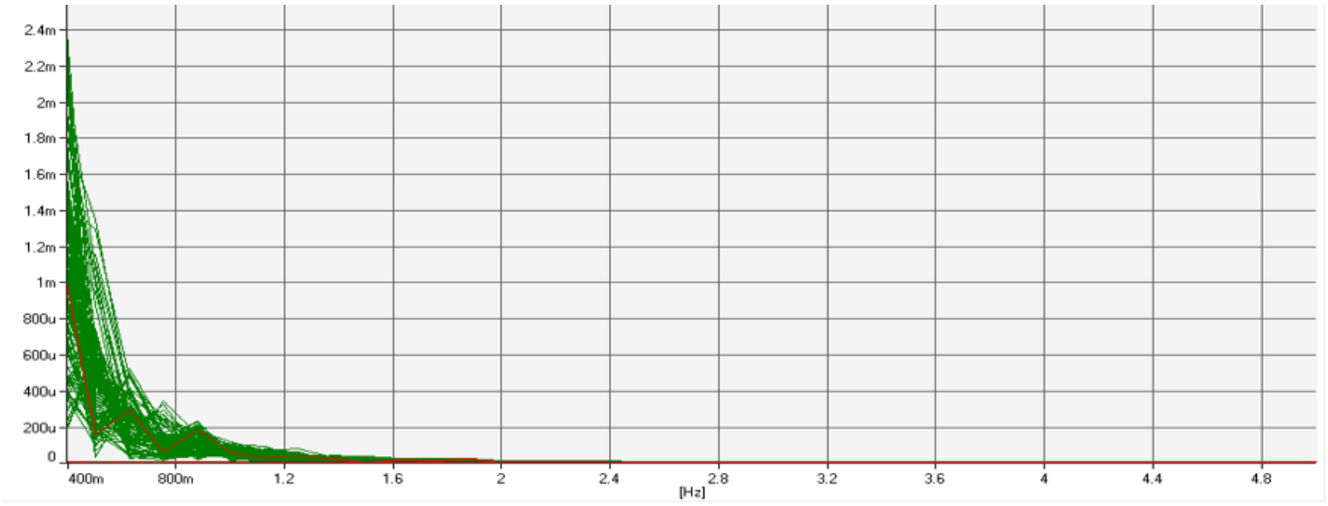


Fig. 4. Autospectrum (Signal 1) Working Measurement 2: Multi-buffer 1: FFT Analyzed

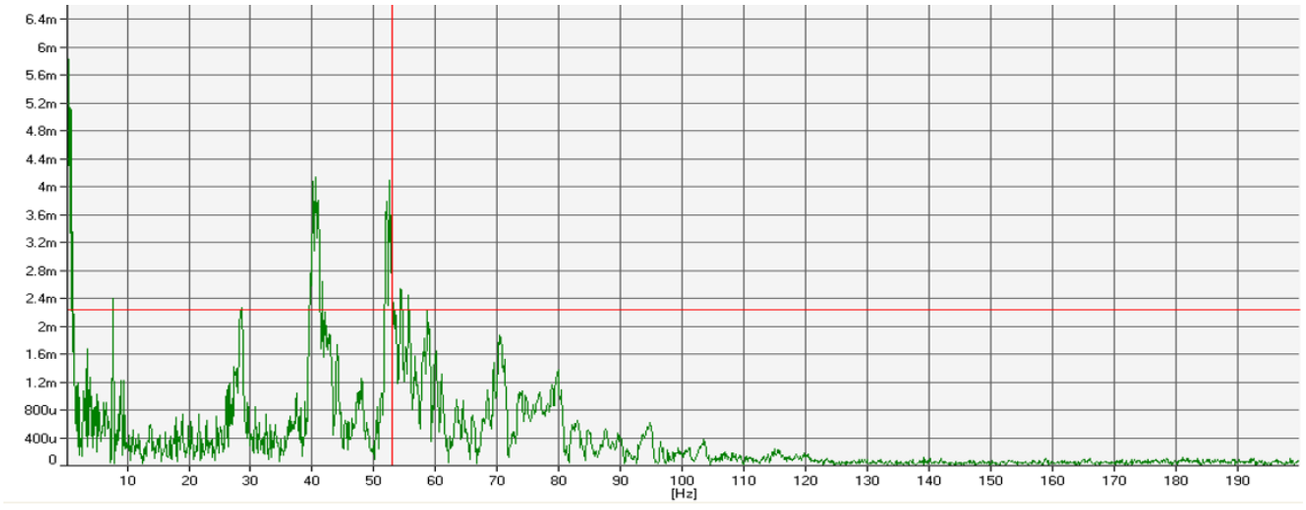


Fig. 5. Autospectrum (Signal 1) Working Measurement 2: Multi-buffer 1: FFT Analyzed

A total of 300 recordings were made at 400 ms.

The dynamic characteristics of the bridge were identified in the frequency domain, covering a range of 52.39 s.

The resolution in the frequency domain is 125 mHz and in the time domain in 1.953 ms.

Under the action of mobile loads of the road traffic on the bridge, the following response spectrum was recorded.

The first 10 frequencies were identified: 1.125 Hz, 1.5 Hz, 3 Hz, 7.625 Hz, 13.63 Hz, 16.13 Hz, 18.75 Hz, 28.38 Hz, 40.37 Hz, and 52.38 Hz (Fig. 5).

The fundamental frequency of the value was identified f_1=1.125 Hz.

By double integration of the previously obtained accelerations, the values of the vertical displacements are obtained.

The maximum dynamic range is 2.4 mm (Fig. 4).

5.3 *Conclusion of level measurements*

From the analysis of measurements performed, shows the following:

1) Improving the durability requests of bridge structure through the application of an integrated permanent and active monitoring system.

2) The identification of the most relevant degradation processes and mechanisms, specific to the structure of this bridge.

3) The projection of a data acquisition and transmission system to a central monitoring unity.

4) The projection of a data processing and analysis system. The experimental program consists of the calibration in a lab and in situ of the processing and analysis system of the data acquired in situ - suspended bridge over an arm of the Danube River.

5) The integration of the information obtained within the surveillance and revision works.

6 CONCLUSIONS

The aim of SHM system is the improved knowledge of the current state and long-term behavior of bridges in Romania. The monitoring system must integrate the actual practice mainly based on visual inspections and combines the response of a number of different reliable sensors, installed on the structure to monitor the progress of damage, with enhanced realistic deterioration models. The system and the sensors were developed to cover the parameters for the most important deterioration mechanisms: corrosion of reinforcement in bridges, carbonation of concrete, freeze-thaw cycles, alkali-silica reaction and mechanical damage, as well as the changes in the structures behavior and safety: static deformation, strains; crack widths and vibrations. In order to be able to identify the warning levels, the monitoring process must be equipped with a data base including mathematic models for each degradation process, and also an evaluative characteristic process of the latter.

In the moment in which the monitoring systems signals the surpassing of an alert level regarding a degradation process, the process of structural identification will begin. This process consists of the application of 3 successive phases: dynamical testing, identification of the dynamical characteristics and calibration of a 3D calculation model built from finite elements. The dynamic testing is realized by exercising the structure with the help of an electrodynamics vibrator or special impact hammer, according to the size and static scheme of the bridge. The testing enables the identification of the dynamic characteristics through modal analysis in the field of frequencies. The calibration of the calculation model enables the comparison of the value between the dynamic characteristics determined at the specific moment and the values determined at a previous time; the significant differences established between the values of the dynamic characteristics identified in different moments, indicate the presence on the monitored structure of a major degradation process. From this moment it begins the application of the structural identification process by calibrating the calculation model in order to enable the exact establishment both of the place in which the process of degradation manifests, and of the consequences over the monitored structure. According to the severity with which the process of degradation manifests over the element of the transportation structure, it starts a protection protocol which can impose speed and weight reductions, increasing the distance between vehicles, closing certain circulation lines, directing the firemen, the police of the SMURD teams, towards the monitored bridge, and finishing with closing the traffic on the bridge and the precise indication of the duration of closure, of the possible deviation routes and of the reparation and/or consolidation necessary works.

REFERENCES

Catbas Necati, Kijewski-Correa Tracy, Aktan Emin, 2013, Structural Identification of Constructed Systems. Approaches, methods and technologies for effective practice of ST-ID. American Society of Civil Engineering.

Comisu C.C. 2006. Mobile lab for dynamic testing and diagnosis of bridges for highways. Research program CEEX 309/2006, Faculty of Civil Engineering of Iasi - CNCSIS, Romania.

Haritos N., Qwen J. S. 2004. The Use of Vibration Data for Damage Detection in Bridges: A Comparison of System Identification and Pattern Recognition Approaches, *Structural Health Monitoring*, No. 3, 141.

Karbhari M. Vistasp, Lee L. S-W, 2009, Vibration-based damage detection techniques for structural health monitoring of civil infrastructure system, in Structural health monitoring of civil infrastructure systems. Woodhead Publishing Limited, Cambridge, UK, ISBN 978-1-84569-392-3.

Khoo L.M., Mantena P.R., Jadhav P. 2004. Structural Damage Assessment Using Vibration Modal Analysis. *Structural Health Monitoring*, No. 3, 177.

Malm, R., and Sundquist, H. (2010). "Time-dependent analyses of segmentally constructed balanced cantilever bridges." Eng. Struct., 32(4), 1038–1045.

Robertson, I. (2005). "Prediction of vertical deflections for a long-span prestressed concrete bridge structure." Eng. Struct., 27(12), 1820–1827.

Sousa, H., Cavadas, F., Henriques, A., Bento, J., Figueiras, J. (2013) Bridge deflection evaluation using strain and rotation measurements; Smart Structures & Systems 11(4): 365-386.

Sousa, H., Costa, B., Henriques, A., Bento, J., Figueiras, J. (2016) Assessment of traffic load events and structural effects on road bridges based on strain measurements, Journal of Civil Engineering and Management, 22(4): 457-469.

Swartz R.A., Lynch J.P., 2009, Wireless sensors and networks for structural health monitoring of civil infrastructure systems, in Structural health monitoring of civil infrastructure systems. Woodhead Publishing Limited, Cambridge, UK, ISBN 978-1-84569-392-3.

Maintenance, Safety, Risk, Management and Life-Cycle Performance of Bridges – Powers, Frangopol, Al-Mahaidi & Caprani (Eds)
© 2018 Taylor & Francis Group, London, ISBN 978-1-138-73045-8

Deformation Monitoring of a Simply Supported Railway Bridge under Varying Dynamic Loads

K. Faulkner, F. Huseynov, J. Brownjohn & Y. Xu
Vibration Engineering Section
University of Exeter, Exeter, UK

ABSTRACT: Structural health monitoring is a useful tool for evaluating the condition of bridges, with permanent systems installed on bridges which form vital links on the major transport network. The economic cost of the monitoring systems limits their installation on smaller bridges which make up the wider transport network. A short-term monitoring system can be quickly installed and adjusted to suit the requirements of individual bridges. These systems are ideal for rural regions with a high number of single span bridges on isolated road and rail networks. This report will review a single span bridge on a private heritage railway under loading from passing steam engines, including the Flying Scotsman. Acceleration data are used to determine the rotations and deflections of the bridge deck. To verify the data, deflection measurements at mid-span were recorded using a video-based measurement system. The deflection measurements from the accelerometers correlate with the video imagery measurements.

1 INTRODUCTION

1.1 *Bridge Failures*

Bridge failures pose a significant risk to human life but can also have a major economic impact on the affected regions. The collapse of the I-35 W bridge in Minnesota, US in 2007 killed 13 people and led to a loss of US$17 million in 2007 and US$43 million in 2008, excluding any of the indirect costs (Deng et al. 2015). Across Europe the infrastructure is ageing, with an estimate of 30% of bridges exceeding 100 years of age (Connolly et al. 2016). In the UK, a review of the railway infrastructure during the period of 1846 to 2013 by van Leeuwen & Lamb (2014) attributed 138 bridge and culvert failures to flooding alone. A more recent report identified that 25% of the 603,168 bridges in the United States are rated as deficient by the Federal Highways Agency (FHWA) (Elsaid & Seracino 2012). Elsaid & Seracino (2012) further reported that the American Association of State Highway and Transport Officials (AASHTO) identified in 2009 that 50% of the bridges in the US are over 40 years and without sufficient knowledge of their current condition. A detailed review of the causes and mechanisms of bridge failure was performed by Deng et al. (2015).

Structural health monitoring (SHM) of large multi-span bridges is becoming increasingly commonplace, with systems been retrofitted to older bridges and with complex data acquisition systems installed on new builds. A review of SHM techniques was carried out by Webb et al. (2014) who categorised SHM into five categories; (1) anomaly detection, (2) sensor deployment studies, (3) model validation, (4) threshold check and (5) damage detection. Sohn and Farrar (2001) further categorised damage detection into five categories, building on previous work performed by Rytter (1993): (1) identification of the presence of damage in a structure, (2) localisation of the damage, (3) identification of the type of damage, (4) quantification of the severity of the damage and (5) prediction of the remaining service life of the structure.

There is a recent trend towards damage detection, particularly towards identifying damage through a decrease in the natural stiffness of a structure. Brownjohn et al. (2011) reviewed vibration-based damage detection techniques, but determined that for damage detection, vibration-based methods are not suitable for all but the most severe cases of damage. This study will instead follow the form of a sensor deployment study, with the intention to measure a series of parameters to determine the performance of the bridge under varying loading conditions.

Predominantly SHM systems are installed on long span bridges, which are vital links on major

transport routes, due to the cost of both installing the instrumentation and also the processing cost required to correctly interpret the data. This study will focus on a short span bridge on a heritage railway, as the bridge is representative of a large number of the smaller bridges which make up the wider transport network across the country, particularly in rural areas. The aim is to eventually develop a system that can be easily transported between a number of bridges and can be quickly adapted to fit the testing requirements of each bridge.

2 WEST SOMERSET RAILWAY

The West Somerset Railway (WSR) is the longest heritage railway in England, with almost 23 miles of track servicing 10 stations. The railway, located in South West England, was opened in 1862 and was originally servicing villages between Taunton and Watchet. The service was further expanded in 1874 as far as Minehead.

The route was closed by National Rail in 1971 but re-opened in 1976 to service local routes with predominantly diesel locomotives. By 1986, the railway was operating as a heritage railway using mainly steam-powered locomotives, travelling between Bishops Lydeard and Minehead. The railway predominantly operates through the Spring to Autumn months, with additional special services in place throughout the year.

2.1 *Mineral Line Bridge*

The Mineral Line Bridge, located to the west of Watchet station, was originally designed to carry the route over the West Somerset Mineral Railway, which now operates as a bridleway open to the public. The bridge is a 14.8 m steel girder single span bridge, with two masonry abutments and with a single track running on it. The abutments are orientated with a skew angle of $60°$ to the main beams of the bridge.

The bridge was originally constructed in the 1870s of wrought iron plate girders, carrying a timber deck supporting the ballasted track bed. The abutments were constructed from stone. A comprehensive maintenance and repair programme to the bridge was carried out in 2011.

2.2 *Locomotives*

The service is predominantly serviced by steam-powered locomotives, but a small number of diesel continue to operate on the route. The largest and most powerful locomotive owned by the WSR is the Raveningham Hall, weighing 76.4 tonnes with a single axle load of 17 tonnes.

Table 1: Steam locomotive details

Locomotive	Year Built	Length [m]	Gross Weight [tonnes]
Flying Scotsman	1923	21.3	97.8
Raveningham Hall	1944	19.2	76.4
7F Class 2-8-0 53808	1925	17.9	65.8



Figure 1: Flying Scotsman locomotive passing over the Mineral Line bridge

Every year the National Railway Museum loans the Flying Scotsman locomotive for special tours across the country and in September 2017 the locomotive came to the WSR. The Flying Scotsman has a gross weight of 97.8 tonnes and a varying axle load of 4 to 11 tonnes. Table 1 presents an overview of all the steam locomotives used during the experiment. The weight indicated in Table 1 is the gross weight of the engine when full, but does not include the tender behind. The Flying Scotsman and Ravenington Hall are depicted in Figure 1 and 2, respectively.

The direction of travel for the train determined the position of the locomotive and the tender. In the Watchet to Minehead direction, the engine preceded the tender and on the return route the tender was at the front of the train. The orientation of the engine and the tender is summarised in Table 2. The times for the train are adjusted to the nearest 5 minute mark.

3 METHODOLOGY

There were two aims for this study:

1. to determine the rotation of the bridge deck under varied loading conditions;

2. to determine deflection at mid-span under the loading conditions.

3.1 *Rotation*

Inclinometers are the most common method used to measure the angle of rotation of an object, but can only be used to measure the rotation with respect to

Table 2: Locomotives passing on track

Train	Time	Locomotive	Direction	Locomotive Configuration	Number of Carriages
1	11:15	Raveningham Hall	BL - MN	Engine	8
2	12:00	Diesel	MN - BL	-	3
3	12:50	Flying Scotsman	MN - BL	Tender	8
4	13:40	Raveningham Hall	MN - BL	Tender	8
5	14:50	Flying Scotsman	BL - MN	Engine	8
6	15:30	7F Class 2-8-0 53808	MN - BL	Engine	7
7	16:10	Raveningham Hall	BL - MN	Engine	8
8	17:30	Flying Scotsman	MN - BL	Tender	8

Notes:
BL : Bishops Lydeard
MN : Minehead

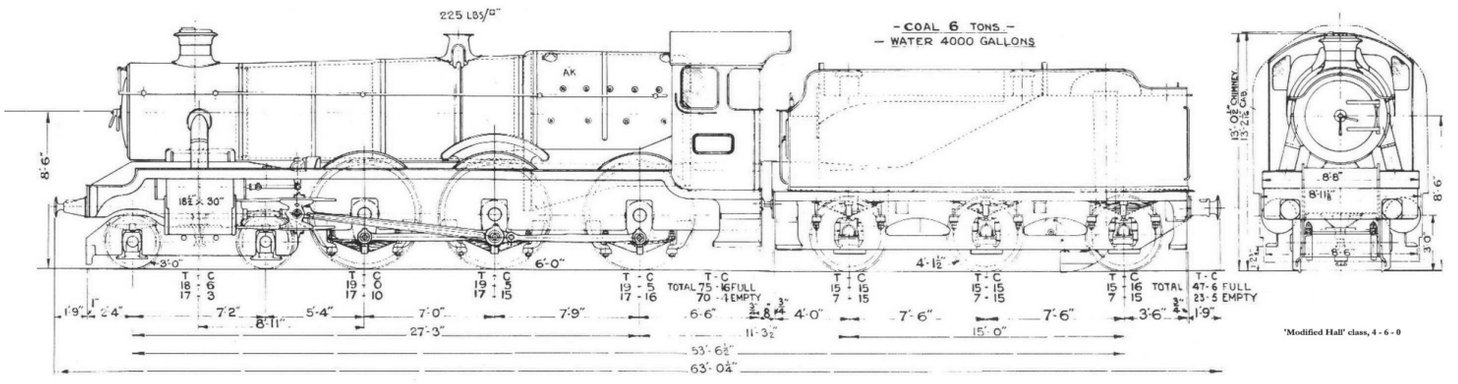


Figure 2: Schematics of the Raveningham Hall locomotive

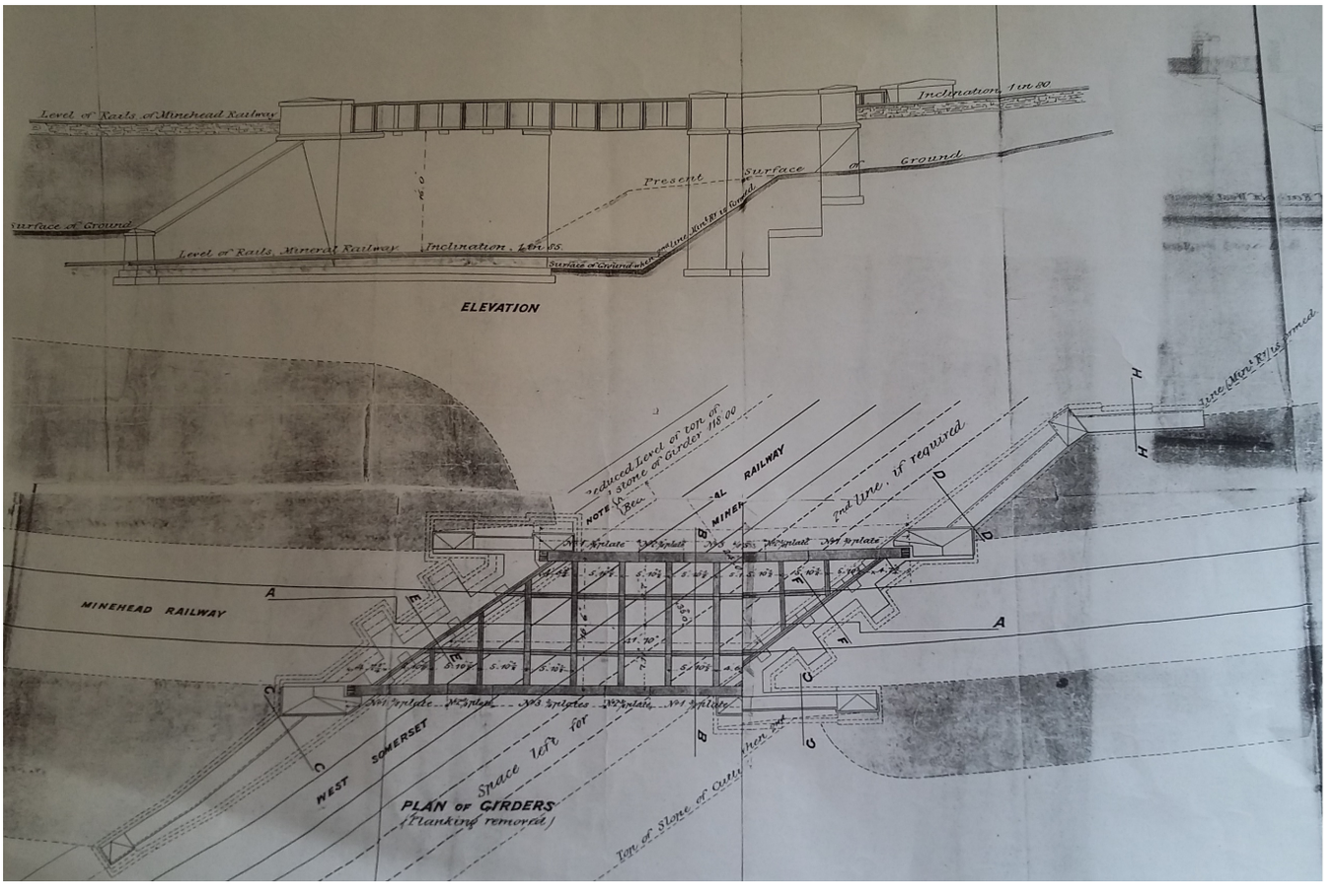


Figure 3: Plan and elevation of the Mineral Line bridge

gravity. Gyroscopes are frequently used in aerospace and navigational industries but have limited use in structural health monitoring to date. Sung et al. (2013) recommend gyroscopes as a method of refining damage detection techniques at hinged supports of bridges using the measured angular velocity.

For this study, accelerometers were used to define the angles of rotation in place of inclinometers. For this study, a single axis of acceleration was used to determine the angle of rotation. The rotation is determined by projecting the gravity vector on the axes of acceleration.

3.2 *Deflection*

The deflection of the bridge was determined using the accelerometers positioned in Figure 4 and confirmed against the deflections measured using Imetrum cameras. The following procedure for calculating deflection is derived from the method presented by Helmi et al. (2015).

Helmi et al. (2015) proposed a method of deflection calculation using accelerometer and strain gauges. The method can be used without strain gauges if a sufficient number of inclination sensors are installed on the bridge. With 5 test measurement points along the length of the 14.8 m bridge span, accelerometer data is sufficient to calculate the deflection for this testing scenario. Their method is reproduced in the following paragraphs.

The rotation along the beam is a measurable parameter and can be explained as a n^{th} order polynomial, expressed as

$$\varphi = a_1 x^n + a_2 x^{n-1} + \cdots + a_i x^{n-i+1} + \cdots + a_n x + a_{n+1} \quad (1)$$

where φ is the angle of rotation, x is the distance along the bridge and a_i is the polynomial coefficient.

Deflection, δ, at any point along the bridge can be determined from the following relationship:

$$\delta = \int \varphi dx \quad (2)$$

Therefore deflection can be calculated by integrating Equation 1:

$$\delta = \frac{a_1}{(n+1)} x^{n+1} + \frac{a_2}{n} x^n + \cdots + \frac{a_i}{n+2-i} x^{n+2-i} + \cdots + \frac{a_n}{2} x^2 + a_{n+1} x + a_{n+2} \quad (3)$$

If we consider one of the abutments as a reference point, with $x = 0$ and $\delta = 0$, then $a_{n+2} = 0$. Using this, we can simplify Equation 3 to

$$\delta = \frac{a_1}{(n+1)} x^{n+1} + \frac{a_2}{n} x^n + \cdots + \frac{a_i}{n+2-i} x^{n+2-i} + \cdots + \frac{a_n}{2} x^2 + a_{n+1} x \quad (4)$$

Using Equation 4, deflection at any point along the bridge can be determined if the polynomial coefficients are known, which is the main advantage of this method. The polynomial coefficients are determined from the following matrices, provided that rotation and deflections are known at $n+1$ or more points:

$$\begin{bmatrix} x_{\varphi 1}^n & x_{\phi 1}^{n-1} & \cdots & x_{\varphi 1} & 1 \\ \vdots & \vdots & \ddots & \vdots & \vdots \\ x_{\varphi i}^n & x_{\varphi i}^{n-1} & \cdots & x_{\varphi i} & 1 \\ \frac{x_{\delta 1}^{n+1}}{n+1} & \frac{x_{\delta 1}^n}{n} & \cdots & \frac{x_{\delta 1}^2}{2} & x_{\delta 1} \\ \vdots & \vdots & \ddots & \vdots & \vdots \\ \frac{x_{\delta k}^{n+1}}{n+1} & \frac{x_{\delta k}^n}{n} & \cdots & \frac{x_{\delta k}^2}{2} & x_{\delta k} \end{bmatrix} \begin{bmatrix} a_1 \\ a_2 \\ \vdots \\ a_n \\ a_{n+1} \end{bmatrix} = \begin{bmatrix} \varphi_1 \\ \vdots \\ \varphi_i \\ \delta_1 \\ \vdots \\ \delta_k \end{bmatrix} \quad (5)$$

4 TEST SET UP

In this section we summarise the equipment used during the testing and the sampling programme. Testing was performed on the 5th September 2017; the first day of the Flying Scotsman special tour on the WSR. The locomotive previously travelled the length of the track on the 29 August at reduced speed to confirm the clearances of the platforms and the bridges was sufficient for the locomotive but the passing of the Flying Scotsman on the 5th September was the first time the locomotive passed at full speed agreed for travel along the route.

The purpose of the study was to examine the Mineral Line Bridge under loading from a number of different locomotives, including the Raveningham Hall and the Flying Scotsman. Whilst all bridges and track along the WSR were analysed prior to the arrival of the Flying Scotsman locomotive, to ensure the WSR met the required capacity, this study measured the performance of the structure to confirm the review.

4.1 *Accelerometers*

A total of 11 single axis Honeywell QA750 inertial grade sensors accelerometers were installed on the bridge deck, with three accelerometers installed at quarter-span, mid-span and three quarter-span to measure the x, y and z channels. A single accelerometer was installed in the longitudinal (x) direction at



Figure 4: Layout of the accelerometers on the deck

each of the supports.

The accelerometers were positioned on the northern side of the bridge deck, with Test Point 1 located on the eastern abutment, increasing to Test Point 5 on the western abutment. The test layout is presented in Figure 4.

4.2 *Measurements with Video Imagery*

The Imetrum measuring system was developed by the University of Bristol to use image processing to accurately determine deflection and strain measurements in structures. The cameras are particularly useful for outdoor environments where it can be difficult to install measuring devices on large structures.

A total of three cameras were installed at site, with one camera positioned to measure deflection at mid-span on the bridge and two cameras positioned to measure deflections on the abutment. The measurements on the abutments are not considered as part of this study. The Imetrum camera layout is presented in Figure 5.

4.3 *Processing*

The data was analysed in MATLAB using the procedures outlined in Section 3. A low pass filter was applied to isolate the accelerations caused by the movement of the train. The data was further smoothed by applying a moving average filter.



Figure 5: Layout of the Imetrum cameras

4.4 *Test Procedure*

Rotation data was calculated from the accelerometers positioned in the horizontal axes. The deflection at mid-span was later determined using the rotation data obtained from the accelerometers and confirmed against the results of the Imetrum camera.

Data collection commenced before the train was due, to allow sufficient time to analyse the bridge under ambient loading before each test. As the exact arrival time at the bridge was not available, the data collection time before the train approached the bridge varied for each train. The running order of the trains and the direction of travel is recorded in Table 2.

Table 3: Measured Rotations

Train	Locomotive	Rotation [deg]
1	Raveningham Hall	0.093
2	Diesel	0.044
3	Flying Scotsman	0.098
4	Raveningham Hall	0.095
5	Flying Scotsman	0.099
6	7F Class 2-8-0 53808	0.081
7	Raveningham Hall	0.089
8	Flying Scotsman	0.108

4.5 *Environmental Considerations*

Weather conditions during the testing were varied throughout the day, with periods of heavy rain intermixed with periods of sunshine. As the sensors are not completely waterproof, a number of tests were performed with plastic bags on the sensors to protect the sensors from excessive rainfall. Whilst every effort is made to limit the amount of air in the bag and to reduce the possibility of buffeting, the bags can cause excess background noise during measurements. During the analysis of the results, the noise produced by the plastic bags was found to be negligible.

5 RESULTS

This section presents the measured rotations and deflections recorded during the aforementioned testing. For each steam locomotive, the measured rotation and deflection plots presents a clear peak for the locomotive followed by smaller peaks of equal amplitude representing the trailing carriages. Within the peak of the locomotive, it is also possible to determine the orientation of the tender and the engine, as the engine is responsible for the larger peak. The reduced diesel locomotive weight results in a measured rotations and displacements similar to the carriages behind.

5.1 *Rotation Data*

Rotation of the bridge under loading was calculated using the method proposed in Section 3.1. The maximum rotation of the bridge under loading from each locomotive is presented in Figure 6. The measured maximum rotation for each loading scenario is presented in Table 3.

Rotation was measured in the longitudinal direction. The maximum rotation was always measured at the abutment furthest away from the approaching trains for the steam engines.

The maximum rotation of $0.108°$ was recorded at Test Point 5, the western abutment, under loading from the Flying Scotsman (Train 8), with the other two passings of the train measuring a rotation of $0.098°$ to $0.099°$.

The Raveningham Hall displayed smaller rotations than the Flying Scotsman locomotive, with a maximum measured rotation of $0.095°$. Though the Raveningham Hall has a greater axle load than the Flying Scotsman, the heavier weight of the Flying Scotsman results in larger rotations.

Only a single measurement was recorded for the 7F Class 2-8-0 53808 steam engine. The maximum rotation measurement recorded for engine was $0.081°$, which was expected for the lighter engine. Following this trend, the maximum measured rotation for the diesel locomotive was significantly smaller, with a maximum deck rotation of $0.044°$.

The same carriages are used to form each train, but it can be seen that the rotations caused by the carriages following the Flying Scotsman are the highest. As each of the Flying Scotsman journeys were operating at full capacity, the increased rotations are likely to be a resultant of the increased live load of these carriages.

5.2 *Deflection Data*

Deflection was calculated at the mid-span of the bridge using the method proposed in Section 3.2. The maximum deflection calculated for each locomotive is presented in Figure 7, plotted against the measured deflections from the Imetrum data. The measured deflection at mid-span and quarter-span for each train is presented in Table 4.

The maximum deflection measured was 7.00 mm for Train 3, the Flying Scotsman. The higher deflection for Train 3 can be attributed to the train travelling at a faster speed during this passing of the train. The speed of the train was determined from determining the entry and exit times of the train on the bridge. Similar to the rotation measurements, the Raveningham Hall deflections measurements were marginally smaller, with a maximum measured deflection of 6.58 mm.

The correlation between the deflection measurements recorded for the Flying Scotsman and the Raveningham Hall indicate that the increased weight of the Flying Scotsman has a negligible effect on the bridge.

The deflection measurements for the carriages exhibit a similar trend to the rotation data, with increased deflections measured for the carriages following the Flying Scotsman locomotive.

Prior to the Flying Scotsman arriving to the railway, essential maintenance was carried out by the bridge owner to ensure the bridge was capable of carrying the increased size of the locomotive.

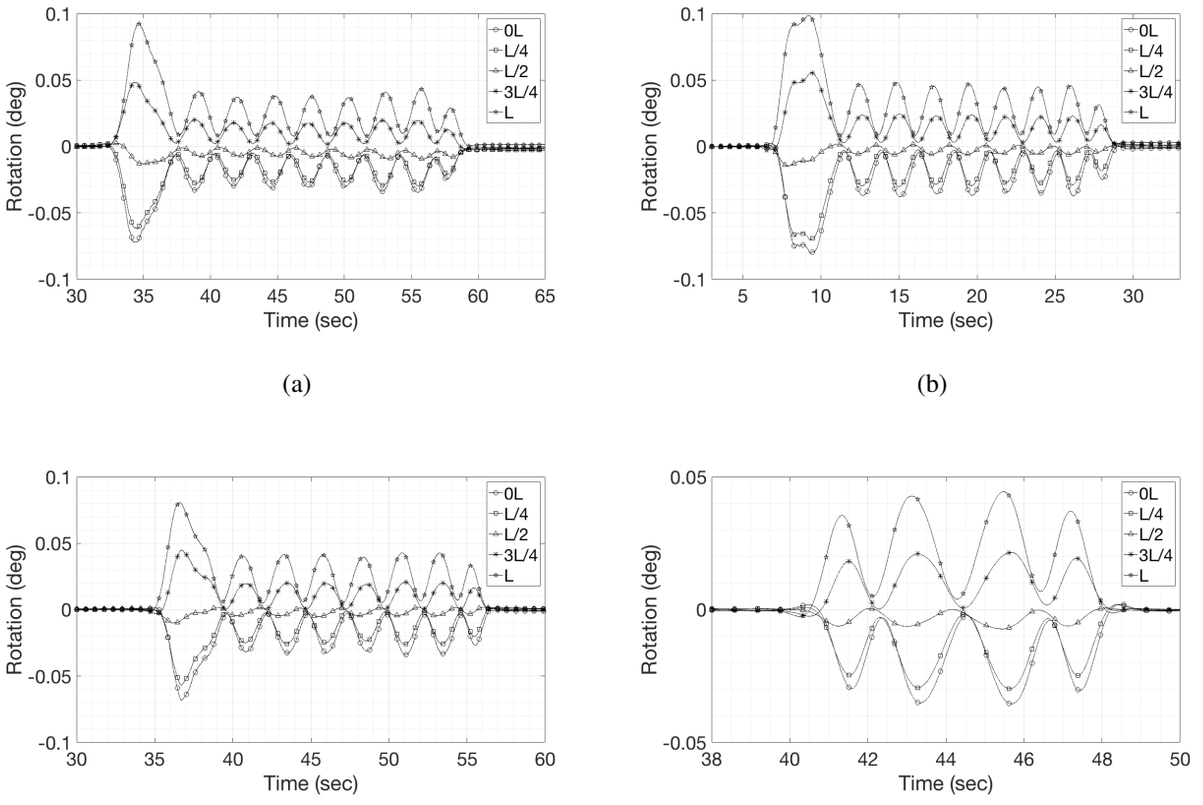


Figure 6: Rotations from accelerometer data under different train loads, (a) Raveningham Hall (Train 1), (b) Flying Scotsman (Train 3), (c) 7F Class 2-8-0 53808 (Train 6) and (d) Diesel (Train 2)

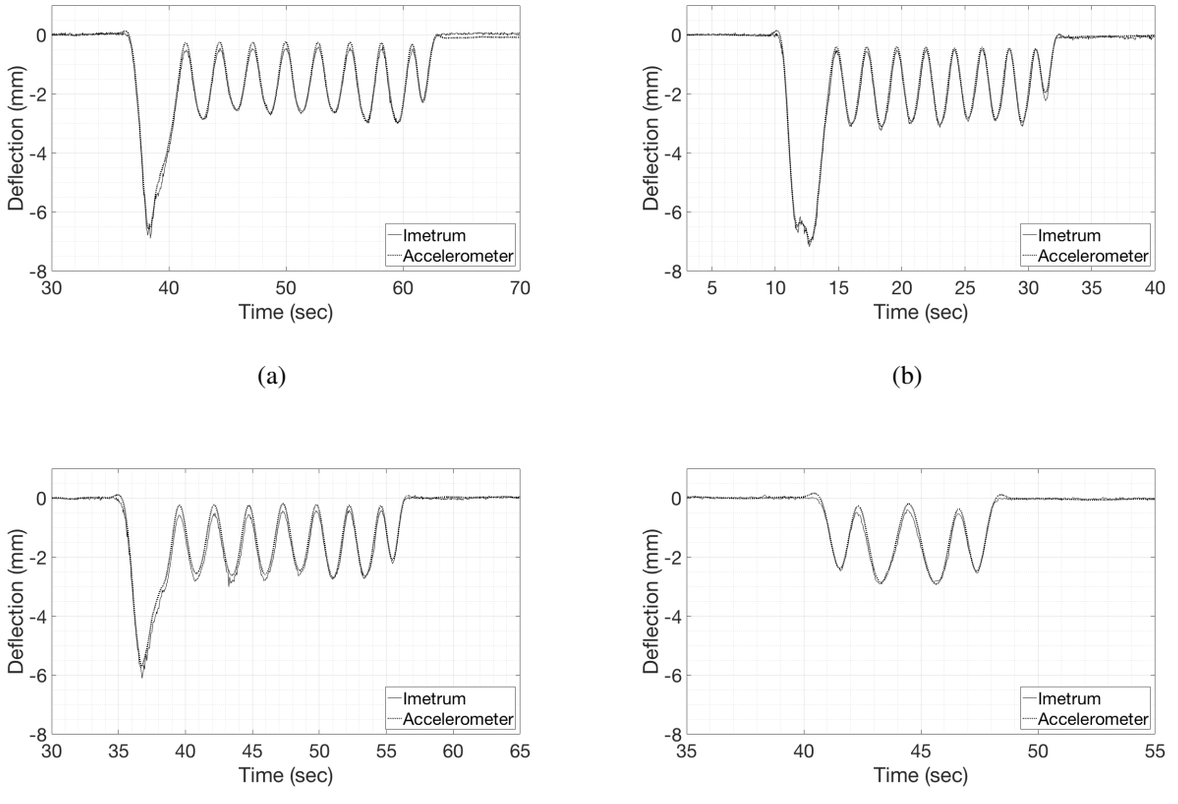


Figure 7: Deflections at mid-span under different train loads , (a) Raveningham Hall (Train 1), (b) Flying Scotsman (Train 3), (c) 7F Class 2-8-0 53808 (Train 6) and (d) Diesel (Train 2)

Table 4: Deflections calculated from measured rotations

Train	Locomotive	Deflection at Mid-Span [mm]
1	Raveningham Hall	6.58
2	Diesel	2.91
3	Flying Scotsman	7.00
4	Raveningham Hall	6.44
5	Flying Scotsman	6.63
6	7F Class 2-8-0 53808	5.70
7	Raveningham Hall	6.16
8	Flying Scotsman	6.80

The results of this study confirm that the bridge has sufficient capacity to carry heavier locomotives than the Raveningham Hall.

6 POTENTIAL FOR FURTHER WORK

The next aim for the study is to construct a stand-alone data monitoring system that is easily adaptable and transportable, to allow for monitoring of the wider transport network.

7 CONCLUSIONS

The purpose of this test was to establish how the Mineral Line bridge performs when subjected to different loading conditions, including the passing of the Flying Scotsman. Accelerometers were situated at five test points along the deck to measure deflections and rotations. The calculated deflection at mid-span was compared against measured deflections from the Imetrum camera positioned at mid-span of the bridge.

The results of the testing showed that the bridge experiences greater magnitude of deflections and rotations under the Flying Scotsman locomotive to those experienced through passage of the other locomotives. The diesel engine, which was the lightest of all the engines, resulted in the lowest measured deflections and rotations.

The correlation between the deflection measured by the Imetrum camera and the deflection calculated using the technique proposed here proves that a small number of accelerometers are sufficient to determine the performance of a bridge under train loading.

8 ACKNOWLDGEMENTS

The team would like to acknowledge the continued support of the West Somerset Railway, particularly David Depoix and Andrew Young.

REFERENCES

Brownjohn, J. M. W., A. De Stefano, Y.-L. Xu, H. Wenzel, & A. E. Aktan (2011). Vibration-Based Monitoring of Civil Infrastructure: Challenges and Successes. *Journal of Civil Structural Health Monitoring 1*(3-4), 79–95.

Connolly, L., A. O. Connor, C. Leahy, & C. Bowe (2016). Monitoring and Maintenance of the Boyne Viaduct. In *Civil Engineering Research in Ireland 2016 (CERI2016)*, Volume 1.

Deng, L., W. Wang, & Y. Yang (2015). State-of-the-Art Review on the Causes and Mechanisms of Bridge Collapse. *Journal of Performance of Constructed Facilities 30*(2).

Elsaid, A. & R. Seracino (2012). Vibration Based Damage Detections of Scour in Coastal Bridges. *Homeland Security Affairs, Supplement 4, Article 2*.

Helmi, K., T. Taylor, A. Zarafshan, & F. Ansari (2015). Reference free method for real time monitoring of bridge deflections. *Engineering Structures 103*, 116–124.

Rytter, A. (1993). *Vibrational Based Inspection of Civil Engineering Structures*. Ph. D. thesis, Aalborg University.

Sohn, H. & C. R. Farrar (2001). Damage Diagnosis using Time Series Analysis of Vibration signals. *Smart Materials and Structures 10*(3), 446–451.

Sung, S. H., J. W. Park, T. Nagayama, & H. J. Jung (2013). A multi-scale sensing and diagnosis system combining accelerometers and gyroscopes for bridge health monitoring. *Smart Materials and Structures 23*(1), 015005.

van Leeuwen, Z. & R. Lamb (2014). Flood and Scour Related Failure Incidents at Railway Assets Between 1846 and 2013. Project W13-4224. *JBA Trust 30*.

Webb, G. T., P. J. Vardanega, & C. R. Middleton (2014). Categories of SHM Deployments: Technologies and Capabilities. *Journal of Bridge Engineering 20*(11).

Maintenance, Safety, Risk, Management and Life-Cycle Performance of Bridges – Powers, Frangopol, Al-Mahaidi & Caprani (Eds)
© 2018 Taylor & Francis Group, London, ISBN 978-1-138-73045-8

DIC-monitoring of full-scale concrete bridge using high-resolution wide-angle lens camera

P.S. Halding, J.W. Schmidt & C.O. Christensen
Technical University of Denmark, Kgs. Lyngby, Denmark

ABSTRACT: Monitoring in combination with proof- and high magnitude load testing can evaluate potentially higher load carrying capacities in existing bridges. However, such in-situ testing provides challenges like limited test-time, difficult calibration under in-situ conditions etc. Consequently, in-situ load-testing significantly amplifies the requirements to monitoring. This paper focuses on results from in-situ DIC-monitoring. The method was used to evaluate deformations- and crack initiation on large concrete bridge surfaces during high magnitude load-testing. DIC-measurements are very susceptible to light, surface texture and contrast, etc. Laboratory testing and preliminary site inspections were done to investigate the measurement conditions. Monitoring was executed with conventional- and wide-angle lens DSLR-cameras positioned underneath the bridge, measuring vertically to the surface. The 2D output from the DIC-software was corrected for wide-angle lens distortions and out-of-plane deflections. The method seems desirable for a more generic use, and has potential for the evaluation of stop criteria.

1 INTRODUCTION

An extensive amount of monitoring approaches have been used during the last decades as a mean to evaluate the structural behavior of in-situ bridge structures in service or during load testing. Monitoring during load testing can be divided into at least two different groups depending on the project scope:

1) *Proof loading*, which includes loading of the structure within the elastic structural domain to demonstrate a certain behavior or capacity. The method is used in a way, which prevent significant damages on bridge structures, and thus enables the structure to remain in service after the load testing.
2) *Failure loading*, where high magnitude load is applied to the bridge to evaluate the response until structural damage have occurred. This enables evaluation of the full structural response, and thus evaluation of boundary conditions, failure modes, crack initiation etc.

Load to failure in conjunction with monitoring can be utilized to more precisely determine stop criteria for future proof load tests of similar bridge types mostly supported by related calibration of theoretical- and FE-models and optimization of probabilistic models.

One promising method for monitoring of concrete bridges during load testing is Digital Image Correlation (DIC), where the concrete surface is photographed before and during loading, and the digital images are analyzed in a computer software to determine deformations- and related strains. This paper presents a novel DIC-monitoring method used on a full-scale In-situ concrete bridge as well as bridge sub-components with wide-angle lens during loading into the failure regime.

1.1 *Digital Image Correlation*

DIC can be seen as an extended version of photogrammetry, and the original technological basis is explained by several researcher (e.g. (Sutton *et al.* (1983) and Bruck *et al.* (1989)). Small subsets (of a predetermined pixel size $X \cdot X$) on digital photographs are analyzed by determining a normalized cross-correlation coefficient, S, based on the image grey level from undeformed, I_u, to deformed shape, I_d:

$$S\left(x, y, u_x, u_y, \frac{\partial u_x}{\partial x}, \frac{\partial u_x}{\partial y}, \frac{\partial u_y}{\partial x}, \frac{\partial u_y}{\partial y}\right) = 1 - \frac{\sum I_u(x,y) I_d(x^*, y^*)}{\sqrt{\sum I_u(x,y)^2 \sum I_d(x^*, y^*)^2}} \quad (1)$$

The parameters, x and y, are coordinates to a point in the undeformed subset, and x^* and y^* are the coordinates of the same point in the subset after translation and deformation:

$$x^* = x + u_x + \frac{\partial u_x}{\partial x}\Delta x + \frac{\partial u_x}{\partial y}\Delta y \quad (2)$$

$$y^* = y + u_y + \frac{\partial u_y}{\partial x}\Delta x + \frac{\partial u_y}{\partial y}\Delta y \quad (3)$$

Δx and Δy are directional components from the center of the subset to a point (x,y) in the subset, see Figure 1.

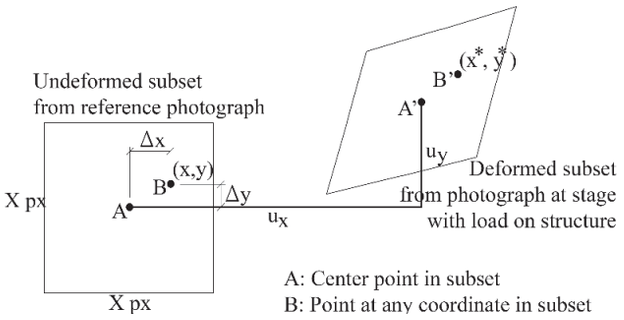


Figure 1: Terminology of undeformed and deformed subsets. Based on figure from Yoneyama & Morimoto (2003).

The displacement from A to A', and B to B' are found by searching for the best displacements and displacement gradients, which minimize the correlation coefficient. This can be done by different approaches such as Newton-Rapson method and Fourier transform (Yoneyama & Morimoto (2003)).

1.1.1 *DIC precision estimates*

Since the grey scale of the photograph is of significant importance for the computation of deflection and strain on surfaces measured by DIC-systems, the surface must have a random pattern of high contrast for DIC software to distinguish the subsets the best way possible. There seem to be no general guidelines or consistent advises available in the literature in regards to pattern types, subset sizes etc. for tests on real structures.

Bornert *et al.* (2009) evaluated DIC errors of digitally deformed computer generated "synthetic" patterns, but they do not apply the results in relation to measurements on real structures, where the type of camera, texture of the surface etc. has a major influence. Fazzini *et al.* (2010) and Wang *et al.* (2011) did similar studies but with actual photographed random patterns manipulated digitally.

Wang et al. showed results for three types of pattern fineness, and there was a relation between pattern fineness, and measurement precision, where a finer pattern showed a better measurement accuracy.

Lecompte *et al.* (2006) reached this conclusion as well with a similar type of experiment. They investigated three sizes of random patterns (mean speckle diameter in pixels: 3, 10 and >10) to conclude that the chosen size of the subsets had to relate to the fineness of the pattern. Best results were detected for small subsets of 13x13 pixels for the fine pattern, and larger subsets of 33x33 pixels for the rough pattern. Furthermore, they realized that the results were only valid for the specific case, and that more systematic research must be conducted for general verification.

Triconnet *et al.* (2009) did experiments with DIC on steel specimens and compared to strain gage data. The focus was on texture influence on the precision and showed a tendency for decreasing uncertainty on strain measurements as the subset size increased.

1.1.2 *DIC in bridge load tests*

For evaluation during actual bridge load testing, DIC-methods have rarely been applied (Yoneyama *et al.* (2007), Tian *et al.* (2013), McCormick, Waterfall & Owens (2014) and Shan *et al.* (2016)).

To the knowledge of the authors, only Yoneyama et al. (2007) and McCormick, Waterfall & Owens (2014) have applied DIC on a larger surface on the side of concrete bridges. McCormick, Waterfall & Owens describe how no random pattern was applied to the surface, and how they still measured both deflections and strains (including crack initiation). Furthermore, they claim that usually, the type of interpolation performed in typical DIC-software gives a precision of between 1/20 and 1/10 pixel.

1.2 *New project with field monitoring*

A new bridge testing project was initiated 2016 in Denmark. The project includes full-scale testing of existing short span (up to 12 m) concrete road bridges (mainly so called "OT-beam bridges") with a novel test rig to apply a high magnitude load in conjunction with conventional- and state-of-the-art monitoring methods. A DIC-system was so far applied to two out of a range of bridges tested in 2016 and 2017. This paper focuses mainly on the method and evaluation of DIC-monitoring during load testing of an in-situ tested bridge in 2017. The project was initiated as a collaboration between the Danish Road Directorate, COWI Denmark, and the Technical University of Denmark.

2 APPLIED DIC-SYSTEM

2.1 *Equipment*

Two DSLR cameras were used: A Canon 6d with a wide-angle lens (Canon EF 16-35mm f/2.8L II USM), to achieve a very large surface for evaluation, and a Canon 550d with a standard lens (Canon EF-S 18-55 IS). Canon 6d had the option of wifi-image transfer. Both cameras were mounted on a tripod pointing perpendicular to the concrete on the bottom surface of the bridge deck. However, this paper only includes results from the wide-angle lens camera in order to elaborate on the novel use- and results gained when using it for DIC-measurements.

The DIC-software used for the photograph analysis was GOM Correlate Professional (2016).

2.2 *Calibration of wide angle lens camera*

It is necessary to correct the direct output from the photographs if strains or in-plane deflections are the purpose of the 2D-analysis. If this is not done, the output deviates from the true deformation values due to non-perpendicular angles from camera to surface, lens distortion of the camera optics, and out-of-plane deflections of the surface (3D-behavior).

2.2.1 *Correction of non-perpendicular angles*

A correction of direct deflection output from DIC-analysis requires information about the camera lens optics. However, it is possible to analytically estimate the level of in-plane deflection correction based on the following method.

Figure 2 shows some of the parameters required for a manual calibration.

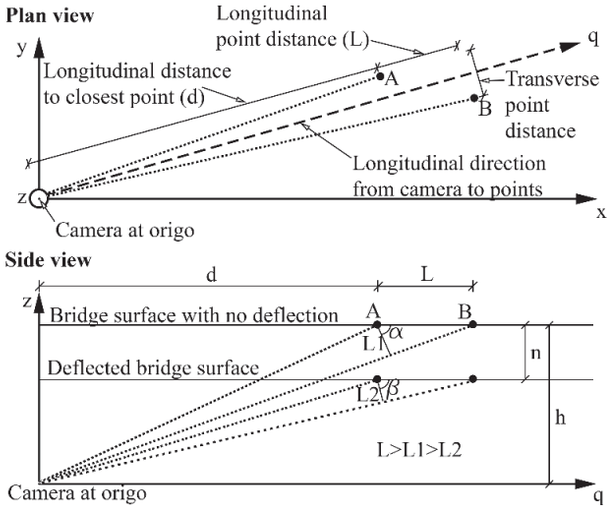


Figure 2: Plan- and side view of points on bridge surface (for strain analysis) and with camera positioned in (0;0;0) pointing in z-direction.

The plan- and side view show two lines from the position of the camera in origo to each of the two points A and B on the underneath surface of the bridge. The in-plane deflection is to be corrected in the direction between the two points. The horizontal distance to the closest point, d, in the longitudinal direction, q, is shown as well as the longitudinal distance between the points, L. L is assumed very small and hence, the triangle with side lengths L and L1, and the corner angle, α, is right-angled. The vertical height (z-direction) from camera to surface is denoted, h, while the downwards deflection of the surface during loading is, n.

2D DIC is typically based on the analysed (small) object being perpendicular to the viewing direction of the camera. When the skew angle on a bigger analysed surface is large in the sides (even more pronounced with wide-angle lens), the deflection output starts deviating from the true value.

When analysing the deflection between points A and B in the figure, the x and y coordinate of the closest point, A, projected to the q-axis is called dx and dy.

$$L1 = L\cos(\alpha) \tag{4}$$

$$\alpha = \operatorname{atan}\left(\frac{\sqrt{dx^2 + dy^2}}{h}\right) \tag{5}$$

$$\text{since } \cos(\operatorname{atan}(x)) = \frac{1}{\sqrt{1 + x^2}} \tag{6}$$

$$L1 = \frac{L}{\sqrt{1 + \left(\frac{\sqrt{dx^2 + dy^2}}{h}\right)^2}} = \frac{L}{\sqrt{1 + \frac{dx^2 + dy^2}{h^2}}} \tag{7}$$

The denominator of L1 (7) is a correction factor to the deflections in the longitudinal direction from camera to the measured points without any out-of-plane deflections occurring (only due to the non-perpendicular angle). The same method applies for L2 (including surface deflection measured by another monitoring instrument during testing) for the triangle L, L2 and angle β, and gives:

$$L2 = \frac{L}{\sqrt{1 + \left(\frac{\sqrt{dx^2 + dy^2}}{h - n}\right)^2}} = \frac{L}{\sqrt{1 + \frac{dx^2 + dy^2}{(h - n)^2}}} \tag{8}$$

The denominator of (8) also takes into account the correction from the extra change in angle due to the out-of-plane surface deflection.

The correction of transverse in-plane deflections between A and B due to a non-perpendicular angle can be estimated as well, but is highly dependent on the camera lens optics. Therefore, a method based on an automatic lens distortion correction is preferable.

Surface strains are not affected by a non-perpendicular angle, since they are determined relative to a length.

2.2.2 *Wide-angle lens distortion*

Applying a wide-angle lens distorts the photographs. This challenge can be overcome by applying an automatic algorithm from Adobe Photoshop (2015), where corrections for a range of different lenses can be applied. The correctness of this method was lab-tested for practical use by capturing photographs of a white surface with a pattern of black squares of 0.1 m.

Figure 3 shows such photograph before and after the lens distortion correction. The unbroken lines are the actual photographed lines of the square pattern, while the dashed lines form an overlay of a geometrically correct pattern. Before the lens correction, the difference between the photographed and the correct patterns is significant, especially near the edges of the image. After the correction, the two patterns are alike. Utilizing this method for correction of lens distortion eliminates the requirement for a manual alteration of deflections due to non-perpendicular angles between camera and surface. The only additional correction of the output now comes down to the out-of-plane deflection of the surface during testing.

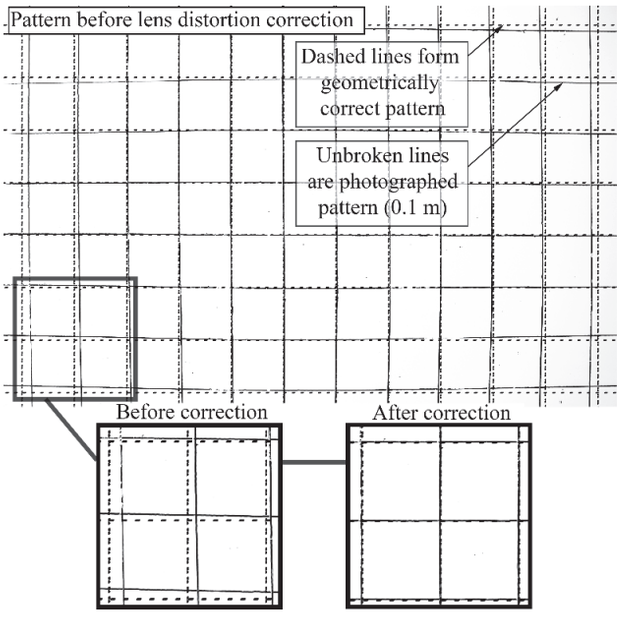


Figure 3: Correction of lens distortion by Photoshop algorithm for the specific wide-angle lens.

2.2.3 *Out-of-plane deflection correction*

When applying DIC in 2D, the assumption is that the distance between camera and surface is constant, which is not the case in the specific bridge tests. The monitored surface deflects out-of-plane, and these deflections must therefore be closely monitored by e.g. lasers or LVDT's for the method to be applicable. Even relatively small deflections can have a large consequence on strain readings, so the correctness of deflection measurements is crucial for the method to work.

The idea behind the out-of-plane deflection correction is depicted in Figure 4.

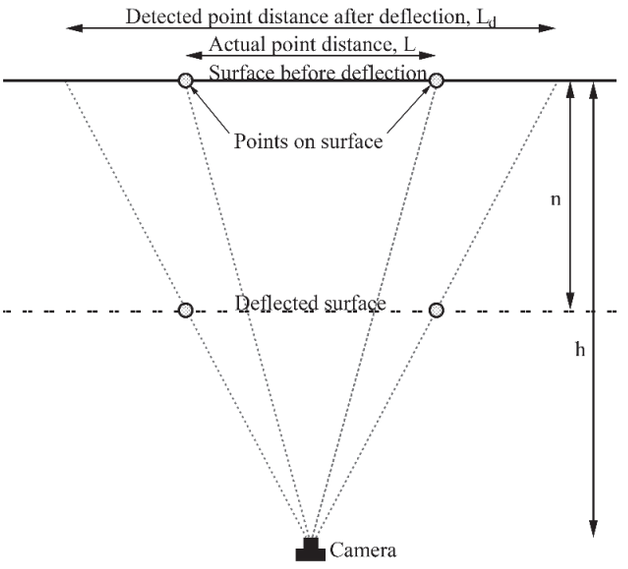


Figure 4: Out-of-plane deflection correction

If the distance from the camera to the surface of the bridge, h, is reduced by the deflection, n, towards the camera, the actual distance between two points on the surface, L, will be detected larger than it is, L_d. By trigonometry the relation between the detected, and actual point distance is:

$$L_d = \frac{L \cdot h}{h - n} \tag{9}$$

The strain alteration from out-of-plane deflection is then determined by:

$$\varepsilon_{oop} = \frac{h}{h - n} - 1 \tag{10}$$

In case of a small deflection compared to the camera to surface distance, the relationship between deflection and altered strain is close to linear. For a deflection of 10 mm for a camera to surface distance of 4 m, the level of strain alteration is 0.25 %.

3 DIC-MONITORED LOAD TESTS

3.1 *Laboratory sub-component testing*

Five double-beams were cut out of an actual bridge (in good condition) for sub-component laboratory testing with DIC. The beam type was similar to that of the in-situ load tested bridge: Overturned T-beams (OT-beams). An additional double-beam was cut out for coupon testing of material properties.

3.1.1 *Test setup*

The load testing was performed as a four-point bending to failure of the components at a rate of 1.7 mm/min. The distance between the loading points for the four-point bending setup was 1.4 m, which is similar to typical axel distances of heavy special vehicles

in the Danish regulations (Danish Road Directorate (2009)). The supports were hinged, and the span was 5.3 m. The setup, as well as the position of the DIC, LVDT's, and strain gages are seen in Figure 5. Three DIC cameras were individually applied to three ranges of the front surface, each at a distance of approximately 1 m. Measuring on the beam side surface meant that no out-of-plane deflections would occur.

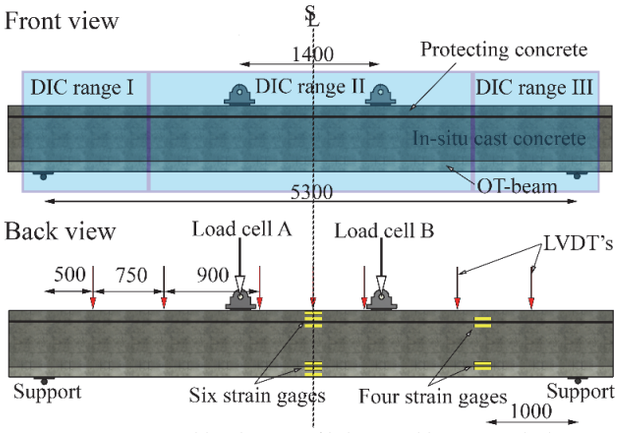


Figure 5: Front and back view of lab-tested beams including position of monitoring equipment. Unit is mm.

Consequently, only lens distortion corrections had to be done. Range II was covered by the wide-angle lens camera, and is the part that is evaluated in this paper. A high-contrast random pattern was applied to the surface of each specimen.

A cross-section of the cut-out beams are shown in Figure 6. The beams consisted of pre-fabricated OT-beams with tested concrete cylinder mean strength of 72 MPa. The in-situ cast concrete above and in-between the beams had a tested mean strength of 41 MPa, which was the same as the protecting concrete layer on top of the beam. A thin membrane of bitumen was applied between the protecting concrete and in-situ cast concrete. The 7 mm in diameter pre-tensioning strands had a 5-percentile strength of 1800 MPa.

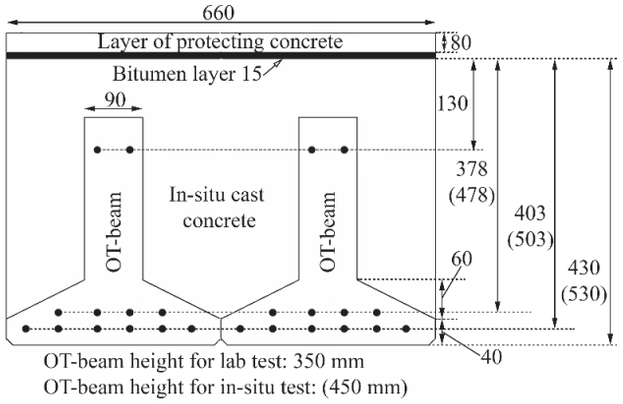


Figure 6: Cross-section of bridge for lab-tests and in-situ tests. Unit is mm.

3.1.2 *Results and evaluation of lab-test*

The lab test showed that the DIC-system could be utilized in detecting cracks on concrete surfaces during load testing with the wide-angle lens camera. Deflection/load-curves from the tested beams are shown with positions of crack detection in Figure 7.

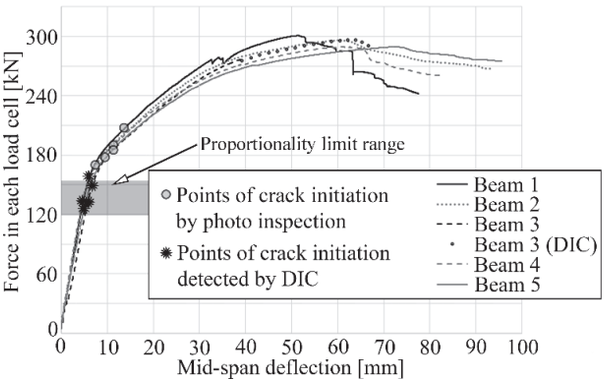


Figure 7: Deflection/load-curves of tested double OT-beams in lab.

Even by thorough inspection of the photographs, the cracks were not detectable until beyond the actual proportionality limit of the load/deflection-curves. When detecting cracks by the DIC-equipment, they were identified in close proximity of the proportionality limit. Furthermore, the applied 50 mm strain gages on the back surface of the specimens (measuring longitudinal strains), verified the DIC-readings of the time of crack initiation. Foil strain gages are not designed for detecting exact crack initiation in tension, and the output was not significantly scattered, but the precision depended on the exact position (in average within 11 % of DIC-measurements).

In Figure 8, an example output from the Beam 5 DIC-evaluation is shown for the point of crack initiation by photograph inspection (183 kN load), and for maximum load (289 kN). The crack initiation load detected by DIC was 128 kN.

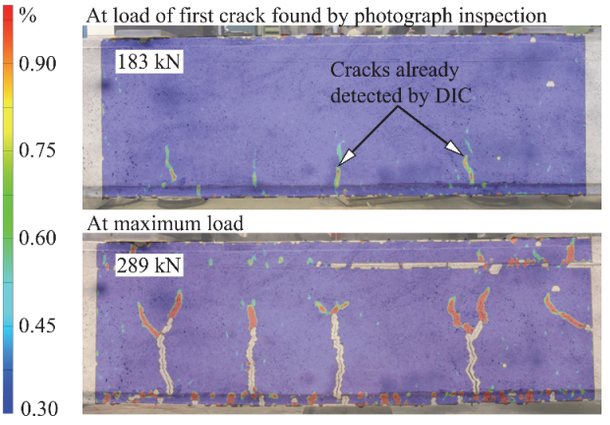


Figure 8: Beam 5 DIC-output at load level 183 kN and 289 kN. Photographed at mid-span by wide-angle lens.

3.2 *In-situ testing*

A full-scale OT-beam bridge was load tested in cold (around freezing point), humid, and windy weather in January 2017. First part of the test was of the full width of the bridge, while the second part was on two strips cut out with a large diamond saw, each with a width of 11 OT-beams.

3.2.1 *Test setup*

A novel loading rig was used to apply the load on the bridge of 9 m span in accordance with the Danish regulations (EN 1991-2 (2003) and Danish Road Directorate (2009, 2010)), see Figure 9. Two cradles

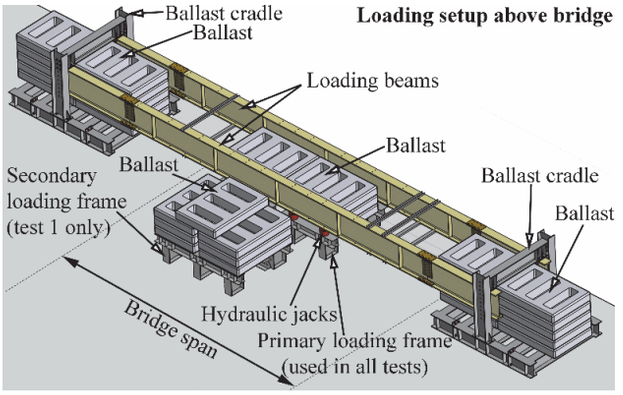


Figure 9: Loading rig with ballast, loading beams, and hydraulic jacks to apply load.

with dead load was positioned above the supports. Between the cradles were two large HE1000B profile steel beams spanning along the bridge span. Specially produced loading frames were placed under the steel beams, in order to apply a precise wheel load. Hydraulic jacks were positioned between the loading frames and the steel beams to apply a controllable static load to the bridge in conjunction with gravity controlled loading from weights. In the test of the full width bridge, an additional load, similar to a second heavy vehicle in the code, was situated next to the loading rig.

Figure 10 shows the position of the DIC-cameras underneath the bridge as well as the position of the load. Strip 1 and 2 had comparable setups, so only strip 1 is shown in the figure. The Canon 6d (wide-angle lens) camera was positioned with a distance to the underneath surface of the bridge of approximately 3.8 m, (whereas the Canon 550d was positioned with a distance of 2.6 m). Deflections were measured by distance lasers, LVDT's and a land surveyor station, and the relevant measuring points are given in Figure 10 as well.

3.2.2 *DIC in-situ results*

The first test concerned DIC measurements performed on the full un-cut bridge structure. The monitoring turned out to be a well-functioning deformation evaluation, but no cracking was detected at the very

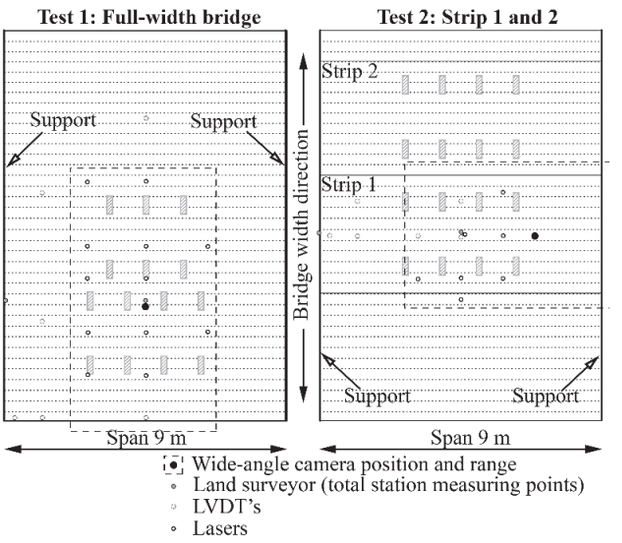


Figure 10: Plan drawings with position of wheel load and deflection- and DIC-measurements.

high magnitude of loading (100 tonne axle load, which was the test rig limit). In the second test, it was decided to cut out longitudinal strips in order to create more simple boundary conditions, to evaluate the effect of asphalt contribution to the capacity, and to verify monitoring accuracy etc.

The strips were successfully loaded to cracking and into the non-linear regime. Strip test 1 was including the asphalt layer, and in strip test 2, the asphalt layer was removed. The precision of each test was evaluated in GOM Correlate Professional at different subset sizes (called facets in GOM), by comparing the first two photographs captured in each test (no load on structure) to see the deviation in longitudinal strain over a defined line on the surface from first to second photograph.

In Figure 11 and 12 a captured photograph from strip test 1 is seen as well as a plot of the precision as function of subset size (both for the wide angle lens camera). The photographs were adjusted in Photoshop to grey scale images with lens distortion cor-

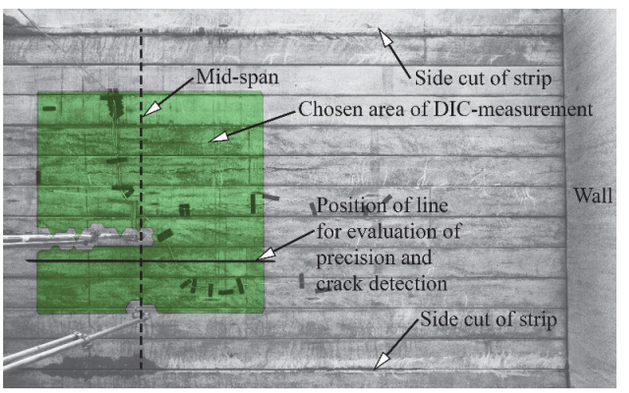


Figure 11: Photograph by wide-angle camera from test 2 strip 1. Location of area for DIC-measurements marked.

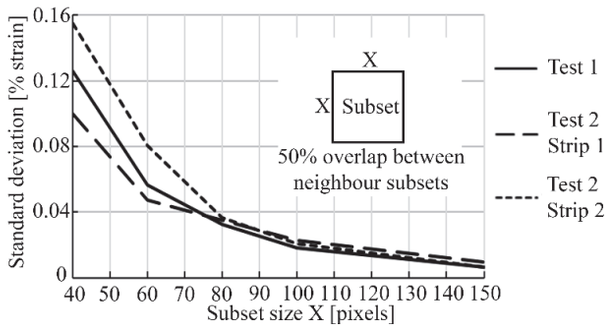


Figure 12: Precision based on deviation between first and second photograph (with no load on bridge).

rection and optimization of the grey level for best possible recognition in GOM Correlate Professional. The Canon 6d with wide-angle lens captured all photographs in all tests by ISO 200 and focal ratio 16.

To directly measure strain values, it is seen that the most reliable data is obtained by using large size subsets in the given example. The directly measured strain value should then subsequently be corrected for out-of-plane deflections.

Cracks were assessed by evaluating contour plots of the longitudinal strains on the surface. Such plots are given in Figure 13 for both strip tests, at the load of first clearly appearing cracking (lines of increased longitudinal tensile strain). The response in the figure has not been corrected for out-of-plane deflection of the OT-beams. The photographic inspection without the DIC-system showed that cracks were not visual until the highest load step was reached.

In Figure 14, a section of 1 m in length (from strip test 1) in direction of the OT-beams is shown. The figure shows data from the longitudinal strain in every point of the section before and after correction

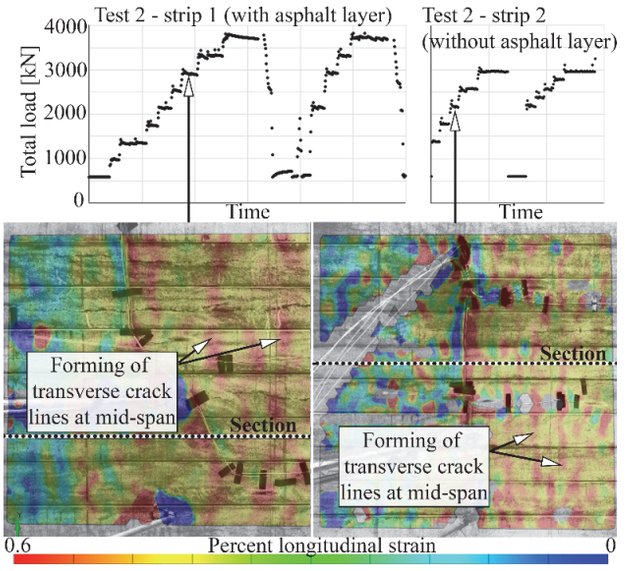


Figure 13: Loading scheme and contour plots of crack initiation without out-of-plane correction.

for out-of-plane deflection of the surface. The measured out-of-plane deflection for the specific load level was 29.5 mm in the left side of the section and 28.0 mm in the right side of the section.

Furthermore, the figure shows the deviation between an analysis based on subset sizes of 80 pixels and 150 pixels. It is seen that using the 80 pixels subset is more precise when determining the position where cracks cross the section. The larger subset size of 150 pixels is too large for fine crack detection in the example.

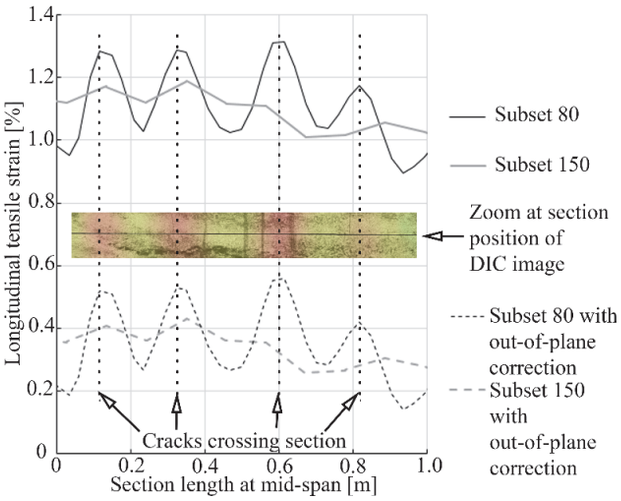


Figure 14: Longitudinal strain of longitudinal section for test 2 strip 1 at first load peak.

4 CONCLUSION

The paper proposes a method for application of a DSLR-camera with wide-angle lens for capturing photographs vertically underneath a concrete bridge during controlled load testing. The method includes correction of lens distortion and out-of-plane deflections of the evaluated surface, which was applied successfully to in-situ tests. Initially, lab-tests were performed of beams during loading (with painted random pattern of high contrast and with no out-of-plane deflection), where crack propagation was followed with the wide-angle lens camera and the lens distortion correction enabled. Later, in-situ tests of a full-scale concrete bridge was performed with the equipment, and both lens distortion correction and out-of-plane deflection corrections were used (and no random pattern was painted on the surface). The results showed that cracks could be found by the wide-angle camera at a distance of approximately 3.8 m with a precision depending on the chosen size of the subsets in the analysis in the DIC-software GOM Correlate. Larger subsets would give a better accuracy, but are too rough for proper crack detection, while a small subset size would give an insufficient accuracy. For the given camera to surface distance a

medium subset size of 80x80 pixels performed well when evaluating deformations- and crack initiations.

5 ONGOING- AND FUTURE WORK

In the project, the DIC wide-angle camera is used together with several other monitoring methods in order to justify the use and consequently optimize it for a more generic purpose.

The method is therefore being evaluated more thoroughly and is compared with the other promising monitoring methods for proof loadings and failure tests of concrete bridges.

The other methods contain e.g. also the regular lens DIC-camera, strain gages, 3D laser scanning, as well as ongoing- and upcoming equipment portfolio which includes tiltmeters, optical fibers and acoustic emission.

AKNOWLEDGEMENTS

The authors would like to thank the project partners at the Danish Road Directorate and COWI for the great cooperation and good ambience in the project. Furthermore, we gratefully acknowledge the contribution from the crane company BMS, and the technical staff at the Technical University of Denmark.

REFERENCES

Adobe. 2015. Photoshop CC.

Bornert, M. et al. 2009. Assessment of Digital Image Correlation Measurement Errors: Methodology and Results, *Experimental Mechanics*, 49(3): 353–370. doi: 10.1007/s11340-008-9204-7.

Bruck, H.A. et al. 1989. Digital image correlation using Newton-Raphson method of partial differential correction, *Experimental Mechanics*, 29(3): 261–267. doi: 10.1007/BF02321405.

Danish Road Directorate. 2009. *EN 1991-2 DK NA:2009 - Annex A*.

Danish Road Directorate. 2010. *Vejledning til belastnings- og beregningsgrundlag*.

EN 1991-2, Traffic Loads on Bridges. 2003.

Fazzini, M. et al. 2010. Study of image characteristics on digital image correlation error assessment, *Optics and Lasers in Engineering*, 48(3): 335–339. doi: 10.1016/j.optlaseng.2009.10.012.

GOM. 2016. GOM Correlate Professional.

Lecompte, D. et al. 2006. Quality assessment of speckle patterns for digital image correlation, *Optics and Lasers in Engineering*, 44(11): 1132–1145. doi: 10.1016/j.optlaseng.2005.10.004.

McCormick, N., Waterfall, P. & Owens, A. 2014. Optical imaging for low-cost structural measurements, *Proceedings of the Institution of Civil Engineers - Bridge Engineering*, 167(1): 33–42. doi: 10.1680/bren.11.00055.

Shan, B. et al. 2016. A Bridge Deflection Monitoring System Based on CCD, *Advances in Materials Science and Engineering*: 1–11. doi: 10.1155/2016/4857373.

Sutton, M. et al. 1983. Determination of displacements using an improved digital correlation method, *Image and Vision Computing*, 1(3): 133–139. doi: 10.1016/0262-8856(83)90064-1.

Tian, L. et al. 2013. Application of digital image correlation for long-distance bridge deflection measurement, Quan, C., Qian, K., and Asundi, A. (eds), *Proceedings of Spie - the International Society for Optical Engineering*, 8769: 87692V. doi: 10.1117/12.2020139.

Triconnet, K. et al. 2009. Parameter choice for optimized digital image correlation, *Optics and Lasers in Engineering*, 47(6): 728–737. doi: 10.1016/j.optlaseng.2008.10.015.

Wang, Y.Q. et al. 2011. Error Estimation of DIC for Heterogeneous Strain States, *Applied Mechanics and Materials*, 70(70): 177–182. doi: 10.4028/www.scientific.net/AMM.70.177.

Yoneyama, S. et al. 2007. Bridge Deflection Measurement using Digital Image Correlation, *Experimental Techniques*, 31(1): 34–40. doi: 10.1111/j.1747-1567.2006.00132.x.

Yoneyama, S. & Morimoto, Y. 2003. Accurate Displacement Measurement by Correlation of Colored Random Patterns, *JSME International Journal Series A*, 46(2): 178–184. doi: 10.1299/jsmea.46.178.

Maintenance, Safety, Risk, Management and Life-Cycle Performance of Bridges – Powers, Frangopol, Al-Mahaidi & Caprani (Eds)
© 2018 Taylor & Francis Group, London, ISBN 978-1-138-73045-8

Monitoring crack width and strain during proof load testing

E.O.L. Lantsoght
Concrete Structures, Delft University of Technology, Delft, The Netherlands
Politecnico, Universidad San Francisco de Quito, Quito, Ecuador
C. van der Veen & D.A. Hordijk
Concrete Structures, Delft University of Technology, Delft, The Netherlands

ABSTRACT: In a proof load test, the applied load is representative of the factored live load, to demonstrate experimentally that the bridge fulfils the code requirements. Signs of distress must be caught with the instrumentation by defining stop criteria. In the literature, several stop criteria for flexure are available. The German guidelines describe, amongst others, a limiting crack width and strain. However, the background of these limiting values is not clear. Therefore, a theoretical approach based on flexural theory is followed. The theoretically derived values are then compared to experimental results obtained from beam experiments. The result of this research work is a limiting value of crack widths and strains that can be used during proof load testing of concrete bridges. The arbitrary stop criteria that were used in the past can now be replaced by stop criteria that are based on the theory of concrete beams in flexure.

1 INTRODUCTION

The majority of the existing bridges in the Netherlands are reaching the end of their originally intended service life, and are subjected to larger live loads than those loads these bridges were originally designed for. Since the mid-2000s, the Dutch Ministry of Infrastructure and the Environment has taken steps to assess its bridge stock. These first assessments (Walraven, 2010, Vergoossen et al., 2013) showed that upon initial assessment, a large number of reinforced concrete bridges do not fulfil the requirements of the currently governing codes NEN-EN 1991-2:2003 (CEN, 2003) for the loads and NEN-EN 1992-1-1:2005 (CEN, 2005) for the capacity of concrete members. Therefore, increasing Levels of Assessment (Lantsoght et al., 2017c, Schlune et al., 2011) for the evaluation of reinforced concrete bridges were proposed. When analytical methods are not sufficient for the evaluation of an existing bridge, or when the uncertainty on the capacity is large (for example as a result of material degradation), proof load testing can be a viable assessment method.

In a proof load test (Anay et al., 2016, Aguilar et al., 2015, Zwicky and Brühwiler, 2015, Casas and Gómez, 2013, Au et al., 2013, Olaszek et al., 2012), the applied load is representative of the factored live load, to demonstrate experimentally that the bridge can sustain this load level. For this reason, it is important to instrument the tested bridge, so that signs of distress can be caught and irreversible damage can be avoided. The threshold values of these measured quantities are called the stop criteria.

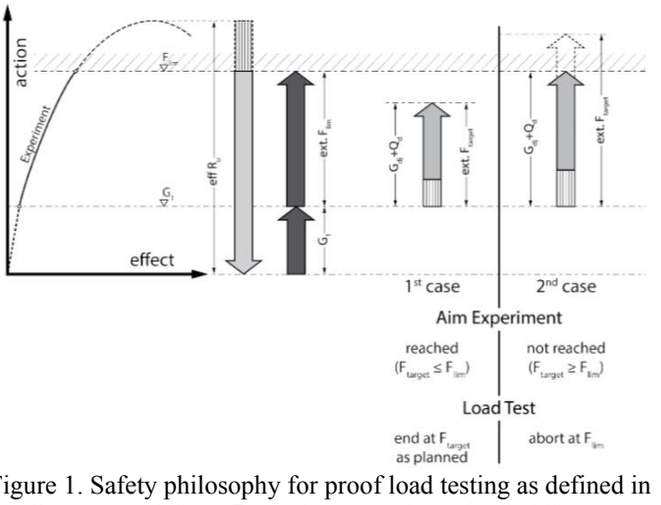


Figure 1. Safety philosophy for proof load testing as defined in the German guideline (Deutscher Ausschuss für Stahlbeton, 2000, Vos, 2016, Lantsoght et al., 2017h).

The safety philosophy for proof load testing is shown in Figure 1. The onset of nonlinear behaviour, which should be captured with the stop criteria, is represented by the load F_{lim}. The load level corresponding to the permanent loads is G_1. The maximum load corresponds to the structural capacity $eff.R_u$. The maximum load that can be applied during a proof load test in order not to have irreversible damage is $F_{lim} - G_1 = ext.F_{lim}$. The load that needs to be applied to the bridge in order to demonstrate that it fulfils the code requirements is $ext.F_{target}$, which corresponds to the factored live loads Q_d and addi-

tional factored superimposed dead loads G_{dj}. If this load is smaller than $ext.F_{lim}$ (1st case in Figure 1), the proof load test is considered successful and it has been shown that the bridge can carry the code-prescribed loads. If, on the other hand, $ext.F_{lim}$ is reached before $ext.F_{target}$, a stop criterion is exceeded before the target load is applied, and further loading than $ext.F_{lim}$ is not permitted. Depending on the largest load level that is reached during the proof load test, it can then be found that the bridge fulfils the requirements for reduced live loads and that a traffic restriction should be imposed.

During the last five years, research at Delft University of Technology has been done to explore the suitability of proof load testing for the evaluation of reinforced concrete slab bridges in shear and flexure. A campaign of pilot proof load tests (Lantsoght et al., 2017f, Lantsoght et al., 2017a, Lantsoght et al., 2017b, Lantsoght et al., 2017d, Lantsoght et al., 2017g), a collapse test (Lantsoght et al., 2017e, Lantsoght et al., 2016a, Lantsoght et al., 2016b, Lantsoght et al., 2016c), additional testing in the laboratory (Lantsoght et al., 2016b, Lantsoght et al., 2017i), and desk research (Lantsoght et al., 2017h) led to the conclusion that proof load testing seems to be a viable option, but that further laboratory testing is necessary to define the stop criteria for shear, and that a theoretical basis for the stop criteria for flexure should be sought. In this paper, the available stop criteria for flexure are improved with a stop criterion that is derived based on flexural theory for reinforced concrete members. As such, the proposed method is suitable for reinforced concrete slab bridges, which often are found not to fulfil the code requirements in the Netherlands.

2 EXISTING STOP CRITERIA FOR FLEXURE

2.1 *German guidelines*

The German guidelines for load testing of concrete structures (Deutscher Ausschuss für Stahlbeton, 2000) are suitable for plain and reinforced concrete buildings subjected to a load test for flexure. The first stop criterion limits the concrete strain ε_c:

$$\varepsilon_c < \varepsilon_{c,lim} - \varepsilon_{c0} \tag{1}$$

with ε_c = the strain measured during proof loading; ε_{c0} = the analytically determined short-term strain in the concrete caused by the permanent loads that are acting on the structure before the application of the proof load and $\varepsilon_{c,lim}$ = 800 $\mu\varepsilon$ for concrete with a compressive strength larger than 25 MPa. The second stop criterion limits the strain in the reinforcement steel ε_{s2}:

$$\varepsilon_{s2} < 0.7\frac{f_{ym}}{E_s} - \varepsilon_{s02} \tag{2}$$

with f_{ym} = the average yield strength of steel on the tension side of the cross-section; E_s = the modulus of elasticity of reinforcing bars; and ε_{s02} = analytically determined strain (assuming cracked conditions) in the reinforcement steel caused by the permanent loads that are acting on the structure before the application of the proof load. For the crack width, w, and the increase in crack width of an existing crack, Δw, the requirements from Table 1 have to be fulfilled. The fourth stop criterion limits the residual deflection in the cracked state to 10% permanent (plastic) deformation after removal of the load.

Table 1. Requirements for crack width for newly developing cracks w and increase in crack width for existing cracks Δw (Deutscher Ausschuss für Stahlbeton, 2000).

	During proof loading	After proof loading
New cracks	$w \leq 0.5$ mm	$\leq 0.3w$
Existing cracks	$\Delta w \leq 0.3$ mm	$\leq 0.2\Delta w$

2.2 *Czech and Slovak codes*

The Czech and Slovak codes (Frýba and Pirner, 2001) describe acceptance criteria that are typically verified after a load test. The first acceptance criterion for a load test is the condition of elastic deformation S_e, with S_{cal} the calculated value:

$$\beta < \frac{S_e}{S_{cal}} \leq \alpha \tag{3}$$

For reinforced concrete bridges, α = 1.10 and β = 0.60. The second acceptance criterion looks at the condition of permanent deformation S_r as a function of the total deformation $S_{tot} = S_r + S_e$:

$$\frac{S_r}{S_{tot}} \leq \alpha_1 \tag{4}$$

with α_1 = 0.25 for reinforced concrete. The third acceptance criterion gives the maximum crack widths as a function of the environmental class, see Table 2.

Table 2: Limitations to crack widths that can occur in a load test for reinforced concrete bridges (Frýba and Pirner, 2001).

Environmental class	Maximum crack width
1 (dry)	0.4 mm
2, 3 (humid)	0.3 mm
4, 5 (aggressive)	0.1 mm

2.3 *Other existing codes and guidelines*

ACI 437.2M-13 (ACI Committee 437, 2013) describes acceptance criteria based on the maximum deflection, residual deflection, deviation from linearity index, and permanency ratio. The deviation from linearity index and permanency ratio can only be used as acceptance criteria when the loading protocol described by ACI 437.2M-13 is used. This loading protocol differs from the protocol recommended for load testing of concrete bridges (Lantsoght et al., 2017i).

The Manual of Bridge Evaluation (AASHTO, 2016) describes the target proof load, but does not quantify stop criteria. This code only mentions that no nonlinear behavior should occur during the test.

Similarly, the Swiss code (SIA, 2011) prescribes that the behavior during the test should be linear, that the residual displacements should be zero, and that the crack width should be "within acceptable limits."

The Polish code (Research Institute of Roads and Bridges, 2008) allows no nonlinear behavior and limits the residual deformations to 20% of the maximum for reinforced concrete bridges.

In Hungary (Hungarian Chamber of Engineers, 2013) a crack width in the concrete of 1 mm is a stop criterion. Under the service loads, the crack width and maximum deflection should not be larger than the limit from NEN-EN 1992-1-1:2005 (CEN, 2005). The residual deformation is limited to 25% of the maximum for reinforced concrete structures.

2.4 *Limitations of existing stop criteria*

As can be seen from the previous sections, in the literature and in existing codes and guidelines, several stop criteria for flexure are available. The German guidelines describe a limiting crack width and strain, as well as other parameters. However, the background of these limiting values is not clear, and the proposed limiting strain seems arbitrary. The proposed limiting crack widths seem to be related to serviceability and durability requirements, which can be exceeded in a short-term proof load test. A theoretical basis, derived from flexural theory, for the stop criteria for flexure is needed.

A limiting strain in the steel reinforcement is not a practical stop criterion, as this criterion requires the removal of the concrete cover in the field, which is often not permitted by the bridge owner.

Many codes describe stop and acceptance criteria based on the largest deflection. However, beam experiments (Lantsoght et al., 2017i, Lantsoght et al., 2016d) indicated that a stop criterion based on a maximum and residual deflection is not reliable. Therefore, stop criteria for the concrete strain and crack width based on flexural theory are derived in this paper.

3 DERIVATION OF THEORETICAL STOP CRITERIA

3.1 *Stop criterion for the limiting flexural strain*

Flexural beam theory is used to derive a stop criterion for flexure, see Figure 2. A beam with an area of reinforcement A_s is studied. The resulting strains are shown in Figure 2b, with ε_c the strain in the concrete under compression, ε_s the strain in the steel and ε_{bot} the strain in the concrete on the bottom. The effective depth is d, the height of the beam h and the height of the compression zone c. Figure 2c shows the stresses, with f_c the stress in the concrete under compression and f_s the stress in the steel. The compressive resultant C and the tensile resultant T are sketched in Figure 2d.

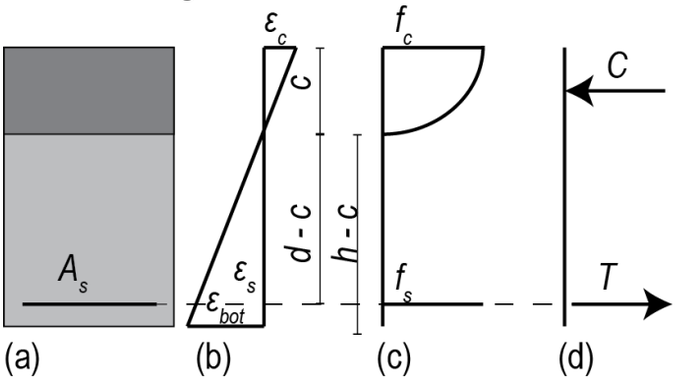


Figure 2. Notations used for derivation of stop criterion based on flexural beam theory: (a) cross-section of beam; (b) strains; (c) stresses; (d) forces.

The strain at the bottom of the cross-section can be calculated as:

$$\varepsilon_{bot} = \frac{h-c}{d-c} f_s \tag{5}$$

To avoid yielding of the steel reinforcement, f_s should be limited to 90% of f_y, the yield strength of the steel, resulting in:

$$\varepsilon_{bot,\max} = \frac{h-c}{d-c} 0.9 \frac{f_y}{E_s} \tag{6}$$

The Young's modulus of steel is E_s. It is then proposed to limit the strain during a field test to 65% of $\varepsilon_{bot,max}$. This maximum strain should be calculated prior to a field test. It is recommended to use Thorenfeldt's stress-strain parabola, see Figure 3. This parabola is described by the following expressions:

$$n_{th} = 0.8 + \frac{f_{cm}}{17.24MPa} \tag{7}$$

$$\varepsilon_0 = \frac{f_{cm}}{E_c}\left(\frac{n_{th}}{n_{th}-1}\right) \tag{8}$$

$$k_{th} = \begin{cases} 1 \text{ if } \dfrac{\varepsilon_c}{\varepsilon_0} \le 1 \\ 0.67 + \dfrac{f_{cm}}{62.07MPa} \text{ if } \dfrac{\varepsilon_c}{\varepsilon_0} > 1 \end{cases} \tag{9}$$

$$f_{c,th} = \frac{0.9 f_{cm} \times n_{th} \times \dfrac{\varepsilon_c}{\varepsilon_0}}{n_{th} - 1 + \left(\dfrac{\varepsilon_c}{\varepsilon_0}\right)^{n_{th} k_{th}}} \tag{10}$$

$$\beta_{th} = \frac{\ln\left(1+\left(\frac{\varepsilon_c}{\varepsilon_0}\right)^2\right)}{\frac{\varepsilon_c}{\varepsilon_0}} \tag{11}$$

$$C = \beta_{th} \times f_{c,th} \times b \times c \tag{12}$$

$$T = A_s \times 0.9 \times f_y \tag{13}$$

The constants n_{th} and ε_0 are material parameters defined by the concrete compressive strength f_{cm} and the Young's modulus of the concrete E_c. The factor k_{th} is a function of the strain ration $\varepsilon_c/\varepsilon_0$. The maximum stress in the parabola is $f_{c,th}$. The average stress is $\beta_{th} \times f_{c,th}$. The resultant of concrete under compression C should equal the resultant of steel under tension T. From this equilibrium, the height of the compression zone c can be found. Once c is known, the value of $\varepsilon_{bot,max}$ can be calculated according to Eq. (6). Then, the maximum strain in the proof load test can be calculated as:

$$\varepsilon_{stop} = 0.65\varepsilon_{bot,\max} - \varepsilon_{c0} \tag{14}$$

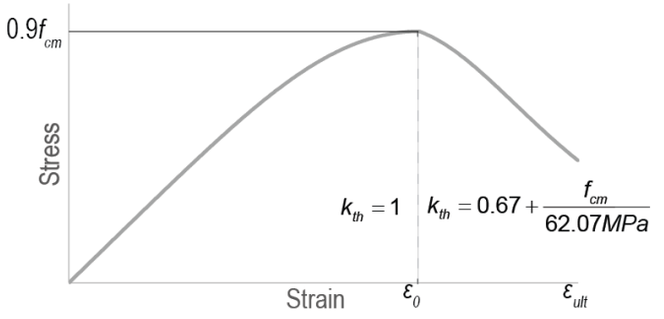


Figure 3. Thorenfeldt's stress-strain parabola.

3.2 *Stop criterion for the limiting crack width*

According to the *fib* Model Code 2010 (fib, 2012), the crack width w can be calculated as:

$$w = 2l_{s,\max}\left(\varepsilon_{sm} - \varepsilon_{cm} - \varepsilon_{cs}\right) \tag{15}$$

$$\varepsilon_{sm} - \varepsilon_{cm} - \varepsilon_{cs} = \frac{\sigma_s - \beta\sigma_{sr}}{E_s} + \eta_r\varepsilon_{sh} \tag{16}$$

With σ_s the stress in the reinforcement steel, σ_{sr} the stress in the steel at cracking, β and η_r terms that depends on the type and duration of loading as given in Table 7.6-2 from the *fib* Model Code 2010 (fib, 2012), and ε_{sh} the shrinkage strain. Since a proof load test is short in duration, it is assumed that no shrinkage occurs during the test and thus $\varepsilon_{sh} = 0$. For short-term loading, the value of $\beta = 0.6$. If the limit of 90% of yielding of the steel is used again for the development of the stop criterion for crack width, then $\sigma_s = 0.9f_y$. The stress at cracking is calculated as:

$$\sigma_{sr} = \frac{f_{ctm}}{\rho_{s,eff}}\left(1 + \alpha_e\rho_{s,eff}\right) \tag{17}$$

The cracking stress can be calculated as (ACI Committee 318, 2014):

$$f_{ctm} = \frac{7.5}{12}\sqrt{f_{cm}} \tag{18}$$

The ratio of the Young's moduli is $\alpha_e = E_s/E_c$. The effective reinforcement ratio $\rho_{s,eff}$ of the fictitious tension tie in the beam depends on the effective height h_{eff}:

$$h_{eff} = 2.5\left(h - d\right) \le \frac{h-c}{3} \tag{19}$$

The effective reinforcement ratio is then:

$$\rho_{s,eff} = \frac{A_s}{b \times h_{eff}} \tag{20}$$

The crack spacing is calculated as:

$$l_{s,\max} = k \times c_{cover} + \frac{1}{4}\frac{f_{ctm}}{\tau_{bms}}\frac{\phi_s}{\rho_{s,eff}} \tag{21}$$

The constant k can be taken as $k = 1$. The concrete cover is c_{cover}. According to Table 7.6-2 from the *fib* Model Code 2010 (fib, 2012), $\tau_{bms} = 1.8f_{ctm}$. The diameter of the reinforcement bars is φ_s. Combining this information, the expression for the maximum crack width can then be determined as:

$$w_{stop} = 2\frac{0.9f_y - 0.6\sigma_{sr}}{E_s}\left(c_{cover} + 0.139\frac{\phi_s}{\rho_{s,eff}}\right) \tag{22}$$

4 BEAM EXPERIMENTS

4.1 *Beams taken from the Ruytenschildt Bridge*

The Ruytenschildt Bridge (Lantsoght et al., 2016b) was tested to collapse in two spans in the summer of 2014. Beams sawn from a span that was not tested were taken to the laboratory for additional testing. Five experiments on three beams were done. Table 3 gives an overview of the geometric properties of the five tested cross-sections. All beams were 6 m long. Beams RSB01 and RSB02 were 500 mm wide and beam RSB03 was 1000 mm wide.

The concrete compressive strength is f_{cm} = 52.2 MPa. The yield strength of the steel is 282 MPa for QR 24 steel, a type of plain reinforcement that was commonly used until the 1960s in the Netherlands.

The beams were tested in three-point bending with a span length of 5 m. For RSB01F and RSB03F, the load was placed at midspan. For RSB02A and RSB02B the distance between the load and support was a = 1.25 m and for RSB03A a = 1.3

m. The load was applied in a cyclic manner. In experiments RSB01F, RSB02A, RSB02B, and RSB03F, a flexural failure was achieved. The load at failure P_{max} is given in Table 4. The results of these experiments can thus be used for the verification of the proposed stop criteria.

Table 3. Properties of cross-sections of the beams taken from the Ruytenschildt Bridge.

RSB	01F	02A	02B	03F	03A
d (mm)	503	515.5	520	521	515
A_c (m^2)	0.290	0.297	0.307	0.596	0.537
Rebar	4Ø22	4Ø22	4Ø22	9Ø22	7Ø22
	4Ø19	4Ø19	5Ø19	8Ø19	8Ø19
ρ_l	0.91%	0.89%	0.96%	0.95%	0.92%

4.2 *Beams cast in the laboratory*

Four experiments on two beams (P804 and P502) reinforced with plain bars and cast in the laboratory were carried out to study stop criteria and the loading protocol for proof load testing (Lantsoght et al., 2017i). Beam P804 had a height of 800 mm, width of 300 mm, and length of 10 m. Beam P502 had a height of 500 mm, width of 300 mm, and length of 8 m. The beams were tested in three point bending, see Figure 4. The span length for beam P502 was 5 m. The load was applied in a cyclic manner to study stop criteria and the required loading protocol in field tests.

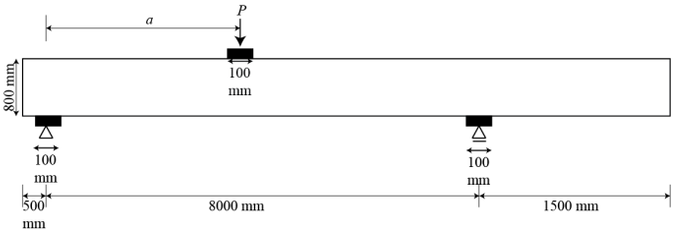


Figure 4. Loading arrangement for beam P804.

The concrete compressive strength of beam P804 is 63.5 MPa and of P502 71.5 MPa. Plain reinforcement bars with a measured yield strength of 297 MPa were used. For beam P804, six reinforcement bars with a diameter of 20 mm were used, and for P502, three bars. The effective depth for P804 was 755 mm and for P502 465 mm. The resulting reinforcement ratio of P804 was 0.83% and of P502 0.68%.

The two experiments in which a flexural failure was achieved are P804A1 and P502A2. The shear span a in P804A1 was 3 m and in P502A2 a = 1 m. The failure load in P804A1 was 207 kN and in P502A2 150 kN.

5 COMPARISON BETWEEN STOP CRITERIA AND EXPERIMENTAL RESULTS

To verify the proposed stop criteria for the concrete strain on the bottom of the cross-section ε_{stop} (Eq. (14)) and for the crack width w_{stop} (Eq. (22)), the results of the experiments in which a flexural failure was achieved are studied.

First, the value of ε_{stop} and w_{stop} are calculated in a spreadsheet. Then, the test results are analyzed to see at which load the stop criteria are exceeded. The results of this analysis are given in Table 4, in which P_{max} is the load at failure in the experiments, P_ε the load for which the strain stop criterion is exceeded, and P_w the load for which the crack width stop criterion is exceeded. "Lim" denotes the percentage of the maximum load at which a stop criterion is exceeded. The lowest load at which a stop criterion is exceeded is marked in grey, as for this load in the field the experiment would be stopped. This value is then also used to calculate Lim.

Table 4. Overview of experimental results and comparison to proposed stop criteria.

Test	P_{max} (kN)	ε_{stop} ($\mu\varepsilon$)	w_{stop} (mm)	P_ε (kN)	P_w (kN)	Lim (%)
RSB01F	276	900	0.177	141	147	51
RSB02A	369	908	0.174	222	224	60
RSB02B	416	903	0.178	235	284	56
RSB03F	607	900	0.170	335	396	56
P804A1	207	910	0.191	120	140	58
P502A2	150	972	0.185	111	92	61

The results of Table 4 show that the resulting strain limit is slightly higher than the limiting strain of $800\mu\varepsilon - \varepsilon_{c0}$ as prescribed by the German guideline (Deutscher Ausschuss für Stahlbeton, 2000). On the other hand, the limiting crack width is slightly smaller than the limits from Table 2 as prescribed by the German guideline (Deutscher Ausschuss für Stahlbeton, 2000).

For the larger beams (RSB beams and P804), the limiting strain criterion is governing. For P502A2, the limiting crack width criterion is governing. The governing stop criterion is exceeded between 51 – 61% of the maximum load. As such, it can be concluded that the proposed stop criteria are conservative and can be used for the preparation of proof load tests for flexure.

6 DISCUSSION

For the stop criteria available in the existing codes and guidelines, the background of the proposed limiting values is not clear. Therefore, a theoretical approach based on flexural beam theory is followed in this paper to derive a stop criterion for the limiting strain and for the limiting crack width. The theoretically derived values were compared to experimental

results obtained testing of beams in the laboratory. The result of this research work is a proposal for the stop criteria for crack widths and strains that can be used during proof load testing of concrete bridges, when the failure mode of flexure is expected. The arbitrary stop criteria that were used in the past can now be replaced by stop criteria that are based on the theory of concrete beams in flexure. The proposed stop criteria are valid for reinforced concrete members. For prestressed concrete members, a similar theoretical derivation could be made.

A possible drawback of the presented stop criteria is that a calculation is required to determine the limiting values, whereas the German guidelines presented a single limiting value. However, linear finite elements and spreadsheets are typically used for the preparation of a proof load test. As such, adding the proposed formulas to the spreadsheets used for the preparation of, for example, the expected load – deflection diagram can be quickly done.

This paper proposes stop criteria for the maximum strain and maximum crack width. For the residual crack width, the limits from the German guideline, see Table 2, could be kept, as also proposed earlier (Lantsoght et al., 2017i).

Note as well that the proposed stop criterion for the limiting crack width is based on expressions for beams reinforced with ribbed bars. This expression is here verified with the results of beams reinforced with plain bars, for which the bond behaviour is different. Further experimental validation of this stop criterion on specimens with ribbed bars is recommended to study if the proposed criterion is generally valid for reinforced concrete.

7 SUMMARY AND CONCLUSIONS

Proof load testing of bridges can be a viable option to demonstrate experimentally that a given bridge fulfils the code requirements. This type of testing requires high loads, and involves higher risks for irreversible damage to the structure or even collapse. Therefore, the structural response of the bridge must be followed closely during a proof load test. When the response exceeds a certain predetermined level, the proof load test needs to be terminated as further loading can result in irreversible damage or collapse. For different types of structural response, these limits are defined as “stop criteria”.

In the currently available codes and guidelines for proof load testing for the failure mode of flexure, stop criteria for flexure are available. These stop criteria are based on a single limiting value, for which a theoretical basis is not directly available.

As earlier analyses indicated that the best results are obtained for stop criteria based on strains and crack widths, this paper aimed at developing a proposal for flexural stop criteria for the strain and crack width based on flexural beam theory. The limiting strain in the concrete is 65% of the strain that corresponds to 90% of the strain at yielding of the steel. The limiting crack width corresponds to the crack width at a stress in the steel of 90% of the yield stress.

To verify the proposed stop criteria, the results from beams taken from the Ruytenschildt Bridge and for beams with plain bars cast in the laboratory, are studied. In total, 6 experiments in which a flexural failure was achieved are used for the analysis in this study.

The comparison between the proposed stop criteria and the experimental results shows that the proposed stop criteria are exceeded prior to failure for all cases (i.e., they work as a stop criterion indeed), and that the stop criteria are exceeded at a load that is 51% - 61% of the failure load. As such, the proposed stop criteria are conservative and can be recommended for the use in proof load tests in which the load is placed at a flexure-critical position.

ACKNOWLEDGEMENTS

The authors wish to express their gratitude and sincere appreciation to the Dutch Ministry of Infrastructure and the Environment (Rijkswaterstaat) for financing this research. The contributions our colleagues Albert Bosman and Yuguang Yang to the experiments described in this paper are gratefully acknowledged. For the desk research on stop criteria, funding was obtained through the program of Chancellor Grants from Universidad San Francisco de Quito. This funding is gratefully acknowledged.

REFERENCES

AASHTO 2016. *The manual for bridge evaluation with 2016 interim revisions,* Washington, D.C., American Association of State Highway and Transportation Officials.

ACI COMMITTEE 318 2014. *Building code requirements for structural concrete (ACI 318-14) and commentary,* Farmington Hills, MI, American Concrete Institute.

ACI COMMITTEE 437 2013. Code Requirements for Load Testing of Existing Concrete Structures (ACI 437.2M-13) and Commentary Farmington Hills, MA.

AGUILAR, C. V., JÁUREGUI, D. V., NEWTSON, C. M., WELDON, B. D. & CORTEZ, T. M. 2015. Load Rating a Prestressed Concrete Double-Tee Beam Bridge without Plans by Proof Testing. *Transportation Research Board Annual Compendium of Papers.* Washington DC.

ANAY, R., CORTEZ, T. M., JÁUREGUI, D. V., ELBATANOUNY, M. K. & ZIEHL, P. 2016. On-Site Acoustic-Emission Monitoring for Assessment of a Prestressed Concrete Double-Tee-Beam Bridge without Plans. *Journal of Performance of Constructed Facilities,* 30.

AU, A., LAM, C., AU, J. & THARMABALA, B. 2013. Eliminating Deck Joints Using Debonded Link Slabs:

Research and Field Tests in Ontario *Journal of Bridge Engineering,* 18**,** 768-778.
CASAS, J. R. & GÓMEZ, J. D. 2013. Load Rating of Highway Bridges by Proof-loading. *KSCE Journal of Civil Engineering,* 17**,** 556-567.
CEN 2003. Eurocode 1: Actions on structures - Part 2: Traffic loads on bridges, NEN-EN 1991-2:2003. Brussels, Belgium: Comité Européen de Normalisation.
CEN 2005. Eurocode 2: Design of Concrete Structures - Part 1-1 General Rules and Rules for Buildings. NEN-EN 1992-1-1:2005. Brussels, Belgium: Comité Européen de Normalisation.
DEUTSCHER AUSSCHUSS FÜR STAHLBETON 2000. DAfStb-Guideline: Load tests on concrete structures (in German). Deutscher Ausschuss fur Stahlbeton,.
FIB 2012. *Model code 2010: final draft,* Lausanne, International Federation for Structural Concrete.
FRÝBA, L. & PIRNER, M. 2001. Load tests and modal analysis of bridges. *Engineering Structures,* 23**,** 102-109.
HUNGARIAN CHAMBER OF ENGINEERS 2013. Guidelines for interventions in Hungary (in Hungarian). Budapest, Hungary.
LANTSOGHT, E., KOEKKOEK, R., YANG, Y., VAN DER VEEN , C., HORDIJK, D. & DE BOER, A. 2017a. Proof load testing of the viaduct De Beek. *39th IABSE Symposium - Engineering the Future.* Vancouver, Canada.
LANTSOGHT, E., VAN DER VEEN, C. & DE BOER, A. 2016a. Shear and moment capacity of the Ruytenschildt bridge. *IABMAS 2016.*
LANTSOGHT, E., VAN DER VEEN , C., HORDIJK, D. & DE BOER, A. 2017b. Recommendations for proof load testing of reinforced concrete slab bridges. *39th IABSE Sympsaium - Engineering the Future.* Vancouver, Canada.
LANTSOGHT, E., YANG, Y., VAN DER VEEN, C., DE BOER, A. & HORDIJK, D. 2016b. Ruytenschildt Bridge: field and laboratory testing. *Engineering Structures,* 128**,** 111-123.
LANTSOGHT, E. O. L., DE BOER, A. & VAN DER VEEN , C. 2017c. Levels of Approximation for the shear assessment of reinforced concrete slab bridges. *Structural Concrete,* 18**,** 143-152.
LANTSOGHT, E. O. L., KOEKKOEK, R. T., HORDIJK, D. A. & DE BOER, A. 2017d. Towards standardization of proof load testing: pilot test on viaduct Zijlweg. *Structure and Infrastructure Engineering***,** 16.
LANTSOGHT, E. O. L., VAN DER VEEN, C., DE BOER, A. & HORDIJK, D. A. 2016c. Probabilistic prediction of the failure mode of the Ruytenschildt Bridge. *Engineering Structures,* 127**,** 549-558.
LANTSOGHT, E. O. L., VAN DER VEEN , C., DE BOER, A. & HORDIJK, D. A. 2017e. Collapse test and moment capacity of the Ruytenschildt Reinforced Concrete Slab Bridge *Structure and Infrastructure Engineering,* 13**,** 1130-1145.
LANTSOGHT, E. O. L., VAN DER VEEN , C., DE BOER, A. & HORDIJK, D. A. 2017f. Proof load testing of reinforced concrete slab bridges in the Netherlands. *Structural Concrete,* 18**,** 597-606.
LANTSOGHT, E. O. L., VAN DER VEEN, C., DE BOER, A. & HORDIJK, D. A. 2017g. Required proof load magnitude for probabilistic field assessment of viaduct De Beek *Engineering Structures,* 148**,** 767-779.
LANTSOGHT, E. O. L., VAN DER VEEN, C., HORDIJK, D. A. & DE BOER, A. 2017h. State-of-the-art on load testing of concrete bridges. *Engineering Structures,* 150**,** 231-241.
LANTSOGHT, E. O. L., YANG, Y., TERSTEEG, R. H. D., VAN DER VEEN, C. & DE BOER, A. 2016d. Development of Stop Criteria for Proof Loading. *IALCCE 2016.* Delft, The Netherlands.
LANTSOGHT, E. O. L., YANG, Y., VAN DER VEEN, C., DE BOER, A. & HORDIJK, D. A. 2017i. Beam experiments on acceptance criteria for bridge load tests. *ACI Structural Journal,* 114**,** 1031-1041.
OLASZEK, P., ŚWIT, G. & CASAS, J. R. 2012. Proof load testing supported by acoustic emission. An example of application. *IABMAS 2012.*
RESEARCH INSTITUTE OF ROADS AND BRIDGES 2008. The rules for road bridges proof loadings (in Polish). Warsaw, Poland.
SCHLUNE, H., PLOS, M. & GYLLTOFT, K. 2011. Safety formats for nonlinear analysis tested on concrete beams subjected to shear forces and bending moments. *Engineering Structures,* 33**,** 2350-2356.
SIA 2011. Existing structures – Bases for examination and interventions SIA 505 269:2011.
VERGOOSSEN, R., NAAKTGEBOREN, M., 'T HART, M., DE BOER, A. & VAN VUGT, E. 2013. Quick Scan on Shear in Existing Slab Type Viaducts. *International IABSE Conference, Assessment, Upgrading and Refurbishment of Infrastructures.* Rotterdam, The Netherlands.
VOS, W. 2016. *Stop criteria for proof loading - The use of stop criteria for a safe use of 'Smart Proof loading'.* M.Sc. Thesis, Delft University of Technology.
WALRAVEN, J. C. 2010. Residual shear bearing capacity of existing bridges. *fib Bulletin 57, Shear and punching shear in RC and FRC elements; Proceedings of a workshop held on 15-16 October 2010.* Salò, Lake Garda, Italy.
ZWICKY, D. & BRÜHWILER, E. 2015. Chillon Viaduct deck slab strengthening using reinforced UHPFRC: Full-scale tests. *In:* F.DEHN, BEUSHAUSEN, H.-D., ALEXANDER, M. G. & MOYO, P. (eds.) *Concrete Repair, Rehabilitation and Retrofitting IV* Leipzig, Germany.

Maintenance, Safety, Risk, Management and Life-Cycle Performance of Bridges – Powers, Frangopol, Al-Mahaidi & Caprani (Eds)
© 2018 Taylor & Francis Group, London, ISBN 978-1-138-73045-8

Twenty years monitoring of a high strength concrete cantilever bridge

E.O.L. Lantsoght
Concrete Structures, Delft University of Technology, Delft, The Netherlands
Politecnico, Universidad San Francisco de Quito, Quito, Ecuador

C. van der Veen
Concrete Structures, Delft University of Technology, Delft, The Netherlands

H. van der Ham
Ministry of Infrastructure and the Environment, Rijkswaterstaat, Utrecht, The Netherlands

A. de Boer
Consultant, The Netherlands

ABSTRACT: In 1997 the Second Stichtse Bridge, a high strength concrete box girder bridge was built in the Netherlands using the balanced cantilever method. At that time, the long-term behaviour of this material (with a cube compressive strength of 75 MPa) was not known. Therefore, it was proposed to monitor the material behaviour and the deflections of the bridge for ten years, and a few properties have been monitored for twenty years. To evaluate the concrete material properties over time, concrete cubes were cast with the segments, and stored inside the bridge at the section locations. These samples have been tested periodically. Also shrinkage measurements were carried out on a concrete sample stored inside the bridge. The deflections of the bridge superstructure have been measured periodically along both edges of the bridge. Based on the available data, it is found that the concrete compressive and splitting tensile strength, as well as the shrinkage deformations, remain constant. The deflections are stabilizing as well.

1 INTRODUCTION

The in-situ balanced cantilever method can be used for the construction of prestressed concrete bridges with a variable height and with a box girder cross-section. Until 1984, these bridges were built in the Netherlands by using lightweight concrete or normal strength normal weight concrete with gravel aggregates. The advantage of using lightweight concrete was the reduction in self-weight, but in practice problems were observed: during construction, the high pressure used to prepare the ducts resulted at some locations also in air and the propagation of cracks in the concrete, which led to spalling of the concrete. As a result, in the 1990s the option of using high strength concrete was explored.

In 1997, the successful construction of the Second Stichtse Bridge, see Figure 1, marked the first application of high strength concrete ($f_{c,cu}$ = 75MPa) in a prestressed concrete balanced cantilever bridge. At that time, the governing codes did not include high strength concrete classes, and there was insufficient knowledge about the long term performance of high strength concrete mixes. For this reason, it was decided to monitor the material properties and overall structural behavior of the Second Stichtse Bridge. The originally planned duration for the monitoring was ten years, but this period was extended to twenty years for a number of parameters.



Figure 1. View of the Second Stichtse Bridge

In particular, the development of the concrete compressive and splitting tensile strength, the effect of creep and shrinkage (including autogenous shrinkage), and the resulting deflections over time were not well-known at the time of design. Estimating the elastic and time-dependent deflections during the construction stages is important to determine the required camber of the main span. Additionally, the creep and shrinkage behavior of the concrete needs to be known to estimate the time-dependent deflections. To analyze these parameters, experiments have been carried out on samples that were cast during construction of the bridge and stored in the bridge, as well as on samples that were cast during construction and then transported, stored, and tested in the Stevin II laboratory of Delft University of Technology. The deflections of the bridge are measured on site.

2 DESCRIPTION OF BRIDGE

The Second Stichtse Bridge was built in the Netherlands in 1997, and was the first prestressed concrete bridge constructed with the balanced cantilever method in high strength concrete. This bridge parallels the First Stichtse Bridge, a prestressed concrete bridge constructed with the balanced cantilever method in lightweight concrete, which opened in 1983. The Second Stichtse Bridge was necessary to double the traffic capacity of the crossing. The goal was to design the Second Stichtse Bridge in such a way that its overall geometry would look similar to that of the First Stichtse Bridge to respect the overall aesthetics. These bridges connect the provinces of Flevoland and Noord Holland and cross a canal that connects the Gooi lake and Eem lake.

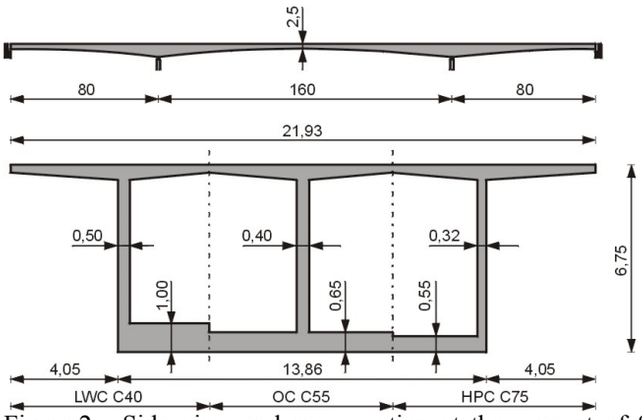


Figure 2. Side view and cross-section at the support of Second Stichtse Bridge. The cross-section compares the necessary dimensions in lightweight concrete, normal concrete, and high strength concrete from left to right (Van der Veen and Kaptijn, 2002).

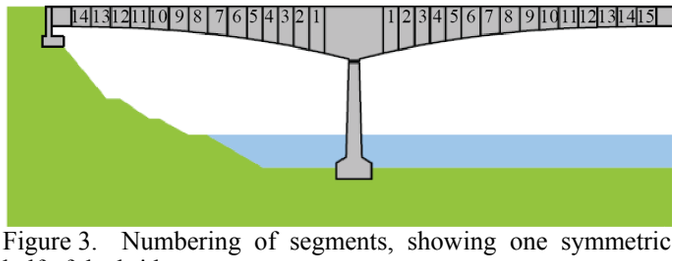


Figure 3. Numbering of segments, showing one symmetric half of the bridge.

The Second Stichtse Bridge has three spans: two end spans of 80 m and a main span of 160 m, see Figure 2. Originally, three designs were developed for comparison (Van der Veen and Kaptijn, 2002): 1) lightweight concrete ($f_{c,cu}$ = 40 MPa, with $f_{c,cu}$ the design concrete cube compressive strength), 2) normal weight normal strength concrete ($f_{c,cu}$ = 55 MPa), and 3) high strength concrete ($f_{c,cu}$ = 75 MPa), as shown Figure 2. The lowest cost was obtained for the design with high strength concrete. Since the dimensions and the weight of the high strength concrete option are smaller than for the normal strength option, larger segments could be developed and the erection time could be shortened by three months. The numbering of the segments is shown in Figure 3. The discussed specimens were cast together with the main span segments.

3 LONG TERM MATERIAL BEHAVIOR

3.1 *Concrete compressive strength*

The concrete compressive strength and the concrete splitting tensile strength have been monitored for twenty years. For this purpose, concrete cubes were cast at the time of construction of the bridge segments, and stored inside the box girder at the position of the respective segments. To determine the material properties, these cubes were retrieved from the bridge, transported to the laboratory, and tested there. This procedure was carried out at 84 days and 124 days after casting, as well as after 1, 2, 5, 10 and 20 years. All results are given in the full measurement report (Lantsoght and van der Veen 2017).

After 10 years of monitoring the results for the compressive strength of high strength concrete, a reduction in the compressive strength of 5% for the cubes stored with segments 8 and 9 was found. It was then concluded that a continued increase in the concrete compressive strength over time cannot be expected for high strength concrete.

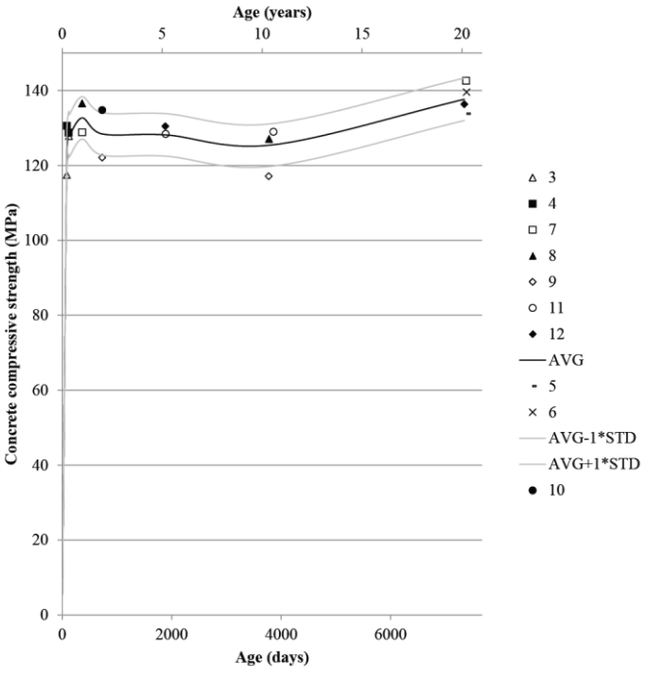


Figure 4. Development of concrete compressive strength over time. The legend shows the number of the segment with which the cubes were cast. Average values of the tested cubes are shown in the figure. The lines of 1 standard deviation above and below the overall average are shown as well.

After 20 years, cubes stored with segments 5, 6, 7 and 12 were tested. The concrete compressive strength as a function of the time is shown in Figure 4, based on the average values of the cubes per segment. These results shown no (further) decrease of the concrete compressive strength, and even indicate

a possible increase over time. It can thus be safely concluded that the compressive strength of high strength concrete does not decrease as a function of time. This conclusion is further reinforced when the variation of the results is taken into account. In Figure 4 the lines of one standard deviation above and below the average value are given. This average value is determined as the average of all cubes tested at a certain age, regardless of the segment. The standard deviation was calculated as 5.67 MPa. Note that this value is slightly larger than the value of 4.88 MPa that is assumed for the cylinder concrete compressive strength in NEN-EN 1992-1-1:2005 (CEN, 2005). From these results, it can be seen that the average value plus one standard deviation after one year (138 MPa) is similar to the average value after twenty years (138 MPa). For finely ground cement, no doubling or tripling of the concrete compressive strength is found over time, which is the case for coarsely ground cement.

3.2 *Concrete splitting tensile strength*

After ten years of monitoring a splitting tensile strength, determined on cubes, of 7 MPa on average was found. Only after two years, temporarily lower values were found (6 MPa). These values are still higher than the average tensile strength of C55/67 concrete, which according to NEN-EN 1992-1-1:2005 should be $f_{ct,m}$ = 4.2 MPa. The general conclusion after ten years of monitoring was that the splitting tensile strength remained constant.

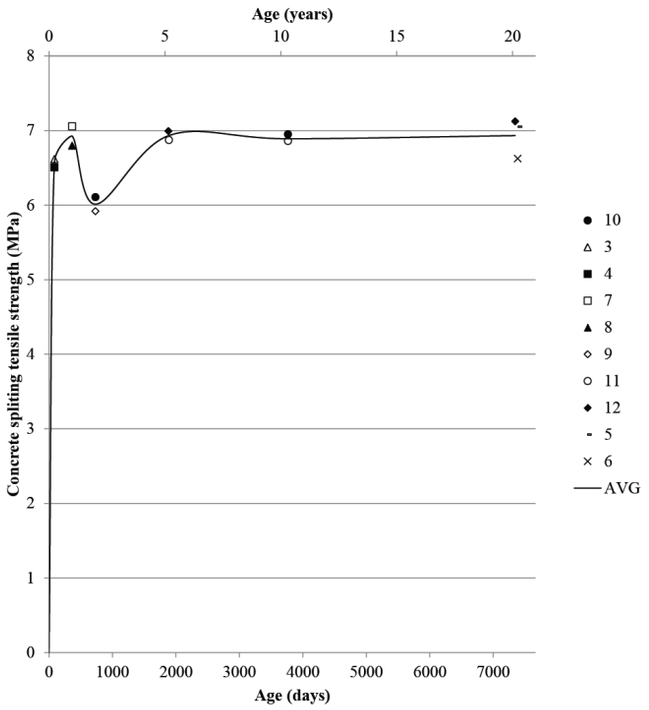


Figure 5. Development of concrete tensile splitting strength over time. The legend shows the number of the segment with which the cubes were cast. Average values of the tested cubes are shown in the figure.

After twenty years, the splitting tensile strength was determined on cubes cast together with segments 5, 6 and 12. These results confirm that the concrete splitting tensile strength determined on cubes remains constant, and about 7 MPa. These results are shown in Figure 5. The line of the average plus and the average minus one standard deviation is not shown in Figure 5, since the relation between the mean and characteristic tensile splitting strength in NEN-EN 1992-1-1:2005 (CEN, 2005) is not determined with a relation that involves the standard deviation.

Another observation that could be made based on the determination of the splitting tensile strength of the concrete over twenty years, is a small increase of the standard deviation on the measured splitting tensile strength. The value increased from about 0.5 MPa during the first years to 0.7 MPa after twenty years.

The general conclusion of monitoring the splitting tensile strength of the high strength concrete mixture for twenty years is that the tensile strength remains constant after five years.

3.3 *Shrinkage*

During the first ten years, shrinkage measurements were taken in the laboratory as well as on concrete blocks stored inside of the bridge box girder. For the specimens stored in the laboratory, the shrinkage strain ε_{sh} is determined for loading high strength concrete of 14 days old and concrete of 1 year old. All specimens were stored at a constant temperature of 20°C and a relative humidity of 50%. For the concrete loaded at 14 days until ten years, a shrinkage strain of $\varepsilon_{sh} = 0.35\times10^{-3}$ was found, and for the concrete load at 365 days old until ten years, a shrinkage strain of $\varepsilon_{sh} = 0.25\times10^{-3}$ was found. The shrinkage effect that was measured in the laboratory was mostly drying shrinkage, since autogenous shrinkage mainly occurs in the first weeks after casting concrete.



Figure 6. Specimen for shrinkage measurements inside box girder.

The specimens that were stored inside the box girder were cast together with segments 13 and 15 and have the same thickness (320 mm) as the web of the box girder. The size of the specimens is 320 mm

× 600 mm × 1000 mm. The deformations are measured at three positions (two on top of the specimen and one on the bottom) over a length of 800 mm. The specimen inside the box girder is shown in Figure 6. The shrinkage deformations are found as the difference between the measured deformations and the deformations caused by temperature variations. The strain caused by the temperature ε_{temp} is determined as:

$$\varepsilon_{temp} = \alpha\left(T_{meas} - T_{ref}\right)l_{meas} \quad (1)$$

with α = 12×10^{-6}/ºC×m, T_{meas} the temperature when the measurement is taken, T_{ref} the reference temperature of 9.7ºC on April 11th 1997 at 11 am when the measurements were started, and l_{meas} the length over which is measured (i.e. 800 mm).

The results of the shrinkage measurements for the specimen cast with segment 13 are shown in Figure 7 and for the specimen cast with segment 15 in Figure 8. As shown in Eq. (1), the effect of the deformations caused by temperature fluctuations needs to be taken into account. No difference between the measurements on the top and bottom of the specimen are observed.

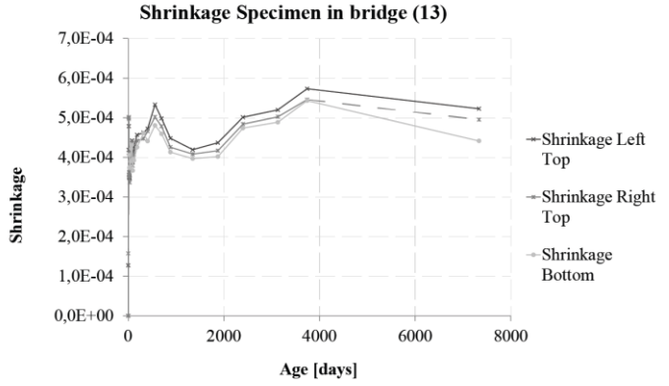


Figure 7. Shrinkage as measured in specimen 13, assuming temperature of 9ºC.

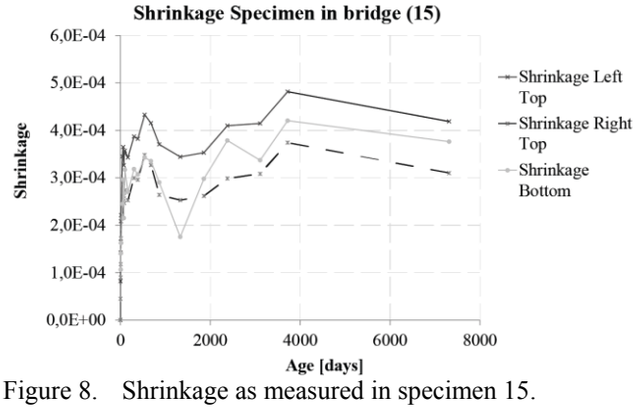


Figure 8. Shrinkage as measured in specimen 15.

During the first ten years of monitoring, the temperature and humidity inside and outside of the box girder were measured. For the measurements after twenty years, the temperature was estimated based on the observations of the Royal Dutch Meteorological Institute (Royal Dutch Meteorological Institute, 2017). The nearest observation stations (Schiphol, Berkhout, De Bilt, Lelystad) reported temperatures on April 26th 2017 at 2 pm ranging between 8.3ºC (De Bilt) and 9.7ºC (Schiphol). An exterior temperature of 9ºC can thus be assumed. This temperature was used to determine the resulting shrinkage strain in Figure 7 and Figure 8.

Since the specimen on which the shrinkage measurements were taken was stored inside of the box girder, the temperature inside may have been larger than the exterior temperature. Based on the measurements of temperature and relative humidity from the first ten years of monitoring, it can be concluded that the difference between the inside and outside temperature is on average 1.5ºC (Van der Veen 2008). The temperature inside of the box girder is more constant than the exterior temperature. The largest temperature differences are observed during winter and summer, and are maximum 9ºC. During the spring months, the largest observed differences between the temperature inside the girder and outside are 5ºC. Therefore, it is assumed that the temperature inside the box girder can have been maximum 14ºC. The results for the shrinkage strain, after a correction for the strain caused by a temperature of 14ºC, are shown in Figure 9.

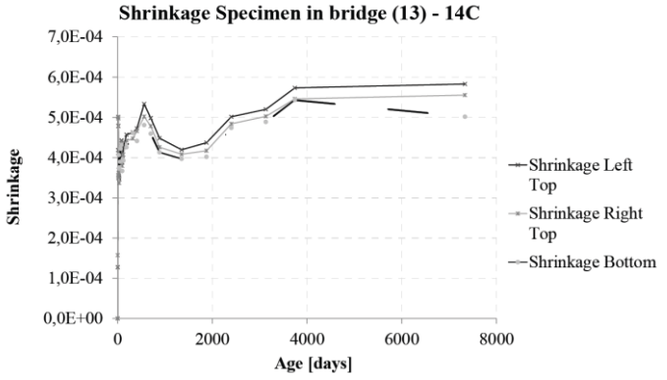


Figure 9. Shrinkage as measured in specimen 13, assuming a temperature of 14ºC.

When a temperature inside the box girder of 9ºC is assumed (Figure 7 and Figure 8), a small amount of swelling of the specimens can be observed after twenty years in comparison with the measurements after ten years. When a temperature inside the box girder of 14ºC is assumed (Figure 9), virtually no difference between the shrinkage strain after ten and twenty years is found. During the first 18 months, a clear increase of the shrinkage strains was observed. Subsequently, a period of swelling of the specimens was observed until three years after casting the concrete. For the time period between three and ten years, a continuous shrinkage is observed in all specimens. this shrinkage process was thus not continued until the concrete reached an age of twenty years. It can thus be concluded that no further increase in shrinkage is observed after twenty years and that the time-dependent deformations have sta-

bilized in the observations between ten and twenty years.

3.4 *10 years of monitoring creep*

The effect of creep is measured in the laboratory as well as on site (De Boer and van der Veen 2012). The creep measurements in the lab are carried out on beams with dimensions of 100 mm × 100 mm × 400 mm, see Figure 10. The length over which the deformations are taken is 200 mm. These measurements are done by using four LVDTs per specimen. The specimens are not sealed, so that the measurements have to be corrected for the effect of shrinkage. The test is carried out in a room with constant temperature of 20°C and RH = 50%.

Three ages of loading the specimens are selected: 14 days, 28 days, and 365 days. For the specimens loaded at 14 and 28 days, a stress of 10 MPa is used, and for the specimen loaded at 365 days 20 MPa. This load level was kept constant for 10 years. The measurements led to the conclusion that a very small creep factor (defined as related to the elastic deformation at 28 days) of between 0.5 and 1.0 is observed for the studied high strength concrete for all ages of loading of the concrete.



Figure 10. Test setup in laboratory for monitoring creep during 10 years.

After ten years, the load was removed from the creep specimens. The occurring deformations during unloading were measured as well. Afterwards, the specimens were loaded to a stress level of 35 MPa (about 30% of the actual measured compressive strength). The behavior during loading was linear elastic and could be used to determine the modulus of elasticity, which was found to increase as the age of the concrete at first loading increased. As such, it is possible to determine the load level that occurred in a sample by loading the sample again. It must be considered that the modulus of elasticity is influenced by the load level and the age of first loading. After unloading, the delayed elastic deformations occurred within 60 minutes after removing the load. These observations are important for the assessment of existing bridges, where the effect of prestressing on the concrete needs to be determined.

To determine the modulus of elasticity, beams of 100 mm × 100 mm × 400 mm are tested under compression. The modulus of elasticity is determined at 1/3rd of the failure load. It is found that for concrete of one year old, the modulus of elasticity is 10% higher than after 28 days.

In addition to the laboratory tests, measurements were taken on the web of the box girder for segments 2, 13, and 15. Measurement points were applied on the box girder. Since a specimen inside the box girder (Figure 6) was monitored for shrinkage, the difference in behaviour between the web and the shrinkage specimen can be attributed to creep. Therefore, the measurements on the web have to be corrected for the effect of shrinkage (determined based on the specimen stored inside the bridge), and the effect of temperature to find the effect of creep. The results for segment 13 for ten years of monitoring are shown in Figure 11. The large increase in the strains at 120 days of age were caused by the casting of the asphalt layer. These results can be used for calculations with for example finite element models.

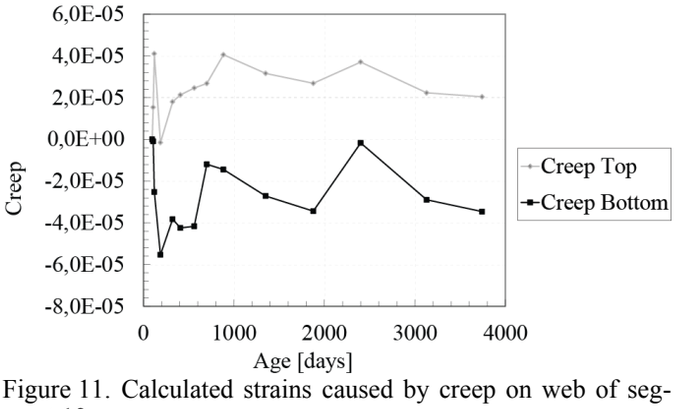


Figure 11. Calculated strains caused by creep on web of segment 13.

4 LONG TERM STRUCTURAL BEHAVIOR

4.1 *Deflection measurements*

At several points in time between 1997 and 2016, the deflections of the bridge have been measured by an external surveyor. Two sets of measurements at 13 positions (on both sides (West and East) of the bridge) are taken, see Figure 12 and Figure 13. The measured deformations are deflections (positive for hogging and negative for sagging) at the second

support (Sup 2), at midspan of the 160 m middle span (Span), and at the third support (Sup 3).

To find the net deflection at midspan, without the effect of the settlements at the support, the effect of all support settlements should be taken into account. A large settlement occurs at support 1; the measured value of this settlement is -22.3 mm in 2016. Such a settlement would result in a hogging at midspan of the main span between supports 2 and 3. To find the hogging or sagging deflection at midspan of the main span, a beam model is used of the box girder modeled as a girder with a variable moment of inertia I.

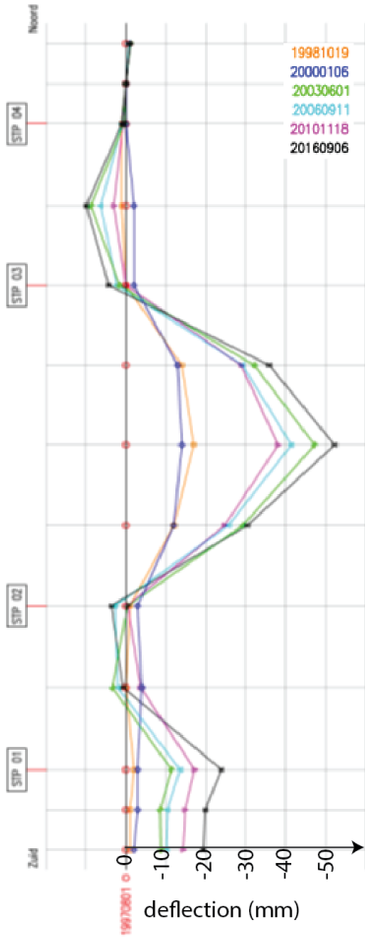


Figure 12. Measured deflection profiles reported in 2016, profile 101-113, with date of measurements in YYYYMMDD format (Sikken, 2016)

The variability in the moment of inertia I results from the changes in the height of the cross-section, as shown in Figure 2. For spans 1 and 3, the height varies parabolically between 2.5 m and 6.75 m. The expression is as follows:

$$h(x) = 6.64\times10^{-4}\frac{1}{m}x^2 + 2.5m \qquad (2)$$

For the central span, the height is also assumed to vary parabolically between the supports and the midspan:

$$g(x) = 6.64\times10^{-4}\frac{1}{m}x^2 - 0.10625\times x + 6.75m \qquad (3)$$

All other properties of the section, required to calculate I, are taken from Figure 2. The top flange is simplified as of constant height, and assumed to be 0.35 m. The value of the Young's modulus of the concrete is taken as E = 46725 MPa, as measured after one year (Van der Veen 2008). In the beam model, elements with a length of 5 m (the largest length of a segment that was used during construction) are used, with a different value of I, calculated based on the different value of the height.

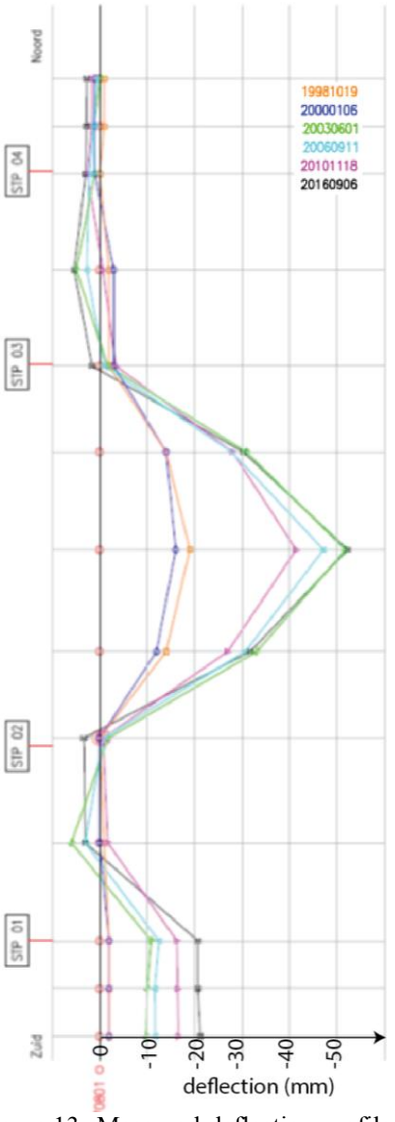


Figure 13. Measured deflection profiles reported in 2016, profile 401-413 (Sikken, 2016).

For the deflection measurements of 2016, the support settlements measured at the four supports resulted in a calculated hogging of 11.35 mm at midspan for the central span. Since a sagging deflection at midspan was measured of -52.25 mm, it can be found that the net deflection equals -63.60 mm.

The effect of the support settlements on the midspan deflection for the central span is calculated for all sets of measurements, see Table 1. These results are then used to calculate the net deflection at midspan of the central span, see Table 2. Additionally, the outside temperature T at the day of the observations as reported by the surveyor is included in Ta-

ble 2. In 2008 (Van der Veen 2008) it was mentioned that the deflections measured in 1999, at a temperature of 8ºC were lower and below the trend of the measurements taken at higher ambient temperatures. Similarly, it can be seen that the deflections measured in 2010, at a temperature of 8-12ºC were lower as well.

The calculated net midspan deflections of the central span can then be shown as a function of the time, see Figure 14. This figure also shows that the increase in deflections between the structure with an age of five years and with an age of twenty years is limited.

Table 1. Average support settlements and midspan deflection

Date DD-MM-YYYY	Sup 1 (mm)	Sup 2 (mm)	Span (mm)	Sup 3 (mm)	Sup 4 (mm)
04-08-1997	0.00	0.00	0.00	0.00	0.00
07-09-1998	-2.00	0.00	-18.00	-1.00	0.50
15-11-1999	-2.50	-1.00	-15.00	-2.50	0.50
17-11-2003	-11.15	-0.60	-49.55	-0.05	0.70
11-09-2006	-13.05	1.45	-44.25	0.65	1.55
18-11-2010	-16.75	-0.40	-39.75	-1.70	1.60
06-09-2016	-22.30	3.95	-52.25	2.95	1.95

Table 2. Calculated effect of support settlements and resulting net deflection at midspan

Date DD-MM-YYYY	Effect (mm)	Net (mm)	*T* (ºC)
04-08-1997	0.00	0.00	21.7
07-09-1998	-0.355	-17.65	17.4
15-11-1999	-2.185	-12.82	8
17-11-2003	2.517	-52.07	23-25
11-09-2006	4.443	-48.69	25
18-11-2010	2.735	-42.49	8-12
06-09-2016	11.35	-63.60	20

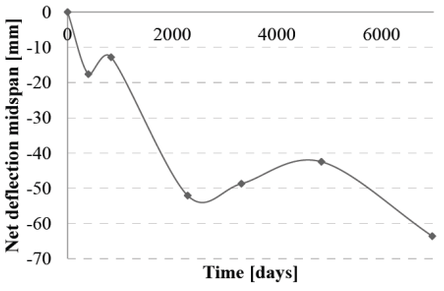


Figure 14. Net deflection at midspan of the central span, corrected for the effect of the support settlements.

For the measured deflections, two conclusions can be drawn. The first conclusion is that the measured deflections are larger when the temperatures are larger, and that this observation should be kept in mind when evaluating the results of the measurements. The second conclusion is that the net deflection at midspan of the central span after twenty years (-63.60 mm) can be considered as small. This deflection is 1/2516 of the span length of 160 m.

4.2 *Comparison to predictions*

During the design stage and after construction of the Second Stichtse Bridge, several predictions have been made of the long-term deflections. The most recent, and most advanced calculations (Louman, 2005), were carried out in TNO Diana Release 8 (TNO DIANA, 2005) using staged execution of the structure and using the modulus of elasticity as a function of the time, the creep as a function of the time and load, related to the actual construction and load scheme of the bridge, and the shrinkage dependent on the time of removing the formwork. The creep and shrinkage models of NEN-EN 1992-1-1:2005 (CEN, 2005), Model Code 1990 (CEB-FIP, 1993) and Han (Han, 1996), a modified model of the Model Code 1990 with the inclusion of parameters for high strength concrete, have been studied. The results for the predictions for 100 years are given in Figure 15a. These are then compared to the measurements in Figure 15b. From this comparison, it can be seen that the predictions using the creep and shrinkage methods of Eurocode 2 and Han give better results than Model Code 1990, which overestimates the long-term deflection.

5 DISCUSSION

The presented results contain unique data with regard to the long-term material and structural behavior of high strength concrete box girder bridges. These results can be used to compare to the strains caused by creep and shrinkage as prescribed by the governing codes, which are determined based on only laboratory test results. Since the presented results are determined based on laboratory specimens as well as on an actual structure, they can be used to improve the assessment practice for existing prestressed high strength concrete bridges. These field data can also be used to optimize the design of high strength concrete balanced cantilever bridges. Future analysis of the bridge can include the material models of the *fib* Model Code 2010 (fib, 2012), and/or using a plane stress model to study shear.

6 SUMMARY AND CONCLUSIONS

In 1997, the Second Stichtse Bridge was the first high strength concrete prestressed box girder bridge constructed using the balanced cantilever method in the Netherlands. At that time, the code provisions did not include high strength concrete classes and the creep function was not considered dependent on the load. Therefore, assumptions with regard to the

long-term concrete behavior had to be made during the design stage.

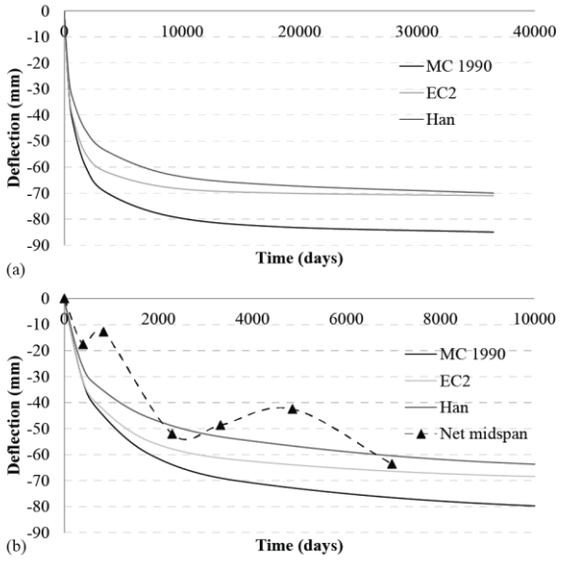


Figure 15. Long-term deflection at midspan of central span: (a) predictions for 100 years (Louman, 2005); (b) comparison between results of twenty years of measurements and predictions

To verify the assumptions with regard to the material behavior, and to learn more about the long-term behavior of high strength concrete in large bridges, a monitoring program was started. The concrete compressive strength and splitting tensile strength were determined based on cubes stored inside the box girder. The effect of shrinkage was determined based on specimens in the laboratory and inside the box girder. The effect of creep was determined from measurements on the web of the box girder. The structural behavior was monitored by measuring the deflections at regular intervals.

After ten years of monitoring, a small decrease of the concrete cube compressive strength was measured. However, the results of testing after twenty years show that the concrete compressive strength remains constant and that there should be no concern with regard to a decrease of the compressive strength.

After twenty years of monitoring the cube splitting tensile strength, it is concluded that this strength has remained constant since the concrete had an age of one year.

After twenty years, the deformations caused by shrinkage have stabilized and are not increasing further. The calculated shrinkage strain does depend on the temperature inside the box girder, which had to be estimated since the temperature and humidity measurements were stopped after ten years of monitoring.

The deflections of the superstructure are determined at regular intervals by surveyors. The analysis in this paper showed that the effect of the support settlement for support 1 resulted in an effect of hogging at the midspan of the central span. When this effect is considered, a net deflection of the central span after twenty years of 63.6 mm is found, which is a small deflection. This value corresponds to the predicted deflections from a finite element model using the long-term material behavior from Eurocode 2 and Han.

ACKNOWLEDGEMENTS

The authors wish to express their gratitude and sincere appreciation to the Dutch Ministry of Infrastructure and the Environment (Rijkswaterstaat) for financing this research work. The help of Fred Schilperoort, Ger Nagtegaal and the late Erik Horeweg during the experiments in the Stevin II laboratory of Delft University of Technology and during the field measurements is also gratefully acknowledged.

REFERENCES

CEB-FIP 1993. Model Code 1990. Lausanne, Switzerland: European Concrete Committee and International Federation for Prestressing.

CEN 2005. Eurocode 2: Design of Concrete Structures - Part 1-1 General Rules and Rules for Buildings. NEN-EN 1992-1-1:2005. Brussels, Belgium: Comité Européen de Normalisation.

DE BOER, A. & VAN DER VEEN , C. 2012. Longterm behaviour of cantilever concrete bridges. *fib symposium 2012.* Stockholm, Sweden.

FIB 2012. *Model code 2010: final draft,* Lausanne, International Federation for Structural Concrete.

HAN, N. 1996. *Time Dependent Behaviour of High Strength Concrete.* Ph.D. Thesis, Delft University of Technology.

LANTSOGHT, E. O. L. & VAN DER VEEN , C. 2017. Twenty years of monitoring the Second Stichtse Bridge in high strength concrete - Measurement Report 2017 (in Dutch).

LOUMAN, F. G. 2005. *Realistic simulation deformation of bridges constructed with the balanced cantilever method - comparsion between Eurocode and current design provisions (in Dutch).* M.Sc., Delft University of Technology.

ROYAL DUTCH METEOROLOGICAL INSTITUTE. 2017. *Hourly weather data for the Netherlands* [Online]. Available: http://www.knmi.nl/klimatologie/uurgegevens/datafiles/350/uurgeg_350_2011-2020.zip. [Accessed 07/06/2017.

SIKKEN, J. 2016. Measurement report deformation measurements Stichts Bridge 26C-100-02-06 Second Stichtse Bridge, Southern bridge over lake Gooi, recorded 20160906 (in Dutch).

TNO DIANA 2005. Users Manual of DIANA, Release 8.1. Delft, The Netherlands.

VAN DER VEEN , C. 2008. Ten years monitoring Second Stichtse Bridge in high strength concrete (in Dutch). Delft, the Netherlands: Delft University of Technology.

VAN DER VEEN , C. & KAPTIJN, N. 2002. Long term behaviour for cantilever bridges in HPC. *fib symposium 2002.* Japan.

Maintenance, Safety, Risk, Management and Life-Cycle Performance of Bridges – Powers, Frangopol, Al-Mahaidi & Caprani (Eds)
© 2018 Taylor & Francis Group, London, ISBN 978-1-138-73045-8

Estimating Climate Effects on Bridge Decks Deterioration

Shuang Liu, Hongping Zhu, Lifei Yang & Muhammad Habib
Huazhong University of Science and Technology, Wuhan, China

ABSTRACT: In this paper, a two-step methodology is proposed to enrich the traditional National Bridge Inventory (NBI) database by taking some environmental information into consideration and estimate climate effects on bridge decks deterioration. The NBI database is firstly extended with more detailed National Oceanic and Atmospheric Administration (NOAA) weather station data which includes temperature, daily temperature difference, relative humidity and freeze-thaw cycles, by means of bridge longitude and latitude records. After that, Different climate factors are used to classify climate regions and the numerical analysis of climate effect on bridge decks deterioration is implemented based on the new database. The results indicate that region 3 with higher freeze-thaw cycles shown a more faster trend on deck deterioration than region 1 and 2. While, when the number of freeze-thaw cycles is less than 80 per year, concrete carbonization caused by temperature and humidity will be the predominant environmental factor for bridge deck deterioration. This proposed method makes the traditional National Bridge Inventory (NBI) database more comprehensive and easy to update and expand, it helps to obtain accurate prediction of the future condition of bridge decks in bridge management system.

1 INTRODUCTION

The condition of the nation's aging bridges has been of the highest concern in recent decades. FHWA estimates that $20.5 billion will need to be invested annually in order to eliminate the United States bridge deficient backlog by 2028. As bridge deck deterioration is one of the primary concerns and cost factors for transportation agencies, the accurate prediction of the future condition of bridge decks becomes an important and urgent task. To accomplish this comprehensive work, the factors that affect the deterioration should be studied thoroughly, which is also a prerequisite of developing deterioration models.

With the aid of NBI database, bridge deck deterioration modeling has been performed by numerous researchers over the year. Many recommended deck deterioration models are built by using third-degree polynomial regression, Markov chain and Weibull-based approach (Bolukbasi et al. 2004; Agrawal et al. 2009; Cruz 2013; Zhang et al. 2003; Scherer and Glagola 1994; Dekelbab et al. 2008), these models describe the relationship between condition rating and bridge age. Some other studies on this topic, account for deck deterioration not only due to bridge age but also other NBI explanatory factors, such as, geometric information, applied load (traffic), and wearing surface information (Ben-Akiva and Gopinath 1995; Mauch and Madanat 2001; Morcous and Hatami 2011; Radovic et al. 2016). These manually selected candidate variables may not be effective for all states and locations and may also exclude potentially important factors. For instance, Wells (1994) recognized the potential differences in deterioration rates of bridge elements due to differences in climatic exposure and operating practices. Dadson (2001) proposed that the region affect the service life of the bridge in Virginia. Kim et al. (2009) found that water is a factor that cannot be ignored during the bridge deterioration analysis. TU Saeed et al. (2017) carried out sensitivity and marginal effects analyses to quantify the effect of the influential factors and found that freeze index, freeze-thaw cycles has a significant adverse effect on bridge condition. Particularly bridge deck is the most immediate component of bridge structure exposed to the harsh conditions of climatic changes, that means it is highly vulnerable to external environment. Damage due to temperature and relative humidity, deicing salts, freeze-thaw cycle induced stresses, fatigue and above all corrosion of rebars, have been confirmed through field tests and numerical modeling (Bremner et al., 2001; Berntsson, L et al. 1995; Gong et al., 2014; Oneill et al., 2001; Nawy, 2008).

Above literature review indicates that a rather spare research can convenient incorporate climate effects into consideration during the bridge deck deterioration. The fundamental reason is that the NBI database lacks environment related items. For this

reason, this paper introduces a two-step methodology to make the traditional NBI database more comprehensive and easy to update and expand.

1. Create NBI and climate database with the aid of SQL server software, and then connect every bridge with the nearest weather station using the information of longitude and latitude. Through these analyses, this paper adds some climate items (temperature, relative humidity, No. of days above 32℃, No. of days below 0℃, freeze-thaw cycles, and No. of daily temperature difference more than 20℃) into the traditional NBI database.

2. Using different climate factors to divide climate zones, and three climatic regions were selected and the deck degradation trends were analyzed and compared.

2 DATA COLLECTION AND DATABASE CONSTRUCTION

2.1 *NBI database*

The National Bridge Inventory (NBI) is a database (FHWA), compiled by the Federal Highway Administration, with information on all bridges and tunnels in the United States. It includes identification information, bridge types and specifications, operational conditions, bridge data (geometric data, functional description, and inspection data). Bridges longer than 20 feet (6.1 meters) used for vehicular traffic is included (Chase et al. 1999).The inventory is developed with the purpose of having a database for bridges to ensure the safety of the traveling public as required by the Federal-Aid Highway Act of 1968 (Graybeal et al. 2002). For further normalization of the NBI data, the FHWA published the Recording and Coding Guide for the Structure Inventory and Appraisal of the Nation's Bridges in 1971. This coding guide outlined the specific bridge elements that are required to be inspected, and provided the guidelines on how to conduct an inspection and records formats.

Based on the NBI coding guide (FHWA 1995), "Condition ratings are used to describe the existing, in-place bridge as compared to the as-built condition." Condition codes are representative of the general condition of the entire component (i.e., deck, superstructure, or substructure). In this rating system, bridge elements condition ratings vary from 0 to 9, and their description for decks is shown in Table 1. These condition ratings are subjective assessments assigned by bridge inspection teams where 9 indicates the best and 0 shows the worst condition.

Table 1. Description of condition rating of bridge decks in NBI

Rating	Description
N	NOT APPLICABLE
9	EXCELLENT CONDITION
8	VERY GOOD CONDITION - no problems noted.
7	GOOD CONDITION - some minor problems.
6	SATISFACTORY CONDITION
5	FAIR CONDITION
4	POOR CONDITION
3	SERIOUS CONDITION
2	CRITICAL CONDITION
1	"IMMINENT" FAILURE CONDITION
0	FAILED CONDITION

To facilitate data storage and extraction, this paper introduced the software Microsoft SQL Server 2008 R2 to convert the ASCII format data to table records. Through the deep study on the original data we found some inconsistencies, such as, the same bridge have two built year records during the inspection period, or a bridge may have the Route_Prefix_005B, Base_Hwy_Network_012 records after year 1996, but before this year may not. Thus, appropriate update is necessary to ensure their consistencies.

The process of data adjustment is done by examining the records for each bridge. All records are selected into one table ordered by structure number and inspection date. Inspection records with the same structure number that show a partial missing of the location, geometric, functional description items will be added by the other complete records. For rebuilt bridges, this data supplement work should be divided into two phases before or after the reconstruction. The flowchart describing method is given in Figure 1.

2.2 *Climate database*

The climate database(CDB) obtains daily weather data for stations all around the United States using the Global Surface Summary of the Day (GSOD) dataset (NOAA). This dataset provides daily mean temperature, maximum temperature, minimum temperature, precipitation, air pressure, mean dew point and wind speed observed for weather stations around the world. These basic data could be used to compute key weather metrics, which are much more important in climate effects analysis, including the actual average annual temperature, relative humidity, No. of days above 32, No. of days below 0℃, freeze-thaw cycles, and No. of daily temperature difference more than 20℃.

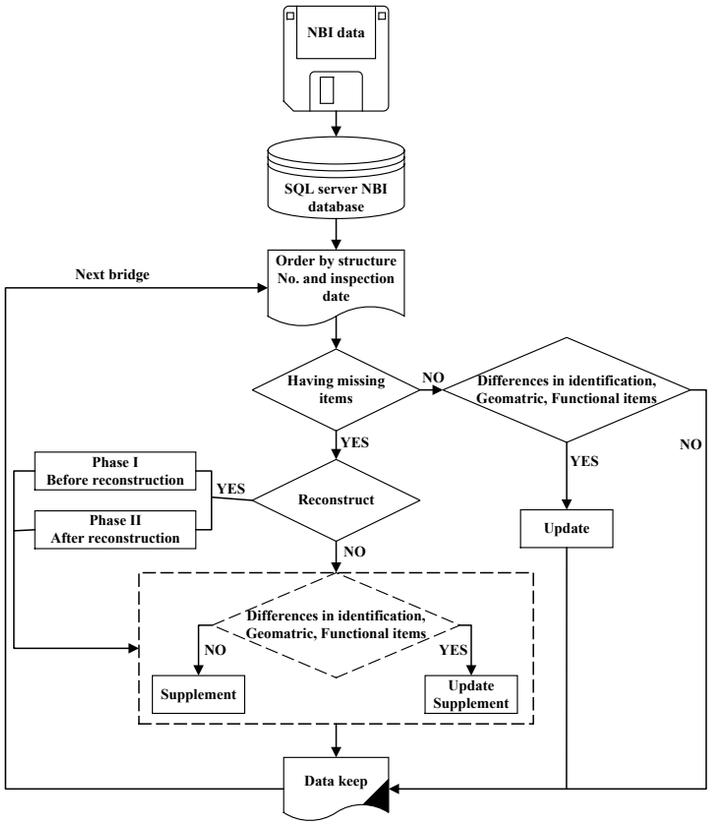


Figure 1. Flowchart for the NBI data adjustment.

Table 2. Derived Climatic Data

Data Element	Monthly		Annual	
	Average	No. of Days	Average	No. of Days
Mean temperature	√	√	√	√
Maximum temperature	√	√	√	√
Minimum temperature	√	√	√	√
No. of days above 32℃		√		√
No. of days below 0℃		√		√
Freeze-thaw cycles		√		√
Relative humidity	√		√	
Daily temperature difference >20℃		√		√

The GSOD set includes thousands of weather stations. In order to determine which stations to use, CDB went through a rigorous process to identify stations with complete data going back to at least the year 1990.

CDB will fill in gaps by averaging the preceding and following days together for occasionally missed data of an individual station for a day or more. This process of averaging values together is consistent with how NCDC fills in gaps for their own datasets and analyses. In the case that an entire month is missing, CDB will use the climate normal value to fill in that month. If a weather station stops reporting data more than five months, then CDB will remove that station from our list.

Based on this integration and processing, there are more than one thousand weather stations used for the United States every year, Figure 2 illustrates the locations of these stations in year 2016 and the number of stations used every year.

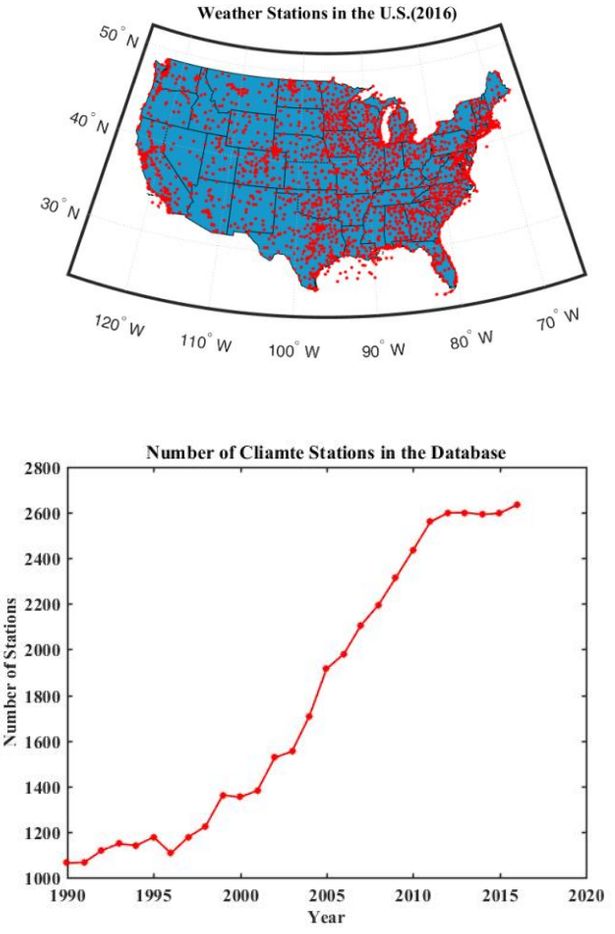


Figure 2. Weather Stations in the USA

2.3 *Database connection*

FHWA's Recording and Coding Guide (FHWA 1995) declared that the structure number(item 8) must be unique for each bridge within the state, and once established should preferably never change for the life of the bridge. At the same time, every NBI bridge has some identification items, such as bridge latitude and longitude information illustrated in item 16, item17 as mentioned in the above chapter. So we can believe that each bridge has a fixed corresponding longitude and latitude. Based on this assumption, the records having no information of longitude and latitude in the early years can be modified and supplemented by the big data analysis from 1992 to 2016. After that, a MATLAB code was written to calculate the nearest weather station for every bridge using its location.

3 CLIMATE EFFECTS ANALYSIS

3.1 *Climatic regionalization*

The freeze-thaw cycle is a main environmental factor which leads to the initiation of cracks and erosion of chloride ion at bridge deck. Figure 3 compares the freeze-thaw cycles recorded from 1992 to 2016 in the database. The figure divides the interstate highway bridges into four parts (less than 40 days; between 40 and 80 days; between 80 and 120 days; more than 120 days) based on the number of freeze-thaw cycles per year. In this division, we use a statistical method that, if the records in a certain interval are more than two-thirds of the total during the bridge inspection period, we determine the bridge into that freeze-thaw interval.

Figure 4 shows the annual mean temperature distribution of the interstate highway bridges. Using the k-means cluster method to divide the bridges into four parts. The cluster centroids are 20.6℃, 16.3℃, 11.4℃ and 7.2℃, respectively. These census data justify the noticeable difference in temperature among the states. This same method was also used to assess the variation of relative humidity in different regions as shown in figure 5, and the centroids are 69.60%, 57.28% and 37.50%, respectively.

According to the climatic regionalization, two representative states per regions (except region 4, In order to control the number of climatic explanatory variables) were selected (Table 3) to do the following analysis.

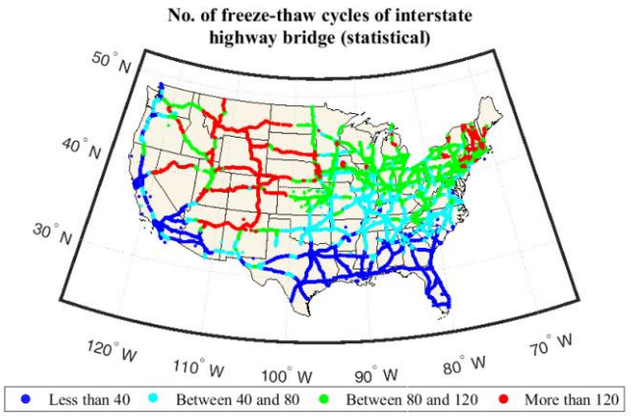


Figure 3. Climatic regionalization based on No. of freeze-thaw cycles per year

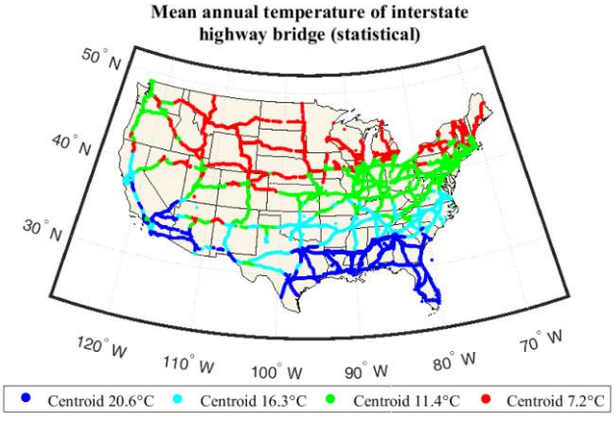


Figure 4. Climatic regionalization based on mean annual temperature

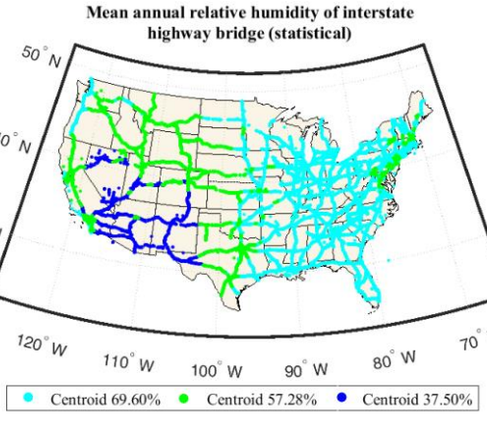


Figure 5. Climatic regionalization based on mean annual relative humidity

Table 3. Bridge data selected

Region	States	No. of freeze-thaw cycles per year	Mean annual temperature (cluster centroid)	Mean annual relative humidity (cluster centroid)
1	Alabama(AL),Georgia(GA)	less than 40	20.6℃	69.60%
2	Tennessee(TN), North Carolina(NC)	between 40 and 80	16.3℃	69.60%
3	Indiana(IN),Ohio(OH)	between 80 and 120	11.4℃	69.60%

3.2 *Data filtering*

In the NBI database, Some bridge elements have undergone major maintenance, rehabilitation, and replacement actions that were not recorded during the service period of the bridge, which may result in erroneous element condition versus age (outliers). For instance, a 50-year-old bridge deck with a condition rating of 9 or 2 or 3 condition rating for a relatively new constructed superstructure (e.g., age 2 years). This kind of phenomenon is much more common in the bridge deck deterioration records, probably because a bridge deck is the most immediate component of bridge structure exposed to the impact of traffic loads and climatic changes. Previous studies(Saito 1988; Markow et al. 1993; Bolukbasi et al. 2004) have shown that decks have a much shorter life than other bridge components. Furthermore, when a bridge is scheduled for reconstruction of its superstructure, the deck will also be replaced along with the other members. In order to eliminate this kind of records, this paper adopts the rules that bridges in the NBI with a date of construction or date of major reconstruction (NBI Item 27) within the past 10 years will not be considered a deficient bridge, will not be eligible for HBRRP funding applies to bridges replaced or reconstructed with any Federal-aid funds. For example, a date of 1976 will be used for the determination until the end of 1985. For the scope of this study, only the highway (excepted county highway) bridges with average daily traffic more than 5000 built during 1981 and 1990 were analyzed.

3.3 *Analysis and results*

Six cases of comparisons between the deterioration rates calculated by average condition rating are considered to demonstrate the climate effects on bridge deck deterioration. These cases show comparison between different regions and highway systems for the following: (1) interstate highway bridge decks without protection in region 1-3; (2) numbered highway bridge decks without protection in region 1-3; (3) state highway bridge decks without protection in region 1-3; (4) interstate highway bridge decks with and without protection in region 3; (5) numbered highway bridge decks with and without protection in region 3; (6) state highway bridge decks with and without protection in region 3.

Figures 7-9 illustrate the variation of average deck condition rating by inspection year. As can be seen from the figures, the deterioration of the bridge decks revealed a trend that region 3 deterioration rate is much faster than the others, while the region 2 is the slowest. The detailed numerical results are presented in table 4. This phenomenon indicates that the deterioration of the deck is relatively rapid when the bridges have experienced more freeze-thaw cycles in the moist environment. Because bridges serviced under this condition have high water content, water held in the pores of cement paste will freeze at low temperatures. As ice occupies a bigger volume than water so expansive forces can be generated, thus can result in surface cracks. More cycles of freezing and thawing result in progressively deeper damage. At

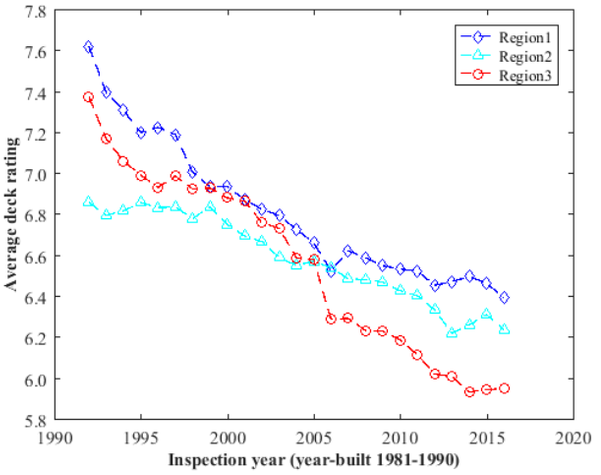


Figure 7. Average condition of the interstate highway bridge decks

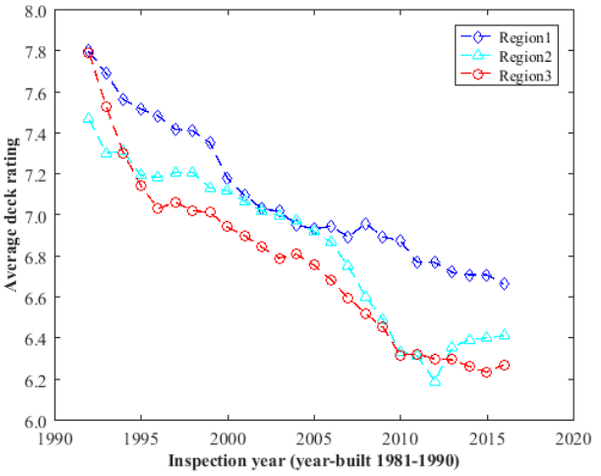


Figure 8. Average condition of the numbered highway bridge decks

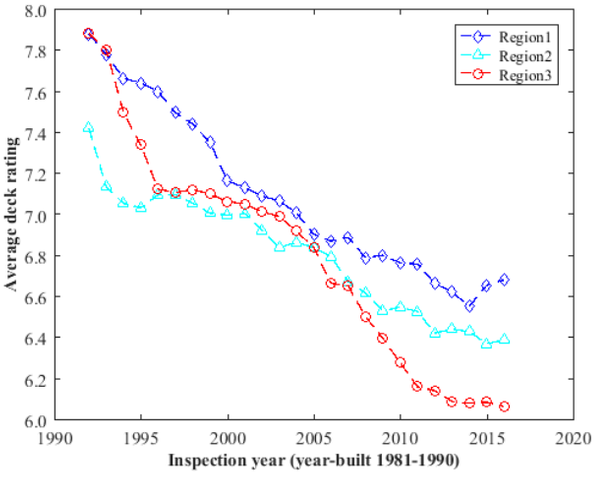


Figure 9. Average condition of the state highway bridge decks

Table 4. Deterioration rates of highway bridge deck condition (without protection)

Region	Interstate highway		Numbered highway		State highway	
	⩾7	Total	⩾7	Total	⩾7	Total
1	-0.084	-0.045	-0.070	-0.052	-0.075	-0.053
2	—	-0.029	-0.035	-0.050	-0.124	-0.038
3	-0.126	-0.060	-0.105	-0.061	-0.083	-0.072

the same time, the more cycles of freezing and thawing mean the greater possibility use of de-icing salts, which can also, accelerates the deterioration process. Comparing region 1 and region 2, the concrete carbonation caused by temperature and humidity will be the predominant environmental factor for the degradation of the bridge deck when the number of days of freeze-thaw cycles are below 80 per year.

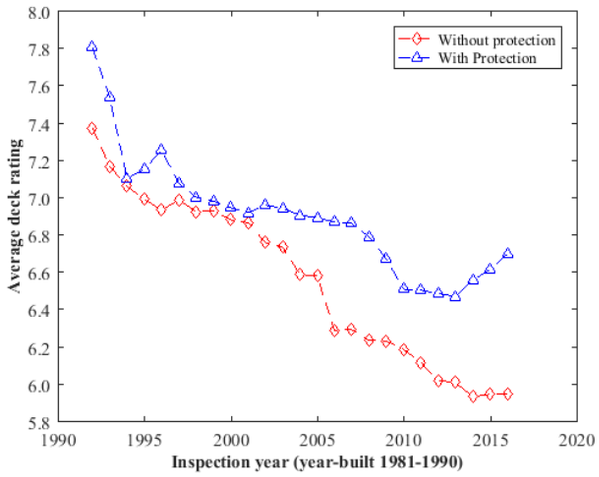


Figure 10. Average condition of the interstate highway bridge decks

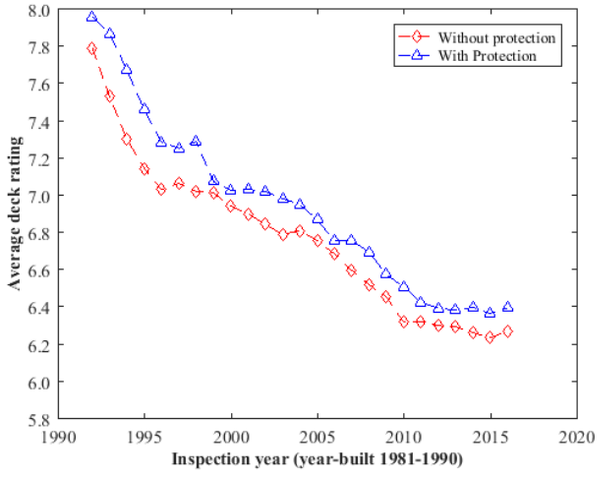


Figure 11. Average condition of the numbered highway bridge decks

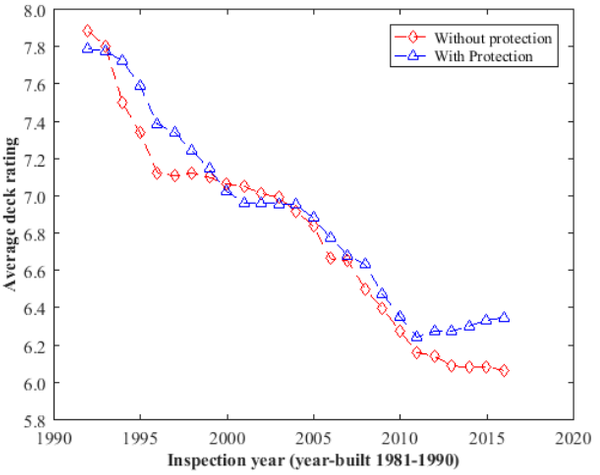


Figure 12. Average condition of the state highway bridge decks

Table 5. Deterioration rates of highway bridge deck condition (with protection)

Region	Interstate highway		Numbered highway		State highway	
	⩾7	Total	⩾7	Total	⩾7	Total
3	-0.351	-0.039	-0.118	-0.062	-0.103	-0.076

In the cold states of region 3, there are bridge decks built with protection measures, such as epoxy-coated reinforcement used in the construction. The deck with protection presents a higher average rating during the inspection period 1992-2016 as shown in figures 10-12. Table 5 presents the deterioration rates of bridge deck with or without protection in three different highway systems. In the interstate highway system, it shows that the decks with protection have a much slower deterioration rate. But in the numbered and state highway systems, the deterioration rates show no significant differences. The reason may be the same as Walker (1998) concluded that epoxy coated reinforcement could be easily damaged in the construction process and that the reduced bond between concrete and epoxy-coated reinforcement increased the widths of flexural cracks。 When the average condition ratings are greater than 7, the deterioration rates exhibit a faster trend than the total, evidenced by the figures 7-12. This can be attributed to two reasons; the duration of a deck in rating 8 and 9 is short (Bolukbasi et al. 2004), and the inspectors tend to record a lower rating to make the element more redundant for the public traffic.

4 SUMMARY AND CONCLUSIONS

This paper has discussed the climate effects on the U.S. highway bridge decks based on the NBI and NOAA database analysis. Data are categorized into four service regions (regions 1-4) in accordance with the number of freeze-thaw cycles per year. Two typical states were selected for regions 1-3 (except region 4, In order to control the number of explanatory variables) to represent the condition ratings of re-

spective regions. Before the factor analysis, this paper proposed a method to connect bridge with NOAA weather stations, this method can be implemented for the real-time NBI climate items updating. The following conclusion are drawn:

Each service region exhibited its own deterioration trend during the inspection year 1992-2016. In area with high freeze-thaw cycles (region 3), the interstate highway bridge deck deterioration rates are much faster (-0.0595) than the region 1 and 2 (-0.0447, -0.0285, respectively).However, in regions 1 and 2 (freeze-thaw cycles less than 80 times per year) it shows that concrete carbonation caused by temperature and humidity will be the predominant environmental factor for the degradation of the bridge deck.These results can be confirmed in the U.S. numbered highway (-0.0517, -0.0493, -0.0610, respectively) and state highway (-0.0533, -0.0384, -0.0719, respectively).

In all highway systems of region 3, the average condition ratings of protected deck (epoxy coated reinforcing) are much higher than the unprotected. but the deterioration rates have no significant change except in interstate highway system, that the protected ones have a slower rates than the unprotected.

The deterioration trends of bridge decks in all service regions indicate that when the average condition is more than seven, the local trends will be faster than the whole.

REFERENCES

Agrawal, A. K., Kawaguchi, A. & Chen, Z. (2010) Deterioration rates of typical bridge elements in New York. *Journal of Bridge Engineering*, 15, 419-429.

Ben-Akiva, M. & Gopinath, D. (1995) Modeling infrastructure performance and user costs. *Journal of Infrastructure Systems*, 1, 33-43.

Bien, J., Elfgren, L. & Olofsson, J. (2007) *Sustainable bridges: assessment for future traffic demands and longer lives,* Dolnoslaskie Wydawnictwo Edukacyjne.

Bolukbasi, M., Mohammadi, J. & Arditi, D. (2004) Estimating the future condition of highway bridge components using national bridge inventory data. *Practice Periodical on Structural Design and Construction*, 9, 16-25.

Bremner, T., Hover, K., Poston, R., Broomfield, J., Joseph, T., Price, R., Clear, K., Khan, M., Reddy, D. & Clifton, J. (2001) Protection of Metals in Concrete Against Corrosion.

Chang, M., Maguire, M. & Sun, Y. (2017) Framework for Mitigating Human Bias in Selection of Explanatory Variables for Bridge Deterioration Modeling. *Journal of Infrastructure Systems,* 23, 04017002.

Chase, S. B., Small, E. P. & Nutakor, C. (1999) An in-depth analysis of the national bridge inventory database utilizing data mining, GIS and advanced statistical methods. *Transportation Research Circular,* 498, 1-17.

Cruz, M. (2013) *Probabilistic service life prediction model for concrete bridge decks*. University of Delaware.

Dadson, D. K. (2001) *Impact of environmental classification on steel girder bridge elements using bridge inspection data*.

Dekelbab, W., Al-Wazeer, A. & Harris, B. (2008) *History lessons from the national bridge inventory. Public Roads*, 71, 30.

Dot, U. (1995) Recording and coding guide for the structure inventory and appraisal of the nation's bridges. US Department of Transportation, *Bridge Management Branch.*

FHWA. *Download NBI ASCII files*. Available: http://www.fhwa.dot.gov/bridge/nbi/ascii.cfm [Accessed May 2, 2016].

Gong, J., Huang, J., Wang, S., Soltesz, S. & Shi, X. (2014) Potential Deicer Effects on Concrete Bridge Decks: Developing Exposure Maps. *Climatic Effects on Pavement and Geotechnical Infrastructure.*

Graybeal, B. A., Phares, B. M., Rolander, D. D., Moore, M. & Washer, G. (2002) Visual inspection of highway bridges. *Journal of nondestructive evaluation,* 21, 67-83.

Hatami, A. & Morcous, G. (2011). *Developing deterioration models for Nebraska bridges*.

Kim, Y. J. & Yoon, D. K. 2009 Identifying critical sources of bridge deterioration in cold regions through the constructed bridges in North Dakota. *Journal of Bridge Engineering,* 15, 542-552.

Mauch, M. & Madanat, S. (2001) Semiparametric hazard rate models of reinforced concrete bridge deck deterioration. *Journal of Infrastructure Systems,* 7, 49-57.

Markow, M. J., Madanat, S. M. & Gurenich, D. I. (1993) Optimal rehabilitation times for concrete bridge decks. *Transportation Research Record.*

Nawy, E. G. 2008 *Concrete construction engineering handbook,* CRC press.

NOAA. *Federal climate complex global surface summary of day data*. Available: http://www.ncdc.noaa.gov/cgibin/res40.pl?page=gsod.html [Accessed May 14, 2016].

Oneill, R., Hill, R. L., Butler, W. B., Cabrera, J. G., Carrasquillo, R. L., Ellis Jr, W. E., Eriin, B. E., Fidjestal, P., Forster, S. W. & Gordon, C. (2001) Guide to durable concrete. *ACI201,* 2, 2-5.

Radovic, M., Ghonima, O. & Schumacher, T. (2016) Data Mining of Bridge Concrete Deck Parameters in the National Bridge Inventory by Two-Step Cluster Analysis. *ASCE-ASME Journal of Risk and Uncertainty in Engineering Systems, Part A: Civil Engineering,* 3, F4016004.

Saeed, T. U., Qiao, Y., Chen, S., Gkritza, K. & Labi, S. (2017) Methodology for Probabilistic Modeling of Highway Bridge Infrastructure Condition: Accounting for Improvement Effectiveness and Incorporating Random Effects. *Journal of Infrastructure Systems,* 23, 04017030.

Saito, M. (1988) The development of a statewide network level bridge management system.

Scherer, W. T. & Glagola, D. M. (1994) Markovian models for bridge maintenance management. *Journal of Transportation Engineering*, 120, 37-51.

Wells, D. T. (1995) Environmental classification scheme for Pontis. *Transportation Research Board Conference Proceedings.*

Zhang, Z., Sun, X. & Wang, X. (2003) Determination of bridge deterioration matrices with state national bridge inventory data. 9th International Bridge Management Conference.

Maintenance, Safety, Risk, Management and Life-Cycle Performance of Bridges – Powers, Frangopol, Al-Mahaidi & Caprani (Eds)
© 2018 Taylor & Francis Group, London, ISBN 978-1-138-73045-8

Railway bridge monitoring system using inertial sensors

P. Olaszek
Road and Bridge Research Institute, Warsaw, Poland

D. Sala
ADAPTRONICA Sp. z o.o., Łomianki, Poland

M. Kokot
ADAPTRONICA Sp. z o.o., Łomianki, Poland

M. Piątek
Technika Obliczeniowa Sp. z o.o., Kraków, Poland

ABSTRACT: The paper presents a railway bridges monitoring system. The system is focused on monitoring of new and old steel bridges. The system is using inertial sensors: inclinometers and accelerometers. These transducers do not require any referential points. The elaboration of the method which uses inclinometers together with an accelerometer for indirect displacement measurement under the dynamic load is the main achievement of the system. Inclinometers are installed in one line on a span and accelerometer at the point of displacement examination. During the passage of a train all the signals from the inclinometers and accelerometer are registered by a central unit and then sent to a server via Internet. A special software platform was developed to test various algorithms of processing the signals registered by the monitored structures during train passages. The system presented herein was checked on arch bridge with span length of 75 m.

1 INTRODUCTION

The dynamics of railway bridges is one of the most complex areas of theoretical analyses and experimental studies – (Frýba 1996, Yang et al. 2004). And the examination of the dynamics of railway bridges located in high speed railway is particularly interesting. Experimental examinations can be carried out under test or service loads. Such tests can be carried out only as one-time test loads conducted for the purpose of structure's acceptance testing or to assess the load capacity of an "old" structure already in use for some time. They can also be carried out as cyclic tests or continuous tests, such as automated monitoring of a structure.

Excessive bridge deformations can endanger traffic by creating unacceptable changes in vertical and horizontal track geometry, excessive rail stresses and vibrations in bridge structures. Excessive vibrations can lead to ballast instability and unacceptable reduction in wheel rail contact forces. Excessive deformations can also affect the loads imposed on the track/bridge system, and create conditions which cause passenger discomfort (EN 1990:2002). Thus, inspection of bridge deformations should be performed with respect to rail safety and passengers' comfort.

It is extremely important to control displacements and accelerations. It should be emphasized here that the measurements of vertical displacements (and especially the measurements of vertical displacements of spans and supports) are one of the most important activities in the process of assessing the structure's technical condition.

They are also one of the most important elements of the process of controlling the structural behaviour during acceptance tests (test loading) before putting a structure into service, as well as during periodic inspections of a structure (every few years).

While the measurements of the accelerations are relatively simple to carry out, the measurements of displacements in an automatic, unattended mode create considerable difficulties. Major difficulties are encountered especially in case of structures with restricted or impossible access to the area under them (bridges over busy roads, railway lines or rivers). In case of spans of great length, the monitoring systems applied nowadays all over the world usually use robotic total stations with the technology of automatic target recognition (ATR) and piezo-technology-based drives as well as GPS (Global Positioning System). Total stations cannot simultaneously measure many points of an examined structure with high accuracy or high sampling rate. In case of observing one point of a bridge it is possible to only perform limited dynamic analysis up to frequency of a few Hz (Cosser et al. 2003, Psimoulis & Stiros 2007, Psimoulis & Stiros

2013). And, a disadvantage of GPS is its obtainable accuracy (Ko & Ni 2005), which limits its usefulness to monitor bridge structures with consider-able displacements.

One of the most important elements of the developed solution is its innovative system of indirect measurement of displacements based on measurements using inclinometers and accelerometers. Many researchers carry out works connected with using for this purpose detectors which do not require a reference point – which are based on inertia. They present works on using accelerometers to measure both accelerations and displacements of bridges under dynamic loads. A disadvantage of this method is the necessity of double integration of an acceleration signal, which can lead to considerable errors in estimating the displacements. There are various methods suggested to correct those errors (Gindy et al. 2008, Sekiya et al 2016, Park et al. 2013), but generally it is not possible to accurately estimate the displacements on the basis of accelerations without additional measurements, for example such as strain gauge measurements (Park et al. 2016).

Many papers were also published related to the application of inclinometers to automatically monitor bridge structures displacements. Most of those papers are limited to measurements under static load. (Olaszek 2014).

Only few of them present the use of inclinometers to determine deflections during static and dynamic load tests (Hou et al. 2005). Works using inclinometers to determine displacements under dynamic load and high-speed train passages are presented in (Hem et al. 2014, Martí-Vargas 2015).

Whereas the method presented here is based on the integration of the signals from inclinometers and accelerometers. Inclinometers are installed in one line on a span and accelerometer at the point of displacement examination. The signals from the inclinometers are used to determine the so called quasi-static component of a displacement, and the signal from the accelerometer to determine a dynamic component. The details of the method of determining displacements will be presented in a separate publication. A similar way of integrating the signals from an inclinometer and an accelerometer, used to determine lateral displacements of a railway bridge support is presented in (Ozdagli et al. 2016).

2 DESCRIPTION OF MONITORING SYSTEM

The developed prototype of the measuring system consists of a central unit and 4 measuring modules. A scheme of the set of equipment is presented in Figure 1.

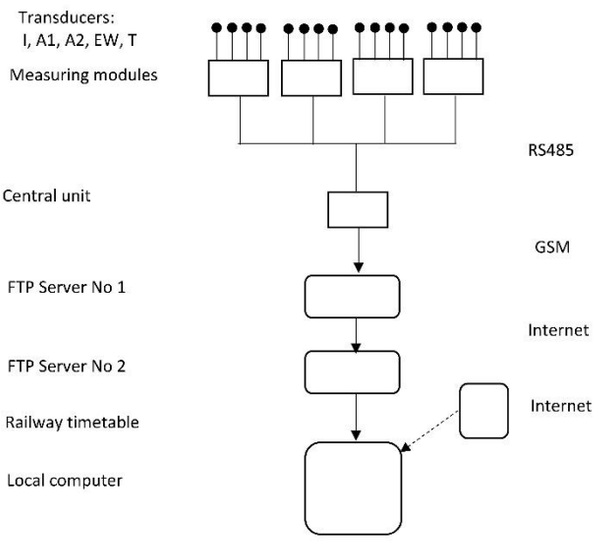


Figure 1. Scheme of the measuring system with indicated methods of data transmission; measuring transducers markings: I – inclinometer, A1 – accelerometer MEMS, A2 – piezoelectric accelerometer, EW – electric wire resistance strain gauge, T - temperature sensor.

Each measuring module comprises an 8-channel, 16-bit analog-digital transducer adapted to operate the following detectors:

- uniaxial gravity inclinometer with measuring range of ±1°;
- MEMS-type three-axis accelerometer with measuring range of ±3g;
- piezoelectric three-axis accelerometer with measuring range of ±5g;
- resistance strain gauge;
- temperature sensor with measuring range from -55°C to +125 °C.

The central unit which controls the measuring module activity consist of a microcontroller, local memory on a SD card, a real-time module and a GSM module. Communication with the measuring modules is established by means of RS485 protocol. The system is equipped with an algorithm of detecting trains' passages, thanks to which a loop of data acquisition is fully automated. The signals registered by the sensors during a train passage are sent as a text file to remote FTP server No. 1. The system works autonomously and the buffer power supply protects from power failures.

In order to ensure data safety, the complete (unprocessed) measuring signals are collaterally copied to server No. 2 located in a different place than server No. 1.

An analysis of the registered signals is made on a local computer using special platform developed in MATLAB environment (MATLAB 2017). The scheme of the platform activity is presented in Figure 2.

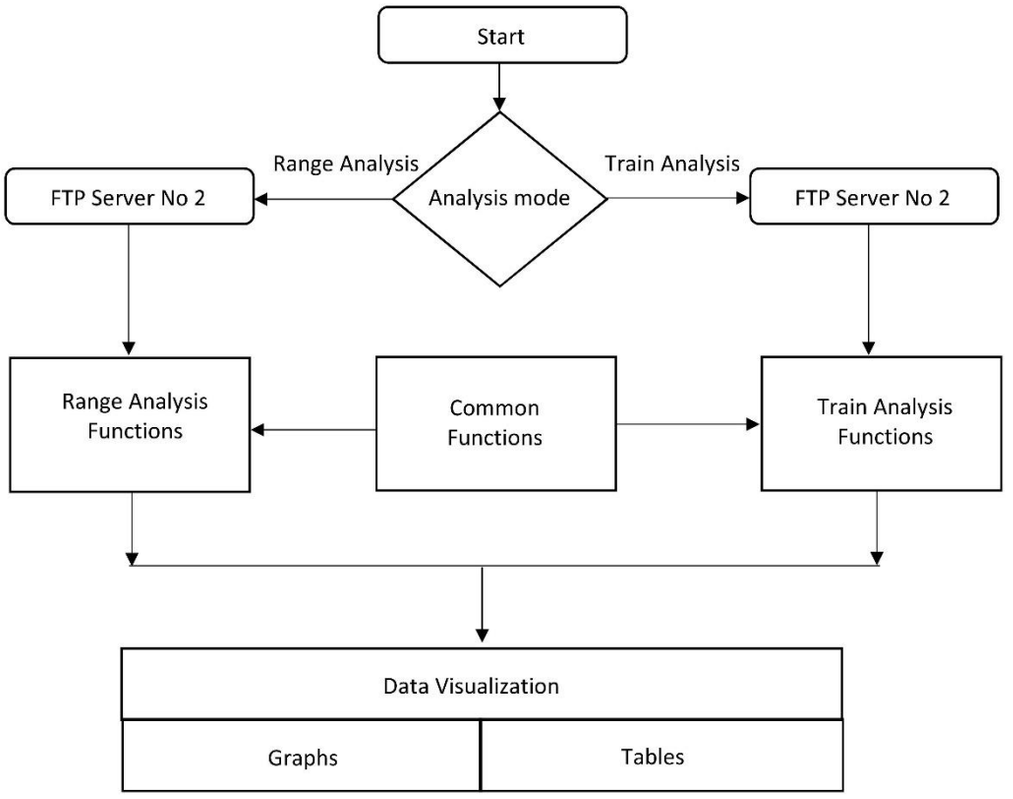


Figure 2. Scheme of platform activity to analyse data from the monitoring.

The platform enables transmission of the measuring data from the FTP server No. 2 to programming variables, and then theirs analyze and visualization in the form of graphs and tables.

The system presented herein was developed for scientific and research purposes and the platform is supposed to facilitate both the creation of new algorithms of processing measuring signals and the analysis of received results. While using the platform, a person who analyses the measuring signals only needs to enter a few commands of the program code in order to program the data readout and visualization of the data processing in the form of graphs or tables. Advantages of using such a developed platform are:

- it is easy to concentrate while creating and algorithm, not programming;
- availability of "ready" functions of processing MATLAB environment signals;
- it is easy to work in many teams while creating different functions for measurement analysis;
- it is easy to handle a big number of measurement data.

The data can be processed in a single train passage analysis mode (train analysis) or in a selected group of trains analysis mode (range analysis). The functions to analyse the measurement results are created in the form of plug-ins – separate files located in proper catalogues (train or range analysis). The trains are identified by the date and time of the initial registration.

After a platform user chooses an individual train passage or a group of trains passage all the functions from the proper catalogue are carried out automatically. The range or analysis functions can use common functions. Sample copies of a computer screen during work with the platform are presented in Figure 3.

The system also uses data about train passages from the Department of Handling the Systems and Individual Timetables, Railway Traffic Management Centre of PKP Polish Railway Company S.A. With respect to the safety requirements in the research and prototype solutions the data are entered to the system in an offline and semi-automatic mode. In the future it will probably be possible to automatically download those data from the PKP PLK SA internal network while developing an application monitoring system.



Figure 3. Sample copies a computer screen during work with the platform: at the top in the mode Train Analysis; at the bottom in the mode Range Analysis.

3 EXAMPLE OF THE BRIDGE MONITORING

The system presented herein was checked on arch bridge located in high speed railway (Fig. 4).

The bridge consists of two new steel arch structures (from 2014 and 2015) with span length of 75.00 m. The arch and the arch tie both have box cross-section. The arch ties are suspended at the arches using 13 pairs of steel hangers. The bridge has ballasted deck, cross-bars from double-tee plate girders and reinforced concrete slab floor. The structure was accepted for train speed up to 250 km/h.



Figure 4. View of the tested bridge: from the side and from the track level.

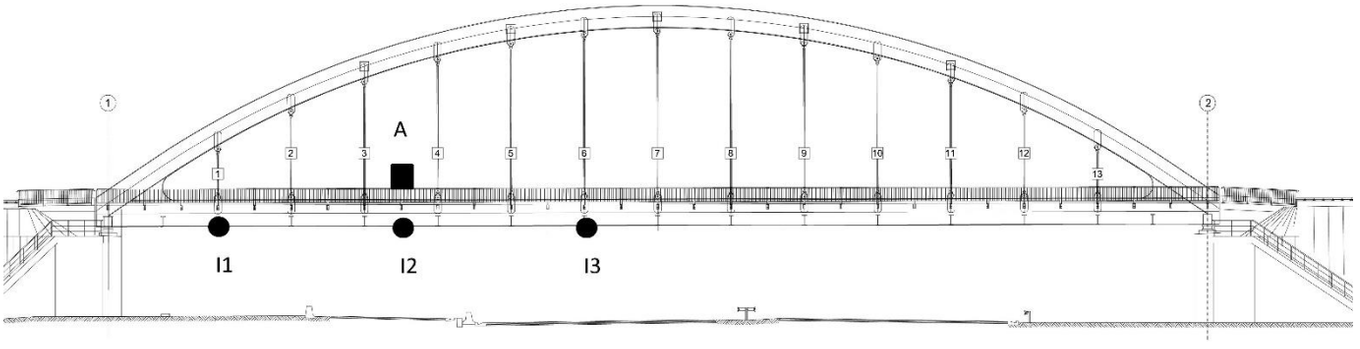


Figure 5. Scheme of inclinometers location (I1, I2, & I3) and accelerometer location (A) for continuous monitoring of the bridge deck.

At the case of arch bridge, the extreme deflection appears at about one a quarter span length. For preliminary testing it was enough to monitor half of the span. Three inclinometers were installed in one line at bridge deck and the accelerometer was located at one a quarter of a span length (Fig. 5).

An example of an analysis of a single registration and indirect determination of displacements is presented in Figure 6. The registration concerned a passenger train passage with the speed of about 160 km/h, consisting of a locomotive EP09 and cars of gross weight 427 tons and length of 246 m (data from the Railway Traffic Management Centre).

The graphs included herein present signals registered by the inclinometers and accelerometer as well as a quasi-static component of the displacement calculated on the basis of the signals from the inclinometers and a dynamic component calculated on the basis of the signals from the accelerometer.

The last graph presents the result of an indirect measurement of displacements compared with the reference time-history registered using a reference method – by means of an inductive transducer.

Relative measurement error using the indirect method in relation to a reference method did not exceed 4% for extreme value.

The installed monitoring system registers measurement data from all passing trains. Recently (September 2017) 35 trains were registered on average during 24-hours. The comparative tests using an inductive transducer were not conducted continuously. Over 6 months, on average once a month, the inductive transducer was installed under various weather conditions to measure displacements caused by passages of various types of passenger trains: separate locomotive and cars or multiple unit trains.

The relative measurement errors determined using the indirect method in relation to a reference method did not exceed 0.5%-7.0% for extreme values. Further works are being carried out in order to improve the accuracy of determining the displacements using the indirect method. The works include examination of different methods of filtering and separating the signals from the inclinometers and the signal from the accelerometer.

It is important to point out here that the tests were carried out with a minimum number of inclinometers. In case of the presented arch bridge 3 inclinometers were used to determine the line of deflection along the half of the span – ultimately it will be necessary to use 6 inclinometers to examine the whole span of such a bridge.

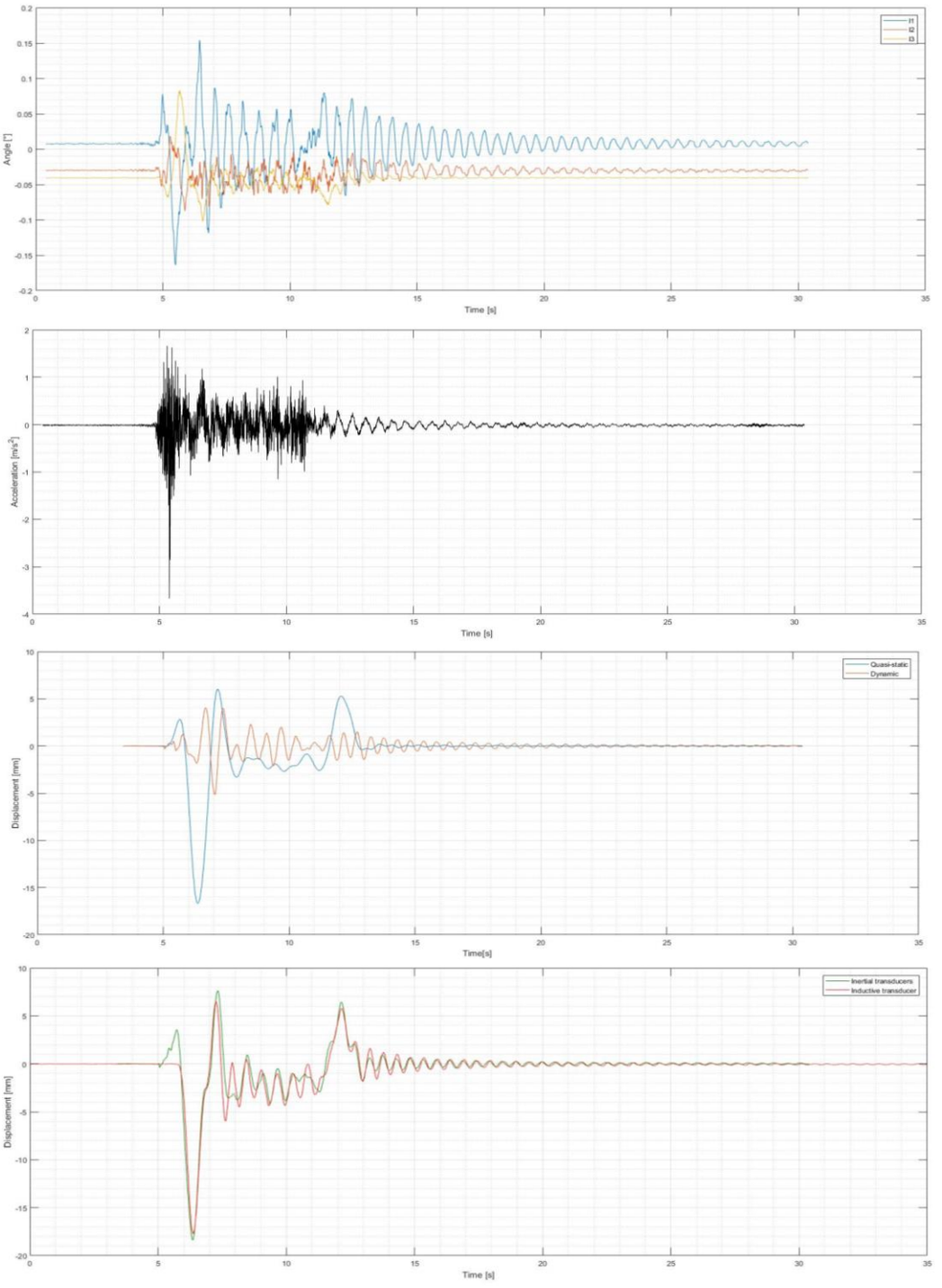


Figure 6. An example of an analysis of a single train; from the top: 1) signals from inclinometers, 2) a signal from an accelerometer, 3) determined quasi-static component (from inclinometers) and dynamic component (from an accelerometer), 4) result of an indirect measurement of displacements compared with the reference time-history registered using a reference method – by means of an inductive transducer.

The continuous monitoring system is supported by periodical total station measurements which aim to control the geometric parameters of the bridge structure in absolute coordinates (in a system connected with the local points of reference).

Figure 7 shows an example of an analysis of a train range monitored during one week. The first two graphs from top present determined values of extreme displacements and accelerations (using 30 Hz low-pass filtering) from all trains that passed during that time.

The displacement values determined by the monitoring system are comparable with the values determined using the numerical modelling (Olaszek et al. 2017).

The determined maximum peak values of bridge deck acceleration (using 30 Hz low-pass filtering) are comparable with the limits for ballasted track 3.5 m/s^2 (EN 1990:2002). In the presented example the registered maximum peak values did not exceed 2.0 m/s^2.

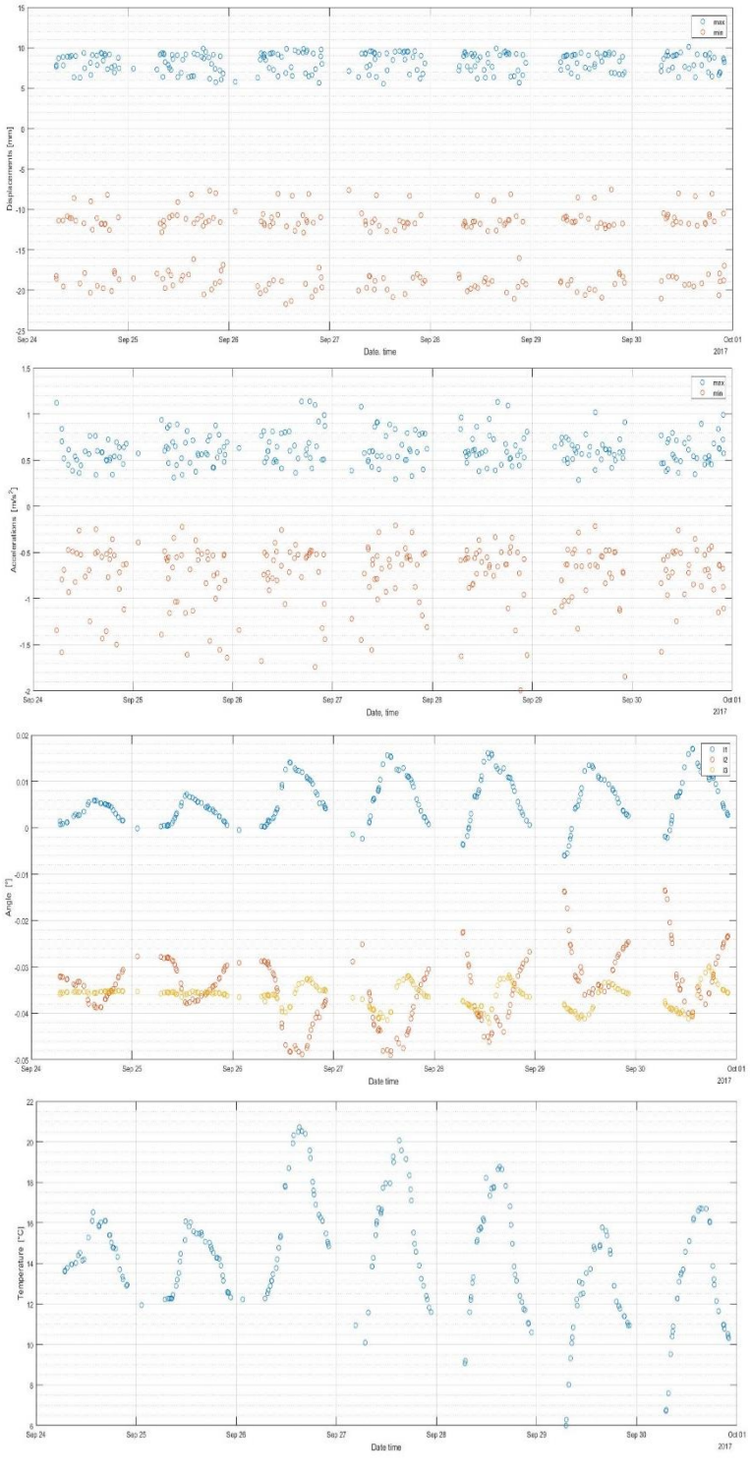


Figure 7. An example of an analysis of a train range monitored during one week: from the top: 1) determined values of extreme displacements, 2) accelerations (using 30 Hz low-pass filtering), 3) angle changes registered without train load (just before a train passage), 4) changes in the average temperature from measurement at a few points of the structure.

Two graphs from bottom (Fig. 7) show angle changes registered without any train load (just before a train passage) as well as changes in the average temperature measured at a few points of the bridge structure.

We can observe here the compliance between the seven-day changes in the angles and the changes in the temperature – maximum daily changes equal to about 10° C.

The numerical analyses of the construction deformations resulting from the changes in the temperature confirmed the conclusions from the monitoring activities – big sensitivity of the construction deformations of local and global character to the changes in the temperature. (Olaszek et al. 2017).

4 CONCLUSIONS

This article presents a bridge structure monitoring system whose main elements are inertial transducers used to determine vertical displacements using an indirect method. The so far tests of the system proved its usefulness for monitoring bridges in high speed railway as well as its possibility to achieve high accuracy while determining displacements using an indirect method.

ACKNOWLEDGEMENTS

The authors would like to thank the members of the team who completed the presented part of the project, including: Eng Robert Czachowski, MSc Eng Małgorzata Mazanek, PhD Eng Tomasz Wierzbicki, MSc Eng Paweł Nurek from the Road and Bridge Research Institute; Prof. PhD, Eng Jan Holnicki – Szulc, PhD, Eng Andrzej Świercz from the Institute of Fundamental Technological Research of the Polish Academy of Science; PhD, Eng Ireneusz Wyczałek from the Institute of Civil Engineering of the Poznań University of Technology; PhD, Eng Przemysław Kołakowski from Adaptronica Sp. z o.o.; MSc Joanna Wyroba from Oprogramowanie Naukowo-Techniczne Sp. z o.o. sp.k., MSc Kazimierz Szadkowski and Directors, Main Engineers and Bridge Diagnosticians from the Railway Track Development and Construction Unit of PKP Polish Railways S.A. in Warsaw and Skarżysko Kamienna.

The project is carried out within the frame of Applied Research Projects, financed by the National Centre for Research and Development in years 2015-2018.

REFERENCES

Cosser, E., G.W. Roberts, X. Meng, and A.H. Dodson. 2003. Measuring the Dynamic Deformation of Bridges Using a Total Station. In *Proceeding of the 11th FIG Symposium on Deformation Measurements, Santorini, Greece*, 25–28.

EN 1990:2002+A1, Eurocode. Basis of structural design.

Frýba, L. 1996. *Dynamics of Railway Bridges*. Thomas Telford Limited.

Gindy, M., R. Vaccaro, H. Nassif, and J. Velde. 2008. A State-Space Approach for Deriving Bridge Displacement from Acceleration. *Computer-Aided Civil and Infrastructure Engineering* 23, no. 4: 281–290.

Hem, X., X. Yang, and L. Zhao. 2014. New Method for High-Speed Railway Bridge Dynamic Deflection Measurement. *Journal of Bridge Engineering* 19, no. 7: 05014004-1–11.

Hou, X., X. Yang, and Q. Huang. 2005. Using Inclinometers to Measure Bridge Deflection. *Journal of Bridge Engineering* 10, no. 5: 564–569.

Ko, J.M., and Y.Q. Ni. 2005. Technology Developments in Structural Health Monitoring of Large-Scale Bridges. *Engineering Structures* 27, no. 12. SEMC 2004 Structural Health Monitoring, Damage Detection and Long-Term Performance Second International Conference on Structural Engineering, Mechanics and Computation (October): 1715–1725.

Martí-Vargas, J.R. 2015. Discussion of "New Method for High-Speed Railway Bridge Dynamic Deflection Measurement" by Xianlong He, Xueshan Yang, and Lizhen Zhao. *Journal of Bridge Engineering* 20, no. 11.

MATLAB 2017. MATLAB - MathWorks. https://www.mathworks.com

Olaszek, P. 2014. Deflection Monitoring System Making Use of Inclinometers and Cubic Spline Curves. In *Bridge Maintenance, Safety, Management and Life Extension*, by Airong Chen, Dan Frangopol, and Xin Ruan, 2305–2312. CRC Press.

Olaszek, P., Świercz, A., Sala, D., Kokot, M. 2017. Monitoring system of high speed railway arch bridge (in Polish). In *Wrocławskie Dni Mostowe 2017,* Poland, Wrocław.

Ozdagli, A.I., F. Moreu, J.A. Gomez, P. Garp, & S. Vemuganti. 2016. Data Fusion of Accelerometers with Inclinometers for Reference-Free High Fidelity Displacement Estimation. In *8th European Workshop On Structural Health Monitoring (EWSHM 2016), 5-8 July 2016,*. Spain, Bilbao.

Park, J.-W., K.-C. Lee, S.-H. Sim, H.-J. Jung & B.F. Spencer. 2016. Traffic Safety Evaluation for Railway Bridges Using Expanded Multisensor Data Fusion. *Computer-Aided Civil and Infrastructure Engineering* 31, no. 10 (October 1): 749–760.

Park, J.-W., S.-H. Sim, H.-J. Jung & B.F.S. Jr. 2013. Development of a Wireless Displacement Measurement System Using Acceleration Responses. *Sensors* 13, no. 7 (July 1): 8377–8392.

Psimoulis, P.A., & S.C. Stiros. 2007. Measurement of Deflections and of Oscillation Frequencies of Engineering Structures Using Robotic Theodolites (RTS). *Engineering Structures* 29, no. 12: 3312–3324.

Psimoulis, P.A., & S.C. Stiros. 2013. Measuring Deflections of a Short-Span Railway Bridge Using a Robotic Total Station. *Journal of Bridge Engineering* 18, no. 2: 182–185.

Sekiya, H., K. Kimura, and C. Miki. 2016. Technique for Determining Bridge Displacement Response Using MEMS Accelerometers. *Sensors (Basel, Switzerland)* 16, no. 2 (February 19).

Yang, Y.B., J.D. Yau, and Y.S. Wu. 2004. *Vehicle-Bridge Interaction Dynamics. With Applications to High-Speed Railways*. World Scientific.

Maintenance, Safety, Risk, Management and Life-Cycle Performance of Bridges – Powers, Frangopol, Al-Mahaidi & Caprani (Eds)
© 2018 Taylor & Francis Group, London, ISBN 978-1-138-73045-8

Non-destructive testing of bridges – health assessment & monitoring

Chetan R. Raikar
Structwel Designers & Consultants Pvt. Ltd., Navi Mumbai, India

ABSTRACT: India has taken major leap into investing in road infrastructure & hence widening of existing roads and bridges is major construction activity. Health Assessment of Bridges hence is an extremely critical task ahead of Central Government and the State Governments of all the States.

As the reliance on infrastructure is growing, the engineered components of transportation infrastructure are aging, deteriorating, and exhausting their capacity to meet the everexpanding operational demands. The mammoth task of inventory preparation and health assessment of all the bridges across the country by is taken up by The Ministry of Transport.

Ensuring operational and structural safety and security of the transportation infrastructure is an essential task. Hence Health assessment and residual / remnant life assessment is needed to be carried out. Load carrying capacity and life cycle cost analysis of existing bridges is yet another area of consultancy needed.

In most cases, job of health assessment is yet left to the experienced engineer who visits the bridge for visual inspection. Sudden collapses of bridges and untimely / unplanned job of major repairs are common. There is a huge loss of human life, fuel and time of commuters due to the same.

Author proposes to cover various Non Destructive Testing (NDT) techniques used in India, methods for health assessment of bridges and few case studies in this article.

Keywords: Non Destructive Testing (NDT) of the bridges, In situ Permeability Tests of concrete, Ground penetrating Radar survey, Infrared Thermography, Load Test of bridges, Metro structures.

PREAMBLE

Health assessment of bridges is scientific process which requires great amount of experience. NDT plays very important role in assessing structural properties of various materials used in the bridges. NDT also assesses the integrity of various structural members of the bridge and their capability to cater to the load which they are expected to. Load rating of existing bridges, structural stability for increased load, and effectiveness of repairs are some of the other areas where NDT plays a major role.

There are several types of NDT to measure various properties of concrete like compressive strength, permeability, stress / strain, integrity, homogeneity, chemical deterioration etc. There are different instruments of NDT available to assess different properties of concrete.

NDT is being practiced in India for around three /four decades or more by now. **Most of the NDT techniques available across the world in developed countries are available in India**. The more advanced countries have long adopted continuous monitoring of stress, deflection/deformation, temperature and other properties of bridge components; in-situ during service life.

DIFFERENCE BETWEEN NDT ON BRIDGES AND ON OTHER STRUCTURES

As we all know, the major difference between loads on a bridge and that on any other structure; is the dynamic nature of the live load a bridge is expected to cater to; during its service life. Other structures like machine foundations also are subjected to dynamic loading of different levels and nature.

NDT on structures other than bridges are carried out, predominantly, to find out residual strength of material of construction like concrete, steel, wood, stone masonry etc. In very few structures (other than bridges); the techniques of NDT for stress measurement, deflection measurement etc; used to measure the structural properties of the members, are required to be deployed. Whereas, in a bridge it is equally important to know stress levels, internal cracking and deflection checks during service life to understand the serviceability of the bridge.

This is a major difference that makes NDT on bridges, entirely a different gamut than the routine

NDT carried out by most laboratories across the country on residential and other structures.

Why NDT on bridges?

Limitations of inspection

Visual inspection is one of the most important aspects of health assessment of structures. It is understood that there are more than 2,50,000 bridges, or more, on National Highways in the country. Surely so, India does not have so many Bridge Inspection Experts to inspect each and every bridge in a reasonable time-frame. The work of visual inspection of the bridges is, therefore, going to be carried out by junior level engineers who may or may not have sufficient and appropriate training to identify distresses by visual inspection.

Even an expert inspector will have several limitations either of access, of time, or of light intensity etc. those that may have limitations of visual assessment.

He/she may also want to additionally confirm the observations and quantify the areas of distresses identified by him/her.

NDT is extremely useful in these situations.

Non-availability of drawings

This is going to be a major challenge faced by the Bridge Engineering Consultants. During the passage of time, important data like drawings & maintenance registers of majority of the bridges has not been retained properly by the owners and the same has been lost.

Geometric survey of physical dimensions of superstructure of any bridge is still an easy task and can be carried out to a great degree of accuracy. Whereas, geometric survey **of substructure of perennial bridges and foundations; just cannot be done without the help of NDT** unfortunately, even NDT techniques have great limitations in supporting the bridge inspector in encompassing this challenge.

Quantum and location of reinforcement and prestressing tendons is another requirement when regression analysis of any bridge is required to be carried out to know its load-carrying capacity or the cause of failure. This task just cannot be completed without any of the most advanced NDT equipments.

Confirmation of visually observed distresses

As mentioned above, an expert bridge inspector would observe several types of distresses in a bridge structure. He/she may want to ignore some of the distresses which would not have any shortterm/long-term bearing on the life or performances of the bridge. Some of the distresses found may be of critical & of urgent / important nature, wherein he/she would suggest immediate measures.

There would be a third type of distress wherein the bridge inspector would like to quantify or reconfirm his/her observations. This is exactly where NDT would provide additional support. Rather, only NDT can bring in completeness to site investigation of health assessment of bridges. It would be prudent to mention here that more than 60% of distress observations by an expert bridge engineer would fall in this category which would need NDT on the same.

To cite some examples; a bridge inspector may want to confirm whether the cracking observed in the wearing course extends into the deck slab too or otherwise. He/she may also want to confirm the exact reason of cracking in concrete whether structural or material, to start with.

There can be several support areas where NDT can support the expert bridge inspector in confirming his observations and can provide extremely valuable data to take him/her further in concluding the health of the bridge structure.

NDT for material strength

NDT provides extremely useful data on strength of materials like concrete, steel etc. used in the construction of the Bridges. Concrete and steel both undergo macro and micro levels of cracking due to various reasons. Chemical infestation, over stressing, fatigue, other age-related distresses, fire, blast, impact due to an accident etc. are some of the reasons that may cause distress in a bridge. Under designed or marginally designed bridge & that is poorly constructed will show early major distress during service-life of the same. NDT will prove to be a useful tool in either altering the condition assessment of the bridge or investigative assessment in case of its early distress/collapse.

NDT for load rating of bridge

There is a constant dilemma in the minds of bridge owners about the current rating of bridges. NDT can be a very useful tool in upgrading or downgrading the rating of a bridge.

NDT on repaired components in bridge structures

Most of the bridges under health assessment would have undergone some form of repair or retrofit during their service-life. The records of **location and quantum of repair may or may not** be available to the bridge inspector. **NDT plays a major role in knowing the effectiveness of earlier repair work carried out**. Delamination **of Polymer modified mortar, Epoxy mortar and** other repair mortars used, delamination and tearing of fibre-wrapping and their effectiveness **in load transfer mechanism of the** bridge.

Table 1 :Non Destructive Tests recommended

Strength tests	Corrosion Assessment & r/f related tests	For detection of cracks/voids/ delamination	Laboratory Tests	Durability Test
• Rebound hammer test • Pull off test • Pull out test • Break off test • Penetration Resistance Test (Windsor Probe) • Core Drilling Method • Permeability Test • Bond Test • Maturity Method • Complete Structural Testing	• Half cell potentiometer • Resistively meter test • Carbonation • Chloride content of concrete • Endoscopy Technique • Covermeter / Rebar Locator	• Ultrasonic Pulse Velocity Test • Infrared thermographic technique • Acoustic Emission techniques • Short Pulse Radar methods • Stress wave propagation methods • pulse echo method • impact echo method • response method • Crack Detection Microscope • Endoscopy Technique • Moisture meter	• Petrography • Chemical analysis • Compressive strength on core sample • Water Permeability • Carbonation	• . Autoclam Permeability Test • Permit ion migration test • Initial Surface absorption test • Rapid chloride migration est

Following are few case studies where Ground Penetrating RADAR, IR and Endoscopy are employed.

GROUND PENETRATING RADAR (GPR / RADAR)

Case Study 1:

Type of Bridge – Stone masonry arch bridge

Year of construction – 1896



Fig. 1: Remote view of river bridge



Fig 2: RADAR survey in horizontal direction on top of Deck Slab

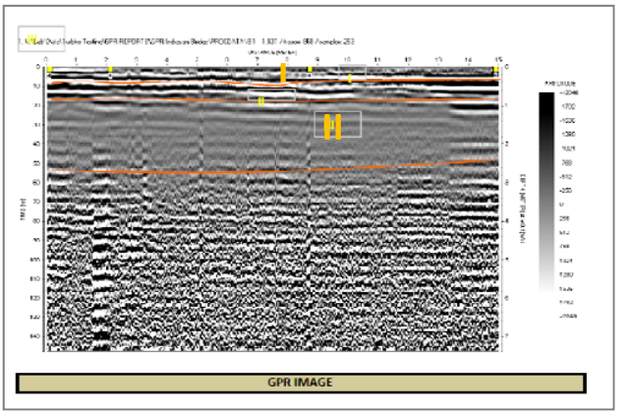


Fig 3: RADAR survey in horizontal direction on top of Deck Slab , I- Bituminous Layer, II Compacted fill

Conclusion:

RADAR tests revealed debonding between Wearing coat (Bituminous layers) and found depth of in filled materials etc.

I.R. (INFRARED THERMOGRAPHY) CAMERA –

Case Study 2:

Type of bridge - Composite structure having RCC Solid Deck Slab rested on Rubble Masonry Piers. The Stone masonry piers are provided at regular intervals in between the abutments.

Year of construction – 1977



Fig. 4: Pier of the bridge under consideration

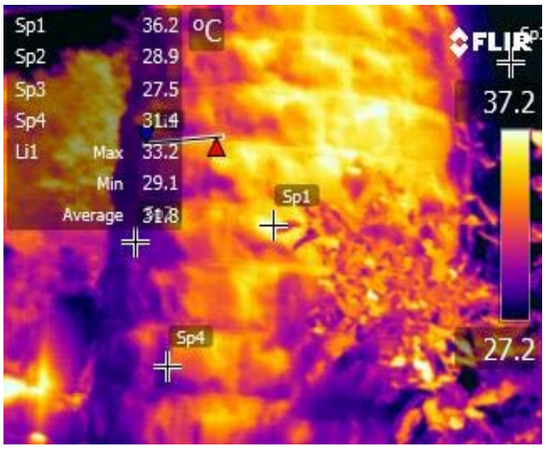


Fig.5: Thermography images of Masonry Piers & Deck slab

Conclusion: I.R. Camera test shows ingress of moisture to the surface of Masonry Piers below Pier caps and soffit of Solid Slabs at some locations.

ENDOSCOPY -

Case Study 3 -

Type of bridge - Composite structure having RCC Solid Deck Slab rested on Rubble Masonry Piers. The Stone masonry piers are provided at regular intervals in between the abutments.

Year of construction – 1977.



Fig.6 Endoscopy of bridge on river.



Fig.7 View under endoscope

Conclusion:

Endoscopy tests revealed voids to the internal area of Masonry at few locations, however Stone Masonry found in intact condition.

Case Study 4-

Location - Bridge on Metro rail

Type of bridge - Cable Stayed Bridge Between two piers (Span length 83 m)

Year of construction - 2013

The load test of bridge is conducted by using train as live load. Total station is used for deflection monitoring as it can measure deflection accurate to 0.2 millimeters. This monitoring system is much easier to set up and use, reducing labor and time requirements. The system has almost no site restrictions. Test conducted for 72 hours, readings are recorded for interval of one hour. Figure 5 illustrates the results of load testing bridge



Fig 8 Deflection monitoring



Fig .9 Close up view of Pylone, prism are fixed at regular interval

Conclusion:

Metro structure successfully passes the trial runs for deflection and stress levels.

References:

1. ASTM D4788-03, "Standard test method for detecting delaminations in bridge decksusing infrared thermography", *American Society for Testing Materials*, 2007.
2. ASTM D6087 - 08
   Standard Test Method for Evaluating Asphalt-Covered Concrete Bridge Decks Using Ground Penetrating Radar
3. Guidelines On Non-Destructive Testing Of Bridges , BS - 103 August, 2009
   B&S Directorate
   Research Designs And Standards Organisation,Lucknow-226011
4. Non Destructive Testing (NDT)]o n Bridges – State Of The Art, by Chetan Raikar, IBMS 2016, 1st Biennial Conference October 2016 – New Delhi
5. Non-Destructive Testing (NDT) of Concrete – For Repair Projects., by Chetan Raikar , The Masterbuilder November 2016

Maintenance, Safety, Risk, Management and Life-Cycle Performance of Bridges – Powers, Frangopol, Al-Mahaidi & Caprani (Eds)
© 2018 Taylor & Francis Group, London, ISBN 978-1-138-73045-8

Rating of Masonry Arch Bridges in USA

A.P. Ranasinghe
Jacobs Engineering
N.Y. Khadbai
Area Engineering
A.K. Ranasinghe
Jacobs Engineering

ABSTRACT:

Arch bridges are amongst the oldest types of bridges used by engineers. Some of the arch bridges built during the Roman Empire are still standing today. Arches have been commonly used in both highway and railroad bridges. Prior to the industrial revolution, arch bridges were built using stones or bricks. Then, steel and concrete arch bridges became more commonly used. The codes and guidelines used for designing these bridges are outdated and may not be compatible with the current design standards and moving load conditions. Many of these arch bridges have been in service for several decades and have experienced significant deterioration. Therefore, it is essential to perform load rating for these bridges to assess their load carrying capacity and evaluate the need for strengthening and repair work. This paper demonstrates the load rating of a major stone arch railroad bridge in the Northeast Corridor of the USA.

1 INRODUCTION

Arch bridges are amongst the oldest types of bridges used by engineers. Some of the arch bridges built during the Roman Empire, such as the Pont du Gard and the Pont Saint Martin, are still standing today. Prior to the industrial revolution, arch bridges were built using stones or bricks. Then, steel and concrete arch bridges became more commonly used. Steel arch bridges offer an economical advantage due to their use in longer spans.

Many of these arch bridges have been in service for several decades and have experienced significant deterioration. These bridges require accurate load rating to assess their condition and evaluate the need for maintenance and rehabilitation work. The load rating of arch bridges can be a challenging task due to the combined effects of axial forces, bending moments, temperature changes, and second-order moments from member buckling.

The codes and guidelines used for designing these bridges are outdated and may not be compatible with the current design standards and moving load conditions. Furthermore, these bridges may have experienced material losses and other deterioration effects that can reduce the load carrying capacity of the bridge. Therefore, it is essential to perform load rating for these bridges to determine the need for strengthening and repair work. This paper demonstrates the implementation of the load rating provisions for a major stone arch railroad bridge in the Northeast Corridor of the USA. The bridge is rated based on the load rating provisions in AREMA Manual for Railway Engineering (2012). The analysis procedure and application of the load rating equations in the code are demonstrated.

2 LOAD RATING METHODOLOGY

The total moment at a node of the arch due to dead and live loads can be written as

$$M_{Total} = (RF) \times (M_{LL+I}) + M_{DL} \quad (1)$$

Where RF is the Rating Factor

The total axial load at a node of the arch due to dead and live loads can be written as

$$P_{Total} = RF \times P_{LL+I} + P_{DL} \quad (2)$$

The eccentricity, $e = (M_{Total}) / (P_{Total})$ (3)

When, e < H / 6, the section is under full com pression as shown by Figure 1. The f_{max} due to dead load and live load (SDL & SLL+I) can be obtained separately by the equation,

f_{max} = P/A + M/S (4)

or f_{max} = P/BH + 6M/BH2 (5)

Where, B = Width of the section = 12”
H = Arch section thickness in inches

When, e > H / 6, the sectio n is not under full com pression as shown by Figure 2 and the joint is open. The f_{max} due to dead load and live load can be obtained separately by the equation,

f_{max} = P / (9H – 18M/P) (6)

AREMA (2012) provides two rating equations each for normal and maximum rating factors.

For normal rating select the lesser of,

(SLN) = [(Sf/1.2) – (SDL)] / [(SLL+I)] (7)

(SLN) = [(Sf) – (SDL)] / [(SLL+I)] (8)

For maximum rating select the lesser of,

(SLN) = [(Sf) – (SDL)] / [(SLL+I)] (9)

(SLN) = [(1.2Sf) – (SDL)] / [(SLL+I)] (10)

Where, Sf = Permissible Stress

It should be noted that ot her force effects such as buoyancy, stream force, longitudinal force, w ind, wind on live load, centrifugal, and friction have been removed from the AREMA equations above. If there are any effects from these, the co mplete AREMA equations should be used and the re sulting bending and axial stresses should be added to SDL appropriately.

A starting value of 0.2 is assum ed for RF in equation 1 and the rating factors given in equations 7 to 10 are calculated. Rating factor is increas ed in steps of 0.2 until the SLN val ue is 1.0 for equation 7 or 8 and also 1.0 for equation 9 or 10. Those RF values will be the normal and the m aximum rating factors for that nod e. This p rocedure will be repeated for other nodes for various li ve load positions along the bridge. This can be easily done by using a Microsoft Excel spreadsheet (2000). The m inimum rating factors from all the nodes from equation 7 or 8 and 9 or 10 will be the normal and maximum rating factors for the bridge.

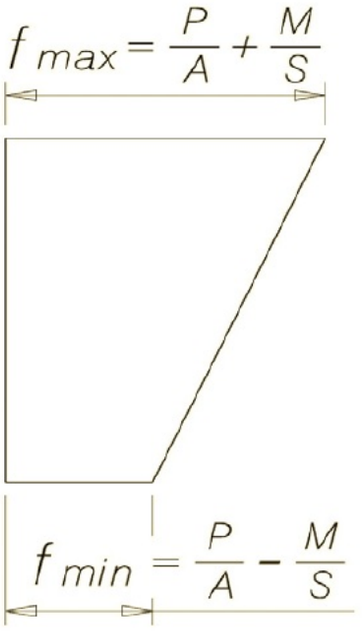


Figure 1. S tress Distribution with Total Com pression.

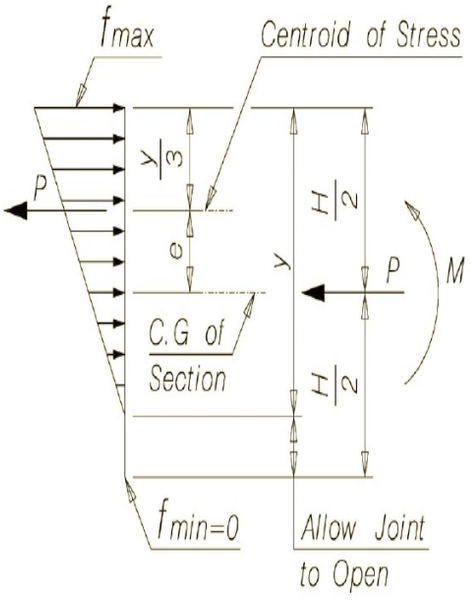


Figure 2. Stress Distribution with the Joint Open at a Node

3 APPLICATION OF THE LOAD RATING METHOD

The load rating process summarized above was applied to the load rating of the Northeast Corridor over Easton Avenue Bridge in New Brunswick, New Jersey, USA. (Figure3). The Northeast Corridor is the busiest rail corridor in the United States. It carries the AMTRAK and other regional rail traffic from Washington DC to Boston via Baltimore, Philadelphia, and New York (Figure 4).

The Northeast Corridor over Easton Avenue Bridge was built in 1902. This stone arch bridge carries four AMTRAK and New Jersey Transit Tracks in New Brunswick, New Jersey (Figure 5). The span length of the bridge is 65 feet and the width is 69 feet. The clear rise of the arch is 10 feet. The thickness of the arch is 4 feet.

The rating process begins by calculating the dead and live load on a one-foot wide section of the arch. Different live loading conditions were produced by moving the train live load over the entire length of the bridge. The bridge was loaded as per AREMA and the live load and impact where applicable. The train live load used was Cooper E80 train load. SDAAD.Pro Software (1998) was used to model the arch and to calculate the axial forces and the corresponding moments at the member nodes of the arch for both dead and live loads. Horizontal soil pressures were applied on the arch. Figure 6 shows the model used. Those loads were used to rate the arch using the method summarized previously. Axial loads and corresponding moments were obtained for two sets of soil pressures with Ke equal to 0.33 and 1.0. Table1 shows a summary of the results. The normal rating factor for the bridge is 1.4 and the maximum load rating is 1.8



Figure 3. North East Corridor over Easton Avenue Bridge.

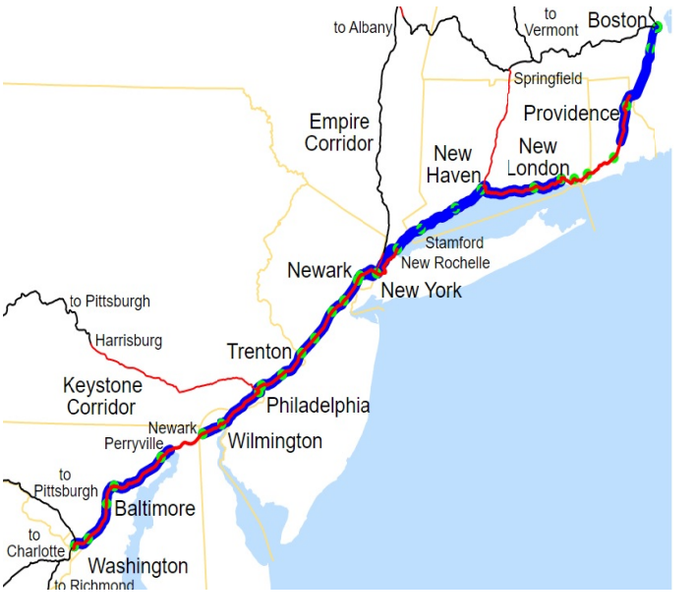


Figure 4. North East Corridor

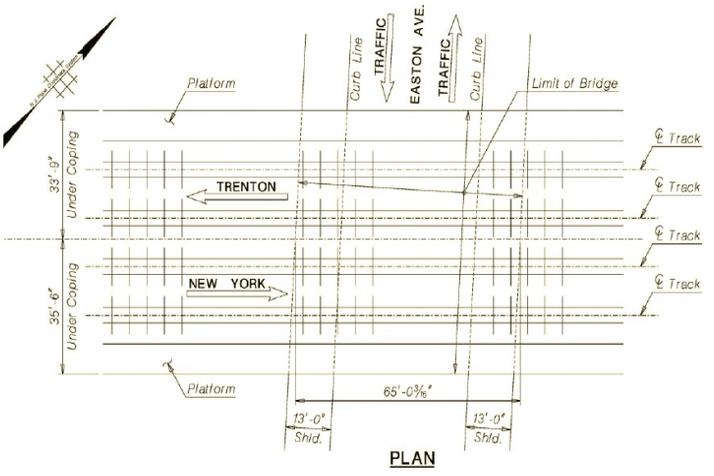


Figure 5. Bridge Plan.

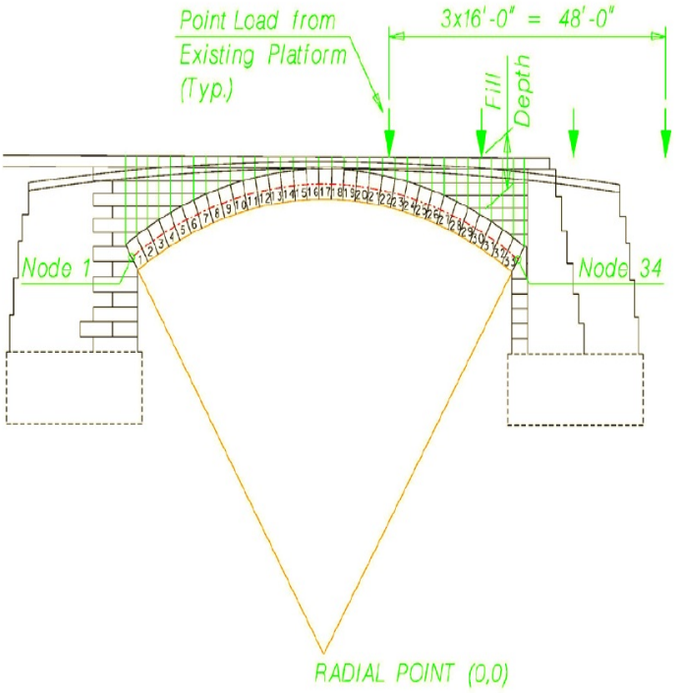


Figure 6. Bridge Model.

Load Rating	ARCH LOADING (DEAD LOADING PLUS LIVE LOADING AS SHOWN BELOW)							
	1/4 SPAN IS LOADED		1/2 SPAN IS LOADED		3/4 SPAN IS LOADED		FULL SPAN IS LOADED	
	Ke = 0.33	Ke = 1.00	Ke = 0.33	Ke = 1.00	Ke = 0.33	Ke = 1.00	Ke = 0.33	Ke = 1.00
NORMAL LOAD RATING	2.4	2.8	1.4	1.4	1.5	1.5	1.5	1.4
MAXIMUM LOAD RATING	2.8	2.8	2.8	2	2	2	1.8	1.8

Table 1 Summary of Results.

4 CONCLUSIONS

Using a standard structural analysis tool (such as STAAD.Pro) to determine member nodal forces, a spreadsheet application (such as Microsoft Excel), and the method for rating summarized in this paper, rating of masonry arch bridges can be done very efficiently and in a standardized fashion.

Also, the effect of deterioration on the arch members, can be efficiently incorporated into the load rating to determine the as-inspected rating.

Further, the method for rating summarized in this paper can be extended to highway bridges also.

5 REFERENCES

American Railway Engineering and Maintenance-of-way Association (AREMA) Manual for Railway Engineering, USA, 2012.

STAADPro Structural Analysis and Design Software Release V, Research Engineers Corporation, Yorba Linda, CA, USA,1998

Microsoft Excel 2000, Microsoft Corporation, Santa Rosa, CA, USA, 1999.

Maintenance, Safety, Risk, Management and Life-Cycle Performance of Bridges – Powers, Frangopol, Al-Mahaidi & Caprani (Eds)
© 2018 Taylor & Francis Group, London, ISBN 978-1-138-73045-8

Monitoring Design for Long-Span Bridges

K. Suzuki
University of Fukui, Fukui, Japan

C. Miki
Tokyo City University, Tokyo, Japan

E. Sasaki
Tokyo Institute of Technology, Tokyo, Japan

A. Tanabe
Nikken Sekkei Civil Engineering LTD, Osaka, Japan

ABSTRACT: This paper presents a Finite Element Analysis(FEA)-based design of a health monitoring system for a structurally complex long-span bridge. The system consists of Bridge Weigh-in-Motion(BWIM), damage detection function and thermal behavior monitoring. To determinate the sensor position for BWIM, the strain response in the floor system is analyzed. Besides, FEA simulations are performed to grasp the damageable parts during an earthquake. Based on the analysis, a sensor arrangement for the bridge is proposed.

1 INTRODUTION

Planning of bridge health monitoring should take account of bridge environment that influences the structural damage or deterioration such as, disaster strikes, traffic volume of heavy trucks and a level of corrosive environment. Reasonable sensor selection, their arrangement and data acquisition would be proposed by considering damage modes. This study describes how to design bridge health monitoring with an example of a large-scale bridge. To identify monitoring items, the bridge condition is divided into in-service one and extreme loading one. For the monitoring for the in-service condition, BWIM is included for the evaluation of fatigue environment. Bearing function is also monitored. For the extreme-loading condition, the proposal of sensor arrangement is based on FEA dynamic simulation to reveal the bridge behavior and damaged bridge components when a strong earthquake strikes.

2 DESIGN CONCEPTS FOR THE MONITORING

As a case study of the monitoring design, Tokyo Gate Bridge(TGB), the construction of which completed in 2012, is targeted. Two reasons why the bridge was targeted as a monitoring design are, firstly it will be difficult to ensure the alternative paths due to its long span and the cross-linking location when a disaster strikes, secondly, structural behavior is unclear due to the characteristic base-isolation system and the application of newly developed high yield point steels. Note that the monitoring system implemented to the TGB is not exactly the same as the proposal of this study because of the bridge administrator's consideration. The TGB connects reclaimed lands in Tokyo bay (Figure 1), aiming to enhance smooth traffic flow in the water front area. Since the site is in only 7km from Haneda Airport, height restriction had to be taken into consideration. In addition, the clearance amounts to 50m for allowing passage of tall ships. By adding aesthetic examination as a symbol of the entryway in Tokyo port into the design, truss structure was chosen in the preliminary design, which reminds us a gantry crane.

There are several concerns about the maintenance management after opening for the TGB. It is anticipated that a large volume of freight cars would use the bridge to avoid traffic congestion in the cen-

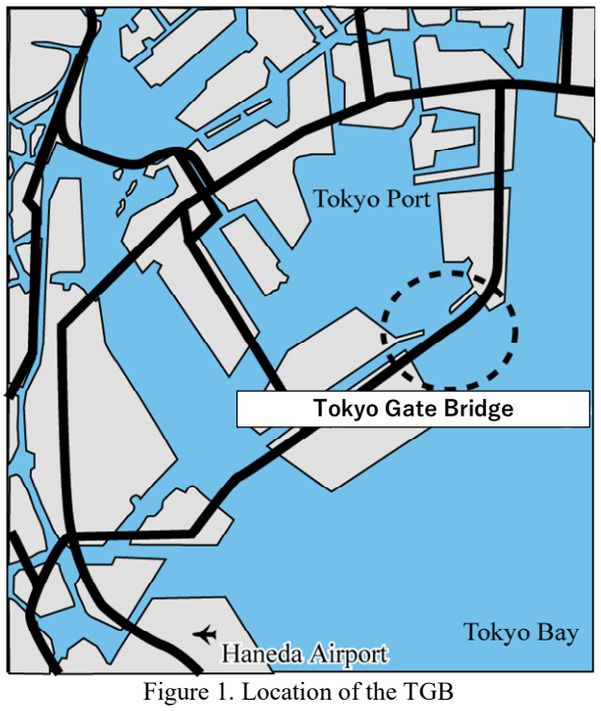
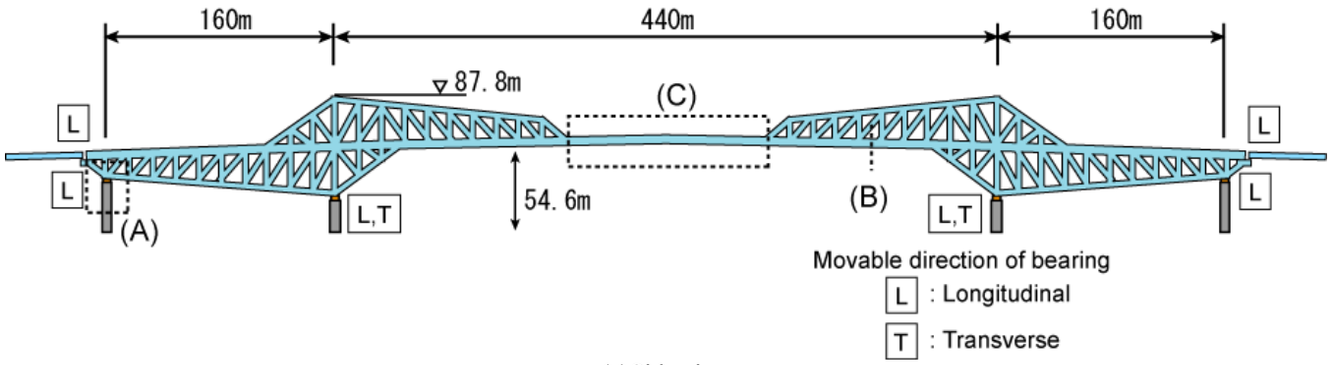
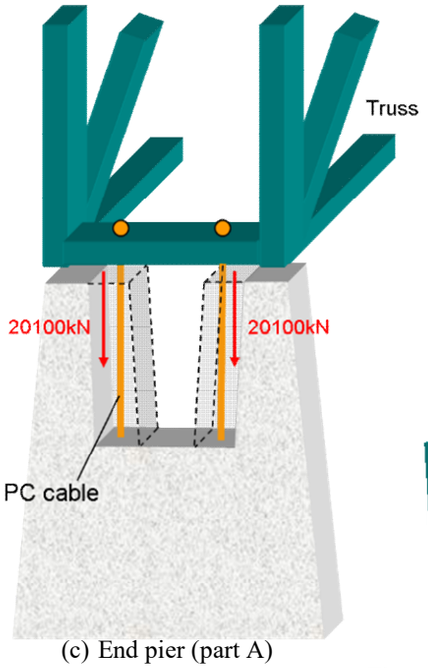


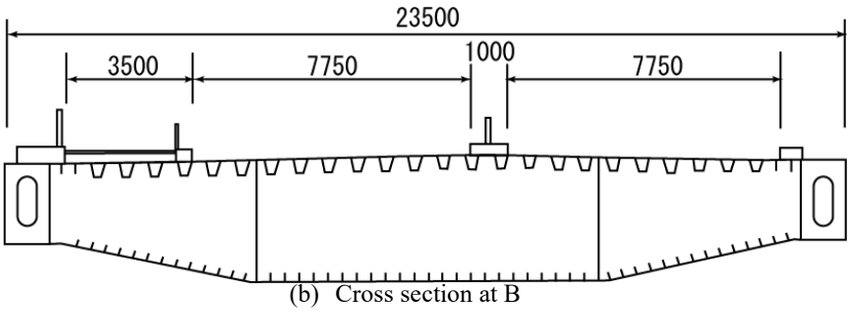
Figure 1. Location of the TGB



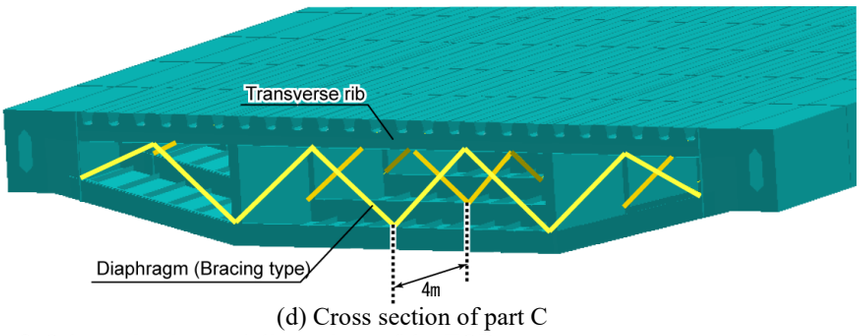
(a)Side view



(c) End pier (part A)



(b) Cross section at B



(d) Cross section of part C

Figure 2. Schematic view and dimensions of the TGB

ter of Tokyo, so that the consideration to fatigue damage is required. As to inspection, the TGB has large inspection areas, and also easy access are difficult in some bridge structures. In addition, Tokyo bay is under harsh condition in terms of disaster, such as an earthquake and a typhoon. Three main aims of the bridge health monitoring system are: (1) to grasp live loads dynamically by using Bridge Weigh-in-Motion (BWIM) for the evaluation of fatigue cause; (2) to diagnose the conditions to control traffic flow promptly in case of the strong level of disasters; (3) to obtain omens of structural degradation in the latent phase with thermal deformation monitoring.

Bridge health monitoring has been developed in three decades, especially for large-scale bridges and newly developed bridges such as integral abutment bridges. In the design of the structural health monitoring system, the selection of sensors, the sensor arrangement, and the data transfer are crucial. Koh et al. (2005) introduced a damage detection system in Gwangan bridge. In the system, health condition was investigated with some laser displacement meters. In suspension bridges, vibration responses in suspension bridges are considerable, Nagayama et al. (2005) proposed an identification method of structural integrity in a suspension bridge by using ambient vibration with accelerometers. In large-scale bridges, structural behaviors have been monitored with much regard for thermal deformation. Kobayashi et al. (2007) evaluated correlativity of temperature change, obtaining the structural behavior in the box girder bridge with thermometers in the box and displacement meters in the bearings. The monitoring system of Orange and Wendell Bridge (Sergio et al. 2007), the type of which is an integral abutment bridge, acquired bridge responses due to temperature for three years. In the meantime, utilization of higher speed network for structural health monitoring has been attempted.

3 BRIDGE DESCRIPTION

The main bridge consists of three-span continuous box girder built in truss structure (Figure 2). It is a 440m length interior span and two 160m long exterior spans for a total bridge length of 760m. The approach bridges adjacent to the main bridge are multi-span continuous box girder, which consists of 120m

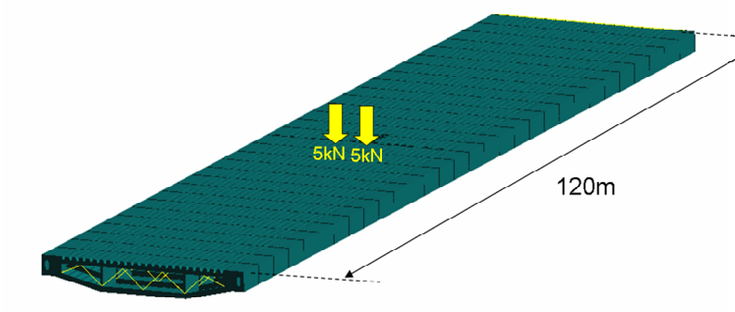


Figure 3. FE model

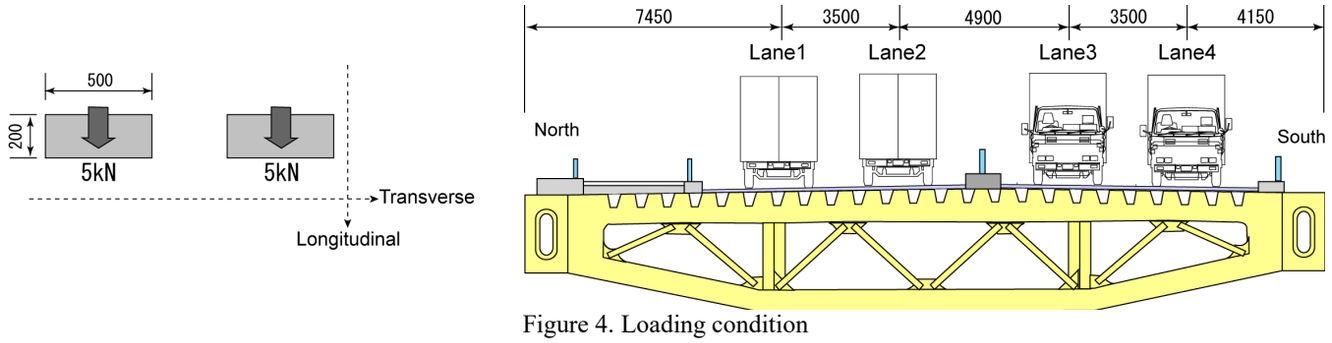


Figure 4. Loading condition

of each span. The one on the east wing is four curved spans and the other one on the west wing extends three straight spans.

The TGB has particular structures. First, in order to reduce weight of metal and save the maintenance cost for bearings supporting a deck, middle chord of the truss integrated with the box girder and orthotropic steel deck structure is adopted (Figure 2-c), instead of the conventional design in which a deck is placed on the lateral member of the truss. The integrated box girder is stiffened with a diaphragm of a sway bracing type tightly arranged every 4m intervals (Figure 2-d). This makes considerable constraints and stiffness in the floor system. Second, the trussed structure supporting the box girder induces negative reaction force at MP1 and MP4. As a countermeasure towards it, tie down cables with 20100(kN) in each are installed (Figure 2-a). Third, in the main bridge, isolation bases are employed on all the piers. The adoption of base isolation is based on the following reasons. 1) Since the piers are short in the large structural system, it may be difficult that effective plastic hinges arise in an extreme loading condition. 2) Deformation induced from plastic hinges is hard to get back to the former condition, because the dead loading acting on MP2 and MP3 exceeds 300,000(kN) in total and the tie down cables at MP1 and MP4 leads to 20,100 (kN) loading in each bearing. Lastly, for the purpose of damage control, side blocks of the bearings on MP1 and MP4 are designed to break when lateral force becomes 20,000(kN). Due to the above structural features, the behavior of the TGB can be complex.

4 SENSOR ARRANGEMENT FOR BWIM

Referring to the suggested BWIM instrumentation in an orthotropic steel deck (Kobayashi et al. 2003), trough ribs right under the axle passage position and a transverse rib are recommended as sensor installation points. The former is to obtain the information of axle positions, and the latter is to calculate the vehicle's weight. In the floor system of the TGB, the strain response in transverse rib might be insufficient due to the connected sway-bracing type diaphragm. Static FEA herein is used to consider suitable installation points, which provide strain data for total weight of the vehicle. Two requirements for the sensor position are that strain responses due to live loads are to be: (1) large as compared with circumjacent positions, (2) less sensitive to differences in vehicles' running positions to transverse direction.

Figure 3 illustrates the Finite Element(FE) model. The model represents a center part of the main bridge. The loading condition shown in Figure 4 is simulating a couple of tires. On each lane, a total of 10kN load is shifted to a transverse direction every 100mm up to 500mm.

Figure 5 shows the analysis results on the Lane 1, Lane 3 and Lane 4, respectively. Minus on the horizontal axes in those graphs means north side and plus on that means south. Two points indicated by the triangle mark means focusing points where strain response is large when the loading position is zero in transverse. About these parts, focusing was paid to two parts showing remarkable strain response in comparison with other ones.

In the Lane 1 (Figure 5), the strain response at position (A) is large. When a running position shifts to -300mm, the response decreases 40%. In contrast, the response of (B) is small in any position compared with (A), and the effect by the running positions is stable. Since the fluctuation of strain re-

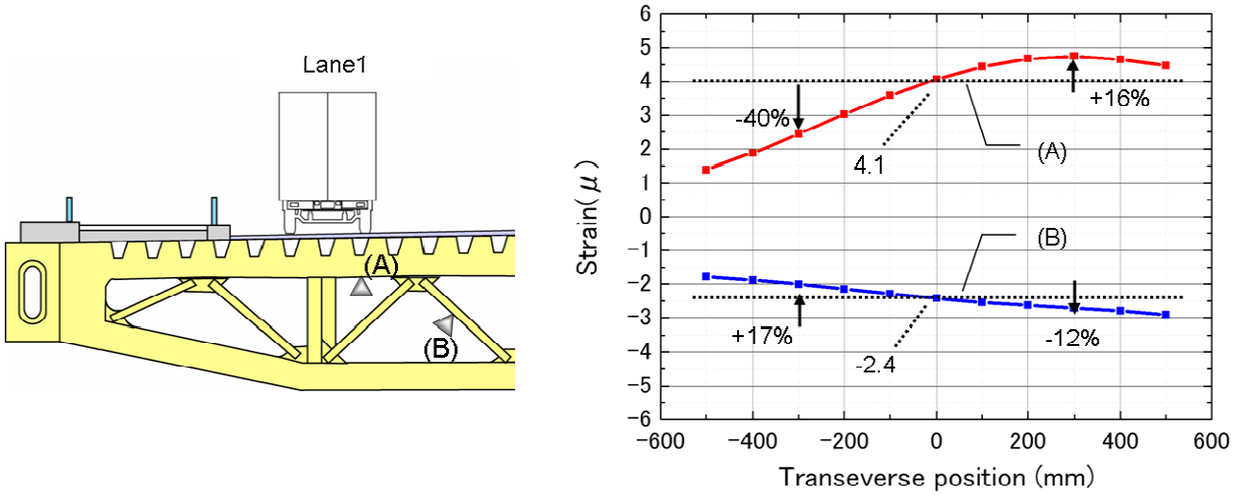


Figure 5. Strain response when loaded on the Lane 1

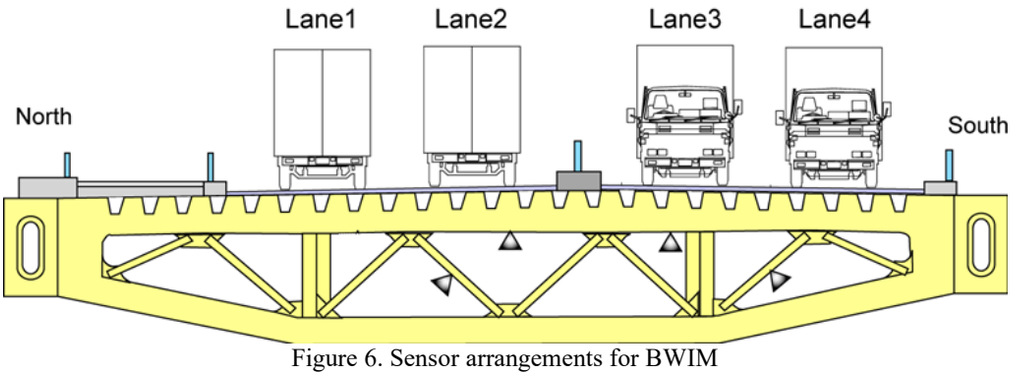


Figure 6. Sensor arrangements for BWIM

sponse at position (A) is significant, BWIM in Lane 1 is performed using strain data of position (B).

The response in the Lane 2 is sufficiently obtained in the transverse rib. The installation part for the Lane 2 is right under the reference running position.

As for the Lane 3 and Lane 4, similar analysis cases are performed; then, the sensor arrangement is determined. Finally, the sensor arrangements for weight-of-vehicle calculation is proposed as shown in Figure 6.

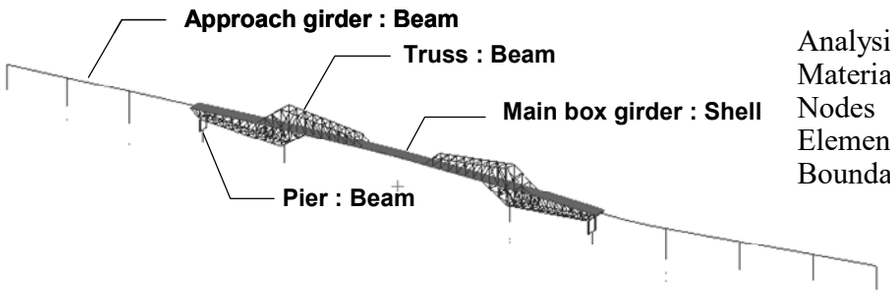
5 MONITORING DESIGN FOR DAMAGE DETECTION IN EXTREME LOADING CONDITION

In arrangement of sensors, it is necessary to duplicate the bridge behavior, including its nonlinearity, and then damaged area, the modes, and the sequence of the damage must be identified. FEA herein simulates damage occurrence, including the effects of the base isolation, tie-down cables, truss-box integrated structure and the damage control in the side blocks in the model.

5.1 *Finite element model*

In order to grasp critical parts during an earthquake, FE dynamic analysis was employed. The FE model involved the possibility of pounding effects between the bridge and the neighboring approach bridges due to the difference of eigenfrequencies, the FE model included approach bridges in both sides. In the model, shell elements were employed to take the torsion effects and local deformation into consideration. The truss members, piers and the approach bridges were modeled with beam elements as shown in Figure 7.

The applied base isolation system was illustrated in Figure 8. This system called “friction isolator” consists of a sliding part and a rubber buffer. In the sliding part, an interface plate covered with Teflon bottomed in the superstructure slides on a stainless-steel plate and the friction effects of the sliding is expected to have damping effects. The friction coefficient in the model is uniformly 0.15 to simplify dynamic analysis in design. The rubber buffer carries horizontal loads with linear restoring. Assuming these actions, the bearings are modeled by using connecter elements in ABAQUS with the constitutive law shown in Figure 9.



Analysis code : ABAQUS
Material : Linear condition
Nodes : 259988
Elements : 266493
Boundary : Full fixity at end points

Figure 7. FE model

For the pounding effects, pounding springs were defined in the model. Figure 10-a shows the spring model for expansion gap. For the pounding effects and constraint effects by seismic restrainers, the spring shows infinitive stiffness when the gap between the main bridge and the approach bridge reach 1300mm.

Bearings at MP1 and MP4 fix transverse movement of the superstructure with side blocks. This was modeled by using a spring element as shown in Figure 10-b. Considering 10mm gap between the shoe and the side block, the maximum response in the model is shown at 10mm. The side blocks ruptures when 20000kN acts

Structural damping in the propagation of earthquake motion was defined with the Rayleigh damping. The coefficients of the mass matrix and the stiffness matrix are determined from the modal participation factors and effective mass value obtained by eigenvalue analysis.

For the input of earthquake motion, the great hanshin earthquake recorded at the Higashi Kobe bridge and the assumed minami-kanto earthquake were used. In advance to the dynamic analysis, ground propagation analyses of those earthquakes were carried out, and then surface displacement waves were obtained. Accordingly, the surface wave contains the property of ground under each pier. The surface waves were input from the bottom of each pier through a ground spring and a ground dashpot.

Since the difference of mode value between longitudinal and transverse direction in large-scale bridges can be large, angle of incidence of an earthquake may affect those response. In this study, each wave was inputted, changing the angle of incidence as a parameter from 0 degree to 315 degrees every 45 degrees (Figure 11).

5.2 *Results and discussions*

Of the two earthquakes used as input waves, no damage was seen in the case of the assumed minami-kanto earthquake regardless of the angle of incidence.

In contrast, in the case of the great hanshin earthquake, damage was induced in the side blocks in the bearings on MP1 and MP4 and the lateral

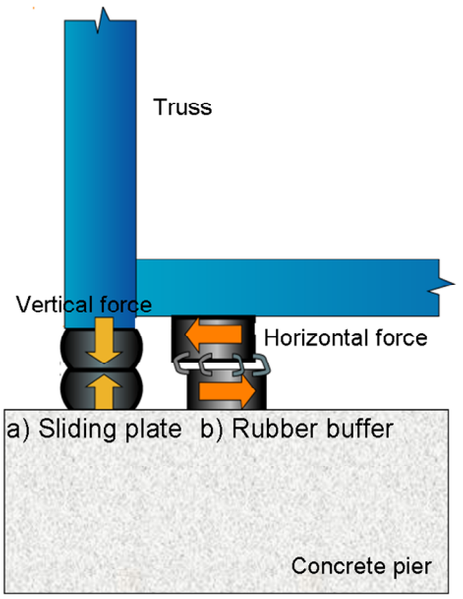
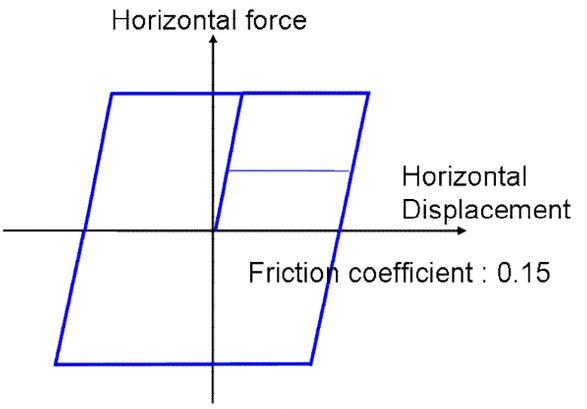
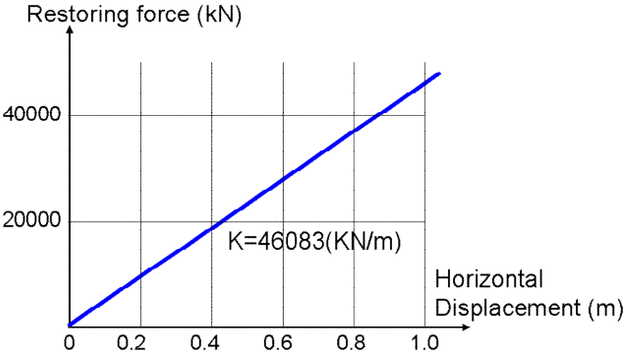


Figure 8. Schema of the base isolation

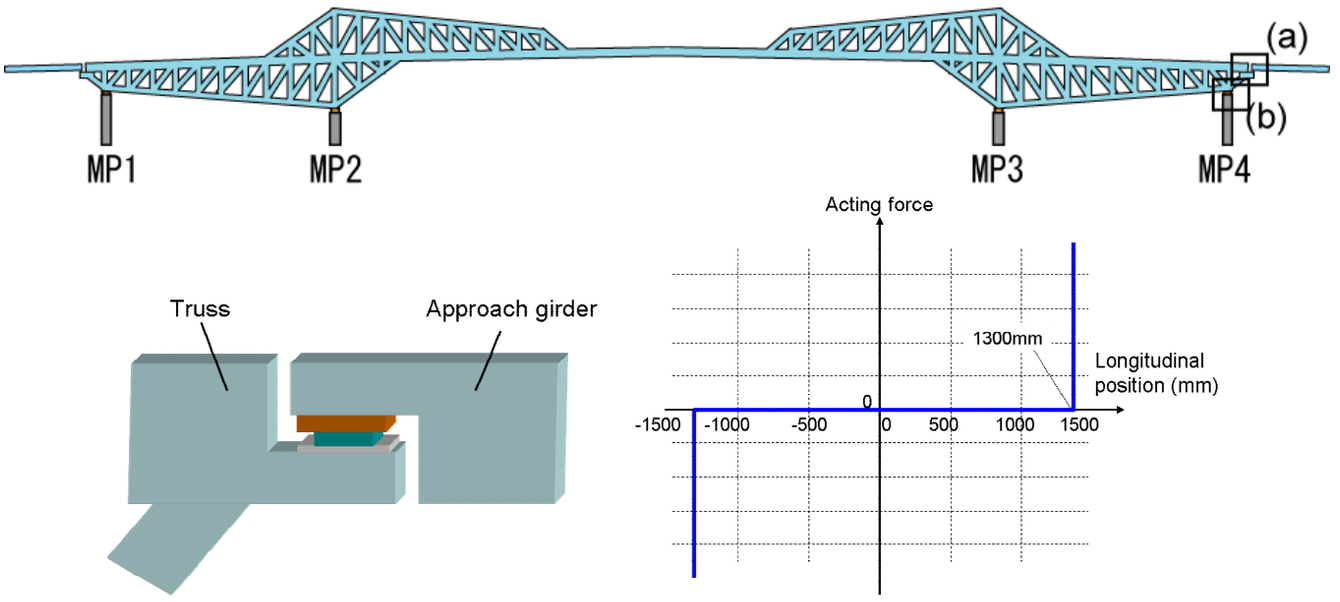


(a) Sliding plate

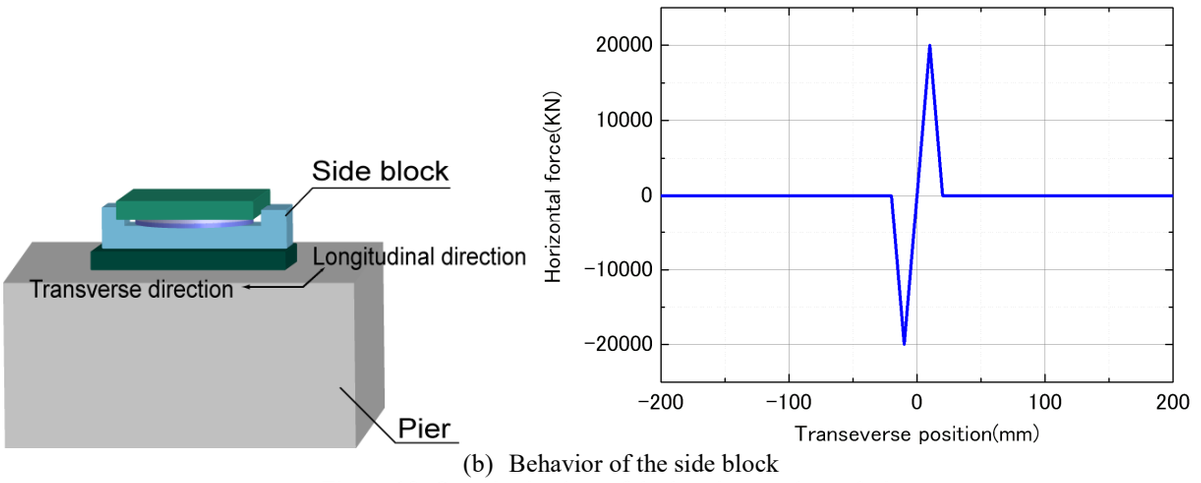


(b) Rubber buffer

Figure. 9 Constitutive law of the seismic base isolation



(a)Spring model for the connection point



(b) Behavior of the side block

Figure 10. Constitutive law of the bearings at the end piers

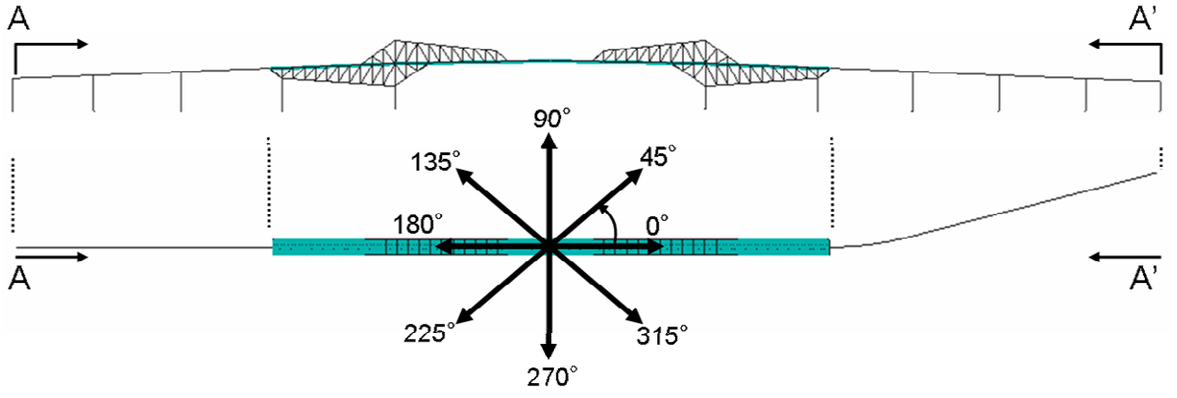


Figure 11. Input of the earthquake

bracings in lower chords. The damage aroused in the case of 0 degree, 45 degrees, 180 degrees and 225 degrees of angle of incidence. There was difference in the angle cases of damage occurrence as explained in Fig.14. The side blocks were damaged in the mentioned four angle cases. As opposed to it, damaged lateral bracings were different by the case.

In case of 45 degrees and 225 degrees, the largest number of members was damaged. The following discussion is mainly mentioned based on the harshest case.

Figure 12 shows the relative displacement in a transverse direction of the bearing at MP1. At the moment of 9.1 seconds from the analysis start, the behavior of the superstructure and that of substruc-

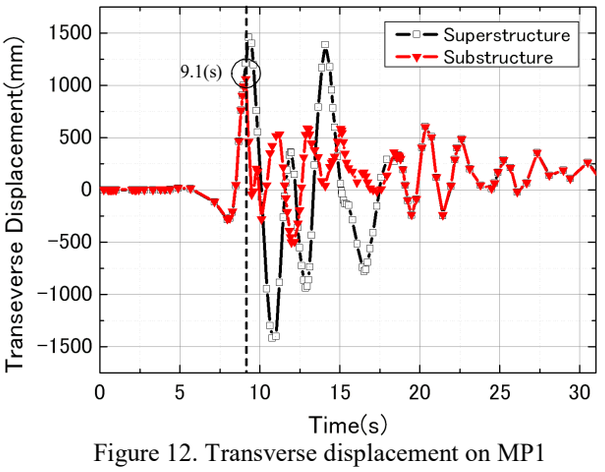


Figure 12. Transverse displacement on MP1

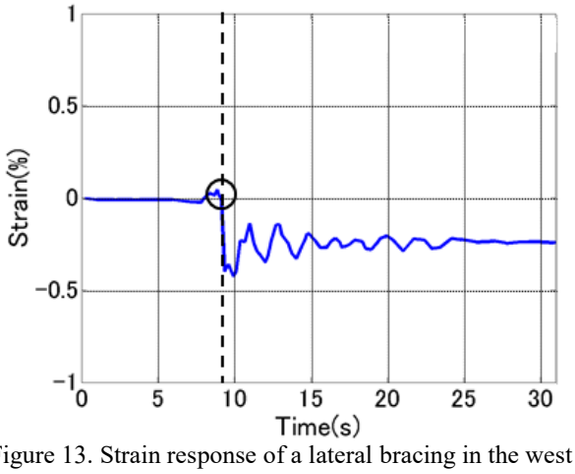


Figure 13. Strain response of a lateral bracing in the west side

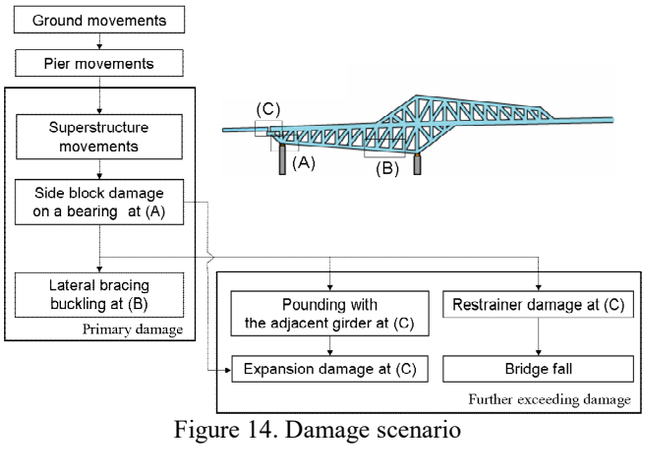


Figure 14. Damage scenario

ture started to show different response. This means that the side blocks fixing a transverse direction was broken at the time. Figure 13 shows the strain responses of lateral bracings at the lower chords. Notice that the moment when compressive damage occurred was right after the moment when the side blocks of the bearings damaged. The same damage scenario occurred at MP4 as well.

Although pounding effects at expansions were concerned, the damage of the adjacent approach bridge did not occur in all cases.

5.3 *Damage scenario*

From the result of the analysis, a damage scenario is drawn in Figure 14 with the order of events. The damage identified in the analyses is defined as primary damage herein. In the scenario, the ground shaking acts on the bases, then the piers are shaken. Due to the behavior of piers, damage arises in the side blocks of the bearings that fix transverse movement of the superstructure. When the side blocks are damaged, relative displacement in transverse direction occurs between the superstructure and the substructure on MP1 and MP4. As a result, lateral bracing buckling and damage in expansions are caused. As a further exceeding damage, pounding effects with adjacent bridges and damage in seismic restrainers can be led. In the considered further exceeding damage, the damage in seismic restrainer can lead bridge fall in the worst case.
In the procedure, it is clear that the damage in the side blocks is a trigger to the subsequent damage cases.

6 A PROPOSAL OF BRIDGE MONITORING

Based on the analysis results and discussions on the damage scenario, this study proposes the TGB health monitoring system. From the viewpoint of sensor durability, fiber optic sensors are appropriate to the structural monitoring system. This monitoring system uses FBG (Fiber Bragg Grating) strain sensors for BWIM and OTDR (Optical Time Domain Reflectometer) system for damage detection in extreme loading condition. Figure 15 illustrates the bridge instrumentation.

For BWIM, FBG strain sensors were employed in the box girder of the central part of the main span. In addition to the four strain sensors for the weight calculation arranged in the targeted diaphragm in the center, eight strain sensors are arranged in the trough ribs for grasping axle location of the vehicle. These sensors are installed at the position left 2m to the longitudinal direction before and behind of the BWIM instrumented diaphragm.

As for the damage detection in extreme loading condition, it is required to detect transverse transition of superstructure accompanied with the damage of the side blocks in the bearings on MP1 and MP4. About the lateral bracings, the damage mode was total buckling, and the detecting regions are too large, so that it is very difficult to detect them. This monitoring arranges the sensors only in side blocks and use the sensors as a trigger of damage initiation. The OTDR system is arranged in all bearings, which are fixed in transverse direction by side blocks.

In addition, 5 FBG sensors are arranged for the temperature measurement of the box and one FBG strain sensor is arranged in the bottom flange to de-

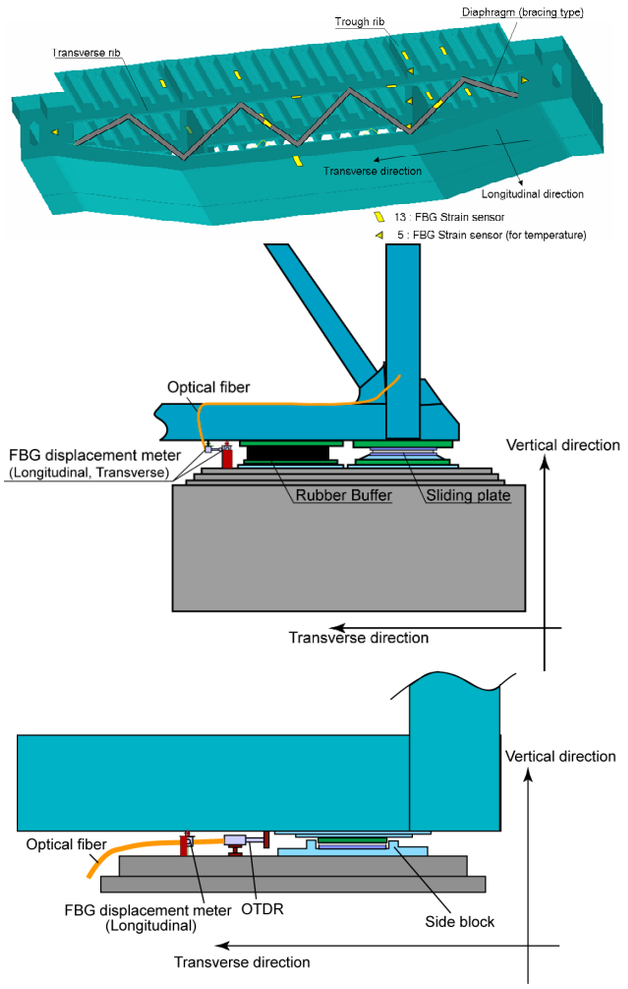


Figure 15. Sensor arrangements

tect thermal deformation. The thermal deformation is monitored with the FBG displacement sensors arranged in all bearings to movable directions.

The all sensors are connected by optical fibers. The optical fiber itself plays a roll of damage detection in this monitoring system. In case the optical fiber was cut, the location is able to be pinpointed from a remote station. Therefore, optical fibers run in the whole bridge to detect large deformation and breakage of the member.

Figure.16 illustrates the system flow from the data acquisition to indicated items by the monitoring system. In case OTDR detects the damage in the side blocks, the system immediately executes road closure and simultaneously indicates damaged parts.

7 CONCLUDING REMARKS

This paper described a design of a heath monitoring system for a base-isolated large-scale bridge. FEA revealed the structural responses, damage modes and those relations. Then, the sensor arrangement was proposed. Followings are the concluding remarks.

(1) For the sensor arrangement of BWIM, the effect of shift of the vehicle's running position on strain responses is clarified by using static FEA. The identified desirable points where the strain response is relatively large and less sensitive to the running position are: 1) in the bracings of the diaphragm for Lane 1 and Lane 4; 2) in the transverse rib for Lane 2 and Lane 3.

(2) The nonlinear dynamic FEA simulated the bridge behaviors, including the inelastic hysteretic property for the sliding part in the base isolation and the effects of attack angle of the earthquake. The results revealed that damage occurs initially at the side blocks in the bearings and secondary at the lateral bracings. Therefore, it is most important to detect damage of the side blocks which is the trigger of the subsequent damage procedure.

REFFERENCES

Brena, S. F., Bonczar, C., Civjan, S.A., DeJong, J.T., and Crovo, D.S., Evaluation of Seasonal and Yearly Behavior of an Integral Abutment Bridge. J. Bridge Engng ASCE, 2007, 12 :296-305.

Kobayashi, Y., Miki, C., and Tanabe, A., Health Monitoring Utilizing Thermal Deformation for Box Girder Bridge with Orthotropic Deck System. Journal of JSCE A, 2006, 62, 794-807, 2006, 62:794-807.

Koh, H.M., Kim, S., and Choo,J.F., Recent Development of Bridge Health Monitoring System in Korea. Sensing Issues in Civil Structural Health Monitoring Springer Netherlands, 2005:33-42.

Nagayama, T., Abe, M., Fujino, Y., Ikeda, K., Structural Identification of a Nonproportionally Damped System and Its Application to a Full-Scale Suspension Bridge, J. Struct. Engng ASCE, 2005, 131:1536-1545.

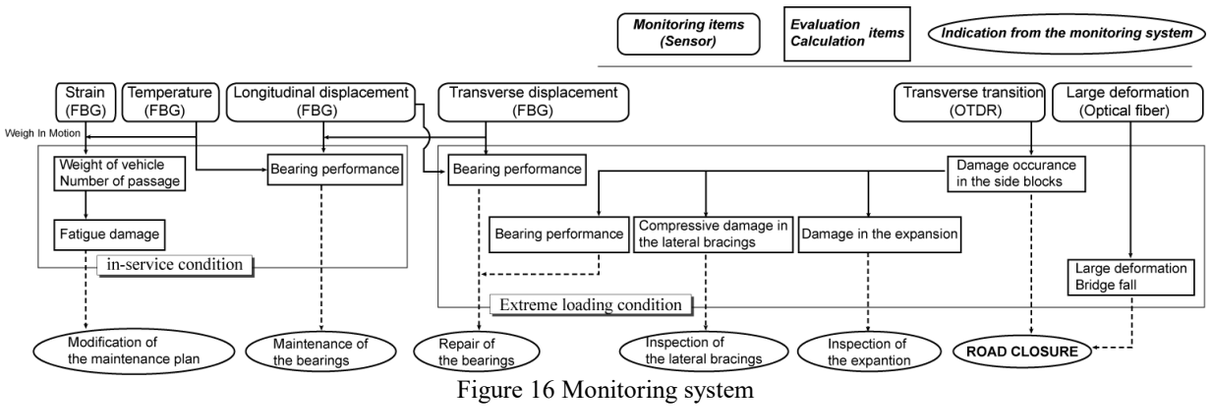


Figure 16 Monitoring system

Maintenance, Safety, Risk, Management and Life-Cycle Performance of Bridges – Powers, Frangopol, Al-Mahaidi & Caprani (Eds)
© 2018 Taylor & Francis Group, London, ISBN 978-1-138-73045-8

Testing of bridge structures using laser scanning method

W. Anigacz & D. Beben
Faculty of Civil Engineering and Architecture, Opole University of Technology, Opole, Poland
J. Kwiatkowski
J&L Consulting Jacek Kwiatkowski, Opole, Poland

ABSTRACT: The objective of the study was to compare and assess suitability of laser scanning method to determine geometric changes of the bridge structures. The laser scanning method was tested at two suspension bridges. First was a technological bridge (Chorula, Poland) with effective main span of 165 m, and second one was a historic cast iron bridge (Ozimek, Poland) with span of 27.7 m. The first measurements were conducted using a FARO Focus 3DX130 scanner. In the case of the second bridge (Ozimek), the results clearly indicate that reduced the distance to the bridge (40 m) allows to obtain satisfactory results, i.e. a full inventory of the bridge elements. Taking into account the above experience, the authors decided to use for the technological bridge examinations a Trimble TX8 scanner. It turned out that the Trimble TX8 scanner allows to obtain the technological bridge displacements under static loads. For the results analysis and point cloud pro-cessing, specifically designed the Trimble Real-Works 10.2 program was used. The software provides a complete solution to efficiently register, analyse, model and create deliverables using data from virtually any source. The software also allows for the automatic interpolation of the markers centre, which in this study constituted the measurement targets and white reference spheres (the same as in the photogrammetric method). The subsequent scans are matching to characteristic points (measurement targets and white reference spheres) in such a way that the next measurement sessions can be topologically consistent. This allows for significantly reduction of the working time on the measurement object. The obtained results were verified by the tachymetric method using the TC 2002 instrument. The presented approach to the bridge testing using scanner method can help in the bridges diagnostic, especially in the case there are not the technical project, for example for old bridges.

1 INTRODUCTION

Inventory measurements are usually performed on bridges in order to confirm project assumptions or as diagnostic tests to provide their proper maintenance. The results of bridge inspection are the basic source of information about technical conditions and occurred damages. They are obligatory in most countries all around the world and are performed on the basis of systematic strategy of transport infrastructure control. Typical measurements and research are usually conducted manually by bridge inspectors in several selected points. Most of inventory work requires a direct contact with structure, what, in some circumstances, may cause problems with object research availability and often requires scaffolding which increases inventory costs. In many cases of bridges, particularly historic ones, there is a lack of project documentation. It is a serious problem during modernization and/or conservation work. Inventory work performed with traditional methods is quite time consuming, especially when objects have complicated and complex structure, e.g. a truss structure. Non-contact tests methods of engineering structures have lately become very popular, for example the interferometric method (Anigacz et al. 2016, Beben 2011, Beben & Anigacz 2017) enables the bridge displacement monitoring even from a few hundred meters. Tachymetric and photogrammetric methods also experience revival thanks to modern equipments and computer analysis of results (Anigacz et al. 2018, Beshr 2015, Jauregui et al. 2003). The laser scanning method gives the possibility of obtaining a point cloud (Berényi et al. 2009, Kwiatkowski 2014, Shen-En 2012, Tang et al. 2006, Truong-Hong et al. 2016) and, as a result, this method may be successfully used in inventory of various engineering objects, particularly the ones with difficult access. Such action can be defined as a reverse engineering.

In this article the authors decided to verify the laser scanning method on the example of two suspension bridges. They analysed measurement capabilities of this method, i.e. the authors checked inventory work quality with the use of laser scanner

on a technological bridge (object #1) and historic cast iron bridge (object #2). Fast expanding measurement techniques, especially geodetic ones, in particular mass measurements enable obtaining complete information about an object and changes in its geometry. The measurements were conducted using FARO Focus 3DX130 and Trimble TX8 scanners.

2. SHORT DESCRIPTION OF BRIDGES

The studied structure no. 1 is a two-pylon steel suspension bridge over the Oder River intended for connecting the marl mine with cement factory with the transport line (Fig. 1). The bridge comprises five spans – four outmost flood spans and the river span. The structure of the transport gallery is suspended with hangers under the main bearing cables distributed over two pairs of pylons.

The load-carrying structure with span of 165.00 m is suspended on cables. The total length of the entire bridge structure is 285.00 m. The bridge was designed as a structure suspended on two steel pylons, through which a set of 2×6 bearing cables of 48 mm diameter. An orthotropic plate is placed directly on the longitudinal beams. The pylons with high of 26.50 m are supported by hinged steel bearings on reinforced concrete foundations. The cables are connected to the pylon in a fixed manner through a head and screwed connections that enable moving the cables on the pylon tip. The bridge is intended for transporting the limestone output with a belt conveyor placed in the transport gallery. Weight of the output transported through the bridge is 900–1100 Mg/hour, and the speed of the belt conveyor movement was 2 m/s.



Figure 1. Side view on the bridge in Chorula.

Object #2 is a historic suspension bridge in Ozimek (Fig. 2). Nowadays the bridge is intended for pedestrian traffic on the Mala Panew river. It was built in 1827 and is the oldest cast iron suspension bridge in Continental Europe. It is a suspension chain bridge completely made of iron (cast iron). Following this parameter it should be acknowledged as the oldest bridge of this type in the world existing till today. An older existing iron suspension bridge was built between 1819 and 1826 over the Menai Strait in Wales, however it is suspended on stone pylons. The parameters of the bridge are: a span – 27.7 m, axial spacing of pylons – 31.5 m, width of a bridge deck – 6.6 m. Complete renovation of the bridge was carried out between 2009 and 2010. It was disassembled, renovated and re-assembled. The bridge construction was strengthened with steal ropes.



Figure 2. Side view on the bridge in Ozimek.

3. RESEARCH METHODOLOGY

One of the most important factors determining a method selection is geometric specifics of an object. The analysed cases are linear objects with major spans of 165 m (bridge #1) and 27.7 m (bridge #2) in length. The span of a bridge is important because accurate determination of measurement point decreases with the increase of the distance. It should be considered in measurements of such type. The study was conducted after forty year of service of the bridge #1 and after a complete renovation of the bridge #2 carried out in 2010. The displacements of bridge #1 was observed during regular continuous 12-hour service loading. A displacements of river span was monitored. In the second case, due to the fact that the bridge is only a pedestrian crossing, the author used a laser scanning method as an inventory tool. The tests on both bridges were conducted for different distances between a scanner and a tested object, i.e. for the bridge in Chorula – about 110 m and for the one in Ozimek – 40 m.

a)



b)



Figure 3. View on the bridges in Ozimek and Chorula during testing using scanner: a) FARO Focus 3D X130, b) Trimble TX8.

The laser scanning method is a relatively new measurement method by means of which quasi-constant, spatial representation of a tested object can be obtained. It results in obtaining spatial point clouds of external surface of an object observed from the scanner position, i.e. in a central position. The accuracy of results depends mainly on the distance between a scanner and an object. In a last few years fast development of laser scanning has been observed. A scanner uses a laser beam which is reflected from the tested object and comes back to the scanner. The distance is determined by the difference in phase of sent and reflected radius. During the measurement a scanner can rotate 360 degrees horizontally. The horizontal and vertical angle settings of the scanner mirror and the information about measured distance are converted into local coordinates in the real time. FARO Focus 3DX130 scanner was used for the bridge testing (Fig. 3a) which measures to 1 million points per second and allows to create clouds exceeding a billion points. The producer's declared accuracy of distance measurement is ±2 mm and the angular resolution is 0.009° (0.16 [mrad].). Further scans are adjusted to characteristic points in the way the next measurement sessions are topologically coherent. It significantly reduces the fieldwork time.

It should be emphasized that the quality of the scan of the technological bridge was in the upper limit of this scanner coverage, i.e. 100-120 m. As it turned out later this limitation did not allow to obtain reliable results using this scanner. Taking into account the above experience, the authors decided to use for the bridge examinations a Trimble TX8 scanner (Fig. 3b).

This scanner measures up to 1 million of points per second and allows to create clouds of over a billion of points. The maximum scan range is 120 m, but it can be increased to 340 m. The wavelength of the laser is 1.5 μm and the scan frequency is equal 1 MHz. The declared accuracy of the measurement of the distance was ±2 mm, and angle resolution is 0.004° (0.08 [mrad]). The standard unit of resolution is dpi, so it means a dot per inch of the length. In the technical applications where the elements of the studied structures are located in different distances from the scanner, the angle resolution is the more convenient to use than the dpi which constantly changing with the change of the distance. The comparison of catalog data shows that the Trimble TX8 scanner has twice the angular resolution than the FARO Focus 3DX130 scanner.

For the results analysis and point cloud processing, specifically designed the Trimble RealWorks 10.2 (2017) program was used. The software provides a complete solution to efficiently register, analyze, model and create deliverables using data from virtually any source. The software also allows for the automatic interpolation of the markers center,

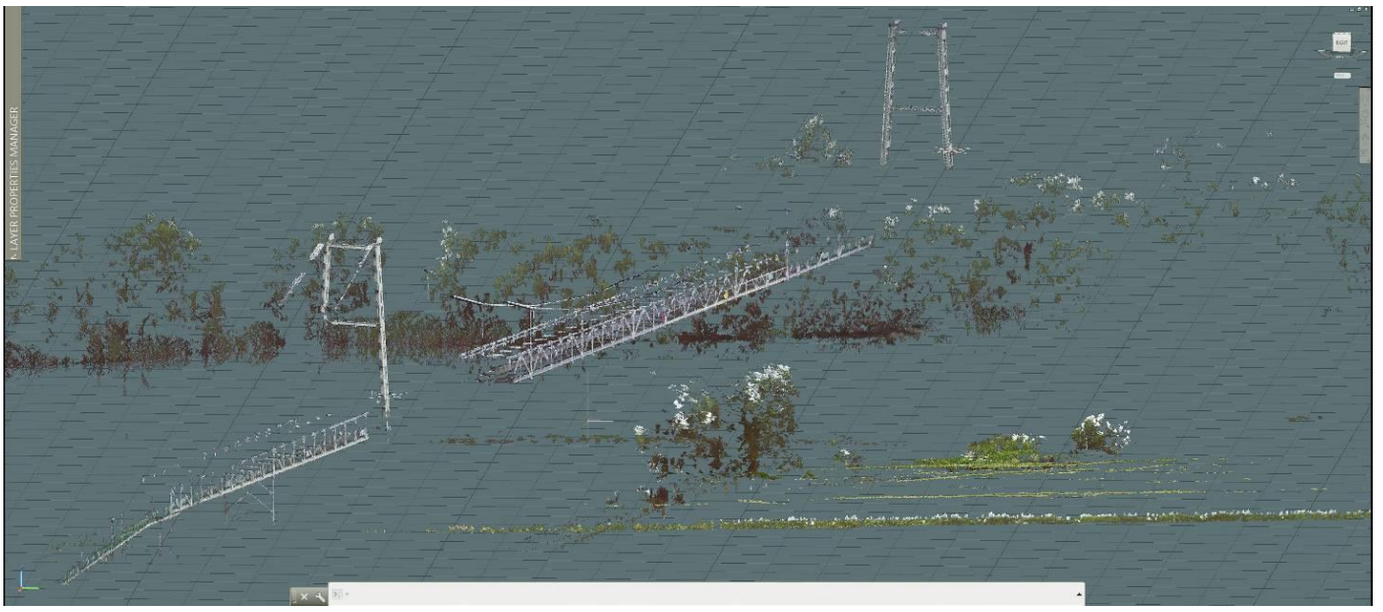


Figure 4. Scan of suspension bridge in Chorula using FARO Focus 3D X130 scanner.

which in this study constituted the measurement targets and white reference spheres (the same as in the photogrammetric method). Data from a scanner of such type are obtained in the .fls format. Conversion to the .rcs format was conducted with the ReCap360 software. Files with the extension .rcs are read by all the AutoDesk applications. The subsequent scans are matching to characteristic points (measurement targets and white reference spheres) in such a way that the next measurement sessions can be topologically consistent. This allows for significantly reduction of the working time on the measurement object (Kwiatkowski 2014).

The elaborated technology is particularly useful for a topologically complex structures. Automatically displaying colors using a calibrated map of the differences between scans (e.g. without and with load) allow to select the points on which should pay more attention.

4. TESTS RESULTS

During elaboration of results the scans were adjusted to characteristic points on a particular bridge in a way the following measurement sessions were topologically coherent. It significantly reduces the fieldwork time. It turned out that in case of the bridge #1 (in Chorula) the approach is inappropriate. The quality of the bridge scan was in the upper limit of reference range, i.e. 100-120 m. During the result analysis it occurred that the quality (points density) of a



Figure 5. Scan of suspension bridge in Ozimek using FARO Focus 3D X130 scanner.



Figure 6. 3D panoramic view of connected point clouds (FARO Focus 3D X130 scanner) for the Ozimek bridge.

scan is too low. Moreover, analysing the laser scanning bridge #1 test results it was stated that due to the lack of correlation (too big differences) with the results obtained from other methods the correctness is open to doubt (Fig. 4).

One of the most significant reasons of uncertain results of dislocation obtained from Faro Focus 3DX130 laser scanning was too large distance from the bridge #1 as well as the fact that the suspension bridge has an openwork structure which requires scans of bigger density than the ones obtained from the used scanner. To verify the test, the same scanner was used to conduct inventory work of a historic (the oldest in Europe) suspension cast iron bridge in Ozimek on the Mala Panew river. The tests were conducted at much shorter distance between the scanner and the bridge, i.e. 40 m. The recorded point cloud density allowed to identify the elements (details) of the bridge and in the result fully satisfactory results of bridge inventory were obtained (Figs 5-7).

As it was mentioned before, because of unsatisfactory measurement results taken with Faro Focus



Figure 7. Top view of the bridge in Ozimek using the FARO Focus 3D X130 scanner.

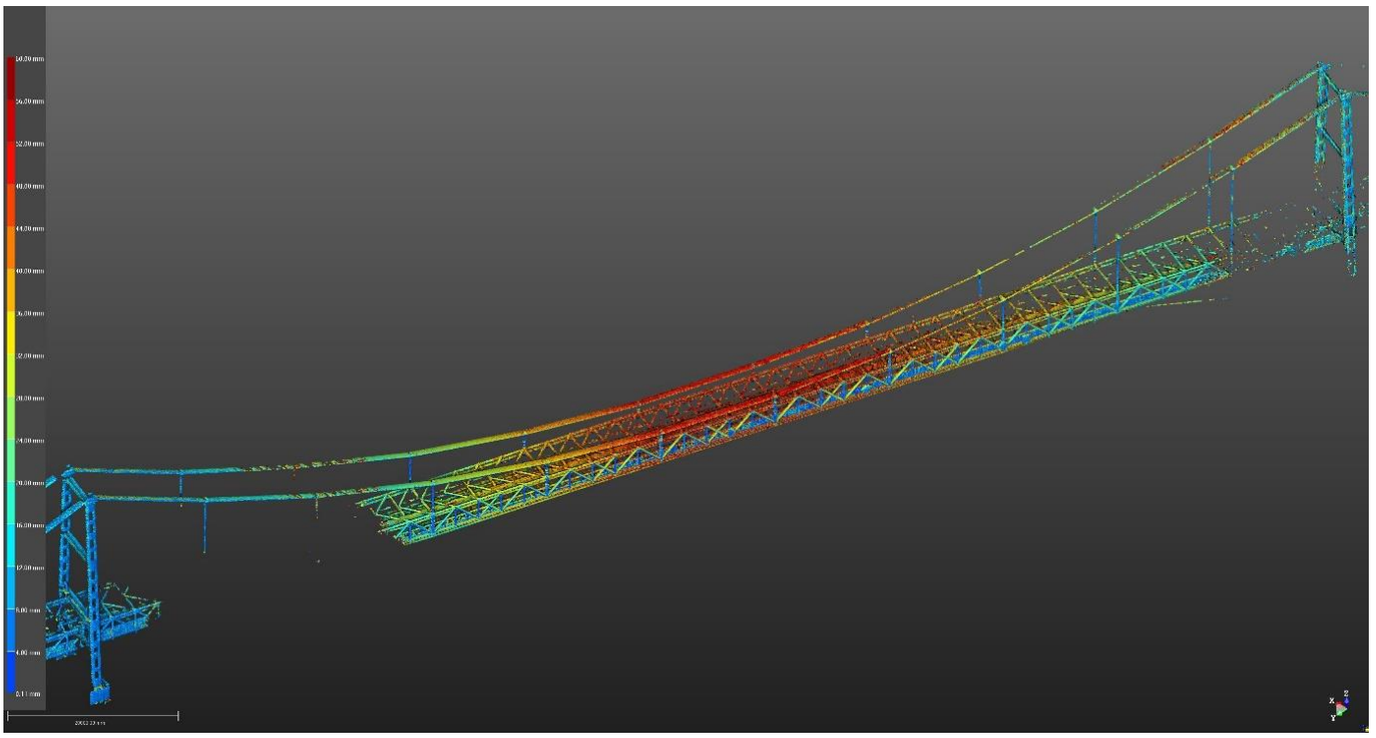


Figure 8. Chorula bridge deflections shown with using colours (a Trimble TX8 scanner).

3DX130 scanner, it was decided to repeat testing of the bridge #1 with the use of a different scanner, i.e. Trimble TX8 which has a wider range (up to 340 m). The obtained results of displacement from static load are satisfactory and fully convergent with the reference method (tachymetry method). Figure 8 presents an example bridge #1 scan with displacements as a map of colours. The red colour means the biggest displacements and the navy blue – the smallest ones. Maximum displacements of 49 mm were obtained in the middle of the main span and were recorded in a suspension cables and lower parts of transport gallery. Figure 9 shows the details of the Chorula bridge in the middle part of structure obtained by using a Trimble TX8 scanner. Table 1 presents the values of bridge 1 vertical displacements obtained by three compared methods for static load (conveyor belt with marl was stopped on the bridge).

The recorded laser scanner measurement session of the suspension bridge in Ozimek was supplemented with photogrammetric images of pixel size 0.5 mm (Fig. 10) and DISTO rangefinder direct

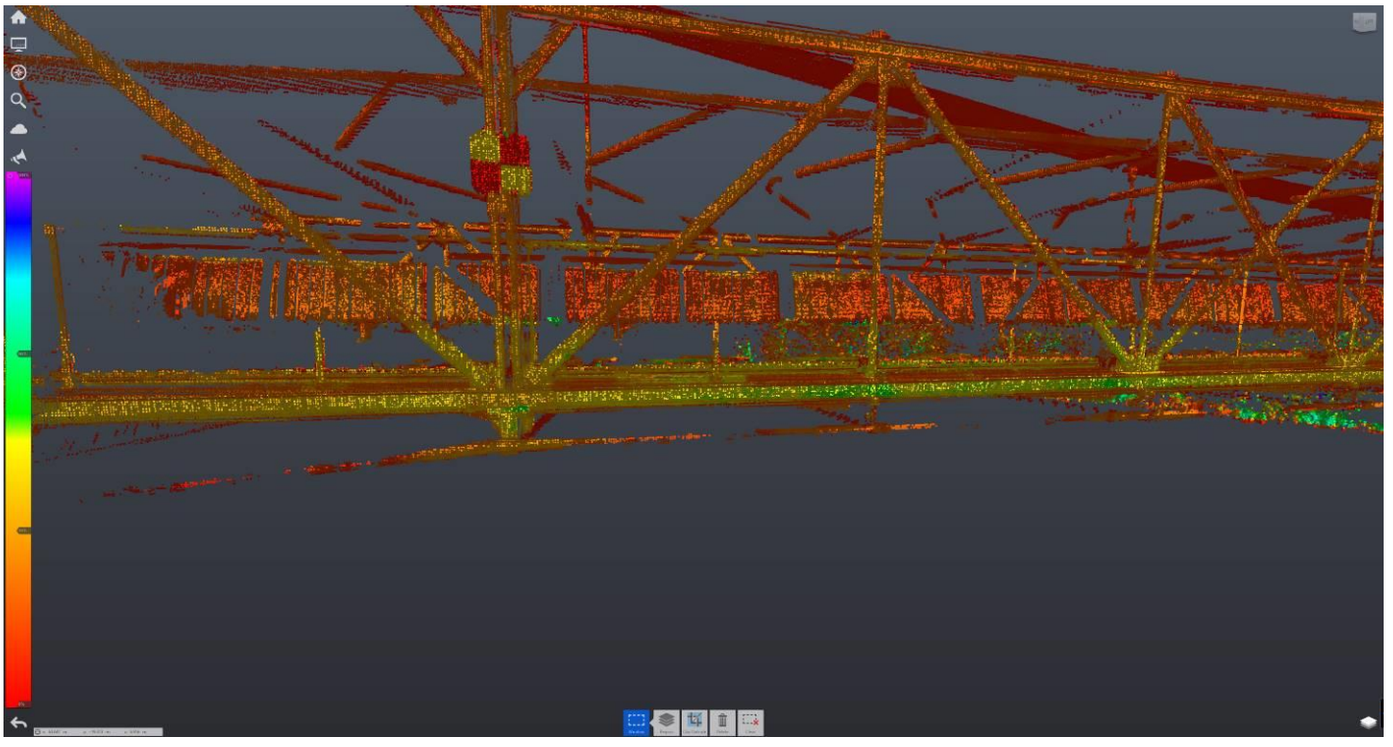


Figure 9. View of details of the Chorula bridge using a Trimble TX8 scanner.



Figure 10. The photogrammetric image of the bridge in Ozimek.

measurement. Considering the difficulties in distinguishing characteristic points, the differences between laser scanning results, photogrammetry and rangefinder measurements not exceeding 7 mm on the whole bridge length should be treated as fully acceptable.

Table 1. Comparison of the maximum registered displacements of the suspension bridge #1.

Measurement method	1/4 of span (mm)	1/2 of span (mm)	3/4 of span (mm)
Tachymetry	24.0	49.1	37.7
Photogrammetry	18	60	46
Laser scanning (FARO scanner)	*	*	*
Laser scanning (Trimble scanner)	19	49	38

Note: * - previous results obtained with the laser scanning using other scanner have been regarded as uncertain (too high discrepancy in comparison to other methods).

The bridge measurements in Chorula, was done with a Trimble TX8 scanner. Point clouds for the unloaded and loaded state clouds were obtained with a resolution of 5.7 mm at a distance of 30 m. This gave about 500 million of measurement points for a single scan. The unloaded state, has been registered on 5 measuring spheres to the loaded state with accuracy under 1 mm using the Trimble RealWorks Advanced Plant software version 10.3 (2017). Visualization of the deviation cloud between the unloaded and loaded state was obtained through an authoritative optimization approach that was then used for comparative analysis in the Trimble RealWorks Advanced Plant 10.3 (2017).

5. CONCLUSIONS

As a result of two suspension bridges measurements conducted with the use of laser scanning method, the following conclusions can be drawn:

1. Laser scanning method in case of Chorula bridge displacements measurements required the application of an adequate scanner, i.e. Trimble TX8. The results are convergent with the reference – tachymetry method. The use of Faro Focus 3DX130 scanner appeared to be less precise. It was the result of too large distance between the scanner and the bridge and too small angular resolution of a scanner (point density).
2. The measurements conducted on the bridge in Ozimek unequivocally indicate that decreasing the distance to a bridge (up to about 40 m) allows to obtain fully satisfactory inventory results. The scans present structure details with sufficient resolution and accuracy.
3. The obtained measurement results unequivocally indicate that there is no universal measurement device (a scanner) for different type of structures including bridges. Each time, before conducting such measurements, the type of a structure, its dimensions and estimated distance from a scanner should be considered. Thus it should be emphasised that the accuracy declared by producers is not always coherent with actual measurements. It is indicated in this paper, and one of the reasons could be a type of bridge construction, texture and colour of the surface.
4. The laser scanning method (the equipment and software) are currently one of the most expensive method of measurements. It would be ideal to use various methods (laser scanning, photogrammetry, tachymetry, and interferometry) at the same time when the bridge is examined.
5. The elaborated technology is particularly useful for a topologically complex structures like a truss bridges. Automatically displaying colors using a calibrated map of the differences between scans (e.g. without and with load) allow to select the points on which should pay more attention.

REFERENCES

Anigacz, W., Beben, D. & Kwiatkowski, J. 2016. Analysis of suitability of new measurement technologies to examine changes in geometric parameters of a suspension bridge. In T.N. Bittencourt, Dan M. Frangopol, & A. Beck (eds), *Maintenance, Monitoring, Safety, Risk and Resilience of Bridges and Bridge Networks*: 2204-2211, London: Taylor & Francis Group.

Anigacz, W., Beben, D. & Kwiatkowski, J. 2018. Displacements monitoring of suspension bridge using geodetic techniques. In J.P. Conte, R. Astroza, G. Benzoni, G. Feltrin, K.J. Loh, & B. Moaveni (eds), *Lecture Notes in Civil Engineering: Experimental Vibration Analysis of Civil Structures*: 331-342, Springer.

Beben, D. 2011. Application of the interferometric radar for dynamic tests of corrugated steel plate (CSP) culvert. *NDT & E International* 44 (5): 405–412.

Beben, D. & Anigacz, W. 2017. Dynamic testing of railway metal culvert using geodetic methods. In *J. Melcer & K. Kotrasova (eds.), Dynamics of Civil Engineering and Transport Structures and Wind Engineering; Proc. intern. conf., Trstená, Slovak Republic, May 21-25, 2017.* MATEC Web of Conference.

Berényi, A., Lovas, T., Barsi, A. & Dunai, L. 2009. Potential of terrestrial laser scanning in load test measurements of bridges. *Periodica Polytechnica Civil Engineering* 53(1): 25-33.

Beshr, A.A.A. 2015. Structural deformation monitoring and analysis of highway bridge using accurate geodetic techniques. *Engineering* 7: 488-498.

Jauregui, D.V., White, K.R., Woodward, C.B. & Leitch K.R. 2003. Noncontact photogrammetric measurement of vertical bridge deflection. *Journal of Bridge Engineering* 8(4): 212–222.

Kwiatkowski, J.L. 2014. *Construction life cycles monitoring of industrial installations verified by hybrid bulk measurement techniques*. Doctoral dissertation, Opole University of Technology (supervisor: Anigacz, W., auxiliary supervisor: Beben, D.), Opole, Poland.

Shen-En, C. 2012. Laser Scanning Technology for Bridge Monitoring. In J. Apolinar Munoz Rodriguez (ed.), *Laser Scanner Technology*: 71-92. Rjeka: InTech.

Tang, P., Akinci, B. & Garrett J.H. 2006. Laser scanning for bridge inspection and management. *IABSE Symposium Weimar 2006*, pp. 17–24.

Trimble Realworks 10.2 User Guide. 2017. *https://www. trimble.com/3d-laser-scanning/realworks.aspx.*

Truong-Hong, L., Falter, H., Lennon, D. & Laefer, D.F. 2016. Framework for Bridge Inspection with Laser Scanning. In *East Asia-Pacific Conference on Structural Engineering and Construction, January 6-8, 2016,* Ho Chi Minh City, Vietnam.

SPECIAL SESSIONS

SS01: Perturbations on SHM results due to environmental changes

Organizers: M. Baessler, F. Hille, W.H. Hu & G. Morgenthal

Maintenance, Safety, Risk, Management and Life-Cycle Performance of Bridges – Powers, Frangopol, Al-Mahaidi & Caprani (Eds)
© 2018 Taylor & Francis Group, London, ISBN 978-1-138-73045-8

A study on diverse strategies for discriminating environmental from damage based variations in monitoring data

M. Baeßler & F. Hille
Department Safety of Structures
Bundesanstalt für Materialforschung und -prüfung (BAM), Germany.

ABSTRACT: Right from the beginning of applying SHM to bridge structures it was obvious that environmental based perturbations on the measurement significantly influence the ability to identify structural damage. Strategies are needed to classify such effects and consider them appropriately in SHM. Various methods have been developed and analyzed to separate environmental based effects from damage induced changes in the measures. Generally, two main approaches have emerged from research activity in this fields: (a) statistics based tools analyzing patterns in the data or in computed parameters and (b) methods, utilizing the structural model of the bridge taking into account environmental as well as damage based changes of stiffness values. With the back-ground of increasing affordability of sensing and computing technology, effort should be made to increase sensitivity, reliability and robustness of procedures, separating environmental from damage caused changes in SHM measures. The contribution describes both general strategies and points out their advantages and drawbacks. As basis, a review on relevant methods was conducted. The aim of the study is to classify approaches for separating damage describing information from environmental based perturbations in dependency of the SHM objective. And such, it is intended to describe a best practice in designing concepts for monitoring infrastructure, naturally effected by environmental influences.

1 INTRODUCTION

Conducting vibration based investigations on the steel-concrete composite Alamosa Canyon bridge in New Mexico, a research group of the Los Alamos National Laboratory reported in (Farrar et al. 1997, Cornwell et al. 1999) about significant variations of approximately 5% in the first mode frequency during a 24 h time period. They also observed similar variations for the frequencies of the other modes. Also investigating the influence of vehicle loads passing on the bridge but did not find a significant effect on the measured modal frequencies of the bridge. Another bridge, investigated by this research group was the I-40 Bridge over the Rio Grande in New Mexico, a steel-concrete composite bridge with welded steel girders. Artificial damage was induced to the bridge by making various torch cuts in the web and flange of the steel girders. In (Farrar and Jauregui 1996) it is reported that the effect of damage to the first three eigenfrequencies is in the same range then the effect of varying temperature.

Liu and DeWolf (2007) investigated the effect of temperature on modal variability of a three-span box girder reinforced concrete bridge. For the duration of one year they measured the dynamic response of the bridge to ambient excitation with accelerometers. They analyzed the first three modes and they found the maximum measured difference in the first three eigenfrequency during the year of about 5-6%. They proposed fitting a linear line to characterize the relationship between temperature and eigenfrequencies for the first three modes. Also on a skewed three-span box girder (Wahab and De Roeck 1997) investigated the seasonal effects of temperature variations and also reported changes in natural frequencies up to 5%. Fraser et al. (2010) determined the temperature based variations of the first four eigenfrequencies of a four-span concrete box girder bridge. The study revealed frequency variations of 7-13%. Peeters et al. (2001) determined the temperature based variations of the first four eigenfrequencies of Z-24 bridge, a post-tensioned concrete box girder bridge in Switzerland. The study revealed frequency variations of 14-18%.

Xu and Wu (2007) studied also the temperature based effect on mode shape curvature of a three-span cable-stayed bridge by numerical simulation and compared the effect of dam-age and temperature variations on these modal properties. They showed variations of the modal frequencies in the bridge of 2%

under variation in temperature of 40K and variations in the mode shape curvatures of 1-8% at different locations along the bridge. They also showed that frequency changes due to damages, induced in the bridge girders and cables, were less than those due to temperature variations. To eliminate the masking effect of temperature based variations on damage detection and condition assessment procedures in SHM different approaches have been proposed in the last decades by the research community. Generally, two different approaches are pursued, first utilizing statistical models to filter out the temperature induced perturbations on the monitoring data and second, utilizing physical models to compute the effect of varying temperature on the behavior of the structure. This paper shows an overview about ways gone to accounting for temperature as well as a set of questions regarding temperature loading, as occurred during application of SHM on bridge structures.

2 STATE OF THE ART

2.1 *Methods based on statistical models*

Statistical methods are solely based on measurement data without using any geometrical or material information describing the behavior of the observed structure. To eliminate the effect of varying environmental perturbation in time series signals and in damage indicating feature time series, data is processed utilizing statistical models. For sustaining robust and reliable results, continuous monitoring in an appropriate measurement period, generally several years, is mandatory.

During the recent decades, several algorithms utilizing different statistical models are adapted and analyzed by the research community. Principally, two different approaches can be distinguished, including or not including the environmental factors into the computation.

One of the most common used underlying statistical models are regression models (Laory et al. 2011, Peeters et al. 2001, Xia et al. 2012). Sohn et al. (1999) used a multiple linear regression model to vibration measurement data and analyzed, if new processed natural frequencies that model at a defined confidence level. Also in (Magalhes et al. 2012) a multiple linear regression model is used to remove the effects of environmental and operational based variations on a concrete arc bridge, taking into account 8 concrete temperature and one air temperature signals. Further, auto-regressive models (AR) and their derivatives are used to account for the relation between measured or processed structural parameters and temperature. Peeters et al. (2001) applied an auto-regressive model with an exogenous input (ARX) to detect damage on the Z-24 bridge utilizing vibration measurements. In (Omenzetter and Brownjohn 2006) the application of auto-regressive integrated moving average model is proposed to detect damage from strain measurement.

Since it is partial challenging to measure the acting environmental parameter statistical models were utilized which do not include direct measurements of these variables but instead treat them as embedded but hidden variables (Shokrani et al. 2016). Several statistical techniques have been developed to normalize data for filtering out periodical, temperature related effects.

In (Yan et al. 2005a, Yan et al. 2005b) the principal component analysis (PCA) is applied to separate the temperature effect and successfully detect damage on experimentally and numerically generated data. Figueiredo et al. (2011) proposes auto-associative neural networks (AANN) to characterize the dependency of the features on the unobserved environmental factors by treating it as hidden intrinsic variables in the network architecture. Kullaa (2003) and Lms and Kullaa (2007) employ factor analysis (FA) for removing varying effects from environmental influences. Factor analysis performs a decomposition of the correlation matrix of observed features.

In (Basseville et al. 2010) a subspace based damage detection method is extended by two statistical algorithms for handling the temperature effect. One approach updates the null-subspace of a matrix built on a reference model by data from different temperature scenarios. A second proposed approach handles the temperature effect as a nuisance parameter rejecting the temperature effect.

2.2 *Methods based on physical Models*

To identify and describe damage robust and reliable by structural health monitoring the utilization of physical models is mandatory. Especially when taking into account the environmental influence related variations in the structures response, the distribution of stiffness parameters of the structure need to be considered for localization and quantification of damage. The application of physical model often is a complex and costly for several reasons. To determine the distribution of stiffness related structural proper-ties of a civil engineering structure in an adequate detailedness and accuracy can be very challenging. Also, on the computational level, the solution of the model updating intrinsic inverse problems might also be a demanding task.

Physical model based approaches for the identification of structural damage with the consideration temperature caused disturbances are described in several publications. Rohrmann et al. (2000) analyzed the vibration response of the Westend bridge in Berlin using a used a thermo-mechanical model. It is shown, that the influence of the temperature depending stiffness of the asphalt layer is significant.

Meruane and Heylen (2012) developed a physical model based damage detection procedure which employs a genetic algorithm for optimization to solve the

inverse problem. They successfully tested the method on simulated and experimentally generated data of the steel-concrete composite I-40 bridge.

Gonzales et al. (2013) investigated a ballasted concrete railway bridge in north Sweden and proved large dependencies of the dynamic response by the temperature variations in the ballast and the ground, especially during frost. For model updating a Bayesian updating scheme was employed.

3 THERMAL STRESSING OF STRUCTURES

3.1 *Influences on the temperature field in bridge structures*

To include the effect of temperature loading to the computation of structural responses it is necessary to account for the influencing thermal processes and principles. For determination of the temperature field in a structure, the heat transfer on the structures surfaces together with the boundary conditions by the surrounding environment is decisive. Heat transfer describes the exchange of thermal energy between the physical systems and consists out of the three general parts: conduction, convection and radiation. The heat transfer of a structure exposed to the natural atmosphere is dependent on the following influences: ambient air temperature, wind speed, rain, ice, humidity, global radiation of the sun (direct and diffuse radiation), reflection of the global radiation of the sun, atmospheric radiation, radiation of the environment and reflection of the radiation, heat radiation of the component as well as evaporation and condensation (Figure 1).

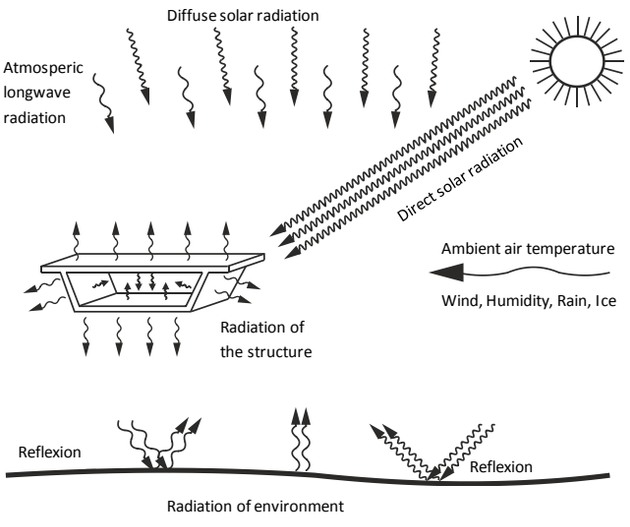


Figure 1: Influences on the heat transfer process

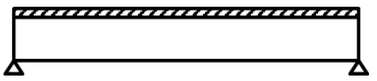
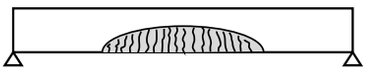
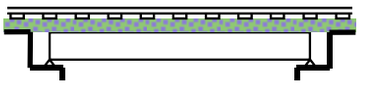
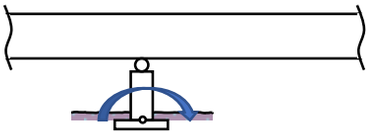
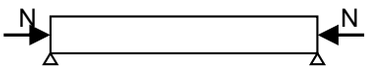
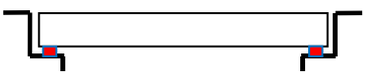
To determine the temperature field of a structure, the knowledge of the measured meteorological data in its characteristic course of the day and of the year as well as realistic data of the thermo-physical material characteristics such as emission coefficients, thermal conductivity or specific heat capacity are necessary.

But even accounting for the general thermal parameters in the temperature field computation, especially for comparative studies one should be aware, that most of the processes are transient and thus two equal states of temperature distribution on a bridge structure are hardly feasible.

3.2 *Thermal structural behavior*

Temperature changes on structural members cause mechanical stresses due to the thermal coefficient of expansion. For bridges, which generally act as beam-like structures, this can affect non-constrained strains, constrained and inherent thermal stresses as well as translational and/or rotational displacements of structural components or of the total structure. In reinforced concrete structures, thermal stresses can lead to the formation of cracks and therefore to temperature depending varying structural cross-sections (stiffness).

Table 1: Temperature influence on structural components.

a) Asphalt layer: strong dependency of stiffness on temperature 
b) Reinforced and prestressed concrete: stiffness can vary for E depends on temperature and humidity and cracks or coupling joints might open with temperature 
c) Ballasted Track: stiffness changes with temperature 
d) Structure soil interaction: stiffness at columns and at abutments can be frost dependent 
e) Axial forces: for constrained slender structures, axial forces and vibration modes are coupled 
f) Bearings: typical bearing materials can behave temperature dependent 

If the material behavior of a homogeneous region itself is temperature-dependent (e.g. asphalt layer),

additional considerations are necessary to assess the effect of the temperature field.

The compilation of temperature influences on structural components in Table 1 is based on experiences from bridge measurements combined with theoretical considerations.

4 EXAMPLES

4.1 *Indifferent: temperature-dependent behavior is low or eliminable*

Especially in the case of bridges that are free of constraints it is to be expected that the temperature influence can be neglected. Although, task depending, it can be necessary to eliminate the influence of temperature.



Figure 2: View and cross-section of Putlitz Bridge in Berlin

Figure 2 shows the view of the Putlitz Bridge in Berlin and its cross-section. Longterm measurements at the bridge deck have resulted in large temperature-dependent movements of the bridges end sections (Figure 3). The structure responds to the temperature effects with significant deformations. However, a consideration of the vibration behavior over the temperature of the structure shows only a weak influence of the temperature (Figure 4). It shows, that in this case an influence of the temperature on the load bearing behavior is negligible.

Performing load monitoring traffic induced strain and temperature signals can be separated without loss of information. The longterm daily and annual periodic variations then don't have to be accounted for.

4.2 *System identification of a temperature-dependent structural behavior*

Measurements are also carried out to identify a dynamic structural behavior. In the case of a dynamic structural analysis, there is no verification to the safer side, the dynamic behavior of the structure must be considered in its actual limits to take account of resonance effects.

For example, according to DIN EN 1990 A2 or DIN 1991-2 the dynamic behavior of the railway

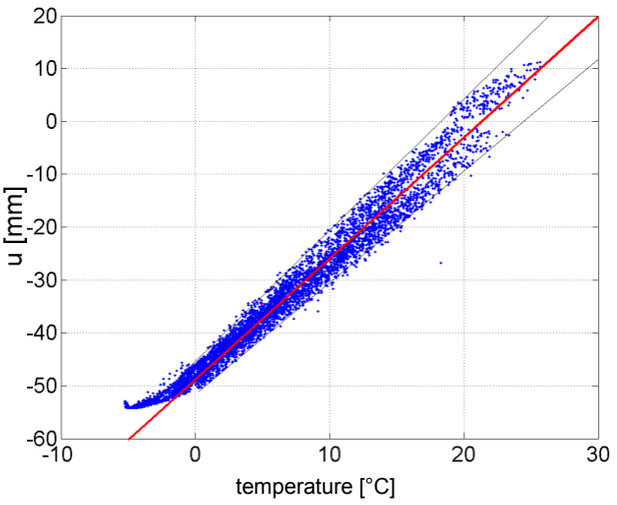


Figure 3: Temperature related movement of end sections of Putlitz Bridge

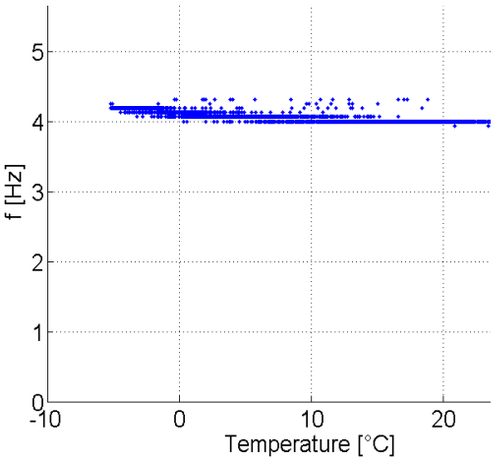


Figure 4: Temperature related natural frequency of Putlitz Bridge

bridges during the train crossing must be considered for the safety verification of high-speed railway bridges. Particularly, regarding fatigue and the limitation of maximum acceleration amplitudes of the bridge deck, considerable dependencies on modal parameters of the bridge structure can occur. In addition to the vehicle-related aspects such as axle loads and clearance as well as driving speed, realistic data of the bridge structures stiffness is fundamental. Structural measurements can be used to identify the real structural behavior.

However, it has been shown that the seasonal variation of the bridge stiffness parameter of have a strong effect on the dynamic response of the bridge structure. Gonzales et al. (2013) and Zabel et al. (2007) have reported on these seasonal influences in particular and determined the temperature-dependent behavior of the superstructure as decisive. However, an experimental proof of the described temperature dependent stiffness changes of the ballast superstructure still does not exists. Although, regardless of the physical matter, it is important to determine the structural behavior over the complete temperature range. Struc-

tural measurements are of great importance.

4.3 *Assessment of load bearing capacity*

The aim of Structural Health Monitoring (SHM) is the measurement based assessment of the load-bearing capacity of a structure.

In detail that means to detect damage, to identify changes in load bearing capacity and to determine the safety level. It is essential to correctly evaluate temperature influences. The basic principles of an SHM strategy are shown in Figure 5.

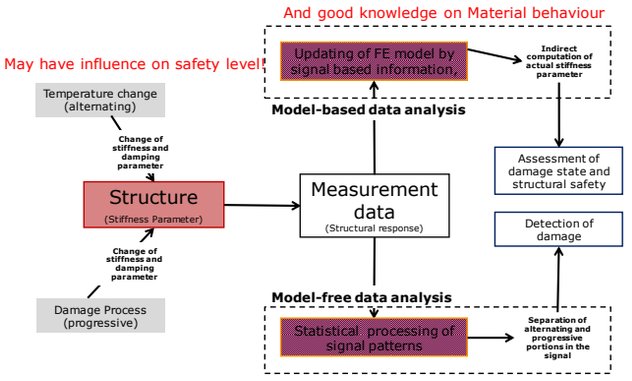


Figure 5: Schematic diagram of Structural Health Monitoring

Generally, the main challenge of a global state monitoring is the provision of an adequate sensitivity of the damage detection methodology for essential damage scenarios. Damages in their initial stage on robust structures as reinforced and prestressed bridges are normally not activated by existing traffic load. Accordingly, no changes in the stiffness ratios are detectable, and thus the damage cannot be detected by means of a measurement of global structural parameters based on the dynamic response. This situation must always be considered in planning monitoring systems for bridge structures.

For a physical model based monitoring of the structural state, a model in high quality is required to provide a connection between system identification and monitoring variables on the one hand and the related load-bearing evaluation on the other hand. For a typical reinforced concrete cross section, this also means that temperature dependent changes in the load bearing behavior must be assessed correctly. Figure 6 shows two cases: In case (1), the structure reacts stiffer due to the carrying effect of the asphalt layer. In terms of safety evaluation, however, this stiffness share is not taken into account. In case (2), the change in the load bearing behavior during crack formation, for example from temperature dependent constraints and inherent stresses, is shown. In the sense of safety assessment, this leads to a reduction of the load bearing capacity in the sense of stability assessment. Those distinctions are elementary for an evaluation.

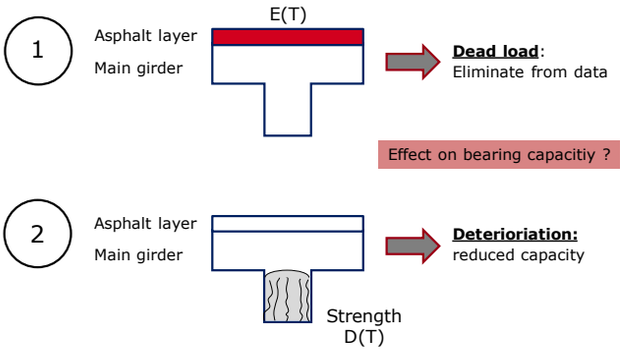


Figure 6: Stiffness changes with different relevance for structural safety

4.4 *Changing the stress situation and the load on coupling joints*

Due to constrained and internal stress conditions on reinforced concrete cross sections, changes in the stressing can occur. In particular in coupling joints, the durableness of the coupling element needs to be verified. Due to poor planning principles for temperature loading of bridges in earlier times, this issue has to be taken into account in particular in the cases of existing structures.



Figure 7: Westend bridge, Berlin

The Westend Bridge in Berlin (Figure 7), which is heavily traffic loaded for several decades, had suffered a series of damage since its erection. This repeatedly required strengthening actions to ensure an adequate load bearing capacity over time. Among other defects, it was found that the coupling joints of the bridge deck had opened. Under the influence of external loads and temperature changes, significant changes in the joint width were observed during inspection and finally monitored by measurement. It was found that, from a certain temperature the crack width of the joint increased disproportionately under traffic load. At the same time, selected vibration measures increased erratic. Obviously, the stress caused by traffic at high temperatures activates additional nonlinear deformation components, which lead to changes in the static dynamic system and are reflected in the additional expansion of the coupling joints. This effect can cause a strong fatigue-inducing effect on the prestressing reinforcement in the region of the coupling joints, especially as at the same time a corrosive attack of the tendons in the coupling joints

has been determined.

Furthermore, it was observed that during the summer months longitudinal cracks were formed in the floor and side slabs of the box girder, which most likely are originated in a temperature induced exceeding of the concretes tensile strength in these areas. The reason for those relatively high tensile stresses is the unfavorably flat cross section of the box girder bridge deck.

Here too, the question arises, to which amount those longitudinal cracks affect the static system (the stiffness of the box girder) and, in particular, lead to a change in the stress conditions under traffic loading.

4.5 *Physical relations from correlations*

For the evaluation of the structural behavior as a function of the temperature loading of a bridge it-self, it is important to establish a relationship be-tween the temperature load and the changed behavior of the structure. From the example of the frequency monitoring over several years at the Westend Bridge there is a significant dependency between frequency and temperature. However, the structure itself is conceivably unfavorable for a corresponding analysis. The flat cross section of the bridge deck is influenced by several non load carrying structural components such as caps, railings and asphalt layer. Due to the compact, multi-celled design, temperature load causes severe constraints within the cross section, which were not considered adequate in the bridges design. In addition, there are non-distinctive boundary conditions for further elements such as the columns, which are also influenced by the seasonal measures.

In order to understand the structural behavior, various attempts have been made in the past to model the structure. Among others a system identification of the thermal model was conducted using real meteorological data. In general, a very good conformity of the model based with the measurement based determined temperatures in the webs of the box girder was achieved. On this base temperature curves and derived parameters such as temperature gradients could be determined for several months periods.

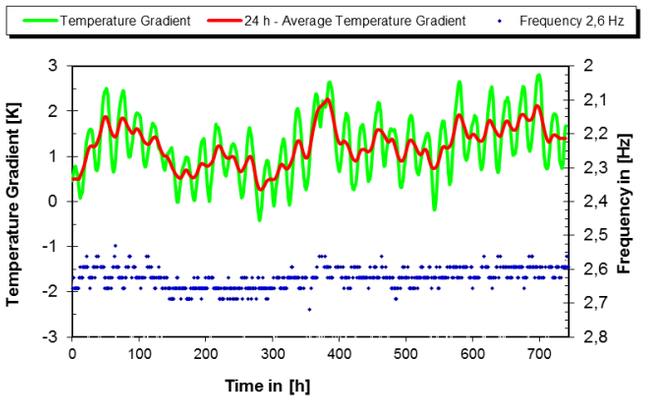


Figure 8: Vertical temperature gradients and natural frequency at 2.6 Hz

However, the example of the Westend bridge shows with the exemplary illustrations in Figure 8 for the temperature gradient and Figure 9 for the mean asphalt temperature that a simple and significant correlation between temperature characteristics and the measured values of the natural frequency in the given resolution is difficult. It is shown, that from the correlation of individual parameters alone a unique mode of action cannot be derived. It becomes comprehensible that probably several influences on the structural behavior do overlap. In the present case, the complex numerical model has too many influencing factors, so that a direct derivation of a temperature dependent structural behavior is not possible.

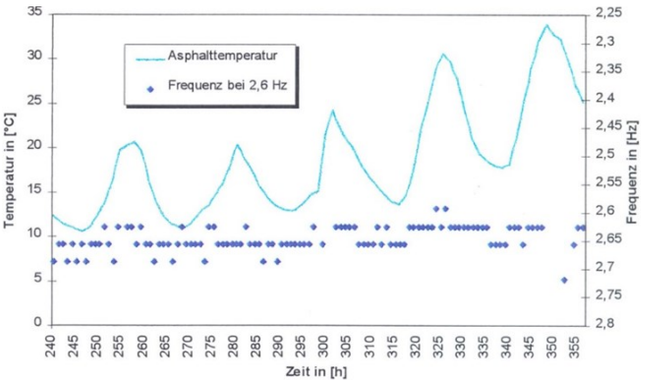


Figure 9: Asphalt temperature and natural frequency at 2.6 Hz

4.6 *Statistical Assessment*

If a simple correlation cannot be represented and a complete physical interpretation is not possible, (physical) model free statistical methods show that structural changes can be derived from longterm measurements. Although there won't be quantitative information of the present safety level, the added value exists for significant variations in the structural response can indicate damage based structural changes.

Utilizing statistical analysis of measured values or of signal-analytic computed dynamic parameters, it is possible to separate temperature-dependent periodic variations from changes caused by damage in the structure. Thereby the structural parameters of the system (geometry, material) and the corresponding physical model remain completely unconsidered. This can reach to a significant advantage compared to the (physical) model-based consideration of temperature influences, since in practice it is difficult or impossible to model the structure in sufficient accuracy. Since only changes in the time signals are analyzed by statistical methods, they are particularly suitable for long-term monitoring of civil engineering structures.

Hu et al. (2015) evaluates dynamic parameters of the Westend Bridge in Berlin for a period of 14 years (Figure 10). The non-linear relationship between the natural frequencies and temperature is determined utilizing a polynomial regression function of 4. order to

remove the temperature effect. For detecting structural changes in the system, the resulting residual is then examined by means of the novelty detection methodology. As shown in Figure 11, a change in the damage index can be shown statistically. Distinct changes in the index show the user that significant changes occurred in the chain from structural reaction to measure recording.

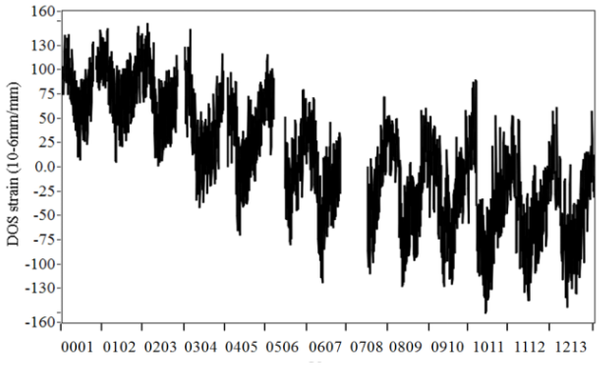


Figure 10: Decrease of strain in the prestressed cable

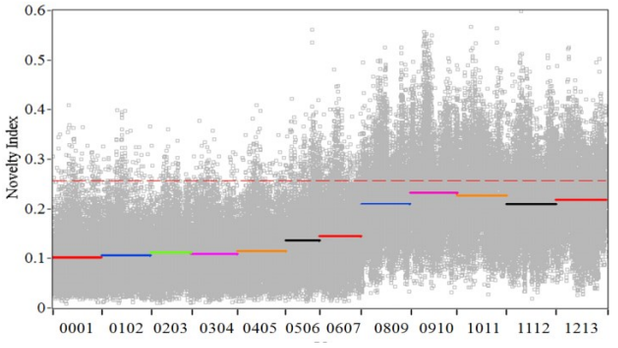


Figure 11: Variation of novelty index

5 CURRENT ACTIVITY

A better understanding of the physical behavior and how it is affected by temperature is crucial for an improvement of strategies dealing with environmental effects in SHM. Current research at BAM includes physical testing of specific materials and construction types relevant for bridge structures using laboratory test devices for thermo-mechanical loading. The aim is to classify and predict the various influence factors as given in table 1. Furthermore, research is focusing on damage detection methods with localization to specify where structural changes take place (Bhuyan et al. 2017, Viefhues et al. 2017). The influence on structural reaction needs to be understood for each individual bridge structure. Also, strategies for elimination or allowance of environmental effects have to be robust regarding measurements at real structures affected by complex environmental issues and other boundary conditions. As a first step research is under way with a test bridge (Figure 12) including various measurement devices and possibilities for loading and



Figure 12: Test (bridge) structure BAM project BLEIB

structural changes like lowering the prestressing. The future focus will also be on additional monitoring of exemplified real bridge structures sensitive to temperature loading.

6 CONCLUSIONS

On the basis of various examples, it was discussed how thermal stresses in a building monitoring system are visible and how they are to be assessed. In particular, the influence on the condition assessment in the sense of stability is often a great difficulty. For example, a fundamental possibility is to keep a load-bearing structure always at its weakest phase, that is, usually in the summer. As shown, statistical methods may also be suitable for detecting load-bearing changes.

Improved detection algorithms and improved physical models defining the mechanical behavior of structures are regarded as essential future tasks.

The acceptance of vibration-based methods for the detection and localization of damages in practical application is solely dependent on the ability to eliminate influences from changing environmental and operating conditions, but in particular from the temperature. Since the stochastic methods for damage detection and localization, which have become more and more important in recent years, use the (statistical) characteristic of the measured data implicitly, the development, adaptation and application of statistical algorithms to eliminate the varying environmental influences are obvious.

On the other hand, the seasonal influence on building surveys is presented in a large number of publications, and often reasoned physical connections are shown for the behavior. As a rule, however, the statements are not experimentally verified and of a rather general nature (“asphalt reacts temperature-dependent”). Objective-specific connections, determined, for example, by an attempt at representatives in the climate chamber, could be very helpful.

REFERENCES

Basseville, M., F. Bourquin, L. Mevel, H. Nasser, & F. Treyssde (2010). Handling the temperature effect in vibration moni-

toring: two subspace-based analytical approaches. *Journal of Engineering Mechanics 136*(3), 367–377.

Bhuyan, M., E. Viefhues, M. Dhler, Y. Lecieux, L. Mevel, F. Hille, & F. Schoefs (2017). Output-only subspace and transfer matrix-based damage localization and quantification. In *7th International Operational Modal Analysis Conference*, Ingolstadt, Germany.

Cornwell, P., C. R. Farrar, S. W. Doebling, & H. Sohn (1999). Environmental variability of modal properties. *Experimental Techniques 23*(46), 45–48.

Farrar, C. R., S. W. Doebling, P. J. Cornwell, & E. G. Straser (1997, 3.-6. February). Variability of modal parameters measured on the alamosa canyon bridge. In *Proceedings of the 15th International Modal Analysis Conference*, Orlando, FL., pp. 257–263.

Farrar, C. R. & D. Jauregui (1996). Damage detection algorithms applied to experimental and numerical modal data from the i-40 bridge. Technical Report LA-13074-MS, Los Alamos National Laboratory.

Figueiredo, E., G. Park, C. R. Farrar, & K. Worden (2011). Machine learning algorithms for damge detection under operational and environmental variability. *Structural Health Monitoring 10*(6), 559–572.

Fraser, M., A. Elgamal, X. He, & J. P. Conte (2010). Sensor network for structural health monitoring of a highway bridge. *Journal of Computing in Civil Engineering 24*(1), 11–24.

Gonzales, I., M. lker Kaustell, & R. Karoumi (2013). Seasonal effects on the stiffness properties of a ballasted railway bridge. *Engineering Structures 57*(Supplement C), 63–72.

Hu, W.-H., S. Said, R. Rohrmann, W.Rcker, .Cunha, & A. Rogge (2015). Vibration-based structural health monitoring of a highway bridge based on continuous dynamicsamic measurements during 14 years. In *ISHMII 7*.

Kullaa, J. (2003). Is temperature measurement essential in structural health monitoring? In *4th International Workshop on Structural Health Monitoring*, Stanford, CA, USA.

Laory, I., T. N. Trinh, & I. F. Smith (2011). Evaluating two model-free data interpretation methods for measurements that are influenced by temperature. *Advanced Engineering Informatics 25*(3), 495.

Liu, C. Y. & J. T. DeWolf (2007). Effect of temperature on modal variability of a curved concrete bridge under ambient loads. *Journal of Structural Engineering ASCE 133*, 1742–1751.

Lms, V. & J. Kullaa (2007). Nonlinear factor analysis in structural health monitoring to remove environmental effects. In *6th International Workshop on Structural Heath Monitoring 2007*, Stanford, CA, USA.

Magalhes, F., A. Cunha, & E. Caetano (2012). Vibration based structural health monitoring of an arch bridge: From automated {OMA} to damage detection. *Mechanical Systems and Signal Processing 28*(0), 212 – 228. Interdisciplinary and Integration Aspects in Structural Health Monitoring.

Meruane, V. & W. Heylen (2012). Structural damage assessment under varying temperature conditions. *Structural Health Monitoring 11*(3), 345–357.

Omenzetter, P. & J. Brownjohn (2006). Application of time series analysis for bridge monitoring. *Smart Material and Structures 15*, 1129–138.

Peeters, B., J. Maeck, & G. D. Roeck (2001). Vibration-based damage detection in civil engineering: excitation sources and temperature effects. *Smart Materials and Structures 10*(3), 518–527.

Rohrmann, R., M. Baeßler, S. Said, W. Schmid, & W. Rücker (2000). Structural causes of temperature affected modal data of civil structures obtained by long time monitoring. In *XVIII. Int. Modal Analysis Conference (IMAC)*, San Antonio, TX, USA.

Shokrani, Y., V. K. Dertimanis, E. N. Chatzi, & M. Savoia (2016, 27 - 30 May 2016). Structural damage localization under varying environmental conditions. In *11th HSTAM International Congress on Mechanics*, Athens, Greece.

Sohn, H., M. Dzwonczyk, E. Strazer, & et.al (1999). An experimental study of temperature effect on modal parameters of the alamosa canuon bridge. *Earthquakeuakeuake Engineering and Structural Dynamicsamics 28*, 879–897.

Viefhues, E., M. Dhler, F. Hille, & L. Mevel (2017). Stochastic subspace-based damage detection with uncertainty in the reference null space. In *11th International Workshop on Structural Health Monitoring*, pp. 1007–1014.

Wahab, M. A. & G. De Roeck (1997). Effect of temperature on dynamic system parameters of a highway bridge. *Structural Engineering International 7*(4), 266–270.

Xia, Y., B. Chen, S. Weng, Y.-Q. Ni, & Y.-L. Xu (2012, May). Temperature effect on vibration properties of civil structures: a literature review and case studies. *Journal of Civil Structural Health Monitoring 2*(1), 29–46.

Xu, Z. D. & Z. Wu (2007). Simulation of the effect of temperature variation on damage detection in a long-span cable-stayed bridge. *Structural Health Monitoring 6*, 177–189.

Yan, A. M., G. Kerschen, P. De Boe, & J. C. Golinval (2005a). Structural damage diagnosis under changing environmental conditions - part 1: linear analysis. *Journal of Mechanical Systems and Signal Processing 19*, 847–864.

Yan, A. M., G. Kerschen, P. De Boe, & J. C. Golinval (2005b). Structural damage diagnosis under changing environmental conditions - part 2: local pca for nonlinear cases. *Journal of Mechanical Systems and Signal Processing 19*, 865–880.

Zabel, V., M. Brehm, & C. Bucher (2007). Seasonal changes of the dynamics of railway bridges with steel girders embedded in concrete. In *Experimental Vibration Analysis for Civil Engineering Structures (EVACES'07)*, Porto, Portugal.

Maintenance, Safety, Risk, Management and Life-Cycle Performance of Bridges – Powers, Frangopol, Al-Mahaidi & Caprani (Eds)
© 2018 Taylor & Francis Group, London, ISBN 978-1-138-73045-8

Automated operational modal analysis of a lively footbridge for tracking long term dynamic behaviour

De-hui Tang & Wei-hua Hu & Jun Teng
Harbin Institute of Technology Shenzhen Graduate School, ShenZhen, China
Elsa Caetano & Álvaro Cunha
Faculty of Engineering (FEUP), University of Porto, Porto, Portugal

ABSTRACT: A continuous dynamic monitoring system was installed at Pedro e Inês footbridge, located in Combra, Portugal, in 2007 by the CONSTRUCT/Vibest research group from the Faculty of Engineering of the University of Porto (FEUP). Such a system was further developed for research purpose by implementing an automated operational modal analysis procedure, in order to track the footbridge's long term dynamic properties and detect early structural modifications. Modal parameters are identified by automated Covariance based Stochastic Subspace Identification (SSI-COV) technique. Their variations are tracked and the influence of temperature is analyzed. With the final purpose of detecting potential structural modifications at an early stage, the Multiple Linear Regression (MLR) method is employed to effectively eliminate temperature effects. Novelty analysis on the residual errors of the MLR model is established to provide a statistical structural health index. During five years from 2007 to 2012, a clear deviation of the proposed health indicator suggests a slight long term modification of the footbridge.

1 INTRODUCTION

The new Pedro e Inês Footbridge was developed along the two banks of the Mondego River at Coimbra, Portugal, and opened to pedestrian traffic in April 2007. The total length of the bridge is 275 meters, consisting of a main shallow arch with 110 m chord and two half arches with chords of 95 m and 70 m.

A special feature of the bridge is the anti-symmetry of both arch and deck cross section along the longtitudinal axis in Figures 1. This particular geometry leads to the existence of a central plaza at mid-span and results in a complex torsional behaviour under vertical loads.

The central arch is supported by two groups of vertical piles with a depth of about 30 meters. The silt/clay soil layers beneath the river bed have poor mechanical characteristics and the horizontal stiffness provided by these foundations is low. Consequently, the arch-effect is expected to be reduced, leading to mixed arch/girder behaviour. The supports provided at the abutments and at the left bank intermediate column allow the longtitudinal displacement of the deck and block the transverse movements [1].

The east abutment contains two 6 meter spaced support alignments (alignment 1 and 2, Figure 3 and Figure 4). For structural reasons it was found adequate to establish symmetrical bridge behaviour in relation to the west side of the structure. For that purpose, a clamped support condition was designed. A vertical downward displacement was imposed in alignment 2 with resource to a post-tensioning system. The bridge deck was locked with bearing support devices which are free to move longitudinally. With this mechanism a binary of forces V was created providing a clamped support for the deck in the east abutment [1].

In order to investigate the long behaviour of the footbridge under operational conditions, six uniaxial piezoelectric accelerometers (PCB model 393C) are installed at the positions corresponding to the lateral and vertical TMDS. Five of them (AV1-AV3, AV5-AV6) are used to measure vertical acceleration while the last one (AT4) is used to measure the lateral response at mid span in Figure 2. Meanwhile, temperature sensors are installed to provide temperature data of ambient environment.

All the accelerometers are connected to a signal conditioning located at the east abutment. Then a digital computer which contains an analogue to digital converter is designed to store the resulting signals.

The integrated long-term dynamic acquisition system continuously records the structural response from the 6 accelerometers with a sampling frequency in 100Hz and 6 temperature sensors with a sampling frequency of 1/3600 Hz. The latest acceleration and temperature files are sent to a computer located at FEUP which is connected to internet. For faster

transmission, the acceleration signals are decimated to 20Hz. The system has been in operation from 1st of June 2007 to 1st of June 2012 and in particular has transmitted five years of continuous data except for occasional interruptions due to small technical problems.

To ensure a good performance of the stabilization diagram, the data in one hour is used for automatic identification of the natural frequencies, mode shapes and modal damping ratios based on Covariance-driven Stochastic Subspace Identification (SSI-COV) methods [2,3].



Figure 1. Pedro e Inês footbridge

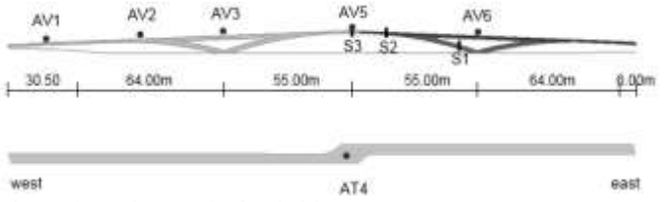


Figure 2. Pedro e Inês footbridge

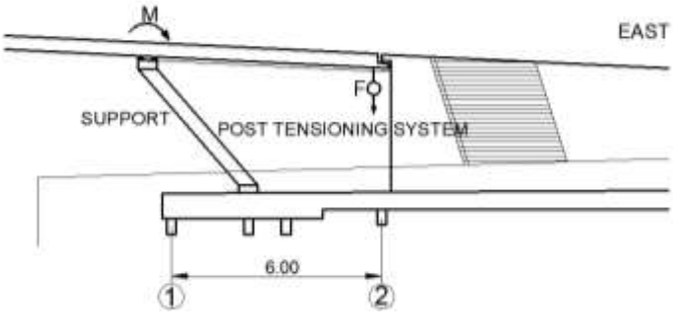


Figure 3. Imposed vertical displacement

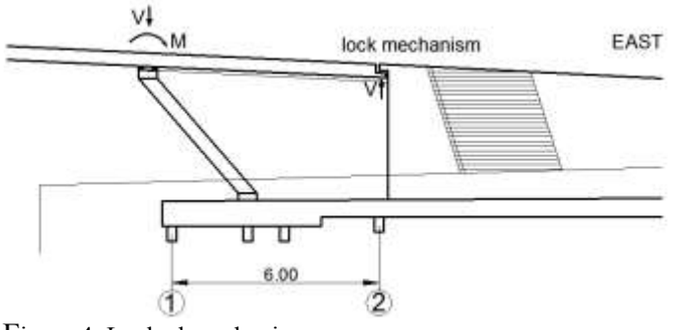


Figure 4. Locked mechanism

2 AUTOMATIC SSI-COV ALGORITHM

The automatic system identification procedure based on SSI-COV algorithm is implemented in the CSMI toolkit. It comprehends two steps: construction of stabilization diagram and cleaning of stabilization diagram.

2.1 *Construction of stabilization diagram*

Correlation functions with a maximum length of i points is used to estimate the state-space model. The minimum and maximum system order is m, n respectively and the stable poles are set in a fixed increment j (m, n, j). Poles are defined as stable pole when the relative differences in the natural frequency (δf), modal damping ratio ($\delta\xi$) and modal assurance criterion (MAC) values between poles of adjacent orders are below the following threshold values:

$$\delta f \le 1\% \tag{1}$$

$$\delta\xi \le 10\% \tag{2}$$

$$(1 - MAC) \times \% \le 5\% \tag{3}$$

In addition, the stable poles having unrealistic damping ratios (e.g. $\xi \ge 10\%$) are discarded.

2.2 *Cleaning of stabilization diagram*

As shown in the Figure 5, the stable poles are concentrated around the structural natural frequencies, while the spurious or numerical poles which interfere with the automated estimation of modal parameters are isolated. Irregular numerical poles between 2~4 Hz may induced by human walking, running and jumping and a few regular spurious poles may result from ambient noises. Comparing with the stable poles, the spurious poles distribute discretely, therefore, these spurious poles can be sort out by treating all poles between minimum and maximum order as follows:

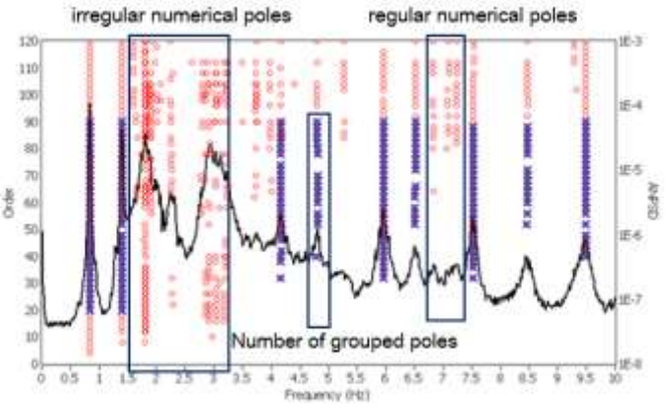


Figure 5. Stabilization diagram

(a) According to the different modal parameters represented by the poles in the minimum order, Poles are divided into different groups; (b) In the (m+j) order, if the relative difference of modal parameters is smaller than the threshold prescribed in (1), the new poles are incorporated into the corresponding groups, however, if there are any poles in (m+j) order which do not match with any groups defined in

the previous step, a new group is defined; (c) Applying Step (b) to the poles from ($m+2j$) to the maximum order and ensuring all poles are grouped; (d) Counting the number of poles inside each group and averaging all the modal parameters of the same group. (e) Finally, setting the threshold for the numbers of poles p, the groups whose poles numbers are smaller than the threshold are removed.

The parameters (*i, j, m, n* and *p*) which used for the automated modal identification in each application are defined according to the quality of the continuous dynamic monitoring results. The modal parameters are estimated by averaging the frequencies, damping ratio and mode shape vectors within the selected groups of poles.

2.3 *Automatic SSI-COV algorithm*

The modal parameters are identified from vibration signals acquired from the 6 accelerometers installed in the new Pedro e Inês Footbridge. In order to facilitate the automatic signal processing, three successive setup files acquired in 20 minutes are concatenated to obtain a one hour response file and obtain more stable results. The parameters *i, j, m, n* and *p* is optimizing to 1024, 2, 20, 90 respectively for the automatic signal processing program. An averaged normalized Power Spectrum Density (ANPSD) plot is overlapped 50% to reflect frequency domain information.

As shown in Figure 5, a very clear alignments of stable poles can be found in the frequency ranges 0-1.5Hz and 4-10Hz. The automatic SSI-COV algorithm capture all the natural modal frequencies automatically.

3 VARIATIONS OF TEMPERATURE, VIBRATION LEVEL AND FREQUENCY

Temperature at different positions has a similar trend. The sensor TC mounted on the south surface of the mid-span of the bridge has shown to provide the highest correlated temperature with the natural frequency estimates (9.428Hz) than other temperature sensors according to [3]. Therefore, temperature data provided by TC has been selected to investigate the temperature effects in Figure 6.

The annual change in temperature has the same tendency, and the temperature reached its maximum of 38.5℃ in July, 2007, while the minimum value of -1.8℃ occurred in December, 2009.

Figure 7 shows the variations of frequencies identified of the 9th bending modes over five years. An obvious trend can be found that the annual frequency estimates changes regularly. It may be concluded that temperature is the main environment factor in this footbridge which can affect the natural frequencies in higher modes easily.

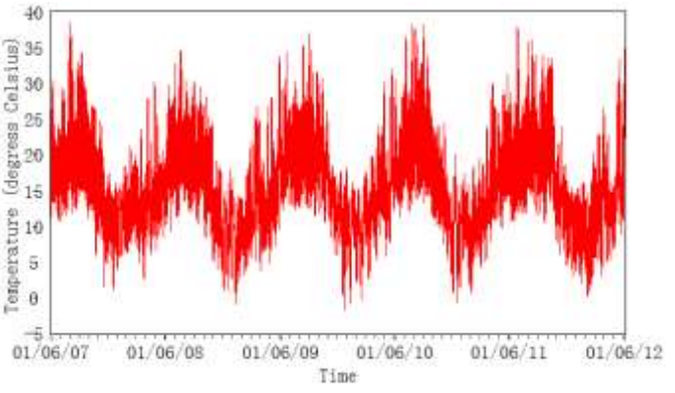


Figure 6. Variation of the temperature from 1st June 2007 to 1st June 2012

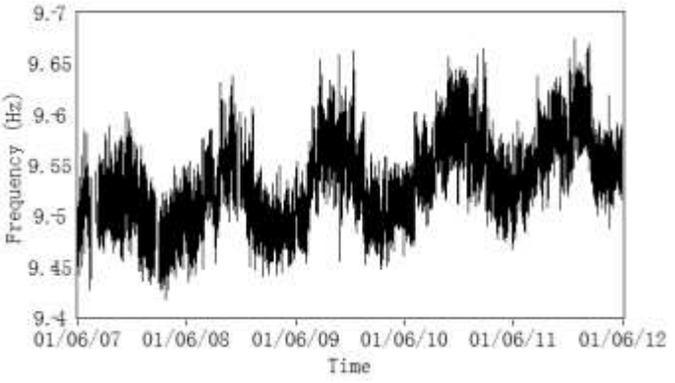


Figure 7. Variation of the estimated frequency from 1st June 2007 to 1st June 2012

4 DETECTION OF STRUCTURAL MODIFICATION DURING 5 YEARS

In the current research, the multiple linear regression (MLR) is used to remove the nonlinear influences of the temperature on the identified frequencies [4]. By selecting the mathematical model established by MLR method, the residual matrix with the environmental and operational effects has been removed. Novelty Detection technique which is simply to identify from measured data if a machine or structure has deviated from normal condition can be applied now to detect early structural modifications [5].

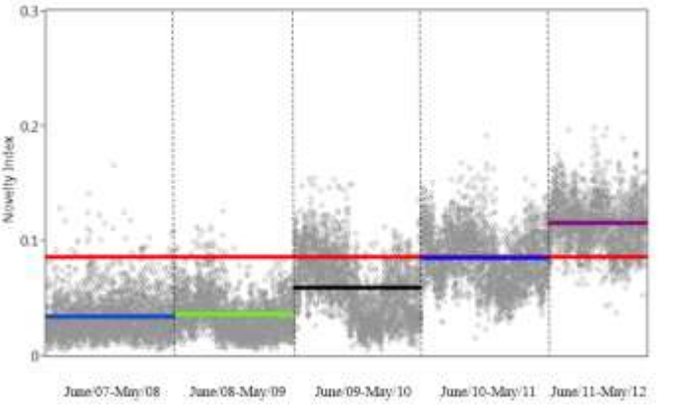


Figure 8. Calculated novelty indices and center lines using frequencies in 5 years

An internal representation Novelty Index (NI) is first built when the structure is under healthy conditions covering one full cycle of environmental and operational variations, and then data are subsequently examined to observe the possible occurrence of significant departure from the normal condition by using the outlier analysis. The Novelty Index (NI) can be defined as its Euclidean norm and is shown in Figure 8.

5 DISCUSSION OF RESULTS

Two possible reasons may have led to the increase of frequencies in each mode and need to be further investigated based on numerical simulation. On the one hand, given the small displacements and loads applied to the footbridge, the horizontal support, which was already modelled as a spring to calibrate the initial numerical model, may have become stiffer and contributed to aggravate the clamping effect at the east abutment.
On the other hand, the silt/clay soil layers beneath the river bed have poor mechanical characteristics but are designed to resist horizontal force produced by the central arch. The horizontal stiffness of the equivalent spring elements used to model the piles may have changed slowly under long-term load effects.

6 CONCLUSION

This paper briefly describes the Pedro e Inês Footbridge and its monitoring system. Data obtained from the system from 1st June 2007 to 1st June 2012 is shown to illustrate the relationship between temperature and frequency estimated, and a linear correlation between temperatures and frequency estimates is observed.
In addition, MLR method and Novelty Detection technique are applied in the paper to eliminate the environmental and operational effects on frequencies and reveal the early modification of structure. Although the possible reason for this modification requires further investigation, the results partially prove that the vibration monitoring system can capture early structural changes.

7 REFERENCES

Dimande, A. & Pimentel, M. & Felix, C & Figueiras, J. 2010. Monitoring System for Execution Control Applied to a Steel Arch Footbridge. *Structure and Infrastructure Engineering* 8(3): 277-294.

Peeters, B. 2000. System Identification and Damage Detection in Civil Engineering. Department of Civil Engineering, Katholieke Unversiteit Leuven, Belgium.

Hu,W.H & Moutinho C. & Caetano E. & Magalhaes F. & Cunha A. 2012. Continuous dynamic monitoring of a lively footbridge for serviceability assessment and damage detection. *Mechanical Systems and Signal Processing* 33: 38-55.

Montgomery, D.C. & Peck, E.A. & Vining, G.G. 2012. Introduction to linear regression analysis. In John Wiley & Sons INC. In New Jersey

Manson, G. 2002. Environment insensitive features for damage detection. Proceedings of the IES conference, Swansea, UK

Maintenance, Safety, Risk, Management and Life-Cycle Performance of Bridges – Powers, Frangopol, Al-Mahaidi & Caprani (Eds)
© 2018 Taylor & Francis Group, London, ISBN 978-1-138-73045-8

Damage detection under environmental variability using Bayesian virtual sensing

J. Kullaa
Metropolia University of Applied Sciences, Helsinki, Finland

ABSTRACT: Structural health monitoring is based on output-only vibration measurements. In order to get an early warning of structural failure, the signal-to-noise ratio of the measurement data should be high. This can be achieved by applying virtual sensing to a redundant sensor network. A Bayesian estimate of the signal of each sensor in the network was derived and proved to be more accurate than the actual measurement. Virtual sensor data replace the actual measurements in damage detection. Another issue is the environmental or operational influences, which can mask the effects of damage. They can be removed by acquiring training data under different conditions and utilizing correlation between the measured quantities. The measurement of the underlying variables is not necessary. Numerical simulations were performed for a structure subject to unknown random excitation and various environmental effects. Damage detection was performed in the time domain using the virtual sensor data.

1 INTRODUCTION

Structural health monitoring is based on output-only vibration measurements acquired by a sensor network. Changes in the dynamic characteristics are interpreted as an indication of damage. Because damage is often local, its effect on the dynamic characteristics is relatively small. In order to get an early warning of structural failure, the signal-to-noise ratio (SNR) of the measurement data should be high. With a large number of low-cost sensor nodes, the data accuracy may have to be compromised. Another issue is the environmental or operational variability, which affects the vibration characteristics of the structure and can thus mask the effects of damage.

Damage detection can be applied in the time-domain or in the feature-domain.

Feature-domain detection is probably more popular because of the following reasons. Statistical analysis is straightforward, because the features are "static". The features are compact: they need less storage capacity. Also, structural engineers are familiar with modal parameters, natural frequencies, mode shapes and damping.

Time-domain detection has also many advantages: The data dimensionality is relatively low (equal to the number of sensors), while the amount of data is very large (the number of samples). This is advantageous in statistical analysis. No system identification is needed, which reduces one possible source of error. The measurement variables are directly related to sensors, making it also possible to localize damage.

Environmental or operational variability affects the data in both domains. Many experimental studies have demonstrated the environmental effects on the dynamic characteristics of large civil engineering structures (Wahab & Roeck 1997; Farrar et al. 1997; Alampalli 1998; Cornwell et al. 1999; Peeters & de Roeck 2000; Rohrmann et al. 2000; Darbre & Proulx 2001; Kullaa 2002). The main underlying effect in most studies is temperature. Also in the last two references, respectively, the influence of the water level in the dam and the humidity on the wooden structure have been identified.

Because the underlying environmental or operational variables are not all known and their effects on the data are often complex, it may be difficult to build a model that predicts the variability in the data. Alternatively, the effects of environment can be removed using the vibration data alone by applying multivariate statistics, provided the data dimensionality is high enough to make the measurements redundant.

Many techniques have emerged to remove environmental or operational effects into account without measuring the underlying variables (Kullaa 2002, 2003, 2004, 2006a, 2009a, 2014; Manson 2002; Sohn et al. 2003; Vanlanduit et al. 2005; Yan et al. 2005a, b; Basseville et al. 2006; Yan & Go-

linval 2006; Lämsä & Kullaa 2007; Gorinevsky et al. 2007; Cross et al. 2011).

The same approach can be taken both in the time-domain and in the feature-domain. The number of static features must be higher than the number of underlying environmental or operational variables. The dimensionality in the time-domain must be higher, because the signals have normal time-variation in addition to the variability in the dynamic characteristics due to environmental or operational effects. Specifically, the number of sensors must be higher than the number of active modes plus the number of underlying variables when using time-domain analysis.

The environmental or operational influences are taken into account by acquiring training data under different conditions. Utilizing the correlation between the variables in the training data, those underlying influences can be eliminated. It is assumed that the sensor network is redundant, so that each sensor reading can be estimated using the covariance model. The residuals (the difference between the measured and estimated variables) are used in damage detection.

If the measurement data are very noisy, small damage may remain undetected. Therefore, a high SNR is important to get an early warning. This can be achieved e.g. by using high-quality sensors or by applying virtual sensing (VS) techniques to a redundant sensor network. In Bayesian VS, the signal of each sensor in the network is estimated using the whole sensor network data. Using Bayes' rule, the estimate can be shown to be more accurate than the actual measurement. Virtual sensing uses the same idea as in the removal of environmental or operational influences from the data discussed above. However, VS is applied independently to each measurement. Once processed, the data still include the prevailing dynamics and environmental or operational influences, as well as the effects of damage. Measurement error is only reduced. The measurement data are replaced with the virtual sensor data in the damage detection algorithm.

Empirical virtual sensing is traditionally used for sensor validation and sensor fault identification (Ray & Luck 1991; Dunia et al. 1996; Dunia & Qin 1998; Kerschen et al. 2005; Friswell & Inman 1999; Abdelghani & Friswell 2004, 2007; Hernandez-Garcia & Masri 2008; Kullaa 2006b, 2007, 2009b, 2010, 2013). Assuming the sensor network is redundant, it is possible to estimate the signal of a single sensor using the remaining sensors in the network. In the present study, all sensors in the network are used to reconstruct the sensor under investigation, including the sensor's own signal. Bayes' rule gives an optimal weighting to all sensors resulting in virtual sensors with the highest accuracy.

This paper is organised as follows. Bayesian virtual sensing is introduced in Section 2 and the posterior mean and variance are derived for the measured quantity of each sensor in the network. The virtual sensors are shown to be more accurate than the corresponding hardware. The strategy of using virtual sensors in damage detection is described in Section 3. In Section 4, numerical simulations are performed for a structure subject to unknown random loads and various environmental effects. Noisy response is measured with a sensor network. Damage detection is performed in the time domain using the virtual sensor data. The performance is compared to the case in which raw measurements are used instead. Finally, concluding remarks are given in Section 5.

2 BAYESIAN EMPIRICAL VIRTUAL SENSING

Virtual sensing techniques estimate quantities of interest using the available physical sensors. Empirical virtual sensing is based on available historical measurements of the same quantity that is being estimated. These measurement data are used to estimate the correlation between the measured quantities. Empirical virtual sensing uses regression techniques that can be implemented using different statistical methods, for example linear regression or neural network regression.

2.1 *Measurement model*

Consider a sensor network measuring p simultaneously sampled variables $\mathbf{y} = \mathbf{y}(t)$ at time instant t. Each measurement $\mathbf{y}$ includes independent measurement error $\mathbf{w} = \mathbf{w}(t)$:

$$\mathbf{y} = \mathbf{x}_m + \mathbf{w} \tag{1}$$

where $\mathbf{x}_m = \mathbf{x}_m(t)$ are the true values of the measured degrees of freedom. The objective is to find a less noisy estimate for the true values $\mathbf{x}_m$ utilizing the noisy measurements $\mathbf{y}$ from the sensor network.

2.2 *Bayes' rule*

From Bayes' rule,

$$p(\mathbf{x}_m \mid \mathbf{y}) = \frac{p(\mathbf{y} \mid \mathbf{x}_m)\, p(\mathbf{x}_m)}{p(\mathbf{y})} \tag{2}$$

This, however, cannot be evaluated, because the distributions are not available. To proceed, only a subset of the physical sensors is estimated by partitioning each observation into observed variables $\mathbf{v}$ and estimated variables $\mathbf{u}$ (typically a single sensor u). The partitioned variables are

$$\mathbf{y} = \begin{Bmatrix} \mathbf{y}_u \\ \mathbf{y}_v \end{Bmatrix},\ \mathbf{x}_m = \begin{Bmatrix} \mathbf{x}_{m,u} \\ \mathbf{x}_{m,v} \end{Bmatrix},\ \mathbf{w} = \begin{Bmatrix} \mathbf{w}_u \\ \mathbf{w}_v \end{Bmatrix} \tag{3}$$

Measurement error $\mathbf{w}$ is assumed to be zero mean, independent of $\mathbf{x}_m$, with a known covariance matrix

$$\boldsymbol{\Sigma}_w = E(\mathbf{w}\mathbf{w}^T) = \begin{bmatrix} \boldsymbol{\Sigma}_{w,uu} & \boldsymbol{\Sigma}_{w,uv} \\ \boldsymbol{\Sigma}_{w,vu} & \boldsymbol{\Sigma}_{w,vv} \end{bmatrix} \tag{4}$$

where $E(\cdot)$ denotes the expectation operator. After partitioning, all distributions are conditioned with $\mathbf{y}_v$. Bayes' rule becomes

$$\begin{aligned} p(\mathbf{x}_{m,u} \mid \mathbf{y}) &= p(\mathbf{x}_{m,u} \mid \mathbf{y}_u, \mathbf{y}_v) \\ &= \frac{p(\mathbf{y}_u \mid \mathbf{x}_{m,u}, \mathbf{y}_v) p(\mathbf{x}_{m,u} \mid \mathbf{y}_v)}{p(\mathbf{y}_u \mid \mathbf{y}_v)} \\ &= \frac{p(\mathbf{y}_u \mid \mathbf{x}_{m,u}) p(\mathbf{x}_{m,u} \mid \mathbf{y}_v)}{p(\mathbf{y}_u \mid \mathbf{y}_v)} \end{aligned} \tag{5}$$

The distributions in (5) can be evaluated as shown in the following.

2.3 *Likelihood*

Assuming Gaussian noise $\mathbf{w}$, the likelihood is obtained using Equation 1:

$$\begin{aligned} p(\mathbf{y}_u \mid \mathbf{x}_{m,u}) &= N(\mathbf{y}_u \mid \mathbf{x}_{m,u}, \boldsymbol{\Sigma}_{w,uu}) \\ &\propto \exp\left[-\frac{1}{2} (\mathbf{y}_u - \mathbf{x}_{m,u})^T \boldsymbol{\Sigma}_{w,uu}^{-1} (\mathbf{y}_u - \mathbf{x}_{m,u}) \right] \end{aligned} \tag{6}$$

2.4 *Evidence*

For simplicity but without loss of generality, assume zero-mean variables $\mathbf{y}$. The partitioned data covariance matrix $\boldsymbol{\Sigma}_y$ is

$$\boldsymbol{\Sigma}_y = E(\mathbf{y}\mathbf{y}^T) = \begin{bmatrix} \boldsymbol{\Sigma}_{y,uu} & \boldsymbol{\Sigma}_{y,uv} \\ \boldsymbol{\Sigma}_{y,vu} & \boldsymbol{\Sigma}_{y,vv} \end{bmatrix} \tag{7}$$

The precision matrix $\boldsymbol{\Gamma}_y$ is defined as the inverse of the covariance matrix $\boldsymbol{\Sigma}_y$ and is also written in partitioned form:

$$\boldsymbol{\Gamma}_y = \boldsymbol{\Sigma}_y^{-1} = \begin{bmatrix} \boldsymbol{\Gamma}_{y,uu} & \boldsymbol{\Gamma}_{y,uv} \\ \boldsymbol{\Gamma}_{y,vu} & \boldsymbol{\Gamma}_{y,vv} \end{bmatrix} \tag{8}$$

A linear minimum mean square error (LMMSE) estimate for $\mathbf{y}_u \mid \mathbf{y}_v$ is obtained by minimizing the mean-square error (MSE) and can be computed either using the covariance or precision matrix (Kullaa 2010, Bishop 2006). If each sensor signal is estimated in turn, the formulas based on the precision matrix result in a more efficient algorithm (Kullaa 2010). The expected value of the estimated variable is:

$$\hat{\mathbf{y}}_u = E(\mathbf{y}_u \mid \mathbf{y}_v) = -\boldsymbol{\Gamma}_{y,uu}^{-1} \boldsymbol{\Gamma}_{y,uv} \mathbf{y}_v = \mathbf{K}\mathbf{y}_v \tag{9}$$

where $\mathbf{K} = -\boldsymbol{\Gamma}_{y,uu}^{-1} \boldsymbol{\Gamma}_{y,uv}$, and the error covariance MSE is

$$\operatorname{cov}(\mathbf{y}_u \mid \mathbf{y}_v) = \boldsymbol{\Gamma}_{y,uu}^{-1} \tag{10}$$

Notice that the covariance is the error compared to the noisy measurement, not to the noiseless (true) value.

The evidence $p(\mathbf{y}_u \mid \mathbf{y}_v)$ is also Gaussian with the mean and covariance from Equations 9 and 10, respectively:

$$\begin{aligned} p(\mathbf{y}_u \mid \mathbf{y}_v) &= N(\mathbf{y}_u \mid \mathbf{K}\mathbf{y}_v, \boldsymbol{\Gamma}_{y,uu}^{-1}) \\ &\propto \exp\left[-\frac{1}{2} (\mathbf{y}_u - \mathbf{K}\mathbf{y}_v)^T \boldsymbol{\Gamma}_{y,uu} (\mathbf{y}_u - \mathbf{K}\mathbf{y}_v) \right] \end{aligned} \tag{11}$$

The evidence is merely a normalizing factor, independent of $\mathbf{x}_{m,u}$. However, evidence will be utilized in damage detection to remove the environmental or operational effects, which will be discussed in Section 3.

2.5 *Prior*

The prior distribution $p(\mathbf{x}_{m,u} \mid \mathbf{y}_v)$ is obtained from the measurement model (1) by partitioning and conditioning:

$$p(\mathbf{y}_u \mid \mathbf{y}_v) = p(\mathbf{x}_{m,u} \mid \mathbf{y}_v) + p(\mathbf{w}_u) \tag{12}$$

from which the prior mean is

$$\begin{aligned} E(\mathbf{x}_{m,u} \mid \mathbf{y}_v) &= E(\mathbf{y}_u \mid \mathbf{y}_v) - E(\mathbf{w}_u) \\ &= E(\mathbf{y}_u \mid \mathbf{y}_v) = \mathbf{K}\mathbf{y}_v \end{aligned} \tag{13}$$

and the prior covariance is obtained from

$$\operatorname{cov}(\mathbf{y}_u \mid \mathbf{y}_v) = \operatorname{cov}(\mathbf{x}_{m,u} \mid \mathbf{y}_v) + \boldsymbol{\Sigma}_{w,uu} \tag{14}$$

from which

$$\begin{aligned} \boldsymbol{\Sigma}_{\text{prior},uu} &= \operatorname{cov}(\mathbf{x}_{m,u} \mid \mathbf{y}_v) \\ &= \operatorname{cov}(\mathbf{y}_u \mid \mathbf{y}_v) - \boldsymbol{\Sigma}_{w,uu} = \boldsymbol{\Gamma}_{y,uu}^{-1} - \boldsymbol{\Sigma}_{w,uu} \end{aligned} \tag{15}$$

The prior distribution is also Gaussian:

$$\begin{aligned} p(\mathbf{x}_{m,u} \mid \mathbf{y}_v) &= N(\mathbf{x}_{m,u} \mid \mathbf{K}\mathbf{y}_v, \boldsymbol{\Sigma}_{\text{prior},uu}) \\ &\propto \exp\left[-\frac{1}{2} (\mathbf{x}_{m,u} - \mathbf{K}\mathbf{y}_v)^T \boldsymbol{\Sigma}_{\text{prior},uu}^{-1} (\mathbf{x}_{m,u} - \mathbf{K}\mathbf{y}_v) \right] \end{aligned} \tag{16}$$

Notice that the prior is not subjective. It is the distribution of the exact quantity, estimated without using the corresponding sensor signal.

2.6 *Posterior*

The posterior distribution (5) is obtained by some manipulation, resulting in

$$
\begin{aligned}
&p(\mathbf{x}_{m,u} \mid \mathbf{y}) = c_1 p(\mathbf{y}_u \mid \mathbf{x}_m) p(\mathbf{x}_{m,u} \mid \mathbf{y}_v) \\
&= c_2 \exp\Bigg[-\frac{1}{2}(\mathbf{y}_u - \mathbf{x}_{m,u})^T \boldsymbol{\Sigma}_{w,uu}^{-1} (\mathbf{y}_u - \mathbf{x}_{m,u}) \\
&-\frac{1}{2}(\mathbf{x}_{m,u} - \mathbf{K}\mathbf{y}_v)^T \boldsymbol{\Sigma}_{\text{prior},uu}^{-1} (\mathbf{x}_{m,u} - \mathbf{K}\mathbf{y}_v) \Bigg] \\
&= c_2 \exp\Bigg[-\frac{1}{2}(\mathbf{x}_{m,u} - \hat{\mathbf{x}}_{m,u})^T \boldsymbol{\Sigma}_{\text{post},uu}^{-1} (\mathbf{x}_{m,u} - \hat{\mathbf{x}}_{m,u}) \Bigg]
\end{aligned}
\tag{17}
$$

where c_1 and c_2 are constants and the posterior covariance $\boldsymbol{\Sigma}_{\text{post},uu}$ is

$$
\boldsymbol{\Sigma}_{\text{post},uu} = \text{cov}(\mathbf{x}_{m,u} \mid \mathbf{y}) = (\boldsymbol{\Sigma}_{w,uu}^{-1} + \boldsymbol{\Sigma}_{\text{prior},uu}^{-1})^{-1} \tag{18}
$$

and the posterior mean is

$$
\hat{\mathbf{x}}_{m,u} = E(\mathbf{x}_{m,u} \mid \mathbf{y}) = \boldsymbol{\Sigma}_{\text{post},uu} (\boldsymbol{\Sigma}_{w,uu}^{-1} \mathbf{y}_u + \boldsymbol{\Sigma}_{\text{prior},uu}^{-1} \mathbf{K}\mathbf{y}_v) \tag{19}
$$

Notice that the MSE of the posterior (18) is always less than that of the measurement error, $\boldsymbol{\Sigma}_{w,uu}$. Therefore, the posterior mean is more accurate than the actual measurement.

Equation 19 can also be written in the following form.

$$
\hat{\mathbf{x}}_{m,u} = \begin{bmatrix} \boldsymbol{\Sigma}_{\text{post},uu} \boldsymbol{\Sigma}_{w,uu}^{-1} & \boldsymbol{\Sigma}_{\text{post},uu} \boldsymbol{\Sigma}_{\text{prior},u}^{-1} \mathbf{K} \end{bmatrix} \begin{Bmatrix} \mathbf{y}_u \\ \mathbf{y}_v \end{Bmatrix} = \mathbf{a}_u^T \mathbf{y} \tag{20}
$$

where $\mathbf{a}_u^T$ is

$$
\mathbf{a}_u^T = \begin{bmatrix} \boldsymbol{\Sigma}_{\text{post},uu} \boldsymbol{\Sigma}_{w,uu}^{-1} & \boldsymbol{\Sigma}_{\text{post},uu} \boldsymbol{\Sigma}_{\text{prior},uu}^{-1} \mathbf{K} \end{bmatrix} \tag{21}
$$

Equation 20 shows that the posterior mean is a weighted sum of the measurements of all sensors in the network.

Generally, the predicted DOFs **u** may include several variables. In the sequel, **u** is one-dimensional including one sensor only. For each sensor u, a corresponding row vector $\mathbf{a}_u^T$ is computed. All these vectors can be assembled in a coefficient matrix **A** to estimate all virtual sensors simultaneously:

$$
\hat{\mathbf{x}}_m = \mathbf{A}\mathbf{y} \tag{22}
$$

where each row u of matrix **A** represents the corresponding sensor.

A diagonal covariance matrix is assumed with variances (18) in the corresponding row u.

2.7 *Application of virtual sensing*

Bayesian virtual sensing is applied to each measurement separately. Each measurement is assumed to be acquired under constant environmental or operational condition, so that the dynamic characteristics remain the same during the whole measurement period. Because the measurement period is typically of the order of a few seconds or minutes, this assumption is often valid. Therefore, the differences between measurements due to environmental or operational variability or damage remain in the data. The noise is only reduced.

Virtual sensors are then used in subsequent damage detection as follows.

3 DAMAGE DETECTION

Virtual sensors are used in damage detection as if they were physical hardware. The measurement data are replaced with the virtual sensor data ($\mathbf{y} \leftarrow \hat{\mathbf{x}}_m$). The damage detection algorithm used in this paper is briefly outlined. Each sensor in turn is estimated using the remaining sensors in the network. The residuals for each sensor are then generated:

$$
\boldsymbol{\varepsilon}_u = \mathbf{y}_u - \hat{\mathbf{y}}_u \tag{23}
$$

where $\mathbf{y}_u$ is a vector of virtual sensor data (Equation 19 or 20) and $\hat{\mathbf{y}}_u$ is the evidence mean (9), identified using training data (virtual sensors) from the undamaged structure. The training data consist of several measurements in order to take different environmental or operational conditions into account. Specifically, the data covariance matrix (7) is estimated using all training data. The environmental or operational influences can be eliminated using correlation between the features (Kullaa 2009a). Once damage occurs, the correlation structure does not fit the experimental data producing a larger residual, which will then trigger an alarm.

All residuals are standardized according to the training data. All samples, training and test data, are subjected to principal component analysis (PCA). The first principal component (PC) is retained in order to find the direction with the largest change in the data space, which is supposed to indicate damage. If the first PC scores of the residuals are not normally distributed and the distribution is unknown, a generalized extreme value distribution can be used regardless of the data distribution (Worden et al. 2002). The scores are divided into subgroups (of size n = 100) and the subgroup minima and maxima are recorded. Extreme value distributions are identified for both the subgroup minima and maxima of the in-control samples (training data). The control limits are computed to these distributions by choosing the probability of exceedance (here 0.001). The extreme values are plotted on a control chart (Montgomery 1997) to see if the test samples exceed the control limits thus indicating damage.

4 NUMERICAL EXAMPLE

As a structural health monitoring example, consider a simply-supported beam with length 1.4 m, a uniform rectangular cross-section of 50 mm × 5 mm (Fig. 1). The beam was also supported with a spring

612.5 mm from the support, with the spring constant k depending non-linearly on temperature:

$$k = k_0 + aT^3 \tag{24}$$

where k_0 = 100 kN/m, a = –0.8 (with compatible units), and T is temperature with a uniform random distribution between –20 and +40°C.

The beam was divided into three sections of equal length. The Young's modulus E_i at each section of the beam had a linear relationship with a corresponding independent and dimensionless unknown environmental variable z_i:

$$E_i = E_0 + \sigma_i z_i, \quad i = 1,2,3 \tag{25}$$

where E_0 = 207 GPa, z_i are standardized Gaussian variables: $z_i \sim N(0,1)$, and the standard deviations σ_i of different sections were: σ_1 = 5 GPa, σ_2 = 3 GPa, and σ_3 = 7 GPa.

The structure was modelled with 144 simple beam elements and one spring element. Independent random excitations with different realizations in each measurement were applied to the structure at three points (Fig. 1). Transverse acceleration was measured at 47 equidistant points along the beam. Gaussian noise was added to each sensor. The sampling frequency was 571 Hz and the number of samples in each measurement was 2859. The first 50 measurements were from the undamaged structure. A slow environmental variability was assumed, justifying a constant environment during each measurement.

As a conclusion, the environmental or operational variability thus introduced originated from (1) a variable spring with a non-linear relationship between temperature and the spring constant, (2) three regions with independently varying Young's moduli, and (3) independent random loads at three points.

Damage was a decrease in the beam depth at the spring support in two elements along a total length of 19.4 mm (Fig. 1). This type of damage could represent local corrosion around the spring joint. The height of the beam varied in five different levels: 4.5, 4, 3.5, 3, and 2.5 mm. Each damage level was monitored with two measurements at variable unknown environmental conditions.

The training data were the first 100,000 samples including almost the first 35 measurements. These were also used to design the control charts. The first principal component scores of the residuals (Equation 23) were plotted on the extreme value statistics (EVS) control chart using subgroups of size 100 (Kullaa et al. 2016).

Different amount of noise and different sensor arrangements were studied. A comparison was made between the proposed method using virtual sensors and a similar method but using raw measurements.

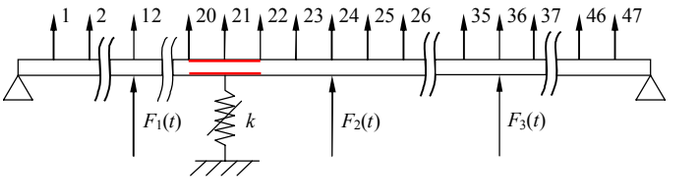


Figure 1. Beam structure with a variable spring. 47 sensors and 3 independent loadings. Damage location is shown in red.

First, optimal sensor placement (OSP) was performed using the effective independence algorithm (EFI) (Kammer 1991, 1992) starting from the initial sensor network with all 47 sensors and removing one sensor in each round until the required number of sensors remained.

In the first case, all 47 sensors were used. A high noise level, σ_w = 0.5 m/s^2 was added to all sensors. Figure 2 shows the EVS control chart when using the raw measurement data and Figure 3 is the corresponding control chart when using the virtual sensors. It can be seen that damage could not be detected from the original noisy data, whereas after noise reduction, four largest damage levels were detected and only the lowest level remained undetected. Occational false alarms appeared during one measurement. This is probably due to the fact that this measurement took place under a high temperature not present in the training data.

In the subsequent cases, the noise level was set to σ_w = 0.1 m/s^2. The effect of the number of sensors was studied using 10, 15, and 20 sensors at optimal positions (according to EFI).

Using raw measurements, hardly any damage levels could be detected with 10 sensors (Fig. 4), whereas damage levels 4 and 5 were detected with 15 or 20 sensors (Figs 6, 8).

Using virtual sensor data, damage levels 2–5 were detected with 10, 15, or 20 sensors (Figs 5, 7, 9). It is interesting that the performance did not improve much when increasing the number of virtual sensors. This may be because the extreme values do not seem identically distributed between measurements within the training data (Figs 5, 7, 9). The virtual sensors were estimated separately in each measurement, which may have resulted in different posterior distributions. Moreover, EFI may not have produced optimal sensor positions for damage detection.

On the other hand, when using the measurement data directly, the extreme values were more identically distributed (Figs 4, 6, 8), which is clearly an advantage in statistical analysis. However, despite the differences in the distributions, virtual sensors outperformed the raw measurements in damage detection. The investigation of different posterior distributions between the measurements is left for the future.

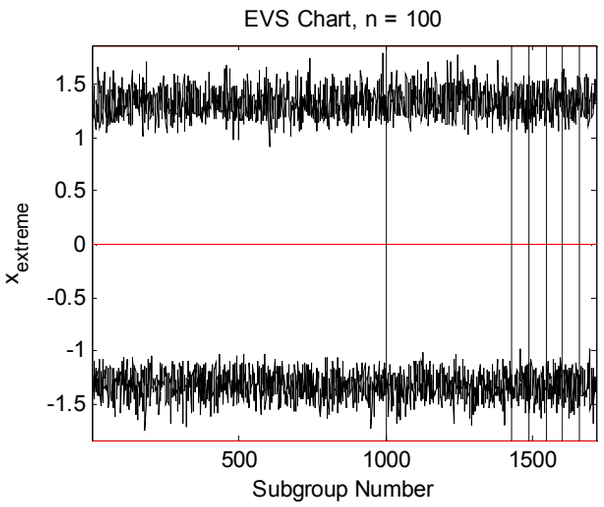


Figure 2. EVS control chart using raw measurements with 47 sensors. σ_w = 0.5 m/s^2. The data before the leftmost vertical line were used as training data, and the other vertical lines indicate the five damage levels with an increasing severity.

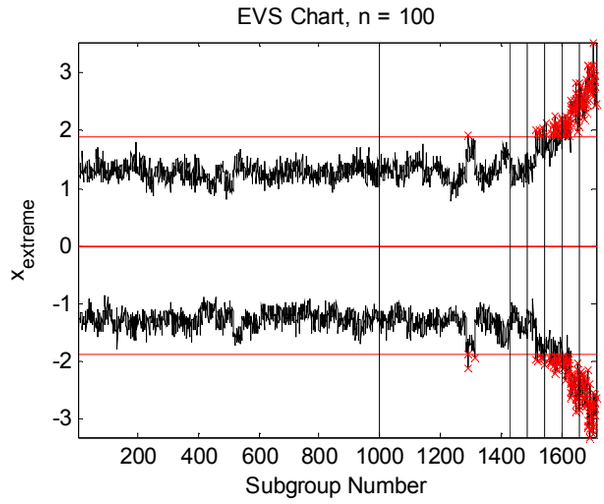


Figure 3. EVS control chart after noise reduction using 47 sensors. σ_w = 0.5 m/s^2.

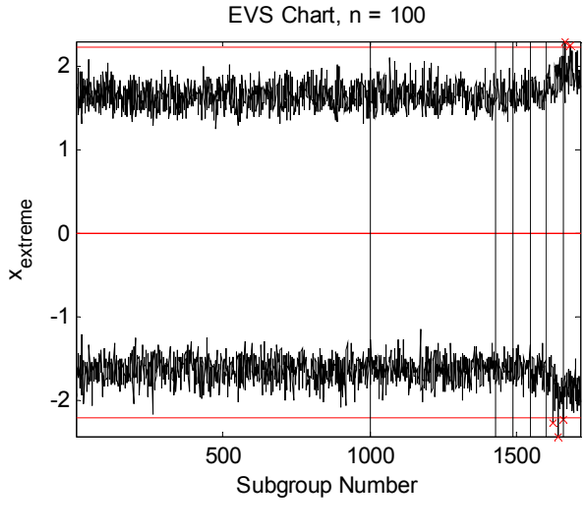


Figure 4. EVS control chart using raw measurements with 10 sensors. σ_w = 0.1 m/s^2.

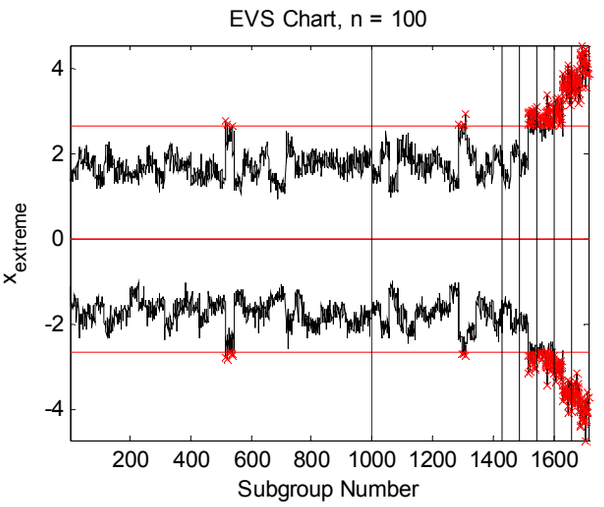


Figure 5. EVS control chart after noise reduction using 10 sensors. σ_w = 0.1 m/s^2.

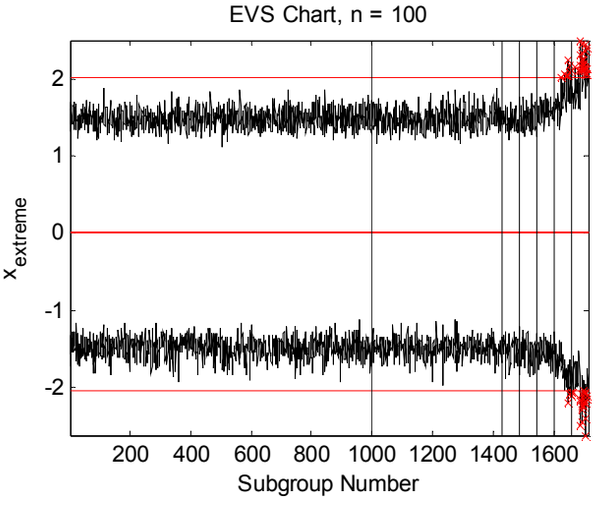


Figure 6. EVS control chart using raw measurements with 15 sensors. σ_w = 0.1 m/s^2.

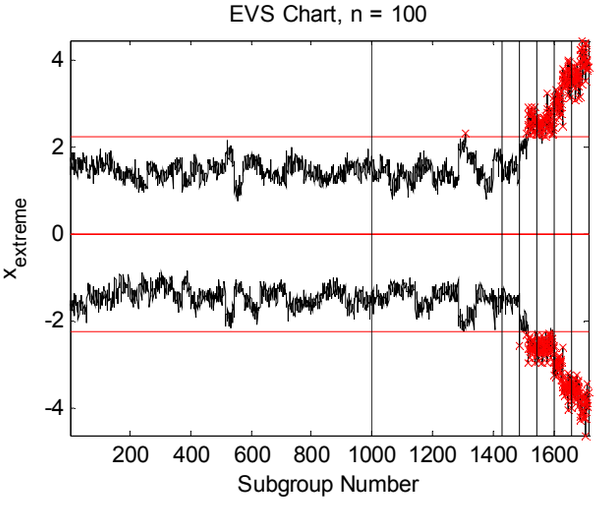


Figure 7. EVS control chart after noise reduction using 15 sensors. σ_w = 0.1 m/s^2.

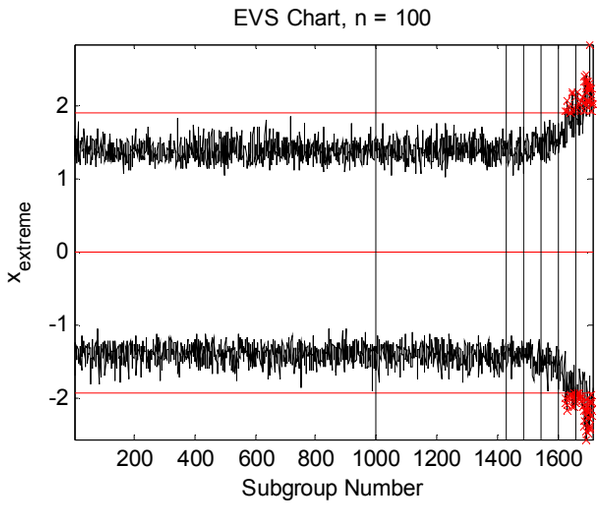


Figure 8. EVS control chart using raw measurements with 20 sensors. $\sigma_w = 0.1$ m/s^2.

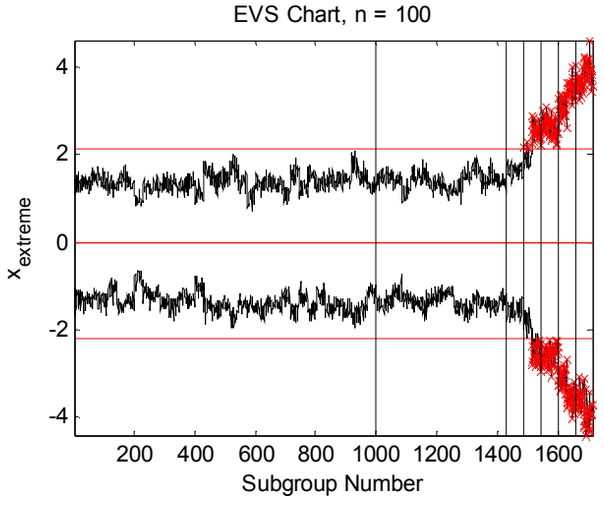


Figure 9. EVS control chart after noise reduction using 20 sensors. $\sigma_w = 0.1$ m/s^2.

5 CONCLUSION

Bayesian virtual sensing was applied to vibration-based structural health monitoring to reduce the measurement error in the sensor network. Bayesian virtual sensors are more accurate than the corresponding hardware and can replace the actual measurement data in any damage detection algorithm.

Damage detection was made in the time-domain. Environmental or operational influences were removed from the data using correlation between the measured variables. The residual was generated by subtracting the evidence mean from the virtual sensor data. The first principal component of the residual was then used as a damage-sensitive feature. An extreme value statistics control chart with appropriate control limits and subgroup size was plotted for damage detection.

Damage detection under variable environmental or operational conditions was successful, and the measurement of the underlying variables was not necessary. Virtual sensors outperformed the raw measurements in damage detection, making early warning more plausible.

The training data must include the underlying effects and the sensor network must be redundant. Experimental validation of the proposed method was left for a future study.

REFERENCES

Abdelghani, M. & Friswell, M.I. 2004. Sensor validation for structural systems with additive sensor faults. *Structural Health Monitoring* 3: 265–275.

Abdelghani, M. & Friswell, M.I. 2007. Sensor validation for structural systems with multiplicative sensor faults. *Mechanical Systems and Signal Processing* 21: 270–279.

Alampalli, S. 1998. Influence of in-service environment on modal parameters. In: *Proceedings of the 16th International Modal Analysis Conference, Santa Barbara, California, 1998*: 111–116.

Basseville, M., Bourquin, F., Mevel, L., Nasser, H. & Treyssède, F. 2006. Merging sensor data from multiple temperature scenarios for vibration-based monitoring of civil structures. In A. Güemes (ed.), *Proceedings of the third European Workshop on Structural Health Monitoring, Granada, Spain, July 5–7, 2006*: 759–506. DEStech.

Bishop, C.M. 2006. *Pattern recognition and machine learning*. Springer.

Cornwell, P., Farrar, C.R., Doebling, S.W. & Sohn, H. 1999. Structural testing series: Part 4. Environmental variability of modal properties. *Experimental Techniques* 23(6): 45–48.

Cross, E.J., Worden, K. & Chen, Q. 2011. Cointegration: a novel approach for the removal of environmental trends in structural health monitoring data. *Proceedings of the Royal Society A* 467: 2712–2732.

Darbre, G.R. & Proulx, J. 2001. The need for system identification techniques using ambient vibration data recorded on large dams. In: *Proceedings of the International Conference on Structural System Identification, Kassel, Germany, September 5–7, 2001*: 205– 213.

Dunia, R., Qin, S.J., Edgar, T.F. & McAvoy, T.J. 1996. Identification of faulty sensors using principal component analysis. *AiChe Journal* 42: 2797–2812.

Dunia, R. & Qin, S.J. 1998. Joint diagnosis of process and sensor faults using principal component analysis. *Control Engineering Practice* 6: 457–469.

Farrar, C.R., Doebling, S.W., Cornwell, P.J. & Straser, E.G. 1997. Variability of modal parameters measured on the Alamosa Canyon Bridge. In: *Proceedings of IMAC-XV: A Conference on Structural Dynamics, Orlando, Florida, 1997*: 257–263.

Friswell, M.I. & Inman, D.J. 1999. Sensor validation of smart structures. *Journal of Intelligent Material Systems and Structures* 10: 973–982.

Gorinevsky, D., Kim, S.-J., Boyd, S., Gordon, G., Beard, S. & Chang, F.-K. 2007. Optimal estimation of accumulating damage trend from series of SHM images. In Fu-Kuo Chang (ed.), *Proceedings of the 6th International Workshop on Structural Health Monitoring, Stanford, CA, September 11–13, 2007*: 1340–1346. DEStech.

Hernandez-Garcia, M.R. & Masri, S.F. 2008. Multivariate Statistical Analysis for Detection and Identification of Faulty Sensors Using Latent Variable Methods. *Advances in Science and Technology* 56: 501–507.

Kammer, D.C. 1991. Sensor placement for on-orbit modal identification and correlation of large space structures. *Journal of Guidance, Control, and Dynamics* 14: 251–259.

Kammer, D.C. 1992. Effects of noise on sensor placement for on-orbit modal identification of large space structures. *Journal of dynamic systems, measurements and control—Transactions of the ASCE* 114 (3): 436–443.

Kerschen, G., De Boe, P., Golinval, J.-C. & Worden, K. 2005. Sensor validation using principal component analysis. *Smart Materials and Structures* 14: 36–42.

Kullaa, J. 2002. Elimination of environmental influences from damage-sensitive features in a structural health monitoring system. In D.L. Balageas (ed.), *Proceedings of the First European Workshop on Structural Health Monitoring, Paris, France, July 10–12, 2002*: 742–749. DEStech.

Kullaa, J. 2003. Is temperature measurement essential in structural health monitoring? In Fu-Kuo Chang (ed.), *Proceedings of the 4th International Workshop on Structural Health Monitoring, Stanford, CA, September 15–17, 2003*: 717–724. DEStech.

Kullaa, J. 2004. Latent variable models to eliminate the environmental effects in structural health monitoring. In R. Flesch, H. Irschik & M. Krommer (eds.), *Proceedings of the Third European Conference on Structural Control, Volume II, Vienna, Austria, July 12–15, 2004*: S5-55–58.

Kullaa, J. 2006a. Removing non-linear environmental influences from structural features. In A. Güemes (ed.), *Proceedings of the third European Workshop on Structural Health Monitoring, Granada, Spain, July 5–7, 2006*: 635–642. DEStech.

Kullaa, J. 2006b. Sensor fault identification and correction in structural health monitoring. In Sas, P. and De Munck, M. (eds.), *Proceedings of ISMA2006, International Conference on Noise and Vibration Engineering, Leuven, Belgium, September 18–20, 2006*: 873–884.

Kullaa, J. 2007. Sensor fault identification and correction in vibration-based multichannel structural health monitoring. In Fu-Kuo Chang (ed.), *Proceedings of the 6th International Workshop on Structural Health Monitoring, Stanford, CA, September 11–13, 2007*: 606–613. DEStech.

Kullaa, J. 2009a. Eliminating environmental or operational influences in structural health monitoring using the missing data analysis. *Journal of Intelligent Material Systems and Structures* 20(11): 1381–1390.

Kullaa, J. 2009b. Three models for sensor validation. In Fu-Kuo Chang (ed.), Proceedings of the 7th International Workshop on Structural Health Monitoring, Stanford, CA, September 9–11, 2009: 529–536. DEStech.

Kullaa, J. 2010. Sensor validation using minimum mean square error estimation. *Mechanical Systems and Signal Processing* 24: 1444–1457.

Kullaa, J. 2013. Detection, identification, and quantification of sensor fault in a sensor network. *Mechanical Systems and Signal Processing* 40: 208–221.

Kullaa, J. 2014. Structural health monitoring under nonlinear environmental or operational influences. *Shock and Vibration* 2014.

Kullaa, J., Magalhães, F., Cunha, Á. 2016. Structural health monitoring and damage detection of an arch bridge using a minimum mean square error estimator. In J. Bakker, D.M. Frangopol, K. van Breugel (eds.), *Life-Cycle of Engineering Systems: Emphasis on Sustainable Civil Infrastructure. Proceedings of the Fifth International Symposium on Life-Cycle Civil Engineering (IALCCE 2016). Delft, The Netherlands, 16–19 October 2016*: 777–784. London: Taylor & Francis.

Lämsä, V. & Kullaa, J. 2007. Nonlinear factor analysis in structural health monitoring to remove environmental effects. In Fu-Kuo Chang (ed.), *Proceedings of the 6th International Workshop on Structural Health Monitoring, Stanford, CA, September 11–13, 2007*: 1092–1099. DEStech.

Manson, G. 2002. Identifying damage sensitive, environment insensitive features for damage detection. In: *Proceedings of the Third International Conference on Identification in Engineering Systems, Swansea, 2002*: 187–197.

Montgomery, D.C. 1997. *Introduction to statistical quality control, 3rd edition*. New York: Wiley.

Peeters, B. & De Roeck, G. 2000. One year monitoring of the Z24 Bridge: Environmental influences versus damage effects. In: *Proceedings of IMAC-XVIII: A Conference on Structural Dynamics, San Antonio, Texas, February 7–10, 2000*: 1570–1576.

Ray, A. & Luck, R. 1991. An introduction to sensor signal validation in redundant measurement systems. *IEEE Control System Magazine* 11: 44–49.

Rohrmann, R.G., Baessler, M., Said, S., Schmid, W. & Ruecker, W.F. 2000. Structural causes of temperature affected modal data of civil structures obtained by long time monitoring. In: *Proceedings of IMAC-XVIII: A Conference on Structural Dynamics, San Antonio, Texas, February 7–10, 2000*: 1–7.

Sohn, H., Worden, K. & Farrar, C.R. 2003. Statistical damage classification under changing environmental and operational conditions. *Journal of Intelligent Materials Systems and Structures* 13(9): 561–574.

Vanlanduit, S., Parloo, E., Cauberghe, B., Guillaume, P. & Verboven, P. 2005. A robust singular value decomposition for damage detection under changing operational conditions and structural uncertainties. *Journal of Sound and Vibration* 284: 1033–1050.

Wahab, M.A. & De Roeck, G. 1997. Effect of temperature on dynamic system parameters of a highway bridge. *Structural Engineering International*, No. 4: 266–270.

Worden, K., Allen, D., Sohn, H. & Farrar, C.R. 2002. Damage detection in mechanical structures using extreme value statistics. In: *SPIE Proceedings, Vol. 4693, 9th Annual International Symposium on Smart Structures and Materials, San Diego, CA, 2002*: 289–299.

Yan, A.-M., Kerschen, G., De Boe, P. & Golinval, J.-C. 2005a. Structural damage diagnosis under varying environmental conditions—Part I: A linear analysis. *Mechanical Systems and Signal Processing* 19: 847–864.

Yan, A.-M., Kerschen, G., De Boe, P. & Golinval, J.-C. 2005b. Structural damage diagnosis under varying environmental conditions—Part II: local PCA for non-linear cases. *Mechanical Systems and Signal Processing* 19: 865–880.

Yan, A.-M. & Golinval, J.-C. 2006. Null subspace-based damage detection of structures using vibration measurements. *Mechanical Systems and Signal Processing* 20: 611–626.

Maintenance, Safety, Risk, Management and Life-Cycle Performance of Bridges – Powers, Frangopol, Al-Mahaidi & Caprani (Eds)
© 2018 Taylor & Francis Group, London, ISBN 978-1-138-73045-8

Assessment of MEMS-based sensors for inclination measurements

S. Rau & G. Morgenthal
Chair of Modelling and Simulation of Structures, Institute of Structural Engineering, Bauhaus University Weimar, Weimar, Germany

ABSTRACT: The condition assessment of critical infrastructure subjected to various environmental effects and extreme loadings such as aeging bridges becomes increasingly important. Monitoring provides the possibility to evaluate the structural performance and identify damage. Sensor-based monitoring systems typically measure accelerations, strains, displacements and inclinations. Whilst piezo-electric sensors are most commonly used in Structural Health Monitoring (SHM) systems, MEMS (microelectromechanical systems) based sensors are growing in popularity because they are small and inexpensive. Novel miniaturized accelerometers can be used to measure local rotation on a structure to determine the deformation state. In this paper, the effect of temperature and long-term stability of a MEMS-based accelerometer are systematically investigated on uncased and encased sensors. Possibilities for compensation are described, while several questions arise from the measured data, which are also presented. It is shown that due to the imperfection of the novel MEMS-based sensor, uncertainty is incorporated in the measurement. The application of these sensors during the construction of cable-stayed bridges is discussed.

1 INTRODUCTION

The condition assessment of bridges subjected to various environmental effects, extreme loading as well as aging becomes increasingly important. Structural Health Monitoring (SHM) provides the possibility to evaluate the structural performance and to identify damage on existing structures. Modern SHM concepts for long-span bridges integrate various types of sensors such as accelerometer, strain gauges, corrosion and load cells, GPS sensors and inclinometer amongst others. Additionally, anenometers, temperature sensors and hygrometers are utilized to determine environmental effects, which influence the measured accelerations, strains, displacements and inclinations. Temperature, wind and external vibrations manipulate recorded signals and further lead to deviations in the extracted parameters that describe the structural condition.

In the past few years MEMS (microelectromechanical system) based sensors are growing in popularity because they are small and inexpensive. For SHM purposes, most commonly piezo-electric sensors are used as they ensure reliable measurements and good long-term stability. Since the quality of MEMS-based sensors is increasing, new fields of application become possible. Apart from vibration measurements MEMS-accelerometer can be utilized to sense local rotations when applied to a structure.

Literature related to MEMS sensors is mainly focused on the technological development and not on the metrological performance, which is critical for application of these novel sensor types for monitoring of structures. Especially, the effect of temperature changes needs to be known, to allow for an appropriate compensation. The long-term stability of the sensors is impaired by sensor drift. In this regard, drift is the occurrence of slowly increasing changes of the measured quantity, e.g. acceleration or inclination, due to aging of the sensor leading to self-induced losses in accuracy.

In the present paper, the effect of temperature and the long-term stability of MEMS-based accelerometer used for inclination measurement are systematically investigated. In order to ascertain the suitability, the accuracy of uncased and encased sample sensors are determined. Suitable measures for temperature and drift compensation are discussed. Several questions arise from the data evaluation. These questions will be presented in the paper. It will be shown that due to the imperfectness of the novel MEMS-based sensor, uncertainty is incorporated in the measurement.

In existing cable-stayed bridges, inclinometer or tilt meter are applied to monitor local rotations of the pylon. As the pylon experiences small inclinations, highly accurate sensing is necessary. However, during construction of cable stayed bridges in balanced

cantilever method, large displacements at the tip of the deck appear. To ensure bridge girder alignment and correct stress distribution in the load-carrying elements, displacements of the bridge girder are monitored by tacheometric survey. Inclinations are the derivative of displacements. Since the girder experiences large deflections also inclinations are significant. Therefore, the question arises whether MEMS-based inclinometer, comprising measurement uncertainty, can be used as an additional method to determine deflections. Thereby the uncertainty in the measurement will yield uncertainty in the reconstructed deflected shape.

2 MEMS-BASED INCLINATION SENSORS

2.1 *MEMS-sensors*

Microelctromechanical systems (MEMS) are a key technology which nowadays has a wide application in automotive industry, automation and health sector allowing for economic monitoring and control within different processes. Mostly accelerometer, gyroscopes and pressure sensors are used. The MEMS-sensors are a few millimeters in size and most of the sensors integrate an electro-mechanical signal conversion and evaluation circuit within the chip. For SHM purposes piezo-electric sensors are most commonly used. In comparison to them, MEMS-based sensors grow in popularity because they are small, inexpensive and easy to include in embedded systems and cheap wireless sensor networks.

2.2 *Inclination sensing using accelerometer*

MEMS-based accelerometer can be used to determine inclinations. Thereby, the rotation with respect to gravity is measured when the sensor is stationary. The principle of the rotation sensing is schematically shown in Figure 1. At an inclined position the sensor measures the vectorial portion of the gravitational acceleration at the individual axes, which can be interpreted directly in terms of the inclination relative to a horizontal position.

The rotation angle φ can be determined based on the acceleration measured in the horizontal axis:

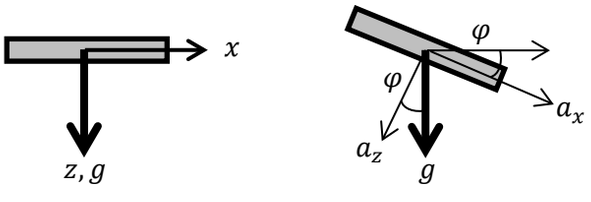


Figure 1. Principle of inclination sensing using accelerometer: initial position (left) and rotated position by angle φ (right).

$$\varphi = \arcsin\left(\frac{a_x}{1g}\right). \quad (1)$$

In the context of SHM, the inclinations to be measured are within the range of a few degrees for the most cases. Therefore, the sensors typically measure within a range of ±3° to ±5°.

Further, it should be noted that a sensor applied to the structure will not be fully aligned with the horizon. As a consequence the relative rotation regarding an initially displaced position has to be measured. The difference in the observed rotation will be the inclination as displayed in Equation (2) and Figure 2.

$$\Delta\varphi = \varphi_1 - \varphi_0 \quad (2)$$

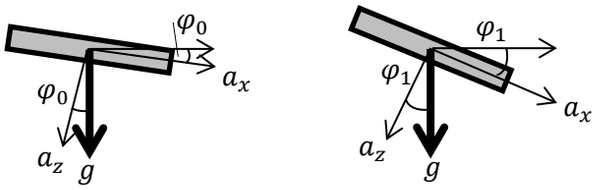


Figure 2. Determination of the relative rotation of the accelerometer: initial state (left) and displaced state (right).

2.3 *Sensor characteristics*

The studied MEMS-based accelerometer is using capacitive sensing techniques to detect accelerations, i.e. a motion-induced change of the position of the internal mass will result in a change of the capacity, which is converted in an electric signal.

The sensing element is produced using air gap insulated microstructure (AIM) technology, thus providing low noise, small cross-axis sensitivity and minimized parasitic capacitance (First Sensor 2016). Special modifications and signal processing methods are employed in this type of sensor to maximize its accuracy. With a temperature range of -45°C to 85°C and an adjustable measurement range (±1° to ±30°) along with a 24 bit analog-digital-conversion, the sensor is generally suitable for monitoring purposes on bridges. It should be noted that the novel MEMS-accelerometer is at design stage and not yet manufactured in mass production. The accuracy of the sensors and the long-term stability were investigated in order to evaluate the applicability of that sensor type for SHM purposes.

The MEMS-sensor is biaxial and measures accelerations in the two horizontal axes. The absolute acceleration can be determined from the electric output signal, which is expressed in terms of a digital integer value in LSB (least significant bit). Since the output signal Out is linear dependent on the applied acceleration a, the relation can be described by Equation (3):

$$Out = K_1 \cdot a + K_0 , \quad (3)$$

where K_1 is the slope and K_0 is the intercept of a linear function. Applying the parameter K_1 and K_0, which are also called Scale-Factor and Bias, the acceleration a can be obtained by Equation (4), wherefrom the angle of rotation can be determined by Equation (1).

$$a = \frac{Out - K_0}{K_1} , \quad (4)$$

Scale-Factor and Bias are sensor-specific and have to be determined by a calibration process under controlled environment. Using high precision turntables, the characteristic curve of the MEMS-accelerometer, wherefrom Scale and Bias are defined, can be found.

In comparison with high-quality piezo-electric sensors, the seismic mass is small and therefore MEMS-based sensors possess a worse signal-to-noise ratio. The noise density is typically 0,4m°/$\sqrt{\text{Hz}}$, i.e. for a measurement with 100 samples per seconds the RMS noise is about 4m° (First Sensor 2016). At that stage, no internal filters are applied to reduce noise. For sensing inclinations at quasi-static state it is assumed that the through averaging the noise-term can be cancelled out. The MEMS-accelerometer also possesses a temperature sensor, which is necessary to allow for temperature compensation further on.

2.4 *Investigation on temperature*

The characteristic relation between signal output and displacement of the seismic mass is affected by temperature as the Young's modulus of the silicon sensing element changes. The temperature effect on Scale-Factor and Bias was investigated in a laboratory test. It was thereby found, that the Scale-Factors and the Bias changes over the regarded temperature range from -15°C to 65°C.

Investigations were conducted for uncased and encased sensors. The thermal effect on the measured inclination is exemplarily shown for two encased sensors in Figure 3. Thereby a horizontally aligned sensor is assumed. It can be seen, that different sensors feature different behavior.

2.5 *Investigations on drift*

Further the long-term stability of the novel MEMS-based accelerometer was investigated on uncased and encapsulated sensors during HTOL (high temperature operation life) test. Thereby the sensors are tested for 1000 hours at an elevated temperature of 80°C in order simulate aging. Assuming a mean operating temperature of the sensor of 25°C (at the sensing element) the test duration corresponds to an equivalent operation time of 8 years. From the test it was evident that there is a great variation between the individual samples. Drift was found to be from –50m° to +50m° over the equivalent life time of the samples.

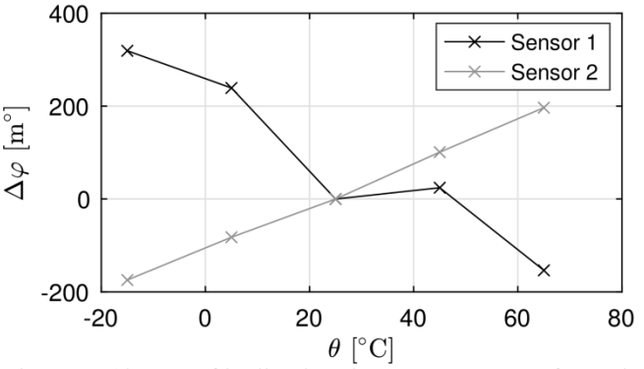


Figure 3. Change of inclination due to temperature for an horizontal aligned sensor at initial temperature of 25 °C.

Especially the great variation of the sensor performance between the different samples creates challenges for real applications. Without any further compensation of temperature and drift the accuracy of the sensor won't be better than ±50m°.

3 SHORT-TERM MEASUREMENTS

A three point bending test on a reinforced concrete beam has been performed to study the performance of the MEMS-based inclinometer. The beam with a dimension of 12 by 20 cm was reinforced with one rebar Ø 14 mm. The beam was simply supported and was loaded with a point load at midspan which was introduced by a hydraulic cylinder. At midspan an inductive displacement transducer (IDT) measured the deflection. The experimental setup is schematically shown in Figure 4.

The inclinations at both supports were recorded by the MEMS inclinometers which were further compared to measured rotations of high quality reference tilt meter. Both inclinometers were mounted to a base plate glued at the top of the beam. The reference sensor had a range of ±3° and a resolution of less than 0.3m°. The range of the MEMS-sensor was set to ±5°. For data acquisition, a microcontroller was used.

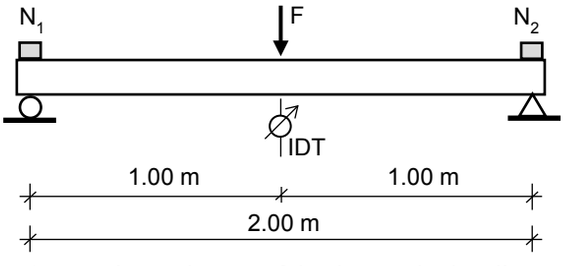


Figure 4: Experimental setup of the three-point bending test.

The load was introduced stepwise by loading ramps. At each ramp, the load was increased by 2.5 kN and the desired load level was held constant for 30 seconds. Initial cracking of the beam was observed at 7 kN at midspan. The beam was further loaded up to 31 kN where the beam reached yielding of the rebar.

A comparison of the inclinations measured by the MEMS-inclinometer and the reference tilt meter is shown in Figure 5 for the different load level. At each load level the average inclination was calculated, which is used therein. As the inclination data of the MEMS-sensor was recorded with a sampling rate of 100 Hz averaging was performed at the load level where the loading was static to eliminate the sensor noise.

Generally, there is a good agreement between the measured inclinations at both supports. For a better comparison, the absolute and relative deviation of the MEMS-inclinometer from the reference tilt meter is provided in Figure 6. It can be seen that the relative deviation is below $\pm$2m° on average with maximum deviations of 4.5m°. However, the relative deviation is smaller than 1 % except of the smallest load level, where the discrepancy can be attributed to the smaller level of inclinations.

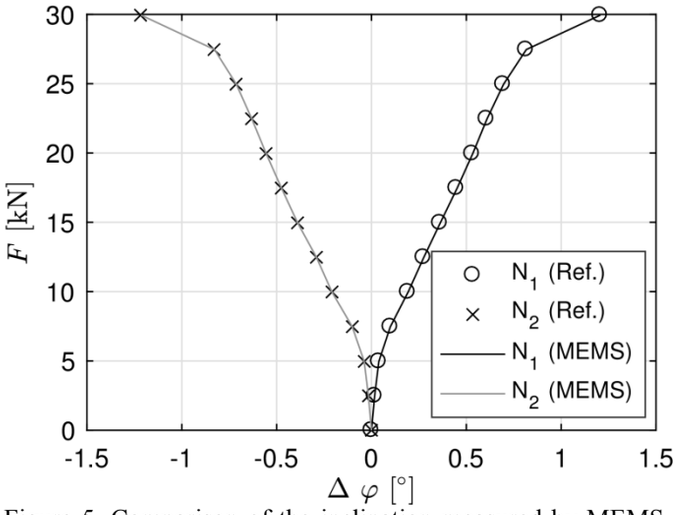


Figure 5. Comparison of the inclination measured by MEMS-inclinometer and reference tilt meter.

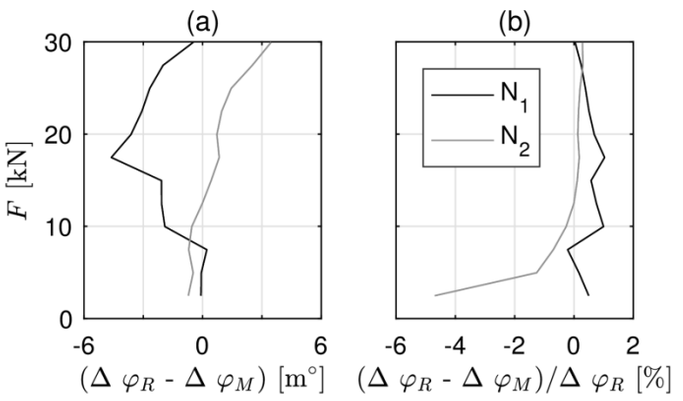


Figure 6. Absolute (a) and relative (b) deviation of the measured inclinations (R – Reference; M – MEMS).

During the test, there was a constant temperature and no significant warming of the sensors has been observed. Therefore, temperature effects as well as drift have not been studied here.

By means of a numerical model the inclinations at the supports have been calculated assuming homogeneous material properties leading to identical rotations at the support regarding their magnitude. However, small differences between the two measured rotations have been observed in the test. The nonlinear numerical model therefore comprises small uncertainty.

Applying the relation between the load-induced rotation at the support and the midspan deflection, which was obtain from the numerical simulation, the deformation u at midspan based on the recorded inclinations of the MEMS-sensor were determined. The comparison of the numerically obtained deflections and the measured deflections is shown for the different load level in Figure 7. It should be noted that the determination process includes model inaccuracies mentioned above such that the deviations cannot solely be attributed to the inclination measurement. The absolute deviation of the determined deflections tend to increase on the higher load levels, however, up the 15 kN, which signifies the serviceability limit state (SLS) of the tested beam, the deviations are within 0,25 mm.

In the flexural test, where inclinations up to 1.2° where applied to the specimen, good agreement between the measurements of the MEMS-based inclinometer and a high quality reference sensor was achieved. The observed difference was in the order of 2m° on average. The test showed the general applicability of the MEMS-devices for inclination sensing whilst containing measurement uncertainty.

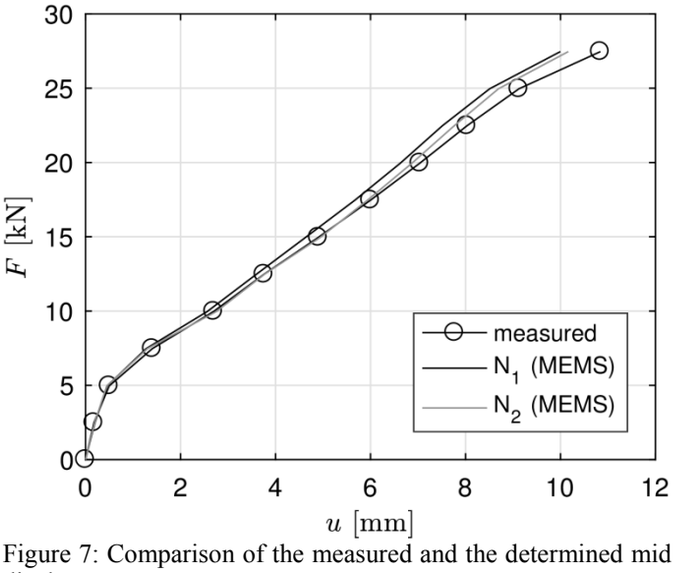


Figure 7: Comparison of the measured and the determined mid displacements.

4 LONG-TERM MEASUREMENTS

In order to observe the long-term stability of the novel MEMS-based accelerometer, several tests have been conducted using uncased and encased sensors under different environmental conditions. All the tests have in common that no rotation was applied to the sensor itself.

4.1 *Measurement with uncased MEMS-sensor*

In a first test the sensors have been mounted to a steel plate, which was rigidly connected to a massive steel platform resting on an individual block foundation. In the laboratory, a relative constant temperature was maintained. The sensor was configured for a range of ±1,7° to allow for high accuracy. The inclination in one axis and the temperature at the sensing element was recorded over the course of 80 days by an uncased sensor. In Figure 8 the time histories of the temperature and the measured inclination are shown. There is a clear similarity between the temperature and the measured inclination. As the temperature decreases the inclination decreases. Also the smaller temperature rises and descents appear correspondingly in the measured rotations. It is therefore assumed that the measured change in inclination, which is physically not present, is mainly introduced by temperature. The effect was then compensated assuming a linear temperature dependency leading to the time history of temperature compensated inclinations in Figure 9. Therein, the maximum deviation to the presumed non-rotating state lies below ±5m° over the course of 80 days.

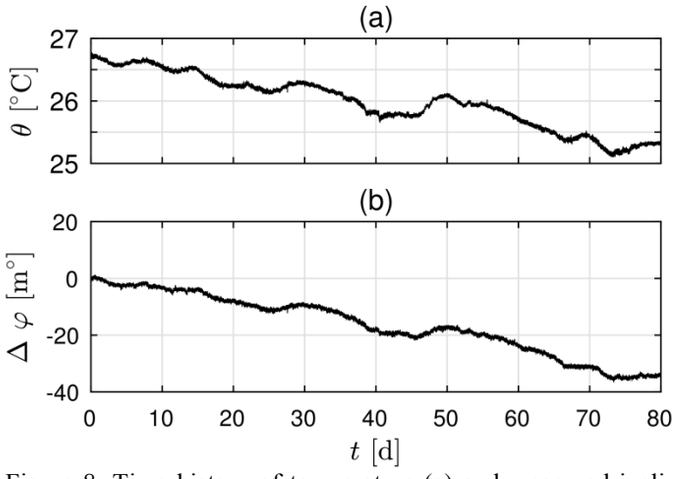


Figure 8: Time history of temperature (a) and measured inclination without compensation (b) until day 80.

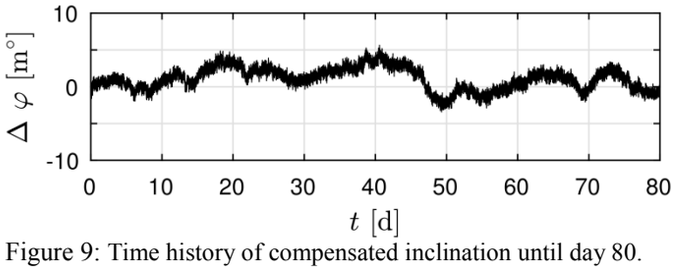


Figure 9: Time history of compensated inclination until day 80.

The relation of the sensor's output signal to the temperature is shown in Figure 10. Thereby, the start of the measurement is colored in black and the end is represented in grey. For a perfectly linearly temperature dependent, drift-free sensor there should be a clear linear relationship. However, at around 25.7°C and 26.2°C small level changes can be observed, yielding 3 different zones with different individual slopes. Here arises the question where these smaller jumps originate from. In Figure 8 (a) it can be seen that for these temperatures at day 26 and 46 temperature rises occurred.

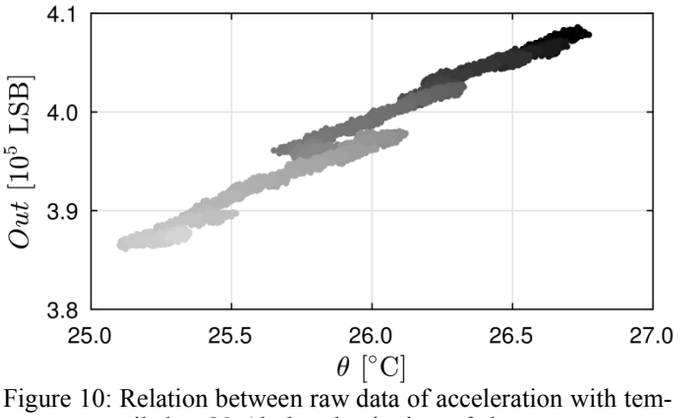


Figure 10: Relation between raw data of acceleration with temperature until day 80 (dark – beginning of the measurement; light – end of measurement)

After the period of 80 days the sensor broke and had to be replaced. The time history of the temperature and the recorded inclinations measured by the replacement sensor, starting at day 91, is provided in Figure 11. Again, a clear dependency between measured inclination and the temperature curve can be observed over the period of 208 days. This also applies to the second part of the measurement where greater variations in the temperature were present. A linear compensation of the temperature has been applied to the inclinations. By that, maximum deviations of 7m° were determined. Looking at the relation of the signal output to the temperature, two effects can be seen. At the beginning of the measurement (black area) there is some kind of warming-up stage of the sensor, where the initial slope is different from the overall slope during the measurement. At a later stage, a downward shift of the sensor's output signal can be observed. As the slope remains the same, this could be attributed to a change in the Bias K_0. However, at this stage it cannot be determined whether that observed signal shifts can be solely related to sensor drift. The temperature compensation by higher order approaches does not seem to be suited, as a short-termed shift appears yielding ambiguous results.

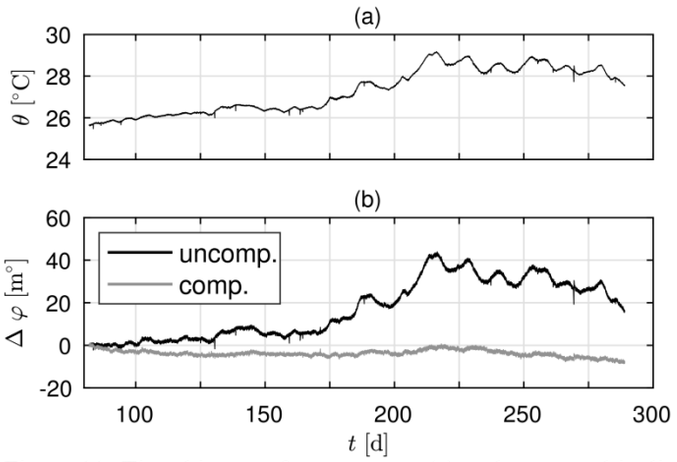


Figure 11: Time history of temperature (a) and measured inclination compensated and uncompensated (b): day 91 - 288

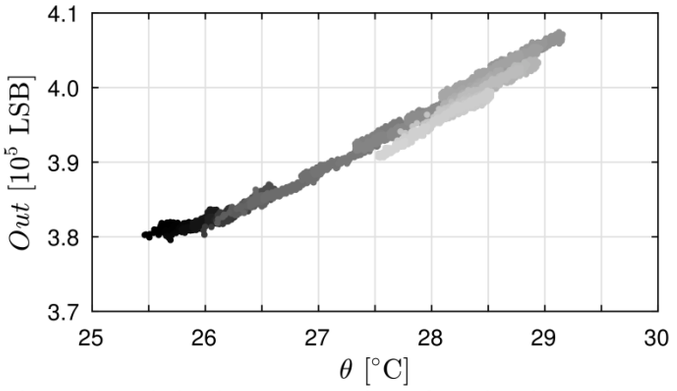


Figure 12: Relation between raw data of acceleration with temperature: day 91 – 288 (dark – beginning of the measurement; light – end of measurement)

4.2 *Measurements with encased MEMS-sensor*

Prior to an installation at a tower-like structure two encased MEMS-based accelerometer have been tested for long-term stability in a controlled environment. Two inclination sensors were housed with a casing whose material possesses a low thermal expansion coefficient. Both sensors measure rotations and temperature at the sensing element. The test was conducted in a lab with constant temperature of 20°C. It is again assumed, that no physical rotation of the sensors, mounted to a heavy steel angle, is applied or induced. Both sensors measure the rotation in different, orthogonal axes. The recorded time histories of the temperature and the inclination over the measurement period of 37 days are depicted in Figure 13. While the inclinations increase continuously, the temperature is increasing throughout except the period between day 25 and 30.

From a temperature calibration of the manufacturer the thermal effect on the Scale-Factor and Bias on the encased sensors was available. In Figure 3 the temperature-induced change of inclination of both encased sensors is shown in relation to an initially horizontally aligned sensor at 25°C. It should be noted, that the effect changes as the sensor is displaced from its initial position due to the trigonometric function in Equation (1). The inclinations before and after temperature compensation are compared in Figure 14.

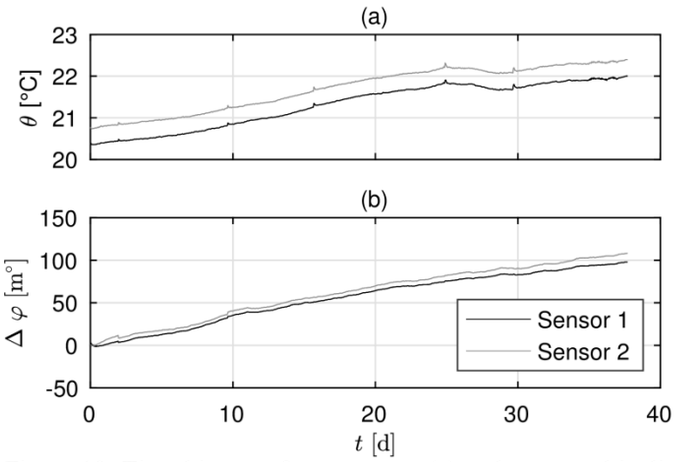


Figure 13: Time history of temperature (a) and measured inclination (b) of two encased MEMS-sensors.

It becomes clear that the temperature has a small effect on the measured deviation from the non-rotated state. In case of the examined, encased sensors temperature has a minor effect. After compensation the inclination of sensor 1 is reduced by 20% of the initial deviation and for sensor 2 it has increased. Since the sensors were mounted to a rigid body, the remaining deviations must be attributed to sensor drift. From HTOL-test (see Section 2.5) the drift was assumed to be linear. Here, linear drift compensation may be applied, but to some extend a flattening can be seen. Therefore a better approximation may be done by root functions.

For determination the long-term stability and quantity of the drift of a MEMS-based sensor in future tests, it is proposed that the sensor is tested under different temperature conditions. These tests should incorporate slow temperature changes including warmer as well as colder phases compared to a reference temperature. If also faster temperature changes are expected for the service life, they have to be imposed also during initial testing.

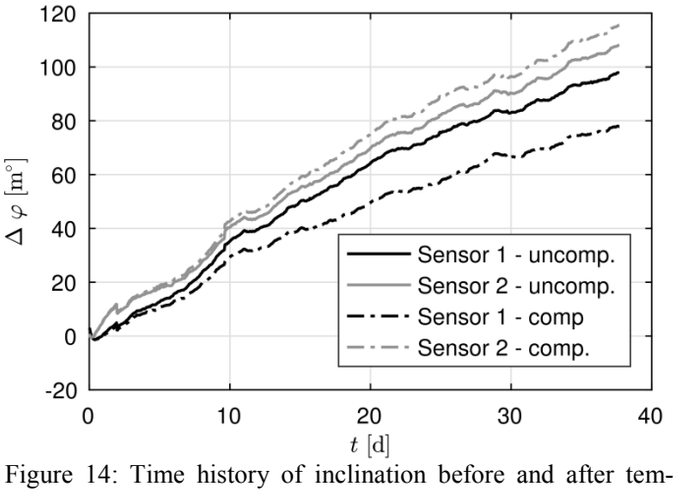


Figure 14: Time history of inclination before and after temperature compensation.

5 MEASUREMENT AT TOWER-LIKE STRUCTURE

The encased MEMS-based accelerometers were installed at a tower-like structure to measure the inclinations under real environmental conditions. Also a reference system based on high quality inclinometers with a range of ±3° and an accuracy of 0.3m° was installed. The inclinations in orthogonal horizontal directions of the structure N_1, N_2 and the temperature were recorded (see Figure 15). The temperature variation can be clearly seen. However, if considering the inclination of the reference sensor, it is also evident, that a drift effect is overlaid in the measured inclinations of the MEMS-inclinometer. The drift seems to be a linear up to day 75, after which the temperature decreases and the growth of the deviation is reduced. The question arises whether the drift reduces after a certain period or the reduction is due to the lower temperature level.

Since the drift was observed to decrease over time an exponential function $f(t)$ was fitted to the raw measurement data as indicated in Figure 16.

$$f(t) = a * e^{-b/t} \qquad a, b > 0 \tag{4}$$

Comparing the measured inclinations of the reference sensor in Figure 15 (b) and the compensated time history of the MEMS-inclinometer in Figure 16, it can be seen that the two curves are still different. The inclinations determined from the MEMS sensors, still contain temperature variations of ±10m° which do not appear in the reference time history. However, the diverging behavior in between the two axis N_1 and N_2 can be observed in both curves. The difference has approximately the same magnitude.

It can be concluded that due to the drift and the fact, that there is no precise information about the drift and how to compensate, the investigated MEMS accelerometer are not yet applicable for long-term monitoring at long-span bridges until now.

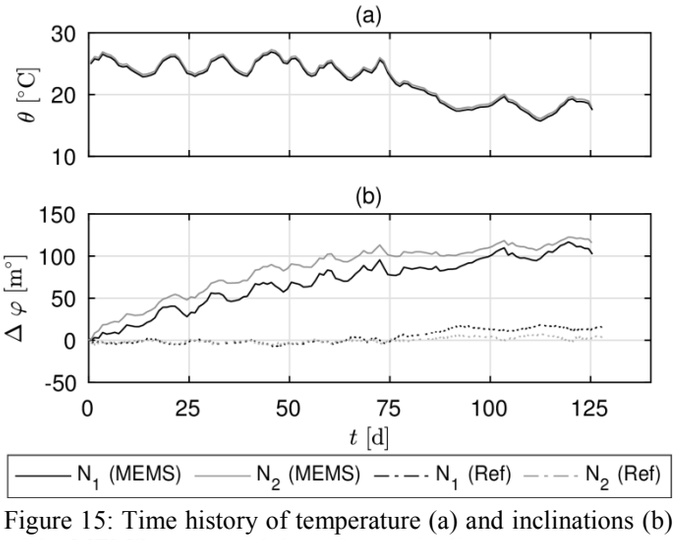


Figure 15: Time history of temperature (a) and inclinations (b) of the MEMS-sensor and the reference inclinometer.

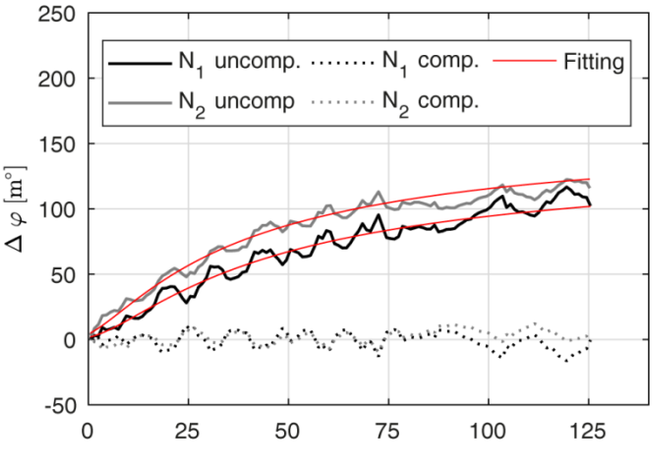


Figure 16. Time histories of the inclinations before and after compensation and indication of the fitting.

More research about the sensor drift needs to be carried out in order to answer the question, what the driving factors for sensor drift are and how an appropriate compensation can be conducted to obtain reliable results. However, in Section 3 it was demonstrated that during short-term measurements the accuracy was less than 5m° throughout all load stages during the bending test, where inclinations up to 1.3° were imposed to a beam. The application for short-term measurements seems therefore possible.

6 POSSIBLE APPLICATION

During the construction of cable-stayed bridges the measurement of stay-cable forces and deflections of the bridge girder are important to ensure bridge girder alignment and desired stress distribution in all bridge components. Right after new deck segments are lifted and before new stay cables are installed, large displacements at the tip of the cantilevered deck occur. Tacheometric survey is used to determine the displacements of the deck.

The inclination is the derivative of the displacement. As large deflections at the cantilever occur also significant inclinations are present during deck construction. Here, the question arises whether the MEMS-based sensors can be utilized in short-term measurements to determine deflections.

Bridge deflections can be evaluated based on polynomial functions, where local inclination measurements are used to define the slope of deflection curves at discrete locations. This method has been studied by Burdet 2000, Xingman 2005 and Zhang 2016. Besides inclinometer Sousa 2013 also applied strain gauges in the estimation process.

The applicability of the MEMS-based accelerometer shall be exemplarily shown for the Stonecutters Bridge, which is located in Hongkong and has a total length of 1596 m with a main span of 1018 m. The cable-stayed bridge was built with balanced cantilever method. At the stage when the longest cantilever (506.4 m) was constructed, the deck experienced

large deflections (Morgenthal 2010). The tip of the cantilever was displaced by more than 3 m yielding rotations of more than 2° (2,000m°). The numerically determined deflected shape and the corresponding inclinations are given in Figure 17.

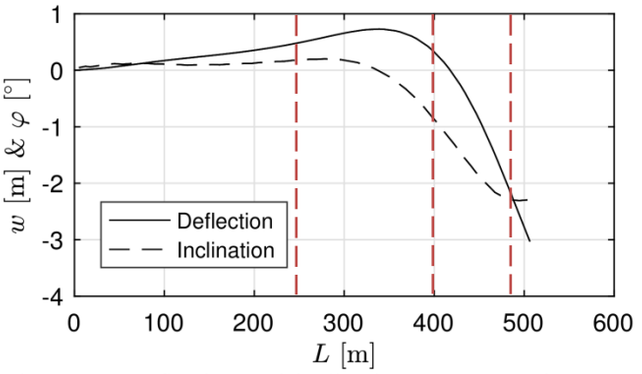


Figure 17. Deflection and inclination at construction stage of Stonecutters Bridge (Morgenthal 2010).

Three possible inclinometer positions are indicated with dashed lines in Figure 17. Being aware of the uncertainty that is related with the MEMS-based inclinometer, the estimation process will result uncertainty in the deflected shape, which can be visualized by envelopes. Since the MEMS-based inclinometers are low-cost compared to standard piezoelectric sensors, also the usage of multiple sensor shall be explored in the context of reduction of the uncertainty in the estimated deflections. Considering the increasing quality of the MEMS-based it is believed that MEMS-inclinometer can be used for bridge monitoring purposes in the near future when significant rotations are present.

7 CONCLUSIONS

The paper presented investigations on the temperature dependency and the drift on novel MEMS-based accelerometer utilized for inclination sensing. Different sensor behavior was observed. Firstly, there are great variations among the individual sensors in terms of temperature dependency as well as sensor drift. Secondly, in a long-term laboratory test, where small and slow temperature variations were observed, the temperature effect seemed to have a significant influence on the raw inclinations. Applied to a tower-like structure, where larger and faster temperature changes were present, the sensor drift had a dominant influence. The questions arising from the data evaluation have been presented in this paper. The imperfection of the miniaturized sensors was shown. The measurement of inclinations with MEMS-based sensors incorporates uncertainties. A flexural test of a beam showed up to 5m° deviations from reference measurements, when inclinations up to 1.2° where applied. One possible application during erection of cable-stayed bridges for short-term measurement to evaluate the deflected shape has been presented.

8 REFERENCES

Morgenthal G., Sham, R. & West, B. 2010. Engineering the Mainspan Construction of Stonecutters Bridge, *ASCE Journal of Bridge Engineering* 15: 144-152.

Xingmin, H., Xueshan, Y. & Qiao, H. 2005. Using Inclinometers to measure bridge deflection. *ASCE Journal of Bridge Engineering* (10): 564-569.

Rau, S. & Morgenthal, G. 2017. An assessment framework for sensor-based detection of critical structural conditions with consideration of load uncertainty. *Structures* (12): 168-178.

Morgenthal, G., Rau, S., Taraben, J., & Abbas, T. 2017. Determination of stay-cable forces using highly mobile vibration measurement devices. *ASCE Journal of Bridge Engineering* (in print).

Wedel, F., Käding, M. & Marx, S. 2017. Belastungsversuche an den Talbrücken der Eisenbahnneubaustrecke Erfurt-Leipzig. In Baessler, M., Rogge, G. & Schiefelbein, N., *Proc. Messen im Bauwesen 2017*, BAM, Berlin, 21-37, ISBN: 978-3-9818270-8-8

Burdet, O. & Zanella, J.-L. 2000. Automatic Monitoring of Bridges using Electronic Inclinometers. *Proc. 16th IABSE congress, Lucerne*. 1574-1581(8)

First Sensor AG 2016. Preliminary Data Sheet of Sensors based on the S-Series "SX-XX.S1.C-XX". Highly Precise Inclinometers and Accelerometer for Inertial Sensor Applications. Version 09/2016

Sousa, H. & Henriques A. A. 2013. Bridge deflection evaluation using strain and rotation measurements. *Smart structures and systems* (11): 365-386

Zhang, W.; Sun, L. M. & Sun, S. W. 2016. Bridge-Deflection Estimation through Inclinometer Data Considering Structural Damages. *Journal of Bridge Engineering*. 22(2): 04016117

Maintenance, Safety, Risk, Management and Life-Cycle Performance of Bridges – Powers, Frangopol, Al-Mahaidi & Caprani (Eds)
© 2018 Taylor & Francis Group, London, ISBN 978-1-138-73045-8

Fine temperature effect analysis based time-varying dynamic properties evaluation of long-span suspension bridges in natural environments

J.S. Zhu
Key Laboratory of Coast Civil Structure Safety of Ministry of Education, Tianjin University, Tianjin, P.R. China

Q.L. Meng
School of Civil Engineering, Tianjin University, Tianjin, P.R. China

ABSTRACT: The dynamic properties of long-span suspension bridges were studied based on fine temperature effect analysis and thermal-eigenvalue problem. The heat transfer between structure and surrounding air was related to wind speed, atmospheric environment and thermal properties of ground surface. Temperature variations in cables and uneven heat transfer coefficients on the pylon were obtained with multi-scale modeling and CFD (Computational Fluid Dynamics) method, respectively. Then, based on the fine temperature distribution, the effect of temperature variations, temperature gradient and material properties on the structural dynamic properties were comparatively analyzed in different seasons. Consistent with other researches, an overall decrease in modal frequency was observed with the increase in temperature. Bur for long-span suspension bridges, the dynamic properties were mainly caused by the thermal stress and the corresponding deformations. The novelty of this work lies in the accurate description of the thermal gradient field, as well as the refined mechanical representation of time-varying thermo-dynamic properties for suspended-cable structures.

1 INTRODUCTION

During the service life of bridge structures, the local damage, as well as seismic behavior can be reflected by the changes in dynamic properties. Therefore, a successful condition assessment relies heavily on prediction accuracy of vibration properties. However, structural natural frequencies are sensitive to the complicated and changeable environments, such as temperature and humidity (Xia et al. 2006). Recently, more and more researches have focused on the effect of temperature gradient on the vibration properties of bridges (Zhou et al. 2014). If temperature-induced variations are not fully understood, structural identification may be determined with deviations and the proper maintenances will be missed.

However, most researches were based on relatively simplified numerical model and hypothetical temperature distribution. Although the fine numerical model and real temperature gradient were taken into account in some researches, only simply girder bridges were mainly focused on (Xia et al. 2011, Nandan et al. 2014, Carboni et al. 2012). Actually, with high flexibility and geometric nonlinearity, the local vibration induced by external excitations is highly obvious for long-span suspension bridges. Unfortunately, the effect of ambient factors on the dynamic properties of long-span suspension bridges is not very clear. Also, suspension bridges were usually simplified as a 3-D beam-shell element model (Wang et al. 2010) and the thermal boundaries were applied in a relatively simple way (Westgate et al. 2014) in some researches. So the temperature gradient and corresponding thermo-dynamic properties have not been studied finely for long-span suspension bridges.

2 THE THERMO-ELASTO-DYNAMIC PROBLEM

2.1 *Fine prediction of temperature distribution for suspension bridges under solar radiations*

2.1.1 *The simulation technique*

The fine simulation technology for predicting temperature distribution in the bridge proposed by Zhu (Zhu et al. 2017) was applied, including fine modeling, thermal loads package and 3-D sheltering algorithm. Based on the technology, some components were equivalent mechanically and the fine model of the suspended bridge was established. 3-D sunshine sheltering status on every surface was updated by calculating the transient solar elevation angle and hour angle in every time increment.

2.1.2 *Multi-scale modeling and temperature-varying in cables*

Many gaps among the internal steel strands exist in main and hanger cables. The air in these gaps, hav-

ing low thermal conductivity, decreases the heat transfer rate in cables. In order to obtain the equivalent thermo-physical parameters by an extensible way, temperature fields in two scale models of cable, containing the steel strand fine model and the steel strand equivalent model, were firstly analyzed. Then seasonal temperature variations in some characteristic cross sections of cables were calculated using the equivalent thermo-physical parameters. Finally, through four temperature points in characteristic cross sections, the spatial temperature-varying in the cables (cable model) was interpolated. Figure 1 describes the multi-scale modeling for cables.

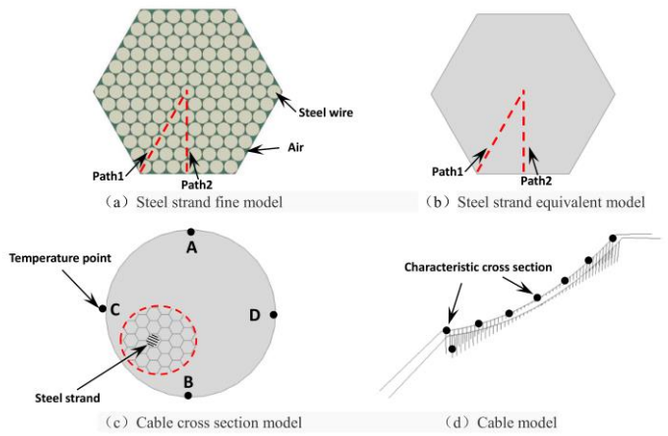


Figure 1. Multi-scale modeling of cables

2.1.3 *Surface transfer coefficient obtained with CFD method*

By establishing 2-D numerical model, which consisted of representative cross sections of python and surrounding air, the conservation equations of mass, momentum, and energy were solved.

2.2 *The thermo-dynamic properties of suspension bridges: finite element method*

Modal properties were provided by solution of the following eigenvalue problem:

$$(K-\omega^2 M)\phi = 0 \tag{1}$$

where M = the global mass matrix; K = stiffness matrix; ω is natural frequency vectors.

2.3 *The decomposition of stiffness matrix K*

Owing to the temperature effect, stiffness matrix K was decomposed into five parts: K_{ini}, the initial stiffness matrix without considering the temperature effect; the: dK_E^T matrix, corresponding to temperature dependence of elastic constants; dK_S^T matrix, which was induced by thermal stress, reflected by the so-called stress stiffening effect; dK_ε^T matrix, indicating the geometric nonlinearity effect and the temperature-induced deformation of bridges; dK_M^T matrix, caused by rigid motion of local materials, especially for cables. So the eigenvalue equation was rewritten:

$$[(K_{ini}+dK_E^T+dK_S^T+dK_\varepsilon^T+dK_M^T)-\omega^2 M]\phi = 0 \tag{2}$$

3 APPLICATION EXAMPLE

3.1 *The suspension bridge*

A suspension bridge (in Zhangjiakou, China) with 720m-length steel-concrete composite girder (see Fig. 4) is located at 109.6º E and 23.6º N, with an azimuth of 40.657º. The 33.6m-width girder is composed of transverse I-shaped steel beams, on which 20cm-thickness concrete slab and 3cm-thickness asphalt pavement are placed. The main cables, with 1/9.5 rise-to-span ratio and 18% internal porosity, contain 91 high strength steel wire strands. Each strand is also composed of 1275 25mm-diameter high strength steel wires. The 107.8m-height pylon was cast into gate-shaped frame.

3.2 *Numerical model*

Based on the mechanical equivalence for steel girder and cables, fine numerical model of the suspension bridge was established (see Fig. 2). The fine modeling not only involved the global features of bridges, such as the azimuth and location, but also contained the local configurations of components including the normal vectors of all surfaces, inclined angles of the outer surfaces, and the sheltering relationships.

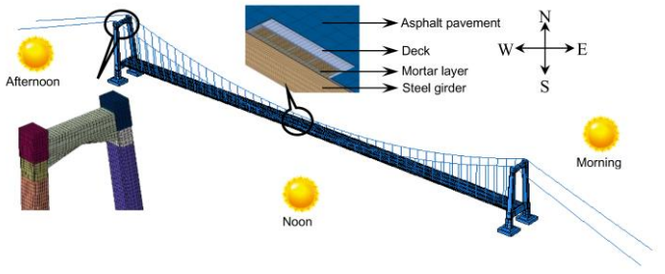


Figure 2. Finite-element model of example suspension bridge

3.3 *Climatic and boundary*

Thermal loads on bridge surfaces were classified into short-wave and long-wave radiations (Zhu et al. 2017), such as direct radiation, diffuse radiation, reflected radiation, atmospheric counter radiation, water radiation and surface radiation. Different from thermal loads, thermal boundaries were treated as the heat convection between surfaces and ambient air (Kehlbeck, in press).

To consider the seasonal effect, four representative days were investigated: the spring equinox, the summer solstice, the autumnal equinox, and the winter solstice (see Table 1).

Table 1. Climate at the bridge site.

Season(Date)	MaxT (℃)	MinT (℃)
Spring(15th April)	19	5
Summer(15thJuly)	30	19
Autumn(15thSeptember)	17	4
Winter(15thJanuary)	-1	-12

* MaxT represents the maximum temperature; MinT represents the minimum temperature

4 APPLICATION RESULTS

4.1 *Fine temperature distribution of suspension bridge*

4.1.1 *Temperature variations in the cables*

Based on a range of thermo-physical parameters, 2-D thermal transfer analysis was conducted in steel strand fine model and the steel strand equivalent model. Then, the equivalent thermo-physical parameters were determined by fitting temperature variations along two paths (see Fig. 1) between both models. The equivalent thermal conductivity and specific heat capacity along the path 1 were 26.2 W/(m℃) and 509.8J/(Kg℃) respectively, close to equivalent parameters 26 W/(℃) and 507.7J/(Kg℃) along path 2, so the finally parameters were selected as mean values of the two paths. Compared with the 50.7 W/(m℃) (Westgate et al. 2014) and 38 W/(m℃) (Fan et al. 2017) from previous test, the equivalent thermal conductivity was lower, which were within the reasonable range.

The temperature variations in cable cross section at different time are plotted in Figure 3(a)-(d). The simulated temperature variations were verified by the measurement temperature on a truncated main cable from Xihoumen Bridge [see Fig. 3(e)] (Yu et al. 2010). The point B was close to the ground during the measurement in which the ground radiation was not clear, so that the temperature variation at point B was different from the measured value during 10~25h. Apart from the difference above, the simulation temperature variations showed reasonable consistency with the field-measured data.

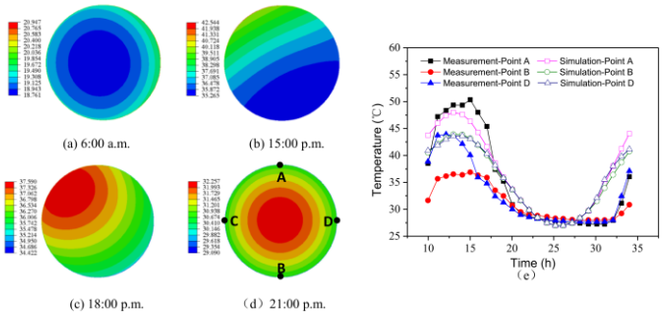


Figure 3. (a)-(d) Temperature distributions in cross section of mid-span main cable at different time (unit: ℃); (e) Contrasts between the simulated temperature and that from Xihoumen bridge

4.1.2 *Non-uniform heat transfer coefficients on the pylon*

As the application of convection heat transfer coefficients, we averaged the coefficients along the surface with the same normal direction, which were classified as east, south, west and north directions. The uneven heat transfer coefficients were quantized on the surface of pylon based on the environmental factors (see Fig. 4).

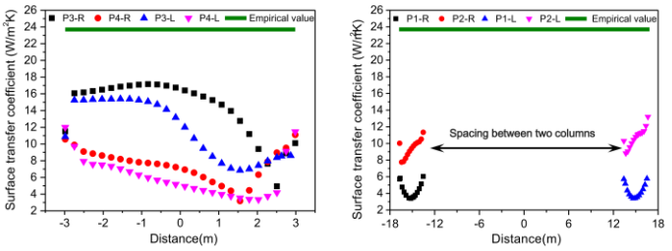


Figure 4. The surface heat transfer coefficients at section (at the height of 10.78m) in winter

4.1.3 *Non-uniform temperature distribution due to the sheltering effect*

Due to the mutual-sheltering, temperature on asphalt deck and pylon locally decreased about 15℃ and 10℃ respectively. The temperature distributions at 10:00 a.m. and 12:10 p.m. in the summer were shown in Figure 5. With the self-sheltering, temperature difference between the sunny and shady face of pylon gradually increased to 7℃ from 6:00 to 18:00. The cap of pylon was buried in soil without any solar radiations (in permanent sheltering).

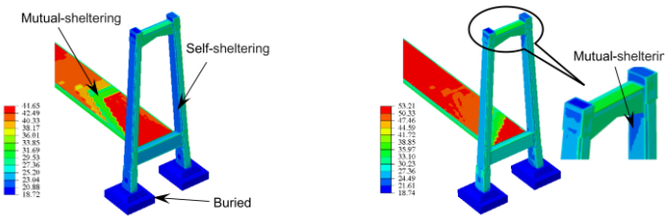


Figure 5. Temperature distributions of the stiffening girder and the main tower at different time in July 15th (unit: ℃)

4.2 *Thermo-dynamic properties of suspension bridge*

4.2.1 *The influence of temperature variations*

In this section, the temperature dependence of concrete elastic modulus was defined as Equation 3 (Xia et al. 2011). Furthermore, the varying elastic modulus for steel, asphalt and cables were listed in Table 2. For all building materials, the elastic modulus almost decreased with the rise of temperature.

$$E(T) = E_{20°C}(1.09 - 0.0045T) \quad (3)$$

where T = temperature of the material; $E_{20°C}$ = Young's modulus of concrete at the temperature 20 ℃.

Table 2. Temperature-dependent elastic modulus of building materials

Temper-ature(℃)	Elastic modulus(MPa)		
	Steel	Asphalt	Cables
-10	-	25000	-
15	206000	16250	164800
20	-	6000	-
38	-	2000	-
100	180250	0	144200

Since the maximum daily temperature difference in four seasons was almost equal, the winter and summer solstice were selected to study the mechanism of thermo-dynamic properties of bridges in extreme temperature situation. Figure 6 shows the daily variations of natural frequencies corresponding to the first four order of bending vibration modes, V1-V4 represent 1-4th vertical bending modes.

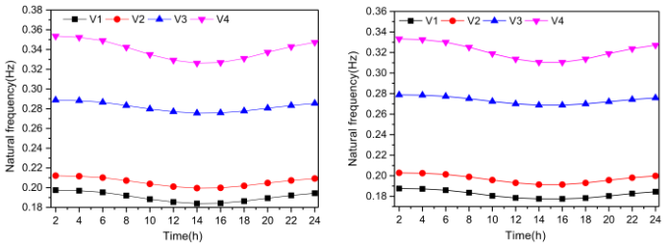
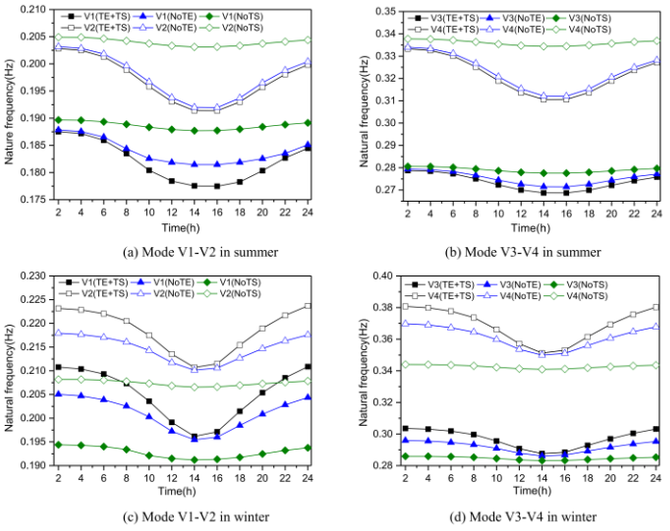


Figure 6. Daily variations of natural frequencies

Whatever seasons and vibration modes, the nature frequencies trended to decrease during 2-14h and increase during 14-24h. Since air temperature reached the maximum value at 14h, it was easier deduced that the modal frequencies decreased with the increase in temperature.

4.2.2 *The influence of material properties*

In order to study the temperature-dependence of materials, three circumstances were considered: (1) All temperature-dependent materials were included; (2) The temperature-dependence of elastic modulus of all materials were removed; (3)The expansion coefficient of all materials were set to 0, which meant no thermal stress induced by solar radiations. The daily variations of natural frequencies of the first four order bending vibration modes under three circumstances is plotted in Figure 7, TE and TS represent case1 and case 2 respectively.



(a) Mode V1-V2 in summer (b) Mode V3-V4 in summer

(c) Mode V1-V2 in winter (d) Mode V3-V4 in winter

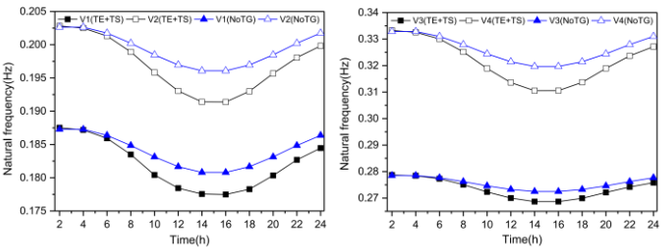
Figure 7. Daily variations of natural frequencies

For all vibration modes as shown, the daily variations of natural frequencies draw back slightly (-1.35% for V1; 0.24% for V1; -0.75% for V1; 0.132% for V1) if elastic modulus remained constant. Smaller elastic modulus of materials corresponded to lower structural natural frequencies. However, the frequencies nearly unchanged when thermal stress was not considered, indicating that the thermo-elasto-dynamic problem was mainly governed by the stress stiffening and geometric nonlinearity effect for long span suspension bridges.

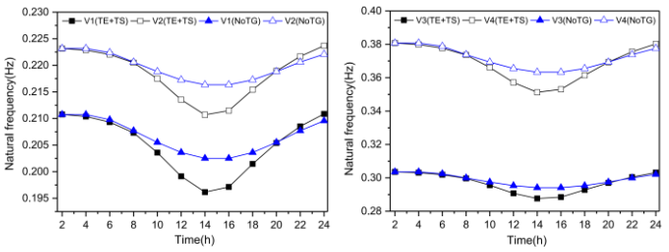
4.2.3 *The influence of temperature gradient*

The thermal loads and convection boundaries on the bridge surfaces were removed to eliminate internal temperature gradients. Air temperature was applied to the whole suspension bridge, in which the reference temperature of expansion coefficient was based on the design (15℃). The daily variations of natural frequencies without temperature gradient (TG) are plotted in Figure 8, only V1-V4 vibration modes were contained.

The influence of temperature gradients in the suspension bridge was obvious, although there were considerable decrease in natural frequencies. The reason that more contributions in winter might be relate to the higher stiffness of concrete and asphalt.



(a) Mode V1-V2 in summer (b) Mode V3-V4 in summer



(c) Mode V1-V2 in winter (d) Mode V3-V4 in winter

Figure 8. Daily variations of natural frequencies

5 DISCUSSION

The dynamic properties of bridges are affected by both local structural configuration and elastic constants of the materials. But unlike simple girder bridges mentioned in previous researches, the thermo-elasto-dynamic problem of suspension bridges are mainly governed through the stress stiffening and geometric nonlinearity effect. This means minimizing the temperature-induced deformation of suspension bridge can effectively control the meaningless variations in the structural modal parameters.

6 CONCLUSION

In the present study, a simulation technology is proposed to predict fine temperature distribution on suspension bridges. Temperature variations in cables and no-uniform surface transfer coefficient on the pylon were obtained with multi-scale modeling and thermal-fluid simulation method, respectively. On the basis of that, the time-varying thermo-dynamic properties were comparatively analyzed. Some conclusions were drawn from the technology application:

(1) With multi-scale modeling, the equivalent thermo-physical parameters of cables could be obtained (For cables in this paper, thermal conductivity=26.1W/(m℃) and specific heat capacity=508.7 J/(Kg℃)).

(2) Due to inverse air flow, the surface transfer coefficients were seriously uneven on the surface of pylon. Therefore, a great deviation would be produced if the heat transfer coefficient was considered uniform on the pylon surface.

(3) With the sheltering effect, temperature on the asphalt pavement and pylon locally decreased about 15℃ and 10℃ respectively. Temperature difference between the sunny and shady face of pylon gradually increased to 7℃.

(4) Under solar radiations, the modal frequencies of suspension bridge decreased with the increase in temperature, the percent of maximum decrease was 6.9%.The influence of temperature gradients was also obvious (The maximum percent of contribution was 44% in winter).

7 ACKNOWLEDGEMENTS

This research project has been supported by National Science Fund of China (51578370) and the National Science Fund of Tianjin (16JCZDJC40300 and 16YFZCSF00460). These supports are gratefully acknowledged.

8 REFERENCES

Carboni, B. & Lacarbonara, W. 2012. A three-dimensional continuum approach to the thermoelastodynamics of large-scale structures. *Engineering Structures*: 40: 155-167.

Fan, H. & Tian, H. 2017. Model test study of change mechanism of temperature and humidity in main cable of suspension bridge. *Bridge Construction*: 47(2):42-47 [in Chinese].

Kehlbeck, F. 1981. Effect of solar radiation on bridge structure. *Chinese Railway Press Ltd.*

Nandan, H. & Singh, M.P. 2014. Effects of thermal environment on structural frequencies: Part I–A simulation study. *Engineering Structures*: 81: 480-490.

Wang, H. & Li, A. & Li, J. 2010. Progressive finite element model calibration of a long-span suspension bridge based on ambient vibration and static measurements. *Engineering Structures*: 32(9): 2546-2556.

Westgate, R. & Koo, K.Y. & Brownjohn, J. 2015. Effect of solar radiation on suspension bridge performance. *Journal of Bridge Engineering ASCE*: 20(5): 04014077.

Xia, Y. & Hao, H. & Zanardo, G. & Deeks, A. 2006. Long term vibration monitoring of an RC slab: temperature and humidity effect. *Engineering Structures*: 28(3): 441-452.

Xia, Y. & Xu, Y.L. & Wei, Z.L. & Zhu, H.P. & Zhou, X.Q. 2011. Variation of structural vibration characteristics versus non-uniform temperature distribution. *Engineering Structures*: 33(1): 146-153.

Yu, M.D & Shen, R.L. 2010. Research on temperature field of main cable section of Xihoumen bridge. Journal of Architecture Civil Engineering: 27(3):53-58 [in Chinese].

Zhou, G.D. & Yi, T.H. 2014. A summary review of correlations between temperatures and vibration properties of long-span bridges. M*athematical Problems in Engineering:* 2014(1):1-19.

Zhu, J.S. & Meng, Q.L. 2017. Effective and fine analysis for temperature effect of bridges in natural environments. *Journal of Bridge Engineering ASCE*: 22(6): 04017017.

Maintenance, Safety, Risk, Management and Life-Cycle Performance of Bridges – Powers, Frangopol, Al-Mahaidi & Caprani (Eds)
© 2018 Taylor & Francis Group, London, ISBN 978-1-138-73045-8

Inverse analysis using compatible displacements

Jun Lei & Dong Xu
Tongji University, Shanghai, China

Jose Turmo
Universitat Politècnica de Catalunya, Barcelona, Spain

ABSTRACT: To avoid potential life and economic loss, structural health monitoring has become increasingly important for bridge systems. As a key component of structural health monitoring, structural system identification (SSI) tries to identify the structural parameters through the measured response. However, due to the ill-posedness of inverse analysis, the estimation of parameters is greatly affected by measurement errors. To alleviate the adverse effect of errors, the relations among the displacements in beam structures (for instance bridges), compatibility conditions, are derived analytically via a symbolical approach. Then a set of compatible displacements is obtained by an optimization procedure that finds the closest compatible deformation shape to the measured one. The final estimations of the parameters are obtained by providing the compatible displacements to SSI. The proposed method is validated by the numerical simulations on a simply supported bridge and on a continuous bridge.

1 INTRODUCTION

As a powerful tool for condition assessment, Structural System Identification (SSI) has drawn great attention in the past decades. SSI can be summarized as structural parameter estimation using discrete measurements of the structural response.

Based on different criteria, SSI methods are categorized as dynamic or static, parametric and non-parametric, deterministic and probabilistic.

In the parametric methods, the parameters directly represent the physical parameters (e.g. elastic moduli, areas, flexural/torsional inertias), like the ones used in finite element models. Non-parametric methods use basis functions to regress the response of the structure, e.g. autoregressive models (Su et al. 2014; Huang et al. 2009; Mei et al. 2016; Lakshmi et al. 2016) or rational fractional polynomials (Okada et al. 2006).

Concerning probabilistic SSI, mainly the Bayesian approach, posterior distributions of the parameters are obtained by updating the assumed distributions of the parameters with discrete measurements of the response (Beck & Katafygiotis 1998; Zhang et al. 2016; Sun et al. 2015; Beck & Au 2002; Behmanesh & Moaveni 2015). The estimates of the parameters might be obtained by point estimate (e.g. mean, median) or interval estimate (confidence interval) based on the posterior distributions of the parameters. On the contrary, deterministic method tries to pinpoint a unique solution of the problem (Lozano-Galant et al. 2013; Sun et al. 2013; Law & Yong 2011; Marano et al. 2011; Raich & Liszkai 2012; Eskew & Jang 2017; Sevillano et al. 2016; Jeong et al. 2013). In both probabilistic and deterministic methods, optimization technique is closely involved. The objective of the optimization might be minimizing the discrepancy between the measurements and the predicted response, e.g. displacements(Sevillano et al. 2016; Marano et al. 2011), acceleration (Marano et al. 2011), mode shapes and frequencies (Eskew & Jang 2017; Jeong et al. 2013), or maximizing the sensitivity of the frequency response functions (Raich & Liszkai 2012).

Observability method (OM) is a mathematical method dealing with the existence and the uniqueness of the solution of system of equations (or a subset of it) (Castillo et al. 2007). The first application of OM in SSI using static tests is introduced in (Lozano-Galant et al. 2013). In the proposed formulation, a finite element model (FEM) of the structure has to be defined first. Subsequently, the equilibrium equaitons are obatined. A series algebraic operations are applied in the resulting system so that the known and the unknown information will be well separated on different sides of the equations. This known information may include the applied external loads, the meausrements of the structural response (deflections, rotations), the boundary conditions. The unkonwn may include the structural parameters, the unmeasured displacements, the reactions. Hereafter, this system of equations is referred as the observability equations. From the perspective of SSI, the

observablity of structural parameters is related to the question that whether the solution or a subset of it can be uniquely determined with a given measurement set. This can be solved by checking the null space of the coefficient matrix of the observability equations.

2 STRUCTURAL SYSTEM IDENTIFICATION BY OBSERVABILITIY METHOD

2.1 *Equilibrium equations from direct analysis*

First, a FEM for the structure to be analyzed is defined according to the desired accuracy. This is related with the number of parameters and the available measurements. The more parameters assumed, the more measurements required. The equilibrium equations can be given as follows:

$$K \cdot \delta = f \tag{1}$$

$$\begin{pmatrix} K_{00}^{p\times r} & K_{01}^{p\times s} \\ K_{10}^{q\times r} & K_{11}^{q\times s} \end{pmatrix} \begin{Bmatrix} \delta_0^{r\times 1} \\ \delta_1^{s\times 1} \end{Bmatrix} = \begin{Bmatrix} f_0^{p\times 1} \\ f_1^{q\times 1} \end{Bmatrix} \tag{2}$$

In Eq. (1), K, δ and f, respectively, represent the global stiffness matrix, the nodal displacements and the nodal forces. For a 2D model with beam elements, all the entries in the global stiffness matrix K are composed of the characteristics of the beams (i.e. length L, elastic moduli E, area A and inertia I). Displacements δ include horizontal displacements u, vertical deflection v and rotation w whereas the quantities in the concentrated forces f include horizontal forces H, vertical forces V and moments M. Hence, all the quantities involved in the equations are {*E, A, I, L, u, v, w, H, V* and *M*}. From these, some of them are known and some are unknown. The known and the unknown quantities are indicated by the subscripts 1 and 0 in Eq. (2), respectively

In direct analysis, it is assumed that the parameters {*E, A, I* and *L*} for every element are known and thereby the global stiffness matrix is always available for structural analysis. Regarding displacements δ, except for the displacements of the restrained nodes, δ_1,at the boundary, the displacements of the remaining free nodes, δ_0, are unknown. In addition, with respect to the forces f, except for the applied external forces f_1, the reactions f_0 at the boundaries are unknown. In direct analysis, these unknowns, i.e. f_0 and δ_0, will be solved in Eq. (1). In SSI by OM, which is an inverse analysis, the assumption that the length L and the applied static external force f_1 are known still applies. Besides, since a subset of the displacements of the free nodes are measured in real-life, the set of known displacements δ_1 is enlarged. Then elastic moduli, E, areas, A, inertias, I, and the remaining unknown displacements δ_0 are to be determined. It should be noted that one of the main objective of SSI is to assess the condition of the structure. That is, the estimations of axial stiffnesses *EA* and flexural stiffnesses *EI* are of primary importance. In order to reduce unknowns, *EA* and *EI*, instead of being regarded as the product of two unknowns, are regarded as one unknown.

To carry out SSI by OM, Eq. (2) needs to be transformed into an equivalent form, Eq. (3), by several algebraic operations.

$$B \cdot z = \begin{bmatrix} K_{10}^{q\times r} & 0^{q\times p} \\ K_{00}^{p\times r} & -I^{p\times p} \end{bmatrix} \begin{Bmatrix} \delta_0^{r\times 1} \\ f_0^{p\times 1} \end{Bmatrix} = \begin{Bmatrix} f_1^{q\times 1} - K_{11}^{q\times s}\delta_1^{s\times 1} \\ -K_{01}^{p\times s}\delta_1^{s\times 1} \end{Bmatrix} = D \tag{3}$$

These operations include the separation of the columns, wherein some entries are the sum of different variables, into several single columns related with different variables, the elimination of duplicated variables, the merge of associated columns, extracting the measured displacement from original δ and place them into the associated columns (Lozano-Galant et al. 2013). In the resultant system of equations, regarding the physical meaning of the unknowns, these unknowns are of two types: (1) those unknowns containing the information of displacements, *u, v* or *w*, or stiffnesses, *EA* or *EI*, or the products of both, (*EAu, EAv, EAw, EIu, EIv* or *EIw*); or (2) the unknown reactions at the boundaries, *H, V* and *M*. In the coefficient matrix, only the known quantities, i.e. the measured displacements (might be *u, v* or *w*) and the length of the elements, *L*, remain. Meanwhile, the entries of the vector on the right side of the equation, D, are the result of the external loads f_1 and the equivalent nodal forces, might be $K_{11}\delta_1$ or $K_{01}\delta_1$. The transformation from Eq. (2) to Eq. (3) collects all unknowns in z and renders both B and D known.

However, due to the existence of errors, Eq. (3) does not necessarily have an exact solution. This is to say, system of equations presented in Eq. (3) is not always compatible. In fact, to yield a solution of Eq. (3), D must satisfy some conditions. That is, the null space N of matrix B has to satisfy that $N \cdot D = 0$. If this holds, Eq. (3) is compatible; otherwise, no solution exists (Castillo et al. 2007).

The structure of the general solution (the set of all solutions), z_g, of Eq. (3) is presented in Eq. (4).

$$z_g = z_p + \boldsymbol{N} \cdot \rho = \begin{Bmatrix} \delta_0^* \\ f_0 \end{Bmatrix}_p + \boldsymbol{N} \cdot \rho \tag{4}$$

The general solution z_g is the sum of a particular solution z_p, and the product of a vector of arbitrary values, ρ, and the null space of the coefficient matrix B in Eq. (3), N. The particular solution z_p can be obtained by dividing the vector D by the coefficient

matrix B. This operation can be achieved in many commercial packages, like Matlab (The MathWorks 2015) and Mathematica (Wolfram 1999). $N{\cdot}\rho$ is the set of all solutions of the associated homogeneous system of equations (a linear space of solutions, wherein the columns of N are vectorial bases, and the entries of the vector ρ are arbitrary values functioning as the coefficients of all possible linear combinations). If any row of the null space N is composed of only zeros, then the scalar in the same row of the product of $N{\cdot}\rho$ will also be zero, and thereby the particular solution specifies the unique solution of this unknown. Namely, any unknown associated with a null row in the null space N is observable, i.e. it exists and it is determined and unique. One special case is that the null space $\mathcal{1}$ of coefficient matrix B does not exist. This means that all the unknowns are observable.

3 COMPATIBILITY CONDITION

In order to demonstrate the idea of compatibility condition, consider the simply supported beam in Figure 1.

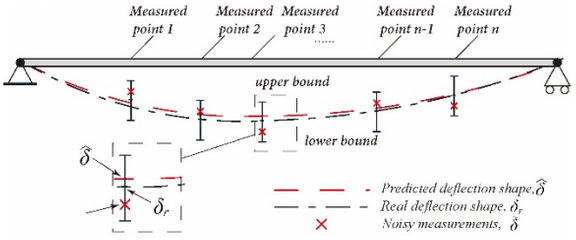


Figure 1. Compatibility condition

The true deflection shape, $\boldsymbol{\delta_r}$, of the structure is indicated by the red dot-dashed line. Due to the physical law, the true displacements should following some compatibility conditions.

However, measurement errors are inevitable in real-life. Assuming that the measurement error follows the normal distribution, the measured displacements $\tilde{\delta}$ can be given as:

$$\tilde{\delta} = (1 + E_{level} \cdot \xi) \cdot \delta_r \tag{5}$$

where E_{level} is the error level in percentage and ξ is a random number following the normal distribution with zero mean and standard deviation of 0.5.

Due to the existence of measurement errors, the measured displacements (indicated by the crossed circle) do not lie on the true deflection shape. Hence, violation of the physical law that the true deformation should satisfy, which is referred as the incompatibility, arises. To smooth away the incompatibility in the measurements, the compatibility conditions among the displacements are derived by the SSI by OM in this section.

3.1 *Derivation of the compatibility condition*

The example of an 18-m simply supported beam is used to show the derivation of the compatibility condition and the associated FEM is given in Figure 2. This FEM has 18 beam elements and the length of each element is 1m. These elements are numbered as 1 to 18 from left to right.

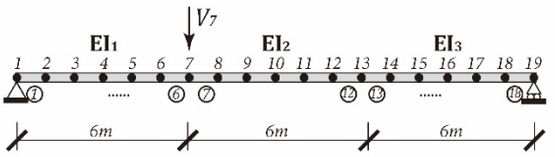


Figure 2. The finite element model for the 18-m simply supported beam

The flexural stiffnesses for elements 1~6, 7~12 and 13~18 are EI_1, EI_2 and EI_3, respectively. The measurable displacements in this structure include 17 deflections, v_2 to v_{18}, and 19 rotations, w_1 to w_{19}. In order to derive the symbolical expression for the unknowns, the essential measurement sets are used (Lei, Nogal, et al. 2017). Without loss of generality, the derivation of this relationship using a given measurement set of three measurements $\{w_7, v_{10}, w_{13}\}$ is exemplified here.

Applying the algebraic operations mentioned in section 2.1, the observability equations corresponding to the measurements $\{w_7, v_{10}, w_{13}\}$ can be obtained. In this system of equations, the unknowns includes the reactions V_1 and V_{19}, the structural parameters EI_1, EI_2 and EI_3, and the coupled variables (e.g. EI_1v_2, EI_1v_3, EI_2v_7…). In the null space of the coefficient matrix, it is found that all the rows related with EI_2 and associated products (i.e. EI_2v_7~ EI_2v_{13}, and EI_2w_8~ EI_2w_{12}) are zeros. This is to say, unknowns EI_2, EI_2v_7~ EI_2v_{13}, and EI_2w_8~ EI_2w_{12} are observable when $\{w_7, v_{10}, w_{13}\}$ are measured. Also, reactions, V_1 and V_{19} are also observable since this is a statically determinate structure. However, all the other variables are not observable.

By solving the observability equations symbolically using Gaussian elimination, a particular solution for all unknowns can be obtained. For instance,

$$\widehat{EI_2} = \frac{18V_7L}{\frac{(w_7 - w_{13})}{L}} \tag{6}$$

$$\widehat{EI_2v_7} = -\frac{3V_7L^3(25w_7 - 12v_{10} + 11w_{13})}{2(w_7 - w_{13})} \tag{7}$$

where the hat, ^, indicates an estimation of the unknowns. The deflection of node 7, v_7, can be obtained by dividing $\widehat{EI_2v_7}$ with $\widehat{EI_2}$. The result is presented in Eq. (8), which specifies the compatible condition that $\{v_7, w_7, v_{10}$ and $w_{13}\}$ should satisfy.

$$12v_7 - 12v_{10} + 25w_7 + 11w_{13} = 0 \quad (8)$$

Similarly, the explicit geometrical relations among different displacements, i.e. the compatibility conditions, can be obtained for the elements within the same element. This is to say, they can be found among the displacements of nodes 1~7 for elements of EI_1 and among the displacements of nodes 13~19 for elements of EI_3. From the previous paragraph, it is clear that displacements of the elements with the same parameter is dependent of three displacements within these elements (being aware that boundary conditions can reduce this number). In the more general case, from the results at element level, at least a set of 7 adequate measurements will be needed. For example, $\{w_1, w_3, w_8, v_9, w_{11}, w_{15}$ and $w_{19}\}$. $\{w_1, w_3\}$ for EI_1, $\{w_8, v_9, w_{11}\}$ for EI_2 and $\{w_{15}, w_{19}\}$ for EI_3. Further, it should be noted that the compatibility condition at the joint nodes should be the same. That is, four more equations can be imposed in this case, which are $v_7(w_1, w_3)=v_7(w_8, v_9, w_{11})$, $w_7(w_1, w_3) = w_7(w_8, w_{11})$, $v_{13}(w_8, v_9, w_{11})=v_{13}(w_{15}, w_{19})$ and $w_{13}(w_8, w_{11})=w_{13}(w_{15}, w_{19})$. Combining all compatibility equations and these four additional equations leads to a system of four equations and seven unknown displacements, the unknowns can be reduced to three displacements that is denoted as the condensed measurement set later. Note that, the number of measurements in this condensed set is the same as the number of parameters. When only three measured displacements are available, the compatibility among these displacements can always be satisfied strictly and a particular set of structural parameters exactly leading to these displacements are always available.

Until now, every displacement in the FEM in Figure 1.c can be expressed as function of $\{w_1, v_9$ and $w_{19}\}$. The associated expression for $\mathbf{EI}_1$, $\mathbf{EI}_2$ and $\mathbf{EI}_3$ can be obtained using these displacements.

3.2 *Imposing compatibility condition*

From 3.1, it is seen that all the displacements within the structure can be expressed by the condensed set. Also, some displacements are measured during the non-destructive static test. Hence, to remove the incompatibility in the measurements, an optimization procedure can be applied. The objective function (see Eq. (9)) of the optimization is the square sum of the proportional deviation of the i^{th} compatible displacements, $\hat{\delta}_i$, from the i^{th} measured measurements, $\tilde{\delta}_i$. N_m is the number of available measurements. The best estimates of the stiffnesses can be determined by providing the optimal $\hat{\delta}_s$ to SSI by OM.

$$F(\hat{\delta}_s) = \sum_{i=1}^{N_m} \left(\frac{\hat{\delta}_i}{\tilde{\delta}_i} - 1\right)^2 = \sum_{i=1}^{N_m} \left(\frac{f(\hat{\delta}_c)}{\tilde{\delta}_i} - 1\right)^2 \quad (9)$$

A flowchart summarizing all the procedures mentioned above can be found in (Lei, Xu, et al. 2017).

4 APPLICTION OF THE PROPOSED METHOD

4.1 *Example 1: Simply supported beam*

In this part, the method is applied in the structure depicted in Figure 2. The effect of the number of measurements, error levels and loading cases are studied.

4.1.1 *Effect of number of measurements*

Regarding the number of measurements, N_m, Three different measurement sets are considered here. $\{v_3, v_5, v_7, v_9, v_{11}, v_{13}, v_{15}, v_{17}\}$ (N_m=8), $\{v_3$~v_5, v_7, v_9~v_{11}, v_{13}, v_{15}~$v_{17}\}$ (N_m=11) and $\{v_2$~$v_{18}\}$ (N_m=17). Errors are introduced by Eq. (5). The results are presented in Figure 3. In addition, the result without applying compatibility condition is also provided when measurement set N_m=8 is used.

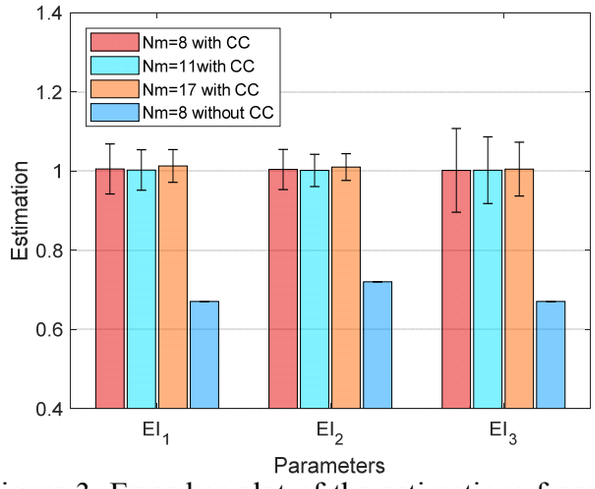


Figure 3. Error bar plot of the estimations from different measurement set with/without compatibility condition (CC).

It is found that the parameters are greatly underestimated using the SSI by OM with redundant measurements. Also the associated variation is very large and hence not shown here. When compatibility conditions are imposed, it is seen that 8 measurements are sufficient to estimate EI_1 and EI_2 accurately with a low dispersion of the estimate. In the case of EI_3, a slight overestimate of 1.3% is observed, which is acceptable. However, the coefficient of variance of the estimates in EI_3 is 0.112, which might not be negligible. When the number of measurement increases, both the mean and the COVs of the normalized estimates of the stiffnesses decrease. With regard to the mean of the estimate, mean of the normalized parameters becomes closer to one and the improvement in EI_3 is relatively large while the improve-

ments in EI_1 and EI_2 are smaller. In Figure 2.b, the drop of COV for EI_3 is roughly twice the drop of COV in EI_1 and EI_2 when the number of measurements increases. However, despite the fact that using more measurements will reduce the extent of dispersion, the COV of the estimates of EI_3 using 17 measurements is still higher than the COV of the estimates of EI_1 using 8 measurements.

4.1.2 *Effect of loading cases*

The effect of the loading case is studied by changing the location of the loads. The studied structure is the one depicted in Figure 2. Nine loading cases are studied here. For each loading case, a vertical load is applied at one point ranging from node 2 to node 10, as indicated in Figure 4. The measurement set $\{v_3, v_5, v_7, v_9, v_{11}, v_{13}, v_{15}, v_{17}\}$ (N_m=8) is used here. Measurements are marked by the red arrows in this figure. For each of these load cases, 2000 measured displacements are generated using Eq. (5) with the error level of 4%, and are taken as input into SSI by compatible OM.

The mean and the coefficient of variation for the 2000 estimations are summarized in Figure 4.

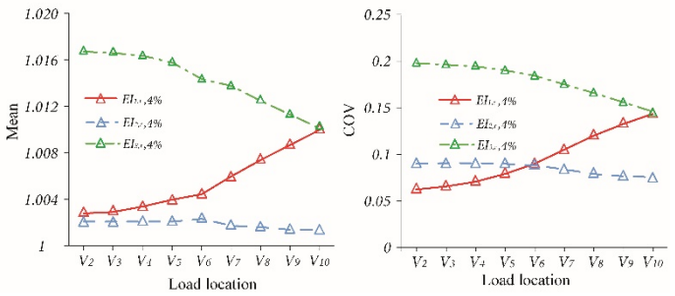


Figure 4. Mean and coefficient of variations of the estimations using $\{v_3, v_5, v_7, v_9, v_{11}, v_{13}, v_{15}, v_{17}\}$ with 4% errors

When the structure is subjected to V_2, the flexural behavior of elements of EI_1 is quite activated. The associated mean for EI_1 is 1.003, which is insensitive to errors. However, in the case of EI_3, a higher overestimation can be observed when high errors exist in the measurements. The associated mean for EI_3 is 1.017. It should be noticed that the flexural behavior of the elements of EI_3, i.e. elements 13~18, is not activated much in this load case. When the load moves from node 2 to node 10, the curvature of the elements of EI_1 decreases while the curvature of the elements of EI_3 increases. Correspondingly, an overestimation of EI_1 arises and escalates while the overestimation of EI_3 becomes less severe. Similar variation is found in the COV of EI_1 and EI_3 in Figure 4.b. For the loading case V_{10}, EI_1 and EI_3 have the same mean. This is because the curvature for elements of EI_1 and the curvature for elements of EI_3 are the same in this load case. Also, the COV of both EI_1 and EI_3 are the same. The flexural behavior of elements of EI_2 is quite activated under each load case. Consequently, the mean and the COV of EI_2 are lower than those of EI_1 and EI_3. When the load moves from node 2 to node 10, which is to become closer to the elements of EI_2, the curvature of these elements becomes even bigger. As a result, a small but perceptible improvement is seen in both the mean and the COV of EI_2 In conclusion, it is advisable to apply different load cases to study different zones of the beam.

5 CONCLUSIONS

This paper proposes a novel approach for identifying compatibility conditions, the relations among displacements, in beam - like structure using observability method. By solving an underdetermined system of equations formulated by compatibility conditions, it is shown that all displacements in a beam - like structure are functions of a subset of these displacements. Then, an optimization procedure is introduced to reduce the measurement errors by minimizing the square sum of the proportional deviation of the measured displacements and those compatible displacements. The effectiveness of this method is validated in a simply supported beam. A two span continuous bridge example will be presented during the conference.

REFERENCE:

Beck, J.L. & Au, S.-K., 2002. Bayesian Updating of Structural Models and Reliability using Markov Chain Monte Carlo Simulation. *Journal of Engineering Mechanics*, 128(4), pp.380–391.

Beck, J.L. & Katafygiotis, L.S., 1998. Updating Models and Their Uncertainties. I: Bayesian Statistical Framework. *Journal of Engineering Mechanics*, 124(4), pp.455–461.

Behmanesh, I. & Moaveni, B., 2015. Probabilistic identification of simulated damage on the Dowling Hall footbridge through Bayesian finite element model updating. *Structural Control and Health Monitoring*, 22(3), pp.463–483.

Castillo, E. et al., 2007. Observability in linear systems of equations and inequalities: Applications. *Computers and Operations Research*, 34(6 SPEC. ISS.), pp.1708–1720.

Eskew, E.L. & Jang, S., 2017. Remaining stiffness estimation of buildings using incomplete measurements. *Structural Control and Health Monitoring*, 24, p.e1899.

Huang, C.S. et al., 2009. Identification of time-variant modal parameters using time-varying autoregressive with exogenous input and low-order polynomial function. *Computer-Aided Civil and Infrastructure Engineering*, 24(7), pp.470–491.

Jeong, M., Choi, J.-H. & Koh, B.-H., 2013. Performance evaluation of modified genetic and swarm-based optimization algorithms in damage identification problem. *Structural Control and Health Monitoring*, 20(6), pp.878–889.

Lakshmi, K., Rao, A.R.M. & Gopalakrishnan, N., 2016. Singular spectrum analysis combined with ARMAX model for structural damage detection. *Structural Control and Health Monitoring*.

Law, S.S. & Yong, D., 2011. Substructure methods for structural condition assessment. *Journal of Sound and Vibration*, 330(15), pp.3606–3619.

Lei, J., Nogal, M., et al., 2017. Constrained observability method in static structural system identification. *Structural Control and Health Monitoring*, p.2040e.

Lei, J., Xu, D. & Turmo, J., 2017. Static structural system identification for beam-like structures using compatibility conditions. *Structural Control and Health Monitoring*, p.e2062.

Lozano-Galant, J.A. et al., 2013. Application of observability techniques to structural system identification. *Computer-Aided Civil and Infrastructure Engineering*, 28(6), pp.434–450.

Marano, G.C., Quaranta, G. & Monti, G., 2011. Modified Genetic Algorithm for the Dynamic Identification of Structural Systems Using Incomplete Measurements. *Computer-Aided Civil and Infrastructure Engineering*, 26(2), pp.92–110.

Mei, L., Mita, A. & Zhou, J., 2016. An improved substructural damage detection approach of shear structure based on ARMAX model residual. *Structural Control and Health Monitoring*, 23(2), pp.218–236.

Okada, R. et al., 2006. Rational polynomial approximation modelling for analysis of structures with VE dampers. *Journal of earthquake engineering*, 10(1), pp.97–125.

Raich, A.M. & Liszkai, T.R., 2012. Multi-objective optimization of sensor and excitation layouts for frequency response function-based structural damage identification. *Computer-Aided Civil and Infrastructure Engineering*, 27(2), pp.95–117.

Sevillano, E., Sun, R. & Perera, R., 2016. Damage evaluation of structures with uncertain parameters via interval analysis and FE model updating methods. *Structural Control and Health Monitoring*.

Su, W.C., Liu, C.Y. & Huang, C.S., 2014. Identification of instantaneous modal parameter of time-varying systems via a wavelet-based approach and its application. *Computer-Aided Civil and Infrastructure Engineering*, 29(4), pp.279–298.

Sun, H. et al., 2015. Statistical Regularization for Identification of Structural Parameters and External Loadings Using State Space Models. *Computer-Aided Civil and Infrastructure Engineering*, 30(11), pp.843–858.

Sun, H., Luş, H. & Betti, R., 2013. Identification of structural models using a modified Artificial Bee Colony algorithm. *Computers & Structures*, 116, pp.59–74.

The MathWorks, I., 2015. *Matlab Primer* 2015b ed., https://www.mathworks.com/help/pdf_doc/matlab/getstart.pdf.

Wolfram, S., 1999. *The MATHEMATICA ® Book* 4th ed., Cambridge University Press.

Zhang, F.L. et al., 2016. Structural health monitoring of Shanghai Tower during different stages using a Bayesian approach. *Structural Control and Health Monitoring*, 23(11), pp.1366–1384.

SS02: Continuous bridge monitoring and damage detection

Organizers: A. Miyamoto, E. Brühwiler, R. Kiviluoma & P. Hradil

Maintenance, Safety, Risk, Management and Life-Cycle Performance of Bridges – Powers, Frangopol, Al-Mahaidi & Caprani (Eds)
© 2018 Taylor & Francis Group, London, ISBN 978-1-138-73045-8

Combined structural and traffic monitoring of steel suspension bridge

P. Hradil & K. Koski
VTT Technical Research Centre of Finland

ABSTRACT: The present paper discusses the possibility of using structural monitoring sensors such as strain gages attached to the main girders of steel bridges to collect the data about the traffic on the bridge deck. Obtaining useful data is challenging task since the load is typically transferred from the deck to the main load-carrying structure through several intermediate structural members. The main parameters affecting the reliability of such results are the number, position and type of sensors used. The additional requirements might lead to a more complicated planning of the bridge instrumentation. On the other hand, this method can result in substantial savings in planned monitoring systems and will increase the value of monitoring data from already instrumented bridges. The method is demonstrated on a steel suspension bridge located in western Finland.

1 INTRODUCTION

Structural monitoring of long-span road and railway bridges is a common approach to continuously collect data about strains, deflections and other parameters on specific locations of the load-carrying structure. At the same time, the bridge can be instrumented to monitor the traffic, especially weights, speeds and axle distances of passing vehicles. In both cases, the amount of data is usually huge, and many methods have been recently developed to evaluate the results in a real time. However, sensors intended for traffic monitoring are typically close to the surface, while the structural sensors are attached to the load-carrying structural members.

The goal of this study was to develop a calculation method to predict the mass of passing vehicles from multiple measured strains on the bridge and to calibrate its parameters to the existing loading tests.

The demonstration case is for the presented approach is steel suspension bridge in Kirjalansalmi that has been continuously monitored more than seven years. The bridge has a long history of repeated loading test, which are very useful for the calibration of traffic monitoring algorithms. Kirjalansalmi Bridge is owned and maintained by Finnish Transport Agency (Liikennevirasto) that is acknowledged here for its support for the development and prototyping of the monitoring methods and associated software.

2 KIRJALANSALMI BRIDGE

Kirjalansalmi Bridge (Figure 1) is a suspension bridge situated in south-western part of Finland near the city of Turku. The bridge was built in 1963. It is spanning 220 m between the towers and its 12.7 m wide deck is supported by the system of steel truss girders. Most of the truss connections are welded or riveted with heavy connection plates, and therefore are susceptible to the fatigue damage. The bridge supporting system has been renovated in 2005. As the result, the whole deck is now placed on the rubber bearings inserted between the longitudinal secondary beams and cross girders.



Figure 1 Kirjalansalmi Bridge

The bridge was instrumented with strain gauges, deflection sensors and video camera. The whole system was originally maintained and controlled by VTT's computer that collected the strain and displacement data continuously every 10 minutes and if the strain reached the critical level, a 30 seconds long "event" was recorded with the sampling frequency 100 Hz. The video was recorded at the same time and saved together with the measured data.

3 BRIDGE WEIGHTING IN MOTION METHOD

We proposed a simple equation to obtain the estimated vehicle mass from the measured strain, vehicle length and its relative position to the sensor. We have optimized the equation parameters to minimize the prediction error of selected sensors (see Table 1) against the results of loading tests (see Table 2). It should be noted that the sensor names might have been different during the test loads.

Table 1. Selected sensors location

Sensor	Girder	Position
Sg01	West	Upper Chord, North (1/4 span)
Sg08	East	Upper Chord, North (1/4 span)
Sg25	East	Upper Chord, North (1/4 span)
Sg31	West	Upper Chord, South (3/4 span)
Sg32	East	Upper Chord, South (3/4 span)

It can be seen that sensors Sg01 and Sg08 (or Sg25), are symmetrical as well as Sg31 and Sg32. Therefore, their data can be used for the estimation of transverse position of the vehicle.

The prediction equations are based on 112 existing loading tests from 1998 (Tirkkonen, 1999), 2000 (Tirkkonen, 2001), 2005 (Hakola, 2005) to 2007 (Hakola, 2008, Lampi, 2007), 2009 (Hakola and Mäkinen, 2010, Turunen, 2009), 2013 (Hakola et al., 2014a) and 2016. The tests were performed with 1 to 4 vehicles driving either at walking speed (static tests) or up to 60 km/h (dynamic tests). The total load was between 60 and 276 t.

Table 2. Loading tests

Date	Static tests	Dynamic tests	Speed (km/h)	Weight (t)
11.9.1998	4	4	10 – 60	61 – 174
20.9.2000	6	7	0 – 60	99 – 198
11.8.2005	5	5	5 – 60	154 – 213
30.8.2007	6	7	40 – 60	61 – 122
29.10.2009	10	9	40 – 60	60 – 127
3.9.2013	12	3	60	61 – 276
29.9.2016	n/a	18	60	76
7.10.2016	n/a	16	60	76

The measurements in 1998 and 2000 were performed before the installation of the rubber supports under the bridge secondary beams. Therefore, their results do not accurately correspond to the current situation and are excluded from the calibration of the weight-in-motion calculation model.

The prediction is limited to the data obtained by the selected sensors (see Figures 2 and 3). Therefore, the best prediction of the vehicle mass, speed and position would be in the studied ranges of test loads. However, the extrapolation of the results for lighter or faster vehicles is also possible and it is used in the real-time evaluation of the measured data.

The sensor Sg25 has more data reported than Sg08 and because both are placed in the same location, only Sg25 was be used in the evaluation of vehicle's mass, speed and direction. The calculation parameters are, however, calibrated for both sensors in case that one of them will be removed in the future.

3.1 *Basic equations*

We have reviewed the basic weighting-in-motion (WIM) equation applied in Kirjalansalmi Bridge (Hakola and Halonen, 2013, Hradil, 2016) and modified it to the format used in Jännenvirta Bridge (Hakola et al., 2014b, Hradil, 2015), which is more reflecting the physical meaning of the measured parameters. The general form of the WIM calculation is in Eq. (1).

$$m = A\bar{\sigma}\,, \tag{1}$$

where $\bar{\sigma}$ is the stress range of the equivalent load moving in the center of the bridge with negligible (infinitely small) speed. The correction for the load position is given by coefficient k and the effect of vehicle speed is taken into account by the factor δ with the speed measured directly from the difference between stress peaks of two sensors on the opposite side of the bridge.

$$m = A\frac{\sigma - Bk}{\delta} \tag{2}$$

Since the equation is calibrated on four sensors, the predicted mass is the weighted average from all of the sensors:

$$m = \sum_{i=1}^{4} m_i w_i \tag{3}$$

with the weighting factors w proportional to the total error R of the predictions in all of the evaluated loading tests:

$$w_i = \frac{1/R_i}{\sum_{j=1}^{4} 1/R_j} \tag{4}$$

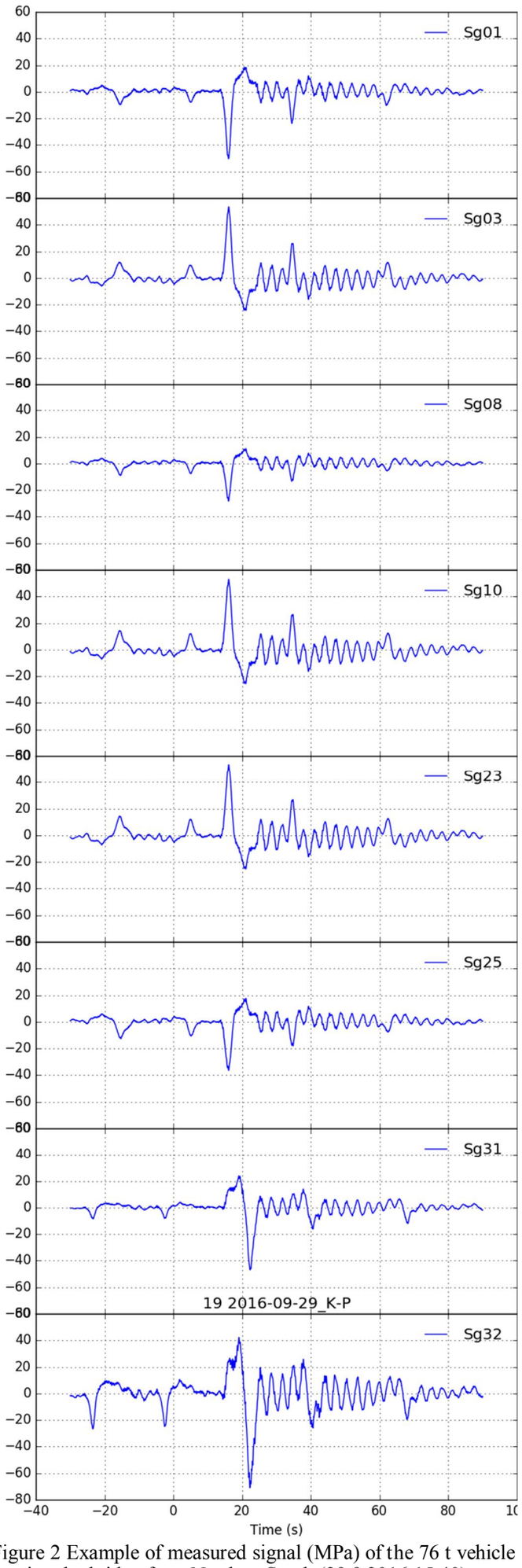


Figure 2 Example of measured signal (MPa) of the 76 t vehicle passing the bridge from North to South (29.9.2016 15:40)

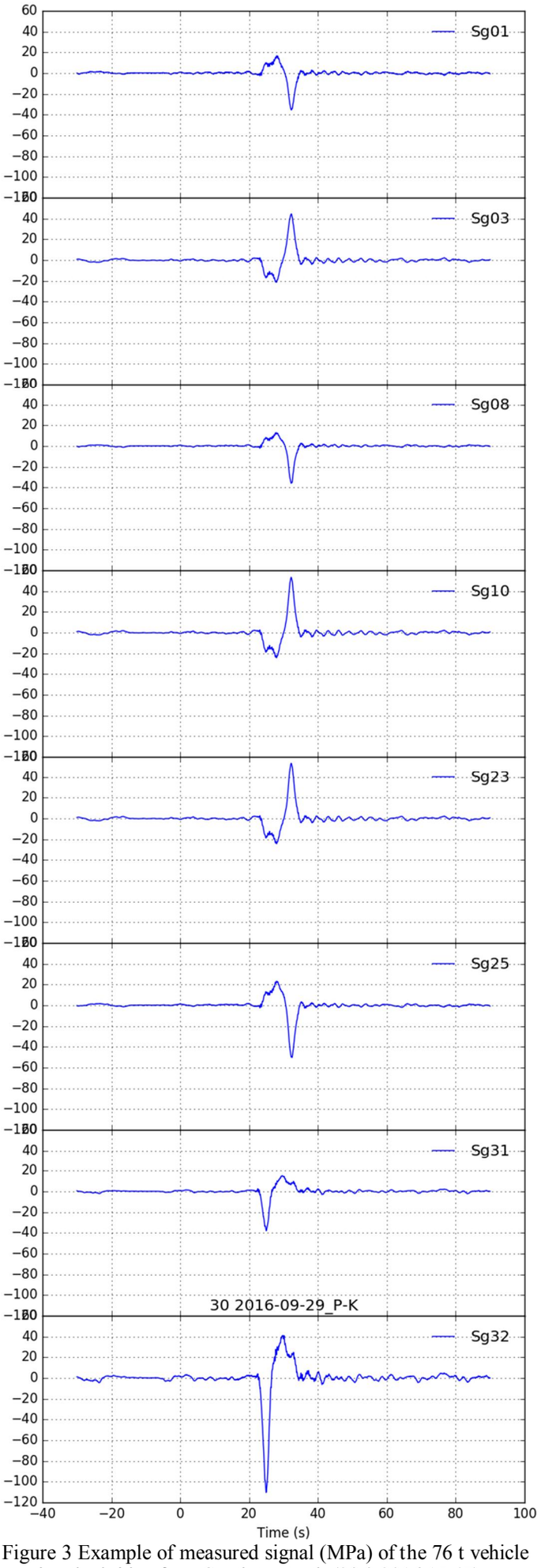


Figure 3 Example of measured signal (MPa) of the 76 t vehicle passing the bridge from South to North (29.9.2016 15:47)

The average prediction error R_i in Equation (4) is based on the sum of squares of particular errors $r_{i,j}$ in prediction for sensor i and test j:

$$R_i = \frac{1}{n}\sqrt{\sum_{j=1}^{n} r_{i,j}^2} \quad (5)$$

where n is the number of loading tests valid for the i-th sensor.

3.2 *Effect of the vehicle speed and position*

The dynamic reduction factor δ of measured stress range should be 1 in the static tests. Additionally, it is assumed that the factor is growing proportionally to the vehicle speed v, resulting in the following equation:

$$\delta = Cv + 1 \quad (6)$$

The coefficient C from Eq. (6) is calibrated on the loading tests, with the same weight, length and position of the vehicle.

Similarly, the coefficient B for the position of the vehicle in the transverse direction was calibrated on the loading tests, when the same vehicles were driving at different bridge sides. As a result, also coefficient A was determined from those tests. Linear approximation was used in both cases.

3.3 *Prediction of the vehicle speed and position*

The data from symmetrically placed sensors served as an estimation of the vehicle transverse position. The transverse factor k was then calculated based on the following equation:

$$k = \frac{A_E\sigma_E/\delta_E - A_W\sigma_W/\delta_W}{A_E B_E/\delta_E - A_W B_W/\delta_W} \quad (7)$$

where indexes E and W correspond to the east and west side of the bridge respectively. This coefficient is typically equal to 1 or -1 if the vehicle is in the middle of eastern lane or western lane respectively, but in reality the value ranges between -1.2 and 1.2.

4 EFFECT OF THE VEHICLE SPEED

In order to assess the vehicle speed, a series of tests with the identical load and position on the bridge was needed. Moreover, the tests with multiple vehicles in the row were excluded, because the gap between the vehicles was too significant to be neglected, and the resulting stress ranges were lower at higher speeds.

Table 3. Loading tests applicable for the speed calibration

Loading tests	Weight (t)	Position index	Speed (km/h)	Sensors used
2009-2, 11, 13	63	0	0, 40, 60	01,08,25
2009-9, 18	72	0	0, 40	01, 08, 25
2009-10, 19	72	-1	0, 40	01, 08, 25
2013-3, 13, 14	61	1 to 1.2[1)]	0, 60	25

[1)] vehicle driving near the bridge edge

Table 3 shows that there is a lack of data needed for the individual calibration of each sensor. The data quality is also relatively low. Therefore, a single parameter was calculated to be used in all locations.

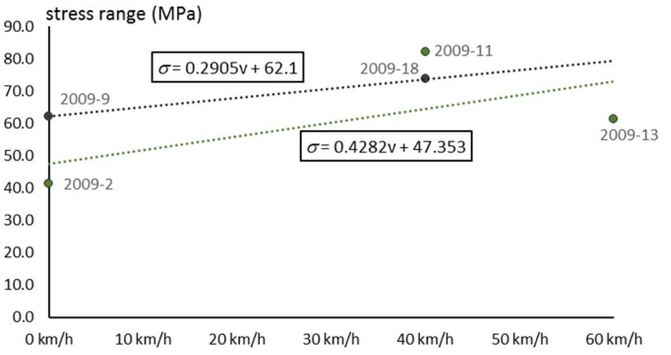


Figure 4. The effect of vehicle speed on sensor Sg01

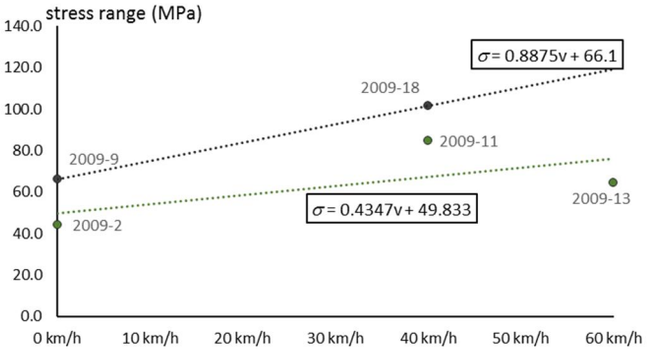


Figure 5. The effect of vehicle speed on sensor Sg08

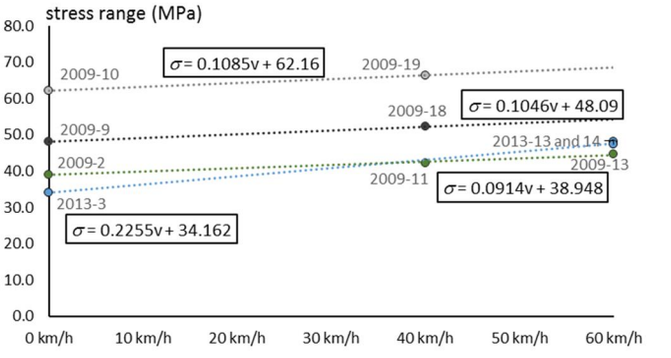


Figure 6. The effect of vehicle speed on sensor Sg25

The results in Figures 4 to 4 are expressed as:

$$\sigma = c_1 v + c_2 \quad (8)$$

Then the dynamic factor δ can be calculated as:

$$\delta = Cv + 1, \text{ where } C = c_1/c_2 \quad (9)$$

The weighted average of the factor C is 0.00621 h/km based on the available loading tests results.

5 EFFECT OF THE VEHICLE POSITION

The position of the load in the transverse direction affects the measured stress ranges. Therefore, coefficient B had to be calibrated on the loading tests with different position of the same load crossing the bridge at the same speed.

Table 4. Loading tests applicable for the vehicle position calibration

Loading tests	Weight (t)	Position index	Speed (km/h)	Sensors used
2007-1a, 1b, 1c	62	-1, 0, 1.2[1)]	-	01, 08
2009-2e, 2f	127	-1, 1	40	01, 08
2013-1, 2, 3	61	-1.2[1)], 0, 1.2[1)]	-	25
2016-1 to 34	76	-1, 1	60	all

[1)] vehicle driving near the bridge edge

It was assumed that the relation between the stress range σ and coefficient k is linear. The results are shown in Figures 6 to 11 and Table 5.

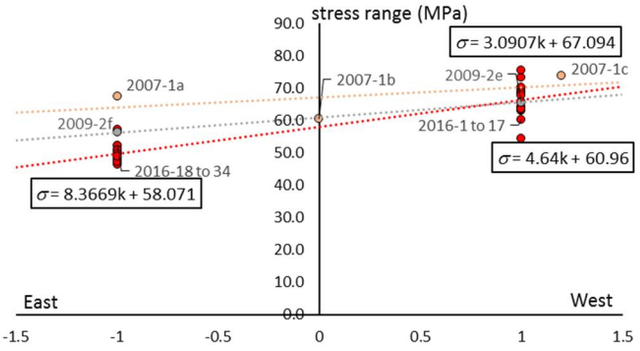


Figure 7. The effect of vehicle position on sensor Sg01

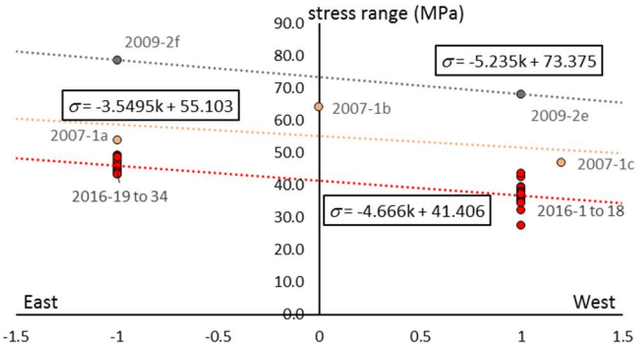


Figure 8. The effect of vehicle position on sensor Sg08

The results in the graphs are expressed as stress range σ being a function of position index k:

$$\sigma = c_3 k + c_4 \tag{10}$$

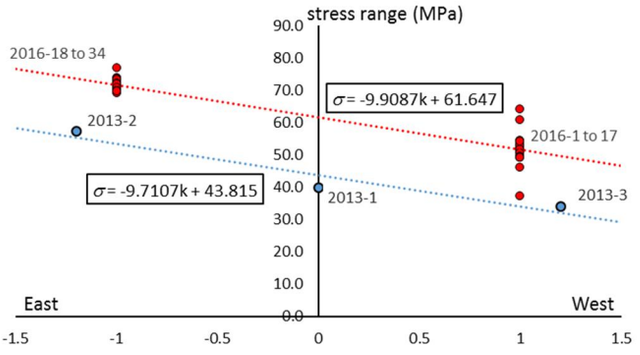


Figure 9. The effect of vehicle position on sensor Sg25

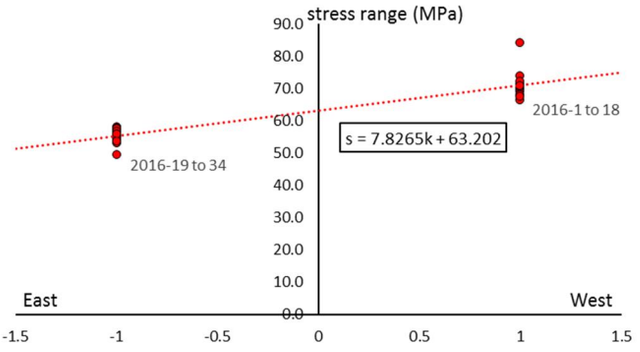


Figure 10. The effect of vehicle position on sensor Sg31

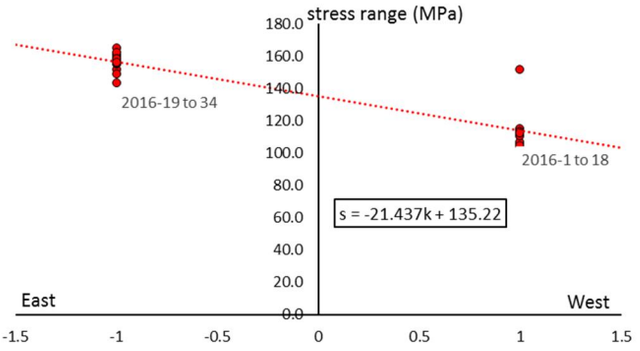


Figure 11. The effect of vehicle position on sensor Sg32

After substituting Eq. (1) in this relationship, one can obtain:

$$A = \frac{\delta m}{c_4} = \frac{(0.00621v + 1)m}{c_4} \text{ and } B = c_3 \tag{11}$$

Table 5 shows the weighted average values of the main equation parameters A (of the vehicle weight) and B (related to the vehicle transverse position). The negative value of B in sensors Sg08, Sg25 and Sg32 corresponds to their placement on the opposite side of the bridge than the other sensors (Sg01 and Sg31).

Table 5. Average coefficients A and B for different sensors

	Sg01	Sg08	Sg25	Sg31	Sg32
A (t/MPa)	1.78	2.58	1.72	1.71	0.80
B (MPa)	7.92	-4.71	-9.95	7.83	-21.44

6 PREDICTION OF THE VEHICLE POSITION AND WEIGHT

Since there is possible to recognize one sensor couple on the north side of the bridge and another couple one on the south side, the position index k is average from two factors calculated according to Eq. (7). This Equation can be, however, simplified because of the single parameter C used in the calculation of the dynamic effect δ. From the two options of north-east located sensors, Sg25 was selected. Then the calculation of the k factor turns into:

$$k = 0.5\left(\frac{A_{SG25}\sigma_{SG25} - A_{SG01}\sigma_{SG01}}{A_{SG25}B_{SG25} - A_{SG01}B_{SG01}} + \right. \\ \left. + \frac{A_{SG32}\sigma_{SG32} - A_{SG31}\sigma_{SG31}}{A_{SG32}B_{SG32} - A_{SG31}B_{SG31}} \right) \quad (12)$$

The optimized parameters produced the set o f five Equations (13) to (17); one for each sensor.

$$m_{01} = 1.78\left(\sigma_{SG01} - 7.92k\right)/(0.00621v + 1) \quad (13)$$

$$m_{08} = 2.58\left(\sigma_{SG08} + 4.71k\right)/(0.00621v + 1) \quad (14)$$

$$m_{25} = 1.72\left(\sigma_{SG25} + 9.95k\right)/(0.00621v + 1) \quad (15)$$

$$m_{31} = 1.71\left(\sigma_{SG31} - 7.83k\right)/(0.00621v + 1) \quad (16)$$

$$m_{32} = 0.80\left(\sigma_{SG32} + 21.44k\right)/(0.00621v + 1) \quad (17)$$

The weights estimated at each sensor from the measured stress ranges were compared to the real weights of the loading tests. The average prediction errors and the corresponding weighting factors are presented in Table 6.

Table 6. Average prediction error R, the weighting factor w and the number of loading tests n used for its calibration at different sensors

	Sg01	Sg08	Sg25	Sg31	Sg32
R (t)	5.81	5.61	8.29	3.79	4.41
w	0.220	-	0.154	0.337	0.290
n	34	34	55	34	34

Then the estimation of the vehicle mass will be based on the following equation:

$$m = 0.22m_{01} + 0.154m_{25} + 0.337m_{31} + 0.29m_{32} \quad (18)$$

7 VALIDATION OF THE RESULTS

The position of the vehicle on the bridge was calculated using Equation (11). The results are presented in Table 7. It can be concluded that the prediction is good; however, it is based only on the tests with 76 t vehicle when all four sensors were active.

Table 7. Validation of predicted position of the vehicle

Test	Predicted k	Reported position index
2016-1	0.97	1
2016-2	0.88	1
2016-3	0.99	1
2016-4	0.95	1
2016-5	0.95	1
2016-6	1.01	1
2016-7	1.05	1
2016-8	0.90	1
2016-9	0.89	1
2016-10	0.94	1
2016-11	0.98	1
2016-12	1.09	1
2016-13	0.96	1
2016-14	0.97	1
2016-15	0.99	1
2016-16	0.96	1
2016-17	0.95	1
2016-18	-1.08	-1
2016-19	-0.96	-1
2016-20	-1.07	-1
2016-21	-1.04	-1
2016-22	-1.11	-1
2016-23	-1.02	-1
2016-24	-1.03	-1
2016-25	-1.09	-1
2016-26	-1.16	-1
2016-27	-1.03	-1
2016-28	-1.01	-1
2016-29	-0.99	-1
2016-30	-1.07	-1
2016-31	-1.10	-1
2016-32	-1.10	-1
2016-33	-1.13	-1
2016-34	-0.97	-1

The proposed calculation was then validated against the measured data from Hakola (2010) and Tirkkonen (1999). The dynamic factors δ from the Equation (1) are also presented in the Table 8.

Table 8 Validation of the vehicle weight prediction

Test	dynamic factor δ	Predicted weight	Measured weight
2016-1	1.50	72 t	76 t
2016-2	1.47	73 t	76 t
2016-3	1.45	74 t	76 t
2016-4	1.47	72 t	76 t
2016-5	1.44	75 t	76 t
2016-6	1.46	74 t	76 t
2016-7	1.48	74 t	76 t
2016-8	1.48	84 t	76 t
2016-9	1.46	76 t	76 t
2016-10	1.45	73 t	76 t
2016-11	1.45	72 t	76 t
2016-12	1.44	70 t	76 t
2016-13	1.42	73 t	76 t
2016-14	1.45	68 t	76 t
2016-15	1.46	73 t	76 t
2016-16	1.43	73 t	76 t
2016-17	1.46	74 t	76 t
2016-18	1.41	78 t	76 t
2016-19	1.40	76 t	76 t
2016-20	1.38	73 t	76 t
2016-21	1.40	75 t	76 t
2016-22	1.41	79 t	76 t
2016-23	1.39	78 t	76 t
2016-24	1.41	77 t	76 t
2016-25	1.41	77 t	76 t
2016-26	1.40	75 t	76 t
2016-27	1.42	76 t	76 t
2016-28	1.41	75 t	76 t
2016-29	1.37	80 t	76 t
2016-30	1.39	76 t	76 t
2016-31	1.41	74 t	76 t
2016-32	1.43	74 t	76 t
2016-33	1.42	73 t	76 t
2016-34	1.42	72 t	76 t

8 IMPLEMENTATION IN REAL-TIME MONITORING

The evaluation of real-time data is based on the same inputs and produces the same kind of outputs as the previous versions described in Hradil (2016). However, its internal calculation is now based on the data from four sensors, and therefore the calculation time is proportionally longer.

The real-time data has many disadvantages compared to the load test results. The measured ranges are often biased by several vehicles passing over the bridge at the same time and the typical weights of the vehicles are smaller than the test loads. Those two factors contribute to the fact that many times the identification of all four corresponding signal peaks is impossible. Therefore, the methodology described in this paper was improved to provide results also for the cases with three, two or even a single sensor measurement. It should be noted that such results tend to be less accurate.

The statistics about traffic on the bridge are presented in Figures 12 to 14. They represent the distribution of calculated vehicle weights and speeds during one month. The barcode chart in Figure 14 shows the traffic density during the day.

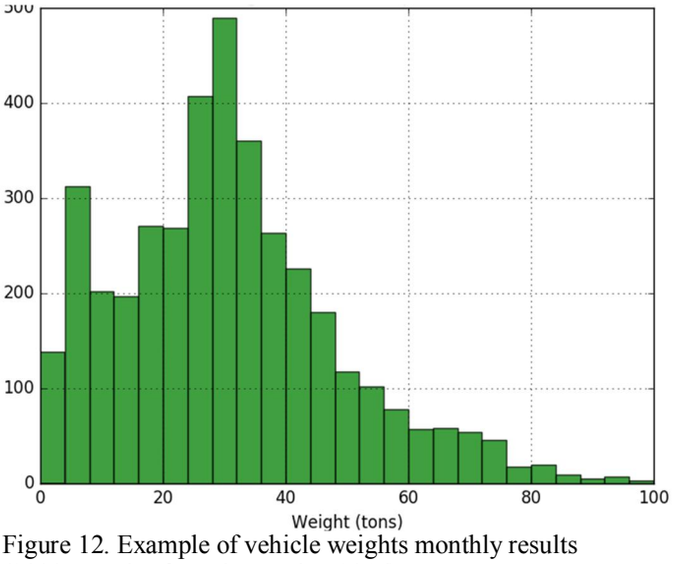


Figure 12. Example of vehicle weights monthly results (3899 samples from September 2016)

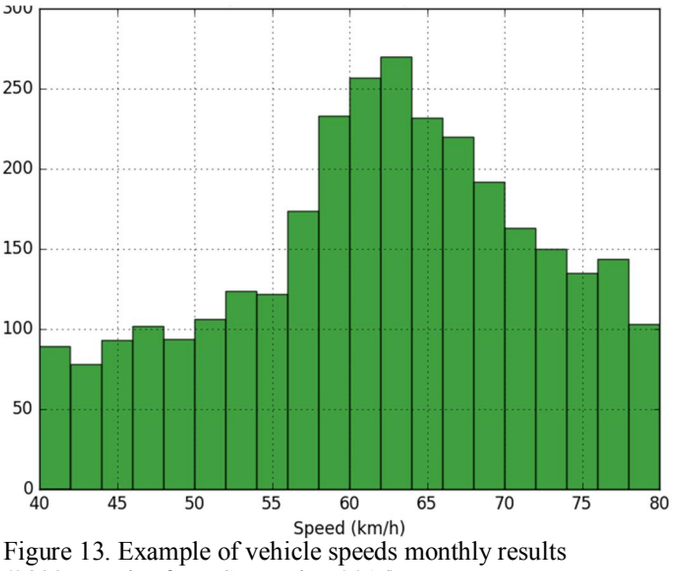


Figure 13. Example of vehicle speeds monthly results (3899 samples from September 2016)



Figure 14. Example of registered events density daily results (22.9.2016)

9 CONCLUSIONS

The weighting-in-motion calculation method was adapted from the previous Kirjalansalmi Bridge calculations (Hradil, 2016), improved and tested on Jännenvirta Bridge (Hradil, 2015) and extended with the effect of vehicle speed obtained from multiple sensors. The weighted average of results based on the optimization errors was also introduced because of data originating from multiple sensors. The method was validated against the real load tests on which it was calibrated.

It can be concluded that the results of the proposed weight calculation show relatively good correlation to the loading tests. The accuracy of the results is sufficient for the purpose of long-term monitoring of the traffic on the bridge deck. Since the bridge was already instrumented to monitor the structural loads on the main girder, the presented data were obtained without any additional sensors and, in fact, without a need to physically visit the bridge.

ACKNOWLEDGEMENTS

We would like to thank to Timo Tirkkonen from Finnish Transport Agency for the loading tests data from 2016 and overall support throughout this study. Our thanks also belong to Pekka Toivola, Markko Turunen and Mikko Lampi from Savcor Oy, who have provided access to the data from their real-time structural monitoring of Kirjalansalmi Bridge.

REFERENCES

Hakola, I. 2005, Kirjalansalmen riippusillan koekuormitus vuonna 2005, Research notes, RTE4656/05, VTT Technical Research Centre of Finland, Espoo, Finland.

Hakola, I. 2007, Kirjalansalmen riippusillan koekuormitus vuonna 2007, Research notes, VTT-S-00207-08, VTT Technical Research Centre of Finland, Espoo, Finland.

Hakola, I. 2010, Kirjalansalmen riippusillan koekuormitusten ja laskennan yhteenvetoraportti vuonna 2010, Research report, VTT-R-05937-10, VTT Technical Research Centre of Finland, Espoo, Finland.

Hakola, I., Halonen, M. 2013, SITUEL – Life Cycle and Safety in Bridges and Tunnels, Research report, VTT-R-01949-13, VTT Technical Research Centre of Finland, Espoo, Finland.

Hakola, I., Halonen, M., Mäkinen, J., Hradil, P. 2014a, Kirjalansalmen riippusillan koekuormitus vuonna 2013, Research report, VTT-R-01168-14, VTT Technical Research Centre of Finland, Espoo, Finland.

Hakola, I., Halonen, M., Mäkinen, J., Hradil, P. 2014b, Jännenvirran sillan koekuormitus vuonna 2013, Research report, VTT-R-01127-14, VTT Technical Research Centre of Finland, Espoo, Finland.

Hakola, I., Mäkinen, J. 2010, Kirjalansalmen riippusillan koekuormitus vuonna 2009, Research report, VTT-R-01385-10, VTT Technical Research Centre of Finland, Espoo, Finland.

Hradil, P. 2015, Jännenvirta Bridge weighting in motion, Research report draft, VTT Technical Research Centre of Finland, Espoo, Finland.

Hradil, P. 2016, Implementation of Kirjalansalmi Bridge monitoring evaluation script to the new environment, Research report, VTT-R-00509-16, VTT Technical Research Centre of Finland, Espoo, Finland.

Lampi, M. 2007, Kirjalansalmen rasitustesti 30.8.2007, Technical report, Futurtec.

Tirkkonen, T. 1999, Kirjalansalmen sillan tutkimukset vuonna 1998, Research notes, RTE573/99, VTT Technical Research Centre of Finland, Espoo, Finland.

Tirkkonen, T. 2001, Kirjalansalmen sillan mittaukset vuonna 2000, Research notes, RTE3118/01, VTT Technical Research Centre of Finland, Espoo, Finland.

Turunen, M. 2009, Kirjalansalmen rasitustesti 29.10.2009, Savcor Futurtec Technical report, Savcor Tempo Oy, Mikkeli, Finland.

Maintenance, Safety, Risk, Management and Life-Cycle Performance of Bridges – Powers, Frangopol, Al-Mahaidi & Caprani (Eds)
© 2018 Taylor & Francis Group, London, ISBN 978-1-138-73045-8

"Pocket-Monitoring" for the fatigue safety verification of bridge members in steel and reinforced concrete

E. Brühwiler
Swiss Federal Institute of Technology (EPFL), Lausanne, Switzerland

ABSTRACT: The fatigue safety of the reinforced concrete deck slab of a sixty-year-old steel-concrete road viaduct as well as the riveted steel girders of a 130 year old railway bridge was questioned based on the results of conventional assessment consisting in "re-calculation" using traffic models given by codes. Subsequently, examination of the fatigue action effect was performed using data obtained from "pocket-monitoring" which is a rational and ready-to-use, cost-effective monitoring device. The "pocket-monitoring" concept for the determination of fatigue action effects in the two present cases revealed fatigue relevant stresses that were lower than the fatigue limit of the critical fatigue details. Consequently, there is no fatigue damage in these details, and the fatigue relevant element of the two bridge structures is safe for a next long service duration of unrestricted traffic loads. The large discrepancy in the results between the presented monitoring method and conventional assessment is attributed to over-conservative code provisions.

1 INTRODUCTION

1.1 *Motivation*

In many countries, civil structures have been in service already for several generations. As part of the transportation infrastructure, bridges add value to the public economy. Therefore, there is high interest in economic performance while providing unrestricted use (e.g. without limitation of traffic loads). Obviously, there is a need to extend the service life of civil structures significantly beyond 70 to 100 years (which often is the arbitrarily presumed service life of structures).

Structural engineers were educated to design and build new structures. When they deal with existing structures, they perform so-called "assessments" or "re-calculations" like for the design of new structures. Many of these structural engineers implicitly think that the lifespan of a bridge is finite and similar to the one of a human being, i.e. 70 to 100 years. The same structural engineers often consider a bridge that is in service for more than 50 years as being "old". Implicitly it is assumed that an "old" bridge needs to be dismantled, and any "repair" or "retrofit" to survive the "remaining service life" (of maybe 20 years) would be the goal.

This irrational approach is outdated, also because for economic and technical reasons, it is neither justified nor possible to replace existing structures simply because they reach what might be considered their "design life" (of 70 to 100 years).

Instead, when dealing with existing structures in terms of future service duration, the structural engineer has to device ways to examine and – if necessary – enhance the existing structure in view of a second service duration, rather than demolishing and replacing the existing structure by a new one (Brühwiler 2017).

In addition to the cost argument, often there are significant cultural values involved in existing structures, and these cultural values have to be respected accordingly, not only for the interest of society but also for the sake of the structural engineering culture and profession.

1.2 *Limits of conventional assessment*

The current approach to "assess" the structural safety of existing bridges, is similar to the methodology used for the design of a new bridge, i.e. a load model (supposed to represent traffic loads) is imposed on a (computational) structural model in order to calculate sectional forces and deformations, to obtain the so-called action effect. These are then compared with the resistance of the structural members. These calculated results are often obtained without visiting the existing bridge to evaluate its condition.

In some countries, the current methodology for existing structures is awkwardly called "re-calculation" referring to the fact that the structure was first calculated when it was designed. This term betrays the way of thinking, and actually, the current approach is

rightly called "assessment". The existence of the existing structure is not exploited, and thus this pure calculation method – even when precisely performed using refined models – cannot produce better than "guesswork". Obviously, the current "assessment" approach should be abandoned.

1.3 *Objectives*

This paper suggests a novel methodology with the objective to exploit the existence of the existing bridge structure to determine the effective structural performance, f.ex. in terms of fatigue behavior.

The basic idea is to accurately determine in-situ structural behavior (rather than calculating it) in order to be able to perform more precise and realistic verification of structural and fatigue safety. The ultimate goal is to avoid or limit construction intervention to a strict minimum while verifying sufficient fatigue safety allowing for a second long future service duration. We call this approach examination engineering (short: Examineering). "Examineering" is a concept allowing to leave the outdated "assessment" approach.

More specifically, this paper highlights a methodology to examine the fatigue safety of existing bridges using explicitly data obtained from "pocket-monitoring" of structural behaviour of fatigue relevant elements of the existing bridge. The benefits of the proposed methodology are illustrated by means of two recent applications in Switzerland.

2 DETERMINATION OF ACCURATE ACTION EFFECTS BY MONITORING

2.1 *Basic concept*

The contemporary approach to existing structures is based on updating, which means collecting and exploiting detailed in-situ information from the existing structure while reducing uncertainties in structural parameters (Brühwiler et al. 2012, SIA269 2011).

The controlling parameters are determined as precisely as needed following a stepwise procedure with increasing focus on details. The structural safety verification is performed using updated values, called examination values.

The notion of degree of compliance n is introduced in the deterministic verification of the structural safety:

$$n = \frac{R_{d,updated}}{E_{d,updated}} \quad (1)$$

where $R_{d,updated}$ and $E_{d,updated}$ are the examination values of resistance and action effect, respectively.

The degree of compliance is a numerical statement showing the extent to which an existing structure fulfils the structural safety requirements. This formulation not only gives the information whether the structural safety is fulfilled. It also indicates by how much the verification is fulfilled (or not). The latter is necessary for the evaluation of results and in view of the planning of interventions.

In the context of this paper, monitoring of structural behavior has the general objective to determine more accurately effective action effects in terms of measured strains (stresses), displacements or accelerations, acting on structural elements.

2.2 *Stepwise procedure*

In a first step of verification on Level 1 (general ex-amination), the examination value of action effect $E_{d,updated}$ is determined using updated load models (for permanent and live loads) which are applied to a structural model to obtain sectional forces, stresses and strains, i.e. action effects, through structural analysis (Fig. 1).

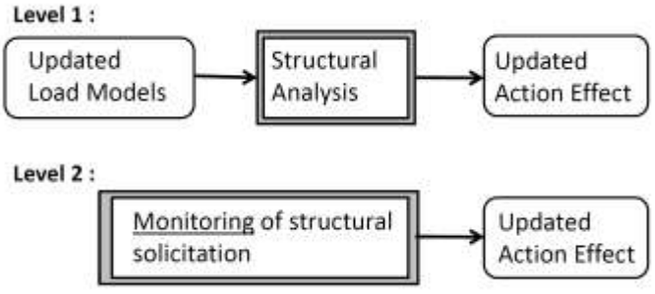


Figure 1. Determination of updated action effect.

This approach is analogous to the one generally applied for the design of new structures. The first objective is to identify critical sections and structural elements. Secondly, this simple and pragmatic approach may already lead suitable results, i.e., showing that structural safety is fulfilled).

If the safety verification is not conclusive on Level 1, further updating needs to be performed on Level 2 in a detailed examination by performing monitoring of action effects due to live loads (Fig. 1). In this way, action effects are directly measured by monitoring while significantly reducing uncertainties inherent with the approach on Level 1.

However, it may not be possible to obtain monitored data directly from critical cross sections determinant for the structural safety verification. In addition, action effect due to permanent load (dead load) is not recorded by monitoring.

Structural analysis using refined numerical models is thus needed to "translate" monitored data to sections determinant for the structural safety verification (Fig. 2) and to determine the solicitation of the existing structure due to permanent loads.

Consequently, the use of structural models changes its significance when compared to structural analyses for the design of new structures.

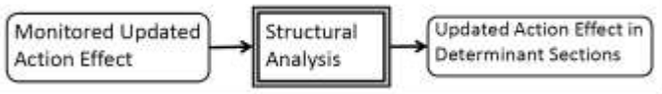


Figure 2. Translation of monitored data to sections determinant for structural safety.

In addition, monitored data are used to calibrate the structural model with the objective to obtain as accurate sectional forces as possible reducing thereby un-certainty usually implied in structural models. Such a calibrated structural model may then be used to determine, for example, fatigue action effects of future traffic scenarios.

It is interesting to note that following the approach on Level 2, no more load model is needed since solicitation of structural elements is directly recorded which obviously is the most direct and reliable information to verify structural safety.

The structural safety requirements imposed on an existing structure need to be clearly defined. Monitoring of action effects on structural elements reduces uncertainties. Yet, some safety margin must be respected, either by considering some partial safety factor or, in the case of fatigue safety verification, by some criterion of target level of acceptable fatigue damage.

2.3 *Pocket Monitoring*

An important feature of existing bridge safety verification is that the existing bridge can be monitored to determine the real 'action effects' it experiences. The advent of cheap and high storage capacity hardware in recent years means that direct measurement of elemental action effects via structural monitoring is now a viable option.

Monitoring can overcome limitations of accurately modelling in-service behavior. For example, material properties may change over time and secondary elements may reduce the stress levels in the structural parts that can provide uncertainty in modelling but these effects are inherent in the measured data.

"Pocket-monitoring" is a rational and ready-to-use structural monitoring tool of reasonable cost that will be used on a routinely basis by the structural engineer commissioned to perform an examination of an existing structure. "Pocket-monitoring" is opposed to many structural monitoring methods that are elaborate, complex, expensive and thus finally uninteresting for practical application. "Pocket monitoring" includes a straightforward low cost measuring equipment that any structural engineer is supposed to be equipped with (in addition to numerical codes for structural analysis).

In this way, structural monitoring shall become as self-evident for the structural engineer as f.ex. software of Finite Element models which nowadays are used on a routinely basis.

"Pocket-monitoring" is also a counter argument against current practitioners' perception of monitoring and so-called "structural health monitoring" as being complex, costly and not yet ready for practical application.

The potential of "pocket-monitoring" will be illustrated by means of the following two examples.

3 EXAMPLE 1: RC DECKS SLAB OF A STEEL – CONCRETE COMPOSITE BRIDGE

3.1 *Motivation and objectives*

A 182m long steel–concrete composite road viaduct built, in service for 60 years, was "assessed" with regards to its structural and fatigue safety (Fig. 3).



Figure 3. Steel – concrete composite road viaduct from 1957, located in Switzerland: overall view and test truck on the viaduct.

The up to 17cm thin reinforced concrete slab acts in the longitudinal direction in composite action with the two steel boxes (Fig. 4). In the main load bearing transverse direction, the slab is fixed by means of steel rebars welded to the top flange of the two steel boxes. The span in the transverse direction is 7.1m apart (equal to the distance between the axes of the two boxes).

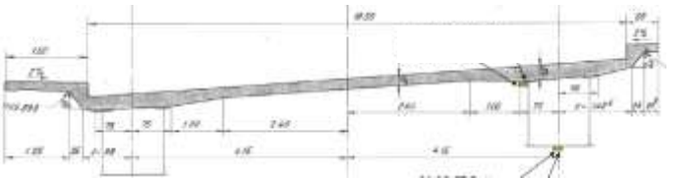


Figure 4. Cross section of the viaduct.

The assessment of the structure was performed using the updated load model according to the Swiss Standard for existing structures (SIA 269/1 2011), thus following Level 1 according to Fig. 1.

The assessment revealed sufficient structural and fatigue safety for the steel structure. The reinforced concrete slab however did not fulfil the safety verifications. In particular, there was uncertainty about the effectiveness of the fixation of the slab on the boxes since the calculated stresses in the rebars significantly depend on the degree of fixity of the slab with the boxes.

Subsequently, it was decided to proceed to an examination by means of pocket-monitoring instrumentation. The objectives were to determine the effective structural behavior, in particular the degree of fixity of the slab, as well as the fatigue relevant stresses in the steel rebars.

3.2 *Monitoring system*

The monitoring followed three steps: 1) installation of the measurement system, 2) load test for calibration of the measurement system, 3) permanent recording of measured values during 12 months.

Remark: In reality, a more complete system of measuring sensors was deployed on the structure in order to exploit measurement results for research purpose. In this paper, only the results as obtained by the "pocket-monitoring" are presented.

3.2.1 *Installation of the measurement system*

Two identical arrangements of sensors were installed in two slab zones of the cross sections at mid-span of two different spans. The acquisition system consisted of three apparatuses, one for electrical strain gauges, one for thermocouples and one serving as unit for storing the continuously recorded data by means of a portable computer. This equipment was safely placed in a solid container fixed to one pier of the viaduct. The monitoring was supervised through internet connection.

Electrical strain gauges (in half-bridge configuration and 5-wire mounting to compensate temperature effects) were installed directly on 4 rebars of each slab zone (after carefully chiseling off of the cover concrete) at the bottom face of the slab (Fig. 5). In addition, strain gauges were also mounted on the flanges and webs of the steel boxes. All strain gauges were protected from humidity by means of a silicone gel and covered with an isolating pad. Measurement frequency was 100Hz.

With this strain gauge arrangement, longitudinal and transversal deformation of the slab is measured and could be related to the deformation measurements of the steel boxes.

In order to account for temperature effects on the structure and on the strain gages, thermocouples were installed at locations close to the strain gages to measure the temperature about 4 centimeters inside the concrete of the slab.

In addition, LVDTs (linear variable differential transducers) were installed to measure the deflection of the slab.

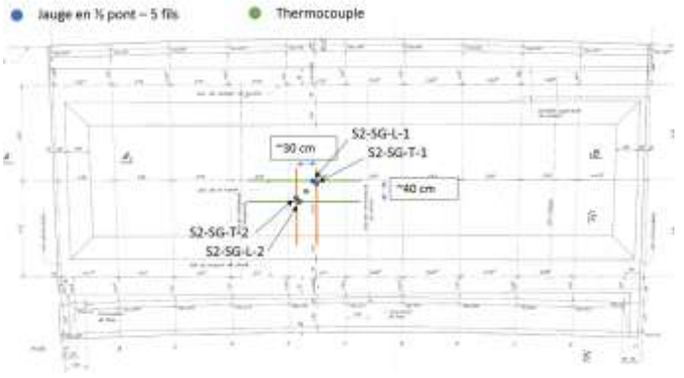


Figure 5. Arrangement of strain gauges on rebars and thermocouples (temperature sensors).

3.2.2 *Load test*

A load test was performed using a loaded truck with 5 axles (Fig. 3) of exactly known load and spacing, totaling a load of 400kN (which is the maximum admissible load on this road). This test track circulated on predefined trajectories on the slab and at different speeds. During the truck passage, regular traffic was temporarily interrupted.

The measurements due to the truck passage served as reference for the measurements obtained from regular traffic. These measurements also served to calibrate a refined FE-Model of the structure to investigate the degree of fixity of the slab.

3.2.3 *Long term monitoring*

Long-term monitoring during 303 days (in the period from August 2016 to July 2017), i.e. there were some interruptions of measurements due to problems with power supply and big data storage.

This monitoring campaign allowed to obtain the histogram of stress amplitudes due to the passage of vehicles due to the effective road traffic that was used for the fatigue evaluation of the RC slab. First fatigue evaluation was already done with the collected stress amplitudes after one month. (Remark: For research purposes, the measurement system is still active.)

3.3 *Results*

The recorded strain amplitudes due to the traffic action effect only were transferred into stress ranges using Hooke's law and a modulus of elasticity of the steel rebar of 205GPa. Rainflow method was used to determine stress amplitudes and number of cycles (Fig. 6).

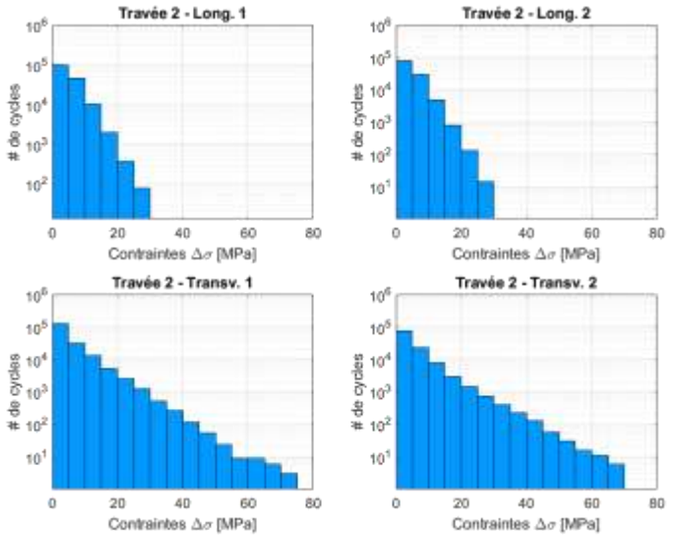


Figure 6. Annual histograms of tensile stress amplitudes for the four instrumented rebars at one slab zone (Fig. 5).

As expected, recorded tensile stresses in the longitudinal slab direction were significantly smaller than the ones in the transverse direction. Largest recorded stress amplitudes were 70MPa, which is a relatively small value with respect to the fatigue strength of straight rebars.

The indication of relatively small stresses was already obtained after the load test and first weeks of readings. This first information was important for the owner to take appropriate action.

The results from the truck load test were used to calibrate a detailed FE Model for the analysis of structural behavior. It was confirmed that the RC slab is fully fixed to the two steel boxes. Full fixity is however only provided if there is no fatigue damage.

3.4 *Verification of fatigue safety*

Verification of fatigue safety is basically following a stepwise procedure consisting of two levels:

- Level 1: verification with respect to the fatigue limit of the considered rebars,
- Level 2: damage accumulation calculation using Palmgren-Miner Law and the appropriate S-N-curve for the rebar detail.

Verification of the fatigue safety of concrete under compression and shear stress amplitudes was not performed. The fatigue related stresses in the concrete of the present slab are significantly lower than 50% of the compressive strength and thus concrete fatigue is not relevant.

Regarding the *fatigue strength of the rebar details*, the values according to the Swiss Standard (SIA269/2 2011) were assumed. In the present case, two different details need to be verified:

- for straight rebars at the bottom face of the slab at mid-span, a fatigue strength (detail category) of 150MPa at 2 million cycles with a slope of m=4 for the fatigue resistance line in the double logarithmic S-N diagram; this results in a fatigue limit at 120MPa (at 5 million cycles).
- for welded rebar at the top flange of the steel box, a fatigue resistance category of 70MPa with a fatigue limit at 56MPa was assumed.

For both details, the assumed fatigue strengths are conservative. Literature indicates higher fatigue resistance, in particular in the domain of small stress amplitudes, f.ex. (Tilly 1979). Therefore, higher values for the fatigue limit could be justified.

Nevertheless, the *fatigue verification* was performed with the conservative fatigue strength values for the two rebar details:

Straight rebars: The results shown in Fig. 6 show measured stress amplitudes smaller than 70MPa and thus significantly smaller than the fatigue limit. Consequently, the fatigue safety of the rebars at mid-transverse span of the slab experienced most likely no fatigue relevant stresses during the previous service life. The fatigue damage is negligible. The fatigue verification is thus fulfilled at Level 1 with respect to the fatigue limit.

Welded rebars: Since the fatigue strength of the rebars welded on the top flange of the steel boxes is significantly lower than for straight rebars, stress amplitudes at this critical detail was performed. Measured stresses were "extrapolated" to this critical detail by means of a detailed FE analysis of the slab – box system. The determined stress amplitudes in the welds were 25% higher than the ones measured in the straight rebars at mid-span. Since these extrapolated stress amplitudes are higher than the fatigue limit of 56MPa, Level 2 fatigue verification was needed. Palmgren-Miner fatigue damage calculation was performed leading to values of about 10^{-3} per year, which is close to zero. Information from the literature suggests a detail category of 100MPa to be more realistic than the assumed one of 70MPa, which would lead to negligible accumulated fatigue damage. It could be concluded that also the critical welded rebar details most likely do not present any fatigue damage and guarantee thus full fixity of the slab.

Temperature effects often have a significant effect on the overall structural behavior and thus on stress levels in the rebars of the slab. These temperature effects need to be carefully considered in order to precisely identify the stress amplitudes due to traffic effects. In the present case of the reinforced concrete slab of the composite structure, it was necessary to analyze measured data over one year in order to reliably capture the effect of seasonal temperature variation on stress amplitudes in the rebars.

3.5 *Findings*

The pocket-monitoring campaign revealed relatively small fatigue related stress amplitudes in the critical steel rebar details. The reinforced concrete slab shows no fatigue damage after 60 years of service duration. Future long-term service duration of the viaduct is thus feasible.

This result is in strong contradiction to the calculated results from the assessment. The discrepancy could be explained by the assumed over-conservative fatigue load model and conservative assumptions for the structural model and the fixity of the RC slab on the steel boxes.

4 EXAMPLE 2: RIVETED STEEL GIRDERS OF A RAILWAY BRIDGE

4.1 *Motivation and objectives*

The 93m long railway bridge in Switzerland is in service for 120 years (Fig. 7). The riveted early steel bridge structure consists of an arch of 48m span and 14.8m rise over a river. The structure is carrying a single lane open, normal-gauge railway track that is fixed to two parallel girders of 0.86m constant height and being 1.8m apart.

These girders have a regular span of 10.0m and are supported by columns and at the arch crown. These girders were designed as single span girders but for constructive reasons some details provide a certain continuity over the supports of the girder system. The bridge abutments are built in natural stone masonry.



Fig. 7. Riveted steel railway bridge built in and in service since 1897; this bridge has a high value as cultural heritage structure.

The assessment of the bridge structure at Level 1 was performed using the updated rail traffic model according to the Swiss Standard for existing structures (SIA269/1 2011). The calculated results showed sufficient structural and fatigue safety for the arch and the columns. Sufficient structural safety at ULS (sectional resistance) was also obtained for the girders assumed as single span girders. However, the fatigue safety could not be verified under these assumptions.

Subsequently, it was decided to proceed to an examination by means of "pocket-monitoring". The objectives were to measure the fatigue relevant stresses in the girders and to determine the effective structural behavior of the girder system in terms of a continuous girder system under service loading.

4.2 *Monitoring system*

Because of easy access, the first span near one abutment was chosen to install the monitoring system (Fig. 8) in May 2017.



Figure 8. Edge girder field and scaffold for access to the monitoring system (sensor locations indicated by red rectangles).

During one day, 18 sensors consisting of 14 strain gauges, 2 clip gauges (to measure gap opening displacement between two girders above the support) and 2 temperature gauges, were installed together with two data amplifier/acquisition systems including a portable computer for data storage. Four cross sections, one at mid-span and three close to the intermediate girder support above the first column, were equipped (Fig. 9). The frequency of measurement was 300Hz.

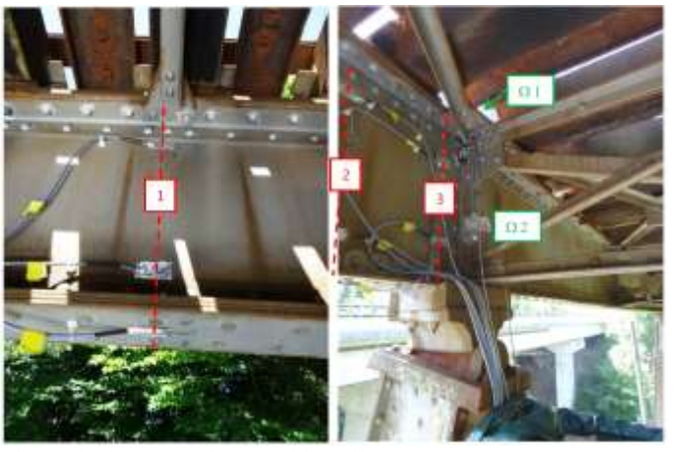


Figure 9. Cross sections and installed sensors.

Continuous measurement readings of train passages were recorded during 4 weeks only. Because of the present type of lightweight structure, it could be anticipated that seasonal temperature effects would not

significantly affect the overall structural response of the bridge structure. This assumption was confirmed by equal histograms of recorded stress amplitudes after 1, 2 and 4 weeks.

In addition, the bridge is exclusively used by only two different types of passenger trains. There are no freight trains. This led to repetitive readings of similar values.

4.3 *Results*

The bending moments deduced from the measured strains evidenced structural behavior similar to a continuous girder system.

The recorded strain history of the train passages showed no dynamic effects (Fig. 10). This is rather surprising since dynamic effects may be expected in the case of an open railway track fixed to a lightweight structure. However, the effect of continuous rails of good surface quality seems to have a favorable effect.

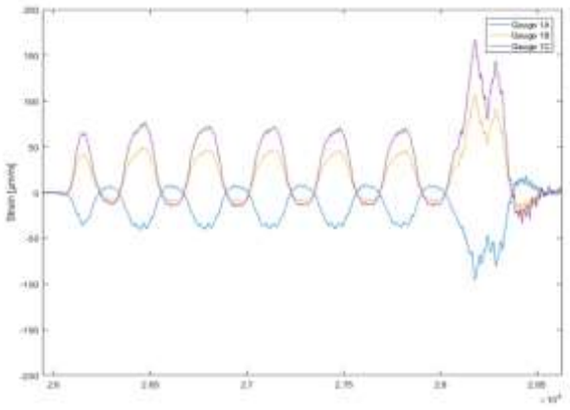


Figure 10. Strain versus time record (structural response) due to the passage of a train hauled by a locomotive (with 4 axles of 200kN) followed by passenger wagons (Fig. 8).

The histogram of fatigue relevant stress amplitudes in the critical cross section at the bottom flange at mid-span of the girder revealed relatively small maximum stress values of 42.5MPa (Fig. 11).

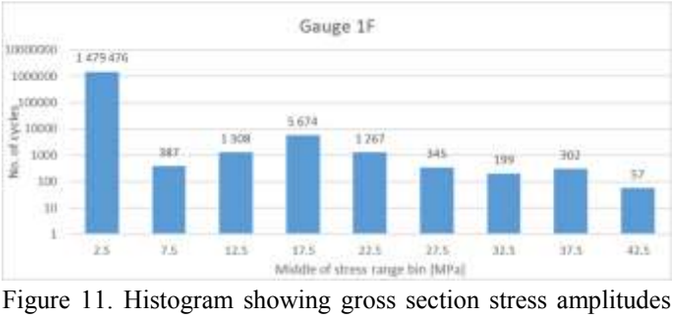


Figure 11. Histogram showing gross section stress amplitudes measured during 4 weeks in the critical cross section at mid-span of one girder.

4.4 *Verification of fatigue safety*

Again, the concept of stepwise verification was applied with the first objective, at Level 1, to verify the measured stress amplitudes with respect to the fatigue limit of the critical detail.

According to the Standard (SIA 269/3 2011), the fatigue detail category for the riveted girder is 80MPa with a fatigue limit of 56MPa.

The measured gross section stress values were modified for considering net section stresses leading a maximum fatigue stress amplitude of 52MPa to be considered for the verification.

In addition, past railway traffic was analyzed in terms of axle loads and axle configurations of previous trains. The railway owner has no plans to increase the trainloads in the mid-term future. From this follows, that most likely there was and will be no fatigue stress amplitude larger than 52MPa.

The fatigue safety on Level 1 with respect to the fatigue limit is verified graphically according to Figure 12:

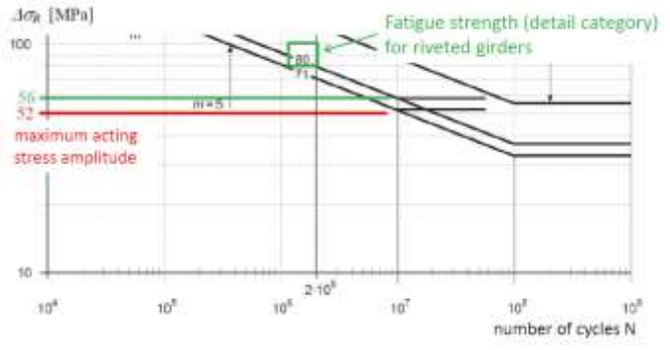


Figure 12. Graphic fatigue verification of the riveted girder, at Level 1, with respect to the fatigue limit.

4.5 *Findings*

Similar to the first example, the pocket-monitoring campaign revealed relatively small fatigue related stress amplitudes in the critical riveted details at the bottom flange of the girder and for the details in the support zone over the column.

These determined fatigue stresses are smaller than the fatigue limit of the detail, and thus there is no fatigue damage in the riveted structure even after 120 years of service duration.

In addition, the measurements allowed unveiling the real structural behavior of the girder system.

Again, these findings are in strong contradiction with the "re-calculation" in the context of the assessment. The discrepancy was explained by the over-conservative rail traffic load model given in (SIA 269/1 2011), the absence of dynamic effects and conservative assumptions in the structural analysis model.

5 DISCUSSION

The two examples show that regarding existing bridges, a greater source of uncertainty lies in the *modeling of traffic loading* and the determination of

the action effects arriving in the structural elements, i.e. in the steel rebar and in the riveted joint detail.

In recent years, increasingly sophisticated approaches have emerged for load effect estimation using traffic simulations incorporating Weigh-in-Motion (WIM) data which form the basis of load models in design and "assessment" codes. While vital for design of new bridges, these codes are based on generic heavy vehicle data from a range of locations and therefore may not always represent the site conditions at the existing bridge under investigation. In addition, codes include provisions for illegally overloaded vehicles which could be reduced substantially through adequate policing (on roads and also on railways).

"Re-calculation" using "assessment" codes are therefore to over-conservative, in particular in the context of fatigue safety verification. Current methods should thus be replaced by more realistic methodology relying on data from monitoring of real structural behavior of the existing bridge in question.

Regarding *sensor technology for monitoring*, electric strain gauges, like the ones used in the presented two examples, actually suffer from a bad reputation. Strain gauges are considered as an "old technology" that is not reliable on the long-term (excessive drift) and too difficult to compensate for temperature effects. As a result, strain gauges are not used for monitoring or they are used only for very short periods of measurements.

Our experience is that correctly installed and protected, temperature compensated strain gauges withstand a full year (and longer) of measurements without significant drift or any other non-structural effect. In addition, a defect resulting from poor glued bonding or welding of the gauge and local magnetic interferences would be immediately visible on the signal.

If temperature and long-term effects are reliably mastered using strain gauges fully compensated for drift and temperature, measurement uncertainties are limited and the measurement results are precise and reliable (Loraux 2018).

6 CONCLUSIONS

The methodology of "pocket-monitoring" has been introduced to examine the fatigue safety of critical details of existing bridges. The following conclusions are:

The monitoring allows to determine real structural behavior and realistic fatigue relevant stresses. In addition, uncertainty in structural behavior could be reduced and refined numerical structural models could be calibrated to account for real behavior. Monitoring thus allows to gain much more precise and realistic information.

The two presented pocket-monitoring devices turned out to be relatively easy to install and robust, leading to reliable readings.

Overall, examination by means of pocket monitoring is highly economic since the results in both presented examples showed largely sufficient fatigue safety, and thus no intervention is needed (while conventional "assessment" by "re-calculation" recommended costly interventions).

7 REFERENCES

Brühwiler E. 2017. "Getting more out of existing structures", *Khan Distinguished Lecture Series*, February 17 2017, Lehigh University, Bethlehem PA, USA: http://www.lehigh.edu/~infrk/2017/frk17bruhwiler.html

Brühwiler E., Vogel T., Lang T., Lüchinger P. 2012. Swiss standards for existing structures. *Structural Engineering International 22(2),* IABSE Zurich, pp.275-280.

Loraux C. 2018. Long-term monitoring of existing wind turbine towers and fatigue performance of UHPFRC under compressive stresses, PhD Thesis No 8404, Swiss Federal Institute of Technology (EPFL) Lausanne, Switzerland.

Standard SIA 269 2011. *Existing structures – Bases for examination and interventions.* Swiss Society of Engineers and Architects (SIA), Zurich.

Standard SIA 269/1 2011. *Existing structures – Actions.* Swiss Society of Engineers and Architects (SIA), Zurich.

Standard SIA 269/2 2011. *Existing structures – Concrete structures.* Swiss Society of Engineers and Architects (SIA), Zurich.

Standard SIA 269/3 2011. *Existing structures – Steel structures.* Swiss Society of Engineers and Architects (SIA), Zurich.

G. P. Tilly – Fatigue of steel reinforcement bars in concrete: a review. 1979

Maintenance, Safety, Risk, Management and Life-Cycle Performance of Bridges – Powers, Frangopol, Al-Mahaidi & Caprani (Eds)
© 2018 Taylor & Francis Group, London, ISBN 978-1-138-73045-8

Structural risk assessment and management through the capture of dynamic movement.

M. Kudrenko
Mainmark, Melbourne, Australia

ABSTRACT: Mainmark have introduced the STRAAM system of full scale structural integrity assessment and continuous monitoring for dams, buildings and bridges into Australia and New Zealand. Advances in measuring extremely low amplitude vibrations combined with methods for extracting the unique dynamic signature have now enabled the rapid measurement of the response of steel and concrete structures. The STRAAM method utilises the normal traffic conditions and wind loads on the structure to measure the frequency response of the structure. This allows the quick calibration of Finite Element Models that can be used to accurately assess the strength of the structure. Furthermore, this information allows asset owners to efficiently track changes in the capacity of their structures due to aging, impact, earthquake or flood activity through changes in the vibration of the structure and associated natural frequencies, mode shapes and damping ratios.

1 INTRODUCTION

1.1 *Mainmark and STRAAM*

Mainmark have partnered with STRAAM Group from New York to introduce the STRAAM structural risk assessment and management system for structures into Australia and New Zealand. The STRAAM system allows for rapid, non-invasive assessment of a structure's current status.

1.2 *Non-intrusive & non-destructive assessments*

The testing of steel and concrete structures using high technology has become fast, cheap and precise. At the same time, it is non-intrusive and gives both basic information and information that would be difficult to obtain by conventionally assessments. This has been enabled by the use of induced vibration testing of a series of structures both in Europe and the USA. With the increasing availability of high precision accelerometers, microscopic movements of structures can be recorded and analysed. As a result, it is possible to use the simple methodology associated with naturally occurring excitation to decode the state of health of the structure and view its performance objectively.

2 DYNAMIC MEASURMENTS

2.1 *Philosophy of assessment with STRAAM*

With the developments of electronics and sensor technology, the ability to record very precise measurement properties of monolithic structures has led to a rationale for the management of such facilities with a methodology that enables the augmentation and enhancement of traditional visual inspections (Jeary et al).

Newton's second law of motion is used for the basis of the equations of structures in dynamic motion. This is also applied to a structures individual modes of vibration. The equation to express this sort of motion, under each mode 'r', can be presented as:

$$m_r = \frac{\hat{\mathrm{F}}_r}{\hat{x}_r \, 8 \, \zeta_r \, \pi^2 \, f_{r^2}} \qquad (1)$$

Where, the displacement is x_r from mode 'r' for and applied for of F_r. The dampening ratio is f_r and the frequency of resonance is F_r.

2.2 *Dampening and displacement*

For application however we are generally most interested in the dampening value and the displacement per unit force value; the reason being is that a dampening value is used as a parameter to give the measurement of energy dissipation on a structure, where the displacement per unit force allows for a comparison with the requirements of design construction. As the modal mass, m_r, does not change in the elastic regime for any single mode, measurements of non-linear dampening characteristics and frequency of resonance provide

the necessary information to compare the capacity ratio to the demand. Every structure type has a characteristic vibration modes, which requires that the deflected mode shape that is representative of mode 'r' also needs to be assessed as all of the above parameters apply to individual modes of vibration. For this reason, this method can be applied to many types structures whether they contain stone, steel, timber or concrete.

2.3 *Forced excitation*

Previous works of calibrating forced excitation against natural excitation have existed for some time now (Ellis et al) and the calibration of the non-intrusive simple methodology against the induced vibration approach is detailed here. As a result, it has made it possible to use the simple methodology associated with naturally occurring excitation to decode the state of health of structures. A typical methodology for the induced vibration testing can be described as follows:

1. Vibrators were located a strategic sections of a structure. The frequency of excitation is incremented sequentially and a response/frequency curve was obtained;
2. A frequency of resonance is selected and the vibrators are set to operate at this frequency;
3. An accelerometer is taken to various locations of interest, in turn, and the vibration amplitude is measured at each position, both longitudinally and across the structure;
4. The vibrators are suddenly switched off, and the ensuing decay of oscillation is used to estimate the damping ratio for this mode of vibration;
5. Steps 2, 3 and 4 are repeated for each resonance in turn;
6. The vibrators are redeployed in different locations and Steps 1-5 inclusive were repeated for further modes of vibration;
7. Step 6 was repeated with a further redeployment of the vibrators
8. A recording of the ambient response was made for a period of about 12 hours.

A certain amount of background vibration is observed which, on occasions, made the measuring of the lower frequency responses rather difficult.
For the use of ambient excitation step 8 only is required, although the necessary recording time is dictated by the lowest frequency of resonance of the structure.

2.4 *Utilising natural excitation*

The methodology requires a force to be applied to the structure. Because a series of structures were tested using induced vibration testing (with a large vibrator system), and these results were correlated against the response of structures from naturally occurring forces, then the non-intrusive methodology has been calibrated in the most precise way possible. Examples of naturally occurring forces include wind, traffic and micro-seismic activity. Because of the precision of the instrumentation used it is no longer necessary to wait for an event such as an earthquake for the state of health of the structure to be assessed. In this way regular or continuous monitoring can also be used to show the gradual ageing process for the structure. Such detailed information allows the management of facilities and the planning of necessary maintenance that is informed by measurement. This type of measurement is capable of discerning information about problem areas of a structure that are not apparent to a visual observation, and therefore offers a significant advantage over a more conventional type of inspection. This type of measurement can also be performed quite quickly structure and is economically efficient.

In practice, the force can be applied from natural sources such as air movement, traffic or other human agency.

The following describes the response of as single degree of freedom (mode 'r').

$$\boldsymbol{X_r} = \frac{F_r}{8 f_r^2 \zeta_r M_r \pi^2} \tag{2}$$

Where for mode 'r'
M is the participating mass
f is the frequency of resonance
F is the force
Ϛ is the damping ratio of mode r

Thus the displacement per unit force can be defined as:

$$\frac{X_r}{F_r} = \frac{1}{8 \zeta_r f_r^2 M_r \pi^2} \tag{3}$$

- The displacement per unit force is inversely proportional to the damping times the stiffness.
- If the modal mass is unchanging, and the mode shape is unchanging then for a given frequency and damping for a mode 'r' the displacement per unit force will remain unchanged up to the elastic limit.
- In practice there may be small changes in the frequency of resonance (as a function of amplitude – not as a function of time). There

will be changes to damping with amplitude. However, we can compensate for such effects by measuring the non-linear damping.

2.5 *Dynamic response to 'dynamic signature'*

There are several system-level parameters which aid in the conversion from dynamic response (acceleration records) to Dynamic Signature, and identification of damage in a structure during a STRAAM structural assessment. These include:

1. Gross migration of frequency of resonance away from the expected response. In particular, the loss of stiffness in each mode of vibration can be estimated by comparing the differences in measured frequencies of resonance from the expected values. Lower frequencies indicate a loss of stiffness in a particular mode of vibration.
2. Spectral bifurcations whereby a principal mode of vibration shows signs of splitting into several modes of vibration. This indicates that the structure is forming mechanisms and that local resonances are forming.
3. Changes in modal amplitude ratios can be tracked over time to show indications of changes to particular modes of vibration which can indicate that parts of the structure are responding differently from previously. Inferences of damage or strengthening can be made utilizing these changes along with other observations.
4. Energy dissipation as measured through the nonlinear damping parameter. Damping values which are higher than expected are clear indications that energy is being dissipated through cracking, rubbing of structural members or unexpected soil-structure interaction (foundation damage). This measure generally requires a long duration of measurement such as that obtained with continuous monitoring in order to establish the full amplitude dependent damping behaviour.

3 DIGITAL SIGNAL PROCESSING

3.1 *Baseline Spectral Response Analysis*

The on-site measurements of acceleration are processed using standard and proprietary digital signal processing (DSP) techniques to facilitate the extraction of relevant dynamic properties of the structural system. The main output of the DSP process is the decomposition of the time-series acceleration data into its frequency content (Power Spectral Density). The spectrum is interpreted to identify the modes of vibration (frequencies of resonance, amplitudes and modal ratios) of the structure. This forms the baseline Dynamic Signature and is essentially a fingerprint of how the structure is currently behaving with resonances appearing as isolated peaks in the plots. This baseline Dynamic Signature provides the datum with which future dynamic responses can be compared for assessment of changes to the structure's performance.

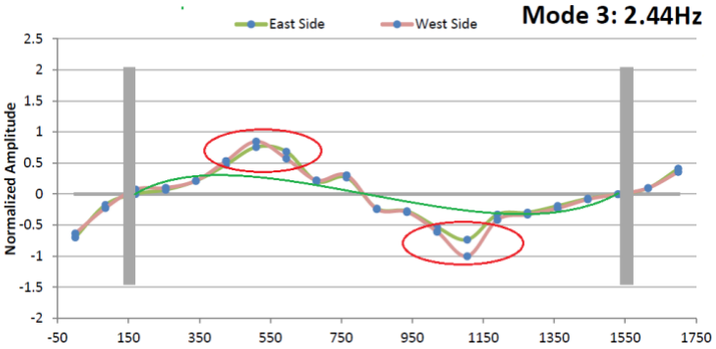


Figure 1. Example of a 2nd Order mode showing stiffness anomalies

3.2 *'Baseline' methodology*

STRAAM uses a systematic approach, called the STRAAM Protocol, to understand how a structure behaves and for developing the best approach of monitoring the structure for an assessment and then long term monitoring. The STRAAM Protocol involves several steps necessary to establish the baseline Dynamic Signature of the structure:

1. Step 1 (Site Survey, Photos, Drawings, Reports) is to gather field information so that the monitoring plan will achieve the project goals efficiently and the transfer of design drawings and photos. This is accomplished through interaction with project stakeholders prior to data recording.
2. Step 2 (Structural Model and Frequency Range Identification) we will use the existing FEM (or construct our own internally) to understand the expected response, mode shapes and frequency ranges for the structure. Additionally, it can help locate areas of the structure which will provide the greatest response for our instruments. This is all integrated into an advanced monitoring plan that is designed to best achieve the project goals.
3. Step 3 (Data collection/ Signal Conditioning) we proceed to the field to capture response information from the structure in an efficient and effective manner. When monitoring, we record acceleration with highly sensitive acclerometers (along the X, Y and Z axis) and temperature at a rate of 200 samples per second for the acceleration, and 1 sample per second for the temperature. The sensitivity of

the instruments allows STRAAM to capture low amplitude response information to be used for analysis. Local excitation (wind loading and nearby traffic for example) is all that is require to capture acceleration response, although known force can also be applied to drive excitation.

We then proceeded with steps 4-7 of the STRAAM Protocol where we process the data into the response spectra and compare the dynamic resonant frequencies in various modes and various conditions. This iterative process completely correlates the measured response with the expected response from the model. For most structures, the baseline data recoding can be completed in as little time as a day.

3.3 *Continuous monitoring methodology*

Continuous monitoring of a structure follows similarly to that of the baseline recording of a structure, however the data collection phase remains on going for the duration of the project. This is useful as it allows for the real time monitoring of structures and how their dynamic response may change over time due to external influences. Examples of this could be nearby constructions works or seismic events impacting structures foundations, the effect of a severe weather event or even the increase in loading on structural elements.

4 RECENT STRAAM APPLICATIONS

4.1 *Bridge Spanning Dandenong Creek, VIC*

A Super-T, duel lane single span bridge crossing Dandenong Creek in Victoria required ground works to correct sunken approach slabs to the bridge deck.

The STRAAM system was used at this site before works to calibrate a FEM model using a known load passing over the bridge. The bridge then has sensors strategically placed to capture the baseline dynamic signature of the structure and then monitor in real-time the dynamic effects of the ground correction works on the bridge.

This gave the ground works contractor certainty in knowing they were not causing damage to the bridge as a result of there earth works.

4.2 *Camperdown Childcare Centre, NSW*

The Guardian Early Learning Centre in Camperdown, New South Wales is an inner-city childcare facility that provides day care for children from infants to pre-school age. Due to its urban location, the centre wanted to utilise its roof area to create an extra play space for the children.

The rooftop had been added onto the building's original roof structure as an open space area that could be walked on. The Guardian Early Learning Centre wanted to add landscaping and additional play equipment to the rooftop area, while ensuring it remained within Australian Standards for safety.

Adding higher loads, such as saturated soils and other landscaping materials that might hold water, could significantly increase the loading on the roof. The Guardian Early Learning Centre had limited information on the roof's design capacity and needed to understand, with certainty, how much load the roof could safely bear to help determine landscaping decisions.

The consulting engineer engaged Mainmark to provide a structural capacity assessment of the roof using its unique Structural Risk Assessment and Management (STRAAM) technology. Mainmark recorded the building's natural vibration frequency and determined a baseline dynamic signature, then performed a random decrement algorithm (RANDEC) to evaluate the direct measure of the structure's non-linear damping response.

Data was collected over the course of two days and analysed to determine the roof's likely performance under additional loads. Based on the results, the Guardian Early Learning Centre has could proceed safely with its landscaping project.

4.3 *Hong Kong Office Building*

During the construction of a MTR rail tunnel, a partial collapse of the ground at the face of the TBM occurred. This ground movement was observed as a loss of support at a high rise office building approximately 400 m away from the TBM location. The movement of the office building was perceivable, and damage to the façade was observed. The building was evacuated at the time.

The STRAAM sensors were monitoring the structure at the time to determine the structural condition of the building. The random decrement graph (damping vs amplitude) picked up the loss of capacity in the structure. At the time of the event, the structure exhibited significant loss of damping at low amplitudes, indicating probable loss of load bearing at the supports due to the ground movement.

In the following month, the low amplitude damping improved for the structure, most likely due to load redistribution through the concrete frame. The high amplitude damping was approximately 10%

lower after the event; which represents a 10% loss in wind loading, usually the critical load case for Hong Kong structures. However, the building had sufficient over design to cope with the 10% loss.

4.4 *High School, Houston*

A three storey, brick high school was assessed using STRAAM prior to a substantial redevelopment. The purpose was to conduct a Dynamic Baseline Assessment that could be then used to monitor the risk as the redevelopment progressed and to observe the efficiency of the redevelopment after it was completed.

The modes of vibration were identified for the structure. The frequency and damping values obtained indicate the building is generally in good condition, without significant damage.

Anomalies were identified at a few locations. Vertical movement on the north elevation indicates a possible concern with soil conditions or foundations at this location; a possible source of future façade cracking if not addressed. A remnant low amplitude response at the third floor of the centre stairwell suggests a possible crack between the third floor and the roof at this location. The identification of these anomalies, showing some degradation in specific areas, were inputs to the redevelopment works.

4.5 *Bridge 329, Chicago*

Bridge 329, owned by the Illinois Highway Authority. carries traffic in an area near Chicago in the USA. The bridge is a four-lane highway with a further lane acting as a hard shoulder. The deck of the bridge is supported by 10 precast, pre-stressed girders that are standard for this type of bridge.

The purpose of the investigation of the dynamic behaviour of Bridge 329 on the Illinois Highway Authority's Network was to investigate whether the bridge was behaving normally or whether it had suffered unseen damage due to an electric current that flowed through the bridge. STRAAM performed a finite element calibration exercise on the bridge. The STRAAM measurements of the bridge were undertaken in a single day in December 2009.

The calibration exercise was detailed and accurate to within 5%. The simplicity of the structure and of its behaviour showed that producing models of such structures are accurate and simple. The finite element model is adjusted by changing the element masses and stiffnesses until the predicted frequencies of vibration correlate well with the measured frequencies from the field. The target is to have the model correspond to within 5% of the fundamental frequency and within 10% of the other lower order recorded frequencies.

The assessment determined the bridge was working within the elastic range and performing as designed.

5 CONCLUSION

Structural risk management assessment and management provide by Mainmark through STRAAM allows for rapid, real time assessment and then reporting of structures. Through measurements of highly sensitive accelerometers and strategic placement, a baseline record of the structure can be obtained and built into a finite element model and calibrated against the structures recorded response, greatly increasing the accuracy of the generated model. From the FEM, serviceability and loading conditions can then be modeled and assessed to allow for the concerned parties to have objective information regarding their asset and make informed decisions based on the actual condition of the structure.

6 REFERENCES

Jeary A.P., Winant T, Bunyan J. Some of the measurement of vibration intensity for the assessment of Building Structures. ASCE 8th Foresics Conference. Performance of the Built Environment. Miami Florida. November 2015.

Ellis, B.R., Jeary, A.P. and Severn, R.T.: Integrity monitoring of dams by dynamic tests, *Proceedings of the International Conference on Safety of Dams*, Coimbra, Portugal, p147-152, Apr 1984.

Deinum, P.J., Dungar, R., Ellis, B.R., Jeary, A.P., Reed, G.A.L., Severn, R.T.: 841255 Variations tests on Emosson arch dam, Switzerland, *Earthquake Engineering Structural Dynamics*, Vol 10, No 3, p447-470, May-Jun 1982 and *International Journal of Rock Mechanics and Mining Science & Geomechanics Abstracts*, Vol 21, Issue 1, pA29, Feb 1984.

Maintenance, Safety, Risk, Management and Life-Cycle Performance of Bridges – Powers, Frangopol, Al-Mahaidi & Caprani (Eds)
© 2018 Taylor & Francis Group, London, ISBN 978-1-138-73045-8

Continuous structural health monitoring for short and medium span bridges

A. Miyamoto
Professor Emeritus of Yamaguchi University, Ube, Japan
(Visiting Professor of EPFL, Lausanne, Switzerland)

ABSTRACT: In this paper, although there are some useful monitoring methods for short and medium span(10-20m) bridges based on the qualitative or quantitative information, mainly two advanced structural health monitoring systems are described to review and analyses the potential of utilizing the long term health monitoring in safety assessment and management issues for short and medium span bridge. The first system is a special designed mobile in situ loading device (vehicle) for short and medium span road bridges to assess the structural safety (performance) and derive optimal strategies for maintenance using reliability based method. The second system is a long term health monitoring method by using public buses as part of a public transit system (called "bus monitoring system") to be applied mainly to short and medium span bridges, along with a safety index, namely, "characteristic deflection" which is relatively free from the influence of dynamic disturbances due to such factors as the roughness of the road surface, and a structural anomaly parameter.

1 INTRODUCTION

It is becoming an important social problem to make maintenance and rehabilitation of the existing short and medium span(10-20m) bridges because there are a huge amount of short and medium span bridges in service in the world. This paper describes a frontier of continuous bridge health monitoring system for not only a rational bridge health monitoring system incorporate with the information and communication technologies for lifetime management of the existing short and medium span bridges but also a data collecting system designed for bridge health monitoring of mainly short and medium span bridges. In this paper, although there are some useful monitoring methods for short and medium span bridges based on the qualitative or quantitative information, mainly two advanced structural health monitoring systems are described to review and analyses the potential of utilizing the long term health monitoring in safety assessment and management issues for short and medium span bridge. The first is a special designed mobile in-situ loading device (vehicle) for short and medium spam road bridges to assess the structural safety (performance) and derive optimal strategies for maintenance using reliability based method. In here, the concept of experimental safety evaluation will be discussed; the loading vehicle for short and medium span road bridge testing as well as essential operating experiences gained in practice will be described (Gutermann & Schröder 2013, Gutermann et al. 2003). The second is a long term health monitoring method using public buses as part of a public transit system (called "bus monitoring system") to be applied mainly to short and medium span bridges, along with a safety index, namely, "characteristic deflection" which is relatively free from the influence of dynamic disturbances due to such factors as the roughness of the road surface, and a structural anomaly parameter (Miyamoto & Yabe 2012). In here, it will be described the details of how to assess the bridge condition by public bus vibration measured in operating on an Ube City bus network in Japan, as a specific example for verify the system.

2 IN-SITU SAFETY EVALUATION SYSTEM BY A LOADING VEHICLE

As one of the useful data collecting systems related to structural safety assessment such as load carrying capacity or durability in existing bridge site, a German research team dealt with an unique experimental safety evaluation system (loading vehicle and measuring equipment) by in-situ loading tests for mainly short and medium span bridges (Gutermann & Schröder 2013, Gutermann & Schröder 2012). In order to optimize the assessment procedure, methods and equipment of the system have been established for increasing refinement and complexity from following points of view:

① to adequate the formulation of a German national technical guideline for loading tests (DAfStb 2000); load tests up to service load (e.g. under normal traffic operation) ,

② to make clear the assessment procedure of the actual load carrying capacity may prove directly by using a special designed loading vehicles and special loading technology for mainly short and medium span bridges , and

③ to determine the structural safety experimentally by performing an in-situ loading test without causing any damage which would impair the safety or the durability of the target bridge.

2.1 *Concept of the Experimental Safety Evaluation by an In-situ Loading Vehicle, BELFA*(Gutermann & Schröder 2013)

For purpose of experimental safety evaluation in-situ for a target bridge as a structural health monitoring system, a special designed (mobile) loading vehicle has been developed for performing loading tests at the road bridge site in a more effective way (Gutermann 2003). It is named "*BELFA*" after the German word "Belastungsfahrzeug" for loading vehicle and may be moved on public roads. It allows conducting these experiments without the cost and timing consuming construction of reaction frames [*www.belfa.eu*]. The project was funded by the Bundesministerium für Bildung und Forschung BMBF (about 1.85 million euros). The loading vehicle as the final design, *BELFA*, consists of a tractor truck with 4 axels and a special semi-trailer with 5 axles as shown in Fig. 1. *BELFA* has 80 tons in total weights, the length amount to 22.5 m in transportation mode and up to 35.5 m in testing mode (see Table 1). It may be also used to apply loads up to 1500 kN so that the common load levels and loading diagrams can be conducted (e.g. in Germany: bridge class 60, which is the highest bridge class in the German standard DIN 1072). As shown in Table 1, *BELFA* has generally the technical limitations that a span of target bridges has to be less than 18m, that is short and medium span bridge, and to be smaller than Germany bridge class 60 loads as the maximum applied load in-situ.

As the operation sequence, the loading vehicle, *BELFA* is driven to the target bridge using its own tractor truck. A special driving permission is needed every time since *BELFA* has over length and overweight. It stops in front of the bridge where the truck is pulling out the front part while the rear axles are blocked. The saddle score of the truck can be reduced additionally by de-airing the pneumatic shock absorption of the last three axles. Thus the truck may cross the bridge, which load carrying capacity is still unknown, with the lowest possible weight. To ensure a riskless crossing it is expedient to assess the structural behavior using the measurement equipment that was installed before. When the first of the rear axles is reaching the bridge, they are blocked again and the middle part is pulled out, too. *BELFA* is placed in the right position and fixed in the desired length. The maximum distance between these supports amounts to 18 m which limits the span of the bridges to be tested to this length. The correct position and length is important since the centre of mass must be in accordance with the planned loading positions. Afterwards all axles are de-aired and are fixed to the vehicle chassis in order that all of the masses were usable as counter-force for the test loading. Four hydraulic jacks, two in the front and two in the rear, are lifting up the whole vehicle so that it serves like a reaction frame. Now starts the self-driving deck crane, which can be moved in the longitudinal direction, to place entrained weights on the chassis. If this weight is not sufficient for compensating the test loads applied, additional ballast weight is required. For that, an on-board water bag may be

Table 1. Essential data of *BELFA* (Gutermann & Schröder 2013)

Length in transportation mode:	22.5 m
Max. length in working position:	35.5 m
Max. distance between supports	18.0 m
Total weight	approx. 84.5 t
Max. test load (without additional dead freight)	approx. 750 kN
Max. permissible test load	1500 kN

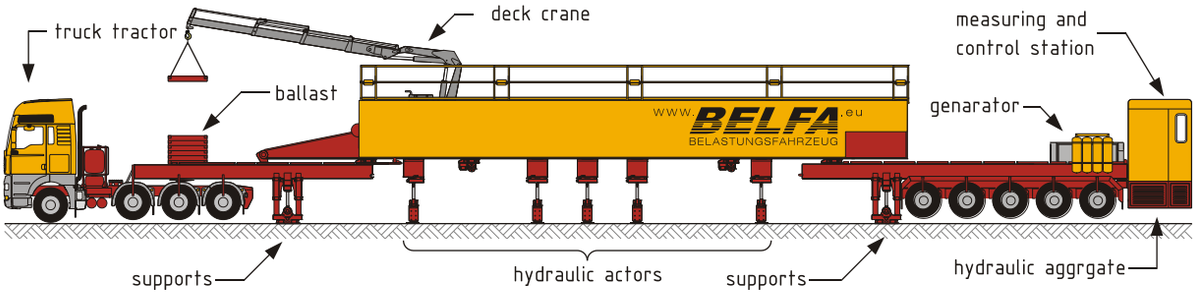


Figure 1. Basic elements of *BELFA* in working position (Gutermann & Schröder 2013)

filled with up to 20 tons of water. If still the reaction force is too low, the *BELFA* may be anchored at the bridge supports by using high-strength steel bars or may be ballasted additionally with external weight. Doing so, the centre of mass must be adjusted to the desired position. The hydraulic actors were moved to the test position, which may be at any point between the supports, and their load distribution beams were lowered to the pavement.

During a load test at the bridge site as shown in Fig. 2, the existing bridge components such as main girders and slabs with an unknown effective load carrying capacity is assessed. Though the effects of loading on the bridge (e.g. deformations) can be measured, the magnitude of the present dead load as well as the ultimate strength is unknown. All equipment must work electronically and has to be integrated in an online measurement system to ensure that the critical load level is definitely identified, which is characterised by beginning damage processes. The experimental safety evaluation without causing any damage is tied to two important technical prerequisites:

① The application of the test loads has to be undertaken in a way that sudden failure of the structure is avoided even in the case of unexpected damage.

② During test loading, the behaviour of the structure has to be monitored continuously and evaluated in real time (e.g. deformations and micro crack formation). In this way, critical load levels are identified and the loading program may be altered in order to avoid damage to the structure. Limit criteria have to be determined prior to the test according to the recommendations (DAfStb 2000).

The best results concerning a safety evaluation are obtained if the structural behaviour above the service load level can be assessed experimentally.

2.2 *Safety Assessment and Application to Actual Bridges* (Gutermann & Schröder 2013)

The German guideline for loading tests (DIN 1072 1985) shows the equation how to calculate the applied test load, $ext\ F_{target}$ for the target bridge,

$$ext\ F_{target} = \sum_{j>1} \gamma_{g,j} \cdot G_{k,j} + \gamma_{q,1} \cdot Q_{k,1} + \sum_{i>1} \gamma_{q,i} \cdot \psi_{o,i} \cdot Q_{k,i} \quad (1)$$

where,

$0{,}35\ G_{k,1} \leq ext\ F_{target} \leq ext\ F_{lim}$,

$G_{k,1}$:Characteristic value of existing structural permanent action,

$G_{k,j}$:Characteristic value of additional self-weight *j,*

$Q_{k,1}$, $Q_{k,I}$:Characteristic value of variable action (traffic loads) respectively of main variable action *i,*

$\gamma_{g,j}$: Partial safety factor of permanent action *G,*

$\gamma_{Q,1}$, $\gamma_{Q,I}$: Partial safety factor of variable action *Q,*

$\psi_{o,I}$: Combination coefficient in case of several variable action *Q.*

The particular values for partial safety factors and for combination coefficient can be found in pertinent recommendations or national appendices (DIN EN 1990 2010). However one special feature of load tests is that the target bridge exists and the self-weight is already acting. Thus this safety margin must not be included in the calculation of the test target load $ext\ F_{target}$ ($\gamma_{g,I}$=1.0). Dynamic effects also are considered by increasing the variable action using a dynamic coefficient, φ which is dependent on the bridge span. The maximum value of φ is 1.4 for short bridges and cannot fall below 1.0 if the span exceeds 50 m (DIN 1072 1985).

During the loading test, influential factors can reduce the stress level, thus the attempted load conditions in the structure are not reached, e.g.

- system influences (part restraint, abutment settlement, lateral distribution),
- structural layers (sealing, slope/safety concrete, pavement concrete, road surfaces),
- formation of the cantilevers and caps (incl. solid railings),
- ambient influences (e.g. temperature).

If they do not have the same permanent effect on the structure, the test target load must be increased by an overload ΔF to compensate this reduction (Gutermann 2004). Then the effective applied test load for the target bridge is $ext\ F_{target}=F+\Delta F$ and generates the stress level in the structure to be verified according to the recommendations. Prior investigations have shown that e.g. pavement acts as a quasi-monolithic strengthening of the structure.

As an example of applying the *BERFA* in-situ loading system to the target bridge which constructed in 1970 and crossed a river in Germany (BS-bridge) with a span of 12 m length. Its cross section consisted of 19 prestressed precast concrete beams which were completed with poured in-situ concrete. Identical loading tests (place and magnitude) were performed in the following conditions of the bridge structure (see Fig. 3):

① initial condition(1),

② after removing the asphalt(2),

③ after removing asphalt and protection/sloping concrete(3),

④ after removing asphalt, protection/sloping concrete, pavement concrete(4).

As a result, Fig. 3 shows the load deflection curves of first loading cycle at midspan under above

four conditions. In this case the determined overload factor was 1.04 (ΔF=0.04 × F) taking only the influence of asphalt into account. Further studies have shown that the coefficient can rise up to 1.26. In the case of constant factors such as restraint effects from concrete joints or earth resistance on the abutments, it is presumed that this influence has the same favourable effects for the residual use period. These influences do not have to be taken into account in the form of an overload and can be used therefore as potential for a higher experimental bridge rating.

3 HEALTH MONITORING SYSTEM BY USING PUBLIC BUSES

In order to properly maintain numerous short and medium span bridges in Japan by conducting periodic inspections, it is necessary to develop an easy-to-use and efficient bridge monitoring system (Chang et al. 2014). The author is developing a short and medium span bridge monitoring system for detecting deterioration in safety and other performance of existing bridges by use of under-rear-wheel-spring acceleration sensors installed on fixed-route buses (called "bus monitoring system") (Miyamoto & Yabe 2012). The proposed monitoring system represents a monitoring system, to be applied mainly to short and medium span bridges, making use of a fixed-route bus operated as part of a public transit system. The aim of the proposed system is to detect the transition from the "acceleration stage," in which the safety performance of a bridge sharply declines because of aging, to the "deterioration stage". This paper presents the result of a three-year field test of the bus monitoring system conducted by using an in-service fixed-route bus in Ube City, Japan. For the bus monitoring system, "characteristic deflection" was defined as an indicator that may be useful in efficiently detecting a structural anomaly of a bridge. For the purpose of examining the sensitivity of characteristic deflection, the effect of artificial damage (bridge guardrail removal) on characteristic deflection was evaluated by using an out-of-service bridge being removed.



Figure 2. View of in-situ loading test by BELFA for an existing bridge (Gutermann & Schröder 2013)

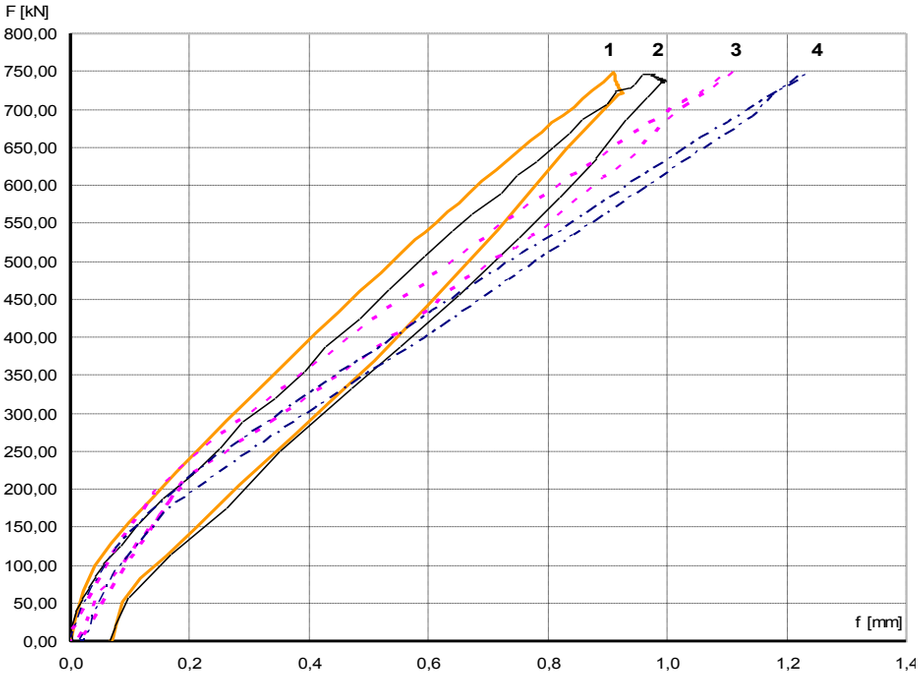


Figure 3. Example of load deflection curves at midspan by BELFA under four various conditions *(Gutermann & Schröder 2013)*

3.1 *Principle & Outline of Bus Monitoring System*

The bus monitoring system has been developed by the method of monitoring short and medium span bridges by using fixed-route buses operated as part of public transport systems. Fig. 4 illustrates a basic concept and damage detection flow of the bus monitoring system. Main reasons why the use of fixed-route buses, which are large and heavy vehicles, was considered are as follows:

① If a large vehicle about 10 m in length is used for on-the-move measurement on a short or medium span bridge, that vehicle is likely to be the only vehicle passing over the bridge at point in time.

② In order to make a short or medium span bridge, whose stiffness is relatively high, it is necessary to use a reasonably heavyweight vehicle.

③ Large vehicles used to vibrate bridges make it easier to reproduce measuring conditions such as travel time, route, frequency of passages and vehicle speed.

④ By using a fixed-route bus equipped with acceleration sensors, main short and medium span bridges in the area of interest can be monitored on a regular basis. By so doing, monitoring cost would be substantially less than in the case where sensors were installed at all bridges.

⑤ Power for the measuring devices can be supplied from the power supply available in the bus.

The vertical displacement, $\delta_a(t)$ of the bridge and the bus under its rear wheel springs is an estimated deflection obtainable by integrating the vertical acceleration waveform twice. That displacement can be expressed, as the sum of (1) the static displacement, $\delta_{sa}(t)$ dependent on bridge stiffness and bus weight, (2) a non-steady-state vibration component having a stochastic nature characterized as a Gaussian process attributable to a rough road

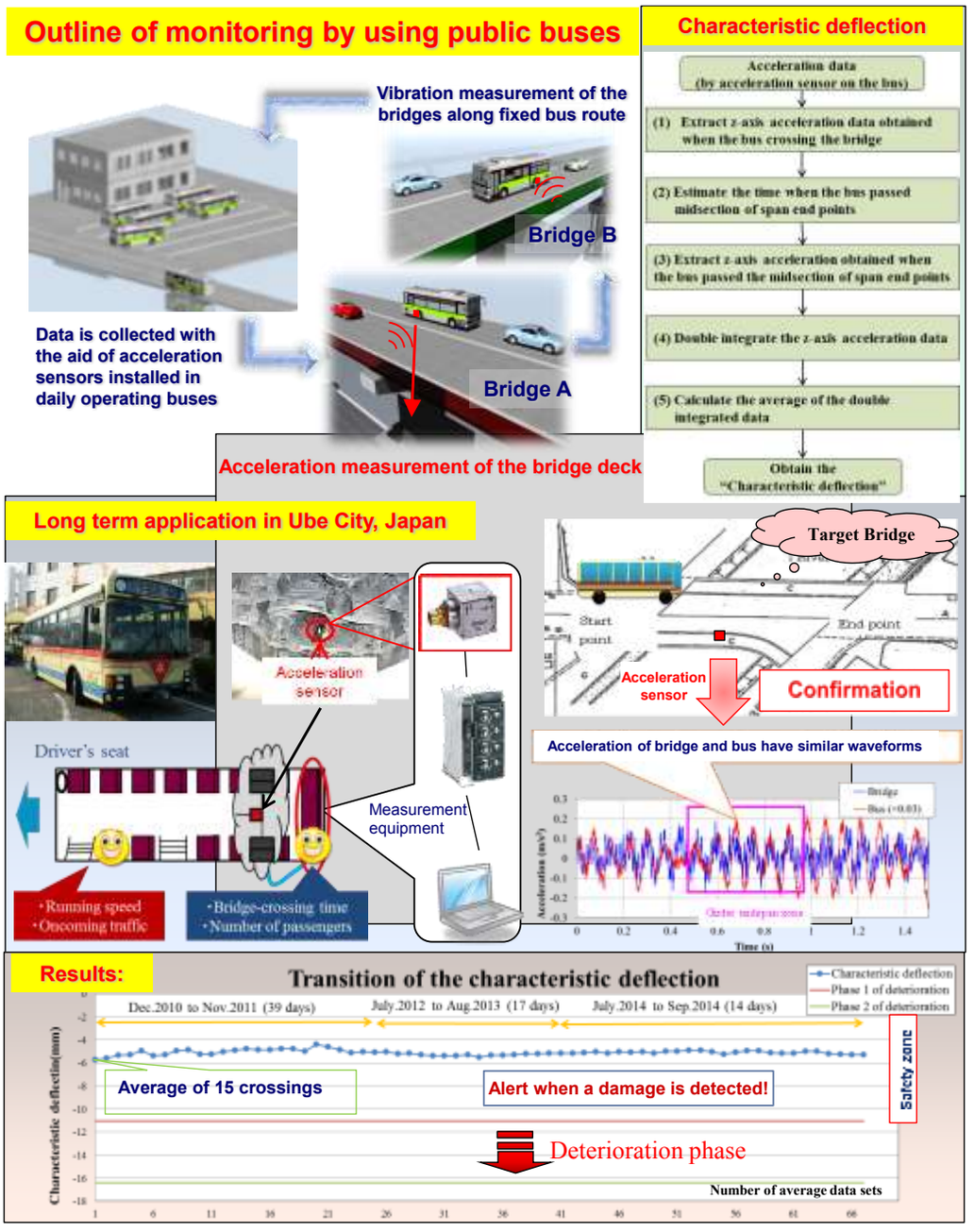


Figure 4. Basic concept and damage detection flow of the bus monitoring system

surface and having a mean value of 0, (3) vibration components governed by the equation of motion such as the bridge and the vehicle, and (4) external disturbance factors, $\delta_x(t)$ due to differences in the operating conditions of the bus and differences in data extraction and processing methods, as follows:

$$\delta_a(t) = \delta_{sa}(t) + S_r(\Omega, t) + \int_{-\infty}^{+\infty} X(f) \cdot e^{2\pi f t i} df + \delta_x(t) \quad (2)$$

where,

$S_r(\Omega, t)$: density function of road roughness,
Ω: spatial frequency of road surface,
$X(f)$: Fourier coefficient.

For the purposes of this study, characteristic deflection, μ_a (Miyamoto & Yabe 2012) is defined as the estimated deflection obtained from Eq. (2) averaged in the bridge section of the road. Studies have shown that characteristic deflection can be made to converge to the extent that anomaly evaluation results are not affected by increasing the number of samples, N, by using the central limit theorem, in order to allow for the influence of various external disturbance factors, $\delta_x(t)$, including the operating conditions of the bus. In this study, the authors used the moving average method to process characteristic deflection data and see what happens. In the moving average method, averages are calculated for incrementally shifted data sections. Fig. 5 shows standard deviations of characteristic deflection values obtained by calculating characteristic deflection averages for incrementally shifted data sections. As shown in Fig. 5, as data sections become larger, standard deviations tend to decrease. It can also be seen that after data section size exceeds a certain limit, standard deviations do not change significantly thereafter. This indicates that by the moving average method mentioned above, the variability of characteristic deflection values decreased and converged so that anomalies can be detected by observing such changes.

3.2 *Long-term Health Monitoring on Bus Routes in Ube City, Japan*

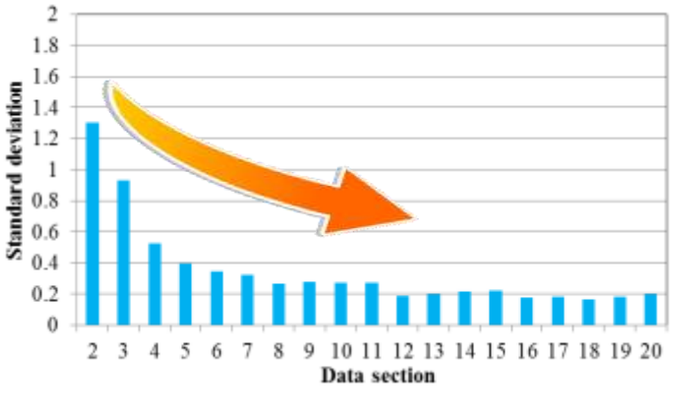


Figure 5. Changes in standard deviation estimated by the moving average method



Figure 6. Fixed-route bus & sensor for long-term field testing

3.2.1 *Field test*

As a long-term application of the bus monitoring method of measurement, a field test utilizing Ube City's bus routes has been underway. The long-term experiment, which uses fixed-route buses being operated in the city, has been continued for about three years since December 2010 and is supposed to be continued in the years to come. Fig. 6 shows the fixed-route bus used in the experiment and the under-rear-wheel-spring acceleration sensors installed to the bus. The acceleration sensors were bonded to the under-rear-wheel-spring section of the bus and was coated with epoxy resin for protection over a long period of time. The sensors used consisted of a triaxial acceleration sensor and uniaxial acceleration sensors (backups). These sensors were oriented along the direction of travel of the bus (X-axis), the transverse direction (Y-axis) and the vertical direction (Z-axis). The acceleration sensor cables were passed through the floor drain of the bus. Thus, the acceleration sensors are connected to the data logger and the computer in the bus so that the vibration of the bus crossing the bridge can be monitored in real time. Although the acceleration sensors, the data logger and the computer are designed to be powered by the power source of the bus, in the experiment a portable rechargeable battery was used. Table 2 lists main bridges of interest located on the bus routes and summarizes data on those bridges. As an example of measurement data, this paper shows the measurements results obtained from the Shingondai Bridge (see Fig. 7), one of the bridges (prestressed

Table 2. Target bridge data

Bridge name	Completed in	Type of superstructure			Span length (m)	Bridge length (m)
Jase Bridge	1976	Span No.	Start point side 1	Prestressed concrete slab bridge (pretensioned slab)	18.0	85.0
			2	Prestressed concrete slab bridge (pretensioned slab)	16.0	
			3	Prestressed concrete slab bridge (pretensioned slab)	18.0	
			4	Prestressed concrete slab bridge (pretensioned slab)	14.0	
			End point side 5	Prestressed concrete slab bridge (pretensioned slab)	19.0	
Shiratsuchi Daini Bridge	1933 (estimated)	Span No.	Start point side 1	Reinforced concrete (T-girder)	7.0	15.8
			End point side 5	Reinforced concrete (T-girder)	7.0	
Shingondai Bridge	June 1998	Girder bridge (other)			22.4	23.6

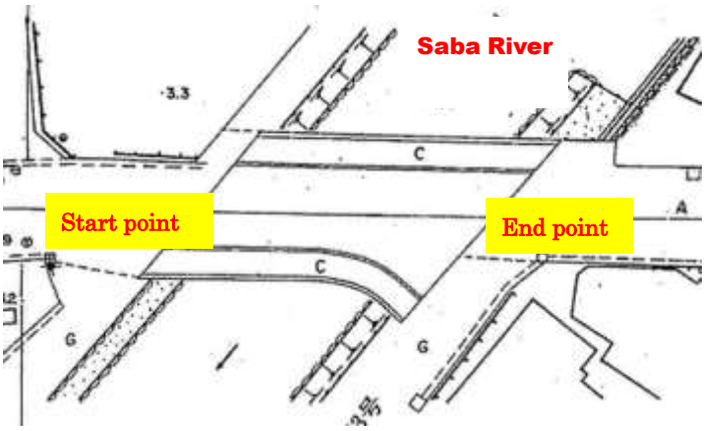


Figure 7. Plan view of Shingondai Bridge in Table 2

concrete(PC) girder bridge) managed by Ube City, Japan on the bus routes.

3.2.2 *Characteristic deflection calculation method*

This section describes how to calculate characteristic deflection, an indicator of bridge performance used by the bus monitoring system. A flow diagram for the calculation of characteristic deflection following measurement data acquisition is shown in Fig. 4, and each step is described in detail below. The steps (1) through (5) shown below correspond to the numbers shown in Fig. 4.

3.2.3 *Extract data on vertical acceleration during bridge crossing*

Extract data on vertical acceleration during the crossing of the bridge from the acceleration measurement data by referring to the combination of the time at which the bus crossed the bridge and GPS data.

3.2.4 *Estimate the time when the bus passed midspan points*

The extracted data on acceleration during the crossing of the bridge include data on strong vibrations recorded at bridge joints. It is therefore necessary to use girder midspan acceleration data that do not include such joint vibration data. The time when the midspan point of a girder is passed can be estimated by extracting data for between-joint data meeting certain criteria such as time intervals (sec) and the number of waves. Since, however, acceleration data vary considerably in magnitude depending on such factors as the operating conditions of the bus, it may be difficult to identify joint-zone data. In order to accurately estimate the time when the midspan point of a girder is passed, attention was paid to deflection estimates that can be obtained by integrating vertical acceleration data twice.

3.2.5 *Extract midspan vertical acceleration data*

Extract the midspan vertical acceleration data determined as described in Step (2) (see Fig. 4). Fig. 8 shows an example of both side expansion joints and midspan portions of vertical acceleration data. In the example shown in Fig. 8, a portion of midspan region data corresponding to about 0.8 sec (about 10 waves) was identified as data to be extracted. The most important thing in calculating the characteristics deflection is to determine the range of data to be extracted according to such criteria as the number of waves and time(sec) and extract acceleration waveforms from the same regions every time.

3.2.6 *Integrate extracted acceleration data twice*

Extracted acceleration data are converted to velocity by the first integration and to displacement by the second integration. At this step, the vertical displacement obtained by integrating vertical

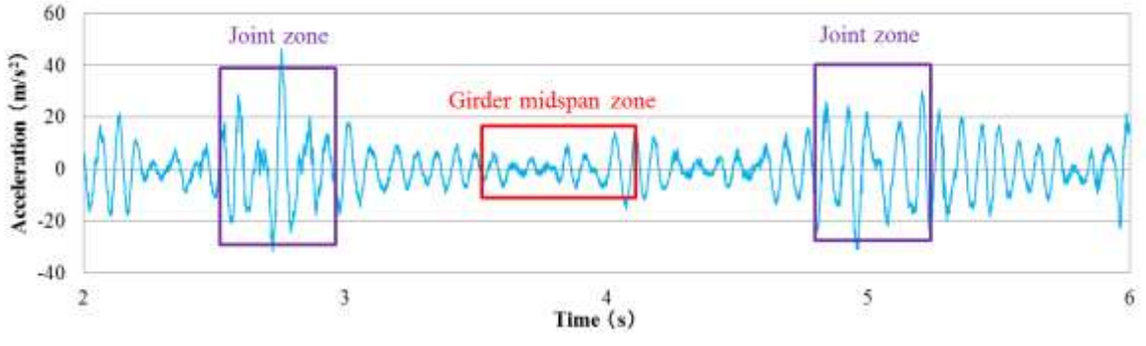


Figure 8. Example of determination of acceleration data extraction range

acceleration twice is taken as an estimated deflection.

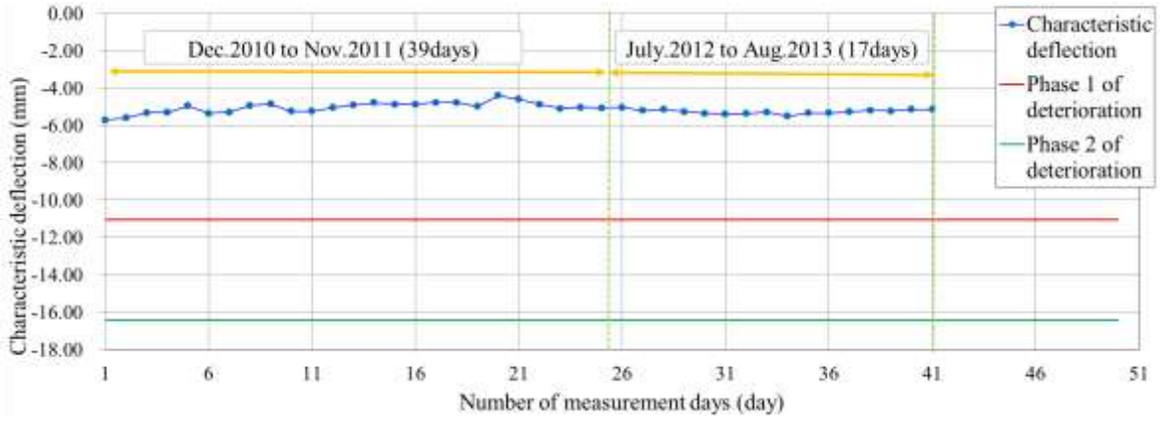
3.2.7 *Average estimated deflection*

Calculate characteristic deflection by averaging the deflection estimates shown in the graph obtained at Step (4) in the direction of time (Fig. 4).

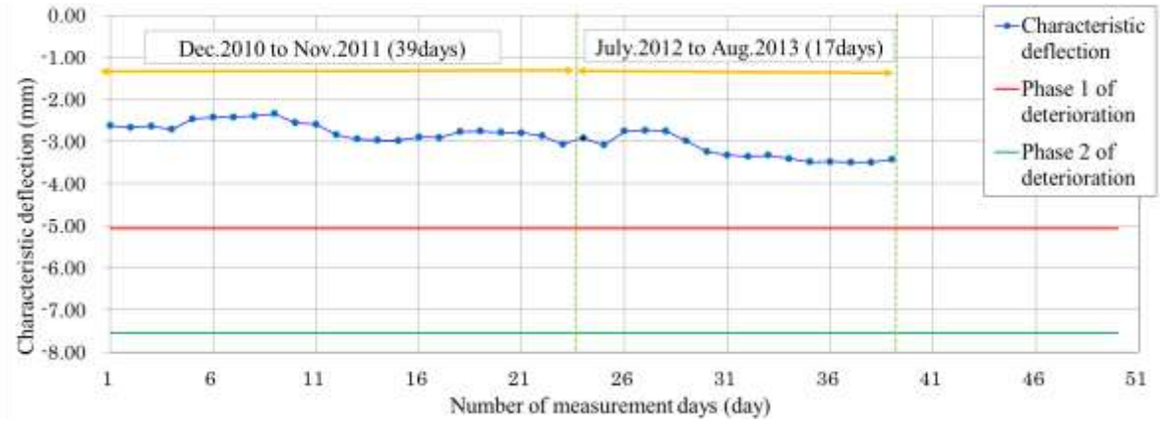
3.2.8 *Test results and discussions*

First of all, let us consider whether or not it is possible, in the event of a structural anomaly of the bridge of interest, to detect the anomaly from the under-rear-wheel-spring acceleration response of the bus. In a previous study, vibration analysis using FSWT (Frequency Slice Wavelet Transform), a time–frequency analysis method, was conducted to analyze acceleration response (Yan et al. 2009). The FSWT analysis of the girder-midspan and under-rear-wheel-spring acceleration responses conducted in this study indicated that the under-rear-wheel-spring region of the bus was always vibrating at around 12 Hz, regardless of whether or not the bus was crossing the bridge. On the other hand, with respect to the acceleration response of the bridge, it has been confirmed that the girder-midspan region of the bridge was actually vibrating at around 12 Hz (Yabe et al. 2012). Fig. 4 shows the acceleration responses of the under-rear-wheel-spring region of the bus and the girder midspan region of the bridge observed when the bus passed the girder midspan section of the bridge. It can be seen that in terms of the magnitude of acceleration response, the two waveforms show a fair degree of similarity although the under-rear-wheel-spring response values tend to be larger. From these results, it can be concluded that the vibration properties of the bridge of interest can be identified according to the under-rear-wheel-spring vibration of the bus.

Next, let us consider characteristic deflection calculation results. Figs. 9(a) and (b) show changes in characteristic deflection at the Shingondai Bridge during the initial and return trips, respectively, of the bus calculated from the measurement data obtained during a total of 56 days in 2010 to 2013. There are differences in the number of data sets between initial trip data and return trip data because there were some invalid cases such as a case in which the bus stopped on a bridge. The data shown in Figs. 9(a) and (b) were obtained by applying a serious deterioration threshold specifying the limit of the degree of seriousness of bridge anomalies. In this connection, it has been found that characteristic deflection increases to 193% in the event of deterioration that causes the introduced prestressing force to decrease by 50% and to 286% in the event of deterioration that causes the introduced prestressing force to decrease by 90%. It was therefore decided to calculate the average of the



(a) Tokonami→Nishikiwa Gakkomae



(b) Nishikiwa Gakkomae→Tokonami

Figure 9. Long-term changes in characteristic deflection (Shingondai Bridge)

characteristic deflection values obtained from the first 15 measurements and use the characteristic deflection value equal to 1.93 times the average value as the threshold level for Phase 1 deterioration (red line) and the characteristic deflection value equal to 2.86 times the average value as the threshold level for Phase 2 deterioration (green line). The actual procedure is to measure characteristic deflection on a continual basis and, if the threshold level is reached or exceeded, suspect the occurrence of some kind of serious damage to the bridge of interest and conduct visual inspection immediately. Inspection needs to be conducted when characteristic deflection has reached or exceeded the threshold level on the initial or return trip. Characteristic deflections in "Data Section 15" obtained by the moving average method are shown in Fig. 9, where a single characteristic deflection point represents the average of 15 measurement results. Comparison of Figs. 9(a) and (b) reveal that characteristic deflection values differ between the initial trip and the return trip. This is thought to be because the Shingondai Bridge is not symmetrical as shown in Fig. 7. Long-term changes in characteristic deflection showed little change although Fig. 9(a) shows slight changes. In contrast, Fig. 9(b) shows that the lowest value of characteristic deflection decreased gradually. Nevertheless, in both cases, the serious deterioration threshold was not reached or exceeded. It can therefore be concluded that serious damage has not yet occurred on the initial trip route or on the return trip route.

4 CONCLUDING REMARKS

Bridge health monitoring using the latest information technology and sensors will be becoming more challenging issues in the future for maintenance and rehabilitation of existing bridges. In this paper, although several methods are available for monitoring and assessment of existing short and medium span bridges, two advanced structural health monitoring systems were introduced.

In the first part of this paper, as one of the advanced data collecting system for experimental safety evaluation developed by German research team, a special designed in-situ loading vehicle, *BELFA* which is available for assessment quantitatively of load carrying capacity of the target bridge was discussed as a structural health monitoring system at the bridge site. The proposed method was applied to a few actual existing concrete bridges in a rural area of Germany as a specific example to verify its effectiveness. As the results, it will be able to make a rational periodical health monitoring system for existing short and medium span bridges, and then the method helps bridge administrators to establish the rational maintenance strategies.

In the second part, as one solution to the problem for condition assessment of existing short and medium span reinforced and prestressed concrete bridges, a new long term monitoring method using a public bus as part of a public transit system (bus monitoring system) was introduced, along with safety indices, namely, characteristic deflection, which is relatively free from the influence of dynamic disturbances due to such factors as the roughness of the road surface, and a structural anomaly parameter. Moreover, the details of not only how to assess the bridge condition by public bus vibration measured in operating on Ube City bus network as a specific example for verify the system but also what kind of consideration we need to apply the system to existing bridges in overseas country were discussed.

The author would hope that this paper would be of some help in this field in the future.

5 REFERENCES

Chang, K.C., Kim, C.W. & Kawatani, M. 2014. Feasibility Investigation for a Bridge Damage Identification Method through Moving Vehicle Laboratory Experiment, *Structure and Infrastructure Engineering*, Taylor & Francis, **10**(3), 328-345.

DAfStb (Ed). 2000. Recommendation; Guideline for Load Testing of Concrete Structures. Beuth Verlag.

DIN 1072. 1985. Short and Medium Span Bridges, Load Assumptions, German guideline.

DIN EN 1990. 2010. Eurocode: Basis of Structural Design.

Gutermann, M. & Schröder, C. 2013. Loading Vehicle BELFA – development and experience gained in 10 years of practice –, *Structural Health Monitoring and Maintenance of Short- & Medium-Span Bridges*, Yamaguchi University, Ube, Japan, **5**, pp. 1-17.

Gutermann, M., Slowik, V. & Steffens, K. 2003. Experimental Safety Evaluation of Concrete and Masonry Bridges, *International Symposium NDT-CE 2003 in Berlin*.

Gutermann, M. & Schröder, C. 2012. Existing Structures - old and disused - Experimental Approaches for Extension of Lifetime, *Proceedings of 50th Annual Conference on Experimental Stress Analysis*, Tábor, Czech Republic.

Gutermann, M. 2003. Ein Beitrag zur experimentell gestützten Tragsicherheitsbewertung von Massivbrücken, *Dresden Technical University*.
(http://nbn-resolving.de/urn:nbn:de:swb:14-1062059931515-51848 (8.12.2013))

Gutermann, M. 2004. An Article on Experimental Assessment of Structural Safety of Solid Bridges, *Proceedings of ICEM12; 12th International Conference on Experimental Mechanics*, Politecnico di Bari, Italy.

Miyamoto, A. & Yabe, A. 2012. Development of Practical Health Monitoring System for Short- and Medium-Span Bridges based on Vibration Responses of City Bus, *Journal of Civil Structural Health Monitoring, International Society for Structural Health Monitoring of Intelligent Infrastructure (ISHMII,)*, **2**(1), 47-63.

Yan, Z., Miyamoto, A. & Jiang, Z. 2009. Frequency Slice Wavelet Transform for Transient Vibration Response Analysis, *Mechanical Systems and Signal Processing*, **23**(5), 1474-1489.

Yabe, A., Isoda, S., Nagata, M. & Miyamoto, A. 2012. Field Test on Short/Medium Span Bridge Monitoring System based on Public Bus Vibration, *Proceedings of the 67th Annual Conference of the Japan Society of Civil Engineers*, **VI-232**.

Maintenance, Safety, Risk, Management and Life-Cycle Performance of Bridges – Powers, Frangopol, Al-Mahaidi & Caprani (Eds)
© 2018 Taylor & Francis Group, London, ISBN 978-1-138-73045-8

A strain sensor based monitoring and damage detection system for a two-span beam bridge

P. Waibel & O. Schneider & H.B. Keller
Institute for Applied Computer Science
Karlsruhe Institute of Technology (KIT), Karlsruhe, Germany.

J. Müller & O. Schneider
Büro für Strukturmechanik GmbH, Coburg, Germany.

S. Keller
Institute of Photogrammetry and Remote Sensing
Karlsruhe Institute of Technology (KIT), Karlsruhe, Germany.

ABSTRACT:
Structural analyses of old and often already damaged bridges are expensive and time-consuming. Hence, there is a huge demand for structural health monitoring systems that can be retrofitted on existing bridges to achieve information if damages jeopardize a future use. The authors present a data-driven analyzing method for detecting and assessing structural damages in a two-span concrete beam bridge that is equipped with distributed strain sensors below the decks of the bridge segments. The method makes use of bridge excitations caused by single vehicles (with unknown load and velocity) along both spans and their induced strains at various sensor locations.
Computer simulations of vehicle crossings over a bridge model with varying damage scenarios are used to validate the method. Supporting validations are conducted based on data of a real national highway bridge, which has been approved for scientific experiments including the infliction of damages. Results are promising in effectively detecting and assessing different damages using the proposed method.

1 INTRODUCTION

Bridges are critical infrastructure elements, for safety reasons and due to their economic importance. However, the average age of bridges in Germany (already about 40 years) is increasing. Additionally, higher traffic frequencies and increased vehicle sizes and weights have changed the loading conditions of these bridges. Both aspects raise the number and severity of structural damages in bridges (BASt, 2017). Structural analysis of bridges taking into account damages are expensive and time-consuming. Thus, there is a high demand for low-cost (semi-) automated structural health monitoring systems that can be retrofitted on existing bridges.

The data analyzing method presented in this contribution enables the detection, localization and assessment of structural damages in a two-span beam bridge. COTS strain sensors, which are installed below the decks of the bridge spans provide the data basis. Frequently occurring single truck crossings with unknown velocity and weights are used as excitation of the bridge. Extracting data-based features from the measured time series data allows to distinguish between damage severities and damage locations. Our method makes use of the characteristics of two-span beam bridge structures, which lead to specific strain data.

The method is validated with computer simulations of vehicle crossings of a FEM bridge model, in which damages with varying severities and locations were taken into account. Data of a real national highway bridge that has been approved for scientific experiments provide the basis to prove the applicability of the developed method. I.e. after closing the bridge for public traffic, structural damages have been gradually inflicted into the bridge in between numerous bridge crossings.

Eventually, the authors demonstrate that the presented sensor system combined with the developed analysis method allow a subsequent upgrade of existing two-span beam bridges with an effective structural health monitoring. Thus, this approach represents an economic solution for retrofitting bridges with a monitoring and damage detection system.

1.1 *Related Work*

Four categories of structural health monitoring systems are usually distinguished, where most systems fall into the first three categories (Rytter, 1993):
Detecting the damage (1), localizing the damage (2), quantifying the damage severity (3), and predicting the remaining service life (4).

Many methods of structural health monitoring analyze the measured vibration response of the structure. The relation between physical properties and

modal parameters forms the basis of these approaches (e.g. Doebling et al., 1998; Fan & Qiao 2011). Besides these methods that are relying on sensor installations on a bridge, numerous methods exist, which extract dynamic properties of a bridge structure from the dynamic response of a crossing vehicle. (e.g. Yang et al., 2004 & Malekjafarian et al., 2015)

1.2 *Paper outline*

In Section 2 the authors describe briefly the test bridge and the sensor system, which provide the basis for the development of the algorithms. Section 3 addresses the bridge model and the simulation properties. In Section 4 the experiments at the test bridge are outlined. The developed algorithms for the detection and assessment of structural damages are described in Section 5. Section 6 addresses the results of the validation with simulation data and experimental data.

2 TEST BRIDGE

A national highway bridge in Germany has been selected as test bridge based on its representative properties as well as for technical measurement reasons. The bridge type is a pre-stressed two-span beam structure with two lanes (Fig. 1). The length of the bridge is 50 meters and the width is 10 meters. The year of construction is 1962. The bridge is part of a rural arterial road and consequently under intensive usage of about 20,000 vehicles of various types per day.

A scheduled reconstruction of the bridge during the project duration has offered the unique possibility to conduct destructive experiments with the infliction of controlled damages into the bridge. After the bridge closure for public usage, dummy vehicle crossings have been performed.



Figure 1. Test bridge.

2.1 *Sensor system*

The sensor system consists of 18 linear strain gauges (HBM 1-LY41-50/120) which are installed below the deck of the bridge and which are connected to a universal amplifier (HBM QuantumX MX840B and MX1615B).

The measuring range of the strain sensor is -50,000 to 50,000µstrain with a measuring accuracy of ±0.02µstrain. The recording frequency of the sensor data is 200 Hz.

Figure 2 illustrates the position and label of each instrumented sensor on the bridge.

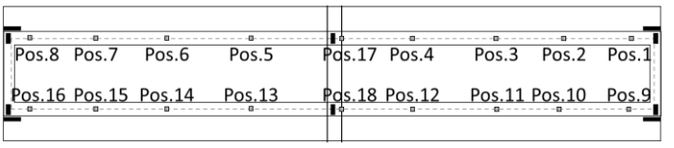


Figure 2. Strain sensor positions below bridge.

3 NUMERICAL MODEL AND SIMULATION

The validation of the algorithms required the development of a bridge model with the possibility to consider structural damages as well as simulations of vehicle crossings. The test bridge described above provides the basis for the FEM mathematical bridge model. Statistical traffic data constitutes the preparation of the vehicle bridge crossing simulation data.

3.1 *Bridge model parameters*

The bridge model has been built with the finite element analysis and CAD software SOFiSTiK. Two calculation models have been developed for structural dynamic analysis: A simplified model consisting of 40 beam elements and a more detailed 3D model consisting of about 2,000 shell elements for nonlinear analysis. Figure 3 depicts the cross section of the bridge. The bridge supports are roller bearings and hence abutments are not taken into account.

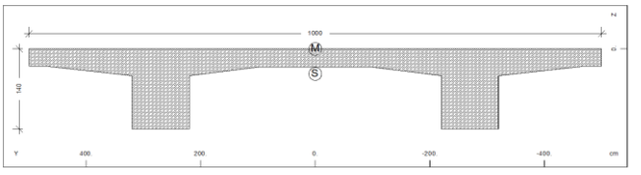


Figure 3. Cross-section of bridge model.

Two commonly occurring structural damages with increasing severity are modelled:

Damage 1 is located above the central bridge bearing. Damage 2 is located at a center span. (Fig. 4)

The severities of both damages are subdivided into four increments: Severity 1 (5%), severity 2 (20%), severity 3 (35%) and severity 4 (50%). The percentage indicates the partial loss of each element's load-bearing capacity.

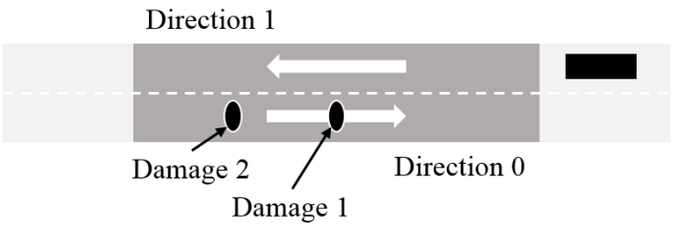


Figure 4. Damage locations in simulation data.

3.2 *Vehicle parameters*

Based on preliminary results, the data of single vehicle crossings of heavy trucks are considered as data basis for the simulations. Therefore, the simulations focus on bridge crossings of 5-axis trucks to build up this data basis. It is possible to detect single vehicle crossings of heavy trucks based on strain data amplitudes easily. Additionally, many single truck crossings occur at the test bridge especially during the night. Therefore, focusing on single truck crossings does not represent a strict restriction for the monitoring system. The vehicle crossings are simulated with varying vehicle characteristics that are derived on statistical traffic data (Geissler, 2014).

In order to cover a wide range of scenarios, the variation of vehicle characteristics in the simulation data comprises the following properties:

- Weight
- Length
- Vehicle velocity: Mean 60km/h; Standard deviation 9.5km/h
- Wheelbase
- Natural frequencies of wheel suspensions
- Attenuation constants of wheel suspensions
- Vehicle width
- Deviation from ideal track

All simulated vehicle bridge crossings follow *direction 1* (Fig. 4).

To validate the performance of the developed method with respect to the detection and assessment of bridge damages, the following number of simulations of vehicle crossings in different damage classes have been conducted:

- 800 vehicle crossings with no damage (Damage class: 0)
- 4x90 vehicle crossings with damage 1 in four severity steps (Damage classes : 1.1, 1.2, 1.3, 1.4)
- 4x90 vehicle crossings with damage 2 in four severity steps (Damage classes : 2.1, 2.2, 2.3, 2.4)

Figure 5 illustrates the variance in the simulation data (undamaged bridge) for the sensor at position 3.

The entire vehicle crossing simulation data comprises 1520 vehicle crossings with 1400 data points (corresponding to 0…7s) for each sensor (sensor position 1…17; data of sensor 18 is corrupt).

4 TEST BRIDGE EXPERIMENTS

Due to the officially scheduled reconstruction of the test bridge, there has been the unique opportunity for running extensive custom experiments with the bridge. These numerous experiments have included the manual infliction of damages into the bridge as well as the excitation of the bridge with a 20t vehicle passing the bridge repeatedly.

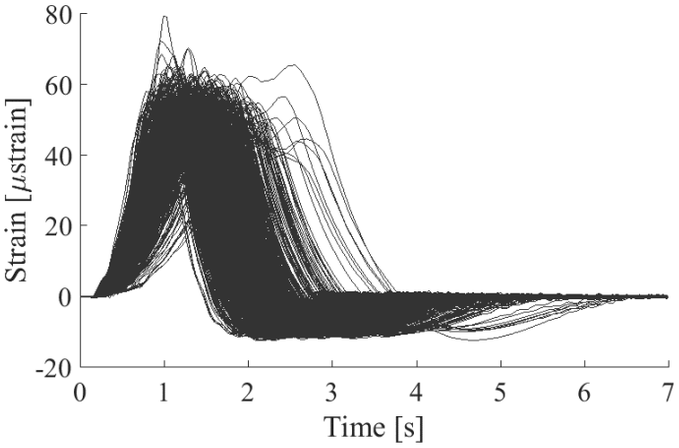


Figure 5. Strain values at sensor position 3 of all simulated bridge crossings with damage class 0 (undamaged bridge model)

Currently, a part of the acquired experimental data have been preprocessed and analyzed. Available preprocessed data includes experiments with cutting tendon cables, corresponding to damage 2 in the simulation data. This damage could be the consequence of a hydrogen embrittlement under real conditions (Fig. 6). In Figure 7 the cutting of tendon cables is shown.



Figure 6. Damage location in experimental data.

The following data sets have been recorded:

- 25 vehicle crossings without damage (Damage class: 0),
- 25 vehicle crossings with three removed tendon cables (Damage class: 3.1) and
- 23 vehicle crossings with six removed tendon cables (Damage class: 3.2).

5 METHOD

In this section, the authors describe the data processing steps that are required to discriminate different damage classes based on the simulation and the experimental data.



Figure 7. Cutting of three tendon cables at the test bridge.

Figure 8 shows a typical signal of a vehicle crossing of the analyzed two-span beam bridge. As the vehicle enters the bridge, the strain value increases at the span where the sensor is located. After leaving the span to the next bridge segment, the strain value gets negative. This measurable feedback to the other segment is caused by the two-span beam structure's lever action across the middle support. Utilizing this inherent property forms the basis of two extracted features. After the vehicle passage, the free oscillations of the bridge without exciting force i.e. the damped natural frequencies are analyzable. Two extracted features are based on these signal parts.

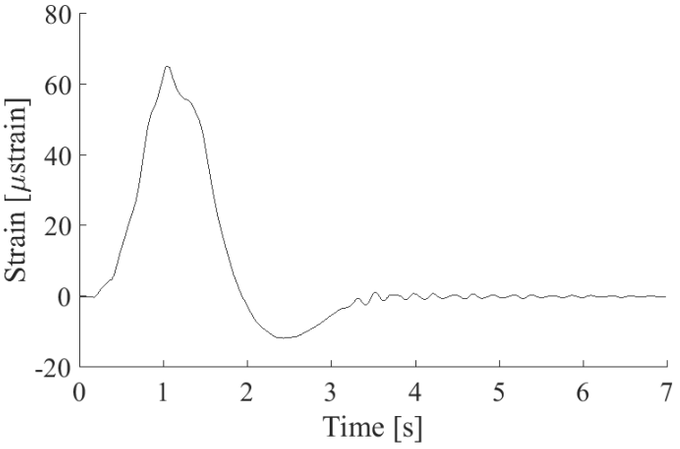


Figure 8. Simulated strain signal at sensor position 5 of one vehicle crossing (damage class: 0).

At first, a data preprocessing step is required to normalize the data sets. Subsequently, the feature extraction is executed which aims to reduce the data dimension to few characteristic features. These features should still possess all the information about bridge damages and damage locations and exclude all irrelevant information. This property is evaluated for four extracted features using an analysis of variances approach.

5.1 *Data Preprocessing*

In order to acquire data sets of the sensor signals similar to the one in Figure 8 for the real bridge experiments, an event detection is implemented. This event detection uses ring buffering and a peak detection in the data sets. Prospectively, the event detection could be upgraded to automatically detect, segment and classify single truck crossings.

Due to various reasons, such as temperature effects or sensor drifts, the measured strain values can be biased. In order to normalize the data, this bias has to be removed from the data sets. The applied method calculates the median strain value of the data before and after the excitation by a vehicle bridge crossing and subtracts it from the analyzed data set. The normalized data can be used for further processing steps.

5.2 *Feature extraction*

Each data set of one vehicle bridge crossing consists of a time series with 1,400 data points. This can be regarded as a 1,400-dimensional feature space, in which each data set reflects one position. Distinguishing between different damage classes means finding clusters of data sets in this high-dimensional feature space. However, this approach does not offer insight into the data structure. E.g., it is not clear, if minor variations end up in different classes. In addition, vehicles with different weights would end up in different clusters. The variation in the data caused by different vehicle masses or velocities are obviously higher than the variation caused by small damages.

In an online system, vehicle mass and vehicle velocity are unknowns. Therefore, it is appropriate to extract features from the data that are independent of the vehicle's mass and velocity. These features should still contain all the information about the bridge damages and allow an accurate discrimination of the different damage classes. Mathematically speaking, the extraction of one feature from the data is a reduction of the data dimension from 1,400 to one.

Here, we propose four features and evaluate their performance afterwards. The first two features are based on the data after the excitation by the vehicle, i.e. after the vehicle has passed the bridge. For this reason, an automatic detection of the point of time, when a vehicle leaves the bridge in the analyzed time-series data is implemented. The third and the fourth feature are based on the entire signal and use ratios to ensure independence from velocity and mass.

- Exponential decay

The upper and lower envelope of the decaying signal are calculated using the Hilbert transformation. A curve fit is implemented which estimates the parameters a and b of the following equation for both envelopes.

$$y(t) = a \cdot e^{-b \cdot t} \quad (1)$$

The exponential decay constant b is similar for both upper and lower envelope. Thus, the extracted feature f_1 is the exponential decay constant b of the upper envelope.

- Natural frequencies

Using the Fourier transformation, the natural frequencies of the bridge can be estimated. In the bridge model, the first mode is at 4.175 Hz. Assuming there are damage-based variations in the modal properties, the first mode is extracted as feature f_2. The implemented algorithm detects the frequency with the highest power spectrum amplitude between 4 and 5 Hz in the data sets.

- Min/max-ratio

The min/max-ratio reflects the quotient of the absolute value of the minimum strain and the maximum strain value during one bridge crossing of a vehicle.

$$f_3 = \frac{|\min(\varepsilon)|}{|\max(\varepsilon)|} \quad (2)$$

Using the ratio, there is no influence by vehicle mass and velocity since the mass and velocity influences the minimum and maximum equally and can thus be eliminated from the quotient.

- Area ratio

The feature area ratio is the quotient of the summarized positive strain and the summarized negative strain in one data set.

$$f_4 = \frac{\left| \sum_{k=t_{ss,1}}^{t_{ss,2}} \varepsilon(t_k) \right|}{\left| \sum_{k=t_{os,1}}^{t_{os,2}} \varepsilon(t_k) \right|} \quad (3)$$

Here, $t_{ss,1}$ indicates, when the vehicle enters the same bridge span where the sensor is located. The vehicle leaves this bridge segment at $t_{ss,2}$. The point in time when the vehicle enters the span where the sensor is not present is $t_{so,1}$ and it leaves this segment at the point in time $t_{so,2}$. Depending on sensor location and vehicle direction the parameters $t_{ss,2}$ and $t_{so,1}$ or $t_{so,2}$ and $t_{ss,1}$ are equal.

5.3 *Feature evaluation*

In order to evaluate the extracted features, the analysis of variances method (ANOVA) is conducted. This method examines whether (and if so how) the expectation values of the measured feature values vary in different damage classes. It is based on the calculation of the ratio between the inner-class variation and the variation between classes. A subsequent test for statistical significance allows determining, whether the classes differ significantly or not and hence defines the quality of a feature.

It is assumed that the prerequisite of ANOVA - measurement data follow a normal distribution- is fulfilled. As the evaluation measure the following value is used

$$Q = 1 - \frac{SSW}{SSB + SSW} \quad (4)$$

where *SSW* reflects the *S*um of *S*quares *W*ithin groups and *SSB* is the *S*um of *S*quares *B*etween groups. A value of Q close to one means that the feature's performance to discriminate all classes is high. A value close to zero means the feature is not suited for discriminating different damage classes (damage severity and damage position).

6 RESULTS AND DISCUSSION

The features described in Section 5 are calculated for the simulation data as well as for the experimental data. The calculation of the ANOVA-based quality measure Q is additionally subdivided into each sensor position. Hence, the evaluation of the results allows defining the best combination of sensor position and extracted feature regarding the discriminability of the damage classes.

6.1 *Simulation data*

The ANOVA-based measures Q for each feature at each sensor position are presented in Table 1. The features f_1 and f_2 yield values near zero for all sensor positions, reflecting a low potential to discriminate the different damage classes. Due to its location at the center bearing, sensor position 17 is not suitable for calculating the exponential decay.

The results of feature 3 and feature 4 range above 0.7 for several sensors and almost reach 1 for their combinations: sensor pos. 4/5 and feature 4.

In Figure 9 the box plots for feature f_4 at sensor position 5 is shown. Each damage class possesses a different median value and has low inner-class variances. Discriminating the damage classes is easily achievable via simple thresholding.

Figure 10 depicts the results of the feature min/max ratio f_3 for sensor position 7.

Table 1. Results of feature evaluation for the simulation data represented by the measure Q which ranges from 0 (worst) to 1 (best). The maximum values of each feature/sensor combination are highlighted.

Sensor pos.	f_1	f_2	f_3	f_4
1	0.01	0.02	0.02	0.88
2	0.02	0.01	0.59	0.60
3	0.01	0.04	0.75	0.79
4	**0.07**	0.02	0.75	0.97
5	0.01	0.03	0.74	**0.99**
6	0.02	0.02	0.65	0.78
7	0.01	0.01	**0.82**	0.74
8	0.04	0.05	0.21	0.86
9	0.01	0.05	0.62	0.85
10	0.02	0.03	0.11	0.09
11	0.02	0.06	0.32	0.31
12	0.03	**0.07**	0.11	0.38
13	0.04	0.07	0.03	0.18
14	0.03	0.07	0.31	0.36
15	0.01	0.05	0.24	0.26
16	0.01	0.05	0.32	0.73
17	N/A	0.0	0.01	0.01

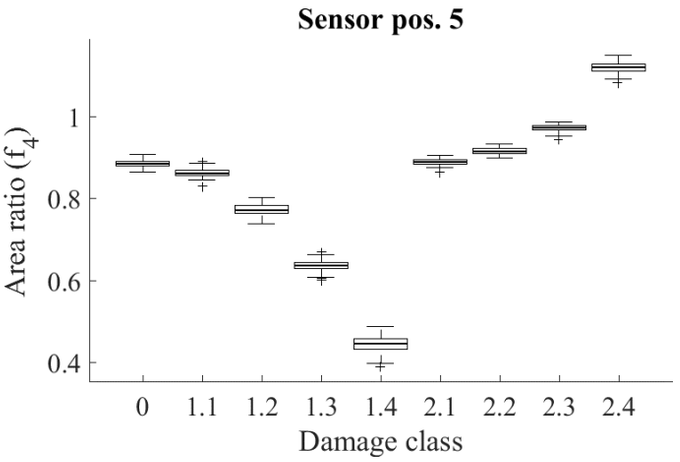


Figure 9. Box plot of feature area ratio f_4 for sensor at position 5 based on simulation data.

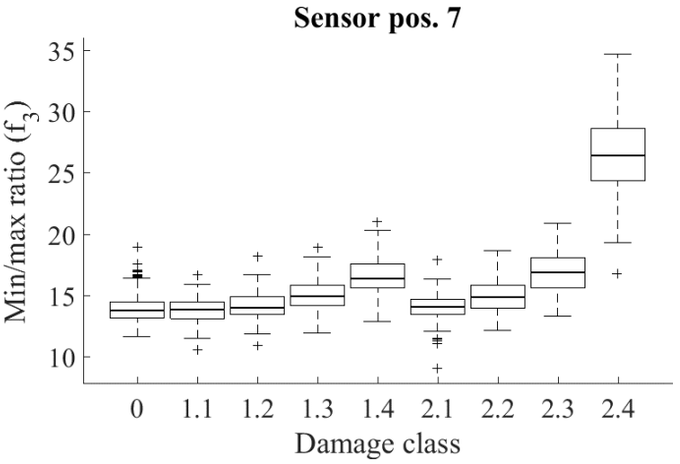


Figure 10. Box plot of feature min/max ratio f_3 for the sensor at position 7 based on simulation data.

6.2 *Experimental data*

Facing experimental sensor data, it turned out that the extraction of the exponential damping factor is not reliable when it is exclusively based on strain data. Figure 11 shows a signal after the vehicle passage. Fitting envelopes into this signal part fails to yield reasonable results.

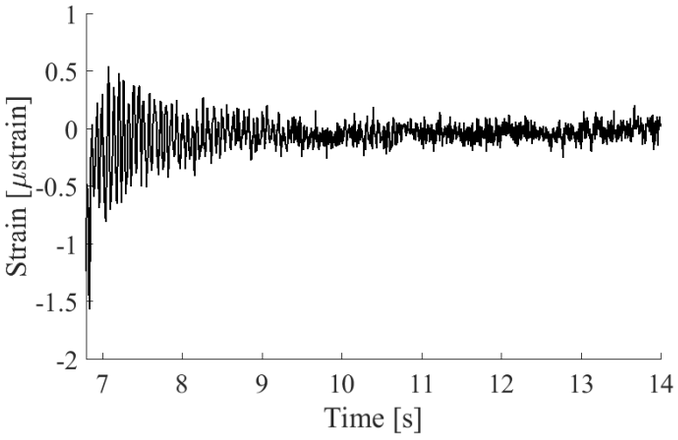


Figure 11. Sensor signal after the vehicle left the bridge (experimental data).

In Table 2 the results of the feature evaluation are presented. Regarding the experimental data, the feature min/max ratio f_3 performs slightly better than the feature area ratio f_4. Both are near 1 for specific sensor positions; therefore, they offer a high discriminability between the damage classes. The performance of the frequency-based feature f_2 reaches only low values for Q through all sensor positions. The damping factor f_1 is not analyzed in the experimental data.

Table 2. Results of feature evaluation for the experimental data represented by the measure Q which ranges from 0 (worst) to 1 (best). The maximum values of each feature/sensor combination are highlighted.

Sensor pos.	f_1	f_2	f_3	f_4
1	N/A	0.11	0.88	0.83
2	N/A	0.02	0.08	0.02
3	N/A	0.02	0.83	0.79
4	N/A	**0.15**	0.90	**0.92**
5	N/A	0.13	**0.96**	0.90
6	N/A	0.03	0.86	0.75
7	N/A	0.15	0.76	0.49
8	N/A	0.01	0.80	0.48
9	N/A	0.13	0.28	0.16
10	N/A	0.03	0.37	0.02
11	N/A	0.03	0.41	0.65
12	N/A	0.01	0.63	0.38
13	N/A	0.02	0.93	0.81
14	N/A	0.10	0.79	0.80
15	N/A	0.06	0.42	0.23
16	N/A	0.05	0.10	0.12
17	N/A	0.07	0.25	0.43
18	N/A	0.06	0.65	0.63

Box plots of the best sensor position for the features min/max ratio f_3 and area ratio f_4 are presented in Figure 12 and Figure 13. Similar to the simulation data, the different damage classes turn out to be well discriminable. In both features the different damage classes are reflected by different median values in combination with low variances.

6.3 *Discussion*

The results demonstrate that the applied feature extraction allows a reduction of the high dimensional data to single dimension variables, while still keeping and even emphasizing the differences between various damage classes. This approach works with both ratio-based features. The features based on the free oscillations of the bridge resulted in a poor discriminability using strain sensor data.

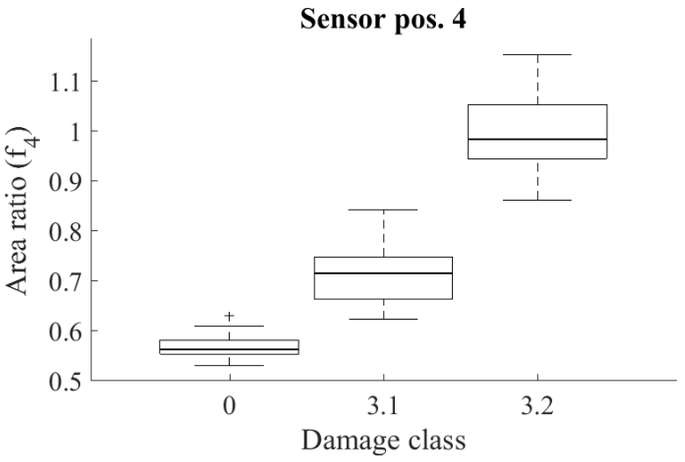


Figure 12. Box plot of feature min/max ratio f_4 for the sensor at position 4 based on experimental data.

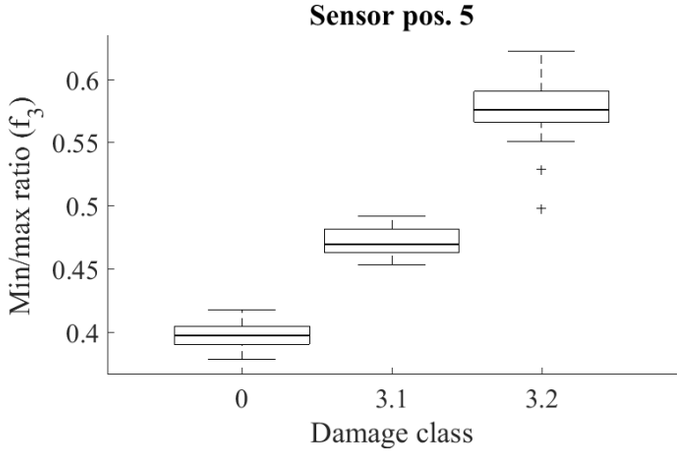


Figure 13. Box plot of feature area ratio f_3 for the sensor at position 5 based on experimental data.

Extracting the features area ratio or the min/max ratio, it is possible to discriminate damage severities and damage locations with only one strain sensor at a specific position.

Still, a few restrictions have to be retained at the current state of the method devolvement. Two damage classes in the simulation data and one in the experimental data have been considered. Further damage scenarios could result in similar feature values and therefore prevent a successful classification. Nevertheless, the authors assume that an adequate classification could follow up by using more than one sensor in the classification step. The presented approach considers so far vehicle passages in just one direction. Adding information by integrating vehicle crossings could additionally improve the performance. In future research, the authors address these additional aspects.

Compared to traditional visual inspections of the bridge, the presented approach offers several advantages. Once the sensor system is installed, data is acquired 24/7. This allows a continuous tracking of the bridge state with little effort. In addition, the system represents a low-cost solution for bridge monitoring, as it requires only few strain sensors and an analysis unit for data processing, data archiving and data access.

7 CONCLUSION

A structural health monitoring system for bridges requires the reliable detection, localization and assessment of damages in the bridge structure. In this paper, an approach for a two-span beam bridge based on strain sensor data and subsequent data processing is proposed. The authors demonstrate that the extraction of features based on strain sensor data at specific sensor positions achieves a high performance in discriminating different damage locations and severities. Using ratios in the data signals, the extracted features are independent from vehicle masses and vehicle velocities, two variables that are usually unknowns in real traffic scenarios.

The method is validated with simulation data as well as with experimental data from a real bridge with inflicted damages. The validation results demonstrate the applicability of the developed method.

ACKNOWLEDGMENTS

This work was supported by the Federal Ministry of Education and Research of Germany (BMBF) through the project i.bridge. The authors thank the Institute of Sensor and Actuator Technology (ISAT) and the company ci-Tec, which are also project partners within the i.bridge project.

REFERENCES

BASt, 2017. Brückenstatistik - Altersstruktur nach Brückenflächen.

Doebling, S.W. & Farrar, C.R. & Prime, M.B. 1998. A Summary Review of Vibration-Based Damage Identification Methods. *Identification Methods, The Shock and Vibration Digest* 30: 91–105.

Fan, W. & Qiao, P. Z. 2011. Vibration-based damage identification methods: a review and comparative study. *Structural Health Monitoring* 10(1): 83–111.

Geissler, K. 2014. Handbuch Brückenbau. Ernst & Sohn Berlin.

Malekjafarian, A. & McGetrick, P.J. & OBrien, E.J. 2015. A Review of Indirect Bridge Monitoring Using Passing Vehicles. *Shock and Vibration* (2015): Article ID 286139.

Rytter, A. 1993. Vibration Based Inspection of Civil Engineering Structures. PhD thesis. Aalborg University, Denmark.

Yang, Y.-B. & Lin, C. W. & Yau, J. D. 2004. Extracting bridge frequencies from the dynamic response of a passing vehicle. *Journal of Sound and Vibration* 272(3-5): 471–493.

Maintenance, Safety, Risk, Management and Life-Cycle Performance of Bridges – Powers, Frangopol, Al-Mahaidi & Caprani (Eds)
© 2018 Taylor & Francis Group, London, ISBN 978-1-138-73045-8

Automatic Data Collection System for Structural Health Monitoring

Akito Yabe, Tetsuya Iye
KOZO KEIKAKU Engineering Inc. Tokyo, Japan
Ayaho Miyamoto
Yamaguchi University Yamaguchi, Japan

ABSTRACT: In Japan, a great number of short and medium span bridges is managed by local government on a limited budget and limited number of expert engineers. More reasonable and efficient than conventional visual inspection or monitoring systems methods of the condition assessment have been needed. Therefore, a method of the condition assessment system based on monitoring data from public bus vibration was developed for existing short span (10m～20m span length) RC bridges. Due to the fact that this system is only composed of an acceleration sensor and a manual operation data collection system, a reasonable and efficient automatic data collection system is considered. In this paper, a method of automatic data collection system using GPS sensor is proposed. This system which is installed on the public bus changes a manual and non-efficient operation into an automatic and low cost one.

1 INTORODUCTION

1.1 *Summary of the condition assessment system based on monitoring data from public bus*

In Japan, about 70 percent of nearly 670,000 bridges were constructed in the 1960s and 1970s. Most of them are short- or medium-span (10–20 m) bridges. This great number of short and medium span bridges is managed by local government on a limited budget and limited number of expert engineers. That is why, the number of carried out inspections is insufficient. In the future, due to reconstruction of government finances and declining birth rate the bridge management will become even more difficult. Therefore more reasonable and efficient than conventional visual inspection or monitoring systems methods of the condition assessment have been needed. In view of such situation a method of the condition assessment system based on monitoring data from public bus vibration as shown in **Figure 1** was developed for existing short span RC bridges. This system has applied a method of extracting safety indices, namely "Characteristic Deflection" (shortened to CD) which is relatively free from the influence of dynamic disturbances due to such factors as the unevenness of the road surface, and a structural anomaly parameter. The system is only composed of an acceleration sensor and a manual operation data collection system. While measuring the acceleration of bus vibration, an operator has to be on the bus to make a note of a time when the vehicle is passing over the target bridge. After measuring, CD is extracted from acceleration data by manual operation. Due to the operating cost of this process, an automatic data collection system seems to be more reasonable and efficient monitoring system. This paper focuses on a method of automatic data collection system using Global Positioning System (GPS). This system is pinpointing bus's position by GPS sensor data and detecting ups or downs of a road. If the bus is over the target bridge, this system automatically measures acceleration data. It is expected that this automatic data collection system will enable to create low cost bridge management system.

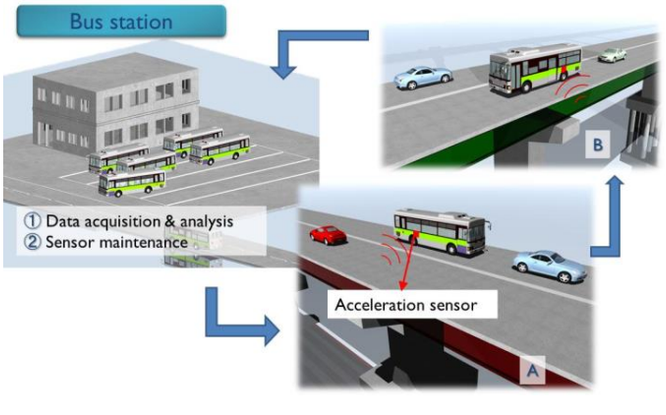


Figure 1. Concept of bus monitoring system for short- and medium-span bridges.

1.2 *Concerning the theory of "Characteristic Deflection"*

The calculating CD process is one of the rational methods for extracting damage/deterioration-related information from measured rear wheel vibrations of a bus without being affected by the dynamic characteristics of the bridge and the vehicle and the road surface profile. A summary of the rationale for extracting CD is shown **Figure 2**.

The rear wheel vertical vibration $\delta_a(t)$ of a bus running at a constant speed can be expressed as the sum of static displacement $\delta_{sa}(t)$, which is dependent on the measured rear wheel vertical vibration of the bus, and dynamic displacement $\delta_{da}(t)$, which is dependent on the road surface profile and the vibration characteristics of the bridge and the vehicle:

$$\delta_a(t) = \delta_{sa}(t) + \delta_{da}(t) \quad (1)$$

If it is assumed that the unevenness of the road surface can be expressed as a steady-state random Gaussian process with an average value of 0 and that dynamic displacement including bridge–vehicle interaction is ergodic and Fourier-series-expandable, the dynamic displacement $\delta_{da}(t)$ can be expressed as their sum:

$$\delta_{da}(t) = S_r(\Omega, t) + \int_{-\infty}^{+\infty} X(f) \cdot e^{2\pi f t i} df \quad (2)$$

where

$S_r(\Omega, t)$: density function for unevenness of road surface.

Ω: spatial frequency of road surface profile.

$X(f)$: Fourier coefficient.

In Eq. (2), the sample mean in the second term is 0. The mean of a sufficient number (N) of samples obtained from $\delta_{da}(t)$ can be expressed as

$$\frac{\sum_{t=1}^{N} \delta_{da}(t)}{N} \fallingdotseq 0 \quad (3)$$

Next, k samples are taken from measured values obtained from $\delta_a(t)$, and their mean is expressed as : $\overline{\delta a\ (t)}$

$$\overline{\delta a\ (t)} = \frac{\sum_{j=1}^{k} \delta_a(j)}{k} \quad (4)$$

Because the sample mean follows a normal distribution in accordance with the central limit theorem, $\overline{\delta a\ (t)}$ converges to a certain value (μ_a). For the sample mean $\delta_a(j)$ of a sufficient number (n) of samples, the following equation holds true:

$$\mu_a = \frac{\sum_{i=1}^{n} \overline{\delta a\ (t)}_i}{n} = \frac{\sum_{i=1}^{nk} (\delta_a(j))_i}{nk} \quad (5)$$

Sampling is made so that there is no overlap in the samples. If N is sufficiently large for $nk = N$ and $t = 1 \sim N$, the following approximation can be made:

$$\mu_a \fallingdotseq \frac{\sum_{t=1}^{N} \delta_a(j)_t}{N} \quad (6)$$

This expresses the mean displacement of the rear axle of the bus passing over the bridge. From Eqs. (1) and (3), the following equation can be derived:

$$\mu_a \fallingdotseq \frac{\sum_{t=1}^{N} \delta_{sa}(t)}{N} \quad (7)$$

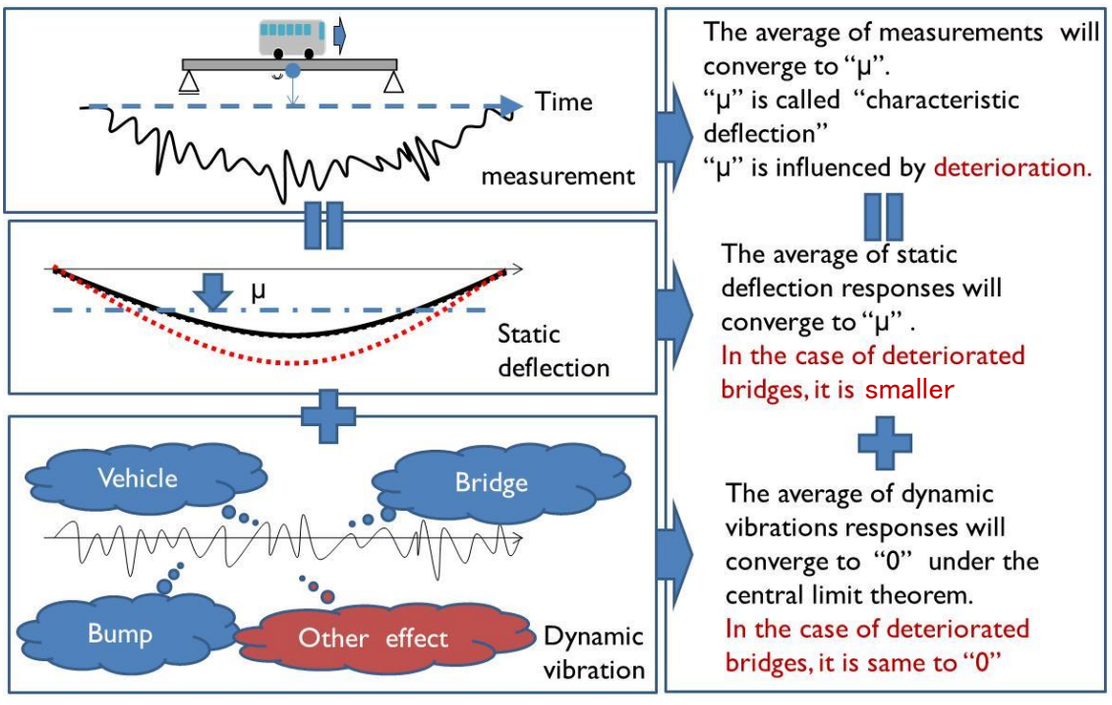


Figure 1. A summary of the rationale for extracting CD

This means that the mean displacement of the rear axle of the bus passing over the bridge obtained from a sufficient number (N) of samples can be extracted as a value, μ_a (referred to as "Characteristic Deflection value"), that is relatively free from the influence of the vibration characteristics of the bridge and the vehicle and the dynamic displacement due to the unevenness of the road surface. Since the values of μ_a are extracted from measurements taken when the bridge under consideration is in a sound condition, values extracted from a measurement taken after the occurrence of deterioration or damage are represented by μ_a'Then, the following equation can be defined :

$$\alpha = \frac{\mu_a'}{\mu_a} \qquad (8)$$

The rate of change α expressed by Eq. (8) is defined as the structural anomaly parameter. After a given value of α is set, the characteristic deflection is monitored continuously. When the characteristic deflection has exceeded a certain limit, it can be detecting that the bridge of interest has moved from the acceleration stage to the deterioration stage.
From the above, CD was calculated based on the law of classical mechanics such as Hooke's law and statistical feature data. If the condition is satisfied which means Hooke's law influence is greater than others in measured rear wheel vibrations, only CD has the significant information of damage/deterioration. Therefore, rear wheel vibrations have to be measured by a heavy vehicle such as a bus.

2 SUMMARY OF AUTOMATIC DATA COLLECTION SYSTEM

2.1 *Composition of automatic data collection system*

Conventional data collection system is composed by an acceleration sensor, a data logger, a personal computer and a battery. This system data logging sampling frequency is 1000Hz, so collecting a huge number of acceleration data is impossible. The system is operated manually. That is why, when measuring the acceleration of bus vibration, one operator is always checking whether the bus is approaching the target bridges, while another operator is responsible for pushing the start button and making a note of a time when the bus enters the target bridge. New data collection system is created by adding GPS sensor and USB camera to the conventional system, as presented in Figure 3. An acceleration sensor and a GPS sensor performance are shown in **Table 1.** GPS sensor has two operating functions. One function is detecting that the bus is approaching the target bridges with detecting the ups or downs of a road. Another function is a trigger for the start of measuring the acceleration of bus vibration.

2.2 *A method of the target bridge detection*

In the case of detecting the measurement target bridge using GPS data there are three important aspects: detection of approaching to the target bridge, detection of the ups or downs and relation with acceleration data. A detection method of vehicle approaching to the target bridge is shown in **Figure 4**. The two position area data were prepared for picking up GPS in the automatic data collection system in order to detect the ups or downs and solve a time lag of data acquisition. As shown in Figure 3, when the bus is going into the Picking up area 1 on the ups side lane, the system state becomes "Ready". Later, when it is going into the Picking up area 2, the system state becomes "Measurement Start". An acceleration data is logging time to pass the bridge. When in the state of "Measurement" in the area 2, the trigger is off to change the state.



Figure 3. A new automatic data collection system.

Table 1. An acceleration sensor

Acceleration sensor	
Manufacturer	Fuji Ceramics co.
Type	Piezoelectric
Frequency Performance	3Axis 1Hz～
Sampling Frequency	1000Hz

Table 2. A GPS sensor

GPS sensor	
Manufacturer	ZMP Inc.
Survey Accuracy	3m CEP(50%)
Frequency Performance	5Hz
Sampling Frequency	5Hz

After logging data, the state becomes “Idle” and waiting to become “Ready” in the next area. On the bottom of the figure, a bus approaching from another direction is presented. The system is able to detect the ups or the downs and detect approaching the target bridge.

The system has data base of relation between picking up area numbers and the all target bridges. That is why, every measured data is linked to the target bridge with a time stamp.

2.3 *An automatic data collection system program*

An automatic data collection program flow is shown in **Figure 5**. This program is composed of three modules and one database. These modules are a picking up area verification module, a state management module, an acceleration logging module and target bridges position data base.

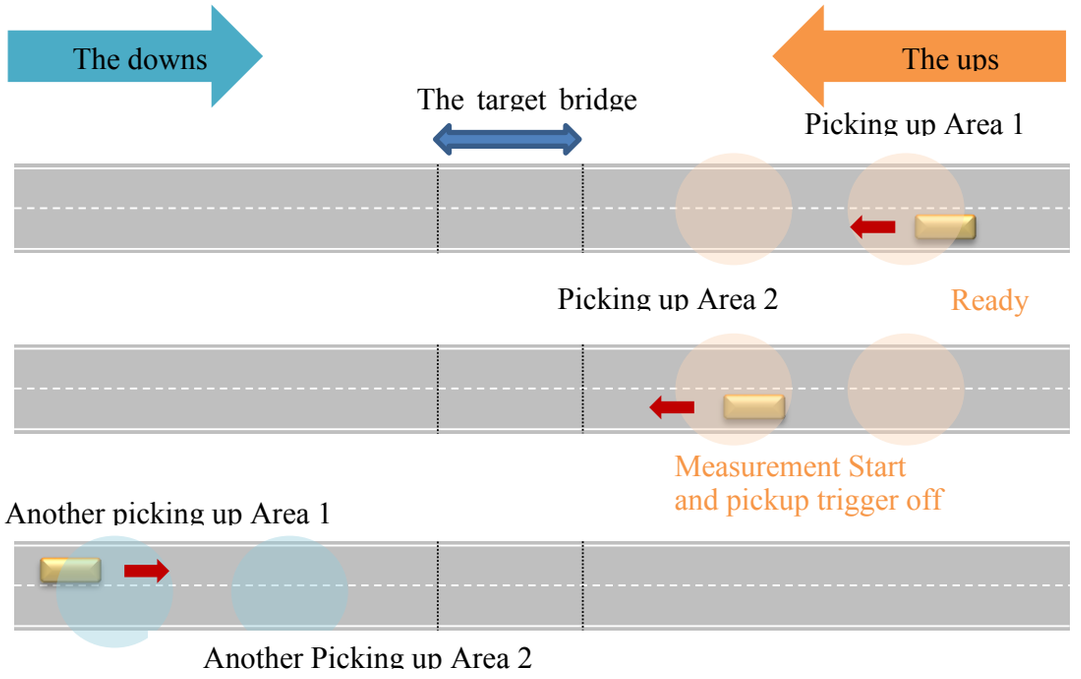


Figure 4. A detection method of vehicle approaching the target bridge

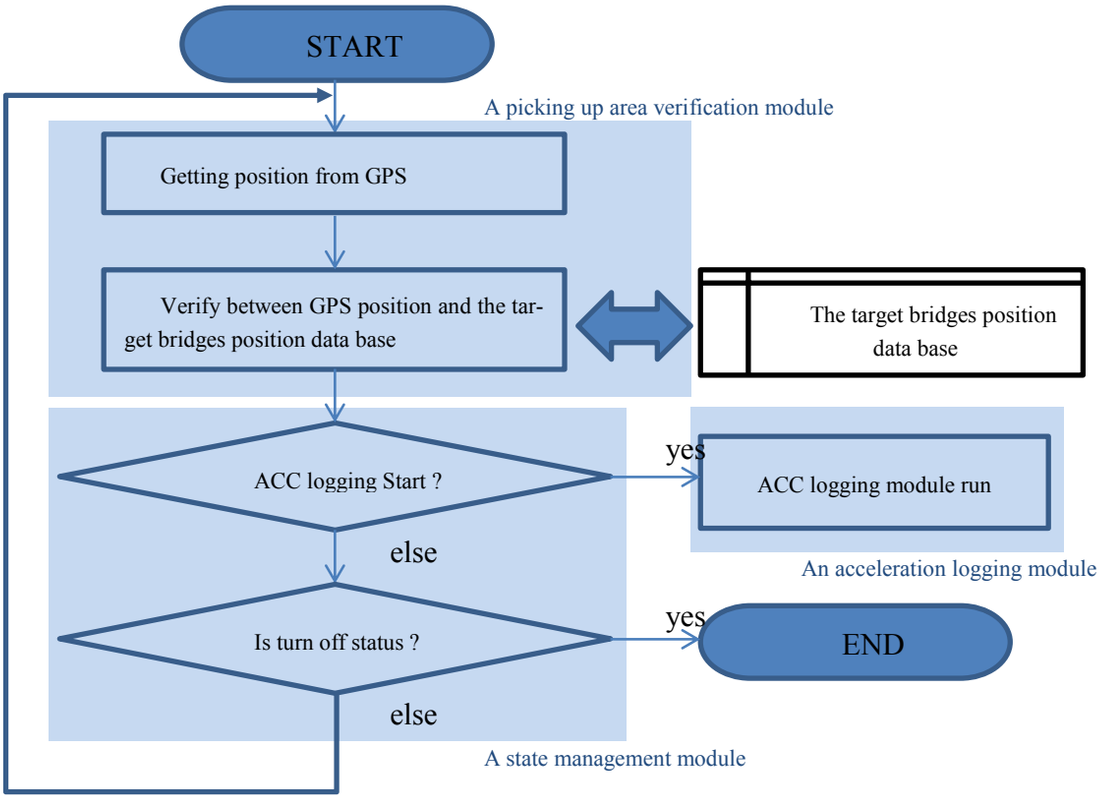


Figure 5. An automatic data collection program flow bridge

A picking area verification module is verifying GPS data and target bridges position while running. A state management module is changing system states in order of passed picking area numbers. An acceleration logging module saves acceleration data according to state management module. This program substitutes manual operations for an automatic cooperation of modules. The target bridges position data base has 5 major items. Their items are shown in **Table 3.**

3 TEST OF AUTOMATIC DATA COLLECTION SYSTEM

3.1 *Data collecting test on "Shingondai-bridge"*

In this case the operating city bus was used. The one-day route of a city bus in the Ube city is shown in Figure 6. The field test started at 7:00 and ended at 19:00. The data collecting test was carried out on "Shingondai-bridge" (Figure 7). The position of "Shingondai-bridge" is presented by a red circle on the Figure 6. "Shingondai-bridge" was constructed in ~~at~~ 1998. This bridge is a simple girder bridge with 22.4m span. In this test case a radius of a picking up circle area is 40m. The distance between Area1, Area2 and the target bridge was set to 50m. These radiuses and distances depend on GPS sampling frequency and the bus running speed. In this test, this system was used to collect data for several seconds while passing through "Shingondai bridge" and identifying the up line and the down line automatically (Figure 8).
Figure 9 shows trajectories of passing through "Shingondai bridge" by this system. Figure 10 shows the one of the acceleration data of passing through "Shingondai bridge".

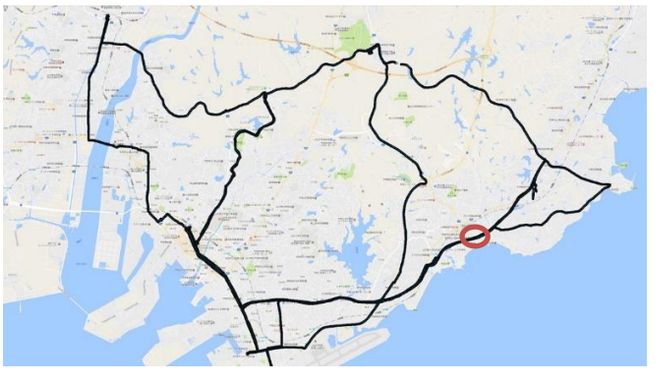


Figure 6. The one-day route of a city bus in the Ube city.



Figure 7. Shingondai-bridge.

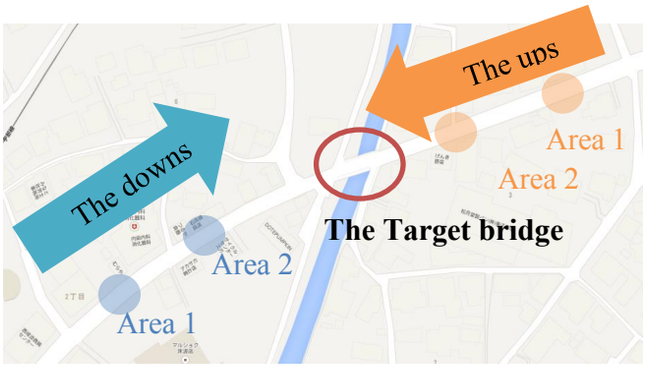


Figure 8. Shingondai-bridge location.

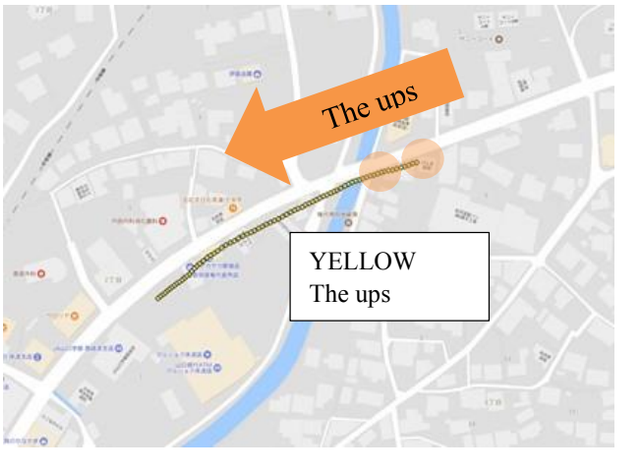


Figure 9. Trajectories of passing through "Shingondai bridge" by this system.

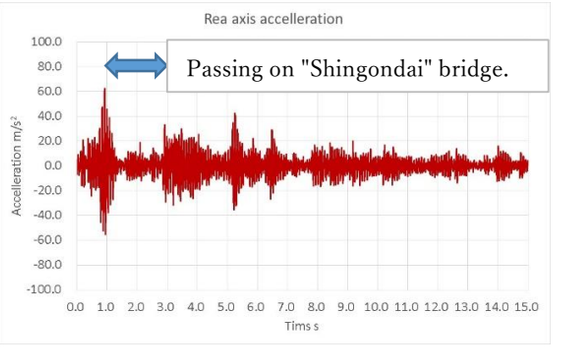


Figure 10. One of the acceleration data of passing through "Shingondai bridge" ~~by this system~~.

3.2 *Testing the completely automatic data collection system*

In the case of Ube city bus, system needed another power supply other than the vehicle battery and human operation at starting and ending. That is why an automatically start-up and shut-down function was needed. In order to implement this function, we focused on the car accessories power supply. A diagram for realizing the function is shown in Figure 11. It needs two BIOS functions on the personal computer which are "(a)power on when AC is detected" and "(b)initiate automatic shutdown when AC is removed". This test was carried out on "Ougi brige" from 17 May 2017 until 12 July 2017 at Kawasaki in Kanagawa Prefecture (Figure 12). Implementation of these functions was tested on a crane car (13) during a one-month trial period. The purpose was to check and eliminate potential errors which could create problems on the city bus, largely impacting transportation infrastructure. Figure 14 is shown the fuse box of the crane car. This system was suppled power from accessories power supply. Figure 15 shows the component of data collection system. This is composed ~~by~~ of PC, a logger unit and GPS unit connected to USB. This component is fixed strictly for anti-theft. This system was left while for around a month in the car.

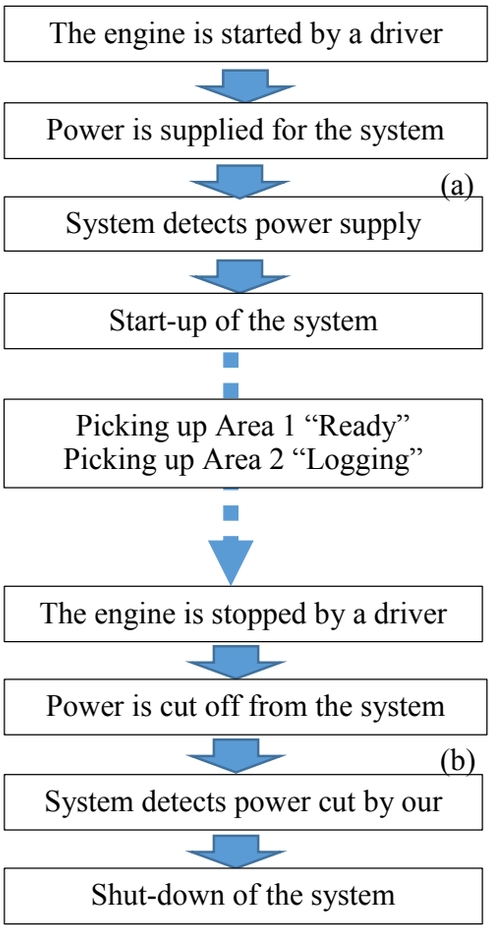


Figure 11. A diagram for automatical~~ly~~ start-up and shut-down function.



Figure 12. Ougi-bridge location.



Figure 13. A crane car used in the test.



Figure 14. The fuse box of the crane car.

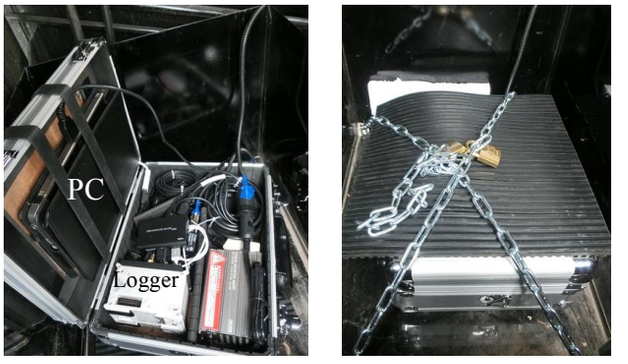


Figure 15. Components of the system.

Figure 15 shows components of used system. Figure 16 shows trajectories of passing through "Ougi bridge" by the system. The system also succeeded in collecting data automatically without human operation.

4 CONCLUSION

This paper focused on a method of automatic data collection system using GPS, and introduced an automatic data collection program. Systems were tested in the field with good results. Main conclusions reached the results of verification experiments and are summarized as follows:

1) Under certain conditions using GPS is feasible for the automatic data collection system.

2) A running to the ups or the downs is able to ~~detect~~ be detected by picking up Area1 and Area2 in this system.

3) Under certain conditions using power supply from the vehicle is feasible for the completely automatic data collection system.

The automatic data collection system has some problems which will be solved in the future. What is more, it is important to answer to the following questions. What are the rational parameters for this system for any kind of the bridge? What kind of method should be applied to transfer the huge data from this system? How to extract CD from acceleration data automatically?



Figure 16. Trajectories of passing through "Shingondai bridge" by this system.



Figure 17. Trajectories of passing through "Ougi bridge" by this system.

REFERENCES

- Japan Ministry of Land, Infrastructure, Transport and Tour-ism, http://www.mlit.go.jp/road/sisaku/yobohozen/yobo2_3.pdf,2011
- Ayaho Miyamoto, Akito Yabe: Bridge Condition Assess-ment based on Vibration Responses of Passenger Vehi-cle, Journal of Physics(CS), Vol.305(1), pp.1-10, 2011.7.
- Lin C.W. and Yang Y.B. (2005) "Use of a passing vehicle to scan the fundamental bridge frequencies: an experi-mental verification. Engineering Structures, 27, 1865-1878.
- Yabe, A, Araki, H, and Miyamoto, A. 2008. Application of traffic vibration simulator to damage detection for bridge maintenance, IABSE Conference on Information and Communication Technology for Bridges, Buildings and Construction Practice, June 4-6, Helsinki.
- Yabe, A and Miyamoto, A. 2010. Bridge Maintenance, Safe-ty, Management and Life-Cycle Optimization, CRC Press (A Balkema Book), IABMAS'2010, Pennsylvania, USA
- Yabe, A. 2013. Automatic Data Collection System for Inno-vative Bridge Health Monitoring based on Public Bus Vibration, CSHM-5, Ube, JAPAN

SS03: Bridge safety, maintenance and management under hazards and changing climate

Organizers: Y. Dong, M. Soliman & D.M. Frangopol

Maintenance, Safety, Risk, Management and Life-Cycle Performance of Bridges – Powers, Frangopol, Al-Mahaidi & Caprani (Eds)
© 2018 Taylor & Francis Group, London, ISBN 978-1-138-73045-8

Vulnerability of bridges exposed to coastal hazards and climate change

G.P. Balomenos
Rice University, Houston, Texas, USA

S. Kameshwar
Oregon State University, Corvallis, Oregon, USA

B. Bass, J.E. Padgett, P. Bedient
Rice University, Houston, Texas, USA

ABSTRACT: Many bridges in the United States (US) are located in areas prone to storm surge and sea level rise. Past events have highlighted the structural vulnerability of these structures when subjected to hurricanes, triggering the development of fragility models for bridges subjected to hurricane-induced surge and waves. However, parameterized fragility models are lacking for a range of different bridge configurations to enable rapid application across a region and/or to explore climate change effects on bridge damage risks. In addition, fragility models assuming the same superstructure across a bridge for developing fragility curves may not provide full information on vulnerability given that different types of superstructures may exist within a single bridge. Thus, this study assesses the fragility of individual spans for different bridge classes subjected to storm surge and waves. The bridge deck is modeled as a grillage and wave force time-history analysis is conducted on bridge models from each class generated through Latin hypercube sampling. Logistic regression is applied to derive parameterized fragilities given hurricane intensity measures. This paper then incorporates the new models in a case study along the Houston-Galveston region of Texas for storm scenarios with and without sea level rise. The results show the variation in failure probability across different bridge classes and the dependence of these differences on the intensity of the hazard. In addition, the results reveal the anticipated increase in failure probability that may be expected with alternative climate change scenarios in which sea level rise is incorporated in the hurricane hazard model used for the scenario risk assessment.

1 INTRODUCTION

Bridges are a vital component of the transportation network to ensure connectivity in areas damaged by natural hazards (Padgett et al., 2008). Past events have highlighted the structural vulnerability of bridges when exposed to natural hazards, e.g. hurricanes, with dramatic consequences to the functionality of the transportation network (Gidaris et al., 2017). For example, Hurricane Katrina in 2005 caused significant damaged to bridges with an overall cost of repair/replace over $1 billion (Padgett et al., 2008). Many bridges located in the Houston-Galveston region of Texas were damaged by storm surge and waves produced by Hurricane Ike in 2008 (Stearns and Padgett, 2011). Therefore, bridge damage related to coastal events have increased the interest of the scientific community for quantifying the vulnerability of the bridge structures. A discussion of these studies is provided below, while a more thorough review can be found in Gidaris et al. (2017).

Padgett et al. (2012) developed empirical fragilities for water crossing multi-span simply supported (MSSS) concrete girder bridges subjected to hurricane hazards, for the Mississippi and Louisiana Katrina exposed region. These fragilities were developed through a statistical analysis for four damage states and a single hurricane hazard, i.e. the empirical probability of the bridge being in or exceeding a damage state was conditioned on the hurricane surge elevation.

Ataei and Padgett (2012) proposed a probabilistic framework for bridge deck unseating when subjected to hurricane hazards. The proposed framework uses analytical expressions for estimating the uplift probability of each bridge span. Then, the bridge failure is estimated in series, i.e. uplift of any span constitutes bridge failure. The authors applied the framework to a number of bridges located in the Houston-Galveston region of Texas. For the developed fragilities the probability of deck unseating was conditioned on two hurricane hazard intensity measures, i.e. wave height and relative surge elevation. In addition the authors developed a rapid-approximation fragility model that depends on the bridge span mass per unit length and estimates the probability of failure using an analytical expression with coefficients derived based on regression analysis.

Kameshwar and Padgett (2014) proposed a multi-hazard risk assessment framework for highway

bridges. The proposed multi-hazard framework was implement to MSSS concrete girder bridges in South Carolina for both earthquakes and hurricanes. A single damage state was considered similar to Ataei and Padgett (2012), i.e. bridge failure estimated in series based on deck uplift/unseating. However, a nonlinear dynamic analysis was performed using OpenSees (Mazzoni et al., 2006), i.e. bridge models were subjected to wave force time histories, contrary to Ataei and Padgett (2012) where the bridge models were subjected to static analysis. In addition, the bridge failure probability was conditioned on three parameters, namely surge height, wave height and bridge height.

Ataei and Padgett (2015) proposed a numerical model which takes into account the fluid-structure interaction (FSI) for evaluating bridge fragility in hurricane events. The model was utilized for a water crossing MSSS concrete girder bridge in the Houston area. A single damage state was considered, i.e. deck uplift, and the probability of the bridge failure was conditioned on wave height and relative surge elevation.

Anarde et al. (2017) proposed an integrated model for assessing bridge vulnerability exposed to hurricanes. The authors investigated the effect of climate change on local geomorphology and associated changes in storm surge and waves. Thus, the model takes into account landscape changes, e.g., erosion, associated with sea-level rise to examine the effects of these changes for a number of bridges surrounding Freeport in Texas, using already developed fragility models from previous studies.

This study focuses on developing improved fragility models, i.e. parameterized for a range of different bridge configurations, and to examine the effects of climate change on bridge vulnerability using these improved models. Different types of superstructures may exist, even within a single bridge. Therefore, existing models may not fully capture the bridge behavior under coastal hazards. Thus, instead of developing bridge class fragilities or those appropriate for only an individual bridge, this study develops parameterized fragility models that capture the dynamics of the problem and can be applied to a whole portfolio of bridges with varying details and superstructures. Two bridge classes are examined, i.e. MSSS concrete girders and MSSS steel girders, for a portfolio of MSSS bridges located in the Houston-Galveston region of Texas. The bridge superstructure, i.e. deck and girder, is modeled as a grillage, instead of a spine used in the previous studies, and the bridge models are subjected to wave-time histories using OpenSees. A single damage state is considered, i.e. individual deck uplift, and the probability of the deck uplift is conditioned on bridge parameters, e.g. deck width, length, etc., and on two hurricane-related hazards, i.e. surge height and wave height. Given the significant and growing development along the coast in regions subjected to sea level rise (Nicholls et al., 1999, Crosset et al., 2004), an illustration of the application of these parameterized fragility models for alternative sea level rise conditions is shown.

2 BRIDGES MODELING OF HURRICANE RESPONSE

In this study, the response of bridges subjected to hurricane wave and surge loads is assessed using nonlinear dynamic analysis. For this purpose, a general three-dimensional bridge model is created in OpenSees (Mazzoni et al., 2006), which can be used for bridges with different superstructure types. Next, transient analysis is performed to assess the response of the bridge model subjected to wave and storm surge loads. Details on bridge, load, and response modeling are presented in the following sub-sections

2.1 *Bridge modeling*

Deck unseating has been observed to be the most common cause of structural failure in bridges subjected to hurricane wave and surge loads (Padgett et al., 2008, Stearns and Padgett, 2011, Padgett et al., 2012). This type of failure is predominantly observed in simply supported spans, situated at low elevation, wherein several individual deck spans are unseated. Considering this failure mode, bridges can be considered as a series systems of spans where failure of even a single span leads to bridge failure. Therefore, this study models individual spans whose fragilities can be later combined in series to assess the overall fragility of a bridge. The modeling approach adopted herein is further supported by recent analysis of structural layouts and plans of bridges, conducted by the authors, in the Houston-Galveston region. The analysis shows that within a single bridge, superstructure characteristics change from one span to another, such as girder size and girder type. This observation indicates that modeling individual bridge spans with potentially different characteristics and re-combining them as a series system may be more realistic in comparison to modeling an entire bridge with the same superstructure characteristics.

The Opensees model of an individual span consists of a bridge deck, bearings, bridge bents and, foundations. The deck is modeled using a grillage (Hambly, 1976) where the longitudinal element (along the length of the bridge) represent girders and the transverse elements (along the width of the bridge) represent the deck slab. The deck is discretized along the length at a spacing of 1.0 m and the discretization along the transverse direction is governed by the number of girders in the bridge deck. The spacing for longitudinal discretization is determined by evaluating the maximum spacing that leads to convergence

of the total hurricane loads on the bridge deck. Since the deck usually acts as rigid body during deck unseating, the grillage elements are modeled using elastic beam column elements with appropriate section and material properties, which are considered to be variables whose effect on the hurricane response will be studied in the following sections. The bridge deck is placed on top of the bearing assembly situated on the bent cap. The commonly observed elastomeric bearings are modeled using a steel type material to represent the elastomeric pad and a hysteretic material to model the steel dowels in the bearing assembly. Bearing properties such as stiffness of the elastomeric pad and the strength of the dowel bars are considered as variables. The bent cap and the columns are modeled with rectangular and circular beam column elements, respectively, modeled using fiber sections. The fiber section comprises of three different layers that represent the un-confined cover concrete, the confined core concrete, and the longitudinal reinforcement. The effect of transverse reinforcement is incorporated in the properties of the confined concrete following Mander (Mander et al., 1988). Herein, column diameter (D_c), column height (H_c), concrete strength (f_c), yield stress of reinforcing steel (f_y), and reinforcement ratios, longitudinal (ρ_l) and transverse (ρ_t), are also included as variables. The pile foundations are modeled using non-linear springs in translational and rotational directions. The characteristics of the foundation springs are assumed to be uncertain. Since this study primarily focuses on deck unseating failure of simply supported spans, the vertical and torsional degrees of freedom are constrained at the foundation nodes. In order to facilitate modeling deck unseating response, node to node contact elements are used in the finite element model. These contact elements are incorporated between the deck and the bridge bent. The properties of the contact elements are calibrated to ensure that the bridge characteristics are not altered significantly. Additional details on modeling of bridge components can be found in Nielson (2005) and Kameshwar and Padgett (2014).

2.2 *Load modeling*

The OpenSees finite element bridge model described above is subjected to time varying hurricane wave and surge loads. The maximum wave loads on bridge decks are obtained using AASHTO guidelines (AASHTO, 2008). These maximum loads are used along with a modified version of the phenomenological hurricane wave and surge load model proposed by Ataei at al. (2010) to obtain the wave and surge load time history. The load model proposed by Ataei et al. (2010) cannot be directly applied to bridge decks modeled using a grillage because it provides the total horizontal and vertical loads acting on a bridge deck; for a grillage deck model, loads at every girder is required. Therefore, considering the wave velocity and girder spacing, the phenomenological load model is modified to obtain the time history of loads acting on every girder. Using the modified load model, different load time series are obtained for each girder. The magnitude of these loads depends on relative bridge clearance (Z_c) which is the difference between the deck height and the still water level, i.e. Z_c is negative when the deck is submerged; wave period (T) and wave height (H_w), in addition to bridge superstructure type. Herein, Z_c and H_w are considered as variables while T is considered to be uncertain.

2.3 *Response*

Using the finite element bridge span model and the surge and wave load model, dynamic analyses are conducted to evaluate the deck unseating performance. Herein, the bridge deck is subjected to loads from a single wave during the transient analysis. At each time step, the displacements of the deck nodes are recorded to identify unseating failures. The recorded deck node displacements are also used to identify and separate models where transient analysis did not converge due to numerical issues from models where transient analysis fails due to large deck displacements. Finally, the deck response is characterized by using a binary variable which is assigned a value equal to one when unseating is observed and a value equal to zero when unseating is not observed.

3 FRAGILITY MODELING

Using the binary deck unseating response along with the bridge and wave characteristics this study develops logistic regression based fragility models. For this purpose, a machine learning based approach is used. First, key variables that might affect the deck unseating behavior are identified, e.g. deck length (L), deck width (W), slab thickness (h), girder cross-section area (A_{gd}), girder weight (W_{gd}), number of girders (n_{gd}), Z_c, H_w. Next, an experimental design is set up to uniformly span the space of these variables; herein Latin hypercube sampling is used to generate 256 combinations of parameter values. For each combination, a finite element model is developed and the time history of loads is obtained following the procedure described in the previous section. The binary bridge deck unseating response is obtained, for all parameter combinations, by performing non-linear dynamic analysis. Using binary response and the key variables, a logistic regression model is trained to predict the binary response for given values of input variables. Additional information on training logistic regression model can be obtained from Hosmer and Lemeshow (2000). Using the final logistic regression model, the failure probability can be obtained for a given set of bridge and wave load parameters as:

$$p_f\left(uplift \mid X, IM\right) = \frac{\exp\left(g\left(X, IM\right)\right)}{1+\exp\left(g\left(X, IM\right)\right)} \quad (1)$$

where X = bridge parameters; IM = hazard parameters, i.e. H_w and Z_c; and $g(X,IM)$ = polynomial which represents the logarithm of odds in favor of deck unseating. Herein, a stepwise regression method is adopted to ensure that only the most influential parameter combinations are included in $g(X,IM)$.

4 PERFORMANCE ASSESSMENT OF BRIDGES IN HOUSTON-GALVESTON

4.1 *Hurricane scenarios*

In this study, two hurricanes that result in 100-yr and 500-yr surge levels, respectively, are simulated under baseline, i.e. existing sea level conditions, as well as 2050 and 2100 sea level rise (SLR) scenarios. This analysis does not take into account dynamic changes in storm characteristics that may additionally occur due to climate change, which can alter the characteristics (i.e. size and intensity) of the 100-yr and 500-yr storms simulated. Nonetheless, the sea level rise scenarios put into context any increases in surge levels and wave heights that may occur for the simulated storms. The peak surge and wave response for this suite of six storms was determined utilizing the tightly coupled Advanced CIRCulation and Simulating WAves Nearshore (ADCIRC+SWAN) model (Luettich and Westerink, 2004). The two hurricanes were obtained from the Federal Emergency Management Agency's (FEMA's) suite of Upper TX Coast storms utilized for their surge risk analysis (USACE, 2011, FEMA, 2017), and are referred to as Storm 033 and Storm 036. Storm's 033 and 036 result in roughly 100-year and 500-yr surge levels for present day conditions, respectively, based on comparisons against FEMA's most recent surge frequency analysis (Ebersole et al., 2015). The sea level rise conditions for the year's 2050 (0.437 m increase in sea level) and 2100 (1.367 m increase in sea level) are based on mean estimates from the National Oceanic and Atmospheric Administration (NOAA) (Sweet et al., 2017).

4.2 *Bridge inventory*

A set of bridges are selected from the Houston-Galveston region of Texas. This area is located in the Upper Texas Gulf Coast, an area prone to hurricane events and vulnerable to storm surge (Torres et al., 2017). The National Bridge Inventory (NBI, 2017) does not contain enough information regarding parameters required for assessing bridge vulnerability exposed to coastal hazards. Thus, a database was developed through a detailed review of the bridge plans for the area of interest. From this database a subset of bridges with concrete and steel girders was extracted to retrieve structural details, e.g. deck width, deck length, etc., for each bridge class. Table 1 gives an indication of the typical range of these parameters and the bounds for which the LHS for fragility analysis was conducted.

Table 1. Bounds for bridge parameters.

Parameter	Range (concrete girder)	Range (steel girder)
Deck length (L)	6.1-27.4 m	9.1-27.4 m
Deck width (W)	6.6-18.6 m	6.1-18.3 m
Slab thickness (h)	0.11-0.25 m	0.15-0.42 m
Girder c/s area (A_{gd})	0.18-0.51 m^2	0.07-0.49 m^2
Girder weight (W_{gd})	4.18-11.98 kN/m	5.4-37.7 kN/m
Number of girders (n_{gd})	2-17	2-18

4.3 *Risk assessment*

Using logistic regression, the logit function for the uplift of a concrete girder is estimated as:

$$g(X,IM) = 9.78 - 9.24Z_c + 2.31H_w - 80.63h - 0.51n_{gd} + 21.33H_w h \quad (2)$$

Similarly, the logit function for the uplift of a steel girder is estimated as:

$$g(X,IM) = 316.78 - 18.91Z_c + 7.36H_w + 1.77\times10^{-4}W - 4393.7h + 5.19Z_cH_w - 7.96\times10^{-4}Wh - 2.75Z_c^2 + 18{,}826h^2 - 25{,}953h^3 \quad (3)$$

Fragility surfaces are plotted using the derived logit functions for bridges with concrete (Figure 1) and steel (Figure 2) girders, showing the uplift probability conditioned on Z_c and H_w. Fragility analysis indicates that there is a variation in the uplift probability between the two examined bridge classes. For example, there is 33.63% probability for a 0.1 m submerged concrete girder bridge to experience uplift if subjected to a wave height of 1 m, while this probability is 8.26% for a steel girder bridge (Figure 3). This difference can reach up to 30.12% for a wave height of 1.25 m (Figure 4). Thus, considering the same superstructure across a bridge for developing fragility curves may not provide full information on vulnerability.

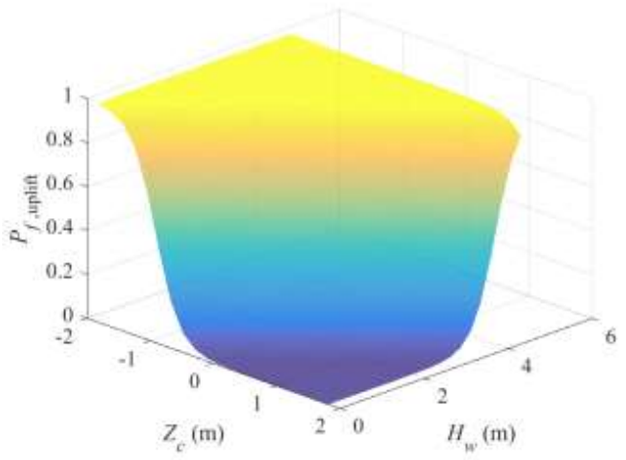


Figure 1. Fragility surface for concrete girder.

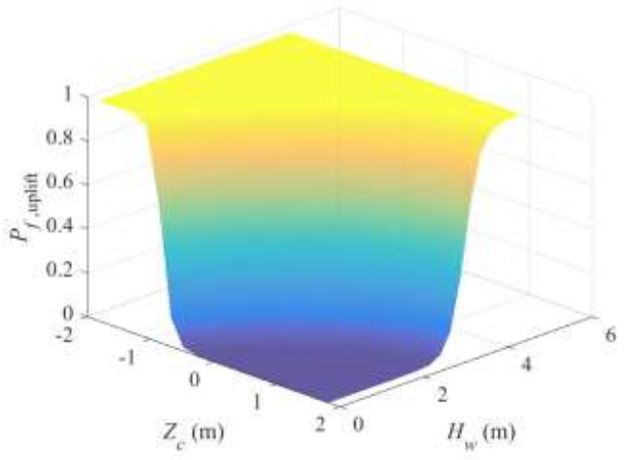


Figure 2. Fragility surface for steel girder.

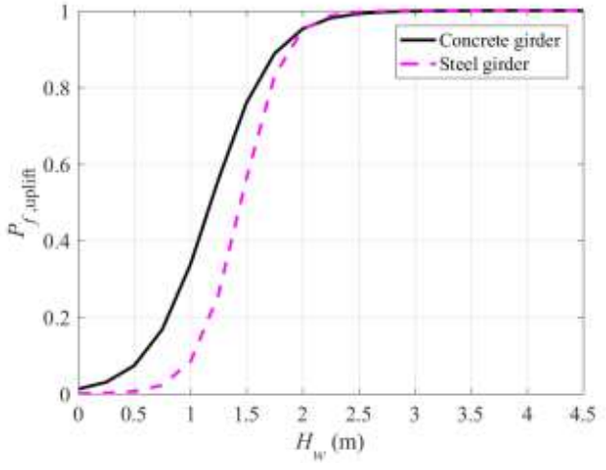


Figure 3. Uplift fragility for Z_c=-0.1 m.

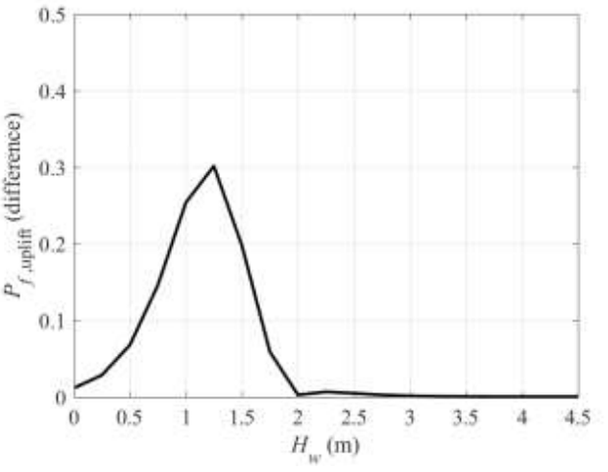


Figure 4. $p_{f,uplift}$ difference between concrete and steel girder for Z_c=-0.1 m.

Then, the conditional probabilities of uplift failure are calculated for the bridges of the examined inventory using the aforementioned logit functions and for current or projected H_w and Z_c. The analysis results indicate that future sea level rise will increase the uplift failure probabilities for both Storm 33 and Storm 36 scenarios. For example, there is a high uplift probability for 35 concrete girder bridges to experience uplift in 2050 if they will be subjected to surge and waves caused by a 100-yr storm, while this number increases to 42 bridges using 2100 sea level projection (Figure 5). In a similar manner, there is an increase in the number of bridges with high uplift probability, i.e. more than 75%, if subjected to storm surge and waves cause by a 500-yr hurricane in 2050 and 2100 (Figure 6). Future storm scenarios indicate an expected increase in the uplift probability for bridges with low current vulnerability. For instance, bridges with failure probability less than 5% (Figure 7), are expected to be more vulnerable in year 2100 (Figure 8) due to storm surge alterations caused by climate change.

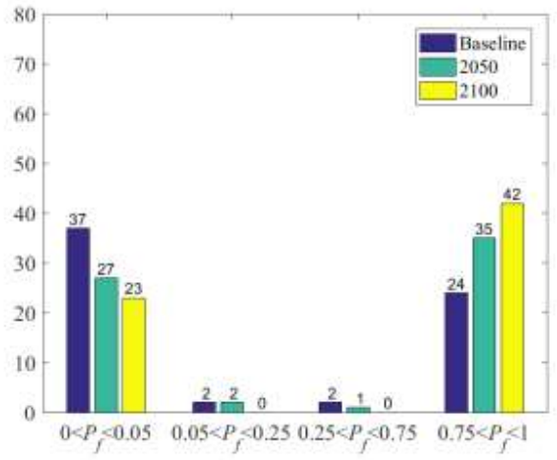


Figure 5. Number of concrete girder bridges within specific bounds of failure probability: Storm 33 scenarios.

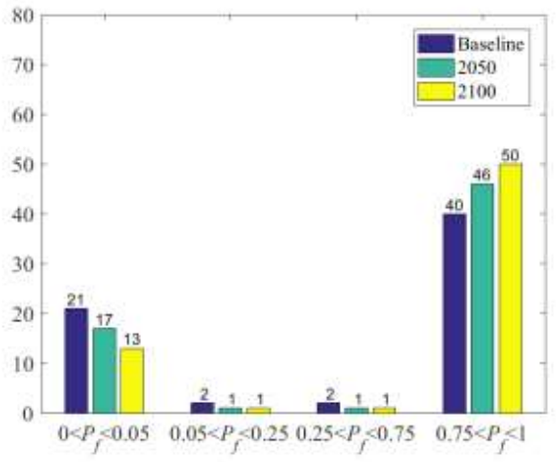


Figure 6. Number of concrete girder bridges within specific bounds of failure probability: Storm 36 scenarios.

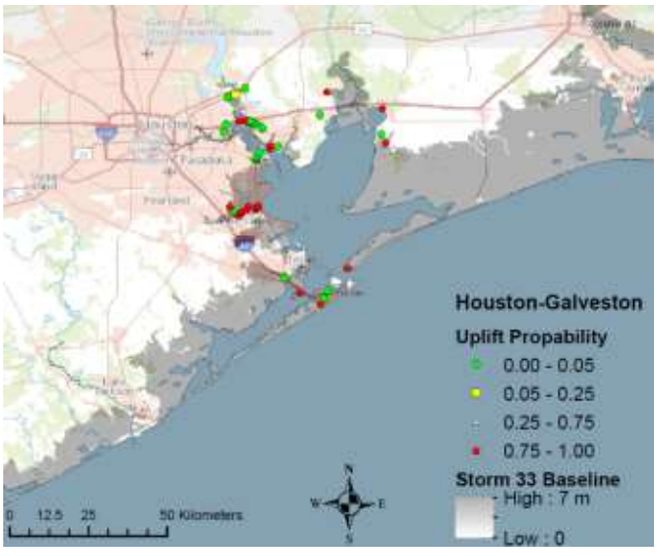


Figure 7. Uplift probability of concrete girder bridges in Houston-Galveston for Storm 33 Baseline scenario.

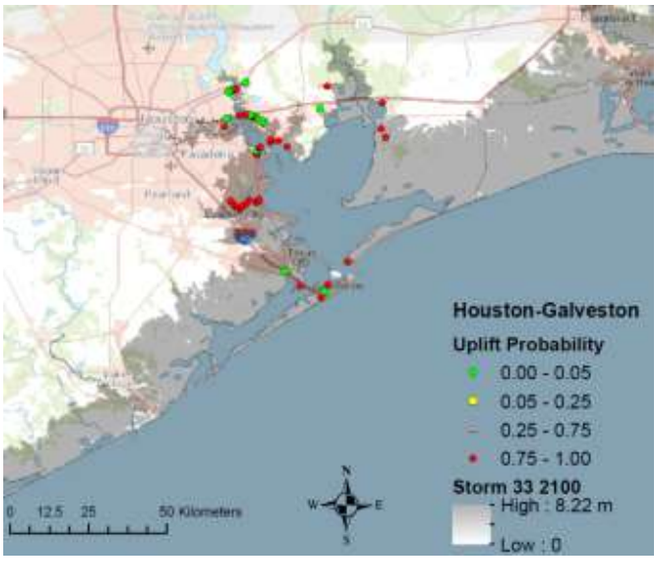


Figure 8. Uplift probability of concrete girder bridges in Houston-Galveston for Storm 33 2100 scenario.

The examined steel girder bridges are in locations not significantly affected by the future sea level rise. Thus, results for this bridge class related to uplift probabilities for current and projected sea level conditions are not reported.

5 CONCLUSIONS

This study examines the vulnerability of bridges exposed to hurricane-induced surge and waves. First, the study addresses a gap in parameterized fragility for a range of different bridge configurations to enable hurricane risk assessment across a region. Thus, a set of bridges are selected from the Houston-Galveston region of Texas and two bridges classes are investigated, i.e. bridges with concrete and steel girder superstructures. Nonlinear dynamic analysis is conducted, i.e. considering wave force time-history, on bridge models from each class generated through Latin hypercube sampling. Then, parameterized fragilities are derived to express the probability of deck unseating given bridge class and hurricane intensity measures. The results indicate that both bridges are prone to uplift damage with the increase of the storm surge although the differences in the uplift probability between the examined bridge classes varies depending on the intensity of the hurricane.

This study further investigates the application of the fragility models for risk assessment of a regional portfolio of bridges in Texas for storm scenarios with and without sea level rise, allowing exploration of climate change effects on bridge damage risks. The results indicate that future sea level rise will further increase the uplift risk of the concrete girder bridges exposed to a hurricane with the same characteristics. Future work will include more superstructure types, e.g. box girder, slab, and will address issues such as system response with spatial variability of wave.

6 ACKNOWLEDGEMENTS

The authors grateful acknowledge the support of this research by the Shell Center for Sustainability and by the Houston Endowment under the Severe Storm Prediction, Education, and Evacuation from Disasters (SSPEED) Center. The authors also acknowledge the support provided by the National Science Foundation under grant number OISE-1545837. Any opinions, findings, and conclusions or recommendations expressed in this material are those of the authors and do not necessarily reflect the views of the sponsors.

7 REFERENCES

AASHTO. 2008. *Guide specifications for bridges vulnerable to coastal storms.* Washington, DC.

Anarde, K. A., Kameshwar, S., Irza, J. N., Nittrouer, J. A., Lorenzo-Trueba, J., Padgett, J. E., Sebastian, A. & Bedient, P. B. 2017. Impacts of Hurricane Storm Surge on Infrastructure Vulnerability for an Evolving Coastal Landscape. *Natural Hazards Review,* 19**,** 04017020.

Ataei, N. & Padgett, J. E. 2012. Probabilistic modeling of bridge deck unseating during hurricane events. *Journal of Bridge Engineering,* 18**,** 275-286.

Ataei, N. & Padgett, J. E. 2015. Influential fluid–structure interaction modelling parameters on the response of bridges vulnerable to coastal storms. *Structure and infrastructure engineering,* 11**,** 321-333.

Ataei, N., Stearns, M. & Padgett, J. 2010. Response sensitivity for probabilistic damage assessment of coastal bridges under surge and wave loading. *Transportation Research Record: Journal of the Transportation Research Board***,** 93-101.

Crosset, K. M., Culliton, T. J., Wiley, P. C. & Goodspeed, T. R. 2004. Population trends along the coastal United States: 1980-2008. *National Oceanic and Atmospheric Administration (NOAA).* Coastal Trends Report Series: Government Printing Office.

Ebersole, B. A., Massey, T. C., Melby, J. A., Nadal-Caraballo, N. C., Hendon, D. L., Richardson, T. W. & Whalin, R. W. 2015. *Interim Report – Ike Dike Concept for Reducing Hurricane Storm Surge in the Houston-Galveston Region.* Jackson State University, Jackson, MS.

FEMA 2017. Flood insurance study—Harris County, Texas and incorporated areas. *Federal Emergency Management Agency (FEMA).* Flood Insurance Study Number 48201CV001E. Washington, DC.

Gidaris, I., Padgett, J. E., Barbosa, A. R., Chen, S., Cox, D., Webb, B. & Cerato, A. 2017. Multiple-hazard fragility and restoration models of highway bridges for regional risk and resilience assessment in the united states: state-of-the-art review. *Journal of structural engineering,* 143**,** 04016188.

Hambly, E. C. 1976. *Bridge deck behaviour*, London: Chapman and Hall.

Hosmer, D. W. & Lemeshow, S. 2000. *Applied logistic regression,* New York, NY., John Wiley & Sons.

Kameshwar, S. & Padgett, J. E. 2014. Multi-hazard risk assessment of highway bridges subjected to earthquake and hurricane hazards. *Engineering Structures,* 78**,** 154-166.

Luettich, R. A. & Westerink, J. J. 2004. *Formulation and numerical implementation of the 2D/3D ADCIRC finite element model version 44. XX*, Citeseer.

Mander, J. B., Priestley, M. J. & Park, R. 1988. Theoretical stress-strain model for confined concrete. *Journal of structural engineering,* 114**,** 1804-1826.

Mazzoni, S., McKenna, F., Scott, M. H. & Fenves, G. L. 2006. OpenSees command language manual. *Pacific Earthquake Engineering Research (PEER) Center,* University of California**,** Berkeley, CA.

NBI. 2017. *National Bridge Inventory Database.* (http://nationalbridges.com/).

Nicholls, R. J., Hoozemans, F. M. & Marchand, M. 1999. Increasing flood risk and wetland losses due to global sea-level rise: regional and global analyses. *Global Environmental Change,* 9**,** S69-S87.

Nielson, B. G. 2005. *Analytical fragility curves for highway bridges in moderate seismic zones.* Georgia Institute of Technology, Atlanta, GA.

Padgett, J., DesRoches, R., Nielson, B., Yashinsky, M., Kwon, O.-S., Burdette, N. & Tavera, E. 2008. Bridge damage and repair costs from Hurricane Katrina. *Journal of Bridge Engineering,* 13**,** 6-14.

Padgett, J. E., Spiller, A. & Arnold, C. 2012. Statistical analysis of coastal bridge vulnerability based on empirical evidence from Hurricane Katrina. *Structure and infrastructure engineering,* 8**,** 595-605.

Stearns, M. & Padgett, J. E. 2011. Impact of 2008 Hurricane Ike on bridge infrastructure in the Houston/Galveston region. *Journal of Performance of Constructed Facilities,* 26**,** 441-452.

Sweet, W., Kopp, R., Weaver, C., Obeysekera, J., Horton, R. M., Thieler, E. R. & Zervas, C. 2017. Global and regional sea level rise scenarios for the United States. *National Oceanic and Atmospheric Administration (NOAA).* Technical Report NOS CO-OPS 083. Silver Spring, MD.

Torres, J. M., Bass, B., Irza, J. N., Proft, J., Sebastian, A., Dawson, C. & Bedient, P. 2017. Modeling the Hydrodynamic Performance of a Conceptual Storm Surge Barrier System for the Galveston Bay Region. *Journal of Waterway, Port, Coastal, and Ocean Engineering,* 143**,** 05017002.

USACE 2011. Flood Insurance Study: Coastal Counties, Texas. Intermediate Submission 2: Scoping and Data Review. *US Army Corps of Engineers (USACE).* Washington, DC.

Maintenance, Safety, Risk, Management and Life-Cycle Performance of Bridges – Powers, Frangopol, Al-Mahaidi & Caprani (Eds)
© 2018 Taylor & Francis Group, London, ISBN 978-1-138-73045-8

Probabilistic multi-hazard assessment of seismic and scour effects on bridge structures

Z. Chen
School of Computing and Engineering, University of Missouri-Kansas City, USA
X. Guo
College of Civil Science and Engineering, Yangzhou University, Yangzhou, Jiangsu, China

ABSTRACT: This paper proposes a probabilistic framework for assessing seismic and scour effects on existing river-crossing bridge structures. The unique features of this framework include the conjunct use of probabilistic scour and seismic hazard modeling, and the definitions of seismic-scour integrated fragility and demand hazard models. Probabilistic assessment is then performed to evaluate the seismic-scour effects on a representative bridge model. The fragility results for the chosen bridge model reveal that scour tends to be beneficial in reducing structural damage at slight to moderate seismic intensities and to be detrimental in increasing collapse potential at high-level intensities. The demand hazard curves further quantify probabilistically the occurrence of local damage and global collapse, and systematically reveal the complex effects of scour as a hydraulic hazard on bridge structures.

1 INTRODUCTION

There are over 484,500 highway bridges built over river channels in the U.S., among which over 20,904 are regarded scour-critical (Hunt, 2009). A distinct feature of flood-induced scour is that once it starts forming around a foundation, it may accumulate or vary over the bridge's service life. Hence it is intuitive that a potentially more severe risk is that scour is combined with other extreme hazards, such as earthquakes, which may threaten bridges serving in both earthquake and flooding active regions, such as Alaska and California in the U.S.

Towards a multi-hazard approach to assessing the conjunct effects of earthquakes and flooding-induced scour on the vulnerability of bridges, a probabilistic approach to bridge scour analysis is required due to its inherent uncertainties in the first place. In two recent papers, a general approach to probabilistic scour hazard modeling was reported, which is built upon deterministic scour estimation by considering model bias and random errors (Bolduc et al., 2008, Briaud et al., 2013). Furthermore, Briaud et al. (2013) concluded that for shallow foundations supporting bridge structures, the design scour depth needs to be 2.0 ~ 2.5 times of the HEC-18 estimates to ensure that the probability of exceeding the estimated scour depth be less than 0.001, even that both HEC-18 (Sand and Clay) methods are considerably conservative compared with measured bridge scour data. Besides probabilistic scour assessment for bridge foundations, however, these two efforts did not address the multi-hazard effects on a bridge as a system if earthquakes are involved.

For a system-level multi-hazard assessment of seismic and scour effects (termed *seismic-scour effects* hereafter), a number of efforts are found. Wang et al. investigate the vulnerability of scoured pile-foundation supported bridges through probabilistic fragility surface analysis (Wang et al., 2012). However, in their work, scour was treated deterministically. In Dong et al. (2013), a multi-hazard assessment approach was used to study bridge performance considering time-variant structural deterioration; however, scour uncertainty was not considered either (Dong et al., 2013). Prasad and Banerjee investigated the seismic risk of four example bridges considering scour variations (Prasad and Banerjee, 2013, Banerjee and Prasad, 2011). While studying the characteristics of seismic fragility curves, however, only system-level displacement-based demands (i.e. drift demand at the deck level) were used, which led to the conclusion that scour always increases seismic fragility. Several recent efforts are found on probabilistic calibration of load-resistance factors that are used to combine scour condition with seismic and other design forces (Ghosn et al., 2004, Alipour et al., 2012, Wang et al., 2014).

No quantitative and probabilistic framework is found to date that is able to comprehensively assess the conjunct seismic-scour effects on river-crossing bridge's vulnerability. In the following, a probabilistic framework is proposed that aims to output seis-

mic-scour integrated fragility and probabilistic demand hazard. The focus is then on the experimental results and observations based on a simple shallow-foundation supported bridge model, followed by the conclusions in the last section.

2 PROBABILISTIC METHODOLOGY

For assessing performance and vulnerability of structures considering seismic hazards, two probabilistic analysis tools are usually employed, which are probabilistic seismic fragility analysis (PSFA) and probabilistic seismic demand analysis (PSDA). PSFA can been applied to identify the probability of a defined limit-state (e.g. structural damage or collapse) conditional on one or multiple measures of seismic intensity (Karim and Yamazaki, 2003, Shinozuka et al., 2000, Nielson and DesRoches, 2007, Hwang et al., 2001). PSDA is used to assess structural vulnerability by estimating the annual probability of a structural demand exceeding a varying demand parameter without conditioning on the input hazard (Bazzurro and Cornell, 1994, Cornell et al., 2002). The output of PSDA model is a demand hazard curve that is analogous to a seismic hazard curve (from probabilistic seismic hazard analysis, PSHA). Since the demand hazard curve is an essential component of the probabilistic performance-based seismic design framework (Cornell and Krawinkler, 2000), PSDA has been frequently used for assessing building structures (Luco, 2002, Tothong and Luco, 2007) and bridge structures (Tondini and Stojadinovic, 2012, Mackie and Stojadinovic, 2001).

Different from general multi-hazard analysis wherein two or more hazards appear as joint occurrence of two independent events that may be generalized as external forces applied to structures (but independent to structures), earthquake and scour should be treated distinctly. Different from loading-based hazards, scour primarily leads to modification of the geometric boundary condition of the soil-foundation-structure (SFS) bridge system. This boundary modification further results in reduction in foundation stiffness, and nonlinear foundation bearing and lateral capacities as demonstrated previously. To account for such changes, a system-level modeling approach needs to be adopted considering SFSI subjected to dynamic loadings (e.g., earthquakes). This in turn leads to an unfavorable situation, wherein the SFS bridge system is not invariant; rather, it is subject to significant modification in terms of foundation impedance and nonlinear capacities due to the varying scour (treated as a hazard).

2.1 *Mean-Scour Seismic Fragility Modeling*

The seismic fragility or the probability of structural damage given a seismic *IM* can be modeled as a conditional probability, $P(Z>z^* \mid IM)$, where z^* is a specifically defined value of the demand variable. The expression $Z > z^*$ defines a limit state that indicates occurrence of a certain level of damage or even collapse. For measuring the seismic intensity, a sufficient *IM* should be chosen. Peak ground acceleration (PGA) is often used as an objective scalar measure of seismic intensity. When a structure is considered, the spectral displacement (Sd) and spectral acceleration (Sa) defined at the structure's modal period (Tn) are two commonly used measures. In this paper, Sa is adopted; particularly, Sa measured at the fixed-base first-mode period of the bridge model is used

When the sample values of *IM* and *Z* are available, a fitting function in terms of $IM = x$ is usually used to fit the conditional probability $P(Z>z^* \mid IM)$, denoted by $\Psi(x)$. The most popular approach is to enforce a monotonically increasing function bounded by [0, 1], such as the Lognormal cumulative distribution function $\Psi(x)$ (Shinozuka et al., 2000), to fit the data set of $\{(Z>z^*)_i, IM_i \mid i = 1 \ldots N\}$:

$$\Psi(x) = P(Z > z^* \mid IM = x) \approx \Phi\left(\frac{\ln x - \mu}{\beta}\right) \quad (1)$$

where μ and β are the mean and standard deviation parameters of the Lognormal cumulative function, respectively. Based on the sample data, a general approach to parameter estimation is the maximum likelihood estimation (MLE) method (Baker, 2015). This method is adopted in this paper and formulation details are found in Baker (2015).

When scour depth (*SD*) is considered in seismic fragility analysis, an easy treatment is to compute seismic demands using the SFS bridge model that incorporates a designated scour condition in terms of a deterministic *SD* value, y^*:

$$\Psi(x) = P(Z > z^* \mid IM = x, SD = y^*) \approx \Phi_{y^*}\left(\frac{\ln x - \mu}{\beta}\right) \quad (2)$$

The expression in Eq. 2 represents the seismic fragility considering a deterministic scour depth, wherein the uncertainties come from external seismic inputs and possibly from structural materials.

If one considers scour as a type of hazard and then treats scour depth as a random variable, a bivariate fragility model becomes of interest:

$$\Psi(x, y) = P(Z > z^* \mid IM = x, SD = y) \quad (3)$$

If the conditional probability model in Eq. 3 is fitted by a bivariate Lognormal function, a fragility surface model is achieved. A fragility surface model has its merit in expressing the true fragility of a structure when multiple hazards are affecting the structure (Lee and Rosowsky, 2006) or multiple parameters are used to describe one hazardous effect (Seyedi et al., 2010). As implied in Eq. 6, one may consider fitting the conditional probability by a bivariate function in terms of both seismic intensity and scour depth as independent variables and then study the resulting seismic-scour

fragility surface. However, a significant difference of scour effects from seismic effects as illustrated previously is that scour may cause beneficial effects (i.e. reduction of force demands). This implies that the fragility when partially conditional on scour may decrease as the scour depth increases. With the fragility partially depending on seismic measure *IM* (which often designates a monotonic increasing relation), the resulting fragility surface from Eq. 3 may be non-monotonic, which causes difficulty in interpreting such a surface. To retain the traditional simplicity in a fragility curve, it is more straightforward to marginalize out the scour depth as a random variable. Based on the law of total probability, one has

$$P(Z > z^* | IM = x) = \int P(Z > z^* | IM = x, SD = y) f_{SD}(y) \mathrm{d}y = \mathbf{E}_{SD}[\Psi(x, y)] \quad (4)$$

$$P(Z > z^* \mid IM = x) \approx \Phi_{MS}\left(\frac{\ln x - \mu}{\beta}\right) \quad (5)$$

where $f_{SD}(y)$ is the probability density function for the scour depth as a random variable and **E**[] defines the mathematical expectation operator. In Eq. 4, the seismic fragility is defined by integrating out scour depth as a random variable, which is equivalent to the mathematical mean of the bivariate fragility upon the scour depth distribution. Due to this analytical meaning, a notion of *mean-scour* (MS) fragility is proposed in this paper. In the meantime, the analytical expression of the mean-scour fragility $P(Z > z^* \mid IM = x)$ means that the fragility model can be directly estimated by fitting the simulated data set using the Lognormal model in Eq. 5.

2.2 *Seismic-Scour Integrated Demand Modeling*

Traditional PSDA assesses the performance of a structure by probabilistically predicting the seismic response in terms of the probability of exceedance for a limit state defined by $Z > z$, where z is a varying demand value. The resulting function, $H_z(z) = P(Z > z)$, is termed probabilistic demand hazard model. In the original efforts [e.g. (Bazzurro and Cornell, 1994)], a probabilistic demand hazard model (or strictly speaking the mean annual frequency of the exceedance event for a response demand) is evaluated based on the summation over seismic sources described by magnitudes and site distance. In more recent literature, a probabilistic demand hazard model for evaluating the seismic performance of a structure has been defined in a continuous form (Cornell et al., 2002):

$$H_Z(z) = \int P(Z > z \mid IM = x) \mid \mathrm{d}H_{IM}(x) \mid \quad (6)$$

where $P(Z > z \mid IM = x)$ defines the likelihood that the structural demand Z exceeds a post-elastic demand value z, and $\mathrm{d}H_{\mathrm{IM}}(x)$ defines the derivative of the seismic hazard model (the absolute sign is necessary since the derivative is negative).

It is noted that Eq. 6 considers one (seismic) hazard. If flooding-induced scour as a hazardous condition is considered, the integrated seismic-scour demand hazard, denoted by $H_{SS}(z)$, is proposed, which is based on a simple extension of Eq. 6:

$$H_{SS}(z) = \iint P(Z > z \mid IM = x, SD = y) \mathrm{d}H_{IM}(x) \mathrm{d}H_{SD}(y) \quad (7)$$

where $H_{IM}(x)$ and $H_{SD}(y)$ are the probabilistic seismic hazard and scour hazard models, respectively. The demand hazard model in Eq. 7 involves probabilistic models of seismic and scour hazards. The two hazard models are introduced below.

2.3 *Probabilistic Seismic Hazard Analysis*

The probabilistic seismic hazard analysis (PSHA) attempts to define the probability of exceedance (POE) for an IM variable x that is exceeded annually, denoted by $H_{IM}(x)$. In practice, PSHA can be analytically conducted for a given site; for example, analytical formulation was given based on empirical attenuation models and probabilistic calculation was based on a Lognormal distribution assumed for a seismic intensity measure (Field, 2005). In addition, seismic hazard models can be obtained from the web portal of the United States Geological Survey (USGS) for a given site in the United States (USGS, 2015). One key step in PSHA is to select an appropriate seismic *IM* type. Traditionally, peak ground acceleration (PGA) and spectral acceleration (Sa) at a certain natural period (T_n) are commonly used (Kafali and Grigoriu, 2007). In this paper, the USGS' seismic hazard model in terms of SAs is adopted.

2.4 *Probabilistic Scour Hazard Analysis*

For local bridge scour (scour around bridge foundation), two primary estimation methods exist as described in Hydraulic Engineering Circular No. 18 (Arneson et al., 2012), which is termed the HEC-18 Sand and HEC-18 Clay. The HEC-18 Clay method was developed at the Texas A&M University, which was designed to predict scour depths in cohesive fine-grained soils (e.g. clay) and was once termed the SRICOS-EFA method (Briaud et al., 1999). Using the HEC-18 Clay method, the scour depth is the function of time over the period of the hydrograph. First, this method predicts the maximum scour $\hat{y}_{\max}$ as:

$$\hat{y}_{\max} = 0.18R^{0.635} \quad (8)$$

where R is Reynolds number equal to vD_p/υ , v is the upstream velocity, D_p is diameter of the pier, and υ is the water viscosity (10^{-6} s/m^2 at 20^{o}C). The time-dependent scour depth, denoted by $\hat{y}_t$, is defined by linking the maximum scour depth in Eq. 1, the time at

which a given velocity is applied, and the initial rate of scour:

$$\hat{y}_t = \frac{t}{\frac{1}{\dot{y}_i} + \frac{t}{\hat{y}_{\max}}} \quad (9)$$

where t with a unit of year is the time over which a given velocity is applied and $\dot{y}_i$ denotes the initial rate of scour.

Based on the deterministic estimation described in Eq. 8 and 9, multiplicative correction factors are considered to account for the bias and random errors inherent in the deterministic models, which leads to the probabilistic scour modeling (Bolduc et al., 2008) and is termed probabilistic scour hazard analysis in this paper (PScHA to be different from PSHA).

In Bolduc et al (2008), by adopting a Lognormal distribution for scour depth, the probabilistic scour depth is formulated in a Logarithm expression:

$$\mathrm{Log}[y_t] = \mathrm{Log}[\theta_y] + \mathrm{Log}[\hat{y}_t] + \sigma_y \mathbf{N}(0;1) \quad (10)$$

where θ_y is a parameter accounting for the model bias; $\hat{y}_t$ is the deterministic and time-dependent scour estimation from Eq. 9; $\mathbf{N}(0;1)$ represents a Normal random variable with zero mean and unit variance; σ_y is therefore the standard deviation of the Lognormal variable y_t. This implies that when these deterministic parameters, θ_y, $\hat{y}_t$ and σ_y are available, a probability density function for the distribution of the scour depth can be defined using a Lognormal distribution, denoted by $f_{SD}(y_t)$ in this paper. Given $f_{SD}(y)$, the scour hazard can be analytically expressed as $H_{SD}(y_t) = 1 - \int_0^{y_t} f_{SD}(y)\mathrm{d}y$. Similar to the seismic hazard curve, this model when depicted as a curve quantifies the probability of exceeding a scour-depth value at a bridge site; the only distinction is that different from the annual POEs as used in a seismic hazard model, a scour hazard model defined above is calculated at a certain year of service.

3 EXPERIMENTAL RESULTS

3.1 *Simple Bridge Model*

The bridge chosen in this paper has a shallow foundation system with a full embedment depth that is constructed in a hard-soil (e.g. cohesive clay) river bed. The bridge has three spans of concrete decks supported by two concrete columns. Such a bridge is commonly used in practice for short-span river passing when the foundation soil is relatively hard (e.g. clay) (Kimmerling et al., 2002). In addition, by analyzing a shallow foundation-supported bridge model, the probabilistic assessment can be readily conducted. It is noted, nevertheless, the framework developed and demonstrated in this paper can be easily adapted for assessing existing bridges with deep foundation systems (e.g. piles) in soft-soil river bed provided a finite-element (FE) based SFS model is provided. Fig. 1 illustrates the bridge model, which was used in the author's previous work (Guo and Chen, 2015). The bridge is a three-span (27m+36m+27m) continuous structure supported by two piers on two separate shallow foundations. The height of the circular piers is 9.0 m with the diameter of 1.4 m. The steel ratio of the column is about 1.3%. The foundation is constructed on hard clay with a density of 1700 kg/m^3 and with a small-strain shear wave velocity of 260 m/s. The thickness of the foundation is 2.4 m, with the transverse width being 2.8 m and the longitudinal length being 3.3 m, respectively. The original embedment depth of foundations is 4.0 m. The simplified configuration of the bridge is shown in Fig. 1. A three-dimensional finite-element (FE) model for the bridge is developed to simulate the bridge using the OpenSees framework (Mazzoni et al., 2005). The FE modeling and the details about beam-column elements, footing elements, material uncertainties, sampling scheme, and the nonlinear time-history analysis details are found in this work as well. Particularly, we consider a target service period of 50 years among its 75-year design life. The purpose is to mimic the situation of an existing bridge that is subject to progressive scour after 50 years of service.

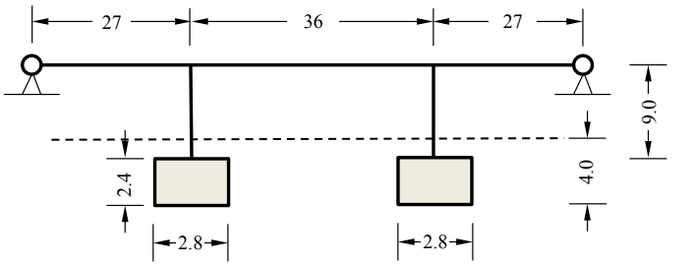


Figure 1. Bridge configuration (unit: m).

3.2 *Demand Variables*

A variety of response demand parameters can be extracted. In this paper two demand variables are considered in the following fragility and demand modeling.

1) Local strain ductility: defined as the ratio of the strain demand ($|\epsilon_{max}|$) at the base of the concrete pier to the compressive yielding strain (ϵ_y) of the concrete, $\mu_s = |\epsilon_{max}| / \epsilon_y$. Since the local strain at the surface is proportional to the curvature, $\epsilon = \rho\, r$, where r is the diameter of the circular column, one can define an equivalent local curvature ductility demand. Hereinafter, local strain ductility demand (μ_s) is used.
2) System drift ductility: defined as the ratio of the transverse system drift demand at the mid-span of the bridge deck ($|u_{max}|$) to the bridge's yielding drift (u_y) at the fixed-end boundary condition, $\mu_d = |u_{max}| / u_y$. For the bridge model

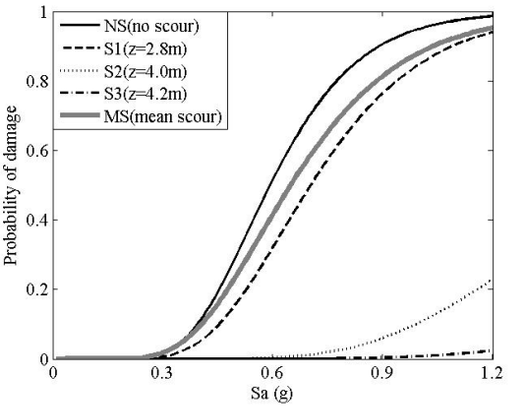
considered herein, the yielding drift is about 6.1 cm.

The local strain ductility demand μ_s reflects the degree of local inelasticity occurred to the bridge's concrete piers. For bridge structures, the ranges for using local strain ductility demand to characterize different damage levels are well defined [e.g. (Choi et al., 2004)]. In general, when given a limit state of $\mu_s > 1$, it implies the onset of local damage or indication of slight damage. Larger threshold may be used to define higher-level structural damage, such as $2 < \mu_s < 4$ for moderate damage or $\mu_s > 4$ for extensive damage. Fragility models resulting from these higher-level damage limit-states are not reported in this paper. The system drift ductility demand indicates the degree of global displacement, which in general consists of structural deformation and foundation-induced rigid-body motion (e.g. sliding and rocking) as a SFS system. In this paper, if μ_d is larger than seven ($\mu_d > 7$), the onset of system collapse limit-state is defined (usually a drift ductility of 5 ~ 10 is used to define bridge collapse in the literature; herein a median value of 7 is used) (Dutta and Mander, 1998, Kim and Feng, 2003). We particularly note that for a scoured SFS bridge, it may be biased to define a limit-state using the system-level ductility demand to indicate structural damage in local members. Especially when considering an extreme scour, a limit-state in the range of $2 < \mu_d < 3$ may be dominated by the rigid-body displacement from the substructure with linear-elastic or insignificant inelastic structural deformation; in this case, structural damage may not reach to the expected level (e.g. $\mu_s < 1$).

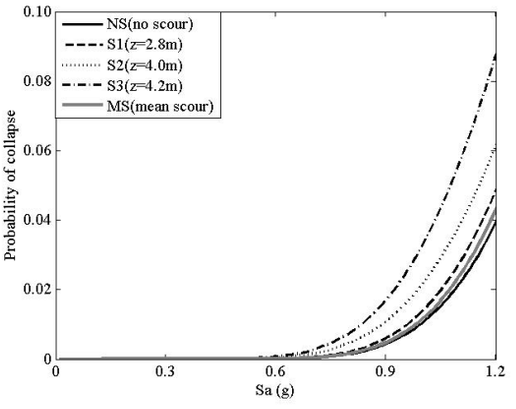
3.3 *Fragility Analysis Results*

Based on the limit states defined previously, Fig. 2(a) shows the probability of local damage defined by $\mu_s > 1$ considering four designated scour-depth values (No scour; Scour S1 with z= 2.8 m; S2 with z= 4.0 m; S3 with z= 4.2 m). In addition, the mean-scour (MS) fragility curve according to Eq. 5 is shown as well. Fig. 2(b) uses the same configuration for plotting the fragility curves in terms of the defined collapse limit-state ($\mu_d > 7$). It is noted that material uncertainties are not considered in the two fragility illustrations in Fig. 2.

Fig. 2(a) indicates that the probability of damage is insignificant (less than 10%) if Sa (T1) < 0.33 g (equivalently corresponding to an annual POE of 9.2×10^{-3}, which is the Expected Earthquake design level). In addition, at the NS (i.e. z = 0 m) and the S1 level of scour depth (i.e. z = 2.8 m), the probability of damage quickly approaches to a high probability (> 50%) when the spectral acceleration becomes larger than 0.5 g (or an equivalent 0.38% annual POE). The general trend is that if the scour depth increases when the *IM* is greater than 0.33 g, the probability of damage decreases significantly. Especially, when the scour reaches the full-depth of the foundation (S2), the probability of damage dramatically reduces; for example, at Sa (T1) = 1.19 g (about 4.1×10^{-4} annual POE or subject to the MCE-level earthquake), the probability of damage is around 5%, whereas it is 95% compared with the N1 case (z = 2.8 m). This observation is consistent with the aforementioned literature that softened foundations in the context of seismic soil-structure interaction tend to lead to less structural damage or smaller base-shear force demands (Ghosn et al., 2004). However, it should be pointed out that when the bridge is subjected to high-intensity earthquakes and greater scout depths, the potential threat is system collapse. Therefore, it is rational to state that increasing scour depth is only beneficial when subjected to weak to moderate-intensity earthquakes (e.g. in the case of the bridge model herein, Sa(T1) < 0.8 g).



(a)



(b)

Figure 2. Fragility model at different scour depths without considering material uncertainties: (a) probability of structural damage at the column base; and (b) probability of system collapse.

Fig. 2(b) shows the probability of collapse defined based on the drift ductility demand at the bridge deck. This figure indicates that the probability of collapse increases as the scour depth and the seismic intensity levels increase. Specifically, the conditional probability of collapse is close to zero when Sa (T1) < 0.7g. Nonetheless, the probability of collapse rises for each scour condition when Sa (T1) > 0.7g. For a NS system, the probability of collapse is 4 % if Sa (T1) = 1.19 g or considering a MCE level earthquake. By

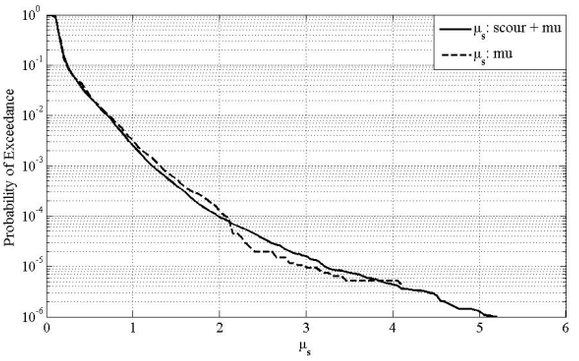
contrast, the corresponding probability for a scour system with the scour depth of 4.2m is about 9%, which is about 2.25 times of that for the NS system. Accordingly, scour is detrimental by increasing the probability of collapse at all levels of ground motions, but much significantly when the seismic intensity approaches to the MCE level.

The above fragility curves are constructed at designated scour conditions (NS, S1, S2, and S3). However, for an in-service bridge, its scour depth may be completely unknown; therefore, one may not be able to designate a scour depth. Based on Eq. 5, Fig. 2(a) and (b) also report the resulting MS fragility curves. First, one can observe that the MS fragility curve at either of the limit states lies between the fragility curve at the S1 condition (z = 2.8 m) and the one at the NS condition (no scour or z = 0 m), although it is worthy to mention that this observation depends on the probabilistic scour hazard modeling at a specific site.

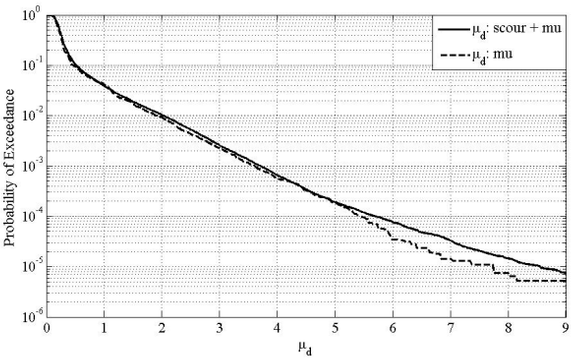
Second, similar observations in the trend of the MS curves as *IM* increases are still seen compared with the curves at the designated scour depths. Considering the smaller difference of the MS fragility curves from the curves at the S1 condition yet significant difference from the curves at the S2 and S3 conditions, one may assert that scour survey is critical in terms of the potential high risk resulting from a possibly greater scour depth. Nonetheless, if an accurate scour depth is not available, the proposed probabilistic MS fragility modeling becomes instrumental to quantitatively assess the seismic-scour effects.

3.4 *Demand Analysis Results*

The seismic-scour integrated demand hazard curves can be approximated as expressed in Eq. 7. With the two ductility demand measures, Fig. 3 reports the demand hazard curves, wherein the vertical axis indicates the probability of exceeding a demand variable that is marked in the horizontal axis (which is either μ_s or μ_d). The two illustrations in Fig. 3 provide a comparison between the cases of considering scour vs. not considering scour (in both cases, material uncertainties, denoted by 'mu', are considered). Among them, Fig. 3(a) illustrates the demand hazard curves in terms of the local strain ductility variable; whereas Fig. 3(b) presents the system drift-ductility hazard curves.



(a)



(b)

Figure 3. Probabilistic demand hazard curves considering scour and material uncertainties (denoted by 'mu') vs. considering 'mu' only: (a) strain ductility demand hazard curves; (b) drift ductility demand hazard curves.

First of all, the demand hazard curves in Fig. 3 reveal the effects of scour as a source of hazard on the bridge structure. In terms of the local strain ductility μ_s in Fig. 3(a), the POEs in the range of $\mu_s < 2.1$ indicates that scour lowers the probability of structural damage in bridge piers, which is consistent with the previous fragility study. However, in the range of $2.1 < \mu_s < 4.1$, scour increases the probability of damage, which is not revealed in the fragility study since such limit-state of $2 < \mu_s < 4$ is not defined. It is noted that in both ranges, scour effect is insignificant due to the fact that scour-depth (*SD*) as a random variable has been integrated out numerically; therefore, it should be roughly regarded as a 'mean' effect of the scour. In terms of the system drift ductility μ_d in Fig. 2(b), the overall trend is that the probability of exceeding any specified μ_d increases due to the consideration of scour. This is especially evident when μ_d is greater than 5. This implies that at larger drift ductility levels, wherein the likelihood of system collapse is defined, scour tends to increase the probability of system collapse. Due to these observations, we state that the probabilistic demand hazard modeling provides a more comprehensive approach to evaluating the effects of scour on the seismic response and the vulnerability of bridge structures.

4 CONCLUSIONS

This paper proposes a comprehensive probabilistic framework for assessing the effects of scour on seismic response of existing bridge structures. Through a case-based assessment using a representative bridge model, several important observations are quantitatively revealed. These include:

1. The fragility curves at designated scour depths or the proposed mean-scour seismic fragility curves indicate that scour tends to be beneficial in reducing structural damage at slight to moderate seismic intensities. However, concern should be raised at strong seismic intensities, wherein even with a lowered probability of structural damage, the collapse potential is significantly increased due to scour.
2. The demand hazard curves systematically reveal the complex effects of seismic attacks and scour conditions on exceeding any local structural deformation or system drift demands. These effects include that scour lowers the probability of exceeding a local strain ductility demand at small values compared to the case where scour is not considered; but increases the probability of exceedance at larger demand values. In the meantime, scour systematically increases the probability of exceedance at any system drift ductility level, and more significantly at a larger demand level; or equivalently, scour in general increases the likelihood of system collapse when compared with the case of no consideration of bridge scour.
    1) Material uncertainties can be ignored if solely for evaluating the effects of scour. If ignored, the proposed framework provides a computationally efficient approach to performing integrated seismic-scour assessment for bridge structures. However, if material uncertainties considered, computational cost is much increased since more parametric finite-element models are included, which results in excessive nonlinear static pushover analysis in the framework. To mitigate this, one may choose a small and unique set of ground motions (e.g. only one motion is used in this paper) at different seismic intensity levels.

To this end, we envision that the proposed probabilistic framework and the associated numerical implementation in this paper may provide a rapid means for assessing the conjunct seismic and scour effects on existing river-crossing bridges. We further note that the proposed probabilistic framework can be adopted to assess the effects of flood-induced scour on other bridge types (e.g. deep-foundation supported bridges in soft soils), provided that a finite-element based nonlinear model for the bridge is available.

5 ACKNOWOLGEDGEMENT

The author appreciates the funding from a project supported by the University of Missouri Research Board. The second author gratefully acknowledges the support from the grants from National Natural Science Foundation of China (Grant Number 51708484). In addition, the authors thank for the reviewers for providing constructive comments that greatly help improve the studies in this paper.

6 PREFERENCES

ALIPOUR, A., SHAFEI, B. & SHINOZUKA, M. 2012. Reliability-Based Calibration of Load and Resistance Factors for Design of RC Bridges under Multiple Extreme Events: Scour and Earthquake. *Journal of Bridge Engineering,* 18**,** 362-371.

ARNESON, L., ZEVENBERGEN, L., LAGASSE, P. & CLOPPER, P. 2012. Evaluating scour at bridges. *Hydraulic Engineering Circular No. 18,* Publication No. FHWA-HIF-12-003.

BAKER, J. W. 2015. Efficient analytical fragility function fitting using dynamic structural analysis. *Earthquake Spectra,* 31**,** 579-599.

BANERJEE, S. & PRASAD, G. G. 2011. Analysis of Bridge Performance under the Combined Effect of Earthquake and Flood - Induced Scour. *In:* M.A., B. (ed.) *Vulnerability, Uncertainty, and Risk: Analysis, Modeling, and Management.* ASCE.

BAZZURRO, P. & CORNELL, C. A. 1994. Seismic hazard analysis of nonlinear structures. I: Methodology. *Journal of Structural Engineering,* 120**,** 3320-3344.

BOLDUC, L. C., GARDONI, P. & BRIAUD, J.-L. 2008. Probability of exceedance estimates for scour depth around bridge piers. *Journal of geotechnical and geoenvironmental engineering,* 134**,** 175-184.

BRIAUD, J.-L., GARDONI, P. & YAO, C. 2013. Statistical, risk, and reliability analyses of bridge scour. *Journal of Geotechnical and Geoenvironmental Engineering,* 140**,** 04013011.

BRIAUD, J.-L., TING, F. C., CHEN, H., GUDAVALLI, R., PERUGU, S. & WEI, G. 1999. SRICOS: Prediction of scour rate in cohesive soils at bridge piers. *Journal of geotechnical and geoenvironmental engineering,* 125**,** 237-246.

CHOI, E., DESROCHES, R. & NIELSON, B. 2004. Seismic fragility of typical bridges in moderate seismic zones. *Engineering Structures,* 26**,** 187-199.

CORNELL, C. A., JALAYER, F., HAMBURGER, R. O. & FOUTCH, D. A. 2002. Probabilistic basis for 2000 SAC federal emergency management agency steel moment frame guidelines. *Journal of Structural Engineering,* 128**,** 526-533.

CORNELL, C. A. & KRAWINKLER, H. 2000. Progress and challenges in seismic performance assessment. *PEER Center News,* 3**,** 1-3.

DONG, Y., FRANGOPOL, D. M. & SAYDAM, D. 2013. Time - variant sustainability assessment of seismically vulnerable bridges subjected to multiple hazards. *Earthquake Engineering & Structural Dynamics,* 42**,** 1451-1467.

DUTTA, A. & MANDER, J. Seismic fragility analysis of highway bridges. Proceedings of the INCEDE-MCEER Center-to-Center Project Workshop on Earthquake Engineering Frontiers in Transportation Systems, 1998. 22-23.

FIELD, E. 2005. *Probabilistic seismic hazard analysis (PSHA): A primer* [Online]. Available: http://www.opensha.org/ [Accessed].

GHOSN, M., MOSES, F. & WANG, J. 2004. NCHRP Report 489: Design of Highway Bridges for Extreme Events. *Transportation Research Board, Washington, DC*.

GUO, X. & CHEN, Z. 2015. Lifecycle multihazard framework for assessing flood scour and earthquake effects on bridge failure. *ASCE-ASME Journal of Risk and Uncertainty in Engineering Systems, Part A: Civil Engineering,* 2**,** C4015004.

HUNT, B. E. 2009. Monitoring scour critical bridges: A Synthesis of Highway Practice (NCHRP Synthesis 396). Transportation Research Board.

HWANG, H., LIU, J. B. & CHIU, Y.-H. 2001. Seismic fragility analysis of highway bridges. Urbana, IL: Mid-America Earthquake Center.

KAFALI, C. & GRIGORIU, M. 2007. Seismic fragility analysis: Application to simple linear and nonlinear systems. *Earthquake Engineering & Structural Dynamics,* 36**,** 1885-1900.

KARIM, K. R. & YAMAZAKI, F. 2003. A simplified method of constructing fragility curves for highway bridges. *Earthquake engineering & structural dynamics,* 32**,** 1603-1626.

KIM, S.-H. & FENG, M. Q. 2003. Fragility analysis of bridges under ground motion with spatial variation. *International Journal of Non-Linear Mechanics,* 38**,** 705-721.

KIMMERLING, R. E., BACHUS, R. C., MAYNE, P. W., SCHEIDER, J. A. & ZETTLER, T. E. 2002. Geotechnical Engineering Circular No. 6, Shallow Foundations (FHWA-IF-02-054). Washington, DC: Federal Highway Administration.

LEE, K. H. & ROSOWSKY, D. V. 2006. Fragility analysis of woodframe buildings considering combined snow and earthquake loading. *Structural Safety,* 28**,** 289-303.

LUCO, N. 2002. *Probabilistic seismic demand analysis, SMRF connection fractures, and near-source effects.* Ph.D., Stanford University.

MACKIE, K. & STOJADINOVIC, B. 2001. Probabilistic seismic demand model for California highway bridges. *Journal of Bridge Engineering,* 6**,** 468-481.

MAZZONI, S., MCKENNA, F., SCOTT, M. H. & FENVES, G. L. 2005. OpenSees command language manual. *Pacific Earthquake Engineering Research (PEER) Center*.

NIELSON, B. G. & DESROCHES, R. 2007. Seismic fragility methodology for highway bridges using a component level approach. *Earthquake Engineering & Structural Dynamics,* 36**,** 823-839.

PRASAD, G. G. & BANERJEE, S. 2013. The Impact of Flood-induced Scour on Seismic Fragility Characteristics of Bridges. *Journal of Earthquake Engineering,* 17**,** 803-828.

SEYEDI, D., GEHL, P., DOUGLAS, J., DAVENNE, L., MEZHER, N. & GHAVAMIAN, S. 2010. Development of seismic fragility surfaces for reinforced concrete buildings by means of nonlinear time-history analysis. *Earthquake Engineering & Structural Dynamics,* 39**,** 91-108.

SHINOZUKA, M., FENG, M. Q., LEE, J. & NAGANUMA, T. 2000. Statistical analysis of fragility curves. *Journal of Engineering Mechanics,* 126**,** 1224-1231.

TONDINI, N. & STOJADINOVIC, B. 2012. Probabilistic seismic demand model for curved reinforced concrete bridges. *Bulletin of Earthquake Engineering,* 10**,** 1455-1479.

TOTHONG, P. & LUCO, N. 2007. Probabilistic seismic demand analysis using advanced ground motion intensity measures. *Earthquake Engineering & Structural Dynamics,* 36**,** 1837-1860.

USGS. 2015. *Seismic Design Maps & Tools* [Online]. Available: http://earthquake.usgs.gov/hazards/designmaps/ [Accessed].

WANG, Z., PADGETT, J. E. & DUEÑAS-OSORIO, L. 2014. Risk-consistent calibration of load factors for the design of reinforced concrete bridges under the combined effects of earthquake and scour hazards. *Engineering Structures,* 79**,** 86-95.

WANG, Z., SONG, W. & LI, T. Combined fragility surface analysis of earthquake and scour hazards for bridge. Proceedings of 15th world conference on earthquake engineering, 2012 Lisbon, Portugal.

Maintenance, Safety, Risk, Management and Life-Cycle Performance of Bridges – Powers, Frangopol, Al-Mahaidi & Caprani (Eds)
© 2018 Taylor & Francis Group, London, ISBN 978-1-138-73045-8

Reliability based corrosion damage assessment for concrete bridge decks under a changing climate

L.I. Peng & M.G. Stewart
Centre for Infrastructure Performance and Reliability, The University of Newcastle, Australia

ABSTRACT: A changing climate may alter the environment during the concrete structures' service life, especially in the longer term. According to the latest Intergovernmental Panel on Climate Change (IPCC) climate projections that temperature and carbon dioxide concentration in the atmosphere are likely to increase significantly by the end of this century. These changes may cause an acceleration of carbonation-induced deterioration processes and consequently a decline of the safety, serviceability and durability of concrete infrastructure. Carbonation-induced deterioration of Reinforced Concrete (RC) bridge decks under a changing climate is investigated in this study. Two latest IPCC climate projection scenarios, i.e. RCP 8.5 and RCP 4.5 emission scenarios, are used here representing possibly high and medium greenhouse gas emission scenarios. The spatial time-dependent reliability analysis is used to include not only the uncertainty of climate projections, deterioration processes and predictive models, but also the spatial variability in material properties and dimensions. The likelihood and extent of corrosion damage is estimated by tracking the evolution of the corrosion process across a bridge deck using Monte Carlo Simulations, and it is more or less affected by the changing climate depending on locations. Case studies of RC bridge decks are presented considering effects of construction methods, climate conditions and design specifications for Australian and Chinese bridges. The findings provide a basis for the development of climate adaptation through the design of concrete bridges, as well as an assessment of the optimal timing and extent of maintenance measures of concrete bridge asset management plans.

1 INSTRUCTIONS

The deterioration rate of RC structures depends on the construction processes employed and the composition of the materials used, as well as the environment. The influences of a changing climate may be potentially important factors for asset management, because it may alter the exposure environment of the structure, and change factors known to affect the corrosion of steel reinforcing bars. The latest Intergovernmental Panel on Climate Change (IPCC) assessment report (2013) indicated a significant increase of CO_2 concentration in the atmosphere which will induce temperature increases to at least 2°C by 2100. Rising temperatures will increase rates of carbonation penetration, as well as the corrosion rate. Changes in relative humidity (RH) will affect corrosion process as well. Peng & Stewart (2016) improved carbonation models by considering the effects of temperature and RH on diffusion coefficient, site-dependent CO_2 levels, and considering RH as a time-dependent variable. Time-dependent RH effects on corrosion rate are also considered (Peng & Stewart 2014). Due to the spatial variability of workmanship, environmental and other factors, it is recognized that the material and dimensional properties of a concrete structures will not be homogeneous. To consider the spatial variability of concrete material properties and concrete cover, and to predict probability and extent of corrosion damage of RC components subject to carbonation induced corrosion, a spatial time-dependent reliability method can be used (Peng & Stewart 2014).

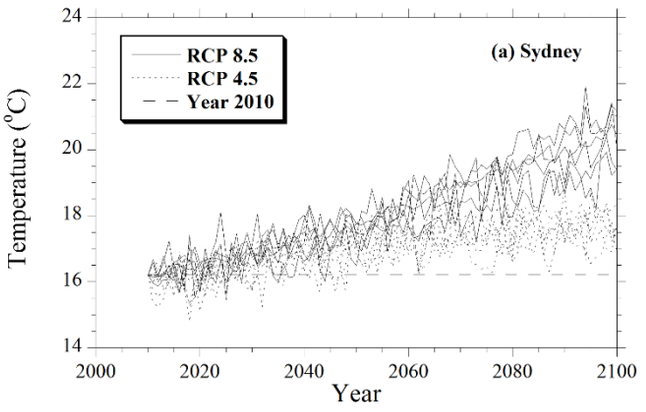
In this paper, two emission scenarios are considered, i.e. RCP 8.5 and RCP 4.5 which represent high and medium greenhouse gas emission scenarios, respectively. RC bridge decks in an Australian city Sydney and a Chinese city Kunming are chosen as a case study to include the effects of construction methods, climate conditions and design specifications. The spatial time-dependent reliability analysis includes the time-dependent climate scenarios and deterioration processes, as well as a large number of random variables and spatial random fields of material properties and dimensions. The surface of concrete structures is discretized into many elements and the likelihood and extent of corrosion damage is calculated by tracking the evolution of the corrosion process of each element using Monte Carlo simula-

tion. Climate adaptation and/or maintenance strategies based on the analysis could provide insights into this problem for policy makers and society (e.g., Stewart & Deng 2015).

2 CLIMATE PROJECTIONS

The IPCC Fifth Assessment Report (2013) uses Representative Concentration Pathways (RCPs) to represent possible CO_2 emission scenarios. The four RCPs, RCP 2.6, RCP 4.5, RCP 6, and RCP 8.5, are named after a possible range of radiative forcing values in the year 2100 (2.6, 4.5, 6.0, and 8.5 W/m^2, respectively). The scenarios RCP 8.5 and RCP 4.5 are used in this study, representing high and medium emission scenarios, respectively. Additionally, an emission scenario based on the Year 2010 CO_2 level of 389 ppm is also considered to provide a reference for other emission scenarios.

To project spatially dependent temperature increases in the future under different emission scenarios, various climate models or Atmosphere-Ocean General Circulation Models (AOGCMs) have been developed based on physical principles at the continental scale. To find the full range of possible values, it is necessary to use multiple models to take into account the uncertainties of models in any impact assessment (Peng & Stewart 2016). Six GCMs are used to project temperature and RH change from 2010 to 2100. Two cities are selected: (a) Sydney, Australia; and (b) Kunming, China. Both cities are major urban centers. The projected annual average temperatures and RH for the six GCM projections, for RCP 8.5 and RCP 4.5 emission scenarios for Sydney and Kunming are shown in Figures 1 and 2. It can be found that there is a large variability between model projections, which makes climate projections particularly challenging. On the other hand, the climate and temperature and RH change trend projections for Sydney and Kunming are similar.



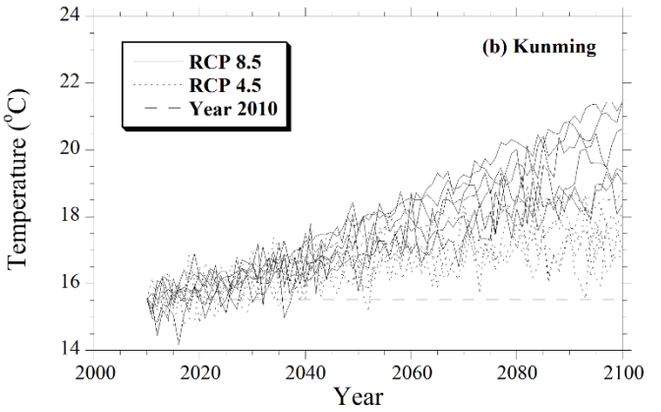


Figure 1. Projected annual average temperatures for the six GCM (BCC-CSM1.1, MIROC5, IPSL-CM5A-LR, CSIRO-MK3.6.0, CNRM-CM5 and ACCESS1.0) projections for RCP 8.5, RCP 4.5 and Year 2010 emission scenarios, for (a) Sydney and (b) Kunming.

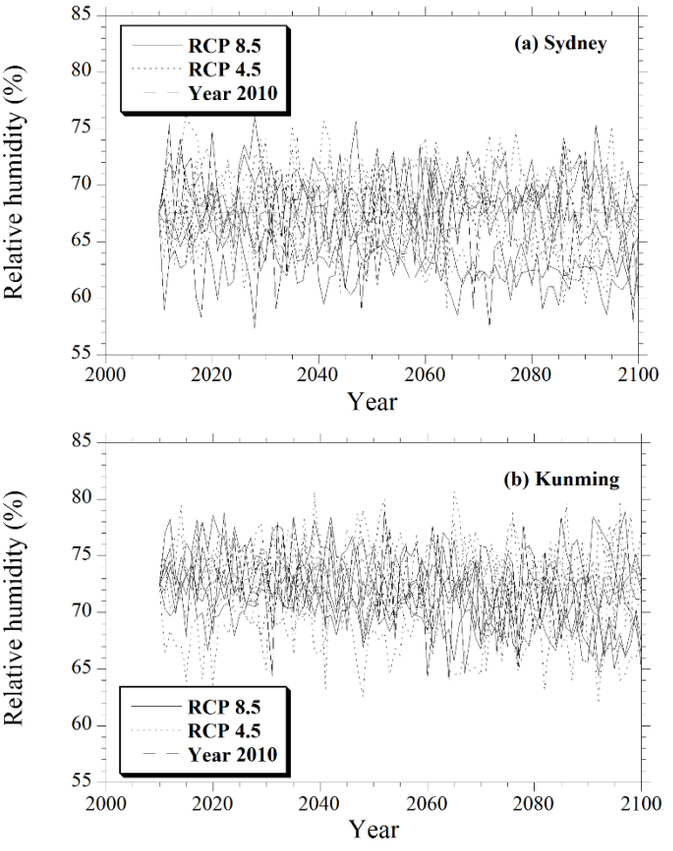


Figure 2. Projected annual average relative humidity for the six GCM (BCC-CSM1.1, MIROC5, IPSL-CM5A-LR, CSIRO-MK3.6.0, CNRM-CM5 and ACCESS1.0) projections for RCP 8.5, RCP 4.5 and Year 2010 emission scenarios, for (a) Sydney and (b) Kunming.

3 CARBONATION INDUCED CORROSION AND DAMAGE

The carbonation induced corrosion process normally consist of three stages: (i) corrosion initiation (T_i, assumed as the time when carbonation depth reaches reinforcement bar); (ii) crack initiation (T_{1st}, time to first cracking-hairline crack of 0.05mm width); (iii) crack propagation (T_{sev}, time for crack to develop

from crack initiation to a limit crack width, w_{lim}). Therefore, the time to corrosion damage (severe cracking or spalling) T_{sp} is the sum of T_i, T_{1st} and T_{sev}.

3.1 *Carbonation induced corrosion*

The carbonation penetration process is simulated as a diffusion process, considering a wide range of influencing parameters including CO_2 concentration, temperature and RH etc. Peng & Stewart (2016) considered the carbonation process as a steady state process modelled by Fick's First Law, and considered time-dependent CO_2 concentration, temperature and RH effects. The carbonation depth model is modified as

$$x_c(t) = \sqrt{\frac{2D(t)}{a}\int_{2010}^{t} f_T(t) f_{RH}(t) k_{site} C_{CO_2}(t) dt}\left(\frac{t_0}{t-2009}\right)^{n_m} \quad t \geq 2010 \quad (1)$$

$$D(t) = D_1 (t-2009)^{-n_d} \quad (2)$$

$$a = 0.75 C_e C_a O \alpha_H \frac{M_{CO_2}}{M_{C_aO}} \quad \alpha_H \approx 1 - e^{-3.38 w/c} \quad (3)$$

where t is defined in calendar years starting from 2010, assuming the bridges goes into service in the year 2010; $x_c(t)$ is the carbonation depth at time t; $C_{CO2}(t)$ is the time-dependent increase in atmospheric CO_2 concentration (10^{-3} kg/m^3); k_{site} is factor to account for increased CO_2 levels in non-remote environments; $f_T(t)$ is time-dependent change in diffusion coefficient due to changes in temperature; $f_{RH}(t)$ is time-dependent change in diffusion coefficient due to changes in RH; D(t) is CO_2 diffusion coefficient in concrete calibrated for time period 2010 to t; D_1 is CO_2 diffusion coefficient at t=2010; n_d is the age factor for the CO_2 diffusion coefficient; t_0 is one year; C_e is cement content (kg/m^3); CaO is CaO content in cement (0.65); α_H is a degree of hydration, the degree of hydration for ordinary Portland cement (OPC) after more than 400 days is estimated as Eq.(3); M_{CaO} is molar mass of CaO and equal to 56 g/mol; and M_{CO2} is molar mass of CO_2 equal to 44 g/mol. The CO_2 diffusion can be hindered by rain with elapsed time because of pore blocking of water in concrete skin, the age factor for microclimatic conditions n_m associated with the frequency of wetting and drying cycles is n_m=0 for sheltered outdoor, and n_m=0.12 for unsheltered outdoor exposures (Yoon et al. 2007). The functions for k_{site}, $f_T(t)$ and $f_{RH}(t)$ are detailed in Peng & Stewart (2016).

3.2 *Corrosion propagation*

When carbonation depth reaches the reinforcing bar, corrosion initiates (T_i) where T_i is the year when the carbonation depth exceeds the concrete cover. The corrosion rate is variable and highly dependent on exposure conditions and atmospheric situations. For instance, the optimum RH for corrosion is 70-80%, and then corrosion rate decreases as RH increases due to reduced diffusion of oxygen through the concrete (Neville 1995). A model that includes RH and temperature effects on corrosion rate proposed by Breysse et al. (2013) shows that a lower RH will decrease corrosion rate when RH is less than the reference RH:

$$i_{corr}(RH,T) = i_{corr\cdot ref}(RH_{ref},T_{ref}) e^{0.0312(RH-RH_{ref})} e^{-4736\left(\frac{1}{273.15+T}-\frac{1}{273.15+T_{ref}}\right)} \quad (4)$$

where a reference state is RH_{ref}=80%, and T_{ref}=20°C.

In the present study, the reference corrosion rate is denoted as $i_{corr-20}$ and is assumed lognormally distributed with statistical parameters given by Duracrete (1998), where a corrosion rate of 1 μA/cm^2 = 0.0116 mm/year. For sheltered moderate humidity exposure environment, the mean carbonation corrosion rate ($i_{corr-20}$) is 0.172 μA/cm^2, and the standard deviation is 0.086 μA/cm^2. These values take into account the concrete grades suggested for the corresponding exposure classes. This is likely to be a conservative assumption as corrosion rate will generally decrease with time due to the build-up of rust products thus impeding the corrosion process (Vu & Stewart 2000).

3.3 *Crack initiation (T_{1st}), severe cracking (T_{sev}) and corrosion damage (T_{sp})*

The time to crack initiation, T_{1st} is estimated by a model proposed by El Maaddawy & Souki (2007). It should be noted, that the accuracy of the time to corrosion damage (T_{sp}, $T_{sp}=T_i+T_{1st}+T_{sev}$) is dominated by the accuracy of time to corrosion initiation (T_i) and the time to crack propagation (T_{sev}, time for crack to develop from crack initiation to a limit crack width), and so damage risk predictions are relatively insensitive to the crack initiation model (Stewart & Mullard 2007).

The definition of how 'excessive' the crack width depends on individual conditions and asset owner policies; in this paper, concrete structures will be regarded as 'severely cracked' when crack width reaches a crack width of 1.0 mm. Mullard and Stewart (2011) have modelled rate of crack propagation which enables the time for a crack to develop from crack initiation to a limit crack width. Since corrosion rate is a time-dependent function of temperature and RH then time to corrosion damage is corrected for a time-variant corrosion rate instead of a time-invariant (constant) corrosion rate, for more details see Peng & Stewart (2016).

4 SPATIAL TIME-DEPENDENT RELIABILITY ANALYSIS

Reinforced concrete construction involves various processes including concrete batching, onsite dimensional set out, reinforcement placement, compaction of the concrete and curing. The nature of these processes introduces the potential for substantial variability of concrete quality due to variations in work practices. The spatial variability of concrete cover, concrete strength, diffusion coefficient and binding capacity are included in the analysis.

Random field theory can be used to model the spatial variability of these parameters. Therefore, a RC bridge deck or a surface can be represented by a 2D random field. In a random field, the surface is discretized into k identical elements of size Δ and the random variables within the random field are statistically correlated based on the corresponding correlation function (Vanmarcke 1983). The midpoint method is used to represent an element by the value at the centroid of that element and this value is assumed to be constant within the element.

The spatial correlation between elements in a random field can be described by the correlation function which defines the exact pattern of decay of the variance. The correlation function $\rho(\tau)$ determines the correlation coefficient between two elements separated by distance (τ) and is representative of the spatial correlation between the elements. As the distance between correlated elements becomes smaller the correlation coefficient approaches unity as defined by the correlation function, and likewise as the distance increases the correlation coefficient reduces.

The Gaussian correlation function has been widely used in engineering applications, including spatial modelling of RC structures, and as such it shall be used herein to model the spatial correlation of elements within a random field (Der Kiureghian & Ke 1988, Sudret 2008, Mullard & Stewart 2009). The Gaussian (or squared exponential) correlation function used herein is

$$\rho(\tau)=\exp\left[-\left(\frac{|\tau_x|^2}{d_x^2}\right)-\left(\frac{|\tau_y|^2}{d_y^2}\right)\right] \quad (5)$$

where $d_x=\theta_x/\sqrt{\pi}$ and $d_y=\theta_y/\sqrt{\pi}$; θ_x and θ_y are the scales of fluctuation for a two-dimensional random field in x and y directions, respectively; and $\tau_x=x_i-x_j$ and $\tau_y=y_i-y_j$ are the distances between centroid of elements i and elements j in the x and y directions, respectively. Once the stochastic random field is defined, Monte Carlo simulation methods are used to generate random variables for each element and the spatially variable parameters of each element are then defined using the correlation function. Monte Carlo simulation can also predict the deteriorated state of each element (T_i, T_{sp}) at every time interval.

4.1 *Proportion of a concrete surface subject to corrosion damage*

Corrosion damage is defined as the time when concrete cover reaches a limit crack width of 1.0 mm. Therefore, the proportion of concrete surface severe corrosion damage at time t (d_{crack}) for each Monte Carlo simulation realization is

$$d_{\text{crack}}(t)=\frac{n\left[t>T_{sp(j)}\right]}{k}\times 100\% \quad (6)$$

where $T_{sp}(j)$ is the time to corrosion damage of element j, and n[] denotes the number of elements for which $t> T_{sp}(j)$.

4.2 *Probability that at least x% of concrete surface has damaged*

The probability that at least x% of concrete surface has damaged at time t is

$$\Pr\left(d_{crack}(t)\geq x\%\right)=\int_{x\%}^{100\%} f_{d_{crack}}(d_{crack},t)\,\mathrm{d}\,d_{crack} \quad (7)$$

where $f_{dcrack}(d_{crack},t)$ is the multi-dimensional probability distribution of $d_{crack}(t)$ obtained from Monte Carlo simulation analysis for each time step t, a value of $d_{crack}(t)$ is calculated and after many simulations the probability distribution $f_{dcrack}(d_{crack},t)$ for every combination of t and $d_{crack}(t)$ will be inferred. As will be shown later $f_{dcrack}(d_{crack},t)$ is highly non-Gaussian and so percentile values of $f_{dcrack}(d_{crack},t)$ can only be predicted from simulation methods (Stewart & Mullard 2007).

5 CASE STUDY: RC BRIDGE DECKS IN SYDNEY AND KUNMING

5.1 *Structural configuration*

According to national code requirements, concrete cover requirements and concrete properties are not constant, generally, depending on the grade of concrete, and the exposure class. Environmental exposure in Australia is classified by the Australian Concrete Structures Code AS5100.5-2004 as three climatic zones (arid, temperate and tropical). Similarly, the environmental exposures in China are also classified for three climatic areas, as severe cold area, cold area and temperate area (JTG.D62-2004). The selected sites of Sydney and Kunming represent temperate climates in both codes. Note that RC structures are assumed to use ordinary Portland cement concrete, and standard formwork and compaction.

Concrete inside buildings in a dry environment, concrete surfaces subject to long-term rain in unsheltered exposures, and RC permanently submerged in water generally have a low carbonation rate. However, concrete inside buildings with moderate air

humidity, and external concrete sheltered from rain have higher likelihood of carbonation (Peng & Stewart 2016). The upper side of bridge deck is usually protected by wearing surface from water ingress and subsequent damage, however, the bottom side of bridge deck should be considered as external concrete sheltered from rain.

The durability design requirements specified in AS5100.5-2004 and JTG.D62-2004 relate to minimum concrete cover and concrete compressive strength, and assume standard formwork and compaction. The exposure classification conditions can be referred from AS5100.5-2004, JTG.D62-2004 and Peng (2015). For RC bridges in Sydney which are 50 km from coast, exposure classification A is appropriate to use. Note that RC structures close to the coast in Sydney have higher cover and are much less susceptible to carbonation induced corrosion. The exposure classification for RC bridge decks in the inland city of Kunming is exposure classification I. The durability requirements for a RC bridge deck in Sydney and Kunming are shown in Table 1. Note that the concrete compressive strengths in Chinese standards are based on cube compressive strengths. The bar diameter is assumed to be 20 mm, in practice, it can be other values of course, but corrosion damage risks are not sensitive to bar diameter (Peng & Stewart 2016).

Table 1. Durability design specifications (AS5100.5-2004, JTG.D62-2004) and deterioration models for bridges.

Class	w/c ratio	C_e (kg/m^3)	Mean D_1	Mean n_d	Cover (mm)	F'_c * (MPa)
A	0.56	320	2.22	0.24	35	25
I	0.55	275	2.22	0.24	30	C25

* C represents cube compressive strength.

5.2 *Spatial and stochastic variables*

A 2D random field is applied to simulate the RC bridge decks considering the spatial variability of concrete cover, concrete strength, and CO_2 diffusion coefficient and binding capacity. In this study, these four parameters are modelled as stationary random fields with respect to space. Random and spatial variables modelled as non-stationary can be included in the analysis if more realistic structural configurations are to be modelled.

Data to characterize the spatial correlation of concrete dimensional, material property and corrosion parameters is limited (Stewart & Mullard 2007, Sudret 2008, Na et al. 2013). The scale of fluctuation, θ, defines the distance over which correlation persists in a random field. Vanmarcke (1983) proposed various methods for the calculation of the scale of fluctuation for stationary random fields. These methods, however, require large amount of spatial data and although this has been collected in some cases, typically the scale of fluctuation is estimated using engineering judgment. However, due to a scarcity of reliable field data of concrete cover, concrete compressive strength, CO_2 diffusion coefficient and binding capacity, the scales of fluctuation in the x and y directions (θ_x, θ_y) are estimated based on previous studies as summarized in Table 2 (Sudret 2008, Na et al. 2013). Because the scales of fluctuation are not identical, the four random fields need to be generated separately. Stewart and Mullard (2007) found that chloride induced corrosion damage probabilities are not overly sensitive if the scale of fluctuation varies from 1.0 to 3.0 m for concrete cover. Nonetheless, more effort is needed to characterize the scale of fluctuation, as well as the shape of the correlation function, with more confidence.

The size of the discretized element is usually defined based on practical and analytical considerations. Sterritt et al. (2001) suggested that the element size should be in the range of 0.1 to 0.75 m. Therefore, element size Δ=0.5 m is chosen herein. The RC slab is 10 m long and 10 m wide, providing a total area of 100 m^2. The deck size, however, can be adjusted to fit needs.

To account for the random variation of basic parameters in structural analysis, the statistical description of the variability of material properties of reinforced concrete slabs is required, see Table 3 (Peng & Stewart 2014). Concrete strength is time-variant, and the time-dependent increase in concrete compressive strength after one year using the ACI method is f_c=1.162f_c(28) where f_c(28) is the 28-day in-situ compressive strength (Stewart 1996). Time-dependent gains in strength beyond one year are not considered in the present analysis. The difference between cast in-situ and precast concrete compressive strength is minor (Wiśniewski et al. 2012). The statistics of concrete cover are based on Australian and Chinese field surveys (McGee 1999, RGRRCSM 1985), and the results are also partly listed in Table 3. Only results for cast in-situ concrete are presented in this paper.

Table 2. Random field parameters.

Parameter	Distribution	Mean	COV	θ (m)
Concrete cover	Truncated normal	Table 3	Table 3	2
Concrete strength f_c	Truncated normal	Table 3	Table 3	1
Diffusion coefficient D_1	Lognormal	Table 1	σ=0.15	2
Binding capacity a	Lognormal	Eq. (3)	0.3	2

Table 3. Statistical parameters for corrosion parameters, material properties and dimensions.

Parameters	Mean	COV	Distribution
concrete cover (cast in situ)			
AU	C_{nom}+6 mm	σ=11.5 mm	Truncated normal*
CN	$0.90C_{nom}$	0.3	Truncated normal*
$f_c(28)$			
AU: N32	1.06F'c	0.152	Truncated normal**
CN: C25	0.90F'c	0.196	Truncated normal**
f_t	$0.53(f_c)^{0.5}$	0.13	Normal
E_c	$4600(f_c)^{0.5}$	0.12	Normal
n_d	0.242	0.12	Normal
ME(r_{crack})	1.04	0.09	Normal
δ_0	15 μm	0.1	Normal
k_{site}			
Urban area	1.14	0.08	Truncated normal***
Suburban area	1.07	0.06	Truncated normal***
Rural area	1.05	0.04	Truncated normal***

* truncated at 8 mm. ** truncated at 0 MPa. *** truncated at 1.0. AU: Australia. CN: China.

5.3 *Results*

The mean carbonation depths of sheltered and unsheltered RC bridge decks in Sydney and Kunming are shown in Figures 3-4 and are based on the average of six GCM projections. Due to the long-term effects of the wetting and drying cycles, the mean carbonation depths for unsheltered section are reduced significantly compared to sheltered section. Therefore, the analysis to follow will focus on sheltered RC bridge deck section. The RCP 8.5, RCP 4.5 and the Year 2010 emission scenarios have a significant effect on carbonation depths, and carbonation depths for RCP 8.5 and RCP 4.5 emission scenarios can be increased by up to 5.5 mm by 2100. For example, for bridges in Sydney, the RCP 8.5 emission scenario increases carbonation depth by approximately 34% when compared to the reference Year 2010 CO_2 emissions, whereas the RCP 4.5 increases carbonation depths by 13%. The COV of carbonation depth increases from 0.05 in 2010 to 0.08 by 2100. Carbonation depth for RC bridges in Sydney is very close to those in Kunming. Because both cities have similar temperature and RH projections, as well as the similar durability design requirements. The differences of design requirement between RC bridges in Sydney and Kunming are concrete cover and cement content, however, concrete cover thickness will not influence the carbonation process and the results show that the carbonation process is not sensitive to cement content.

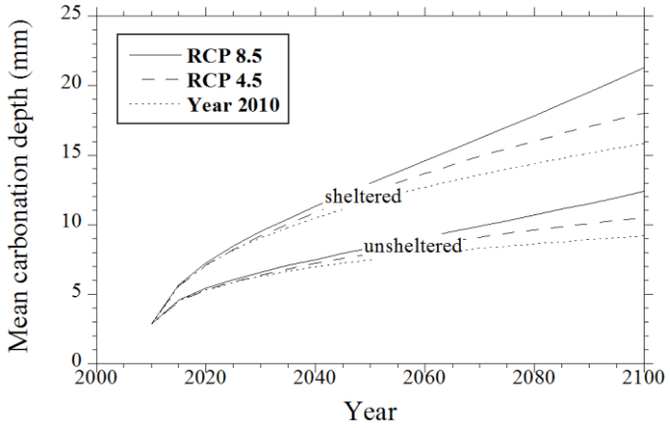


Figure 3. Mean carbonation depth of bridge decks in Sydney under all emission scenarios.

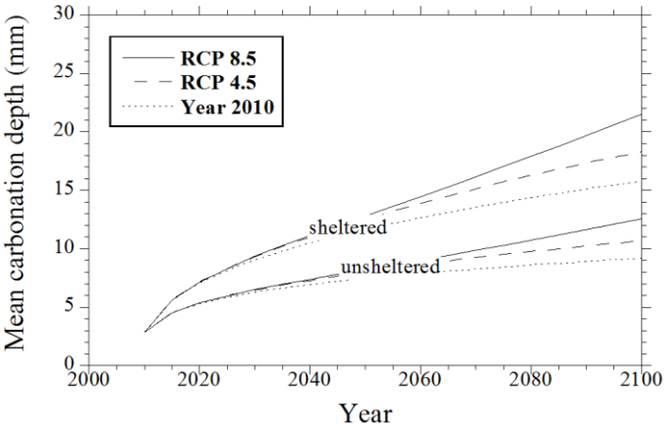


Figure 4. Mean carbonation depth of bridge decks in Kunming under all emission scenarios.

Carbonation depth increases with time. When the carbonation depth reaches the surface of reinforcing bar then corrosion is initiated. Therefore, the extent of corrosion initiation is mainly determined by carbonation depth and concrete cover. Figures 5-6 present the mean extent of corrosion initiation for cast in-situ sheltered RC bridge decks in Sydney and Kunming. The elements that are corrosion initiated for RCP 8.5 emission scenario can be twice as much for the reference Year 2010 emission scenario. In Sydney, less than 5% of the sheltered concrete surface of bridge decks will start corrosion by the end of this century, even under RCP 8.5 emission scenario; while the extent is about 25% for sheltered RC bridge decks in Kunming. As the carbonation depth are predicted to be very similar for bridge decks in both cities, so concrete thickness plays a significant role in initiate corrosion process. The big difference of extent of corrosion initiation for cast in-situ sheltered RC bridge decks are mainly due to higher durability requirements on concrete cover (Table 1) and better construction quality for Australian structures (Table 3).

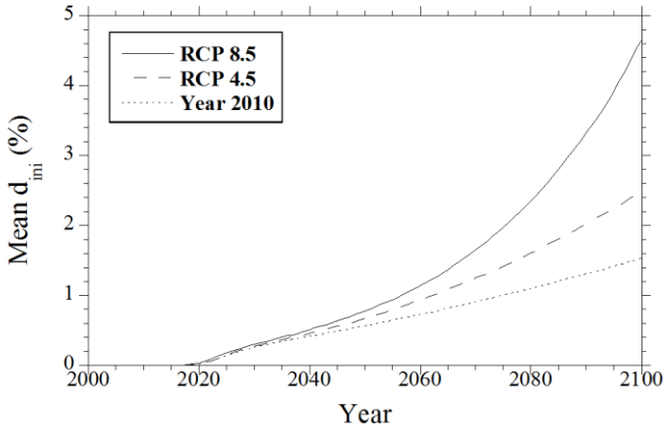


Figure 5. Mean extent of corrosion initiation of bridge decks in Sydney under all emission scenarios.

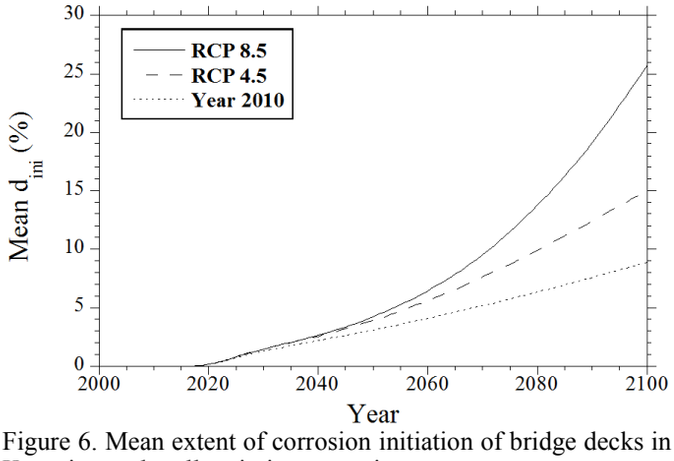


Figure 6. Mean extent of corrosion initiation of bridge decks in Kunming under all emission scenarios.

After corrosion is initiated, the corrosion process is dominated by the corrosion rate. Figures 7-8 present the mean proportion of surface corrosion damage for cast in-situ sheltered RC decks in Sydney and Kunming under all emission scenarios. Less than 0.5% of the concrete surface will be damaged for RC bridge decks in Sydney, for RCP 8.5 emission scenario by 2100. The five times larger corrosion initiation extent for RC bridge decks in Kunming subsequently lead to about ten times larger corrosion damage extent compared to those in Sydney, for RCP 8.5 emission scenario by 2100. Climate change may cause more severe corrosion damage. The RCP 8.5 emission scenario is predicted to cause around twice as much corrosion damage extent in RC bridge decks in Kunming compared to Year 2010 emission scenario. In practical terms, this is equivalent to expecting that up to an additional 2% of all concrete surfaces by 2100 will be damaged and in need of maintenance or repair, because of a changing climate. The differences between results of RCP 8.5 and Year 2010 emission scenario for RC bridge decks in Sydney are relatively lower. Overall, the extents of corrosion initiation and corrosion damage for RC bridge decks in Sydney and Kunming are quite low compared to RC buildings which generally have lower durability requirements (Peng 2015).

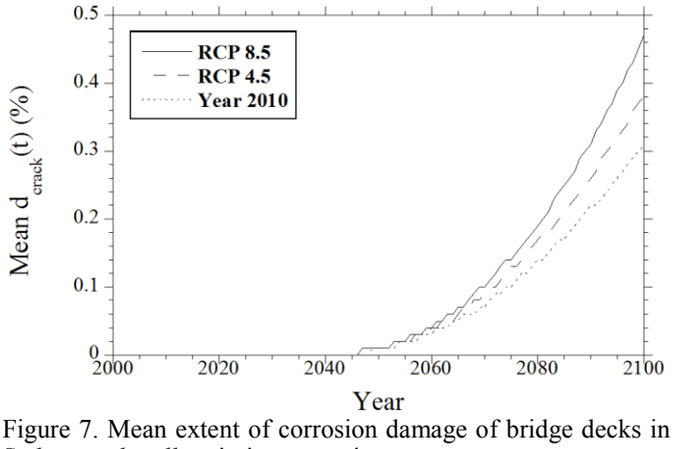


Figure 7. Mean extent of corrosion damage of bridge decks in Sydney under all emission scenarios.

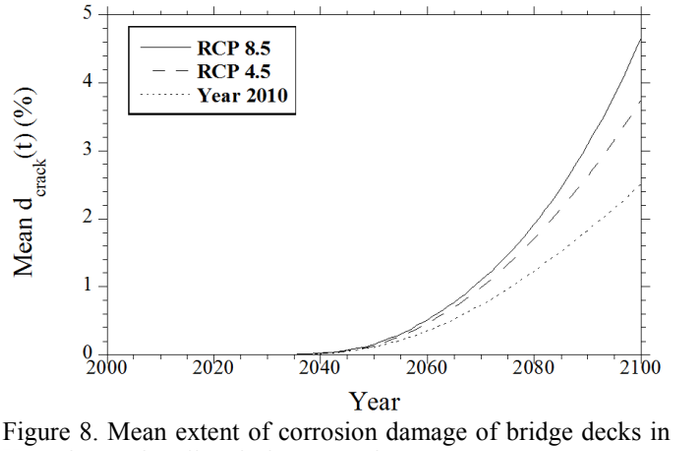


Figure 8. Mean extent of corrosion damage of bridge decks in Kunming under all emission scenarios.

The histograms of proportion of surface corrosion damage for cast in-situ sheltered RC decks $f_{dcrack}(d_{crack},t)$ is highly non-Gaussian (Peng 2015, Peng & Stewart 2014). The likelihood of no or little damage is significantly high, but it will decrease with time. However, even by 2100, the probability of significant damage is still low. Since the extent of corrosion damage can be predicted with time, inspection intervals and repair threshold can be determined to optimize resources to make sure structures to stay at an acceptable safety and service level. On the other hand, the analysis can be used to develop climate adaptation measures in the design stage, considering cost benefit effects of alternative climate adaptation measures to minimize life-cycle costs of structures (e.g., Peng & Stewart 2015).

6 CONCLUSIONS

The paper has described a spatial time-dependent reliability analysis of the carbonation induced corrosion deterioration of RC bridge decks under a changing climate. The spatial random fields of concrete cover, concrete strength, CO_2 diffusion coefficient and binding capacity are included whilst other material and corrosion parameters are treated as dependent spatial or random variables. Time-dependent CO_2, temperature and RH effects on carbonation

depth and corrosion rates are included. The results from the spatial time-dependent reliability analysis were presented in terms of likelihood and extent of surface corrosion damage, for RC bridge decks in an Australian city Sydney and a Chinese city Kunming. It was found that a changing climate can cause the extent of damage to increase by up to 2% for RC bridge decks in Kunming. RC bridge decks in Sydney are under much less risk to carbonation induced corrosion damage mainly due to higher durability requirements and better construction quality on concrete cover. The analysis can be used to optimize investment on maintenance strategies and develop climate adaptation measures in the design stage, which provide insights into this problem for policy makers and community.

7 ACKNOWLEDGEMENTS

The authors acknowledge the World Climate Research Program's Working Group on Coupled Modelling, which is responsible for CMIP, and we thank the climate modelling groups (listed in Figs 1-2 of this paper) for producing and making available their model outputs. For CMIP, the US Department of Energy's Program for Climate Model Diagnosis and Intercomparison provided coordinating support and led the development of software infrastructure in partnership with the Global Organization for Earth System Science Portals. The authors express their appreciation to Xiaoming Wang and Stacey Dravitzki of CSIRO for providing climate data.

8 REFERENCES

AS5100.5-2004. *Bridge design Part 5: concrete*. Standard Australia, Sydney.

Breysse, D., Chaplain, M. & Marache, A. 2013. Simulation of synthetic climate at local scale as a mean to assess the impact of climate change on infrastructures, *Proceedings of Safety, Reliability, Risk and Life-Cycle Performance of Structures and Infrastructures (ICOSSAR2013), New York, NY, USA*. CRC Press, Boca Raton, FL, USA.

Der Kiureghian, A. & Ke, J.B. 1988. The stochastic finite element method in structural reliability. *Probabilistic engineering mechanics* 3(2): 83–91.

DuraCrete. 1998. *Modelling of degradation, DuraCrete – Probabilistic performance based durability design of concrete structures*, EU – Brite EuRam III, Contract BRPR-CT95-0132, Project BE95-1347/R4-5.

El Maaddawy, T. & Soudki, K.A. 2007. A model for prediction of time from corrosion initiation to corrosion cracking. *Cement and Concrete Composite* 29(3): 168–175.

IPCC. 2013. *Climate change 2013: the physical science basis. Contribution of working group I to the fifth assessment report of the intergovernmental panel on climate change*. Cambridge University press, Cambridge, UK and New York, NY, USA.

JTG.D62-2004. 2004. *Code for design of highway reinforced concrete and prestressed concrete bridges and culverts*. Beijing: Ministry of Communication of the People's Republic of China. (In Chinese).

McGee, R. 1999. Modelling of Durability Performance of Tasmanian Bridges. *ICASP8 Applications of Statistics and Probability in Civil Engineering. R.E. Melchers and M.G. Stewart (eds),* 1: 297-306.

Mullard, J.A. & Stewart, M.G. 2009. Stochastic assessment of timing and efficiency of maintenance for corroding RC structures. *Journal of structural engineering* 135(8): 887–895.

Mullard, J.A. & Stewart, M.G. 2011. Corrosion-induced cover cracking: new test data and predictive models. *ACI Structural Journal* 108(1): 71–79.

Na, U.J., Kwon, S. & Chaudhuri, S.R. et al. 2012. Stochastic model for service life prediction of RC structures exposed to carbonation using random field simulation. *KSCE Journal of civil engineering* 16(1): 133–143.

Neville, A. 1995. Chloride attack of reinforced concrete: an overview. *Materials and Structures* 28(2): 63–70.

Peng, L. 2015. *Spatial time-dependent reliability analysis of carbonation induced corrosion damage to RC structures under a changing climate and cost-benefit analysis of climate adaptation strategies*. PhD thesis.

Peng, L. & Stewart, M.G. 2014. Spatial Time-Dependent Reliability Analysis of Corrosion Damage to Concrete Structures under a Changing Climate. *Magazine of Concrete Research* 66(22): 1154-1169.

Peng, L. & Stewart, M.G. 2015. Damage risks and cost-benefit analysis of climate adaptation strategies of RC structures in Australia. *Concrete in Australia* 41(3): 36-47.

Peng, L. & Stewart, M.G. 2016. Climate change and corrosion damage risks for reinforced concrete infrastructure in China. *Structure and Infrastructure Engineering* 12(4): 499-516.

RGRRCSM (Research Group on Reliability of Reinforced Concrete Structural Members). 1985. Investigation and statistical analysis of the dimensional tolerances of reinforced concrete structural members. *Journal of building structures* 6(4): 2–9. (In Chinese).

Sterritt, G., Chryssanthopoulos, M.K. & Shetty, N.K. 2001. Reliability-based inspection planning for RC highway bridges. *Safety and risk in engineering* 32(10): 3279–3287.

Stewart, M.G. 1996. Serviceability reliability analysis of reinforced concrete structures. *Journal of structural engineering ASCE* 122(7): 794–803.

Stewart, M.G. & Mullard, J.A. 2007. Spatial time-dependent reliability analysis of corrosion damage and the timing of first repair for RC structures. *Engineering Structures* 29(7): 1457–1464.

Stewart, M.G. & Deng, X. 2015. Climate Impact Risks and Climate Adaptation Engineering for Built Infrastructure. *ASCE-ASME Journal of Risk and Uncertainty in Engineering Systems, Part A: Civil Engineering* 1(1):04014001.

Sudret, B. 2008. Probabilistic models for the extent of damage in degrading reinforced concrete structures. *Reliability engineering and system safety* 93(3): 410–422.

Vanmarcke, E. 1983. *Random Fields: Analysis and Synthesis*. MIT Press, Cambridge, MA, USA.

Vu, K.A.T. & Stewart, M.G. 2000. Structural reliability of concrete bridges including improved chloride-induced corrosion models. *Structural Safety* 22(4): 313–333.

Wiśniewski, D.F., Cruz, P.J.S. & Henriques, A.A.R. et al. 2012. Probabilistic models for mechanical properties of concrete, reinforcing steel and pre-stressing steel. *Structure and Infrastructure Engineering* 8(2): 111-123.

Yoon, I.S., Copuroglu, O. & Park, K.B. 2007. Effect of global climatic change on carbonation progress of concrete. *Atmospheric Environment* 41: 7274-7285.

Maintenance, Safety, Risk, Management and Life-Cycle Performance of Bridges – Powers, Frangopol, Al-Mahaidi & Caprani (Eds)
© 2018 Taylor & Francis Group, London, ISBN 978-1-138-73045-8

Risk-Informed Assessment of Climate Change by Considering Deterioration and Hazards

Y.H. Li[1] and Y. Dong[1]
[1]: Department of Civil and Environmental Engineering, The Hong Kong Polytechnic University, Kowloon, Hong Kong, China

ABSTRACT: Life-cycle probabilistic life-cycle risk assessment of coastal bridges under typhoon hazard is progressively gaining attention. Though damage of coastal bridges during typhoon-induced wave and surge impacts has been widely investigated, probabilistic models are lack of research to characterize the bridge vulnerability and the consequent life-cycle loss. This paper aims to provide a framework of probability-based life-cycle risk assessment of coastal bridges under typhoon hazard and to propose an analytical method to estimate the typhoon-induced life-cycle loss. The proposed methodology can benefit the society to manage risks of coastal bridges during typhoons. The investigations focus on deck unseating failure mode, which is a primary damage pattern for simply supported bridges during typhoons. The proposed methodology is applied to an existing bridge to ensure the feasibility.

1 INTRODUCTION

Highway bridges may be subjected to hazards such as floods, earthquakes, and hurricanes during their service life. Storm surge can cause significant flooding in coastal areas, which could overwhelm infrastructure systems. Overall, hazard risk assessment is of vital importance to ensure structural safety and functionality during the service life of civil infrastructure systems (Frangopol 2011; Dong and Frangopol 2015). Typhoons, also known as hurricanes and tropical cyclones, can cause destructive damage to civil infrastructures and lead to severe casualties and economic losses. Landfalling typhoons become major hazards for coastal regions associated with extreme rainfall, winds and storm surge. Hurricane Katrina is one of the deadliest tropical cyclones in the natural hazard history of the United States, which left over 1,800 deaths with a total loss of more than $125 billion in 2005 (Graumann *et al.* 2005). In China, annual typhoon landfall is up to 7 on average, resulting in significant annual damage loss of $5.6 billion US dollars (Elliott *et al.* 2015). Furthermore, a large number of field observations emphasized the vulnerability of coastal bridges failed during the Typhoon Songda (2004), Hurricane Ivan (2004) and Ike (2008). During typhoon activities, storm surge and the induced inundation destroyed coastal bridges significantly. The subsequent repairs and replacement account for a large proportion of the typhoon hazard financial losses. Hence, research on coastal bridges vulnerable to typhoon hazard is necessarily required to benefit the society in enhancing the preparedness and awareness prior to extreme typhoon events. Additionally, recent research suggested that global climate change may increase the intensity and frequency of typhoons. For instance, warming climate may increase the average intensity of tropical cyclones by 2-11% worldwide by 2100 and the projected global sea level rise may reach 0.21 to 0.82m by the year of 2100 (Webster *et al.* 2005; Emanuel 2008; Knutson *et al.* 2010). Cumulative evidences indicate that the existing coastal bridges are exposed to higher damage risks during future extreme typhoons. All these facts have received an increasing attention from researchers, insurers and policy-makers, which requires a comprehensive probability risk assessment of typhoon hazard damages on coastal bridges.

The impact of typhoons on bridges mainly arises from storm surge and wave-induced loading. The consequent horizontal and vertical uplift forces produce excessive horizontal and vertical displacements at supports. When these displacements surpass the restraint at supports, superstructure becomes unsupported and eventually deck unseating appears. Deck unseating failure is recognized as the most primary damage for simply supported bridges (Kulicki 2010). Although an increasing amount of recent research has been conducted in terms of coastal bridges under typhoon hazard, the investigations of probabilistic risk assessment considering both deck

unseating failure and typhoon wind speed are still lacking. Studies of the corresponding typhoon-induced damage loss for existing bridge are also limited. Recently, Wang *et al*. (2017) suggested a method for hurricane damage loss assessment from the perspective of insurers and proposed a hurricane vulnerability analysis considering the wind speed as well as model uncertainty. Though this work stated hurricane occurrence process can be modeled as Poisson process, this study fails to reflect Poisson process and Poisson distribution clearly in the computation steps. In another typhoon risk investigation, Lin and Shullman (2017) successfully applied the stationary and non-stationary Poisson process model to estimate the hurricane arrivals. However, this research investigated the hurricane induced surge and flooding for New York City and mainly focused the expected annual damage consequences rather than the long-term loss. To overcome these deficiencies, this paper introduces a probabilistic life-cycle assessment framework of coastal bridges vulnerable to typhoons and proposes a new method for typhoon damage loss estimation. A flowchart of the assessment procedures of bridges vulnerable to typhoon hazard is shown in Figure 1.

This probability-based life-cycle framework mainly consists of three stages: hazard analysis of typhoons, structural vulnerability of the given bridge under typhoons and the corresponding typhoon-induced damage loss. The hazard analysis targets the distribution of typhoon arrivals and the distribution of typhoon wind speed. The vulnerability assessment focuses on bridge deck unseating damage because this failure mode is the most predominant for coastal simply supported bridges. The following damage consequence evaluation estimates the total damage loss of the reconstruction of the bridge based on analytical method. A case study of a practical simply supported bridge in New Jersey is conducted to illustrate the proposed approach and to identify the uncertainty on the evaluation consequences.

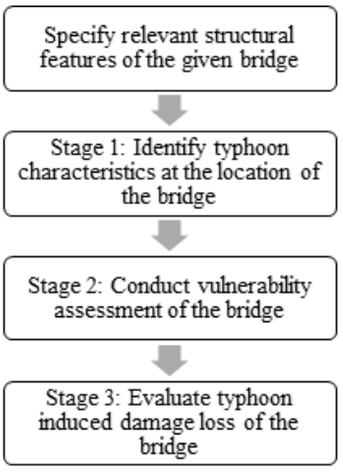


Figure 1. Flowchart of time-variant structural performance assessment process under hazard effects

2 TYPHOON HAZARD EFFECTS

Typhoon hazard analysis is the first stage in the risk assessment process, which provides the probabilistic descriptions of hazard characterization. In this section, typhoon occurrence process and hazard quantification are introduced.

2.1 *Stochastic typhoon process*

For a specific region with given climate environment, storm arrivals can be assumed to be conditionally independent, because the interactions between each typhoon event are comparatively small and require more scientific understanding. Researchers suggested a Poisson process to model the typhoon occurrence process (Onof *et al.* 2000; Elsner and Bossak 2001; Vanem 2011). If the future climate is assumed as stationary, the typhoon arrival process is assumed to be stationary Poisson process. Otherwise, a non-stationary Poisson process is considered instead. These two processes are also named as homogenous and non-homogeneous Poisson process (also known as stationary and non-stationary Poisson process). For a homogenous Poisson process, the typhoon arrival process is with a fixed and constant arrival rate λ. The probability of k (k = 0, 1, 2 …) typhoon events occur within the time interval (0, T) with the mean occurrence rate λ gives

$$\Pr\left(N_T = k\right) = \frac{\left(\lambda T\right)^k}{k!}\exp\left(-\lambda T\right) \qquad (1)$$

The nonhomogeneous Poisson process takes into account the arrival rate varying with time with a notation of $\lambda(t)$. Hence, the probability becomes

$$\Pr\left(N_T = k\right) = \frac{\left(\int_0^T \lambda\left(t\right)dt\right)^k}{k!}\exp\left(-\int_0^T \lambda(t)dt\right) \qquad (2)$$

2.2 *Typhoon wind speed probabilities*

The typhoon hazard can be characterized by the probabilities distribution of the typhoon wind speed. It is usually suggested to adopt the probability information based on a given location, but reference information from adjacent areas or other similar regions can be used if lack of data resources. The research probability distribution of extreme wind speed has been progressively developed in the last two decades (Simiu and Scanlan 1996; Vickery *et al.* 2010; Simiu 2011). A parametric modeling of typhoon wind speed was carried out by Yeo *et al.* (2013), which suggested that typhoon speed can be assumed as Weibull distribution. Accordingly, the cumulative distribution function (CDF) and the corresponding probability density function (PDF) in a nonhomogeneous (parameters are time independent

if for homogeneous situation) process with time-variant parameters $u(t)$ and $\alpha(t)$ gives

$$F_v(v,t) = \Pr(V < v) = 1 - \exp\left[-\left(\frac{v}{u(t)}\right)^{\alpha(t)}\right] \quad (3)$$

$$f_v(v,t) = \frac{\partial F_v(v,t)}{\partial v} = \exp\left[-\left(\frac{v}{u(t)}\right)^{\alpha(t)}\right]\frac{\alpha(t)}{u(t)}\left(\frac{v}{u(t)}\right)^{\alpha(t)-1} \quad (4)$$

3 VULNERABILITY

The following vulnerability analysis is the second stage in the risk assessment, which refers to estimating the probability of failure of coastal bridges against the given typhoon hazard. In structural safety analysis, structural failure typically occurs when the demand exceeds capacity. The limit state is applied to indicate the boundary between desired and undesired performance, at which the capacity equals to the demand. This paper focuses on the predominant deck unseating failure mode for simply supported coastal bridges during typhoons. Deck unseating failure takes place when the capacity of bridge superstructure at supports (capacity C) fails to resist the uplift forces (demand D) caused by storm wave loadings. Therefore, the probability of failure can be written as

$$P_f = P[(C-D) < 0] \quad (5)$$

Deck unseating occurs when the typhoon-induced uplift forces unseat the superstructure vertically and horizontal wave forces dislocate the deck from substructure. These loadings can be determined from both computational modeling and empirical methods. The computational approach refers to the computational fluid dynamic (CFD) method, which gives numerical simulations of three-dimensional hydrodynamic modelling. CFD program can be adopted to analyze the wave structure interactions such as computing the wave-induced forces on bridges decks. Jin and Meng (2011) conducted a study using CFD software Flow-3D to investigate wave forces on the superstructure of coastal bridges but stated that this CFD method was relatively time-consuming. A two-dimensional potential flow modeling was proposed alternatively in their research. Seiffert *et al.* (2014) later suggested a CFD program OpenFOAM calculating solitary wave forces on bridge decks based on the theory of Euler equations. However, for the probabilistic analysis, this numerical method is not computationally efficient to obtain the probability of failure.

Hydrostatic empirical relations were introduced at an early stage by Wang (1970), Overbeek and Klabbers (2001) and McConnell *et al*. (2004). Similar estimations for the vertical uplift and horizontal forces were developed by Douglass *et al.* (2006) depending on the maximum water level elevation and deck clearance height. Americana Association of State Highway and Transportation Officials developed guide specifications for bridges vulnerable to coastal bridges (AASHTO 2008) and this guidance presented a series of equations calculating maximum vertical force, maximum horizontal force and the corresponding overturning moment. This paper adopts AASHTO model to estimate the wave-induced forces upon a bridge.

The vertical loading on bridge superstructure contributes to deck unseating failure. According to AASHTO, the maximum quasi-static vertical force can be computed. The significant wave height and wave period are required values to compute the demand of bridge deck. These two items are characterized by different geographical locations and are replied on fetch length, average water depth and wind stress factor. Experimental studies conducted by AASHTO gives the relationship between the significant wave height and the maximum wave height. Thus, the uplift demand on bridge is the sum of the maximum quasi-static vertical force and vertical slamming force, while the capacity purely equals to the weight of the structure if there are no additional retrofitting measures provided for bridges vulnerable to typhoon loads. The limit state function for the deck unseating failure of coastal bridge is

$$g_{typhoon} = F_w - \left(F_{v-\max} + F_s\right) \quad (6)$$

where F_w is self-weight; $F_{v\text{-}max}$ is maximum quasi-static vertical load; and F_s is vertical slamming force. As stated in the last section, the typhoon wind speed follows a Weibull distribution, which means the demand of bridge varies with the hurricane wind speed and eventually results in the change of probability of failure of the bridge system. This vulnerability model associated with typhoon wind speed aims to characterize the potential of occurrence of bridge deck unseating damage caused by typhoon winds. Monte-Carlo simulation is then applied to this limit state function to obtain the probability of failure

4 LIFE-CYCLE LOSS

The annual risk and life-cycle loss assessment of bridges under hazards is presented in this section. Probability-based evaluation of the typhoon hazard consequences is the last stage of a risk assessment, which is significantly essential for insurers and policy makers to manage the risk loss of coastal communities. Poisson process model is commonly used to model the typhoon arrival process, which consists of homogenous and nonhomogeneous computation

methods. The major difference between these two methods is the definition of occurrence rate (storm arrival frequency in this case, described as intensity function). The homogeneous approach defines a stationary occurrence rate in the Poisson process, while the nonhomogeneous approach gives a time-variant occurrence rate. Details will be provided in formulas with explanation in this section. In both approaches, life-cycle damage loss of bridge under typhoon hazard is considered over the lifespan of the structure. It is assumed that the post-hazard bridges are completely reconstructed to the pre-damage state before the next typhoon event. Since the distribution type of the damage loss is uncertain, expectation, standard deviation (SD) and coefficient of variation (COV) of the total loss are focused to identify the characteristics of this probability distribution. It is defined total time of interest equals to the lifespan of the bridge. Each storm that happens within this time horizon has an index notation. All the future damage loss is transformed into present value through a discount rate. The total annual hazard loss is computed by summing up all the metrics associated with repair, time, fatalities, operating, and environmental losses. Accordingly, the annual total hazard loss can be computed as (Dong *et al.* 2013)

$$L_{tot}(t) = L_{REP}(t) + L_{OL}(t) + L_{TL}(t) + L_{FA}(t) + L_{ENV}(t) \quad (7)$$

where L_{REP} is annual repair loss; L_{OL} is annual operation loss; L_{TL} is annual time loss; L_{FA} is annual fatalities loss; and L_{ENV} is annual environmental loss of a bridge subjected to a hazard. Generally, there are both aleatoric and epistemic uncertainties involved in hazard assessment and consequence evaluation (Ang and Tang 2007). These uncertainties should be considered in this probabilistic total loss assessment framework. Given the distribution parameters, these random variables can be generated using MATLAB (MathWorks 2014). By performing numerical simulation, the expected value and dispersion of the sustainability metrics can be obtained. Considering the time effects on structural performance, the total life-cycle hazard loss can be computed as (Dong and Frangopol 2017a)

$$LCL_T = \sum_{i=1}^{N(T_{\text{int}})} L_{tot}(t_k) \cdot e^{-rt_k} \quad (8)$$

where T_{int} is the investigated time interval (years); $N(T_{int})$ is the random number of events that occur during time interval T_{int} and expected value of $N(T_{int})$ equals λT_{int}; λ is the mean occurrence rate of hazard; $L_{tot}(t_k)$ is the expected total loss at time t_k under hazard; and r is the constant monetary discount rate. The relation between $L_{k,tot}$ and time t can be computed. Subsequently, the total life-cycle loss can be compute.

Given to the homogeneous Poisson process, occurrence of typhoon is modeled with a stationary (time-independent) occurrence rate. The expectation becomes

$$E[TL(t_{\max})] = \frac{\lambda E[L]}{\alpha}[1 - e^{-\alpha t_{\max}}] \quad (9)$$

and the standard deviation gives (Dong and Frangopol 2017b)

$$SD[TL(t_{\max})] = \sqrt{\frac{\lambda E[L^2]}{2\alpha}[1 - e^{-2\alpha t_{\max}}]} \quad (10)$$

The nonhomogeneous Poisson process analysis is applied to model the typhoon arrival when the effect of climate and built environment changes are considered. This approach is with a time-variant occurrence rate. The expectation and standard deviation of the nonhomogeneous case are

$$E[TL(t_{\max})] = \frac{\int_0^{t_{\max}} \lambda(t)dtE[L]}{\alpha t_{\max}}[1 - e^{-\alpha t_{\max}}] \quad (11)$$

and the standard deviation gives

$$SD[TL(t_{\max})] = \sqrt{E[TL({t_{\max}}^2)] - (E[TL(t_{\max})])^2} \quad (12)$$

5 NUMERICAL EXAMPLE

The proposed framework is applied to an existing highway bridge. The time-variant annual hazard loss and life-cycle loss of this two-span concrete simply supported bridge is investigated throughout its service life. The bridge is located at the intersection of Bailey Ave. and US Highway 101. The bridge has two spans of equal length (47.3 *m*) and carries two lanes of traffic in each direction. The schematic layout of the bridge, with the length of 94.6 *m* and the width of 19.2 *m*, is shown in Figure 2. The lifetime is assumed to be 75 years. The failure mode considered in this paper assumes that failure occurs at the deck or/and any two neighboring girders.

According to the proposed risk assessment framework, hazard and vulnerability analysis are conducted based on the introduced methodology. The probability of deck unseating failure of bridge in terms of the given typhoon hazard is computed as 0.005. As for the life-cycle consequences assessment, there are also several preliminaries to be addressed. The deck unseating damage cost equals to the replacement of superstructures with a value of US$ 1,283,200 since deck unseating failure is measured as the only failure mode. In Poisson process model, the item of damage loss is a random variable. Hence, the damage loss equals to the product of deck unseating loss and the probability of deck unseating failure. Another key element in the typhoon-induced bridge loss estimation is the occurrence rate, which refers to the intensity function of the Poisson

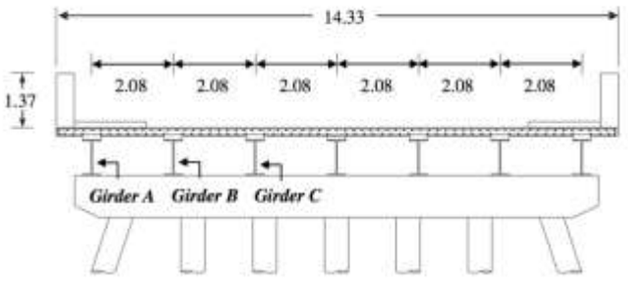


Figure 2. Section view of the bridge under investigation

process. Previous research gave limited evidence to demonstrate the specific correlation between typhoon frequency and time, thus a linear relationship is assumed for the intensity function, with an initial occurrence rate of 0.245/year. This intensity function assumes typhoon frequency increases by 5% over a period of 100 years. A constant discount rate is taken as 3% to transfer the future damage loss to the present. Given the design period of 70 years for the bridge, major characteristics of life-cycle cost in terms of expectation, standard deviation and coefficient of variation are shown in Table 1. In both homogeneous and nonhomogeneous cases, the COV values are larger than 1, which indicates the probability distribution of damage loss is high-variance. In reliability analysis, robustness adaptation is required for further research.

Table 1. Expectation, standard deviation and COV of the proposed life-cycle cost estimation

Occurrence model	Expected US $	Standard deviation US $	Coefficient of variation (COV)
Homogeneous	45,981	49,084	1.06
Nonhomogeneous	126,448	142,788	1.13

6 CONCLUSIONS

This paper proposes a framework to develop costal bridges vulnerable to typhoons based on the probabilistic life-cycle assessment in hazard, vulnerability and consequences evaluation aspects. A typical simply supported bridge was investigated. The proposed analytical approach successfully estimated typhoon-induced consequences by identifying the main distribution characteristics of the damage loss of an existing bridge. This approach could further provide insurers and policy-makers references to manage bridges against typhoon risks in coastal regions. The expected bridge life-cycle cost showed a high-variance distribution, which requires further robustness adaptation investigations to address this issue. Further work can be performed associated with uncertainties of the proposed model by introducing uncertainty indicator to quantifying the distribution type. Additionally, optimization management of bridges can be further conducted after this life-cycle assessment to mitigate the consequence loss during typhoons.

ACKNOWLEDGEMENTS

The study has been supported by The Hong Kong Polytechnic University under Start-Up Fund (1-ZE7Q) is gratefully acknowledged. The opinions and conclusions presented in this paper are those of the authors and do not necessarily reflect the views of the sponsoring organization. The opinions and conclusions presented in this paper are those of the authors and do not necessarily reflect the views of the sponsoring organization.

REFERENCES

AASHTO. (2008). *AASHTO guide specifications for bridges vulnerable to coastal storms*. Washington, DC.

Dong, Y., Frangopol, D.M., and Saydam, D. (2013). Time-variant sustainability assessment of seismically vulnerable bridges subjected to multiple hazards. *Earthquake Engineering and Structural Dynamics*, 42(10), 1451-1467.

Dong, Y., and Frangopol, D.M. 2015. Risk and resilience assessment of bridges under mainshock and aftershocks incorporating uncertainties. *Engineering Structures*, 83, 198-208.

Dong. Y., and Frangopol, D.M. (2017a). Probabilistic life-cycle cost-benefit analysis of portfolios of buildings under flood hazard. *Engineering Structures*, 142, 290-299.

Dong, Y., and Frangopol, D.M. (2017b). Adaptation optimization of residential buildings under hurricane threat considering climate change in a life-cycle context. *Journal of Performance of Constructed Facilities*, 31(6), 04017099, 1-10.

Douglass, S.L., Chen, Q., Olsen, J.M., Edge, B.L., and Brown, D. (2006). *Wave forces on bridge decks*. Coastal Transportation Engineering Research and Education Center, Univ. of South Alabama, Mobile, Ala.

Elsner, J.B., and Bossak, B.H. (2001). Bayesian analysis of U.S. hurricane climate. *J Clim* 14:4341–4350.

Emanuel, K. (2008). The hurricane-climate connection. *Bull Amer Meteor Soc* 89: ES10–ES20.

Elliott, R.J.R., Strobl, E., and Sun, P. (2015). The local impact of typhoons on economic activity in china: a view from outer space. *J Urban Econ* 88:50–66.

Frangopol, D.M. (2011). Life-cycle performance, management, and optimization of structural systems under uncertainty: accomplishments and challenges. *Structure and Infrastructure Engineering*, 7(6), 389-413.

Graumann, A., Houston, T., Lawrimore, J., Levinson, D., Lott, N., McCown, S., Stephens, S., and Wuerts, D. (2005). Hurricane Katrina: A climatological perspective-Preliminary report. *Technical Rep. No. 2005-01*, NOAA's National Climate Data Center, Washington, D.C.

Jin, J., and Meng, B. (2011). Computation of wave loads on the super- structures of coastal highway bridges. *Ocean Eng.*, 38(17–18), 2185–2200.

Kulicki, J.M. (2010). Development of the AASHTO guide specifications for bridges vulnerable to coastal storms.

Proc., 5th Int. Conf. on Bridge Maintenance, Safety and Management, *IABMAS 2010*, 2837–2844.
Knutson, T.R., McBride, J.L., Chan, J., Emanuel, K., Holland, G., Landsea, C., Held, I., Kossin, J.P., Srivastava, A.K., and Sugi, M. (2010). Tropical cyclones and climate change. *Nature Geoscience*, 3(3), pp.157-163.
Lin, N., and Shullman, E. (2017). Dealing with hurricane surge flooding in a changing environment: part I. Risk assessment considering storm climatology change, sea level rise, and coastal development. *Stochastic Environmental Research and Risk Assessment*, pp.1-22.
McConnell, K., Allsop, W., and Cruickshank, I. (2004). *Piers, jetties and related structures exposed to waves: guidelines for hydraulic loadings*. Thomas Telford.
Overbeek, J., and Klabbers, I.M. (2001). Design of jetty decks for extreme vertical wave loads. *In Ports' 01: America's Ports: Gateway to the Global Economy*, pp. 1-10.
Onof, C., Chandler, R.E, Kakou, A., Northrop, P., Wheater H.S., and Isham, V. (2000). Rainfall modelling using Poisson-cluster processes: a review of developments. *Stoch Environ Res Risk Assess* 14(6):384–411.
Ross, S.M. (2000). Introduction to probability models. Academic press.
Simiu, E., and Scanlan, R.H. (1996). Wind effects on structures. Wiley.
Simiu, E. (2011). Design of buildings for wind: A guide for ASCE 7-10 standard users and designers of special structures. John Wiley & Sons.
Seiffert, B., Hayatdavoodi, M., and Ertekin, R. C. (2014). 'Experiments and computations of solitary-wave forces on a coastal-bridge deck. Part I: Flat plate', Coastal Engineering 88(June), 194–209.
Vanem, E. (2011). Long-term time-dependent stochastic modelling of extreme waves. *Stoch Environ Res Risk Assess* 25(2):185–209.
Vickery, P.J., Wadhera, D., Galsworthy, J., Peterka, J.A., Irwin, P.A., and Griffis, L.A. (2010). Ultimate wind load design gust wind speeds in the United States for use in ASCE-7. *Journal of structural engineering,* 136(5), pp.613-625.
Wang, H. (1970). Water wave pressure on horizontal plate. *Journal of the Hydraulics Division*, ASCE 96(10), 1997–2016.
Wang, C., Zhang, H., Feng, K., and Li, Q. (2017). Assessing hurricane damage costs in the presence of vulnerability model uncertainty. *Natural Hazards*, 85(3), pp.1621-1635.
Webster, P.J., Holland, G.J., Curry, J.A., and Chang, H.R. (2005). Changes in tropical cyclone number, duration, and intensity in a warming environment. *Science*, 309(5742), pp.1844-1846.
Yeo, D., Lin, N., and Simiu, E. (2013). Estimation of hurricane wind speed probabilities: Application to New York City and other coastal locations. *Journal of Structural Engineering*, 140(6), p.04014017.

Maintenance, Safety, Risk, Management and Life-Cycle Performance of Bridges – Powers, Frangopol, Al-Mahaidi & Caprani (Eds)
© 2018 Taylor & Francis Group, London, ISBN 978-1-138-73045-8

Climate change and potential impact on the seismic vulnerability of highway bridge structures

M. Mortagi & J. Ghosh

Department of Civil Engineering
Indian Institute of Technology Bombay, India

ABSTRACT: The past decade has witnessed significant research progress towards quantifying the seismic vulnerability of aging highway bridges. However, majority of existing literature assumes deterioration rate to be independent of the repercussions stemming from climate change along the bridge service life. In this regard, recent advances on this topic indicate a potential time-dependent shift in average temperature and relative humidity that may influence the degradation mechanism of structural members. Consequently, the influence of climate change on the seismic fragility of bridges need to be evaluated. This study proposes a framework to evaluate the vulnerability of highway bridges under different scenarios considering earthquake hazard, aging and deterioration, and global warming due to climate change. Results reveal that throughout the lifetime of the bridges, the seismic vulnerability consistently increases due to corrosion deterioration and the effect is further pronounced when the influence of potential climate change is incorporated within the fragility assessment methodology.

1 INTRODUCTION

Global warming and climate change are considered as a passive sides of the continued increase in the emissions of greenhouse gases, such as carbon dioxide (CO_2). Recently, soon after the industrial revolution, CO_2 concentration has substantially increased by approximately 0.5% per year (Yoon at el. 2007). Present studies in this area have shown that, increasing level of CO_2 emissions may lead to a rise in temperature (Stewart & Deng 2014). For instance, Peters at al. (2013) shows that by the year 2100 the mean temperature may increase by 4-5°C if the CO_2 emissions continue to record at the high end of emissions scenarios. There are different scenarios to estimate and define the future climate change according to the intergovernmental panel on climate change (IPCC 2007). These scenarios are represented in different categories according to the CO_2 emissions which relate to changes in population growth rate, economy, energy and technology (Stewart et al. 2012). The increase of atmospheric CO_2 concentration has a direct influence on the increase of carbonation depth and temperature that may increase the corrosion rate for carbonation induced corrosion (Stewart et al. 2010). For instance, Zhou et al. (2014) used the CO_2 diffusion as a coefficient in calculating the carbonation depth in their model. On the other hand, the CO_2 emissions and an associated increase of atmospheric temperature may also indirectly influence chloride induced corrosion due to an increase of atmospheric temperature, as elaborated next.

Past research on chloride induced corrosion deterioration of reinforced concrete structures has underlined the sensitivity of chlorides ingress in the concrete matrix to increase in temperature and humidity (Xi et al. 1999, Chen et al. 2006). Accounting for such effects within the climate change context is particularly important since global warming may lead to a time-dependent shift in average temperature and relative humidity (Bastidas-Arteaga et al. 2010, 2013, Stewart et al. 2011, 2012). Until now, a majority of existing literature on chloride induced corrosion assumes a constant or time-dependent deterioration rate that is independent of variations in temperature and humidity along the bridge service life. Recently, Bastidas-Arteaga et al. (2010, 2013) adopted a stochastic approach to demonstrate the impact of global warming and weather effects on chloride ingress in concrete. Using future projections of climate change manifested through alterations in temperature and relative humidity, these studies estimated the increased likelihood of deterioration in aging structures. While these future projections were studied under the "expected" and "pessimistic" climate change scenarios, sub-categories such as seasonal variation effects were also accounted for. Stewart et al. (2011) considered the CO_2 concentration and temperature as the main factors in increasing concrete deterioration and damage risks to different structures. It was found that, due

to climate change and global warming, the damage risks due to chloride induced corrosion increase by approximately 10%.

The primary focus of this paper involves the impact assessment of potential climate change effects on the seismic fragility curves of highway bridge located in moderate to high seismic zones. While recent investigations by Choe et al. (2008 , 2009), Ghosh & Padgett (2010), among others, have underlined the marked increase of seismic fragility due to corrosion deterioration, the individual influence of projected temperature and humidity changes needs further exploration.

To achieve the above objective, the impact of lifetime environmental exposures such as temperature change, humidity and chloride concentration on the corrosion initiation time and corrosion rates is considered first. Next the impact of climate change is demonstrated on the fundamental equations governing corrosion deterioration. Furthermore, based on a future climate change scenario, the influence of aging and climate change is estimated on the column seismic performance of a case-study multi-span continuous steel girder bridge (MSC steel girder bridge) located in the Central and Southeastern United States as illustrated in Section 4. The paper ends with conclusions and recommendations for future work.

2 CHLORID INDUCED DETERIORATION MODELING

Deterioration of reinforced concrete (RC) structures, especially bridges, resulting from chloride induced reinforcement corrosion has been observed as one of the most significant durability problems. Sources of chlorides may stem from application of the deicing salts, particularly in cold regions or proximity to the marine atmosphere. Common manifestations of this deterioration mechanism includes, but are not restricted to, the following:

1. Reduction in steel cross-section area.
2. Cracking and spalling the cover concrete.
3. Degradation of cover strength.
4. Deterioration of steel-concrete interface bond strength.
5. Decreasing the RC structures service life.

This section briefly describes some of the commonly adopted chloride induced deterioration models to estimate corrosion initiation time and corrosion rates.

2.1 *Corrosion initiation time*

Several studies are available in literature that estimate the corrosion initiation time (t_i) of RC structures exposed to a chloride laden environment (Duracrete 2000, Bertolini et al. 2004, Choe et al. 2009). Based on Fick's second law of diffusion and calibration to laboratory test data, t_i can be calculates as shown in Equation (1):

$$t_i = \left\{ \frac{x^2}{4k_c k_e k_t D_0 (t_0)^{n_{cl}}} \cdot\cdot \left[erf^{-1}\left(1 - \frac{C_{cr}}{C_s}\right)\right]^{-2} \right\}^{\frac{1}{(1-n_{cl})}} \quad (1)$$

where k_e is the environmental factor, k_t is the influence of test methods while estimating the chloride diffusion, k_c is the curing factor, t_0 is the age of concrete when the compliance test is implemented, D_0 is chloride diffusion at t_0, n_{cl} is the age factor, C_s and C_{cr} are surface and critical chloride concentration respectively, and *erf* is the Gaussian error function.

2.2 *Rate of corrosion*

In RC structures, following corrosion initiation a reduction in rebar area is typically observed. This rate of reduction can defined in terms of a corrosion current density, i_{corr}, (in $\mu A/cm^2$) or annual metal loss per unit surface area, $r_{corr,}$ (in $\mu m / year$). The rate of corrosion is sensitive to the surrounding relative humidity. In low humidity, the electrical resistivity of concrete controls $r_{corr.}$ On the other hand, when the ambient humidity is high, r_{corr} is primarily affected by the availability of oxygen at the cathode (Tuutti 1982, Yalsyn et al. 1996, Vu & Stewart 2000, Bastidas-Arteaga 2009). For RC structures, it is often observed that the water cement ratio (*w/c*), cover depth (*x*) and environmental conditions (temperature and humidity) directly or indirectly affect the availability of oxygen to corrode the steel rebars. Based on experimental results, Vu & Stewart (2000) investigated a corrosion rate model (Equation 2) that couples the effect of *w/c* and *x* on the corrosion rate at reference environmental conditions. These reference conditions correspond to a temperature of 20 °C and 75% relative humidity.

$$i_{corr,0} = \frac{37.8(1 - w/c)^{-1.64}}{x} (\mu A / cm^2) \quad (2)$$

where *x* is the cover depth (in *cm*).

A number of studies have reported that r_{corr} is a time-dependent parameter and typically reduces with time owing to the following reasons (Tuutti 1982, Yalsyn et al. 1996, Vu & Stewart 2000, Bastidas-Arteaga 2009, Liu & Weyers 1998):

1. The steel surface rust products reduce the diffusion of iron ions away from the steel surface.
2. The reduction of the ratio among the cathode and anode.

According to Liu & Weyers (1998) data, a time dependent model for r_{corr} was developed by Vu & Stewart (2000), as represented in Equation (3).

$$i_{corr}(t_p) = i_{corr,0} \times 0.85 \times t_p^{-0.29} \quad (3)$$

where t_p is time from corrosion initiation and $i_{corr,0}$ can be evaluated by Eq. (2).

2.3 *Time-dependent reduction in embedded steel area*

The reduced diameter of the reinforcement bar at time t after initiation time, can be computed as (Stewart et al. 2010):

$$d(t) = d_0 - 0.0232 \int_{t_i}^{t} i_{corr}(t)dt \quad (4)$$

where d_0 is the initial diameter (in mm). Consequently, the area of reinforcement steel, for equal diameter bars, according to uniform corrosion can be estimated as:

$$A(t) = \begin{cases} n d_0^2 \dfrac{\pi}{4} & for\ t \le t_i \\ n(d(t))^2 \dfrac{\pi}{4} & for\ t_i < t < t_i + (d_o / r_{corr}) \\ 0 & for\ t \ge t_i + (d_o / r_{corr}) \end{cases} \quad (5)$$

3 CHLORIDE INDUCED DETERIORATION MODELING CONSIDERING THE INFLUENCE OF CLIMATE CHANGE

This section of the paper will highlight the likely influence of climate change on the basic corrosion deterioration models elaborated in the previous section.

3.1 *Influence on Initiation time*

Recently, multiple researchers have investigated the effect of environmental conditions, i.e. temperature (T) and relative humidity (RH), on initiation time due to chloride induced corrosion. For instance, a model of initiation time which couples the T and RH effects was reported by Allampallewar et al. (2008), El Hassan et al. (2010). This model is represented as:

$$t_i = \left\{ \frac{x^2}{4D_c(T,RH)(t_0)^{n_{cl}}} \cdot\cdot \left[erf^{-1}\left(1 - \frac{C_{cr}}{C_s}\right)\right]^{-2} \right\}^{\frac{1}{(1-n_{cl})}} \quad (6)$$

where $D_c(T,RH)$ *is expressed as:*

$$D_c(T,RH) = D_{c,ref}\ F_1(T) F_2(RH) \quad (7)$$

where $D_{c,ref}$ is the chloride diffusion at reference condition, reference temperature (20 °C) and humidity (RH=100%) (Allampallewar et al. 2008, Nielsen et al. 2003, El Hassan et al. 2010). The factors $F_1(T)$ and $F_2(RH)$ are represented in Equations (8) and (9).

$$F_1(T) = \exp\left[\frac{U_c}{R}\left(\frac{1}{T_{ref}} - \frac{1}{T}\right)\right] \quad (8)$$

$$F_2(RH) = \exp\left[1 + \frac{(1-RH)^4}{(1-RH_c)^4}\right]^{-1} \quad (9)$$

where U_c and R are the activation energy of chloride diffusion process (in kJ/mol) and the gas constant (8.314 J mol^{-1} K^{-1}) respectively, T_{ref} and RH_c are the reference temperature taken as *296 K* (20 °C*)* and reference humidity at which $D(RH_c)$ = 0.5D(100%) (Nielsen et al. 2003), taken as 0.75, T is the current absolute temperature of concrete (K) and finally, RH is the pore relative humidity.

3.1.1 *Improved corrosion initiation time model*

In this paper, the corrosion initiation time is estimated according to Eq. (7) after accounting for the environmental conditions. So, the initiation time model couples the effect of time, temperature, humidity and the environmental condition as shown in Equation (10).

$$t_i = \left\{ \frac{x^2}{4k_e k_c k_t D_c(T,RH)(t_0)^{n_{cl}}} \cdot\cdot \left[erf^{-1}\left(1 - \frac{C_{cr}}{C_s}\right)\right]^{-2} \right\}^{\frac{1}{(1-n_{cl})}} \quad (10)$$

3.2 *Rate of corrosion*

In the present work, the effects of temperature, relative humidity and chloride concentration on the rate of corrosion are incorporated besides the effect of w/c, cover and time as shown in Equation (11) (Guo 2011)

$$i_{corr}(t) = \frac{37.8(1-w/c)^{-1.64}}{x} \times 0.85 \ldots \ldots \times t_p^{-0.29} \times f_{RH} \times f_T \times f_{Cl} \quad (11)$$

where f_T, f_{RH} and f_{Cl} are the temperature, relative humidity and chloride factor respectively.

The next sections will illustrate the impact of temperature (f_T), relative humidity (f_{RH}) and chloride concentration (f_{Cl}) on the rate of corrosion. One should note that the *w/c* and *x* are assumed to be 0.5 and 38.1 mm, respectively.

3.2.1 *Influence of temperature on corrosion rate*

Past research indicates an increase in corrosion rate at elevated temperatures. For instance, Stewart et al. (2011) note that an increase in temperature by 2 °C may cause an increase in the corrosion rate up to 15%. The relationship between temperature and corrosion rate has also been investigated by Duracrete (2000) as shown in Equations 12 and 13. This model underlines the influence of temperature on corrosion rate at reference test temperature of 20 °C ($i_{corr,20}$)

$$i_{corr} = i_{corr,20}\left[1 + K\left(T(t) - 20\right)\right] \tag{12}$$

where

$$K \begin{cases} 0.025 & if \quad T(t) < 20° \\ 0.073 & if \quad T(t) > 20° \end{cases} \tag{13}$$

Another model describing this relationship was reported by Pour- Ghaz et al. (2009) and Virmani et al. (1983) as:

$$i_{corr} = i_{corr,20} \times f_T \tag{14}$$

where

$$f_T = e^{2283\left(\frac{1}{284} - \frac{1}{T}\right)} \tag{15}$$

where T is the temperature in *Kelvin*.

Figure 1 illustrates the effects of these models on the rate of corrosion. The present work considers he second model for computing the temperature factor.

3.2.2 *Influence of humidity on corrosion rate*

Past experiments by researchers have revealed that when the RH of concrete is less than 50%, the corrosion rate is low and below 35% rust formation halts owing to the high electrical resistance of concrete. On the other hand, corrosion rate is found to be highest between 70% to 90% RH. Additionally, while, there is an exponentially increase in corrosion rate from 50% to 70% RH, there is a rapid drop from 90% to full saturation (Balafas et al. 2010). This primarily occurs because at very high relative humidity, the rate at which oxygen reaches the surface of reinforcement is typically low (Balafas et al. 2010). Based on these observations, the RH factor f_{RH} can be estimated as shown in Equation 16 and demonstrated in Figure 2 (Guo 2011):

$$f_{RH} = e^{-6000\,(RH - 0.75)^6} \tag{16}$$

The relationship between corrosion rate, T and RH, according to Eq. (11), is presented in Figure 3.

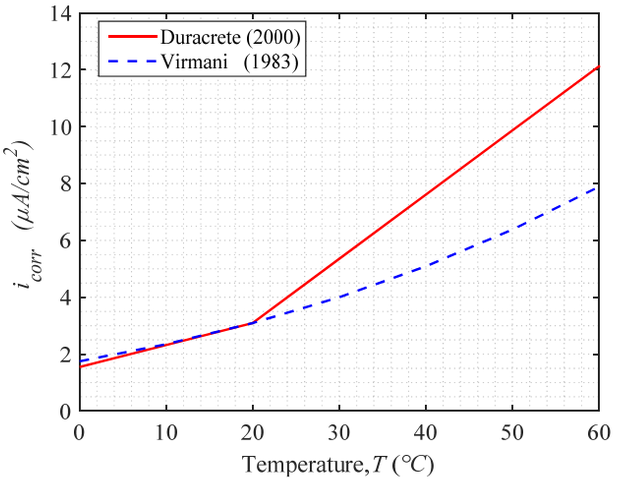


Figure 1. Variation of corrosion rate with temperature.

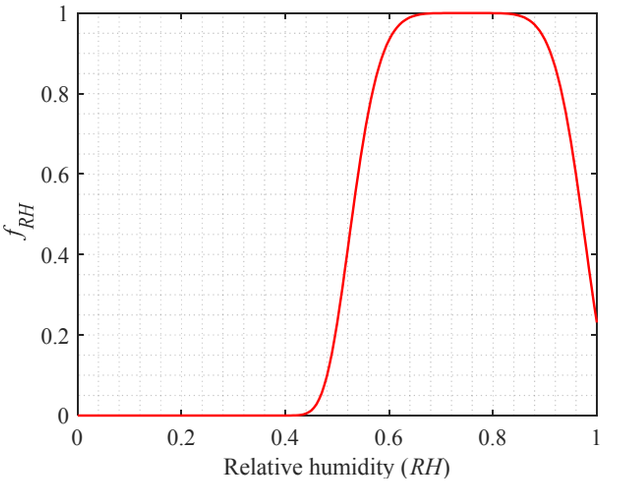


Figure 2. Variation of the relative humidity factor f_{RH} (t) with relative humidity (RH) (Guo 2011).

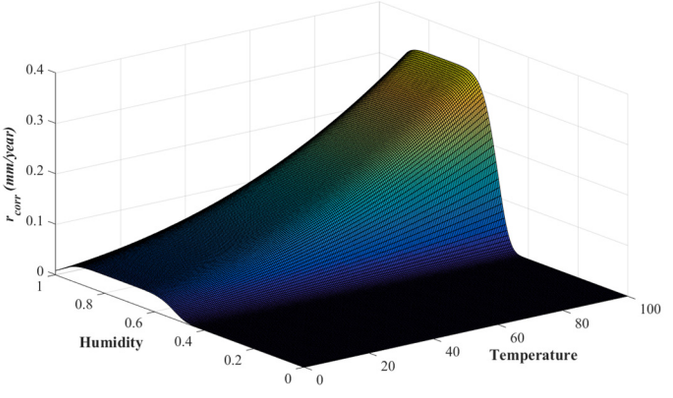


Figure 3. Joint impact of Temperature (T) and Relative Humidity (RH) on corrosion rate (r_{corr})

3.2.3 *Influence of chloride concentration (Cl) on corrosion rate*

Besides assessing the influence of climate change alone, this study also investigates the increase in chloride concentration at the rebar interface along the service life of the structure. The increase in chloride concentration can result in an increase of corrosion rate (Liu & Weyers 1998). This primarily occurs due to the increase in concrete conductivity following an increase in chloride concentration. Besides, in the corrosion process, chlorides accelerate the electrochemical reactions by altering the concrete resistivity when the chloride concentration at the steel surface reaches to the critical chloride concentration. Consequently, the chloride factor, f_{Cl}, can be estimated according to chloride concentration, Cl, and the critical chloride concentration (C_{cr}). The chloride factor can be computed, based on the Liu & Weyers (1998) approach, as follows (Guo 2011):

$$f_{Cl} = \frac{Cl + C_{cr}}{2C_{cr}} \tag{17}$$

Figure 4 shows the estimated chloride factor, f_{Cl}, following initiation time.

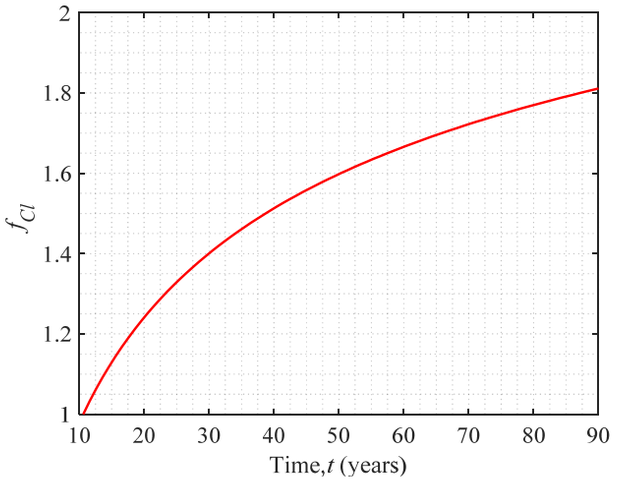


Figure 4. Variation of the chloride factor, f_{Cl} over the time.

4 SEISMIC FRAGILITY UNDER CLIMATE CHANGE

In the past, little attention has been paid to the impact assessment of climate change on the seismic vulnerability of bridge structures. This section investigates the effect of climate change on the seismic behavior of deteriorating multispan continuous steel girder bridge located in South Carolina within Central and Southeastern US (CSUS). This study assumes the corrosion induced deterioration to be localized within the bridge columns, although other studies have underlined potential deterioration of other bridge components, such as bearings (Lindquist 2008).

4.1 *Bridge characteristics and modeling*

The general description of the geometric configuration of the bridge is given in Figure 5. The bridge consists of three spans of 25.10 m length and deck width of 9.53 m. The bridge has two bents, each bent with two columns of 3.93 m height. The column section is 914.4 mm in diameter with 12 #29 (25.58 *mm* diameter) rebars. The finite element modeling of the bridge is developed using OpenSees, following the recommendations by Nielson (2005). The model also considers the uncertainty of the modeling parameter, i.e. yield strength of steel and concrete, bridge component behavior, mass, damping, loading direction. The uncertainty of these parameters and their probability distributions are adopted in this study from Nielson (2005). For nonlinear time history analysis, the two synthetic suites of ground motions developed by Wen & Wu (2001) and Rix & Fernandez (2004) are used to evaluate the bridge seismic performance as adopted by other researchers in the past for bridges in CSUS (Nielson 2005, Padgett 2007).

4.2 *Climate change scenario and environmental conditions*

This study considers three scenarios for vulnerability evaluation: without climate change, expected climate change scenario and pessimistic climate change scenario. Bastidas-Arteaga et al. 2010 defined these scenarios for a period of 100 years as a reference period. For expected scenario, the temperature and relative humidity increases up to 2.5 °C and 5% from reference values, while for the pessimistic scenario, the change in temperature and relative humidity increases up to 6.5 °C and 10 % respectively. For the considered case study bridge location (Charleston, South Carolina, USA), the initial environmental conditions i.e. temperature and relative humidity are assumed to be 19 °C and 73% (see Figure 6) as per past recorded data (U.S. climate data). Figure 7 illustrates the impact of these different conditions on the corrosion rate. The modeling parameters associated with the corrosion initiation time calculated as 10.63 years using Equation 10, can be found in Duracrete (2000) and Choe et al. (2008).

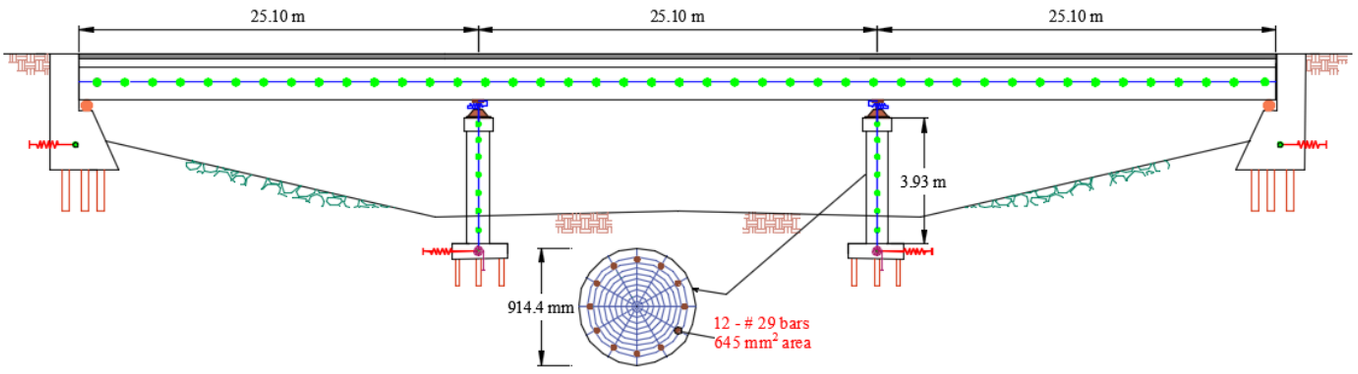


Figure 5. Elevation view of the 3-D nonlinear analytical finite element model of the case-study MSC steel girder bridge.

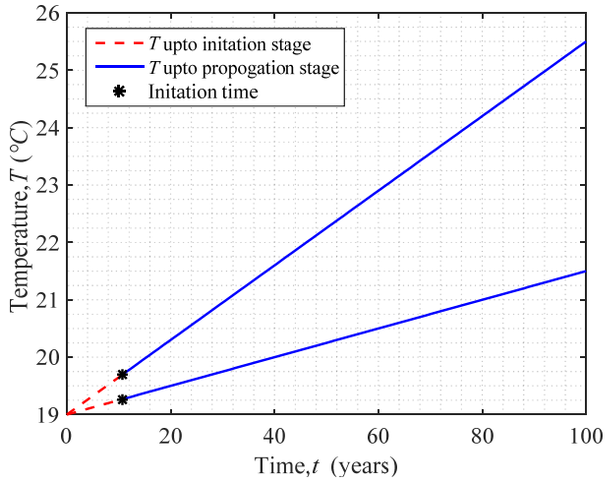


Figure 6. Increase in temperature for two scenarios (expected and pessimistic) along the service life (100 years) of the bridge.

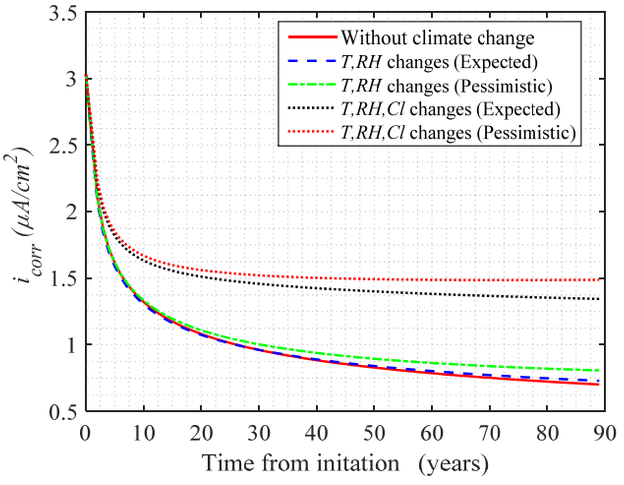


Figure 7. The corrosion rate for the considering case studies.

4.3 *RC bridge column deterioration*

4.3.1 *Loss of reinforcing steel area*

As a consequence of time-dependent corrosion of the RC column, the area of steel bars reduce throughout the lifetime of the bridge. The area loss of reinforcing steel is computed for different climate change cases assuming uniform time-dependent corrosion deterioration model along with a coefficient of variation (COV) of 0.2.

4.3.2 *Reduction in cover concrete strength*

The cracking of concrete cover is caused by the internal tensile forces from the accumulation of expansive rust products. The internal strength is generated as a result of expansive rust products and it leads to various problems. For instance, the formation of cracks leads to an acceleration of corrosion rate and a reduction in the steel cross-section. Furthermore, it may cause a loss in the structure ductility and a reduction in the concrete cross-sectional area (Rao et al. 2016). The model used to estimate the reduction in cover strength is adopted from Rao et al. (2016) and can be expressed as:

$$f_{co}^{*}(t) = \frac{f'_{co}}{1 + \dfrac{0.31416\ \varepsilon_{co} n_{bars}\left[D_{in} - D(t)\right]}{D_{col}}} \tag{18}$$

where f'_{co}, ε_{co} are the peak compressive stress and its corresponding strain respectively, n_{bars} is the number of bars, D_{col} is the undamaged column width, $D(t)$ is the diameter of corroded steel bars and D_{in} is the initial diameter of the steel bars. Details on the reduction in cover strength and the definitions of theses parameters can be found in Rao et al. (2016). The results show a significant decrease in cover concrete strength up to 80% for the time-dependent corrosion model, increasing to 82.7% when temperature and humidity effects are considered and up to about 88% when the influence of chloride concentration is accounted.

4.4 *Seismic fragility of case-study bridge columns under varying case-study conditions*

The seismic fragility curves for bridge columns are developed considering the same approach as mentioned in Nielson & DesRoches (2007). This research focused on estimating the seismic fragility curves for bridge column only, while leaving impact assessment

of climate change on bearings and overall bridge system as future work. To carry out the probabilistic analysis, first nonlinear time history analysis is conducted to develop probabilistic seismic demand models are estimated using linear regression. These demand models are compared with the lognormal limit state capacities of the column for different damage state, i.e. slight, moderate, extensive, and complete, to develop seismic fragility curves as (Nielson & DesRoches 2007):

$$P\left[DS > ds \middle| IM \right] = \Phi\left[\frac{\ln(IM) - \lambda}{\zeta} \right] \quad (19)$$

where $P\left[DS > ds \mid IM \right]$ is the conditional probability of exceeding damage state (DS) for given intensity measure of ground motion (IM) that is taken as peak ground acceleration (PGA), λ and ζ are the natural logarithm of the median IM value and the dispersion parameter for the bridge component fragility, and $\Phi[\cdot]$ is the standard normal probability integral.

Addressing the present purpose, the vulnerability of the bridge under a multi-hazard threat scenario considering earthquake hazard, aging and deterioration, and global warming due to climate change is evaluated. The seismic fragility curves are developed for six different scenarios listed as follows:

1. As-built (no corrosion).
2. Time-dependent (t) corrosion only (No impact of T, RH, Cl concentration)
3. Time, T and RH (Expected scenario).
4. Time, T and RH (Pessimistic scenario).
5. Time, T, RH, Cl concentration (Expected).
6. Time, T, RH, Cl concentration (Pessimistic).

For the above scenarios, Figure 8 shows the seismic fragility curves at 100 years for the case-study bridge column corresponding to the complete damage state. A preliminary review across all cases and damage states reveals similar dispersions for fragility estimates. Consequently, median estimates are used as an indicator to represent the impact of time-dependent aging (t), temperature (T), relative humidity (RH) and Cl concentration on the fragility estimates. For instance, the results reveal that the median PGA decreases by approximately 13.82 % due to aging compared to pristine conditions. This percentage decreases further to 17.08% if the effect of T and RH are considered according to the expected scenario and to 17.52% for the pessimistic scenario. When considering the effect of Cl concentration in conjunction with T and RH, the reduction in the medians emerge as 19.48% and 20.24% for the expected and pessimistic scenarios, respectively. These results underline the criticality of accounting for the impact of climate change and increasing chloride concentration on the seismic fragility of aging bridge structure.

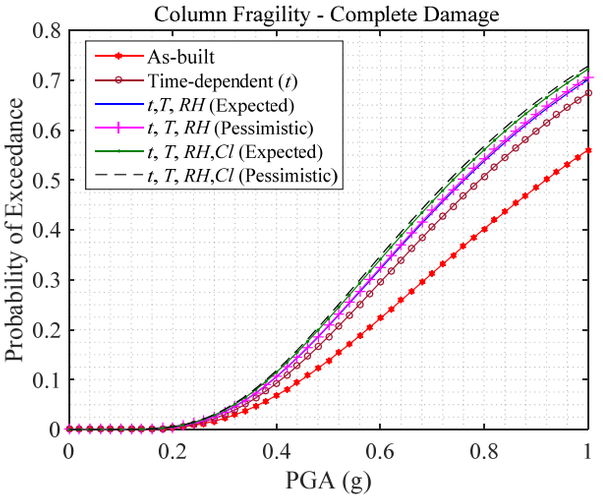


Figure 8. Seismic fragility curves of the bridge columns for different climate change scenarios.

5 CONCLUSIONS

This paper provides a framework to evaluate the vulnerability of highway bridges under a multi-hazard threat scenario considering earthquake hazard, corrosion deterioration, and global warming due to climate change. First, the influence of temperature, relative humidity and the chloride concentration on the rate of corrosion is investigated. Results indicate sensitivity of initial corrosion rate to temperature and relative humidity underlining the need to incorporate these effects within corrosion rate models. Consequently, improved and updated corrosion rate models are used in conjunction with two climate change (expected and pessimistic), to estimate the effect of temperature and humidity on bridge deterioration and subsequent fragility.

For a case-study multispan continuous steel girder bridge located in marine–splash exposure condition within South Carolina, USA a 6.6% reduction in the steel bars diameter is observed for time-dependent aging alone. This percentage further reduces to 8.1% and 12.4% when the effects of climate change (temperature and relative humidity variation), and increasing chloride concentration along with climate change are respectively considered for the pessimistic scenario. One should note that these percentage changes are sensitive to the initial conditions of temperature and relative humidity. In addition to rebar area reduction as a primary manifestation of corrosion deterioration, this study also considers change in cover strength as a secondary effect.

Finally, the impact of aging and climate change on the column seismic performance at the different damage states for the considered case-study is illustrated. For the different climate change scenarios and chloride concentration levels, this study develops seismic fragility curves following a full probabilistic analysis of the case-study bridge that considers uncertainty in ground motions, corrosion parameters, and material and modeling parameters. Results reveal substantial impact of climate change and subsequent increase in chloride concentration across all damage states. For instance, after 100 years of chloride exposure, the median estimates for complete damage state decreases by 13.82% (compared to pristine conditions) due to

time-dependent aging alone. Consideration of temperature and relative humidity effects reveals a further decrease to 17.08% and 17.52% for the expected and pessimistic scenarios respectively. Lastly, considering climate change effects along with increasing chloride concentration leads to a reduction in the median estimates by as large as 19.48% and 20.24% for the expected and pessimistic scenarios, respectively.

6 REFERENCES

Allampallewar, S.B. & Srividya, A., 2008. *Corrosion Performance of Reinforced Concrete Member along Indian Coasts*: Effect of Temperature & Relative Humidity. International Journal of Performability Engineering, 4(3), pp.285-292.

Balafas, I. & Burgoyne, C.J., 2010. *Environmental effects on cover cracking due to corrosion*. Cement and Concrete Research, 40(9), pp.1429-1440.

Bastidas-Arteaga, E., 2009. *Probabilistic service life modeling of RC structures subjected to the combined effect of chloride-induced corrosion and cyclic loading* (Doctoral dissertation, Universidad de los Andes).

Bastidas-Arteaga, E., Schoefs, F., Stewart, M.G. & Wang, X., 2013. *Influence of global warming on durability of corroding RC structures: A probabilistic approach.* Engineering Structures, 51, pp.259-266.

Bastidas-Arteaga, E., Chateauneuf, A., Sánchez-Silva, M., Bressolette, P. & Schoefs, F., 2010. *Influence of weather and global warming in chloride ingress into concrete: A stochastic approach*. Structural Safety, 32(4), pp.238-249.

Bertolini, L., Elsener, B., Pedeferri, P., Redaelli, E. and Polder, R.B., 2013. *Corrosion of steel in concrete: prevention, diagnosis, repair*. John Wiley & Sons.

Chen, D. & Mahadevan, S., 2008. Chloride-induced reinforcement corrosion and concrete cracking simulation. Cement and Concrete Composites, 30(3), pp.227-238.

Choe, D.E., Gardoni, P., Rosowsky, D. and Haukaas, T., 2009. *Seismic fragility estimates for reinforced concrete bridges subject to corrosion.* Structural Safety, 31(4), pp.275-283.

Choe, D.E., Gardoni, P., Rosowsky, D. & Haukaas, T., 2008. *Probabilistic capacity models and seismic fragility estimates for RC columns subject to corrosion.* Reliability Engineering & System Safety, 93(3), pp.383-393.

Duracrete. (2000). *Probabilistic Performance Based Durability Design of Concrete Structures: Final Technical Report*. The European Union – Brite EuRam III

El Hassan, J., Bressolette, P., Chateauneuf, A. & El Tawil, K., 2010. *Reliability-based assessment of the effect of climatic conditions on the corrosion of RC structures subject to chloride ingress.* Engineering Structures, 32(10), pp.3279-3287.

Ghosh, J. & Padgett, J.E., 2010. *Aging considerations in the development of time-dependent seismic fragility curves.* Journal of Structural Engineering, 136(12), pp.1497-1511.

Guo, Y., 2011. *Assessing the seismic performance of corroding RC bridge columns* (Doctoral dissertation).

IPCC. 2007. Climate Change 2007: The Physical Science Basis. Contribution of Working Group I to the Fourth Assessment Report of the Intergovernmental Panel on Climate Change S. Solomon et al. (eds). Cambridge, UK and New York, NY, USA: Cambridge University Press.

Lindquist, L. 2008. "Corrosion of steel bridge girder anchor bolts." MS thesis, Georgia Institute of Technology, Atlanta, Georgia.

Liu, T. & Weyers, R.W., 1998. *Modeling the dynamic corrosion process in chloride contaminated concrete structures.* Cement and Concrete Research, 28(3), pp.365-379.

Nielsen, E.P. & Geiker, M.R., 2003. *Chloride diffusion in partially saturated cementitious material.* Cement and Concrete Research, 33(1), pp.133-138.

Nielson, B.G., 2005. *Analytical fragility curves for highway bridges in moderate seismic zones* (Doctoral dissertation, Georgia Institute of Technology).

Nielson, B.G. & DesRoches, R., 2007. *Analytical seismic fragility curves for typical bridges in the central and southeastern United States*. *Earthquake Spectra, 23(3), pp.615-633.*

Padgett, J.E., 2007. *Seismic vulnerability assessment of retrofitted bridges using probabilistic methods* (Doctoral dissertation, Georgia Institute of Technology).

Peters, G.P., Andrew, R.M., Boden, T., Canadell, J.G., Ciais, P., Le Quéré, C., Marland, G., Raupach, M.R. & Wilson, C., 2013. *The challenge to keep global warming below 2°C*. Nature Climate Change, 3(1), p.4.

Pour-Ghaz, M., Isgor, O.B. & Ghods, P., 2009. *The effect of temperature on the corrosion of steel in concrete. Part 1: Simulated polarization resistance tests and model development.* Corrosion Science, 51(2), pp.415-425.

Rao, A.S., Lepech, M.D., Kiremidjian, A.S. & Sun, X.Y., 2017. *Simplified structural deterioration model for reinforced concrete bridge piers under cyclic loading*. Structure and Infrastructure Engineering, 13(1), pp.55-66.

Rix, G. J. & Fernandez, J. A. (2004). *Earthquake Ground Motion Simulation.*

Stewart, M.G. & Deng, X., 2014. *Climate impact risks and climate adaptation engineering for built infrastructure.* ASCE-ASME Journal of Risk and Uncertainty in Engineering Systems, Part A: Civil Engineering, 1(1), p.04014001.

Stewart, M.G, Wang, X., & Nguyen, M.N. 2012. *Climate change adaptation for corrosion control of concrete infrastructure.* Structural Safety 35(0): p.29–39.

Stewart, M.G., Wang, X. & Nguyen, M.N., 2011. *Climate change impact and risks of concrete infrastructure deterioration*. Engineering Structures, 33(4), pp.1326-1337.

Stewart, M.G. & Peng, J., 2010. *Life-cycle cost assessment of climate change adaptation measures to minimise carbonation-induced corrosion risks.*

Tuutti, K., 1982. Corrosion of steel in concrete.

U.S climate data. "US climate data – Temperature, Precipitation, Sunshine and Snowfall." <https://www.usclimatedata.com/climate/south-carolina/united-states/3210> (Oct. 14, 2107).

Virmani, Y.P., Clear, K.C. & Pasko Jr, T.J., 1983. *Time-to-corrosion of reinforcing steel in concrete slabs. Volume 5. Calcium nitrite admixture or epoxy-coated reinforcing bars as corrosion protection systems.* Report for July 1980-December 1982 (No. PB-84-195239; FHWA/RD-83/012). Federal Highway Administration, Washington, DC (USA).

Vu, K.A.T. & Stewart, M.G., 2000. *Structural reliability of concrete bridges including improved chloride-induced corrosion models.* Structural safety, 22(4), pp.313-333.

Wen, Y.K. & Wu, C.L., 2001. *Uniform hazard ground motions for mid-America cities. Earthquake spectra*, 17(2), pp.359-384.

Xi, Y. & Bažant, Z.P., 1999. Modeling chloride penetration in saturated concrete. Journal of Materials in Civil Engineering, 11(1), pp.58-65.

Yalcyn, H. & Ergun, M., 1996. *The prediction of corrosion rates of reinforcing steels in concrete*. Cement and Concrete Research, 26(10), pp.1593-1599.

Yoon, I.S., Çopuroğlu, O. & Park, K.B., 2007. *Effect of global climatic change on carbonation progress of concrete*. Atmospheric environment, 41(34), pp.7274-7285.

Zhou, Y., Gencturk, B., Willam, K. & Attar, A., 2014. *Carbonation-induced and chloride-induced corrosion in reinforced concrete structures.* Journal of Materials in Civil Engineering, 27(9), p.04014245.

SS04: Structural health monitoring for infrastructure asset management

Organizers: J. Li, X.-W. Ye, T.-H. Yi & H.P. Chen

Maintenance, Safety, Risk, Management and Life-Cycle Performance of Bridges – Powers, Frangopol, Al-Mahaidi & Caprani (Eds)
© 2018 Taylor & Francis Group, London, ISBN 978-1-138-73045-8

Traffic Load Modelling for Urban Highway Bridges using Weigh-in-Motion Data

T.L. Huang, J.J. Liao & J. Zhong
School of Civil Engineering, Central South University, Changsha 410075, China
J.W. Zhong
Wuhan Bridge Science Research Institute LTD, Wuhan 430034, China
H.P. Chen
Department of Engineering Science, University of Greenwich, Chatham Maritime, Kent, ME4 4TB, UK

ABSTRACT: In this study, using the weigh-in-motion (WIM) data collected from an operational long-span urban highway bridge structural heath monitoring (SHM) system located in Wuhan, China, the statistical characteristics of gross vehicle weight (GVW), axle weights and spacing of axles are obtained, and then a statistical fatigue traffic load model for urban highway bridges is also proposed based on the Miner linear accumulated damage hypothesis and the effective fatigue damage principle. The proposed statistical fatigue traffic model can be used for bridge fatigue design and assessment. On the basis of the types of vehicles, (1) Considering the double or multi-modal distribution characteristics of the traffic GVW, the statistical parameters of the double or multi-modal Gauss distribution are estimated using expectation maximization (EM) algorithm; (2) Considering the single or multi-modal distribution characteristics of the traffic axle weight, the statistical parameters of the single or multi-modal Gauss distribution are estimated using EM algorithm; (3) The expectation and standard deviation of the spacing of axles are directly calculated; (4) Considering the statistical characteristics of the weight and spacing of axle, a statistical fatigue traffic load model for urban highway bridges is proposed based on the Miner linear accumulated damage hypothesis and the effective fatigue damage principle.

1 INTRODUCTION

1.1 *Introduction of WIM and traffic load model*

In the past decades, the structural health monitoring (SHM) techniques have been developed and applied in civil infrastructures such as bridges. As the important part of the bridge SHM systems, the weigh-in-motion (WIM) systems are normally adopted as the tool for surveying the condition of the traffic and for formulating the traffic load model (Jacob 2005, Jacob et al. 2010).

The bridge vehicle load model can be normally divided into two types, i.e., the vehicle load model for calculating the traffic load effect of bridge and the fatigue vehicle load model for fatigue analysis of bridge structures (Getachew and Obrien, 2007, O'Connor and Eichinger, 2007). Furthermore, the vehicle load model can be divided into two categories. The first type of models belong to the static model, which bases on the statistical analysis of the traffic load data. Based on the measured traffic load data, the key parameters of the traffic load model such as the gross vehicle weight (GVW), the axle weight, the speed of vehicle and the spacing of vehicle are theoretically analyzed and studied. The distribution functions of these parameters are obtained, and then the vehicle load models for specific regions are established. The second type of model, which bases on the probability and stochastic theory. By simulating the construction of the corresponding dynamic random traffic flow and the load effect analysis, the vehicle load models, which considers versatile parameters, such as the impact of vehicle lateral position, the random characteristics of the vehicle parameters are established.

In this paper, using the WIM data collected from the Wuhan Junshan Yangtze River Bridge SHM system located in Wuhan, China, the composition of vehicles, the statistical characteristics of the GVW, the axle weights and the axle spacing are obtained. Then the maximum value of the traffic load for the designated reference period are deduced. At last, a statistical fatigue traffic load model for urban highway bridges is also proposed based on the Miner linear accumulated damage hypothesis and the effective fatigue damage principle, which are suitable for the fatigue analysis of the bridge structures.

2 STATISTICAL TRAFFIC LOAD MODEL BASED ON MULTI-MODAL GAUSSIAN DISTRIBUTION

2.1 *Theoretical background: Multi-modal Gaussian distribution*

For any n time moments $t_1, t_2, \cdots, t_n$, the random variables $X(t_1), X(t_2), \cdots, X(t_n)$ obey the joint normal distribution, then the random process $X(t)$ is the Gaussian process with a joint probability density function,

$$f_X = \frac{1}{\sqrt{2\pi} \times \sqrt{|C_X|}} \exp\left[-\frac{(x-\mu_X)^T}{2C_X}(x-\mu_X) \right] \quad (1)$$

where μ_X is the mean matrix, C_X is the covariance matrix. The joint probability density function (PDF) of this Gaussian random process is determined by its mean $\mu_X(t_i), (i=1,2,\cdots,n)$ and covariance $C_X(t_i, t_j), (i, j=1,2,\cdots,n)$.

In cases where each of the underlying random variables $X(t_1), X(t_2), \cdots, X(t_n)$ is continuous, the outcome variable $X(t)$ will also be continuous and its joint PDF is sometimes referred to as a mixture PDF. The cumulative distribution function (CDF) and the PDF if it exists can be expressed as a convex combination (i.e. a weighted sum, with non-negative weights that sum to 1) of all individual CDFs and PDFs. These individual distributions that are combined to form the mixture distribution are called the mixture components, and the weights associated with each component are called the mixture weights. The number of components in mixture distribution is often restricted to being finite.

For a mixture distribution which is composed of n components, the weights of the components are

$$\alpha_1, \alpha_2, \cdots, \alpha_n, \sum_{i=1}^{n} \alpha_i = 1 \quad (2)$$

The PDFs of the components are $f_1(x), \cdots, f_n(x)$ and the joint PDF of the mixture distribution is

$$f(x) = \alpha_1 f_1(x) + \alpha_2 f_2(x) + \cdots + \alpha_n f_n(x) \quad (3)$$

When each of the individual distributions $f_1(x), \cdots, f_n(x)$ is Gaussian distribution,

$$f_i(x) = \frac{1}{\sqrt{2\pi}\sigma_i} \exp\left(-\frac{(x-\mu_i)^2}{2\sigma_i} \right), (i=1,2,\cdots,n) \quad (4)$$

Therefore, the mixture distribution $f(x)$ is also a Gaussian distribution.

2.2 *Data pre-processing*

According to the "Highway Law" and the relevant laws or regulations of China, the axle weight of vehicles travelling on the road should meet the requirements of the road engineering technical standard, i.e., "Limits of dimensions, axle load and masses for road vehicles (GB1589-2004)", and the rules of the Ministry of Communications of China, i.e., "Guidelines for toll collection on toll roads". In addition, considering the overload phenomenon of different vehicles in the actual road operational condition, a few rules have been applied for removing the abnormal WIM data, which are listed as follows,

(1) To exclude the vehicles with GVW less than 8kN or greater than 1500kN.

In the provisions of the "Guidelines for toll collection on toll roads", the GVW of six-axle trucks is limited below 490kN. However, the GVW of the actual operational vehicles are normally overloaded 200%, i.e., about 1000kN. On this basis, extra 50% overload is considered. So the limit for the vehicles with GVW greater than 1500kN is made.

(2) To exclude the vehicles in which the number of axles are not two, three, four, five and six. This is because that the proportion of the other axle number are very scare in China.

(3) To exclude the vehicles with the axle weight less than 3kN or greater than 720kN.

In the provisions of the "Guidelines for toll collection on toll roads", the axle weight of six-axle trucks is limited below 240kN. However, the axle weight of the actual operational vehicles are normally overloaded 200%, i.e., about 48kN. On this basis, extra 50% overload is considered. So the limit for the vehicles with axle weight greater than 720kN is made.

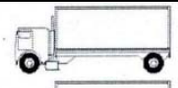
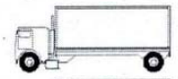
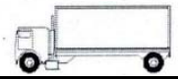
(4) To exclude the vehicles in which the number of axle is not identical with the type of the vehicle.

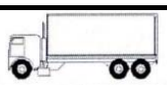
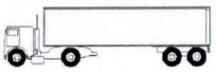
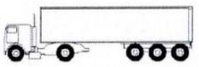
(5) To exclude the vehicles in which the sum of the axle weight is not identical with the GVW.

2.3 *Statistical analysis of WIM data*

The vehicle WIM data of the Wuhan Junshan Yangtze River Bridge on August 2013 are collected and analyzed. The statistical results of the composition of the vehicles are shown in Table 1.

Table 1. The composition of the vehicles.

Models	Illustration	Numbers	Proportion
Two-axle Mini-bus		305481	0.517
Two-axle truck		89942	0.152
Two-axle bus		9758	0.017

Three-axle truck		35331	0.060
Four-axle truck		27826	0.047
Five-axle truck		7023	0.012
Six-axle truck		115120	0.195

The GVW histogram of the vehicles is shown in Figure 1. It can be obviously seen that the distribution of the GVW of vehicles exhibits multi-peak characteristics. The peak values of the vehicle are distributed in the ranges at 2,000 kg - 8,000 kg, 10,000 kg - 24,000 kg, 24,000 kg - 66,000 kg, and three obvious peaks are concentrated in 3,000 kg, 16,000 kg and 54,000 kg. The proportion of the light vehicles less than 6,000 kg are more than 60%.

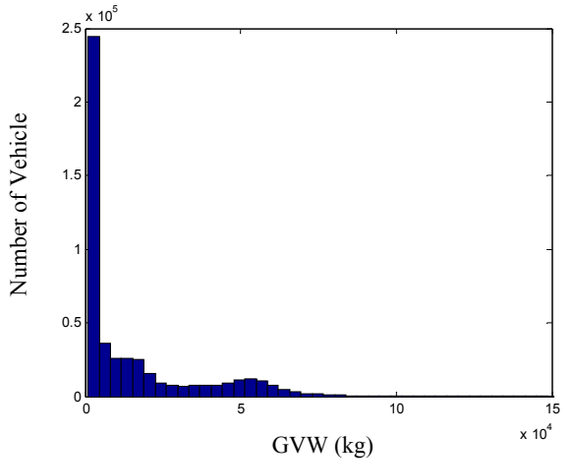
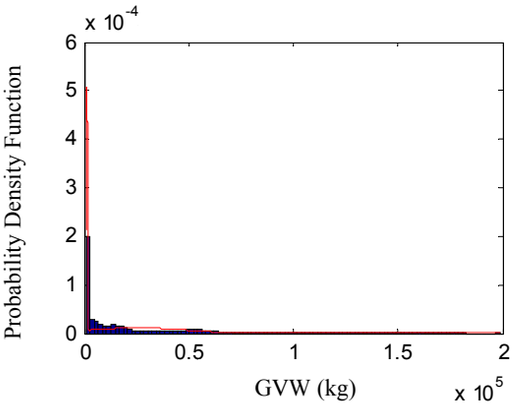
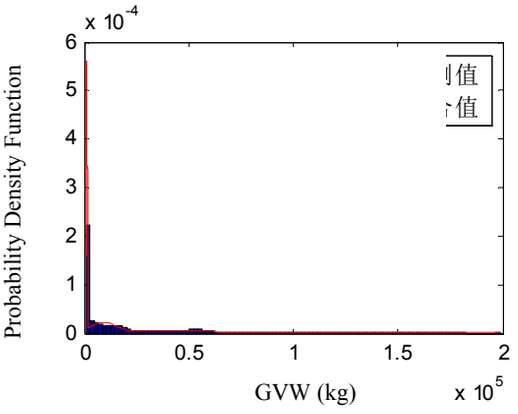


Figure 1. The histogram of GVW.

Normally, the mixture Gaussian or Weibull distribution model are used to fit the probability density function of the GVW of vehicles. There are several ways to solve the mixture distribution model parameters, such as the nonlinear least squares fitting method, which solves the model parameters of a multi-modal mixture Gaussian distribution cumulative distribution (Mei et al. 2004, Guo et al. 2011, Lan et al. 2011). In this study, the expectation maximization (EM) algorithm is adopted to fit the PDFs of the double and triple Gaussian distribution for the GVW of the vehicles, as shown in Figure 2. Compared with the double and triple Gaussian distributions, it can be seen that the triple Gaussian distribution is more effective for fitting the PDF of the GVW, and the distribution can be verified by the K-S check with 95% guarantee level.

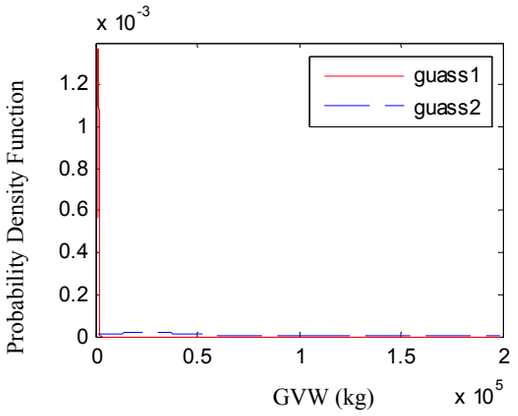


(a) Double mixture Gaussian distribution

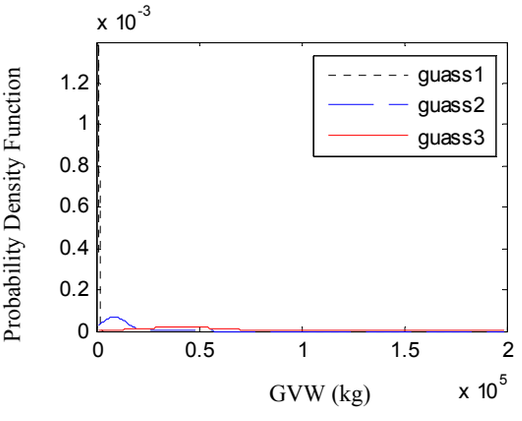


(b) Triple mixture Gaussian distribution

Figure 2. The fitted probability density function (PDF) for the GVW of the vehicles using mixture Gaussian distribution.



(a) Double Gaussian distribution



(b) Triple Gaussian distribution

Figure 3. The components of the double and triple Gaussian distribution.

The components of the double and triple Gaussian distribution are shown in Figure 3 and the corresponding weight, mean and standard deviations are listed in Table 2. As shown in Figure 3, it is clearly seen that the shape of the components of the double and triple Gaussian distribution are different. For the double Gaussian distribution, the means and the standard deviations are 11093 kg, 44026 kg and 5639 kg, 20245 kg, respectively. For the triple Gaussian distribution, the means and standard deviations are: 9852 kg, 31622 kg, 46110 kg and 4767 kg, 16590 kg, 23499 kg, respectively.

Table 2. Fitted parameters of the mixture Gaussian distribution.

Distribution parameter	Weight α	Mean μ	Standard deviation σ
Double	0.5030	11093	5639
	0.4970	44026	20245
Triple	0.3911	9852	4767
	0.3084	31622	16590
	0.3005	46110	23499

The measured cumulative distribution function (CDF) and the fitted CDF by using the triple Gaussian distribution are shown in Figure 4. As shown in Figure 4, the fitted curve is almost the same as the measured curve. It shows that the triple Gaussian distribution can be used to fit the distribution of the GVW of the vehicles.

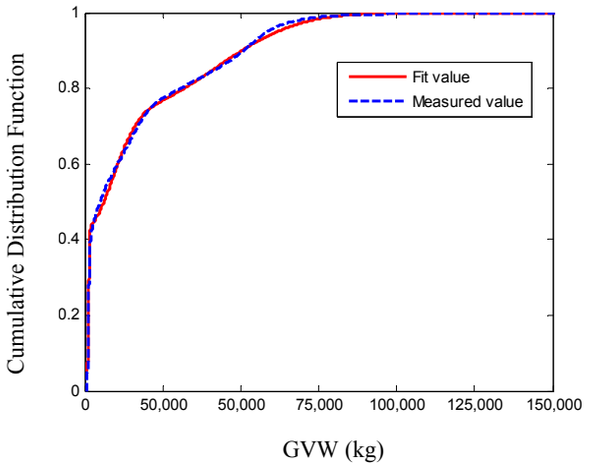


Figure 4. The measured and fitted cumulative distribution function (CDF).

3 ESTIMATION OF THE VEHICLE LOAD EXTREME BASED ON EXTREME VALUE TYPE I DISTRIBUTION

3.1 *Principles of extreme estimation using extreme value type I distribution*

According to the provision of the "General Specification for Design of Highway Bridges and Culverts (JTG D60-2015)", the bridge design reference period is 100 years in China. In this study, it is assumed that the maximum value of the vehicle load in one day can be used to represent the maximum value of the vehicle load in one year. Therefore, a 100-day WIM data are collected and used for the estimation of the vehicle load extreme for bridges in the design reference period. As we known, the composition of the vehicles has very obviously regional characteristics. It is more reasonable to estimate the extreme of the vehicle load based on the measured WIM data for assessing the conditions of bridges.

Many researches have shown that the probability distribution of the vehicle load can be represented by a variety of distributions. The extreme value type I distribution can be a better description.

If the amount of data is big enough and defining X_M as the maximum of a set of random variables X, then X_M can be taken as a new random variable. When $n \to \infty$, it can be proved that the distribution of the random variable X_M is the exponential distribution in the condition that the random variable X obeys the exponential distribution, the normal distribution or the Weibull distribution.

$$F_M(x) = \lim_{n\to\infty}\left[F(x)\right]^n = exp\left\{-exp\left[-\alpha(x-\beta)\right]\right\} \tag{5}$$

where α and β are the distribution parameters of the extreme value type I distribution. The mean and the standard deviation are

$$\begin{aligned} \mu_x &= 0.57722/\alpha + \beta \\ \sigma_x &= 1.28255/\alpha \end{aligned} \tag{6}$$

The corresponding PDF $f(x)$ and the CDF $F(x)$ are

$$f(x) = \alpha e^{-\alpha(x_e-\beta)} e^{-e^{-\alpha(x_e-\beta)}} \tag{7}$$

$$F(x) = \exp(-\exp(-y)),\ y = \alpha(x_e - \mu) \tag{8}$$

Where α and μ are parameters which can be represented as the mean value μ_X and the standard deviation σ_X

$$\mu = \mu_X - 0.5772/\alpha \tag{9}$$

$$\alpha = \pi/(\sqrt{6}\sigma_X) \tag{10}$$

Eqs. (9) - (10) can be changed as the following form,

$$y = -\ln(-\ln(F(x_e))) \tag{11}$$

$$x_e = \mu + (1/\alpha)y \tag{12}$$

3.2 *Estimation of the extreme of the vehicle load*

Based on the Gumbel extreme value theory and the assume that the observed extreme values are independent of each other, it is possible to obtain,

$$F(T = t_0) = F^n(T = t_d) \tag{13}$$

where $F(T = t_0)$ is the extreme distribution of the year, $F(T = t_d)$ is the extreme distribution of the design reference period, $t_d = 100$ years.

Based on the Eq. (7) to Eq. (13), one can obtain,

$$\exp\left\{-\exp\left[-y(T = t_d)\right]\right\} = \left\{\exp\left\{-\exp\left[-y(T = t_0)\right]\right\}\right\}^m \tag{14}$$

Using the Eq. (8) and Eq. (14), one can obtain the following equations,

$$\frac{1}{\alpha(T = t_d)} = \frac{1}{\alpha(T = t_0)} \tag{15}$$

$$\mu(t = t_d) = \mu(t = t_0) + \frac{1}{\alpha(T = t_0)}\ln\left(\frac{t_d}{t_0}\right) \tag{16}$$

As we know $t_0 = 1$, $t_d = 100$, if $\mu_d = \mu(t = t_d)$ and $\alpha_d = \alpha(T = t_d)$ are obtained, the extreme value distribution can be determined as follow,

$$F(x_e) = \exp(-\exp(-y)) \tag{15}$$

The determination of μ_d and α_d can be obtained by using the following steps,

(1) Based on the rules on Section 2.1, to remove the unreasonable WIM data.

(2) To extract the daily extreme value of the processed data and arrange them from small values to large value, then an arrangement of extreme data $\{x_i\}, (i = 1, 2, \cdots, n)$ is obtained,

(3) To calculate the non-exceeding probability of each extreme load $\{P_i\}, (i = 1, 2, \cdots, n)$ and to define a new variable $\{y_i\}, (i = 1, 2, \cdots, n)$

$$P_i = i/(n+1), (i = 1, 2, \cdots, n) \tag{16a}$$

$$y_i = -\ln(-\ln P_i), (i = 1, 2, \cdots, n) \tag{16b}$$

(4) Setting $\{y_i\}, (i = 1, 2, \cdots, n)$ as the horizontal axis and $\{x_i\}, (i = 1, 2, \cdots, n)$ as the vertical axis, a fitted straight line is obtained by using the linear least squares method. The slope of the straight line $1/\alpha_0$ is and the intercept is μ_0 when $y = 0$.

(5) Then the parameters μ_d and α_d can be determined by substituting the values of μ_0 and α_0 into Eqs. (15) - (16).

(6) At last, the extreme distribution of vehicle load in the design reference period can be obtained by substituting the values of μ_d and α_d into Eq. (8).

Following the above steps, the parameters are calculated by using the WIM data, i.e., $\alpha_0 = \alpha_d = 4.7834 \times 10^{-4}$, $\mu_0 = 1.7638 \times 10^5$ and $\mu_d = 1.8601 \times 10^5$. The estimated CDF of vehicle load is shown in Figure 5.

Taking the value at the 0.95 locus of the cumulative distribution function (CDF) curve $F_{X,\max}(X)$, the estimated maximum value of vehicle load in the design reference period is $x_{0.95} = 1922.2$ kN.

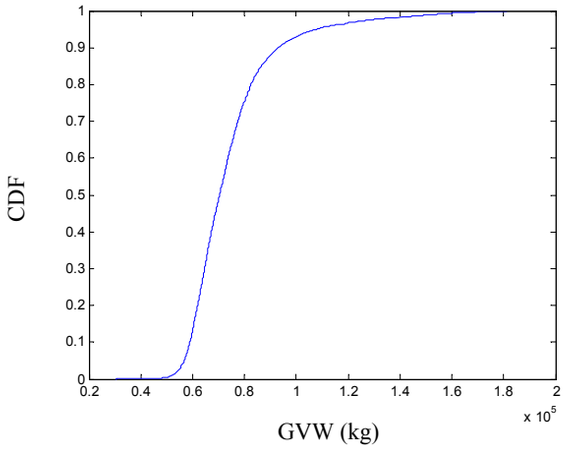


Figure 5. The estimated cumulative distribution function (CDF).

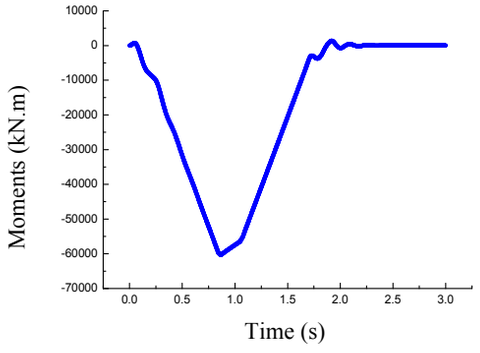
4 FATIGUE VEHICLE LOAD MODEL BASED ON WIM DATA

4.1 *Finite element analysis of the number of stress cycle*

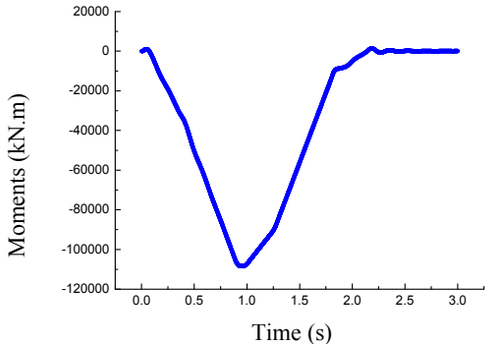
In this study, a finite element (FE) simple support beam bridge model with span of 32 meters is established by using ANSYS software. The vehicle load is simplified as a set of concentrated forces and applied to the simply supported girder bridge model. By adopting the move load method, the moment response time-history curves at the mid cross-section of this simply supported beam are shown in Figure 5. In these calculation, the vehicle speed is measured according to the actual condition. The average vehicle speed of different types of vehicle are shown in Table 3 and the calculation time interval is 0.01s.

Table 3. The average vehicle speed of different types of vehicle.

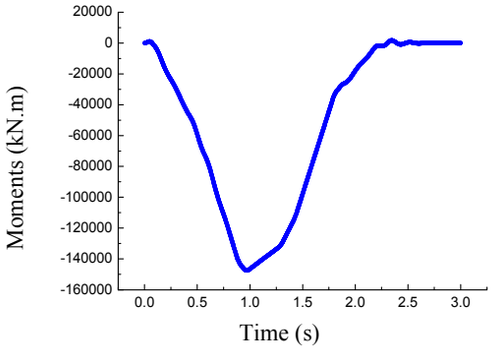
Axle type	speed（km/h）
Two axles	69.26
three axles	64.84
Four axles	65.99
Five axles	67.04
Six axles	64.99



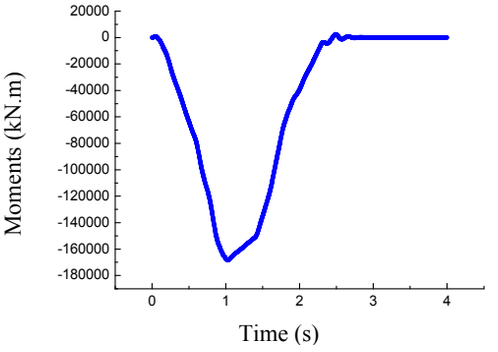
(a) Two-axle vehicle



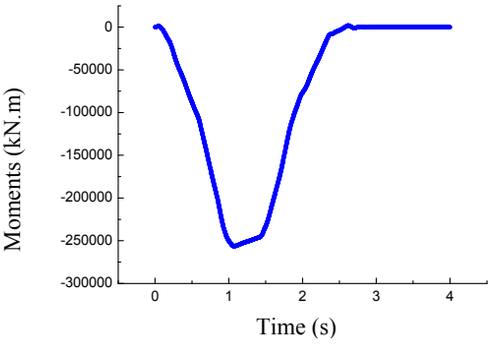
(b) Three-axle vehicle



(c) Four-axle vehicle



(d) Five-axle vehicle



(e) Six-axle vehicle

Figure 5. The mid-span moment response time-history curves of a 32m simply supported beam under different types of vehicle.

As shown in Figure 5, the bending moment time-history curves during the passing of each vehicle have only a big moment cycle and some very small cycles, no matter how many axles the vehicle have. Due to the effect of the dynamic effect, the maximum value of the moment is not generated when the vehicle reaches the mid-span, but is slightly delayed. In addition, for this 32m simple supported beam bridge, when the axles pass, the curve of the bending moment curves are almost the same, but the values are different, which shows that the bending moment curves are not affected by the wheelbase and the axle weight distribution. Therefore, for this 32m simply supported beam bridge, the number of fatigue stress cycles caused by each axle can be simplified to 1, and the maximum bending moment or stress amplitude can be calculated according to a set of concentrated forces acted on the most unfavorable position of the influence line.

4.2 *Fatigue damage analysis of vehicles with different axles*

Only considering the largest moment induced by the six-axle vehicles, the formula of the equivalent stress amplitude is listed as follows,

$$S_{eq}=\left(\sum_{i=1}^{k}n_i S_i^{\ m}\Big/N\right)^{\frac{1}{m}} \tag{17}$$

where S_i is the magnitude of the stress amplitude decomposed by the rain flow counting method; n_i is the magnitude of the actual magnitude of the stress amplitude of S_i; N is the total number of stress amplitude decomposed by rain flow counting method; m is a parameter determined by the S-N curve. For steel structures, m is normally taken as 3.

The equivalent moment is calculated as follows,

$$M_D=\left(\sum f_i \bullet (M_{ri})^3\right)^{1/3} \tag{18}$$

where M_D is the equivalent moment, and f_i is the frequency where the moment M_{ri} appears.

In order to compare the contribution of each axle to structural fatigue damage, the damage ratio D_r can be used to represent the contribution rate of each type of vehicle to structural fatigue damage. Here the damage ratio is the ratio of the damage caused by the axle to all the car to the structure which indicates the cumulative damage caused by fatigue. The calculation formula is listed as follows,

$$D_r=\frac{D_i}{D_{all}}=\frac{n_i S_i^m}{n_{all}S_{all}^m}=\frac{n_i M_i^m}{n_{all}M_{all}^m} \tag{19}$$

where D_i is the cumulative damage caused by the vehicles with i axles, D_{all} is the cumulative damage caused by all vehicles, n_i is the number of cycles caused by the vehicles with i axles, n_{all} is the number of cycles caused by all vehicles, S_{Di} is the stress amplitude caused by the vehicles with i axles, S_{all} is the stress amplitude caused by all vehicles. Based on the rules of the AASSTO specification about the fatigue details, m = 3 is adopted in this article.

The equivalent bending moment of the 32m span simply supported beam and the damage ratio of vehicles with different axles are shown in Table 4.

It should be noted that the composition of the vehicles listed in Table 4 is different with the ones in Table 1. The reason is that all vehicles below 3 tons are not considered for fatigue analysis. As shown in Table 4, although the proportion of vehicles with two-axle is 29.78%, the damage ratio to the bridge is only 10.91%. On the contrary, although the proportion of vehicles with six-axle is 44.53%, the damage ratio to the bridge is 68.89%. It is seen that the six-axle vehicles are the main factor for the fatigue damage to the bridge. Therefore, the six-axle vehicle is adopted as the prototype of standard fatigue vehicle.

Table 4. The equivalent bending moment and the damage ratio of vehicles with different axles.

Number of axles	Proportion	Amplitude of moment (kN•m)	Cycles	Damage ratio
Two	29.78%	61.06	76155	10.91%
Three	12.82%	109.53	32798	8.43%
Four	10.37%	148.49	26523	9.24%
Five	2.50%	169.12	6383	2.53%
Six	44.53%	257.81	113893	68.89%
Total	1		255752	1

4.3 *The standard fatigue vehicle model*

The prototype of standard fatigue vehicle is shown in Figure 6. If the GVW of this vehicle is W, then the axle weights are 0.12W, 0.14W, 0.2W, 0.2W, 0.17W and 0.17W, respectively. The wheelbases are 3.2m, 1.5m, 7.0m, 1.3m and 1.3m, respectively.

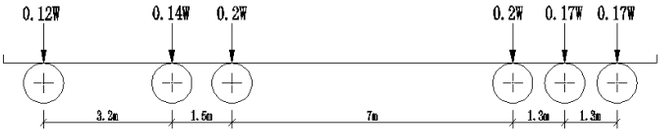


Figure 6. The prototype of standard fatigue vehicle.

The equivalent weight of the standard fatigue vehicle can be calculated through the superposition of each axle weight by using Eq. (20).

$$W_{ej}=\left[\sum\left(f_i W_i^3\right)\right]^{\frac{1}{3}} \tag{20}$$

Where W_{ej} is the equivalent weight of the standard fatigue vehicle; W_i is the equivalent weight of the vehicle with i axles; f_i is the frequency ratio of the vehicle with i axles. Based on the WIM data, the equivalent weight of the standard fatigue vehicle is 36216 kg. Therefore, the axle weight has been allocated by using the ratio of the prototype of standard fatigue vehicle. For convenience of use, the equivalent weight and the axle weight has been slightly adjusted. Then the standard fatigue vehicle model for the urban highway bridges located in Wuhan, China is proposed and shown in Figure 7.

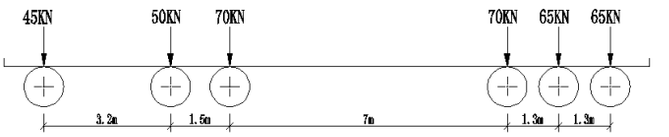


Figure 7. The standard fatigue vehicle model for the urban highway bridges located in Wuhan, China.

5 CONCLUSIONS

In this paper, based on the WIM data collected from the Wuhan Junshan Yangtze Bridge, the mixed Gaussian distribution model is adopted to fit the probability density function of the GVW. The results show that the triple Gaussian distribution is more effective for fitting the PDF of the GVW, and the distribution can be verified by the K-S check with 95% guarantee level. Based on the extreme value type I distribution, the estimated maximum value of vehicle load in the design reference period is 1922.2 kN. Based on the fatigue analysis on a 32m simple supported beam bridge, a six-axle standard fatigue vehicle model for the urban highway bridges located in Wuhan, China is proposed.

ACKNOWLEDGEMENTS

The authors are grateful for the financial support from the Natural Science Foundation of China (Grant No. 51478472) and the Natural Science Foundation of Hunan Province, China (Grant No. 2015JJ2176).

REFERENCES

Getachew, A., Obrien, E. J. 2007. Simplified site-specific traffic load models for bridge assessment. *Structure and infrastructure Engineering*, 3(4), 303-311.

Guo T., Frangopol D. M., Han D., and Chen Y. 2011. Probabilistic assessment of deteriorating pre-stressed concrete Box-Girder bridges under increased vehicle loads and aggressive environment, *Journal of Performance of Constructed Facilities*, 25(6), 564-576.

Lan C., Li H., and Ou J. 2011. Traffic load modelling based on structural health monitoring data. *Structure & Infrastructure Engineering*, 7(5), 379-386.

Jacob, B., O'Brien, E. J. 2005. Weigh-in-motion: Recent developments in Europe. *In 4th International Conference on Weigh-in-Motion-ICWIM4, Taipei, Taiwan, 20-23rd February, 2005.*

Jacob, B., Feypell-de La Beaumelle, V. 2010. Improving truck safety: Potential of weigh-in-motion technology. *IATSS research*, 34(1), 9-15.

Mei G., Qin Q., and Lin D.-J. 2004. Bimodal renewal processes models of highway vehicle loads. *Reliability Engineering and System Safety*, 83(3), 333-339.

O'Connor, A., Eichinger, E. M. 2007. Site-specific traffic load modelling for bridge assessment. *Proceedings of the Institution of Civil Engineers-Bridge Engineering*, 160(4), 185-194.

Maintenance, Safety, Risk, Management and Life-Cycle Performance of Bridges – Powers, Frangopol, Al-Mahaidi & Caprani (Eds)
© 2018 Taylor & Francis Group, London, ISBN 978-1-138-73045-8

Acceleration Response Analysis of a Long-span Steel Arch Bridge Subjected to High-speed Trains Integrating SHM Data

H.L. Li, Y.L. Ding, H.W. Zhao & S.T. Hou
Key Laboratory of C&PC Structures of the Ministry of Education, Southeast University, Nanjing 210096, China

ABSTRACT: In recent years several long-span bridges have been constructed and put into service in China's high-speed railway lines. These bridges usually cross the major rivers of China which serve as vital shipping channels. The long-span structure becomes the superior and sometimes even sole scheme to carry high-speed tracks over the rivers without impacting the water transportation at the bridge site. High-speed trains require stable and smooth geometries of the tracks on long-span bridges to achieve successful and safe passages. Nevertheless, the above mentioned track geometries can be threatened by multiple stressors, e.g., high-speed trains, wind, temperature, among others. Structural health monitoring (SHM) systems have been applied to the long-span bridges, aiming to collect real-time information about both the stressors and structure responses. This information can be used to investigate the performance of bridge structures, and eventually to ensure the running safety of high-speed trains. In this context, the present paper examines the acceleration responses of a long-span steel arch bridge, i.e., the Nanjing Dashengguan Yangtze River Bridge, under operating high-speed train loads. This unique long-span railway bridge and its SHM system are introduced. A coupled dynamic model of the high-speed vehicle and bridge structure system is subsequently developed. Acceleration responses at the typical locations resulting from the coupled dynamic analysis are compared to the SHM data. It is found that at several specific velocity values the maximum accelerations of the bridge produce respective peaks through the parametric study on train speeds. This interesting phenomenon calls for more detailed investigation on the concerned topic in the future.

1 INTRODUCTION

High-speed rails, as a fast, safe, and comfort transportation means, have been constructed more and more in the worldwide. Taking China as an example, a high-speed railway network with the total mileage of about 20,000 km has been completed by the end of 2015. This network connects every city that has a population larger than half million in the middle and eastern China. High-speed rails are currently extending to the western mountainous and eastern coastline areas, where railway lines have to cross some deep valleys and/or broad waterways. Consequently, more and more long-span bridges have been constructed and put into service in high-speed railway lines.

These long-span bridges are required to provide sufficient rigidity to maintain stable and smooth geometries of the tracks, since the high-speed trains are sensitive to the changes of track geometries. Nevertheless, the above mentioned track geometries can be threatened by multiple stressors, including high-speed trains, wind, temperature, and so on. Structural health monitoring (SHM) can serve as an effective tool for collecting real-time information about both the stressors and structure responses (Ko and Ni 2005; Catbas et al. 2008; Feng and Feng 2016). This information can be utilized to evaluate the performance of bridges (Leander et al. 2010; Magalhães et al. 2012). Moreover, online early-warnings may also be realized based on the data obtained from SHM (Ding et al. 2017).

On the other hand, SHM systems can provide reliable calibrations for the theoretical and/or numerical models. Although field measurements are normally considered as real reflections of stressors and load effects, numerical methods play a key role in investigating the scenarios that have not been included in SHM. Dynamic responses of the railway bridges subjected to high-speed trains can be computed by establishing coupled train-bridge model (Li et al. 2015, 2016, 2017). Time histories of displacement and acceleration obtained from the numerical coupling model are subsequently used to assess the performance of bridges (Xia et al. 2012).

In this paper, a preliminary investigation is conducted on a unique long-span steel arch bridge for high-speed railways, i.e., the Nanjing Dashengguan

Yangtze River Bridge, with emphasis on acceleration responses. A coupled high-speed train and bridge system model is established to numerically characterize accelerations of the bridge deck. These computational results are compared with the measurements obtained from SHM. Some discussions are presented along with the acceleration results.

2 DASHENGGUAN YANGTZE RIVER BRIDGE AND SHM SYSTEM

2.1 *Bridge description*

The Dashenguan Yangtze River Bridge (see Fig. 1) is located in the southwest suburb area of Nanjing, crossing the longest river in China, the Yangtze River. The bridge is a continuous steel truss structure with six spans which are, respectively, 108 m, 192 m, 336 m, 336 m, 192 m, and 108 m (see Fig. 2). In particular, two largest spans of 336 m are constructed in terms of steel truss arch, allowing the navigation of huge ships with a 32 m clearance. The Dashenguan Yangtze River Bridge carries six railway tracks on three rail lines. They are, respectively, Beijing-Shanghai (B-S) high-speed railway line, Shanghai-Wuhan-Chengdu (S-W-C) railway line, and Nanjing Metro line S3. The steel arch cross-section and lane arrangement are shown in Fig.3. It is designed that high-speed trains in the Beijing-Shanghai high-speed railway line run through the bridge at the speed up to 300 km/h. The design load of the six tracks is more than 600 kN/m along the longitudinal direction of the bridge, which becomes the largest design load among high-speed railway bridges all over the world.



Figure 1. Photograph of the Dashengguan Yangtze River Bridge.

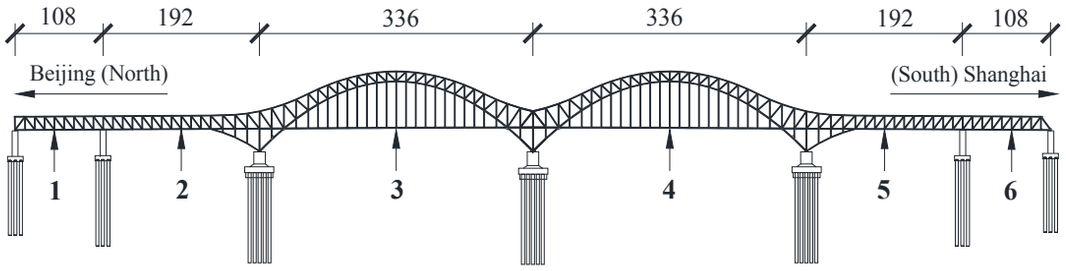


Figure 2. Span arrangement and acceleration monitoring cross-sections (Units: m)

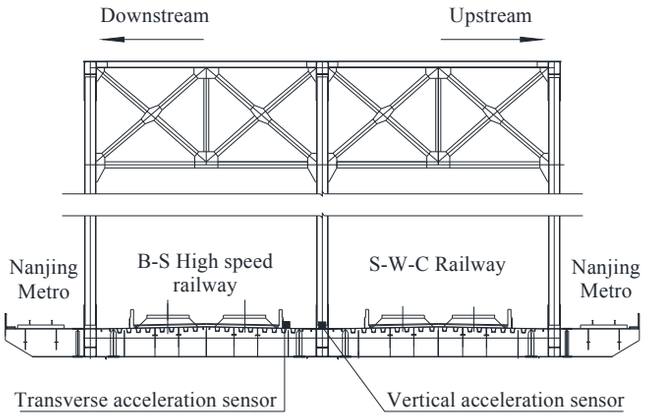


Fig. 3. Locations of the acceleration sensors

2.2 *Acceleration monitoring system*

A long-term SHM system was installed on the Dashengguan Yangtze River Bridge. In this monitoring system, acceleration sensors are employed to measure the dynamic responses of the bridge. The monitoring cross-sections associated with the bridge acceleration responses are shown in Fig. 2. Six cross-sections are instrumented, among which cross-section 1 is on the assisted span on the Beijing side, cross-section 2 is on the side span on the Beijing side, cross-section 3 is on the middle span on the Beijing side, cross-section 4 is on the middle span on the Shanghai side, cross-section 5 is on the side span on the Shanghai side, and cross-section 6 is on the assisted span on the Shanghai side. A vertical acceleration sensor is employed at cross-sections 1 and 6. A vertical acceleration sensor and a transverse one are employed at cross-sections 2, 3, 4 and 5. The locations of acceleration sensors in their monitoring cross-sections are further shown in Fig. 3. The sampling rate of the acceleration sensors is 200 Hz. In addition, Speedometers are also included in the SHM system on the Dashengguan Yangtze River Bridge to monitor the train speeds.

3 COUPLED TRAIN-BRIDGE SYSTEM MODEL

In order to simulate the dynamic acceleration histories of the Dashengguan Yangtze River Bridge under high-speed trains, a coupled train-bridge model is established to conduct numerical analysis. The coupled system model consists of a 3D train model, a 3D bridge model established through the direct stiffness method, and a wheel-rail interaction model.

3.1 *Train model*

High-speed trains running in the China's railway lines are usually composed of eight or sixteen vehicles. Herein, it is assumed that these vehicles are independent from each other. Each vehicle consists of a car body, two bogies, and four wheel-sets. These rigid-body components are connected by the primary and/or secondary suspension systems. The suspension systems are modeled as springs and dashpots. Each car body or bogie has five degrees of freedom (i.e., swaying, rolling, yawing, floating, and pitching); whereas each wheel-set has four degrees of freedom (i.e., swaying, rolling, yawing, and floating) (Li et al. 2016). Using the Lagrange's equation, the dynamic equation of motion of the vehicle can be expressed as

$$\mathbf{M}_v\ddot{\mathbf{X}}_v + \mathbf{C}_v\dot{\mathbf{X}}_v + \mathbf{K}_v\mathbf{X}_v = \mathbf{P}_v \qquad (1)$$

where $\mathbf{M}_v$, $\mathbf{C}_v$, and $\mathbf{K}_v$ are, respectively, the mass, damping, and stiffness matrices of the vehicle model, which are related to the dimensional and mechanical parameters of the vehicle (e.g., spring and damping coefficients of the suspension systems) and usually change with vehicle types; $\mathbf{P}_v$ is the vector of dynamic forces acting on the vehicle model, which is dependent on the adopted wheel-rail interaction model; and $\mathbf{X}_v$, $\dot{\mathbf{X}}_v$, and $\ddot{\mathbf{X}}_v$ represent, respectively, the displacement, velocity, and acceleration vectors.

3.2 *Bridge FE model*

For such a long-span arch bridge, finite elements can be an effective tool to formulate the equation of motion of the bridge. In the present analysis, a 3D FE model of the Dashengguan Yangtze River Bridge is established through the ANSYS software (see Fig. 4). In this model, BEAM188 elements are used to model the arch ribs, hangers, and stiffeners of the box girders. The crossbeams of box girders and floor slab are simulated with SHELL181 elements. There are a total of 59,760 nodes and 112,706 elements in the FE model. Frequencies and shapes of the fundamental modes of shape obtained from the FE model can be found in Zhao et al. (2016). The numerical modal parameters agree with the field test counterparts well.

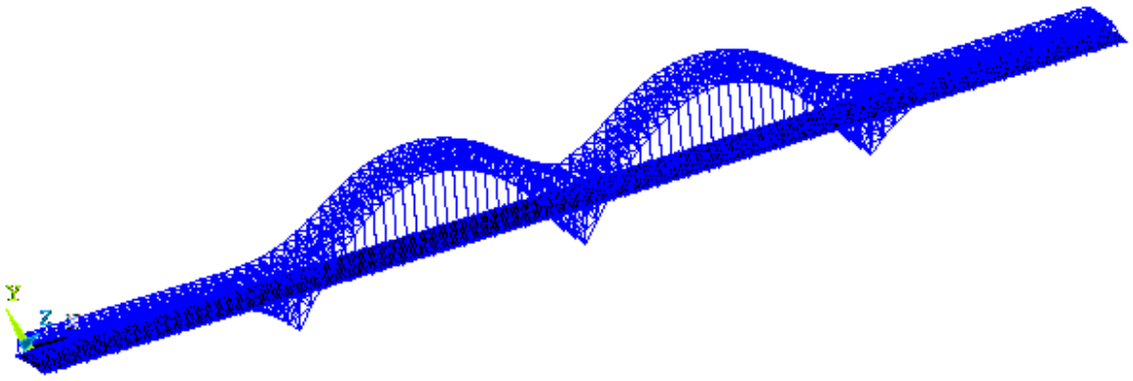


Figure 4. FE model of the Dashengguan Yangtze River Bridge

In this paper, the equation of motion of the Dashengguan Yangtze River Bridge is generated via the direct stiffness method, based on the above men-

tioned FE model. The bridge equation of motion can be written as

$$\mathbf{M}_b\ddot{\mathbf{X}}_b + \mathbf{C}_b\dot{\mathbf{X}}_b + \mathbf{K}_b\mathbf{X}_b = \mathbf{P}_b \quad (2)$$

where $\mathbf{M}_b$, $\mathbf{C}_b$, and $\mathbf{K}_b$ are, respectively, the mass, damping, and stiffness matrices of the bridge, which are obtained from the FE model; $\mathbf{X}_b$, $\dot{\mathbf{X}}_b$, and $\ddot{\mathbf{X}}_b$ are the displacement, velocity, and acceleration vectors of bridge nodes in terms of geometric coordinates, respectively; and $\mathbf{P}_b$ is the vector of dynamic forces acting on the bridge by the running train.

3.3 *System equation of motion*

How to solve $\mathbf{P}_v$ and $\mathbf{P}_b$ on the right-hand side of Equations (1) and (2) is the key issue associated with these equations. $\mathbf{P}_v$ and $\mathbf{P}_b$ are determined by wheel-rail interactions. The interactions can be characterized through assumed wheel-rail contact relationship, i.e., the wheel-rail interaction model. Various models have been proposed in literature (Zhai et al. 2010) to determine $\mathbf{P}_v$ and $\mathbf{P}_b$.

In the present analysis, the linear wheel-rail interaction model proposed in Zhang et al. (2010) is used to establish the vectors $\mathbf{P}_v$ and $\mathbf{P}_b$. Specifically, the vertical wheel-rail forces are related to motions of the bridge deck and track irregularities since wheel-sets are assumed to have the same motion as the bridge deck in the vertical direction. The lateral wheel-rail forces depend on the relative motion of wheel and rail, and track irregularities based on the Kalker's creep theory. Therefore, both $\mathbf{P}_v$ and $\mathbf{P}_b$ are associated with the motion of the vehicle and bridge deck, and track irregularities. If the terms related to the motion of the vehicle and bridge deck in $\mathbf{P}_v$ of Equation (1) and $\mathbf{P}_b$ of Equation (2) are moved to the left-hand side of the equations, the equation of motion of the train-bridge system can be expressed as

$$\begin{bmatrix} \mathbf{M}_v & 0 \\ 0 & \mathbf{M}_b \end{bmatrix} \begin{Bmatrix} \ddot{\mathbf{X}}_v(t) \\ \ddot{\mathbf{X}}_b(t) \end{Bmatrix} + \begin{bmatrix} \mathbf{C}_{vv} & \mathbf{C}_{vb} \\ \mathbf{C}_{bv} & \mathbf{C}_{bb} \end{bmatrix} \begin{Bmatrix} \dot{\mathbf{X}}_v(t) \\ \dot{\mathbf{X}}_b(t) \end{Bmatrix} + \begin{bmatrix} \mathbf{K}_{vv} & \mathbf{K}_{vb} \\ \mathbf{K}_{bv} & \mathbf{K}_{bb} \end{bmatrix} \begin{Bmatrix} \mathbf{X}_v(t) \\ \mathbf{X}_b(t) \end{Bmatrix} = \begin{Bmatrix} \mathbf{F}_v \\ \mathbf{F}_b \end{Bmatrix} \quad (3)$$

where $\mathbf{C}_{vb}$ and $\mathbf{C}_{bv}$, and $\mathbf{K}_{vb}$ and $\mathbf{K}_{bv}$ are, respectively, parts of the system damping and stiffness matrices arising due to the coupling effects of the train and bridge subsystems; and $\mathbf{F}_v$ and $\mathbf{F}_b$ = force vectors associated with track irregularities. Equation (3) can be solved through implicit numerical integration methodology, such as the Newmark-β method. An in-house procedure has been developed on the MATLAB platform to numerically solve the system equation of motion.

4 ACCELERATION RESULTS AND DISCUSSION

4.1 *Track irregularities*

Coupled dynamic analysis is conducted with respected to the high-speed train and Dashengguan Yangtze River Bridge system. Track irregularities adopted in the coupling analysis are generated from the German track irregularity spectra, which can be expressed as (Xia et al. 2012)

$$S_v(\Omega) = \frac{A_v\Omega_c^2}{(\Omega^2+\Omega_r^2)(\Omega^2+\Omega_c^2)} \quad (4a)$$

$$S_a(\Omega) = \frac{A_a\Omega_c^2}{(\Omega^2+\Omega_r^2)(\Omega^2+\Omega_c^2)} \quad (4b)$$

$$S_c(\Omega) = \frac{A_v\cdot b^{-2}\cdot\Omega_c^2\cdot\Omega^2}{(\Omega^2+\Omega_r^2)(\Omega^2+\Omega_c^2)(\Omega^2+\Omega_s^2)} \quad (4c)$$

$$S_g(\Omega) = \frac{A_g\Omega_c^2\Omega^2}{(\Omega^2+\Omega_r^2)(\Omega^2+\Omega_c^2)(\Omega^2+\Omega_s^2)} \quad (4d)$$

where S_v(W), S_a(W), and S_g(W) are respectively the power spectral density (PSD) functions of vertical profile, alignment, and gauge irregularities (m^2/(rad/m)); S_c(W) is the PSD function of cross-level irregularities (1/(rad/m)); A_v=4.032$\times10^{-7}$, A_a=2.119$\times10^{-7}$, and A_g=5.32$\times10^{-8}$ are the roughness coefficients (m^2·rad/m); Ω_c= 0.8246, Ω_r=0.0206 and Ω_s=0.4380 are the cutoff frequencies (rad/m); and b is the half of the distance between the right and left rail centers.

4.2 *Acceleration time histories*

Acceleration time histories of cross-sections 1, 2, and 3 (see Fig. 2) from the health monitoring are extracted. These accelerations were induced by high-speed trains with 245 km/h speed that ran towards Shanghai in the B-S high-speed line. The trains consist of eight vehicles. Acceleration responses at the monitored locations are computed by using the coupled train-bridge system model. The integration time step employed in solving the system dynamic equation of motion is 0.005 s which is equal to the sampling frequency of the monitoring system. Figs. 5-7 show the time histories of vertical accelerations obtained from the monitoring system and numerical simulation.

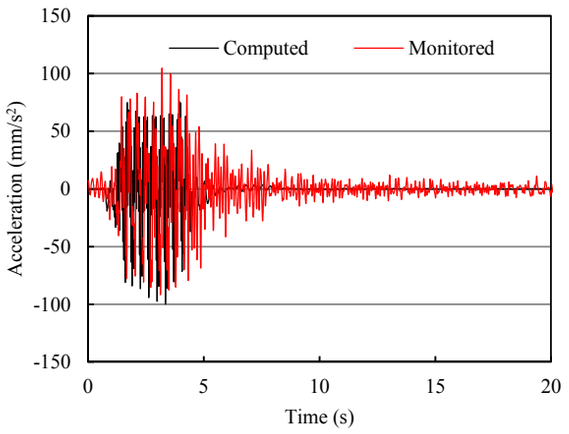


Fig. 5 Comparison of monitored and computed vertical acceleration time histories at cross-section 1

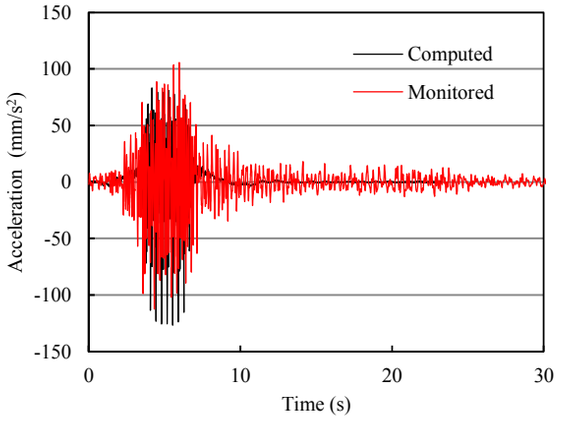


Fig. 6 Comparison of monitored and computed vertical acceleration time histories at cross-section 2

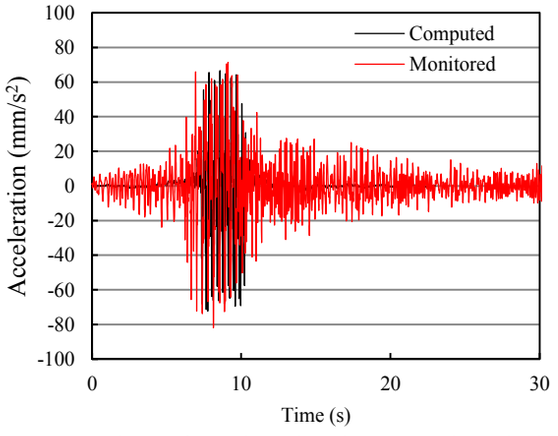


Fig. 7 Comparison of monitored and computed vertical acceleration time histories at cross-section 3

From Fig. 5, it can be seen that the two sets of acceleration time histories are generally close to each other. Amplitudes of the field data above the horizon are larger than the numerical counterparts. Both sets of data show that accelerations are within the prescribed values.

Some differences between the computed and monitored results can be observed in Figs. 6 and 7, mainly since the track irregularities used in the coupled dynamic analysis are numerically generated and do not necessarily reflect the actual smoothness of steel rails on the Dashengguan Yangtze River Bridge. Moreover, track irregularities can cause random vibrations within the high-speed train and bridge system. Consequently, different acceleration time histories will be measured even if a high-speed train running through the Dashengguan Yangtze River Bridge several times under exactly the same conditions (e.g., train speed, environmental temperature, and so on).

4.3 *Acceleration amplitudes*

It is detected in the SHM system that high-speed trains run through the Dashengguan Yangtze River Bridge at various speeds mainly ranging from 200 km/h~300 km/h. Accordingly, acceleration responses at cross-sections 1, 2, and 3 are computed with respect to different train speeds (i.e., 200 km/h ~ 300 km/h). Train composition and track irregularities are identical with those used in section 4.2. Acceleration amplitudes are further displayed in Figs. 8-10, since amplitudes, instead of time histories, can impact the running safety of high-speed trains.

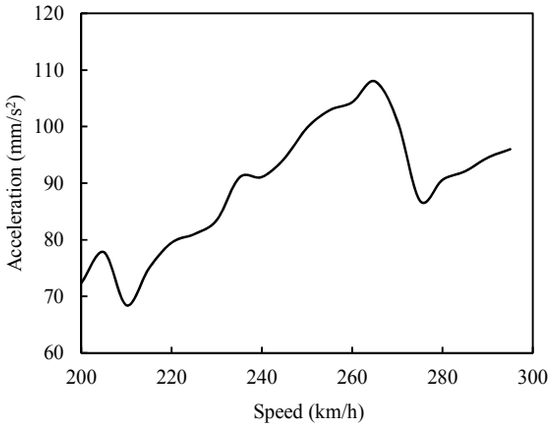


Fig. 8 Variation of amplitude of the vertical acceleration with train speed at cross-section 1

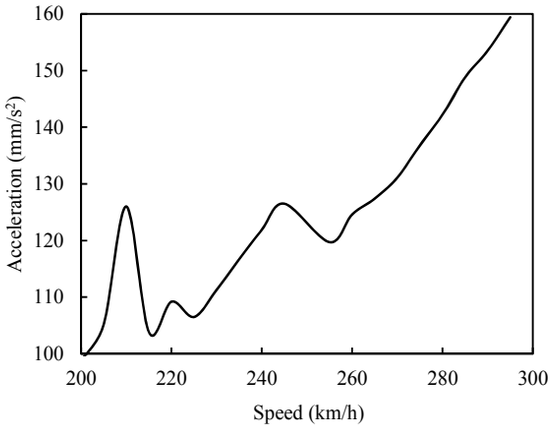


Fig. 9 Variation of amplitude of the vertical acceleration with train speed at cross-section 2

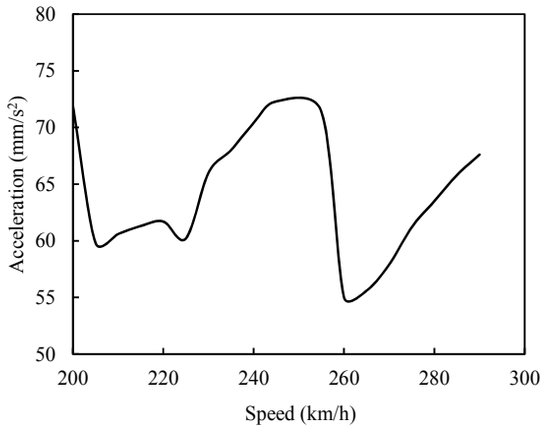


Fig. 10 Variation of amplitude of the vertical acceleration with train speed at cross-section 3

It can be observed in the figures that train speed has significant influence on the bridge acceleration responses. Both peaks and valleys are present in the three acceleration-speed curves. These peaks and valleys may be caused by vibration resonance and cancellation of the train-bridge system (Xia et al. 2014; Yang et al. 2004). In addition, the three acceleration-speed curves are quite different from each other. This implies that all critical cross-sections should be examined to ensure that accelerations of the Dashengguan Yangtze River Bridge are within the prescribed limits under various train speeds.

5 SUMMARY

The high-speed railway network is extending to the western mountainous and eastern coastline areas of China, in which the high-speed railways confront some deep valleys and broad waterways. Long-span bridges provide an effective option to overcome the abovementioned natural barriers. However, high-speed trains are sensitive to the track deformations. How to maintain the geometries of tracks which may be impacted by multiple stressors including high-speed train loads on these unique long-span bridges has been a challenge to researchers and engineers. SHM systems can help obtaining the real-time information about both the stressors and responses of long-span bridges. As an effective alternative, numerical calculations are able to consider loading cases that are not covered by the field monitoring.

As a preliminary study, this paper examines the acceleration responses of a unique long-span railway bridge for high-speed rails, the Dashengguan Yangtze River Bridge, by establishing the coupled train-bridge system model. A 3D train model, 3D bridge FE model, and wheel-rail interaction model considering the effects of track irregularities are incorporated in the system model. Time histories of the bridge accelerations are obtained and compared with the data collected from the SHM system. Acceleration amplitudes are further computed with the help of the coupled system model. Both the time history and amplitude results show that acceleration responses of the examined bridge comply with the code.

Track irregularities are the main cause of random vibrations within the train-bridge system. Time histories shown in Figs.5-7 only represent one sample, and therefore, some differences are observed between the computed sample and the measured sample (see Fig. 6 and 7). It is anticipated that statistical analysis can facilitate reducing the gaps between the numerical and monitoring results. Statistical acceleration-speed curves will provide more useful information, based on which vibration resonance and cancellation phenomena associated with the Dashengguan Yangtze River Bridge can be further investigated.

ACKNOWLEDGEMENTS

This study is supported by the National Natural Science Foundation of China (Grant 51708112).

REFERENCES

Catbas F.N., Susoy M. & Frangopol, D.M. 2008. Structural health monitoring and reliability estimation: Long span truss bridge application with environmental monitoring data. Engineering Structures, 30(9): 2347-2359.

Ding, Y.L., Zhao H.W., Deng L., Li A.Q. & Wang M.Y. 2017. Early warning of abnormal train-induced vibrations for a steel-truss arch railway bridge: case study. *Journal of Bridge Engineering, ASCE* 22(11): 1-12.

Feng, D.M. & Feng, M.Q. 2015. Vision-based multipoint displacement measurement for structural health monitoring. *Structural Control & Health Monitoring,* 23(5): 876-890.

Ko, J.M. & Ni, Y.Q. 2005. Technology developments in structural health monitoring of large-scale bridges. *Engineering Structures* 27(12): 1715-1725.

Leander, J., Andersson, A. & Karoumi, R. 2010. Monitoring and enhanced fatigue evaluation of a steel railway bridge. *Engineering Structures* 32(3): 854-863.

Li, H.L., Frangopol, D.M., Soliman, M. & Xia, H. 2016. Fatigue Reliability Assessment of Railway Bridges Based on Probabilistic Dynamic Analysis of a Coupled Train-Bridge System. *Journal of Structural Engineering, ACSE* 142(3): 1-16.

Li, H.L., Soliman, M., Frangopol, D.M. & Xia, H. 2017. Fatigue damage in railway steel bridges: approach based on a dynamic train-bridge coupled model. *Journal of Bridge Engineering, ACSE* 22(11): 1-9.

Li, H.L., Xia, H., Soliman, M. & Frangopol, D.M. 2015. Bridge stress calculation based on the dynamic response of coupled train-bridge system. *Engineering Structures* 99: 334-345.

Magalhães, F., Cunha, A., & Caetano, E. 2012. Vibration based structural health monitoring of an arch bridge: from automated OMA to damage detection. *Mechanical Systems and Signal Processing*, 28: 212-228.

Xia, H., De Roeck, G. & Goicolea, J. M. 2012. *Bridge vibration and controls: New research*, Nova Science, New York.

Xia, H., Li, H.L., Guo, W.W. & De Roeck, G. 2014. Vibration resonance and cancellation of simply supported bridges under moving train loads. *Journal of Engineering Mechanics, ASCE*, 140(5), 04014015.

Yang, Y. B., Lin , C. L ., Yau, J. D. & Chang D.W. 2004. Mechanism of resonance and cancellation for train-induced vibrations on bridges wi th elastic bearings. *Journal of Sound and Vibration*, 269(1-2): 345-360.

Zhai, W.M, Wang K.Y. & Cai C.B. 2010. Fundamentals of vehicle-track coupled dynamics. *Vehicle System Dynamics*, 47(11): 1349-1376.

Zhang, N., Xia, H., Guo, W. W. & De Roeck, G. 2010. A vehicle bridge linear interaction model and its validation. *International journal of structural stability and dynamics*, 10(2): 335-361.

Zhao, H.W., Ding, Y.L., An, Y.H. & Li, A .Q. 2016. Transverse dynamic mechanical behavior of hangers in the rigid tied-arch bridge under train lo ads. *Journal of Performanceof Constructed Facilities, ACSE* 31(1): 1-16.

Maintenance, Safety, Risk, Management and Life-Cycle Performance of Bridges – Powers, Frangopol, Al-Mahaidi & Caprani (Eds)
© 2018 Taylor & Francis Group, London, ISBN 978-1-138-73045-8

Optimal weight problem for response sensitivity-based damage identification

Junxian Zhou & Li Wang & Zhong-Rong Lu*
Department of applied mechanics and engineering
Sun Yat-sen University, Guangzhou, P.R.China

ABSTRACT: The response sensitivity approach has been shown to be effective for structural damage identification. The goal function involved is of the form $g(\boldsymbol{\alpha}) = \|\boldsymbol{R}(\boldsymbol{\alpha}) - \hat{\boldsymbol{R}}\|^2_{\boldsymbol{W}}$ with $\boldsymbol{R}(\boldsymbol{\alpha})$ denoting the response function derived via governing equations with given parameters $\boldsymbol{\alpha}$ and $\hat{\boldsymbol{R}}$ the measured data. In many cases of response sensitivity analysis, the weight matrix $\boldsymbol{W}$ is simply set to be de identity matrix and few studies have been presented alone on how to properly choose the weight matrix. This paper tries to present a simple theoretical and numerical investigation on the optimal weight problem for response sensitivity-based damage identification with measurement and model errors. By minimizing the expectation of the squares error in identification results, the optimal weight matrix is found to be $\boldsymbol{W}^{opt} = c\boldsymbol{Q}_R^{-1}, c > 0$ when only measurement errors is involved with covariance $\boldsymbol{Q}_R$. Futher analysis shows that the optimal weight matrix can also make the 'relative error' - square root of expectation of squares relative error in every individual damage parameter minimized. What's more, if model errors, such as errors in the damping and load parameters are additionally considered, the optimal matrix is $\boldsymbol{W}^{opt} = c(\boldsymbol{Q}_R + \boldsymbol{S}_\beta \boldsymbol{Q}_\beta \boldsymbol{S}_\beta^T)^{-1}, c > 0$, where $\boldsymbol{Q}_\beta = E[\boldsymbol{\varepsilon}_\beta \boldsymbol{\varepsilon}_\beta^T]$ and $\boldsymbol{S}_\beta = \nabla_\beta \boldsymbol{R}(\boldsymbol{\alpha}^{ex}, \hat{\boldsymbol{\beta}})$ with $\boldsymbol{\varepsilon}_\beta$ being model errors of the model parameters $\hat{\boldsymbol{\beta}}$. Numerical tests on a plane frame are conducted to see the effect of the proposed optimal weight matrix.

1 INTRODUCTION

Reliable, efficient and non-destructive identification of damage in structures is central to structural health monitoring. Physically damage often arising due to environmental aggressions, possibly unexpected loads and material creep etc, mainly causes a loss of structural stiffness. Therefore, the main task of structural damage identification is to inversely identify the damage locations and intensities from the measured data, e.g. acceleration, displacement responses, eigenfrequencies and/or eigen modes of a structure. Typically, such a procedure belongs to a class of inverse problems and is often modeled as a nonlinear weighted least-squares optimization problem between measurement data and theoretic data. Among the many methods to solve the nonlinear least-squares optimization problem, the sensitivity-based approaches (Chen & Maung 2014, Lu & Law 2007, Lu & Wang 2017) have shown its effectiveness.

In principle, the success of the sensitivity-based approaches is based on the sensitivity analysis and usage of regularization techniques (Lu & Wang 2017). Over the years, considerable work has been focused on the development and application of the sensitivity-based approaches for damage identification in various kinds of structures and with various types of the measured data. Generally speaking, eigenfrequencies and eigen modes is most used for damage identification because they are easily accessed. However, the low-frequency modal data usually obtained in modal tests is insensitive to small or local damage (Link & Weiland 2009). In contrast, as pointed out by Link and Weiland (Link & Weiland 2009), time domain response data from impact tests carries high-frequency information and is sensitive to damage even if the damage is local (Cattarius & Inman 1997); this indicates that time domain response data is beneficial for the detection of local and small damage compared with the modal data. With the time domain data, Lu and Law (Lu & Law 2007) proposed to use response sensitivity analysis for damage identification, and later, Lu and Wang (Lu & Wang 2017) enhanced the response sensitivity approach so that even large damage can be identified. In addition, Link and Weiland(Link & Weiland 2009) conducted an elaborate comparative study for sensitivity-based damage identification using modal data and using time domain response data, for with the latter was shown to be superior in damage identification.

In this paper, the sensitivity-based approaches using the time data (Lu & Wang 2017) is followed up for further investigation. As mentioned above, the objective function is of the weighted least-squares form for which the residual between the measured data and the implicitly derived data and the selection of weighting matrix are concerned. However, limited attention has been paid to the choice and effect of the weight matrix for the weighted nonlinear least-squares optimization problems. It is noteworthy that the weight matrix shall be carefully selected. On the one hand, different kinds of data—displacement, velocity, acceleration or eigenfrequency correspond to different dimensions. Without properly defined weight matrix, equivalent replacement of dimensions, e.g. $1m$ replaced by 10^3mm may lead to quite different objective functions and different identification results thereof. To avoid this, the scaling effect behind the weight matrix should be implicated. On the other hand, when the measured data is at different levels of errors, the weight matrix should be chosen such that large error corresponds to less weight. Primitively, there have already been some reasonable choices of the weight matrix (Friswell & Mottershead 1995, Silva, Maia, Link, & Mottershead 2016, Govers & Link 2010), such as being the reciprocal of the covariance matrix of the measured data. Particularly, in sensitivity-based model updating, proper choice of the weight matrix in each updating step may even pose the equivalent effect of regularization (Friswell & Mottershead 1995, Govers & Link 2010). In this paper, the main aim is to present a thorough view on the optimal choice and the specific effect of the weight matrix for response-sensitivity-based damage identification. Distinct to the work in (Friswell & Mottershead 1995, Govers & Link 2010), the weight matrix herein for the nonlinear least-squares optimization problem does not change during the iterative identification procedure and does not intend to pose the regularization effect; rather, it tries to render the expectation of the squares error of the final identified results minimized. Moreover, in addition to the measurement errors, the model errors such as the external load are also considered and how to properly choose the weight matrix in such cases is also addressed. The remainder of the paper is structured as follows. Section 2 briefly states the underlying damage identification problem. In Section 3, how to choose the optimal weight matrix with measurement and model errors is specifically analyzed. In Section 4, a plane frame numerical example is studied in detail to see the effect of the proposed optimal weight matrix and final conclusions are drawn in Section 5.

2 THEORY

2.1 *Finite element model*

Consider a general finite element model of a linear elastic time-invariant structure, governed by the following dynamic equations,

$$\begin{aligned} &\boldsymbol{M}\ddot{\boldsymbol{d}} + \boldsymbol{C}\dot{\boldsymbol{d}} + \boldsymbol{K}\boldsymbol{d} = \boldsymbol{P}(t) \\ &\boldsymbol{d}(0) = \boldsymbol{d}_0, \dot{\boldsymbol{d}}(0) = \dot{\boldsymbol{d}}_0 \end{aligned} \tag{1}$$

where $\boldsymbol{M}, \boldsymbol{K}, \boldsymbol{C}$ are the system mass, damping and stiffness matrices, respectively. $\boldsymbol{d}$, $\dot{\boldsymbol{d}}$, $\ddot{\boldsymbol{d}}$ represent the displacement, velocity and acceleration responses of the structure and $\boldsymbol{d}_0$, $\dot{\boldsymbol{d}}_0$ are initial displacement and velocity. $\boldsymbol{P}$ denotes the external load vector. Usually, the stiffness matrix $\boldsymbol{K}$ is an affine function of the parameters $\boldsymbol{\alpha} \subset R^m$, i.e., $\boldsymbol{K} = \boldsymbol{K}(\boldsymbol{\alpha}) := \boldsymbol{K}_0 + \sum_{j=1}^{m} \alpha_j \boldsymbol{K}_j$. The damping matrix $\boldsymbol{C}$ is assumed to be the Rayleigh damping, that is, $\boldsymbol{C} = a_1\boldsymbol{M} + a_2\boldsymbol{K}$ with a_1,a_2 being two positive coefficients. In practice, given a set of $\boldsymbol{\alpha}$, the responses (including displacement, velocity and acceleration) of the structure are often obtained by the Newmark method.

2.2 *Sensitivity analysis*

The sensitivity of responses $\boldsymbol{d}, \ddot{\boldsymbol{d}}$ with respect to the parameter α_k can be derived from the following equation

$$\begin{aligned} &\boldsymbol{M}\frac{\partial \ddot{\boldsymbol{d}}}{\partial \alpha_k} + \boldsymbol{C}\frac{\partial \dot{\boldsymbol{d}}}{\partial \alpha_k} + \boldsymbol{K}\frac{\partial \boldsymbol{d}}{\partial \alpha_k} = -\boldsymbol{K}_k(\boldsymbol{d} + a_2\dot{\boldsymbol{d}}), \\ &\frac{\partial \boldsymbol{d}}{\partial \alpha_k}(0) = 0, \frac{\partial \dot{\boldsymbol{d}}}{\partial \alpha_k}(0) = 0 \end{aligned} \tag{2}$$

As is seen, the governing equation for $\frac{\partial \boldsymbol{d}}{\partial \alpha_k}$ is in the same form with the original motion equation (1) except that the force function $\boldsymbol{P}(t)$ is replaced by $-\boldsymbol{K}_k(\boldsymbol{d} + a_2\dot{\boldsymbol{d}})$ and initial conditions are set to zero. Still, the response sensitivity $\frac{\partial \boldsymbol{d}}{\partial \alpha_k}, \frac{\partial \ddot{\boldsymbol{d}}}{\partial \alpha_k}$ can be computed by the Newmark method.

2.3 *Objective function of damage identification*

Now assume that the measured response data $\boldsymbol{R}$ at observed time points $t_j = 1, 2, \cdots, l$ is stored in a vector with the form $\hat{\boldsymbol{R}} = \begin{pmatrix} \hat{\boldsymbol{d}}_i \\ \hat{\ddot{\boldsymbol{d}}}_j \end{pmatrix} = \begin{pmatrix} [\hat{u}_i(t_1), \hat{u}_i(t_2), \cdots, \hat{u}_i(t_l)]^T \\ [\hat{\ddot{u}}_j(t_1), \hat{\ddot{u}}_j(t_2), \cdots, \hat{\ddot{u}}_j(t_l)]^T \end{pmatrix}$, where the displacement and acceleration measurement points can be different and the number of measuring points can

be more than one. Theoretically, given the damage parameters $\boldsymbol{\alpha}$, the measured quantities $\boldsymbol{R}(\boldsymbol{\alpha})$ can be implicitly computed as $\boldsymbol{R} = \begin{pmatrix} \boldsymbol{d}_i(\boldsymbol{\alpha}) \\ \ddot{\boldsymbol{d}}_j(\boldsymbol{\alpha}) \end{pmatrix} = \begin{pmatrix} [u_i(t_1), u_i(t_2), \cdots, u_i(t_l)]^T \\ [\ddot{u}_j(t_1), \ddot{u}_j(t_2), \cdots, \ddot{u}_j(t_l)]^T \end{pmatrix}$.

In damage identification, the aim is to identify $\boldsymbol{\alpha}$ from the measured data which forms a inverse problem and can be formulated as minimization of the following objective function—weighted least-squares of the error in measured quantities,

$$\begin{aligned} \min g(\boldsymbol{\alpha}) &= (\hat{\boldsymbol{R}} - \boldsymbol{R}(\boldsymbol{\alpha}))^T \boldsymbol{W} (\hat{\boldsymbol{R}} - \boldsymbol{R}(\boldsymbol{\alpha})) \\ &= \|\hat{\boldsymbol{R}} - \boldsymbol{R}(\boldsymbol{\alpha})\|^2_{\boldsymbol{W}} \end{aligned} \tag{3}$$

where $\boldsymbol{W}$ is a positive-definite weight matrix. Different weight matrix $\boldsymbol{W}$ could result in different damage identification results and how to properly choose such a weight matrix will be addressed in Section 3. In what follows, how to solve the damage identification problem (3) with response data via the sensitivity analysis is presented.

2.4 *Enhanced response sensitivity approach*

Problem (3) is a typical nonlinear optimization problem and therefore, it should be solved iteratively. A common yet simple manner to cope with such a nonlinear least-squares problem is to linearize $\hat{\boldsymbol{R}} - \boldsymbol{R}(\boldsymbol{\alpha})$ at a given $\bar{\boldsymbol{\alpha}}$, that is

$$\hat{\boldsymbol{R}} - \boldsymbol{R}(\boldsymbol{\alpha}) = \delta \boldsymbol{R}(\bar{\boldsymbol{\alpha}}) - \boldsymbol{S}(\bar{\boldsymbol{\alpha}}) \delta \boldsymbol{\alpha} \tag{4}$$

where $\delta \boldsymbol{\alpha} := \boldsymbol{\alpha} - \bar{\boldsymbol{\alpha}}$ is the *update* of $\boldsymbol{\alpha}$, $\delta \boldsymbol{R}(\bar{\boldsymbol{\alpha}})$ is called the residual between the measured data $\hat{\boldsymbol{R}}$ and the derived data $\boldsymbol{R}(\bar{\boldsymbol{\alpha}})$, and $\boldsymbol{S}(\bar{\boldsymbol{\alpha}})$ is the first-order sensitivity matrix, possessing the following form

$$\boldsymbol{S}(\bar{\boldsymbol{\alpha}}) = \bigtriangledown_{\boldsymbol{\alpha}} \boldsymbol{R}(\bar{\boldsymbol{\alpha}}) := \begin{pmatrix} \frac{\partial \boldsymbol{d}_i}{\partial \alpha_1}, \frac{\partial \boldsymbol{d}_i}{\partial \alpha_2}, \cdots, \frac{\partial \boldsymbol{d}_i}{\partial \alpha_m} \\ \frac{\partial \ddot{\boldsymbol{d}}_j}{\partial \alpha_1}, \frac{\partial \ddot{\boldsymbol{d}}_j}{\partial \alpha_2}, \cdots, \frac{\partial \ddot{\boldsymbol{d}}_j}{\partial \alpha_m} \end{pmatrix} \tag{5}$$

where the sensitivity analysis(2) is involved. Then, a linear least-squares minimization problem for update $\delta \boldsymbol{\alpha}$ can be invoked

$$min\ \hat{g}(\delta \boldsymbol{\alpha}, \bar{\boldsymbol{\alpha}}) := \|\delta \boldsymbol{R}(\bar{\boldsymbol{\alpha}}) - \boldsymbol{S}(\bar{\boldsymbol{\alpha}}) \delta \boldsymbol{\alpha}\|^2_{\boldsymbol{W}} \tag{6}$$

However, problem(6) is often ill-posed and therefore the Tikhonov regularization is utilized where the regularization term $\lambda \|\delta \boldsymbol{\alpha}\|^2$ with $\|\cdot\|$ denoting the usual L^2 norm and λ a small nonnegative regularization parameter is added to (6). Under this circumstance, the update $\delta \boldsymbol{\alpha}_\lambda$ becomes

$$\delta \boldsymbol{\alpha}_\lambda = arg\ min \|\boldsymbol{S}(\bar{\boldsymbol{\alpha}}) \delta \boldsymbol{\alpha} - \delta \boldsymbol{R}(\bar{\boldsymbol{\alpha}})\|^2_{\boldsymbol{W}} + \lambda \|\delta \boldsymbol{\alpha}\|^2 \tag{7}$$

$$\Rightarrow \delta \boldsymbol{\alpha}_\lambda = [\boldsymbol{S}(\bar{\boldsymbol{\alpha}})^T \boldsymbol{W} \boldsymbol{S}(\bar{\boldsymbol{\alpha}}) + \lambda \boldsymbol{I}]^{-1} \boldsymbol{S}(\bar{\boldsymbol{\alpha}})^T \boldsymbol{W} \delta \boldsymbol{R}(\bar{\boldsymbol{\alpha}})$$

The trust-region restriction is additionally enforced by properly determining the regularization parameter λ. For simplicity, the steps of enhanced response sensitivity approach are given in Table 1 and for more details, refer to (Lu & Wang 2017).

3 OPTIMAL WEIGHT MATRIX UNDER MEASUREMENT AND MODEL ERRORS

3.1 *Optimal weight matrix under measurement errors*

Assume that the measured data is subject to normally distributed noise as the following form,

$$\hat{\boldsymbol{R}} = \boldsymbol{R}(\boldsymbol{\alpha}^{ex}) + \boldsymbol{\varepsilon}_R \tag{8}$$

where $\boldsymbol{\alpha}^{ex}$ represent the exact damage parameters and $\boldsymbol{\varepsilon}_R$ is the measured error vector pertaining to the Gaussian distribution subject to zero means and positive definite covariance $E[\boldsymbol{\varepsilon}_R \boldsymbol{\varepsilon}_R^T] = \boldsymbol{Q}_R$. An optimal weight matrix shall render the expectation of squares of the identification errors $E[(\boldsymbol{\alpha}^* - \boldsymbol{\alpha}^{ex})^T (\boldsymbol{\alpha}^* - \boldsymbol{\alpha}^{ex})]$ minimized. To go further, the goal function $g(\boldsymbol{\alpha})$ (3) is further analyzed by linearization,

$$\begin{aligned} g(\boldsymbol{\alpha}) &= \|\boldsymbol{R}(\boldsymbol{\alpha}^{ex}) + \boldsymbol{\varepsilon}_R - \boldsymbol{R}(\boldsymbol{\alpha}))\|^2_{\boldsymbol{W}} \\ &= \|\boldsymbol{\varepsilon}_R - \boldsymbol{S}(\boldsymbol{\alpha}^{ex}) \cdot (\boldsymbol{\alpha} - \boldsymbol{\alpha}^{ex}) + h.o.t\|^2_{\boldsymbol{W}} \end{aligned} \tag{9}$$

where $h.o.t$ represents higher order terms that are negligible with respect to $\boldsymbol{\varepsilon}_R$ when $\boldsymbol{\alpha}$ is in the vicinity of $\boldsymbol{\alpha}^{ex}$. Note that $\boldsymbol{\alpha}^*$ is in the vicinity of $\boldsymbol{\alpha}^{ex}$, this means,

$$\boldsymbol{\alpha}^* - \boldsymbol{\alpha}^{ex} \approx [\boldsymbol{S}^T \boldsymbol{W} \boldsymbol{S}]^{-1} \boldsymbol{S}^T \boldsymbol{W} \boldsymbol{\varepsilon}_R := \boldsymbol{L}_W \boldsymbol{\varepsilon}_R \tag{10}$$

where $\boldsymbol{L}_W = [\boldsymbol{S}^T \boldsymbol{W} \boldsymbol{S}]^{-1} \boldsymbol{S}^T \boldsymbol{W}$. Then, one can has

$$\begin{aligned} E[(\boldsymbol{\alpha}^* - \boldsymbol{\alpha}^{ex})^T (\boldsymbol{\alpha}^* - \boldsymbol{\alpha}^{ex})] &\approx E[\boldsymbol{\varepsilon}_R^T \boldsymbol{L}_W^T \boldsymbol{L}_W \boldsymbol{\varepsilon}_R] \\ &= tr(\boldsymbol{L}_W \boldsymbol{Q}_R \boldsymbol{L}_W^T) \end{aligned} \tag{11}$$

where $tr(\cdot)$ is the trace operator and the last equality arises due to $E[\boldsymbol{\varepsilon}_R \boldsymbol{\varepsilon}_R^T] = \boldsymbol{Q}_R$.

Theorem 1

The optimal choice of $\boldsymbol{W}$ to minimize $F(\boldsymbol{W}) := tr(\boldsymbol{L}_W \boldsymbol{Q}_R \boldsymbol{L}_W^T)$ is

$$\boldsymbol{W}^{opt} = c \boldsymbol{Q}_R^{-1}, c > 0 \tag{12}$$

and then,

$$F(\boldsymbol{W}^{opt}) = tr([\boldsymbol{S}^T \boldsymbol{Q}_R^{-1} \boldsymbol{S}]^{-1}). \tag{13}$$

Proof

Table 1: Algorithmic details for enhanced response sensitivity approach

-set initial damage parameters $\boldsymbol{\alpha}^1$ as those of the intact structure,
-fix error tolerance *RelErr* (e.g., = 10^6) for convergence criterion,
-fix the maximum number of iterations *Nmax*(e.g.,=100),
-fix trust-region parameters ρ_{cr} (e.g.,=0.5) and $\gamma > 1$(e.g.,=2)
-fix the maximum number of steps for trust-region procedure *Ntr*,(e.g.,=10,)
-load the measured data $\hat{\boldsymbol{R}}$ and user-defined weight matrix $\boldsymbol{W}$,
-for k=1:*Nmax*
 -solve(1) to get $\boldsymbol{R}(\boldsymbol{\alpha}^k)$,
 -compute the residual $\delta\boldsymbol{R} = \hat{\boldsymbol{R}} - \boldsymbol{R}(\boldsymbol{\alpha}^k)$,
 -do sensitivity analysis (2) to get the sensitivity matrix $\boldsymbol{S}(\boldsymbol{\alpha}^k)$,
 -use L-curve method to get the initial regularization parameter $\lambda = \lambda_L(\alpha^k)$,
 -for i=1:*Ntr* %Trust-region procedure
  -$\lambda = \gamma^{i-1}\lambda_L(\alpha^k)$,
  -compute the update $\delta\boldsymbol{\alpha} = [\boldsymbol{S}^T(\boldsymbol{\alpha}^k)\boldsymbol{W}\boldsymbol{S}(\boldsymbol{\alpha}^k) + \lambda\boldsymbol{I}]^{-1}\boldsymbol{S}^T(\boldsymbol{\alpha}^k)\boldsymbol{W}\delta\boldsymbol{R}$
  -solve (1) to get $\boldsymbol{R}(\boldsymbol{\alpha}^k + \delta\boldsymbol{\alpha})$,
  -computer new residual $\delta\boldsymbol{R}_{new} = \hat{\boldsymbol{R}} - \boldsymbol{R}(\boldsymbol{\alpha}^k + \delta\boldsymbol{\alpha})$,
  -calculate the agreement indicator $\rho = \frac{\|\delta\boldsymbol{R}\|^2 - \|\delta\boldsymbol{R}_{new}\|^2}{\|\delta\boldsymbol{R}\|^2 - \|\delta\boldsymbol{R} - S(\boldsymbol{\alpha}^k)\delta\boldsymbol{\alpha}\|^2}$,
  -if $\rho \geq \rho_{cr}$ break,
 -end for
 -update damage parameters $\boldsymbol{\alpha}^{(k+1)} = \boldsymbol{\alpha}^k + \delta\boldsymbol{\alpha}$,
 -if $\|\delta\boldsymbol{\alpha}\|/\|\boldsymbol{\alpha}^{k+1}\| \leq RelErrbreak$.
-end for

Herein, the auxiliary matrix $\boldsymbol{L}_W$ rather than $\boldsymbol{W}$ is used for later derivation. A remarkable feature of $\boldsymbol{L}_W$ is

$$\boldsymbol{L}_W\boldsymbol{S} = \boldsymbol{I}. \tag{14}$$

Then, the problem becomes an equality constrained optimization problem and the Lagrangian multipliers $\boldsymbol{\Theta}$ are introduced to deal with the constraints (14),

$$\ell(\boldsymbol{L}_W, \boldsymbol{\Theta}) = tr(\boldsymbol{L}_W\boldsymbol{Q}_R\boldsymbol{L}_W^T) + tr((\boldsymbol{I} - \boldsymbol{L}_W\boldsymbol{S})\boldsymbol{\Theta}). \tag{15}$$

Optimization of $\ell(\boldsymbol{L}_W, \boldsymbol{\Theta})$ over $\boldsymbol{L}_W$ leads to,

$$\boldsymbol{L}_W = \frac{1}{2}\boldsymbol{\Theta}^T\boldsymbol{S}^T\boldsymbol{Q}_R^{-1}. \tag{16}$$

Then, combination of (14) and (16) yields,

$$\boldsymbol{\Theta} = 2(\boldsymbol{S}^T\boldsymbol{Q}_R^{-1}\boldsymbol{S})^{-1} \tag{17}$$

Along with (16), optimal $\boldsymbol{L}_W$ is found to be

$$\boldsymbol{L}_W^{opt} = (\boldsymbol{S}^T\boldsymbol{Q}_R^{-1}\boldsymbol{S})^{-1}\boldsymbol{S}^T\boldsymbol{Q}_R^{-1}. \tag{18}$$

Further considering, the definitions of $\boldsymbol{L}_W$ and $\boldsymbol{F}(\boldsymbol{W})$, equations (12) and (13) in theorem 1 follows naturally.

Theorem 2

Introduce an order operator $\preceq$ (or inversely $\succeq$) for two symmetric matrix $\boldsymbol{A}, \boldsymbol{B} \in R^{N\times N}$ as follows,

$$\boldsymbol{A} \preceq \boldsymbol{B} \Leftrightarrow \boldsymbol{v}^T\boldsymbol{A}\boldsymbol{v} \leq \boldsymbol{v}^T\boldsymbol{B}\boldsymbol{v}, \forall\boldsymbol{v} \in R^N \tag{19}$$

In the sense of the order operator $\succeq$, covariance of the identification errors $E[(\boldsymbol{\alpha}^* - \boldsymbol{\alpha}^{ex})(\boldsymbol{\alpha}^* - \boldsymbol{\alpha}^{ex})^T] = \boldsymbol{L}_W\boldsymbol{Q}_R\boldsymbol{L}_W^T$ would also arrive at a minimum under the optimal weight matrix $\boldsymbol{W}^{opt} = c\boldsymbol{Q}_R^{-1}$, i.e.,

$$\boldsymbol{L}_W^{opt}\boldsymbol{Q}^R(\boldsymbol{L}_W^{opt})^T = [\boldsymbol{S}^T\boldsymbol{Q}_R^{-1}\boldsymbol{S}]^{-1} \preceq \boldsymbol{L}_W\boldsymbol{Q}_R\boldsymbol{L}_W^T, \tag{20}$$
$$\forall \quad positive\,definite\,\boldsymbol{W}.$$

Proof

For an arbitrary positive definite weight matrix $\boldsymbol{W}$, one can have

$$\boldsymbol{L}_W = \boldsymbol{L}_W^{opt} + \Delta\boldsymbol{L} \tag{21}$$

with $\Delta\boldsymbol{L}$ satisfying $\Delta\boldsymbol{L}\cdot\boldsymbol{S} = 0$. Recalling the Definition of $\boldsymbol{L}_W^{opt}$ in (16), it is also found that

$$\boldsymbol{L}_W^{opt}\boldsymbol{Q}_R\Delta\boldsymbol{L}^T = 0. \tag{22}$$

With equations (21) and (22), there holds

$$\begin{aligned}\boldsymbol{L}_W\boldsymbol{Q}_R\boldsymbol{L}_W^T &= (\boldsymbol{L}_W^{opt} + \Delta\boldsymbol{L})\boldsymbol{Q}_R(\boldsymbol{L}_W^{opt} + \Delta\boldsymbol{L})^T \\ &\succeq \boldsymbol{L}_W^{opt}\boldsymbol{Q}_R(\boldsymbol{L}_W^{opt})^T = [\boldsymbol{S}^T\boldsymbol{Q}_R^{-1}\boldsymbol{S}]^{-1}\end{aligned} \tag{23}$$

3.2 *Additional considerations on model errors*

The model parameters $\boldsymbol{\beta} = [\beta_1, \beta_2, \ldots, \beta_n]^T$ are also taken in account herein in addition to the damage parameter $\boldsymbol{\alpha}$. For structures, the modal parameters $\boldsymbol{\beta}$ may include the mass density in the mass Matrix $\boldsymbol{M}$

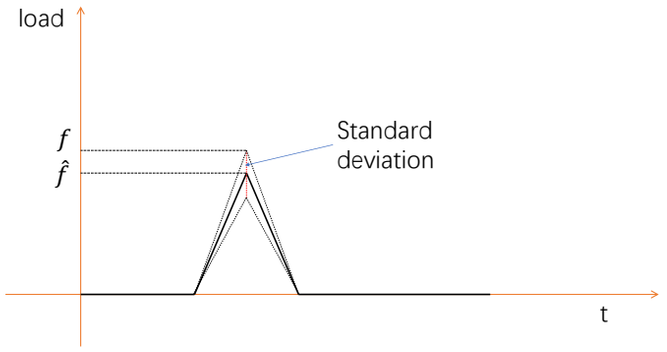


Figure 1: Schematic illustrations for impact load

and the amplitude of an impact load in the load vector $\boldsymbol{P}$, etc. The known values $\hat{\boldsymbol{\beta}}$ pertains to

$$\hat{\boldsymbol{\beta}} = \boldsymbol{\beta}^{ex} + \boldsymbol{\varepsilon}_{\beta} \tag{24}$$

where $\boldsymbol{\beta}^{ex}$ is the unknown exact model parameters and $\boldsymbol{\varepsilon}_{\beta}$ represent the errors subject to Gaussian distribution with zero means and covariance $E[\boldsymbol{\varepsilon}_{\beta}\boldsymbol{\varepsilon}_{\beta}^{T}] = \boldsymbol{Q}_{\beta}$. $\boldsymbol{\varepsilon}_{\beta}$ and $\boldsymbol{\varepsilon}_{R}$ are independent from each other. The derived data under the parameters $\hat{\boldsymbol{\beta}}$ is expressed as $\boldsymbol{R}(\boldsymbol{\alpha}, \hat{\boldsymbol{\beta}})$. In this way, the goal function (3) becomes

$$g(\boldsymbol{\alpha}) = \|\hat{\boldsymbol{R}} - R(\boldsymbol{\alpha}, \hat{\boldsymbol{\beta}})\|^2_{\boldsymbol{W}} \tag{25}$$

To further estimate the covariance of the identification errors $\boldsymbol{\alpha}^* - \boldsymbol{\alpha}^{ex}$, similar to equations(9)-(11). The linear Taylor expansion is applied to the goal function for $\boldsymbol{\alpha}$ in the vicinity of $\boldsymbol{\alpha}^{ex}$,

$$\begin{aligned} g(\boldsymbol{\alpha}) &= \|R(\boldsymbol{\alpha}^{ex}, \boldsymbol{\beta}^{ex}) + \boldsymbol{\varepsilon}_R - \boldsymbol{R}(\boldsymbol{\alpha}, \hat{\boldsymbol{\beta}})\|^2_{\boldsymbol{W}} \\ &\approx \|\boldsymbol{\varepsilon}_R - \boldsymbol{S}_{\beta}\boldsymbol{\varepsilon}_{\beta} - \boldsymbol{S} \cdot (\boldsymbol{\alpha} - \boldsymbol{\alpha}^{ex})\|^2_{\boldsymbol{W}} \end{aligned} \tag{26}$$

where $\boldsymbol{S} = \bigtriangledown_{\alpha}\boldsymbol{R}(\boldsymbol{\alpha}^{ex}, \hat{\boldsymbol{\beta}}), \boldsymbol{S}_{\beta} = \bigtriangledown_{\beta} R(\boldsymbol{\alpha}^{ex}, \hat{\boldsymbol{\beta}}) := [\frac{\partial \boldsymbol{R}(\boldsymbol{\alpha}^{ex}, \hat{\boldsymbol{\beta}})}{\partial \beta_1}, \frac{\partial \boldsymbol{R}(\boldsymbol{\alpha}^{ex}, \hat{\boldsymbol{\beta}})}{\partial \beta_2}, \ldots, \frac{\partial \boldsymbol{R}(\boldsymbol{\alpha}^{ex}, \hat{\boldsymbol{\beta}})}{\partial \beta_n}]$. Minimization of (26) yields,

$$\boldsymbol{\alpha}^* - \boldsymbol{\alpha}^{ex} \approx \boldsymbol{L}_W(\boldsymbol{\varepsilon}_R - \boldsymbol{S}_{\beta}\boldsymbol{\varepsilon}_{\beta}) \tag{27}$$

where L_W is of the same form with that in (10). Note that $\boldsymbol{\varepsilon}_R - \boldsymbol{S}_{\beta}\boldsymbol{\varepsilon}_{\beta}$ are also pertaining to Gaussian distribution with zero means and the follwing covariance,

$$E[(\boldsymbol{\varepsilon}_R - \boldsymbol{S}_{\beta}\boldsymbol{\varepsilon}_{\beta})(\boldsymbol{\varepsilon}_R - \boldsymbol{S}_{\beta}\boldsymbol{\varepsilon}_{\beta})^T] = \boldsymbol{Q}_R + \boldsymbol{S}_{\beta}\boldsymbol{Q}_{\beta}\boldsymbol{S}_{\beta}^T. \tag{28}$$

Refer to the proof of the optimal weight matrix in Section 3.1, the optimal weight matrix herein under both measurement and model errors is found to be

$$\boldsymbol{W}^{opt} = c(\boldsymbol{Q}_R + \boldsymbol{S}_{\beta}\boldsymbol{Q}_{\beta}\boldsymbol{S}_{\beta}^T)^{-1}, c > 0 \tag{29}$$

However, difficulty would arise for sensitivity analysis of $\boldsymbol{S}_{\beta} = \nabla_{\beta}\boldsymbol{R}(\boldsymbol{\alpha}^{ex}, \hat{\boldsymbol{\beta}})$, because the required $\boldsymbol{\alpha}^{ex}$ is unknown. To circumvent this difficulty, the approximate damage parameters $\tilde{\boldsymbol{\alpha}}^*$, that are obtained through damage identification with the weight matrix $\boldsymbol{W} = c\boldsymbol{Q}_R^{-1}$ and are often good approximations of $\boldsymbol{\alpha}^{ex}$, are adopted for computation of the sensitivity matrix $\boldsymbol{S}_{\beta}$ and the optimal weight matrix (29) thereof.

The next section considers the load parameters with model error to investigate the influence of the model error. So here the derivation of sensitivity of time response with respect to load parameters is discuss. Considering an impact load of the triangle form in Figure(1), assume that the real peak value f is of the form $f = \hat{f}(1 + \beta_f)$ where $\hat{f}$ is the known/measured peak value and β_f is the percentage noise and in this way, the load vector shall be parameterized as $\boldsymbol{P} = \hat{\boldsymbol{P}}(1 + \beta_f)$. For the dynamic equations(1), the sensitivity of response with respect to β_f yields

$$\begin{aligned} &\boldsymbol{M}\frac{\partial \ddot{\boldsymbol{d}}}{\partial \beta_f} + \boldsymbol{C}\frac{\partial \dot{\boldsymbol{d}}}{\partial \beta_f} + \boldsymbol{K}\frac{\partial \boldsymbol{d}}{\partial \beta_f} = \frac{\partial \boldsymbol{P}}{\partial \beta_f} = \hat{\boldsymbol{P}}, \\ &\frac{\partial \boldsymbol{d}}{\partial \beta_f}(0) = 0, \frac{\partial \dot{\boldsymbol{d}}}{\partial \beta_f}(0) = 0 \end{aligned} \tag{30}$$

Usually, the initial state of the structure is at rest and then, after comparison between (1) and (30), the sensitivity $\frac{\partial \boldsymbol{R}}{\partial \beta_f}$ is simply obtained as

$$\frac{\partial \boldsymbol{R}}{\partial \beta_f} = \begin{pmatrix} \hat{\boldsymbol{d}}_i \\ \hat{\dot{\boldsymbol{d}}}_j \end{pmatrix} \tag{31}$$

4 NUMERICAL TESTS

A simple plane frame is studied to verify the proposed optimal weight matrix. The algorithm in Table 1 is adopted for damage identification and the algorithmic parameters *RelErr, Nmax,* ρ_{cr}, γ, *Ntr* are taken as the values in the following brackets. For model parameters (only load parameter is considered in here), the known impact load $\hat{\boldsymbol{P}}$ are given and the exact values $\boldsymbol{P}^{ex}$ is obtained as $\boldsymbol{P}^{ex} = \hat{\boldsymbol{P}}(1 + \beta_f)$

A single-span plane frame structure as shown in Figure 2 is studied herein to see the effect of weight matrix. Geometric parameters are: the height and width of the frame $H = 1.2m$ and $L = 0.6m$, and the rectangular cross-section dimensions $b = 0.01m$ and $h = 0.02m$. The properties of the intact frame are: the mass density $\rho = 2.7 \times 10^3 kg/m^3$ and the elastic modulus $E = 6.9 \times 10^{10} N/m^2$. As for the finite element modeling, the frame is uniformly divided into 11 Euler-Bernoulli beam elements with 12 nodes each with three DOFs where x-,y-translational and rotational displacements at the kth node are denoted by u_k, v_k, θ_k. Practically, the fixed nodes 1 and 12 of the frame are modeled with the same large support stiffness $\hat{k}_t = \hat{k}_v = 1.5 \times 10^{10} kN/m$ and $\hat{k}_\theta = 1.5 \times 10^9 kN \cdot m/rad$.

Table 2: Damage identification scenarios for plane frame structure

Damage scenario	Damage location(element no.)	Reduction in elastic modulus	Measurement(with noise)	Model error
1	9,10	20%,25%	$\ddot{u}_2(2\%)$,$u_2(10\%)$,$\ddot{u}_9(10\%)$	———
2	2,4,8	20%,20%,15%	$\ddot{u}_2(2\%), \ddot{u}_4(10\%), \ddot{u}_{11}(10\%)$	$F(t)(2\%)$

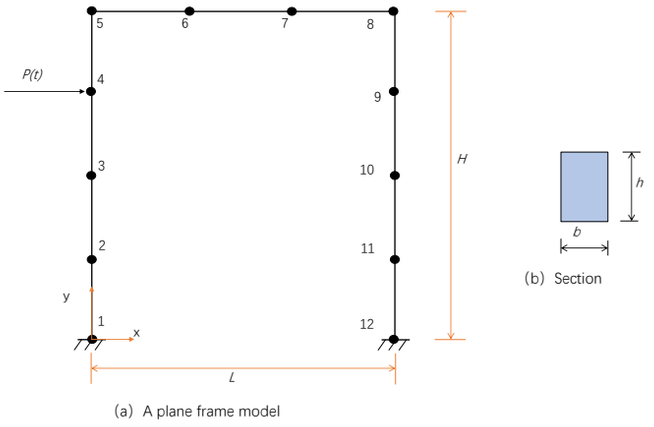


Figure 2: A plane frame model: mesh, load and boundary conditions

In this example, the first two frequencies of the intact frame are found to be 13.095 and 57.308Hz and for simplicity, the first two modal damping ratios are both assumed to be 0.01. Then, the Rayleigh coefficients are $\hat{\alpha}_1 = 1.3395s^{-1}$ and $\hat{\alpha}_2 = 4.52 \times 10^{-5}s$ so that the damping matrix $\boldsymbol{C} = \hat{\alpha}_1\boldsymbol{M} + \hat{\alpha}_2\boldsymbol{K}$ is obtained. As for the external load, the horizontal impact load enforced at 4 node is as follows:

$$\boldsymbol{P}(t) = \begin{cases} 1900 * (t - 0.05) & (0.05s < t < 0.1s) \\ 1900 * (0.15 - t) & (0.1s < t < 0.15s) \end{cases} \tag{32}$$

For this example, the simulated data-displacements or accelerations is obtained from numerical simulation during the time period [0,4s] with a sampling rate of 500Hz. The measured data $\hat{\boldsymbol{d}}_i, \hat{\ddot{\boldsymbol{d}}}_j$ is obtained by addition of measurement errors to simulated data $\boldsymbol{d}_i, \ddot{\boldsymbol{d}}_j$ that is taken from $\boldsymbol{R}(\boldsymbol{\alpha}^{ex}, \boldsymbol{\beta}^{ex})$.

If no model error exists, the optimal weight matrix $\boldsymbol{W}^{opt} = c\boldsymbol{Q}_R^{-1}$ and the identity weight matrix $\boldsymbol{W}^{id} = \boldsymbol{I}$ are used for comparison; while if model errors are considered, the identity weight matrix $\boldsymbol{W}^{id} = \boldsymbol{I}$, the quasi-optimal weight matrix $\boldsymbol{W}^{quasi} = c\boldsymbol{Q}_R^{-1}$ and the optimal weight matrix $\boldsymbol{W}^{opt} = c(\boldsymbol{Q}_R + \boldsymbol{S}_\beta \boldsymbol{Q}_\beta \boldsymbol{S}_\beta^T)^{-1}$ would be adopted for comparative purpose. The identified damage parameters can be obtained by the enhanced response sensitivity approach in Table 1. 20 sets of the measurement data and exact model parameters data when considering model errors will be generated by Monte Carlo sampling. The elastic modulus in the 11 elements are treated as the damage parameters to be identified.

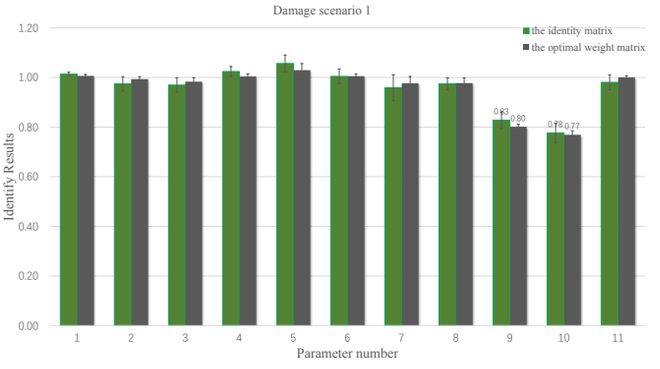


Figure 3: Bar graph with means and standard deviations for damage identification of Scenario 1

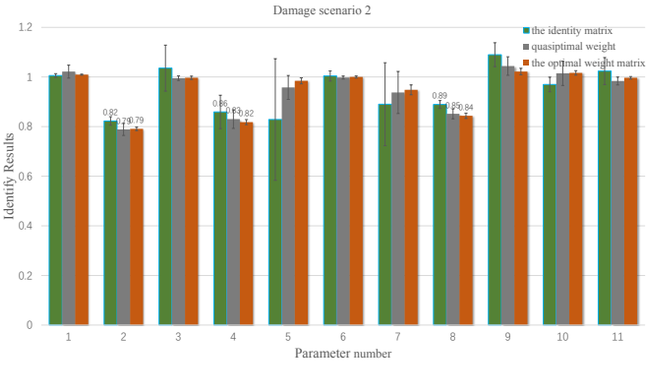


Figure 4: Bar graph with means and standard deviations for damage identification of Scenario 2

Scenario 1 use accelerations and displacements and consider different measurement error levels for accelerations/displacements at different positions (see Table 2). This scenario is assumed to be free from model errors. Based on the Monte Carlo sampling and damage identification algorithm in Table 1, damage parameters can be identified and detailed results on means and standard deviations of individual damage parameters are shown in Figures 3 where ' identified results' refer to $\frac{\alpha_k^*}{\alpha_k^{intact}}$ where α_k^{intact} denotes the parameter before damage. The benefits brought by the optimal weight matrix are obvious since more accurate averages and less standard deviations are obtained under the optimal weight matrix.

Scenario 2 adopts accelerations and additionally take the model errors into account, the Gaussian noise of level 2% is added to the impact load. Along with the Monte Carlo sampling and the enhanced response sensitivity approach, identification results for 20 sampling data sets are obtained with the three specific weight matrices. Statistical bar graphs for the two scenarios are depicted in Figures 4.

For Scenario 2, the result indicates that with the

load error, the identity weight matrix may lead to significant identification errors , while the quasi-optimal weight concerning merely the measurement errors can gain acceptable good identification results and nearly perfect identification results are obtained using the optimal weight matrix where both the measurement and model errors are considered.

5 CONCLUSIONS

In this paper, the selection of the optimal weight matrix has been discussed in case of measurement and model errors. By resorting to the criterion that the optimal weight matrix should minimized the expectation of squares error in identification results, the optimal weight matrix is found to be inversely proportional to the covariance of measurement errors when only measurement errors are considered. In case of model errors, the same criterion shows that the optimal weight matrix depends not only on measurement errors, but also on model errors along with sensitivity to model parameters. Further analysis finds that the optimal weight matrix can also render the 'relative error' of every individual damage parameter minimized. Then, numerical tests on a plane frame is conducted and results show that the optimal choice of the weight matrix can work as expected to improve the accuracy of the damage identification results when different levels of measurement errors(or model errors) or different types of response data are invoked.

ACKNOWLEDGMENTS

This work was supported by the National Natural Science Foundation of China under Grants (11572356), Guangdong Province Natural Science Foundation (2015A030313126), the Fundamental Research Funds for the Central Universities(17lgjc42), and the Guangdong Province Science and Technology Program (2016A020223006). Such financial aids are gratefully acknowledged.

REFERENCES

Cattarius, J. & D. J. Inman (1997). Time domain analysis for damage detection in smart structures. *Mechanical Systems & Signal Processing 11*(3), 409–423.

Chen, H. P. & T. S. Maung (2014). Regularised finite element model updating using measured incomplete modal data. *Journal of Sound & Vibration 333*(21), 5566–5582.

Friswell, M. & J. E. Mottershead (1995). *Finite Element Model Updating in Structural Dynamics*. Kluwer Academic Publishers,.

Govers, Y. & M. Link (2010). Stochastic model updating-covariance matrix adjustment from uncertain experimental modal data. *Mechanical Systems & Signal Processing 24*(3), 696–706.

Link, M. & M. Weiland (2009). Damage identification by multi-model updating in the modal and in the time domain. *Mechanical Systems & Signal Processing 23*(6), 1734–1746.

Lu, Z. R. & S. S. Law (2007). Features of dynamic response sensitivity and its application in damage detection. *Journal of Sound & Vibration 303*(1-2), 305–329.

Lu, Z. R. & L. Wang (2017). An enhanced response sensitivity approach for structural damage identification: convergence and performance. *International Journal for Numerical Methods in Engineering 111*(13), 1231–1251.

Silva, T. A. N., N. M. M. Maia, M. Link, & J. E. Mottershead (2016). Parameter selection and covariance updating. *Mechanical Systems & Signal Processing s 70-71*, 269–283.

Maintenance, Safety, Risk, Management and Life-Cycle Performance of Bridges – Powers, Frangopol, Al-Mahaidi & Caprani (Eds)
© 2018 Taylor & Francis Group, London, ISBN 978-1-138-73045-8

A mesoscopic analysis of chloride diffusion with adaptive mesh refinement

Zichao Pan, Dalei Wang, Rujin Ma & Airong Chen
Department of Bridge Engineering
Tongji University, China

ABSTRACT: The chloride induced rebar corrosion is a big thread to reinforced concrete (RC) structures in the ocean, coastal area, and where the deicing salt is used. A mesoscopic numerical analysis of the chloride diffusion process in RC structures can give a full chloride profile in the concrete with the consideration of material heterogeneity, but also requires a lot of computational efforts which is usually unacceptable in a 3D numerical simulation. In this paper, the technique of adaptive mesh refinement (AMR) is integrated into the classic finite element method (FEM) for the chloride diffusion problem. The main idea of the integrated method is to refine the grid based on a predefined refinement criterion step by step during the whole analysis until the required precision of the solution is reached. A computer program is developed to evaluate the efficiency of the novel mesoscopic method for both 2D and 3D chloride diffusion problems. The result shows that the numerical method with AMR can greatly improve the efficiency of the simulation while the precision of the solution in key areas can be ensured as well.

1 INTRODUCTION

The chloride penetration is one of the most significant threads to reinforced concrete (RC) infrastructures in coastal areas and cold regions where the deicing-salt is used. During the chloride penetration process, chloride ions will accumulate at the surface of rebars. When the local chloride content reaches a threshold called "critical chloride content" (Angst, Elsener, Larsen, & ystein Vennesland 2009), rebars will start to corrode with extra prerequisites such as water and oxygen. The safety and service performances of the entire structure will also decrease due to loss of effective cross-sectional area and strength of rebars and bonding strength between rebars and concrete. Thus, the initiation of rebar corrosion is an important signal during service life of RC structures.

To estimate the initiation time of rebar corrosion, numerous efforts have been taken in both experimental and theoretical researches. The latter can be further categorized into the analytical approach where the Fick's law is often used (Zhou 2016, Zhou 2014), and the numerical simulation method which is more flexible and with a wider application. So far, most of early researches were conducted at macro-scale, where the concrete is considered as a homogeneous and isotropic material. With uniform exposure conditions which are often assumed in analysis, the chloride ions will transport into concrete with no spatial variability, which is contrary to some experimental observations (Angst & Polder 2014). The reason is that the concrete is actually a heterogeneity material which is composed of aggregate, cement paste and interfacial transition zone (ITZ) at meso-scale. The transport path of chloride ions will be distorted by the impermeable aggregates, which can result in the spatial variability of chloride penetration due to the random aggregate structure (RAS), i.e., random shape and position.

To investigate the characteristics of chloride penetration at meso-scale, related researches in recent years have been conducted (Pan, Xin, & Chen 2014, Zheng, Zhou, Wu, & Jin 2012, Pan, Chen, & Xin 2015). Some important conclusions are also available, e.g., aggregates with a larger aspect ratio can effectively decrease the chloride diffusivity of concrete (Pan, Xin, & Chen 2014, Zheng, Zhou, Wu, & Jin 2012). But difficulties are also found during these researches. One of the biggest problems is that it is difficult to obtain a mesh with high quality of the meso-scale model for numerical analysis such as finite element analysis (FEA). Due to the geometrical complexity of aggregate shape and tiny spacings between aggregates with a high volume fraction, the free mesh method provided by some commercial softwares will often fail. An alternative approach is to map a prepared mesh with regular element (triangle and square for instance) onto the meso-scale

model, and attribute different material properties to elements according to their positions in the meso-scale model, e.g., completely inside an aggregate or cement paste, partially occupied by an aggregate. This mapping mesh method can always succeed regardless of the geometrical complexity of aggregate shape, but the mesh size should be small enough, and usually smaller than the minimum size of aggregates, which will significantly increase the amount of computational work, especially in a three-dimensional (3D) analysis.

To decrease the computational burden in a mesoscopic analysis of chloride transport problem, the technique of adaptive mesh refinement (AMR) can be introduced. The general philosophy of AMR is to improve the accuracy of numerical solutions by starting the analysis on a coarse initial mesh and then refining the mesh based on the refinement criteria. So far, AMR has been already successfully applied in Calculated Fluid Dynamics (CFD) (Rossi, Cotela, Lafontaine, Dadvand, & Idelsohn 2013, Antepara, Lehmkuhl, Borrell, Chiva, & Oliva 2014) and mechanical behaviors of structures such as fracture (Khoei, Moslemi, Ardakany, Barani, & Azadi 2009, Park, Paulino, Celes, & Espinha 2012, Khoei, Eghbalian, Moslemi, & Azadi 2013) and dynamic response under earthquake (Sun & Li 2016). The overall aim of AMR is to obtain a balance between accuracy and computational efficiency in numerical simulations.

This paper mainly provides an AMR-based finite element method (FEM) to simulate the chloride diffusion in concrete at meso-scale. The detailed implementations of AMR in FEM, e.g., element hierarchy, are described in the first part of the paper. Then, the method is applied into both steady and transient analysis of chloride diffusion problems. The refinement criteria which determines the critical elements to be further refined is proposed and tested. Some benchmarks are also conducted to compare the computational efficiency between AMR-based FEM and normal FEM.

2 MODELS AND METHODS

2.1 *Meso-scale model of concrete*

At meso-scale, concrete is considered as a composite material which can be divided into the cement paste as the homogeneous matrix, the aggregate as the inclusion, and ITZ as the interface between cement paste and aggregate. The ITZ is usually modeled as a soft shell with identical thickness around aggregate. Thus, the meso-scale model of concrete is mainly determined by the characteristics of aggregates, i.e., the shape and position. The shape of real aggregates is so complicated that it is often assumed as some realistic geometries such as sphere, ellipsoid, polyhedron, geometry described by spherical harmonics (Garboczi 2002).

The size of each aggregate in the meso-scale model of concrete should be determined according to the aggregate gradation, e.g., the Fuller's gradation, equal volume fraction (EVF) gradation. For non-spherical shapes, aspect ratios should be also properly decided to realistically model the aggregate shape. Generally, the aspect ratio can be defined based on the sizes of the bounding box of the aggregate. For example, the aspect ratios of an ellipsoid can be simply defined as $\xi_1 = a/b$ and $\xi_2 = b/c$, where a, b and c are the major, medium and minor radii of the ellipsoid. The orientations of each aggregate are usually considered as random variables following a uniform distribution in the range of $[0, 2\pi]$.

When the shapes of all aggregates are determined, the next step is to determine the aggregate position which is often called "aggregate packing". As solid particles, aggregates are not allowed to be overlapped with one another. Thus, separation checks are needed to determine proper position of each aggregate in the meso-scale model. The algorithm of separation check differs for different shapes of aggregates. For example, for spherical shape, it is only needed to calculate the distance between centers of two aggregates and compare it with the radii of these two aggregates. For the other shapes, the algorithms will become much more complicated, e.g., ellipsoid (Wang, Wang, & Kim 2001), spherical harmonics (Qian 2012). The overall packing procedure can follow a classic "take and place" method (Wang, Kwan, & Chan 1999). When an aggregate is to be placed into the meso-scale model, it is checked whether this aggregate is overlapped with any aggregate which is already in the meso-scale model by using the corresponding algorithm of separation check. If so, the aggregate is taken out and dropped into the meso-scale model again until all separation checks are passed. To eliminate the "wall effect" caused by the boundary of meso-scale model on the aggregate packing, the periodic boundary condition can be applied (Qian 2012).

2.2 *AMR scheme*

2.2.1 *Mesh hierarchy*

To decrease the computational efforts, the mesoscopic analysis is usually conducted in a representative volume element (RVE) instead of the entire component or structure. The size of REV (L) should be large enough to fully cover the characteristics of material heterogeneity. In the case of concrete, it is recommended that L should be at least 3 to 5 times larger than the maximum size of aggregates.

The AMR procedure used in this paper can be described by Fig. 1. To start with, an initial coarse mesh which only has one element is given in Fig. 1(a). The initial mesh can be named as level 0 mesh. In Fig. 1, this single element is divided into four elements by generating and connecting new nodes in the middle of

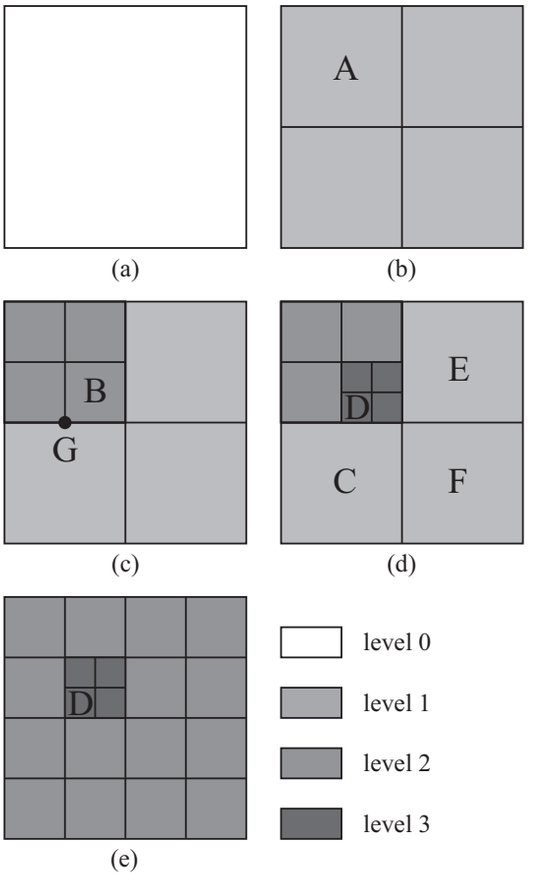


Figure 1: A schematic of 2D AMR and different levels of elements.

each side of the element. The newly created elements result in the mesh of next level, namely level 1. In Fig. 1(c), element A which belongs to level 1 mesh can be further refined to level 2. This procedure can continue to any levels. But it is required that the difference of mesh levels between any two adjacent elements can never exceed one level. Thus, the mesh in Fig. 1(d) is not allowed in AMR, as elements C and D belong to the level 1 and 3 meshes, respectively, with a difference of two levels. If element B in Fig 1(c) needs to be refined, elements C, E and F in Fig. 1(d) should be firstly refined to level 2, as shown in Fig. 1(e).

2.2.2 *Transitional element*

During AMR procedure, new nodes are added in the middle of the side of elements on the mesh of higher level, e.g., node G in Fig. 1(c). These "mid-nodes" can result in the inconsistent nodal solutions of chloride ions in FEA between the adjacent elements. A possible solution of this problem is to apply the multiple-point constraint (MPC) to eliminate the DOFs on mid-nodes from the final matrix solver of linear equations. But this approach requires some additional modifications to the old computer program we developed previously, especially when the sparse matrix is used. Thus, we used another approach, i.e., transitional elements, to solve the problem of inconsistent nodal solutions on mid-nodes. According to the number and positions of mid-nodes, different transitional elements are formed inside the element on the higher

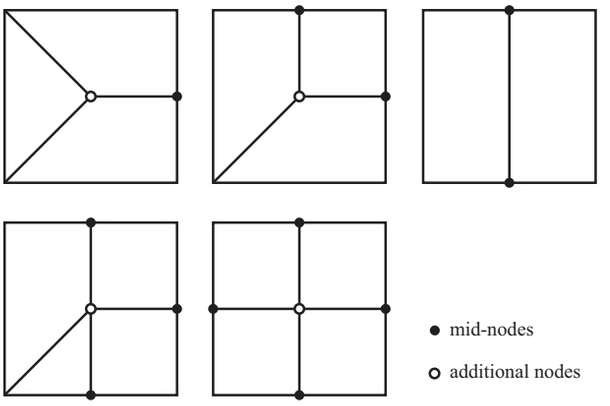


Figure 2: A schematic of additional nodes and transitional elements due to mid-nodes.

level, as shown in Fig. 2. The disadvantage of this approach is that extra nodes should be generated inside the element, which may increases the number of DOFs in the final matrix solver. But these extra nodes can also result in a smooth transition of nodal solutions between elements of different levels.

2.3 *FEM for chloride diffusion problem*

2.3.1 *Transient analysis*

The governing equation of the chloride diffusion can be obtained by the Fick's 2nd law:

$$\frac{\partial \phi}{\partial t} = D_x \frac{\partial^2 \phi}{\partial x^2} + D_y \frac{\partial^2 \phi}{\partial y^2} + D_z \frac{\partial^2 \phi}{\partial z^2} \tag{1}$$

where ϕ is the nodal solution of chloride content, D_x, D_y, D_z are apparent chloride diffusivity in three directions, respectively. For an isotropic material, $D_x = D_y = D_z = D_{\text{app}}$.

In mathematics, Eq. (1) is similar to the governing equation for thermal conductivity. Thus, it can be numerically solved by FEM for thermal conductivity as demonstrated in some textbooks, e.g. (Reddy & Gartling 2000). The final matrix system of linear equations can be expressed as:

$$\boldsymbol{C}\dot{\boldsymbol{\phi}} + \boldsymbol{K}\boldsymbol{\phi} = \boldsymbol{P} \tag{2}$$

where matrices $\boldsymbol{C}$ and $\boldsymbol{K}$ are analogy to the specific heat and conductivity matrices in thermal transfer problem, respectively. This matrix equation can be discretized in time domain and transformed to:

$$\overline{\boldsymbol{K}}\boldsymbol{\phi}_{n+1} = \overline{\boldsymbol{Q}}_{n+1} \qquad (n = 0, 1, 2, ..., M) \tag{3}$$

where $\overline{\boldsymbol{K}}$ and $\overline{\boldsymbol{Q}}_{n+1}$ are:

$$\overline{\boldsymbol{K}} = \boldsymbol{C}/\Delta t + \theta \boldsymbol{K} \tag{4}$$

$$\overline{\boldsymbol{Q}}_{n+1} = [\boldsymbol{C}/\Delta t - (1-\theta)\boldsymbol{K}]\boldsymbol{\phi}_n + (1-\theta)\boldsymbol{P}_n + \theta \boldsymbol{P}_{n+1} \tag{5}$$

where $\theta = 1/2$ is used (the Crank-Nicolson method). By the above equations, the nodal solutions of chloride content can be obtained step by step based on a given initial condition, i.e., $\boldsymbol{\phi} = \boldsymbol{\phi}_0$

2.3.2 *Steady analysis*

In a steady analysis, the nodal solutions of chloride content is irrelevant to time. Thus, Eq. (1) is simplified as:

$$D_x\frac{\partial^2\phi}{\partial x^2}+D_y\frac{\partial^2\phi}{\partial y^2}+D_z\frac{\partial^2\phi}{\partial z^2}=0 \tag{6}$$

and the final matrix equation is simply:

$$\boldsymbol{K\phi}=\boldsymbol{P} \tag{7}$$

2.3.3 *Initial and boundary conditions*

In most cases, it can be assumed that no chloride ions present inside fresh concrete where river sand is used. Thus, the initial condition can be simply:

$$\boldsymbol{\phi}_0=0 \tag{8}$$

The boundary conditions of chloride diffusion problem at meso-scale mainly contain two types, i.e, the Dirichlet (Γ_ϕ) and Neumann (Γ_q) boundary conditions:

$$\phi=\phi_b \quad \text{on} \quad \Gamma_\phi \tag{9}$$

$$\partial\phi/\partial\overrightarrow{n}=q \quad \text{on} \quad \Gamma_q \tag{10}$$

where $\overrightarrow{n}$ is the unit vector normal to the boundary. For the Neumann boundary condition, it is usually assumed that $q=0$. In this case, $\boldsymbol{P}$ in Eqs. (2) and (7) does not exist, i.e., $\boldsymbol{P}=0$.

2.4 *Refinement criterion*

When the nodal solutions of chloride content are obtained on the mesh of level n, for each element , the chloride content inside the element can be calculated based on the nodal solutions and shape functions:

$$\phi(\xi,\eta,\zeta)=\sum_{i=1}^{n}\phi_i\cdot N_i(\xi,\eta,\zeta) \tag{11}$$

where ϕ_i is the nodal solutions, n is the number of nodes in the element ($n=3,4$), (ξ,η,ζ) are the local coordinates of the element, N_i is the shape function. Then, the local field distribution of chloride content in each element is compared with that obtained from the previous level of mesh to calculate the error and define the refinement criterion:

$$\varepsilon=\frac{\int(\phi^{l+1}-\phi^l)\mathrm{d}\Omega}{\Omega}>\varepsilon_0 \tag{12}$$

where Ω is the area (2D) or volume (3D) of the element, ε_0 is the predefined critical value.

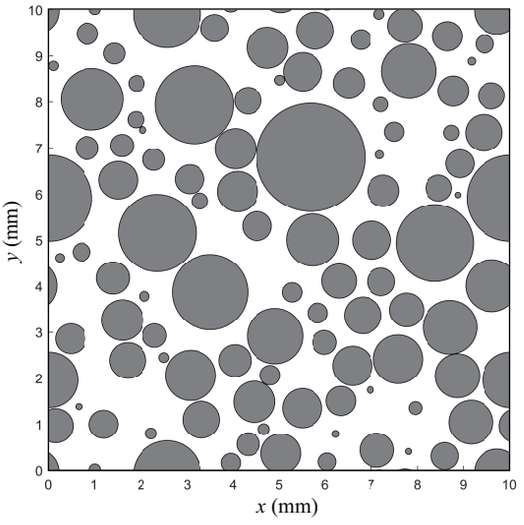


Figure 3: Meso-scale model for benchmarks of steady and transient analysis.

3 BENCHMARKS

Consider the meso-scale model shown in Fig. 3 which is a slice from a 3D model in REV of size $10\times10\times10$ mm^3. Both of steady and transient analysis are conducted in this model to compare the results and efficiency between AMR-based FEM and normal FEM. For the steady analysis, the boundary conditions are:

$$\phi(y=0)=1.0 \quad \phi(y=10)=0.0 \tag{13}$$

$$\partial\phi/\partial\overrightarrow{n}(x=0.0)=\partial\phi/\partial\overrightarrow{n}(x=10.0)=0.0 \tag{14}$$

while for the transient analysis, the boundary conditions are:

$$\phi(y=0)=1.0 \quad \partial\phi/\partial\overrightarrow{n}(y=10.0)=0.0 \tag{15}$$

$$\partial\phi/\partial\overrightarrow{n}(x=0.0)=\partial\phi/\partial\overrightarrow{n}(x=10.0)=0.0 \tag{16}$$

In both of steady and transient analysis, the apparent chloride diffusivity of cement paste is $D_{\text{cp}}=0.0864$ mm^2/d (1.0×10^{-12} m^2/s which represents a small chloride diffusivity of cementitious materials), while the diffusivity of ITZ (D_{ITZ}) is assumed as 5 times larger than D_{cp} (Zheng, Zhou, Wu, & Jin 2012) due to its higher porosity and percolation effect (Winslow, Cohen, Bentz, Snyder, & Garboczi 1994, Bentz, Hwang, Hagwood, Garboczi, Snyder, & Scrivener 1994).

3.1 *Steady analysis at meso-scale*

The results of steady analysis at different mesh levels are shown in Fig. 4. During the AMR procedure, the program can automatically identify the critical elements to be refined based on the refinement criterion in Eq. (12). The results show that most of these critical elements are located at the surface of aggregates.

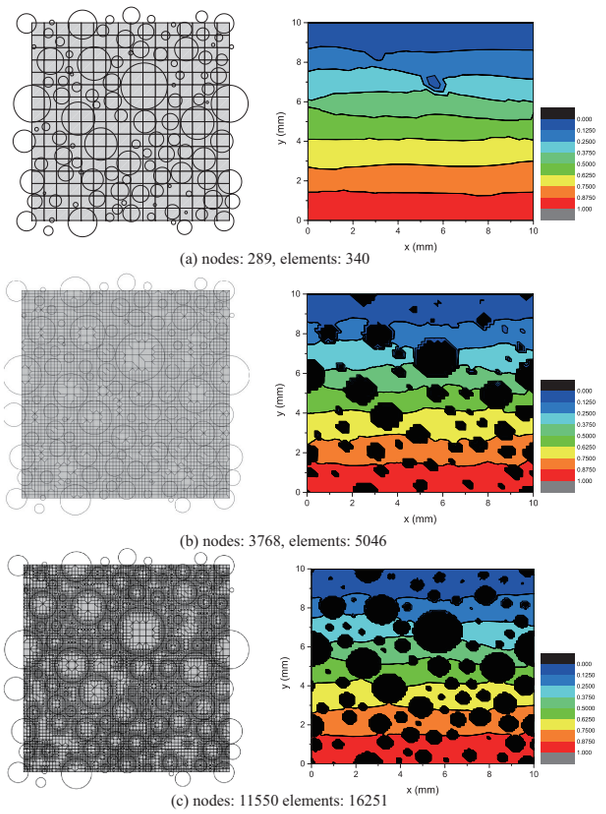


Figure 4: A benchmark of steady analysis of chloride diffusion at meso-scale with AMR.

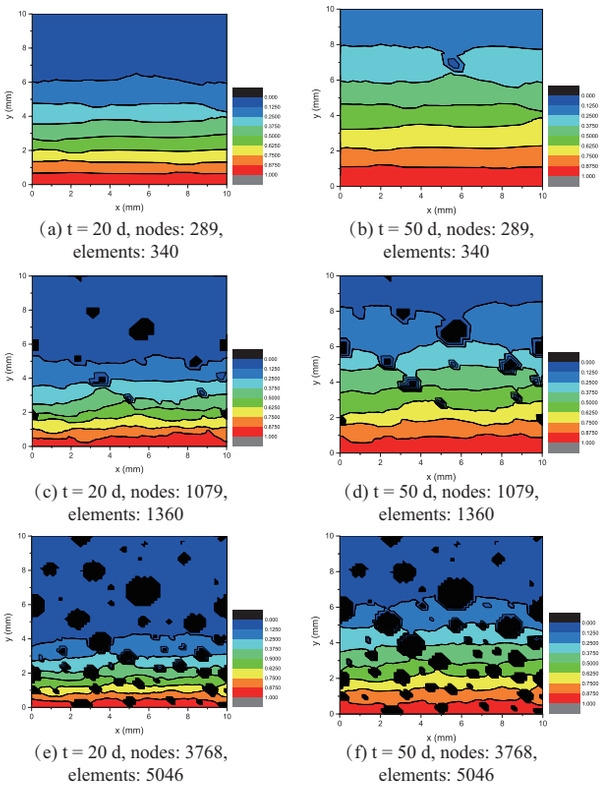


Figure 5: A benchmark of transient analysis of chloride diffusion at meso-scale with AMR.

By refining the critical elements to higher levels of mesh, the effect of aggregates on the field distribution of chloride content, as well as the transport path, becomes more and more significant.

Base on the field distribution of chloride content at meso-scale, we can further calculate the chloride flux in each element and determine the equivalent apparent chloride diffusivity of the REV for structural durability design at macro-scale by following the procedure in (Pan, Xin, & Chen 2014).

3.2 *Transient analysis at meso-scale*

The transient analysis starts from an initial condition $\phi_0 = 0.0$ by assuming that no initial chloride ions, e.g., the chloride ions in sea sand, are mixed in fresh concrete. The whole transient analysis lasts for 50 time steps with $\Delta t = 1$ d. The field distributions of chloride content at time $t = 20$ d and $t = 50$ d obtained at different levels of mesh are plotted in Fig. 5. Similar to the steady analysis, the critical elements are also found at the surface of aggregates, and as mesh level increases, the effect of aggregates on chloride diffusion process becomes more obvious.

3.3 *Efficiency analysis*

To analyze the efficiency of AMR-based FEM, the number of DOFs in AMR-based mesh and uniform mesh in the above benchmarks are compared in Fig. 6. As can be seen, when the mesh level reaches 9, the number of DOFs in uniform mesh will dramatically increase with the mesh level, while the number

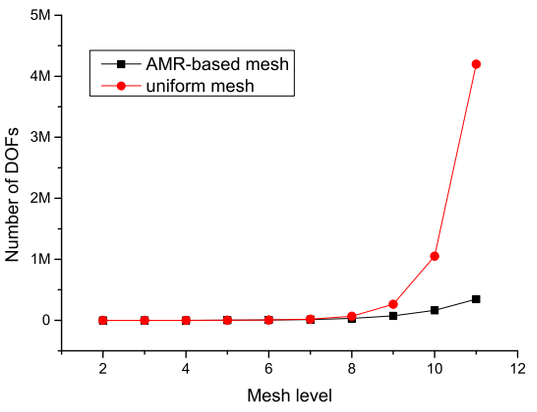


Figure 6: A comparison between number of DOFs of AMR-based mesh and uniform mesh.

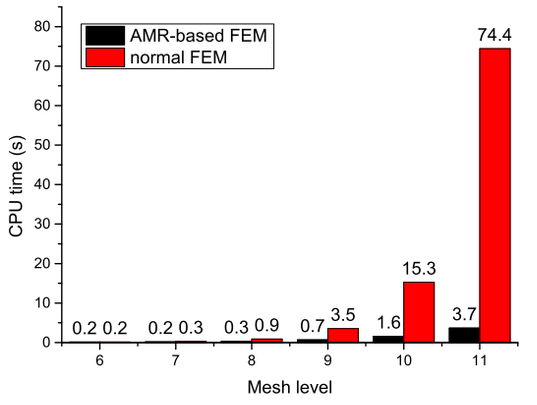


Figure 7: A comparison between CPU time of AMR-based FEM and normal FEM in steady analysis.

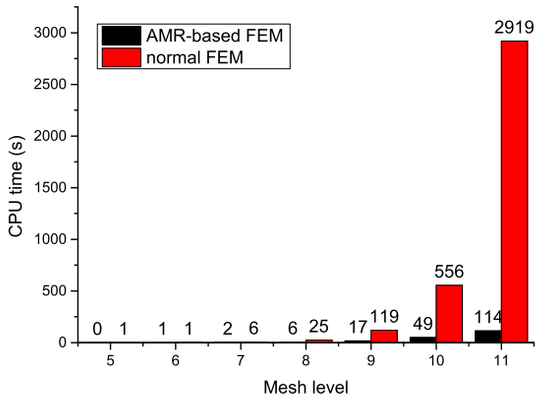


Figure 8: A comparison between CPU time of AMR-based FEM and normal FEM in transient analysis.

of DOFs in AMR-based mesh just shows a slight increase.

The CPU time to conduct the whole numerical simulation, including mesh formation, element refinement, global matrix formation, solver of sparse matrix system, etc., is also compared between AMR-based FEM and normal FEM, as shown in Fig. 7 and Fig. 8 for steady and transient analysis, respectively. Due to the adaptive mesh, the CPU time needed by AMR-based FEM does not change too much with different requirements of the solution precision.

4 DISCUSSIONS

Although the above benchmarks successfully demonstrate the advantages of AMR-based FEM in efficiency of simulation in chloride diffusion at meso-scale, there are still some problems in the current method and developed programs, which will be pointed out and briefly discussed as follows.

4.1 *ITZ modeling*

The ITZ is a special microstructure in cementitious materials in that it has a much higher porosity than bulk cement paste and extremely small thickness, i.e., $10 \sim 50$ μm (Ollivier, Maso, & Bourdette 1996, Scrivener & Nemati 1996). This huge discrepancy between geometrical sizes of ITZ and aggregate makes it difficult to explicitly model ITZ in a numerical simulation. Some researches homogenized the aggregate and its ITZ into an equivalent "aggregate" (Zheng, Zhou, Wu, & Jin 2012), while some researches deliberately increase the thickness of ITZ used in the numerical simulation, e.g., 1.0 mm (Du & Jin 2014), to avoid the difficulty in modeling ITZ.

In the current research, the ITZ is modeled by a classic approach, i.e., assigning ITZ material properties to the interface elements which are partially occupied by aggregates and cement paste. Thus, during the AMR procedure, the ITZ thickness decreases due to the smaller size of elements on the higher level mesh. Furthermore, the geometrical boundaries, as well as the volume fraction, of aggregates in the finite element model is different from that in the original meso-scale model due to the "saw-toothed" effect from the mapping mesh method. Although this effect can be decreased by a refined mesh, it cannot be completely eliminated theoretically.

The above improper modeling of ITZ well explains why the critical elements to be refined in the benchmarks in Section 3 are almost all found at the surface of aggregates. Actually, it is found in the benchmarks that the error calculated by Eq. (12) does not obviously decrease during mesh refinement. Thus, the current program can only terminate the analysis when the mesh level reaches a predefined one or the ITZ thickness (size of interfac elements) meets the requirement of the real thickness observed in experiments. This approach differs from the error control and convergence criterion in classic AMRs. To solve this problem, a better modeling of ITZ in the mass transport issue of cementitious materials by AMR-based FEM should be found.

4.2 *3D AMR-based FEM*

Just as an illustration, the benchmarks in Section 3 are only conducted in 2D. But the proposed method and developed program can be extended to 3D with a more complex data structure and preprocessor. In 3D, the efficiency of AMR-based numerical method can be expected to be further increased compared with a 2D AMR-based method. But a detailed benchmark is not conducted here, as the computation requirements in normal FEM exceed the capacity of computers we used. When the AMR-based method is extended to 3D, the data structure used in the computer program should be carefully optimized. Otherwise, the efficiency of AMR will be slowed down due to the frequent data processing between different levels of mesh.

5 CONCLUSIONS

This paper mainly developed an AMR-based FEM to simulate the chloride diffusion in concrete at meso-scale. The detailed implementations of AMR, FEM in solving chloride diffusion problem and refinement criterion are demonstrated. With the developed program, benchmarks of 2D steady and transient analysis of chloride diffusion at meso-scale were conducted to compare the efficiency between AMR-based FEM and normal FEM. The results showed that AMR could greatly decrease the CPU time needed by FEA, especially in a extremely refined mesh. Furthermore, some problems in the current method and developed program, e.g., improper modeling of ITZ, error control, convergence criterion, data structures, were pointed out and briefly discussed. Through this research, it is

expected to develop a platform for efficient simulation of mass transport process in porosity materials at the scales where the heterogeneity needs to be considered.

6 ACKNOWLEDGMENT

This research is supported by National Natural Science Foundation of China (grant No.: 51608377, 51378383), which is appreciated here.

REFERENCES

Angst, U., B. Elsener, C. K. Larsen, & ystein Vennesland (2009). Critical chloride content in reinforced concrete a review. *Cement and Concrete Research 39*(12), 1122 – 1138.

Angst, U. M. & R. Polder (2014). Spatial variability of chloride in concrete within homogeneously exposed areas. *Cement and Concrete Research 56*(2), 40–51.

Antepara, O., O. Lehmkuhl, R. Borrell, J. Chiva, & A. Oliva (2014). Parallel adaptive mesh refinement for large-eddy simulations of turbulent flows. *Computers and Fluids 110*, 48–61.

Bentz, D. P., J. T. G. Hwang, C. Hagwood, E. J. Garboczi, K. A. Snyder, & N. B. K. L. Scrivener (1994). Interfacial zone percolation in concrete: Effects of interfacial zone thickness and aggregate shape. *Mrs Proceedings 370*.

Du, X. & L. Jin (2014). Meso-scale numerical investigation on cracking of cover concrete induced by corrosion of reinforcing steel. *Engineering Failure Analysis 39*(4), 21–33.

Garboczi, E. J. (2002). Three-dimensional mathematical analysis of particle shape using x-ray tomography and spherical harmonics: Application to aggregates used in concrete. *Cement and Concrete Research 32*(10), 1621–1638.

Khoei, A. R., M. Eghbalian, H. Moslemi, & H. Azadi (2013). Crack growth modeling via 3d automatic adaptive mesh refinement based on modified-spr technique. *Applied Mathematical Modelling 37*(12), 357–383.

Khoei, A. R., H. Moslemi, K. M. Ardakany, O. R. Barani, & H. Azadi (2009). Modeling of cohesive crack growth using an adaptive mesh refinement via the modified-spr technique. *International Journal of Fracture 159*(1), 21–41.

Ollivier, J. P., J. C. Maso, & B. Bourdette (1996). Interfacial transition zone in concrete. *Advanced Cement Based Materials 2*(1), 30–38.

Pan, Z., A. Chen, & R. Xin (2015). Spatial variability of chloride and its influence on thickness of concrete cover: A two-dimensional mesoscopic numerical research. *Engineering Structures 95*, 154–169.

Pan, Z., R. Xin, & A. Chen (2014). Chloride diffusivity of concrete: Probabilistic characteristics at meso-scale. *Computers and Concrete 13*(2), 187–207.

Park, K., G. H. Paulino, W. Celes, & R. Espinha (2012). Adaptive mesh refinement and coarsening for cohesive zone modeling of dynamic fracture. *International Journal for Numerical Methods in Engineering 92*(1), 1–35.

Qian, Z. (2012). *Multiscale Modeling of Fracture Processes in Cementitious Materials*. Ph. D. thesis, Delft University of Technology.

Reddy, J. N. & D. K. Gartling (2000). *The finite element method in heat transfer and fluid dynamics*. CRC Press,.

Rossi, R., J. Cotela, N. M. Lafontaine, P. Dadvand, & S. R. Idelsohn (2013). Parallel adaptive mesh refinement for incompressible flow problems. *Computers and Fluids 80*(1), 342–355.

Scrivener, K. L. & K. M. Nemati (1996). The percolation of pore space in the cement paste/aggregate interfacial zone of concrete. *Cement and Concrete Research 26*(1), 35–40.

Sun, B. & Z. Li (2016). Adaptive mesh refinement fem for seismic damage evolution in concrete-based structures. *Engineering Structures 115*, 155–164.

Wang, W., J. Wang, & M. S. Kim (2001). *An algebraic condition for the separation of two ellipsoids*. Elsevier Science Publishers B. V.

Wang, Z. M., A. K. H. Kwan, & H. C. Chan (1999). Mesoscopic study of concrete i: generation of random aggregate structure and finite element mesh. *Computers and Structures 70*(5), 533–544.

Winslow, D. N., M. D. Cohen, D. P. Bentz, K. A. Snyder, & E. J. Garboczi (1994). Percolation and pore structure in mortars and concrete. *Cement and Concrete Research 24*(1), 25–37.

Zheng, J. J., X. Z. Zhou, Y. F. Wu, & X. Y. Jin (2012). A numerical method for the chloride diffusivity in concrete with aggregate shape effect. *Construction and Building Materials 31*(6), 151–156.

Zhou, S. (2014). Modeling chloride diffusion in concrete with linear increase of surface chloride. *Aci Materials Journal 111*(5), 483–490.

Zhou, S. (2016). Analytical model for square root increase of surface chloride concentration and decrease of chloride diffusivity. *Journal of Materials in Civil Engineering 28*(4), 04015181.

Maintenance, Safety, Risk, Management and Life-Cycle Performance of Bridges – Powers, Frangopol, Al-Mahaidi & Caprani (Eds)
© 2018 Taylor & Francis Group, London, ISBN 978-1-138-73045-8

Bridge Displacement Monitoring using Acceleration Measurement for Efficient Bridge Management

Y. Umekawa & H. Suganuma
TTES, Inc., Tokyo, Japan

ABSTRACT: In this study, the concept of efficient bridge management system focused on monitoring bridge displacements has been proposed for maintaining numerous middle length bridges in rural government of Japan. In order to monitor displacement easily, a displacement estimation method has been proposed using measured acceleration data. The applicability of the proposed method then has been verified trough the filed measurement using the loading truck. Finally, the management system has been proposed and its application scheme also has been introduced for further actual operations in local districts in the future.

1 INTRODUCTION

1.1 *Background*

Numerous civil infrastructures, which were constructed during the rapid economic growth of Japan, have rapidly been aged or deteriorated and so much attention has been paid to the maintenance of infrastructures. With regards to bridges, there are over 700 thousand bridges in Japan. Therefore, it is necessary to develop efficient maintenance technologies such as Structural Health Monitoring (SHM) systems for satisfactory management of these existing bridges.

Almost 70% of total bridges are managed by local government districts, and these bridges are mainly short or medium length (~50m). In addition, local governments have serious problems such as insufficient financial and human resources, as well as technical shortage. Hence, it is essential to manage as many bridges as possible with minimum cost and effort, leading to the concept of the minimum monitoring system.

In particular, for bridge structures, it is important to measure displacement in relation to loadings such as passing vehicles, as bridge displacement can be used to ensure the application limit of bridges. Moreover, displacement is directly related to stiff nesses of bridges and therefore bridge displacement can be used to understand the tendency of how existing bridges will deteriorate by monitoring change of bridge displacements induced by the known weight of the passing vehicles.

In this study, by considering the implementation cost and applicability in field measurements, an acceleration based displacement monitoring system has been proposed as namely minimum monitoring system. For simple and easy usage, displacement is estimated by numerical integration of acceleration data, which is measured from one acceleration sensor by the proposed method in this study. Next, the field measurement based on loading tests using trucks, have also been conducted for a simple and medium length existing bridge to measure displacements and accelerations from an acceleration sensor attached at the main girder.

From the results of the field measurement, estimated displacements have been compared to directly measured displacements using a contact displacement sensor, and the accuracy of the proposed method has been verified. This study has verified the applicability of the minimum monitoring system for efficient management of bridges. The application scheme of this monitoring system has then been introduced for further actual operation in local government districts.

2 PORPOSAL OF BRIDGE DISPLACEMENT ESTIMATION METHOD

2.1 *Displacement measurement for bridge structures*

As the aforementioned background, bridge displacement is of great importance for monitoring the bridge behavior or for assessing its structural safety, serviceability and integrity, as structural deterioration and damages are mainly caused by dynamic loadings from heavy vehicles passing over bridges.

Direct displacement measurement systems, such as contact displacement sensors and laser displace-

ment sensors, are very expensive and not applicable for bridges as these displacement sensors must require fixed points for reference as well as power supplies. Therefore, although these reference-based sensors are accurate, their practical application for bridge monitoring is not efficient due to implementation costs and limited accessibility. In other measurement system, Global Position System (GPS) or vision-based systems enable reference-free displacement measurements, but their accuracy is not reliable and their installation cost also cannot be considered cost-effective either (Nakamura, 2000, Lee, 2006).

On the contrary, accelerometers are commonly used for SHM of bridges considering they are cost effective and easy to install without the need of any reference points in the recent researches. In addition, recent developments in Micro Electro-Mechanical Systems (MEMS) based sensors have encouraged accelerometers to develop also, by becoming wireless, small, cheaper and more accurate. Therefore, indirect displacement estimation methods, using measured accelerations, have been proposed as an effective method for bridge monitoring systems instead of using direct displacement measurements.

2.2 *Difficulties in bridge displacement estimation from acceleration measurement*

However, double integration of measured acceleration results in not reliable displacement estimation with an unacceptably large drift error due to inherent their sensor noise. Therefore, in order to estimate displacement accurately by using double integration, low frequency noise components must be removed to avoid large estimation errors.

To overcome this difficulty of integrating measured accelerations, Park et al (Park, 2005) proposed an initial velocity estimation method where displacement is estimated using boundary conditions, such as an assumed initial velocity or initial zero displacement, to reduce the effect of large drift. However, this method divides measured acceleration into several segments such as the dynamic and static responses and then integrates each segment to improve the accuracy of the pseudo static displacement estimation. Considering the actual traffic situations on in-service bridges, this estimation method is not applicable for automated displacement determination as the time of passing vehicles remains unknown.

In another study, Richard et al (Richard 2006, Velde 2006, Kandula 2012) estimated bridge deflections by assuming bridge vibrations as the sum of exponentially damped sinusoids. Using this method, noise free acceleration could be obtained and then integrated to displacement. However, this estimation method has to utilize large matrix calculations with Singular Value Decomposition (SVD)-based algorithms, which can cause high calculation cost. Instability also arises when analyzing measured accelerations from MEMS-based sensors because these sensors include much more sensor noise than other sensors.

Lee et al (Lee 2010) developed a Finite Impulse Response (FIR) filter for indirect displacement estimation from measured accelerations, but this integration filter only focuses on the zero-crossing displacement under a passing train and ignored the pseudo static displacement. In parallel, Park et al (Park 2013) proposed an acceleration-based displacement sensor using the smart sensor Imote2 platform. Using this sensor, displacement can be automatically calculated by the proposed FIR filter-based method. The applicability of acceleration-based displacement estimation has great potential to obtain displacement information of even large bridge structures. These recent approaches aim at performing intelligent on-board computing by using wireless monitoring systems with smart sensors and consequently, full-scale bridge monitoring is able to provide more meaningful information.

Umekawa et al (Umekawa 2015) have proposed an integration method using a wavelet transformation and the effectiveness of the proposed method has been verified for analyzing changes of bridge displacement. As the similar approach, and Sekiya et al (Sekiya 2016) have focused on the cause of integration error and represent the importance of selecting acceleration sensors for displacement estimation, and also proposed the method named “free vibration method” using multiple acceleration sensor to detect the entrance and the exit of passing vehicles onto the girder and integrate free vibration and induced displacement by passing vehicles separately.

Even though several displacement estimation methods have been proposed to date, the difficulty of integrating in the lowest frequency regions has yet to be improved, because of high density noise which comes from mechanical and/or thermal effects. This problem is also caused by variety of noise densities in the accelerometer specifications used for analyses. Moreover, the pseudo static displacements induced by passing vehicles are not zero-crossing responses but half-length waves and so it is difficult to evaluate this kind of vibration.

Taking into account the aforementioned integration problems and studies, this paper presents an integration method with auto calculating algorithm from measured acceleration by only one accelerometer. The proposed method is demonstrated using measured acceleration data sets and estimates bridge displacement of an in-service bridge in local government districts. To validate the applicability and accuracy of this integration method, the estimated displacement results are verified by comparing to measured displacements.

2.3 *Proposed method for bridge displacement estimation*

In this study, the target of bridge displacement is basically for only one passing vehicle, as bridge displacement regarding to the known weight should be evaluated to monitor change of the response with time. In addition, bridges in local districts have few amount of traffic and therefore it is not so important to evaluate displacement induced by continuously passing vehicles.

Displacement is induced by a passing vehicle as shown in Figure 1. When the vehicle pass onto a bridge girder, pseudo-static displacement which is a half-length wave and mainly lower frequency based on the passing time, happens to the loading direction and this displacement can be theoretically obtained by double integration of acceleration data.

However, measured acceleration data inherently includes sensor noise and this sensor noise become significant integration error in the process of integration and also this sensor noise cannot be separated by filtering because this sensor noise exist in all frequency domain. Therefore, this estimation error should be removed to estimate displacement accurately. However, this integration error does not linearly increase in the time domain as the density of sensor noise also fluctuate in time because of the mechanical instability of sensors, and therefore it is not possible to estimate simply.

The outline of the proposed method is as shown in Figure 2. Firstly, measured acceleration is theoretically integrated twice to obtain displacement (Figure 2a) following this equation below in time domain.

$$d = \int_0^T \left[\int_0^\tau a(\tau) d\tau \right] dt + v_0 + d_0$$

where d : displacement, a : acceleration, v : velocity, v_0 :initial velocity, d_0 : initial displacement.

Measured acceleration data $a_{measured}$ includes measurement error caused by sensor noise e_i as following the equation.

$$a_{measured} = a_{real} + e_i$$

This integrated displacement includes the estimation error caused by sensor noise as shown in the following equation.

$$d_{estimated} = d_{real} + \sum_0^t \sum_0^t e_i dt^2 + \sum_0^t e_i dt$$

However, this estimation error is basically caused by mechanical behavior of sensors such as temperatures changes and so always not stable. Therefore, it cannot be considered possible to define the model of this estimation error as equation.

Hence, in this proposed method, from the displacement, the entrance and the exit of passing vehicle is detected in time domain, as the displacement induced by passing vehicle can be considered as a local change and distinguished from the estimation error (Figure 2b).

The estimation error can be estimate by using the integrated result by polynomial spline estimation (Figure 2c) and finally the estimated displacement can be estimated be removing the estimated integration error in time domain (Figure 2d)

This applicability and accuracy of this method has been verified by the field measurement using the loading trucks.

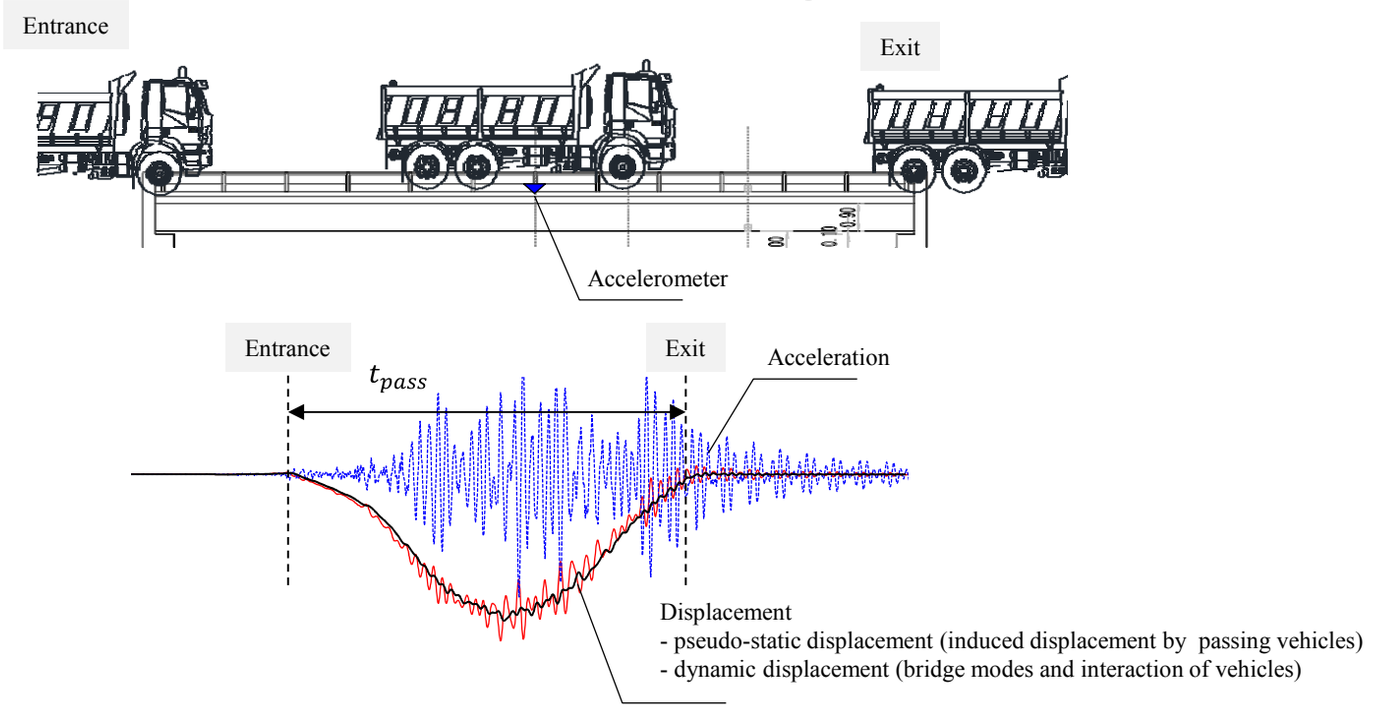


Figure 1. Outline of bridge displacement estimation from measured acceleration

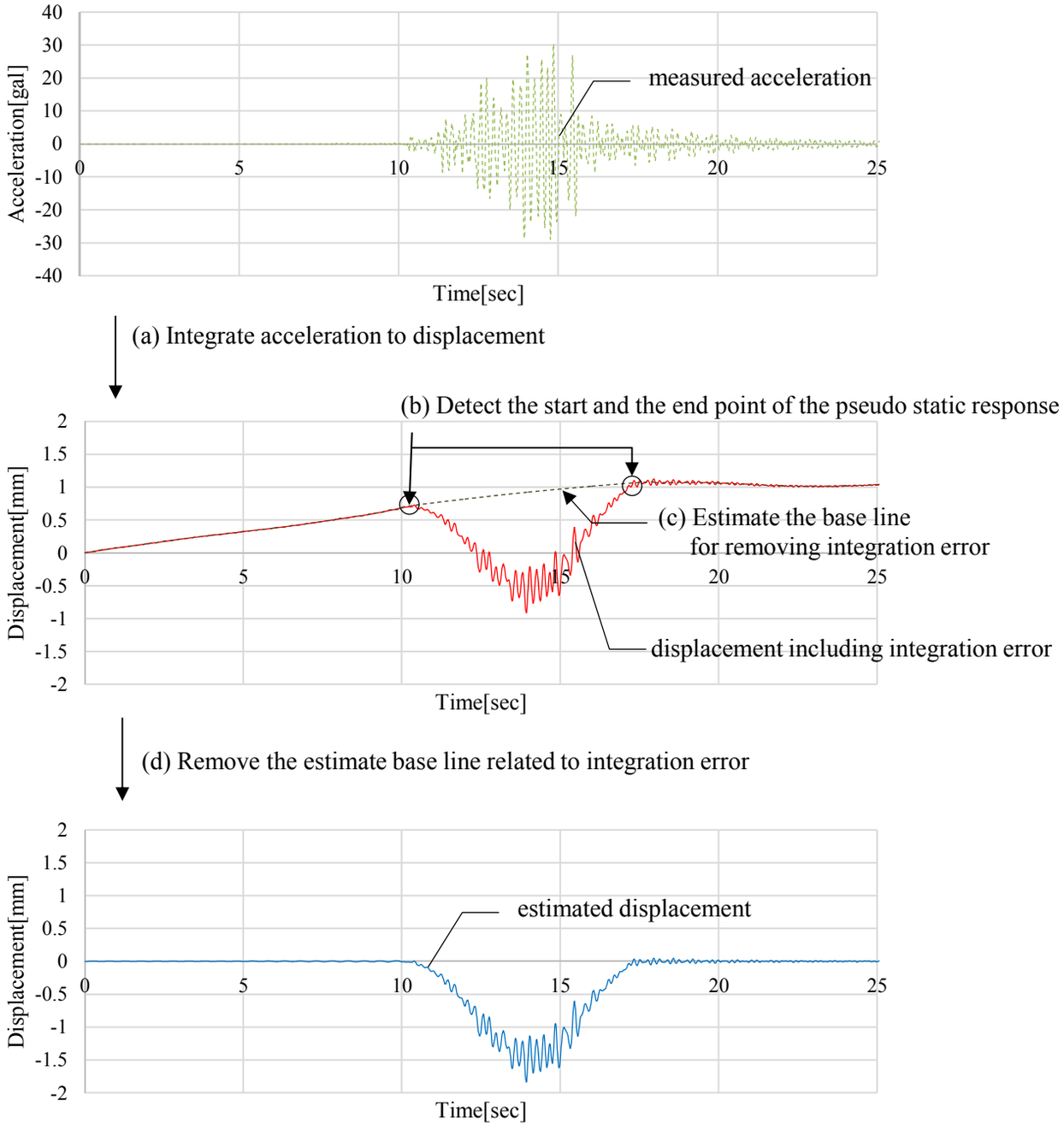


Figure 2. Conceptual outline of the proposed method

3 FIELD LOADING TEST

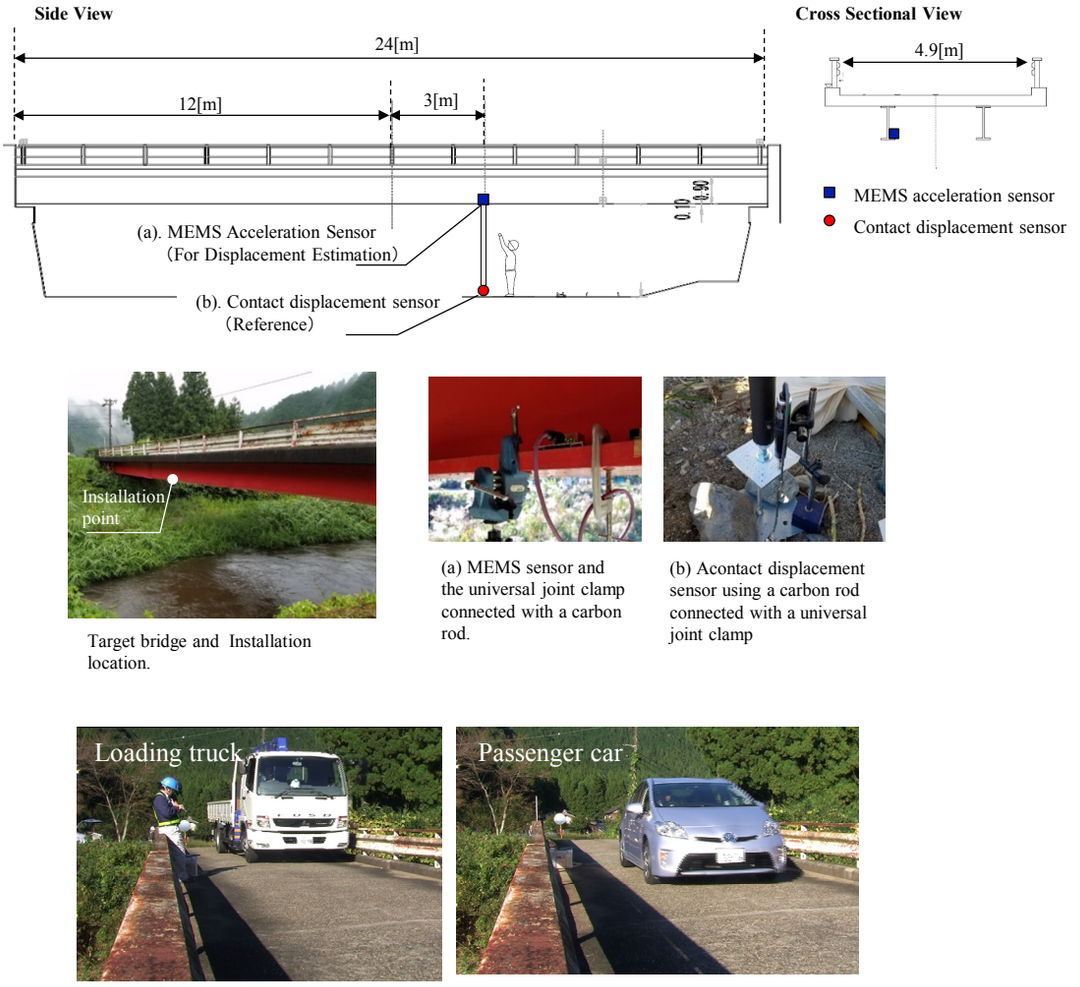
3.1 *Target bridge and field measurement*

The target bridge is a steel girder bridge, with one lane as shown in Figure 3. The span length is 24[m] and the effective width is 4.9[m]. This target bridge was selected as local bridges have commonly short or medium length span (~50m) and are located in low-traffic area.

MEMS acceleration sensor was attached at the installation point, lower flange of the girder with magnet sensor base plate. The carbon rod connected with a universal joint, was attached at the same location. The top of this rod has the plate to be measured by a contact displacement sensor attached on the ground. The detailed specification of these sensors is shown in Table 1.

Contact displacement sensor was also installed as reference data to verify estimation results using acceleration data by comparing these data. These sensors were connected to the same data logger with sampling frequency of 100[Hz].

Loading test was conducted using 2axles Truck and a passenger car, which were prepared for inducing enough large displacement to be evaluated. The total weights of these vehicles are 6.2[ton] and 1.5[ton]. The speed of loading test was conducted with around 20[km/h] as there is no space to get faster speed around the target bridge.



Target bridge and Installation location.

(a) MEMS sensor and the universal joint clamp connected with a carbon rod.

(b) Acontact displacement sensor using a carbon rod connected with a universal joint clamp

Figure 3. Target bridge and the detail of measurement equipment

3.2 *Verification of estimated displacement by using the proposed method*

The displacement induced by the loading vehicles was measured by a contact displacement sensor, and estimated from measured acceleration data by the proposed method. The verification results can be shown in Figure 4. These results show the bridge displacement estimated from the acceleration data by using the proposed method, and the high correlation can be seen between these data. In the case that the loading truck passed through the girder, the maximum displacement was 1.64[mm] and the frequency of this induced pseudo-static displacement was about 0.05[Hz] (passed time = 9[sec]). In this frequency band, it is difficult to obtain the accurate integration results because the larger integration error happens if the frequency of noise is lower than 1[Hz]. In another case that a passenger car passed through the girder, the maximum displacement was around 0.3[mm], and this result shows the high applicability even for small displacement and it is difficult for other displacement sensors to measure accurately this order of small displacement.

The estimation errors were calculated as three times of standard deviation (3σ) of the difference between measured and estimated displacements in each case, and represents that the displacements

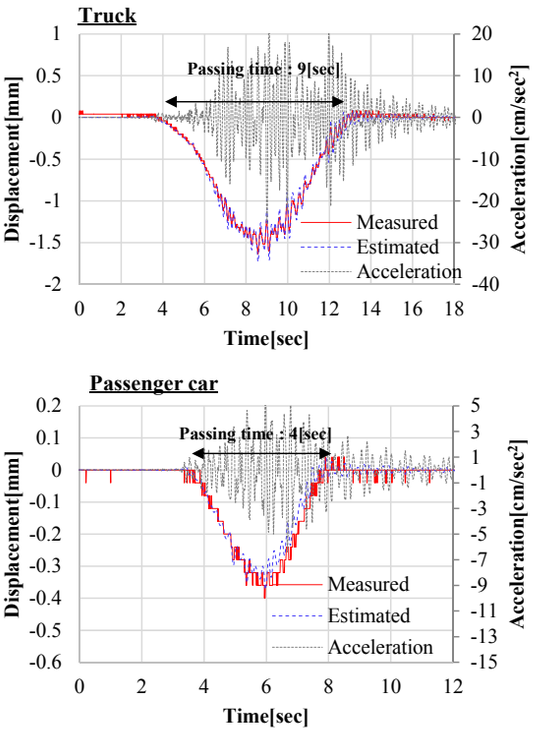


Figure 4. The results of bridge displacement estimation of a loading truck and a passenger's car

could be estimated from a measured acceleration data with high accuracy as shown in Table 2. There are

Table 1. The details of sensor specifications

Type	Range	Frequency band	Resolution
MEMS accelerometer	±5[G]	0.1 – 20[Hz]	0.06[μG]
Contact displacement sensor	±25[mm]	0 – 5[Hz]	0.05[mm]

Table 2. The evaluation of estimated results and its accuracy

Case	Type	Total weight[kg]	Measured displacement [mm]	Estimated displacement [mm]	3σ [mm]
1	Truck	6,200	1.60	1.64	0.20
2			1.68	1.62	0.24
3			1.64	1.74	0.25
4			1.76	1.75	0.30
5			1.52	1.52	0.29
6			1.80	1.9	0.22
7			1.64	1.73	0.10
8			1.72	1.77	0.20
9			1.72	1.79	0.19
10	Car	1,500	0.33	0.36	0.07
11			0.29	0.32	0.08
12			0.32	0.36	0.07

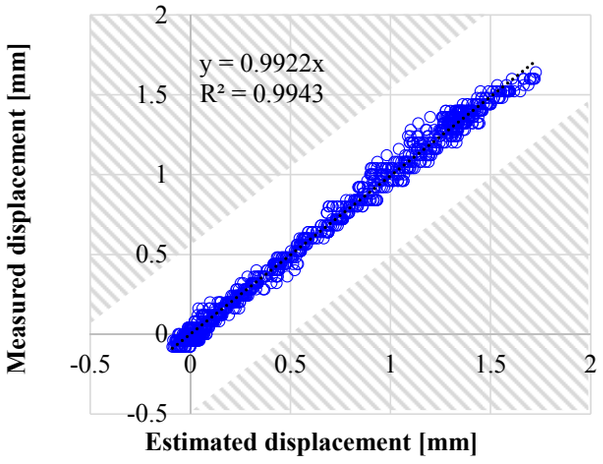


Figure 5. The comparison of measured and estimated results (Case 1: Truck)

still few errors between them, but this difference is caused by differences between each sensor specification of the applicable frequency bandwidth. Also, comparing the estimated and measured displacement in the case 1, these displacements can be seen as a linear relationship as shown in Figure 5. The difference of these displacements are under 0.2[mm] at any sampled time.

Hence, from the measured data by the conducted loading test, the applicability and the accuracy of this proposed method could be verified by comparing to measured displacements as referential data.



Figure 6. The base plate and the sensor plate attached on wheel guard

4 APPLICATION OF THE MINIMUM MONITORING SYSTEM

4.1 *Preparation for the installation of measurement equipment*

The minimum monitoring system requires only one acceleration sensor as acceleration is possible to provide the information of bridge natural frequencies of bridges, and displacements induced by passing vehicles. As acceleration can be installed on the girder by using the base plate, which enables to measure acceleration from on the girder, on wheel guard of bridges as shown in Figure 6. By anchoring this base plate, it is possible to measure acceleration data easily by attaching the sensor plate to this base plate.

4.2 *The development of this proposed system for application*

In order to make this system applicable for local government districts, it is important to design the system which anyone can easily use. According to the recent development of the network infrastructure services such as Cloud services, many things have been connected with the internet, which idea is called by Internet of Thing (IoT). The sensors con-

nected with the internet server to analysis measured data by this proposed method and then these data and results can be stored in data storage by using high secure data transmission. This data is also connected with map location service to efficiently manage the data and the bridge interactively. The prototype device is developed as shown in Figure 7.

4.3 *The actual operation of this proposed system*

The actual application scheme of this proposed system is as shown in Figure 8. The brief outline of actual operations of this proposed method is below.

1) As the initial setup for preparing measurements, the base plate is attached at the center of wheel guards of bridges.
2) Next, when field measurements are conducted, IoT devices including MEMS sensor with the sensor plate, is attached to the base plate.
3) After this preparation, the loading vehicle passes through bridges and then acceleration data are measured at the same time.
4) Measured data is uploaded and stored to Could server through M2M communication with GPS location information, and simultaneously measure data are analyzed by Could computing engine including the proposed analysis algorithm. After measurements are finished, these devices are collected and these base plates are covered until next measurement.

By using the devices temporary and measuring as many bridges as possible at the same time, it is possible to inspect bridge behaviors with reducing maintenance cost of bridges. This system can be considered capable of enabling to support the problems such as cost, human resource and technical shortage in local government districts. In addition, the proposed system has been developed as WEB application (Infra Studio) and this application enables people who have less technical knowledge to manage stored these monitoring data.

5 CONCLUSION

The purpose of this study is to propose a bridge displacement estimation method by using one acceleration data to develop applicable displacement measurement method. A bridge estimation method has been proposed, and has been applied to measured accelerations from an in-service bridge in a local district. The results have then been verified by comparing the estimated displacements to measured displacements measured using a contact displace-

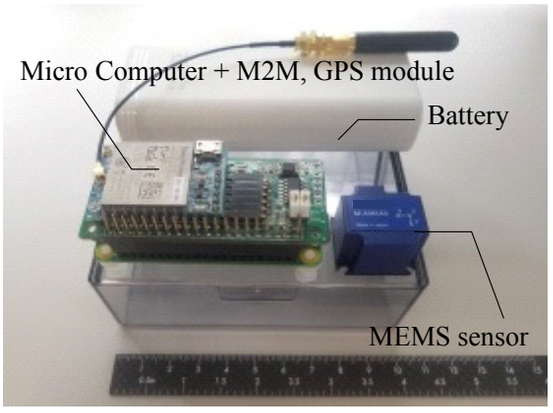


Figure 7. The prototype device for efficient measurement of acceleration data

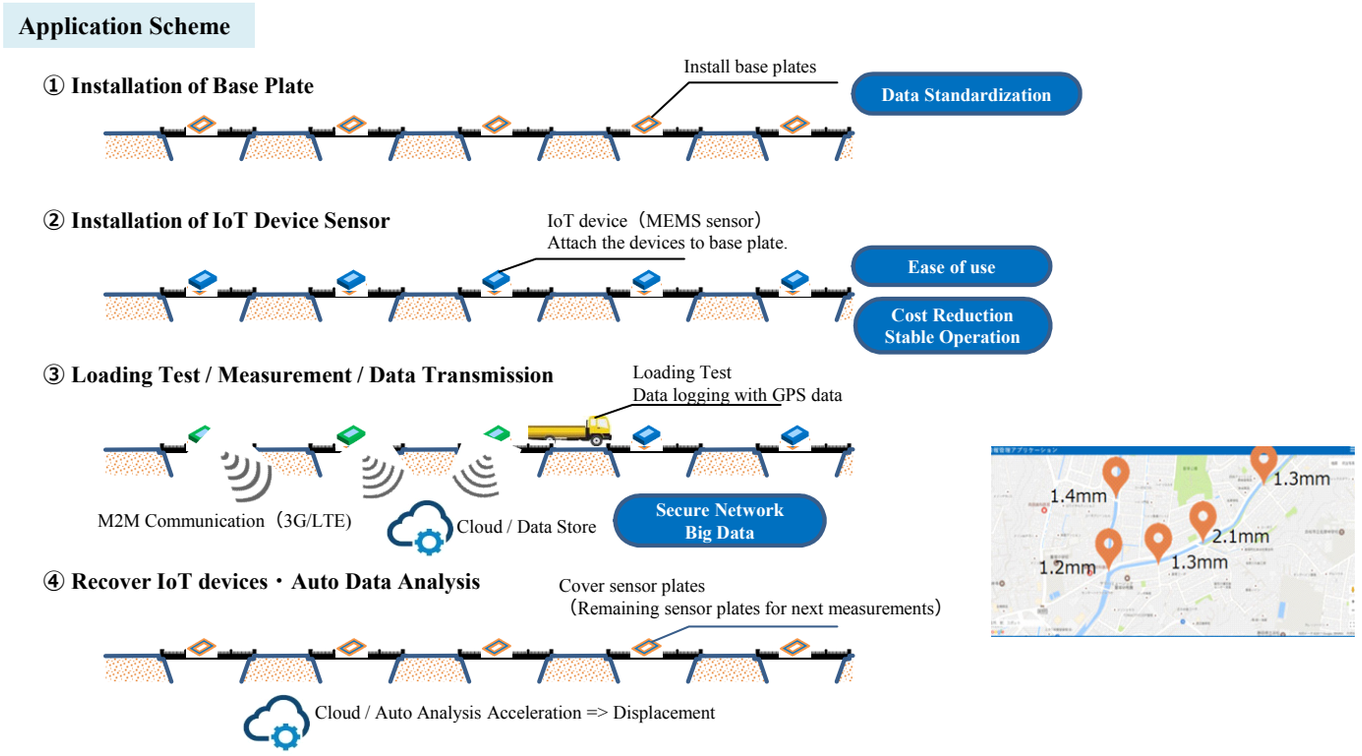


Figure 8. The application scheme of the proposed monitoring system for actual operation

ment sensor. In addition, for applying this proposed method as the minimum monitoring system, the actual operation procedure has been considered and also the bridge monitoring system including data storage and analysis engine has been developed. The results can be summarized as follows.

1) A bridge displacement estimation method has been proposed, and its applicability has been verified trough field measurement regarding to the light amount of the traffic amount such as the prepared loading trucks.
2) The accuracy of the proposed method has been verified by comparing estimated displacements to measured displacements. The estimation error has been validated as three times of standard deviation of difference between their data.
3) The concept of the minimum monitoring system has been introduced and then the actual operation procedures have been considered. The applicability of this system has been developed by using the Cloud network system.

The applicability of this proposed method has been verified. However, this proposed method has been developed for measuring bridge displacement basically when a single passing vehicle pass through short or medium span length bridges and therefore the proposed method should be developed for continuous and complex traffic situations for applying to many kinds of bridge structures. By developing the IoT device, more efficient measurement and maintenance of bridge could be possible. Considering efficient bridge management system, the knowledge of civil engineering and the application of ICT technologies should be connected.

REFERENCES

Nakamura, S. 2000 GPS Measurement of Wind-Induced Suspension Bridge Girder Displacements, Journal of Structural Engineering, pp.1413-1419.

Lee J-J., and Shinozuka M., 2006, A vision based system for remote sensing of bridge displacement, NDT & E International 39, pp.425-431.

Park K-T., Kim S-H., Park H-S., and Lee K-W., 2005, The determination of bridge displacement using measured acceleration, Engineering Structures 27, pp. 371–378.

Richard J V., Mayrai G, Hani N., and Jana V., 2006, An Algorithm for Estimating Bridge Deflection from Accelerometer Measurements", Signals, Systems and Computers, pp.540-544.

Velde, J., Gindy, M., and Nassif, H., 2006, Estimation of Bridge Displacements from Measured Acceleration Records, XXIII Southeastern Conference on Theoretical and Applied Mechanics (SECTAM), Mayaguez, Puerto Rico.

Kandula, V., DeBrunner, L., and Rambo-Roddenberry, M. 2012, Field testing of indirect displacement estimation using accelerometers, Proceedings of the Conf. Record of the 46th Asilomar Conf. Signals, Systems, and Computers

Lee, H.S.; Hong, Y.H.; Park, H.W., 2010, Design of an FIR filter for the displacement reconstruction using measured acceleration in low-frequency dominant structures, Int. J. Numer. Methods Eng. v82, pp.403-434.

Park J-W., Sim S-H., Jong H-J., and Spencer JR F. B., 2013 Development of a Wireless Displacement Measurement System Using Acceleration Responses, Sensors 2013, v. 13, pp. 8378–8392.

PARK K-T., KIM S-H., PARK H-S., and LEE K-W., 2005, The determination of bridge displacement using measured acceleration, Engineering Structures 27, pp. 371–378.

Umekawa. Y., Sasaki. E., 2015, Evaluation of Vehicular Induced Displacement by Using Wavelet Transformation from Wireless Acceleration Measurement, IABSE Symposium Report, IABSE Workshop Helsinki.

Sekiya, H.; Kinomoto, T.; Miki, C. 2016, "Technique for Determining Bridge Displacement Response Using MEMS Accelerometers", Sensors, v16, 1882.

Infra Studio: http://infra-studio.com/

Maintenance, Safety, Risk, Management and Life-Cycle Performance of Bridges – Powers, Frangopol, Al-Mahaidi & Caprani (Eds)
© 2018 Taylor & Francis Group, London, ISBN 978-1-138-73045-8

Guide for a Successful Monitoring Project from Finland

J. Wuorenjuuri
VR Track Oy, Helsinki, Finland

Monitoring structures is one of the main fields of structural engineering in the future. Monitoring project have many challenges. It requires more skills and more knowledge from all partners involved in the monitoring project. In the past, it has been difficult to see monitoring as a project. The roles have been unclear in monitoring process, results have not been so clear for decision makers. The purchaser of monitoring has not been able to get the information he thought he would get. And the monitoring costs have been a surprise. But the fact is that monitoring costs are reducing all the time and the results are greatly just as good as the purchaser himself knows how to buy these services. In Finland to help purchasers to build a successful project a Bridge Monitoring Guide was introduced in 2016.

1 NEED FOR MONITORING GUIDE

1.1 *Background*

The Bridge Monitoring Guide is drawn up to assist purchasers in monitoring of bridges and to form engineering problems into monitoring projects. The guide presents the contents and the process of the monitoring project and how to run a successful project through. At the same time, a separate Bridge Monitoring Handbook is introduced to assist designers, consultants, and expert companies to plan the monitoring projects as service providers.

As more monitoring companies and service providers come to the field of monitoring, also purchasers must be able to meet the requirements of procurement of effective monitoring results.

Information generated by bridge monitoring projects must serve effectively the decision making relating to bridge management and usability issues. Unified methods of purchasing and quality assurance activities improve these goals and help achieving cost-effectiveness of monitoring objectives and reduce unnecessary monitoring.

This Bridge Monitoring Guide can be used for monitor projects to road, rail, light traffic, and street bridges. The guide may also be used, as applicable, for other engineering structures. The Guide serves as help for procurement procedures and quality assurance. The Guide describes the monitoring methods, the monitoring project process, the quality control, and safety issues of the monitoring project, and can be used to monitor both new and existing bridges. The Guide also includes general guidelines for test loading of bridges.

1.2 *Terminology*

It was also very important in the Bridge Monitoring Guide to define the words, roles, and documents in a Monitoring project.

One of the main challenges has been, that when purchaser buys a monitoring service, he expects results from the monitoring report. But often comes up to be disappointed, when the monitoring project only gives raw data as a report. Of course, the purchaser needs to also buy the analyzing service from an expert.

Also, there has been problems, that the known problem has been monitored using unsuitable monitoring method. It is like getting answers to different questions that originally the purchaser had in mind. It is up to the purchaser to know what he is buying and what should be included into a Monitoring Project to get the right results.

1.3 *Basis for monitoring*

Monitoring is a method of structural engineering that produces numerical information about the actual behavior of the structure. Monitoring supplements the conventional inspections of the bridge by pro-

ducing information that can be utilized and compared later in determining bridge loads, service life, comfort and damages, and the assessment of design solutions. Monitoring is not a substitute for bridge inspections, but can be incorporated into the inspection system. The monitoring of the bridge condition aims to give the information needed for most cost-effective repair or construction measure.

The repair and construction measures are usually based on solutions, which are very dependent on good quality data. By improving this data for example by monitoring, a more cost-effective outcome is possible. Monitoring can be also executed several times if needed.

The monitoring projects to solve bridge capacity issues is mainly related to situations where the axle and total weights of heavy traffic and the stresses they cause are to be determined in advance. In these monitoring projects, mainly known loads are used and the goal is to find a connection between the actual behavior of the structure and the calculated model. The focus of capacity related monitoring is in the final phase of the monitoring project, which is the analysis of the results. Monitoring can be used to produce bridge behavior information about normal permissible weights and special transports.

Bridge monitoring can provide information to determine bridge life. In the analysis phase of the monitoring project, the relationship between the original design life and a more accurate estimate of the current lifetime can be specified, based on the measured conditions and the deterioration issues of the bridge. This information can be used either for the choice of the repair principles or for the safe end of the bridge for use.

In addition to the capacity and deteriorations analysis, monitoring can be used other purposes such as to provide information on the usability, comfort levels or vibrations of the bridge or the general development of bridge standards. In addition, monitoring can provide information on new innovative design or construction solutions if needed to verify special structures.

Mostly, monitoring is related to the use of the bridge, but monitoring can also be executed during the construction phase for quality management purposes of construction works. The duration of monitoring can vary from one-time monitoring to continuous monitoring of the entire bridge lifespan. Monitoring can also be restricted to specific structural parts or it may be localized to damaged points.

Monitoring can consist of one project called a Monitoring Project and a monitoring program consists of several Monitor Projects. The monitoring project consists of three components: monitoring planning, monitoring implementation and analysis of monitoring results. The implementation part of the monitoring is the inspection activity at the bridge site.

2 MONITORING NEEDS AND GOALS

The decision to monitor a bridge must be based on monitoring needs. Monitoring is an option when the available information of a bridge cannot achieve the desired target state. Monitoring needs can be related to bridge damages, bearing capacity, lifetime, comfort, and development. There may be a need for monitoring may already before the bridge is built, but often the monitoring need arises after the construction phase when the bridge is in use. The need to monitor the condition of a bridge often comes up after special inspections or known failures and the need for monitoring of the bearing capacity is linked to capacity calculations.

Bridge monitoring must be a systematic activity that is performed according to the instructions given. The results should be stored in a database or a bridge register and in a unified mode, so the data can be used later without special programs.

The monitoring need must be a starting point for a monitoring plan. The monitoring plan defines the monitoring project and the form of implementation. The Monitor Project should produce enough new information so that the target state of a bridge can be achieved cost-effectively. To collect the right information, monitoring must include goals for the implementation and the analysis phases, so that the original target is reached. These goals must be defined in the monitoring plan. The purpose of goals for monitoring is also to reduce unnecessary monitoring.

The goals of the monitoring implementation and analysis phases must be defined at the beginning of the monitoring plan. Since setting of goals has a significant impact on the costs of monitoring, they can be specified during the monitoring plan phase, with more accurate information about the more exact monitoring methods and their costs. Setting targets for monitoring is most effective when it is done in co-operation between the purchaser and the main monitoring consultant of a Monitoring Project. The goals of Monitoring must be set so that they are achievable. Also, multiple simultaneous goals can be set for monitoring.

A Monitoring Project does not include the actual bridge repairs or modifications. The Monitoring Project only produces more measurement data,

which is supplemented by information on the load bearing capacity and damage analysis models of a bridge. The design for bridge repairs or modifications is part of the post-monitoring activities that can be taken to reach the target state of a bridge. A Monitoring Project gives information to the decision maker on the investment needs

3 MONITORING METHODS

3.1 *General*

The monitoring method describes the continuity and duration of the monitoring performed in the Monitoring project. There are three monitoring methods: continuous, periodic and single monitoring projects. The monitoring method does not directly describe the scope of monitoring.

The selection of the monitoring method influences the most to the duration of the monitoring. In addition, it affects the installation of measuring devices and sensors, the implementation of monitoring and the cost of monitoring. As a basic rule, continuous monitoring has the highest cost and single monitors have the lowest costs.

3.2 *Continuous monitoring*

Continuous monitoring is a continuous measurement of the bridge without interruption. The continuous monitoring may take several years and often it will permanently install the sensors in the structure. Continuous monitoring is the most productive and often cost-effective monitoring.

In continuous monitoring, attention should be paid to the early stages of the Monitoring Project and, if necessary, monitoring, especially for long-term operation, maintenance and calibration capabilities of sensors and measuring devices. Continuous monitoring can track time-dependent quantities. Moving the measurement data from the subject to the monitoring results analyzer can happen continuously and automatically or intermittently for example once a day.

3.3 *Periodic monitoring*

In periodic monitoring, the bridge is monitored in sequences. The length of the period to be measured and the length of the period can be short or long for up to several years. The spacing between periods may be regular or irregular, and repairs or modification to the bridge can be made between the periods. Periodic monitoring is particularly suited to ensuring the success of repairs to the bridge. Periodic monitoring can be used to monitor time-dependent variables.

In the early stages of the Monitoring Project, in the periodic monitoring phase, attention should be paid especially to the calibration of sensors and measuring devices.

3.4 *Single monitoring*

In single monitoring, the bridge is monitored for only one period. Single monitoring will change into periodic monitoring if it is renewed later, for example, after bridge repairs. The possibility of periodic monitoring should already be identified in the monitoring plan to consider the repeatability of the measurement arrangements and possible re-installation of the sensors. The duration of a single monitoring may be some weeks. For example, information about continuous heavy traffic and its effects on the bridge can be obtained. However, during single monitoring, the condition of the bridge is not expected to change, so it is not possible to generate data on time-dependent quantities.

3.5 *Selection of monitoring method*

Selection of the monitoring method is the responsibility of the purchaser of the Monitoring Project. The monitoring method generates a significant part of the cost of monitoring and substantially affects the information produced by monitoring. The choice of monitoring method depends on the need for monitoring, the target state of a bridge, the cost of monitoring and the usefulness of the results obtained. Different monitoring methods can often be used to achieve the goals. Selecting a monitoring method is always bridge-specific and case-specific.

In case of a damaged bridge all monitoring methods can be used. Continuous monitoring and periodic monitoring techniques can be used to distinguish time-dependent factors from monitoring results. In single monitoring, it is important to use a sufficiently large load of normal traffic if the test load is not used. The monitoring of the development of a damage requires continuous or periodic monitoring. In assessing the significance of damage, the monitoring method should be chosen based on possible new information that can be produced and monitoring costs.

In the case of the determination of axle loads (= permissible axle and total weights), periodic and single monitoring can be used to monitor the bridge. Changing the permissible axial and total weights is often subjected to test loads, and single monitoring can be used to verify the load carrying capacity. Continuous monitoring is often not cost-effective in the estimation of bearing capacity, but it can be used to monitor the performance of a bridge repairs or increasing permissible loads on bridge.

Information related to estimate the remaining lifetime of a bridge, can be generated by all monitoring methods. Single monitoring cannot produce information about factors that change over time. In single monitoring the lifetime review is only related to the information produced by the test loading. Periodic or continuous monitoring can be used to produce accurate continuous information for estimating service life.

The most appropriate monitoring method and the cost of monitoring is usually made more accurate during monitoring planning. When the information and goals are defined, the main monitoring consultant of the monitoring must specify the various monitoring options for the purchaser so, that the target status defined by the purchaser can be achieved after the Monitoring Project. Selection of the monitoring method should also consider the available Monitoring Project implementation scenarios.

4 SCOPE OF MONITORING

4.1 *General*

The scope of the monitoring describes the resources used to plan, implementation and analyzing the results of the Monitoring Project. The scope of the monitoring involves the use of the monitoring technology, the number of measuring devices used and the analysis of the monitoring results. The monitoring project has three different scopes: limited, extensive, and extra extensive. Selecting the scope of monitoring is part of the task of the purchaser.

The scope can be selected during the monitoring project or can be refined when the monitoring plan is completed and the purchaser has more information about the monitoring. The scope of monitoring affects the number of measuring points and measurement techniques.

4.2 *Extra-extensive monitoring*

In addition to the phenomenon under examination, the extra-extensive monitoring provides detailed information on the actual behavior of the entire bridge. More than one measurement technique and very many measurement channels is used to monitor the same phenomenon in an extra-extensive monitoring to model the actual behavior of the bridge.

4.3 *Extensive monitoring*

In extensive monitoring, information is provided in addition to the item under consideration, and the overall real behavior of the bridge. There may be several measurement techniques and several measurement channels is used.

4.4 *Limited monitoring*

In limited monitoring, information is provided only on the phenomenon under review. In a limited monitoring, only one measurement technique is used to generate information. The measurement channels are usually up to 20, but a simple method can be used to analyze the monitoring results.

4.5 *Selecting the Scope of Monitoring*

The scope of monitoring plays a major role in the cost of monitoring the project. The scope of the monitoring is always based on the most cost-effective scope option. In selecting the scope, the purchaser must estimate the amount and reliability of the data generated by the monitoring in relation to the cost of monitoring. The scope of monitoring should always be chosen so that the information can be used reliably to achieve the target state with an analytical model.

The importance of the bridge should be evaluated when selecting the scope of the monitoring. Significance means the importance of a bridge or bridge type on the transport network. In addition, it is necessary to evaluate the possible replacement of the bridge. With a large replacement cost, extensive monitoring can help achieve cost savings if the renewal of the bridge can be postponed to the future or even demolished after use.

5 MONITORING PROJECT

5.1 *General*

The Monitoring Project is a set of monitoring issues and processes. The Monitoring Project includes all three aspects of the monitoring (planning, implementation, and analysis of results), the documents of each sub-area and the contracts between the parties involved. The whole monitoring project is designed to provide the necessary additional information to achieve the defined target state.

The monitoring project has three main forms of implementation (divided monitoring, centralized monitoring, and shared monitoring). Implementation forms determine the roles and tasks of the parties involved in the monitoring project. The suitability of the implementation forms for the monitoring project depends on the monitoring method, the duration of the monitoring and the resources available.

Choosing the right choice for the implementation method is intended to ensure the quality and cost-effectiveness of Monitoring Project. A Monitoring Program consists of several Monitoring Projects. It is important that the measurement and analysis results are stored in a systematic database.

5.2 *Roles of the monitoring project*

The Monitoring Project includes different roles for the various parties involved, which include responsibilities in the areas of the monitoring project. Responsibility is defined as a set of issues, the role of which being the same. In one project, the same company or person can have more roles. For example, in centralized monitoring, in addition to its role of the main monitoring consultant can have roles as the main monitor planner and monitoring results analyzer.

Each project must have at least the following roles:
- Purchaser
- The main monitor consultant or planner
- The monitoring implementer
- The monitoring results analyzer
- The monitor expert of Purchaser
- Safety Coordinator

The Project options for Monitoring can be as in the following 5.3 – 5.5.

5.3 *Project option 1: Divided Monitoring Project*

Divided monitoring is the most common form of monitoring. There are three parties involved in divided monitoring during the entire monitoring project: the purchaser, the main consultant of monitoring and the monitoring implementer. In addition to these parties, the project may include sub-consultants. In the divided monitoring, the monitoring results are analyzed for the main consultant of monitoring. There may be more monitoring implementers if the Monitoring Project is periodic and lasts for a long time.

Divided monitoring can be applied to conventional Monitoring Projects, which can be both short and long. From the purchasers point of view, divided monitoring usually requires less contract documents because the monitoring process can be purchased mainly with the plan main monitoring consultant. For the purchaser, the greatest risk is that the implementation of the monitoring must be realized as planned.

5.4 *Project option 2: Centralized Monitoring Project*

Centralized monitoring is a lightweight Monitoring Project for the Purchaser. In addition to the purchaser, there is only one company in a Centralized Monitoring Project. One company is involved in the planning, implementation and analyzing of the monitoring results. In a Centralized Monitoring Project, the information link between the contract partners is more straight forward, and the risks caused by the communication between the partners are small.

A Centralized Monitoring Project is suitable for monitoring cases where the role of the purchaser in the monitoring project is kept to a minimum and where the monitoring content is clear. A Centralized Monitoring Project requires extensive contract documents from the Purchaser because the entire monitoring project is usually purchased at the beginning of the project. Additionally, the purchaser must have expertise in monitoring to evaluate the measurement techniques proposed and the suitability of the monitoring implementer.

5.5 *Project option 3: Shared monitoring Project*

A Shared Monitoring Contract is a purchaser-oriented mode for a Monitoring Project. In a Shared Monitoring Project, a different partner performs each aspect of monitoring. In addition to the purchaser, the Monitoring Project, the main monitoring consultant, the monitoring implementer, and the monitoring results analyst participate in the monitoring project. Long-term monitoring projects may have more monitoring implementers.

A Shared Monitoring Project is recommended to be used only in long-term monitoring projects where other Monitoring Project forms cannot be used due to the length of the Monitoring Project. It is recommended for the purchaser to use a monitoring expert consultant in a Shared Monitoring Project.

The major risks of a Shared Monitoring Project are the flow of information between the partners and complexity of project management. The separation of the Monitor Planner and the Monitoring Results Analyzer according to a Shared Monitoring Project raises the risk that the analysis of the monitoring results does not correspond to the monitoring plan. In Shared Monitoring Projects, the quality and content of plans and design documents is an important factor in successful Monitoring Project.

5.6 *The risks of a monitoring project*

The monitoring project involves risks that depend on the complexity of monitoring and its implementation. Risks occur in all three areas of monitoring. Risks can be divided into risks associated with management, planning and implementation. Risk analyzes are part of the risk management. Risks can be controlled by selecting the most appropriate monitoring method and form of project.

The risks associated with planning and implementation of monitoring depend mainly on the objectives of monitoring and on the complexity of the monitoring target. The risks of planning and implementation are mainly managed through monitoring plans that the purchaser accepts and the partners have sufficient professional skills. The risks of a Monitoring Project vary from one project to another. A general risk may also be lack of experience or lack of skills of chosen partners.

6 CONTENTS OF THE MONITORING DOCUMENTATION

6.1 *General*

The main monitor planner of the monitoring is responsible for determining the points to be examined by professional judgment so that reliable data are obtained from the condition and operation of the structures. The implementer of the monitoring is responsible for the reliability of measurement results and the long-term performance of sensors and other instruments. To ensure the reliability of the results, calibrations and related measurements must be made in continuous monitoring. The planner of the monitoring determines the level of accuracy for which measurements to be achieved.

The monitoring project includes the following documents:

- Contracts
- Monitoring Plan
- Safety plan
- Implementation plan
- Measurement Report from implementer
- Monitoring Report from Analyzer of results

In some cases, these requirements can be lowered if the project is small in scope or does not include structural monitoring. In a Centralized Monitoring Project, the Monitoring plan, Safety plan and Implementation plan can be combined into a single document.

Devices used for monitoring must be serviced and calibrated in accordance with their manufacturer's instructions. The documentation of the calibration data must be up-to-date.

Monitoring projects usually change during the way, so it is important to agree on the unit prices to possible modifications by the purchaser. The relevant structural drawings should also be available at the bridge site. It is also necessary to agree that the information is available for purchaser, project partners and possibly the maintenance partners during and after the project.

In case of continuous Monitoring Projects, different partners have different practices regarding the ownership of measuring instruments. The contract documents must specify whether the buyer is purchasing the measuring equipment and who owns them after the monitoring project. In principle, measuring instruments are part of the monitoring provider and their rental price should be included the implementation of the monitoring.

7 QUALITY MANAGEMENT

7.1 *Organization and staff*

The various partners involved in the monitoring must announce in their tenders the structure and organization of the monitoring service, as well as the duties and powers of those responsible for the implementation of the work. Persons participating in monitoring projects must meet requirements of purchaser for skills and safety levels. Continuity of competence must be ensured.

The quality assurance must be a part of the Monitoring Project. Usually the main monitoring consultant has the role of to ensure the quality of the Monitoring Project unless otherwise agreed.

7.2 *Subcontractors*

The subcontractor must meet the same organizational and personnel requirements as what is required from the main monitoring contract partners. The subcontractor must comply with the quality assurance procedure of the monitoring contract partners. Also, safety requirements must be met.

7.3 *Quality assurance*

The purchaser requires a quality assurance procedure documented by the monitoring partners. The quality assurance procedure will be reviewed at the first meeting. The partners implementing the monitoring system will make its own quality control in accordance with its quality assurance process.

Quality interim reporting during the audit period is done as agreed in the first meeting. A summary of the supplier's internal quality assurance and its results are presented to the purchaser in the final monitoring report. In small assignments communication and reporting can be agreed separately.

8 WORK SAFETY

8.1 *General*

All safety and performance issues in monitoring must comply with the requirements and instructions the purchaser as well as of laws and regulations and other governmental regulations. The laws set out the responsibilities and obligations of the employer, as well as the rights and obligations of the employee.

Monitoring is a form of structural inspections and the execution must be based on the safety regulations, procedural instructions, and safety instructions of the Finnish Transport Agency's guidelines. Monitoring is not construction work that has additional safety requirements. The Monitoring Project must have a Safety Coordinator appointed by the purchaser, who is responsible for the safety and health measures during the preparation, design and implementation phase of the project. The Safety Coordinator may be a from organization of purchaser or a consultant. A Safety plan that manages occupational safety must be always drafted.

There are also requirements for safety equipment and tools that can be used on a bridge site. Bridges in road environments have safety qualification requirements for all workers. Railway bridges require also Safety qualification for all workers. At bridge site that cross both road and railways, workers must have both qualifications.

8.2 *Transport arrangements*

Traffic arrangements are included in the monitoring order unless otherwise stated in the contract of the Monitoring Project. The safety document prepared by the purchaser also presents issues and requirements regarding traffic safety and traffic arrangements.

The monitoring implementer can either buy traffic arrangements as a comprehensive service for specialized companies or implements arrangements with their own resources. The organizer of the traffic arrangements must be named in the monitoring implementation plan.

The organizer of the traffic arrangements must always draw up a written traffic control plan. The traffic control plan is part of the monitoring implementation plan that must be approved by the purchaser. A notice of work that influence traffic must be made to the responsible Traffic Center in advance.

9 CONCLUSIONS

The main message to Monitoring Projects is that they should be well organized, management of the project has to be effective to get exact and useful information from monitoring. Monitoring is too expensive and time consuming, that it is waste of resources if the project does not produce enough information or it produces a lot of additional information that no one can use.

The purchaser has to have enough information and vision to make a good Monitoring project. he must know what to demand even if he does not understand the technical aspects of monitoring. The Bridge Monitoring Guide, that has been introduced in Finland to help purchasers to put together a monitoring project after a problem of capacity, damages or service life deficiencies has been detected. It is very important to understand, that monitoring is a helpful tool in decision making, especially when costs of aging infrastructure is getting higher every year.

The key issues are:
- clear project plan
- the choice of monitoring method
- the choice of scope of monitoring
- the scope of monitoring project type
- risk management
- quality management
- safety management
- the choice of skilled people

The cost of monitoring has reduced to a good level, and it will continue to do so. In Finland, there are many successful Monitoring Projects that have met the needs of wise decision making. Some projects are to understand the behavior of a bridge with special details or with damaged parts. Or to help decide to renew or repair methods. This is economical solution for a good infrastructure.

10 REFERENCES

Finnish Transport Agency. 2016. Siltojen monitorointiohje lo_2016-18. Helsinki. Finland

Maintenance, Safety, Risk, Management and Life-Cycle Performance of Bridges – Powers, Frangopol, Al-Mahaidi & Caprani (Eds)
© 2018 Taylor & Francis Group, London, ISBN 978-1-138-73045-8

Bending-Shear Fatigue Behavior of Concrete Girder Bridges

Ming Yuan & Donghuang Yan & Yun Liu
Changsha University of Science & Technology, Changsha, China

ABSTRACT: Under the bending-shear condition, the diagonal crack of web will appear in concrete box-girder bridge when principal tensile stress of tensile-shear zone concrete exceeds principal stress limit value. The overall objective of this study is to develop a calculated method for the fatigue behavior of web under bending-shear of concrete box-girder bridge. First, some basic conceptions and calculation methods of concrete fatigue theory are introduced. Next, the time-history curves of bending moment, shear force and principal tensile stress in typical section have been achieved. Then the effects of vehicle speed and heavy vehicles for the equivalent principal tensile stress on web of box-girder are discussed. Finally, the reliability index is established to assess the fatigue life for existing concrete box-girder bridge. Some conclusions are drawn on the basis of the current research.

1 INTRODUCTION

The vehicle speed and overloading vehicles increase with the development of traffic. For service bridges, concrete microscopic cracks may occur and propagate by cyclic load. Under the bending-shear condition, the diagonal crack of web will appear in concrete box-girder bridge when principal tensile stress of tensile-shear zone concrete exceeds principal stress limit value (AASHTO 2002, JTG D64-2004 2004). Especially for the concrete box-girder bridge with small-medium span, the compressive stress value of principal tensile stress reserve generally small under dead load condition. Considered the effect of live load, the changes of principal tensile stress amplitude are more significant. Therefore, calculating principal tensile stress accurately under vehicles cyclic load is a challenging problem for fatigue life assessment and prediction.

Several studies have been proposed for concrete flexural fatigue (Shi & Yao 1990, Zhu 2011,Gaspar & Stucchi 2013, Sousa et al. 2013). These methods do not directly associate the bending-shear fatigue behavior. The overall objective of this study is to develop a calculated method for the fatigue behavior of web under bending-shear of concrete box-girder bridge. First, some basic conceptions and calculation methods of concrete fatigue theory are introduced. In combination with actual traffic volume of two typical highways, five typical kinds of vehicles are chosen as vehicle load spectrum of concrete box-girder bridges. Next, the time-history curves of moment, shear force and principal tensile stress in typical section have been achieved. The principal tensile stress spectrum at the web of box-girder is acquired by Rain-flow counting method. According to Miner linear fatigue damage rule, the equivalent principal tensile stress spectrum is proposed for fatigue life assessment and prediction. Then the effects of vehicle speed and heavy vehicles for the equivalent principal tensile stress on web of box-girder are discussed. Finally, the reliability index is established to assess and predict fatigue life for existing concrete box-girder bridge.

2 CALCULATED METHOD

2.1 *Vehicle load spectrum*

Many vehicle load spectrum for fatigue of the steel bridge have been obtained. Especially in Britain, the United States and other European countries, steel bridge fatigue load spectrums have been developed successfully and widely used. Combined with the actual traffic volume of highway bridge (Ju & Fan 1994). The following characteristics of vehicle load can be analysed by a certain method. The vehicle has various types, because the axle load, wheelbase, track width and total weight are different.The vehicle loads are processed according to the following principles:

1) According to the statistics of actual traffic, the same amount of axle is classified according to the vehicle load (the original load spectrum).
2) In each kind of vehicle load, according to the fre-

quency of the axle and axle load, and the equivalent axle load of each type of each axis can be found. Based on Miner equivalent fatigue accumulation rule (Gaspar & Stucchi 2013, Sousa et al. 2013), an equivalent conversion on the axle load is conducted, and then equivalent total weight has been obtained. The jth axis load of the equivalent vehicle is shown as

$$W_{ej} = (\sum f_i W_{ij}{}^m)^{1/m} \quad (1)$$

Where, f_i is the relative frequency from the same kind of vehicle, W_{ij} is the axle load, m is the slope of material S-N curve.

3) Wheelbase is generally be calculated by weighted method. C_j is the jth wheelbase of the vehicle load, it is shown as

$$C_j = \sum f_i \, C_{ij} \quad (2)$$

Where C_{ij} is the jth wheelbase of the ith vehicle load.

2.2 *Principle tensile stress spectrum*

The principle tensile stress spectrum of prestressed concrete box-girder bridge is calculated by vehicle-bridge coupling vibration model. The specific steps are list as follows:

1) According to the circumstance of bridges in roads, statistics of various models of axle load, the vehicle weight and traffic are surveyed.

2) Fatigue vehicle model is defined according to the statistics and classification of different models. Then the simulation models are computed.

3) Through the program of vehicle-bridge coupling vibration model, the time history for bending moment and shear force of bridge is concluded, and then the time history for principle tensile stress is achieved.

4) According to the drain sump method or the rain-flow counting method, the load effects $\Delta\sigma_e$ are acquired.

2.3 *Equivalent principle stress amplitude*

Because the internal force or stress course is discrete under axle load, the required stress amplitude cannot be directly applied in the analysis of fatigue performance and fatigue life prediction. It needs to simplify according to the Miner linear fatigue damage rule equivalent simplification. The formulas of the equivalent stress amplitude are shown as Eq. 3 ~Eq. 8.

The variable amplitude stress of bridge under vehicle load is divided into k parts S_{r1}, S_{r2},..., S_{rk}, its corresponding cycles n_1, n_2, n_3,..., n_k, assuming that the bridge structure or component under constant stress level S_{r1}, S_{r2},..., S_{rk}, the corresponding fatigue life N_1, N_2,..., N_k, under the effect of amplitude stress S_{ri}, the bridge structure or component have fatigue damage after cycles. According to the Miner linear cumulative damage rule,

$$D = \sum_{i=1}^{k} \frac{n_i}{n_k} = \frac{n_1}{N_1} + \frac{n_2}{N_2} + \cdots + \frac{n_k}{N_k} = 1 \quad (3)$$

According to the formula of constant amplitude fatigue $N(\Delta\sigma)^m = C$, m is the slope of S-N curve.

$$\sum n_i (S_{re})^m = C \quad (4)$$

$$N_i (S_{ri})^m = C \quad (5)$$

According to Eq. 3 and Eq. 4

$$\sum n_i / N_i = (S_{ri})^m / (S_{re})^m \quad (6)$$

According to Eq. 6 and Eq. 3

$$\sum \frac{n_i}{N_i} = \sum \frac{n_i}{\sum n_i} \bullet \frac{(S_{ri})^m}{(S_{re})^m} = \sum \alpha_i \bullet \frac{(S_{ri})^m}{(S_{re})^m} = 1 \quad (7)$$

Then, the equivalent stress amplitude is represented as

$$S_{re} = [\sum_{i=1}^{n} \alpha_i S_{ri}^m]^{1/m} \quad (8)$$

Where,

S_{re} -- the equivalent stress amplitude (MPa);

α_i -- the frequency of stress amplitude S_{ri};

S_{ri} -- stress amplitude (MPa);

m -- Material constant, generally value 3.0.

2.4 *Evaluation of fatigue life*

In view of the fatigue life evaluation and prediction, there are generally two kinds of methods to evaluate the fatigue life of bridge in the practical application. One method is using fatigue test data to evaluate the fatigue life by analysing fatigue curve. Another method is using the theory of fatigue crack propagation to evaluate the fatigue life.

Structural fatigue reliability index can be calculated as

$$\beta = \frac{\lg \Delta\sigma_R + 2S_R - \lg \Delta\sigma_e}{\sqrt{S_R^2 + S_e^2}} = \frac{\lg \Delta\sigma_R + 2S_R - \lg(k_1 k_2 k_3 \sqrt[m]{100/T\Delta\sigma})}{\sqrt{S_R^2 + S_e^2}} \quad (9)$$

$$= \beta_0 + \frac{(\lg T - \lg 100)/m}{\sqrt{S_R^2 + S_e^2}}$$

$$T = 10^{[2 - m(\beta_0 - \beta)\sqrt{S_R^2 + S_e^2}]}$$

Where, β_0 is the goal of fatigue reliability index, S_R, S_e is the standard deviation.

3 DEMONSTRATION EXAMPLE

3.1 *Example of vehicle load spectrum*

Traffic volume survey is a statistics on a road of various kinds of vehicles and vehicle weight, through the investigation of road traffic. It can be used for study the change of the traffic volume (vehicle type, such as the distribution of the van), and provide ref-

erence for bridge design.

Actual traffic volume of two typical highways are combined and discussed. According to the statistics of actual traffic volume, vehicle load was classified by the same number of axles, the equivalent axle load and average wheelbase was calculated according to the Eq. (1) and Eq. (2). In order to simplify the load parameters of the vehicle model, the average equivalent axle load and average wheelbase are made following adjustments: 1) the equivalent axle load take multiples of 5 kN. 2) the average wheelbase take multiple of 0.5 m, as shown in Table 2.

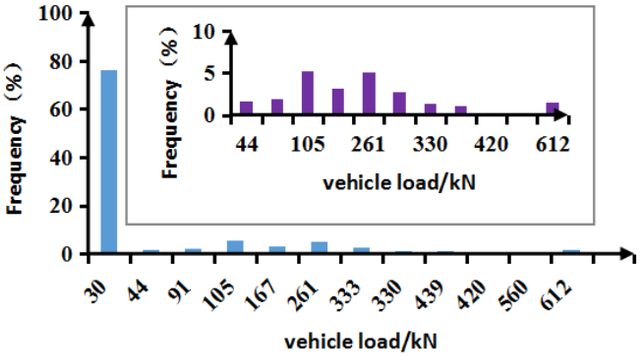
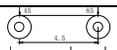
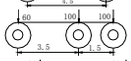
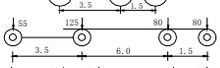
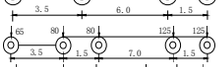


Figure 1. A bridge vehicle load distribution histogram in 2008

Table 1. The calculation results of the equivalent axle load, average wheelbase

Vehicle model number	Axle number	Equivalent axle load (kN)	Average wheelbase (m)
M1	2	42 83	4.42
M2	3	61 100 100	3.55 1.32
M3	4	53 123 82 82	3.35 5.92 1.24
M4	5	66 78 78 125 125	3.14 1.35 7.12 1.30
M5	6	51 120 120 107 107	3.20 1.35 5.66 1.20 1.20

Table 2. A bridge load spectrum in 2008

Vehicle model number	Graphic (The axle load: kN, wheelbase: m)	Total weight (kN)	The ratio of the total traffic volume(%)
M1		130	11.89
M2		260	5.03
M3		340	4.08
M4		475	1.24
M5		610	1.43
	Total		23.67

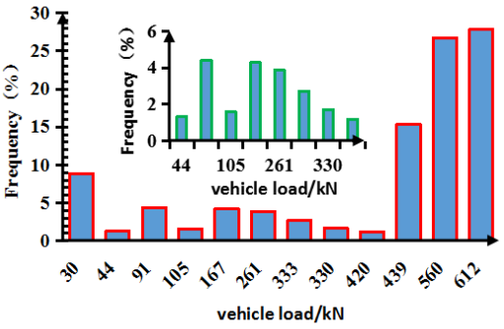


Figure 2. A highway bridge vehicle load distribution histogram in 2010

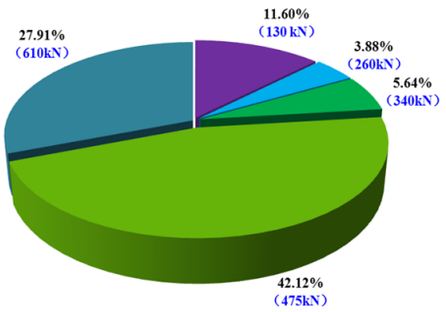


Figure 3. A highway bridge load distribution histogram in 2010

3.2 *Example of PC box-girder bridge*

The proposed methodology is demonstrated in this section for the fatigue analysis of a PC box-girder bridge. The bridge cross section under consideration is given subsequently in Figure. 4. The cross section form is single box section, span L=40 m, beam height H=2.2 m, top plate width B=13.0 m, bottom plate width D=9.0 m. The chamfer size of top plate is 20×60 cm, the chamfer size of bottom plate is 20×40 cm, the cantilever length of box girder is 2.0 m, web plate thickness is 0.4 m, the thickness of top plate is 0.25 m and bottom plate is 0.22 m.

C50 concrete is applied in the upper main bearing structure of bridge, the axial compressive strength standard value f_{ck}=32.4MPa, the axial compressive strength design value f_{cd}=22.4MPa. The prestressed steel strand with high strength and low relaxation is applied, the tensile strength standard values f_{pk}=1860MPa, diameter d=15.20mm, area S=139.0mm^2, modulus of elasticity E_p=1.95×105MPa.

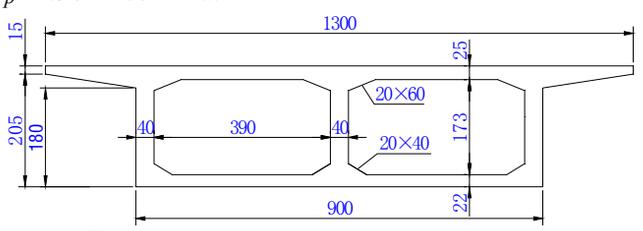


Figure 4. The cross section of simply supported beam

A program of vehicle-bridge coupling vibration model is applied to calculate the mid-span bending moment and shear force time history. Combined with the rain-flow counting method, then the princi-

pal tensile stress spectrum of control points on the box girder web is obtained, as shown in Fig.5 and Fig. 6. It is descried that: (1) The small stress amplitude of load spectrum 1 is taken relatively major proportion, and the high stress amplitude of load spectrum 2 is taken relatively major proportion; (2) Compared load spectrum 1 with load spectrum 2, its principal tensile stress is changed with the speed variation, and principal tensile stress amplitude also increased.

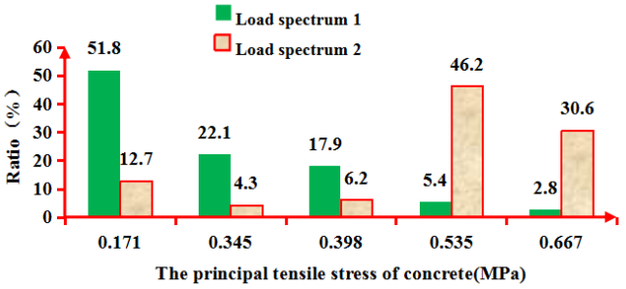


Figure 5. The position 3# of principal tensile stress spectrum on box girder web plate (vehicle speed is 10 m/s)

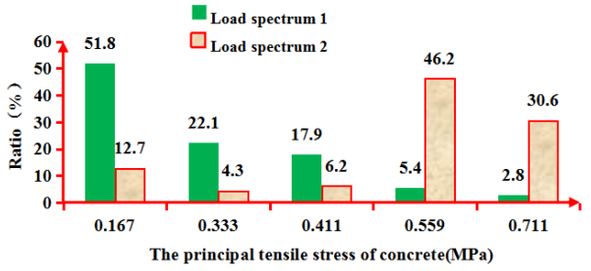


Figure 6. The position 3# of principal tensile stress spectrum on box girder web plate (vehicle speed is 50 m/s)

The equivalent principal tensile stress amplitude of 3# position on the box girder web is studied under different vehicle speed and heavy traffic volume, based on load spectrum 1and load spectrum 2. It is represented as follows as Figure 7~Figure 10. It can be descried that the equivalent principal tensile stress amplitude increases with vehicle speed and traffic volume growth. The heavy traffic volume affects the change of equivalent principal tensile stress amplitude obviously.

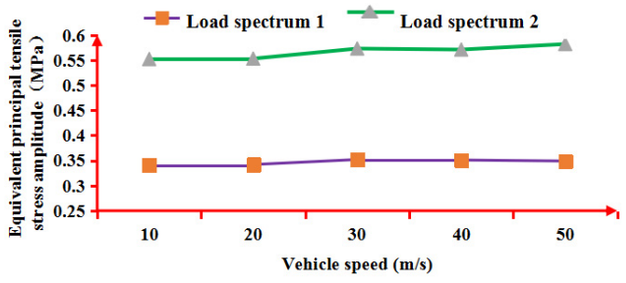


Figure 7. The equivalent principal tensile stress amplitude of 3# position on the box girder web under different vehicle speed

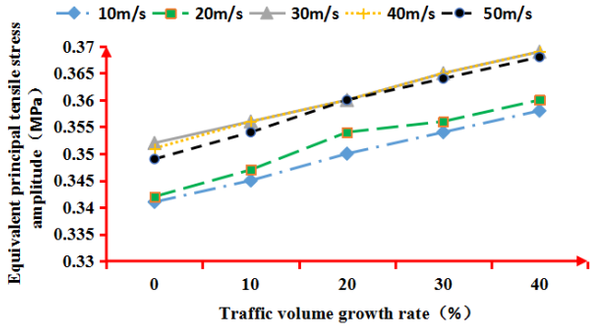


Figure 8. The equivalent principal tensile stress amplitude of box girder web under increased heavy traffic volume

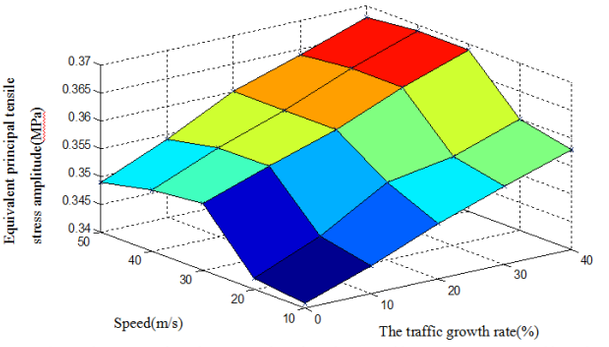


Figure 9. The equivalent principal tensile stress amplitude of 3# position on the box girder web plate under different vehicle speed and heavy traffic volume (load spectrum 1)

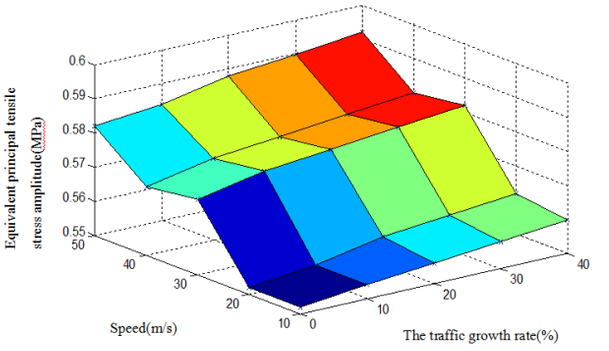


Figure 10. The equivalent principal tensile stress amplitude of 3# position on the box girder web plate under different vehicle speed and heavy traffic volume (load spectrum 2)

The reliability index under two load spectrums considering vehicle speed and heavy traffic volume are discussed. The parameters of reliability index are list as S_R=0.12MPa, S_e=0.066 (load spectrum 1), S_e=0.082 (load spectrum 2), $\Delta\sigma_R$=1.06MPa. The calculation values of reliability index and fatigue life are shown as Figure 7~Figure 10. The reliability index of bridge decreases according to the increase of vehicle speed and heavy traffic volume.

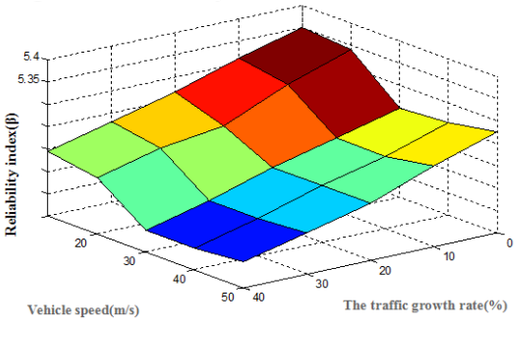


Figure 11. The reliability indexes considering the different vehicle speed and increased heavy traffic volume (load spectrum 1)

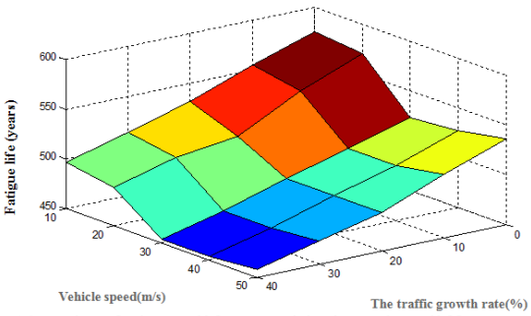


Figure 12. The fatigue life considering the different vehicle speed and increased heavy traffic volume (years) (load spectrum 1)

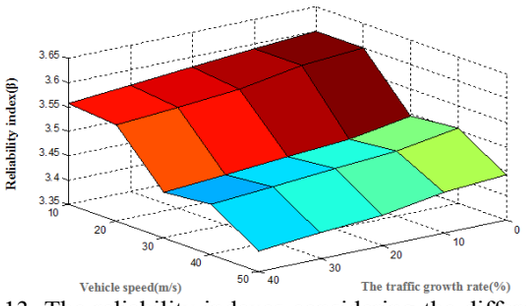


Figure 13. The reliability indexes considering the different vehicle speed and increased heavy traffic volume (load spectrum 2)

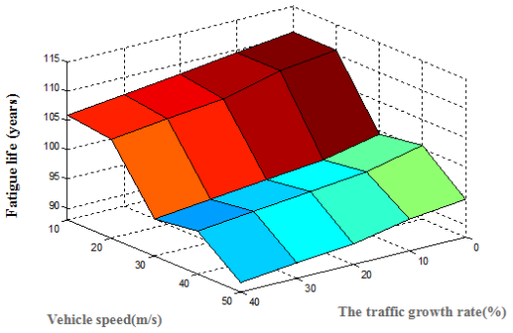


Figure 14. The fatigue life considering the different vehicle speed and increased heavy traffic volume (years) (load spectrum 2)

4 CONCLUSIONS

In this study, a calculated method for the fatigue behaviour of web under bending-shear of concrete box-girder bridge is proposed. Several conclusions are drawn on the basis of this study:

(1）Considering the growth of vehicle speed and heavy vehicle traffic volume, the principle tensile stress and equivalent principal tensile stress increase with the vehicle speed. The heavy vehicle traffic volume effect on principal tensile stress and equivalent principal tensile stress obviously, which increase with heavy vehicle traffic volume. The varieties of equivalent principal tensile stress amplitude are affected extremely when considering the vehicle speed and heavy traffic volume at the same time.

(2) Based on the equivalent principal tensile stress amplitude on the web of box girder, the fatigue life of PC simply supported box-girder bridge is evaluated under vehicle load. The growths of vehicle speed and heavy vehicle traffic volume affect the reliability index and fatigue life. The heavy vehicle traffic volume has significant influence on reliability index under bending-shear of box-girder bridge.

References

American Association of State Highway and Transportation Officials (AASHTO). 2012. *LRFD bridge design specifications*, 6th Ed., AASHTO, Washington, D.C.

Gaspar, R. & Stucchi, F. R. 2013. Web design of box girders concrete bridges. *Engineering Structures*, 57, 267-275.

Gomez, M. P. & Anderson, W. E. A. 1961. A rational analytic theory of fatigue. *Trend in engineering*, 13(1), 9-14.

Ju, Y. & Fan, C. 1994. Fatigue cumulative damage theory study. *Journal of Harbin engineering college*. 27(5)115-120.

Li, C. & Ma, C. 1997. The diagonal shear strength test study of concrete beams under varying amplitude repeated load. *Journal of taiyuan university of technology*, (28): 33-36.

Okamura H. & Farghaly, S. 1979. Shear Design of Reinforced Concrete Beams for Static and Moving Loads. *Proceedings of Japan Society of Civil Engineers*, 287:127-136.

Price, K.M. & Edwards A.D. 1971. Fatigue Strength in Shear of Prestressed Concrete I-Beams. *Journal of ACI*, 68(4).

Shi, X. & Yao, Z. 1990. Bending fatigue properties of cement concrete. *China Civil Engineering Journal*, 23(3):11-22.

Sousa, C. et al. 2013. Fatigue analysis of box-girder webs subjected to in-plane shear and transverse bending induced by railway traffic. *Engineering Structures*, 54, 248-261.

The Ministry of Communications. 2004. *Highway reinforced concrete and prestressed concrete bridge design code*. Beijing: China communication press.

Zhu, H. 2011. Fatigue test and residual life prediction method study of highway simply-supported reinforced concrete bridge. [Central south university PhD thesis], *Changsha: Central south university*, 56-83.

SS05: Self-sensing and connected infrastructures for a smart transport future

Organizer: F. Giustozzi

Maintenance, Safety, Risk, Management and Life-Cycle Performance of Bridges – Powers, Frangopol, Al-Mahaidi & Caprani (Eds)
© 2018 Taylor & Francis Group, London, ISBN 978-1-138-73045-8

Global Instrumentation, Vehicle, Track and Bridge on operation railway of MRS Logistic Railway

Rodolfo Montoya
Railway Bridge Consultant, MRS L ogistic and Pontifical Catholic University of Rio de Janeiro, Rio de Janeiro, Brazil
Luiz Fernando Martha
Associate Professor in Civil Engin eering. Pontifical Ca tholic University of Rio de Janeiro, Rio de Janeiro, Brazil

ABSTRACT: The uncertainties of the design, execution and maintenance are clearly revealed in the increase of the dynamic impact on the structures. In the maintenance of the bridges we can observe that each factors are relevance on the total value impact dynamic projected or expected. Knowing each percentage of importance, facilitates the process of maintenance of each responsible area, this was initially done intuitively to be able to locate where the trigger of the problem was. Theoretically we lack parameters to obtain the variables that allow us to use an adequate analysis of reliability. However, it was necessary to approach the problem experimentally, by assembling a known vehicle, on a bridge, track and instrumented vehicle, isolating known defect patterns, to be able to measure the relevance of each variable within the dynamic amplification. This global instrumentation project is certainly the first instrumentation in Brazil, isolating defects of the vehicle, track and bridge, more interestingly, the whole company managed to work together with a common purpose that was the efficient maintenance of bridges. We obtained the importance of each parameter, final coefficient of experimental dynamic impact measured for each bridge, with the transmissibility levels of each transition zone of the system. It was also obtained the reduction that each parameter is responsibility in the total residual life of the structure, being able to convert this into monetary numbers and a more real decision making.

1 INTRODUCTION

Dynamic impact management has parameter importance in the management of bridges following prioritization. We can verify the importance of each parameter in isolation to be able to reduce risks and levels of uncertainty so we can be able to maintain a more efficient maintenance input (Figure 1).

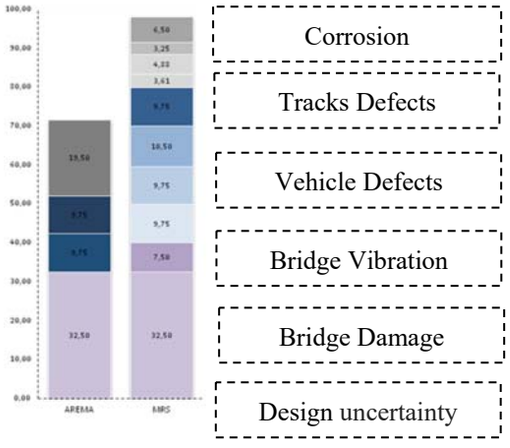


Figure 1 – Dynamic Impact Variable

We observed that we have different parameters that participate in this dynamic impact and each of them has relevance in maintenance. The main ones are listed below:

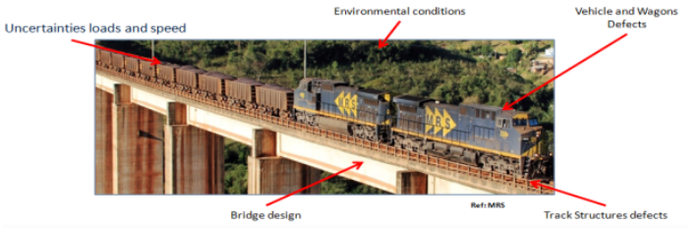


Figure 2 – Uncertainties Railway Bridges

2 DYNAMIC IMPACT MANAGING

2.1 *Loading Deviation*

The loading deviation brings a reduction in the capacity over the structural life of the bridge, which does not mean that the structure can collapse, but that it will reduce the useful fatigue life of the bridge because of the differences of each axis applied in the structures, which increases the stress response peaks for unbalanced loading, so the structure response is at higher cycles (Figure 3).

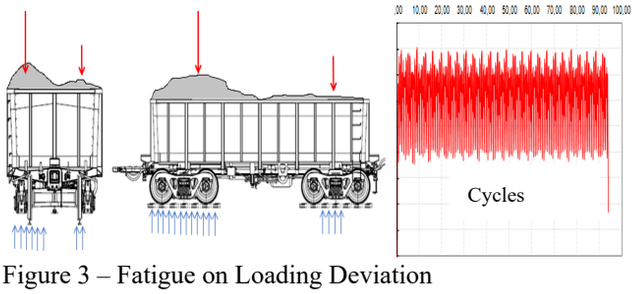


Figure 3 – Fatigue on Loading Deviation

In order to verify the importance of a vehicle passing with loading deviation, different bridges were numerically modelled and a vehicle with different deviations travelled noticing that there are some deviations loading configurations that do not affect the bridges in a certain span. Thus, we can determine a maximum load deviation for each bridge with a certain configuration as shown in Figure 4.

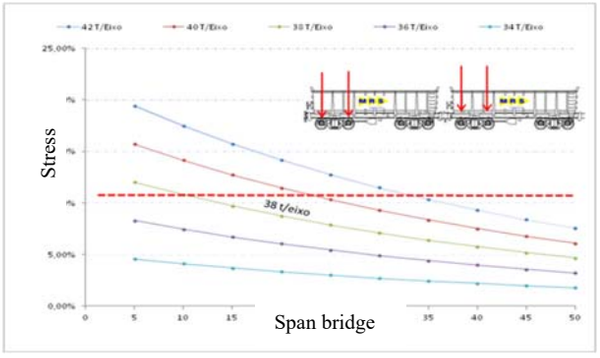


Figure 4 – Different Span to Loading Deviation Analysis

2.2 *Uncertainties of Execution, design and quality control*

The uncertainties of execution, design and quality control are the most difficult ones to control because in every project there are security factors that depend very much on the experience of the designer. In execution we often have changes to reduce costs. The worst is that these changes still often decrease the quality of the work (Figure 5).

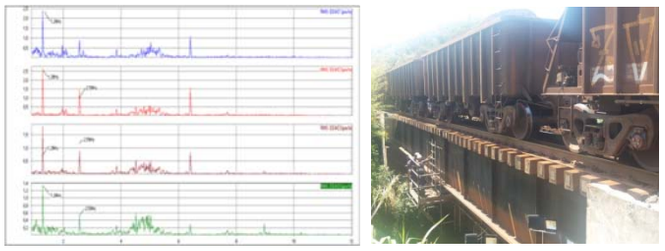


Figure 5 – Instrumentation Bridge to calibrate models

The way to mitigate these uncertainties is to raise the actual dimensions of the structure and to instrument it in order to know how it is actually behaving and what its utilization factor is.

2.3 *Track and Vehicle Defects*

Track and Vehicle Defects greatly amplify the dynamic impact on the structure, measure instrumentation, and achieve an impact factor of 2,00 times the static value (Merheb, 2017). Spring faults in vehicles have high importance for the future maintenance of the bridge as well as road
defects (Figure 6).

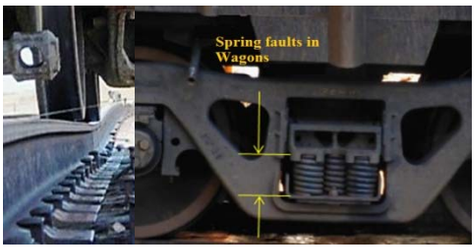


Figure 6 – Defect Vehicle and Tracks

2.4 *Vehicle Speed*

The velocity of the vehicle influences the response of the structure directly. It is known that the greater the speed the greater the dynamic impact, and the smaller the bridge span the greater the dynamic impact. We can observe that in certain structural configurations it is more efficient to increase velocity than to decrease velocity because there is a correct relationship between velocity and structure response. However, as a standard, we find that, for railroad trains, velocities that lead to resonance when there is damage in the structure floats between 30 and 50 km/h (Figure 7).

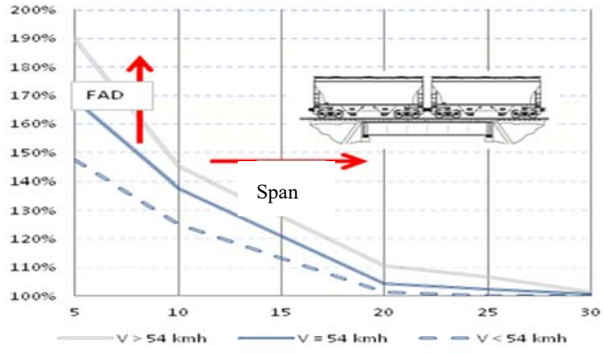


Figure 7 – Impact of speed on Span Bridge

2.5 *Damage Structure and Dynamic Response*

Damage to the structure will lead to less inertia, hence a different structural response; this can be observed in the vibration modes of the structure.



Figure 8 – Damage Bridge Inspection to New Plan Bridge

Local damage change can lead to dynamic impact amplification by up to 30% of global risk in the structure, (Figure 8).

All these values were guided separately, based on the experience and research in the different railway companies.

It is very relative and qualitative, so we can observe that initially after a benchmarking with different railroads and areas we get the values.

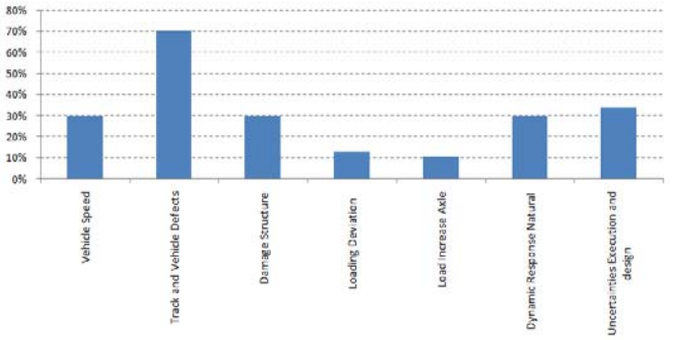


Figure 9 – Initial Model Dynamic Propose

In our management of maintenance, these values were used as parameters and maintenance indicators, allowing managing our budgets and responsibilities of each area, this development also leveraged a need to calibrate each parameter, thus increasing the need to experimentally implement bridges, vehicles and tracks. A model was thus created to instrument all variables controlled and to quantify each parameter.

3 GLOBAL INSTRUMENTATION PROCEEDS

As a part of the PhD thesis of the Principal Author, global vehicle, bridge and bridge instrumentation will be performed to obtain calibrated information of each parameter enabling to have a calibrated model. This is also important for verifying each vehicle defect or pathway as it influences the dynamic response of the structure. Different damages will be planned for the track and for the vehicle in order to seek the most unfavourable case and trying to isolate every request to calibrate the numerical model of the bridges and obtaining a greater reliability. Figure 22 shows, finally, the instrumentation global planning.

The influence of the accumulated damages, load deviation of each wagon, road defects, as well as pathologies in the structures and dynamic response of the vehicle are studied. These parameters influence the dynamic factor, such as fatigue, speed, mass, stiffness and damping of the vehicle. the same, etc.

Two bridges of different characteristics are being instrumented to evaluate each defect and influence of each parameter on the dynamic impact, this will be possible by performing an overall instrumentation, of all these parameters isolating each defect and evaluating them separately, in order to obtain a matrix of damage and defect that allows to be introduced later in the matrix of decision and prioritization.

The instrumentation model is presented below, where the steps of vehicle, track and bridge instrumentation are shown.

Considering the mobile load associated with the passage of vehicles at different speeds, the damage obtained and, where necessary, local damage will be used to evaluate the fatigue and the remnant service life, exhaustion of the connections and consequent redistribution of efforts, proposing a method hybrid that takes advantage of the best characteristics of each method studied.
The configuration of the vehicle will be carried out in the following manner, following isolation assumptions of each variable that influences the dynamical impact amplification process.

The first block formed by the locomotive and 4 wagons, will be composed of GDU type wagons, in perfect conditions, in this block will be instrumented the trick near the locomotive, where the vertical movement of the springs and dynamic response of the same will be observed.

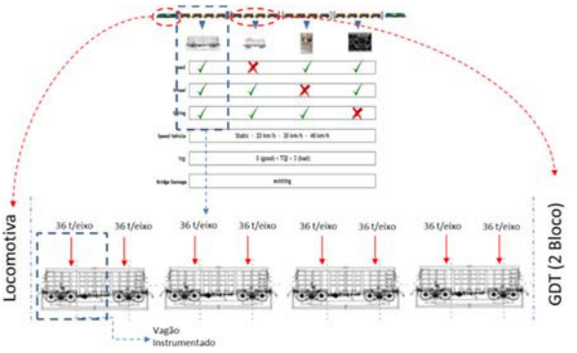


Figure 10 – First Block Vehicle Instrumentation

The instrumentation proposed in the spring was configured with two accelerometers, two extensometers and one LDVT, to visualize the vertical displacements and the internal tensions of the spring. The second block is formed to isolate the deviation in the load, so a deviation with a maximum of 11% difference between imbalance tricks will be performed so that it does not cause danger in the operation of the vehicle.

The values were obtained from historical load logs obtained by the company, so a composition was created that allows simulating the maximum deviation found and verifying the voltage increases in the track and in the bridge.

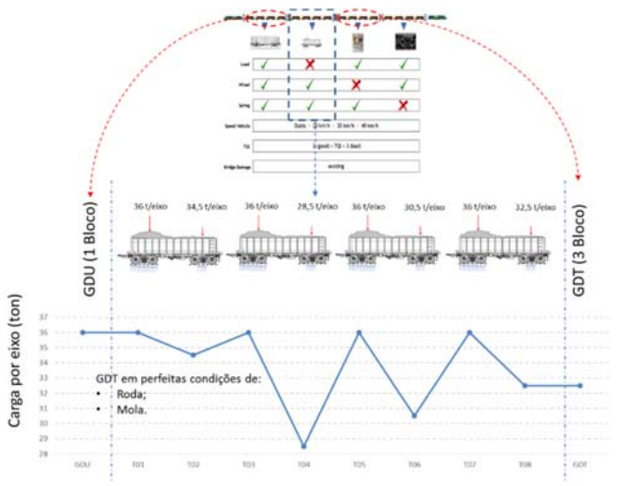


Figure 11 – Second Block Vehicle Instrumentation

In the third block we isolated the problems found in the wheels, these defects are classified by impact rates, being the same:

- Take up to 225 KN;
- Media up to 330 KN;
- Record up to 450 KN;
- Very high up to 550KN.

In the railroad it is very difficult to find the last case, because when a wheel fault generates 450 KN is immediately removed from the service. In this case, the highest value found before the test will be placed.

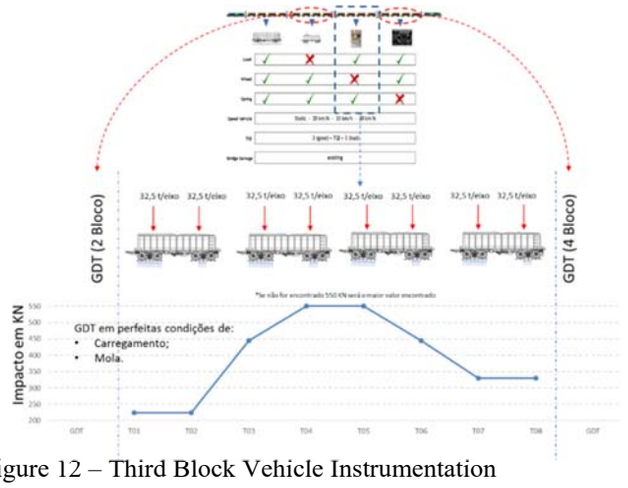


Figure 12 – Third Block Vehicle Instrumentation

Finally, the last block will be where we have demade spring insulated in the vehicle, it was configured by the residual capacity of use, so were divided into solid spring (0% capacity), spring with 10%, 15% and 20% capacity.

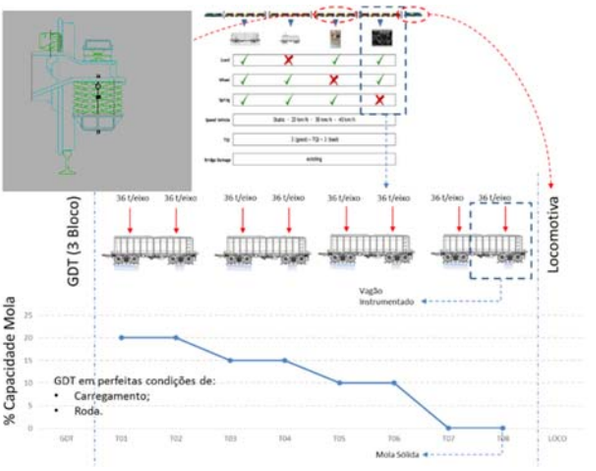


Figure 13 – Last Block Vehicle Instrumentation

4 BRIDGES, VEHICLES AND TRACKS INSTRUMENTATION CHARACTERISTICS

The different effects of wheel, spring and loading were placed in each block of the instrumented vehicle in order to isolate the defects and the impact that each of them generates on the structure. Thus we can observe the configuration of the vehicles for the test.

The vehicle was loaded in the configuration presented in the previous chapter and different passages with different speeds were made to calibrate the whole numerical model;



Figure 14 – Loading deviation

The springs were calibrated by withdrawing or including springs lacking the ability to absorb the dynamic impingement on the bridge.



Figure 15 – Different types of damage spring

The wheel defects are defects obtained from the maintenance, produced by the use of them over time, obtained a maximum value of 330 KN, it is not exceeded for reasons of operational safety.



Figure 16 – Different types of damage wheel

4.1 *Bridge Instrumentation*

The Bridge analyzed, studied and evaluated is the Bridge Belizário River, located at km 097+327 Km of the Center Line, in the municipality of Mendes/ RJ, It has a span of 26,30 meters with a metal beam with full welded profile. The Bridge analyzed, studied and evaluated is the Bridge Itinguçu located at km 019+795 Km, in Mangaratiba, it has a span of 39.34 meters of inverted beam metal.

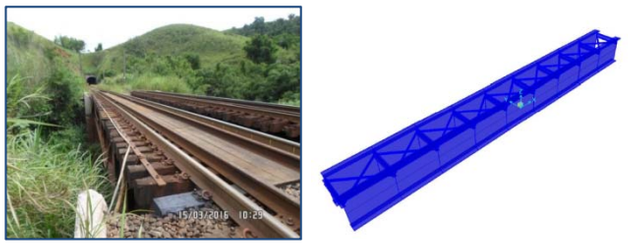


Figure 17 – Bridge Belizario Instrumentation

In the case of the Belizario bridge it was instrumented with road defects on the bridge and transitions, later maintenance was carried out on the track and again instrumented with the same test vehicle in order to isolate the effects of the defects of the permanent track.



Figure 18 – Bridge Itigunçu Instrumentation

The instrumentation of the bridge was with extensometry and accelerometry, locating the sensors in places that have the highest displacement, vibration and stress indexes, so we can obtain data to calibrate our numerical models. The instrumentation project is also aligned with the instrumentation tracks, to be able to stay in the same instrumentation points and then make comparisons to obtain the dynamic coefficients.

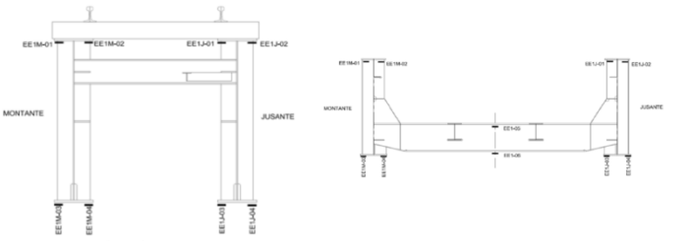


Figure 19 – Instrumentation Project

The instrumentation was also acquiring the real trains that travel on the bridge, thus performing a continuous instrumentation for approximately 2 weeks.



Figure 20 – Sensors Installation on Bridge

4.2 *Vehicle and Spring Instrumentation*

The instrumentation of the vehicle was carried out in order to observe the load deviation, wheel and spring defects, as these variables influence the dynamic impact of the structure.



Figure 21 – Spring Model Instrumentation

4.3 *Track Defects Instrumentation*

The track was instrumented exactly in the places where the bridge was also instrumented, so as not to lose information, as well as in the transition, the sensors in this case are pressure sensor specific, being able to obtain real values of dynamic loading.



Figure 22 – Damage on track and instrumentation

5 RESULTS

The frequency of inspections will largely depend on the expertise and experiences of the technician, for it was recommended to conduct a brief survey on the different standards and railways. Each railway will have the frequency that best suits the scene, conditions and economic partners interests. Figure 20

Finally, with this instrumentation and analyzing the results, we can visualize the importance of each defect on the amplification of the dynamical impact on the tensions of the main elements of the bridges, and we can even simulate the loss of life of the fatigue produced by each variable.

Thus obtaining a management tool for each variable and consequently each area responsible for it.

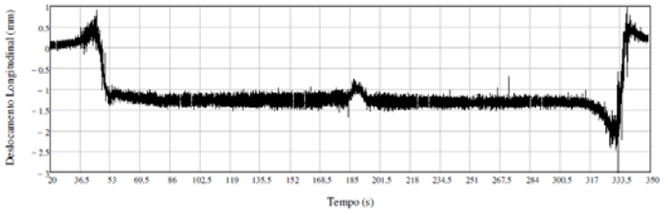


Figure 23 – Resultsxxxx

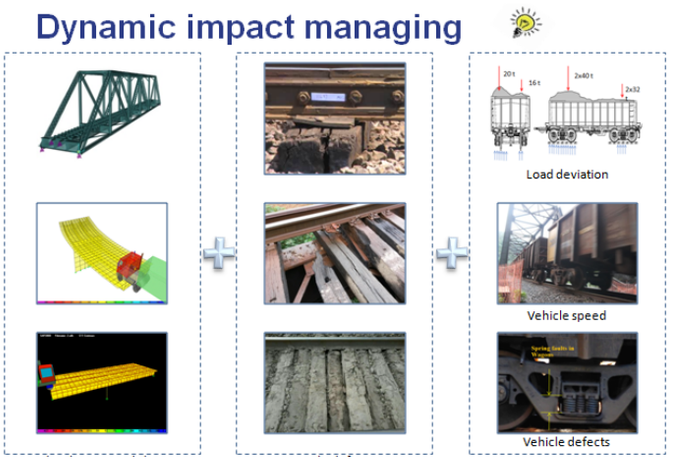


Figure 24 – Results xxxx

6 CONCLUSIONS

The frequency of inspections will largely depend on the expertise and experiences of the technician, for it was recommended to conduct a brief survey on the different standards and railways. Each railway will have the frequency that best suits the scene, conditions and economic partners interests. Figure 20 shows a new vision of all bridge railways. Later to, the fatigue analysis and visual inspection damage, we can see different defects and solutions for each railway.

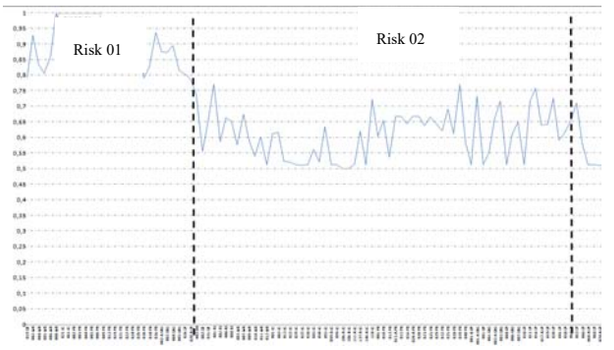


Figure 25 – Map of Risk railway

The results of prioritization are easy to manipulate by Excel, allowing the calculation of annual budget. Using the prioritization techniques was considered more effective to achieve management of railway assets, minimizing risks and planning resources properly.

The fatigue analysis and visual inspection damage, we can see different defects and solutions for each railway and allow to create a maintenance planning;

The visibility to dynamic impact managing and uncertain, we allow minimizes the effect of the dynamic impact and us to have an adequate control of all the operation and maintenance on the bridge;

Using the prioritization and reliability techniques was considered more effective to achieve management of railway assets, minimizing risks and planning resources to time of rehabilitation.

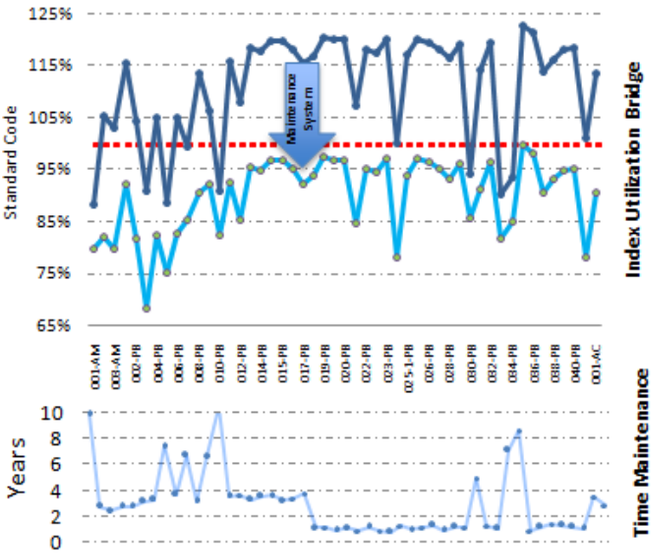


Figure 26 – Influence of Impact Dynamic

Having the visualization of the variables that influence the dynamic impact, we can observe and act in a targeted and precise way for each section, which minimizes the effect of the dynamic impact and allows us to have an adequate control of all the operation on the bridge. Figure 21 shows a diagram of the railroad with the percentages of use for each bridge, being able to understand accurately what the main

problems in the bridge are, either concerning maintenance, road or vehicle.

7 ACKNOWLEDGMENTS

Thanks for Pontifical Catholic University of Rio de Janeiro, MRS Logistic and Montoya Alves Engenharia.

8 REFERENCES

Montoya, R.; et al. Vale Infrastructure Guide. 2011;
AREMA. Manual for Railway Engineering. 2013;
Montoya, R. Cartool fatigue. 2009;
Afonso, D. Check the Bridges Fatigue Steel Railway. 2007;
Montoya, R, Prioritization of the time rehabilitation in railway bridges based on risk and fatigue index, 2017;
Merheb, A. Dynamic Loads Evaluation in Existing Railroad Infrastructure Under Increasing Axle Loads and Speed, 2017;
Modern Railway Track (2nd edition) By Coenraad Esveld 2001.

Maintenance, Safety, Risk, Management and Life-Cycle Performance of Bridges – Powers, Frangopol, Al-Mahaidi & Caprani (Eds)
© 2018 Taylor & Francis Group, London, ISBN 978-1-138-73045-8

Pervasive Fibre-Optic Sensor Networks in Bridges: A UK Case Study

L.J. Butler[1, 2], M.Z.E.B. Elshafie[1, 3] and C.R. Middleton[1]

[1]*Department of Engineering, University of Cambridge, Cambridge, United Kingdom*
[2]*Lloyd's Register Foundation Programme on Data-Centric Engineering, The Alan Turing Institute*
[3]*Visitor at the Department of Civil and Architectural Engineering, Qatar University, Qatar*

ABSTRACT: Integrating fibre-optic sensor networks in a newly-constructed infrastructure assets enables data-driven performance assessment during its construction and throughout its operational life. As part of a multi-million pound railway infrastructure redevelopment project, two new railway bridges were instrumented with an extensive network of both discrete (fibre Bragg gratings or FBGs) and distributed (based on Brillouin optical time domain reflectometry or BOTDR) fibre optic sensors to measure both strain and temperature throughout construction and in-service. Completed in 2016 in Staffordshire UK, both 'self-sensing' bridges contain more than 500 fibre Bragg grating sensors and over 600 metres of distributed fibre optic sensor cabling. This paper describes the sensing technologies employed, installation techniques for improving sensing robustness, the monitoring programme and objectives, data processing methods and assumptions, and the primary monitoring findings of this project. Results related to measurements of prestress losses in prestressed concrete girders, estimates of steel girder deflection using FBGs and videogrammetry, and assessments of percentage utilisation of critical superstructure elements are presented. In terms of future directions, BIM-based environments which incorporate sensor elements and an emerging field of research known as *Data-Centric Engineering* are introduced as tools to better manage, maintain and learn from the information generated from self-sensing infrastructure.

1 INTRODUCTION AND BACKGROUND

Smart infrastructure results from the combination of physical (i.e. bridges, tunnels, roads, etc.) and digital (i.e. sensors, internet of things, GIM, etc.) infrastructure, leading to more reliable information to enable better, cheaper and faster decision making (CSIC 2016).

From a U.K. perspective, there are a number of challenges facing the infrastructure management sector. In particular, these challenges include, pressures to maintain adequate levels of asset performance under shrinking financial budgets; aging assets which require ever-increasing maintenance and upgrading; tighter government regulations requiring greater accountability and risk assessment; and the unknown future effects of climate change (ICE 2017). To combat these challenges, smarter infrastructure is required. It has been estimated that the smart infrastructure sector has the potential to create opportunities worth anywhere between £2.4 and £4.8 trillion ($3.2 and $6.3 trillion) globally (CSIC 2016).

Within the envelope of smart infrastructure systems is the concept of 'self-sensing' (or 'sensory') structures. These structures use measurements from embedded sensing systems to provide information on their internal state (Measures 1992). Any structure can be converted into a 'self-sensing' structure whether the sensor system is installed during construction or long after the structure has been in operation. Bridges are good candidates for implementing a sensing system as they represent critical assets within road and rail networks and their long-term in-situ performance, particularly how they deteriorate, has not been well categorized. Therefore, sensing systems, at a minimum, should be designed to function reliably in the long-term. Most importantly, sensor and monitoring systems in general should not be implemented before defining the purpose of monitoring for a particular asset or application. Further guidance on structural health monitoring (SHM) system selection for bridges is provided in Vardenega et al. (2016), Webb et al. (2015) and Middleton et al. (2016).

First appearing in the early 1990s, fibre optic based sensor systems have been installed to monitor a variety of bridge types around the world. In Australia, fibre optic sensors (fibre Bragg gratings) installed externally in combination with digital image correlation techniques were used to measure strain during load testing of a prestressed concrete girder bridge (Gowripalan et al. 2016). Similar bridge

monitoring studies which incorporate the use of fibre optic sensing have been undertaken in Canada (Tennyson et al. 2001; Regier and Hoult 2014), the United States (Cardini and DeWolf 2009; Glisic 2012), Sweden (Jemli et al. 2003), Portugal (Costa and Figueiras 2012), China (Chan et al. 2006) and India (Scott et al. 2013). Compared with electrical-based sensors, FOS have several advantages including being corrosion resistant, having higher accuracy, good long-term stability and requiring less cabling (and therefore reduced interrogator channel requirements).

In the U.K., while traditional SHM systems have been deployed across various large-scale bridge projects, the use of fibre optic sensing has been very limited (Webb et al. 2017; Lydon et al. 2017). This paper presents a new fibre-optic-based bridge sensing case study. Completed in April 2016, the Stafford Area Improvements Programme (SAIP) involved a major upgrade and redevelopment on the West Coast Main Line near Crewe including the construction of 11 new bridges.

An Innovate UK and EPSRC-funded research project in collaboration with the Staffordshire Alliance (Network Rail, Laing O'Rourke, Atkins, and VolkerRail) and the University of Cambridge's Centre for Smart Infrastructure and Construction (CSIC) constructed, to the authors' current knowledge, the most densely-instrumented 'self-sensing' railway bridges in the U.K. Two of the 11 new bridges (one steel composite and one prestressed concrete) constructed as part of the SAIP were extensively instrumented as prototypes containing durable, permanent, fibre-optic based strain monitoring systems.

This paper provides an overview of the monitoring system and sensing technologies, innovative techniques for improving sensing system robustness, data processing and analysis assumptions, and the primary monitoring findings. Additional insight is provided into new tools related to self-sensing infrastructure and the emerging research area known as data-centric engineering.

2 SELF-SENSING BRIDGE PROTOTYPES

2.1 *Description of bridge structural systems*

Intersection Bridge 5 is a steel half-through skewed (22.6º) railway bridge formed by two 2.2 metre deep main I-girders with composite concrete deck supported on transverse steel cross beams. It carries two new lines of ballasted track and forms the primary structure in the SAIP as it crosses the existing West Coast Main railway line. It has a single skew span of 26.8 metres and is simply-supported on piled abutments. To provide lateral buckling restraint of the top I-girder flanges, U-frames consisting of vertical stiffeners at corresponding moment-connected steel cross beam locations are provided at every three metres. This bridge type was selected for this application to achieve construction depth requirements.

Underbridge 11 is a prestressed concrete girder bridge with infill concrete deck simply-supported on elastomeric bearings on piled abutments. The 11.2 metre span carries one line of ballasted track over a minor watercourse. Seven prestressed concrete (PC) TY7 internal beams and two PC TYE7 edge beams form the main superstructure. The 0.7 metre deep PC beams were precast offsite 6 months prior to being erected on the abutments. A 200 mm thick reinforced concrete deck slab and solid concrete infill in between the PC beams were cast in-situ. Transverse tie bars were installed across the deck through web opening holes in the PC beams. An additional concrete slab bridge was constructed adjacent to Underbridge 11 which forms part of a pedestrian footpath. This bridge type was selected for this particular application because it promoted offsite manufacture and led to reduced erection times and construction costs. Figure 1 depicts the completed self-sensing bridges.



(a) Intersection Bridge 5



(b) Underbridge 11

Figure 1. Completed self-sensing railway bridge prototypes

2.2 *Sensing system technology*

Fibre optic sensors (FOS) are typically grouped within two main categories: discrete and distributed.

This research study involved the combined use of both types of FOS, discrete FOS known as fibre Bragg gratings and distributed FOS based on optical time domain reflectometry (OTDR).

Bragg gratings are written into the core of an optical fibre typically using an excimer laser. The refractive index at the grating locations are altered compared with the adjacent fibre. This creates a dielectric mirror which reflects laser (ultraviolet) light at a specific frequency. Typically, several (up to 20 or greater) FBGs can be written each with different Bragg wavelengths along a single fibre. When an FBG is stretched, the grating period shifts which results in a change in wavelength of the reflected ultraviolet light (Kreuzer 2006). This change in wavelength is then converted to an equivalent change in strain. The FBGs used as part of this study were formed using a draw tower process and were coated with glass fibre reinforced polymer coating for added robustness during installation. Sensor arrays with up to 20 FBGs at one metre spacing were produced. Using an optical fibre interrogator combined with an optical fibre multiplexer, both produced by Micron Optics, it was possible to record strain changes at 250 Hz of up to 320 individual FBG sensors simultaneously.

Distributed FOS sensors, on the other hand, have the ability to measure strain changes along the entire length of a fibre optic cable. Based on the optical time domain reflectometry (OTDR) technique, an optical pulse (laser light) is shone down an optical fibre where a photodetector measures the amount of backscattered light in the fibre. Knowing the speed of light, the time information is converted to distance. One particular backscattered light component known as Brillouin scattering, carries information about the temperature and amount of strain in the fibre based on its wavelength shift; this is known as Brillouin Optical Time Domain Reflectometry (BOTDR) (Glišić and Inaudi 2007). The BOTDR cable used as part of this study was a steel-reinforced single-mode low bend loss fibre. Strain values are averaged over a 50 cm length are taken at steps of 5 cm along the entire cable. Unlike FBG sensors, BOTDR based sensing is not suitable for capturing dynamic strain changes as measurement times of 5 minutes or greater are typical depending on the length of cable.

FOS are particularly sensitive to temperature changes (i.e. index of refraction is altered and the glass fibre expands or contracts) and therefore, various compensation techniques are required in order to isolate temperature effects and obtain mechanical strains. Separate temperature-compensation FO sensors for both the FBG and BOTDR FOS were implemented on this project to account for these effects.

2.3 *Sensor topologies and installation*

On Underbridge 11, a combination of FBG and BOTDR sensors were employed. Figure 2 depicts an overview of the sensor topology for Underbridge 11. A primary objective of the monitoring programme was to assess and compare the strain measurements provided by both systems.

In total, six of the nine prestressed concrete (PC) beams were instrumented along the top and bottom prestressing strands with 10 strain FBGs, 6 temperature FBGs and both strain and temperature BOTDR sensing cables. All PC beam instrumentation was completed at the pre-casting facility following prestressing of the strands before pouring of the concrete. The early-age behaviour of the beams was then assessed prior to their erection on the bridge abutments (refer to Butler et al. 2016 for further details). Additional sensors were then installed along the top layer of reinforcing in the concrete deck (6 FBGs) and along the transverse ties (4 FBGs) at both midspan and quarterspan locations (refer to Figure 2). Sensors were secured to the prestressing strands and reinforcing steel using plastic ties spaced at approximately 300 mm.

Only FBG sensors were installed on Intersection Bridge 5 as depicted in Figure 3. The main west and east girders were instrumented with 20 strain and temperature compensating FBGs along both the top and bottom flanges. Two cross beams, one at midspan and one near the end (skew) span were also instrumented with 7 strain and temperature FBGs along the top and bottom flanges. At the instrumented cross beam locations, 7 strain and temperature FBGs were installed within the transverse concrete deck along the top layer of reinforcing steel. One of the web stiffeners forming part of the midspan U-frame was also instrumented with 6 vertically oriented FBGs (4 strain and 2 temperature). Following cleaning and abrasion of the surface of the steel superstructure, the FBG sensors were attached using a structural adhesive. The final surface painting system was then applied by the bridge contractor following sensor installation. FBGs installed within the concrete deck were attached to the reinforcing steel using plastic cable ties spaced at approximately 300 mm.

The most vulnerable component of the installed fibre optic sensor networks are the splices between both the primary sensor array and the routing cables and optical connectors. For this reason, a series of special splice protector designs were devised in the laboratory prior to sensor deployment. Combined with the ruggedized coatings applied to the sensor cabling, the final installed sensor network has so far

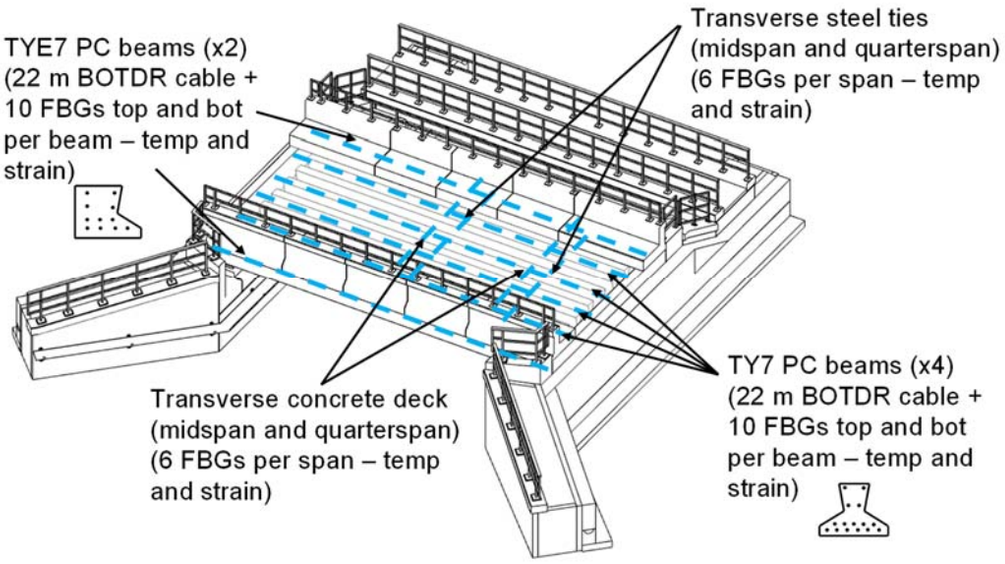


Figure 2. Sensor topology for Underbridge 11

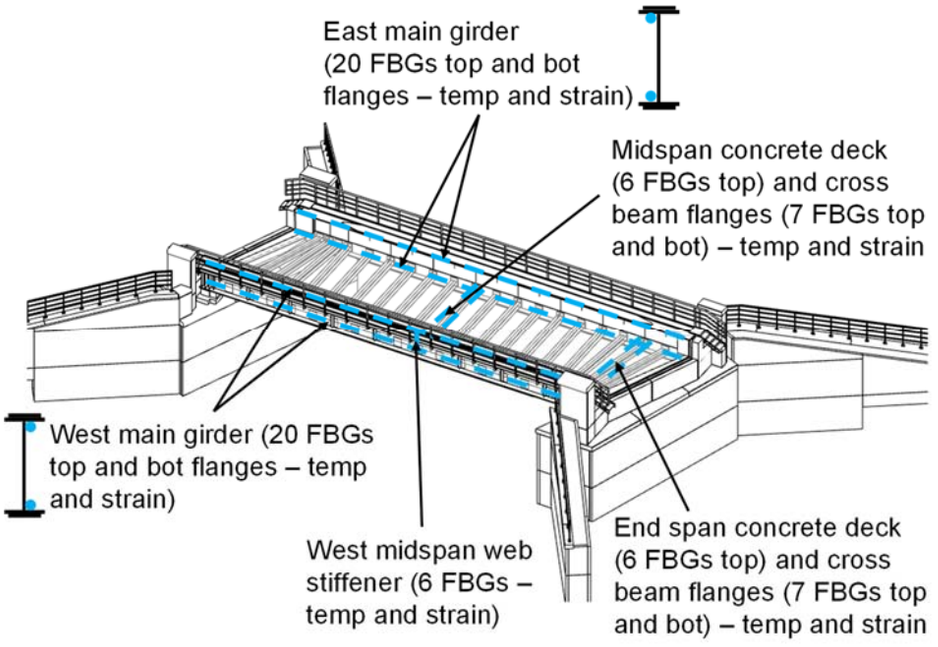


Figure 3. Sensor topology for Intersection Bridge 5

proven to be highly resilient during its first two years in operation.

3 MONITORING RESULTS AND DISCUSSION

The installation of the monitoring systems for both bridges was completed by the fall of 2015 and both bridges were opened to rail traffic by March 2016. Since their opening, two additional monitoring visits occurred in July 2016 and one year later in July 2017. The following section presents an overview and discussion of some of the key findings to date.

3.1 *Prestress losses in PC beams (Underbridge 11)*

A primary focus of monitoring Underbridge 11 was to assess the early age and long-term prestress losses within the PC beams. In particular, the strain changes measured from the FBG sensors were used to estimate the change in prestress during the first two years of the internal TY7 (average of two) and external TYE7 (average of two) PC beams as presented in Figure 4.

Changes in prestress were calculated based on the interpolated strains acting through the centroid of the prestressing steel. Note that baseline stress values were taken from a time immediately prior to detensioning of the prestressing strands. The total measured change in prestress for the TY7 and TYE7 PC beams between January 2015 and July 2017 were 211 MPa and 165 MPa, respectively. The values of long-term prestress losses calculated using Eurocode 2 (according to EN 1992-2, BSI 2004) are presented in Butler et al. (2016). The total (120 year) estimated

prestress losses for the TY7 and TYE7 PC beams were 275 MPa and 267 MPa, respectively. Therefore, the measured prestress changes for the TY7 and TYE7 PC beams were 77% and 62% of the Eurocode 2 estimated ultimate losses, respectively. Based on the estimated change in prestress from the FBG strain measurements, it appears that the loss of prestress in the TYE7 beams (average of two beams) is greater than the loss in the TY7 beams (average of two beams).

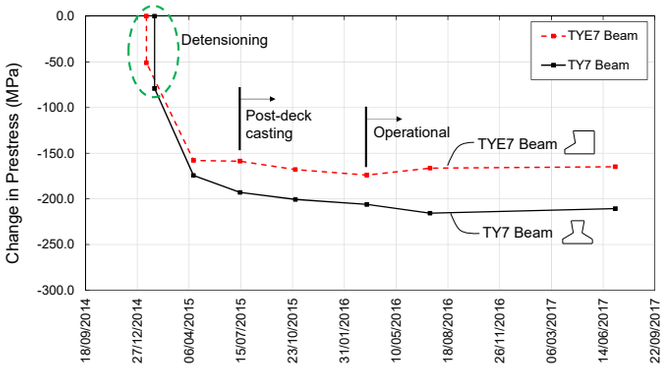


Figure 4. Estimated change in prestress in PC beams from FBG strain measurements

This difference in prestress losses appears to stem from greater elastic shortening losses during the detensioning process. Based on Figure 4 it appears that the value of the prestress losses increase slightly after the bridges become operational. It is suspected that ambient effects (i.e. temperature, relative humidity, wind, etc.) may account for these anomalies however, further research is required to better understand this effect.

In comparing discrete versus distributed fibre optic sensor technology, a previous study by the authors reported that the FBG and BOTDR measured strains during the first six months following beam casting were similar (Butler et al. 2016).

3.2 *Steel girder deflections under live loading (Intersection Bridge 5)*

Strain measurements taken from the FBG sensors (ε_{FBG}) installed along the top and bottom flanges of the two main girders were used to estimate the midspan deflections under passing trains. Based on the assumption of Euler-Bernoulli beam bending and using linear regression to fit a set of polynomial basis functions ($a_i\varphi_i$) to the curvature calculated from the strain data, double integration was performed numerically to obtain estimates of the girder's vertical deflection at a given time t_i, $w(x,t_i)$, along the total length L, of the girder. The midspan deflection ($w_{midspan}(t_i)$) at a given time t_i, is then reported as $W(L/2,t_i)$. This procedure is repeated for each time step (in this instance at 250 times per second which is equivalent to the FBG sensor acquisition rate) and for each FBG top and bottom pair (20 in total per girder). A summary of the algorithm was implemented using Matlab and is outlined below:

For t_j = 0 to t_{final} (based on size of data file)
  For i = 1 to n (= number of FBGs)

$$\frac{|\varepsilon(x)_{top}| + |\varepsilon(x)_{bot}|}{z} = k(x)_{FBG} \rightarrow k(x)_{POLY} = \sum_{i=1}^{n-1} a_i\varphi_i(x)$$ Linear regression

$$\frac{\partial^2 w(x)}{\partial x^2} = -\left(\frac{1}{z}\right)\varepsilon(x) = k(x) = -\sum_{i=1}^{n-1} a_i\varphi_i(x)$$ Equate to Euler-Bernoulli beam formulation

$$w(x) = -\sum_{i=0}^{n-1} a_i\psi_i(x) + Ax + B$$ Numerical double integration

$$A = \left(\frac{1}{zL}\right)\sum_{i=1}^{n-1} a_i[\psi_i(L) - \psi_i(0)]$$ Calculate integration constants from beam boundary conditions

$$B = \left(\frac{1}{z}\right)\sum_{i=1}^{n-1} a_i\psi_i(0)$$

  End i

$$w_{midspan}(t_i) = w(L/2, t_i)$$ Calculate midspan deflection

End t_j

This methodology is similar to methods reported by Vurpillot et al. (1996) and Todd et al. (2000). It was assumed that the girder was simply-supported implying a vertical deflection of zero at both ends. A third-order polynomial was chosen as a basis function and was found to provide an adequate fit to the calculated curvature data. To validate the FBG-calculated deflection results, an advanced videogrammetry system produced by Imetrum was used to measure the midspan deflection of the east main girder when a 4-car passenger train passed over the bridge (refer to Figure 5 and Figure 6).



Figure 5. Videogrammetry system setup for measuring midspan deflection of east main girder

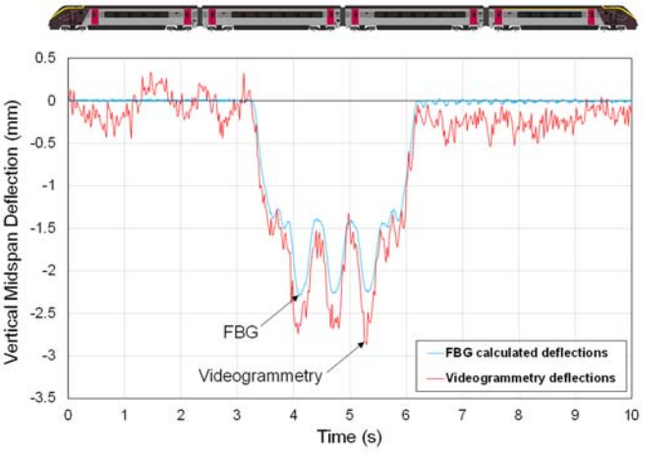


Figure 6. Midspan deflection of east main girder versus time using FBG back-estimated and videogrammetry measurements

The FBG-estimated midspan deflection results followed a very similar deflection profile as compared to the videogrammetry based results. On average, the maximum (corresponding to the peak deflection values in Figure 6) midspan deflections measured using the videogrammetry system were 18% higher than those estimated from the FBG strain measurements. This difference may be due to inherent errors in measurement of the videogrammetry system and also due to errors which arise within the back-calculation of deflection via double integration of the FBG-strain measurements. While additional monitoring data from both the FBGs and videogrammetry are required, the initial results of these two deflection estimation methods seem promising.

3.3 *Percentage utilisation assessment*

A primary benefit of integrating sensing within a structure is the ability to estimate and assess levels of performance in-service. In particular, the FBG sensors installed within Intersection Bridge 5 along the top and bottom flanges of the main girder can be used to estimate the curvature and moment demand under average daily rail loading. Calculated moment demand envelopes can then be generated and updated as more data is collected. As an example, Figure 7 presents the moment demand envelopes for both main girders based on FBG strain data collected from 12 trains passing over the bridge over a period of 8 hours. During this period, only two passenger train types, Class 350 'Desiro' and a Class 221 'Super Voyager' passed over the bridge. Note that the measurement results seem to indicate a sensor malfunction on the east main girder possibly due to localized debonding.

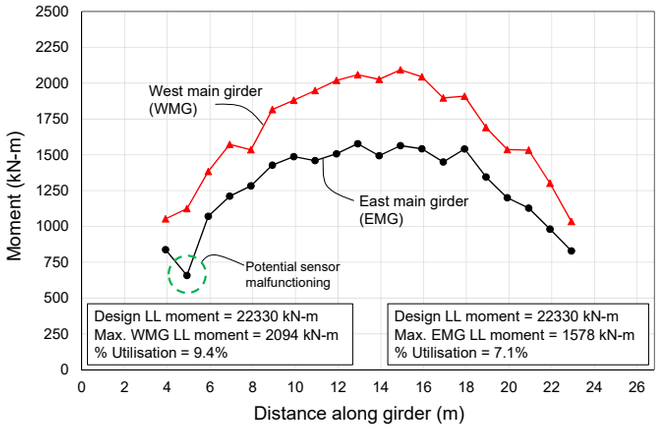


Figure 7. FBG estimated moment demand envelopes for the main girders on Intersection Bridge 5

To provide an estimate of the percentage utilisation of each girder considering the data collected from the 12 trains, the (ultimate) design live load moment capacity of the girder section must be calculated. Using Eurocode design equations (BSI 2005, 2006) for calculating the capacity of the main I-girders and based on previous studies by the authors (Delgado et al. 2017) the design moment capacity under live loading ($M_{DES,LL}$) is 22.3 MN-m. Therefore, based on the sensor data-generated moment envelopes, the west main girder and east main girder have percentage utilizations of 9.4% and 7.1%, respectively. Note that the west main girder appears to be consistently supporting a higher proportion of the live loading compared with the east main girder. This may be due to additional vertical loads induced from the track curvature which creates slightly unbalanced loading on the west track. Another potential explanation for this difference may stem from the dominant rail traffic patterns on the bridge in which more heavily-loaded (e.g. Class 221 versus Class 350 train types) passenger trains tend to travel on the west line (in this case southbound). This would have the effect of skewing the moment demand envelopes. Therefore, future research will include collecting and processing data from a larger number of trains. Daily, weekly, monthly and seasonal effects will also be considered when revising and interpreting the percentage utilisation estimates.

4 FUTURE TOOLS FOR LONG-TERM MONITORING OF SELF-SENSING BRIDGES

This monitoring project has highlighted the variety of information that can be captured for assessing bridges when they are constructed with an integrated sensing system. It has also revealed that if self-sensing structures are to be widely adopted across all levels of infrastructure then consideration of the long term management, analysis and interpretation of the information generated is critical. The following sections introduce two new areas of research currently being explored for increasing the value of monitoring data.

4.1 *Sensing-integrated BIM models*

Building information models (BIM), are digital representations of physical assets which are typically employed during the design and construction phases. However, there is growing interest to leverage BIM in facilities and asset management (Burcerik-Gerber 2012). Preliminary work has been completed in developing BIM elements for sensors which can store continuous strain and temperature data from FBGs, BOTDR or other sensor types and provide a visualization directly within the BIM model (Delgado et al. 2017). This proposed approach will enable engineers and asset managers to use a common interface in which they can use the information generated during an asset's operation. In terms of long-term inspections, this approach can help to avoid subjectivity, increase reliability, and provide an integrated long-term data management system.

4.2 *Data-centric engineering*

Through a collaboration between the Lloyds Register Foundation funded program on Data Centric Engineering (DCE) at the Alan Turing Institute and the Cambridge Centre for Smart Infrastructure and Construction (CSIC) at the University of Cambridge, a multi-disciplinary team of engineers and data scientists are working to characterize and analyse the vast quantities of dynamic strain data gathered from the self-sensing bridges and other structures.

DCE may be viewed as an approach for learning about engineering structures which leverages physics-based (e.g. finite element) models which are updated based on sensor data and statistical (data-driven) models that incorporate prior knowledge of the physical asset. This combined model would provide the self-sensing structure with a 'digital twin' which would exist alongside the asset and be updated and refined throughout its service life (Lau et al. 2018a).

This collaboration has thus far developed streaming statistical models and temporal de-trending techniques which have been successfully applied to large, continuously recorded strain data sets collected from Intersection Bridge 5 (Lau et al. 2018b).

It is envisioned that merging concepts such as sensing-integrated BIM models and 'digital twins' will provide powerful future platforms on which to build additional value into the data generated from condition monitoring systems.

5 CONCLUSIONS

This paper has discussed the creation of two fibre-optic based self-sensing railway bridge prototypes. The bridges included Underbridge 11, an 11.2 metre prestressed concrete girder bridge with a cast in-situ concrete deck, and Intersection Bridge 5, a 26.8 metre steel half-through skewed I-girder bridge with a composite concrete deck. Discussions of the sensor technologies employed along with the installation techniques and sensor topologies are presented. Based on two years of collected monitoring data, the primary findings of this study include:

1. Pertaining to the prestressed concrete girder Underbridge 11, a comparison of the measured prestress losses in the internal (TY7) beams and the external (TYE7) edge beams indicated a higher prestress loss for the TYE7 beams in their first 2 years in-service. Based on the change in prestress, the TY7 and TYE7 beams had reached 77% and 62%, respectively of the Eurocode 2 predicted long-term losses.

2. Two methods for estimating the midspan deflection of the Intersection Bridge 5 east main girder under live loading were investigated as part of this study. The first method involved applying an algorithm which considered Euler-Bernoulli beam theory and moment-curvature relationships to calculate vertical deflection using FBG-measured horizontal strains. In addition, a videogrammetry system was also deployed to measure deflections of the east main girder. It was found that both methods produced similar time-deflection profiles however, the videogrammetry deflections were on average 18% greater than those estimated from the FBG strain measurements. While additional monitoring data is required, these initial results were found to be promising.

3. Based on the monitoring data collected from 12 passenger trains passing over Intersection Bridge 5, moment demand envelopes for both main girders were derived in order to compare with the design live load moment capacity. Based on their moment envelopes, the west and east main girders' structural utilization percentages under live load were 9.4% and 7.1%, respectively. It was noted however, that further monitoring is planned to develop a larger moment demand envelope data set that will also consider the effect of environmental factors such as temperature on the measure moment demand.

This paper concludes with a discussion of current advances in BIM models which are capable of storing, managing and visualizing data obtained from sensor systems. A new area of research referred to as data-centric engineering is introduced where research efforts are currently underway to integrate finite element models with advanced statistical models for data generated from self-sensing bridges.

ACKNOWLEDGEMENTS

The authors would like to acknowledge EPSRC, Innovate UK and the Lloyd's Register Foundation for funding this research through the Centre for Smart Infrastructure and Construction (CSIC) Innovation and Knowledge Centre and the Alan Turing Institute. Research related to installation of the sensor system was carried out under EPSRC grant no. EP/L010917/1. Data related to this publication is available at the University of Cambridge data repository.

REFERENCES

Becerik-Gerber B., Jazizadeh F., Li N., and Calis G. 2012. Application Areas and Data Requirements for BIM-Enabled Facilities Management. *J. Constr. Eng. Manag.*, American Society of Civil Engineers, 138(3), 431–442.

BSI. 2004. EN 1992-1-1:2004 Eurocode 2: Design of concrete structures. Part 1–1: General rules and rules for buildings. British standards institution, Chiswick, U.K.

BSI. 2005. BS EN 1994-2:2005 Eurocode 4: Design of composite steel and concrete structures. Part 2: General

rules and rules for bridges. British standards institution, Chiswick, U.K.

BSI. 2006. BS EN 1993-2:2006 Eurocode 3: Design of steel structures. Part 2: steel bridges. British standards institution, Chiswick, U.K.

Butler L.J., Gibbons N., He P., Middleton C.R. and Elshafie M.Z.E.B. 2016. Evaluating the early-age behaviour of full-scale prestressed concrete beams using distributed and discrete fibre optic sensors. *Construction and Building Materials*, 126: 894 – 912.

Cardini A.J. and DeWolf J.T. 2009. Long-term structural health monitoring of multi-girder steel composite bridge using strain data. *Journal of Structural Health Monitoring*, 8(1): 47 – 58.

Centre for Smart Infrastructure and Construction (CSIC). 2016. Smart infrastructure: getting more from strategic assets. White paper: 7 pgs.

Chan T.H.T., Yu L., Tam H.Y., Ni Y.Q., Liu S.Y. 2006. Chung W.H., and Cheng L.K. Fiber Bragg Grating Sensors for Structural Health Monitoring of Tsing Ma Bridge: Background and Experimental Observation. *Engineering structures*, 28:648 – 659.

Costa B.J.A. and Figueras J.A. 2012. Evaluation of a strain monitoring system for existing steel railway bridges. *Journal of Constructional Steel Research*, 72: 179 – 191.

Delgado J.M.D., Butler L.J., Brilakis I., Elshafie M.Z.E.B. and Middleton C.R. 2017. Structural performance monitoring using data-driven and dynamic BIM environments. *ASCE Journal of Computing in Civil Engineering*. In press.

Glišić, B., and Inaudi, D. 2008. *Fibre optic methods for structural health monitoring*. John Wiley & Sons. 262 pgs.

Gowripalan N., Li J. & Wang J.J. 2016. Monitoring of bridges using fibre optic sensors (FOS) and digital image correlation (DIC) techniques – an Australian perspective, *Concrete in Australia 42(2)*: 55 – 59.

Institution of Civil Engineers (ICE). 2017. Intelligent assets for tomorrow's infrastructure: guiding principles. ICE guidance paper. London U.K., 28 pgs.

Jemli M.E., Karoumi R., and Lanaro R. 2003 Monitoring of the New Årsta Railway Bridge Using Traditional and Fibre Optic Sensors. *Smart Structures and Materials*, 5057: 279 – 288.

Kreuzer M. 2006. Strain measurement with fiber Bragg grating sensors. HBM, Darmstadt, S2338.

Lau F-D.H., Butler L.J., Adams N.M., Elshafie M.Z.E.B., and Girolami M.A. (2018a). The role of statistics in data-centric engineering. *Statistics and Probability Letters*, Special Issue on the Role of Statistics in the Era of Big Data. Article in press.

Lau F-D.H., Adams N.M., Girolami M.A., Butler L.J. and Elshafie M.Z.E.B. (2018b). Real-time statistical modelling of data generated from self-sensing bridges. *Journal of Smart Infrastructure and Construction*, Proceedings of the Institution of Civil Engineering, Themed Issue on Big Data Analysis. Article in press.

Lydon M., Robinson D., Taylor S.E., Amato G., O'Brien E.J. & Uddin N. 2017. Improved axle detection for bridge weigh-in motion systems using fiber optic sensors. *Journal of Civil Structural Health Monitoring*, 7: 325 – 332.

Measures R.M., LeBlanc M., Liu K., Ferguson S., Valis T., Hogg D., Turner R. & McEwen. 1992. Fiber optic sensors for smart structures. *Optics and Lasers in Engineering* 16: 127 – 152.

Middleton C.R., Fidler P.R.A., and Vardanega P.J. (2016). *Bridge monitoring: a practical guide*, Thomas Telford Limited, ICE Publishing, 120 pages.

Regier R. and Hoult N.A. 2014. Distributed strain behaviour of a reinforced concrete bridge: case study. *ASCE Journal of Bridge Engineering*, 19(12): 1 – 9.

Scott R.H., Banerji P., Chikermane S., Srinivasan S., Basheer P.A.M., Surre F., Sun T. & Grattan K.T.V. 2013. Commissioning and evaluation of a fiber-optic sensor system for bridge monitoring. *IEEE Sensors Journal*, 13(7): 2555–2562.

Tennyson R.C., Mufti A.A., Rizkalla S., Tadros G. & Bemokrane B. 2001. Structural health monitoring of nnovative bridges in Canada. *Smart Materials and Structures*, 10: 560 – 573.

Todd M.D., Johnson G.A., Chang C.C. 2000. Real-time girder deflection reconstruction using a fibre Bragg grating system. *Proc. IMAC XVIII: a Conf. on Structural Dynamics*, 1313 – 1319.

Vardanega P.J., Webb G.T., Fidler P.R.A. & Middleton C.R. 2016. Assessing the potential value of bridge monitoring systems. *Bridge Engineering, Proceedings of the Institution of Civil Engineers*, 169(BE2):126 – 138.

Vurpillot S., Inaudi D., Scano A. 1996. Mathematical model for the determination of vertical displacement from internal horizontal measurements of a bridge. Smart systems for bridges, structures, and highways. *SPIE Smart Structures and Materials*, 2719:46 – 53.

Webb G.T., Vardanega P.J. & Middleton C.R. 2015. Categories of SHM deployments: technologies and capabilities. *ASCE Journal of Bridge Engineering*, 20(11): 1 – 12.

Webb G.T., Vardanega P.J., Hoult N.A., Fidler P.R.A., Bennet P.J. & Middleton C.R. 2017. Analysis of fibre-optic strain-monitoring data from a prestressed concrete bridge. *ASCE Journal of Bridge Engineering*, 22(5): 1 – 14.

Maintenance, Safety, Risk, Management and Life-Cycle Performance of Bridges – Powers, Frangopol, Al-Mahaidi & Caprani (Eds)
© 2018 Taylor & Francis Group, London, ISBN 978-1-138-73045-8

Shear force-based method for detecting vehicle speed and axle spacing

Lu Deng
Key Laboratory for Damage Diagnosis for Engineeri ng Structures of Hunan Province, Hunan University, Changsha, Hunan 410082, China

Wei He
College of Civil Engineering, Hunan University, Changsha, Hunan 410082, China

Yang Yu & C.S. Cai
Department of Civil and Environmental Engineering, Louisiana State University, Baton Rouge, Louisiana，70803，USA

ABSTRACT: Bridge weigh-in-motion (BWIM) system uses the bridge as a scale to estimate vehicle weights. For BWIM systems, reliable axle detection is a prerequisite for the accurate identification of axle weights and GVW. The existing nothing-on-road (NOR) BWIM systems typically use additional sensors, such as the free-of-axle-detector (FAD) sensors, for axle detection. However, these NOR axle detection strategies were reported to be only suitable for certain types of bridges and susceptible to wheel transverse positions. In this study, a equivalent shear force (ESF) method is proposed to identify vehicle speed and axle spacing by using the flexural strain signal recorded from the weighing sensors. Compared to the existing NOR BWIM systems, the proposed method does not require additional sensors for axle detection, which reduces the cost and facilitate the installation of BWIM systems. The effectiveness and accuracy of the proposed method are demonstrated through numerical simulations using three-dimensional vehicle-bridge coupled analysis.

1 INSTRUCTION

The Bridge weigh-in-motion (BWIM) offers an efficient way for vehicle overweight enforcement and traffic monitoring using an instrumented bridge (Moses 1979; Zolghadri et al. 2016). The obtained traffic in-formation is valuable for the management of transportation networks and safety assessment of bridges (Lydon et al. 2016; Jacob & O'Brien 2005). In the past several decades, great efforts have been spent on developing new BWIM algorithms and improving the identification accuracy of BWIM systems (Peters 1984; Jacob & O'Brien 1998; WAVE 2001; O'Brien et al 2009; Žnidarič et al. 2015). A comprehensive state-of-the-art review of existing BWIM algorithms and instrumentation was presented by Yu et al. (2016).

In order to identify the axle weights and gross vehicle weight (GVW), accurate axle detection is required by most BWIM systems. Typically, a BWIM system includes weighing sensors and axle detecting devices (Moses 1979). Axle detection can be pavement based using sensors installed on the road sur-face such as tape switches, pneumatic tubes, and piezoceramic sensors. Although pavement-based axle detection can usually achieve good accuracy, they are not ideal for BWIM applications as they are not durable and can cause interruption of traffic (WAVE 2001; Chatterjee et al. 2006; Zhao et al. 2014). In order to eliminate the use of axle detectors on the road surface, the concept of nothing-on-the-road (NOR) systems and the free-of-axle detector (FAD) algorithms were introduced in the Weighing-in-Motion of Axles and Vehicles for Europe (WAVE) project (WAVE 2001). The FAD method uses FAD sensors in addition to weighing sensors to measure the local bridge responses which contain the information of vehicle axles. However, the FAD methods are only suitable for certain types of bridges and are susceptible to the transverse position of wheels (O'Brien et al. 2012; Ieng SS et al. 2012; Kalin et al. 2006). Aiming to overcome these disadvantages, alternative axle detection strategies have been developed for NOR BWIM systems. For example, O'Brien et al. (2012) and Bao et al. (2016) used shear strains to identify vehicle axles. Lydon et al. (2017) developed a NOR BWIM system based on advanced fiber optical sensors. Ojio et al. (2016) proposed a contactless BWIM system using roadside vision systems to monitor and identify vehicle speed and axle spacing.

For bending moment-based BWIM systems, it is beneficial to directly extract axle information from the global strain signals. Kalhori et al. (2017) identified vehicle axles using the peak-to-peak approach which utilizes flexural strains, though some axles might be missed under some circumstances. Yu et al. (2015) used wavelet transformation of the bridge global response for axle detection. Nevertheless, it is usually difficult to directly identify vehicle axles from the global strain signal of bridges because the global bridge response is less sensitive to individual

vehicle axles compared with local bridge responses. In addition, signal processing techniques were adopted by some researchers to improve the accuracy of axle detection. Kalin et al. (2006) utilized a band-pass filter to isolate individual axles. Wall et al. (2009) calculated the second derivative of bending moments for vehicle speed and axle spacing identification. However, this method is susceptible to measurement noises. Wavelet analysis, as a powerful pat-tern recognition technique, has also been applied for axle detection by some researchers (Chatterjee et al. 2006; Yu et al. 2015; Dunne et al. 2005; Lechner et al. 2010). Nevertheless, this technique is susceptible to the errors in the original signal (Lydon et al. 2016).

In this study, a novel equivalent shear force (ESF) method was proposed to estimate vehicle speed and axle spacing. This method directly uses the flexural strain signals acquired from weighing sensors to de-tect the vehicle axles. In order to demonstrate the effectiveness and accuracy of the proposed ESF meth-od, extensive numerical simulations based on a three-dimensional (3D) vehicle-bridge coupled analysis are conducted. The impacts of various factors on the ac-curacy of the proposed method are also examined.

2 BRIDGE-VEHICLE COUPLED SYSTEM

2.1 *Dynamic Equation of Bridge and Vehicle*

The dynamic equations of motion of bridge and vehicle can be expressed as following:

$$M_b \ddot{d}_b + C_b \dot{d}_b + K_b d_b = F_{bv} \tag{1}$$

$$M_v \ddot{d}_v + C_v \dot{d}_v + K_v d_v = F_{vb} + F_{vg} \tag{2}$$

where M_b, M_v, C_b, C_v, K_b, and K_v are the mass, damping, and stiffness matrices of the bridge and the vehicle, respectively; d_b and d_v are the displacement vectors (in the vertical direction) of the bridge and the vehicle, respectively; F_{bv} and F_{vb} are the vectors of the wheel-road contact forces acting on the bridge and the vehicle, respectively; and F_{vg} is the gravity force vector of the vehicle.

Utilizing the force and displacement compatibility at the contacting points between the bridge and the vehicle, the motion equations of the bridge and the vehicle can be coupled as follows:

$$\begin{bmatrix} M_b & \\ & M_v \end{bmatrix} \begin{Bmatrix} \ddot{d}_b \\ \ddot{d}_v \end{Bmatrix} + \begin{bmatrix} C_b & C_{bv} \\ C_{vb} & C_v \end{bmatrix} \begin{Bmatrix} \dot{d}_b \\ \dot{d}_v \end{Bmatrix} + \begin{bmatrix} K_b & K_{bv} \\ K_{vb} & K_v \end{bmatrix} \begin{Bmatrix} d_b \\ d_v \end{Bmatrix} = \begin{Bmatrix} F_{br} \\ F_{vr} + F_{vg} \end{Bmatrix} \tag{3}$$

where C_{bv}, C_{vb}, K_{bv} and K_{vb} are time dependent terms related to the tire-road contact forces; and the subscript r denotes road surface roughness which will be introduced in the following section. The details of deriving the above equations can be found in (Deng & Cai 2010a) and (Deng & Cai 2010b) and are not introduced here for the sake of brevity.

2.2 *Road Surface Condition*

Road surface roughness is a main source of excitation for the vibration of bridge-vehicle system. It can be described by a zero-mean stationary Gaussian stochastic process which can be generated through its power spectral density function. The International Organization for Standardization (ISO 1995) classified the road surface condition (RSC) based on different roughness coefficients. Based on the ISO classification, a total of four different road surface conditions, namely, smooth, very good, good, and average, were considered in the present study, with corresponding roughness coefficients of 0, 5×10^{-6}, 20×10^{-6}, and 80×10^{-6} m^3/cycle, respectively.

2.3 *Solving the BVI problem*

Eq. (3) can be solved using numerical integration algorithms. A Matlab program was developed to solve the BVI problem using the Newmark-β method in the time domain. The BVI model has also been validated using field measurements by Cai et al. (2007) and Deng and Cai (2011). The strain of the bridge can be calculated based on the bridge dynamic displacement responses by:

$$\varepsilon = B \cdot d_b \tag{4}$$

where B is the strain-displacement relationship matrix assembled with the derivatives of the element shape functions with respect to x, y, and z, and can be derived following a standard finite element formulation process.

3 METHODOLOGY FOR DETECTING VEHICLE SPEED AND AXLES

3.1 *Equivalent Shear Force Method*

Figure 1 (a) shows a linear-elastic beam AB with arbitrary support conditions. P, Q, and O are three consecutive points on beam AB while point O is located at the middle of points P and Q. l_A, l, and l_B are the length of segments AP, PQ and QB, respectively. The reaction forces of the beam AB are represented by M_A, M_B, F_A, and F_B, which are functions of x, as shown in Figure 1(a).

When the beam AB is subjected to a concentrated force F applied at a distance of x from point A, the

bending moment at positions P and Q of the beam AB can be expressed as:

$$M_P = M_A(x) + M_P^F, \quad M_Q = M_A(x) + M_Q^F$$
$$M_P^F = \begin{cases} F_A(x)l_A - F(l_A - x), & 0 \le x < l_A \\ F_A(x)l_A, & l_A \le x < l_A + l + l_B \end{cases} \quad (5)$$
$$M_Q^F = \begin{cases} F_A(x)(l_A + l) - F(l_A + l - x), & 0 \le x < l_A + l \\ F_A(x)(l_A + l), & l_A + l \le x < l_A + l + l_B \end{cases}$$

From Eq. (5), the following two variables can be defined and derived:

$$V^E(x) \triangleq \frac{M_Q - M_P}{l} = G(x) + F_A(x)$$
$$G(x) = \begin{cases} -F, & 0 \le x < l_A \\ -F(1 - \frac{x}{l}), & l_A \le x < l_A + l \\ 0, & l_A + l \le x \le l_A + l + l_B \end{cases} \quad (6)$$

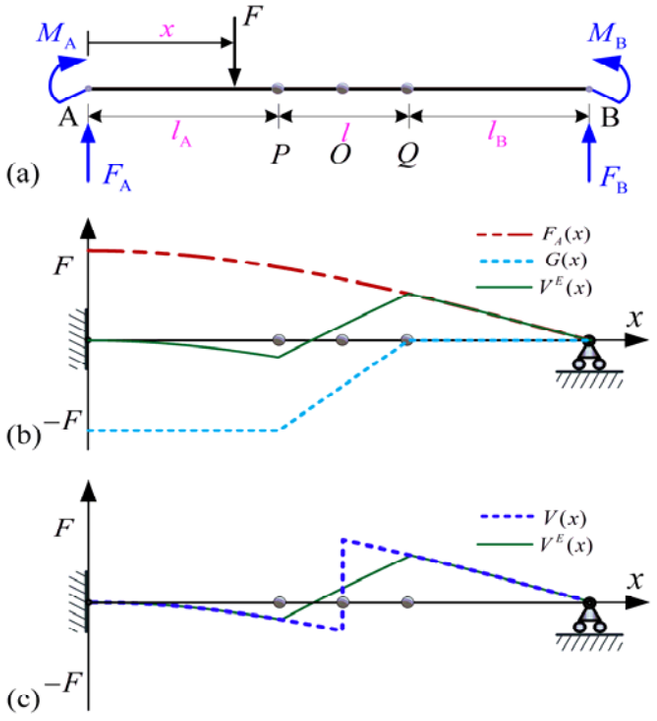


Figure 1. Schematic of the ESF method: (a) beam AB with arbitrary boundary conditions; (b) the influence lines of $F_A(x)$, $G(x)$, and $V^E(x)$; (c) the influence line for the shear force at point O and the ESF of segment PQ.

For the purpose of illustration, the influence lines for $F_A(x)$, $G(x)$, and $V^E(x)$ for a beam with a fixed support on the left end and a roller support on the right end are obtained based on Eq. (6) by assuming F=1, and the results are plotted in Figure 1 (b). It can be seen that $V^E(x)$ has two sudden changes of slope corresponding to a valley and a peak on its influence line.

In fact, based on the theory of mechanics of materials, V^E, which is derived by the moments at points P and Q as shown in Eq.(6), is an approximation of the shear force at point O:

$$V^E \approx V = \frac{dM}{dx} \quad (7)$$

Therefore, V^E is called the equivalent shear force of PQ hereafter. The influence line of the shear force V at point O and the influence line of the ESF of PQ are plotted in Figure 1 (c). When points P and Q approach point O, the ESF curve shown in Figure 1 (c) will converge to the shear force at point O.

3.2 *Axle Detection*

The sudden changes of the slope of V^E can be used to identify axle passing. Firstly, two segments P_1Q_1 and P_2Q_2 were selected as shown in Figure 2. The lengths of the two segments are denoted as l_1 and l_2, respectively. The distance between the centers of the two segments is L, as shown in Figure 2. Then, the ESF of the two segments can be obtained using Eq. (6). Based on the characteristic of the ESF, if a N-axle vehicle passes the bridge, there will be N groups of valleys and peaks on the ESF of a segment. Thus, the axles can be identified as the number of valleys or peaks on the ESF curve. The vehicle speed can be predicted using the time lag between the ESFs of the two segments and the known distance L. It should be noted that, theoretically, the vehicle speed can be identified using the time lag between the valley and the peak. However, in reality, the dynamic effect and measurement noises tend to shift the peaks and valleys away from their theoretical locations, making it difficult to accurately identify the vehicle speed using only one segment. Therefore, two segments with a center spacing of L were used for identification.

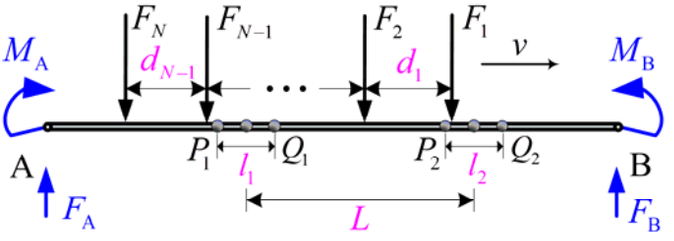


Figure 2. Two beam segments for axle detection.

Figure 3 shows the static bending moment and the ESF of two segments of a simply-supported beam AB subjected to two moving loads with a spacing of d. The x axis represents the location of the first axle and the y axis represents the bending moments or the ESF. From Figure 3, the number of axles can be identified by counting the number of valleys (t_{11}^1 and t_{21}^1 relative to P_1 on V_1^E, or t_{11}^2 and t_{21}^2 relative to P_2 on V_2^E) or peaks (t_{12}^1 and t_{22}^1 relative to Q_1 on V_1^E, or t_{12}^2 and t_{22}^2 relative to Q_2

on V_2^E). Then, the vehicle speed can be predicted as:

$$v = \frac{L}{\Delta T} = \frac{L}{\frac{t_{s1}^2 + t_{s2}^2}{2} - \frac{t_{s1}^1 + t_{s2}^1}{2}}, \quad s = 1 \text{ or } 2 \tag{8}$$

where ΔT is the time lag between ESF1 and ESF2 and it can be automatically determined by using an alternatively cross-correlation algorithm proposed by Kalin et al. (2006). After the vehicle speed is obtained, the axle spacing can be easily calculated as:

$$d = v\left(\frac{t_{21}^s + t_{22}^s}{2} - \frac{t_{11}^s + t_{12}^s}{2}\right), \quad s = 1 \text{ or } 2 \tag{9}$$

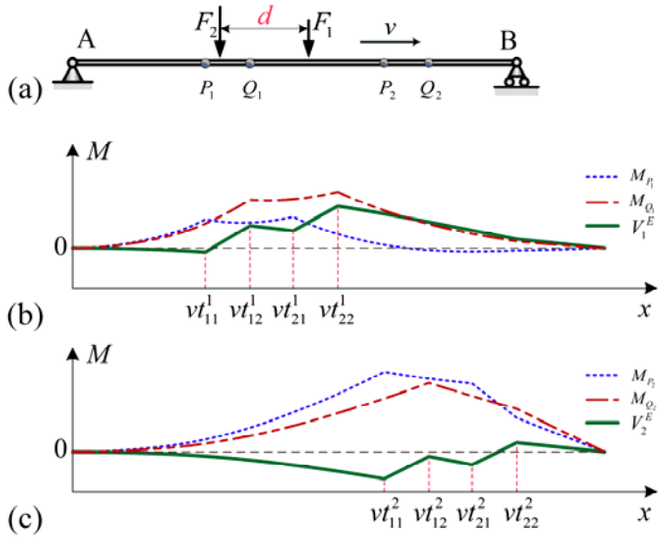


Figure 3. Bending moment and ESFs of a beam: (a) a simply-supported beam AB subject to two moving loads; (b) the static moments at P_1 and Q_1, and ESF of P_1Q_1 (V^E_1); (c) the static moments at P_2 and Q_2, and ESF of P_2Q_2 (V^E_2).

Based on the above discussion, it can be seen that two groups of measurement points, with two points in each group, are needed to identify the vehicle speed and axle spacing. Nevertheless, in practice, only three measurement points are needed since the two segments can share one measurement point located in the middle. In addition, it should be mentioned that the ESF method can only be used to identify axles whose spacing is larger than the spacing of the two adjacent measurement points. For those closely-spaced axles (for example, an axle group), the proposed method may automatically treat them as one single axle in the identification process.

In-service bridges under routine traffic loads can normally be considered as linear-elastic systems. Namely, the global bending moment is linearly related to the flexural strain. Taking a multi-girder bridge for example, the total global bending moment of the bridge at a cross section can be calculated based upon the recorded normal strain as follows:

$$M_s = \sum_{i=1}^{n} EW_i \varepsilon_{s,i}, \; s = \{P_1, Q_1, P_2, Q_2\} \tag{10}$$

where E is the modulus of elasticity of the bridge material, Wi is the section modulus of the ith girder, and $\varepsilon_{s,i}$ is the normal strain of the ith girder at section s. However, it was found in this study that using the strain information from all girders is not necessary since the strain from one particular girder that bears a significant portion of vehicle loads can fulfill the requirement of identifying the vehicle speed and axle spacing, even under different transverse locations of the moving vehicle. Therefore, there is no need to install sensors on all girders in the lateral direction, and the strain information from the girder that bears the largest amount of vehicle loads was selected in the present study, namely:

$$V_j^E = \frac{M_{Q_j} - M_{P_j}}{l_j} = \frac{EW}{l_j}\left(\varepsilon_{Q_j} - \varepsilon_{P_j}\right) \tag{11}$$

Since $\frac{EW}{l_j}$ is a constant scalar, for the sake of convenience, ESF is redefined by ignoring the constant using Eq. (12) in the following analysis:

$$\text{ESF}_j = V_j^E \Big/ \frac{EW}{l_j} = \varepsilon_{Q_j} - \varepsilon_{P_j} \tag{12}$$

4 NUMERICAL SIMULATIONS

4.1 *Case Description*

4.1.1 *4.1.1. Bridge model*

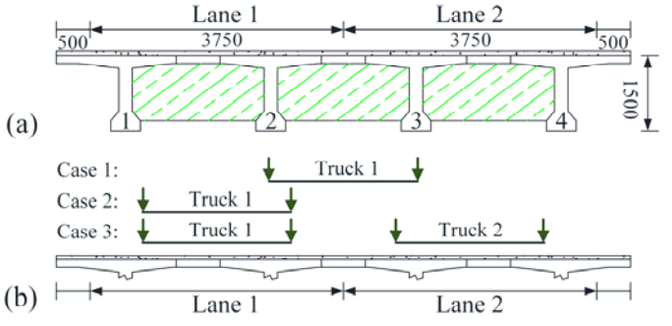


Figure 4. (a) Bridge cross section (unit: mm); (b) Considered loading cases.

In the present study, a multi-girder bridge with four identical T-beams was used in the numerical simulations. The bridge's cross section and the selected loading positions are plotted in Figure 4. The bridge was modeled using solid elements in ANSYS. The finite element model of the bridge is shown in Figure 5. In the simulation study, three measurement stations with an equal spacing of 2m are selected on the soffit of Girder 2 which bears the largest proportion of vehicle loads. As shown in Figure 5, the three

measurement stations are denoted by A, B, and C where station B is located at the mid-span. The ESFs of AB and BC were then calculated using the longitudinal strains collected from those stations.

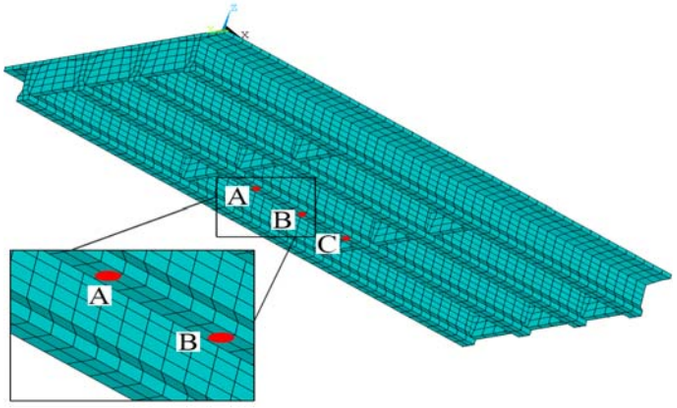


Figure 5. FE model of the bridge and locations of the measurement stations.

4.1.2 *Vehicle Model*

In the numerical study, three typical highway trucks were adopted. Figure 6 shows the axle configuration of the three trucks. Each truck was modeled by mass-spring-dashpot systems. Detail properties of the three vehicles can be found in (Harris 2007; Shi and Cai 2009; Wang and Liu 2000; Zhang et al. 2006; Zhou and Chen 2015). In the simulation, five vehicle speeds from 10 m/s to 30 m/s with an increment of 5 m/s, four different road surface conditions including smooth, very good, good, and average, and three loading cases including both single vehicle cases and cases with multiple vehicle presence were considered to simulate different scenarios of truck passing. Table 1 summarizes the parameters considered in the numerical simulation.

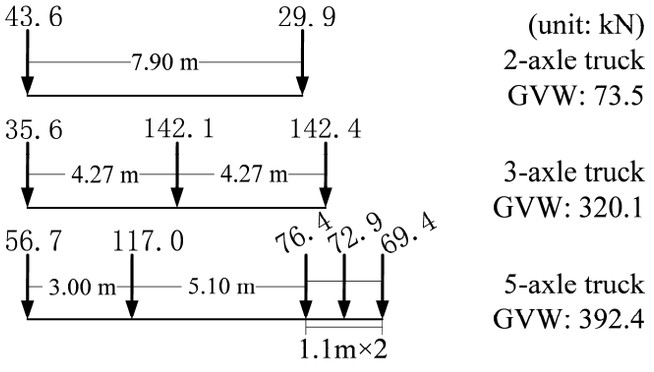


Figure 6. Axle weight distribution of the three trucks (Note: GVW=gross vehicle weight).

Table 1. Values of Parameters Considered in the Numerical Simulation

Parameter	Value
Speed (m/s)	10, 15, 20, 25, 30
Roughness	Smooth, very good, good, average
Truck type	2-axle truck, 3-axle truck, 5-axle truck
Loading case	1: one truck along the centerline of the bridge
	2: one truck along the centerline of Lane 1
	3: two trucks in both traffic lanes

4.2 *Identification Results for Single-Vehicle Cases*

For the single-vehicle cases, the truck either travelled along the centerline of the bridge or along the center of the left lane. Figure 7 shows the typical longitudinal strain responses and the calculated ESFs under the passage of the 2-axle truck. Figure 8 shows the ESFs of Girder 2 and the detected peaks and valleys under the passage of each truck at the speed of 20 m/s. For the purpose of demonstration, only a few typical cases were plotted. From Figure 8, it can be seen that clear peaks and valleys are observed and that the number of peaks and valleys is the same as the number of vehicle axles except for the case of the 5-axle truck where only three peaks or valleys are found. For the 5-axle truck, the three rear axles are closely spaced, which resulted in only one identifiable peak and valley. It should be mentioned that the difficulty in identifying closely-spaced axles has been reported by many researchers. Usually, the closely-spaced axles, such as a tandem or tridem axle group, are identified as a single axle by most BWIM systems. In the present study, the three rear axles of the 5-axle truck are treated as a single axle with a weight of 218.7 kN. The equivalent axle spacing between the second axle and the rear axle group is calculated as:

$$\mathrm{AS}_2' = \sum_{i=3}^{5} \mathrm{AW}_i \left(\sum_{j=2}^{i-1} \mathrm{AS}_j \right) \Bigg/ \sum_{i=3}^{5} \mathrm{AW}_i \tag{13}$$

where AW_i is the weight of the ith axle and AS_j is the spacing between the (i-1)th axle and the ith axle. Using the proposed method, the vehicle speed and axle spacing were calculated. For each RSC, five vehicle speeds were considered and for each set of RSC and each vehicle speed, ten runs with ten randomly generated road surface profiles were performed using the BVI simulation. Then, the root mean square (RMS) of the ten results is calculated for the error analysis. Table 2 gives the RMSs of the relative errors (%) in the identification results. For the sake of brevity, the results of 3-Axle truck are omitted.

From Table 2, it can be seen that: (1) the proposed method can effectively identify the vehicle speed and axle spacing. The RMSs of the identification errors are all within five percent for the vehicle speed and axle spacing; (2) vehicle speed does not seem to have a significant impact on the identification accuracy; (3) RSC affects the identification accuracy as rough surface tends to induce more vibrations and decrease the identification accuracy. Nevertheless, the identification results still show a satisfactory degree of accuracy under the average RSC.

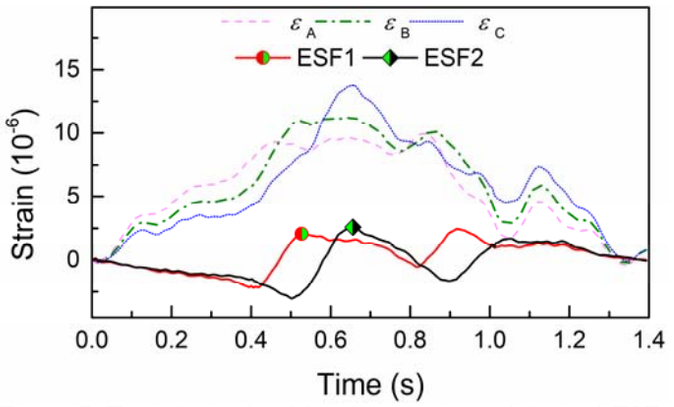


Figure 7. Typical simulated bending strains and derived ESFs (Loading case 1, 2-axle truck, v = 20 m/s, average RSC).

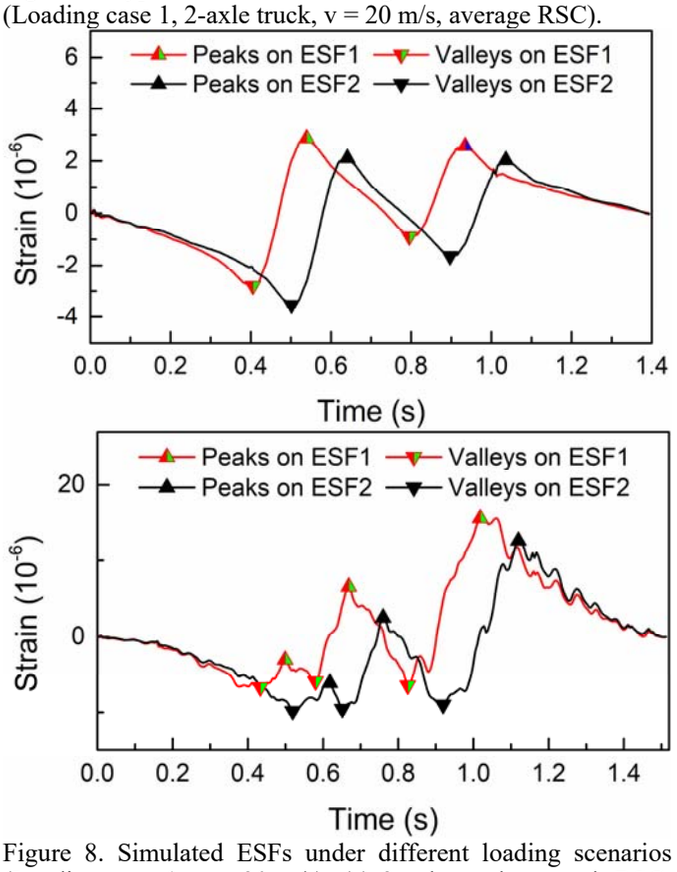


Figure 8. Simulated ESFs under different loading scenarios (Loading case 1, v = 20 m/s): (a) 2-axle truck, smooth RSC; (b) 5-axle truck, average RSC.

In addition, the identification results for loading case 2 are very similar to those for loading case 1 when measurement stations are selected on Girder 2 and thus they are not presented here for the sake of brevity. Meanwhile, in order to investigate the effect of the transverse location of the measurement stations, three measurement stations with the same longitudinal location as those on Girder 2 were selected on Girder 3 and Figure 9 shows the bending strain time histories and the ESFs for the 5-axle truck passing at a speed of 20 m/s under loading case 2. It can be seen that the ESFs of Girder 3 do not show clear peaks or valleys, making it infeasible to identify the vehicle axles. This is because when the vehicle was positioned in Lane 1, the shear forces induced on Girder 3 is so small that the peaks and valleys are not easily identifiable. This also indicates that two groups of measurement stations are required for each traffic lane in order to capture the information of all vehicles passing over the bridge. Also, the ESF signal under different traffic lanes can potentially be used to determine the traveling lane of the vehicle.

Table 2. The RMS of the Relative Identification Errors (%) of the Three Trucks (Loading case 1)

RSC	True speed (m/s)	RMS of identification error (%)				
		2-Axle truck		5-Axle truck		
		Speed	AS	Speed	AS_1	AS_2
Smooth	10	0.31	0.16	0.21	2.29	2.38
	15	0.78	0.38	0.93	2.79	1.54
	20	0.68	0.01	0.68	2.73	1.81
	25	1.30	0.63	0.16	1.06	1.64
	30	2.22	0.77	0.37	2.97	0.62
Very Good	10	1.62	1.63	1.06	1.89	1.21
	15	0.70	0.90	2.06	2.09	1.69
	20	1.34	0.87	1.75	2.00	2.01
	25	0.51	0.89	1.12	1.29	1.43
	30	1.82	0.82	1.23	2.82	1.41
Good	10	1.25	1.03	1.32	2.03	0.84
	15	0.48	1.23	1.28	2.04	1.60
	20	1.07	0.89	1.56	1.73	2.85
	25	1.24	1.13	1.58	2.43	2.97
	30	1.40	1.51	1.10	2.52	2.46
Average	10	1.03	2.03	1.12	2.49	2.26
	15	1.39	2.22	2.41	1.70	2.98
	20	2.49	3.03	1.42	3.03	2.44
	25	1.83	1.63	1.99	4.05	2.56
	30	1.52	2.03	1.80	2.94	3.68

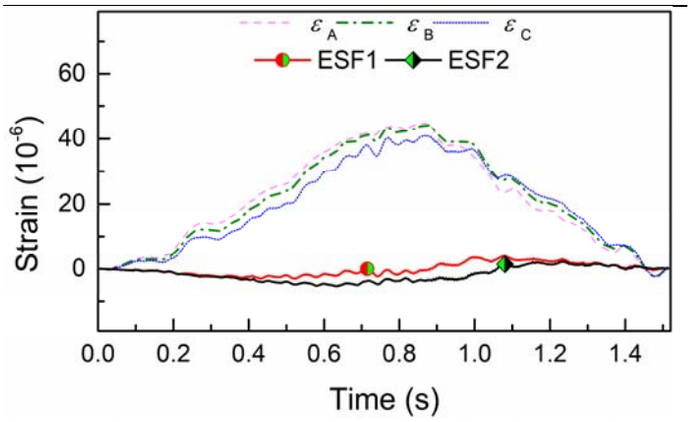


Figure 9. Simulated bending strain and ESF of Girder 3 (Loading case 2, 5-axle truck, v = 20 m/s, average RSC).

4.3 *Identification Results for Cases with Multiple Truck Presence*

In this study, a loading case with a 2-axle truck traveling in Lane 1 and a 3-axle truck traveling in Lane 2 were considered, as presented in Figure 4 (c). In order to represent the real traffic, three driving plans were developed and summarized in Table 3.

Figure 10 shows the time history of the simulated strain response and the ESFs for Girder 2 and Girder 3 following the first driving plan. The two trucks were set to travel at 20 m/s with a headway distance of 5 m and average RSC was used. From Figure 10, it can be seen that the peaks and valleys on the ESF time histories for both girders can still be clearly identified when the two trucks passed over the bridge simultaneously. For Girder 2, the ESF shows two groups of peaks and valleys corresponding to

the 2-axle truck while for Girder 3, the ESF shows three groups of peaks and valleys corresponding to the 3-axle truck. The RMS of relative identification errors (%) for two trucks traveling at the same and different speeds are summarized in Table 4 and Table 5, respectively. It can be seen that good accuracy was achieved in the identified vehicle speed and axles for both trucks, suggesting that the proposed method is able to deal with cases with multiple vehicle presence.

Table 3. Driving Plans of Two Trucks in Different Lanes (Loading Case 3).

Driving plan	Description
1	Two trucks enter bridge at the same time at the same speed (from 10 to 30 m/s)
2	Two trucks travel at the same speed (from 10 to 30 m/s) with headway distance of either 5m or 10m.
3	Two trucks enter bridge at the same time while the speed of the 2-axle truck was kept at 20 m/s but the 3-axle truck's speed varies from10 to 30 m/s.

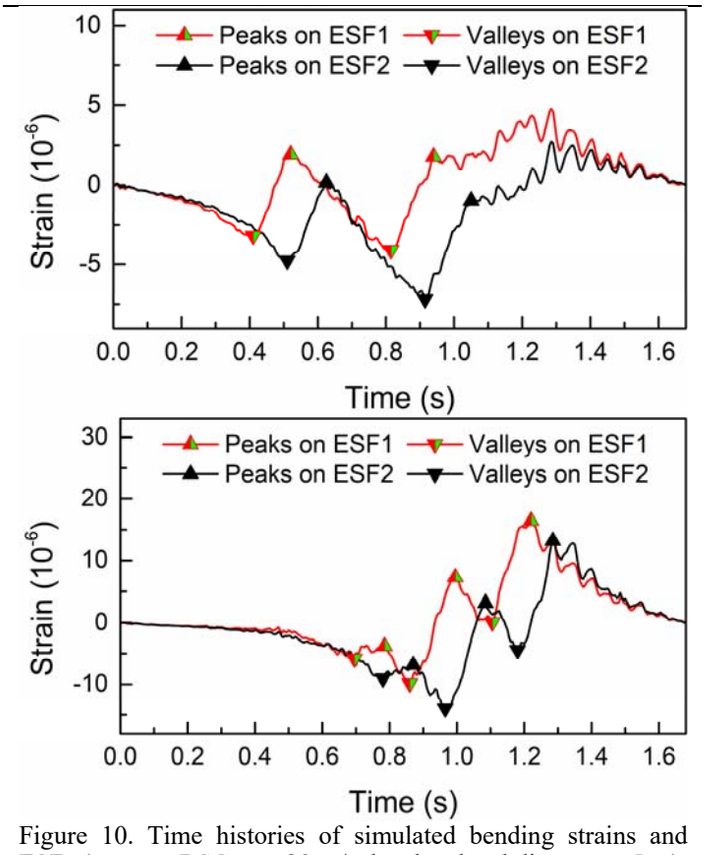


Figure 10. Time histories of simulated bending strains and ESFs (average RSC, v = 20 m/s, head-to-head distance = 5 m): (a) Girder 2; (b) Girder 3.

Table 4. RMS of Relative Errors of Identification Results of Two Trucks Traveling at the Same Speed

Head-to-head distance(m)	Speed (m/s)	RMS of Relative Errors (%) 2-Axle Truck v	2-Axle Truck AS	3-Axle Truck v	3-Axle Truck AS1	3-Axle Truck AS2
0	10	0.90	1.54	1.07	1.90	1.86
	15	1.05	0.83	1.44	0.92	1.83
	20	1.03	1.11	1.15	1.71	2.04
	25	1.25	1.56	1.94	0.95	1.30
	30	0.92	0.95	1.55	1.81	1.56
5	10	1.50	1.39	1.02	1.88	1.29
	15	1.51	1.80	1.56	2.53	1.68
	20	2.26	2.25	1.14	2.07	2.63
	25	1.03	2.23	2.21	2.29	2.45
	30	2.60	1.85	1.53	1.56	1.77
10	10	0.87	1.04	0.76	2.40	2.52
	15	0.86	2.05	1.44	1.29	1.37
	20	1.13	0.76	2.03	2.77	1.53
	25	1.33	1.77	1.96	2.85	1.94
	30	2.47	1.71	1.89	1.49	2.46

Table 5. RMS of Relative Errors of Identification Results of Two Trucks Traveling at Different Speeds

Speed (m/s)		RMS of Relative Errors (%)				
Truck 1	Truck 2	2-Axle Truck v	2-Axle Truck AS	3-Axle Truck v	3-Axle Truck AS1	3-Axle Truck AS2
20	10	2.35	1.71	0.66	2.04	1.60
	15	1.45	1.89	1.51	1.79	1.62
	20	1.03	1.11	1.15	1.71	2.04
	25	1.14	2.09	1.57	2.17	1.91
	30	1.66	1.68	1.43	1.53	2.03

5 SUMMARY AND CONCLUSIONS

In this study, a novel axle detection strategy, i.e., the equivalent shear force method, was proposed to identify the speed and the axle spacing of moving vehicles on bridges. The proposed ESF method utilizes the global bending strains of bridges to achieve axle detection and thus can be used for the NOR BWIM systems. Numerical study was conducted to demonstrate the performance of the proposed ESF method. The identification results showed that the proposed ESF method can provide accurate and reliable axle detection for the NOR BWIM systems. The effects of measurement location, vehicle speed, vehicle's lateral position, road surface condition, and multiple vehicle presence on the identification accuracy were investigated. Based on the results obtained, the following conclusions can be drawn: (1) in order to identify vehicles traveling in a particular lane, strain sensors need to be installed underneath that lane; (2) the vehicle's speed and lateral position do not affect the identification accuracy; (3) the identification accuracy decreases as the RSC worsens. Nevertheless, the identification accuracy is still acceptable under the average RSC; (4) the ESF method is able to identify vehicle speed and axle spacing under the cases with multiple vehicle presence.

Compared with traditional NOR axle detection methods such as the FAD methods, the ESF method uses the global bending response of bridges and is thus applicable to most bridges whose dominant internal force is bending moment under vehicle loading. Furthermore, the ESF is not susceptible to the lateral position of the vehicles and can also be used to identify multiple vehicle presence. These advantages make the ESF method a reliable strategy of axle detection for commercial NOR BWIM systems. Future studies will focus on developing algorithms for automatic identification of vehicle axles using

the ESF method and testing the performance of the ESF method in full-scale experiments.

ACKNOWLEDGMENTS

The authors acknowledge the financial support provided by the National Natural Science Foundation of China (Grants 51478176 and 51778222), the funding provided by the Hunan Communications Research Institute and the financial support provided by China Scholarship Council.

REFERENCE

Bao T, Babanajad SK, Taylor T, Ansari F. 2016. Generalized Meth-od and Monitoring Technique for Shear-Strain-Based Bridge Weigh-in-Motion. *Journal of Bridge Engineering* (*ASCE*). 21:04015029.

Cai CS, Shi X, Araujo MS, Chen S. 2007. Influence of Approach Span Conditions on Vehicle-Induced Dynamic Response of Slab-on-Girder Bridges: Field and Numerical Simulations. *Transportation Research Board 86t h Annual Meeting*, Washington DC.

Chatterjee P, Obrien E, Li Y, González A. 2006. Wavelet domain analysis for identification of vehicle axles from bridge measurements. *Computers & Structures*. 84:1792-801.

Deng L, Cai CS. 2010a. Development of dynamic impact factor for performance evaluation of existing multi-girder concrete bridges. *Engineering Structures*. 32(1), 21-31.

Deng L, Cai CS. 2010b. Identification of Dynamic Vehicular Axle Loads: Theory and Simulations. *Journal of Vibration & Control*. 16:2167-94.

Deng L, Cai CS. 2011. Identification of Dynamic Vehicular Axle Loads: Demonstration by a Field Study. Journal of Vibration & Control. 17:183-95.

Dunne D, O'Brien EJ, Basu B, Gonzalez A. 2005. Bridge WIM systems with Nothing On the Road (NOR). *International Conference on Weigh-In-Motion*, 4th, Taipei.

Harris NK, O'Brien EJ, González A. 2007. Reduction of bridge dynamic amplification through adjustment of vehicle suspension damping. *Journal of Sound & Vibration*. 302:471–85.

He W, Deng L, Shi H, Cai CS, Yu Y. 2016. Novel Virtual Simply Sup-ported Beam Method for Detecting the Speed and Axles of Moving Vehicles on Bridges. *Journal of Bridge Engineering* (*ASCE*). 04016141.

Ieng SS, Zermane A, Schmidt F, Jacob B. 2012. Analysis of B-WIM signals acquired in Millau orthotropic viaduct using statistical classification. *6th International conference on weigh-in-motion* (*ICWIM 6*), Dallas. p. 43-52.

ISO-8608. 1995. Mechanical Vibration-Road surface profiles Reporting of measured data. *International Organization for Standardization* (*ISO*), Geneva.

Jacob B, O'Brien E. 1998. European specification on weigh-in-motion of road vehicles (COST323). *Second European conference on w eigh-in-motion of road vehicles,* Lisbon. 14-6.

Jacob B, O'Brien E. 2005. Weigh-in-motion: recent developments in Europe. *4th International Conference on Weigh-In-Motion*, Taipei.

Kalhori H, Alamdari MM, Zhu X, Samali B, Mustapha S. 2017. Non-intrusive schemes for speed and axle identification in bridge-weigh-in-motion systems. *Measurement Science and Technology*. 28:025102.

Kalin J, Žnidarič A, Lavrič I. 2006. Practical implementation of nothing-on-the-road bridge weigh-in-motion system. *9th International symposium on heavy vehi cle weights and dimensions*, Pennsylvania.

Lechner B, Lieschnegg M, Mariani O, Pircher M, Fuchs A. 2010. A Wavelet-Based Bridge Weigh-In-Motion SysTem. *International Journal on Sm art Sensing & Intelligent Systems*. 3(4).

Lydon M, Taylor SE, Robinson D, Mufti A, Brien EJO. 2016. Recent developments in bridge weigh in motion (B-WIM). *Journal of Civil Structural Health Monitoring*. 6:69-81.

Lydon M, Robinson D, Taylor SE, Amato G, Brien EJO, Uddin N. 2017. Improved axle detection for bridge weigh-in-motion systems using fiber optic sensors. *Journal of Civil Structural Health Monitoring*. 7:325-32.

Moses F. 1979. Weigh-in-motion system using instrumented bridges. *Transportation Engineering Journal*. 105:233-49.

O'Brien EJ, Rowley CW, González A, Green MF. 2009. A regularized solution to the bridge weigh-in-motion equations. *International Journal of Heavy Vehi cle Systems*. 16:310-27.

O'Brien E, Hajializadeh D, Uddin N, Robinson D, Opitz R. 2012. Strategies for axle detection in bridge weigh-in-motion systems. *6th International Conference on Weigh-In-Motion* (*ICWIM 6*), Dallas.

Ojio T, Carey CH, O'Brien EJ, Doherty C, Taylor SE. 2016. Contact-less Bridge Weigh-in-Motion. *Journal of Bridge Engineering* (*ASCE*). 21(7):04016032.

Peters R. 1984. AXWAY-a system to obtain vehicle axle weights. *Australian Road Research*. 12: 10-8.

Shi X, Cai C. 2009. Simulation of Dynamic Effects of Vehicles on Pavement Using a 3D Interaction Model. J*ournal of Transportation Engineering*. 135:736-44.

Wall CJ, Christenson RE, Mcdonnell AMH, Jamalipour A. 2009. A Non-Intrusive Bridge Weigh-in-Motion System for a Single Span Steel Girder Bridge Using Only Strain Measurements. *Girder Bridges*.

Wang TL, Liu CH. 2000. Influence of Heavy Trucks on Highway Bridges. Report No. FL/DOT/RMC/6672-379.

WAVE. 2001. Weighing-in-motion of axles and vehicles for Europe (WAVE). Report of work package 1.2, *Laboratoire Central des Ponts et Chaussées*, Paris;

Yu Y, Cai C, Deng L. 2015. Vehicle axle identification using wavelet analysis of bridge global responses. *Journal of Vibration and Control*. 1077546315623147.

Yu Y, Cai C, Deng L. 2016. State-of-the-art review on bridge weigh-in-motion technology. *Advances in Structural Engineering*. 19:1514-30.

Zhang Y, Cai CS, Shi X, Wang C. 2006. Vehicle-Induced Dynamic Performance of FRP versus Concrete Slab Bridge. *Journal of Bridge Engineering (ASCE)*. 11:410-9.

Zhao H, Uddin N, Shao X, Zhu P, Tan C. 2014. Field-calibrated influence lines for improved axle weight identification with a bridge weigh-in-motion system. *Structure & Infrastructure Engineering*. 11:1-23.

Zhou Y, Chen S. 2015. Fully coupled driving safety analysis of moving traffic on long-span bridges subjected to cross-wind. *Journal of Wind Engineering & Industrial Aerodynamics*. 143:1-18.

Žnidarič A, Turk G, Zupan E. 2015. Determination of strain correction factors for bridge weigh-in-motion systems. *Engineering Structures*. 102:387-94.

Zolghadri N, Halling MW, Johnson N, Barr PJ. 2016. Field Verification of Simplified Bridge Weigh-in-Motion Techniques. *Journal of Bridge Engineering* (*ASCE*). 21(10):04016063.

Maintenance, Safety, Risk, Management and Life-Cycle Performance of Bridges – Powers, Frangopol, Al-Mahaidi & Caprani (Eds)
© 2018 Taylor & Francis Group, London, ISBN 978-1-138-73045-8

Virtual design of adaptive road-bridge-types in a comprehensive 5D-BIM assessment

M. Nöldgen
Cologne University of Applied Sciences, Cologne, Germany
J. B. P. Lim
University of Auckland, Auckland, New Zealand
S. Giebat
Schüßler-Plan Ingenieurgesellschaft mbH, Düsseldorf, Germany

ABSTRACT: Currently, new processes are being developed for the model-driven design of structures which make use of the upcoming means of digitalization, such as object-oriented-modeling (OOM), interconnecting Web-based Server-Architecture, Machine-Algorithms for design and fabrication procedures. Relevant Building Information is modeled over the lifecycle which means that data is available and disposable and no longer "hidden" in documents (i.e. design is no longer document driven). New processes focus on the optimization of engineering tasks in the design of structures, such as definition of initial requirements, construction and simulation (optimize geometry and material consumption), time scheduling and cost estimation. BIM principle: Information should be assigned and used without any redundancies in all phases and processes of the product life-cycle. This contribution picks up the idea of comprehensive parametric product templates in combination with an implicit design technology as it is widely used in the production industry for an automated but still strongly adaptive design. These techniques are very helpful especially in the preliminary design of road bridge structures.

1 INTRODUCTION

With the ongoing digitalization and automation of construction processes, the thought arises, that the same can be done for the planning process of bridge models. By creating template models, the earlier stages of the planning process can be automated. Creating and using templates offers various advantages compared to current planning methods. The main one is that they can be used repeatedly, reducing planning costs and time drastically. Draft designs of bridges can be created within hours. Including the correct placement, dimensions and alignment, as well as related documents such as drafts, bill of material, and sustainability evaluations. At the draft design stage objects of the model are accurately represented, whilst lacking details such as screws, welds and reinforcement. Details like that are only available as annotations (LOD300).

This paper explains the core concept behind a parametric, adaptive road bridge model that is created project unspecific and can hence be used as a template for multiple projects featuring a similar bridge design. It can adapt to local requirements and different gradients by allowing alterations to the corresponding parameters.
After using the template, the draft design becomes available straight away. It contains documents such as tables, text files and drawings. All of which are connected to the main model and automatically update on changes. Giving the user live feedback, on how alterations may affect the bridges' sustainability, appearance and cost.

The thought behind a parametric, adaptive design is to create a BIM-model that can be used multiple times, instead of creating a new bridge model for every construction project. This approach is especially viable for standardized bridge designs, since their layout only varies in detail and thus requiring less changes to the parameter. The currently underutilized functionality of creating such a model with associativity will become increasingly important in the future. In other branches, such as the aviation and automobile industry, this modeling technique is already used a lot with highly beneficial results.

2 METHODOLOGY

This paper focuses on using new BIM-processes in early design and including them into a composite bridge model template. An example is used to study the effects in a relevant application in practice, see Figure 1. The goal is to have a parametric, adaptive bridge model with a maximum grade of automation in bridge design. This model can be used for multiple projects as a template. It provides an instant adjustment to local requirements. It also includes the preparation of the structural analysis of the bridge as well as other documents (drafts, tables etc.). All documents related to the model automatically adapt to changes of the parameters. This model can be used repeatedly for different projects, since the parameters can be easily modified to fit local requirements and thus making the initial design process cheaper, quicker and less error-prone.

At first, the basic structure of the model is shown and compared to the use of a parametric, adaptive bridge design to current designing methods, pointing out the advantages and disadvantages of using a parametric, adaptive bridge design with an implicit geometry description. An implicit geometry description saves all methods of an object in a hierarchical construction history. This is contrary to most BIM-systems working with an explicit or hybrid geometry description that only saves the final geometric attributes. The implicit geometry description offered by sophisticated CAD software is a necessity for the creation of a bridge template and subsequent individual modification and detailing, see Section 2.

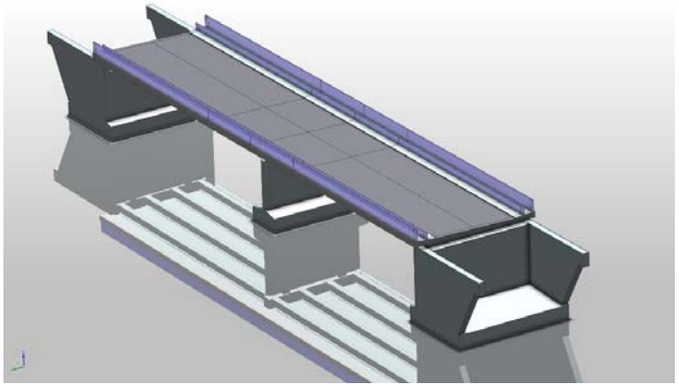


Figure 1: Composite Road-Bridge Type developed as a parametric, adaptive template Building Information Model

In Section 3, the challenges and advantages of the new approach are described. The creation of a model that can be used as template, results in a higher work load at first sight. However, the use of parametric adaptive, bridge models proofs to offer great potential in multiple reuse cases. It can greatly cut early project planning times. This makes its use a valid option for standardized bridge structures, but not for the creation of individual bridge designs. Overall it proves to be the next step for designing standardized bridge models satisfying today´s demands for faster and cheaper design processes.
In this Section the technical background of a template driven parametric top-down modeling based in a history-based CAD-process is explained in detail.

Section 4 presents how an adaptive building information model can reduce the planning times of a bridge, taking away the time intensive process of creating a draft design as well as preparing further planning processes. Therefore, it allows a less labor-intensive planning process. In addition, a quality improvement comes with the use of the template. Functions such as pre-dimensioning cost estimation and sustainability rating can be easily integrated into the template.

2.1 *Requirements for a parametric adaptive template driven modeling of road bridges*

For route-bound infrastructures such as bridges it seems to be clearly advantageous to choose a top-down modeling strategy as most components are dependent on the alignment and fixed by outer constraints such as crossing routes or as-built-infrastructures.
In preliminary design, a rather less detailed model (Level of Detail (LoD) 300) is needed which can easily (and ideally automated) adapt to different positions and shapes to several variants of alignments. Hence there is a strong need of flexibility in positioning and form fitting.
At the same time adjacent information such as technical documentation, drawings, structural analysis, bill of material and costs, time-sheets and sustainability values directly result from the model properties.

2.2 *Parametric Top-Down Modeling Technique*

The most common method to describe an object oriented 3D model is the Boundary Representation Method. This method only saves information on the geometric attributes, leaving out any information on the creation process so that there is no adaptivity given.
Sophisticated CAD software allow for a more flexible Procedural Method. As the name already suggests, this method saves the procedure of the creation process in a timeline.
With the procedural method the engineer has a tool to create and individually modify all individual parameters and features in design in pre- and post-processing. It allows for the manipulation of every step that was involved in the creation of the model. This is imperative for the use as a template, since it requires alterations of the modeling history. The modeling history can be edited at any given point

before and after applying the template which is a strong benefit in the preliminary design phase of a road bridge.
In a so-called "control" part file the guiding geometrical information such as the alignments, planes of main axes and master sketches are created and stored. From this control part file the necessary information is referenced to other work part files where the 3D-object modeling of individual components (superstructure, pillars etc) is finally generated. The advantages of such a top-down master-model strategy are a good overview and central adaptivity of all important parameters, such as the alignment and the cross-section which might be changed several times in early project phases. In addition, the assembly allows for the potential to install a centralized template.
Furthermore, simultaneous engineering of bridge components is possible as all major information may be linked from the master-part and then processed individually in separate work part files while the master-model can be protected by read-only.

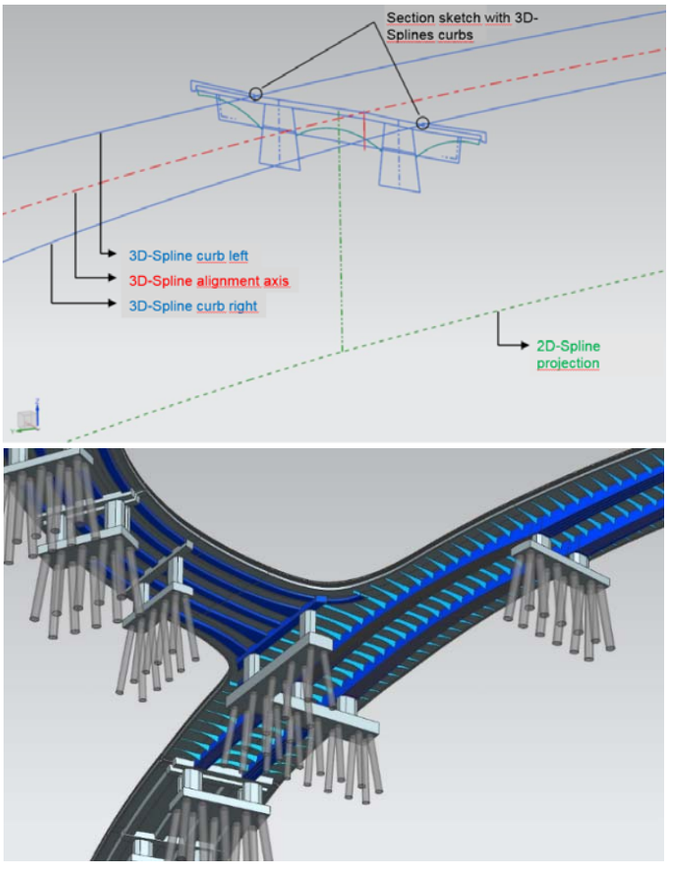


Figure 2: upper: "Control" part-file: Three Alignments which define the widening road surface and a parametric cross section guided by the alignments; lower: completed 3D-model of the bridge structure based on referenced control objects and parameters [6]

Figure 2 (upper) shows the three spatial alignments which were integrated in this project to define the widening road surface in 3D. The three alignments are "cut" into the cross-sectional space in order to guide the variable composite cross-section of the bridge which is set up by additional structural parameters. The main alignment ("3D-Gradiente") is projected in the x-y-space for the definition of main axes and planes.

2.3 *Adaptivity in implicit CAD*

Changes to the model are mostly applied to the control assembly which shall contain all relevant parameters and features to be adapted in a preliminary design. The other reloaded objects automatically adapt to the changes due to the associations. Associations between two objects are not allowed to be bi-directional, exchanging information back and forth to keep the content consistent.

However, a successful adaption to individual boundary conditions affords a high flexibility also in modification and detailing of the related geometry in all work parts. For this purpose, sophisticated implicit modeling techniques are needed which have the full set of parameters and features even after the preliminary template modeling has been finished.

2.4 *Template Driven Design*

The template collects a set of relevant parameters and features to be modified during the modeling process which are located in the model control part-file. The studies show that the template has to be worked out thoroughly in advance by the designing engineer to avoid conflicts in design.
In the presented study the following parameters were chosen:

- Coordinates for alignment-curves
- Crossing-angle of alignments
- Main-Spans for each field individually
- Type of cross-section
- Structural height (Steel-girder)

Those parameters can be adapted within a template by inserting individual values, given values, functions or automated rules. Obviously, upper and lower boundary conditions should be given to ensure reasonable solutions and quality.
Once updated the template allows for the automated adaption of the instant creation of drafts, cost estimates, bill of material and sustainability ratings (See also section 4). To obtain the required data most elements were created with a level of development of 300 according to the description made by the American Association of Architects [2]. This means that 'the quantity, size, shape, location, and orientation of the element as designed can be measured directly from the model without referring to non-modeled information such as notes or dimension call-outs.' Unlike regular execution planning, the model can be used as groundwork for the further planning.

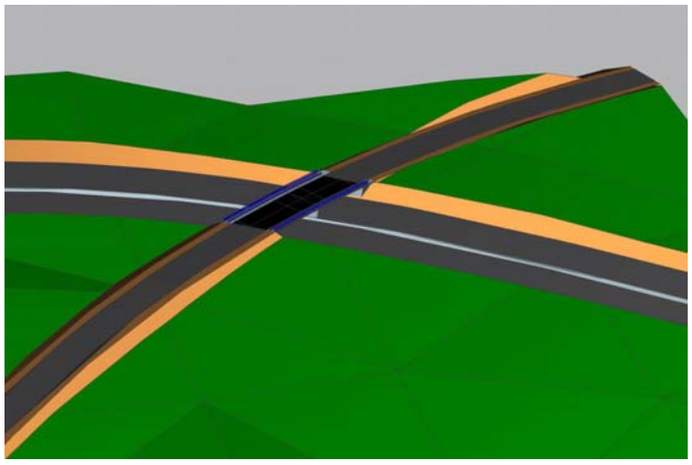


Figure 3. Parametric Two-Span Bridge adapted to a crossing regular Highway in terrain

The model can easily be applied to any given requirements. The integrated product template studio offers a fast and simple way to change the bridges' parameters. It gives live feedback on the status of the parameters requirements, assuring that all values are correct and recommending possible corrections.
There are, however, a few issues which would require an intense preparatory work to be automated. One of those is the adaption to the digital terrain model. The number of variations possible in this adaption of abutment and DEM seems to make automation ineffective. It is recommended to adapt this manually within the implicit post-processing and detailing, for example for the construction pit that should interact with the terrain. Furthermore, depending on the client´s demands, the gradient might be manually inserted as well. Alternatively, the bridge can also be aligned using coordinates that can be inserted in the product template studio.

3 RESULTS AND FINDINGS

3.1 *Issues*

The automation in model design does not come without issues. As it is always the case when switching to a new method of planning, getting used to it can take a while. Using the procedural method requires an intense preparatory work before starting modeling in the beginning. Unlike the regular Boundary-Representation-Method, with the sole purpose of creating objects with the correct attributes, the creation of a parametric, adaptive design requires the user to consider in what sequence the features work and interact in advance.
Since changes to the bridges parameter force the software to recalculate all objects which get affected by these changes, it must be assured that the changes get applied in the correct sequence. Using a hierarchical order helps to keep the sequence consistent.
Furthermore, the model history should be clearly structured to assure that the used features can be easily manipulated. This requires clear conventions every planner must follow.
It becomes evident that the initial creation of the template is much slower than creating a non- associative model. But the increased effort is well worth it as it becomes evident in the next section.
Finally, current software independent data exchange formats do not allow the exchange of method information. Thus, the template is solemnly usable with one software product ('closed BIM').

3.2 *Advantages*

There are many advantages using a model template. First and foremost, the enormous time savings, since creating a model only requires modifications to the initial template parameters. The conceptual and draft design phase in a regular BIM phase usually require a lot of effort compared to the conventional planning process. Using the template allows reducing the effort for the first planning stages to a minimum.
Later stages take similar time as in a regular BIM process. The draft and concept design in a regular BIM process usually take more time then in a conventional planning process, moving the planning expenses to the earlier stages. Unlike the conventional planning process, where the draft design is not further used, BIM processes utilize the draft design without any breaks in the information flow. This saves time in the execution planning.
Additionally, to the reduction of planning errors generally coming with the application of BIM, this method reduces the amount of errors even further. Since, errors that occur due to issues with the template can be corrected to prevent them in future projects.
Current fee structures often do not distinguish between draft designs created in a BIM process and designs in conventional planning. It is thereby favoring the conventional planning process, since it is less time intensive and therefore cheaper. The template fixes this imbalance since it takes away plenty of the effort from the early planning stages, see Fig. 4.
Most objects are created without any associativity between each other, except the one to the control assembly, which means they can be easily separated. This can be utilized by distributing objects among several employees and companies at the same time without worrying about clashes (concurrent engineering). This reduces the time for the execution-planning as well, assuring an even quicker model creation and subsequent process.

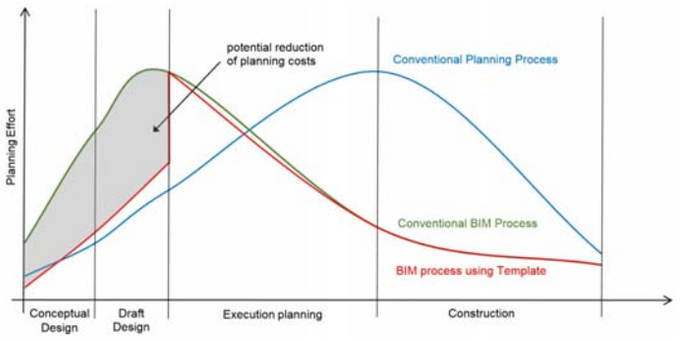


Figure 4. Difference of template driven parametric bridge design to other planning procedures

4 AUTOMATION WITH PARAMETRIC, ADAPTIVE BIM TEMPLATES

4.1 *Drawings as derivatives*

The geometry is stored and maintained in a "work" part file, the so-called the master-model (master part). Simulations, 2D/3D-Derivatives (e.g. as drawings or 3D-visualizations) and even the adjacent structure, the assembly of all bridge components, reference to the master-model. The decisive advantage: Any changes conducted in the master-part will update via associations as long as they were defined consistently.

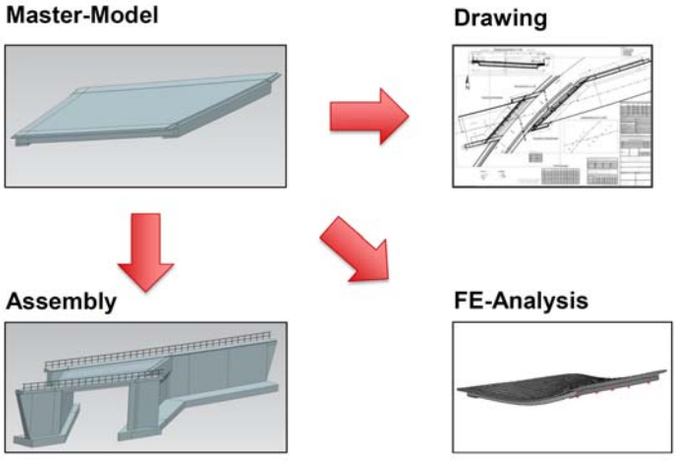


Figure 5. Master-model-concept of a bridge superstructure, drawings, FEA and assemblies receive all geometrical information from the master-part [7]

In 3D-Design, drawings are no longer main products but derivatives of the 3D-Model. Drawings are derived by defining a section plane in the model which is subsequently placed on a 2D-plan. The drawing part files are fully associative to the model as they are positioned upwards to the hierarchical structure. The associativity is unidirectional from master to slave so that changes have to be performed in the master-model.

As the 3D-Model follows the alignment sections have to be defined on curved surfaces.
The authors strongly recommend to modify these current regulations for 2D-drawings with respect to the potential and capability of 3D-models [8]. As a clear advantage compared to 2D-drawings, 2D-derivatives of 3D-models represent real sections and can be positioned everywhere in the 3D-model. This evidently leads to a better understanding, consistency and accuracy.
Hence the authors recommend to increase the number of 3D-sections. Sections which are modified or coupled with others lose associativity to the 3D-model! An example is shown in the next figure 6.

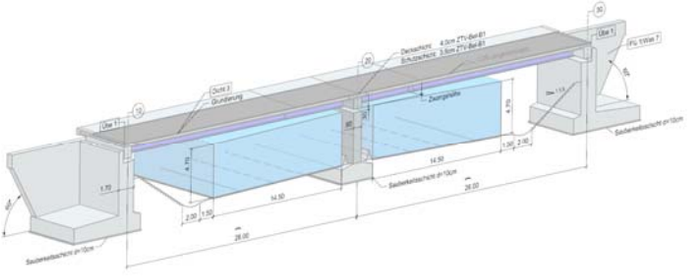


Figure 6. Curved longitudinal section in the 3D-Model, guided by the spatially curved alignment projected in vertical direction. Product Manufacturing Information illustrate the regulatory information (Attributes) [8]

For a further automation, manufacturing drawings can be extracted from the model whilst not only geometrical but also manufacturing information can be integrated in the model and supplied for the following production processes, logistics and erection. Figure 7 shows an example of prefabricated concrete elements automated in construction order and driven by the model. The attributes were assigned to the individual master-parts and visualized by so-called Product-Manufacturing-Information (PMI) in NX.

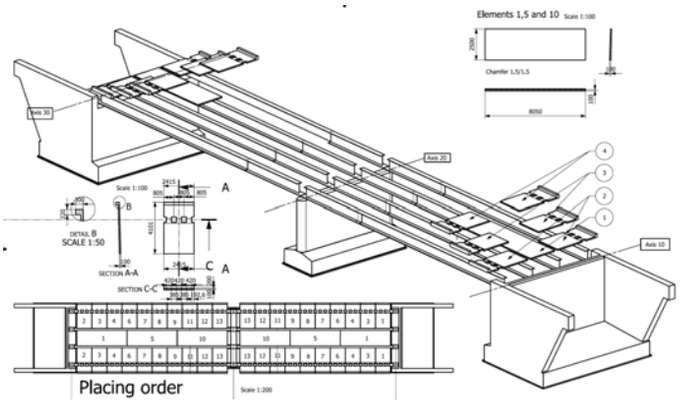


Figure 7. Manufacturing drawing for the logistic and erection of prefabricated R/C bridge deck elements

Current software independent data exchange formats allow for the exchange of such manufacturing

information. Thus, the template is generally usable with any BIM software product (‘open BIM’).

4.2 *BIM2FEM Embedded Structural Analysis*

The technical background of Building Information Modelling (BIM) is a relational database where objects such as 3D-parts, semantic data, drawings and simulations are linked. BIM is a model-driven process, so that a master-model-concept is a common technique in CAD/CAM software applications [4, 5].

The geometry is stored and maintained in the master-part. Simulations, 2D-Derivatives (Drawings) and even the adjacent structure, the assembly of all bridge components, reference to the master-model. The decisive advantage: Any changes conducted in the master-part will update via the references.

Based on the master-model-concept, the first and most important engineering task in the proposed method is to enrich the geometry of a structural component by well-chosen geometrical and statical constraints for the subsequent Finite-Element-Analysis (FEA), see Figure 8.

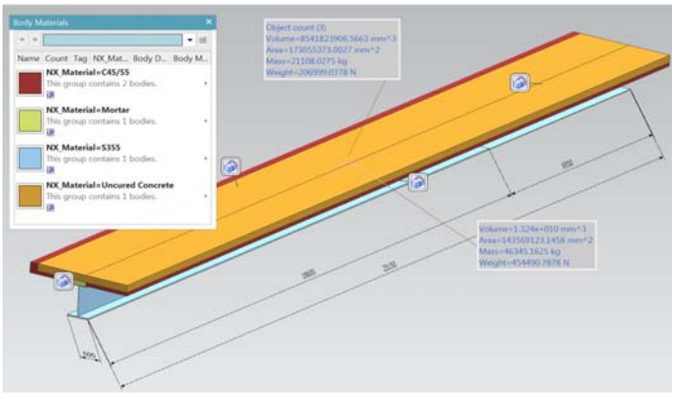


Figure 8. 3D-CAD Model enriched with geometric and static boundary conditions and Attributes for the subsequent simulation

Apart from the automatic generation of the finite element mesh, the calculation of the necessary cambering of the steel girder was integrated into the model as well. The resulting deflection graph as seen in Figure 1 is loaded back into the main model to create the optimal precamber for the steel girder. As the rest of the model, the calculation automatically adapts to changes of the parameter. It can also be considered to add the pre-dimensioning to the process using iteration steps. This can reduce the time effort since the geometry of the elements do not require modifications later. It also improves the sustainability, since a geometry optimization is often not done to the full extend.

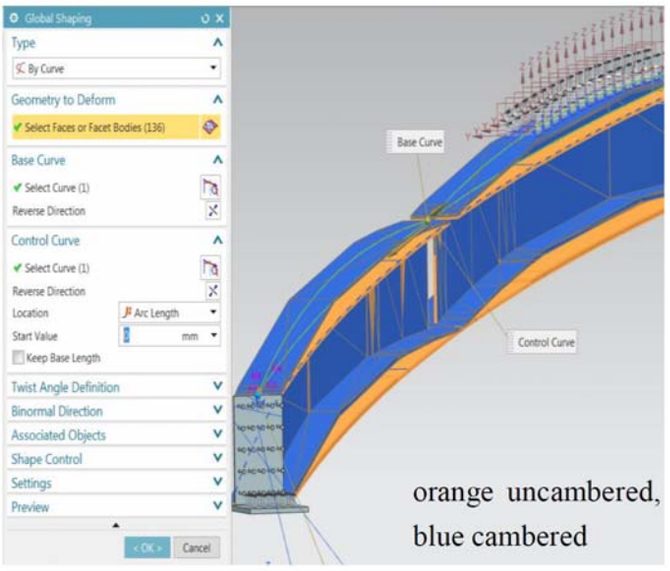


Figure 9. Cambering calculated in CAE updated in 3D-CAD-Geometry for the further production process

The system was meshed using a tetrahedral mesh, since it is the most versatile mesh and more importantly the only one not necessarily requiring mesh dependent boundary conditions. This comes as great advantage, since boundary conditions bear the risk of getting lost upon geometry changes. The forces for the dead loads were included by measuring them in the master model and afterwards linking them as parameter into the calculation. All forces and boundary conditions were applied to the geometry itself instead of the mesh to keep the adaptivity.

4.3 *Sustainability*

The Building Information Model can be used to rapidly evaluate different concepts. With the linked sustainability and estimation results there is an instant feedback. For this study, the sustainability of two different girder types (bridge type 3 (BT3): open, welded profile vs. bridge type (4) open, rolled profile) were compared.

It can be pointed out, that the different girder shapes had little impact on the environmental impact, even though the steel beams make up for ~10% of the carbon dioxide emissions of the super structure. The welded steel beam performed slightly better due to its optimized shape.
For the evaluation of the bridges sustainability reference bridges were used. The evaluation was done in consideration of the span width. The bridge was compared to other composite bridges, since they generally have an inferior environmental impact compared to concrete bridges. The environmental impact of the materials was determined using aggregated cause-effect data from ‘eco balance of bridges’

[3]. Overall the bridge had slightly lower CO_2 emissions than the average reference bridges.

Table 1. Sustainability life-cycle inventory

SP*	GE	EC	RMC	W	SW
Unit/m² bridge surface	tCO_2	GJ	t	t	t
BT 3 52m	391	3.500	1.385	250.2	3.1
BT 4 52m	391	3.505	1.387	250.5	3.1
Literature [3]	422	3.9	1.2	279.7	1.3

* GE Greenhouse Effect
EC Energy Consumption
RMC Raw Material consumption
W Waste
SW Special Waste
BT Bridge Type No. Length
SP Sustainability Parameter

5 CONCLUSION

It can be assumed that it will become increasingly important in the future to create automated building information models of standardized structures. Such models can be used repeatedly and optimized along the way. The planning method minimizes errors and maximizes the speed in which a construction is planned. It allows to compensate the disadvantages typical for the early planning stages of BIM models. It must be emphasized that the major requirements for a successful application of 3D-CAD in road-bridge design are

- Template concept according to BIM-Use-Cases
- An implicit (procedural) CAD-tool based on Constructive Solid Geometry
- Top-Down modeling and control part files
- Timeline history for parameters and features
- Well sorted Associations and part-structures
- Template for Human-Machine-Interaction

The presented study already shows the great potential of having a parametric, adaptive bridge model template. Whereas this model only includes elements for the draft design it can be expected that more and more planning elements such as drawings, manufacturing data, structural simulations or reporting files such as the bill of material and sustainability records may be included into the template, dependent on how often the bridge design is used. Currently implicit modeling structures are not completely supported by Open BIM concepts, this might change in the future, making it possible to automate the entire life-cycle process.

The report shows only the beginning of an adaptive, parametric model. More and more planning elements can be added to the model. Including not only the execution planning, but also product lifecycle management, information on the required maintenance. The post construction 3D-model can be marked with 3D- annotations, giving information on the condition of each element. By using hyperlinks, various kinds of information (photos, protocols, processes) can be included to the model as well, it thereby becomes easier to find the problematic areas on subsequent inspections. Damages can be directly evaluated with regards to construction information included in the model and even the demolition planning can be simplified.

6 REFERENCES

[1] Nöldgen, M.: *BIM im Brücken- und Ingenieurbau*, Springer Vieweg Verlag, 2016

[2] BIM Forum: *Level of Development Specification Version 20125* published by BIM Forum URL: www.bimforum.org/lod

[3] Lünser, H.: *Ökobilanz im Brückenbau,* Springer Birkhäuser, 1998

[4] Unigraphics: *3D CAD/CAM and PDM sof tware*, Aircraft Engineering and Aerospace Technology, 72(4), 2000

[5] Kolonay, R. M.: *Physics-based distributed collaborative design for aerospace vehicle development and technical assessment*, 20th ISPE Conference, 2013

[6] Nöldgen, M.; Harder, J.: *BIM: Design Embedded Simulation of Road Bri dges*, IABSE Symposium 2016, 21.-23.09.2016, Conference Proceedings, Stockholm, Sweden

[7] Nöldgen, M.; Bach, A.: *BIM in Bridge Design – 3D-Modeling, Design Embedded FE-Simulation and Drawings, A large scale project in a Port Area* , 4th 5D-Conference 25th-26th October 2016, Conference Proceedings, Konstanz, Germany

[8] Nöldgen, M.; Bach, A.: *BIM-gerechter Entwurf von Brücken – Grundlagen, Methodik und technische Anforderungen*, Hauptaufsatz, Bauingenieur 2017, S. 407-415, Band 92, 2017

Maintenance, Safety, Risk, Management and Life-Cycle Performance of Bridges – Powers, Frangopol, Al-Mahaidi & Caprani (Eds)
© 2018 Taylor & Francis Group, London, ISBN 978-1-138-73045-8

TRUSS-ITN methods for detecting bridge damage from response to traffic

A. González, D. Martínez, E.J. O'Brien & M. Casero
University College Dublin, Dublin, Ireland

J.J. Moughty & J.R. Casas
Universitat Politécnica Catalunya, Barcelona, Spain

M. Vagnoli, R. Remenyte-Prescott & J. Andrews
University of Nottingham, Nottingham, UK

F. Huseynov & J. Brownjohn
Full Scale Dynamics Ltd., Exeter, UK

ABSTRACT: The performance of four methods in establishing whether a bridge has experienced damage or not from the response to the crossing of a vehicle, is assessed within the Marie Skłodowska-Curie Innovative Training Network titled TRUSS (Training in Reducing Uncertainty of Structural Safety, http://trussitn.eu, 2015-2019). The first and second methods extract vibration based damage sensitive features and apply a Bayesian Belief network respectively from/to bridge accelerations to determine the occurrence of damage. A third method based on bridge rotations applies bridge weigh-in-motion concepts to detect damage from estimated vehicle's weights. Finally, a fourth method derives bridge curvature and damage from the vehicle response. A blind test based on the responses of a complex vehicle-bridge interaction theoretical model is carried out to assess performance. The estimations of damage by each method are collected independently and compared to the exact solution.

1 INTRODUCTION

1.1 *TRUSS innovative training network*

TRUSS (Training in Reducing Uncertainty in Structural Safety) is a Marie Skłodowska-Curie Innovative Training Network (ITN) funded by the European Union under the Horizon 2020 Programme aiming to address some of the needs by operators managing infrastructure. The overall approach of TRUSS ITN is to integrate 14 Individual Research Projects (IRPs) into the overall network collaboration, which is encompassed by two thematic research clusters: (i) buildings, energy and marine infrastructure and (ii) rail and road infrastructure. At the most basic level, there is a number of bilateral collaborations, centred around each IRP. An Early Stage Researcher (ESR) is recruited for each IRP and assigned a doctoral studies panel composed by experts from at least two European countries, including both academic and industrial participation. Structural safety and Structural Health Monitoring (SHM) is a broad area of investigation and while training within TRUSS provide ESRs with an overall understanding and advanced skills, IRPs respond to specific needs for a particular infrastructure type. Detailed info about TRUSS can be found in González (2017).

1.2 *Damage detection for bridges*

Within the rail and road infrastructure cluster, there are four IRPs focused on the development of methods for detecting damage in a bridge from the response to traffic. The inputs for three of these methods are the response of sensors directly attached to the bridge when crossed by a vehicle: bridge accelerations for both an approach based on vibration parameters (VIB) and a Bayesian Belief Network (BBN), and bridge rotations for a Bridge Weigh-In-Motion (B-WIM) – based approach. The input for the fourth method is the response of displacement sensors mounted on the vehicle (i.e., drive-by) traversing the bridge. Therefore, blind test comparisons based on a vehicle-bridge interaction (VBI) theoretical model are carried out to assess performance. Section 2 defines the simulation model employed to gather input responses as required by each method. Section 3 describes the background of each damage detection method. Each method is tested at a different research institution. Damage is identified, located and quantified for scenarios that are unknown a priori. The solutions to these scenarios, distinguished by location and severity of damage, road roughness, and vehicle weight and speed, are discussed in Section 4. Finally, Section 5 provides conclusions.

2 VEHICLE-BRIDGE INTERACTION MODEL

2.1 *Bridge model*

The bridge is modelled as a beam-and-slab with 0.9 m deep precast concrete beams and a 0.16 m thick continuous structural slab on top of them. The struc-

ture is 20 m long and 10 m wide (Figure 1), allowing to accommodate two traffic lanes. There are a total of 10 longitudinal beams spaced by 1 meter and placed symmetrically with respect to the bridge centerline. The slab is discretized into 1 m x 1 m plate Finite Elements (FEs), with the exception of the rows of plate elements closest to the edge that have a size of 1 m (long.) x 0.5 m (trans.). Each of the 10 longitudinal beams is discretized into 1 m long 20 elementary beams. I.e., the bridge model has a total of 220 plate elements and 200 beam elements. The bridge is simply supported in all beams at both ends.

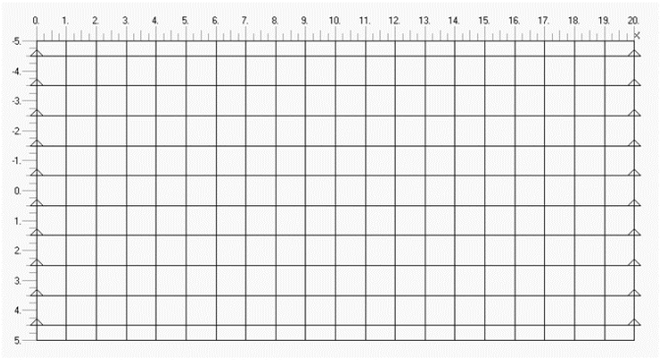


Figure 1. Plan view of bridge model.

The section of the longitudinal beams has a second moment of area of 0.108 m^4 for those beam elements closest to the supports (i.e., longitudinal coordinate x between 0 m and 1 m, and between 19 m and 20 m), and of 0.0685 m^4 for the rest of beam elements (i.e., x between 1 m and 19 m). All bridge material has been assumed to have a density of 2500 kg/m^3 and Poisson's ratio of 0.15. The slab has longitudinal and shear moduli of $31x10^9$ and $13.48x10^9$ N/m^2 respectively. The beams have a modulus of elasticity of $34x10^9$ N/m^2 and shear modulus of $14.78x10^9$ N/m^2. Regarding global dynamic properties, a 3% modal damping is adopted and the first natural frequencies of the bridge model are 6.13 (longitudinal), 7.14 (torsional), 9.27 (torsional) and 12.34 (torsional) Hz.

2.2 *Vehicle model, road profile and interaction*

The configuration of the vehicle is a typical European 5-axle articulated truck with rear tridem. The overall length of the truck, including front and rear frame overhangs, is 14.9 m. The distances between the 1st axle and the remaining four axles are 3.6 m, 9.93 m, 11.24 m, and 12.55 m, i.e., spacings between consecutive axles of 3.6, 6.33, 1.31 and 1.31 m. The transverse distance between two wheels of an axle is 2 m. In all scenarios, the vehicle travels from left to right, with inner and outer wheels located along the path at 0.5 m and 2.5 m respectively from bridge centerline in Figure 1.

The truck is modelled using vertical elements that consist of stiffness springs and damping elements whereas horizontal elements are made of bars and/or rigid elements. Mass elements are used to model the body masses of the tractor and the trailer which are rigidly connected to the frame. More details on the truck model can be found in González et al (2015). Table 1 provides dynamic properties for stiffness and damping of the tire and suspension corresponding to each individual wheel of an axle. A single tire is assumed for the 1st axle while two tires are considered for other axles. Two different Gross Vehicle Weights (GVWs) are tested. For the first truck model, namely vehicle A (fully-loaded), GVW adds up to 40 tons while for the second truck model B (half-loaded), the GVW is 25 tons. The distribution of GVW to individual wheel weights can be found in Table 1. Body frequencies of the truck oscillate between 1.4 and 4.1 Hz and axle roll and hop frequencies between 10.5 and 15.6 Hz.

Table 1. Wheel properties

Wheel	Static		Dynamic			
	A	B	Tire		Suspension	
	kN	kN	kN/m	kNs/m	kN/m	kNs/m
1st axle	31.87	28.83	1000	3	1800	5
2nd axle	53.94	35.10	2000	3	500*	0*
3rd axle	36.77	19.55	2000	3	1800	5
4th axle	36.77	19.55	2000	3	1800	5
5th axle	36.77	19.55	2000	3	1800	5

* Air suspension in 2nd axle. All other axles have steel susp.

The interaction between vehicle and bridge is implemented using a Lagrange multiplier technique (González 2010). A 'very good' road profile according to ISO standards is added to the bridge surface and to a 50 m approach length. The profile consists of 101 spatial waves between 0.01 cycles/m and 4 cycles/m with a geometric spatial mean of $0.5x10^{-6}$ m^3/cycle and phases randomly generated for each wave. The road profile remains the same in all runs, except for three test scenarios.

2.3 *Calibration data*

The response of the bridge to 4 simulated runs is provided for calibrating each damage detection algorithm. The same vehicle is driven at 20 and 30 m/s with two different gross vehicle weights (25 and 40 tons) as a result of altering the body mass of the trailer (Table 1). Algorithms 1 (VIB) and 2 (BBN) are provided with accelerations at nine bridge locations with coordinates (5,-2.5), (10,-2.5), (15,-2.5), (5,-0.5), (10,-0.5), (15,-0.5), (5,2.5), (10,2.5) and (15,2.5) related to Figure 1, where the first coordinate refers to the longitudinal direction (i.e., three simulated sensor locations in longitudinal sections at ¼, ½ and ¾ of the bridge span). Algorithm 3 (B-WIM) is provided with rotations at six bridge locations with coordinates (0,-2.5), (20,-2.5), (0,-0.5), (20,-0.5), (0,2.5) and (20,2.5) (i.e., three simulated sensor locations at both support ends). Finally, algorithm 4 (drive-by) is provided with displacements of the vehicle for the contact wheel point and immedi-

ately above the wheel for each of the 10 wheels. The difference between these two points aims to simulate the profile measurements by a Traffic Speed Deflectometer (TSD) (Rasmussen et al 2002). For the calibration runs, the bridge is assumed to be healthy, i.e., all elements maintain the properties given in Section 2.1.

2.4 *Test data*

A total of 16 different simulations are conducted in order to test the ability of the algorithms to detect, locate and quantify damage (Table 2). Damage is modelled as % stiffness loss at selected beam elements. The location given in the table corresponds to the central part of the damage in the affected beams (in m from the first support), which extends 1.5 m at both sides. All damages have a total width as specified in Table 2 and a total length of 3 m with the maximum % stiffness loss taking place along the meter in the middle of the affected length and then, decreasing gradually until becoming zero. The percental values in Table 2 are calculated with respect to the stiffness (modulus of elasticity multiplied by second moment of area) of the entire cross-section.

Table 2. Test data

Test	Vehicle		road	Damage scenario (L = 20 m)			
No.	Speed m/s	truck type		location m	width m	stiffness-loss percentage	lane*
1	20	A	2	3L/4	5	8.0%	2
2	30	B	3	Healthy			
3	30	A**	1	L/4	5	6.0%	2
4	20	B **	2	Healthy			
5	20	A	1	5L/8	5	8.0%	1
6	30	B	1	L/8	5	12.1%	1
7	30	A	1	L/2	5	10.0%	2
8	20	B	1	L/2	5	6.0%	2
9	20	A	1	3L/8	5	12.1%	1
10	30	B	1	2L/3	10	16%	1-2
11	22.5	A	1	L/3	10	20.1%	1-2
12	27.5	B	1	L/3	5	10.0%	1
13	30	A	1	5L/8	5	8.0%	2
14	20	B	1	5L/8	10	16.0%	1-2
15	20	A	1	L/3,3L/4	10,5	11.9%,12.1%	1-2,1
16	30	B	1	3L/8,2L/3	10,5	24.2%,8%	1-2,2

* While lane 1 corresponds to the half of the bridge where the vehicle is travelling, lane 2 corresponds to the opposite half. Lane 1-2 corresponds to the full width of the bridge.
** Twice the value of suspension stiffness given in Table 1.

It is important to keep in mind that variations in the test data with respect to calibration data can be attributed not only to damage but also to one or a combination of the following sources: (i) location and severity of damage, (ii) change in road roughness, (iii) change in vehicle dynamic properties, (iv) change in vehicle gross mass, and (v) change in vehicle speed. Other than these causes of change, parameters of the VBI model remain the same as in calibration runs. All road profiles have a 'very good' road class, but those labelled with different numbers correspond to different amplitude and distribution of the road irregularities. Calibration data has been obtained with the road labelled '1' in Table 2. Road labels '2' and '3' correspond to geometric spatial means of $2\text{x}10^{-6}$ and $8\text{x}10^{-6}$ m^3/cycle respectively. The parameters in Table 2 remain hidden to the contributors, except for those algorithms requiring speed and GVW to operate. The latter could be obtained on site, i.e., via a Pavement-based WIM (P-WIM) system or nothing-on-the-road B-WIM system.

3 DESCRIPTION OF ALGORITHMS

3.1 *Using vibration parameters*

The damage identification method proposed in this section is based on the logical utilization of vibration data to obtain parameters that can discern structural changes without prior knowledge of structural properties. The use of vibration parameters as damage sensitive features provides an alternative to standard modal-based damage sensitive features which can suffer under changing environmental and operational conditions and are generally further limited in accuracy when applied to short non-stationary signals, such as those assessed herein, as their methodology assumes linear structural behaviour and signal stationarity (Moughty & Casas, 2017a). A number of vibration parameters have been shown to demonstrate damage sensitivity when assessed under ambient conditions (Mougty & Casas, 2017b), such as Cumulative Absolute Velocity, i.e., the summed integral of all absolute acceleration values of the response history, generally used to determine site specific earthquake energy.

$$CAV = \int_0^t |\ddot{x}(t)|dt \tag{1}$$

Destructive Potential Factor is another earthquake energy based feature that also accounts for frequency characteristics by including the variable ν_0 - number of zero crossings per unit of time.

$$P_D = \frac{\frac{\pi}{2g}.\int_0^\infty \ddot{x}(t)^2\ dt}{{\nu_0}^2} \tag{2}$$

Vibration Intensity is also a vibration energy based feature, but utilizes a Fourier based frequency.

$$I = \frac{\int_0^t |\ddot{x}(t)|dt}{f} \tag{3}$$

All of the above vibration parameters utilize energy, while two also incorporated a frequency denominator, the premise of which is that given constant conditions and loading, a structure will exhibit an increase in vibration energy when damaged and a reduction in vibration frequency, resulting in a synergistic damage detection relationship. The application of the aforementioned vibration parameters to the current case study first requires some regression procedures to establish the various ancillary varia-

bles in the 16 test runs such as vehicle velocity, weight and road profile. Beginning with *vehicle velocity*, one can take advantage of the three sensors located along the vehicle path to obtain the times of impact of the front wheel through the use of a high pass filter that is sufficiently designed to suppress all structural and vehicle dynamic behavioral frequency signatures (> 200 Hz), leaving only high frequency noise and impacts at sensor locations, as Figure 2 demonstrates for a 20 m/s case, with first wheel impact times labeled.

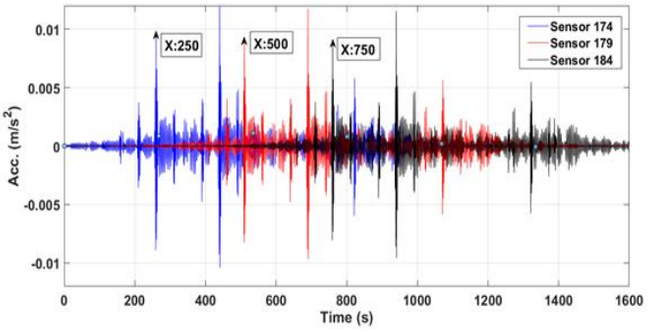


Figure 2. First wheel impact times for sensors along vehicle path (20 m/s case).

Vehicle weight is assumed to be either 25 tonnes or 40 tonnes and classification is conducted using Peak Ground Displacement Values. Road profile condition is determined by isolating the frequency content associated with the vehicle/road profile interaction in the three sensors along the vehicle path by obtaining their Cross Spectral Density (CSD) and comparing it to the CSD for the three sensors on the opposite side of the bridge where the vehicle/road profile interaction is less evident. Figure 3 presents the CSD comparison for a 20 m/s vehicle velocity case, where it can be seen that a distinct deviation in frequency content exists above 40 Hz, indicating that the vehicle/road profile induced vibration for the 20 m/s cases is predominantly associated with, but not limited to, frequencies > 40 Hz. The same can be said of frequencies > 60 Hz for vehicle velocity of 30 m/s. A change in road profile can be assessed by comparing the CAV of the filtered data of the calibration case and test case.

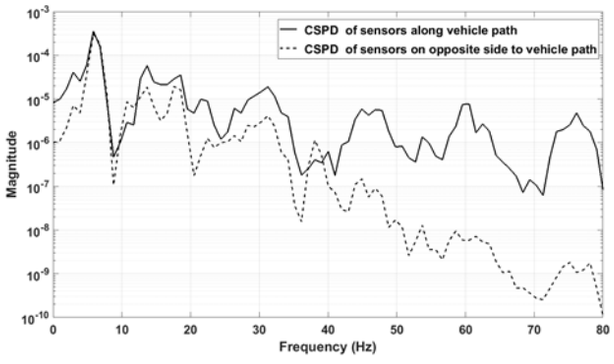


Figure 3. CSD of sensors along vehicle path and opposite side of bridge (20 m/s case).

Once all ancillary variables have been established in all test cases, the presence of damage can be assessed by first normalizing the calibration vibration parameters before obtaining the percentage difference at each sensor location for each test case. This will provide an estimate of both damage presence and location. The determination of stiffness loss is not feasible through energy based parameters, however the degree of damage severity can be determined in a relative sense, i.e. from no damage to greatest damage.

3.2 *Using a Bayesian belief network*

A BBN approach is proposed for condition monitoring and fault detection of bridges. In fact, the adoption of BBN for SHM purpose is limited. However, a BBN-based approach can provide an assessment of the bridge health state every time when new evidence of the bridge behavior becomes available, and consequently the health state of the bridge can be monitored continuously by taking account of all kind of uncertainties, which are not accounted for by FE model updating and machine learning methods. Conversely, BBN are able to manage different sources of uncertainties, such as incomplete knowledge of the actual health state of the bridge (i.e. epistemic uncertainties) and such as the degradation mechanism of the bridge, which is initiated at unknown time (i.e. aleatory uncertainties). At the same time, interdependencies between different bridge elements can be evaluated by a BBN approach (Franchin et al. 2016, Vagnoli et al. 2017).

A BBN method is developed by defining two parts: i) a graphical visualization part, which is composed of nodes and arcs; ii) a quantitative part, which is composed of Conditional Probabilities Tables (CPT). The nodes represent the elements of the bridge of which the bridge manager would like to monitor the health state, whereas the arcs are directed links between different nodes and they represent the influence of the parent node (i.e. the node from which the arc departs) on the health state of its child (the node to which the arc is directed) (Vileiniskis et al. 2016). It is worth noting that the accuracy of a BBN approach strongly depends on the definition of the CPTs, which quantify the conditional probabilistic relationship between connected nodes, i.e., the influences between different elements of the bridge.

A reliable BBN is developed by performing a detailed analysis of the bridge structure, in order to describe the bridge elements of interest, the measurement system on the bridge, and the possible influences between different bridge elements. Therefore, the BBN approach aims to monitor continuously the health state of the bridge during a long period of time, rather than in a short period. Indeed, the CPTs, which can be defined initially by using historical datasets, visual inspection reports, simulation of

an FE model of the bridge under study or relying on expert judgement, can be updated every time when new evidence of the bridge behaviour is available. Finally, it should be noted that the BBN can assess the health state of the whole bridge, by monitoring the health state of its elements, and, at the same time, assess the health state of each bridge element by monitoring the health state of the whole bridge (Siraj et al. 2015).

The BBN of the beam-and-slab bridge is developed by assuming that each beam of the bridge can be divided into five smaller elements of 4 m length. For example, Figure 4 shows only the BBN part for the beams of the bridge at 4.5 m and 3.5 m for clarity. The five parent nodes (B_*i*_E_*j*, where *I* =1, 2, …, 10, and *j* = 1, 2, …, 5), which are shown within the dashed box, represent the five elements of each beam. The health state of each beam element is influenced by the condition of its neighbour elements, as shown by the B_*i*_E_*j*_1 nodes within the dotted box in Figure 4. In a similar way, the health state of a beam is influenced by the health state of its 5 smaller elements (Beam_*i* nodes), and the health state of the neighbour beams, as shown by the beam_*i*_1 nodes in Figure 4. Finally the health state of the whole bridge is assessed by considering the health state of each beam and their smaller elements.

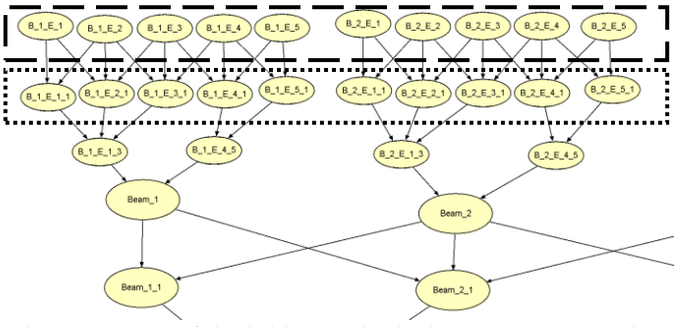


Figure 4. BBN of the bridge. Only the beams at 4.5 m and 3.5 m of the bridge are shown for clarity.

The CPTs of the BBN are evaluated by defining three possible health states for each node, and developing an expert elicitation process, due to the fact that datasets and information about the bridge behaviour are not available. If measurements of the bridge behaviour, historical datasets and visual inspection reports were available, the CPTs would have been defined by merging these different sources of information, and a more reliable BBN would be developed. The BBN monitors the health state of the bridge by providing a probability for each health state of each bridge element, and thus of the whole bridge. Indeed, when new evidence of the bridge behaviour is provided by the measurement system, it is compared with the reference behaviour of the bridge, i.e. the behaviour of the healthy bridge, and then the health state of the parent nodes is updated accordingly. Simultaneously, the updated state of the root parent nodes is propagated through the BBN, and the health state of each longitudinal beam, and of the whole bridge, is updated. In this way, the health state of the bridge is monitored by observing the evolution of the probabilities of the bridge health state over time, and the causes of the changes of the bridge health state are identified.

3.3 *Using Rotations for Bridge Weigh-in-Motion*

It is well known that the change in rotation between two points along the length of a bridge structure is equal to the area under that part of the curvature diagram, i.e., the area under the *M/EI* diagram where *M* is moment and *EI* is flexural stiffness. Hence any reduction in flexural stiffness due to damage should result in an increase in the area under the curvature diagram. This area can be measured using inclinometers installed on the bridge.

Broadly speaking, damage can be identified by an increase in rotation. However, rather than looking directly at rotation values, which are influenced by the applied load or moment, the method proposes to process those rotation values with a B-WIM algorithm to estimate the weight of each passing vehicle. B-WIM is a system that uses the response of a structure under a traversing vehicle to back-calculate its axle weights. The algorithm is based on the bridge's influence line. During installation, the influence line of the structure is obtained by back-calculating the influence ordinates from the response to a vehicle of known weights and axle configuration using a process described by OBrien et al (2006). If damage had occurred, it is expected that the B-WIM algorithm will suggest an increase in the predicted weights.

A P-WIM system can be installed at the bridge site to determine the actual weights of vehicles crossing the bridge. Then the ratio of GVW predicted by P-WIM and B-WIM systems will be used as damage indicator. This approach is similar to that proposed by Cantero & González (2014), except that the B-WIM system used in their study is based on strain measurements, which is sensitive only to damage near the vicinity of the sensors, and as result, it is only applicable to structurally indeterminate bridges (i.e., integral bridges). As rotations are affected by stiffness at points remote from the sensors, the concept proposed here is also applicable to determinate bridges.

The influence lines of rotation are calculated at each sensor location using responses due to a 5-axle calibration truck (Section 2.2). Figure 5 shows a typical rotation time history. The response of the bridge consists of dynamic and static components. Moving average filtering is applied on the raw data to smooth out the dynamic response. Figure 5 shows the raw data (in solid blue line) for a sensor placed at the left-hand support, on the south side of the bridge, 2.5 m away from the bridge centerline in the transverse direction (sensor coordinates: (0,2.5)). The filtered rotation data is shown in red. The dashed black

curve represents the predicted static response of the bridge, obtained as a linear combination of the influence line and the axle weights. It can be seen that the static response due to the estimated weights fit the 'measurements' with a high degree of accuracy. The contributions of the individual axles are shown in dashed pink lines.

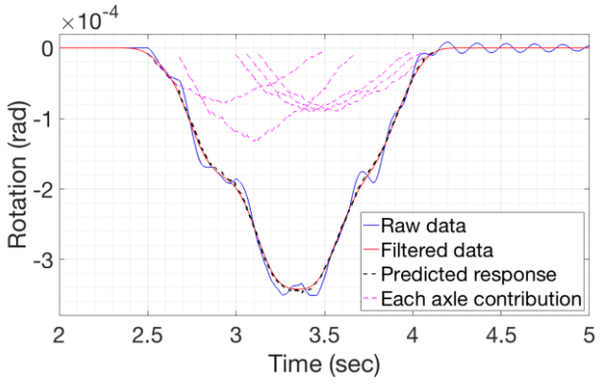


Figure 5. Recorded and predicted rotation time histories for calibration run with truck A travelling at 20 m/s.

Table 3 gives the calculated changes in GVW found using the rotation data recorded at each sensor location for four calibration runs. It can be seen that the proposed method accurately calculates the GVW with no more than 0.7% variation.

Table 3. % change in predicted GVW for the calibration runs.

Run No	(Actual – Predicted)/Actual GVW (%)					
	Sensor coordinates: x(m),y(m)					
	0,-2.5	20,-2.5	0,-0.5	20,-0.5	0,2.5	20,2.5
1	0.3	0.2	0.3	0.2	0.3	0.2
2	0.2	0.2	0.2	0.2	0.3	0.2
3	0.0	0.0	0.0	0.3	0.2	0.5
4	0.6	0.6	0.6	0.7	0.6	0.7

Table 4 gives the changes in inferred GVW for the 16 blind test response histories. Test nos. 5-10 and 13-16, indicated in bold text in Table 4, are damaged test scenarios according to the algorithm. The damaged location is identified by analyzing the magnitude of change in GVW obtained from each sensor. It was found out that sensors placed closer to a damage location are more sensitive to detect damage than the sensors placed further away. Further analyses were carried out where it was concluded that variations in GVW for test nos. 1-4 and 11-12 are either due to the change in road profile or vehicle dynamic properties.

3.4 *Using curvatures from vehicle deflections*

Flexural stiffness or curvature (2nd derivative of deflection) is increasing in popularity for damage detection and location purposes (Catbas et al. 2008). Curvature can be calculated by the ratio of bending moment to stiffness or by the second derivative of deflection measurements.

Table 4. % change in predicted GVW for the blind test runs.

Test No	(Actual – Predicted)/Actual GVW (%)					
	Sensor coordinates: x(m),y(m)					
	0,-2.5	20,-2.5	0,-0.5	20,-0.5	0,2.5	20,2.5
1	0.6	2.3	0.5	1.3	0.4	0.5
2	0.3	0.4	0.2	0.6	0.2	0.5
3	1.8	0.7	1.3	0.7	0.7	0.5
4	-0.2	-0.1	-0.2	0.0	-0.1	0.0
5	**1.2**	**1.3**	**1.4**	**2.0**	**1.7**	**2.7**
6	**0.9**	**0.8**	**1.6**	**0.9**	**3.6**	**0.8**
7	**2.5**	**3.3**	**1.4**	**1.8**	**0.7**	**1.1**
8	**1.6**	**2.0**	**1.0**	**0.9**	**0.6**	**0.4**
9	**2.1**	**2.0**	**3.2**	**2.0**	**4.4**	**2.4**
10	**2.2**	**4.2**	**1.9**	**3.6**	**1.8**	**3.2**
11	4.4	2.6	4.0	1.9	3.8	1.7
12	2.2	2.0	3.2	2.2	4.3	2.4
13	**1.5**	**3.0**	**0.9**	**1.7**	**0.6**	**1.0**
14	**2.6**	**4.2**	**2.3**	**3.3**	**2.1**	**3.0**
15	**3.5**	**2.7**	**3.5**	**3.7**	**3.5**	**5.4**
16	**7.2**	**7.4**	**6.0**	**4.7**	**5.3**	**3.3**

OBrien et al (2017) use Instantaneous Curvature (*IC*) to locate damage in noisy conditions. In this paper, *IC* is calculated from the relative deflections obtained by subtracting the deflection under the tyre contact point and the displacement of the point of the wheel just above the tyre measured from a stiff bar representing an axle of the vehicle model defined in Section 2.2. Damage is estimated using both the healthy (i.e., calibration) and the potentially damaged (i.e., test) signal using curvatures. The inputs to the algorithm in this paper are vehicle displacements. In practise, a TSD is a vehicle that could be used to take vertical velocity readings on pavements that would facilitate to determine their deflection (Rasmussen et al. 2002). However, the application of TSD for damage detection on bridges is still at an early stage of development.

IC is based on deflection measured at three locations on the bridge at any given time. For the vehicle under investigation, data under each axle of the vehicle can have unequal distances between axles. The central difference method is used to estimate curvature (Singh & Bhadauria 2009). In ideal circumstances, *IC* is calculated using absolute deflections relative to a global reference. A more realistic alternative is to measure the relative deflections of the bridge relative to the vehicle. *IC* is dependent on the position *x* of the vehicle on the bridge and the time *t*. These parameters are related through the velocity of the vehicle. Traditional definition of curvature considers calculation at a time instant and *IC* was prepared according to this procedure. In order to locate damage in this test, the absolute value of the difference in *IC* between the healthy and the damaged cases denoted by *AD* is used:

$$AD = |IC_{Dam} - IC_{Hea}| \quad (4)$$

where IC_{Dam} = damaged instantaneous curvature; and IC_{Hea} = corresponding healthy curvature. A val-

ue of *AD* higher than $1x10^{-6}$ is a clear indicative of damage as shown by Figure 6.

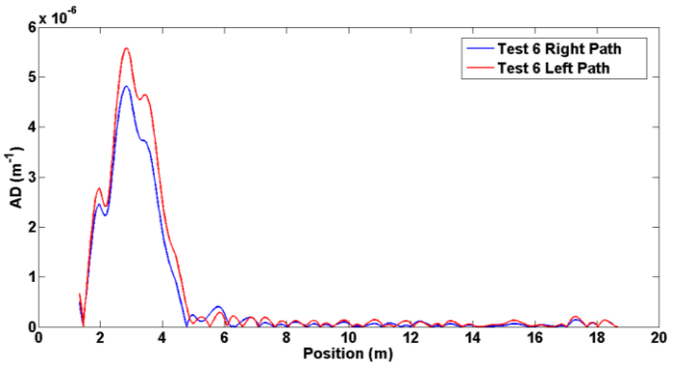


Figure 6. *AD* results for test no. 6 (Table 2).

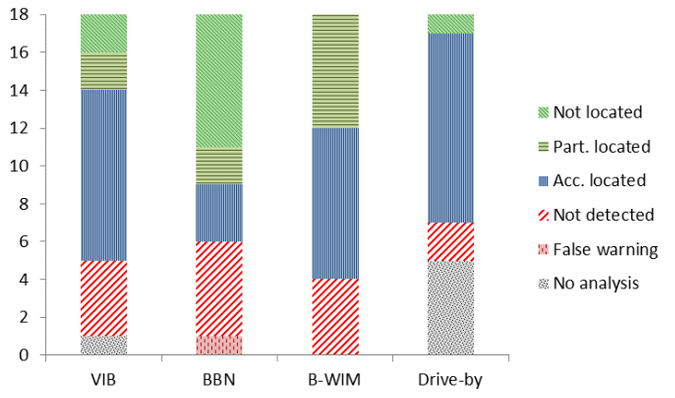


Figure 7. Comparison of performance by each algorithm.

Damage can easily be located around 3 m from the left support in this figure. The magnitude of *AD* provides information about how close is the damage to the wheel path and the intensity of the damage. *AD* can oscillate between 10^{-7} to 10^{-4}, but damage detection cannot be guaranteed if values are too low.

4 TESTING

Generally speaking, all algorithms achieve location of damage along the longitudinal direction *x*, while VIB, BBN and B-WIM -based methods try to locate damage transversally too. Therefore, they meet requirements for level II damage detection techniques that are able not only to stablish if damage has occurred, but to also simultaneously determine the location of damage. Figure 7 shows the outcomes of the algorithms classified into the following categories: damaged being 'not located', 'partially detected', 'accurately detected', 'not detected', 'false warning' (or misidentified), and 'no analysis'. The latter category addresses those instances in which an algorithm cannot evaluate the data due to changes in road roughness, vehicle properties or speed that do not match the conditions in the calibration run. 'False warning' refers to the case when the bridge is deemed to be damaged when, in reality, changes in the response are due to causes other than damage. 'Not detected' are situations when damage goes unnoticed to the algorithm. The first three categories in the legend of Figure 7 refer to tests in which it is successfully established that damage has occurred but: (i) the location of the identified damage differs completely from the actual location damage ('Not located'), (ii) the proposed range of damage intersects partially with the actual damage or it is significantly wider, thus including several non-damaged elements ('Part. located'), and (iii) damage is located within 1 m of its true position ('Acc. located'). In Figure 7, location refers always and exclusively to the longitudinal position of the damage along the bridge. It must be noted that a total of 18 instances are identified in the figure, since both test nos. 15 and 16 (Table 2) include two damage locations.

VIB locates damage both longitudinal and transversally with high rate of success. It can be seen from Figure 7 that damage is detected longitudinally in 13 of 18 cases (72%). Among those 13 cases, damage is partially or accurately located 85% of times. In contrast to other algorithms, identification of the half of the bridge affected by damage is always successful. On the downside, in the case of multiple damages, the algorithm is only able to detect one of them.

The BBN stablishes prior probabilities of damage using the four calibration runs and then, following an analysis of the variation of those probabilities, evaluates whether damage has occurred in the bridge or not. The BBN is able to analyze all the proposed tests (damage detected in 12 of 18 cases, i.e., 67% success); however, successful location of the damage is scarce. The algorithm tends to place the damage in the central elements of the bridge, which may indicate that, while it is capable of detecting damage, it has more difficulties on locating it. Nonetheless, one strength of this method is its probabilistic approach towards the solution, which could allow for further improvements if a larger calibration sample was available for defining CPTs.

The B-WIM algorithm is able to detect damage both transversally and longitudinally, although it sometimes identifies as damage a wider area than in reality. In addition, when damage affects all the width of the bridge, the method tends to concentrate the damage exclusively on the half of the bridge opposite to the vehicle path. Nonetheless, as shown in Figure 7, the algorithm shows a 78% rate of success, with 14 out of 18 cases where damage is accurately or partially located.

Drive-by detects damage in 11 cases (61%). This is somewhat expected as there are 5 test scenarios (nos. 1, 2, 4, 11 and 12) where the algorithm is unable to analyze and assess the data. However, damage is accurately predicted in 77% of those 11 cases where an analysis is feasible. It must be highlighted that when damage is located on the vehicle path, the algorithm is always able to accurately locate it. The cases where the algorithm is not able to detect damage correspond to the damage being located on the

other side of the bridge (i.e., test no. 8). However, if this damage was large enough (test no. 7), the method is still able to warn of the presence of the damage. Location of damage is however limited to its longitudinal position due to the conditions of the test. In this regard, it is necessary to note that the other three algorithms based on sensors placed on the bridge are provided with data concerning several transversal locations across the deck section, while the drive-by algorithm only uses data from the vehicle driving along a fixed path in one half of the bridge. If the vehicle was driven in the other half of the bridge, there could be potential for the drive-by system to also estimate the transverse location of damage.

5 CONCLUSIONS

This paper has presented four novel damage detection algorithms, developed within the Marie Skłodowska-Curie TRUSS ITN, which can be used either for SHM or routine bridge inspections. Given that accelerometers are relatively common, economical and easy to install, accelerations have been used as input to two algorithms. An alternative algorithm has used bridge rotations that can be obtained via inclinometers. Unlike strain sensors, which are mainly attached at bridge midspan, inclinometers can be installed on the soffit of the deck at abutment locations without bridge or lane closures. Ultimately, drive-by does not require placing any sensor in the bridge at all. However, a hi-tech instrumented vehicle must be used in order to obtain the curvature of the road surface through vertical velocity readings with sufficiently high resolution.

Overall, the B-WIM algorithm has appeared to be the most successful in establishing if damage has occurred (14 damages); followed by VIB (13), BBN (12) and drive-by (11). B-WIM has also been able to locate those identified 14 damages (i.e., adding predictions labelled partially and accurately), while VBI (11 located) and drive-by (10 located) show a slightly smaller rate of success. There have been aspects where B-WIM is outperformed by other algorithms, i.e., VIB has given the best performance in providing the transverse location of damage. In addition, the longitudinal range of damage predicted by B-WIM has often been on the safe side. Interestingly enough, drive-by has provided the best results in precisely locating the longitudinal position of damage, i.e., 10 times compared to 9 and 8 times using VIB and B-WIM respectively.

ACKNOWLEDGEMENTS

This project (http://trussitn.eu) has received funding from the EU's Horizon 2020 research and innovation programme under the Marie Skłodowska-Curie grant agreement No. 642453.

REFERENCES

Cantero, D. & González, A. 2014. Bridge damage detection using Weigh-in-Motion technology. *Journal of Bridge Engineering* 20(1): 1–10.

Catbas, F. N., Gul, M. & Burkett, J.L. 2008. Conceptual damage-sensitive features for structural health monitoring: laboratory and field demonstrations. *Mechanical Systems and Signal Processing* 22(7): 1650-1669.

Franchin, P., Lupoi, A., Noto, F. & Tesfamariam, S. 2016. Seismic fragility of reinforced concrete girder bridges using Bayesian belief network. *Earthquake Engineering and Structural Dynamics* 45(1): 29-44.

González, A. 2010. Chapter 26: Vehicle-bridge dynamic interaction using finite element modelling. In D. Moratal (eds), *Finite Element Analysis*: 637-662. Croatia: InTech.

González, A. 2017. Developments in damage assessment by Marie Skłodowska-Curie TRUSS ITN project. *Journal of Physics: Conference Series* 842(1): 012039.

González, A., Covián, E. & Casero, M. 2015. Impact of superimposed and truck live load on modal characteristics of short-span bridges. In M. López Aenlle et al (eds.), *Operational Modal Analysis Conference (IOMAC 2015); Proc. 6th intern. Confer., Gijon (Spain), 10-14 May 2015*.

Moughty, J.J. & Casas, J.R. 2017a. A state of the art review of modal-based damage detection in bridges: development, challenges, and solutions. *Applied Sciences* 7(5): 510

Moughty, J.J. & Casas, J.R. 2017b. Performance assessment of vibration parameters as damage indicators for bridge structures under ambient excitation. In *Proceedings of 10th International Conference on Structural Dynamics (EURODYN 2017), Rome, Italy, 10-13 September 2016.*

OBrien, E.J., Quilligan, M.J. & Karoumi, R. 2006. Calculating an influence line from direct measurements. *Proceedings of the Institution of Civil Engineers - Bridge Engineering* 159: 31–34.

OBrien, E.J., Martinez, D., Malekjafarian, A. & Sevillano, E. 2017. Damage detection using curvatures obtained from vehicle measurements. *Journal of Civil Structural Health Monitoring* 7(3): 333-341.

Rasmussen, S., Krarup, J.A. & Hildebrand, G. 2002. Non-contact deflection measurement at high speed. In *Bearing Capacity of Roads, Railways and Airfields; Proc. 6th intern. Confer., Lisbon, Portugal, 2002*.

Singh, A.K. & Bhadauria, B. 2009. Finite difference formulae for unequal sub-intervals using Lagrange's interpolation formula. *Int. Journal of Mathematical Analysis* 3(17) 815-827.

Siraj, T., Tesfamariam, S. & Dueñas-Osorio, L. 2015. Seismic risk assessment of high-voltage trans-formers using Bayesian belief networks. *Structure and Infrastructure Engineering* 11:929–943.

Vagnoli, M., Remenyte-Prescott, R. & Andrews, J. 2017. Railway bridge structural health monitoring and fault detection: State-of-the-art methods and future challenges. *Structural Health Monitoring* 1-37.

Vileiniskis, M., Remenyte-Prescott, R., Rama, D. & Andrews, J. 2016. Fault detection and diagnostics of a three-phase separator. *Journal of Loss Prevention in the Process Industries* 41: 215-230.

SS06: Advances in corrosion modelling of steel bridges

Organizer: M. Mahmoodian

Maintenance, Safety, Risk, Management and Life-Cycle Performance of Bridges – Powers, Frangopol, Al-Mahaidi & Caprani (Eds)
© 2018 Taylor & Francis Group, London, ISBN 978-1-138-73045-8

Structural Reliability Analysis of Corroding Steel Bridges Using Random-Field Representation

Vahid Aryai & Mojtaba Mahmoodian
Department of Civil Engineering, RMIT University, Melbourne, Australia

Nima Vahidi Ferdowsi & Farid Ariai
Department of Computer Engineering, Ferdowsi University of Mashhad, Mashhad, Iran

ABSTRACT: The functional safety of steel bridges is of great importance for governments and infrastructure managers. This functionality is, however, affected by natural aging and environmental threads such as corrosion. Corrosion can play major role in steel bridge failure; mainly by reducing the thickness of bridge girders or by forming pits on the steel surface which consequently affects the structural integrity of the bridge. In this study, an innovative technique for representation of corrosion has been used when applying a multi-failure reliability analysis method. To this aim, the distribution of corrosion pits is modelled by a 2D random field and then, the generated surface is incorporated with a Monte-Carlo reliability analysis method to predict the service life of in-service steel bridge girders.

Keywords: Steel bridge, random field, non-linear corrosion, serviceability prediction, Monte-Carlo simulation

1 INTRODUCTION

Bridges are among the most important transportation infrastructures which play an important role in transporting people and goods worldwide. Reliability of in-service bridges dropped over years, affected by external factors such as corrosion and loading. The combination of corrosion and loading can cause failure of bridges which costs millions of dollars for asset owners. According to a report by NACE [2], corrosion cost of highway bridges to US economy has been estimated at $8.3 billion, which forms 37% of overall corrosion costs to US infrastructures. These costs can be reduced by implementing a proper maintenance strategy that is based upon the results of an accurate reliability analysis.

Most of the determining factors in a reliability analysis, such as corrosion factors, load parameters, mechanical properties, etc., show high degrees of randomness which needs to be addressed in accordance. Such randomness limits applicability of deterministic methods for reliability assessment of structures. The issue indicates the necessity of applying the probabilistic methods when running a reliability analysis. Throughout the literature, service life prediction of corrosion affected steel bridges has been done by considering the impact of cross-section loss due to corrosion on overall operation of the bridge. Sharifi and Paik [3] studied the effect of corrosion on ultimate strength of steel girders. The corrosion loss was modelled using power-law formula and First Order Reliability Method (FORM) was employed to evaluate the reliability analysis of a steel-box girder over time. The study showed that, simultaneous impact of dead-load, live-load and corrosion cause a drastic reduction in safety and reliability of steel bridge girders. This approach, except for the reliability analysis method and also the selected limit-states, has been widely used by other researchers [4-6] for the structural assessment and service-life prediction of steel and reinforced concrete bridges and buried pipelines. The researches, however, fell short in accurate representation of the geometrical characteristics of corrosion, where the authors ignored the spatial variability of corrosion over the steel surface.

It has been proved that, considering the spatial variations of corrosion instead of its uniform representation can highly affect the result of a reliability analysis [7,8]. Random field theory, has been demonstrated to be able to model a corroded surface considering its correlation structure. This method has been successfully used for modelling spatial distribution of pits in reinforced concrete bridges [7], in cast-iron pipeline corrosion modelling [8] and also in naval engineering for modelling corrosion in ship's hull [9].

The first step in implementation of a reliability analysis is to select proper limit-states which represent the common failure modes in the studied infra-

structure. Several failure modes are suggested to be examined when studying reliability of steel bridge girders, among them the deflection, shear and flexural failure are of greater importance [1,5]. In regards with the reliability analysis methods, Since FORM and Second Order Reliability Method (SORM) methods require linearization of limit-state functions and also are unable to deal with lognormal random variables, Monte-Carlo simulation can be a good alternative. This method is, however, computationally demanding even for today's computers.

Once the reliability assessment technique has been determined, engineers are often encountered with the task of identifying the component that has the most effect on the system's overall performance. I shape steel girders of utmost importance when studying the reliability of steel bridges, since many catastrophic bridge failures were reported to be subjected to failure of these components [10,11]. In this research, corrosion depth on a steel bridge girder is modelled by 2D random field that is discretised based on Karhunen–Loève (K-L) series expansion. A Monte-Carlo simulation is then used for evaluation of three limit-states (flexural, shear and deflection) and also for generation of random fields and random variables. The final goal is to find the service life of an in-service corrosion affected girder as the critical component of the steel bridge. A parametric sensitivity analysis is also performed to compare the importance of involved parameters in service-life prediction of the steel girder.

2 PROBLEM FORMULATION

Corrosion of steel girders is a time-variant process. The power law formula (Equation (1)) can be used for measuring corrosion depth over time in which the constants 'a' and 'b' are obtained from regression analysis of inspection data. In this paper, corrosion factors (i.e., a and b in Equation (1)) are selected based on assumption.

$$\Delta = at^b \tag{1}$$

As discussed in the introduction section, deflection, shear and flexural are the critical failure modes Therefore, the limit-states for deflection, shear and flexure are selected to be evaluated in this study. A limit state is a condition of a structure beyond which the relevant design criteria is violated. The following equation shows the general form of the limit state for a structure subject to a time-variant deteriorating process such as corrosion:

$$G(R,S,t) = R(t) - S(t) \tag{2}$$

In equation 2, $G(R,S,t)$ is a limit state function, $S(t)$ is the stress affecting the limit state requirement at time t, and $R(t)$ is the resistance of the structure at time t. When the stress becomes greater than the resistance of the structure, the failure occurs. The failure criteria are selected so that; deflection failure occurs when the deflection at the middle of the span excesses the allowable deflection. Moreover, flexural failure occurs if the flexural moment becomes more than the flexural resistance. As for the shear failure, shear force excesses the shear resistance of the steel section. Formulations of the stresses and resistances can be found in Table 1.

Limit states	Stress	Resistance
Flexural	M_S	$M_\sigma = f_y Z_P$
Shear	τ_S	$\tau_R = 0.6 f_y A_P$
Deflection	$\Delta_S = \frac{P\left(l^3 + l/2 - 6.5\right) \times \left(3l^2 - l^2/4 - 42.25 + 6.5l\right)}{48EI}$	Δ_R

Table 1. Stress and resistance formulations for the three failure modes [1].

The combined effect of the aforementioned failure modes is also considered as a system failure, which is obtained by considering the failure modes as the serviceability failure modes and by applying the following formulation, in which P_{f1}, P_{f2} and P_{f3} are probabilities of deflection, flexural and shear failure respectively:

$$P_f(t) = 1 - \left[\left(1 - P_{f1}P_{f2}P_{f3}\right)\right] \tag{3}$$

To deal with uncertainty associated with the random parameters involved in this research, a Monte-Carlo Simulation is used. The Monte-Carlo method uses random sampling for simulating a large number of experiments. In this method value of each random variable (x) and also the generated random fields for each time step are selected and then the limit state function (G (x)) is evaluated. Failure is defined so that the limit state function is violated (i.e. for the negative values of G (x)). This process is repeated continuously; dividing the number of failures by the total number of iteration, *N*, obtains the estimated probability of failure:

$$P_f \sim \frac{1}{N}\sum_{j=1}^{N} I'\left(G(x_j) < 0\right) \tag{4}$$

In equation 4, *I'* is 1 if $G(x_j) < 0$ or is 0 if $G(x_j) \geq 0$ and $j = 1 \ldots, N$ is the indicator of samples. The generated sample size is a determining fac-

tor in the accuracy of the Monte Carlo Simulation. The smaller probability of failures requires larger sample size to obtain an accurate simulation result.

The geometry of a corroded surface can be modelled mathematically using random field theory. Based on K-L expansion method, a random field $X(x)$, can be represented with a sequence of uncorrelated random variables $\xi_i,\ i, r_o \in \mathbb{N}$ [12]

$$\hat{X}(x) = \mu(x) + \sum_{i=1}^{r} \sqrt{\lambda_i}\xi_i\phi_i(x). \quad (5)$$

Where $\mu(x)$ is mean function, r_0 is number of terms in the series with largest eigenvalues, ξ is a set of uncorrelated standard normal random variables and, λ and $\phi(x)$ are eigenvalues and eigenfunctions of covariance kernel. The correlation between random variables of the random field is captured using the autocorrelation function which is a function of the distance between points in the domain and the correlation length. In this research, a typical exponential squared autocorrelation function has been used.

3 WORKED EXAMPLE

In this paper, a 20m span of a typical railway steel bridge with concrete filled deck, has been selected as a worked example. Each span is consisted of five steel girders with yield strength of 250 MPA, and dimensions as described in Figure 1 and Table 2. It has been assumed that, the girder is under the effect of both dead load and live load. The load due to the weight of concrete deck, overhead structure and the weight of steel girder itself are considered as the dead loads. On the other hand, axle loads of trains crossing the bridge is treated as the random live load. To represent the most extreme scenario, two trains are considered to cross the bridge at the same time and the placement of axle forces on the studied girder is chosen so that to create the maximum bending M_S and maximum shear τ_S. The statistical characteristics of the dead and live loads have been listed in table 2.

In the current research, the distribution types of the involved random variables are selected based on assumptions, so that the parameters for which no information is available are considered as normal, and the parameters for which the negative values of mean and coefficient of variation are not physically admissible are chosen Lognormal. In addition, the corrosion depth is presented by random field. Table 2 represents the values of the involved parameters in the failure criteria.

Symbol	Definition	Value	Mean	COV (%)	Distribution
E	Modulus of elasticity of girder, kPa	---	213.74×10^6	1.0	Normal
a	Multiplying constant	---	0.4	0.25	Normal
b	Exponential constant	---	0.5	0.30	Normal
l	Length of span, m	---	20	0.1	Normal
Δ_R	Allowable deflection, m	---	0.031	0.1	Normal
L	Live load, kN	---	120	30	Normal
T_1	Girder dimensions, cm	---	28	0.1	Normal
T_2	Girder dimensions, cm	---	18	0.1	Normal
T_3	Girder dimensions, cm	---	28	0.1	Normal
H	Girder dimensions, cm	---	250	0.1	Normal
P	Axle load to the girder, kN	140	---	---	---
D	Dead load, kN/m^2	20	---	---	---
r_o	Number of truncated terms in the K-L	50	---	---	---
Z_P	Effective section modulus, m^3	0.078	---	---	---
A_P	Web area, m^2	0.015	---	---	---
F_y	Yield stress, MPa	250	---	---	---

Table 2. Definition, values and type of variables involved in the research

The probability of failure is calculated for each nodes of the discretised random field and the failure is counted as soon as the failure occurs in the first node of the field. The following section provides the results of the analysis.

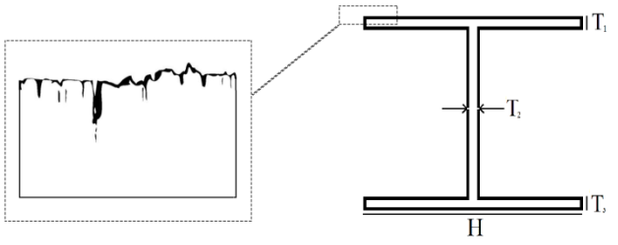


Figure 1. Dimensions of the steel grid; the values of T_1 to T_3 are reduced by equation 1 over time.

RESULTS AND DISCUSSION

Figures 2 to 5 present the results of the proposed methodology with an algorithm developed in MATLAB® R2017a environment. Considering the failure threshold to be 0.002, it can be seen from figure 2 that, the system failure is likely to occur after 90 years, while shear failure, the first failure mode that reaches the threshold, is occurred 10 years later. Flexural and shear failure contribute more to the failure of the girder as a whole. Moreover, the deflection failure is unlikely to occur before 400 years, which shows the importance of consideration of the first two failure mode in design code of steel girders.

To study the impact of steel grade and the corrosion factors on reliability of the girder, a sensitivity analysis has been conducted by changing the values of three parameters; steel grade, multiplying and exponential constants while keeping the rest of variables constant. Results of the sensitivity analysis of steel grade, and the corrosion factors can be found in figures 3 to 5. The figures reveal the significance of the impact of the corrosion exponential constant on overall failure condition of the girder, so that adding one unit to its numerical value can extend the service-life by 400 years (Figure 5). To a lesser extent, the multiplying factor should be taken care of by the analyst, since for the same scenario, the service-life is extended by 90 years. Among all of the studied

parameters in this research, steel grade shows the least impact on the reliability of the steel girder.

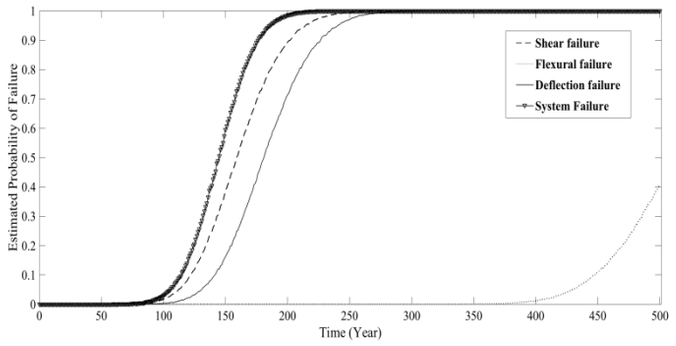


Figure 2. Estimated probability of failure over time for shear, flexural, deflection and system failure.

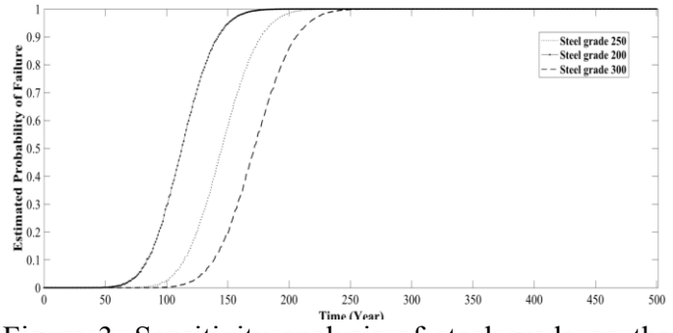


Figure 3. Sensitivity analysis of steel grade on the system probability of failure.

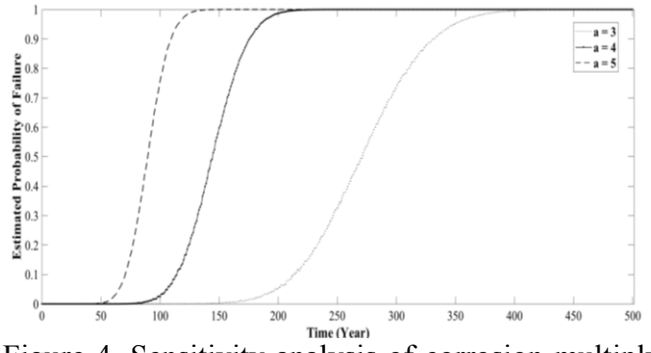


Figure 4. Sensitivity analysis of corrosion multiplying constant on the system probability of failure.

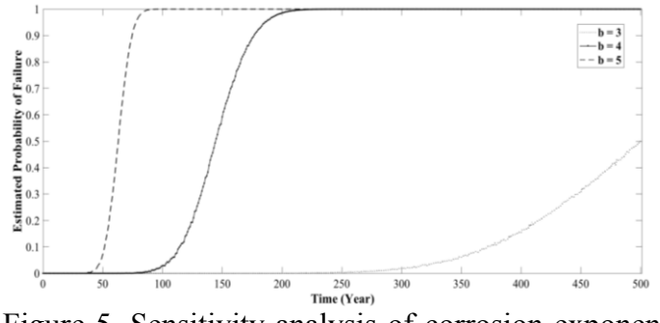


Figure 5. Sensitivity analysis of corrosion exponential constant on the system probability of failure.

Generally speaking, this study shows the importance of random variables on the system failure of steel girders, as well as the significant impact that the corrosion process can have over time. Although the proposed methodology is an applicable service life prediction method, there is still research required to improve it. An issue that needs to be addressed in the future research is that, the method ignored the correlation among limit-states when utilizing equation 3. On the other hand, the method assumed that the correlation structure of the random fields remains constant over time, while, it has been proved that the correlation structure of a corroding surface changes with time [8]. This issue can be solved by developing a time-dependent correlation length model. That, however, requires field data consisted of 3D scanned geometry of a corroding steel girder over time, which is a challenging task to obtain.

CONCLUSION

In this paper, a time-dependent reliability analysis method that considers the spatial variability of corrosion has been applied for service-life prediction of an in-service steel bridge girder. The method incorporated random field theory into an existing time-dependent Monte-Carlo reliability analysis method to make it more realistic yet simplistic. It was shown by a worked example that; the method is applicable on steel bridge elements. A parametric sensitivity analysis also performed to measure the importance of three selected parameters on overall failure of the girders. The results indicated that a greater care should be taken when selecting the values of corrosion factors for a reliability analysis. The proposed methodology enables asset managers to plan more efficient maintenance strategy for the bridge girders. Since maintenance strategies are mainly involved in finding a balance between probability of failure and the cost of reducing the risk, an optimal maintenance strategy can be achieved using the probability of failure estimation from the presented method and determining failure cost by stakeholders.

REFERENCES

[1] Darmawan, M.S., Refani, A.N., Irmawan, M., Bayuaji, R. and Anugraha, R.B., 2013. Time dependent reliability analysis of steel I bridge girder designed based on SNI T-02-2005 and SNI T-3-2005 subjected to corrosion. *Procedia Engineering*, *54*, pp.270-285.

[2] NACE international (The corrosion society), https://www.nace.org/ (Accessed October 2017).

[3] Sharifi, Y. and Paik, J.K., 2011. Ultimate strength reliability analysis of corroded steel box girder bridges. *Thin-Walled Structures*, *49*(1), pp.157-166.

[4] Czarnecki, A.A. and Nowak, A.S., 2008. Time-variant reliability profiles for steel girder bridges. *Structural Safety*, *30*(1), pp.49-64.

[5] Mahmoodian, M., Alani, A. and Tee, K.F., 2012. Stochastic failure analysis of the gusset plates in the Mississippi river bridge. *International Journal of Forensic Engineering*, *1*(2), pp.153-166.

[6] Mahmoodian, M. and Aryai, V., 2017. Structural failure assessment of buried steel water pipes subject to corrosive environment. *Urban Water Journal*, pp.1-8.

[7] Stewart, M.G., 2012. Spatial and time-dependent reliability modelling of corrosion damage, safety and maintenance for reinforced concrete structures. *Structure and Infrastructure Engineering*, *8*(6), pp.607-619.

[8] Aryai, V. and Mahmoodian, M., 2017. Spatial-temporal reliability analysis of corroding cast iron water pipes. *Engineering Failure Analysis*, *82*, pp.179-189.

[9] Teixeira, A.P. and Soares, C.G., 2008. Ultimate strength of plates with random fields of corrosion. *Structure and Infrastructure Engineering*, *4*(5), pp.363-370.

[10] Hamutçuoğlu, O.M. and Scott, M.H., 2009. Finite element reliability analysis of bridge girders considering moment–shear interaction. *Structural Safety*, *31*(5), pp.356-362.

[11] Czarnecki, A.A. and Nowak, A.S., 2007, March. Reliability-based evaluation of steel girder bridges. In *Proceedings of the Institution of Civil Engineers-Bridge Engineering* (Vol. 160, No. 1, pp. 9-16). London: [Thomas Telford], c2003-.

[12] Schmidt, V. ed. (2014). Stochastic geometry, spatial statistics and random fields: models and algorithms (Vol. 2120). Springer.

Maintenance, Safety, Risk, Management and Life-Cycle Performance of Bridges – Powers, Frangopol, Al-Mahaidi & Caprani (Eds)
© 2018 Taylor & Francis Group, London, ISBN 978-1-138-73045-8

Corrosion risks: assessment of enclosed spaces, monitoring real bridges

M. W. K. Bowers
Arup, London, United Kingdom

ABSTRACT: Enclosed spaces created by box sections in long (and short) span steel deck bridges are often perceived as high risk spaces for corrosion requiring design mitigation. This risk is often poorly defined and leads to onerous requirements for mitigation and corrosion protection. Anecdotal evidence and prior research suggests the real corrosion risk in such spaces is much less than anticipated.

Accepted practice around the world for long span structures of this type is to use de-humidification systems to control the environment to less than a critical relative humidity. It is assumed these systems offer a life cycle cost benefit compared to painted steelwork which is assumed to require relatively frequent maintenance.

This paper presents results, over eighteen to twenty-four months, the environment within this type of enclosed space (one structure with a de-humidification system and two without) by means of monitoring temperature, relative humidity and surface wetness. Where possible this data was correlated with external weather data to understand how the internal environment reacts to the external conditions.

1 INTRODUCTION

Corrosion in spaces created by long and short span bridge decks and other high volume enclosed spaces in bridges or other structures, is often perceived as a risk requiring design mitigation. The risk is often poorly and conservatively defined leading to onerous requirements for mitigation and corrosion protection.

Anecdotal evidence and prior research experience suggest real corrosion risks and maintenance in such spaces is much less than anticipated. Arup investigated the environments within enclosed bridge spaces and based on this work we now have a better understanding of environmental conditions within enclosed spaces and can recommend appropriate corrosion mitigation.

2 ACCEPTED PRACTICE

2.1 *Long-span structures*

For long-span bridge decks, accepted practice in many parts of the world is to use dehumidification plant to condition the space to a relative humidity (RH) below which corrosion cannot occur. The value of RH can vary but is often relatively low; around 45%. The use of dehumidification adds complexity to the original construction and leaves the bridge owner with additional costs associated with running and maintaining the plant. These costs can be significant and the usual RH limits mean the plant runs for long periods of time to ensure the limit is not exceeded in all parts of a structure.

It is often assumed that dehumidification offers a life cycle cost benefit over painting the steel because of a perceived need to maintain the paint system. It is also assumed that the life to maintenance of paints within decks is comparable to that of external surfaces and that complete repainting is required approximately every 20 years; this is expensive given the very large areas and often difficult with access in confined spaces

2.2 *Short-span structures*

For short span bridges the preferred options for control of corrosion within decks and boxes is the provision of a corrosion allowance (additional thickness

to the steel that can corrode over the life of the structure without affecting integrity) and a paint system. Often the assumed corrosion risk and mitigation is overstated by assuming more severe service environments than occur in practice.

3 STRUCTURES INVESTIGATED

Arup have undertaken research at 3 existing long span structures in the United Kingdom to assess the performance, service environments and corrosion risks within these spaces.

At each structure an initial survey was carried out to understand the overall condition and note any evidence of corrosion, standing water or water ingress.

3.1 *Tay Road bridge*

The Tay Road bridge is a twin box long spanning bridge that has 42 piers with a total length of 2.25 kilometers in Dundee, Scotland. The Tay Bridge has no dehumidification system in the spans.

The internal box sections show no signs of wetting or corrosion at any point along either span, even in the end spans which are more open to the environment. The steel shows no sign of corrosion.



Figure 1. Tay Road Bridge

3.2 *Cleddau Bridge*

The Cleddau Bridge is a single box long spanning bridge that has 5 piers with a total length of 0.8km in Pembroke Dock, Wales. The Cleddau Bridge has no dehumidification system in the spans.

The internal box sections show signs of localized surface corrosion. This localized corrosion is not of structural significance, and is located at areas where there appears to have been water ingress, such as around external vents, service penetrations and bulkheads. There is no evidence of condensation or corrosion from condensation on surfaces.

The bridge has not been fully repainted since it was built in 1975. Areas of localized repainting have occurred where new steel has been added. At the time of inspection, there were plans to work through the bridge to maintain the limited areas of corrosion and coating deterioration.



Figure 2. Cleddau Bridge

3.3 *Humber Bridge*

The Humber Bridge is a single box suspension bridge spanning 2.2km across the Humber, just outside of Kingston upon Hull. The Humber Bridge has a dehumidification system.

During the walkthrough of the bridge deck, locations of standing water were noted around penetrations in the deck. This water is regularly cleaned out and the dehumidification system prevents it becoming surface condensation. No areas of corrosion were observed.

The entry sections to the span are not included in the dehumidification system. Monitoring on this structure included both the dehumidified and open sections of the deck. This allowed a direct comparison of the environments and the conditions achieved by the dehumidification system.



Figure 3. Humber Bridge

4 MONITORING

The study looked to monitor relative humidity (RH), temperature and surface wetness. During the planning of the project there was a discussion as to whether wireless loggers should be used. It was decided that manual retrieval of data was better as it allowed for visual inspection of the spaces at roughly six month intervals.

In each bridge, RH and temperature were monitored for a period of 18 to 24 months starting in 2012. The period originally was to be 12 months to capture all seasons and the perceived wettest times of the year. It became possible to continue the monitoring to capture the spring and autumns seasons twice and therefore giving a more complete data set.

Each structure had 3 or 4 monitoring locations over the complete span, located to take account of possible different environments due to the bridge orientation (N-S or E-W), structural features, or in the case of the Humber Bridge, humid and dehumidified zones.

A photograph of the typical monitoring set up can be found in figure 4.

4.1 *Relative humidity and temperature equipment*

Relative humidity and temperature were logged using a *Testo 174H Mini Data Logger*. These loggers took readings every 30 minutes regardless of condition and had no trigger levels. The time between visits was set by the battery life and number of measurements recordable by the internal logger.

4.2 *Time of wetness equipment*

Time of wetness (ToW) was logged using a *Madge-Tech LF101A Data Logger*. This device activate when moisture is present on the leaf and creates a potential across the dielectric sensor. These loggers had trigger values that were calibrated on various wetness levels to ensure they triggered and began recording when surface wetness was present (+-0.2mV). When placing these loggers around the bridge decks, in general they were placed in locations that appeared to have water ingress or areas of surface corrosion.

4.3 *External conditions*

External weather data, where available was taken from the closest weather station or obtained from the bridge management.

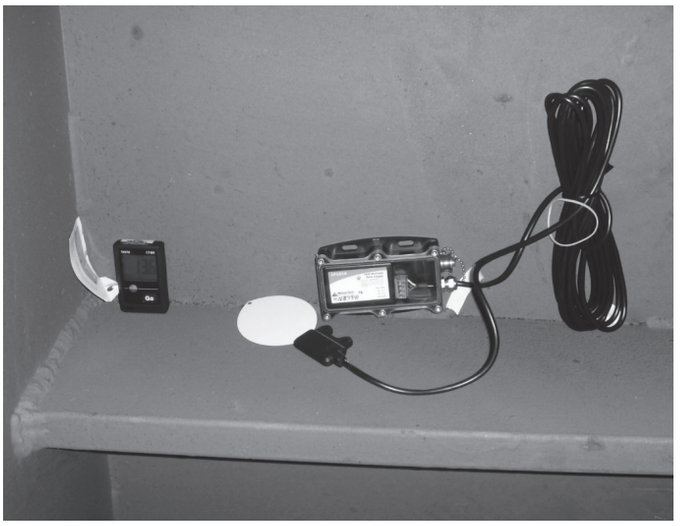


Figure 4. Equipment in place at the Humber Bridge

5 RESULTS OF INTERNAL ENIRONMENT MONITORING

The following is a summary of the results observed on site at the three bridges.

5.1 *Relative Humidity*

The relative humidity levels observed at the bridges is detailed in table 1. Along with the minimum, maximum and mean information from each bridge, the time above various levels of relative humidity are also an important metric when considering corrosion and can be found in table 2.

Table 1. Minimum, maximum, and mean relative humidity at the three bridges.

	Relative Humidity [%]		
Bridge	Min	Max	Mean
Cleddau	36	97.1	74.9
Humber (dehumidified)	13.4	82.2	37.6
Humber (open section)	27.2	94.3	67.7
Tay	30.9	98	75.7

Table 2. Time above 40, 60 and 80% RH in the three bridges.

	Time above RH level [%]		
Bridge	>40%	>60%	>80%
Cleddau	99.2	89	37.8
Humber (dehumidified)	44.7	1.4	0
Humber (open section)	97.8	72.5	19.4
Tay	99.7	93.9	33.9

5.2 *Temperature*

The temperatures observed at the bridges is detailed in table 3.

Table 3. Minimum, maximum, and mean temperature at the three bridges.

	Temperature [°C]		
Bridge	Min	Max	Mean
Cleddau	-1.9	22.9	11.8
Humber (dehumidified)	-4.4	37.7	12
Humber (open section)	-5.5	32.1	11.2
Tay	-2.2	27.8	9.4

5.3 *Surface Wetness*

No periods of wetness were recorded at the locations observed during the project.

6 COMPARISON WITH EXTERNAL DATA

For this paper, it is important to understand the relationships between internal and external conditions of the bridges. Figure 5 and 6 show a comparison of temperature and relative humidity for the month of April 2013 and figures 7 and 8 a single day from the period of May 2013.

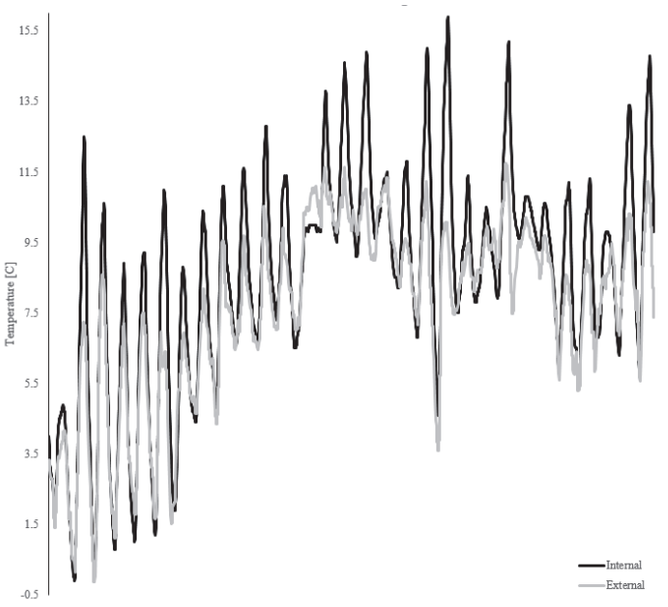


Figure 5. Comparison of internal and external temperature at Cleddau Bridge (April 2013)

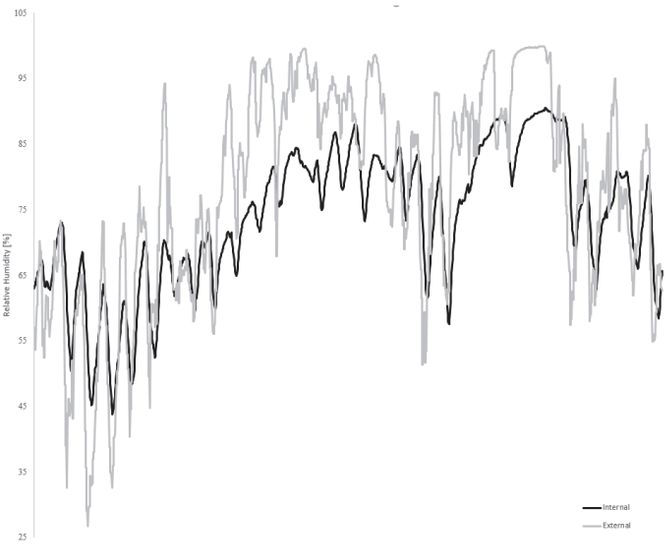


Figure 6. Comparison of internal and external relative humidity at Cleddau Bridge (April 2013)

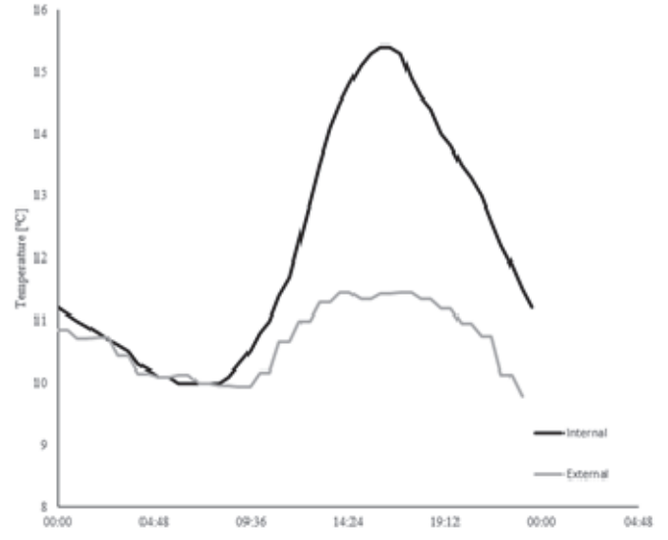


Figure 7. Comparison of internal and external temperature at Cleddau Bridge (5-May-2013)

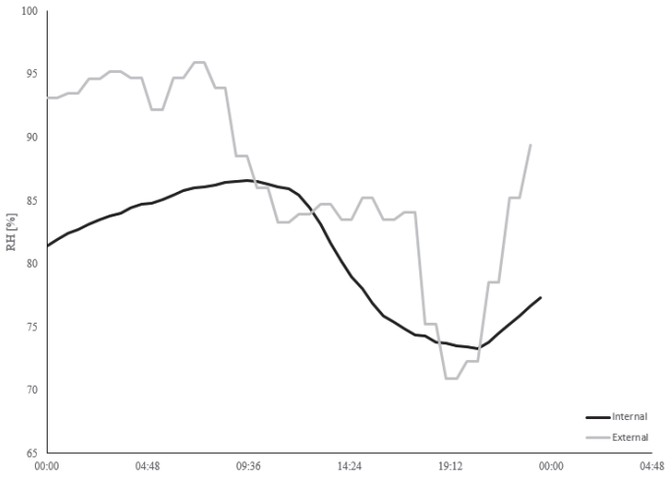


Figure 8. Comparison of internal and external relative humidity at Cleddau Bridge (5-May-2013)

7 DISCUSSION: OBSERVED EVIRONMENT

The inspections of all structures show that corrosion within deck spaces is not a significant risk. Both the Tay and Cleddau Bridges are protected with a primer which has received only partial maintenance during the 40-year service life. This information is consistent with anecdotal, based on the experiences of the current bridge managers. Where corrosion was found in the inspected structures it was at isolated locations and had not resulted in significant loss of section. Corrosion was found where water could pond and often this was associated with ingress through poorly sealed or maintained details such as penetrations into the deck space that allowed water ingress rather than the formation of condensation.

All three structures are typical of modern bridge fabrication, at least in respect of the environments created within the decks. The decks may be 'nominally sealed' and prevent direct ingress of the weather (sun, rain and wind) none were airtight or hermetically sealed. It is assumed that in all cases the bridges could 'breathe' and allow some exchange of air between the internal and external environment.

The observations of low incidence and significance of corrosion was consistent with environmental monitoring. ToW sensors did not record any significant water formation on any surfaces within any of the three structures. It was found that the RH and temperature within the bridge deck changes slowly compared to the external conditions. The relatively slow changes in internal environment with significant lag relative to external changes suggests conditions are close to equilibrium. The risk of condensation within such spaces is low and that the conditions required for condensation are different to those in an external environment, or on the external surface of the structure.

During the monitoring period, there was only one instance, based on the external conditions when condensate could have formed on the internal surface but none was recorded on the ToW sensor. This occurred in November 2013 and indicates that water deposition did not occur, or it did not occur in a location where sensors were present.

It is often assumed the critical RH below which corrosion will not occur is in the range of 40 to 70%; the relatively low RH to cause corrosion is due to the deposition of the air borne pollutants on the surface, particularly chlorides, sulfur dioxide and dust particles. These pollutants are hydroscopic and absorb moisture from the atmosphere at RH values well below saturation. It is clear from this research and previous studies undertaken at the Transport Research Laboratory(TRL)[1][2] that this range of 40 – 70% is likely inappropriate for internal spaces. The critical RH is probably very close to saturation and those conditions occur rarely in closed spaces on bridges in temperate climates. The TRL work and this research is also consistent with other research in related environments such as those found in modern vented cavity wall construction[3][4].

Internal spaces of bridge decks are not exposed to the weather nor wind borne contaminants that could settle on the internal surfaces. This accounts for the high RH required to cause corrosion and why no ToW was measured within the three structures during the monitoring period, even with the RH exceeded the assumed limits.

The absence of pollutants and relatively stable environments within bridge decks and other large volume spaces show that corrosion risks are much lower than often assumed in design. The design assumption is that condensate can form for long periods and that conditions within the structure (in terms of RH and temperature) will be very similar to the external conditions due to a free exchange of air. The monitoring has shown this is not the case. Condensation may and probably does at time form in these spaces, but the frequency and duration of both are low. This results in low ToW (measured in hours per year) and low annual corrosion rates.

8 DISCUSSION: CORROSION RISKS

The internal RH and temperature values (annual mean) allow an estimation of corrosion risk using the method given in *ISO 9223:2012*. To do so requires an estimation of deposition rates of pollutants, sulfur dioxide and chloride. Given these pollutants are essentially wind borne and the internal surfaces of bridge decks are protected from the wind, these deposition rates are likely low. Again, this is consistent with observations regarding time ToW and previous research. Therefore, one can assume a low

deposition rate for both pollutants, of lower bound S and P classes of *ISO 9223:2012.*

The results of the calculation are shown in table 4. The values for corrosion rate would put all the boxes (except the dehumidified Humber box) in the mid-range of the C2 class (corrosion rate 1.3 to 25 microns per year). This being said, the method of calculation has potential errors which are listed as -33% to +50%; allowing for this error, the boxes still fall in the C2 class.

It should be noted that even with a dehumidification system the bridge falls into this C2 category, all be it at the lower end.

The calculation gives the rate for the first year and it is highly likely that the rate over subsequent years would gradually decrease and eventually stabilize after 20 to 25 years.

The calculation has used the data from a single monitoring point which would give the most conservative corrosion rate and not the fully averaged values given in tables 1 and 3.

Table 4. Calculation to ISO 9224 to determine corrosion loss per year from measured conditions.

Bridge	RH [%]	Temp [°C]	Corrosion rate per yr. [microns]	
Cleddau	76.1	10.1	10	(+50% 15)
Humber (dehumidified)	38.7	12.1	3.8	(+50% 5.8)
Humber (open section)	67.7	11.2	8	(+50% 12)
Tay	76.9	9.82	10.1	(+50% 15)

9 DISCUSSION: CORROSION PROTECTION

If the corrosion risk within large volume spaces is low, the risk requires relatively modest measures to mitigate it. The options for protection are:

- Use of a paint specification
- Use of a corrosion allowance
- Use of dehumidification
- A combination approach

9.1 *Paint specifications*

Experience shows that primer only paint specifications provide effective and very long term protection (at least 40 years) with minimum requirements for maintenance of the paint. This performance is understandable given that steel within these spaces is not exposed to damaging UV light from the sun or exposed to long periods of wetness.

Where maintenance has been observed to any coatings in the deck spaces it has been to relatively small areas and has not required a complete removal or replacement of paint on the steel surface.

It follows that a modern paint specification would provide long term protection to internal spaces and would have very low maintenance requirements.

9.2 *Corrosion allowance*

The low risk of corrosion within bridge spaces means that effective protection could be provided with almost a nominal corrosion allowance of, say, 1mm on the section thickness. However, design standards may take a more conservative view. For example, the UK National Annex to *EN 1993-2* suggests, in the best case, a 2mm allowance to be added which could be significant when added to all internal surfaces. The assumption appears to be that condensation (and therefore surface wetness) is a more regular occurrence than is found in practice.

9.3 *Dehumidification*

This research has shown there is little justification for dehumidification of internal bridge spaces in temperate climates. The corrosion risks do not warrant the use of this method and the assumptions on which it has been based look doubtful. The cost argument largely relates to an assumption on the long term performance, and therefore maintenance of paint coatings within the deck space. Those assumptions are directly contradicted by this research and anecdotal evidence from other structures. The assumed RH limit below which corrosion will not occur is also questionable. This research is consistent with the previous research of others and indicates the RH limit is much closer to saturation than the assumed range of 40 – 70%.

9.4 *A combined approach*

Arguably the most effective protection to the internal parts of a structure can be provided by combinations of a paint specification, with an assumed practical life (not life to first maintenance) of 50 years and a nominal corrosion allowance of 1mm. This would assume minor maintenance of the coating but no complete replacement over the life of the structure.

An alternative for longer span structures, that provides a degree of redundancy is the use of a paint specification backed up with a dehumidification system. In this case it would be the recommendation that the trigger value for this system to turn on be set to a value of 90% or higher. This would limit the period for which the plant operated but would provide redundancy if conditions within the structure differed significantly from those assumed. The critical RH could, in the future, be reduced.

10 CONCLUSIONS

This research has shown:

That environments found in long span bridge decks are relatively stable and change much more slowly (with respect to RH and temperature) than the external environments.

That the risk of condensation and long periods of surface wetness in bridge decks is much lower than anticipated.

That corrosion risks within bridge decks and other large volume spaces is much lower than usually assumed in design.

That modest paints specifications (essentially a primer only specification) provide very effective and long term protection within bridge spaces and do not require significant maintenance.

That the use of dehumidification of decks and other large volume spaces is not the preferred option for corrosion control.

The preferred option for corrosion control in decks and other spaces is the use of a primer only paint specification and a nominal corrosion allowance.

11 REFERENCES

[1] Mackensie, M. 1991. Transport and Road Research Laboratory Research Report 293

[2] Vassie, P. I. 1987. Corrosion of structural steelwork in bridge enclosures, box sections and anchorage chambers. British Corrosion Journal vol.22 no.1

[3] Hudson, R. M. The corrosion of Structural Steelwork in the cavity walls of buildings

[4] SCI P262 2009. Durability of light steel framing in residential buildings.

Maintenance, Safety, Risk, Management and Life-Cycle Performance of Bridges – Powers, Frangopol, Al-Mahaidi & Caprani (Eds)
© 2018 Taylor & Francis Group, London, ISBN 978-1-138-73045-8

Effect of Corrosion on Mechanical Properties of Steel Bridge Elements

L. Li, M. Mahmoodian, and C. Q. Li
School of Engineering, RMIT University, AUSTRALIA (E-mail: s3500237@student.rmit.edu.au, mojtaba.mahmoodian@rmit.edu.au, shiwei.zhou@rmit.edu.au, chunqing.li@rmit.edu.au)

ABSTRACT: Corrosion of steel is a worldwide issue which potentially affects structural integrity of bridges. This research presents the results of comprehensive lab tests on the stress effect on corrosion and the combined effect of stress and corrosion on the mechanical properties of steel bridge elements. G250 mild steel specimens, commonly used for bridge construction, are used for analysis. Both stressed and non-stressed specimens are immersed in acid solutions to simulate corrosion progress. The stress effect on corrosion rate (mass loss) is studied. The combined effect of stress and corrosion on mechanical properties is also studied. Hydrogen concentration is monitored for stressed and non-stressed steel during corrosion to find the mechanism of the degradation of mechanical properties. The outcome of this research can help bridge engineers and asset managers to better model corrosion and more accurately assess the structural integrity of corrosion affected steel bridges.

1 INTRODUCTION

Corrosion is a major concern for steel bridge structures. Corrosion can lead to losses of cross sections and reduction of mechanical properties, including yield strength, ultimate strength, and ductility (Garbatov et al. 2014). It reduces service life of bridges and makes the bridges vulnerable to failure (Chen 2007, Li et al. 2017). In most of the cases, bridge steel is simultaneously stressed under loading and is subjected to corrosion (Wang et al. 2014). Therefore, it is vital to model and quantify the corrosion behavior and corrosion impact of steel under stress and corrosion combined environment, in order to optimize maintenance, repair, and rehabilitation of steel bridges.

Stress leads to the decrease of corrosion resistance of steel (Javaherdashti et al. 2006, Ren et al. 2012, Xu & Cheng 2012). In details, Revie (2008) and Li & Cheng (2008) pointed out that passive oxide films are formed before and during corrosion which provides a protective layer for steel against corrosion. The applied stress ruptures the passive oxide films and enhances the dissolution rate at steel surface. In addition, stress also causes deformation on steel surface, which increases the surface energy and makes corrosive solution easier to cover the steel surface (Ren et al. 2012)

The interaction of stress and corrosion also results in the reduction of mechanical properties of steel (Revie 2008, Marcus 2011). On one hand, as mentioned earlier, stress plays a key role in the rupture of the passive oxygen films and the initiation of the micro plastic deformation at grain boundaries. They are directly related to initiation and propagation of stress corrosion cracking (Li & Cheng 2008). On the other hand, hydrogen embrittlement becomes more serious when steel is stressed (Revie 2008, Eggum 2013). This is because stress causes more cracks and voids within steel that favors the diffusion and residence of hydrogen atoms.

Despite the previous researches on the effect of stress on the corrosion rate of steel, the review of the literature highlights the limitations in the current knowledge. To begin with, literature mainly focuses on the acceleration effect of plastic stress on corrosion. However, in most of the real cases, steel is subjected to elastic stress (70% to 80% of the yield strength) under serviceability load, and there is lacking knowledge on the effect of elastic stress on corrosion. Ren et al. (2012) and Wang et al. (2014) indicated that elastic stress attributes to the surface energy increment, which subsequently increases the corrosion rate of steel. However, Xu & Cheng (2012) pointed out that the application of elastic stress has no effect on the corrosion rate of steel. To examine these conflicting views, the current research carries out a comprehensive experiment to investigate the effect of elastic stress on corrosion rate.

Next, as mentioned above, stressed steel is more susceptible to stress corrosion cracking and hydrogen embrittlement than non-stressed steel (Revie

2008, Marcus 2011). It is expected that the reduction of mechanical properties is more significant for stressed steel than non-stressed steel under similar corrosion environment. However, very limited literature compared the level of degradation of mechanical properties between stressed and non-stressed steel. In addition, the combined effect of corrosion and stress on mechanical properties has been studied mainly for pipeline steel, high tensile stress, and stainless steel (Li & Mahmoodian 2013, Mahmoodian & Li 2017a, b), as the case in Cheng (2007) and Liu et al. (2008), there is almost no relevant research focusing on the corrosion of mild steel under the stress and corrosion combined environment. The mild steel, however, has been widely used for bridge construction (Yakel & Azizinamini 2005).

In addition, according to literature, it is reasonable to assume that there are more hydrogen atoms penetrating into steel when steel is stressed at the same corrosion time. Nonetheless, the hydrogen concentration between stressed and non-stressed steel has not been compared at the same corrosion environment in the previous literature.

This paper presents a comprehensive experimental program to achieve three objectives: (1) to investigate effect of elastic stress on corrosion of mild steel, (2) to quantify the degradation of mechanical properties under stress and corrosion combined environment, and (3) to measure the increase of hydrogen concentration during corrosion to determine the mechanism of degradation of mechanical properties.

G250 mild steel, a steel used commonly for bridge construction, is used in this study. Simulated corrosion tests are conducted by immersing both stressed and non-stressed steel specimens in acidic solutions. Mass loss and mechanical properties of specimens after each stage of immersion are measured. In addition, hydrogen concentration has been measured for both stressed and non-stressed steel after each stage of corrosion.

2 EXPERIMENTAL SET UP

2.1 *Sample Preparation*

The test specimens were taken from Grade 250 mild steel. This type of steel is commonly used for the construction of bridges and other common steel structures. All the specimens were fabricated according to ASTM E8 (2016), shown in Figure 1. The specimens were wrapped with acid resistant tapes at both ends, so that corrosion only takes place in the tested area (i.e., 50mm gauge length in the middle)

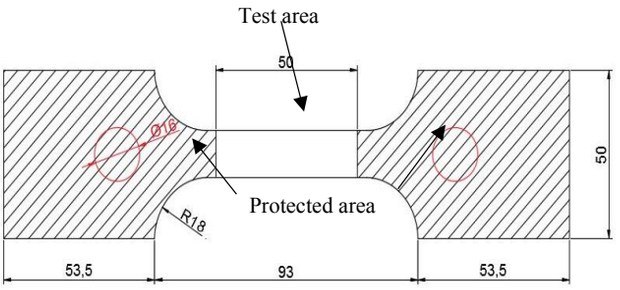
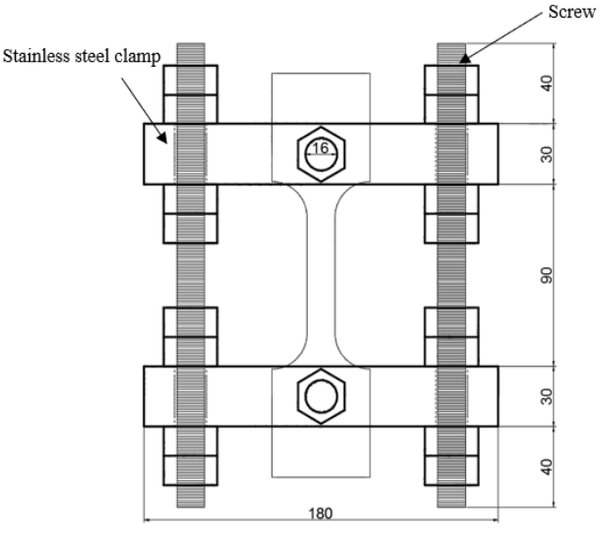


Figure 1. Specimen for tensile test (Units: mm)

2.2 *Design of stress system*

The steel specimens were stressed up to 70% of yield strength (220Mpa). This percentage was determined based on the ratio between serviceability load and ultimate load referring to AS5100.2 (2017). Specimens were stressed through clamp and jig system designed as Figure 2a. The system is composed of two 1800mm×30mm×26mm grade 904 stainless steel plates and four M16 high tensile steel screws. Specimens were stretched by tensile test machine and then screws were fixed to maintain the stress (Fig. 2b). The clamp and jig systems were wrapped with acid resistant tape and then coated with Vaseline (Fig. 3b). This is to prevent the corrosion of clamp and jig system. In addition, the distance between the stainless-steel clamps was measured constantly during corrosion to control the releasing of stress.



(a) Design of clamp and jig system (Units: mm)



(b) Stress process of the specimen

Figure 2. Details of clamp and jig system

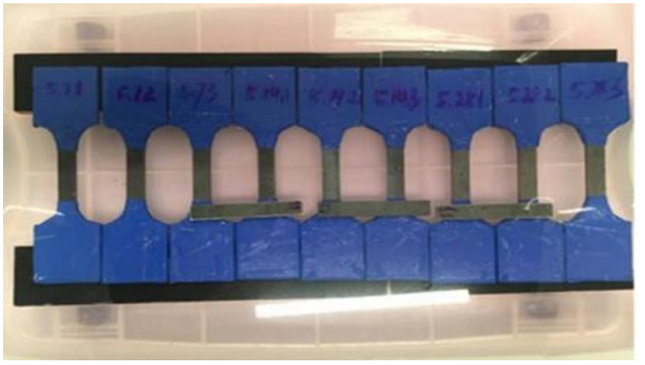
2.3 *Immersion test*

Corrosion simulation was carried out through acid immersion test following ASTM G31-72 (2004). Hydrochloride acid (HCl) was selected as the immersion solution, consistent with the literature (Revie 2008, Eggum 2013). Two HCl solutions at different pHs were chosen for the corrosion simulation, namely HCl with pH=2.5 and HCl with pH=5. In particular, the solution with pH=5 well simulates the natural corrosion of bridge steel according to Liu et al. (2014). The solutions with pH=2.5 were chosen to accelerate corrosion within the given time frame of the project.

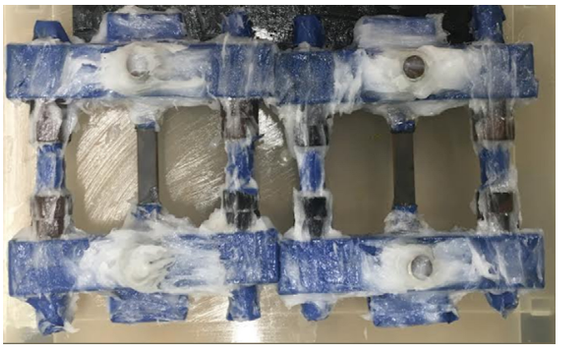
The immersion duration was set as 7, 14, and 28 days. For stressed and non-stressed cases, there were 4 specimens for each immersion time, where 3 specimens went through tensile test and 1 specimen was taken for hydrogen concentration measurement. Specimens were weighed before and after corrosion to determine mass loss as an indication of corrosion rate. The test plan is shown in Table 1 and the immersion test set up is shown in Figure 3.

Table 1. Test plan for tensile test and hydrogen measurement test

Solution	Stress (Mpa)	Immersion duration (days)	Number of specimens	
			Tensile test	Hydrogen measurement
Before immersion	0	0	3	1
pH=5	0/220	7	3	1
		14	3	1
		28	3	1
pH=2.5		7	3	1
		14	3	1
		28	3	1



(a) Non-stressed specimen



(b) Stressed specimen ready to immerse in acid

Figure 3. Set up of immersion test

2.4 *Hydrogen measurement*

Hydrogen concentration was measured for stressed and non-stressed steel specimens after each stages of corrosion. Hydrogen concentration tests were performed using Barnacle cell according to ASTM F 1113-87 (2017). The set up for hydrogen measurement is shown in Figure 4. In theory, Barnacle cell takes hydrogen containing steel as the anode, and uses a nickel/nickel oxide electrode as the cathode.



Figure 4. Set up of hydrogen concentration test

For the measurement, steel specimens were exposed to 0.2 Molar sodium hydroxide (NaOH) so-

lutions restored in Teflon cell. Hydrogen gas and atoms within steel reacted within hydroxide (NaOH) solutions and the current of reaction was recorded after 30 minutes to calculate hydrogen concentration, following Equation 1.

$$I_p = FC_0(D/\pi t)^{1/2} \quad (1)$$

where I_p is the current density, F is the Faraday constant (96485.3 C/mol), C_0 is the hydrogen concentration, t is the recording time (30mins by standard), D is the diffusion coefficient for mild steel (2.5×10^{-8} cm/s^2).

2.5 *Tensile test*

Tensile test was conducted according to ASTM E8 (2016). The cross-head speed was set as 1.1 mm/s for entire specimens. Yield strength, ultimate strength and failure strain were measured through tensile test.

3 RESULTS AND DISCUSSION

3.1 *Mass loss versus time*

The mass losses of steel specimens as a function of time for both stressed and non-stressed specimen are shown in Figure 5. From Figure 5, for non-stressed specimens, mass loss is 1.42% in pH=5 HCl and 3.77% in pH=2.5 HCl, whist for stressed specimens, mass loss is 1.33% in pH=5 HCl and 2.55% pH=2.5 HCl after 28 days' immersion. The results indicate that a higher concentration of acid favors the corrosion process, and there is an acceleration in corrosion rate when specimens are stressed. The findings are in agreement of the previous literature (Ren et al. 2012).

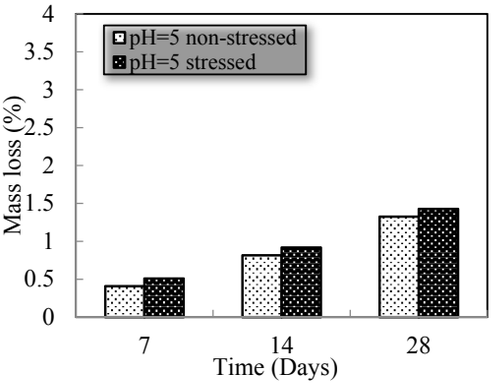
The result indicates the applied elastic stress can increase the corrosion rate of steel. Corrosion is an electrochemical process and corrosion rate increases with the decreases of electrochemical potential (Ren et al. 2012). Electrochemical potential can be reduced by the applied stress due the following reasons: (1) Passive oxide films are formed before and during corrosion and the reactions are shown from Equation 2 to Equation 5. Stress ruptures the passive oxide films. At the film rupture site, galvanic corrosion occurs between the exposed steel and the surrounding oxide films (Revie 2008, Marcus 2011). This leads to the decrease of the electrochemical potential. (2) With the presence of stress, the surface energy of steel increases and this reduces electrochemical potential by making the acid solution easier to attach and cover the steel surface (Ren et al. 2012). (3) When the presence of stress, local stress concentration leads to the plastic deformation at grain boundaries. The plastic deformation decreases the activation energy of anodic dissolution and subsequently decreases the electrochemical potential. In addition, plastic deformation at grain boundaries can further rupture the passive oxide films and reduce the corrosion resistance (Revie 2008, Marcus 2011).

$$Fe + 4H_2O \leftrightarrow Fe_3O_4 + 8H^+ + 8e^- \quad (2)$$

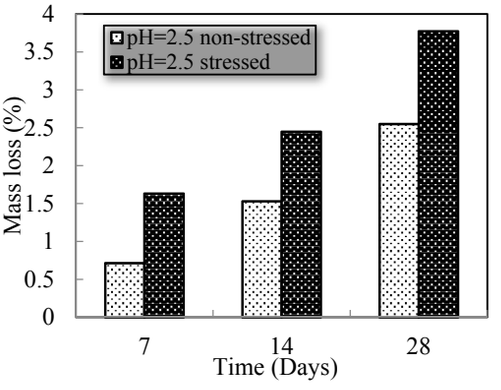
$$2Fe_3O_4 + H_2O \leftrightarrow 3Fe_2O_3 + 2H^+ + 2e^- \quad (3)$$

$$3Fe^{2+} + 4H_2O \leftrightarrow Fe_3O_4 + 8H^+ + 2e^- \quad (4)$$

$$2Fe^{2+} + 3H_2O \leftrightarrow Fe_2O_3 + 6H^+ + 2e^- \quad (5)$$



(a) pH 5



(b) pH 2.5

Figure 5. Mass loss versus time

3.2 *Hydrogen concentration versus time*

Figure 6 shows hydrogen concentration grows during corrosion, and the concentration is higher for stressed specimens than none-stressed samples at the same immersion time. In details, after 28 days' immersion, hydrogen concentration increases from 0 to 0.78ppm in pH=5 HCl and to 1.97 ppm in pH=2.5 HCl for none-stressed specimens. For stressed specimens, the concentration increases to 1.17ppm and 2.58ppm in these two solutions respectively.

The hydrogen concentration grows more rapidly for stressed specimens than none-stressed samples at the same immersion time. There are two explanations: On one hand, corrosion is a combination of oxygen reduction (Eq .6 and Eq.7) and hydrogen evolution reaction (Eq. 8 and Eq.9) (Revie 2008, Marcus 2011). Hydrogen gas (H_2) is released in hydrogen evolution reaction, which can diffuse in steel and cause the increase of hydrogen concentration. Stress accelerated corrosion and makes more hydrogen gas release at steel surface (Eggum 2013). In addition, hydrogen evolution reaction plays a more dominant role on the corrosion reaction at pits and cracks. Stress ruptures the passive oxide films, favors localized corrosion, and makes more pits and cracks formed on the surface. This subsequently enhances hydrogen evolution reaction and makes more hydrogen release and diffusion into steel (Eggum 2013).

Oxygen Reduction Reaction (ORR):

$$1/2O_2 + 2H_3O^+ + 2e \rightarrow 3H_2O \text{ Acid} \quad (6)$$

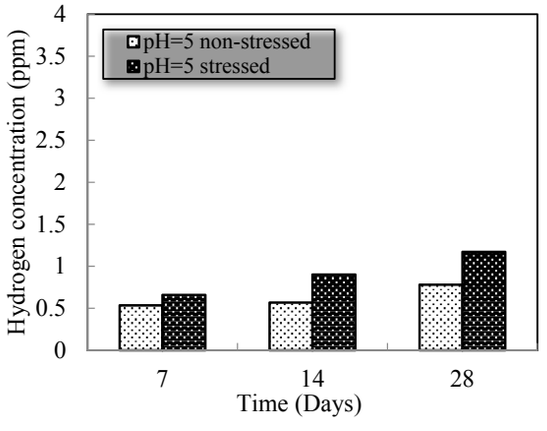
$$1/2O_2 + H_2O + 2e \rightarrow 2OH^- \text{ Neutral alkaline} \quad (7)$$

Hydrogen Evolution Reaction (HER):

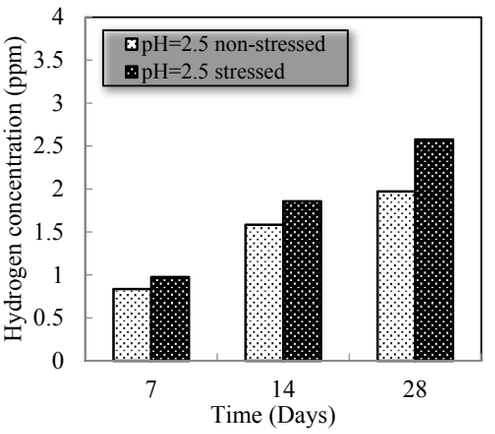
$$H_3O^+ + e \rightarrow 1/2H_2 + H_2O \text{ Acid} \quad (8)$$

$$H_2O + e \rightarrow 1/2H_2 + OH^- \text{ Neutral, alkaline} \quad (9)$$

On the other hand, hydrogen atoms in the acid solutions can be absorbed by steel and this also increases hydrogen concentration. Stress favors the absorption of hydrogen atoms by increasing the surface energy on the steel surface. Stress also creates more dislocations and voids inside steel that traps hydrogen atoms (Eggum 2013).



(a) pH= 5



(b) pH= 2.5

Figure 6. Hydrogen concentration versus time

3.3 *Mechanical properties versus time*

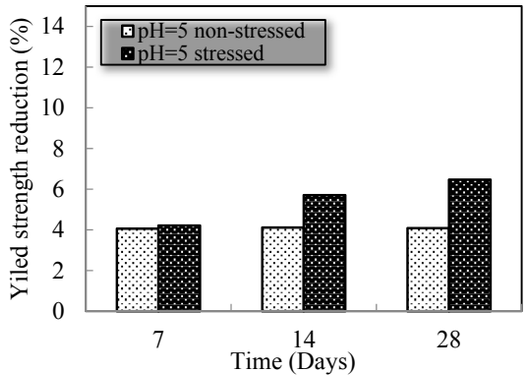
The stress effect on yield strength and ultimate strength is determined in two ways according to Seica & Packer (2004), one emphasized the importance of section loss, surface roughness and corrosion products (rust) on the degradation of mechanical properties. Original cross-section area is used to determine the yield strength and ultimate strength of corroded specimens (Fig. 7 and Fig. 8). This is referred to "as original" condition. The other one focused on the corrosion effect on metallic mechanical properties only. The area of reduced cross-section by corrosion is used to determine yield strength and ultimate strength of corroded specimens (Fig. 9 and Fig. 10). This is referred to "as is" condition.

As shown from Figure 7 and Figure 8, there is a significant reduction in yield strength and ultimate strength for "as original" condition. The reduction is more significant for stressed specimens than non-stressed specimens at the same immersion time. To be specific, in pH=5 HCl, yield strength reduces by 4.08% for non-stressed steel and 6.47% for stressed steel after 28 days' immersion. In pH=2.5 HCl, the yield strength reduces by 4.70% for non-stressed steel and 7.58% for stressed steel after 28 days' immersion. In addition, the ultimate strength for non-stressed and stressed specimens reduces by 3.72% and 12.33% in pH=5 HCl, and 4.12% and 13.63% in pH=2.5 HCl after 28 days' immersion.

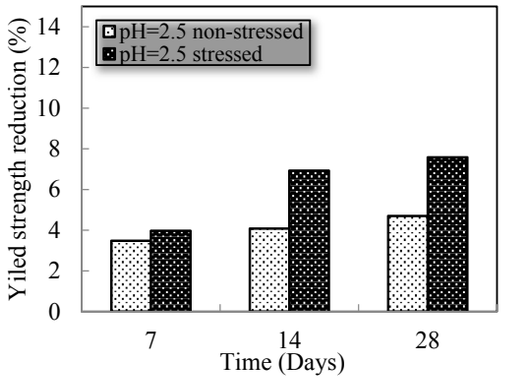
There is no notable change in yield strength and ultimate strength for "as is" condition (Fig. 9 and Fig. 10). This is because corrosion only affects 0.2mm below the steel surface for the 6mm thickness specimens (Revie 2008). In this way, the reduction of the resistance (flexure and shear resistance) of steel after corrosion is mainly caused by the loss of cross section, the increase of surface roughness, and the formation of corrosion products of the steel surface (Revie 2008).

However, there is a significant reduction in steel ductility. From Figure 11, failure strain (ductility) reduces by 14.4% and 36.6% in pH=5 HCl and pH=2.5 HCl respectively for non-stressed condition and reduces by 29.0% and 40.9% for stressed conditions. The reduction of failure strain is a combined effect of hydrogen embrittlement, element composition changes, grain size changes, and residual stress concentration caused by pitting corrosion.

Since the concentration of hydrogen within steel is increased more rapidly with the presence of stress, the reduction of failure strain is more serious for stressed steel than non-stressed steel at the same corrosion time. In addition, stress plays a key role in the rupture of the passive oxygen films and the initiation of the microplastic deformation at grain boundaries. This can also lead to more serious reduction of the ductility of steel during corrosion. Due to the reduction in ductility, failure of bridge may occur suddenly without any signs, and the bridge steel can be more vulnerable to fatigue failure (Revie 2008)

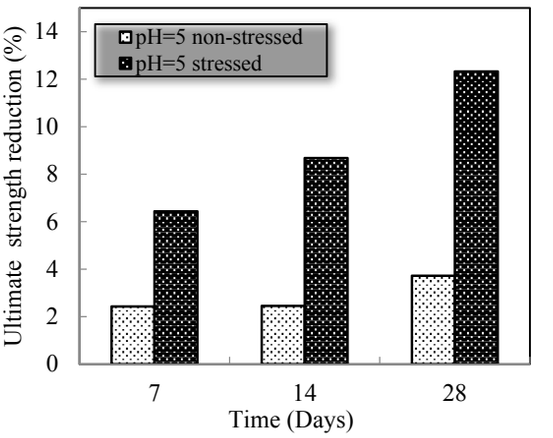


(a) pH =5

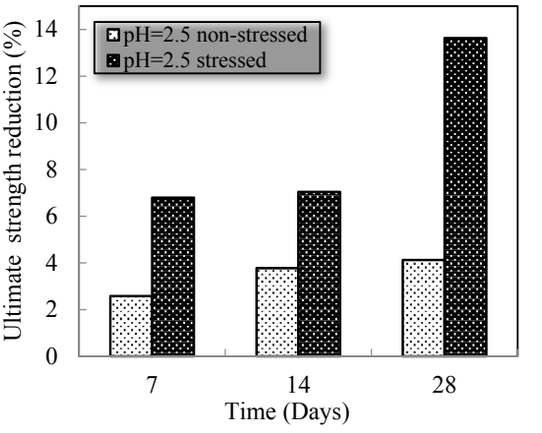


(b) pH =2.5

Figure 7. Yield strength reduction versus time (as original)

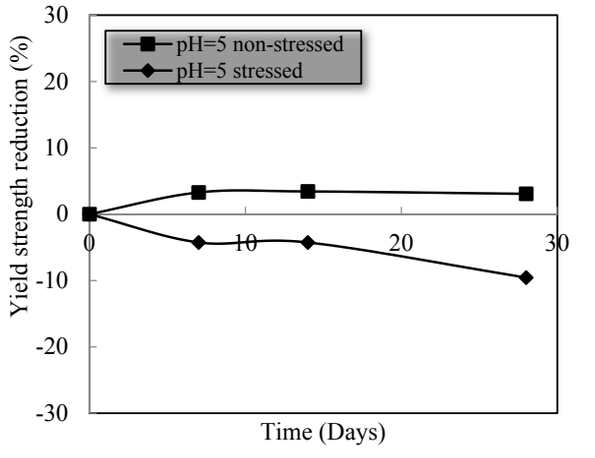


(a) pH =5

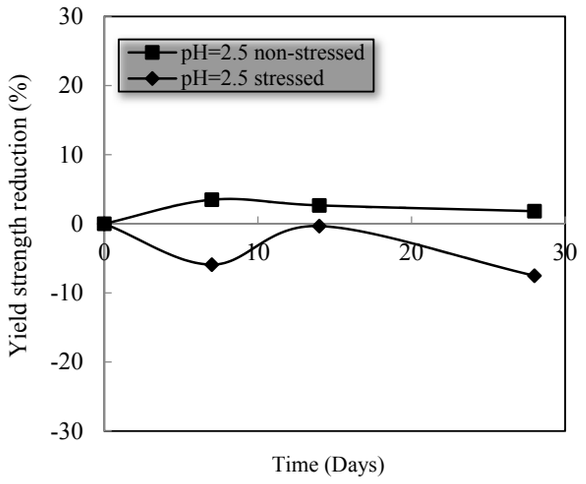


(b) pH =2.5

Figure 8. Ultimate strength reduction versus time (as original)

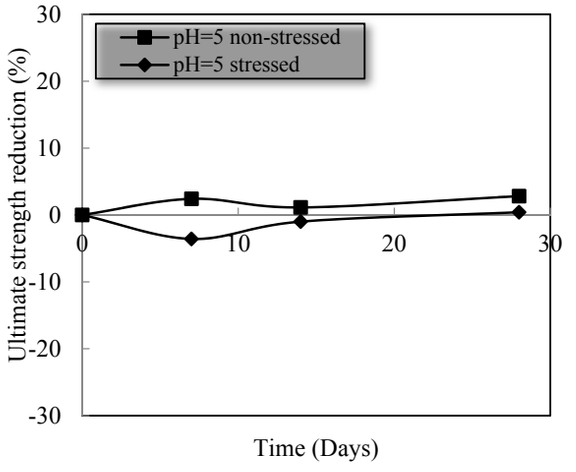


(a) pH =5

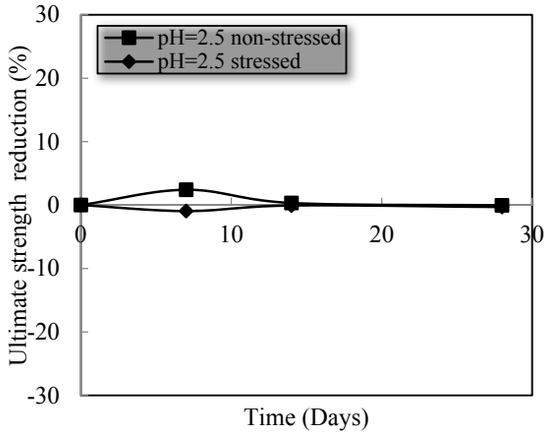


(b) pH=2.5

Figure 9. Yield strength reduction versus time (as is)

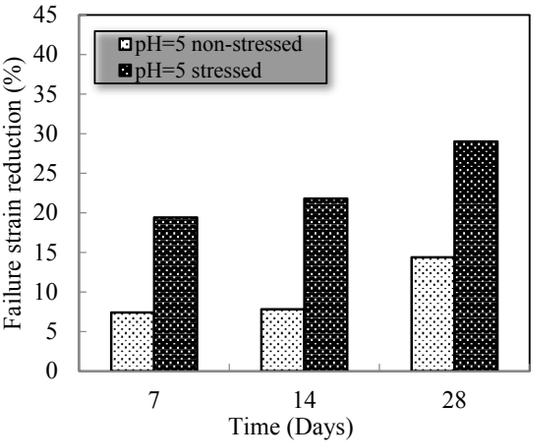


(a) pH =5

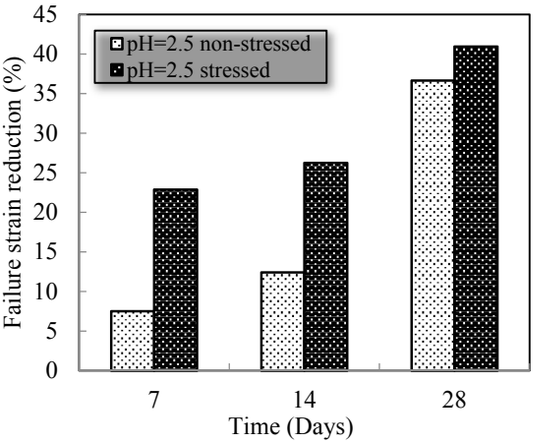


(b) pH=2.5

Figure 10. Ultimate strength reduction versus time (as is)



(a) pH =5



(b) pH =2.5

Figure 11. Failure strain reduction versus time

4 CONCLUSION

The results of a comprehensive corrosion study on bridge steel (mild steel) have been presented in this paper. The stress effect on corrosion rate and hydrogen concentration is quantified. The degradation of mechanical properties is quantified both for stressed and non-stressed steel after corrosion. Two different solutions of hydrochloride acid (HCl), namely pH=5 HCl and pH=2.5 HCl, are used for corrosion simulation test. The tests found that there is acceleration in corrosion rate when steel is stressed. The stressed steel specimens also have higher hydrogen concentration than non-stressed steel at the same immersion time. This indicates that stressed steel is more vulnerable to hydrogen embrittlement during corrosion. In addition, considering the corrosion effect on metallic mechanical properties of steel, corrosion has limited effect on yield strength and ultimate strength, but it can lead to significant reduction on the ductility of steel. The reduction of ductility is al-

so more serious for stressed steel than non-stressed steel at the same immersion time since it has higher hydrogen concentration. The outcome of this research can help bridge engineers and asset managers to understand the corrosion process of steel bridges under stress, and understand the effect of corrosion on the mechanical properties of steel elements of aging bridges.

5 ACKNOWLEDGEMENT

Financial support from Metro Trains Melbourne, Australia and the Australian Research Council under DP140101547, LP150100413 and DP170102211 is gratefully acknowledged.

6 REFERENCE

ASTM E8 / E8M-16a. 2016. *Standard Test Methods for Tension Testing of Metallic Materials*. ASTM International, West Conshohocken, PA, www.astm.org

ASTM G31-72. 2004. *Standard Practice for Laboratory Immersion Corrosion Testing of Metals*. ASTM International, West Conshohocken, PA, www.astm.org

ASTM F1113-87. 2017. *Standard Test Method for Electrochemical Measurement of Diffusible Hydrogen in Steels (Barnacle Electrode)*. ASTM International, West Conshohocken, PA, www.astm.org

AS 5100.2. 2017. *Bridge design, Part 2: Design loads*. Australia Standards.

Cheng, Y. 2007. Analysis of electrochemical hydrogen permeation through X-65 pipeline steel and its implications on pipeline stress corrosion cracking. *International Journal of Hydrogen Energy* 32(9): 1269-1276

Eggum, T. J. 2013. *Hydrogen in Low Carbon Steel: Diffusion, Effect on Tensile Properties, and an Examination of Hydrogen's Role in the Initiation of Stress Corrosion Cracking in a Failed Pipeline.* University of Calgary.

Garbatov, Y., Soares, C. G., Parunov, J. & Kodvanj, J. 2014. Tensile strength assessment of corroded small scale specimens. *Corrosion science* 85: 296-303.

Javaherdashti, R., Raman, R. S., Panter, C. & Pereloma, E. 2006. Microbiologically assisted stress corrosion cracking of carbon steel in mixed and pure cultures of sulfate reducing bacteria. *International biodeterioration & biodegradation* 58(1): 27-35.

Li, M. & Cheng, Y. 2008. Corrosion of the stressed pipe steel in carbonate–bicarbonate solution studied by scanning localized electrochemical impedance spectroscopy. *Electrochimica Acta* 53(6): 2831-2836.

Li, C. Q. & Mahmoodian**,** M. 2013. Risk Based Service Life Prediction of Underground Cast Iron Pipes Subjected to Corrosion. *Journal of Reliab*ility Engineering & System Safety 119: 102-108.

Li, L., & Mahmoodian, M. & Li C. Q. 2017. Structural assessment of an in-service steel viaduct using time variant reliability analysis. *In 12th International Conference on Structural Safety and Reliability, At Technische Universität Wien, Vienna, Austria*.

Liu, Z., Li, X., Du, C., Zhai, G. & Cheng, Y. 2008. Stress corrosion cracking behaviour of X70 pipe steel in an acidic soil environment. *Corrosion Science* 50(8): 2251-2257.

Liu, Y., Wang, Z. & Ke, W. 2014. Study on influence of native oxide and corrosion products on atmospheric corrosion of pure Al. *Corrosion Science* 80: 169-176.

Mahmoodian, M. & Li, C. Q. 2017a. Reliability based service life prediction of corrosion affected cast iron pipes considering multi failure modes. *ASCE Journal of Infrastructure systems*

Mahmoodian, M. & Li, C. Q. 2017b. Stochastic service life prediction and reliability analysis of defected steel pipes, *Journal of Petroleum science and engineering* 151: 434-438.

Marcus, P. 2011. *Corrosion mechanisms in theory and practice*. Crc Press.

Ren, R., Zhang, S., Pang, X. & Gao, K. 2012. A novel observation of the interaction between the macroelastic stress and electrochemical corrosion of low carbon steel in 3.5 wt% NaCl solution. *Electrochimica Acta* 85: 283-294.

Revie, R. W. 2008. *Corrosion and corrosion control*. John Wiley & Sons.

Seica, M.V. & Packer, J.A. 2004. Mechanical properties and strength of aged cast iron water pipes. *Journal of materials in civil engineering* 16(1): 69-77.

Wang, X., Tang, X., Wang, L., Wang, C. & Guo, Z. 2014. Corrosion behavior of X80 pipeline steel under coupling effect of stress and stray current. *Int. J. Electrochem. Sci* 9(8): 4574-4588.

Xu, L. & Cheng, Y. 2012. An experimental investigation of corrosion of X100 pipeline steel under uniaxial elastic stress in a near-neutral pH solution. *Corrosion Science* 59: 103-109.

Yakel, A. J. & Azizinamini, A. 2005. Improved moment strength prediction of composite steel plate girders in positive bending. *Journal of bridge engineering* 10(1): 28-38.

Maintenance, Safety, Risk, Management and Life-Cycle Performance of Bridges – Powers, Frangopol, Al-Mahaidi & Caprani (Eds)
© 2018 Taylor & Francis Group, London, ISBN 978-1-138-73045-8

3D cellular automata based numerical simulation of atmospheric corrosion process on weathering steel

J.S. Zhu, X.Y. Guo & J.F. Kang
School of Civil Engineering, Tianjin University, Tianjin, P.R. China

ABSTRACT: In order to reproduce the atmospheric corrosion process of weathering steel (WS), a three-dimensional (3D) cellular automata (CA) based method was proposed. Firstly, the basic assumptions were made with the purpose of simplifying the complicated corrosion process. Then the evolution rules of atmospheric corrosion were proposed and the MATLAB program was developed. Secondly, the results obtained from the CA model were compared with the basic corrosion laws verified by experiments. Results show that the basic hypotheses and evolution rules are reasonable and the model is reliable, which can be used to describe and to identify the corrosion kinetics, corrosion morphology and distribution characteristics of pits for WS in atmosphere. Finally, the parameter analysis was performed. The CA model can be used to continuously predict the corrosion behaviors of WS in the long-term atmospheric corrosion process.

1 NTRODUCTION

Weathering steels (WS) are increasingly used as engineering materials owing to environmental and economic advantages. The main applications of WS include bridges and other load-bearing structures, such as electricity posts, utility towers, guide rails and roofing, etc (Morcillo et al. 2013 & 2014). Protective rusts which form on the surface of WS at early stages can reduce further rusting. Therefore, WS can be used without painting or after rust stabilizing surface treatment. Being applicable to relatively mild environments such as rural and urban setting, these steels encounter difficulties in coastal areas because airborne salt deposits may generate porous and non-adhesive rusts on their surface (Nishikata et al. 2014). And when the steel structures are subjected to loads, such as bridges under vehicle loads, the protective rust layers may crack or even fall off. In these cases, the rust layers tend to lose protection, resulting in further corrosion of WS, especially pitting corrosion.

In previous studies, the atmospheric corrosion models of WS were established by fitting the long-term corrosion data. The models were mainly based on the empirical formulas (Bohnenkamp et al. 1974, Pourbaix 1982, Wang et al. 2013 & Miura et al. 2017). However, due to the fact that the corrosion data obtained from atmospheric exposure tests are discontinuous, the models cannot dynamically and continuously describe the evolution of corrosion damage of WS over time. Computational simulation technology can be used to achieve the continuous corrosion process of WS. A promising approach for simulating the corrosion evolution process is cellular automata method (Malki et al. 2005). Cellular automaton (CA), originally proposed by Von Neumann (Von Neumann & Burks, 1966), is a discrete dynamical system. It not only exhibits various properties of continuous dynamical systems but also facilitates implementation. These properties make it to be an efficient method to model complex physical and chemical systems (Chopard & Droz, 2005). Recently, extensive works from corrosion science aiming to establish the cellular automata (CA) models of metal corrosion have been done (Lishchuk et al. 2011 & Van der Weeën et al. 2014). However, an in-depth research on the corrosion process and a rigorous analysis of pit development of weathering steel (WS) by cellular automata (CA) method are lacking in civil engineering. The present study seeks to fill this gap.

The main objective of this research is to develop an approach based on 3D CA to simulate atmospheric corrosion evolution of WS by specific rules governing the electrochemical reactions and diffusion. This research consisted in the 3D CA model development, with the purpose of reproducing the actual atmospheric corrosion process of WS. To achieve this goal, the MATLAB program of corrosion evolution was developed. In order to validate the hypotheses made in the model, the results of corrosion damage growth obtained from the CA model were compared with the basic corrosion laws verified by experiments. At last, the parameter analysis was performed.

2 CELLULAR AUTOMATA METHOD

Cellular automata are described as discrete space-time dynamical systems evolving according to certain local rules. And the systems are defined in a discrete space composed of cells with finite states. Basically, the CA represent simple mathematical idealizations of physical systems. In fact, any physical system satisfying differential equations may be approximated as a CA by introducing discrete coordinates and variables, as well as discrete time steps. CA provides a simple framework to describe, simu-

late, and understand the behaviors of complex physical systems. The CA method was developed by researchers in many fields of science (Chopard & Droz, 2005), such as sociology, computer, biology, ecology, geography and physical chemistry, etc. The application of CA in civil engineering was mainly focused on the durability analysis of concrete structures in aggressive environments, such as the diffusion of carbon dioxide and chlorine ion in the concrete (Biondini et al. 2004 & Cao et al. 2012). However, the CA method was barely applied to study the damage evolution of atmospheric corrosion of steel, which could be of practical importance in quantifying corrosion damage and predicting structural integrity in engineering structures. A complete CA system is composed of cells with finite states, cell space, cell neighbors and evolution rules.

3 3D CELLULAR AUTOMATA MODEL OF CORROSION EVOLUTION

3.1 *Basic hypotheses*

In view of the complexities of atmospheric corrosion, some necessary simplifications need to be made. Based on the characteristics of CA model the basic assumptions are made as follows:

1) The corrosion kinetics is governed by the O_2 diffusion. Compared with the diffusion, the rate of chemical reaction is extremely rapid. Once Fe contacted with O_2, they react immediately.

2) The electrolyte film attached to the steel surface remains neutral during the corrosion process. The anode and cathode regions are not distinguished in the electrochemical reaction. And $Fe + 1/2O_2 + H_2O \rightarrow Fe(OH)_2$ is considered as the only chemical reaction equation in which a single corrosion product is produced. The harmful ions and pollutants in the atmosphere, such as chloride ion, sulfur dioxide and carbon dioxide, are not considered to participate in the chemical reactions.

3) It is assumed that the electrolyte film exists on the surface of steel during the whole corrosion process. The O_2 concentration in the electrolyte film remains constant in certain atmospheric environment during the corrosion process. And the H_2O is sufficient which is not consumed during the chemical reactions.

4) A cell represents a set of molecules or atoms. In order to ensure the chemical equilibrium, it is assumed that the number of atoms represented by one Fe cell is twice as many as that of molecules represented by one O_2 cell or H_2O cell.

5) The corrosion products attached to the steel surface can slow down the corrosion rate of WS. Simultaneously, the corrosion products can be dissolved with a certain probability, which will result in the continued corrosion process.

3.2 *Evolution rules of atmospheric corrosion*

3.2.1 *Configuration of cell space*

The CA model describing the atmospheric corrosion mechanisms is defined in a three dimensional cubic lattice with Von Neumann 6-connectivity. The model is composed of a 100×100×100 mesh with constant boundary conditions (on the top and bottom) and periodic boundary conditions (on the front, back, left and right). There are four different kinds of sites involved in the lattice, which are solution site W, oxygen site O, metal site M and product site P. The solution sites occupied by H_2O cells provide the neutral environment for the electrochemical reactions. The oxygen sites, metal sites and product sites are occupied by O_2 cells, Fe cells and $Fe(OH)_2$ cells, respectively. One site is only occupied by one substance based on the exclusion rules. The 3D model and profile are shown in Fig. 1. The upper half of model is the electrolyte in which the O_2 cells are distributed randomly, and the lower half corresponds to the steel substrate. The electrolyte concentration can be defined by the ratio of the sites number O/(O+W), which keeps constant during the evolution process.

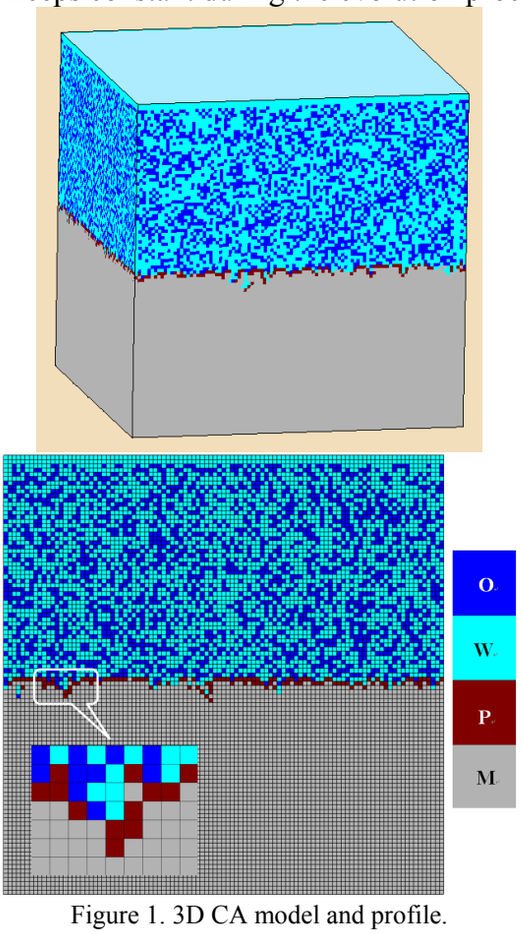


Figure 1. 3D CA model and profile.

3.2.2 *Rules of electrochemical reactions*

According to the previous definition, $Fe + 1/2O_2 + H_2O \rightarrow Fe(OH)_2$ can be expressed by M+O+W→P and P→W. P can be dissolved with probability p, by which the cracking or dissolution of protective rust layers resulting from external factors is simulated.

Based on the basic hypotheses in section 2.1, the reactions can be simplified as M+O→P+O and M+O→O+W, which occur with probability (1-*p*) and *p* respectively. The following rules of reactions are defined.

When M is faced by O, it is dissolved with a fixed probability *p*, causing that M site turns into O and that original O site is occupied by W. Otherwise, P is produced with a fixed probability (1-*p*), causing that M site turns into P and O stays put. However, when M is in contact with any other site, its site keeps unchanged. W site can be occupied by O or P, and P is deposited on the top of M site under gravity and is not affected by any other cell.

3.2.3 *Rules of oxygen diffusion*

Only the oxygen diffusion is considered in this model. A random walk method is used to simulate the diffusion process in the CA model. The rules based on the random walk method conform to the Fick's second law, which had been confirmed by Chopard and Droz (Chopard & Droz, 2005). All the O in the electrolyte simultaneously attempt to jump to the adjacent sites at each time step during the diffusion process. There are three possible outcomes when an O attempts to move to the nearest neighbor site. Firstly, if the adjacent site is occupied by another O, the O stays in place and randomly chooses a direction to face. Secondly, if the adjacent site is W faced by another O or more, the O stays in place and randomly chooses a direction to face. Finally, if the adjacent site is W and no other O face it, the O abandons its current site and swaps with the W and randomly chooses a direction to face.

In summary, during a transition, all the O_2 cells move towards the six directions randomly according to the rules of diffusion. When O_2 cells meet Fe cells, their states will change according to the rules of electrochemical reactions, and the produced $Fe(OH)_2$ cells are deposited under gravity. The MATLAB program is developed to implement the process.

4 MODEL ANALYSIS AND VERIFICATION

The developed model aims at simulating the evolution of atmospheric corrosion of WS, permitting to describe and identify the corrosion kinetics, corrosion morphology and distribution characteristics of pits for WS in atmosphere. For the initial conditions, the lower dissolution probability can be used to describe the formation of a dense and well-adhering rust layer on the surface of WS and the O_2 concentration is mainly related to the environmental parameters. When WS is located in the high relative humidity regions, the electrolyte film on the steel surface can last for a longer time. So the quantity of O_2 reacting with Fe is larger than that in dry environment. As an example, the O_2 concentration *c* and dissolution probability *p* are set as 60% and 0.3 in following analysis, respectively.

4.1 *Corrosion kinetics*

Fig. 2 and Fig. 3 show the variation of average depth and corrosion rate with time steps, respectively. The corrosion rate is equivalent to the variation of average depth per unit time step. In Figs. 2 and 3, the points *A*, *B*, *C* and *D* in curves correspond to the time step 10, 100, 200 and 400, respectively. It is observed that the evolution process of atmospheric corrosion of WS can be divided into four phases: initial phase (before point *A*), rapid growth phase (point *A* to *B*), slow growth phase (point *B* to *C*) and steady phase (after point *C*). In initial phase, the average depth increases linearly with time steps, and the corrosion rate is at a high level. In this phase, the rust layers formed on the surface of WS are porous which cannot provide good protections. Subsequently, the corrosion process proceeds to rapid growth phase, where a great increase in corrosion degree appears. For the WS exposed in atmosphere, the rust layers gradually thicken and the inner rust layers close to substrate begin to become dense. Furthermore, the growing rust layers hinder the O_2 penetration and slow down the diffusion, resulting in the decrease of corrosion rate, as described in Fig. 3. Then the corrosion rate is reduced to point *B*, and the slow growth phase begins. In this phase, the dense protective layers continue to develop and the average depth grows slowly to point *C*. After point *C*, the corrosion rate is close to zero and the average depth keeps virtually unchanged. In steady phase, it is considered that the stable protective layers have formed on WS.

As Bohnenkamp et al. noted in 1974, the corrosion curves of WS obey power function and most of the experimental atmospheric corrosion data has been found to adhere to the following kinetic relationship (Morcillo et al. 2013):

$$C = At^{n} \tag{1}$$

where *C* is the corrosion depth after time *t*, *A* and *n* are constants. *A* is equivalent to the corrosion after the first year of exposure, which is considered as a measure of the initial corrosion resistance of WS. *n* is the time exponent, reflecting the change in average corrosion depth with exposure time and the corrosion evolution of WS. The value of *n* does not affect the corrosion in first year but corrosion in successive years.

In order to determine the relationship between corrosion rate and exposure time, an exponential decrease equation was proposed by M. Morcillo et al. based on a large number of experimental data, as follows:

$$y = A_1 \exp(\frac{-x}{t_1}) + y_o \quad (2)$$

where y is the corrosion rate, x is the exposure time, A_1, t_1 and y_o are constants. In general, the Eqs. (1) and (2) are obtained by fitting the short-term experimental data, and the longest time for WS specimens exposed in atmosphere is about 20 years.

As shown in Figs. 2 and 3, the Eqs. (1) and (2) are used to fit the curve segments which are from point A to C, respectively. The correlation coefficients are 0.9657 and 0.9924, respectively. It is proved that the simulation results agree well with the corrosion laws presented by the experimental results.

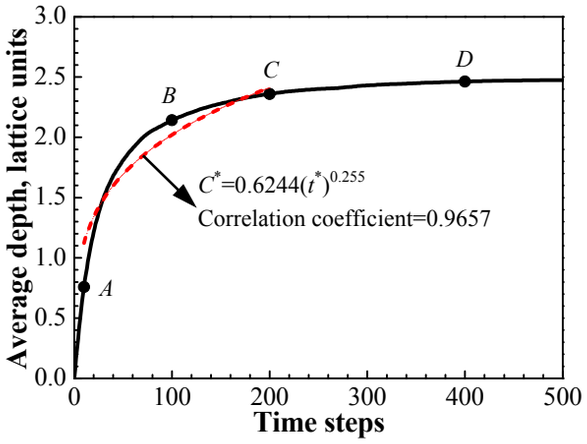


Figure 2. Average depth as function of time steps.

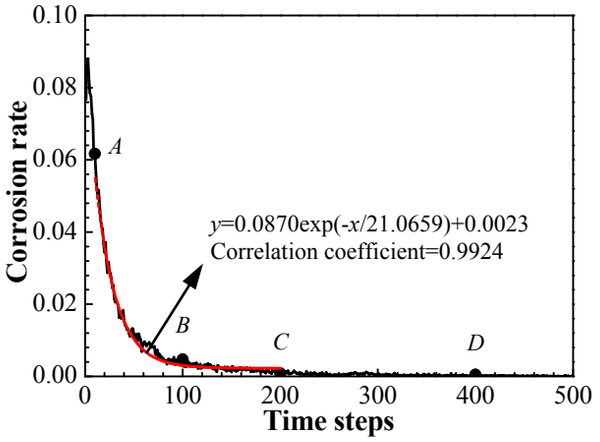


Figure 3. Corrosion rate as function of time steps.

4.2 *Corrosion morphology*

Fig. 4 shows the overall corrosion morphologies of WS at different time steps. At time step 10, the pits initiation is observed and a few of pits with a maximum depth of 4 lattice units appear. With the increase of time steps, the initiated pits grow in size and new pits also begin to initiate. At time step 100, the top layer of entire area is corroded. The pit depth is mainly 1 to 3 lattice units, while only one pit with the depth of 8 lattice units is found. Then more pits reach the 8 lattice units depth. More wide and shallow pits appear at time step 200. Subsequently, the pits area increases with time steps but the average depth for whole sample basically remains constant owing to the increasing protections of rust layers.

Fig. 5 shows the variations in the cross-sectional shape of pits at different time steps. It can be seen that the variations of corrosion depth are consistent with the law described in Figs. 2 and 4. As observed in Fig. 5, the cross-sectional shapes of pits primarily contain: vertical, wide and shallow, elliptical, narrow and deep, subsurface, horizontal and undercutting, etc. These shapes are similar to those presented in ISO 11463. In steady phase, the cross-sectional shapes of pits are mainly wide and shallow, and elliptical.

4.3 *Distribution characteristics of pits*

Fig. 6 shows the distribution characteristics of pits. According to statistical analysis, at time step 10, 62.5 percent of the entire area is corroded, and pits with the depth of 1 to 2 lattice units account for 98.7 percent of all the pits. Subsequently, as time steps increase, the proportion of pits with the depth of one lattice unit begins to decline while the proportion of pits with the depth of 2 to 4 lattice units starts to raise. After 200 time steps, the frequencies of different depth pits tend to be stable. Generally, in terms of time step 100, 200 and 400, the pits with the depth of 1 to 3 lattice units account for 91.7, 85.6 and 84.0 percent, respctively. Based on the previous studies, the pit depth conforms to the Weibull distribution preferentially (Xu et al. 2012). Weibull statistical analysis is based on the weakest link theory about chain, and its cumulative distribution function is as follow (Weibull, 1951):

$$F(x) = 1 - \exp[-(\frac{x-\sigma_u}{\gamma})^m] \quad (3)$$

where x is the pit depth, σ_u is the location parameter, γ is the scale parameter, and m is the shape parameter. σ_u is usually taken as 0 in practical application and the Eq. (3) can be simplified as a function with two parameters. Therefore, the probability density function can be expressed by:

$$f(x) = \frac{m}{\gamma^m} x^{m-1} \exp[-(\frac{x}{\gamma})^m] \quad (4)$$

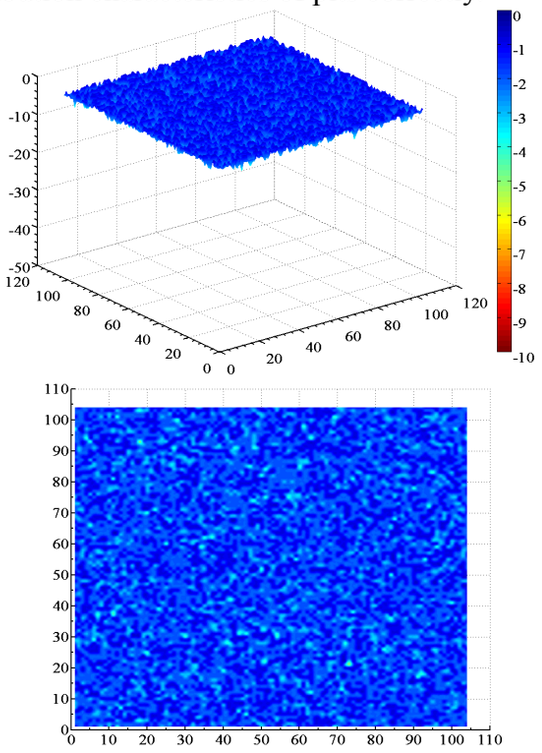
$$\mu = \gamma \cdot \Gamma(1 + \frac{1}{m}) \quad (5)$$

$$\sigma^2 = \gamma^2 \cdot \Gamma(1 + \frac{2}{m}) - \mu^2 \quad (6)$$

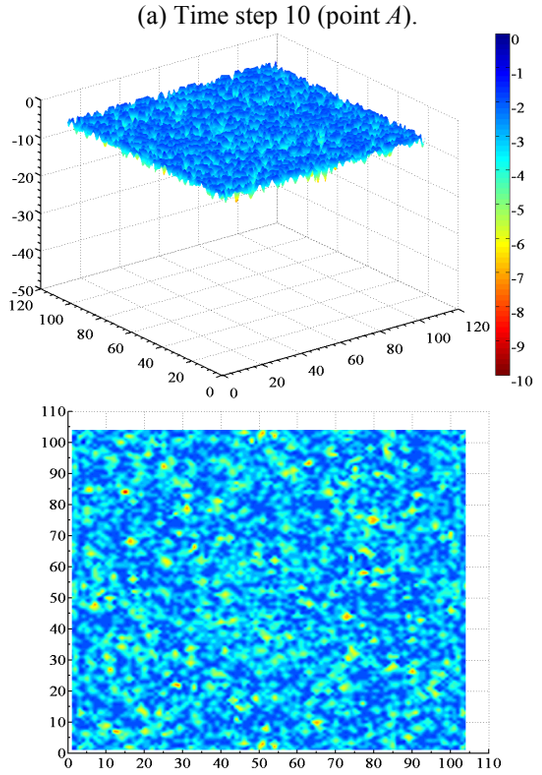
where μ and σ are the mean and standard deviation of pit depth, respectively. Γ corresponds to the gamma function.

In the present study, Eq. (4) is used to fit the distribution of pit depth, as described in Fig. 6. According to m and γ obtained by fitting, Eqs. (5) and (6) are used to calculate μ and σ, respectively. In addition, a comparison between calculation and simulation results is presented in Table 1. It can be observed that Eq. (4) produce good agreement with the distribution of pit depth which is acquired from the CA model, and the mean and standard deviation calculated by equations get close to the simulation re-

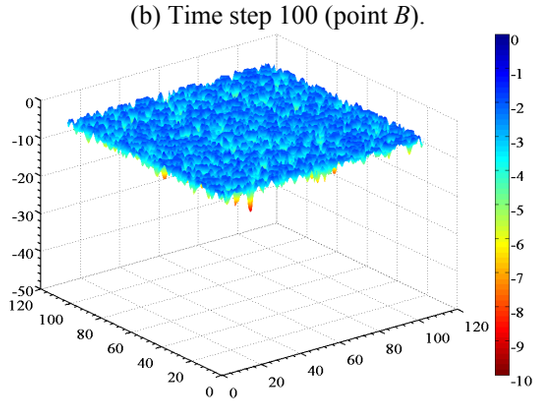
sults. It is proved that the CA model can reflect the distribution characteristics of pits correctly.

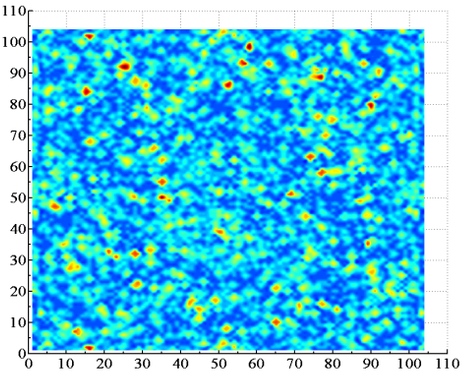


(a) Time step 10 (point *A*).

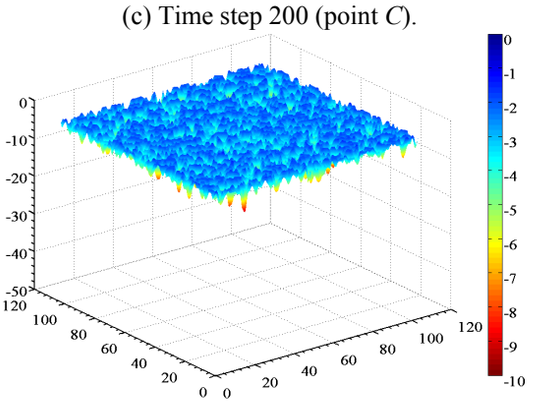


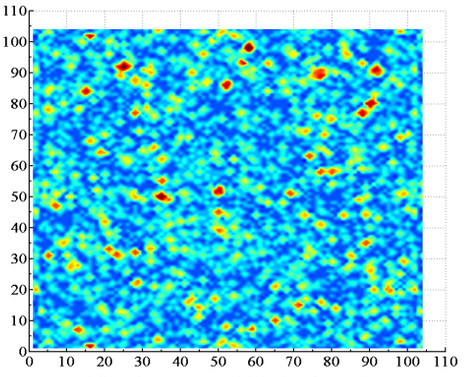
(b) Time step 100 (point *B*).





(c) Time step 200 (point *C*).





(d) Time step 400 (point *D*).

Figure 4. Corrosion morphologies of WS at different time steps.

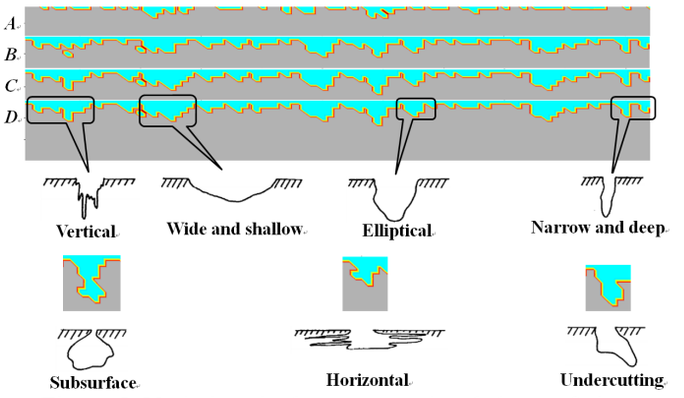


Figure 5. Variations in the cross-sectional shape of pits.

To sum up, the simulation results including the corrosion kinetics, corrosion morphology and distribution characteristics of pits accord with the general atmospheric corrosion laws of WS. It is indicated that the basic hypotheses made in section 3.1 are reasonable and the model is reliable. The 3D CA model can be used to simulate the evolution of atmospheric corrosion for WS effectively.

Table 1 Comparison between calculation and simulation results for statistical characteristics.

Corrosion process	m	γ	Correlation coefficient	Mean μ (Weibull)	Mean μ^* (CA)	μ^*/μ	Standard deviation σ (Weibull)	Standard deviation σ^* (CA)	σ^*/σ
A (time step 10)	2.668	1.269	0.9999	1.1280	1.1813	1.05	0.4555	0.4202	0.92
B (time step 100)	2.264	2.229	0.9984	1.9744	2.0765	1.05	0.9233	0.9830	1.06
C (time step 200)	2.111	2.422	0.9960	2.1451	2.2964	1.07	1.0681	1.1734	1.10
D (time step 400)	2.041	2.466	0.9969	2.1847	2.3616	1.08	1.1214	1.2659	1.13

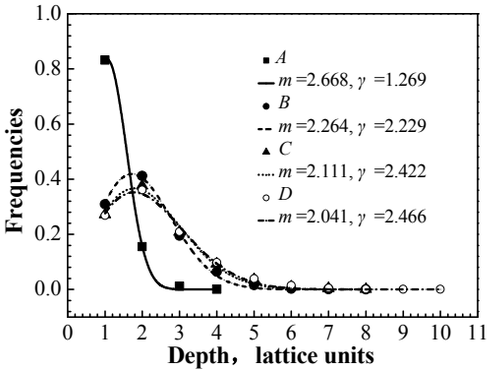
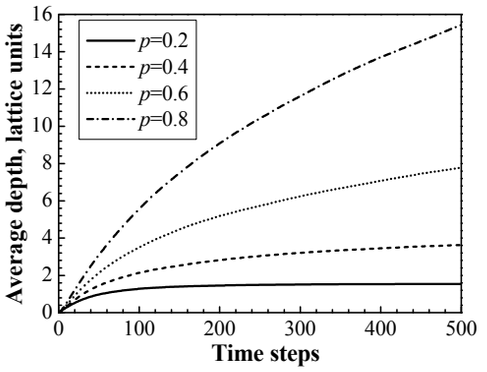
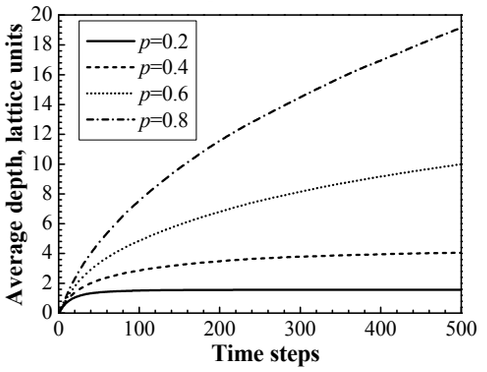


Figure 6. Frequencies of pit depth.

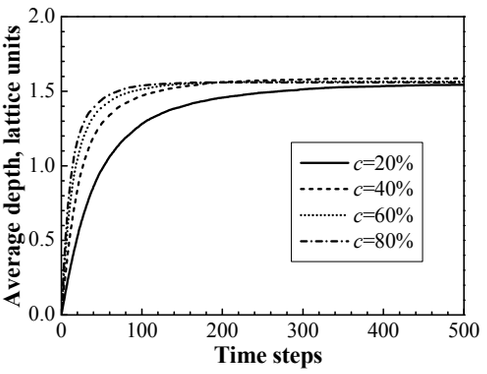


(a) c=20%, p=0.2, 0.4, 0.6, 0.8.

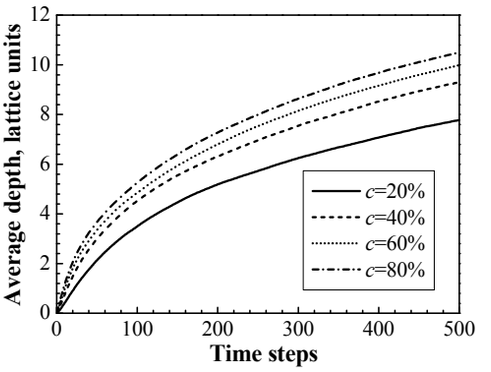


(b) c=60%, p=0.2, 0.4, 0.6, 0.8.

Figure 7. Effects of dissolution probability upon the time dependence of the average depth.



(a) p=0.2, c=20%, 40%, 60%, 80%.



(b) p=0.6, c=20%, 40%, 60%, 80%.

Figure 8. Effects of O_2 concentration upon the time dependence of the average depth.

5 PARAMETER ANALYSIS

The atmospheric corrosion of WS is not a continuous process. Electrochemical corrosion occurs only when the electrolyte film is formed on the surface of steel. It has been proved by experiments that relative humidity is the key parameter influencing the long-term atmospheric corrosion of WS (Gong et al. 2009). The relative humidity can influence the thickness and existence time of electrolyte film, thus further affect the quantity of O_2 reacting with steel. Moreover, temperature can affect the O_2 diffusion through electrolyte film. Hence the influence of relative humidity and temperature on the atmospheric corrosion can be attributed to that of O_2 concentration. The behaviors of rust layers are affected by the chemical compositions of WS, concentration of erosive ions and external loads. The influence of these factors can be attributed to that of dissolution probability. Therefore, the parameters including dissolution probability and O_2 concentration are analyzed in this section.

The effect of dissolution probability and O_2 concentration upon the corrosion kinetics is presented in Fig.7 and Fig.8, respectively. It can be seen that the dissolution probability has a significant impact on the corrosion rate. The corrosion rate increases with the dissolution probability, which leads to the differences of average depth for different dissolution probabilities. And with the increase in time steps, the differences get larger and larger. In addition, it requires more time steps to reach the steady phase in terms of the larger dissolution probability. As observed in Fig.8, the O_2 concentration has an effect on the early stage corrosion rate but has no effect on

the final corrosion state. With the increase of O_2 concentration, the time steps that it takes to reach the steady phase decreases. In general, the final corrosion damage of WS is determined by the dissolution probability, while the O_2 concentration only affects the time steps required to reach the final corrosion state.

6 CONCLUSIONS

The objectives of this study were to reproduce the atmospheric corrosion process of WS at the mesoscopic scale and obtain the macroscopic expression of cumulative corrosion damage. The following conclusions are obtained by the intensive analysis:

(1) The simulation results conform to the general atmospheric corrosion laws of WS. Therefore, the basic hypotheses and evolution rules of corrosion are reasonable and the model is reliable. 3D CA method is presented as a useful tool with the application of simulation of atmospheric corrosion process. It can permit to describe and identify the corrosion kinetics, corrosion morphology and distribution characteristics of pits for WS in atmosphere.

(2) The evolution process of atmospheric corrosion of WS can be divided into four phases: initial phase, rapid growth phase, slow growth phase and steady phase. In initial phase, the average depth increases linearly with time steps. In second phase, the growing rust layers hinder the oxygen penetration, which results in the decrease of corrosion rate. Subsequently, the dense protective layers continue to develop. In steady phase, as the corrosion rate is close to zero, it is considered that the stable protective layers have formed on WS.

(3) During the evolution process, many metastable pits cannot grow into stable pits because of the protections of rust layers. The surface morphologies of stable pits develop from ellipse to diamond with the increase of time steps. In general, the simulated morphology can be seen as a realistic representation of multi-pit corrosion damage and the CA model can reflect the distribution characteristics of pits correctly.

(4) The final corrosion damage of WS is determined by the dissolution probability, while the oxygen concentration only affects the time required to reach the final corrosion state.

ACKNOWLEDGEMENTS

This work presented here is supported by the National Science Fund of China (51578370) and the National Science Fund of Tianjin (16JCZDJC40300 and 16YFZCSF00460). Any opinions, findings and conclusions or recommendations expressed in this paper are those of the authors and do not necessarily reflect those of the sponsor.

REFERENCES

Biondini, F., Bontempi, F., Frangopol, D. M. & Malerba, P. G. 2004. Cellular automata approach to durability analysis of concrete structures in aggressive environments. *Journal of Structural Engineering* 130(11): 1724-1737.

Bohnenkamp, K., Burgmann, G. & Schwenk, W. 1974. Corrosion atmospherique de l'acier doux, Exposition de l'acier aux intemperies, *Galvano-Organo* 445: 587-589.

Cao, J., Wang, Y. F., Li, K. P. & Ma, Y. S. 2012. Modeling the diffusion of chloride ion in concrete using cellular automaton. *Journal of Materials in Civil Engineering* 24(6): 783-788.

Chopard, B. & Droz, M. 2005. *Cellular automata modeling of physical systems*. Cambridge University Press, Cambridge.

Gong, M., Yu, Z. X. & Chen, L. 2009. *Metal Corrosion Theory and Corrosion Control*, Chemical Industry Press, Beijing (in Chinese).

ISO 11463: 1995. Corrosion of metals and alloys-Evaluation of pitting corrosion.

Lishchuk, S.V., Akid, R., Worden, K. & Michalski, J. 2011. A cellular automaton model for predicting intergranular corrosion. *Corrosion Science* 53(8): 2518-2526.

Malki, B. & Baroux, B. 2005. Computer simulation of the corrosion pit growth. *Corrosion Science* 47(1): 171-182.

Miura, S., Murase, M., Okamoto, T., Dang, D. T. & Iwasaki, E. 2017. Corrosion behavior and applicability of weathering steel in vietnam. *Journal of Materials in Civil Engineering* 29(4): 04016264.

Morcillo, M., Chico, B., Díaz, I., Cano, H. & Fuente, D. D. L. 2013. Atmospheric corrosion data of weathering steels. A review. *Corrosion Science* 77(12): 6-24.

Morcillo, M., Díaz, I., Chico, B., Cano, H. & Fuente, D. D. L. 2014. Weathering steels: From empirical development to scientific design. A review. Corrosion Science 83(7): 6-31.

Nishikata, A., Zhu, Q. & Tada, E. 2014. Long-term monitoring of atmospheric corrosion at weathering steel bridges by an electrochemical impedance method. *Corrosion Science* 87(5): 80-88.

Pourbaix M. 1982. The linear bilogaritmic law for atmospheric corrosion. In Ailor, W.H. (ed.), *Atmospheric corrosion*, The Electrochemical Society, John Wiley and Sons, New York, 107-121.

Van der Weeën, P., Zimer, A.M., Pereira, E.C., Mascaro, L.H., Bruno, O.M. & De Baets, B. 2014. Modeling pitting corrosion by means of a 3D discrete stochastic model. *Corrosion Science* 82: 133-144.

Von Neumann, J. & Burks, A.W. 1966. *Theory of Self-reproducing Automata*, University of Illinois Press, Urbana.

Wang, Z. F., Liu, J. R., Wu, L. X., Han, R. D. & Sun, Y. Q. 2013. Study of the corrosion behavior of weathering steels in atmospheric environments. *Corrosion Science* 67(2): 1-10.

Weibull, W. 1951. A statistical distributions function of wide applicability. *Journal of Applied Mechanics* 13(2): 293-297.

Xu, Y. D., Qian, C. X. & Sun, J. Y. 2012. Evolution and distribution of corrosion pits in reinforcing bars under coupled chemo-mechanical attacks. *Journal of Southeast University (Natural Science Edition)* 42(3): 492-497 (in Chinese).

Maintenance, Safety, Risk, Management and Life-Cycle Performance of Bridges – Powers, Frangopol, Al-Mahaidi & Caprani (Eds)
© 2018 Taylor & Francis Group, London, ISBN 978-1-138-73045-8

Structural performance of bridges under deterioration processes: Bicentenario Bridge

J.D. González & F.A. Cerda
University of Concepción, Concepción, Chile

ABSTRACT: Over time, bridges reduce their expected performance levels to environmental and mechanical effects under service loads or extreme events. This research presents a methodology to include corrosion and fatigue deterioration processes in the bridge analysis. In addition, performance and reliability assessments of the structure over time are conducted based on current design standards: strength, fatigue and serviceability. Uncertainties related to estimation of vehicle load, properties of the materials and parameters associated with corrosion are included by means of a probabilistic distribution.

These techniques are applied to a real case study, the Bicentenario Oriente Bridge, currently under construction in Concepción, Chile. The steel girders of a particular span are studied and by means of a fault tree analysis the reliability of the system is calculated by reliability at element level. This analysis allows an evaluation of the proposed methodology and verification of the expected diagnoses for bridges with similar structure.

1 INTRODUCTION

In Chile, there are around 12,000 bridges, which require a periodic evaluation of their structural condition. Due to the earthquake of 2010, of the 100 bridges that suffered damage, 20 collapsed. Currently, the integrity of all structures and their possible performance in face of future events are not known (Tang 2010).

Structural health monitoring (SHM) aims to predict and reduce the risks associated with different levels of structural damage by studying its structural condition with periodic reviews, sensor implementation, and subsequent analysis and interpretation of data.

In civil engineering, the application of SHM arises from the need of private and governmental industries to detect damage to their infrastructure early in order to generate an increase in safety of human lives and to decrease the economic impact associated with structures out of operation (Farrar & Worden 2006).

Civil structures, due to their inherent vulnerability are prone to deterioration through corrosion, fatigue and physical damage over their life-cycle. This can lead to unsatisfactory performance under service loads, natural disaster or extreme events.

The study of the condition of the structure over time allows the prediction of the remaining useful life and the incorporation of maintenance strategies to ensure that the structure operates over a range of minimum performance.

2 PERFORMANCE MODEL

One way to study the structural condition is by applying a performance model that includes the effects of degradation over time. Similarly, one way of assessing structural performance is through the reliability index associated with the limit states of the current design standard.

Throughout structures life-cycle, their initial performance level decrease reaching unsatisfactory levels due to environmental and mechanical factors over time under service loads or extreme events.

It is necessary to have maintenance that corrects the problems presented in the structure in order to increase the lifetime and reduce the costs associated with maintaining operating structure, which increases the values of the performance indicator.

Because the condition of the structure decreases over time, the accumulated deterioration until time t can be defined as $D(t)$. The rate of degradation can change drastically over time due to variations in environmental conditions, material properties, use loads, among other. For a case where there is no maintenance, the performance indicator can be written as:

$$V(t) = \max\{V_o - D(t), 0\} \quad (1)$$

where $V(t)$ is the performance indicator; V_o is the remaining life of the system at time t equal 0; and $D(t)$ is the accumulated deterioration at time t.

In Figure 1, a performance curve is presented with the application of a corrective maintenance at time t_f. It is observed that $V(t)$ is the performance indicator; $D(t)$ is the accumulated deterioration at time t; t_f is the time at witch limit performance is reached; k^* is the limit performance. It is observed that when the performance indicator reaches the acceptable limit value, a corrective maintenance is performed (Sánchez-Silva et al. 2016).

According to Sánchez-Silva & Klutke (2016), continuous degradation models can be divided into progressive and shock-based. The progressive degradation consists in that the capacity of the structure decreases continuously linearly or non-linear in time. The expression is presented below:

$$V(t) = V_o - \int_0^t \delta(\tau) d\tau \quad (2)$$

where V_o corresponds to the remaining life of the system at time t equal 0; $\delta(t)$ is the rate of deterioration; t is the domain of integration.

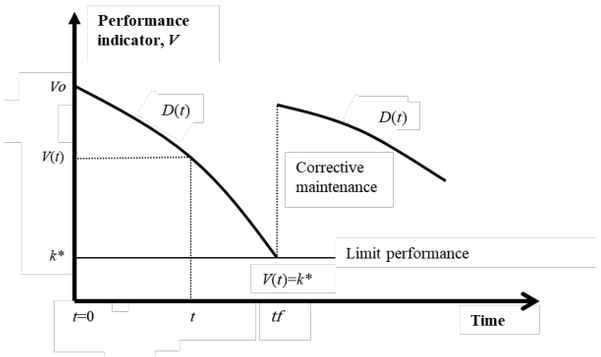


Figure 1. Description of system performance over time (Sánchez-Silva et al. 2016).

On the other hand, shock-based degradation is caused by extreme events such as earthquakes, tsunamis, fires, etc. These events cause a significant change in the physical properties of the system over a short period of time. The expression representing it is shown below:

$$V(t) = V_o - \sum_{i=1}^{Ni} Y_i \quad (3)$$

where Y_i corresponds to the random variable that describes the deterioration caused by event i; N_i is the ith event.

Frequently, both degradation processes occur simultaneously throughout the structure life-cycle. The expression is presented below:

$$V(t) = V_o - \int_0^t \delta(\tau) d\tau - \sum_{i=1}^{Ni} Y_i \quad (4)$$

2.1 *Reliability index and probability of failure*

The structural condition can be presented by reliability or probability of failure associated with a limit state. The latter consists of an event whose occurrence must be avoided to ensure proper behavior of the structure. Due to the uncertainties present in the lifetime of the structure, resistance and demand should be considered as random variables.

For a structural element, the resistance is represented over time by $R=R(t)$, the demand by $S=S(t)$ and the performance function by $g=g(t)$ with $g(t)=R(t)-S(t)$. Considering r_k y s_k as the results of the variables $R_k=R(t_k)$ y $S_k=S(t_k)$, respectively, the probability of failure at time $t=t_k$ can be evaluated by integrating the density function in the fault domain. The expression is presented below:

$$P_f(t_k) = P[R_k < S_k] = P[g \le 0] = \int_{\tau_k} f^k_{R,S}(r,s) dr ds \quad (5)$$

As an alternative way, the structural safety can be evaluated by the reliability index $\beta_k=\beta(t_k)$.

$$\beta(t_k) = \frac{\mu_{R,k} - \mu_{S,k}}{\sqrt{\sigma^2_{R,k} + \sigma^2_{S,k} - 2\rho_k \sigma_{R,k} \sigma_{R,k}}} \quad (6)$$

where μ and σ correspond to the mean and standard deviation, respectively; and ρ_k corresponds to the correlation between R and S.

If resistance and demand are normal variables, the probability of failure and the reliability index are related by the following expression:

$$P_f(t_k) = \phi(-\beta_k) \quad (7)$$

where $\phi(\cdot)$ corresponds to standard normal cumulative probability function.

Figure 2 presents the probabilistic distribution of resistance and demand of the structure (Soliman 2015).

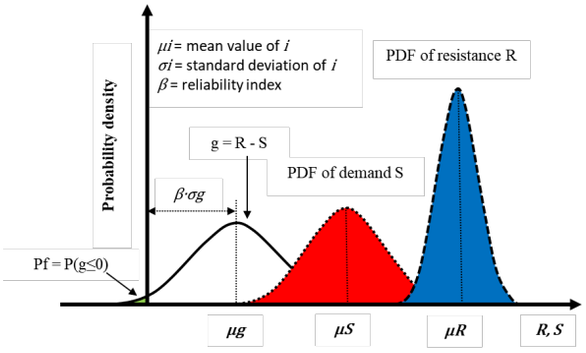


Figure 2. Concept of probability of failure and reliability index (Soliman 2015).

Soliman (2015) presents the resistance and demand values as probabilistic distributions with a mean and standard deviation. In the same way, the probability of failure is represented as the area where $g \leq 0$.

2.2 *Corrosion model*

The corrosion models mainly present the effect of uniform corrosion on the structural elements, being the main cause of this phenomenon the accumulation of water and salt on the steel surfaces (Kayser & Nowak 1989a). These models consist of the representation of the loss of surface at the cross-sectional and longitudinal level of the element that generates a loss of area, inertial and stiffness.

Corrosion severity depends on the properties of the material (material alloys), local atmosphere (temperature and relative humidity) and exposure conditions such as initial climate, exposure duration, orientation, exposure angle, time of wetness, atmospheric pollutants, de-icing salt.

Klinesmith et al. (2007) developed a model of atmospheric corrosion taking into account four environmental variables (wetness, sulfur dioxide, salinity and temperature). The expression is presented below:

$$Y(t) = A\, t^{B} \left(\frac{TOW}{C}\right)^{D} \left(1 + \frac{[SO_2]}{E}\right)^{F} \left(1 + \frac{[Cl]}{G}\right)^{H} e^{J(T + T_O)} \tag{8}$$

where Y is the corrosion loss in μm; t is the exposure time in years; TOW is the time of wetness in h/year; SO_2 is the concentration of sulfur dioxide in μg/m^3; Cl is the chloride deposition rate in mg/m^2/day; T is the environmental temperature in °C; and A, B, C, D, E, F, G, H, J, T_o are empirical coefficients.

Figure 3 shows dark areas where corrosion patterns usually occurs in steel girder bridges (Kayser & Nowak 1989b). It can be seen that the surface with corrosion near the supports occurs throughout the web height. In the middle zone, corrosion occurs in the lower quarter web height.

Kayser & Nowak (1989b) identified the areas where the highest values of corrosion were produced due to the presence and accumulation of surface water, temperature, salinity, among others.

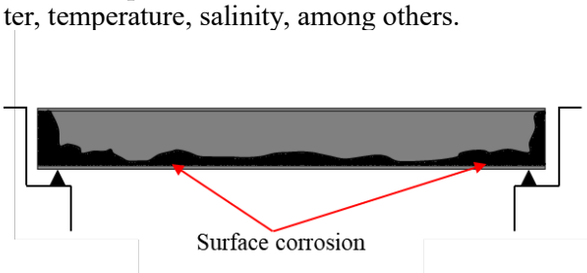


Figure 3. Corrosion pattern of a steel girder bridge (Kayser & Nowak 1989b).

By combining information on location and corrosion ratio together with the structural analysis of the elements for the calculation of stresses, a structural condition degradation model can be generated which indicates performance over the structure life-cycle.

2.3 *Limit states and loads*

All structures have basic requirements: safety against collapse and satisfactory performance over its lifetime. Likewise, stability, strength, functionality and durability requirements must be met. Limit states usually define the various ways in which a structure does not meet these basic requirements. If the structure does not exceed one of the limit states, it is considered that it no longer fulfills the functions for which it was designed.

AASHTO LRFD Bridge Design Specifications consider factors for each load and for each nominal resistance. The vehicle loads can be represented in three types: design truck, design tandem and design lane load.

For the evaluation of the structural performance, the reliability index was calculated by means of the limit states of Strength I, Fatigue and Service II (ASSHTO LRFD).

3 STRUCTURAL MODELING

A structural model is generated that allows the analysis of a composite steel beam, where input data correspond to the initial dimensions and cross-section of the element, corrosion values, distribution of corrosion on the elements and the permanent and transient loads, among others. Corrosion penetration was represented on a yearly time scale.

After applying the respective factors, the effects of service loads are compared with the values of limit states presented in AASHTO LRFD and reliability index of the elements is calculated.

The structural model of the composite beam is performed using the OpenSees (Open System for Earthquake Engineering Simulation) software that incorporates within its commands and library the representation of structural elements through the use of finite elements.

The finite element model generates structural behavior data through different corrosion scenarios for the beam elements. The model consists on the representation of a composite element (steel beam and concrete slab). This consists of the representation of the cross-section with rectangular and linear elements in order to give them different material properties. The first elements are called patch quad and represents the steel beam and the concrete of the reinforced concrete slab; the second elements are called layer straight and are used to represent the re-

inforced steel of a section of a reinforced concrete slab.

The behavior of the beam is represented discreetly; each level of corrosion corresponds to one year of use of the structure. The AASHTO LRFD standard indicates that design life of a bridge should be at least 75 years. However, Feyermuth (2009) indicates that bridges must have a minimum service life of 100 years under appropriate maintenance actions but without large repairs. For each of the year of study, iteration is generated to the model that includes corrosion, cross-sections and previous results.

The input data of the model correspond to: properties of the materials, length of the elements, types of support, cross-sections, corrosion values and loads with their respective factors depending on the limit state.

The applied load on the model correspond to dead loads due to structural components and wearing surfaces; to vehicle loads by design lane load and design truck, represented as distributed and punctual load, respectively.

The output data of the model are stresses, deformations, displacements and forces at the points of interest.

Figure 4 presents a flowchart of the structural modeling process and calculation of reliability index by means of the limit states of Strength I, Fatigue and Service II. It is possible to observe the case of deterioration considered and the factors involved in the calculation of the penetration of corrosion.

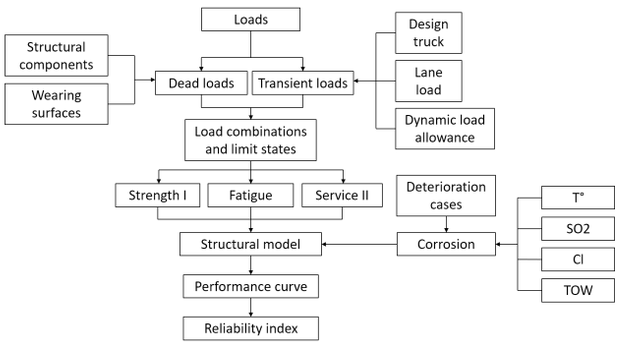


Figure 4. Flowchart of the modeling process and obtaining results.

As mentioned, the behavior of an element under the effects of corrosion is represented by a loss of thickness in the different elements of steel girder cross-section (flange and web).

The formulation of the corrosion pattern presented by Kayser & Nowak (1989b) with the corrosion values extracted from Klinesmith et al. (2007) is carried out by using the finite element tool by means of cross-sections of the fiber type for the representation of the beam and slab elements.

In this study, the corrosion representation is made by removing the affected zones of the steel section for each level of corrosion, both in the web and in the bottom flange along the beam. Figure 5 shows modeling of the cases without corrosion and with corrosion in middle sector and the supports. It can be observed that the painted areas represent the corrosion in the steel element, according to the patterns presented by Kayser & Nowak (1989b).

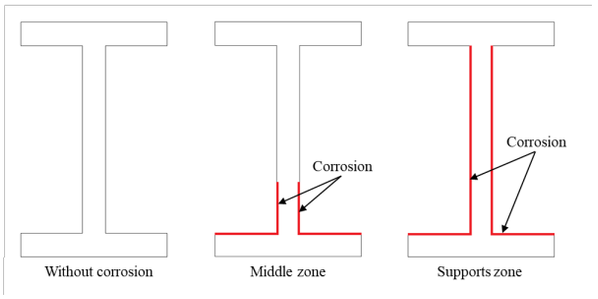


Figure 5. Corrosion scenarios for the steel beam represented in the model.

4 CASE STUDY

The methodology was applied to the Bicentenario Oriente Bridge in its structure located to the east side, currently under construction in Concepción, Chile. The objective of the road project is to increase connectivity between Concepción and San Pedro de la Paz. The bridge is represented by a simply supported span.

The structure is represented by the model previously explained in OpenSees software. The inputs are the dimension and materials of the elements; the permanent and transient loads given by the weight of the elements and the vehicular loads; and corrosion values for each damage scenario.

The distribution coefficient that represents the effect of the loads in the structure is incorporated in OpenSees by means of a 3D model.

4.1 Characteristics of the structure

The total length of the bridge is 1490m between north and south abutments. These points are connected to the main streets through access structures. The bridge has two traffic lanes 3.5 m wide each. Figure 6 presents the location of the Bicentenario Oriente Bridge over the Biobío river.

The structure is composed of 3 girder spans with lengths ranging between 39.60 m and 40.66 m. The span to be studied has a length of 39.72 m and is supported by piers C10 and C11. The spacing between longitudinal girders is 3.5 m. The length of each girder is 39.52.

The steel girders vary their cross-section longitudinally. The thickness of the flange increases as the center of the span is reached. Four zones are generated with different cross-section for each half girder. The three elements that compose the span have the

same characteristics. Figure 7 shows the four zones representing half of each girder. It is possible to emphasize that the girders are symmetrical with respect to their middle point. They are made of A573 Gr 50 steel with yield strength of 345 MPa.

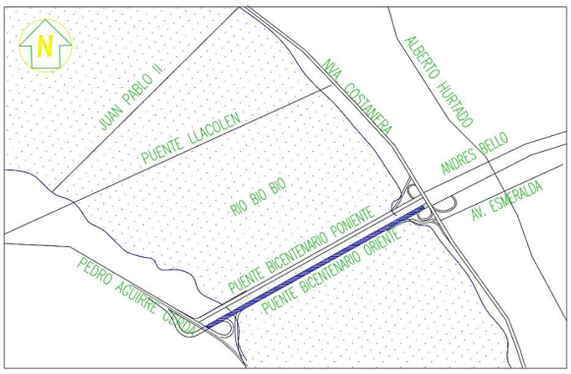


Figure 6. Location of Bicentenario Oriente Bridge, Chile (Public Works Ministry, Chile).

Table 1 shows the dimensions of the four zones representing half of the element.

Table 1. Dimensions of each cross-section of the girder.

Dimension	Zone 1	Zone 2	Zone 3	Zone 4
	mm	mm	mm	mm
Length	8760	1000	4000	6000
Top flange width	400	400	400	400
Top flange thickness	20	20	30	30
Web depth	2000	2000	2000	2000
Web thickness	12	12	12	12
Bottom flange width	500	500	500	500
Bottom flange thickness	30	38	38	50

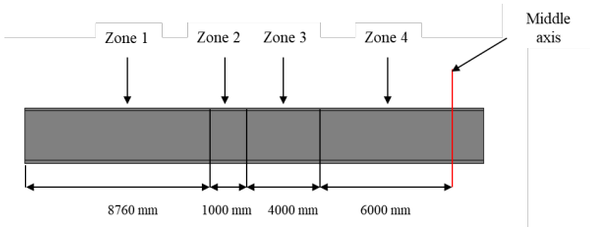


Figure 7. Cross-sections of the girder (Public Works Ministry, Chile).

4.2 *Corrosion values*

The mean penetration values are given by expression presented by Klinesmith et al. (2007). The values of temperature, time of wetness, sulfur dioxide concentration and chloride deposition rate correspond to data representative of Concepción.

Figure 8 shows the increase in penetration of the element surface as the years of exposure increase.

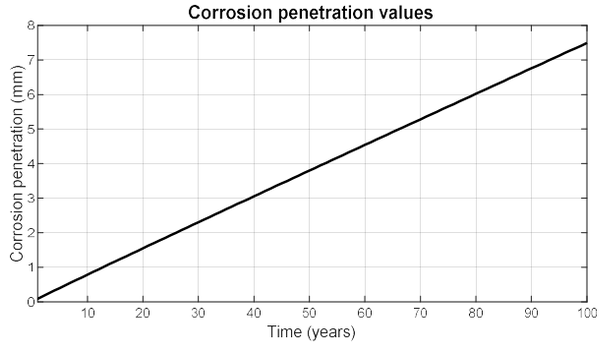


Figure 8. Penetration of corrosion on the surface of the element.

4.3 *Variability in loads*

Due to the consideration of design loads as operation loads in the bridge lifetime, it is necessary to add stochastic characteristics that consider the variability of them in the operation of the structure.

The average values considered in the study are those extracted from the software by means of the analysis with input of the properties and loads presented in the previous sections with their respective load and distribution factors.

In the same way for the values of resistance, it is considered variability associated to the properties of the materials, corrosion parameters, atmospheric conditions, construction of the structure, among others.

Table 2 shows the values of the coefficients of variation considered in the reliability index calculations.

Table 2. Coefficient of variation values for permanent loads, transient loads and strength.

Load	CV
Permanent	0.10
Transient	0.20
Resistance	0.05

5 RESULTS

In the next section it is presented the results obtained from the analysis of the elements of the study case structure for interior and exterior girder.

5.1 *Limit state Strength I*

The strength limit state compares the ultimate moment acting on element with nominal moment that is a function of the plastic moment and corresponds to resistance.

Figure 9 shows the nominal moment values for the largest cross-section of the element corresponding to the middle zone (zone 4) for interior and exterior girder. The degradation of the resistance in rela-

tion to the time of exposure to the effects of corrosion can be observed. The slope difference is produced by the location of the neutral axis in each girder member due to the different concrete areas in each composite section. In the same way, the latter justifies the higher values for the interior girder.

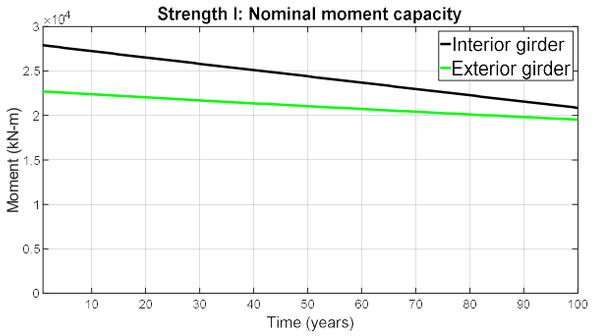


Figure 9. Nominal moment, cross-section zone 4, Strength I.

The reliability index is presented in Figure 10. It is observed that due to the expressions present in the calculations of the limit states, the reliability index curves for each element have the same characteristics as the nominal moment curves. Limits are not reached with the study period. However, a much higher rate of decrease for the interior girder can be noted.

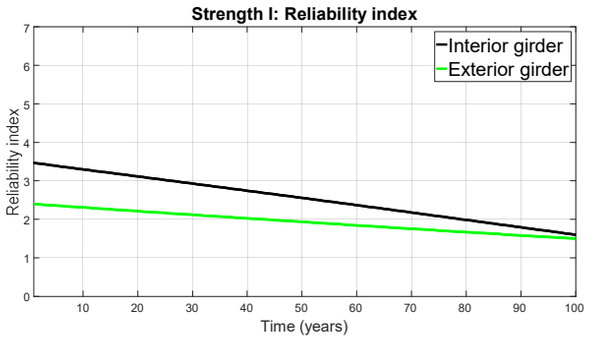


Figure 10. Reliability index, Strength I.

5.2 *Limit state Fatigue*

The fatigue limit state compares the stress range with the stress limits for each number of cycles.

Figure 11 (logarithmic scale) shows the stress range limit curve for the detail studied on the bridge girder. This curve includes finite and infinite load-induced fatigue life.

The reliability index is presented in Figure 12. It is observed that due corrosion the stress in the elements increases and the reliability index decreases for each load cycle. The first zone of the curve correspond to finite life fatigue (logarithmic) and the second to infinite life fatigue (linear). The exterior girder has lower values due to the greater demand generated by the fatigue truck.

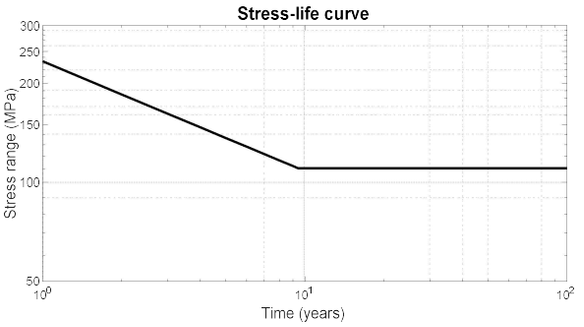


Figure 11. Stress-life curve, Fatigue.

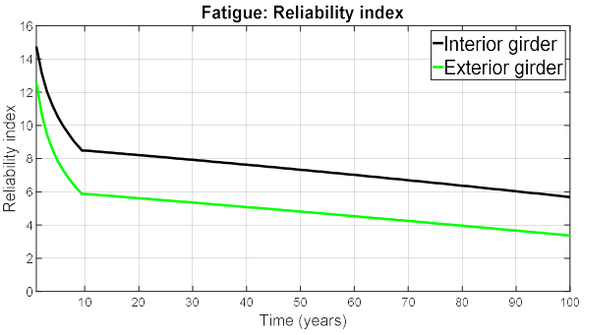


Figure 12. Reliability index, Fatigue.

5.3 *Limit state Service II, permanent deformations*

If loads are applied above the elastic limit, the material acquires permanent deformations and the element does not recover its original shape when removing the loads.

In the limit state of Service II, the calculation of permanent deformations is made by the tensions in the steel sections.

Figure 13 shows the maximum stress values within the life of the bridge. An increase in values is observed due to loss of cross-section of elements. Also, it is observed that the values of stresses are close enough to the yield strength of the steel of 345 MPa. The values are higher in the interior girder due to the transverse distribution of the vehicle load.

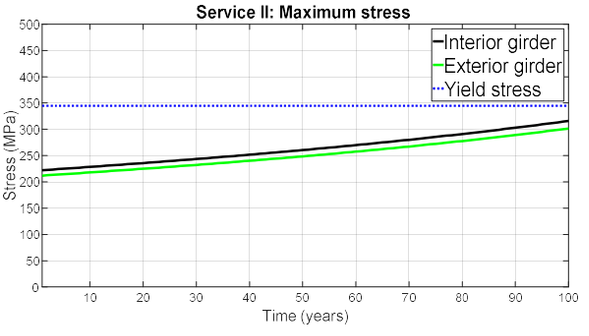


Figure 13. Maximum stress, Service II, Permanent deformations.

Figure 14 shows the reliability index values. It is observed that the values approach zero. The exterior

girder has higher values due to its lower stress demands.

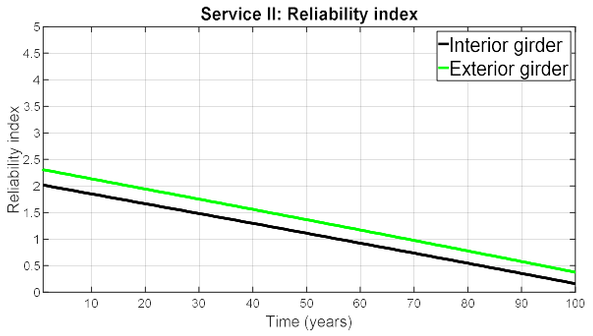


Figure 14. Reliability index, Service II, Permanent deformations.

5.4 *Limit state Service II, elastic deformations*

It consists of the deformation of the elements produced by the loads of use: design truck and lane load. The vehicle load must include the dynamic impact load.

From Figure 15 it can be seen that the interior girder has major deformations. On the other hand, the maximum deformation limit is not reached.

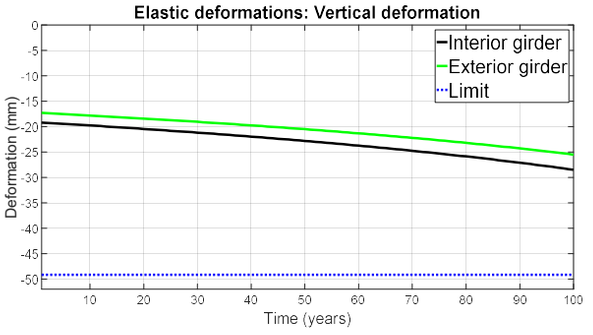


Figure 15. Vertical deformations, Service II, elastic deformations.

Figure 16 shows the reliability index values. It is concluded that the reliability index reaches values above the limit and, therefore, the probability of failure is low throughout the lifetime of the structure.

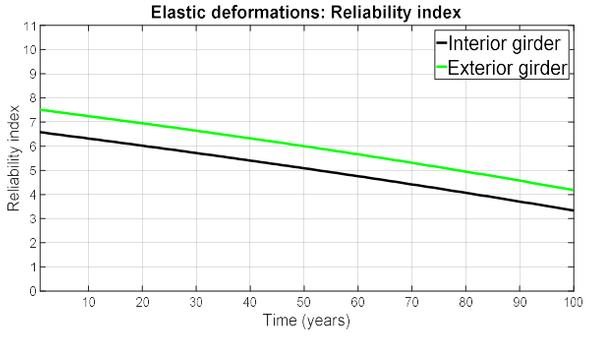


Figure 16. Reliability index, Service II, Elastic deformations.

5.5 *Overall limit state*

The overall reliability index of the structure corresponds to the graph of all limit states studied. Its purpose is to present a reliability value at the structure level that corresponds to the lowest value according to the possible failure scenarios. In this case, the system is series so if any of the girders fails, the system will fail.

From Figure 17, it can be seen that Service II limit state presents the lowest reliability values and controls the structure condition. In more detail, the interior girder is the one that has a high probability of surpassing the limit stress in the bottom flange and not fulfilling the conditions of service.

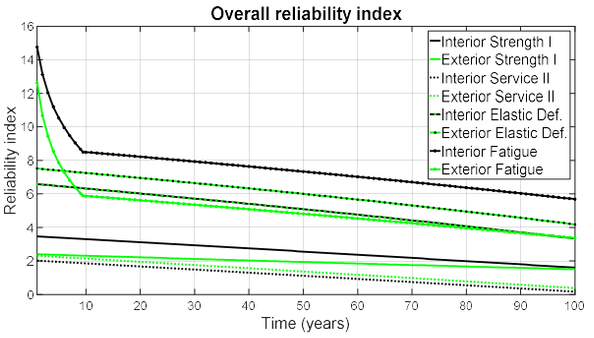


Figure 17. Overall reliability index.

6 CONCLUSIONS

Through the present research, it is proposed a methodology for the evaluation of the structural performance under process of corrosion degradation through the use of a finite element model for a steel girder and concrete slab bridge. For this purpose, software was used to generate different damage scenarios that represented the time of exposure to corrosion degradation agents. A period of 100 years was considered as service life of the structure and by means of the reliability index the structural condition was analyzed over time under current design standards.

When applying the methodology to the case study, a span of the Bicentenario Oriente Bridge, it was obtained that the evaluated limit states corresponding to strength, fatigue and serviceability were not exceeded within the operational life of the structure.

It was possible to corroborate that the properties of the elements are affected in relation to the time of exposure to corrosion degradation agents. The values of cross-section and resistance of the elements decreased and the values of stress and deformations increased.

The limit state of Service II is the one that controls the performance of the structure because it presented the lowest values in lifetime. In the same

way, the interior girder evidenced the greater solicitations because it supports the greater proportion of the traffic lanes.

The limit states of Strength I and Fatigue were not reached with the studied period, being the probability of failure low in the analysis. Despite this, the exterior girder showed the lowest values of reliability.

In relation to the above, it was concluded that the effects of corrosion degradation did not reduce the structure design life. However, these effects acting in conjunction with other degradation agents such as reinforced concrete corrosion or extreme events such as earthquakes, tsunamis, fires, can generate performance values below the expected limits.

The generated model can be updated with observations generated with visual inspections related to the advance of corrosion and other damage conditions. Also the parameters of the corrosion model must be calibrated for local conditions.

The predictive capacity of the model can be improved by calibrating the load and data models of the structure based on data measured in the field with the installation of sensors.

7 REFERENCES

American Association of State Highway and Transportation Officials (AASHTO) 2014. *AASHTO LRFD Bridge Design Specifications (6th Ed)*. Washington, DC: American Association of State Highway and Transportation Officials

Farrar, C.R. & Worden, K. 2013. *Structural health monitoring: a machine learning perspective*. Hoboken, New Jersey: John Wiley & Sons.

Freyermuth, C. 2009. Service life and sustainability of concrete bridges. *ASPIRE The Concrete Bridge Magazine* 3(4): 12-15.

Kayser, J. & Nowak, S. 1989a. Capacity loss due to corrosion in steel-girder bridges. *ASCE Journal of Structural Engineering* 115(6): 1525-1537.

Kayser, J. & Nowak, S. 1989b. Reliability of corroded steel girder bridges. *Journal of Structural Safety* 6(1): 53-63.

Klinesmith, D., McCuen, R. & Albrecht, P. 2007. Effect of environmental condition on corrosion rates. *ASCE Journal of Materials in Civil Engineering* 19(2): 121-129.

Mazzoni, S., McKenna, F., Scott, M., Fenves, G. et al. 2006. *OpenSees Command Language Manual. Pacific Earthquake Engineering Research Center*. California: University of California Berkeley.

Sánchez-Silva. M., Frangopol, D., Padgett, J. & Soliman M. 2016. Maintenance and operation of infrastructure systems: review. *ASCE Journal of Structural Engineering* 142(9): F4016004-1 – F4016004-16.

Sánchez-Silva, M. & Klutke, G 2016. *Reliability and Life-Cycle Analysis of Deteriorating Systems*. New York: Springer.

Soliman, M. 2015. *Life-cycle Management of civil and marine structures under fatigue and corrosion effects* (PhD Thesis). Bethlehem, Pennsylvania: Lehigh University.

Tang, A. K., & Eidinger, J. M. 2010. *Chile Earthquake of 2010: Lifeline Performance*. Reston, Virginia: American Society of Civil Engineers.

Maintenance, Safety, Risk, Management and Life-Cycle Performance of Bridges – Powers, Frangopol, Al-Mahaidi & Caprani (Eds)
© 2018 Taylor & Francis Group, London, ISBN 978-1-138-73045-8

Predictive modelling of the deterioration of Australian state bridge network

H.D. Tran & S. Setunge
RMIT University, Melbourne, Australia
Y-C. Koay & H. Luczak
VicRoads, Melbourne, Australia

ABSTRACT: Road bridges are life line structures essential to ensure community mobility. Management of an aging bridge network on limited resources can be a challenge for the state authorities. Prediction of future condition states of bridges at component level is essential to optimise maintenance actions and ensure the safety and serviceability of the network. This is the first step in developing an advanced management strategy. A research project funded by the Australian Research Council in partnership with the Roads Corporation of Victoria (VicRoads) and conducted at RMIT University in Melbourne examined the level 2 visual inspection data collected by over 4-5 inspection cycles with the objective of predicting deterioration of bridge components. The quality and quantity of the data were analyzed and observed to be adequate for developing component level deterioration prediction models. A range of deterioration prediction methods including the deterministic models and stochastic models were examined to understand the validity of the different methods in predicting the deterioration of bridge components using visual inspection data. A case study with a demonstration on concrete open girder is investigated for the well-known linear models and the commonly used Markov deterioration model. The results show that the Markov model can produce more reasonable prediction than the linear model when presented with short time inspection data. Furthermore, preparation of valid data is also important to ensuring accurate and sensible prediction from deterioration models. This study also shows that the issue of first inspection has significant impact on predictive outcomes and thus should be carefully considered in preparation of valid data.

1 INTRODUCTION

1.1 *Background*

Bridges are important infrastructure assets because they have intensive capital investment, and play a crucial role in transportation network for ensuring well being of population. After many years of service, bridge structures are aging and deteriorating, which become hazard to traffic users in the event of structure failures or falling apart. Because bridge structures are public assets, the asset management of bridge structures requires not only ensuring safe and serviceability throughout their service life but also cost-effective maintenance, rehabilitation and replacement program (MRR).

It has been a common practice that bridge structures are routinely inspected to detect damages and defects before repair, rehabilitation and replacement can be carried out. The inspection intervals and detail levels of inspections are varied among bridge management agencies. The norms are 3 levels of inspection with level 1 of screening with interval 3-6 months, level 2 of visual detail with interval 2-3 years and level 3 of in-depth for specific cases.

It has been increasingly recognized that deterioration models of bridge structures provide useful information of deterioration rate and prediction of future condition of bridge structures. Such information is important for asset management of bridges structures in terms of timely and cost-effective inspection and maintenance program, and reliability analysis for prioritization and long-term management.

Intensive industry surveys (Ryan T. W. et al, 2012, Principal Bridge Engineers, 2014) and research works (Moomen, 2016, Goyal, 2015, Jamali et al., 2013) have been carried out to understand the cause of deterioration, contributing factors and to model the deterioration process for current and future prediction. In brief, summary points are as follows:

The cause of deterioration is specific to material of bridge structures. For example, fatigue is often with steel and creep is often with concrete.

Contributing factors to deterioration include traffic volume, exposure to corrosive soil and air and so on.

Deterioration process can be single or combined processes such as stress corrosion cracking in steel

and coupled with random damage events such as flooding and earthquake.

Deterioration models are divided into knowledge-based, data-driven and mechanism-based models. Few bridge management agencies use knowledge and experience to determine future deterioration from inspected defects (Safia et al., 2013). The data-driven models use the inspection data to predict the future deterioration (Agrawal et al., 2010, Bu, 2013, Edirisinghe et al., 2013). The mechanism-based model is based on deterioration mechanisms such as corrosion of reinforcing steels (Jamali et al., 2013, Lu et al., 2011).

1.2 *Aims and Objectives*

This study aims to compare the predictive deterioration between the deterministic linear and the stochastic Markov models, which are data-driven deterioration models. The deterministic linear model is well known for its ease of use and implementation. However, it is criticized for failure to capture the uncertainty of deterioration process, which can be addressed by the stochastic Markov model. The data-drive model is chosen over the physical model because it is attempted to utilize the level 2 inspection data, which are available and supplied by VicRoads, a bridge management agency in Australia through a collaborative research project on bridge deterioration modelling. The physical models are considered more advanced and accurate but they require intensive and detailed data that are costly and difficult to obtain. Therefore, they are not selected in this study.

The objectives of this study are:

i. To describe the level 2 inspection data of the case study with VicRoads, that are used for the deterioration models
ii. To present how valid data are compiled for deterioration models
iii. To compare the predictive deterioration between the linear and Markov models.

2 DESCRIPTION OF CASE STUDY

2.1 *Overview*

VicRoads is the registered business name of the Roads Corporation in Victoria State of Australia (www.vicroads.com.au). It is a Victorian statutory authority established under the Transport Act 1983 and continued in the Transport Integration Act 2010. One of VicRoads' core services is to plan, develop and manage the arterial road network, including roads, bridges, culverts, traffic signs and so on.

The bridge management of VicRoads is supported through its RAS, which is a computerized and web-based 2D database. RAS contains basic data of 6207 structures including bridges, culverts and tunnel with their attributes such as number of spans, length and width. The oldest structure was built in 1899. RAS also stores 261324 records of level 2 inspections as of 2017. The first recorded inspection was 1995.

The VicRoads's inspection practice is published in open-access inspection manual (Principal Bridge Engineers, 2014), which basically has 3 levels of inspection. Level 1 inspection is considered a screening inspection with maximum interval of 6 months. The level 2 inspection is a routine inspection with typical interval of 2 years and level 3 is an in-depth inspection for special cases.

A 2-year collaborative research project between VicRoads and RMIT University has been established to develop deterioration models using level 2 inspection data for bridge structures. The outcomes of this project could provide justifying for future state funding of bridge management and also provide support for more effective and efficient asset management program.

2.2 *Level 2 Inspection data*

The VicRoads' inspection manual describes the breakdown of bridge structures into superstructures and substructures and into structure elements such as piles, decks and bearings. Each bridge element is coded by their function and one of 5 types of material (i.e. timber, steel, prestressed, concrete and others). For example, the 2C mean open girder/stringer with concrete material.

The level 2 inspection provides condition rating for individual elements based on their inspected defects as per inspection guidelines. The condition rating is a 1-4 scale with one being good and 4 being worst. The condition state percentage distribution is used to provide inspection reports. For example, an inspection report of [90% 10% 0% 0%] of 2C means 90% of the open girders is in condition 1, 10% in condition 2 and 0% in condition 3 and 4. Some key notes of inspection are:

Widening section of structure is treated as a separate structure. This means the same structure ID will have separate structures known as N (original), L (left widening) or R (right widening) with corresponding inspection records.

The inspection report also indicates location of defects and quantity but not in a consistent and standardized format.

3 COMPILATION OF VALID DATA

3.1 *Missing data*

For bridge structures, 639 out of 6207 structures have missing built year, which are then removed from valid pool of data for deterioration model.

For inspection records, 6827 out of 261324 inspection records have missing widening data (i.e. N, L or R are not specified), which then removed from the valid pool of data.

The valid pool of data then contains 5568 structures and 246997 inspection records.

3.2 *Bridge widening*

It has been found that the widening of bridge was carried out for many bridges, noting that additional new structures are often added to support the widening section but the material of new structures need not be the same with the existing structures. Therefore, the widening sections are treated as separate structures to the original bridge structures but both are operated in the same working environments. However, the construction year of widening is not recorded in RAS and thus the result of first inspection cannot be used to compare with the constructed year but can be used to compare with the subsequent inspections.

3.3 *Inspection twice*

It has been found that 2 inspection records by different inspectors are reported for the same year. For example, the 2C open girder was found to have 87 inspection-twice out of 757 inspection records. It is decided to remove one of two inspections from the valid pool of data.

3.4 *Condition improvement*

It has been found that condition of elements is improved at the second or else inspections after the first inspection. Some improvements are [60% 40% 0% 0%] at 1999 became [90% 0% 10% 0%] in 2002. This is unacceptable because percentage in condition 1 cannot be increased unless maintenance was conducted. There are 160 condition improvement out of 757 inspections.

It is decided to remove inspections with condition improvement from the valid pool of data. However, the subsequent inspection is still kept and the inspection with condition improvement becomes the new reference year.

3.5 *Abnormal condition distribution*

It has been found that a small portion of inspection records show abnormal condition distribution. One abnormal example is [90% 0% 0% 10%] because for the same structure elements under the same working environments, it seems abnormal to have such a significance difference in the deterioration. However, there are only 8 such cases out of 757 inspection records of 2C (for example).

It is decided to remove such abnormal cases of inspections from the valid pool of data.

3.6 *First inspection*

The average built year is 1972 with standard deviation of 21 years. However, the first recorded inspection year was 1995. It is not sure whether any maintenance action had been conducted from built year until first inspection record. Taking example of the 2C open girder, it has been found that there are 239 first inspections out of 757 inspections and 144 out of 239 cases shows 100% in condition 1.

Another study (Ackah 2016) has found the similar issue. One solution is to use a 5-10 years difference form the first inspection records as acceptable built year. To ensure reliable data, the effect of first inspection records on the outcome of deterioration modeling will be investigated in this study.

3.7 *Repeat inspection*

It has been found that repeat inspections occur from the first inspection until 2017. However, the inspection intervals are not consistent even for the same structure. To utilize the repeat inspection, the following assumptions are used:

i. Deterioration is treated over unit time of 1 year and therefore different inspection intervals are not an issue.
ii. Repeat inspections that show unchanged condition 1 are treated as one inspection record from the start of inspection until the last inspection. This would increase the time stay in condition 1, a critical concern that was found in a published study and will be explained later in this study. For example, a series of repeat inspection at 1999, 2001, 2003 and 2005 showing unchanged condition 1. This series would become one inspection record between 1999 and 2005 showing time of 6 years staying in condition 1 instead of 3 inspection records with 2 years staying in condition 1.

3.8 *Unchanged condition*

It has been found that unchanged condition occurs at inspection and mostly at condition 1. For example, the condition is still 1 at inspection in 1999 and then 2002. From deterioration process point of view, if the rate of deterioration is very slow, it can be assumed to be constant because visual inspection could not identify such small changes. The unchanged condition is not suitable for deterioration models such as linear regression and Gamm process models that require strictly increasing deterioration. This issue is investigated in this study.

4 DETERIORATION MODELS

4.1 *Linear regression model*

Equation 1 shows the linear relation between bridge condition (output) with age (input factors) (Agrawal et al., 2010). More input factors can be added into Equation 1 in a similar manner.

$$Y=a_0 + a_1 * age + \varepsilon \quad (1)$$

where a_0 is constant coefficient, a_1 is slope coefficients of age (year) and ε is measurement error assumed to have zero mean and independent constant variance.

The interpretation of Equation 1 is that a) for the case of one input and one output, the relation is a straight line; b) for the case of two and more inputs, the relation is a plane and hyper-plane; c) the linear relation means constant deterioration rate over time; d) measurement error means that for the same values of inputs, every time the output is measured or assessed, the output value might not be the same due to equipment sensitivity or human subjectivity; e) deterioration is increasing with age, meaning unchanged condition is not valid.

For calibrating or estimating the model coefficients, the least square method is often used to minimize the error term between the observed output and model output.

The predictive performance of the linear model is often assessed using the coefficient of determination R^2 between observed values and model outputs.

4.2 *Markov model*

The Markov model is based on the stochastic theory of Markov chain (Madanat et al., 1995), which describes a system that can be in one of several condition states at any time, and it can stay still or move to another state at each time step with some transition probabilities. This theory is well suited for observation of level 2 condition data of bridge elements because the snapshot inspection reveals the condition state at the time of inspection and the unchanged and changed condition states over time can be captured with the transition probabilities.

The most important property of the Markov chain is that the probability of movement depends only on the current condition regardless of the history of movement, called memoryless property. This means that a) the currently known condition can represent for the accumulated deterioration up to the current time and b) the future condition does not depend on how long it stays in previous conditions. This property is well suited for long life assets such as concrete. In the opposite is usage-based assets such as light bulbs and machineries in which their future condition depends on how long they have been used in the past.

The Markov model is mathematically expressed as a matrix M of transition probabilities:

$$M = \begin{bmatrix} P_{11} & P_{12} & P_{13} & P_{14} \\ P_{21} & P_{22} & P_{23} & P_{24} \\ P_{31} & P_{32} & P_{33} & P_{34} \\ P_{41} & P_{42} & P_{43} & P_{44} \end{bmatrix} \quad (2)$$

where P_{ij} is the probability of moving from a condition state i to a condition state j over a unit time step. In this study, P_{ij} is assumed zero if i>j meaning improved condition is not modeled due to lack of maintenance data.

The memoryless property and the theory of total probability can be used to predict the probability vector $[P_1\ P_2\ P_3\ P_4]$ at any future time T, given the known current condition with certainty or probabilities $[C_1\ C_2\ C_3\ C_4]$ as shown in the Chapman-Kolmogorov Equation:

$$[P_1\ P_2\ P_3\ P_4] = [C_1\ C_2\ C_3\ C_4] * M^T \quad (3)$$

Equation 3 is a matrix multiplication of current condition with the transition matrix powered to future time T. To utilize Equation 3, the transition matrix M of Equation 2 needs to be estimated. Among several calibration/estimation techniques, this study uses the proven Bayesian Markov chain Monte Carlo simulation technique (Micevski et al., 2002) to estimate the transition matrix M of the Markov model. In brief, the Bayesian technique transforms the unknown elements Pij of the transition matrix M into a multivariate distribution by using observed data, Equation 3 and the Bayesian theory. The Markov chain Monte Carlo simulation is then used to generate sampling data of the elements, which become the estimator of the unknown elements. The details can be referred to Micevski et al. (2002).

The predictive performance of the Markov model is commonly validated using the Chi-square test on a separate dataset that is not used in the calibration of the Markov model (Micevski et al., 2002). The validation dataset is often randomly selected from 15-20% of the entire dataset.

5 RESULTS

The deterioration models in Section 4 are applied to the case study and the results are demonstrated for the concrete open girder 2C.

5.1 *Effect of first inspection*

To investigate the effect of first inspection, the dataset of all inspection is compared against the dataset of second up inspection (i.e. first inspection data is removed) in both linear and Markov models.

Table 1 show that the Markov model passes the fitness test for both datasets. The negative values for R^2 of the linear model on both datasets indicate the poor fitness of linear model and the linear model should not be used.

Table 1. Results of fitness test for Markov and linear models for percentage prediction on condition 1.

Data	Markov model	Linear model
	Chi-Square test	R^2 Value
All Inspection data	55.8<85.9	-0.544
Second up inspection data	7.8<67.5	-0.247

The calibrated transition matrix for old bridge is shown as a demonstration in equation 4 and 5 for all-inspection and second-up inspection.

$$M(all) = \begin{bmatrix} 0.9934 & 0.0052 & 0.0008 & 0.0006 \\ 0 & 0.9984 & 0.0009 & 0.0007 \\ 0 & 0 & 0.9972 & 0.0028 \\ 0 & 0 & 0 & 1 \end{bmatrix} \quad (4)$$

$$M(second) = \begin{bmatrix} 0.9894 & 0.0082 & 0.0018 & 0.0006 \\ 0 & 0.9889 & 0.0104 & 0.0007 \\ 0 & 0 & 0.9991 & 0.0009 \\ 0 & 0 & 0 & 1 \end{bmatrix} \quad (5)$$

Despite the unacceptable fitness of linear models, Figures 1 and 2 can still be used to illustrate the significant effect of first inspection. This effect shows that linear model is sensitive to the range of calibration data. In Figure 1, the observed data cover a wide range of age up to 100 years and thus the prediction make more reasonable sense as compared to Figure 2.

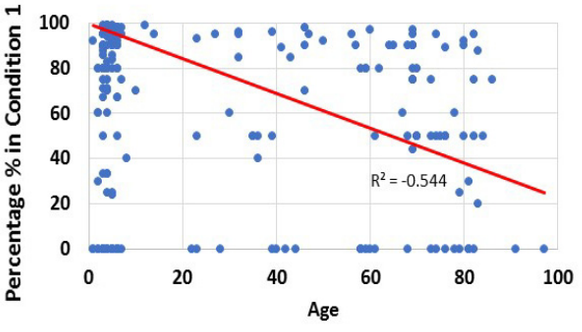


Figure 1. Linear model fitted with all inspection data for percentage in condition 1

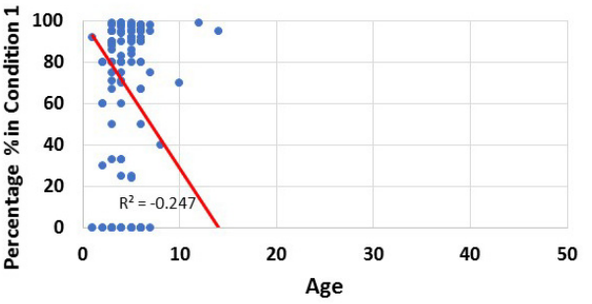


Figure 2. Linear model fitted with second up inspection data (first inspection removed) for percentage in condition 1.

Figures 3 and 4 show the effect of first inspection on Markov model. It appears that the removal of first inspection makes the deterioration faster. For example, at the age of 100 years, the percentages in condition 1are 45% and 18% and 20% and 30% in condition 4 for all-inspection and second-up inspection respectively,

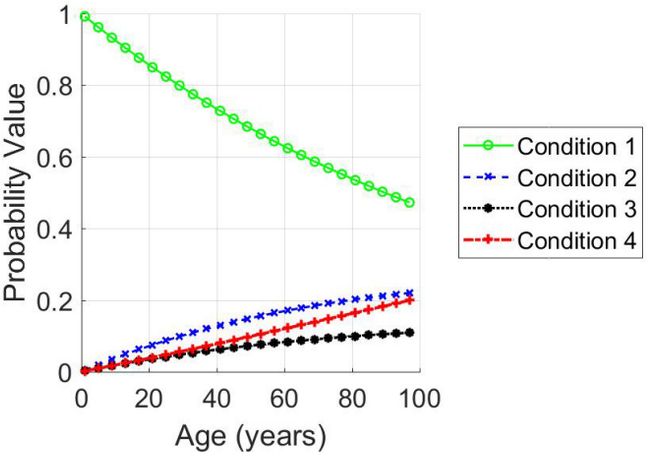


Figure 3. Markov model on all inspection data.

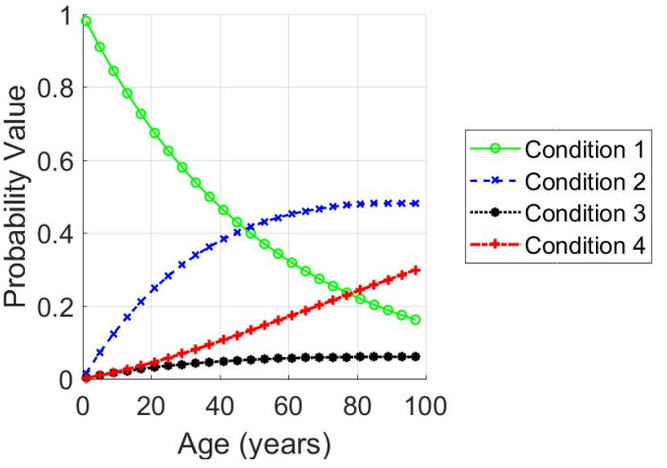
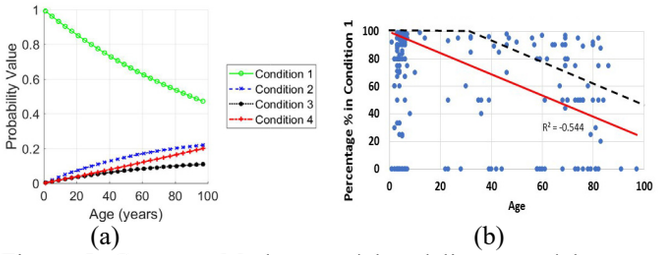


Figure 4. Markov model on second up inspection (i.e. first inspection removed)

5.2 *Effect of unchanged condition one*

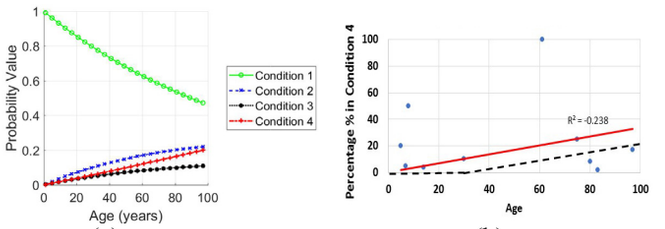
To study the effect of unchanged condition 1 on linear model, the unchanged condition 1, which is removed from the calibration dataset of the linear model, is used to calculate the average time staying in condition 1. The revised linear model as shown with dash line of Figure 5b has 2 segments. The first segment is horizontal line, representing for the time staying in condition 1, which is calculated as 31 years. The second segment is the deterioration line, which is similar to the calibrated shown in Figure 1. Figure 5a is the replot of Figure 3 for ease of comparison.

It can be seen from Figure 5a and 5b that the revised linear model is quite similar to the condition 1 of the Markov model. The concept of 2-segment linear model is further applied to condition 4 as shown in Figure 6, which also shows the similarity between Markov model and 2-segment linear model.



(a) (b)

Figure 5. Compare Markov model and linear model on percentage in condition 1 for all inspection data



(a) (b)

Figure 6. Compare Markov model and linear model on percentage in condition 4 for all inspection data

5.3 *Model comparison*

The Markov model passes the fitness test while the linear model fails as shown in Table 1. The poor fitness of the linear model can be seen in Figure 1 where observed data have high uncertainty as shown with the un-patterned scattering. Instead of trying to fit an impossible line through the observed percentage in condition 1 with age, the Markov model takes a different approach by capturing the percentage changes between condition states. Furthermore, the Markov model and the 2-segment linear model have similar rate of deterioration as shown in Figures 5 and 6. However, for the case of removing first inspection, the linear model shows much faster rate of deterioration than that of the Markov model. This highlights another shortfall of linear model when range of observed data is unable to cover the range of prediction. This also shows the good generality of Markov model in such cases.

6 DISCUSSION

This study is limited to the case of concrete material with a demonstration on open girder 2C. However, the methodology can be extended to all bridge elements with different material.

The effect of contributing factors such as traffic volume and exposure condition will be investigated in further studies.

This study shows the weakness of the linear model and thereby supports the use of stochastic Markov model in modelling deterioration of bridge elements.

Despite the advantage, the Markov model still shows deterioration in the first few years. This is considered unrealistic as found in a previous study (Sobanjo and Thompson, 2011). The previous study claimed that the new structures are expected to stay in condition 1 for the first 10-30 years before transitioning into deteriorated conditions. If all structures follow this pattern then Markov model should be applied to the data after transition start. If some new structures start to move to condition 2 after few years due to unknown causes such as uncertainty of material batch, inconsistent construction practice or damage event, then the Markov model can reflect that. Therefore, it is not the shortfall of the Markov model but how valid data is compiled for the deterioration models.

The comparison between Markov model and other stochastic models such as Gamma process model (Edirisinghe et al., 2013) will be conducted in further works.

7 CONCLUSION

Deterioration models can significantly improve the efficiency of asset management of bridge networks. This study presents a methodology of preparing valid data for deterioration model. This is an important step that is often overlooked and results in poor prediction.

This study also compares the deterministic linear model against the stochastic Markov model. The demonstration on a concrete open girder shows that the Markov model is more suited than the linear model.

Further investigations will be conducted to study the effect of contributing factors, and to compare against other stochastic models.

8 REFERENCES

Ackah , K. E. 2016. *Weibull-Based Deterioration And Preservation Models For Florida Bridges.* Master, Florida State University

Agrawal, A., Kawaguchi, A. & Chen, Z. 2010. Deterioration Rates of Typical Bridge Elements In New York. *Journal of Bridge Engineering,* 15**,** 419-429.

Bu, G. 2013. *Development of An Integrated Deterioration Method For Long-Term Bridge Performance Prediction.* Phd Thesis, Griffith University.

Edirisinghe, R., Setunge, S. & Zhang, G. 2013. Application of Gamma Process For Building Deterioration Prediction. *Journal of Performance of Constructed Facilities,* 27**,** 763-773.

Goyal, R. 2015. *Development of A Survival Based Framework For Bridge Deterioration Modeling With Large-Scale Application To The North Carolina Bridge Management System.* Phd Thesis, University of North Carolina At Charlotte.

Jamali, A., Angst, U., Adey, B. & Elsener, B. 2013. Modeling of Corrosion-Induced Concrete Cover Cracking: A Critical Analysis. *Construction And Building Materials,* 42**,** 225-237.

Lu, C., Jin, W. & Liu, R. 2011. Reinforcement Corrosion-Induced Cover Cracking And Its Time Prediction For Reinforced Concrete Structures. *Corrosion Science,* 53**,** 1337-1347.

Madanat, S., Mishalani, R. & Ibrahim, W. H. W. 1995. Estimation Of Infrastructure Transition Probabilities From Condition Rating Data. *Journal of Infrastructure Systems, Asce,* 1**,** 120-125.

Micevski, T., Kuczera, G. & Coombes, P. 2002. Markov Model For Storm Water Pipe Deterioration. *Journal of Infrastructure Systems,* 8**,** 49-56.

Moomen, M. 2016. *Deterioration Modeling of Highway Bridge Components Using Deterministic And Stochastic Methods.* Master Thesis, Purdue University.

Principal Bridge Engineers 2014. Road Structures Inspection Manual Melbourne: Vicroads.

Ryan T. W. Et Al 2012. Bridge Inspector's Reference Manual (Birm). Us: Fwha.

Safia, M., Sundquista, H., Karoumia, R. & Racutanu, G. 2013. Development of The Swedish Bridge Management System By Upgrading And Expanding The Use of Lcc. *Structure And Infrastructure Engineering,* 9**,** 1240–1250.

Sobanjo, J. O. & Thompson, P. D. 2011. Enhancement of The Fdot's Project Level And Network-Level Bridge Management Analysis Tools Final Report. Florida State University.

SS07: European standardization of quality specifications for roadway bridges

Organizers: J.R. Casas & J.C. Matos

Maintenance, Safety, Risk, Management and Life-Cycle Performance of Bridges – Powers, Frangopol, Al-Mahaidi & Caprani (Eds)
© 2018 Taylor & Francis Group, London, ISBN 978-1-138-73045-8

Quality Specifications for Roadway Bridges in Europe

Joan R. Casas
UPC-BarcelonaTech, Barcelona, Spain

Jose C. Matos
ISISE, University of Minho, Guimaraes, Portugal

ABSTRACT: In Europe, there is a large disparity from country to country regarding the way performance indicators are quantified and goals and quality controls specified. The main objective of COST Action TU-1406 is to establish quality specifications for roadway bridges that could be accepted on a European basis. The application of these common specifications will be highly dependent on the changes in philosophy and operational methods (inspection, testing,…) that the new specifications will require in the future as a result of their implementation. Therefore, to reduce to a minimum the possible reluctance of operators to change the actual performance indicators and the methods to obtain them and also to take advantage of the existing background and knowledge and the data-bases available after a lot of years of use, it is mandatory that the new homogenized quality specifications proposed as result of the Action are based on the actual practice.

1 INTRODUCTION

In the past few years, significant worldwide research has been done regarding condition assessment of roadway bridges. Obtained values from visual inspection or non-destructive testing, which provide information regarding the assessed bridge condition state, are compared with previously established goals. As a result, there are currently several methodologies to assess the bridge condition. More recently, the concept of performance indicators (PI) was introduced, simplifying the communication between consultants, operators and owners. However, large deviations continue to exist on how these indicators are defined and obtained and, therefore specificactions are required for a standardization of this procedure. For a standardized procedure, for example, quality control plans (QCP) are further important instruments which are based on the previously mentioned PIs and pre- specified PI-goals. However, these performance goals are difficult to obtain, as they are highly subjective as they reflect the user and societal requirements. Recently, COST Action TU1406 emerged with the main ambition of developing a guideline for the establishment of QCPs in roadway bridges in Europe, by integrating the most recent knowledge on performance assessment procedures with the adoption of specific goals (Casas, 2016a,b, Matos, Casas, & Fernandes, 2016). This guideline will focus on bridge maintenance and life-cycle performance at two levels: (i) performance indicators (PIs), (ii) performance goals (PG). The primary goal is, among others, to update and adapt existing PI tables to guarantee a state-of-the-art PI based bridge assessment technology in Europe. Performance indicators related to sustainability will also find place in such new assessment standards. By developing new approaches to quantify and assess bridge performance, as well as quality specifications to assure expected performance levels, it is expected that bridge management strategies will be significantly improved and homogeneized all across Europe, enhancing asset management of aging structures in Europe.

The main challenges in the development of a quality control plan for highway bridges are the following:

- Quality assurance and control is important in all industrial fields and construction industry is no exception. Bridge management is a part of construction industry activities that ensures that the bridge attains the desired service life and quality level.

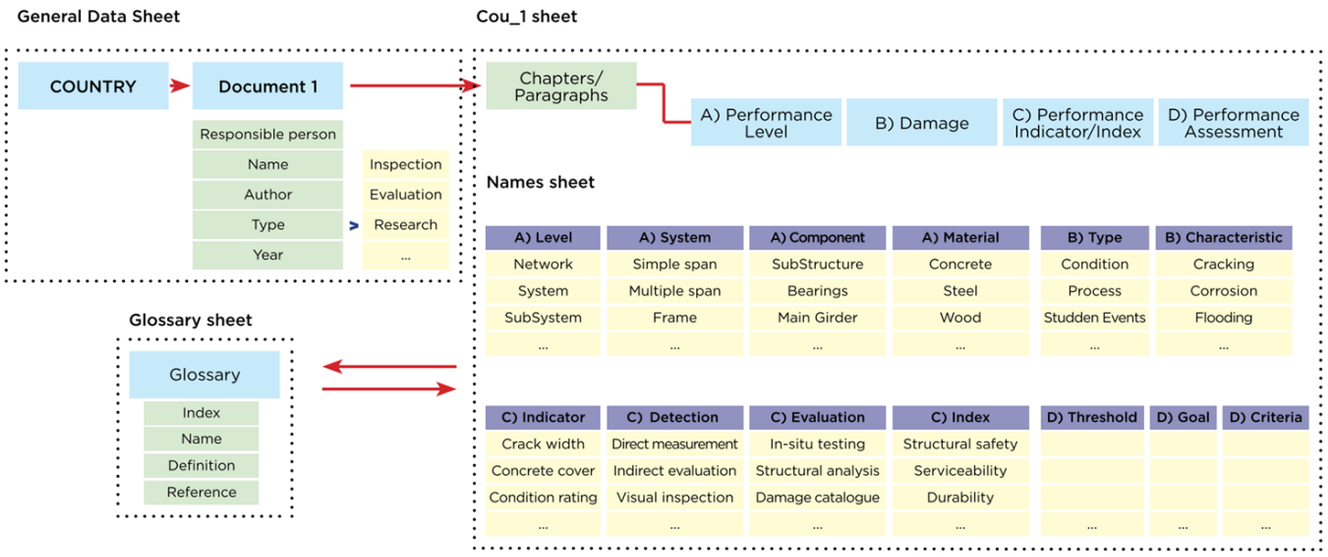


Figure 1. Structure of the Performance indicators database for the survey process

- Important parts of any BMS are quality assurance and control plans that must provide the basis for quality data acquisition and processing. Reliable data related to the condition of the structures is essential for all further processes, however ensuring continuously the quality of this data is a demanding task, as the data acquisition is mainly based on periodic visual inspections. Data processing and decision models, on the other hand, are dependent on preselected criteria and decision methods. A well-designed decision model will yield reliable result through the lifetime of its use.
- The third component of quality assurance and control in bridge management is maintenance planning. Bridges differ in size, condition, structural design, materials used etc., therefore these specific features need to be acknowledged in the maintenance plans. Designing unique plan for every bridge is irrational and designing a general plan for all bridges impossible. Additionally, optimizing maintenance for individual bridge may worsen optimization on the network level and viceversa. A compromise has to be made in order to implement a quality plan successfully into practice.

2 COST ACTION-TU1406

Infrastructure managers are facing now conflicting requirements to improve the availability and serviceability of aging infrastructure, while the maintenance planning is constrained by budget restrictions.

Many research efforts are ongoing, for the last few decades, ranging from development of bridge management system, optimization models, life cycle cost analysis, to big data analysis and implementation of artificial intelligence models into decision support tools. Since transport infrastructure is presenting crucial factor for the economy and societal development, it is not only subject to technical requirements,
but it is also required to keep up with societal and economic requirements.

Therefore, bridge maintenance planning should accommodate multiple performance goals (PGs) which need to be quantified by various performance indicators (PIs) and key performance indicators (KPIs)

Through WG1 activities, the development of a PIs database had been defined as an essential component of COST TU1406. The preliminary works developed into the working group indicated that an extended systematic screening on practical national inspection and evaluation documents was necessary in order to obtain a consistent and conclusive information associated with PIs, PGs and performance thresholds (PTs) from each COST partner country.

The core of the survey process for obtaining PIs and corresponding key performance indicators (KPI) is given in Figure 1. The two COST nominated persons per country, together with the infrastructure operators and owners chose beforehand the relevant documents (e.g. inspection, evaluation, research etc.) from which the PIs, and related information were extracted. A user interface (UI) served for a systemized data collection and it also allowed a relative flexible treatment of the number of data sets and PIs (unrestricted data input), which of course varies a lot from one to the other document.

The results of the screening process that involved a total of 36 countries, were partly heterogeneous and with a number of overlapping terms. This mainly results from a free interpretation leeway and different know-how of experts in visual inspections, performance evaluation, performance assessment and decision making in the participating countries. The previously sketched data collection process resulted in a list of more than 700 terms that were considered as related to performance indicators according to the inspection and assessment documents, which was later clustered and homogenized. The screening results were used for a homogenization process by the WG1 core group and the nominated persons from each country were asked again to verify their performance and damage specific inputs, by comparing them with the homogenized and categorized terms. These homogenized data were the baseline for all further studies and quantifications and provide also the basis for an effective comparison of performance quantities between countries.

From this process resulted a shorter list of 385 terms, grouped in 11 clusters from defects to rating and loads. The list was considered, not as a final list of PIs, but as a list of terms that can be related with PIs (PI related terms as addressed in WG1 Report). Assuming that not all the 385 terms can be considered as PIs as this high number will make the objective of the Action unpractical, a new practical based categorization of the terms had been performed. The following four categories of terms were considered: performance indicators (PIs), damage processes (DPs), observations (OBS) and other data (OD). A fifth category was considered, related with non-interceptable processes, once they are out of the scope of this group. The sixth category considered was labelled as Combined Performance Indicator, trying to cluster terms that reflect general properties of a structure and may be derived, among other ways, from the combination of several PIs. As an example, the term bridge condition was considered in this category since one can assume that it can be derived from all the other PIs. (Amado & Hajdin, 2017; Strauss et al., 2016). The distribution of the 385 PIs related terms through the 8 categories above defined is shown in Table 1 (Amado & Hajdin, 2017). The complete categorization of terms can be found in the COST TU1406 WG1 report.

In order to move on with the reduction of the list of PIs, an expert group was asked to specify PIs according to the following points: Measurable? Quantifiable? Target value available? Valid for ranking? Allow decision with economic implications?. These questions are based on the definition of performance indicator that was agreed within the COST Action: performance indicator is a measurable and quantifiable parameter, related to the bridge performance, that can be directly compared with a target measure of a performance goal (absolute measure of performance) or can be used for ranking purposes, among a bridge population (relative measure of performance), in the framework of a Quality Control Plan or life-cycle management (decisions and actions involving economic resources)

Table 1. Distribution of the 385 PI related terms through 8 different categories

Categories	Number of PI related Terms
Performance Indicator	17
Performance Indicator-Redundant	7
Damage Process	27
Damage Process - Redundant	13
Observation	245
Other Data	33
Non-Interceptable Processes	16
Combined PI	27
Total	385

In order to assess performance goals, Key Performance Indicators (KPIs) need to be defined, at strategic and tactical level. Those KPIs are determined from a number of PIs collected at an operational level. For the purpose of this Action, the PIs are determined at at the bridge element level.

At the end, approximately 100 extricated PIs are further related with one or more of the key performance indicators (KPIs) defined in Working Group 2 (WG2): reliability (R), availability (A), maintainability (M), safety (S), security (Se), environment (E), costs (C), health (H), politics (P), rating/inspection (I). A further process is required for categorization of PIs in relation to PGs and PTs at different levels: component (CL), system (SL), network (NL); taking into account different aspects: technical (Tech), sustainability (Sust) and socio-economic (SoEc).

The screening process and the expert questionnaire made it possible to assign the performance indicators to component (CL), system (SL) and network level (NL), and to assign the PIs to the spider tails or KPIs, as presented in Figure 2. The assignment shown in the figure refers to five selected countries (Austria, Chile, Croatia, Portugal and Spain). This information is available in a similar form for the other countries in the WG1 Report. Figure 2 shows the spider diagram indicating the KPIs and the country specific assigned PIs obtained from the expert analyses as presented above. The green areas in Figure 2 represent the most favorable rate and the red areas should alarm the bridge operator and require immediate intervention.

As some times they could be contradictory (increasing of safety also derives in increase of cost, for instance), bridge performance goals should be set as a multi-objective system, taking into account different

aspects of bridge and network performance. The basis of the approach is the work developed so far in the Netherlands. Netherlands' Rijkswaterstaat (RWS) has developed RAMS SHEEP concept, which additionally to RAMS (Reliability, Availability, Maintainability and Safety) defines the following aspects: Security, Health, Environment, Economics and Politics [7], where each criterion is defined as follows:

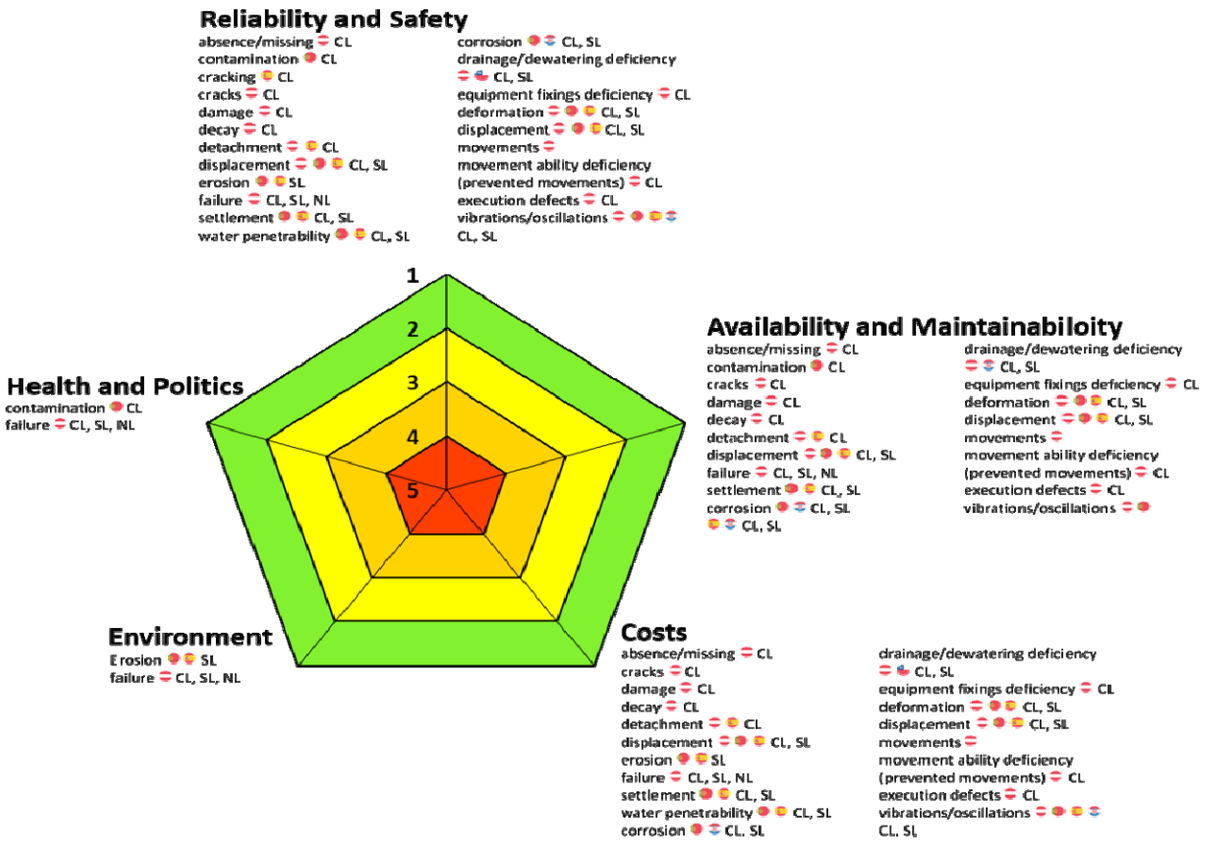


Figure 2. The spider diagram indicating the KPIs and the country specific assigned PIs and/or observations and damages.

- Security: related to the safety of a system regarding to vandalism and unreasonable human behavior.
- Health: being related to physically, mentally and socially defined aspects.
- Environment: concerns the physical environment requirements
- Economics: regarding the relationship between cost and value.
- Politics: concerning political-administrative and social requirements.

In Figure 3, the process of the multiple performance goals assessment is presented, also showing the transition from a system to the network level.

In order to get the optimum quality control plan, Multi-criteria decision-making (MCDM) provides a systematic approach to combine these inputs with benefit/ cost information and decision-maker or stakeholder views to rank the alternatives. MCDM is used to identify and quantify decision-maker and stakeholder considerations about various (mostly) non-monetary factors in order to compare alternative courses of action. Hierarchy structure for linking multi-objective bridge performance goals, covering most of the previously mentioned aspects with performance indicators is required. Possible result of multi-criteria assessment of different bridge maintenance alternatives represented in a spider diagram as in Figure 2 can be finally used for a decision making about the optimal maintenance or design solution.

Alternatively, the multiple performance criteria can be combined into a so-called utility function, in which all the criteria are brought into a single scale. In order to transform the various out into a single (mostly monetary) scale it is necessary to establish weight factor for the individual types of criteria.

Some of the weight factors are available in some countries (for example weight factor for traffic delays, noise, injuries etc.), depending on the selection of criteria, some weight factor may still need to be developed. In the development of the weight factors the starting point can be taken in the qualitative approach mentioned above, from which the apparent relative weight can be deducted

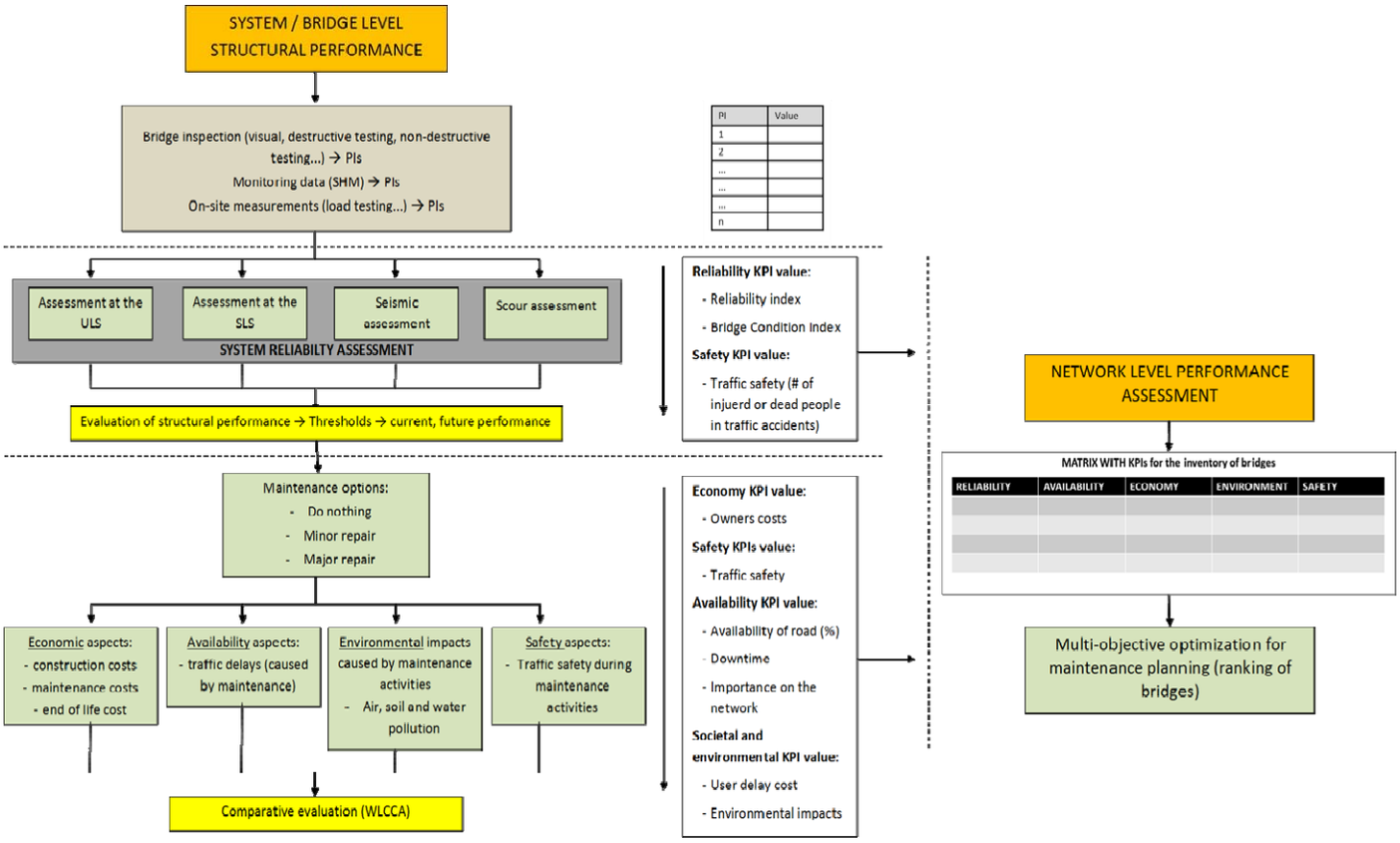


Figure 3. Overview of the process for performance goals assessment and transition from system to network level

Once the possible outcomes have been brought to a single scale, the best decision can be found as a formal optimized decision process, in which option with the maximum "utility" shall be selected as the recommended decision.

Utility theory provides a measure of preferences of a decision maker over a group of alternatives (Ishizaka, Nemery 2013). Based on the six axioms of utility theory, Multi-attribute utility theory (MAUT) is introduced by (Keeney, Raifa 1993). MAUT provides a systematic approach to reduce the qualitative values of various attributes (i.e. performance indicators) into utility functions. The obtained utility scores are then aggregated based on the relative importance of attributes. The final score assign a ranking to each alternative based on either minimization or maximization function. In other words, MAUT assigns the relative importance of performance indicators (e.g. condition, cost, etc.), while comparing number of bridges. These bridges are often referred as alternatives in MAUT.

MAUT involves the single decision maker who is willing to make certain trade-off among the performance goals while exposed with uncertainty and risk (Keeney, Raiffa 1993). The uncertainty is usually originated because of unavailable and dynamic nature of data, and involvement of number of stakeholders. For instance, in the bridge planning the exact estimation on number of users affected due to maintenance activity is difficult to define. MAUT integrates a body of mathematical utility models and a range of decision assessment methods in order to assist in decision ranking problem (Thevenot et al. 2006). The single attribute utility function is calculated for each performance aspect, which reflects the risk attitude of the decision maker.

In WG2 of TU1406 COST Action, a web-based tool was developed to apply the multi-objective optimization. The developed tool have implemented one of the method of MCDA namely Multi-Attribute Utility Theory (MAUT) by using the R Utility package (Reichert, Schuwirth, & Langhans, 2013). The tool as well as further information on the treatment of performance goals within the Action can be found in Stipanovic et al. 2017.

Finally, quality specifications or quality controls should be defined in WG3. The quality control framework includes the following goals:

- Reliability: including the probability of structural failure (structural safety) or operational failure (serviceability)
- Availability: the proportion of time a system is in a functioning condition. In our case is the additional travel time due to imposed traffic regime on the bridge
- Safety (not structural safety): minimize or eliminate the harm people during the service life of the bridge
- Economy: minimize life-cycle cost
- Sustainability: environmental friendliness

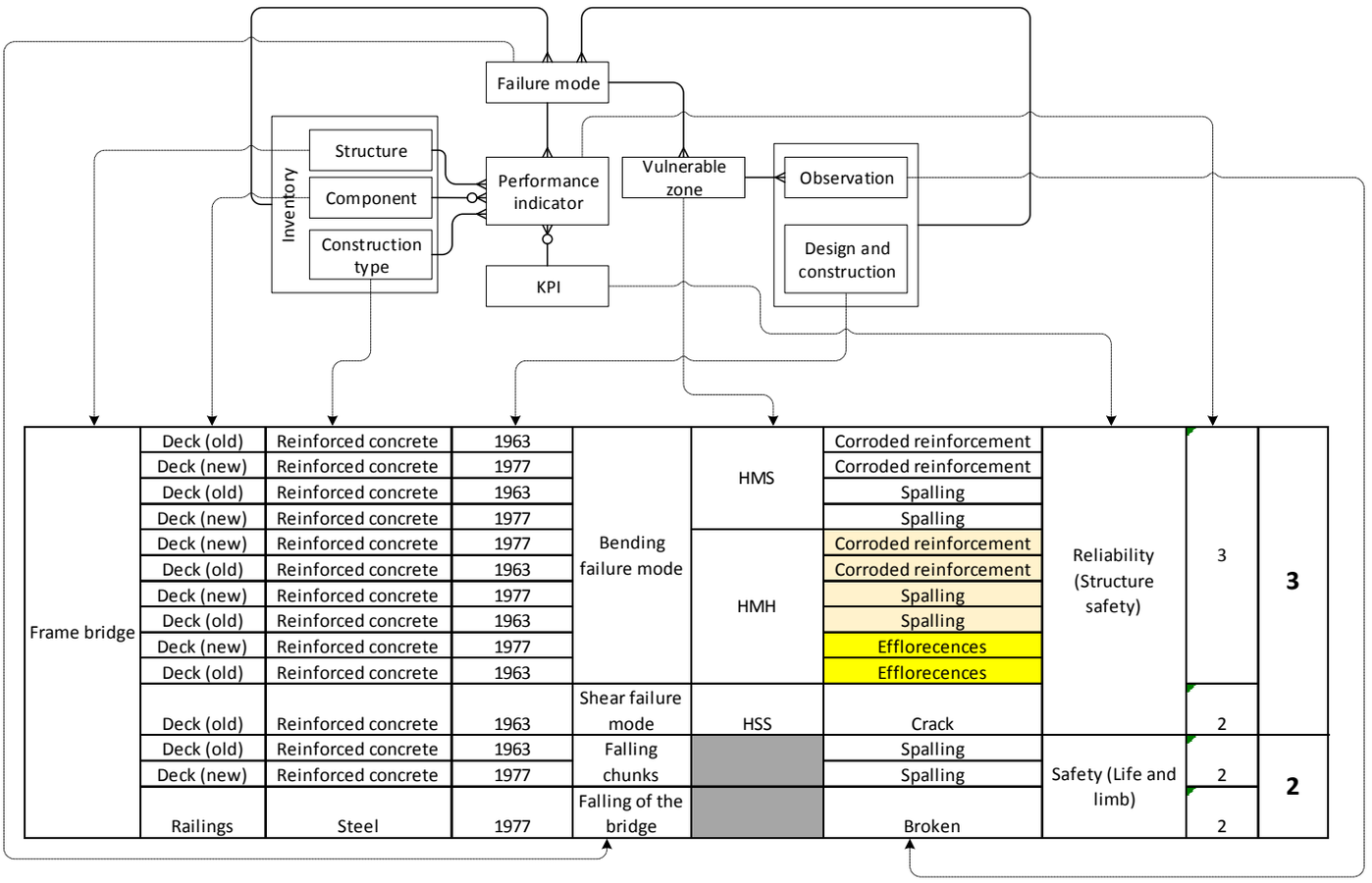
The quality control plan is divided in 2 groups:

- Static (snap shot) control: to inspect and investigate the bridge and determine whether the reliability (structural safety and serviceability) and the safety are met. This is the basis for the decision making on actions.
- Dynamic control: Based on the static control and including the plan and actions to execute in order to ensure the long term fulfillment of safety and serviceability goals. The goals to achieve are related to availability, economy and sustainability as it includes the feasible maintenance scenarios that define costs and availability over certain time frame by using reliability and safety forecasts.

Because the reliability goal should be checked against feasible failures, the practical application of the method has divided global group of bridges into the following bridge types: frame, arch, continuous beam, so for each type the most vulnerable zones can be identified and the corresponding performance indicators related to reliability observed and/or quantified. For instance, regarding a frame type bridge, the regions close to mid-span and supports will be those selected for a reliability analysis. This division also helps in the process of selecting the best maintenance policy. For instance, for the frame bridge shown in Figure 4, the corresponding flowchart and assigned values of reliability and safety based on the visual inspection is presented in Figure 5. The maximum value for both KPIs is 5. In this case, the values obtained are 3 for reliability and 2 for safety. The goals of availability, economics and sustainability are governed by maintenance scenarios. In fact, the snapshot assessment of availability and costs are of none or little interest. Therefore, the feasible maintenance scenarios (do nothing, preventive and corrective) are defined. Regarding availability indicator, each maintenance intervention requires certain traffic regime, which may include closure for certain type of vehicles or lane closure or narrower lanes. The normal traffic regime can be assigned with the maximum performance value. The other traffic regimes can be ranked by the additional travel time they cause for the road users. This additional travel time can be also monetized according to the guidelines given in the WG2 report. The selected intervention scenario is obtained based on the MAUT approach as previously explained. In WG2 report a case study showing a practical application to define the best maintenance scenario for a group of bridge (network level) is presented.



Figure 4. Frame bridge: one span, reinforced concrete



Frame bridge	Deck (old)	Reinforced concrete	1963	Bending failure mode	HMS	Corroded reinforcement	Reliability (Structure safety)	3	3
	Deck (new)	Reinforced concrete	1977			Corroded reinforcement			
	Deck (old)	Reinforced concrete	1963			Spalling			
	Deck (new)	Reinforced concrete	1977			Spalling			
	Deck (new)	Reinforced concrete	1977		HMH	Corroded reinforcement			
	Deck (old)	Reinforced concrete	1963			Corroded reinforcement			
	Deck (new)	Reinforced concrete	1977			Spalling			
	Deck (old)	Reinforced concrete	1963			Spalling			
	Deck (new)	Reinforced concrete	1977			Efflorecences			
	Deck (old)	Reinforced concrete	1963			Efflorecences			
	Deck (old)	Reinforced concrete	1963	Shear failure mode	HSS	Crack		2	
	Deck (old)	Reinforced concrete	1963	Falling chunks		Spalling	Safety (Life and limb)	2	2
	Deck (new)	Reinforced concrete	1977			Spalling			
	Railings	Steel	1977	Falling of the bridge		Broken		2	

Figure 5. Flowchart and results corresponding to bridge in figure 4

3 CONCLUSIONS

After an exhaustive analysis of the data obtained in the research carried out, it was concluded that different countries have different definitions of PIs and how they are obtained. Due to the existence of different interpretations, an additional clustering and homogenization process was required. From this procedure it was possible to verify that all countries have a PI, named condition index, condition rating or deterioration index, mainly obtained through visual inspections. Although in some cases this is the only existing PI used, there are countries, like Denmark or The Netherlands, in which operators and bridge owners are currently using other relevant indicators. In Denmark, concepts like remaining service life, robustness, safety index-reliability and vulnerability are addressed. On the other hand, in The Netherlands, the performance is evaluated by the RAMSSHEEP (reliability, availability, maintainability, safety, security, health, environment, economics and politics) approach, where risk is used to obtain
social, environmental, economic and political indicators.

How collecting PIs used across Europe was presented. The aim was to establish good practices on the definition of QCPs for roadway bridges. This should be the basis for the future proposal of the definition of PIs that could be adopted and used all over Europe.

The methodology is based on a deep analysis of the existing bridge management policies and available documents for inspection and evaluation existing in European countries and the main PIs used, with the objective to define a common group of quality specifications and control plans that can be assumed by all these countries. The gathered data from European countries was further analyzed and systematized.

As the focus on an efficient delivery of network performance increases, so does the interest in the relations between societal goals, performance indicators for both the road network and bridges or bridge elements. The implementation of asset management should increase the integration of network and bridge performance requirements. Network or even societal goals tend to be rather broad in their defini-

tion. Furthermore, there is often no exclusive relationship between performance indicators set at a lower level and goals at a higher level. An important notion is that in many countries, the main focus of bridge management is still the condition assessment of the particular objects or elements thereof.

The objective of the COST TU 1406 Action is to investigate the way bridge PIs and KPIs are collected and quantified, how performance goals are specified across Europe, and finally to produce guideline documents linking collection and quantification of PIs, KPIs, performance goals, standards, and practices to decision making processes. This paper shows an overview of performance goals at different levels, from high-level strategic decisions to low-level, system-specific requirements developed within the Action. The paper also explains how other performance aspects, like traffic safety, availability, economy, environmental and societal impacts could be quantified and used for the multi-objective bridge performance goals assessment. At the end, 5 performance goals and corresponding KPI´s were defined: Reliability, Availability, Safety, Economy and Sustainability and based on them, the Quality Control plans are defined. These, in turn, are divided into static (point in time) and dynamic (maintenance plans) control. In the current practice, in most countries, the condition state or the condition index is used as an unique KPI, instead of reliability and safety.

4 ACKNOWLEDGEMENTS

This article is based upon the work from COST Action TU-1406, Quality specifications for roadway bridges, standardization at a European level (BridgeSpec), supported by COST (European Cooperation in Science and Technology).

5 REFERENCES

Amado, J., & Hajdin, R. 2017. : Basis for the development of Quality Control Plans for Arch Bridges *Proceedings of the Joint COST TU1402 – COST TU1406 – IABSE WC1 Workshop*. Zagreb: University of Zagreb.

Casas, J.R. 2016a. European Standardization of Quality Specifications for Roadway Bridges: an Overview. *Proceedings of IABMAS 2016*. Foz do Iguaçu (Brasil): Taylor and Francis.

Casas, J.R. 2016b. Quality control plans and performance indicators for highway bridges across Europe. *Proceedings of the 5th International Sympos ium on Lifecycle Civil Engineering.* Delft (The Netherlands): Taylor and Francis.

Ishizaka, A., & Nemery, P. 2013. *Multi-criteria decision analysis: methods and sof tware*. New York: John W iley & Sons.

Keeney, R. L., & Raiffa, H. 1993. *Decisions with multiple objectives: preferences and value trade-offs.* Cambridge university press

Matos, J.C., Casas, J.R., & Fernandes, S. 2016. COST Action TU1406 Quality Specifications for Roadway Bridges (BridgeSpec). *Proceedings of IABMAS-2016* , Foz do Iguaçu (Brasil): Taylor and Francis.

Reichert, P., Schuwirth, N., & Langhans, S. 2013. Constructing, Evaluating and Visualizing Value and Utility Functions for Decision Support. Environmental *Modelling and Software*,46:283–91.

Stipanovic, I., Chatzi, E., Limonggelli, M., Gavin, K., Allah Bukhsh, Z., Skaric, S., Palic, S., Xenidis, Y., Imam, B., Anzlin, A., Zanini, M., Klanker, G., Hoj, N., Ademovic, N. 2017. *WG2 Technical Report: Performance Goals for Roadway Bridges of Cost action TU 1406*. Brussels: COST

Straus, A., , Mandic, A., Campos, J. & Casas, J. R. 2016. *WG1 Technical Report: Perf ormance indicators for roadway bridges of Cost Action TU1406.* Brussels: COST.

Strauss, A., Vidovic, A., Zambon, I., Dengg, F., Tanasic, N., & Matos, J.C. 2016. Performance indicators for roadway bridges. *Proceedings of IABMAS-2016.* Foz do Iguaçu (Brasil): Taylor and Francis

Thevenot, H. J., Steva, E. D., Okudan, G. E., & Simpson, T. W. 2006. A multi-attribute utility theory-based approach to product line consolidation and selection. In ASME 2006 *International Design Engineering Technical Conferences and Computers and Inf ormation in Engineering Conference:*441-450. American Society of Mechanical Engineers.

Maintenance, Safety, Risk, Management and Life-Cycle Performance of Bridges – Powers, Frangopol, Al-Mahaidi & Caprani (Eds)
© 2018 Taylor & Francis Group, London, ISBN 978-1-138-73045-8

Quality specifications and performance indicators for road bridges in Europe

Alfred Strauss
Department of Civil Engineering and Natural Hazards, University of Natural Resources and Life Sciences, Peter-Jordan-Straße 82, 1190 Vienna, Austria

Sérgio Fernandes
ANSER Lda., Jardim Dr. Rodrigues Ferreira 50 – 1 C, 4780-367 Santo Tirso, Portugal

Joan R. Casas
UPC-BarcelonaTech, Jordi Girona 1-3, 08034 Barcelona, Spain

Lisa Mold
Department of Civil Engineering and Natural Hazards, University of Natural Resources and Life Sciences, Peter-Jordan-Straße 82, 1190 Vienna, Austria

José C. Matos
Civil Engineering Department, Campus de Azurém, Minho University, 4800-058 Guimarães, Portugal

ABSTRACT: Across Europe, multiple management systems were developed with the aim of managing roadway bridges in an efficient manner. Although being generically similar, the condition assessment process, based in the assessment of performance indicators which are compared with performance goals in order to evaluate the accomplishment of established quality control plans, can be identified as one difference among them. This leads to the existence of multiple different methodologies for assessing the bridge condition, and consequently to a considerable variation in roadway bridges quality. COST Action TU1406 aims to achieve the European economic and societal needs by standardizing the condition assessment and maintenance level of roadway bridges. For such purpose it would be required to establish the specific recommendations for the quantification of performance indicators, the definition of standardized performance goals and, finally, a guideline for quality control plans.

Keywords: *performance indicator, performance goal, quality control plan, roadway bridge, asset management*

1 INTRODUCTION

In the past few years, significant worldwide research has been done regarding condition assessment of roadway bridges, specifically through the use of non-destructive tests, monitoring systems and visual inspection techniques. Obtained values, which provide information regarding the assessed bridge condition state, are then compared with previously established goals. As a result, there are currently several methodologies to assess the bridge condition. A similar problem was addressed with roadway pavements in the past. Although this was a worldwide problem, in Europe it was solved through COST Action 354 "Performance indicators for pavements' (COST 354, 2004). More recently, the concept of performance indicators (PI) was introduced, simplifying the communication between consultants, operators and owners. However, large deviations continue to exist on how these indicators are obtained and, therefore specific actions are required for a standardization of this procedure. For a standardized procedure, for example, quality control plans (QCP) are further important in-

struments which are based on the previously mentioned PIs and pre-specified PI-goals. However, these PI-goals are difficult to obtain, as they are highly subjective. A first very good generalized overview of the current methodologies to assess the bridge condition is given in the report by Hooks and Frangopol, (2013). In addition, bridge performance measures in relation to the goals of bridge projects is available in Adams and Kang (2009). As can be seen in Table 1 the authors listed a set of PIs, including a classification depending on the level of analysis: cross section (CS), component (CO) or/and system (SY). It should be mentioned, that the operators are already using some of these PIs intensively, while others are still in a conceptual phase. It is, however, endeavored that road authorities can collect experience as soon as possible with these indicators. An assistance to this process is provided by the publication of Ghosn et al. (2016), where he presents a complete and comprehensive description of available reliability-based PIs.

Recently, COST Action TU1406 emerged with the main ambition of developing a guideline for the establishment of QCPs in roadway bridges, by integrating the most recent knowledge on performance assessment procedures with the adoption of specific goals (Matos, 2016; Matos, Casas, & Fernandes, 2016). This guideline will focus on bridge maintenance and life-cycle performance at two levels: (i) performance indicators (PIs), (ii) performance goals (PG). The primary goal is, among others, to update and adapt existing PI tables to guarantee a state-of-the-art PI based bridge assessment technology in Europe. Performance indicators related to sustainability will also find place in such new assessment standards. By developing new approaches to quantify and assess bridge performance, as well as quality specifications to assure expected performance levels, it is expected that bridge management strategies will be significantly improved, enhancing asset management of aging structures in Europe. The target groups and end users who will exploit the outcome of the COST TU1406 action are: (i) public/private owners, as their assets will be maintained in an upscale level; (ii) operators, as standardized procedures for reducing maintenance costs, guaranteeing the same quality-level, will be introduced; (iii) design and consultant engineers, as the assessment of roadway bridges performance will be established in a uniform way, according to the developed guideline; (iv) equipment and software companies, as a new perspective will be given, regarding the most suitable equipment and software for the assessment of roadway bridges; (iv) academics, and researchers and engineers, as they will take an advantage of their involvement in the guideline preparation; (v) students, as they will benefit from COST tools (e.g. training schools) and from the contact with different stakeholders involved in this Action; (vi) relevant European, international and national associations, with which the main outcomes of this Action will be shared; and (vii) standardization bodies and code writers, which will benefit from the developed guideline. More details and backgrounds are discussed in Matos (2016) and Matos et al. (2016).

2 OBJECTIVES

Based on the previously outlined specifications to assure expected performance levels and to assure a significant improvement in bridge management strategies, the following objectives have been defined in the COST TU1406 action:

(1) to develop, for the first time in Europe, a guideline for the establishment of QC plans (QCPs) for roadway bridges at a European level. The Action aims to achieve the European economic and societal needs by standardizing the condition assessment and maintenance level of roadway bridges;

(2) to examine the possibility of incorporating new indicators related to sustainable performance of roadway bridges as well as research performance indicators PIs which are still in the process of definition.

(3) to establish detailed recommendations for assessing PIs, technical as well as sustainable, and for characterizing associated specific goals.

(4) the claim of a European PI database, which is associated with the following sub-tasks: (a) the systematization of available knowledge associated with existing QC plans for bridges at an European level and the characterization of associated PIs and PGs; (b) the exploration of the up-to-date knowledge on PIs, including technical, environmental, economic and social indicators; (c) the definition of quality specifications through the definition of performance goals PGs, quarantine a required performance level; (d) the development of detailed examples for practicing engineers on the assessment of PIs as well as

in the definition of PGs - these are to be integrated into a guideline; (e) the flexibility of the DB to incorporate present and future operational and research based PIs and PGs of the COST countries

For an efficient achievement of the above-defined objectives, a linear work process was defined, which is divided into the following work packages as presented by Casas (2016) and Matos et al. (2016): *WG1: "Performance indicators"*. The goal was to explore those PIs of bridge structures, in the course of international research cooperation, which capture the mechanical and technical properties and its degradation behavior, already partly covered by code specifications. Considerations also include: natural aging, quality of the material; service life design methods; sustainable indicators; environmental, economic and social based indicators, performance profiles. The final result is the implementation of a PI database for

Europe with flexibility to accommodate country-specific requirements. Further information on this WG can be found in Strauss and Ivanković (2016). Objectives of WG1 are therefore, among others, the characterization of bridge PIs, which can address: (a) the safety: the load factor, and the reliability index to ultimate limit state (ULS); (b) the serviceability: the condition index, and the reliability index to serviceability limit state (SLS); (c) the availability, and robustness; (d) the costs: the total life cycle costs (LCC), and values related to durability aspects; and (e) aspects of environmental efficiency: CO2 footprint; *WG2: "Performance goals"*. The objective was to provide an overview of existing PGs for the indicators previously identified in WG1, and to develop technical recommendations which will specify the PGs. These goals will vary according to technical, environmental, economic and social factors. Further information on this WG can be found in Stipanovic and Klanker (2016); *WG3: "Quality Control Plans"*. Bridge quality control (QC) is actually restricted to the design and construction phases and are achieved by complying with existing design code requirements. When it comes to existing bridges, despite the age, location or even the current condition state, QC is performed according to existing design codes or the owner/operator expertise. There is no uniform procedure to assess existing bridge state condition. Therefore, there is a real need to establish a guideline for performing the QCPs for existing bridges. This plan should be based on multilevel procedures, from simple visual inspections to in-depth investigations, and on the level of doubts with regard to bridge performance. It should also define at which time intervals QC is necessary, and which condition the more detailed investigations or corrective actions are necessary. Based on the results of WG1 and WG2, as well as on survey of existing approaches in practice, the objective of WG3 is to provide a methodology with detailed step-by-step explanations for the establishment of QCPs for different bridge types. The QCP has to establish PGs, which are user/society related, e.g.: traveling time; traffic allowance; safety level; comfort/serviceability; Further information on this WG can be found in Hajdin (2016).

3 SYSTEMATIZATION OF AVAILABLE KNOWLEDGE ABOUT PIS

3.1 *General*

In a first step, associated with the targets of WG1 to WG3, a technical survey among the COST TU1406 participating countries was carried out in order to clarify: (a) what is already being done around Europe in the field of bridge management strategies and performance based concepts; and b) what is considered necessary for enhancement. These surveys focused on guidelines, inspection documents, evaluation and assessment documents already in use by the infrastructure operators and documents from the research area.

Thus, the extracted PIs could already been categorized in PIs already in use, PIs on the way to be in use, and research based PIs. The surveys were made possible with the help of the networks created in the course of COST TU1406. These networks include people from different stakeholders (such as infrastructure operators, consultants and owners of infrastructure facilities, universities, institutions in the field of infrastructure facilities) and from various scientific disciplines (e.g. on-site testing, visual inspection, monitoring, structural engineering, structural analyses sustainability, etc.). The motivation for this first process step was based on the following very important findings: (a) The bridges performance is very good in most European countries and the infrastructure owners or operators are doing a very good work; (b) It is important to learn the stakeholders strategies in order to improve and enhance (if required) their procedures and rules; (c) The implementation of a common methodology across Europe, with flexibility to accommodate country-specific requirements, needs to know what is being done now. Too many changes will reluctance make bridge owners and operators reluctant to process the harmonized methodology in their daily work. In addition, the new harmonized methodology cannot be disregarded.

3.2 *First phase of the process of data collection*

As can be seen from Figure 1, a kind of closed questionnaire concerning predefined performance indicators PIs based on former characteristics and the country-specific situations was carried out in the first round. The following widely agreed PGs were used to define those PIs that where of interest for the survey and with respect to bridge management strategies: PIs in connection with (a) the safety, (b) the functionality (serviceable), (c) the availability (to the user), (d) the total life-cycle cost of bridges, and (e) the environmental impact. In particular following PIs where stressed: (I) Concerning the safety: the load factor, the safety factor, and the reliability index to ULS; (II) Concerning the serviceability: the condition index, and the reliability index to SLS; (III) Concerning the availability goal: robustness (the bridge should be minimally affected by external conditions not specifically foreseen during design), and resilience (the bridge should be quickly recovered from any undesired disruption); (IV) Concerning of being economically viable: the total life-cycle cost, and the durability aspects values (a more durable bridge will be an inexpensive bridge to maintain), such as the diffusivity coefficient of chlorides in concrete, and the permeability of concrete cover; (V) Concerning the goal of being environmentally friendly: CO2 footprint.

The first survey phase provides the following findings among others, which are also discussed in a more comprehensive way in Casas (2016) and Strauss et al. (2016). It was of high importance in this first survey phase (a) that the original documents were also made available (important passages marked in color) since different translations led to a very high number of e.g. management strategies or assessment methods, which proved to be not correct when inquiring and considering the original documents, and (b) to differentiate between the operational and the research-based documents in order to allow objective proposals for enhancements.

3.3 *Second phase of the process of data collection*

The COST TU1406 Geneva Workshop was held in September of 2015 to define further essential steps of the WG1 group. The goal was the clearer differentiation between the already applied concepts and documents and the research-based approach. Each WG member was asked to participate in the workshop, and (b) to prepare a poster or oral presentations with the following objectives: (1) Extract from the available documents in each country the most important (> 8) PIs; (2) show the formulation and the procedure on how to obtain the PI; (3) show the thresholds with respect to each PI, if available; (4) show the goals with respect to each PI, if available; (5) characterize, based on their experience, if the indicated or proposed PI are already applied by owners, operators, experts, …, and in which project phases; (6) characterize those groups that are important PI, but not applied now, or not applied now and needing further research in order to become fully implementable.

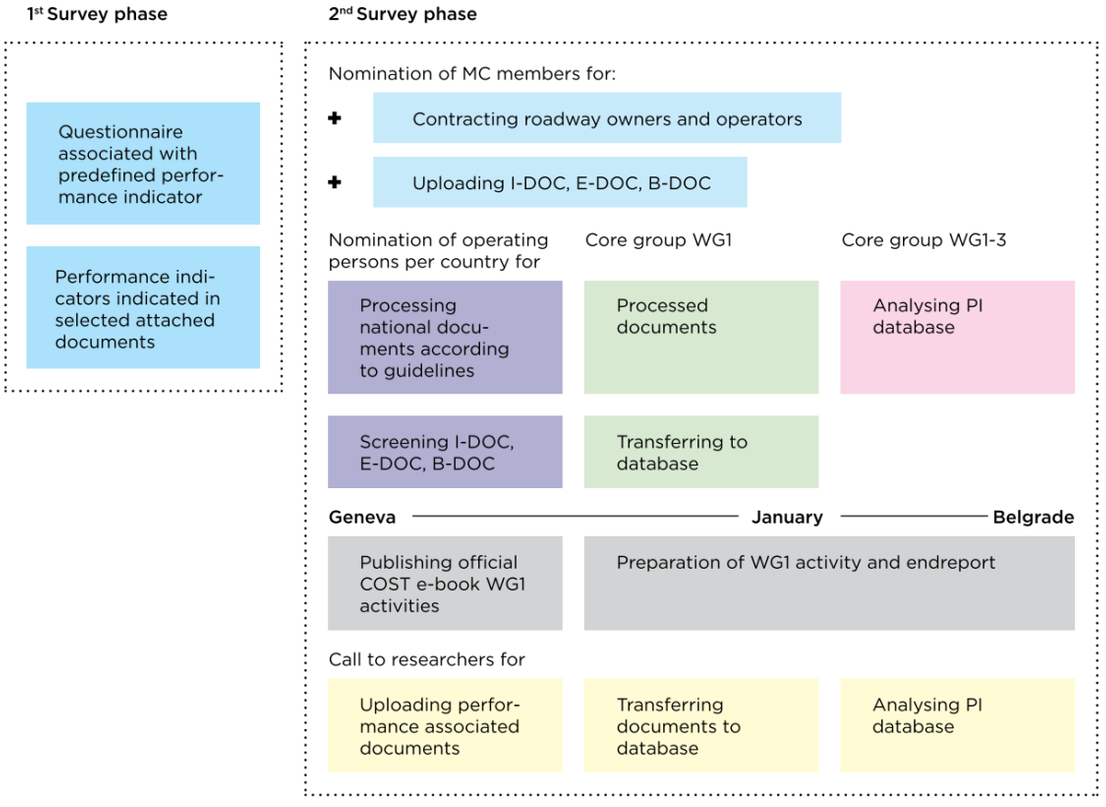


Figure 1. Technical survey on performance indicators

The workshop in Geneva indicated that an extended systematic screening on practical national inspection and evaluation documents is necessary in order to obtain a consistent and conclusive information associated with PIs, PGs and performance thresholds (PTs) from each COST partner country. Two responsible persons were nominated for each COST partner country, whereas the management committee (MC) member (1st person) had the responsibility to build up the contact to the infrastructure operators and owners in order to determine with them the afore mentioned relevant documents, and the 2nd nominated national expert (2nd person) had the responsibility to process the screening of the documents of its country and to fill up the PI-database, which is described in more detail in the next section.

3.4 *Performance indicators database for the survey process*

Through WG1 activities, the development of a PIs database had been defined as an essential component of COST TU1406. The core of the survey process for

obtaining PIs and corresponding key performance indicators (KPI) is given in Figure 2. As mentioned previously the two COST nominated persons together with the infrastructure operators and owners chose beforehand the relevant documents (e.g. inspection, evaluation, research etc.) from which the PIs, and related information were extracted. A user interface (UI) served for a systemized data collection and it also allowed a relative flexible treatment of the number of data sets and PIs (unrestricted data input), which of course varies from one to the other document very much.

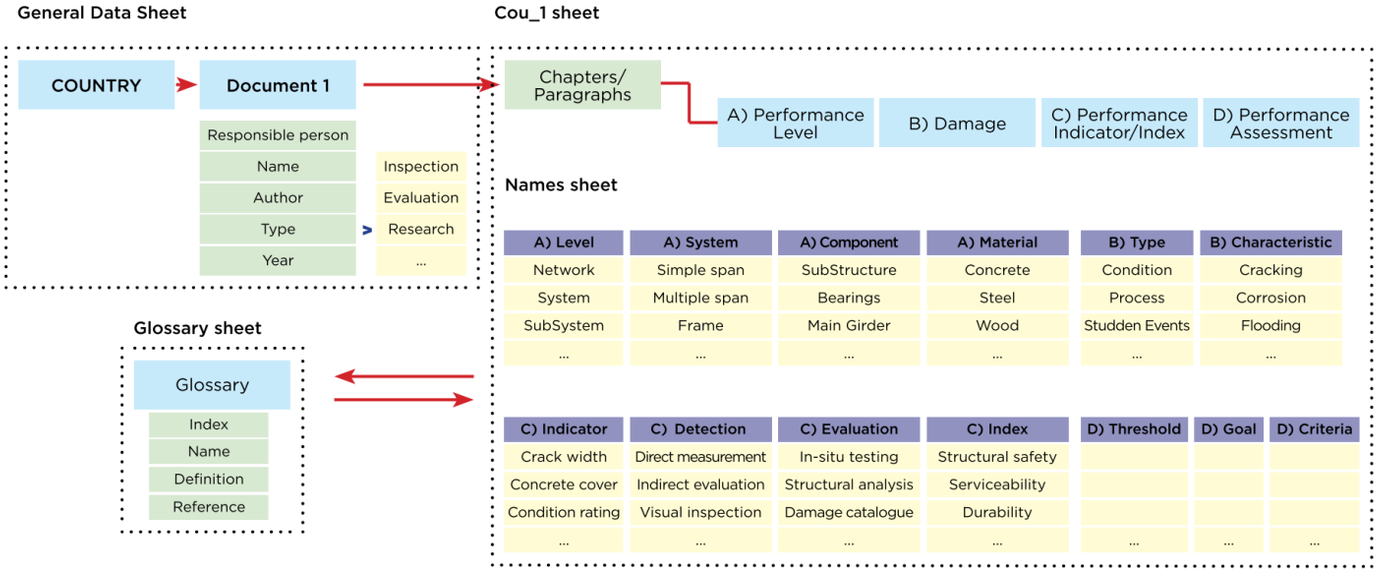


Figure 2. Structure of the Performance indicators database for the survey process

The UI for the survey is structured in MS Excel (see Figure 4), where the information may be stored in four groups: (i) Performance Level; (ii) Damage Processes (DP); (iii) PI/Index; and (iv) Performance Assessment. Besides this data, there is an opportunity to add additional references and specific information about a group element (e.g. evaluation process, formula, Figure, etc.). The background for this structure comes from screening of the Austrian national document (Bundesministerium für Verkher, Innovation und Technologie, 2011) and two documents from United Kingdom (County Surveyors Society CSS, 2004). The performance indicators database for the survey process is divided into several documents as shown in Figure 4. In order to support on the interface in the screening process, a Glossary of key terms is required to store the information and terminology related to PI, PG, PT and PM. Such Glossary has been prepared on the basis of the information from German and Austrian documents (BASt, 2015, Bundesministerium für Verkehr, Innovation und Technologie, 2011). During the screening process it was updated by national specific information on the one side in their own language, and on the other side in English. The Glossary is acting as a background document, whose definitions are used to support the filling of the data base.

In a "Damages Sheet" the nominated persons were able to fill in the national damages which are not comprised in the Glossary. All prepared interfaces for the screening of national relevant documents were prepared with the aim of being user friendly and allowing the free input. In the Glossary this was made possible by adding the sheet "New terms". Here, the users were free to add additional concepts, definitions, explanations and keywords in relation to PIs, goals, thresholds, criteria and methods (Figure 4). At present in the data surveying process, 36 countries are included.

3.5 *Homogenization Process*

The results of the screening process were partly heterogeneous and with a number of overlapping terms. This mainly results from a free interpretation leeway and different know-how of experts in visual inspections, performance evaluation, performance assessment and decision making. The screening results were used for a homogenization process by the WG1 core group and the nominated persons from each country, were asked again to verify their performance and damage specific inputs, by comparing them with the homogenized and categorized terms. These homogenized data were the baseline for all further studies and quantifications and provides also the basis for an effective comparison of performance quantities between countries.

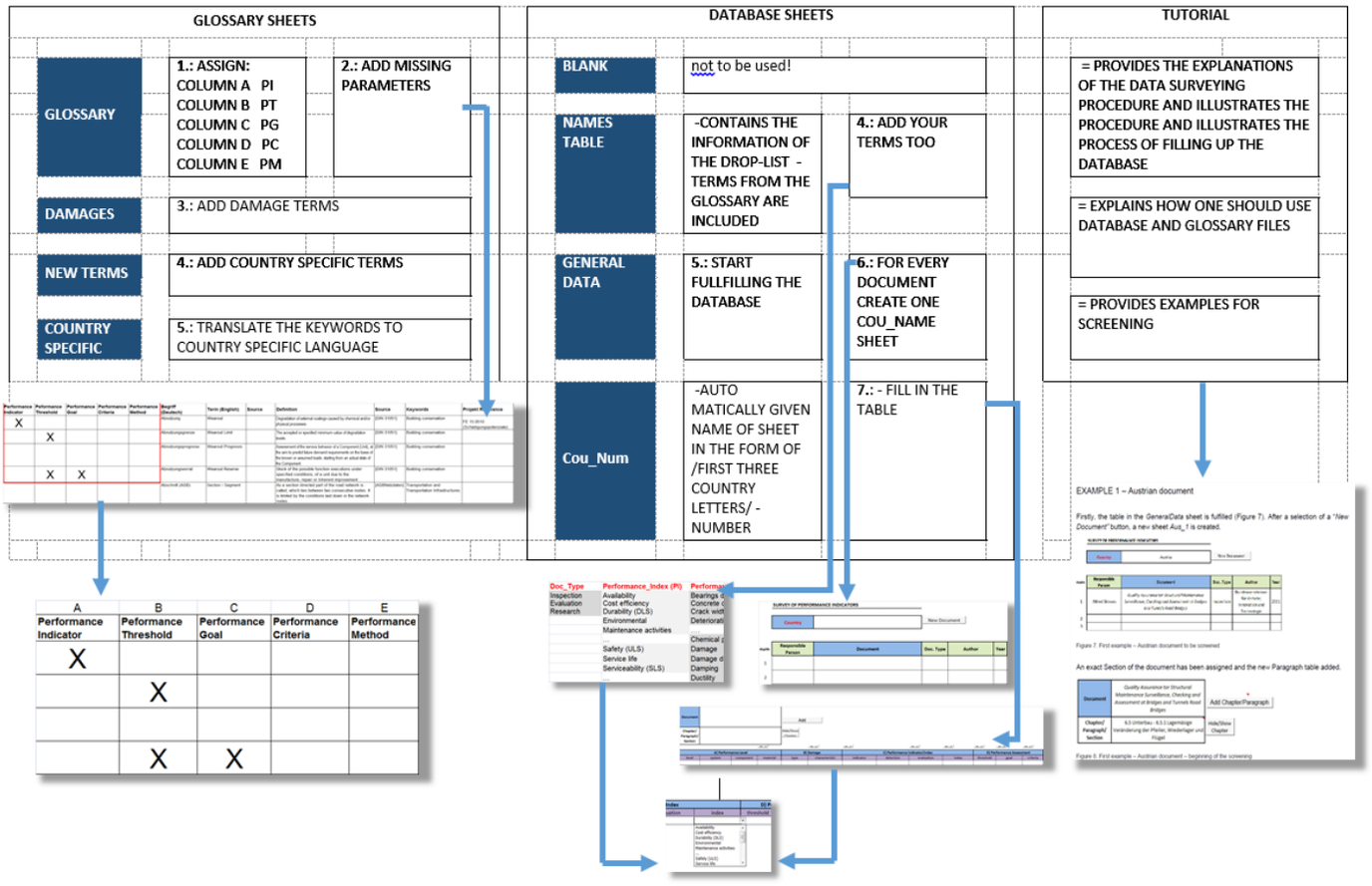


Figure 3. Performance indicators database for the survey process and its associated documents-B

3.6 *Findings from the process of data collection*

The previously sketched data collection process resulted in a list of more than 700 terms, which was later clustered and homogenized. From this process resulted a shorter list of 385 terms, grouped in 11 clusters from defects to rating and loads. The list was considered, not as a final list of PIs, but as a list of terms that can be related with PIs (PI related terms as addressed in WG1 Report). Assuming that not all the 385 terms can be considered as PIs a new practical based categorization of the terms had been performed. The following four categories of terms were considered: performance indicators (PIs), damage processes (DPs), observations (OBS) and other data (OD). A fifth category was considered, related with non-interceptable processes, once they are out of the scope of this group. The sixth category considered was labelled as Combined Performance Indicator, trying to cluster terms that reflect general properties of a structure and may be derived, among other ways, from the combination of several PIs. As an example, the term bridge condition was considered in this category once one can assume that it can be derived from all the other PIs. (Amado & Hajdin, 2017; Strauss & Ivanković, 2016). The distribution of the 385 PIs related terms through the 8 categories above defined is shown in Table 2 (Amado & Hajdin, 2017). The complete categorization of terms can be found in the COST TU1406 WG1 report.

Regarding DPs, Bień and Gładysz-Bień (2016) proposed three main groups of degradation mechanisms (DM) in arch bridges, related with physical, chemical and biological phenomena. In Table 4 the list of DMs considered by these authors was compared with the list of DPs resulted from the categorization of terms proposed in the WG1 report. A correlation could also be found for most of the terms. One single term referred in the bibliography could not find a synonym in the present proposal, which was the term Leaching. It's also important to note that, in some cases, several Damages Processes related terms could be found for the same DMs.

3.7 *Assessment of Performance Indicators*

As shown in the framework for the establishment of QCPs (Hajdin, 2016), its intended to translate the assessment made for each PI through a performance value (PV), based in a qualitative approach that can

be applicable also in a quantitative manner. Independently from the tool used to achieve this goal, event trees, fault trees, Bayesian Networks or others, it was understood that each PI is related with certain DPs and that this latter category is related with certain observations. The conjugation of these relations with other information such as the level of assessment, structure type, element, time and other data (comprising measurements, material properties, etc.) will allow to determine a certain PV.

4 PERFORMANCE INDICATORS VS. KEY PERFORMANCE INDICATORS

4.1 *General*

It was agreed, among the TU1406 community, that PI is a measurable and quantifiable parameter related to the bridge performance that can be compared with a target measure of a PG or can be used for ranking purposes among a bridge population in the framework of a QCP or life-cycle management (which includes decisions and actions involving economic resources). To evaluate certain performance indicator, performance thresholds (PT) or criteria must be set. A threshold value constitutes a boundary for purposes such as: a) monitoring (e.g. an effect is observed or not), b) assessing (e.g. an effect is low or high), and c) decision-making (e.g. an effect is critical or not). A criterion is a characteristic that is relevant for the choice between processes e.g. such as maintenance actions or others. Although the interaction of different PIs is inevitable, their categorization into technical, sustainable and socio-economic indicators through component, system and network level is proposed in order to more easily identify the level of their influence to a certain KPI related to PG.

In order to move on with the reduction of the list of PIs, an expert group was asked to specify PIs according to the following points: Measurable? Quantifiable? Target value available? Valid for ranking? Allow decision with economic implications?.

At the end, approximately 100 extricated PIs are further related with one or more of the key performance indicators (KPIs) defined in WG2: reliability (R), availability (A), maintainability (M), safety (S), security (Se), environment (E), costs (C), health (H), politics (P), rating/inspection (I). A further process is required for categorization of PIs in relation to PGs and PTs at different levels: component (CL), system (SL), network (NL); taking into account different aspects: technical (Tech), sustainability (Sust) and socio-economic (SoEc).



Figure 4. Terms obtained from the entire screening process of the operational documents in connection with performance assessment of bridge structures

Figures 5 show the terms obtained from the entire screening process of the operational documents in connection with performance assessment of bridge structures. From these figures it can be seen which of the overall terms are documented and also used in bridge engineering in five selected countries: Austria,

Chile, Croatia, Portugal and Spain. In addition a separation of the terms in "2º Level PIs, 2ºPI; Damage Process, DP_; Non-interceptable processes, NIP; Observation, OBS; Other data, OD; Performance Indicator, PI" was defined in cooperation with WG2 and WG3 as can be seen from the superscript next to the terms in order to allow the setup of an efficiently manageable QC. More details are discussed in the report of WG3. The PIs are considered as elements that are related to the KPIs of the "RAMSSHEEP" spider, as presented in the next paragraph. The coloring of the terms as can be seen in Figures 5 and 6, refers to the local or object classification. Finally, the remaining country-specific consideration, in addition to the 5 countries shown in Figures 5 and 6, can be found in the WG1 report.

Figure 5 and 6 shows the terms extracted from the inspection and evaluation documents for the respective category defined previously. It is striking that the number of actually characterized PIs is only 29 of the 385 terms.

The screening process and the expert questionnaire made it possible to assign the performance indicators to component (CL), system (SL) and network level (NL), as shown in Table 6 and to assign the PIs to the spider tails or KPIs. The assignment shown here for the five selected countries is available in a similar form for the other countries in the WG1 Report. Figure 7 shows the "RAMSSHEEP" spider indicating the KPIs and the country specific assigned PIs obtained from the expert analyses as presented above.

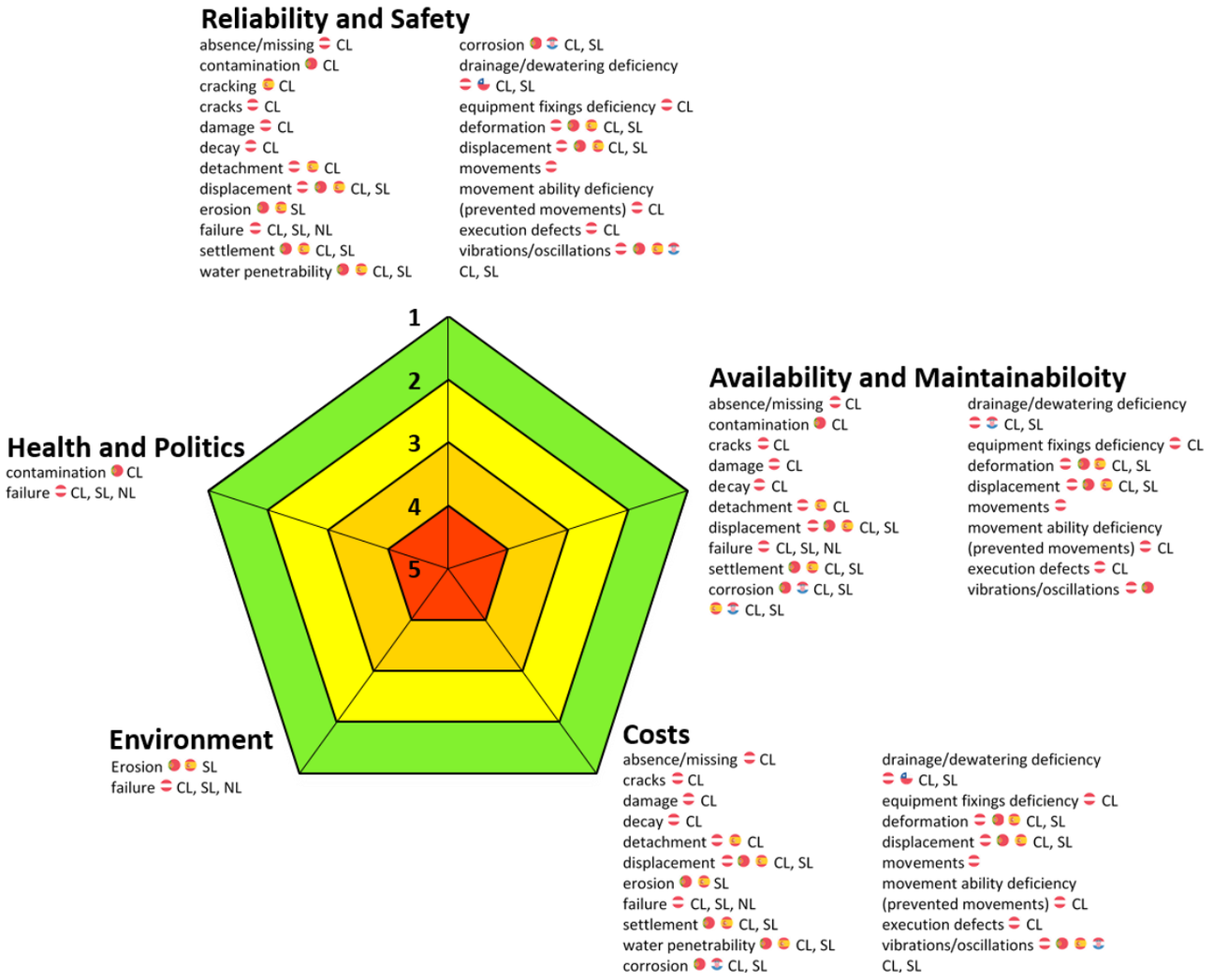


Figure 5. The "RAMSSHEEP" spider indicating the KPIs and the country specific assigned PIs

Further process will require allocation of rating value (1-5, as in table 1) and weighting factor (whose values are still to be defined) to each PIs related to five main groups of KPIs which are established in relation to requirements of the WG2 and WG3. The final rating and weighting will reveal overall rating (with rating factors r_{SRS}, r_{AM}, r_C, r_E and r_{HP}) of each of the five most important KPIs groups. The green areas in Fig. 7 represent the most favorable rate and the red areas should alarm the bridge operator and require immediate intervention.

5 PERFORMANCE INDICATORS DATABASE FOR THE ASSESSMENT PROCESS

5.1 *Relational Database Structure*

A relational database is a set of tables containing unique instances of data fitted in predefined categories, which, due to the established relations, allows users to view information as needed. A considerable amount of information was provided from the screening process. Although this data was gathered in a structured manner, it is dispersed through multiple files, becoming rather difficult to manage, analyze or compare. Therefore, in order to overcome such restrictions, a relational database with an organization structure represented in Figure 8 was developed.

The information included in the "GeneralData" sheets, concerning the documents titles from where the data was retrieved, was introduced in the "srv_op_doc" table. This data is related to its respective country through the foreign key "country_id". The "Cou_num" sheets from the Excel workbooks contains the screened data, organized per document chapter. In the relational database, this information was inserted in the "srv_op_chapter" table, concerning the documents chapters, and in the "srv_op_record", that contains all the findings. The homogenization data was inserted in the "srv_hmg" table. All the remaining tables concern the data given in the "Names_Table" sheet which feed the dropdown lists included in the "Cou_num" sheets and are linked to the main tables through foreign keys.

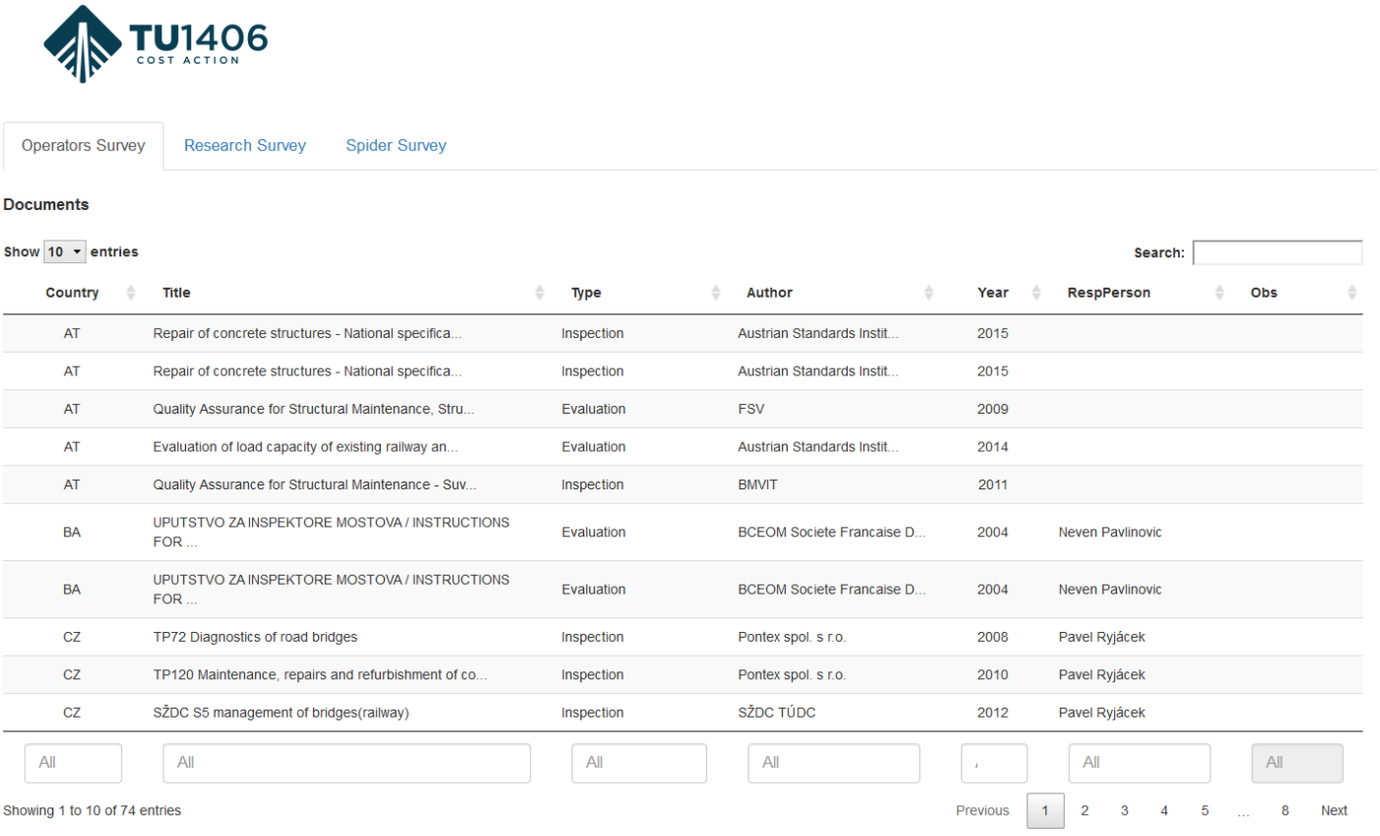


Figure 6. User interface

In addition to the database development, and due to the high number of documents provided by the countries involved, several routines were developed. They allow to read the information from the Excel files and insert it in the database in a systematic way.

5.2 *User Interface*

The development of a database by itself brings many advantages to all organizations. However, given that the management of such tool is not very user friendly to those with no experience in such field, a visual interface is required. From this perspective, a UI capable of displaying the information contained in the database was also developed. Given all technologies available, and considering those currently in use by COST Action TU1406 (see Figure 9).

6 CONCLUSIONS

In this paper, an overview of COST Action TU1406 with incidence in the work and the methodology adopted within WG1 to achieve the purpose of collecting PIs used across Europe was presented. The aim was to establish good practices on the definition

of QCPs for roadway bridges. This should be the basis for the future proposal of the definition of PIs that could be adopted and used all over Europe.

The methodology is based on a deep analysis of the existing bridge management policies existing in European countries and the main PIs used with the objective to define a common group of quality specifications and control plans that can be assumed by all these countries. The gathered data from European countries was further analyzed and systematized. Thereby, the existing roadway bridges in EU member countries are managed not only country-specific but also in a consolidative manner.. Although showing an European initiative, the proposed methods in this paper can be also applied to other countries in the world, where homogeneity in QC of existing roadway bridge stock is needed, in order to facilitate the existence of a roadway network that allows the communication and transportation from one region to another in a safe, reliable and cost-effective way.

Although it was possible to reach a high level of satisfaction with the obtained results, more work is still needed. It will be necessary to have a selection of the most relevant PIs for achieving KPIs for an optimal QCP within the bridge management and also to allocate them with appropriate weights to set different levels of importance between them. The next step is the definition of the technical recommendations for the specification of PGs based on existing ones for the indicators discussed in this study.

7 REFERENCES

Adams, T.M., & Kang, M.K. (2009). Sensitivity Analysis of Bridge Health Index to Element Failure and Element Conditions, Project completed for the Midwest Regional University Transportation Center with support from the Wisconsin Department of Transportation.

Amado, J., & Hajdin, R. (2017). *Proceedings of the Joint COST TU1402 – COST TU1406 – IABSE WC1 Workshop: Basis for the development of Quality Control Plans for Arch Bridges*. Zagreb: University of Zagreb.

Berichte der Bundesanstalt für Straßenwesen (BASt). (2015). Intelligente Brücke – Schädigungsrelevante Einwirkungen und Schädigungspotenziale von Brückenbauwerken aus Beton, Schünemann Verlag. Germany (in German)

Bień, J., & Gładysz-Bień, M. (2016, October). *Gerontology of* Arch Bridges. Paper presented at the proceedings of the 8th International Conference on Arch Bridges, Wroclaw, Poland.

Bundesministerium fürVerkehr, Innovation und Technologie. (2011). Quality Assurance for Structural Maintenance; Surveillance, Checking and Assessment of Bridges and Tunnels; Road Bridges. Vienna, Austria. (in German)

Casas, J.R. (2016). Maintenance, Monitoring, Safety, Risk and Resilience of Bridges and Bridge Networks: European Standardization of Quality Specifications for Roadway Bridges: an Overview. London: Taylor and Francis.

Casas, J.R. (2016, October). Quality control plans and performance indicators for highway bridges across Europe. In proceedings of the 5th International Symposium on Lifecycle Civil Engineering, Delft, The Netherlands.

COST 354 MoU: European Cooperation in the field of Scientific and Technical Research – COST. (2004). Memorandum of Understanding for TUD COST Action 354.

COST Action TU1406 MoU: European Cooperation in the field of Scientific and Technical Research – COST. (2014). Memorandum of Understanding for COST Action TU1406.

County Surveyors Society CSS. (2004). Addendum to: CSS Guidance Note On Bridge Condition Indicators. Volume 2: Bridge Inspection Reporting. Lincoln, United Kingdom.

Ghosn, M., Frangopol, D., McAllister, T., Shah, M., Diniz, S., Ellingwood, B., Manuel, L., Biondini, F., Catbas, N., Strauss, A., & Zhao, X. (2016). Reliability-Based Performance Indicators for Structural Members. Journal of Structural Engineering, doi:10.1061/(ASCE)ST.1943-541X.0001546.

Hajdin, R. (2016). Maintenance, Monitoring, Safety, Risk and Resilience of Bridges and Bridge Networks: Quality control plans on roadway bridges. London: Taylor and Francis

Hooks, J., & Frangopol, D.M. (2013). Bridge Performance Primer, Report of the Long-Term Bridge Performance (LTBP) Program of the Federal Highway Administration FHWA

Matos, J.C. (2016, October). An overview of COST Action TU1406, Quality Specifications for Roadway Bridges (BridgeSpec). In proceedings of the 5th International Symposium on Lifecycle Civil Engineering, Delft, The Netherlands.

Matos, J.C., Casas, J.R., & Fernandes, S. (2016). Maintenance, Monitoring, Safety, Risk and Resilience of Bridges and Bridge Networks: COST Action TU1406 Quality Specifications for Roadway Bridges (BridgeSpec). London: Taylor and Francis.

Stipanovic, I., & Klanker, G. (2016). Maintenance, Monitoring, Safety, Risk and Resilience of Bridges and Bridge Networks: Performance goals for roadway bridges. London: Taylor and Francis.

Strauss, A., & Ivanković, A. M. (2016, April). Performance indicators for road bridges – categorization overview. Paper presented at the WG meeting of COST Action TU1406 Quality specifications for roadway bridges, standardization at a European level, Belgrade, Serbia

Strauss, A., Vidovic, A., Zambon, I., Dengg, F., Tanasic, N., & Matos, J.C. (2016). Maintenance, Monitoring, Safety, Risk and Resilience of Bridges and Bridge Networks: Performance indicators for roadway bridges. London: Taylor and Francis.

Zimmermann, T., Strauss, A., Bergmeister, K. (2010). Numerical investigation of historic masonry walls under normal and shear load. Construction and Building Materials. Volume 24, Issue 8, Pages 1385-13

Zimmermann, T., Strauss, A., Lehký, D., Novák, D., Keršner, Z. (2014) Stochastic fracture-mechanical characteristics of concrete based on experiments and inverse analysis. Construction and Building Materials Volume 73, Pages 535-543

8 ACKNOWLEDGEMENTS

This article is based upon work from COST Action TU1406, Quality specifications for roadway bridges, standardization at a European level (BridgeSpec).

Maintenance, Safety, Risk, Management and Life-Cycle Performance of Bridges – Powers, Frangopol, Al-Mahaidi & Caprani (Eds)
© 2018 Taylor & Francis Group, London, ISBN 978-1-138-73045-8

Quality control plan for RC bridges exposed to flooding events

N. Tanasic
University of Belgrade, Faculty of Civil Engineering, Serbia
R. Hajdin
Infrastructure Management Consultants, Zurich, Switzerland

ABSTRACT: The state-of-the-art bridge management practice do not adequately account for flooding and related local scour, thus fail to provide crucial information to viably mitigate consequences of bridge failures. The current policies in practice, which are solely based on visual inspections, need to be updated with efficient, preferably quantitative methodologies for a comprehensive and timely screening of vulnerable bridges. The research is aimed at application of key performance indicators which consider relevant data for assessment of vulnerability to local scour. Herein, particularly bridge exposure and bridge resistance are assessed. The latter involves failure modes, an essential ingredient for evaluation of a probability of failure, which is related to the indicator of reliability. The guidelines are necessary for inspection of bridge vulnerable zones i.e. segments that have the key role in resistance to failure. The practical evaluation of the reliability class is presented for RC girder bridges, which support elaboration of adequate quality control plans.

1 INTRODUCTION

The current bridge management (BM) practice in planning of adequate maintenance actions for bridges endangered by flooding hazards cannot provide satisfactory results, as it mostly relies on the lessons learned in the aftermath of failures. In Europe, related BM procedures are qualitative and not comprehensive. In most cases, they are based solely on visual inspections (Tanasic & Hajdin, 2017a), which was confirmed within ongoing research project COST TU1406 (Matos et al., 2016). In the U.S., the consideration of flooding hazard in decision-making is based on qualitative ratings of specific National Bridge Inventory (NBI) items. Still, some U.S. states additionally apply own methodologies, which take into consideration more thorough inspection procedures and involve vulnerability assessments (e.g. New York State Department of Transportation, 2003).

In the last two decades, the risk-based approaches are being developed to address the flooding impact on bridges and transportation infrastructure. In the HYRISK approach (Pearson et al., 2002), the total consequences of a bridge failure are thoroughly elaborated. This methodology accounts for a bridge foundation type and static system, but uses the information on past failures as the basis for estimation of the probabilities of failure. Recently, this approach is suggested to be updated to account for soil erodibility at bridge sites, as a major determinant of a scour related failures (Bones et al., 2017). In Khelifa et al. (2013) the risk-based approach is presented, where the NBI items are used to account for climate change effect on the frequent occurrences of flood and related rising of the probability of failures.

There is not many software that account for risk analysis of bridges exposed to flooding events. In HAZUS-MH (Federal Emergency Management Agency, 2007) and Road Risk (Swiss Federal Road Office, 2011) a coincidence analysis between the geographic extents of flooding and infrastructure location is performed. Although, different flooding scenarios may be considered, the structure resistance and indirect of consequences of failure are not elaborated.

Currently, the main research need in assessment of flooding impact on inadequate bridge performance, are investigation and application of performance indicators (PI) that may timely identify scour-susceptible bridges (Brown et al., 2014). In Tanasic & Hajdin (2017c), the threat of flooding hazard in the Serbian road network was assessed in the light of a flooding event in May 2014. The motivation was to provide the principal steps for an upgrade of current BM procedures, and the novel, vulnerability-based approach was suggested to identify endangered bridges that to be examined in more detail.

The ongoing European research project COST TU1406, elaborates quality control (QC) plans for roadway bridges, by accounting for uncertainties of

interceptable and non-interceptable (i.e. sudden) processes that can significantly affect a bridge performance. The adopted approach involves application of key performance indicators (KPIs), based on RAMSSH€EP approach (Rijkswaterstaat, 2012). The first task within the COST project comprised survey of relevant PIs used by national road agencies (Strauss et al., 2016). In the second task, performance goals were investigated (Stipanovic et al., 2017), while in the third task, the report on the quality control plan is being prepared (Hajdin et al., 2017 and Linneberg et al., 2017).

In the scope of this paper are the relevant findings of the COST project related to failures due to flooding hazard and related local scour which is regarded as a sudden process. The influence of possible failure modes of girder bridges on the probability of a failure, and their relation to the KPI of Reliability is elaborated.

2 THE RELEVANT DATA SET FOR ASSESSMENT OF A THREAT OF LOCAL SCOUR

All bridge types regardless of age, static system or materials may be affected by a flooding hazard, where foundations of bridge substructures and bridge embankments may be exposed to the process of local scouring. Eventually, there is removal of supporting soil at foundations, while the soil and the bridge structure jointly resist this adverse action until the bridge fails under its own dead load (Tanasic, 2015). This bridge resistance still waits to be adequately accounted in the current BM practice, in order to avoid an overestimation of vulnerability.

The observations that are commonly used in the assessment of local scour are related to the visual appearance of foundations, embankments and an area beneath a bridge. These are not by themselves an effective PI and only have significant value if noticed timely, as they can relate to a probability of failure. There are direct observations, which can point out a problem with local scour, such as substructure settlement/rotation and resulting localized damage (e.g. cracks) at joints, bearings and other bridge elements. These indicate that a failure has already occurred, thus an immediate attention i.e. adequate repairs are necessary. For a BM practice, these types of observations can trigger inspection of yet undamaged bridges, with a similar hydrology data, but still cannot be used as a reliable indicator for estimation of failure rate.

Any type of damage on structural elements, which is not a result of a foundation displacement/rotation, are of interest as it may decrease bridge resistance to an oncoming flooding event. Here, the importance of two parameters: damage location and its severity (e.g. area/depth affected) must be determined for diverse bridge types and their elements in order to conduct a comprehensive analysis on possible bridge failure modes, which is elaborated in section 4.

The scour depth is an observation/indicator that may be directly measured, monitored or indirectly evaluated by empirical formulas. The choice of the right approach is based on available resources (e.g. budget, available data and equipment, etc.) and engineering judgement which mostly relies on experience. In practice, visual inspection can trigger either monitoring/measuring of scour depth or a countermeasure instalment, but this cannot be regarded as a reliable diagnostic method since scour can be a sudden process. Also, indirect evaluations of scour depth are applied to complement the decision-making process, but this require additional effort and resources. In the related empirical formulas, customary practice is to model uncertainties of the relevant parameters with probability distributions (Johnson & Dock, 1998).

Although the information on the scour depth entangles the data on flooding magnitude, channel properties, soil properties and substructure geometry, it must be coupled with relevant data on bridge type and demand (e.g. traffic volume) for reliable decision making. It is evident that a risk-based methodology is a feasible approach to adequately consider a flooding hazard in BM. The emphasis is on a simple, yet comprehensive approach, which relies on existing information and inexpensive, but reliable inspection procedures. It should include the most relevant data, and these may be structured in three groups:

1. Exposure to a local scour at substructures
   - Flood magnitude & duration
   - Water channel geometry & properties
   - Debris/ice potential
   - Soil erodibility
   - Piers & abutments type/geometry, position and alignment in respect to a water flow
2. Resistance to failure modes induced by local scour at substructures
   - Soil cover
   - Geotechnics properties of soil
   - Type/detailing of sub/superstructures
   - Location & severity of a damage on relevant bridge elements
3. Consequences related to failure modes
   - Loss of life & limb
   - Costs of repairs or replacement
   - Down time
   - Network & traffic data to include indirect costs of failure

A major drawback for a practice-ready approach are diverse types & levels of uncertainties related to this data. Although most of this information are not usually stored in a bridge database, it exists up to an extent in a bridge design documentation or in other databases (e.g. hazard and traffic related data). Even-

tually, some data may be inferred based on an experience (e.g. reinforcement detailing) or surveyed in a one-time inspection. For a full risk-based approach, an estimation of the flood magnitudes that will affect a bridge is required, which is an overkill for BM practice. It is far more convenient to adopt a certain flooding magnitude (e.g. 100-year flood), a related scenario, e.g. local scour at a pier, and apply a vulnerability approach (Tanasic & Hajdin, 2017c), which is briefly presented in following section.

3 VULNERABILITY ASSESSMENT AND KEY PERFORMACE INDICATORS

From a BM perspective, the vulnerability may be defined as the expected total consequences of inadequate bridge performance caused by a hazard (e.g. flooding) of a certain magnitude (Birdsall). Here, the formula which defines this relationship is given as:

$$V_n^s = P_n^s \cdot (DC_n + IC_n) \quad (1)$$

where: $V_n^s =$ the vulnerability of a bridge with respect to a flooding event of a specific magnitude *s* and a chosen failure mode *n*; $P_n^s =$ the conditional probability of a bridge failure in the chosen failure mode *n*, with the respect to a flooding event of a specific magnitude *s*; $DC_n =$ direct consequences with respect to the chosen bridge failure mode *n*; and $IC_n =$ indirect, mostly traffic related consequences with respect to the chosen bridge failure mode *n*.

The vulnerability is a comprehensive PI for decision-making, with respect to a failure due to a hazard, that identifies and ranks the bridges that need to be investigated in more detail. It considers the resistance of a bridge to local scour action related to the flooding of a certain magnitude. The essential ingredient for its evaluation are the failure modes, which account for partial damage or a collapse. However, the adequate vulnerability approaches are beyond the scope of the COST project.

In the approach of the COST action, the focus is on evaluation of KPIs: Reliability, Availability, Safety, Economics as the most viable for the elaboration of QC plans. The failure modes are required for evaluation of the probability of a bridge failure, which is in a direct relationship with the KPI of Reliability. The direct consequences of a failure, related to loss of life and limb, are required to assess the KPI of Safety, while the KPIs of Availability and Economy are dependent on the chosen mitigation actions. The indirect consequences of a failure and direct costs of bridge repair/replacement due to a failure, are not accounted for in the evaluation of the KPIs within the COST.

4 BRIDGE FAILURE MODES AND VULNERABLE ZONES

In the analysis of failure modes (FMs), the influence of specific bridge elements on the bridge resistance needs to be addressed. The FMs are usually discussed in the light of observed damage (e.g. May et al., 2002, Briaud et al., 2010 and Ettema et al., 2011), but the differentiation between diverse bridge types and specific damages, and an explanation how the related failures occur, have not been provided.

The resistance of a bridge to a flooding event is primarily dependent on analysed scenarios (e.g. a local scour at a middle pier). For each scenario, the possible FMs are governed by the soil cover at an affected substructure and the combined resistance of a soil-bridge system. Here the foundation soil geotechnical properties have a key role, due to large safety factors in the design. Secondary, but not unimportant is the engaged superstructure resistance governed by the type/properties of bearings/joints and main girder (Tanasic & Hajdin, 2015). The main FM types and the key elements of girder bridges, which reflect on how much bridge resistance can be engaged, are listed in Table 1., while the related examples are given in Figure 1.

The failure mode type 1 (FM1) is the most dangerous since it may cause progressive collapse (Figure 1.a), provided that the design of the main girder is not failure/collapse safe to a damage to one of the supports (e.g. FM4 in Figure 1.d). The FM2 may occur if the top of the pier of an affected foundation is not restrained to a movement in the horizontal plane, by design or due to a poor condition state of bearings. This FM is common for multiple-single span bridges e.g. in Figure 1.b. The FM3 is "the most desired" case, since the requirement for failure is that the foundation soil and the structure need to deplete their joint resistance to a partial loss of the support at the affected substructure foundation (Figure 1.c).

Regarding Table 1., the clear and concise guidelines are necessary for inspection of bridges and in particular, their vulnerable zones. The vulnerable zones comprise bridge segments, which have a crucial role in resistance to a failure due to local scour at substructure foundation/s (Figure 2.). Here, the soil cover at substructures is included. Any type and severity of a damage at vulnerable zones is of interest, as it may decrease the overall bridge resistance to an oncoming flooding event i.e. increase the probability of a failure.

Table 1. Key bridge elements for girder bridge resistance to local scour and failure modes (FMs)

Bridge element	Attention	Resistance to a failure mode	Failure Mode
Affected substructure	Inadequate detailing or condition	Structure governed	1
Bearing/joint at the top of the affected substructure	Inadequate detailing or condition	Soil governed (low superstructure effect)	2
Bearings/joints at other substructures	Horizontal displacement free or restrained	Combined soil-bridge resistance	3
Main girder	Detailing	Combined soil-bridge resistance	3
Main girder	Detailing	Failure safe	4

a)



b)



c)



d)



Figure 1. Failure mode types related to Table 1. a) FM1: Inadequate pier/foundation detailing, Serbia, 2014; b) FM2: Failure of a multiple single span bridge, Canada, 2009; c) FM3: Local scour at a pier, Serbia, 2016; d) FM4: Pier washed away and no collapse, Serbia, 2016.

5 THE ASSESSMENT OF RELIABILITY

The semi-quantitative approach is presented, where the Reliability class with associated matrix (Figure 4.) is defined via Exposure class and Resistance class. The Exposure class aims to grade the threat of a certain flooding scenario and related local scour. The Reliability class aims to account for diverse bridge types, their characteristic FMs and a temporal aspect i.e. information update on the condition in the vulnerable zones. For the case were there are several substructures affected, the assessments of Exposure and Resistance classes are performed for each substructure separately, to estimate which is the case that has the highest Reliability class.

5.1 *Assessment of Exposure class*

There are four exposure classes on the vertical axis of the matrix in Figure 4.b, where one denotes the lowest, and four the highest exposure of a bridge. The main data for this assessment comprise an extreme flood hydrograph, river channel properties/geometry and information on foundation soil type/erodibility.

The first class denotes bridges with substructures that are not in a floodplain for the adopted extreme flood (e.g. return period of 100 years), whereas the second class implies that a substructure is going to be in a contact with water. Still, this does not necessarily involve local scour. Thus, an assessment of the soil erodibility should be performed on site or in a laboratory in a one-time inspection, or assessed indirectly, which is further elaborated.

Two parameters are commonly used to describe threshold value for soil erosion rate of 0.1mm/hr – the critical shear stress at the soil interface (τ_c) or the critical velocity for initiation of erosion (V_c). Their application depends on the methodology for indirect evaluation of local scour, and here the two approaches, given in (Florida Department of Transportation, 2010) and (Briaud et al., 2011), are suggested to use for coarse-grained and fine-grained soil, respectively. Any other approach may be used, but preferably it should account for temporal aspect of local scour i.e. evolution of its magnitude over flood duration, to provide a more realistic values of possible scour depths.

The transition from the second to the third Exposure class implies that the mean approach velocity of flow upstream V, for the adopted extreme flood, can induce soil erosion. To evaluate V, the information on river channel geometry (cross section and slope) and the Manning coefficient are necessary. In the absence of reliable data for an investigated location, these may be verified easily in one-time inspection. The V_c may be either evaluated based on the median soil particle diameter (D_{50} > 0.01mm) and critical soil particle shear velocity (Melville & Coleman, 2000) or conser-

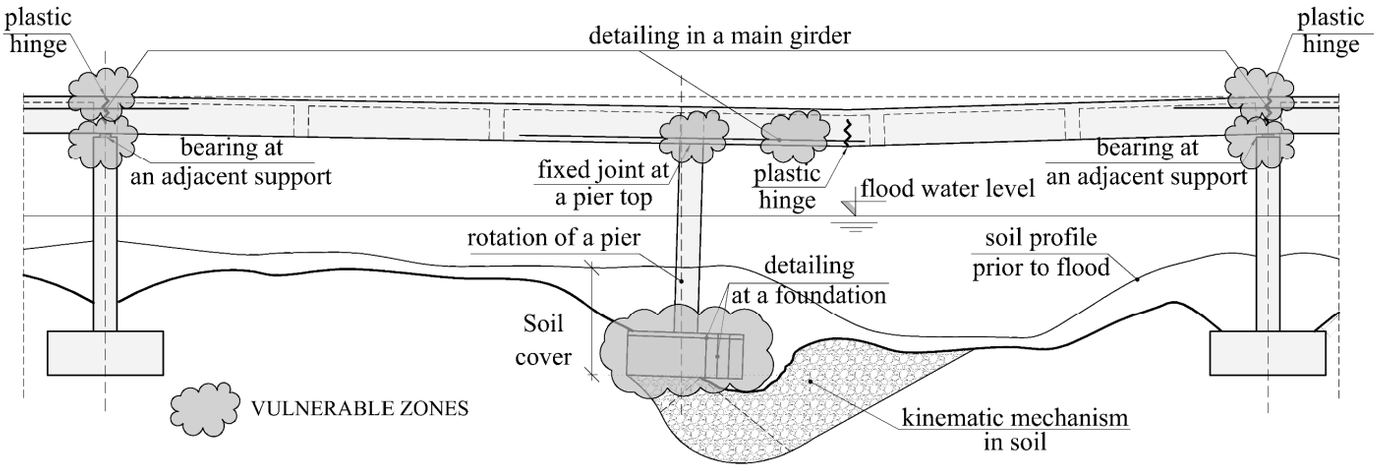


Figure 2. Multiple-span girder bridge and its vulnerable zones and an example of a failure mode due to local scour at a pier - adapted from (Tanasic & Hajdin, 2017b)

vatively accounted for the recognized soil type by using erosion function charts (Briaud et al., 2011), that can be also used for estimation of the τ_c.

If a bridge is in the class three and have a history of flooding events, it should be classified in the fourth class. Also, the fourth class of exposure may be selected if there are conditions on site, which may exacerbate local scour (e.g. debris/ice, flow constriction, etc.), but cannot be readily accounted in the indirect evaluation of local scour.

5.2 *Assessment of the Resistance class*

The resistance of a bridge to local scour is graded in five classes (horizontal axis of matrix in Figure 4.), where one denotes the highest and five the lowest resistance. The main data for this assessment comprise possible FMs and condition of bridge elements in vulnerable zones, including the height of a soil cover.

A bridge is initially categorized in a class based on a relevant failure mode and foundation type (Figure 3.). By design, the bridges with deep foundations are clearly more resistant to a failure, but here FMs which involve pile buckling should be considered (Ramey & Brown, 2004). For shallow foundations, the ultimate extent of scour cavity beneath the foundation level govern the probability of failure (Tanasic, 2015), which is accounted for in FMs in Table 1.

The bridges with countermeasures are categorized in the first class, if the condition of these protective measures is good. Otherwise, their presence is ignored. Transition to a higher class (a lower resistance) is possible in a case where a condition of a segment, which is in a vulnerable zone (Figure 2.), becomes worse, i.e. may affect the possible FMs.

When the Exposure class is equal three or higher, the update of resistance class is possible when the soil cover at a substructure reaches a predefined threshold. For this assessment, a potential local scour depth at an affected substructure may be indirectly evaluated via well-established scour evaluation formulas (Arneson et al., 2012). An example of thresholds for the soil cover is given in Figure 4.a, which is based on the adopted extreme event magnitude. The update of resistance class is considered conservative, as the related evaluation formulas tend to overestimate local scour depths observed on-site. Nevertheless, it is regarded as sufficiently accurate and comprehensive for practice, provided that the failure modes are adequately considered.

The common situation in practice is that the data on foundation type/geometry is unknown and it cannot be reliably obtained from the available project documentation, date of construction, design code, etc. The bridges with unknown foundations are to be treated as bridges with shallow foundations i.e. can be initially categorized in a class three, four or five (provided the main girder is not failure safe).

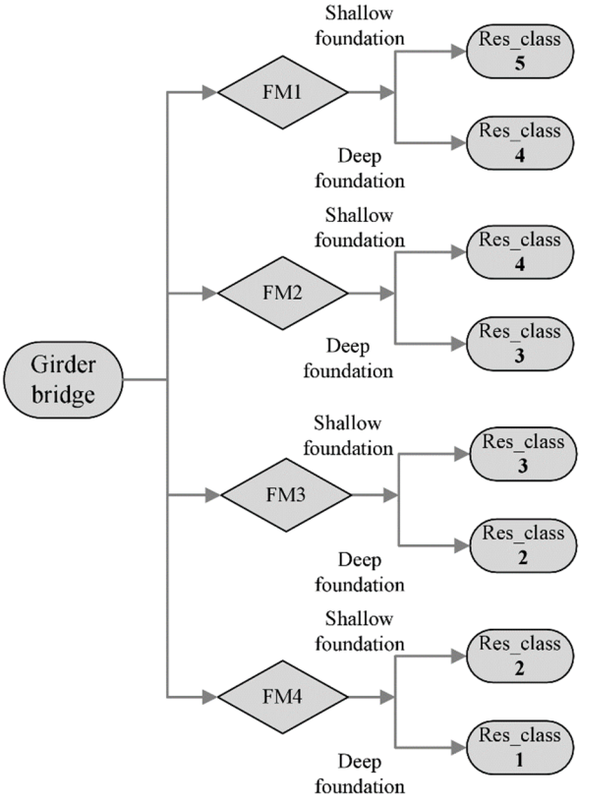


Figure 3. Relationship between failure mode (FM) types (Table 1.) for girder bridges and their initial resistance classes.

Another issue is the soil cover at bridge substructures, and here both foundation depth and the actual soil cover at the affected foundation can be unknown. If the Exposure class for these bridge substructures is equal or higher than three, their initial Resistance class should be increased by one (five is the max. value).

5.3 *Assessment of Reliability class*

The given matrix (Figure 4.b) provides a practical solution for the semi-quantitative assessment of reliability, where all relevant information on a bridge exposed to a local scour event is considered. The main advantage of the presented approach over the current practice is a possibility to account for the resistance of specific bridge types via failure modes. This provides a more realistic assessment of a threat of failures and thus lead to elaboration of adequate QC plans.

The presented reliability assessment has a potential to be upgraded in a full quantitative approach, which would provide a more detailed differentiation between the given reliability class thresholds.

a) **Update of the Resistance class**

3	$L_s < 0.5\ S_c$	three and more consecutive flooding events
4	$0.5\ S_c > L_s > S_c$	two consecutive flooding events
5	$L_s > S_c$	one flooding event

*L_s = Indirectly evaluated local scour depth

*S_c = Soil cover; (for deep foundations = max. allowed for a pile buckling failure mode

b) **Reliability class**

high	medium	low	very low	critical

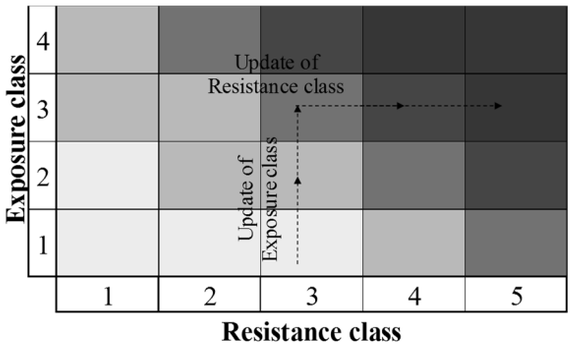


Figure 4. An example of a Reliability class matrix a) Update of the resistance class via evaluation of local scour depth; b) Legend and reliability class matrix

6 CONCLUSION

The current decision-making in bridge management related to flooding hazards, relies mostly on visual inspection and assessment of a substructure exposure to local scour, while the bridge resistance is usually ignored. The ongoing research is oriented towards application of comprehensive performance indicators in practice to reliably anticipate bridge failures in oncoming flooding events and aid in adequate mitigation of the related threat.

Here, the research within COST TU1406 action aims to account for both the interceptable and non-interceptable processes in elaboration of quality control plans, by application of the RAMSSH€EP methodology. The key performance indicators (KPI), which are selected to be further elaborated in a practice ready approach are: Reliability, Safety, Availability, and Economics. For a flooding hazard, it is evident that risk-based assessments are necessary. There is a need to set a basis for application of these approaches in the future. It is suggested to account for a vulnerability assessment as it considers all relevant data: exposure to the hazard magnitudes, related bridge's resistance and total consequences.

The essential ingredient in a vulnerability assessment is probability of a bridge failure due to local scour. It is directly related to the KPI of Reliability, and governed by the bridge exposure to a local scour and the bridge resistance which is accounted with relevant failure modes. The relationship of a bridge type to a failure mode is based both on the inherent and time dependent properties (e.g. condition) of key bridge elements which are in vulnerable zones.

The semi-quantitative approach was suggested to assess the Reliability, where a Reliability class is obtained via Exposure class and the Resistance class. The main parameters that Exposure class accounts are: extreme flooding magnitude, information on soil erodibility and complications on a bridge site which can exacerbate scour. The Resistance class considers failure modes and general foundation type, which govern the initial classification, and the height of soil cover at an affected substructure. The latter may additionally update the resistance class when compared to indirectly evaluated local scour depth.

The presented approach is going to be extended within a COST action to account for frame and arch bridges and their characteristic failure modes.

7 ACKNOWLEDGEMENTS

The research presented in this paper is based on a COST TU1406 research project - "Quality specifications for roadway bridges, standardization at a European level", and the work of its Work Group 3. The information on bridge in the example is obtained with the courtesy of Serbian Road Directory – Sector for maintenance of state roads and Sector for informatics systems in transportation. The authors would like to thank Tamara Komarica and Momčilo Veljović for their cooperation.

REFERENCES

Arneson, L.A., Zevenbergen, L.W., Lagasse, P.F. & Clopper, P.E. 2012. *Evaluation of Scour at Bridges, Fifth Edition, Federal Highway Administration Report FHWA-HIF-12-003, Hydraulic Engineering Circular No. 18*. Washington, D.C.: U.S. Department of Transportation.

Birdsall, J. 2009. PhD. Thesis number 4251: The Responsive Approach: an Integrated Socially-Sustainable Technically-Optimal Decision Model. Lausanne: Swiss Federal Institute of Technology.

Bones, E., Garrow, B. & Sturm, T. 2017. Incorporating Soil Erodibility Properties into Scour Risk-Assessment Tools Using HYRISK. *Journal of Infrastructure Systems 23(3)*.

Briaud, J. L., Hurlebaus, S., Chang, K.A., Yao, C., Sharma, H., Yu O.Y., Darby, C., Hunt, B. E. & Price, G.R. 2010. *Report 0-6060-1: Realtime monitoring of bridge scour using remote monitoring technology*. Austin: Texas Department of Transportation.

Briaud, J.L., Chen, H.C., Chang, K.A., Oh, S.J., Chen, S., Wang, J., Li, Y., Kwak, K., Nartjaho, P., Gudaralli, R., Wei, W., Pergu, S., Cao, Y.W. & Ting, F. 2011. *Summary Report: The Sricos – EFA Method*. College Station: Texas A&M University.

Brown, M., Gomez J., Hammer, M. & Hooks, J. 2014. *Report FHWA-HRT-14-052: Long-Term Bridge Performance High Priority Bridge Performance Issues*. Rutgers: The State University of New Jersey, The Center for Advanced Infrastructure and Transportation.

Ettema, R., Constantinescu, G. & Melville, B. 2011. *Evaluation of Bridge Scour Research: Pier Scour Processes and Predictions. NCHRP Web-Only Document no.175*. Washington, D.C.: Transportation Research Board of the National Academies.

Florida Department of Transportation 2010. *Bridge Scour Manual*. Tallahassee: Florida Department of Transportation.

Federal Emergency Management Agency.2007. *HAZUS-MH MR3 - Multi-Hazard Loss Estimation Methodology - Flood Model - Technical Manual*. Washington D.C.: Federal Emergency Management Agency.

Hajdin, R., Tanasic, N., Kusar, M., Amado, J. 2017. A novel Quality Control Framework for the management of existing bridges. *IABSE Symposium Report, IABSE Symposium Vancouver: Engineering the Future, 19-23 Sept. 2017. pp. 304-311 (8)*. Zurich: IABSE.

Johnson, P.A. & Dock, A.D. 1998. Probabilistic bridge scour estimates. *Journal of Hydraulic Engineering ASCE 124(7): pp. 750–754*.

Khelifa, A., Garrow L. A., Higgins M.J. & Meyer M.D. 2013. Impacts of climate change on scour-vulnerable bridges: Assessment based on Hyrisk. *Journal of infrastructure systems (19): pp. 138 – 146.*

Linneberg, P., Masovic, S., Hajdin, R. 2017. Quality Control Plans for Girder and Frame Bridges. *IABSE Symposium Report, IABSE Symposium Vancouver 2017: Engineering the Future, pp. 2651-2658(8).* Zurich: IABSE.

Matos, J., Casas, J.R. & Fernandez, S. 2016. COST Action TU1406 Quality Specifications for Roadway Bridges (BridgeSpec). Bittencourt, Frangopol & Beck (ed.), *Maintenance, Monitoring, Safety, Risk and Resilience of Bridges and Bridge Networks*. London: Taylor & Francis Group. ISBN978-1-138-02851-7.

May, R.W.P., Ackers, J.C. & Kirby, A.M. 2002. *Manual on scour at bridges and other hydraulic structures, C551.* London: Construction Industry Research and Information Association.

Melville, B. W. & Coleman, S.E. 2000. *Bridge scour*. Littleton: Water Resources Publications, LLC.

New York State Department of Transportation 2003. *Hydraulic Vulnerability Manual*. New York, New York State Department of Transportation.

Pearson, D., Stein S. and Jones J. S. 2002. *Hyrisk methodology and User Guide*. Washington: Federal Highway Administration.

Ramey, G. E. & Brown, D. A. 2004. *Research Project 930-585: Stability of highway bridges subject to scour*. Auburn: Alabama Department of Transportation, Department of Civil Engineering, Auburn University.

Rijkswaterstaat. 2012. Leidraad RAMS—sturen op prestaties van systemen (in Dutch). Den Haag: Ministerie van Verkeer en Waterstaat.

Stipanovic, I., Chatzi, E., Limongelli, M. Gavin, K., Bukhsh, Z.A., Skaric Palic, S., Xenidis, Y., Imam, B., Anzlin, A., Zanini, M., Klanker, G. Hoj, N., Ademovic, N. 2017. *WG2 technical report: Performance Goals for Roadway Bridges of COST Action TU 1406*. Available on-line: http://www.tu1406.eu/wp-content/uploads/2017/11/tu1406_wg2.pdf. ISBN: 978-3-900932-41-1

Strauss, A. Mandić-Ivanković, A., Matos, J & Casas J. 2016. *WG1 technical report: Performance indicators for roadway bridges of COST Action 1406*. Available on-line: http://www.tu1406.eu/wp-content/uploads/2016/10/COST_TU1406_WG1_TECH_REPORT.pdf. ISBN: 978-3-900932-41-1

Swiss Federal Road Office 2011. *Technical Manual Road Risk 1.0 - Software for Assessment of natural hazards on national roads* (in German). Bern: Department for Environment, Transport, Energy and Communication, The Swiss Federal Road Office.

Tanasic, N. & Hajdin, R. 2015. Resistance of the soil-bridge model to local scour action. Presented at 94th Annual Meeting of the Transportation Research Board, Washington D.C., 11-15 January 2015.

Tanasic, N. 2015. PhD. Thesis: Vulnerability of reinforced concrete bridges exposed to local scour in bridge management. Belgrade: Faculty of Civil engineering, University of Belgrade.

Tanasic, N. & Hajdin, R. 2017a. Performance indicators for bridges exposed to a flooding hazard. *The Value of Structural Health Monitoring for the reliable Bridge Management*; e-book of *Joint COST TU1402 – COST TU1406 – IABSE WCI Workshop, Zagreb, 2-3 March 2017. Zagreb:* Faculty of Civil Engineering, University of Zagreb. ISBN 978-953-8168-08-6

Tanasic, N. & Hajdin, R. 2017b. Vulnerability: The Top-Level Performance Indicator for Bridge Exposed to Flooding Hazards. *TRB's E-Circular 224: Eleventh International Bridge and Structures Management Conference, Mesa, 25-27 April 2017.* Washington, D.C.: Transportation Research Board of the National Academies.

Tanasic, N. & Hajdin, R. 2017c. Management of RC bridges with shallow foundation exposed to local scour. *In Journal of Structure & Infrastructure Engineering, Special Issue: Bridge analysis, design, assessment, monitoring and management.* doi:10.1080/15732479.2017.1406960

Maintenance, Safety, Risk, Management and Life-Cycle Performance of Bridges – Powers, Frangopol, Al-Mahaidi & Caprani (Eds)
© 2018 Taylor & Francis Group, London, ISBN 978-1-138-73045-8

Monitoring in management of roadway bridges

J. Bień, T. Kamiński & M. Kużawa
Wrocław University of Science and Technology, Poland

ABSTRACT: The paper presents review of monitoring methods applied in bridge engineering as well as proposal of a unified classification of the monitoring procedures − based on suggested standardized criteria. Implementation of the monitoring tools in Bridge Management Systems is also presented. State of the art related to practical applications of such systems is illustrated and expected development trends in this area are discussed. Proposed solutions are based on results of the European international research projects as well as on long-term experience in design and implementation of the Bridge Management Systems in Poland.

1 INTRODUCTION

Road asset management is a task of great responsibility, since it involves vital assets to the community. Roadway bridge structures are complex physical systems consisting of many heterogeneous components.

Management of operation and maintenance of bridges requires efficient system of structure condition monitoring. Generally, monitoring system can be defined as arrangement of all activities that are performed with the goal to collect data for bridge condition assessment as a background for competent management.

Monitoring of bridge structures is an interdisciplinary activity that requires expert knowledge from different disciplines: structure inspection, non-destructive testing, structural and electronic engineering, modelling and simulation techniques, data processing, communication and archiving techniques, software design and implementation techniques. Since all these disciplines can hardly be covered by a single expert, monitoring is an activity that is essentially based on cooperation of a group of experts in very different engineering fields and backgrounds. A common detailed analysis and planning as well as communication between the experts is required for a successful monitoring activity.

Creation and development of effective bridge monitoring systems is a subject of research in many countries as well as was a topic of a number of the international research projects, e.g.:

- Bridge Management in Europe (BRIME 97-2220), Deliverable D8, Bridge Management and Condition Monitoring, 1999,
- Bridge Management in Europe (BRIME 97-2220), Deliverable D11, Modelling of deterioration, 1999,
- Integrated Monitoring Systems for Durability Assessment of Concrete Structures – SMART STRUCTURES, Final Report, European Commission, Brite EuRam III Programme, 2002,
- Smart Structures. Integrated Monitoring Systems for Durability Assessment of Concrete Structures, Project Report, 2002.
- Corrosion of Steel in Reinforced Concrete Structures – COST 521. Final Report, Eds. Cigna R. et al., European Commission, Directorate-General for Research, 2003,
- Improving Assessment, Optimisation of Maintenance, and Development of Database for Masonry Arch Bridges, Research Project, UIC, 2007.

At the moment one of the largest international research projects focused on roadway bridge monitoring and management is COST Action TU1406 "Quality specifications for roadway bridges, standardization at a European level" (www.tu1406.eu).

The main objective of the Action is to develop a guideline for the establishment of quality control plans in roadway bridges, based on specific performance indicators. These indicators can be qualitative or quantitative based, and they can be obtained by means of the monitoring systems.

By developing new approaches to quantify and assess the bridge performance, as well as quality specifications to assure an expected performance level, bridge management strategies based on efficient monitoring systems will be significantly improved, enhancing asset management of ageing structures.

2 MONITORING STRATEGIES

Monitoring can be generally defined as an act of acquiring, processing, communicating and archiving information about the actions on structure and/or the action effects on a structure over a given period of time (Bień et al. 2004, Watanabe E. 2010). Forms of bridge condition monitoring can be divided into two main categories (Fig. 1). The first category of monitoring procedures comprises regular as well as irregular (special) inspections based on visual examination and results of the non-destructive testing (NDT) and/or semi-destructive testing (SDT). The inspections are performed regardless of the structure loads by means of various types of NDT & SDT techniques (Bray D.E. & McBride D. 1992, Cartz L. 1999, Hellier Ch.J. 2001, Helmerich R. 2007, Malhorta V.M. & Carino N.J. 2003, Wenzel H. 2005). In majority of existing Bridge Management Systems the regular inspections are performed on basic level (every year) and on advanced level (every 5 years). This category of load-independent monitoring is usually applied to all bridge structures. Detailed procedures and requirements are defined in national regulations (Bień et al. 2016, Helmerich R. et al. 2012).

The second category of monitoring actions includes observation of bridge structure response to loads by means of installed technical measuring equipment. A technical monitoring system is a data acquisition and processing unit which continuously and autonomously provides real-time information about a structure or a structural component. This type of monitoring should contribute to an exact estimation of the bridge condition, which is impossible to achieve with inspections only.

In this category static and dynamic controlled proof loads can be distinguished (Bień et al. 2015) as well as short- and long-time technical monitoring under normal road traffic and natural environmental conditions. Predefined proof load tests are usually applied before opening a new bridge structure to traffic or after completing major rehabilitation works. Short- and long-term monitoring are based on application of transducers for sensing physical or chemical quantities along with programmable electronic equipment for acquiring, processing and communicating data as well as utilization of algorithms that define how data acquisition, processing and communication is performed. Short-term monitoring (usually 24 hours to few days) is executed by means of temporally installed sensors, while the long-term monitoring requires permanently mounted system.

The overall objective of technical monitoring is to improve the knowledge on the real behaviour of structures, supporting inspections and recognizing of unapproachable areas. The information obtained by monitoring can be used for very different purposes:

- identification of bridge loads and environmental impacts,
- monitoring of bridge reactions on loads and other influences,
- recognition of bridge degradation processes and structural performance,
- documentation of bridge history and prediction of a remaining life-time.

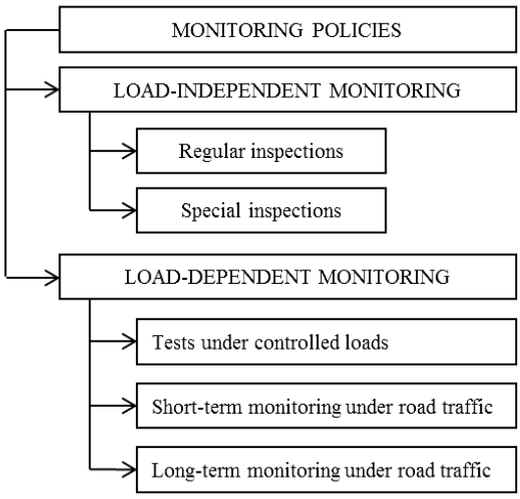


Figure 1. Basic forms of monitoring applied in bridge management.

Depending on the goal of analysis the following types of technical monitoring systems can be distinguished (Table 1):

- Action monitoring – allowing assessment of the magnitude as well as the spatial and temporal distribution of specific forces acting on a structure or a structural component, including traffic loads and environmental impacts (Hildebrand M. et al. 2008).
- Reaction monitoring – allowing assessment of the state of displacement, stress/strain level and distribution in a structure as well as vibration parameters: frequency, velocity, amplifications, damping caused by traffic loads and other influences (Cunha A. et al. 2007, Doebling et al. 1996).
- Performance monitoring – allowing to evaluate whether a structure or a structural component meets the performance requirements under specific or any actions, defined by the performance indicators (Enright M.P. & Frangopol D.M. 2000).
- Health monitoring – monitoring allowing the real-time assessment and prediction of the health condition of a structure or a structural component by means of their safety and serviceability indicators (Wenzel H. 2009).

Each monitoring system has to be designed individually, taking into account specific problems of the observed bridge structure. In practice each specific implementation is usually a mixture of categories listed in Table 1.

Table 1. Types of technical monitoring systems and expected effects.

Type of monitoring system	Monitoring effects
Action monitoring	Characteristics of all loads acting on a bridge structure Geometry and speed of vehicles Changes of traffic structure on the bridge Environmental influences (temperature, wind, humidity, earthquakes, etc.) Monitoring of overloaded transports Monitoring of accidents on the structure and in the neighbourhood
Reaction monitoring	Displacements, strains, stresses, vibration frequency, velocity and amplifications, etc. of structural elements Verification of theoretical analyses Modal parameters of the structure Dynamic amplification factors Material effort level
Performance monitoring	Identification of critical values of measured quantities Detection of bridge defects based on modal parameters changes Monitoring of parameters of defects (location, extent, intensity) Assessment of bridge technical condition and serviceability
Health monitoring	Changes of bridge technical condition and serviceability History of loads and environmental influences (temperature, wind, humidity, earthquakes, etc.) Observation of degradation processes progress (e.g. depth of concrete carbonation, corrosion advancement, etc.) Determination of input values for degradation models Remaining life-time prediction

Application of advanced monitoring systems to all bridge structures is not technically needed and would be economically not feasible. The technical monitoring is usually limited to the following situations:

- record-breaking long-span structures,
- bridges with innovative structural and/or material solutions,
- very important bridge structures, strategic components of transportation system,
- damaged structures awaiting rehabilitation or replacement,
- selected reference bridge structures, representative for the national bridge asset, monitored for creation and verification of degradation models.

In each case a monitoring of all bridge components with sensors is not necessary. Therefore, the technical monitoring process has to be restricted to a limited number of components which could affect the safety, durability and resistance of the bridge. In the scope of the investigation especially defects previously identified should be monitored and changes should be analysed.

3 MONITORING TECHNOLOGIES

Diverse purposes of monitoring procedures require application of problem specific technologies which differ substantially from each other. Classification of the technologies can be based on:

- frequency of inspections/measurements including:
  - continuous observation with defined frequency of measurements,
  - periodical observations with predefined schedule and program,
  - irregular observations/measurements dependent on specified conditions;
- type of monitored occurrences:
  - physical parameters,
  - chemical processes,
  - biological phenomena.

In the case of the load-independent monitoring based on inspections a wide range of the non-destructive testing methods and semi-destructive testing methods can be used. Classifications of the most popular NDT methods and techniques, which do not in any way breach the integrity of the tested structures (Hoła J. et al. 2015, Kühn B. et al. 2008) are presented in Table 2.

Table 2. Classification of NDT methods and techniques.

Testing methods	Measuring techniques
Optical methods	Visual inspection Endoscopy Microscopy Geodesy CCTV
Acoustic methods	Acoustic emission Impulse response Impact-echo Parallel seismic Ultrasonic techniques Ultrasonic tomography
Radiological methods	Radiographic techniques Computer tomography
Electromagnetic methods	Electromagnetic induction Radar techniques Magnetic techniques Electric potential/resistance techniques
Laser methods	Laser static techniques Laser dynamic techniques
Sclerometric methods	Static techniques Dynamic techniques
Thermographic methods	Passive techniques Active techniques

In Table 3 classification of the semi-destructive testing (SDT) methods, requiring material samples to be taken or any other minor breach of structural integrity, is shown. In this classification physical, chemical and biological methods applied during field and laboratory tests are distinguished.

Table 3. Classification of SDT methods and techniques.

Testing methods	Measuring techniques
Field tests	
Physical methods	Pull-out/pull-off tests
	Penetration tests
	Water resistance test
	Pressure techniques(flat-jack test, water penetration test, etc.)
Chemical methods	Rainbow/pH tests
	Chloride test
	Alkali test
	Electroanalytical tests
Biological methods	Macroscopic techniques
	Microscopic techniques
Laboratory tests	
Physical methods	Physical parameters of materials based on tests of specimens
	Computer tomography techniques
Chemical methods	Quantitative analytical techniques
	Electroanalytical techniques
	Spectral analyses
	Chromatography analyses
Biological methods	Advanced microscopic analyses
	"In vitro" culture techniques

In monitoring of bridge structures by means of installed technical measuring equipment wide range of measuring techniques and sensors can be engaged (Bischoff R. et al. 2007, Maia N.M.M. et al. 2003, Wenzel H. 2005). Typical tools applied for monitoring of forces acting on a structure are presented in Table 4.

Table 4. Monitoring of loads and environmental impacts.

Physical quantity	Measuring techniques and sensors
Live loads	Wheel pressure sensors
	TV/video cameras
Temperature	Thermocouples
	Thermistors
	Electrical resistance thermometers
	MEMS sensors
Humidity	Hygrometers
	MEMS sensors
Wind	Anemometers
Water flow	Water level sensors
	Water velocity sensors

For observation of bridge structure reactions to traffic loads and other influences as well as for bridge performance and health monitoring the following physical and chemical quantities are taken into account (Cunha A. et al. 2007, Doebling S.W. et al. 1996, Hildebrand M. et al. 2008, Watanabe E. et al. 2010, Wenzel H 2005, Wenzel H. 2009):

- linear and angular displacements,
- strain and stress level,
- vibration velocity, acceleration, frequency,
- crack opening changes,
- forces in bearing, cables, etc.,
- quantities specific for degradation processes.

The most popular measuring techniques and types of sensors used in bridge monitoring technical systems are presented in Table 5.

Table 5. Measuring techniques and types of sensors used in monitoring of bridge structure performance.

Physical or chemical quantity	Measuring techniques and sensors
Linear displacement	Geodetic techniques
	Mechanical sensors
	Inductive sensors
	Vibrating wire sensors
	Capacitive sensors
	Eddy current sensors
	Fibre optics sensors
	Laser techniques
	Radar techniques
	Hydraulic sensors
Angular displacement	Inclinometers
	Fibre optics sensors
	MEMS sensors
Strain/stress	Electrical resistance gauges
	Fibre optics sensors
	Vibrating wire sensors
	MEMS sensors
Vibration velocity and acceleration	Piezoelectric sensors
	Capacitive sensors
	Inertia sensors
	Inductive sensors
	Radar techniques
	Laser techniques
	MEMS sensors
Crack opening	Mechanical sensors
	Inductive sensors
	Fibre optics sensors
	Vibrating wire sensors
Bearing/cables reactions	Electrical resistance gauges
	Piezoelectric sensors
	Vibrating wire sensors
Degradation processes	Acoustic emission sensors
	Chloride level sensors
	Sensors of pH level
	Corrosion sensors

4 MONITORING IMPLEMENTATION AND OPERATION

General scheme of implementation procedure of long-term monitoring system based on sensors is presented in Figure 2. In the first step the goals of the monitoring system should be defined as a basis for the system architecture design. After detailed designing of all components and installation of the whole system on the bridge the testing procedure should be performed. Experimental values should be compared to results achieved by means of theoretical model of the structure (Bień J. 2011). Testing process should also confirm that bridge performance indicators can be observed using the monitoring system.

In the case of positive results of the testing the monitoring system can be accepted for operation. During long-term action of the system some maintenance activities are often necessary, including modifications of the system elements and improvements of the bridge theoretical model engaged in analysis of monitoring results.

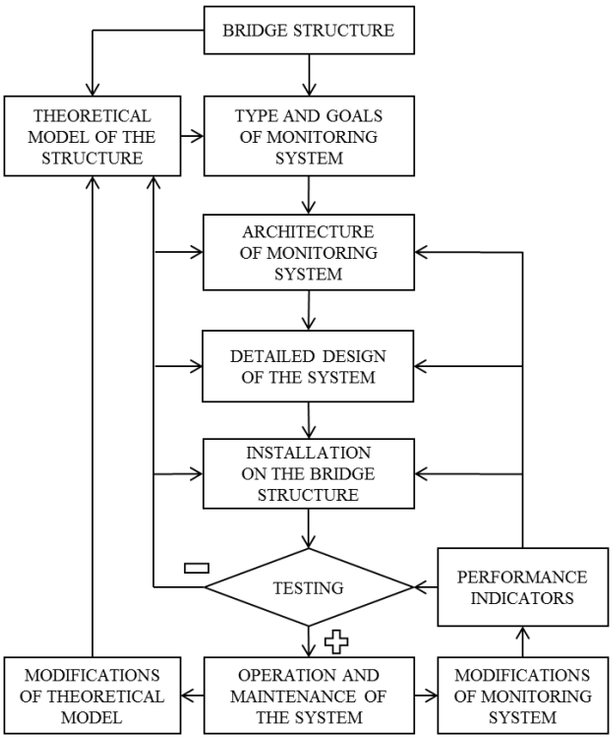


Figure 2. General scheme of monitoring system implementation.

Contemporary bridge monitoring systems are often equipped with knowledge-based expert tools supporting processing and analysis of experimental data as well as supporting decisions in management of bridge operation and maintenance (Bień J. & Rawa P. 2004). Taking into account fast development of the Information Technology (IT) we can expect that in the near future the bridge monitoring systems will be a part of the unified Building Information Management (BIM) process (Chang-su Shim et al. 2017).

Operation scheme of an advanced monitoring system is presented in Figure 3. The basic components of the systems are:

- measuring system with equipment transmitting data to acquisition module,
- data processing module using theoretical model of the structure for analysis and interpretation of measurements,
- module responsible for presentation of output data, often equipped with visualization tools,
- expert system supporting decisions in management of bridge operation and maintenance by means of information collected in data and knowledge base (Bień J. et al. 2010, Kamiński T. et al. 2013).

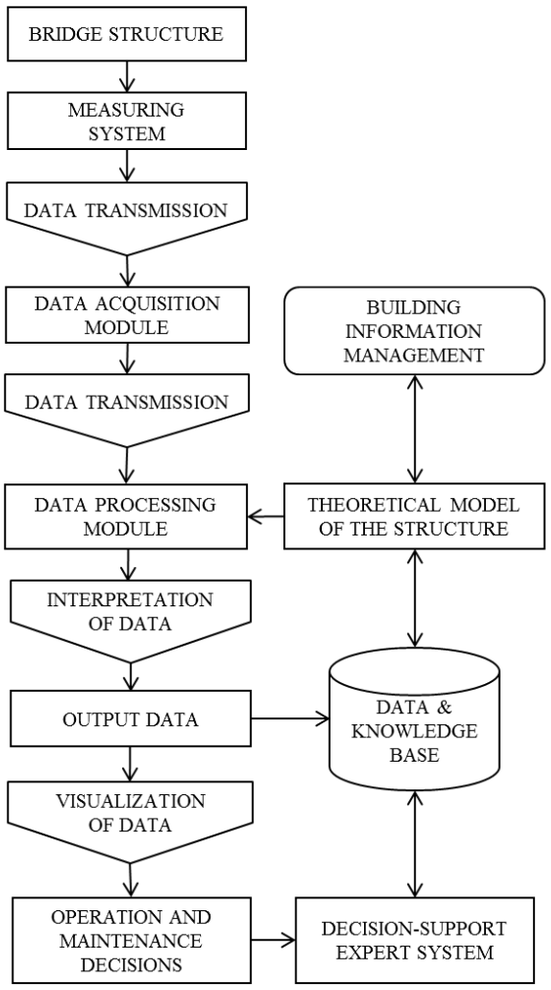


Figure 3. Operation scheme of monitoring system supported by knowledge-based expert system.

5 CONCLUDING REMARKS

Monitoring of bridge structures' condition plays more and more important role in management of roadway bridge infrastructure. Structural health monitoring is one of the diagnostic tools evaluated within the COST Action TU1406 "Quality specifica-

tions for roadway bridges, standardization at a European level" as a significant instrument in bridge quality control. It may be carried out both in a permanent way by means of built-in gauges mounted on a structure as well as within systematic inspections and arranged tests of a limited duration with application of external measuring devices.

The main objectives of monitoring processes in bridge management can be formulated as follows:

- on-line observation of bridge technical condition and serviceability based on predefined performance indicators,
- analysis of changes in structure response to loads focused on detection and identification of defects,
- acquiring of input values for individual lifetime model for monitored bridge helpful in operation and maintenance planning,
- cognitive analysis of bridge structures behaviour for improvement methods of designing, modelling and analysis, maintenance, optimization of costs, etc.

Proposed terminology with definitions of basic terms as well as classifications of types of monitoring systems with measuring methods and techniques create an approach to unification of this bridge engineering area on an international level as a part of the COST Action TU1406.

6 REFERENCES

Bień J. 2011. Modelling of structure geometry in Bridge Management Systems. *Archives of Civil and Mechanical Engineering* 11(3): 519-532.

Bień J., Kamiński T., Kużawa M. 2015. Validation of numerical models of concrete box bridges based on load test results, *Archives of Civil and Mechanical Engineering* 15(4): 1046-1060.

Bień J., Krzyżanowski J., Rawa P., Zwolski J. 2004. Dynamic Load Tests In Bridge Management. *Archives of Civil and Mechanical Engineering* 4(2): 63–78.

Bień J., Kużawa M., Bień B. 2010. To See is to Know: Visualization in Bridge Inspection and Management: 567-574, *5th International Conference on Bridge Maintenance, Safety and Management*. Philadelphia.

Bień J., Kużawa M., Gładysz-Bień, Kamiński T. 2016. Quality control of road bridges in Poland, *8th International Conference on Bridge Maintenance, Safety and Management, IABMAS 2016, Foz do Iguaçu, Brasil:* 971-978.

Bień J., Rawa P. 2004. Hybrid Knowledge Representation in BMS, *Archives of Civil and Mechanical Engineering* 4(1): 41-55.

Bischoff R., Meyer J., Feltrin G. 2007. Low power wireless sensor network for long term structural health monitoring, In Bień J., Elfgren L., Olofsson J. (eds), *Sustainable Bridges – Assessment for Future traffic Demands and Longer Live*: 397-407, Dolnośląskie Wydawnictwo Edukacyjne.

Bray D.E., McBride D. 1992. *Nondestructive Testing Techniques*. New York: John Wiley & Sons.

Cartz L. 1999. *Nondestructive testing. Radiography. Ultrasonics. Liquid Penetrant. Magnetic Particle. Eddy Current*. ASM International.

Chang-su Shim, Hwirang Kang, Ngoc Son Dang and Deokkeun Lee, 2017. Development of BIM-based bridge maintenance system for cable-stayed bridges. *Smart Structures & Systems* 20(6): 697-708.

Cunha A., Caetano E., Magalhaes F. 2007. Output-Only Dynamic Testing of Bridges and Special Structure. *Structural Concrete* 8(2): 67-85.

Doebling S.W., Farrar C.R., Prime M.B., Shevitz D.W. 1996. *Damage Identification and Health Monitoring of Structural and Mechanical Systems from Changes in Their Vibration Characteristics, A Literature Review*. Los Alamos National Laboratory, LA-13070-MS.

Enright M.P., Frangopol D.M. 2000. Survey and Evaluation of Damaged Concrete Bridges, *Journal of Bridge Engineering* (1): 31–38.

Hellier Ch. J. 2001. *Handbook of nondestructive evaluation*. McGraw-Hill.

Helmerich R., Bień J., Cruz P. 2007. A guideline for inspection and condition assessment including the NDT-toolbox. In Bień J., Elfgren L., Olofsson J. (eds), *Sustainable Bridges – Assessment for Future traffic Demands and Longer Live*: 93-104, Dolnośląskie Wydawnictwo Edukacyjne.

Helmerich R., Niederleithinger E., Trela Ch., Bień J., Bernardini G. 2012. Multi-tool inspection and numerical analysis of an old masonry arch bridge, *Structure and Infrastructure Engineering* 8(1): 27-39.

Hildebrand M., Biliszczuk J., Berger A. 2008. Monitoring System for a Cable-Stayed Bridge in Plock, *17th Congress of IABSE, Creating and Renewing Urban Structures*, *Chicago, September 17-19*.

Hoła J., Bień J., Sadowski L., Schabowicz K. 2015. Non-destructive and semi-destructive diagnostics of concrete structures in assessment of their durability. *Bulletin of the Polish Academy of Sciences, Technical Sciences* 63(1): 87–96.

Kamiński T., Bień J., Bień B. 2013. An expert tool for assessment of damaged masonry arch bridges. *7th International Conference on Arch Bridges, Trogir – Split, Croatia*: 691-698.

Kühn B. et al. 2008. Assessment of Existing Steel Structures: Recommendations for Estimation of Remaining Fatigue Life. *JRC Scientific and Technical Reports*.

Maia N.M.M., Silva J.M.M., Almas E.A.M., Sampaio R.P.C. 2003. Damage Detection in Structures: From Mode Shape to Frequency Response Function Methods, *Mechanical Systems and Signal Processing* 3(17).

Malhorta V.M., Carino N.J. 2003. *CRC Handbook on nondestructive testing of concrete*, CRC Press.

Watanabe E., Furuta H., Yamaguchi T., Kano M. 2010. On longevity and monitoring technologies of bridges – a survey study by Japanese Society of Steel Construction: 64-71, *5th International Conference on Bridge Maintenance, Safety and Management*. Philadelphia.

Wenzel H. 2005. *Ambient Vibration Monitoring*, J. Wiley & Sons Ltd.

Wenzel H. 2009. *Health Monitoring of Bridges*, J. Wiley & Sons Ltd.

Maintenance, Safety, Risk, Management and Life-Cycle Performance of Bridges – Powers, Frangopol, Al-Mahaidi & Caprani (Eds)
© 2018 Taylor & Francis Group, London, ISBN 978-1-138-73045-8

Bridge Management in Australia and New Zealand: Current Approaches and Future Needs

M.M. Melhem & C. Caprani
Department of Civil Engineering, Monash University, Clayton, Victoria, Australia

A. Ng
VicRoads Asset Services, Kew, Victoria, Australia

ABSTRACT: This article presents a review of the management of existing road bridges within Australia and New Zealand. Currently, the approaches to bridge management vary between the nine regional road jurisdictions. Different performance measures are applied, and different road bridge management systems are used. A uniform approach and agreement of the performance goals is desirable. Hence, the future needs required for these jurisdictions will also be discussed. Achievement of a uniform system not only provides an efficient way for bridge management of road bridges, but also allows quality assurance for their design life of 100 years and beyond.

1 INTRODUCTION

1.1 *Importance of Bridge Management*

Bridges are a fundamental component of the road transport infrastructure, linking communities and enhancing network productivity. But with aging infrastructure, increasing traffic demand, larger heavy vehicles, funding constraints, and other problem hazards, there is increasing need for quality assurance for the existing road bridges during their design life (Geiger *et al.,* 2005). For Australian and New Zealand bridges, the design life is 100 years (AS5100.1, 2017), one of the longest design lives internationally. Therefore, it is a significant task for both countries to assure performance goals are met to provide an efficient and effective transport network.

Performance goals can be on three different levels (Stipanovic *et al.*, 2017). At the operational level, performance goals for the individual road bridges and their components are considered. The tactical level includes part of the road network, such as series of bridges forming a major highway. And the strategic level considers the entire road bridge network and connectivity. For each of these levels, a range of performance goals can be present. Cost Action TU1406 indicate performance goals are that a road bridge or road bridge network should be safe, functional (serviceable), available, cheap and environmentally friendly (Straus & Mandic Ivankovic, 2016). Netherlands' Rijkswaterstaat (RWS) have considered a RAMS-SHEEP approach for road bridges; reliability, availability, maintainability, safety, security, health, environment, economical, political (Casas & Matos, 2017).

To measure whether these performance goals are being met, key performance indicators are compared to performance targets. The performance indicators are described through performance measures. Examples of performance measures at the operational level include condition rating, and at the strategic level include level of service. The process of measuring performance indicators to compare with targets to assess performances is best facilitated by road bridge management systems (BMSs).

A BMS assists with information collection, storage and analysis of bridges in a road network and is designed to support decision-making about funding quality assurance works that ensure road bridges met performance goals (Austroads, 2009). Database modules provide information on the performance of the bridge network and interact with predictive models to output results that assist in the planning of any future works program. Examples around the world include "AASHTOWare" Bridge Management (formally PONTIS), BRIDGIT, and OBMS (Austroads, 2013). The road bridge management process is an ongoing cyclic process. That is, after the works program is completed, the relevant database modules are updated, and the predictive models interact with the modules once again.

1.2 *Australian and New Zealand Context*

In Australia and New Zealand, more than 50,000 road bridges are currently in service (Rummey & Dowling, 2004). The road bridge stock is aging,

with the majority of existing road bridges in Australia built immediately after World War II when the country underwent a significant construction boom (Ng *et al.*, 2017).

In addition to the aging problem, Australia is heavily dependent on road freight. Out of the total freight task, 95% is carried by vehicles weighing 4.5 tonnes or more (Department of Infrastructure and Regional Development, 2014) and this road freight task is projected to double after 2030 (Bureau of Infrastructure Transport and Regional Economics, 2013), putting increasing pressure to allow a higher volume, and even heavier, vehicles on Australian road networks.

Over 800 agencies and jurisdictions are responsible for managing road bridges in Australia and New Zealand (Rummey & Dowling, 2004). These include a combination of private and public sectors, local councils, and nine regional road jurisdictions (State Road Authorities or SRAs) (Table 1). The three largest of these road jurisdictions, measured by number of structures managed, are located in the most populous states of Australia; Queensland (Department of Transport and Main Roads – TMR), Victoria (Roads Corporation – VicRoads), and New South Wales (Roads and Maritime Service – RMS)

Table 1. Nine regional road jurisdictions (SRAs) ranked by number of bridges and culverted managed (Sonnenberg, 2014)

Road Jurisdiction (SRA)	Abbreviation
Department of Transport and Main Roads Queensland	TMR
Roads Corporation Victoria	VicRoads
Roads and Maritime Service New South Wales	RMS
Department of Planning, Transport and Infrastructure South Australia	DPTI SA
Department of Infrastructure, Energy and Resources Tasmania	DIERT
Main Roads Western Australia	MRWA
Department of Urban Services Australian Capital Territory	DUS
Department of Infrastructure, Planning and Environment Northern Territory	DIPE NT
New Zealand Transport Agency	NZTA

This article presents a review of the management of existing road bridges within Australia and New Zealand. Currently, the approaches to bridge management vary between the SRAs. Different performance measures are applied and different BMSs are used. Indeed, a uniform approach and agreement of performance goals is desirable, especially with the advent of the national Performance Based Standards for Australia. Hence, the future needs required for these jurisdictions will also be discussed. Achieving a uniform system across these regions not only provides an efficient way for bridge management of road bridges, but also allows quality assurance for their design life of 100 years.

2 CURRENT PRACTICE

2.1 *Approaches to Management*

Since the 1990s, in both Australia and New Zealand, SRAs have been individually adapting bridge management approaches used overseas (Michael, 1994).

Generally, there are two bridge management approaches used in practice: top-down and bottom-up. The top-down approach begins at the strategic level. Quality assurance projects are commissioned for the entire road bridge network based on the needs of stakeholders such as road users, government, and the environment. From the bottom-up, quality assurance is managed by collecting inventory data, such as condition and capacity, from individual road bridges. It is this data that then drives the policies to ensure the bridge network continues to perform in a manner fit for purpose (Austroads, 2013).

When reviewing overseas practice, most SRAs considered the American BMS. In New Zealand, it was found that such a system was too "data hungry", and that given the small number of road bridges managed by NZTA, a simpler system could be applied (Austroads, 2002). Hence, New Zealand adopts a top-down approach to road bridge management. On the other hand, Australia mainly considers a bottom-up approach (Figure 1)

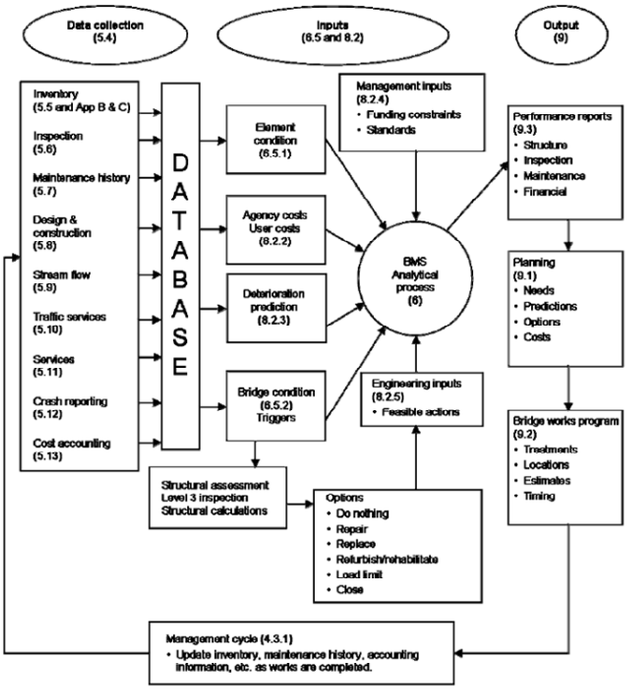


Figure 1. Road bridge management system cyclic approach across Australia and New Zealand (Austroads, 2009)

2.2 *Bridge Management Systems in Australia*

Most of the road jurisdictions in Australia have some form of a database system to capture information about bridge inventory, inspection data, condition reports, and capacity assessments. These systems have slight differences, but all have the same ultimate objective; to assist in planning for commissioning of future performance assurance works.

The earliest reported road bridge management system is that of Main Roads Western Australia (MRWA), operating in the late 1980s. Moreover, the system in the Department of Planning, Transport and Infrastructure South Australia (DPTI SA) is said to be operating for more than 30 years (Austroads, 2002). In 1995, a strategy for managing the performance of bridges in Victoria was introduced by VicRoads (Austroads, 2013). It concluded that a system was required to capture bridge inspections, condition, load capacity, and setting of realistic budget need. As such, the VicRoads bridge management system was developed. It comprises basic modules of inventory with inspection and maintenance recording. Other bridge management systems similarly developed includes those by Roads and Maritime Services, New South Wales (RMS NSW), Transport and Mainroads (TMR), Queensland, and Department of Infrastructure, Planning and Environment, Northern Territory (DIPE NT).

Over the years, these bridge management systems have undergone a series of revisions. One notable change is the move towards coverage of all road structures, and not just bridges. For example, in Victoria the current system is the Road Asset System (RAS), and in Queensland, it is the Structural Assets Management System (SAMS).

2.3 *Inspection Manuals*

As shown in Figure 1, inspections are necessary in the road BMS. They provide an up-to-date inventory for the structure, including its condition and capacity. Indeed, each SRA have developed inspection manuals as part of their road BMS. Often, these documents form part of the relevant laws for the region (for example, the *Road Management Act 2004* in Victoria). Additionally, local government road agencies within the state are likely to use their regional road jurisdictions inspection manual for the management for their local road bridges.

A tiered approach to inspections is outlined in the manuals for the largest three regional road jurisdictions; VicRoads, RMS and TMR (Sonnenberg, 2014). There are minor differences between these three road jurisdictions. Notably, VicRoads and TMR follow three levels of inspections, whereas RMS follows four levels.

Level 1 inspections are practically a drive-by inspection of the structure to ensure it is still functioning with no obvious gross defects. This simply updates the road bridge inventory. This occurs once every 6 months in Victoria, between 6 to 12 months in Queensland, and according to road maintenance in New South Wales.

Level 2 inspections are condition assessments based on close visual inspection conducted by an inspector. Some road jurisdictions conduct accreditation program for their inspectors. Based on the individual element condition ratings, the bridge condition is quantified, using an approach discussed later. The frequency of these inspections depends on the structure type, condition, and location.

Level 3 investigations are detailed engineering studies performed by structural engineers, which may include material testing to quantify structural integrity issues. For Victoria and Queensland, Level 3 includes structural analysis to quantify the load-carrying capacity of the road bridge. Whereas, Level 4 assessments in New South Wales quantify the load-carrying capacity of the road bridge, including proof loading tests. They are conducted when deemed required.

At first, these inspection manuals considered bridge structures only, but nowadays inspection manuals also provide guidance for all road asset structures. Other changes include guidance for higher level inspections, and clarity for condition inspection of structural elements that were not made of steel or concrete (VicRoads, 2014).

2.4 *National Standard*

When a national code for the design for new bridges was drafted in the early 2000s, the need for a section covering the assessment of existing bridges was vital. Indeed, the first edition of the Australian Standard AS5100 (2004) included *Part 7: Rating of Existing Bridges* to achieve this aim. The standard outlines how rating for a bridge is calculated for load-capacity estimation. It became the basis for Level 3 (or Level 4 for RMS) investigations.

The 2004 AS5100 code had some limitations, including limited information about the methods of assessment for different materials, such as masonry, for example. Often road agencies would refer to international standards to perform the higher-level investigation (Shoghi & Giufre, 2017). The code recently (2017) underwent an update to provide a clear methodology on how bridge assessments are to be conducted. In particular, the order in which condition assessments and capacity assessment are performed is clarified (Figure 2). Additionally, the methods for testing of different material types are detailed in *Part 8* of the Standards.

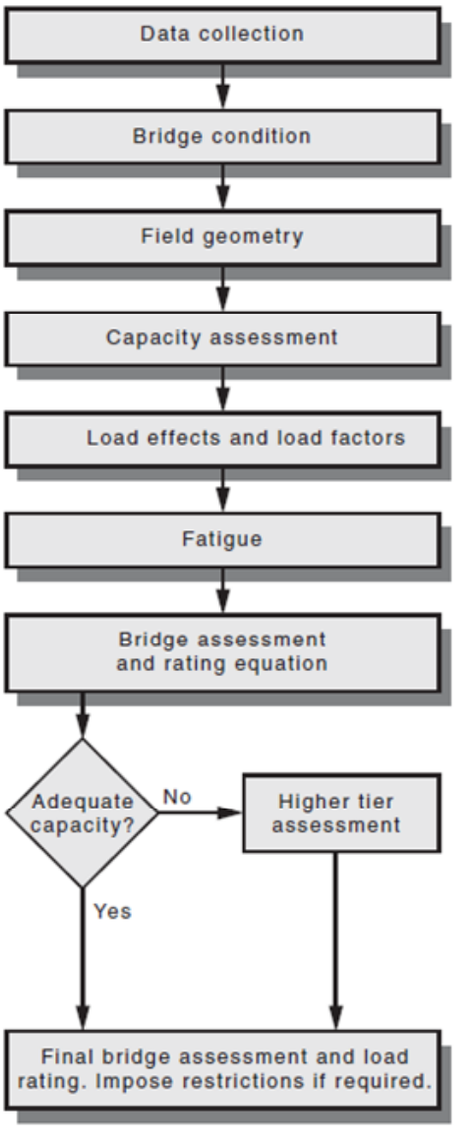


Figure 2. Australian and New Zealand Bridge Capacity Assessment Flowchat (AS 5100.7, 2017).

3 PERFORMANCE MEASURES

3.1 *Performance Goals to Indicators*

The performance goals for the individual road jurisdictions in Australia/New Zealand are not explicitly documented. This is different to other international bodies such as Netherlands' Rijkswaterstaat . However, Austroads (2009), the association of Australian and New Zealand road jurisdictions, have concluded the main performance goals for road bridge networks are:

- Functionality: minimum traffic delays;
- Safety: safe for intended use;
- Aesthetics: maintenance of an acceptable appearance;
- Sustainability: no backlog of repairs, and;
- Economic: keeping costs to a minimum.

The suggested key performance indicators by Austroads (2009) for measuring these goals are:

- Condition;
- Reliability;
- Remaining life;
- Risk;
- Socio-economic, and;
- Sufficiency indicators.

The extent to which the suggested indicators are applied as performance measures varies across the nine regional jurisdictions. As alluded to earlier, the bridge management practises across the jurisdictions are often at the operation level (bottom-up), which would suggest strong usage of the above performance measures. Nevertheless, the quantitative targets for these indicators is limited: it appears that subjective rankings are instead used for decision-making about future maintenance works.

3.2 *Condition Ratings*

Condition ratings are visual inspections of the elements that make up the road bridge to provide a measure of the condition for the structure. This in turn advises whether the performance goals of functionally and aesthetics are being met. Across all jurisdictions, condition ratings are performed as part of Level 2 inspections. The individual components of the bridge are visually inspected and then quantified based on a scaled rating system.

Most states in Australia use a 1 to 4 condition state rating for individual elements on a bridge, with 1 being as-built and 4 being poor (Austroads, 2013). NZTA uses five condition states, where the last state is complete failure of the component. Similarly, TMR has a condition state 5, but used for when the entire structure is rated as unsafe – it is not used at the component level. Only DPTI SA has a more significant difference to the other authorities: eight element conditions ratings are used, 0 to 6, and 9 (Not Applicable, Very Good, Good, Adequate, Poor, Very Poor, No rating, Unsafe).

After assessment of individual components, the overall bridge rating is then quantified. However, this step is conducted differently by the road agencies. For example, VicRoads applies a weighted average method, the Bridge Condition Number (BCN). It is an average rating for the clustered group of elements that are weighted based on the perceived importance in the structure. This results in a bridge condition index from 100 to 0, with 0 being as-built (Austroads, 2013). Figure 3 shows the BCN publically available for road bridges in Victoria. Alternative methods for bridge conditions include the RMS Bridge Health Indicators (BHI): it is qualitative method, reporting the bridge as either "Poor", "Fair" or "Good" based on the condition state and importance of the element under consideration.

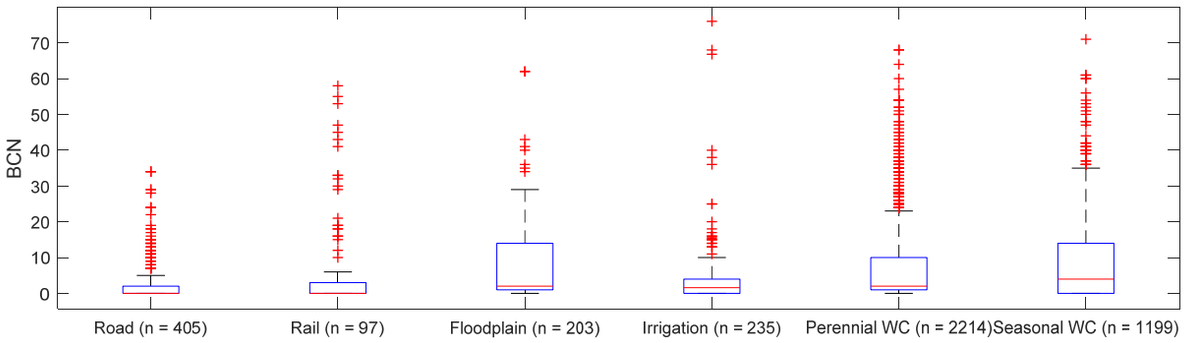


Figure 3. Published Bridge Condition Number (BCN) for "Road Over" Bridges in Victoria indicating current bridge conditions. (WC = Watercourse) ('n' = sample size) (Reference: VicRoads Data).

It is important to note that element condition ratings are a subjective process. However, authorities have in recent years enacted approaches to reduce this subjectivity, namely: (1) training and certification of bridge inspectors; (2) inspection manual guidance, such as photographic examples of different condition ratings for elements. Ultimately though, there are no quantitative measurements at Level 2 inspections – with the minor exception of crack widths.

3.3 *Sufficiency Indicators*

Aside from condition, there are other bridge sufficiency measures. Austroads (2004) suggested bridge width, bridge vertical clearance, and bridge load capacity. These parameters indicate the level of functionality for the road network.

Bridge width in the road network context refers to the percentage of bridges not providing the target trafficable carriageway width for the location. These targets vary between each road jurisdictions and depend on the local circumstances and route strategy. Additionally, each road authority specifies their target clearance for road bridges depending on local circumstances and route strategy.

Bridge load capacity for the network is the number of bridges with live load capacity less than the legal requirement. AS5100.7 (2017) presents a multi-tiered approach for capacity assessment (Figure 2). The load rating factor (*RF*) is nationally recognised as the first-basis for measuring load capacity. The rating factor is expressed as:

$$RF = \frac{\text{Available capacity for traffic load effects}}{\text{Load effects of nominated rating vehicle}} \quad (1)$$

where the structural capacity of the existing bridge is determined using the relevant contemporary design standards. However, alternative measures are used by the regional road jurisdictions for heavy vehicle access considerations. For example, as a proxy for capacity estimation, the live load model used for the bridge design is used in some cases. As an example of this approach, VicRoads applies the Critical Ratio algorithm when determining if a heavy vehicle is approved for restricted travel (Caprani & Ng, 2017);

$$CR = \frac{\text{Proposed vehicle load effects}}{\text{Reference load effects}} \quad (2)$$

The standard also allows load capacity measures using results of field investigation, and test loading in the field. The extent of these vary depending on the regional road jurisdictions.

3.4 *Strategic Measures*

Condition ratings and sufficient indicators are example of bottom-up performance measures. Data from individual bridges are combined to provide an indicator of the state of network. Bottom-up bridge management is common in Australia, but top-down performance measures are also used.

Life-cycle cost analysis can help identify the most economical action from a series of possible alternatives. Austroads (2013) presents the following model for the life-cycle cost for bridges:

$$LCC = DC + CC + MC + RC + UC + SC \quad (3)$$

where DC is the design cost, CC is the construction costs, MC is the maintenance cost, RC is the rehabilitation cost, UC is the user cost, and SC is the salvage cost.

Risk-based analyses have recently been introduced into the road BMS for particular SRAs. The risk is calculated as the product of the probability of failure and consequence of failure, which in turn comprised of tabulated factors that depend on the bridge properties. The probability of component failure (PCF) is expressed as:

$$PCF = LF \times RF \times CF \times IF \times EF \quad (4)$$

where LF is the loading factor (the type and number of vehicles), RF is the resistance factor (material type of different components), CF is the condition

factor, IF is the inspection factor and EF is exposure factor. The probability of system failure is calculated as follows:

$$PSF = \frac{\sum PCF}{n} \quad (5)$$

where n is the number of components in a system. Moreover, the consequence of failure is expressed as:

$$COF = HC + EC + TC + NC + RC \quad (6)$$

where HC is the human consequence (based on annual daily traffic), EC is the environmental consequence, TC is the traffic access consequence (detour distance), NC is economic consequence for replacement, and RC is the road class.

Other indicators, include the level of service for the network, and political motivators such as improving higher productivity freight vehicle (HPFV) access on the network.

4 FUTURE NEEDS

4.1 *Towards Unification*

As has been seen, there are many different approaches in road bridge management and variations in the performance measures across the regional road jurisdictions in Australia and New Zealand. While the latest edition of AS5100.7 provides clear definition on what is to be conducted for a bridge assessment, there is clearly still much room for the individual agencies to adopt their own method. Nevertheless, it is increasingly recognized that a unified approach would be beneficial. This comes on the back of other developments, such as the advent of the National Heavy Vehicle Regulator in Australia, who sets nationally applicable Performance Based Standards (PBS) for trucks.

A unified approach requires agreement of all road agencies and jurisdictions on whether three level or four levels of inspections are required, the scaling for the condition rating system, and the approach for measuring the overall bridge condition. Clear performance goals and prescribed performance targets are also required to achieve unification. Currently, a ranking approach is used for allocation of funds for future works.

Agreement on a unified approach would lead to the development of a single inspection and management manual applicable for all road bridges in Australia and New Zealand. Such harmonization would facilitate ready understanding of needs across all jurisdictions, and would reduce barriers for consultants to operate across jurisdictional lines.

Austroads Project BS.B.C.008 was initiated to develop a consistent approach and methodology for Australia (Rummey & Dowling, 2004). It concluded that the RMS approach to bridge management is most suitable. That is, a four-tiered level of inspection and modified version of the BHI to be used for bridge condition. In addition, the Austroads Bridge Task Force is currently proposing an investigation into the best approach to implement harmonisation.

4.2 *Improved Performance Measures*

Visual inspections for condition measures are prone to subjectivity, and can be particularly redundant if the process is sub-contracted outside the road jurisdictions. Therefore, SRAs should consider adopting structural health monitoring (SHM), weigh-in motion (WIM), and other recent technologies to quantitatively measure bridge performances. Such approaches are already adopted internationally. However, the use of such technologies have only been recently applied locally, with the latest version of AS5100.7 promoting the use of SHM in one clause.

A key point, not clearly addressed, is how condition measures can be used to determine the effective reduction in load-carrying capacity. Some international codes have developed different rules for assessment of existing structures to those used for the design of new structures. AS5100 does not follow this approach and states the structural capacity of existing components is to be determined using the relevant design standards. Thus, future revisions of the national standard should consider adopting different methods for the assessment of existing structures.

4.3 *Alternative Performance Indicators*

Deterministic bridge ratings provide a quick, efficient, and thus economical measure of bridge performance. However, ratings contain uncertainty as input parameters are subject to randomness and so may not reveal the true performance level. The use of a probabilistic approach can consider these uncertainties. Nowadays, bridge standards such as the American, Canadian, Danish, Swiss and British codes have moved away from traditional deterministic load rating processes and allow the use of reliability analysis for bridge performance assessments (Wisniewski *et al.*, 2012). The reliability index (β) as performance indicator for a limit state is commonly used internationally. AS5100 is yet to adopt this change. The reliability index can be considered for both safety and serviceability limit states, and at the element, or structure level. Ongoing work at Monash University and other international universities is attempting to extend this to the road network level as well.

A key hurdle to the adoption of an overarching safety-based framework is that the use of probabilistic methods for bridge assessment in Australia is not facilitated in AS5100:2017. While the 2004 edition

simply focused on the use of rating factors for performance assessment, the 2017 edition encourages the use of higher-tier assessments (Figure 2). However, details on what constitutes higher-tier assessments is limited. The Austroads Project TP1952 is currently investigating current SRA's methods that go beyond the current AS5100.7 and what international methods may be appropriate in an Australian context (Ng *et al.,* 2017). The early stages of this project have suggested that probabilistic methods and reliability indices are the basis of a framework to ensure safety whilst moving beyond deterministic evaluation.

4.4 *Updated Bridge Management Systems*

Deterioration models are an important aspect of BMS for maintenance optimisation. Based on the inspection data, deterioration models can provide an estimate of the deterioration rates. Typically, the probability of a structure or element moving from one state (condition rating) to another are estimated using Markov chains. This approach uses a matrix encapsulating transition probabilities which must be calibrated based on historical data. The problem with this approach is that by the time sufficient historical data is available to properly calibrate the transition matrix, the moment to take benefit of preventative maintenance has passed.

A survey conducted by Austroads (2002) concludes that none of the nine regional road jurisdictions use such models in their BMS. Research between universities and these jurisdictions are presently underway (Austroads, 2013). Hence, there are ambitions for inclusion of these models in their bridge management systems. It is important that the adoption of this approach is carefully calibrated using a combined laboratory data and field data approach to avoid the problem of timing mentioned above.

5 SUMMARY

Approaches to bridge management vary across the different road jurisdictions in Australia and New Zealand. While they all aim to achieve the same outcome, different performance measures are used for the different performance indicators to determine whether adequate performance exists across the bridge network. While the process towards unification has begun, clear performance goals with set targets, improved performance measures, alternative performance indicators such as the reliability index, and improvements to the existing bridge management systems are required. This will not only provide an efficient way for bridge management of road bridges locally, but also allows improved quality assurance for the remaining useful life of a bridge.

REFERENCES

Austroads. (2002). *Bridge Management Systems The State of the Art*. Sydney.

Austroads. (2004). *Guidelines for Bridge Management - Structure Information*. Sydney.

Austroads. (2009). *Guide to Asset Management - Part 6 : Bridge Performance*. Sydney.

Austroads. (2013). *Bridge Management Using Performance Models*. Sydney.

Bureau of Infrastructure Transport and Regional Economics. (2013). *Australian Infrastructure Statistics Yearbook 2013*.

Caprani, C. C., and Ng, A. (2017). A Vehicle Assessment Tool for Access Decision Support. *Austroads Bridge Conference*.

Casas, J. R., and Matos, J. C. (2017). Standardization of quality control plans for highway bridges in Europe: COST Action TU 1406. *IOP Conference Series: Material Science and Engineering*, *236*, 012051.

Department of Infrastructure and Regional Development. (2014). *Freightline 1 – Australian freight transport overview*.

Department of Transport and Main Roads. (2016). *Structures Inspection Manual*. Brisbane.

Geiger, D., Wells, P., Bugas-Schramm, P., and Love, L. (2005). *Transportation Asset Management in Australia, Canada, England, and New Zealand*. Alexandria.

Michael, K. (1994). Building Bridges for the Future. *Austroads Bridge Conference*.

Ng, A., Rooke, A., and Pape, T. (2017). Austroads Project TP1952 – Higher order assessments for existing bridges. *Austroads Bridge Conference*.

Roads and Maritime Services. (2006). *Bridge Inspection Procedure Manual*. Sydney.

Rummey, G. D., and Dowling, L. B. (2004). Towards a Uniform Bridge Management System for Australia and New Zealand. *Austroads Bridge Conference*.

Shoghi, A., and Giufre, A. (2017). Assessment of the High Street Masonry Arch Bridge over Merri Creek for New Class Trams and Road Vehicle Loadings. *Austroads Bridge Conference*.

Sonnenberg, A. (2014). Australian Bridge Inspection Process. *Small Bridges Conference*.

Standards Australia. (2017a). *AS 5100.1-2017: Bridge design - Scope and general principles*. Sydney: Standards Australia.

Standards Australia. (2017b). *AS 5100.7-2017: Bridge design - Bridge assessment*. Sydney: Standards Australia.

Standards Australia. (2017c). *AS 5100.8-2017: Bridge design - Rehabilitation and strengthing of existing bridges*. Sydney: Standards Australia.

Stipanovic, I., Chatzi, E., Limonggelli, M., and Gavin, K. (2017). *WG2 Technical Report: Perfomance Goals for roadway bridges of Cost Action TU1406*. Brussels.

Straus, A., and Mandic Ivankovic, A. (2016). *WG1 Technical Report: Perfomance indicators for roadway bridges of Cost Action TU1406*. Brussels.

VicRoads. (2014). *Roads Structures Inspection Manual*. Melbourne.

Wiśniewski, D. F., Casas, J. R., and Ghosn, M. (2012). Codes for Safety Assessment of Existing Bridges — Current State and Further Development. *Structural Engineering International*, *4*, 552–561.

Maintenance, Safety, Risk, Management and Life-Cycle Performance of Bridges – Powers, Frangopol, Al-Mahaidi & Caprani (Eds)
© 2018 Taylor & Francis Group, London, ISBN 978-1-138-73045-8

Repair and Retrofitting of Bridges under IBMS protocol

Sitarama Sagi Raju
Managing Director, IBMS, IDDC Engineers Pvt. Ltd.

Tumati Kiran kumar
Junior Bridge Engineer, IBMS, IDDC Engineers Pvt. Ltd

ABSTRACT: At present there are 169758 structures in Indian Bridge Management System (IBMS) on total 2.5% of national road network. Out of 169758 structures 36673 bridges which include minor, Major bridges. Based on the IBMS Rating system, we have identified 6551 bridges which are under distress condition (either structurally or functionally) and require either immediate attention or planned inspection.

Many a times even after taking all the due precautions and all quality control measures, bridge structures deteriorate. Generally the causes of distress on bridges are classified into three categories, such as Aggression by Mechanical elements, Aggression by Physical elements and Aggression by Chemical elements. From the above mentioned reasons, structure may be predominantly affected by Aggression by Chemical element from the day one it is constructed. Within the IBMS rating system, we prepare the probability matrix which will give us the Deterioration Time (Δt).

Based on the above mentioned cause of deterioration, we find out Primary cause of deterioration and Secondary cause of deterioration. Based on this cause of distress an appropriate principle is applied in order to suggest or recommend the repair/rehabilitation methodology.

1 INTRODUCTION

Bridges form one of the most important infrastructure facilities in the world. As a component asset management program, the Indian bridge management system (IBMS) facilitates performance-based and data-driven project planning by storing historical bridge data, including bridge characteristics, inspection data, rating information, uses deterioration models and economic models to predict future needs when optimizing network-level and project-level decisions. In world-wide phenomena the cause of deterioration is due to inadequate design & construction, overloading, lack of adequate maintenance, atmospheric effect and unseen abnormal floods, earthquakes etc. Effectiveness in detection and characterization of major deterioration types: delamination, concrete degradation, reinforcement corrosion, and cracking.

Bridge Management system are used to monitor and making a decision‟s regarding maintenance, preservation, and repair, subject to budget constraints. Defining general processes and addressing distress, diagnosis of the cause, proposing remedial measures and the corresponding principles and methods. It generates detailed inventory data and condition ratings of assets, ensuring the dynamics of deterioration process are captured.

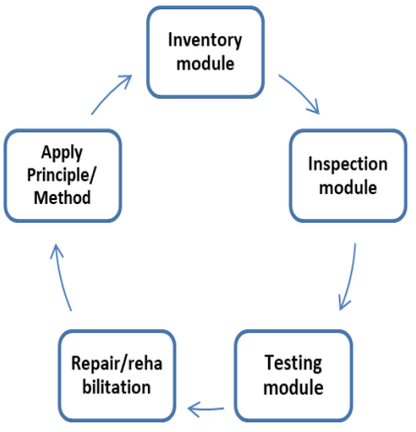


Figure 1. IBMS Life Cycle

IBMS use the principle of "FRWD" (First repair the worst damage) to ensure the entire bridge inventory is rendered in safe in a phased manner. IBMS applies a technical logic to manage the bridge assets during its life cycle.

2 FRAMEWORK FOR CONSIDERING IBMS PARAMETERS

Bridge has a unique identity number which is link with state code, RTO Zone, highway number, chainage and bridge number that gives national identity for every National highway bridges in India. To deep findings, picking precise location details in the form of latitude and longitude is being collected in auto mode using Ground Positioning System that accurate location of bridge. Engineering properties of bridge design, materials and other technical details of the bridge are being collected. In data collection Structural data, functional data and socio-economic data is collected on basis of rating system. Rating is between 0-9 conditions which are deciding the importance of bridge.

3 APPROCH FOR RATING SYSTEM

For Structural data, we consider Integral-Non Integral Deck, Super structure, Sub-structure and Scour. For functional data Bank & channel, waterway adequacy & deck geometry etc., are taken into account. For Socio- Economic, daily traffic, economic growth, environmental impact etc., are collected. For every component rating „0" is worst condition and „9" is excellent condition each rating has descriptive details is presented. In every rating system is accumulating with alpha numeric string. Based on performance of rating will decide bridge condition either bad or good in technically. Deep finding for inventory data apply classified filter to view data by as structural form, material of construction, type of bridge, loading as per IRC, age of bridge, traffic lane on bridge, crossing feature, length of bridge, width of carriage way.

Over viewing bridge inspection report details that gives all the details with component wise such as structural data, approach details, protection works, foundation, superstructure, substructure details, bearing & pedestals, expansion joints, drainage system & wearing coat, etc.,

Based on this inventory rating codes, IBMS analyse the data and indicates the bridge which needs further investigation which is in depth or detailed study using various Non- Destructive test procedures. A detailed remedial plan is defined for each bridge tested.

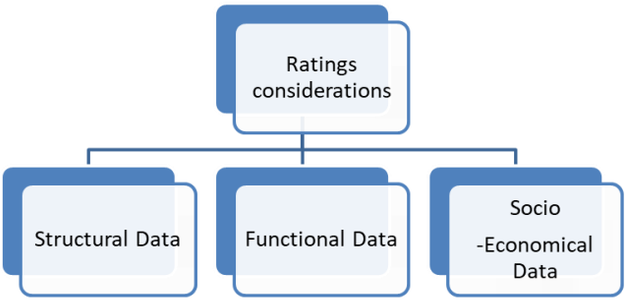


Figure 2. Rating Module

4 EVALUATING DISTRESS BRIDGES BASED ON RATINGS

In the first task, inventory data and rating is completed, the same is required to be validated during the inspection stage.

The second task during Bridge Inspection, the Bridge Inspection Engineer has to ascertain the ratings provided during inventory. This provides for in built validation of data collected during inventory. Based on the observations of the bridge parameters and the environment and traffic condition existing at bridge location, it is essential for the bridge Inspection engineer to reassess the rating provided by the Inventory engineer. This procedure fulfils the need for self-validation of all data that ensures that data used by IBMS in processing is correct and validated. Inventory compiles Structural rating (SR), Functional rating (FR) & Socio-Economical rating (SER). If structural rating (SR), are below 5 then either of the three conditions (C1, C2, and C3) are applied.

1. Where C1 applies if SPi $\leq$2, where i=1 to 4 then immediate attention
2. Where C2 applies if SPi $\leq$5 and $\geq$2 where i=1 to 4 Planned inspection within 6 months
3. Where C3 applies if SPi $\geq$6, where i=1 to 4 Inspection only as per schedule

From out of 35504 bridges, 6764 bridges are distressed condition. As below given table no of distressed bridges which have structural rating is below 5. For Immediate attention bridges which are responding for repair immediately because bridges are totally deteriorated, it may cause to economic loss. Planned Inspection which rating is 3, 4 & 5 is needed to test and if any distress identified then repair to notified. Inspection as per schedule is need to Re-inspected again next year to evaluate if it deteriorates testing proposed if not again inspection.

S.no	Type of bridge	No.of Bridges	No of distressed Bridges	Planned Inspec-tion	Immediate atten-tion
1	Extra-Long Bridge	1744	296	11	285
2	Major Bridge	3395	664	24	640
3	Minor Bridge	31534	5591	113	5478

Table 1. List of Distress Bridge

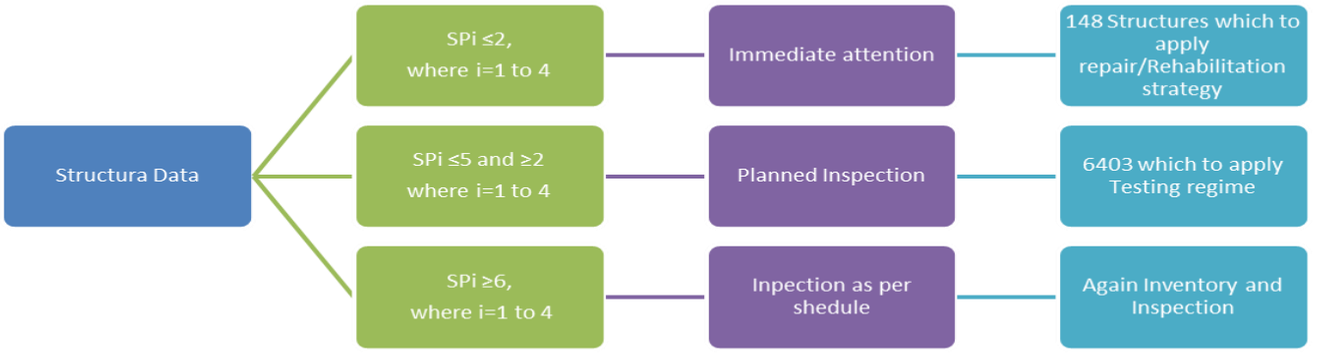


Figure 3. Flow chart shows decision making to identify distress bridges based on ratings

5 RENDERING BRIDGE SAFE

1. Cause Identification
2. Deterioration time identity
3. Applicability of MRSR

5.1 *Data Processing and Identification of cause*

The third task during the inspection process is to complete the prognosis of distress in bridge if any distress is observed. To be able to do this, it is critical that the Bridge Inspection Engineer to understand the various deterioration processes and what type of distress causes this deterioration process to happen.

The Distress in bridge is any situation; that is not designed and has occurred. Deterioration is the manifestation or propagation of this distress in a continuous manner to cause alarm. Bridge Inspection Engineer based on his expertise and knowledge will judge the reason for the distress to have occurred and this form the prognosis of distress. The main cause of distress which sometimes results in manifestation of other type of distress or is severe is called the primary cause of distress. The subsequent distress that gets manifested or resultant due to primary distress is called secondary distress. Distress can occurs in specific and localized manner as much as it can occur in the overall structure. The final distress map of the bridge may be a result of multiple causes (primary cause and secondary cause) and combined effect of both primary and secondary causes. This could at times make it difficult to determine the correct primary cause. Primary cause can be defined as the cause that is seen to the maximum and has resulted in most extensive distress from among the all the other causes.

Ideally it is better to eliminate the causes rather than identify the cause. This could result in a matrix of causes. From among these identified causes, the primary cause can be confirmed if not properly identified initially.

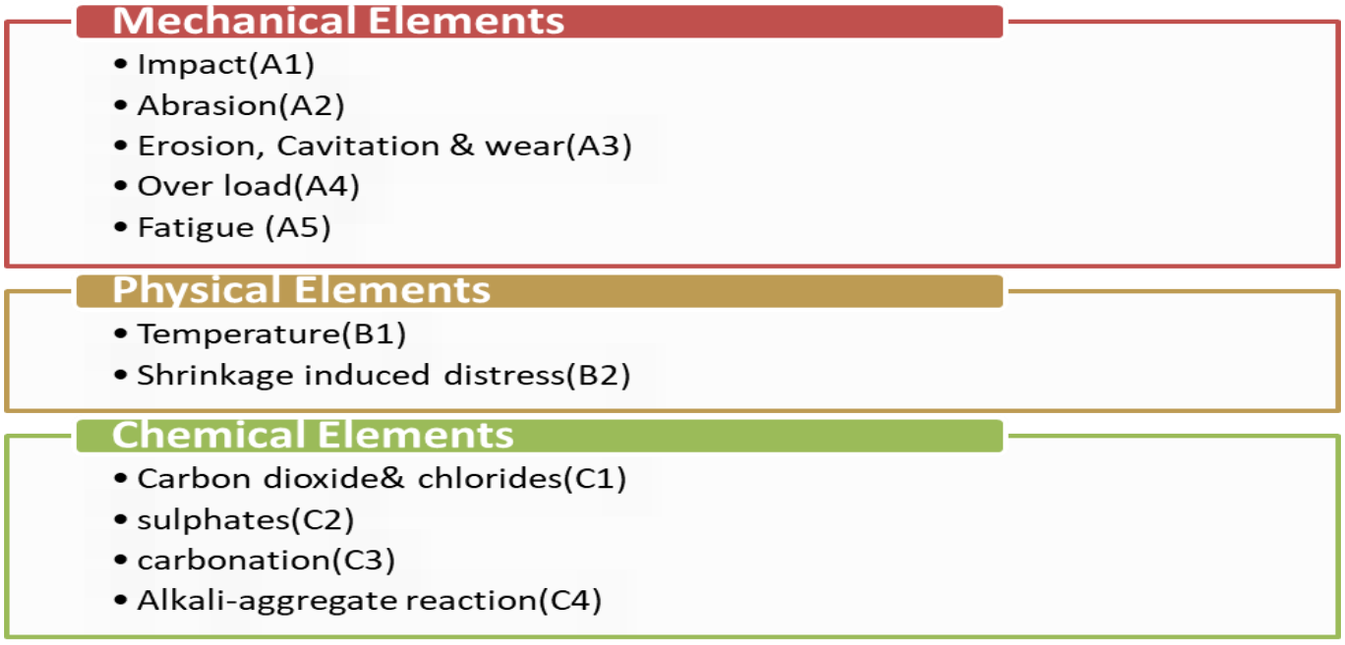


Figure 4. Causes Identification

5.2 *Identification of deterioration time*

By above defined causes is to be able to capture the combined effect of each of the process, based on site condition testing engineer will assign the rating number to each of the process and then combine these rating in the form of a **Deterioration Matrix P.**

$$\mathbf{P}= [\textit{Mechanical} \quad \textit{Physical} \quad \textit{Chemical}]$$

$$P=\begin{pmatrix} A1 & B1 & C1 \\ A2 & B2 & C2 \\ A3 & 0 & C3 \\ A4 & 0 & C4 \\ A5 & 0 & 0 \end{pmatrix}$$

This deterioration matrix is then converted to deterioration probability matrix. As per Rating system for every cause ratings are to be consider from "1" to "9" which stand 1 stands for worst and 9 is good [X1,X2,X3… X9) for each rating has description details. Rating 9 is good condition, so there is no possibility of deterioration X= [X9-1, X9-2, X9-3….X9-9]. Once the probability matrix is formed, the vertical column summation yields the impact probability of one particular process on the deterioration of the bridge. Input data is essential which is based on ratings allotted to the bridge based on site condition. Summation of all matrixes rating to get probability of deterioration in each clause of matrix P = [X9-1/X, X9-2/x….. X9-9/x]

The summation of Mechanical, Physical and Chemical process is should equal to 1

Year of deterioration T = Chemical Probability * Δt + Physical Probability * Δt + Mechanical Probability * Δt

$\therefore$ Δt is the deterioration time. It is based on the total impact such as overloading, environmentally effect.

5.3 *Applicability of MRSR*

5.3.1 Maintenance:

Maintenance is needed to preserve the intended load carrying capacity of the bridge to ensure correct functioning, aesthetic appearance and continued safety. It excludes any work leading to improvement of the structure by strengthening or by widening to carry heavier loads or wider gauge. It consists of the prevention of deterioration by normal causes, wear, and damage through accidents, vandalism and built-in imperfections. Maintenance deserves great attention. Maintenance is to be performed in a systematically way because it has been proved to be the most economical. All structures should be designed and constructed with consideration of both capital expenditure and predictable maintenance cost.

IBMS has in place over 150+ routine maintenance procedures (RMM), over 100+ detailed maintenance procedures (DMM) and frequently maintenance procedure (FMM)

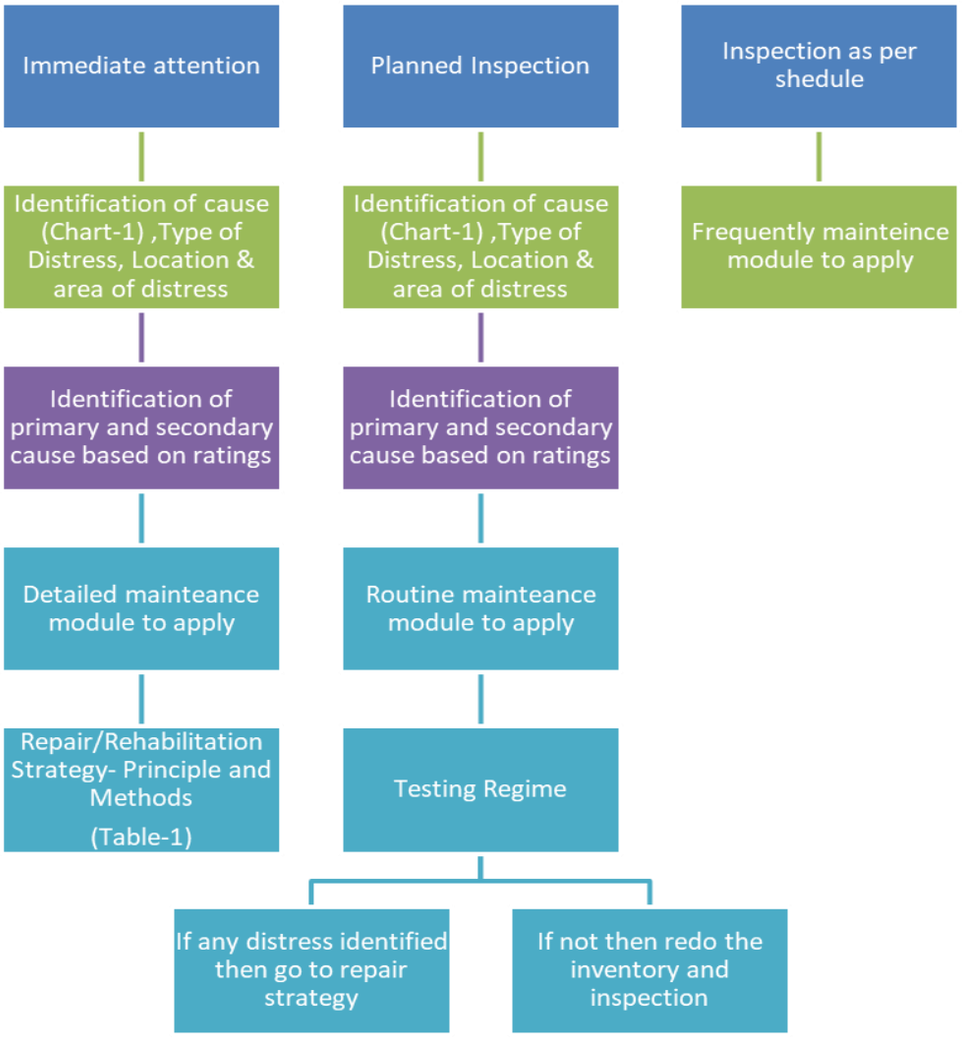


Figure 4. Protocol for MRSR

5.3.2 Repair/Rehabilitation:

IBMS has its immediate goal (2015-2020) to render all bridges safe and during subsequent period of time to increase the efficiency of bridge management. With this as the goal and focus, it is important that the choice of repair strategy is adopted. Based on the cause of defect/ distress, the primary and secondary cause of distress is identified. There are 24 tests that have a proper testing procedure and test results should adequately confirm the cause of distress. Similarly other contributory causes for distress are identified and the overall deterioration process is defined.

During identification of the cause of distress, laminar behaviour of the bridge is to be accounted for most the distress affects the lamina of the bridge component. Such effect could cause the surface lamina of the component to deteriorate faster than the section. Such effects are to be recorded and accordingly the repair strategy is to be selected.

Once the principle cause is identified, certain principles only can be adopted to address that cause. However as the bridge structure is massive, contributory factors and principle factor could be affecting the bridge in certain specific areas/ locations. In such cases the locations and cause will dictate the repair principle. Certain principle of repair need to applied to the whole bridge structure to enhance the performance of the bridge and such principles have to be applied post all other repair principles are applied.

Certain principle of repair need to applied to the whole bridge structure to enhance the performance of the bridge and such principles have to be applied post all other repair principles are applied In such cases the locations and cause will dictate the repair principle. Certain principle of repair need to applied to the whole bridge structure to enhance the perfor-

mance of the bridge and such principles have to be applied post all other repair principles are applied. Appropriate method of repair is very critical in the longevity in the performance of the repair section. IBMS follows a protocol which defines first the principle of repair for each of the cause of distress.

While detailed specification of each of the suggested method needs to be evolved, the basic principle followed is described herein under.

The specification which is product / system specific shall include the performance requirements for the product and the system to be used. Most of the product/ system fall under the generic of Chemical.

Based on ratings, cause of distress and nature of distress identification proper remedial principle will be adopted.

Sl. No.	Cause of Distress	Nature of Distress	Principal Possible Measures for Remedy
		(I) Distress in Concrete	
1	**(A) Mechanical** Impact, Overloading, Movement, Settlement, Explosion, Vibration, Seismic	Cracking Delamination Spalling Disintegration	1. **Crack Filling:** By Injection of suitable grouting and/or filler material after sealing them, Active cracks due to corrosion, ASR or foundation settlement etc. Should not be injection grouted. 2. **Concrete Restoration:** By Hand applied mortar, Spraying of mortar (Guniting), Spraying of concrete (Shotcreting), Recasting of concrete, Replacement of old element by new one 3. **Structural Strengthening:** By Addition of new reinforcement externally, Bonding of steel plates, Wrapping/Bonding by Fibre Reinforced Plastic (FRP), Encasing the member partly or wholly either by concrete or by mortar or ultra-high performance concrete reinforced or non-reinforced, Addition of new reinforcement by drilling holes & embedding in concrete, Pre-stressing by external cables.
2	**(B) Chemical** Alkali Aggregate Reaction, Aggressive Agents (Acids, Salts (sulphates, phosphates, etc.), Biological Activities		1. **Protection against Ingress:** By Sealing & Injection of cracks (for dormant / dead cracks only), of cracks, Impregnation of surface, Application of membranes, Surface coating, providing external panels. **2. Moisture Control:** By Coating of the exposed surface, Cladding over the surface, Impregnation of hydrophobic material. **3. Increasing Resistance to Chemicals:** By Overlays, Coatings, Impregnation
3	**(C) Physical** Shrinkage, Erosion, Wear and Tear, Fire		1.Protection against ingress 2.Moisture control 3.Structural strengthening 4.Increasing Physical Resistance: By Overlays, Coatings, Impregnation

(II) Distress in Reinforcement and Pre-stressing		
Carbonation of Concrete	Uniform Corrosion: Cracking & Delamination	1. Preserving or restoring passivity 2. Control of Anodic areas.
Corrosive contaminants: Sodium chloride, Calcium chloride & Others	Pitting & Stress corrosion: Spalling & Cracking	1.Cathodic control 2.Cathodic protection 3.Chloride of anodic areas 4.Restoring passivity
Severe progress of corrosion due to above effects	Scaling of steel: severe loss of surface area	Local replacement of steel reinforcement or part or full replacement of the member

Table 2. Remedial Principles based on causes

5.3.3 Strengthening

Strengthening operations aim at restoring the bridge to its original service level it once had and has now lost. In some cases this consists of giving the bridge the service level which was intended, but could not be attained because of deficiencies in the original design and/or construction. The procedures require design inputs and cannot be generalised. The design of these remedial measures needs in-depth analysis of the present status of the bridge component that needs to be strengthening and details of its original condition. Various techniques are available for strengthening of bridges and some of them are recent advances like use of FRP and similar materials.

5.3.4 Replacement

Replacement is to be carried out when the whole structure or at least its major components are required to be replaced, Replacement are essential at times when the age of the bridge has advanced and the bridge show distress where the cost effectiveness of the rehabilitation or strengthening is not economically feasible.

6 CONCLUSION

IBMS has attempted to adopt a logical flow of process to be used to define the various maintenance, rehabilitation, strengthening or replacement procedures. The basis of such decision making rests on the dynamics of the bridge and its condition defined just before the decision is required to be taken. At time, the decision is triggered due to deterioration process and in such case the logical sequence would be try and prevent the bridge from further deterioration.
IBMS aims to render all bridges safe by application of MRSR modules to the bridges few at a time (presently using the FRWD protocol to bridges whose rating is below 3) and once all bridges are rendered safe (rating above 5), the efforts would be directed to improve on the efficiency of the management of bridges by ensuring all bridges have repeat rating above 6 and would only require timely maintenance.
The quantification can also be automated once the as built drawings of the bridges are available and then on this drawing we superimpose the distress. The future of IBMS shall involve application of BIM (Bridge Information Modeling) to IBMS.

Technology exploitation is the motto of our IBMS and hence we are looking for future trends that can be applied to this process.

7 REFERANCES

- Sachin joshi 2008 on "Bridge Asset Management Program" - Indian Road Congress.
- "Standard Specifications and Code of Practice for Road Bridges, Section-II Loads and load combinations"- IRC:6-2016.
- "European Standards" - EN-1504.
- "Quality specifications for roadway bridges, standardization at a European level" - TU1406.
- "Guidelines on Techniques for Strengthening and Rehabilitation of Bridges" - IRC SP: 40-1993.

SS08: Construction management issues in bridge engineering and construction

Organizer: M. Nasser Darwish

Maintenance, Safety, Risk, Management and Life-Cycle Performance of Bridges – Powers, Frangopol, Al-Mahaidi & Caprani (Eds)
© 2018 Taylor & Francis Group, London, ISBN 978-1-138-73045-8

The construction of the new Tappan Zee Bridge

R.D. Csogi, PE
Greenman-Pedersen, Inc., Babylon, New York

ABSTRACT: Construction for the original Tappan Zee Bridge started in March 1952 and the bridge opened to traffic on December 15, 1955. The original bridge was designed to last only 50 years due to material shortages during the Korean War at the time of its construction. The aging bridge bears an average of 138,000 vehicles per day, substantially more traffic than its designed capacity. The new Tappan Zee Bridge is being constructed just to the north of the original structure. It is a 3.1 mile twin crossing comprised of low marine viaduct Approaches, and features twin cable-stayed bridges over the shipping channel. The new bridge has a fully integrated Health Monitoring system designed to monitor the structure for its full 100 year service life. The construction cost is valued at $3.98 billion.

1 INTRODUCTION

The new Tappan Zee Bridge is being constructed over the Hudson River literally yards to the north of the existing bridge … for a specific reason. First the location of the original Bridge has to be explained. The site of the original bridge is at the Hudson River's second-widest point at 3.1 miles wide.

The reason the site was chosen was to have it be as close as possible to New York City, while staying out of the 25-mile range of the Port Authority's influence, thus ensuring that revenue from collected tolls would go to the then newly created New York State Thruway Authority, and not the Port Authority. In order to maintain jurisdiction over the new Bridge, The Thruway Authority had no choice to build to the north.

With the location determined, next was the size, capacity and use of the replacement structure. The new crossing consists of two parallel structures built 32 feet apart from one another. This space and the parallel structures are designed to accommodate a rapid transit system in the future.

The South Bridge contains 4 lanes of vehicular traffic with adjoining emergency breakdown lanes, and carries eastbound traffic. The North Bridge also contains 4 vehicular lanes with adjoining emergency lanes. In addition, there is a shared pedestrian and bicycle pathway which is behind barriers and protected from the vehicle lanes. Also contained within the pedestrian/bikeway area are viewing "bump out" overlook pods at 6 location along the length of the Bridge.

The centerpiece of the new parallel crossings are the cable-stayed Main Span Bridges. Each cable-stayed bridge spans 1,200 feet over the Hudson River shipping channels. Each bridge has 4 concrete Towers that reach a height of 419 feet. Each bridge has 96 stay cables ranging in length from 190 to 623 feet (See Figure 1).

The new Tappan Zee Bridge is being designed and constructed under a Design/Build Agreement between the New York State Thruway Authority and Tappan Zee Constructors, LLC (TZC).



Figure 1. Artist Rendering of the New Tappan Zee Bridge

This consortium consists of Fluor Enterprises, American Bridge Company, Granite Construction Northeast, Traylor Brothers, and the major subcontractor, HDR serving as the Designer. Their winning bid was $3.1 billion, construction began in the Spring of 2013, and the proposed contract completion date is currently August 15, 2018.

2 THE DESIGN

In the traditional Design-Bid Build (DBB) arena, a design is developed to allow numerous Contractors to bid on a singular design. It incorporates common foundation, span length, deck systems elements that are common to most Constructors. Utilizing the Design-Build (DB) model, Contractors and designers are free to entertain designs that suit the Contractor's means and methods without the constraints of the DBB model.

The secret to Tappan Zee Constructor's winning bid was ultimately tied to their unique means and methods, or namely their one of a kind floating crane, the Left Coast Lifter. The Left Coast Lifter was built for the American Bridge/Fluor joint venture, which was the lead contractor on the new Oakland Bay Bridge in San Francisco, California.

The Left Coast Lifter is built on a barge hull. The barge was built in Portland, Oregon by U.S. Barge, LLC and ferried to Shanghai, where it was fitted with a shear-leg crane manufactured by Shanghai Zhenhua Port Machinery Co. Ltd. The completed sheerleg was ferried back to the United States on a semi-submersible heavy-lift ship. The shear-leg crane on Left Coast Lifter has a 328-foot long boom, weighing 900 tons with a 1,900 lift capacity. It is the largest barge crane ever used on the U.S. West Coast (See Figure 2).



Figure 2. The Left Coast Lifter erecting an Approach Span tri-girder segment.

With its lifting capacity of 1,900 tons, it allowed the designer to design bridge elements such as girders to unusually long lengths. On the Approaches, the typical span length is 350 feet from pier to pier. The superstructure girder design was driven by the capacity of the Left Coast Lifter. Each span consists of five 12 foot deep welded plate girders. The girders are fabricated in either 3 or 2 girder sets at a fabrication facility on the Hudson River just outside of Albany, New York. The girder sets are fabricated complete with all cross bracing, scuppers, and utility conduits. They are barged downstream to the work site and lifted onto the piers in either 2 or 3 girder units (See Figure 2).

The design of the foundations and substructure also relied on large modular units that also could be lifted with the Lifter. Due to the large amount of muck and soft soils that comprise the Hudson River bottom, the pile lengths were typically 360 feet in length, and 4 to 6 feet in diameter, with 1" thick steel walls. While not unusual for these soil types and large pier to pier span lengths, what was unusual was that these piles were fabricated in 180 foot segments and required only 1 welded splice.

In keeping with the use of modular components, the Pier Caps were precast off-site, barged to the pier stem locations on the Hudson River, and lifted with the Lifter. These Pier Caps were massive and most weighed in at 200 tons. Being of a trapezoidal shape, this saved a lot of intricate onsite forming on the river, and eliminated weather dependencies for the foundation work.

From the beginning, Tappan Zee Constructors decided to begin the design effort with Building Information Modeling (BIM) technology, and utilize this model throughout the fabrication and construction process. BIM enabled designers to visualize the structure in three dimensions and from infinite vantage points. This visualization can identify potential design conflicts early in the process and allow designers to discover efficiencies that can help reduce cost and improve construction scheduling. The BIM design model also helped to quantify and organize the materials needed for this project.

The open structure of the BIM model allows all project participants to coordinate their specific aspect of the design or construction. This includes the Prime designer, HDR, and all of its sub-consultants, as well as the Prime contractor, TZC, and all of their sub-contractors, and the Owner, the Thruway Authority. For example, Welsbach Electric Corp. used the BIM model to configure the installation of the bridge's electrical conduits and wiring. This was coordinated with the production of the crossing's steel girders.

Once the bridge is complete and operational, the BIM model will be utilized by future maintenance

crews. Each of the approximately 500,000 bridge elements can be viewed with links to pertinent design and maintenance information. Maintenance crews will be able to view the model from mobile devices, laptops or desktop computers. This will allow the crews to see every piece of the bridge at every possible angle.

3 MOBILIZATION

Before a single pile was driven or a single cubic yard of concrete was placed, an enormous amount of mobilization and preparatory work was required for this one of a kind bridge project. Multiple staging areas and equipment yards were constructed on both sides of the River. Field Offices and crew changing facilities were either built or reconfigured from existing buildings that were leased for the project. In all, these facilities were expected to support over 5,000 workers, engineers and other support staff for the duration of the project.

One such building that was procured after the Contract Execution between TZC and the NYSTA, was an on-site building to house the Designer's design staff and Contractor's procurement and management staff. These two entities were co-located under one roof to facilitate the numerous meetings that were required to ensure the speedy completion of the new bridge's design.

Other mobilization efforts that were being accomplished were the pre-construction geotechnical investigations both on land, and on several barge-based operations for additional engineering analysis of the river bottom. Dredging began in the shallow areas adjoining the riverbanks to support the staging of barge-mounted cranes and equipment. Over 800,000 cubic yards of material was removed from these areas. To compliment riverbank staging areas and to minimize the dredging efforts, two temporary construction trestles were built. Each totaling 1,000 feet in length and extended out into the Hudson River parallel to the alignment of the new Approaches.

The Left Coast Lifter was on its way from San Francisco via the Panama Canal to a shipyard downstream from the Tappan Zee near Jersey City. It spent several months moored there where it was modified for the specific needs of the project. This work included rigorous lift testing, precise tuning, careful inspections and installation of a new state of-the-art computer operating system complete with touch screen controls.

In addition, perimeter environmental monitoring stations were installed near both the Rockland and Westchester County shorelines as part of the New Tappan Zee Bridge Project's Environmental Performance Commitments (EPC). These commitments are intended to monitor, minimize and mitigate potential adverse effects related to construction noise, vibration and air quality associated with the project.

Noise was monitored very closely during construction. Highly sophisticated monitoring devices were installed at locations near the project site to ensure that construction activities are performed without exceeding allowable sound levels. The monitoring devices record the level of sound and automatically report back to the engineers should noise levels even approach a level not to be exceeded and then display the results online.

Finally, survey work was proceeding both on land and on the Hudson River for both control and foundation layout. Much of this work utilized the existing bridge structure as control and had to be accurately surveyed to verify as-built coordinates.

4 FOUNDATION WORK

Foundation work began with the development of an acceptable work plan that incorporated environmental considerations, a test pile program, and a quality assurance/control verification process. There are two basic components for the Approach Span Pier and Main Tower foundations … the concrete-filled steel piles, and a pile cap which consists of a precast slab unit which serves as the bottom form and steel modular forms to create a "tub" for each pile cap. These tubs are lifted and positioned atop each pile cluster at a pier location, fitted with reinforcement cages and filled with concrete (See Figure 3).

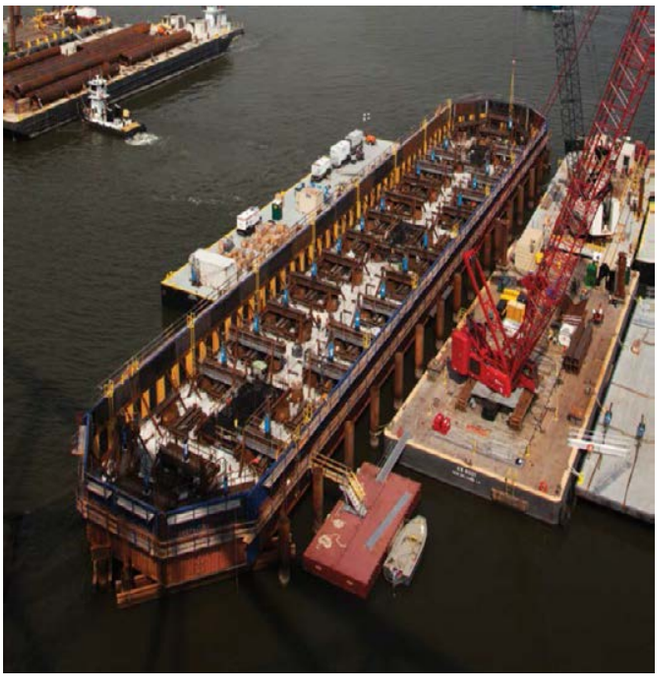


Figure 3. Main Tower Pile Cap Formwork

There are 1,000 piles that are utilized for the new Tappan Zee Bridge. In total, there are 41 Approach Span Piers and 2 Main Tower Piers. The Main Tower piles are 6 feet in diameter and the Approach Span Piers rest on 4 foot diameter Piles.

Some are driven to bedrock where it was located high enough to be reached. This occurred on the Westchester side of the Hudson River where the bedrock was approximately 150 feet below the river surface. On the Rockland side, it was approximately 700 feet below the river surface. These piles were designed as friction piles, some reaching 360 feet in length.

The largest cluster of piles were for the four Main Tower structures which are the major support structures for the twin cable-stayed bridges. The two Main Tower Piers were built large enough so the two side by side Towers share the singular pile cap. Each Tower foundation pile cap sits on 64 six foot diameter piles. Each Tower foundation pile cap measures 320 long by 60 feet wide, and is 14 feet thick.

The Main Tower piles were driven using a template, a 4600 barge-mounted Ringer crane, both a vibratory and impact hammers, and bubble curtain units for environment compliance. The Main Tower piles were installed in halves with the lower segment being 170 feet in length and weighing 70 tons. The upper segment was 110 feet and weighed 52 tons. The two halves were joined with a full penetration weld.

Each pile segment was lifted into the template guide and allowed to sink under its own weight approximately 40 feet into the mucky river bottom. The pile was tapped several times with the hammer to displace any fish in the vicinity, and the bubble curtain activated to deaden the driving noise for the aquatic life. The piles were conventionally driven to the required blow count.

The pile cap "tubs" (previously described) were lowered over the protruding piles with strand jacks, and rested on collars installed at the appropriate elevation. The rebar was set into position and the tubs were filled with 20,000 CY of concrete.

A unique feature to these operations were the use of floating concrete batch plants. Utilizing three floating concrete plants during the peak of construction was also a key aspect to TZC's competitive low bid. These plants were highly mobile and allowed TZC to deliver 125 cubic yards of concrete per hour (per plant) at any location on the Hudson River.

Imagine the logistics of having to move traditional concrete trucks to points on the river. Also imagine the number of these trucks that were removed from the Thruway and local roads by utilizing these floating batch plants.

In addition, these plants also included several environmentally-conscious features. An advanced air quality system reduced dust from escaping the plants during production and highly efficient, clean engines reduced emissions. All systems on the plant and its accompanying support barge were be painstakingly contained to prevent spillage into the river.

5 SUBSTRUCTURE WORK

The second year of the project saw substructure begin in earnest. Working with 130 barges fitted with cranes and various types of equipment and materials, work progressed on the Approach Span Piers and Main Towers.

Building atop the completed pile caps each of the Approach Span Pier stems were conventional formed with modular forms. These forms were completed to the required height and lowered around pre-tied and stacked reinforcement cages. The taller piers were constructed in segments by filling the lower segments with concrete, curing, and restacking to form the upper segment.

Once these stems were complete, the Lifter would erect the precast Pier Caps onto the stems. These Pier Caps were prefabricated by Coastal Precast Systems in Chesapeake, VA and were barged to the project site. These caps were trapezoidal shaped and weighed approximately 200 tons.

By far the most noticeable substructure elements for the new Tappan Zee Bridge crossing are the Main Towers for the twin cable-stayed bridges. Each Tower leg cants outward from the base until it reaches its final height of 419 feet. Each pair of legs are tied together at the final roadway elevation with a massive, precast concrete crossbeam weighing 700 tons (See Figure 4).



Figure 4 – Main Tower Construction with Precast Concrete Crossbeam in Position

Tower leg construction begins with the use of modular steel "jump forms". The jump forms, were positioned on the Main Tower pile caps, and enabled construction of the open concrete towers to take their shape. Crews used a series of climbing tower cranes and catwalks to install steel reinforcement and to cast the concrete. As each segment is completed, the forms "jump" to the next level via a screw jacking system, allowing the next segment to be built on top of the preceding one.

Each jump form is composed of two different forms, one internal form and one external. The external form moves upward ahead of the internal form, providing a safe area for workers to install rebar cages. While the rebar is installed, the internal form remains with the previous segment of the tower until the next segment is ready to be filled with concrete. The internal form is moved upward and both forms are then joined together, acting as casting chamber (See Figure 4).

6 SUPERSTRUCTURE WORK

Once the pier construction advances to a point where there are a substantial number completed, the erection of the steel superstructure begins. The steel superstructure actually begins at a fabrication facilities located in Pennsylvania, North Carolina and Virginia. They are welded steel plate girders that range in length from 350 to 410 feet, and are typically 12 feet deep.

They are shipped to a TZC assembly yard located at the Port of Coeymans on the Hudson River in Albany County. At the assembly yard, the girders are connected in either 3 or 2 girder units, or assemblies. Each girder assembly is bolted together with cross frames and all appurtenances including electrical, communication, etc. conduits. In all, 100,000 tons of steel were used to create 134 girder assemblies.

Each assembly is barged 95 miles from Coeymans to the bridge site. The first 410 foot, 850 ton assembly was set on June 17, 2015 using the Lifter. The Lifter utilizes a custom designed lifting frame which employs 4 hydraulic rams located at the 4 corners of the frame (See Figure 2). This allows the girder assemblies to be "pitched and yawed" to precise elevations to accurately set the assemblies on the bearings (See Figure 5).

The erection of the girder assemblies using the Lifter was a very unique operation. The Lifter does not have the ability to rotate its derrick type boom. It can only raise and lower the boom to change the pick radius, raise and lower the lifting frame and attached load. The Lifter's positioning system is comprised of four anchors positioned off each of the four corners of the barge hull, and connected with winch lines. By reeving in and bailing out via these winch lines, the Lifter can be accurately turned and positioned to pick up or position its load. All of the positioning capability for the Lifter is carefully controlled by its pilot, and assisted by way of GPS and computer enhanced controls.

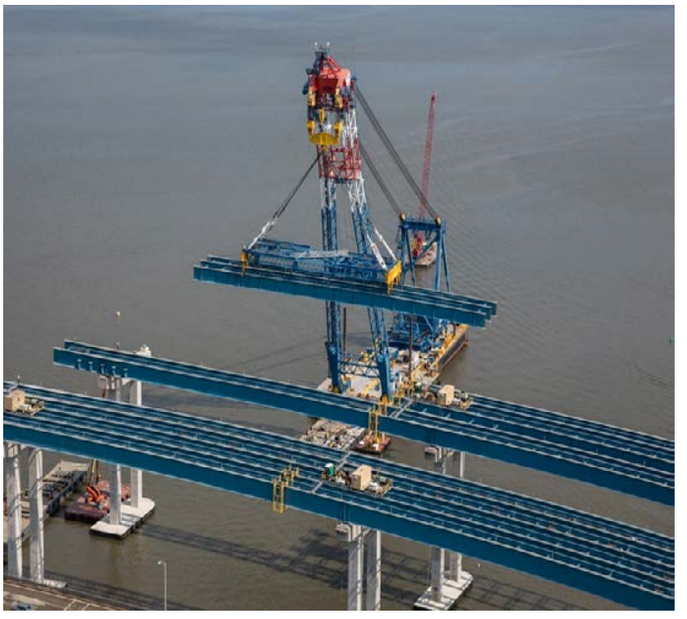


Figure 5 – Girder Assembly Erection Using the Lifter and the Hydraulically Controlled Lifting Frame

Most, but not all of the girder assemblies could be erected using the Lifter, and were traditionally erected on land by crawler cranes in smaller assemblies … except for one. On the Westchester side of the Hudson River is the first river pier, a land pier and the Westchester Abutment. Between the land pier and the first river pier lies the Metro-North Hudson Line railroad tracks. Running along the Hudson River banks, this extremely busy commuter line serves as a major transportation link between Westchester and New York City.

Land based cranes could not be positioned within the Metro-North right of way and effectively erect the Approach girders without fouling the track areas. Track shut downs would be limited and only allowed during minimal off-peak, nighttime periods. TZC developed an alternative girder installation method, they launched the girder assemblies over the Metro-North track areas.

The process began by erecting individual beams into a girder assembly on land and rolling it on a specially-designed track system just east of the Westchester Abutment, These assemblies were pushed west over the railroad tracks toward the first pier in the river. As the operation progressed, additional girders were connected and pushed westward until the assembly reached the first river pier. The entire operation took approximately three months, and work over the Metro-North tracks occurred during three Friday overnights. This approach maxim-

ized safety for both workers and the public and minimizes any potential impact to Metro-North Railroad and its passengers. Construction activities were suspended when trains passed through the area, and resumed when given the "all clear" instruction by Metro-North.

Following the girder assembly erection were the precast deck installation. In keeping with the modular approach to building the new Tappan Zee Bridge, over 6,600 precast deck panels were cast at off-site facilities and trucked to the Port of Coeymans fabrication facility and then barged to the work site.

Weighing as much as 74,000 pounds each, the approach span deck panels are 12 feet long, range between 22 and 45 feet wide and nearly 11 inches thick. When fully assembled, the deck panels for both the approach and main spans will comprise a surface area of more than 65 acres. The individual panels are joined together by pouring concrete around the galvanized steel reinforcement that extends out from each panel. The final driving surface will consist of a 1-inch Rosphalt overlay which will ensure durability and a safe, even ride for drivers (See Figure 6).



Figure 6 – Precast Deck Unit Installation on the Approach Spans

The final superstructure type is the twin cable-stayed structures. Work began with the installation of four large pre-assembled sections of steel, weighing nearly 340,000 pounds each, atop the main span crossbeams. These steel segments allowed the Main Span team to build out from the towers one section at a time, attaching stay cables to the structure along the way.

The new bridge utilized 192 stay cables to support the eastbound and westbound roadways on the main span. Crews first installed the casing with a single steel strand in place. Once the material is secured to anchor points in the main span towers and the steel girders of the road deck, workers installed additional strands through the casing, parallel to one another. The process continued until the casing is filled with strands.



Figure 7 – Erection of the Main Span Cable-Stayed Superstructure

Each side of the eight towers has 12 pairs of stay cables, ranging in length from 190 to 623 feet. The completed 2,230-foot main span supports a total of 74 million pounds of steel and concrete (See Figure 7).

7 CONCLUSIONS

Besides the construction of the actual bridge crossing, there are many more aspects to this project. For example, there are 36 existing buildings that are associated with the existing Tappan Zee Bridge. They range in function from NY State Police facilities to maintenance buildings. Some of these facilities will be maintained or replaced by TZC during the life of the project.

The facility component for the new Tappan Zee Bridge includes a new NYSTA consolidated maintenance and administration facility, a new facility for the New York State Police, and several electrical, communications and storage facilities. In addition, a temporary joint NYSTA/State Police facility will be established until construction of the new facilities are completed.

On August 25, 2017, 4 lanes of traffic from the existing Tappan Zee Bridge were shifted to the northernmost new bridge. This allowed a portion of the existing crossing to be demolished and the remaining tie in areas to be completed on the north-

ernmost new bridge. On October 6, 2017 when these areas were complete, the remaining 4 lanes of traffic were shifted to the new northernmost bridge. In this configuration, the new bridge carried all traffic from the original Tappan Zee Bridge.

Using the Lifter, demolition began on the existing bridge Approaches to allow the final tie in construction for the southerly new bridge to be completed. Demolition of the existing Tappan Zee Bridge will continue throughout 2018, and the second new bridge will be completed by June 2018.

Once complete, the 4 eastbound lanes will be shifted onto the newly completed bridge. This will be the final configuration with the eastbound and westbound traffic situated and separated on the two independent bridge crossings. The 100 year lifespan of the new Tappan Zee Bridge will begin.

REFERENCES

New York State Thruway Authority, 2013, Geotechnical Investigations, *The New NY Bridge Project Newsletter,* Issue 01, 2013: 8-12

New York State Thruway Authority, 2014, New York's Monumental Lifter, *The New NY Bridge Project Quarterly Magazine,* Fall 2014: 3-8

Maintenance, Safety, Risk, Management and Life-Cycle Performance of Bridges – Powers, Frangopol, Al-Mahaidi & Caprani (Eds)
© 2018 Taylor & Francis Group, London, ISBN 978-1-138-73045-8

A case study of early cracks of a concrete pylon

J.Song & X.F.Shi
Department of Bridge Engineering, Tongji University, Shanghai, China

ABSTRACT: The durability of concrete pylon is one of the key issues in the maintenance of cable-stayed bridges. However, a lot of wide cracks were produced at construction stage of many pylons, which may lead to a decrease in durability. The causes of cracks of a concrete pylon were studied in this paper. Firstly, the thermal parameters are identified by temperature test, and FEA method are adopted for simulation. It is proved that the hydration heat has a significant effect on cracking. The cracks are divided into two kinds: surface cracks and internal cracks. The surface cracks are caused by the sudden cooling during the formwork removal stage. The internal cracks are caused by the excessive temperature difference between segments. The analysis can provide reference for the prevention, treatment and maintenance of such structural.

1 INSTRUCTIONS

Pylon is a key component of the bridge with cable bearing system. Generally, it is built with segmental pouring method. According to the survey, the pylon is prone to produce a large number of cracks (Ma and Wang, 2002, Jing and Li, 2000, Gan, 2004) in construction stage, which seriously affects the appearance quality of structure. Part of the cracks has significant width, which may lead to a decline in structural durability.

The exorbitant hydration temperature in one of the main causes of cracks(Liu and Hu, 2017, Honorio et al., 2015). The control technology has been established in mass concrete, (ACI, 2007). However, crack control is not carried out much in the construction of pylon.

This paper mainly discusses the crack causes of a concrete pylon. After the construction of a segment, a large number of cracks were detected. The finite element model is established, which parameters are obtained by fitting the measured temperature, to verify the causes of cracks. The result of FEA simulation demonstrate that the main causes are the high temperature and lack of preventive measures.

The surface cracks are caused by the sudden cooling during the formwork removal stage. The internal cracks are caused by the excessive temperature difference between segments.

The deep cracks have adverse effects on structural durability and should be concerned in such structures. The case study in this paper can provide a reference for the prevention, analysis and maintenance of cracks.

2 DETAILS OF PYLON AND CRACKS

2.1 *Details of pylon*

This paper studies the lower part of the pylon. The total height of the lower part is 151.48m, horizontally divided into two limbs. The size of one limb is shown in Fig. 1. Longitudinal and horizontal dimensional proportion is 7:2. The middle of the section is hollowed. The solid area on both sides is 3×4m, and the thin wall is 8×1.5m.

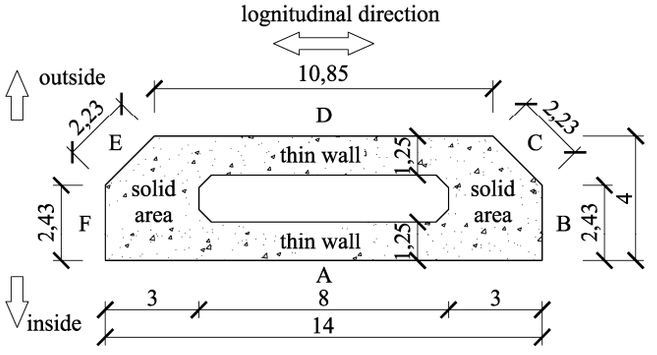


Figure 1. Size of section (unit: m)

The pylon used C50 grade concrete. Material consumption for one square: cement 336kg, fly ash 96kg, mineral powder 48kg, sand 714kg, gravel 1072kg, water 154kg. The adiabatic temperature rise is 58.3℃. The pylon is built segmentally. The height of one segment is between 4 to 6m. The outer surface is formed with WISA formwork (the material is wood), and the inner cavity is formed with steel formwork.

2.2 *Details of cracks*

This segments did not take any temperature control measures. The pouring height is 4.5m. The formwork were removed 4 days after pouring, and cracks are detected 10 days after pouring. The crack distribution are shown in Fig. 2.

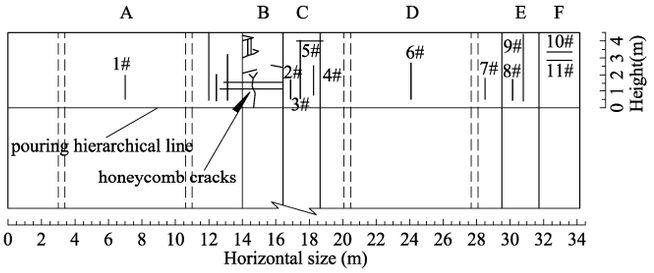


Figure 2. Unfolded surface of crack distribution

A and D are the outer surfaces of the thin wall. Vertical crack 1# and 6# are distributed in the center of these surfaces. The cracks rise from the interface of two layers of concrete with the height 2~3m and the width 0.1mm.

There are lots of cracks distributed on the surfaces of the solid area, such as B, C, E, F and sides of A and D. The side B is full of cracks, and most of the cracks are short with the width 0.05mm. There are 4 cracks in side C, 3 in longitudinal direction with crack length 1 to 4m and the crack width varies from 0.04 to 0.12mm. Another crack is distributed horizontally with crack length 1.4m and crack width 0.01mm. There are two longitudinal cracks distributed in side E, the crack length varies from 1.3～4m and the crack width is about 0.04mm. There are two horizontal cracks distributed in side F, its crack length is 1.5m and the crack width is about 0.09mm.

The detection shows that the cracks are characterized by large number and random distribution. The number of cracks in the solid area are more than that of the thin wall. The cracks on the solid area tend to be random, with different directions like horizontal, vertical and oblique, also the distribution is uneven. The cracks on the thin wall are more regularity, but the crack width is wider than solid areas.

3 CAUSE ANALYSIS OF CRACKS

3.1 *Finite element model*

Adopt ANSYS to establish finite element model of three segments of pylon. Single segment height is 4.5m. Considering the symmetry of the structure, half model is established. Element type of thermal analysis is Solid70. When stress analysis is conducted, the element is converted to Solid45. See the features of model and element in Fig.3.

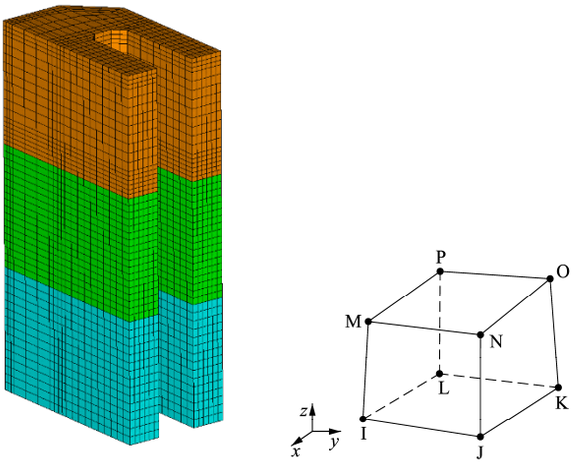


Figure 3. Finite element model and element characteristics

3.2 *Identification of parameters*

The basic formula of temperature calculation are as follow (Zhu, 2012, Kaviany, 2002):

$$\rho c\frac{\partial T}{\partial t}=k\nabla^2 T+\frac{dQ}{dt} \tag{1}$$

$$Q=Q_0\left(1-e^{-\gamma t}\right)=c\rho T_{abs}\left(1-e^{-\gamma t}\right) \tag{2}$$

where, T =temperature, t =time, ρ = density, c = specific heat capacity, λ = heat conductivity coefficient, Q = quantity of heat, Q_0 = total heat of concrete hydration reaction, γ = hydration reaction rate, and T_{abs} = increase in adiabatic temperature.

The concrete heat conduction equation requires a limit to the first and third boundary conditions. The first boundary condition is used to describe the initial temperature field of concrete pouring. The third boundary condition is used to describe the surface heat loss when the concrete makes contact with the fluid.

$$T\left(0\right)=T_0\left(x,y,z\right) \tag{3}$$

$$q=-\lambda\frac{\partial T}{\partial n}=\beta\left(T-T_f\right) \tag{4}$$

where, q = heat loss on a concrete surface, $\boldsymbol{n}$ =the outer normal direction on the surface, T_f = the fluid temperature, and β = convective heat transfer coefficient.

Table 1. Value of parameters

Para.	Value*	Para.	Value*	Para.	Value*
c	960	$T_{0,\ \text{pylon}}$	25	$\beta_{\text{wood formwork}}$	2
λ	2.33	T_{water}	22	$\beta_{\text{steel formwork}}$	5
γ	1.5	T_{air}	25	$\beta_{\text{top surface}}$	10
T_{abs}	58.3	β_{pipe}	380	β_{surface}	10

* In addition to temperature in degrees Celsius, the other parameters are used in international units.

The parameters are fitted by temperature monitoring. The final parameters are shown in Table 1. The

water temperature of the pipe and the air temperature are using the average value.

The measured data and simulation results are compared in Fig. 4.

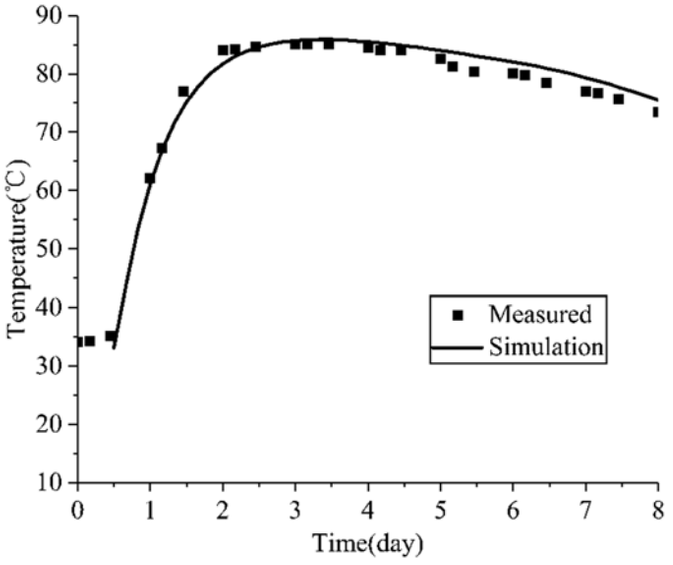


Figure 4. Actual measured data and simulation results

The heat transfer coefficient of the exposed surface (under shade) is calculated by using the following formula (Liu, 2006):

$$\beta_{surface} = 3.46v + 6.02 \tag{5}$$

where, v = the wind speed, here adopt 1m/s.

The coupling effect of temperature and material characteristics should be considered in early age concrete, and the relevant model of CEP-FIP is used to calculate.

$$t_T = \sum_{i=1}^{n} \Delta t_i \exp\left[13.65 - \frac{4000}{273 + T(\Delta t_i)/T_0}\right] \tag{6}$$

where, t_T = the temperature adjusted concrete age which replaces t in the corresponding equations, Δt_i is the number of days where a temperature T prevails, $T(\Delta t_i)$ is the temperature during the time period Δt_i, T_0=1℃.

Creep is calculated by relaxation coefficient. The relaxation coefficient is used to describe the phenomenon that the stress decreases gradually with the extension of time when the concrete is subjected to the forced strain.

$$\varepsilon(t) = \frac{\sigma(\tau_0)}{E(\tau_0)} + \sigma(\tau_0)C(t,\tau_0) + \int_{\tau_0}^{t} J(t,\tau)\frac{d\sigma(\tau)}{d\tau}d\tau \tag{7}$$

When the strain in formula 7 remains constant, the formula can be written as follows:

$$\sigma(\tau_0)C(t,\tau_0) + \int_{\tau_0}^{t} J(t,\tau)\frac{d\sigma(\tau)}{d\tau}d\tau = 0 \tag{8}$$

When $\sigma(\tau_0)$=1, the relaxation coefficient can be solved by formula 8. The relaxation coefficient provided by the literature is adopted here (Zhu 2012):

$$\begin{aligned} K(t,\tau) = 1 &- \left(0.25 + 0.25\tau^{-0.4}\right)\left[1 - e^{-0.2(t-\tau)}\right] \\ &- \left(0.15 + 0.3\tau^{-0.4}\right)\left[1 - e^{-0.006(t-\tau)}\right] \end{aligned} \tag{9}$$

where, $K(t,\tau)$ = relaxation coefficient when moment τ is loaded into moment t. $\sigma(t)$ = residual stress at t moment. $\sigma(\tau)$ = transient stress at τ moment.

The relaxation coefficient curve is shown in Fig.5.

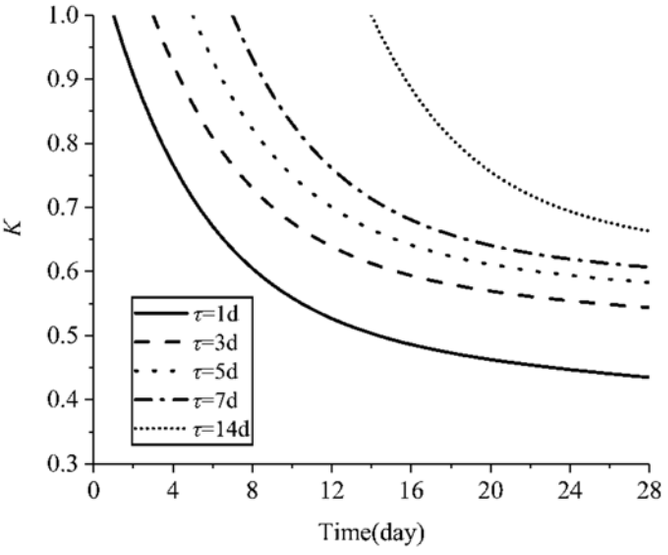


Figure 5. The relaxation coefficient

Time effects are also considered. The relative strength and the modulus of elasticity of concrete at various ages can be estimated form formula 10 to 13 (CEB-FIP, 2010).

$$f_{tk}(t) = \beta_{cc}(t) f_{tk} \tag{10}$$

$$\beta_{cc}(t) = \exp\left\{0.25\left[1 - \left(\frac{28}{t}\right)^{1/2}\right]\right\} \tag{11}$$

$$E_{ci}(t) = \beta_E(t) E_{ci} \tag{12}$$

$$\beta_E(t) = \left[\beta_{cc}(t)\right]^{0.5} \tag{13}$$

where, $f_{tk}(t)$ = the mean concrete strength at age of t days, f_{tk} = the mean strength after 28 days, $E_{ci}(t)$ = the modulus of elasticity at an age of t days, E_{ci} = the modulus of elasticity at an age of 28 days, $\beta_{cc}(t)$ and $\beta_E(t)$ are coefficients which depends on the age of concrete t, t = the age of concrete adjusted according to formula 6.

In addition, the stress calculation takes into account the gravity and the construction step. The value of elastic modulus and tensile strength of 28 days are obtained by experiment. E_{ci} =5.36×10^{4}MPa, f_{tk} =3.9MPa.

3.3 *Causes of cracks*

The temperature of the internal of the solid, the surface of the solid and internal of the thin wall are shown in Fig. 6.

The internal of the solid and internal of the thin wall are affected by high hydration heat, and the temperature rose up to 70~78 ℃ within 2 days. Then under the influence of natural cooling, the solid area cools slowly, thin wall cools faster simultaneously.

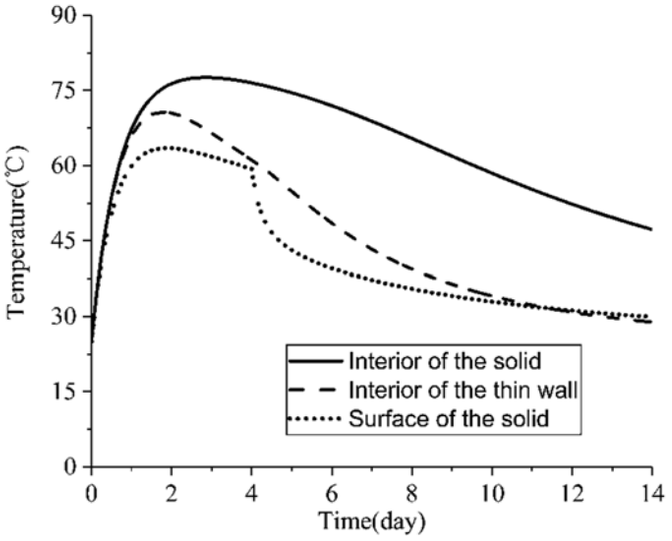


Figure 6. Temperature variation curve of typical position

The maximum temperature of surface is 64 ℃. After the formwork is removed in the fourth day, the temperature decreases sharply to 15℃ within 1 day.

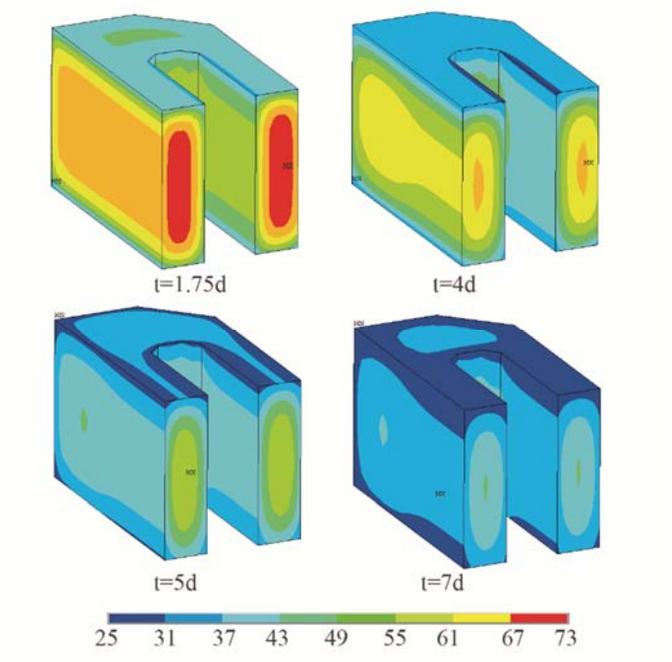


Figure 7. The change of temperature field (Unit:℃)

In fact, the structure is affected by non-uniform temperature field which changes with time. There are mainly 4 stages, as shown in Fig.7. The first stage is the temperature rising stage, when the internal is generally in high temperature state, and the temperature of the surface is much lower. The second stage is cooling stage, the heat is emitted from the surface, and the internal and surface temperature are gradually cooled. The third stage is rapid cooling stage, after the removal of formwork, the temperature of surface decreases sharply. The last stage is chill stage, the surface and interior temperature approach the ambient temperature gradually.

There are two kinds of temperature difference for pylon, one is the temperature difference between the current segment and base segment, and the another is the temperature difference between the internal and the surface. Due to the inhomogeneity of temperature field distribution, the temperature effect is complex. Only the solid finite element method can reflect the specific influences of these two kinds of effects. The stress results are shown in Fig.8.

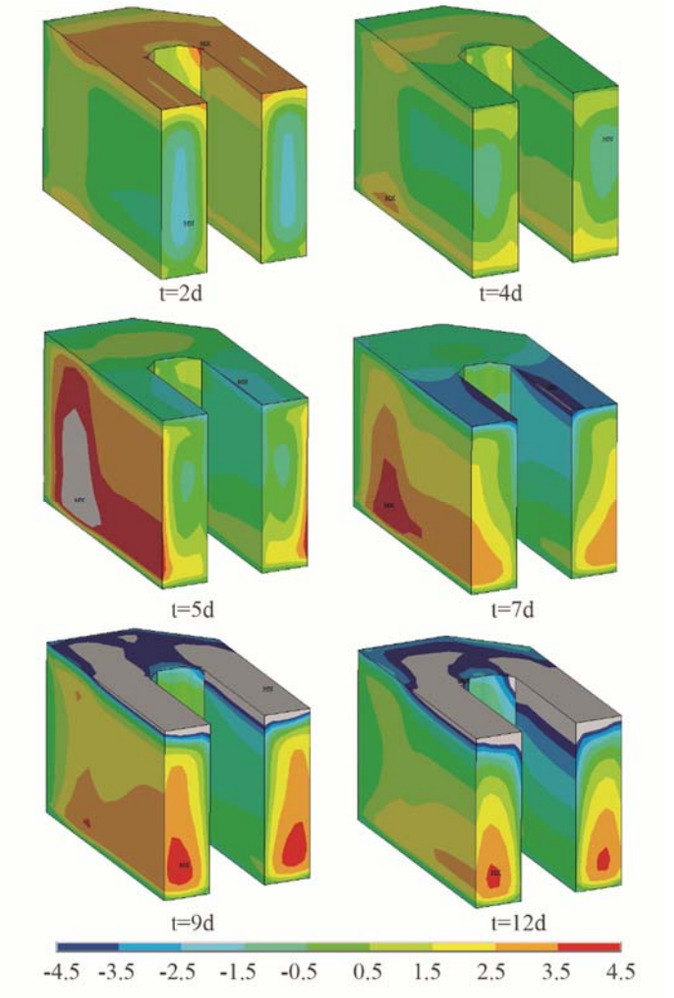


Figure 8. The horizontal stress distribution (Unit: MPa)

Temperature rise stage (0~2d): The internal of the thin wall is compressed, and the temperature gradient of surface produces small tensile stress.

Cooling stage (2~4d): The internal compressive stress gradually decreases, and tension occurs in the joint surface.

Rapid cooling stage (5d): The surface temperature decreases rapidly, the tensile stress exceeds 4.5MPa, and the tensile effect of solid is larger than that of thin wall.

Chill stage (5~10d): The temperature continues to decrease, when the temperature of the upper segment rises. The temperature difference causes the gradual expanding internal tensile.

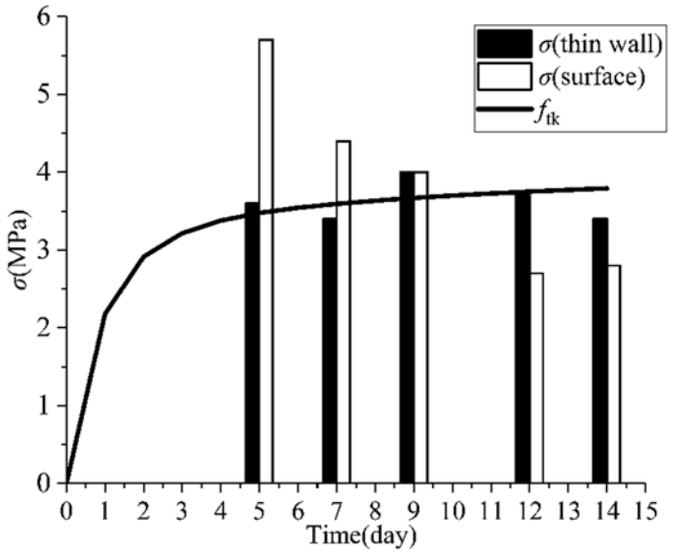


Figure 9. Tensile stress and tensile strength

The stress results are consistent with the crack detection results. The assumed crack development process is: after the formwork removes (5~7d), the cracks appear on the surface of the solid area, and the vertical cracking occurs on the surface of the thin wall. There are only 1 vertical crack on the thin wall, which may be caused by the stress releasing after the cracking. As the temperature continues to decrease (9d), cracks extend to the interior. The tensile stress and tensile strength are summarized in Fig. 9.

3.4 *Discussion*

As can be seen from the analysis, the crack is mainly produced in the form removal stage. However, insulation measures are adopted in some pylons, which may inhibit the creation of cracks.

Adopt the same finite element model to calculate the stress under the condition of heat preservation.

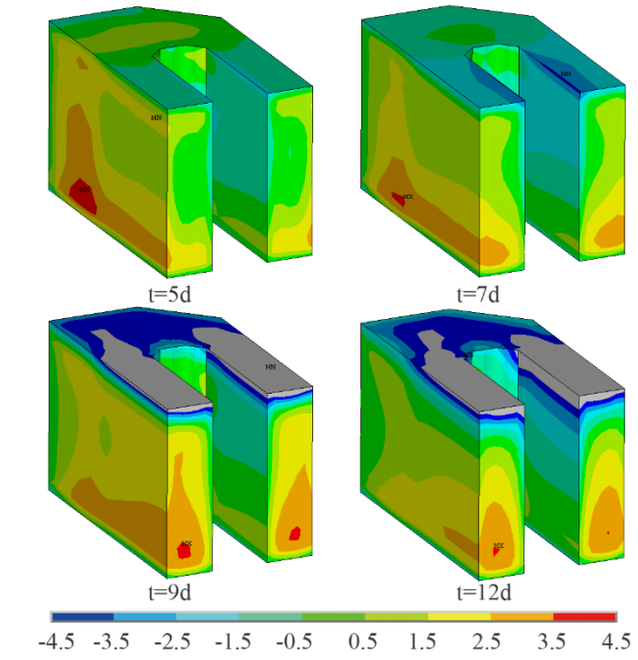


Figure 10. The stress under thermal insulation condition

After the template was removed on day 5, the surface stress was significantly reduced compared to the uninsulated condition. The surface stress of the solid is reduced to 3.5MPa, and the surface stress of the thin wall is reduced to 2.6MPa.

With the cooling process, the internal tensile stress of the thin wall increases gradually. And the stress reached a peak of 3.6MPa on the 9th day, as shown in Fig.10.

The insulation measures can only reduce the number of cracks, but may not avoid the cracks. Moreover, the risk of internal cracks is not reduced for the thin wall.

Reduce the temperature rise of the pylon could be an effective method to control thermal cracks. Fig.11 shows the stress when the adiabatic temperature rise is adjusted to 40℃. The surface stress is reduced to below 4MPa, and the internal stress of the thin wall is reduced to less than 3MPa.

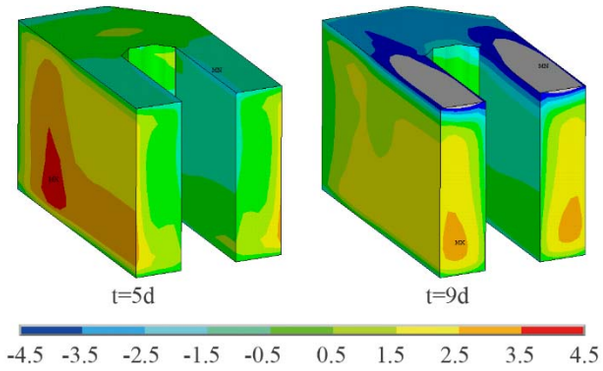


Figure 11. The stress after reducing temperature rise

A series of control measures have been adopted: (1) 0 to 2 days: using pipe cooling to decrease the temperature rise. (2) 4 day: remove the formwork and wrap the segments with oilcloth. (3) 4-14 days: keep the oilcloth sealed to make the temperature drop slowly. (4)14 day: end the protection. No cracking occurs in subsequent sections, and the early cracks in the bridge pylon can be avoided.

4 CONCLUSION

The causes of cracks of a concrete pylon are mainly discussed in this paper, and the conclusion is as follows:

1) The pylon is characterized with quick temperature rise and higher temperature, which are the main causes of the surface cracking and the internal cracking.

2) The surface cracks are generated in the formwork removal stage, resulting from sudden temperature decrease. The internal cracks of the thin wall are generated in chill stage, caused by inter-segment constraints.

3) The control measures are applied in the subsequent segments, and no cracks are occurred.

Hydration heat is one of the main causes of cracks. Some cracks may develop deep and have adverse effects on structural durability. The analysis of this paper can provide reference for the prevention, treatment and maintenance of such structural.

5 REFERENCES

ACI (2007). Report on thermal and volume change effects on cracking of mass concrete. *ACI 207.1R-07*. American.

CEB-FIP (2010). CEB-FIP Model Code 2010. Breat Britain: Redwood Books.

GAN, Y. P. (2004). Analysis and Cracks Treatment of the substructure of the Pylon in Yiling Cable-stayed Bridge. *Transportation Science and Technology,* 3**,** 51-53.

HONORIO, T., BARY, B. & BENBOUDJEMA, F. (2015). Factors affecting the thermo-chemo-mechanical behaviour of massive concrete structures at early-age. *Materials and Structures,* 49**,** 3055-3073.

JING, B. L. & LI, S. L. (2000). Study on Crack Control of the North Tower of Jingzhou Yangtze River Highway Bridge. *East China Highway,* 6**,** 26-27.

KAVIANY, M. (2002). *Principles of heat transfer,* New York, John Wiley & Sons Inc.,.

LIU, J. Y. & HU, G. W. (2017). Research on the Control Technoloy in Cracking Prevention of 100 Meter High H-type Cable Tower. *Journal of railway engineering society,* 1**,** 60-66.

LIU, Z. Q. (2006). *Research for Convection Heat Transfer on the Surface of Concrete Structure.* Master, Tongji University.

MA, C. S. & WANG, P. (2002). Analysis of Crack Causes of Certain Bridge Tower. *Highway,* 8**,** 44-47.

ZHU, B. F. (2012). *Temperature Stress and Temperature Control of Mass Concrete,* Beijing, China Water & Power Press.

Maintenance, Safety, Risk, Management and Life-Cycle Performance of Bridges – Powers, Frangopol, Al-Mahaidi & Caprani (Eds)
© 2018 Taylor & Francis Group, London, ISBN 978-1-138-73045-8

A case study of using a support vector machine on bridge inspection data

Arong & S. Murakami
Head Office for Information Management of Gifu University, Gifu City, Gifu Prefecture, Japan
Yiliguoqi
Mechanical and Civil Engineering Division of Gifu University, Gifu City, Gifu Prefecture, Japan

ABSTRACT: In Japan, regional governments manage 70% of all road bridges (over 700,000 road bridges), and half of these bridges will be in their service life in the near future. However, regional governments lack the resources (in finances, specialists, and technologies) that are needed to maintain this many bridges. Therefore, it is necessary to develop a practical method of bridge integrity evaluation to assess the degree of a bridge superstructure's structural health. This paper proposes a bridge integrity evaluation method by applying support vector machines (SVMs) of artificial intelligence (AI) techniques. This paper proposes that bridge integrity evaluation methods provide bridge inspectors and engineers with a more reliable and efficient bridge structural health assessment approach.

1 INTRODUCTION

1.1 *Background*

Japan has over 700,000 road bridges; 70% of these bridges are situated on the regional roads and are managed by regional governments. Many of these regional bridges were constructed during the high economic growth period (from the mid-1950s to the early 1970s), and about 40% of these bridges will be over 50 years old in 10 years (The Road Committee of the Panel on Infrastructure Development 2014). Furthermore, regional governments' maintenance budgets are limited. Regional governments usually have a shortage of financial resources, specialists, and technologies. Thus, developing practical bridge maintenance programs for regional governments is an important issue. To address this issue, this paper proposes using artificial intelligence (AI) techniques to analyses a priority assessment of structure's inspection items; this will assist bridge engineers when they assess a bridge's integrity. This would be a great approach for regional governments.

1.2 *Overview and scope of the study*

For a bridge management system (BMS), there are three modules: management, assessment, and maintenance. Management always controls inspection data. Assessment is used to analyse the condition of quality, life cycle cost, cost benefits, and the priority of a bridge's maintenance. The maintenance module is the result of management and assessment when conducting efficient site works. Each BMS depends on their efficient bridge inspections. Bridge inspectors use their judgment to evaluate and appraise maintenance problems and critical deterioration on site. This responsibility is based on the assumption that the individual bridge inspector has a sound understanding of bridge inspection, maintenance, and rehabilitation requirements (Arong et al. 2014).

Additionally, in 2007, the Minister of Land, Infrastructure, Transport and Tourism (MLIT) started a subsidy program for regional governments to establish long-term bridge maintenance programs. In this program, prefectures conduct bridge inspection programs that follow the MLIT's protocol; bridges on arterial routes that carry large volumes of traffic are inspected periodically for every five years. However, some regions still do not inspect their bridges; others conduct inspections, but inspection protocol and quality are not standardized (Masahiro et al. 2013). According to the Regular Inspection Procedure for Road Bridge (2014), which is regulated by the MLIT, the Gifu Prefecture conducts regular inspections (every five years) of all bridges that span longer than 2 meters once.

Over the past few years, several experimental studies on the evaluation of bridge integrity with AI techniques have been carried out by researchers. Reviewing the techniques in Japan, Oishi H analysed slope data using the support vector machine (SVM) of an AI technique; this was done to evaluate a risk of dangerous spots for sediment related disaster by learning the data of each slope. The results showed that an SVM can evaluate a risk with higher precision than a conventional rating method (Oishi et al. 2007).

Chikata Y compared an SVM with learning vector quantization (LVQ) to examine the evaluation of bridge integrity with pattern recognition (Chikata et al. 2007). Sugimoto H proposed estimating the synthetic safety of infrastructures by using an SVM (Sugimoto et al. 2009). The Yuki K research group analysed the inspection and repair records of bridges' expansion joints with an SVM; this was done to evaluate judgement criteria for repairing civil engineering structures. Due to the Yuki K study, the setting method using an SVM is an effective tool for the maintenance management plan of civil engineering structures; this is because the method has high integrity due to the structure's evaluation by a professional engineer (Yuki et al. 2012). In the above studies, the SVM was introduced; it can be an effective tool for the maintenance management plan of civil engineering structures. Regional governments face a lack of economic resources and bridge maintenance engineers; as a result, researchers are focusing on numerical simulations using an SVM to estimate bridges' integrity and the priority of their maintenance repairs. However, it is almost impossible to replace bridge experts with AI techniques when estimating bridge integrity in the current situation regarding technical. Therefore, studying the weight of inspection items' priority, which uses the SVM to estimate bridge integrity to assist regional governments, is vital for the maintenance of bridge infrastructure.

In this study, we propose the efficient health integrity evaluation method for bridge structure members. We applied an SVM to determine the weight priority of inspection items; this was done to assist regional governments in assessing bridges' integrity. The SVM was used to classify bridge structure members' health. The input data were the deterioration degrees of items in the detailed site inspection on structure member; the output data were the bridge structural members' degree of health. As a numerical example, 124 pieces of inspection data of the steel composite girder bridge in the Gifu prefecture were used. Keeping a balance between correctly classified accuracy and Receiver Operating Characteristic (ROC) curves enabled the weight assessment of the bridge structure members' inspection items to combine. It was found that the combined weight of bridge structure members' inspection items provides bridge inspectors and maintenance engineers with a more reliable and efficient bridge structural health assessment approach.

2 THEORETICAL BACKGROUND

2.1 *Introduction to SVMs*

An SVM is a type of binary supervised machine learning. It is also a type of AI algorithm. Recently, SVMs have received a great deal of attention, and they demonstrated excellent performance in terms of pattern classification. SVMs are based on the induction principle of structural risk minimization, which aims to minimize a test error by controlling two contradictory factors: a functional risk from empirical data and a capacity for the set of real-valued functions (Cortes et al. 1995; Vapnik et al. 1998).

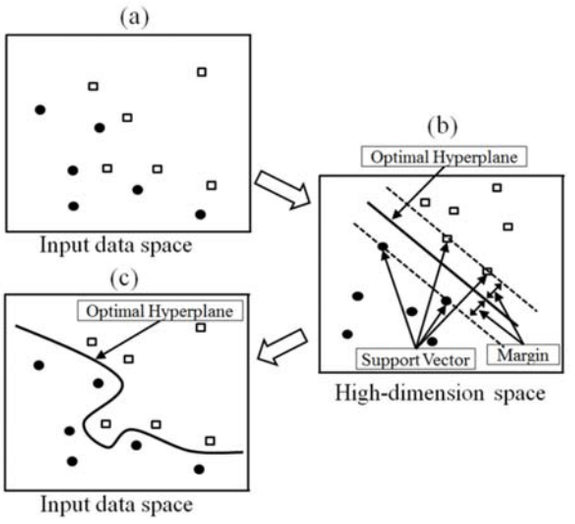


Figure 1. SVM concept diagram

An SVM algorithm aims to find the optimal separating hyperplane that effectively separates the data points into the labelled classes (see Fig. 1). Let us consider that we have a binary classification problem. Fig.1-(a) shows a mapping input space of non-separable data points. For convenience, we can assume the labels are +1 (positive examples) or –1 (negative examples). What follows χ denotes a vector with a component x_i. The notation x_i will denote the i^{th} vector in a dataset $\{(x_i y_i)\}_{i=1}^{n}$, where y_i is the label associated with x_i. The naive way of making a non-linear classifier out of a linear classifier is to map our data from the input space χ to a feature space F using a non-linear function $\Phi: \chi \rightarrow F$ (see Fig.1-(b)). SVMs operate by finding a linear hyperplane that separates the positive and negative examples with a maximum interclass distance or margin. The discriminant function in the feature space F can be considered as follows (Ben-Hur et al. 2010):

$$f(x) = \sum_{i=1}^{n} \alpha_i \kappa(x, x_i) + b \tag{1}$$

where b is the model bias. Note that only those points that lie closest to the hyper-plane have α_i and consist the support vectors. In the case of non-separable data, a soft margin hyperplane is defined to allow errors ξ_i (slack variable) in classification. Hence, the optimization problem is formulated as follows (Ben-Hur et al. 2010):

$$\underset{w,b}{\text{minimize}} \frac{1}{2}\|w\|^2 + c\sum_{i=1}^{n}\xi_i \qquad (2)$$
$$subject \quad to: y_i\left(w^T x_i + b\right) \geq 1-\xi_i, \xi_i \geq 0.$$

where $\xi_i \geq 0$ are slack variables that allow an example to be in the margin ($0 \leq \xi_i \leq 1$, also called a margin error) or to be misclassified ($\xi_i > 1$). Since an example is misclassified if the value of its slack variable is greater than 1, $\sum_i \xi_i$ is a bound on the number of misclassified examples. Our objective of maximizing the margin, i.e., minimizing $\frac{1}{2}\|w\|^2$ will be augmented with a term $C\sum_i \xi_i$ to penalize misclassification and margin errors. The trade-off between maximization of the margin and minimization of error is controlled by cost parameter C (Burges et al. 1998; Drosou et al. 2014). In this way, classification is performed by the optimal hyperplane at a high-dimensional space. As a result, the nonlinear separation is performed in the original input space (see Fig.1-(c)).

In a nonlinear case, a kernel function is introduced to map the low-dimensional input space to the high-dimensional feature space. There are many possible choices of the kernel functions, such as the linear, polynomial, radial basis function (RBF), and sigmoid function. In this study, the RBF kernel (Gaussian kernel) given by the following function was used:

$$f(x) = \sum_{i=1}^{n} \alpha_i \kappa(x, x_i) + b \qquad (3)$$

where $\gamma > 0$ is a parameter that controls the width of Gaussion. When designing an SVM, one must choose a kernel function, set kernel parameters γ, and determine a soft margin constant C (penalty parameter). The Grid algorithm is an alternative to finding the best C and γ when using the RBF kernel function (Ben-Hur et al. 2010).

In this study, we decided to classify the bridge structure members' health into two classes ("Good" and "Poor") and then training the model.

2.2 *The ROC curve*

The ROC curve was introduced by the signal processing community in order to evaluate the capability of a human operator; this was done to distinguish an informative radar signal from noise. The ROC curve has mostly been used in the medical decision-making community to assess the usefulness of diagnostic tests (Rakotomamonjy et al. 2004).

Traditionally, the evaluation of a learned model is done by minimizing the estimation of a generalization error or some other related measures. However, the accuracy (the rate of correct classification) of a classifier is the most frequently used performance measurement (Rakotomamonjy et al. 2004). The ac-curacy can be obtained from the confusion matrix, as shown in Table 1. The accuracy can be considered as follows:

$$Accuracy = \frac{TP+TN}{TP+FP+FN+TN} \qquad (4)$$

where TP (True Positives) is positive records that correctly predicted as positive. FN (False Negatives) is positive records that incorrectly predicted as negative. FP (False Positive) is negative records that in correctly predicted as positive. TN (True Negatives) is negative records that correctly predicted as negative.

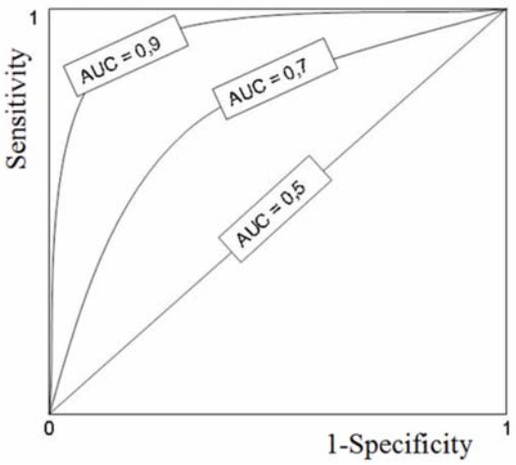


Figure 2. The ROC curve (refer Simundic et al. 2012)

Obtaining the optimal balance classification ability is described effectively in terms of sensitivity (or true positive rate or positive class accuracy) and specificity (or true negative rate or negative class accuracy) as follows:

$$Sensitivity = \frac{TP}{TP+FN} = 1 - Type\ II\ error \qquad (5)$$

$$Specificity = \frac{TN}{TN+FP} = 1 - Type\ I\ error \qquad (6)$$

More precisely, sensitivity measures the proportion of actual positives that are identified correctly. Specificity measures the proportion of actual negatives that are identified correctly.

Table 1. Confusion matrix

		Predicted Class	
		Positives	Negatives
Actual Class	Positives	TP	FN
	Negatives	FP	TN

Table 2. Interpretation of the AUC Curves (refer Simundic et al. 2012)

AUC	Diagnostic Accuracy
0.9-1.0	Excellent
0.8-0.9	Very good
0.7-0.8	Good
0.6-0.7	Sufficient
0.5-0.6	Bad
<0.5	Test not useful

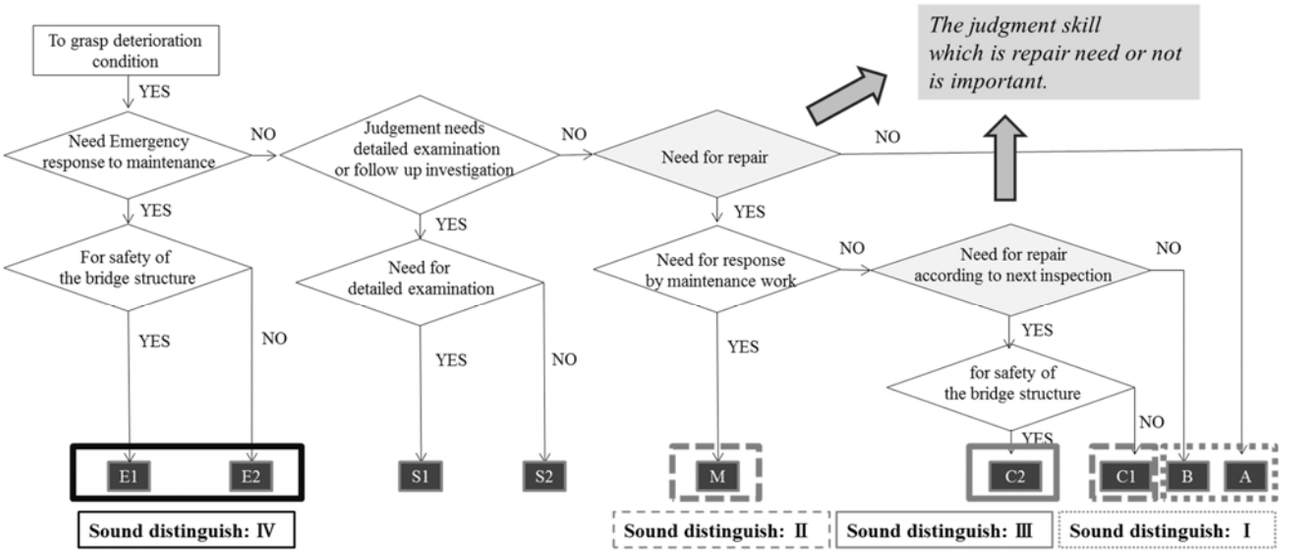


Figure 3. Sound distinguish flow

In addition, the trade-off between sensitivity and specificity can be represented graphically as an ROC curve. It can be understood as a plot of the probability of correctly classifying the positive examples against the rate of incorrectly classifying true negative examples. The ROC curve can be constructed by plotting these pairs of values on the graph with 1-specificity on the x axis and sensitivity on the y axis. In fact, when the data are strongly unbalanced, accuracy may be misleading, since the all-positive or all-negative classifier may achieve a very good classification rate. Situations in which datasets are unbalanced arise frequently in real-world problems; in these cases, model evaluation is done with criteria other than accuracy. Metrics extracted from ROC curves, such as the area under the ROC curve (AUC), can be a good alternative for model evaluation; this is because the ROC curve can determine the difference between errors on positive or negative examples (Rakotomamonjy et al. 2004).

Ana-Maria Simundic's (Simundic et al. 2012) study on diagnostic accuracy shows the shape of an ROC curve, and the AUC helps us estimate how high the discriminative power of a test is. The area under the curve can have any value between 0 and 1, and it is a good indicator of the overall quality of the test. A perfect diagnostic test has an AUC of 1.0, whereas an excellent test has an AUC around 0.9 to 1.0, a very good test has an AUC around 0.8 to 0.9, a good test has an AUC around 0.7 to 0.8, a sufficient test has an AUC around 0.6 to 0.7, a bad test has an AUC around 0.5 to 0.6, and a useless test has an AUC of 0.5 or less than 0.5. Generally, the relation between AUC and diagnostic accuracy (as described in Table 2) and the ROC curve can be plotted like in Fig. 2 (Simundic et al. 2012). In our study, the AUC rating was determined according to Table 2.

3 CASE STUDY ON SMALL AND MEDIUM BRIDGES

3.1 *Visual inspection of bridges*

There are approximately 700,000 road bridges in Japan, and ministerial orders stipulate that close visual inspections of all components should be conducted every five years (Tamakoshi et al. 2015). The Gifu Prefecture tried a unique bridge inspection method by remote viewing with binoculars; they also created a unique bridge inspection manual (Road Maintenance Division of Gifu Prefecture Government 2010) to ensure appropriate inspection accuracy (Hosoe et al. 2006).

According to the Regular Inspection Procedure for Road Bridge (2014), which is regulated by the MLIT, all bridges in Japan with a span longer than 2 meters must be inspected at least once every five years. In response to this, the Gifu Prefecture revised the Revision Bridge Inspection Manual (Ministry of Land, Infrastructure, Transport and Tourism 2014; Road Maintenance Division of Gifu Prefecture Government 2016). To plan the priority maintenance scheme, the bridge's integrity and degree of deterioration are needed in order to make engineering decisions. Maintenance urgency ratings are diagnoses given by experienced engineers in a very subjective manner, recommending necessary actions that should be completed by the next inspection (Masahiro et al. 2013).

For every structural member in each bridge span, the results of a sound diagnosis can be categorized into one of four ranks, which are listed in Table 3. In the new criteria, a bridge's sound diagnosis has four levels, which are Ⅰ, Ⅱ, Ⅲ and Ⅳ, corresponding to the conventional criteria. In the conventional criteria, a bridge's sound diagnosis has five levels, which are

denoted in Arabic numerals as 5, 4, 3, 2, and 1, respectively. The flow of remedial work urgency ratings is shown in Fig. 3. From the flow, bridge need for response by maintenance work and also bridge need for repair according to next inspection shows a bridge inspector's required knowledge and judgement skill, which helps determine whether the bridge's owners need to repair the bridge. It is important to distinguish the soundness rank as being Ⅰ, Ⅱ, or Ⅲ.

In our study, we followed the conventional criteria to classify structure members' degree of health. Table 4 shows the standard for classifying inspected members. Additionally, we focused on the main girder of the single-span steel girder bridge as well as the multi-span continuous steel girder bridges. Table 5 shows the standard deformation type. We only examined steel members (steel girders) in this study.

Table 3. Diagnosis of soundness in Gifu prefecture

New Criteria		Description	Refer Conventional Criteria	
Ⅰa	Good	No obstacle to the function of the structure.	5	Health
Ⅰb			4	Almost health
Ⅱ	Preventive maintenance phase	There is no obstacle to the function of the structure, but it is desirable to take preventive maintenance.	3	Start repair: Deterioration occurs
Ⅲ	Early rehabilitation phase	There is a possibility that the function of the structure may be hindered, so a rehabilitation strategy must be taken.	2	Intermediate repairs required: Large deterioration
Ⅳ	Emergency repair phase	Presence of an obstacle to the function of the structure, or a possibility of occurrence is extremely high. An urgent action must be taken.	1	Possible structure failure: Critical deterioration

Table 4. Standard of classifying inspected members

Damage classification					
superstructure			substructure	bearing	others
Main girder	Cross beam	slab			

Table 5. Standard deformation type

Material type	Deformation type
Steel member	Corrosion, crack, fracture, others
Concrete member	Cracks, cracks on the slab, others
others	Dysfunction of bearing, others

3.2 *Numerical analysis results using the SVM*

In this study, we statistically analysed the two categorized levels of health; the classified levels ("Good" and "Poor") were found on the main girder of steel girder bridges; this was based on actual bridge inspection data from the Gifu Prefecture. In this study, the priorities of the inspection items through the SVM analyses are examined using the bridge structural health assessment by professional inspector. These analyses were obtained through the SVM analysis software Waikato environment for knowledge analysis (WEKA) version 3.9. We conducted this experiment by using the classification solver in a library for support vector machine (LIBSVM) with a grid search optimal parameter. The input data were the degree of deterioration for each span girder's inspection item, and the output data were the main girder's degree of health. As a numerical example, 124 pieces of inspection data of steel bridges in the Gifu Prefecture were used. We represented a "Good" health class with "Y" if the health rating of conventional criteria was equal to or greater than 4. If the health rating was less than 4, it was "Poor". For the inspection data of this study, health integrity was assessed by seven inspectors. The inspection attributes and class label are shown in Table 6. The optimal parameter is shown in Table 7.

Table 6. List of features and class label

Feature	X_1	section location: 1 = edge part, 0 = middle of span, -1 = intermediate support
	X_2	construction year, years
	X_3	painting year, years
	X_4	deformation of main girder (health rating: 1, 2, 3, 4, 5)
	X_5	missing bolt (health rating: 1, 2, 3, 4, 5)
	X_6	abnormality of joint gap (health rating: 1, 2, 3, 4, 5)
	X_7	deterioration of corrosion protection (health rating: 1, 2, 3, 4, 5)
	X_8	corrosion in main girder (health rating: 1, 2, 3, 4, 5)
Label	Y	poor (health rating: 1, 2, 3), good (health rating: 4, 5)

Table 7. Parameter C and γ

Inspector	C	γ
Training data	1000	1.0
Testing data	1000	1.0

In this study, we used feature combinations to indicate some relationships. Because all feature meanings were available, we were able to manually identify some useful pairs of features. We used the training data, which was from an experienced inspector, to test the effectiveness of different feature combinations by predicting the class label of "Y". To estimate a feature's importance, we exploited the performance measurement of AUC, which was conducted for each combined feature.

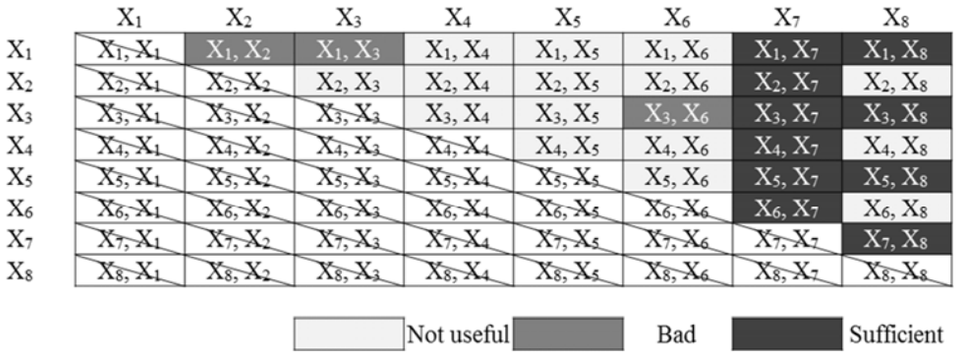


Figure 4. Useful attribute combines

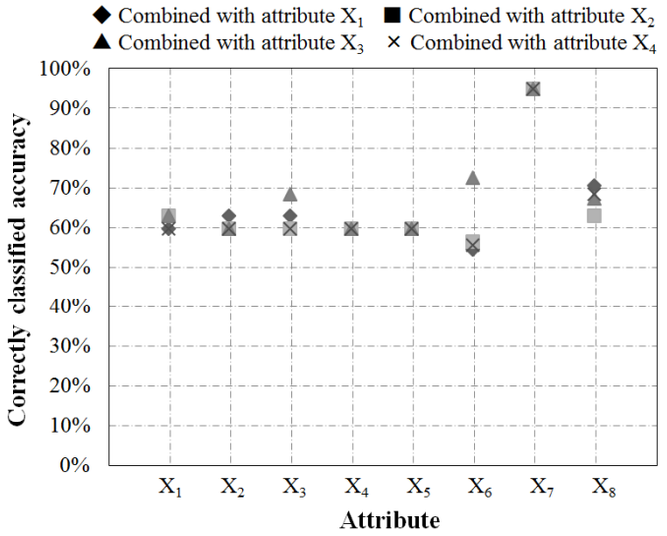


Figure 5.1. Correctly classified accuracy of combined attribute X_1, X_2, X_3, X_4

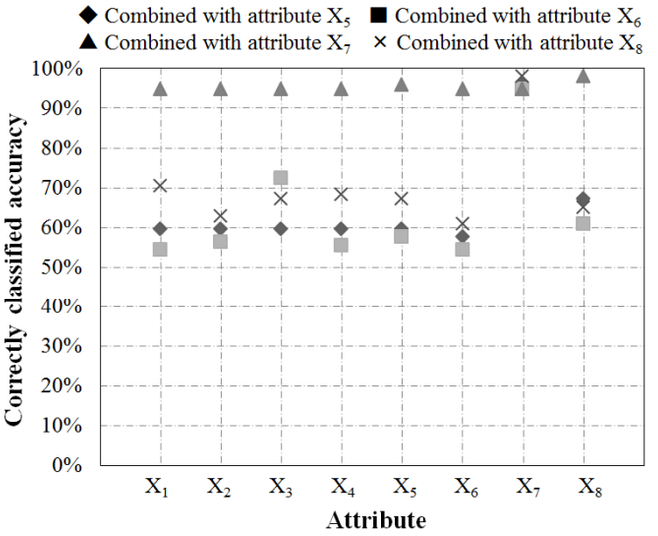


Figure 5.2. Correctly classified accuracy of combined attribute X_5, X_6, X_7, X_8

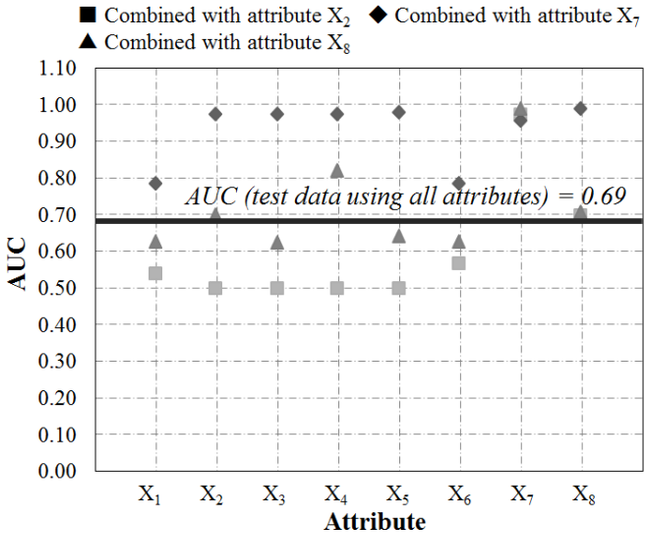


Figure 6.1. AUC of good level (health rating:4,5) which combined with attribute X_2, X_7, X_8

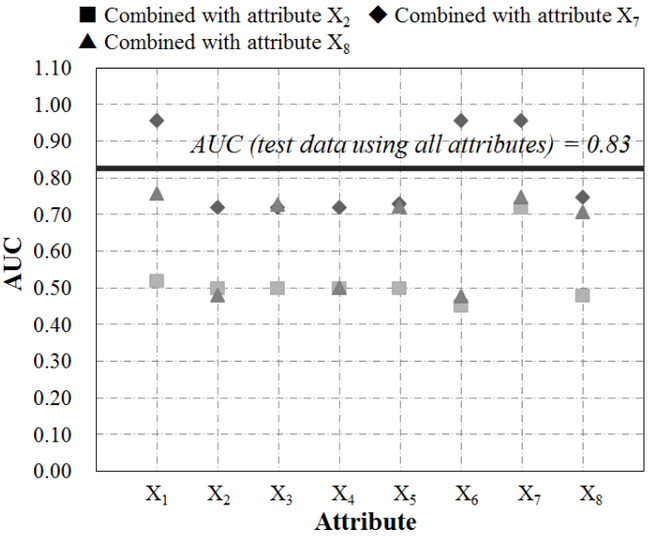


Figure 6.2. AUC of poor level (health rating:1, 2, 3) which combined with attribute X_2, X_7, X_8

In additional, the two-combined feature opportunity set contained eight features, and, in this study, it had 28 settings of two-combined features in order to perform the analyses. The useful feature combinations were tested and shown in Fig. 4. A dark black block denotes a sufficient (useful) feature combination. A black block denotes a bad feature combination. A light black block denotes a feature combination that is not useful. Fig. 5.1 shows the results of correctly classified accuracy when the other attribute combining X_1 (section location), X_2 (construction year), X_3 (painting year), and X_4 (de-formation of main girder). Based on the Fig. 5.1 shown results, it can be seen that X_1, X_2, X_3, and X_4, combining with attribute X_7 (deterioration of corrosion protection)

gives a high accuracy of correct classification. Fig. 5.2 shows that the other attribute combining X_5 (missing bolt), X_6 (abnormality of joint gap), X_7 (deterioration of corrosion protection), and X_8 (corrosion in main girder) resulted in correct classification accuracy. Based on the Fig. 5.2 shown results, it can be seen that X_5, X_6, X_7, and X_8, combining with attribute X_7 (deterioration of corrosion protection) gives high accuracy of correct classification. Based on the above results, attribute X_7 (deterioration of corrosion protection) gives more meaningful to assess the priority of inspection items.

Table 8. The AUC result of good level (health rating:4, 5)

	X_1	X_2	X_3	X_4	X_5	X_6	X_7	X_8
X_1	0.50	0.54	0.55	0.50	0.31	0.59	0.78	0.63
X_2	0.54	0.50	0.50	0.50	0.50	0.57	0.97	0.70
X_3	0.55	0.50	0.66	0.36	0.35	0.58	0.97	0.62
X_4	0.50	0.50	0.36	0.50	0.50	0.58	0.97	0.82
X_5	0.31	0.50	0.35	0.50	0.50	0.61	0.98	0.64
X_6	0.59	0.57	0.58	0.58	0.61	0.52	0.78	0.63
X_7	0.78	0.97	0.97	0.97	0.98	0.78	0.96	0.99
X_8	0.63	0.70	0.62	0.82	0.64	0.63	0.99	0.71

Table 9. The AUC result of poor level (health rating:1, 2, 3)

	X_1	X_2	X_3	X_4	X_5	X_6	X_7	X_8
X_1	0.50	0.52	0.52	0.50	0.74	0.42	0.96	0.76
X_2	0.52	0.50	0.50	0.50	0.50	0.45	0.72	0.48
X_3	0.52	0.50	0.66	0.72	0.73	0.79	0.72	0.73
X_4	0.50	0.50	0.72	0.50	0.50	0.44	0.72	0.50
X_5	0.74	0.50	0.73	0.50	0.50	0.45	0.73	0.72
X_6	0.42	0.45	0.79	0.44	0.45	0.52	0.96	0.48
X_7	0.96	0.72	0.72	0.72	0.73	0.96	0.96	0.75
X_8	0.76	0.48	0.73	0.50	0.72	0.48	0.75	0.71

Depending on whether the data are unbalanced, correctly classified accuracy may be misleading; this is because the all-good or all-poor classifier may achieve a very good classification rate. We must use the ROC curve (and the AUC) to differentiate between errors on good or poor examples. Fig. 6.1 shows the AUC result of a good level, which has the other attribute combining X_2 (construction year), X_7 (deterioration of corrosion protection), and X_8 (corrosion in main girder). The good level of the AUC result using all attributes is equal to 0.69. In good classification, the combination of X_3X_2, X_4X_2, and X_5X_2 gives, results close to 0.5. Fig. 6.2 shows the AUC result of a poor level, which has the other attribute combining X_2 (construction year), X_7 (deterioration of corrosion protection), and X8 (corrosion in main girder). The poor level of the AUC result using all attributes is equal to 0.83. In poor classification, the combination of X_1X_2, X_3X_2, X_4X_2, X_5X_2, X_6X_2, and X_8X_2, gives results close to 0.5. Base on the Ana-Maria Simundic's (Simundic et al. 2012) study on diagnostic accuracy (see Table 2.), the AUC results around 0.5-0.6 gives a bad test result. So the useful feature combinations were X_1X_7, X_2X_7, X_3X_7, X_4X_7, X_5X_7, X_6X_7, X_1X_8, X_3X_8, X_5X_8, and X_7X_8. The AUC result's details are shown in Tables 8 and 9.

4 DISCUSSION

Feature importance and selection can give an objective utility of features. We need to manually create an objective utility feature of inspection items. Above the SVM numerical results, a useful feature combination denote in Fig. 4. The other attribute combine with attribute X7 (deterioration of corrosion protection) gives important effectiveness assessment of inspection site work for regional government's inspector.

The concept of a proposed diagnostic optimization method for bridge integrity is described in Fig. 7. Regional governments are constantly distressed by the lack of a maintenance budget and maintenance experts. This proposed diagnostic optimization method can assist regional governments in determining bridges' health and integrity, which are generally decided by own experience of each maintenance experts.

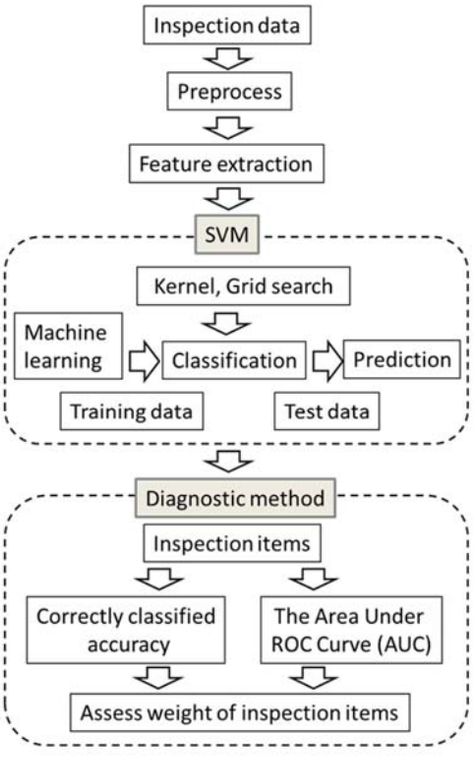


Figure 7. Concept diagram of sound diagnosis

5 CONCLUSION

In this study, we obtained a useful feature combination of inspection items by using a machine learning

algorithm. According to the SVM analysis, the correctly classified accuracy and the AUC can obtain the effectiveness assessment of different feature combinations by using an experienced inspector's training data to predict the class label. Thus, this proposed bridge integrity evaluation method can help and assist regional governments determine bridges' degree of health.

REFERENCES

Arong. Murakami, S. & Hosoe, I. 2014. A proposal for weighted optimization method on bridge health integrity through corroded steel bridge infrastructure. *Proceeding of 7th International Conference on Bridge Maintenance, Safety and Management (IABMAS 2014), Shanghai, 7-11 July 2014*.

Ben-Hur, A. & Weston, J. 2010. A user's guide to support vector machines. *Data Mining Techniques for the Life Sciences*: 223-239.

Bridge Periodical Inspection Manual (Japanese). 2014. Ministry of Land, Infrastructure, Transport and Tourism. http://www.mlit.go.jp/road/ir/ir-council/pdf/yobo3_1_6.pdf

Bridge Periodical Inspection Manual (Japanese). 2016. Road Maintenance Division of Gifu Prefecture Government. http://www.pref.gifu.lg.jp/shakaikiban/doro/doroiji/11657/index_57545.data/1-02_kyoutuu.pdf

Burges, C. 1998. A tutorial on support vector machines for pattern recognition. *Data Mining and Knowledge Discovery, Kluwer Academic* 2: 121-167.

Chikata, Y. Aso, K. Kameda, J. & Kido, T. 2007. Applicability of SVM and LVQ to evaluation of bridge integrity (Japanese). *Journal of Applied Computing in Civil Engineering* 16: 175-184.

Cortes, C. & Vapnik, V. 1995. Support-vector networks. *Machine Learning* 20: 273-297.

Drosou, K. Georgiou, S. Koukouvinos, C. & Stylianou, S. 2014. Support Vector Machines Classification on Class Imbalanced Data: A Case Study with Real Medical Data. *Journal of Data Science* 12: 727-754.

Hosoe, I. Kato, N. & Morimoto, H. 2006. Scenario for rational maintenance and management of bridges. *10th International Conference on Inspection, Appraisal, Repair and Maintenance of Structures, Hong Kong*: 207-214.

Masahiro, S. & Takashi, T. 2013. Bridge inspection standards in Japan and US. *Proceedings of the 29th US - Japan Bridge Engineering Workshop, Tsukuba Japan, 11-13 November 2013.*

Oishi, H. Kobayashi, H. Yun, Y. Tanaka, H. Nakayama, H. & Furukawa, K. 2007. Evaluation of the danger of slops in view of the effective value of measure constructions using support vector machine (Japanese). *Journal of Japan Society of Civil Engineers (Ser. F)* 63: 107-118.

Rakotomamonjy, A. 2004. Optimizing area under ROC curve with SVMs. *Proceedings of 1st international workshop on ROC Analysis in Artificial Intelligence, Spain*: 71-80.

Recommendations for Full-scale Maintenance of Aging Roads. 2014.: The Road Committee of the Panel on Infrastructure Development. https://www.mlit.go.jp/road/road_e/pdf/recommendation.pdf (reference day 2017.10.17)

Simundic, A. 2012. Diagnostic Accuracy-Part 1: Basic Concepts. *Journal of Near-Patient Testing & Technology* 11: 6-8.

Sugimoto, H. Ichima, K. Abe, J. & Furukawa, K. 2009. On synthetic health evaluation of infrastructure by SVM and its application to ranking of structures (Japanese). *Journal of Japan Society of Civil Eng*ineers (Ser. A) 65: 658-669.

Tamakoshi, T. Shiratom, M. Yokoi, Y. Mabuchi, T. & Yabu, M. Guidelines for periodic road structure inspections. http://www.nilim.go.jp/english/annual/annual2015/pdf_file/43.pdf (reference day 2017.10.17)

Vapnik, V. 1998. *Statistical Learning Theory.* New York: Wiley-Interscience.

Yuki, K. Kobayashi, H. Ohishi, H. Sugimoto, H. Iida, T. & Furukawa, K. 2012. Evaluation for judgement criteria of repair on civil engineering structure by support vector machine (Japanese). *Journal of Japan Society of Civil Engineer Ser. F4 (Construction and Management)* 68: 52-61.

Maintenance, Safety, Risk, Management and Life-Cycle Performance of Bridges – Powers, Frangopol, Al-Mahaidi & Caprani (Eds)
© 2018 Taylor & Francis Group, London, ISBN 978-1-138-73045-8

Evaluation of slab lifting strategies for maintenance of middle slabs in double-deck tunnels

S.M. Kim, Y.K. Cho & B.K. Park
Kyung Hee University, Yongin, Korea

ABSTRACT: The major difference between double-deck tunnels and general tunnels is the existence of middle slab in double-deck tunnels. Both sides of the middle slab lie on the brackets along the longitudinal direction and the bearing pads between slab and bracket may need to be replaced for maintenance. In this case, part of the middle slab needs to be lifted for the replacement of the bearing pads. The objective of this study is to evaluate slab lifting strategies of the middle slab in double-deck tunnel when replacement of bearing pads lying between slab and bracket is needed. The middle slabs have been divided into three different sections as normal, expansion joint, and emergency passageway sections. At each section, several different slab lifting methods have been applied and analyzed to investigate the stress distribution in the slab and to evaluate the maximum tensile stresses. The analysis results show that the optimal slab lifting method that reduces the maximum tensile stresses of the slab is different depending on the section type of the middle slab.

1 INSTRUCTION

Double-deck tunnels (Fig. 1) are of interest in many countries recently because of their advantage in economics and construction. Some of them include Fuxing tunnel in China, M30 tunnel in Spain, SMART tunnel in Malaysia, A86 tunnel in France, Istanbul Strait Road tunnel in Turkey (Arlet 2012, Kannapiram 2005, Kim, 2010, Santhiman & Weei 2006). Other countries such as the Netherlands, Russia, USA, Australia, and Korea also have recently opened or planned double-deck tunnels.

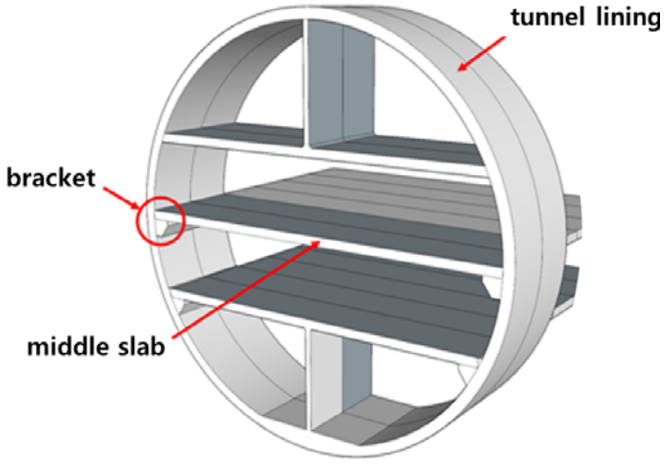


Figure 1. Middle slab in double-deck tunnel

The major characteristic of the double-deck tunnel is the existence of middle slab as shown in Figure 1 (Park et al. 2017). Both sides of the middle slab lie on the brackets along the longitudinal direction and the bearing pads between slab and bracket may need to be replaced for maintenance. In this case, part of the middle slab needs to be lifted for the replacement of the bearing pads.

Several different methods to replace bearing pads can be considered. For bridge slabs, the entire width of the slab can be lifted to replace bearing pads as shown in Figure 2. For beams, each supporting point can be lifted as shown in Figure 3. For some cases as shown in Figure 4, many lifting devices can be used all together.

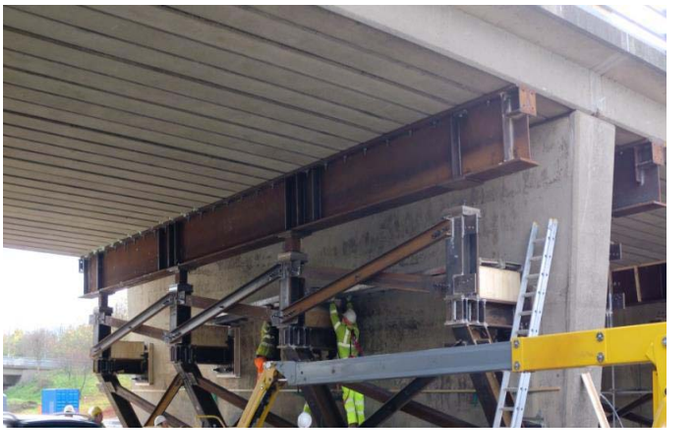


Figure 2. Bridge slab lifting (Freyssinet 2017)



Figure 3. Beam lifting (Constructionspecifier 2017)



Figure 4. Lifting using multiple devices (Heavyliftnews 2017)

The objective of this study is to evaluate slab lifting strategies of the middle slab in double-deck tunnel when maintenance such as replacement of bearing pads lying between slab and bracket is needed. Several different slab lifting methods have been applied and analyzed to investigate the stress distribution in the slab and to evaluate the maximum tensile stresses.

2 ANALYSIS MODEL

The middle slabs have been divided into three different sections as shown in Figures 5-7: normal section, expansion joint section, and emergency passageway section. The finite element models of those middle slab sections have been developed using a finite element analysis program (ABAQUS 2007) and Figure 8 shows a half of the finite element model of the emergency passageway section. The slab thickness is 400 mm and the longitudinal length of the slab considered in this study is 100 m. Both side edges of the slab are simply supported along the longitudinal direction. Only the dead weight of the slab is considered as the applied load since the traffic is not allowed when the slab lifting work is being conducted.

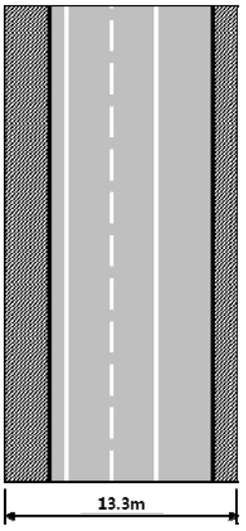


Figure 5. Normal section of middle slab

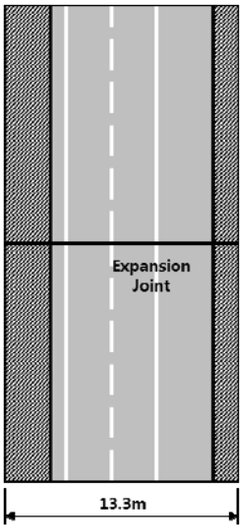


Figure 6. Expansion joint section of middle slab

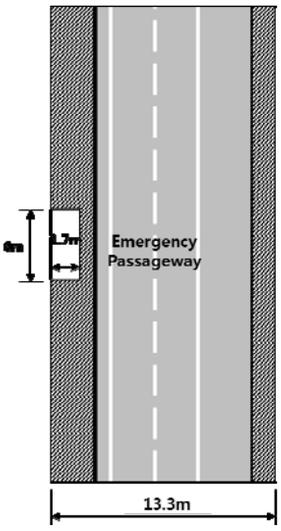


Figure 7. Emergency passageway section of middle slab

The major parameters of the slab lifting methods are basically the number of lifting points and the distances between the lifting points as shown in Figure

9. Lifting at one side and at both sides of the slab are also considered as shown in Figure 10.

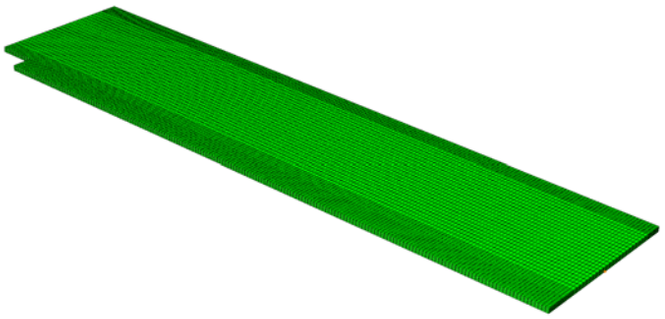
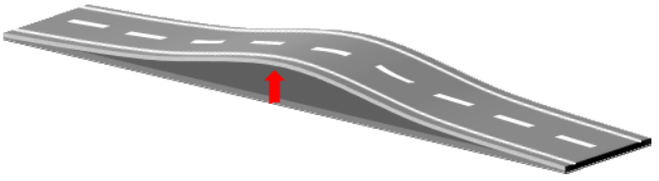
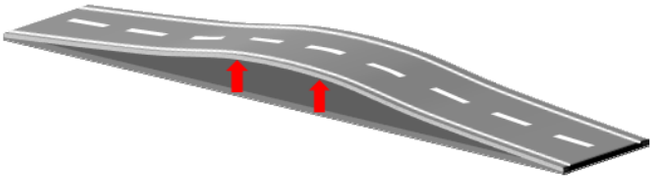


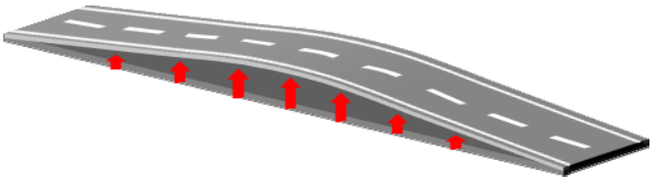
Figure 8. Analysis model of emergency passageway section of middle slab



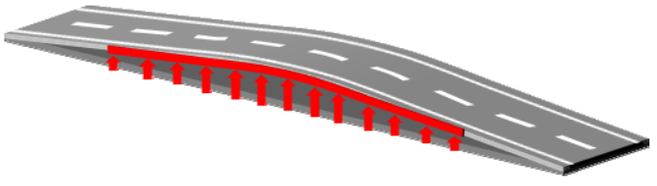
(a) One-point lift



(b) Two-point lift

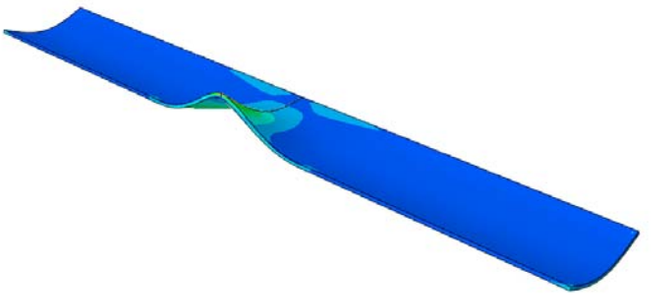


(c) Seven-point lift

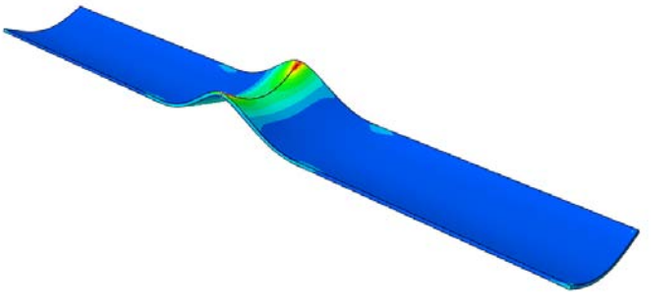


(d) Continuously distributed lift

Figure 9. Slab lifting methods under different lifting points



(a) One-side lift



(b) Both-side lift

Figure 10. One- and both-side lifts

3 ANALYSIS RESULTS

3.1 *Stresses at normal section of middle slab*

In order to find the stresses when the middle slab is lifted at the normal section to replace bearing pads, several lifting methods are considered as listed in Table 1. The numbers of lifting points considered in this study are 1, 2 and 7. A continuously distributed lifting method is also considered using Equation (1) even though this method cannot be applied in practice. The maximum lifting height is 50 mm at the center of the lifting points. The distance between the lifting points for 2-point lifting method is 2 m. The distances to the lifting points from the center for 7-point lifting method are -12, -8, -4, 0, 4, 8, 12 m.

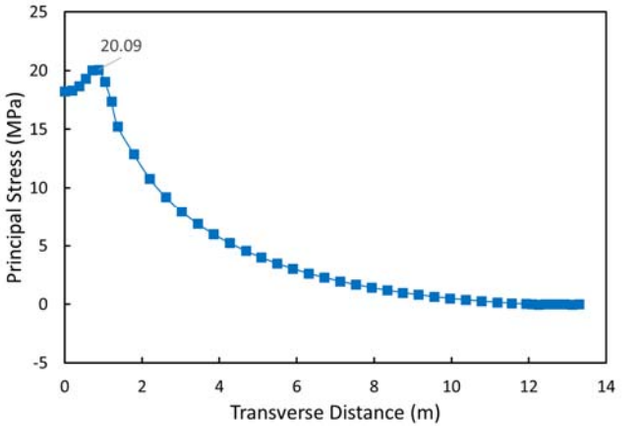
$$D(z) = 0.025 \times \cos\left(\frac{z \times \pi}{25}\right) + 0.025 \quad (1)$$

Table 1. Lifting methods at normal section

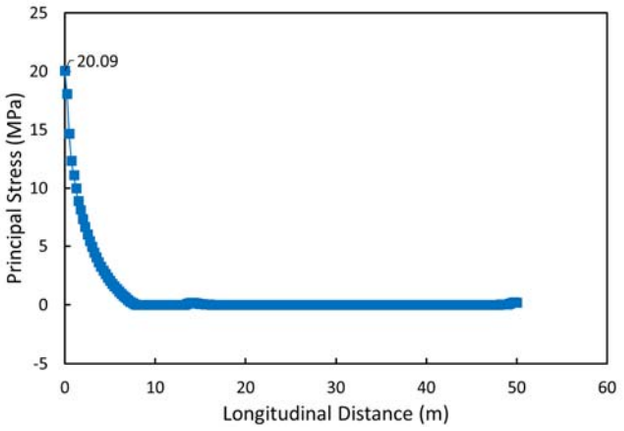
Lifting points	One-edge lift	Both-edge lift
1	T-1E-1P	T-2E-1P
2	T-1E-2P	T-2E-2P
7	T-1E-7P	T-2E-7P
Distributed	T-1E-D	T-2E-D

Figure 11 shows the principal stresses along the transverse and longitudinal directions when the mid-

dle slab is lifted at one-side edge using 1-point lifting method. In the transverse direction, the maximum stress occurs at the lifting point and the stress becomes gradually smaller as the transverse distance increases from the lifting point. In the longitudinal direction, the maximum stress occurs at the lifting point and the stress decreases rapidly as the distance from the lifting point increases up to about 7 m and then no stresses are observed after the distance.



(a) Along the transverse direction



(b) Along the longitudinal direction

Figure 11. Principal stresses at normal section of middle slab under T-1E-1P

The analyses have been performed to find the maximum stresses under the lifting methods listed in Table 1 and the results are shown in Figure 12. Generally, as the number of lifting points increases, the maximum stresses become smaller. For the same number of lifting points, the maximum stresses under both-side lifting methods are generally smaller than those under one-side lifting methods. For one-side and both-side lifting methods, the smallest maximum stresses occur when the continuously distributed lifting method is applied. However, that method cannot be applied in practice because the supporting beam to lift the slab cannot be fabricated to exactly match the curvature of the slab. If the curvature of the slab is smaller than that of the supporting beam, just the center of the beam will support the slab and this case will be the same as the 1-point lift. On the other hand, if the slab curvature is larger than that of the supporting beam, the slab is lifted at both ends of the beam. Therefore, the 7-point lifts at both sides of the middle slab will be the most appropriate method to reduce the slab stresses under the slab lift for replacement of bearing pads.

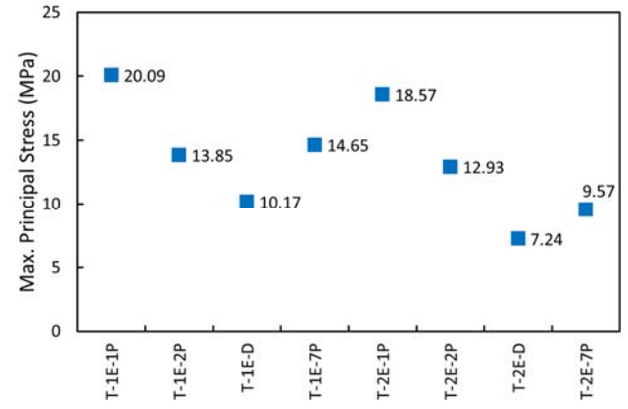


Figure 12. Maximum stresses at normal section of middle slab

3.2 *Stresses at expansion joint section of middle slab*

The stress distribution of the middle slab when the slab is lifted at the expansion joint section is also investigated. The lifting methods considered at the expansion joint section are listed in Table 2. The 1-point lifting method represents the slab lift conducted at the expansion joint. The 2-point lifting method is that the lifting is conducted at 1 m left and 1 m right from the expansion joint, so it is actually 1-point lift at 1 m apart from the expansion joint. The same situation happens on the 7-point lifting method, and just 4 points are lifted from the expansion joint to one direction.

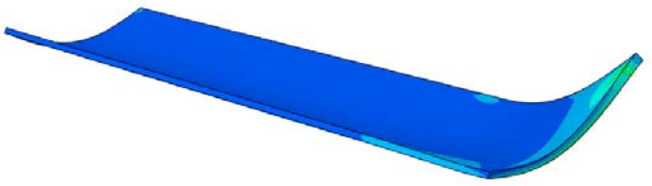
Table 2. Lifting methods at expansion joint section

Lifting points	One-edge lift	Both-edge lift
1	EJ-1E-1P	EJ-2E-1P
2	EJ-1E-2P	EJ-2E-2P
7	EJ-1E-7P	EJ-2E-7P
Distributed	EJ-1E-D	EJ-2E-D

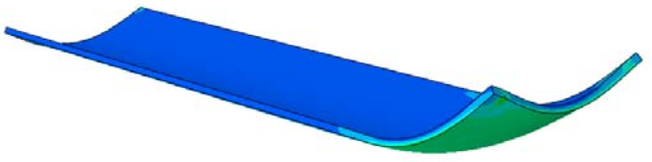
Figure 13 shows the typical deflected shapes and stress distribution when the middle slab is lifted at the expansion joint section under the one-side and both-side lifting methods.

The maximum stresses under different lifting methods listed in Table 2 are obtained and the results are shown in Figure 14. The both-side lifts show smaller stresses compared with the one-side lifts when the number of lifting points is the same. The smallest maximum stress occurs when the mid-

dle slab is lifted at both side and two points, one each from the expansion joint, are lifted. This result is different from the result at the normal section. The smallest maximum stress at the normal section occurs when the continuously distributed lifting method is chosen, as previously examined.



(a) One-side lift



(b) Both-side lift

Figure 13. Deformation and stresses of expansion joint section

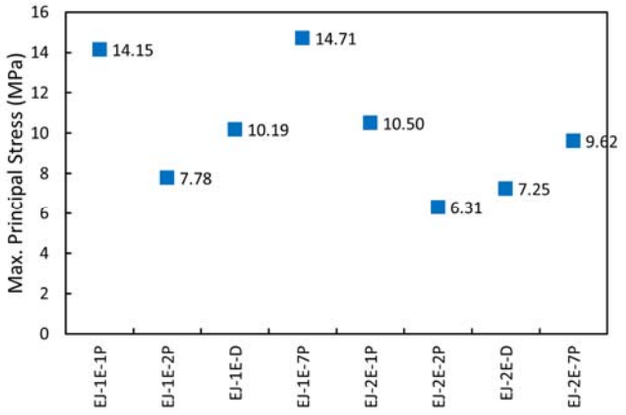


Figure 14. Maximum stresses at expansion joint section of middle slab

3.3 *Stresses at emergency passageway section of middle slab*

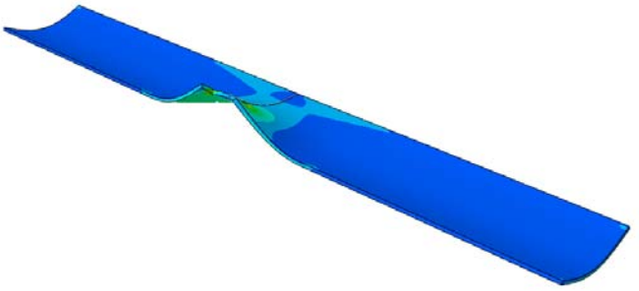
The stresses of the middle slab are also analyzed when the slab lifting is conducted at the emergency passageway section of the middle slab. The primary difference of the emergency passageway section from the normal section is the existence of the empty space at one side of the slab for movement between upper and lower levels. The slab lifting methods considered at the emergency passageway section are listed in Table 3. For the continuously distributed lifting method, Equation (2) is used at the passageway side (stair side) and Equation (1) shown previously is used at the opposite side (non-stair regular side). The distances between lifting points of the 2-point lifting method are 2 m and 8 m for the regular side and the passageway side, respectively. The 7-point lifting method at the regular side is the same as that for the normal section, and the 6-point lifting method is applied at the passageway section. In this case, the distances to the lifting points from the center of the passageway are -12, -8, -4, 4, 8, 12 m.

$$D(z) = 0.025 \times \cos\left(\frac{z \times \pi}{13} - \frac{\pi}{4}\right) + 0.025 \quad (2)$$

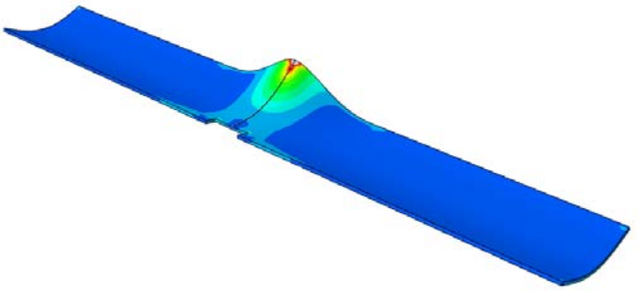
Table 3. Lifting methods at emergency passageway section

Lifting points	One-edge lift (stair side)	One-edge lift (regular side)	Both-edge lift
1	EPS-1E-1P	EPR-1E-1P	-
2	EPS-1E-2P	EPR-1E-2P	-
6 or 7	EPS-1E-6P	EPR-1E-7P	EP-2E-7P
Distributed	EPS-1E-D	EPR-1E-D	EP-2E-D

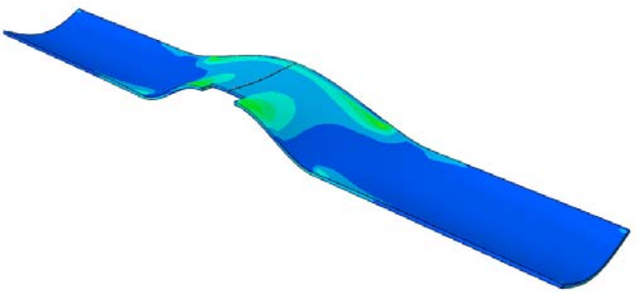
Figure 15 shows the typical deflected shapes and stress distribution of the middle slab when the slab is lifted at the emergency passageway section under the stair-side, regular-side, and both-side lifting methods.



(a) Stair-side lift



(b) Regular-side lift



(c) Both-side lift

Figure 15. Deformation and stresses of emergency passageway section

The maximum stresses of the middle slab when the slab is lifted using the methods listed in Table 3 are analyzed and shown in Figure 16. For one-side lifts, the maximum stresses are smaller when the regular side is lifted compared with the stair side lifting if the number of lifting points is the same, except for the 1-point lifting method. If the continuously distributed lifting methods are applied, the maximum stresses are the smallest. However, as mentioned previously, the continuously distributed lifting method is not practically used. Therefore, if the both sides are lifted at the same time with 7 lifting points at the regular side and 6 lifting points at the stair side, the maximum slab stresses can be reduced.

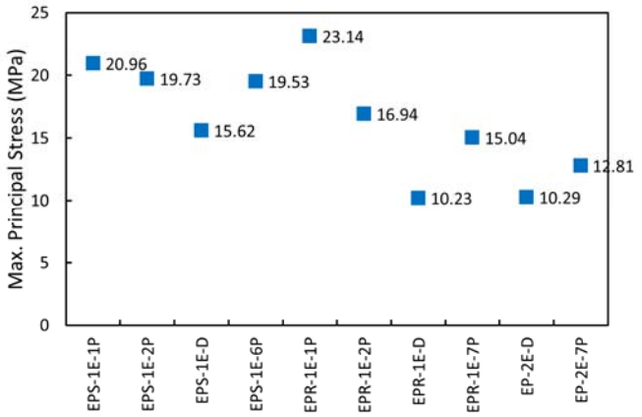


Figure 16. Maximum stresses at emergency passageway section of middle slab

4 SUMMARY AND CONCLUSIONS

This study was performed to evaluate slab lifting strategies of the middle slab in double-deck tunnel when the bearing pads between the slab and bracket are needed to be replaced with new ones. Several different slab lifting methods were examined at different sections of the middle slab to find the minimal stress occurrence during the slab lifting work. The main conclusions from this study are as follows:

- The optimal slab lifting method that reduces the maximum tensile stresses of the slab is different depending on the section type of the middle slab.
- At the normal section of the middle slab, the multiple-point lifting, such as the 7-point lifting, at both sides of the slab is the most appropriate to reduce the maximum tensile stress of the slab.
- At the expansion joint section of the middle slab, the 2-point lifting, one each from the expansion joint, at both sides of the slab is the most acceptable method.
- At the emergency passageway section of the middle slab, the multiple-point lifting at both sides of the slab, such as the 7-point lifting at the regular side and the 6-point lifting at the passageway side, is the most appropriate.
- At any section of the middle slab, the slab lifting at both sides at the same time is recommended since it decreases the maximum tensile stresses of the slab compared with the slab lifting at just one side of the slab.
- If the optimal slab lifting methods are considered depending on the section type of the middle slab, the economical design of the middle slab can be achieved.

ACKNOWLEDGEMENTS

This research was supported by Development of Design and Construction Technology for Double Deck Tunnel in Great Depth Underground Space (14SCIP-B088624-01) from Construction Technology Research Program funded by Ministry of Land, Infrastructure and Transport of Korean government. The authors wish to express their gratitude for the financial support.

REFERENCES

ABAQUS. 2007. User's Manual Version 6.7, Hibbit, Karlsson & Sorensen, Inc., Pawtucket, R.I.

Arlet, A. 2012. Tunnel A86 Duplex: A Private Initiative, International Seminar on Long Road Tunnels. World Road Association-PIARC. Chile.

Constructionspecifier 2017. Accessed on internet on October 25, 2017. https://www.constructionspecifier.com/bearing-pad-durability-in-precast-concrete-garages/.

Freyssinet 2017. Accessed on internet on October 25, 2017. http://freyssinet.co.uk/freyssinet-ltd-continues-to-excel-at-bridge-bearing-replacement-contracts-10-october-2011/.

Heavyliftnews 2017. Accessed on internet on October 25, 2017. http://www.heavyliftnews.com/transport/100-axle-lines-tianjie-spmts-assist-3200t-giant-bridge-section-roll-on-the-barge.

Kannapiram, R.K.M. 2005. A Study and Evaluation on SMART Project, Malaysia. Ph.D. Dissertation. University of Southern Queensland.

Kim, S.H. 2010. Large Tunnels for Transportation Purposes and Face Stability of Mechanically Driven Tunnels in Soft Ground. Ph.D. Dissertation. The University of Texas at Austin.

Park, H.B., Cho, Y.K., Lee, Y.H., Kim, S.M. 2017. Analysis of the Fundamental Behaviors of the Middle Slab in a Double-Deck Tunnel for Design Guide Development. *International Journal of Highway Engineering* 19(1): 63-72.

Santhiman, M.S. & Weei, L.H. 2006. ITS of SMART. PIARC International Seminar on Intelligent Transport System (ITS) in Road Network Operations, Kuala Lumpur, Malaysia.

Maintenance, Safety, Risk, Management and Life-Cycle Performance of Bridges – Powers, Frangopol, Al-Mahaidi & Caprani (Eds)
© 2018 Taylor & Francis Group, London, ISBN 978-1-138-73045-8

Research and application of maintenance for a combined highway-railway bridge

Jun Fu, Tao Zhang , Zhibin Li
School of transportation, Wuhan University of Technology, Wuhan, China;
Qingjun Ding
School of material, Wuhan University of Technology, Wuhan, China;
Jiabiao Huang
Yichang Hong yuan road construction inspection & management corporation, Yichang,China

ABSTRACT: This paper explores the feasibility of using a composite deck system with Hybrid Fiber Reinforced Lightweight Aggregate Concrete (HFRLAC), shear studs on Orthotropic Steel Deck (OSD) to reconstruct the Zhicheng Yangtze River Combined Highway-Railway Bridge(HRCB)， without disrupting train traffic. The mix of HFRLAC were introduceed. The fatigue test for the scale model of composite deck pavement was carried out under equivalent loading. The Finite Element Analysis(FEA) was conducted based on the simplified deck pavement. The field tests results and service condition have proved the maintenance for the HRCB is effective since 2013.

KEYWORDS: combined highway-railway bridge;maintenance;composite deck system ; HFRLAC; shear studs; FEA; scale model and field test.

1 INTRODUCTION

Many bridges in service appear to have operational problems (Imam & Righiniotis, 2010). A large number of studies that feature reasonable maintenance decisions and choosing the proper maintenance scheme have been carried out (Dan & Biondini, 2014). However, there is only a few researches involving the maintenance for highway-railway combined bridges.

Due to the nature of the structural characteristics of a combined highway-railway bridge, weight reduction are important for the bridge safety.Lightweight aggregate concrete could greatly reduce the dead loading for a bridge, and it will be widely used if the brittleness could be eliminated. Fibers can significantly enhance the lightweight aggregate concrete (Hassanpour, Shafigh & Mahmud, 2012; Victor, 2007).Experimental results showed that even low content fibers could remarkably improve properties such as the splitting tensile strength, flexural strength, and toughness (Balendran, Zhou, Nadeem & Leung, 2002; Shi & Riefler, 2005). Studies found that the addition of hybrid steel fibers and polypropylene fibers,can greatly improve the mechanical properties of lightweight aggregate concrete made with natural pumice (Huo, Shen & Cui, 2007; Düzgün, Gül & Aydin, 2005). Altun & Aktaş (2013) successfully developed a high performance PVA (polyvinyl alcohol) fiber reinforced lightweight concrete (FRLWC) that showed high flexural strength, high flexural ductility, and excellent toughness.

Zhicheng Yangtze River Combined Highway-Railway Bridge (“Zhicheng Bridge”) ,built in 1971 China, is a steel truss continuous girder bridge with total span 1280m(Fig.1-2). The original highway deck pavement of Zhicheng Bridge is made up of 12cm C30 reinforced concrete slab, 4cm concrete layer, and covered with 1.5cm asphalt sand layer (Fig.3). Inspections showed that the original bridge deck pavement was damaged seriously(Fig.4)

This paper foucsed on the maintenance of combined highway-railway bridge using composite deck pavement based on the HFRLAC & shear studs ,where the scheme were verified by finite element analysis, scale model and field test.

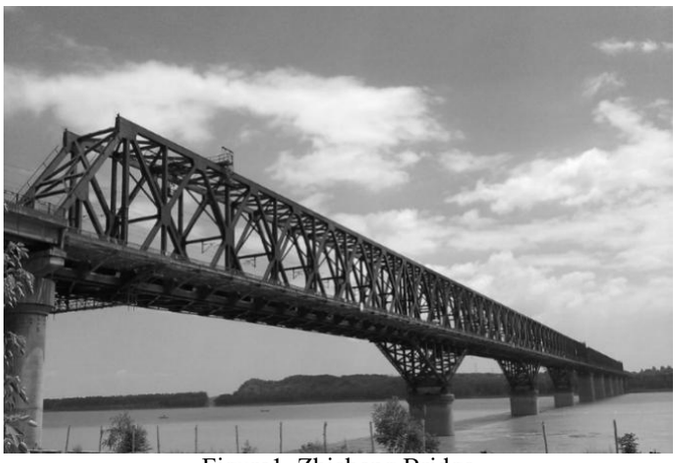


Figure1. Zhicheng Bridge

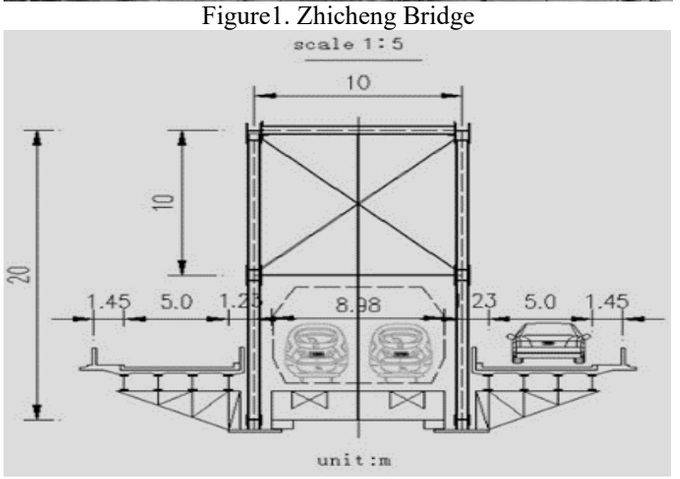


Figure2. Cross-section

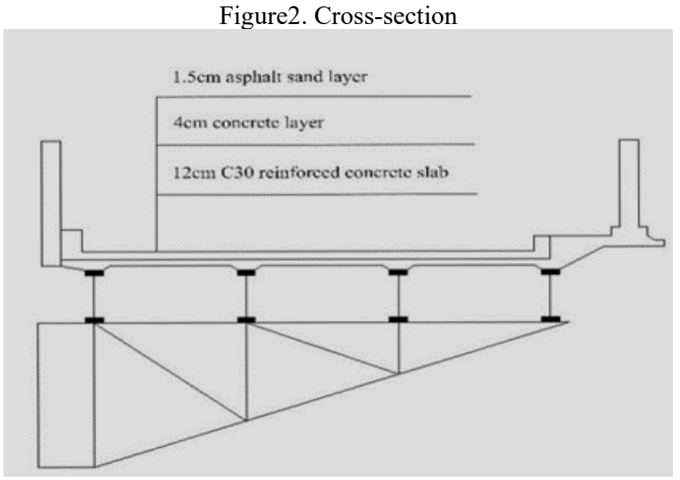


Figure3. Original highway deck pavement



Figure4. Deck pavement damage

2 MAINTENACE SCHEME & FEM

2.1 *Maintenance of Zhicheng Bridge*

For the maintenance of Zhicheng Bridge，a new orthotropic steel deck (Fig.5(a)), with the pavement consisting of HFRLAC, shear studs,mesh reinforcement & a stress absorbing waterproof layer between the HFRLAC layer and the SMA layer. The details of the deck pavement can be seen from Fig.5(b)

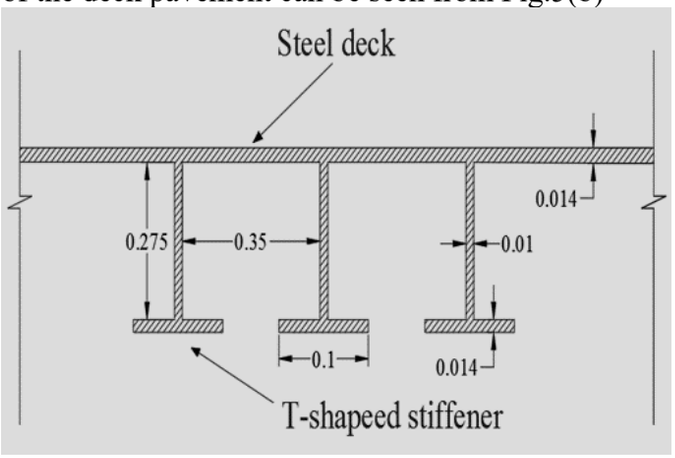


Figure 5(a). The new OSD

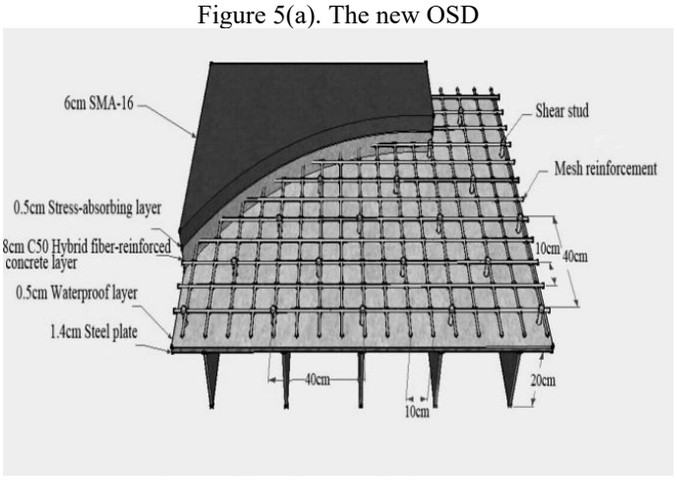


Figure 5(b). The new deck pavement

2.2 *FEM of Zhicheng Bridge*

In this study, a global FEM(Fig.6 & Fig.7) for the Zhicheng Bridge was built. The shear studs & mesh reinforcement has been dealt with equivalently in the HFRLAC. The Shell63 element was used to simulate OSD, HFRLAC and SMA. The truss and triangle brackets were simulated by Beam188 element. The boundary conditions of the model were the same as those of the actual bridge. Table 1 showed the parameters of FEM for the deck pavement.

Table 1. Parameters of the deck pavement

Parameters	Elastic modulus E / Pa	Thickness h / m	Poisson's ratio μ	Density ρ /（$kg \cdot m^{-3}$）	Bending stiffness D/（$kN{\cdot}m^2$）
Orthotropic Steel Deck	2.10E+11	0.014	0.3	7850	3769
HFRLAC	3.50E+10	0.08	0.25	2470	19911
SMA	1.00E+09	0.06	0.25	2400	320

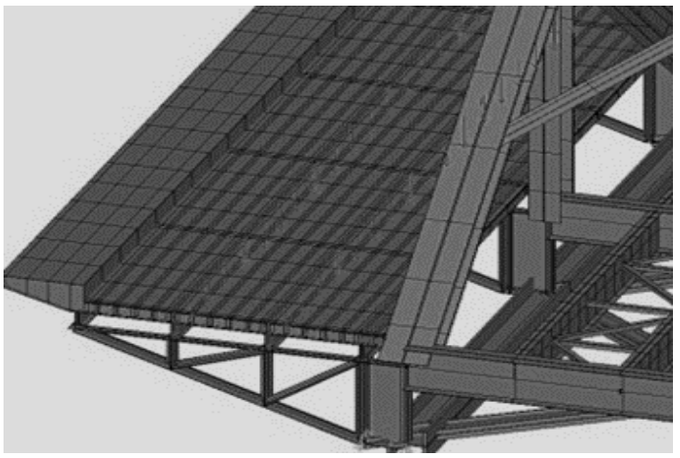


Figure 6(a) Vehicle loads

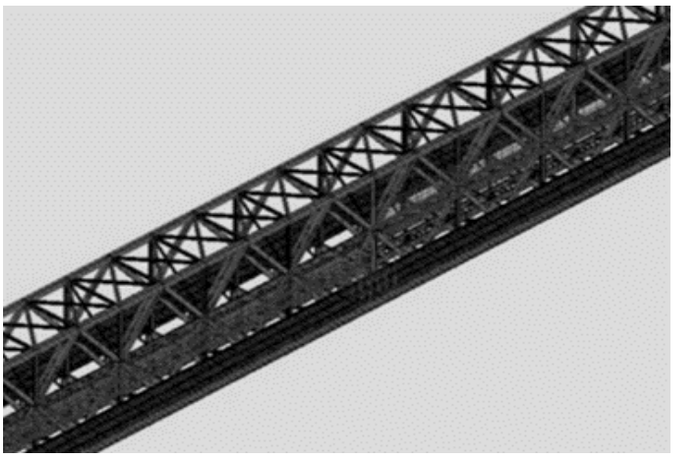


Figure 6 (b) Train loads

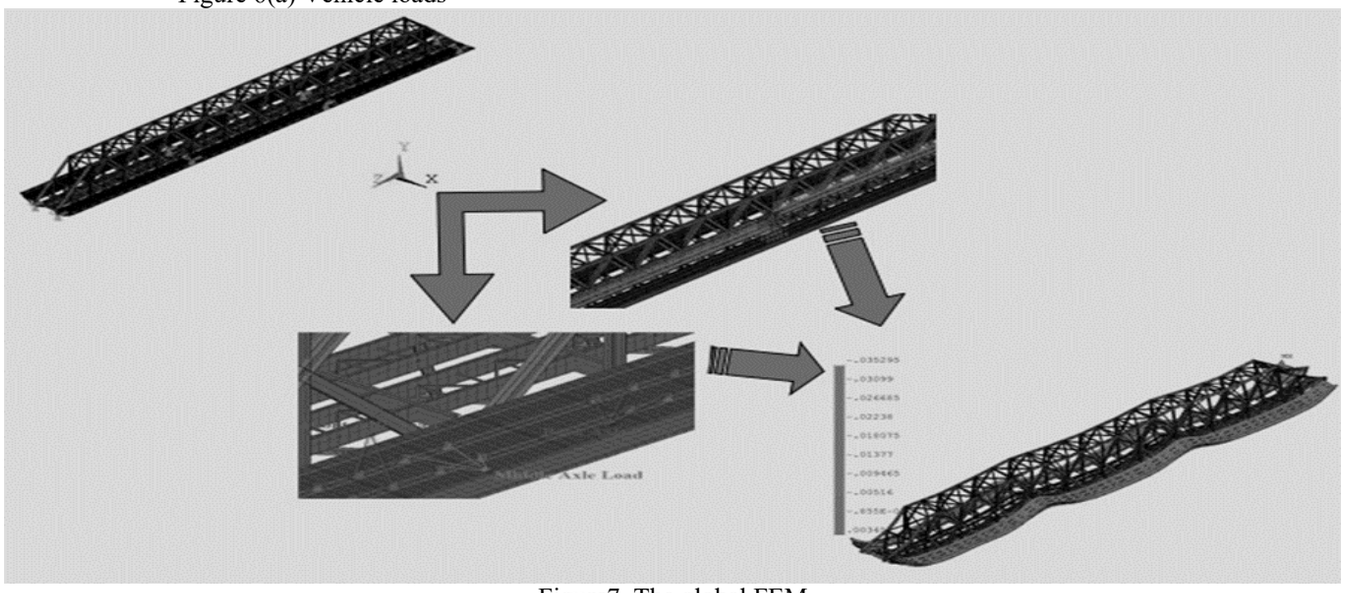


Figure7. The global FEM

3 HFRLAC MIX & PROPERTIES

Table 2. HFRLAC mix

Cementing material (kg/m^3)		Fine aggregae (kg/m^3)	Ceramsite (kg/m^3)	Water (kg/m^3)	Water Reducing admixture (kg/m^3)	Flexibil-izer (kg/m^3)	Hybrid fibers (kg/m^3)	
Cement	Pulverized fly ash						Steel fibers	Polyacrylonitrile fibers
500	50	680	530	150	12.1	10.0	60	0.8

Table 3. The properties of HFRLAC

Elastic modulus /Gpa	Apparent density kg/m^3	Compressive strength /MPa			Shrinkage rate ($\times10^{-4}$)		Tensile strength /MPa		Toughness index η_{20}
		3d	7d	28d	28d	90d	3d	28d	
28	1950	55	59.1	67.6	0.9	1.5	5.0	5.3	25.5

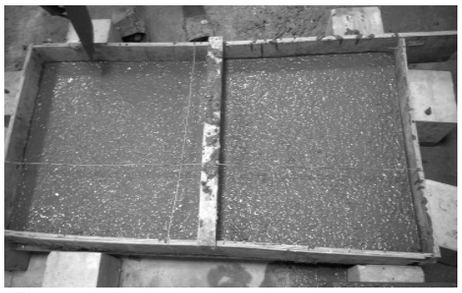


Figure 8. Lightweight concrete

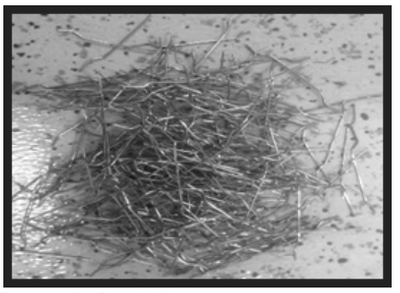


Figure 9. Steel fibers



Figure10. Polyacrylonitrile fibers

4 SCALE MODEL TEST & CONSTRUCTION

4.1 *Scale model test*

In this experiment, the fatigue performance of n ew pavement structure was determined using an MTS fatigue testing machine at a scale of 1:2 c ompared with the actual deck pavement. The ma ximum load capacity of the test machine is 100 0kN, load measurement accuracy is less than 0.5 %, and the machine has an applied load frequen cy range of 0.01~30Hz. The test procedure can be summaryzed as follows: a stress level of 0.7 and a cyclic stress ratio of 0.1 was selected; t he loading frequency was set at 10Hz and the c yclical load was applied. The test was automatic ally stopped after a cycle count of 2 million wa s reached. The stress level was increased and th e test was repeated. At each stress level, 3 tensi le fatigue specimens were made The test results showed that the fatigue cycles exceed 2 million times, which can meet the requirements of brid ge service

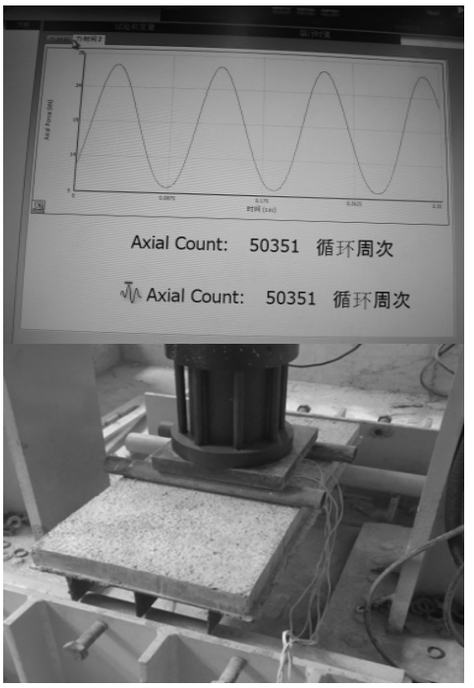
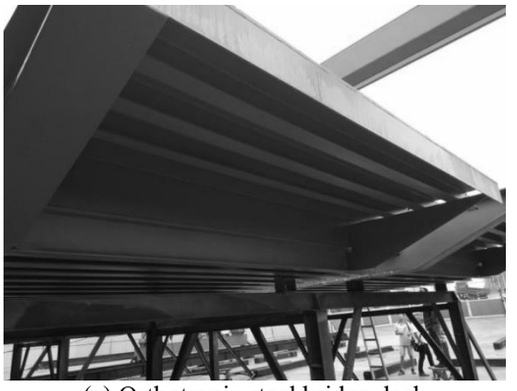


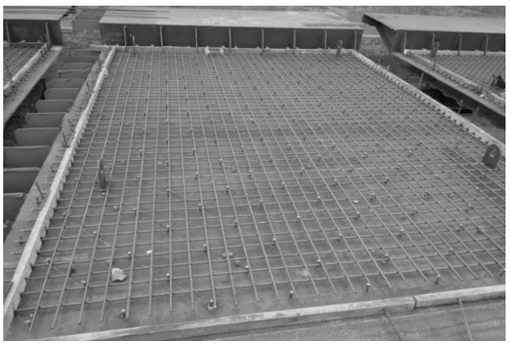
Figure 11. Scale model test



4.2 *Construction*



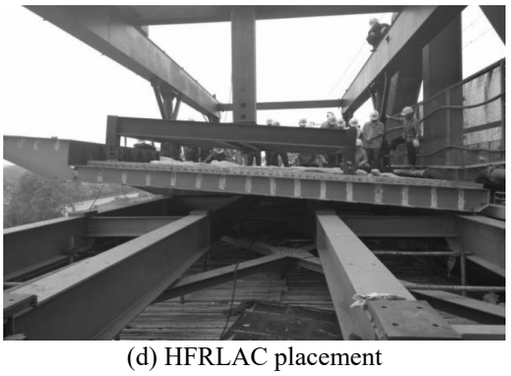
(a) Orthotropic steel bridge deck



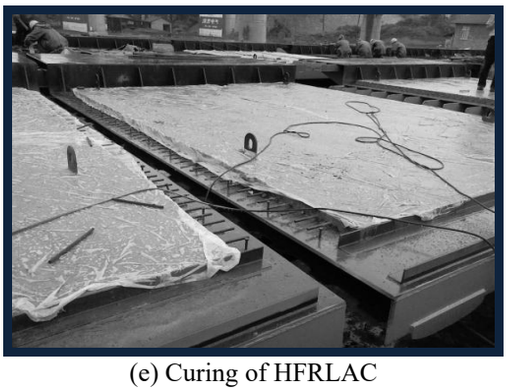
(b) Shear studs + mesh reinforcement



(c) Installation of orthotropic steel deck placement



(d) HFRLAC placement



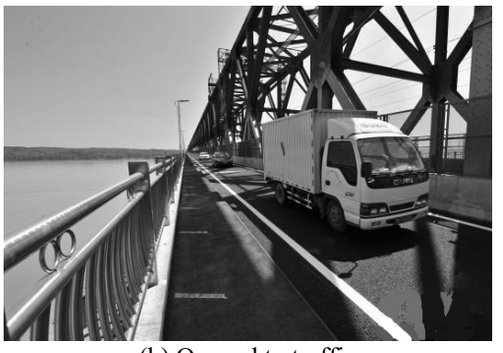
(e) Curing of HFRLAC



(f)Broom finish of HFRLAC



(g) Installation of bridge deck



(h) Opened to traffic

Figure 12. Construction of composite deck pavement

Figure 12 showed the maintenance for the combined highway-railway bridge with HFRLAC and shear studs.And after successful application,the Zhicheng Yangtze River Combined Highway-Railway Bridge has been in service for 5 years.

5 RESULTS AND DISCUSSION

5.1 Strain results

The results of finite element analysis, presented in Figure 13, showed that the maximum longitudinal tensile strain and the maximum transverse tensile strain of the bridge deck pavement under different loads were less than the allowable value of the materials. Figure 14 showed the calculated vertical displacement of deck pavement under different loads. The maximum displacement of the bridge deck pavement under coupled loads of vehicle and train is 5.16 cm, which was almost the same as measured results

From Table 5, the maximum stress values of the bars after maintenance were not only lower than the corresponding values before maintenance, but also less than the allowable stress value. This difference dispalyed that the safety of the bridge was increased after the reconstruction work. According to the calculation results, the strain and displacement of deck pavement and the stress of truss, are all satisfied with the design requirements.

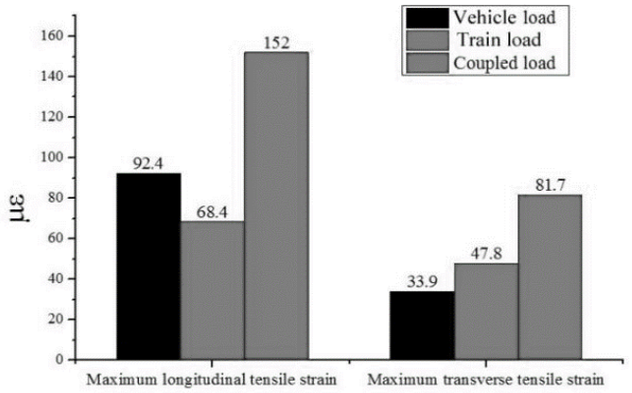


Figure 13. Strain results

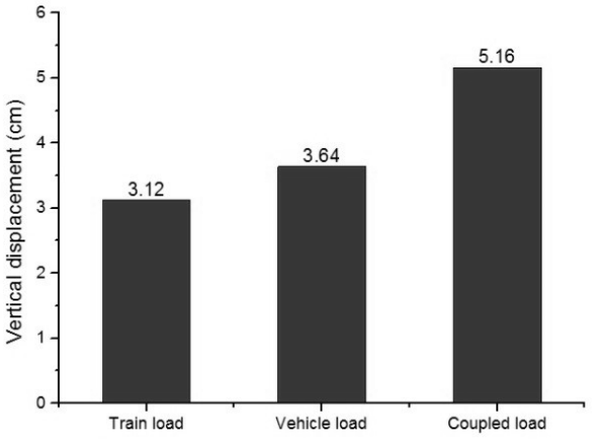


Figure 14. Vertical displacement results

5.2 comparision between New pavement & Original pavement

Figure 15 showed the values of vertical displacement resulting from the coupled train & vehicle loads before and after the maintenance. It was clear that all verdital dispalacement of new pavement scheme was smaller than the original one.So the Zhicheng bridge is benefical from the new deck pavement with more safe allowable.

As shown in Figure 16 ,there were 6 measuing points in Zhicheng bridge for the comparsion of strain.The theoretical strain values were greater than the measured values, which indicateed that the bridge had a great redundancy after the maintenance.

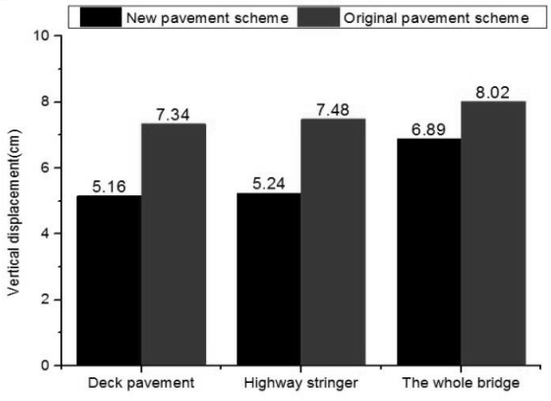


Figure 15. Comparison of Vertical displacement

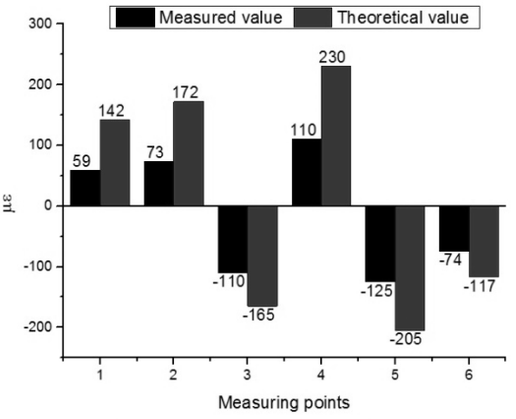


Figure 16. Comparison of strain

6 CONCLUSIONS

The composite deck pavement,based on OSD, HFRLAC and shear studs,could proviod a new idea for combined highway-railway bridge maintenance.

FEM analysis,scale model testing & field test proved the maintenance could meet the design requirements under the coupled loading of vehicles and train.

According to the comparision between New pavement & Original pavement, the composite deck pavement design & construciton could be suitable for combined highway-railway bridge maintenance,espially without disrupting train traffic.

REFERENCES,

Imam, B. M., & Righiniotis, T. D. (2010). Fatigue evaluation of riveted railway bridges through global and local analysis. Journal of Constructional Steel Research, 66(11), 1411-1421.

Dan, M. F., & Biondini, F. (2014). Bridge design, maintenance and management. Structure & Infrastructure Engineering, 10(4), 419-419.

Hassanpour, M., Shafigh, P., & Mahmud, H. B. (2012). Lightweight aggregate concrete fiber reinforcement–a review. Construction and Building Materials, 37, 452-461.

Victor C, L. I. (2007). Progress and application of engineered cementitious composites. Kuei Suan Jen Hsueh Pao/ Journal of the Chinese Ceramic Society, 35(4), 531-536.

Balendran, R. V., Zhou, F. P., Nadeem, A., & Leung, A. Y. T. (2002). Influence of steel fibres on strength and ductility of normal and lightweight high strength concrete. Building and environment, 37(12), 1361-1367.

Shi, C., Wu, Y., & Riefler, M. (2005). Properties of fiber-reinforced lightweight concrete. Special Publication, 226, 123-134.

Huo, J., Shen, X., & Cui, Q. (2007). Study on physical and mechanical properties of hybrid fiber

reinforced lightweight aggregate concrete. New Building Materials.
Düzgün, O. A., Gül, R., & Aydin, A. C. (2005). Effect of steel fibers on the mechanical properties of natural lightweight aggregate concrete. Materials Letters, 59(27), 3357-3363.
Altun, F., & Aktaş, B. (2013). Investigation of rein forced concrete beams behavior of steel fiber added lightweight concrete. Construction & Building Materials, 164(38), 575-581

SS09: CIM: Community Information Modeling – The new frontier of civil engineering

Organizers: G.P. Cimellaro, M. Domaneschi & S. Mahin

Maintenance, Safety, Risk, Management and Life-Cycle Performance of Bridges – Powers, Frangopol, Al-Mahaidi & Caprani (Eds)
© 2018 Taylor & Francis Group, London, ISBN 978-1-138-73045-8

Fuzzy Based Tool to Measure the Resilience of Communities

O. Kammouh, A. Zamani Noori, M. Domaneschi, G.P. Cimellaro
Politecnico di Torino, Italy

ABSTRACT: Last decades have been characterized by an increasing number of disasters all over the world. Therefore, the concept of community resilience has attracted the attention of the scientists who started to explore and assess the ability of communities to recover after undesirable events. In this work, a method for assessing the earthquake community resilience based on the PEOPLES framework is presented. PEOPLES is a framework that defines community resilience using seven dimensions. Each of the dimensions is defined through a set of indicators to describe the different aspects of resilience. The exact evaluation of the indicators is usually not possible due to the lack of deterministic data related to the damaged system after the disaster. The proposed method exploits a knowledge-based fuzzy modelling to allow the quantitative evaluation of the PEOPLES indicators taking into account uncertainties. The output of the implemented fuzzy method is a resilience index.

1 INTRODUCTION

According to "The International Disaster Dataset" (EM-DAT), the number of natural disasters and the corresponding number of people affected, with related economic losses, have shown an upward trend in the last years. This implies that communities are often not sufficiently resilient to natural catastrophes. Consequently, the concept of resilience has been deepened in the engineering field to assess the ability of a community to recover after an undesirable event. Indeed, since the adoption of the Hyogo framework in (Manyena 2006), strategies involved in hazard planning and disaster risk reduction have experienced a paradigm shift from a vulnerability assessment approach to a resilience-based approach (Mayunga 2007).

Since the concept of resilience is applicable in several disciplines, different definitions are available in the literature. Cimellaro et al. (2016) have conducted a comprehensive review on this topic. In their work, the resilience definition provided by Bruneau et al. (2003) emerges: resilience is "the ability of social units to mitigate hazards, contain the effects of disasters when they occur, and carry out recovery activities in ways to minimize social disruption". This definition has been later improved by Cimellaro et al. (2010) who define resilience as: "a function indicating the capability to sustain a level of functionality or performance for a given building, bridge, lifeline network, or community, over a period defined as the control time (T_C) that is usually decided by owners, or society (usually is the life cycle, life span of the system etc.)". Thus, resilience can be defined analytically as the area under the serviceability performance curve $Q(t)$ of a system, normalized accordingly to the considered control time (T_C):

$$R = \int_{t_1}^{t_r} \frac{Q(t)}{T_C}\, dt \tag{1}$$

where R is the resilience index; $Q(t)$ is the system functionality at time t; t_1 is the moment when the disturbance occurs and the system functionality drops from its initial value q_0 to q_1; t_r is the moment when the initial serviceability is completely recovered and equal to q_r; T_C is the control time. Figure 1 shows the performance curve derived using Equation 1. The serviceability $Q(t)$ ranges between 0% and 100% to indicate the complete absence of functionality of the service and its complete effectiveness, respectively.

Here, community resilience is evaluated exploiting a novel method, which benefits from the PEOPLES framework (Renschler et al. 2010, Cimellaro et al. 2016). PEOPLES is a layered framework: each dimension is divided into components, and each component is divided again into a set of indicators. (Kammouh et al. 2017b) conducted a comprehensive review on community resilience indicators that led to identifying 115 of them. They also proposed a method to transform the framework from a qualitative to a quantitative model through the measure-

ment of indicator parameters. However, in specific scenarios, some indicators may be difficult to obtain and quantify, as well as the interdependency among them. In order to track and represent such uncertainties, a method that enhances the one proposed by Kammouh et al. (2017b) is presented herein. The method introduces a fuzzy logic-based modelling of PEOPLES indicators that accounts for the uncertainties involved in the assessment process.

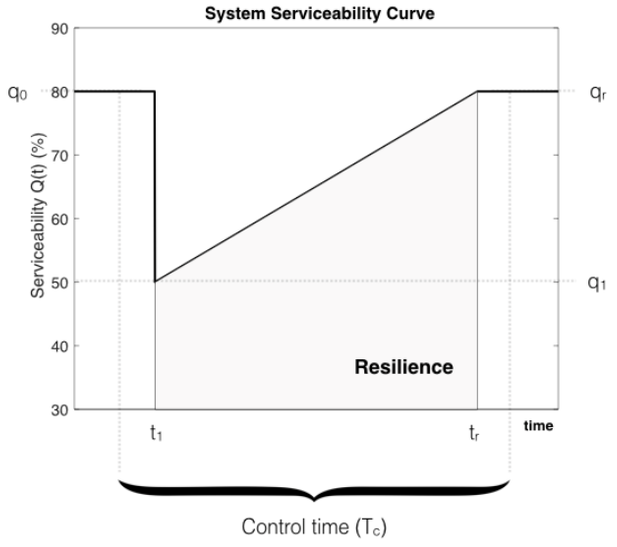


Figure 1. Example of a serviceability function and resilience evaluation.

2 PEOPLES FRAMEWORK

Challenges to make the concept of resilience operational have been addressed by Cimellaro et al. (2016) who defined the so called PEOPLES framework. The framework has been developed at the Multidisciplinary Center of Earthquake Engineering Research (MCEER) and has enhanced the initial research on resilience characteristics. By evaluating the functionality performance of community components (both in time and space), this framework guarantees a qualitative assessment of the community resilience. The acronym "PEOPLES" stands for seven community dimensions:

1 Population and demographics: it includes parameters that describe the social-economic composition of the community. This dimension measures the social vulnerability that could hinder the functionality of the emergency and recovery systems (e.g. population density, age distribution, presence and integration of minorities and socio-economic status.)
2 Environment and ecosystem: it estimates the capability of the environment and of the ecosystem to get back to its pre-hazard conditions. It includes water, air and soil assessments as well as a measure of the biodiversity and the sustainability relations.
3 Organized government services: it covers the services that the government guarantees before and after an extreme event. A great importance is given to the mitigation and recovery processes, which include the preparedness to hazards and all disaster risk reduction measures.
4 Physical infrastructure: it considers the buildings and facilities that are the prevalent interests of civil engineers and traditional resilience analysis. Particularly, two different aspects are analyzed in this dimension: facilities, which includes housing and services which are not crucial for the emergency response, and lifelines, which instead consists of the services that are of vital importance for the management of critical situations.
5 Lifestyle and community competence: This dimension takes into account the capability of a community to face problems by means of political partnerships. This includes both the abilities of a community (i.e. the skills of their components) and its perceptions (i.e. the judgements and feelings that a community has on itself.)
6 Economic development: it describes the economic situation of the community. It can be easily divided in two terms, a static component, which measures the present economic condition, and a dynamic one, which instead takes into account the development and economic growth of the community.
7 Social-cultural capital: This last dimension contains an evaluation of the community's attitude to react to disasters and to return to the pre-event conditions. It includes a lot of subcategories that measure the people's commitment in the community and the social-cultural heritage.

3 FUZZY LOGIC

Zadeh (1965) introduced the concept of fuzzy set and the theory behind it. This theory comes with the absence of any mathematical framework that is able to describe the complexity and vagueness included in processes where human intervention is significant. While in the crisp logic the variables belong only to one class, in the fuzzy logic a variable x can be a member of several classes (fuzzy sets) with different membership grades (μ). Thus, each fuzzy set is characterized by a membership function that associates to any input x a real number (μ) ranging between 0 (x does not belong to the fuzzy set) and 1 (x completely belongs to the fuzzy set) (Zadeh 1965). The strength of inference systems based on fuzzy logic relies on the following two main aspects:

– fuzzy inference systems can handle both descriptive (linguistic) knowledge and numerical data;

– fuzzy inference systems exploit approximate reasoning algorithm to formulate relationships between inputs by which uncertainties can be propagated throughout the whole process (Tesfamariam & Saatcioglu 2008a)

Designing a fuzzy logic-based system follows two fundamental steps: 1) defining the membership functions and the fuzzification process; 2) designing the fuzzy inference system. Fuzzy methods have been widely developed and applied in several fields (Ross 2009). In the context of earthquake engineering, fuzzy methods have been exploited in different applications (e.g. (Tesfamariam & Saatcioglu 2008a, b, Tesfamariam & Saatcioglu 2010, Tesfamariam & Sanchez-Silva 2011, Tesfamariam & Wang 2011)). Fuzzy methods have been widely used also for developing structural control systems (Casciati et al. 2004). A clear procedure for the application of fuzzy logic can be found in (Tesfamariam & Saatcioglu 2008b).

A fuzzy logic system (FLS) can be defined as the nonlinear mapping of an input data set to a scalar output data. A FLS consists of four main parts: fuzzifier, rules, inference engine, and defuzzifier (Figure 2).

The process of fuzzy logic is: a crisp set of input data are gathered and converted to a fuzzy set using fuzzy linguistic variables, fuzzy linguistic terms and membership functions. This step is known as fuzzification. Afterwards, an inference is made based on a set of rules. Lastly, the resulting fuzzy output is mapped to a crisp output using the membership functions, in the defuzzification step.

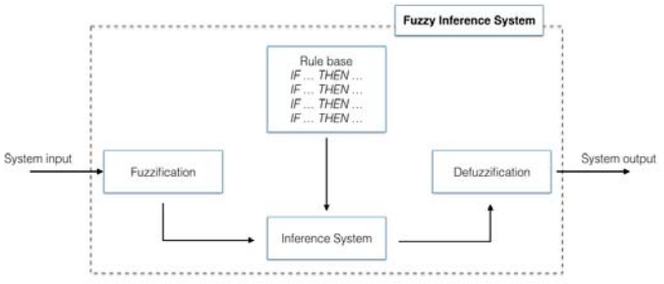


Figure 2. The Fuzzy inference system

3.1 *Fuzzification*

The basic input parameters have a range of values that can be clustered into linguistic quantifiers, for instance, very low (VL), medium low (ML), medium (M), medium high (MH) and very high (VH). The process of assigning linguistic values is a form of data compression and it is called *granulation*. The fuzzification step converts the input values into a homogeneous scale by assigning corresponding membership functions with respect to their specified granularities (Tesfamariam & Saatcioglu 2008b).

Membership functions are used in the fuzzification and defuzzification steps of a FLS, to map the non-fuzzy input values to fuzzy linguistic terms and vice versa. A membership function is used to quantify a linguistic term. Note that, an important characteristic of fuzzy logic is that a numerical value does not have to be fuzzified using only one membership function. In other words, a value can belong to multiple sets at the same time. There are different forms of membership functions such as triangular, trapezoidal, piecewise linear, Gaussian, or singleton. The most common types of membership functions are triangular, trapezoidal, and Gaussian shapes. The type of the membership function can be context dependent and it is generally chosen arbitrarily according to the user experience (Mendel 1995).

3.2 *Fuzzy Rules*

The fuzzy rule base (FRB) is derived from heuristic knowledge of experts or historical data to define the relationships between inputs and outputs. The most common type is the *Mandami* type, which is a simple IF-THEN rule with a condition and a conclusion. For instance, considering two inputs, the i^{th} rule has the following formulation:

$$R: IF\ x_1\ is\ A_1\ AND\ x_2\ is\ A_2\ THEN\ y\ is\ B \quad (2)$$

where x_1 and x_2 are the inputs variable, A_1 and A_2 are input sets, y is the output, B is the output set. The completeness of a fuzzy model is determined by the description of the behaviour for all possible input values and requires a large number of rules. The rule base is the union of all the rules:

$$R = \bigcup_{i=1}^{n} R_i = R_1\ ALSO\ R_2\ ALSO \ldots ALSO\ R_n \quad (3)$$

In some cases it is possible to regulate the degree of influence of each rule on the final output. This can be done by adding weightings based on priority or consistency, in a static or in a dynamic way.

3.3 *Fuzzy Inference System (FIS)*

After evaluating the result of each rule, the results are combined to obtain a final output. This process is called *inference*. Several accumulation methods can be used to combine the results of the individual rules. The maximum algorithm is generally used for accumulation. The evaluations of the fuzzy rules and the combination of the results of the individual rules are performed using fuzzy set operations. The operations on fuzzy sets are different with respect to the operations on non-fuzzy sets.

3.4 *Defuzzifcation*

After the inference step, the overall result is a fuzzy value. This result should be defuzzified to obtain a final crisp output. This is the purpose of the defuzzifier component of an FLS. The defuzzification represents the inverse of the fuzzification process. It is performed according to the membership function of the output variable. There are several techniques to perform the defuzzification such as centre of gravity, centre of area, and mean of maximum methods.

4 METHODOLOGY

Recently, (Kammouh et al. 2017b) have developed a novel method to assess the resilience of communities based on the PEOPLES framework. The researchers provided a way to analytically quantify the resilience of communities through the use of indicators. A list of 115 resilience indicators representing the different aspects of a community have been identified. A full list of indicators can be found in (Kammouh et al., unpubl) while a part of the list can be found in (Kammouh et al. 2017b). Each indicator has been defined and computed using a set of parameters: the functionality before the disaster (q_0), the functionality after the disaster (q_1), the functionality after the restoration phase (q_r), and the recovery time (T_r) (see Figure 1). Moreover, a target value (TV) has been identified for each indicator in order to normalize q_0, q_1 and q_r between 0 and 1 to have a computable and comparable dataset. Then, a serviceability function for the whole community is derived from the aggregation of these measurements, where the weighting scheme is defined according to the indicator importance. Finally, the community resilience is computed as the area under the community serviceability curve using Equation (1).

The methodology previously described represents a major break-through in the context of community resilience evaluation. In spite of being very simple, it can be applied to large communities and can serve as a powerful tool in preliminary decision-making processes related to natural catastrophic events. Nevertheless, this method is operable only if indicators can be numerically quantified, which may not be the case in some scenarios.

In this paper, a method that enhances the one proposed by (Kammouh et al. 2017b) is proposed. The method exploits a fuzzy logic-based modelling of PEOPLES indicators in order to deal with uncertainties and missing knowledge. In the following, the fuzzy modelling of PEOPLES indicators and the evaluation of community resilience using information gathered through the fuzzy inference system are discussed. Different approaches are proposed to match different levels of complexity, starting from a two-parameter approach then four-parameter approach and ending with a full translation of the PEOPLES framework. The proposed methodologies are not fully interchangeable and so only one of them should be selected in accordance with the needed details level.

5 TWO-PARAMETER APPROACH

This approach adopts only two of the four serviceability parameters described before, namely serviceability initial drop q^* (previously referred to as q_0) and recovery time T^* (previously referred to as T_0). Fuzzy parameters have been chosen based on the research by (Bruneau et al. 2003) who describes the resilience of a system using the following three indicators: reduced failure probability; reduced consequences from failure; reduced time to recovery. The reduced failure probability has not been taken into account as it is not easily related to the herein adopted mathematical definition of resilience, which considers only the failure consequence q^* and the repair time T^*. Figure 3 presents a hierarchy of the two-parameter approach where both *time* and *initial drop* variables are used as inputs for the fuzzy system. The inputs are combined using a set of rules to obtain the output variable *fuzzy resilience*. The fuzzy output is defuzzified to get a crisp value that serves as a resilience index for the corresponding indicator.

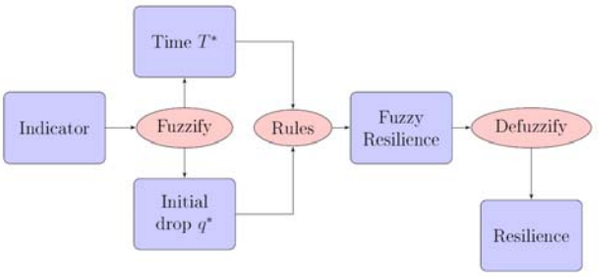


Figure 3. Schematic representation of the two-parameter approach.

5.1 *Evaluating the initial serviceability drop q^*:*

In the authors' opinion, two trapezoidal membership functions can be reasonably adopted in the present case. They are termed as "High" and "Low". The fuzzification used for q* is [High; Low]→[(0, 0, 0.35, 0.65); (0.35, 0.65, 1, 1)]. The membership functions are graphically shown in Figure 4.

5.2 *Evaluating the recovery time T^*:*

When speaking of recovery, the intent is the *full* recovery. Outperforming, or non-complete recovery, as indicated by (Cimellaro et al. 2010), are not generally predictable and therefore they are not included here. For the time variable T^*, three membership functions are suggested by the authors, namely: "short"; "long"; and "very long". The time variable

is normalized based on a 3-year time span, which is normally the time reference for civil applications (i.e., 3 years corresponds to 1 on the horizontal axis). Figure 5 shows the membership functions chosen by the authors. The membership functions are not symmetrical as they have been constructed to the favor of the "Long" and "Very Long" memberships. That is, high range of values of the restoration time T^* variable corresponds to the membership functions "Long" and "Very Long".

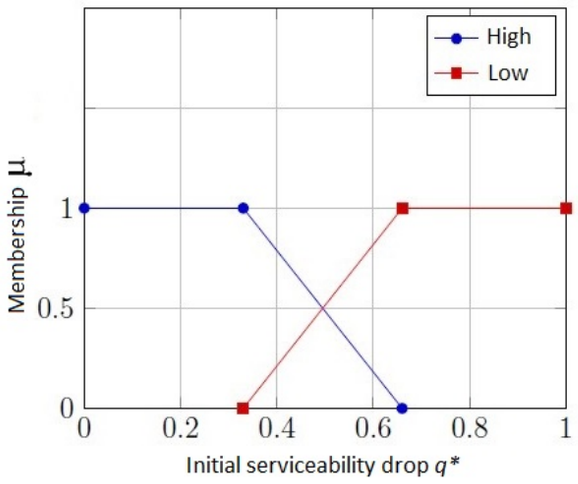


Figure 4. Membership functions for the serviceability variable q^*.

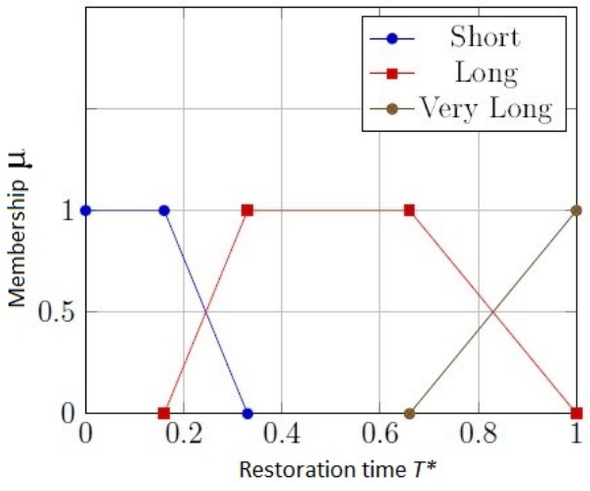


Figure 5. Membership functions for the downtime variable T^*.

The aim is to translate the given input variables (q^* and T^*) into one resilience measure R. This measure is itself fuzzy and so it is defined by a membership function. The chosen membership functions are depicted in Figure 6. Following the fuzzy approach, it is possible to define an output value calculated from the provided inputs on basis of a set of rules. The rules adopted in this study to relate the inputs and the output are shown in Table 1.

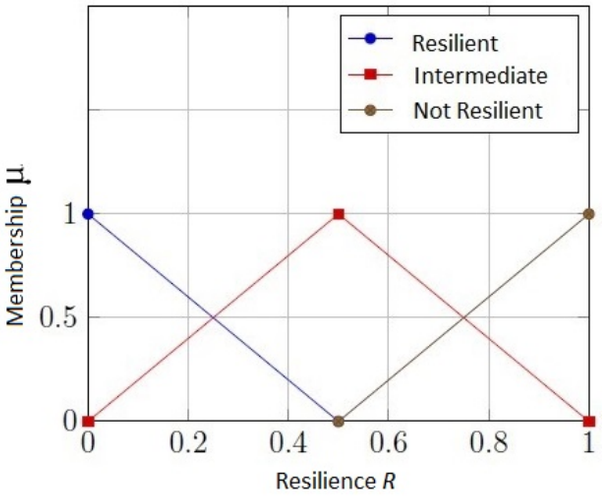


Figure 6. Membership functions for the resilience variable R.

Table 1. Fuzzy rule base for resilience.

T^*	q^*	R
short	high	resilient
Long	high	resilient
Very long	high	intermediate
Short	low	intermediate
long	low	not resilient
Very long	low	not resilient

5.3 *Defuzzification*

The fuzzy output variable is translated (defuzzified) into a numerical value that serves as a measure for resilience. Different methods for defuzzification can be used (Manyena 2006) such as center of gravity, weighted average, mean-max, center of largest area etc. The use of one method rather than another is dependent on the application. Here, the center of gravity method given in Equation 4 is used.

$$CoA = \frac{\int_{x_{min}}^{x_{max}} f(x) \cdot x \, dx}{\int_{x_{min}}^{x_{max}} f(x) \, dx} \quad (4)$$

where $f(x)$ is the function that shapes the output fuzzy set after the aggregation process and x stands for the real values inside the fuzzy set support ([0, 1]).

5.4 *Weighting*

The methodology introduced above applies to each indicator apart. It is often the case to aggregate different indicators into a single measure (i.e. community resilience) through a hierarchical structure. Usually, indicators contribute differently towards resilience and this necessitates weighting them according to their contribution. Different weighting schemes can be applied (Kammouh et al. 2017a, Kammouh et al., in press, Kammouh et al. 2017b). The one used in (Kammouh et al. 2017b) is here

adopted. This can be performed by simply allocating an importance factor (I) ranging between 1 and 3 to each indicator then applying the weighted average rule as follows:

$$R = \frac{\sum_{i=1}^{N} I_i R_i}{\sum_{i=1}^{N} I_i} = \sum_{i=1}^{N} w_i R_i \quad (5)$$

where R is the community resilience measure, R_i is the resilience measure of the i^{th} indicator, I_i is the corresponding importance factor (which can be scaled to preference), and w_i is the weighting factor of the i^{th} indicator. The difference with what was proposed in (Kammouh et al. 2017b) is that in this methodology the serviceability functions are translated into a resilience value before applying the weighting method (Figure 7). This simplifies the fuzzy system as it reduces the number of variables that need to be handled. Another approach that considers the weighting factors within the fuzzy system is introduced later in the paper.

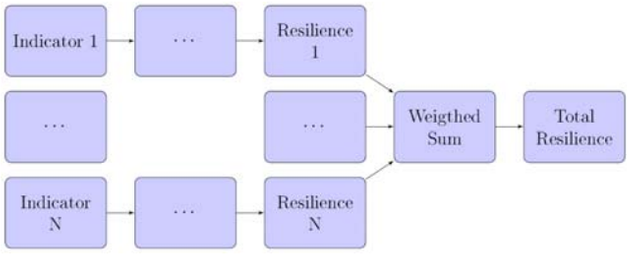


Figure 7. Hierarchical scheme of the fuzzy system with the weighting process.

Practical examples on the application of the fuzzy method to several case studies can be found in (Tesfamariam & Saatcioglu 2008a, b, Tesfamariam & Saatcioglu 2010). The same procedure is applied in this research but with the new variables and membership functions.

6 FOUR-PARAMETER APPROACH

Considering only two parameters to represent a resilience indicator may in some cases be insufficient, thus affecting the mentioned benefits of using the Fuzzy approach. Moreover, this may oversimplify the problem especially when specific information about the structure itself is available and to be added. For this reason, in certain cases it may be beneficial to build up the resilience curve from fuzzy parameters other than the recovery time and the initial drop. In fact, it has been pointed out by Comerio (2006) that further distinction in the repair time is possible. According to his work, the following parameters should be taken into account:

- Construction repair time;
- Mobilization time;
- Economic conditions of the interested region;

The mobilization time in particular, labelled as "irrational" in (Comerio 2006) (e.g. financing, workforce availability, relocation of functions or regulatory changes), is often not properly accounted for and therefore it should be given a special attention when evaluating downtime.

These three indicators may be fuzzyfied with a structure similar to the one adopted for the recovery time T^*. The result is similar to what shown previously with the only difference that new rules and membership functions are to be assigned to the new variables. When resilience measures are calculated, weighting is performed to obtain the system (community) resilience.

7 FULL PEOPLES

Most of the concepts described previously remain valid here. The only difference is that the approach introduced in this section includes the weighting of the variables within the fuzzy system. Normally, choosing adequate weighting factors is subjective and includes uncertainty. Although the inclusion of the weighting factors within the fuzzy system may add additional complexity as more variables are considered, it is certainly beneficial as it solves the uncertainty problem related to the weighting factors. To do that, two alternatives are proposed:

- Include the importance factor in the definition of the rules governing the fuzzy logic. In other words, assign rules such that the output is strongly related to the indicators with highest importance;
- Translate the importance factor into a fuzzy variable itself and include rules for it.

In both cases, rules have to be adapted to account for the importance factors. In the former case, rules are firmly tight to the particular application (i.e. hard to modify and not flexible); the latter case is, in this respect, more flexible but at the cost of additional complexity since additional rules have to be added to include the effect of the importance factor. This approach will be further developed and case studies will be added in future work. Figure 8 shows the logic flow where the weighting process is included as a separate variable in the first step before fuzzification:

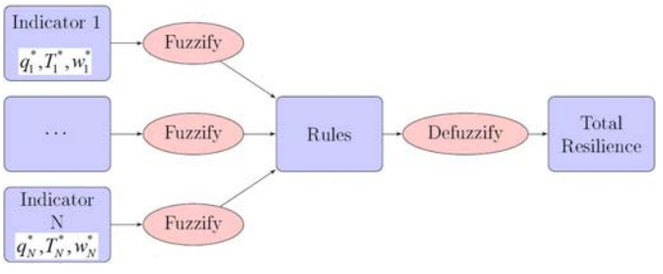


Figure 8. Full PEOPLES approach general hierarchical scheme with the weighting process included in the fuzzy system as a separate variable.

8 CONCLUSION

This paper extends the work previously done on the PEOPLES framework to evaluate the resilience of communities. It takes advantage of the fuzzy theory to account for the uncertainties involved in the evaluation of the PEOPLES' indicators. Different approaches are herein proposed depending on the level of complexity sought and the application type. The former considers only two fuzzy variables and it is intrinsically simple. However, oversimplification can affect the accuracy of the community resilience evaluation. A more comprehensive approach which includes a larger number of parameters with essential benefits in the resilience assessment at the cost of more demanding computational efforts is proposed. Possible developments in the application of weighting factors are also suggested for aggregating different indicators into a single community resilience measure.

9 ACKNOWLEDGMENT

The research leading to these results has received funding from the European Research Council under the Grant Agreement n° ERC_IDEAL RESCUE_637842 of the project IDEAL RESCUE—Integrated Design and Control of Sustainable Communities during Emergencies.

10 REFERENCES

BRUNEAU, M., CHANG, S. E., EGUCHI, R. T., LEE, G. C., O'ROURKE, T. D., REINHORN, A. M., SHINOZUKA, M., TIERNEY, K., WALLACE, W. A. & WINTERFELDT, D. V. (2003) A Framework to Quantitatively Assess and Enhance the Seismic Resilience of Communities. *Earthquake Spectra,* 19**,** 733-752.

CASCIATI, F., DOMANESCHI, M. & FARAVELLI L. (2004) Design and Implementation of a Pointer System Controller. *Nonlinear Dynamics*, 36, 203-215.

CIMELLARO, G. P., REINHORN, A. M. & BRUNEAU, M. (2010) Framework for analytical quantification of disaster resilience. *Engineering Structures,* 32**,** 3639-3649.

CIMELLARO, G. P., RENSCHLER, C., REINHORN, A. M. & ARENDT, L. (2016) PEOPLES: A Framework for Evaluating Resilience. *Journal of Structural Engineering,* 142**,** 04016063.

COMERIO, M. C. (2006) Estimating downtime in loss modeling. *Earthquake Spectra,* 22**,** 349-365.

KAMMOUH, O., DERVISHAJ, G. & CIMELLARO, G. P. (2017a) A New Resilience Rating System for Countries and States. *Procedia Engineering,* 198**,** 985-998.

KAMMOUH, O., DERVISHAJ, G. & CIMELLARO, G. P. (in press) A quantitative framework to assess resilience and risk at the country level. *ASCE-ASME Journal of Risk and Uncertainty in Engineering Systems, Part A: Civil Engineering, in press*.

KAMMOUH, O., NOORI, A. Z., CIMELLARO, G. P. & MAHIN, S., Resilience Evaluation Of Urban Communities Based On Peoples Framework. *ASCE-ASME Journal of Risk and Uncertainty in Engineering Systems, Part A: Civil Engineering, Unpub*.

KAMMOUH, O., NOORI, A. Z., RENSCHLER, C. & CIMELLARO, G. P. (2017b) Resilience quantification of communities based on PEOPLES framework. *16th World Conference on Earthquake.* Santiago.

MANYENA, S. B. (2006) The concept of resilience revisited. *Disasters,* 30**,** 434-450.

MAYUNGA, J. S. (2007) Understanding and applying the concept of community disaster resilience: a capital-based approach. *Summer academy for social vulnerability and resilience building,* 1**,** 16.

MENDEL, J. (1995) Fuzzy logic systems for engineering: a tutorial. *Proceedings of the IEEE.*

RENSCHLER, C. S., FRAZIER, A. E., ARENDT, L. A., CIMELLARO, G. P., REINHORN, A. M. & BRUNEAU, M. (2010) *A framework for defining and measuring resilience at the community scale: The PEOPLES resilience framework*, MCEER Buffalo.

ROSS, T. J. (2009) *Fuzzy logic with engineering applications*, John Wiley & Sons.

TESFAMARIAM, S. & SAATCIOGLU, M. (2008a) Risk-based seismic evaluation of reinforced concrete buildings. *Earthquake Spectra,* 24**,** 795-821.

TESFAMARIAM, S. & SAATCIOGLU, M. (2008b) Seismic risk assessment of RC buildings using fuzzy synthetic evaluation. *Journal of Earthquake Engineering,* 12**,** 1157-1184.

TESFAMARIAM, S. & SAATCIOGLU, M. (2010) Seismic vulnerability assessment of reinforced concrete buildings using hierarchical fuzzy rule base modeling. *Earthquake Spectra,* 26**,** 235-256.

TESFAMARIAM, S. & SANCHEZ-SILVA, M. (2011) A model for earthquake risk management based on the life-cycle performance of structures. *Civil Engineering and Environmental Systems,* 28**,** 261-278.

TESFAMARIAM, S. & WANG, Y. (2011) Risk-based seismic retrofit prioritization of reinforced concrete civic infrastructure: Case study for state of Oregon schools and emergency facilities. *Natural Hazards Review,* 13**,** 188-195.

ZADEH, L. A. (1965) Fuzzy sets. *Information and control,* 8**,** 338-353.

Maintenance, Safety, Risk, Management and Life-Cycle Performance of Bridges – Powers, Frangopol, Al-Mahaidi & Caprani (Eds)
© 2018 Taylor & Francis Group, London, ISBN 978-1-138-73045-8

Resilience Assessment of City-Scale Transportation Networks Using Monte Carlo Simulation

O. Kammouh, A. Cardoni, S. Marasco & G.P. Cimellaro
Department of Structural, Geotechnical & Building E ngineering, Politecnico di Torino, Corso Duca degli Abruzzi 24, 10129, Turin, Italy

S. Mahin
Department of Civil & Environmental Engineering, Unive rsity of California Berkeley, Davis Hall, Berkeley, USA

ABSTRACT: To improve the resilience of critical infrastructure systems, their intrinsic properties need to be understood and their resilience state needs to be identified. In the literature, several methods to evaluate networks' reliability and resilience can be found. However, the applicability of these methods is usually restricted to small-size networks. In this paper, the transportation network of a large-scale virtual city is considered as a case study. A random removal strategy of the links (roads) is applied to simulate the network's failure. The network reliability is then calculated using the Destruction Spectrum (D-spectrum) method and a Monte Carlo approach has been developed to generate failure permutations that are necessary for the evaluation of the D-spectrum. In addition, the Birnbaum Importance Measure (BIM) has been adopted in this study to determine the importance of the network's components. The methodology adopted in this study can be also extended to all network-based systems. The paper also introduces resilience indicators as a soft tool to predict the performance and the serviceability of the transportation networks.

1 INTRODUCTION

Good physical connectivity in the urban and rural areas is essential for the economic growth of communities. Because of its intensive use of infrastructures, the transport sector is considered an important component of the economy and a common tool used for development. Transport networks need to provide a continuous service for communities, and this necessitates a good understanding of their resilience and reliability states. For instance, understanding how the topology of the network changes under disruptive events can be fundamental in the decision making process. It could also speed up rescue operations and help in evaluating cascading effects on other interdependent networks. This paper explores mostly the reliability of large scale networks. Reliability is a very broad concept and its application is extended to all engineering fields. In general terms, network reliability can be defined as the probability of connecting the nodes of the network (Chang & Li 2014). Other authors consider reliability as the quality of the transportation system in terms of optimal travel time, i.e. the probability that a trip between two nodes takes less than a certain time (Immers et al. 2002). Another widely used concept is the capacity reliability, which is the probability that the network capacity can accommodate a certain traffic volume at a required level of service (Chootinan et al. 2005, Chen et al. 2013, Niu et al., 2017). Reliability has also been studied under specific situations, such as the emergency response, using both ideas of travel time and level of service (Edrissi et al. 2015). Looking at graph theory, Guidotti et al. (2017) have used the connectivity measures as a tool to determine whether a network is reliable or not.

In this work, the reliability of the transportation network of a large scale virtual city is evaluated. The reliability definition adopted in (Gertsbakh & Shpungin 2008, Gertsbakh & Shpungin 2012, Gertsbakh & Shpungin 2016) is considered in this study. According to the researchers, reliability is related to the probability that some nodes, called terminals, remain connected. Thus, the system fails when the terminals are no more connected. The terminal nodes are strategic nodes with pre-defined survival probabilities assigned by the competent authorities. Knowing these probabilities helps greatly in improving the network (Peeta et al. 2010). However, it can be rather difficult to have access to such data. For this reason, a different failure criterion has been chosen in this work. Moreover, another performance parameter, the Birnbaum Importance Measure (BIM), is considered to study the behavior of the analyzed network. This parameter represents the importance of the network's components (Gertsbakh & Shpungin 2012); that is, components with a high BIM index are vulnerable components. The determination of the reliability and BIM indexes is relatively simple for small networks, but when ap-

plied to a large-scale road transportation network, the computational effort becomes a significant aspect to take into account.

The paper also introduces various resilience indicators of transport networks that can serve as a soft tool to predict and assess the resilience and functionality of the transportation system. The indicators are still not exhaustive and they mainly cover the physical aspect of the network only. Further work will be developed to consider organizational and managerial aspects of the network.

The paper is structured as follows: a brief introduction of the performance indexes with their equations is presented in section 2. Section 3 introduces some strategies to overcome the computational issues. A case study is presented in section 4, where the description of the network and the obtained results are provided. Finally, resilience indicators for transport networks are proposed in section 5.

2 NETWORK RELIABILITY AND COMPONENTS' IMPORTANCE

2.1 *Destruction spectrum*

The Destruction spectrum, or simply D-spectrum, is a representation of a network's structure and its failure definition (Gertsbakh & Shpungin 2009). The system in Figure 1 is used to introduce the concept of the D-spectrum. The nodes in the system are assumed reliable while the edges are unreliable; that is, only edges are subject to failure. In this example, the system's failure is defined as the loss in connectivity between the terminal nodes *a* and *c*.

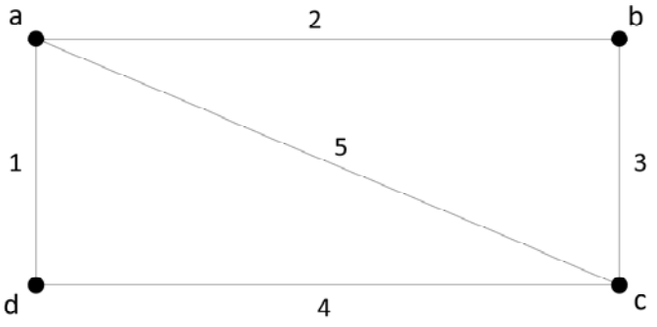


Figure 1. A simple network with two critical nodes.

The system's failure can be reached through different sequences of failing components. For instance, if the edges (1; 2; 5; 3; 4) fail, the two nodes *a* and *c* become disconnected, and thus the system fails. Another permutation leading to the same result can be (3; 5; 4; 1; 2). The failing component at which the system becomes down is called the anchor of the permutation. In the two permutations above, edges 5 and 4 are the anchors respectively. The total number of failure permutations in a system is *k!,* where *k* is the number of unreliable elements. After identifying all failure permutations, the D-spectrum set of the network is computed as follows:

$$D = \left\{ d_1 = \frac{x_1}{k!}, d_2 = \frac{x_2}{k!}, ..., d_k = \frac{x_k}{k!} \right\} \quad (1)$$

where d_i is the i^{th} component of the spectrum, x_i is the total number of permutations whose anchor's order is i, k is the total number of unreliable components. It is obvious from the equation above that the summation of all elements is 1 ($\Sigma_i\, d_i = 1$).

It is worth to note that the failure probability of each edge is not considered in the D-spectrum. One may simply consider a random removal of the edges in the sense that all edges have the same failure probability. Otherwise, a strategic edge removal can be considered but it requires additional analyses. For instance, in transportation networks, the removal of an edge (road) may be linked to the level of damage of the adjacent buildings. This requires fragility analysis to determine the level of damage that each building is subject to.

2.2 *Network reliability*

Generally, a network can be considered reliable when it offers a certain level of service or performance, even during emergency situations. Most of the reliability definitions that can be found in the literature deal with the concept of reliability in probabilistic terms. According to the definition of Gertsbakh & Shpungin (2008), each element of the network (nodes and edges) is given a probability p of being available and a probability $q = 1 - p$ of being unavailable. All these probabilities contribute in the determination of the network's reliability. The formulation used to calculate the reliability index *R(N)* is given in Equation (2). This one is valid when all unreliable components have the same failure probability.

$$R(N) = 1 - \sum_{i=1}^{k} y_i \frac{k!\, q^i\, p^{k-1}}{i!(k-i)!} \quad (2)$$

where y_i is the cumulative D-spectrum, given by the following equation:

$$y_i = \sum_{b=1}^{i} d_b \quad (3)$$

2.3 *Components' importance*

The Birnbaum Importance Measure (BIM) is a parameter that describes the importance of network's components. The vulnerability of the components is what determines their corresponding value of BIM.

This measure can be a tool to identify the critical components of a network in order to strengthen them. The following equation is used to compute the BIM index of a single component *j*:

$$BIM_j = \sum_{i=1}^{k} \frac{k!(z_{i,j} q^{i-1} p^{k-i} - (y_i - z_{i,j}) q^i p^{k-i-1})}{i!(k-i)!} \quad (4)$$

where $z_{i,j} = Z_{i,j} / k!$, in which $Z_{i,j}$ is the number of permutations satisfying two conditions: (a) if the first *i* elements of the network are down, then the network is down; (b) element *j* is among the first *i* elements of the permutation. By doing some manipulation, the expression in Equation (4) can be written in a different form, shown in Equation (5). It is worth to note that both reliability and BIM indexes share a common factor in their equations, and this provides a unique characteristic to compute both indexes in a single operation.

$$BIM_j = \sum_{i=1}^{k} \frac{k! q^i p^{k-1}}{i!(k-i)!} \cdot \left(\frac{z_{i,j}}{q} - \frac{y_i - z_{i,j}}{p} \right) \quad (5)$$

3 METHOD: APPLICATION TO LARGE-SCALE NETWORKS

Theoretical reliability analyses are not always applicable to large problems. For instance, the applications of the above mentioned equations are limited to small networks with defined number of components. This is due to the presence of *factorial* in the denominator of the spectrum set (Eq.(1)). The same problem appears when computing the reliability index *R*, although we know in advance that this is a number between 0 and 1, regardless of the network's size. In this section, we present strategies to apply the D-spectrum to large scale networks and compute the reliability index and BIM-spectra.

3.1 *D-spectrum for large scale networks: a Monte Carlo approach*

We propose the use of a Monte Carlo approach to generate the failure permutations needed to compute the D-spectrum. Hereafter, the algorithm of the Monte Carlo simulation is presented.

Algorithm: Generate permutations and compute the D-spectrum

1) Define a failure criterion for the network (e.g. percentage of failed components, number of disconnected nodes, etc.).
2) Start a permutation counter (n = 1).
3) Choose a component (edge or node) randomly from 1 to k and store it (i.e. the chosen number represents a failed component).
4) Check if the network's failure criterion defined in step 1 is met:
   a. If yes, store the permutation and go to step 5;
   b. If no, choose another number from 1 to k excluding the numbers previously chosen and then go back to step 4.
5) Set n = n + 1 and repeat the steps 3 and 4 for *M* times to generate *M* permutations.
6) Group the permutations according to their anchor's value (i.e. the anchor value coincides with the vector's length of the permutation).
7) Compute the D-spectrum using Equation (1).

In case of targeted removal, the network's components should be linked with given failure probabilities or lifetime distributions. In this case, step 3 is adjusted so that the removal process is not random.

3.2 *Reliability and BIM indexes for large scale networks: incremental computation*

Practically, computing the reliability and BIM indexes is not possible for moderate to large networks. The reason is that both numerator and denominator in the second term of the reliability index (Eq.(2)) and in the first term of the BIM index (Eq.(5)) are too large. However, it is known in advance that the reliability index is a number that ranges between 0 and 1 regardless of the network's size. Symbolic calculation represents an effective tool to solve such kind of numerical problems. Also, a more compact writing of the equation has been used. Defining *M* as shown in Equation (6), it is possible to rewrite the expressions of reliability and BIM indexes (Eqs 7-8).

$$M_i = \frac{k! q^i p^{k-i}}{i!(k-i)!} \quad (6)$$

$$R = 1 - \sum_{i=1}^{k} y_i \cdot M_i \quad (7)$$

$$BIM_j = \sum_{i=1}^{k} M_i \cdot \left(\frac{z_{i,j}}{q} - \frac{y_i - z_{i,j}}{p} \right) \quad (8)$$

4 CASE STUDY: THE TRANSPORTATION NETWORK OF A VIRTUAL CITY

4.1 *Network definition*

The road transportation network of a virtual city has been modeled as an undirected graph (Figure 2). An undirected graph *G = (V, E)* consists of a set of vertices (or nodes), representing the intersections, together with an edge set *E*. The elements belonging to *E* are called edges or links, and represent the roads of the network. In an undirected graph every pair of

nodes is connected, so each path can be passed through in both directions. Actually, a road map would be a directed graph, as the streets have a certain way. However, in emergency conditions, it is likely that respecting the directions becomes a secondary aspect.



Figure 2. The transportation network of the virtual city.

The road transportation system consists of 19,614 edges connecting 15,012 nodes. Mathematically, the network has been described with an adjacency matrix A, which is a square matrix with a side dimension equal to the number of the nodes. The elements inside A can be either 1 or 0. If $a_{i,j} = 1$, it means that there is a connection (road) between node i and node j, while 0 means that the two nodes are not linked. Since the graph is not directed, the resulting adjacency matrix is symmetric. This matrix allows to describe and modify the topology of the network and to automate all the calculations.

4.2 *Network's failure criterion*

The definition of the failure criterion is strictly related to the reliability of the network. Despite its importance, there is not a unique definition for the failure criterion of a network. Gertsbakh & Shpungin (2008) proposed the criterion of terminal connectivity; that is, if critical nodes are disconnected, the network becomes down. This criterion is applicable to small scale networks, but when dealing with large networks a huge computational effort would be needed to identify whether the nodes are connected or not. In this work, a simpler network failure criterion is adopted. The network is considered unavailable when at least 5% of the nodes are isolated (not connected to any edge).

4.3 *Results*

The methodology introduced in section 3 has been applied to the case study. Due to the large size of the analyzed network, the results are not shown using vectors or matrices, but rather using graphs.

First, the above mentioned algorithm has been used to generate the failure permutations of the edges. The number of permutations considered in this case study is 3.5 million. The generated permutations have been subsequently used in the calculation of the D-spectrum. The result of the D-spectrum is shown in Figure 3. It can be clearly seen that there are only few non-zero elements in the distribution, and they are all gathered in a small range. The distribution of the D-spectrum is a perfectly normal distribution confirming that the assumed number of permutations was large enough to represent the problem. The location of the distribution's peak depends greatly on the chosen failure criterion of the network and on the number of components forming the network. More study will be dedicated to know the reason of having a normal distribution and to identify the effect of the failure criterion and number of components on the position of the distribution's peak. Moreover, looking at the definition of the D-spectrum, the sum of all its elements is 1. This is verified in Figure 4, which shows the distribution of the cumulative D-spectrum.

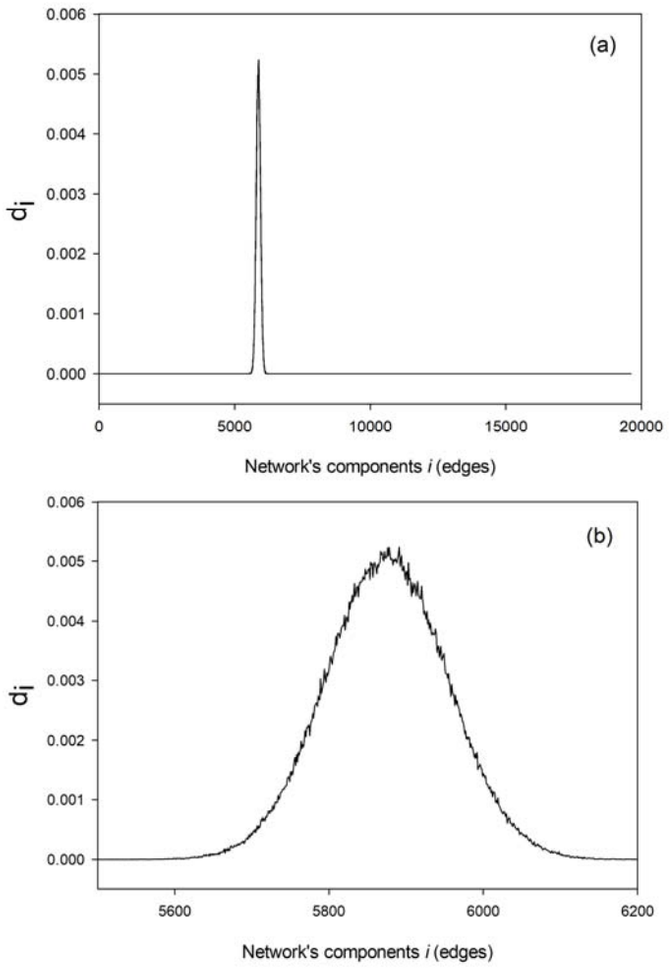


Figure 3. (a) The D-spectrum of all components of the case study network; (b) a zoomed view at the distribution peak.

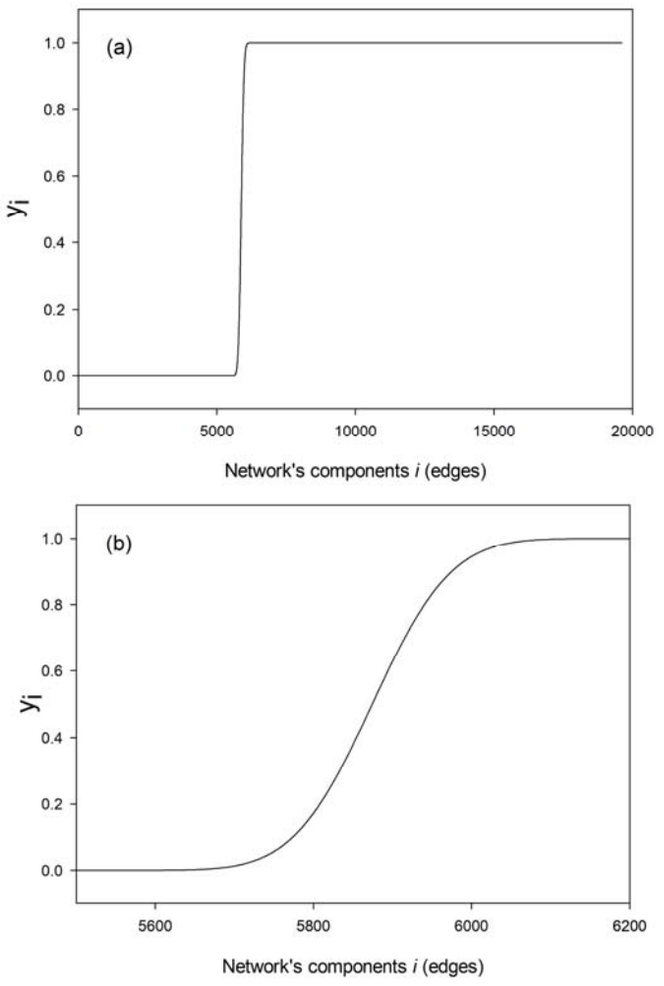


Figure 4. (a) The cumulative D-spectrum of all components of the case study network; (b) a zoomed view at the transitional part.

Following the D-spectrum, the BIM index of the network's components and the network reliability index *R* have been evaluated. The BIM index results of the networks' components have been normalized with respect to the maximum value. Figure 5 shows the BIM results of the first 100 components. The BIM indexes of the other components range between the upper the lower bounds, 1 and 0.98 respectively. This implies that the variance in the results is very small. In fact, the importance index of the edge is ruled by the network configuration and the failure probability of the edge. In our network, we considered an equal failure probability for the edges, which was represented by the random removal process. The small difference in the importance of the edges was only due to the network's configuration.

The reliability of the network was computed using Equation (7). It is worth to mention that the network reliability depends mainly on the following factors: (a) the network size (number of components in the network *k*); (b) the component's failure probability *q*; (c) the network's failure criterion (embedded in the cumulative D-spectrum term *y*); (d) and the network's topography (embedded in the cumula-

tive D-spectrum term *y*). The reliability of the analyzed network was found to be 46%. However, this number considers equal failure probabilities for all network components. This is rarely the case because usually the effect of disruptive events on a network system is not spatially uniform.

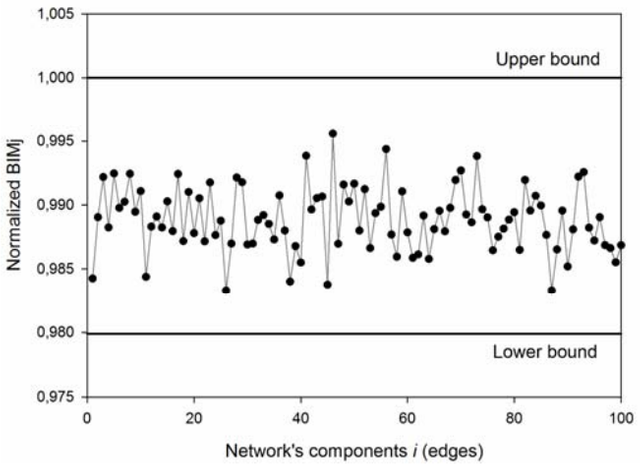


Figure 5. The BIM spectra of the network's components.

5 RESILIENCE INDICATORS FOR TRANSPORTATION NETWORKS

Indicators are quantifiable variables that represent selected characteristics of resilience (Cimellaro et al., 2016; Cutter 2016). Generally, individual indicators can be combined to create a single resilience index (Kammouh et al. 2017b). The index illustrates the multi-dimensional nature of resilience by aggregating multiple indicators, but also condenses its complexity into a single numeric value.

To study the resilience of a critical infrastructure, it is important to tackle the different resilience aspects of the system (Cimellaro et al., 2010, Cimellaro et al., 2015). For example, having a well-planned transportation network can result in a non-resilient system if the organizational and the managerial aspects are not considered. The user-behavior aspect can also contribute in the overall resilience of the analyzed system. While non-physical components are fundamental to study the resilience of transport networks, in this work only the physical aspect in considered.

The functionality of the physical aspect of transportation infrastructure has a great impact on the resilience of entire system. The physical aspect can be divided into two main parts: the inherent physical characteristics of the traffic and the network topography, which is the geometry of the network that defines the location of the links (i.e. roads, subway lines, path, bridges, etc.) and nodes (i.e. intersections, stations, etc.).

The physical characteristics of transportation infrastructure includes factors like resisting strength, pavement condition, road width, number of lanes, lighting system, safety elements, etc. All of these attributes and basic elements control the proper function of transport system, especially when it is under rare events, such as earthquakes, floods, hurricanes, landslides, etc. (which have long-term effect) and frequent events like traffic accidents, road maintenance (which temporarily disable intended function) (Soltani-Sobh et al. 2016).

Generally, an infrastructure with enough redundant capacity can minimize the impact of adverse events and keep the system in a relatively stable state. For example, when a car accident occurs on a road with emergency lanes or with a Variable Message Signs (VMS), travelers can use the extra lane or change to an alternative way that is suggested by the VMS before getting stuck in the traffic. Moreover, the degradation of the road environment influences the driving conditions, which affect the road capacity and result in the failure of the whole system.

In addition to the physical characteristics, the degree of betweenness and connectivity of the network system should be considered to assess the resilience of transportation networks. The concept of *betweenness* quantifies the number of shortest paths that pass through a node (Leu et al. 2010). As shown in Figure 6, node *A* has the highest betweenness among all four nodes. In a previous study, it was proved that a failure of the node with the highest betweenness can cause the maximum damage to the network because it reduces the efficiency and the survivability of the entire system (Zhang et al. 2011). Moreover, Steiglitz et al. (1969) proposed that the residual connections between nodes can increase the performance of the network. In other words, the more number of reliable passageways between an origin and a destination, the more resilient is the transportation system.

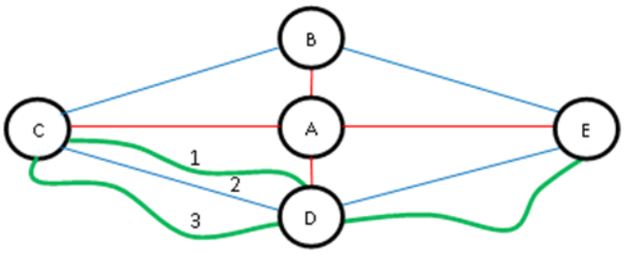


Figure 6. An illustration of the concept of connectivity and betweenness.

This is illustrated in Figure 6, where links 1, 2, 3 represent three alternative paths connecting the two nodes *C* and *D*. So, users would have alternative choices when one of the three routes is closed. This implies that the system has a high redundancy, which is the ability to remain (nearly) unchanged with disturbance.

Table 1 shows an extended list of resilience indicators that describe the physical system of the transportation network. Most of the indicators have been collected from the literature while some of them have been proposed by the authors. The indicators are grouped under different components representing the major aspects of the system. Each of the indicators is accompanied by a *measure* that allows the analytical evaluation of the indicator. Each measure is normalized with respect to a fixed quantity, the target value (*TV*), which is an essential quantity defined by the authority to provide a baseline to measure the corresponding indicator. Moreover, the indicators have been identified by their nature: 'Static indicator (S)' assigned to indicators that are not affected by the perturbation/disaster, and 'Dynamic indicator (D)' assigned to the indicators whose value/serviceability changes after the event.

Indicators must be weighted according to their contribution towards the resilience of the system. Kammouh et al. (2017a) introduced and exemplified three weighting methods for resilience indicators based either on the dependence tree analysis or on the spider plot analysis (Kammouh et al. 2017a, Kammouh et al., in press).

Table 1. Components and indicators of the physical system of transportation networks.

Component/ indicator	**Measure (0≤value≤1)**	**Reference**	**Nature**
1-Links/Connectors			
-Accessibility	Number of links/passageways per destination ÷ TV	(Ip & Wang 2011)	D
-Road density	Number of alternative links between an origin and destination ÷ TV	(Jenelius 2009)	D
-Road width	Average width of road ÷ TV	(Jenelius 2009)	S
-Lanes of road	Number of lanes available ÷ TV	(Litman 2006)	D
-Link (road, track, etc.) condition	% links with full functionality during the event	*	D
2-Vehicles			
-Mode of transport	Number of multi-mode choices per destination ÷ TV	(Ip & Wang 2011)	D
-Service level	Average speed of vehicles in normal condition ÷ TV	*	S
-Characteristics of vehicles	Degree of preference of specific vehicles (regarding performance, comfort level, etc.)÷ TV	*	S
3-Other Facilities/Structures			
-Quality of facilities	1-(% deficiency of facilities in past events ÷ TV)	(Tamvakis & Xenidis 2012)	S
-Critical components	Number of roundabout/emergency lanes ÷ TV	*	S
-Maintenance of facilities	Number of maintenance during an interval of period ÷ TV	(Tamvakis & Xenidis 2012)	S
-Essential infrastructure robustness	% infrastructures that remained operational during emergencies in past events	(Reduction 2012)	S
-Traffic load capacity	Number of excessive capacity (emergency lanes, tracks, airlines, etc.) ÷ TV	(Cox et al. 2011)	D
-Urban form	Number of city centers per 100,000 people ÷ TV	(Mishra et al. 2012)	S
-Size of network (connectivity)	Number of connectivity of intersection ÷ TV	(Zhang et al. 2011)	D
-Size of network (betweenness)	1-(Number of betweenness of intersections ÷ TV)	(Zhang et al. 2011)	D
4-Accessories			
-Tool kit inside vehicles	1-(Presence of tool kits, like extinguisher, escape hammer, etc.); 0 (otherwise)	*	S
-Path environment	Number of safety elements (isolation strips, traffic lights, etc.) per km ÷ TV	(Soltani-Sobh et al. 2016)	S
5-Serviceability			
-Characteristics of traffic lines	Frequency and capacity of each line ÷ TV	(Dorbritz 2011)	D
-Travel time reliability	number of punctual service assisted by control system ÷ total number of service	(Leu et al. 2010)	S

* Indicator proposed by the authors

6 CONCLUDING REMARKS

This paper presents a methodology to evaluate multiple performance indexes for large scale networks. In the literature, several methods to evaluate networks reliability and resilience can be found. The application of such methods to large scale networks is not feasible due to the computational complexity. In this paper, the case of large scale networks is tackled. The case study considered in this work is the transportation network of a virtual city. First, the road map of the city is transformed into an undirected graph, which consists of 15,012 nodes and 19,614 edges. A random removal strategy of the edges is applied as a failure mechanism until the network's failure point is reached. The network reli-

ability is then calculated using the Destruction Spectrum (D-spectrum) method assuming the same failure probability for all edges. A Monte Carlo approach is used to generate failure permutations which are necessary for evaluating the D-spectrum. In addition, the network's edges have been ranked from the most to the least important by applying the Birnbaum Importance Measure (BIM). To overcome the computational obstacles, an algorithm and calculations techniques have been presented and discussed. The results obtained in this study are used to identify the vulnerable components of the network. The vulnerable components are the ones that should be focused on to improve the overall resilience of the infrastructure. The analysis concept adopted in this study is applicable to all network-based infrastructure systems such as water, gas, transportation, etc. Future work is geared towards replicating the analysis methodology to the case of strategic edge removal. The edge removal mechanism will be linked to the buildings' damage assuming a certain destructive event. The paper also proposed a list of resilience indicators for transport networks that describe the physical aspect of the system. Future studies will focus on identifying other indicators related to other aspects of the transportation infrastructure.

ACKNOWLEDGEMENTS

The research leading to these results has received funding from the European Research Council under the Grant Agreement n° ERC_IDEAL RESCUE_637842 of the project IDEAL RESCUE—Integrated Design and Control of Sustainable Communities during Emergencies.

REFERENCES

Chang, S. & Li, L. Reliability analysis of highway and transportation network with paths failure. Advanced Research and Technology in Industry Applications (WARTIA), 2014 IEEE Workshop on, 2014. IEEE, 50-53.

Chen, A., Kasikitwiwat, P. & Yang, C. 2013. Alternate capacity reliability measures for transportation networks. *Journal of Advanced Transportation,* 47**,** 79-104.

Chootinan, P., Wong, S. C. & Chen, A. 2005. A reliability-based network design problem. *Journal of Advanced Transportation,* 39**,** 247-270.

Cimellaro, G. P., Renschler, C., Reinhorn, A. M., and Arendt, L. (2016). "PEOPLES: a framework for evaluating resilience." *Journal of Structural Engineering, ASCE*, 142(10), DOI: 10.1061/(ASCE)ST.1943-1541X.0001514.

Cimellaro, G., Tinebra, A., Renschler, C., and Fragiadakis, M. (2015). "New Resilience Index for Urban Water Distribution Networks." *Journal of Structural Engineering, ASCE*, 10.1061/(ASCE)ST.1943-1541X.0001433 , C4015014.

Cimellaro, G. P., Reinhorn, A. M., and Bruneau, M. (2010). "Framework for analytical quantification of disaster resilience." *Engineering Structures*, 32(11), 3639–3649.

Cox, A., Prager, F. & Rose, A. 2011. Transportation security and the role of resilience: A foundation for operational metrics. *Transport policy,* 18**,** 307-317.

Cutter, S. L. 2016. The landscape of disaster resilience indicators in the USA. *Natural hazards,* 80**,** 741-758.

Dorbritz, R. Assessing the resilience of transportation systems in case of large-scale disastrous events. Proceedings of the 8th International Conference on Environmental Engineering, Vilnius, Lithuania, 2011. 1070-1076.

Edrissi, A., Nourinejad, M. & Roorda, M. J. 2015. Transportation network reliability in emergency response. *Transportation Research Part E-Logistics and Transportation Review,* 80**,** 56-73.

Gertsbakh, I. & Shpungin, Y. 2008. Network reliability importance measures: combinatorics and monte carlo based computations. *WSEAS Transactions on Computers,* 7**,** 216-227.

Gertsbakh, I. B. & Shpungin, Y. 2009. *Models of Network Reliability: Analysis, Combinatorics, and Monte Carlo* , CRC Press, Inc.

Gertsbakh, I. B. & Shpungin, Y. 2012. Using D-spectra in network Monte Carlo: estimation of system reliability and component importance. *Recent Advances in System Reliability.* Springer.

Gertsbakh, I. B. & Shpungin, Y. 2016. *Models of network reliability: analysis, combinatorics, and Monte Carlo*, CRC press.

Guidotti, R., Gardoni, P. & Chen, Y. 2017. Network reliability analysis with link and nodal weights and auxiliary nodes. *Structural Safety,* 65**,** 12-26.

Immers, B., Yperman, I., Stada, J. & Bleukx, A. 2002. Reliability and robustness of transportation networks. *Problem survey and examples*.

Ip, W. H. & Wang, D. 2011. Resilience and friability of transportation networks: evaluation, analysis and optimization. *IEEE Systems Journal,* 5**,** 189-198.

Jenelius, E. 2009. Network structure and travel patterns: explaining the geographical disparities of road network vulnerability. *Journal of Transport Geography,* 17**,** 234-244.

Kammouh, O., Dervishaj, G. & Cimellaro, G. P. 2017a. A New Resilience Rating System For Countries and States. *Procedia Engineering,* 198**:** 985-998.

Kammouh, O., Noori, A., Renschler, C. & Cimellaro, G. P. 2017b. Resilience quantification of communities based on PEOPLES framework. *16th World Conference on Earthquake, 9-13 January 2017.* Santiago.

Kammouh, O., Dervishaj, G. & Cimellaro, G. P. Quantitative Framework to Assess Resilience and Risk at the Country Level. *Journal of Risk and Uncert ainty in Engineering Systems,* (in press).

Leu, G., Abbass, H. & Curtis, N. 2010. Resilience of ground transportation networks: a case study on Melbourne. *33rd Australasian Transport Research Forum Conference, 29 September - 1 October.* Canberra.

Litman, T. 2006. Lessons from Katrina and Rita: What major disasters can teach transportation planners. *Journal of Transportation Engineering,* 132**,** 11-18.

Mishra, S., Welch, T. F. & Jha, M. K. 2012. Performance indicators for public transit connectivity in multi-modal transportation networks. *Transportation Research Part A: Policy and Practice,* 46**,** 1066-1085.

Niu, Y.-F., Gao, Z.-Y. & Lam, W. H. 2017. Evaluating the reliability of a stochastic distribution network in terms of minimal cuts. *Transportation Research Part E: Logi stics and Transportation Review,* 100**,** 75-97.

Peeta, S., Salman, F. S., Gunnec, D. & Viswanath, K. 2010. Pre-disaster investment decisions for strengthening a highway network. *Computers & Operations Research,* 37**,** 1708-1719.

Reduction, U. N. O. F. D. R. 2012. *How to Make Cities More Resilient: A Handbook for Local Government Leaders: a Contribution to the Global Campaign 2010-2015: Making Cities Resilient-My City is Getting Ready!*, UNISDR.

Soltani-Sobh, A., Heaslip, K., Stevanovic, A., El Khoury, J. & Song, Z. 2016. Evaluation of transportation network reliability during unexpected events with multiple uncertainties. *International journal of disaster risk reduction,* 17**,** 128-136.

Steiglitz, K., Weiner, P. & Kleitman, D. 1969. The design of minimum-cost survivable networks. *IEEE Transactions on Circuit Theory,* 16**,** 455-460.

Tamvakis, P. & Xenidis, Y. 2012. Resilience in transportation systems. *Procedia-Social and Behavioral Sciences,* 48**,** 3441-3450.

Zhang, J., Xu, X., Hong, L., Wang, S. & Fei, Q. 2011. Networked analysis of the Shanghai subway network, in China. *Physica A: Statistical Mechanics and its Applications,* 390**,** 4562-4570.

Maintenance, Safety, Risk, Management and Life-Cycle Performance of Bridges – Powers, Frangopol, Al-Mahaidi & Caprani (Eds)
© 2018 Taylor & Francis Group, London, ISBN 978-1-138-73045-8

Seismic Resilience of Electric Power Networks in Urban Areas

S. Sordo, M. Domaneschi, G.P. Cimellaro
Department of Structural, Geotechnical & Building Engineering, Po litecnico di T orino, Corso Duca degl i Abruzzi 24, 10129, Turin, ItalyPolitecnico di Torino, Italy

S. Mahin
Department of Civil & E nvironmental Engineering, University of Califor nia Berkeley, Davis Hall, Berkeley, USA

ABSTRACT: Recent natural disasters have raised the question of how communities can recover from extreme events. In the last decade, the research has been focusing on analyzing interdependencies between different networks. This paper deals with the distribution power network, developing a method to estimate a realistic grid of a virtual city called "Ideal City" freely inspired to the city of Turin in Italy. A software called Matpower, developed by the Joint Research Center, has been used for the load flow analysis of the power network. Fragility curves, repair costs and downtime are evaluated using FEMA's database. Finally, a strategy to improve the network resilience is proposed considering the complexity of the environment.

1 I NTRODUCTION

Seismic resilience of urban areas is one of the central topics in the actual scientific fields. Many recent disasters consolidated the idea that much still needs to reduce human and economic losses due to earthquakes.
One of the most affected networks, especially in the first hours after the event, is the electrical distribution network. Indeed, the first news that media report is that a considerable number of people is left without electric supply.
This aspect complicates situations that are already difficult by isolating communications from large parts of the cities, slowing down the rescue and making it harder for people to resume normal lives. It should not be forgotten that the quick restoration of such networks in critical conditions, for example by replacing key elements such as transformers, can have very high costs. Therefore, careful analysis of the electricity grid is mandatory. In this paper the authors present some suggestions for dealing with this kind of problem evaluating the network resilience, possible countermeasures for overcoming issues and improvements.
This paper on electric network is part of a larger study on a virtual city called Ideal City (Zamani Noori et al. 2017) that is developed to be a resilience based designed community. This town is freely inspired to the city of Turin that is a town of about one million inhabitants in North-West Italy.
This study is related on the EPN (Electrical Power Network) but it is focused on the electrical distribution system. The electricity grid starts with generation stations located many kilometers far from urban centers. It continues with the transmission system that usually surrounds the cities and ends with the distribution network directly to the consumers.
The network components in terms of fragility curves are studied. Repair costs and time are also estimated and, finally, the improvement of the network resilience is evaluated.
The power network can be affected not only by earthquakes but also by tornadoes that is the first cause of failure of electricity in USA in terms of MW lost. Indeed, NIST-funded Center for Risk-Based Community Resilience Planning (Unnikrishnan & van de Lindt 2016) explains how the EPN of Centerville, a Virtual Community Testbed of approximately 50.000 people in a Midwestern State, can be studied and losses analysis performed.
This type of approach is not present only in the American or European literature, but it is now a very actual theme in other countries. For example, an interesting work by Arghavani (2017) can be reported. This is a prototype model to analyze the seismic resilience of the transmission grid of the city of Qom, an Iranian center of quite a million citizen. Iran is a high seismic zone and the researchers have built a simplified model of the network implementing also some emergency scenarios. It is a connectivity analysis, i.e. a binary statement 0 or 1, in which some lines fall, and the response of the grid in terms of recovery time is represented by using a gamma cumulative distribution function.
This type of investigation started years ago, from 2004 when Professor Shinozuka (Shinozuka et al. 2004, Shinozuka et al. 2007) studied the resilience

of integrated power and water system of the LADWP (Los Angeles Department of Water and Power). A database related to the effects of several previous events, e.g. the 1994 Northridge earthquake, is used. In this research, the critical points of the distribution network are the transformers and the associated fragility curves. The correct spatial distribution of PGA is modelled within a Monte Carlo approach. The authors computed risk curves of power supply, households without power, economic losses and some system performance criteria.
Finally, it is worth underlining how resilience of distribution network isn't only a university topic. It is also strictly regulated by law. Last year, within the end of March, all Italian DSOs (Distribution System Operators) have been required to deliver a resiliency plan of their networks to national authority for electricity gas and water.

2 METHODOLOGY

2.1 *Model of the network*

The first problem of the present study is the paucity of data. Information about distribution buses of an urban network is very difficult to collect. Sensible data are usually not shared because security standards or economic interest may be compromised. So, the idea is to try to find an electric grid compatible with the map of Ideal City. The approach selected is summarized in Figure 1.

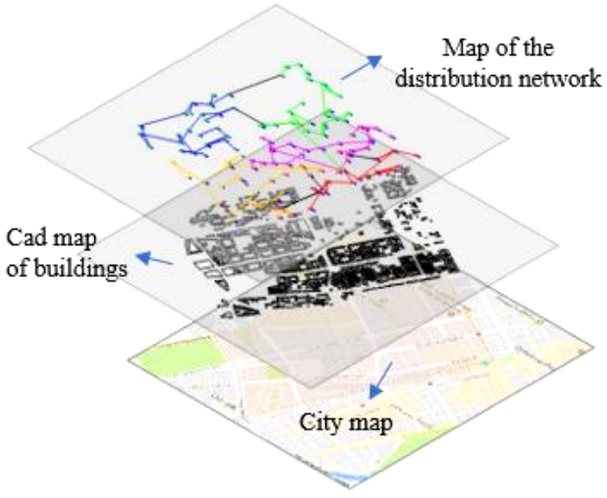


Figure 1. Sketch of the approach

Designing the power supply network for one million people is a critical task. Therefore, a literature review of existing case studies has been performed for selecting a solution that has been adapted to an Ideal City sample.
The European Commission in collaboration with the Distribution System Operators Observatory of JRC (Joint Research Center) released a technical report (Prettico et al. 2016) about representative networks. They have collected data from 79 out of 190 European DSOs that are representative of the 70% of the electricity supplied by all DSOs serving over 100,000 customers. They distribute more than 2,000 TWh of electricity to over 200 million customers per year, covering a total area of more than 3 million square km. This report has been used to build 36 indicators about network structure, network design and distributed generation. From 10 of such indicators, representative distribution networks have been obtained using RNM (Reference Network Model). This is a useful software for large scale distribution planning developed by the Universidad Pontificia Comillas (Domingo et al. 2011).
In the present paper, the "urban" network from JRC database is used for the most densely populated districts and the "semi-urban" ones in the surrounding areas of Ideal City.
The second step consists in making this network independent from the map that JRC has used to realize the model. Information about HV (high voltage), MV (medium voltage) and LV (low voltage) buses with coordinates, branches, electric parameters and protections are provided. In order to apply this realistic network to Ideal City, LV data are relevant only for defining the total amount of consumers, not for their real positions. So, only HV and MV buses are explicitly considered in the model. Finally, the network model is rebuilt writing a new description.
The network has been strictly controlled using Matpower6.0, a package of MATLAB M-files employed for solving power flow problems and developed by PSERC (Power Systems Engineering Research Center) at Cornell University (Zimmerman et al. 2011).
The method for the network performance analysis consists in the computation of the load flow on the entire damaged grid. In this way, a higher precision respect to a simpler and faster connectivity analysis (Arghavani 2017) is provided. Matpower nonlinear analyses are solved through the Newton Raphson (NR) algorithm.
In the AC power flow problem (Zimmerman et al. 2011), the nodal bus injections are defined through those related to loads and generators. The power balance equations are expressed in complex matrix form as

$$g_S\left(V, Sg\right) = S_{bus}\left(V\right) + S_d - C_g S_g = 0 \qquad (1)$$

where $S_{bus}(V)$ is the complex power injections as functions of the complex bus voltages V, S_d are constant power loads, S_g is the generator injections and the C_g is the connection matrix.
This problem can be split into its real P and reactive Q components:

$$g_P\left(\theta, V_m, P_g\right) = P_{bus}\left(\theta, V_m\right) + P_d - C_g P_g = 0 \quad (2)$$

$$g_Q\left(\theta, V_m, Q_g\right) = Q_{bus}\left(\theta, V_m\right) + Q_d - C_g P_g = 0 \quad (3)$$

where θ is the voltage angle and V_m is the voltage magnitude. The power flow problem could be a set of equations in the form

$$g\left(x\right) = 0 \quad (4)$$

and in particular

$$g\left(x\right) = \begin{bmatrix} g_P\left(\theta, V_m, P_g\right) \text{ for PV and PQ buses} \\ g_Q\left(\theta, V_m, Q_g\right) \text{ for PQ buses} \end{bmatrix} \quad (5)$$

where PQ buses are pure load buses and they represent the major part of all of network buses. In these elements P and Q are defined, but θ and V_m must be calculated.
PV buses are connected to the generator and they are a small part of all buses. In these elements P and V_m are defined, but Q and must be calculated (Grainger & Stevenson 1994). Is also important to specify the value of x, as:

$$x = \begin{bmatrix} \theta \text{ for all buses except Reference bus} \\ V_m \text{ for PQ buses} \end{bmatrix} \quad (6)$$

where the Reference bus is the slack bus and it is considered as the number one of the network. In this element, $\theta = 0^o$, V_m is known but P and Q must be computed.
So, a nonlinear system (Dharamjit & Tanti 2012) with n_{pv} + n_{pq} equations and unknowns (n is the number of PV or PQ buses) results. Solving by x, it's possible to determine the generator real power injections at the reference bus and generator power injections.
These solutions are provided using the iterative NR's method. Starting from an initial trial solution, at each iteration, a tolerance must be smaller than a predetermined threshold. So, the passages are these:
It starts with

$$\left[g(x)\right] = \begin{bmatrix} \tilde{} \\ g \end{bmatrix} \quad (7)$$

the solution at first iteration is

$$\left[x\right] = \left[x^{(0)}\right] = \left[x^{(k)}\right] \quad (8)$$

The tolerance is computed as

$$\left[\varepsilon^{(k)}\right] = \begin{bmatrix} \tilde{} \\ g \end{bmatrix} - \left[g\left(\left[x^{(k)}\right]\right)\right] \quad (9)$$

If the tolerance doesn't become smaller than the threshold, the function $[g(x)]$ is represented as a series, involving the Jacobian matrix computed at $[x]=[x^{(k)}]$. They can be written as $[J^{(k)}]$. Finally

$$\left[g\left(\left[x^{(k)}\right]\right)\right] + \left[J^{(k)}\right] \cdot \left[\Delta x^{(k)}\right] = \begin{bmatrix} \tilde{} \\ g \end{bmatrix} \quad (10)$$

and so

$$\left[J^{(k)}\right] \cdot \left[\Delta x^{(k)}\right] = \left[\varepsilon^{(k)}\right] \quad (11)$$

The NR's method linearizes the nonlinear system and, therefore, the Jacobian matrix is composed by constant values function of the unknown variables.
After the modelling of the network, the load flow is computed through the MATLAB code. If the NR's method converges (Figure 2) and the power restraints are respected, the grid is properly designed.

```
Newton's method power flow converged in 5 iterations.

Converged in 0.78 seconds
```

System Summary					
How many?		How much?	P (MW)	Q (MVAr)	
Buses	166	Total Gen Capacity	1000.0	-1000.0 to 1000.0	
Generators	1	On-line Capacity	1000.0	-1000.0 to 1000.0	
Committed Gens	1	Generation (actual)	89.5	37.9	
Loads	164	Load	88.5	26.5	
Fixed	164	Fixed	88.5	26.5	
Dispatchable	0	Dispatchable	-0.0 of -0.0	-0.0	
Shunts	0	Shunt (inj)	-0.0	0.0	
Branches	170	Losses (I^2 * Z)	1.00	11.35	
Transformers	1	Branch Charging (inj)	-	0.0	
Inter-ties	0	Total Inter-tie Flow	0.0	0.0	
Areas	1				

	Minimum	Maximum
Voltage Magnitude	0.984 p.u. @ bus 3192	1.002 p.u. @ bus 3160
Voltage Angle	-6.52 deg @ bus 3192	0.00 deg @ bus 1
P Losses (I^2*R)	-	0.32 MW @ line 1-3160
Q Losses (I^2*X)	-	10.81 MVAr @ line 1-3160

Figure 2. Example of convergence with the NR's method and restraints for a hypothetic network.

2.2 *Resilience Index*

The Italian Regulatory Authority for Electricity Gas and Water suggests to compute the resilience of an electric grid focus on the risk of disabling users in case of hazard or extreme weather conditions (The Italian Regulatory Authority for Electricity Gas and Water, 2017).
This index is called IRI and is calculated as

$$IRI = NUD \cdot PD \quad (12)$$

where NUD is the number of LV users disabled and PD is probability of disservice. This chance is

$$PD = 1 / TR \quad (13)$$

where TR is the return time of the event, calculated in accordance with the European standard CEI EN 50341 (EN 50341-2-13). For a safe calculation we will take 50-years as return time.
An assessment of resilience can be obtained by computing the inverse of the risk index, thus obtaining

$$IRE = TR / NUD \quad (14)$$

where IRE is the resilience index, or calculating the integer over time of the IRI index.
Another resilience rating can be given in term of ENS (Energy Not Supplied) to highlight the power delivered before the event and the time it takes to restore it.

2.3 *Fragility and Restoration*

The first assumption of this study is to concentrate the fragility of the network in medium voltage substations (Figure 3).



Figure 3. Typical indoor MV substation.

To model their fragility researchers have used the HAZUS®-MH MR5 (FEMA 2002) that provides sets of fragility curves for unanchored elements. This means that the components are assumed without any seismic protection and designed with normal requirements. This hypothesis is introduced because the goal is to estimate the worst-case scenario's probability of exceedance.
Medium voltage substations are composed by important equipment as transformers, switches, circuit breakers etc. Furthermore, they are assumed as installed in buildings, so they can be also affected by the structural damages. Table 1 reports the damage conditions.

Table 1. Description of damage states

Damage state	Description
Complete	component OR building 100% damaged
Extensive	component OR building 70% damaged
Moderate	component OR building 40% damaged
Minor	component OR building 5% damaged

Fragility curves of the components implement the PGA (Peak Ground Acceleration in [*g*]) as seismic intensity parameters. They are lognormal function defined through logarithmic mean λ and logarithmic standard deviation ß. Table 2 summarizes the implemented fragility curves parameters. Figure 4 depicts the resulting fragility functions.

Table 2. Fragility parameters for medium voltage substations with unanchored components (Cavalieri et al. 2014).

Damage state	λ	ß
Complete	-0.69	0.4
Extensive	-1.2	0.4
Moderate	-1.61	0.5
Minor	-2.3	0.6

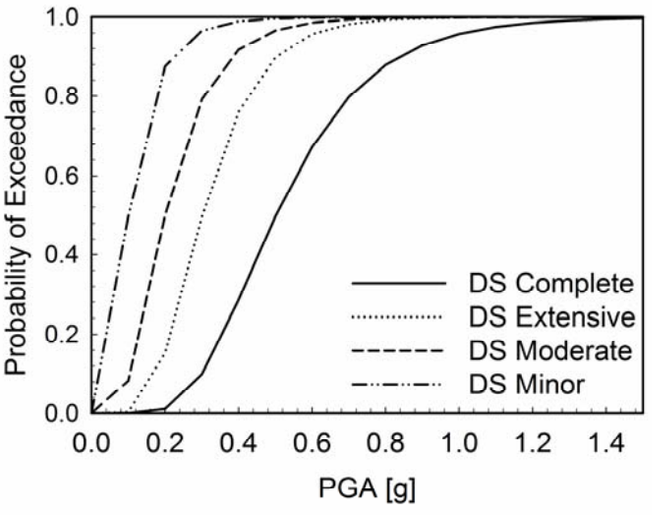


Figure 4. Fragility curves for medium voltage substations with standard components

The simulation considers an increasing set of PGAs and the resulting outcomes of the network are evaluated. In these scenarios, MV substations failed and consumers are without power.
The resilience of the system is evaluated in terms of MW lost due to people without electricity for a certain period, costs and time due to repair activities. About the restoration consequences, authors refer to HAZUS Technical Manual (FEMA 2002). Figure 5 reports the adopted restoration functions.

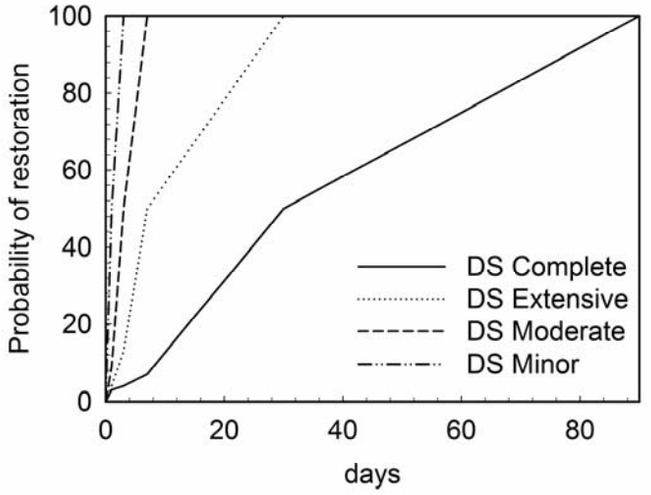


Figure 5. Discretized Restoration Functions for electric substations

In the restoration analyzes the focus is moved on transformers (Figure 6) because they can be considered the most critical substations components.



Figure 6. Typical MV/LV distribution transformer.

In general, (Cataliotti 1983-1999) they are electromagnetic induction static facilities, which modify power values from a primary circuit (receiver) to a secondary one (deliver)

Distribution transformers MV/LV have a three-column core, concentric windings, wire-wired conductors for small sections, flat for the major. They can be classified according to many parameters such as insulating material with which they are protected from high operating temperatures, depending on the service and cooling mode. In this case, however, they have been classified according to the nominal power that can be delivered. There are five classes of transformers (Prettico et al. 2016) as reported in Table 3.

Table 3. Classes of transformers and type of network in which are present

Transformers power (kVA)	Network
100	Semi-urban
250	Semi-urban
400	Semi-urban, Urban
630	Semi-urban, Urban
1000	Semi-urban, Urban

About transformers costs, authors refer to PACT, a FEMA tool to analyze the seismic performance assessment of structural and non-structural components (FEMA P-58-3 2016). Data are given in US dollar (USD) but they have been converted in euros (€) with 1.2 as exchange rate (Figure 7).

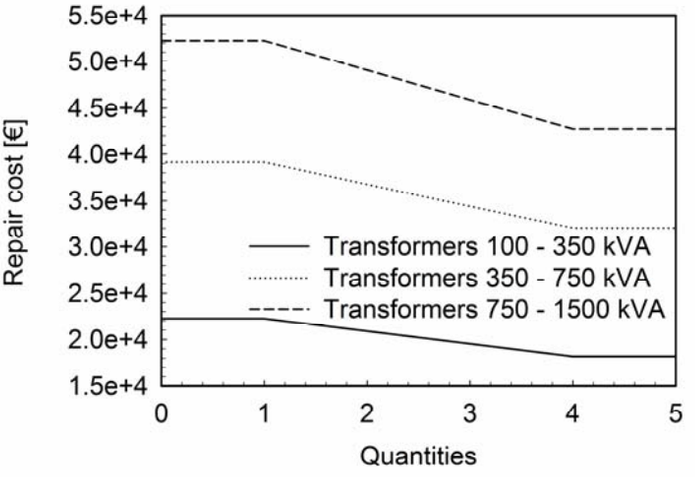


Figure 7. Repair cost of transformers related to their quantities

It is also important to take into account the correlation between the damage state and the transformers serviceability and power availability, as Table 4 summarizes.

Table 4. Relation damage state – power supply

Damage state	Serviceability	Power
Complete	Not repairable	No
Extensive	Operational after repairs	No
Moderate	Operational without repairs	Reduced
Minor	Operational without repairs	Reduced

3 APPLICATION

3.1 *Network description*

The case study employed for the application of the method consists in the Ideal City's district of Crocetta. It is a very central and urbanized area of Turin, full of residential buildings, offices and schools such as the university Politecnico di Torino. The population is about 40,000 people. During the day, such number of population increases.

So, the "urban" network from the JRC database is employed and adapted to the Crocetta's case, being

suitable for about 50,000 users. Figure 8 shows the satellite image of the considered district.



Figure 8. Crocetta's picture from the satellite with its borders highlighted in red

The grid is composed by five feeders, which supply 12735 housing units (supposing a mean of 4 people per unit) and 38 MV consumers. There is only one HV/MV substation from 132 to 20 kV with 80 MVA of rated power and 126 MV/LV substations from 20 to 0.4 kV (Prettico et al. 2016). About the latter 126 MV/LV substations, they are detailed in Table 5.

Table 5. Number of transformers per each class

Rated power (kVA)	Number
1000	34
630	52
400	40

This distribution network is presented in Figure 9, while Figure 10 shows the overlap of the same grid with the district map, as obtained by some simplification from the real map of Turin (Zamani Noori et al. 2017).

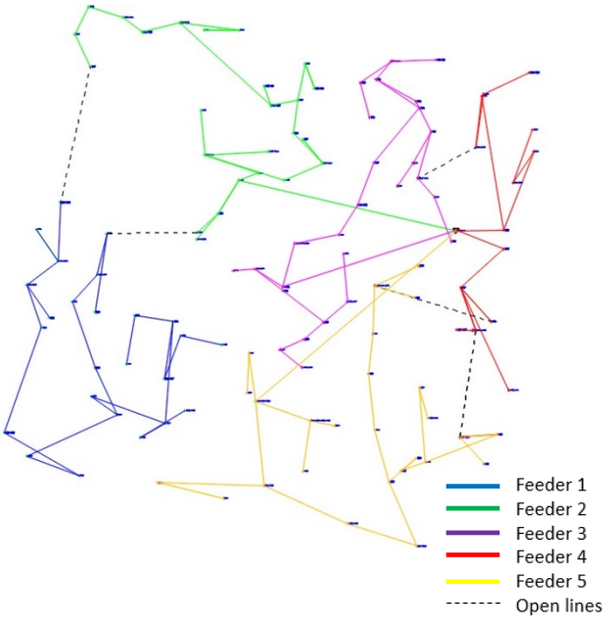


Figure 9. Urban network with MV buses in evidence

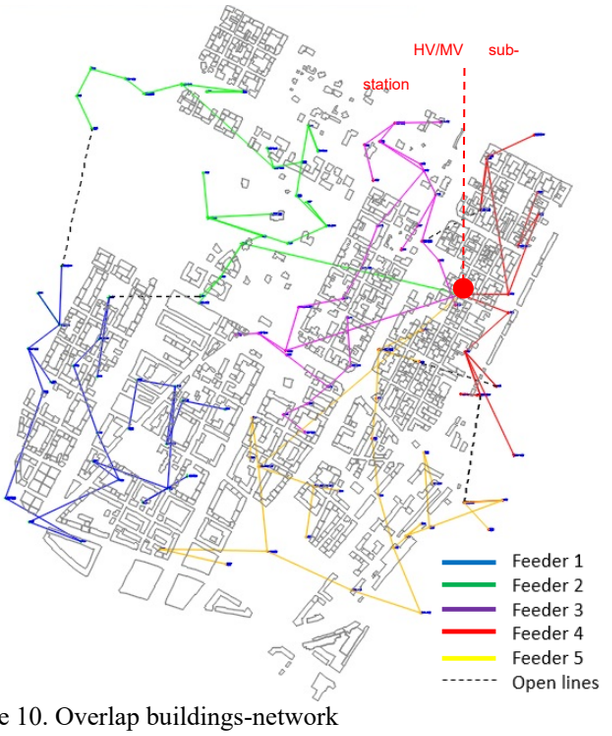


Figure 10. Overlap buildings-network

3.2 *Crocetta fragility and resilience*

In this work, repair costs and down time analysis are evaluated, so it is supposed to refer to a "damage state" situation for the network. In particular, "extensive" damage in Table 4 (with NO power and "Operational after repairs" conditions) for the network is considered. It is assumed that power can be feed only after grid restoration, which consists in components repairing. Indeed, resilience is studied for limited damage conditions, not for complete damage of components and buildings.

Looking at the correspondent fragility curve (Figure 4) it is clear that up to 0.2g the grid does not suffer

any damage. From 0.3g level, substations have the 50% probability of exceedance and with a 0.5g this percentage goes to about 90%.
So, an event with a magnitude between 0.3g-0.5g, can cause the power interruption and the steps until the complete restoration are considered for the present application.
Observing the repair time for MV buses, that is the substation (Figure 5), there is more than 50% chance of having the complete restoration in less than 10 days. In the following, the transformers case is analyzed in detail and the repairs specifications (FEMA P-58-3 2016) are shown is in steps (Table 6).

Table 6. Steps of repairs

After	Transformers repaired
4 days	400 kVA
6 days	400, 630 kVA
7 days	400, 630, 1000 kVA

To give an assessment of resilience we calculate the IRI risk index, if the event occurs at the hypothetic day 2 of a simulation. (Figure 11)

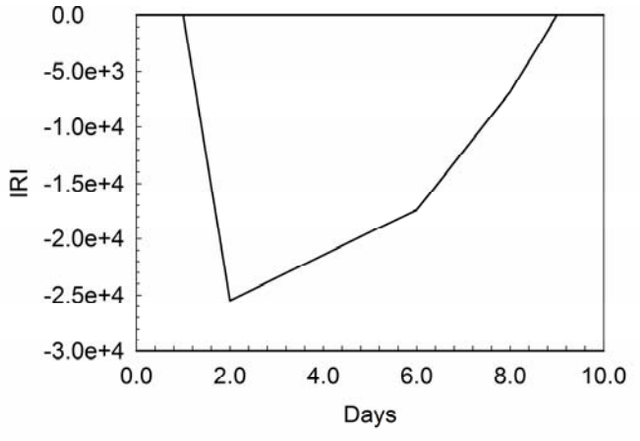


Figure 11. IRI index

A second evaluation can be given in terms of lost energy, the ENS trend is as follows (Figure 12).

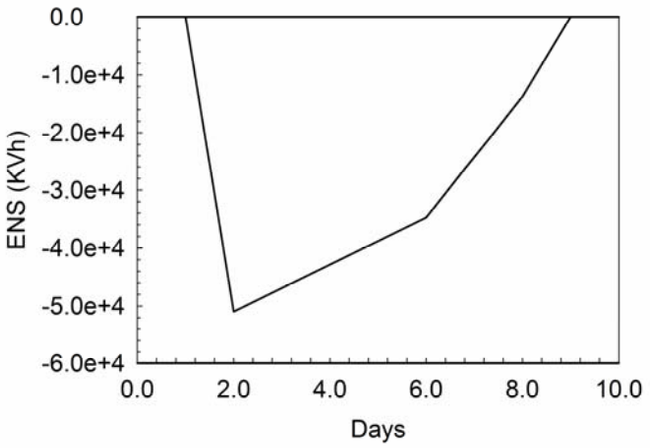


Figure 12. ENS per day

3.3 *Cost analysis and improvements*

As has been shown, a week is necessary for the complete restoration and this implying a huge loss of power. For an assignment of 4 kWh per user, the total amount for a district of the Ideal City, as the Crocetta case, consists in about 0.3 GWh. Considering the typical single-band price of 0.065€/kWh, the economic losses amount over 20,000 €. Accounting the repairs costs, losses further increase.

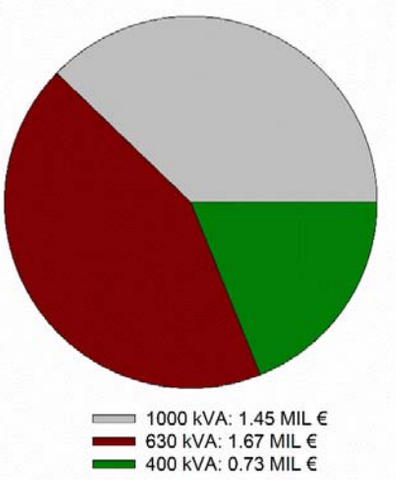


Figure 13. Transformers repair costs repartition

As reported in Figure 13, for the PGA in the range 0.3g-0.5g, the total amount of costs for the transformers consists of 3.85 million euros. Adding the ENS costs with those ones from the restoration of the electrical equipment, 4-5 million euros result.
To improve network resilience, it may be useful to employ substations specifically designed for seismic conditions. Indeed, they are characterized by different fragility curves (Figure 14) with respect to the standard case in Figure 2. Fixing 0.5g PGA, the standard case defines about 90% probability of failure while the seismic case 50%. So, an essential difference can be highlighted.

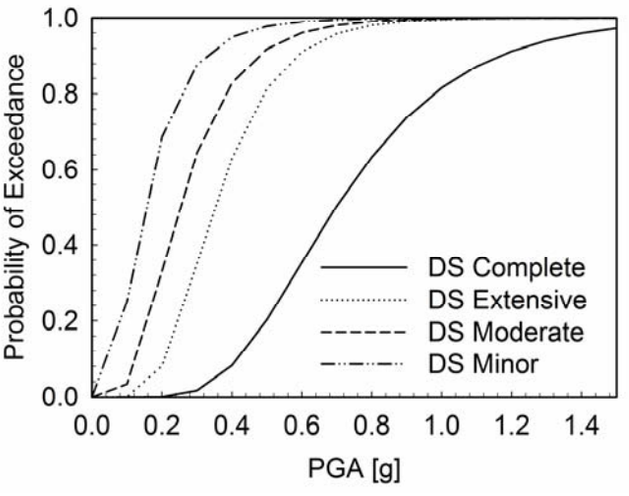


Figure 14. Fragility curves for medium voltage substations with seismic components

Finally, the networks interdependency has to be taken into account following the approach developed by Cimellaro et al. (2016). The fragility of electrical components is connected to failure's probability of buildings system in the district, where substations are installed. Besides, the electric network failure itself induces a series of cascading effects, as summarized in the scheme of Figure 15.
This research team (Cimellaro et al. 2016, Zamani Noori et al. 2017, Cimellaro et al. 2017) is deepening the cascading effects at the urban scale, creating a macroscale model through finite element (FE) analysis of buildings structures, debris and through connectivity matrices of the networks nodes.

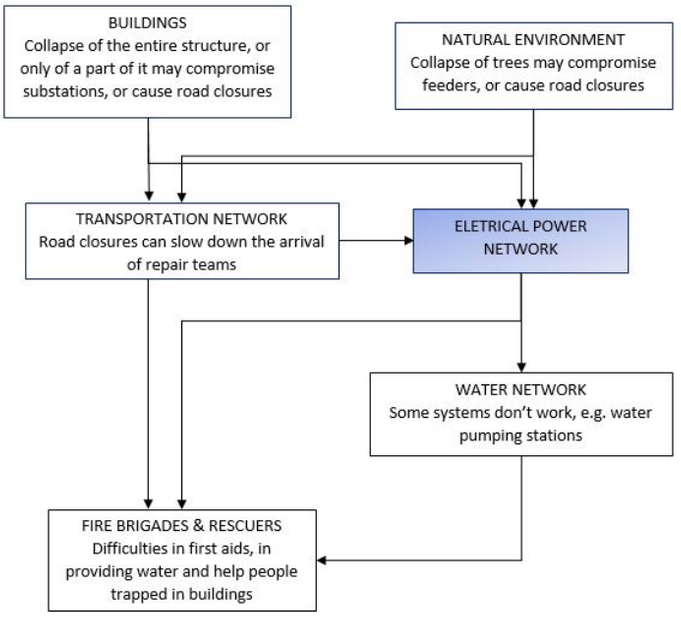


Figure 15. At the top of the figure is shown the indirect fragility of the power grid. At the bottom are presented some cascading effects triggered by blackouts or power reductions.

4 CONCLUSION

This paper is proposing a new methodology to estimate the performance and its inherent resilience of a power distribution network.
The steps are the following: (i) referring to electrical characteristics of urban representative network. (ii) Adapting the data to a specific map focusing on MV buses. (iii) Applying an earthquake hazard with a certain PGA. (iv) Estimating the grid response using fragility curves of MV substations and finally (v) determining the economic losses with repair costs and time curves.
Furthermore, measures for improving resilience are suggested by employing seismic retrofits in substations. The interaction of EPN with other networks is also mentioned and will be studied in further researches in the future.

5 AKNOWLEDGMENT

The research leading to these results has received funding from the European Research Council under the Grant Agreement n°ERC_IDEal reSCUE_637842 of the project IDEAL RESCUE—Integrated DEsign and control of Sustainable CommUnities during Emergencies.

6 REFERENCES

Arghavani, M. 2017. Seismic resilience of the electricity transmission grid of Qom in Iran: analysis of a prototype model. Teheran: International Institute of Earthquake Engineering and Seismology.

Cataliotti, V. 1983-1999. *Impianti elettrici vol. I, II and II I*, Palermo: S.F. Flaccovio.

Cavalieri, F., Franchin, P. & Pinto, P.E. 2014. Fragility functions of electric power stations. *SYNER-G: Typology Definition and Fragility Functions for Physical Elements at Seismic Risk* 27: 157-185. Berlin: Springer.

Cimellaro, G.P., Renschler, C., Reinhorn, A.M. & Arendt, L. 2016. PEOPLES: a framework for evaluating resilience. *Journal of Structural Engineering.*

Cimellaro, G.P., Domaneschi, M., Mahin, S. & Scutiero, G. 2017. Exploring simulation tools for urban seismic analysis and resilience assessment. *6th International Conference on Computational Methods in Structural Dynamics and Earthquake Engineering - COMPDYN 2017*, Rhodes Island, Greece.

Dharamjit & Tanti, D.K. 2012. Load Flow Analysis on IEEE 30 bus System. *International Journal of Scientific and Research Publications* 2 (11).

Domingo, C.M., Román, T.G.S., Sánchez-Miralles, Á., González, J.P.P. & Martínez, A.C. 2011. A reference network model for large-scale distribution planning with automatic street map generation. *IEEE Transaction on Power Systems* 26 (1): 190–197.

FEMA P-58.3.1. PACT Performance Assessment Calculation Tool, *Version 2.9.65*. Washington: Federal Emergency Management Agency.

FEMA P-58-3 2016. Provided Fragility Data. *Seismic Performance Assessment of Buildings, Volume 3 - Supporting Electronic Materials and Ba ckground Documentation*. Washington: Federal Emergency Management Agency.

FEMA 2002. Earthquake loss estimation methodology HAZUS®-MH MR5 Advanced Engineering Building Module-Technical and User's Manual. Washington: Federal Emergency Management Agency.

Grainger, J. J. & Stevenson, Jr. W. D. 1994. *Power System Analysis*. New York: McGraw-Hill.

Guidotti, R., Chmielewski, H., Unnikrishnan, V., Gardoni, P., McAllister, T. & van de Lindt J. 2016. Modeling the resilience of critical infrastructure: the role of network dependencies. *Sustainable and Resilient Infrastructure* 1 (3-4): 153-168.

MATLAB and Statistics Toolbox, *Release 2012b*, Natick: The MathWorks Inc.

Prettico, G., Gangale, F., Mengolini, A., Lucas, A. & Fulli, G. 2016. Distribution System Operators Observatory: From European Electricity Distribution Systems to Representative Distribution Networks. Luxembourg: Publications Office of the European Union.

Shinozuka, M., Dong, X., Chen, T.C. & Jin, X. 2007. Seismic performance of electric transmission network under component failures. *Journal of Earthquake Engineering and Structural Dynamics* 36 (2):227-244.

Shinozuka, M., Chang, S. E., Cheng, T. C., Feng, M., O'Rourke, T., Saadeghvaziri, M. A., Dong, X., Jin, X., Wang, Y. & Shi, P. 2004. Resilience of Integrated Power and Water Systems. *MCEER Research Progress and Accomplishments, Report MCEER-04-SP01*: 65-86. Buffalo: Multidisciplinary Center for Earthquake Engineering Research.

The Italian Regulatory Authority for Electricity Gas and Water, 2017. *Act March 7 2017 2/2017-DIEU*.

Tinney, W. F. & Hart, C. E. 1967. Power Flow Solution by Newton's Method. *IEEE Transactions on Power Apparatus and systems* 86: 1449-1460.

Unnikrishnan, V. U. & van de Lindt, J. W. 2016. Probabilistic framework for performance assessment of electrical power networks to tornadoes. *Sustainable and Resilient Infrastructure* 1 (3-4): 137-152.

Zamani Noori, A., Marasco, S., Kammouh, O., Domaneschi, M. & Cimellaro, G.P. 2017. Smart cities to improve resilience of communities. Brisbane: SHMII-8 Conference (in Press)

Zimmerman, R. D., Murillo-Sanchez, C. E. & Thomas, R. J. 2011. Matpower: Steady-State Operations, Planning and Analysis Tools for Power Systems Research and Education. *IEEE Transactions on Power Systems* 26 (1): 12-19.

Maintenance, Safety, Risk, Management and Life-Cycle Performance of Bridges – Powers, Frangopol, Al-Mahaidi & Caprani (Eds)
© 2018 Taylor & Francis Group, London, ISBN 978-1-138-73045-8

Seismic resilience of bridges in transportation networks

M. Domaneschi, G. Scutiero, G.P. Cimellaro
Politecnico di Torino, Turin, Italy
A.A. Khalil
Applied Science International LLC, USA
C. Pellecchia, E.M. Ricciardi
ASI EUROPE SRL, Italy

ABSTRACT: A disproportionate collapse can be avoided by improving collapse resistance, reducing the vulnerability of the structure or increasing structural robustness. While vulnerability depends on the individual structural components, robustness depends on the whole structural system. Besides collapse resistance, a disproportionate collapse can also be prevented by reducing the exposure of the structure to external actions. Robustness of buildings and bridges is defined as the insensitivity of a structure to the initial damage. Such characteristic has been recognized as a desirable in structural systems, being able to exclude progressive and disproportionate collapses. The robustness of bridges is investigated in this research work at the numerical level by employing a model of a cable-supported bridge. Several earthquake records are employed for the robustness assessment of the bridge at increasing intensity. The role of the redundancy in the structural scheme of the bridge is then evaluated as the strategic measure for limiting disproportionate collapses and improving robustness. Furthermore, solutions for reducing the time for recovering functionality, after the damage occurrence, are also evaluated and discussed within a resilient community framework. Indeed, this study can provide valuable information that can facilitate decision making, enhance planning for disaster mitigation and recovering of critical infrastructures as the transportation network, reducing social and economic losses.

1 INTRODUCTION

In recent years several studies on progressive collapse have been developed. Much attention was paid for buildings, leaving the bridges' field still uncharted. The failure of one structural element can lead to the failure of further structural elements and thus to the collapse of large structural sections or the entire structure. In many cases, the initial triggering event and the resulting damage are disproportionate (Haberland et al. 2012). According to design codes, reducing the vulnerability of the structure or by increasing its the robustness, the collapse due to local effects can be avoided. For cable-stayed bridges, collapse resistance is primarily achieved by robustness (Haberland et al. 2012). Although such systems possess a high degree of static indeterminacy and internal continuity, their redundancy and robustness deserve careful consideration. The cable failure constitutes a local effect that may take like result a progressive collapse. The loss of cables can lead to overloading and rupture of adjacent cables. The cables are easily accessible and exposed to accidental or malicious action; their cross section is relatively small which makes it difficult to provide with specific local resistance; a cable loss could happen nearly instantaneously producing an impulsive dynamic loading; the system might respond in a non-ductile manner. When a catastrophic event such as an earthquake occurs in a bridge, the distance between the cables plays a fundamental rule in term of robustness. The prevention of disproportionate collapse of cable-stayed bridges is of major concern as such structures are of high economic value and their collapse would be accompanied by a large loss of human life (Wolff & Starossek 2010). The importance of providing system redundancy was also highlighted by the collapse of the Mississippi River Bridge in Minneapolis (Salem & Helmy 2017), Minnesota in 2007, in which the whole bridge, which has been classified as non-redundant by the National Transportation Safety Board (NTSB) (2008), catastrophically collapsed after the failure of a gusset plate connection. This paper examines the response of a current stay-cable bridge for progressive collapse. A model of the bridge through Applied Element Method (AEM) is implemented and validated. A solution in order to avoid the disproportionate collapse and increase robustness and redundancy is analyzed and discussed.

2 CASE STUDY

2.1 *Applied element method*

The proposed study investigates the progressive collapse of a real bridge through the nonlinear dynamic analysis. For this research an Applied Elements Method (AEM) based software is used. The AEM is an innovative modeling method adopting the concept of discrete cracking (Applied Science International 2017). Through two decades of continuous development, AEM was proven to be the method that can track the structural collapse behavior passing through all stages of the application of loads: elastic stage, crack initiation and propagation in tension-weak materials, reinforcement yielding, element separation, element collision (contact), and collision with the ground and with adjacent structures. The possible analysis domain of AEM method in comparison to FEM method is shown in Figure 1. Although the FEM is accurate and reliable for analysis of continuum structures, the onset of element separation is difficult to automate and modeling of debris collision is time consuming.

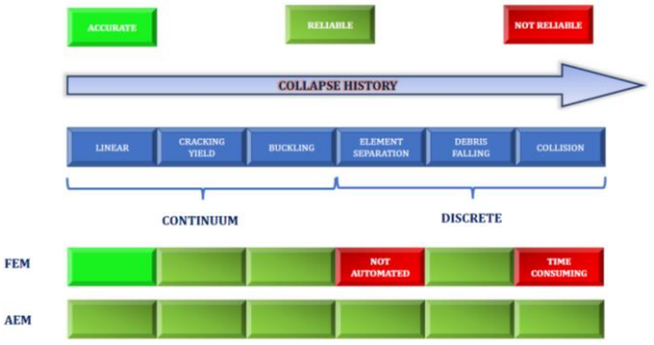


Figure 2. Modeling of structure to AEM.

With AEM, the structure is modeled as an assembly of small elements, which are made by dividing the structure virtually, as shown in Figure 2. The two elements shown in Figure 2 are assumed to be connected by one normal and two shear springs located at contact points, which are distributed around the elements edges. Each group of springs completely represents stresses and deformations of a certain volume as shown in Figure 2.

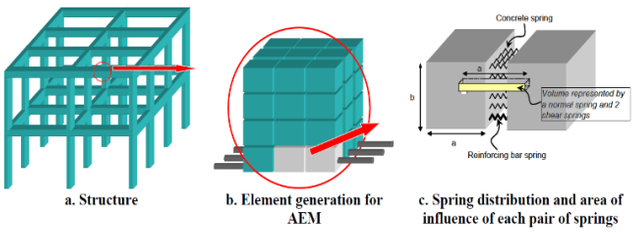


Figure 2. Modeling of structure to AEM.

These springs reflect the different material properties; strain stresses and failure criteria are all calculated and estimated using these springs.

2.2 *AEM for bridge*

Using the AEM method the cables of the bridge can be implement like link members. The link member is a special spring that has the ability to connect two separate solid elements with any angle of inclination as shown in Figure 3. The link member hence carries only axial stresses.

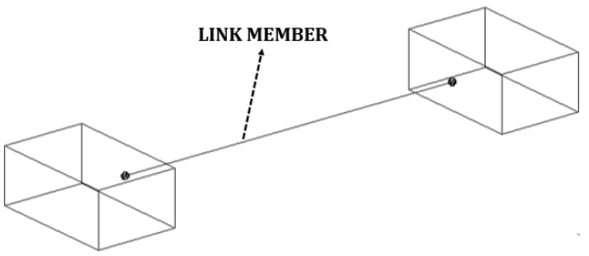


Figure 3. AEM link member.

In order to obtain a real performance of cables, a "tension-only bilinear material" is assigned. As shown in Figure 4, the bilinear material behaves linearly up to the yielding point without any plastic deformations in normal stresses. After yielding point, plastic deformations take place and the stress-strain relation beaves linearly up to failure. After failure, the strength drops to zero but springs remain till they reach separation strain where the elements are separated from each other and springs no longer exist. A stress-softening parameter is used after failure. Tension-only bilinear material is a special case of the bilinear material where the elements can carry only tensile stresses.

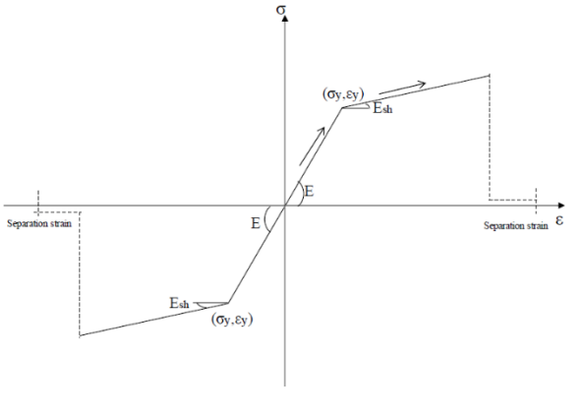


Figure 4. stress-strain of a bilinear material.

The reinforcing steel bars into concrete are modeled by springs that represent the material properties, exact location and dimensions of the bars. The generation of these springs is automatically performed in the software Extreme Loading for Structure (2017).

2.3 *Description of the case study*

The analyzed bridge is described by Li et al. (2014). Yong-he bridge is one of the first cable-stayed bridges constructed in mainland China (Fig.5). It has two main spans of 260 m and two side spans of 25.15 + 99.85 m each. The bridge is 510 m long and 14.5 wide. The towers, connected by two transverse beams, are 60.5 m tall. There is a total of 88 pairs of cables containing steel wires of 5 mm in diameter. Each cable can contain from a minimum of 69 to a maximum of 199 steel wires. To validate the AEM model a comparison with the FEM model, described by Li et al (2014) is performed (Figure 6).



Figure 5. Yong-he Bridge, China

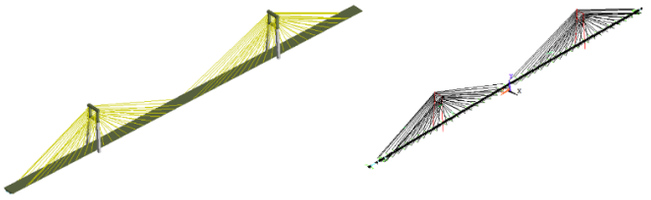


Figure 6. AEM model vs FEM model.

Static and dynamic comparison are made. The shape modes obtained by two models are analyzed. They are computed using the stiffness matrix obtained by the static analysis. The criterion used to verify the correlation between modes is the *modal assurance criterion* (MAC). According to Pastor et al. (2012), the Modal Assurance Criterion is a statistical indicator that is most sensitive to large differences and relatively insensitive to small differences in the mode shapes. The MAC is calculated as the normalized scalar product of the two sets of vectors $\{\phi_A\}$ and $\{\phi_X\}$. The resulting scalars are arranged into the MAC matrix.

$$MAC(r,q) = \frac{|\{\varphi_A\}_r^T\{\varphi_x\}_q|^2}{(\{\varphi_A\}_r^T\{\varphi_A\}_r)(\{\varphi_x\}_q^T\{\varphi_x\}_q)} \quad (1)$$

The MAC takes value between 0 (representing no consistent correspondence) and 1 (representing a consistent correspondence). Values larger than 0.9 indicate consistent correspondence whereas small values indicate poor resemblance of the two shapes. Seven shape modes are taken into account as shown in Table 1.

Table 1. Shape modes. Vertical symmetrical = V.S., vertical asymmetrical =V.A., transverse asymmetrical = T.A.

Mode	Frequency-FEM	Frequency AEM	Shape	ΔFrequency	MAC
	Hz	Hz	-	%	-
1	0.417	0.416	V.S.	0.24%	0.991
2	0.593	0.643	V.A.	-7.78%	0.978
3	0.877	1.012	V.S.	-13.34%	0.945
4	1.044	1.297	V.A.	-19.51%	0.946
5	1.089	1.349	V.S.	-19.27%	0.930
6	1.213	1.515	V.A.	-19.93%	0.889
7	0.311	0.280	T.A.	11.07%	0.928

In Figures 7-13 the mode shapes obtained through FE code and AE code are represented.

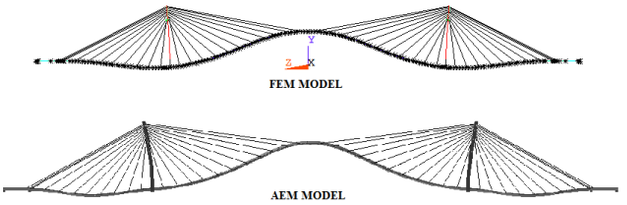


Figure 7. 1th mode shape (V.S.).

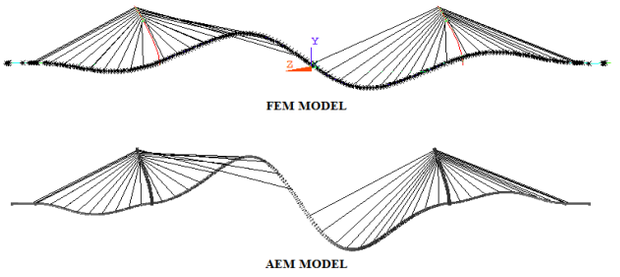


Figure 8. 2nd mode shape (V.A.).

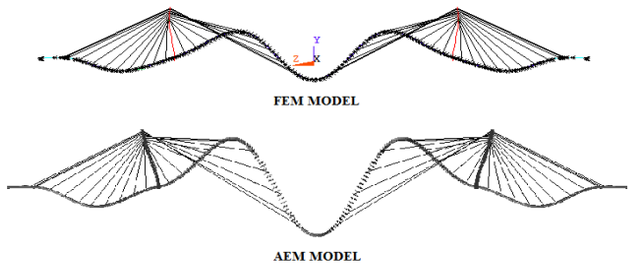


Figure 9. 3rd mode shape (V.S.).

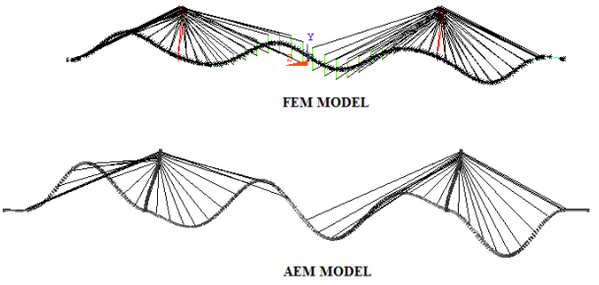


Figure 10. 4th mode shape (V.A.).

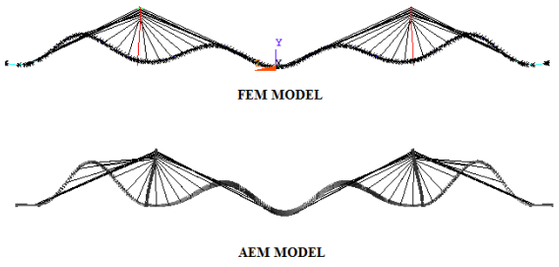


Figure 11. 5th mode shape (V.S.).

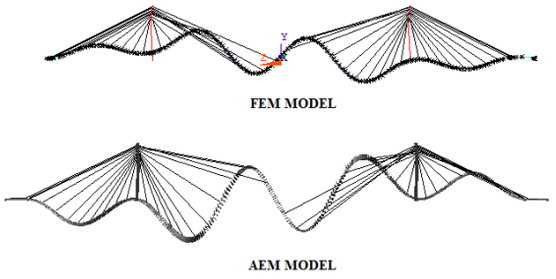


Figure 12. 6th mode shape (V.A.).

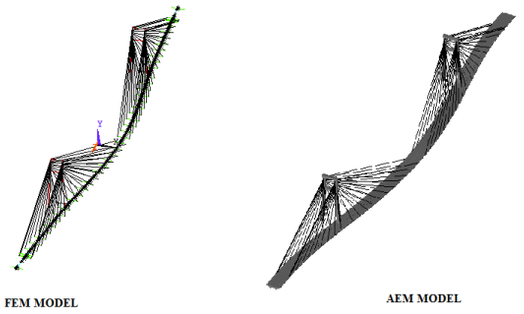


Figure 13. 7th mode shape (T.A.).

The static comparison is based on the node displacement along the symmetry axis of the bridge. The displacement is due to dead load. The values obtained are shown in table 2. In Fig.14 a graphic comparison is reported.

Table 2. Vertical displacement

Model	Displacement Z	Δ
	M	%
FEM	0.178	9
AEM	0.163	

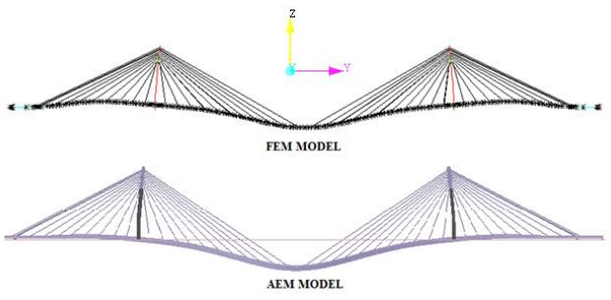


Figure 14: Deformation FEM vs deformation AEM.

3 ROBUSTNESS AND REDUNDANCY

Anitori et al. (2013) have discussed several competing approaches for the deterministic evaluation of structural robustness and redundancy. Robustness is defined as the insensitivity of a structure to an initial damage (Starossek and Haberland 2010). Restelli (2007) evaluates robustness using indicators that are related to the global displacement of a structure composed of parallel members, using

$$\rho = \frac{s_0}{s_d} \qquad (2)$$

where s_0 is the displacement of the undamaged system; and s_d is the displacement of the damaged system. This index decreases from 1 and approaches to 0 as damage spreads within the system. The purpose of this parameter is to evaluate the system susceptibility to degrading damages spreading through the structural elements. A no damaged structure, in elastic field, subject to dynamic action, presents a robustness chart as shown in Figure 15. On the horizontal and vertical axes respectively, the time and the robustness index are reported.

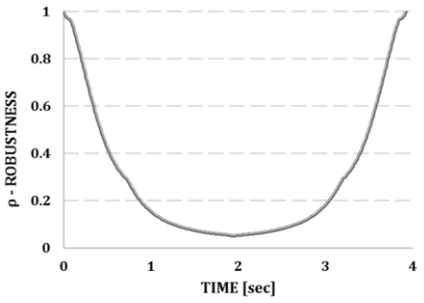


Figure 15: Robustness curve.

Accordingly with Eq. 2, as increasing the displacements decreases the robustness. In addition, as decreasing the dynamic actions, the structure tends to initial configuration and robustness to one. If the structure is damaged the ascending part of robustness curve is reduced or total absent due to the presence plastic deformations. As reported by Ghosn & Moses (1998) and Liu et al. (2000), structural redundancy is defined as the capability of the system to continue to carry load after the failure of one main member. They proposed three different indices. As reported in Figure 16, two indices are related to the overloading of the originally intact bridge configurations of the structure and are defined as the ability of the structural system to resist collapse and/or avoid the loss of structural functionality. The third index is calculated for a damaged configuration of the structure and permits evaluation of the capability of the system to carry some emergency load after the damage of one main member.

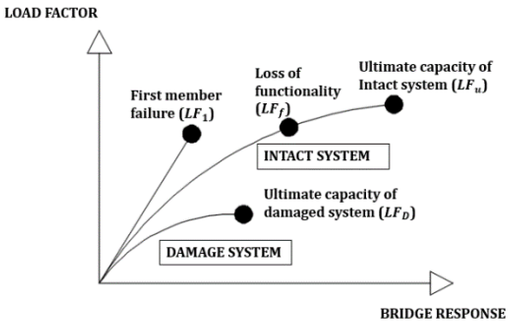


Figure 16: Load measures needed to calculate the redundancy of bridge systems.

These parameters compare the system's capacity to the capacity of the system to resist first member failure, making them applicable for evaluating alternative designs, because current bridge engineering practice is based on member design criteria. These indices are defined in terms of the *system reserve ratios* (Liu et al. 2000) such as R_u, R_f, R_d for the ultimate, functionality and damaged condition limit states, respectively. They are given by following equations:

$$R_u = LF_u/LF_1 \quad (3)$$
$$R_f = LF_f/LF_1 \quad (4)$$
$$R_d = LF_d/LF_1 \quad (5)$$

where LF_1 is the load that causes the failure of the first member; LF_u is the load that causes collapse of the system; LF_f is the load that causes the functionality limit state of the initially intact structure to be exceeded; and LF_d is the load factor that causes the collapse of a damaged structure that has lost one main member. In this paper, an algorithm is implemented to extend this methodology to the case of a time history analysis. Indeed, the methodology presented by Liu et al. (2000) is related to push over analysis, so to the nonlinear static domain. For nonlinear dynamic analyses the load factor cannot be used and a different approach has to be developed.

In the first step of the proposed procedure the accelerogram is converted to positive values only, as shown in Figure 17.

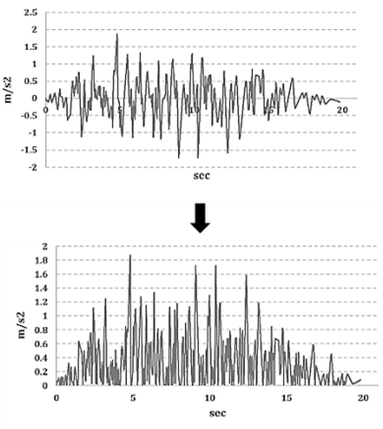


Figure 17. Algorithm – first step.

In the second step, the obtained accelerogram is integrated between 0 and the time corresponding to the failure of the first member (Fig. 18), to compute an equivalent value for LF_1. Integrating between the time corresponding to the failure of the first member and the system collapse time, an equivalent value of LF_d is obtained. In similar way it is possible to calculate also LF_f and LF_u.

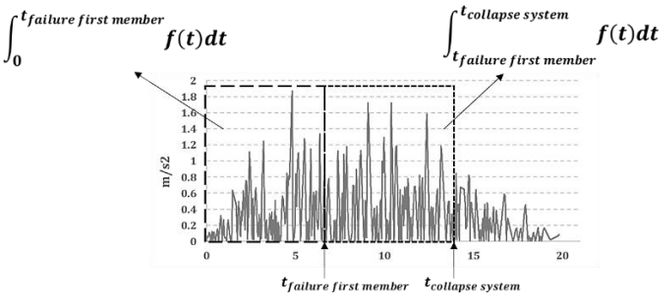


Figure 18. Algorithm – second step.

In other words, to satisfy the target redundancy level, the accelerogram's area that causes the system to collapse or lost functionality must be a percentage higher than the accelerogram's area that causes the first component failure.

4 SEISMIC RESPONSE SIMULATION

4.1 *Seismic simulation of Yong-he Bridge with current cables-configuration*

The loss of a cable is investigated by nonlinear dynamic analyses in the time domain, taking into account large deformations. This direct time integration is used to solve the equation motion. Haifan (1983) analyzed the influence of phase-difference effect on the earthquake response of the Yong-he Bridge. The accelerogram calculated by Haifan (1983) is used for the analyses (Figure 19). It is compatible with design spectrum of China Code.

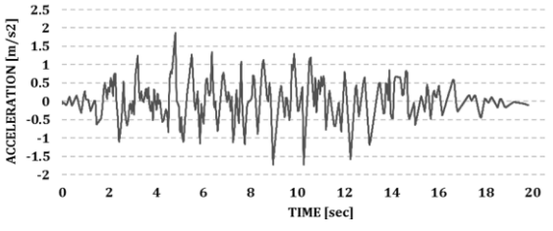


Figure 19. Haifan (1983) accelerogram.

The AEM simulation of the bridge with the dynamic action in Figure 19 results in a disproportionate collapse, as shown in Figure 20.

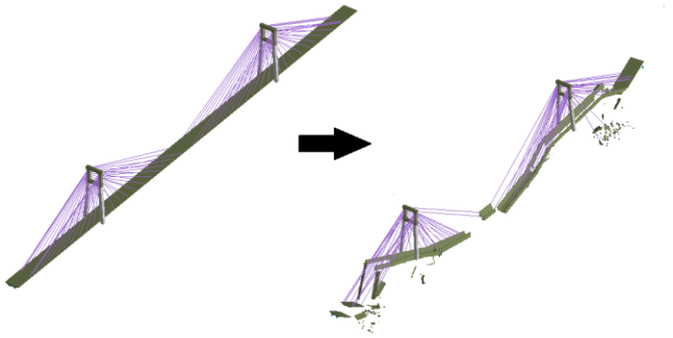


Figure 20. AEM simulation – disproportionate collapse.

In order to identify the source of the collapse, the stresses, in the highlighted cables in Figure 21, are analyzed.

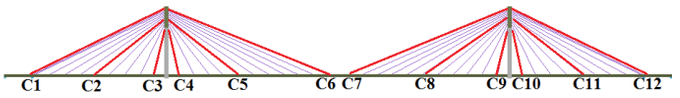


Figure 21. Cables analyzed.

In Table 4 the max values of stresses in the cables are shown.

Table 4. Normal stress cables

Cable	σ_{MAX}	$time(\sigma_{MAX})$
	Kg/cm^2	sec
C1	3648	6.2
C2	3664	11.3
C3	3857	13.1
C4	4166	13
C5	4679	12
C6	4677	6.2
C7	4679	7.5
C8	4676	8
C9	4440	8.8
C10	3629	5.1
C11	3957	16
C12	3646	6

As reported by Li et al., the design stress for the cables is about 4600 Kg/cm^2. From charts, it results that the Cable C6 fails at 6 seconds. Fig.22-23 show the stress in cables C6-C7 obtained by AEM simulation.

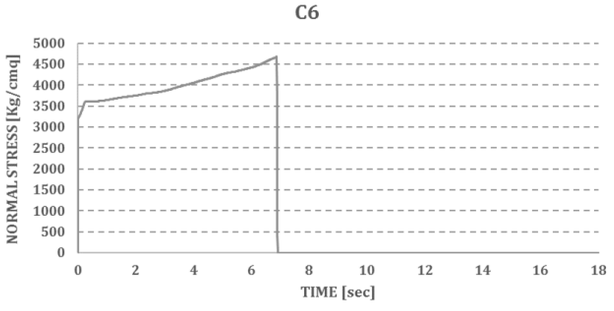


Figure 22. Normal stress cable C6.

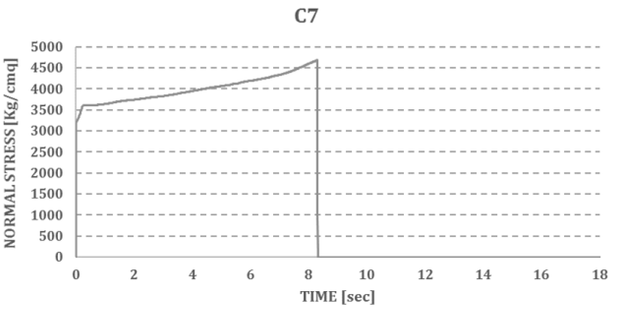


Figure 23. Normal stress cable C7.

The failure of cables C6 and C7 cause the overloading and the consequently ruptures in the adjacent cables. The loss of cables, which leads to a reduction of the capacity of the supporting system, increases the risk of the global failure of the structure. As a result, the bridge collapse due to ground motion cannot be avoided. Some authors indicate that this phenomenon occurs when the distance between the first failure cable and the adjacent cables is about 10 meters (Wolff & Starossek 2010). In Figure 24, the robustness variation with respect to time is reported. After the failure of the cable, the robustness decreases until the collapse of the entire bridge (disproportionate collapse). In Table 5, the redundancy values are shown.

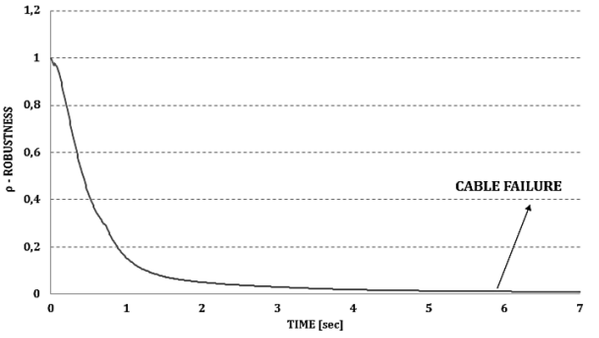


Figure 24. Robustness chart.

Table 5. Redundancy values

Redundancy	
	-
R_u	1.71
R_f	1.09
R_d	1.21

4.2 *Seismic simulation of Yong-he Bridge with new cables-configuration*

A new configuration for the center span stays is proposed to improve the bridge response, as shown in Figure 25. The geometrical distance between the cables is decreased. For cables adjacent to C6 and C7, the distance between the cables is 8 meters while for the cables adjacent to C4 and C9 it is 10 meters. This configuration allows to decrease the stress in cables C6 and C7 that are responsible of the disproportionate collapse (previous section).

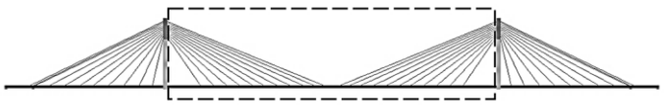


Figure 25. New cables configuration.

As shown in Figure 26, with this new configuration the disproportionate collapse is avoided. The failure of the main girder is due to high tensile stresses in the concrete.

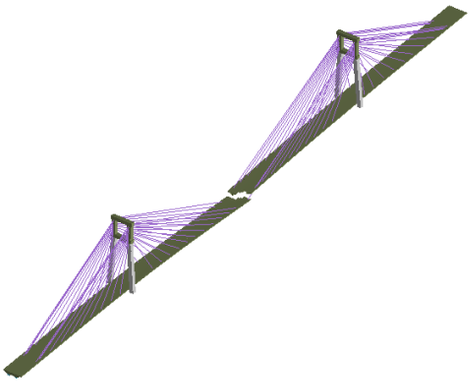


Figure 26. AEM simulation – collapse bridge.

In Figures 27-28 the stresses in cables C6 and C7, the responsible of the disproportionate collapse in the previous bridge configuration, are reported. In the new configuration, stays' failure are not verified.

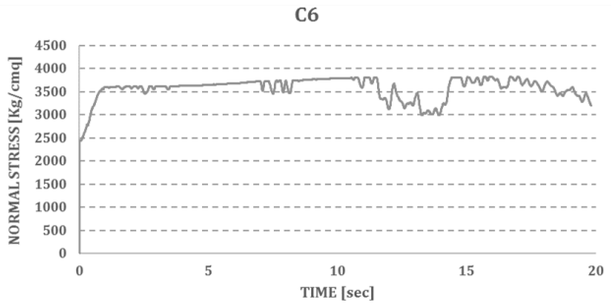


Figure 27. Normal stress cable C6.

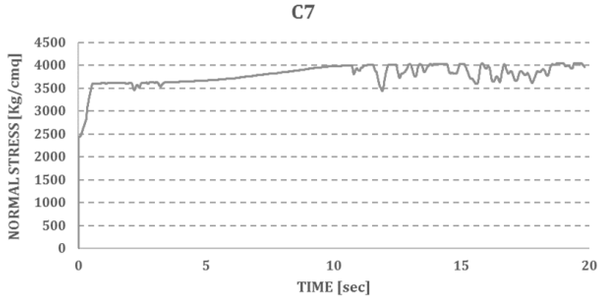


Figure 28. Normal stress cable C7.

The lateral strength of the reinforced concrete deck is abruptly reduced after reaching its ultimate deformation due to the rupture of rebar or the concrete crushing. In Table 6 the max values of the stresses in the cables are shown. They are far to the ultimate limit.

Table 6. Normal stress cables

Cable	σ_{MAX} Kg/cm^2
C1	3803
C2	3784
C3	3715
C4	3742
C5	3788
C6	3815
C7	4041
C8	3700
C9	3731
C10	3748
C11	3726
C12	3709

The deck displacements are extracted and, according to Restelli (2007), the robustness is calculated for each time step as shown in Figure 29. Table 7 reports the redundancy values calculated.

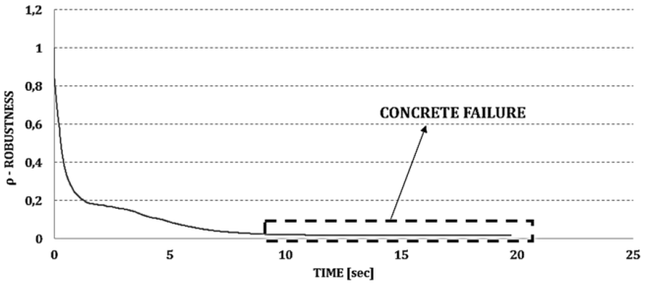


Figure 29. Robustness chart.

Table 7. Redundancy values

Redundancy	-
R_u	4.34
R_f	2.71
R_d	3.37

Comparing the values of Tables 5 and 6, a remarkable improvement in terms of redundancy is highlighted. Table 8 compares the redundancy values in terms of percentage improvements of the new bridge configuration with respect to the original configuration.

Table 8. Redundancy comparison

Redundancy	Δ Redundancy %
R_u	39.4
R_f	40.2
R_d	35.9

Furthermore, in the new configuration, the robustness also results higher than robustness measured in the previous configuration (Figures 24 and 29).

5 CONCLUSIONS

The problem of disproportionate collapse of an existing cable-stayed bridge is investigated through nonlinear dynamic analysis and the Applied Element Method. The analyses show that the bridge cannot sustain the failure of more than two cables without showing a disproportionate collapse. Conversely, it can be avoided through a new cables-configuration. This is closely connected with robustness and redundancy improvements. However, the new configuration results not enough in order to guarantee the functionality of cable-stayed bridge after a strong motion event, because the stresses in the bridge deck compromise the structural stability. Therefore, additional strengthening would be necessary in the main girder for overcoming that issue and avoiding functionality losses. This work can support decision-makers to explore the performance of bridge structures in seismic affected area, to plan strategies and resilience improvements to minimize both losses and recovery time.

6 ACKNOWLEDGEMENTS

The research leading to these results has received funding from the European Research Council under the Grant Agreement n° ERC_IDEAL RESCUE_637842 of the project IDEAL RESCUE-Integrated Design and Control of Sustainable Communities during Emergencies.

7 REFERENCES

Anitori, G., Casas, J.R. & Ghosn, M. (2013) Redundancy and Robustness in the Design and Evaluation of Bridges*: European and North American Perspectives, Journal of Bridge Engineering*, 18 (12), pp. 1241-1251.

Applied Science International, LLC (ASI) (2017), *Extreme loading for structures Theoretical Manual*

Extreme loading for structures 5.0 (2017), Applied Science International, LLC (ASI)

Ghosn, M., & Moses, F. (1998). "Redundancy in highway bridge superstructures." *NCHRP Rep. 406, Transportation Research Board*, Washington, DC.

Haberland, M., Haß, S. & Starossek, U. (2012) Robustness assessment of suspension bridges Bridge Maintenance, Safety, Management, Resilience and Sustainability - *Proceedings of the Sixth International Conference on Bridge Maintenance, Safety and Management*, pp. 1617-1624.

Haifan, X (1983). Earthquake analysis of cable-stayed bridges under the action of travelling waves. *Journal of Tongji University*.

Li, S., Li, H., Liu, Y., Lan, C., Zhou, W. & Ou, J. (2014) SMC structural health monitoring benchmark problem using monitored data from an actual cable-stayed bridge, *Structural Control and Health Monitoring*, 21 (2), pp. 156-172.

Liu, W. D., Ghosn, M., Moses, F., & Neuenhoffer, A. (2000). "Redundancy in highway bridge substructures." *NCHRP Rep. 458, Transportation Research Board*, Washington, DC

Domaneschi, M., Martinelli L. & Perotti F. (2016), "Wind and earthquake protection of cable-supported bridges", *Proceedings of the Institution of Civil Engineers - Bridge Engineering*, 169(BE3), 157–171.

Domaneschi, M. & Martinelli L. (2016), "Earthquake resilience-based control solutions for the extended benchmark cable-stayed bridge", *Journal of Structural Engineering, ASCE*, 142 (8), art. no. 4015009.

Domaneschi, M., Martinelli L. & Po E. (2015), "Control of Wind Buffeting Vibrations in a Suspension Bridge by TMD: hybridization and robustness issues", *Computers and Structures*, 155, 3-17.

Pastor, M., Binda, M. & Harčarik, T. Modal assurance criterion (2012) *Procedia Engineering*, 48, pp. 543-548

Restelli, S. (2007). "Measure of structural robustness of deteriorating systems." *Degree thesis, Politecnico di Milano*, Milan, Italy (in Italian).

Salem H.M. & Helmy H.M. (2014), Numerical Investigation of the Collapse of the Minnesota I-35W Bridge – *Engineering Structures*, PP 635-645, Vol.59

Starossek, U. & Haberland, M., (2010). Disproportionate Collapse: Terminology and Procedures. *Journal of Performance of Constructed Facilities*, 24 (6), 519-528.

Wolff, M. & Starossek, U. (2010) Cable-loss analyses and collapse behavior of cable-stayed bridges Bridge Maintenance, Safety, Management and Life-Cycle Optimization - *Proceedings of the 5th International Conference on Bridge Maintenance, Safety and Management*, pp. 2171-2178.

Maintenance, Safety, Risk, Management and Life-Cycle Performance of Bridges – Powers, Frangopol, Al-Mahaidi & Caprani (Eds)
© 2018 Taylor & Francis Group, London, ISBN 978-1-138-73045-8

Resilience Framework for Seaport Infrastructure: Theory and Application

A. Balbi & M. P. Repetto
University of Genoa, Italy

O. Kammouh & G.P. Cimellaro
Politecnico di Torino, Italy

ABSTRACT: The efficient movement of goods is crucial to the economic growth of communities. This makes the existence of seaports essential for the marine transportation system. Due to their natural location, ports are continuously threatened by natural hazards such as wind action, which necessitates a continuous monitoring and assessment for their performance. The work presented here aims at assessing the resilience of ports against natural disasters. This is done by identifying the performance and the recovery rate of such infrastructure during the period following the event. The research commenced with gathering information about the port's main components that are influenced by natural hazards. The collected data has been compiled in the form of indicators, which have been filtered and grouped under four dimensions in the proposed "PORT framework". Each of the indicator has been allocated a *measure* to enable its quantitative evaluation. The aggregation of the indicators' values allows identifying the port resilience.

1 INTRODUCTION

Ports are a main component of the physical infrastructure of coastal communities. Despite their importance, they are often overlooked in the disaster resilience engineering. Seaport infrastructure is fundamental for marine transportation at both local and national scales. Normally, ports are significantly exposed to natural and manmade disasters (Kron 2011), which necessitates assessing their resilience and performance in order to set mitigation plans for extreme disruptive events.

Although much effort has already been made to boost research on resilience measurement (Cimellaro et al., 2010), there is still no acceptable method for the evaluation of the resilience of large infrastructure systems like ports, and there are still challenges in developing real evaluation strategies.

Different kind of approaches are presented in the literature to measure the seaport resilience: some consider specific scenarios in their studies to measure the performance of given port components, such as the destruction of quays under a seismic event (Safieezadeh et al.2014), while others focus on identifying port performance indicators (e.g. number of TEU's (Twenty-foot Equivalent Unit), tons of dry and liquid bulk material (Pant et al. 2014), etc.), which are used to build performance evaluation frameworks (Berle et al. 2011, Baker et al 2013, Heinsen et al. 2014, Kurapati et al 2015, Mohd Salleh et al. 2015, Gharehgozli et al 2016, Mcintosh et al. 2017). Both kind of approaches have advantages and disadvantages. The first one considers a thorough investigation of a single problem but it does not capture the complexity of the different scenarios that may affect the activity of the port, like communication or organizational problems, and it often only tackles the resilience of structural elements of the port, like berth or cranes. The second approach, on the other hand, uses several generic indicators to determine the resilience of ports. The indicators are assessed independently at a given time without considering their interdependency. In this type of approaches, no final port resilience measure has been proposed in previous work and so the overall performance of the port has not been identified. Indeed, the existing resilience approaches do not actually measure the resilience but rather the performance of ports because resilience is a dynamic process that needs to be assessed for a given period of time following the perturbation and not only at a given instance of time.

The approach introduced in this paper fulfills the mentioned shortcomings by proposing a framework that covers all the significant aspects of port activities at both structural and organizational levels. The interdependency among the ports' elements is consid-

ered through the use of weighted indicators. The final output of the framework is a dynamic port resilience measure.

2 METODOLOGY

Measuring the seaport resilience under natural hazards such as wind actions is a challenging task. Although the use of indicators is perceived as an important instrument to measure resilience, developing a standardized set of resilience indicators is clearly challenging for such a dynamic, constantly reshaping and context-dependent concept.

Among the various resilience approaches in the field of engineering, the ones proposed by Bruneau et al. (2003) and Cimellaro et al. (2016) are the most suitable for developing a resilience framework for port infrastructure. For the purpose of this study, the resilience definition given by Bruneau (2003) is considered: resilience is "the ability of community units to mitigate hazards, contain the effects of disasters when they occur, and carry out recovery activities in ways to minimize disruption and mitigate the effectors of further events".

Kammouh et al. (2017c) proposed a novel method for evaluating community resilience. The method starts by collecting all community resilience indicators found in the literature and then allocating them into homogeneous components, classified under seven dimensions (Kammouh et al. 2017c, Kammouh et al., unpubl). A measure is assigned to each indicator allowing it to be quantified. The measure is not represented by a scalar value but rather a normalized continuous function that marks the serviceability of the community in time (Figure 1). All measures are weighted according to their contribution in the overall resilience assessment. The methodology takes as inputs the indicators' serviceability before and after a given hazard and turns as an output the serviceability curve of the community as well as a resilience measure. The resilience is then computed as the area under the serviceability function for a defined control time (T_1 -T_f) following the disaster (Figure 1).

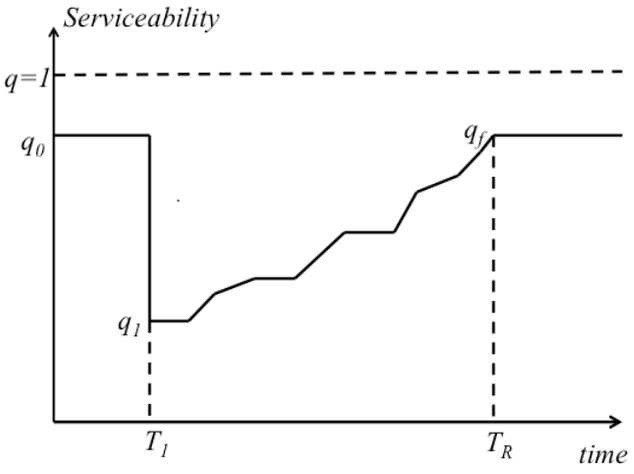


Figure 1. The concept of Serviceability function: q_0 initial serviceability, T_1 disaster event time, q_1 post-disaster serviceability, q_f final serviceability after T_R

The method proposed in this paper is inspired by the work previously done in (Kammouh et al. 2017c) as it uses the same algorithm. However, a new and exhaustive list of indicators that are applicable only for port infrastructures is introduced in this paper.

The identification of a set of port-specific indicators was fundamental for identifying the main ports elements that could be influenced by the natural hazards. This task has been completed through a wide literature research on port indicators and several visits to the VTE (Voltri Terminal Europa), the main container terminal of the Port of Genoa and one of the most important in the Mediterranean area. The collected data have been compiled in the form of *indicators*, which have been filtered and classified under a set of *components*. Finally, the components have been grouped under four *dimensions*: Physical Infrastructure, ICT and Equipment; Organization and Business Management; Resources and Economy Development; and Territory, Environment and Stakeholders, summarized under the acronym "PORT" (Table 1). Each indicator has been assigned a measure to make it quantifiable and then weighted according to its interdependency with the other indicators.

Table 1 Dimensions and components of the PORT framework

Physical Infrastructure, ICT and Equipment	**Resources and Economy Development**
1.1 Quay Cycle	3.1 Financial Flows
1.2 Trucks Cycle	3.2 Financial Services
1.3 Rail Cycle	3.3 Port Business and Costs
1.4 Yard	3.4 Employment Services
1.5 Port Buildings	
1.6 Containers	
1.7 Port Utility Services	
1.8 Technical Services Availability	
Organization and Business Management	**Territory, Environment and Stakeholders**
2.1 Terminal Policy	4.1 External Physical Access
2.2 Internal and External Communication	4.2 Environment Sustainably
2.3 Human Resources	4.3 Reputation
2.4 Resources Planning	
2.5 Risk Assessment and Mitigation	
2.6 Preparedness, Response and Recovery	

Several weighting techniques exist in the literature (Kammouh et al. 2017a, Kammouh et al., 2017b, Kammouh et al. 2017c). At this stage, the weighting

factors are assumed in the range between 1 and 3 on the basis of qualitative judgment. Future work will be addressed to a quantitative definition of such factors Table 1 lists the dimensions and the components of the PORT framework.

3 PORT FRAMEWORK STRUCTURE

Figure 2 shows a simple scheme of the port areas and the principal activities that are adopted in this work as indicators. Three cycles (train, quay and trucks cycles), the yard and the buildings are the main intermodal areas of the Port, where the most important activities are carried out. Containers are moved from the Quay Cycle to the Yard and to the Trucks and Train Cycles in order to be shipped through the external Railway and Roadway System and vice versa.

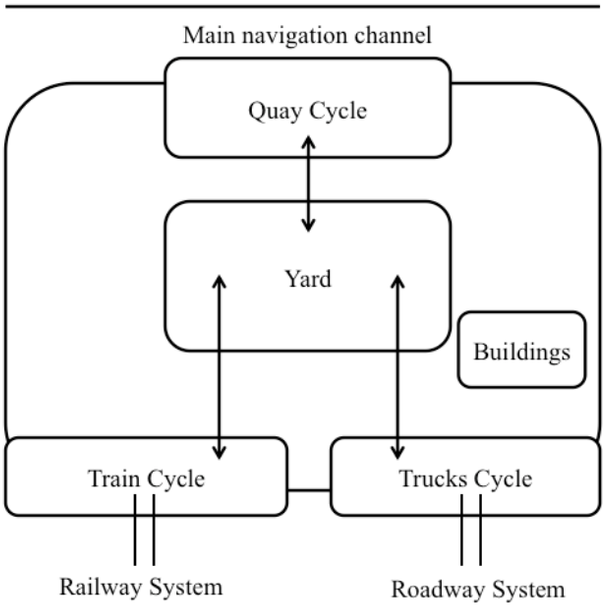


Figure 2. Schematic representation of different port area ort Areas and their interconnections.

A full list of dimensions, components, and indicators can be found in Appendix. In this table, a measure has been assigned to each indicator to allow its quantitative evaluation. The measures have been defined in close collaboration with the port experts to insure that the proposed data actually exists in the port terminals databases.

TV is the "Target Value" of the indicator, usually defined by the terminal experts and safety&security manager. This quantity is used as a baseline to normalize the measures. For instance, if we consider the measure "Quay gantry cranes low profile (indicator 1.1.1 in Appendix), the output of the measure would be *the daily number of TEUs handled by port cranes low profile type*. The output in its current shape can not be combined with other measures until it is normalized. This is done by dividing over the corresponding *TV*. In this case, *TV* represents the *ideal number of TEUs that the crane can handle as expected by port operators*. This operation (normalization) allows comparing and considering different heterogeneous variables related to different port aspects, such as physical infrastructure, port communications and the economic resources

I is the importance factor of each indicator which is determined according to the indicator's contribution in the overall resilience assessment.

Nat describes the nature of the indicator: The indicators can be either Static (*S*) or Dynamic (*D*). Static indicators are the ones that are not affected by the disastrous event and their values do not change after the disaster, while Dynamic indicators are the ones whose values change after the disaster's occurrence.

In the following, each dimension with selected components (in **bold**) and indicators (in *italic*) are described in details.

3.1 *Physical Infrastructure, ICT and Equipment;*

Eight components are considered to describe this dimension: **Quay Cycle**, **Trucks Cycle**, **Train Cycle**, **Yard**, **Port Buildings**, **Containers**, **Port Utility systems** and **Technical Services Availability**. The first four components represent the areas where the most important operations of the port take place. The critical elements needed to run the operations in the mentioned port areas have been investigated. The "crane" has been spotted as the most critical element to run most operations in the different port zones. That is, in case of crane interruption, most port activities break in.

In the **Quay Cycle**, cranes are placed on rails near the dock for loading and unloading goods from the ships. Their configuration is designed to meet specific height limits, especially when the port is close to an airport. Two different crane types are considered: *quay gantry cranes low profile type* and *quay gantry cranes gooseneck type*. These two types of cranes are therefore chosen as indicators for the Quay Cycle component.



Figure 3. VTE's quay gantry cranes - gooseneck type

In the **Trucks Cycle**, which is the area where the containers are loaded and unloaded to and from the *trucks*, there are the *rubber-tired gantries (RTGs*), which are mobile gantry cranes mounted on rubber tired used to stack the containers in the yard

In the **Train Cycle**, cranes are placed near the railroad tracks of the port area. They are defined as *Rail-Mounted Gantries cranes* and they are equipped with tracks in order to move easily along the length of the *freight train*.

In the **Yard**, to facilitate the internal container storage movements, cranes can be mounted both on Rubber or Rail as *Rubber-tired gantries* and *Rail-Mounted Gantries* respectively. For each of these elements, the most representative measure is "the daily number of congested containers". This measure applies to both loaded and unloaded containers. In addition, the two elements: *Prime Mover* and *Reach Strakes* are necessary for the internal movement in the terminal area (i.e., to move the TEUs from one cycle to another or to carry them to the rubber vehicles in the storage yard) and therefore they are chosen as additional indicators.

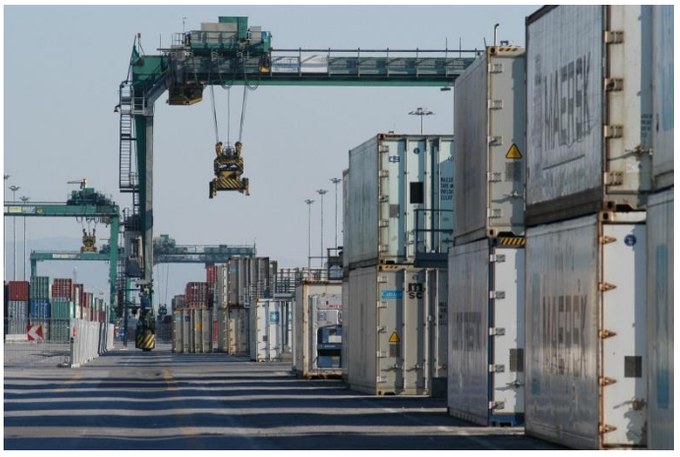


Figure 4. The Yard with the rubber-tired gantries and rail-mounted gantries

Buildings serviceability is determined according to their resistance. An event that significantly reduces the building capacity implies the building's closure or destruction, with consequences on both the human life and the port activity.

The **Containers** are fundamental for organizing the entire port activity. Containers can be stored in temperature controlled environments and they can be either empty or full. *Empty container*, in particular, is chosen as an indicator for the **Containers** component due to their critical role during emergencies, where the goods in the damaged containers are moved to the empty ones. Other indicators for this component can be found in Appendix.

The **Utilities,** such as *gas* and *electricity*, are critical for the operation of the port cranes. *Electricity* is crucial also for the operation of *ICT* equipment (informational and communication technology), which is essential for the internal management of the port handling and storage.

The availability of **Technical Services** facilities represent a main component to run the port activities. If these services are absent or unavailable, the entry of ships into the dock becomes more complex or even impossible. Therefore, **Technical Services** has been chosen as a component for this dimension.

3.2 *Organization and Business Management;*

Port Organization activity components are divided into two main categories: ordinary organization practices and extraordinary organization practices. Ordinary organizational practices are: **terminal policies**, **internal and external communications**, **human resources**, and **resources planning**. Extraordinary organizations are related to **risk assessment and mitigation**, **response preparation and reconstruction**.

Terminal Policy: considers the *Health and Safety Executive* (HSE), which measures the effect of the perturbation on the workers' safety and health. It also considers the serviceability of the *Informational Technology system,* which plays a central role in the port main activities (e.g. the operation of the *cranes)*. For example, a computer system block can lead to the immediate cessation of all port activities as it becomes impossible to know the location, destination, and contents of the containers. It is measured with "the number of *IT* block events that cause the port activities to stop". Another indicator is the *Terminal security,* which depends on the ISPS code (International Ship and Port Facility Security Code). Destructive events cause the terminal security to be weakened as the level of control is reduced.

Internal and external communication plays an important role in the port organization serviceability. One of the most weighted indicators for this component is the *internal terminal communication indicator* (location, destination, and container contents), known as EDI connectivity (Electronic Data Interchange).

The component **Human resources** is divided into four indicators: *operational personnel*, *staff planning operational activities*, *supervisory staff* and *Manning of Dockers*. In the scenario of a destructive event, the *operational personnel* indicator becomes particularly sensitive due to the fluctuation in the amount of work carried out.

Resources Planning: concerns the *Berth Window occupancy delays*, the average permanence of a container within the yard (*Turnaround Time*) and the *berth occupancy rate*.

The second part of the components related to this dimension concern the **assessment and mitigation of risks** and the **preparation and allocation of resources** to mitigate the effects of the disaster event. These components are present in Appendix but are not described in the paper.

3.3 *Resources and Economy Development*

Ports usually require good **Financial Flows** to allow the investments in port activities. For ports, investments are fundamental to ensure their competitiveness and serviceability. Measuring the financial flow is crucial in order to evaluate the serviceability of a port system and its potential to expand and develop. Investments for which a capital is required may be of several types, superstructures such as cranes, maintenance and drainage, and expansion of the storage space. An additional effect of the destructives event on the financial capabilities of a port is the difficulty to access the *Financial Services.*

The **Port business** component is related to those indictors through which the economic outlook of a port is commonly assessed. The most relevant indicator for **port business** is the number of containers (*tonnage*) that is handled annually by the port.

3.4 *Territory, Environment and Stakeholders*

In this last component, the port elements that are located outside the port terminal are considered: the **access routes** to the port terminal, the quality of the environment **(environment sustainability)** and the port's social **reputation**. The first component concerns the serviceability of access roads such as the *highway access infrastructure*, the *incoming rail,* and the *navigation channel* through which ships depart and arrive. The environmental sustainability of the port activity includes the *quality of air*, *water* (can be reduced by ship spills), and *noise pollution,* which can have a strong impact on the surrounding citizenship.

The impact of the port activity on the citizens' lives may seriously affect the *port's social image*. This indictor is of special importance to the port terminal operators as it can lead to the closure of port activities in extreme cases.

4 CONCLUSION

This paper introduces a resilience measurement tool for seaports. The introduced PORT framework consists of a large number of resilience indicators that cover the main aspects of a port activity and management. A wide literature review has been made and several port experts and port authority personnel have been interviewed in order to conclude the presented indicators list.

Future work aims at defining quantitatively the weighting factors and validating the proposed framework by applying it to a real case study, such as the Genoa port. A user-friendly software tool in which the above methodology is implemented will also be introduced.

5 ACKNOWLEDGMENT

The research leading to these results has received funding from the European Research Council under the Grant Agreement n° ERC_IDEAL RESCUE_637842 of the project IDEAL RESCUE—Integrated Design and Control of Sustainable Communities during Emergencies. The research has also been financially supported by "Compagnia di San Paolo" Project "Wind monitoring, simulation and forecasting for the smart management and safety of port, urban and territorial systems" (grant number 2015.0333, ID ROL: 9820),. Authors gratefully acknowledge PSA Voltri-Pra QSE & Risk Management Manager Stefano Mordeglia, who gave valuable information about the critical aspects of seaports..

REFERENCES

Becker, A. H., Matson, P., Fischer, M., & Mastrandrea, M. D. (2015). Towards seaport resilience for climate change adaptation: Stakeholder perceptions of hurricane impacts in Gulfport (MS) and Providence (RI). *Progress in Planning*, *99*, 1-49.

Berle, Ø., Asbjørnslett, B. E., & Rice, J. B. (2011). Formal vulnerability assessment of a maritime transportation system. *Engineering & System Safety*, *96*(6), 696-705.

Bruneau, M., Chang, S. E., Eguchi, R. T., Lee, G. C., O'Rourke, T. D., Reinhorn, A. M., & Von Winterfeldt, D. (2003). A framework to quantitatively assess and enhance the seismic resilience of communities. *Earthquake spectra*, *19*(4), 733-752.

Cimellaro, G. P., Reinhorn, A. M., and Bruneau, M. (2010). "Framework for analytical quantification of disaster resilience." *Engineering Structures*, 32(11), 3639–3649.

Cimellaro, G.P., Renschler, C., Reinhorn, A.M. & Arendt, L. (2016), PEOPLES: A Framework for Evaluating Resilience. *Journal of Structural Engineering*: 04016063.

Cutter, S. L., Burton, C. G., & Emrich, C. T. (2010). Disaster resilience indicators for benchmarking baseline conditions. *Journal of Homeland Security and Emergency Management*, *7*(1).

Cutter, S. L., Barnes, L., Berry, M., Burton, C., Evans, E., Tate, E., & Webb, J. (2008). Community and Regional Resilience: Perspectives from Hazards, Disasters, and Emergency Management. *Community and Regional Resilience Initiative (CARRI) Research Report*, *1*.

de Langen, P., Nidjam, M., & van der Horst, M. (2007). New indicators to measure port performance. *Journal of Maritime Research*, *4*(1), 23-36.

Gharehgozli, A. H., Mileski, J., Adams, A., & von Zharen, W. (2017). Evaluating a "wicked problem": a conceptual framework on seaport resiliency in the event of weather disruptions. *Technological Forecasting and Social Change*, *121*, 65-75.

Hanson, S., Nicholls, R., Ranger, N., Hallegatte, S., Corfee-Morlot, J., Herweijer, C., et al. (2010). A global ranking of port cities with high exposure to climate extremes. *Climatic Change*, 104(1), 89– 111.

Hsieh, C. H., Tai, H. H., & Lee, Y. N. (2014). Port vulnerability assessment from the perspective of critical infrastructure interdependency. *Maritime Policy & Management*, *41*(6), 589-606.

Kammouh, O., Dervishaj, G. & Cimellaro, G. P. (2017a) A New Resilience Rating System for Countries and States. *Procedia Engineering,* 198**,** 985-998.
Kammouh, O., Dervishaj, G. & Cimellaro, G. P. (2017b) A quantitative framework to assess resilience and risk at the country level. *ASCE-ASME Journal of Risk and Uncertainty in Engineering Systems, Part A: Civil Engineering*.
Kammouh, O., Noori, A. Z., Cimellaro, G. P. & Mahin, S., Resilience Evaluation Of Urban Communities Based On Peoples Framework. *ASCE-ASME Journal of Risk and Uncertainty in Engineering Systems, Part A: Civil Engineering, Unpub*.
Kammouh, O., Noori, A. Z., Renschler, C. & Cimellaro, G. P. (2017c) Resilience quantification of communities based on PEOPLES framework. *16th World Conference on Earthquake.* Santiago.
Kron, W. (2013). Coasts: the high-risk areas of the world. *Natural hazards*, *66*(3), 1363-1382.
Kurapati, S., Lukosch, H., Verbraeck, A., & Brazier, F. M. (2015). Improving resilience in intermodal transport operations in seaports: a gaming approach. *EURO Journal on Decision Processes*, *3*(3-4), 375-396.
Pant, R., Barker, K., Ramirez-Marquez, J.E. & Rocco C.M. (2014) Stochastic measures of resilience and their application to container terminals. *Comput&Ind Eng*; 70:183–94.
Pitikilis, K., (2011), Systemic Seismic Vulnerability and Risk Analysis for Buildings*, Lifeline Networks and Infrastructures Safety Gain.*
Mansouri, M., Nilchiani, R., & Mostashari, A. (2010). A policy making framework for resilient port infrastructure systems. *Marine Policy*, *34*(6), 1125-1134.
Morris, L. L. (2017). Ports Resilience Index: Participatory Methods to Assess Resilience (Doctoral dissertation).
McIntosh, R. D., & Becker, A. (2016, February). Towards a Comparative Index of Seaport Climate-Risk: Development of Indicators from Open Data. In *American Geophysical Union, Ocean Sciences Meeting 2016, abstract# EC34B-1170*.
Na, U. J., & Shinozuka, M. (2009). Simulation-based seismic loss estimation of seaport transportation system. *Reliability Engineering & System Safety*, 94(3), 722-731.
Mohd Salleh, N., Riahi, R., Yang, Z., and Wang, J. (2015). "Supply Chain Risk Management in the Container Liner Shipping Industry from a Strategic Point of View." *European Journal of Business and Management*, 7(24), 155-163.
Rose, A. 2007. Economic resilience to natural and man-made disasters: multidisciplinary origins and contextual dimensions. *Environ Hazard*; 7(4):383–98.
Shafieezadeh, A. & Burden, L. I. 2014. Scenario-based resilience assessment framework for critical infrastructure systems: case study for seismic resilience of seaports. *Reliability Engineering & System Safety* 132: 207-219.
Southworth, F., Hayes, J., McLeod, S., & Strauss-Wieder, A. (2014). *Making US Ports Resilient as Part of Extended Intermodal Supply Chains* (No. Project NCFRP-37).
Thoresen, C. A. (2003). Port designer's handbook: recommendations and guidelines. Thomas Telford.
UNISDR. How to Make Cities More Resilient: A Handbook for Local Government Leaders : a Contribution to the Global Campaign 2010-2015 : Making Cities Resilient - My City is Getting Ready! United Nations Office for Disaster Risk Reduction, 2012 Disaster Risk Reduction, 2012.

APPENDIX

Dimension/ component/indicator	Measure (0 ≤value ≤1)	Ref	I	Nat
1. Physical Infrastructure, ITC, Equipments			3	
1.1 Quay Cycle			3	
- Quay gantry cranes low profile type	Daily n° of TEUs loaded and unloaded ÷ TV	Morris 2017 Thoresen 2003	3	D
- Quay gantry cranes gooseneck type	Daily n° of TEUs loaded and unloaded ÷ TV	Morris 2017 Thoresen (2003)	3	D
1.2 Trucks Cycle			3	
- Trucks	Daily n° of Trucks Served ÷TV	Soutworth et al.2014	2	D
- Rubber-tired gantries (RTG)	Daily n° of TEUs loaded and unloaded ÷ TV	Morris 2017 Thoresen 2003	3	D
1.3 Train Cycle			3	
- Trains	Daily n° of Train operated ÷ TV	Soutworth et al.2014	3	D
- Rail-mounted gantries	Daily n° of TEUs loaded and unloaded ÷ TV	Morris 2017 Thoresen 2003	3	D
1.4 Yard			3	
- Rubber-tired gantries	Daily n° of TEUs loaded and unloaded ÷ TV	Morris 2017 Thoresen 2003	3	D
- Rail-mounted gantries	Daily n° of TEUs loaded and unloaded ÷ TV	Morris 2017 Thoresen 200)	3	D
- Reach Stackers	n° of Reach Stackers available ÷ n° of Reach Stackers needed	Morris 2017	2	D
- Prime mover	n° of prime mover available ÷ n° of prime mover needed	Morris 2017	2	D
1.5 Port Buildings			3	
- Docks	Resistance of the structure	Soutworth et al.2014 Thoresen 2003	3	D
- Administration buildings office	Resistance of the structure	Soutworth et al.2014	2	D

- Operation Control Room	Resistance of the structure	**	3	D
- Maintenance buildings	Resistance of the structure	**	1	D
- CFS	Resistance of the structure	Na&Shinozuka 2009	3	D
1.6 Containers			3	
- IMO Goods	n° of IMO TEUs handled ÷ n° of TEUs demanded, per cycle	**	2	D
- Reefer	n° of Reefer TEUs handled ÷ n° of TEUs demanded, per cycle	Soutworth et al.2014	2	D
- Empty Containers	n° of undamaged empty TEUs handled÷ n° of empty TEU's demanded, per cycle	**	3	D
- FCL	n° of FCL handled ÷ n° of TEUs demanded, per cycle	Soutworth et al.2014	3	D
1.7 Port Utility Systems			2	
- Power line/Electricity sub-station	KW/h provided to the port's cranes and equipment÷ KW/h needed	Beker et al. 2015	3	D
- Liquid fuel system	l of Liquid fuel provided to the yard equipment÷ l needed	Pitikilis 2011	3	D
- Fiber Optics	1 (if it is active), 0 (otherwise)	Beker et al. 2015	2	D
- Phone lines	1 (if it is active), 0 (otherwise)	Beker et al. 2015	1	D
- Sewer lines/(waste water system)	1 (if it is active), 0 (otherwise)	Beker et al. 2015	1	D
- Water utility	1 (if it is active), 0 (otherwise)	Beker et al. 2015	1	D
- Fire-fighting plant	1 (if it is active), 0 (otherwise)	Pitikilis 2011	1	S
1.8 Technical Services Availability			1	
- Pilots	1 (if it is active), 0 (otherwise)	Beker et al. 2015	2	D
- Thug Boats	1 (if it is active), 0 (otherwise)	**	2	D
- Mooring	1 (if it is active), 0 (otherwise)	**	2	D
Organization and Business Management			3	
2.1 Terminal Policy			3	
- HSE	n° of monthly professional Illnesses ÷ TV	de Langen et al. 2007*	1	S
- IT Policy	n° of monthly events stopped operations ÷ TV	Hsieh et al. 2013*	3	S
- Security organization (ISPS Code)	n° of monthly security incidents ÷ TV	de Langen et al.2007	2	S
- Delegation of authority	1 (if there is), 0 (otherwise)	de Langen et al.2007	1	S
2.2 Internal and External Communication			2	
- Terminal and Shipping Companies Communication	1 (if there is), 0 (otherwise)	Berle et al. 2011	2	S
- Terminal and Port Authority Communication/Coast Guard	1 (if there is), 0 (otherwise)	Berle et al. 2011	1	S
T- erminal and Trucks Company Communication	1 (if there is), 0 (otherwise)	Berle et al. 2011	2	S
- Terminal/Shipper&Forwarders Communication	1 (if there is), 0 (otherwise)	Berle et al. 2011	2	S
- Internal Terminal Communication (EDI connectivity)	1 (if there is), 0 (otherwise)	de Langen et al.2007	3	S
2.3 Human Resources			2	
- Availability of ops staff	n° of ops personnel available/ n° personnel needed for each enabling	Berle et al 2011*	3	D
- Planning of ops staff	n° of personnel supervising terminal÷ TV	Berle et al 2011*	2	D
- Supervising of ops staff	n° of personnel responsible for managing and performing transloading operations ÷ TV	Berle et al 2011*	2	D
- Manning of Dockers (to cover peaks)	n° of Manning of Dockers personnel available÷ n° personnel needed for each enabling	Berle et al. 2011*	2	D
2.4 Resources Planning and Location			2	
- Delays	1- ((n° of ships arrived at port at the berthing window - n° of ship allowed to enter into the port) ÷ n° of ships arrived at port)	Baker 2015	2	D
- Turnaround time	days of average warehousing of TEUs÷ TV	de Langen et al.2007	2	D
- Berth occupancy rate	n° of ships ÷ n° of quay available location	de Langen et al.2007	2	D
2.5 Risks Assessment and Mitigation			3	
- Policy/Risk appetite definition/Targets	1 (if there is), 0 (otherwise)	**	2	S
- Identification of hazards	1 (if there is), 0 (otherwise)	**	2	S
- Evaluation of risks	1 (if there is), 0 (otherwise)	**	2	S
- Mitigation countermeasures	% port area covered by a recent hazard mitigation plan	**	3	S

- Improvement Plan	% financial resources to carry out risk reduction activities ÷ TV	**	3	S
- Monitoring&Audit	% essential port elements that are under regular monitoring and audit programs	**	3	S
- Management review	1 (if there is), 0 (otherwise)	**	1	S
- Mitigation spending	Ten year average per m^2 spending for mitigation projects ÷ TV	Rose 2012	3	S
- Exposure to hazard protective resource	% building infrastructure not in high hazard zones	Cutter 2017	3	S
- Protective Resources	% of port area that consists of wind-breaks/wave breaks	Cutter 2008	2	S
- Essential infrastructure resistance	% of essential structures that remained operational during emergencies in past events	UNISDR 2007	3	S
- Essential infrastructure assessment	% essential infrastructures that are under regular assessment programs	***	3	S
- Accuracy of building codes	% designed structural damage – % actual structural damage (from past events)	***	3	S
2.6 Preparedness, Response and Recovery			3	
- Terminal Emergency Response Plan	1 (if there is), 0 (otherwise)	**	3	S
- Training and drills of emergency squad	1 (if there is), 0 (otherwise)	**	2	S
- Accrual for crisis management supporting the restoration	1 (if there is), 0 (otherwise)	**	2	S
- Disaster risk reduction measures integrated into post-Disaster recovery and rehabilitation activities	1 (if there is), 0 (otherwise)	**	3	S
- Contingency plan degree including an outline strategy for post-disaster recovery and reconstruction)	1 (if there is), 0 (otherwise)	**	2	S
- Emergency external services	1 (if there is), 0 (otherwise)	**	2	S
- Crisis Communication Plan	1 (if there is), 0 (otherwise)	**	1	S
- Temporary facilities	1 (if there is), 0 (otherwise)	***	2	D
Resource and economic development			2	
3.1 Financial Flows			2	
- Access to capital and investment for dredging, safety measures and expansion	capital accessed/ capital needed	Berle et al. 2011	2	S
- Revenues, access to capital and liquidity to invest in warehouses, storage yards and connecting infrastructure	capital accessed ÷ capital needed	Berle et al. 2011	2	S
- Access to capital, liquidity and revenue to fund operations and investments in superstructure	capital accessed ÷ capital needed	Berle et al. 2011	2	S
- Access to capital, liquidity and revenue to fund operations and expansion of infrastructure	capital accessed ÷ capital needed	Berle et al. 2011	2	S
3.2 Financial Services			1	
- Difficulties in obtaining insurance	0 (if there are), 1 (otherwise)	***	1	S
- Hazard Insurance Coverage (Risks uninsurable)	% of port elements covered by insurance program	Cutter 2014	1	S
3.3 Terminal Business and Costs			3	
- Tonnage	total monthly of goods tons moved ÷ TV	Beker 2015	3	D
- Revenue to Terminal	monthly revenue to port ÷ TV	Beker 2015	3	D
- Operations continuity	1 (if there is), 0 (otherwise)	Beker 2015	3	S
- Respect of pre-storm business plans	1 (if there is), 0 (otherwise)	Beker 2015	1	S
I- nvestment growth	% of investment growth ÷ TV	***	3	D
Territory Envirorment and Stekeholders			2	
4.1 External Physical Access			3	
- Roadway Systems	1 (if there is), 0 (otherwise)	Pitikilis 2011	3	S
- Railway Systems	1 (if there is), 0 (otherwise)	Pitikilis 2011	3	S
- Main Navigation Channel	1 (if there is), 0 (otherwise)	Beker 2015	3	S
4.2 Environment Sustainably			2	
- Noise pollution	1-(noise pollution index (NPI) ÷ TV)	***	2	D
- Air quality	1-(air quality index (AQI) ÷ TV)	***	3	D
- Water Quality	1-(water quality index (WQI) ÷ TV)	***	3	D
- Waste management	1 (if there is), 0 (otherwise)	***	1	S
- Debris field cleaning	0 (if there is), 1 (otherwise)	***	2	S
4.3 Reputation			3	
- Social image of the port	1-(Social Image index (SII) ÷ TV)		3	D

* Indicator found in literature but strongly modified after meetings with port experts
** Indicator found after interviews with port experts and port authority personnel
*** Indicator proposed by the authors

Maintenance, Safety, Risk, Management and Life-Cycle Performance of Bridges – Powers, Frangopol, Al-Mahaidi & Caprani (Eds)
© 2018 Taylor & Francis Group, London, ISBN 978-1-138-73045-8

Seismic damage assessment of a virtual large-scale city model

M. Domaneschi, S. Marasco, G. Scutiero, A. Zamani Noori, O. Kammouh, V. Taurino, G.P. Cimellaro
Department of Structural, Geotechnical & Building Engineering, Politecnico di Torino, Corso Duca degli Abruzzi 24, 10129, Turin, ItalyPolitecnico di Torino, Italy.

ABSTRACT: Recent social developments and economic transformation have changed the engineering design approach from building design level towards community design level (city, region, country). The latter approach involves modeling of interconnections between different systems (buildings, transportation, water network, etc.) rather than designing the buildings individually. Thus, new analysis tools are expected to be developed to simulate the complex response of a community subsequently to disasters. The need of such rational tools is the object of this research work. Two different numerical approaches to simulate the response of a large-scale built environment after a seismic scenario are explored by developing multipurpose numerical codes. A district of a virtual city is considered as a case study and the level of damage for built environment is estimated. This work could be the first step for further urban loss analysis, e.g. through agent-based models that could be updated online with the proposed simulation.

1 INTRODUCTION

Disaster events devastate the nature and human beings of a community. When a catastrophic event such as an earthquake occurs in a built environment, the consequential structural damage may cause high losses (casualties, repair costs, and repair time). The main goal of the paper is the seismic damage evaluation on the built environment through dynamic analysis. For seismic damage assessment of an urban area, computer-based simulation has become the most feasible and efficient methodology for scientific research and engineering application (Lu & Guan 2017). Given large-scale and complicated structural system, a computational model with balanced accuracy and efficiency is critical for earthquake disaster simulation. In this study two methodologies, based on the tri-linear and bi-linear backbone curve, are compared to evaluate in detail the seismic performance of the regular buildings.

Many studies claimed that the tri-linear backbone curve model can accurately represent the building's response in terms of inter-story (Vamvatsikos & Cornell 2005, Shi 2014). The first proposed approach is based on a nonlinear multi degrees of freedom system (MDOF) developed by Marasco et al. (2017). Nonlinear MDOF shear models are recognized able to satisfactorily capture the nonlinear properties of multi-story buildings, predict the Engineering Demand Parameters (EDPs), and assess a reasonable level of damage (Lu et al. 2014, Xu et al. 2014). The second methodology, developed by Cimellaro et al. (2017), is based on a simplified approach to obtain an equivalent single degree of freedom system (SDOF) through linear hypothesis.

The proposed methods have the ability to output the displacement contours for different time steps, thus making it possible to generate an animation of the building seismic responses. According to the Hazus (2012), the seismic damage is classified into five levels: slight, moderate, extensive, and complete damages. The same district of a virtual city model, called Ideal City, freely inspired to the city of Turin in Italy, is developed for evaluating the seismic effects at increasing intensities through proposed methodologies. It will be the starting step for further urban loss analyses, e.g. through agent-based models, which will be updated with respect to performance losses.

2 METHODOLOGY

2.1 *High fidelity model (HFM)*

The proposed methodology is discussed by Marasco et al. (2017). In this approach, the inter-story behavior of a regular building is simulated through a tri-linear backbone curve (Figure 1). The three main points of the curve are evaluated using a nonlinear static approach for a MDOF system. To achieve this goal, a MATLAB algorithm has been developed considering

the uncertainties on the geometric and mechanical parameters used in the analyses. Variation of the parameters within an acceptable range is considered through a Monte Carlo Simulation (MCS) obtaining a set of tri-linear backbone curves for each building.

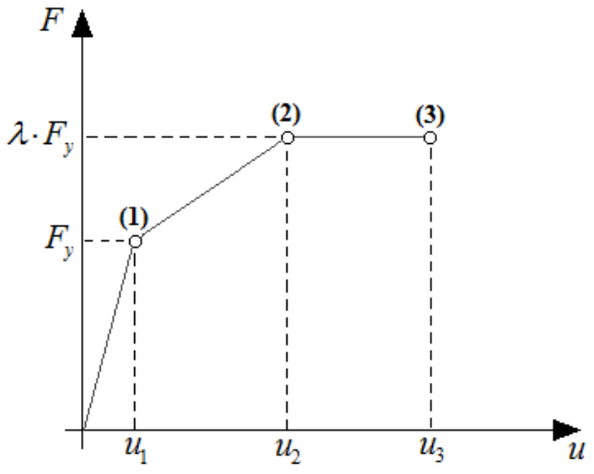


Figure 1. Tri-linear backbone curve.

The ranges of the main building's parameters are selected according to the knowledge level of the building. In addition, the deterioration of the mechanical properties (such as strength and elastic modulus of concrete) is taken into account through the aging equation proposed by Eurocode 2 (EC2 2004) according to the year of construction. Once the Matlab algorithm evaluates the tri-linear backbone curve at each step of MCS, the SAP2000 API is used to apply to all the buildings the data set obtained by the algorithm. This automated procedure is capable of reducing the computational time and analyze the dynamic responses dispersion caused by the data uncertainty. Therefore, the mean response and associated dispersion for each building within the virtual city can be estimated.

This approach is suitable to allow a decision-maker the ability to explore how their community responds to a disruptive event and quantify the mean performance of buildings and their uncertainty in the dynamic response after a hazard. Assimilating the dynamic nonlinear response of a structural system to a unique backbone curve leads to analyze the building as a nonlinear equivalent Single Degree Of Freedom (SDOF) model. The SDOF system simplification allows for a reduction in the computational efforts needed to assess the response of a large number of structures.

Finally, the hysteresis is considered according to the Takeda model (Takeda et al. 1970), as implemented inSAP2000. Figure 2 shows in detail the software data flow used in the simulations.

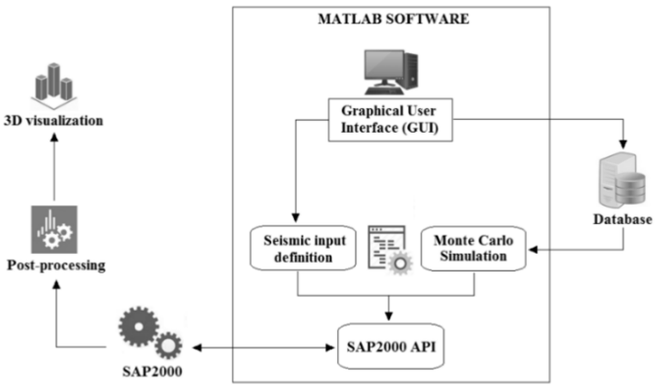


Figure 2. Software data flow.

According to the maximum drift, the structural damage is assessed for each building and the associated level of damage is evaluated (slight, moderate, extensive, complete). A 3D visualization tool is also provided, which shows the dynamic response of the building within the virtual.

2.2 *Simplified approach model (SAM)*

The proposed methodology is presented in Cimellaro et al. (2017). The building behavior is reproduced through a single degree of freedom (SDOF) model within a multipurpose FE software (Figure 3). A SOLID185 Element (eight nodes) represents the structure in ANSYS. It is fixed to the ground and has the same section of the real building's footprint. The mass is concentrated on the top of the building's model.

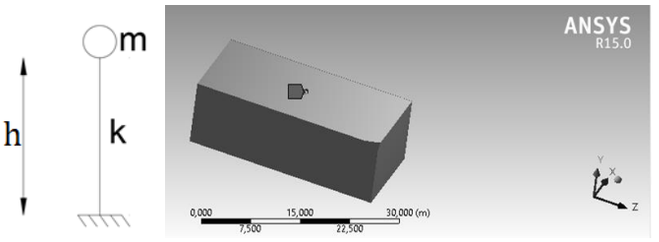


Figure 3. SDOF model and 3D visualization.

A self-weight for floor of 11 KN/m^2 is adopted accordingly with a widely accepted range of 10-12 KN/m^2. The period of structure (T) and equivalent SDOF stiffness of the building (k) are calculated by following:

$$T = CH^{3/4} \tag{1}$$

$$K = \left(\frac{2\pi}{T}\right)^2 m_{tot} \tag{2}$$

$$K = \frac{GA_s + 3EI}{H + H^3} \rightarrow E \tag{3}$$

where C is computed by Eurocode 8 (1998), H is the building's height in meter, m_{tot} is the mass in Kg, T is the period of the first vibration mode in seconds,

K is the stiffness of building, G is the shear modulus, and E is the elasticity modulus. The total mass is given by:

$$m^* = \sum m_i . \varphi_i \quad (4)$$

where m_i is the mass for floor and it can be assumed equal to 11 KN/m^2 and φ_i is the eigenvector of the building at floor i. Importing a 3D-GIS file into the FE code, the geometrical model of the regular buildings in a single step can be defined. Figure 4 exemplifies the general procedure for performing the solid FE mesh of the ideal city.

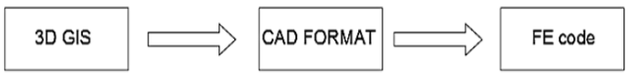


Figure 4. Method to import the geometrical model in a FE software.

The discretization of all buildings through this approach results very useful for both the polygonal visualization of the virtual city and, at the same time, for limiting the computational costs (low number of degrees of freedom). The seismic damage is classified as slight, moderate, extensive/complete. To assess the seismic damages of buildings through a linear approach, the force-based damage criterion in Xiong et al. (2016) is exclusively adopted. Thus, the bi-linear backbone curve consists in two key points (Figure 5).

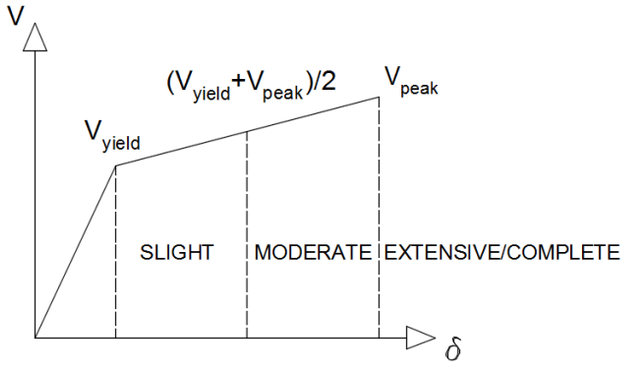


Figure 5. Bi-linear backbone curve.

The first one corresponds to yielding that is the turning point between the linear and the nonlinear behavior. According to Xiong et al. (2016), it is calculated such as:

$$V_{yield} = \Omega_1 V_{design} \quad (5)$$

where Ω_1 is the yield overstrength ratio of RC frames. As reported by HAZUS, a value of Ω_1 equal to 1,1 is adopted. The second point is the peak one corresponding to the peak strength.

$$V_{peak} = \Omega_2 V_{design} \quad (6)$$

To determine Ω_2, the statistical analysis is performed by Xiong et al. (2016) on RC frames designed following the Chinese seismic design code. For base shear forces that exceed the V_{peak} in Figure 5, the resulting damage is assumed in the range extensive/complete. Because, through a linear analysis, the displacement associated to highly nonlinear structural response can not be reasonably evaluated. The resultant base shear strength is calculated for each building and compared with the limit values in Figure 5.

3 DISTRICT SEISMIC RESPONSE SIMULATION

3.1 *Case study description*

A medium-size district of a virtual city model, called Ideal City, freely inspired to the city of Turin in Italy, has been considered to firstly assess the overall procedure and the structural behavior during an earthquake. The district is situated in Turin and contains nine regular buildings (Figure 6 and Table 1). Structures with "L" shape in reality are parts of buildings with a rectangular shape divided by a seismic joint.

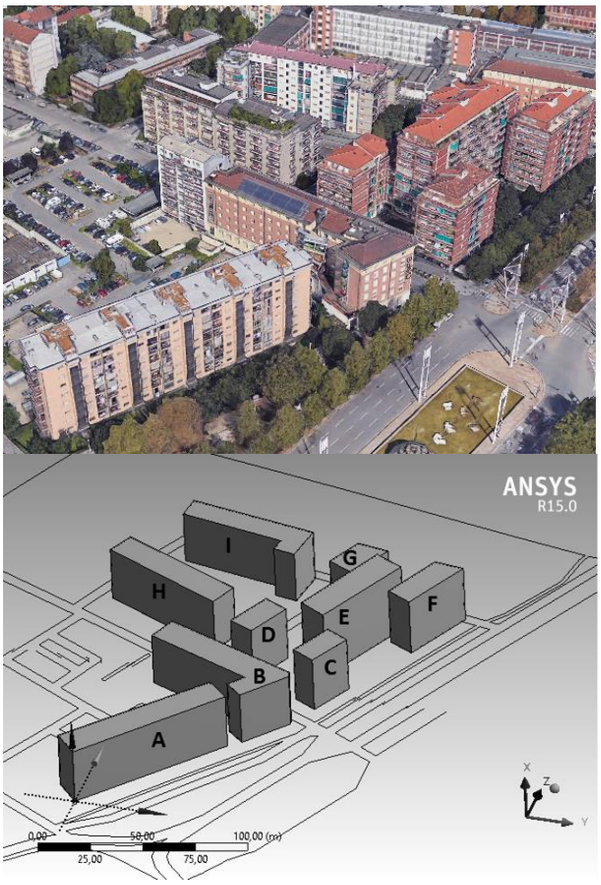


Figure 6. Case study buildings.

SIMQKE_GR software is used for generating the seismic acceleration input (Figure 7) as function of the geographical coordinates of the city, the soil type, the topography of the area, the total duration of the ground motion. The seismic input is applied to the virtual city at increasing intensities as shown in Table 2.

Table 1. Geometric building parameters.

Building	Height	Area
	m	m^2
A	28.9	1258
B	27.4	1242
C	29	293
D	29	319
E	36	810
F	28.4	475
G	28.4	323
H	28	951
I	28.4	862

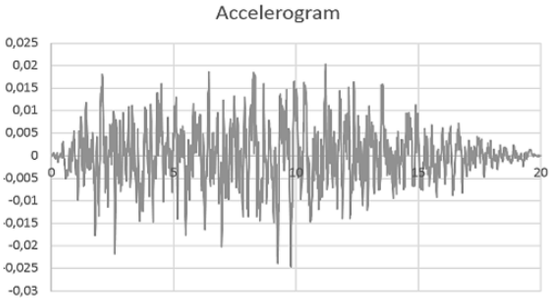


Figure 7. Generated accelerogram.

Table 2. Peak ground acceleration (PGA) for a constant duration Dr=20s.

Input Motion	PGA
	m/s2s^2
1	0.02
2	0.06
3	0.1
4	0.2
5	0.28
6	0.38
7	0.46

3.2 *Damage assessment by HFM*

Figure 8 shows the HFM results for different input motions corresponding to each building. On the horizontal and vertical axes respectively, the number of input motion and the maximum displacements on the top of the building values for the seven input motions are reported. The damage levels of the buildings for the different input motions are reported (S: slight, M: moderate, E: extensive, C: complete) in Table 3.

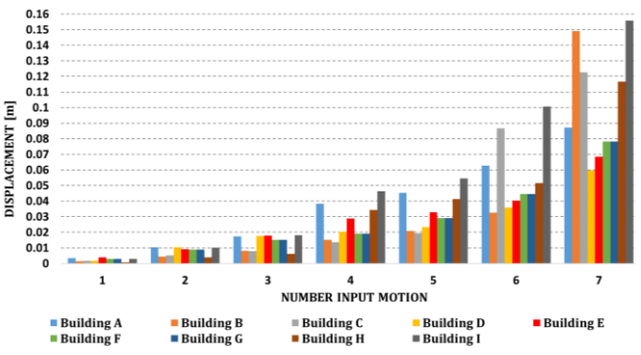


Figure 8. Maximum displacements evaluated by HFM.

Table 3. Damage state through HFM: S=slight, M=moderate, E=extensive, C=complete.

Building	Input motion number						
	1	2	3	4	5	6	7
A	<S	<S	<S	<S	<S	S-M	M-E
B	<S	<S	<S	<S	<S	S-M	M-E
C	<S	<S	<S	<S	<S	M-E	M-E
D	<S	<S	<S	<S	<S	S-M	M-E
E	<S	<S	<S	<S	<S	S-M	M-E
F	<S	<S	<S	S-M	S-M	S-M	M-E
G	<S	<S	<S	<S	S-M	M-E	M-E
H	<S	<S	<S	S-M	M-E	M-E	E-C
I	<S	<S	<S	S-M	S-M	M-E	M-E

3.3 *Damage assessment by SAM*

The results obtained by SAM for different input motions for each building are reported in Figure 9 in terms of maximum displacements. Obviously, being computed through linear analyses, they are halved with respect to those of HFM in Figure 8. Again, on the vertical axis, the maximum displacements on the top of each building are reported, while on the horizontal axis the number of input motion.
Table 4 reports the damage level for different input motions corresponding to each building of the district. Figure 10 illustrates an example of building visualization provided by SAM.

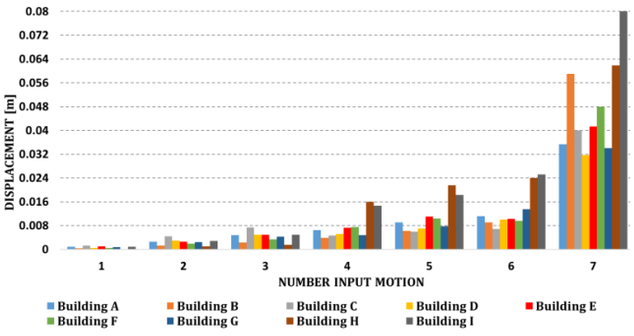


Figure 9. Maximum displacements evaluated by SAM.

Table 4. Damage state through SAM: S=slight, M=moderate, E=extensive, C=complete.

Building	Input motion number						
	1	2	3	4	5	6	7
A	<S	<S	<S	<S	<S	S	S-M
B	<S	<S	<S	<S	<S	S	M
C	<S	<S	<S	<S	<S	S-M	M
D	<S	<S	<S	<S	<S	S	S-M
E	<S	<S	<S	S	S	S	S-M
F	<S	<S	<S	S	S	M	M
G	<S	<S	<S	S	S	S-M	M
H	<S	<S	<S	S	S	S-M	S-M
I	<S	<S	<S	S	S	M	M

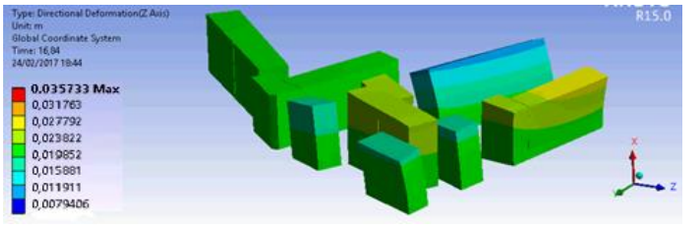


Figure 10. Example of visualization provided with SAM.

3.4 *Comparison between methodologies*

From the comparison between the outcomes of the two methodologies, similar responses can be found at the lowest input levels that are mainly characterized by linear behavior. For higher input motions, the linear response method by Cimellaro et al. (2017) obviously underestimates the displacements as shown in Figure 11 to Figure 19. Dynamic equilibrium equations are solved using direct integration method.

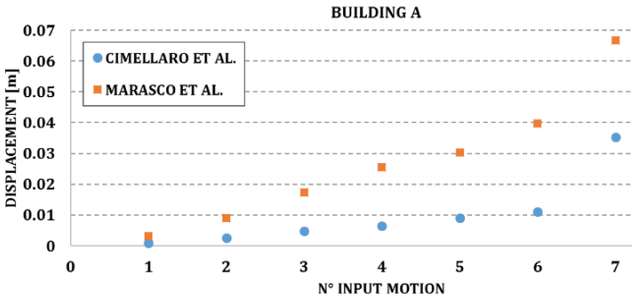


Figure 11. Comparison between two methods (Building A).

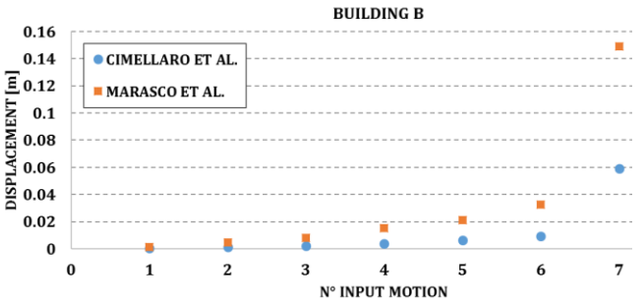


Figure 12. Comparison between two methods (Building B).

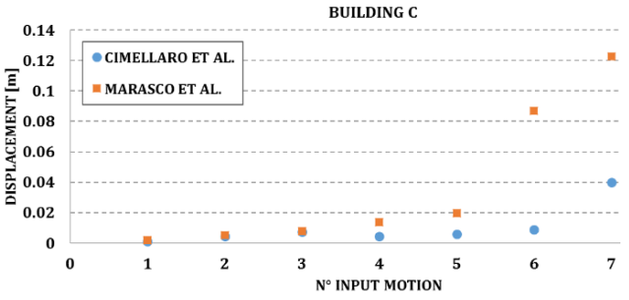


Figure 13. Comparison between two methods (Building C).

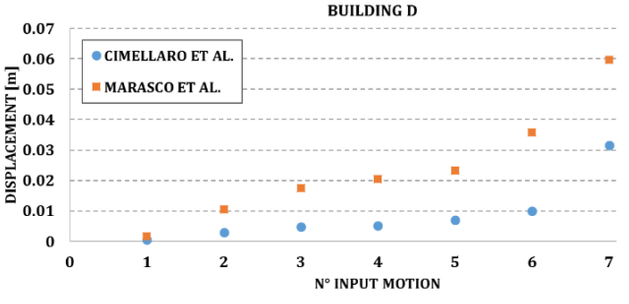


Figure 14. Comparison between two methods (Building D).

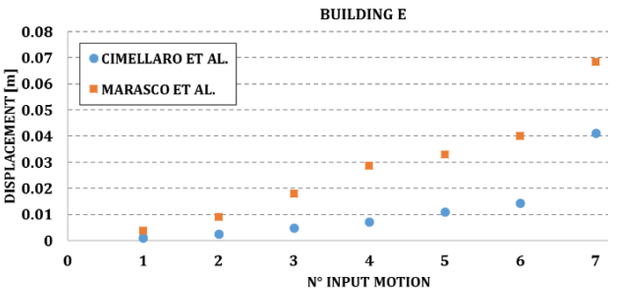


Figure 15. Comparison between two methods (Building E).

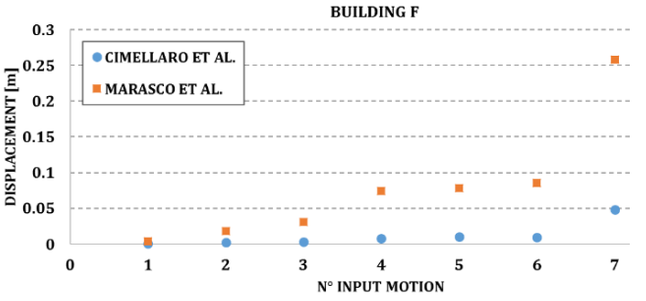


Figure 16. Comparison between two methods (Building F).

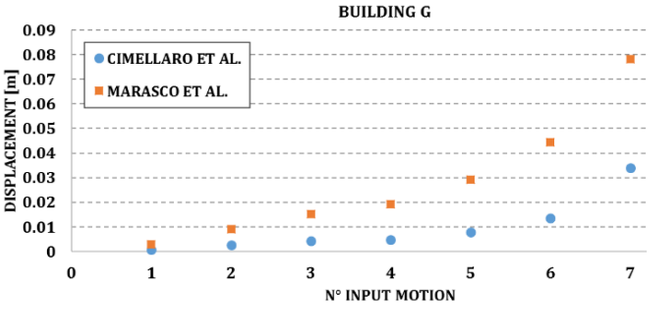


Figure 17. Comparison between two methods (Building G).

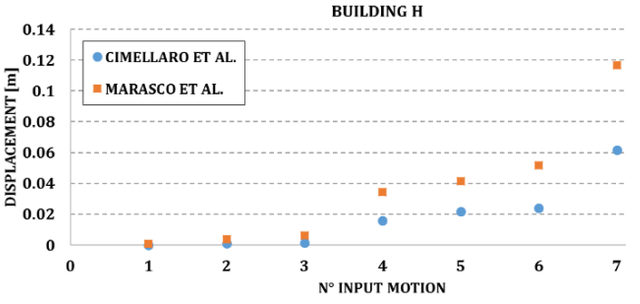


Figure 18. Comparison between two methods (Building H).

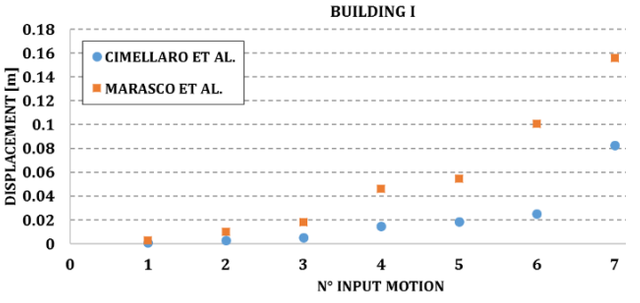


Figure 19. Comparison between two methods (Building I).

The natual vibrating periods of the equivalent SDOF models of both the methodologies are shown in Table 5. The SAM periods are lower than those obtained by HFM method, consistently with the adopted different methodologies. Indeed, in HFM the parameters of the equivalent SDOF are computed through 3D nonlinear dynamic analysis of the buildings.

HFM estimates the base shear (F_{yield}) and top displacement (u_{yield}) values corresponding to the formation of the first plastic hinge. Thus, the secant stiffness of the equivalent SDOF is given by:

$$K = \frac{F_{yield}}{u_{yield}} \tag{7}$$

Differently, SAM evaluates the equivalent SDOF stiffness (k) according to Eurocode 8 (see Equation 1 and Equation 2).

Table 5. Period equivalent SDOF

Building	T-High fidelity model	T-Simplified approach
	Sec	Sec
A	0.86	0.68
B	0.77	0.57
C	0.80	0.68
D	0.81	0.66
E	0.87	0.76
F	0.83	0.60
G	0.90	0.64
H	0.84	0.62
I	0.74	0.66

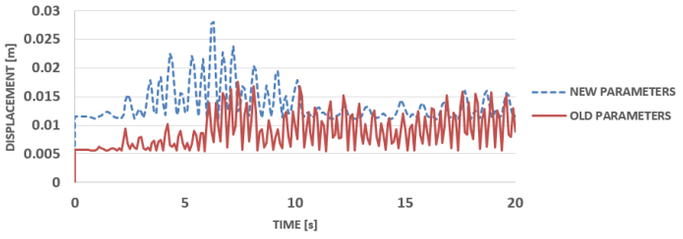


Figure 20. Displacements Building H – SAM

In order to deepen the comparison between the two methodologies, the building H is implemented in the linear SAM approach using the mechanical parameters computed by HFM. Figure 20 depicts the new displacements compared with those previous obtained through SAM employing input motion 4. The maximum displacement computed with new parameters, tends to solution computed with HFM.

Increasing the intensity of the input motion in HFM, the buildings' displacements belong to the nonlinear domain. As shown by previous results on damage state in HFM (Table 3), for PGA greater than 0.1g, buildings F, H, and I highlight elastic-plastic response and slight-to-moderate damage levels. Consistently, SAM also highlight modifications in the damage level with respect to lower input intensity levels but limited to slight damages.

Figure 21 depicts the linear and nonlinear response characteristics of SAM and HFM respectively. Accordingly to the linear approach, the displacements increase proportionally to the magnitude of seismic actions. Keeping constant a generic force (F) in plastic field, the displacement (u_2) of a nonlinear model is larger than the displacement (u_1) of a linear model.

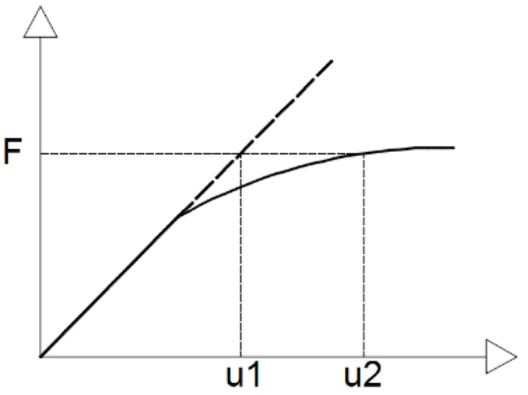


Figure 21. Linear model vs. nonlinear model

A further comparison is done in order to clarify the deviation between the two methodologies during the input motion 7. Table 6 summarizes the drift ratios obtained where HFM highlights larger responses consistently with the adopted nonlinear approach.

Table 6. Drift ratios for input motion n°7.

Building	HFM	SAM
	-	-
A	0.54	0.12
B	0.55	0.22
C	0.54	0.14
D	0.40	0.10
E	0.19	0.11
F	0.70	0.18
G	0.43	0.12
H	0.53	0.21
I	0.56	0.28

The study by Xiong et al. (2016) has been originally developed for predicting damage conditions through nonlinear time-history analysis. This hypothesis justifies the limited damaged levels in Table 4 with respect to Table 3.

Furthermore, the damage assessment method in SAM adopts a force criterion only. This assumption is reasonable at the earlier stage of seismic damage, when the stiffness of the structure is high and a small variation in deformation will lead to a significant change in the internal forces. For structural conditions beyond the peak shear force V_{peak} , the damage is assumed in the range "extensive/complete".

A further development of the present study will be focused on the modification of the trilinear curve by Xiong et al. (2016), for adapting the original methodology to the adoption of linear structural analyses.

The HFM method evaluates each building individually through nonlinear analysis. Tri-linear backbone

curves are accordingly defined. Despite the different approaches to simulate the buildings response, both methods evaluate compatible levels of damages for the considered case study.

4 CONCLUSION

Two different approaches to implement dynamic time history analyses for damage assessment in a built environment of a virtual city are proposed. The simplified linear approach model (SAM) reduces the computational time but underestimates the damage states with respect to the high-fidelity model (HFM). This last is based on a nonlinear approach with higher computational costs with respect to SAM.
Both the methodologies are reasonable simplified approaches in order to calculate the damage state in built environment as long as the buildings are perfectly regulars. Therefore, they can give a significant contribution to disaster resilience analysis and prevention in urban areas through numerical implementation in the virtual city models. Furthermore, they are capable to significantly reduce the computational time in large dimension models reducing the total number of degrees of freedom.
The proposed methodologies can support decision-makers to explore how their communities respond to a disaster event, quantify the performance of buildings, and to plan the better resilience-building strategies to minimize losses and the recovery time.

5 ACKNOWLEDGEMENTS

The research leading to these results has received funding from the European Research Council under the Grant Agreement n° ERC_IDEAL RESCUE_637842 of the project IDEAL RESCUE-Integrated Design and Control of Sustainable Communities during Emergencies.

6 REFERENCES

Ansys Inc., Canonsburg, PA, United States, 2015.

Baglio, M., Marasco, S., and Cimellaro, G. P. (2017). "Simulating earthquakes using artificial spectrum-compatible ground motions." *6th International Conference on Computational Methods in Structural Dynamics and Earthquake Engineering (COMPDYN2017)*15-17 June 2017, Rhodes Island, Greece.

Cimellaro, G. P., Domaneschi, M., and Mahin, S. (2017). "Exploring simulation tools for urban seismic analysis and resilience assessment." *6th International Conference on Computational Methods in Structural Dynamics and Earthquake Engineering (COMPDYN2017)*15-17 June 2017, Rhodes Island, Greece.

Cimellaro G.P., Domaneschi M., Mahin S. & Scutiero G. 2017, Exploring simulation tools for urban seismic analysis and resilience assessment, *COMPDYN 2017*.

Cimellaro, G. P., Renschler, C., Reinhorn, A. M., and Arendt, L. (2016). "PEOPLES: a framework for evaluating resilience." *Journal of Structural Engineering, ASCE*, 142(10), DOI: 10.1061/(ASCE)ST.1943-1541X.0001514.

Cimellaro, G., Tinebra, A., Renschler, C., and Fragiadakis, M. (2015). "New Resilience Index for Urban Water Distribution Networks." *Journal of Structural Engineering, ASCE*, 10.1061/(ASCE)ST.1943-1541X.0001433 , C4015014.

Cimellaro, G. P., Reinhorn, A. M., and Bruneau, M. (2010). "Framework for analytical quantification of disaster resilience." *Engineering Structures*, 32(11), 3639–3649.

EC2 2004. Design of concrete structures-Part 1-1: General rules and rules for buildings. European Committee for Standardization, Bruxelles, BG.

Eurocode-8 1998, UNI ENV 1998, Design of structures for earthquake resistance.

HAZUS 2012. FEMA - Multi-hazard loss estimation methodology. Washington, DC.

Lu, X.& Guan, H. 2017. Earthquake Disaster Simulation of Civil Infrastructures: From Tall Buildings, *Springer Nature, Singapore.*

Marasco, S., Zamani-Noori, A., and Cimellaro, G. P. (2017). "Keynote Lecture: Resilience Assessment for the Built Environment of a Virtual City." *6th International Conference on Computational Methods in Structural Dynamics and Earthquake Engineering (COMPDYN2017)*15-17 June 2017, Rhodes Island, Greece.

Matlab R2017, The MathWorks, Inc., Natick, Massachusetts, United States.

SAP 2000 2015, Computer and Structures Inc, Berkeley, California.

SIMQKE_GR, Piero Gelfi, University of Brescia, Italy

Takeda, T.M. 1970, Reinforced Concrete Response to Simulated Earthquakes. ASCE, *Journal of the Structural Division, Vol. 96*, No. ST12, pp. 2557 – 2573.

Vamvatsikos, D. 2002, C.A. Cornell, Incremental dynamic analysis. *EarthqEngStructDyn* 31 (3):491–514.

Xiong C., Lu X., Lin X., Xu Z. Ye & L. 2016. Parameter Determination and Damage Prediction of Multi-Story Buildings. *Journal of Earthquake Engineering*, 00, 1-25. Johnson, H.L. 1965. Artistic development in autistic children. Child Development 65(1): 13-16.

SS10: Assessment and evaluation of deteriorated bridges

Organizers: H.K. Kim & J.R. Casas

Maintenance, Safety, Risk, Management and Life-Cycle Performance of Bridges – Powers, Frangopol, Al-Mahaidi & Caprani (Eds)
© 2018 Taylor & Francis Group, London, ISBN 978-1-138-73045-8

Seismic retrofit of truss bridge for highway and railway

T. Hanai, T. Tamura & Y. Hirayama
Honshu-Shikoku Bridge Expressway Co. Ltd. (HSBE), Japan

ABSTRACT: For the steel truss portion of the Hitsuishijima viaduct, seismic performance evaluation was conducted and it was found that some members were damaged. Although the replacement of all the road deck bearings by isolation bearings was initially planned, scaffolding installation over the rail lines was limited within only three hours at midnight and heavy protection was required. In order to minimize work over the rail lines, isolation of truss girder was studied, which is unprecedented method for the highway-railway combined bridges in Japan. For the truss girder isolation, i) structural feasibility, ii) constraining effect of long rail, and iii) the running safety of the train were studied. By this method, the retrofit became minimal and economical.

1 INTRODUCTION

The Seto-Ohashi Bridges are highway-railway combined bridges and consists of three suspension bridges, two cable-stayed bridges, and truss bridges and viaducts. The construction of the Bridges started in 1978, and the Bridges were opened to traffic in 1988 as a first direct link between Honshu and Shikoku Island among three routes of Honshu-Shikoku Bridges. The Bridges were designed by original seismic design code. In the original seismic design code, although a plate boundary earthquake with magnitude of 8 was considered, an inland near field earthquake was not considered. And there is concern that large-scale earthquakes which are larger than that of the original design, would occur in the near future. Therefore seismic retrofit of the Seto-Ohashi Bridges started in 2013 and will be completed by 2020. As a seismic retrofit measure of the steel truss portion of the Hitsuishijima viaduct (hereinafter referred to as "truss bridge"), isolation of truss girder, which is unprecedented method for the highway-railway combined bridges in Japan, was selected. In this paper, selection process of the truss girder isolation and technical consideration to realize the method are explained.

2 EVALUATION OF TRUSS BRIDGE

The truss bridge is adjacent to the prestressed concrete viaduct portion and consecutive cable-stayed bridges, Hitsuishijima Bridge and Iwakurojima Bridge, in the north and south respectively (Figure 1). The truss bridge has simply supported truss girder with span length of 100m (Figure 2).



Figure 1. Hitsuishijima Island

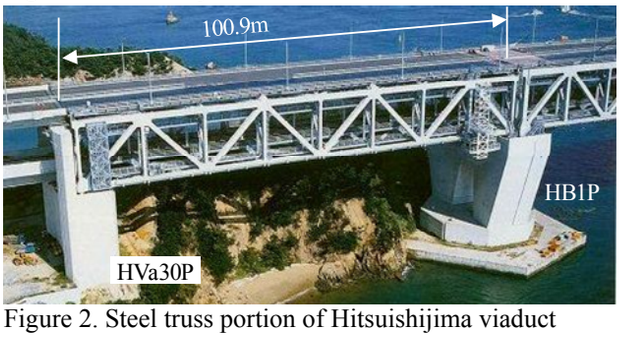


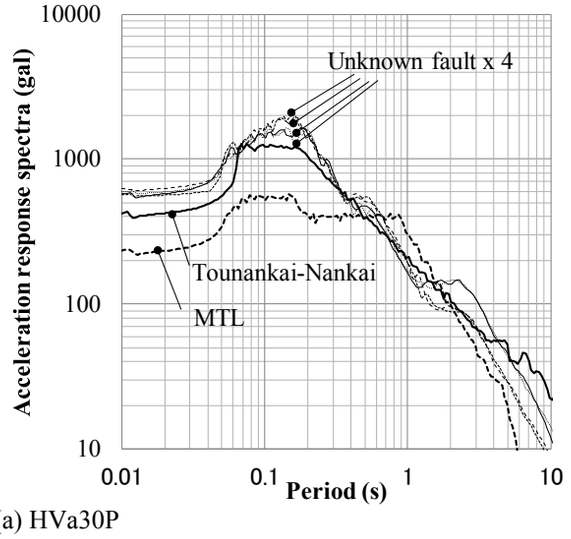
Figure 2. Steel truss portion of Hitsuishijima viaduct

Seismic performance evaluation of the truss bridge was conducted based on the Specification for Highway Bridges (JRA 2012) that is a Japanese standard for highway bridge design.

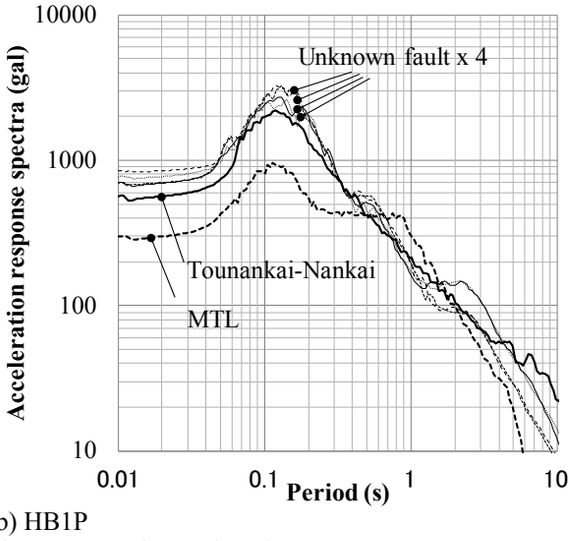
Seismic ground motions of the large-scale earthquakes (Level 2 earthquake) used for the seismic evaluation and seismic retrofit design are shown in Figure 3. They are the ground motions at the base of

the pier foundations calculated from the rock outcropping motions on the bedrock whose S-wave velocity is about 1500m/s by the one-dimensional wave propagation method. Two types of scenario earthquakes were considered. One is the Tounankai-Nankai Earthquake which is plate boundary earthquake with a magnitude of 8.6, the other is an earthquake with a magnitude of 7.5 coming from the Median Tectonic Line (hereinafter referred to as MTL) which is an inland active fault and is located about 35km from the bridge. A fault model for the Tounankai-Nankai Earthquak is shown in Figure 4. In addition to the two types of scenario earthquakes, four types of seismic ground motions generated by unknown fault earthquakes with a magnitude of 6.8 occurring just beneath the site were considered. This means the consideration for the possibility that an unknown inland active fault might exist near the site. All the seismic ground motions were estimated by a hybrid method (Green's function method + 3D finite difference method or discrete wave number method).

Analytical model used for the evaluation and retrofit design is shown in Figure 5. For the truss members and piers, nonlinear fiber elements are used. The road decks, road deck bearings, rail girders, and rail girder bearings are modeled with linear element. In the analysis, geometric nonlinearity is also considered.



(a) HVa30P



(b) HB1P

Figure 3. Level 2 earthquake

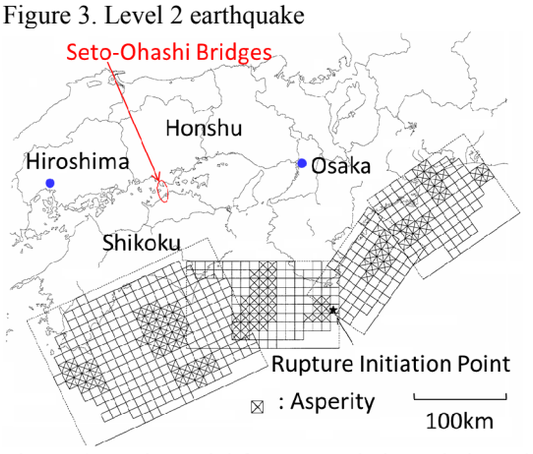


Figure 4. Fault Model for Tounankai-Nankai Earthquake

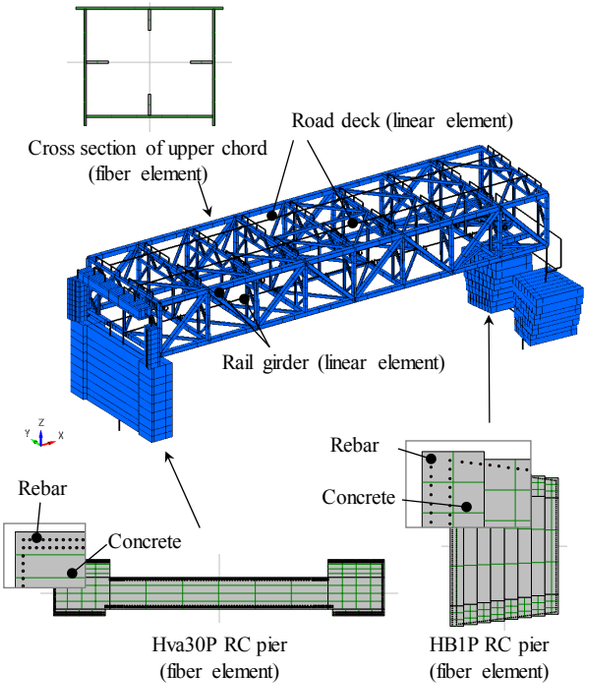


Figure 5. Analytical model

Evaluation result of the truss bridge is shown in Figure 6 and Table 1. It was found that the damages occur in the truss member near the supports and road girder bearings. Horizontal members above rail lines in the floor truss are also damaged. Because these members are immediately above the railway lines

and support overhead lines (Figure 7), maintenance work is conducted exclusively by the railway operator and workable time is limited within a few hours at midnight. Since the retrofit of these members is virtually impossible in reality, alternative schemes are studied.

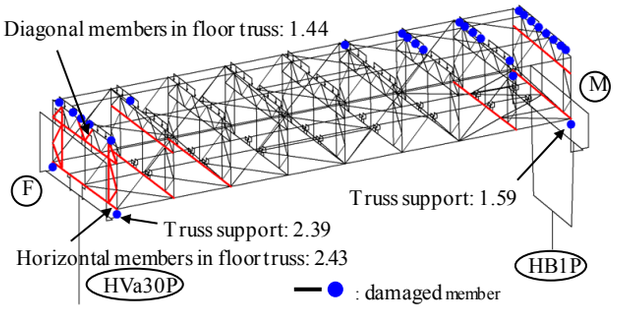


Figure 6. Evaluation result of truss bridge (response / allowable value)

Table 1. Evaluation result of truss bridge

Member	Evaluation	Number of damaged member
Truss girder		
Upper chord	0.51	0/16
Lower chord	0.56	0/16
Diagonal	0.64	0/16
Vertical	0.93	0/18
Floor truss		
Horizontal	**2.43**	**8**/27
Other	**1.44**	**12**/151
Upper lateral	0.86	0/18
Lower Lateral	0.98	0/23
Truss girder bearing		
(displacement)		
HB1P (longitudinal)	0.74	0/2
(strength)		
HVa30P		
vertical		
bearing	0.62	0/2
pullout	0.00	0/2
horizontal		
longitudinal	**1.24**	**2**/2
transverse	**2.39**	**2**/2
HB1P		
vertical		
bearing	0.42	0/2
pullout	0.00	0/2
horizontal		
transverse	**1.59**	**2**/2
Road deck bearing		
(displacement)	**1.14**	**18**/64
(strength)		
longitudinal	**1.91**	**5**/8
transverse	**1.02**	**1**/72
RC pier		
HVa30P		
bending (L)	0.62	
shear (L)	0.61	
bending (T)	0.25	
shear (T)	0.58	
HB1P		
bending (L)	0.52	
shear (L)	0.59	
bending (T)	0.46	
shear (T)	0.58	

Evaluation: response / allowable value

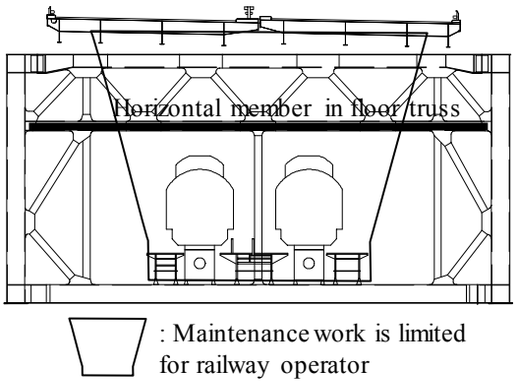


Figure 7. Damaged horizontal member

3 ALTERNATIVES OF SEISMIC RETROFIT

To avoid the retrofit of the horizontal members above the rail lines, alternative schemes were studied.

3.1 *Distribution of horizontal force in road deck supports*

By the replacement of road deck bearings by rubber bearings, inertial force of the road deck will be distributed. Result is shown in Figure 8. Although the number of damaged members is reduced, damage of the truss girder bearings remain. Without reinforce method of truss girder bearings, this scheme is not feasible.

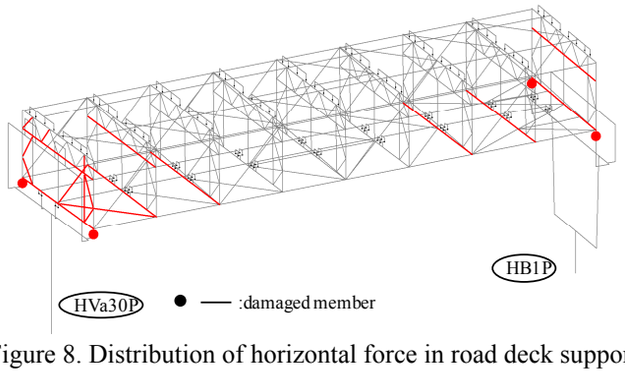


Figure 8. Distribution of horizontal force in road deck supports

3.2 *Road deck isolation*

By the replacement of road deck bearings by isolation bearings, inertial force transmitted from road decks to truss girder will be reduced and damages in the truss members will be reduced. However, all the truss members will not be saved by the road deck isolation only. Additional reinforcement of the truss members is required (Figure 9).

The replacement of the road deck bearings requires installation of scaffoldings and protections. Since these works are conducted above the railway lines, there are many restrictions during the retrofitting work.

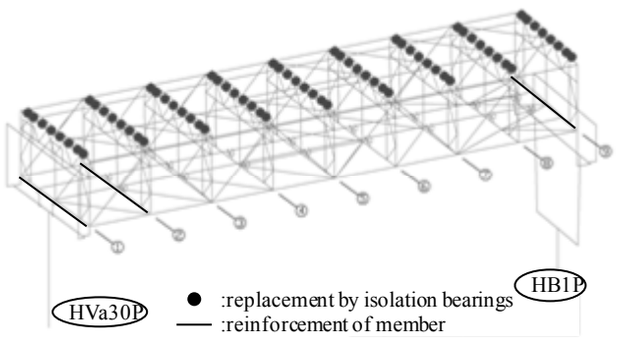


Figure 9. Retrofit by road deck isolation

3.3 *Truss girder isolation*

In this scheme, original hinged supports (Figure 10) for truss girder will be replaced by the rubber isolation bearings (Figure 11). The isolation bearings absorb seismic force and the inertial force acting on road deck and truss girder will be reduced to protect truss members from damage. Since this scheme reduce the work above the railway lines, it will reduce the retrofit cost compared with the road deck isolation scheme. However, since the scheme is unprecedented for highway-railway combined bridges in Japan, it requires technical consideration.

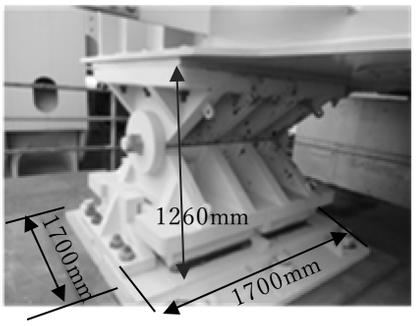


Figure 10. Original hinged support for truss girder

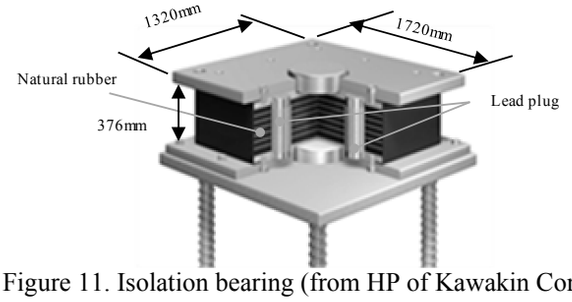


Figure 11. Isolation bearing (from HP of Kawakin CoreTech)

4 STUDIES FOR TRUSS GIRDER ISOLATION

In order to realize truss girder isolation, several issues were studied.

4.1 *Structural feasibilities*

Since the bridge is supported by two bearings at each end, reaction force becomes large and the required area for the rubber bearings becomes large. By assessing the current live load and dead load, it is confirmed that the required area for the rubber bearing is under the manufacturer's limit.

If the uplift force occurs during earthquake, function of isolation bearing cannot be taken into account (JRA 2012). By the calculation during earthquake, it is confirmed that the uplift will not occur and the bearing can be designed.

Because of the large area of rubber bearing, size of the upper shoe becomes larger than the current one. To accommodate this problem, steel saddle can be used to transmit reaction force (Figure 12).

For the replacement of the bearings, the truss girder is jacked up. It is confirmed that the jack up is possible with the reinforcement of truss members near jack points.

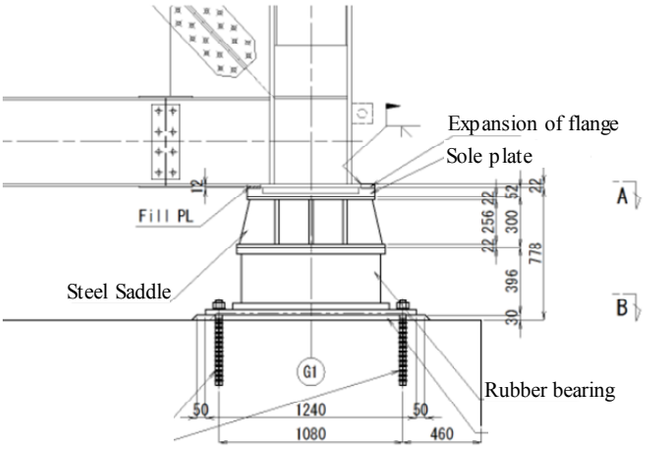


Figure 12. Rubber bearing with steel saddle

4.2 *Constraining effect of long rail*

Since the rail line is continuous to the adjacent concrete viaduct, longitudinal constraining effect of the long rail in the truss girder isolation is concerned. To clarify this effect, analysis using simple model was conducted (Ikeda et al. 2014). Analytical model is shown in Figure 13. Constrain between rail and structure is modeled by the nonlinear hysteresis model proposed in Ikeda 2014. Adjacent concrete viaduct has total length of 1,165m and 29 spans (4+4+3+8+10). It has very complicated structures such as two-level rigid frame and the soil conditions varies for each section. Therefore, instead of using full bridge model, the simplified model was used. The adjacent concrete viaduct was modeled as one-degree-of-freedom system with spring and mass. Total mass of the viaduct was used for the 1DOF mass. Spring constant was calculated by the target natural periods of 0.5s, 0.65s, and 0.8s. Target natural periods are selected referring natural periods of the viaduct.

Natural periods of the bridge are shown in Figure 14. By the constraining effect of long rail, natural period decreases by 13%. However, variation of the natural period of adjacent viaduct does not affect much.

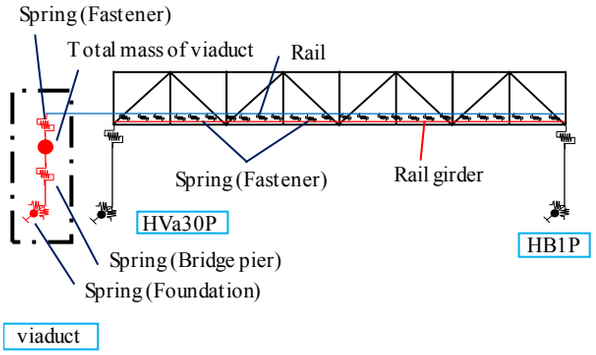


Figure 13. Analytical model

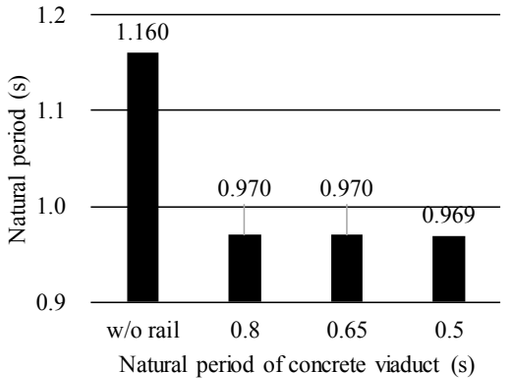


Figure 14. Natural period of the bridge

Response in the truss member is shown in Figure 15. The value in the figure is response divided by the allowable value. The response increases as natural period of concrete viaduct decreases. Even in the worst case, response is under the allowable value.

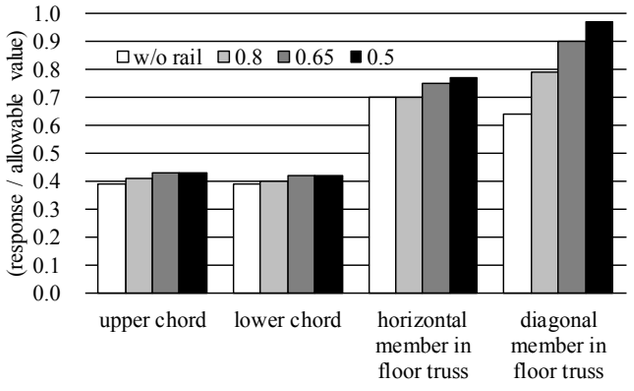


Figure 15. Response of the truss members

The number of damaged road deck bearings is shown in Figure 16. By the constraining effect of long rail, longitudinally-fixed road deck bearings at above Hva30P are damaged. With the increase of the natural period of the concrete viaduct, the number of damaged bearings decreases.

By the parametric study, it was found that damage becomes large when the natural period of adjacent concrete viaduct decreases. The natural period of the concrete viaduct ranges from 0.3 to 0.95. However, since the closest portion of the viaduct has the natural period of 0.75s, 0.65s is used for the seismic retrofit design.

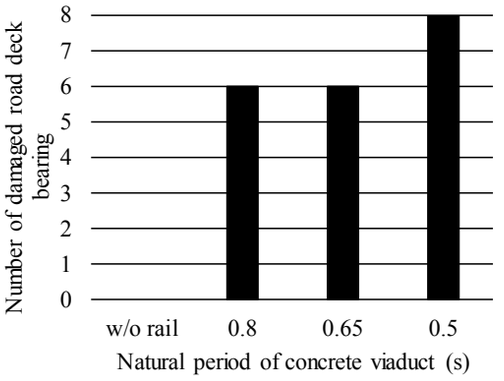


Figure 16. Number of damaged road deck bearings

4.3 *Running safety of train*

4.3.1 *Running safety of train during earthquake*

Running safety of the trains during the earthquake with high probability of occurrence for the bridge service life (Level 1 earthquake) shall be examined for the structure after the truss girder isolation according to the RTRI 2012. Using the analytical model, acceleration of each support point of rail girders were calculated with Level 1 earthquake. Acceleration data is then integrated to obtain displacement and vertical angle change at each support point. The result is shown in Figure 17. By the truss girder isolation, vertical angle change increases from about 1/1000 to 2/1000. However, the values are far below the critical value of 6/1000.

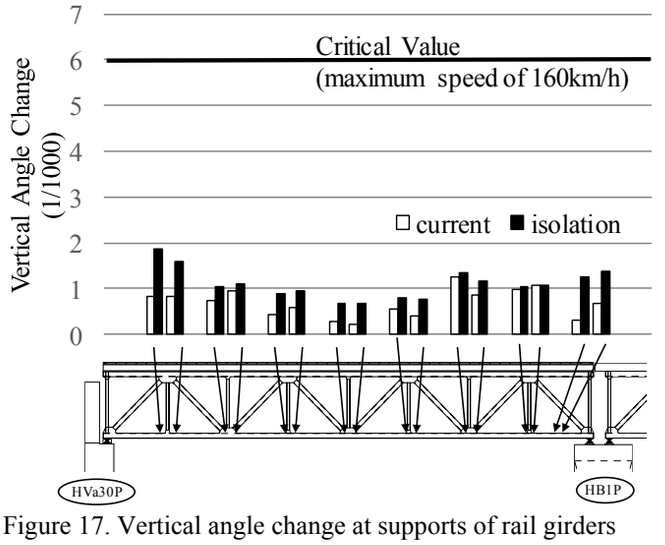


Figure 17. Vertical angle change at supports of rail girders

With Vehicle Dynamics Simulator (Miyamoto et al. 1998), behavior of train car under Level 1 earthquake was analyzed. The Simulator can input longitudinal, transverse, and vertical vibration and simulate jumping of the train car and large roll motion. Since it is confirmed that the results of single car model and formation model are similar, single car model was used. The model is shown in Figure 18.

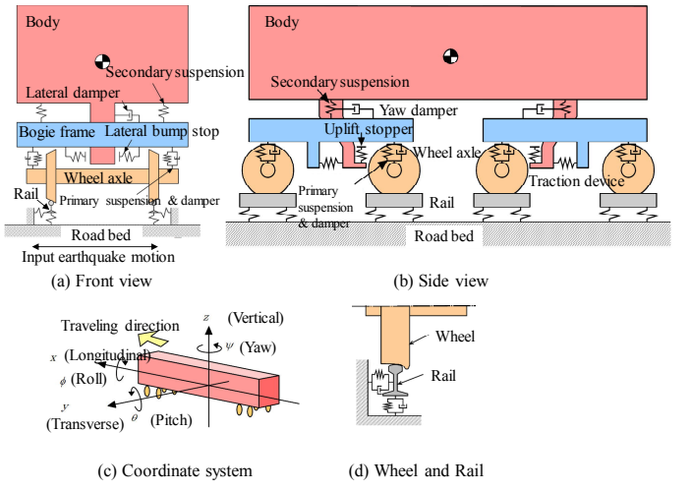
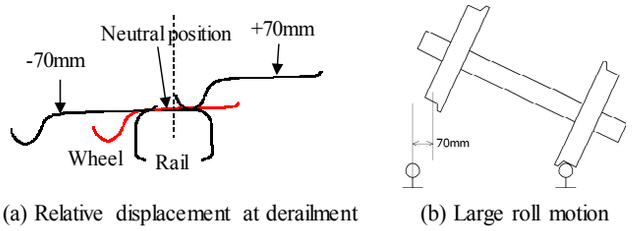


Figure 18. Simulation model

Derailment was judged by the relative displacement between wheel and rail. When this displacement reaches ±70mm, it is judged to be derailed (Figure 19).

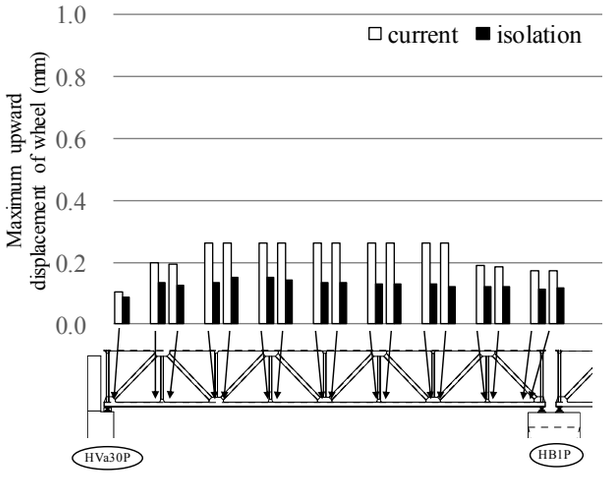


(a) Relative displacement at derailment (b) Large roll motion

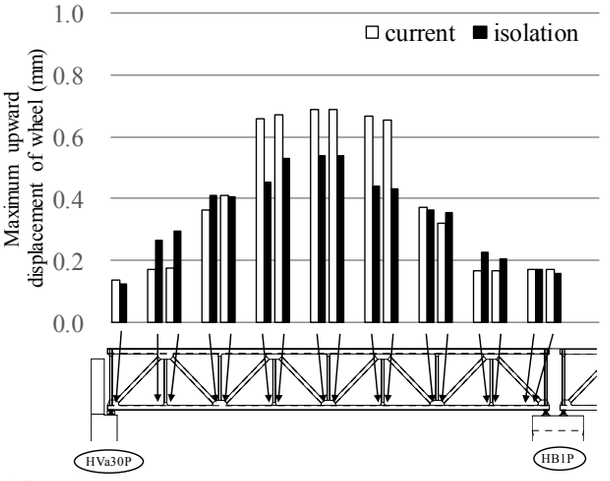
Figure 19. Criteria of derailment

In the analysis Japanese bullet train (Shinkansen) and local train operating on Seto-Ohashi Briges were examined. For the local train, mass of passengers were also taken into account. Input seismic motion is the one calculated for the previous analysis for vertical angle change.

Results are shown in Figure 20. For all the cases, maximum upward displacements are less than 1mm, far below the critical value of 70mm. All the movements were caused by transverse movement of the wheel and the wheels were not detached from rail (Figure 18 (a)). For bullet train, displacement becomes small by the truss girder isolation. For local train, effect of the isolation varies.



(a) Bullet train (Shinkansen)

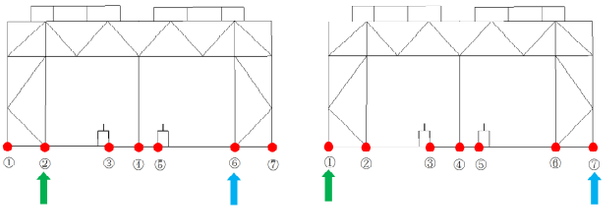


(b) Local train

Figure 20. Maximum upward displacement of wheel

4.3.2 *Running safety during bearing replacement*

During the replacement of bearings, the vertical displacement of the rail must be smaller than the value specified by the railway operator. In order to examine this, forced upward displacement is applied at jack point until the reaction force of the replaced bearing becomes zero and calculate the vertical displacement of the rail. Jack points for each end are shown in Figure 21. Calculated vertical displacement of rail is shown in Table 2. It was found that the vertical displacement of the rail is well under the specified displacement limit.



(a) Hva30P (b) HB1P

Figure 21. Jack points

Table 2. Vertical displacement of rail

(mm)

	HVa30P		HB1P	
	East	West	East	West
Jack up amount	18.9	15.4	9.0	8.5
Displacement of rail	2.1	1.4	3.4	3.2
Specified limit	16	16	38	38

5 SEISMIC RETROFIT

From the above mentioned study, “truss girder isolation + reinforcement of road deck bearings” are selected as the seismic retrofit scheme for the steel truss portion of the Hitsuishi viaduct (Figure 22). The outline of the retrofit is as follows.

– For the isolation of the truss girder, current four hinged bearings for the truss girder are replaced

with isolation bearings (spring confined lead rubber bearings).
- For the replacement of the truss girder bearings, portions of floor truss and lower chord are reinforced for jack up.
- Eight road deck bearings above HVa30P are reinforced.
- For the settlement prevention devices (concrete blocks), vertical members in floor truss are reinforced in HB1P. For HVa30P, since the location of settlement prevention devices coincide with jack point, additional reinforcement is not required.

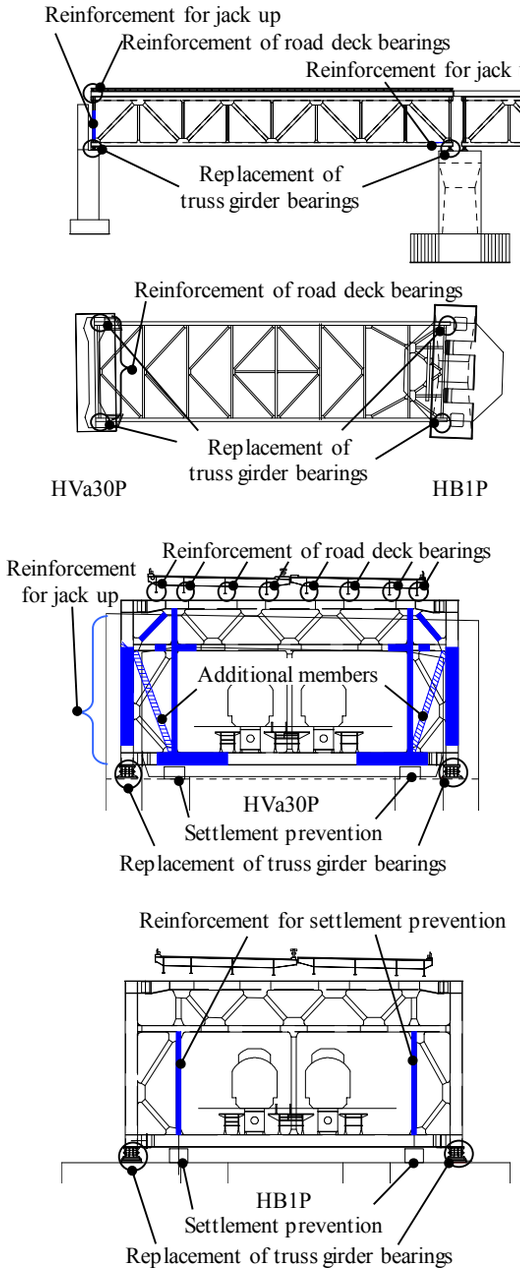


Figure 22. Seismic retrofit

6 CONCLUSION

As the seismic retrofit of truss bridge for highway and railway, truss girder isolation, which is unprecedented method for highway-railway combined bridges in Japan, was studied. For the retrofit design, constraining effect of long rail was taken into account. And it was confirmed that the running safety of train is secured after the truss girder isolation. Seismic retrofit work began in 2017 and will complete in 2018.

REFERENCE

Ikeda, M., Toyooka, A., Iemura, H., Iwata, S., Murata, K., & Ichikawa, A 2014. Effects of track structures on seismic behavior of railway bridges supported by isolation rubber bearings. *Journal of JSCE*, Vol. 70, No. 1, 1-16

Japan Road Association 2012. *Specification of highway bridges*. Japan Road Association

Miyamoto, T., Ishida, H., & Matsuo, M 1998. The dynamic behavior of railway vehicle during earthquake (Vehicle Dynamics Simulation on Track Vibrating in Lateral & Vertical Directions). *Transactions of JSME C,* Vol.64, No. 626, 3928-3935

Railway Technical Research Institute 2012. *Design Standards for Railway Structures and Commentary (Seismic Design).* Maruzen

Maintenance, Safety, Risk, Management and Life-Cycle Performance of Bridges – Powers, Frangopol, Al-Mahaidi & Caprani (Eds)
© 2018 Taylor & Francis Group, London, ISBN 978-1-138-73045-8

Safety assessment of bridges for transportation of power plant generator

I.Y. Paik & K.H. Jeong
Gachon University, Songnam, Korea

M.K. Jun & J.H. Jeong & S-H. Hong
Wonju Regional Construction and Management Administration, Wonju, Korea

H. Koo
Korea Institute of Civil Engineering and Building Technology, Goyang, Korea

R.C. Lee
SQ Engineering, Seoul, Korea

ABSTRACT: In this paper, the case of the transportation of an extremely heavy equipment of the combined heat & power generator is presented with the application of the live load factor for the assessment of the bridge for the special permit vehicle. The live load model (KL510) of the domestic highway bridge design code is used as the nominal live load and the statistical characteristics of the load model are reviewed for the application of the evaluation for the special permit vehicle. An example of the special permit for the modular transporter vehicle which carries an extremely heavy equipment for a power plant facility is presented. After the precision safety diagnosis with load test and the numerical analysis using a commercial finite element program, most of the bridges are short of the capacity and needed additional strengthening. After the completion of the transportation, a manual for permit process of the extra-heavy vehicle operation was written.

1 INTRUDUCTION

As the national economy develops, the industries are expanding and the technical capacities for transportation are increased. The demand for transporting larger or heavier cargo is continuously emerging. Also, the transportation of importing cargo which is not under the domestic weight or size regulation is inquired. These transporting vehicles might operate beyond the level of the ordinary traffic situation for which the safety level of the road facilities are designed and maintained. This is a very important issue in securing public safety for the road facilities and traffic.

The limitation criterion on vehicle operation is essential for the safety of the road structure, traffic, and environment. It is necessary for the road in conducting the inherent functions such as smooth transportation of logistics as a core network of a nation. Accordingly, most countries are establishing and operating limitation criterion on the size and weight of the vehicles considering each country's situation.

Generally, the limitation criterion on the weight of the vehicle driving on the road is divided into the axial weight limitation criterion and the gross weight limitation criterion. In this context, the limitation criterion of the axial weight is aimed at securing the safety of the road pavement, and the limitation criterion of the gross weight is based on the engineering theory and policy judgment for the purpose of securing the safety of the road structure, especially the bridge structure.

The size and weight of the vehicle that runs on the road in accordance with the Road Law in Korea are specified as limited to 2.5m in width, 4.0m (or 4.2m) in height, 16.7m in length, 10ton in axle weight and 40ton in gross weight. The purpose of restricting the operation of the over-sized or over-weighted vehicle is to preserve the road structure and to prevent the danger caused by the operation of this vehicle on the road.

According to the National Energy Basic Plan, the construction of the energy development complex is continuously increasing. In this paper, the case of the transportation of the combined heat & power generator is presented. The application for the permit to transporting the generator and the major equipment for a combined heat and power plant was requested in 2016 in Wonju Regional Construction and Management Administration. As the total weight of the equipment is about 1,200 tons, the application was rejected at the beginning and the alternative transportation via water channel had been recommended.

After considering the difficulties in other means of transportation and the public contribution of the power plant, the regional administration conditionally accepted the transportation. The applicant is required to verify that the safety of the road facilities and traffic is secured. In order to secure the safety of the road structures due to the over-weighted vehicle passage, the checking items for securing the structural safety of the bridges and the buried structures were examined by conducting the precision safety diagnosis before and after passing the structures. If necessary, the appropriate strengthening of the structure is designed and conducted.

After a complicated work between the administration, applicant and engineers, the transportation is completed (MLTM 2017a). The regional administration examined the existing regulations of the process for permit vehicle and wrote a manual for improving the efficient management of either restriction or permission of vehicle operation based on the experience of the transportation of the generator (MLTM 2017). The contents are summarized in this paper.

2 SAFETY ASSESSMENT FOR PERMIT VEHICLE

2.1 *Safety in design live load*

The Korean highway bridge design code (KHBDC) adopts the limit state design method and the live load model was determined based on the statistical and probabilistic study on t he domestic measured data. The safety margin in the design of the bridge is mainly achieved from the conservative selection of the live load and the load and resistance factors applied in the design combination.

The live load model of KHBDC is KL-510 and is composed of a standard truck model with four axles multiplied by 0.75 and a uniformly distributed load as shown in Figure 1. The weight and distance of axes were determined after a series of statistical study on the measured domestic truck data. (KIBSE 2015) The equivalent truck traffic to KL-510 is presented in Paik & Jeong (2017) and briefly summarized.

A reliable data measured from WIM system for highway vehicles in Korea was obtained. The statistical analysis method was applied to the data to estimate the weight for a 100-year design life of bridges. The moments obtained by applying the estimated weight are compared with KL-510.

The weight and type of vehicle model that yields the same load effect as KL-510 were obtained. The vehicle type which governs the load effect on bridges are the cargo truck with five axles. Depending on the span length, the single truck and the serial trucks govern the load effect. Figure 2 shows the consistency of the load effect by the statistically estimated trucks compared to the KL-510. Figure 3 shows the weight of the single truck which governs the moment for 15 meter span. Similarly, Figure 5 shows the weights of the two trucks in series for 30 meter span.

It is assumed that the distance between two back-to-back trucks is 5m with no impact and the distance between three back-to-back trucks is 15m each and the impact is 10%.

In order to consider the multi-lane loading condition, the statistically estimated load effect by the parallel two trucks is compared to that of KL-510. The two lane moment effect is shown in Figure 5. It shows that the KL-510 is very consistent with the statistically estimated truck load effect

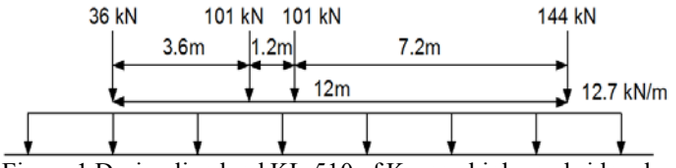


Figure 1 Design live load KL-510 of Korean highway bridge design code

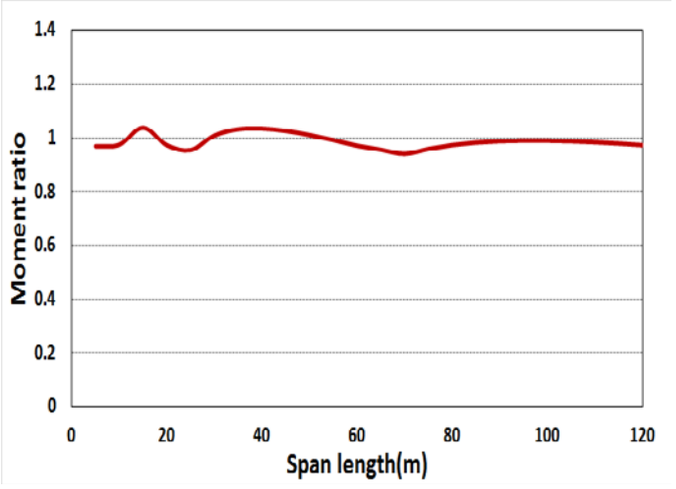


Figure 2 Moment ratio of statistically estimated truck to KL-510

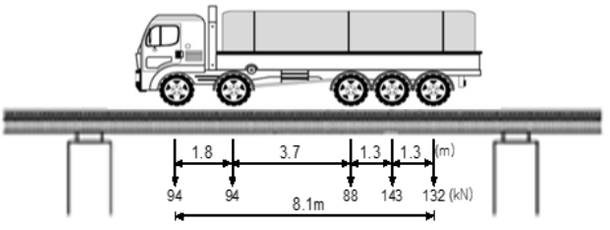


Figure 3 Estimated weight of a single truck on 15m bridge

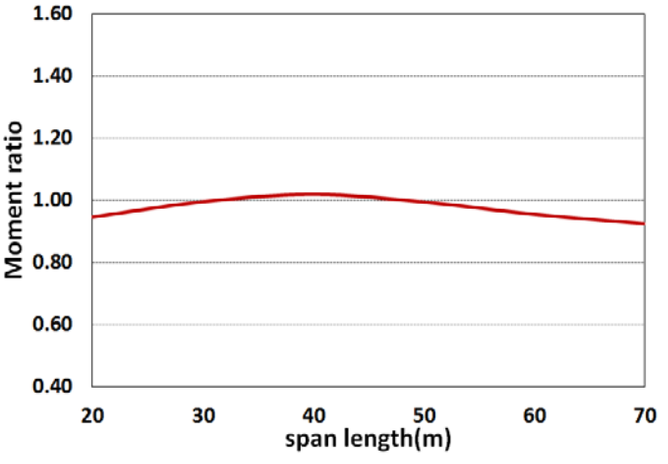


Figure 4 Moment ratio by estimated two serial trucks on two lane loading to KL-510

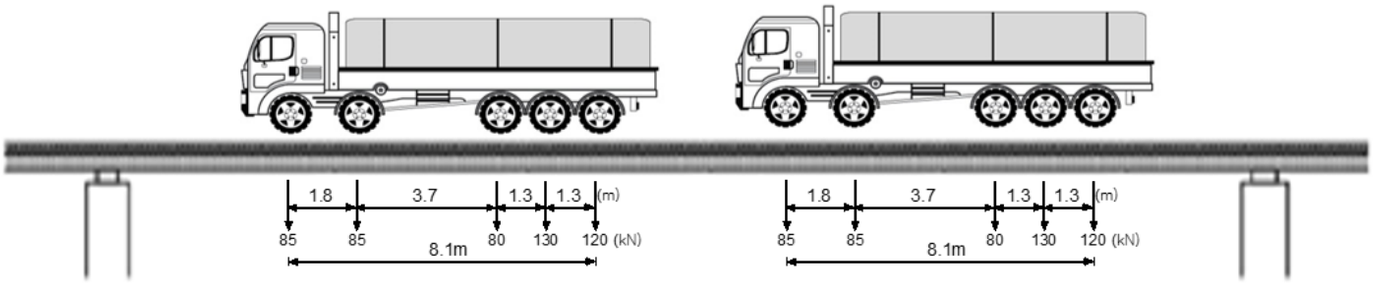


Figure 5 Estimated weight of two serial trucks on 30m bridge

2.2 *Live load factor for special permit vehicle*

The target reliability index for an existing bridge is usually lower than the target reliability index for a new bridge. This is because the uncertainty concerning the load and the bridge are reduced. Also, it is reflected that the cost required to increase the safety rate of the existing bridge is remarkably higher than that of the new bridge.

The design life of KHBDC is 100 years, and the target reliability index is 3.7. The design satisfies the target reliability by applying a live load factor of 1.80. On the other hand, the live load factor for a permit vehicle is 1.40. The Manual for Bridge Evaluation (AASHTO 2011) proposes a live load factor of 1.15 for the special permit with escorted crossing. As the weight of each axle of the permit vehicle transporting the generator was weighed on site, the uncertainty of the load from the vehicle was greatly reduced. For the safety check for the bridges on the route, the live load of 1.30 was applied.

3 EVALUATION OF BRIDGES FOR TRANSPORTATION OF GENERATOR

Precision safety diagnosis was carried out for all the bridges and buried structures on the route. The evaluation process followed the guidelines for the safety inspection and precision safety diagnosis (KISC 2008).

The precision safety diagnosis procedure is as follows. The possible route for transportation and the dimension and specification of the vehicle were collected and analyzed. The road surface inspection and the condition evaluation of the facilities on the route were carried out. The load test by testing trucks was carried out for the structures.

After the evaluation, it was decided that 13 bridges were strengthened by installing the temporary supports and 6 were bypassed among 20 bridges on the transporting route.

Structural behaviors were tested and measured by applying testing truck loads to the actual bridges and the results were compared with that of the structural analysis. Based on the safety assessment, the temporary supports were installed on the bottom of the bridge.

An example of the evaluation process is as follows. The example bridge located on the transportation route is a reinforced concrete slab bridge as shown in Figure 6. It is a 2-span continuous bridge and the total length is 20 m and the width is 19.5 m.

The total length of the vehicle was 38.6m and the width was 5m as shown in Figure 7. The vehicle regulation for protecting the safety of the road facility and traffic is 16.7m in length and 2.5m in width. In addition the height of the transporting trailer was 6.1m which is much higher than the height limitation of 4.0m for protecting the cross-road structures including overpass.

The weight of the transporting modular trailer was double checked by measuring all the axles by the portable weight meters at the site. The total weight of the vehicle specified on the application for permit was 469 tons and the measured value was 491 tons which was 4.6% higher than the application and was accepted. The total weight of the trailer was extremely larger than 40tons limitation for a single vehicle. As there were 12 tires in one row in the direction of the width of the trailer and the width and length of the trailer was much larger than the ordinary single vehicle, the weight density applied by the trailer to the bridge structure might be somewhat relieved but was still much too large.

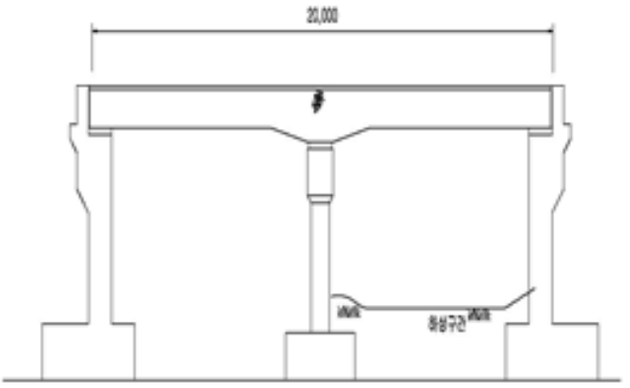


Figure 6 Longitudinal section of the example slab bridge

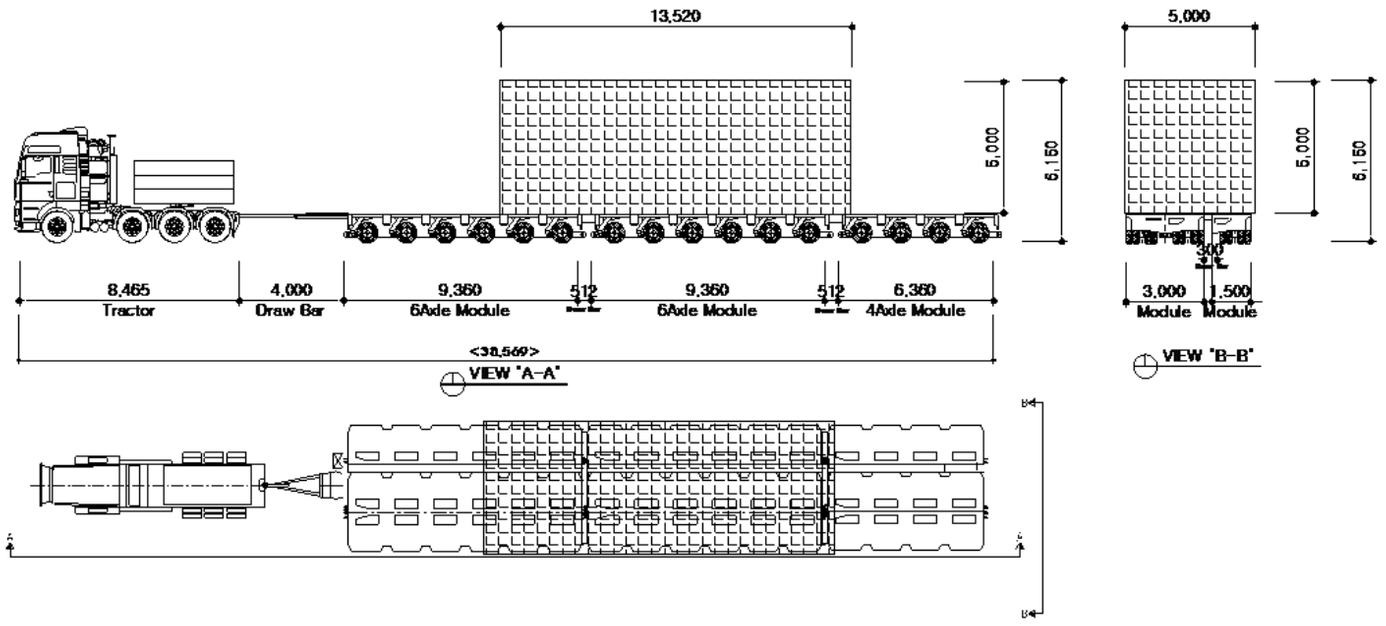


Figure 7 Dimension of the modular trailer transporting the generator

The numerical analysis was performed by using a commercial finite element program Midas Civil 2016. The bending moment diagram of the slab due to the modular trailer is shown in Figure 8. It was evaluated that the factored member force generated by the heavy load on the upper slab was larger than the design strength of the section. For this example bridge, the shear force near inner support much exceeded and the negative moment was below the capacity of the slab. Therefore, it was judged that the strengthening of the slab through the lower support was required when the heavy vehicle passes through.

The temporary support was designed and installed under the slab with the foundation of the support treated as shown in Figure 9.

Figure 10 shows the predicted displacement from the result of the numerical analysis for the supported slab bridge. After installing the support the shear force on the slab decreased and the resulted within the capacity of the bridge. The negative moment also decreased and fell within the capacity of the section.

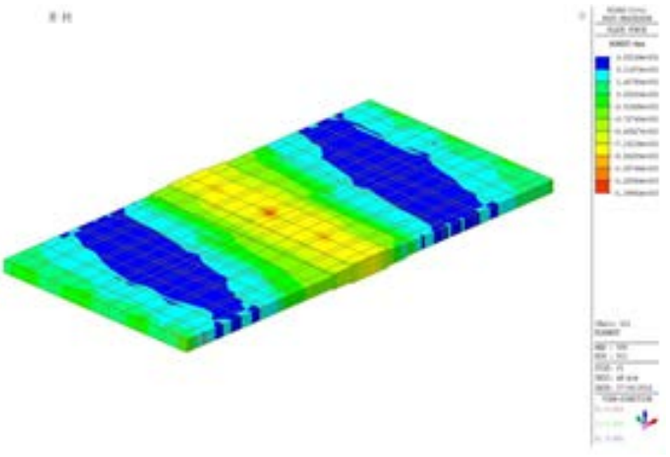


Figure 8 Bending moment diagram of slab bridge subject to modular trailer

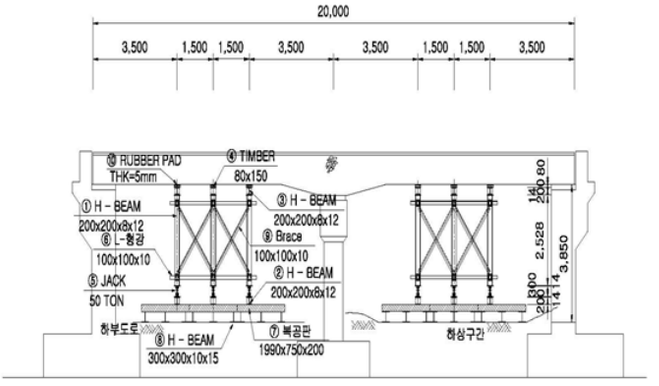


Figure 9 Longitudinal Section of the supported slab bridge

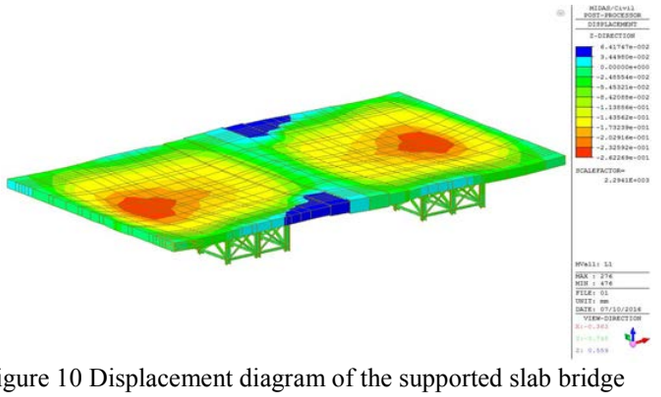


Figure 10 Displacement diagram of the supported slab bridge subject to modular trailer

4 TRANSPORTATION OF GENERATOR

The actual transportation was finally permitted after all the relevant regional authorities over the route to operate the vehicle were agreed. The agreement came after the preliminary measures for the operation of the permissible vehicle such as the measures for securing the road facilities and traffic safety, organizing the emergency action plan and insurance etc. were all met.

The specially permitted vehicle operated in the state where the person in charge of the relevant authority and the safety manager are present at the operation site. The applicant should operate an emergency service organization that could act as a control tower at the permitted vehicle operation site and report the operation result of the permitted vehicle to the road management office.

After completion of the transportation of the combined heat & power generator, the safety inspection and the pavement status survey was conducted within one month. The current status of the road facilities were compared with those before transportation and the maintenance and reinforcement should have been carried out in case of damage.

Bridges, culverts, etc., were subjected to safety diagnosis by specialty companies. No additional damages were observed except in some repaired sections. The inspection showed there were no serious defects that could impair the safety of the facilities

In order to secure traffic safety during the permit vehicle operation and to prevent and respond quickly to possible accidents, a number of supporting vehicles such as guide vehicles, spare cars, working vehicles, and ambulance are arranged in front of and behind the permit vehicle as shown in Figure 12.

5 CONCLUSION AND MANUAL OF PERMIT PROCESS FOR HEAVY TRANSPORTATION

After the consultation and review period for about 4 months (March to June) and the preparation process for about 4 months (July to November) afterwards, about 200km of transportation was completed.

In relation to the special permit for the operation of a super large and heavy vehicle, the present law stipulates the entity of the permission, object of the permission, authority for issuing the permission condition, and kind of document required for permission application and approval condition through Road Law. However, there is a limit to the operation of a special permit system for operating very large and heavy vehicles only by the current applicable regulations. In particular, the problems due to lack of procedural and method specificity for securing the safety of both of the road structure and traffic act as a big obstacle in the operation of the system.

In order to improve these problems, several things were proposed. First, the applicant should implement and establish various reviews and plans necessary for the operation of the permit vehicle before applying for the special permit. Second, the Road management office conducts document screening and permission reviewing. Third, only after passing the relevant review, the field demonstration and proactive measures should be conducted. Fourth, under the control of the control tower, the vehicle shall be operated according to the authorized vehicle operation plan. Fifth, after completion of vehicle operation post-measures should be carried out.

The followings are the procedures and methods that were established to the special permits for the operation of extra-large and heavy-weight vehicles considering road structure and traffic safety.





Figure 11 Transportation of generator

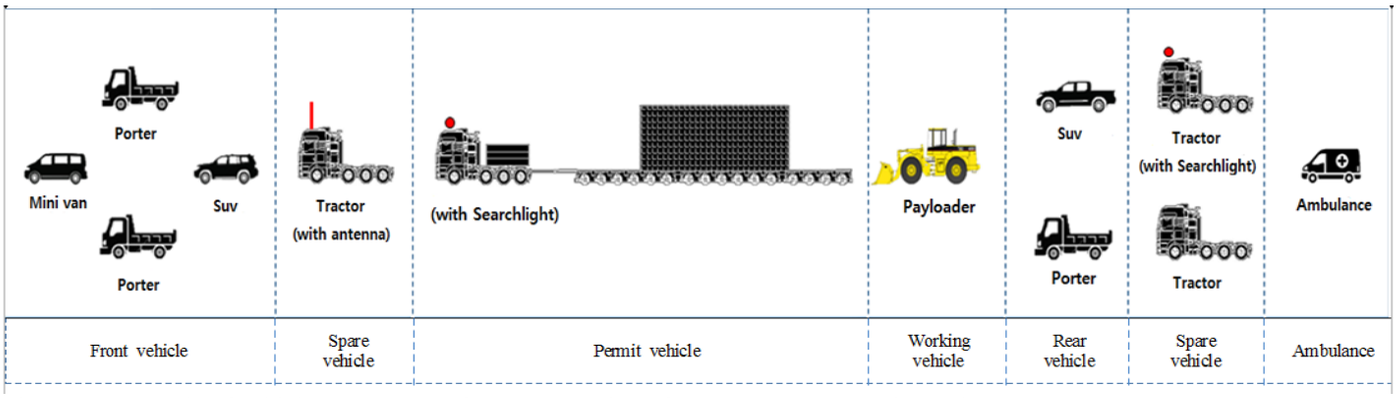
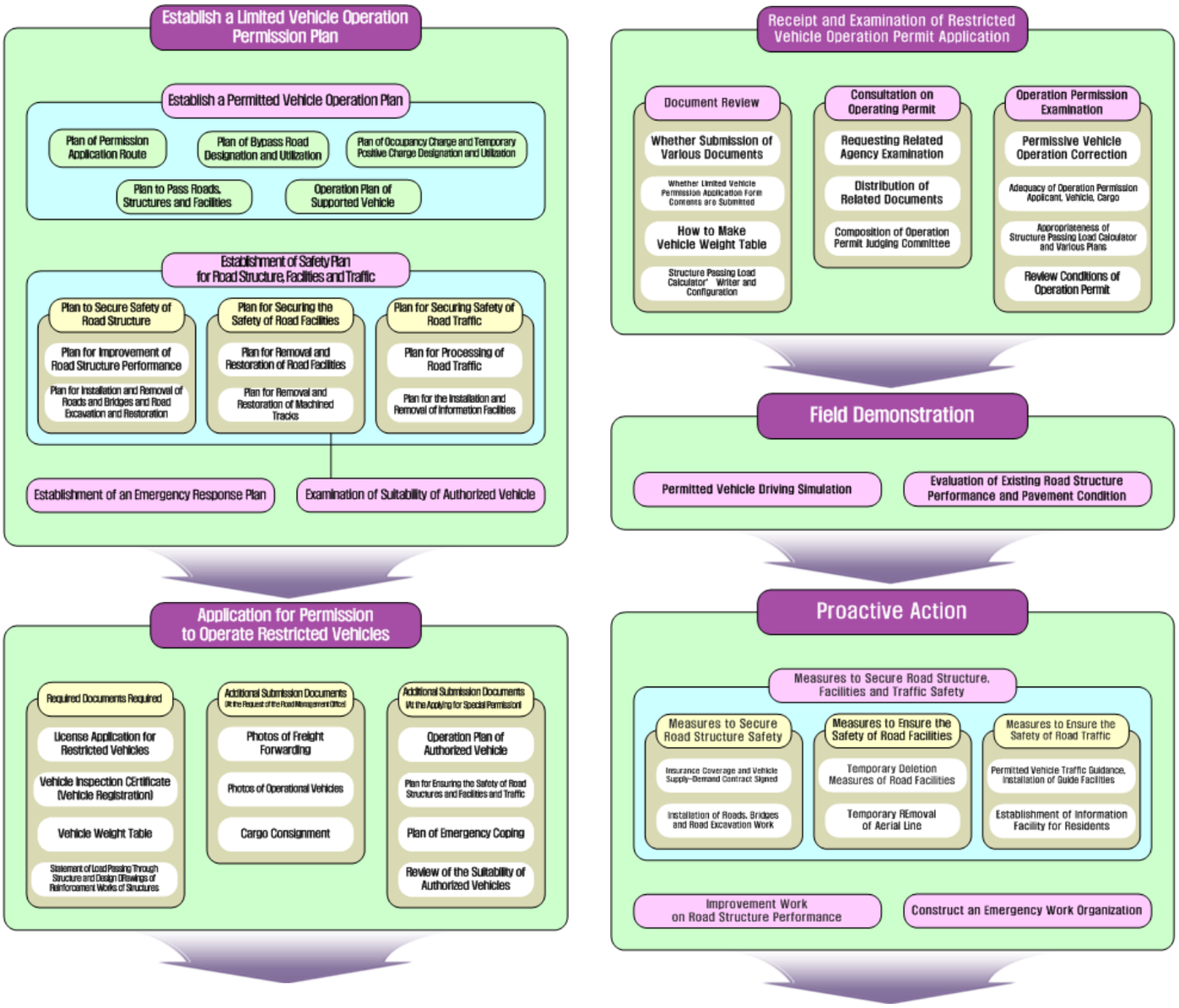


Figure 12 Example of vehicle arrangement for transportation of generator on mountain road



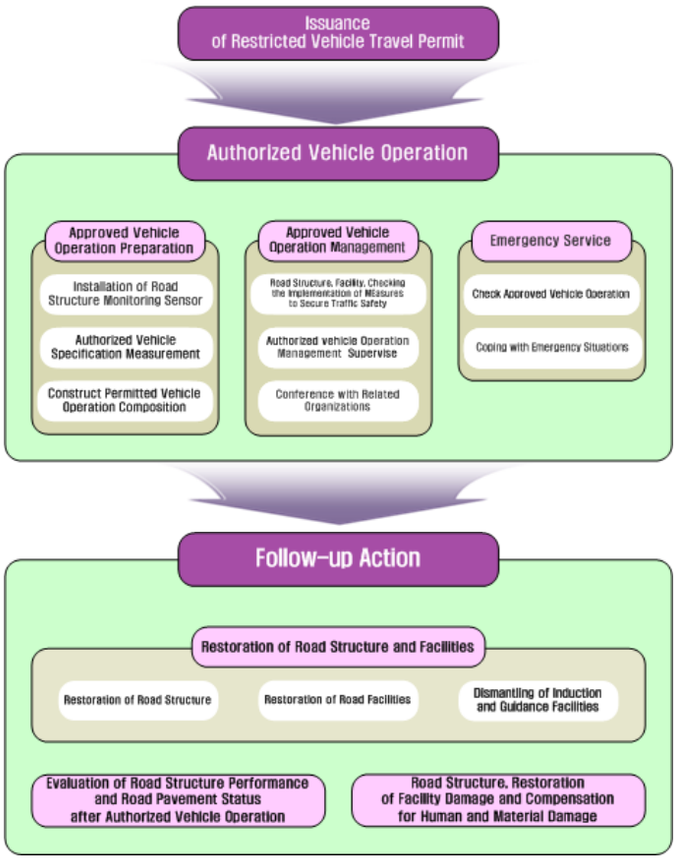


Figure 13 Permit process for heavy transportation

6 ACKNOWLEDGEMENTS

This research was supported by a grant (18SCIP-B128569-02 2) from Smart Civil Infrastructure Research Program funded by Ministry of Land, Infrastructure and Transport of Korean government.

7 REFERENCE

AASHTO. 2011. *The Manual for Bridge Evaluation*, 2nd ed. American Association of State Highway and Transportation Officials.

KIBSE & KBRC. 2015. *Commentary on Highway Bridge Design Code (Limit State Design Method)*, Korean Institute of Bridge and Structural Engineers and Korea Bridge Design & Engineering Research Center.

KISC. 2008. *Guidelines for Safety Inspection and Precision Safety Diagnosis*, Korea Infrastructure Safety Corporation.

Paik, I.Y. & Jeong, K.H. 2017. Analysis of Moment Effect of Bridge Design Live Load KL-510 by Statistical Analysis of WIM Data of Expressway, *Journal of Korean Society of Steel Construction*, Vol. 29, No. 6.

WRCMA. 2017a. *Casebook of the Heaviest Transportation in Korea*, Wonju Regional Construction and Management Administration of Korea Ministry of Land, Infrastructure and Transport.

WRCMA. 2017b. *Manual of Special Permit for Extra Large and Heavy Transportation*, Wonju Regional Construction and Management Administration of Korea Ministry of Land, Infrastructure and Transport.

Maintenance, Safety, Risk, Management and Life-Cycle Performance of Bridges – Powers, Frangopol, Al-Mahaidi & Caprani (Eds)
© 2018 Taylor & Francis Group, London, ISBN 978-1-138-73045-8

Evaluation of adhered sea-salt particle amount to bridge, anti-adhesion countermeasures

A. Toktorbai uulu & H. Katsuchi, H. Yamada
Department of Civil Engineering,
Yokohama National University, Yokohama, Japan

ABSTRACT: Bridges located near coastal areas are easy to get decreased their service life by corrosion attack. Airborne sea-salt particles adhered to bridge surfaces are the most influential and they are the reason for a significant section deterioration of bridge members. This paper investigates the amount of adhered sea salt particles at various parts of bridge girder surfaces. As a methodology, a wind-tunnel test was conducted. Bridge model was tested at the two kinds of wind velocity: 5.4m/s & 3.5m/s. Phenol particles were ejected as a role of sea-salt particles. Clearance effect was also tested at three different heights. Results showed the differences of adhered particle amounts at different part of girder surfaces. Finally, four possible methods are proposed to decrease the amount of adhered particles inside the bridge girders.

1 INTRODUCTION

Nowadays, the importance of bridge maintenance has been increasing. The reason is that the age of infrastructures, especially bridges, is getting old in the developed countries as well as in Japan. The bridges located near coastal areas are easy to get decreased their service life by corrosion attack. The governing factors of corrosion are temperature, humidity and various dusts on the surfaces. Among them, the adhered sea-salt particles are the most influential and they are the reason for a significant section deterioration of bridge members. Hence, for the efficient maintenance program, it is necessary to evaluate the behavior of the airborne sea salt particles at different part of a bridge deck.

It was reported that the site painting criteria or applicable criteria for weathering steel: the weathering steel is safe from corrosion and does not need painting if the amount of the adhered sea-salt particles to the bridge surface is less than 0.05mg/dm²/day (mdd) (Ohya 2009).

Because of the negative effect of the airborne sea salt particles for the steel bridges, on-site measurements of the amount of airborne sea salt particles have been carried out. There are two main methods that are extensively used in order to measure the amount of airborne sea salt particles in Japan. One is so-called "Doken tank" method (Public Works Research Institute method), the other one is the dry gauze method. The "Doken tank" method uses the special sampler tank to collect the airborne sea salt particles. The dry gauze method grabs particles with its dry gauze-patch which is exposed near bridge surfaces. However, from only the results, it is difficult to evaluate how much airborne sea salt particles can be adhered to the surfaces of a bridge when equipment is fixed in one position. Therefore, various methods have been developed to predict the detailed behaviors of airborne sea-salt particles by other researchers. For example, Obata et al. (2008) proposed a numerical framework to predict the adhesion behavior of sea-salt particles on a bridge surface. Moreover, they made an in situ observation in order to estimate the concentration and amount of airborne sea-salt particles. Iwasaki et al. (2007) proposed an observation method to estimate the level of partial corrosion of a bridge exposed to airborne sea-salts. Besides, they conducted a numerical simulation to compare the simulation data with their observation data. Hasebe et al. (2015) developed an experimental method to estimate the amount of the adhesion to the surface of a bridge model by ejecting a mist included salt particles.

Our work was to evaluate the adhesion behavior of sea-salt particles at the bridge girder and investigate the amount of adhered airborne sea-salt particles at different part of bridge girder surfaces by wind-tunnel which has unique test facilities. Additionally, CFD analysis was carried out for further understanding the wind-tunnel experiment results. Finally, four kinds of countermeasures were proposed to decrease the amount of the sea-salt particle's adhesion at the inside of bridge girders.

2 WIND-TUNNEL EXPERIMENT

2.1 *Experimental settings and conditions*

An open wind-tunnel with unique test facilities of Yokohama National University (YNU) was used for the measurement of the airborne sea-salt particles' behaviors. Figure 1 shows the general view and the inside of working section of the wind-tunnel in YNU. The size of the working section is 1.3m wide and 1.3m high. Figure 2 illustrates the experiment setting. In the wind-tunnel test, phenol particles were ejected from the ejection nozzle to the model bridge side as a role of sea-salt particles since their properties are close to the real sea-salt particles. As a target bridge, a highway four I-shaped steel girder bridge was chosen and its model was made up at the scale of 1/60. The model bridge was tested at two kinds of wind velocity: 5.4m/s and 3.5m/s which are the annual wind speed of Naha city (Okinawa prefecture) and Yokohama city, respectively. The reason of choosing Okinawa is that many bridges are suffering from corrosion in Okinawa due to the sea-salt particles because they are located close to ocean. Wind-tunnel experiment settings, conditions and other parameters are shown in table 1. Phenol particles were ejected for 2 minutes and 5 times at the same conditions. Before starting the test, the adhesive tapes with the size of 1cm² was attached to the parts of model bridge girder surfaces in both sides at the parts of top flange, web top, web center, web bottom and both surfaces of bottom flange to capture the particles colliding with girder surfaces. Figure 3 illustrates the positions of the attached tapes at the each part of girder surfaces.

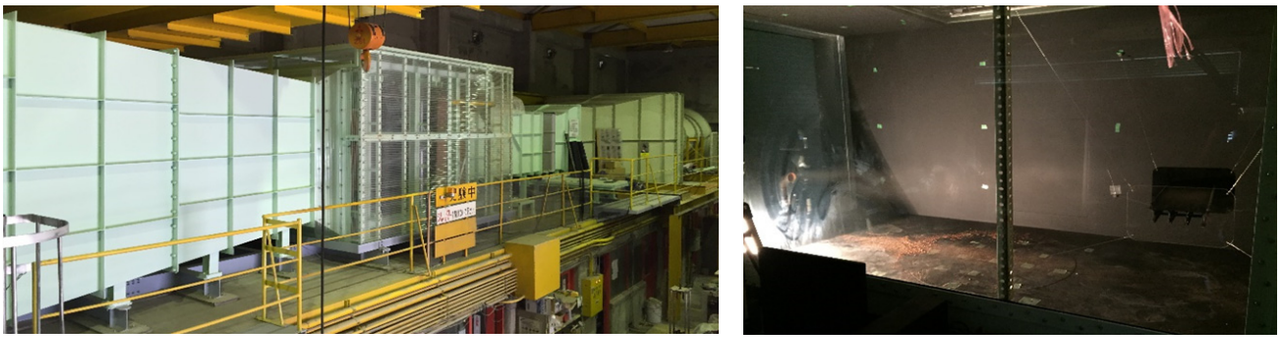


Figure 1: General view of YNU wind-tunnel (left) and its working section (right)

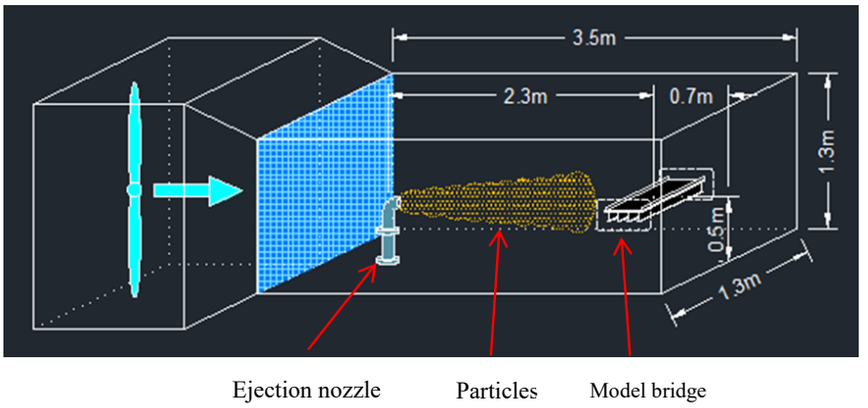


Figure 2: Experiment settings

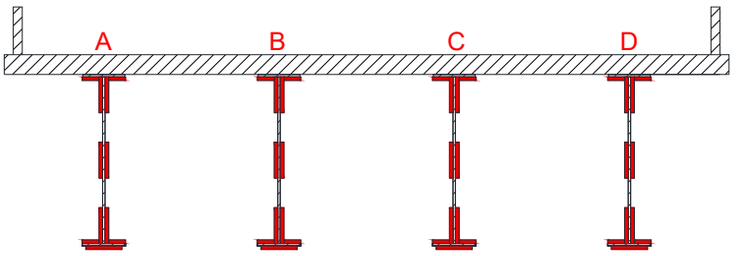


Figure 3: Positions of attached adhesive tapes on girder surfaces.

Table 1: Wind-Tunnel experiment settings and conditions

Settings	size and conditions
Working section	1.3m x 1.3m
Model scale	1/60
Blockage ratio	5%
Ejected particle	Phenol particles
Wind velocity	5.4m/s and 3.5m/s
Temperature	17ºC

2.2 *Reference test*

In order to check the uniformity of the particle flow ejecting from the nozzle, a reference model was tested before starting a test for the bridge model. The reference model which has a same height with the model bridge girder was fixed at the same height with the ejection nozzle. Adhesive tapes were attached to upside, middle and down side of the reference model surface. The model was tested at 5.4m/s three times (3 cases) repeatedly at the same ejection time that mentioned before. Figure 4 shows the adhered particles to the upside, middle and down side. The results showed that the differences in the amount of adhered particles are not significant. It indicates that the incoming particles are uniform (figure 5). Table 2 shows the average value of three cases and the ratio of amounts of adhered particles between them. Converted values into mdd were shown as well. The middle part has 4% more adhered particles and 12% more particles obtained from the down side. Obviously, particles mostly adhered to down parts because of the gravity force and wind load when the positions of the nozzle and model were located at the same level.

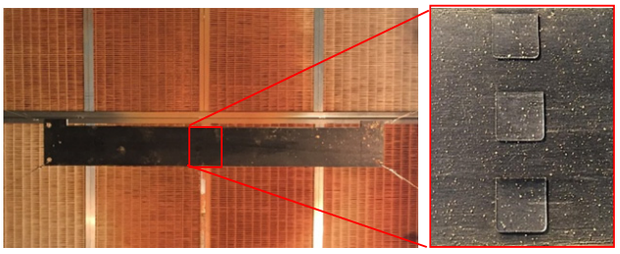


Figure 4: Fixed reference model (left) and illustration of adhered particles to the tape surfaces (right).

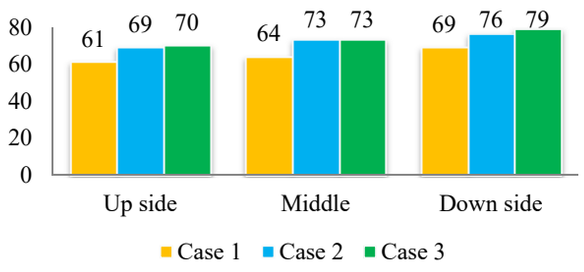


Figure 5: Reference model test results- amount of adhered particles at three cases

Table 2: Amount of adhered particles to reference model

Ref. model surfaces	Average	Ratio	Converted into mdd
Upside	67	1.0	10.9
Middle	70	1.04	11.4
Downside	75	1.12	12.2

2.3 *Model bridge test*

After making sure that the income flow is uniform, the model bridge was fixed at the same position where the reference model was fixed. First, it was tested at the wind velocity 5.4m/s for the particle ejection time mentioned before. After finishing the experiment the amount of adhered particles was calculated from the each tape. Repeatedly, this experimental procedure was conducted 5 times at the same conditions. Thereafter, the average value of the amount of adhered particles of five cases was taken to get more accurate results. These sequences of experiments were applied for the wind velocity 3.5m/s as well. Figure 6 illustrates the amounts of the adhered particle distributions of the both wind velocities.

From the results it is shown that, at the wind velocity 5.4m/s has a slightly higher amount of adhered particles comparing with the wind velocity 3.5m/s. Front surfaces of both cases have an extremely large amount of adhered particles. It is because of the direct collision. However most of them may be washed down by the rain. It is important to estimate the amount of adhered particles inside bridge girders where no exposure to the rain. As for the inside, particles mostly adhered to the rear standing girders; those are the surfaces between “C” and “D”. This can be assumed that, for the stream separated from the leading edge it is hard to roll in between the anterior standing girders: “A” and “B”. On the other hand, it is easier to roll in between the rear standing girders.

2.4 *With clearance effect*

Some bridges and overpasses located in the urban area or over the small rivers may have a low clearance (distance between the down surface of a bridge or overpass till the water or earth surface). Bridges with this kind of a low clearance might have significant adhered airborne sea-salt particles due to the earth effect. This time, the model bridge with three kinds of clearance heights: 3m, 6m and 9m was tested in the wind-tunnel. An artificial floor was installed as a role of “earth” and the distance between the artificial floor surface and the lower part of the model bridge was regulated at each case of test according to the heights of clearances. The experimental conditions are same with the previous test. The clearance effect was tested only at the wind velocity 5.4m/s. Figure 7 illustrates the adhered particle distribution of three clearance heights.

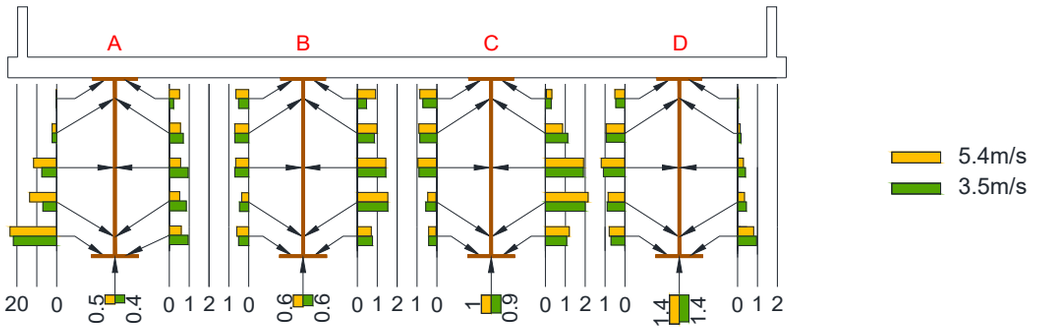


Figure 6: Adhered participle distributions (unit: mdd)

The results indicate that, the biggest amount of adhered particles was calculated from the case of the highest clearance (9m). It can be assumed that, the more space under the bridge, the bigger amount of the airborne sea-salt particles may attach to the bridge girder surfaces (range is up to 9m). However, as for the bottom flange surfaces, the biggest number of the adhered particles can be seen on the second girder "B", and the lowest is on the forth girder "D" (excluding first girder "A") in case of the lowest clearances (3m). As the clearance height is going to increase, the amount is changing to opposite. Specifically, in case of 6m clearance, the amounts of adhered particles are almost equal at the each bottom flange surfaces excluding first girder "A". In case of 9m clearance, the biggest amount is obtained from the last girder "D". This phenomenon can be explained as when the clearance is low, the separated stream from the leading edge is accelerated as it passes a narrow space under the bridge. Accordingly, the accelerated particle stream instantly (depending on wind speed) goes up and attaches to the closest object (girder "B"). When it has a higher clearance, the separated stream passes wider space under the bridge and mostly reattach to the ending part of bridge deck ("D"). Hence, the amounts of adhered particles at these bottom flange surfaces vary highly due to the different clearance heights.

Results of clearance effect (clearance 3m) were compared with the real observation data. Iwasaki and Nagai observed the amount of the adhered particles to the web surfaces of the bridge near the Niigata city with the clearance height of 2m (Figure 8). Since, our particle ejection time and density differed from the observation, we will compare only the distribution tendencies of adhered particles to the web surfaces. Thus, the observation data has the biggest amounts of adhered particles at the web-center. In our experiment, we obtained the biggest amounts of adhered particles from the web-center as well (figure 9).

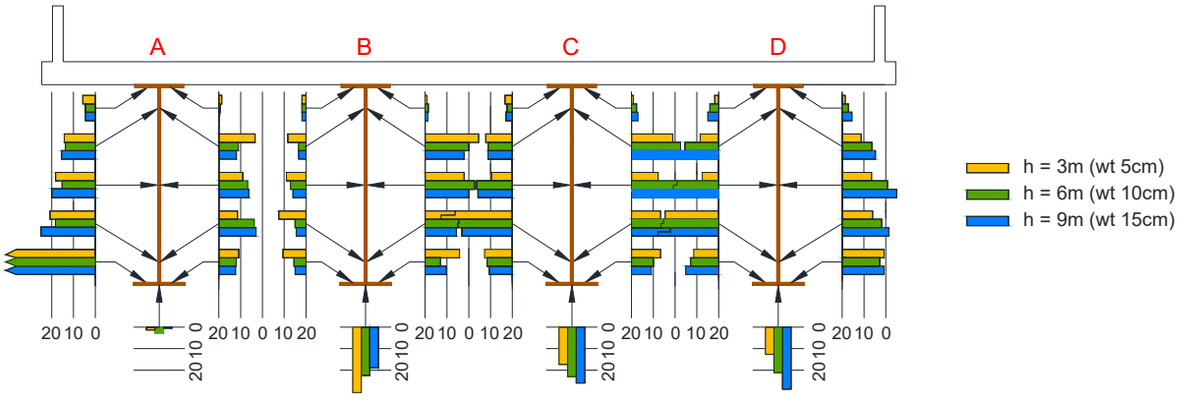


Figure 7: Adhered particle distributions of three clearance heights (unit: mdd)

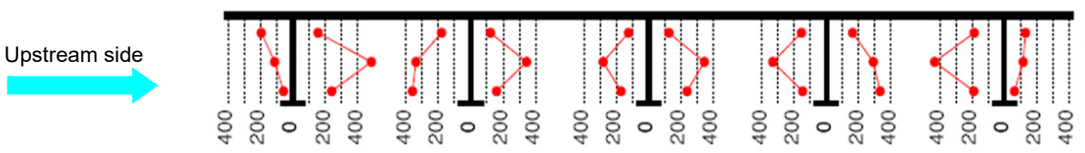


Figure 8: Observation data of adhered amount of airborne sea-salt particles (unit: mg/m²) (Iwasaki et al. 2007)

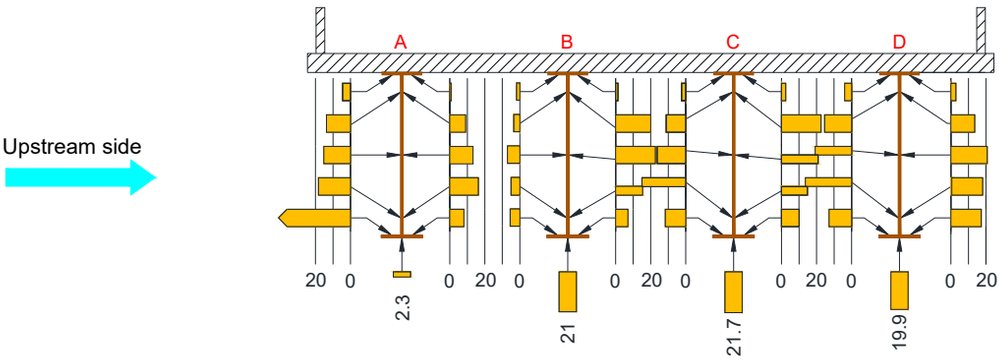


Figure 9: Clearance 3m, adhered particle distribution graph.

3 NUMERICAL SIMU-LATIONS

3.1 *CFD analysis settings and conditions*

For further understanding the results of the wind-tunnel experiments, CFD (Computational Fluid Dynamics) analyses were performed. The visualization of the flow around the bridge girders was illustrated by CFD, which is difficult to obtain from the experimental work. Numerical analyses were performed using the CFD software program STAR-CCM+ that is able to simulate micro particles and their adhesion to solid surfaces. Figure 10 shows the domain size and notations of analyses which followed the recommendations of Sohankar (1998). According to his recommendations, the distance between inlet and model is 15D (D is a height of model) and the distance between the model until outlet is 25D. The height of domain region is 25D. Top wall was set as slip boundary. Bottom wall was set as slip boundary as well, but in case of "Clearance effect check", it was changed into non-slip boundary. Inflow stream is set uniform along the inlet boundary and the outlet boundary is set as where a pressure gradient is equal to zero along any stream lines. All the bridge surfaces are modelled as non-slip boundaries. The geometric dimensions of the model bridge were chosen to be same with the bridge model of wind-tunnel experiment. As for the meshing domain, the tetrahedral mesher was selected. The mesh size around the CAD model is much finer, 0.25cm. Fine mesh is important around the model for the more accurate visualization of flow. Then mesh size is going to be bigger (1cm and 5cm) as going far from the model area as shown in the figure 11. Non-steady state air flow analysis of 20 seconds was carried out for every simulation. After initial 7 seconds, 100 units of particles per one parcel representing the sea-salt particles are injected uniformly from the inlet every 1 second. It should be noted that the concentration of airborne particles is inversely proportional to wind speed under this particle injection condition. The other conditions of analysis are given in Table 3. The size 10μm of particle is determined according to the sea-salt particle originated from the ocean. The density was set 2.2 x 10^3 kg/m³. Wind velocities: 5.4m/s and 3.5m/s and the temperature applied to analyses are same with wind tunnel experiment settings. Relative humidity was set 0% since it has a negligible effect.

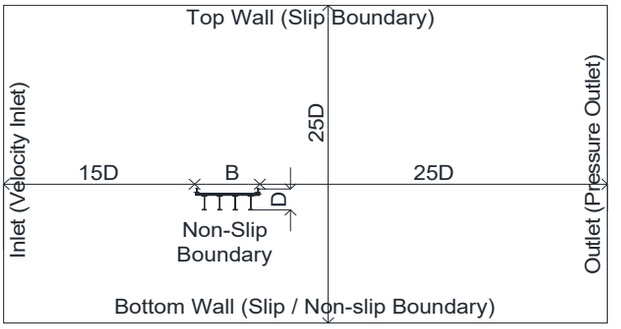


Figure 10: Domain size and notations

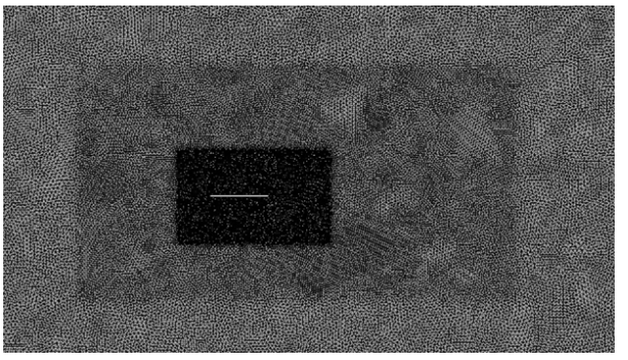
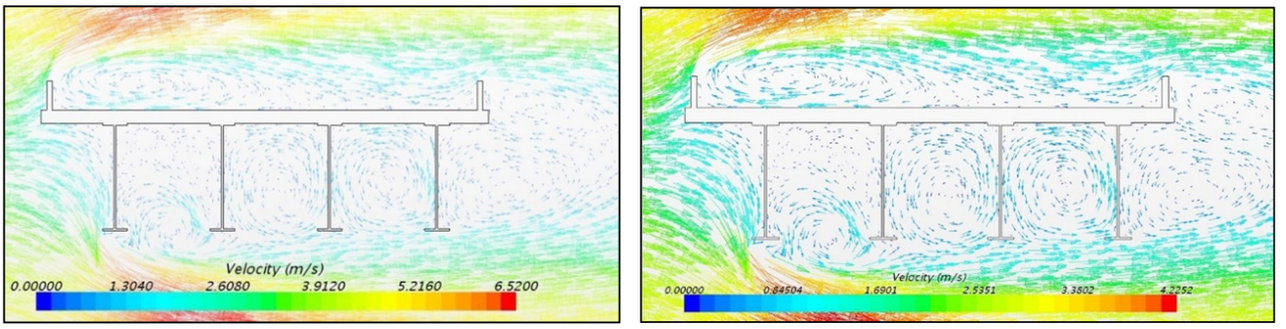


Figure 11: Tetrahedral domain mesh. Total cell numbers: 151471cells.

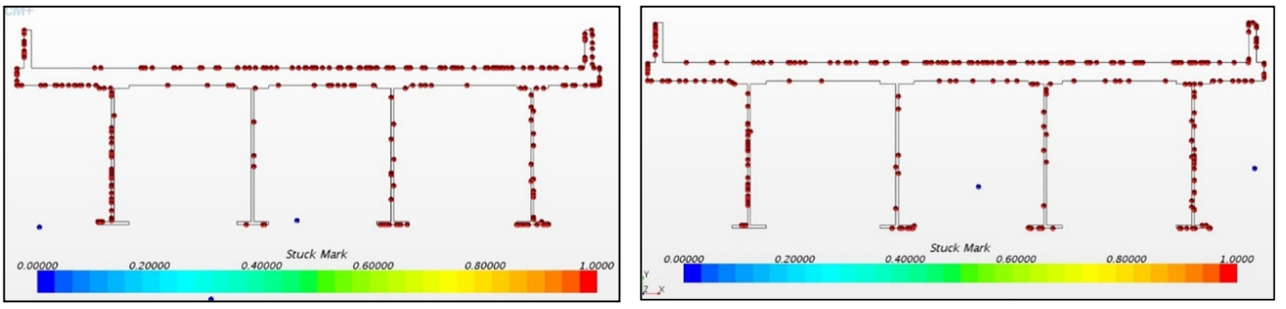
Table 3: CFD settings and parameters

Settings	Properties
Diameter of particles	10 μm
Density of particles	2.200x10³ kg/m³
Density of air	1.205x10³ kg/m³
Relative humidity	0%
Incoming speed	5.4m/s, 3.5m/s
Input particles' amount	0.05mdd/s
Particles motion equation	Lagrangian approach
Flow motion equation	Navier-Stokes equations



(a) (b)

Figure 12: Air velocity magnitude distribution: (a) wind velocity: 5.4 m/s; (b) wind velocity: 3.5 m/s



(a) (b)

Figure 13: Adhered particles to the bridge surfaces: (a) wind velocity: 5.4 m/s; (b) wind velocity: 3.5 m/s

3.1.1 *Simulation results*

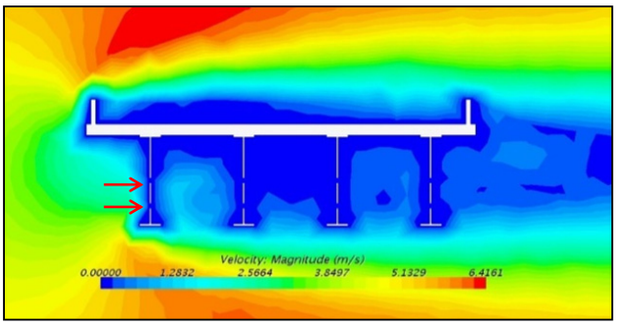
Figure12 illustrates the air velocity magnitude distributions of the two kinds of wind velocities: 5.4m/s and 3.5m/s around the bridge deck. The red areas on the top and bottom indicate the highest flow velocities, the green areas on the front and after red areas represent intermediate velocities and the blue color arrows around the bridge deck and inside of bridge deck indicate the lowest velocity magnitude distributions. In figure 13, the red points illustrate the image of adhered airborne sea-salt particles to the bridge surfaces. A comparison of the results showed no noticeable differences of the adhered particles distributions between the CFD analysis and experimental work.

3.2 *Countermeasures*

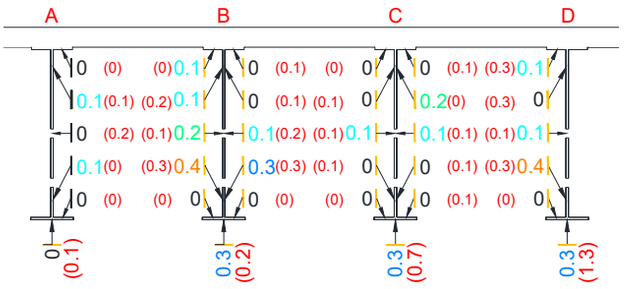
Four possible methods in order to decrease the amount of adhered airborne sea-salt particles inside the bridge girders were investigated by the CFD methodology as shown in figures 14-17. The pictures on left side of each figure illustrate the derived results for the air velocity magnitude distribution. The flow direction of airborne sea-salt particles affected depending on these air velocity magnitudes. For instance, particles mostly attached where the higher air velocity magnitude shown around the model bridge. The pictures on right side show the results of the quantitative amounts of adhered particles of each method. The red colour numbers are present the amount of adhered particles in case of normal bridge without countermeasures. They were written in order to compare with the amounts of the countermeasures those were written in other colour numbers. Specifics of each countermeasure and their results are explained below.

3.2.1 *First method: Hole in girder*

Occasionally, a hole is open on the girders of bridges in order to pass through a water pipe, gas pipe or cables. Obviously, they consider the strength and safety of bridge girders. Following this, we tried to make holes with a diameter of 10cm at the centre and lower part of webs of bridge model section. It is expected that some incoming particles may pass together with an air flow through these holes of webs and the amount of adhered particles to the girder surfaces will be reduced. As shown in figure 14, the amount of adhered particles reduced inside the girders but not significantly.

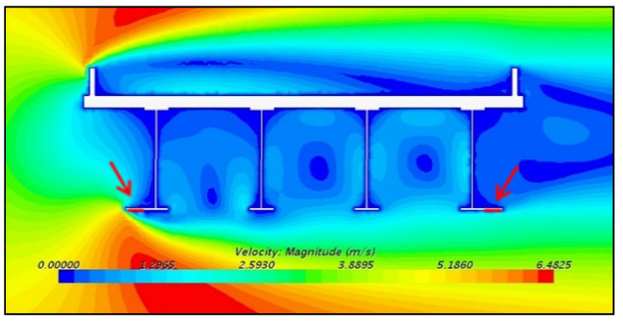


Air velocity magnitude distribution

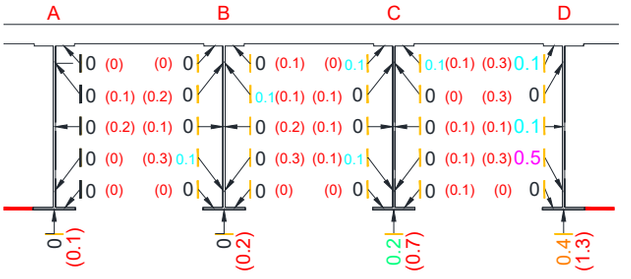


Quantitative amount of adhered particles

Figure 14: First method: Hole in girder

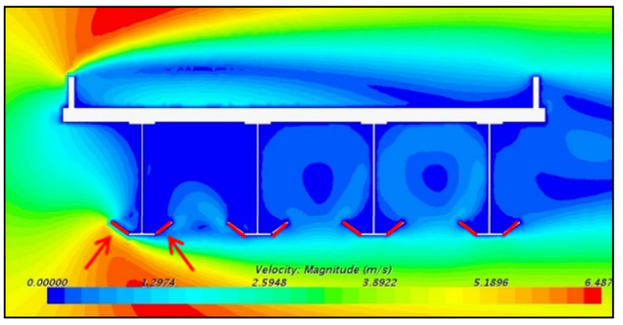


Air velocity magnitude distribution

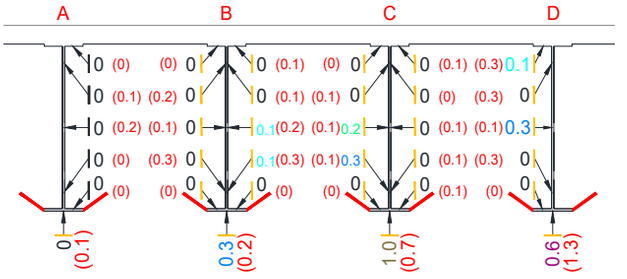


Quantitative amount of adhered particles

Figure 15: Second method: Adding members at inflow and outflow sides

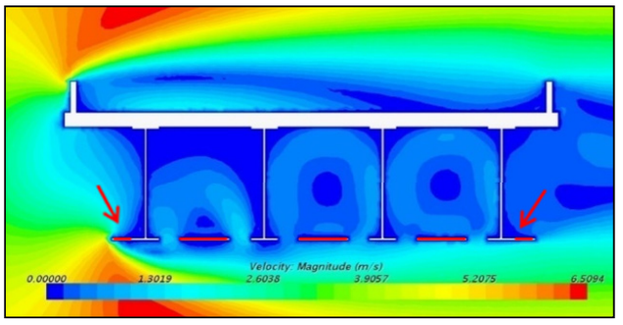


Air velocity magnitude distribution

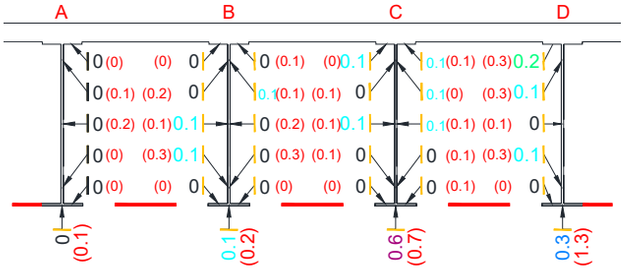


Quantitative amount of adhered particles

Figure 16: Third method: Adding members at bottom flanges with an angle of 35º



Air velocity magnitude distribution



Quantitative amount of adhered particles

Figure 17: Fourth method: Adding members at bottom side between the girders

3.2.2 *Second method: Adding members at inflow and outflow sides*

With a 50cm length a member (stainless steel, aluminium or other metals that do not rust) can be added horizontally to the bottom flanges at inflow side and outflow side symmetrically. The purpose is to separate the incoming flow largely and create difficulty for this to roll inside the girders. Figure 15 shows the image of added member with the results of simulation. As shown in the results, the number of adhered particles significantly decreased but inflow side of last girder has still a slightly adhered particles.

3.2.3 *Third method: Adding members at bottom flanges with an angle of 35°*

Members with an angle of 35 degree are added to the bottom flanges at inflow side and outflow side of every girder to suppress the flow of particles coming to the inside of girders. Figure 16 shows the results of the air velocity magnitude distribution and the adhered particles inside the girders. The Figure indicates a good result but not better than the second method.

3.2.4 *Fourth method: Adding members at bottom side between the girders*

Added members in front side and rare side are same with the second method but additional members with a length of around 1 meter added between the girders as shown in figure 17. The purpose is to decrease the scope of particles entering to inside girders. Closing all gaps completely would be the best choice, but the bridge owner needs to maintain inside the girders. Hence, a space that human or equipment can enter inside is necessary. The result shows not a big change comparing with the second method.

Among the four cases of countermeasures, the second method showed the best result. Simply by adding members at inflow and outflow sides symmetrically, it was able to decrease the biggest amount of adhered particles inside the bridge girders.

4 CONCLUSIONS

The study has investigated the adhesive behaviours of the sea-salt particles to the girders of four I-shaped steel girder bridge. Based on experimental and numerical analyses, the following conclusions can be highlighted:

- Both the experimental test and the numerical simulations showed that the higher the wind speed is the bigger number of the adhered particles to the bridge surfaces is obtained.
- Amount of adhered particles with the clearance effect had a good agreement with the observation data. The amounts on the down flanges are highly variable depending on the clearance height.
- The visualization of the airflow and the distribution of sea-salt particles to bridge surfaces were derived by CFD.
- A comparison of the results showed no noticeable differences of the adhered particle distributions between the CFD analysis and experimental work.
- Methods of countermeasures confirmed that by adding members to a bridge, it is possible to decrease the amount of adhered particles to the girder surfaces. Among them, the second method showed the best result.

5 REFERENCES

Goto, S., Aso, T. & Miyamoto, A. 2005. An analysis of the relationship between adhesive sodium and rust thickness on weathering steel bridges. *Steel-Structure Symposium, 2005.*

Haque, M. N., Katsuchi, H., Yamada, H. & Nishio, M. 2014. Strategy to Develop Efficient Grid System for Flow Analysis around Two-Dimensional Bluff Bodies. *KSCE Journal of Civil Engineering* (0000) 00(0):1-12

Hasebe, H., Sakakibara, Y., Yamaya, K., Sone, R., Haruki, Y. & Nomura, T. 2015. Wind tunnel experiment to estimate the amount of airborne sea salt adhering to the surface of a bridge. *14th International Conference on Wind Engineering.*

Iwasaki, E. & Nagai M. 2007/03. Estimation of marine salt behavior around the bridge section. *JSIE*, Vol. 53A

Iwasaki, E., Ito, S., Kojima, Y. & Nagai, M. 2010. Estimation of airborne sea salt around a bridge section by numerical simulation. *Journal of the Japan Society of Civil Engineers*, A-66-4, 752-766, (in Japanese).

Obata, M., Hasegawa, T. Nagata, K. & Goto, Y. 2008/03. Numerical simulation of sea salt particulate matter adhesion on bridge surfaces by two- phase flow analysis. *JSCE,* Vol.54A, (in Japanese).

Ohya, M. & Takebe M. 2009. Applicability of a New Method for Selecting Weathering Steel for Bridges*. Corrosion in Marine and Saltwater Environments,* 3 214th ECS Meeting, Vol. 16 (43) pp. 87-99

Okinawa General Bureau- Development Construction Department, Civil Engineering and Construction Department, *Manual of steel bridge painting in Okinawa area.* 2008.

Public Works Research Institute (PWRI), 1985. *National-wide survey of chloride particle distribution conveyed with sea wind,* Technical Report (I)–(IV).

Ronald, Ch., Katsuchi, H., Yamada, H. & Sasaki, E. 2012/03. Study on estimation of amount of airborne sea salt around bridge deck. *JSIE*, Vol.58A

Sohankar, A., Norberg, C. & Davidson, L. 1998/01. Low-Reynolds-number flow around a square cylinder at incidence: study of blockage, onset of vortex shedding and outlet boundary condition. *International Journal for Numerical Methods in Fluids,* Vol. 26, No. 1, pp. 39-56,

Maintenance, Safety, Risk, Management and Life-Cycle Performance of Bridges – Powers, Frangopol, Al-Mahaidi & Caprani (Eds)
© 2018 Taylor & Francis Group, London, ISBN 978-1-138-73045-8

Influence of collision on structural performance of steel girder

E. Yamaguchi, Y. Tanaka & H. Tsuji
Kyushu Institute of Technology, Kitakyushu, Japan

ABSTRACT: An overpass is occasionally damaged by a truck running underneath. Typical collision damage in a steel girder bridge includes the deformation of a main girder, the buckling of a transverse stiffener and the removal of a transverse stiffener from the web. The influence of the damage on the safety of the bridge needs be judged. Yet it is not always an easy task, since the load-carrying capacity of a girder damaged by collision has not been studied much. The first author has been involved in the evaluation of a highway steel girder bridge damaged by collision. Based on the data obtained from that bridge, the load-carrying capacity of the deformed girder is studied numerically in the present study. To be specific, the deformation of the main girder due to collision is reproduced by the finite element analysis and the deformed steel girder is loaded to evaluate the load-carrying capacity. The result indicates that as far as the damage is confined to the deformation of the girder, the collision does not threaten the safety of the bridge even when the deformation is quite large.

1 INTRODUCTION

Occasionally a truck running on a highway collides with a bridge across the highway. It is required to evaluate the influence of the accident on the bridge to ensure the safety of traffic on it. However, study on such influence appears very limited. As a result, the bridge tends to be attended overly.

In Japan, the construction of railways preceded that of highways. Therefore, the clearances under quite a few railway bridges do not satisfy the current requirement, which leads to more collisions of trucks with railway bridges. Some technical reports on collision damage in railway bridges are available in the literature (Nieda & Suzuki 2000, Suginoue et al. 2006, Nakayama et al. 2008 among others). Most of those technical papers describe only damages and the first-aid measures employed without touching on the safety issues such as the influence on the stiffness and the load-carrying capacity. The investigation by Nakayama et al. (2008) is one of a very few studies on the influence of collision damage on the load-carrying capacity of the damaged main girder.

Nakayama et al. (2008) first studied the characteristics of collision damage in the steel railway bridge. They stated that out of 14 damaged bridges, eight bridges were subjected to severe damage such as the deformation of track, the fall from the bearing and crack in the main girder, which have resulted in the immediate closure of those railway bridges. The remaining six girders underwent only the deformation of the main girders. The major deformations of those six girders were found to be classified into three groups: local upward deformation of the lower flange, horizontal deformation of the lower flange and the combination of the two. Focusing on the damages of the first two groups, Nakayama et al. (2008) have investigated the load-carrying capacity of the deformed girder experimentally and numerically. To that end, they prepared three girder specimens. The span of each girder was 5360 mm long and the difference between the three girder specimens lies in the initial deformation: one had no deformation, another girder had a locally upward displacement of the lower flange up to 78 mm and the lower flange of the other girder was displaced horizontally up to 27 mm. These initial deformations were decided referring to the maximum values they observed in the actual railway bridges damaged by the collision. Their research results have revealed that the damages they considered have insignificant influence on the load-carrying capacity. They have observed the tendency that the collision increased the capacity. They stated that a possible reason for this phenomenon was the strain-hardening due to the deformation caused by the collision.

The first author has been involved in the safety evaluation of a highway steel bridge damaged by collision. The damage of the main girder was severer than the one investigated by Nakayama et al. (2008). Yet no cracks in the web plate and no significant damage around the bearings were found. The main



Figure 1. Damaged bridge.



Figure 2. View from underneath.

concern was therefore the load-carrying capacity of the damaged girder. The present paper deals with this issue.

2 OVERVIEW OF BRIDGE

The highway bridge to be studied is a single-span steel girder bridge across an expressway and was damaged by collision (Fig. 1). The bridge is 29.8 m long and the span is 29.0 m long. The superstructure consists of two main girders and orthotropic deck. The main girder has transverse stiffeners while the orthotropic deck has longitudinal stiffeners and cross girders. Lateral struts are also installed to support two pipes. The view of the bridge from underneath is given in Figure 2.

3 DAMAGE

Only one of the main girders was found damaged. This is because the expressway below the damaged part of the bridge is uphill. The lower flange and the web were displaced outward, as is shown schematically in Figure 3. The cross girders set in the upper

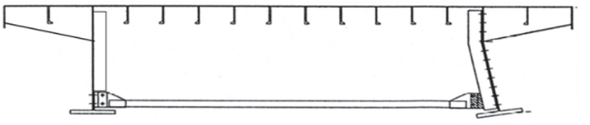


Figure 3. Deformation due to collision.

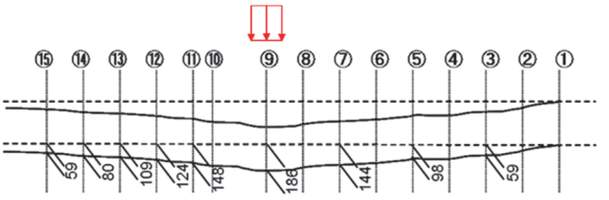


Figure 4. Horizontal displacement of lower flange.

part of the web restricted the web deformation only to the lower part. The residual horizontal displacements of the lower flange due to the collision were measured, the results of which are presented in Figure 4.

29 transverse stiffeners are welded to each web in addition to those at the bearings. The cross section having the transverse stiffener is given the number; the section closest to the abutment A2 is Section 1 and the section closest to the abutment A1 is Section 29. The circled numbers in Figure 4 correspond to those section numbers.

Figure 4 indicates that the largest horizontal displacement was caused around Section 9, which is 8.8 m away from the A2 bearing. A truck must have collided with around Section 9. The displacement at Section 9 is 186 mm, which is 1/156 of the span length. Note that the residual displacement of the girder studied by Nakayama et al. (2008) is 1/199 of the span length and that the Japanese design specifications (Japan 2012) requires the initial deflection to be less than 1/1000 of the member length.

The deformation of the main-girder web and the lower flange are not the only damage. In addition to them, some transvers stiffeners were bent and/or buckled; some welded connections between the transvers stiffeners and the web were fractured, separating the transvers stiffeners from the web; and some bolted connections between the transvers stiffeners and the lateral struts were broken, separating the lateral struts from the transverse stiffeners.

4 COLLISON LOAD

It was observed that the lateral strut at Section 11 was separated from the transverse stiffener and that it was held between the two main girders. Since the residual horizontal displacement at Section 11 is 148 mm, the phenomenon can be created if and only if the maximum horizontal displacement of the lower flange at Section 11 due to the collision had been equal to or

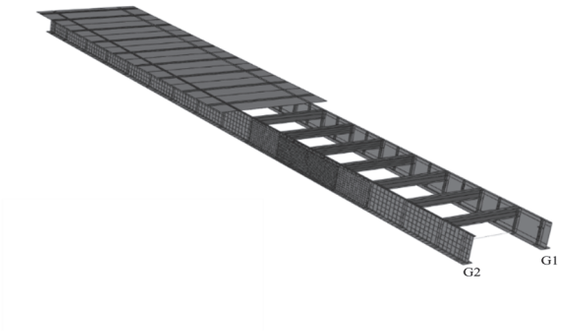


Figure 5. Finite element mesh.

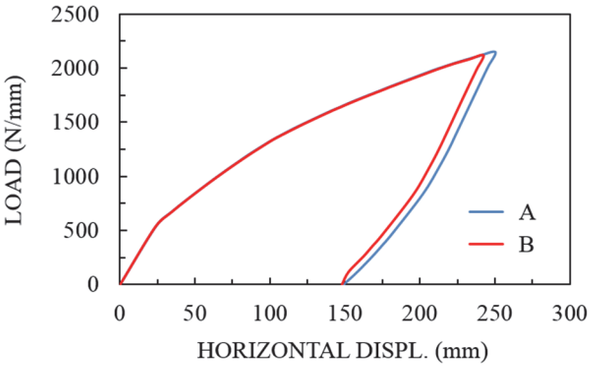


Figure 6. Horizontal load- lower-flange displacement curve at Section 11.

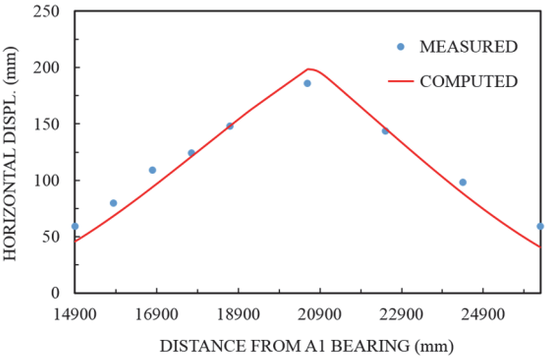


Figure 7. Horizontal displacement of lower flange.

greater than 148 mm while the residual displacement would have been smaller than 148 mm if not for the lateral strut at Section 11.

Herein the static load that can cause the above situation is estimated by the finite element analysis that takes into account the material and geometrical nonlinearities. This load has the effect virtually equivalent to the collision and so it is called the collision load in this study. For this analysis, ABAQUS (Dassault 2008) is used. Shell elements are employed for all the members except for the lateral struts that are modelled by beam elements. Since major deformation of the web is in the lower part and the primary role of the orthotropic deck is to provide the main girders and the cross girders with the clamped edge, the deck is modelled as a very stiff plate for the sake of simplicity. The finite element mesh is shown in Figure 5.

Steel used for the bridge is SM490Y specified in Japan Industrial Standard. Young's modulus E is 205 GPa and Poisson's ratio 0.3. Yield stress is 365 N/mm^2 for the plate thickness t less than 16 mm and 355 N/mm^2 for 16 mm $\leq$ t < 40 mm. Beyond the yield stress, the uniaxial material stiffness is assumed to be E/100. The elastic-plastic behavior of von Mises type with the kinematic hardening rule is assumed.

As noted earlier, the largest horizontal displacement was found around Section 9 (Fig. 4). The coating on the bottom surface of the lower flange was scratched out near Section 9. It is then legitimate to conclude that the collision had happened in this portion.

In the present study, based on the observation of the scratch on the coating of the lower flange, the collision load is assumed to be the uniformly distributed load over 400-mm range, as the red arrows in Figure 4 indicate. With this load, various analyses are conducted and it is found that once the load is increased up to 2145 N/mm, the total removal of the load leaves the displacement of 148 mm. The load-displacement curve A in Figure 6 represents this mechanical behavior. The curve A also shows that the displacement is 148 mm at 1650 N/mm. Therefore, the collision load must be between 1650 N/mm and 2145 N/mm for the lateral strut at Section 11 to be sandwiched between the main girders.

The lateral strut at Section 11 was found bent by 8 mm. The finite element analysis of this member under axial load is conducted using shell elements and the axial load that causes the 8-mm deflection turns out to be 45 kN.

The bridge is then analyzed again together with the point load of 45 kN, the reaction from the lateral strut, at the lower flange of Section 11. It is found that the collision load of 2120 N/mm leaves the horizontal displacement of 148 mm with the presence of the point load: the load-displacement curve B in Figure 6 is the result with the point load of 45 kN at the lower flange of Section 11. The computed residual horizontal displacement of the lower flange is plotted together with the measured displacement in Figure 7. Fairly good agreement is observed, confirming the validity of the present analysis.

5 INFLUENCE OF COLLISION DAMAGE

5.1 *Load-carrying*

To evaluate the influence of the damage caused by the collision, the load-carrying capacity of the damaged girder by itself is computed by the nonlinear finite element analysis. The girder to be analyzed here is taken out of the bridge deformed by the collision



Figure 8. Loading condition.

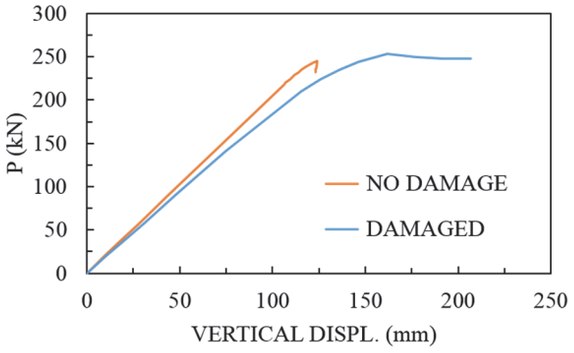


Figure 9. Load P – vertical displacement relationships at Point C (influence of damage).

load in the previous section.

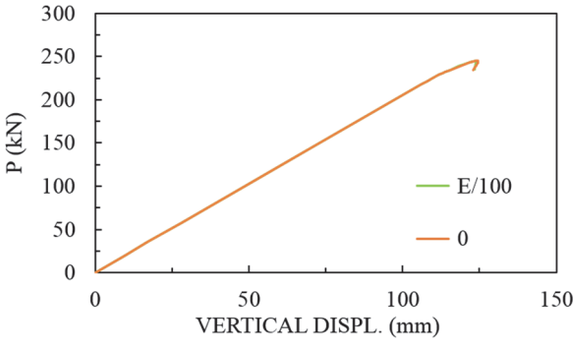
The girder is simply supported. The out-of-plane displacement, the rotation around the vertical axis and the rotation around the girder axis (torsion) are constrained along the top of the girder. As shown in Figure 8, two point-loads are applied at the top ends of Sections 8 and 10, as the severest damage is around Section 9. Point C is located at the bottom of the web at the center between Sections 8 and 10. To quantify the influence of the damage, the original (intact) girder is also analyzed.

The numerical results in terms of the load P and the vertical displacement at Point C are presented in Figure 9. The figure shows that while the stiffness is reduced by 8%, the 3% increase in the maximum load, from 243.0 kN to 253.0 kN, is observed. The intact girder exhibits little nonlinear behavior, but the damaged girder undergoes nonlinear response rather extensively.

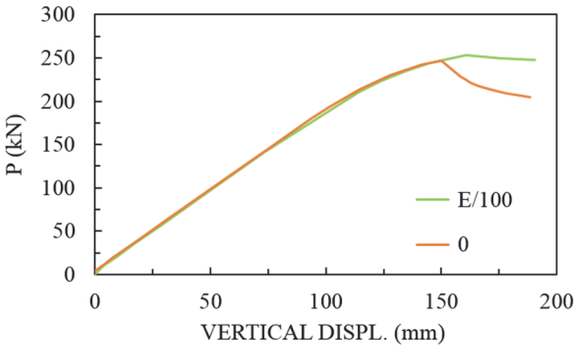
Nakayama et al. (2008) conducted the similar study and observed the same phenomenon of the increase in the load-carrying capacity due to the collision damage. Their study is based on the girder which has the largest horizontal displacement of 1/200 of the span length. This magnitude is just about the maximum they observed in their investigation of the damaged railway bridges. Note that the damage in the present study is 1.4 times larger than theirs.

5.2 *Effect of strain-hardening*

Nakayama et al. (2008) have suggested that the increase in the load-carrying capacity is caused by the strain-hardening associated with the plastic deformation due to collision. To study the effect of strain-hardening, the numerical analysis is conducted,



(a) Intact girder



(b) Damaged girder

Figure 10. Load P – vertical displacement relationships at Point C (influence of plastic modulus).

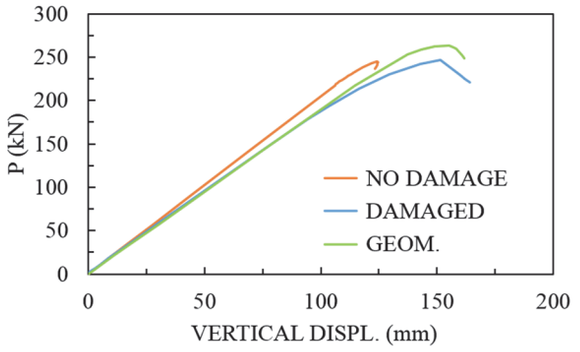
assuming zero second slope in the uniaxial material behavior in addition to E/100.

The numerical results in Figure 10 show that the load-carrying capacity of the intact girder is 245.0 kN for 0 and E/100 while those of the damaged girders are 246.7 and 253.0 for 0 and E/100, respectively. The load-carrying capacity becomes larger with the increase of the plastic modulus. But the load-carrying capacity has increased from 245.0 kN to 246.7 kN even when no strain-hardening is assumed. This result indicates that the phenomenon of the increase in the load-carrying capacity due to the collision damage cannot be explained well from the viewpoint of the strain-hardening.

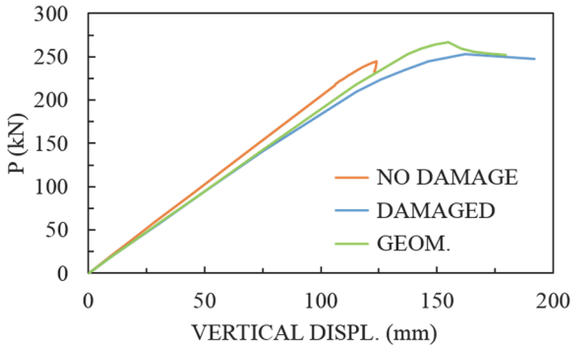
5.3 *Effect of configuration change*

The difference between the intact girder and the damaged girder lie in the residual stress and the geometrical configuration. To see the influence of the configuration change solely, the residual stress is eliminated from the damaged girder and then analyzed. The results are shown in Figure 11 as GEOM together with the others.

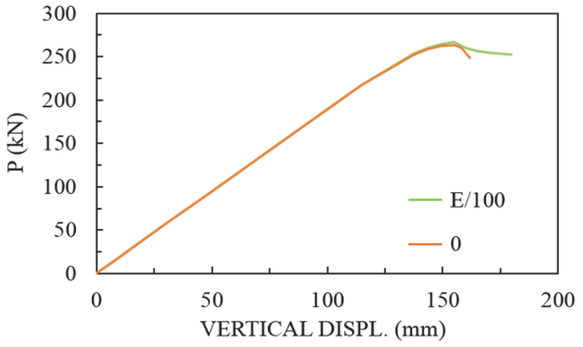
Regardless of the magnitude of the second slope, the initial stiffness is the same as that of the respective girder analyzed in the previous section, the one with both the residual stress and the configuration change (DAMAGED). The change in the configuration is



(a) Zero second slope



(b) Second slope of E/100



(c) Influence of plastic modulus (GEOM.)

Figure 11. Load P – vertical displacement relationships at Point C (influence of configuration change).

therefore the main cause for the reduction in the stiffness. Even in the case of the zero second slope, the load-carrying capacity increases from 245.0 kN to 262.9 kN. Hence, it can be stated that the configuration change must be responsible for the increase in the load-carrying capacity.

The residual stress influences the plastification quite much. With the presence of the residual stress, plastic deformation starts in smaller load while without the residual stress, the maximum load is reached with little plastic deformation, resulting in the small influence of the second slope on the load-carrying capacity (Fig. 11(c)).

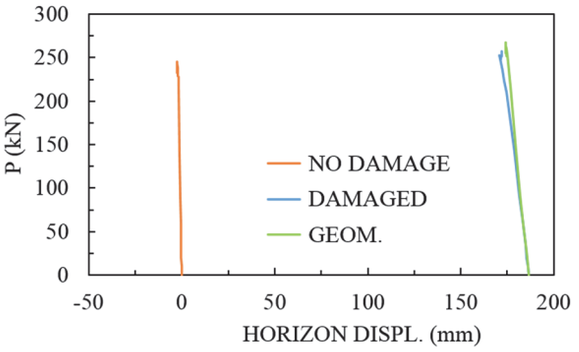


Figure 12. Load P – horizontal displacement relationships at Point C (E/100).

5.4 *Mechanical Behavior*

Figure 12 shows the relationship between the load P and the horizontal displacement at Point C. Except the intact girder, the horizontal displacement is not zero even before the loading, i.e. at P = 0, which represents the collision damage. With the point-loads increasing, those horizontal displacements tend to decrease: the deformed girders are returning to the original positions. The phenomenon is caused by the tensile stress acting in the bottom flange. The mechanical behavior of the deformed girder is thus quite different from that of the intact girder.

6 CONCLUDING REMARKS

The influence of the deformation of the steel bridge girder due to collision was studied. Through the nonlinear finite element analysis, the collision load was identified first, which gave the residual horizontal displacement of the lower flange comparable to that of the actual bridge. The influence of the damage due to the collision was then investigated. While the initial stiffness was found reduced by 8%, the bending strength becomes 3% larger. The subsequent analyses showed that the phenomenon was attributable to the configuration change that led to a quite different mechanical behavior from that of the original girder.

From the results thus obtained, it may be concluded that the deformation of the girder doesn't necessarily threaten the safety of the bridge. It needs be noted, however, that there is a chance that the damage other than deformation, if found, may lead to a completely different conclusion.

ACKNOWLEDGEMENTS

The financial support for the present study, Grant-in-Aid for Scientific Research (C) (KAKENHI, No. 15K06184), is gratefully acknowledged.

REFERENCES

Dassault Systemes Simulia Corp. 2008. *User's Manual, ABAQUS Ver. 6.8*. Dassault Systemes Simulia Corp.

Japan Road Association 2012. *Specifications for Highway Bridges: Part 2 Steel Bridges*. Japan Road Association.

Nakayama, T. et al. 2008. Residual load carrying capacities of riveted steel girders subjected to collision deformation. *Structural Engineering*, JSCE 54A: 68-79.

Nieda, H. & Suzuki, H. 2000. The pier overturning accident of inspect and restoration on the steel railway bridge. *Proceedings of Annual Conference of Japan Society of Civil Engineers* 55(IV): 604-605.

Suginoue, T. et al. 2006. First-aid measures of steel girder deformed by collision. *Proceedings of Annual Conference of Japan Society of Civil Engineers* 61(IV): 331-332.

Maintenance, Safety, Risk, Management and Life-Cycle Performance of Bridges – Powers, Frangopol, Al-Mahaidi & Caprani (Eds)
© 2018 Taylor & Francis Group, London, ISBN 978-1-138-73045-8

Sectional Analysis of Corroded Wires in Chloride-contaminated Tendon

C.H. Yoo & S.H. Bong & H.K. Kim
Department of Civil and Environmental Engineering, Seoul National University, Seoul, South Korea

Y.C. Park
Institute of Construction and Environmental Engineering, Seoul National University, Seoul, South Korea

ABSTRACT: In bridges which had a tendon-like structural member, the corrosion is a main cause of deterioration of the structural resistance. For assessing the effect of corrosion in tendon, the transition of corroded section should be identified. For this purpose, strand samples were collected from prestressed concrete bridge site which had suffered the corrosion caused by chloride contamination. By utilizing camera and macro lens, corroded wire sections are scanned as pictures. Based on these pictures, the geometric properties of corroded wire sections such as pit angle and pit depth are analyzed. The corrosion of wire spreads rapidly with tangential direction at the early stage of corrosion. As the corrosion grows, the main direction of corrosion is changed to radial direction. Furthermore, the uncertainties of pit angle and maximum pit depth decrease as the corrosion of wire progresses. This research can help the modeling the corrosion in corroded wire under chloride contamination.

1 INTRODUCTION

In bridges which had a tendon-like structural member, the corrosion is a main cause of deteriorating the structural resistance. For assessing the effect of corrosion in tendon, the transition of corrosion in corroded section should be identified. Val and Melchers (1997) and Hartt and Lee (2016) assumed the shape of corrosion without verifying actual deformation of corroded section for assessing the effect of corrosion.

For identifying the shape of corrosion, 3D scanning technique was utilized in Kashani et al. (2013). However, this method is hard to apply in 7-wire strand because there is inner space in strand to which the sight of 3D scanner cannot reach. Therefore, this paper adopts taking a close-up pictures of corroded wire sections. From these pictures, the geometric properties of the corroded wire and the corrosion characteristics of the corroded tendon are analyzed.

2 DATA OF CORRODED WIRE SECTIONS

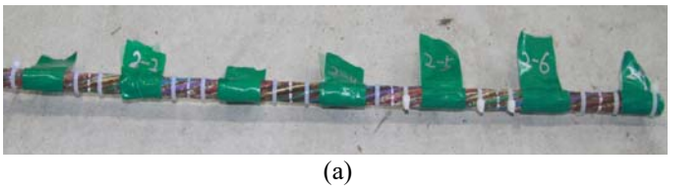
2.1 *Strand samples*

Strand samples were collected from prestressed concrete bridge site. The tendons of this bridge site has suffered chloride contamination with grout void occurred from bleeding of grout. Strand samples were selected whether there is a visible corrosion. Strand samples were cut into about 1m length for conducting fatigue test (Park et al., 2017). Corroded wire sections were investigated after this fatigue test.

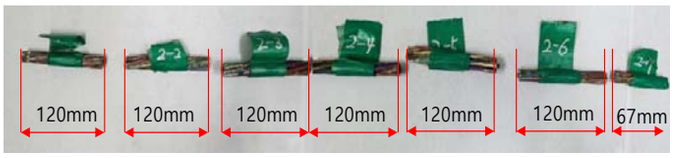
For acquiring more wire section samples, strand samples were sliced into several number of pieces. The number of pieces is determined with considering the geometric form of strand and wire as shown in Figure 1. The twisted angle α around which outer wires wind center wire is about 82.5°. The radius of outer wire and center wire, r_o and r_c, are 2.5mm and 2.6mm, respectively. The length for putting outer wire in place is 243mm ($=2\pi r_h \tan\alpha$). With considering this length, strand samples were divided into 8 pieces which have about 120mm length. Figure 2 indicates the strand sample before and after cutting.



Figure 1. Geometric form of strand and its cross-section



(a)



(b)

Figure 2. Strand sample (a) before cutting, (b) after cutting

2.2 *Close-up photos*

Before extracting the information of corroded wire sections, one more preprocess for converting corroded wire sections to information of corroded surface is needed. Gonzalez et al. (1995) used a scale for measuring weight loss and a micrometer for measuring pit depth. Kashani et al. (2013) used a 3D scanning optical measurement technique and developed 3D solid models of corroded bars. The method used by Gonzalez et al. (1995) is good for pulling out the information related with average weight loss within samples, but hard to discover individual characteristics of corrosion surface. The method employed by Kashani et al. (2013) is effective in catching detail characteristics of corrosion surface. However, this method is difficult to apply in 7-wire strands because there is unobservable space where sight of 3D scanner cannot reach in 7-wire strands. Therefore, the method with utilizing camera and macro lens is selected. This method can check distinct corrosion boundary of corroded wire sections.

The configuration for taking close-up photos is represented in Figure 3. Camera with macro lens can classify the precise corrosion boundary as shown in Figure 4.

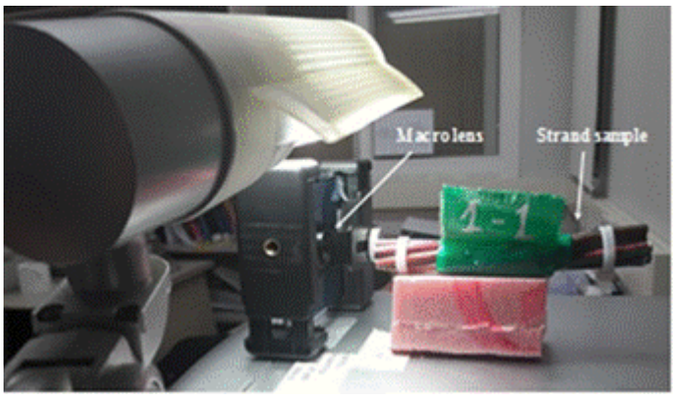


Figure 3. Configuration of taking close-up photos

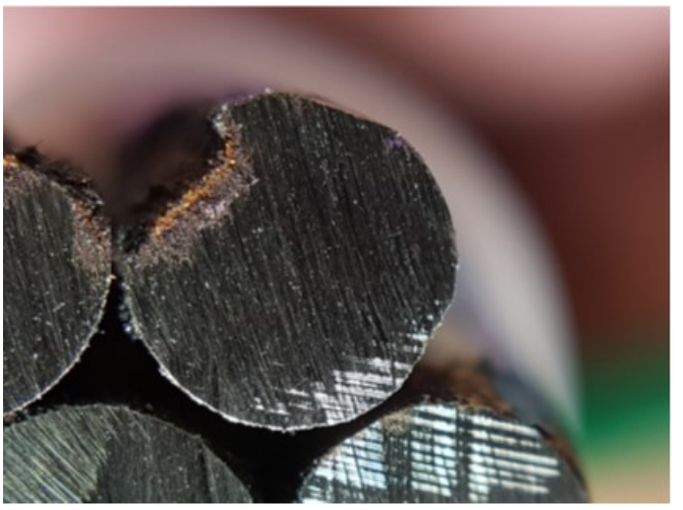


Figure 4. Example of close-up photo

2.3 *Geometric properties of corroded wire sections*

The shape of corroded boundary was identified from close-up photo of corroded wire sections. Two geometric properties as shown in Figure 5, pit angle θ and pit depth d, were extracted from close-up photos. Pit angle θ represents a tangential length of corrosion surface. Pit depth d is defined as a radial distance between outline of wire and corroded surface. In here, the maximum value among pit depth, $d_{\max}$, derived as Eq. (1) is mainly used in the analysis.

$$d_{\max} = \max\left(d_1, d_2, ..., d_n\right) \tag{1}$$

where $d_1, d_2, ..., d_n$ are pit depths obtained in same wire section.

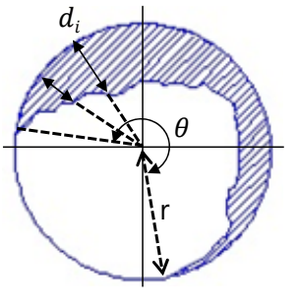


Figure 5. Geometric properties of corroded wire section

3 RESULTS AND DISCUSSIONS

3.1 *Pit angle and maximum pit depth of corroded wire sections*

The pit angle θ and pit depth $d_{\max}$ for each corroded wire sections were extracted from close-up photos. Corrosion was founded by total 90 wires. The results are represent in terms of average and coefficient of variation (COV) of pit angle and maximum pit depth in Figure 6 and 7, respectively. As can be seen in Figure 6, pit angle grows rapidly compared with maximum pit depth in the early phase of corrosion. On the contrary, maximum pit depth becomes deeper in the late phase of corrosion. This means that the direction of corrosion progress toward tangential direction at the early of corrosion stage. As the corrosion grows, the main direction of corrosion is changed to radial direction. Figure 7 describes that the variation of pit angle and maximum pit depth among wires decreases as the section loss increases.

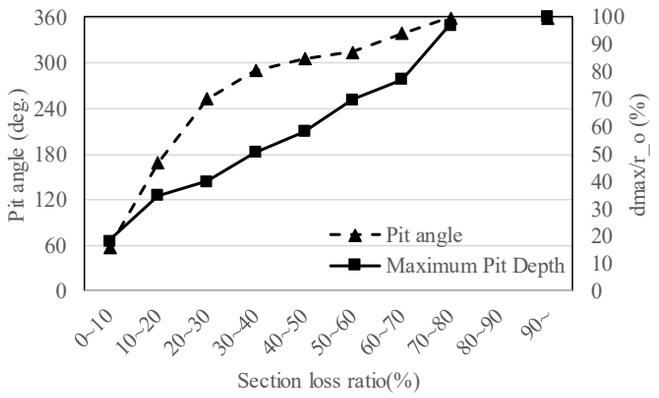


Figure 6. Average of Pit angle and pit depth versus section loss ratio

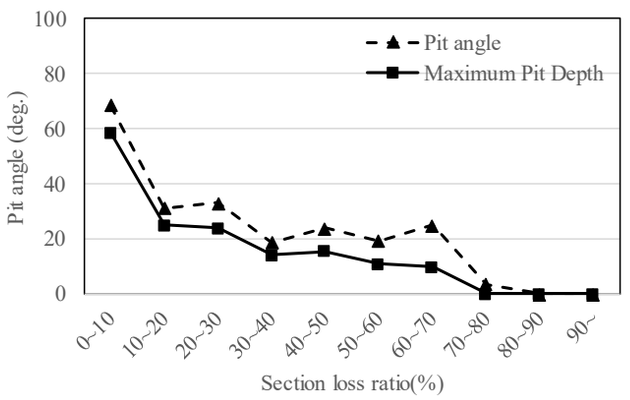


Figure 7. COV of Pit angle and pit depth versus section loss ratio

3.2 *Dispersion rate of corrosion in strand*

The corrosion characteristics of strand is analyzed with 47 corroded samples in the unit of strand. For this purpose, the section loss ratio which equals to section loss over cross-section of wire are calculated against the number of corroded outer wires and as shown in Figure 8. It can be shown that the section loss ratio increase as the number of corroded outer wires increase.

When only one outer wire is corroded among 6 outer wire, whole corrosion in strand is occurred in one wire. So its dispersion rate is 100%. If there are two corroded outer wire with same sectional loss, both wire has 50% of dispersion rate. Figure 9 represents a dispersion rate of corrosion in strand samples. It can be said that corrosion of strand is dispersed as the number of corroded outer wires increase

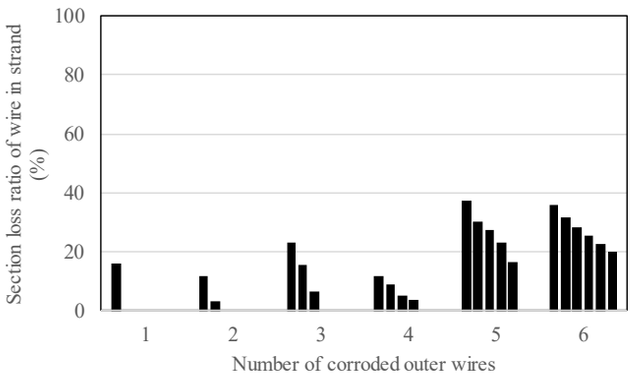


Figure 8. Section loss ratio versus the number of corroded outer wires

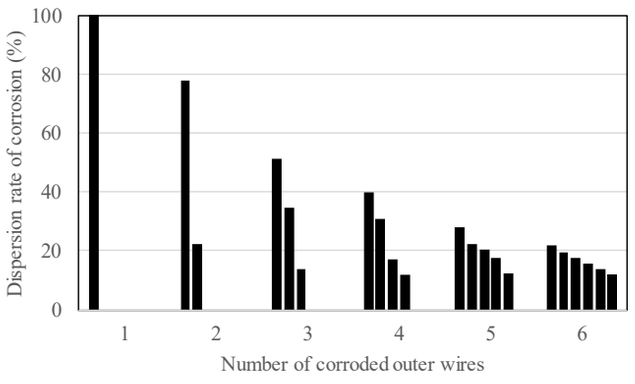


Figure 9. Dispersion ratio versus the number of corroded outer wires

4 CONCLUSIONS

Strand samples were collected from prestressed concrete bridge site which has suffered corrosion cause by chloride contamination. By utilizing camera and macro lens, corroded wire sections are scanned as pictures. Based on these pictures, the geometric properties of corroded wire sections such as pit angle and pit depth and the corrosion characteristics in strands are analyzed. The corrosion of wire spreads rapidly with tangential direction at the early stage of corrosion. As the corrosion grows, the main direction of corrosion is changed to radial direction. Furthermore, the uncertainties of pit angle and maximum pit depth decrease as the corrosion of wire progresses. In terms of corrosion of strand, the number of corroded outer wires shows an increasing tendency as corrosion grows. Also, it can be said that corrosion of strand is dispersed as the number of corroded outer wires increase.

This research can help the corrosion modeling of the corroded wire under chloride contamination.

ACKNOWLEDGEMENT

This study and presentation were supported by grants(17SCIP-B119964-02) from the Ministry of Land, Infrastructure and Transport of the Korean Government.

REFERENCES

Gonzalez, J.A., Andreade, C., Alonso, C. and Feliu, S. 1995, Comparison of rates of general corrosion and maximum pitting penetration on concrete embedded steel reinforcement, *Cement and Concrete Research*, 25-2: 257-264

Hartt, W.H. and Lee, S.K. 2016. Projecting Corrosion-Induced Bridge Tendon Failure Resulting from Deficient Grout: Part I : Model Development and Example Results, *Corrosion*, 72-8: 991-998.

Kashani, M.M., Crewe, A.J. and Alexander, N.A. 2013, Use of a 3D optical measurement technique for stochastic corrosion pattern analysis of reinforcing bars subjected to accelerated corrosion, *Corrosion Science*, 73: 208-221.

Park, Y. C., Yoo, S. M. and Kim, C. Y. (2017). Fatigue Performance Evaluation of Severely Corroded Steel Strands. Paper presented at the 39th IABSE Symposium, Vancouver, Canada.

Val, D.V. and Melchers, R.E. 1997. Reliability of deterioration RC slab bridges, *Journal of Structural Engineering*, 123-12: 1638-1644.

Maintenance, Safety, Risk, Management and Life-Cycle Performance of Bridges – Powers, Frangopol, Al-Mahaidi & Caprani (Eds)
© 2018 Taylor & Francis Group, London, ISBN 978-1-138-73045-8

GA-based Model Updating for Existing Bridges

J.C. Kim
Byucksan Engineering, Seoul, Korea

J. Yoon & S. Shin
INHA University, Incheon, Korea

ABSTRACT: In this research, a model updating technique based on GA(genetic algorithm) is developed and applied to an existing PS concrete girder bridge. Usually, numerical model updating requires long hours of optimization process and has troubles in accessing to a reliable target solution. To reduce the computational time and improve the accessibility, we developed a program whose whole process runs only in *Matlab* environment. The parameters used in the proposed model updating process include the design range of the crossover probability, mutation probability, and the step parameter adjusting the amount of increment of the parameter. It was confirmed that the model updating performance is improved when the gene arrangement of the chromosome is closely related to the property of an actual bridge and the static and dynamic characteristics are well applied to the fitness function. The importance of selecting parameter values was determined by complex model formation and the design range of reasonable parameters of the current model.

1 INTRODUCTION

According to the 2017 survey of Korean MLIT (Ministry of Land, Infrastructure, and Transport), about 10% of existing bridges in Korea are over 30 years old but the statistics will jump to more than 30% after 10 years from now on. Therefore, a reasonable and reliable way of evaluating existing bridges is critical to the safety and maintenance of existing bridges in Korea.

In evaluating a bridge, some formalized processes are already known to us; including investigation, NDT, loading tests, and evaluation of load rating, etc. In evaluating the load-carrying capacity of a bridge, an analytical model for the bridge should be determined. The methods of such model updating for bridge structures can be classified as direct methods and iterative methods. The direct methods include methods based on NN(neural network) and GA(genetic algorithm). Because direct methods simply minimize numerical errors in the system matrix so that it is difficult to have any physical meaning in the finally obtained model for a structure (Baruch and Itzhac 1978). In iterative methods, sensitivity matrix is usually utilized to search for optimal stiffness and mass properties. This approach is effective in improving the structural characteristics but it is difficult to apply for a complex structure because every parameter should be updated based on the sensitivity matrix (Mottershead and Friswell 1993). To overcome such problems in both methods, a model updating scheme was developed by combining a GA and commercial software for structural analysis (Kim 2016). However, one handicap of this approach is still the computation time required in running the repetitive process between independent GA program and a commercial software.

In this paper, a similar computational process is proposed between a GA program and structural analysis program but runs all in *Matlab* environments. The developed program has been examined through an application to a PS concrete girder bridge and the results are summarized.

2 APPLICATION OF GENETIC ALGORITHM

2.1 *Operation process*

The process of GA is illustrated in the left column of Figure 1; starting from the generation of initial population to elite strategy and termination criteria.

In creating initial population, the research created evenly distributed random numbers and utilized uniform pseudo-random sampling method to determine individual population (Ripley 1981, Maaranen *et al*. 2007).

The fitness function $f(x)$ is defined by the combination of an objective function $J(x)$ and a penalty function $p(x)$.

$$\textit{Minimize} \quad f(x) = \max \frac{1}{J(x) + p(x)} \tag{1}$$

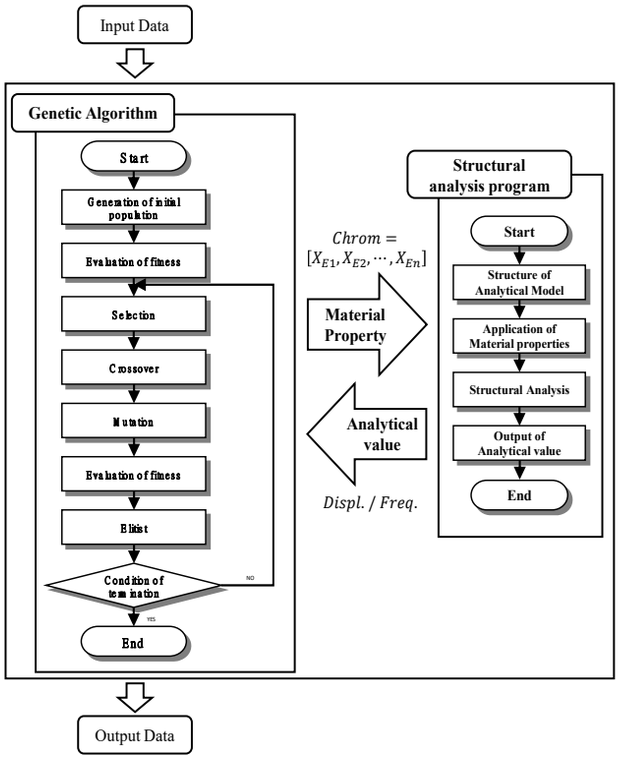


Figure 1. Process of GA-based analytical model updating.

For the penalty function, a variable penalty method of Eq.(2) by Cho(1999) was applied by indicating the increase of penalty factor as the number of population increases.

$$p(x) = (r \cdot k)^2 \sum_{i=1}^{m} g_i^2(x), \quad (k = 1, \ldots, n) \tag{2}$$

where r = penalty factor, k = number of population, n = total number of population, m = number of constraints, $g_i(x)$ = violation of constraints which equals to 0 when it satisfies the penalty function.

To select population, the gradient-like reproduction scheme by Jin and Joo(2000) was applied. For the cross-over, the homo-sexuality scheme by Yang and Kim(1995) was applied. For the mutation, a modified uniform or dynamic mutation scheme by Eq.(3) was applied.

$$X_i = \begin{cases} a_i + (UB - a_i) \cdot \lambda \cdot step_k & (\tau = 0) \\ a_i - (a_i - LB) \cdot \lambda \cdot step_k & (\tau = 1) \end{cases} \tag{3}$$

where UB = upper bound, LB = lower bound of design value X_i, λ = random number between 0 and 1, a_i = the i-th design variable among the mutation values, and $step_k$ = input variable defined by Eq.(4) between 0 and 1.

$$step_k = \left\{(step)^{1/n}\right\}^{k-1}, \quad (k = 1, \ldots, n) \tag{4}$$

When the fitness of the current generation is lower, a simple elite strategy is applied by changing the best fit in the current generation and the best fit in the previous generations (De Jong 1975).

Table 1. GA parameters suggested in the previous researches.

Parameters	Chung (2007)	Lee* (2000)	Grefenstette (1986)	Schaffer (1989)	De Jong (1975)
Population	30~200	-	30~100	20~30	50~100
Crossover Probability	.6~.95	.4~.8	.45~.95	.75~.95	.6~.95
Mutation Probability	.005~.01	.002~.05	.01	.005~.01	.001~.01

* When the mutation probability is 0.05, the design point tends to flow to the next optimal solution.

Table 2. Range of design parameters (Kim 2016)

Parameters	Population Size	Crossover Probability	Mutation Probability	Step
Design Range	30	0.1~0.9	0.01, 0.05 0.1	1, 0.1 0.01, 0.001

2.2 *Design parameters*

Because there is no clear theory about the effect of parameter values on the performance of genetic algorithms, the crossover, mutation, and the parameters at each step were determined through trial and error and summarized in Table 2 based on the previous researches shown in Table 1.

2.3 *Process of GA-based model updating*

GA-based model updating program is divided by two parts; one of GA part and the other of structural analysis as shown in Figure 1. Both parts of programs are developed in *Matlab* environments in this research. A lot of feedbacks are iterated with different initial populations. Because a stand-alone internal structural analysis program instead of using a commercial software was utilized, a lot of communication time in connecting GA program and analysis program could be saved.

Input data include information on initial parameters, fitness function, and initial analytical model for a bridge. Output prints the improved gene sequence of material characteristics.

3 APPLICATION TO A PSC GIRDER BRIDGE

3.1 *Overview of the PSC girder bridge*

A PS concrete girder bridge of a simple span as shown in Figure 2 was selected for tests. The length of the simple span part of the bridge is 30 m and the width of the section is 12.6 m. The bridge locates in an express highway in Korea. The total length of the bridge including the test span is 273 m of seven spans.

Detail dimensions of the span and sections are in Figure 3. In addition, the locations of LVDTs and accelerometers for the tests are also given.



Figure 2. Overview of the PS concrete girder bridge.

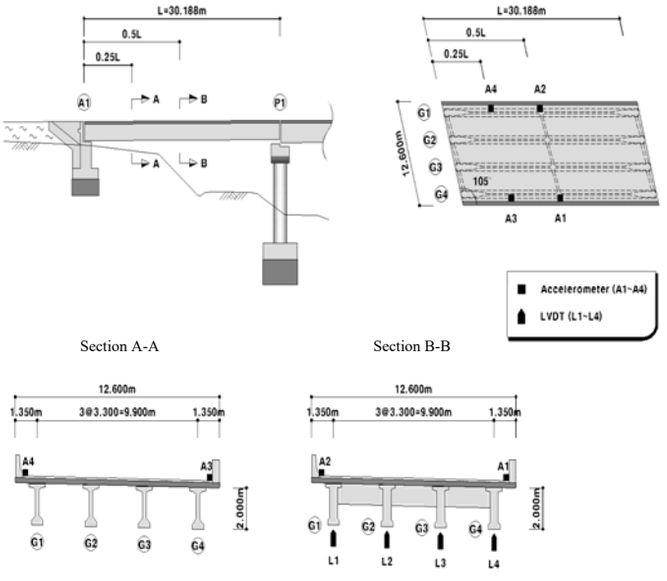
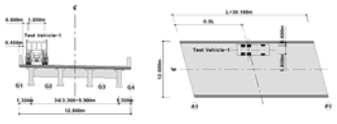
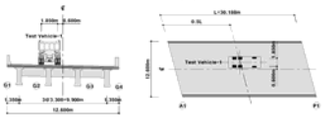


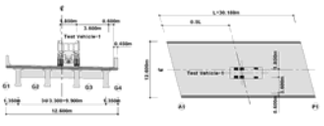
Figure 3. Bridge dimensions and sensor layout.



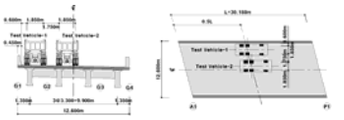
(a) Load Case 1



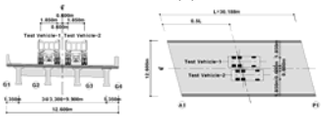
(b) Load Case 2



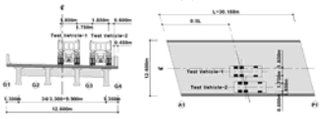
(c) Load Case 3



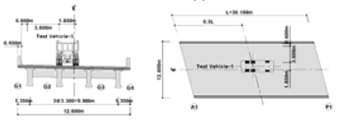
(d) Load Case 4



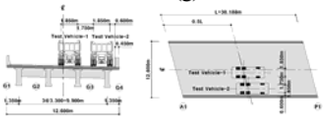
(e) Load Case 5



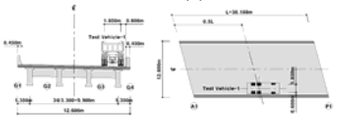
(f) Load Case 6



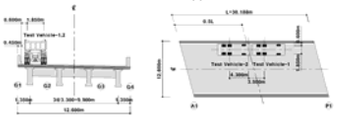
(g) Load Case 7



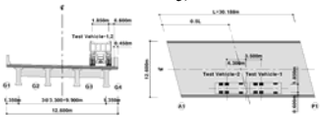
(h) Load Case 8



(i) Load Case 9



(j) Load Case 10



(k) Load Case 11

Figure 4. Load case for the loading tests

3.2 *Loading test*

Static and dynamic loading tests were carried out with measuring sensors of Figure 3. For static loading tests, eleven different load cases were considered. The loading cases are illustrated in Figure 4. Static deflections were measured at each girder in the mid-span and natural frequencies were identified

from the measured accelerations as summarized in Table 3 and Table 4.

Dynamic loading tests were carried out with different truck speeds of 10~100 km/hr. The natural frequencies in Table 4 were averaged from the identified modal data of different speeds.

Table 3. Mid-span deflection for load case (mm)

Load case	G1	G2	G3	G4
LC 1	1.667	0.950	0.240	0.002
LC 2	0.897	1.120	0.643	0.232
LC 3	0.418	0.860	1.021	0.514
LC 4	2.356	2.004	1.048	0.323
LC 5	1.190	1.885	1.775	0.918
LC 6	0.455	1.168	1.955	1.885
LC 7	0.680	1.075	0.798	0.327
LC 8	0.306	0.744	1.097	0.651
LC 9	0.034	0.285	0.909	1.379
LC 10	2.858	1.662	0.467	0.004
LC 11	0.028	0.517	1.600	2.546

Table 4. Identified natural frequencies (Hz)

Mode 1	Mode 2	Mode 3
5.924	7.149	9.889

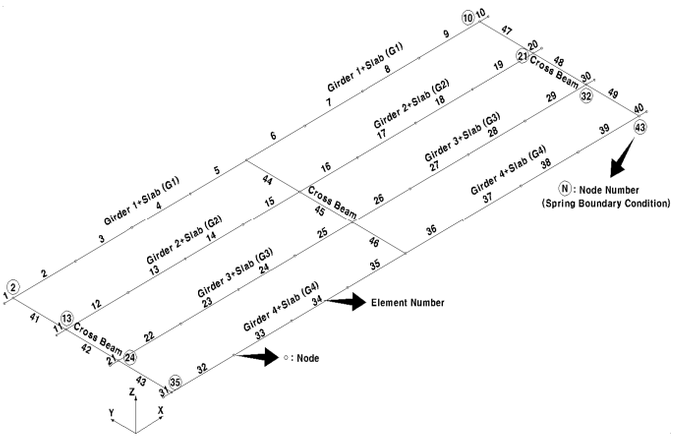


Figure 5. Grid model for the PSC girder bridge

3.3 *Analytical model for the PSC girder bridge*

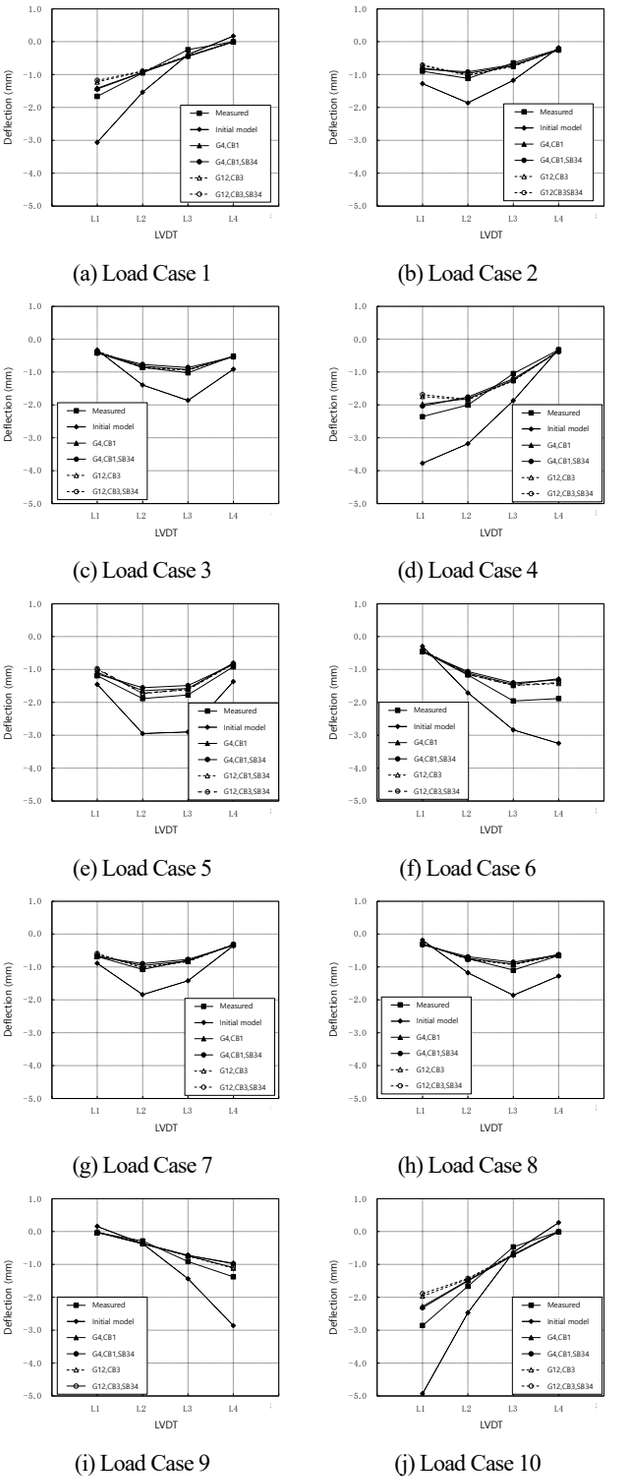
A simple grid model using 3-D frame elements as shown in Figure 5 was utilized to represent the bridge. The deck system and the prestressing tendons were not separately considered in the model. Rather its stiffness was included in the girder elements. The number of nodes are 44 and 40 composite elements and 9 crossbeams were modeled. The supports were replaced by spring elements as additional parameters.

Two fitness functions were applied for the model by only using measured static displacements (case 1) and by using both measured static displacements and the identified first natural frequency (case 2).

$$f(x_i) = a_i f_1(x_i) + b_i f_2(x_i) = a_i \sum_{k=1}^{n_i} \left(\sum_{l=1}^{m_i} \left(\frac{\delta_{k,l}^{\text{int}} - \delta_{k,l}^{anl}}{\delta_{k,l}^{\text{int}}} \right)^2 \right) + b_i \left| \frac{f_r^{\text{int}} - f_r^{anl}}{f_r^{\text{int}}} \right| \quad (5)$$

With constraints of

$$g_k(x_i) = a_i f_{1,k}(x_i) - 0.1 \le 0 \qquad g(x_i) = b_i f_2(x_i) - 0.1 \le 0 \quad (6)$$



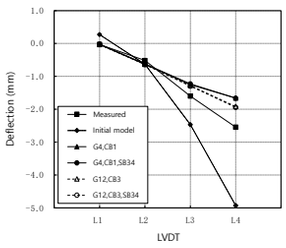
(a) Load Case 1 (b) Load Case 2

(c) Load Case 3 (d) Load Case 4

(e) Load Case 5 (f) Load Case 6

(g) Load Case 7 (h) Load Case 8

(i) Load Case 9 (j) Load Case 10



(k) Load Case 11

Figure 6. Comparison of girder deflections in case 2.

For case 1: $a_i = 1$, $b_i = 0$, and case 2: $a_i = 1$, $b_i = 1$. For case 2, the estimated deflections at each girder in the mid-span were compared with the initial and the measured deflections in Figure 6.

Table 5. Deflection errors of case 1 ($a_i = 1$, $b_i = 0$) (%)

Load case	model 1	model 2	model 3	model 4
1	2.725	2.527	6.333	7.592
2	1.615	1.943	1.959	2.306
3	0.510	1.594	0.413	0.444
4	2.044	1.768	4.143	4.857
5	1.346	2.224	1.085	1.260
6	6.927	7.121	4.831	5.244
7	0.640	1.408	0.419	0.544
8	1.590	2.775	1.311	1.421
9	7.624	7.253	3.685	4.168
10	3.763	3.409	**8.024**	**9.435**
11	**9.899**	**9.937**	5.485	5.097
Average	3.517	3.814	3.426	3.852

Table 6. Deflection errors of case 2 ($a_i = 1$, $b_i = 1$) (%)

Load case	model 1	model 2	model 3	model 4
1	1.773	1.847	5.943	7.538
2	1.482	1.248	1.701	2.250
3	0.477	0.065	0.350	0.495
4	1.344	1.353	3.689	4.794
5	1.195	0.474	0.790	1.294
6	6.602	5.837	4.418	5.151
7	0.734	0.403	0.290	0.527
8	1.431	0.778	1.268	1.491
9	7.705	7.186	3.315	3.944
10	2.363	2.244	**7.300**	**9.390**
11	**9.997**	**9.584**	4.517	4.650
Average	3.191	2.820	3.053	3.775

Table 7. The minimum objective function depending on the design range of the crossover probability

Crossover Probability	Minimum objective function Average	more than 10 freq. numbers
0.1	2026.87	27.08
0.2	4542.99	30.21
0.3	1870.06	21.88
0.4	1877.91	23.96
0.5	1549.53	15.63
0.6	**1116.64**	**10.42**
0.7	2355.66	12.50
0.8	4199.64	20.83
0.9	1576.62	12.50
Average	2346.21	19.44

Table 8. The minimum objective function depending on the design range of the mutation probability

Mutation Probability	Minimum objective function Average	more than 10 freq. numbers
0.01	2564.12	22.57
0.05	**1637.24**	**18.40**
0.31	2837.28	17.36
Average	2346.21	19.44

Table 9. The minimum objective function depending on the design range of step

Step	Minimum objective function Average	more than 10 freq. numbers
0.001	2015.39	17.13
0.01	3397.58	23.15
0.1	2349.16	21.30
1.0	**1622.72**	**16.20**
Average	2346.21	19.44

Figure 6 shows that static deflections at 4 girders are getting closer to the measured deflections as model is updated by the proposed algorithm.

The errors between the measured and estimated static deflections at each load case are summarized in Table 5 and Table 6 with 4 different models. Applied models are (1) model 1 with parameters of 4 girders and 1 crossbeams, (2) model 2 with parameters of model 1 plus 10 support springs, (3) model 3 with parameters of 12 composite sections plus 3 crossbeams, and (4) model 4 with parameters of model 3 plus 34 spring elements. At each model applied, the maximum deflection error is less than 10%, which satisfies the KCI guideline (2010). From Table 5 and Table 6, it can be observed that deflection errors by case 2 using both static deflection and natural frequency are smaller than those by case 1.

3.4 *Selection of optimal parameters*

The parameters considered in the study include crossover probability, mutation probability, and step parameters. By comparing the fitness function according to different design values, the performance of the genetic algorithm was compared.

As the crossover probability increases, more crossover is taking place and thus searching capability improves. Table 7 summarizes the calculated minimum objective function depending on the design rage of the crossover probability. Table shows the best performance when the probability is 0.5, 0.6, and 0.9.

As the mutation probability increases, the probability of converging to the global optimal solution is increased by generating various genes. However, it should be noted that the result will be equal to that of random search, if it is too big. Table 8 shows that the minimum objective function could be obtained when mutation probability is 0.05.

Step is a parameter that controls the magnitude of crossover and mutation increments. When it is equal to 1.0, the increment is uniform. When it is less than 1.0, the increment decreases so that the local search capability can be improved. Table 9 shows that the

performance is the best when the step is equal to 1.0 with a long array. When the array becomes shorter with less than 1.0, the performance improves better with step of 0.001.

4 CONCLUSIONS

A modified GA program for updating analytical models is proposed and applied to a simply span PS concrete girder bridge. To improve an analytical model, measured static deflections and the first natural frequency were used in defining the fitness function in the study. In addition, the performance of the algorithm was evaluated with different range of design parameters of crossover probability, mutation probability, and the step size.

In the study, a grid model using 3-D frame elements for the PS concrete girder bridge was improved by using four gene arrays. In updating analytical model for the actual bridge, the error rate of the fitness function was small in the case of the models 3 and 4 rather than the other two models. It is concluded that even if the computation time may be longer, the results will be improved with gene arrays close to the actual situation.

Two different fitness functions were tested in the study: one only with static deflections and the other with static deflections and natural frequencies. In overall, the case of using both measured data of static deflections and modal frequencies provides a little smaller error in the determined deflections. However, the error gap is negligibly small.

Use of spring elements at the supports could improve the estimation error with smaller error in deflection estimation in most of the test cases. But in some load cases, errors were rather larger than those without considering the spring elements at the supports. However, in general, it can be concluded that the error behavior can be improved by using an analytical model that can consider the boundary condition effects.

ACKNOWLEDGEMENTS

This research was supported by a grant(18SCIP-B128569-02 2) from Smart Civil Infrastructure Research Program funded by Ministry of Land, Infrastructure and Transport of Korean government.

REFERENCES

Baruch, M. and Itzhac, Y. 1978. Optimal Weighted Orthogonalization of Measured modes. *AIAA Journal*. 16(4): 346-351.

Cho, Y.S. 1999. Development of Genetic Algorithms for Efficient Constraints Handling. MS thesis. Hanyang University.

Chung, J.H. 2007. Application of Multi-Objective Genetic Algorithms for Planning of Detention Facilities. Ph. D. dissertation. Knu University.

Grefenstette, J.J. 1986. Optimization of Control Parameters for Genetic Algorithms. *IEEE Transactions on Systems, Man, and Cybernetics*, IEEE. 1(SMC-16): 122-128.

KCI. 2010. Safety Evaluation Criteria and examples of existing Concrete Bridges.

Lee, D.G. 2000. A study on the modified real-valued genetic algorithm using an improved crossover with meiosis and MIN/MAX operation. Ph. D. dissertation. Yonsei University.

De Jong, K.A. 1975. Analysis of the behavior of a class of genetic adaptive systems. Ph.D. thesis, University of Michigan, Ann Arbor.

Jin, G.G. and Joo S.R. 2000. A Study on a Real-Coded Genetic Algorithm. *Journal of Institute of C ontrol, Robotics and Systems* . 6(4): 268-275.

Kim, J.C. 2016, Development of a Mutation Operator of a Real-coded Genetic Algorithm for Model Updating of Existing Bridges. Ph.D. thesis, Inha University.

Maaranen, H., Miettinen, K. and Penttinen, A. 2007. On initial populations of a genetic algorithm for continuous optimization problems. *Journal of Global Optimization*. 37: 405-436.

Mottershead, J.E. and Friswell, M.I. 1993. Model updating in structural dynamics - A survey. *Journal of Sound and Vi bration*. 167(2): 347-375.

Ripley, B.D. 1981. Spatial Statistics. John Wiley & Sons. New York.

Schaffer, J.D., Caruana, R.A., Eshelman, L.J. and Rajarshi Das 1989. A Study of Control Parameters Affecting Online Performance of Genetic Algorithms for Function Optimization, Proc. 3rd Int. Conf. on Genetic Algorithms and Their Applications. 51-60.

Yang, Y.S. and Kim, G.H. 1995. A Real Code Genetic Algorithm for Optimum Design. *The Journal of the Computational Structural Engineering Institute of Korea*. 8(2), 123-132.

SS11: Life-cycle structural redundancy, robustness and resilience of bridges under multiple hazards

Organizers: F. Biondini & D.M. Frangopol

Maintenance, Safety, Risk, Management and Life-Cycle Performance of Bridges – Powers, Frangopol, Al-Mahaidi & Caprani (Eds)
© 2018 Taylor & Francis Group, London, ISBN 978-1-138-73045-8

Survey on life-cycle structural performance indicators for bridges

F. Biondini
Department of Civil and Environmental Engineering, Politecnico di Milano, Milan, Italy
D.M. Frangopol
Department of Civil and Environmental Engineering, ATLSS Center, Lehigh University, Bethlehem, PA, USA

ABSTRACT: A survey on life-cycle performance of civil structure and infrastructure systems has been conducted among researchers and experts from universities, industries, engineering firms and agencies active in the field of life-cycle civil engineering. The survey was aimed at gathering information about successful practices and explore avenues to overcome obstacles to filling the gap between theory and practice. The results of the survey were reported in the January 2018 issue of the ASCE Journal of Structural Engineering. In this paper, the survey database is further processed considering only the group of respondents working in the bridge engineering sector to investigate the role of life-cycle performance indicators in design, assessment and maintenance of deteriorating bridges. The main results are presented and discussed with emphasis on the need to incorporate life-cycle concepts, criteria and methods in bridge structural design codes, standards and guidelines.

1 INTRODUCTION

The economic growth and sustainable development of countries require to preserve and possibly improve the safety, serviceability, reliability, redundancy, robustness and resilience of critical structures and infrastructure facilities under uncertainty. Considering the high impact of aging and deterioration processes and their interaction with other multiple natural and man-made hazards, structural engineering is undergoing a profound change towards a life-cycle oriented design philosophy. This is particularly important for bridges and infrastructure systems, as pointed out by rating systems such as the Report Card for America's Infrastructure issued by the American Society of Civil Engineers (ASCE 2017): "The U.S. has 614,387 bridges, almost four in 10 of which are 50 years or older. 56,007 – 9.1% – of the nation's bridges were structurally deficient in 2016, and on average there were 188 million trips across a structurally deficient bridge each day. While the number of bridges that are in such poor condition as to be considered structurally deficient is decreasing, the average age of America's bridges keeps going up and many of the nation's bridges are approaching the end of their design life. The most recent estimate puts the nation's backlog of bridge rehabilitation needs at $123 billion."

Guiding policies and support decision-making processes are hence necessary for reliable design of durable bridges and rational planning of maintenance, repair, or replacement of existing bridges. Relevant advances have been accomplished in the fields of modeling, analysis, design, maintenance and management of deteriorating bridges and infrastructure systems (Frangopol 2011, Biondini & Frangopol 2016a). These advances are based on a rational approach to life-cycle design of structures and infrastructures. However, further efforts are necessary to filling the gap between theory and practice and foster the incorporation of life-cycle concepts in structural design codes, standards and specifications.

In fact, the codified procedures for bridge design generally refer to the structural performance in terms of structural safety and reliability. However, when aging and deterioration are considered, the evaluation of the system performance should account for additional performance indicators aimed to provide a comprehensive description of the life-cycle structural resources (Barone & Frangopol 2014, Biondini 2009, Biondini et al. 2008, 2014, 2015, Biondini & Frangopol 2014, 2016a, 2017, Frangopol & Saydam 2014, Frangopol & Soliman 2016, Frangopol et al. 2017, Ghosn et al. 2010, 2016a, 2016b, Okasha & Frangopol 2010, Saydam & Frangopol 2011, Zhu & Frangopol 2012, among others).

In addition, the progressive and/or sudden deterioration of structural performance develops under significant uncertainties related to material and geometrical properties, damage mechanisms, mechanical and environmental stressors, inspection and monitoring outcomes, maintenance and repair interventions, life-cycle cost models and decision making processes. A probabilistic approach for a proper modeling

of these uncertainties and of their propagation over time is therefore essential to quantify the life-cycle structural performance, safety, reliability and risk of bridges and infrastructures (Frangopol 2011).

To this purpose, research and applications are promoted within the Structural Engineering Institute (SEI) of ASCE by the Technical Council (TC) on Life-Cycle Performance, Safety, Reliability and Risk of Structural Systems (Frangopol & Ellingwood 2010). The archival work product of the SEI/ ASCE TC for the first five years of existence is presented in a recent collection of papers representing the consensus as to the current state of the art in life-cycle performance assessment and risk-informed decision making in structural engineering (Biondini & Frangopol 2016a, Ghosn et al. 2016a, 2016b, Lounis & McAllister 2016, Sánchez-Silva et al. 2016). Recent activities of SEI/ASCE TC included a special project approved by the SEI Technical Activities Division Executive Committee for the development of a state of the art report outlining the current status and research needs in the fields of life-cycle of civil structure and infrastructure systems (Biondini & Frangopol 2016b). The tasks of the special project included a survey to investigate the level of development and implementation of criteria, methods and tools in this field. The main results of the survey were presented in Biondini & Frangopol (2018). In this paper, the survey database is further processed considering only the group of respondents active in the bridge engineering sector and the results are presented and discussed with emphasis on the role of the life-cycle bridge performance indicators and the need for their incorporation in design codes and implementation in design practice.

2 SURVEY

The survey was disseminated to about 400 individuals, including members of the SEI/ASCE Technical Council, members of the International Association for Life-Cycle Civil Engineering (IALCCE), and other selected experts from universities, industries, engineering firms and agencies active in the field of life-cycle civil engineering. The survey included about 50 questions. The objective was to obtain information about the development and the implementation of criteria, methods and tools for life-cycle design and assessment of civil structure and infrastructure systems and to gather information about successful practices, and explore avenues to overcome real and perceived obstacles to filling the gap between theory and practice. The percentage of respondents was about 20%. In particular, 68 of the respondents (85%) are working in the bridge engineering sector. In the following, a brief summary of the main findings based on the survey data associated only with this group of respondents is presented.

3 PERFORMANCE INDICATORS

Aging and deterioration are complex phenomena that mainly include corrosion, fatigue, aging, chloride penetration and carbonation processes, and other causes of environmental damage such as alkali-silica reaction, erosion, sulfate attack and frost attack, among others. The evaluation of the aging and deterioration effects on bridges and related structural facilities should account for multiple deterministic and probabilistic time-variant performance indicators aimed at providing a comprehensive description of the life-cycle structural resources and detect the possible occurrence of critical failures.

In addition to the classical concepts of structural safety, serviceability and reliability, there are other important time-variant structural performance indicators that can be effectively related to the possible occurrence of local and global failures, including structural redundancy and failure times, structural robustness, and system resilience (Biondini 2012, 2009, Biondini et al. 2014, 2015, Biondini & Frangopol 2008, 2014, 2016a, 2017, Bocchini et al. 2015, Decò et al. 2013, Dong & Frangopol 2015, 2016, Ghosn et al. 2016a, 2016b, among others).

Structural redundancy denotes the ability of the system to redistribute among its members the loading which can no longer be sustained by damaged members after the occurrence of a local failure. The load redistribution capacity is a desirable structural feature to ensure suitable system performance under accidental actions and extreme events, but the concept can be extended over time to account for the time-evolution of the redistribution mechanisms due to deterioration processes. However, structural redundancy refers to a prescribed point in time and does not provide a measure of the failure rate, which depends on the damage scenario and damage propagation mechanism. Failure times should be computed to this purpose and the time interval between subsequent failures, such as the first local failure and structural collapse, could represent an effective indicator of the damage tolerance of the system and its ability to be repaired after local failures.

The terms redundancy and robustness are often used as synonymous, but they refer to different system performance. Structural robustness is the ability of the system to suffer an amount of damage not disproportionate with respect to the causes of the damage itself. According to this definition, a measure of robustness should arise by comparing the system performance in the original state, in which the structure is fully intact, and in a perturbed state, in which a prescribed damage scenario is applied. Robustness is generally evaluated with respect to damage suddenly provoked by accidental actions and abnormal loads. However, depending on the damage propagation mechanism, aging and progressive deterioration may also involve disproportionate effects.

Finally, resilience can be related to the capability of structures, infrastructures, and communities, to withstand the effects of extreme events and recover efficiently the original performance and functionality. Resilience is often investigated with reference to damage and disruption caused by seismic events. In this context, a life-cycle approach is necessary because aging and structural deterioration can modify the seismic performance and functionality and, consequently, make the system resilience depending on the time of occurrence of the seismic event.

4 IMPLEMENTATION

The brief overview on structural performance indicators emphasizes the importance of considering a suitable set of indicators for a comprehensive evaluation of the life-cycle bridge performance. The survey results listed in Table 1 show that this is clearly perceived by bridge engineers. In fact, life-cycle performance indicators provide the essential metrics to support and properly instruct the decision making process underlying actions regularly applied in practice for bridge management by organizations such as agencies and authorities. This includes effective inspection procedures, evaluation and rating systems, maintenance and repair plans, as indicated by the survey results listed in Table 2.

Table 1. Time-variant system performance indicators to be considered for life-cycle analysis of bridges.

Indicators	Responses	Percentage
Safety	59	86.8%
Serviceability	52	76.5%
Reliability	51	75.0%
Redundancy	27	39.7%
Robustness	29	42.6%
Resilience	44	64.7%
Sustainability	36	52.9%
Other	5	7.4%

Table 2. Activities applied with regular frequency in organizations such as agencies and authorities.

Indicators	Responses	Percentage
Inspection	39	57.4%
Evaluation/Rating	39	57.4%
Maintenance/Repair	28	41.2%
Other	7	10.3%

Life-cycle analysis of bridges is developed in practice considering different structural performance indicators and by using different tools, models, and/or resources. The survey results listed in Table 3 indicates that the use of probabilistic methods in bridge engineering is predominant due to the need of handling uncertainties.

Table 3. Tools and resources for life-cycle analysis of bridges.

Indicators	Responses	Percentage
Probabilistic methods	39	57.4%
Engineering judgement	32	47.1%
Guidelines provided by codes	31	45.6%
Guidelines provided by owners	18	26.5%
Guidelines outlined by companies or agencies abroad	14	20.6%
Other	9	13.2%

However, there is also a tendency to mitigate the lack of knowledge on the uncertainty involved in the problem by using engineering judgement and relying on design codes and, when available, guidelines provided by owners or outlined by companies or agencies abroad. In fact, in most cases (74%) official guidelines to regulate the implementation of life-cycle criteria and methods are not available to practitioners. Moreover, Table 4 shows that advances in the standardization of the life-cycle design procedures for bridges should be complemented with an increasing awareness of the society, political system, industries, and owners.

Table 4. Factors to be improved for promoting life-cycle analysis of bridges in design practice.

Indicators	Responses	Percentage
Design codes and standards	51	75.0%
Design guidelines	44	64.7%
Owners awareness	34	50.0%
Social and political awareness	31	45.6%
Industry awareness	18	26.5%
Other	1	1.5%

Future directions to accomplish these goals in bridge engineering are the selection of the pertinent codes/standards/specifications/guidelines such as ASCE/SEI 7-16 (2017), AASHTO (2010), and EUROCODES (2002), that could serve, if appropriate provisions will be implemented, as a vehicle to consider life-cycle concepts in design practice.

5 CONCLUSIONS

The results of the survey indicate a significant gap between research advances and applicative implementation of life-cycle performance indicators in the design, assessment, and maintenance of bridges under uncertainty. The availability of bridge design codes, standards and specifications incorporating life-cycle concepts and addressing life-cycle methods and procedures is extremely important and represents an important target to be accomplished for the successful implementation in practice of a modern and rational life-cycle oriented probability-based approach to bridge engineering.

ACKNOWLEDGEMENTS

The support from the SEI Technical Activities Division Executive Committee is gratefully acknowledged, with special thanks to Robert Nickerson, SEI Board of Governors and SEI TAD Executive Committee Contact of the Technical Council. Special thanks are due to Andrea Titi of Politecnico di Milano for the dedicated work and contributions to the development of the survey. The information available from previous surveys conducted by ASCE are also gratefully acknowledged, particularly the ASCE survey on Utilization of Life-Cycle Cost Analysis and Performance Based Design, organized by Dan M. Frangopol, Mohamed Soliman and Samantha Sabatino, Lehigh University, and the SEI/ASCE TC TG2 TG3 survey on Implementation of Risk-Based Methods for the Design of Structure and Infrastructure Systems, organized by Michel Ghosn, City College of New York, Ming Liu, U.S. Department of the Navy, and Bruce R. Ellingwood, Colorado State University.

REFERENCES

AASHTO, 2010. *LRFD Bridge design specifications*, American Association of State Highway and Transportation Officials, Washington, DC, USA.

ASCE, 2017. *Report card for America's infrastructure*, American Society of Civil Engineers, Reston, VA, USA.

ASCE/SEI 7-16 2017. *Minimum design loads for buildings and other structures*, American Society of Civil Engineers, Reston, VA, USA.

Barone, G., Frangopol, D.M., 2014. Reliability, risk and lifetime distributions as performance indicators for life-cycle maintenance of deteriorating structures, *Reliability Engineering & System Safety*, 123, 21-37.

Biondini, F., 2009. A measure of lifetime structural robustness, *ASCE/SEI Structures Congress*, Austin, TX, USA, April 30-May 2, 2009. In: *Proceedings of the Structures Congress 2009*, L. Griffis, T. Helwig, M. Waggoner, M. Hoit (Eds.), American Society of Civil Engineers, USA.

Biondini, F., 2012. Discussion of the paper: Time-variant redundancy of ship structures, by Decò, A., Frangopol, D.M., Okasha, N.M., *Society of Naval Architects and Marine Engineers Transactions*, SNAME, **119**, 40.

Biondini, F., Camnasio, E., Palermo, A., 2014. Lifetime seismic performance of concrete bridges exposed to corrosion. *Structure and Infrastructure Engineering*, Taylor & Francis, **10**(7), 880-900.

Biondini, F., Camnasio, E., Titi, A., 2015. Seismic resilience of concrete structures under corrosion. *Earthquake Engineering and Structural Dynamics*, John Wiley & Sons, **44**(14), 2445–2466.

Biondini, F., Frangopol, D.M., 2008. Probabilistic limit analysis and lifetime prediction of concrete structures. *Structure and Infrastructure Engineering*, Taylor & Francis, **4**(5), 399-412.

Biondini, F., Frangopol, D.M., 2014. Time-variant robustness of aging structures. Chapter 6 in: *Maintenance and Safety of Aging Infrastructure*, Y. Tsompanakis, D.M. Frangopol, (Eds.), CRC Press, 163-200.

Biondini, F., Frangopol, D.M., 2016a. Life-cycle performance of deteriorating structural systems under uncertainty: Review, *Journal of Structural Engineering*, ASCE, 142(9), F4016001, 1-17.

Biondini, F., Frangopol, D.M., 2016b. Life-cycle performance of civil structure and infrastructure systems, *Structure Magazine*, Joint Publication of NCSEA/CASE/SEI, C3 Ink, October, 40-41, Reston, VA, USA.

Biondini, F., Frangopol, D.M., 2017. Time-variant redundancy and failure times of deteriorating concrete structures considering multiple limit states, *Structure and Infrastructure Engineering*, 13(1), 94-106.

Biondini, F., Frangopol, D.M., 2018. Life-cycle performance of civil structure and infrastructure systems: Survey, *Journal of Structural Engineering*, ASCE, 144(1), 06017008, 1-17.

Biondini, F., Frangopol, D.M., Malerba, P.G., 2008. Uncertainty effects on lifetime structural performance of cable-stayed bridges, *Probabilistic Engineering Mechanics*, Elsevier, **23**(4), 509-522.

Bocchini, P., Frangopol, D.M., Ummenhofer, T., Zinke, T., 2014. Resilience and sustainability of the civil infrastructure: Towards a unified approach, *Journal of Infrastructure Systems*, ASCE, 20(2), 04014004, 1-16.

Decò, A., Bocchini, P., Frangopol, D.M., 2013. A probabilistic approach for the prediction of seismic resilience of bridges, *Earthquake Engineering and Structural Dynamics*, 42(10), 1469-1487.

Dong, Y., Frangopol, D.M. 2015. Risk and resilience assessment of bridges under mainshock and aftershocks incorporating uncertainties, *Engineering Structures*, 83, 198-208.

Dong, Y., Frangopol, D.M., 2016. Probabilistic time-dependent multi-hazard life-cycle and resilience assessment of bridges considering climate change, *Journal of Performance of Constructed Facilities*, ASCE, 30(5), 04016034, 1-12.

EUROCODES 2002. *Basis of design and actions on structures. BS EN 1990:2002*. British Standards Institution, London, UK.

Frangopol, D.M., 2011. Life-cycle performance, management, and optimization of structural systems under uncertainty: Accomplishments and challenges, *Structure and Infrastructure Engineering*, Taylor & Francis, 7(6), 389-413.

Frangopol, D.M., Dong, Y., Sabatino, S., 2017. Bridge life-cycle performance and cost: Analysis, prediction, optimization, and decision-making, *Structure and Infrastructure Engineering*, 13(10), 1239-1257.

Frangopol, D.M., Ellingwood, B.R., 2010. Life-cycle performance, safety, reliability and risk of structural systems, Editorial, *Structure Magazine*, Joint Publication of NCSEA, CASE, SEI, C3 Ink, March, 7, Reston, VA, USA.

Frangopol, D.M., Saydam, D., 2014. Structural performance indicators for bridges. Chapter 9 in *Bridge Engineering Handbook* - Second Edition, Vol. 1 Fundamentals, W-F. Chen and L. Duan, eds., CRC Press, 185-205.

Frangopol, D.M., Soliman, M., 2016. Life-cycle of structural systems: recent achievements and future directions, *Structure and Infrastructure Engineering*, 12(1), 1-20.

Ghosn, M., Dueñas-Osorio, L., Frangopol, D.M., McAllister, T.P., Bocchini, P., Manuel, L., Ellingwood, B.R., Arangio, S., Bontempi, F., Shah, M., Akiyama, M., Biondini, F., Hernandez, S., Tsiatas, G., 2016a. Performance indicators for structural systems and infrastructure networks, *Journal of Structural Engineering*, ASCE, 142(9), F4016003, 1-18.

Ghosn, M., Frangopol, D.M., McAllister, T.P., Shah, M., Diniz, S., Ellingwood, B.R., Manuel, L., Biondini, F., Catbas, N., Strauss, A., Zhao, X.L., 2016b. Reliability-based performance indicators for structural members, *Journal of Structural Engineering*, ASCE, 142(9), F4016002, 1-13.

Ghosn, M., Moses, F., Frangopol, D.M., 2010. Redundancy and robustness of highway bridge superstructures and substructures, *Structure and Infrastructure Engineering*, 6(1-2), 257-278.

Lounis, Z., McAllister, T.P., 2016. Risk-based decision making for sustainable and resilient infrastructure systems, *Journal of Structural Engineering*, ASCE, 142(9), F4016005, 1-14.

Okasha, N.M., Frangopol, D.M., 2010. Time-variant redundancy of structural systems, *Structure and Infrastructure Engineering*, 6(1-2), 279-301.

Sánchez-Silva, M., Frangopol, D.M., Padgett, J., Soliman, M., 2016. Maintenance and operation of infrastructure systems under uncertainty: Review, *Journal of Structural Engineering*, ASCE, 142(9), F4016004, 1-16.

Saydam, D., Frangopol, D.M., 2011. Time-dependent performance indicators of damaged bridge superstructures. *Engineering Structures*, 33(9), 2458-2471.

Zhu, B., Frangopol, D.M., 2012. Reliability, redundancy and risk as performance indicators of structural systems during their life-cycle, *Engineering Structures*, Elsevier, 41, 34-49.

Maintenance, Safety, Risk, Management and Life-Cycle Performance of Bridges – Powers, Frangopol, Al-Mahaidi & Caprani (Eds)
© 2018 Taylor & Francis Group, London, ISBN 978-1-138-73045-8

Seismic resilience of road bridges: lessons learned from the 14 November 2016 Kaikōura Earthquake

A.I. Sarkis & A. Palermo
University of Canterbury, Christchurch, New Zealand
O. Kammouh & G.P. Cimellaro
Politecnico di Torino, Turin, Italy

ABSTRACT: The 14th of November 2016 Kaikōura Earthquake sequence has highly affected the transport infrastructure in New Zealand. From the perspective of life-safety, the overall bridge performance was satisfactory; however, based on the observed undesirable sub-system performance of the damaged bridges, further investigation into possible improvements of the current design philosophy was warranted.
This paper describes the structural performance of the most severely damaged bridges during the Kaikōura Earthquake. The study is based on observations made during site inspections, on subsequent computational analyses performed and on a functionality database collected during the period following the event. The paper also introduces resilience indicators as a tool to predict the lifecycle performance and functionality of bridges. Finally, conclusions on the resilience and functionality of the bridges in the aftermath of the earthquake are raised, highlighting the main performance issues and suggesting strategies and technologies to enhance their seismic resilience during future events.

1 INTRODUCTION

The Kaikōura earthquake, with a moment of magnitude equivalent to M_w=7.8, occurred two minutes after midnight on the 14th of November 2016 (NZST). The epicenter was about 60km south-west of the town of Kaikōura, New Zealand (NZ), while the hypocenter was at a depth of approximately 15km. The event was a summation of multiple fault ruptures over a large spatial domain, and its complexity has resulted in the reassessment of many assumptions about earthquake processes.

The transportation network of the entire northeast portion of the South Island was badly affected. In this area, there are over 268 State Highway (SH) bridge structures, most of which are made of reinforced concrete, and 636 local road bridge structures (Palermo et al., 2017).

The performance of bridges during major earthquakes is of interest for reviewing the assumptions that are made during the seismic design or assessing the structure and its approaches. Therefore, the overall aim of this paper is to present general observations for the performance and resilience shown by the most severely damaged road bridges in the Kaikōura Earthquake, and to open the discussion on how to improve seismic resilience of road bridges during future events.

The four bridges covered by the present paper are located within 5km radius of one another and within 11km of the township of Waiau, which is the closest town to the earthquake epicenter. Except for the Wandle River Bridge, which is on a shallow soil site, the bridges are situated on sites underlain with deep layers of dense gravels and sand, and it is likely that they were subjected to similar intensity of ground shaking (Wood & McHaffie, 2017). Table 1 shows the main general information of the four bridges analyzed, together with a map of their location in Figure 1/

Table 1. Bridges assessed in the present report

Bridge Name	Year of design	Length	Number of spans	High-way	Distance of epicenter
		m			km
Lottery River	1984	123	6	Inland Route	11
Lower Mason River	1984	164	8	Inland Route	7
Mason River	1979	197	12	River Road	5
Wandle River	1987	51	3	Inland Route	13

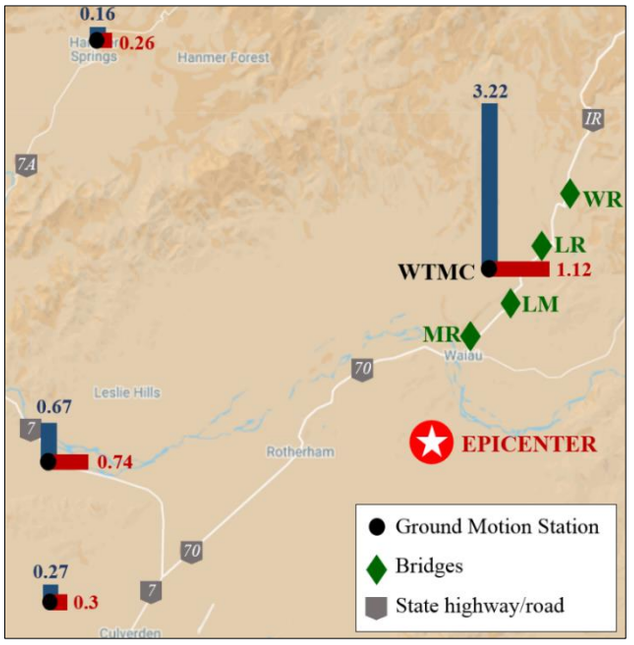


Figure 1. Map of bridges analyzed in the Hurunui District with the maximum measured PGA

2 EARTHQUAKE GROUND MOTIONS

During the Kaikōura earthquake, there was a large spatial variation in the shaking intensity, even within the moderate distances within the same district. When judging the level of damage to bridges, on top of the earthquake intensity, the variation in the design philosophy and the seismic detailing need to be taken into account as they can dictate either desirable or undesirable performance.

Figure 2 shows the geometric mean (of the two horizontal components) of the 5% damped elastic horizontal pseudo-spectral accelerations measured in Te Mara Farm Waiau station (WTMC), located close to Waiau (see Figure 1). Overlaid are the NZ elastic design spectra used during three design eras. The present day elastic design spectra was taken from NZS1170.5:2004, it was obtained for a Bridge Manual Importance Level 2 (1/1000-year annual probability of exceedance, ULS) structure, soil class C, and having a Hazard factor Z = 0.45, with no near fault effects. The two oldest design spectra, based on working stress design, were taken from Kaiser et al. (2017), and modified for compatibility with limit state design by Palermo et al (2017).

The bridges studied were designed in the period ranging from 1980 to 1987, hence, using the design spectra from the 1965-1987 era. The corresponding design spectra was greatly exceeded, as it can be seen in Figure 2. Most bridges had elastic periods of vibration within the range of 0.2 s to 1.0s, which is the period of vibration where the ground shaking at WTMC exceeded even the modern design spectra (Figure 2). The bridges had a transverse period of vibration in the range of 0.2s to 0.6s and the pseudo-spectral acceleration experienced by these bridges greatly exceeded 1.5g.

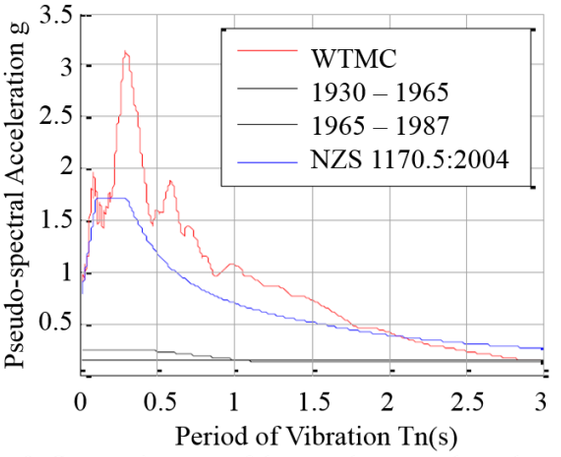


Figure 2. Geometric mean of the pseudo-spectral acceleration measured at WTMC strong motion station (Palermo et al., 2017)

3 STRUCTURAL PERFORMANCE AND DAMAGE

3.1 *Structural configuration of the bridges*

The Lottery River, Lower Mason River, Mason River, and Wandle River bridges (Figure 3) are structurally similar to one another. They are all multi-span precast concrete bridges supported on single column piers with hammer head pier caps. Further structural details are summarized in Table 2.

Table 2. Main structural details and main damage summary for the four bridges under study (Wood & McHaffie, 2017)

Bridge Name	Superstructure	Pier type	Pier founda-tion	Main damage
Lottery River	Continuous RC deck, joint at middle pier, twin 20m prestressed I beams	Single column	Single cylinder	Severe hinging in columns & buckling of column rebar
Lower Mason River	Continuous RC deck, joint at middle pier, twin 20m prestressed I beams	Single column	Single cylinder	Severe hinging in columns & fracture/buckling of column rebar
Mason River	Five 16m pretensioned double core deck units	Single column	Steel H pile group	Hinging in columns, superstructure joint damage
Wandle River	Five 16m pretensioned double core deck units	Single column	Single cylinder	Severe hinging in columns - Bridge demolished

In the way they resist lateral loading, the Lottery River (Figure 3a) and Lower Mason (Figure 3b) bridges are identical. The transverse interaction has been isolated by the omission of transverse shear keys at the central pier (Palermo et al., 2017). In addition, they use a rudimentary form of seismic isolation under transverse loading such that they can displace

an appreciable amount on the supporting elastomeric bearings before contacting the shear keys. As a result, the bridges make use of the low lateral stiffness of the bearings to elongate the period of the structure.



Figure 3. Bridges under study: (a) Lottery River Bridge; (b) Lower Mason River Bridge; (c) Mason River Bridge; (d) Wandle River Bridge (Palermo et al., 2017).

The longitudinal interaction between each half of the bridge has been isolated by a movement joint with knock off detail. The deck beams are tied together longitudinally except over the central pier. The beams rest on wide seats, thus, all piers resist longitudinal lateral loading, except the central pier, which is effectively much more flexible. Until the beams contact the shear keys, the overall transverse response can be thought of as rigid body translation of each half of the superstructure.

Similarly, the Mason River Bridge (Figure 3c) is split in two with a central movement joint. There are transverse shear keys at the abutments and internal longitudinal shear keys and linkage bars over all of the piers except the central pier. At the central pier, provision is made for longitudinal movement with loose linkage bars but steel plate lateral support stubs cast into the piers restrain the transverse movement. Therefore, the overall transverse response can be thought of as the deck having a curved displaced shape where the largest transverse displacement occurs at the central pier (Palermo et al., 2017).

The Wandle River Bridge (Figure 3d) is curved in plan and has a slope in the longitudinal direction. Linkages, shear keys and elastomeric bearings restrain the transverse and longitudinal movement over the piers, but only linkage bars resist both the transverse and longitudinal movement at the abutments. Longitudinal movement towards the backfill at the abutments is resisted by the abutment back-wall which is cast against the beams.

3.2 *Bridge performance and observed damage*

At the Lower Mason Bridge, all piers, except for the central, formed fully developed plastic hinges (PH) at the base. As mentioned, the central pier is located below a movement joint in the deck and has shear keys restraining the superstructure. Extensive cover spalling and a significant number of buckled and fractured longitudinal bars were seen. Pier damage at the Lottery River Bridge was similar but without an evidence of bar fracture. Figure 4 illustrates the damage patterns found on the column rebar of both bridges.

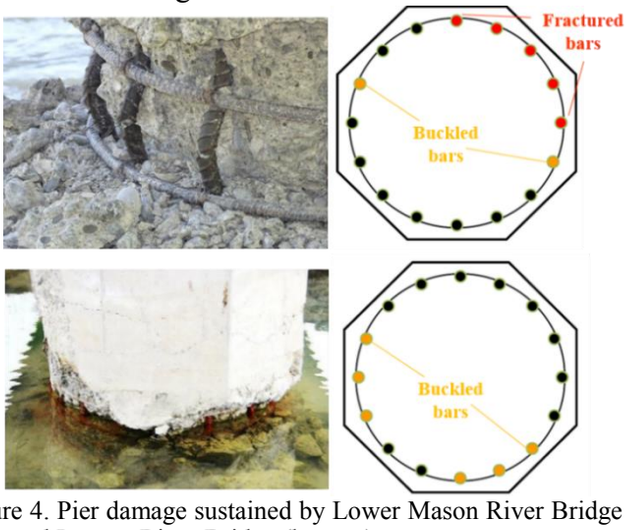


Figure 4. Pier damage sustained by Lower Mason River Bridge (top) and Lottery River Bridge (bottom).

Together with the PH zones, observed damage common to both bridges, Lower Mason and Lottery, included: damage to the knock-off block at the central

pier movement joint, failure of the abutment knock-off blocks; residual displacement of most of the elastomeric bearing pads at the piers and abutments; and residual displacements at the central pier and abutment movement joints. Damage to the abutments is illustrated in Figure 5.

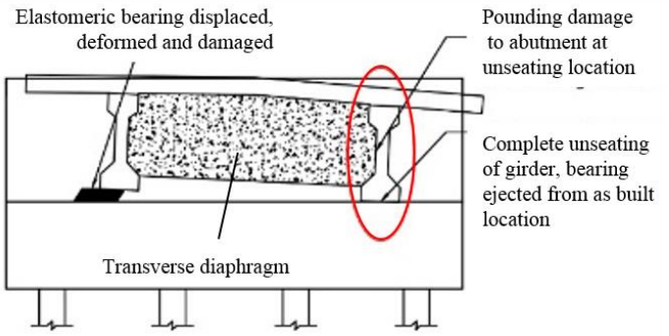


Figure 5. Abutment damage schematics for the Lower Mason River Bridge (modified from: Palermo et al, 2017)

Similar damage observations were made for the Mason River Bridge, where the deck joints had opened or closed, and pier PH with bar buckling and concrete spalling were observed with increasing degree of damage towards the central pier. The pier damage pattern was interesting at this bridge as concrete spalling and rebar exposure occurred mainly at the face of the piers facing south, and tended to be more in the longitudinal loading direction.

The damage observed to the Wandle River Bridge was extensive, and included: separation between the hollow core deck units at the south end of the bridge; translation of deck units in the downstream direction; hinging and rotating of piers towards the upstream side (up to 7° rotation); opening of the deck joints at the abutments, along with significant approach damage (Figure 6).

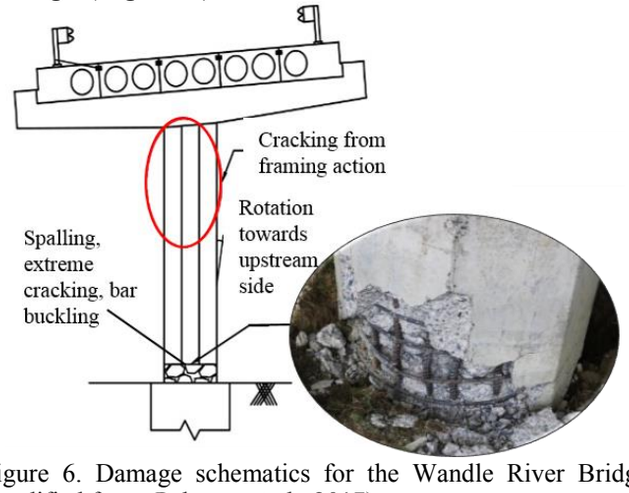


Figure 6. Damage schematics for the Wandle River Bridge (modified from: Palermo et al., 2017)

The displacement capacities for the bridges were estimated by Wood & McHaffie (2017) using a tributary mass type Displacement Based Design (DBD) analysis of a single pier, at the Damage Control Limit State (DCLS). They are compared in Table 3 with the displacement demand for transverse direction loading estimated from spectra computed from the WMTC records.

Table 3. Displacement capacity and WMTC demand

Bridge Name	DCLS Capacity	Demand from WMTC Records	Ratio Capacity/ Demand	Secant Period at WMTC Demand
	mm	mm		s
Lottery River	130	300	0.43	2.1
Lower Mason River	160	290	0.55	2.2
Mason River	180	130	1.38	1.1
Wandle River	180	350	0.51	1.8

Based on the assumption that the WMTC records are a reasonable representation of the bridge site ground motions, the displacement demands on the bridges were considerably greater than the DCLS capacity displacements, explaining the severe damage observed in the PH zones.

It can be concluded that the piers performed well, as they developed PH at the pier bases and went through the expected failure mechanism. However, significant instability was visible in the Wandle Bridge, where most likely all orthogonal motions were interacting with the bridge structure, causing large displacements and separation gaps between some of the deck beam units.

4 RECOVERY PROCESS

After the earthquake, the priority was to restore access to Kaikōura Township and surroundings, which were cut off by earthquake damage, and establish a safe and reliable alternative route. To achieve this, the Inland Route, via Waiau, was identified as the best option since the main route, through SH1, was completely blocked due to landslides.

It took 38 days after the earthquake to reopen the Inland Route. This was mainly due to earthquake induced damage on the road such as significant rock fall and slips that needed to be cleared, in addition to the associated construction activity which also contributed to the hazard. The bridges were able to be reopened, to some level of service, within a few days. However, it took up to three months to complete their repairs. It is important to highlight that repairs to the bridges so far are considered temporary in some extent and permanent restoration of the bridges is to be planned

In general terms, the bridge structures withstood the earthquake sequence well, demonstrating considerably robustness. However, many bridge approaches were damaged due to settlement and horizontal movement, thereby making some bridges

impassable. Approach reconstruction through the placement of fill and resealing quickly made the majority of these road bridges usable again.

Figure 7 illustrates the recovery rate of the Inland Route and the bridges under study during the first one hundred days following the earthquake using the maximum speed allowance as a functionality indicator for normal, Class 1, vehicles. The earthquake occurred at 12:02 am on the 14th of November, causing the Inland Route to be immediately closed by the Civil Defense Emergency Management. The route remained closed until it was given access for the NZ Defense Force convoys to get through with emergency supplies to Kaikōura, on November 25th, 12 days after the earthquake (point A in Figure 7).

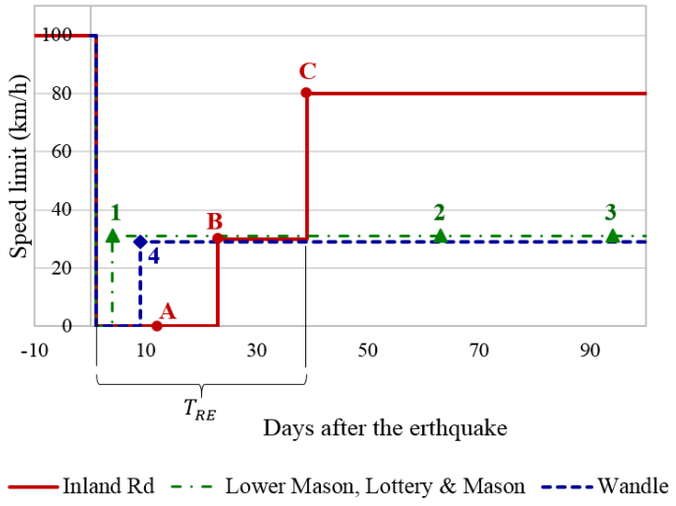


Figure 7. Functionality based on the maximum speed limit for the Inland Route and the four bridges under study.

The route remained fragile and hazardous, closed to the general public until the 6th of December, day 23 after the earthquake (point B in Figure 7), when controlled emergency and resident access was allowed with a speed limitation of 30km/h, 70% less than the pre-earthquake speed limit of 100km/h. Works undertaken during these days to make the severely damaged road safe enough included clearing the road of more than fifty slips, stabilizing slopes, and assessing the damage to the bridges.

It was only until the 21st (point C in Figure 7) of December when the public were granted unrestricted access to the Inland Road, bringing the first unrestricted road connection back to Kaikōura, for a total recovery time T_{RE} of 38 days after the earthquake.

The Lower Mason River Bridge was opened to traffic on November 17th, day 4 after the earthquake, (point 1 on the graph) with a speed restriction of 30km/h and a sign "one heavy vehicle at a time". Overweight vehicles were to use the adjacent ford that was installed on the day after the earthquake. Prior to opening the bridge, the following works had been completed: detailed inspection of the bridge, removal and appropriate filling of the knock off device at the central expansion joint, and approach repairs and re-levelling. To reinstate the original seismic capacity, a pile jacketing was issued for all pier columns, which was finished around mid-January (point 2 in Figure 7). After the pile jacketing was completed, the one-heavy-vehicle-at-a-time restriction was removed but the 30km/h restriction remained due to the uneven road surface.

The recovery process for the Lottery Bridge was very similar to the Lower Mason, since they share similar structure type and damage. Pier columns were unable to be inspected on the first days after the earthquake due to the bed and water level, yet, damage was anticipated to be less than at Lower Mason due to the shorter bridge columns. Excavation of pier piles occurred on November 25th confirming that damage was of a lesser extent, and pier jacketing was issued and completed around mid-February (point 3 in Figure 7).

Likewise, the Mason River Bridge shared the same timeline, however no security works have been carried out on this bridge as the earthquake damage was considered not to affect the serviceability of the structure. Investigation is currently underway to expose bridge piers and replace buckled bars.

For the Wandle River Bridge, decision was made on November 15th to install a Bailey bridge upstream with a 33m span. Installation was completed by November 21st and opened to traffic on the 22nd, nine days after the earthquake (point 4 in Figure 7). The Bailey bridge was able to be erected so quickly, within eight days, because New Zealand Transport Agency (NZTA) maintains an emergency stock of Bailey bridges with a contractor also in place to respond in the event of emergencies. The Bailey bridge provided largely unrestricted access across the Wandle River, however, a 30km/h speed restriction was installed due to the alignment and to provide impact protection to the bridge. The Wandle Bridge was demolished in May 2017 and a new bridge design is programmed with a low priority for 2018.

Permanent recovery works on the bridges have been given a low priority. The initial response works intended to restore an acceptable level of service for the Inland Route that would enable access into and out of Kaikōura following the November earthquake. Once this was achieved, the priority of works was switched to recovering SH1. There is also reluctance to undertake further significant work on the Inland Route, as this route acts as a bypass to SH1 to access Kaikōura from the south.

It is important to note that while the route may have been at open, pre-earthquake speed limits of 100km/h, heavy vehicles would still have to comply with lower speed requirements. Additionally, all bridges are single lane, therefore, it is unlikely that even normal vehicles were travelling across the bridges at maximum speed.

5 HOW TO PREDICT STRUCTURAL RESILIENCE?

The NZ South Island transportation network had a resilient response, as it counted with alternative routes connecting locations, allowing to restore access to isolated communities within a relatively reasonable time. On the other hand, access to Kaikōura was closed during the first 23 days for the general public, what makes us wonder, resilience for whom?

Furthermore, in terms of bridge performance, the bridge structures withstood the earthquake sequence well. Bridges demonstrated considerably robustness and hence resilience as, even if damaged, they allowed the transit of vehicles and therefore to reinstate functionality in the route. But, as they are still awaiting for permanent repairs to be undertaken, what is the current damage resistance capacity or probability of failure? Can we expect them to show resilience for future events? What leads us to the question, how can we assess and predict structural resilience?

5.1 *Resilience assessment*

In studies dealing with seismic hazard, resilience can be considered as a performance indicator that quantifies the residual functionality along with the effort in responding to the seismic event (Deco et al, 2013). In this conceptual approach, performance can range between 0 and 100%. In case of an earthquake, usually serviceability of a structure drops to a lower level, being 0% a complete loss of service, followed by a recovery process after the disaster, and then finishes when there is a restoration of the serviceability to its "normal" performance level. This characterization of system performance leads to a broader conceptualization of resilience, where a resilient structure can be understood as one with the ability to present reduced chances of failure, reduced consequences from failures and reduced recovery time (Bruneau et al, 2003).

Within the *Technical Guidance for Engineering Assessments* (2017) in NZ, structural resilience is defined as the ability of the structure to continue to perform in earthquake shaking beyond an Ultimate Limit State (ULS) shaking demand level. Therefore, the bigger the space between the point of onset of nonlinear behavior and the point of brittle behavior of the structure, which would lead to collapse, the more resilient is a structure. Structural resilience can be thought as an inherent characteristic of structures designed to the new codes or even older well designed structures, as their performance will follow the desirable hierarchy of element failures, which was the case of the bridges under study. There can be the case where a structural system has a low resilience and is susceptible to sudden reduction in their performance and functionality as the earthquake shaking increases beyond a particular value.

Measuring resilience has been an exploding field of inquiry in the past decade. Disaster resilience assessment approaches fall into three primary categories: indicators, scorecards, and tools (Cutter, 2015). In the following section the assessment of resilience through the use of indicators will be further discussed.

5.2 *Resilience indicators for road bridges*

Indicators are quantifiable variables that represent selected characteristics of resilience (Cutter, 2015). Generally, individual indicators can be combined to create a resilience index (Kammouh et al. 2017b). The index illustrates multi-dimensional nature of resilience by aggregating multiple indicators, but also condenses its complexity into a single numeric value.

Recent bridge design codes consider performance uncertainty by including specific factors in the computation of structural resistance and load. However, this does not comply the uncertainties in loading and deterioration processes which make the prediction of lifecycle performance of bridges so complex. Prediction of time-dependent bridge performance under uncertainty may require the use of several indicators, thus, it is important to select adequate indicators to evaluate and predict the structural performance and functionality of bridges.

Significant research has been done on quantifying structural performance with deterministic and probabilistic indicators (Frangopol & Saydam, 2014). For example, system reliability measures, such as the probability of failure or the reliability index, are adequate for quantifying the safety of a structure with respect to ultimate limit states, but the system redundancy index is required to evaluate the availability of warning before a system's failure (Frangopol & Saydam, 2014). Additionally, performance indicators related to damage tolerance of structures, such as vulnerability and robustness are essential to consider for bridges under deterioration together with the indicators related to system safety.

Subsequently, it is required to consider multiple indicators when evaluating the seismic resilience of a bridge. Indicators must be weighted according to their contribution towards the resilience of the system, so that resilience is quantified as a normalized value of the area inside the enclosed shape made by linking the adjacent indicators weights or scores. Kammouh et al. (2017a) introduced and exemplified three weighting methods for resilience indicators based either on the dependence tree analysis or on the spider plot analysis (Kammouh et al. 2017a, Kammouh et al., in press).

Table 4 shows some examples of resilience indicators for bridges. They have been divided into two categories, 'soft' and 'hard' indicators, according to the difficulty involved in their measurement. Soft

indicators, in general, can be determined qualitatively through surveys, data compilation or specific sample procedures, whereas hard indicators would require a higher effort, whichever computational, numerical or probabilistic. They can be calculated using mathematical formulas and/or matrices in order to approximate and understand the characteristic of the system under study.

Table 4. Examples of 'soft' and 'hard' type of resilience indicators for bridges

Soft Indicators	Hard Indicators
Speed Limit	Safety factor
Travel time	Reliability index
Physical access	Probability of failure
Weight allowance	Redundancy index
Operative utility systems	Vulnerability
Condition Ratings	Robustness

Indicators can be measured at a member or a component level, an overall structure or a system level, and a group of structures or a network level. For example, when evaluating stability problems, the performance is normally quantified at a member level, and normally, this is enough to ensure an adequate level of safety. However, when evaluating resilience, a member level approach might not provide the necessary information about the overall performance of the bridge or the bridge network.

6 LESSONS LEARNED

Since all bridges were subjected to similar ground motions, it is informative to compare the damage to them and the design features that influenced their structural performance and resilience. The following sections summarize the main issues raised and lessons learned from study of these bridges.

6.1 *Bridge intervention and route recovery*

An acceptable level of service was able to be restored within a short period of time. This can be attributed to a combination of a number of factors:

- Both NZTA and the Hurunui District Council, entities in charge of the bridges, had a Bridge Consultant (Opus International Consultants) in place to respond in the event of an emergency.
- The Bridge Consultant was familiar with the affected bridge stock and had information readily available through an established and maintained Bridge Information System.
- Network contractors (Downer and Sicon) were in place to respond in the event of an emergency.
- Emergency procedures in place to coordinate a response, inspections and works.
- Emergency bridge stock and contractor in place to erect Wandle Bailey Bridge.
- Clients, Consultant and Contractors experienced from Canterbury Earthquake Sequence on 2010-2011.
- Very knowledgeable client able to make informed decisions.

6.2 *Bridge response and behavior*

In modern design, there is a tendency to design more efficient structures, with longer spans and reduced foundations with a reliance on acceptable damage and dissipation through the use of PH. While this was largely observed on the bridges on the Inland Route, a few things that eventuated were undesirable such as the buckling and the fracture of the reinforcement and the large residual deformations for Wandle Bridge.

In this event, older bridges that had not been designed to modern standards performed better than expected. The likely reason for this is that these structures were designed with a greater level of redundancy, thanks to their shorter spans, more piers and more piles for the foundations.

For the Inland Route around the Waiau area, the earthquake demands from the Kaikōura Earthquake were severe, in excess of a 1000 year return period. As such, it is considered a significant earthquake with a low probability of occurring in the bridges' typical design life. On more critical routes, such as SH1, the design philosophy tends to shift towards designing to meet higher importance levels. For bridges on critical routes, the design would typically be for a return period of 2500 years at the DCLS and a return period in the order of 10 000 years at the Collapse Limit State.

6.3 *Reparability and influence of the structural form*

The structural scheme can play a part in the repair strategy, costs and hence resilience. In the case of monolithic bridges, repair of PH should be considered at the design stage. On the Lottery and Lower Mason bridges, the 1.5m diameter cylinder foundations located directly beneath the 1.0m diameter columns of the piers simplified the repair (Figure 8a). New reinforcement could be doweled into the existing pile and the pier re-cast, restoring the moment capacity of the column (Figure 8b). In contrast, for the Mason Bridge, repair is more difficult due to the shape and size of the pier cap (Figure 8c), as the geometry will make it very difficult to dowel in additional bars in and re-cast concrete. The result will be a significant repair cost and potential downtime for the structure.

Designing and detailing monolithic connections taking into account the repair strategy for different design level events would optimize the recovery after an earthquake event. Furthermore, if the bridges were designed for damage avoidance, incorporating energy dissipation and reparability, performance and recovery of the bridges could be improved. Hence, full restoration on the functionality of the route could be accomplished immediately after the earthquake.



Figure 8. Plastic hinge repair: (a) PH in Lower Mason Bridge; (b) repair of PH by epoxy grout bars; (c) geometry at Mason River Bridge PH zones.

7 CONCLUSIONS

Resilience indicators for bridges are important tools for predicting and evaluating the structural performance and functionality of bridges given a seismic event. They can help to characterize the basic elements of the structure under analysis and thus help to raise the awareness on the benefits of mitigation technologies and strategies, and making the business case for understanding the investments and results of enhancing resilience at different scales. This paper provides a general conceptualization of resilience indicators as a starting point for future research to be undertaken on the prediction of structural performance and resilience of bridges.

A brief overview of the structural performance and resilience shown by the most severely damaged bridges during the Kaikōura Earthquake has been given. At the time of initial inspection, the bridges were rapidly assessed and were generally only open to emergency traffic. Since then, temporary repair works allowed public access through these routes; however, long term repair or replacement strategies are still being considered by the managing authorities. From the perspective of life safety we can consider the overall performance as satisfactory.

The bridges, even if damaged, behaved as expected from design and allowed to reinstate transit of vehicles and restore the functionality in the route. This made possible to restore access to isolated communities within a relatively reasonable time of 23 days, thanks to the availability of an alternative route which has worked as a bypass. However, was this a satisfactory performance in a seismically active developed country or do we need to improve our current design philosophy so that we can warrant enhanced resilience during future events?

8 REFERENCES

Bocchini, G; Rais, A; Brando, M; Giovinazzi, S; Palermo, A & Crowley, H. 2017. Earthquake-Induced Physical Damage and Functional Impact on Bridges: Learning from the Mw 6.2 Christchurch Earthquake (New Zealand). *Journal of Earthquake Engineering*, (Under review).

Bradley, B; Razafindrakoto, H & Polak, V. 2017. Ground-motion observations from the 14 November 2016 Mw7.8 Kaikōura, New Zealand Earthquake and insights from broadband simulations. *Seismological Research Letters*, 88(3): 740-756.

Bruneau, M; Chang, S; Eguchi, R; Lee, G; O'Rourke, T; Reinhorn, A; Shinozuka, M; Tierney, K; Wallace, W & Winterfeldt, D. 2003. A Framework to Quantitatively Assess and Enhance the Seismic Resilience of Communities. *Earthquake Spectra*, 19(4): 733-752.

Cutter, S. 2015. The landscape of disaster resilience indicators in the USA. *Natural Hazards*, 80(2):741-758.

Deco, A; Bocchini, P & Frangopol, D. 2013. A probabilistic approach for the prediction of seismic resilience of bridges. *Earthquake Engineering & Structural Dynamics*, 42(10): 1469-1487.

Frangopol, D & Saydam, D. 2014. Structural Performance Indicators for Bridges. *Bridge Engineering Handbook: Fundamentals*, 185-205

Kaiser, A; Balfour, N; Fry, B; Litchfield, N; Gerstenberger, M; D'Anastasio, E; Horspool N; McVerry, G; Ristau, J; Bannister, S; Christophersen, A; Clark, K; Power, W; Rhoades, D; Masser, C; Hamling, I; Wallace, L; Mountjoy, J; Kaneko, Y; Benites, R; Van Houtte, C; Dellow, S; Wotherspoon, L; Elwood, K & Gledhill, K. 2017. The 2016 Kaikōura, New Zealand, earthquake: preliminary seismological report. *Seismological Research Letters*, 88(3): 727-739.

Kammouh, O; Dervishaj, G & Cimellaro, G. 2017a. A New Resilience Rating System For Countries and States. *Procedia Engineering,* 198**:** 985-998.

Kammouh, O; Dervishaj, G & Cimellaro, P. 2017. Quantitative Framework to Assess Resilience and Risk at the Country Level. *Journal of Risk and Uncertainty in Engineering Systems,* (in press).

Kammouh, O; Noori, A; Renschler, C & Cimellaro, G. P. (2017b) Resilience quantification of communities based on PEOPLES framework. *16th World Conference on Earthquake.* Santiago.

Palermo, A; Liu, Rais, A; McHaffie, B; Andisheh, K; Pampanin, S; Gentile, R; Nuzzo, I; Granerio, M; Loporcaro, G; McGann, C & Wotherspoon, L. 2017. Performance of Road Bridges during the 14 November 2016 Kaikōura Earthquake. *Bulletin of the New Zealand Society for Earthquake Engineering*, 50(2): 253-270.

The Seismic Assessment of Existing Buildings. Technical Guidelines for Engineering Assessments (1st ed.). 2017. New Zealand: New Zealand Society for Earthquake Engineering.

Wood, J & McHaffie, B. 2017. *Performance of State Highway Bridges in the 2016 Kaikōura Earthquake: Five Bridges Located Near the Epicentre at Waiau. Report prepared for: NZ Transport Agency.* Christchurch: John Wood Consulting.

Maintenance, Safety, Risk, Management and Life-Cycle Performance of Bridges – Powers, Frangopol, Al-Mahaidi & Caprani (Eds)
© 2018 Taylor & Francis Group, London, ISBN 978-1-138-73045-8

Renewal-theory-based Life-cycle Risk Assessment of Bridge Deck Unseating under Hurricanes

David Y. Yang & Dan M. Frangopol
Department of Civil and Environmental Engineering, ATLSS Engineering Research Center, Lehigh University, 117 ATLSS Drive, Bethlehem, PA 18015-4729, USA

ABSTRACT: Hurricanes pose a major threat to coastal bridges. For bridge superstructures, hurricane-induced surge and wave loads can lead to bridge deck unseating, which has been identified as the most common failure mode for coastal bridges under hurricanes. This paper proposes a novel method for life-cycle risk assessment of coastal bridges under this hazard. The proposed method considers both capacity deterioration of unseating-resistant systems (e.g. connection dowels) and the reoccurrence of hurricanes in the service life of bridges. Renewal theory is leveraged to consider repairs after deck unseating failure. A prestressed concrete box-girder span is used to illustrate the proposed method. Based on the assessment, it is found that non-deteriorating unseating-resistant systems can significantly reduce the life-cycle risk of bridge unseating.

1 INTRODUCTION

Coastal bridges are vulnerable to hurricanes and hurricane-induced floods. Recent hurricane events (e.g. hurricanes Harvey and Irma in 2017) revealed that the failure of bridges under these events hinders prompt hazard response and post-hazard recovery, posing devastating losses and long-lasting consequences to the afflicted communities. For bridge superstructures, hurricane-induced surge and wave loads can lead to bridge deck unseating. Based on a recent review on causes and mechanisms of bridge failure, deck unseating under hurricanes and hurricane-induced floods is one of the most common causes of bridge failure during the period 1989 to 2000 in the United States (Deng et al. 2016).

Apart from hurricane hazards, coastal bridges are also located in a very corrosive environment that can lead to severe deterioration of bridge performance. According to the latest report card by American Society of Civil Engineers (ASCE 2017), 9.1% of the nation's bridges are structurally deficient. Many of these bridges are situated along the coastline. Therefore, the deterioration of bridge capacity against deck unseating should be considered in the risk assessment process.

Due to the high consequences of bridge failure under hurricanes, extensive studies have been dedicated to this topic, including modeling of hurricane-induced loads on bridges, bridge response under these loads, likelihood of deck unseating, and risk assessment and mitigation (e.g. Ataei & Padgett 2013a; Mondoro et al. 2016). However, most of the existing studies deal mainly with the likelihood and risk of deck unseating under one possible hurricane event and its surge and wave loads. The analyses usually end with the fragility curves/surfaces of bridges under hurricanes. Structural deterioration and reoccurrence of hurricane events in the bridge's service life have not been properly considered. Recently, Mondoro et al. (2016) conducted a life-cycle risk analysis that considered structural deterioration and modeled hurricane occurrence as a binomial process. However, this study did not account for the repairs of bridge deck after unseating failure. In addition, the deterioration of unseating-resistant systems themselves was not considered.

In this paper, a novel method for life-cycle risk assessment of bridge deck unseating is proposed based on renewal theory. The reoccurrence of hurricanes is modeled as a Poisson process. To include post-hazard repairs into the life-cycle analysis, the proposed method uses renewal-reward processes to model the occurrence of unseating failures and the associated repairs. Pitting corrosion in dowel bars (i.e. a typical unseating-resistant system in concrete bridges) is also taken into account. A prestressed concrete box-girder span is used to illustrate the application of the proposed method. It is acknowledged that various corrosion-resistant materials (e.g. stainless steel and fiber reinforced polymer) have been applied in aggressive environments to enhance the long-term performance of bridges (Soliman & Frangopol 2015; Yang & Teng 2018). Therefore, the cost-effectiveness of using these new materials in unseating-resistant systems is also investigated based on the proposed method.

2 HURRICANE-INDUCED LOADS ON BRIDGE SUPERSTRUCTURE

2.1 *Hazard analysis*

Hurricane hazards can be quantified by the associated wind speeds. In probabilistic analysis and risk assessment of hurricanes, the wind speed can be considered in two approaches. The first approach is based on the statistics of maximum annual gust wind speed. The characteristics of hurricanes are then considered by modifying the obtained statistical model (Peterka & Shahid 1998). The end-product of this approach is a probability distribution of annual wind speed that can be used in fragility and risk analyses (Stewart 2003; Li and Ellingwood 2006; Mondoro et al. 2016; Dong and Frangopol 2017). The second approach is to directly analyze the records of tropical cyclones including hurricanes and hurricane-akin phenomena such as tropical storms and tropical depressions for a specific region. The results of this analysis are the site-specific return period and the statistical distribution of wind speed associated with a tropical cyclone event (Li et al. 2016).

In this paper, the second approach is used in the proposed method. Compared to the first approach, it is believed that the statistics of the wind speed in the second approach should better match the applicable scope of the model of hurricane-induced loads presented in the following subsection. It should also be noted that, in order to obtain a full range of wind speeds, the second approach uses data from all tropical cyclones, including less critical events to deck unseating such as tropical storms and tropical depressions. Therefore, the proposed method uses probabilistic transformation to obtain the wind distribution in a more relevant event and its associated return period. Specifically, if a minimal wind speed v_{min} is specified, the conditional probability distribution density function (PDF) of wind speed can be expressed as

$$f'_V(v) = \frac{f_V(v)}{1 - F_V(v_{min})} \quad \text{for } v \geq v_{min} \tag{1}$$

where $f'_V(\cdot)$ is the conditional PDF of wind speed; $f_V(\cdot)$ is the original PDF of the wind speed obtained using the second approach; $F_V(\cdot)$ is the original cumulative distribution function (CDF) of the wind speed. The return period of the wind speed following the PDF in Equation 1 can be then calculated by the following equation:

$$T_{hurr} = \frac{T_{cycl}}{1 - F_V(v_{min})} \tag{2}$$

where T_{cycl} is the return period of tropical cyclones; T_{hurr} is the return period of hurricanes with a minimal wind speed v_{min}. For instance, the wind speed distribution and the return period of a hurricane in category 3 and above can be obtained using Equations 1 and 2, respectively, with $v_{min} = 50$ m/s.

Conversely, if the return period of a hurricane is specified, the associated minimal wind speed can be determined by the following equation:

$$v_{min} = F_V^{-1}\left(1 - \frac{T_{cycl}}{T_{hurr}}\right) \tag{3}$$

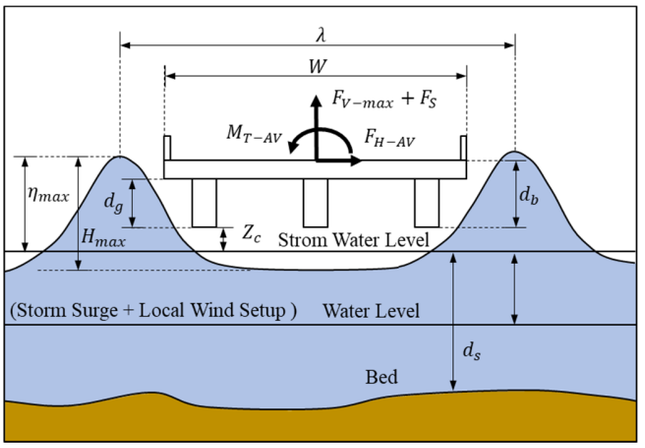
where $F_V^{-1}(\cdot)$ is the inverse function of $F_V(\cdot)$. The wind distribution can then be obtained using Equation 1.

2.2 *Hurricane-induced surge and wave loads*

Hurricanes, along with their associated heavy precipitation, can induce high waves and surge storms that pose threats to bridge superstructures. Hurricane-induced surge and wave loads can be attributed to various factors including buoyancy, drag and inertia forces, forces associated with added mass, and vertical slamming forces, among others. Quantification of these loads on bridges requires considerable numerical modeling, systematic experiments and on-site observations. Various studies have been conducted based on the hindsight of disastrous hurricanes, hydrodynamic experiments, and numerical simulations using computational fluid dynamics (e.g. Douglass et al. 2006; Chen et al. 2009; Jin & Meng 2011; Ataei & Padgett 2015; Do et al. 2016). Results from serveral of these studies have been instilled in the first design guidelines for coastal bridges vulnerable to hurricane-induced storms, released by the American Association of State Highway and Transportation Officials (AASHTO 2008). In this paper, the model in AASHTO (2008) are used to consider the hurricane-induced surge and wave loads on bridge superstructures.

Based on AASHTO (2008), bridge superstructures under hurricane-induced surge and waves are subjected to a horizontal force representing drag and inertia forces, a vertical force representing uplifting and wave slamming, and a moment due to uneven distributed forces under the bridge deck. These loads are shown schematically in Figure 1. For bridge deck unseating, the most critical force contributing to the failure is the maximum total vertical force, i.e. the summation of the maximum uplifting force F_{V-MAX} and the vertical wave slamming force F_S (Ataei & Padgett 2013b). AASHTO (2008) provided detailed computation procedures that start with the prediction of significant wave height and wave period and end with the calculation of F_{V-MAX} and F_S. Due to space limitation, specific equations are not presented herein. Nevertheless, related parameters are summarized, as shown in Figure 1. It should be noted that the obtained vertical load involves many uncertainties. Probabilistic analyses including both aleatory and epistemic uncertainties can be found in Ataei & Padgett

(2013b) and Mondoro et al. (2016). Their studies are followed herein to consider these uncertainties given the occurrence of a hurricane.



η_{max}	=	wave crest height above storm water level
H_{max}	=	maximum wave height
λ	=	wave length
d_s	=	storm water depth at the bridge
d_b	=	girder height + deck thickness
d_g	=	girder height
Z_c	=	positive or negative distance from storm water level to the bottom of the girder
W	=	deck width

Figure 1. Hurricane-induced loads and their controlling parameters [adapted from AASHTO (2008)]

3 MODELING OF TIME-DEPENDENT CAPACITY

3.1 *Unseating-resistant systems*

The resistance to the aforementioned hurricane-induced loads decides the capacity of the bridge superstructure against unseating failure. The vertical resistance of a superstructure includes its self-weight and the resistance provided by unseating-resistant systems such as dowels, shear keys, and tie-downs, among others. Retrofitting measures, e.g. drilling holes in bridge deck, can also be used to reduce the demand side of the unseating risk. A brief description of these systems can be found in Mondoro et al. (2016). In this paper, the analysis is focused primarily on the vertical resistance provided by the dowels connecting the bridge superstructure and the abutment. A typical dowel setup in a concrete bridge is shown in Figure 2.

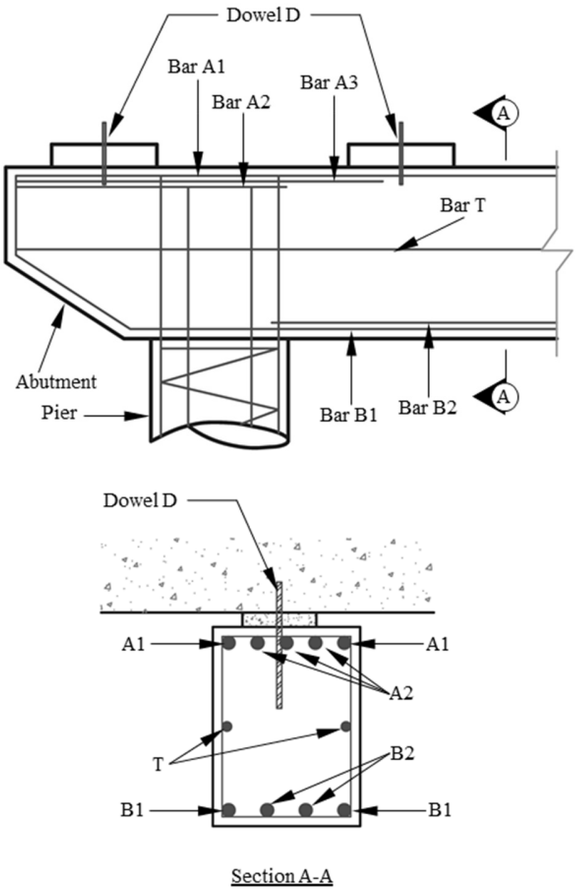


Figure 2. Typical dowel anchorage [adapted from Ataei & Padgett (2013b)]

The capacity of the dowel anchorage can be determined based on the design specification of American Concrete Institute(ACI 2014). It is assumed herein that the embedment length of the dowel is greater than the required development length. Therefore, the pullout strength is controlled by the yield strength of the dowel bar and can be calculated using the following equation (ACI 2014):

$$F_D = n_D \cdot A_{se} f_y \tag{4}$$

where F_D is the total pullout strength provided by all dowels; n_D is the number of dowels; A_{se} is the area of one dowel bar; f_y is the yield strength of the dowel bar. Therefore, the total capacity against unseating failure, including self-weight and dowel resistance, can be expressed as

$$F_c = F_{sw} + F_D \tag{5}$$

in which

$$F_{sw} = \left(d_d W + A_g n_g\right)\gamma_c \cdot L_s \tag{6}$$

where F_c is the capacity; F_{sw} is the self-weight; d_d is the deck thickness; A_g is the area of one girder; n_g is the number of girders; γ_c is the unit weight of reinforced concrete; L_s is the span length.

3.2 *Deterioration due to corrosion*

As mentioned previously, coastal bridges are located in a highly corrosive environment due to airborne chloride and seawater splashes. Chloride-induced corrosion is detrimental at cracks and interfaces where chloride ions and other reactants can easily reach the surface of steel bars. It can be seen from Equation 4 that the corrosion can lead to the reduction of bar areas and consequently the decrease of pullout strength.

Corrosion of steel bars can occur in two forms: uniform corrosion and pitting corrosion (Val & Melchers 1997). For coastal bridges above seawater, pitting corrosion is of more relevance. In order to consider the capacity deterioration due to corrosion, the remaining area of a corroded bar is estimated by the following equation (Val & Melchers 1997):

$$A_r = \begin{cases} A_{se} - A_1 - A_2 & \text{if } p(t_{corr}) \le \dfrac{D_0}{\sqrt{2}} \\ A_1 - A_2 & \text{if } \dfrac{D_0}{\sqrt{2}} < p(t_{corr}) \le D_0 \\ 0 & \text{if } p(t) > D_0 \end{cases} \tag{7}$$

in which

$$p(t_{corr}) = 0.0116 \cdot t_{corr} \cdot i_{corr} \cdot R_{pit} \tag{8}$$

$$A_1 = \frac{1}{2}\left[\theta_1 \left(\frac{D_0}{2}\right)^2 - a\left|\frac{D_0}{2} - \frac{p(t_{corr})^2}{D_0}\right|\right] \tag{9}$$

$$A_2 = \frac{1}{2}\left[\theta_2 p(t_{corr})^2 - a\frac{p(t_{corr})^2}{D_0}\right] \tag{10}$$

and

$$a = 2p(t_{corr})\sqrt{1 - \left[\frac{p(t_{corr})^2}{D_0}\right]} \tag{11}$$

$$\theta_1 = 2\arcsin\left(\frac{2a}{D_0}\right) \tag{12}$$

$$\theta_2 = 2\arcsin\left[\frac{a}{p(t_{corr})}\right] \tag{13}$$

where A_r is the remaining area; D_0 is the diameter of the uncorroded bar; t_{corr} is the time after corrosion initiation in years; $p(t_{corr})$ is the pitting depth in t_{corr}; i_{corr} is the corrosion current density in μA/cm^2; R_{pit} is the pitting factor (Val & Melchers 1997; Stewart & Al-Harthy 2008). It is assumed herein that the corrosion initiates instantly due to the existence of concrete-to-concrete interface (see Figure 2). Therefore, the time of corrosion t_{corr} is equal to the exposure time. The reduction of yield strength due to corrosion is also considered using the following equation (Du et al. 2005):

$$f_y(t) = \left[1 - \frac{0.5(A_{se} - A_r)}{A_{se}}\right] \cdot f_{y0} \tag{14}$$

where $f_y(t)$ is the yield strength at time t; f_{y0} is the yield strength of the uncorroded bar.

By considering the cross-section and yield strength reduction due to corrosion, time-dependent capacity against unseating failure can be determined using Equations 4 and 5, in which the resistance provided the dowels is time-dependent. Similar to the hurricane-induced loads, uncertainties are considered for the modeling of capacity.

Recently, corrosion-resistant materials such as stainless steel and fiber reinforced polymer have been applied in aggressive environments to reduce or even eliminate the adverse effects of corrosion. Although the use of these materials usually indicates a higher initial cost, it has been shown that the life-cycle cost, considering maintenance, is lower than the structures with conventional steel (Soliman & Frangopol 2015; Yang & Teng 2018). In this study, the application of these materials in risk mitigation is investigated. For brevity, it is directly assumed that the cross-sectional area of the dowel and its yield strength does not change with time.

4 LIFE-CYCLE RISK OF REPAIRABLE SYSTEMS

Life-cycle risk is defined herein as the expected consequences of bridge deck unseating during the bridge's service life. As can be realized from the previous sections, the life-cycle risk of deck unseating should account for the reoccurrence of hurricanes and the deterioration of unseating-resistant systems when applicable. Conventionally, life-cycle risk of structures under hazards is usually determined based on the annual risk, as represented by the following equation (Decò & Frangopol 2011):

$$\bar{R}_{f,0}(t_L) = \sum_{i=1}^{t_L} C_{f,i} P[F|H_i] P[H_i] \tag{15}$$

where $\bar{R}_{f,0}$ is the life-cycle risk; t_L is an integer representing the service life of the bridge; $C_{f,i}$ is the monetary consequences in year i; $P[F|H_i]$ is the probability of failure given a hazard occurs in year i; $P[H_i]$ is the probability of hazard occurrence in year i. This formulation implies that the hazard occurrence follows a binomial process with discrete time interval of one year. Another important implication of Equation 15 is that the structure is abandoned after the failure. Therefore, Equation 15 calculates the expected consequences up to the first failure within the time horizon t_L.

For deck unseating, such an implication is invalid because after deck unseating, a new superstructure is most likely to be reinstated. In reliability engineering, such a system is referred to as a repairable system. For a deteriorating but repairable system, its life-cycle risk cannot be determined using Equation 15 as $P[F|H_i]$ is, in this case, related to the failure history of the system. However, if it is assumed that the repair action restores the capacity to its original level, the life-cycle risk can be obtained based on renewal theory, with which the occurrence of unseating failure and its associated repair action is modeled as a renewal-reward process. One realization of this process is shown schematically in Figure 3.

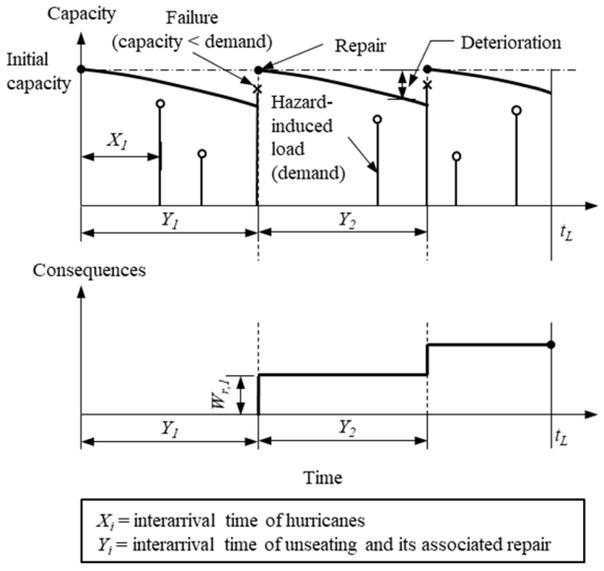


Figure 3. Life-cycle performance of repairable systems under hazards

Based on renewal theory, the expected life-cycle consequences (i.e. risk) of a deteriorating but repairable system can be expressed as (Yang & Frangopol 2017)

$$r_f(t_L) = E\left[\sum_{i=1}^{N_r(t_L)} W_r \cdot e^{-\alpha T_{r,i}}\right] = \int_0^{t_L} w_r \cdot e^{-\alpha\tau} dU(\tau) \tag{16}$$

where $r_f(t_L)$ is the life-cycle risk; $E[\cdot]$ is the expectation operator; $N_r(t_L)$ is the number of unseating failures (and the associated repairs); W_r is the monetary consequences (cost) due to the unseating failure and repair; α is the discount rate of money; $T_{r,i}$ is the time of occurrence of the ith unseating failure; w_r is the mean value of W_r; $U(\cdot)$ is the renewal function of the renewal process of unseating occurrence. The renewal function describes the expected number of event occurrence and can be expressed as

$$U(t) = E[N_r(t)] = \sum_{m=1}^{\infty} \Psi^{(m)}(t) \tag{17}$$

where $\Psi(t)$ is the time-dependent failure probability up to time t; $\Psi^{(m)}(\cdot)$ is the m-fold convolution of $\Psi(\cdot)$. In this paper, the following two-degree polynomial function is used to represent the capacity deterioration:

$$C(t) = k - bt - at^2 \tag{18}$$

where $C(t)$ is the time-dependent capacity; k is the initial capacity; a and b are parameters of the deterioration function. It also hypothesized that the magnitude of demand associated with each hurricane event follows exponential distribution with rate parameter μ. Based on these assumptions, the value of $\Psi(t)$ can be determined using the following closed-form expression:

$$\Psi(t) = 1 - \exp[-\lambda \cdot \varphi(t) \cdot \exp(-\mu k)] \tag{19}$$

in which

$$\varphi(t) = -\left.\frac{\sqrt{\pi} e^{-\frac{\mu b^2}{4a}} \operatorname{erf}\left(-\sqrt{-\mu a} \cdot x + \frac{\mu b}{2\sqrt{-\mu a}}\right)}{2\sqrt{-\mu a}}\right|_{x=0}^{x=t} \tag{20}$$

where λ is the occurrence rate of hurricanes; $\operatorname{erf}(\cdot)$ is the error function. If the system does not deteriorate (e.g. due to the use of corrosion-resistant dowels), $\Psi(t)$ can be expressed as

$$\Psi(t) = 1 - \exp[-\lambda t \cdot \exp(-\mu k)] \tag{21}$$

As mentioned previously, the capacity is a random variable due to the various uncertainties involved. Therefore, the life-cycle risk considering the capacity uncertainties can be expressed as

$$\bar{R}_f(t_L) = \int_0^{\infty} r_f(t_L|k) \cdot f_K(k) dk \tag{22}$$

where $\bar{R}_f(t_L)$ is the expected life-cycle risk considering all uncertainties; $r_f(t_L|k)$ the expected life-cycle risk given the initial capacity k, which can be determined using Equations 16-21; $f_K(\cdot)$ is the PDF of initial capacity. In general, sampling method is needed for the evaluation of Equation 22.

It should be noted that the assumptions mentioned above should be verified for a specific application. In more general cases, closed-form expressions similar to Equations 19-21 are no longer guaranteed to exist. Efficient sampling methods such as that in Yang et al. (2017) may become the only feasible option to evaluate the time-dependent failure probability $\Psi(t)$ and the integral in Equation 22.

5 ILLUSTRATIVE EXAMPLE

The proposed method is illustrated using a 15.2 m simply supported span from a prestressed concrete box-girder bridge located in a coastal region. The water depth below the bridge is 3 m. The span is subjected to hurricanes with the fetch length equal to 50 km. For hurricane events, their return period and the distribution of wind speed are obtained from Li et al. (2016). Specifically, the wind speed follows Weibull distribution with shape and scale parameters equal to 2.06 m/s and 35.9 m/s, respectively. The return period associated with this wind speed is 4.08 years. For reasons mentioned previously, the tropical cyclone statistics are converted to hurricanes with a return period equal to 20 years. The hurricane-induced loads are determined based on the AASHTO design specifications. The variables used in the analysis are summarized in Table 1 (Ataei & Padgett 2013b). The time horizon of interest is 100 years.

Table 1: Variables for capacity and demand modeling

(a) Deterministic variables

Variable	Value	Variable	Value
W	10.9 m	d_a	0.38 m
d_d	0.12 m	D_0	32 mm
n_a	2	n_D	4
A_a	0.58 m^2	i_{corr}	2 μA/cm^2

Note: W = span width; d_d = deck thickness; n_g = number of girders; A_g = cross-sectional area of one girder; d_g = height of one girder; D_0 = diameter of dowels; n_D = number of dowels; i_{corr} = corrosion current density.

(b) Parameter of random variables

Variable	Mean	COV	Distribution
f_{y0}	413 MPa	0.08	Lognormal
f_c	25 MPa	0.15	Normal
R_{pit}	7.17	0.19	Gumbel

Note: f_{y0} = initial yield strength; f_c = concrete strength; R_{pit} = pitting factor.

Based on the hurricane statistics, the demand upon each hurricane occurrence is modeled using Monte Carlo simulation. Figure 4 shows the histogram of the simulation results. It can be seen that the demand follows exponential distribution approximately. The mean value and median value of the load are 588.53 kN and 407.94 kN, respectively.

By virtue of the capacity and deterioration models, the time-dependent capacity against unseating failure is modeled using Monte Carlo simulation. The evolution of the capacity is presented in Figure 5. Equation 18 is used to fit the deterioration of mean capacity. The obtained values for a and b are 0.06178 and 1.473, respectively.

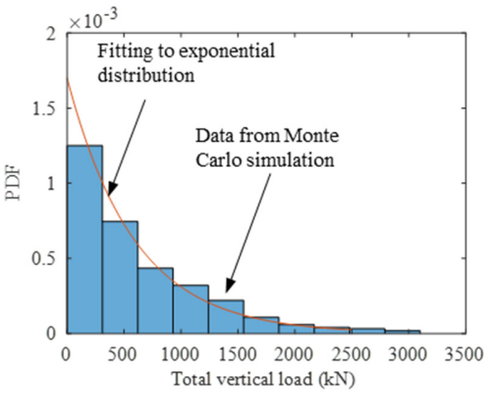


Figure 4. Probabilistic analysis of hurricane-induced loads

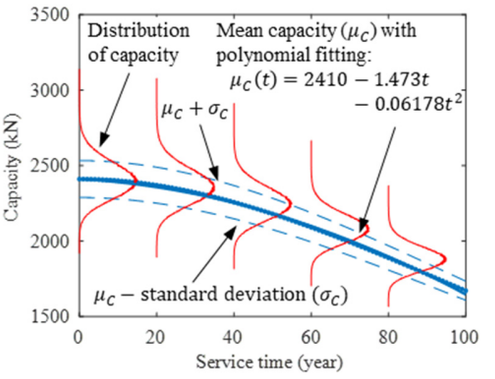


Figure 5. Probabilistic analysis of capacity deterioration

The samples of the initial capacity generated herein can be further used to carry out the integration in Equation 22. The convergence of this integration is shown in Figure 6, in which both deteriorating and non-deteriorating dowels are considered based on Equations 19 and 21, respectively. The discount rate of money is assumed to be 0, indicating that the nominal interest rate is the same as the expected inflation rate (Mondoro et al. 2016). In the analysis, the expected cost associated with unseating failure is assumed to be 100 monetary units, i.e. $w_r = 100$. It can also be regarded as a percentage value to the real monetary cost. The obtained risks for deteriorating and non-deteriorating systems are 16.05 and 8.57 monetary units, respectively. Since no discount rate is considered, the obtained results indicate that the expected numbers of unseating failures in 100 years are 0.161 and 0.086 for deteriorating and non-deteriorating dowels, respectively.

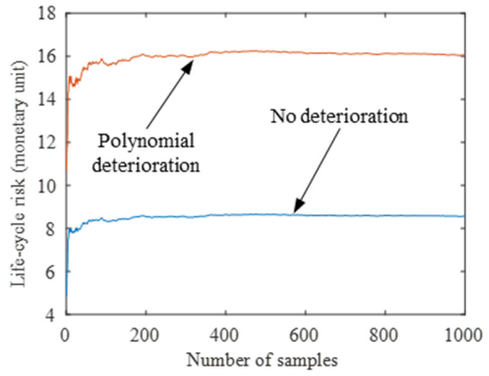


Figure 6. Monte Carlo simulation of unseating risk

In order to quantify the economic benefit of dowels in risk mitigation, the life-cycle risk of the same span without any dowels is also analyzed. In this case, the capacity side of the problem includes only the self-weight, and no deterioration is applicable. The obtained life-cycle risk is 111.35 monetary units, indicating that, on average, the number of unseating failures in 100 years is around 1.11 if no dowels are provided. Therefore, both deteriorating and non-deteriorating unseating-resistant systems can considerably mitigate the life-cycle risk of deck unseating under hurricanes. The economic benefits of both systems can be quantified by subtracting the risks with dowels from that without dowels. In particular, the benefits of deteriorating and non-deteriorating systems are 95.3 and 102.78 monetary units, respectively. If the failure cost is perceived as percentage value (100%), non-deteriorating systems can further reduce 7.48% of the failure cost compared to deteriorating systems. As the cost of deck unseating failure is usually considerably higher than the cost of dowels, the higher initial cost of non-deteriorating dowels can be well justified.

6 CONCLUSIONS

In this paper, a new method is proposed for life-cycle risk assessment of bridge deck unseating under hurricanes. The uncertainties from both demand and capacity sides are taken into account. The proposed method considers both hurricane reoccurrence as a stochastic process and capacity deterioration due to pitting corrosion. Life-cycle risk is formulated for (non)deteriorating but repairable systems based on renewal theory. A number of conclusions are drawn:

1. Unseating-resistant systems are important for risk mitigation of coastal bridges under hurricanes. The benefit of such systems can well outweigh the associated cost.
2. For unseating-resistant systems, capacity deterioration should be considered in the risk assessment. The use of non-deteriorating systems shows better cost-effectiveness in risk mitigation despite the higher initial cost.
3. Occurrence of unseating failures and the associated consequences can be modeled as a renewal-reward process. As a result, life-cycle risk of repairable systems can be assessed using renewal theory. In the most general sense, sampling-based methods are needed for risk assessment.
4. Future work based on the proposed method should consider climate change effects. This can be achieved by hazard analysis pivoting on general climate models and by extending the current risk formulation to nonstationary processes.

7 ACKNOWLEDGEMENTS

The support by grants from (a) the National Science Foundation (NSF) Award CMMI-1537926, (b) the U.S. Federal Highway Administration (FHWA) Cooperative Agreement Award DTFH61-07-H-00040, and (c) the U.S. Office of Naval Research (ONR) Awards N00014-08-1-0188, N00014-12-1-0023, and N00014-16-1-2299 is gratefully acknowledged. Opinions presented in this paper are those of the authors and do not necessarily reflect the views of the sponsoring organizations.

REFERENCES

AASHTO, 2008. *Guide Specifications for Bridges Vulnerable to Coastal Storms*, Washington, D.C.: American Association of State Highway and Transportation Officials (AASHTO).

ACI, 2014. *Building Code Requirements for Structural Concrete*, Detroit, MI: American Concrete Institute (ACI), ACI 318.

ASCE, 2017. *Report Card for America's Infrastructure*, American Society of Civil Engineers (ASCE).

Ataei, N. & Padgett, J.E., 2013a. Fragility assessment of coastal bridges under hurricane events using enhanced probabilistic capacity models. In C. P. Jones & L. G. Griffis, eds. *Advances in Hurricane Engineering: Learning from Our Past - Proceedings of the 2012 ATC and SEI Conference on Advances in Hurricane Engineering*. Miami, FL, 691–702.

Ataei, N. & Padgett, J.E., 2013b. Probabilistic modeling of bridge deck unseating during hurricane events. *Journal of Bridge Engineering*, 18(4): 275–286.

Ataei, N. & Padgett, J.E., 2015. Influential fluid–structure interaction modelling parameters on the response of bridges vulnerable to coastal storms. *Structure and Infrastructure Engineering*, 11(3): 321–333.

Chen, Q., Wang, L. & Zhao, H., 2009. Hydrodynamic investigation of coastal bridge collapse during Hurricane Katrina. *Journal of Hydraulic Engineering, ASCE*, 135(3): 175–186.

Decò, A. & Frangopol, D.M., 2011. Risk assessment of highway bridges under multiple hazards. *Journal of Risk Research*, 14(9): 1057–1089.

Deng, L., Wang, W. & Yu, Y., 2016. State-of-the-art review on the causes and mechanisms of bridge collapse. *Journal of Performance of Constructed Facilities, ASCE*, 30(2): 4015005.

Do, T.Q., van de Lindt, J.W. & Cox, D.T., 2016. Performance-based design methodology for inundated elevated coastal structures subjected to wave load. *Engineering Structures*, 117: 250–262.

Dong, Y. & Frangopol, D.M., 2017. Adaptation optimization of residential buildings under hurricane threat considering climate change in a lifecycle context. *Journal of Performance of Constructed Facilities, ASCE*, 31(6): 4017099.

Douglass, S.L., Chen, Q., Olsen, J.M., Edge, B.L. & Brown, D., 2006. *Wave Forces on Bridge Decks*, Mobile, Alabama: Coastal Transportation Engineering Research and Education Center, University of South Alabama.

Du, Y.G., Clark, L.A. & Chan, A.H.C., 2005. Residual capacity of corroded reinforcing bars. *Magazine of Concrete Research*, 57(3): 135–147.

Jin, J. & Meng, B., 2011. Computation of wave loads on the superstructures of coastal highway bridges. *Ocean Engineering*, 38(17): 2185–2200.

Li, Q., Wang, C. & Zhang, H., 2016. A probabilistic framework for hurricane damage assessment considering non-stationarity and correlation in hurricane actions. *Structural Safety*, 59: 108–117.

Li, Y. & Ellingwood, B.R., 2006. Hurricane damage to residential construction in the US: Importance of uncertainty modeling in risk assessment. *Engineering Structures*, 28(7): 1009–1018.

Mondoro, A., Frangopol, D.M. & Soliman, M., 2016. Optimal risk-based management of coastal bridges vulnerable to hurricanes. *Journal of Infrastructure Systems, ASCE*, 23(3): 4016046.

Peterka, J.A. & Shahid, S., 1998. Design gust wind speeds in the United States. *Journal of Structural Engineering, ASCE*, 124(2): 207–214.

Soliman, M. & Frangopol, D.M., 2015. Life-cycle cost evaluation of conventional and corrosion-resistant steel for bridges. *Journal of Bridge Engineering, ASCE*, 20(1): 6014005.

Stewart, M.G., 2003. Cyclone damage and temporal changes to building vulnerability and economic risks for residential construction. *Journal of Wind Engineering and Industrial Aerodynamics*, 91(5): 671–691.

Stewart, M.G. & Al-Harthy, A., 2008. Pitting corrosion and structural reliability of corroding RC structures: Experimental data and probabilistic analysis. *Reliability Engineering and System Safety*, 93(3): 373–382.

Val, D. V. & Melchers, R.E., 1997. Reliability of deteriorating RC slab bridges. *Journal of Structural Engineering*, 123(12): 1638–1644.

Yang, D.Y. & Frangopol, D.M., 2017. Life-cycle management of deteriorating civil infrastructure considering resilience to lifetime hazards: A general approach based on renewal-reward processes. (submitted).

Yang, D.Y. & Teng, J.G., 2018. Steel-RC structures versus FRP-reinforced seawater sea-sand concrete structures: Lifecycle cost comparison. In *Proceedings of the 9th International Conference on Fibre-Reinforced Polymer Composites in Civil Engineering (CICE 2018)*. Paris, (submitted).

Yang, D.Y., Teng, J.G. & Frangopol, D.M., 2017. Cross-entropy-based adaptive importance sampling for time-dependent reliability analysis of deteriorating structures. *Structural Safety*, 66: 38–50.

Maintenance, Safety, Risk, Management and Life-Cycle Performance of Bridges – Powers, Frangopol, Al-Mahaidi & Caprani (Eds)
© 2018 Taylor & Francis Group, London, ISBN 978-1-138-73045-8

Life-cycle seismic resilience of aging bridges and road networks considering bridge capacity correlation

L. Capacci & F. Biondini
Department of Civil and Environmental Engineering, Politecnico di Milano, Milan, Italy

ABSTRACT: The definition of proper design, maintenance, and management policies for aging structural facilities is a strategic priority for communities exposed to multiple natural hazards. In this paper, the probabilistic life-cycle seismic resilience of aging bridges and road networks is investigated by means of a congestion-based performance measure. The level of structural deterioration and seismic damage associated with different limit states is related to traffic restrictions that are progressively removed depending on the recovery times of each bridge in the network. This approach is applied to reinforced concrete (RC) bridges exposed to chloride-induced corrosion and different earthquake scenarios in terms of magnitude and epicenter location. Simple road networks with series and parallel bridge configurations are investigated considering different levels of bridge seismic capacity correlation. The results show the effectiveness of the proposed framework in quantifying the detrimental combined effects of bridge structural deterioration and seismic damage and the influence of bridge seismic capacities correlation on the life-cycle resilience of road networks with different connectivity patterns.

1 INTRODUCTION

During the last decades, the consequences of natural catastrophes showed how communities are largely affected by disruption and downtime of critical infrastructures induced by mechanical damage and loss of functionality of key structural facilities. The impact of distressing events on infrastructure systems has recently intensified along with the increase in complexity and interdependency of lifelines in modern communities (Faturechi & Miller-Hooks 2014).

Structures and infrastructure systems are called to guarantee adequate life-cycle performance under the interdependent harmful effects of sudden extreme events, such as earthquakes, and continuous deterioration processes (Biondini & Frangopol 2016). In order to improve the capability of infrastructure systems to cope with multiple interacting hazards, resilience has recently gained a prominent importance in design and assessment of aging structural facilities, as well as in the definition of risk mitigation programs. Indeed, the concept of resilience relies on the need to quantify the effectiveness of proactive interventions and emergency response in promptly and efficiently restoring the integrity and operability of damaged facilities to recover the pre-event system functionality (Bruneau *et al.* 2003, McDaniels *et al.* 2008, Bocchini *et al.* 2012, Ouyang *et al.* 2015, Ayyub 2015).

In this context, the assessment of the operability of bridge networks under emergency activities is a fundamental task to ensure optimal life-cycle management of road transportation systems (Zhou *et al.* 2010, Chang *et al.* 2012, Decò *et al.* 2013, Ertuğay *et al.* 2016, Capacci *et al.* 2016). Along with the network topology (Bocchini & Frangopol 2012) and hazard scenario (Baker & Jayaram 2008), the functionality and resilience of road networks depend on the correlation between the time-variant performance of the exposed structures. Furthermore, the correlation between bridge failures can be addressed based on their surveyed conditions, network topology, and functional road classes (Rokneddin *et al.* 2013).

In this paper, the probabilistic life-cycle seismic resilience of aging bridges and road networks is investigated by means of a congestion-based performance measure. The correlated seismic capacities of spatially distributed reinforced concrete (RC) bridges exposed to chloride-induced corrosion are assessed to define the time-variant damage probability under different earthquake scenarios. The post-event seismic damage and its progressive restoration due to recovery actions are related to vehicle transit limitations

and traffic analyses are carried out to assess the functionality of the road network from the event occurrence up to the complete recovery. A probabilistic measure of multi-hazard life-cycle seismic resilience is hence proposed to assess the impact at the network scale of structural aging, earthquake scenario, and bridge seismic capacity correlation. In particular, simple road networks with series and parallel bridge configurations are investigated to show the effectiveness of the proposed framework in quantifying the detrimental effects of both structural deterioration and seismic damage and the influence of correlation between bridge seismic capacities on the life-cycle resilience of transportation infrastructure systems.

2 SEISMIC ASSESSMENT OF RC BRIDGES

2.1 *Time-variant effects of corrosion*

The main effect of corrosion in RC structures is the reduction of the cross-section of reinforcing steel bars (Bertolini *et al.* 2004). The steel mass loss is quantified by a time-variant damage index $\delta_s = \delta_s(t) \in [0;1]$. Corrosion may also affect the ductility of steel bars. This effect is related to the steel mass loss by means of a reduction of the steel ultimate strain capacity $\varepsilon_{su}=\varepsilon_{su}(\delta_s)$, as shown in (Biondini & Vergani 2015). It is worth noting that the formation of oxidation products may lead to propagation of longitudinal splitting cracks and concrete cover spalling (Biondini & Vergani 2015, Biondini & Frangopol 2016). However, deterioration of concrete induced by corrosion is not considered as a critical issue for the applications presented in this paper. Corrosion initiation is associated with a critical threshold of chloride concentration C_{cr} and corrosion rate is related to the concentration $C=C(t)$ by means of a damage rate coefficient q_s. Fick's laws of diffusion are used to describe the chloride ingress process and the diffusion equations are solved numerically by means of cellular automata. Further information about diffusion simulation and damage modelling can be found in Biondini *et al.* (2004) and Biondini & Vergani (2015).

2.2 *Bridge limit states and seismic fragilities*

The life-cycle seismic capacity of RC bridges is investigated under uncertainty by means of time-variant fragilities $P^E_{s,b}=P^E_{s,b}(t_b)$, which provide the probability of exceedance of a limit state s_b given the occurrence of a seismic event of intensity i_b at time t_0, where $t_b=t_0-t_{c,b}$ is the bridge age and $t_{c,b}$ is the bridge construction time (Capacci *et al.* 2018b). The peak ground acceleration is assumed as seismic intensity measure. The bridge seismic capacity is evaluated based on incremental dynamic analysis (Vamvatsikos & Cornell 2002). The damage measure is associated with the maximum drift $\theta_{\max,b}$, defined as the maximum ratio of the bridge pier top displacement to the pier height. The attainment of the damage states s_b is associated with the following time-variant drift thresholds $\theta_{s,b}$ (Capacci 2015):

- Slight Damage (SD, s_b=1): $\theta_{1,b}=\theta_{y,b}$;
- Moderate Damage (MD, s_b=2): $\theta_{2,b}=\theta_{y,b}+0.3\theta_{p,b}$;
- Extensive Damage (ED, s_b=3): $\theta_{3,b}=\theta_{y,b}+0.6\theta_{p,b}$;

with $\theta_{p,b}=\theta_{u,b}-\theta_{y,b}$, and where $\theta_{y,b}$ and $\theta_{u,b}$ are the mean values of the drift at first yielding and ultimate bending curvatures, respectively, at the base of the bridge piers. The time-variant drift thresholds $\theta_{y,b}$ and $\theta_{u,b}$ are computed by means of non-linear static (push-over) analysis. In addition, the bridge is assumed to suffer No Damage (ND, s_b=0) if $\theta_{\max,b}<\theta_{1,b}$, and to reach the limit state of Structural Collapse (SC, s_b=4) when the dynamic equilibrium under ground motion is no longer fulfilled.

The probabilistic analysis is performed by Monte Carlo simulation and the results of the incremental dynamic analyses are processed by assuming lognormal distribution of the fragility functions:

$$P^E_{s,b} = P(s_b \mid i_b, t_b) = \Phi\left(\frac{\ln i_b - \lambda_{s,b}(t_b)}{\zeta_{s,b}(t_b)}\right) \quad (1)$$

where Φ is the cumulative distribution of a normal variate, and $\lambda_{s,b}$ and $\zeta_{s,b}$ are the mean and standard deviation, respectively, of the natural logarithm of the seismic capacity associated with damage state s_b.

2.3 *Seismic hazard and network damage*

The seismic demand is evaluated based on the ground motion prediction equation proposed in Bindi *et al.* (2011). The seismic intensity i_b at the site $\mathbf{x}_b$ of the b-th bridge in the network is related to the earthquake scenario in terms of magnitude M and focal distance between bridge site $\mathbf{x}_b$ and epicenter location $\mathbf{x}_e$ (Biondini *et al.* 2017, 2018a).

The combination of bridge initial damage levels in a given network is defined by means of an integer index s based on the ordered selection without repetitions of the damage states s_b of each bridge:

$$s = 1 + \sum_{b=1}^{N_b} \left(N_{s,b}\right)^{N_b-b} \cdot s_b \quad (2)$$

where N_b is the total number of bridges and $N_{s,b}$ is the number of possible damage states of the b-th bridge.

Along with the seismic scenario, defined in terms of magnitude M and epicenter location $\mathbf{x}_e$, the time-variant probability of occurrence of the s-th damage combination depends on both location $\mathbf{x}_b$ and age t_b of each bridge, as well as on the correlation between the seismic capacity of each pair of bridges. The conditional probability of occurrence of the s-th damage combination can hence be expressed as follows:

$$P_s = P(s \mid M, \mathbf{x}_e, \mathbf{x}_b, t_b, \boldsymbol{\rho}) \quad (3)$$

where $\boldsymbol{\rho}$ is a correlation matrix that collects the linear correlation coefficients of each pair of bridge seismic capacities.

3 RESILIENCE OF ROAD NETWORKS

3.1 *Traffic flow and travel time*

The performance of road networks can be assessed based on the traffic flow response, given the Origin-Destination traffic demand and the network topology. The travel time c_{ij} of the road arc *i-j* can be expressed as a function of the related vehicle flow per unit of time f_{ij}. The flow depends on the arc practicability in terms of practical capacity $f^{cr}_{ij}=n_L(v_{cr}/d_{\min})$ and travel time at free flow $c^0_{ij}=L_{ij}/v_{\lim}$, where: L_{ij}=arc length; n_L=number of open lanes; $d_{\min}$=minimum allowed distance between vehicles associated with the arc road class; v_{cr}=critical speed; v_{lim}=speed limit (either maximum $v_{\max}$ or minimum $v_{\min}$). More detailed information on the traffic model and the relationship between travel time and traffic flow can be found in Capacci (2015).

3.2 *Type of users and traffic limitations*

The traffic capacity of a road arc may be impaired by traffic restrictions applied to regulate the transit on damaged bridges (Mackie & Stojadinović 2006). Three different types of traffic users and related traffic flows are considered: light vehicles, f_l; heavy vehicles, f_h; emergency vehicles, f_e. Traffic limitations on the *b*-th bridge are identified by a decision variable d_b based on the following $N_{d,b}=5$ traffic restrictions (Biondini *et al.* 2015):

- No Restrictions ($d_b=0$): the traffic on the bridge is regular and the speed limit v_{lim} corresponds to the maximum allowed speed *0*;
- Weight Restriction ($d_b=1$): heavy vehicles are forbidden, i.e. $f_h=0$, and the speed limit is reduced to $v_{\min}$.
- One Lane Open Only ($d_b=2$): light and emergency vehicles can transit on only one lane, i.e. $n_L=1$;
- Emergency Access Only ($d_b=3$): the transit of emergency vehicles only is allowed, i.e. $f_l=0$;
- Closure ($d_b=4$): no vehicles can transit over the bridge, i.e. $f_e=0$ or $n_L=0$.

The decision variables $d_b=k$ with $k>1$ are inclusive of the traffic restrictions associated with $d_b<k$. The network restriction combination is defined by means of an integer index *d* in terms of the decision variable d_b, consistently with the criterion proposed for the network damage combinations:

$$d = 1 + \sum_{b=1}^{N_b} \left(N_{d,b}\right)^{N_b - b} \cdot d_b \tag{4}$$

3.3 *Traffic analysis and network functionality*

The vehicle flow f_{ij} of any road arc *i-j* can be identified based on the user-equilibrium condition enforced by the Wardrop's gravitational model (Wardrop 1952), which consists in the minimization of the total travel time *TTT* of all the users of the road network. More details concerning with the traffic analysis, the solution of the related optimization problem and the definition of total travel time $TTT_d=TTT(d)$ under traffic restriction combinations can be found in Bocchini & Frangopol (2011) and Biondini *et al.* (2015).

The functionality level $Q_d=Q(d)\in[0;1]$ of the road network associated with the combination *d* of traffic restrictions is defined as follows (Capacci 2015):

$$Q(d) = \frac{TTT_u}{TTT_d} \tag{5}$$

where $TTT_u=TTT(d=1)$ is the total travel time in unrestricted conditions, i.e. no traffic regulations are applied to any bridge. It is worth noting that the condition of unrestricted transit with $TTT_d=TTT_u$ and $Q=1$ is fulfilled both before the seismic event occurrence and after full recovery of all the bridges.

3.4 *Bridge recovery process*

In the aftermath of a seismic event, each bridge in the network may suffer an initial loss of seismic capacity, leading the road managers to enforce a serviceability limitation. In particular, the traffic restriction $d_b=k$ is applied to the *b*-th bridge if the earthquake induces the damage state $s_b=k$ (Capacci *et al.* 2016)

The idle time $\Delta t_{i,b}$ represents the interval between the occurrence time t_0 and the repair initiation for the *b*-th bridge. In the following, the idle time is neglected and the repair actions of each bridge in the network are assumed to start at time t_0.

The bridge recovery process develops over a series of time steps depending on the initial damage and the specific recovery strategy. The partial recovery times $t_{p,b}$ are related to time instants in which the attainment of intermediate seismic capacity thresholds allows the enforcement of less severe traffic limitations up to the complete reopening of the bridge to all users. In particular, $p=1,\ldots,N_{j,b}$, where $N_{j,b}$ is the total number of jumps in the network recovery process. The final recovery time $t_{r,b}$ is associated with the completion of the repair actions. During the recovery process, each initial traffic limitation $d_b=k$ with $k>0$ is partially released leading to a sequence of progressively less severe restrictions $d_b=h$ with $h<k$. The full serviceability of the bridge, i.e. $d_b=0$, is reached at time $t_{r,b}$.

3.5 *Network recovery process*

At the network level, the repair activities carried out on each bridge lead to define a constant stepwise model for the progressive restoration of the functionality (Padgett & DesRoches 2007). In this way, the road network functionality is described by a discrete set of values associated with the network restrictions *d*, from the initial damage to the fully restored state. The recovery function of network functionality over a time interval $\Delta t_h=(t_h-t_0)$, where t_h is a given horizon time, is hence defined in stepwise form as follows:

$$Q(t) = Q_j, \quad t_j \le t < t_{j+1} \ \forall j \in [0; N_j] \tag{6}$$

where t_j=t_h for j=N_j+1 and N_j=$\sum_b N_{j,b}$ is the total number of jumps in the network recovery process.

A seismic event striking the road network at time t_0 would cause a sudden drop of functionality from the pre-event level to Q_0=Q(d=s) under the traffic restrictions imposed by the initial damage combination s of the bridges. Therefore, post-event restoration activities lead to progressive functionality jumps from Q_{j-1} to Q_j at time t_j with j=1,…,N_j.

3.6 *Resilience levels and resilience measure*

The resilience level R_s associated with the network damage combination s is defined as the average integral of the network functionality over the recovery time interval Δt_h. Considering the stepwise form of the network recovery function, the resilience integral can be reduced to the following sum:

$$R_s = \frac{1}{\Delta t_h} \sum_{j=1}^{N_j} Q_j \Delta t_j \tag{7}$$

where Δt_j= t_j–t_{j-1} is the j-th recovery time step.

The resilience measure R of the road network is inspired by the concept of expected utility (Ang & Tang 1984) and obtained by weighing the resilience levels R_s of the N_s network damage combinations with the corresponding damage probabilities:

$$R = \sum_{s=1}^{N_s} P_s \cdot R_s \tag{8}$$

4 APPLICATION

4.1 *RC box girder bridge*

The four-span continuous RC bridge shown in Figure 1 is considered (Mander *et al.* 2007). The total length of the bridge is 200 m, with spans of 50 m, as shown in Figure 1a. The height of the piers is 14 m. Figure 1b shows the box girder cross-section of the deck. The piers have circular cross-section and are reinforced with 36 steel bars with 30mm-diameter, as shown in Figure 1c. Concrete and steel nominal strengths are f_c=40MPa and f_{sy}=450MPa, respectively.

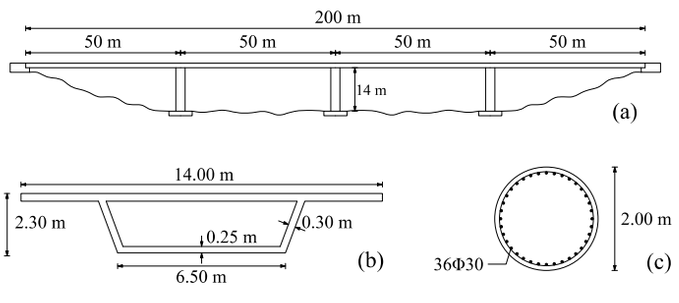


Figure 1. RC box girder bridge: (a) longitudinal profile; (b) deck cross-section; (c) pier cross-section with reinforcement layout.

The bridge piers are exposed to a chloride diffusive attack on the external surface, with nominal chloride concentration C_0=3% [wt.%/c]. A nominal diffusivity coefficient D=15.8×10^{-12} m^2/sec is assumed for concrete. The corrosion damage propagation is evaluated by assuming a nominal damage rate coefficient q_s=(0.02 year^{-1})/C_0, with corrosion initiation related to the attainment of a nominal critical threshold of concentration C_{cr}=0.6wt.%/c.

4.2 *Bridge seismic fragilities under corrosion*

Concrete strength f_c, steel strength f_{sy}, viscous damping ξ, diffusivity D, steel damage rate q_s, surface chloride concentration C_0 and critical chloride concentration C_{cr} are assumed as uncorrelated random variables with prescribed density distributions. The life-cycle fragility analysis is carried out by Monte Carlo simulation based on Latin Hypercube Sampling. The nonlinear time-history dynamic analyses are performed in each realization for a set of 10 artificial earthquakes generated to comply with the elastic response spectrum given by Eurocode 8 for soil type B (CEN-EN 1998). Further details on both the probabilistic modeling and simulation process can be found elsewhere (Capacci 2015, Capacci *et al.* 2016).

Figure 2 shows the time-variant drift thresholds based on the mean values of the drift limits $\theta_{y,b}$ and $\theta_{u,b}$ at first yielding and ultimate, respectively. It is noted that corrosion damage significantly reduces over time the pier displacement ductility. Figure 3 shows the lognormal best fitting of the corresponding time-variant fragility curves over a 100-year lifetime with steps of 10 years. The bridge seismic capacity against the occurrence of first yielding is slightly affected by corrosion. However, the effects of structural deterioration lead to a substantial decrease of bridge seismic capacity for any damage state s_b>1.

4.3 *Road networks and resilience levels*

The road networks shown in Figures 4a and 5a with bridges in series (S) and parallel (P), respectively, are considered. The networks include one Origin and one Destination, two identical bridges B_1 and B_2 built at time $t_{c,b}$=0 at a relative distance of 10km, and a secondary road to detour the traffic flow.

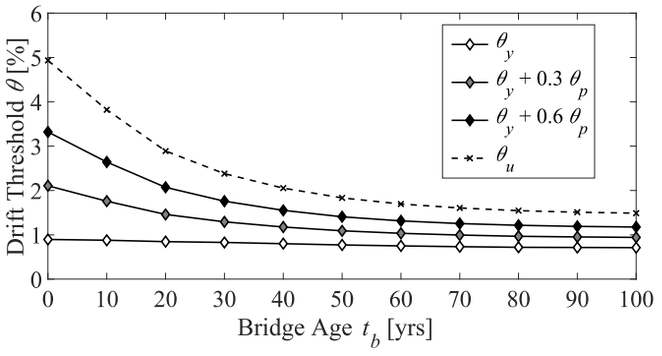


Figure 2. Drift ratios associated with different thresholds.

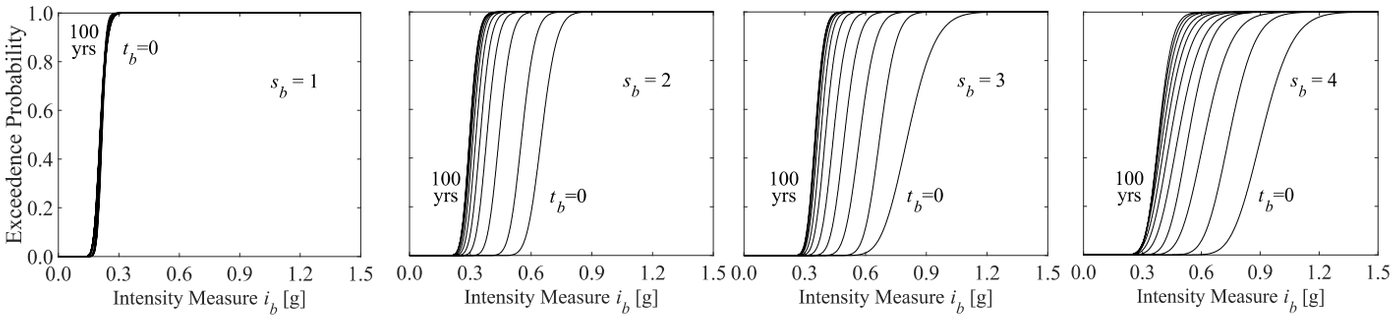


Figure 3. Time-variant seismic fragility curves for a seismic event occurring at bridge age from t_b=0 to 100 years with time steps of 10 years: (a) Slight Damage, (b) Moderate Damage, (c) Extensive Damage, and (d) Structural Collapse.

Given a Cartesian coordinate system $\mathbf{x}=(x,y)$ with origin $\mathbf{x}_c=(0,0)$ in the bridge network centroid and x-axis aligned with the O-D nodes, the coordinates of the bridges are (km): $\mathbf{x}_{b=1}=(-5,0)$ and $\mathbf{x}_{b=2}=(5,0)$ for system S; $\mathbf{x}_{b=1}=(0,-5)$ and $\mathbf{x}_{b=2}=(0,5)$ for system P. Table 1 summarizes the main traffic parameters, with v_{cr}=65 km/h and $d_{\min}$=30 m/cars. The two networks have similar total travel times. Traffic restrictions are applied to the bridges according to the initial damage state and post-event recovery enforcing stepwise increments in the network functionality. Partial and final recovery times are listed in Table 2.

The bar charts shown in Figure 4b and 5b provide the resilience levels for the network damage combinations. The functionality of network S is affected by any damage scenario in which at least one bridge suffers significant damage (Figure 5a), since redundancy is given by the detour only. Conversely, the functionality of network P is significantly reduced only if both bridges are extensively damaged (Figure 5b).

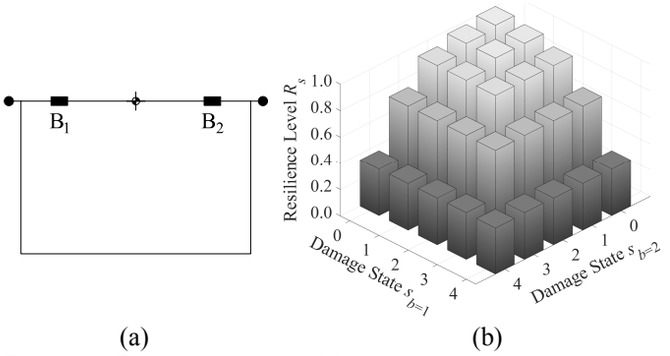


Figure 4. Road network S: (a) connectivity layout with two bridges in series, and (b) bar chart of the resilience levels.

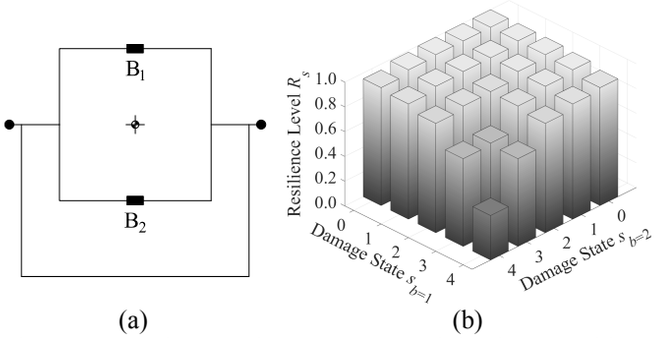


Figure 5. Road network P: (a) connectivity layout with two bridges in parallel, and (b) bar chart of the resilience levels.

Table 1. Traffic parameters of networks S and P.

	Highway in S	Highways in P	Side Road
L [km]	15	18	60
n_L	3	3	2
$v_{\max}$ [km/h]	130	130	90
$v_{\min}$ [km/h]	70	70	50

Table 2. Bridge recovery times for each damage state.

	$t_{p=1,b}$ [days]	$t_{p=2,b}$ [days]	$t_{p=3,b}$ [days]	$t_{r,b}$ [days]
s_b=1	-	-	-	30
s_b=2	39	-	-	90
s_b=3	82	103	-	180
s_b=4	165	218	262	360

4.4 *Seismic resilience of the road networks*

The seismic resilience of the two road networks S and P is evaluated considering different levels of bridge seismic capacity correlation. Consistently with the procedure for the fragility analysis, the network damage probabilities P_s are retrieved by Monte Carlo simulation based on Latin Hypercube Sampling for a sample of 5000 realizations of correlated bridge seismic capacities. Figures 6 and 7 show the 3-D surfaces and the related 2-D contour maps of the resilience $R=R(\mathbf{x}_e)$ of the networks S (Figure 6) and P (Figure 7), for a seismic event with magnitude M=6.75 occurring at time t_0=40 years based on a square grid of epicenters with grid size of 0.2 km. Three levels of linear correlation ρ are considered for the bridge seismic capacities: (a) $\rho = 0$, (b) $\rho = 0.5$, and (c) $\rho = 1$.

The most critical earthquake scenarios for the network S are associated with epicenter locations close to one of the bridges, for all levels of correlation, because of the limited system redundancy. However, the impact of the lack of redundancy is partially mitigated by the bridge capacity correlation when the epicenter is close to the network centroid. In fact, in this case the likelihood of having at least one bridge severely damaged increases as correlation decreases.

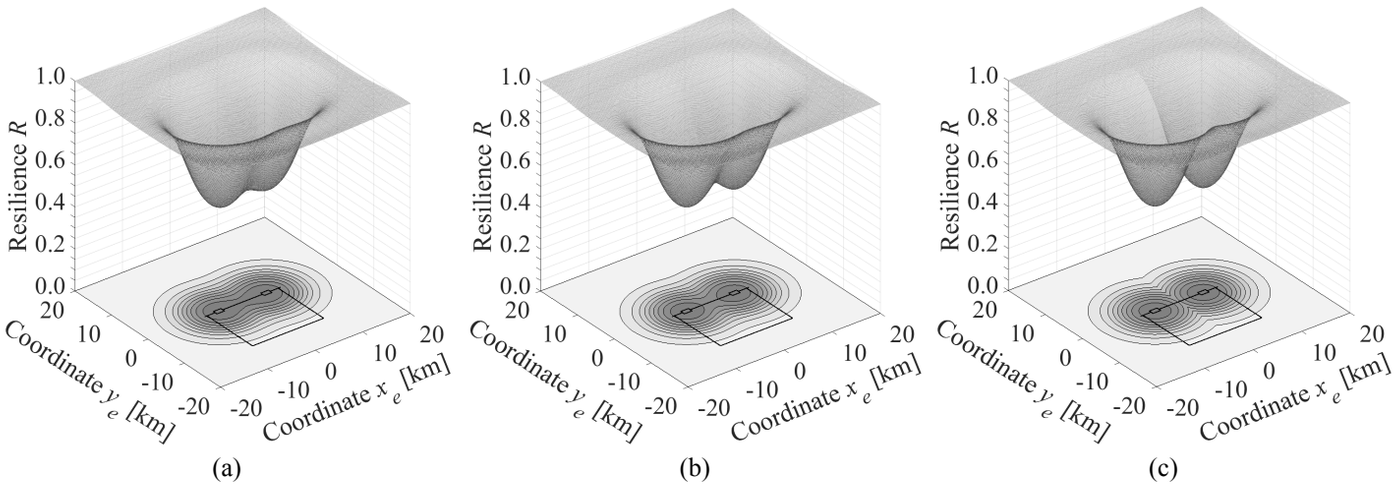


Figure 6. Road network S. Resilience R versus the epicenter location $\mathbf{x}_e=(x_e,y_e)$ of a seismic event occurring at time t_0 = 40 years with earthquake magnitude M=6.75 for different levels of bridge seismic capacity correlation: (a) ρ=0, (b) ρ=0.5, and (c) ρ=1.

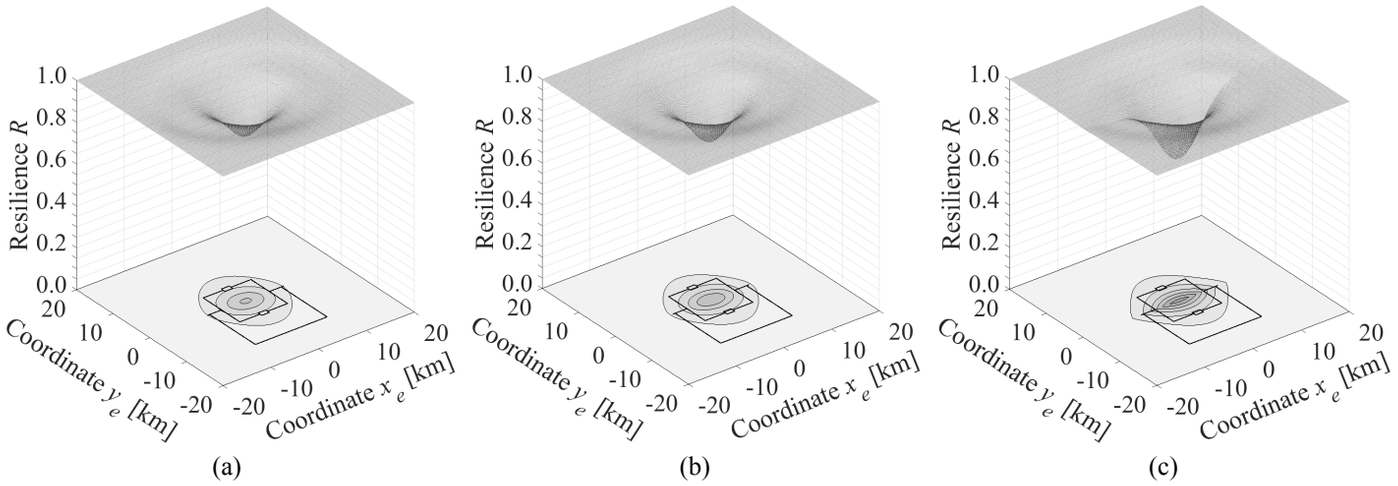


Figure 7. Road network P. Resilience R versus the epicenter location $\mathbf{x}_e=(x_e,y_e)$ of a seismic event occurring at time t_0 = 40 years with earthquake magnitude M=6.75 for different levels of bridge seismic capacity correlation: (a) ρ=0, (b) ρ=0.5, and (c) ρ=1.

Conversely, the most critical earthquake scenarios for the network P are associated with epicenter locations close to the network centroid. This tendency is exacerbated by the correlation of bridge seismic capacities, since for these scenarios the likelihood of having both bridges severely damaged increases with the correlation level.

The influence of the earthquake epicenter location and bridge seismic capacity correlation can be appreciated also from the diagrams illustrated in Figures 8 and 9, which show the seismic resilience R versus the epicenter distance $d_e=\|\mathbf{x}_e-\mathbf{x}_c\|$ from the network centroid along the direction at angle $\alpha_e=\arcsin[(y_e-y_c)/d_e]$ with the x-axis. The resilience curves are shown for $\alpha_e=0$ and $\pi/2$, occurrence times t_0=20, 40 and 60 years, and earthquake magnitudes M=6.25, 6.50 and 6.75. With respect to the contour maps shown in Figures 6 and 7, the diagrams in Figures 8 and 9 show that the role of correlation may be emphasized over time due to structural deterioration and for increasing seismic magnitude. However, the effect of correlation may be substantially reduced under the combined effects of severe corrosion and seismic damage.

In order to show the role of correlation of the bridge seismic capacities over the life-cycle, the following time-variant resilience sensitivity index is defined for the investigated S and P road networks:

$$\Delta r_\rho(M,\mathbf{x}_e,t_0)=\frac{R_\rho-R_{\rho=0}}{R_{\rho=0}} \tag{9}$$

where R_ρ is the network seismic resilience associated with a linear correlation coefficient ρ. Figure 10 shows the resilience sensitivity index Δr_ρ for ρ=1, i.e. $\Delta r_{\rho=1}$, versus the occurrence time t_0 for epicenter location in the network centroid, i.e. $\mathbf{x}_e=\mathbf{x}_c$, and different magnitudes M=6.25, 6.50 and 6.75. These results confirm the opposite trends obtained for the series system S, with $\Delta r_{\rho=1}>0$, and the parallel system P, with $\Delta r_{\rho=1}<0$. Moreover, in both cases the correlation effects tend to increase at the beginning of the service life, after about 10 years, when corrosion damage propagates. However, this tendency is reversed over time under severe deterioration for increasing seismic hazard since both bridges are likely to suffer extensive seismic damage regardless of the level of correlation of their seismic capacities.

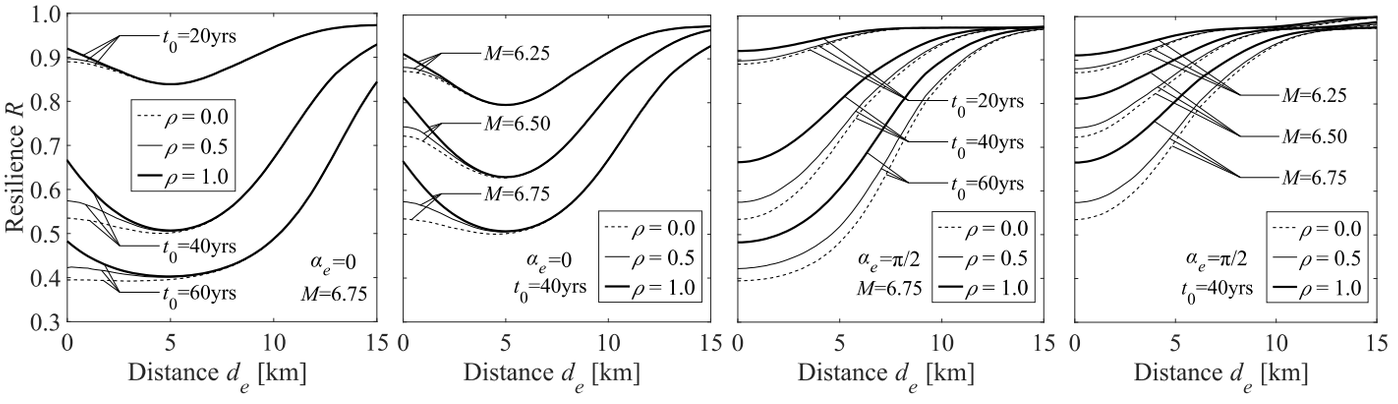


Figure 8. Road network S. Resilience R versus epicenter distance d_e from the network centroid for different angles α_e=0 and π/2, earthquake magnitudes M=6.25, 6.50 and 6.75, and occurrence times t_0=20, 40 and 60 years.

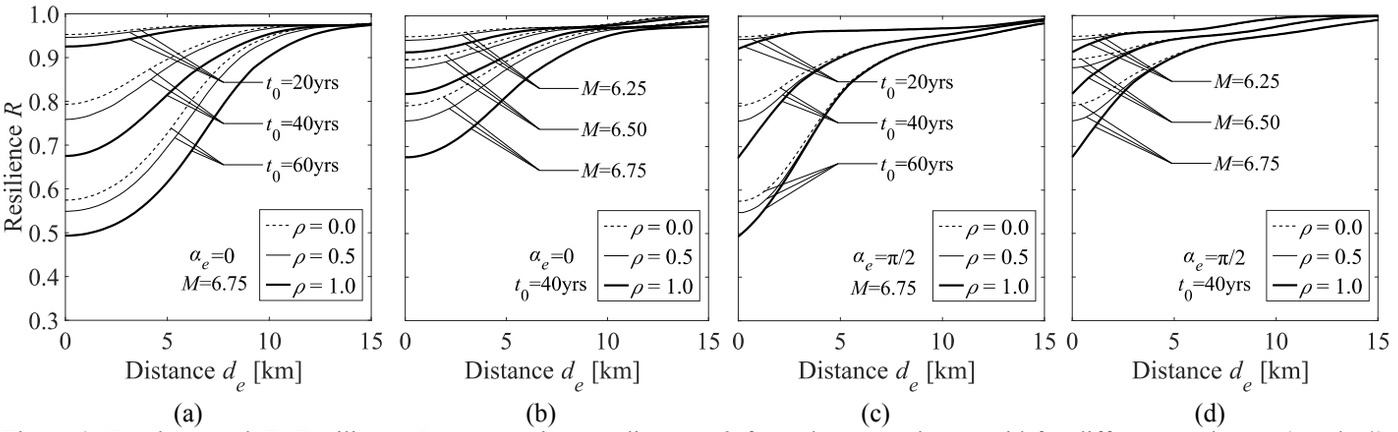


Figure 9. Road network P. Resilience R versus epicenter distance d_e from the network centroid for different angles α_e=0 and π/2, earthquake magnitudes M=6.25, 6.50 and 6.75, and occurrence times t_0=20, 40 and 60 years.

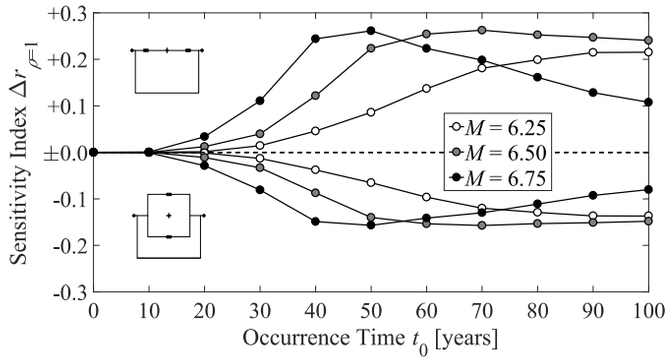


Figure 10. Resilience sensitivity index Δr_ρ for ρ=1 versus the occurrence time t_0 with epicenter location in the network centroid, i.e. $\mathbf{x}_e$=$\mathbf{x}_c$, and different magnitudes M=6.25, 6.50, 6.75.

5 CONCLUSIONS

A multi-hazard probabilistic framework for life-cycle resilience assessment of road transportation networks with spatially distributed RC bridges exposed to chloride-induced corrosion and different earthquake scenarios has been presented. Simple road networks with series and parallel bridge configurations have been investigated to quantify the detrimental effects of both structural deterioration and seismic damage, as well as the influence of bridge seismic capacity correlation, on the life-cycle seismic resilience of transportation infrastructure systems.

It has been shown that for series bridge networks, which rely on detour routes to ensure a certain degree of redundancy, the most critical earthquake scenarios are associated with epicenters close to the bridges. The impact of the lack of redundancy can be partially mitigated by correlation between bridge seismic capacities when the epicenter is relatively far from the bridges. In fact, in this case the likelihood of having at least one bridge severely damaged tends to increase as correlation decreases. Conversely, for parallel bridge networks the most critical earthquake scenarios are associated with epicenters close to the network centroid. This is emphasized by bridge capacity correlation, since in these scenarios the likelihood of having the correlated bridges severely damaged increases with the correlation level. Moreover, for the investigated series and parallel networks the correlation effects tend to increase under moderate levels of structural deterioration. However, over time the combined effects of severe corrosion and seismic damage may significantly reduce such effects. This highlights the importance of a multi-hazard life-cycle-oriented probabilistic approach to seismic resilience assessment of bridges and road infrastructure networks.

REFERENCES

Ang, A.H.S. & Tang, W.H. 1984. *Probability Concepts in Engineering Planning and Design.* Volume II: *Decision, Risk, and Reliability*. John Wiley & Sons, New York, NY, USA.

Ayyub B.M. 2015. Practical resilience metrics for planning, design, and decision making. *ASCE-ASME Journal of Risk and Uncertainty in Engineering Systems, Part A: Civil Engineering*, 1(3): 04015008.

Baker, J.W. & Jayaram, N. 2008. *Effects of spatial correlation of ground motion parameters for multi-site seismic risk assessment: collaborative research with Stanford University and AIR*. Final Technical Report for U.S. Geological Survey National Earthquake Hazards Reduction Program.

Bertolini, L., Elsener, B., Pedeferri, P. & Polder, R. 2004. *Corrosion of steel in concrete*, Wiley-VCH, Weinheim, Germany.

Bindi, D., Pacor, F., Luzi, L., Puglia, R., Massa, M., Ameri, G. & Paolucci, R. 2011. Ground motion prediction equations derived from the Italian strong motion database. *Bulletin of Earthquake Engineering*, 9(6): 1899-1920.

Biondini, F., Bontempi, F., Frangopol, D.M. & Malerba, P.G. 2004. Cellular automata approach to durability analysis of concrete structures in aggressive environments. *Journal of Structural Engineering* ASCE 130(11): 1724-1737.

Biondini, F., Camnasio, E. & Titi, A. 2015a. Seismic resilience of concrete structures under corrosion. *Earthquake Engineering and Structural Dynamics*, 44(14): 2445-2466.

Biondini, F., Capacci, L. & Titi A. 2015b. Seismic resilience of bridges and highway networks. *16th Congress of the Italian Association of Earthquake Engineering*, L'Aquila, Italy, September 13-17, 2015.

Biondini, F., Capacci, L & Titi, A. 2016. Seismic resilience of aging bridges and evolving road networks. *5th International Workshop on Design in Civil and Environmental Engineering*, Rome, Italy, October 6-8, 2016.

Biondini, F., Capacci, L. & Titi, A. 2017. Life-cycle resilience of deteriorating bridge networks under earthquake scenarios. *16th World Conference on Earthquake Engineering*, Santiago of Chile, Chile, January 9-13, 2017.

Biondini F., & Frangopol D.M. 2016. Life-cycle performance of deteriorating structural systems under uncertainty: Review, *Journal of Structural Engineering*, 142(9): 1-17.

Biondini, F. & Vergani M. 2015. Deteriorating beam finite element for nonlinear analysis of concrete structures under corrosion. *Structure and Infrastructure Engineering*, 11(4): 519-532.

Bocchini, P., Decò A. & Frangopol D.M. 2012. Probabilistic functionality recovery model for resilience analysis. *6th Int. Conference on Bridge Maintenance, Safety and Management* (IABMAS 2012), Stresa, Italy, July 8–12, 2012. In: *Bridge Maintenance, Safety, Management, Resilience and Sustainability*, F. Biondini, D.M. Frangopol (Eds.), CRC Press/ Balkema, Taylor & Francis Group, London, UK, 2012.

Bocchini, P. & Frangopol, D.M. 2011. A stochastic computational framework for the joint transportation network fragility analysis and traffic flow distribution under extreme events. *Probabilistic Engineering Mechanics*, 26(2): 182-193.

Bocchini, P. & Frangopol, D.M. 2012. Optimal resilience- and cost-based postdisaster intervention prioritization for bridges along a highway segment. *Journal of Bridge Engineering*, 17(1):117–129.

Bruneau, M., Chang, S.E., Eguchi, R.T., Lee, G.C., O'Rourke, T.D., Reinhorn, A..M, Shinozuka, M., Tierney, K., Wallace, W.A. & Winterfeldt, D.V. 2003. A framework to quantitatively assess and enhance the seismic resilience of communities. *Earthquake Spectra*, 19(4): 733-752.

Capacci, L. 2015. *Seismic resilience of bridge networks*. MSc Thesis, Politecnico di Milano, Italy.

Capacci, L., Biondini, F. & Titi, A. 2016. Seismic resilience of aging bridges and transportation networks. *8th Int. Conference on Bridge Maintenance, Safety and Management* (IABMAS2016), Foz do Iguaçu, Brazil, June 26-30, 2016. In: *Maintenance, Monitoring, Safety, Risk and Resilience of Bridges and Bridge Networks*, T.N. Bittencourt, D.M. Frangopol, A. Beck (Eds.), CRC Press/Balkema, Taylor & Francis Group, London, UK.

Capacci, L. & Biondini, F. 2018a. Role of the earthquake scenario on life-cycle seismic resilience of aging bridge networks. *16th European Conference on Earthquake Engineering*, Thessaloniki, Greece, June 18-21, 2018.

Capacci, L. & Biondini, F. 2018b. Effects of structural deterioration and infrastructure upgrading on the life-cycle seismic resilience of bridge networks. *IABSE Conference "Engineering the Developing World"*, Kuala Lumpur, Malaysia, April 25-27, 2018.

CEN-EN 1998-1 (2004). *Eurocode 8: Design of structures for earthquake resistance – Part 1: General rules, seismic actions and rules for buildings*. European Committee for Standardization, Brussels, Belgium.

Chang, L., Peng, F., Ouyang, Y., Elnashai, A.S., & Spencer, B.F. 2012. Bridge seismic retrofit program planning to maximize postearthquake transportation network capacity. *Journal of Infrastructure System*, 18(2): 75-88.

Decò, A., Bocchini, P. & Frangopol, D.M. 2013. A probabilistic approach for the prediction of seismic resilience of bridges. Earthquake. *Engineering and Structural Dynamics*, 42(10): 1469–1487.

Ertuğay, K., Argyroudis, S. & Düzgün, H.Ş. 2016. Accessibility modeling in earthquake case considering road closure probabilities: A case study of health and shelter service accessibility in Thessaloniki, Greece. *International Journal of Disaster Risk Reduction*, 17:49-66.

Faturechi, R. & Miller-Hooks, E. 2015. Measuring the performance of transportation infrastructure systems in disasters: a comprehensive review. *Journal of Infrastructure Systems*, 21(1): 04014025.

Mackie, K.R. & Stojadinović, B. 2006. Post-earthquake functionality of highway overpass bridges. *Earthquake Engineering and Structural Dynamics*, 35(1): 77-93.

Mander, J.B., Dhakal, R.P., Mashiko, N. & Solberg K.M. 2007. Incremental dynamic analysis applied to seismic financial risk assessment of bridges. *Engineering Structures*, 29(10): 2662-2672.

McDaniels, T., Chang, S., Cole D., Mikawoz, J. & Longstaff, H. 2008. Fostering resilience to extreme events within infrastructure systems: Characterizing decision contexts for mitigation and adaptation. *Global Environmental Change* 18(2): 310-318.

Ouyang, M., Dueñas-Osorio, L. & Min, X. 2012. A three-stage resilience analysis framework for urban infrastructure systems. *Structural Safety*, 36-37: 23-31.

Padgett, J.E. & DesRoches, R. 2007. Bridge functionality relationships for improved seismic risk assessment of transportation networks. *Earthquake Spectra*, 23(1): 115-130.

Rokneddin, K., Ghosh, J., Dueñas-Osorio, L. & Padgett J.E. 2014. Seismic Reliability Assessment of Aging Highway Bridge Networks with Field Instrumentation Data and Correlated Failures, II: Application. *Earthquake Spectra*, 30(2): 819-843.

Vamvatsikos, D. & Cornell, C.A. 2002. Incremental dynamic analysis. *Earthquake Engineering & Structural Dynamics*, 31(3): 491-514.

Wardrop, J.G. 1952. Some theoretical aspects of road traffic research. *ICE Proceedings, Engineering Divisions*, 1(3): 325-362.

Zhou, Y., Banerjee, S. & Shinozuka, M. 2010. Socio-economic effect of seismic retrofit of bridges for highway transportation networks: a pilot study. *Structure and Infrastructure Engineering*, 6(1-2): 145-157.

Maintenance, Safety, Risk, Management and Life-Cycle Performance of Bridges – Powers, Frangopol, Al-Mahaidi & Caprani (Eds)
© 2018 Taylor & Francis Group, London, ISBN 978-1-138-73045-8

Time-Dependent Probability of Exceeding Restoration Levels in Resilience Analysis

F. Nocera & P. Gardoni
University of Illinois at Urbana-Champaign, Urbana, IL, USA
G.P. Cimellaro
Politecnico di Torino, Turin, Italy

ABSTRACT: Resilience typically refers to the ability of a system to adapt to changing conditions, withstand and rapidly recover from disruptions due to extreme/rare events. This paper proposes a methodology to predict the recovery process of a selected system given past recovery data and estimate the probability of exceeding a target value of functionality at any time. A Bayesian inference is used to update the model parameters as new data become available while the recovery process is in progress. The methodology is general and can be applied to continuous recovery processes such as those of economic or natural systems, as well as to discrete recovery process such as those of engineering systems. As an illustration, the proposed methodology is implemented considering a bridge restoration following seismic damage.

Keywords: Decision Support, Metrics, Recovery, Reliability analysis, Resilience.

1 INTRODUCTION

Civil infrastructure enable the movement of goods, services, and resources to communities (Corotis 2009; Ellingwood et al. 2016; Gardoni et al. 2016). Civil infrastructure are vulnerable to natural and anthropogenic hazards. Past disasters have showed their vulnerability and emphasized the relevance of risk mitigation and management (Murphy and Gardoni 2006; Gardoni and LaFave 2016; Gardoni et al. 2016). Natural hazards (such as floods, earthquakes, and hurricanes), and anthropogenic hazards (such as accidents and terrorist attacks) may cause damage to civil infrastructure, leading to loss or reduction in functionality of the infrastructure.

The concept of resilience has gained relevance in the recent past as a desirable feature for communities (Bruneau et al. 2003; McAllister 2013; Caverzan and Solomos 2014; Ellingwood et al. 2016; Guidotti et al. 2016, 2017; Sharma et al. 2017). In the last fifteen years, researchers have connoted the resilience using several definitions and proposing several approaches to measure resilience in different areas (e.g., engineering, and social science). Resilience, in general, has been defined as the ability of systems to recover after disturbances (e.g., Bruneau et al. 2003; Cimellaro et al. 2010a; Bocchini et al. 2012). The recovery process can be described using *recovery curves*, which play a key role in terms of defining the resilience of a system. The recovery curve captures the changes in the performance of a disturbed system over time, and describes how the system recovers toward a desired system state. Neglecting the occurrence of hazards while the recovery is in progress, the recovery curve is, in general, a non-decreasing function. Different studies have attempted to define recovery curves for different engineering systems subject to hazards (e.g., Cimellaro et al. 2010b; Decò et al. 2013; Titi et al. 2015; Bonstrom and Corotis 2016). The recovery curves are defined based on qualitative descriptors such as the preparedness of communities, which can impact the recovery process. However, the recovery curves are not modeled explicitly as functions of influencing variables that shape the recovery process (e.g., available resources). Furthermore, the recovery curves do not account for the underlying uncertainties and, as a result, it is not possible to estimate the probability of reaching or exceeding a target percentile of interest of the ultimate desired state (i.e., target value of functionality.) Finally, it is not clear how additional information that might become

available while the recovery is in process (such as current progress of the work or increased resource availability) may modify the recovery models and affect/reduce the uncertainty involved (Sharma et al. 2017). Sharma et al. (2017) addressed partially these limitations, proposing a mathematical formulation to model the recovery curves based on the work plan of activities involved in the recovery process. As a result, while the work on individual activities may proceed continuously over time, the changes in the system state occur at discrete points in time when a set of activities is completed. As further discussed in Section 2, Sharma et al. (2017) also introduced a set of metrics, analogous to the moments of a random variable, to quantify the resilience of a system.

This paper proposes a methodology to predict the recovery process of a selected system given past recovery data, and estimate the probability of reaching or exceeding a target value of functionality at any time. The proposed methodology is general and can be applied to different domains, e.g. economical, natural, and engineering systems. Specifically, in the engineering domain, the proposed methodology can be used i) in a reliability-based design to make design decisions and ii) in identifying recovery strategies both with the objective of achieving a target value of functionality within a desired time with a specified level of probability for a given hazard.

In the proposed methodology, we first obtain estimates of the resilience metrics defined according to Sharma et al. (2017) using recovery data for different systems. The uncertainties in the estimates are captured by the joint probability density function (PDF) of the resilience metrics. Parametrized recovery curves are then introduced to model the time-varying recovery process and the joint PDF of the model parameters in the recovery curves is obtained as a function of the joint PDF of the resilience metrics. Then, the joint PDF of the model parameters are used to define the variability in the possibly recovery curves, which is used to evaluate the probability of reaching or exceeding a desired target value of functionality by performing a reliability analysis (Ditlevsen and Madsen 1996; Gardoni 2017). Furthermore, we propose to include the Bayesian inference to update the model parameters, combining prior information with the objective information from the new data as they become available during the recovery process. As an illustration of the proposed methodology, we consider a bridge restoration following seismic damage.

Following this introduction, Section 2 reviews mathematical formulations for resilience analysis. Section 3 shows the proposed methodology. Section 4 includes the numerical example to illustrate the proposed methodology. Finally, Section 5 concludes the article.

2 REVIEW OF MATHEMATICAL FORMULATION FOR RESILIENCE ANALYSIS

Mitigation planning and the allocation of resources in pre- and post-disruption scenarios mostly depend on the resilience analysis of engineering systems (Gardoni et al. 2016). In resilience analysis, the performance of a system (e.g., the system functionality), typically indicated as $Q(t)$, is a time-dependent function that defines the system state (Cimellaro et al. 2010a; Bocchini et al. 2012; Bonstrom and Corotis 2016; Sharma et al. 2017). The functionality of a system may experience an instantaneous drop due to an external shock, such as a natural or anthropogenic hazard (Kumar and Gardoni 2014; Kumar et al. 2015; Jia and Gardoni 2017a,b). After the occurrence of the hazard, recovery activities retrieve the system functionality to a desired level, which may be below, same or better than the pre-disruption value (Ayyub 2014, 2015).

Recovery curves capture the changes in the system functionality and define how the system recover to achieve the desired level of functionality at the end of the recovery process. To quantify the resilience, number of researchers (e.g., Bruneau and Reinhorn 2007; Cimellaro et al. 2010b; Bonstrom and Corotis 2016) have defined a measure as a function of the integral over time of the recovery curves. The first attempts to measure the resilience showed the relevance of quantifying resilience in an objective way. These contributions provided partial information on the resilience of a system (Sharma et al. 2017). For instance, Bruneau et al. (2003) introduced the resilience index R, computed as the area of the region bounded by the recovery curve. Chang and Shinozuka (2004) proposed to quantify resilience as the conditional probability of meeting a desired level of performance, in terms of residual functionality and time to recover, given a seismic event. However, as Sharma et al. (2017) noted, such metrics provide only an incomplete description of resilience, showing that these metrics might provide the same value of resilience in the case of different recovery processes. In response to this limitation, Sharma et al. (2017) introduced a set of partial descriptors of the recovery curve as new resilience metrics in analogy with the partial descriptors commonly accepted in probability and statistics (e.g., mean and standard deviation of a random variable). These resilience metrics have two important features: i) the partial descriptors are simple with clear interpretations, and ii) any subset of partial descriptors can be expanded systematically to include higher order descriptions to eventually fully characterize the resilience of a system. Sharma et al. (2017) called $Q(t)$ the cumulative resilience function (CRF). In the case the CRF is a continuous and differentiable function of the time, we can define the

resilience density function (RDF) q as its time derivative. Instead, in the case the CRF is not continuous and differentiable, we can define a resilience mass function (RMF) to describe changes in the recovery as a step-wise function. Based on these definitions, they introduced the center of resilience ρ and the resilience bandwidth, χ as two fundamental partial descriptors. In most cases, ρ and χ are sufficient to characterize a recovery curve, as well as the mean and the standard deviation are able to fully describe a probability density function. Sharma et al. (2017) also introduced higher order of partial descriptors, such as the skewness of the recovery ψ that measures the symmetry of the recovery process around the center of resilience ρ. The analogy between the resilience metrics and the moments in statistics is consistent with the analogy between the CRF, RDF, RMF and the cumulative distribution function (CDF), the probability density function (PDF) and the probability mass function (PMF) of a random variable.

3 PROPOSED METHODOLOGY

This section describes the proposed methodology to predict a probable recovery curve and to estimate the probability of reaching or exceeding a target value of functionality at any time.

In general, the work progress for civil structures and infrastructure is described through a continuous function over time (Klinger and Susong 2006; Gardoni et al. 2007); conversely, the state of a system experiences a change after the completion of a set of activities (Sharma et al. 2017). Therefore, the functionality of a system can be described as a step-wise function with jumps at the completion of each set of activities (Sharma et al. 2017). This behavior is typical for civil structures and infrastructure, or more generally, engineering systems, whereas the recovery curve of natural systems (e.g., recovery and resilience of tropical forests (Cole et al. 2014; van Leeuwen 2008)) might be a continuous function. The proposed methodology is general and can be applied to both processes described by step-wise and continuous recovery curves. The methodology has the following four steps:

Step 1: Obtaining the joint PDF of the resilience metrics. The first step consists in collecting historical recovery data and obtaining estimates for the resilience metrics reviewed in Section 2. Then, we can construct the joint PDF of the resilience metrics with prescribed marginals and covariances (Liu and Der Kiureghian, 1986).

Step 2: Obtaining the joint PDF of the parameters of the recovery curve. The second step calls for introducing parametrized recovery curves to model the time-varying recovery process. We consider a parametrized CRF to describe the recovery process over time of a general performance measure in the following form:

$$Q(\boldsymbol{\Theta},\tau) = Q(\boldsymbol{\theta},\tau) + \sigma\varepsilon \tag{1}$$

where $\boldsymbol{\Theta} = (\boldsymbol{\theta},\sigma)$ is a set of unknown model parameters that needs to be estimated; $\boldsymbol{\theta} = (\theta_1,\ldots, \theta_n)$; and $\sigma\varepsilon$ is an additive model error term of Q (additivity assumption), in which σ is the standard deviation of the model error, assumed not to depend on τ (homoskedasticity assumption), and ε is a standard normal random variable (normality assumption). The homoskedacity and the normality assumptions can be satisfied using an appropriate variance stabilizing transformation from the parametrized family of transformations introduced by Box and Cox (1964). Mathematically, we can write the n^{th} resilience metric, $\rho^{(n)}$, as follows:

$$\rho^{(n)} := \frac{\int_0^{T_R} \tau^n q(\tau)\, d\tau}{\int_0^{T_R} q(\tau)\, d\tau} \tag{2}$$

where T_R is the recovery time, that is the time needed to achieved the desired level of functionality; and $q(\tau)$ is the instantaneous rate of recovery progress (i.e., the resilience density function (RDF).

We can then use compute the joint PDF of the model parameters $\boldsymbol{\Theta}$ based on the joint PDF of the resilience metrics (Hogg et al. 2012). Let the set (ρ, χ,..., $\rho^{(n)}$) follow a joint PDF $f_{\boldsymbol{P}}$ (ρ, χ,..., $\rho^{(n)}$) on a support set C. Based on the definition of the resilience metrics, the resilience metrics are a function of $\boldsymbol{\theta} = (\theta_1,\ldots, \theta_n)$, in the support set D, such that $\rho = k_1(\theta_1,\ldots, \theta_n)$, $\chi = k_2(\theta_1,\ldots, \theta_n)$, up to $\rho^{(n)} = k_n(\theta_1,\ldots, \theta_n)$. We evaluate the Jacobian given by

$$\mathrm{J} = \begin{bmatrix} \frac{\partial\rho}{\partial\theta_1} & \frac{\partial\rho}{\partial\theta_2} & \cdots & \frac{\partial\rho}{\partial\theta_n} \\ \frac{\partial\chi}{\partial\theta_1} & \frac{\partial\chi}{\partial\theta_2} & \cdots & \frac{\partial\chi}{\partial\theta_n} \\ \vdots & \vdots & \ddots & \vdots \\ \frac{\partial\rho^{(n)}}{\partial\theta_1} & \frac{\partial\rho^{(n)}}{\partial\theta_2} & \cdots & \frac{\partial\rho^{(n)}}{\partial\theta_n} \end{bmatrix} \tag{3}$$

and its determinant $|\boldsymbol{J}|$, and then write the joint PDF of $\boldsymbol{\theta}$ as

$$f_{\boldsymbol{\theta}}(\theta_1,\ldots,\theta_n) = \begin{cases} f_{\boldsymbol{\theta}}[k_1(\theta_1,\ldots,\theta_n),\ldots, \\ k_n(\theta_1,\ldots,\theta_n)]\,|J| & (\theta_1,\ldots,\theta_n)\in D \\ 0 & \text{elsewhere} \end{cases} \tag{4}$$

We can now derive the expected recovery curve accounting for the relevant uncertainties based on the distribution of the parameters in Eq. (1).

Step 3: Estimating the probability of reaching or exceeding a target percentile of interest of the ultimate desired state. Once we obtained $Q(\boldsymbol{\Theta},\tau)$, we can estimate the probability of reaching or exceeding a target value of functionality at any time using the conventional rules of the reliability analysis (Ditlevsen and Madsen 1996; Gardoni 2017). We define the limit-state function $g(\boldsymbol{\Theta},\tau)$ as follows:

$$g(\boldsymbol{\Theta},\tau) = Q(\boldsymbol{\Theta},\tau) - Q_T \tag{5}$$

where Q_T is the target percentile of interest of the ultimate desired state, Q_∞. We introduce the time-dependent function $H(\tau)$ that expresses the probability that of reaching or exceeding a target value of functionality at any time as

$$H(\tau) = 1 - \mathbb{P}\left[g(\boldsymbol{\Theta},\tau) \le 0 \middle| \tau \right] \tag{6}$$

Figure 1 shows the conceptual representation of the function $H(\tau)$ over time.

We also propose to use the results from the first order reliability analysis to estimate confidence bounds on the estimate in Eq. (6). Following Gardoni et al. (2002), the variance of the reliability index $\beta(\boldsymbol{\Theta},\tau)$ can be written as

$$\sigma_\beta^2(\tau) \approx \nabla_{\boldsymbol{\Theta}} \beta(\tau) \boldsymbol{\Sigma}_{\boldsymbol{\Theta}\boldsymbol{\Theta}} \nabla_{\boldsymbol{\Theta}} \beta(\tau)^T \tag{7}$$

where $\nabla_{\boldsymbol{\Theta}}\beta(\tau)$ is the gradient of $\beta(\boldsymbol{\Theta},\tau)$ computed at the mean value, and $\boldsymbol{\Sigma}_{\boldsymbol{\Theta}\boldsymbol{\Theta}}$ is the posterior covariance matrix. Therefore, we obtain the one standard deviation bounds, representing approximately 15% and 85% probability levels as

$$\left\{ \Phi\left[-\tilde{\beta}(\tau) - \sigma_\beta(\tau) \right], \Phi\left[-\tilde{\beta}(\tau) + \sigma_\beta(\tau) \right] \right\} \tag{8}$$

where $\tilde{\beta}(\tau)$ is the mean of the reliability index.

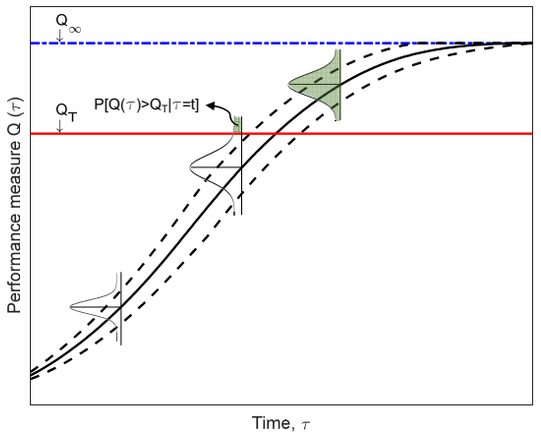


Figure 1. Conceptual representation of probability of reaching or exceeding a target value of functionality at any time

Step 4: Updating the model parameters as new data become available. The fourth step includes the Bayesian inference to update the model parameters, combining prior information with the information from the new data as they might become available during the recovery process. The Bayesian inference allows adjusting the previous prediction based on the observed data in terms of the actual recovery process (Gardoni et al. 2007).

Based on the availability of new data while the recovery process advances, we propose to update the state of knowledge of the parameters $\boldsymbol{\Theta}$ (Gardoni et al. 2002; Gardoni et al. 2007) as described in Step 4 of the proposed methodology. Mathematically, we can write the posterior distribution $f'(\boldsymbol{\Theta})$ as (Box and Tiao, 1992)

$$f'(\boldsymbol{\Theta} \mid \mathbf{Q}) = \kappa L(\boldsymbol{\Theta} \mid \mathbf{Q}) f(\boldsymbol{\Theta}) \tag{9}$$

where κ is a normalizing factor; $L(\boldsymbol{\Theta}|\mathbf{Q})$ is the likelihood function that contains the objective information on $\boldsymbol{\Theta}$; and $f(\boldsymbol{\Theta})$ is the prior distribution, reflecting the state of knowledge about $\boldsymbol{\Theta}$ prior to obtaining the observations $\mathbf{Q} = (Q_1,\ldots,Q_m)$, considering the time at which they are measured.

Furthermore, (9) can be used every time additional information is available to update the model. Therefore, if n independent set of observations are available, we can write as follows:

$$f(\boldsymbol{\Theta} \mid \mathbf{Q}_1,\ldots,\mathbf{Q}_k) \propto L(\boldsymbol{\Theta} \mid \mathbf{Q}_k) f(\boldsymbol{\Theta} \mid \mathbf{Q}_1,\ldots,\mathbf{Q}_{k-1}) \quad k = 2,\ldots,n \tag{10}$$

The prior distribution incorporates the status of knowledge based on previous experiences or engineering judgments. We propose to adopt the joint PDF computed in Eq. (4) as the prior distribution of $\boldsymbol{\theta} = (\theta_1,\ldots,\theta_n)$. Generally, considering the set of parameters $\boldsymbol{\Theta} = (\boldsymbol{\theta},\sigma)$, $\boldsymbol{\theta}$ and σ are assumed independent.

The likelihood function allows transferring the observed information into the model. The benefits of using this approach is in the possibility of including lower, upper and equality data (Gardoni et al. 2002, 2007). A lower bound datum is defined as an observed lower bound Q_t at time τ; an upper bound datum is defined as an observed upper bound Q_t at time τ; an equality datum is defined as the recorded state during the recovery process at time τ. Thus, based on the normality assumption, we write the likelihood function as (Gardoni et al. 2002)

$$\begin{aligned} \mathrm{L}(\boldsymbol{\theta},\sigma) \propto & \prod_{\substack{\text{equality} \\ \text{data}}} \left\{ \frac{1}{\sigma} \varphi\left[\frac{Q_t - Q(\boldsymbol{\theta},\tau)}{\sigma} \right] \right\} \\ & \times \prod_{\substack{\text{lower bound} \\ \text{data}}} \left\{ \Phi\left[-\frac{Q_t - Q(\boldsymbol{\theta},\tau)}{\sigma} \right] \right\} \\ & \times \prod_{\substack{\text{upper bound} \\ \text{data}}} \left\{ \Phi\left[\frac{Q_t - Q(\boldsymbol{\theta},\tau)}{\sigma} \right] \right\} \end{aligned} \tag{11}$$

where $\varphi(\cdot)$ is the standard normal PDF, $\Phi(\cdot)$ is the standard normal CDF, and Q_t is the recorded datum.

The main benefits of the proposed methodology are that the predictive Q is simply defined as a function of resilience metrics, and the prediction can take

advantage of collected data both before and during the recovery process.

4 EXAMPLE

This section illustrates the proposed methodology considering the recovery process of a typical RC bridge subject to a seismic excitation.

4.1 Example: Discrete Recovery Curve for a Single Column Single Bent Bridge

As previously discussed, the functionality of engineering structures can be described as a step-wise function with jumps occurring when a set of activities associated with a change in functionality is completed. In this section, we illustrate the proposed methodology using a typical reinforce concrete (RC) bridge damage by a seismic excitation. Figure 2 shows the configuration of the considered bridge (single column, single bent).

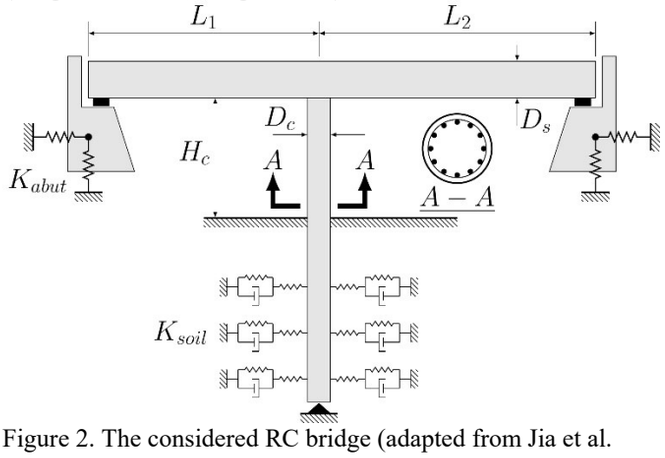


Figure 2. The considered RC bridge (adapted from Jia et al. 2017)

As for the first step of the proposed methodology, we obtain the estimates of the first two resilience metrics, ρ and χ, and their marginal distributions. Based on the observed data, we assume that ρ and χ follow a lognormal distribution, whose parameters are listed in Table 1.

Table 1. Distribution parameters of the resilience metrics

Resilience metric	λ	ξ
ρ	–0.94	0.22
χ	1.14	0.20

Then, we construct the joint PDF of the resilience metrics with the prescribed marginal distributions and covariances. Figure 3 shows the pair (ρ, χ) and their correlation. Most of the data follow in the zoomed range and the correlation coefficient is estimated as illustrated in Fig. 3.

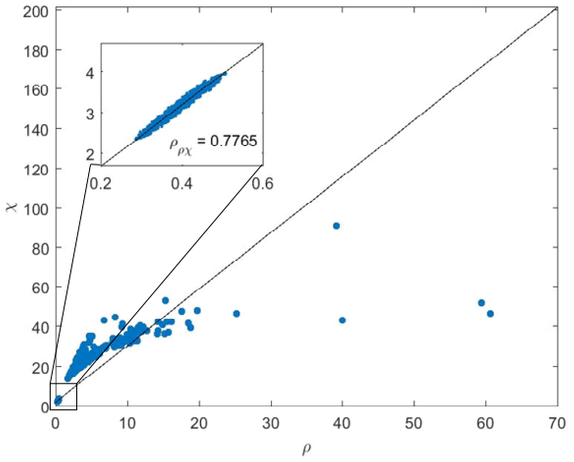


Figure 3. Correlation between the adopted resilience metrics

Then, we introduce a parametrized recovery curve to describe the changes in a selected performance indicator over time. The performance indicator considered in this example is the instantaneous reliability index β. We assume there is only one recovery step that restores the reliability of the bridge, as described in Sharma et al. (2017). Consequently, the mathematical model can be expressed in the form:

$$Q(\boldsymbol{\Theta},\tau)=\begin{cases}\theta_0 & \tau<\theta_1\\ Q_\infty & \tau\geq\theta_1\end{cases} \tag{12}$$

where θ_0 is the residual reliability index after the occurrence of the hazard and before the completion of the recovery, and θ_1 is the time at which the reliability index reaches the ultimate desired state Q_∞. Based on the definition of the resilience metrics, the variables θ_0 and θ_1 can be written as a function of the resilience metrics. Specifically, Figure 4 shows the RMF of the adopted parametrized recovery curve.

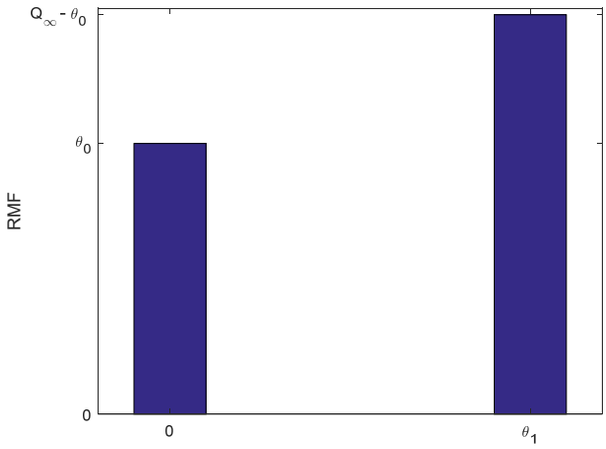


Figure 4. RMF of the adopted parametrized recovery curve

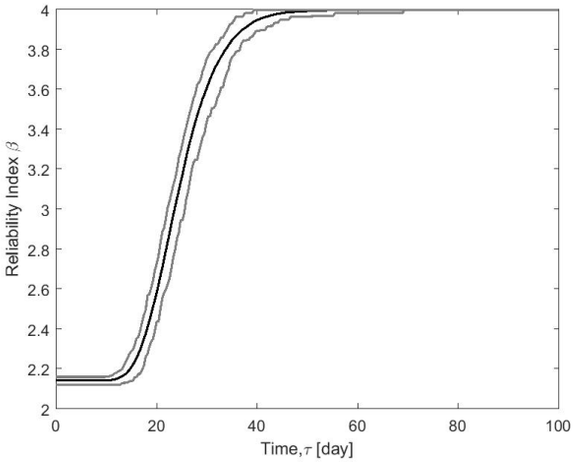


Figure 5. Mean value and corresponding 95% confidence band of the recovery curve

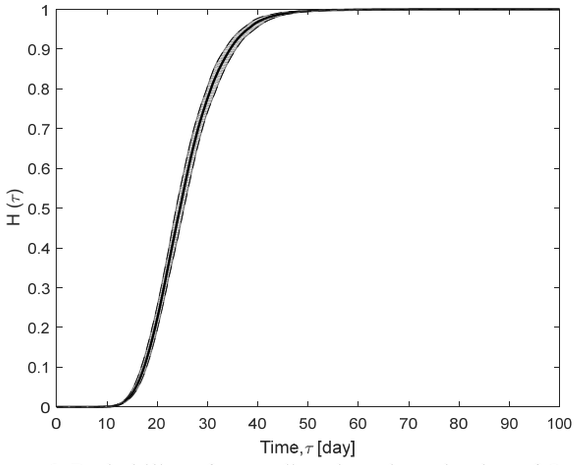


Figure 6. Probability of exceeding the selected value of Q_T = 3.5

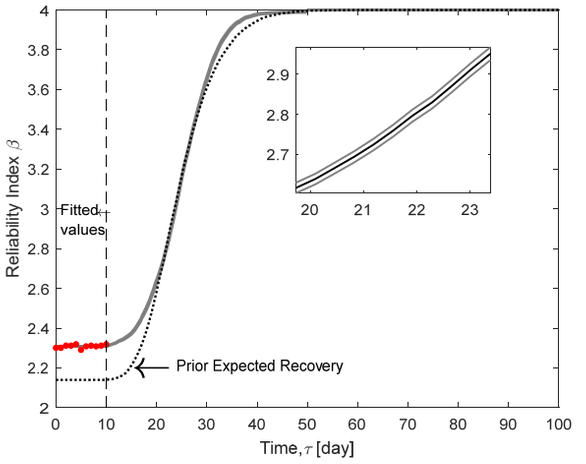


Figure 7. Mean value and corresponding 95% confidence band of the recovery curve after updating the model parameters

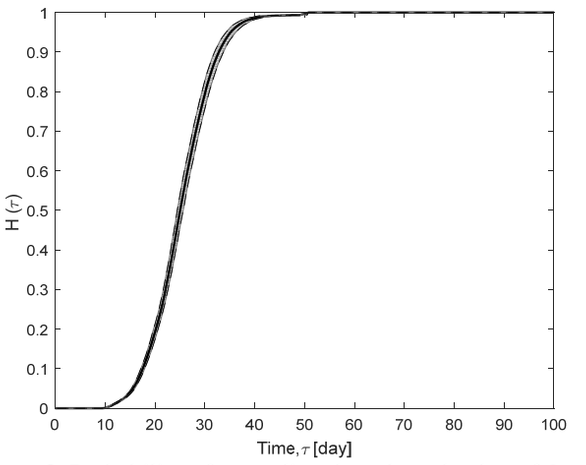


Figure 8. Probability of exceeding the selected value of Q_T = 3.5 after updating the model parameters

Following the proposed methodology, we obtain the joint PDF of the parameters of the recovery curve and the corresponding expected recovery process in terms of the instantaneous reliability index β. Consequently, we estimate the probability of reaching or exceeding a target value of functionality at any time, setting for example $Q_T = 3.5$.

Figure 5 shows the expected changes of the instantaneous reliability over time. Figure 6 shows the probability of exceeding the selected value of Q_T. The figure also presents the confidence band due to the statistical uncertainty in $\boldsymbol{\Theta}$.

To illustrate Step 4 of the propose methodology, we assume that after the occurrence of the hazards, we collect data on the state of damage for the first ten days and we update the model parameters. As a result, we obtain the new expected recovery process and the corresponding probability of reaching or exceeding the same value of the target functionality at any time, as shown in Figure 7 and 8.

5 CONCLUSIONS

This paper proposed a probabilistic methodology to predict a probable recovery curve of a system after the occurrence of a hazard and to estimate the probability of reaching or exceeding target percentile of interest of the ultimate desired state. The methodology consists of four steps.

Based on historical data, first we estimate resilience metrics associated to typical recoveries. Then, parameterized recovery curves are introduced and the joint probability density function (PDF) of the model parameters is obtained using general rules of probability theory as a function of the distribution of the resilience metrics. Then, a reliability analysis is used to estimate the probability of reaching or exceeding a target percentile of interest of the ultimate desired state. The proposed methodology also incorporated a Bayesian updating procedure to update the estimates as new data might become available. The paper showed the proposed methodology by model-

ing the recovery of a typical reinforced concrete (RC) bridge.

ACKNOWLEDGEMENTS

This work was supported in part by the National Science of Foundation (NSF) under Award No. 1638346 and by the National Institute of Standards and Technology (NIST) through the Center for Risk-Based Community Resilience Planning under Award No. 70NANB15H044.
The research leading to these results has also received funding from the European Research Council under the Grant Agreement n° ERC_IDEAL RESCUE_637842 of the project IDEAL RESCUE-Integrated Design and Control of Sustainable Communities during Emergencies.
Opinions and findings presented are those of the writers and do not necessarily reflect the views of the sponsor.

REFERENCES

Ayyub, B. M. 2014. Systems resilience for multihazard environments: Definition, metrics, and valuation for decision making. *Risk Analysis* 34(2): 340–355.

Ayyub, B. M. 2015. Practical resilience metrics for planning, design, and decsion making. *Journal of Risk Uncertainty in Engineering Systems, Part A: Civil Engineering* 1(3): 04015008.

Bocchini, P., Decò, A., and Frangopol, D. M. 2012. Probabilistic functionality recovery model for resilience analysis. *Bridge Maintenance, Safety, Management, Resilience and Sustainability*, Biodini and Frangopol (Eds): 1920–1927.

Bonstrom, H., and Corotis, R. B. 2016. First-Order Reliability Approach to Quantify and Improve Building Portfolio Resilience. *Journal of Structural Engineering* 142(8): C4014001.

Box, G. E. P., and Cox, D. 1964. An analysis of transformations. *Journal of the Royal Statistical Society: Series B* 26: 211-252.

Box, G. E. P., and Tiao, G. C. 1992. *Bayesian inference in statistical analysis*. John Wiley & Sons.

Bruneau, M., Chang, S. E., Eguchi, R. T., Lee, G. C., O'Rourke, T. D., Reinhorn, A. M., Shinozuka, M., Tierney, K., Wallace, W. A., and von Winterfeldt, D. 2003. A Framework to Quantitatively Assess and Enhance the Seismic Resilience of Communities. *Earthquake Spectra* 19(4): 733–752.

Bruneau, M., and Reinhorn, A. 2007. Exploring the Concept of Seismic Resilience. *Earthquake Spectra* 23: 41-62.

Caverzan, A., and Solomos, G. 2014. Review on resilience in literature and standards codes for critical built-inrastructures. *JRC Science and Policy Report*.

Chang, S. E., and Shinozuka, M. 2004. Measuring Improvements in the Disaster Resilience of Communities. *Earthquake Spectra* 20(3): 739–755.

Cimellaro, G. P., Reinhorn, A. M., and Bruneau, M. 2010a. Seismic resilience of a hospital system. *Structure and Infrastructure Engineering* 6(1): 127–144.

Cimellaro, G. P., Reinhorn, A. M., and Bruneau, M. 2010b. Framework for analytical quantification of disaster resilience. *Engineering Structures* 32(11): 3639–3649.

Cole, E. S. L., Bhagwat, S. A, and Willis, K. J. 2014. Recovery and resilience of tropical forests after disturbance. *Nature Communications* 5(1): 59–65.

Collins English Dictionary Complete and Unabridged edition 12th edition. (2014)

Corotis, R. 2009. Societal issues in adopting life-cycle concepts within the political system. *Structure and Infrastructure Engineering* 5:3906.

Decò, A., Bocchini, P., and Frangopol, D. M. 2013. A probabilistic approach for the prediction of seismic resilience of bridges. *Earthquake Engineering & Structural Dynamics* 42(10): 1469–1487.

Ditlevsen, O., and Madsen, H. O. 1996. *Structural reliability methods*, Wiley, New York.

Ellingwood, B. R., Cutler, H., Gardoni, P., Peacock, W. G., van de Lindt, J. W., and Wang, N. 2016. The Centerville Virtual Community: a fully integrated decision model of interacting physical and social infrastructure systems. *Sustainable and Resilient Infrastructure* 1(3–4): 95–107.

Gardoni, P., Der Kiureghian, A., and Mosalam, K. M. 2002. Probabilistic Capacity Models and Fragility Estimates for Reinforced Concrete Columns based on Experimental Observations. *Journal of Engineering Mechanics* 128(10): 1024–1038.

Gardoni, P., Mosalam, K. M., and Der Kiureghian, A. 2003. Probabilistic seismic demand models and fragility estimates for RC bridges. *Journal of Earthquake Engineering* 7(Special Issue 1): 79–106.

Gardoni, P., Reinschmidt, K. F., and Kumar, R. 2007. A probabilistic framework for Bayesian adaptive forecasting of project progress. *Computer-Aided Civil and Infrastructure Engineering* 22(3): 182–196.

Gardoni, P., and LaFave, J. M. (Eds.) 2016. *Multi-hazard Approaches to Civil Infrastructure Engineering*, Springer International.

Gardoni, P., Murphy, C., Rowell, A., (Eds.) 2016. *Societal Risk Management of Natural Hazards*, Springer.

Gardoni, P. (Ed.) 2017. *Risk and Reliability Analysis: Theory and Applications*. Springer International Publishing.

Guidotti, R., Chmielewski, H., Unnikrishnan, V., Gardoni, P., McAllister, T., and van de Lindt, J. 2016. Modeling the resilience of critical infrastructure: the role of network dependencies. *Sustainable and Resilient Infrastructure* 1(3–4): 153–168.

Guidotti, R., Gardoni, P., and Chen, Y. 2017. Network reliability analysis with link and nodal weights and auxiliary nodes. *Structural Safety* 65: 12–26.

Hogg, R. V., McKean, J. W., and Craig, A. T. 2012. *Introduction to Mathematical Statistics*. 7th Edition, Prentice Hall College Div.

Jia, G., Tabandeh, A., and Gardoni, P. 2017. Life-Cycle Analysis of Engineering Systems: Modeling Deterioration, Instantaneous Reliability, and Resilience. *Risk and Reliability Analysis: Theory and Applications*,

P. Gardoni, (Ed.), Springer International Publishing.

Jia, G., and Gardoni, P. 2017a. State-dependent stochastic models: A general stochastic framework for modeling deteriorating engineering systems considering multiple deterioration processes and their interactions. *Structural Safety* (under review).

Jia, G., and Gardoni, P. 2017b. Stochastic life-cycle analysis: Renewal-theory life-cycle analysis with state-dependent deterioration stochastic models. *Reliability Engineering and System Safety* (under review).

Klinger, M., and Susong, M. 2006. *The construction project : phases, people, terms, paperwork, processes*. American Bar Association.

Kumar, R., and Gardoni, P. 2014. Renewal theory-based life-cycle analysis of deteriorating engineering systems. *Structural Safety* 50: 94–102.

Kumar, R., Cline, D., and Gardoni, P., 2015. A stochastic framework to model deterioration in engineering systems. *Structural Safety* 53: 36-43.

Liu, P-L., and Der Kiureghian A. 1986. Multivariate Distributions Models with Prescribed Marginals and Covariances. *Probabilistic Engineering Mechanics* 1(2): 105-112.

McAllister, T. 2013. *Developing Guidelines and Standards for Disaster Resilience of the Built Environment: A Research Needs Assessment*. Gaithersburg, MD.

Sharma, N., Tabandeh, A., and Gardoni, P. 2017. Resilience analysis: a mathematical formulation to model resilience of engineering systems. *Sustainable and Resilient Infrastructure* DOI: 10.1080/23789689.2017.1345257.

Titi, A., Biondini, F., and Frangopol, D.M. 2015. Seismic resilience of deteriorating concrete structures. *Structures Congress*.

Van Leeuwen, W. J. D. 2008. Monitoring the effects of forest restoration treatments on post-fire vegetation recovery with MODIS multitemporal data. *Sensors* 8(3): 2017-2042.

Maintenance, Safety, Risk, Management and Life-Cycle Performance of Bridges – Powers, Frangopol, Al-Mahaidi & Caprani (Eds)
© 2018 Taylor & Francis Group, London, ISBN 978-1-138-73045-8

Computational Investigation on the Piers of a U-Slab Bridge under Raising Flood Intensity

M. Nasim & S. Setunge & H. Mohseni & SW. Zhou
RMIT University, Melbourne, Australia

ABSTRACT:
The resistance to flood and debris loading is a critical parameter affecting the design of bridges under flood loading. For instance, bridges partially or completely immersed into water in extreme flood will result in very notable hydrodynamic loads on decks and piers. Based on previous studies on the nature of the pressure resulted from the water flow on the structure, we herein investigate the performance of pier under raising intensity of flood using finite element analysis. In addition, we evaluate the effect of bed fixity and the different damage levels of the pier. Furthermore, the probability of the damage in various levels of flood loading is also summarized and analyzed, which will be helpful for enhancing the resilience of the road infrastructures.

1 INTRODUCTION

1.1 *Background*

Flooding caused around $50 billion damages in the U.S. in the 1990s according to the National Weather Service (NWS) estimation (NWS-HIC 2001). Although flood damage fluctuates considerably from year to year, estimates reveal that the trend is still increasing over the past century (Pielke Jr and Downton, 2000).

There are far higher structural and environmental uncertainties, which must be considered when assessing existing bridges. Most concrete structural failures occur during the construction phase or due to massive ecological calamities (Khan, 2014). Based on the Melbourne Water (2005) reports, most costly natural disasters in Australia from 1967 to 1999 are riverine flooding (average $314 million annually) and severe storms ($284.2 million) (Melbourne and Water, 2005). Over the last 30 years, numerous bridges were damaged by flooding. The Schoharie Creek Bridge (Storey et al., 2003) in New York destroyed in 1987. The Hatchie Bridge (Cao et al., 2009) in Tennessee destroyed in April 1989, and the Hintze Ribeiro Bridge (Sousa J.J. and Bastos L., 2013) in Portugal damaged in 2001. The damages to these bridges are entirely or partially attributed to the losses to piers. A vast number of bridges are built across rivers, and usually, the water flow forces on the structure are calculated by the approaches mentioned in the design standards. The acceptable structural design and damage assessment related to the well understanding of each element of the bridge behaviour and the damage mechanisms of each part.

Floods can cause bridges to collapse in a few different ways. Severe floods, such as rapid onset and flash flooding, can cause rivers and creeks to overflow, picking up debris such as trees, cars and parts of houses in the process. When the river passes under a bridge, the high water level smashes the debris into the bridge. The shear impact of the debris can cause immediate bridge failure, or the weight of the debris piled up combined with the immense force of the fast-flowing water pushing on it can cause the bridge to fail more gradually.



Figure1. Bridge collapse cause by Cumbria floods (BBC2009)

Inverted U-slab bridges are one of the most vulnerable and old concrete bridge structures in Australia, specifically in Victoria, based on the Vic-Roads reports (Vicroads, 2014). The piers are slender and fragile to the effect of scour and flood pressure notably when the debris outstandingly increases the pressure on the thin elements of the bridge. Hughes et al. (2007), Investigated the soil subgrade modulus effect on a pile bent's pushover buckling capacity on scoured bridges, under axial loads and a small amount of lateral load has insignificant force except when the soil module is very low (Hughes et al., 2007). Fiang et al. (2015) analysed the impact of extreme scour on the buckling stability of bridge piles in soft layered clay. Schambeau et al. (2014) expanded a screening tool to evaluate the buckling failure of the bridge timber pile bent in extreme scour. Lin et al. (2012) employed the integrated

analysis method to assess the lateral response and the buckling capacity of a bridge pile group to assess the susceptibility of bridges to scour, before, during, or after a scour event (Lin et al., 2012). The significance of stability analysis in the maintenance of the existing bridges has to do with scouring which may cause catastrophic bridge failures (Jackson et al., 1991). The nonlinear stability of the pile group foundation under the scour phenomena are studied, and the soil properties and the soil-structure interaction of the pile are taken into account (Zhao Zhong, 1999) and found that the soil properties have a significant influence on the buckling behaviour of the piles.



Figure 2. Kiewa Valley Highway Bridge, Broken Pier and Debris, December 2010 (Vicroads, 2014)

1.2 *Structural stability*

In civil engineering area, stability means the power of the structure to withstand for an identified time all the loads and forces that may be brought to bear on it. Generally, structures may lose their stability in two ways: buckling and flutter, depending on the system and its environment, as far as static methods are concerned. Buckling of structures is a phenomenon in which an existing state of equilibrium or type of behaviour of the structure subjected to apply compressive loading may suddenly change into a new equilibrium state or a new type of reaction. Stability equations for discrete models may be constructed using various devices. For FEM models only energy methods are practical. All techniques eventually lead to matrix stability equations that take the form of an algebraic Eigenproblem. Reaching a critical point may lead to immediate destruction (collapse) of the structure. Excessive lateral drifts cause visual or functional sagging, failure or cracking on the structure

The plastic limit state of a structure of the perfectly-plastic material, “pl”, is the state in which for the first time in the loading history the displacements, u_i, can increase under constant external forces, if geometrical changes are disregarded. Stability can also be defined regarding the total potential energy Π of the structure. Recall that the sum of the strain energy, U, stored in the deformed elastic body and the loss of the potential of the generalized external forces, If the total potential energy increases during a virtual displacement, then the equilibrium configuration is defined to be stable. If the sum of strain energy decreases or remains unchanged, the configuration is unstable (Yoo and Lee, 2011).

1.3 *Pushover Analysis*

Structural behaviour can be monitored with the nonlinear static analysis in which the load is applied incrementally to the structure. Nonlinear static methods of analysis (pushover) establish the capacity curve of a structure. In pushover analysis procedures, the behaviour of the structure is character bed by a capacity curve. In general, when nonlinear response develops in the pushover analysis, the displacements of the element will increase disproportionately with increasing load (Hernandez-Montes et al., 2004). ABAQUS offers a general framework for material failure modelling that allows the combination of multiple failure mechanisms acting simultaneously on the same material. Material failure refers to the complete loss of load-carrying capacity that, results from progressive degradation of the material stiffness. The stiffness degradation process is modelled using damage mechanics (Systèmes, 2013).

2 VERIFYING MODEL OF THE CONCRETE BEAM USING CONCRETE DAMAGE PLASTICITY (CDP)

2.1 *Concrete and steel reinforcement*

A damaged stage is the stage where plans are made to detect a problem in the structure so that it could be taken care of before the occurrence of a fault (Worden and Dulieu-Barton, 2004). The compressive model used in this study translates the stress-strain behaviour of concrete is the concrete damaged plasticity (CDP) model (Carreira and Chu, 1985). However, in this study, tensile concrete modelling was the focus, so a suitable compressive model was chosen, which depended on the modulus of elasticity and the compressive strength of concrete. The concrete damaged plasticity (CDP) model is capable of carrying out the static and dynamic analysis of RC members with bars embedded. The model includes isotropic material, which accounts for tensile cracking and the compressive crushing modes. The model is also capable of stiffness degradation with the irreversible damage that occurs during the fracture process (Rodríguez Soler et al., 2013). For the CDP model, the default values of the

dilation angle, eccentricity, fb0/fc0, K and viscosity parameter were used as 35, 0.1, 1.16, 0.667 and 0.01, respectively. These parameters were also used with some variations in other models (López-Almansa et al., 2014, Kmiecik and Kamiński, 2011). Two types of steel reinforcement were used. Plain bars with 6 mm diameter were used for the top reinforcement and transverse reinforcement while 10 mm bars were used as the primary tension reinforcement. The properties of the steel reinforcement are from (Hanif et al., 2016)

2.2 *Finite element simulation*

A model of a simply supported reinforced concrete beam with multiple cracks is developed to examine its use for damage detection and structural health monitoring using commercial software ABAQUS 6.14. The model illustrates some nonlinearity in the static response of damaged beam. The force-displacement relationship in the model has been compared with the experimental model studying on the crack model for damage detection in reinforced concrete structure (Hamad et al., 2011). The model's nonlinear behaviour shows a very close trend to the experimental model's behaviour under static loading. Figure 3 shows how the analysis trend is close to the experimental response.

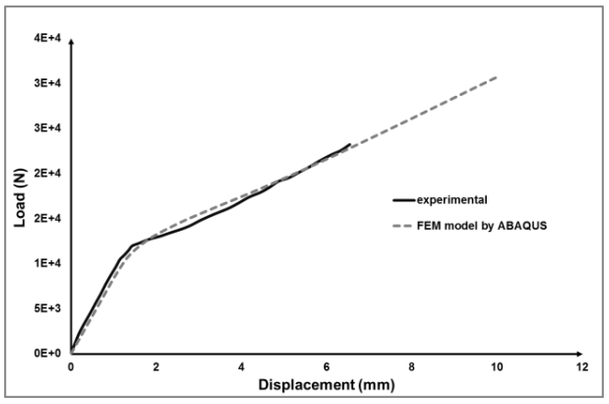


Figure 3: static load-displacement curve for mid-span cracked region

The cracking pattern was compared with the analytically developed flexural model, which is capable of detecting damage through non-linearity in Figure 4 and Figure 5. The reason for crack investigating crack propagation was to validate the capability of the present study for mixed-mode crack formation. The significant cracks seemed to be significantly vertical to match the cracking pattern predicted by similar research.

From the results 11.5 KN forces is the crack appearance phase in the beam, and from the next pushover analysis result, which can be seen in Figure 4, the approximate maximum load that the beam can take is 45 KN. It is comparable with the maximum pressure capacity overtaken by Hanif (Hanif et al., 2016).

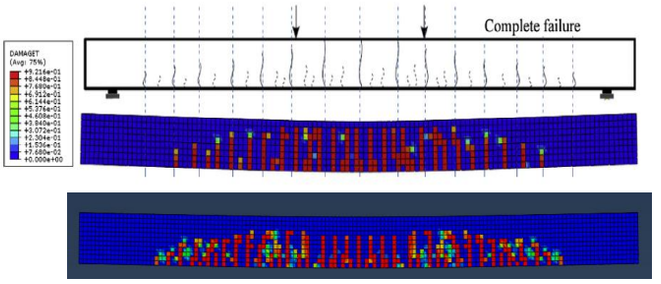


Figure 4: comparison of simulated cracking pattern (below) with Hamad et al., (Hanif et al., 2016, Hamad et al., 2011)(above) and Hanif et a.,l (Hanif et al., 2016) (middle)

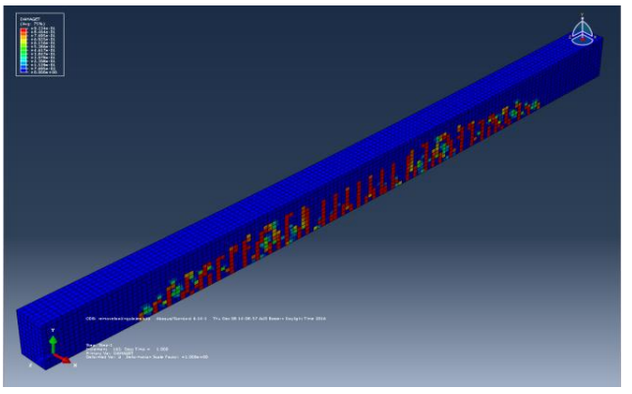


Figure 5: 3-D simulated cracking pattern for 4-point load from ABAQUS

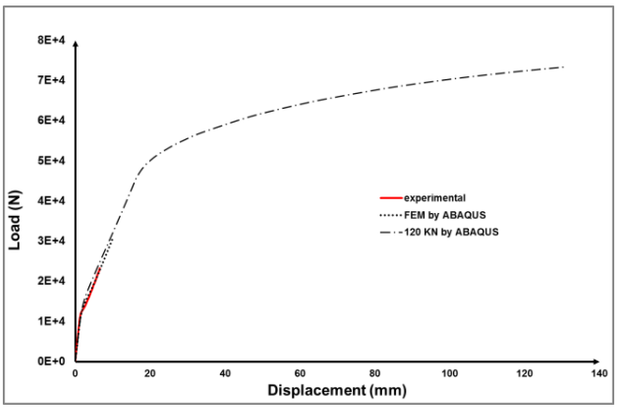


Figure 6: static load-displacement curve for mid-span (envelope curve)

3 SIMULATION AND METHODOLOGY

3.1 *FE simulation and nonlinear analysis*

The verified model in the previous phase is similar to the bridge pier, so the model is decided to be used to recognise the model's behaviour under flood loading as a uniform pressure on its face.

There are two models which the first model is fix in the foundation and is pin for the second model, and

both can rotate from the top. And actually, the piers connection to the superstructure is a simple connection (Vicroads, 2014). The concrete and steel properties are described in table 1 and 2.

Table 1: Mechanical properties of steel reinforcement

Bar type	Diameter (mm)	f_y (MPa)	E_s (MPa)	ε_s	ν	ρ kg/m^3
Plain bars	6	393.600	208,000	0.25	0.3	7850
Main bars	10	540.800	199,200	0.32	0.3	7850

Table 2: Mechanical properties of concrete

Density Tonne/mm^3	f_{cu} MPa	f_{ct} MPa	E_c MPa	ν –
2.4E−9	36.5	3.65	26957.85	0.15

The concrete properties and all damage plasticity models have assumed as well as Hanif et al. (2014). Commercial software ABAQUS 6.14 was used for the analysis. The selected pier is shown in Figure 6. The static push-over analysis is performed with the incremental static load as a percentage of damage. The approximate maximum pressure that the beam can take is 45 KN. The total load was incrementally applied in increments of approximately 10–15% of the maximum load and was specified as the percentage of damage.

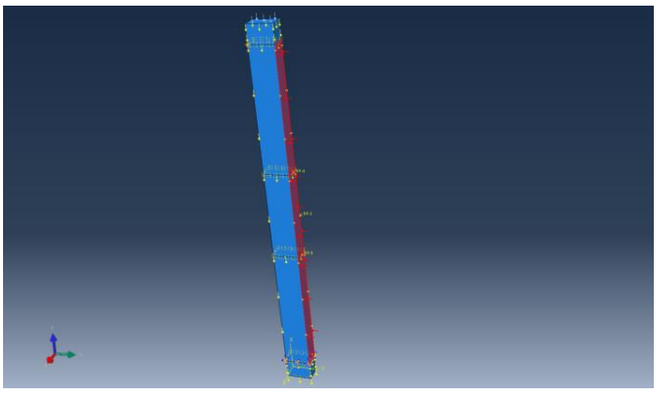


Figure 7: Piers simulation using ABAQUS and the water flow pressure applied on the front face

Based on the previous study on the pressure behaviour of the water flow around a rectangular pier as a case study (Nasim M. et al., 2015), the water flow pattern as a uniform is reasonable for different water flow velocities. Based on this survey the pressure distribution assumed as a uniform pattern along the pier model. The pressure is considered 1 (MPa), in which the force is applied to the model from 0 to 1 incrementally. The piers weight is taking into consideration in the analysis as well as the piers axial load capacity which is calculated based on the axial load capacity of the beam-column theories. Mesh sensitivity analysis has been done to verify the model in the previous phase of verification.

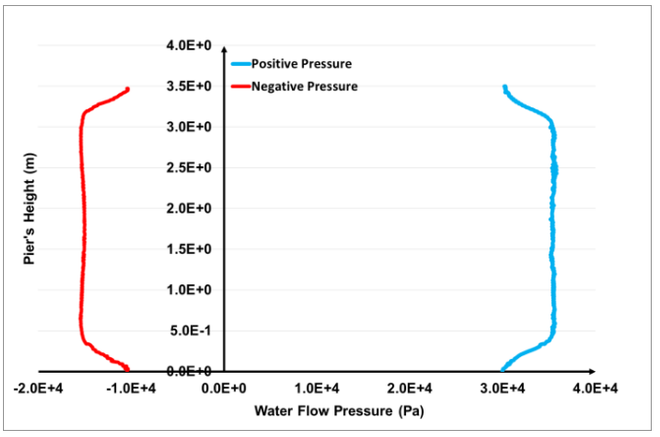


Figure 8: water flow pressure pattern along the pier's height when the water flow velocity is 6.5 m/s.

The boundary condition is a pin at the top of the pier as the pier and superstructure connection is a simple connection and the bed fixity is assumed as a fix when the bed fixity is hard enough and is considered as a pined model to show the very loose soil condition. 3 degrees of freedom are used for the simply supported end. In the analysis, deformation can be represented by three independent displacements (DOF).

3.2 *Methodology*

The beam behaviour under 4 point loads can describe the different damage phases, for example, the first changes in the load-displacement curve are the crack initiation phase in which the system stiffness is decreasing.

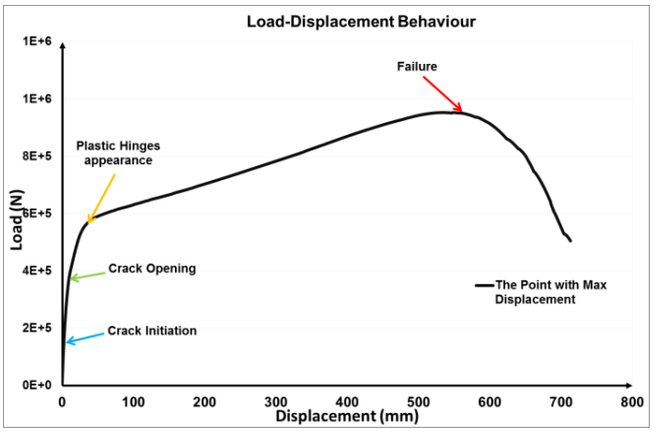


Figure 7: static load-displacement curve for mid-span Maximum load undertaken (envelope curve)

The model's pushover analysis under four-point loads, more than its capacity can give us an idea of the structure's damage levels. Figure 7 is the load-displacement of the mid-span of the beam, and it shows how it is behaving under 4 pints load. Form this curve the four different levels of damage to the

structure is definable. The first level of damage which is crack initiation phase is when the structure's stiffness, which is the curve's slope, is degrading due to increasing the load. The first bifurcation on the envelope curve is the critical load of the structure. The second degradation of the curve slope occurred after second bifurcation point, is when the cracks are starting to be opened and nonlinearity if the concrete is appearing the third phase of damage is when the reinforcement is beginning to yield, and then the nonlinearity of the structure is recognisable. From this level of damage the plastic hinges can appear, and due to that, the structures' stiffness is dramatically decreasing. When plastic hinges appear it does not mean the overall instability of the Structure, while it can tolerate more lateral load, but it shows that the structure is not stiff enough to withstand for the lateral loads and by exceeding the load large displacements can occur. Although plastic hinges appearance is very critical in the structural design and is a fundamental level of damage for all structure still it gives some ideas of replacing the element, on the other hand by increasing the load the element is supposed to be failed when the very bid displacements happen. The structural failure or instability of the structure is happening when the load-displacement curve reaches the ultimate load capacity in which after that point the structural stiffness is the Eigenvalue of the stiffness matrix is zero and then it gets negative. This level of damage is called the instability phase in which the structure has no more capacity to tolerate excess loading.

In this research, a pier has been nonlinearly analysed in two ultimate bed fixity to consider how the bed fixity can affect the structural stability under flood loading. Apart from these two types of the modelling the axial load of the pier, resulted from the superstructure's weight and the other loads, are assumed to be compared in both models. The nonlinear analysis considering all nonlinearity of the geometry and material conducted on the models, and the results compared.

4 NONLINEAR ANALYSIS AND DISCUSSION

4.1 *Stability analysis*

In work described here, a finite element approach has been employed to obtain the regions of damages and instability. Nonlinear analysis can represent the model's different stage of damage while in the linear path you can deliver just a Euler buckling load in which it can be much far from the real damage states (Yoo and Lee, 2011).

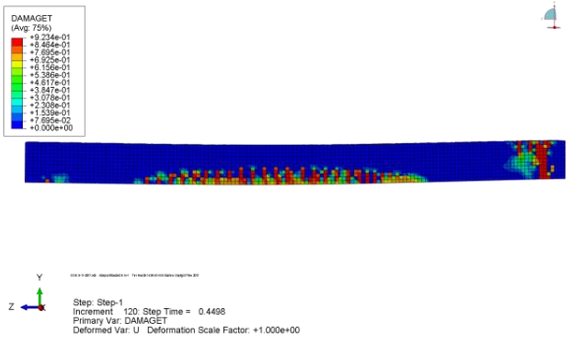


Figure 9: damage state of the fix-pin ended model when it is in 45% of loading

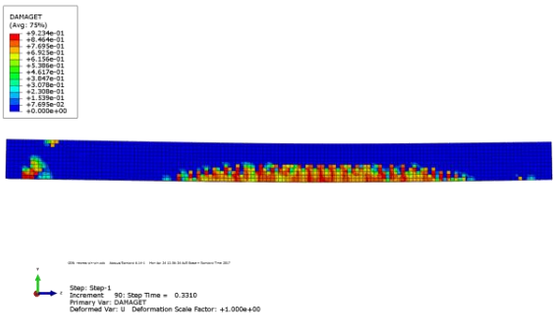


Figure 10: damage state of the pin-pin ended model when it is in 33% of loading

Figure 9 and 10 illustrate the cracks propagation along the pier during flood increasing pressure. Figure 9 is the pier with very hard bed layer of soil in which it can be assumed as a fixed bed, while figure 10 represents a very loose soil. The 2 model analysed under flood loading, pier's weight and the allowable axial load for the element, considering the P-Δ effect (Baji et al., 2012). The axial load helps the buckling happening earlier, and the ultimate load capacity of the structure will be decreased. The two models analysed for the same water pressure loading with the 0.01 initial increments. The crack pattern of both figures 9 and 10m shows that the crack pattern doesn't have specific different unless in the stiffed soil model the bed area is at the risk of damage. It considered that the loss is starting from support area of the fixed support and then the mid-height starts to be damaged the same as the very loose soil condition. The comparison between both models' initial behaviour with the load-deflection response, illustrated in figure 11. As it can be seen the initial stiffness of the models is slightly different in which in the linear zone before any damage happening the in the stiffed soil the elastic stiffness of the structure is 21% more than the loose soil.

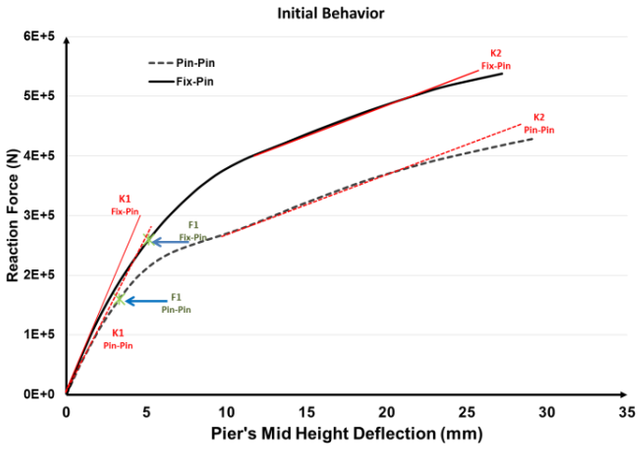


Figure 11: Load-Deflection initial behavior of the structures (envelope curve)

In the first phase of the structural behaviour, there is an elastic behaviour in which the slopes of the curves represent the elastic stiffness of the structures. This stage is called crack initiation phase. As it can be seen in the fix-pin model, this parameter, K_1, is about 6.7E+4 while it is about 5.27E+4 for the pin-pin model. The initial stiffness K_1 of the models are slightly different in which in the linear zone before any damage happening, in the stiffed soil the elastic stiffness of the structure is 21.4% more than the loose soil. The structural response is changing from elastic to elastic-plastic phase reaching to the F_1, at the first bifurcation pion. Crack in the pin-pin model is starting to appear when the horizontal reaction forces in the element reach to 260 KN, F_1, while in the fix-pin model the crack initiation force is about 160 KN, F_1, which is 38.5% less than the F_1 in the rigid soil.

By increasing the water flow pressure on the structure, incrementally, the structural behaviour enters to the second phase of crack propagation and rising. This step starts with a very significant reduction in the structural stiffness. The second bifurcation point loads the second critical load of the structure. For example, the second stiffness, K_2, of the fix-pin model is about 58% of initial stiffness K_1 while it is reduced about 82% in the pin-pin model. In this phase, it can be seen that there is a much-closed stiffness for both models, just 7.8% of the difference. This reduction is happening due to the presence of reinforcements. This phase shows that after crack initiation the behaviours are much closed to each other. In this phase, 85% of the fix-pin and 82.3% pin-pin model's stiffness are dropping which is a considerable decrease in the stiffness. It shows that how cracks can affect the rigidity and applicability of a structure.

Reaching F_2 in both models is the point that the structural behaviour is about to behave plastically. In other words, the structural response is about to be a ductile and very slight increase in water flow pressure can lead a very significant deformation of the damaged area. This means that in the model some plastic hinges have appeared which can reduce the stiffness of the structure dramatically. From the curve above, F_2, loads of plastic hinges occurrence are 556 KN for the stiffed soil condition and about 474 KN for the soft soil condition. These loads are representing 17.2% difference in both model, and it shows that the capacity of the soft soil is still lower than the stiffed soil. In this phase, 92.2% of the fix-pin and 93% pin-pin model's stiffness are dropping which is a very significant reduction. Although the stiffness's of 2 models have 19.6% difference, it seems they are parallel, and it means that in this stage of loading the structure's behaviour is close to each other. This scenario of the damage is ending buy getting the ultimate load of 951 KN and 837 KN for end fixed and end pined model alternatively. After getting ultimate loads, the negative stiffness means that the structure has no more capability of load increasing, so the structure is getting unstable in this case.

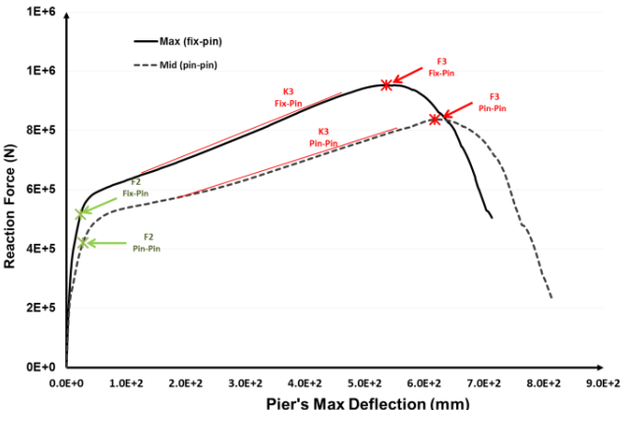


Figure 12: Load-Deflection behavior of the structures (envelope curve)

Table 3 provided all data regarding the structural behaviour during water flow increases.

Table 3: Structural Load-Deflection Parameters

	K1	F1 (N)	K2	F2 (N)	K3	F3 (N)	%(K1-K2)/K1	%(K2-K3)/K2
PIN-FIX	6.70E+04	2.60E+05	10106	5.56E+05	808.4	951910	8.49E+01	92.00079161
PIN-PIN	52686	1.60E+05	9315.5	474362	649.32	836825	82.31883233	93.02968171
2 Models Difference	2.14E+01	3.85E+01	7.82208589	1.72E+01	19.6784	12.089903	-	-

In table 4 the water flow velocity related to these critical values of the forces and pressures has been calculated based on the equation proposed by AS5100 (Standards Australia, 2017).

Table 4: Critical Water Flow Pressures and Velocities

	F1 (N)	P1(Mpa)	V1 (mm/s)	F2 (N)	P2(Mpa)	V2(mm/s)	F3(N)	P3(Mpa)	V3(mm/s)
PIN-FIX	2.60E+05	7.41E-01	3.1	5.56E+05	1.58E+00	4.54	951910	2.71199	5.9
PIN-PIN	1.60E+05	4.56E-01	2.4	474362	1.35E+00	4.18	836825	2.38412	5.5

The structure chosen in this research is slender, and that's why the very low pressure of water flow due to low velocity can cause damage.

From above description, it is concluded that the methodology can provide the deformation related to the different damage scenarios for different kinds of bed fixity. For example, just 3.1 (mm) deformation of the element can cause cracks on the structure in soft soil model, and in the stiff soil foundation, it starts when it gets to 2.8 (mm) which is pretty close to the soft soil model. Cracks will be opened, and plastic hinges are appearing when the deformation is getting to 22 (mm) in fix-pin model and 32 (mm). After plastic hinges, appearance, the model behaves very ductility, and they are failing when the fix-pin model is 53(cm), and the failure value for the soft soil model is 61 (cm). These values and all values described above can give us an idea to calculate damage mechanisms in different water flow velocities.

4.2 *Damage probability*

The probability of the damage in structure cab is described with damage parameter defined by ABAQUS for reinforced concrete. The parameter determined by the ratio of the module of elasticity in each step to the initial module of elasticity (Systèmes, 2013). Figure 13 describes damage parameter for specific critical elements in both soft and stiff soil model. As it can be seen, the pin-pin model is vulnerable in comparison with the fix-pin model for both models the damage is zero when loading is starting, but its value is dramatically increased in the soft soil model as it gets maximum value from 4% of total load to 13% of the whole load. While in the fix-pin model damage in the element starts when it got 9% of total load and increased to a maximum value of the loss when 40% of the total load is applied to the structure. From this outputs, it is considering how the bed fixity can affect the damage behaviour of the elements. In the soft soil, the crack grows dramatically while its growth in the fixed model is little slower.

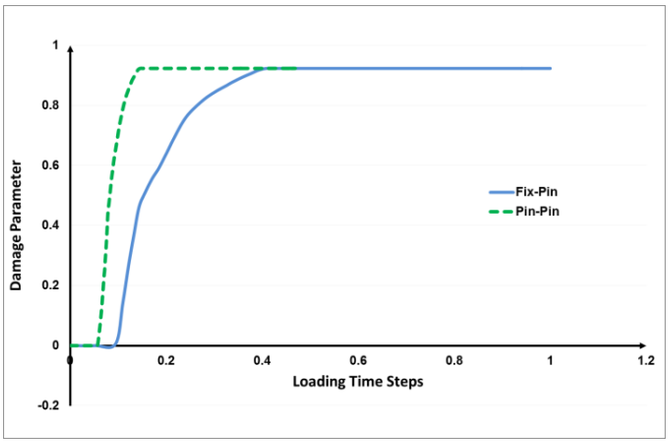


Figure 13: Critical element's damage behavior in both models

Damage parameter is a parameter to understand how the damage can grow in an element but is not able to consider the different damage levels or considering whole structures, so for the future; it is recommended to study more on the damage indices to find the probability of the structures.

5 CONCLUSIONS

The resistance to flood and debris loading is a critical parameter affecting the design of bridges under flood loading. Based on the previous study on the nature of the pressure resulting from the water flow on the structure, various finite element simulation and pushover analysis have been conducted to generalise how the pier would behave under flood intensity raising. The model is verified by an experimental study on the model from literature, and this structure is identified to be examined with the finite element method to figure out the water flow effect on the structural behaviour. Followed by, the effect of bed fixity is discussed in this paper, and the different damage levels of the pier are defined and evaluated in each model. The probability of the damage in various levels of flood loading is studied and based on the research in this area following outcomes are considerable.

- Based on the behaviour of the structure and the reduction on the structural stiffness the different levels of damage can be defined from crack initiation to crack opening and plastic hinges appearance and finally the total failure of the structure.

- Soft soil model has lower critical loadings in different levels of damage while the correspondent load has more significant values of deformation in soft soil model.

- Stiffness reduction is more in the fix-pin model rather than pin-pin model in the first damage occurrence. The decrease in structural stiffness is getting more, in the pin-pin model in the second stiffness reduction.

- Damage behaviour of the structure shows that failure happens after a very significant ductility manner of the concrete element. The real damage can be considered when the model starts its plastic deformation.

The methodology the outcomes can be useful to decide vulnerability assessment of a real structure and enhancing the resilience of bridges during flood disaster.

ACKNOWLEDGMENT

This research is supported by RMIT University and granted by Bushfire and Natural Hazard CRC.

REFERENCES

BAJI, H., RONAGH, H. R., SHAYANFAR, M. A. & BARKHORDARI, M. A. 2012. Effect of second order analysis on the drift reliability of steel buildings. *Advances in Structural Engineering,* 15**,** 1989-1999.

CAO, M., LIU, Z. & MENG, J. 2009. Statistical analysis and reflections on bridge deficiencies and disasters in the United States. *Highway,* 7**,** 162-167.

CARREIRA, D. J. & CHU, K.-H. Stress-strain relationship for plain concrete in compression. Journal Proceedings, 1985. 797-804.

HAMAD, W. I., OWEN, J. S. & HUSSEIN, M. F. M. 2011. A flexural crack model for damage detection in reinforced concrete structures. *Journal of Physics: Conference Series,* 305**,** 012037.

HANIF, M. U., IBRAHIM, Z., JAMEEL, M., GHAEDI, K. & ASLAM, M. 2016. A new approach to estimate damage in concrete beams using non-linearity. *Construction and Building Materials,* 124**,** 1081-1089.

HERNANDEZ-MONTES, E., KWON, O.-S. & ASCHHEIM, M. A. 2004. An energy-based formulation for first-and multiple-mode nonlinear static (pushover) analyses. *Journal of Earthquake Engineering,* 8**,** 69-88.

HUGHES, D., RAMEY, G. E. & HUGHES, M. L. 2007. Effects of extreme scour and soil subgrade modulus on bridge pile bent buckling. *Practice Periodical on Structural Design and Construction,* 12**,** 96-108.

JACKSON, L. E., THOMPSON, P. L. & RICHARDSON, E. Hatchie River and Schoharie Creek Bridge Failures. Hydraulic Engineering, 1991. ASCE, 202-208.

KHAN, M. A. 2014. *Accelerated Bridge Construction: Best Practices and Techniques*, Elsevier.

KMIECIK, P. & KAMIŃSKI, M. 2011. Modelling of reinforced concrete structures and composite structures with concrete strength degradation taken into consideration. *Archives of civil and mechanical engineering,* 11**,** 623-636.

LIN, C., BENNETT, C., HAN, J. & PARSONS, R. L. 2012. Integrated analysis of the performance of pile-supported bridges under scoured conditions. *Engineering structures,* 36**,** 27-38.

LÓPEZ-ALMANSA, F., ALFARAH, B. & OLLER, S. Numerical simulation of RC frame testing with damaged plasticity model. Comparison with simplified models. Second European Conference on Earthquake Engineering and Seismology, Istanbul, Turkey, 2014.

MELBOURNE & WATER 2005. Flood Management and Drainage Strategy. Victoria: Port Philip and Westernport Region.

NASIM M. , MOHSENI H. , SETUNGE S. , ZHOU S. & DISSANAYAKE A.P. 2015. A Comparison of the Effect of Pier Shape on Flood Loading on Bridges. *ABC2015 Conference* Melbourne: Austroad

PIELKE JR, R. A. & DOWNTON, M. W. 2000. Precipitation and damaging floods: trends in the United States, 1932–97. *Journal of Climate,* 13**,** 3625-3637.

RODRÍGUEZ SOLER, J., MARTINEZ CUTILLAS, F. J. & MARTI RODRIGUEZ, J. 2013. Concrete constitutive model, calibration and applications.

SOUSA J.J. & BASTOS L. 2013. Multi-temporal SAR interferometry reveals acceleration of bridge sinking before collapse. *Natural Hazards and Earth System Sciences,* 13**,** 659-667.

STANDARDS AUSTRALIA 2017. Bridge Design-Design Loads. *AS 5100.2:2017.* Austarlian Standards.

STOREY, CHRIS, DELATTE & NORBERT 2003. Lessons from the collapse of the schoharie creek bridge. *Forensic Engineering***,** 158-167.

SYSTÈMES, D. 2013. ABAQUS User's & Theory Manuals—Release 6.14-1, Providence, RI, USA.

VICROADS 2014. Road Structures Inspection Manual. VicRoads Technical Services.

WORDEN, K. & DULIEU-BARTON, J. 2004. An overview of intelligent fault detection in systems and structures. *Structural Health Monitoring,* 3**,** 85-98.

YOO, C. H. & LEE, S. 2011. *Stability of structures: principles and applications*, Elsevier.

ZHAO ZHONG. 1999. *Stability of Pile Groups.* PhD, University of Minnesota.

SS12: Centenary bridges – An insight into construction and technology history

Organizers: P. Cruz & P.G. Malerba

Maintenance, Safety, Risk, Management and Life-Cycle Performance of Bridges – Powers, Frangopol, Al-Mahaidi & Caprani (Eds)
© 2018 Taylor & Francis Group, London, ISBN 978-1-138-73045-8

The dream of building bridges over the Tagus River mouth in Lisbon

P.J.S. Cruz
Lab2PT, School of Architecture, University of Minho, Guimarães, Portugal

ABSTRACT: The Tagus is the longest river in the Iberian Peninsula (in the southwest corner of Europe, comprising most of the Portuguese and Spanish territories) and it forms a wide estuary at its mouth near Lisbon. The need for a permanent bridge between Lisbon and the south bank of the river had long been felt and several solutions have been proposed since the 19th century. However, the construction of the first bridge crossing the river in that area only occurred in the second half of the 20th century. This work represents an opportunity to pay a tribute to the engineers involved in the design and construction of those bridges and to give a valuable insight into construction and technology history.

1 INTRODUCTION

Théophile Seyrig (1843-1923) was an associate of Gustave Eiffel in the firm *Eiffel et Ce.*, from 1869 to 1881. In that period he designed the daring arch of Maria Pia Bridge crossing the River Douro in Porto, built between 1876 and 1877 (Fig. 1). At that time it was the greatest span in the world (160 m). The iron arch was built without falsework, using only suspended cables. It was also one of the first times, if not the first, that calculation on the wind effect was accurately made using a hitherto unused method (Cruz & Cordeiro, 2001).

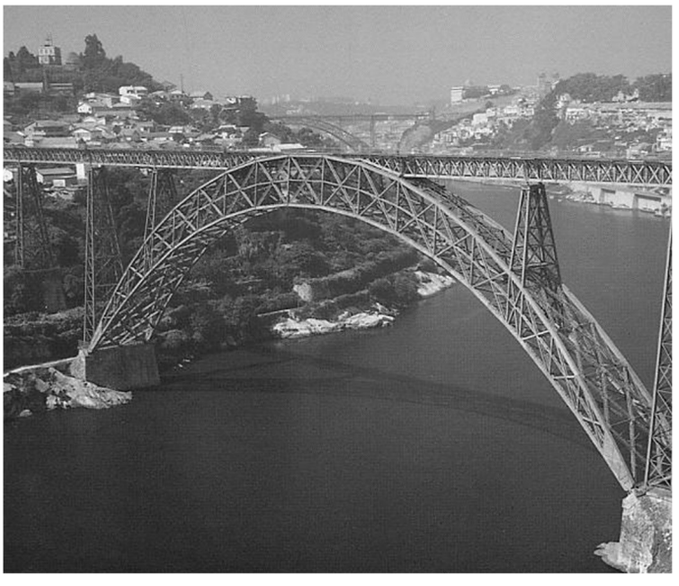


Figure 1. Maria Pia Bridge in Porto.

It was with this bridge that Gustave Eiffel and his company advanced considerably towards international recognition. It also provided them with the necessary experience and accuracy to produce a similar project seven years later - the famous Garabit Viaduct over the Truyère in the Massif Central, near Saint-Flour, in France. It had a 165 m span (five more metres than Maria Pia Bridge). Gustave Eiffel adapted most of the plans of the Portuguese bridge to the French one (Marrey, 1982).

Théophile Seyrig submitted a proposal for the Luiz I Bridge, over the River Douro in Porto, comprised by two metal decks supported by a large iron arch and by five pillars (Fig. 2).

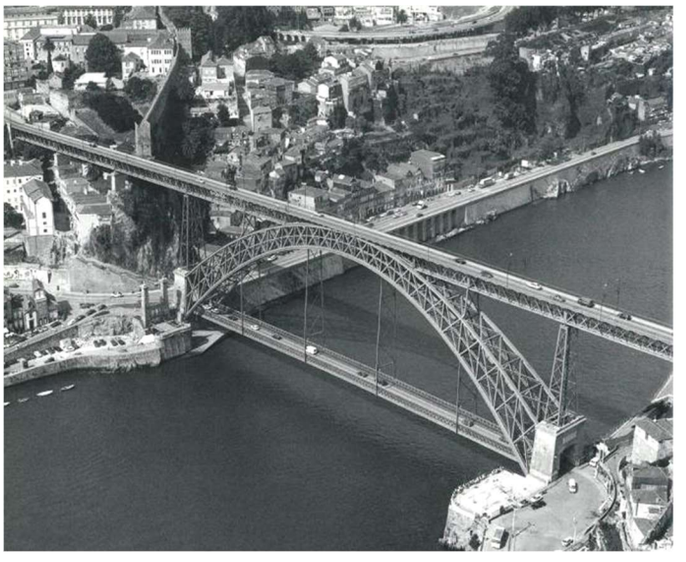


Figure 2. Luiz I Bridge in Porto.

The arch is composed by two divergent parabolic curves, with a chord of 172 m and a rise of about 44.6 m (Cruz, 2016). This bridge still holds the record for the world's largest iron arch. The construction company was a Brussels-based firm called *Société Anonyme de Construction et des Ateliers de Willebroeck*. In December 1881 the official inauguration of the work took place, and on October 1886 the upper deck was opened.

The Tagus River rises in the Sierra de Albarracín of eastern Spain, passes close to Madrid and forms part of the border with Portugal before flowing into the Atlantic Ocean in Lisbon (Fig. 3).



Figure 3. Map of Portugal identifying the Tagus and Douro rivers and the cities of Lisbon and Porto.

In the last two decades of the 19th Century several solutions were proposed to build a bridge between Lisbon and the south bank, being the most relevant the one presented in 1889 by Edmond Bartissol (1841-1916) and Théophile Seyrig. It was a multi-span metal railway solution, with a total length of 2310 m, which at that time would become the longest bridge in Europe (Fig. 4).

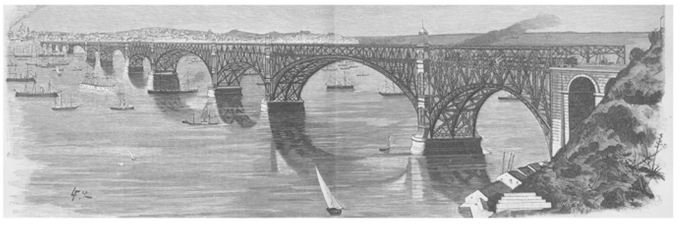


Figure 4. Solution proposed by Bartissol and Seyrig.

The bridge would leave the Rocha Conde de Óbidos towards the castle of Almada, giving way to the railway line that will leave the Rossio station to connect with that of Barreiro, in a 15.5 kilometers route (Fig. 5).

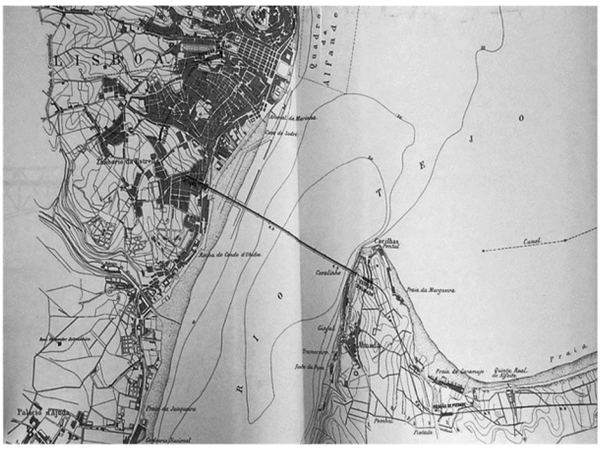


Figure 5. Location of the bridge proposed by Bartissol and Seyrig.

Although Bartissol's enjoyed a strong reputation in public works this project was not approved. Bartissol was responsible for the organization of the railway in Galicia (north-west region of Spain) between 1871 and 1875. In 1875 he moved to Portugal as a representative of *Financière de Paris*. He then undertook major projects, namely those to build the Beira Alta railway line, which crossed Portugal from east to west, as well as many other constructions including bridges and tunnels using innovative techniques for that time. The long-awaited bridge would only come fifty years after Edmond Bartissol's death.



Figure 6. First phase of the 25 de Abril Bridge view.

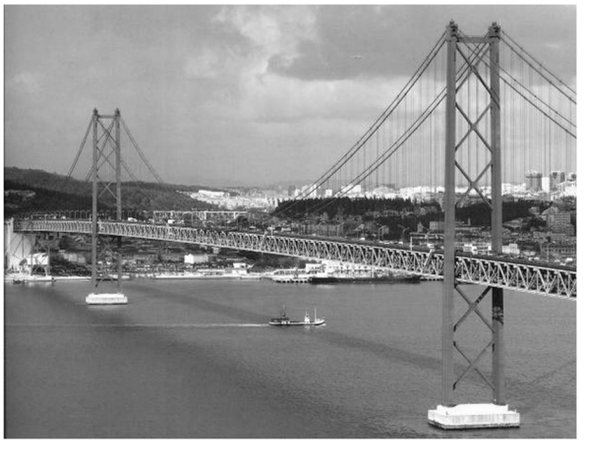


Figure 7. Second phase of the 25 de Abril Bridge view.

The construction of a long steel suspension bridge started in November 1962. The planned implementation period was fifty-one months, ending in February 1967. However, it was possible to shorten this period by six months, opening the bridge to traffic in August 1966. The central span of the suspended bridge was 1012.88 m length.

The project foresaw that, in the first phase, the bridge was exclusively for roadway traffic (Fig. 6) and that later, in a second phase, the installation of the railway could occur.

It was necessary to wait three decades so that in 1996 the works of widening the roadway platform and the inclusion of the railway line could begin. In November 1998 the roadway platform with six car lanes would open to traffic. In July 1999 the exploration of the railway line began (Fig. 7).

2 THE 19TH CENTURY PROJECTS

The aspiration to connect the two banks of the River Tagus began in the second half of the nineteenth century, with a design proposed in 1876 by the Portuguese engineer Miguel Pais, which provided a link between the Grilo area in Lisbon and Montijo in the south bank. The project consisted in a double deck for road and rail traffic with 74 central spans which were 60 m long and the two end spans which were 48 m long. Since then several projects have dreamed a bridge to connect Lisbon with the south bank of the Tagus River (Fig. 8).

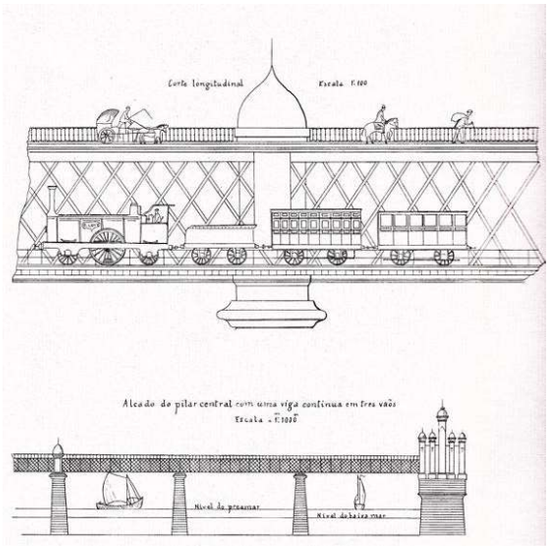


Figure 8. Solution proposed by Eng. Miguel Pais, 1876.

Other projects were proposed by:
- The American Lye, 1888;
- Bartissol and Seyrig, 1889 (Fig. 4);
- André de Proença Vieira, 1890;
- Maschinenbau-Actien-Gesellschaft, a company from Nuremberg, 1890 (Fig 9).



Figure 9. Location of the bridge in the Tagus estuary.

3 THE 20TH CENTURY BRIDGES

3.1 *25 de Abril Bridge*

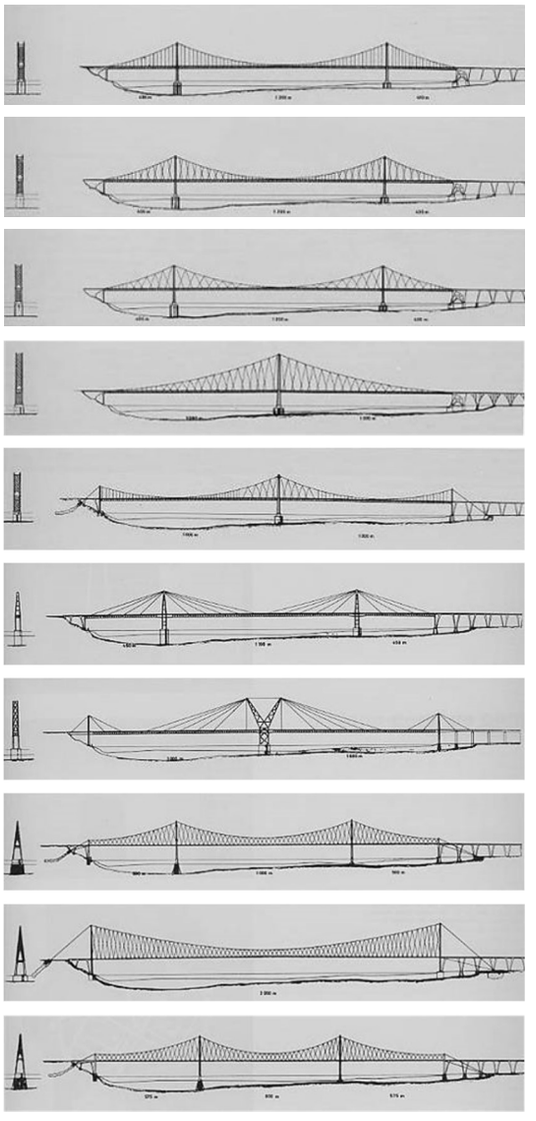
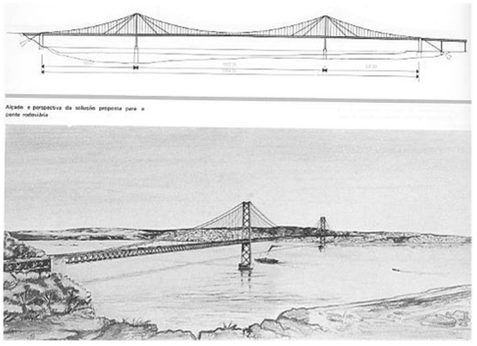


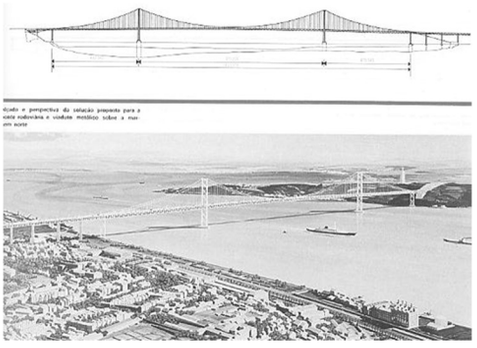
Figure 10. Theoretical reference solutions for the design of the bridge structure (GPT, 1966).

In the 1950's there was a strong demographic and industrial growth in the District of Lisbon, which led to considering the possibilities of using the Tagus southern bank lands. Thus in June 1953 a national commission was set up to work out roadway and railway links between Lisbon and the southern bank.

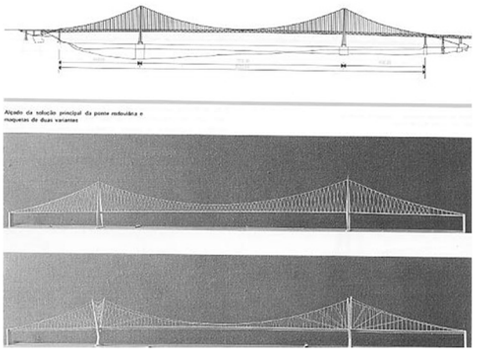
At the initiative of the Office of the Bridge over the Tagus, between 1959 and 1960, a group of national technicians prepared a study and presented a set of ten theoretical solutions for the structure of the bridge (Fig. 10).



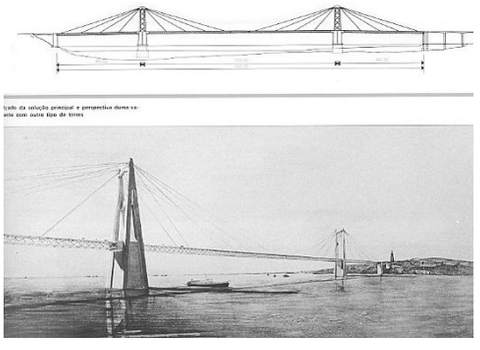
d) Proposal 4 - Professor Kurt Klöppel.



c) Proposal 3 - Steinman, Boynton, Gronquist & London Comp.



b) Proposal 2 - Professor Chadenson.



a) Proposal 1 - Professor Albert Caquot.

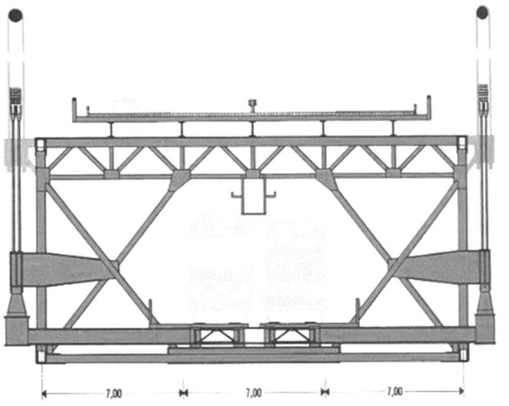
Figure 11. Bridge over the Tagus River in Lisbon, proposals submitted to the competition (GPT, 1966).

Four proposals were presented to the international public tender (Fig. 11).

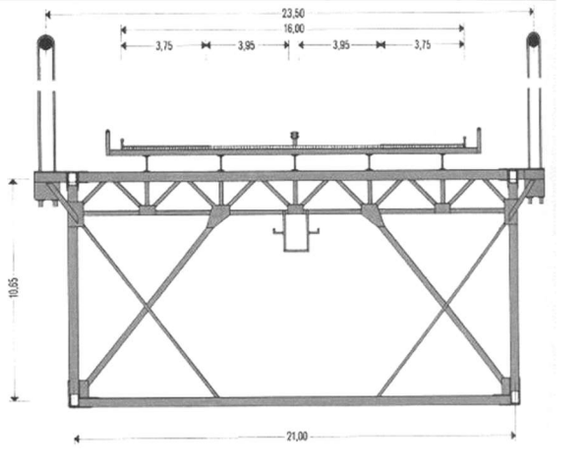
Proposal 1 had the lowest costs for the road crossing, whereas proposal 3 was the only one which had a quotation to consider for the mixed roadway and railway bridge and an offer for the external financing covering the entire cost of the work.

In May 1960 the Portuguese Government decided that the work was provisionally adjudicated to competitor number 3 and in February 1961 signed the contract for the execution of the work.

A definitive project was presented in November 1961. It was approved in May 1962 by the Public Works Council and finally adjudicated. The United States Steel International (New York) Inc. based in New York was the prime contractor that associated a significant number of other companies. Thus Steinman, Boynton, Gronquist & London, Consulting Engineers designed the bridge. The Tudor Engineering Company designed the foundations and was responsible for the seismic studies. The American Bridge Division of U.S. Steel Corporation built the steel towers and all the superstructure of the suspension bridge.



b) Phase 2.



a) Phase 1.

Figure 12. Cross section of the stiffness beam (GPT, 1966).

As mentioned before, the project foresaw two phases. In the first one the bridge would be exclusively for roadway traffic and would consist of towers

and anchors, suspension cables and hangers that would support the rigidity beam (Fig. 12a). In a second stage the installation of the railway would be achieved by adding a supplementary structure consisting of two secondary continuous cables, several inclined cables and a beam settled inside the rigidity beam. The shape and location of these reinforcing elements would allow their future installation without interfering with the traffic in the roadway platform tanker (Fig. 12b) (GPT, 1966).

The central span of the suspended bridge was 1012.88 m, the lateral spans were 483.42 m and each margin span was about 100 m. The towers were 190.47 m high (Fig. 13).

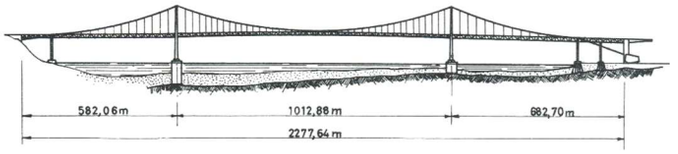


Figure 13. Bridge elevation (GPT, 1966).

The construction began in November 1962. The execution period was estimated to be 51 months, ending in February 1967. However, it was possible to shorten this period by six months and open the bridge to traffic in August 1966, under the name of Salazar Bridge. In 1974 the name would change to 25th of April Bridge.

The upper platform, running 70 m above water, started carrying 4 car lanes, two in each direction, with a dividing guardrail. In July 1990, this guardrail was removed giving way to a fifth reversible lane. In November 1998, the platform was extended to the present six lanes. The first railway crossing would take place in June 1999.

Contrary to what was envisaged by Professor Albert Caquot for the second phase, instead of adding inclined cables to the suspension system, the installation of only two secondary cables was preferred (Fig. 7).

For the installation of the railway deck in the north access viaduct (*Viaduto de Alcântara*) the designer, Professor António Reis, from GRID, opted for a composite solution of steel I beams connected with diaphragms and assembled by incremental launching from both ends (Fig. 14).

The metallic structure was fabricated in the south bank and transported to the site in segments consisting of "half" sections, 16 m and 20 m long (Fig. 15). These segments were connected transversely by welding the diaphragms in situ, after which the horizontal bracings were installed at the level of the lowest flange. The deck was incrementally launched from the north in a length of 452.6 m (Reis, 1997). The cross-section of the superstructure consisted of two I-beams, with a 4500 mm space between webs of. The webs had a constant thickness of 25 mm and the flanges varied between 40 mm in the spans up to 120 mm in the sections over the supports. The width of the flanges varied between 800 mm and 1300 mm. The diaphragms were 6.4 m apart and 20 mm thick with two flanges of 600×30 mm.

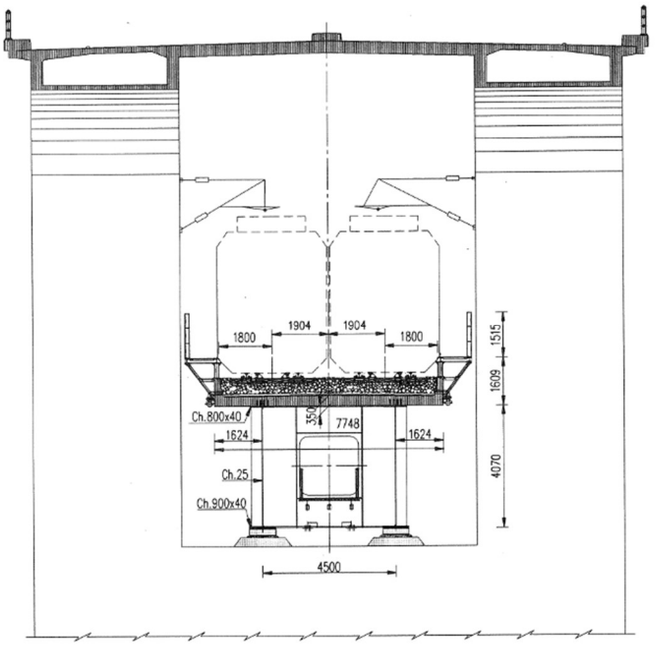


Figure 14. Railway deck in the north access viaduct (Reis, 1997).



Figure 15. North access viaduct - segments consisting of a half section.

The concrete slab was 0.35 m thick and connected to the steel beams by 22 mm diameter studs. Longitudinally the structure works had a beam with two continuous segments of 392.3 m and 526.6 m, separated by an expansion joint (Reis, 1997).

3.2 *Vasco da Gama Bridge*

To avoid that the main traffic between the northern and southern regions had to cross Lisbon and to reduce the traffic in the 25 de Abril Bridge, in April 1994, Lusoponte consortium has been selected to build the Vasco da Gama Bridge. It integrated the fol-

lowing companies: Kvaerner Construction International Limited; Campenon Bernard SGE; Bento Pedroso Construções, S.A.; Somague – Sociedade de Construções, S.A.; Sociedade de Construções H. Hagen, S.A.; Teixeira Duarte – Engenharia e Construções, S.A.; EDIFER – Construções Pires Coelho e Fernandes, S.A.).

The design contract was awarded to a consortium comprising the companies Kvaerner Technology, Europe Etudes Gecti (EEG), *Consultores para Obras, Barragens e Planeamento* S. A. (COBA) and *Projectos de Pontes e Estruturas Especiais* (PROPONTE).



Figure 16. Vasco da Gama Bridge (http://memoria-expo98.com/en/vasco-da-gama-bridge/).

The project was verified by Tejo Ponte Control, a consortium of *A2P Consult - Estudos e Projectos*, Hyder Consulting, *Provia Consultores de Engenharia* and Tudor Engineering.

The Vasco da Gama Bridge is the longest bridge in Europe, with a total length of 12.4 km, including 0.8 km for the main bridge and 11.6 km in viaducts and carries six road lanes (Fig. 16). The curved layout of the bridge enhanced the possible paths of large vessels.

The bridge has a life expectancy of 120 years, having been designed to withstand wind speeds of 250 km/h and to hold up to an earthquake 4.5 times stronger than the historical 1755 Lisbon earthquake (which had an estimated magnitude of 8.5-9.0 on the moment magnitude scale).

The cable-stayed bridge has a central span of 420.2 m and side spans of 204.6 m. The height of the central pylons is 150 m and the deck gives a clearance of 47 m above water level on the navigation channel called North Channel. The deck is a steel-concrete composite structure consisting of a 0.25 m thick prestressed reinforced concrete slab laying on steel transverse beams, spaced at 4.42 m intervals, and two main side solid concrete girds where 2×24 pairs of stays are linked to the pylons.

The H-shaped north and south pylons stand on foundations designed to withstand impact from a 30,000 tonne ship travelling at the cruise speed of 12 nuts. The deepest foundation piles, up to 2.2 m in diameter, were driven down to 95 m under mean sea level.

The construction began in February 1995 and it was opened to traffic in March 1998, two months before the opening of Expo 98, the World's Fair that celebrated the 500th anniversary of the discovery of the sea route from Europe to India by Vasco da Gama.

4 THE THIRD TAGUS CROSSING

4.1 *Introduction*

A decade after the opening of the Vasco da Gama Bridge Portugal strongly committed itself to the construction of three mega projects: a high-speed rail network (Fig. 17), a Third Tagus Crossing and a new airport in the metropolitan area of Lisbon.

The new bridge would accommodate four railway lines, two for the high-speed railway line Lisbon-Madrid, two for Iberian gauge conventional railway lines, and six roadway lanes, three in each direction.



Figure 17. High-speed rail network (www.expresso.pt).

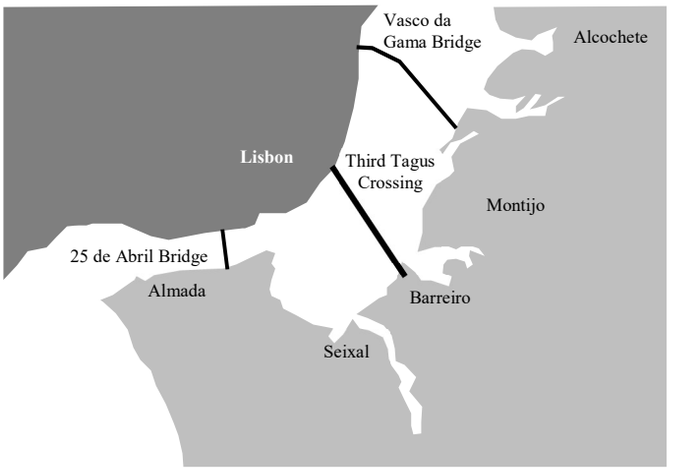


Figure 18. Location of Third Tagus Crossing.

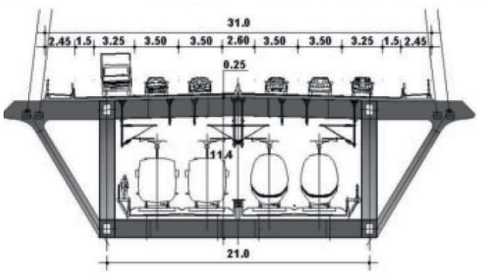
After many studies and discussions about the location of these new infrastructures, in 2008 was selected the Chelas-Barreiro corridor (Fig. 18).

4.2 *Reference design*

Under the initiative of the RAVE - *Rede Ferroviária de Alta Velocidade, S.A.* (High Speed Railway Network), in 2009 a reference design of the new bridge developed by Grid (coordination and structures), Consulgeo (geotechnical studies) and Fialho Rodrigues (geology) was presented. The adopted solution was a cable-stayed structure which had a composite double deck with a total length of 3.7 km, a main span of 600 m and a 200-metre high pylon (Fig. 19).

4.3 *The international public tender*

The international public tender for the construction and concession of the high-speed rail infrastructure in the section between Poceirão and Lisbon, which included the construction of the Third Tagus Crossing between Chelas and Barreiro, was launched in March 2009.



b) Cross section.



a) Elevation.

Figure 19. Preview of the Third Tagus River Crossing Bridge, in Lisbon (GRID, 2009 & Reis, 2008).

With a length of 34 km, the Lisbon-Poceirão section was prepared for mixed traffic (passengers and goods) and had a maximum speed of 200 km/h on the third Tagus crossing and in the Barreiro tunnel and 350 km/h on the rest of the line.

In January 2010, RAVE announced that the two consortia had moved to the negotiation stage of the international public tender:

- *Tave Tejo* consortium, which included the Spanish *FCC - Fomento de Construcciones y Contratas* (26%), the Portuguese *Ramalho Rosa-Cobetar* (1%) and *Conduril* (9%), the Italian *Impregilo* (25%) and *Cimolai* (4%), as well as the holding company *EHST - European High Speed Trains* (35%). The design companies were Adão da Fonseca Engenheiros Consultores, Ideam & Fhecor;
- *Altavia* consortium, which included the Portuguese *Mota-Engil* (17.38%), *Somague* (14.64%), *Teixeira Duarte* (14.64%), *MSF* (10.98%), *Opway* (10.98%), *Esconcesions* (5%), *BPI* (6%), *BES* (1%), banco *Invest (*0.75%) and *Alves Ribeiro - Consultoria de Gestão* (2.25%) and the French *Vinci* (16.38%). The design companies were Arcadis, LCW, A2P, PCA and Betar together with Lavigne & Cheron Architects.

The Altavia solution consisted of a cable-stayed bridge near the Lisbon bank, two bowstrings over the two navigation channels and trusses in the remaining crossing, with a total length of 8 km and a main span of 540 m.

A third proposal, by Elos Consortium, did not reach the negotiation stage. The consortium included the Portuguese Soares da Costa, Brisa, Lena Bento Pedroso, Edifer, Zagope, BCP and Caixa Geral de Depósitos, the Spanish Iridium - Concesiones de Infraestructuras, of the ACS group, and the North American company Babcock & Brown Limited.

According to the preliminary report of the selection board, the price difference of the two tenders, initially 300 million euros, increased to 509 million euros due to adjustments made by the evaluation committee, related with the net adjusted value, which included "construction, maintenance and financial costs". The proposal of the *Tave Tejo* consortium increased from 1870 million euros to 1964 million euros while the proposal of the *Altavia* consortium increased from 2166 million euros to 2473 million euros.

The consortium *Altavia* contested the preliminary evaluation report stating that the proposal by the *Tave Tejo* group did not meet all the specifications requirements - construction of the high-speed line, the third crossing of the Tagus and the north and south accesses of the new bridge.



Figure 20. Tave Tejo solution.

In May 2010, the Government decided to cancel the tender due to the global financial and economic crisis.

The *Tave Tejo* solution is a double steel truss cable stayed bridge with an overall length of 8184 m (Fig. 20). It consists of an 1140-metre long main bridge, two access viaducts of 540 and 950 m and 47 intermediate spans with a total length of 5554 m. The cable-stayed bridge pylons height is 198 m. The width of the road deck is 28.37 m and of the railway deck is 19.00 m.



b) The superstructure of the remaining crossing.



b) Bow-strings over the two navigation channels.



a) Cable-stayed bridge near the Lisbon bank.

Figure 21. Altavia solution.

The *Altavia* solution consists of a cable-stayed bridge near the Lisbon bank, two bowstrings over the two navigation channels and trusses in the remaining crossing, with a total length of 8 km and a main span of 540 m (Fig. 21).

For the railroad crossing a cable-stayed bridge was proposed near the Lisbon bank, two bowstrings over the two navigation channels and trusses in the remaining crossing. The pylons are 190 m high and the foundations are 70 m deep by piles with a diameter of 2.5 m.

5 CONCLUSIONS

It is worth recognizing the outstanding contribution of landmark bridges to the valorisation and development of the territories in which they are implemented.

This work describes the dream of building bridges over the wide estuary of the Tagus River mouth in Lisbon since the 19th Century.

The great diversity of the audacious technical solutions proposed undoubtedly deserves a worldwide diffusion and recognition.

REFERENCES

Cruz, P.J.S. & Cordeiro, J.M.L. 2001. *The Porto Bridges*. Porto: Editora Civilização (in Portuguese).

Cruz, P.J.S. 2016. Extending the Life of Centenary Metal Bridges, In Bittencourt, Frangopol & Beck (eds.), *Maintenance, Monitoring, Safety, Risk and Resilience of Bridges and Bridge Networks*; *Proc. intern. symp.*. Foz do Iguaçu, Brazil, 26-30 June 2016, London: Taylor & Francis Group.

GPT. 1966. *The Salazar Bridge*, Gabinete da Ponte sobre o Tejo, Lisbon (in Portuguese).

GRID, SA, 2009. *Third Tagus River Crossing: Main Bridge – Base Case Design* (in Portuguese).

Marrey, B. 1982. *Gustave Eiffel, Engineer-Builder*, Paris: Pour la Science (in French).

Reis, A.J. 1997. Steel and composite bridges: developments and achievements. In Lamas, Cruz & Calado (eds.), *Steel and Composite Construction, Proc. nat. symp.,* Porto, 20-21 November, 1997, Porto: cmm (in Portuguese).

Reis, A.J. 2008. Composite bridges: Options and design issues. In Cruz, Simões da Silva & Schröter (eds.), *Steel Bridges. Advanced Solutions and Technologies; Proc. intern. symp*.. Guimarães, 4-6 June 2008.

Santana, F. & Calado, R.H. 1999. *Vasco da Gama Bridge*. Lisbon: GATTEL – Gabinete da Travessia do Tejo em Lisboa.

Souza, J.F. 1906. *Still the fluvial station of the lines of the south and southeast - Annotations to a representation* (in Portuguese).

Maintenance, Safety, Risk, Management and Life-Cycle Performance of Bridges – Powers, Frangopol, Al-Mahaidi & Caprani (Eds)
© 2018 Taylor & Francis Group, London, ISBN 978-1-138-73045-8

Articulated and continuous cantilever bridges after a century of experience

P.G. Malerba
Dept. of Civil and Environmental Engineering, Politecnico di Milano, Milano, Italy

ABSTRACT: Cantilever bridges made of steel, reinforced and prestressed concrete, with their diverse arrangements, have given a fundamental contribution to the development of bridge construction. Many of these bridges, built more than a century ago, are still in service. Such an extended period of use allows us to ascertain their performances over time and also to highlight their most common draw-backs. With the hindsight of a century and a half of accrued experience, this paper will present an overview of how these bridges are performing today under the wear of time and increasingly heavy traffic intensities.

1 HISTORICAL AND TECHNICAL BACKGROUND

1.1 *State-of-the-art engineering in the XVIII century*

The material characteristics, the building technologies and the theoretical know-how of the past centuries were quite different from those we have today.

About the materials, the industrial process to produce cast iron was perfected at the end of the eighteenth century, while steels with modern characteristics were patented in the middle of 1800. In the second half of the nineteenth century new technologies were proposed: it is this period that Coignet, Monier, and others performed the first experiments on reinforced concrete. E. Freyssinet patented the prestressed concrete technology in 1928. Between 1933 and 1936, Abeles made the first experiments on partially pre-stressed beams and decks.

About the theoretical knowledge, mechanical sciences and theory of structures made a fundamental breakthrough in the nineteenth century. In particular, in the middle of 1800 many studies were devoted to truss structures. Starting from the experiences of trussed wooden bridges and roofs, practitioners and scholars foresaw the possibility of new developments thanks to the exploitation of the superior characteristics of new materials. Remarkable was the contribution of Squire Whipple, who presented one of the first thorough analysis of the behavior of trussed beams (bowstring truss) and proposed to use cast iron for compressed members and wrought iron for tensioned ones. These studies resulted in the construction of longer bridges, many of which served railways lines and allowed to overpass remarkable spans, supporting high traffic loads.

1.2 *The origin of continuous articulated bridges (Gerber type Bridges)*

In a few years, these experiences led to the introduction of new, ingenious arrangements, that brought about what we can collectively describe as articulated or cantilever bridges.

In its first configuration, a cantilever bridge is a continuous bridge having hinges in specific sections, typically at points of contraflexion.

G. H. Gerber designed the innovative Haßfurt Brücke, completed in 1866 and considered the first modern cantilever bridge. This bridge is made of a girder over three spans (29.90 + 37.90 + 29.90 = 77.70 m), having two hinged joints in the central span, which is thus supported by the two lateral cantilevering beams.

The first cantilever bridge in the USA, the "Kentucky River Bridge", designed by G.F. Bouscaren and C. S. Smith (Wilcox 1898), was completed in 1877. It is a three-span bridge ($3 \times 114.27 = 91.4 + 160.0 + 91.4 = 342.8$ m), with two hinges located in the side spans, at a 22.9 m distance from the piers axes.

The "Niagara Cantilever Bridge" was designed by C. C. Schneider and completed in December 1883. Once again, the bridge consists of three spans: two side spans of 114.3 m each and a 36.6 m central span. The two hinges are located in the central span.

These early examples came to characterize specific subtypes of articulated bridges: bridges with hinges located in the side spans are called Kentucky

type bridge, while Niagara type bridges are those having hinges in the central span.

The most notable cantilever bridge of the nineteenth century is the Firth of Forth Bridge, whose construction began in 1881 and was completed in 1890. The bridge was designed by Sir J. Fowler and Sir B. Baker and has a total length of 2,467 km. It consists of two main spans, each 520 m long, having a width of 37 m at the piers and 9.8 m at center; the towers are 110 m tall.

Since then, the cantilever scheme became one of the most common solutions for long-span bridges subjected to heavy loads.

The reasons for the success of the cantilever bridges are many: first, they are or can be easily reduced to statically determined structures. Even if theories and methods to deal with statically indeterminate structures were available at the end of the nineteenth century, dealing with statically determined structures was advantageous in that allowed to obtain reliable and straightforward analytical results and to simplify the search for the maxima and minima of the internal forces. The fact that foundations settlements did not influence the structure behavior was another significant advantage, so were the possibility of arranging specialized equipment for intermediate construction stages, no need of falseworks that would obstruct rivers or canals during construction, and shorter construction times.

1.3 *The introduction of pressed R.C. cantilever bridges*

The first Gerber type bridges were built as steel trusses. The advent of reinforced concrete saw the construction of many R.C. Gerber bridges, but only on very short spans. Only the diffusion of the prestressing technology, after 1950, made it possible to lengthen the spans of the girders, and concrete structures became competitive.

It is worth noting that, notwithstanding the change in construction material and technologies, one hundred years of experience steered designers once again towards Gerber type/cantilever structures. This was not only due to the advantages recalled previously, which still stood, but also to the initial difficulties in obtaining a reliable analysis of the effects of time-dependent behaviors. As a consequence, this scheme was still widely used until the last decades of the twentieth century.

The balanced cantilever erection technique became the most diffused construction method and new girder arrangements, such as the one having a single hinge in the central sections, were introduced.

As known, and excluding particular cases, present standards suggest the use of fully continuous girders over articulated structures.

Other attempts to obtain continuous jointless girders, but maintaining a simple static scheme, are the so-called tie-deck girders, composed of several simply-supported spans, connected through short continuity slabs.

2 THE EVOLUTION OF CANTILEVER BRIDGES

We maintain a distinction between steel and concrete cantilever bridges.

2.1 *Trussed cantilever steel girders*

As already recalled, between the end of 1800 and the beginning of 1900, medium-long girder bridges for both railway and road networks were designed as steel trusses. Relatively simple and statically determined schemes, the so-called “Gerber type” girders, were obtained through the introduction of hinges in suitable points along the spans. Apart from the panel geometry of the truss, the element which differentiates these bridges was the arrangement of the articulations at the internal supports, carrying the suspended ends of a span. The set of bearing supports at one end must remain fixed, allowing rotation only, while the supports at the other end must permit translational longitudinal movement as well as rotation of the ends of the superstructure. Therefore, the supports typically comprise of a fixed hinge bearing support and a roller, or of a rocker-roller or pendulum type expansion bearing.

Figure 1 shows the layout of a bridge rebuilt in 1953. It is a trussed bridge with a double deck, the upper one serving a railway and the lower one a road. The bridge has a west span of 44.00 m, a central span of 56.00 m and an east span of 45.00 m. The mechanisms supporting the central span are located at a distance of 11.20 m at either side of the two central piers and are composed by a couple of pin supports on the west side (Fig. 2) and by a couple of pendula (rockers) on the east side (Fig. 3). Figure 4 shows the roller support at a pier.

In many cases, the pendulum is an oscillating strut, whose length is equal to the depth of the girder, with one end connected to the upper stringer of the supported span and the other to the lower stringer of the cantilever. Figure 5 shows the oscillating pin and hanger assembly, working like a pendulum, between the upper and lower chords belonging to a bridge opened in 1908 and identically rebuilt after the Second World War in 1947. The bridge is 1097 m long. Its central part, 607 m long, is made of Gerber trusses, spanning 75.25 m and supported by masonry piers. The expansion supports lie at a distance of 15.14 m from the nearest pier.

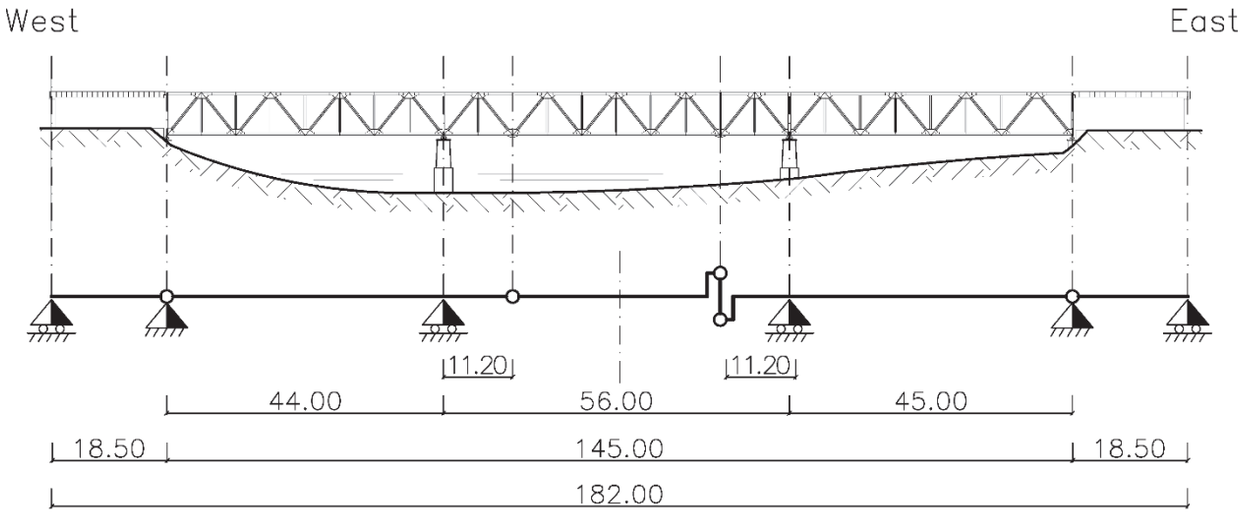


Figure 1. Layout of a truss bridge having the upper deck serving a railway and the lower one a road (rebuilt in 1953).

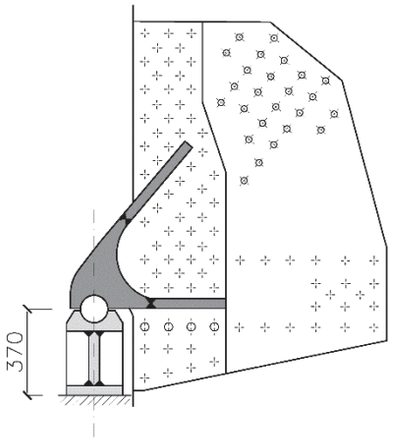


Figure 2. Scheme of the pin support on the west side of the bridge shown in Figure 1.

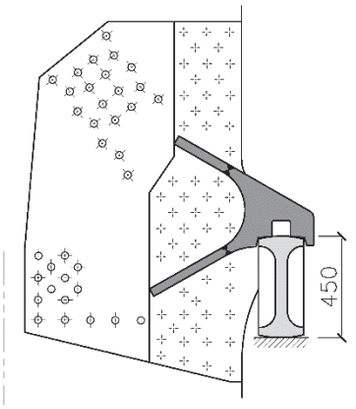


Figure 3. Scheme of the pendulum (rocker) on the east side of the bridge shown in Figure 1.



Figure 4. The roller bearing in correspondence of a pier of the bridge shown in Figure 1.

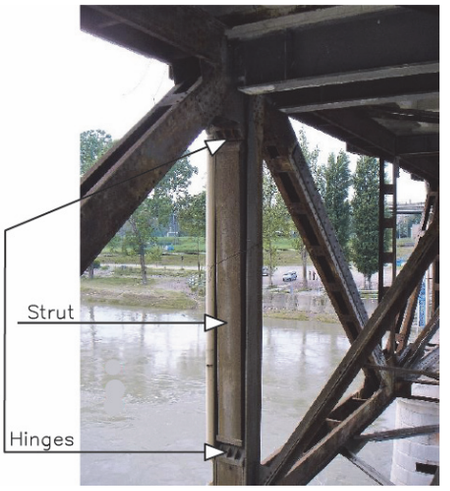


Figure 5. Pin and hanger assembly working as a pendulum between the upper and lower chords in a bridge rebuilt in 1947.

2.2 *Reinforced and prestressed cantilever concrete girders*

From the beginning of the XX century, with the improvement of the reinforced concrete technology, several multi-spans R.C. cantilever bridges were constructed. The length of both cantilevers and suspended spans were limited and, in any case, shorter than those of trussed steel bridges. Their use in railways was uncommon.

The spread of the prestressing technology allowed a remarkable increase in spans that could now exceed 100 m. The three main schemes for reinforced and prestressed cantilever concrete girders are briefly recalled in the following (Mathivat 1983).

2.2.1 *Articulated systems with suspended spans*
In this scheme, the central span is sustained by the two cantilevers projecting from the piers. Basic arrangements are shown in Figure 6 and correspond to those already defined as Niagara (Fig. 6a) or Kentucky (Fig. 6b) type bridges. In European countries, the mechanisms used at the joints for materializing the articulation are called "Gerber hinges". One end of the suspended span is simply supported, while the other end lies on sliding supports, which allow the horizontal displacements due to length changes in the beams caused by time-dependent and temperature effects. Both supports permit rotations. The main advantages of this configuration are a clear and straightforward static scheme (since they are statically determined structures) and the avoidance of spurious effect due to settlements of the foundations.

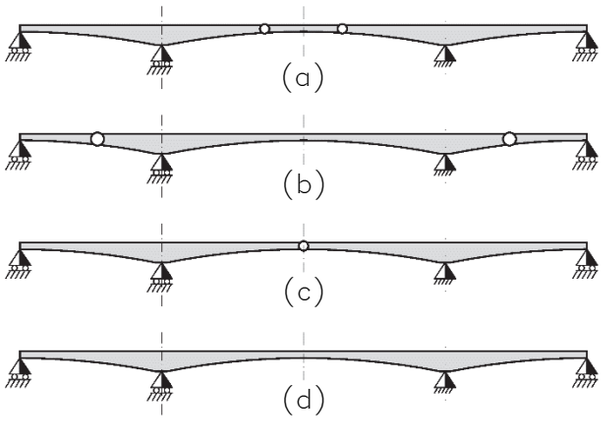


Figure 6. Cantilever bridges basic arrangements: (a) Niagara type; (b) Kentucky type; (c) hinged cantilever; (d) cantilever made continuous.

2.2.2 *Partially articulated systems with hinged cantilevers*
In this arrangement, after the erection phase, the ends of the cantilevers are connected by a key central hinge (Fig. 6c). The bending moment at midspan is zero. The central hinge transmits shearing forces, allows relative rotation between the two ends of the cantilevers and, through a suitable design, allows a free expansion of the girder. The design develops from a simple initial model because the structure is statically determined under the combined effects of self-weight and prestressing. Once the central hinge has been incorporated, the structure becomes statically indeterminate with respect to additional loads due to finishing works and traffic loads. In the final configuration, the statically indeterminate forces for each span are the vertical shear forces exchanged at the central hinge.

2.2.3 *Cantilever systems made continuous*
After the erection phase, the two adjacent cantilevers are connected, rendering them fully collaborating and the girder continuous (Fig. 6d). This type of bridges may be cast on scaffoldings and then prestressed, or build through the so-called balanced cantilever method. In such second case, the adjacent cantilevers are connected by concreting the central segment and then prestressing the girder with cables running along its whole length. Among the three schemes (articulated, partially articulated, continuous) the continuous one is at present the best solution. In fact, many cantilever bridges built according to the other two schemes have over time been modified and rendered continuous.

2.3 *Different joint types for reinforced and prestressed concrete girders*
In these structures, the joints must transmit high-intensity forces from the cantilever to the suspended structure, while also allow suitable relative movements between the coupled structures. These forces are localized over small areas, resulting in highly concentrated stresses. For iron and steel bridges, it was natural to resorts to devices like those used for heavy mechanical machinery. Bearing and expansion supports, rollers, rockers, and sliders are mechanical devices, involving special manufacturing techniques (Fig. 7). The main body of the supports are cast and then worked with a milling cutter, lathe, and borer machines and, in the end, the working surfaces are hardened with chemical and thermal treatments.

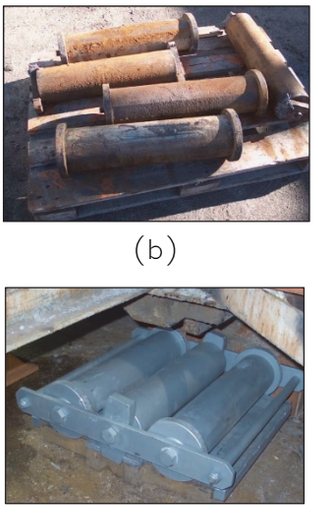


Figure 7. (a) Schemes of bearing and expansion supports used in iron/steel bridges; (b) roller bearings of a railway steel truss after 75 years of service; (c) the new rollers ready to substitute the old ones.

For concrete bridges the situation was different. For short spans, lead pads and elastomeric bearings were initially used. For longer cantilever girders there were attempts to design hinges and rockers with blocks of high strength concrete and special reinforcement arrangements, but in the end, the most

common solution exploited joint connections like those of steel bridges. Nowadays pot bearings, made of an elastomeric disc confined between a steel pot and a circular piston, with or without upper sliding guides, are used.

In truth, for R.C. and P.C. cantilever bridges with articulations, the main problem is the force transmission from the bearing or connecting devices to the body of the structure. The most frequent solution uses joints made of a couple of opposite corbels, like those shown in Figures 8 and 10.

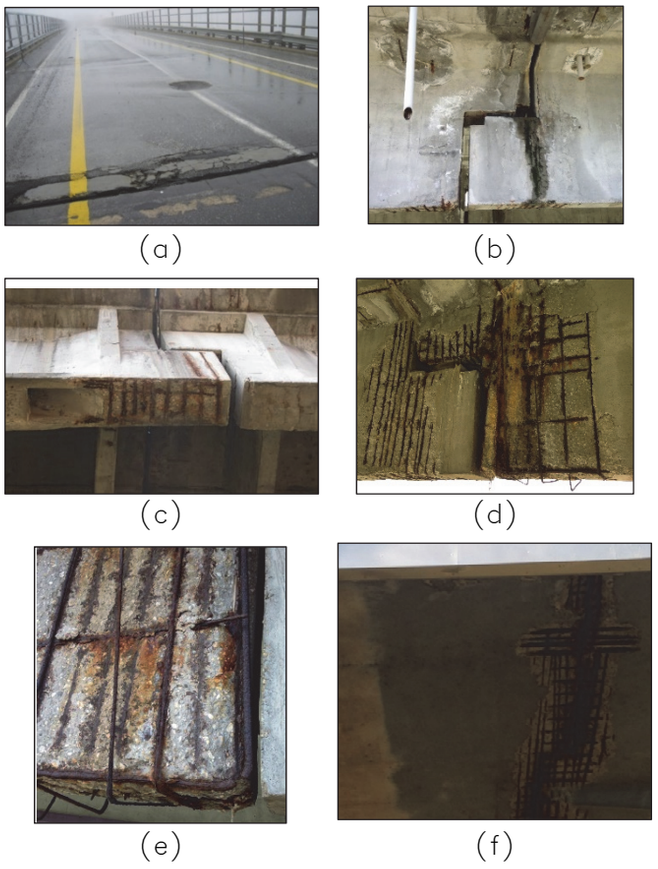


Figure 8. Articulated joints in R.C. Bridges: (a) malfunctioning joints lead to platform cracking; (b-f) the cumulative effects of malfunctionings in the joints and drainage systems cause water leakages that foster reinforcement corrosion.

For girders with hinged cantilevers, the key connections are usually made of massive steel blocks, whose sliding interfaces must be carefully milled and refined. Moreover, the two elements of the key must be assembled with small tolerances, to avoid gaps between the contact surfaces (Fig. 9).

3 IN-SERVICE BEHAVIOUR AND MOST COMMON TYPE OF DAMAGES

3.1 *Common damages*

Cantilever structures have proved to be fundamental in increasing span lengths and introducing new construction techniques. Many of these bridges, now more than one century old, are still in service.

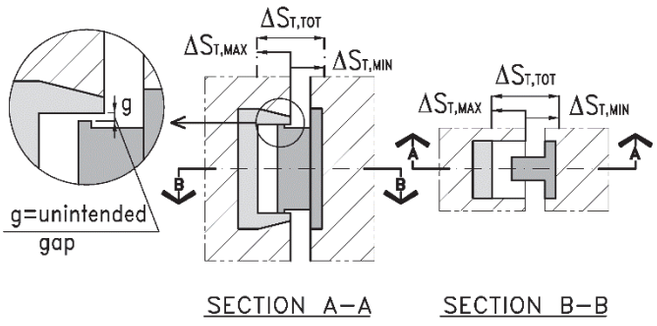


Figure 9. Example of a key central hinge in a R.C. bridge. The occurrence of an unintended gap makes the dowel action discontinuous and causes severe dynamic and hammering effects.

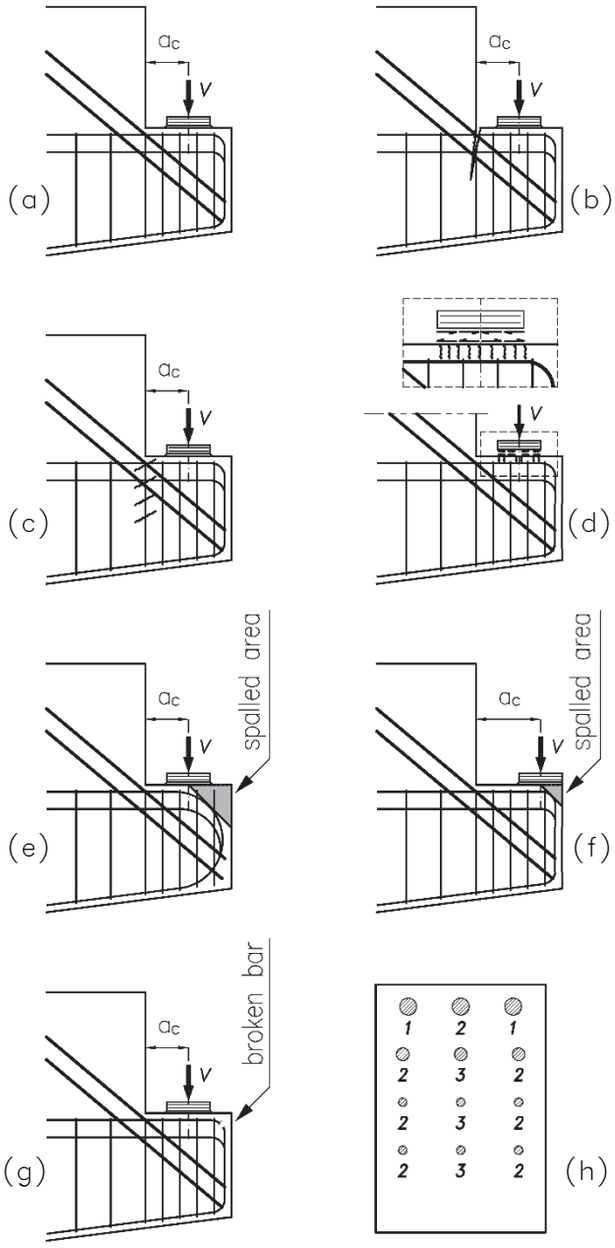


Figure 10. Recurring problems in R.C. Gerber corbels: (a) layout of the typical R.C. corbel; (b) flexural crack; (c) shear cracks; (d) cracking below the bearing pad; (e) incorrect reinforcement layout; (f) incorrect positioning of the bearing pad; (g) breakage at the bend of an exposed corroded bar; (h) sequence of activation of corrosion in rebars (1, 2, 3): the bars closest to the lateral surfaces are the most vulnerable, while internal bars provide an important reserve of strength.

This extended period of use allows us to ascertain their performances over time and to highlight, also, their most significant drawbacks. Such a posteriori evaluation is not intended as a critic of a praiseworthy past, but rather as an opportunity for examining their most common weaknesses, so as to conceive and design practical solutions to extend their service life.

In medium-long span bridges built over the last 150 years, the most common damages are those typical of old structures. They are mainly due to aging and lack of maintenance and can be summarized as surface wearing, with onset and diffusion of steel corrosion and, for R.C. bridges, cracks formation.

3.2 *Typical damages in cantilever girders*

Paying specific attention to cantilever girders, we can today affirm that some design criteria that appeared reasonable in the past, have resulted in dangerous preconditioning in later stages of the structure's life.

Many typical malfunctions have been triggered by: (a) initial choice of static scheme; (b) joints design; (c) an insufficient analysis of time-dependent effects (shortening, excessive deflections); (d) incorrect use of prestressing in governing the static and deformed configuration of the structure.

3.3 *Joints and their static and functional effects*

Joints articulations need to work as hinges. For the same geometry and loading conditions, articulated girders are statically/kinematically equivalent to continuous ones, if the articulations are placed at sections with zero bending moment in the corresponding continuous scheme. These hinges allow relative rotations between the two ends of the cantilevers and permit free longitudinal expansions of the girder. For a given loading condition (e.g. self-weight and permanent loads), the optimal hinge position can be easily determined.

It must be pointed out that small changes in hinge location and/or in loading distribution induce minor changes in the displacement as well as in the corresponding internal forces distributions, but relevant changes in the local relative rotations between the edges of a joint.

In girders with a key central hinge, in case the two edges of the joint end up being separated by an unintentional gap (identified with *g* in Fig. 9), the dowel action becomes discontinuous, causing severe dynamic and hammering effects.

Hence, from the functional point of view, the presence of internal hinges and joints causes slope discontinuities in the road profile and, under permanent loads, such kinks are progressively increased by time-dependent effects (Figs 11a, b).

Local discontinuities foster dynamic effects, reduce ride comfort (Fig. 8a) and cause severe damages to both bearing devices and their interfaces with the main structure. Moreover, the increase in the dynamic effects on the cantilever beams induces fatigue stresses in the upper rebars and tendons for negative moments.

In the end, repeated relative rotations between the joint edges damage the drainage and sealing systems, causing water to leak on underlying surfaces and corrosion of the nearby reinforcement (Figs 8b-f).

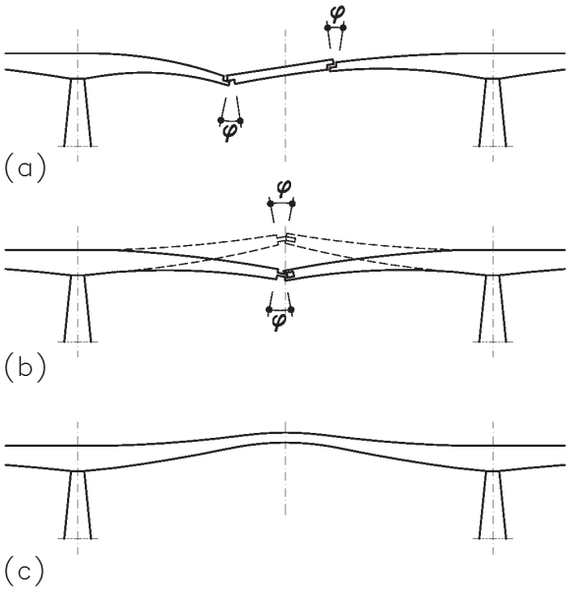


Figure 11. Time-dependent effects magnify irregularities: (a) abnormal slope in the central span (redrawn from Mathivat); (b) significant relative rotation (kink) at the central hinge (redrawn from Mathivat); (c) loss of planarity in a continuous girder.

3.4 *A focus on Gerber corbels*

Leakage of salted water from the platform causes the damaging effects shown in Figure 8, i.e spalling of concrete cover, corrosion of the bars, breakage at the bends of smaller bars like external stirrups. Other damaged states are shown in Figure 10 and consist of flexural or shear type cracks (Figs 10b, c); surface cracking immediately below and nearby the bearing pad (Fig. 10d); spalling of the corner due to an incorrect reinforcement shaping (larger bars involve larger radius of bend, Fig. 10e); spalling of corner due to incorrect bearing pad positioning (too close to the edge, Fig. 10f); breakage at the bend of exposed corroded bars (Fig. 10g). With reference to a hypothetical corbel section, Figure 10h shows the sequence of activation (1, 2, 3) of the corrosion effects The bars closest to the lateral surfaces are more vulnerable to corrosion than the interior bars, that, if present, remain an important reserve of strength.

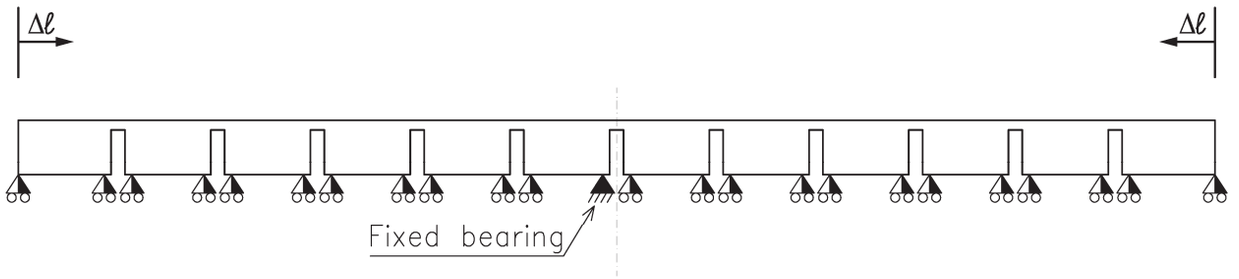


Fig. 12. Scheme representing a so-called "tied-deck girder" or "kinematic chain girder".

Gerber joints or corbel failures were at the basis of many ruinous bridge collapses. In steel bridges, corrosion states reduce the area and the stiffness of the pendulum struts, and lead to states of local instability, with consequences on the whole structure.

In R.C. bridges, the worsening of the damage states previously described may lead to the breakage of the corbel, causing the loss of its supporting action.

Small corbels are more vulnerable. The strut and tie models assumed for their design are reliable if the bottle-shaped struts volume is sufficiently larger than the material sizes of the aggregates, bars, and their bend radius. Moreover, corbels of limited dimensions make it difficult to accurately arrange the bars, resulting in structural details with congested reinforcement.

3.5 *Quasi-continuous bridges (tie-deck girders)*

A so-called "tied-deck girder" or "kinematic chain girder" is a viaduct composed of a train of simply-supported decks, longitudinally connected through short and flexible continuity slabs (Fig. 12). By avoiding joint devices between the spans, such scheme makes the carriageway continuous.

Dealing with long-span bridges, the time-dependent effects (shortening) and temperature excursions, cause longitudinal displacements which increase from the fixed point towards the free ends. In the design phase, it must be verified that, for the worst expected shortening over time, the upper plate of the bearing device will still be insisting on the lower one with a wide-enough contact area.

Experience showed that this might not be sufficient. In multi-span tied-deck-slab bridges, the shortening effects may cause significant changes in the local diffusion mechanisms in the contact zones of the bearing supports. These zones belong to the ends of the beams, where the prestressing action diffuses and stabilizes over a length nearly equal to the depth of the beam itself. In a proper design arrangement, the diffusion the stresses from the bearing supports superimposes the diffusion zone of prestressing, creating a biaxial compression zone. When the relative displacement of the sliding plates of the bearing device is such that the stress field due to the support reactions rest outside that of the biaxially compressed area, a wedge collapse may occur (Fig. 13). This local failure of a zone interested by very intense forces may create further and severe consequences and even lead to the collapse (Malerba 2016).

3.6 *Continuous prestressed bridges. Excessive deflections*

In the beginning, the design of these bridges was mainly focused on the erection stage, checking the stress distributions for the different configuration assumed during the erection and computing the corresponding deflections. As known, the deck is progressively uprising, until, in the final stages, the weight of the last segments and their higher lever arms lower the girder and it reaches the final (straight) trim, expected for the closure.

Excessively simplified analyses of creep and shrinkage effects and incorrect use of prestressing in governing statics and deformed configuration of the structure caused excessive deflections over time, with loss of functionality. Many drawbacks proved to be caused by the action of the upper cables, introduced for strengthening the girder, but adversely affecting its deformed configurations (Krístek et al. 2006). The conventional assessment of the time-dependent behavior of prestressed cantilever-built bridges uses tools of analysis based on deterministic criteria and assumes that all the factors involved are known and certain data. As known, the expected attitude of this type of bridges results from the antagonist roles of self-weight and prestressing. The final value of the deflections results from the difference of two large and opposite numbers, representing downward and upward deflections, which strongly depend on several uncertainties due to environmental factors, material characteristics, pre-tensioning forces in the tendons and erection technologies. As recently shown (Malerba 2012, Briccola 2017) through probabilistic analyses, such uncertainties have a significant influence on the deformational behavior. Both deflections and their variance increase with time and they may strongly modify the vertical attitude of the structure.

These effects are emphasized when the prestressing is applied only a few days after curing.

Acknowledging the existence of possible diverging behaviors and the intensity of their effects allows us not only to explain some excessive deformation experienced under permanent loads but also to draft solutions to make this type of structures more stable and safer.

3.7 Inspection and maintenance

Hinges, joints and any other type of articulation are vulnerable and expensive devices, characterized by a life cycle that is very short with respect that of the bridge. For these reasons, they require specific inspection and maintenance activities. In case of damages and failures, they are difficult to place and replace and strongly condition the operational costs.

4 CONCLUSIONS

Cantilever bridges have given a fundamental contribution to the development of bridge construction. Their performances over time allow highlighting their most common draw-backs, design solutions to extend their service life and define criteria to improve the design of new bridges.

For existing cantilever bridges, it is important to respect a rigorous and effective inspection and maintenance plan. Any intervention in case of incipient damage must not only repair but also try to increase the robustness of the weakest details and check the subsequent effects on the whole structure.

For new bridges, according to location, soil characteristic, costs and expected construction times, it is better to avoid articulated girders and an extensive use of joints, and to privilege continuous structural schemes.

In the design stage of continuous prestressed bridges, the uncertainties due to time-dependent effects pay a relevant role. For this reason, it is advisable to prearrange empty ducts for additional prestressing cables, to be used in contrasting unfavorable time-dependent effects. The layout of these cables must be designed according to the set of possible diverging schemes.

To prolong the structure service life and enhance its robustness, it is important always to predispose systems that facilitate inspection and maintenance operations and allow to recover potential drawbacks due to malfunctioning of special devices such as drainage systems, joints and bearing supports.

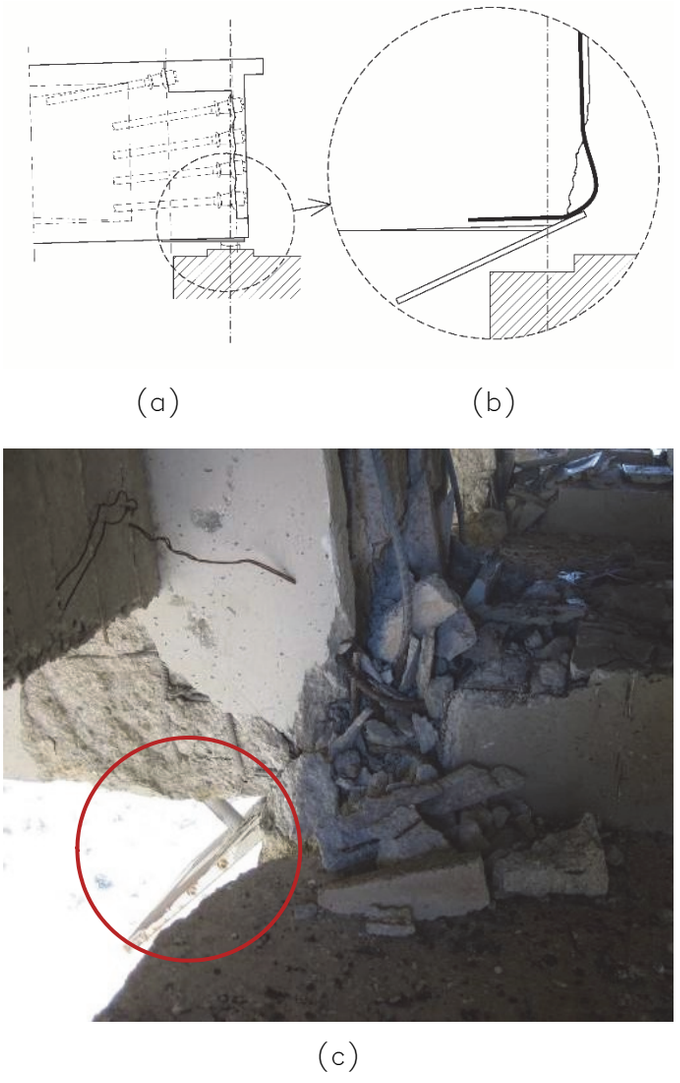


Fig. 13. Detail of a collapse occurred when the bearing pad had reached its maximum displacement: (a) layout of the prestressing tendons; (b) concrete spalling occurs in the corner, the bars undergo buckling and the bearing device upper plate rotates; (c) the final stages of an actual collapse (the bearing device upper plate is highlighted by the red circle).

REFERENCES

Briccola, D. 2017. Sensitivity analysis of bridge structures to time-dependent effects. PhDISSD Thesis, Politecnico di Milano (Italy). Supervisor: P. G. Malerba.

Krístek,V., Bažant, Z.P., Zich, M. & Kohoutková, A. 2006. Box Girder Bridge Deflections, *Concrete Intern.* Vol. 28, No. 1: 55-63.

Malerba, P.G. 2011. Stable and Diverging Time-Dependent Behaviours in some types of Bridge Structures, *Proceedings of the 2011 World Congress on Advances in Structural Engineering and Mechanics, Seoul, 18-23 September 2012.* Daejeon: Techno-press.

Malerba, P.G., Quagliaroli, M. & Scaperrotta, D. 2016. A Collapse induced by shortening in a Multispan Viaduct, *Proc. of the 8th Int. Conf. on Bridge Maintenance, Safety and Management (IABMAS2016), Foz do Iguaçu, 26-30 June 2016. CRC Press.*

Mathivat, J., 1983. *The Cantilever Construction of Prestressed Concrete Bridges*. Hoboken: J. Wiley & Sons. ISBN 0471103438

Wilcox, R.M., 1898. *Theory and calculation of cantilever bridges*. D. Van Nostrand Company.

Maintenance, Safety, Risk, Management and Life-Cycle Performance of Bridges – Powers, Frangopol, Al-Mahaidi & Caprani (Eds)
© 2018 Taylor & Francis Group, London, ISBN 978-1-138-73045-8

Whipple's 1841 Bowstring Truss – World's First Scientifically Designed Truss Bridge

I. A. Nitschke
Historic Preservation Advisory Committee, Town of Claverack, NY, USA

F. E. Griggs Jr.
Distinguished Member ASCE, Historic Bridge Consultant, 30 Bradt Road, Rexford, NY, USA

ABSTRACT: The Whipple Bowstring Truss bridge (patented in 1841), was the first bridge truss design in the world that used scientific principles, by Squire Whipple, who published them in the 1847 book: A Work on Bridge Building. Designed for the Enlarged Erie Canal in New York State (1836-1862), hundreds of Whipple Bowstring Truss bridges were built for the canal and other waterways. One such bridge was the Shaw Bridge, built in 1870, for the New York City to Albany Post Road over the Claverack Creek, in the idyllic Hudson Valley. This bridge is one of only eight of the vintage Whipple Bowstring Truss bridges left, the lone one in its original location and the only double span. It clearly exemplifies the robust original design, including the use of cast iron for compression members, wrought iron for tension members, and a wooden deck that could be replaced without affecting the strength of the bridge. Since the Shaw Bridge is uniquely in its original location, it also has its original masonry abutments (and pier). Despite being used for 120 years and closed for over 25 years, the bridge is in remarkably good condition, which speaks well for its original design and materials (19th century cast and wrought iron being more rust resistant than most modern steel). Whipple's importance cannot be overstated. Besides clearly documenting theoretical principles for bridge design for the first time, he promoted the use of prefabricated components, life-cycle costing, and was important for the Enlarged Erie Canal and early railway industry, helping make New York City become a world leader. The bridge is clearly eligible for Historic Civil Engineering Landmark status and this paper argues it is a World Heritage Bridge candidate. The meticulous restoration of the Shaw Bridge will be a fitting tribute to the genius of Squire Whipple.

1 INTRODUCTION

In a quiet picturesque area of Columbia County, in the renowned Hudson Valley of New York State, there is a charming double-span iron bowstring truss bridge over a scenic trout stream – the Claverack Creek. Currently it is neglected and closed, but this bridge, the Shaw Bridge, was designed by the famous 19th century engineer, Squire Whipple, and was once an important bridge on the main Post Road that connected America's financial centre (New York City) to New York State's capital (Albany). This paper tells the story of the world-renowned Shaw Bridge and the modest gentleman who designed it.

2 SQUIRE WHIPPLE – THE GENIUS BEHIND THE DESIGN OF THE SHAW BRIDGE

2.1 *Young Squire Whipple's Inspirations, Education, and Training (1804-1839)*

Squire Whipple was born in Massachusetts in 1804, the ninth son of a farmer and mill owner. The young Whipple was exposed to the latest construction techniques and materials and methods used to power mills of all kinds. When he was 13, his family moved to a farm in New York State. Whipple was a voracious reader who had a passion for learning but little or no interest in farming. He was a good student and at an early age became a schoolteacher at the local one-room schoolhouse. He became a vegetarian and would not use horses or oxen as beasts of burden. Fortunately, his father had developed another water-powered mill that kept Squire occupied and gave him the skills of a carpenter, tinsmith, blacksmith, and jointer. He experimented with electricity, played the violin every day, and attended nearby Hartwick Seminary and Fairfield Academy for several terms in the mid 1820s. In 1828 he studied law in a local lawyer's office while also working on his father's mills.

After receiving the best common school education available, in 1830 he graduated from Union College in Schenectady, New York after one year of study. He spent the decade of the 1830s working on various railroads and the Erie Canal enlargement. When work was slow, he designed, built, and sold mathematical instruments such as transits and engineer's levels and drafting equipment (Griggs 1988, 2002, 2005, 2015).

2.2 *Mature Squire Whipple's Productive Years (1840-1860)*

In 1841, Whipple designed and built a weigh lock scale with a capacity of 300 tons to weigh the enlarged canal boats in Utica, New York, which was adopted elsewhere. This was the largest weighing device in the country at the time.

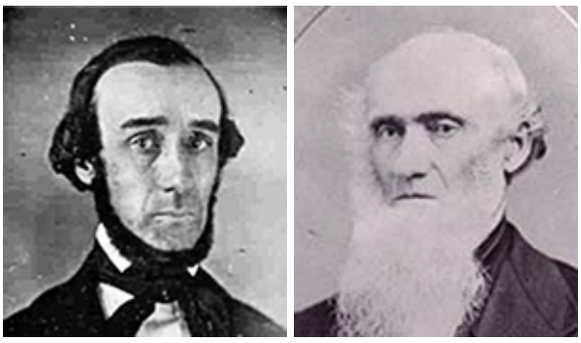


Figure 1 Squire Whipple (a) Young (b) Senior

Whipple became interested in the design and construction of bridges. He knew that wooden bridges on the original Erie Canal had a short life and the new, wider canal would require longer span bridges. So he devised methods to study bridge designs using various materials including iron. These investigations led to his design of the elegant bowstring truss that used cast iron for compression members, wrought iron for tension members, and a wooden deck that could be replaced without affecting the strength of the bridge. He applied for and was issued a patent, April 24, 1841. See Figure 2.

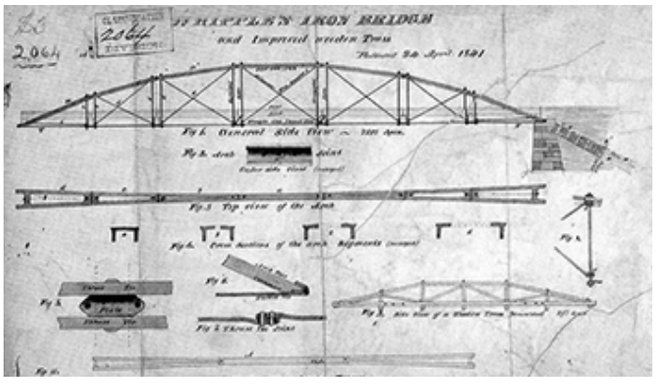


Figure 2. Whipple's Patent Drawings 1841

Whipple tried to convince the Canal Commissioners that a bridge built of iron was a good long-term investment (thus becoming a pioneering advocate of life-cycle costing), but they were reluctant to trust a new material for their bridges. To illustrate the stability and strength of his bridge, Whipple had one built at his own expense on a vacant lot in Utica, New York near the offices of the Canal commissioners, and when the wooden First Street Bridge in Utica fell, they finally approved the construction of his bridge. Between 1842 and 1870, hundreds of Whipple Bridges were built over the Erie and its branch canals, either by Whipple or to his patent, as his design was eventually adopted by the Canal Commissioners as the standard bridge to cross the canals of the state. See Figure 3 for an example.



Figure 3. Lithograph of Whipple's Bowstring Bridge in Syracuse NY, one of hundreds built over the Enlarged Erie Canal.

Others (like the Shaw Bridge) were built over waterways in the United States and one was even built in Japan (devised by Socichirro Matsumoto a Japanese 1876 graduate of Rensselaer Polytechnic Institute in Troy, New York). Frequently, contractors would build to his patent without paying patent fees, so he never received large sums of money from builders using his patent (Griggs 1988, 2002, 2005, 2015).

Whipple wanted to share his discoveries with the world and to bring credibility and respect to bridge building, so in 1846 he wrote *An Essay on Bridge Building: containing analyses and comparison of the principal plans in use with investigations as to the best plans and proportions and the relative merits ofwood and iron for bridges*. It included an analysis of the bowstring truss and other bridges, including the trapezoidal form. Whipple's decision to write this essay was probably based on his intention to show that his bowstring truss was the best form available in terms of efficient use of material but he found instead "each of the three forms – the arch, and the trapezoidal with and without verticals, possessed certain practical advantages entitling each to preference in respective cases". The 47-page essay marked the beginning of analytical truss design, and the following year it was made part of his 1847 seminal book *A Work On Bridge Building: consisting of two essays, the one elementary and general, the other giving original plans and practical details for iron*

and wooden bridges (Whipple 1847). For the first time anywhere in the world, this book presented the correct methods of analyzing and designing a truss using the properties of the latest appropriate materials. His technique, now known as the method of joints, is still the way that truss analysis is taught. He used both trigonometry and geometrical construction – the force polygon method – to find his member forces.

Between 1848 and 1850 Whipple designed and built several short span iron bridges for the New York and Erie Railroad. Though successful these bridges were removed after another iron bridge (not of Whipple's design) collapsed in 1850. Undaunted, in 1852-53 Whipple went on to design and build the first successful long span trapezoidal railroad bridges in West Troy and Utica, NY. This double intersection design was the most common railroad truss bridge until the 1890s, being built over western rivers with spans over 150 m (Griggs 1988, 2002, 2005, 2015).

2.3 *Senior Squire Whipple Continues to Make Major Contributions (1861-1888)*

About 1860 Whipple turned his business over to his nephew J. M. Whipple but took on a few jobs including designing and building trapezoidal bridges, swing bridges, and lift bridges. In December 1872, he designed and patented the first vertical lift bridge in the United States and built one over the Erie Canal in Utica.

Whipple continued to update and expand his first book with an Appendix in 1869 and wrote a more formal book on bridge building (first printed in 1872 then reprinted until 1899): *An Elementary and Practical Treatise on Bridge Building, An Enlarged and Improved Edition of the Author's Original Work.* (Whipple 1872). He contributed several articles to American Society of Civil Engineers (ASCE) Journals, and was the first person, after the post-Civil War rebirth of ASCE, to be named an Honorary Member of the Society in 1868.

Whipple died on March 15, 1888 at the age of 84 and was buried in the Albany Rural Cemetery leaving his widow Anna and no children. His obituary in *Engineering News* noted "The death of Squire Whipple… removes from the engineering world a man who by his individuality and originality practically created the modern art of bridge construction; not only in substituting iron for wood in bridges but in also pointing out the law governing the distribution of strain in framed structures and the proper proportioning of the various members in such structures".

3 THE WORLD FAMOUS, CHARMING, AND NEGLECTED SHAW BRIDGE

3.1 *The Shaw Bridge, Built along a Main Highway, is Named, and Photographed (1870-1930)*

The vital Albany to New York Post Road changed paths over its 300-year history but by 1870 it crossed the Claverack Creek via a double-span bowstring truss bridge later named the Shaw Bridge. The bridge builder (J. D. Hutchinson) and construction date (1870) are clearly established by the inscription embossed along the top of each of the four cast iron trusses, see Figure 4. John D. Hutchinson (1842-1897) and his father John S. Hutchinson (1814-1870) built more than 50 bridges using the patented Whipple design but defaulted on paying fees to Whipple (after a small down payment), resulting in lengthy court cases that were settled with a paltry sum paid by New York State.



Figure 4. Shaw Bridge inscription: "J. D. HUTCHINSON, BUILDER TROY, N.Y 1870"



Figure 5. Postcard of the Shaw Bridge south portal, looking north

Traditionally, local bridges were named after the owner of the nearest farm. In 1879, William Shaw, having made a fortune from his import-export business in Brooklyn, New York, purchased the farm next to the bridge, and the bridge became known as the "Shaw Bridge".

Later, the bridge was photographed, featured on a postcard with caption: "Bridge at Claverack, near Hudson, NY", and widely distributed, see Figure 5. The back of the postcard has the Trade Mark Litho-Chrome, Germany, which dates the postcard to the period 1906-1909, so the

photograph for the postcard was taken when the bridge was essentially in original condition. Note that the wooden deck reaches through the trusses. This is consistent with "New York State Canals – 1871 – Specification of the Manor of Constructing Whipple's Patent Iron Arch Truss Bridge Superstructure" (reproduced in Allen 1973). The postcard and official Specification are the fundamental documents that will be used to carefully restore the Shaw Bridge to its original condition.

3.2 *The Shaw Bridge is Bypassed, Repaired, Celebrated, and Finally Closed (1931-1989)*

"When the present State Route 9H was constructed in 1931, this remnant of the Old Post Road…became a little used road belonging to the Town of Claverack…However, when the hurricane of September 21, 1938, struck, the Shaw Bridge was one of the few in all Columbia County that was passable". In 1956 the bridge was condemned then repaired and reopened. Ten years later (1966), measured drawings of the deck provided an accurate list of materials to replace the wood stringers and deck, the last time they were replaced. On September 6, 1980, a ceremony celebrated the Shaw Bridge's listing on the National Register of Historic Places. This event included speeches emphasizing the historical importance of the bridge and a parade across the bridge led by a horse-drawn buckboard, followed by 1922 Essex Speedster, 1923 Studebaker, 1924 Ford, 1922 White truck, 1929 Ford truck, and 1930 Ford truck. However, despite significant support, by June 1989 the bridge was closed to motorized vehicle traffic because of "structural deficiencies".

3.3 *Attempts to Open the Shaw Bridge are Initially Unsuccessful but Finally Begin to Succeed (1990-Present)*

During 1990, various newspaper articles reported that the Town of Claverack was seeking funds to repair the Shaw Bridge. Cost of the restoration could be as much as $330,000. Meetings were attended by Van Wyck Lane residents interested in seeing the bridge preserved. One neighbor suggested the span be rehabilitated and reopened only to pedestrian traffic in order to preserve "the tranquil character of our neighborhood". By August 1990 it was announced that the state would grant $146,650 for half the cost of repairs. However, the town and county failed to come to an agreement on matching the state grant and the grant expired.

Meanwhile, in the summer of 1994, Jet Lowe, the famous Historic American Engineering Record (HAER) photographer, photographed the Shaw Bridge. However, in November 1995, the county engineer stated there are "no plans to re-open Van Wyck Lane over the Claverack Creek at this time". Thirteen years later, Wikipedia recorded how the famous bridge had become overgrown with vines and weeds. In 2010, several photos by Rick Ehrenberg (see Figure 6) conveyed the deplorable state of this important bridge to the Claverack Town Supervisor, stating "As the only known Whipple twin-span bowstring in the world, it would be a shame – no, crime, really – to NOT properly restore this bridge. It is a living piece of history, from a time when America's technical, engineering, and manufacturing prowess were just starting to bloom – and Squire Whipple was at the forefront".



Figure 6. Shaw Bridge. Photo by Rick Ehrenberg 2010

This led, in 2011, to clearing of the vegetation from the bridge by the Town Highway crew and photo documentation of the bridge by HistoricBridges.org, culminating in a proposal to the Preservation League to fund a Historic Structure Report, which, alas, was rejected. A second (this time successful) proposal was sent to the Preservation League in 2012, which resulted in the development of reports by engineering consultants Ryan-Biggs Associates and coauthor of this Dr. Francis Griggs Jr. These reports were then used to prepare a New York State Consolidated Funding Application (CFA) to restore the bridge in 2014. Unfortunately, the 2014 application was rejected. In 2016 a revised application was submitted and this time it was successful. With CFA money ($170,000) now available, it is expected that matching money, material and in-kind services will finally result in the initiation ofthe restoration of the Shaw Bridge.

3. DESCRIPTION OF THE CURRENT STATE OF THE SHAW BRIDGE

3.1 *Overview*

Whipple had a fondness for the first bridge he designed – the bowstring truss. He wrote: "The arched truss, moreover, may, by some, be thought to have a more graceful and agreeable appearance than the cancelled truss. I will not take upon myself to decide on this point, except by remarking, that, to a person who comprehends the principles and properties of different kinds of structures, in a case where strength is the grand desideratum, that plan of structure which secures this in the greatest degree, with the least amount of material and expense, will generally excite the most pleasing sensations in the mind" (Whipple 1847). The charming Shaw Bridge closely follows the bowstring truss design patented by Squire Whipple. Despite being neglected for so long, the bridge is in remarkably good condition, which speaks well for its original design and materials (19th century cast and wrought iron being more rust resistant than most modern steel).

The two-span, single-lane bridge has an overall length of about 50 m and a roadway width of about 3.2 m. Each of the identical pony trusses spans 25.4 m over the Claverack Creek. The bridge is currently closed to both vehicular traffic and pedestrians.

Wrought iron or steel floorbeams (additional testing would be required to determine if they are wrought iron or steel) are 23 cm deep and span about 4 m between the centerline of the trusses. The floorbeams support wood stringers, which are spaced at about 0.5 m on center and support a 6.4 cm thick wood deck. The trusses and the ends of the wood stringers are supported on stone masonry abutments and on a single stone masonry pier between the southern and northern span. Claverack Creek at normal water levels flows entirely under the southern span of the bridge.

3.2 *Condition of Cast Iron Top Chords & Junction Blocks*

Top chords are in excellent condition. The joints between segments are generally full bearing. Evidently in the past it was thought the segments were shifting with respect to one another and three retainer plates were added (on the east and west trusses of the south span and the west truss of the north span). It would be preferable to remove the retained plates in the rehabilitation of the spans. A small hairline crack was observed on the east truss of the south span where someone had attached a railing bracket and connected a steel bar across the crack. This is not a serious structural problem but it would be desirable to repair the crack in a less obvious way. Where non-historic railings have been welded or dowelled to the cast iron between the two spans, these will be removed and the holes repaired. The largest unknown is the condition of the ends of the chords that have been encased in concrete at the abutments and pier. It is unlikely that the cast iron has been damaged by the encasing (but the lower wrought iron chords could be, see below), but, in any case, all the top chords will be examined after the concrete is removed.

Junction blocks appear to be in a solid, uncracked, condition.

3.3 *Condition of Wrought Iron Lower Chord Loops, Vertical Rods, Diagonal Rods, Metal Beams, Metal Diagonal Cross Bracings*

Lower chord loops appear to be in good condition and in full contact with the cast iron junction blocks as there were no observed loose members. The largest unknown is, again, at the ends where they have been encased with concrete and where they enter the top chord casting. This area will be investigated closely when the concrete is removed and when the structure is cleaned and any cake or pack rust is removed.

Vertical rods appear to be in good condition except in areas where they have been bent, probably from some vehicle crossing the bridge. In other Whipple Bridges there has been some necking from corrosion where the vertical rods pass into the cast iron junction blocks. All of these areas will be reexamined after the structure is cleaned and any cake or pack rust is removed.

Diagonal rods are in good condition except, in a few cases, where they are severed or bent. Many of the diagonals are loose and will need to be tightened. As with the verticals, necking down of the section can occur where the diagonals enter the cast iron junction blocks, so it is probable that some of the ends of these elements may have to be replaced. All of these areas will be reexamined after the structure is cleaned and any cake or pack rust removed.

Beams appear to be in fairly good condition. Some rusting on the top flanges is apparent. It is believed that after cleaning they will be reusable.

Diagonal cross bracings are in good condition. The turnbuckles will have to be cleaned and restored to operating condition.

3.4 *Condition of Wood Stringers, and Wood Deck*

Wood stringers and decking must all be replaced. The non-original deck structure (designed to be replaced) was last installed in 1966. The new deck will more accurately reproduce the original, referencing the circa 1900 Postcard and the New York State Canals – 1871 – Specification (Allen 1973).

4. TREATMENT RECOMMENDATIONS

4.1 *Historic Preservation Objectives*

The U.S. National Parks, Secretary of the Interior, Standards for the Treatment of Historic Properties will be followed (Weeks & Grimmer 1995). These common sense historic preservation principles are intended to promote historic preservation best practices that help to protect irreplaceable cultural resources. The four treatment approaches of the Standards are: Preservation, Rehabilitation, Restoration, and Reconstruction. The treatment for the Shaw Bridge will follow the Restoration approach, which focuses on the retention of materials from the most significant time in the bridge's history (circa 1870 to 1900), while permitting the removal of materials from other periods (like guardrails, non-original wooden deck and stringers).

4.2 *Standards for Restoration of Historic Properties*

A property will be used as it was historically or be given a new use, which reflects the property's restoration period.

Materials and features from the restoration period will be retained and preserved. The removal of materials or alteration of features, spaces, and spatial relationships that characterize the period will not be undertaken.

Each property will be recognized as a physical record of its time, place, and use. Work needed to stabilize, consolidate and conserve materials and features from the restoration period will be physically and visually compatible, identifiable upon close inspection, and properly documented for future research.

Materials, features, spaces, and finishes that characterize other historical periods will be documented prior to their alteration or removal. Distinctive materials, features, finishes, and construction techniques or examples of craftsmanship that characterize the restoration period will be preserved.

Deteriorated features from the restoration period will be repaired rather than replaced. Where the severity of deterioration requires replacement of a distinctive feature, the new feature will match the old in design, color, texture, and, where possible, materials.

Replacement of missing features from the restoration period will be substantiated by documentary and physical evidence. A false sense of history will not be created by adding conjectural features, features from other properties, or by combining features that never existed together historically.

Chemical or physical treatments, if appropriate, will be undertaken using the gentlest means possible. Treatments that cause damage to historic materials will not be used.

Archeological resources affected by a project will be protected and preserved in place. If such resources must be disturbed, mitigation measures will be undertaken.
Designs that were never executed historically will not be constructed (Weeks & Grimmer 1995).

4.3 *Rationale for Using Standards for Restoration of the Shaw Bridge*

Restoration is warranted because the Shaw Bridge is a nationally significant resource – a rare survivor of the revolutionary design by engineering genius Squire Whipple – and it was constructed during a period when the road it carried was the most important main highway between New York City and New York State's capital, Albany. The Shaw Bridge's historical importance was recognized in 1980 when it was listed on the National Register and, it is generally agreed, it is eligible for Historic Civil Engineering Landmark status and possibly a potential World Heritage Bridge (see Section 5). Other considerations for the Restoration choice are the remarkably good physical conditions of the bridge with excellent original material that is largely intact with few alterations to the historical structure. The proposed pedestrian, bicycle, (and occasional horses and horse-drawn vehicles) use is also consistent with the original use before automobiles. Other sensitive issues are code requirements that need to be taken into consideration, but if hastily or poorly designed, code-required actions may jeopardize the bridge's materials as well as its historic character. For the Shaw Bridge, expensive

abatement of lead paint requires particular care if important historic finishes are not to be adversely affected. One of the first investigations will be to assess how much of the iron is covered by actual lead paint and explore alternatives to paint removal, especially in the unlikely event that the paint does not contain lead. Finally, the need to meet accessibility requirements (like handrails) under the Americans with Disabilities Act of 1990 will be designed to minimize material loss and visual change to the historic bridge (Weeks & Grimmer 1995).

4.4 *Work Recommendations*

The project will be guided by recommendations from the Historic Structure Report outlined in the New York State Proposal to restore the Shaw Bridge and overseen by New York Office of Parks, Recreation and Historic Preservation using the following tasks:

Task 1: Supervise & Administer the Project
Task 2: Re-Point Stone Masonry Abutments & Pier
Task 3: Remove Concrete Encasements At Truss Bearing, Highway Railing, Wood Stringers, & Decking & Replace With Temporary Planking
Task 4: Remove & Dispose Of Lead Paint & Rust
Task 5: Repair & Paint All Metal Truss Members & Beams
Task 6: Fill Pier Scour Hole & Protect With Stone
Task 7: Replace Wood Stringers & Deck

5. DISCUSSION & CONCLUSION THAT THE SHAW BRIDGE IS A POTENTIAL WORLD HERITAGE BRIDGE

The first Whipple Bowstring Truss bridge was designed, built, and patented by New York State engineering genius Squire Whipple in 1841, using scientifically based mathematical principles. In 1846-7 Whipple put these ideas into print in the book A Work on Bridge Building, the first time in the world that a scientific work correctly analyzed the stresses in a truss. Whipple is recognized as the father of iron-bridge building in America and has had a profound influence on the history of American civil engineering. The majority of the hundreds of Whipple Bowstring Truss bridges that were built were along the Enlarged Erie Canal, opening up the west and playing a key role in the rising dominance of New York City as America's most important city. They were essential to the success of the Erie Canal since they reconnected cities, villages, hamlets, and farm fields that grew up around the canal without impeding canal traffic. Similarly, the well-placed double-span Shaw Bridge (that extended over a wide part of the Claverack Creek) on the Albany New York Post Road provided a vital link, especially during winter months when the Hudson River was frozen and during periods of flooding when other bridges were closed.

Of the hundreds of original Whipple Bowstring Truss bridges built, only eight* are known to survive. Six are in New York State (Shaw Bridge, Black River Canal Bridge, Ehrmentraut Farm Bridge, Normanskill Farm Bridge, Union College Bridge, and Vischer Ferry Bridge); one is in Ohio (Rodrick Bridge); and one is in Japan (Hachiman Bridge). Coauthor Francis Griggs Jr. has been involved in the restoration of three of the eight historical Whipple bowstring truss bridges: Black River Canal (2001), Union College (1980), and Vischer's Ferry (1997).

* Note: Four completely new (2008-2015) Whipple Bowstring Truss bridges were built in Buffalo, New York, at the cost of millions of dollars. However, these bridges were factory-made and assembled differently than the way Whipple designed them, so cannot be considered true historical bridges. The bridges are major tourist attractions on the Buffalo waterfront, which has the stylized Whipple Bridge logo:



Of the eight historical Whipple bowstring truss bridges, the Shaw Bridge is the best example of this world-famous bridge: it is the only double-span Whipple Bowstring Truss left and the only one in its original location with all the original metal structure, stone abutments, and stone pier virtually intact. Only the badly rotted wooden stringers and deck (replaceable by design) are not original. The wooden stringers and deck will be reconstructed according to the circa 1900 color postcard photo and the New York State Canals – 1871 – Specifications. As such, the restored Shaw Bridge has the potential to become a world-class bridge.

To be included on the World Heritage List, sites must be of outstanding universal value and meet at least one out of ten selection criteria (see http://whc.unesco.org/en/criteria/ for the complete criteria list). The Shaw Bridge satisfies the following four selection criteria: (i) To represent a masterpiece of human creative genius; (ii) To exhibit an important interchange of human values, over a span of time or within a cultural area of the world, on developments in… technology; (iv) To be an outstanding example of a type of … technological ensemble which illustrates a significant stage in human history; and (vi) To be directly or tangibly associated with events or living traditions, with ideas, or with beliefs, with artistic and literary works of outstanding universal

significance (preferably used in conjunction with other criteria) … The protection, management, authenticity and integrity of properties are also important considerations.

The status of the Shaw Bridge as a world-class historic bridge is confirmed by three publications that follow.

First, before the Shaw Bridge closed, it was included in the book Great American Bridges and Dams by Donald L. Jackson with a foreword by renowned historian David McCullough (Jackson 1998). Several New York City bridges were in this book, including world famous 1883 Brooklyn Bridge, 1917 Hell Gate Bridge, and 1931 George Washington Bridge. Upstate New York was represented by three bridges: 1870 Shaw Bridge, 1855 Blenheim Covered Bridge (destroyed by the 2011 tropical storm Irene), and 1927 Peace Bridge (Buffalo).

Second, in an important article (DeLony 1996) "Context for World Heritage Bridges", Eric DeLony (former chief of the National Park Service, Historic American Engineering Record), listed five potential world heritage bridges for New York State: 1860 Central Park Cast-Iron Arches, 1867 Normanskill Whipple Bowstring Truss Bridge, 1883 Brooklyn Bridge, 1886 Poughkeepsie Cantilever Bridge, and 1917 Hell Gate Bridge. The reason for DeLony's choice of the Normanskill Bridge over the Shaw Bridge may have been the extensive documentation of the Normanskill Bridge by HAER in 1969 (Allen 1973), unlike the Shaw Bridge, which was not known at the time of the 1969 study. (Although DeLony would have been aware, in 1996, of Jet Lowe's 1994 photographs of the Shaw Bridge). As noted above, the Shaw Bridge is in its original location. But DeLony appears to contradict himself and make a special exception for the Normanskill bridge (which has been moved twice to the current location and does not have its original abutments) when he states: "A World Heritage bridge, like other properties, must meet the test of authenticity in design, materials, workmanship, or setting" [emphasis added]. The relocation of the Normanskill bridge from its original location and foundations negatively impacts the authenticity of its setting. The setting of the Shaw Bridge, still standing on its original abutments and pier, along the once vital Albany Post Road over the bucolic Claverack Creek, has a much greater authentic setting than the relocated Normanskill farm bridge. Besides, the Shaw Bridge has two spans while the Normanskill Bridge has only one.

Third, in the oversize book of photos Bridges, A history of the world's most famous and important spans by Judith Dupré, with an introductory interview by celebrated architect Frank O. Gehry (Dupré, 1997) only four New York State bridges are photographed and listed: Brooklyn Bridge, Hell Gate Bridge, George Washington Bridge, and Albany (Normanskill) Whipple Bowstring Truss Bridge. Again, the Normanskill Bridge was probably chosen because of the extensive HAER documentation conducted in 1969, but the Shaw Bridge, when restored, has a much greater claim to fame than the Normanskill Bridge.

REFERENCES

Griggs, Jr, F. (1988, 2002, 2005, 2015) A Forerunner in Iron Bridge Construction: An Interview With Squire Whipple, *Civil Engineering Practice*, Fall 1988, pp. 21-35; Squire Whipple – Father of Iron Bridges, *Journal of Bridge Engineering*, May/June 2002, pp. 146-155; Squire Whipple, *Structure Magazine*, September 2005, pp. 58-60; Historic Structures: The Whipple Bowstring Truss, *Structure Magazine*, January 2015, pp. 46-48

Whipple, S. (1846) *An Essay on Bridge Building*, H. Curtiss, Utica, NY, 1846; A Work on Bridge Building, H. H. Curtiss, Utica, NY, 1847; An Elementary and Practical Treatise on Bridge Building, D. Van Nostrand, New York 1872. [Digitized by Google].

Allen, R. S. (1973) Whipple Cast- and Wrought-iron Bow-string Truss Bridge 1867", Historic American Engineering Record, (HAER NY-4) Smithsonian Studies in History and Technology, Number 26, 1973, Specifications of the Whipple Truss Bridge, p. 149.

Weeks, K. D. & Grimmer, A. E. (1995) *The Secretary of the Interior's Standards for the Treatment of Historic Properties with Guidelines for Preserving, Rehabilitating, Restoring & Reconstructing Historic Buildings*, U.S. Department of the Interior, National Park Service, Washington, D.C., 1995, pp. 117-166.

Jackson, D. L. (1988) *Great American Bridges and Dams*, NY, John Wiley & Sons, 1988, 126-127.

Delony, E. (1996) Context for World Heritage Bridges, *International Council on Monuments and Sites (ICOMOS) and The International Committee for the Conservation of the Industrial Heritage (TICCIH)* 1996, pp. 1, 8, 15.

Dupré, J., Bridges (1997) *A history of the world's most famous and important spans*, New York, Black Dog & Leventhal Publishers, 1997, pp. 50-51.

Maintenance, Safety, Risk, Management and Life-Cycle Performance of Bridges – Powers, Frangopol, Al-Mahaidi & Caprani (Eds)
© 2018 Taylor & Francis Group, London, ISBN 978-1-138-73045-8

The Use of Machine Learning Techniques to Assess Damage in Critical Infrastructure

M.A. Terra, R. A. Pereira Junior, L. F. M. Sanchez & M. Noel.
University of Ottawa, Ottawa, ON, Canada

W. R. Junior
Construtora Cunha Braga, Sao Paulo, SP, Brazil

ABSTRACT: Over the past decades researchers have tried to develop protocols to assess the current condition (diagnosis) and the potential for further expansion/distress (prognosis) of aging critical infrastructure. Among promising techniques, particular attention was given to quantitative microscopic procedures such as *the Damage Rating Index (DRI)*. However, those techniques were found to be quite time-consuming and relied on the experience of petrographers able to properly judge their outcomes. It has been found that *Machine Learning (ML)* techniques might be used for efficient damage assessment in concrete. With the aid of modern software and some custom programming, petrographers could provide some "training" to the computer to diagnose concrete distress mechanisms. This paper discusses the potential use of ML to appraise damage in critical infrastructure. Validation is made with data obtained from laboratory test specimens with different amounts of damage from AAR. Preliminary results illustrate the promising character of ML in diagnosing AAR-affected concrete, which may also be suitable for other types of deterioration.

1 INTRODUCTION

Civil infrastructure is very critical for society, connecting a nation's businesses, communities and people, driving the economy, and improving the quality of life of human beings. Usually, civil concrete infrastructure is designed with a lifespan, so-called "service-life", of 50-75 years depending on the code used for designing and the structure type (i.e. dams, bridges, tunnels, stadiums, etc.). It is known that several critical structures are reaching the end of their expected service life, and thus actions should be taken in order to either manage/guarantee their performance over their last few years in service or extend their expected lifespan. Moreover, several of those structures present clear signs of distress due to numerous damage mechanisms which might very likely decrease their performance down to unacceptable thresholds (Figure 1).

In this context, alkali-aggregate reaction (AAR) is one of the most important damage mechanisms affecting the performance of concrete infrastructure worldwide (Fournier and Bérubé 2000, Sanchez et al. 2015). AAR is normally divided in two distinct mechanisms; the so-called alkali-silica reaction (ASR) and alkali-carbonate reaction (ACR).

- ASR is a chemical reaction between unstable silica minerals phases from the aggregates used in concrete and the alkali ions found in the concrete pore solution. It is by far the most common reaction mechanism found in concrete around the world (Fournier & Bérubé 2000).
- ACR is a chemical mechanism that happens in concrete in the presence of limestone and/or dolomite aggregates. Currently, there is no consensus in the technical society on the real mechanisms causing ACR-induced expansion and damage. Yet the dedolomitization of dolomite seems to be one of the potential causes (Grattan-Bellew et al. 2010, Fournier & Bérubé 2000).

One of the biggest challenges in civil engineering nowadays is to identify the cause and the extent of distress, to establish the correlation between the reductions in mechanical properties, physical integrity, durability and performance of the affected material, to evaluate possible structural implications and also their potential for further deterioration. Those are critical steps in the selection of management actions on the above structures (Sanchez et al. 2015, Grattan-Bellew & Danay 1992, Grattan-Bellew & Mitchell 2006, Rivard et al. 2000).


Figure 1: Concrete block damaged by AAR- Quebec,Canada.

Over the past decades, engineers and researchers have tried to develop tools and procedures to assess the current condition (diagnosis) and the potential for further expansion/distress (prognosis) of concrete damaged by AAR. Among promising techniques, particular attention has been given to the Damage Rating Index (DRI), a semi-quantitative petrographic method, as well as to some quantitative image analysis techniques through the use of fluorescent epoxy dyes (Rivard et al. 2000, Sanchez et al. 2015). However, although very interesting, those techniques are quite time consuming and more importantly always rely on experienced petrographers able to properly judge the outcomes of the methods. Otherwise, it has been identified that a number of *Machine Learning* (ML) techniques might be used for efficient assessment of damage in concrete. However, very few data is available in the literature on the use of ML systems for diagnosing concrete affected by AAR.

The primary objective of the current study is to explore the potential of ML techniques for the assessment of critical concrete infrastructure such as bridges. It is anticipated that these techniques could eventually be used to diagnose problems in concrete bridge structures through an automated analysis of their distress features, and possibly even to provide a prognosis of future damage. While the methodology presented herein focuses specifically on concrete distress caused by AAR, the approach used could very likely also be used to evaluate other mechanisms (e.g. corrosion of steel reinforcement, freeze-thaw damage, delayed ettringite formation, etc.). This work thus provides a preliminary basis for identifying and isolating the effects of multiple distress mechanisms that may be present together in a single sample, a task which is currently very difficult to assess through manual methods.

2 BACKGROUND

2.1 *Microscopic tools for assessing AAR damage*

To evaluate AAR-induced expansion and damage, several mechanical and microscopic tools were developed in the past decades. Among them, the Damage Rating Index (DRI) is one of the most promising tools. The DRI is a microscopic analysis performed with the use of a stereomicroscope (15-16x magnification) where damage features generally associated with AAR are counted through a 1 cm² grid (i.e. 10 x 10 mm units) drawn on the surface of a polished concrete section (Sanchez et al. 2017, Villeneuve & Fournier 2012, Dunbar & Grattan-Bellew 1995). The number of counts corresponding to each type of petrographic feature are then multiplied by a weighting factor, whose purpose is to balance their relative importance towards the mechanism of distress, in this case AAR. The factors used in the method were selected on a logical basis, but relatively arbitrarily (Sanchez et al. 2015, Villeneuve & Fournier 2012); they were recently modified in order to reduce the variability between the petrographers performing the test (Villeneuve & Fournier 2012). Ideally, a surface of at least 200 cm² should be used for DRI analysis, and it may be greater in the case of mass concrete incorporating larger size aggregate particles. However, for comparative purposes, the final DRI value is normalized to a 100 cm² area.

It has been shown that the DRI correlates well with measurements of expansion and damage caused by AAR in concrete presenting different compressive strengths and incorporating a wide range of reactive aggregates (Sanchez et al. 2015, Rivard et al. 2000). Yet, the microscopic technique is also quite time-consuming, which could be at least partially improved by the use of automated techniques such as machine learning processes (Pereira Junior & Inkpen 2017, Azam & Gavrilova 2017). Furthermore, DRI values depend largely on the skill and experience of the researcher, and thus may be considered somewhat subjective. By training computers to perform automated analyses, more consistent and objective results might be expected.

2.2 *Machine Learning (ML)*

Machine Learning (ML) is a field of artificial intelligence that provides systems the ability to automatically learn and improve from data without following only explicitly programmed instructions. ML algorithms operate by building a model based on inputs and using that to make predictions or decisions.

ML is employed in a range of computing tasks where programming explicit algorithms is infeasible. ML is commonly classified in three types:

1. **Supervised Learning**: It is the ML task of inferring a function from labeled training data as an input, generalizing to unseen situations. The algorithm will learn the relationship between the images and their associated numbers, and apply that learned relationship to classify completely new images (without labels) that the machine hasn´t seen before (Maini V., 2017);
2. **Unsupervised Learning**: It is the ML task of inferring a function to describe hidden structure from unlabeled data. The algorithm is left to their own devices to discover and present what must be the structure in the data such as groupings or rules that describe portions of the data (Hinton et al., 1999); and
3. **Reinforcement Learning**: It is a type of ML algorithm that allows an agent to decide the best next action on its current state, by learning behaviours. It is a goal-oriented learning based on interaction with environment. It is not about discovering which action to take, but instead must discover which action will yield the maximum reward. (Auer et al. 2010) and (Sutton et al., 1998).

More specifically dealing with images, and whatever is the type of ML selected, it involves three steps as described below:

- *Image Recognition*

Human brain makes vision an easy task. It doesn't take any effort for humans to distinguish a lion from a jaguar, read a sign or recognize a human's known face. But these are actually hard problems to solve with a computer: they only can make it because our brains are incredibly good at understanding images. In the last few years, the field of ML has made tremendous progress on addressing these difficult issues. In particular, it has been found that a model called deep convolutional neural network (CNN) can achieve reasonable performance on hard visual recognition tasks, matching or even exceeding human performance in some domains (Abadi et al. 2015).

- *Model Building*

The Clarifai API (Sood, 2017) offers image and video recognition as a service, using artificial intelligence to recognize the visual content. API is built around the idea that input parameters are sent (microscopic images of concrete, for example) to the service and it returns predictions based on a model built specifically for a given purpose. A model is a processing block that converts inputs parameters (e.g. images) to predictions (e.g. concepts, bounding boxes, etc.). When an input parameter is implemented in the model, it will return the predictions that the model captures on the input parameter provided.

- *Training, Testing and Evaluating the Model*

Training process include the creation and association of concepts for each type of implemented images, with their specific classifications, building a model. Testing and Evaluating processes estimate how well the built model has been trained, calculating its accuracy results.
Currently, there are a number of available ML tools which are able to process and recognize any information such as images once they are well-trained (Matsumoto 2017, Krizhevsky et al. 2012). These tools might be used for specific purposes in civil engineering, for instance, to detect AAR-induced expansion and damage. Normally, the best ML approaches use mathematical models such as convolutional neural networks (CNN) which are powerful techniques for recognizing images (Azam & Gavrilova 2017, Pereira Junior & Inkpen 2017, Krizhevsky et al. 2012). Their ability can be set by varying the number, depth, and amplitude of images. However, very few trials with the use of CNN were made to detect distress in concrete so far.

3 SCOPE OF WORK

As previously discussed, there is a lack of fast, economical, and reliable tools to assess damage in concrete, and ML techniques seem to be a promising solution. This project aims to develop an automated tool to assess the diagnosis and prognosis of AAR-affected concrete through the use of ML systems. First, with the use of a stereomicroscope, a number of pictures were taken of different AAR crack types, presenting different features and development stages as per the DRI. Then, ML systems through the use of CNN algorithms were implemented to detect the type and progress of damage in an automated fashion. Accuracy in the detection is assessed and if needed, a greater number and more detailed depth & amplitude of images are analysed so that a target accuracy is reached. Figure 2 illustrates the process of ML to detect AAR damage proposed in this work.

4 METHODOLOGY

The process of sample fabrication, ML training and data gathering used in this research contains 8 steps that are described hereafter.

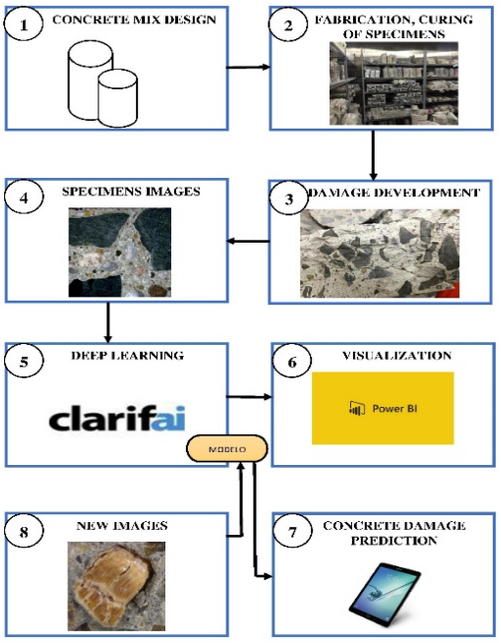


Figure 2: ML system.

4.1 *Concrete Mix Design*

Twenty four concrete cylinders (i.e. 100mm by 200 mm in size) containing two different reactive aggregates (i.e. coarse - NM and fine – Tx), presenting distinct reactive levels) and three levels of compressive strengths (i.e. 25, 35 and 45 MPa) were cast. Non-reactive aggregates (D and UL), respectively coarse aggregates and sand were also added to Tx and NM mixes. The concrete mixtures were mix-designed to contain the same amount of cement paste and aggregates in volume (i.e. from one mix to another). All concrete mixes were made with the same conventional (CSA Type GU, ASTM type I) high alkali (0.88 % Na2Oeq) Portland cement. Reagent grade NaOH was used to raise the total alkali content of the mixtures to 1.25% Na2Oeq, by cement mass, for accelerating the expansion process due to AAR. Table 1 presents the concrete mixtures used in this research.

Table 1: Concrete mixtures used in this research.

Mixtures	Materials	25MPa	35MPa	45MPa
	Cement	314	370	424
	Water	192	174	157
Tx + D	Sand	790	790	790
	Coarse Ag.	1029	1029	1029
NM+UL	Sand	714	714	714
	Coarse Ag.	1073	1073	1073

4.2 *Fabrication, curing, and testing of specimens*

After casting, the specimens were placed for 48h in the moist curing room. Small holes, 5 mm in diameter by 15 mm long, were then drilled in both ends of each of the test cylinders and stainless steel gauge studs were glued in place, with fast-setting cement slurry, for longitudinal expansion measurements. Following completion of the first 48h at 23°C, the "0" length reading was performed and the specimens were placed in a sealed plastic (22 liters) containers lined with a damp cloth (4 cylinders per bucket). All buckets were then stored at 38°C and 100% R.H., and all of the test cylinders were monitored regularly for length variations. Periodic axial measurements were made as per ASTM C 1293 (ASTM C1293 2008). The specimens were then monitored until they reached the expansion levels selected for the project (i.e. 0.05± 0.01%, 0.12± 0.01%, 0.20± 0.01% and 0.30± 0.01%). Finally, the specimens were first cut in two along their axis, and then polished for microscopic analyses.

A polishing device, which uses diamond-impregnated rubber disks (nº. 50 (coarse), 100, 400, 800, 1500 to 3000 (very fine), was used for obtaining surfaces of appropriate quality for DRI assessment (Sanchez et al 2015, Sanchez et al 2017).

4.3 *Damage Rating Index and Image analysis*

A semi-quantitative petrographic analysis, using the DRI, was performed on specimens from each concrete mixture at the various expansion levels studied and presented in Section 4.2, according to the method described by Villeneuve & Fournier (2012).

Actually, the crack counting within the aggregate particles were performed on particles down to 1 mm in size, so that the distress coming from reactive sands might be well assessed (Sanchez et al. 2015, Sanchez et al, 2016, Sanchez et al. 2017).

Once the DRI was performed, pictures using a high-quality camera attached to the stereomicroscope were taken from some of the "squares" (i.e. 1cm^2) used in the DRI analysis, for a total of 100 cm^2

Thus, a total of ≈ 8 pictures were taken per specimen (i.e. 200 total), which enabled the development of a large database of images with two different types of mechanisms (i.e. AAR coming from the reactive coarse aggregates and sand), three concrete strengths and several different crack features as by Sanchez et al. 2015 and highlighted in Table 2. Figure 3 illustrates some of the different features captured by the camera.

Table 2: Damage features accounted in the DRI analysis and deep learning process.

Petrographic features	Abbreviation
Cracks in coarse aggregate	CCA
Opened cracks in coarse aggregates	OCA
Crack with reaction product in coarse aggregate	OCAG
Coarse aggregate debonded	CAD
Disaggregate/corroded aggregate particle	DAP
Cracks in cement paste	CCP
Cracks with reaction product in cement paste	CCPG

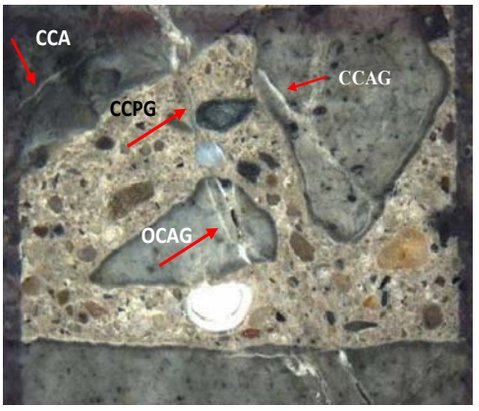


Figure 3: Petrographic features captured by the camera in the DRI analysis (Sanchez et al. 2015)

4.4 *Deep Convolutional Neural Network*

The implementation of the machine learning process for the detection of AAR-induced expansion and damage was performed through the use of CNN models. A Convolutional Neural Network (CNN) is a class of supervised learning with deep, feed-forward artificial neural networks that has been successfully applied to analyzing visual imagery (Krizhevsky et al. 2012, Ciresan et al. 2011).

Basically, the first need is to teach the computer how each petrographic feature looks like before it being able to recognize a new object. In a supervised learning, the more a feature the computer sees, the better it gets in recognizing that feature. This task can be carried by labeling the images, and the computer will start recognizing patterns present in a specific damage taken from distressed concrete that are absent from other ones and will start building its own cognition.

These models are able to identify the crack's pattern and quantity in the different concrete mixtures at distinct expansion levels. Several existing models were tested and the best CNN was selected for the project. Furthermore, trials to create a brand new model optimized for the current specific purpose were also performed.

Figure 4 illustrates the basic blocks of the CNN process, consisting of the input layer (convolution), hidden-layers (pooling layers and fully connected layers) and the output layer (classification ranked by scores). To do so, the image is broken up into a number of tiles (convolution). Now we have to apply a technique to reduce the dimensions of an image (by taking the maximum pixel value of a grid) and to make the model more generic, predicting what each tile is individually. Finally, the computer tries to predict which damage feature is in the image based on the prediction of all the tiles. This allows the computer to parallelize the operations and detect the object regardless of where it is located in the image.

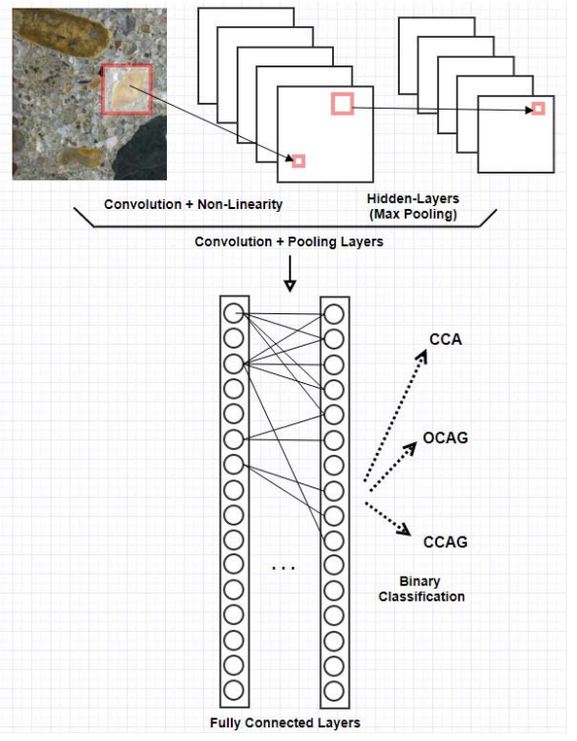


Figure 4: Convolutional Neural Network for Image Classification.

4.5 *Visualization*

In the visualization step, a Business Intelligence system was developed, preparing data for analysis, developing and running queries against that data gathered, and creating reports, dashboards and data visualization to make the analytical results available for the evaluation of our ML system.

4.6 *New Images*

New separated images should also be prepared in a similar manner as described in Section 4.3 to be directly used for prediction purposes by the system for validation.

4.7 *Damage Prediction*

The last step is the damage prediction itself. It consists of using the system for real situations. Thus, users provide new "microscopy concrete images" as input parameters of the model, which will be tested and evaluated by the system, using the deep learning techniques as per Section 4.4.

5 PRELIMINARY RESULTS

Trying to fit the model to the training data and hope it would accurately work for the real data it has never seen before is not appropriate. So, some kind of assurance that the model has got most of the patterns from the data correct, and its not picking up too much on the noise (Gupta P., 2017).

In order to estimate how accurately a machine learning model will perform in practice, it is usually executed a cross-validation step. It has two sub-processes: *Training* and *Testing*. The *Training* process is used for training a model. Then, the trained model is applied in the *Testing* process.

The performance of the model is measured during the *Testing* phase. It was implemented a 5-split cross-validation process to train and forecast damage in concrete due to AAR, detailed as follows:

1. Set aside a random 20% subset of the training data and designate as a test set (40 from 200 images);
2. Train a new model with the remaining 80% of the training data (160 from 200 images);
3. Pass the test set data through this new model to make predictions;
4. Compare the predictions against the test sets actual labels; and
5. Repeat steps 1) through 4) across 5-splits to average out the evaluation results.

The average results obtained in the evaluation process are presented in Table 3. The concept, its accuracy score, the number of prediction attempts, and the total labeled concepts associated with 200 pre-trained images are illustrated in Table 3.

Table 3: Concrete Pathology Model Evaluation

Concept	***Accuracy***	***Predictions***	***Pre-Trained***
DP	1.000	0	6
CCA	0.742	36	174
CCP	0.671	16	73
CCPG	0.651	6	26
OCA	0.590	26	125
OCAG	0.496	13	36
None	0.533	1	9
Total	***Avg:0,664***	***46***	***449***

Analyzing the data above, one may verify that, for example, the cracks in the cement paste (CCP) achieved around 67% of accuracy in the evaluation the process of predicting this type of damage with the current deep learning model. Moreover, in this case, 73 pre-trained images were used with this concept, and 16 predictions of CCP over 40 images were performed (first step of the 5-split cross-validation process), each one having zero or multiple concepts. It is worth noting that a total of 7 concepts (DP, CCA, CCP, CCPG, OCA, OCAG and None), and 449 concept labels (each image can be associated to zero, one or more concepts) are associated with 200 pictures in the current dataset.

Usually, to achieving satisfactory results in the evaluation process, it often requires thousands of images to be trained for an unknown model, such as the one proposed in this research. The more labeled images we have to train, the more accurate the predicted result tends to be. Despite that, Table 3 shows that preliminary and encouraging results with an average of 66.4% of accuracy on predicting the correct concepts associated to images were obtained using only 449 labeled concepts and 200 pictures.

6 DISCUSSION AND APPLICATION OF ML FOR ASSESSING DAMAGED STRUCTURES

6.1 *Robert-Bourassa/Charest Bridge*

Robert-Bourassa/Charest (RBC) overpass was a highway bridge structure (Quebec, Canada) that was built in 1966 using an alkali-silica reactive (ASR) limestone aggregate. The bridge was made of a bridge deck (BD) resting on reinforced concrete Y-shaped columns (C), themselves supported by massive foundations blocks (FB) (Figure 5) (Sanchez et al. 2016).Over the last decades, many signs of distress developed on the various elements of the structure. This included extensive steel corrosion and concrete delamination/spalling at the level of the deck; map cracking, scaling, disaggregation and pop-outs affecting the massive concrete foundations due to ASR and freeze-thaw (FT) cycles; and concrete spalling and steel corrosion on the columns and foundations exposed to salt-water spray from traffic on the Robert-Bourassa highway (Bérubé et al. 2005). Numerous laboratory tests methods, including the DRI, were performed on RBC cores extracted from its different structural members (FB vs C vs BD) presenting different environmental/exposure conditions (surface vs core; exposed vs non-exposed) and orientation (vertical vs transversal vs longitudinal), which highlighted the different damage

degrees found at different locations (Sanchez et al. 2014).



Figure 5: Robert-Bourassa/Charest overpass after nearly 50 years in service.

6.2 *Damage Rating Index Results*

Figure 6 presents the microscopic responses of the cores assessed through their DRI numbers. All of the samples contained closed cracks within the aggregate particles (CCA). CCA cracks are likely caused during aggregate production (e.g. crushing, sieving, etc.) and weathering, and may not be related to ASR progress. However, open cracks with and without gel within the aggregate particles (OCA and OCAG, respectively) are indeed ASR damage features. Likewise, cracks in the cement paste with and without gel (CCP and CCPG) are also caused by ASR. As seen in Figure 5, greater DRI numbers are found for the FB specimens, followed by BD and C cores. Furthermore, greater damage was obtained for exposed cores, compared to non-exposed ones for the FB samples. Likewise, surface specimens presented more damage than internal samples.

In the BD cores, damage varied according to the core's orientation. Vertical cores presented greater damage than the longitudinal and transverse specimens, which, unlike the mechanical analyses, showed similar results. Samples from the deck top showed lower damage than ones from the bottom. C samples also presented lower damage degrees than FB and BD cores, which may be linked to the amount of reinforcement present in those members. The results illustrated in Figure 6 showed that non-negligible differences of damage degrees are found in the different members of RBC, which confirms the need of quantitative damage tools (such as the DRI) for a better selection of rehabilitation procedures according to their respective current distress. However, although thorough, the above analyses were quite time-consuming and somewhat expensive due to the amount of hours of analysis spent by petrographers.

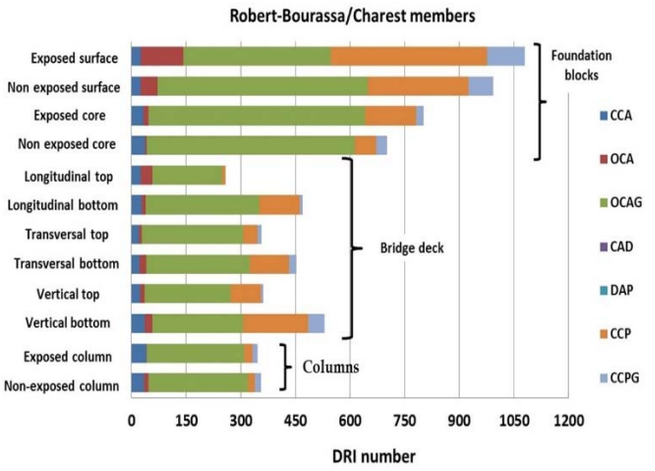


Figure 6: DRI numbers obtained on RBC cores extracted from distinct structural components, environmental and orientation conditions.

Otherwise, if those quantitative microscopic could be somehow automated through the use of reliable ML techniques, fast and low cost analyses might be accessible for the evaluation of critical infrastructure, at least for initial screening which would be extremely cost-beneficial.

7 CONCLUSIONS AND FUTURE WORK

Most of the aging infrastructure worldwide are currently under critical conditions, either approaching the end of their service-lives or presenting clear signs of distress due to numerous damage mechanisms (or even both!). In Canada and around the globe, AAR is one of the most harmful damage mechanisms and various concrete structures are currently suffering from this issue. Otherwise, in a globalized world as nowadays, time is one of the most important variables in engineering decision making and thus fast, low cost and reliable techniques for diagnosing the damage type and extent and prognosis of the potential of future distress is extremely desired. The scientific contribution of this project is to work on a very little-explored field in civil engineering which is the use of machine learning to automate damage evaluation in concrete towards the development of better procedures to detect and enhance the durability of affected aging structures.

In this work, concrete mixtures presenting two different types of reactive aggregate and three different compressive strengths were tested through DRI and ML tools. Preliminary results show an encouraging average of 66.4% of accuracy obtained using only 200 images. Future works will intend to extend this work using a larger number of images as well as testing the ML adopted protocol for assessing RBC overpass in its distinct structural components. Correlations with DRI results will be made (Figure 6) and the reliability of the new proposed technique will

be tested. Finally, a new CNN procedure is already being developed so that the precision of the evaluations might be raised to at least 80%.

REFERENCES

- Abadi, M., Agarwal A., Barham P., Brevdo E., Chen Z., Citro., Corrado G.S., Davis A., Dean J., M. Devin M., Ghemawat S., Goodfellow I., Harp A., Irving G., Isard M., Jia Y., Jozefowicz R., Kaiser L., Kudlur M., Levenberg J., Man´e D., Monga R., Moore S., Murray D., Olah C., Schuster M., Shlens J., Steiner B., Sutskever I., Talwar K., Tucker P., Vanhoucke V., Vasudevan V., Vi´egas F., Vinyals O., Warden P., Wattenberg M., Wicke M., Yu Y., Zheng X., (2015). Tensor Flow: Large-scale machine learning on heterogeneous systems.
- ASTM (2008). Standard test method for determination of length change of concrete due to alkali-silica reaction. ASTM International.
- Auer P,. Jaksch T., Ortner R. (2010). Near-optimal regret for reinforcement learning. Journal of Machine Learning Research. vol. 11, pp. 1563-1600.
- Azam S., Gavrilova M. (2017). Person Identification Using Discriminative Visual Aesthetic, pp. 15–26. Cham: Springer International Publishing.
- Bérubé M., Smaoui N., Fournier B., Bissonnette B., Durand B. (2005). Evaluation of the expansion attained to date by concrete affected by alkali–silica reaction. Part III:Application to existing structures. NRC Research Press.
- Ciresan, Dan; Ueli Meier; Jonathan Masci; Luca M. Gambardella; Jurgen Schmidhuber (2011). Flexible, High Performance Convolutional Neural Networks for Image Classification. Proceedings of the 22nd International Joint Conference on Artificial Intelligence – vol. 2, pp. 1237–1242.
- Dunbar P., Grattan-Bellew P. (1995). Results of damage rating evaluation of condition of concrete from a number of structures affected by ASR. CANMET/ACI International Workshop on Alkali-Aggregate Reactions in Concrete, 257–266.
- Fournier B., Bérubé M. (2000). Alkali-aggregate reaction in concrete: a review of basic concepts and engineering implications. Can J. Civ. Eng., 167–191.
- Grattan-Bellew P., Danay A. (1992). Comparison of laboratory and field evaluation of AAR in large dams, proc. of the international. Canadian Electrical Association & Canadian National Committee.
- Grattan-Bellew P., Mitchell, L. (2006). Quantitative petrographic analysis of concrete the damage rating index (DRI) method, a review, Proc. Marc-Andre Berube Symposium on AAR in concrete. CANMET/ACI Advances in Concrete Technology Seminar, 321–334.
- Grattan-Bellew P., Mitchell, L., Margeson, J., Min D. (2010). Is alkali-carbonate reaction just a variant of alkali-silica reaction ACR=ASR? Cement and Concrete Research (10), 556–562.
- Gupta, P. (2017). Cross-Validation in Machine Learning. Towards Data Science: Visiting Concepts, Ideas and Codes. URL: http://towardsdatascience.com.
- Hinton, Geoffrey; Sejnowski, Terrence J., eds. (1999). Unsupervised Learning: Foundations of Neural Computation. MIT Press. ISBN 0-262-58168-X.
- Krizhevsky A., Sutskever I., Hinton.G. (2012). Imagenet classification with deep convolutional neural networks. Advances in Neural Information Processing Systems-Curran Associates, Inc (25), 1097–1105.
- Maini V.; Sabri S. (2017). Machine Learning for Humans, Part 2.1: Supervised Learning. Update 9/2/2017
- Matsumoto T., S. A. (2017). Development of an automatic detector of cracks in concrete using machine learning. Sustainable Civil Engineering Structures, and Construction Materials, SCESCM-Procedia Engineering (171), 1250–1255.
- Mehryar Mohri, Afshin Rostamizadeh, Ameet Talwalkar (2012). Foundations of Machine Learning, The MIT Press ISBN 9780262018258.
- Pereira Junior R. A., Inkpen D. (2017). Using Cognitive Computing to Get Insights on Personality Traits from Twitter Messages, pp. 278–283. Cham: Springer International Publishing.
- Rivard P., Fournier B., Ballivy G., (2000). Quantitative assessment of concrete damage due to alkali-silica reaction (ASR) by petrographic analysis. 11th International Conference on Alkali-Aggregate Reaction, 889.
- Sanchez L.F.M, Fournier B, Jolin M., Bastien J. (2014). Evaluation of the stiffness damage test (SDT) as a tool for assessing damage in concrete due to ASR: Test loading and output responses for concretes incorporating fine or coarse reactive aggregates. Cement and Concrete Research (56), 213–229.
- Sanchez L.F.M, Fournier B, Jolin M., Duchesne J. (2015). Reliable quantification of AAR damage through assessment of the damage rating index (DRI). Cement and Concrete Research (67), 74–92.
- Sanchez L.F.M, Fournier B, Jolin M., Bastien J., Mitchell D. (2016). Practical use of the Stiffness Damage Test (SDT) for assessing damage in concrete infrastructure affected by alkali-silica reaction. Construction and Building Materials (125), 1178-1188.
- Sanchez L.F.M, Fournier B, Jolin M., Mitchell D., Bastien J., (2017). Overall assessment of alkali-aggregate reaction (AAR) in concretes presenting different strengths and incorporating a wide range of reactive aggregate types and natures. Cement and Concrete Research (93), 391–411.
- Sanchez, L. F. S., Fournier, B., Bastien, J., Mitchell, D., Noel, M. 2016. Overall assessment of an ASR affected overpass “Robert-Bourassa/Charest” after nearly 50 years in service. International Conference on Bridge Maintenance, Safety and Management.
- Sood, G. (2017). Clarifai: R Client for the Clarifai API. R package version 0.4.2.
- Sutton R., Barto A. (1998). Reinforcement Learning: An Introduction. MIT Press. ISBN 0-262-19398-1.
- Villeneuve V., Fournier B., (2012). Determination of the damage in concrete affected by ASR - the damage rating index (DRI), proceedings. 14th International Conference on Alkali aggregate Reaction in Concrete (electronic).

Maintenance, Safety, Risk, Management and Life-Cycle Performance of Bridges – Powers, Frangopol, Al-Mahaidi & Caprani (Eds)
© 2018 Taylor & Francis Group, London, ISBN 978-1-138-73045-8

Shear Capacity of an Existing RC Bridge Deck Slab: FE Analysis Using Continuum Elements

Jiangpeng Shu

Postdoctoral fellow, Norwegian University of Science and Technology, Trondheim, Norway

ABSTRACT: For reinforced concrete (RC) slabs without shear reinforcement, shear and punching can be the governing failure mode at the ultimate limit state if subjected to large concentrated loads. Shear and punching of RC slabs without shear reinforcement has been a challenging problem in assessment based on current standards. To examine a previously developed enhanced analysis approach, this study was conducted by applying a "Multi-level Assessment Strategy" to a 55-year old RC bridge deck slab subjected to concentrated loads near the main girder in a field failure test. The differences between analysis methods at different levels of assessment was discussed regarding one-way shear and punching shear behavior of the slab. The influences of parameters such as boundary conditions, location of concentrated loads and shear force distribution were investigated.

1 INTRODUCTION

Existing infrastructure represents a substantial part of societal assets and existing bridges represent a huge capital that needs to be well administrated (SB-LRA, 2007). Bridge deck slabs are among the most exposed bridge parts and are often critical to damage (SB-ICA, 2007). One-way shear and punching shear may be the governing failure mode in reinforced concrete slabs without shear reinforcement when subjected to large concentrated loads. Currently, building codes of practice, such as ACI (ACI, 2014) and Eurocode 2 (CEN, 2004), provide several approaches to check the two-way punching strength of flat concrete slabs. However, previous studies have shown that existing models provided by design provisions are too conservative and that enhanced assessment methods can reveal higher load-carrying capacity (SB-LRA, 2007). Consequently, it is important to evaluate current code methods and provide recommendations for improvement.

In order to provide a systematic approach for the assessment of RC slabs, Plos et al. (2016) has developed a "Multi-level Assessment Strategy" which provides recommendations for the assessment of RC slabs using analytical and finite element (FE) models; see Figure 1. The strategy is based on the principle of successively improved evaluation in structural assessment. Accordingly, the assessment of the load-carrying capacity with associated structural response can be conducted through the following levels and methods:

- (I) Simplified analysis
- (II) 3D linear FE analysis
- (III) 3D non-linear shell FE analysis
- (IV) 3D non-linear FE analysis with continuum elements and fully bonded reinforcement
- (V) 3D non-linear FE analysis with continuum elements including the slip between reinforcement and concrete.

Case studies have shown that more advanced methods based on non-linear FE analyses normally yield an improved understanding of the structural response and are capable of demonstrating higher, yet conservative, predictions of load-carrying capacity (Plos et al., 2016; SB-4.5, 2007).

The aim of this study was to examine the highest level of Multi-level Assessment Strategy (Plos et al., 2016) and modelling methods developed by Shu et al. (2015; 2016) and to investigate the response of a real structure in engineering practice. A full-scale field test has been carried out to a 55-year RC bridge (Bagge, 2014; Bagge et al., 2014; 2015); the deck slab was subjected to concentrated load near one of the main girders which led to a shear type failure of the slab. The highest level of Multi-level Assessment Strategy was then used to evaluate the capacity and response of the slab with respect to one-way shear and punching shear capacity. Furthermore, the difference of failure modes between pure one-way shear and punching shear was studied and the influencing factors, e.g. boundary conditions, arching action and load distribution, in the model were investigated. The choice of effective width to calculate the one-way shear resistance was discussed based on the shear force distribution.

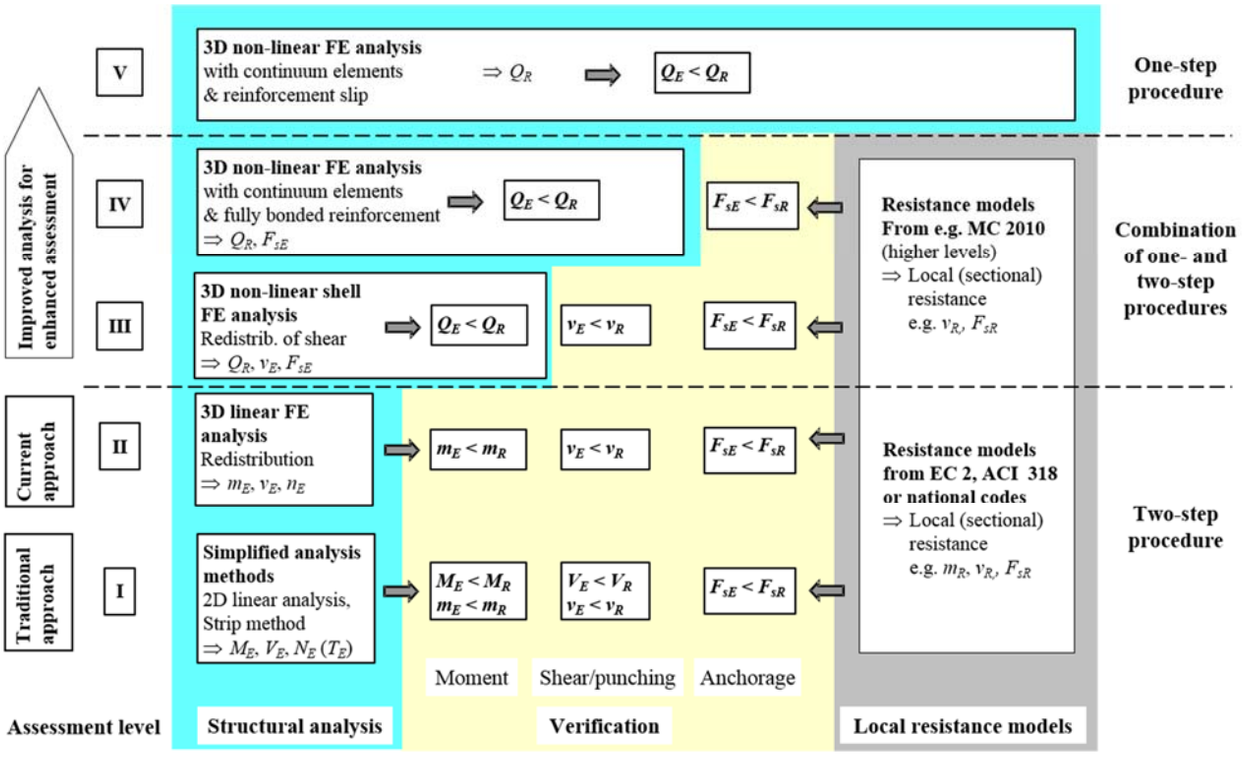


Figure 1. Multi-level Assessment Strategy of reinforced concrete bridge deck slabs; Plos et al. (2016).

2 DESTRUCTIVE TEST

The Kiruna Bridge was a continuous five-span structure with a total length of 121.5 m. The superstructure, 15.6 m wide, consisted of three longitudinal prestressed girders connected with a reinforced concrete slab at the top which had integrated curbs at each side. It was inclined longitudinally and transversally, and was also partly curved longitudinally. Due to the length of the bridge, the superstructure was segmentally cast-in-place and prestressed using a BBRV post-tensioning system. At the abutments, the superstructure was supported on bearings while reinforced concrete columns, with a joint at the base formed the intermediate supports.


Figure 2. Photo of the bridge

At an age of 55 years in 2014, the bridge was subjected to an extensive in-situ field test program; see Figure 5. The test load setup and dimension of the loading plate is determined according to Load Model 2 in EC 1 (CEN, 2003). A single axle load applied on specific tire contact areas which covers the dynamic effects of the normal traffic on short structural members. The load was applied to the bridge, using a longitudinally positioned simply supported load distribution beam and a forced-controlled hydraulic jack supported by wire thread through a drilled hole

in the deck slab and anchorage in the bedrock. At the supports of the load distribution beam, 2.0 m apart, the load was transferred to the upper surface of the bridge deck slab (paving removed) through under-grouted steel plates (350 × 600 mm^2).

In order to monitor the structural behavior of the bridge during the test, applied force and deflections were measured. The force was derived from the oil pressure in the hydraulic jack and draw-wire sensors were instrumented to the bridge to measure deflections relative to the ground. Deflections were measured at the bottom surface of the deck slab centrically underneath the load application and at the corresponding longitudinal position at the base of the adjacent girder. Moreover, the midspan deflection was measured for each girder.

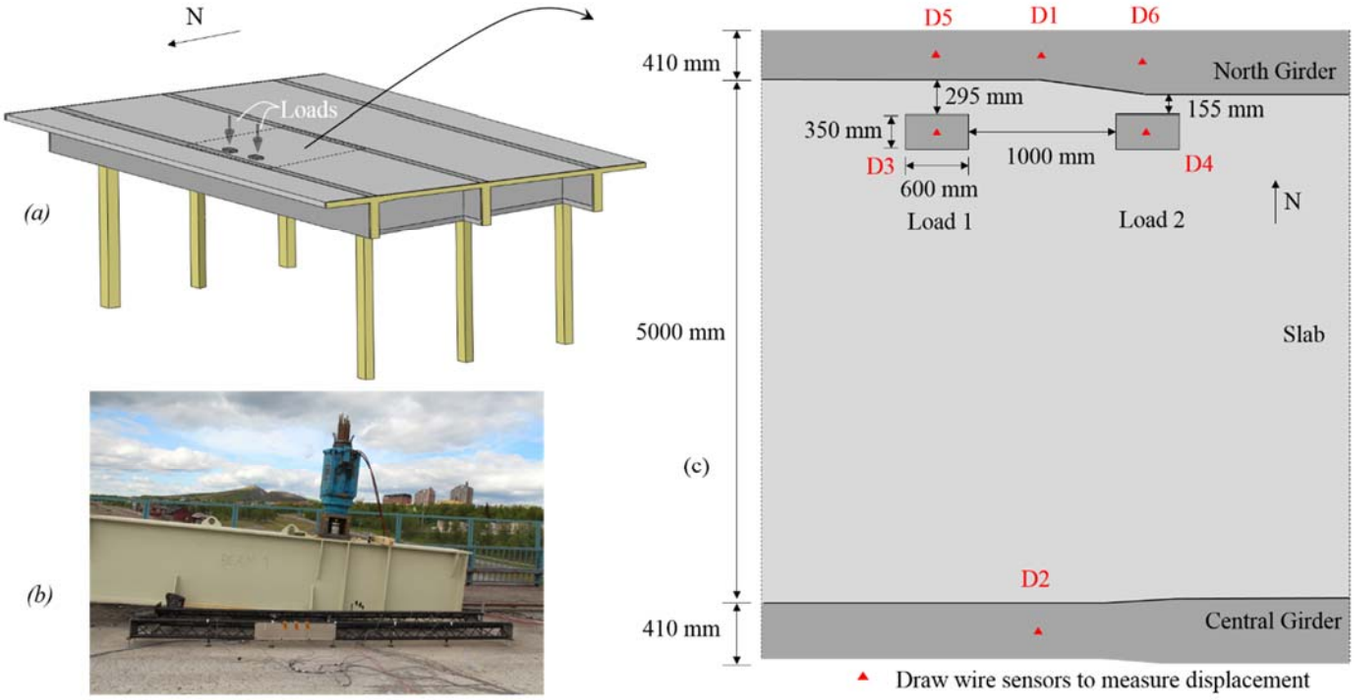


Figure 3. (*a*) Isometric view of layout of loading plates, (*b*) photo of field test, loading beam and hydraulic jack, and (*c*) layout of loading plates and measurement points for displacement.

In the test, considerable deflection of the girders occurred and, at a load of $Q_{u.exp}$ = 3.32 MN (1.66 MN for each loading plate), the slab suddenly, without any warning, failed with a combined failure mode of one-way shear and punching shear. The failure was initiated between one of the loading plates and the girder, and propagated on either side of the plate, thus, producing a U-shaped failure surface.

3 FE ANALYSIS

3.1 FE model

In the FE model, the tested span including columns was modelled by a detailed 4-node brick element model and the remaining part of the bridge was modelled using 2-node beam elements as displayed in Figure 4(*a*). At least 8 elements were used in the thickness direction to sufficiently reflect the flexural behaviour (Shu et al., 2015). For the part of the bridge modelled with beam elements. The part modelled with brick elements was connected to the part modelled with beam elements assuming that the connected cross-section, perpendicular to the beam main axis, remained plane and un-deformed, with the same rotations and deflections as the connected beam element. The reinforcement was included in the model as fully bonded embedded reinforcement bars, in accordance with the layout in the original drawings.

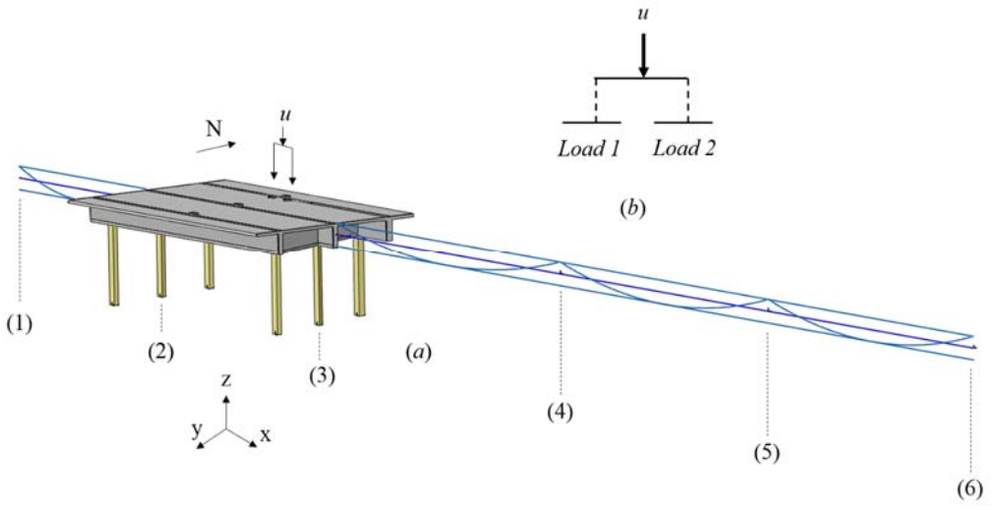


Figure 4. FE analyses: (a) non-linear FE model of the tested bridge, showing supports 1-6 (b) Load distribution system for displacement controlled loading.

The bridge was simply supported at the end abutments and at the bottom of the columns at support 2 and 3. Supports 1-5 were constrained for displacement in vertical, transverse and longitudinal directions of the bridge but support 6 was allowed displacement in longitudinal direction. The bridge was preloaded with concentrated loads above the girders before the concentrated load was applied to the slab. The analysis was carried out using a Quasi-Newton iteration method based on force and energy convergence criteria, with a tolerance of 0.01.

3.2 Material model

In all calculations, material parameters were obtained from the in-situ tests or from calculation see Table 1. For the material model, concrete was modelled using a fracture energy based total strain crack model; see Figure 5.

For the material model used in the non-linear FE analysis at levels III and IV, concrete was modelled using a constitutive model based on non-linear fracture mechanics using a smeared rotating crack model based on total strain (TNO, 2015). In this approach, the crack width w is related to the crack strain ε_{cr} perpendicular to the crack via a characteristic length called crack band width h_b. The advantage of this method is that the formulation remains local and the algorithmic structure of the FE code would require only minor adjustments, limited to the part of the code responsible for evaluations of the stress (and stiffness) corresponding to a given strain increment (Jirásek, 2012). The crack band width was assumed to be equal to the mean crack distance since the reinforcement was modelled as fully bonded (Shu et al., 2015). A tension softening curve according to Hordijk (1991) was used; see Figure 5 (*a*). The behavior of concrete in compression was described by an isotropic damage constitutive law and the stress-strain relationship used were based on Thorenfeldt et al. (1987); see Figure 5 (*b*).

Table 1. Input material parameters of concrete

Items	Calculation method	Values
Poisson's ratio	MC2010	$v = 0.15$
Tensile strength	MC2010 concerning reduction	$f_{ctm} = 2.0$ MPa
Fracture energy	MC2010	$G_f = 140$ Nm/m^2
Mean crack distance	EC2	$h_b = 219$ mm

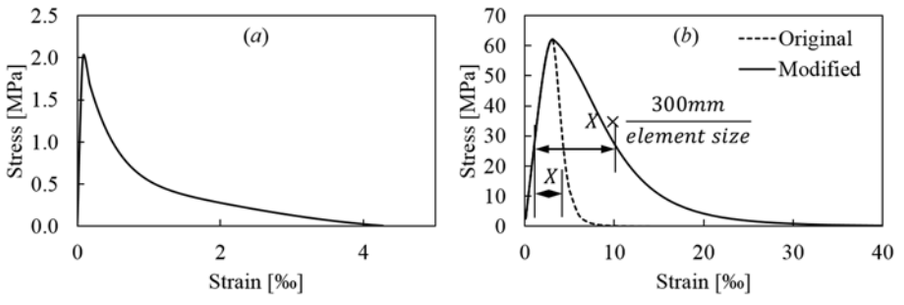


Figure 5. Materiel model of concrete: (a) response in tension; (b) response in compression

4 RESULTS AND DISCUSSION

4.1 Load-carrying capacity and failure modes

Load-deflection relationship from the continuum non-linear FE analysis are compared to corresponding relationship from experiment in Figure 6. The deflections were taken from the model at the same position as in the experiment. It shows the comparison of 6 measurement points on girders and slab. A good agreement between continuum NLFEA and experiment was observed for both stiffness and final capacity.

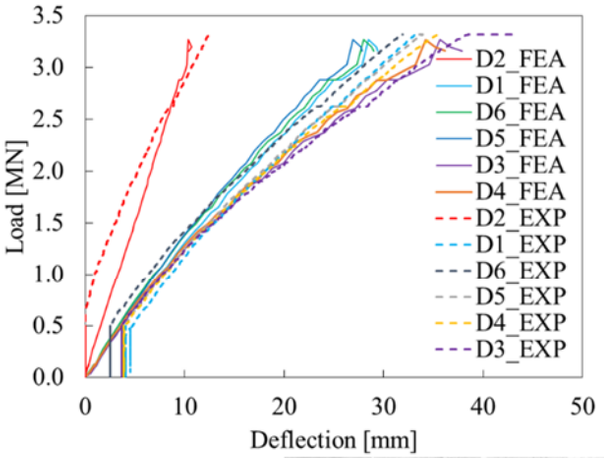


Figure 6. Load-deflection relationship for level IV analysis, compared to experimental results.

The crack pattern at the bottom and top of the bridge deck slab after experiment is displayed in Figure 7 (*a*) and (*b*) respectively. This indicates that it was a combination of one-way shear and punching shear failure. Figure 7 (*c*) and (*d*) illustrates the strain based crack pattern at the bottom of the slab and an isometric view with a cross section of the slab from the continuum FE analysis one loading increment before failure happened. In the FE analysis, at approximately 60% of failure load, a large shear crack was developed between the loading plates and the girder. Just before the punching failure occurred, another shear crack developed on the other side of the loading plates and the failure occurred. At failure, the cracking in the FE analysis corresponded closer to a one-way shear failure than to a punching failure. In the experiment, shear failure occurred only adjacent to load 1 and no major shear crack was registered close to load 2. However, in the non-linear FE analysis, the failure crack propagated from load 1 to load 2, even though it was initiated adjacent to load 1.

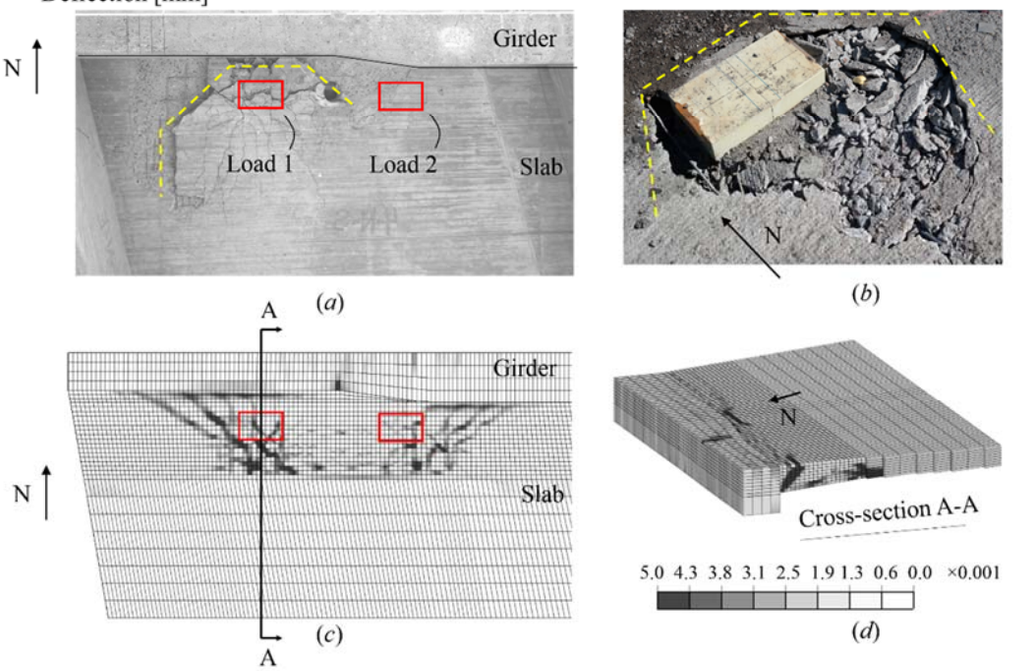


Figure 7. Photo of crack pattern at the final load level in the experiment (*a*) at the bottom of slab in experiment and (*b*) crack pattern near load 1 at the top of slab in experiment; Strain based crack pattern from continuum non-linear FE analysis: (*c*) at the bottom of slab and (*d*) at the isometric view of cross-section.

4.2 The influence of arching actions

The arching action is important and needs to be taken into account when assessing the load carrying capacity with respect to shear, when loads are acting close to supports. The internal compression strut will become steeper the closer to the support the load is acting and, as a consequence, the shear capacity will increase. The arching action is accounted for in EC2 (CEN, 2004) and MC2010 (fib, 2013). In addition, Natario et al. (2014) has shown that the load action of shear force can be even further reduced, and suggested that the reduction factor should be modified

to $\beta = a_v/2.75d \leq 1$. A recent research conducted by Rombach and Henze (2017) even suggested $\beta = a_v/3d$. However, compared to arching action of beams (Kani, 1966; Muttoni & Ruiz, 2008; Campana et al., 2013), this increase in capacity is not as remarkable for slabs because the direct load transfer is counteracted by a decrease in effective width when the load acts closer to the support of a slab (Lantsoght et al., 2014)

In the bridge test, the distance from the edge of the loads to the edge of the girder were only 1.09d and 0.6d for load plate 1 and load plate 2, respectively. To study the influence of arching action, the loads were gradually moved further away (100 mm per step) from the girder in the level IV model (see Figure 8(*a*) and Table 2. The load on position 1 was the same as in the field test. The nominal shear strength (excluding influence of b_w, d and f_{cm}) were calculated assuming a pure one-way shear failure and compared to laboratory test results obtained by Natario et al. (2014) and Lantsoght et al. (2014); see Figure 8 (*b*). From the analysis results, it was observed that the shear capacity decreased when loads were moved further away from the support. When the loading plates were placed in position 4, the failure mode even changed from shear to bending failure. The results are similar to findings by the other researchers (Lantsoght et al., 2014; Natário et al., 2014), but the decrease in capacity was smaller than expected. There are two causes that could explain this difference. Firstly, the tested slabs of Natario et al. (2014) and Lantsoght et al. (2014) had almost purely one-way shear action, while the slab of the tested bridge with its long-stretched supports on the girder activated a three dimensional load-carrying mechanism. Secondly, the tested slab was loaded with two loads but the failure occurred adjacent to load 1 only. However, the cracking around load 2 influenced the failure at load 1, which was also reflected in the shear force distribution, discussed in the next section.

Table 2. Variation of load positions, shear span ratios and load-carrying capacity from the analysis of the tested bridge

Load positions	loading plate 1			loading plate 2			Capacity [MN]
	d_1 [mm]	a_{v1} [mm]	a_{v1}/d_1	d_2 [mm]	a_{v2} [mm]	a_{v2}/d_2	
1	270	295	1.09	259	155	0.60	3.28
2	262	395	1.51	259*	255	0.98	2.72
3	253	495	1.96	253	355	1.40	2.34
4	244	595	2.44	244	455	1.86	2.00

* The d_1 and d_2 were takes at critical section using 45 degree shear crack inclination. Load plate 2 is positioned closer than d_2 from the girder, so the critical section is assumed to be at the edge of the girder.

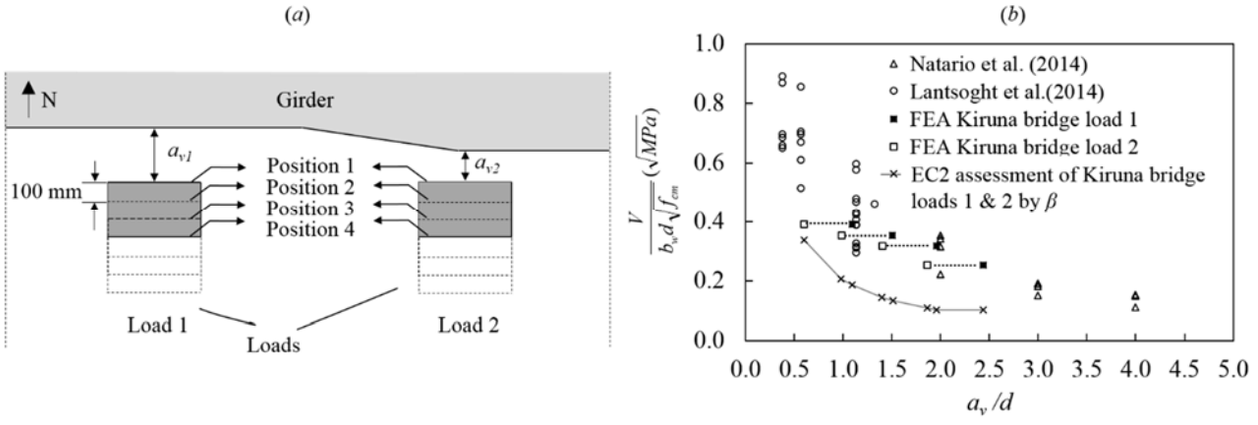


Figure 8. (a) Variation of load positions in the analysis of the tested bridge; grey color indicates original position in field test (b) nominal shear capacity of the slab subjected to loads at different positons, with comparison to literature (Lantsoght et al., 2014; Natário et al., 2014).

In Figure 9, the shear force per unit length along a line in the longitudinal direction of the bridge close to the girder is presented for different load levels. A clear shear force redistribution was observed for the shear force near loading plate 1: the shear force close to loading plate increased fast as the applied load increased at low load levels ($Q/Q_u \leq 0.8$), but stopped to increase at higher load levels ($Q/Q_u > 0.8$). Instead, the shear force in the adjacent region increased faster. Similar observation was also presented for the reaction force along a slab support by Natario et al.(Natário et al., 2014).

According to French practice (Chauvel et al., 2007), the effective width for shear force distribution should be limited to the area within 45 degree angles from the edges of the loaded area. The shear force within this region (grey shadow) was observed to be much higher than the adjacent region.

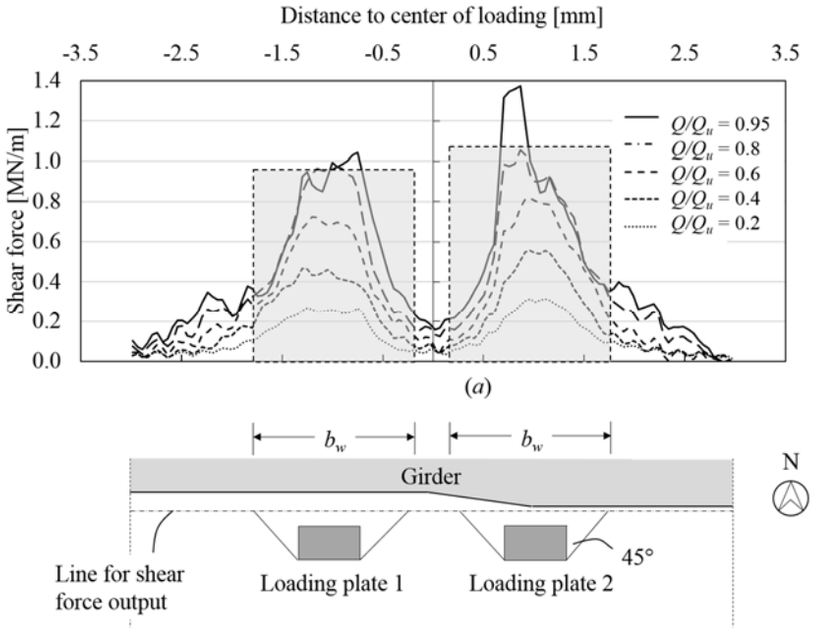


Figure 9. Unitary shear force across a line parallel to the girder, from FE analysis with continuum elements.

5 CONCLUSIONS

The tested RC bridge deck slab failed in a combination of one-way shear and punching shear. This kind of shear type failure as well as structural response of the slab could be reflected using continuum nonlinear FE analyses with a model including the entire bridge with reasonable simplifications.

a. The extent of the FE model, as well as the assumption of boundary conditions for the tested slab has significant influence on the analysis results.
b. The location of applied load plays an important role. When the load was moved further away from the closest girder in the continuum FE analysis, the load-carrying capacity with respect to shear was decreased until the failure mode changed to bending failure.
c. In addition, the analysis of shear force distribution also shows that the method using a 45 degree distribution to define effective width is reasonable and the failure mode in

ACKNOWLEDGEMENT

The authors would like to acknowledge the financial support from The Swedish Transport Administration (Trafikverket). Also thanks to Luossavaara-Kiirunavaara AB (LKAB) and Hjalmar Lundbom Research Centre (HLRC), which supported the experiment. Furthermore, the authors thank the colleagues in the Swedish Universities of the Built Environment, i.e. Chalmers University of Technology, Royal Institute of Technology (KTH), Lund University (LTH) and Luleå University of Technology (LTU), for the fruitful cooperation in the project.

REFERENCES

ACI, 2014. Building Code Requirements for Structural Concrete and Commentary. Farmington Hills, Mich: ACI American Concrete Institute.

Bagge, N., 2014. Assessment of Concrete Bridge: Models and Tests for Refined Capacity Estimation. Luleå University of Technology, Luleå.

Bagge, N., Nilimaa, J., Blanksvärd, T., Elfgren, L., 2014. Nord. Concr. Res. 51, 63–83.

Bagge, N., Shu, J., Plos, M., Elfgren, L., 2015. Punching Capacity of a Reinforced Concrete Bridge Deck Slab Loaded to Failure, in: Nordic Concrete Research: Residual Capacity of Deteriorated Concrete Structures. Oslo, Norway, pp. 57–60.

Campana, S., Anastasi, A., Fernández Ruiz, M., Muttoni, A., 2013. Mag. Concr. Res. 65, 386–404.

CEN, 2003. Eurocode 1 - Actions on structures - Part 2 - Traffic loads on bridges. CEN European Committee for Standardization, Brussels, Belgium.

CEN, 2004. Eurocode 2: Design of concrete structures - part 1-1: General rules and rules for

buildings. CEN European Committee for Standardization, Brussels, Belgium.
Chauvel, D., Thonier, H., Coin, A., Ile, N., 2007. CEN/TC 250.
fib, 2013. Model Code for Concrete Structures 2010. International Federation for Structural Concrete (fib), Lausanne.
Hordijk, D.A., 1991. Local approach to fatigue of concrete.pdf. Delft University of Technology, Delft, Netherlands.
Jirásek, M., 2012. Modeling of localized inelastic deformation. Czech Technical University in Prague, Prague.
Kani, G., 1966. ACI Struct. J. 63.
Lantsoght, E., Veen, C., Walraven, J., 2014. ACI Struct. J. 275–284.
Muttoni, A., Ruiz, M.F., 2008. ACI Struct. J. 105, 163–172.
Natário, F., Fernández Ruiz, M., Muttoni, A., 2014. Eng. Struct. 76, 10–23.
Plos, M., Shu, J., Zandi, K., Lundgren, K., 2016. Struct. Infrastruct. Eng. 13, 223–241.
Rombach, G.A., Henze, L., 2017. Shear Capacity of Concrete Slabs Without Shear Reinforcement Under Concentrated Loads Close to Support, in: FIB Symposium 2017. Maastricht, pp. 676–683.
SB-ICA, 2007. Guideline for Inspection and Condition Assessment. Sustainable bridges: Report.
SB-LRA, 2007. Guideline for Load and Resistance Assessment of Existing European Railway Bridges. Sustainable Bridges: Report.
Shu, J., Fall, D., Plos, M., Zandi, K., Lundgren, K., 2015. Eng. Struct. 101, 439–449.
Shu, J., Plos, M., Johansson, M., Zandi, K., Nilenius, F., 2016. Eng. Struct.
TNO, 2015. Diana finite element analysis, User's Manual -- Release 9.6, TNO DIANA BV. Delft.

Maintenance, Safety, Risk, Management and Life-Cycle Performance of Bridges – Powers, Frangopol, Al-Mahaidi & Caprani (Eds)
© 2018 Taylor & Francis Group, London, ISBN 978-1-138-73045-8

Rehabilitation of timber bridge piles using a wrapping system

R. Borzou & W. Lokuge
School of Civil Engineering and Surveying, University of Southern Queensland, Springfield, QLD4300

ABSTRACT: The majority of the thousands of timber bridges around Australia are more than 50 years old and strengthening and rehabilitation of deteriorated timber bridges is a strong financial commitment. Therefore it is a timely concern to investigate the rehabilitation process involved. The maintenance cost of timber bridges are affected significantly by a number of deterioration mechanisms, which require a systematic approach for diagnosis and treatment. The techniques used to rehabilitate timber bridges vary depending on the deterioration mechanism and location. This research aims at investigating the techniques used in timber pile rehabilitation. The main deterioration mechanism studied in this research is the splitting. An experimental program was carried out to investigate the strength enhancement due to a FRP wrapping system combined with two types of filler material, Crane Rail Grout (CRG) and Underwater Cementitious Grout (UCG). Hardwood timber of grade F27 with 150 mm diameter and 300 mm high samples were used in the testing program. Three levels of damage were introduced to the total height, samples were wrapped with FRP system and tested for compression. Load and displacement curves were developed based on the experimental results.

1 INTRODUCTION

Current timber bridge stock in Australian roads are definitely having timber piles as its primary structural support. Road authorities are making every effort to maintain these aging bridges. Dismantling older timber bridges and replacing them with concrete or any other material may not be the best option for most of the timber bridges. Therefore, rehabilitation techniques are being researched, commercialized and implemented on bridges around Australia. Eccentric and concentric loads on timber piles were analysed experimentally and analytically in the past (Borello 2009; Borello et al. 2010).

Fibre composites such Fibre Reinforced Polymer (FRP) laminates with their inherent properties which offer great tensile strength benefits than those of steel, timber and concrete in vast varieties of environmental conditions. These conditions can range from tidal/splash waves, high moisture environments and fluctuating thermal conditions. The combination of FRP laminate with an infill annulus material offers deteriorated timber sections greater lateral confinement, resulting in larger axial load capacities. Not only does the FRP laminate offer high tensile strength, but also offers a protection from biological attack for submerged timber pile cases.

This research paper focuses on a repair method for decayed timber piles, for bridges, boardwalks and jetties using FRP jacketing technology. Due to durability, pumpability, workability and compressive strength requirements, Crane Rail Grout (CRG) and Underwater Cementitious Grout (UCG) were selected as the filler materials in this study. The combination of material offers an all-round (360 degree) confining pressure. This significantly increases the strength of the pile. Therefore, this repair method will be tested and validated throughout this paper.

Currently information about splitting due to thermal expansion is lacking and in dire need of research and testing. New piles can be cut and posted onto the old piles but this solution can often be costly. Therefore, a new technique currently on the market offer a helpful solution. Wrapping the deteriorated pile while still under axial load reduces time and cost of the project. This solution consists of a GFRP wrap spaced approximately 20 mm with corner bar spacers that are attached to the existing pile. The wrap is sealed with an underwater resin that will eliminate any moisture from entering the fill material and ultimately to the existing pile. Usually an underwater cementitious grout is used to fill the 20-mm annular space as its material properties are extremely high. After 7 days the fill material will reach approximately 90% of its maximum 28 days strength. After 7 days the compressive strength should be approximately 100 MPa. This is just one example of rehabilitation that can be seen dominat-

ing the market for its ease of use, strength benefits and cost effectiveness.

2 TIMBER PILE DETERIORATION

There are many ways that can initiate a timber bridge deterioration. Once started it will spread due to many other reasons as well.

2.1 *Main deterioration methods*

Weathering is the main cause of timber pile deterioration as moisture can inhibit the pile causing thermal expansion to occur. The result of this is cracking along the fibres, opening the timber for fungal decay to start breeding.The principal cause of weathering is the excessive exposure of moisture content. When wood is unprotected from external factors, moisture can be absorbed in both the cell walls and the cell cavities of the timber. Some researchers (Mohammadi et al. 2014) suggested that a moisture content greater than 20% decay will start taking place whereby Austroads guide to bridge technology (Austroads 2009) believes that decay will start taking place at 15% moisture content.

Austroads (2009) reported that decay is the rotting of timber because of fungal attacks. Timber piles are subjected to weathering conditions such as water and temperature. As a result, the nature of the pile is to shrink. This shrinkage results in large internal stresses. The outcome of this action causes splits to form in the timber pile. These splits are a pathway for fungal decay to take effect. The fungal decay will make its way to the centre of the untreated timber pile.

Termites is another means that a pile can deteriorate rapidly. Termites are generally found in the northern tropical belt of Australia (Austroads 2009). The Damage caused by termites is much more rapid growing than that of fungi ((Mohammadi et al. 2014). It is less common to see termite attack to occur in durable hardwoods without some sort of pre-existing fungal decay. This is due to the fact moisture is present which is excellent conditions for termite growth (Mainroads 2014). There are many marine borer species, and each species has a different habit and ability to attack timber piles in different coastal regions (Cookson 1986).

Timber piles that are submerged beneath the water surface can be inhabited by marine organisms. It has been noted that these organisms become more severe in subtropical waters than in colder waters (Bootle 1983).

Austroads (2009) defines a split as separation along the grain extending right through the member. Splitting is caused by thermal expansion, fluctuations of moisture content and overloading. Most splitting is due too wet and dry cycles. It can be noted that Austroads (2009) agree that moisture content and thermal expansion are the main causes for splitting or checking along the grain of the timber pile. Overloading is another contributing factor for the cracking or splitting of timber piles. Queensland timber bridge maintenance manual (MainRoads-Queensland 2004) stipulates that cracks may be aggravated by overloading vehicular collision. Overloading cause splitting to start from the bearing area and travels upwards to the timber girder. Once again, the splitting can be seen to run along the grain.

2.2 *Rehabilitation techniques*

From previous studies, it is evident that rehabilitation of timber piles around Australia is a necessity in maintaining the structural integrity of timber bridges. There is approximately 12,075 timber bridges that currently or in future need maintaining for the given defects outlined above. There are several timber pile rehabilitation methods available around Australia.

2.2.1 *Posting repair method*

This procedure meant the deteriorated affected pile was removed completely and replaced with a new surface treated pile to stop weathering or decaying issues. Epoxy grouting is used to join the new section to that of the old section. In some cases, the repair methodology required shoring to support the pile from becoming weak or unstable. This method of repair was tested under axial compression loading. The results were credible with maintaining ultimate strength and axial stiffness after the repair had taken place. These tests did not evaluate combined axial and lateral loads on the repair procedure.

2.2.2 *Splicing*

Splicing is a simple and cost-effective solution for the rehabilitation of deteriorated timber piles. This process entails cutting and posting a new section replacing the old deteriorated pile. The material used in splicing can either be timber or steel straps approximately 15 cm in length (Mohammadi et al. 2014). This section is connected by long metal screws. Lap splicing is extremely low cost, effective but will not last the test of time. This is a short-term fix with the intentions of implementing a better repair technique in the coming years. Austroads (2009) and Mohammadi et al (2014) agree that lap splicing should be avoided where possible. In addition, it is stated (Kim & Andrawes 2016) that this method will have catastrophic consequences if the pile is subjected to a bending moment. This was evident in a bridge collapse in Illinois, USA.

2.2.3 *Grout/ epoxy injection*

Another effective low cost and durable repair is grout or epoxy injection. This technique leaves a

proportion of the timber exposed. When using epoxy injection some sort of confinement needs to be incorporated (Emerson 2004). For example, using a FRP wrap in conjunction with an epoxy will suffice. According to railway and track structures, grout injection has the strength capabilities to increase the service life of the timber piles to approximately 15 – 20 years. Epoxy injection requires approximately 30 min to 5 hours drying time (Avent et al. 1978). Then the injection ports can be sanded smooth then painted for aesthetics purposes. This injection method can be used for both structural and semi structural components of timber bridges.

2.2.4 *Concrete jackets*

Concrete jackets are another method of rehabilitating a deteriorated timber piles. A steel cage is placed around effected area of the existing timber pile. Jackets can be formed using 25 – 50 mm (Mohammadi et al. 2014) thick coat shotcrete reinforced with steel caging. This method has its downfall as concrete is likely be subjected to external factors such as acids, alkalize or salt in ground water. This may cause drastic effects such as cracking and spalling (Mohammadi. et al. 2014). This will cause exposure of the steel cage resulting in corrosion and loss of cross sectional area. If cross sectional area is reduced then strength and durability will be reduced. Austroads (2009) also suggests concrete jacketing as a repair method but does not go into detail about how the repair should be carried out or implemented.

2.2.5 *FRP wrapping*

Fibre-Reinforced Polymer is another method of rehabilitating defected or decayed timber piles. Polymer resins plays as the matrix which helps bind fibre reinforcements together. Another advantage of using the FRP wrapping technique is that the resin used to bind the material can eliminate future deterioration. One matrix combination study conducted at the University of Manitoba used Glass Fibre-Reinforcement Polymers (GFRP) and grout shells to restore axial loads. This technique places a grout shell approximately 50 mm thick around the affected area. Then the GFRP is wrapped around the grout to create a seal. When tested the pile showed positive results restoring and in some cases increasing the compressive strength.

Cut and post is another technique (Caiza et al. 2012) where the rotten or deteriorated section is cut and reposted with a new timber section. A FRP wrap and grout shell completes the retrofit when the old timber section meets the new. Results shows that this technique will increase the compressive strength of the timber pile.

Recent technology such as FRP wrapping is becoming more and more frequent because of its strength improvements. Alongside this, FRP can be easily installed/fitted on site without and need for machinery. Therefore, this method seems to be the best method of rehabilitating timber piles.

Previous attempts and testing has been achieved in this field but more data is required to gain a defined method of procedure. Results vary in what percentage axial compression will increase when using the FRP wrapping method. Therefore, further testing is essential in accurately proving how FRP wrapping can increase the structural integrity to that of a normalized defected pile.

3 EXPERIMENTAL PROGRAM

The experimental program was designed to test short timber columns with FRP wrapping and a filler. Total number of samples tested in this project is 16. Testing of one control sample (no damage), 3 unwrapped samples with 3 damage levels, 3 samples strengthened using underground cementitious grout (duplicate) and 3 samples strengthened using crane rail grout (duplicate) comprised the experimental program.

3.1 *Materials*

The timber samples were sourced by University of Southern Queensland while the filler and FRP wrapping were provided by Quakewrap Australia. Material quantities used are summarized in Table 1.

Table 1. Material quantities

Material	Quantity
F27 timber (150 mm diameter)	4.8 m
Cementitious Grout	50 L
Crane rail grout	50 L
FRP laminate	7.5 m^2
Underwater Resin 220UR	2.2 L

3.1.1 *Timber*

Grade F27 cylindrical timber samples having approximate dimensions of 150 mm diameter and 300 mm length were used in this experimental program.

3.1.2 *Filler*

The two filler materials used were crane rail grout and underwater cementitious grout. Both filler materials will reach approximately 90% of its compressive strength after 7 days (Figure 1).

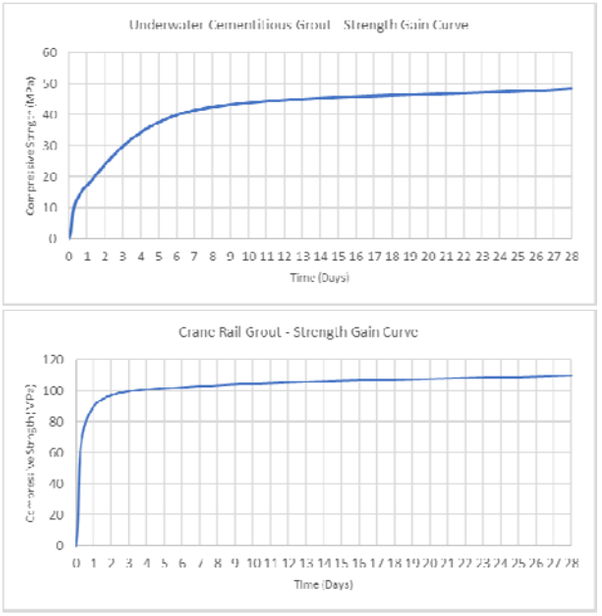


Figure 1. Strength development of filler

3.1.3 *FRP wrapping system*

PileMedic™ PLG60.60 is the FRP laminate used in the wrapping system. It has bidirectional fibres providing strength in both longitudinal and transverse directions. Properties of FRP are shown in Table 2.

Table 2. Material properties

Material	Max strength MPa
Underwater cementitious grout	48.3 (compression)
Crane rail grout	110 (compression)
Fibre Reinforced Polymer (FRP)	3.8 (tension)
Underwater Resin 220UR	418 (tension)

3.2 *Sample preparation*

All the samples were cut into approximately 300 mm lengths, weighed and the dimensions were recorded. Splitting was introduced into all the samples except the control sample.

3.2.1 *Damage levels*

Timber Bridge Detail Inspection Guidelines (Mainroads 2014) from Main Roads Western Australia states a severe vertical split would be greater than 5 mm in width and extending more than a meter in length. Some splits may be wider than 5 mm but have shorter length or vice versa. This was the only information found about the splitting measurements through inspection of deteriorated timber piles. The length of split gained from inspection extends greater than 1 m. Therefore, the split used in this research runs the entire length of the sample (≈300 mm). These two parameters will be maintained throughout experimental procedure. Split depth will be adopted at depths of full radius, 2/3 radius and 1/3 radius Figure 2.



Figure 2. Defect induced samples

Samples were then wrapped by the FRP laminate (Figure 3) and the filler was introduced into the annulus (Table 3)



Figure 3. FRP wrapping process

Table 3. Annulus details

Material	Annulus thickness mm
Underwater cementitious grout	20
Crane rail grout	20
Fibre Reinforced Polymer (FRP)	3
Underwater Resin 220UR	2

3.3 *Testing*

All the samples ready to be tested are shown in Figure 4 and they are to be tested using the SANS compression testing machine to find the maximum load/stress of the timber piles. Samples were attached with the strain gauges too to get the strain values in addition to the strains getting from the ma-

chine. A sample ready to be tested in the machine is shown in Figure 5.



Figure 4. Samples ready for testing



Figure 5. Sample in the compression-testing machine

Recorded data included the load and the displacement from the testing machine and the strain values from the data acquisition system 5000.

4 RESULTS AND DISCUSSION

Figure 6 shows the load deformation curves for the control sample, and the samples with defects. All these samples are unwrapped. The machine has the capacity of 2000 kN and it was calibrated to be used only for 1800 kN. Hence, the sample without any defect (control) could not reach its maximum capacity.

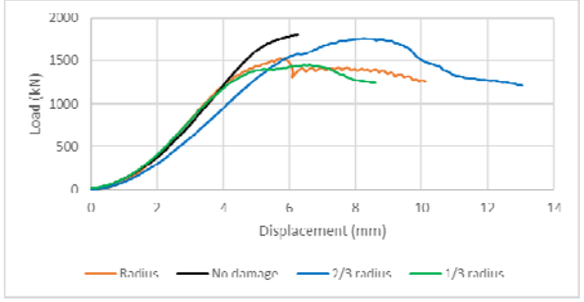


Figure 6. Load deformation for control samples

Figure 7 shows the load deformations curves for underwater cementitious grout (samples did not reach their capacity). However it is clear from Figures 6 and 7 that the deformation with FRP wrapping and cementitious filler is less than the deformation observed for unwrapped samples.

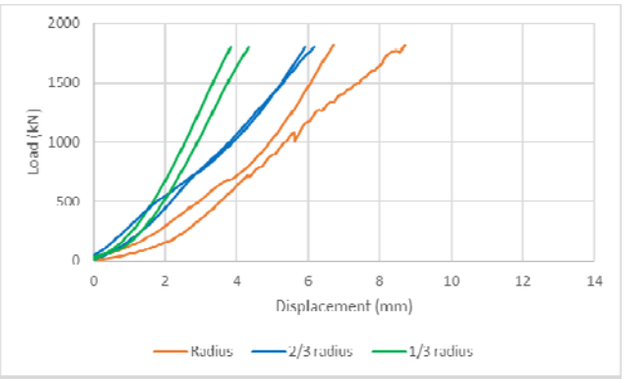


Figure 7. Load deformation curves for cementitious grout

Figure 8 shows the load deformation curves for the samples wrapped with FRP and crane rail grout as the filler. Comparing with Figure 7, it can be observed that samples with crane rail filler will reach a higher ultimate deformation than the samples with cementitious grout filler.

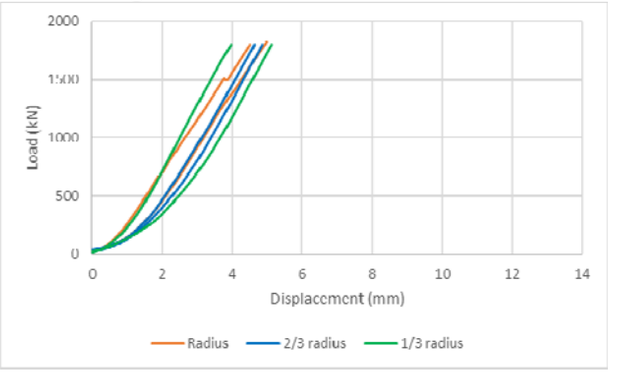


Figure 8. Load deformation curves for crane rail

5 CONCLUSIONS

Several conclusions can be drawn from this study. All defected control samples produced a failure and showed higher axial deformation. Due to the limitation of the capacity of the compression testing machine, no conclusions can be made regarding the failure load of the wrapped samples. However the observed curves show that the timber short columns can effectively be confined using the proposed FRP wrapping system and the 2 fillers (cementitious grout and crane rail grout). This is shown by the much higher expected failure load and the increased anticipated deformation from the observed curves. Further work is planned to test similar samples using a higher capacity-testing machine.

ACKNOWLEDGEMENT

The authors wish to acknowledge the support given by Mr Tony White and Mr Bede O'Rourke from Quakewrap Australia.

REFERENCES

Austroads 2009, Austroads Guide to Bridge Technology-Part 7 Maintenance and Management of Existing Bridges, Austroads Publication, Sydney, Australia.

Avent, RR, Emkin, LZ & Sanders, PH 1978, 'Behavior of Epoxy Repaired Full-Scale Timber Trusses', *Journal of the Structural Division, ASCE*, vol. 104, no. ST6, pp. 933-51.

Bootle, KR 1983, *Wood in Australia. Types, properties and uses*, McGraw-Hill Book Company.

Borello, DJ, Andrawesa, B, Hajjar, JF, Olson, SM & Hansen, J 2010, 'Experimental and analytical investigation of bridge timber piles under eccentric loads', *Engineering structures*, vol. 32, pp. 2237-46.

Borello, DJ, Andrawes, B., Hajjar, J., Olson, S. M., Hansen, J., and Buenker, J. 2009, *Forensic collapse investigation of a concrete bridge with timber piers*, Illinois Center for Transportation.

Caiza, P, Shin, M & Andrawes, B 2012, *Load Rating and Retrofit Testing of Bridge Timber Piles Subjected to Eccentric Loading*, Illinois Center for Transportation.

Cookson, L 1986, *Marine borers and timber piling options, Research review 1986*, CSIRO Division of Chemical and Wood Technology.

Emerson, RN 2004, 'In Situ Repair Technique for Decayed Timber Piles', *American Society of Civil Engineers Conference Proceedings*, vol. 137, no. 65.

Kim, K-HE & Andrawes, B 2016, *Load Rating and FRP Retrofitting of Bridge Abutment Timber Piles*, Illinois Center for Transportation.

MainRoads-Queensland 2004, *Bridge Inspection Manual*, Department of MainRaods, Queensland.

Mainroads 2014, *Detailed Visual Bridge Inspection Guidelines for Timber Bridges*, Main roads, Western Australia.

Mohammadi, A, Gull, JH, Taghinezhad, R & Azizinamini, A 2014, *Assessment and Evaluation of Timber Piles Used in Nebraska for Retrofit and Rating*, Department of Civil and Environmental Engineering, Florida International University, Miami, Florida.

Maintenance, Safety, Risk, Management and Life-Cycle Performance of Bridges – Powers, Frangopol, Al-Mahaidi & Caprani (Eds)
© 2018 Taylor & Francis Group, London, ISBN 978-1-138-73045-8

Investigating snipe depth in girders and corbels in timber bridges

J. Cohen & W. Lokuge
School of Civil Engineering and Surveying, University of Southern Queensland, Springfield, QLD4300
N. Herath
Department of Infrastructure Engineering, The University of Melbourne, VIC3010

ABSTRACT: There are over 300 timber bridges on Queensland state controlled roads which require constant maintenance as the timber components deteriorate over time. Inspections are done at three levels depending on the necessity. A significant number of the defects are due to poor practices such as excessive sniping of girders and corbels, which contribute to many bridges being rated in poor condition. This causes costs to increase due to increased inspection frequencies and rectification works. The aim of this research is to critically investigate the effect of sniping on the overall structural performance of individual bridge elements. Based on inspection reports for timber bridges, it is understood that sniping is a major issue and it contributes towards the deterioration of the whole member. Structural analysis has been carried out using finite element modelling in Ansys. Finite element modelling allows idealised timber components to be analysed under different loading conditions. This has been used to compare the effect of snipe depth on the structural integrity of timber components such as girders and corbels. As snipe depth increases, stress concentrations form at the snipe resulting in increased risk of splitting. Based on this modelling, some recommendations are made regarding the future assessment of component condition states.

1 INTRODUCTION

Timber has been a popular material for bridge construction in Queensland since colonial times. Many timber bridges remain in service on the Queensland state controlled road network, despite being superseded by prestressed concrete bridges as the preferred bridge type.

The legacy timber bridge network creates many challenges for the authorities in charge of maintenance. The aging timber bridges are being overstressed by increasing traffic loadings. The bridges were all built to obsolete design codes and traffic loadings, meaning they may not have sufficient capacity to handle modern heavy vehicles. While rehabilitation programs and replacement programs are in development, the sheer number of timber bridges on the road network means it will take many years to rehabilitate or replace them all. Therefore, there is a pressing need to maintain the existing network of timber bridges and extend their service lives until the resources become available for rehabilitation or replacement.

Timber bridges suffer from a range of degradation mechanisms which means intensive and costly inspection regimes must be implemented to guarantee continued operation. The scarcity of suitable hardwood timber components also adds upwards pressure to the maintenance costs. Although the uptake of alternative technologies such as glued laminated (Glu-Lam) and fibre reinforced polymer (FRP) girders is currently happening although the process is still extremely slow, at least in Australia. As a naturally occurring product, timber has a high degree of variability, which makes structural analysis difficult. Condition states are often calculated using empirically derived or arbitrary limits, and often depend on the judgement of bridge inspectors.

Due to all of these challenges faced by the timber bridge network, it is a priority to identify ways in which maintenance costs can be reduced while increasing service life. This research project will review the current state of maintenance and rehabilitation practices, in order to identify areas for improvement mainly for girders and corbels.

This research paper reports a numerical investigation on the behavior of timber bridge girders and corbels and attempts to link it with the condition states. Condition states drive the frequency and intensity of bridge inspections, and are used as a basis for justifying rehabilitation and replacement projects. If it can be shown that condition state ratings are too conservative, it may be possible to save considerable amounts of money by reducing the frequency of inspections, and delaying the need for costly replacements.

Timber bridges were relatively cheap and fast to construct, up to 50% of the cost of an equivalent concrete bridge (Crawford 2014), which allowed for the rapid expansion of Australia's nascent road and rail networks. However, timber bridges have a shorter design life (Nicholas 2014) than concrete, and require more in-service maintenance. It is important to recognize the contribution provided by timber bridges in the rapid social and economic expansion of Australia. These bridges were designed to have relatively short service lives, and were never intended to handle present day traffic volumes and loads. The short term benefits of timber such as low cost, availability and ease of construction were the dominant factors influencing early decision makers. However, the popularity of timber in the past has left behind a legacy of ongoing maintenance, rehabilitation and eventual replacement of Australia's timber bridge stock. Slow rates of replacement means there will be a requirement to keep timber bridges in service for decades to come. This requirement is a huge challenge to transportation authorities, who need to minimize the cost of inspecting and maintaining timber bridges, while planning future rehabilitation and replacement programs.

2 TIMBER BRIDGES IN QUEENSLAND

In 2005, there were approximately 500 timber bridges in services on state controlled roads in Queensland. The mean age of timber bridges is approximately 60 years and at current rates of replacement, some of these bridges will need to remain in service for the next 30 to 40 years. All timber truss-type bridges have been removed from service on the Queensland state controlled road network. The remaining timber bridges are mostly timber girder bridges (Roads 2005)(BAM 2005a). These bridges typically include timber piles, headstocks, corbels, girders and decks, although sometimes steel or concrete components are substituted.

3 SNIPING

The Timber Bridge Maintenance Manual (Queensland Department of Transport and Main Roads) acknowledges that sniping is used to allow easy insertion of replacement components. However, this technique can compromise structural integrity and fail to improve the condition state rating of the new component or the bridge as a whole.

Sniping causes stresses to concentrate at the end of the notch, which in turn increases the tendency for longitudinal cracking. Once a component has cracked, the effective sectional depth available to resist bending and shear stress is reduced. This can reduce the overall structural capacity of a component. The tensile strength of timber is lowest perpendicular to the grain. The stresses concentrated at the snipe can thus cause cracking if they result in tensile stress normal to the grain. An excessively deep snipe also reduces the cross sectional area available to resist bending and shear forces.

In order to reduce the concentration of stresses at the snipe, a recommended snipe angle of 1:4 is preferred; however it is a question whether this ratio is strictly adhered to in practice. While this may reduce the concentration of stresses at the snipe, it does not affect the overall reduction in shear capacity due to a decreased cross sectional area.

Excessive sniping of corbels is considered to be less severe as the notch is in compression rather than tension. This reduces the tendency for longitudinal cracking. There is a concern that an excessively deep cut may cause the corbel to lose bending strength and then fail in bending when loaded.

Table 1. Condition states based on snipe depth

Snipe depth		Condition state
Girder	Corbel	
0%	0%	1
<10%	<10%	2
10-15%	10-18%	3
16-30%	19-25%	4

The Bridge Inspection Manual outlines what condition state a component should be placed in based on the observed snipe depth (Table 1). There are other potential defects such as rot or splitting which may result in a component being rated in a worse condition. Generally, the most limiting defect and corresponding condition state are recorded. The presence of other less serious defects is usually recorded in the inspector notes.

The Timber Bridge Maintenance Manual recommends that any girder with a snipe depth greater than 30% of the original sectional depth should be replaced. Anything less than 15% is acceptable, and snipes between 16% and 30% of the depth should be strengthened with anti-splitter bolts (Table 2).

Table 2. Remedial actions for girders and corbels

	Snipe depth	Remedial action
Girder	<15%	None
	16-30%	Anti-splitting bolts
	>30%	Replace
Corbel	<25%	None
	>25%	Strengthen and replace

4 NUMERICAL INVESTIGATION

As identified before, the finite element method (FEM) analysis was performed by modelling girders and corbels to resemble sawn octagonal timber components, as used for Class A timber bridges on Queensland state controlled roads.

4.1 *Model limitations*

Finite element models can only ever represent a simplified version of reality. While there has been a lot of effort made to ensure the models reflect reality as close as possible, there are several limitations to the model:

- Components are idealised based on common lengths and profiles. Where a range of alternatives were available, the most limiting dimensions were chosen, as those were likely to result in the most adverse effects.
- The 3-dimensional Brick models cannot account for the effects from sloping grain or knots in the timber. These are properties that are unique to each individual timber component and their effects are difficult to predict. Timber is assumed to have grains aligned with the longitudinal axis, and free from knots or other defects.
- Timber is a highly variable material. Material elastic properties are derived from the Australian Standards, and may not represent the actual properties of a specific species or piece of timber. Material properties will be discussed further in this paper.
- The models assume that there are no other forms of degradation such as piping, surface checks or rot. It is theoretically possible to model these degradation mechanisms but it would require a much finer mesh, resulting in greatly increased computation time.
- The models do not account for repeated load effects or age-related loss of strength (which may be up to 50% of original strength).
- The angle of snipe is assumed to be 1:4 regardless of snipe depth, but in the real world, the angle of the cut is highly variable due to installation restrictions and workmanship standards.

4.2 *Material properties*

Grey ironbark (*Eucalyptus siderophloia)* is a common timber species used in the region due to its density, strength and resistance to termite. For the purpose of modelling timber bridge components, the properties of grey ironbark were selected from the AS1720.2 (2010). It is assumed the girders and the corbels are unseasoned because bridge timbers were considered to be in an unseasoned state in the past (Heckroodt 2002; Nicholas 2014). The minimum requirements for timber girders according to MRTS87 are a stress grade of F27 and a structural grade of 1. F22 timber is accepted, provided that no defects are visible in the middle third of the member. As corbels are only secondary structural members, the requirements are slightly relaxed. Corbels may be stress grade F22 and structural grade 2. F22 grade Grey Ironbark is modelled as this is the theoretically weaker timber, and should hence produce the most adverse result. F22 timber has a modulus of elasticity parallel to grain of 16000 MPa and modulus of rigidity of 1070 MPa. Orthotropic elastic properties for F22 timber was analysed (Forest Products Laboratory 2010) to develop the following ratios:

Table 3. Properties of grey ironbark

Modulus of Elasticity (MPa)		Modulus of rigidity (MPa)		Poisson ratio	
EL	16000	GLR	1072	ν_{LR}	0.4
ER	1956	GRT	320	ν_{RT}	0.7
ET	1956	GLT	1072	ν_{LT}	0.5
				ν_{RL}	0.05
				ν_{TR}	0.061
				ν_{TL}	0.03

The subscripts L, R and T shown in Table 3 refer to the longitudinal, radial and tangential directions respectively.

4.3 *Model development*

The girders and corbels are modelled to closely resemble sawn octagonal timber components, as used for Class A timber bridges on Queensland state controlled roads using ANSYS finite element software package. Solid 45 elements were selected in modelling the girders and the corbels. Although Class A bridges are now considered obsolete, the components used for maintenance and rehabilitation are of similar dimensions. The model dimensions used in the simulation are shown in Figure 1.

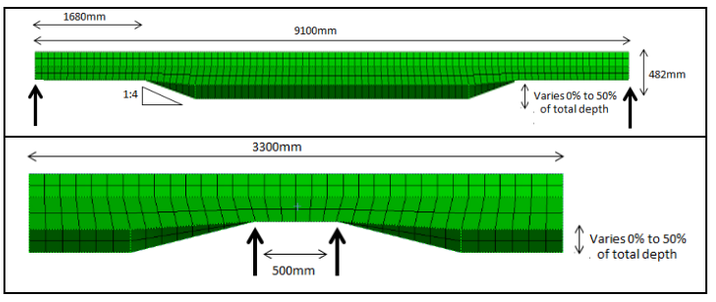
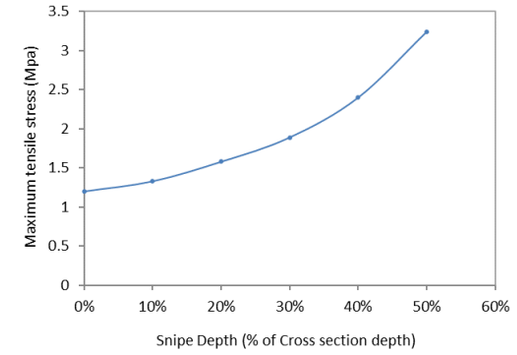


Figure 1. Typical girder and corbel layout

4.4 *Girders*

Six timber girders were investigated; with snipe depths ranging from 0% to 50% of the cross sectional depth and they were assumed to be simply supported at the ends. The maximum tensile stresses and maximum displacements obtained for all considered snipe depth variations were plotted against the snipe depth percentage.

The maximum tensile stresses variation displays an exponential distribution with regards to the increase in snipe depth as shown in Figure 2. Increase in snipe depth from 10% to 50% increases the bending stresses more than twice the stresses at 10% of snipe depth. It is evident that the reduction in effective bending depth in girders causes significant increase in bending stresses. Therefore it is an important aspect to consider the correct snipe depth in design of timber girders. Due to the natural degradation of timber girder strength with time, there is a higher risk associated with old bridges in this aspect.



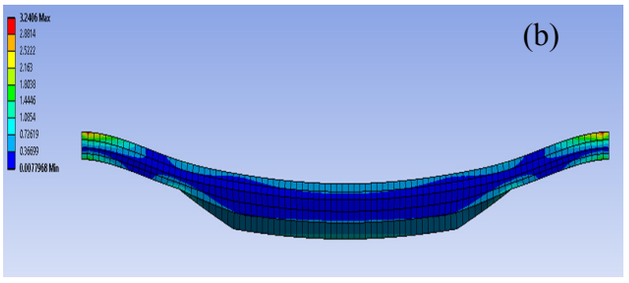
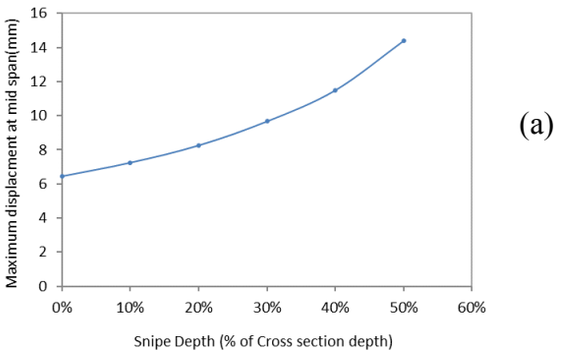


Figure 2. (a) Maximum tensile stress variation with snipe depth, (b) Tensile stresses in girder

Figure 3 shows the variation of maximum displacement at the mid span of the girder with the change of snipe depth. This plot also displays an exponential growth in displacements at the mid span with increase in snipe depth. Increase in snipe depth from 10% to 50% increase the maximum displacement by approximately twice as the displacement at 10%.



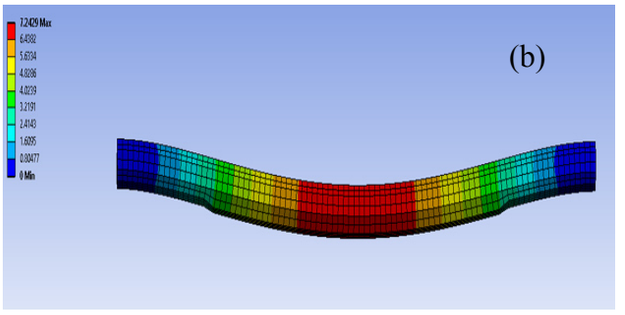


Figure 3. (a) Maximum displacement variation with snipe depth, (b) Maximum displacement in girder

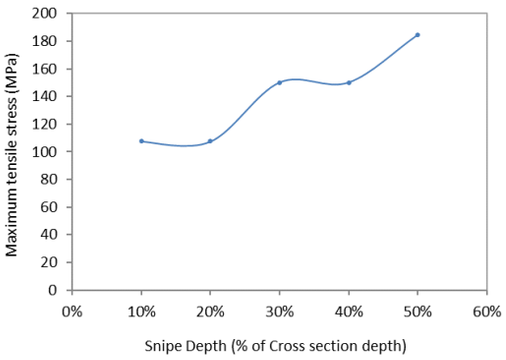
Due to the reduction in effective depth in girders, both stresses and displacements are significantly increased. This could results in splitting of girders and encouraging complete failure at some stage if correct actions are not taken. A potential defense against structural failure is the installation of anti-splitter bolts. These bolts are installed vertically through the girder at locations near the snipes. As the stresses are developed, they are transferred to the steel bolts, which will alleviate the strain in the timber member. The anti-splitter bolts would only be effective where there is enough cross-sectional area remaining to withstand the shear forces at the supports.

4.5 *Corbels*

Similar to girders, five timber corbels were also modelled with snipe depths varying from 10% to 50% of the cross sectional depth and maximum stresses and displacements at the mid span were examined. The most adverse conditions for the corbel occur when the girder load is transferred close to the corbel outstand. This would occur if the girder end had deteriorated, resulting in the support point creeping back towards the end of the corbel. This is basically the structural purpose of the corbel, to offset the effects of deterioration to the ends of the girders, and provide a larger bearing surface for the girders to rest on.

The finite element models only considered performance under an arbitrary loading. Performance is broadly defined by the amount of deflection and the degree to which stresses were concentrating at the snipe. The maximum stresses at the corbel as shown in Figure 4, display a significant increase due to the increase in snipe depth. Large increase in stresses is

observed when the snipe depth exceeded 20%, and there is no much difference in the stresses in change of snipe depth 10% and 20%.



(a)

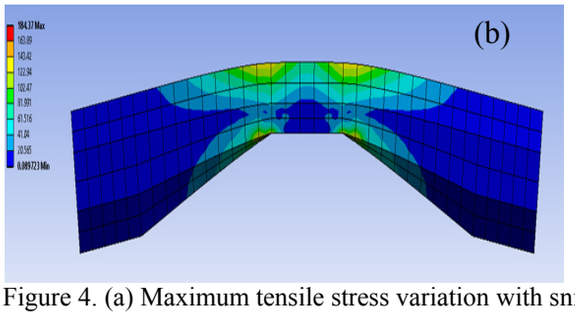
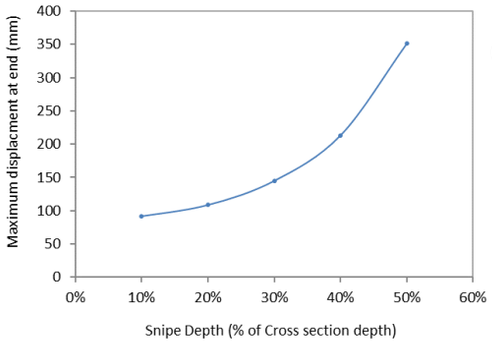


Figure 4. (a) Maximum tensile stress variation with snipe depth, (b) Tensile stresses in corbel

The variation of maximum displacement at the mid span of the corbel was plotted against the snipe depth percentage as shown in Figure 5. An exponential growth is observed due to the increase in snipe depth similar to the behavior of girders and increase of snipe depth from 10% to 50% increases the displacement more than 3 times.



(a)

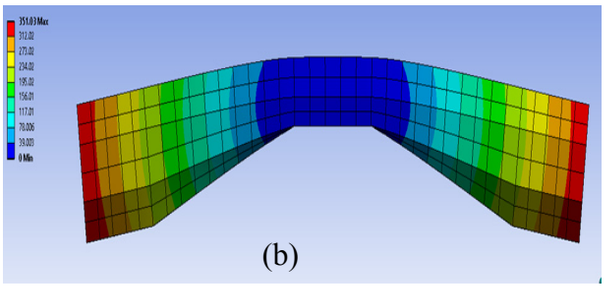


Figure 5. (a) Maximum displacement variation with snipe depth, (b) Maximum displacement in corbel

Considering both stress variation and displacement variations with respect to the increase in snipe depth, it is proposed that reasonable snipe depth for a corbel could be below 20% of the total depth. As per Table 2, remedial action should be taken for corbels with snipe depths greater than 25%. However it is proposed from this study that snipe depth greater than 20% would be a reasonable figure to have some remedial actions corbels.

5 CONCLUSIONS

Having identified sniping as a major area of concern for timber bridges, finite element modelling was used to further investigate this issue. The models were used to simulate the behaviour of girders and corbels with different snipe depths. Preliminary results tend to confirm the TMR restriction on snipes greater than 30% for girders and it is proposed that 20% snipe depth could be sensible for corbels. Condition state ratings, by their nature, are based on observable traits specific to each component. It is a subjective number used in an attempt to quantify some sort of defect. Condition states are not intended to quantify the load capacity of a component or a structure – they merely indicate general condition. For this reason, it is believed that condition states should be used for plotting deterioration trends from natural and mechanical degradation. They are not the ideal way to quantify inbuilt defects such as excessive sniping or point loading, as these defects do not change with time, hence no deterioration curve can be plotted. It is therefore difficult to link condition states to the structural performance of a sniped component. However, due to the history of continuing adequate performance, with no corbel failures attributed to excessive sniping, the case could be mounted to relax the requirements of the Bridge Inspection Manual.

REFERENCES

Crawford, S 2014, 'Timber Bridge Management: Past, Present and Future', in *Engineering and Technology Forum*, Transport Main Roads, Queensland.

Forest Products Laboratory 2010, *Wood Handbook: Wood As An Engineering Material*, [Text (Electronic bk)], General technical report FPL-GTR-113, U.S. Dept. of Agriculture, Forest Service, Forest Products Laboratory, Madison, http://app.knovel.com/web/toc.v/cid:kpWHWEM00F.

Heckroodt, R 2002, 'Guide to the Deterioration and Failure of Building Materials', in *Chapter 5 Deterioration of timber*, Thomas Telford Cape Town, South Africa, pp. 87-105.

Nicholas, A 2014, 'The New Australian Standard AS 5100 Part 9: Timber Bridges', in *9th Austroads Bridge Conference ARRB*, Sydney, New South Wales.

Queensland Department of Transport and Main Roads 2005, *Timber Bridge Maintenance Manual*, Bridge Asset Management, Structures Division, Road System and Engineering, Australia.

SS13: Value of information of SHM for life-cycle management of bridges

Organizers: S. Thöns, M. Stewart, D.G. Lu & A.J. O'Connor

Maintenance, Safety, Risk, Management and Life-Cycle Performance of Bridges – Powers, Frangopol, Al-Mahaidi & Caprani (Eds)
© 2018 Taylor & Francis Group, London, ISBN 978-1-138-73045-8

Sensitivity Analysis of Value of Information Framework

M. S. Khan
IITB-Monash Research Academy
Indian Institute of Technology Bombay, Mumbai, India

S. Ghosh & J. Ghosh
Department of Civil Engineering
Indian Institute of Technology Bombay, Mumbai, India

C. Caprani
Department of Civil Engineering
Monash University, Melbourne, Australia

ABSTRACT: The benefit of structural health monitoring (SHM) can possibly manifest through uncertainty reduction, risk reduction or life-cycle cost reduction. In the absence of a formal framework to establish monitoring benefits, SHM appears only as an additional cost to the stakeholders. This discourages the stakeholders from investing in health monitoring strategies. In the absence of a monetary value for the monitoring benefit, we rely on regulatory provisions to mandate effective structural health monitoring strategies. The value of information (VoI) is one such indicator that tries to formally quantify the benefits of monitoring, through its ability to arrive at optimum decisions with regards to the lifecycle management of structures. Broadly, VoI can be established through graphical methods or through a structural reliability based framework. In this paper, we briefly review the state-of-the-art on the VoI approach in structural engineering. Discussions are provided on the parameters that typically influence the VoI, followed by a case study example for VoI in fatigue cracking of steel structures. Calculations on sobol indices for the sensivitiy analysis help identify critical parameters affecting the VoI output.

1 INTRODUCTION

Structural Health Monitoring (SHM) refers to the various activities and techniques that are employed to establish the state of a structure and assist the stakeholders in adopting the most optimal actions for its management (Chang et al. 2003). The necessity of SHM comes from the fact that the predictions made by structural models are plagued with errors and uncertainties. Hence it becomes crucial to update the model parameters through information coming from structural condition inspections and new optimal decisions are identified (Brownjohn 2007).

The benefit of SHM primarily manifests in the reduction of uncertainties in the model prediction. Additionally, the risks a structure is exposed to can be reduced. Also, by preventing unnecessary maintenance and adopting the most optimal maintenance actions, the lifecycle costs can also be reduced (Frangopol 2011). Once the inspection has been carried out, the actual benefits for SHM can be established. However for the stakeholders, the choice of SHM strategy should be guided by the benefits it is likely to give throughout the service life of the structure.

In the absence of a framework that formally quantifies SHM benefit apriori, the ability of SHM to be beneficial is viewed with skepticism by the stakeholders (Cappello et al. 2016). Under such circumstances, SHM has to be enforced through statutory laws. Additionally, the stakeholders struggle in ranking the different available SHM strategies and this decision is left to the subjective judgement of the stakeholder (Thöns & Faber 2013). Also, it may not always be the case that the adopted SHM strategy is beneficial. Value of Information (VoI) is one such framework that attempts to quantify SHM benefit.

The VoI framework is based on bayesian preposterior analysis (Howard 1966, Raïffa & Schlaifer 1961). The VoI is premised on the idea that the value of any information lies in its ability to guide us to optimal decisions. In simple terms, the VoI is defined as the difference between the expected utility of optimal de-

cisions with and without SHM information (Cappello et al. 2016). Within civil engineering, some studies on VoI are the following - to quantify the benefits of SHM/inspection for particular problems in structural engineering (Thöns and Faber 2013, Straub 2014, Thöns et al. 2015, Qin et al. 2015, Thöns et al. 2017), to rank various SHM instruments (Pozzi & Der Kiureghian 2011), to optimize maintenance strategy (Malings & Pozzi 2017) and to optimize sensor placement (Malings & Pozzi 2016). In order to determine the VoI, typically two kinds of strategies are adopted - either graphical decision model solving strategies like Dynamic Influence Diagram, Markov Decision Processes etc. (Memarzadeh and Pozzi 2016, Straub et al. 2017, Malings and Pozzi 2017) or reliability based simulation methods like Monte Carlo sampling (Pozzi & Der Kiureghian 2011), importance sampling (Straub 2014) etc.

Pozzi & Der Kiureghian (2011) proposed a Monte Carlo based strategy to evaluate VoI. They implemented their algorithm on a simple reliability based model. After evaluating the evolution of VoI with the randomness of the inspection instrument, a range of suitable sensors can be established which cost less than the value they are most likely to deliver over the lifecycle of the structure. Such a methodology could be used to rank different inspection instruments. Straub (2014) extended this work to incorporate sequential decision making for fatigue cracking in a steel component and proposed an importance sampling approach for evaluating VoI. Thöns & Faber (2013) proposed a normalized VoI approach in which the utility function without SHM did not depend on any decision variable and the SHM observations were conditioned upon aleatory and epistemic uncertainties. Thöns et al. (2015) extended their approach for VoI estimation by incorporating updated aleatory and epistemic uncertainties for estimating utility with SHM.

A number of parameters that influence VoI have been observed in different studies. Pozzi & Der Kiureghian (2011), Straub (2014) and Thöns & Faber (2013) have noted that the VoI is higher for a lower randomness of the measurement uncertaintity. Thöns & Faber (2013) also observed a relatively higher influence of failure costs on VoI relative to maintenance costs. Thöns & Faber (2013) and Thöns et al. (2015) observed the influence of low and high model failure probability on VoI. Konakli et al. (2016) investigated VoI for structural systems and concluded that the VoI is higher for a higher component correlation.

Sensitivity Analysis gives crucial insights into the working of complex mathematical models. They are frequently adopted to validate models based on their ability to reflect sensitivities of influential parameters. Once the influential parameters are identified, they can be used to construct metamodels conditioned only on the key input parameters. The parameters of influence of VoI have been identified but there has not been any formal quantification of its sensitivities. This paper presents a brief discussion on the theory of VoI and its parameters of influence. The sensitivity of a VoI framework to a number of parameters is quantified through Sobol indices. The VoI for a steel fatigue crack growth model is established and the sensitivity of VoI is quantified.

2 FORMULATION FOR VALUE OF INFORMATION

Value of information theory is based on the framework of bayesian pre-posterior analysis (Raïffa & Schlaifer 1961). For a detailed exposition on the theoretical framework of VoI, the reader is referred to Thöns (2015) and Konakli et al. (2016). For the purpose of our illustration, a brief presentation of VoI is given below.

Essentially, the VoI is defined as the difference between the expected prior utility and the expected posterior utility for a given decision model. A simple formulation of utility can be done in terms of the cost function $C(a, \mathbf{X})$, where $a \in \mathbf{A}$ is a decision action from the set of all possible decisions in the set $\mathbf{A}$ and $\mathbf{X}$ is a random vector of the input variables of the model $\mathcal{M}$. Hence the prior costs can be represented as:

$$C_{prior} = \mathrm{E}_{\mathbf{X}}\left[C\left(a_{opt}, \mathbf{X}\right)\right] = \min_{a} \mathrm{E}_{\mathbf{X}}\left[C\left(a, \mathbf{X}\right)\right] \tag{1}$$

where a_{opt} is the optimum maintenance action defined by:

$$a_{opt} = \arg\min_{a} \mathrm{E}_{\mathbf{X}}\left[C\left(a, \mathbf{X}\right)\right] \tag{2}$$

where $\mathrm{E}[\cdot]$ is the expectation operator.

In cases where SHM is adopted, observations coming from monitoring/inspections, $\mathbf{y}$, give the updated input parameters $\mathbf{X}'$. A new decision action is taken based on the updated state of the structure and hazard, given by a'_{opt} which in turn gives up an updated estimate of costs called posterior costs, C_{post} . Carrying out the same process for all possible realizations of the monitoring outcomes, $\mathbf{Y}$, gives us the expected posterior costs given by:

$$C_{post} = \mathrm{E}_{\mathbf{Y}}\left[\mathrm{E}_{\mathbf{X}'}\left[C\left(a'_{opt}, \mathbf{X}'\right)\right]\right] \tag{3}$$

$$C_{post} = \mathrm{E}_{\mathbf{Y}}\left[\min_{a} \mathrm{E}_{\mathbf{X}'}\left[C\left(a, \mathbf{X}'\right)\right]\right] \tag{4}$$

$$a'_{opt} = \arg\min_{a} \mathrm{E}_{\mathbf{X}'}\left[C\left(a, \mathbf{X}'\right)\right] \tag{5}$$

Finally, the VoI is defined as the difference between the expected prior costs and expected posterior costs as below:

$$\text{VoI} = C_{prior} - C_{post} \tag{6}$$

VoI can also be presented as a ratio, referred to as Normalized VoI ($NVoI$), normalized with respect to the prior costs as given below:

$$\text{NVoI} = \frac{C_{prior} - C_{post}}{C_{prior}} \tag{7}$$

3 PARAMETERS INFLUENCING VOI

From the brief discussion in Section 2, one can identify a number of parameters that could influence the VoI.

3.1 *Cost model*

It is evident from the formulation of Section 2 that the cost model is an integral part of the VoI framework. Throughout the lifecycle of the structure, the stakeholders can incur costs from three main sources namely - cost of failure, cost of maintenance/repair and the cost of SHM.

The costs of failure includes the direct and indirect consequences of failure incurred by the agency and/or the user. The inspection/monitoring of structures is another significant part of the lifecycle costs and usually precedes any maintenance/repair action which has a cost of its own. However it could be assumed that the inspection is free while determining the VoI and the instrument which gives a higher VoI with the least cost is considered the best of all available options (Pozzi & Der Kiureghian 2011, Straub 2014). Hence such an indirect cost-benefit analysis can be used to rank various SHM strategies under consideration.

Establishing the actual consequences of failure can be a challenging task. The estimates made are subject to a number of approximations related the structure and its utility. Such estimates can also be expected to differ with each structure under consideration, adopted maintenance strategy and degradation model (Faber 2002). Thöns et al. (2015) found that the failure costs contributed significantly to the VoI as opposed to the inspection costs and the repair costs.

3.2 *Decision model*

The other significant aspect of the VoI framework is the decision model. As the structural condition deteriorates, the stakeholders are faced with the question whether to repair or replace the structure. Different types of repair strategies can be adopted depending upon the level of damage within the structure. Additionally, such decisions can be taken multiple times throughout the lifecycle of the structure. This can be modelled as a dynamic decision problem.

Such complexity renders the problem of VoI estimation intractable due to the high computational demands. A more comprehensive maintenance model would contain an essential maintenance as well as a preventive maintenance strategy (Sánchez-Silva et al. 2016). Preventive maintenance strategies are those that are employed to keep the structure operating at a certain specified level. They can be planned on the basis of a threshold level (other than failure) or they can be planned to repeat at a particular time period. Essential maintenance strategies on the other hand are triggered when the structural performance deteriorates below a certain minimum performance threshold (typically failure). However, due to the issues arising from problem complexity, researchers frequently adopt a single decision whether to replace the structure or do nothing in case of a failure at one or two instances during the service life of the structure (Pozzi and Der Kiureghian 2011, Straub 2014, Cappello et al. 2016).

It can also be argued that since the decision models do not capture the actual structural maintenance scenario, the full VoI has not been realized. Additionally, the process of generating synthetic samples of SHM observations entails superimposing an unbiased random error with the model prediction. In other words, the VoI is calculated for the case when SHM informs the stakeholder what he or she already knows through their model prediction but with a slight margin of error. However, this approximate estimate of VoI can be reasonable for practical purposes (Konakli et al. 2016).

3.3 *Probability of failure*

Decisions relating to maintaining a structure are made throughout its lifetime. During this period, the magnitude of different costs incurred especially due to failure vary. Additionally, the time value of money should be accounted for through discounting of future costs. Hence the period within which the structure fails and its probability of failure becomes influential through the interaction between the decisions, time instant and their consequences.

The probability of failure of a structure depends upon a number of other factors such as the type of distribution of demand and capacity, the specifics of structural degradation law, interdependencies between the components of the system etc. Faber & Thöns (2014) and Konakli et al. (2016) noted a clear but complex influence of the annual probability of failure on the estimated VoI.

3.4 *Model uncertainty and errors*

Mathematical models of physical phenomenon are frequently based upon certain approximations of the reality. For example, in structures, degradation processes are frequently modelled as a linear degradation process as an approximation when the actual scenario

might be far more complicated than that. This introduces errors in model predictions.

Additionally a distinction between model errors and model uncertainty can be made. Physical phenomena are highly random. Due to the difficulty in estimating actual values of the parameters governing a phenomena, they are frequently modelled as random variables. These uncertainties in the input parameters are propagated and manifest in the variance of the output variable under consideration.

SHM serves an important purpose in reducing model uncertainties and model errors. Hence the information obtained through SHM and its value would depend upon the extent of model uncertainty and errors. In the cases when the model uncertainty and/or the model error is high, the VoI should be higher and vice versa. However the direct influence of model uncertainties and errors on VoI has not been studied.

The model errors can be accounted through an additive bias (α_0) term, a scaling bias (α_1) term and a randomness term ($\epsilon_{\mathcal{M}}$) as below:

$$m = \alpha_1 \mathcal{M}(\mathbf{X}) + \alpha_0 + \epsilon_{\mathcal{M}} \tag{8}$$

where m is the model prediction and $\epsilon_{\mathcal{M}}$ is a zero mean standard normal variable.

3.5 *Instrument errors*

Instrument errors can arise from human errors and instrument imperfections. The existence of certain environmental factors can also lead to erroneous measurements. Instruments are also characterized by their precision in the form of the smallest measurement they can make.

There can be two types of inspections outcomes - binary output and continuous output. In cases when the structural state is either considered to be safe of failed (or the existence/non-existence of flaws), the SHM adopted can simply return a yes or no. In such cases, the accuracy of the instrument can be modelled using the likelihood matrix with True/False Positive/Negative rate (Omenzetter et al. 2016). In cases when the SHM instrument measures a continuous output, like crack size, Probability of Detection (PoD) curves or instead a model with bias and randomness similar to Equation (8) can be adopted.

It can be argued intuitively that the VoI should be lower for an instrument with higher errors. The evolution of VoI with instrument randomness has been studied by a number of researchers (Pozzi & Der Kiureghian 2011, Straub 2014).

4 SENSITIVITY ANALYSIS EXAMPLE

Sensitivity analysis (SA) is the study of the extent to which input parameters influence a mathematical model. The methods for sensitivity analysis can be divided into three types - local SA, screening methods and global SA. For more details the reader is referred to the work of Saltelli et al. 2004.

The SA of VoI is carried out for the following objectives:

1. To identify the influential parameters
2. To study the extent of influence of parameters of the VoI model
3. To validate the VoI model based on its ability to reflect known influential parameters

SALib is a sensitivity analysis package for python (Herman & Usher 2017). This paper details sensitivity studies of the VoI model as proposed by Straub (2014) using SALib. This section briefly details the VoI framework proposed by Straub (2014) followed by the choice of parameters sensitivity analysis and subsequent calculation of Sobol indices.

4.1 *VoI in fatigue crack growth in steel structures*

Straub (2014) investigated the VoI for the case of fatigue crack growth in steel structures. We adopt the same problem for the purpose of our studies.

A service life of 20 years is assumed for the steel component and divided into 4 periods of 5 year each as follows: 0-5 year, 5-10 year, 10-15 year and 15-20 year. The decision model consists of either replacing the structure at the beginning of each interval ie 0, 5, 10, 15 years or do nothing. The optimum decision the one which gives the minimum expected cost. A single inspection is made at year 5. The expected costs are estimated for the cases of with and without SHM inspection using a Monte Carlo strategy and VoI is calculated. Costs of failure and costs of replacing the component at the beginning of each of these periods is taken into consideration. For more details on the specifics of the problem, the model parameters and the proposed methodology the reader is referred to the original paper (Straub 2014).

The fatigue cracking on a steel component is modelled as per Paris' Laws and the crack depth, l, is given as below:

$$l(\mathbf{X}, t) = \left[\left(1 - \frac{m}{2}\right) C \Delta S^m \pi^{0.5m} \nu t - l_0^{\left(1-\frac{m}{2}\right)} \right]^{\frac{1}{\left(1-\frac{m}{2}\right)}} \tag{9}$$

where C and m are empirical constants, ΔS is the stress range per cycle, ν is the annual cycle rate, l_0 is the initial crack length at zero stress cycles and t is time. The limit state function is given by,

$$G_F(\mathbf{X}, t) = l(\mathbf{X}, t) - l_c \tag{10}$$

where l_c is the threshold crack length.

4.2 *Parameters for study*

For the purpose of SA, 6 variables are considered to vary uniformly between their upper bounds and lower bounds as specified in Table 1. SALib carries out an experimental design as per Saltelli (2002) using the parameters as specified in Table 1. The VoI is evaluated for this design and finally the sobol indices (Section 4.3) are estimated.

In order to study the influence of the cost of repair, a scaling factor SF is adopted. Hence the cost of repair becomes the original cost of repair (Straub 2014) multipled by SF. This SF is varied in the sensitivity studies as a uniformly distributed random variables within the bounds specified by Table 1. The variables μ_{l_0}, $\mu_{\Delta S}$ and l_c are important parameters of the model and can be considered to directly influence the probability of failure of the model. The model errors are not taken into explicit consideration but the coefficient of variation (COV) of ΔS contributes to the model uncertainty. The instrument is considered to be unbiased and characterized by its randomness given by σ_E.

Table 1: Parameters of VoI model for sensitivity analysis

Variable	Lower bound	Upper Bound	Median
SF	0.2	5	2.6
σ_E [mm]	0.75	2	1.75
μ_{l_0} [mm]	0.5	2	1.75
$\mu_{\Delta S}$ [Nmm^{-2}]	50	65	57.5
COV of ΔS	0.15	0.25	0.2
l_c [mm]	40	50	45

4.3 *Sobol Indices for sensitivity*

Sobol indices are indices which are constructed by decomposing the variance of an output random variable Z in terms of its input random variables $X_i \in \mathbf{X}$, where $i = 1$ to d, normalized by the actual variance of Z. The first order indices are given by Equation (11).

$$S_i = \frac{\mathrm{V}_{X_i}\left[E_{X_{\sim i}}\left(Z|X_i\right)\right]}{\mathrm{V}(Z)} \tag{11}$$

Here the notation $X_{\sim i}$ means all variables except X_i. Also, $\mathrm{E}[\cdot]$ denotes the expectation operator and $\mathrm{V}(\cdot)$ denotes the variance operator. Hence the numerator in Equation (11) represents the variance of the expectation of output variable Z by fixing X_i. It measures the effect of varying X_i alone on the variance of Z.

Second order indices can be constructed as below:

$$S_{ij} = \frac{\mathrm{V}_{X_{ij}}\left[\mathrm{E}_{X_{\sim ij}}\left(Z|X_i, X_j\right)\right]}{\mathrm{V}(Z)} \tag{12}$$

Similarly, higher order indices can be constructed. An interesting property of such indices is given below:

$$\sum_{i=1}^{d} S_i + \sum_{i<j}^{d} S_{ij} + ... + S_{12..d} = 1 \tag{13}$$

As the number of input parameters increase, the number of sobol indices increases exponentially. Hence to reduce the computation and directly estimate the total extent of influence an input variable exerts on Y, total order indices are constructed. They are defined below:

$$S_{T_i} = 1 - \frac{\mathrm{V}_{X_{\sim ij}}\left[\mathrm{E}_{X_{ij}}\left(Z|X_{\sim i}\right)\right]}{\mathrm{V}(Z)} \tag{14}$$

S_{T_i} measures the effect of all terms of any order that include X_i on the variance of Z.

4.4 *Sensitivity analysis methodology*

In order to study the sensitivity, three strategies have been adopted. Firstly, the variation of the VoI and $NVoI$ is studied for different values of input parameters are studied. A baseline model is adopted with median values of the parameters as specified in Table 1 is carried out. Additionally, keeping all other parameters constant, the model is evaluated for the upper bound value and the lower bound value for each parameter as specified in Table 1.

In the second and the third strategy, the first order and total order Sobol sensitivity indices are calculated. In the second strategy, the indices are calculated using the Saltelli scheme (Saltelli 2002) implemented in SALib. As per the scheme, the number of samples required for estimation of Monte Carlo estimates of first order and total order Sobol indices are given by $N\left(k+2\right)$, where k is the number of parameters in the study, equal to 6 in our case, and N is an integer that typically ranges between 10 to 1000. For the purpose of this study, $N = 1000$ has been adopted for a reasonably good convergence of first order and total order indices. It should be noted that evaluation of the model is an extremely computationally demanding process, which limits the maximum number of samples that can be adopted for the study.

In the third strategy, the Sobol indices are calculated using Fourier Amplitude Sensitivity Testing (FAST) (Saltelli et al. 1999) implemented in SALib in order to validate the results obtained by Saltelli Scheme. For this strategy, the value of interference parameter adopted is 4 and 390 samples are generated to obtain point estimates of the first order and total order indices.

5 RESULTS AND DISCUSSION

Figure 1 and Figure 2 express VoI and NVoI respectively evaluated at different bounds of the parameters. For the chosen distribution of parameters, it is quite evident that the parameters μ_{l_0}, $\mu_{\Delta S}$ and the COV of ΔS is most significant followed by σ_E. The model remains largely insensitive two SF and l_c.

A similar pattern is observed in the estimated first order (Figure 3 and Figure 4) and total order indices

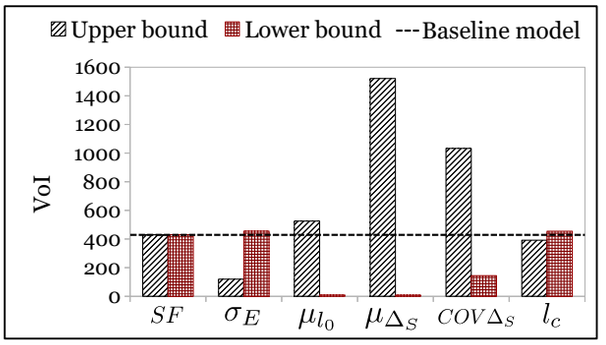


Figure 1: VoI at different bounds of parameters

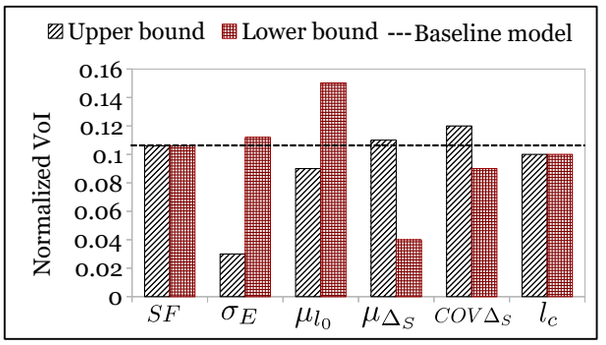


Figure 2: Normalized VoI at different bounds of parameters

(Figure 5 and Figure 6). A quick conclusion that can be drawn from Figures 3, 4 and 5 is that the value of $N = 1000$ gives a reasonably converged estimate of the Sobol indices. However Figure 6 indicates that for total order indices of NVoI, more samples would be required. Also, it can be observed from Figures 3, 4 and 5 that FAST algorithm gives reasonably accurate estimates of Sobol indices are a much smaller computational cost.

Figure 3 and Figure 5 express higher sensitivity indices for the parameters of the underlying physical phenomenon. These parameters directly influence the probability of failure of the structure. The model for cost of failure has a higher consequence when the structure fails earlier during its service life period as opposed to a failure during the later period of its service life (Straub 2014). It implies that the VoI is more pronounced when the consequences of failure are higher and less dependent upon the parameters of inspection instrument quality like σ_E. Hence the

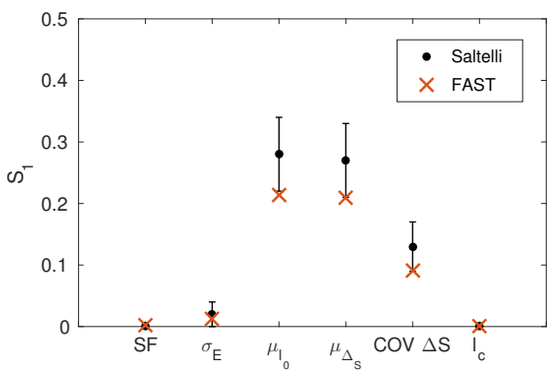


Figure 3: First order Sobol indices for VoI

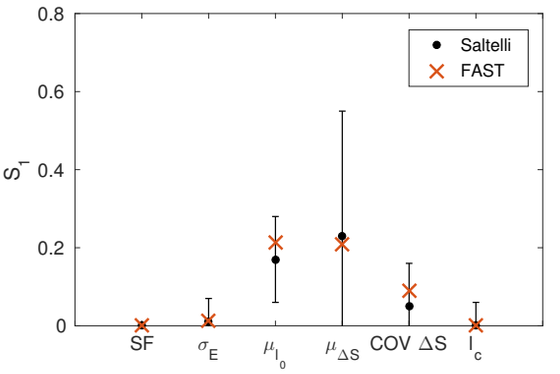


Figure 4: First order Sobol indices for NVoI

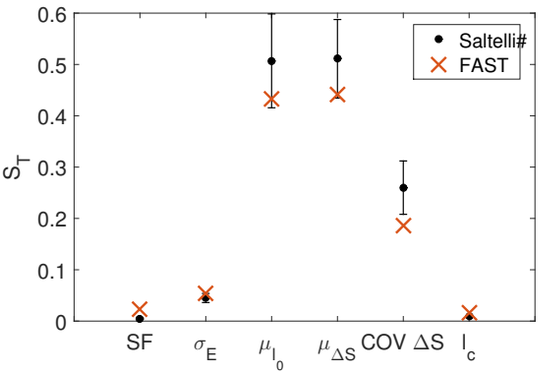


Figure 5: Total order Sobol Indices for VoI

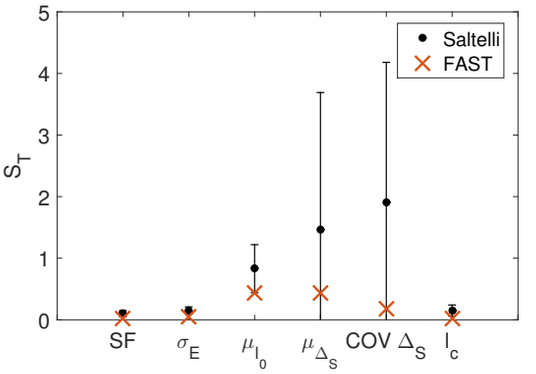


Figure 6: Total order Sobol indices for NVoI

decision to adopt SHM and its consequent benefit is largely a function of the stakes involved.

When the consequences of failure are high, the VoI obtained is also high. However when normalized with respect to the prior costs, the relative difference in VoI is less pronounced as can be noticed by comparing Figure 1 and Figure 2.

As opposed to the parameters μ_{l_0}, $\mu_{\Delta S}$ and the COV of ΔS, σ_E has a relatively lower influence on VoI as shown in Figure 3 and Figure 5. This could be due to the fact that the probability of failure of the structure/component is directly influenced by those other parameters, resulting in a larger variation in VoI. However, from Figure 2 it can be observed that σ_E is a significant variable for the normalised VoI.

SF is found to have negligible sensitivity on VoI and NVoI. It could be due to the fact that as per the cost model adopted, the costs of repair are of 10^2 to 10^1 order less than the costs of failure (Straub 2014). Nonetheless, for the current VoI problem, it would make negligible difference in VoI estimates if the costs of repair were neglected.

The VoI framework shows relatively less sensitivity to the threshold crack length l_c (Figures 3 to 6). This is observed 5because the adopted range of l_c between 40 mm and 50 mm does not impact the 5 year period probabilities of failure significantly.

6 CONCLUSION

This paper details sensitivity analysis of a VoI framework through variance decomposition and estimation of Sobol indices. This sensitivity analysis gives key insights into the working of a complex VoI framework; however, computational demands imposes a significant challenge for such studies.

The VoI framework is found to have a negligible sensitivity towards the cost of repair, whereas the most significant contribution comes from the costs of failure. Hence the repair costs can be neglected for VoI estimations. Additionally, the variables intrinsic to the underlying physical model which directly influence the time/probability of failure of the structure exert a high degree of influence on the model. These variables also show a high nonlinear interaction through their large total Sobol indices (S_T). A simple conclusion that can be drawn from this is that the VoI is largely dependent on the extent of consequences of failure of the structure.

Uncertainty in the underlying physical model, modelled as the coefficient of variation of an input parameter ΔS also exerts a significant influence on the VoI. A high VoI is obtained for higher model uncertainty and vice versa. Among the other significant variables that describe the quality of inspection instrument is the instrument randomness.

The aforementioned conclusions must be deduced while considering the influence of the underlying assumptions of the probabilistic model as well as the cost model. The influence of the choice of probability distribution for the parameters of the underlying physical model has not been investigated. Additionally, the influence of these parameters could become more significant in the case of a cost model that adopts higher consequences of failure.

Further research is required to study the influence of other parameters of influence which have not been covered by this study like model errors. The identification of influential parameters for VoI estimation will aid in the development of metamodels for VoI estimation and, if needed, in a more suitable definition of the VoI.

REFERENCES

Brownjohn, J. (2007). Structural health monitoring of civil infrastructure. *Philosophical Transactions of the Royal Society A: Mathematical, Physical and Engineering Sciences 365*(1851), 589–622.

Cappello, C., D. Zonta, & B. Glisic (2016). Expected utility theory for monitoring-based decision-making. *Proceedings of the IEEE 104*(8), 1647–1661.

Chang, P., A. Flatau, & S. Liu (2003). Review paper: Health monitoring of civil infrastructure. *Structural Health Monitoring 2*(3), 257–267.

Faber, M. (2002). Risk-based inspection: An introduction. *Structural Engineering International: Journal of the International Association for Bridge and Structural Engineering (IABSE) 12*(3), 186.

Faber, M. & S. Thöns (2014). On the value of structural health monitoring. *Safety, Reliability and Risk Analysis: Beyond the Horizon - Proceedings of the European Safety and Reliability Conference, ESREL 2013*, 2535–2544. cited By 0.

Frangopol, D. (2011). Life-cycle performance, management, and optimisation of structural systems under uncertainty: Accomplishments and challenges. *Structure and Infrastructure Engineering 7*(6), 389–413.

Herman, J. & W. Usher (2017). Salib: An open-source python library for sensitivity analysis. *The Journal of Open Source Software 2*(1), 1–2.

Howard, R. (1966). Information value theory. *IEEE Transactions on Systems Science and Cybernetics 2*(1), 22–26.

Konakli, K., B. Sudret, & M. H. Faber (2016). Numerical investigations into the value of information in lifecycle analysis of structural systems. *ASCE-ASME Journal of Risk and Uncertainty in Engineering Systems, Part A: Civil Engineering 2*(3), B4015007.

Malings, C. & M. Pozzi (2016). Value of information for spatially distributed systems: Application to sensor placement. *Reliability Engineering and System Safety 154*, 219–233.

Malings, C. & M. Pozzi (2017). Optimal Sensor Placement and Scheduling with Value of Information for Spatio-Temporal Infrastructure System Management. In *ICOSSAR - 12th International Conference on Structural Safety & Reliability*, Vienna, Austria, pp. 3320–3330.

Memarzadeh, M. & M. Pozzi (2016). Value of information

in sequential decision making: Component inspection, permanent monitoring and system-level scheduling. *Reliability Engineering and System Safety 154*, 137–151.

Omenzetter, P., M. Limongelli, & U. Yazgan (2016). Quantifying the value of seismic structural health monitoring of buildings. *8th European Workshop on Structural Health Monitoring, EWSHM 2016 1*, 510–519.

Pozzi, M. & A. Der Kiureghian (2011). Assessing the value of information for long-term structural health monitoring. *Proceedings of SPIE - The International Society for Optical Engineering 7984*.

Qin, J., S. Thöns, & M. Faber (2015). On the value of shm in the context of service life integrity management. *12th International Conference on Applications of Statistics and Probability in Civil Engineering, ICASP 2015*.

Raïffa, H. & R. Schlaifer (1961). *Applied statistical decision theory*. Studies in managerial economics. Division of Research, Graduate School of Business Adminitration, Harvard University.

Saltelli, A. (2002). Making best use of model evaluations to compute sensitivity indices. *Computer Physics Communications 145*(2), 280–297.

Saltelli, A., S. Tarantola, F. Campolongo, & M. Ratto (2004). *Sensitivity Analysis in Practice*. John Wiley and Sons, Ltd.

Saltelli, A., S. Tarantola, & K. P.-S. Chan (1999). A quantitative model-independent method for global sensitivity analysis of model output. *Technometrics 41*(1), 39–56.

Sánchez-Silva, M., D. Frangopol, J. Padgett, & M. Soliman (2016). Maintenance and operation of infrastructure systems: Review. *Journal of Structural Engineering (United States) 142*(9).

Straub, D. (2014). Value of information analysis with structural reliability methods. *Structural Safety 49*, 75–85.

Straub, D., E. Chatzi, E. Bismut, W. Courage, M. Döhler, M. H. Faber, J. Köhler, G. Lombaert, P. Omenzetter, M. Pozzi, S. Thöns, D. V. Val, H. Wenzel, & D. Zonta (2017). Value of information: A roadmap to quantifying the benefit of structural health monitoring. In *ICOSSAR - 12th International Conference on Structural Safety & Reliability*, Vienna, Austria, pp. 3018–3029.

Thöns, S. (2015). *Proceedings of 1st Workshop on Quantifying the Value of Structural Health Monitoring*. Kongens Lyngby: COST.

Thöns, S. & M. Faber (2013). Assessing the value of structural health monitoring. *Safety, Reliability, Risk and Life-Cycle Performance of Structures and Infrastructures - Proceedings of the 11th International Conference on Structural Safety and Reliability, ICOSSAR 2013*, 2543–2550.

Thöns, S., M. Faber, & D. Val (2017). On the Value of Structural Health Monitoring Information for the Operation of Wind Parks. In *ICOSSAR - 12th International Conference on Structural Safety & Reliability*, Vienna, Austria, pp. 3008–3017.

Thöns, S., R. Schneider, & M. Faber (2015). Quantification of the value of structural health monitoring information for fatigue deteriorating structural systems. *12th International Conference on Applications of Statistics and Probability in Civil Engineering, ICASP 2015*.

Maintenance, Safety, Risk, Management and Life-Cycle Performance of Bridges – Powers, Frangopol, Al-Mahaidi & Caprani (Eds)
© 2018 Taylor & Francis Group, London, ISBN 978-1-138-73045-8

Health monitoring data modeling and reliability prediction of an actual bridge based on ARMA model

D.G. Lu, W.H. Zhang & Z. Zhao
School of Civil Engineering, Harbin Institute of Technology, Harbin, P.R. China

ABSTRACT: An actual CFST arch type bridge located in China which has been installed a health monitoring system, is taken as a test-bed in this paper. To model the health monitoring data and predict the reliability of the structural system, an Auto-Regressive Moving-Average (ARMA) model is introduced in this paper. The Levenberg-Marquarat optimization algorithm is utilized in the parameter. Based on the vertical acceleration data, use of the improved estimation algorithm is made to build the ARMA model. The deflection data of the girders is performed by reliability analysis. In combination with the data obtained by the pressure rings on the suspenders of the bridge, the cable forces are identified, and the ARMA model is established to process and analyze the cable forces. The effects of the variations of strength and diameter of the strands on the reliability assessment of the suspenders are investigated.

1 INTRODUCTION

Since the 1980s, with the rapid development of Chinese economy, a great deal achievements have been made in the field of bridge construction. Meanwhile, like other countries all over the world, the bridge projects in China are facing the bridge accidents. For this reason, many bridge constructions have installed different sizes of health monitoring systems all over the world. Up to now, the technology of the bridge health monitoring system installation has already been well developed (Kim & Pakzad 2007, Roberts & Brown 2005, Koh & Choo 2006, Koh & Lee, H.S 2008). After nearly 30 years of monitoring, a large amount of data has been accumulated, therefore, how to cope with the huge monitoring data accurately and timely becomes a key process of condition assessment and performance prediction of bridges.

The methods of dealing with bridge health monitoring data include time-frequency analysis method, modal analysis method, analytic hierarchy process, genetic algorithm, neural network analysis method, time series analysis method, reliability theory analysis method (Ni & Jinag 2001, Hunag & Shen 1998). However, the theory of modeling and analysis of monitoring data has not yet been developed to maturity.

Time series analysis originated from the forecast, the traditional periodic graph analysis and the correlation analysis to establish non-parametric time series model. An important breakthrough in time series analysis is from nonparametric models to parametric models. ARMA model originated from the AR and MA model, then extended to non-linear Smooth field, etc. (Yule 1927, Walker 1931). After that, the formulation of the maximum entropy spectrum and AR spectrum were proposed (Burg 1967, Parzen 1968). Box and Jenkins proposed the complete framework of ARMA model and a complete set of time-series data modeling, parameterization, testing, prediction and control methods, made an indelible contribution to the timing theory is applied in various fields (Box & Jenkins 1976). From that, lots of research has been focused on this area (Van den Bos 1971, Pisarenko 1973, Pandit & Wu 1978). It has carried out a more comprehensive study on the system identification method of bridge health diagnosis. The research projects include I-40 bridge project and Alamosa canyon (Farrar & Cone 1995, Johnson & Lam 2004, Carden & Brownjohn 2008). Some research focused on modal identification and damage identification (Qin & Zhang 1998) .

In this paper, we take data-driven modeling as an objective, the feasibility of the application of time series analysis method to modeling and analysis of

bridge monitoring data is discussed. The basic ARMA (Auto-Regressive Moving-Average) model in time series analysis is selected to model and analyze the health monitoring data of bridges, and the reliability indices of bridge are calculated based on the proposed ARMA model.

2 ESTABLISHMENT OF ARMA MODEL AND IMPROVED PARAMETER ESTIMATION ALGORITHM

2.1 *Illustration of ARMA model*

When the sequence $\{x_t\}$ has both autoregressive and moving average, the model should also contain both the autoregressive and the moving averaging process, combining the AR and the MA models to get the ARMA model. It is expressed:

$$x_t = \varphi_1 x_{t-1} + \mathrm{L} + \varphi_p x_{t-p} + \varepsilon_t - \theta_1 \varepsilon_{t-1} - \mathrm{L} - \theta_q \varepsilon_{t-q} \quad (1)$$

It can be abbreviated as ARMA (p,q). Where $\{\varepsilon_t\}$ is the white noise sequence, $\varphi_1,\varphi_2,\cdots,\varphi_p$ are the autoregressive parameters of the model, $\theta_1,\theta_2,\ldots,\theta_p$ are the moving average parameters of the model. When the backward operator B is introduced, the equation (1) can be described by the p-order polynomial

$$\Phi(B)x_t = \Theta(B)\varepsilon_t \quad (2)$$

Where,

$$\Phi(B) = 1 - \varphi_1 B - \varphi_2 B^2 - \mathrm{L} - \varphi_p B^p \quad (3)$$

$$\Theta(B) = 1 - \theta_1 B - \theta_2 B^2 - \mathrm{L} - \theta_q B^q \quad (4)$$

$Bx_t=x_{t-1}$, $B^2x_t=x_{t-2}$, …, $B^px_t=x_{t-p}$, $B\varepsilon_t=\varepsilon_{t-1}$, $B^2\varepsilon_t=\varepsilon_{t-2}$, …, $B^q\varepsilon_t=\varepsilon_{t-q}$.

Equation (3) is called the autoregressive feature polynomial, and equation (4) is called the moving average feature polynomial.

2.2 *The process of establishment*

For the observation sequence data $\{x_t\}$ obtained by the signal acquisition system, it should be tested and preprocessed according to relative requirements to meet the conditions for establishing the ARMA model. Through the previous data test and preprocessing, then combine with the characteristics to transform the data form.

If the autocorrelation function and the partial autocorrelation function all have the properties of tailing, then ARMA model modeling is used. In a word, the selection is due to truncated properties of the autocorrelation and partial autocorrelation function. According to the correlation of the sequence $\{x_t\}$, the order of the model can be determined from the truncation of the autocorrelation and the partial autocorrelation function. And then the parameters estimation is the next step of the establishment but it has a few difficulties, the detail will be discussed in the next section.

After the establishment of a time series model from the sample data, we need to test the applicability of the model. The residual sequence can reflect the degree of application to the data when the model is established. Therefore, the residual sequence should be analyzed when the applicability of the model is tested. There are also a variety of applicability test methods, such as R test, F test, D-W test and so on. In this paper, we mainly use D-W test and the correlation graph to test the applicability.

2.3 *The optimization methods of parameter estimation*

Parameter estimation is the key to the modeling process, due to lack information of noise $\{\varepsilon_t\}$, the difficulty of estimating the parameters of the ARMA model is increased. Commonly methods like least squares, etc.

In this paper, we use one of the optimization methods of ARMA model parameter estimation optimization method: Legeven-Marquarat algorithm, a modified algorithm of Gauss-Newton algorithm, which properly combines the Newton method and the steepest descent method. Determine the objective function with the long autoregressive method to estimate the initial value. Then, the parameters of the ARMA model are optimized to speed up the convergence and improve the estimation accuracy.

For ARMA (p,q) model, observation time series can be fitted in mathematical model

$$x_t = f\left(X_t, \beta\right) + \varepsilon_t \quad (5)$$

Where $X_t=[x_{t-1},x_{t-2},\cdots,x_{t-k}]^T$, X_t is the k-dimensional vector of different observations, $\beta=[\varphi_1\ \varphi_2\cdots\varphi_p\ \theta_1\ \theta_2\ \cdots\theta_p]^T$, β is r ($r=p+q$) dimension vector by the estimate parameters, ε_t is the model residual, f is the function relation between X_t and parameter β.

Then the formulation written by vector form

$$x_t = \varphi_1 x_{t-1} + \mathrm{L} + \varphi_p x_{t-p} + \varepsilon_t - \theta_1 \varepsilon_{t-1} - \mathrm{L} - \theta_q \varepsilon_{t-q} \quad (6)$$

Where, $X_t^T=[x_{t-1},x_{t-2},\cdots,x_{t-p},\varepsilon_{t-1},\varepsilon_{t-2},\cdots,\varepsilon_{t-q}]^T$, $\beta=[\varphi_1\ \varphi_2\cdots\varphi_p\ \theta_1\ \theta_2\cdots\theta_p]^T$.

Since ε_{t-1}, ε_{t-2}, $\cdots$, ε_{t-q} are not known but can be obtained by x_{t-1}, x_{t-2}, $\cdots$, x_{t-q}, so X_t^T is a nonlinear term, which leads to the occurrence of the nonlinear term of the parameter β to be estimated. The objective function of the ARMA model is defined as the sum of squares of the residuals of the model

$$S\left(\beta\right) = \sum\nolimits_t \varepsilon_t^2 = \sum\nolimits_t \left[x_t - X_t^T \beta\right]^2 \quad (7)$$

From the viewpoint of model optimization theory, the optimal estimation of β is the problem of finding the minimum value of S(β). The common solution is the least squares method, but it is easy to become a singular matrix in the iterative process. And owing to its higher requirement for the initial value, when the original value far away from the minimum value, it will be difficult to convergence. Therefore, this paper improves the traditional least squares method and applies the Levenberg-Marquarat algorithm to avoid the drawbacks.

3 ILLUSTRATIVE EXAMPLE

For illustrating the above model, an arch-bridge of concrete filled steel tubular bridge, the Yitong River Bridge shown in the Figure 1 which length is 740m, located in the Changchun city, Jilin Province, China, is taken as the test-bed in our paper which is a mid-type concrete-filled steel tubular arch bridge.



Figure 1 The real map of Yitong River bridge.

3.1 *Establish the model based on the vertical acceleration data*

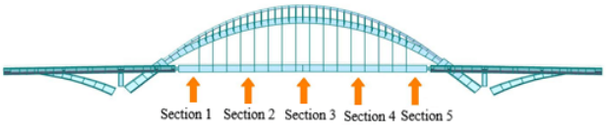
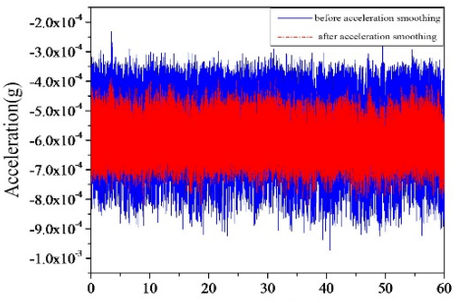
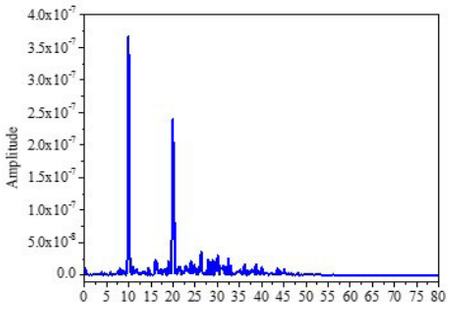


Figure 2 The location of the acceleration sensor

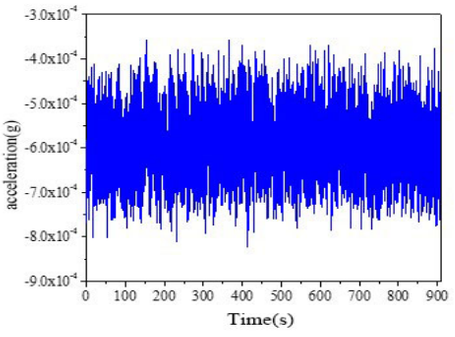
The data acquisition used in this paper is collected by an acceleration sensor mounted across the main beam, the location of the acceleration sensor is shown in Figure 2. Selecting the acceleration sensor channel_07 collection of the main beam vertical acceleration information $\{y_t\}$, sampling step is 0.001s, because the amount of data is too large, only draw the first 60s of data time series. Smoothing the data $\{y_t\}$, removing the short-term fluctuations effects and making the time series curve smooth. Then do the spectral analysis for the smooth data and identify the main frequency. It can find that the signal has two frequency components. The highest is 9.961Hz, the second is 19.922Hz. According the sampling theorem, the resample frequency set as 20Hz. Then do the stationary test, using MATLAB adfTest command to test $\{x_t\}$, find it's a stationary series, considering the first difference and a zero-mean trend removal, obtain the time series difference $\{Dx_t\}$. Plot their autocorrelation and partial autocorrelation coefficient curves. The results are shown in the Figure 3.



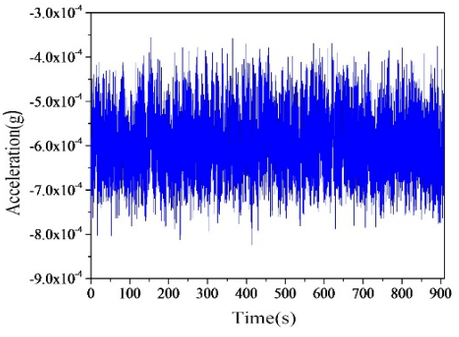
(a) Acceleration smoothing



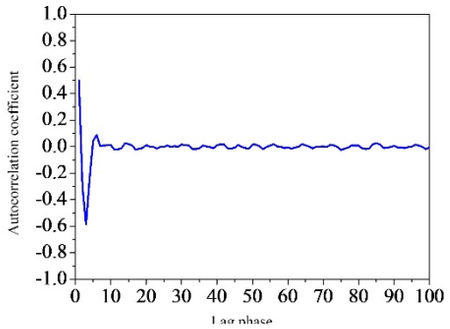
(b) Signal spectrum



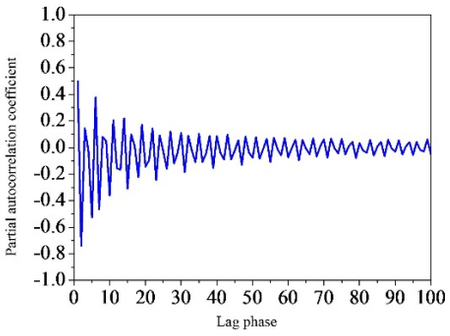
(c) Resampling signal time series



(d) Differential processing data time



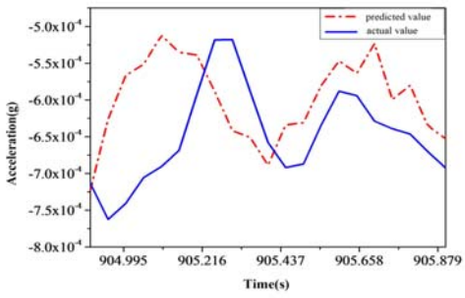
(e) Sample autocorrelation coefficient



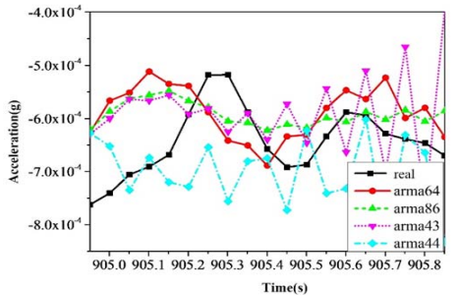
(f) Sample partial autocorrelation coefficient

Figure 3 The results of data selection

Binding order selection criteria and correlation coefficient map, we can determ ine the m odel order and then estim ate the m odel parameters using the former method. Here we show the different m odel order predicting results in the following Figure 4. We see that ARMA(6,4) can simulate the original series trend, the relative error is also properly small.



(b) Prediction comparison

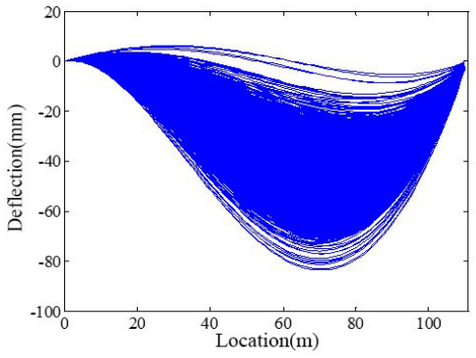


(a) Comparison of different primary order prediction results

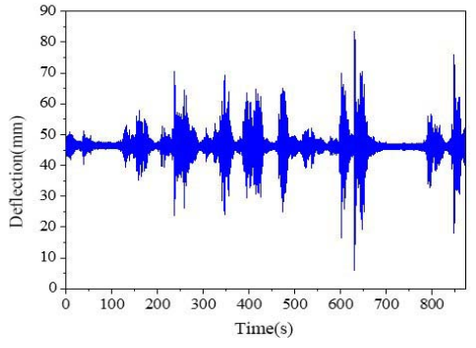
Figure 4 The different model predicting results

3.2 *Serviceability reliability analysis of main girder based on deflection data*

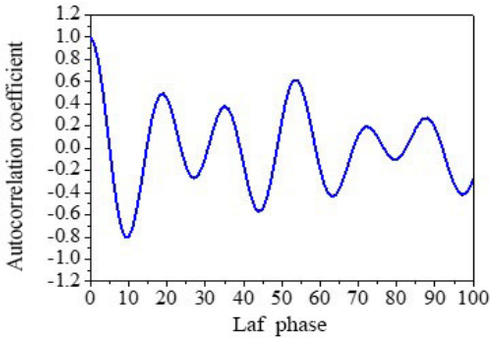
The deflection of the main beam of the Yitong River Bridge is m onitored by the inclinom eter, 5 inclinometers sequentially laid in span length direction of the main beam. Utilizing the m onitoring data, we can obtain the deflection equation. Then pick up the maximum curve at every tim e point follow the code requirements and establish the tim e series sam ple. Similarly as the above step, we can determ ine the model order and estim ate parameters, using the ARMA model to predict, the result are shown as follows Figure 5.



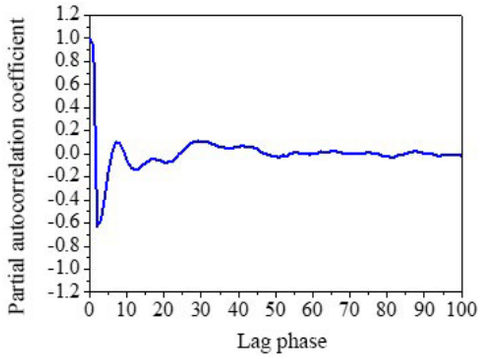
(a) Main beam deflection



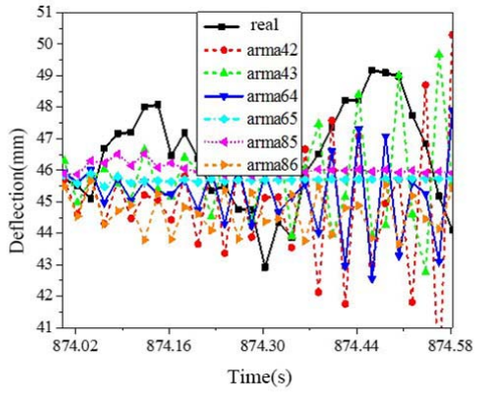
(b) Maximum deflection time series



(c) Sample autocorrelation coefficient



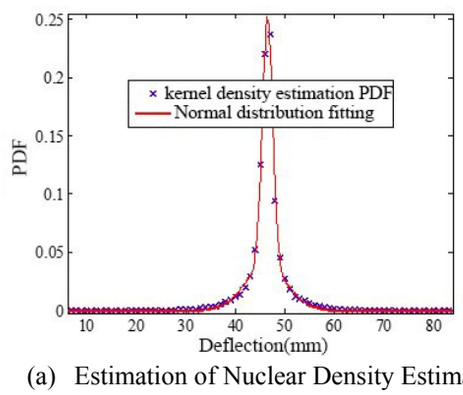
(d) Sample partial autocorrelation coefficient



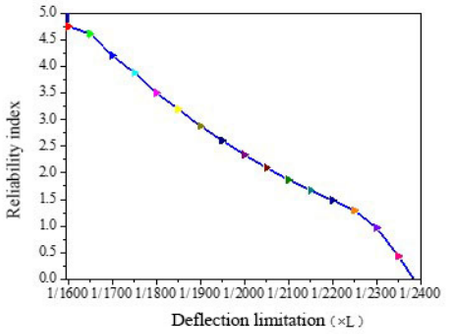
(e) Comparison of predictive effects of primary model

Figure 5 The results of data selection

As for the serviceability reliability analysis of main beam deflection, the kernel density estim ation method is used to estimate the PDF of the deflection data. The m aximum deflection series of the m ain beam is fitted by the dist ribution fitting toolbox in the MATLAB platform and di stribution form is selected as Non-parametric, the kernel selects norm al, and the window width autom atically selects the default optimal window width. Then choosing the MCMC method to sample the deflection data of the main beam, and calculating the serviceability reliability index of the main girder. The results are as follows Figure 6.



(a) Estimation of Nuclear Density Estimation



(b) The reliability index varies with deflection limitation

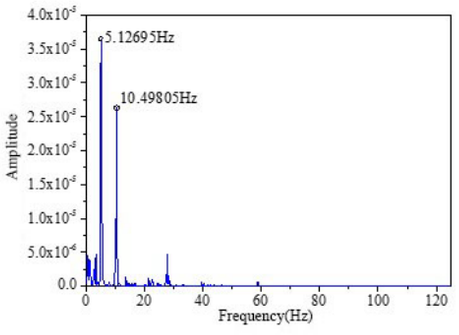
Figure 6 The results of serviceability reliability analysis

It can be seen f rom Figure 6 that the reliability indicator decreases with the increase of the deflection limit level. For the bridge, when the def lection limit is taken as L / 2350, the index is approxim ately 0. Define the lim it between the L / 1800 ~ L / 2300, the indicators corresponding to 3.5077 ~ 0.9688.

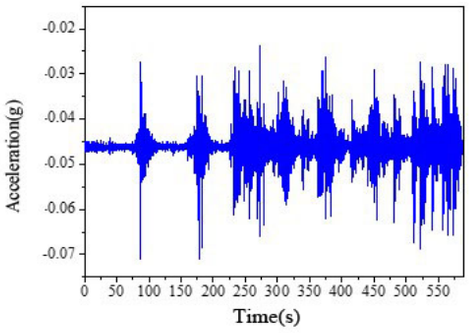
3.3 *Reliability analysis of suspender based on cable force monitoring data*

Using the frequency m ethod to test the cable force, through the ICP sensor installed on the boom (as close as possible to the m iddle of the boom) test structure of the natural vibration frequency, the IMC module connect to the com puter, using artificial or environmental incentives to collect signals, then analysis the first few order vibration frequency and calculate the cable force.

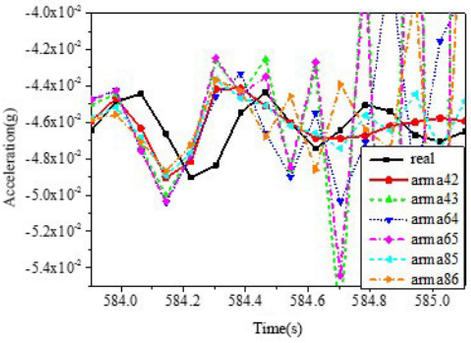
There we choose the m id-span suspenders of the bridge as an example. Like the former analysis steps, smoothing the original data and analyzing the spectral. After resample, the ARMA model is established to process and analyze the cable forces. The relative results are shown in the following Figure 7.



(a) The spectrum of the original data



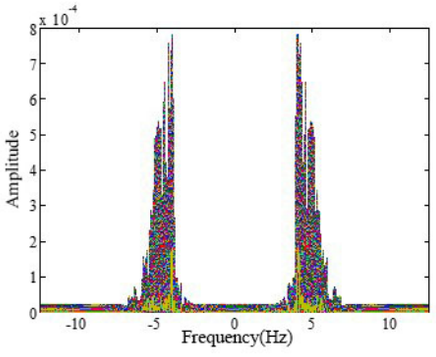
(b) Resample time series



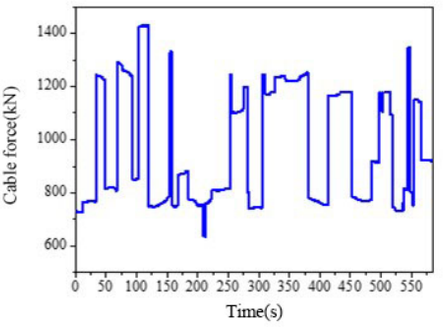
(c)Comparison of prediction effect of each model

Figure 7 The results of data selection

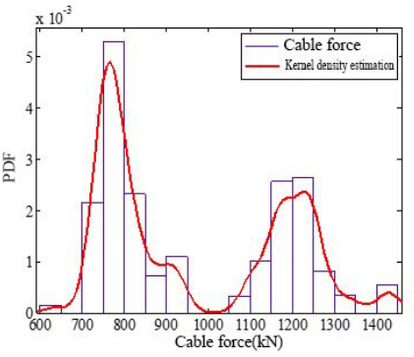
For obtaining the reliability, identif ying the instantaneous frequency and calculating the boom cable force, the results shown in the Figure 8. Then using the kernel density estim ation method to estimate the probability density f unction of the suspender force data, and the reliability indices of the suspender are calculated using the MCMC sim ulation method like the former step.



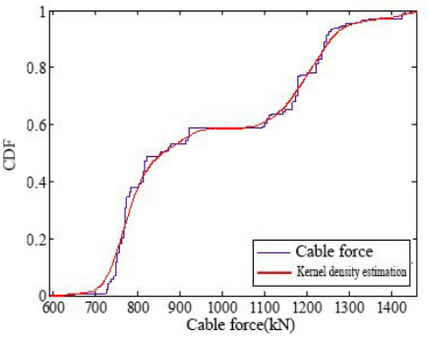
(a) Signal instantaneous spectrum



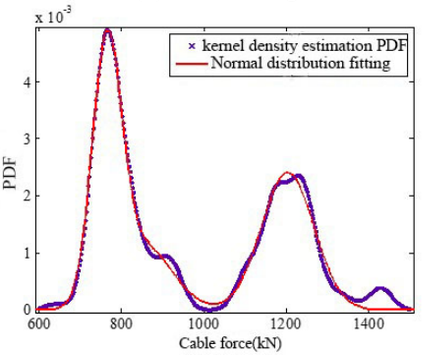
(b) The suspender axial force



(c) PDF Fitting



(d) CDF Fitting

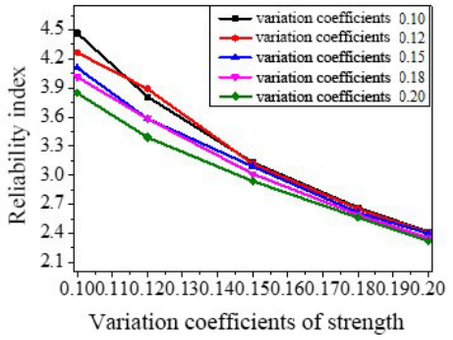


(e) Cable force distribution using kernel density estimation

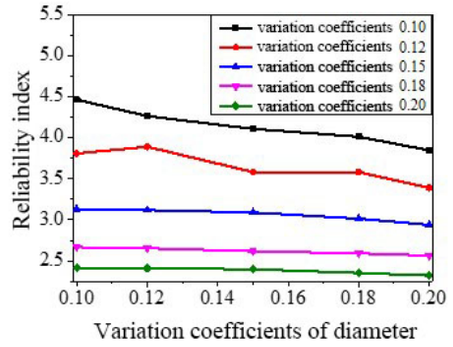
Figure 8 The results of reliability analysis

In fact, the coefficient of variation of the strength and diameter of the strand is very sm all, usually slightly less than 0.1, but due to computer limitation, when the coefficient of variation is given sm all, the

MCMC simulation method will sample too many times. It is difficult to extract the failure state. Therefore, this paper assumes that the both coefficient of variations are 0.1, the MCMC sampling is carried out for 1 million times, and calculate its reliability. We choose the variation coefficients slightly larger than 0.1 to investigate the effects of the variations of strength and diameter on the reliability assessment. The results are shown in the Figure 9.



(a) Effects of the variations of strength



(b) Effects of the variations of diameter

Figure 9 The results of effects analysis

4 CONCLUSION

The details of establishing the ARMA model have been presented, and an improved parameter estimation algorithm is introduced. Compared with the traditional least squares method, the improved method's convergence speed is faster, and the significance of the parameter estimation is also improved.

Based on the vertical acceleration data of the main beam of Yitong River Bridge, the ARMA model is established. It is proposed to combine the order criterion and the time series correlation analysis to determine the order of several possible orders, modeling and comparison, and select the better ARMA model. The results show that the short-term prediction accuracy and trend of ARMA model are relatively high. Time series analysis method is feasible in the field of bridge health monitoring data processing.

Based on the deflection monitoring data, the kernel density estimation method is used to estimate the probability density function of the deflection data of the unconventional distribution, and the MCMC method is used to calculate the reliability indices corresponding to the serviceability limit states. The results show that the reliability indices of the serviceability limit states of the main beam decreases with the increase of the deflection limit.

Based on the data of the boom cable axial force, the ARMA model is established. The probability density function of the cable force is estimated by the kernel density estimation method. The MCMC method is used to calculate the reliability indices of the suspender. Then the effect of the variations of strength and diameter on the reliability assessment is investigated. The results show that the reliability of the Yitong River bridge is good, and the effects of variability of the strength is bigger than that of the cable diameter.

5 REFERENCES

Box, G.E.P. & Jenkins, G.M. 1976. Time Series Analysis: Forecasting and Control. Holden-Day Inc.

Burg, J.P. 1967. Maximum Eutroy Spactral Analysis. Proc. 37th Meeting Society of Exploration Geophysists.

Carden, E.P. & Brownjohn, J.M.W. 2008. ARMA modelled time-series classification for structural health monitoring of civil infrastructure. Mechanical Systems and Signal Processing 22: 295-314.

Farrar, C.R. & Cone, K.M. 1995. Vibration testing of the I-40 bridge before and after the introduction of damage. Proceeding of the 13th International Modal Analysis Conference: 203-209.

Hunag, N.E. & Shen, Z. et al. 1998. The Empirical Mode Decomposition and Hilbert Spectrum for Nonlinear and Non-Stationary Times Series Analysis. Proceedings of the Royal Sociey of London 454: 903-995.

Johnson, E.A. & Lam, H.F. et al. 2004. Phase I IASC -ASCE Structural Health Monitoring Benchmark Problem using Simulated Data. ASCE Journal of Engineering Mechanics 130(1): 3-15.

Kim, S. & Pakzad, S. et al. 2007. Health Monitoring of Civil Infrastructures Using Wireless Sensor Networks. IEEE Information Processing In Sensor Networks: 254-263.

Koh, H.M. & Lee, H.S. et al. Monitoring of Bridges in Korea. Encyclopedia of Structural Health Motoring, John Wiley&Sons, Ltd: 2008-2906.

Koh, H.M. & Choo, J.F. 2006. Applications and Researches in Bridge Health Monitoring Systems and Intelligent Infrastructures in Korea. Structural Health Monitoring and Infrastructure. Ou,Li & duan, Taylor & Francis Group, London:151-160.

Ni, Y.Q. & Jinag, S.F. et al. 2001. Applieation of Adaptive Probabilistic Neual Network to Damage Detection of Tsing Ma Suspension Bridge, Pocreedings of SPIE, Vol. 4337: 347-356.

Parzen, E. 1968. Statistical spectral analysis (single channel case) in 1968. Stanford Univ., Stanford, CA, Tech, Rep.

Pisarenko, V.F. 1973. Retrieval of Harmonics from a Covariance Function. Geophys J.Roy.Astron.Soc.

Pandit, S.M. & Wu, S.M. 1978. Dynamic Data System – A New Modeling Technique. ASME Trans, Series B, 99.

Qin, Q & Zhang, W. 1998. Damage detection of suspension bridges. Proc. of IMAC XVI, Santa Barbara, USA, Feb.2-5:945-951.

Roberts, G.W. & Brown, C. et al. 2005. Deflection Monitoring of the Forth Road Bridge by GPS. ION GNSS 18th International Technical Meeting of the Satellite Division, long beach, CA: 1016-1021.

Van, den Bos, A. 1971. Alternative interpretation of maximum entropy spectral analysis (Corresp.). Information Theory IEEE Transactions on 17.4: 493-494.

Walker, G. 1931. On periodicity in series of related terms. Proceedings of the Royal Society of London, 131(818): 518-532.

Yule, G.U. 1927. On A Method of Investigating Periodicities in Disturbed Series with Special Reference to Wolfer's Sunspot Numbers. Philosph. Trans. Roy. Soc. Ser. A. 226.

Maintenance, Safety, Risk, Management and Life-Cycle Performance of Bridges – Powers, Frangopol, Al-Mahaidi & Caprani (Eds)
© 2018 Taylor & Francis Group, London, ISBN 978-1-138-73045-8

Assessment of Terrorism Risk Mitigation Measures for Iconic Bridges

Sebastian Thöns
Technical University of Denmark, Lyngby, Denmark
Mark G. Stewart
The University of Newcastle, New South Wales, Australia

ABSTRACT: This paper describes the assessment of the cost efficiency of risk mitigation measures for terrorist attacks with Improvised Explosive Devices (IEDs) for an iconic bridge structure. The assessment is performed with a decision theoretical framework building upon very recent advances in the framework of the COST Action TU1402 on Quantifying the Value of Structural Heath Monitoring. The decision scenario is formulated for a decision maker constituting an authority responsible for the societal safety of the infrastructure and consequently the direct risks for the infrastructure owner and the indirect risk due to fatalities and importance of the infrastructure are considered. The mitigation strategies are classified within the decision theoretical context as protection measures, which may be implemented in the design phase of a bridge, and as control, i.e. information acquirement, strategies. The identification of efficient measures for risk mitigation is based on (1) the risk and expected cost based optimization of actions and information and their combination before implementation, (2) on quantifying and assuring significance in risk reduction and (3) on the quantification of the uncertainties associated to the implementation. These criteria ensure a transparent decision and the performance of the measures before strategy implementation. It is found that the decision is relying on the identification of the threat level and that control strategies may be in favor as their costs are adjustable. However, for very high threat levels, bridge protection strategies or protection strategies in combination with control strategies may be more cost efficient.

1 INTRODUCTION

The study of protective measures and their efficiency for terrorist threats constitutes an important topic of research and is challenged by the seemingly permanent terrorist threats and by risk-averse regulative measures e.g. in US (e.g. Stewart and Mueller (2014), Ellingwood (2006), Stewart (2017), Xiao et al. (2017), Mueller and Stewart (2016) and SeRoN Consortium (2012a)). Many aspects like the explosive loading and structural performance modelling (e.g. Xiao et al. (2017), Bedon et al. (2018), Mouritz and Rajapakse (2017) and Netherton and Stewart (2010)), the improvised explosive device performance (e.g. Grant and Stewart (2017)), the design for explosive loads (Stewart (2018)) are extensively covered. However, (1) the combined assessment of the performance of information acquirement strategies with risk mitigation measures and (2) the explicit formulation of the optimization of the risk mitigation strategies in an explicit decision theoretical framework has hardly been performed.

This study aims thus to explicate efficient information acquirement and protective measures for terrorism risk reduction in a decision theoretical framework by utilizing the Bayesian prior and pre-posterior decision theory to assess and optimize the counter-terrorism strategy effectiveness before strategy implementation.

The decision theoretical approach is formulated in Section 2 distinguishing counter terrorism protection measures, which may be implemented in the design phase of a bridge, and control, i.e. information acquirement via surveillance, strategies and accordingly prior and pre-posterior decision analyses. The objective function for the calculation and optimization of the risk and the expected benefits and costs in dependency of the decision variables strategies and information and action parameters of strategies is formulated. Section 3 contains the description of the decision scenarios in the context of Improvised Explosive Device (IED) attacks to large iconic bridges and the development and discussion of the probabilistic information, information precision, action and system states and consequence models for the individual risk mitigation strategies. The results for the protection strategy and control optimization are

shown in Section 4 and the optimal decision variables are explicated and explained. The paper concludes with a discussion of the boundaries of the analysis and insights gained beyond its specifics in Section 5 and with a summary and the conclusions in Section 6.

2 APPROACH

The approach of assessing information and protection measures for structures under terrorism attacks takes basis in the framework for Structural Integrity and Risk Management as developed in Thöns (In Press) and Faber et al. (2017). Figure 1 shows an adapted decision tree distinguishing a do-nothing (i.e. business as usual) branch and risk mitigation strategies with and without additional information acquirements. The branches are classified into choice nodes for decision variables and chance nodes for probabilistic models associated to the choice nodes.

The decisions are based on the maximisation of the benefits, i.e. the minimisation of the expected cost and risk in dependency of the choices, i.e. decision variables. The expected benefit for the strategies without and with additional information: $B_{1,i}\left(a_{i,l}^{\ *}\right)$ and $B_{2,i}\left(i_{i,j}^{*}, a_{i,l}^{\ *}\right)$ respectively, are defined with the strategy-optimal actions $a_{i,l}^{\ *}$ and the optimal information acquirement strategy $i_{i,j}^{*}$. The expected benefit in the do-nothing-branch is denoted with B_0 and its system state $X_m \in \mathbf{X}$.

The expected benefits with no consideration of additional information $B_{1,i}\left(a_{i,l}^{\ *}\right)$ represent a prior decision analysis as they depend solely on the choice of actions $a_{i,l} \in \mathbf{a}_i$ and the – eventually action dependent - probabilistic system state models $X_m \in \mathbf{X}$:

$$B_{1,i}\left(a_{i,l}^{\ *}\right) = \underset{a_{i,l} \in \mathbf{a}_i}{max}\left(E_{X_m}\left[b_1\left(a_{i,l}, X_m\right)\right]\right). \quad (1)$$

The expected benefit with consideration of additional information $B_{2,i}\left(i_i^{*}, a_{i,l}^{\ *}\right)$ is dependent on the vector of information acquirement strategies $i_{i,j} \in \mathbf{i}_i$, their probabilistic outcome models $Z_{i,k} \in \mathbf{Z}_i$ and the strategy dependent set of actions and the system states. In the extensive form, the expectation over the posterior system states is calculated by Bayesian updating (operator E''_{X_m}) and the dependency on the system states is then marginalized with the expectation in regard to the probabilistic information outcomes with the operator $E_{Z_{i,k}}$:

$$B_1\left(i_{i,j}^{*}, a_{i,l}^{\ *}\right) = \underset{i_{i,j} \in \mathbf{i}_i}{max} E_{Z_{i,k}}\left[\underset{a_{i,l} \in \mathbf{a}_i}{max} E''_{X_l}\left[b_{2,i}\left(i_{i,j}, Z_{i,k}, a_{i,l}, X_m\right)\right]\right]. \quad (2)$$

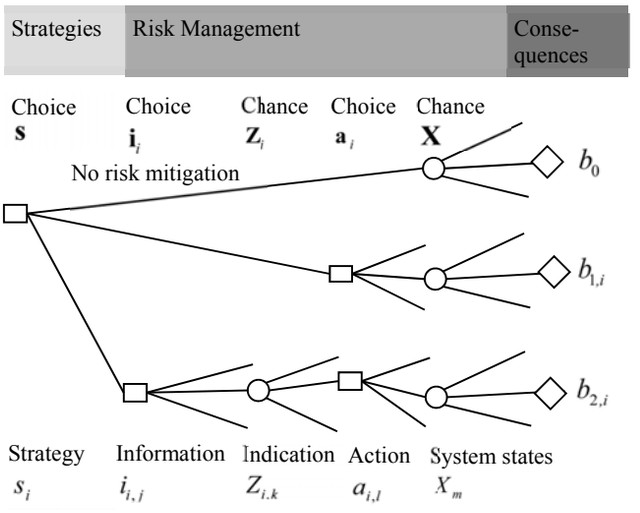


Figure 1: Decision tree for risk mitigation strategies

The value of the strategies may be expressed as the gain in expected benefits due to the identification of the optimal action strategy or the optimal information acquirement and action strategy:

$$V_{s_i} = B_{1,i}\left(a_{i,l}^{\ *}\right) - B_0 \ \text{ or } \ V_{s_i} = B_{2,i}\left(i_{i,j}^{*}, a_{i,l}^{\ *}\right) - B_0 . \quad (3)$$

The measure of significance of these information acquirement and/or action strategies is defined with relating the expected benefit gain to the expected benefit of the no mitigation base scenario:

$$\bar{V}_{s_i} = \frac{B_{1,i} - B_0}{|B_0|} \ \text{ or } \ \bar{V}_{s_i} = \frac{B_{2,i} - B_0}{|B_0|} . \quad (4)$$

3 DECISION SCENARIOS

In the following an iconic bridge with a value of €2.0 Billon or annual cost of €81 Million for a 100 year design life and an interest rate of 4% is considered. The decision maker is a public authority responsible for the safety of a large scale and iconic bridge. The objective of the decision maker is to minimize total risks for society and the bridge users and thus to implement mitigation strategies, which minimize the total risks and expected costs on an annual basis.

Two risk mitigation strategies are distinguished, namely, the implementation of protective measures in bridge design (strategy protect: s_1) and the implementation of a surveillance system in combination with bridge temporary closure during times of high threats (strategy control: s_2) taking basis in Stewart and Mueller (2014) and SeRoN Consortium (2012b).

3.1 *System state model and consequences*

The system states safe and bridge collapse are analyzed. The probability of a collapse is calculated with the probability of a threat $P(T)$, the conditional probabilities of a hazard $P(H|T)$ and collapse of the bridge $P(C|H)$, i.e.:

$$P(C) = P(C|H) \cdot P(H|T) \cdot P(T) \quad (5)$$

The probability of threat can be inferred by looking back to past threats and hazards. However, current threat information should also be accounted for and the estimation of the threat probabilities should be based upon information by police and security services. Such information are usually not public nor accessible by scientists. It should further be considered that large and iconic bridges may attract attackers more than typical highway bridges and it may also attract skilled attackers so that the likelihood of an attack increases (Stewart and Mueller (2014)). Thus, e.g. in US the San Francisco's Golden Gate Bridge or New York's Brooklyn Bridge might be a more tempting target for terrorists as evidenced by the 2002 poorly conceived (and quickly abandoned) plot to sever the stay cables of the Brooklyn Bridge with blowtorches [39].

The quantification of the threat probability in the U.S. based on the publicly known plots would result in 6.7E-6 per bridge per year. The basis are the Brooklyn bridge plot as the only one in 15 years against a large bridge in the U.S. and 1000 large/iconic bridges in the U.S. (Blue Ribbon Panel on Bridge and Tunnel Security (2003)). The 2002 plot to destroy the Brooklyn Bridge was more fanciful than a serious threat. Mueller (2018) summarizes the threat as "in 2002, Iman Faris traveled to New York City under orders from Khalid Sheikh Mohammed to survey possible terror targets within the United States. After basic internet research Faris decided on the Brooklyn Bridge as a potential target and believed that 'gas torches' could be used to bring the bridge down. However after conducting physical reconnaissance of the bridge (which consisted of driving over it once), Faris concluded that an attack was unlikely to succeed because of the bridge's structural design and because of the New York Police Department patrols there, and he never sought to acquire the equipment necessary for such an attack." There may be other threats that we are unaware of, but the threat level is likely to be less than one threat per year. No plots are publically known to the authors in Europe.

The conditional probability of a hazard $P(H|T)$ may be assessed by considering the construction, placement and successful donation of an explosive device. While the technical reliability of an IED detonation is high (Grant and Stewart (2012)), human errors play a significant role and reduce the probability of a successful attack. The past information for Western countries has been studied by Grant and Stewart (2017) for the time period of 1970 to 2013 concluding with success rate of up to 22% and a total average of 8%. Considering that an iconic bridge may be attacked by skilled terrorists, a triangular distribution with a minimum of 0%, a mode of 15% and a maximum of 25% is utilized, see also Stewart (2017).

The probability of a bridge collapse $P(C|H)$ depends on the scenario, i.e. the energy release of the IED charge, its location and the structural system and its robustness. The probability of a bridge collapse is assessed rather high to $P(C|H) = 90\%$ due to (1) skilled terrorist are assumed having being able to design a collapse scenario and (2) iconic bridges may have a highly utilized structural system with a low redundancy. Studies of progressive collapse of e.g. cabled stayed bridges (Das et al. (2016) and Mozos and Aparicio (2010)) point towards a high collapse probability for the assessed scenarios. Further, the need for more robust bridges is acknowledged and approaches can e.g. be found in Lonetti and Pascuzzo (2014).

The consequences of a bridge collapse encompass the property damage to the bridge structure and the vehicles on the bridge as the direct consequences and the costs from fatalities, the bridge reconstruction costs and the importance of the bridge in the road network. Based on EU project Security of Road Transport Networks (SeRoN: SeRoN Consortium (2012b) and SeRoN Consortium (2012c)), the total consequences are calculated to 7 times the bridge value. A Uniform distribution between 5 and 10 is herein used accounting for that the consequences may be significantly higher for iconic bridges and are uncertain.

3.2 *Prior decision analysis: Protective measures in bridge design*

The implementation of protective measures for the design of a bridge can be analyzed with a prior decision analysis and with probabilistic models of the system states and the mitigation actions in conjunction with the consequences and costs.

The protective measures are modelled with the annual costs and the risk reduction performance. Following Stewart and Mueller (2014) and SeRoN Consortium (2012b), a 5.0% additional investment in a protective measure (C_{Prot}) may lead to a risk reduction (ΔR) of 95% and a 3.3% investment may reduce the risk by 75%. These costs are annualized over a period of 100 years and the risk reduction-cost-relationship in Figure 2 is established.

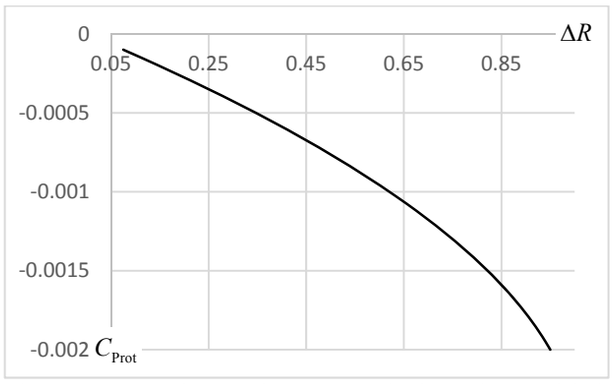


Figure 2: Costs of protective measure in dependency of their risk reduction performance.

The relationship implies that very high risk reduction measures may only be achieved with an over-proportional cost increase. Low to moderate risk reduction maybe achieved with an almost linear cost increase.

The probabilistic model for the protection measure strategy is summarized in Table 1.

Table 1: Probabilistic model for the prior decision analysis on the cost efficiency of protective measures (strategy: protect s_1)

Nodes, states		Consequences	Prob.
Protective actions	a_0	0	-
	$\mathbf{a}_{1,1}$	[-0.0001…0.002]	$\Delta R(\mathbf{a}_{1,1}) = [0.075…0.95]$
System states	X_0	0	$1-P(C)$
	X_1	U(-10.0,-5.0)	$P(C)$

U: Uniform distribution

3.3 *Pre-posterior decision analysis: Surveillance information and bridge closure*

A control strategy encompassing surveillance information in combination with bridge closure and detection actions can be modelled with a pre-posterior decision analysis. For example, if an imminent threat is detected the bridge may be temporally closed to allow for time to apprehend the terrorists or defuse an IED. The surveillance information are described with their detection performance, i.e. the indication and no-indication probabilities of threats in conjunction with the costs of the surveillance system investment and operation. The surveillance information model utilized here covers various strategies from enhanced incident detection (low costs as it may be integrated in the existing systems) to high cost systems with a high detection probability. Consequently, the indication probability given a threat and the no-indication probability given no threat, $P(\mathbf{Z}_{2,1}|T)$ and $P(\mathbf{Z}_{2,0}|\overline{T})$, respectively, are varied between 0.7 and 0.99 (Table 2). The posterior probabilities of bridge collapse $P''(C)$ are calculated with the updated threat probability:

$$P(T|\mathbf{Z}) = \frac{P(\mathbf{Z}|T)\cdot P(T)}{P(\mathbf{Z}|T)\cdot P(T) + P(\mathbf{Z}|\overline{T})\cdot P(\overline{T})} \quad (6)$$

$$\text{with } \mathbf{Z} = [\mathbf{Z}_{2,0}, \mathbf{Z}_{2,1}] \quad (7)$$

The costs of the surveillance systems C_{Surv} increase over-proportional with a higher rate for precise systems as shown in Figure 3.

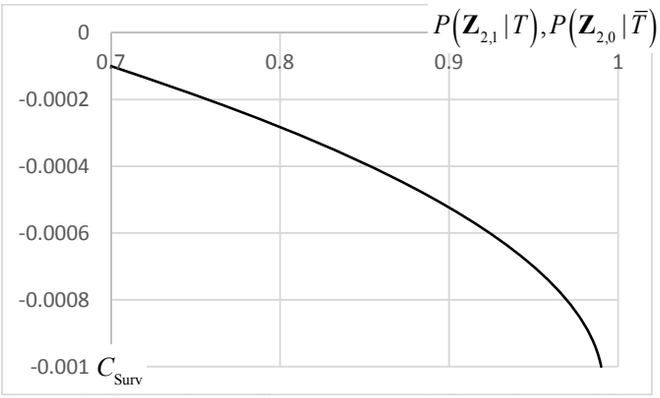


Figure 3: Costs of surveillance systems in dependency of their reliability.

The cost of the bridge closing are calculated with the bridge importance in the traffic network and the associated costs based on SeRoN Consortium (2012b) and SeRoN Consortium (2012c). A bridge closure of 2 days is assumed for attack prevention and eventual explosive charge detection, location and deactivation activities leading to costs of 2.72E-3 per year for the considered bridge. The bridge closure leads to a reduction of the consequences for bridge collapse by reduction of the property damage including a lower number of vehicles on the bridge and consequently a reduction of the costs due to fatalities, bridge reconstruction and traffic diversion. A Uniform distribution between a maximum of 5 and 1 is assumed (Table 2).

Table 2: Probabilistic model for the pre-posterior decision analysis on the cost efficiency of surveillance information (strategy: control s_2)

States	Consequences	Prob.	
i_2	[-1.0E-4… -1.0E-3]	-	
		X_0	X_1
$\mathbf{Z}_{2,0}$	-	[0.7…0.99]	[0.3…0.01]
$\mathbf{Z}_{2,1}$	-	[0.3…0.01]	[0.7…0.99]
$a_{2,0}$	0	-	
$a_{2,1}$	2.72E-3	-	
X_0	0	$1-P''(C)$	
X_1	U(-10.0,-5.0)	$P''(C)$	
$X_1 \mid a_{2,1}$	U(-5.0,-1.0)	$P''(C)$	

U: Uniform distribution

3.4 *Summary of strategies*

Figure 4 contains the detailed decision tree for the analysis of the protection strategy with a prior decision analysis and the control strategy with a pre-posterior decision analysis. It should be noted that the branch $\mathbf{Z}_{2,0} : a_{2,1}$, i.e. bridge closure in case of a no threat indication, is excluded.

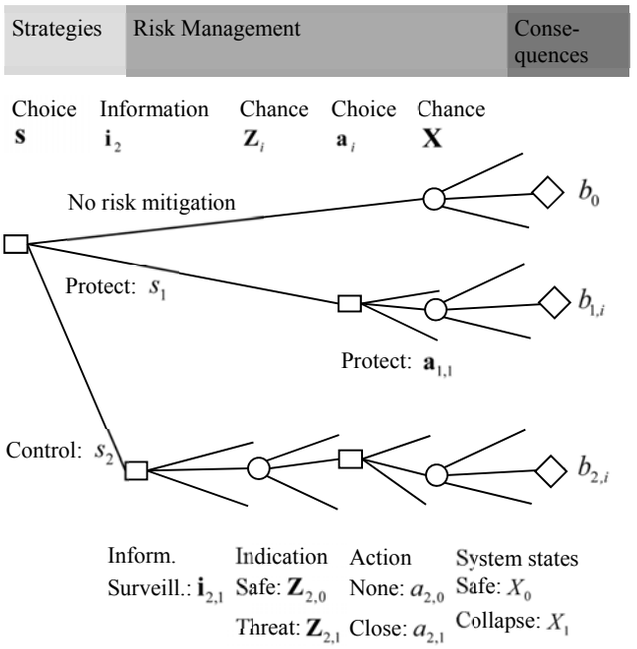


Figure 4: Decision tree for analyzed strategies

4 RESULTS

The established decision scenario is analyzed individually in detail for the protection strategy and the control strategy and then jointly by the explanation of the results and the identification of the optimal protection and/or control strategy on the basis of the minimum risk and expected costs, the strategy significance and success probability. The threat probabilities are chosen so that the protection and control measures just become the optimal decision.

4.1 *Analysis of protective measures*

The analysis and optimization of the protective measures in the design phase is performed for three threat levels. Figure 5 shows the minimum risk and expected costs dependent on the protection risk reduction. A change of the optimal action is indicated when the line becomes horizontal, e.g. at $\Delta R = 0.52$ for an annual threat probability of 1.7E-3 where the optimal action changes from protection to do-nothing. For increasing threat levels, the change of the optimal action shifts towards protection measures with a higher risk reduction and the curves become more peaked.

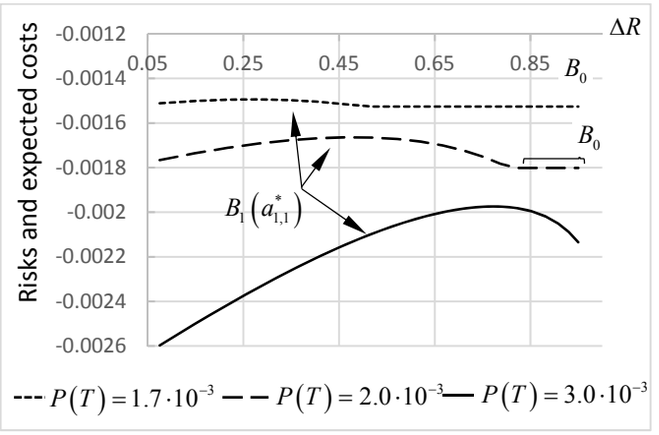


Figure 5: Minimum risks and expected costs in dependency of the protection risk reduction for different threat levels

The probability that the protection measure is cost efficient is calculated to account for the uncertainties in the models as the optimization and decision is based on the expectation. The probability decreases with an increasing risk reduction and increasing costs of the protective measure as well as with decreasing threat probabilities (Figure 6). It is independent of the minimum risk and expected cost in Figure 5.

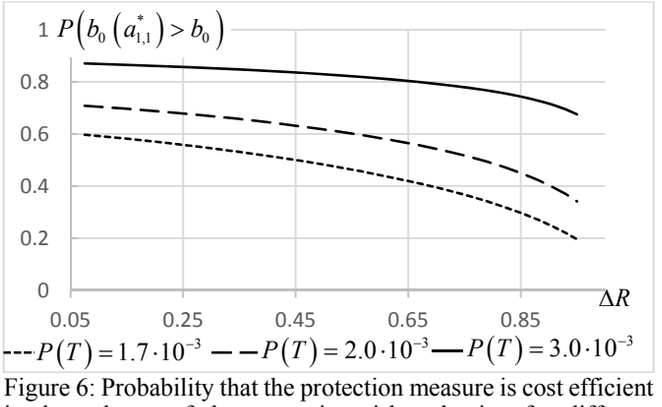


Figure 6: Probability that the protection measure is cost efficient in dependency of the protection risk reduction for different threat levels

The optimal protection measures are identified as the minima in Figure 5 and listed in Table 3. Only for a high threat level, a high level of the protection is optimal despite the over-proportional larger costs. It is noted that the cost efficiency probability of the protection is significantly higher in comparison to lower threat probabilities.

Table 3: Optimal protection strategy for different threat levels

$P(T)$	$\Delta R(a^*_{1,1})$	$C_{\text{Prot}}(a^*_{1,1})$	$P(b_0(a^*_{1,1}) > b_0)$
$1.7 \cdot 10^{-3}$	0.28	0.149%	0.50
$2.0 \cdot 10^{-3}$	0.46	0.166%	0.55
$3.0 \cdot 10^{-3}$	0.79	0.197%	0.77

4.2 *Analysis of surveillance information and bridge closure actions*

The analysis and optimization of the control strategy is performed for an annual threat probability of $P(T)=1.7\cdot10^{-3}$ to $P(T)=3.0\cdot10^{-3}$. Figure 7 shows sharp change of inclination in the curves for the threat probabilities 1.7E-3 and 2.0E-3. Here, the optimal action for a threat indication changes from do-nothing to closure of the bridge. The minimum risks and expected costs are located at relatively high threat indication reliabilities and according costs (see also Figure 3).

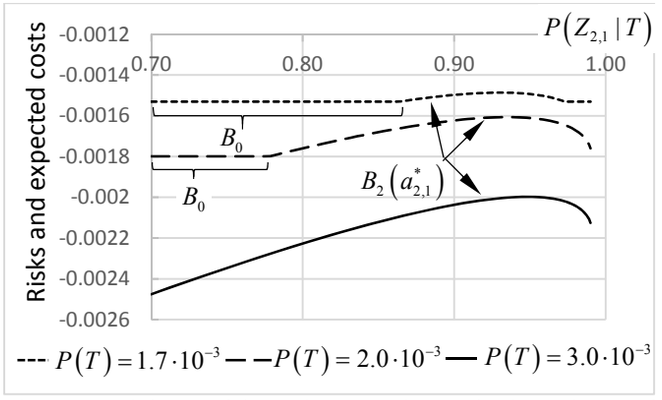


Figure 7: Minimum risks and expected costs in dependency of the surveillance performance for different threat levels

The probabilities that the surveillance and bridge closure strategy is cost efficient, increases with an increasing threat indication probability and corresponding surveillance strategy costs until the minimum risks and expected benefits are reached (Figure 8). The probabilities are highest for the highest threat probability.

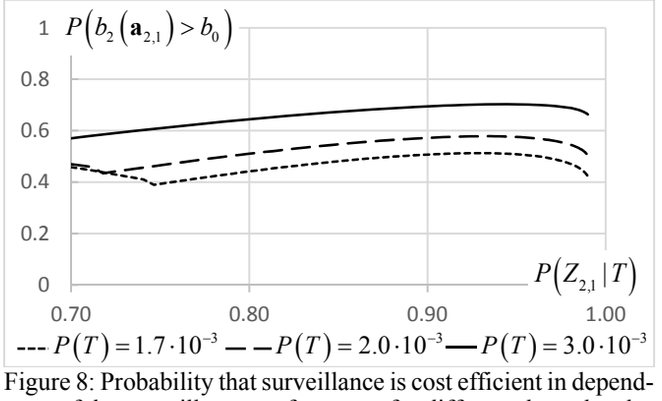


Figure 8: Probability that surveillance is cost efficient in dependency of the surveillance performance for different threat levels

The optimal surveillance strategies for the considered threat levels are very similar in indication reliabilities and associated costs (

Table 4). Only the probability of cost efficiency increases significantly for higher threat probabilities.

Table 4: Optimal surveillance strategy for different threat levels

$P(T)$	$P^*(Z_1\|T)$	C^*_{Surv}	$P(b_2(a^*_{2,1})>b_0)$
$1.7\cdot10^{-3}$	0.93	0.062%	0.51
$2.0\cdot10^{-3}$	0.94	0.064%	0.58
$3.0\cdot10^{-3}$	0.95	0.069%	0.70

Table 5 contains the identification of the optimal strategy for risk mitigation based on the minimum risk and expected costs together with the measures of significance as the relative value of the strategy, shown in Eqn. (4). Both risk mitigation strategies namely protection and control are risk and expected costs optimal for an annual threat probability of $1.7\cdot10^{-3}$. However, the measure of significance is very low, i.e. the implementation of a protection and control strategy reduces only insignificantly the risks and expected costs.

For a threat probability of $2.0\cdot10^{-3}$, the control strategy is more cost efficient with a significance of 10.7% risk and expected cost reduction in comparison to the do-nothing strategy. It is also noted that the probability of cost efficiency is slightly higher for the control strategy (see Table 3 and

Table 4).

A very significant risk and expected cost reduction of 26.0% and more can be achieved for an annual threat probability of $3.0\cdot10^{-3}$ for both strategies where the protection strategy leads to slightly lower risks and expected cost as well as a higher probability of cost efficiency.

Table 5: Expected benefits and measures of significance and optimal protection strategies (bold)

$P(T)$	Protect: s_1		Control: s_2	
	B_1	$\bar{V}_{s_1}$	B_2	$\bar{V}_{s_2}$
$1.7\cdot10^{-3}$	**$-1.49\cdot10^{-3}$**	**<1.00%**	**$-1.49\cdot10^{-3}$**	**<1.00%**
$2.0\cdot10^{-3}$	$-1.66\cdot10^{-3}$	7.60%	**$-1.61\cdot10^{-3}$**	**10.7%**
$3.0\cdot10^{-3}$	**$-1.97\cdot10^{-3}$**	**26.9%**	$-2.00\cdot10^{-3}$	26.0%

5 DISCUSSION

The efficiency of risk mitigation measures is largely dependent and the analysis is highly sensitive to the threat levels. Any decision should thus be based on knowledge of the threat levels. If the historical statistics, see Section 3.1, are considered leading to annual threat probabilities of 1.0E-5 or lower, no mitigation strategy is cost efficient.

Beyond the specifics of the decision analysis and taking into account the variation of the threat levels throughout the long service life of a bridge, it should be noted that the cost efficiency of surveillance can

be influenced by pausing operation for periods with low threat levels as this contributes largely to the annual costs. Hence, changing threats point to flexible and surveillance based systems. However, co-benefits for protective measures may be found e.g. in a higher earthquake resistance (Stewart (2017)).

A combination of protection and control strategies constitutes an attractive option for very high threat probabilities. However, for the analyzed threat probabilities, a combination will not be efficient, as the risk reduction by the protective measure will result in lower absolute values not being able to accommodate for the expected cost of the protection strategy.

6 SUMMARY AND CONCLUSIONS

This paper contains a cost efficiency assessment of risk mitigation measures for terrorist attacks with Improvised Explosive Devices (IEDs) for a large span and iconic bridge structure. The assessment is performed within a decision theoretical framework building upon very recent advances in the frame of the COST Action TU1402 on Quantifying the Value of Structural Heath Monitoring.

The decision scenario is formulated based on an authority responsible for the societal safety of the infrastructure and consequently the direct risks for the infrastructure owner and the indirect risk due to fatalities and importance of the infrastructure are considered. The risk mitigation strategies are classified within the decision theoretical context as protection measures, which may be implemented in the design phase of a structure, and as control, i.e. information acquirement, strategies. Whereas the protection measures can be analyzed with a prior decision analysis, the analysis of additional information requires a pre-posterior decision analysis and an appropriate modelling of the information before its acquirement.

The identification of efficient measures for risk mitigation is based on

1) The risk and expected cost based optimization of actions and information and their combination before implementation,
2) On quantifying and assuring significance in risk reduction and
3) On the quantification of the uncertainties associated to the strategy implementation.

All three criteria ensure a transparent decision and the performance of the measures at the decision point in time before implementation.

Specifically, it has been found in the analysis of protective measures:

- High performance and expensive protection measures are cost efficient for higher threat levels (larger than $3.0 \cdot 10^{-3}$). The probability of cost efficiency is higher than 0.77.
- For lower threat levels (between $2.0 \cdot 10^{-3}$ and $3.0 \cdot 10^{-3}$), low cost protective measures with a risk reduction of about 25% to 45% may be implemented.
- Below a threat level of $2.0 \cdot 10^{-3}$ protective measures should not be implemented as the probability of their efficiency is equal or lower than 50% and the risk and expected cost reduction is insignificant.

In contrast to the optimal protection strategies, the optimal control strategies are most efficient with relatively high costs and an associated high indication reliability.

- The optimal control strategies are relatively insensitive to the considered threat probabilities and may thus be identified very clearly. The optimal control strategies should have an indication reliability higher than 93% with annual costs equal to 0.062% (or higher for higher indication reliabilities) per year per bridge.
- For threat probabilities between $2.0 \cdot 10^{-3}$ and $3.0 \cdot 10^{-3}$, the control strategy has a slightly better performance than protective measures in terms of minimum risks, significance and success probability.
- Below a threat level of $2.0 \cdot 10^{-3}$ control strategies should not be implemented as the probability of their efficiency is equal or lower than 51% and the risk and expected cost reduction is insignificant.

Decision analyses in general and in conjunction with their complexity and computational demands should contain or provide interfaces (as with this paper) to (1) sophisticated models such as e.g. for the structural performance modelling for explosive loadings, (2) non-public (e.g. threat) information and (3) sophisticated information acquirement performance models. In return, these models and information should be available in the format, quality, and relevance required by the decision analysis to ensure transparent, consistent and sustained decisions. The interface design, the model development and availability are seen as the most challenging aspects for the further evolution of decision analyses and their implementation, however, with a clear and substantial potential to benefit society.

ACKNOWLEDGEMENTS

The COST Action TU1402 on Quantifying the Value of Structural Health Monitoring (www.cost-tu1402.eu) is gratefully acknowledged for the inspiring discussions, contributions and workshops across the scientific and engineering disciplines with researchers, industrial experts and representatives of infrastructure operators, owners and authorities.

The visiting fellowship provided by the Centre for Infrastructure Performance and Reliability at The

University of Newcastle for the first author is gratefully acknowledged.

7 REFERENCES

BEDON, C., ZHANG, X., SANTOS, F., HONFI, D., KOZŁOWSKI, M., ARRIGONI, M., FIGULI, L. & LANGE, D. (2018) Performance of structural glass facades under extreme loads – Design methods, existing research, current issues and trends. *Construction and Building Materials,* 163**,** 921-937.

BLUE RIBBON PANEL ON BRIDGE AND TUNNEL SECURITY (2003) Recommendations for Bridge and Tunnel Security, US Federal Highway Administration (FHWA).

DAS, R., PANDEY, A. D., SOUMYA, MAHESH, M. J., SAINI, P. & ANVESH, S. (2016) Progressive Collapse of a Cable Stayed Bridge. *Procedia Engineering,* 144**,** 132-139.

ELLINGWOOD, B. R. (2006) Mitigating Risk from Abnormal Loads and Progressive Collapse. *Journal of Performance of Constructed Facilities,* 20**,** 315-323.

FABER, M. H., QIN, J., MIRAGLIA, S. & THÖNS, S. (2017) On the Probabilistic Characterization of Robustness and Resilience. *Procedia Engineering,* 198**,** 1070-1083.

GRANT, M. & STEWART, M. G. (2012) A systems model for probabilistic risk assessment of improvised explosive device attacks. *International Journal of Intelligent Defence Support Systems,* 5**,** 75-93.

GRANT, M. J. & STEWART, M. G. (2017) Modelling improvised explosive device attacks in the West – Assessing the hazard. *Reliability Engineering & System Safety,* 165**,** 345-354.

LONETTI, P. & PASCUZZO, A. (2014) Vulnerability and failure analysis of hybrid cable-stayed suspension bridges subjected to damage mechanisms. *Engineering Failure Analysis,* 45**,** 470-495.

MOURITZ, A. P. & RAJAPAKSE, Y. D. S. (Eds.) (2017) *Explosion Blast Response of Composites*, Woodhead Publishing.

MOZOS, C. M. & APARICIO, A. C. (2010) Parametric study on the dynamic response of cable stayed bridges to the sudden failure of a stay, Part I: Bending moment acting on the deck. *Engineering Structures,* 32**,** 3288-3300.

MUELLER, J. E. (2018) Terrorism Since 9/11: The American Cases. http://politicalscience.osu.edu/faculty/jmueller/since.html.

MUELLER, J. E. & STEWART, M. G. (2016) *Chasing Ghosts - The Policing of Terrorism,* New York, USA, Oxford University Press. ISBN:

NETHERTON, M. D. & STEWART, M. G. (2010) Blast Load Variability and Accuracy of Blast Load Prediction Models. *International Journal of Protective Structures,* 1**,** 543-570.

SERON CONSORTIUM (2012a) Security of Road Networks: Final Report. Final Report

SERON CONSORTIUM (2012b) Security of Road Networks: Risk Assessment. D500

SERON CONSORTIUM (2012c) Security of Road Networks: Validation. D600

STEWART, M. G. (2017) Risk of Progressive Collapse of Buildings from Terrorist Attacks: Are the Benefits of Protection Worth the Cost? *Journal of Performance of Constructed Facilities,* 31**,** 04016093.

STEWART, M. G. (2018) Reliability-based load factor design model for explosive blast loading. *Structural Safety,* 71**,** 13-23.

STEWART, M. G. & MUELLER, J. (2014) Terrorism Risks for Bridges in a Multi-Hazard Environment. *International Journal of Protective Structures,* 5**,** 275-289.

THÖNS, S. (In Press) On the Value of Monitoring Information for the Structural Integrity and Risk Management. *Computer-Aided Civil and Infrastructure Engineering***,** n/a-n/a.

XIAO, W., ANDRAE, M., RUEDIGER, L. & GEBBEKEN, N. (2017) Numerical prediction of blast wall effectiveness for structural protection against air blast. *Procedia Engineering,* 199**,** 2519-2524.

Maintenance, Safety, Risk, Management and Life-Cycle Performance of Bridges – Powers, Frangopol, Al-Mahaidi & Caprani (Eds)
© 2018 Taylor & Francis Group, London, ISBN 978-1-138-73045-8

Evaluation of fatigue crack propagation considering the modal superposition technique

C.S. Horas & G. Alencar & R. Calçada
CONSTRUCT-LESE, University of Porto, Faculty of Engineering, Portugal

A. Jesus
INEGI, University of Porto, Faculty of Engineering, Portugal

ABSTRACT: In large Civil Engineering structures, such as bridges, the fatigue damage assessment is highly conditioned by the computational demands of global and detailed local models required to properly analyse the structural behaviour under cyclic loads. The dynamic analysis using direct time-integration algorithms is unfeasible in most of the cases, which leads to the necessity of considering the modal superposition concepts for such applications in order to increase the efficiency and accuracy of investigations concerning the fatigue crack propagation problem. In this regard, Albuquerque et al. (2012; 2015) proposed and implemented a computational algorithm aiming at predicting the remaining fatigue life of cracked details. Although, despite its computational efficiency, additional and relevant improvements may be proposed in order to allow precise and detailed fatigue analyses compatible with the pace of design, maintenance and strengthening operations of new or existing aged bridges.

1 INTRODUCTION

The planned railway network in Europe demands the existence of a considerable number of infrastructures, such as bridges and tunnels. Naturally, with the increase of the speed of circulation, the requirements for a safe operation on railway lines are more restricting, leading to the necessity of designing new structures or strengthen the existing ones. In Europe, there are, approximately, 300000 railway bridges and 3500km of railway tunnels that are close to or over the end of their planned service life. The replacement on a large scale of such number of infrastructures would not be economically feasible or realistic. Therefore, an extension of their service life shall be a major priority (European Union 2015).

Among the most important structural issues, fatigue is a particularly relevant cause of concern regarding the structural integrity of existing and operating bridges. The consciousness of fatigue phenomena only arose some decades ago, which means that when the first metallic bridges were designed this behaviour was not taken into account. Such drawback, led to a vast number of operating bridges where no structural verifications regarding cyclic loadings were carried out. This situation implies that the performance of such structures shall be carefully monitored in order to avoid global or local structural failures. As abovementioned, the development of monitoring systems, considering the recent improvements on numerical modelling capabilities, is essential to avoid fatigue cracks or control their propagation, to estimate the residual life of existing structural components and assess the necessity of strengthening operations.

Several methodologies have been proposed in the most important standards and guidelines in order to evaluate the fatigue damage (BSI 1980; AASHTO 2012; Hobbacher 2016). The approach based on nominal stresses and S-N curves is the most used one. Although, several of its limitations have been pointed out, being particularly important the impossibility of assessing the evolution of the fatigue cracking in existing structural members (Horas et al. 2016). In this regards, alternative approaches based on the Fracture Mechanics principles have been suggested to assess the crack propagation issues (Albuquerque et al. 2012).

Understanding cracks propagation under cyclic loadings, from the material scale until the occurrence of a global or local structural failure, have been possible due to the evolution of Fracture Mechanics principles. Most of fatigue analyses based in such concepts underlies on the Paris law (Paris et al. 1961) which suggests that, on elastic domain and for a stable propagation regime under constant amplitude loading, the fatigue crack propagation rate, da/dN, may be related to the corresponding stress intensity factor range, ΔK.

Several implementations of the Fracture Mechanics concepts have been performed in distinct engineering areas using numerical models based on the Finite Element Method (FEM). In such cases, the direct time-integration of the dynamic problem may be achieved implementing algorithms such as the Newmark (Bathe 1996) and Hilbert-Highes-Taylor (HHT) (Chung & Hulbert 1993). Although, such approaches usually require the computation of an enormous number of load steps which leads to unattainable computational requirements when local detailed analyses are needed. In this context, the modal superposition appears as a most efficient solution for investigating the crack growth over the time (Albuquerque et al. 2015; Horas et al. 2017).

In the Civil Engineering context, the difference between the global scale of structures (metres or kilometres) and the localized occurrence of fatigue phenomenon may be a relevant issue for accurate numerical investigations. This multi-scale problem may be overcome considering submodelling techniques which allow combining relevant simplifications of the global numerical model without neglecting the precise calculation of local stress and strain fields, indispensable to evaluate the fatigue damage (Kiss & Dunai 2000; Li et al. 2007; Teixeira 2015; Albuquerque 2015).

Taking into account the presented framework, it is important to develop advanced numerical tools to evaluate the structural integrity of large railway bridges in the different stages of their lifetime. Therefore, the aim of this paper is to suggested improvements to the computational algorithm proposed by Albuquerque et al. (2012;2015), based on modal superposition concepts, in order to maximize its computational efficiency and make its application compatible with the pace of design, maintenance and strengthening operations typical of large Civil Engineering structures.

2 THEORETICAL BACKGROUND

The theoretical concepts underlying the approached strategy to investigate the fatigue damage related to crack propagation issues, linking the modal superposition and Linear Elastic Fracture Mechanics principles, are detailed in the present section.

2.1 *Modal superposition concepts*

A structural system subject to cyclic loadings presents a dynamic behaviour extremely dependent on both the structural and loading characterization. If, for a certain time step, t, the mass, stiffness, damping and acting nodal forces are known, the dynamic response may be computed considering direct-time integration algorithms or the modal superposition technique. In such conditions, the dynamic behaviour of the structural system with N degrees of freedom may be defined by NxN simultaneous equations:

$$M.\ddot{u}(t) + C.\dot{u}(t) + K.u(t) = F(t) \quad (1)$$

where, associated with the N degrees of freedom, M is the mass matrix, C the damping matrix and K the stiffness matrix, each with NxN dimension. Also, for a certain time instant, u(t), u̇(t) and ü(t) are, respectively, the displacement, velocity and acceleration matrices and F(t) the nodal forces matrix, each of them defined by Nx1 terms.

When a loaded structure remains elastic and its properties are constant along the time, the systems of equations (1) may be decoupled into N independent equations which may be individually solved (Clough & Penzien 1975):

$$\ddot{Y}_j(t) + 2w_j.\xi_j.\dot{Y}_j(t) + {w_j}^2.Y_j(t) = f_j(t) \quad (2)$$

where, for the j^{th} mode of vibration, $Y_j(t)$ and $f_j(t)$, are, respectively, the matrix of modal coordinates and matrix of nodal forces, related to the N degrees of freedom. Also, w_j and ξ_j are modal quantities, respectively, the frequency and the damping coefficient.

Albuquerque et al. (2012) suggested the concept of modal stress intensity factor to evaluate the crack propagation integrating successively the Paris law. Such approach allows calculating the stress intensity factor time-histories, K(t), as the sum of static and dynamic parts, respectively, K_{sta} and $K_{dyn}(t)$, naturally related to the static and dynamic stresses, σ_{sta} and $\sigma_{dyn}(t)$. Therefore, K(t), may be computed as follows:

$$K(t) = K_{sta} + K_{dyn}(t) \quad (3)$$

$$K_{sta} = Y.\sigma_{sta}.\sqrt{\pi a} \quad (4)$$

$$K_{dyn}(t) = Y.\sigma_{dyn}(t).\sqrt{\pi a} \quad (5)$$

where, Y is a parameter associated with the geometrical characteristics of the structure and crack. According to the presented concepts, the $\sigma_{dyn}(t)$ may be calculated according to:

$$\sigma_{dyn}(t) = \sum_j \sigma_j \,.\, Y_j\,(t) \quad (6)$$

In equation (6), σ_j is defined as the modal stress dependent on the j^{th} modal shape, $Y_j(t)$. Considering equations (5) and (6), the concept of modal stress intensity factor may be defined:

$$K(t) = K_{sta} + \sum_j K_j \,.\, Y_j\,(t) \quad (7)$$

The reasoning underlying the definition of modal stress intensity factor may be extended to other local parameters such as stresses, strains or energetic quantities. Thus, equations (3) and (7) may be re-written in a general form:

$$\psi(t) = \psi_{stat} + \sum_j \psi_j \,.\, Y_j\,(t) \tag{8}$$

where, ψ is a generic fatigue quantity, ψ_{stat} the part associated with the static loading and ψ_j the modal quantity related to the j^{th} modal shape. Naturally, as demonstrated by equation (8), the modal superposition concepts may be extended to different local parameters related to the fatigue crack initiation and crack propagation damages.

2.2 *Propagation of fatigue cracks*

As demonstrated by Horas et al. (2017) and Albuquerque et al. (2012), respectively, for fatigue crack initiation and crack propagation, the numerical analysis of cracking phenomena requires a well-defined fatigue model.

According to the loading characterization, pure or mixed-mode crack propagation may occur. Regarding, the uniaxial ones, mode I (opening mode), mode II (sliding mode) and mode III (tearing mode) may be defined. Logically, equation (7) may be adjusted to calculate the corresponding K values:

$$K_I(t) = K_{I,stat} + \sum_j K_{I,j} \,.\, Y_j\,(t) \tag{9}$$

$$K_{II}(t) = K_{II,stat} + \sum_j K_{II,j} \,.\, Y_j\,(t) \tag{10}$$

$$K_{III}(t) = K_{III,stat} + \sum_j K_{III,j} \,.\, Y_j\,(t) \tag{11}$$

where, K_I, K_{II} and K_{III} are the stress intensity factors related to the defined pure propagation modes. For simple loading conditions, as already mentioned, Paris et al. (1961) established a relation to characterize the influence of the stress intensity factor range, $\Delta K = K_{max} - K_{min}$, on the crack propagation rate, da/dN:

$$\frac{da}{dN} = C.\Delta K^m = C.(Y.\Delta\sigma.\sqrt{\pi a})^m \tag{12}$$

where, C and m are material parameters. Although, generally complex structures such as bridges are subjected to complex dynamic loadings which give origin to mixed-mode propagation. In such cases, Tanaka (1974), among others, proposed the concept of equivalent stress intensity factor, K_{eq}, for mixed-mode (I+II) cases:

$$K_{eq}(t) = \sqrt[4]{K_I^4(t) + 8K_{II}^4(t)} \tag{13}$$

Associated with $K_{eq}(t)$, the histogram of $\Delta K_{eq,i}$ in function of the respective number of cycles, n_i, may be obtained considering a cycle counting method as the rainflow (Matsuishi & Endo 1968). Therefore, taking into account equation (12) and (13), the value of the crack increment, Δa, may be calculated integrating the Paris law:

$$\Delta a = \sum_i n_i \, C \Delta K_{eq,i}{}^m \tag{14}$$

Subsequently, the crack path may be defined considering a crack branching criteria. One of the most implemented is the maximum tangential stress criterion (MTS) suggested by Erdogan & Sih (1963). Applying this approach, the kink-angle time-history, $\theta(t)$, may be obtained as follows:

$$\theta(t) = \cos^{-1}\left(\frac{3K_{II}^2(t) + \sqrt{K_I^4(t) + 8K_I^2 K_{II}^2(t)}}{K_I^2(t) + 9K_{II}^2(t)}\right) \tag{15}$$

where, θ is the angle between a certain crack plane at the instant of time *t* and the crack initial plane, being its signal determined according to the classical local coordinate system of Fracture Mechanics and considering the value of K_{II} (θ is positive is K_{II} is negative).

Once defined $\Delta K_{eq,i}$ and n_i, the equivalent kink angle, $\bar{\theta}$, may be calculated through a weighted average function (Fracture Analysis Consultants 2011):

$$\bar{\theta} = \frac{\sum_i^n \frac{da}{dn}(\Delta K_{eq,i})\theta_i(K_I, K_{II})}{\sum_i^n \frac{da}{dn}(\Delta K_{eq,i})} \tag{16}$$

Considering equations (14), (15) and (16), for each $\Delta K_{eq,i}$ and n_i, Δa and the associated $\bar{\theta}$ may be computed allowing to define completely the cracking path.

2.3 *Submodelling*

In general, for large structures the global numerical model is able to properly reproduce the dynamic global behaviour, even when built with beam or shell elements discretized with coarse meshes. However, when local analyses are required, much more refined local modelling, using shell or volumetric elements, are needed. Such detailing is difficult to achieve using only the global model. Therefore, submodelling techniques, which allow considering the global-local interaction between numerical models, may be implemented. Among the submodelling techniques, the shell-to-solid is particularly useful since the displacement fields obtained at the global model are inputted into the submodel considering the appropriate shape functions without any geometrical constraints (Silva 2015; Albuquerque 2015).

2.4 *Computational workflows: single and parallel computing processes*

The presented theoretical concepts may be implemented integrated into computational algorithms. Albuquerque et al. (2012; 2015) proposed a workflow to assess fatigue cracking problems based on the modal superposition principles and single computing. Such computational algorithm is outlined in Figure 1 and may be summarized in the following steps:

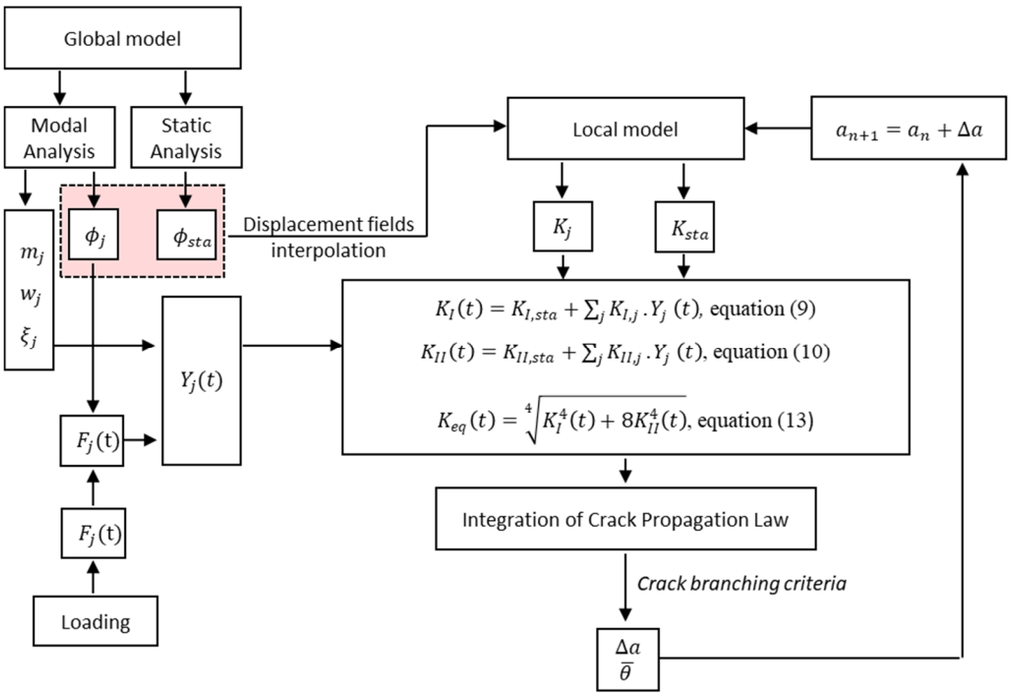


Figure 1. Computational algorithm for crack propagation analysis (with submodelling)

i. Calculation of the displacement fields due to the static loading, Φ_{stat}, corresponding static stress intensity factor, K_{stat}, and consistent sign;
ii. Modal analysis of the structure obtaining, for each j^{th} vibration mode, the value of K_j and corresponding sign. Computation of modal frequencies, ω_j, modal masses, m_j, mode shapes, Φ_j, and definition of modal damping coefficients, ξ_j;
iii. Evaluation of the dynamic loading, F(t), and determination of the modal forces, $F_j(t)$;
iv. Calculation of the modal coordinates time-histories, $Y_j(t)$;
v. Displacement field interpolation;
vi. Computation of K(t) for a certain crack length, a_n, applying equations (9), (10) and (13), being $K_I(t)$ equal to zero when its value is negative because contact (crack closure) algorithms are not considered at the crack faces;
vii. Application of the rainflow counting method in order to calculate $\Delta K_{eq,i}$ and n_i;
viii. Integration of the selected crack propagation law, e.g. equation (14) (Castro & Meggiolaro 2009);
ix. Evaluation of Δa and $\bar{\theta}$ allowing the subsequent modification of the local cracked model, considering the new crack length, a_{n+1};
x. Re-initiation of the cyclic process until the stop criterion is reached, generally the material toughness, K_c, or geometric constraints.

The described workflow may be applied to multiple complex dynamic events, e.g. successive passages of trains. Although, for the sake of computational efficiency, when multiple trains are considered, it is advisable adopting constant crack increments between iteration, Δa_{inc}. Therefore, the increase of the crack due to a block of trains (e.g. daily trains) should be scaled by $B_n=\Delta a_{inc}/\Delta a$, being B_n the number of loading blocks needed to achieve Δa_{inc}.

The presented algorithm is based on a single computing approach. However, if the modal superposition principles are adopted, the previously described step vi. is a decoupled process and for each j^{th} vibration mode only one independent calculation is required. Thus, a multiple computing process may be implemented allowing to perform such step multiple times at the same time. In Figure 2, a scheme of the main concepts behind the parallel computing is presented. In mathematical terms, the number of parallel processes is only limited by the considered number of j^{th} vibration modes, although, due to computational restrains, a small and controlled number of parallel processes are generally adopted.

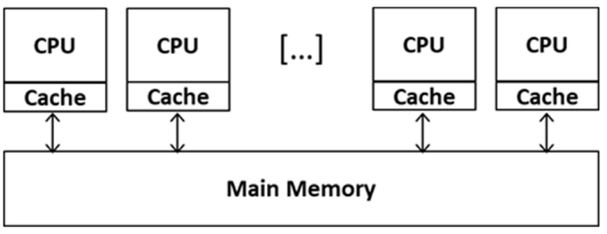


Figure 2. Scheme of a shared memory multiprocessing

3 IMPLEMENTATION IN A CASE STUDY

In the present paper, the results obtained after implementing the described approach, to assess the fatigue crack propagation in a complex welded detail of a Portuguese railway bridge, are presented. A special focus is given to the improvements in the computational efficiency achieved after considering the parallel computing.

3.1 *Alcácer do Sal bridge*

The structure analysed is a bowstring metallic bridge, located in the Lisboa-Algarve railway connection, composed of 3 spans with 160 m suspended by tension rods. The cross-section is materialized by a concrete deck lying over a trapezoidal box-girder. Also, at the connection between the deck and the tension rods, additional steel diaphragms linked to 2 diagonal strings provide supplementary strength. Such diagonals are 600mm wide and present a thickness of 35mm.

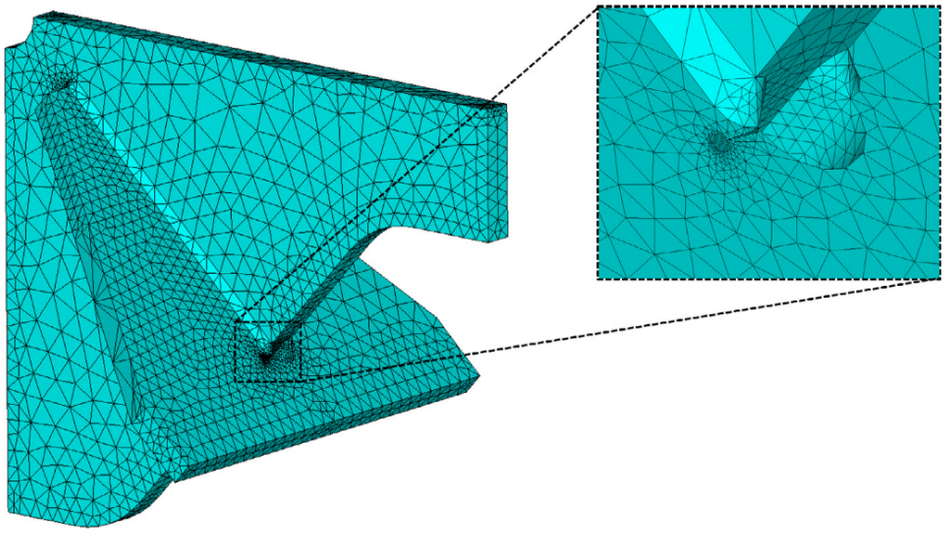
Albuquerque et al. (2015) performed initial fatigue studies in the Alcácer do Sal bridge. For such purposed, the authors developed a global model, conceived with beam and shell elements, and local numerical models, built with volumetric/solid elements. A shell-to-solid submodelling technique was considered. In order to determine the most fatigue-prone detail, initial static analyses were carried out and the denominated diaphragm 51 was identified as the critical one. At the toe of its weld filament, a high-stress concentration was found, which allowed concluding that a potential small defect would increase the possibilities of locally starting a cracking phenomenon. Thus, at such location and considering that the approached methodology aims at investigating the crack propagation process, a small initial defect was considered (Figure 3).



a) partial view of the bridge



b) steel diaphragm and diagonal strings



c) submodel of the welded detail

Figure 3. Partial view of the bridge and developed local numerical model (Albuquerque 2015)

3.2 *Dynamic analysis assumptions*

In modal superposition analyses, a constant modal damping ratio, ξ, of 0.5% was assumed for all the considered vibration modes as proposed by EN1991-2 (CEN 2003) for steel and composite bridges. The remaining modal properties, ω_j and m_j, were computed according to the structural characteristics.

The fatigue model was defined considering experimental investigations performed on specimens with thickness and material properties similar to the assumed cracked detail. In such tests, the material toughness, K_c, equal to 1434 MPa$\sqrt{mm}$ was determined as the limit for the stable propagation regime (Carvalho et al. 2014). Also, a value of 63 MPa$\sqrt{mm}$ was defined for the stress intensity factor threshold, ΔK_{th}, with basis on the suggestions of BS7910 (BSI 2013) (Table 1).

Table 1 - Adopted parameters for fatigue analysis

C	m	ΔK_{th} (MPa.$\sqrt{mm}$)	K_c (MPa.$\sqrt{mm}$)
9.93×10^{-14}	3.14	63	1434

Previously, Albuquerque et al. (2015) assumed an initial defect of 15 mm and considered the contribution of 1500 vibration modes. In the present paper, an initial crack length of 1 mm was considered, which is believed to be a better approximation to the beginning of the crack propagation. Regarding the number of modes, it is easily understandable that in a large structure a considerable number of vibration modes does not contribute to the value of the stress intensity factor at the crack front. Therefore, considering equation (7), a parametric analysis was performed in order to evaluate the contribution of each mode to the stress field at the assumed cracked area. A cut-off limit, ΔK_{cf}, was defined below which the contribution of a certain mode was disregard (Table 2).

Table 2 - Parametric analysis

ΔK_{cf} (MPa.$\sqrt{mm}$)	0.10	0.15	0.20	0.25
No. of modes	808	685	697	540

In Table 2, the number of vibration modes as a function of the cut-off stress intensity values are presented. When a reduced number of modes was considered a good agreement with the previous analysis results, taking into account 1500 modes, was stated comparing the values of $K_I(t)$, $K_{II}(t)$ and $K_{eq}(t)$ obtained from different calculations. Considering the presented results and seeking to found a compromise between the accuracy of results and computational efficiency, 685 vibration modes were adopted in the investigations detailed in the present paper. In order to have some figures, using a personal computer with a processor 3.4GHz i7-6700 CPU and 16 GB of RAM memory, after 29 increments and 64 hours of computation the value of K_c was achieved, on the other hand, when 685 modes were accounted for, time was reduced to 28 hours.

3.3 *Fatigue life predictions*

The assessment of the fatigue damage in the assumed cracked detail was performed considering the heavy traffic-mix, proposed in EN1991-2 (CEN 2003), and the real traffic circulating on the bridge evaluated by Albuquerque (2015). Also, as already mentioned, values of 15 mm and 1 mm were considered as initial defects.

Regarding the parallel computing analyses, considering 685 vibration modes, 4 parallel processes were defined, the first 3 considering 171 vibration modes and the last one the remaining modes.

Figure 4 presents the numerical crack propagation path when the critical toughness was achieved at the crack tip.

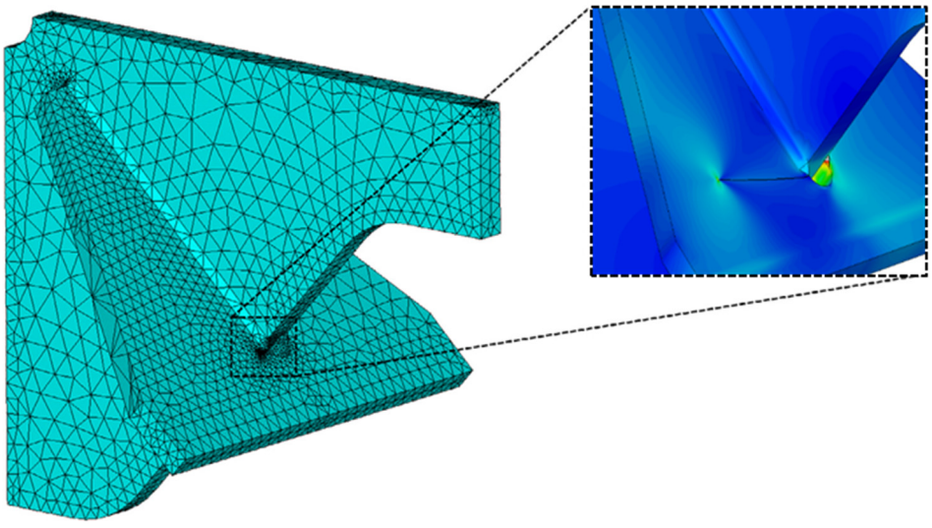


Figure 4. Crack propagation path: 685modes, iteration 29

Table 3 – Remaining fatigue life predictions (single and parallel computing)

Analysis	No. of modes	Traffic scenario	a_i (mm)	nº iterations	Computational time	Remaining life
(1)	1500	Heavy traffic-mix: EN1991-2 (CEN 2003)	15	29	64 hours	1 year and 10 months
(2)	685	Heavy traffic-mix: EN1991-2 (CEN 2003)	15	29	28 hours	1 year and 10 months
(3)	685	Real traffic: Albuquerque (2015)	15	32	33 hours	39 years and 8 months
(4)	685	Heavy traffic-mix: EN1991-2 (CEN 2003)	1	31	27 hours	2 years and 1 months
(5)	685	Real traffic: Albuquerque (2015)	1	35	33 hours	44 years

In Table 3, the main results accomplished after the performed analyses are detailed. Regarding the computational times, the efficiency when multiples processes were admitted increased significantly, being the calculation times 40% lower in such cases. Although, due to the depletion of the hardware capacity, as it is easily understandable, a linear relation between the adopted number of processes and the decreased of the computational time were not found. Naturally, the improvement of the personal computer capabilities should allow minimizing the required analysing time.

In which concerns to the remaining life results, threatening predictions were achieved when the standard traffic was assumed. Such data, besides proving that the actual traffic is considerably lower than the normative prescriptions, showed that a small defect due to accidental reasons or defective construction may put in risk the structural integrity at short time. However, it is important to highlight that such predictions are only valid when the crack initiation phase is completely developed. Aditional calculations, which are out of the scope of the present paper, showed that even the loading of the heavy traffic-mix is not severe enough to start a fatigue cracking phenomenon in the most stressed spot of the assumed cracked detail (Horas et al. 2018).

In general, the obtained results stress the importance of advanced numerical tools for design, maintenance and strengthening operations. Also, the hazard which a small defect represent for a fatigue-critical detail was demonstrated, highlighting the necessity of proper monitoring systems, in which the improved and investigated computational algorithm may be integrated, to control the structural performance of existing and operating bridges.

4 CONCLUSIONS

The improved methodology based on the modal superposition principles and Fracture Mechanics concepts, for fatigue assessment, proved to be appropriate for cracked details under mixed-mode (*I+II*) complex loadings.

With the main goal of investigating the assumed cracked detail of the Alcácer do Sal railway bridge, a set of analyses were performed considering different initial crack length assumptions and distinct traffic scenarios. If a small defect exists, the achieved results when the standardize traffic is considered may put in cause the global S-N methodology proposed in EN1993-1-9 (CEN 2005).

As concerns the computational efficiency, the reduction of the considered number of vibration modes and the adoption of the parallel computing were found to be major improvements. The achieved calculation times are within the pace of design, maintenance and strengthening operations typical of large Civil Engineering structures such as bridges.

5 ACKNOWLEDGMENTS

This work was financially supported by: Project POCI-01-0145-FEDER-007457 - CONSTRUCT - Institute of R&D In Structures and Construction funded by FEDER funds through COMPETE2020 - Programa Operacional Competitividade e Internacionalização (POCI) – and by national funds through FCT - Fundação para a Ciência e a Tecnologia; PD/BD/114101/2015. Also, the authors gratefully acknowledge the financial support for this work provided by CNPq - Brazilian Science Foundation; fellowship number 203662/2014-8.

6 REFERENCES

AASHTO, 2012. *LRFD Bridge Design Specifications* 6th ed., Washington, D.C.: American of State Highway and Transportation Offcials.

Albuquerque, C., 2015. *Advanced Methodologies for the Assessment of the Fatigue Behaviour of Railway Bridges*. Porto: Faculty of Engineering of the University of Porto.

Albuquerque, C. et al., 2015. An efficient methodology for fatigue damage assessment of bridge details using modal superposition of stress intensity factors. *International Journal of Fatigue*, 81, pp.61–77. Available at: http://www.sciencedirect.com/science/article/pii/S014211231500211X.

Albuquerque, C., de Castro, P.M.S.T. & Calçada, R., 2012. Efficient crack analysis of dynamically loaded structures using a modal superposition of stress intensity factors. *Engineering Fracture Mechanics*, 93, pp.75–91. Available at: http://www.sciencedirect.com/science/article/pii/S0013794412002639.

Bathe, K.-J., 1996. *Finite Element Procedures*, New Jersey: Prentice Hall Inc.

BSI, 2013. BS7910: Guide to methods for assessing the acceptability of flaws in metallic structures.

Carvalho, D. et al., 2014. Fatigue behaviour of structural steels. Comparison of strain-life and fatigue crack propagation data. In *9º Congresso Nacional de Mecânica Experimental*. Aveiro.

Castro, J.T.P. de & Meggiolaro, M.A., 2009. *Fadiga técnicas e prática de dimensionamento estrutural sob cargas reais de serviço*, [S.l.: s.n.].

CEN, 2003. Eurocode 1: Actions on structures. *Part 2: Traffic loads on bridges*.

Chung, J. & Hulbert, G.M., 1993. A time integration algorithm for structural dynamics with improved numerical dissipation: the generalized-α method. *Journal of Applied Mechanics*, 60(2), pp.371–375.

Clough, R.W. & Penzien, J., 1975. *Dynamics of structures*, McGraw-Hill.

Erdogan, F. & Sih, G.C., 1963. On the Crack Extension in Plates Under Plane Loading and Transverse Shear. *Journal of Basic Engineering*, 85(4), p.519. Available at: http://fluidsengineering.asmedigitalcollection.asme.org/article.aspx?articleid=1431534.

European Union, 2015. Decision of the Adoption of the Shift2Rail Master Plan. *Report: Strategic Masterplan*.

Fracture Analysis Consultants, I., 2011. Franc3D Reference Manual.

Hobbacher, A., 2016. Recommendations for Fatigue Design of Welded Joints and Components, Cham: Springer International Publishing. Available at: http://link.springer.com/10.1007/978-3-319-23757-2.

Horas, C.S. et al., 2016. Application of Modal Superposition Technique in the Fatigue Analysis Using Local Approaches. In *Procedia Engineering*. Gijón, Spain.

Horas, C.S. et al., 2017. Application of the modal superposition technique combined with analytical elastoplastic approaches to assess the fatigue crack initiation on structural components. Engineering Fracture Mechanics, 185, pp.271–283. Available at: http://linkinghub.elsevier.com/retrieve/pii/S001379441630707X [Accessed July 14, 2017].

Horas, C.S. et al., 2018. Development of an efficient approach for fatigue crack initiation and propagation analysis of bridge critical details using the modal superposition technique. Engineering Failure Analysis, accepted, in press.

Kiss, K. & Dunai, L., 2000. Stress history generation for truss bridges using multi-level models. *Computers & Structures*, 78(1–3), pp.329–339. Available at: http://www.sciencedirect.com/science/article/pii/S0045794900000791.

Li, Z.X. et al., 2007. Multi-scale numerical analysis on dynamic response and local damage in long-span bridges. *Engineering Structures*, 29(7), pp.1507–1524. Available at: http://www.sciencedirect.com/science/article/pii/S0141029606003282.

Matsuishi, M. & Endo, T., 1968. Fatigue of metals subjected to varying stress. In *Proceedings of the Kyushu Branch of Japan Society of Mechanical Engineers*. Fukuoka, pp. 37–40.

Paris, P., Gomez, M. & Anderson, W., 1961. A Rational Theory of Fatigue. *The Trend in Engineering*, 13, pp.9–14.

Silva, A., 2015. *Advanced Methodologies for the Fatigue Analysis of Representative Details of Metallic Bridges*. Porto: Faculty of Engineering of the University of Porto.

Tanaka, K., 1974. Fatigue crack propagation from a crack inclined to the cyclic tensile axis. *Engineering Fracture Mechanics*, 6(3), pp.493–507. Available at: http://www.sciencedirect.com/science/article/pii/0013794474900071.

Teixeira, R.M., 2015. *Metodologias para Modelagem e Análise da Fadiga em Ligações Rebitadas com Aplicação em Pontes Metálicas Ferroviárias*. São Paulo: Escola Politécnica da Universidade de São Paulo.

Maintenance, Safety, Risk, Management and Life-Cycle Performance of Bridges – Powers, Frangopol, Al-Mahaidi & Caprani (Eds)
© 2018 Taylor & Francis Group, London, ISBN 978-1-138-73045-8

Inspection and Assessment of One of Australia's Earliest Masonry Bridges

D. McDonnell
Arup, Sydney, Australia

D. Ashurst
Arup, Midlands, UK

I. Berger
Heritage Professional, Sydney, Australia

ABSTRACT: Lennox Bridge is a sandstone arch bridge located on Church Street over the Parramatta River in the Parramatta CBD in New South Wales. The Bridge was constructed in 1839 and is the second oldest road bridge still in operation in Australia, after Lansdowne Bridge completed in 1836. The bridge was widened with a reinforced concrete arch in 1935 and new portals were constructed through the abutments in 2014. The bridge is owned by City of Parramatta Council, managed by Roads and Maritime Services and listed on the State Heritage Register in NSW.

Parramatta Light Rail Stage 1 (PLR) is a new 12 km long light rail system that will operate between Westmead and Carlingford through the Parramatta CBD where the light rail will cross Lennox Bridge. A condition assessment of the bridge was undertaken as part of the asset assurance process for the retained assets in the light rail corridor. The condition assessment comprised combined geotechnical and structural investigations and a structural assessment. This paper discusses the asset assurance process and highlights the lessons learned for future applications.

1 INTRODUCTION

1.1 *The project*

Lennox Bridge is a masonry arch bridge located on Church Street over the Parramatta River in the Parramatta CBD in New South Wales. The Bridge was constructed in 1839 and is the second oldest road bridge in operation in Australia. The bridge is owned by City of Parramatta Council (CoPC) and Roads and Maritime Services (RMS) is responsible for the operation and management of the Bridge.

Parramatta Light Rail Stage 1 (PLR) will run from Westmead and Carlingford through the Parramatta CB where the light rail corridor will travel along Church Street and traverse Lennox Bridge.

Lennox Bridge comprises a single elliptical arch with a span of approximately 23.2 metres. The fabric of the original approach spans and arch spandrels consists of ashlar masonry and the voussoir stones of the arch are edged blocks (RMS, 2012). The bridge is 11.9m wide and was completed in two stages, the first 6.4m and the second 5.5m wide.

The bridge has undergone a number of significant modifications since. Sections of the stone arch were strengthened internally in 1901-2 for the new Parramatta-Baulkham Hills tramway. A cantilevered steel pedestrian footway was added to the western (upstream side) bridge in 1912 (RMS, 2012). The bridge was widened on the western side in 1935 by the addition of a reinforced concrete arch with stone facing which replaced the pedestrian footway installed in 1912.

In 2014 portals were introduced through the abutments of the bridge in order to improve access to and along the Parramatta River. The concrete balustrade on the eastern elevation was replaced with a new masonry parapet as part of this works.

PLR will connect Westmead and Carlingford via the Parramatta CBD. Lennox Bridge will form part of the light rail corridor and is one of a number of retained bridges in the new light rail corridor. A geotechnical and structural investigation of the 1839 bridge and a structural assessment was undertaken as part of the asset assurance process for PLR. This paper will discuss this process and outcomes.

2 HISTORY AND CONTEXT

2.1 *David Lennox*

David Lennox was born into a farming family at Ochiltree, Ayrshire in Scotland on 9 February, 1788.

In Britain, Lennox had worked on the vast Highland Roads and Bridges construction programme that was overseen by Thomas Telford. He was then engaged as a stonemason on the pioneering suspension bridge over the Menai Straits in North Wales designed by Telford before achieving the status of master mason in 1823. He spent a couple of years working on swing-bridges on the Gloucester and Sharpness Canal, followed by three years as foreman mason for the contractor John Cargill building Telford's iconic masonry arch bridge on the Severn at Over near Gloucester which was completed in 1829 (Alsop, 2014).



Figure 1 Portrait of Lennox taken in 1843 (then aged 55) (courtesy of Parramatta Visitors Centre).

Following his wife's death in 1828, compounded by a severe financial recession in Britain leading to mass unemployment, Lennox made the decision to emigrate to New South Wales. He landed at Sydney on 11 August 1832, carrying with him drawings of the bridges he had worked on, together with testimonials and letters of introduction which included one from Telford himself (RMS, 2012). One of Lennox's letters of introduction led to a meeting with the Surveyor-General of New South Wales, Thomas Mitchell (1792-1855) who secured for him the appointment of "Superintendent of Bridges" in 1832. His major outputs in NSW were Lapstone Bridge (1833), Berrima Bridge (1836), Lansdowne Bridge (1836) as well as Queens Wharf at Parramatta (1835) and the Liverpool Dam (1836). He transferred to Victoria in a similar position and retired there in 1853 following his construction of the Prince's Bridge across the Yarra River, a 150ft masonry arch which when completed in 1850 was among the longest and flattest arch bridges in the world.

2.2 *Former bridges on the site*

The location where Church Street crosses the Parramatta River is the site of the earliest documented river crossing in the Parramatta District, dating from the earliest years of the colonial settlement. Three bridges have been built on or immediately adjacent to this site which consequently possesses a high degree of archaeological potential.

Major Grose constructed a timber bridge at the end of Church Street across Parramatta River in 1794. The bridge was washed away in 1795, and replaced with a timber girder bridge, with stone piers. This bridge connected the early township to the area north of the river including the gaol, which was completed in 1797. During this period, the bridge at Church Street was referred to as The Gaol Bridge.

By the 1820s, the bridge was known as "Parramatta Bridge". It was in a state of serious disrepair by 1826, requiring temporary timber trestle supports.

2.3 *Design*

The last major bridge that Lennox designed and built in NSW was over the Parramatta River in Church Street, Parramatta. In September 1835 Governor Bourke's rejection of his design for the bridge triggered a dispute between Lennox and his superiors about the size and appearance of the bridge which delayed its construction by a year, causing Lennox to complain, 'I am tired of it before the work is commenced'. Eventually Bourke accepted his design for a 76ft span arch.

Lennox later wrote that Westgate Bridge at Gloucester was 'nearly the same in all respects as that at Parramatta'. Robert Smirke's Westgate Bridge had been completed in 1816 on a site less than a mile from Over Bridge, so Lennox would have had many opportunities to inspect it. It was demolished in the 1970s; photographs suggest the two bridges were only superficially similar.

Construction began in November 1836, using the centering from the Lansdowne Bridge, adjusted to the new span, and was completed in 1839. The Bridge was named Lennox Bridge by the Parramatta Council in 1867.

2.4 *Construction*

Lennox sourced the stone for the bridge from a quarry behind the Parramatta Female Factory. The Female Factory was a workhouse and was located in

what are now the grounds of Cumberland Hospital close to the bridge site.



Figure 2. Westgate Bridge at Gloucester built 1816, the inspiration for the design of Lennox Bridge.

Various gangs of masons and labourers were used on the different parts of the bridge structure. The more detailed arch work and double curved abutments was carried out by the bridge gangs, who were the most skilled members of the convict workforce (RMS, 2012). Labour issues slowed down construction as the Royal Engineers regularly requisitioned the bridge gang to work on the Parramatta barracks and gaol.

Lennox's plan was ' to build one half of the arch at one time and make the road passable over that part, until the other is completed'. The first completed section of the bridge was opened to traffic in September 1838 (RMS, 2012).

Lennox Bridge was the only bridge he built in NSW in an urban setting and it appears he took steps to ornament it. The central buttresses, arch keystone and certain horizontal string courses were constructed of a whiter stone as a deliberate act of the original design.



Figure 3. Lennox Bridge western elevation in 1930 highlighting the two tone colour scheme (RMS Photo Collection).

Lennox utilized a system of "hollow spandrels" whereby the roadway was carried by stone slabs supported on masonry walls over the arch barrel, forming voids which reduced the weight of backfill and created internal galleries that enabled construction surveillance of the arch and spandrel walls. This device had been used by Telford on Over Bridge and may possibly have been used by Lennox on the Prince's Bridge also.

The gallery design method as well as the two stages of construction, accounted for the greater cost of Lennox Bridge over and earlier bridge of Lennox design in NSW , the Lansdowne Bridge (RMS, 2012). The out turn cost of the Lansdowne Bridge £1083 pounds, whereas Lennox Bridge cost £1797 despite the fact that he reused the centering manufactured for the Lansdowne Bridge (RMS, 2012).

The western wing walls, which are now concealed behind the 1934 bridge were curved in plan.

2.5 *Alterations*

Located on the main north-south route of the Parramatta CBD the bridge has undergone a number of alterations reflecting the changing needs of the community. Sections of the stone arch were strengthened internally in 1901-2 to enable the Bridge to carry the new Parramatta-Baulkham Hills tramway. The tramway was extended to Castle Hill in 1905. The tramway across the Bridge opened on 18 August 1902 and closed in 1927.

The bridge was widened in 1935 by the addition of a reinforced concrete arch on the western side. The face of the concrete arch is covered with a stone façade.

The original design is still visible on the eastern side, the only alteration being the replacement of the original parapet with a concrete balustrade which was subsequently replaced with a new parapet in 2014.



Figure 4. Lennox Bridge General showing all three arches.

In 2014 Parramatta City Council commissioned the design and construction of pedestrian portals through the abutments of Lennox Bridge as part of the Parramatta City River Strategy to provide con-

tinuous level access via a shared path along the river to Parramatta Park. Excavation revealed, am ongst other things, an un-m ortared wall which appears to have been built to retain the fill supporting the road when the first half of the original bridge was being built. In addition the rem ains of a pier of the former timber beam bridge at the crossing were identified.

The balustrade on the eastern side of the bridge was replaced with a stone parapet m ore in keeping with the original design intent.

3 GEOTECHNICAL AND STRUCTURAL INVESTIGATION

3.1 *Boreholes*

A total of 8 boreholes were drilled to characterize the ground profile and identify the founding depths and materials of the bridge. Down-hole geophysics techniques were used in 6 of these boreholes, located in the riverbank areas next to each of the two abutments.

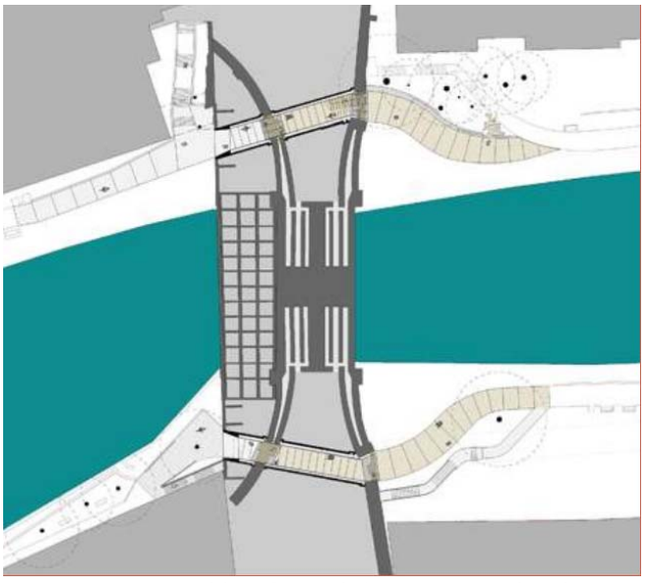


Figure 5. Lennox Bridge General Arrangement showing portals through the bridge. The curved wi ngwalls that were concealed by the 1935 western additi on are evident as are the internal galleries on Eastern (1839) bridge (Hill Thalis Architects, 2014)

Based on previous knowledge of the ground conditions in the area, it was known that the ground profile beneath each river bank was expected to com - prise a sequence of alluvial deposits over sandstone bedrock. It was anticipated that the bridge foundations (both for the older sandstone bridge and the later concrete bridge) were founded on the bedrock, but this, and the compositon of the abutments, needed to be verified (Arumugam et al, 2017).

3.2 *1839 Bridge Abutment Boreholes*

Two boreholes were drilled adjacent to the two bridge abutments on the eastern side of the bridge. The first borehole was drilled approxim ately 1m from the abutm ent and the second positioned approximately 4m away. The purpose of the first borehole (1 m away) was to carry out down-hole geophysics using Borehole Ground Penetrating Radar (BGPR) aimed at identifying the founding depth of the bridge abutm ent. The purpose of the second borehole (4 m away) at each side was to provide a benchmark BGPR profile (Arum ugam et al, 2017). This is discussed further below.

Two boreholes were drilled through the abutm ents in order to characterize the abutm ent materials and confirm the founding depth. The boreholes were drilled through the asphalt of the road, fill m aterials followed by sandstone blocks and into the founding bed rock. The roughly rectangular-shaped sandstone blocks are separated by irregularly spaced lim e mortar joints with a variable thickness ranging f rom 30 mm to 150 m m (Arumugam et al, 2017). The borehole terminated in sandstone bedrock. A section through the south abutment is shown in Figure 6.

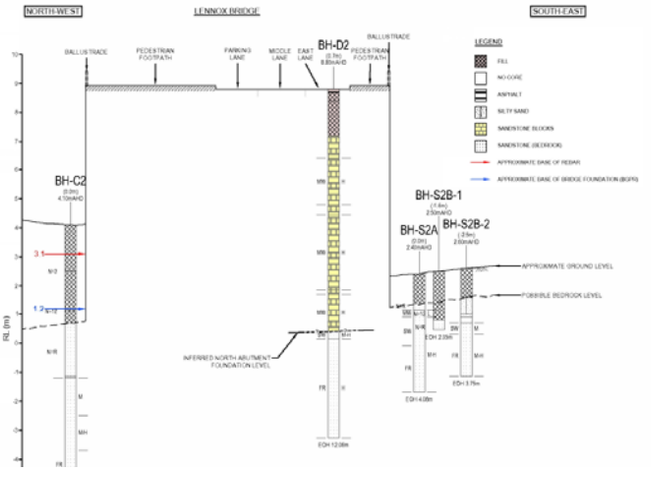


Figure 6. Section showing boreholes through the abutment (Arumugam et al 2017)

3.3 *1935 Bridge Abutment Boreholes*

On the western side of the bridge adjacent to the reinforced concrete arch, a single borehole was undertaken adjacent to each abutment, 1 metre from the edge of the wall. A downhole magnetometer probe was to detect the presence of steel reinforcement within the concrete foundation and infer the base of the bridge foundation (Arumugam et al, 2014). The approximate level of the base of the reinforcement in the foundation is indicated in Figure 5 by the red horizontal line on the left hand side of the figure.

3.4 *Trial pits*

Two trial pits were excavated through the pavement of the bridge deck approximately. The dimensions of trial pits were 0.8 m x 0.6 m x 0.8 m (length x breadth x depth). The goal of the trial pits was to characterize the fill material between the pavement and the upper surface of the stone arch. The pits were manually excavated using lightweight pneumatic tools as a precautionary measure. The pits revealed that the fill material is variable containing boulders and gravelly sand above the stone deck slab that forms the roof of the galleries (Arumugam et al, 2014).

3.5 *Borehole Ground Penetrating Radar*

The Borehole Ground Penetrating Radar (BGPR) survey was completed in four (4) boreholes on the eastern side of the bridge with the aim of identifying the depth of the bridges' sandstone foundation.

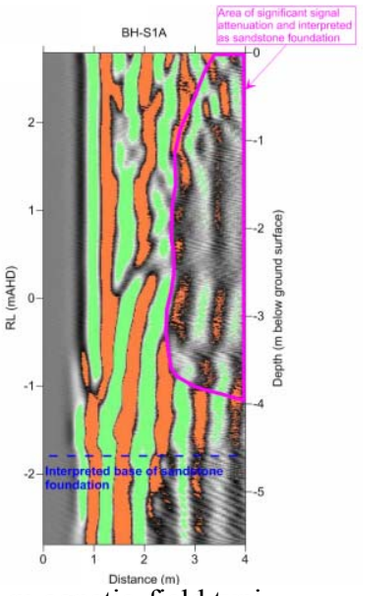
The BGPR method is similar to surface GPR methods in that it passes radio frequency electromagnetic energy pulses into the ground. However, the equipment is deployed down a vertical borehole and signals are radiated omni-directionally, thus sampling a cylindrical shaped volume of material down the borehole with a radius (i.e. depth of penetration) that is dependent on the dielectric properties of the material. Reflection of BGPR energy occurs at interfaces where contrasting electrical properties exist, such as sub-surface construction layers and natural ground. Where either a large reflector or signal attenuation occurred, this was interpreted as a result of the sandstone foundation of the bridge (Arumugam et al, 2014).

These results of the BGPR corresponded with the geotechnical boreholes drilled through the bridge. The approximate level of the base of the sandstone foundation is indicated in Figure 5 by the horizontal red line of the left hand side of the section.

3.6 *Downhole Magnetometer Testing*

Downhole magnetometer testing was performed on the western side of the bridge to identify the depth to the base of steel reinforcement in the foundation of the 1935 reinforced concrete bridge.

Downhole magnetic testing is a passive method based on the measurement of localised perturbations to the Earth's magnetic field. These perturbations may be caused by geological features and buried ferrous targets (e.g., pipes, cables, drums, iron sheets, steel reinforcement). Downhole magnetic testing was completed in-situ using pre-drilled, PVC cased boreholes.



The vertical component of the magnetic field typically provides the clearest indication of the base of the steel reinforcement in the bridge foundation and hence the approximate depth of the foundation. Magnetic anomalies present in the data generally indicate the approximate base of the steel reinforcement, see Figure 7.

Figure 7. Sample BGPR profile with interpretation (Arumugam et al, 2017)

3.7 *Ground Penetrating Radar (GPR) Survey of the bridge deck*

As part of the overall investigation a surface-based GPR survey of the bridge deck was completed to identify the depth of the stone deck and assess the fill material beneath the road pavement.

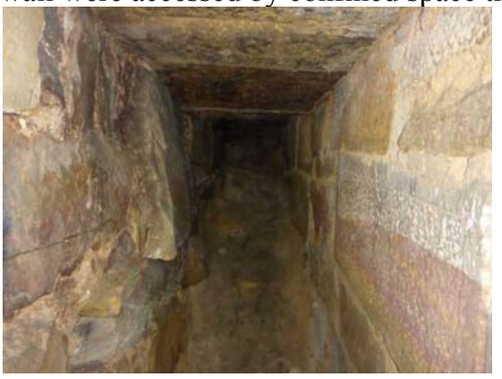
GPR data were collected along six (6) profiles parallel to the existing bridge alignment approximately 1.5m apart. The GPR identified several variations in the fill material as well as larger boulder size objects within the fill (Arumugam et al 2017).

3.8 *Structural Investigation*

The accessible sandstone surfaces of the abutments of the 1839 bridge was visually examined and tap tested locally for evidence of deterioration.

A petrographic analysis of intact lime mortar samples extracted by coring below the ground surface was undertaken to analyze the mineral composition and the presence of iron oxides.

The northeastern galleries behind the external spandrel wall were accessed by confined space trained



personnel.

Figure 8. View looking southwards in the northeastern gallery system

4 STRUCTURAL ASSESSMENT

4.1 *Arch Assessment under light rail vehicle loading*

The structural capacity of the masonry arch barrel was assessed using the arch analysis software Limit State RING 3.2.

A second model was developed using LS-DYNA to assess the bridge dynamic behavior, the response to horizontal loading and as a verification of the RING model.

4.2 *Load Model*

A load model representative of the actual rolling stock was used for the assessment.

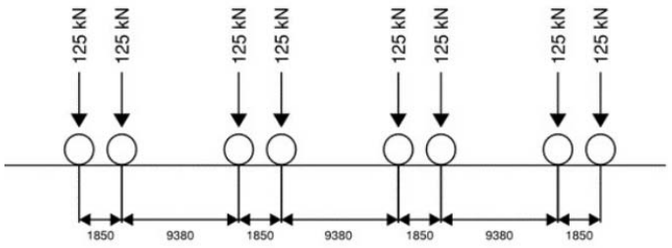


Figure 9. 45m LRV Loading Configuration

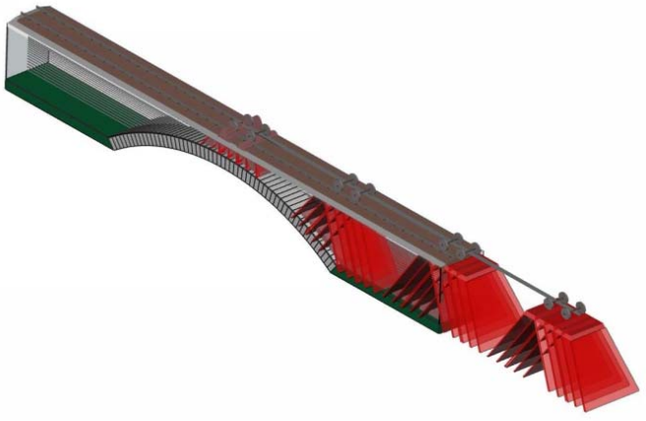


Figure 10. RING Analysis model

Two light rail tracks, northbound and southbound were assumed. Horizontal loading (braking, traction, nosing) were also considered.

Fatigue loading was also considered. Fatigue failure of a masonry arch bridge has not been positively identified to date, although there is some anecdotal evidence in the UK that repeated application of heavy loads could accelerate the deterioration of masonry arch bridges (CIRIA 2006). Laboratory experiments indicate an endurance limit for cyclic loading of about 50% of the static load strength, although there is some scatter in results (Roberts, Hughes and Dandamundi, 2004), (Melbourne, Tomor and Wang, 2004). For masonry arch bridges in the UK supporting highways, the current assessment code indicates that it "will be prudent" to limit the regularly applied loads to half the ultimate failure load (Highways Agency, 2001).

4.3 *Load factors and combinations*

Load factors and combination from AS 5100.7 (Standards Australia, 2017) were used.

4.4 *Material characteristics*

The masonry fabric material properties were based on the results of tests of core samples from sandstone masonry units extracted on the boreholes taken through the bridge deck. The core samples were tested for uniaxial compressive strength in accordance with AS 4133.4.2.2 (Standards Australia, 2013) with results in the range 16.9 – 19.3 MPa. The samples were also tested for deformability in accordance with AS 4133.4.3.2 (Standards Australia, 2013) and the secant modulus results were approximately 5 GPa.

4.5 *Strength Assessment Findings*

The outcome of the load rating of the masonry arch was that the arch barrel has significant residual resistance capacity to support the vertical and horizontal loading applied by light rail (2 LRV's, one travelling in each direction). The assessment included a series of sensitivity analyses to account for residual uncertainties in some of the parameters.

4.6 *Vibration Analysis*

In general, unless the bridges are structurally unsound or have decorative elements that are fragile in nature, vibration due to rail operation is not expected to cause damage to masonry arch structures of the type commonly found in the UK and similar to Lennox Bridge (CIRIA 2006).

As PLR is a light rail line with continuous welded rail the risk is further reduced as both of these factors reduce the dynamic loading applied to the bridge structure from rail operation.

A vibration analysis of the arch was carried out using LS-DYNA. No significant increase in structural

stresses were observed in the analysis indicating that dynamic effects are small.

Damage to the bridge structure from construction induced vibration is considered a higher risk that should be mitigated through appropriate selection of construction methodology, tools and work methods by the contractor. Recommended construction vibration limits are provided for heritage masonry structures.

4.7 *Masonry wing-walls assessment*

The light rail corridor is outside the zone of influence of the masonry wing walls however an assessment of the walls was carried out as part of the integrity assessment and will inform the management of the structural integrity of the bridge during construction.

4.8 *Hydraulic Assessment*

The bridge site has been subject to a number of significant floods since records began in 1795 including a massive flood event in 1988.

A flood retarding basin was constructed following plans by the Upper Parramatta River Catchment Trust in the mid 1990's (RMS, 2012). This alleviated flooding (but did not eliminate) flooding at the bridge site (RMS, 2012). The foreshore walkways were flooded in 2011.

A 2002 dive inspection revealed that a number of the blocks in the lower permanently submerged section of the abutment had been displaced outward and some were missing as a result of progressive scouring of the bedrock (RMS, 2012). This was later visually confirmed when the river was drained at this location (RMS, 2012). The damaged zone extended for approximately 10m.



Figure 11. Southern abutment scour damage (Fretwell Photography, 2002)

A scour remediation programme was undertaken in 2002 whereby the damage due to the scour hole and displaced blocks were plugged through a combination of grout injection and patch repair.

An inspection of the repair and an independent hydraulic assessment is underway at the time of writing.

4.9 *Services*

Several services cross the bridge including a water main installed in 2014 and managed by Sydney Water Corporation. The potential risk to the structural integrity of masonry arch bridges posed by water services is well documented (RAIB, 2017). A protection plan will be developed for the services including the watermain as part of the PLR construction phase to address the risk of damage to the watermain.

5 CONSERVATION MANAGEMENT

A detailed and comprehensive conservation management plan (RMS, 2012) has been developed by RMS. The plan provides detailed recommendations for the management of the structure including technical requirements for tasks such as mortar repair, stone surface repair, cleaning of graffiti etc. along with frequencies, protocols and workflows for maintenance and interventions.

6 CONCLUSIONS

The Lennox Bridge is a culturally significant heritage listed bridge. It is important to the people of Parramatta, both as a transport link, and as a piece of the local heritage. It has often been used as a popular symbol of the Parramatta City Council, the Local Government area in which it is located.

Lennox Bridge embodies the development of Parramatta from a semi-rural township to a major regional city and reflects the changing needs of the local community over more than 150 years (RMS, 2012).

The bridge will become part of the Parramatta Light Rail Stage 1 rail corridor. As part of the asset assurance process for PLR an investigation and structural assessment was carried out.

The assessment assessed the structural integrity of the bridge under the change of use imposed by the light rail system. The outcome of the assessment is that the bridge has sufficient residual capacity to support light rail.

The findings of the assessment will be used to inform the management of structural integrity and the fabric of this historic bridge during the design and construction of the PLR.

The bridge has comfortably handled a number of changes of use over the years from horse drawn traffic to motorized vehicles to trams. In the future it will transition to carrying 21st century light rail vehicles and become a key component of the new Parramatta light rail system.

7 ACKNOWLEDGEMENTS

The permission and support of the TfNSW PLR team and RMS Asset Management is gratefully acknowledged in the preparation of this paper.

7.1 *References*

Arumugam, Y., Hitchcock, P., Rohleder, R., Stewart, S. 2017. *A Case study – Geotechnical and geophysical investigations of an old stone heritage bridge at Parramatta, Greater Western Sydney NSW, Australia.*

Alsop, P.F.B. (2010) *David Lennox: Volume 1: The early years 1788-1833*. Geelong: published privately.

Alsop, P.F.B. (2014a) *David Lennox: Volume 2: The middle years 1833-1844*. Geelong: published privately.

Roads and Maritime Services, Sydney Region Asset Management Branch, 2012. *Conservation Management Plan, Lennox Bridge over Parramatta River, Parramatta*.

Selkirk, H. (1920) David Lennox: the bridge builder and his work. *Journal of the Royal Australian Historical Society* 6 (5), 201-243.

Standards Australia, 2017. *AS 5100.7 Bridge Design, Part 7: Assessment*

Standards Australia, 2013. *AS 4133.4.2.2 Methods of testing rocks for engineering purposes. Method 4.2.2: Rock strength tests – Determination of uniaxial compressive strength – Rock strength less than 50 MPa*

Standards Australia, 2013. *AS 4133.4.3.2 Methods of testing rocks for engineering purposes. Method 4.3.2: Rock strength tests – Determination of the deformability of rock materials in uniaxial compression – Rock strength less than 50 MPa*

CIRIA 656, 2006. *Masonry Arch Bridges: Condition Appraisal and Remedial Treatment.*

Roberts, Hughes and Dandamudi, 2004. *Progressive damage to masonry arch bridges caused by repeated traffic loading Phase2: Final Report.*

Melbourne, Tomor and Wang, 2004. *Cyclic load capacity and endurance limit of multi-ring masonry arches".*

Highways Agency, 2001. *Highway structrures: Inspection and Assessment. Assessment of highway bridges and structures. DMRB Volume 3 Section 4 Part 4 (BA 16/97).*

Rail Accident Investigation Branch. *Rail Accident Report, Partial collapse of a bridge onto open railway lines at Barrow upon Soar, Leicestershire 1 August 2016*

SS14: Resilience of bridges to climate change, natural & man-made hazards

Organizers: A.J. O'Connor & M. Nogal

Maintenance, Safety, Risk, Management and Life-Cycle Performance of Bridges – Powers, Frangopol, Al-Mahaidi & Caprani (Eds)
© 2018 Taylor & Francis Group, London, ISBN 978-1-138-73045-8

Seismic Performance of Bridges with Rocking Piers in Hanshin Expressway

Kyoko Azumi
Hanshin Expressway Company Limited, Osaka, Japan
Koichi Sugioka
Hanshin Expressway Company Limited, Osaka, Japan
Nobuhiro Mitsukawa
CTI Engineering Company Limited, Osaka, Japan

ABSTRACT: In April 2016, an earthquake of magnitude 7.3 occurred in Kumamoto Prefecture in Japan. Due to the strong tremor, a bridge with rocking piers collapsed. The rocking piers have pivot bearings both on top and bottom ends. As this structure is designed to only support vertical force, once the horizontal displacement occurs, the whole bridge structure would become unstable. In this study, one of same rocking pier bridges in Hanshin Expressway is focused on for seismic stability. Firstly, dynamic analysis for the whole bridge is carried out, and based on the results the retrofitting design is proposed. In the study, it is found that the reaction force of the existing bridge deduced significantly after the retrofitting. The dynamic analysis made after retrofitting proves that the response values of the entire bridge system remains unchanged.

1 INTRODUCTION

In April 2016, a magnitude 7.3 earthquake hit Kumamoto Prefecture located in the western Japan. Due to the strong lateral tremor, 4 bridges over expressway were damaged, and one of them collapsed and blocked the expressway as shown in Figure 1. The collapsed bridge has rocking piers with pivot bearing on top and bottom ends. As such rocking pier structure is designed to only support vertical force without horizontal support function, once the horizontal displacement occurs, the whole bridges structure would become unstable.
For safety concern, the national government ordered that the bridge managers should promptly propose an adequate solution of retrofit or removal of same rocking pier bridges.
In this study, dynamic analysis is carried out for grasping seismic performance of the bridge with rocking piers in Hanshin Expressway. Based on the results, improvement methods are proposed.

2 BRIDGE OVERVIEW

Table 1 and Figure 2 show the inventory data and the side and plan view of the target bridge respectively. Substructures of the bridge have 5 piers, and the middle pier (P3) owns 3 rocking columns with the alignment angle of 45° to the superstructure. P3 owns hinge bearings both on upper and bottom ends of the columns. The rest bearing conditions are fixed at P4 and movable at others. The bridge is in parallel with and over a bridge managed by another road authority, and P3 is situated on the central pier (Pier B) of the bridge which is situated in the river. Figure 3 shows the front view of P3 and Pier B.
There are multiple numbers of rocking pier bridges in Hanshin Expressway. Before Kumamoto Earthquake occurred, all of the rocking piers have finished their retrofitting to match with the utmost seismic level (hereafter referred as “Level 2” which is prescribed in the Japanese Design Specifications for Highway Bridges, 2012. Therefore, the rocking piers of the target bridge have a precondition of strengthening by column deviation prevention system (Komoto et al. 2005).
Moreover, the column other piers of the bridge has been retrofitted: P1 (reinforced concrete pier) is jacketed with steel plates, and P2, P4 and P5 (steel rigid-frame pier) are filled with concrete to increase ductility strength.

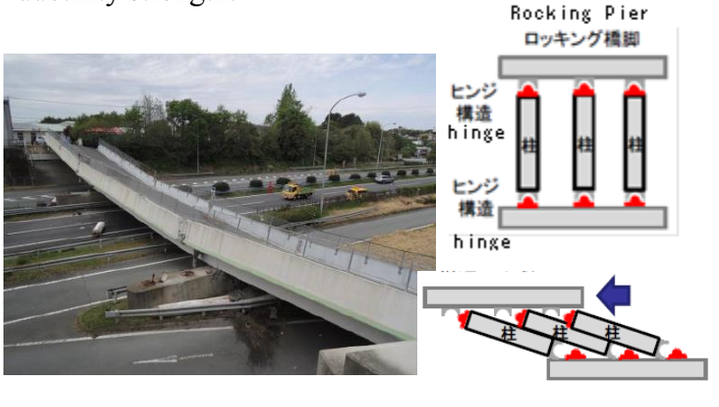


Figure 1. Disaster of Rocking Piers.

Table 1. Inventory Data of the Target Bridge.

Structure	4-span continuous steel box girder bridge
Bridge Length	208.000m
Span	47.5+58.124+55.876+45.555m
Substructure	P1: reinforced concrete pier P2,P4,P5:steel rigid-frame pier P3: bridges consist of 3 rocking piers
Completion	1979
Location	Osaka, Japan
Owner	Hanshin Expressway Co., Ltd

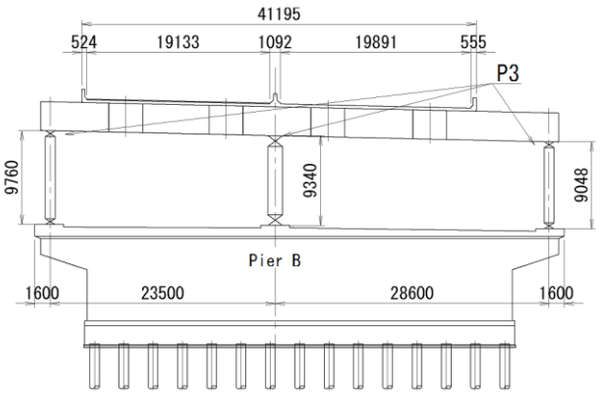


Figure 3.Cross-section of P3 and Pier B.

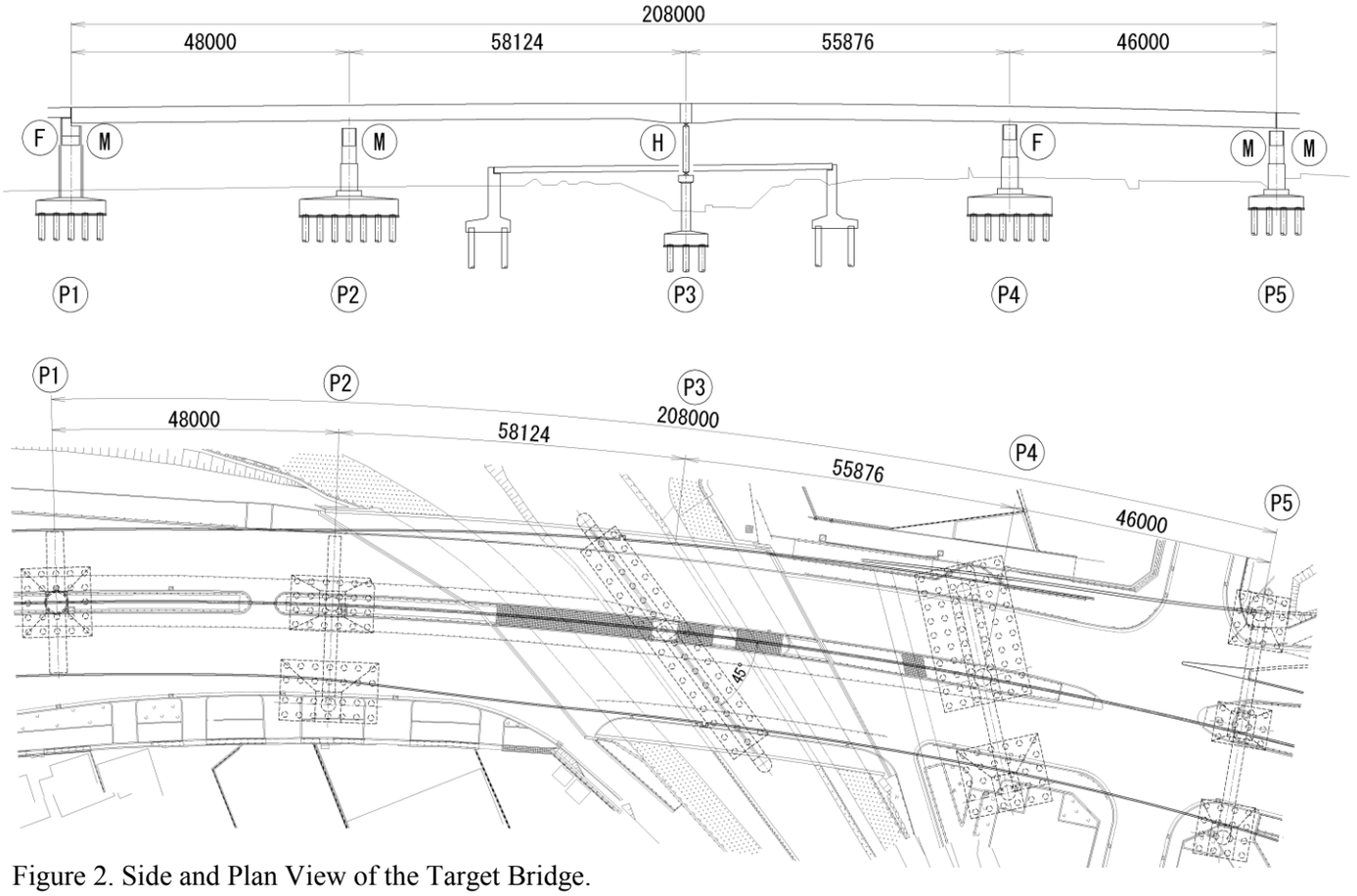


Figure 2. Side and Plan View of the Target Bridge.

3 ANALYTICAL POLICY

Before the confirmation of current seismic performance of the bridge, it is necessary to determine the bridge's seismic performance requirement. According to the Japan Specifications for Highway Bridges (Japan Road Association, 2012), collapsing of entire bridges must be avoided in case of Level 2 earthquake while fixable partial damage is allowed. This performance requirement is the outcome for improving rocking piers. Concretely, the entire bridge shall be changed to self-standing structural system.

When the 3 rocking columns of P3 become unstable, it is highly likely that the whole bridge may be collapsed. Therefore in the study, dynamic analysis is carried out for grasping seismic performance of the entire bridge system. Based on the results and the aforementioned seismic performance goal, appropriate retrofitting methods are proposed.

4 DYNAMIC ANALYSIS

4.1 *Analytical models*

3-Dimensions non-linear dynamic analysis was conducted for grasping seismic performance of the target bridge. Analysis software program is TDAP III (Ver3.05_01). Table 2 shows the given analytical conditions, and Figure 4 shows the analytical model.

In the model making, superstructure is modeled by elements of alignment considering it is consisted of linear members. Meanwhile piers are considered as non-linear members since they are expected to yield.

Steel piers are modeled by fiber element, and concrete piers are modeled by M-Φ element in which beams are element of alignment and columns are nonlinear element of beam (Japan Road Association, 2002). Estimated non-linear characteristics are shown in Figure 5 and Figure 6. Boundary condition of upper and bottom ends of rocking piers is modeled as pin connection. Foundation is modeled by element of linear springs which is concentrated on the foundation center.
The pier modelling also takes the previous seismic retrofitting into consideration. Bearings are modeled by linear springs and they bearing do not collide with girders even if they displace beyond the allowable limit.

4.2 *Input earthquake motion*
In this analysis, standard acceleration waveform is used for ground type II according to Japan Specifications for Highway Bridges.

4.3 *Limit states*
Limit state for each bridge member is shown in Table 3.

4.4 *Eigenvalue analysis*
Eigenvalue analysis is the method for grasping vibration characteristics of structure. Representative vibration mode in the eigenvalue analysis is shown in Figure 7. Natural period in the first transversal mode is about 1.09 seconds, and the effective mass ratio is 8 %. In this case, the vibration mode of superstructure indicates the vertical direction. The period in the second transversal mode is 0.92 second, and the effective mass ratio is 12 %. In this case, the vibration mode is that the deformation of superstructure is relatively small while all the piers except P3 move greatly.

Table 2. Conditions of Dynamic Analysis.

Analysis method		Time history response analysis program
Eigen value analysis		Sub space method
Integration		Newmark－β methods (β ＝0.25)
Attenuator		Rayleigh attenuator
Time interval of integration		0.002 second
element	Superstructure	elements of alignment
	Steel pier	element of fiber
	Reinforced concrete pier	M-Φ element
	Bearing	element of linear springs
Restoring model	Steel pier	Bi-linear
	Reinforced concrete pier	Tri-linear

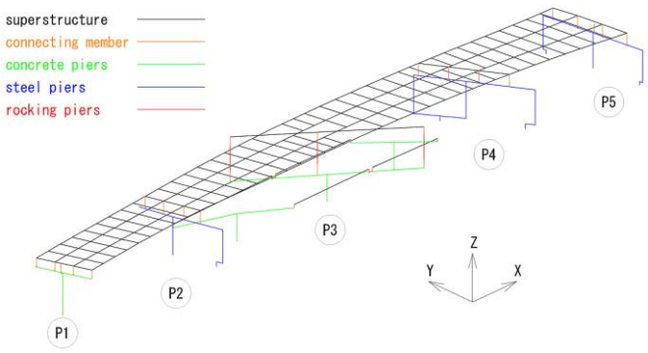


Figure 4. Model of Dynamic Analysis.

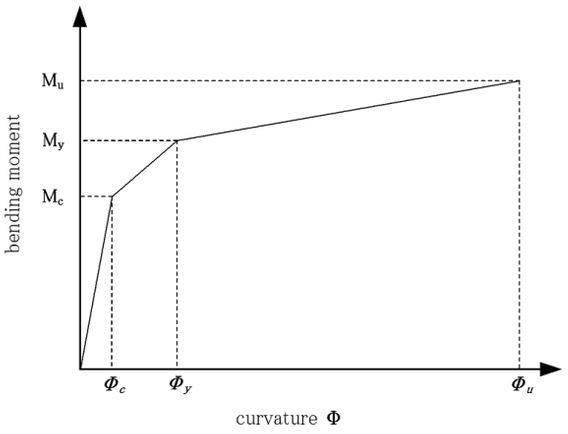


Figure 5. Nonlinear Modelling (Reinforce concrete Pier).

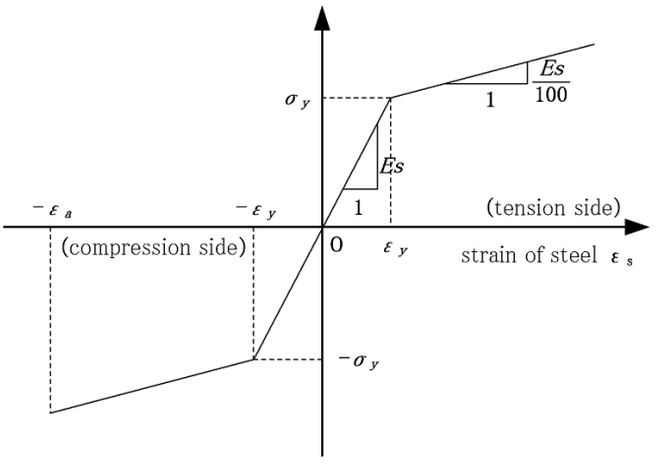
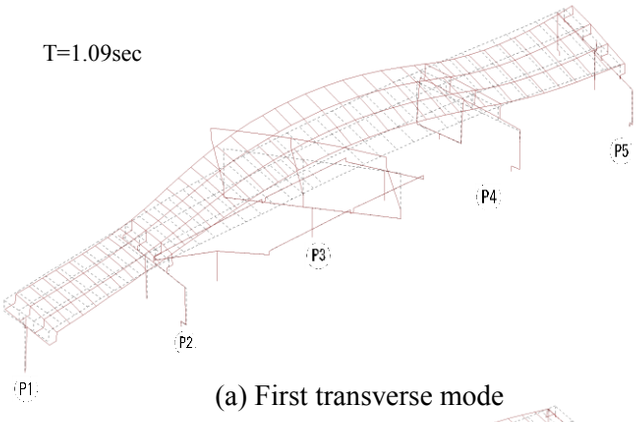


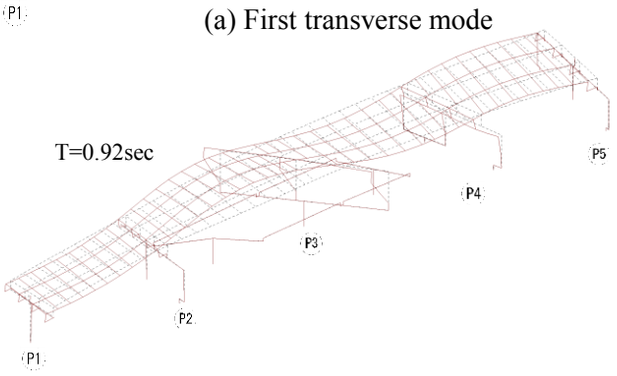
Figure 6. Non-linear Modelling (Steel Pier).

Table 3 Limit State.

	Limit State	
Super-structure	Not to be exceeded elastic area	
Bearing	Stress	Not to be exceeded elastic area
	Displace-ment	Not to collide with girders
Sub-structure	Retrofit easily	
founda-tion	Keep plasticized secondary	



(a) First transverse mode



(b) Second transverse mode

Figure 7. Representative Vibration Mode.

4.5 *Analysis result*

In this analysis, vibration input direction is superstructure's axial direction and transversal direction. In addition, skewed axial and transversal direction of P3 is also added.

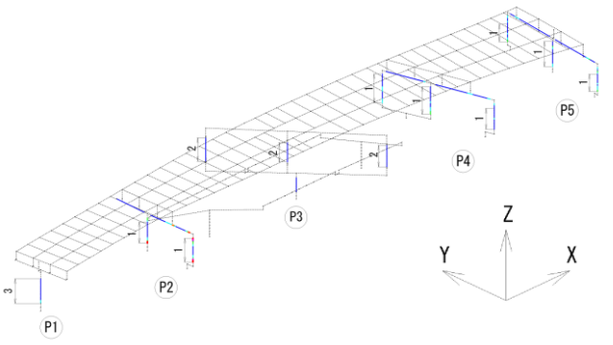
Figure 8 show the analysis results in terms of the ratio of allowable value by response value. In this figure, colors legends show the excess degree of strain. For example, in the case of concrete pier, this blue member means that the strain of the concrete pier is within an allowable value.

Since the target bridge has a one-fix support (P4) system, the response's excessive ratio for P4 tends to be larger than that of other piers. Pier B which supports P3 has a relatively big supporting redundancy and it is regarded safe even if one side of hinge bearing of P3 is changed to be fixed.

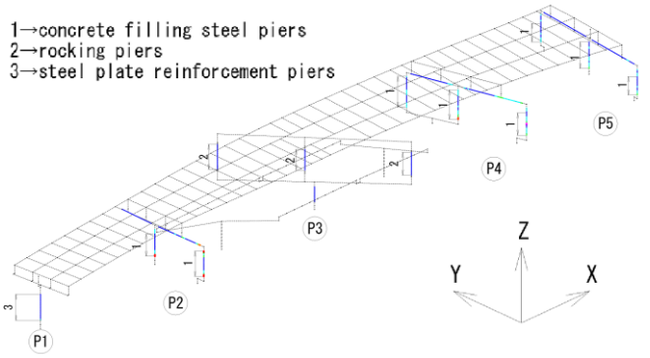
5 IMPROVEMENT METHODOLOGY

Improvement methods for P3 are proposed for preventing its partial destruction from leading to a whole bridge collapse. As a possible solution, it can be considered that additional safeguard structure supports dead load in case the rocking piers become unstable. However, it is difficult to be constructed because P3 is on Pier B and has a limited space.

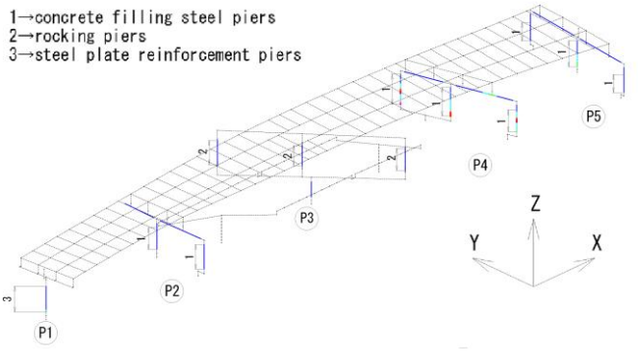
Therefore, as another option as shown in Figure 9, it is proposed and examined that P3 is transformed to a self-standing structure where the upper end bearings are replaced with sliding bearings and the lowerare changed to rigid-connecting structures.



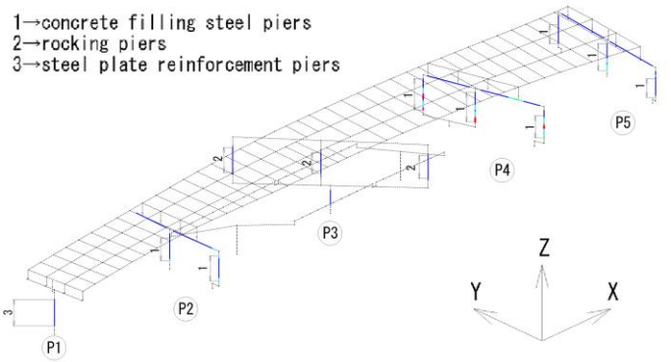
(a) Bridge axial direction



(b) Bridge transversal direction



(c) P3 beam axial direction



(d) P3 beam transversal direction

	concrete pier	steel pier (rectangular section)	steel pier (circular section)
Level 1 : 0.00 ~ 1.00	↑ within allowable value		
Level 2 : 1.00 ~ 2.00	↓ over allowable value	↓ plasticizing	↓ plasticizing
Level 3 : 2.00 ~ 5.00			
Level 4 : 5.00 ~ 7.00			
Level 5 : 7.00 ~ 7.50		↑ within allowable value	
Level 6 : 7.50 ~ 8.80		↓ over allowable value	↑ within allowable value
Level 7 : 8.80 ~			↓ over allowable value

Figure 8. In-situ Structure Analysis Result.

The profiles of the sliding bearings are shown in Table 4.

Figure 10 shows the results dynamic analysis after the P3 improvement is carried out. In a similar fashion with in-situ bridge system, the post-improvement structure shows the excessive ratio of P4 is larger than that of other piers while the response value has no significant difference between the old and the new.

However rocking piers improvement makes Pier B less safe, its response values does not exceed the allowable value. In case of using sliding bearings, it is concerned that excessive bending moment is generated because the lower end is fixed. However, the moment value is less than the allowable value for Pier B beam.

Therefore, the practicality and seismic upgrading of rocking piers improvement using sliding bearing can be confirmed. Moreover, as shown in Table 5, the horizontal displacement of sliding bearings after the improvement is about 50cm, which proves the functionality of sliding bearing.

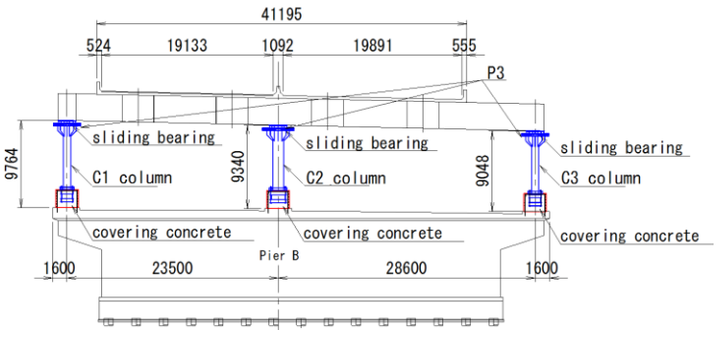
Table 4. Profiles of Sliding Bearing.

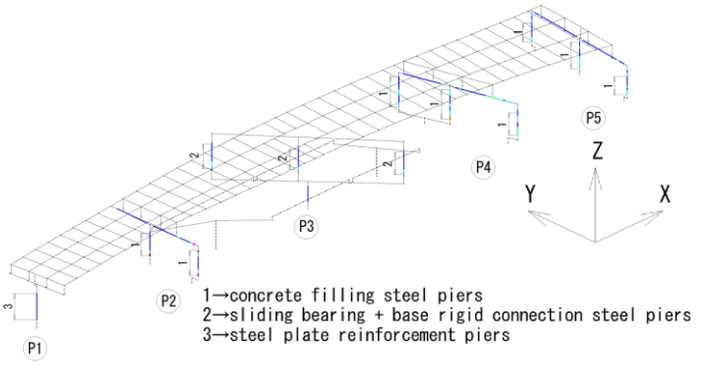
spec	Sliding plate of stainless steel	
Planer shape	Left and right column	2.150×2.350m
	center column	2.500×2.700m
Friction coefficient	μ=0.05	

Table 5. Displacement of Sliding Bearings.

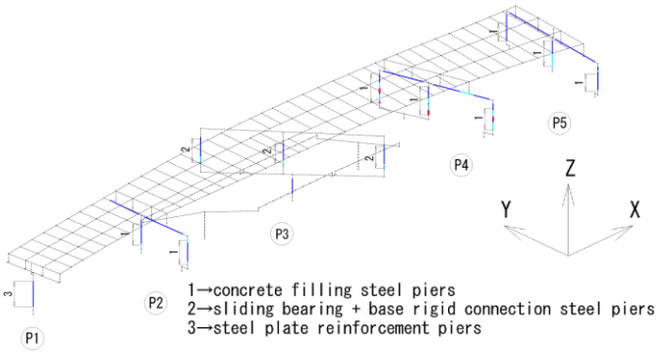
	P3-C1 column	P3-C2 column	P3-C3 Column
Maximum displacement	0.504	0.525	0.464

Figure 9. Improved structure.

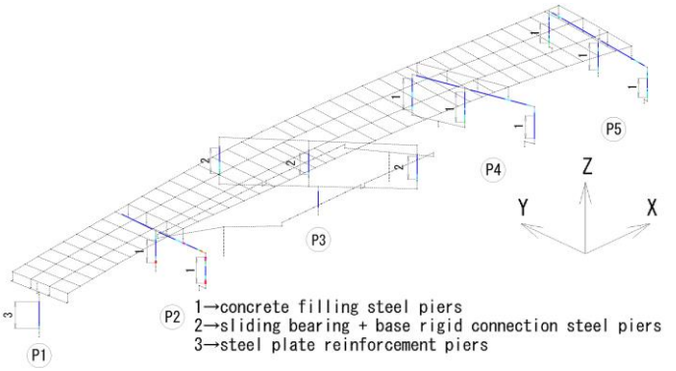




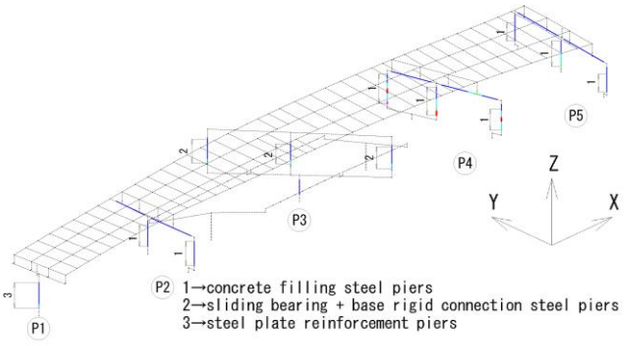
(a) Bridge axial direction



(b) Bridge transversal direction



(c) P3 beam axial direction



(d) P3 beam transversal direction

	concrete pier	steel pier (rectangular section)	steel pier (circular section)
Level 1 : 0.00 ～ 1.00	↑ within allowable value		
Level 2 : 1.00 ～ 2.00	↓ over allowable value	↓ plasticizing	↓ plasticizing
Level 3 : 2.00 ～ 5.00			
Level 4 : 5.00 ～ 7.00			
Level 5 : 7.00 ～ 7.50		↑ within allowable value	
Level 6 : 7.50 ～ 8.80		↓ over allowable value	↑ within allowable value
Level 7 : 8.80 ～			↓ over allowable value

Figure 10. Improve Structure Analysis Result.

6 CONCLUSIONS

Dynamic analysis targeted for rocking pier bridge system is conducted to identify the seismic performance, and the comparison between the in-situ structure and the improved structure evaluates the validity of the improvement method. The followings are key findings obtained by the analysis:

(1) In-situ structure

The excessive ratio of response value on fixed P4 of the bridge tends to be larger than that of other movable piers. Meanwhile since P3 with rocking columns which is on the relatively big and stable Pier B of surface street bridge, it is found that the hinge connection can be transformed into fixed connection by relying on its supporting redundancy.

(2) Improved structure

Under the given condition that the improvement of rocking piers should be considered on the limited area, it is proposed that hinge connections are replaced with sliding bearings on the upper ends and changed to rigid connection on the lower ends. And the dynamic analysis examines the validity of this improvement method confirms that it can keep the same level of the seismic performance compared with in-situ structure. Moreover, the functionality of sliding bearings used in the improvement is confirmed by checking their displacements.

7 REFERENCE

Komoto, K., Yonezawa, Y., Suzuki, T., Takei, K., & Honda, T. 2005. Seismic retrofitting for the Kizugawa bridge on Hanshin expressway, *28th JSCE Earthquake Engineering Symposium* (in Japanese)

Japan Road Association. 2012. *Design Specifications for Highway Bridges Part 5 Seismic Design.* Tokyo: Maruzen Co. Ltd. (in Japanese)

Japan Road Association. 2002. *Design Specifications for Highway Bridges Part 5 Seismic Design.* Tokyo: Maruzen Co. Ltd. (in Japanese)

Maintenance, Safety, Risk, Management and Life-Cycle Performance of Bridges – Powers, Frangopol, Al-Mahaidi & Caprani (Eds)
© 2018 Taylor & Francis Group, London, ISBN 978-1-138-73045-8

Resilience Assessment of Highway Bridges using SMA-based Isolation Bearings

Y. Dong[1], Y. Zheng[2] & Y.H. Li[1]
[1]: Department of Civil and Environmental Engineering, The Hong Kong Polytechnic University, Kowloon, Hong Kong, China
[2]: Department of Bridge Engineering, Tongji University, Shanghai, China

ABSTRACT: Nowadays, shape memory alloy (SMA) has been adopted within the design and retrofit of highway bridges to improve the seismic performance. The performance benefit associated with the SMA bridges has not been well recognized and the relevant study is still needed. This paper aims to apply the resilience assessment to the comparative performance assessment of novel bridges using SMA. The corresponding structural performance on basis of fragility analysis and resilience are addressed. The proposed approach is applied to highway bridges with SMA-cable-based bearings.

1 INTRODUCTION

SMAs are generally associated with high strength besides the super-elasticity and energy dissipation; thus (DesRoches *et al*. 2004; Song *et al.* 2006). SMA could be implemented to resist the high seismic load without significant permanent residual deformations. In this paper, SMA is adopted within the highway bridges to improve the seismic performance under earthquake hazard. The application of SMA within the bridge seismic mitigation process has been studied previously. SMA-cable/bar restrainer was used to replace the steel bar restrainer and was installed at in-span hinge or interface between the girder and abutment. In the previous study, Choi *et al*. (2005) developed an isolation device that integrated SMA wires with rubber/elastomeric bearing to reduce the permanent residual deformation of the bridges under earthquakes. Xue and Li (2007) proposed a rubber bearing installed with pre-tensioning SMA-wires and applied it to a lattice shell structure for seismic mitigation. In this paper, a novel frictional sliding bearing with SMA-cable, which fully takes advantages of the properties of SMAs, such as self-centering, super-elasticity, and energy dissipation is investigated. Another difference from the previous devices with application of SMA is that the SMA-cable is adopted instead of the wire to improve the re-centering capacity of SMA-wire. Additionally, this type of isolation device is more easily to be manufactured and installed. The effects of the proposed SMA-cable-based device on the bridge seismic performance are investigated.

With respective to the hazard management of infrastructures, a widely-recognized indicator is resilience (Frangopol *et al.* 2017). Researchers have turned attention to the challenge of making infrastructure systems more resilient against devastating earthquakes. Resilience is related with the ability of a structural system to mitigate the hazard damage to infrastructures. A methodology to evaluate the seismic resilience of novel bridges is obliged to meet current performance requirements. The seismic resilience associated with novel bridge systems with SMA is investigated in this paper. The computational process is shown in Figure 1. Overall, a perfor-

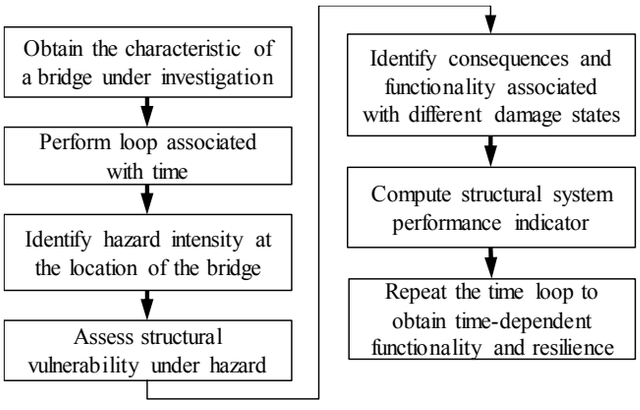


Figure 1. Flowchart of resilience assessment process under hazard effects

mance-based assessment framework that incorporates both resilience and life-cycle engineering is provided in this paper. This framework can be used for making comparison among different alternative designs and retrofit actions.

Overall, an approach to assess the seismic resilience of novel bridge systems is presented in this paper. The structural vulnerability of the novel structural systems is computed based on three-dimensional (3D) nonlinear finite element (FE) models considering the representative hazard scenarios that can happen during the investigated time interval.

2 STRUTURAL SEIMSIC VULNERABILITY USING SMA

Given the chosen seismic ground intensity, the median value of seismic demand can be computed as (Cornell *et al.* 2002; Decò and Frangopol 2013; Dong *et al.* 2013)

$$\ln(EDP) = \ln a + b\ln(IM) \tag{1}$$

where IM is the ground motion intensity indicator and a and b are regression parameters derived from the analytical responses. A 3D FE model can be established using the SAP 2000 (Computers and Structures Inc. 2010) or OpenSees (McKenna *et al.* 2004) to assess the seismic demand. Under a given ground motion intensity IM, the fragility curves can be expressed as (Cornell *et al.* 2002; Zhang and Huo 2009)

$$P[EDP - DI_i \geq 0 | IM] = 1 - \Phi\left(\frac{\ln(DI_i / aIM^b)}{\xi_{EDP|IM}}\right) \tag{2}$$

where $\Phi(.)$ is the standard normal distribution function and $\xi_{EDP|IM}$ is the standard deviation of the logarithmic distribution. The standard deviation of $\ln(EDP)$ under given IM can be computed as (Baker and Cornell 2006)

$$\xi_{EDP|IM} = \sqrt{\frac{\sum_{i=1}^{n}[\ln(EDP_i) - (\ln a + b\ln IM_i)]^2}{n-2}} \tag{3}$$

where n is the number of the selected earthquake ground motions and EDP_i is the seismic response corresponding to the ith earthquake ground motion.

Given the fragility curves of the components, fragility curve of a bridge system can be developed accounting for the relationship between the vulnerable components and assessing structural performance as an overall system. Some studies simply considered the column damage as the performance indicator of bridge system without considering other components. Additionally, Nielson and DesRoches (2007) computed the bridge fragility curves as an event that at least one component exceeds its corresponding damage state. Furthermore, Monte Carlo simulation method can be utilized to conduct the system fragility of bridges. The lower bound is the maximum component fragility and the upper bound is a combination of the component fragilities. These bounds are expressed as follows (Nielson and DesRoches 2007)

$$\max_{k=1}^{m}[P(F_k)] \leq P(F_{\text{sys}}) \leq 1 - \prod_{k=1}^{m}[1 - P(F_k)] \tag{4}$$

where m is the number of the vulnerable component; $P(F_k)$ is the probability failure of the kth component; and $P(F_{\text{sys}})$ is the failure probability of the bridge system.

SMA is a smart and novel material associated with shape memory and super-elasticity properties (Ozbulut *et al.* 2011). The shape memory effect is the ability of SMA to recover its original shape after deformation through a thermal cycling. The super-elasticity effect is described as the ability to recovery from a large strain due to the stress-induced martensitic phase transformations. To reflect the two properties of SMA, a flag-shaped hysteretic model (Tremblay *et al.* 2008) of SMA was shown in Figure 2, in which E_A and E_M are the Young's moduli of the SMA material at austenite and martensite phases, respectively. Given the cross-sectional area and the free displacements in both longitudinal and transverse directions of the SMA-cable, the strain-stress constitutive model of SMA-cable can be established using a one-dimension flag-shaped force-displacement model associated with the proposed isolation device. The more detailed information could be found in Zheng *et al*. (2018).

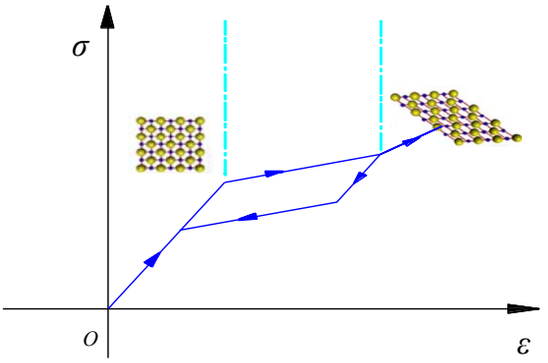


Figure 2. Constitutive hysteretic model of SMA material

3 RESILIENCE ASSESSMENT

Within the last few decades, the occurrence of disruptive, low-probability, high-consequences extreme events across the globe has shifted the focus of scientific communities and decision makers to develop approaches which can improve the resilience of in-

frastructure to disasters. In general, earthquake resilience in civil engineering can be defined as (Bruneau *et al.* 2003) "the ability of social units (e.g., organizations and communities) to mitigate hazards, contain the effects of disasters when they occur, and carry out recovery activities in ways that minimize social disruption and mitigate the effects of future earthquakes". The most widely adopted approach to quantify the resilience of an individual structure, a group of structures, or a network of interrelated structures is to compute the resilience as the integration over time of the functionality (Cimellaro *et al.* 2010; Frangopol and Bocchini 2011)

$$RE = \frac{1}{t_r}\int_{t_0}^{t_0+t_r} Q(t)dt \tag{4}$$

in which $Q(t)$ is the functionality, t_o is the occurrence time of the extreme event, and t_r is the investigated time horizon. The resilience, as computed by Eq. (4), can be illustrated graphically as shown in Figure 3 for one and multiple extreme events during the life-cycle of a system, respectively. The earthquake hazard is emphasized in this keynote paper. Regarding the seismic performance analysis, the first step in seismic vulnerability assessment is to identify the seismic intensity associated with the location of the structural system under investigation (Dong and Frangopol 2015). A specific number of seismic scenarios should be generated within the region of interest. The generated scenarios should be able to approximate the actual seismic activity of the geographical area.

4 NUMERICAL EXAMPLE

The presented approach is applied to a reinforced concrete (RC) bridge with the SMA-cable-based bearing. The relevant performance indicators, such as fragility curves and resilience are investigated and compared with the bridge without using SMA. The bridge investigated herein is a continuous RC bridge with two equal spans as shown in Figure 4. As indicated, the height and the width of the RC two-box girder are 1.2 *m* and 12.5 *m*, respectively. The clear height of the RC column is 7.0 *m*, and the cross section of the RC column is 0.9 *m* × 0.9 *m*.

In order to conduct the nonlinear time-history analysis, a set of 40 ground motion records is selected from Pacific Earthquake Engineering Research Center Ground Motion Database. This suite of selected records covers a wide range of magnitude. The seismic performance of SMA-cable-based bearings and the RC columns, as the most vulnerable

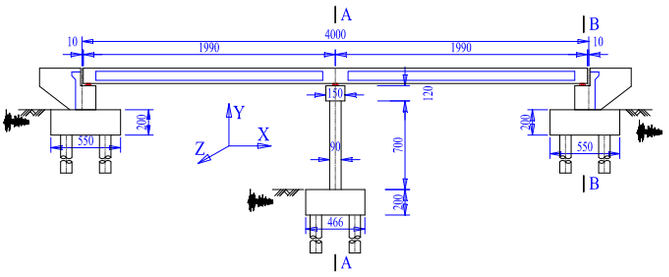


Figure 3. Elevation of the bridge under investigation

components, is investigated and median values corresponding to their appropriate seismic demands are computed using Eq. (1). For the RC column within the bridge, taking the PGA and maximum curvature ductility as the seismic intensity and demand parameter, the two constants *a* and *b* can be obtained based on the linear regression and they are 5.233 and 1.480, respectively.

Given the fragility curves associated with different components, the system-level fragility curve can be obtained. The system failure model proposed by Nielson and DesRoches (2007) is used to compute the system-level bridge fragility curve considering the seismic performance of the columns and bearings. The fragility curves of the bridge system at each damage state compose two parts, i.e., upper and lower bounds. The upper bound indicates the combination of the component fragilities while the lower bound represents the maximum component fragility. The fragility curves associated with moderate and major damage states are plotted in Figure 4. As indicated, the SMA-cable-based bearing can improve the structural performance of the bridge system significantly. At moderate damage state, the upper and lower bounds are much higher than those with SMA.

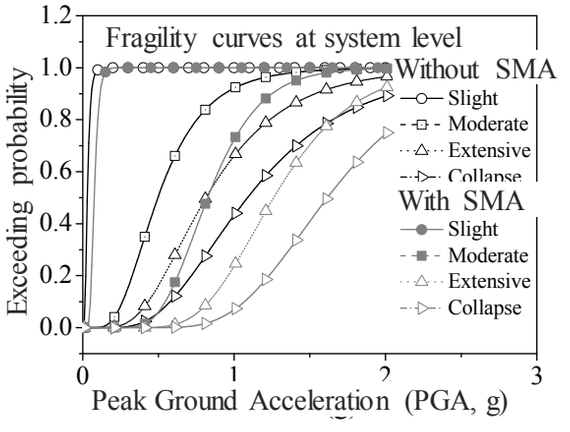


Figure 4. Fragility curves of the bridges with and without using SMA

The resilience of the novel bridges is assessed herein, in which the functionality of bridges considering different damage states should be identified firstly. The following scenarios are considered: immediate access, weight restriction, one lane open only, emergency access only, and bridge closed. Given the hazard intensity, the functionality of the bridges after the earthquake is computed using Eq. (4). The four hazard scenarios are investigated herein, which refer to the 715- and 1450-year return period earthquakes. Hazard curve parameters for the investigated

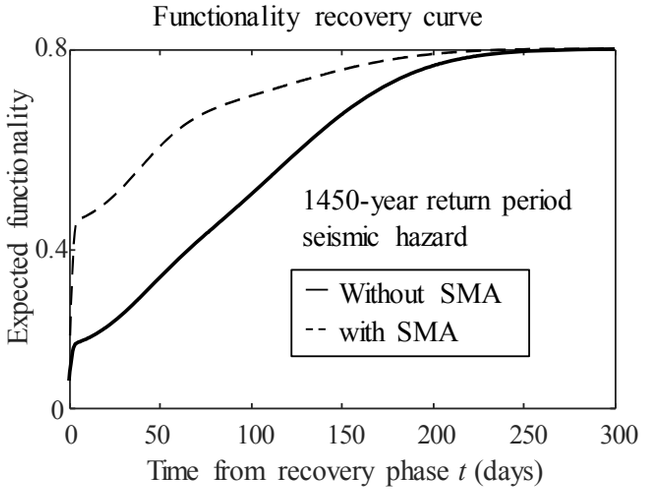


Figure 5. Time-dependent functionality of the bridge under given recovery action

region are based on the United States Geological Survey. The *PGA*s with return period of 715 and 1450 are 0.357 and 0.568, respectively. Given the seismic intensity and fragility curve, the probabilities of the bridge being in different damage states can be obtained, which act as the input for Eq. (4). The expected residual functionalities of the novel bridge under four selected seismic intensities are 0.562 and 0.365, respectively. The recovery path is based on ATC (1999). Accordingly, the bridge functionality restoration process is modeled by a normal cumulative distribution function corresponding to each of the four bridge damage states: slight, moderate, major, and complete. Under the investigated 715 and 1450-year return period earthquake and recovery actions, the functionality of the bridge is shown in Figure 5. As indicated, the functionality of the damaged bridge increases with time and there exists a significant difference between the bridges with and without using SMA. The resilience of the SMA bridges under the investigated seismic hazard intensities is 0.948 and 0.862, respectively. By comparing these values, the resilience of the bridge can be increased of adopting SMA novel system under 1450-year seismic event. As indicated, the performance benefit of resilience associated with SMA increases with a larger investigated hazard intensity.

5 CONCLUSIONS

This paper presents an approach to assess the resilience of novel structural systems with SMA cable-based bearings. The fragility curves associated with the novel bridges with SMA were evaluated by using nonlinear time-history analysis. Resilience under the investigated hazard scenarios were assessed, taking into account hazard recovery pattern. The proposed novel isolation device was applied to a continuous RC bridge. Based on the outcomes, the proposed novel isolation device can improve the seismic performance of the bridge significantly. Thus, the bridges with the proposed SMA devices proved to be effective considering the structural performance associated with bridge failure. The resilience of the novel bridge systems was assessed in this study. The functionality and probability of the bridge in different performance levels were computed to aid the assessment of resilience. The investigated seismic intensity can affect the resilience significantly.

ACKNOWLEDGEMENTS

The study has been supported by The Hong Kong Polytechnic University under Start-Up Fund (1-ZE7Q) is gratefully acknowledged. The opinions and conclusions presented in this paper are those of the authors and do not necessarily reflect the views of the sponsoring organization. The opinions and conclusions presented in this paper are those of the authors and do not necessarily reflect the views of the sponsoring organization.

REFERENCES

ATC (1999). Earthquake damage evaluation data for California. *Technical report ATC-13*. Applied Technology Council.

Baker, J.W., and Cornell, C.A. (2006). Vector-valued ground motion intensity measures for probabilistic seismic demand analysis. *PEER report 2006.08*. Berkeley: Pacific Earthquake Engineering Research Center, University of California Berkeley.

Bruneau M., Chang S.E., Eguchi R.T., Lee G.C., O'Rourke T.D., Reinhorn A.M., Shinozuka M., Tierney K., Wallace W.A., and Winterfeldt D.V. (2003). A framework to quantitatively assess and enhance the seismic resilience of communities, *Earthquake Spectra*, 19, 733-752.

Choi, E., Nam, T., and Cho, B.S. (2005). A new concept of isolation bearings for highway steel bridges using shape memory alloys. *Canada Journal of Civil Engineering*, 32, 957-967.

Cimellaro, G.P., Reinhorn, A.M., and Bruneau, M. (2010). Seismic resilience of a hospital system. *Structure and Infrastructure Engineering*, 6, 127–144.

Cornell, A.C., Jalayer, F., and Hamburger, R.O. (2002). Probabilistic basis for 2000 SAC federal emergency management

agency steel moment frame guidelines. *Journal of Structural Engineering*, 128, 526-532.
Decò, A., Bocchini, P., and Frangopol, D.M. (2013). A probabilistic approach for the prediction of seismic resilience of bridges. *Earthquake Engineering & Structural Dynamics*, 42(10), 1469-1487.
DesRoches, R., McCormick, J., and Delemont, M. (2004). Cyclic Properties of Superelastic Shape Memory Alloy Wires and Bars. *Journal of Structural Engineering,* 130(1), 38-46.
Dong, Y., Frangopol, D.M., and Saydam, D. (2013). Time-variant sustainability assessment of seismically vulnerable bridges subjected to multiple hazards. *Earthquake Engineering and Structural Dynamics*, 42(10), 1451-1467.
Dong, Y., and Frangopol, D.M. (2015). Risk and resilience assessment of bridges under mainshock and aftershocks incorporating uncertainties. *Engineering Structures*, 83, 198-208.
Frangopol, D.M., and Bocchini P. (2011). Resilience as optimization criterion for the rehabilitation of bridges belonging to a transportation network subject to earthquake. *In: SEI-ASCE 2011 Structures Congress*, April 14-16, 2011, Las Vegas, NV.
Frangopol, D.M., Dong, Y., and Sabatino, S. (2017). Bridge life-cycle performance and cost: Analysis, prediction, optimization and decision making, *Structure and Infrastructure Engineering*, Vol 13, No. 10, 1239-1257.
McKenna, F., Fenves, G.L., and Scott, M.H. (2004). OpenSees: Open System for Earthquake Engineering Simulation. Pacific Earthquake Engineering Research Centre, University of California, Berkeley, CA. http://opensees.berkeley.edu.
Nielson, B.G., and DesRoches, R. (2007). Seismic fragility methodology for highway bridges using a component level approach. Earthquake *Engineering and Structural Dynamics,* 36, 823-839.
Ozbulut, O.E., Hurlebaus, S., and Desroches, R. (2011). Seismic response control using shape memory alloys: a review. *Journal of Intelligent Material System and Structures*, 22(14), 1531-1549.
Song, J., and Kang, W.H. (2009). System reliability and sensitivity under statistical dependence by matrix-based system reliability method. *Structural Safety*, 31(2), 148-156.
Tremblay, R., Lacerte, M., and Christopoulos, C. (2008). Seismic Response of Multistory Buildings with Self-Centering Energy Dissipative *Steel Braces. Journal of Structural Engineering*, 134(1), 108-120.
Xue S., and Li X. (2007). Control devices incorporated with shape memory alloy. *Earth. Eng. Eng. Vib*., 6(2),159–169.
Zhang, J., and Huo, Y. (2009). Evaluating effectiveness and optimum design of isolation devices for highway bridges using the fragility function method. *Engineering Structures*, 31, 1648-1660.
Zheng. Y., Dong, Y., and Li, Y. (2018). Resilience and life-cycle performance of smart bridges with shape memory alloy (SMA)-cable-based bearings, *Construction & Building Materials*, Elsevier, 158, 389-400.

Maintenance, Safety, Risk, Management and Life-Cycle Performance of Bridges – Powers, Frangopol, Al-Mahaidi & Caprani (Eds)
© 2018 Taylor & Francis Group, London, ISBN 978-1-138-73045-8

Resilience evaluation of a cable-stayed bridge

H. Gil, K. Han & S. Seo
Super Long Span Bridge R&D Center, Korea Expressway Corporation

J. Park
Korea Expressway Corporation Research Institute, Korea Expressway Corporation

ABSTRACT: A lightning induced fire damaged three stay cables of a cable stayed bridge in Korea. The steel-concrete composite cable st ayed bridge is 990m -long and consists of three cable-stayed spans of 200m + 470m + 200m and two 60m -long end spans. The cable-stayed span is suppor ted by 144 parallel wire strand (PWS) cables. The fire caused by lightning strike led to complete rupture of one stay cable and partial rupture of two more stay cables. The bridge was closed for 15 days to remove and reinstall damaged stay cables. This extreme event provides an opportunity to review the resi lience of the cable-stayed br idge. A resilience of infrastructure is usually def ined as the ability to re duce the magnitude and duration of da mage caused by extreme events. As the number of natural and man-made disasters has increased these days, the vulnerability and resilience of highway bridges need to be evaluate d and improved. The resilience can be evaluated through four "R"s: robustness, redundancy , resourcefulness, and rapidity. In this paper, the resilience of the cable-stayed bridge is evaluated in terms of four "R"s.

1 SEOHAE BRIDGE

The Seohae Bridge, which ope ned to traffic in November 2000, is located approxim ately 65 km south of Seoul and is one of the longest cable-supported bridges in Korea. The tota l length of the bridg e is 7.31 km and it consists of a cable-stayed bridge and two different types of pre- stressed concrete (PSC) box-girder bridges. The cab le-stayed bridge, which is 990-m long, consists of three cable-stayed spans of 200 m + 470 m + 200 m and two 60- m long end spans of simply-supported composite girders (Figure 1).

The deck cross section consists of two longitudinal steel girders spaced 34- m apart, with ste el floor beams between these edge girders at 4.1 m on center, and precast concrete panels. The tw o pylons are H-shaped concrete structur es that reach 186-m above sea level. The three cable-stayed spans are supported by two planes of stay cables each plane contain s 72 cables. The length of stay cables ranges from 54 to 228 m. The stay cables are num bered from 1 to 72, left to right. These cables are m ade up of seven-wire strands with diam eters of 15.2 mm. The strands are galvanized, covered by wa x, individually sheathed, and placed inside a hi gh density polyethylene (HDPE) pipe without grout.

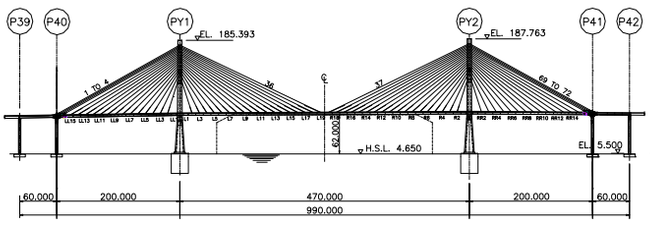


Figure 1. Schematic view of the Seohae Bridge

To monitor the structural response and evaluate the performance of the Seohae Bridge, the structural health monitoring system, called the Seohae S tructural Health Monitoring System (SSHMS), was installed in the year 2000 and have been continuously operated since then. In 2009, the SSHMS was totally renovated due to the deterioration of hardware and software (Gil et al. 2010). Most of the existing sensors such as accelerom eters, temperature sensors, and tiltmeters were replaced during renovation. A real-time kinematic (RTK) GNSS (Global N avigational Satellite System) monitoring system was newly installed to monitor the static and dynamic behavior of the Bridge.

2 CABLE FIRE

Fire is the one of most severe hazards which can lead to partial or total collapse of the bridge. A number bridge fires are reported in the literature (Garlock et al. 2012). It was also reported that two cable-stayed bridges experienced cab le fire and partial

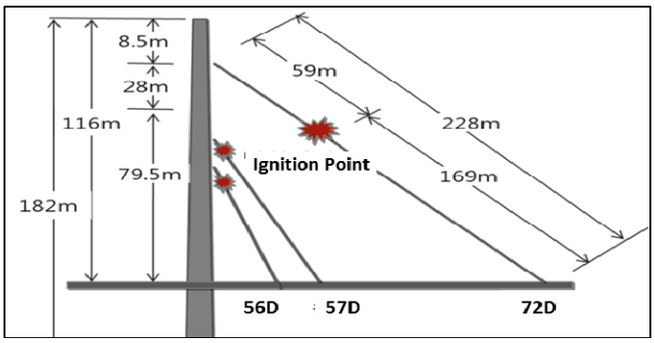


Figure 2. Schematic drawing of ignition point

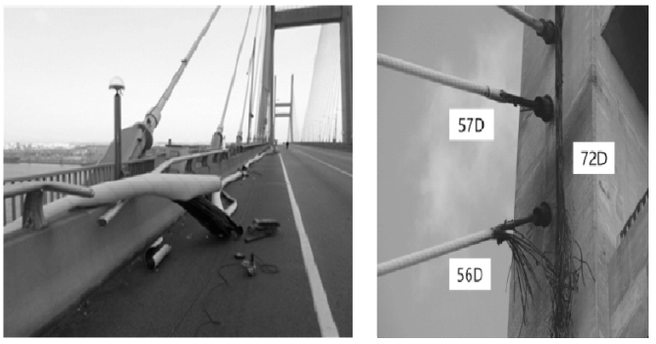


Figure 3. Damaged stay cables

failure (Zoli & S teinhouse 2007). In 2007, a truck carrying coconut caught a fire on the deck of the Mezcala Bridge in Mexico and resulted in the loss of one stay cable. The Rion Antirion Bridge in Greece suffered cable failure due to fire caused by lightning strike in 2005. In both fi res, the HDPE sheathing system for stay cables was poorly suited for suppressing fire but become fire source, if ignited.

During winter thundersto rm on the evening of December 3, 2015, one of the longest upper cab les in the downstream side of the deck, 72D, caused a fire(Fig. 2). The fire star ted almost 80m above the bridge deck and lasted more than two hours. As fire progressed, the 72D cable wa s completely severed. About two-thirds of th e 72D cable dropped on the top of the bridge deck w hile the remaining one-third cable was dangled from the pylon anchorage as shown in Figure 3. The rem aining 72D cable was still under the fire and lead to fire of t wo more cables in the downstream cable plan e, a 56th (56D) cable and a 57th (57D) cable . The fire investigation by fire department concluded that fire was caused by a lightning strike. The detail ed damage investigation also showed that 21 strands out of 37 strands were broken for the 56D cable and 5 strands out of 44 strands were severed for the 57D cable. Becau se of fire and severe damage, the Bridge was immediately closed to traffic and rem ained closed during repair work.

3 RESILIENCE OF INFRASTRUCTURES

Because of global warm ing and clim ate change, infrastructures are more and more exposed to extrem e events such as fire, earthquake, flooding, and scour . These extreme events can lead to severe dam age and collapse of infrastructure. Resilient infrastructure can reduce the risk of severe d amage and co llapse and recovery time. A number of different definitions on the resilience of infrastructure s ystems were given in the literature. Bruneau et al.(2003) conceptualized the seismic resilience as “the ability of both physical and social systems to withstand earthquake-generated forces and dem ands and to cope with earthquake impacts through situation assessment, rapid response, and ef fective recovery strategies”. They also suggested the following four properties of the resilience: robustness, redundancy , resourcefulness, and rapidity. FHWA (Chavel & Yadlosky 2010) issued a framework to reduce the likelihood of possible bridge failures and t hus improve resilience of bridge. PPD-21(2103) defined critical infrastructure resilience as “the ability to prepare for and adapt to changing conditions and withstand and recover rapidly from disruptions”. Caverzan & Solomos (2014) reviewed different definitions on resilience and introduced the following concept: “a function indicating the capability to sustain a level of functionality or performance for a gi ven building, bridge, or community, over a period defined as the control time that is usually decided by owners, or society”. Bocchini el al (2013) com pared conceptual and analytical definition of resilience for civil infrastructures. Alipour (2017) reviewed c oncepts of resilience and defined as the capacity to absorb, a dapt to, and restore after a sudden shock. There is a slight dif ference in the definition of infrastructure resilience but the resilience of infrastructure is typically defined as the ability to reduce the magnitude and duration of damage caused by extreme events.

4 RESILIENCE EVALUATION

As stated earlier, resilience of a system or a structure cannot be easily evaluated quantitatively. The resilience of the Seohae Brid ge against cable fire will be qualitatively evaluated based on the four properties (Bruneau et al. 2003): r obustness, redundancy, resourcefulness, and rapidity . Robustness refers to “strength, or the ability of elem ents, systems, and other units of analysis to withstand a given level of stress or dem and without suffering degradation of loss of function”. Redundancy represents “the extent to which elements, systems, or other units of analysis exist that are subs titutable, i.e., capable of s atisfying functional requirements in the event of disruption, degradation, o r loss of functionality ”. Resourcefulness means “the cap acity to ide ntity problems, establish priorities, and mobilize resources when conditions exist that threaten to disrupt

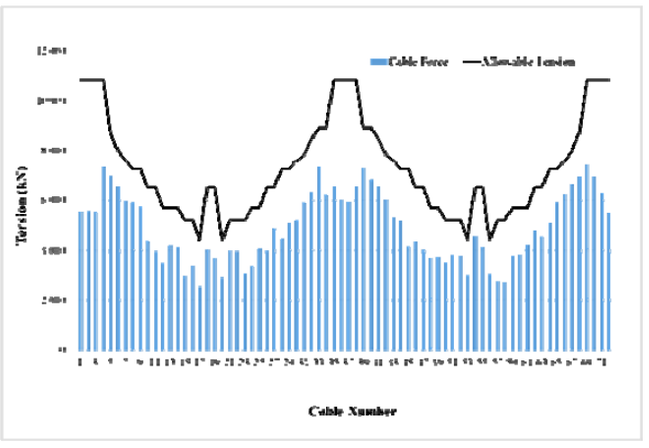
some element, system, or other unit of analysis". Rapidity is "the capacity to meet priorities and achieve goals in a timely manner in order to contain losses and avoid future disruption". It can be concluded that the first two properties, robustness and redundancy, represent how well the structure, the system, or the society is prepared for the sudden events or disasters. The last two properties, resourcefulness and rapidity, consider the response of the organizations or the society to restore the structures after the disasters. In this paper, therefore, the resilience will be assessed by grouping the first two properties together and the last two properties together.

4.1 *Robustness and redundancy*

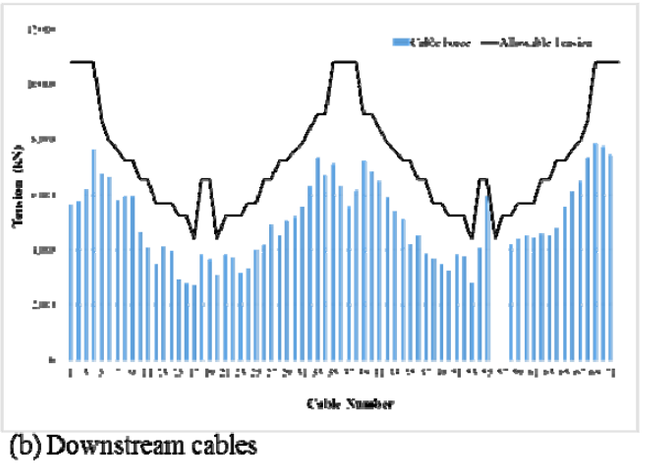
Though the Seohae Bridge was not explicitly considered robustness or redundancy during the design, extreme loads such as earthquake, vessel collision, and typhoon were considered as the part of load cases. It was also stipulated in the special design specification for the Seohae Bridge that the two stay cables can be replaced under traffic restrictions. Two traffic lanes considered to be closed in the direction of the cable replacement. The review of the structural analysis report for the Seohae Bridge confirmed that the replacement of two cables under traffic restriction was considered during design stage, as required in the design specification. The accidental rupture of stay cables were not considered in the special design specification.

To check the structural safety of the fire-damaged bridge, the detailed structural analysis using a three-dimensional finite element model was carried out considering only dead load. It was conservatively assumed that three cables were completely severed. The analysis results given in Figure 4 showed that the tension forces of the cables in the upstream cable plane were barely affected by the fire. The cable forces in the downstream cables near the damaged 56D, 57D, and 72D cables were substantially increased but still lower than allowable tension forces. The analysis results also indicated that the compressive tensile stress of the stiffening girder was substantially increased between the anchorages of the 56D and 57D cables due to cable rupture but lower than allowed stress limit.

The tension force level of the cables was also studied using the health monitoring systems. As stated earlier, the total of 24 accelerometers were installed on stay cables to indirectly measure cable tension level. However, accelerometers are not installed on damaged cables or on neighboring cables except the 69th cable. The accelerometers are also installed on the 37th cables, which are in the opposite side of the pylon and symmetrical to the 72th cables. The measured tension forces of affected cables in upstream and downstream cable planes are compared in Table 1. During fire, the measured tension forces were slightly reduced due to traffic restriction on the Bridge. After fire, the measured tension forces of the cables were slightly changed but well below the maximum allowable tension force of



(a) Upstream cables



(b) Downstream cables

Figure 4. Cable forces after damage

Table 1. Changes in cable tension forces

Cable No.	Before fire (Dec. 3, 2PM)	During fire (Dec. 3, 9PM)	After fire (Dec. 7)	After reopening	
				Dec. 19	Dec. 20
37U*	5,974	5,971 (-3)**	6,065 (91)	6,007 (33)	5,992 (18)
37D*	5,846	5,643 (-203)	5,888 (42)	5,906 (60)	5,890 (44)
69U	7,498	7026 (-472)	7,333 (-165)	7,102 (-396)	7,097 (-401)
69D	6,967	6519 (-448)	7,233 (266)	6,755 (-211)	6,758 (-209)

* U: Upstream cable, D: Downstream cable
** Tension force change compared to pre-fire level

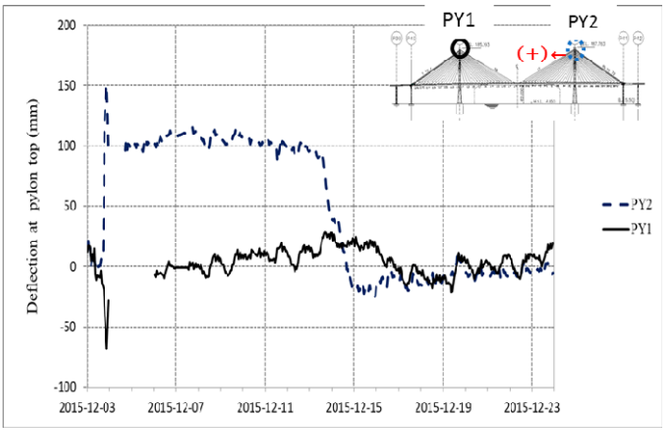


Figure 5. Lateral deflections at the top of pylons

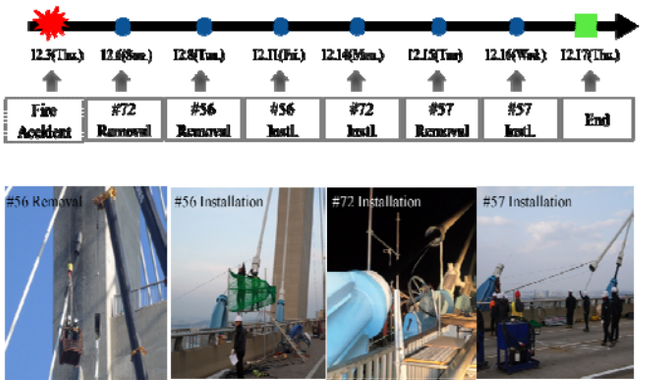


Figure 7. Entire repair work procedure

the cables (10,872kN). After the repair, there seems to be a change in cable forces compare to pre-fire tension force levels.

The deflection of the main pylons and the stiffening girder were also continuously monitored through the structural heath monitoring system. Due to rupture of cables in the side span, the main pylon PY2 with ruptured cables was inclined toward the main span as shown in Figure 5. The inclination of the PY1 main pylon was less than the PY2 pylon but the PY1 pylon also tilted to the main span direction. As the damaged cables repaired, the deflections of the pylons were reduced and returned to its pre-fire state.

The rupture of stay cables caused changes in the geometric profile of the stiffening girder. As illustrated in Figure 6, when the cables were ruptured, the main span deflected downward while side spans, especially the south span, deflected upward. This profile change corresponds to the lateral deflections of the main pylons. However, the lateral deflection of the main pylons and the vertical deflection of the stiffening girder were lower than the allowed limit and did not cause any structural damages. As the cables were replaced, the vertical deflection of the stffening girder was rapidly reduced.

4.2 *Resourcefulness and rapidity*

As stated earlier, the bridge was closed to the traffic immediately due to the concern over structural instability. Even though the detailed structural analysis showed that the damaged bridge can withstand portion of upstream traffic, it was determined to close the Bridge for quick repair work.

Preparation for the repair work started right after the fire was extinguished. It was determined that equipment for stay cable replacement such as monostrand tensioning jacks and stay cable strands are the essential elements for quick repair. A number of heavy lift crawler cranes were also determined to be required to access the cable anchorages in the main pylon and replace damaged cables. Because the Seohae Bridge is the part of strategically important highway networks in Korea with average daily traffic of 88,000 vehicles, all the available resources for stay cable installation in Korea were mobilized to repair the Bridge with the help of Ministry of Land, Infrastructure, and Transport of Korea. To help the repair of the Seohae Bridge, erection equipment and experts for cable-stayed bridges were tapped from other construction sites under the jurisdiction of

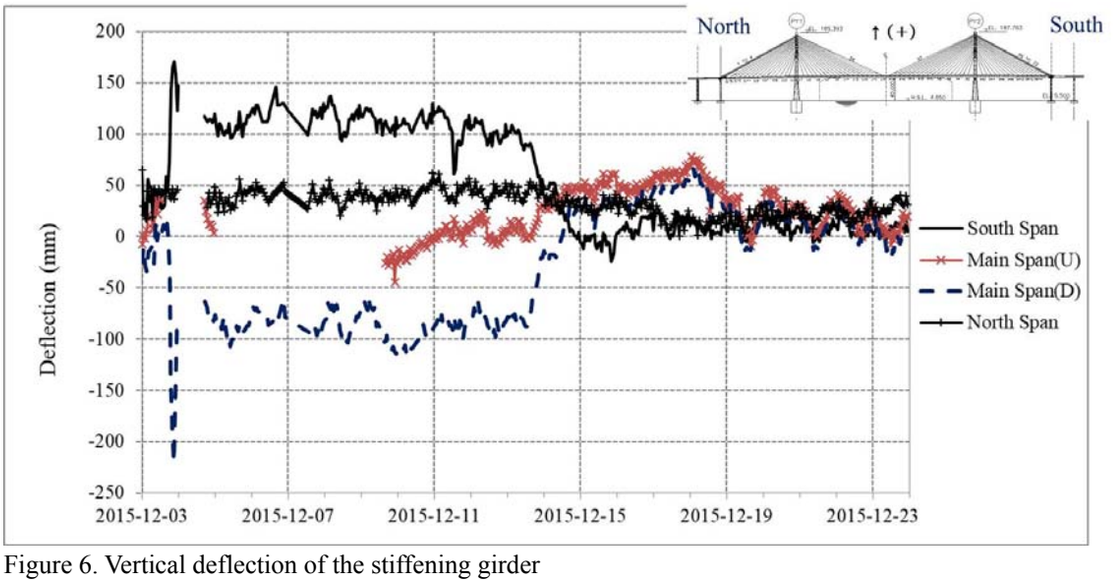


Figure 6. Vertical deflection of the stiffening girder

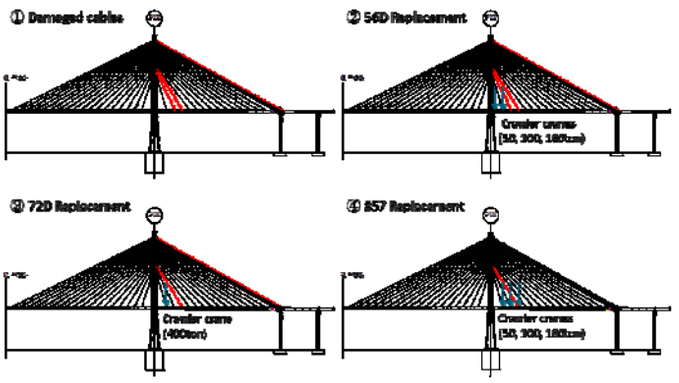


Figure 8. Cable replacement sequence and placement of crawler cranes

Ministry. The strands which were produced for the other cable-stayed bridge were also shifted. As sown in Figure 7, the entire repair work just took 15 days due to quick mobilization of cable installation equipment, material and trained experts in Korea.

At the given time, two or three crawler cranes with large boom length had to be deployed to remove and install stay cables (Fig. 8). The weight of crawler cranes, 490kN (50ton), 980kN (100ton), 1,570kN (160ton), and 3,920kN (400ton), strongly affected the tension force level of the cables and stress level of the stiffening girder. The sequence for removal and installation of stay cables was determined from the detailed structural analysis considering the location and weight of the crawler cranes. The remaining strands of the 56D cable was first removed through de-tensioning and new high strength strands were installed. After the 72D cable was installed, the damaged 57D cable were replaced.

5 CONCLUSION

The lightning caused fire ruptured three stay cables of the 990m long cable stayed bridge in Korea. The bridge was closed to traffic for 15 days and the damaged stay cables were replaced. The resilience of the Bridge against cable failure was qualitatively evaluated in terms of four "R"s: robustness, redundancy, resourcefulness, and rapidity. Due to inherent robustness and redundancy, the Bridge was able to withstand a three-cable failure without a total collapse. The quick repair was possible due to rapid mobilization of available resources for the stay cable erection. Firefighting facilities including fire hydrants and nozzles were newly installed on the cable-stayed bridge to increase resilience. Firefighting drills are also periodically conducted. To prevent further failure of cable-supported bridges due to a lighting strike, the risk of a lightning strike to the cable-supported bridges in Korea was assessed and, if required, lightning protection systems are being installed.

REFERENCE

Alipour, A. 2017. Enhancing resilience of bridges to extreme events by rapid damage assessment and response strategies. *Transportation Research Record: Journal of the Transportation Research Board* (2604): 54-62.

Bocchini, P., Frangopol, D.M., Ummenhofer, T., & Zinke, T. 2014. Resilience and sustainability of civil infrastructures: toward a unified approach. *Journal of Infrastructure System* 20(2): 04014004.

Bruneau, M., Chang, S.E., Eguchi, R.T., Lee, G.C., O'Rourke, T.D., Reinhorn, A.M., Shinozuka, M., Tierney, K., Wallace,W.A., & Von Winterfeldt, D. 2003. A framework to quantitatively assess and enhance the seismic resilience of communities, *Earthquake spectra* 19(4): 733-752.

Caverzan, A. & Solomos, G. 2014. *Review on resilience in literature and standards for critical built-infrastructure*, Joint Research Center, European Commission.

Chavel, B.W. & Yadlosky, J.M. 2011. *Framework for improving resilience of bridge design*. No. FHWA-IF-11-016.

Garlock, M., Paya-Zaforteza, I., Kodur, V. & Gu, L. 2012. Fire hazard in bridges: Review, assessment, and repair strategies. *Engineering Structures* 35:89-98.

Gil, H., Park, J., Cho, J. & Jung, G. 2010. Renovations of structural health monitoring system for Seohae bridge, Seoul, South Korea. *Transportation Research Record: Journal of the Transportation Research Board* (2201): 21-27.

Presidential Policy Directive-Critical Infrastructure Security and Resilience (PPD-21). 2013.

Zoli, T. P. & Steinhouse, J. 2007. Some considerations in the design of long span bridges against progressive collapse. *HNTB, New York, NY, USA*.

Maintenance, Safety, Risk, Management and Life-Cycle Performance of Bridges – Powers, Frangopol, Al-Mahaidi & Caprani (Eds)
© 2018 Taylor & Francis Group, London, ISBN 978-1-138-73045-8

Seismic fragility of highway bridges considering improved bearing deterioration modeling

S. Shekhar & J. Ghosh
Indian Institute of Technology Bombay, Mumbai, India

ABSTRACT: Past literature on seismic fragility assessment of aging highway bridges primarily focus on corrosion of bridge columns, with little attention to deterioration of bridge bearings. Corrosion of bearing assemblies can lead to unexpected behavior under seismic loads. For instance, while corrosion of anchor bolts and keeper plates may lead to reduced bearing lateral strength, accumulation of corrosion byproducts lead to "frozen" or "locked" bearings restraining free movement during earthquake events. Limited studies on the analytical modeling of bearing deterioration often adopt simple and potentially unrealistic assumptions on the degradation mechanism. Addressing these gaps, this study develops improved bearing deterioration models based on available field investigation and experimental data. These models are utilized to study the impact of corroded steel bearings on the component level seismic fragilities of a case-study bridge. Results reveal the criticality of considering realistic bearing degradation models for bridges located in seismic regions and undergoing corrosion deterioration.

1 INTRODUCTION

Civil infrastructure systems such as highway bridges play an essential role in the sustained economic growth and social development of any country. During their service life, critical components of highway bridges maybe exposed to multiple environmental stressors such as corrosion deterioration along with intermittent seismic threats. Multiple bridge components such as columns and bearings (particularly steel bearings) deteriorates over time. Steel bearings including rocker and fixed bearings have been widely used in older steel highway bridges in Central and Southeastern US (CSUS) during the 1950s and 1960s (Saadeghvaziri & Rashidi 1998). These bearings constitute important elements within the bridge system transferring forces from the superstructure to the substructure. However, non-ductile nature of these bearings have exposed their vulnerability during past seismic events (Mander et al. 1996). Failure observed in steel bearings during seismic events includes lateral failure of rocker bearing due to instability in longitudinal direction, anchorage failure of anchor bolt, tearing of keeper plates, among others. These vulnerabilities have led modern design provisions to caution their use in highway bridges and recommend replacement with modern bearings such as elastomeric bearings and PTFE sliding bearings. However, a significant percentage of steel bridges found in CSUS still uses steel bearings (Nielson 2005).

In addition to their seismic vulnerability, corrosion deterioration of these bearings over time can lead to unexpected behavior under seismic loads. For instance, while corrosion of anchor bolts may lead to reduced bearing ultimate lateral strength, accumulation of corrosion byproducts lead to "frozen" or "locked" bearings restraining free movement during earthquake events leading to adverse horizontal forces imparted to the substructure (Silano & Brinckerhoff 1993). While several studies have been carried out in the past to study the impact of corrosion deterioration of bridge columns on seismic fragility assessment, impact of corrosion deterioration of bridge bearings is lacking in the literature. Limited studies on the analytical modeling of bearing deterioration often adopt simple but unrealistic assumptions on the degradation mechanism. For instance, while past literature develops analytical models of aging bridge bearings considering uniform corrosion along the length of the anchor bolt (Ghosh & Padgett 2010), field investigations reveal bolt failure to be primarily dictated by necking at concrete interface due to concentration cell corrosion (Lindquist 2008). Such failure mechanism may severely impact the lateral load capacity of the bearings. Furthermore, experimental tests on corroded bearings by Fan (2014) indicate a reduction in initial stiffness, typically neglected in the past literature.

Moreover, better models on the increase in bearing corrosion due to accumulation of rust debris also needs exploration.

Addressing these gaps, the paper examines the impact of deterioration of steel bearings on seismic fragility of highway bridges by considering improved bearing deterioration model based on past experimental tests and field investigation reports for steel bearings. The next section of this paper elaborates the commonly occurring deterioration mechanisms of steel bearings as observed in past experimental tests and field investigation reports, and presents its influence on bearings load carrying capacity. A representative case-study bridge is presented next along with its analytical model incorporating the deterioration effect of steel bearings. The influence of bearing deterioration on the deterministic seismic response of bridge components is investigated followed by study on seismic fragility assessment. The paper ends with discussions on the results including concluding remarks and opportunities for future research.

2 DETERIORATION OF STEEL BRIDGE BEARINGS

Bridge bearings constitute important elements within the bridge system and provides connection between superstructure and substructure. Under service load conditions, in addition of transferring dead load and traffic load, bearings also accommodate relative movements between the superstructure and substructure caused by thermal action and vehicle braking loads. Also, under extreme lateral loads such as earthquakes, bearings contribute to lateral resistance in both longitudinal and transverse direction.

In Central and Southeastern US, chosen as the case-study region, a large number of steel bridges particularly longer span bridges (>20 m) uses high-type fixed and expansion steel bearings. A high-type fixed bearings permits only rotational movement while an expansion bearing permits both rotational and translational movement. These bearings types have non-ductile properties and are highly susceptible to deterioration when exposed to aggressive environment (Mander et al. 1996). The age-related deterioration of steel bearings manifests itself in variety of forms. For instance, section loss of bearing assemblies causes a reduction in the net area of the bearing available to withstand the gravity load from the superstructure. Reduction of the section especially in the contact region for fixed bearing can cause a decrease in stiffness and strength of the bearing under lateral loads (Fan 2014). These changes can result in unexpected and non-uniform behavior under seismic loads and finally leads to their failure. Reduction in embedded anchor bolts area and thickness of keeper plates over time leads to reduction in lateral load capacity of bearings under earthquake loads in longitudinal and transverse directions. Additionally, buildup of debris and corrosion byproducts also can restrain free movement of a rocker bearing leading to adverse horizontal forces imparted to the superstructure and the substructure and possible overturning of the rocker bearings. To estimate the impact of corrosion on the bridge bearings, the failure modes of the high-type fixed and expansion bearings are studied in the following sub-sections.

2.1 Deterioration of high-type fixed bearings

The failure mode of high-type fixed bearings in the longitudinal direction results from the rocking of the bearing followed by failure of swedged anchor bolts due to prying of the masonry plate. The distribution of forces for a typical fixed bearings along longitudinal direction can be found in Mander et al. (1996) and Ghosh & Padgett (2010) and shown in Figure 1.

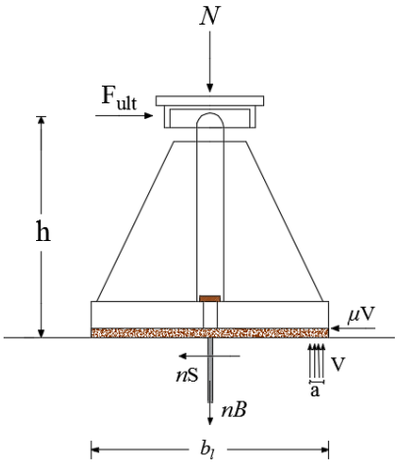


Figure 1. Force distribution mechanism of fixed bearing in longitudinal direction on reinforced concrete pedestal (Mander et al. 1996)

From the equilibrium of forces and moments for longitudinal direction, ultimate strength F_{ult} is found to depend on the dimension of the bearings and also on anchor bolt diameter as:

$$F_{ult}(t) = \frac{0.5 b_l N}{h}\left[\left(1+\frac{nT(t)}{N}\right) - \ldots \right. \\ \left. \ldots \frac{N}{0.85 f_c b_l b_t}\left(1+\frac{nT(t)}{N}\right)^2\right] \quad (1)$$

where, b_l = width of the masonry plate in longitudinal direction; N = axial load on the bearing; h = height of bearing from the concrete pedestal to the sole plate-rocker interface; n = number of anchor bolts; b_t = width of the masonry plate in transverse

direction; f_c = concrete strength of the pedestal and T is the lesser of bond strength (B) and yield strength (S) of the anchor bolt and depend on its diameter d_b.

Due to corrosion along the service life of the bridge, the diameter of the bolt d_b reduces and consequently leads to reduced ultimate lateral strengths for the deteriorated bearings. As explained earlier, this reduction in diameter impacts tensile force T which is minimum of yield strength (S) and bond strength (B) of the anchor bolts. Ghosh & Padgett (2010) assumed the corrosion mechanism of anchor bolts to be similar to the uniform corrosion deterioration mechanism of fully embedded steel reinforcement in the columns. However, field investigations carried by Lindquist (2008) across the state of Georgia in United States reveal that the anchor bolt corrosion is higher at the bolt-concrete interface due to macro-cell formation between the portion of the bolt embedded in the concrete and the portion immediately above the concrete. Consequently, the bolt may fail due to necking at concrete interface especially under lateral loads during earthquakes. Lindquist (2008) concluded that environmental effects such as chloride did not significantly affect anchor bolt corrosion and the median age when anchor bolt corrosion first initiated was found to be approximately 39 years. Results of long-term concentration cell experiments of anchor bolts indicate corrosion rates up to 4 to 6 times more than that of the same bolt in an uncoupled state i.e. bolt completely embedded in concrete. The present study utilizes the above finding for anchor bolt corrosion and thereby assumes higher corrosion rate for necking failure as compared to fully embedded bolt.

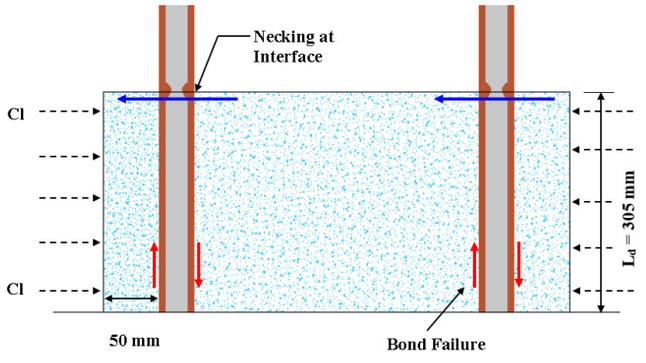


Figure 2. Deterioration mechanisms of anchor bolt.

Figure 2 shows schematic representation of considered reduction in anchor bolt diameter at interface and inside the reinforced concrete (RC) pedestal. Table 1 shows the summary of considered deterioration parameters for calculating reduction in anchor bolt diameter along the service life. For necking failure which typically occurs due to concentration cell corrosion, the initiation time and corrosion rates are adopted from Lindquist (2008). The initiation time for bolts completely embedded in RC pedestal is calculated by assuming the bridge to be located in deicing salt exposure and initiation time is calculated for cover depth of 50 mm (Mander et al. 1996). More details on the adopted formulation of initiation time for deicing salt exposure condition can be found in Thoft-Christensen et al. (1996). The corrosion rate for such exposure is taken from the field study of Whiting et al. (1990), Weyers et al. (1994) and adopted corrosion rate of 0.030 mm/year represent the median of the reported corrosion rates.

Table 1 Description of parameters considered for corrosion of anchor bolts.

Corrosion of fully embedded anchor bolt			
Initiation Time		**Corrosion Rate**	
μ = 15 years	σ = 8 years	μ = 0.030 mm/year	COV = 0.2
Concentration cell corrosion of anchor bolt at interface (Lindquist 2008)			
Initiation Time		**Corrosion Rate**	
μ = 39 years	σ = 12 years	μ = 0.127 mm/year	COV = 0.2

μ = Mean, σ = Standard deviation, COV = Coefficient of variation

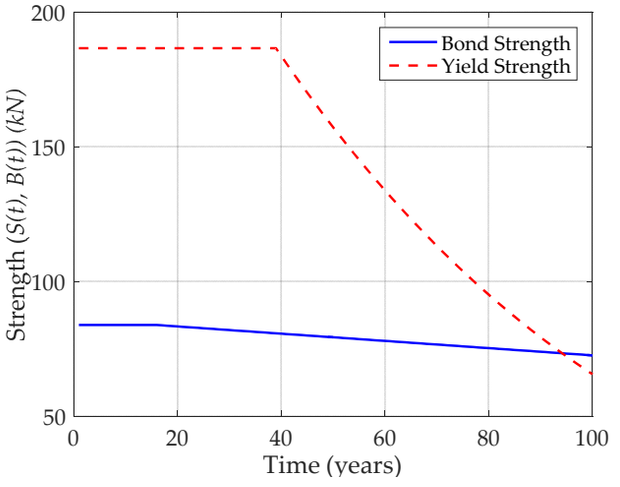


Figure 3. Comparison of time-variant mean value of bond strength (B) and yield strength (S) of anchor bolt due to deterioration of anchor bolt inside concrete and at interface.

Figure 3 shows the time-variant reduction in bond strength (B) and yield strength (S) due to deterioration of anchor bolt inside RC pedestal and at interface. It can be seen that although the rate of deterioration of yield strength (that leads to necking failure) is more, for a majority of service life (up to 85 years), the reduction in ultimate strength (F_{ult}) is govern by bond failure because of its low initial strength. It is noted that Figure 3 only present the mean value of reduction in bond strength and yield strength by considering mean initiation time and

mean corrosion rate from Table 1. The study also consider uncertainty around these values by adopting probabilistic model for initiation time and corrosion rate as shown in Table 1.

In the transverse direction for the fixed bearing, keeper plate failure governs the bearing failure. The experimental test conducted by Mander et al. (1996) reveal that fillet welds on the keeper plates failed in a semi-brittle fashion and neither cracks in the concrete pedestal nor damage to the swedged anchor bolts was observed. The shear strength of anchor bolt is adequate enough to absorb the force transmitted by the keeper plate when rocker strikes it. However, due to corrosion along the service life of the bridge both anchor bolt and keeper plate strength deteriorates and the failure of the bearing is govern by the minimum of the two strength. The reduced shear strength of anchor bolt can be calculated as time-dependent area of the anchor bolt $A_b(t)$ (reduction due to necking at interface) times the yield strength f_y. Additionally, the time-dependent strength of the keeper plate $P(t)$ may be estimated using the yield line theory as shown in Equation 2 (Mander et al. 1996).

$$P(t) = 2\left(\frac{t_p^2(t)}{4} f_{su} + \frac{\left(0.707 t_w(t)\right)^2}{4} f_{su}\right)\left(\frac{L_x}{L_y} + \frac{2L_y}{L_x}\right)$$

$$\text{where, } t_p(t) = t_p - y(t),\ t_w(t) = t_w - y(t) \qquad (2)$$

$$y(t) = At^B$$

where, t_p = 12.7mm, is the as-built thickness of keeper plate, t_w = 12.7mm, is the fillet weld thickness, $t_p(t)$ and $t_w(t)$ is the time-dependent thickness of the keeper plate and fillet weld obtained using the empirical equation provided by Komp (1987) for corrosion of exposed steel members; $y(t)$ is the average corrosion penetration in micrometers and A and B are field test parameters depending on exposure condition (considered here as deicing salt); f_{su} = 400 MPa, is the ultimate strength of keeper plate; L_x and L_y = 127mm and 51mm respectively, is the length and breadth of the keeper plate. Although further details may be found elsewhere, it is worthwhile to note that along the service life of the bridge, the demand placed on the anchor bolt [$P(t)/2$] is lesser than the shear strength of the anchor bolt [$A_b(t)f_y$], thereby the failure in transverse direction is governed by failure of the keeper plate.

2.2 Deterioration of high-type expansion bearings

The high-type expansion (rocker) bearings are designed to allow expansion in longitudinal direction via rocking of the curved bottom of the rocker-masonry plate interface and hinging of sole plate-rocker interface. The response is primarily proportional to the normal reaction indicating that the behaviour obey the laws of classical Coulomb friction and therefore the ultimate lateral strength of the bearing depends on coefficient of rocking friction μ and normal reaction N applied to the bearing. However, along the service life of the bridge corrosion leads to accumulation of excessive corrosion by-products (rusts) along with build-up of dirt and debris. This leads to increase in coefficient of friction that may restrict the rocking motion of these bearings. Mander et al. (1996) reported that under cyclic loading, a locked rocker bearing first performs like a fixed bearing thereby attracting unexpected horizontal forces before the locking condition is broken and the ability to rotate is restored. Marzoi et al. (1983) conducted a set of experiments on steel bearings including rocker bearings to determine effective coefficients of friction under as-built, partly corroded and in-situ conditions (badly corroded and build-up of rust and debris). It was found that the coefficient of friction varies from 0.022 to 0.05 for clean bearing, 0.036-0.055 for partly rusted bearings and 0.121-0.141 for in-situ bearing environment. For time-dependent modeling of increase in coefficient of friction, this study assumes friction coefficient corresponding to clean bearing condition for bridge in pristine state, friction coefficient corresponding to partly rusted bearing condition for 50 year old bridge and friction coefficient corresponding to in-situ bearing condition for 100 year old bridge. Also, a linear variation of coefficient of friction is assumed for in-between years along the service life.

Similar to fixed bearings, the transverse direction failure of expansion bearings is governed by the failure of the keeper plates whose strength can be calculated as indicated earlier in Equation 2. In addition to corrosion of anchor bolts and keeper plates, corrosion of other exposed steel bearings components, such as flanges and webs results in mass loss that affects the bearing initial stiffness. A set of experiments carried by Fan (2014) on salvaged bearings collected from an over 50 year old bridge reveals that a mass loss of 11% of bearing assemblies can lead to reduction in initial stiffness of about 70% for fixed and expansion bearings. In the absence of any further data to support time-dependent modeling of decrease in stiffness due to mass loss, a linearly varying percentage reduction in initial stiffness is assumed for this study starting with 0% for the pristine bridge and 70% for a 100 year old bridge near the end of its service life.

Finally these deterioration affected structural parameters, such as, reduction in ultimate strength, increase in coefficient of friction and decrease in initial stiffness can be incorporated in the analytical modeling of bearings using set of non-linear translational springs. More details about analytical modeling using non-linear springs is provided in the subsequent section through a case-study example.

3 CASE-STUDY BRIDGE

The influence of the identified deterioration mechanisms of the bearings on the seismic response and fragility of highway bridges is assessed for a case-study bridge. This section will first briefly describe the bridge geometry and its finite element modeling followed by detailed impact of bearing deterioration on seismic response of bridge bearings.

3.1 Bridge description and general modeling strategies

This study considers a multi-span continuous (MSC) steel girder bridge type for the case-study example. This bridge type is prevalent in CSUS and accounts for more than 13% of all highway bridges in this region (Nielson 2005). Past studies on this bridge type have highlighted their potential vulnerability under seismic shaking due to inadequate seismic detailing of the columns and non-ductile properties of the steel bearings (Nielson & DesRoches 2007). The bridge geometry consists of three spans with both middle span and end spans of 22.3 m length along with a 10.3 m wide deck consisting of five parallel steel girders in each span. Each bridge bent consist of two 914.4 mm diameter circular columns reinforced with 645 mm^2 longitudinal reinforcement (12 # 29 longitudinal bars, metric size = 28.65 mm) and #13 (metric size = 12.7 mm) transverse stirrups spaced at 307 mm along the length of the column. The load from the superstructure to substructure is transferred using high-type fixed and expansion type steel bearings with fixed bearings placed over the two bents and expansion bearings placed over the two abutments. A three-dimensional high-fidelity finite element model of the case-study bridge is developed using the finite element package OpenSees (McKenna et al. 2000) following the modeling guidelines by Nielson & DesRoches (2007). In order to isolate the impact of corrosion deterioration of steel bearings on seismic fragility estimate, other structural components for the case-study bridge such as columns are assumed to be undeteriorated along the service life of the bridge. While the detailed modeling of deteriorated bearings is presented in subsequent sub-section, an overview of the finite element modeling of the undeteriorated bridge components is presented herein.

As the superstructure remains elastic during the earthquake, the composite action of deck and steel girders are modeled using linear elastic beam-column elements. The column and bent cap are modeled using displacement based beam-column elements with fiber defined cross sections accounting for the steel reinforcement, confined core concrete and unconfined cover concrete. The pounding between abutment-deck is captured using contact elements and nonlinear translational springs are used to model the abutments while the piles at the base of the columns are modeled using lumped translational and rotational springs.

3.2 Finite element modeling of deteriorated bridge bearings

In the present study, the analytical modeling of the bridge bearings depend heavily on the work done by Mander et al. (1996) wherein the researchers tested the response of the steel bearings under reverse cyclic loading. Figure 4 shows the analytical model for the high-type fixed and expansion bearings under pristine condition. A brief overview of the analytical model developed in OpenSees is provided herein while detailed description can be found in Nielson (2005). For fixed bearing in longitudinal direction (denoted here as FBL), *Steel01* material is used to model the prying nature of the masonry plate and *Hysteretic* material is used to capture rocking and stiffness degradation due to anchor bolt failure. It is noted that *Steel01* and *Hysteretic* material are specific to OpenSees only. The two materials are connected in parallel to simulate the overall response. In case of fixed bearing in transverse direction (denoted here as FBT), as stated earlier, the keeper plate fails and no damage to the swedged anchor bolt is expected. While the *Steel01* material is used to model the sliding frictional component until the rocker hits the keeper plate, the *Hysteretic* material is used to model the loading and fracture sequence of the keeper plate. For expansion bearing in longitudinal direction (denoted here as EBL), *Steel01* material is used to model the rocking motion that depends on the normal reaction and coefficient of friction. The response of expansion bearing in transverse direction (denoted here as EBT) is similar to the fixed bearing in transverse and subsequently a similar modeling approach is used.

As explained earlier in Section 2, bearing deterioration due to corrosion leads to reduction in ultimate lateral strength, stiffness and increase in coefficient of friction. Past experimental study on corroded bearings (Fan 2014) have shown that corrosion has negligible impact on the bearing displacement capacities and therefore, this study only consider reduction in stiffness and ultimate load carrying capacity due to corrosion. The time-varying deterioration affected structural parameters are updated in the analytical modeling of the bearings, with the extent of reduction dependent on the point in time along the service life of the bridge. Figure 4 also emphasize the analytical model of the corroded high-type fixed bearings highlighting the decrease in strength and stiffness due to corrosion. The next section use these improved analytical models to demonstrate the impact of deterioration on the seismic response of bridge components.

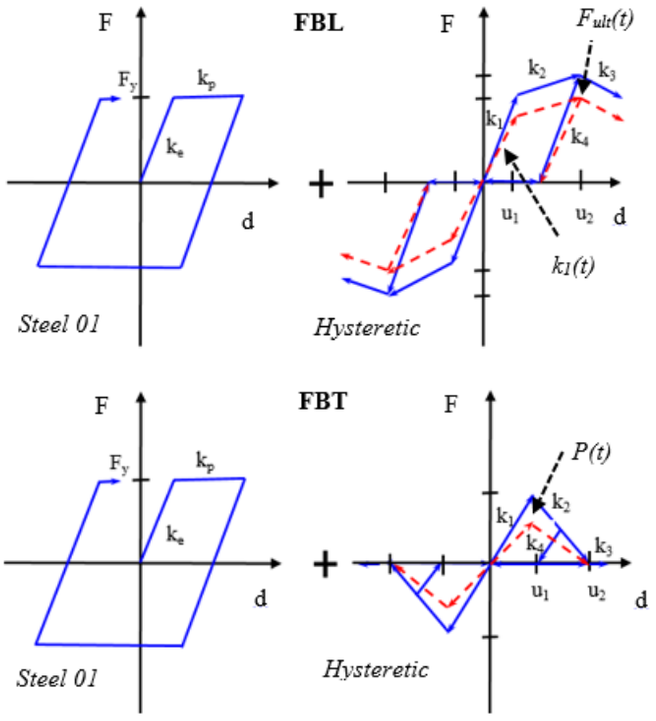


Figure 4. Analytical model of fixed bearing in longitudinal and transverse direction (FBL - Fixed bearing in longitudinal direction, FBT - Fixed bearing in transverse direction).

3.3 Impact of bearing deterioration on seismic response of bridge components

In order to demonstrate the impact of bearing deterioration on the seismic response of bridge components, the case-study bridge is subjected to a ground motion record from the Rix & Fernandez (2004) ground motion suite. This ground motion has peak ground acceleration (PGA) of 0.63 g and duration of 25 s and is first applied along the longitudinal and then along the transverse direction of the deteriorating bridge at different points in time to demonstrate the impact of bearing corrosion on the seismic response of critical bridge components.

Figure 5 shows the longitudinal response of fixed bearings when subjected to longitudinal loading at the beginning (pristine), middle (50 year) and end of service life (100 year). As compared to pristine bridge, 50 year and 100 year old deteriorated bridge results in 39% and 106% increase in deformation. This increase in deformation is expected as deterioration leads to decrease in stiffness and strength of the fixed bearings as explained earlier in Section 2. Fixed bearings in the transverse direction also reveals a consistent increase in deformation due to deterioration of keeper plate leading to its failure at lower force level.

For expansion bearings in longitudinal direction, an increase in yield force by 3% and 27% is observed for 50 year and 100 year old bridge as compared to pristine bridge due to increase in coefficient of friction because of accumulation of rust and debris. This increase in force reduces the deformation in longitudinal direction by 3% and 9% for 50 year and 100 year old bridge. In the transverse direction, expansion bearings experience larger demands due to significant poundings at the abutments. The response is further increased due to reduction in ultimate strength of the keeper plate leading to its failure at lower force and resulting in increase in deformation. Figure 6 shows an increase in deformation by 20% and 70% for 50 year and 100 year old bridge as compared to pristine bridge.

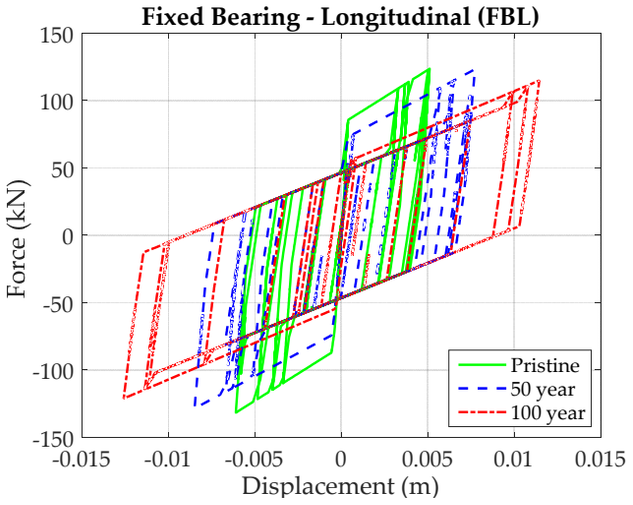


Figure 5. Increase in fixed bearing deformations in the longitudinal direction due to corrosion deterioration.

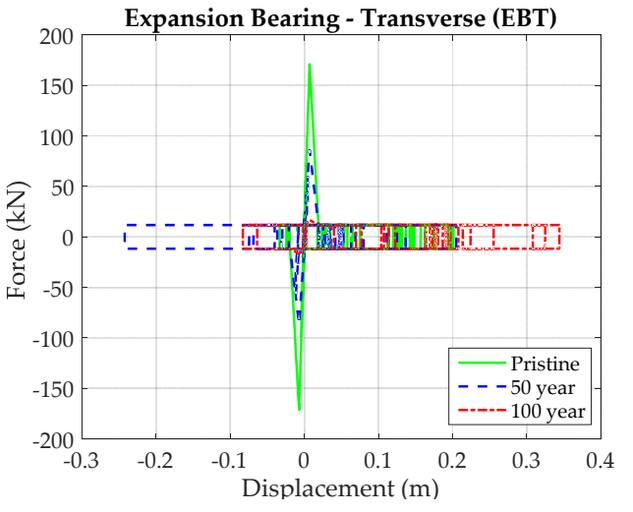


Figure 6. Increase in expansion bearing deformations in the transverse direction due to corrosion deterioration.

While this section focused on the alterations of deterministic bearing response due to deterioration, the subsequent section considers uncertainty in ground motion, material parameters, modeling inputs and deterioration parameters for fragility analysis.

4 IMPACT OF BEARING DETERIORATION ON SEISMIC FRAGILITY

The preceding section presents the time-dependent seismic response of deteriorated bridge component when subjected to single deterministic seismic loading. However, due to inherent randomness in the structural, modeling and deterioration parameters along with ground motion, a full probabilistic analysis is required to determine the effect of bearing corrosion on bridge damage. Typically, the extent of bridge damage is represented by fragility curves that indicate the probability of failure of bridge component given the intensity of ground motion. The time-dependent seismic fragility curves for deteriorated highway bridges are developed using a two-step approach. In the first step probabilistic seismic demand models (PSDMs) for critical bridge components are developed at each point of time along the service life of the bridge. The second step involves the development of component fragility curves using the demand model (obtained in first step) and limit state capacity model of each bridge component.

PSDMs that relates the median peak engineering demand parameter (*EDP*) of the bridge component with the intensity measure (*IM*) of the ground motion are developed by conducting non-linear time history analysis (NLTHA) of the bridge samples using suite of ground motion representative of the case-study region. A synthetic suite of 96 ground motions developed by Wen & Wu (2001) and Rix & Fernandez (2004) representative of the seismicity of CSUS are used in the analysis. To conduct NLTHA, 96 ground motions are paired with 96 statistically different yet nominally identical 3D bridge samples generated using Latin Hypercube sampling considering uncertaility in structural, material and deterioration parameters at different points in time along the service life of the bridge (taken here as 0, 25, 50, 75 and 100 years). Following NLTHA, PSDMs are developed for each bridge component to estimate median seismic demand using the relation given by Cornell & Jalayer (2002).

Following the development of PSDMs for each bridge component, fragilities are evaluated at different points in time along the service life of the bridge to assess the effect of bearing deterioration on seismic vulnerability. The lognormal limit state capacities presented by Nielson & DesRoches (2007) are used in this study. The time-dependent seismic fragility for a particular bridge component *m* and damage state *DS* follows lognormal distribution and estimated as (Nielson & DesRoches 2007):

$$P\left[DS_m(t)\middle|PGA\right] = \Phi\left(\frac{\ln(PGA) - \ln\left(med_m(t)\right)}{\zeta_m(t)}\right) \quad (3)$$

where, $P[DS_m(t)|PGA]$ is the probability of damage state exceedance at time t given a PGA intensity, $med_m(t)$ is the median of lognormal distribution for fragility at time t and $\zeta_m(t)$ is the dispersion of fragility at time t.

Figure 7 shows the increase in seismic vulnerability across all damage states for fixed bearing in transverse direction (FBT) at 75 years of service life. The results are consistent with the observation in deterministic response where increased in deformation is observed for deteriorated bridge due to failure of keeper plates at lower force level. Although not shown here, similar trend of increased vulnerability i.e. decrease in median fragility [$med_m(t)$] (PGA corresponding 50 % failure probability) is observed for fixed bearing in longitudinal direction (FBL) and expansion bearing in transverse direction (EBT). However, rust accumulation and decrease in deformation leads to decrease in vulnerability of expansion bearings in longitudinal direction (EBL).

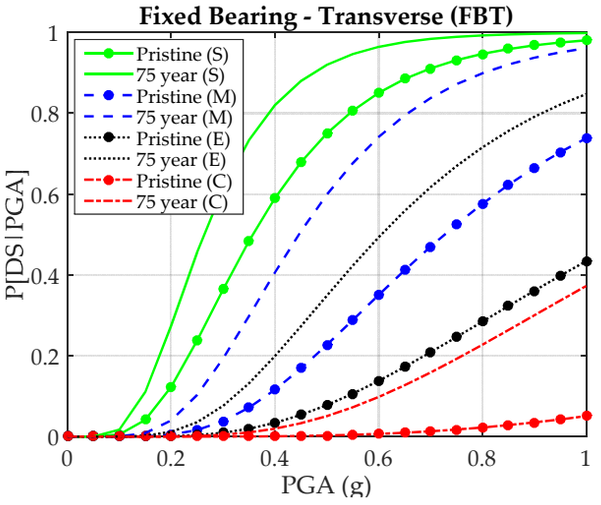


Figure 7. Comparison of fixed bearing transverse (FBT) deformation fragility curves for Slight (S), Moderate (M), Extensive (E), and Complete (C) under pristine and deteriorated state (75 years).

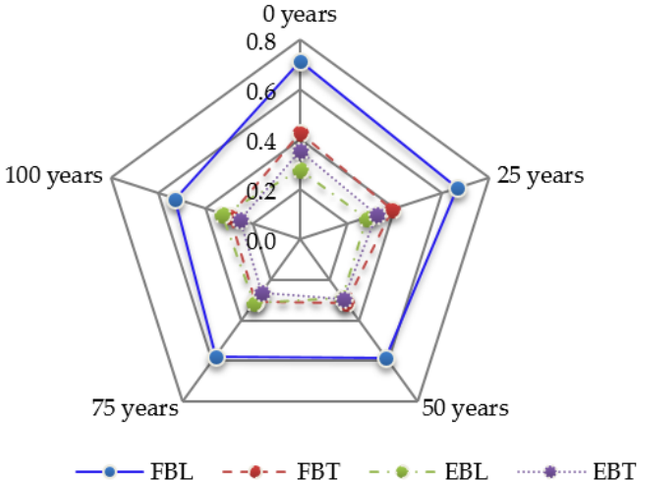


Figure 8. Figure depicting the comparison of time-dependent change in median estimate of fragility (slight damage) for fixed and expansion bearings in longitudinal and transverse direction.

Figure 8 shows the time-dependent change of median fragility for slight damage state for various bearing response. The maximum change (31% decrease in median fragility) is observed in fixed bearing under transverse deformation (FBT). The figure also depicts the ranking of vulnerability of various bearing deformation at each instant of time. For instance, in pristine condition expansion bearing in longitudinal direction (EBL) is most fragile, however at the end of 100 years expansion bearing in transverse direction (EBT) comes out to be more vulnerable of all the considered bearing response. It is also noted that slight reduction in dispersion [$\zeta_m(t)$] is also observed over time indicating reduced uncertainty in predicting median *PGA* for deteriorated bridge state.

5 CONCLUSIONS

The study presents the impact of bearing deterioration on seismic fragility of highway bridges by considering improved bearing deterioration model based on past experimental data and field investigation reports. At the onset, this paper elaborates the commonly occurring deterioration of steel bearings and presents its influence on bearings load carrying capacity. It is observed that corrosion deterioration significantly impacts the ultimate strength and initial stiffness of the bearings along with increase in coefficient of friction. The impact of corrosion deterioration on displacement capacity of the bearing is negligible. To investigate the impact of bearing deterioration on seismic fragility a representative case-study multi-span continuous steel bridge located in Central and Southeastern US is considered. Deterministic analysis reveals that consideration of realistic deterioration mechanisms results in substantial increase in dynamic response of the deteriorated bearings. A full probabilistic analysis considering various uncertainty is conducted to estimate change in seismic fragility of deteriorated bridge components. Except for expansion bearing under longitudinal deformation mode, significant increase in vulnerability is observe for other deformation mode of fixed and expansion bearings. For example, after 100 years of service life, the median value *PGA* for the complete damage state decreases by 61% for expansion bearing under transverse deformation.

Future study in this research will consider the joint impact of considered realistic bearing and column deterioration modeling for estimating component and system fragilities. Also investigation of realistic deterioration modeling on additional bridge types and bearing assemblies such as elastomeric bearings will be considered.

6 ACKNOWLEDGMENTS

This research was funded by Grant Number 14IRTAPSG008 from Industrial Research and Consultancy Centre at Indian Institute of Technology Bombay. The support is gratefully acknowledged.

7 REFERENCES

Cornell, C., & Jalayer, F. 2002. Probabilistic basis for 2000 SAC federal emergency management agency steel moment frame guidelines. *Journal of Structural Engineering* 128(4): 526–533.

Fan, X. 2014. *Characterization of the cyclic behavior of corroded steel bridge bearings and their influence on seismic bridge performance*. Ph.D. Thesis, University of Michigan, Ann Arbor, Michigan.

Ghosh, J., & Padgett, J. E. 2010. Aging Considerations in the Development of Time-Dependent Seismic Fragility Curves. *Journal of Structural Engineering*, 136(12): 1497–1511.

Komp, M. 1987. Atmospheric corrosion ratings of weathering steels—calculation and significance. *Materials performance* 26(7): 42–44.

Lindquist, L. 2008. *Corrosion of steel bridge girder anchor bolts*. M.S. Thesis, Georgia Institute of Technology, Atlanta, GA.

Mander, J. J., Kim, D., Chen, S., & Premus, G. 1996. *Response of steel bridge bearings to the reversed cyclic loading*. Buffalo, NY: Technical Report NCEER 96-0014.

Marzoi, A., Wang, L. R.-L., & Murray, T. M. 1983. Effective coefficient of friction of steel bridge bearings. *Transportation Research Record* 903: 79–86.

McKenna, F., Fenves, G., & Scott, M. 2000. *Open system for earthquake engineering simulation*. University of California, Berkeley, CA.

Nielson, B. G. 2005. *Analytical fragility curves for highway bridges in moderate seismic zones*. Ph.D. Thesis, Georgia Institute of Technology, Atlanta, GA.

Nielson, B. G., & DesRoches, R. 2007. Analytical seismic fragility curves for typical bridges in the central and southeastern United States. *Earthquake Spectra* 23(3): 615–633.

Rix, G., & Fernandez, J. 2004. Earthquake ground motion simulation. <http://geosystems.ce.gatech.edu/soil_dynamics/research/groundmotionsembay>.

Saadeghvaziri, M. A., & Rashidi, S. 1998. Effect of steel bearings on seismic response of bridges in Eastern United States. *6th US national conference on earthquake engineering. EERI*.

Silano, L. G., & Brinckerhoff, P. 1993. *Bridge inspection and rehabilitation*. New York: Wiley-IEEE.

Thoft-Christensen, P., Jensen, F., & Middleton, C. 1996. *Assessment of the reliability of concrete slab bridges*. Dept. of Building Technology and Structural Engineering.

Wen, Y., & Wu, C. 2001. Uniform hazard ground motions for mid-America cities. *Earthquake spectra* 17(2): 359–384.

Weyers, R., Fitch, M., Larsen, E., & Al-Qadi, I. 1994. *Concrete Bridge Protection and Rehabilitation: Chemical and Physical Techniques. Service Life Estimates*. Washington D.C. 357.

Whiting, D., Stejskal, B., & Nagi, M. 1990. *Condition of Prestressed Concrete Bridge Components: Technology Review and Field Surveys*. Washington: Federal Highway Administration.

Maintenance, Safety, Risk, Management and Life-Cycle Performance of Bridges – Powers, Frangopol, Al-Mahaidi & Caprani (Eds)
© 2018 Taylor & Francis Group, London, ISBN 978-1-138-73045-8

Structural Behavior of a Steel-Concrete Composite Beam under Fire Condition

M.S. Kang, H. Pak & J.W. Kang
Hongik University, Seoul, Korea

S.H. Kee
Dong-A University, Busan, Korea

B.J. Choi
Kyonggi University, Suwon, Korea

ABSTRACT: This paper presents a multi-physics analysis framework for estimating thermo-mechanical behavior of structures under fire conditions. The analysis framework consists of three parts. The first part is a fire-driven flow simulation in a rectangular parallelepiped domain which includes fire source and target structure. The fire simulation is conducted using Fire Dynamics Simulator (FDS). From FDS simulation, time history of temperature on the surface of structure is obtained. The second part is the data transfer by an interface model between FDS and thermo-mechanical analyses. By the interface model, the calculated surface temperature from FDS simulation is assigned to the finite element model of the structure for thermo-mechanical analysis. The third part is a nonlinear thermo-mechanical analysis for predicting the structural response under high temperatures. To validate simulation results, structural fire experiments were performed for a real-scale steel-concrete composite beam, whose design was based on the code for nuclear power plant structures of Korea. The calculated time history of displacement at the center of the beam as well as the temperature at sampling points showed good agreement with experimental results. The changes in stiffness, load-carrying capacity, and ductility of the composite beam at elevated temperatures are investigated through parametric studies.

1 INTRODUCTION

Fire is one of the most severe hazards that should be considered in the design and analysis of civil infrastructure such as bridge, tunnel, and nuclear power plant. In recent years, fire in structure has become a major concern according to the rapid increase of urban transportation, which has naturally brought increasing transport of flammable and poisonous materials. In particular, damage or loss of bridge structure due to fire can result in significant social and economic consequences. Therefore, it is important to understand the behavior of structures subjected to fire and investigate structural damage. Recently in the United States and Europe, the performance-based fire resistance design method has been applied for important social infrastructures such as nuclear power plants (Kwon and Jung, 2010). The method sets the fire resistance performance time of a structure considering the type and quantity of combustible materials, the compartment size, and the structural load. In Korea, however, abstract fire resistance regulations have been adopted so far that set the fire resistance performance time of fire zones and apply them to members, rather than systematically performing the fire impact assessment of structures. With this method, it is difficult to establish fire response strategies in the event of a large fire in infrastructures including nuclear power plants and bridges, and it is not easy to verify the integrity of structures. Therefore, we need a total structural behavior assessment technique considering fire size, characteristics of structural materials, and the shape and characteristics of structures. It is not practically easy to assess the deformation and damage of structures due to fire through a full-scale experiment. However, the recent breakthroughs in computer hardware and computational dynamics techniques have enabled calculation of fire flows similar to actual situation and relatively accurate prediction of structural behavior in high temperature conditions. Therefore, it is effective to use computer analysis techniques in order to assess the fire resistance performance of structures for various structural and fire conditions while saving cost required for structural fire experiments.

In this study, a multi-physics structural fire analysis technique to accurately predict structural behavior in a fire is proposed by considering the shape of structure, fire size, and the thermal and mechanical properties of structural materials.

2 NONLINEAR THERMO-MECHANICAL ANALYSIS FRAMEWORK

To predict the behavior of structures exposed to fire, thermal and mechanical properties of structural materials must be reflected. In this study, thermal and mechanical properties of concrete were obtained by

material experiments conducted in the Fire Insurers Laboratories of Korea (FILK) were applied for the thermal and mechanical properties of concrete. For the thermal and mechanical properties of steel, the criteria presented by Eurocode 3 (2005) were used.

To predict the structural behaviors of structures similarly to the actual fire situation, the following three works can be considered to be important: the calculation of thermal flow field from the fire source to the structure, heat transfer analysis to the inside of structure, and structural analysis reflecting the temperature change inside the structure. Because each of these analyses influence the results of other analyses, a method of connecting the previous analysis results to the next analysis is required. This study proposes a fire structure analysis method that can reflect the multi-physics characteristics of thermal flow, heat transfer, and structural system. First, thermal flow field from the fire source to the structure is calculated using the Fire Dynamics Simulator (FDS). Using an interface model between the FDS model and the finite element structural analysis model, the surface temperature of the structure derived from the FDS analysis is applied as the boundary condition of structural analysis. Finally, the fire behavior of structure is calculated by a nonlinear finite element method with the temperature boundary condition and the thermal and mechanical properties of structural materials.

3 MATERIAL PROPERTIES

In general, the thermal and mechanical properties of structures change with temperature. Therefore, the temperature dependence of material properties must be considered to reliably and accurately predict the behavior of structure at high temperatures. Some standards and reports such as ASCE Manual and Reports No. 78 (Lie, 1992), Eurocode 2 (2005) and Eurocode 3 (2005) propose the material properties of steel and concrete at high temperatures based on experimental data. In this study, the criteria presented in Eurocode 3 were used for the thermal and mechanical properties of steel, and the data obtained through the experiments of FILK were applied for the thermal and mechanical properties of concrete.

3.1 *Thermal Properties of Steel*

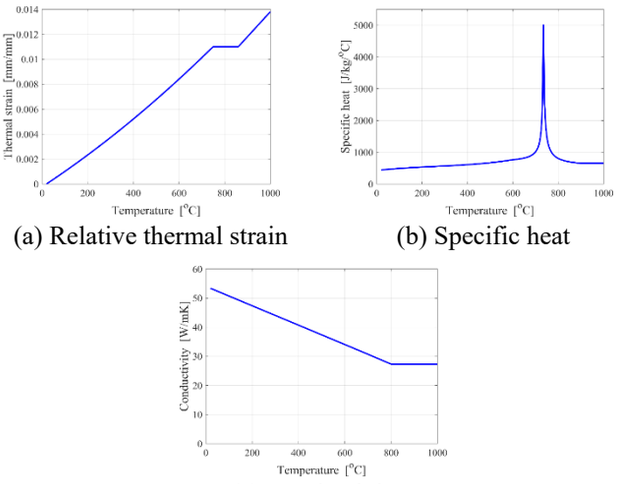
When steel is heated, the thermal properties such as thermal strain, specific heat and conductivity change with rising temperature. Several international standards present the thermal properties of steel based on experimental data. In this study, the equations of the thermal properties of steel and temperature presented by Eurocode 3 (2005) were applied for analysis. Equations (1), (2), and (3) are the relational equations for thermal strain, specific heat, and conductivity, respectively. Figure 1 shows the change of the thermal properties of steel with temperature change.

$$\epsilon_T = \begin{cases} (1.2\times10^{-5})T \\ \quad +(0.4\times10^{-8})T^2 \\ \quad -(2.416\times10^{-4}), & 20℃ < T \le 750℃ \\ (1.1\times10^{-2}), & 750℃ < T \le 860℃ \\ (2\times10^{-5})T - (6.2\times10^{-3}), & \\ & 860℃ < T \le 1200℃ \end{cases} \quad (1)$$

$$C = \begin{cases} 425 \\ \quad +7.73\times10^{-1}T \\ \quad -1.69\times10^{-3}T^2 \\ \quad +2.22\times10^{-6}T^3, & 20℃ \le T < 600℃ \\ 666 + \dfrac{13002}{738-T}, & 600℃ \le T < 735℃ \\ 546 + \dfrac{17820}{T-731}, & 735℃ \le T < 900℃ \\ 650, & 900℃ \le T \le 1200℃ \end{cases} \quad (2)$$

$$\lambda = \begin{cases} 54 - 3.33\times10^{-2}T, & 20℃ \le T < 800℃ \\ 27.3, & 800℃ \le T \le 1200℃ \end{cases} \quad (3)$$

Here, T denotes temperature, ϵ^{th} denotes thermal strain, C denotes specific heat, and λ denotes the thermal conductivity.



(a) Relative thermal strain (b) Specific heat

(c) Conductivity

Figure 1. Thermal properties of steel material

3.2 *Mechanical Properties of Steel*

Eurocode 3 (2005) presents mechanical properties of steel as well as the thermal properties. Eurocode 3 uses several parameters to characterize the stress-strain relationship of steel at specific temperatures. These parameters are yield strain ($\epsilon_{y,T}$), limit strain for yield strength ($\epsilon_{t,T}$), and ultimate strain ($\epsilon_{u,T}$), which have the values of 0.02, 0.15, and 0.2, respectively. Furthermore, the reduction factors in Table 1 are used to define the modulus of elasticity, elastic limit and yield strength at elevated specific temperatures. Each reduction factor can be defined by Eq. (4), (5), and (6) respectively.

Table 1. Reduction factors for stress-strain relationship at elevated temperatures.

T (℃)	Reduction factor of yield strength $(k_{y,T})$	Reduction factor of elastic limit $(k_{p,T})$	Reduction factor of of the modulus of elasticity $(k_{E,T})$
20	1.000	1.000	1.000
100	1.000	1.000	1.000
200	1.000	0.807	0.900
300	1.000	0.613	0.800
400	1.000	0.420	0.700
500	0.780	0.360	0.600
600	0.470	0.180	0.310
700	0.230	0.075	0.130
800	0.110	0.050	0.009
900	0.060	0.0375	0.0675
1000	0.040	0.0250	0.0450

$$k_y,T = f_{y,T}/f_y \tag{4}$$

$$k_{p,T} = f_{p,T}/f_y \tag{5}$$

$$k_{E,T} = E_T/E_0 \tag{6}$$

The constitutive equation is defined as Eq. (11) using the variables a, b, and c defined by Eqs. (8), (9), and (10). The stress-strain relation consists of four steps in total: linear elasticity section, nonlinear section after elastic limit, perfectly plastic, and softening sections. Figure 2 shows this stress-strain relationship presented in Eurocode 3 (2005).

$$\epsilon_{p,T} = f_{p,T}/E_T \tag{7}$$

$$a^2 = (\epsilon_{t,T} - \epsilon_{p,T})(\epsilon_{y,T} - \epsilon_{p,T} + {}^{c}/_{E_T}) \tag{8}$$

$$b^2 = c(\epsilon_{y,T} - \epsilon_{p,T})E_T + c^2 \tag{9}$$

$$c^2 = \frac{(f_{y,T} - f_{p,T}^2}{(\epsilon_{y,T} - \epsilon_{p,T})E_T - 2(f_{y,T} - f_{p,T})} \tag{10}$$

$$\sigma = \begin{cases} \epsilon E_T\,, & \epsilon \le \epsilon_{p,T} \\ f_{p,T} - c + \left(\frac{b}{a}\right)\left[a^2 - (\epsilon_{y,T} - \epsilon)^2\right]^{0.5}, & \epsilon_{p,T} < \epsilon < \epsilon_{y,T} \\ f_{y,T}, & \epsilon_{y,T} < \epsilon < \epsilon_{t,T} \\ f_{y,T}\left[1 - \frac{\epsilon - \epsilon_{t,T}}{\epsilon_{u,T} - \epsilon_{t,T}}\right], & \epsilon_{t,T} < \epsilon < \epsilon_{u,T} \\ 0, & \epsilon = \epsilon_{u,T} \end{cases} \tag{11}$$

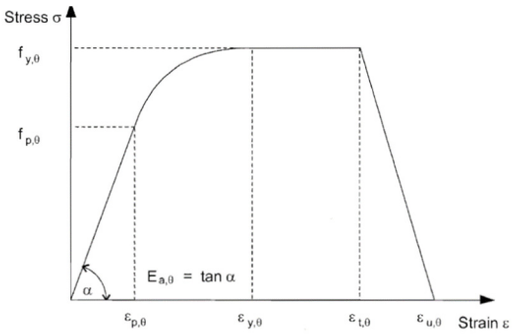


Figure 2. Stress-strain relationship presented in Eurocode 3

For nonlinear thermo-mechanical analysis, the stress-strain relation was applied using Eq. (12) which is the relational equation of yield strength and ultimate strength according to temperature. Figure 3 shows the stress-strain relation of steel applied to nonlinear thermo-mechanical analysis.

$$f_u(T) = \begin{cases} 1.25 f_y(T), & 0℃ \le T < 300℃ \\ f_y(T) \cdot (2 - 0.0025T), & 300℃ < T \le 400℃ \\ f_y(T)\,, & 400℃ \le T \le 1200℃ \end{cases} \tag{12}$$

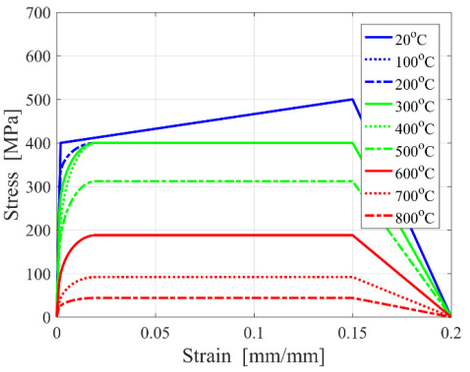
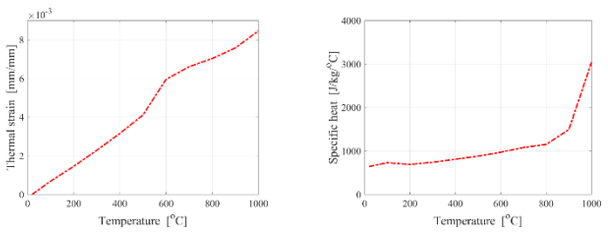


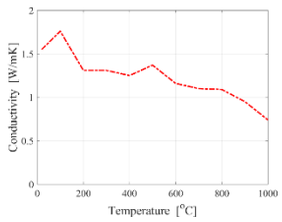
Figure 3. Stress-strain relationship of a steel material

3.3 *Thermal Properties of Concrete*

Thermal and mechanical properties of concrete were obtained by material experiments conducted in Fire Insurers Laboratory of Korea (FILK). Figure 4 shows the thermal properties of concrete that vary with temperature change. When concrete is heated, the thermal strain and specific heat increase overall as the temperature rises, whereas conductivity decreases as the temperature rises.



(a) Relative thermal strain (b) Specific heat



(c) Conductivity

Figure 4. Thermal properties of a concrete material

3.4 *Mechanical Properties of Concrete*

The stress-strain relation of concrete by temperature could be obtained from experiments in the Fire Insurers Laboratory of Korea (FILK). Figure 5 shows the stress-strain relation in the temperature range of 20~800℃. Figure 6 shows that the compressive strength of concrete sharply decreased at 100℃, restored to a similar compressive strength as the value at room temperature, and decreased again as the temperature increased above 300℃.

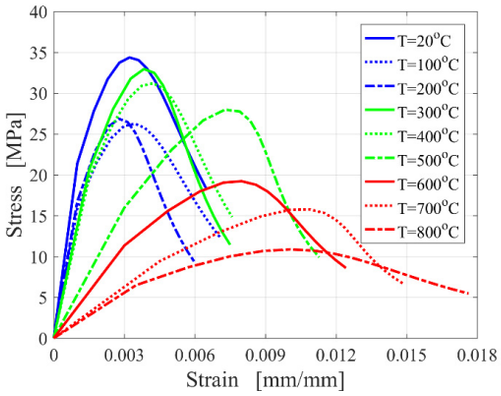


Figure 5. Stress-strain relationship of a concrete material

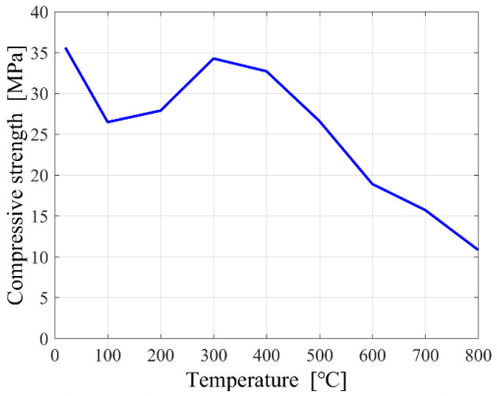


Figure 6. Variation of the compressive strength of concrete with temperature change

4 PLASTIC DAMAGE MODEL

Many plastic models have been proposed for the inelastic analysis of concrete structures showing hardening and softening behaviors when large deformations occur. This study used the plastic damage model proposed by Lee and Fenves (1998) alculates nonlinear behavior considering the loss of strength and stiffness due to concrete cracking.

The plastic damage model is based on the continuum mechanics approach to calculate the behaviors of continuum. In this model, the total strain (ϵ^{total}) consists of elastic strain (ϵ^{el}), plastic strain(ϵ^{pl}), and thermal strain(ϵ^{th}) as shown in Eq. (13).

$$\epsilon^{total} = \epsilon^{el} + \epsilon^{pl} + \epsilon^{th} \tag{13}$$

The plastic response of an undamaged material can be recorded in the effective stress space of the elastic area. The stress-strain relation is defined as Eq. (14), where C_0^{el} is the 4th order isotropic linear elastic stiffness tensor.

$$\sigma = C_0^{\text{el}} : \epsilon^{el} = C_0^{\text{el}} : (\epsilon^{total} - \epsilon^{pl} - \epsilon^{th}) \tag{14}$$

$$\begin{aligned} \sigma &= (1-d)C_0^{\text{el}} : (\epsilon^{total} - \epsilon^{pl} - \epsilon^{th}) \\ &= C^{\text{el}} : (\epsilon^{total} - \epsilon^{pl} - \epsilon^{th}) \end{aligned} \tag{15}$$

The plastic damage model reflects the reduction of the modulus of elasticity due to concrete damages using the damage variable d as shown in Eq. (15). The parameter indicates the concrete damage effect and helps the modeling of inelastic behavior of concrete. Figures 7 and 8 show the responses of uniaxial compression and uniaxial tension for the total strain, respectively.

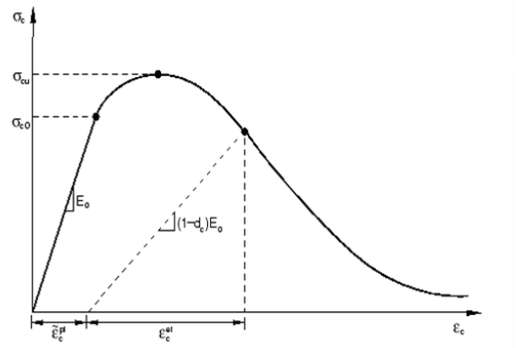


Figure 7. Response of concrete in uniaxial compression

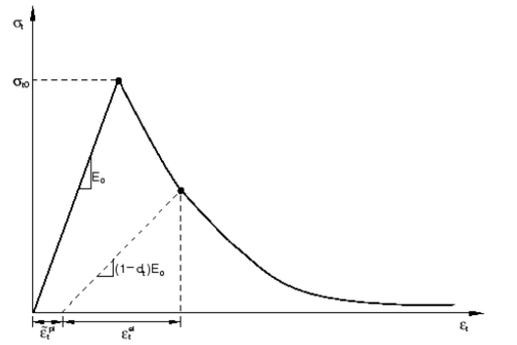


Figure 8. Response of concrete in uniaxial tension

5 RESULTS OF THERMO-MECHANICAL ANALYSIS

5.1 *Nonlinear Thermo-Mechanical Analysis of Representative Volume*

The thermal flow field due to fire from the fire source to the representative volume was calculated through FDS simulation. The temperature history of the representative volume surface exposed to fire could be obtained through fire flow analysis using the FDS model. The domain for FDS simulation is independent from the finite element model domain for thermo-mechanical analysis. In order to apply the surface temperature obtained through FDS simulation in the thermo-mechanical analysis as the boundary condition, a new model is required to send the surface temperature from the FDS model to the new model while sharing the discretization information of each model. In this study, an interface model was developed that sends the time history of the surface temperature at each node of the FDS model to the node of the finite element model at the corresponding location. Using this interface model, preliminary thermo-mechanical analysis was performed by applying the temperature history obtained through thermal flow analysis at each node of the representative volume and the applicability of the nonlinear thermo-mechanical analysis framework was verified.

The representative volume is a cube with a side length of 500 mm and is assumed that the bottom is exposed to fire as shown Fig. 7. The material properties of steel and concrete were applied to the representative finite element model and a pressure was applied to the top surface of the representative volume.

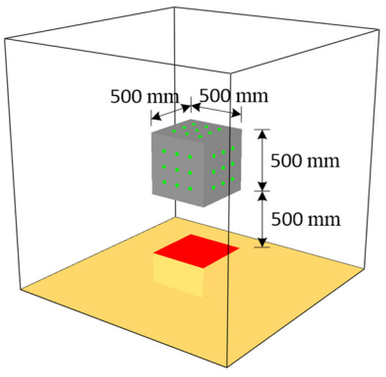
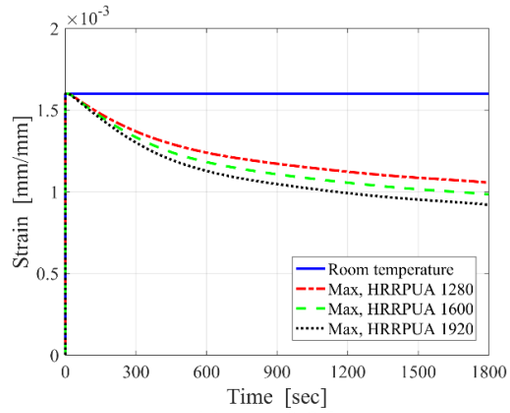
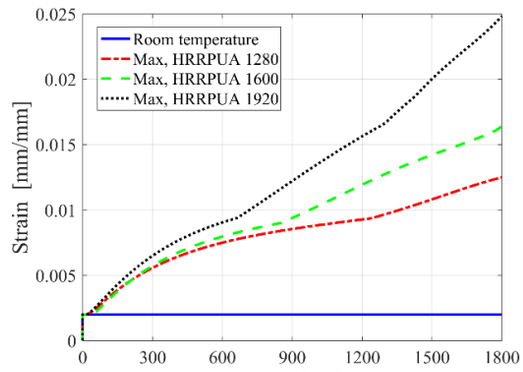


Figure 9. Modeling of a representative volume (RV) structure exposed to fire

Figure 10 (a) and (b) show the time history of compressive strain at the top surface center of the steel representative volume in which a fire occurred. As the maximum heat release rate per unit area (HRRPUA) increased at the pressure of $0.8f_y$, the compressive strain of the representative volume decreases due to the thermal expansion of steel. If the pressure is f_y, even if thermal expansion of the representative volume occurs, the compressive strain of the representative volume increases higher than the yield strain due to the yield of material. Figure 11 (a) and (b) show the time history of compressive strain calculated at the top surface center of the concrete RV in which a fire occurred. At the pressure of $0.4f_u$, thermal expansion occurs in the concrete RV, but the compressive strain increases higher than the strain at room temperature. If the pressure increases to $0.6f_u$, the compressive strain of RV increases much higher than the strain at room temperature due to the ignorable thermal expansion effect.



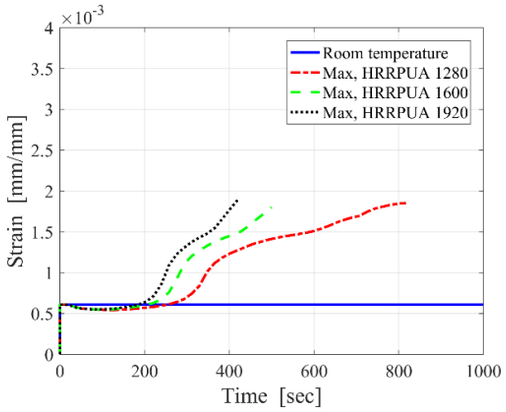
(a) $p = 0.8f_y$



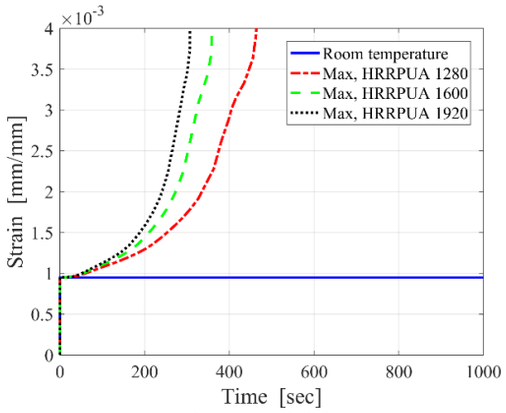
(b) $p = f_y$

Figure 10. FDS-FE fire structural analysis on steel RVs

Figure 11 (a) and (b) show the time history of compressive strain calculated at the top surface center of the concrete RV in which a fire occurred. At the pressure of $0.4f_u$, thermal expansion occurs in the concrete RV, but the compressive strain increases higher than the strain at room temperature. If the pressure increases to $0.6f_u$, the compressive strain of RV increases much higher than the strain at room temperature due to the ignorable thermal expansion effect.



(a) $p = 0.4f_u$



(b) $p = 0.6f_u$

Figure 11, FDS-FE fire structural analysis on concrete RVs

5.2 *Nonlinear Thermo-mechanical Analysis of Steel-Concrete Composite Beam*

A finite element model of the same scale as the specimen was configured based on the design drawing of the steel-concrete composite beam. The slab of the steel-concrete composite beam specimen has a length of 4000 mm and a section of 1000 mm × 210 mm as shown in the design drawing in Figure 12. The steel girder flange has a width of 203.1 mm and a thickness of 13.5 mm, and the web has a height of 320 mm and a thickness of 7.7 mm.

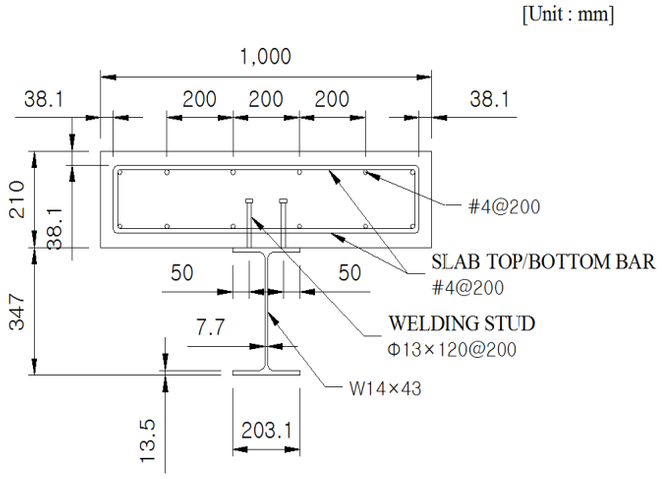


Figure 12. Design drawing of composite beam

The finite element model was created using ABAQUS, a universal finite element analysis application. The steel inside the concrete was modeled as a 3D truss element with 2 nodes (T3D2T), the steel girder as a shell element with 4 nodes (S4RT), and the concrete slab as a 3D solid element with 8 nodes (C3D8T). The number of elements used is 2,226 for steel modeling and 8,000 for concrete slab. The total number of elements for the finite element model is 11,711. Figure 13 shows the finite element models of the steel-concrete composite beam.

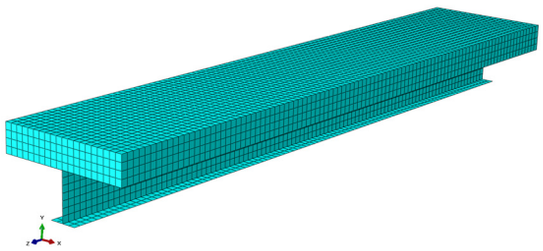


Figure 13. Finite element modeling of the composite beam

Figure 14 shows support and loading conditions of the composite beam. The beam is simply-supported, 5 m long, and loaded by two symmetric concentrated loads each of which is 119.5 kN. The distance between supports is 4.5 m and the distance between the two loading points is 1 m. This loading condition corresponds to a service limit state of the composite beam with no exposure to fire according to concrete design code for nuclear power plant structures in Korea. The bottom part of the composite beam was heated according to standard fire curve (ASTM E119, 2016).

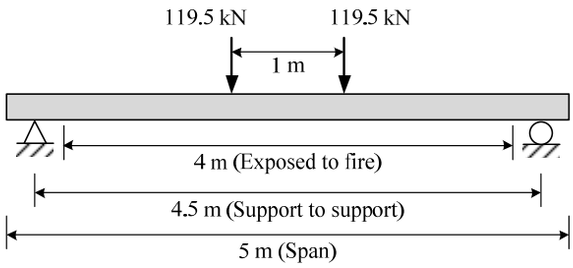


Figure 14. Test configuration

Figures 15 shows the temperature distribution of the steel-concrete composite beam. The temperature of the steel girder and slab bottom to which the standard fire curve had been applied was the highest and the thermal conductivity occurred more easily in the steel girder than in the concrete.

To obtain analysis results similar to the experimental results, the structural relations of steel were varied during the analysis. Concrete thermocouples were installed inside the slab to check the temperature inside the concrete slab. They were installed in 30 mm intervals from the slab bottom as shown in Fig. 16, and the temperature of each thermocouple was compared with the temperature in the thermal analysis results in Fig. 17. Although the thermocouple temperature at slab heights of 80 mm or higher was lower than 100 ℃, which is similar to

the temperature obtained from analysis, the thermocouple temperature at the slab height of 30~80 mm was approximately 100 ℃, which is different from the temperature calculated from thermal analysis. This temperature difference seems to have been caused because the moisture in concrete was evaporated at 100 ℃ during this experiment and the temperature did not increase much.

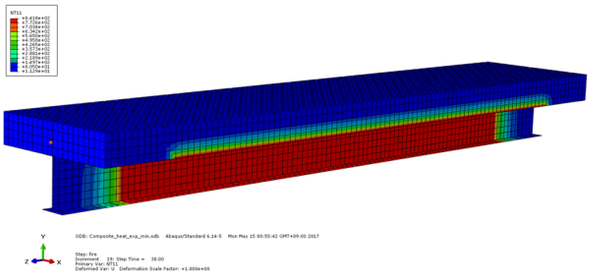


Figure 15. Change of temperature at slab vertical locations

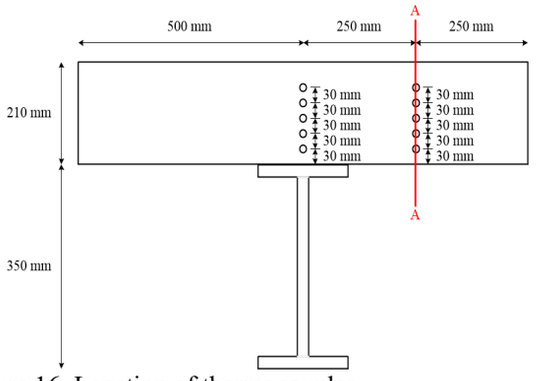


Figure 16. Location of thermocouples

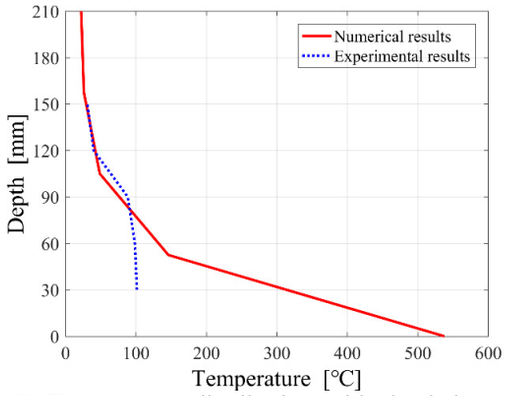


Figure 17. Temperature distribution with depth into the slab (A-A)

To obtain analysis results similar to the experimental results, the structural relation of steel was varied during the analysis. Case 1 shows a linear model in which both the elastic and plastic sections proposed in illam et al. (2009) are linear. Case 2 is the perfectly plastic model as presented in Eurocode 3. Case 3 shows a strain hardening model in Fig. 3. The stress-strain relation of each case is shown in Fig. 18.

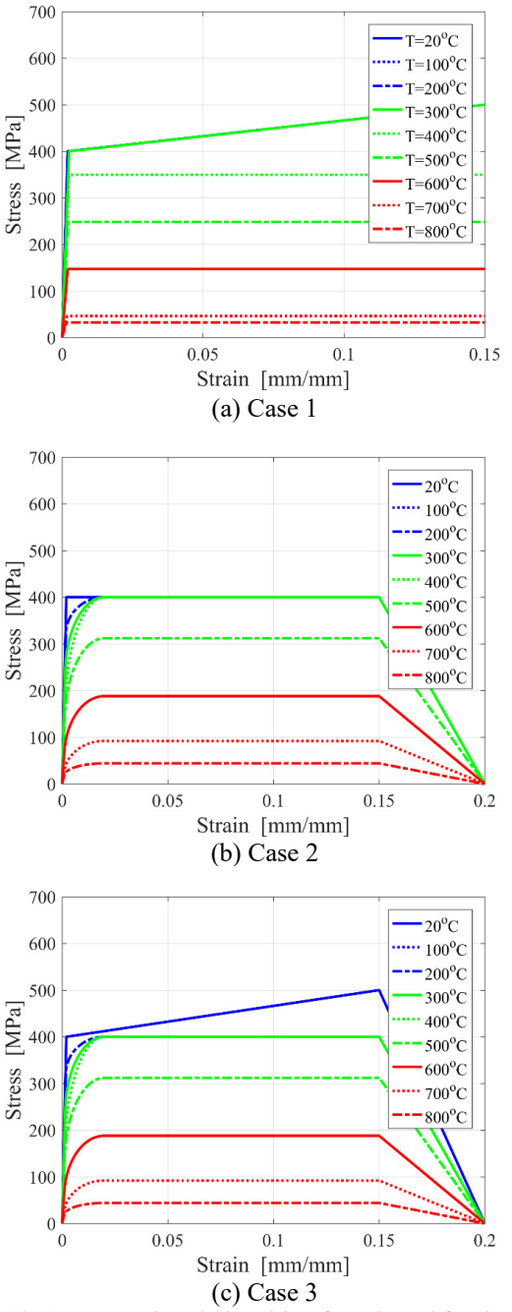


Figure 18. Stress-strain relationship of steel used for the analysis of the composite beam

Figure 19 and 20 show the fire experiment results of the actual steel-concrete composite beam and nonlinear thermo-mechanical analysis results, respectively. Figure 21 confirms that when the strain hardening model is applied to the structural relation of the experimental steel, the experimental results and the analysis results are most similar.



Figure 19. Steel-concrete composite beam after fire experiment

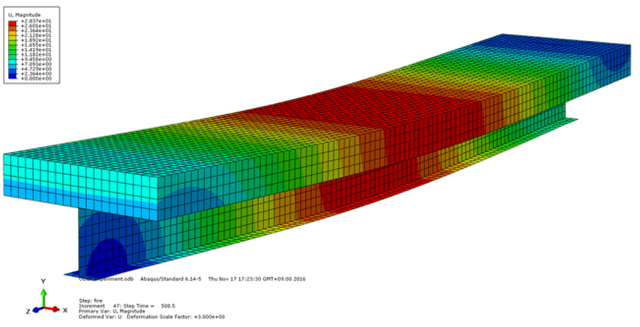


Figure 20. Vertical displacement contour of the composite beam obtained by a structural fire analysis

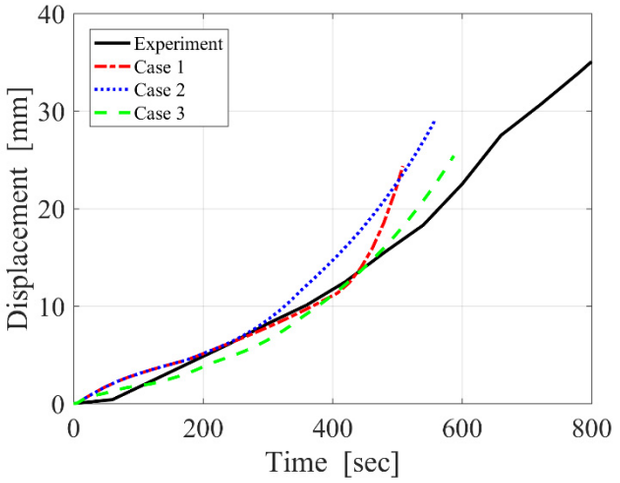


Figure 21. Predicted and measured displacement of the composite beam

6 CONCLUSION

In this study, a thermo-mechanical analysis framework was proposed considering material properties. A fire structure analysis of a RV structure and a steel-concrete composite beam exposed to fire was performed using the framework. The time history of compressive strain for RV structure exposed to fire was obtained as a result of the RV analysis and the applicability of the proposed framework was verified. The time history for the middle displacement on a simple support steel-concrete composite beam exposed to fire was calculated using the framework. The displacement results calculated through thermo-mechanical stress analysis were compared with the displacement results of the actual fire experiment in the FILK. The analysis results are significantly similar to the experimental results, and this verifies the validity of the framework.

7 REFERENCE

Kwon, I. K., & Jung, Y., J. 2010. Cost Analysis for Fire Protection on Structural Members of Residential Steel Building using Fire Engineering Design. *Journal of Korean Institute of Fire Science & Engineering* 24(1): 81-89.

European Committee for Standardization (CEN) 2005. *Eurocode 2: Design of concrete structures part 1-2: General rules - Structural fire design*. Brussels, Belgium: CEN.

European Committee for Standardization (CEN) 2005. *Eurocode 3: Design of steel structures part 1-2: General rules - Structural fire design*. Brussels, Belgium: CEN.

Lie, T. T. 1992. *Structural Fire Protection (Asce Manual and Reports on Engineering Practice) (No 78)*. New York: American Society of Civil Engineers

Willam, K., Xi, Y., Lee, K., & Kim, B. 2009. Thermal response of reinforced concrete structures in nuclear power plants. *A report submitted at College of Engineering and Applied Science.*

ASTM E119 2016. *Standard test methods for fire tests of building construction and materials*. American Society for Testing and Materials.

Lee, J., and Fenves, G. 1998. Plastic-damage model for cyclic loading of concrete structures. *Journal of Engineering Mechanics* 124(8): 892-900.

Maintenance, Safety, Risk, Management and Life-Cycle Performance of Bridges – Powers, Frangopol, Al-Mahaidi & Caprani (Eds)
© 2018 Taylor & Francis Group, London, ISBN 978-1-138-73045-8

The performance estimation of pile-protective structures using simplified collision model

GyeHee Lee
Department of Ocean Civil Engineering
Mokpo National Maritme University, Mokpo, Republic of Korea

ABSTRACT: In this study, a simplified collision model of pile protective structures against a navigation vessel was proposed and verified. The model of pile protective structure was composed by two plastic hinges at below of cap slab and the inside of ground. A equation of motions was developed in considering of the kinematic energy, potential energy and deformation energy in collision event. The developed simplified model was verified by the precise finite element collision analysis of the vessel and the protective structure. The parametric study was performed by using the simplified collision model. As a result, the collision behaviors of the protective structures could be tuned by the control of the inertia mass of capping slab.

1 INTRODUCTION

As the development of bridge technology, long-span bridges are being built across the navigation channels, and new design techniques are adopted in specifications and various collision protective structures are being planned and constructed. Among the various collision protective structures, the pile-type collision protective structure which has the energy dissipation mechanism by the plastic hinge of the pile has the advantage that the efficiency of construction equipment operation and the amount of dissipated energy can be easily controlled. However, since nonlinear behaviors included in the interaction of the pile and the soil, the internal material and the reinforcing bar, and the influence of the upper capping slab must be considered, the precise collision analysis requires a very large analysis model and a expensive analysis cost. This difficulty can be solved by using a simplified collision model which minimizes the degree of freedom which showing the nonlinear behavior of the structure. Using this kinds of simple model, we can develop a design methodology for nonlinear behavior by analyzing the effects of various parameters through a series of iterative analysis.

The development of a simplified model for ship collision had been mainly done in shipbuilding engineering(Sajdak 2004, Tabri 2010). These studies mainly focused on the collision between the ship and the ship, and the changes of ship movement after collision. A simplified collision model between a ship and a bridge was developed and used in the collision analysis for the superstructure of bridges and barges in Korea (Lee 2011). In order to protect a collision of 100000DWT ship, numerical analysis and field test were carried out for 1/15 scale reduction model in the process of designing pile-type collision protective structure(Patsch et al. 2011). They showed that the numerical analysis could simulate the behavior of the file with sufficient accuracy. Zhu et al. evaluated the lateral loading capacity of piles for construction of a ship collision protective structure in a large chamber (Zhu et al. 2012). The static and dynamic $p-y$ curves were calculated from the results of dynamic impact load using pendulum motion and static load using cable. They concluded that it is reasonable to compare the three types of theoretical dynamic $p-y$ curves with the curves obtained from the experiment. This the dynamic $p-y$ curve of the pile and a constant damping ratio were used collision analysis. The damping ratio used this analysis was obtained from the linear dynamic analysis.

In the Korean design code of bridges, the collision force is presented as a function of the mass and velocity of collision ship (Chang 2006). However, the collision force presented in the Korean code shows nonconservative trendy as collision conditions because the formula for the collision force was developed under not enough understanding of ship collision phenomena(Lee & Hong 2011).

Fan et al. proposed a scheme to determine the properties of nonlinear spring of ship bow as collision speed, the spring is a part of mass-spring SDOF model of ship body and bow. The SDOF model was proposed to design a cable-stayed bridge foundation against direct ship collision (Fan et al. 2011). In these

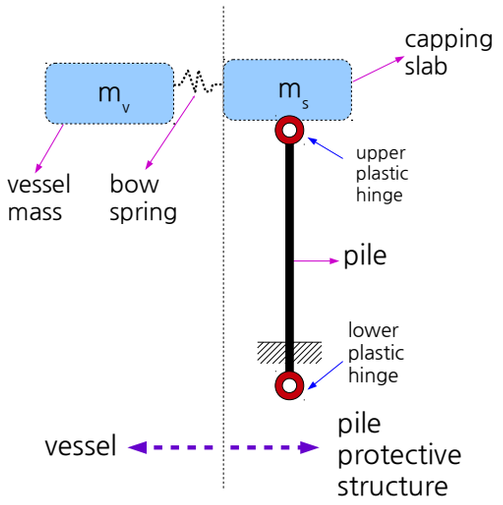


Figure 1: Simplified Collision Model

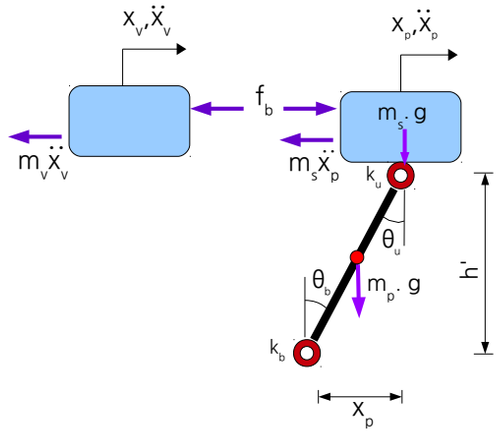


Figure 2: Forces at Collision

studies, they focused on the strain rate of steel bow, and proposed the bow strength curve based on strain rate.

In this study, the equations of the simplified model for effective collision analysis of pile-type protective structure was developed and verified by the results of the precise FEM collision analysis. The energy dissipation characteristics used in the simplified model was obtained from the FEM analysis model.

2 DEVELOPMENT OF SIMPLIFIED MODEL

The following conditions were assumed in the development of the simplified collision model.

- Collisions occur in the plane.
- Ship bow and piles behave plastic-elastically.
- The plastic behavior of the pile is concentrated(plastic hinge).

figure 1 shows the schematic shape of the simplified collision model of the pile-type collision protective structure to derive the equation of motion. The collision ship was simplified to a collision mass(m_v) and a bow spring, which represents the collision force due to the deformation of the bow. A pile-type collision protective structure consists of a capping slab (upper slab) and piles. Here, the capping slab constrains the head of piles to move together and transmit the collision force. Since the heads of piles are tie together by capping slab, its rotational freedoms are ignored. The mass of the slab(m_v) means the mass that resists the collision by inertia force at collision. It was assumed that the group of piles constituting the protective structure has concentrated characteristics.

The force acting on the ship and the guard during collision is shown in figure 2. During the collision, the ship is subjected to inertia force and the reaction force due to deformation of the bow. The equilibrium equation for this is as follows.

$$m_v \ddot{x}_v + f_b = 0 \tag{1}$$

where m_v is the collision mass of the ship, including hydrodynamic additional mass, and f_b is the nonlinear reaction force generated by deformation of the bow, respectively. This reaction force is a function of relative displacements between the ship displacement(x_v) and the structure displacement(x_p). This relative displacement $(x_v - x_p)$ is denoted the deformation of the ship bow.

During the collision process, the movement of the ship and the structure is as follows.

$$(f_b - m_s \ddot{x}_p)h' + g\, x_p(m'_s + \frac{m'_p}{2}) = k_u + k_b \tag{2}$$

where m_s is the mass of the slab, m_p is the mass of the pile group, respectively. The superscript $'$ denote the values in water. $\ddot{x_p}$ is the acceleration of the slab and h' is the vertical height of moment arm from the plastic hinge to the collision point, respectively. If the sum of the moments and the secondary moments of the structure caused by the slab displacement was less than the sum of the plastic moments of both plastic hinges, the protective structure would be stopped. In collision, the total moment resistance of the structure is as follows.

$$M_p = k_u + k_b - (m'_p/2 + m'_s)x_p \tag{3}$$

The horizontal force caused by this moment is as follows

$$f_p = \frac{M_p}{h'} \tag{4}$$

By the equilibrium of horizontal force, (2) can be rewritten

$$m_s \ddot{x}_p + (f_p - f_b) = 0 \tag{5}$$

To solve (1), (5), the following variables are assumed.

$$\left\{ \begin{array}{c} y_1 \\ y_2 \\ y_3 \\ y_4 \end{array} \right\} = \left\{ \begin{array}{c} x_v \\ \frac{dx_v}{dt} \\ x_p \\ \frac{dx_p}{dt} \end{array} \right\} \tag{6}$$

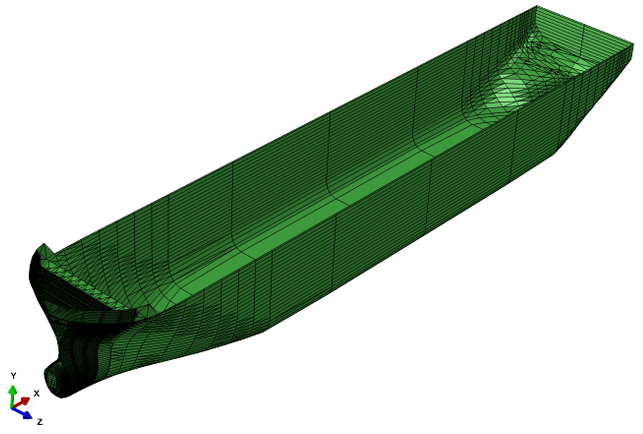


Figure 3: FEM Model of Ship

Substituting (1), (5) to (6), the following equation can be obtained.

$$\begin{Bmatrix} \frac{dy_1}{dt} \\ \frac{dy_2}{dt} \\ \frac{dy_3}{dt} \\ \frac{dy_4}{dt} \end{Bmatrix} = \begin{Bmatrix} y_2 \\ \frac{-f_b(x_v - x_p)}{m_v} \\ y_4 \\ \frac{f_b(x_v - x_p) - f_p(x_p)}{m_s} \end{Bmatrix} \tag{7}$$

Since (7) contains many nonlinear terms, it is hard to solve by the algebraic method, so the solution is calculated numerically. To do this, the fourth-order Runge-Kutta method is used. The application of this method was performed using the *lsode45* function of the numerical analysis package GNU Octave(Eaton et al. 2014).

3 VERIFICATION

3.1 *FEM model*

To verify the developed simplified collision model, nonlinear dynamic collision analysis was performed using commercial FEM package ABAQUS 6.10 (Simulia 2010). The verification FEM model was consist the ship, the protective structure and the ground soil. The ship modeled in verification FEM analysis was the size of 7000GT car carrier and it was modeled by shell elements. The ship bow was modeled by fine meshes, since the collision force would be concentrated. The material and geometric nonlinear behavior in the collision were also considered. The main body was modeled using a shell element, but relatively coarse mesh was used as compared to the ship bow, and elastic behaviors were assumed.

The elastic-plastic material properties were assumed for the bow part and the strain rate effects were considered as follows

$$\frac{\bar{\sigma}}{\sigma_0} = 1 + \left(\frac{\dot{\epsilon}_{pl}}{D}\right)^{\frac{1}{n}} \tag{8}$$

where $\bar{\sigma}$ is the dynamic flow stress, σ_0 is the static flow stress, $\dot{\epsilon}_{pl}$, is the strain rate and D, n are constants

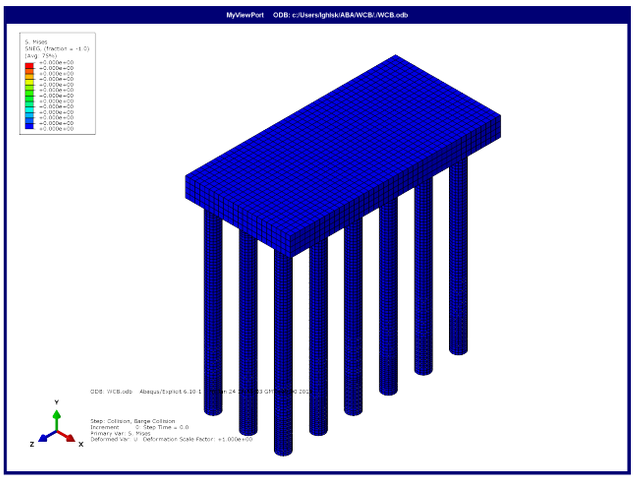


Figure 4: FEM model of protective structure

Table 1: Parameters used in simplified collision model

Mass of Ship (m_v)	1.675E7 kg
Mass of Slab(m_s)	3.544E6 kg
Mass of Piles (m_p)	3.944E5 kg
Dist. of Plastic Hinges (h_p)	23.96 m
Collision Velocity (v_0)	5 m/s

that depend on the material, respectively. In this study, $D = 40.4/sec$, $n = 5$ were used.(Simulia 2010).

The hydrodynamic additional mass was calculated as the design standard (AASHTO 2010). For the efficiency of analysis, the mass scaling which is a technique to increase the critical time step by changing the material density was used for a dense mesh part, that was ship bow. Detailed modeling techniques for other vessels followed the methods developed in previous study(Lee & Hong 2011).

The pile, which is the main energy dissipation mechanism of the pile collision protection structure, was modeled as steel pipe with radius R = 1.0 m. The length of the pile is assumed to be 30 m, and the upper part is assumed to be constrained on the capping slab that is assumed to be an elastic material, and the lower part was assumed to be fixed in bedrock while being penetrated into the soil layer. It was assumed that the soil layer are composed of three layers of clay and sandy soil with a total depth of 10 m. The material of pile was assumed as SS400 steel and material nonlinear behaviors were considered. Nonlinearity of the ground was considered by using nonlinear springs(Lee, Park, & Hong 2012). The objective protective structure was consist of 18 piles and the capping slab confining the piles to dissipate the collision energy of ship.(figure 3)

3.2 *Simplified model*

To verify the developed simple collision model, the collision analysis was performed by the simplified model with the same conditions of FEM model and the two results were compared.

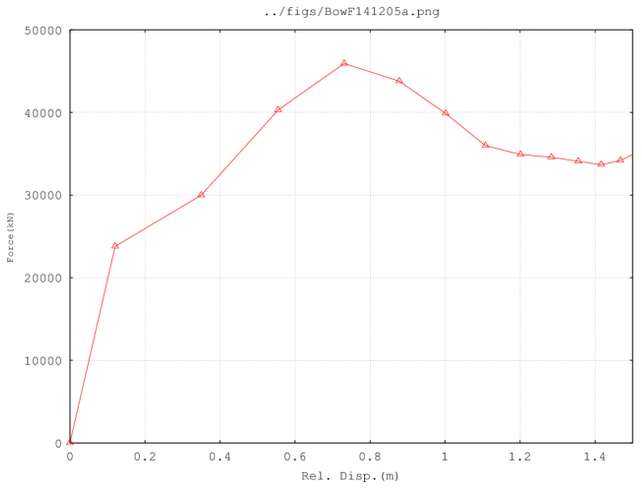


Figure 5: Bow reaction curves used in simplified verification analysis

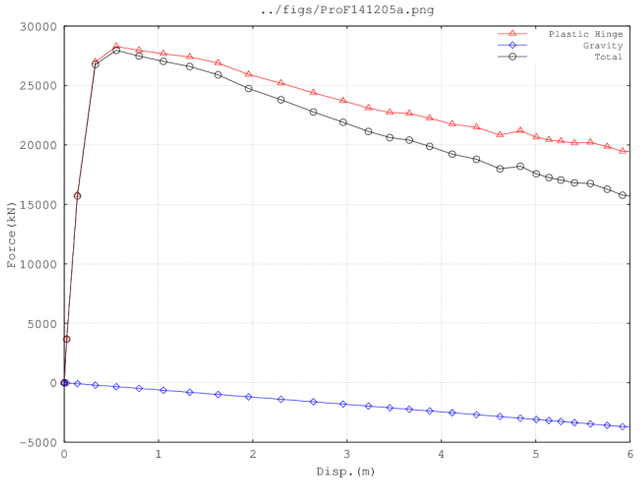


Figure 6: Structure reaction curves used in simplified verification analysis

The analysis parameters applied to the simplified collision model were obtained from the results of FEM analysis and are shown in 1. The location of the plastic hinges were defined as the intersection obtained by extending the center line of the pile which does not cause rotational deformation in the precision analysis.

In collision analysis, both the structure and the ship are subjected acceleration, therefore the force acting between the two objects must be calculated in consideration of the inertia force. In this study, the acceleration history is obtained from the velocity change of the ship bow and the force history during the collision was calculated from the result of the FEM analysis (Lee & Hong 2011). In the resistance curve of the protective structure, the weight of capping slab causing secondary moment according to displacement increases. However, in this verification analysis, the influence of the secondary moment due to the displacement was not considered(figure 6).

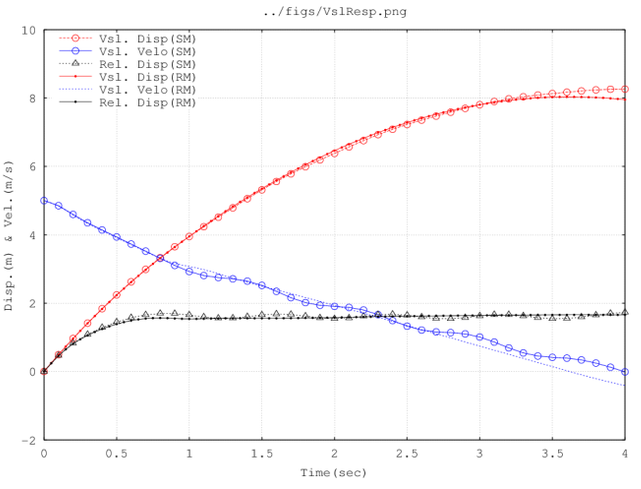


Figure 7: Response comparisons of ship

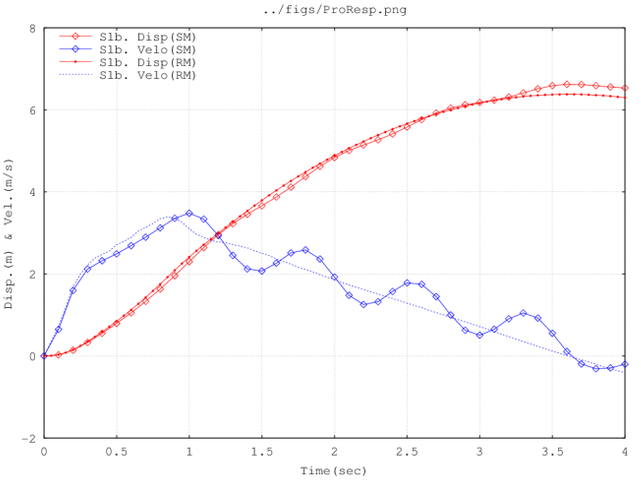


Figure 8: Response comparisons of protective structure

3.3 *Comparison of results*

The collision behaviors of the ship and the protective structure obtained from FEM analysis were compared in displacement and velocity(figure 3.3, 3.3). All responses showed similar results to both analysis. However, in the case of the velocity responses, the vibration shape was appeared compared to FEM analysis, and the collision was terminated at about 3.6 seconds and the recoil occurs in FEM analysis. And it was occurred in about 4 seconds in the simplified analysis The overall analysis results of the simplified model were considered to denote sufficient accuracy for the behavior of the ship.

The collision behavior of the protective structure was similar to that of the ship. However, the vibration phenomenon was more prominent than that of ship in the velocity response. However, the overall tendency was the same and the displacement behavior has a sufficient accuracy.

The change in energy during the collision is shown in figure 10. At the point of collision, all energy was in the form of kinetic energy of the collision ship, but at the start of the collision, this energy was dissipated by the plastic deformation of the bow and the protective

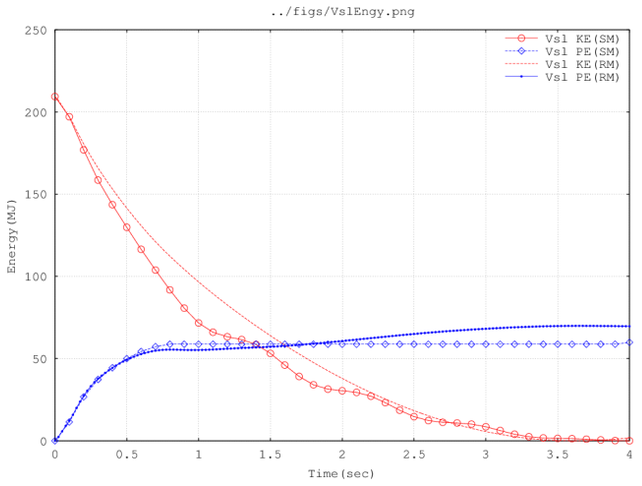


Figure 9: Energy comparisons of ship

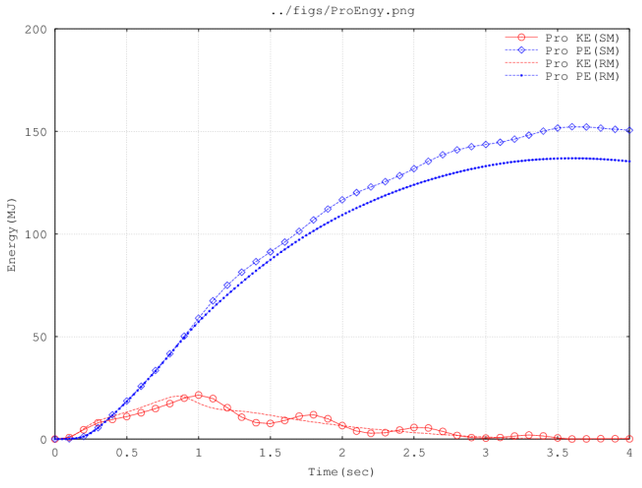


Figure 10: Energy comparisons of protective structure

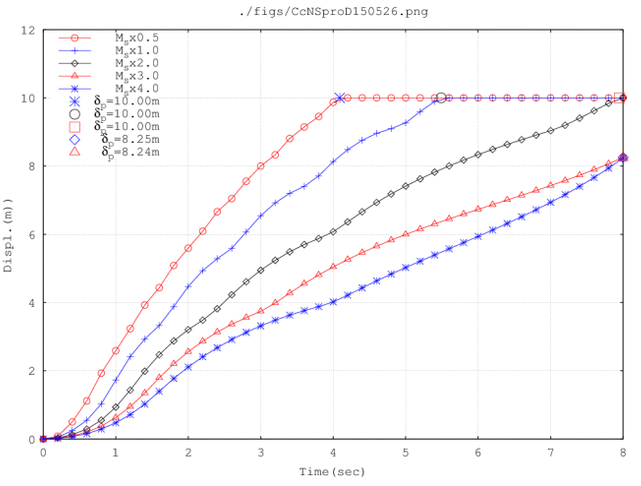


Figure 11: Displacment of protective structure as mass of capping slab

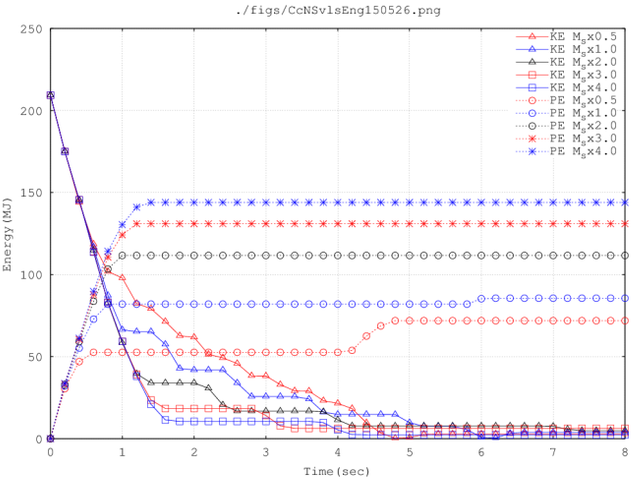


Figure 12: Energy dissipation of vessel as mass of capping slab

structure. The collision energy was mainly dissipated by the plastic deformation of the protective structure.

On the other hand, the kinetic energy of the protective structure was not a large effect on the energy dissipation behavior except for the initial state. The energy change of ship by the simple collision model is very similar to that of FEM analysis except error of kinetic energy due to vibration phenomenon of velocity behavior mentioned above. Overall, however, Of the energy dissipation capacity of the system.

4 PARAMETRIC STUDY

The parametric analysis was performed using the developed simplified model. The characteristics of the plastic hinge considered in the analysis were those of layered pile with diameter of 2m and thickness of 15mm (Lee 2016). The basic collision speed of the ship was assumed 5m/sec, and the bow strength of ship was used that of the verification FEM analysis(figure 6). The maximum displacement of the protective structure was assumed 10 m, considering the case where the displacement of structure was limited by the foundation of the bridge. The other analytical parameters were calculated based on the analytical model used in the verification analysis.

The considered resistance characteristics of the protective structure were the inertia resistance of capping slab mass and the rotational resistance of the plastic hinge. The slab mass was varied from 0.5 to 4 times based on the slab mass(3.543 10^6 kg) of the verification study.

The displacement history of the protective structure is shown in figure 11. When the mass of the slab was less than twice the reference value, the displacement of the protective structure reachees the displacement limit. On the other hand, if the mass of the slab was twice the reference value Or more, the displacement of the protective structure was smaller than the limit value.

In figure 12 shows the amount of dissipated kinetic energy of the ship bow by the plastic deformation. Here, the difference between the kinetic energy and the deformation energy was absorbed as strain energy of the protective structure.

The mass of the slab is not the mass of the structure only but the mass involved in the inertial resistance at collision. The non-structural mass on the slab or the

hydrodynamic added mass of the fluid could be the inertia mass of the slab, and it could be changed easily for the optimal protection design.

5 CONCLUSIONS

In this study, a simplified collision model of pile-type ship protective structure was developed and verified. The pile-type protective structure was modeled as two plastic hinges at the bottom of the upper capping slab and in the ground. The equation of motion including the nonlinear behavior of the bow and the protective structure was derived. The derived equation of motion is numerically analyzed by the Runge-Kutta method. An accurate FEM collision model was constructed considering the nonlinear behaviors at the ship, and the verification was performed by comparing results of two models. As a result, the proposed simple collision analysis model was shown to properly simulate the collision behavior of the pile-type ship collision protection structure. The parametric study was performed by the simplified collision model. As a result, By adjusting the slab mass of the protective structure, the energy dissipation characteristics of the protective structure can be changed greatly. This is a way to easily control the protection ability of the protection structure.

ACKNOWLEDGEMENT

This research was supported by Basic Science Research Program through the National Research Foundation of Korea(NRF) funded by the Ministry of Education(2017R1D1A1B03030253)

REFERENCES

AASHTO (2010). *LRFD Bridge Design Specifications*. AASHTO.

Chang, S. P. e. a. (2006). *Design Guides of Cable Steel Bridges*. Korean Society of Civil Engineers.

Eaton, J. W., D. Bateman, S. Hauberg, & R. Wehbring (2014). *GNU Octave version 3.8.1 manual: a high-level interactive language for numerical computations*. CreateSpace Independent Publishing Platform. ISBN 1441413006.

Fan, W., W. Yuan, Z. Yang, & Q. Fan (2011). Dynamic demand of bridge structure subjected to vessel impact using simplified interaction model analysis and testing of piles for ship impact defenses. *ASCE Journal of Bridge Engineering 16*, 117–126.

Lee, G. (2011). A simplified bridge-vessel collision model considering with the rotational motions of the vessel. *Journal of Korean Society of Civil Engineers 31(2A)*, 43–49.

Lee, G. (2016). Development and verification of simplified collision model for pile protective structures. *Journal of Korean Society of Coastal and Ocean Engineers 28(1)*, 7–12.

Lee, G. & K. Hong (2011). A study for the evaluation of ship collision forces for the design of bridge pier i : Mean collision force. *Journal of Korean Society of Civil Engineers 31(3A)*, 199–206.

Lee, G. H., J. S. Park, & K. Y. Hong (2012). Ship collision behaviors of offshore wind tower on bucket foundation. *Journal of the Korea Society of Disaster Information 8(2)*, 138–147.

Patsch, A., C. Gerbaudo, & A. P. Carlos (2011). Analysis and testing of piles for ship impact defenses. *Journal of The Korean Society of Disaster Information 7(1)*, 75–85.

Sajdak, J. A. (2004). Analyses of ship collisions: Determination of longitudinal extent of damage and penetration. Ph d. thesis, Georgia Institute of Technology.

Simulia (2010). *ABAQUS 6.10 User Manual*. Amsterdam: Simulia Co.

Tabri, K. (2010). Dynamics of ship collisions. Ph d. thesis, Aalto Univ. Denmark.

Zhu, B., R. P. Chen, F. J. Guo, L. G. Kong, & Y. M. Chen (2012). Large-scale modeling and theoretical investigation of lateral collisions on elevated piles. *ASCE Journal of Geotechnical and Geoenvironmental Engineering 138(4)*, 461–471.

Maintenance, Safety, Risk, Management and Life-Cycle Performance of Bridges – Powers, Frangopol, Al-Mahaidi & Caprani (Eds)
© 2018 Taylor & Francis Group, London, ISBN 978-1-138-73045-8

Effect of Slenderness-Ratio Parameter on Seismic Performance of Steel Piers

H. Takezawa & K. Ono
Department of Civil and Environmental Engineering Waseda University, Shinjuku-ku, Tokyo, Japan

S. Okada
IHI Infrastructure Systems Co., Ltd., Minato-ku, Tokyo, Japan

K. Azumi
Hanshin Expressway Company Limited, Minato-ku, Osaka, Japan

ABSTRACT: The slenderness ratio parameter of steel members such as arch ribs is larger than that of usual steel bridge piers. However, previous studies on the seismic performance of steel members with the large slenderness ratio parameter are not sufficient compared with usual steel bridge piers. The purpose of this study is to obtain more results on the load-carrying capacity and the ductility for steel members with the relatively large slenderness ratio parameter based on the elasto-plastic finite element analysis. The validity of the analytical method was confirmed by comparing the analytical results with the previous experimental results. Based on the valid analytical method, the parametric analysis about the width-thickness ratio parameters was conducted and the effect of the slenderness ratio parameter was investigated. Analysis results indicate that the load-carrying capacity and the ductility for steel members decrease as the slenderness ratio parameter increases or the width-thickness ratio parameters increase.

1 INTRODUCTION

The Kobe earthquake in 1995 caused destructive damage to highway bridges. After the Kobe earthquake, a lot of studies for improving the seismic performance and developing the seismic design methods for steel bridge piers were conducted. Based on the useful information obtained from the investigation on seismic performance of steel bridge piers, some methods for estimating the seismic performance of steel bridge piers or steel members have been already proposed. By the way, the slenderness ratio parameter of steel members such as arch ribs is larger than that of usual steel bridge piers. In "*Design Specifications for Highway bridges, part 5, Seismic Design"* (Japan Road Association 2012), the method for estimating the seismic performance of steel members with the relatively large slenderness ratio parameter is proposed($\bar{\lambda} \leqq 0.5$). However, previous studies on the seismic performance of steel members with the large slenderness ratio parameter are not sufficient compared with usual steel bridge piers whose slenderness ratio parameter is not large. For this reason, it is necessary to obtain more information about the elasto-plastic behavior of steel members with the large slenderness ratio parameter by experimental and analytical studies. In this study, the effect of the slenderness ratio parameter on the load-carrying capacity and the ductility was investigated based on the elasto-plastic finite element analysis. First of all, the validity of the analytical method was confirmed by comparing the analytical results with the previous experimental results. Based on the valid analytical method, the parametric analysis about the slenderness ratio parameter and the width-thickness ratio parameters was conducted.

2 OUTLINE OF THE ANALYITICAL METHOD

It is necessary to confirm the validity of the analytical method before investigating the load-carrying capacity and the ductility for steel members by analysis. To confirm the validity of the analytical method, the analysis result was compared with the experimental result in the previous cycle loading experiment (Okada et al. 2010).

2.1 *Analytical program*

For the analysis, an elasto-plastic finite displacement analysis program "CYNAS" (Nishimura et al. 1995; Ono et al. 2016) was used in this study. CYNAS used shell elements. Material constants of a constitutive equation (Azumi. 2016) used in CYNAS can accurately represent steel material properties.

2.2 *Analytical model*

The test specimen (S-44-15) in the previous cycle loading experiment was modeled (Okada et al. 2010). The test specimen has large slenderness ratio

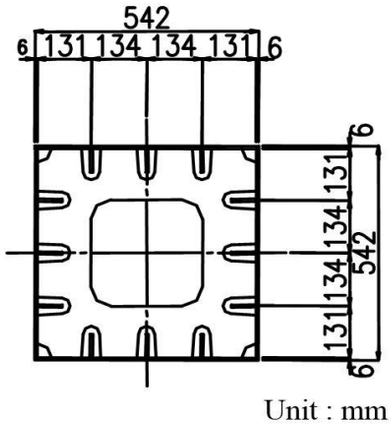


Figure 1. Cross-section of the test specimen(S-44-15).

parameter ($\bar{\lambda}$ =0.51). The values of other parameters are below: R_R =0.53, R_F =0.49, N/N_y =0.11, γ_l/γ_l^* =1.19. R_R and R_F are the width-thickness ratio parameters defined by Equation 2 and Equation 3. N/N_y is the axial force ratio. γ_l/γ_l^* is the stiffness ratio of stiffener. The details of the test specimen (S-44-15) are shown in Table 1. The details of cross-section, side view and analytical model are shown in Figures 1 and 2.

$$\bar{\lambda} = \frac{1}{\pi} \cdot \sqrt{\frac{\sigma_y}{E}} \cdot \frac{2L}{r} \tag{1}$$

$$R_R = \frac{b}{t} \cdot \sqrt{\frac{\sigma_y}{E} \cdot \frac{12(1-\nu^2)}{\pi^2 k_R}} \tag{2}$$

$$R_F = \frac{b}{t} \cdot \sqrt{\frac{\sigma_y}{E} \cdot \frac{12(1-\nu^2)}{\pi^2 k_F}} \tag{3}$$

$$k_F = \begin{cases} \dfrac{(1+\alpha^2)^2 + n\gamma_l}{\alpha^2 \cdot (1+n\gamma_l)} \cdots (\alpha < \alpha_0) \\ \dfrac{2 \cdot (1+\sqrt{1+n\gamma_l})}{1+n\gamma_l} \cdots (\alpha \geq \alpha_0) \end{cases} \tag{4}$$

where σ_y = yield stress; E = Young's modulus; N = axial force; N_y = yield axial force (=$A\sigma_y$); A = cross-section area of column; L = column height (distance from the bottom of the column to the point of application of horizontal load); r = radius of gyration of cross section; b = plate width; t = plate thickness; ν = Poisson's ratio; k_R = buckling coefficient (=$4n^2$); n = number of panel which divided by stiffener; k_F = buckling coefficient of panel between diaphragms defined by Equation 4; α = aspect ratio (=a/b); a = diaphragm height; $\alpha_0 = \sqrt[4]{1+n\gamma_l}$; γ_l = stiffness of stiffener; and γ_l^* = required stiffness of stiffener.

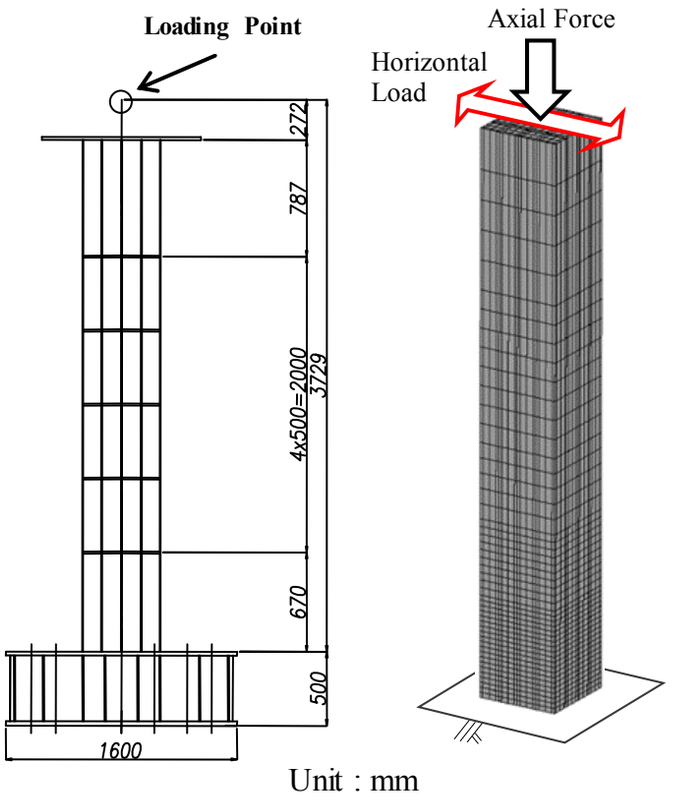


Figure 2. Side view of the test specimen(S-44-15) and analytical model.

Table 1. Details of the test specimen (S-44-15).

Steel type	SM490
Flange width B_F (mm)	542
Web width B_W (mm)	542
Flange thickness t_F (mm)	6
Web thickness t_w (mm)	6
Longitudinal stiffener width b_r (mm)	60
Longitudinal stiffener thickness t_r (mm)	6
Height L(mm)	3729
Number of stiffener	3
Stiffness ratio γ_l/γ_l^*	1.19
Axical force ratio N/N_y	0.11
Slenderness ratio parameter $\bar{\lambda}$	0.51
Width-thickness ratio parameter R_R	0.53
Width-thickness ratio parameter R_F	0.49

2.3 *Analytical conditions*

The steel type of S-44-15 is SM490. Residual stress and initial deflection described in the previous study (Okada et al. 2010) were applied to the analytical models. Residual stress of SM490 and initial deflection are shown in Figure 3 and Figure 4. The cyclic loading pattern of horizontal displacement is shown in Figure 5. After the axical force was loaded, cyclic loading was applied to the top of the model.

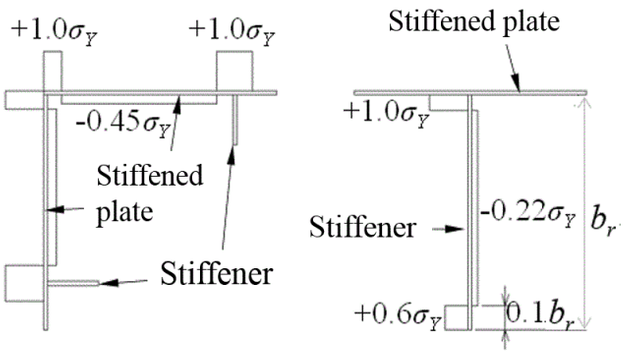


Figure 3. Residual stress(SM490).

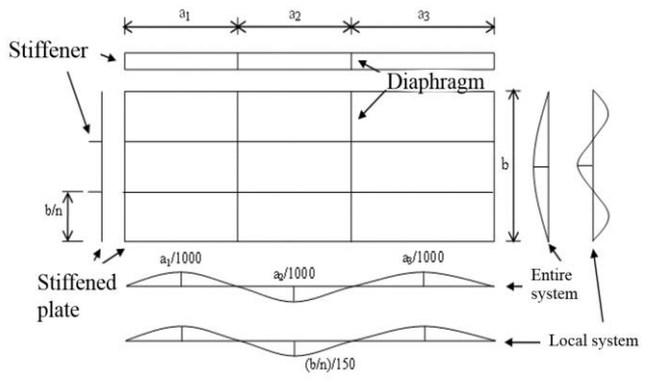


Figure 4. Initial deflection.

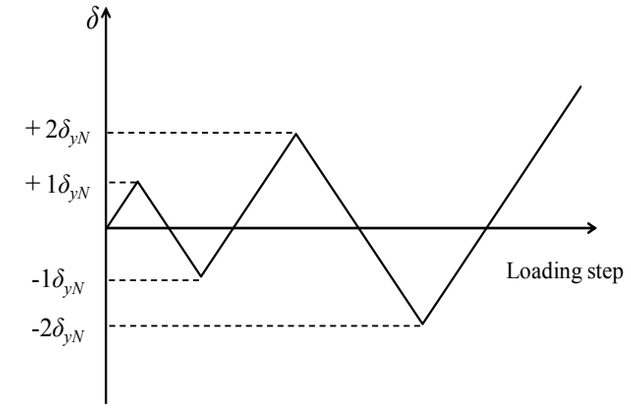


Figure 5. Loading pattern.

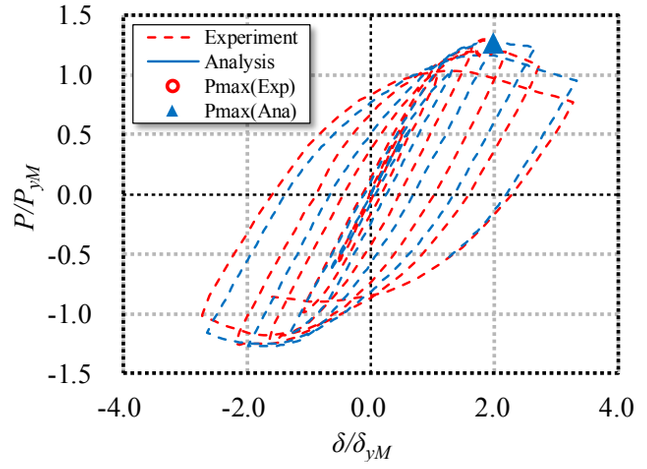


Figure 6. Comparing the analysis result with the experimental result.

Table 2. Details of analytical models.

	P-33-15	P-53-15	P-55-15
Steel type	SM490Y		
Flange width B_F (mm)	900	900	900
Web width B_W (mm)	900	900	900
Flange thickness t_F (mm)	23	14	14
Web thickness t_w (mm)	23	14	14
Longitudinal stiffener width b_r (mm)	150	140	104
Longitudinal stiffener thickness t_r (mm)	30	27	17
Height (mm)	6,000	5,900	6,200
Number of stiffener	2		
Stiffness ratio γ_l/γ_l^*	1.02	2.88	1.02
Axical force ratio N/N_y	0.15	0.15	0.15
Slenderness ratio parameter $\bar{\lambda}$	0.50		
Width-thickness ratio parameter R_R	0.30	0.50	0.50
Width-thickness ratio parameter R_F	0.30	0.30	0.50

$$P_{yM} = \left(\sigma_y - \frac{N}{A}\right) \cdot \frac{W}{L} \tag{5}$$

where W = section modulus.

2.4 *Verification of the analytical method*

The analysis result and the experimental result are compared and shown in Figure 6. The vertical axis is P/P_{yM}. And, the horizontal axis is δ/δ_{yM}. P_{yM} is the yield horizontal load defined by Equation 5. δ_{yM} is the yield horizontal displacement corresponding to P_{yM} on each horizontal load-horizontal displacement relationship. In the Figure 6, the analysis result can express the experiment result adequately up to the maximum horizontal load. Therefore, the validity of the analytical method was confirmed.

3 PALAMETRIC ANALYSIS

The load-carrying capacity and the ductility for steel members with relatively large slenderness ratio parameter were investigated by the elasto-plastic finite displacement analysis.

3.1 *Analytical models*

The details of the analytical models are shown in Table 2. The value of the slenderness ratio parameter $\bar{\lambda}$ is 0.50. For the width-thickness ratio parameters R_R and R_F, the combination values of 0.30 and 0.50 are used. In the case of different width-thickness ra-

tio parameters, the load-carrying capacity and the ductility of steel members were investigated.

3.2 *Analytical method*

The analytical method described in the previous chapter was used. The steel type of analytical models is SM490Y. Therefore, residual stress of SM490Y shown in Figure 7 was applied (Okada et al. 2010). The initial deflection and the loading pattern were the same as those in Figure 4 and Figure 5.

3.3 *Analytical results*

The analysis results of the models in Table 2 are shown in Figure 8. As the cross-sectional area of each analytical model is different, analytical models were compared by using the relationship between P/P_{yM} and δ/δ_{yM}. Consequently, the analysis results indicate that both load-carrying capacity and the ductility of steel members decrease as the width-thickness ratio parameter R_R and R_F increase.

3.4 *Effect of the slenderness ratio parameter*

Based on both the parametric analysis results shown in the section 3.3 and previous analysis results (Okada et al. 2010), the effect of the slenderness ratio parameter was investigated. The previous analytical models have smaller slenderness ratio parameter ($\bar{\lambda}$ =0.20) than the parametric analytical models ($\bar{\lambda}$ =0.50). The details of the previous analytical models are shown in Table 3. In both cases ($\bar{\lambda}$ =0.20 and 0.50), P_{max}/P_{yM} and δ_{max}/δ_{yM} are shown in Figure 9 and Figure 10. The Figure 9 and Figure 10 indicate that both load-carrying capacity and the ductility decrease as the slenderness ratio parameter $\bar{\lambda}$ increases or the width-thickness ratio parameters increase.

Table 3. Details of the previous analytical models (Okada et al. 2010).

	S18-N15	S15-N15	S13-N15
Steel type	SM490Y		
Flange width B_F (mm)	2745	2745	2745
Web width B_W (mm)	2745	2745	2745
Flange thickness t_F (mm)	40	24	24
Web thickness t_w (mm)	40	24	24
Longitudinal stiffener width b_r (mm)	338	309	226
Longitudinal stiffener thickness t_r (mm)	38	35	25
Height (mm)	8078	8015	8226
Number of stiffener	4		
Stiffness ratio γ_l/γ_l^*	1.0	2.8	1.0
Axical force ratio N/N_y	0.15	0.15	0.15
Slenderness ratio parameter $\bar{\lambda}$	0.20		
Width-thickness ratio parameter R_R	0.30	0.50	0.50
Width-thickness ratio parameter R_F	0.30	0.30	0.50

4 CONCLUSIONS

The purpose of this study is to investigate the effects of the slenderness ratio parameter on the load-carrying capacity and the ductility for steel members. The load-carrying capacity and the ductility were investigated based on the elasto-plastic finite element analysis. Before the analysis was conducted, the validity of the analytical method was confirmed by comparing the analysis result with the previous experimental result. The parametric analysis for steel members with relatively large slenderness ratio parameter ($\bar{\lambda}$ =0.50) was conducted in the case of different width-thickness ratio parameters. Furthermore, the effect of the slenderness ratio parameter

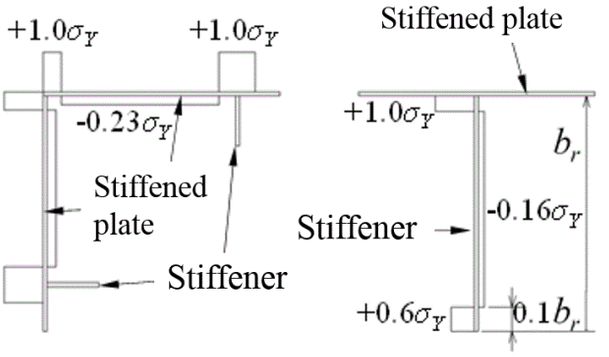


Figure 7. Residual stress(SM490Y).

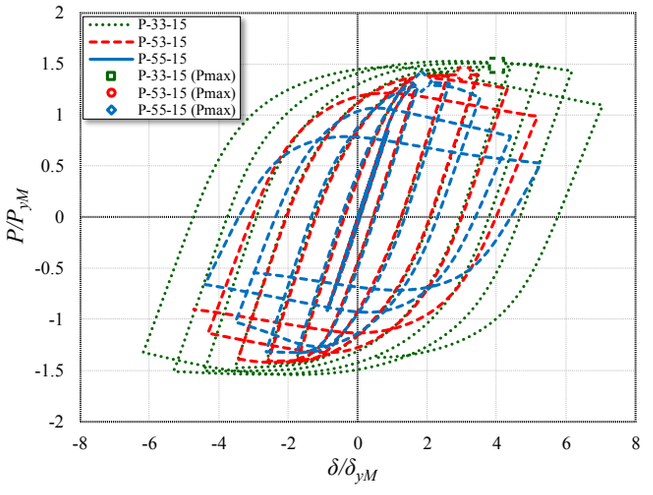


Figure 8. Analysis results of parametric analytical models.

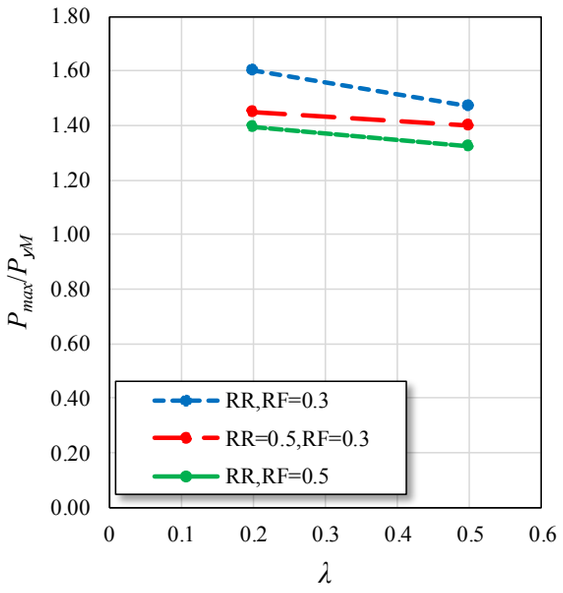


Figure 9. Effect of the slenderness ratio parameter on P_{max}/P_{yM}.

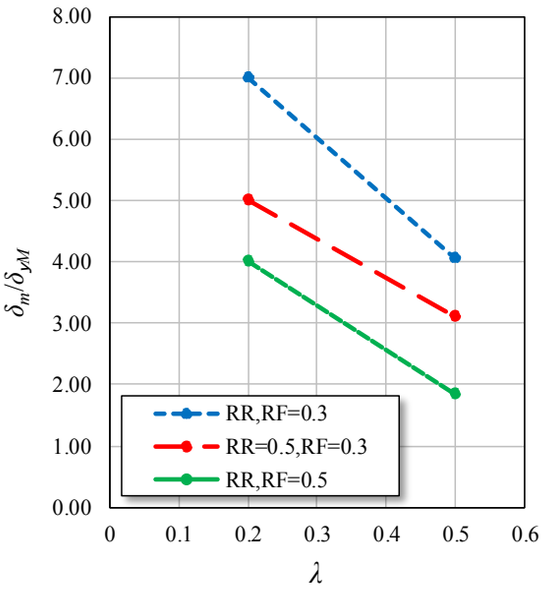


Figure 10. Effect of the slenderness ratio parameter on δ_{max}/δ_{yM}.

was investigated by comparing the parametric analysis results ($\bar{\lambda}$ =0.50) with the previous analysis results ($\bar{\lambda}$ =0.20). Consequently, analysis results indicate that the load-carrying capacity and the ductility of steel members decrease as the slenderness ratio parameter $\bar{\lambda}$ increases or the width-thickness ratio parameters R_R and R_F increase.

5 REFERENCES

Azumi, Kyoko. 2016. Study on Seismic Performance of Arch Rib under High Axial Loading. *Master Thesis, Osaka University*. (in Japanese).

Japan Road Association. 2012. *Design Specifications for Highway bridges part 5 Seismic Design*. Tokyo: Maruzen Co. Ltd. (in Japanese).

Nishimura, Nobuo. Ono, Kiyoshi & Ikeuchi, Tomoyuki. 1995. A constitutive equation for structural steels based on a monotonic loading curve under cyclic loading. *Journal of Japan Society of Civil Engineers* No.513/I-31: 27-38. (in Japanese).

Okada, Seiji. Ono, Kiyoshi. Taniue, Hiroaki. Tokunaga, Munemasa & Nishimura, Nobuo. 2010. Seismic performance of stiffened steel members with rectangular section under high compressive axial force. *Journal of Japan Society of Civil Engineers* A Vol.66 No.3: 576-595. (in Japanese).

Ono, Kiyoshi. Aizawa, Hiroyuki. Miyashita, Takeshi. Yamada, Shinji & Miyazaki, Yasuhiro. 2016. An experimental study on constitutive equation of SBHS400 under cyclic loading. *Proc. 14th East Asia-Pacific Conference on Structural Engineering and Construction* (*EASEC-14*): 1833-1838.

SS15: Latest developments on jointless bridges

Organizers: B. Briseghella, W.P. Yen & B.C. Chen

Maintenance, Safety, Risk, Management and Life-Cycle Performance of Bridges – Powers, Frangopol, Al-Mahaidi & Caprani (Eds)
© 2018 Taylor & Francis Group, London, ISBN 978-1-138-73045-8

Trial design study on integral abutment bridge supported on UHPC-RC segmental pile

G. D. Chen, B.C. Chen and F.Y. Huang
College of Civil Engineering, Fuzhou University, Fuzhou, Fujian, China

Y.Z. Zhuang
College of Civil Engineering and Architecture, Zhejiang University of Technology, Hangzhou, Zhejiang, China

H. Tabatabai
Department of Civil Engineering, University of Wisconsin, Milwaukee, America

ABSTRACT: The commonly used normal reinforced concrete pile (RC) has large stiffness and is not suitable to be used for foundation in integral abutment bridge (IAB). This paper proposes a segmental pile by combining RC pile as its lower portion and UHPC (ultra-high performance concrete) pile as its upper portion in order to increase the lateral flexibility. A trial design of an IAB using this new kind pile is performed in this paper by replacing the original 70cm × 50 (70) cm RC section at the top 3m of pile by 30cm × 30cm UHPC section. FEM of the whole bridge is then established by using software Midas. Analysis result shows that UHPC-RC segmental pile as a new type pile is suitable to be used in IAB.

1 INTRODUCTION

There are three types of jointless bridges, integral abutment bridge, semi-integral abutment bridge and deck extension bridge. Among them, IAB has the largest integrity and best durability without bearing and expansion joint, and it is widely used in the world. However, it is rarely used in China. According to the survey in "Technical Specifications for Jointless Bridges in Fujian", there are only four IABs built or under construction, accounting for 10% of all jointless bridges in China by April 2016. According to the survey reported by United States Department of Transportation in 2004, there are around 9000 IABs built, accounting for 53.3% of all jointless bridges (more than 16900).

The foundation of IAB should be flexible. H-shaped steel pile is widely used in IABs in USA and other countries. But, due to steel corrosion, high price, easy buckling when encountering rock and other shortcomings, they are seldom used in China. In contrast, concrete pile is widely used in China. Because of its large rigidity and poor deformation ability, it is not suitable to be used in IAB, which affects the popularization and application of IAB (Gama 2014).

Therefore, the conception of segmental pile combined with ultra-high performance concrete (UHPC) pile and reinforced concrete (RC) pile is put forward. Specifically, the upper part of the pile using UHPC, with the features of high compressive strength, relatively strong tensile strength and good ductility, can use smaller section to reduce the lateral stiffness and to increase the lateral deformability so as to accommodate the longitudinal deformation of a bridge. The lower part of the pile using RC is used like normal reinforced concrete pile (friction pile or end-bearing pile). This kind of pile is called UHPC-RC segmental pile. The segmental pile could be used in IABs, for it is not only economic, but also meets the requirement of large longitudinal deformation, which provides a new kind of pile for jointless bridge. The use of UHPC in segmental pile not only expands its range of application, but also gets good promotion effect due to its small amount of material consumption and obvious performance.

In order to discuss the feasibility of using UHPC-RC segmental pile in IAB, this paper carries on a trial design on it. Taking the Shangban Bridge as an engineering background, a finite element model with designed segmental piles is established. The internal forces between the trial design bridge and the original bridge are compared so as to provide basic data for further study on UHPC-RC segmental pile in IABs.

2 TRIAL DESIGN

Shangban Bridge is an integral abutment bridge with prestressed concrete, located in Yongchun County of Fujian province. The overall layout is shown in Figure 1. The total length is 137.1m, with the width of 8.5 m. 4 × 30m continuous T-beam is used for the superstructure, and 4 T-beams are arranged side by side transversely. The T-beam girder is 1.8m high. Wet joint is used between the T-beams along the longitudinal direction. The substructure is double column piers with spread foundations. The bridge was opened to traffic in January 2004, and has been

in operation well till n ow. No m ajor maintenance problem has been repo rted in recent decades, for there is no expansion join t or bearing, which shows the advantages of IAB with less or no maintenance.

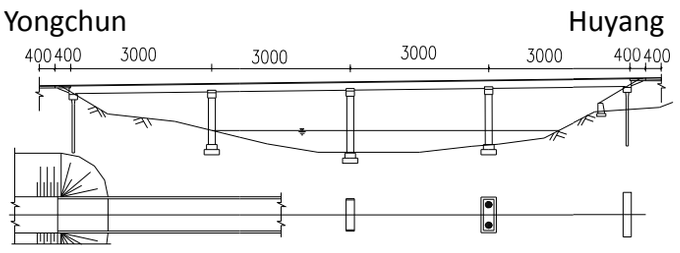


Figure 1. General arrangement diagram of Shangban Bridge (Unit: mm).

Integral abutment is used in Shangban Bridge, which means the girder and abutment are integrated without expansion joint. Low rigidity abutments and digging piles are also used in this bridge. In order to meet the d eformation requirement caused by the temperature difference in the superstructure, a single row of four piles with rect angular cross section bent along their weak axis ar e used for the foundation. The section size is 70cm × 50c m. Within the range of 1m from the top of th e pile down, the section size of the pile varies from 70cm × 50cm to 70c m × 70cm, so as to avoid the potential cracking at th e position where the cross section size changes suddenly. The rectangular pile is m ade of C30 concrete, and the length of the pile is 12.6m. In order to increase the f lexibility of substructure to ens ure that the pile has enough defor mation ability, digging pile is adopted in constr uction, and the loose sandy soil is f illed between th e pile and the origin al soil. The constructional detail of the joint of abutm ent and pile is shown in Figure 2.

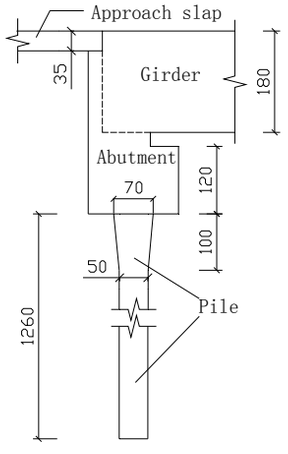
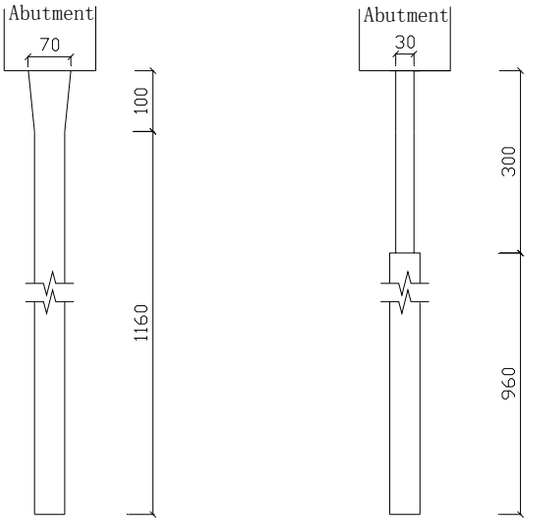


Figure 2. Joint between abutment and its su pporting pile in Shangban Bridge (Unit: cm).

The structure of th e trial-design bridge is the same as that of the original b ridge, except for th e segmental piles. Digging piles and loose sandy soil are also adopted in the tria l design, in order to m eet the flexibility of the substructure. The pile section of original bridge is 70cm × 50cm, and is m ade of C30 concrete (compressive strength is 30MPa, elastic modulus is 30GPa). The pile s of trial design bridge are made of C130 concrete (com pressive strength is 130Mpa, elastic m odulus is 43GPa) on top of piles (Chen 2014, Chen 2016). The RC still keeps approximately the same as the o riginal concrete. According to th e calculation of the vertical load-bearing capacity, the pile cross section for this trial design bridge is 30cm × 30c m for the UHPC part.

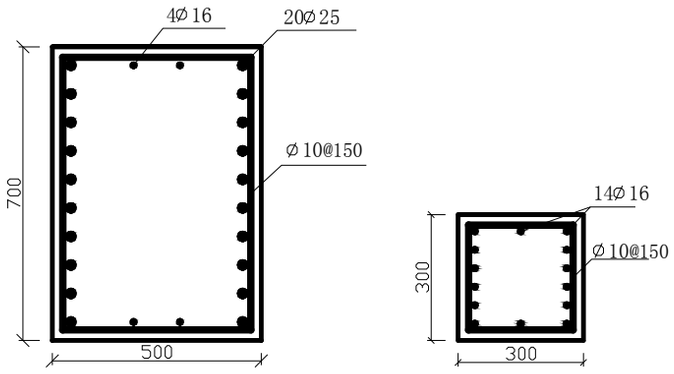
The upper part of the segm ental pile is 3m long UHPC pile, and the lower part is 9.6m long RC pile. The details of the original bridge pile and the trial design bridge pile are shown in Figure 3.



a) Original pile b) Trial design pile

Figure 3. Comparison of piles between original bridge and trial design bridge (Unit: cm).

In the trial design bridge, the arrangem ent of rebar for the RC part pile is th e same as that of the original bridge, as sh own in Figure 4a. The arrangement of rebar for the UHPC part pile is shown in Figure 4b. According to the manual calculation, the flexib ility (the d isplacement of the pile top) of trial design p ile is 2.65 times as much as that of the original pile.



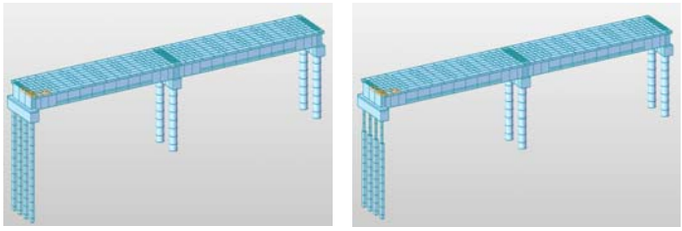
a) RC section b) UHPC section

Figure 4. Reinforcement of pile section

3 FINITE ELEMENT MODEL

3.1 *Summary of modeling*

Software MIDAS is used to build the finite element model of the original bridge and the trial design bridge, as shown in Figure 5. Only half bridge model is shown due to its symmetry. In the model, T-beams, abutments, piles and piers are simulated by beam elements, and the transverse wet joints between the T-beams are simulated by longitudinal beam. The laminated rubber bearing in the bridge modeling is simulated by elastic connection in finite element model. The connection between abutment and girder are simulated by rigid connection in finite element model.



a) FE Modeling of original bridge b) FE Modeling of trial design bridge

Figure 5. Finite element model of original bridge and trial design bridge (only half bridge).

Because the pile foundation of abutments and the spread foundation of piers are embedded with enough depth into rock, the bottoms of piles and piers are simulated by fixity. The finite element model of the original bridge consists of 515 nodes and 687 elements. The number of nodes and elements of the trial design bridge is the same as the original bridge.

The effects of pile-soil interaction and abutment-soil interaction are considered in the model. Pile-soil interaction is simulated by the "m" method adopted in the "Codes for design of ground base and foundation of highway bridges and culverts" (JTG D63-2007), and linear springs take place of the soil around piles by assuming that the soil resistance is proportional to the lateral displacement of the pile at that location. Considering the loose sandy soil around the pile, the coefficient "m" is taken as 15000kN/ m^4. Soil pressure behind abutment is simulated by static soil pressure plus nonlinear spring (only for compression) in the finite element model (Civjan 2007). In order to simulate the bridge more accurately, three phases of construction are divided: simply supported, continuous and completed.

3.2 *Model verification*

The static and dynamic load tests of the original bridge were carried out in the reference (Peng 2001, Peng 2006). The comparison between the measured frequencies of original bridge and the calculated frequencies of finite element model is shown in Table 1. The deviations are less than 10%, which shows that the finite element model can be used to analyze the structural performance of the bridge.

Table 1. Comparison of measured values and calculated values of original bridge frequency.

Mode of vibration	Measured value (Hz)	Calculated value (Hz)	Deviation (%)
Transverse 1st	2.337	2.516	7.7
Transverse 2nd	4.092	3.707	-9.4
Vertical 1st	4.686	4.465	-4.7
Vertical 2nd	5.812	5.326	-8.4
Vertical 3rd	7.337	7.570	3.2

The measured deflection values and finite element values at the mid-span of side span under five load cases are shown in Table 2.

Table 2. Comparison of measured deflection values (A) and finite element values (B) (Unit: mm).

Load case	One car at 1/4 midspan under bias load			Two cars at 1/4 midspan under middle load			One car at midspan under bias load			Two cars at midspan under bias load			Two cars at midspan under middle load		
	A	B	Deviation (%)	A	B	Deviation (%)	A	B	Deviation (%)	A	B	Deviation (%)	A	B	Deviation (%)
Beam 1	1.09	1.17	7.3	1.42	1.52	7.0	2.11	2.25	6.6	3.03	3.27	7.9	2.65	2.76	4.2

Beam 2	0.83	0.89	7.2		1.47	1.56	6.1		1.64	1.76	7.3		2.80	2.87	2.5		2.73	2.84	4.0
Beam 3	0.64	0.68	6.3		1.45	1.56	7.6		1.14	1.21	6.1		2.50	2.56	2.4		2.74	2.84	3.6
Beam 4	0.34	0.36	5.9		1.42	1.52	7.0		0.52	0.55	5.8		1.98	2.12	7.1		2.67	2.76	3.4

It can be seen from Table 2 that the deviations between measured deflection values and finite element values are less than 10%, which means the finite element model used in this paper can accurately simulate the mechanical behaviors of original bridge under static load.

3.3 *Calculation checking of trial design bridge*

The trial design bridge is checked by considering five load combinations as shown in Table 3 (Peng 2009). Load combination I, II, III and IV are the combinations under ultimate limit state, and load combination V is the combination of serviceability limit state, including dead load, secondary dead load and earth pressure at rest.

Table 3. Load combinations.

Load combinations	Safety factors and names of loads
I	1.2 Dead load + 1.0 Prestress + 1.0 Shrinkage creep + 1.4 Vehicle load + 0.75 × 1.4 Temperature load(Up)
II	1.2 Dead load+1.0 Prestress + 1.0 Shrinkage creep + 1.4 Vehicle load + 0.75 × 1.4 Temperature load(Down)
III	1.2 Dead load+1.0 Prestress + 1.0 Shrinkage creep + 0.75 × 1.4 Vehicle load + 1.4 Temperature load(Up)
IV	1.2 Dead load + 1.0 Prestress + 1.0 Shrinkage creep + 0.75 × 1.4 Vehicle load + 1.4 Temperature load(Down)
V	1.0 Dead load + 1.0 Prestress + 1.0 Shrinkage creep + 0.7 Vehicle load(Impact) + 1.4 Temperature load(Down)

The calculation results of the superstructure indicate that both the bending capacity and the shear capacity meet the requirements under ultimate limit state. The crack resisting calculation and deflection calculation also meet the requirements under serviceability limit state.

The calculation results of the substructure indicate that the bearing capability of pile (considered as friction pile) and pile strength (vertical bearing capacity of RC pile and UHPC pile) both meet the requirements (Campione 2010). The maximum crack width appears at the connection joint between pile and abutment, and the width of the crack is 0.18mm which is still less than 0.2mm and meets the requirement for crack width limit.

4 ANALYSIS OF RESULTS

4.1 *Vertical load*

Under the vertical load (dead load and live load), the internal forces in the abutment and the pile of the original bridge and trial design bridge are basically the same. Therefore, only the internal forces of the girders under the vertical load are analyzed in this paper.

4.1.1 *Bending moment of girder under dead load*

Because the structure and the load are symmetrical, only the internal forces in half an bridge are compared. The bridge used the construction method of simply-supported first and being continuous then. The calculation of dead load is carried out in stages. The bending moment of the girder under dead load is shown in Figure 6. The values in the brackets are the bending moment values of trial design bridge.

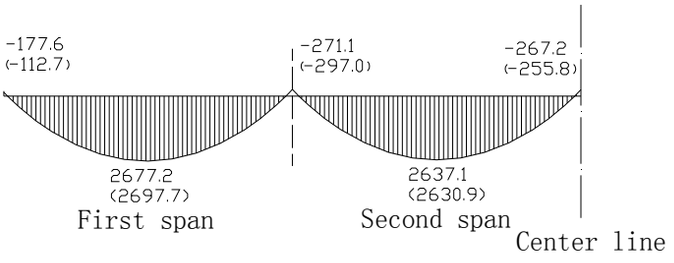


Figure 6. Bending moment of girder under dead load (Unit: kN·m).

It can be seen from Figure 6 that the negative bending moment of the girder at the abutment of the trial design bridge is obviously lower than that of the original bridge under dead load. The value of the trial design is 112.7kN·m, compared to 177.6kN·m of the original bridge, with a decline of 36.5%. By using the segmental pile in the trial design bridge, the bending moment of pile top decreases and it transfers from the top of the pile through the abutment to the end of the girder, thus reducing the negative bending moment of the girder. The segmental pile has little effect to the mid-span bending moment (the value of the first span increases by 0.7% and the value of the second span decreases by 0.2%), which can be ignored.

4.1.2 *Bending moment of girder under vehicle load*

According to "General specifications for design of

highway bridges and culverts" (JTG D60-2015), the bending moment of the girder is calculated by two kinds of vehicle load (bias load and middle load). The bending moment of the girder under bias load and middle load are shown in Figures 7 and Figure 8, respectively. The values in the brackets are the bending moment values of trial design bridge.

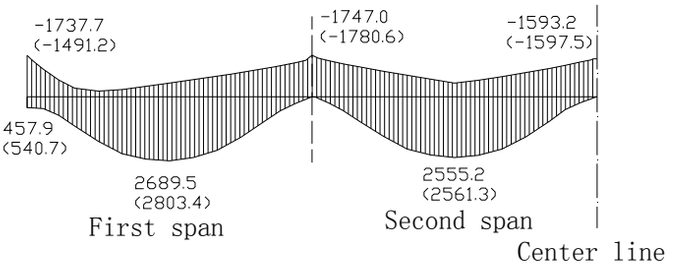


Figure 7. Moment envelop diagram of girder under bias load (Unit：kN·m).

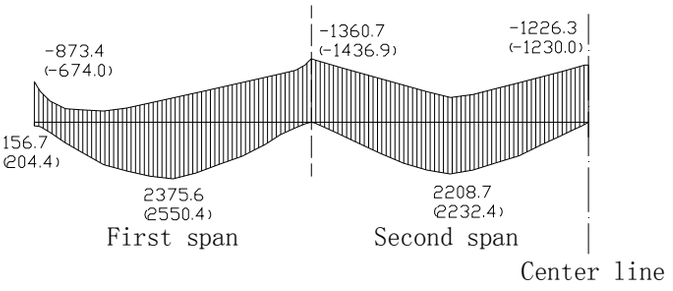


Figure 8. Moment envelop diagram of girder under middle load (Unit：kN·m).

It can be seen that the negative bending moment of the girder at the abutment of the trial design bridge is reduced by 14.2% and 22.8%, respectively, under bias load and middle load. The positive bending moment of the girder is increased slightly. The bending moment of other places changes less than 10%. It indicates that the flexible segmental pile has an advantageous effect on the girder at the abutment under the vehicle load, but has little effect on other places.

4.2 *Temperature load*

Compared to the traditionally jointed bridge, temperature load has a greater impact on the longitudinal deformation of IAB. The temperature effect for IAB is the most influential longitudinal load. Different structures of bridge have different characteristics when temperature drops or rises. The internal forces of girder and pile are greater when temperature goes down, and the internal forces of abutment are greater when temperature goes up. Therefore, this paper will discuss the internal forces in the above three cases. The structural behaviors of the original bridge and the trial design bridge are further explored (Ren 2010).

4.2.1 *Internal force of girder when temperature goes down*

The abutment and the girder are in rigid connection in IABs. When temperature goes down (15°C), the deformation of the girder is affected by the pile under the abutment, and the tensile stress in girder is very unfavorable for concrete material. Therefore, it should be taken into consideration for the internal forces of girder when temperature goes down.

The internal forces of the girder when temperature goes down are shown in Table 4. The bending moment and the axial force of the girder in the trial design bridge are decreased obviously, and the decreased amplitudes are over 40% basically. According to the calculation of finite element model, the displacement at pile top of the trial design bridge is 7.8mm, compared with the about 6.5mm of the original bridge, increased by 20.2%. When temperature goes down, the deformation increases, therefore the axial force and bending moment both decrease greatly.

Table 4. Internal force of girder when temperature goes down.

Internal force	Bending moment at abutment(kN·m)	Axial force at the first span(kN)	Bending moment at the first pier(kN·m)	Axial force at the second span(kN)	Bending moment at the second pier(kN·m)
Original bridge	1277.6	345.3	-288.1	357.9	147.4
Trial design bridge	605.2	174.8	-173.5	187.5	66.8
Amplitude of reduction %	52.6	49.4	39.7	47.6	54.7

4.2.2 *Internal force of pile when temperature goes down*

When temperature goes up, the deformation of IAB is absorbed by the approach slab, backfill and horizontal flexibility of piles. However, when temperature goes down (15 °C), the deformation is only absorbed by the horizontal flexibility of piles. The shear force and the bending moment of piles are

shown in Figure 9 and Figure 10, respectively.

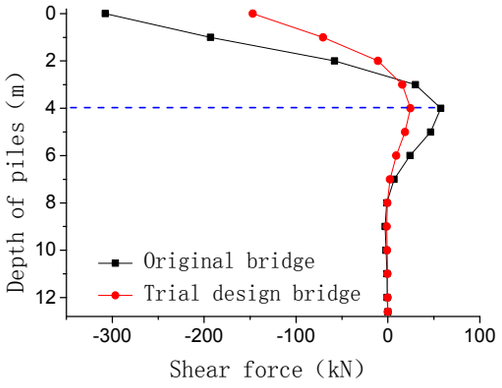


Figure 9. Shear force of piles

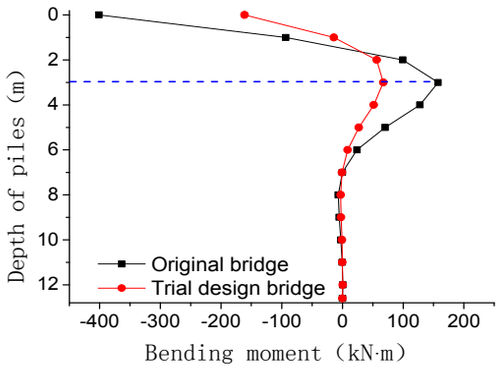


Figure 10. Moment of piles

The internal force distribution along segm ental pile is similar to that of the original pile. By using the segmental pile with smaller horizontal stiffness, the displacement of girder increases, which reduces its internal force. The inflection point of the shear force appears at the depth of 4m, and the inflection point of the bending moment appears at the depth of 3m.

The maximum values of bending mom ent and shear force of the orig inal bridge and trial design bridge appear at the top of the piles, whic h are summarized in T able 5. By using the flexible segmental pile, th e internal forces of the pile are decreased significantly, and the m aximum values of shear force and bending m oment are reduced by 52.2% and 59.8%, respectively.

Table 5. Comparison of intern al forces at the top of piles.

Internal force	Shear force (kN)	Bending momnet (kN·m)
Original bridge	-307.6	-401.2
Trial design bridge	-147.1	-161.2
Amplitude of reduction %	52.2	59.8

4.2.3 *Internal force of abutm ent when temperature goes up*

When temperature goes up (15 °C), the abutm ent moves towards backfill and is subjected to passive earth pressure. The maximum values of shear force and bending m oment appear at the top of the abutment, which are shown in T able 6. The bending moment of abutm ent is linear with he ight of abutment, and the m aximum values of shear force and bending m oment are reduced by 32.6% and 45.8%, respectively, compared with those of the original bridge. According to the calculation of finite element model, the displacement of the pile to p of the trial design bridge is 7.1mm, compared with the that of the original bridge about 6.1mm , increased by 16.4%.

Table 6. Com parison of internal forces at the top of abutments.

Internal force	Shear (kN)	Bending moment (kN·m)
Original bridge	1701.4	3546.2
Trial design	1146.2	1919.9
Amplitude of reduction %	32.6	45.8

5 CONCLUSIONS

(1) This kind of UHPC-RC segmental pile can greatly increase the flexibility of pile foundation and meet the requirem ent of deformation for lar ger spanning integral abutment bridge. Segmental pile is a new type of pile foundati on for IJB, which adapts to the construction situation of China. It is applicable and feasible with a promising future.

(2) The negative bending m oment at the end of girder in the trial design bridge is reduced by 36.5%, compared to the orig inal bridge under dead load. Segmental pile has less influence on the m idspan of girder, which can be ignor ed. Under bias load and middle load, the negative bending moment at the end of girder was reduced by 14.2% and 22.8%. The negative bending moment decreases and the positive bending moment increases in other places, which are not obvious.

(3) For the IABs, when the tem perature goes down,

the axial force and bending moment of girder are significantly reduced. The internal forces of pile are also effectively reduced. The maximum shear force and bending moment of pile occur at the top of pile, and they decrease about 52.2% and 59.8%, respectively. When the temperature goes up, the maximum shear force and bending moment of abutment appear at the top of abutment, and decreased by 32.6% and 45.8%, respectively.

(4) The displacement on the top of the trial design pile is greater than the original bridge, increasing by 16.4% when temperature goes up, and by 20.2% when temperature goes down. By using the segmental pile, the deformation of the superstructure becomes larger and the jointless bridge design length could be longer.

ACKNOWLEDGMENTS

The authors appreciate the support from the Natural Science Foundation of China through Grants Number of 51778147, 51578161 and 51278126 as well as the Zhejiang Provincial Natural Science Fund (LY17E080022）.

REFERENCES

Campione, G., Fossetti, M. & Papia, M. 2010. Behavior of fiber-reinforced concrete columns under axially and eccentrically compressive loads. *ACI Structure J* 107(03): 272–81.

Chen, B.C., Ji, T., Huang, Q.W., et al. 2014. Review of research on ultra-high performance concrete. *Journal of Architecture and Civil Engineering* 31(3): 1-24.

Chen, B.C., Huang, Q.W., Wang, Y.Y., et al. 2016. Design and construction of the first ultra-high performance concrete arch bridge in China. *Journal of China & Foreign Highway* 36(01): 67-71.

Civjan, S.A., Bonczar, C., Brena, S.F., et al. 2007. Integral abutment bridge behavior: Parametric analysis of a Massachusetts Bridge. *Journal of Bridge Engineering* 12(1): 64-71.

David, T. K., Forth, J. P. & Ye, J. 2014. Superstructure behavior of a stub-typeintegral abutment bridge. *Journal of Bridge Engineering* 19 (6).

Dunker, K. F. & Liu, D. 2007. Foundations for integral abutments. Practice Periodical on Structural Design and Construction 12(1): 22-30.

Gama, D. & Almeida, J.F. 2014. Concrete integral abutment bridges with reinforced concrete piles. *Structural Concrete* 15(3): 292-304.

Girton, D. D., Hawkinson, T. R. & Greimann, L. F. 1991. Validation of design recommendation for integral abutment piles. *Journal of Structural Engineering* 117(7): 2117-2134.

Huntley, S. A. & Valsangkar, A. J. 2014. Behaviour of H-piles supporting an integral abutment bridge. *Canadian Geotechnical Journal* 51 (7): 713-734.

Kim, W. & Laman, J. A. 2010. Integral abutment bridge response under thermal loading. *Engineering Structures* 32(6): 1495-1508.

Peng, D.W. & Hong, J.X. 2009. Study on load combination in integral abutment bridge design. *Natural Science Journal of Xiangtan University* 31(03): 112-116.

Peng, D.W., Lin, Z.P. & Hong, M.X. 2006. Study and Practice for jointless bridges. *Highway* (08): 53-62.

Peng, D.W. 2001. Development of jointless bridges. *Journal of Fuzhou University* (02):70-75.

Ren, J.J. & Liu, X.Y. 2010. Occasional forces and displacements of longitudinally coupled ballastless jointless turnout on bridges. *Journal of Southwest Jiaotong University* 18(01): 1-7.

Wang, D. H., Shi, C. J., Wu, Z. M., et al. 2015. A review on ultra high performance concrete: Part II. hydration, microstructure and properties. *Construction and Building Materials* 96: 368-377.

White, D. J., Mekkawy, M., Sritharan S., et al. 2007. Underlying cause for settlement of bridge approach pavement systems[J]. *Journal of Performance of Constructed Facilities* 21(4): 273-282.

Yu, T. L., Sun, X. L. & Zhang, S. F. 2013. Analysis of integral abutment bridge static load test. *Applied Mechanics and Materials* 361-363: 1406-1413.

Maintenance, Safety, Risk, Management and Life-Cycle Performance of Bridges – Powers, Frangopol, Al-Mahaidi & Caprani (Eds)
© 2018 Taylor & Francis Group, London, ISBN 978-1-138-73045-8

Parametric Studies on Seismic Behavior of Integral Abutment Steel Bridges Considering SSI

Q. Zhao & S. Dong & Z. Qi
School of Civil Engineering, Tianjin University, Tianjin, China
Key Laboratory of Coast Civil Structure Safety of Ministry of Education, Tianjin, China
B.C. Chen
School of Civil Engineering, Fuzhou University, Fuzhou Fujian, China

ABSTRACT: The paper focuses on the dynamic and seismic behavior of integral abutment steel bridges considering nonlinear soil-structure interaction, and the effects of design parameters of the integral abutment system on bridge behavior. 3-D finite element model of an integral abutment steel bridge was established with the SAP2000 software, and nonlinear link elements and damper elements were used to model the soil reactions behind the abutment and around the piles. Modal analysis and nonlinear time-history analysis were conducted, with corresponding parametric studies. Results indicate that: Compacting the backfill, increasing the abutment height-to-thickness ratio, and increasing the foundation stiffness will increase the dominant longitudinal frequency of the bridge structure, while H pile orientation has little influence. When satisfying the design requirements and in a reasonable range, compacting the backfill behind the abutment, increasing the abutment height-to-thickness ratio, increasing the foundation stiffness, and orienting the steel H pile to bend about its strong axis can effectively reduce the pile-top displacement, as well as seismic response of girders, abutments and piers, but increasing the foundation stiffness will obviously increase pile-top moment at the same time.

1 INTRODUCTION

Integral abutment bridges are jointless bridges can solve the problem of easily damaged telescopic device (Erhan 2014; Zhao 2011). The integral abutment bridge deck is continuous and connected monolithically with the abutment walls supported typically by a single row of piles to provide the required lateral flexibility to accommodate thermal movements. (Zhao 2011; Wasserman 1996). The advantages of these bridges include reduced maintenance costs compared to traditional jointed bridges with expansion joints and abutment bearings, reduced corrosion and material degradation at the joints (FHWA,1986), increased structural capacity during seismic events (Hassiotis et al, 2006), as well as faster and simpler contraction(Wasserman and Walker, 1996; Hopper and Gomes, 1996).

Under seismic load, Soil-Structure Interaction (SSI) become important due to the lateral movements of the integral abutment bridge together with the abutments is directly reflected on the backfill and foundation soil (Erhan 2014; David 2011). Goel studied earthquake characteristics of integral abutment bridges, and indicated that the bridge has a large deformation resistant capacity in superstructure when the earthquake intensity is low, however the resistance will decrease with the increase of earthquake intensity. (Goel, 1997) Spyrakos studied seismic behavior of integral abutment bridge including soil-structure interaction, in which they assess the significance of soil-structure interaction on the dynamic characteristics and seismic responses of the bridge, and indicated that the existence of backfill had a significant effect on the internal forces and deflection of the abutment, the pile and response of whole bridge. (Spyrakos, 2003)Therefore, it is meaningful to study the nonlinear SSI, and identify the main factors affecting bridge behavior.

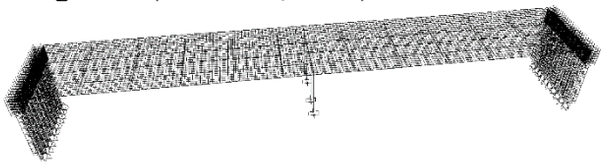
2 FINITE ELEMENT MODEL

This paper focus on the dynamic and seismic performance of the two-span integral abutment steel bridge by mode and nonlinear time history analyses with an emphasis and sensitivity study on the effect of the size and flexibility of abutment, the orientation of H-pile and clay stiffness around the piles. Nine 3-D finite element models of a two-span integral abutment bridge was constructed using SAP2000 software, and the soil-structure interaction (SSI) between the bridge substructure and soil was simulated with spring nonlinear link element and damp element.

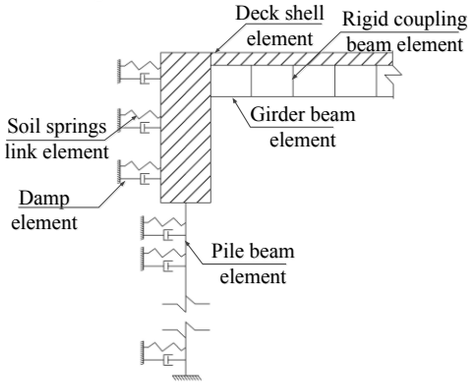
2.1 *Bridge model*

The bridge is a two-span integral abutment bridge with a north span of 42.67 m and a south span of 44.81 m. The bridge superstructure consists of five I-section steel plate girders with a height of 1.63 m and center to center spacing of 2.97 m, supporting a 0.21 m thick concrete deck above. The bridge abutment is composed of a 2970mm high, 910mm thick concrete slab supported each by HP 250x60 steel piles oriented in the strong ax-is bending. The abutment backfilling is a densely-compacted clean sand (φ=40.5°,γ =18.3 kN/m3). The soil around piles is a medium clay (cu=37.5 kPa , γ =14.6 kN/m3). The yield strength of steel used for steel pile and main beam is 345MPa, with the elasticity modulus 200GPa.

The bridge deck and abutments are modeled as shell elements while the main girders, piers, bent cap and piles are modeled as frame elements. The material nonlinearity of the pile and pier is considered in the model and the moment- curvature curve of the plastic hinge is obtained by the cross section designer of SAP2000. A rig-id connection is assumed at the conjunction of the abutments and the piles, as well as the abutment and the steel girders. Rigid linear link elements are used to model the conjunction of the bridge decks and the steel beams. Views of the bridge model and also its abutment details are shown in Figure 1. (SAP2000, 2010)



(a) Finite Element Model of the Two-span Integral Abutment Steel Bridge



(b) Finite Element Model of Abutment Details

Fig. 1 Bridge Model and Abutment Details of the Two-span Integral Abutment Steel Bridge

2.2 *Soil-structure interaction*

The soil around the piles is considered clay, properties of hard clay and medium clay are selected from the ge-otechnical reference (Coduto, 1999) in order to represent soil characteristics. The abutment wall backfilling is considered cohesionless clean sand, properties of loosely-compacted and densely- compacted clean sand are following Coduto et al. (1999). The soil spring elements and damping elements are used to model the soil-structure interactions around the piles and in back of the abutments, as shown in Figure 1(b).

2.2.1 *Springs in back of the abutments*

Based on a comprehensive study on nonlinear soil-abutment interaction for seismic design of bridges by Shamsabadi et al (2007). A simplified hyperbolic force-displacement relation was proposed by EQ (1).

$$F(y_i)=\frac{F_{ult}(2Ky_{\max}-F_{ult})y_i}{F_{ult}y_{\max}+2(Ky_{\max}-F_{ult})y_i} \quad (1)$$

where y = lateral displacement of the abutment; K= average soil stiffness , F_{ult} = maximum abutment Force (per unit length of the wall) developed at a maximum displacement of $y_{\max.}$ For cohesionless soil backfilling F_{ult} can be determined by EQ (2).

$$F_{ult}=0.5\gamma H^2(1-k_v)K_{pe} \quad (2)$$

where γ = soil density; H = height of the abutment; k_v = vertical acceleration coefficient and K_{pe} = seismic passive earth pressure coefficient which can refer to NCHRP 12-70 (2008) to get.

The abutment backfilling is sandy soil with good water permeability. Force displacement relations for unit length of the wall for two cases of densely-compacted clean sand (φ =40.5°, γ=18.3kN/m^3) and loosely-compacted clean sand (φ =37 ° , γ=16.5kN/m^3) backfilling are developed and modeled by nonlinear link elements in FEA model. The *p-y* curve of the soil spring (per unit length behind the wall) is shown in Figure 2.

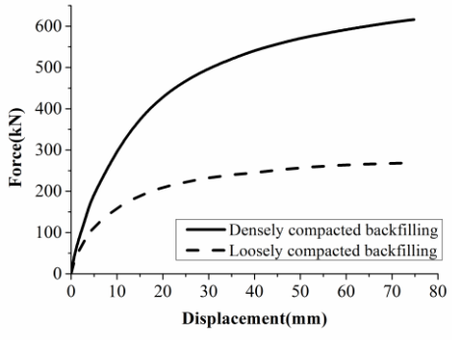


Fig. 2 Force–displacement Relations for Abutment Backfilling

2.2.2 *Springs around the piles*

The procedures given in the American Petroleum Institute (API) are followed to define the *p-y* curves of the soil springs around the piles (American Petroleum Institute, 1993). The ultimate unit lateral bearing capacity of clay p_u is shown by EQ (3):

$$p_u=\begin{cases}3c_u+\gamma X+J\dfrac{c_u X}{D} & X<X_R\\ 9c_u & X\geq X_R\end{cases} \quad (3)$$

where p_u = ultimate resistance; c_u = undrained shear strength; D = pile diameter; γ = effective soil densi-

ty; J = dimensionless empirical constant; X = depth below soil surface and X_R = depth below soil surface to bottom of reduced resistance zone.

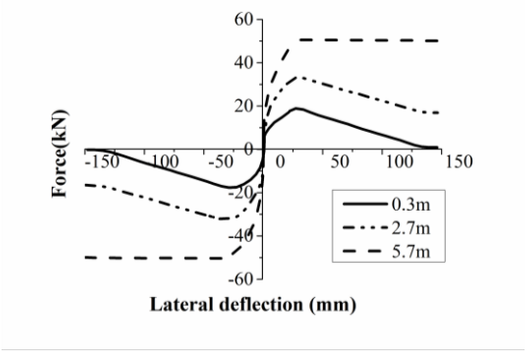
16 groups force displacement relations of the soil springs within range of piles height are developed for two different cases of medium clay (c_u=37.5 *kPa* , γ =14.6 *kN/m*^{3}) and hard clay (c_u=200.0 *kPa* , γ =18.1 *kN/m*^{3}) around the piles. The *p-y* curve of the soil springs at 0.3m, 2.7m and 5.7m below the top of pile are shown in Figure 3.

2.2.3 *Soil damping behind abutments*

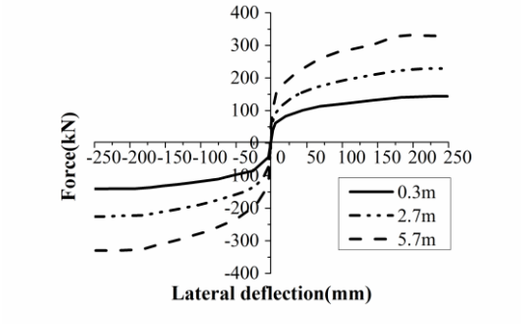
The damping coefficient of abutment backfilling is calculated by the EQ (4) proposed by Jain and Scott (1989).

$$c = \sqrt{\frac{2}{1-\upsilon} G\rho} \tag{3}$$

Where c = damping coefficient; G = soil dynamic shear modulus; ρ = soil density and v = soil Poisson's ratio. The soil dynamic shear modulus of densely-compacted clean sand and loosely-compacted clean sand are 40 MPa and 27 MPa respectively, and the soil Poisson's ratio is 0.3 , the damping coefficient for unit area were 457 kN/(m/s) and 356 kN/(m/s) respectively.



(a) Soft Clay



(b) Hard Clay

Fig. 3 Force–deflection curves of pile springs under cyclic loading

2.2.4 *Soil damping around piles*

The damping coefficient of soil around piles is calculated by the EQ (5) proposed by Anandarajah et al (2005).

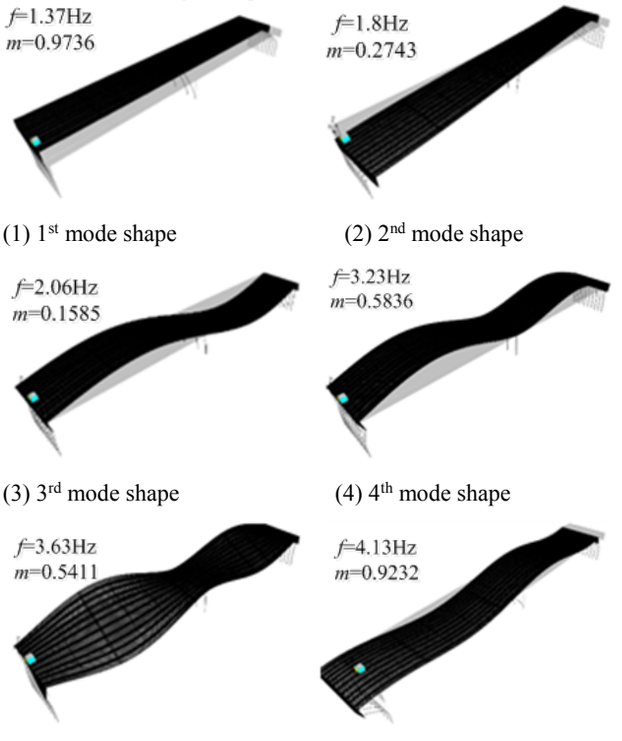
$$c = A\rho V_s \tag{4}$$

where A = tributary area of damping element; ρ = soil density and V_s =soil shear wave velocity. The soil shear wave velocity of soft clay and hard clay are 200 *m/s* and 300 *m/s* respectively, the damping coefficient for unit area of medium clay and hard clay were 292 *kN/(m/s)* and 544 *kN/(m/s)* respectively.

3 DYNAMIC PROPERTIES

The dynamic performance of the integral abutment bridge could be obtained by modal and parameter analysis. The first six mode shapes, natural vibration frequency f as well as participation mass ratio m are shown in Figure 4. The structure and soil properties of influence on the bridge dynamic characteristics including abutment size, pile orientation, levels of soil compaction of abutment backfilling as well as stiffness of soil around piles could be discussed. The parameter analysis are divided into three groups according to abutment size and backfilling properties, related parameter and dominant transverse and longitudinal frequency of model are shown in Table 1.

As shown in Table 1, when the abutment height-to-thickness ratio increased from 1.44 to 3.15 and 3.85, the dominant longitudinal frequency will increase by about 6.5% and 12%, respectively, and the variation of dominant transverse frequency are within 4%. Compacting the backfill behind the abutment will increase the dominant longitudinal frequency by about 16%, but which has no effect on the dominant transverse frequency.



(1) 1st mode shape (2) 2nd mode shape

(3) 3rd mode shape (4) 4th mode shape

(5) 5th mode shape (6) 6th mode shape

Fig. 4 Mode shapes of bridge model

Table.1 Results of dynamic property analysis

	Case	Dominant transverse frequency	Dominant longitudinal frequency
		Hz	Hz
M-1	Medium Clay, Strong axis, Densely, H/T=3.15	1.37	4.13
M-2	Medium Clay, Strong axis, Densely, H/T=1.44	1.32	3.88
M-3	Medium Clay, Strong axis, Densely, H/T=3.85	1.34	4.33
M-4	Medium Clay, Strong axis, Loosely, H/T=3.15	1.37	3.56
M-5	Medium Clay, Strong axis, Loosely, H/T=1.44	1.32	3.34
M-6	Medium Clay, Strong axis, Loosely, H/T=3.85	1.34	3.78
M-7	Medium Clay, Weak axis, Densely, H/T=3.15	1.48	4.08
M-8	Hard Clay, Strong axis, Densely, H/T=3.15	2.12	4.54
M-9	Hard Clay, Weak axis, Densely, H/T=3.15	2.30	4.45

As the H-pile orientation changes from strong axis to weak axis, the longitudinal bending stiffness of pile foundation decreases, but the transverse bending stiffness increases, and the longitudinal dominant frequency decreases by about 3% as well as the transverse dominant frequency increase by about 8%. As the foundation stiffness increases, the longitudinal dominant frequency and the lateral dominant frequency of structure are obviously increases by about 9.5% and 55% respectively. In general, the design parameters of abutment and soil behind abutment have great effect on the longitudinal dominant frequency, while the H-pile orientation and clay stiffness around the pile have great influence on transverse dominant frequency.

4 SEISMIC RESPONSE

In this paper, nonlinear time-history analyses are performed using the scaled component of El Centro earthquake with peak ground acceleration (PGA) equal to 0.215g and the duration is 40s. In order to obtain a better understanding of the seismic response of integral abutment bridges, the peak ground acceleration is adjusted to 0.3g. Figure. 5 shows the acceleration time histories of EI Centro earthquake after PGA adjustment.

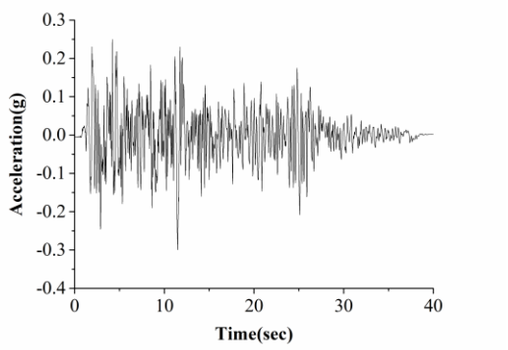
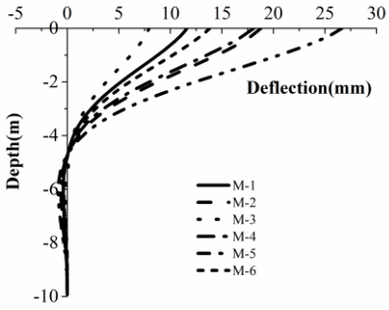


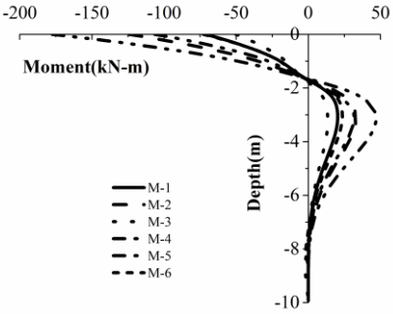
Fig. 5 El Centro Earthquake Record with PGA of 0.3g

4.1 *Abutment size and level of soil compaction of abutment backfilling*

Nonlinear time-history analysis are performed using the finite element model of the integral abutment bridge for the first 6 cases (M1-M6) defined in Table 1. The maximum deflection and moment along the height of pile for the six cases are plotted in Figure 6. The results of parameter analysis are shown in Table 2 and Table 3.



(a) Deflection



(b) Moment

Fig. 6 Pile deflection and moment obtained from the analyses of M1-M6

As shown in Figure 6, the maximum moment of the piles have a positive and negative bidirectional distribution, the absolute maximum moment of the pile appears at the top of the piles. An increase in depth will decrease the maximum moment of piles, and the inflection point of moment appears at about 2 m below the top of pile. Below that level, the reverse maximum pile moment increases gradually and reaches the peak value at about 3 m below the pile top. The peak value can reach 1//3 of the maximum moment at the top of the pile, the moment is trending to zero at about 7 m below the top of the pile, and then reverse, but the reverse maximum displacement along the pile varies within a small range of 2mm.

Table.2 Seismic Response of the Bridge with Different Abutment Height-thickness Ratio

Case	Displacement of pile top	Displacement of abutment top	Moment of pile top	Moment of pier bottom	Maximum moment of abutment	Maximum moment of girder
	mm	mm	kN-m	kN-m	kN-m	kN-m
M-2	18.8	22.2	124.3	1239.8	1586.0	909.7
M-1	11.6	14.5	71.1	818.9	1347.2	746.8
M-3	7.9	9.9	50.2	552.4	1170.5	619.3
M-2&M-1 Diff%	-38.3%	-34.7%	-42.8%	-33.9%	-15.1%	-17.9%
M-1&M-3 Diff%	-31.9%	-31.7%	-29.4%	-32.5%	-13.1%	-17.1%
M-2&M-3 Diff%	-58.0%	-55.4%	-59.6%	-55.4%	-26.2%	-31.9%
M-5	26.7	31.3	177.5	1741.8	3021.3	1260.7
M-4	18.1	23.1	106.5	1310.5	2115.8	1171.2
M-6	13.8	19.6	72.8	1090.8	2281.6	922.3
M-5&M-4 Diff%	-32.1%	-26.1%	-40.0%	-24.8%	-30.0%	-7.1%
M-4&M-6 Diff%	-23.6%	-15.2%	-31.6%	-16.8%	7.8%	-21.3%
M-5&M-6 Diff%	-48.1%	-37.3%	-59.0%	-37.4%	-24.5%	-26.8%

The change of abutment size and abutment backfilling has little influence on the mode of moment and displacement of pile including the shape of moment and displacement, the reverse peak point, the inflection point as well as 0 point position, which only affects the value of peak.

The influence of the change of height-to-thickness ratio of abutment on seismic response of the bridge is shown in Table 2. An increase in abutment height-to-thickness ration will significantly reduce the seismic response of most abutment, pile, pier and main girder, the reduction is depended on increase of height-to-thickness ratio, especially when the backfilling is densely-compacted.It is worth noting that increasing the abutment height-to-thickness ratio (especially when the abutment height increases and the thickness remains constant) or compacting the abutment backfilling may increase temperature stress in the integral bridge because of the soil-structure interaction (SSI) of backfilling and bridge, and make increase in longitudinal stiffness of integral bridge. When the abutment height-to-thickness ratio increases with the abutment thickness decreasing and abutment height is hold constant, there is no remarkable difference of effect of abutment backfilling on bridge and an increase in abutment height-to-thickness will decrease the longitudinal bending stiffness of abutment and temperature stress as well as longitudinal bending stiffness of integral bridge considering SSI. Therefore, in integral bridge structure design, the temperature, seismic and vehicle load should be consider when select abutment height-to-thickness and compacting method.

The influence of the properties of abutment backfilling on seismic response of the bridge is shown in Table 3. As the level of compaction of abutment backfilling decrease, the seismic response of abutment, pile, pier and main girder significantly increase, especially in the case of bigger abutment height-to-thickness, since the compaction of abutment backfilling decreases with average stiffness of abutment backfilling and restraint of structure deformation. The longitudinal seismic behavior of integral bridge depends heavily on the system of abutment and abutment backfilling. The larger the abutment height-to-thickness ratio, the greater the seismic resistance of abutment backfilling and backfilling stiffness. As shown in Table 3, the abutment height-to-thickness ratio have great influence on the maximum displacement and moment of abutment, the maximum displacement at pile top and the moment at pier bottom, and have limited influence on maximum moment of the pile top and the main girder.

Table.3 Seismic Response of the Bridge with Densely and Loosely Compacted Backfill

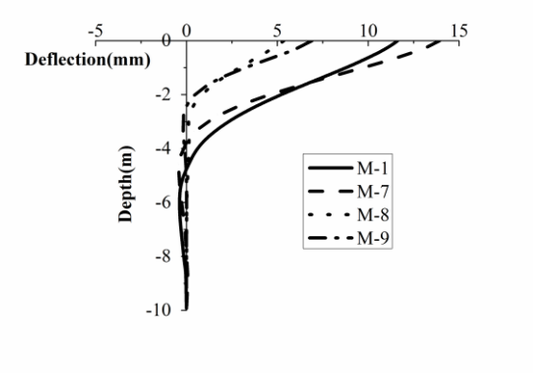
Case	Displacement of pile top	Displacement of abutment top	Moment of pile top	Moment of pier bottom	Maximum moment of abutment	Maximum moment of girder
	mm	mm	kN-m	kN-m	kN-m	kN-m
M-1	11.6	14.5	71.1	818.9	1347.2	746.8
M-4	18.1	23.1	106.5	1310.5	2115.8	1171.2
M-1&M-4 Diff%	56.0%	59.3%	49.8%	60.0%	57.1%	56.8%
M-2	18.8	22.2	124.3	1239.8	1586.0	909.7
M-5	26.7	31.3	177.5	1741.8	3021.3	1260.7
M-2&M-5 Diff%	41.8%	40.9%	42.8%	40.5%	90.5%	38.6%
M-3	7.9	9.9	50.25	52.4	1170.5	619.3
M-6	13.8	19.6	72.8	1090.8	2281.6	922.3
M-3&M-6 Diff%	75.1%	97.9%	45.0%	97.5%	94.9%	48.9%

Comprehensive comparison of the analysis results of M1-M6 shows that seismic response of M-5 is much bigger than other model, the seismic response of model M-3 is the smallest in all models. The differences of displacement of pile top and abutment top as well as the moment of pile top and pier bottom between M-3 and M-5 are more than doubled, and the difference of maximum moment as high as two times or beyond, for M-3 and M-5, respectively. The difference of maximum moment between abutment and main beam is also more than 100%, so it is clear that increasing the abutment height-to-thickness ratio and compacting the abutment backfilling can significantly reduce the seismic response of the structure.

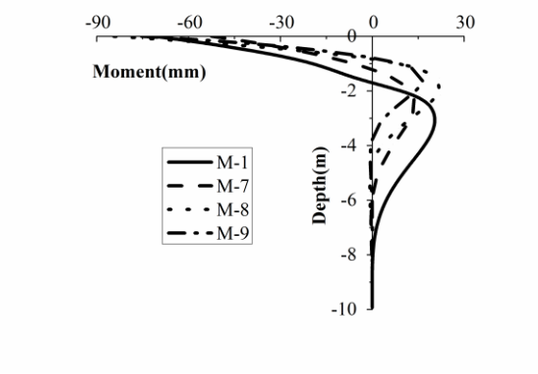
4.2 *Pile orientation and clay stiffness around the piles*

Nonlinear time-history analysis are performed using the finite element model of the integral abutment bridge of the four cases (M-1, M-7-M-9) defined in Table 1. The deflection and moment alonge the height of pile for four cases are plotted in Figure 7. The results of time-history analysis are shown in Table 4 and Table 5.

As shown in Figure 7, pile orientation and soil around the piles have influence on the pile maximum moment, pile displacement and the distribution of moment and displacement including the reverse peak point, the inflection point and 0 point position. The maximum moment of the piles also have a positive and negative bidirectional distribution, the absolute maximum moment of the pile appears at pile top. When the pile bent from about its strong axis to weak axis, the inflection point of moment appears at about 1.2 m below the pile top. When the soil around piles changed from medium clay to hard clay, the influence point of moment appears at about 1 m below pile top, and the reverse peak point of maximum moment, the bending moment and the 0 point position moves upward, especially in hard clay. The properties of soil around piles have a more obvious effect than pile orientation on moment distribution, displacement distribution and peak value, but no obvious effect on peak value of reverse moment.



(a) Deflection



(b) Moment

Fig.7 Distribution of Moment and Displacement along the Pile of Model 1, 7-9

As shown in Table 4, when the pile bent from about its strong axis to weak axis, bending stiffness of pile decreases, flexibility and deformation capacity increases. The maximum displacement at pile top increases 19.8% and the maximum moment of pile top decreases 26.2% for the case of piles in medium clay. And when piles in hard clay, the increase of the displacement at pile top increases, while the decrease of the moment decreases. When the pile bent about its strong axis, the material at pile top is in elastic phase in medium and hard clay, while when the pile bent about its weak axis, the material at pile top is in elastic-plastic phase. Therefore, in the interest of improving the temperature deformation capacity of the integral bridge, it is necessary to note that it will put forward higher requirements for seismic design of pile, abutment and pier when the H steel pile bending about weak axis.

Table.4 Seismic Response of the Bridge with Abutment Pile Bending about Strong or Weak Axis

Case	Displacement of pile top	Displacement of abutment top	Moment of pile top	Moment of pier bottom	Maximum moment of abutment	Maximum moment of girder
		mm	kN-m	kN-m	kN-m	kN-m
M-1	11.6	14.5	71.1	818.9	1347.2	746.8
M-7	13.9	17.1	52.5	962.5	1529.1	805.3
M-1&M-7 Diff%	19.8%	17.9%	-26.2%	17.5%	13.5%	7.8%
M-8	5.4	7.9	84.4	440.2	1276.7	707.2
M-9	6.9	9.0	75.3	498.5	1410.7	623.6
M-8&M-9 Diff%	27.9%	14.5%	-10.7%	13.2%	10.5%	-11.8%

Table.5 Seismic Response of the Bridge with Different Clay Type Around the Pile

Case	Displacement of pile top	Displacement of abutment top	Moment of pile top	Moment of pier bottom	Maximum moment of abutment	Maximum moment of girder
M-1	11.6	14.5	71.1	818.9	1347.2	746.8
M-8	5.4	7.9	84.4	440.2	1276.7	707.2
M-1&M-8 Diff%	-53.4%	-45.5%	18.7%	-46.2%	-5.2%	-5.3%
M-7	13.9	17.1	52.5	962.5	1529.1	805.3
M-9	6.9	9.0	75.3	498.5	1410.7	623.6
M-7&M-9 Diff%	-50.3%	-47.1%	43.5%	-48.2%	-7.7%	-22.6%

As shown in Table 5, as the stiffness of soil around pile become larger, the soil has much effect on the sidewise restraint and respond of bridge displacement decreases, but pile orientation has no effect on this. With the stiffness of soil around piles increasing, the reaction force of soil and moment at pile top increase. When the pile bent about its strong axis, the increase of the maximum moment of main girder is not obvious affected by the soil stiffness.

5 CONCLUSION

The work presented here supports the following conclusions:

In general, abutment size and properties of abutment backfilling have great influence on the dynamic behavior of bridge structures at longitudinal direction, and H-pile orientation and properties of soil around piles have great influence on the dynamic behavior of bridge structures at transverse direction. Compacting the backfill, increasing the abutment height-to-thickness ratio, and increasing the foundation stiffness will increase the dominant longitudinal frequency of the bridge structure, while H pile orientation has little influence. Increasing the foundation stiffness and orienting the H steel pile to bend about its strong axis will increase the dominant lateral frequency of the bridge structure, while abutment dimensions and abutment backfilling have little influence. Calculation results of the nonlinear time-history analysis shows that the maximum moment and displacement of piles have a positive and negative bidirectional distribution, the absolute maximum and displacement of pile appear at pile top, and decrease with the depth increases.

As the height-to-thickness ratio of abutment increases, the seismic response of most abutment, pile, pier and main girder significantly decrease.

An decrease in backfilling compaction will increase the seismic response of abutment backfilling, the seismic response of abutment, pile, pier and main girder. Increasing the abutment height-to-thickness ratio and compacting the backfill behind the abutment could obviously decrease bridge seismic response, but may increase the temperature stress of the integral bridge.

When the pile bent from about its strong axis to weak axis, the deformation capacity and bending stress of pile increase, but maximum moment decrease, maximum displacement and moment at pile top as well as moment at pier bottom obviously increase.

As stiffness of soil around piles increases, moment at pile top increases, but the response of bridge displacement, maximum displacement of pile top and abutment top, moment of pier bottom decrease, and pile orientation have no effect on this.

In meeting the design requirement of integral bridge, it is recommended to use higher height-to-thickness ratio, more flexible abutment and compacted backfill. When the H steel pile is used in abutment foundation, it is suggested that pile bent about the strong axis. Increasing stiffness of soil around piles will decrease bridge displacement and moment of abutment, pier and girder, but increase pile top moment. In a wide temperature different and high earthquake intensity region, seismic response and temperature stress should be taken into comprehensive consideration. The behavior of H-pile and joints of abutment and pile in strong earthquake must continue in-depth detail.

6 REFERENCES

Anandarajah A, Zhang J, Ealy C. 2005. Calibration of Dynamic Analysis Methods from Field Test Data. *Soil Dynamic Earthquake Engineering*, 25 (7–10):763–772.

American Petroleum Institute (API). 1993. Recommended Practice for Planning, Designing, and Constructing Fixed Offshore Platforms—Working Stress Design. 20th Ed., API RP2A-WSD, Washington, D.C.

David TK, Forth JP. 2011. Modeling of soil structure interaction of integral abutment bridges. *World Acad Sci Eng Technol* 78:769–74.

Erhan S, Dicleli M. 2014. Effect of dynamic soil–bridge interaction modeling assumptions on the calculated seismic response of integral bridges. *Soil Dynamics & Earthquake Engineering*, 66(6): 42-55.

Erhan S, Dicleli M. 2015. Comparative Assessment of the Seismic Performance of Integral and Conventional Bridges with Respect to the Differences at the Abutments. *Bulletin of Earthquake Engineering*, 13(2): 653-677.

FHWA/RD-86/102. 1986. Seismic Design of Highway Bridge Foundations. Federal Highway Administration.

Goel, R.K. 1997. Earthquake Characteristics of Bridges with Integral Abutments. Journal of Structural Engineering, ASCE, 123(11): 1435-1443.

Hassiotis, S., Khodair, Y., Roman, E., and Dehne, Y. 2006. Evaluation of Integral Abutments. FHWA-NJ-2005-025.

Hopper, E.J. and Gomes, J.P. 1996. Field Study of an Integral Backwall Bridge. Virginia Transportation Research Council, VTRC 97-T7, October.

Jain SK, Scoott R F. 1989. Seismic Analysis of Cantilever Retaining Walls. Anaheim: Proceedings of Structural Mechanics in Reactor Technology.

NCHRP 12-70. 2008. Seismic Analysis and Design of Retaining Walls, Buried Structures, Slopes and Embankment. National Cooperative Highway Research Program, Transportation Research Board, Washington.

SAP. 2010. Integrated Finite Element Analysis and Design of Structures. Berkeley: Computers and Structures Inc.

Shamsabadi, A., Rollins, K.M. and Kapuskar, M. 2007. Nonlinear SoilAbutment-Bridge Structure Interaction for Seismic Performance-Based. *Design. Journal of Geotechnical and Geoenvironmental Engineering*, *ASCE*, 133(6):707-720.

Spyrakos, C. Loannidis, G. 2003. Seismic Behavior of a Post-Tensioned Integral Bridge Including Soil-Structure Interaction. *Journal of Soil Dynamics and Earthquake Engineering*, Elsevier, 23(1):53-63.

Wasserman EP, Walker JH. 1996. Integral Abutments for Steel Bridges. Tennessee Department of Transportation, Nashville.

Zhao Q, Farahani RV, Burdette EG. 2011. Seismic analysis of integral abutment bridges including Soil-Structure Interaction. *Structures Congress,*2201(-1): 289-303.

Maintenance, Safety, Risk, Management and Life-Cycle Performance of Bridges – Powers, Frangopol, Al-Mahaidi & Caprani (Eds)
© 2018 Taylor & Francis Group, London, ISBN 978-1-138-73045-8

Research on SSI simulation method of integral abutment bridge under earthquake

Qiuhong Zhao
Key Laboratory of Coast Civil Structure Safety of Ministry of Education, and School of Civil Engineering Tianjin University, Tianjin, China.

Jing Qiu & Zeyu An & Zhaoyang Qi
School of Civil Engineering
Tianjin University, Tianjin, China.

ABSTRACT: In order to study the influence of simulation methods of SSI on the seismic analysis of integral abutment bridges, the 3-D finite element model of an integral abutment bridge was established with the SAP2000 software. The seismic responses of a detailed model and a series of simplified models were obtained through nonlinear time history analysis. Results indicate that: The damping of soil has little effect on the seismic response of the integral bridge and the damping of the soil can be neglected in the seismic analysis of the integral bridge. When PGA is 0.15g and 0.3g, the model using "m" method to simplify pile-soil interaction has higher analysis accuracy. And with the increasing of PGA, the analysis accuracy decreases, but with small change. The model using "m" method to calculate the stiffness of soil behind abutment has high analysis accuracy, and with the increasing of PGA, the accuracy has a decreasing trend but with only a little change, and the error is always within reasonable range. The "m" method is considered to be useful to simplify the pile-soil interaction, especially when the PGA is small. The "m" method is also useful to the simplification of the abutment-soil interaction. SSI simplified simulation method should be selected according to the value of PGA of the earthquake, and considering the analysis accuracy of the seismic response of each component, and also should consider the different sensitivity of the seismic response of different component when different simplified simulation method was adopted.

1 INTRODUCTION

According to the statistical bulletin of transportation industry development in 2015 (MOT 2016), the number of highway bridges in China has reached 779,200, of which 695,800 are small and medium bridges, accounting for 89.3% of the total. During the period from 2005 to 2015, 442,600 highway bridges were built in China, of which 383,400 were small and medium-sized bridges, accounting for 86.6%. Therefore, we should pay special attention to the construction and maintenance of small and medium-sized bridges. The bridge pier and abutment are always equipped with expansion joints to absorb the bridge structure deformation. Although the telescopic device is small in size and small in quantity, the cost can account for about 5% of the total cost of the project and the construction cost and late maintenance cost should not be underestimated. In addition, the temperature effect, vehicle load and concrete shrinkage and creep makes the expansion joints easily damaged. This phenomenon will not only affect the driving, but also further lead to the beam end and bearing erosion by acid rain, thus causing great potential safety hazard.

Integral abutment bridge (hereinafter referred to as "integral bridge") is a type of bridge which is put forward to solve the problem of the damage and failure of bridge expansion device in traditional bridges. The abutment is no longer set expansion joints and bearings, but connected into a whole (Chen et al. 2013, Vasheghani-Farahani et al. 2010, Wasserman and Walker 1996). Compared with the traditional bridge, the integral bridge has these advantages (Wasserman & Walker 1996): (1) simple design and construction process and lower cost of life cycle; (2) high integrity of structure, high redundancy and high earthquake resisting ability; (3) reducing the harmful effect of vehicle impact and structural vibration and improving the driving stability.

Due to the cancellation of the expansion device and bearing, expansion deformation of upper structure will transfer to the abutment and its pile founda-

tion, resulting in deformation of soil behind the abutment and around the pile, and the soil will in turn restrain the deformation of abutments and piles, thus affect the response of the integral structure. And the interaction is very complex and highly nonlinear. The complexity and uncertainty of soil properties and the interaction of soil-abutment and soil-pile, to a certain extent, limits the development of the analysis and design method of the integral bridge. In this paper, a three-dimensional finite element model of an integral bridge is established by using different soil-abutment and soil-pile interaction simulation methods, and the influence of the detailed degree of soil structure interaction (Soil-Structure Interaction, abbreviation SSI) modeling on the seismic analysis of the integral bridge is discussed. The research is conducive to achieve an accurate, reliable and moderately simplified SSI simulation method.

2 FINITE ELEMENT MODEL

2.1 *Modeling of bridge structure*

The span of the integral steel bridges is 56.7m and 58.8m, with 9.5m width of concrete pavement and 0.2m thickness of bridge deck. The bridge structure is composed of three steel girders with variable cross section, with 1.7m height in the mid-span, 345MPa yield strength and 200GPa elastic modulus. The abutment is 2.1m height, 1.1m thickness and 9.8m length, with compacted sand backfill behind the abutment and 8 steel pipe piles with an outer diameter of 355mm used at the foundation. Longitudinal profile and abutment connection joint of the bridge are shown in Figure 1.

A three-dimensional finite element model of the bridge is established by using the structural analysis and design software SAP2000 (SAP 2010), as shown in Figure 2. The abutment is simulated by shell element, and the steel beam, pier column, cap and pile is simulated by frame element. The calculation efficiency and the analysis accuracy are taken into account when dividing units, and different element size is used at different parts. Rigid connections was used between abutments and girders and between abutments and piles. Only the vertical displacement at the bottom of the pile is constrained, and relative translation of three directions of the connection between girder and cap beam is constrained. The pier column pile foundation has not been simulated in the model. It is assumed that the bottom of the column is fully rigid and is simulated by restricting the translation and rotation of column bottom joint in all directions, without considering the flexibility of the pile foundation and its influence on the pier column. The damping ratios used in all analyses were 5%.

In terms of material definition, the constitutive relation of concrete is modeled by Mander in SAP2000, and the constitutive relation of steel is modeled by Simple model. Both of the concrete and steel materials are isotropic, assuming that material behavior is unaffected by load direction and material orientation.

2.2 *Detailed modeling of SSI*

Soil is a highly nonlinear material and it shows highly nonlinear characteristics even at very low stress-strain level. In order to simulate the interaction of soil and structure more accurately and comprehensively, in this paper, a series of discrete nonlinear soil spring elements and damping elements are adopted for the simulation of soil-abutment-pile interaction, as shown in Figure 3.

The soil spring element type use the Multi-Linear Plastic. Considering the nonlinear characteristics of the spring, the hysteretic type uses the Takeda hysteretic model.

2.2.1 *Definition of soil spring behind abutment*

Behind the abutment is compacted sandy soil backfill, with 40.5° internal friction angle and $18.3kN/m^3$ density. Shamsabadi et al. (2007) studied the nonlinear interaction of soil and abutments under seismic action and proposed the formula (1) that define the parabolic load-displacement ($p-y$) curve of soil:

$$F(y_i) = \frac{F_{ult}(2Ky_{\max} - F_{ult})y_i}{F_{ult}y_{\max} + 2(Ky_{\max} - F_{ult})y_i}, \tag{1}$$

where y is the lateral displacement of abutment, F_{ult} is the maximum passive earth pressure acting on abutment of unit length when abutment displacement is $y_{\max}$, K is average soil stiffness. For sandy soil, F_{ult} can be calculated by formula (2):

$$F_{ult} = 0.5\gamma H^2 (1 - k_v) K_{pe}, \tag{2}$$

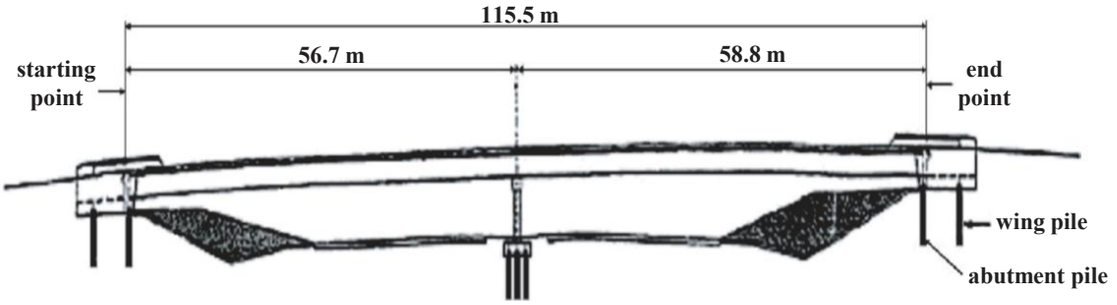
where H is the height of the abutment; γ is soil density, k_v is the vertical acceleration coefficient, K_{pe} is seismic passive earth pressure coefficient, can be obtained from the NCHRP 12-70 report of the National Cooperative Highway Research Program (NCHRP 2009).

2.2.2 *Definition of soil spring around pile*

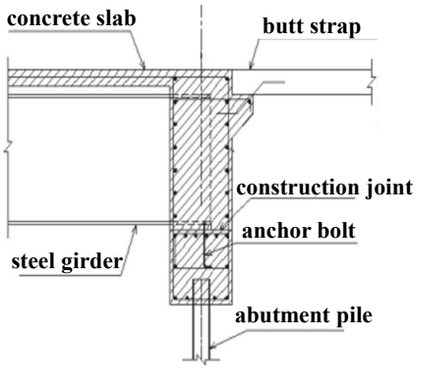
Around the pile foundation is soft clay of which undrained shear strength $c_u = 35.9kPa$, bulk density $\gamma = 14.6kN/m^3$. American Petroleum Institute (API 1977) recommends the method given by Matlock in (Matlock 1970) to define the nonlinear $p-y$ curve of soft clay. The horizontal ultimate strength of soil is p_u:

$$p_u = \begin{cases} 3c_u + \gamma X + J\frac{c_u X}{D} X < X_R \\ 9c_u X \geq X_R \end{cases}, \tag{3}$$

where c_u is undrained shear strength, p_u is horizontal ultimate strength, D is the calculation width of pile;



(a) longitudinal profile



(b) connection joint of integral abutment

Figure 1: Longitudinal profile and abutment connection joint of a two-span integral abutment bridge

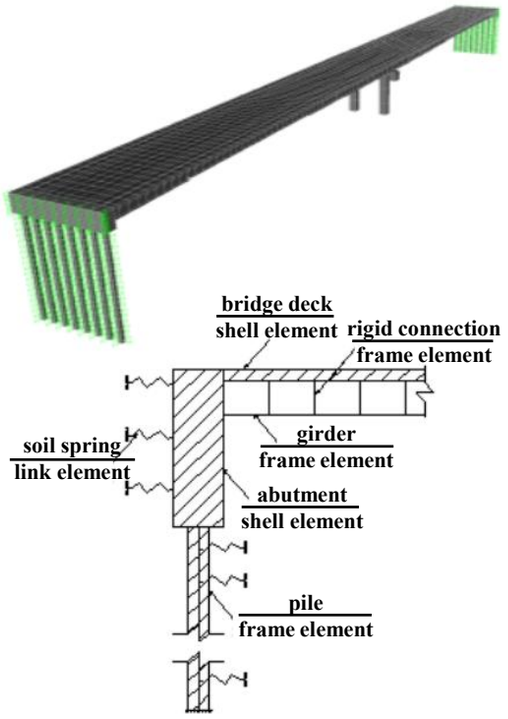


Figure 2: FEM model

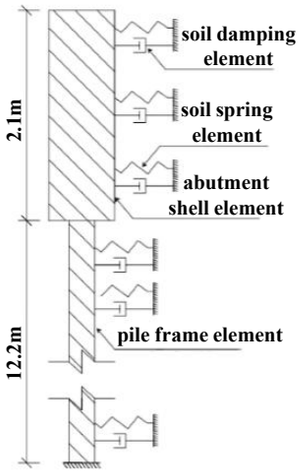


Figure 3: Detailed modeling of soil-structure interaction

J is dimensionless empirical constant; γ is soil density; X is the depth of soil surface to calculation point; X_R is the depth limit of ultimate strength calculation, which can be obtained by formula (4):

$$X_R = \frac{6D}{\frac{\gamma D}{c_u} + J}. \tag{4}$$

After the horizontal ultimate strength of the soft clay (p_u) is determined, the $p-y$ curve under cyclic loading is formed by Figure 4, where y is the actual horizontal displacement, $y_c = 2.5\varepsilon_c D$, ε_c is the corresponding strain when the soil horizontal resistance reaches half of the limit value. The soil spring $p-y$ curves of 0.3 m, 2.7 m and 5.8 m below the pile top are shown in Figure 5.

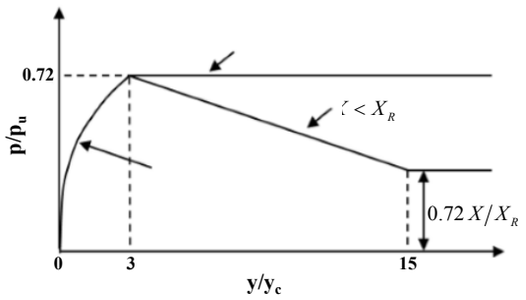


Figure 4: Generation of load-deflection curves for medium clay under cyclic loading

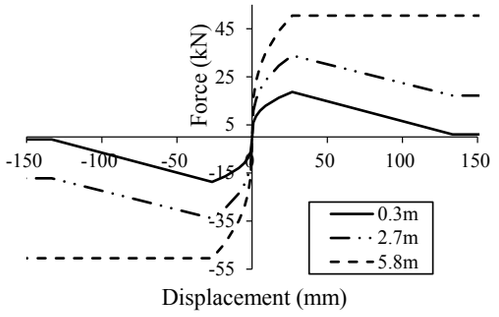


Figure 5: The p-y curve of soil around pile

2.2.3 *Definition of soil damping behind abutment*
The damping coefficient of soil behind abutment is calculated by the formula proposed by Jain & Scott (1989):

$$c = \sqrt{\frac{2}{1-\upsilon}} G\rho, \tag{5}$$

where G is the dynamic shear modulus of soil; c is the damping coefficient of soil; υ is the Poisson's ratio of soil; ρ is soil density. The dynamic shear modulus of compacted sandy soil is $40MPa$, and the Poisson's ratio is 0.3. Therefore, the damping coefficient c of the soil per unit area is $457kN/(m/s)$.

2.2.4 *Definition of soil damping around pile*
The damping coefficient of the soil around the pile is calculated by using the formula proposed by Anandarajah et al. (2005):

$$c = A\rho V_s, \tag{6}$$

where ρ is soil density; V_s is shear wave velocity of soil; A is the damping element dependent area. The shear wave velocity of soft clay is $200m/s$, and the damping coefficient c of the soil per unit area is $290kN/(m/s)$.

2.3 *Simplified modeling of SSI*

The simulation of soil-abutment and soil-pile interaction is simplified and 4 analytical models are established, as shown in Table 1.

Model 1 (referred to as M1) is the detailed model uses the discrete nonlinear soil spring elements and damping elements to simulate the soil-abutment and soil-pile interaction.

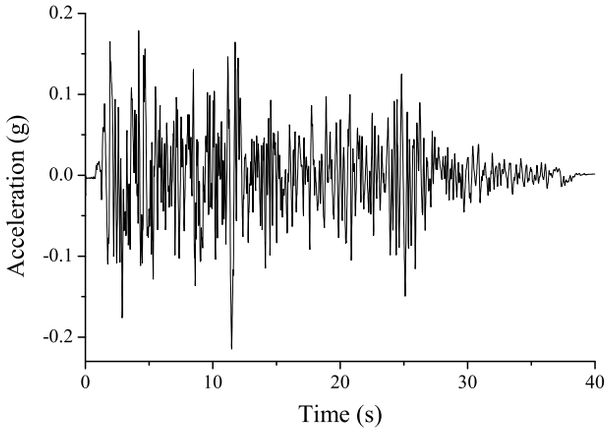


Figure 6: El Centro earthquake record

Model 2 (referred to as M2) removes the damping element of soil behind abutment and soil around pile in M1, without considering the effect of soil damping, therefore, the influence of soil damping on the simulation accuracy of seismic analysis of the integral fridge is analyzed.

Model 3 (referred to as M3) simplify the simulation of the soil around the pile. M3 assumes that the soil is linear elastic and uses the "m" method (CCCC Highway Consultants CO. 2007) to calculate the stiffness of the soil spring, without considering the nonlinear behavior of the soil around the pile. "m" method is simple, widely used and a familiar method for engineers and technicians in China, and it has been applied to the relevant specifications in China.

Model 4 (referred to as M4) simplify the simulation of the soil behind the abutment. M4 assumes that the soil is linear elastic without considering the nonlinear behavior of soil behind the abutment and uses the "m" method to calculate the stiffness of the linear elastic soil spring.

3 THE INFLUENCE OF SSI SIMULATION METHOD ON SEISMIC RESPONSE OF INTEGRAL BRIDGE

In this paper, the structural response of the bridge under different peak ground acceleration (PGA) seismic waves is obtained by nonlinear time history analysis. The horizontal seismic waves used in the time history analysis are the seismic waves of El Centro in the United States, California, with 0.215g PGA and 40s duration, and the seismic acceleration records are shown in Figure 6. The PGA of seismic wave is adjusted to 0.15g, 0.3g and 0.6g respectively in order to investigate the influence of the value of PGA on the accuracy of simplified model analysis.

Table 1: Different modeling methods of soil-structure interaction.

Model	Soil-abutment interaction	Soil-pile interaction
M1	nonlinear spring element + damping element	nonlinear spring element + damping element
M2	nonlinear spring element	nonlinear spring element
M3	nonlinear spring element + damping element	linear spring element (”m” method)
M4	linear spring element (”m” method)	nonlinear spring element + damping element

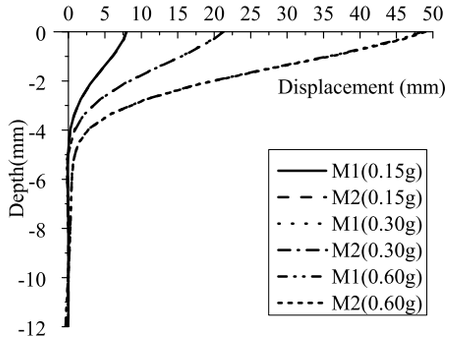


Figure 7: Distribution of displacement along the pile in model 1 & 2

3.1 *Influence of the soil damping*

Distribution of pile displacement of model 1 and model 2 along pile length under different PGA is shown in Figure 7. When PGA is 0.15g, the time history of the pile top bending moment of model 1 and model 2 is shown in Figure 8. Analyses results of the displacement at the top of the pile, displacement at the top of the pier, bending moment at the top of the pile, bending moment at the bottom of the pier, maximum bending moment of the abutment and maximum bending moment of the girder are shown in Table 2.

By comparing the results in Figure 7, Figure 8 and Table 2, it can be found that soil damping has little

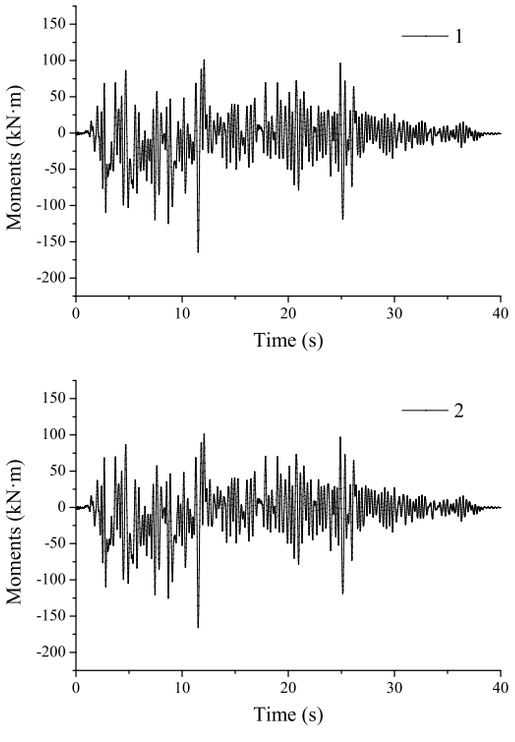


Figure 8: Pile top moment time history at PGA=0.15g of model 1 & 2

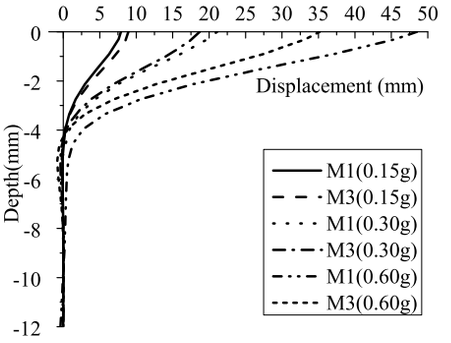


Figure 9: Distribution of displacement along the pile in model 1 & 3

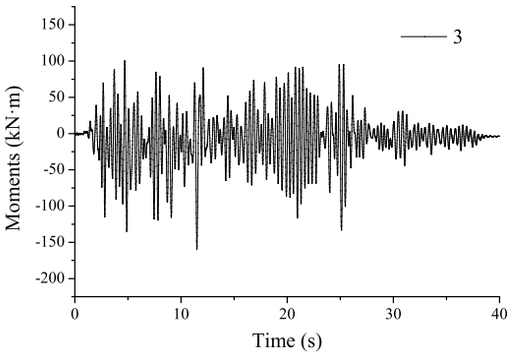


Figure 10: Pile top moment time history at PGA=0.15g of model 3

effect on the seismic response of the bridge. The pile displacement distribution and the time history of pile top bending moment of M1 and M2 are almost the same, with the differences of seismic response of each component less than 1%. Therefore, the damping of the soil can be neglected in the seismic analysis of integral bridge.

3.2 *Influence of simplification of soil-abutment interaction*

Distribution of pile displacement of M1 and M3 along pile length under different PGA is shown in Figure 9. When PGA is 0.15g, the time history of the pile top bending moment of M3 is shown in Figure 10. Analyses results of the displacement at the top of the pile, displacement at the top of the pier, bending moment at the top of the pile, bending moment at the bottom of the pier, maximum bending moment of the abutment and maximum bending moment of the girder are shown in Table 3.

By comparing the pile displacement distribution of model 1 and 3 under different PGA in Figure 9, it can be seen that the results of M3 is close to that of detailed model M1. When PGA is small (PGA=0.15g),

Table 2: Comparison of the bridge seismic response in model 1 and model 2.

Acce.	Model	Pile top disp.	Pier top disp.	Pile top moments	Pier bottom moments	Abutment Mmax	Girder Mmax
		mm	mm	kN·m	kN·m	kN·m	kN·m
0.15g	M1	7.9	6.5	164.5	995.5	755.9	401.7
	M2	8.0	6.6	165.9	1003.0	761.6	404.9
0.3g	M1	21.1	17.9	341.6	1886.9	1792.0	968.8
	M2	21.3	18.0	314.7	1898.2	1805.9	977.1
0.6g	M1	48.5	42.4	362.1	2765.7	3931.1	2233.8
	M2	49.0	42.8	362.1	2768.9	3964.3	2254.0

Table 3: Comparison of the bridge seismic response in model 1 and model 3.

Acce.	Model	Pile top disp.	Pier top disp.	Pile top moments	Pier bottom moments	Abutment Mmax	Girder Mmax
		mm	mm	kN·m	kN·m	kN·m	kN·m
0.15g	M1	7.9	6.5	164.5	995.5	755.9	401.7
	M3	8.9	7.3	159.7	1048.8	714.9	344.6
0.3g	M1	21.1	17.9	341.6	1886.9	1792.0	968.8
	M3	18.7	16.0	298.3	1771.5	1409.6	690.3
0.6g	M1	48.5	42.4	362.1	2765.7	3931.1	2233.8
	M3	35.2	31.1	349.7	2537.8	2678.0	1382.5

M3 slightly overestimated the displacement of pile top (12.6%); at PGA=0.30g, M3 slightly underestimated the displacement of pile top (11.3%); but at PGA=0.60g, the error of M3 reached 27%. Therefore, when the PGA value is large, the influence of soil bridge interaction simulation simplification should be carefully considered.

According to Figure 10, the bending moment of M1 reaches a negative maximum value of $164.5kN \cdot m$ at $t = 11.51s$ and reaches a maximum positive value of $101.1kN \cdot m$ at $t = 12.07s$. The waveform of M3 is consistent with the detailed model M1 and the maximum value of the bending moment is similar, which is $159.7kN \cdot m$ and $164.5kN \cdot m$, with a difference of only 2.9%. But the time to reach the maximum is different. M3 reaches its maximum value at $t = 11.49s$, while M1 at $t = 11.51s$.

With the increasing of PGA, the nonlinear properties of soil are gradually enhanced and the stiffness tends to decrease. M3 uses the "m" method to calculate the stiffness of soil around pile, without considering the nonlinear soil, so the stiffness of soil around pile of M3 tends to increase compared with M1. Therefore, when the PGA increases from 0.15g to 0.3g and 0.6g, the increasing range of displacement of the abutment pile top and the pier top of M3 compared to M1 changes from +12% to -11% and -27%.

By comparing the differences of seismic responses between M1 and M3 in different PGA cases in Table 3, the following conclusions can be drawn: In general, when the PGA is 0.15g, the seismic response of the simplified model M3 is similar with that of the detailed model M1 and the differences of the seismic response of each structural component is below 15%. Which is consistent with the statement that "When the horizontal load on the piles is relatively small, or the displacement of the pile at the mud surface is not more than 10mm, the error of "m" method is small" (CCCC Highway Consultants CO. 2007). But with the increasing of PGA, the accuracy of M3 is decreasing. When the PGA increases to 0.6g, the difference of the result the maximum bending moment of the abutment and the maximum bending moment of the girder between M3 and M1 is 31.9% and 38.1% respectively.

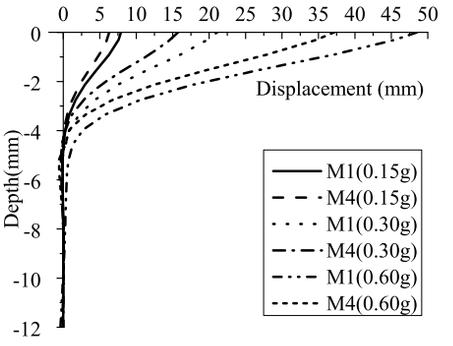


Figure 11: Distribution of displacement along the pile in model 1 & 4

3.3 *Influence of simplification of soil-pile interaction*

Distribution of pile displacement of M1 and M4 along pile length under different PGA is shown in Figure 11. When PGA is 0.15g, the time history of the pile top bending moment of M4 is shown in Figure 12. Analyses results of the displacement at the top of the pile, displacement at the top of the pier, bending moment at the top of the pile, bending moment at the bottom of the pier, maximum bending moment of the abutment and maximum bending moment of the girder are shown in Table 4.

By comparing the pile displacement distribution of M1 and M4 under different PGA, it can be seen that the pile displacement of M4 when PGA is 0.15g is much larger than M1, but with the increasing of PGA,

Table 4: Comparison of the bridge seismic response in model 1 and model 4.

Acce.	Model	Pile top disp.	Pier top disp.	Pile top moments	Pier bottom moments	Abutment Mmax	Girder Mmax
		mm	mm	kN·m	kN·m	kN·m	kN·m
0.15g	M1	7.9	6.5	164.5	995.5	755.9	401.7
	M4	6.3	5.9	134.9	861.3	508.3	308.1
0.3g	M1	21.1	17.9	341.6	1886.9	1792.0	968.8
	M4	15.7	14.7	293.7	1691.0	1134.4	691.9
0.6g	M1	48.5	42.4	362.1	2765.7	3931.1	2233.8
	M4	37.2	34.5	355.1	2698.1	2554.2	1586.5

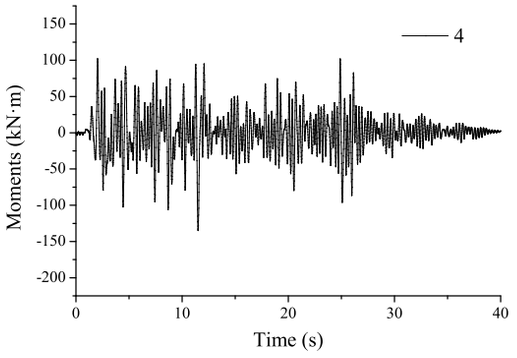


Figure 12: Pile top moment time history at PGA=0.15g of model 4

the results of M4 gradually approach the results of M1. When PGA increases to 0.6g, the pile displacement of M4 is the closest to that of M1 than M3.

According to Figure 12, the bending moment of M1 reaches a negative maximum value of $164.5kN \cdot m$ at $t = 11.51s$ and reaches a maximum positive value of $101.1kN \cdot m$ at $t = 12.07s$. The waveform of M4 is consistent with the detailed model M1 and they all reach the maximum moment at the top of the pile at $t = 11.5s$, $134.9kN \cdot m$ and $164.5kN \cdot m$, respectively, with a difference of 18%.

With the increasing of PGA, the nonlinear properties of soil are gradually enhanced and the stiffness tends to decrease. M4 uses "m" method to calculate the stiffness of soil, without considering the soil nonlinearity, thus overestimated the abutment-soil system stiffness. The analysis error of abutment maximum bending moment is about 35%, but the analysis error of other responses is less than 30%, so the overall analysis accuracy is higher. With the increasing of PGA, the analysis accuracy of M6 has a tendency to decrease, but not very much.

3.4 *Simulation method selection*

Because the difference between the seismic response of the members of M2 (without considering the influence of soil damping) and the detailed model M1 is less than 1%, so the influence of soil damping can be neglected when the seismic analysis of the whole bridge is carried out.

According to the results of different models under different PGA, when PGA is 0.15g and 0.3g, the analysis accuracy of the model using "m" method to simplify the soil-pile interaction (M3) is higher. When the PGA is 0.6g, the accuracy of the model using using "m" method to simplify the soil-abutment interaction (M4) is higher than the model using "m" method to simplify the soil-pile interaction (M3).

By comparing the results of each simplified model and the detailed model, it can be found that the overall analysis accuracy of the simplified model 3 is higher, of which the error is always within a reasonable range. Under different PGA, the average difference between M3 and detailed model M1 of bending moment at the pile top, the bending moment of pier bottom and the pile top displacement is about 6.3%, 6.6% and 17.3% respectively, which is higher than that of M4. The difference of the displacement of pier top, the maximum bending moment of abutment and the maximum bending moment of girder is 16.4%, 19.5% and 27% respectively. The maximum difference between M3 and detailed model, which is 38.1%, occurs in the comparison of maximum bending moment of the girder when the PGA is 0.6g. The overall analysis accuracy of M4 is also relatively high, and the accuracy of the analysis fluctuates little when the PGA changes, and the error always stays within a reasonable range. The maximum difference occurs in the comparison of the maximum bending moment of the abutment when PGA is 0.3g, with the difference of 36.7%.

From the results of each component, the analytical accuracy of pile top displacement, pile top bending moment, pier bottom bending moment and the maximum bending moment of the abutment is higher when using simplified model M3, and the average error of different PGA is 17.2%, 6.3% , 6.6% and 19.5% respectively; The analysis accuracy of the pier top displacement and the maximum bending moment of the girder is higher when the simplified model M4 is adopted, with the average error considering different PGA is 15.2% and 26.9% respectively.

From the point of view of the sensitivity of the component analysis results, when the seismic wave PGA changes, the variational range of analysis accuracy of M3 is greater than M4, in other words, the analysis accuracy of M3 is less sensitive to the seismic wave PGA. And for M3, the variational range of analysis accuracy of maximum bending moment of girder and abutment is greater, which means higher sensitivity, while for M4, the accuracy analysis of pile top bending moment and pier top bending moment changes greatly, which means higher sensitivity.

In conclusion, SSI simplified simulation method should be selected according to the value of PGA of the earthquake, and considering the analysis accuracy of the seismic response of each component, and also should consider the different sensitivity of the seismic response of different component when different simplified simulation method was adopted.

4 CONCLUSION

(1) The damping of soil has little effect on the seismic response of the integral bridge and the damping of the soil can be neglected in the seismic analysis of the integral bridge.

(2) When PGA is 0.15g and 0.3g, the model using "m" method to simplify pile-soil interaction (M3) has higher analysis accuracy. And with the increasing of PGA, the analysis accuracy of M3 decreases, but with small change. However, when the PGA is 0.6g, the model using "m" method to simplify the abutment-soil interaction (M4) has higher accuracy than M3.

(3) The model using "m" method to calculate the stiffness of soil behind abutment (M4) has high analysis accuracy, and with the increasing of PGA, the accuracy of M4 has a decreasing trend but with only a little change, and the error is always within reasonable range.

(4) M3 has higher analysis accuracy in the analysis of the displacement of the pile top displacement, the pile top bending moment, the pier bottom bending moment and the maximum bending moment of the abutment, while M4 has higher analysis accuracy in the analysis of the displacement at the pier top and the maximum bending moment of the girder. When the seismic wave PGA changes, the analysis accuracy of M3 of the maximum bending moment of the abutment and girder changes a lot and the sensitivity is high, while the analysis accuracy of M4 of the pile and pier top bending moment is more sensitive to the seismic wave PGA.

(5) The "m" method is considered to be useful to simplify the pile-soil interaction, especially when the PGA is small. The "m" method is also useful to the simplification of the abutment-soil interaction. SSI simplified simulation method should be selected according to the value of PGA of the earthquake, and considering the analysis accuracy of the seismic response of each component, and also should consider the different sensitivity of the seismic response of different component when different simplified simulation method was adopted.

5 ACKNOWLEDGMENTS

The authors of this paper would like to express their appreciation for the financial support given by the Nature Science Foundation of China (No. 51378340) and Application Foundation and Advanced Technology Research Key Program of Tianjin, China (No. 14JCZDJC40100-2014). Support from the funding agency above is gratefully acknowledged.

REFERENCES

Anandarajah, A., J. Zhang, & C. Ealy (2005). Calibration of dynamic analysis methods from field test data. *Soil Dynamic Earthquake Engineering 25(7)*, 763–772.

API (1977). Recommended practice for planning, designing, and constructing fixed offshore platformsłworking stress design. Technical report, American Petroleum Institute.

CCCC Highway Consultants CO., L. (2007). Design criterion for road bridge culvert base foundation. Technical report, China Communications Press, Beijing, China.

Chen, B., Y. Zhuang, & B. Briseghella (2013). *Jointless Bridge.* Beijing, China: China Communications Press.

Jain, S. & R. Scott (1989). Seismic analysis of cantilever retaining walls. Technical report, Proceedings of Structural Mechanics in Reactor Technology, Anaheim.

Matlock, H. (1970). Correlation for design of laterally loaded piles in soft clay. Technical report, Offshore Technology Conference, Houston.

MOT (2016). Statistical bulletin of transportation industry development in 2015. Technical report, Ministry of Transport of the People's Republic of China.

NCHRP (2009). Seismic analysis and design of retaining walls, buried structures, slopes, and embankments. Technical report, National Cooperative Highway Research Program.

SAP (2010). *Integrated Finite Element Analysis and Design of Structures.* Berkeley: Computers and Structures Inc.

Shamsabadi, A., K. Rollins, & M. Kapuskar (2007). Nonlinear soil-abutment-bridge structure interaction for seismic performance-based design. *Journal of Geotechnical and Geoenvironmental Engineering 133(6)*, 702–720.

Vasheghani-Farahani, R., Q. Zhao, & E. Burdette (2010). Seismic analysis of integral abutment bridge in tennessee, including soil-structure interaction. *Journal of the Transportation Research Board 2201*, 70–79.

Wasserman, E. & J. Walker (1996). *Highway Structures Design Handbook.* American Iron and Steel Institute.

Maintenance, Safety, Risk, Management and Life-Cycle Performance of Bridges – Powers, Frangopol, Al-Mahaidi & Caprani (Eds)
© 2018 Taylor & Francis Group, London, ISBN 978-1-138-73045-8

Seismic Behavior and Cyclic Tests on Integral Abutment–Pile Joints

Qiuhong Zhao[1,2] & Yikang Li[1] & Zhaoyang Qi[1]
1 School of Civil Engineering, Tianjin University, Tianjin, China
2 Key Laboratory of Coast Civil Structure Safety of Ministry of Education, Tianjin, China
Baochun Chen[3]
3 School of Civil Engineering, Fuzhou University, Fuzhou Fujian, China

ABSTRACT: This paper focused on seismic behavior of integral abutment-steel H pile joints through cyclic tests. Six specimens were tested, composing of a steel H-pile embedded inside an inverted "T" shape reinforced concrete block simulating abutment. Design parameters varying as follow: H pile orientation, strong vs. weak axis bending; crumb rubber concrete (CRC) vs. normal concrete, for portion of abutment around pile tip; attaching rubber plates to H pile tip vs. no rubber plates. Test results indicated that: pile orientation had significant influence on seismic performance, energy dissipation and bending capacity for weak axis bending is lower than strong axis bending, while failure displacement and ductility is higher; CRC would reduce concrete cracks, initial stiffness, and slow down stiffness degradation, and reduced total energy dissipation; attaching rubber plates to pile tip protected it from damage. It would reduce initial stiffness and bending capacity, but increased failure displacement and ductility.

1 INTRODUCTION

With the increasing demand for transportation in recent years, the amount of bridge construction increased rapidly. Expansion devices in regular bridges exposure to external environment, including precipitation, dust, and traffic load are liable to damage, while it is difficult to be repaired or replaced. In jointless bridges, superstructure and substructure form an integral connection at the abutment level, expansion devices have been removed. As a result, the maintenance costs can be decreased obviously.

Different form regular bridges, the integral connection transfer moment and shear, and deformations in the superstructure caused by temperature changing and earthquake transfer to the substructure directly. Consequently, the connection of abutment and pile must be taken into seismic design consideration of great importance. In order to reduce loads and deformations transferred from the superstructure to the substructure, flexible piles and foundations are typically recommended to accommodate the loads and deformations.

1.1 *Embedded depth*

The depth of piles embedded in abutments have negligible influence on the integrity of the connection. Piles could bear relatively large lateral deformations while the embedded depth is more than 0.3m. Moment of pile distributes bidirectionally, moment at the top of pile decreases to zero, counter moment increases to a maximum value and decreases to zero gradually in a further step along with the increasing embedded depth (Burdette 1999; Burdette 2003; Burdette 2004), and the seismic performance of integral abutment-pile joints can be improved (Frosch 2009).

1.2 *Pinned connection*

An experimental research revealed that providing a pinned connection of abutment and pile can effectively improve the seismic performance, because the pinned connection accommodates deformations without resulting in excessive stress (Frosch 2009). Sherafati proposed that wrapping the top of the concrete-filled steel tube pile up with a rubber sleeve and embedding the wrapped pile head into the abutment. As a result, lateral stiffness and maximum moment have been decreased, and deformation capacity of the pile has been promoted. Experimental result showed that lateral deformation capacity of pinned connection increased to 3.8 times as much as that of rigid connection (Sherafati 2014).

1.3 *Bending orientations*

In order to reduce the bending stiffness of the pile, studies focused on bending orientations of the pile were conducted. Frosch revealed that the lateral load capacity of piles is larger for strong axis bending, while the lateral displacement capacity is reduced,

and strength degradation restricts the seismic performance of the piles seriously (Frosch 2009). Some studies showed that piles bend along their weak axis can accommodate larger displacement transferred from the superstructure to the substructure, so that piles and abutment can be protected (Chovichien 2004; Girton 1991; Haj-Najib 2002; Thanasattayawibul 2006).

The traditional construction measure of integral abutment-H steel pile joints is embedding the H steel pile into the abutment directly. Due to the high stiffness and bad deformation capacity, the joints tend to be damaged easily. Research on construction measures of integral abutment-H steel pile joints need to be conducted in a further step to improve the seismic performance.

In recent years, rubber consumed massively in China, but cannot be recycled efficiently (Yue 2006). Rational utilization of abandoned rubber has advantages to solve the problem of environment pollution and resources wasting.

In this paper, cyclic tests are conducted on 6 integral abutment-H steel pile joint specimens. Considering 3 aspects which affect the seismic performance of the joints: bending orientation, which is the main factor affecting the stiffness of piles; applying rubberized concrete to the joint region in abutment, so that the elastic modulus and cracks developing of abutment concrete can be reduced (Baoming 2010; Chujie 2008); wrapping rubber plates around the head of H steel pile, deformations from earthquake can be absorbed by rubber plates, and the head of pile can be protected from damage. In a further step, finite element analysis is conducted based on the verification with experimental results. Effects of axial compression ratio, rubber content, yield strength of steel, and thickness of rubber plate on seismic performance of the joint are considered.

2 SPECIMEN DETAILS

2.1 *Specimen design*

Abutment-H steel pile part of a two span integral steel bridge in Tennessee was chosen as the prototype of test specimens, each specimen has the same contour and size. As can be seen from Figure 1, the cross section of abutment is 910×910mm, and HP 246×256×10×10 for the cross section of H steel pile. Six specimens are named as S1 to S6. S1 and S2 are specimens with rigid joint; S3 and S4 are specimens which applying rubberized concrete with 10% rubber content to the joint region in abutment, the depth of concrete-replaced region is 100mm deeper than the embedded depth of steel pile, rubberized concrete mix proportion can be found from Table 1; S5 and S6 are specimens which pasting 25mm thick rubber plates to the head of H steel pile embedded in the abutment. Differences between 6 specimens can be seen from Figure 2.

Table 1. Rubberized concrete mix proportion.

Rubber	Cement	Sand	Stone	Water	Reducer
kg	kg	kg	kg	kg	kg
100	590	412	1030	205.9	0.917

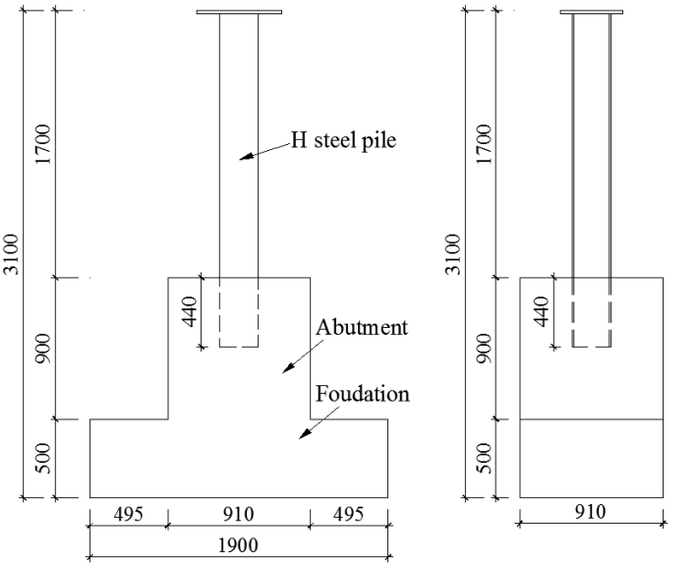


Figure 1. Contour size of specimen.

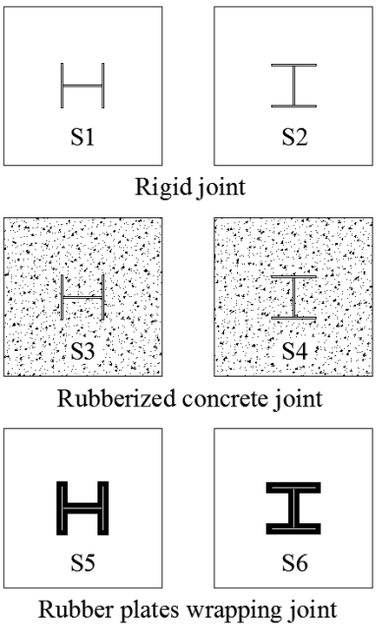


Figure 2. Joint connecting measures.

2.2 *Material properties*

Specimens mainly consist of H steel pile and concrete abutment. Steel grade Q345 was used for the H steel pile, result of steel material tension test can be seen from Table 2. C35 concrete was used for the abutment, measured compression strength of standard cube of ordinary concrete and rubberized con-

crete were 49.5MPa and 31.3MPa. In order to obtain the material mechanical property of rubber plate, reserved 25mm thick rubber plate was cut into 100×100×25mm cuboid, so that the force-displacement curve of rubber plate under compression was obtained by universal test machine, which can be seen from Figure 3.

Table 2. Tension test results of steel materials.

Design grade	Yield strength	Tensile strength	Yield ratio
MPa	MPa	MPa	——
345	391	551.8	0.71

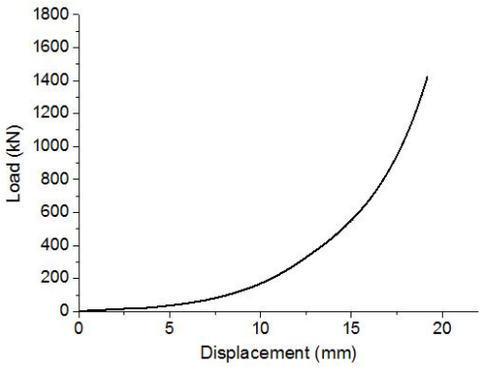
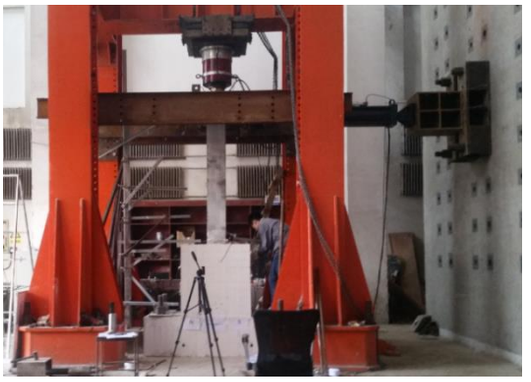


Figure 3. Compression load-displacement curve of rubber plate.

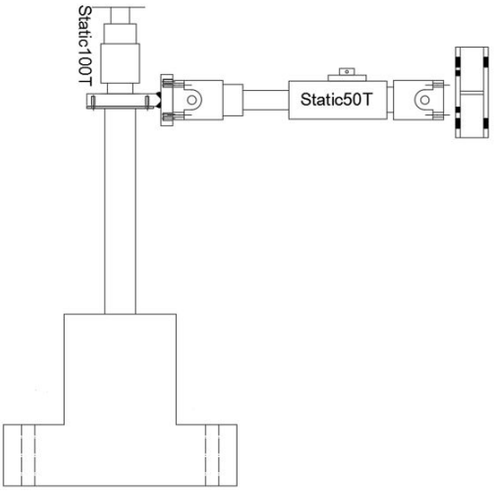
2.3 *Test devices and loading program*

In this test, axial and horizontal loading are adopted to reflect seismic performance of the integral abutment-pile joints under actual stress conditions. Axial load is imposed by a 1000kN vertical jack, which is fixed on the reaction frame but can move in step with the horizontal loading location of the H steel pile. During the test, the axial compression ratio remains a constant of 0.25. Horizontal reciprocating load is imposed by a horizontal actuator which can provide maximum load of ±500kN, and maximum displacement of ±200mm. Arrangement of experimental loading device can be seen form Figure 4.

Figure 5. shows the loading program applied to 6 specimens in this test. Axial load was applied to the specimen and kept a constant before lateral load applied during the test. Displacement-dominated loading was adopted in this test. The first level of loading amplitude and amplitude increment were both 6mm, and each level loaded only once before system yielding, the displacement while system yielding was denoted as d_y. The loading amplitude increment was taken as $0.5d_y$ since system yielding, and each level loaded twice. Once the lateral load bearing capacity declined to 85% of the peak lateral load bearing capacity, it can be considered that the system damaged, and test terminated.



(a) Arrangement of actual loading devices.



(b) Sketch of loading devices.

Figure 4. Test setup.

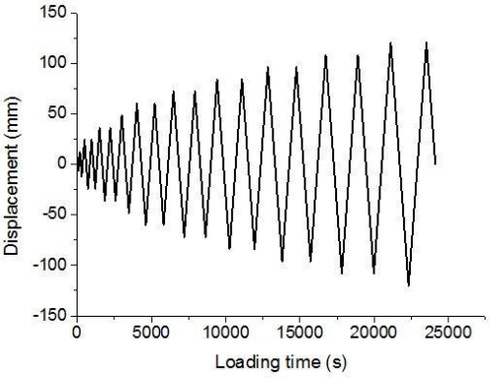


Figure 5. Loading program.

3 DESCRIPTION OF TEST SPECIMENS

Specimen S-1 behaved elastic before the lateral displacement of 24mm. White coating cast from flanges at the bottom of steel pile, concrete cracks carried out at the interface of steel pile and abutment; the specimen began to yield at the displacement of 24mm and reached peak load at 36mm. White coating cast from bottom flanges during yielding to peak bearing capacity stage continuously, concrete cracks developed at the interface of the steel pile and the

abutment; lateral load bearing capacity kept degrading while the lateral displacement increased from 36mm to 72mm, which caused local buckling of the flanges at the bottom of steel pile. The range of buckling extended with the increasing of the applied loading. Consequently, the web yielded and the development of concrete cracks decreased after yielding.

As well as S-1, specimen S-2 yielded at the lateral displacement of 24mm. Concrete cracks carried out with small pieces spalling of white coating at the interface of the steel pile flanges and the concrete; the specimen reached its peak load capacity at the lateral displacement of 48mm. White coating cast severely from the flanges at the bottom of steel pile during the stage of system yielding to system reaching peak load bearing capacity, and lateral load bearing capacity kept degrading while the lateral displacement increased from 48mm to 96mm, the concrete cracks carried out at the abutment where adjacent to the margins of flanges. With the development of lateral load increasing, local buckling of the flanges at the bottom of steel pile developed constantly.

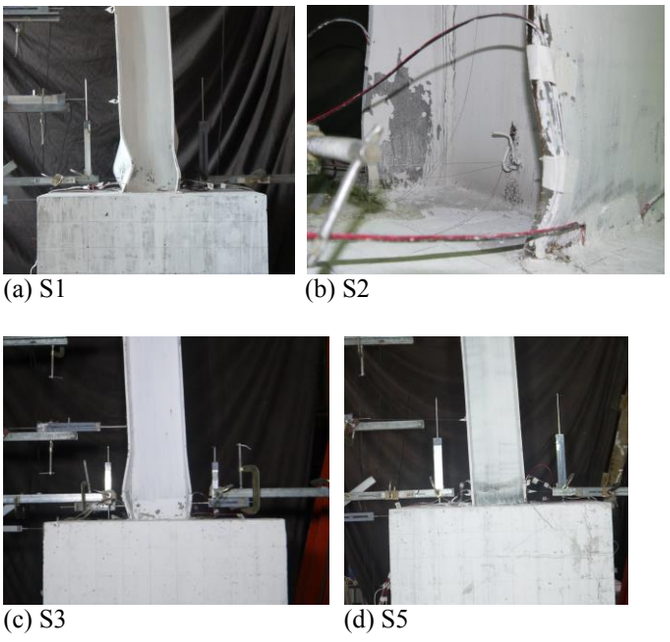
Specimen S-3 yielded while the lateral displacement was 24mm and reached its peak load bearing capacity while the lateral displacement was 48mm as well. Concrete cracks developed but a few at the interface of the steel pile and the abutment since system yielding. The flanges at the bottom of steel pile kept buckling while the lateral displacement increased from 48mm to 84mm, and the range of buckling extended with the increasing of the applied loading. Consequently, the development of cracks reduced after the buckling of web.

Specimen S-4 began to yield while loading to the lateral displacement of 33mm, and reached its peak lateral load bearing capacity at 66mm. White coating cast inattentively from the flanges at bottom of steel pile during yielding to peak bearing capacity stage, flanges began to yield and developed constantly. The specimen was on the stage of failure from 66mm to 99mm, buckling occurred on the flanges of the pile and developed constantly with the applied loading.

Specimen S-5 worked at elastic state before the lateral displacement was 18mm, and an insignificant crack appeared at the abutment where adjacent to the margin of flange. As load keeping on, the specimen reached its peak lateral load bearing capacity at the lateral displacement of 45mm, and concrete cracks developed at the interface of the steel pile and the abutment, and rubber plates were compressed or cracked with the applied loading. Diagonal cracks were visible and developed constantly at the margins of flanges after the specimen reached its peak load bearing capacity. The specimen was on the stage of failure from the lateral displacement of 45mm to that of 90mm. Finally, the abutment appeared severe cracks to damage while the steel pile remained intact.

Specimen S-6 behaved elastic before the lateral displacement of 33mm and no significant phenomenon appeared. As lateral load carrying on, the gap between the margins of flange and the rubber plate got widen gradually, and the specimen reached its peak load bearing capacity at the displacement of 66mm. The specimen was on the failure stage from the lateral displacement of 66mm to that of 99mm, the gap mentioned above got widen in a further step, and the concrete was local fractured at the contacted portion of the rubber plate and concrete while the steel pile remained intact.

Failure modes of typical specimens are shown in Figure 6.



(a) S1 (b) S2

(c) S3 (d) S5

Figure 6. Failure modes of typical specimens.

4 ANALYSIS OF TEST RESULTS

4.1 *Load-displacement performance*

The acquisition of lateral load magnitude could be accomplished with the force sensor erected on the end of the actuator, and the lateral displacement of specimen could be obtained by the displacement sensor which is attached on the top center of the specimen. The load-displacement hysteretic curve of 6 specimens are shown in Figure 7.

The important properties in different stages of force and deformation, for instance, the seismic parameters of strength, stiffness and ductility could be obtained from the envelope curves which are also used for comprehensive assessment of seismic behavior. Envelope curves of all specimens are shown in Figure 8.

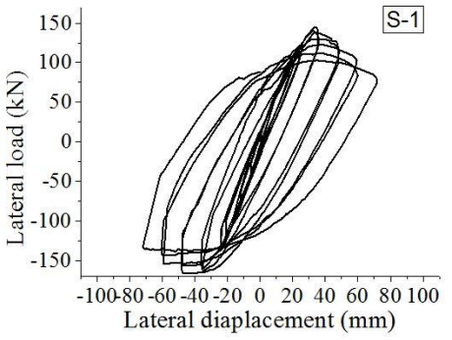
According to the envelope curves above, generalized yield moment method is selected to define the yield load and yield displacement of all specimens. Values of lateral rigidity, yielding value, peak point

value, failure displacement, bearing capacity and ductility ratio of 6 specimens are shown in Table 3.

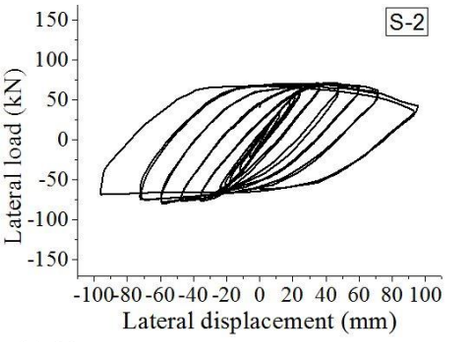
It can be found from the experimental results that the bending axis of steel H pile has a significant influence on ductility performance to system, the differences on rigidity, lateral displacement and bearing capacity are relatively distinct. The lateral stiffness and yielding load of weak axis bending specimen is obviously worse than that of strong axis bending specimen, and the peak lateral load bearing capacity of weak axis bending specimen is relatively small, while the lateral displacements of specimen reaching its peak lateral load bearing capacity and performing to failure are the opposite. The failure lateral drift varies from 1/32 to 1/22 of strong axis bending specimens, while the lateral drift of weak axis bending specimens varies from 1/24 to 1/18. The ductility ratio of strong axis bending specimen is 1.55 on average. Generally, specimens of weak axis bending entered into plastic stage earlier because of the smaller bending stiffness, which caused a larger ductility ratio, 2.65 on average.

It can be found from Figure 7. (a-d), adopting crumb rubber concrete in local region has an insignificant influence on the load-displacement behavior at the beginning of the envelope curves. The difference got pronounced while the lateral load got close to the peak load gradually. Lateral rigidity of specimens decreased obviously by adopting crumb rubber concrete in local region, the average value of lateral rigidity of strong bending axis and weak bending axis dropped respectively from 4.86 and 2.35 to 3.61 and 1.91. It has an insignificant influence on the yield and peak load by adopting crumb rubber concrete in local region as well, but increases relevant lateral displacement. In general, filling rubber in concrete or not has an insignificant influence on the failure load and lateral displacement, the insertion of crumb rubber is not good for ductility promotion of the system.

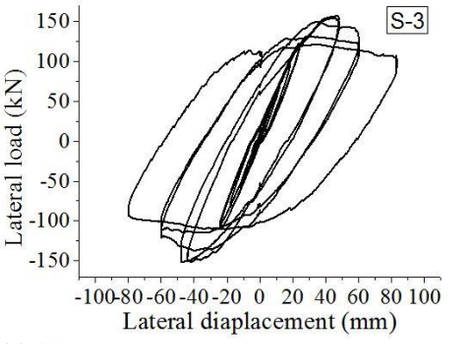
Unlike filling crumb rubber in concrete, wrapping rubber plate has a significant influence on the seismic performance of the system. Compared with adopting crumb rubber concrete in local region, it influences the lateral rigidity remarkably, the average value of lateral rigidity of strong bending axis and weak bending axis dropped from 4.86 and 2.35 to 2.85 and 0.84. The yield load, peak load and failure load are decreased while the failure lateral displacement is increased by wrapping rubber plate, which improves the system ductility to a certain extent. Ductility ratio of strong axis bending specimens increased from 2.2 to 3.2 on average while that of weak axis bending specimens unchanged.



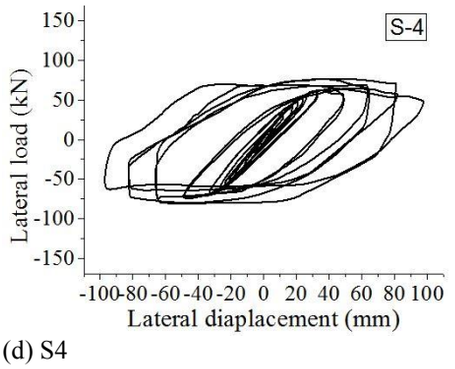
(a) S1



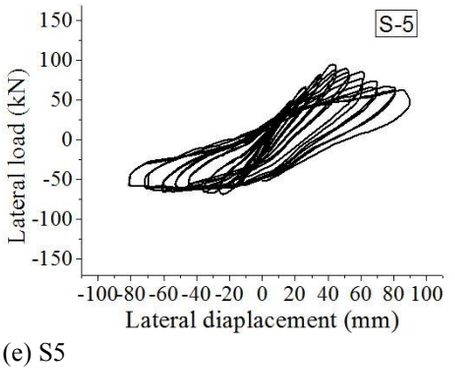
(b) S2



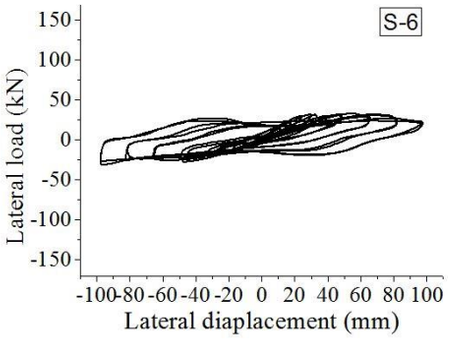
(c) S3



(d) S4



(e) S5



(f) S6

Figure 7. Load-displacement curve.

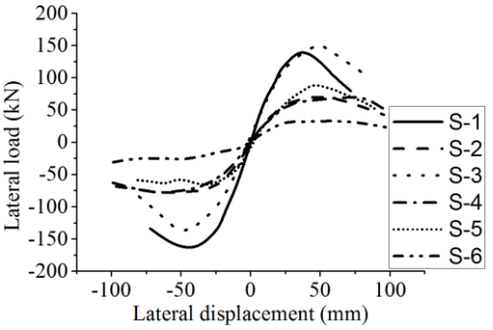


Figure 8. Envelope curve.

Table 3. Seismic performance characteristics of specimens.

Setting		K kN/mm	d_y mm	P_y kN	d_m mm	P_m kN	d_u mm	α rad	μ —
S1	+	4.61	27.3	125.6	36.1	135.2	54.3	1/32	1.99
	−	5.11	28.6	146.2	48.0	163.9	68.7	1/25	2.40
S2	+	2.17	28.3	61.6	47.5	71.4	73.1	1/24	2.58
	−	2.52	27.4	69.1	59.7	79.8	96.7	1/18	3.53
S3	+	4.06	32.2	130.6	48.0	157.1	58.3	1/30	1.81
	−	3.16	45.0	142.2	48.0	148.1	57.9	1/30	1.29
S4	+	1.95	31.2	60.8	82.5	71.4	89.6	1/20	2.87
	−	1.86	37.5	69.7	66.0	79.5	91.0	1/19	2.43
S5	+	2.30	39.4	90.3	42.5	94.8	64.7	1/27	1.65
	−	3.39	16.9	57.3	24.1	69.0	81.1	1/22	4.81
S6	+	1.24	24.5	30.5	55.4	33.3	83.8	1/21	3.42
	−	0.43	44.7	25.6	98.7	30.9	98.7	1/18	—

* K is the lateral stiffness, d_y is the displacement while system yielding, P_y is the lateral load capacity while system yielding, d_m is the displacement while system reaching its peak load capacity, P_m is the peak lateral load capacity, d_u is the displacement while lateral load capacity decreasing to 85% of peak load capacity, α is the ultimate displacement angle, μ is the ductility ratio of the system.

4.2 *Stiffness degradation*

Stiffness degradation reflects the degrading procedure of specimens under cyclic loading, it is an important characteristic in the research of seismic performance. The method of researching stiffness degradation of specimens under cyclic loading process is calculating the secant stiffness of specimens. Stiffness degradation curves of all specimens are shown in Figure 9.

Specimen S-1 and S-3 performed high lateral stiffness level during the initial stage of loading, which is twice than the others, but lateral stiffness dropped rapidly with the increasing lateral displacement. Despite the stiffness degradation of S-1 and S-3 are evident, they are still higher than that of other specimens during the later loading stage. Specimen 2, The lateral stiffness of S-2, S-4 and S-5 are respectively closed during the whole loading stage, while that of S-6 dropped rapidly from initial loading stage to the failure stage, and was always lower than the others.

According to the contrast, the lateral stiffness of strong axis bending specimens are always higher than the lateral stiffness of weak axis bending specimens. Adopting crumb rubber concrete in local region reduces the initial stiffness of specimens but also retards the stiffness degradation, relatively, the lateral stiffness of specimens adopting crumb rubber concrete in local region was higher than specimens adopting ordinary concrete in the whole abutment region during the stage of load bearing capacity decline. Wrapping rubber plate reduces the initial lateral stiffness significantly but it affects the stiffness degradation slightly during the stage of load bearing capacity decline.

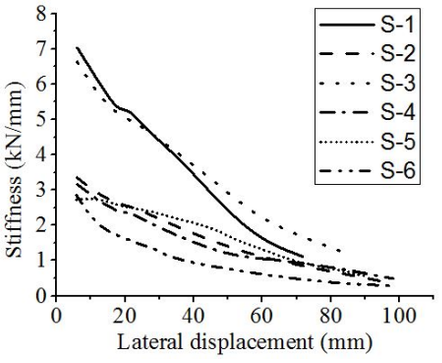


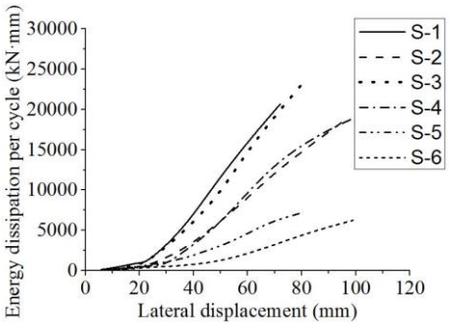
Figure 9. Stiffness degradation.

4.3 *Energy dissipation*

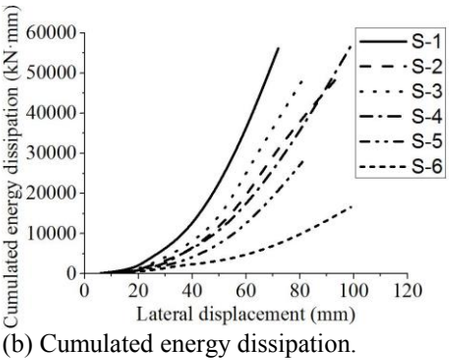
Single-cyclic energy dissipation, cumulated energy dissipation and equivalent viscous damping coefficients are used to indicate the energy dissipation capacity of all specimens under reciprocate pseudo static cyclic loading in this test, and the performance mentioned above are shown in Figure 10.

By comparison, the energy dissipation capacity of strong axis bending specimens are evidently higher than that of weak axis bending specimens. Adopting crumb rubber concrete in local region reduces the single-cyclic energy dissipation capacity at the elastic stage, but the capacity approaches or exceeds the ordinary ones gradually with the lateral load carrying on, which indicates that adopting crumb rubber concrete in local region affects the single-cyclic energy

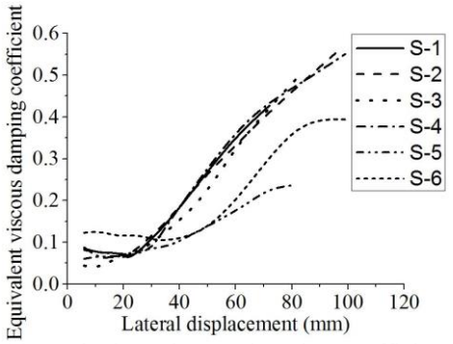
dissipation capacity gradually at the later stage of loading. The cumulated energy dissipation curves reveal that adopting crumb rubber concrete in local region reduces the cumulated energy dissipation capacity, this phenomenon is much more remarkable in specimens with strong axis bending. Wrapping rubber plate distinctly reduces the single-cyclic energy dissipation capacity and the decline tends to increase with the augment of lateral displacement, as well as the cumulated energy dissipation capacity. The comparison of equivalent viscous damping coefficients reveals that adopting crumb rubber concrete in local region has an insignificant influence on damping coefficients, but wrapping rubber plate distinctly reduces damping coefficients.



(a) Single-cyclic energy dissipation.



(b) Cumulated energy dissipation.



(c) Equivalent viscous damping coefficient.

Figure 10. Energy dissipation capacity.

5 CONCLUSIONS

The bending axis of H steel pile has significant influence on seismic performance of the joint. The energy dissipation capacity and stiffness of weak axis bending specimens are worse than that of strong axis bending specimens, on the opposite, the ultimate lateral displacement and ductility of weak axis bending specimens are both higher than that of strong axis bending specimens.

Adopting crumb rubber concrete in local region of the abutment can obviously reduce the concrete cracks, and the lateral load bearing capacity is influenced by the construction measure slightly while the yield displacement is increased, which is not good for the ductility improvement of the system. Due to the material properties of rubber, the initial lateral stiffness could be reduced, and the speed of stiffness degradation could be retarded as well. Adopting crumb rubber concrete in local region of the abutment has insignificant influence on equivalent viscous damping coefficient, while reduces the energy dissipation capacity to a certain extent.

Wrapping rubber plate at the top of steel pile is an efficient way to reduce the initial lateral stiffness of the system without reducing the lateral stiffness at plastic stage obviously. As a result, the lateral load bearing capacity would be reduced distinctly, while the ultimate displacement would be increased, and the ductility would be improved significantly, so that the abutment-pile joint could accommodate lager loads and deformations transferred from the superstructure to the substructure efficiently.

6 ACKNOWLEDGEMENTS

The authors of this paper would like to express their appreciation for the financial support given by the Nature Science Foundation of China (No. 51378340) and Application Foundation and Advanced Technology Research Key Program of Tianjin, China (No. 14JCZDJC40100-2014). Support from the funding agency above is gratefully acknowledged.

7 REFERENCES

Baoming, W. & Wei L. 2010. Research progress of cement concrete containing scrap rubber in abroad. *Concrete* (4): 54-56.

Burdette, E.G. & Deatherage, J H. & Goodpasture, D.W. 1999. Behavior of laterally loaded piles supporting bridge abutments-phase I. Tennessee: Tennessee Department of Transportation.

Burdette, E.G. & Deatherage, J.H. & Goodpasture, D.W. 2003. Behavior of laterally loaded piles supporting bridge abutments-phase II. Tennessee: Tennessee Department of Transportation.

Burdette, E.G. & Howard, S.C. & Tidwell, J.B. 2004. Lateral load prestressed concrete piles supporting integral abutments. *PCI Journal*: 70-77.

Chovichien, V. 2004. The behavior and design of piles for integral abutment bridges. Ph.D. thesis, Purdue Univ., West Lafayette, IN.

Chujie J. & Chuanmei Z. & Wenhua Z. 2008. An overview of the study on rubcrete. *Journal of Chongqing Jianzhu University* 30(2): 138-145.

Frosch, R.J. & Kreger, M.E. & Talbott, A.M. 2009. Earthquake resistance of integral abutment bridges. Purdue Univ., West Lafayette, IN.

Girton, D.D. & Hawkinson, T.R. & Greimann, L.F. 1991. Validation of design recommendations for integral-abutment piles. *Journal of Structural Engineering* 117(7): 2117-2134.

Haj-Najib, R. 2002. Integral abutment bridges with skew angles. Ph.D. dissertation, Univ. of Maryland, College Park, MD.

Sherafati, A. & Azizinamini, A. 2014. Flexible pile head in jointless bridges: experimental investigation. *Journal of Bridge Engineering* 20(4): 04014071.

Thanasattayawibul, N. 2006. Curved integral abutment bridges. Ph.D. thesis, Univ. of Maryland, College Park, MD.

Yue, L. & Ling W. 2006. The research progress of Portland cement concrete containing crumb rubber. *Concrete* (4): 91-93.

Maintenance, Safety, Risk, Management and Life-Cycle Performance of Bridges – Powers, Frangopol, Al-Mahaidi & Caprani (Eds)
© 2018 Taylor & Francis Group, London, ISBN 978-1-138-73045-8

DESIGN AND CONSTRUCTION CHALLENGES OF JOINTLESS BRIDGES IN SEISMIC REGIONS

Bijan Khaleghi, PhD, PE, SE
Adjunct Professor at Saint Martin University
State Bridge Design Engineer, Washington State, USA

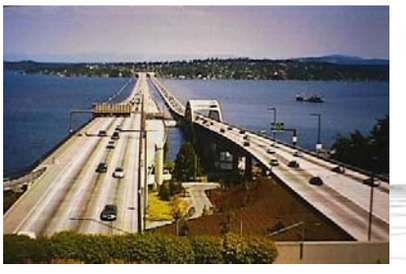
W. Phillip Yen, PhD, PE
Chair, International Association of Bridge Earthquake Engineering, USA

ABSTRACT: Jointless bridges have been used for bridges in the United States for years since the beginning of the National Interstate Highway System in 1950s. Through the intervening years, more and more states have utilized Jointless bridge construction in varying degrees establishing national standards and uniform design policy regarding bridge lengths, skews, details or design procedures. Many states since then have moved toward continuous bridges with jointless integral abutments and piers, as standard design and construction practice.

Jointless bridge superstructures are constructed to work integrally with the abutments. Movements due to creep, shrinkage and temperature changes are accommodated by using flexible beatings or foundation and through incorporating relief joints at the ends of the approach slabs. In addition to reduced maintenance costs, other advantages of jointless bridges include improved structural integrity, reliability and redundancy, improved longterm serviceability, improved riding surface, reduced initial cost, and improved aesthetics. In recent times, jointless bridges have been built in seismically sensitive areas.

This paper will attempt to capture the state-of-practice in the United States, but will lean toward practices favored by the Washington State Department of Transportation (WSDOT) with its long history of continuous bridges in seismic regions. The design and construction practices, seismic design and detailing of jointless bridges have been addressed in this paper.

Key words: Bridge, Continuous, Jointless, Seismic, Concrete, Precast





INTRODUCTION

Jointless bridges are defined as bridges with no expansion joints between the superstructure and the supporting abutments. Because of several problems resulting from the traditional practice, the jointless bridge has been widely adopted.

Precast, prestressed superstructures have an important advantage over both steel and cast-in-place concrete superstructures for jointless bridges. The advantage is that precast, prestressed superstructures experience considerably less thermal movement than steel superstructures, and less long-term movements than cast-in place concrete superstructures. This is because the

manufacturing process for precast members is such that much of the long term shrinkage will have occurred prior to erection and establishment of continuity in the superstructure. Moreover, the amount of creep that will occur over time decreases with increasing age of concrete at time of erection.

Concrete superstructures are less sensitive to temperature changes due to the lag between the air temperature and the interior temperature of a concrete member with its relatively large mass. This phenomenon is reflected in AASHTO LRFD Bridge Design Specifications (AASHTO BDS), which provides lower design temperature variations for concrete superstructures than for steel. In a moderate climate, a concrete superstructure will expand and contract a total of approximately 12 mm per 30 m of bridge length with seasonal temperature variation. However, a steel superstructure will typically expand and contract approximately 25 mm per 30 m of length.

Bridge piers and abutments restrain thermal movements and induce tensile or compressive forces in the superstructure. With properly proportioned piers and abutments these restraint forces are routinely and safely ignored in the design of the superstructure.

Thermal movements of a cast-in-place concrete superstructure are similar to those of a precast, prestressed concrete superstructure. However, creep and shrinkage movements are considerably greater for cast-in-place than for precast superstructures. For these reasons, shrinkage and creep movements of precast, prestressed concrete superstructures are frequently ignored for structures of moderate length. However for longer spans the differential shrinkage between the cast-in-place slab and the precast girder in addition to creep and thermal effects should be considered.

Even though thermal movements in precast, prestressed members are minimal, restraint forces in the superstructure will be present. Flexible jointless abutments and semi-rigid or flexible piers are used to minimize the restraint forces in jointless bridges.

JOINTLESS JOISTLESS BRIDGES

Jointless bridges consist of superstructures, abutments, intermediate piers, and foundations. The design of jointless bridges is generally similar to that of conventional bridge design. Special analysis and design considerations required for jointless bridges are primarily associated with the need to accommodate volumetric changes in the structure, such as thermal movements.

Jointless bridges accommodate superstructure movements without conventional expansion joints. The superstructure is rigidly or semi-rigidly connected to the abutments. Approach slabs, connected to the abutment and/or deck slab with reinforcement, move with the superstructure. Generally, at its junction with the approach pavement, the approach slab is supported by a sleeper slab or grade beam. The superstructure movement here is accommodated using flexible pavement joints.

Jointless construction is well-suited to both single- and multiple-span bridges. For single-span bridges, stability is provided by passive pressure behind the backwall and for multiple-span bridges, intermediate piers contribute to the bridge's stability. Jointless bridges could be founded on piles or shafts or spread footings on soil if the soil is well compacted and the possibility of settlement of the foundation is considered in the design as shown in Figure 1.

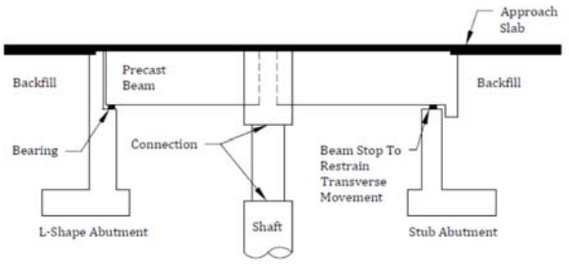


Figure 1. Continuous Jointless Bridge

BENEFITS OF JOINTLESS BRIDGES

Jointless bridges provide substantial reserve capacity to resist potentially damaging overloads by distributing loads along the continuous and full-depth diaphragm at bridge ends. The close tolerances required when utilizing expansion bearings and bridge seats need to conform to girder flange slope and camber corrections, since the girder loads are ultimately carried by the concrete comprising the end diaphragm.

For normal expansion bearing conditions, the ratio of the end-span to the adjacent interior- span length must be held to approximately 0.6, unless uplift conditions are to be accommodated. If uplift can occur, expensive hold-down devices must be added to expansion bearings. Utilizing jointless abutments allows for much shorter end spans, if desired, since the abutment acts as a counterweight and the uplift capacity of the piling maybe used.

Continuity in bridge superstructure provides added redundancy and capacity for all types of catastrophic events. In designing for seismic events, considerable material reductions can be achieved through the use of continuity by negating the need for enlarged seat widths and restrainers. Further, the use of jointless abutments eliminates loss of girder support; the most common cause of damage to bridges in seismic events. Joints introduce a potential collapse mechanism into the overall bridge structure. Jointless abutments have consistently performed well in actual seismic events and have significantly reduced or avoided problems of backwall and bearing damage that are associated with seat-type jointed abutments. The dampening arising from soil-abutment interaction has been proven to significantly reduce the lateral loads taken by intermediate substructure columns and footings. The following limitations may be considered in use of jointless bridges:

1. Limitations on length are concerned with passive pressure effects, stresses in the piles, and the movement capacity of the joint between the approach slab and the approach pavement. Many state departments of transportation limit lengths to 100 m for steel superstructures and 200 m for prestressed concrete superstructures. A few states, like Washington, have successfully used longer lengths.
2. Skew angles have generally been below 45 deg. However some states have used this method of construction extensively and effectively for curved bridges as well as bridges with skew angles up to 75 deg.
3. Jointless bridges require end diaphragms to be supported on flexible foundation types and bearings

DESIGN REQUIREMENT FOR JOINTLESS BRIDGES IN SEISMIC REGIONS

The AASHTO Guide Specifications for LRFD Bridge Seismic Design (LRFD SGS) is a displacement-based requiring bridge to be design with adequate displacement capacity to accommodate earthquake demands. The displacement capacity of bridges is checked using a displacement-based procedure, especially for those bridges located in regions of high seismic risk. The force-based methodology of the LRFD Specifications has also been used in some states with lower seismic demand.

The overall objective of the performance criteria is life safety during a 1,000-year seismic event. Bridges have a low probability of collapse but may suffer significant damage and significant disruption to service. Partial or complete replacement may be required." In a major event, offsets, cracking, reinforcement yielding, and major spalling of concrete are expected. While the 1,000-year return period is judged as applicable to most bridges, higher levels of performance may be required by the bridge owner, as in the case of "critical" or "essential" bridges that provide life safety transportation, bridges that are essential to the economy, or bridges required for local emergency plans. Site- or project-specific design criteria are generally developed for such projects.

The LRFD SGS does not explicitly address the jointless precast, pretensioned or post-tensioned elements. The precast beams made continuous for live loads must have beam–to–beam or beam–to–cap connections that can be expected to remain undamaged during the 1,000-year seismic event. Opening and closing of the bottom flange-to-flange or flange-to-cap joint connection is not permitted.

In the force-based analysis method, a linear elastic multi-modal response spectrum analysis is performed and the force effects in various bridge or structure components are determined. Equivalent static analysis of lateral loads based on a percentage of the dead load is also permitted by some agencies. The capacities of the components are evaluated and the component demand/capacity (D/C) ratios are then calculated. A particular component is said to have adequate capacity if its D/C ratio is less than the permissible force reduction factor, R, for that component.

Pushover analysis addresses typical sources of material nonlinearity as well as geometric nonlinearity. Material nonlinearity includes soil, concrete, soil-structure interaction, and yielding of the reinforcement. Geometric nonlinearity refers to the P-Δ effect. The bridge frame is pushed laterally along both its longitudinal and transverse directions until the target displacement is obtained.

The analysis is incrementally linearly elastic and captures the overall nonlinear behavior of the elements, including soil effects, by pushing the frame laterally to initiate plastic action. Each increment pushes the frame until a plastic hinge forms, and redefines the structural system after each hinge forms until the potential collapse mechanism is achieved.

ABUTMENT TYPES FO R JOINTLESS BRIDGES

The beginning or ending substructure element of a bridge is commonly referred to as an abutment or end bent. There are numerous variations that are used in further describing these units, such as bench-type, spill-through, stub, deep, etc. For consistency within this report, these units will be collectively referred to as abutments, with only minimal added description of their variation in type.

In jointless bridges, the ends of the girders are fixed to the abutments and expansion joints are eliminated at these supports. With the expansion joints eliminated, forces are induced in the substructure due to resistance to thermal movement and to creep and shrinkage that have to be considered in the design of jointless abutments.

While jointless abutments have been used successfully for 50 years, their implementation has not been an exact science, but rather a matter of intuition, experimentation and observation. Inspection of many bridges with failed expansion bearings has revealed that anticipated catastrophic damage has not always occurred.

The most common technique used in foundation design is the p-y method. Using this procedure, pile response is obtained by an interactive solution of differential equations using finite-difference techniques. The soil response is described by a family of non-linear curves (p-y curves) that compute soil resistance p as a function of pile deflection y.

APPROACH SLABS AND BACKFILL

Due to the difficulties in obtaining proper embankment and backfill compaction around abutments, approach slabs are recommended; especially for new construction. Approach slabs offer many benefits other than acting as a bridge between the abutment and more densely compacted embankments. Approach slabs provide a transition from the pavement to the bridge if embankment settlement occurs. Such transitions provide a smooth ride while reducing impact loads to the bridge. Approach slabs also provide greater load distribution at bridge ends, which aids in reducing damage to the abutments; especially from overweight vehicles. Finally, properly detailed approach slabs help control roadway drainage, thus preventing erosion of the abutment backfill or freeze/thaw damage resulting from saturated backfill.

The approach slab must be anchored into the abutment backwall so that it moves in concert with the bridge. Otherwise, cyclic expansions will force the slab to move with the bridge without a mechanism to pull it back when the bridge contracts. As debris fills the resulting opening, repeated cycles will ratchet the slab off its support. The anchorage used to fasten the approach slab should be detailed to act as hinge so that the slab can rotate downward without distress as the embankment settles.

Where the anticipated total movement at an abutment exceeds 12 mm and the approach roadway is asphalt, an expansion joint at the pavement should be considered. The reason for the latter is that larger movements can damage asphalt adjacent to the end of the approach pavement in the expansion cycle. During the contraction phase, a significant gap is created through which water can infiltrate the subgrade. If regular maintenance can be arranged to fill this gap with a suitable joint sealer in cold weather, no joint will be needed.

If expansion joints are provided, the joints should only be located at the roadway end of the approach slab. It is a certainty that the joint system will fail at some future time. If the joint is located between the abutment backwall and the approach pavement, then the slab jacking process mentioned above will occur.

Approach slabs have been found to be one of the most critical components of a jointless bridge. The approach slabs serve two primary purposes:

1. Approach slabs reduce the compaction of the backfill material behind the backwall due to traffic. Control of excessive passive soil resistance to thermal expansion is also achieved.
2. The thermal movements of the system are transferred from the end of the bridge to the point where the approach slab joins the roadway pavement. A flexible pavement joint is provided at this point. In addition, some agencies use plastic sheets or expanded polystyrene boards below the approach slab to provide a positive separation from the subgrade to enhance movement.

SEISMIC DESIGN OF INTEGRAL ABUTMENTS

The participation of abutment walls in providing resistance to seismically induced inertial loads may be considered in the seismic design of bridges either to reduce column sizes or reduce the ductility demand on the columns. Damage to backwall and wingwalls during earthquakes may be considered acceptable when considering no

collapse criteria, provided that unseating or other damage to the superstructure does not occur. The capacity of the abutments to resist the bridge inertial loads shall be compatible with the soil resistance that can be reliably mobilized, the structural design of the abutment wall, and whether the wall is permitted to be damaged by the design earthquake. The lateral load capacity of walls shall be evaluated on the basis of a rational passive earth-pressure theory.

Under earthquake loading, the earth pressure action on abutment walls changes from a static condition to one of two possible conditions:

- The dynamic active pressure condition as the wall moves away from the backfill, or
- The passive pressure condition as the inertial load of the bridge pushes the wall into the backfill.

The governing earth pressure condition depends on the magnitude of seismically induced movement of the abutment walls, the bridge superstructure, and the bridge abutment configuration. The semi integral abutment and corresponding loading diagram is shown in Figure 2.

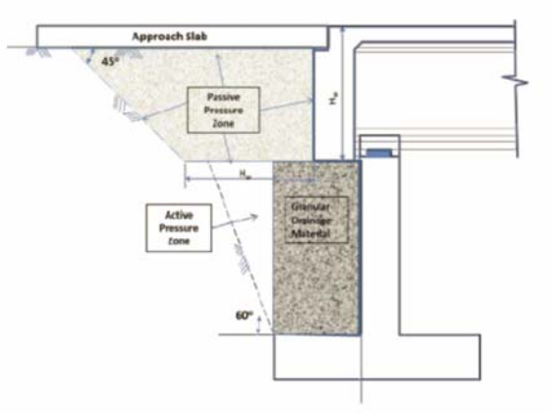


Figure 2. Semi Integral Abutment and Corresponding Loading Diagram

Abutment resistance shall be limited to 70% of the value obtained using the procedure given in the AASHTO SGS. Abutment stiffness, K_{eff}, and passive capacity, P_p, should be characterized by a bilinear or other higher order nonlinear relationship. When the motion of the back wall is primarily translation, passive pressures may be assumed uniformly distributed over the height.

Jointless short span bridges could also be supported by a geosynthetic wall and SE wall. These bridges shall conform to the following requirements:

1. Walls shall be 10 m or less in total height, which includes the retained soil height up to the bottom of the embedded spread footing.
2. For structural earth walls, the front edge of the bridge footing shall be placed 1.2 m. minimum from the back face of the fascia panel. For geosynthetic retaining walls with a wrapped face, the front edge of the bridge footing shall be placed 610 mm minimum from the back face of the fascia panel.
3. The abutment footing shall be covered by at least 150 mm of soil for frost protection.
4. The superstructure of continuous span bridges shall be designed for differential settlement between piers.

ABUTMENT CONNECTION FOR PRECAST JOINTLESS BRIDGES

The typical abutment in regions of moderate and high seismic hazard is a cast-in-place concrete pier wall supported on spread footings, piles, or shaft foundations. Precast beams are often supported on elastomeric bearing pads at end piers. Semi-jointless end diaphragms may be used for shorter bridges. The bearing system is designed for the service load condition but may not be adequate to resist seismic loading. The bearings are designed to be accessible so that the superstructure can be lifted and the bearings replaced after a major seismic event. Approach slabs rest on a notch provided at the superstructure end, thereby providing a ramp up

to and on to the bridge, should soil behind the abutment settle during a seismic event.

This type of end diaphragm eliminates the need for expansion joints at end piers. The gap between the end pier wall and the end diaphragm is designed to be greater than the longitudinal seismic movement requirement for the extreme event limit state, and thermal expansions at the service limit state for bridge lengths less than 150 m.

The minimum displacement requirements at the expansion bearing should accommodate the greater of the maximum displacement calculated from a displacement analysis or a percentage of the empirical seat width, N, specified in Equation 1.

$$N = (8 + 0.02L + 0.08H)(1 + 0.000125S2) \quad (1)$$

where

N = minimum support length

L = bridge length to the adjacent expansion joint, or to the end of the bridge

H = average height of abutment wall supporting the superstructure

S = skew angle of the support measured normal to span, degrees

For SDC D, the beam bearing support length, N, must accommodate the relative longitudinal earthquake displacement demand at the supports or at a hinge within a span between two frames. That length is determined as:

$$N = (4+1.65\Delta_{eq})(1+0.00025S2) \geq 610 \text{ mm} \quad (2)$$

The hinge seat length in "well-balanced frames" (adjacent frames for which the ratio of the natural periods is equal to or greater than 0.7) to be evaluated as follows:

$$N = \Delta_{p/s} + \Delta_{cr+sh} + \Delta temp + \Delta_{eq} + 100 \text{ mm} \quad (3)$$

Where:

Δ_{eq} = relative earthquake loading longitudinal displacement demand

$\Delta_{p/s}$ = displacement due to prestressing

Δ_{cr+sh} = displacement due to creep and shrinkage

Δ_{temp} = displacement due to temperature effects

ABUTMENT LONGITUDINAL RESPONSE FOR SDCS

Abutments designed for bridges in SDC B or C are expected to resist earthquake loads with minimal damage. For seat-type abutments, minimal abutment movement could be expected under dynamic passive pressure conditions. However, bridge superstructure displacement demands may be 100 mm. or more and could potentially increase the soil mobilization.

For SDC D, passive pressure resistance in soils behind jointless abutment walls and backwalls for seat abutments will usually be mobilized because of the large longitudinal superstructure displacements associated with the inertial loads. Two alternatives may be considered:

- Case 1: Earthquake-Resisting System (ERS) without Abutment Contribution. The bridge ERS shall be designed to resist all seismic loads without any contribution from abutments. Abutments may contribute to limiting displacement, providing additional capacity and better performance that is not directly accounted for in the analytical model.
- Case 2: Earthquake-Resisting System (ERS) with Abutment Contribution. In this case, the

bridge shall be designed with the abutments as a key element of the ERS.

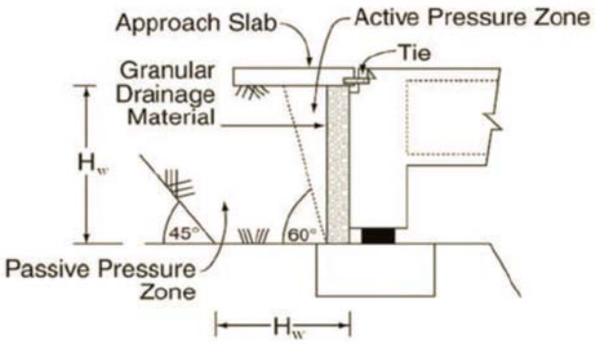


Figure 3. Abutment Stiffness and Passive Pressure

CALCULATION OF BEST ESTIMATE PASSIVE PRESSURE

If the strength characteristics of compacted or natural soils in the "passive pressure zone" are known, then the passive force for a given height, Hw, may be computed using accepted analysis procedures. These procedures should account for the interface friction between the wall and the soil. Therefore, the properties of backfill that is only placed adjacent to the wall in the active pressure zone may not be appropriate as a weaker failure surface can develop in the embankment.

Abutment stiffness, Keff and passive capacity, Pp should be characterized by a bilinear or other higher order nonlinear relationship as shown in Figure 4.

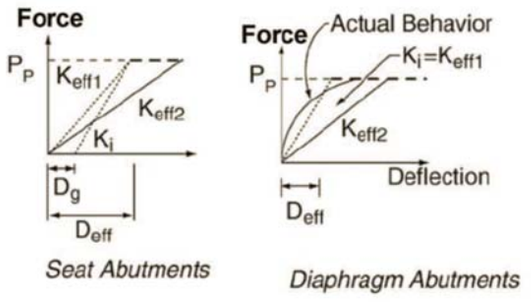


Figure 4. Characterization of Abutment Capacity and Stiffness

An equivalent linear secant stiffness, K_{eff} is required for analyses. For jointless- or diaphragm-type abutments, an initial secant stiffness may be determined as follows:

$$K_{eff1} = \frac{P_p}{(F_w H_w)} \quad (1)$$

If computed abutment forces exceed the soil capacity, the stiffness should be softened iteratively (K_{eff1} to K_{eff2}) until abutment displacements are consistent (within 30 percent) with the assumed stiffness. For seat-type abutments, the expansion gap should be included in the initial estimate of the secant stiffness.

$$K_{eff1} = \frac{P_p}{(F_w H_w + D_g)} \quad (2)$$

where:

P_p = passive lateral earth pressure capacity

H_w = height of backwall

F_w = factor between 0.01 to 0.05 for soils ranging from dense sand to compacted clays

D_g = width of gap between backwall and superstructure

REFERENCES

1. AASHTO LRFD Bridge Design Specifications 7th edition, 2014. Washington, DC.
2. AASHTO. 2009. AASHTO Guide Specifications for LRFD Seismic Bridge Design. Washington, DC
3. WSDOT Bridge Design Manual. Publication no. M23-50. Olympia, Washington.

Maintenance, Safety, Risk, Management and Life-Cycle Performance of Bridges – Powers, Frangopol, Al-Mahaidi & Caprani (Eds)
© 2018 Taylor & Francis Group, London, ISBN 978-1-138-73045-8

Fatigue strength improvement of welded joints using SBHS700 by applying ICR treatment.

Y. Ono & K. Kinoshita
Department of civil engineering in Gifu University, Gifu, Japan

ABSTRACT: In the background of requirements to weight reduction and cost saving, the application of high strength steels in steel bridges has been investigated. However, SBHS700 of 780MPa class steels must particularly grasp with respects to fatigue strength of welded joints. In this study, in order to clarify effects of the fatigue strength improvement by ICR (Impact crack retrofit closure) treatment for SBHS700, fatigue tests continuously carried out using small fatigue specimens of out of plane gusset welded joints, which were removed from a girder specimen of a previous study by gas fusion cutting. Before fatigue tests, compressive residual stress is confirmed with the x-ray diffraction method. The test results indicate that the fatigue strength improvement effects on welded joints treated by ICR treatment was at least 3 classes larger in case of using SBHS700. However, the fatigue strength of one specimen is lower than that of another specimen. Therefore, this paper also presents the result evaluated by using the control method of fatigue strength improvement based on the shape of the deformation area after ICR and the crack initiation can be identified based on the observation for a fractured surface using Scanning Electron Microscope (SEM).

1 INTRODUCTION

The application of high strength steels for steel bridges is one of the most effective approaches on weight reduction and cost saving of production and transport [Gunther. 2005, Konishi et al. 2007 & Miki et al. 2013]. Especially, steels for bridge high performance structures (SBHS) developed newly in Japan have been focused on the application because there is a large number of popularity due to beneficial qualities such as its higher strength, good weldability, and significantly improved fracture toughness. However, the fatigue strength of welded joints dose not generally depend on the tensile strength [Anami et al. 2000]. Therefore, in order to apply high strength steels to steel bridges efficiently, the fatigue strength of welded joints using high strength steels should be improved.

From the background, recent studies [Hanji et al. 2017 & Mori et al. 2010] have showed that the fatigue strength improvement effect such as grinding and peening treatment at the weld toe tends to depend on the steel strength. Therefore, it is necessary to grasp fatigue strength improvement effects on welded joints using SBHS especially for SBHS700 that has over 700 MPa yield strength and higher fatigue strength effect is expected.

In the previous study [Hanji et al. 2014], in order to clarify effects of fatigue strength improvement methods, the fatigue test of a girder specimen using SBHS700 was carried out. Various fatigue strength improvement methods, which can improve the weld toe shape and introduce compressive residual stress, were used on out-of-plane gusset welded joints on the girder specimen and the fatigue test result show fatigue strength improvement of the welded joints. However, the previous study does not quantitatively show the fatigue strength improvement because these improved out-of-plane gusset welded joints have not failed.

In this study, following the previous study [Hanji et al. 2014], in order to clarify the effects, fatigue tests are continuously carried out using small fatigue specimens of out-of-plane gusset welded joints, which were removed from the girder specimen by gas fusion cutting. Before fatigue tests, residual stress in the vicinity of the weld toe was measured by the x-ray diffraction method and compared with previous studies. The target results of this study are ICR (Impact crack retrofit closure) treatment which is one of the peening techniques. This technique has been originally developed for the fatigue life extension by closing the fatigue crack opening [Ishikawa et al. 2010 & Yamada et al. 2015]. The ICR treatment of this study was performed to the base metal besides the weld toe to introduce compressive residual stress, which is proposed by previous studies [Nakano et al. 2015 & Nakanishi et al. 2015]. They showed that the fatigue strength improvement effect could be simply controlled by measuring the deformation area of ICR treatment and the distance between the weld toe and

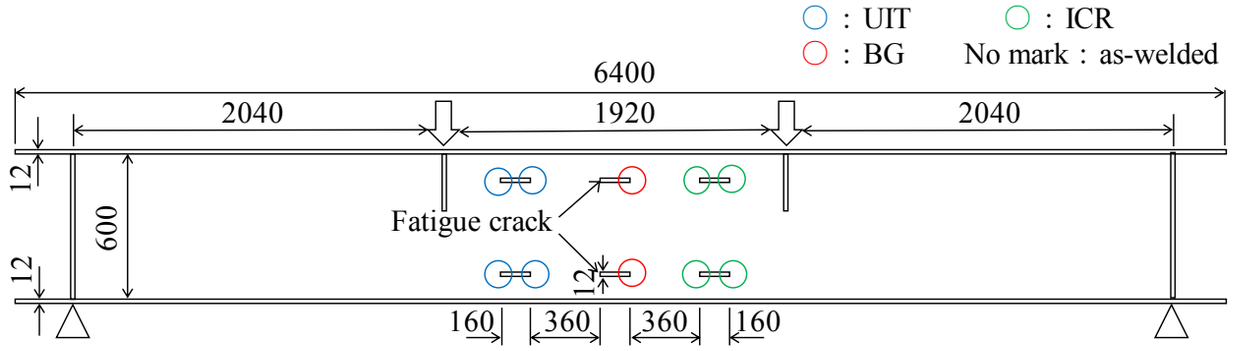


Figure 1. I-shape girder specimen of SBHS700 (unit: mm) [Hanji et al. 2014]

Table 1. Mechanical properties of SBHS700 [Hanji et al. 2014]

Type of steel	Yield stress (N/mm^2)	Tensile strength (N/mm^2)	Elongation (%)	Thickness (mm)
SBHS700	823	846	24	12

Table 2. Chemical compositions of SBHS700 (unit: %) [Hanji et al. 2014]

Type of steel	C	Si	Mn	P	S	Cu	Ni	Cr	Mo	V	B	Pcm
SBHS700	0.06	0.25	1.37	0.004	0.002	0.98	0.98	0.34	0.3	0.04	0.0003	0.24

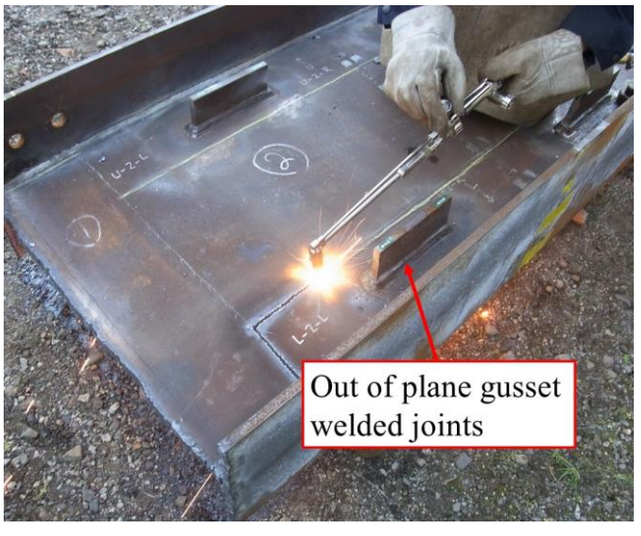


Figure 2. Gas fusion cutting to the girder specimen

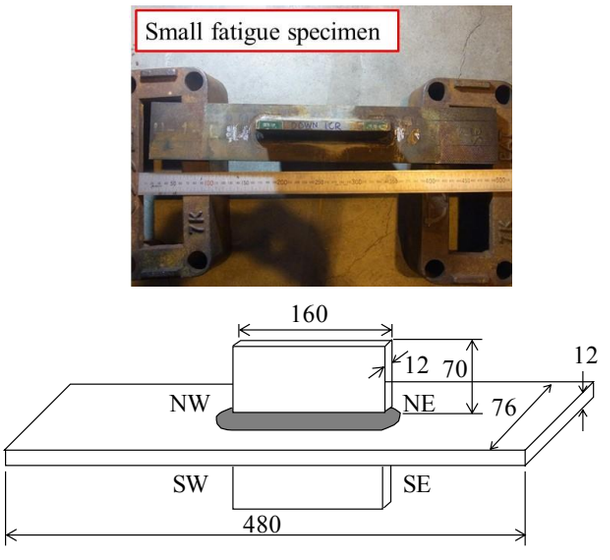


Figure 3. Small fatigue specimen (unit: mm)

the ICR treatment edge. Therefore, these deformation area and distance were measured and fatigue test results were evaluated judging from these factors. In this study, as additional investigation, the crack initiation was identified for the fractured surface with Scanning Electron Microscope (SEM).

2 FATIGUE TEST SPECIMEN

2.1 *Girder specimen of previous study*

Figure 1 shows the SBHS700 I girder specimen. The I girder was 6400 mm long and had a web that was 600 mm wide by 12 mm thick, and flanges that were 300 mm wide by 12 mm thick. A set of six 160 mm*70 mm*12 mm plates were welded 80 mm from the top and the bottom of the web, evenly spaced at 360 mm apart on both sides of the webs as well. According to the previous study, preheating of 50 ℃ was applied to the base metal, and the YM-80C (JIS Z 3312) electrode was used in a CO_2 type of welding. A full penetration welding process was carried out. The weld toe profiles were used by three types of fatigue strength improvement methods, which are BG (Burr Grinding), UIT (Ultrasonic Impact Treatment) and ICR. In the girder specimen, the nominal stress

was constant of 100 N/mm^2 on each gusset and the stress ratio was 0.1. The fatigue test was finished at approximately 1.5 million cycles because both of as-welded gussets failed. Table 1-2 show the mechanical properties and the chemical compositions of SBHS700, respectively.

2.2 *Small fatigue test specimen*

Figure 2 shows condition of gas fusion cutting to the girder specimen. In order to remove out of plane gusset welded joints from the original I girder specimen of SBHS700, gas fusion cutting was utilized. After removing the welded joints from the girder specimen, small fatigue specimens were formed with the wire electric discharge machining device because the gas fusion left the edges of the specimen uneven. Figure 3 shows the geometry and the dimension of small fatigue specimen. In this study, two ICR specimens were named ICR-1, ICR-2, respectively. Each weld toe was named NE, NW, SE, SW.

3 MEASUREMENT RESIDUAL STRESS

3.1 *Measurement condition*

Before fatigue tests, the residual stress was measured in order to confirm how much compressive residual stress was left in the vicinity of the weld toe because there was a fear that it was released in gas fusion cutting to the girder specimen and during forming to small specimens. Figure 4 shows device of measurement residual stress. This is Portable X-ray Residual Stress Analyzer called u-X360s of Pulstec Industrial Co., Ltd. The measurement method was cos α using the Kα radiation of chromium and the collimator size was Φ2 mm. Figure 5 shows the measurement point and direction of residual stress. Residual stress was measured 2 mm away from the treatment edge directly in the center of gusset, 38 mm from either side of the gusset. This was decided in order to compare with results of the previous study that Hanji et al. 2017 had already measured residual stresses of ICR treatment at the same point for out-of-plane gusset welded joints using SBHS700. The measurement was conducted along the longitudinal direction (y-axis) on all four sides of the gusset.

3.2 *Measurement result*

Figure 6 shows the results of measurement residual stress. In this figure, results of previous study and average of each result are also indicated. Compressive residual stresses of previous results are from -420 to -480 MPa. From results of ICR-1 and ICR-2, compressive residual stresses are entirely about from -240 MPa to -600 MPa, indicating that some are about as

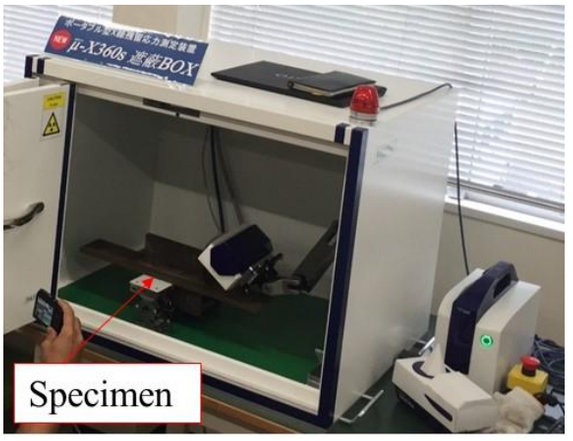


Figure 4. Device of measurement residual stress

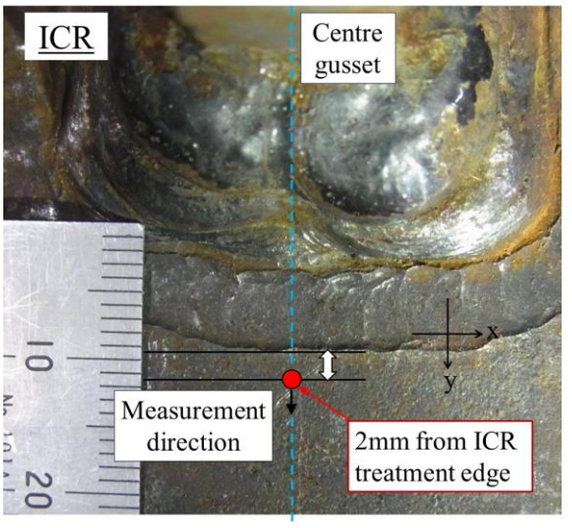


Figure 5. Measurement point and direction of residual stress

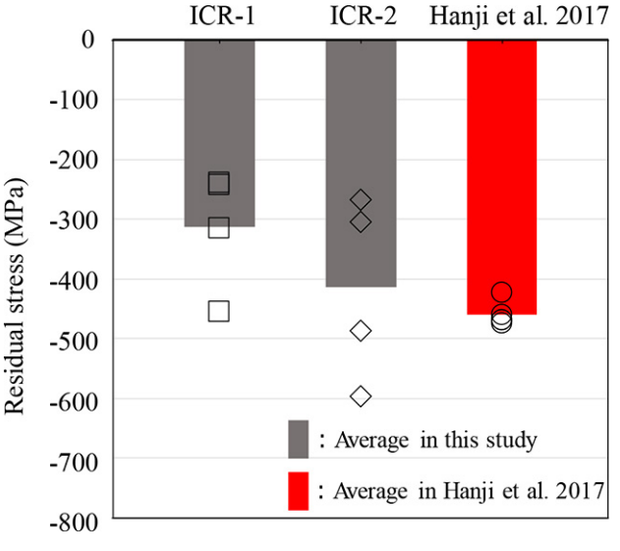


Figure 6. Result of measurement residual stress

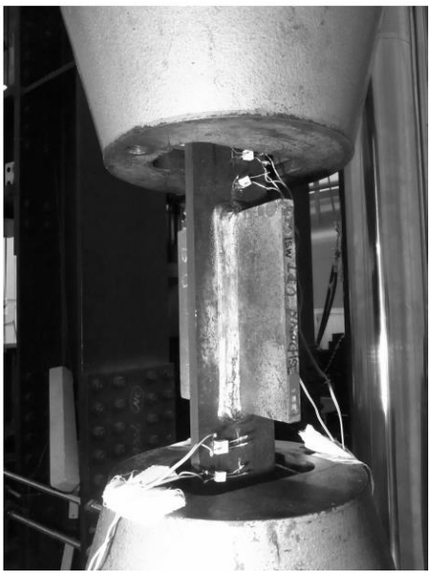


Figure 7. Fatigue test setup

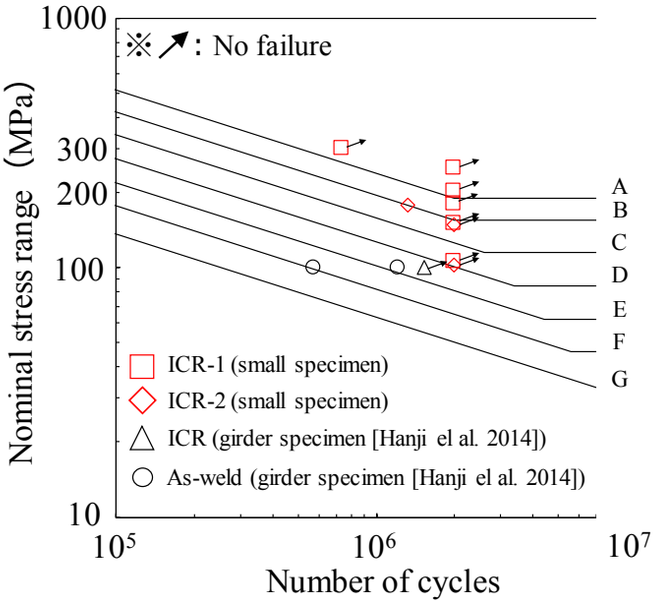


Figure 8. Fatigue test result (S-N curve)

Table 3. Fatigue test result

Specimen	Weld toe condition	Nominal stress range (MPa)	Number of cycles	Note
Girder specimen in Hanji et al. 2014	As-weld	100	575000	
		100	1206000	
	ICR-1	100	>1520000	Fatigue test finished
	ICR-2	100	>1520000	
Small specimen in this study	ICR-1	106	>2000000	
		150	>2000000	
		180	>2000000	
		201	>2000000	
		250	>2000000	
		298	>740310	Crack from base metal Fatigue test finished
	ICR-2	102	>2000000	
		149	>2000000	
		178	1326750	Crack from weld toe

> means no failure

much as and others are at most 50 % lower than that of previous study. As a result, it can be seen that compressive residual stresses at 2 mm from treatment edge of ICR have reserved at least more than half of results in previous study although there might be influence of removing from the girder specimen or forming to small specimen.

4 FATIGUE TEST

4.1 *Test condition*

Figure 7 shows the fatigue test setup. The fatigue tests were performed at room temperature and moisture with a 200 kN material fatigue machine. The specimen experienced an axial tension test and a constant amplitude sine wave, 10 Hz frequency. The stress ratio was approximately 0. Strain gauges were placed on 2 mm and 30 mm from the treatment edge in the center of the gusset. The 2 mm location, which residual stress was measured, was intentionally used to monitor the transition of residual stress and the initiation of a fatigue crack. The 30 mm location was used for the calculation of nominal stress. These locations were repeated for all four sides of gusset specimen. Besides fatigue tests under constant stress range, the beach-mark test was also carried out. During fatigue tests, the stress range was reduced to one half periodically in order to leave beach marks on the fracture surface. First of all, nominal stress range was

100 MPa under the same condition as the fatigue test of the girder specimen. If the fatigue crack did not appear after 2 million cycles, the fatigue test was continued after increasing the nominal stress range.

4.2 *Fatigue test results*

Figure 8 shows the fatigue test results, which are the relationship between the nominal stress range and the number of cycles for ICR-1 and ICR-2. In this figure, the results of the girder specimen [Hanji et al. 2014] and the fatigue design curve proposed by Japanese Society of Steel Structure [JSSC. 2012] are also indicated. Arrow marks mean that there is no fatigue crack within 2 million cycles at each test condition. Detailed fatigue test results such as the nominal stress range and the number of cycles of each specimen are presented in Table 3.

At first, while ICR-1 and ICR-2 were continuously tested under the nominal stress range 100 MPa which was the same condition as the girder specimen, these specimens reached 2 million cycles and the fatigue cracks were not initiated. Therefore, the fatigue strength improvement effect is confirmed as well as the effect of previous study [Hanji et al. 2014].

At second, from the result of ICR-1, in spite of increasing nominal stress range such as 150, 180, 200, 250 MPa, the fatigue cracks were not initiated. The JSSC fatigue strength raises up to A class, and becomes higher than that of As-weld in previous results classifying E and F class. As a result, the fatigue strength of ICR-1 can be greatly improved from 4 to 5 classes, from which could illustrate larger fatigue strength improvement effect in comparison with results of the girder specimen treated by ICR. Eventually, the fatigue crack from base metal in the nominal stress range 300 MPa was initiated, and then the fatigue tests was finished. On the other hand, from the result of ICR-2, when the nominal stress range was increased to 180 MPa, the fatigue crack was initiated. Although the JSSC fatigue strength raises up to B class and improves from 3 to 4 classes, the fatigue strength is lower than that of ICR-1. As a result, it can be shown that fatigue strength improvement effect is larger than that shown in the previous girder specimen even after reforming to small specimens.

Therefore, it is confirmed that the fatigue strength improvement effects on welded joints treated by ICR is at least 3 classes larger in case of using SBHS700 as long as the fatigue test results in this study, whose effects correspond to those in recent studies [Hanji et al. 2017 & Mori et al. 2010].

5 EVALUATION FATIGUE TEST RESULT

Nakano et al. 2015 and Nakanishi et al. 2015 have investigated the fatigue strength of welded joints peened on base metal besides the weld toe using ICR, and they proposed standards of fatigue strength improvement which ensures at least 2 classes larger in case that SM490Y class steels are used and the nominal stress range is under 250 MPa. The standards are based on the configuration of deformation area of ICR treatment and the distance between weld toe and ICR treatment edge, which is the simple and practical quality control. Figure 9 shows shape of specimen around the weld toe treated by ICR. In order to get the deformation area of ICR, silicon like dental impression material is pressed on the treatment area and is cut to the interval of 1 mm thickness, and then the deformation area is measured on the image of these silicon. The distance between weld toe and treatment edge is measured on the image of the surface of specimen. In this paragraph, it is confirmed that whether specimens satisfied with the standards of fatigue strength improvement, or not.

5.1 *Deformation area of ICR*

Figure 10 shows the relationship between the residual stress and the deformation area. In this figure, results of previous study [Nakanishi et al. 2015] using SM490Y class steels are also indicated. The standards of deformation area is that Average depth × width is over 0.7 mm^2 or Maximum depth × width is over 1.0 mm^2. Width is the minimum value out of measurement results. The residual stress on 10 mm away from the weld toe is used in the previous study. Note that this study measured residual stress on 2 mm away from treatment edge but on approximately 10 mm away from weld toe, as shown in Figure 5. Detailed residual stress and shape of deformation area is displayed in Table 4.

From this figure, all results are content with the standard of deformation area regardless of using average or maximum depth. The residual stress of from -200 to -300 MPa is plotted below the line of previous results. On the other hand, the residual stress of from -450 to -600 MPa is plotted above the line, from which implicates that these residual stresses without influence of removing from the girder specimen or forming to small specimen depends on the steel strength because the results are greatly over the line of SM490Y class steels. Therefore, it can be said that the deformation area of ICR-1 and ICR-2 fulfills the standard of fatigue strength improvement although some residual stresses are lower than that of previous study. Incidentally, it can be understood that the residual stress of the weld toe SW where the fatigue crack initiated is plotted above the line of previous study.

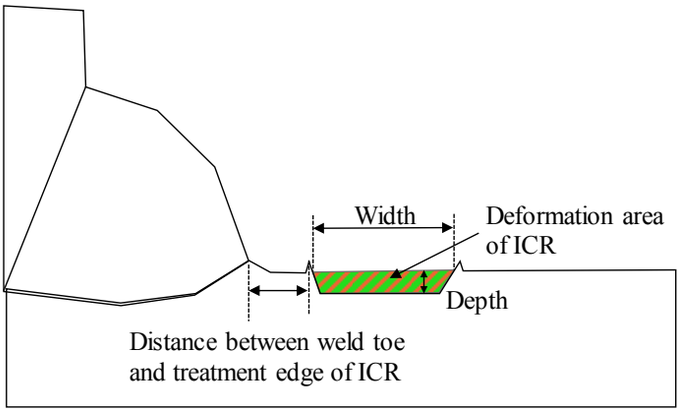


Figure 9. Shape of specimen around weld toe treated by ICR

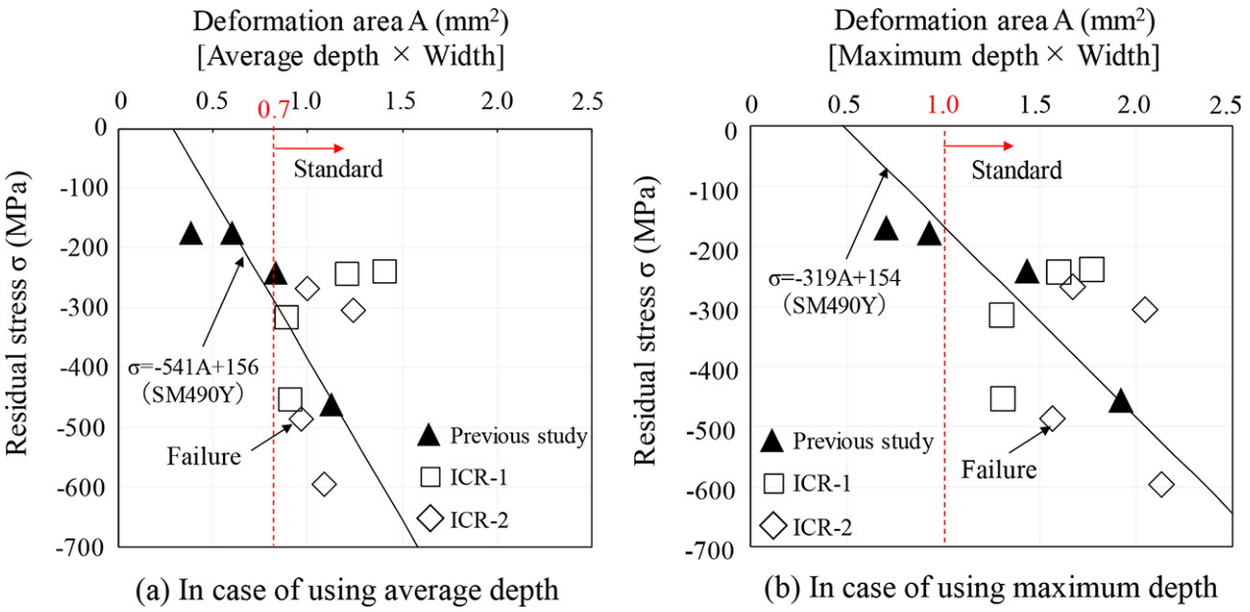


Figure 10. Relationship between residual stress and defamation area

Table 4. Residual stress and shape of treatment area

Specimen	Weld toe	Residual stress (MPa)	Minimum width (mm)	Average depth (mm)	Maximum depth (mm)	Deformation area =Average depth × Width (mm^2)	Deformation area =Maximum depth × Width (mm^2)
ICR-1	NE	-454	4.1	0.22	0.32	0.9 (>0.7)	1.3 (>1.0)
	NW	-243	4.7	0.24	0.32	1.1 (>0.7)	1.5 (>1.0)
	SE	-316	4.7	0.17	0.26	0.8 (>0.7)	1.2 (>1.0)
	SW	-239	3.6	0.27	0.34	1.0 (>0.7)	1.2 (>1.0)
ICR-2	NE	-268	3.8	0.26	0.39	1.0 (>0.7)	1.5 (>1.0)
	NW	-596	3.7	0.30	0.46	1.1 (>0.7)	1.7 (>1.0)
	SE	-305	4.5	0.28	0.38	1.2 (>0.7)	1.7 (>1.0)
	SW	-486	4.0	0.24	0.32	1.3 (>0.7)	1.3 (>1.0)

5.2 *Distance between weld toe and treatment edge*

Figure 11 shows the distance between the weld toe and treatment edge. The standard of the distance is under 2 mm. The distance of each weld toe for ICR-1 is under 2 mm. On the other hand, the distance of the weld toe SW where the fatigue crack initiated for ICR-2 is over 2 mm. Figure 12 shows the failure surface of weld toe SW. It was observed that the fatigue crack initiated at the weld toe. The specimens of this study have a space between the weld toe and the treatment edge, whose space may be formed because welding from both sides is contacted there.

In order to clarify the crack initiation, the observation of fractured surface was conducted using SEM. The result of the observation around crack initiation is indicated in Figure 13. There are some beach marks left on fractured surface, which the crack initiation can be predicted. Expanding the crack initiation area with SEM, it was identified due to finding the radial trail which the fatigue crack propagated. As a result, the crack initiation corresponded to the weld toe which is away the maximum distance 2.1 mm

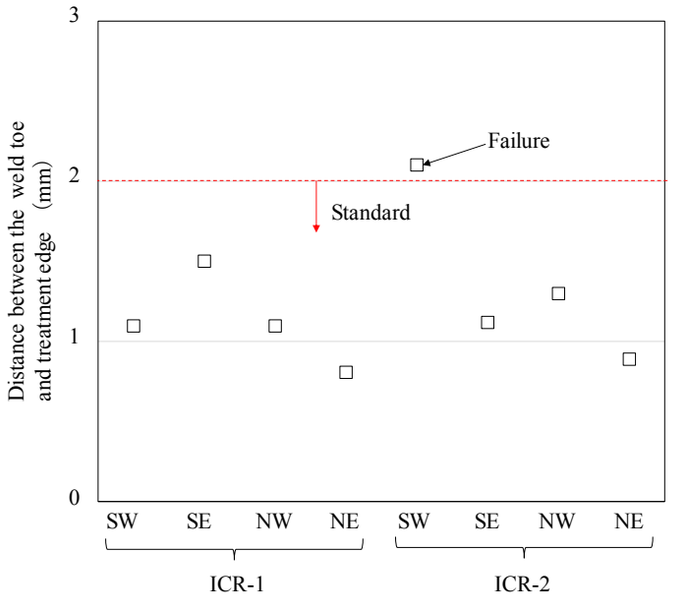


Figure 11. Distance between weld toe and treatment edge

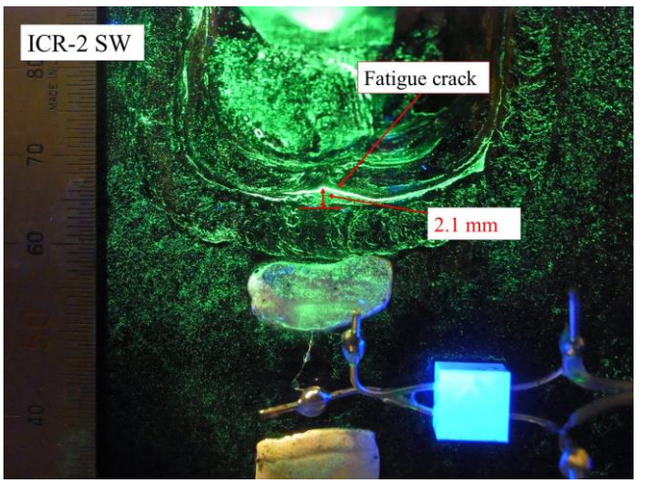


Figure 12. Failure surface of weld toe SW for ICR-2

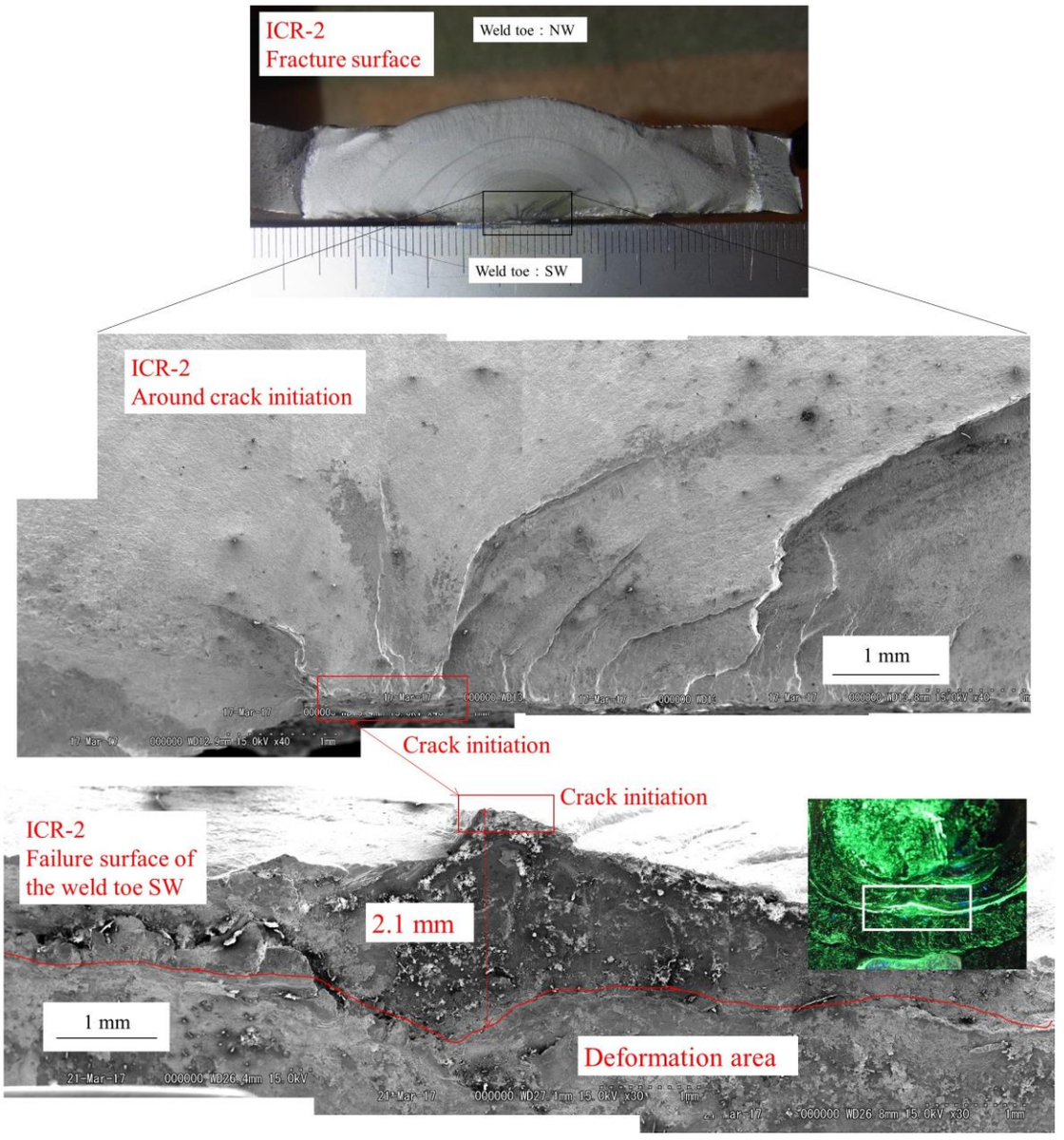


Figure 13. Result of observation for fractured surface around crack initiation

from the treatment edge. Therefore, it can be said that the fatigue strength of ICR-2 was lower than that of ICR-1 because the distance between the weld toe and the treatment edge is over 2 mm, which is the same result that the effect of ICR treatment decreases when the distance is over 2 mm in the previous study.

CONCULUSION

In order to clarify quantitatively the fatigue strength improvement effect on out-of-plane gussets welded joints, these gussets were removed from the previous girder specimen of SBHS700 and the continuous fatigue test was conducted. Before the fatigue test, compressive residual stress was measured and compared with the previous study [Hanji et al. 2017]. In addition, fatigue strength improvement effect was evaluated based on the measurement of the depression shape after ICR as shown in previous studies [Nakano et al. 2015 & Nakanishi et al. 2015]. The observation of crack initiation using SEM was conducted. The conclusions of this study are described as follows.

1 From the measurement of residual stress, compressive residual stress for small fatigue specimens was kept by over one half of that in a previous study even after removing from the girder specimen to gas fusion cutting and reforming to the small specimen.
2 From the fatigue test results, the fatigue strength improvement effect of welded joints treated by ICR is greatly higher. However, the fatigue strength of ICR-2 specimen was from 1 to 2 classes lower than that of ICR-1 specimen. This is the reason that the fatigue strength improvement effect decreases because the distance between weld toe and treatment edge is over 2 mm.
3 The observation of fractured surface using SEM verified that the crack initiation was the weld toe away the maximum distance 2.1 mm from the treatment edge.

ACKNOWLEDGEMEMT

The authors would like to appreciate Prof. Kazuo, Tateishi and Associate Prof. Takeshi, Hanji in Nagoya University and Prof. Anami, Kengo in Shibaura Institute of technology for providing the girder specimen of SBHS700 and Shuichi, Ono, Takayuki, Endo in Japan Construction Method and Machinery Research Institute for transporting the girder and Muneyuki, Uchida in PULSTEC for measuring residual stresses.

REFERENCE

Gunther H-P (ed.). 2005. Use and application of high-performance steels for steel structures. *IABSE-AIPC-IVBH*, Struct Eng Doc 8.

Konishi, T., Takahashi, K. & Miki, C. 2007. Application of high strength steel on steel bridge and its effects on weight reduction. *Journal of JSCE*, No.654/I-52: 91-103. (in Japanese)

Miki, C. & Tai, M. 2013. Fatigue strength improvement of out-of-plane welded joints of steel girder under variable amplitude loading. *Weld World*, No.57: 823-840.

Anami, K., Miki, C., Yamamoto, H & Higuchi, Y. 2000. Fatigue strength of welded joint made of high strength steel and fatigue strength improvement. *Journal of JSCE*, No.675/I-55: 251-260. (in Japanese)

Hanji, T. & Anami, K. 2017. Influence of static strength of steels on fatigue strength improvement of welded joints by toe treatment. *Journal of Structural Engineering*, Vol.63A: 646-658. (in Japanese)

Mori, T., Shimanuki, H. & Tanaka M. 2010. Influence of steel static strength on fatigue strength of web-gusset welded joints with UIT. *Journal of the Japan Welding Society*, Vol.70, No.2: 210-220. (in Japanese)

Hanji, T., Tateishi, K., Ono, S. & Danshita, Y. 2014. Fatigue strength of welded joints using steels for bridge high performance structures (SBHS). *Journal of Structural Engineering*, Vol.60A: 587-595. (in Japanese)

Ishikawa, T., Yamada, K., Kakiichi, T. & Li, H. 2010. Extending fatigue life of cracked out-of-plane gusset by ICR treatment. *Structural Eng./Earthquake Eng., JSCE*, Vol.28, No.1: 21s-28s.

Yamada, K., Ishikawa, T. & Kakiichi T. 2015. Rehabilitation and improvement of fatigue life of welded joints by ICR treatment. *Advanced Steel Construction*, Vol.11, No.3: 293-304.

Nakano, T., Nakanishi, K. & Morikage Y. 2015. Method of improving fatigue strength by peening on base metal and development of mechanized system. *JFE Technical Report*, No.20: 118-124.

Nakanishi, K., Morikage, Y., Kawabata, A. & Tomo, H. 2015. Study on improvement method of fatigue strength of weld joints by hammer peening on base metal. *Journal of JSCE*, Vol.71A, No.1: 10-19. (in Japanese)

Japanese Society of Steel Construction. 2012. Fatigue design recommendations for steel structures. *Gihodo*. (in Japanese)

Maintenance, Safety, Risk, Management and Life-Cycle Performance of Bridges – Powers, Frangopol, Al-Mahaidi & Caprani (Eds)
© 2018 Taylor & Francis Group, London, ISBN 978-1-138-73045-8

Three Bridges with the Same Name "Kömürhan Bridge"

N. Apaydin
General Directorate of Turkish State Highways, Ankara, Turkey
O. Yaldiz
General Directorate of Turkish State Highways, Ankara, Turkey

ABSTRACT: Kömürhan Bridge has a strategic position on the roads connecting the Eastern Anatolia Region with the Central Anatolia and Mediterranean regions in Turkey. As a result of the increasing traffic density between these regions, Kömürhan Bridge has gained more importance nowadays. Throughout the history, there has been more than one bridge in the same name, Kömürhan Bridge, connecting the same places, Malatya and Elazığ. In this paper, one can find the reasons behind the construction of new bridges and also detailed technical information about the them (especially third bridge) constructed at the same location.

1 INTRODUCTION

Kömürhan Cable-Stayed Bridge is planned to be constructed on Euphrates River which is a natural border separating Malatya - Elazığ cities and on 51th km of the existing Elazığ - Malatya State Road (see Figure 1). The geopolitical and strategic importance is great because it is the only point that connects Elazığ and Malatya and provides transition route for 16 cities in Eastern Anatolia Region. Detailed information about the bridges (especially the third bridge) called as Kömürhan Bridge constructed at the same location is given in the paper.

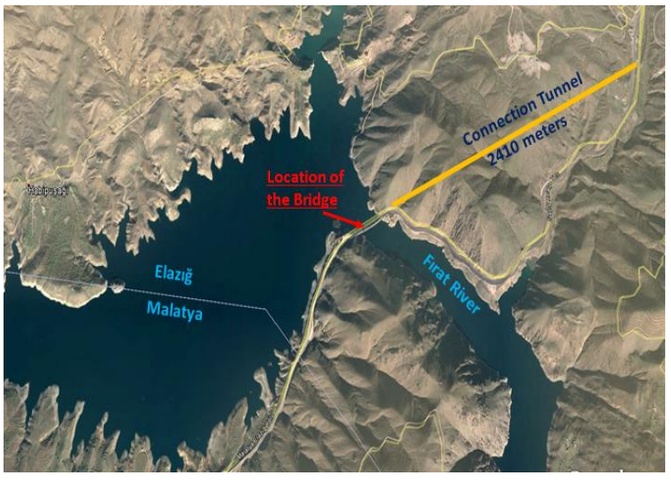


Figure 1: Location of the bridge.

2 HISTORICAL INFORMATION

The historical information and properties of the first two Kömürhan Bridges can be summarized as follows: Before the first Kömürhan Bridge was constructed (until 1930), transportation between Elazığ and Malatya cities was provided only by rafts and boats, and then by a timber bridge built during World War I. However, with the rise of the waters on Euphrates River, the timber bridge was destroyed. Then, the use of the raft and boats started again. For this reason, the need for a permanent bridge was inevitable. A suitable place for the construction was determined at about 12 km east of the destroyed timber bridge. During the design studies, it has been understood that if a concrete bridge were used, water would not be a serious problem while it would cause a considerable difficulty for a steel bridge. In case of using steel bridge, the length of the bridge would be much more compared to concrete one. In addition, due to the difficulties that often arise from the need for frequent painting of a large bridge, reinforced concrete bridge have been preferred although the price is slightly higher. The construction of the first reinforced concrete Kömürhan Bridge began in 1930 and finished in 1932. One of the major importance of the project is that the bridge won the title of the world's sixth largest reinforced concrete bridge as of the period when it was built. According to the design, arched bridge type was considered due to the steep

rocks on both sides of the region (see Figure 2). The bridge was built 33.35 m above the low water level of the river, and the topography made a great difficulty in the construction of the scaffolding. The most difficult part of construction of a long span reinforced concrete bridges is scaffolding. In order to cope with the difficulties created by the topography, a four-cable suspension system was established with a diameter of 32 mm stretched to the towers and the scaffolding of the main span was suspended to those cables. The geometric properties of the bridge are as follows: It consists of two spans in the form of an arch, with a main span length of 108 m, side span lengths of 28 m on both sides and a width of 6.40 m. Main arch is in the shape of hollow box. As for calculation, load carrying capacity calculations were made according to German reinforced concrete norms of 1925.

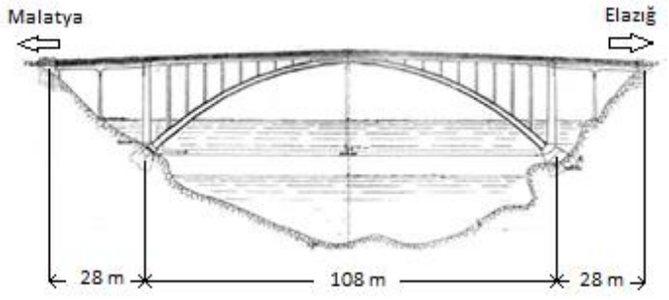


Figure 2: Longitudinal section of the first bridge.

The first bridge has provided transportation in the region for approximately 50 years. However, it was foreseen that this bridge would be under water after the construction of Karakaya Dam. Therefore, it was decided to build a new bridge next to the first one, designed by taking into consideration the dam elevation. The construction began in 1983 and finished in 1986. The major structural importance of this bridge is that was the first bridge constructed by using balanced cantilever method in Turkey. At first, for the new bridge, a project of a gerber-girder system was prepared with a total length of 287 m, a main span of 115 m and side spans of 86 m. However, considering the difficulty of scaffolding of the high piers in the river during the construction, the design was changed and a balanced cantilever method was applied to the project. In the new project, the total length of the bridge was kept same while the main span length was increased. The geometric properties of the second bridge are as follows: The bridge consists of a main span with 135 m length and two side spans with 76 m length each (see Figure 3). The total bridge length is 287 m and the width is 11.50 m. The piers, each 59.50 m in height, consist of variable cross sections with three segments. The cross section width of piers decreases linearly to 8.50 m at the top, with 14.40 m at the bottom. To protect the hydrostatic equilibrium, gaps were left on the walls of piers that allow water

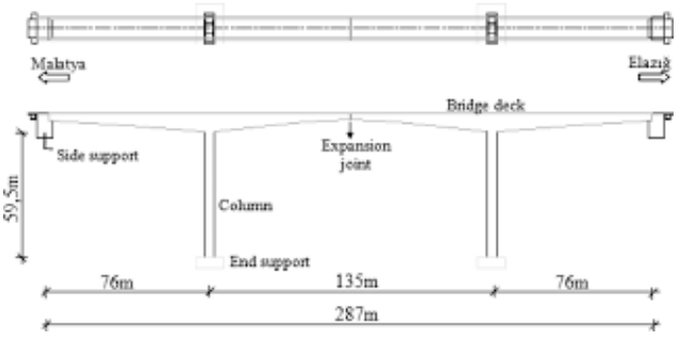


Figure 3: Plan view and longitudinal section of the second bridge.

pass. The deck is composed of 56 segments; all of the them are approximately 5 m in length. Height of the box girder is 9.35 m on the main columns, and it decreases parabolically to 3.5 m at the side supports and 3.0 m at the expansion joint. Design details are as follows: In order to connect deck cantilevers, an expansion joint is formed in the main span of the bridge. In this way, the edge of the cantilever at the main span is free, and the expansion caused by heat and traffic load is allowed. Besides, equivalent movement of the deck in the vertical direction is provided by establishing a connection between two ends for vertical loads. Further, transverse movement is avoided by side wedges.

3 THE NEED FOR THE THIRD BRIDGE

Currently, existing bridge is the only bridge that serves the coming and going, and it is a problematic bridge since it cannot carry traffic density no longer. In order to meet the density arising from the increasing tourism traffic in the region, and to provide advantages such as high geometric standard, comfortable transportation, traffic safety and time saving, it has been decided to build a new bridge. Seven alternative projects were presented to the institution (General Directorate of Highways). Cable stayed bridge alternative design, a single pylon on the Malatya side and a tunnel on the Elazığ side with approach viaducts was selected as suitable. The project was approved by the institution in 2012 and the construction tender was completed in 2013. The Connection Tunnel and Road Construction Work was started in 2014. With this project, a modern state road with a new bridge and tunnel will be built right next to second bridge, while the existing 1 x 1 lane low standard road (having

small curvature radius and too much curve) and second Kömürhan Bridge will be preserved in the region (see Figure 4).



Figure 4: A view of the second and third bridge.

One cannot see all three bridges together since the first bridge is under water currently. However, if there were no water, the view would be as shown in figure 5.

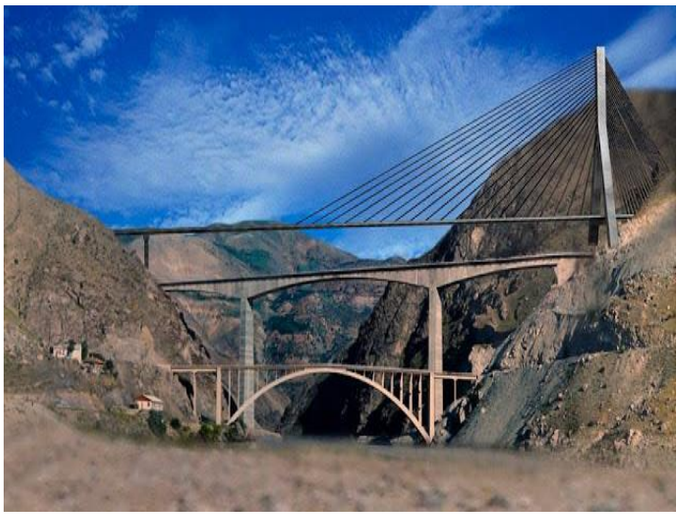


Figure 5: A view of all three bridges side-by-side.

For the construction of third bridge, since it would be very difficult and costly to place the pier in the dam lake, the dam lake had to be crossed with a bridge having a large span. The new Kömürhan Bridge in the project area; will be a kind of bridge called "Cable Stayed" in international literature. This kind is a modern bridge type used for passing large openings as it is on suspended bridges over the Bosphorus in Istanbul.

In addition to the construction of bridge, there is a tunnel construction work in the project area, which has a total length of 4800 m, 2 x 2 lane traffic passing in 2 tubes and each tube is 2400 m in length. Apart from these, the works included are as follows: three floors of total 1200 m^2 closed area construction of police station, earthwork, NATO pipeline displacement, intersection manufacturing, culvert and subway manufacturing, electrical-lighting works, mechanical cold mixture and hot mix asphalt production and guardrail production.

4 PROPERTIES OF THE THIRD BRIDGE

By analyzing the third bridge, the first thing one will notice would be the characteristic features. The bridge has a main span length of 380 m, side span length of 180 m, and total length of 660 m (see Figure 6).

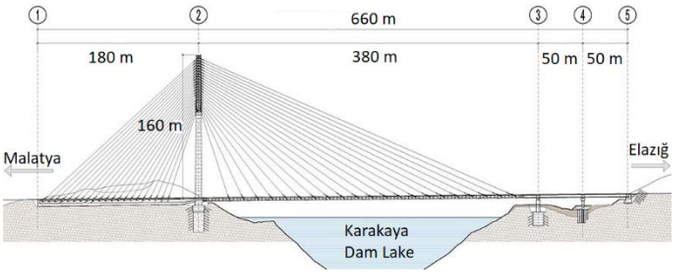


Figure 6: Longitudinal section of the third bridge.

The superstructure is 25 m in width and 3.5 m in height. The side spans are prestressed concrete box and the main span is steel orthotropic box girder (see Figure 7).

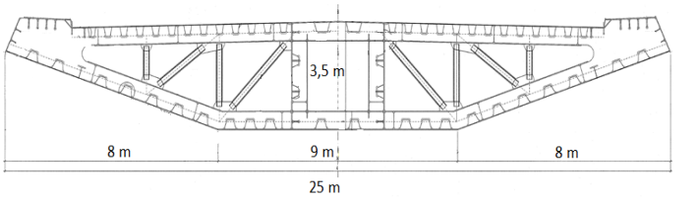


Figure 7: Typical cross section.

The main span consists of a starting segment of 34 m, 21 segment of 16 m and a key segment of 10 m in length. The main span is carried to the pylon with 21 cables. The cables are connected in single plane in the middle of the deck (see Figure 8). The rear cables are connected to the base block with a length of 180 m. The longest cable length is 390 m and the total cable length is 8536 m.



Figure 8: Connection of cables to the pylon.

The ground consists of gabbro and diabase type rock belonging to Kömürhan ophiolites. The pylon is located on two caissons 12 m in diameter and 22.5 m in depth (see Figure 9).

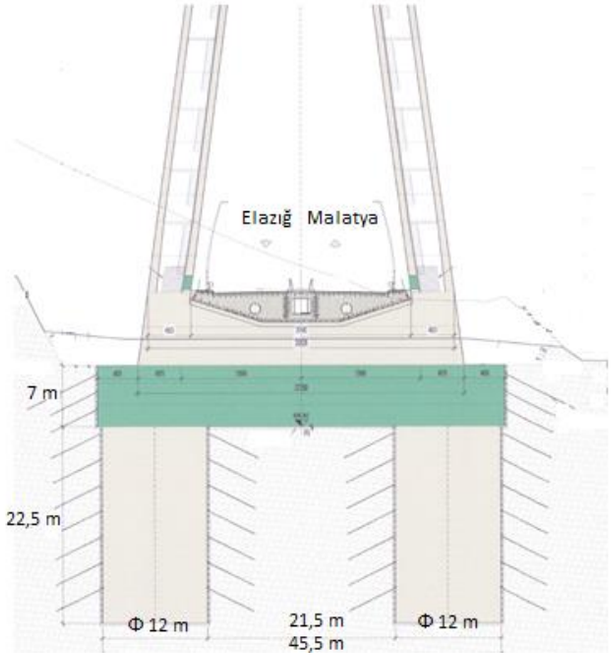


Figure 9: Cross section of caissons.



Figure 10: A view of caisson construction.

5 MATERIALS

The materials used in the construction of the bridge are as follows: C-50 type as concrete material in pylons, C-40 type in post-tensioned slab and C-30 type in other elements. The steel grade used for structural steel as steel material is S355 type and the reinforced concrete steel is S500 type. The cable grade is Gr 1600/1860 f15.7mm- Low Relaxation.

6 TECHNICAL DETAILS

When it comes to technical details, above all, there are two reasons for choosing a single pylon design. The first of these is that there is not enough distance to place the rear cables if another pylon is placed on Elazığ side. The second is that planned pylon location on Elazığ side would be on the backfill, which is the difficulty that the potential support problems will bring about in the dam reservoir.

7 DESIGN OF STRUCTURES

Some of the details about selection of structural system should be clarified. In cable design; a cable layout called "modified fan" was used. ". In this system, the cables are anchored intermittently as close to the top of the tower as possible. Thus, the carrying capacities of the cables can be used to the maximum extent

Moreover, in terms of superstructure design; the choice of the superstructure section greatly affects the entire behavior, construction method and cost of the bridge. The aerodynamic characteristics of the cross section are also important for bridge stability. The selected cross-section provided not only main span to get lighter which result in reduction of cable cross-sections but also it has eliminated the stability problems that can occur in the wind thanks to its high torsional stiffness. On the approach bridge, a cross section of a post-tensioned concrete box was used to cross the 50 m span.

In pylon design, the pylon shape should be aesthetic, sufficiently rigid in the longitudinal and transverse directions to be able to control the displacements in the main span and to provide earthquake safety. In this type of bridges, generally A type, H type and Reverse-Y type pylons are used. Reverse-Y type pylon was used on third Kömürhan Bridge. In this way, the ease of construction was ensured by installing the cables in the upright part of the pylon and also the rigidity against the effects of both earthquake and wind was provided in the transverse direction.

Regarding foundation design; the idealized ground profile in the project area consists of artificial backfill of limited thickness observed locally on the surface and gabbro and diabase type rock units belonging to Kömürhan ophiolites. Pylon and grid line

3 foundations were designed as caisson, 12 m in diameter, grid line 4 foundation was designed as pile,165 cm in diameter and grid line 5-end pier was designed as shallow foundation (see Figure 6: longitudinal section for grid line information).

In the matter of bearing design; the bridge deck is connected to the pylon as fixed end. The main span is designed not to allow shear transfer in grid line 3 and consequently the stability of the bridge is secured in earthquake and wind. The support of the bridge under vertical loads is provided by a pair of spherical bearings on each grid line.

The matters considered below should be noted about the design of the structure. The design of the bridge is based on nonlinear effects. The nonlinear behaviors of the cables under dynamic and moving loads were investigated and stability checks were carried out. In design, time-dependent creep and shrinkage effects are taken into account under the axial load and bending effect (creep effect is effective on reinforced concrete decks and pylons under high pressure).

8 CALCULATIONS

As for the calculations, the matters could be stated as follows: In typical segment calculation; a finite element model of the orthotropic deck between the cables was established and the stresses were checked under various loads. Besides, additional analyzes such as cable replacement and cable breakage have been made.

In deck transverse direction calculation; a finite element model of the orthotropic deck was established and transverse direction analyzes were performed.

When it comes to final calculation, the bridge geometry is adjusted by optimizing the cable forces when the bridge is completed. Stress checks were carried out on superstructure and cables.

9 ANALYSIS

In analysis of construction stages; each stage of the construction and the loads belonging to that stage were identified and analyzed. With this analysis, it is aimed that after the last construction phase, the bridge superstructure and pylon should be as the desired geometry. As a result, cable stresses at each stage are determined.

For earthquake analysis; it can be said that cable stayed bridges are generally less affected by earthquakes. The reason of this is that cable bridges are flexible structures. For this reason, they remain on the right side of the spectrum and they are exposed to lower accelerations during the dominant periods. A number of experiments and analyzes have been carried out in the design phase to optimize the safety of the bridge against earthquake. The bridge was designed not to be damaged at an earthquake level of 2% (recurring time of 2475 years) with a probability of exceeding in 50 years corresponding to General Directorate of Highways' required safety performance level. In addition, considering the possibility of earthquake during the construction of the bridge, the investigation was made according to the earthquake having the probability of exceeding 50% in 50 years (recurrence time of 75 years)

As for the wind analysis; the bridge cross section should be designed to reduce the wind effects aerodynamically. The aerodynamic features of the cross section of third Kömürhan Bridge were analyzed with advanced software. Hence, the critical wind speeds which are to be applied to the bridge and the bridge resonance have been determined. The three-dimensional model prepared for the bridge at 1/60 scale was subjected to the wind tunnel test. During these tests, the aerodynamic characteristics of the deck section and the wind safety of the bridge were investigated. The bridge is expected to stabilize even in the wind, which is at a speed of about 250 km/h.

10 STANDARDS

The main standards and resources used in design are as follows: AASHTO LRFD and Eurocode specifications were used for the design of reinforced concrete, prestressed concrete, steel and composite building elements. AASHTO Guide Specifications for LRFD Seismic Bridge Design was used in the earthquake design of the bridge.

11 CONCLUSION

Finally, expected project main quantities are given below in table 1.

PROJECT MAIN QUANTITIES			
Earth-works	Concrete works	Rein-forcement	Steel works
1.750.000 m³	180.000 m³	6.000 ton	6.650 ton
Cable (strands)	Post-Tensioned Steel Works	Plant Mix Sub-Base and Base	Bitu-minous Hot Mix Asphalt
920 ton	210 ton	120.000 ton	73.000 ton

Table 1: Project main quantities.

When the bridge is completed (in 2018), it will be the world's third largest "single-pylon, cable stayed bridge" with a main span length of 380 m (see Table 2).

Rank-ing	Bridge Name	Country	Year	Main Span Length (m)
1	Zhivopisny	Russia	2007	410
2	New Taipei	Taiwan	2010	400
3	Kömürhan	Turkey	-	380
4	Ada	Serbia	2012	376
5	Margaret Hunt Hill	USA	2012	365
6	Rama VIII	Thailand	2002	300

Table 2: Ranking of the largest single-pylon cable stayed bridges in the world.

It is one of the exemplary projects in Turkey for the construction sector in terms of its technical features and innovations by using large-scale domestic engineering services, domestic technology and domestic workforce. Since the construction is performed by using completely domestic resources, the cost will be at least three times cheaper than the equivalent bridges in the country. Moreover, it is a very important investment for the whole country because it is located on a unique point connecting Elazığ and Malatya as well as the east and west.

REFERENCES

ATLAS, K. (2015, December 07). Retrieved from http://kopriyet.blogspot.com.tr/2015/12/komurhan-koprusu.html#!/2015/12/komurhan-koprusu.html

BRIDGES AND VIADUCTS. (n.d.). Retrieved from http://www.yukselproje.com.tr/wp-content/uploads/2016/10/BRIDGES.pdf

KOMURHAN BRIDGE. (n.d.). Retrieved from http://pipenbaher-consulting.com/project/komurhan/54

KOMURHAN BRIDGE and TUNNEL CONSTRUCTION PROJECT. (n.d.). Retrieved from http://www.gulsanholding.com.tr/en/komurhan-koprusu-baglanti-tuneli-ile-yolu-yapim-isi-en.asp

Bayraktar, A., Sevim, B., Altunişik, A. C., & Türker, T. (2010, May). Finite element model updating of Kömürhan highway bridge based on experimental measurements. Retrieved from https://www.researchgate.net/publication/264150713_Finite_element_model_updating_of_Kmrhan_highway_bridge_based_on_experimental_measurements

SS16: Revised fatigue detail categories for bridges (in European standards)

Organizer: U. Kuhlmann

Maintenance, Safety, Risk, Management and Life-Cycle Performance of Bridges – Powers, Frangopol, Al-Mahaidi & Caprani (Eds)
© 2018 Taylor & Francis Group, London, ISBN 978-1-138-73045-8

Assessment of fatigue tests to review detail categories of EC3

H. Bartsch & M. Feldmann
Institute of Steel Construction, Aachen, Germany

ABSTRACT: The present paper deals with the current status of research activities on the assessment of fatigue tests in order to review detail categories of EC3-1-9. Statistical methods which have been used for a detail classification are outlined shortly. The concept of a well-structured SQL supported data base is presented, which is intended to comprise all known fatigue test series relevant for a fatigue detail classification in the future. Subsequently, an exemplary fatigue evaluation of a longitudinal weld detail is presented. After the selection of expressive fatigue tests series, these have been evaluated for a detail classification by considering the prediction as well as the tolerance interval. Additionally, influences of failure criterion, component size, mean stress and boundary conditions are discussed. The results show, that the selected series partially exhibit distinctively higher fatigue resistances as currently incorporated in Eurocode regulations. Finally, first preliminary numerical simulations for future fatigue tests are presented.

1 INTRODUCTION

In many areas of our infrastructure, as for instance the construction of bridges, fatigue design of steel structures is a major issue. Compared to former national standards, the European standard referring to fatigue design of steel structures (Eurocode 3, 2005) however leads to over conservative and inefficient results. The basis of the fatigue detail categories dates back several decades. Additionally the existing fatigue test database is incomplete and the evaluation methods are outdated. Recent knowledge has mainly not been adopted.

For these reasons, current investigations aim to re-evaluate existing data collections in order to develop recommendations of improved fatigue detail categories for European standards. An elaborate data base structure has been established in order to assess the available fatigue test data in a sophisticated manner. The database enables as well search and selection functions as a user-driven evaluation of test data. A large amount of relevant parameters influencing the fatigue life has been obtained from available sources and incorporated into the database. The documented parameters comprise information on material, welding, environmental influences, loading as well as geometry of the respective details.

With the help of the re-evaluated data base, different possibilities of detail category evaluations have been investigated. In present research activities (Enhancement detail catalouge, 2016), all details of EC3-1-9 (Eurocode 3, 2005) are analyzed. However, for detailed investigations, this paper only focusses on welded built-up sections. Possible influences on the fatigue test results in terms of component characteristics and mean stress have also been considered.

Moreover, numerical investigations demonstrating the true stress distribution in typical connection details are presented. These simulations enable the comparison of commonly applied assumptions according to the nominal stress concept and the therefor conducted fatigue test. For this purpose, future plans contain additional component tests measuring bolt forces and strains in the area of the connection.

2 OUTLINE OF STATISTIC METHODS

In order to ensure a safe derivation of standard values, a series has to be evaluated by statical approaches. However, different methods of statistical analysis for the definition of fatigue resistances are known. By comparing the wording of EC3-1-9 (Eurocode 3, 2005) and the respective background document (Background Documentation Chapter 9, 1989), a contradiction can be noticed. The background document claims that a prediction interval (see section 2.2) has been used to statistically evaluate a fatigue test series. In contrast, according to (Eurocode 3, 2005), test results shall be analyzed by utilizing the tolerance interval (see section 2.3).

In general, the tolerance interval depicts the more conservative limit, allowing for uncertainties in estimates of population statistics. (Schneider & Maddox, 2003)
Among other important issues, the contradiction between EC-3-1-9 and its background document led to current research activities in which a re-evaluation of fatigue data is applied in order to review the current detail categories. The following sections give short outlines of the statistical approaches adopted in the presented investigations.

2.1 *Regression analysis*

In order to derive an S-N-curve out of a fatigue tests series, as a first step a regression analysis is conducted. The regression line establishes a linear correlation between the logarithm of stresses $log\,S$ and number of cycles $log\,N$, which fits bests to the test results. Equation 1 describes the linear regression function in fatigue context: (Schneider & Maddox, 2003)

$$log\,N = log\,A - m \cdot log\,S \tag{1}$$

The slope of the regression line m, can be calculated by the least-square method. However, EC3-1-9 (Eurocode 3, 2005) specifies the slope of S-N-curves for longitudinal stresses, as regarded in the present investigations, to the value three. If the slope is set, only the intercept of the $\log N$ axis $\log A$ has to be determined by the following equation (Kosfeld, et al., 2016):

$$\log A = \frac{1}{n} \cdot \sum_{i=1}^{n} \log N_i + m \cdot \frac{1}{n} \sum_{i=1}^{n} \log S_\mathrm{i} \tag{2}$$

where n = number of single test results. By determining $\log A$, the regression line depicting the characteristic S-N-curve is fully described.

2.2 *Prediction interval*

In the context of design objectives, it has to be ensured that a given proportion of data is located in between specific limits, which have to be determined statistically. Based on existing test results, the prediction interval (equation 3) is utilized to give a forecast on future test results (Schneider & Maddox, 2003):

$$\log\, N_{P\%}^{\pm} = (\log A + m \cdot \log S)$$

$$\pm\, t \cdot \hat{\sigma} \sqrt{1 + \frac{1}{n} + \frac{\left(\log S - \overline{\log S}\right)^2}{\sum_{i=1}^{n} \left(\log S_i - \overline{\log S}\right)^2}} \tag{3}$$

where $\overline{\log S}$ = mean of the n values of $\log S_i$; t = appropriate percentage point of Student's t distribution, with f degrees of freedom; $\hat{\sigma}^2$ = best estimate of the variance of the data about the regression line, which is equal to the sum of squared residuals divided by the number of degrees of freedom f; and f = n − 2 in the case where two coefficients have to be estimated from the data.

Concerning the investigations presented in section 4, one-sided prediction intervals with a confidence of 95% are applied.

2.3 *Tolerance interval*

The tolerance interval is also used to predict future test results on the basis of existing data. However, in comparison to the prediction interval, the tolerance interval makes a statement on a probability of surviving with a certain confidence level. This implies that the tolerance limit estimates a confidence limit on the prediction limit. The expression of the tolerance interval resembles Equation 3, only the value t is substituted by the statistic k, depicting the one-sided tolerance limit factor which can be taken out of tables. (Schneider & Maddox, 2003) During present investigations, one-sided tolerance limits have been calculated for a 75% confidence level of 95% probability of survival. (ISO 12107, 2012)

3 FATIGUE DATA SOURCES AND DATABASE

The established fatigue data base rests upon several fatigue data collections, which have been gathered during a former research activity (Sedlacek, G. et al., unpubl.). These data collections comprise 13 databases of different authors in USA, France, Germany, Japan, Australia and the Netherlands.

During present investigations, the original sources of all these data collections are purchased and analyzed again in a more detailed manner. A new innovative structured data base on SQL basis shall eventually contain about 250 sources comprising about 1100 fatigue test series, only by evaluating data of the former data collection. Prospectively, more recent and expressive fatigue test data will also be included into the data base. For research operations in the near and far future, the data base will be available online, enabling protected user-driven interfaces for queries, evaluations, modifications and maintenances of data.

As a first step in the data preparation, the sources of the former data collections are surveyed. After primary observations of several sources, a large variation of quality could be found. Most of the sources have been published in the 1960s and 1970s. The most recent fatigue investigations being part of the former data collection have been made in 2003.

The newly established innovative data base aims to incorporate any information relevant in case of fatigue issues, as mentioned in the following:

- General information: component, source, general remarks;
- Information on loading: kind of loading, frequency of testing, location of calculated stress range;

– Information on material: steel grades, yield strength, ultimate strength;
– Information on welds: shape, weld symbols acc. to (EN ISO 2553, 2013), number of passes, pretreatments, post treatments, sequence, characteristics of filler material, welding position acc. to (EN ISO 6947, 2011), process acc. to (EN ISO 4063, 2010);
– Information on environmental conditions: temperature, corrosive conditions, humidity;
– Detail specific properties: vary depending on analyzed detail (e.g. thickness of components, span width);
– Test results: stress range, stress ratio, number of cycles to rupture, failure criterion, failure region;

With the help of the structured data base, the therein incorporated information and the coding of appropriate scripts, evaluation of fatigue tests and influencing parameters can be realized easily.

The present paper demonstrates a preliminary evaluation of one exemplary detail appearing in many areas of our infrastructure, as for instance the construction of steel bridges. Table 1 contains an overview of all series and number of tests belonging to welded built-up sections, which are classified into fatigue details in table 8.2 of EC 3-1-9 (Eurocode 3, 2005). This table of the detail catalogue contains different types of longitudinal welds, which are classified into several fatigue details, as for instance automatic and manual fillet or but welds and intermittent welds. Table 1 comprises all purchased data of the existing fatigue data collections (Sedlacek, G. et al., unpubl.).

Table 1. Overview of series on welded built-up sections (table 8.2 (Eurocode 3, 2005)).

Detail	Description	Number of series	Number of tests
②	Automatic fillet welds	6	77
③	Automatic fillet or butt weld carried out from both sides but containing stop/start positions	28	275
⑤	Manual fillet or butt weld	12	70
⑧	Intermittent longitudinal fillet welds	7	38
⑨	Longitudinal butt weld, fillet weld or intermittent weld with a cope hole height not greater than 60 mm	7	36
⑩	Longitudinal butt weld, both sides ground flush parallel to load direction, 100% NDT	2	183
	No grinding and no start/stop	1	100
	With start/stop positions	-	-
Sum		63	779

4 FATIGUE EVALUATION

4.1 *Outsourcing of tests*

By examining the purchased fatigue series in a detailed manner, several crucial aspects have been noticed, which will be outlined in the following section.

Some sources depict secondary sources and contain few detailed information on geometry or material of the tested specimens, making it difficult to review the original data in a detailed way. Oftentimes, important information as for instance weld details or failure criterion are not even noted in the primarily source. Moreover, the documented failure criteria vary to a large extend. Occurring failure criteria are fore instance “Complete fracture”, “Increase in deflection of 0.02 inches”, “Through thickness crack” or the criterion is even unknown, leading to a challenging evaluation of different series. Test results are sometimes only indicated graphically in moderate quality diagrams, leading to inaccurate tabularizing of results. Some test series appear in more than one source and have been incorporated twice into the former data collection. Additionally, some series of the existing data collection have possibly been classified with a wrong detail in former evaluations, which in some cases could only have been found out after researching original publications. What is more, in some cases a distinct classification into one detail is not possible.

In order to gain a first overview of the fatigue test results regarding classification into details, for each detail the most expressive series have been identified. For the identification, the following main criteria have been used:
– Availability of primary or only secondary source
– Availability of test data in tables or only in terms of diagrams
– Expressiveness of failure criterion
– Number of tests
– Possibility of an obvious allocation to a fatigue detail of EC-3-1-9 (Eurocode 3, 2005)

4.2 *Evaluation of fatigue data*

In the following, a first overview of possible evaluations of fatigue series belonging to detail 3 of table 8.2 (Eurocode 3, 2005) is presented. These series comprise welded built-up sections containing longitudinal automatic fillet or butt weld carried out from both sides containing stop/start positions. Table 2 presents an excerpt of this detail in EC3-1-9.

In order to evaluate the most significant series, eight out of 28 available tests series have been selected taking into account the outsourcing criteria named in section 4.1. Other test series have been dropped in this first evaluation because of bad documented secondary sources, totally unknown failure criteria or due to a small number of test results (less than 5 test results per series).

Table 2. Excerpt of detail category table 8.2 detail 3 (Eurocode 3, 2005).

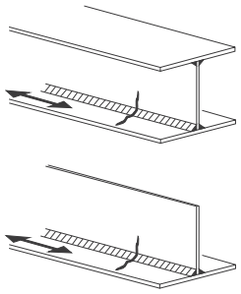
Detail category	Constructional detail	Description
112		3) Automatic fillet or butt weld carried out from both sides but containing stop/start positions.

Table 3 gives information on the eight selected series regarding failure criterion, specimen type, country in which the series have been performed and on the number of tests per series. The eight series originate from three different sources, comprising tests on different types of specimens. Moreover, the series have been conducted in different laboratories and contain different failure criteria as well as different numbers of single tests. This variation leads to a wide distribution and covering of possible influencing characteristics.

Table 3. Selected series of detail 3 in table 8.2 (Eurocode 3, 2005).

Series	Failure criterion	Specimen type	Number of tests	Country
S1*	„Complete fracture“	T-specimen	31	USA
S2*	„Complete fracture“	T-specimen	12	USA
S3*	„Complete fracture“	T-specimen	12	USA
S4**	„Fracture“	T-specimen	21	Germany
S5**	„Fracture“	T-specimen	66	Germany
S6*	„Complete fracture“	I-specimen	9	USA
S7***	“Fracture propagated to half of web”	I-specimen	9	Germany
S8***	“Fracture propagated to half of web”	I-specimen	25	Germany

* (Reemsnyder, 1963)
** (Olivier & Ritter, 1981)
*** (Minner, 1981)

The selected test series have been evaluated separately. As a first step, a linear regression (see section 2.1) has been performed for the defined gradient m, which is incorporated with the value three in S-N-curves in EC-3-1-9 (Eurocode 3, 2005), confer the straight line in Figure 1. Furthermore, the reference value of the fatigue strength $\Delta\sigma_c$ at $N_C = 2$ million cycles has been evaluated by using the two statistical methods:

- Prediction interval (cf. section 2.2) and
- Tolerance interval (cf. section 2.3)

The prediction as well as the tolerance intervals are depicted in Figure 1 for series S1 by dotted and dashed lines.

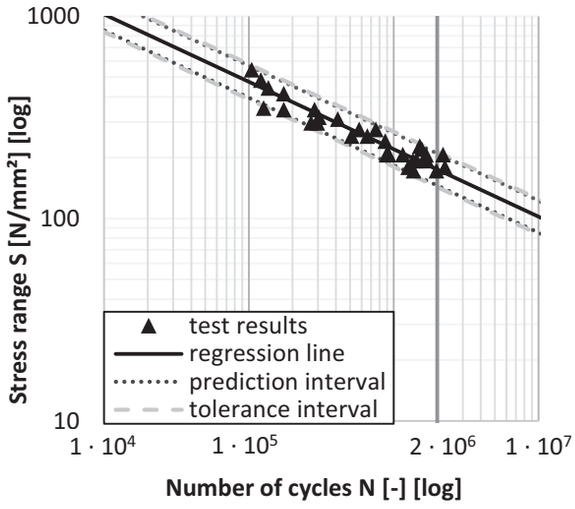


Figure 1. Depiction of test results, regression line, prediction and tolerance interval of S1 (Reemsnyder, 1963).

The evaluation of series S1 results to the following values:

- Prediction interval: $\Delta\sigma_c = 145.7$ N/mm²
- Tolerance interval: $\Delta\sigma_c = 143.1$ N/mm²

As comparison, the detail category of EC3-1-9 (Eurocode 3, 2005) amounts to 112 N/mm², which lies distinctly below the statistically secured values of Series S1.

The presented evaluation progress has been realized for all eight selected series. Figure 2 illustrates the different values of fatigue strength, evaluated by prediction and tolerance intervals, compared to the current EC 3-1-9 (Eurocode 3, 2005) fatigue class and the next higher fatigue level.

As seen in the figure, every series exhibits a sufficient fatigue strength to be classified in the current fatigue class 112. Moreover, six or even seven (if the prediction interval is consulted) series could be classified in class 125, which is the next higher classification.

For further analyses, it has to be remarked that the eight series differ from each other regarding influences on fatigue in many regards. In general, a comparison of all single characteristics of the series is difficult. Too many differences among the properties lead to the inability of isolating interesting influencing parameters on fatigue strength such as component thickness, steel grade or fabrication of welds. However, several independent variables could be investigated, as described in the following sections.

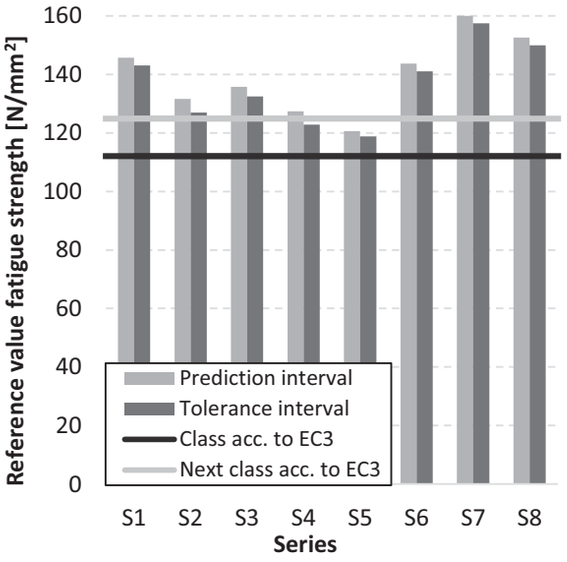


Figure 2. Evaluation of selected series of detail 3 table 8.2 (Eurocode 3, 2005).

4.3 *Influence of failure criterion*

First of all, the different failure criteria depict crucial influencing parameters. The eight selected series of detail 3 in table 8.2 (Eurocode 3, 2005) originate from three different sources, which define failure as "fracture", as "complete fracture" or as "crack, which propagated until reaching half of the web". More detailed information is not given, which makes the comparison of the series and a distinct classification into one fatigue class questionable. Nevertheless, it can be noticed that the series with highest fatigue resistance (S7 and S8) belong to one source and also the two series with weakest results (S4 and S5) originate from a common source, indicating a tendency.

4.4 *Influence of component size*

Apart from the failure criterion, also the type of specimen differentiates among the selected series. The component size can influence the fatigue strength. For specific details, this size effect is already included in EC3-1-9. Investigations have shown that large component tests proved to exhibit lower fatigue resistance than investigations on small specimens (Helms, et al., 1989). Possible mentioned reasons might be:

- Stress mechanical influence: according to fracture mechanics, thicker cracked plates exhibit a lower fatigue life than thinner plates containing the same crack size to thickness ratio.
- Productional influence: In large constructions, higher residual stresses due to welding arise.
- Statistical influence: Because of a larger amount of weld volume, exterior and interior imperfections are more likely in larger structures.

Series S1 to S5 have been performed on small scale T-specimens, whereas larger I-sections have been used for Series S6 to S8. Two series, namely S3 and S6 are the only series directly comparable to each other regarding size effects, since they have been fabricated and tested similarly, except for the type of specimen. The T-specimen of S3 theoretically depicts an extract of an I-specimen tested in S6, as illustrated in Figure 3.

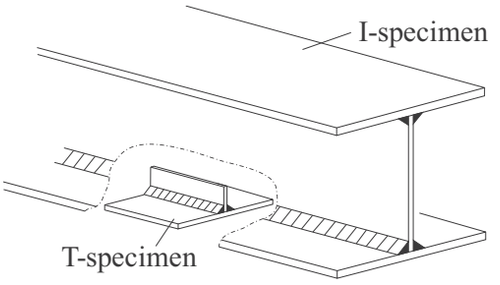


Figure 3. Depiction of I- and T-specimen (Reemsnyder, 1963).

As seen in the evaluation results, the larger I-specimen exhibits a higher fatigue strength than the smaller T-specimen, though. The authors ascribe this effect to the fact that the crack propagation proceeds slower in larger than in smaller specimens, where a through-thickness crack is achieved earlier. (Reemsnyder, 1963) This observation underlines again the importance of the failure criterion, as the crack propagation rate becomes only distinct, if the failure criterion is defined as "fracture". In case of a failure criterion depicting the "first detection of a small crack", a larger specimen might not be advantageous because of the above named influences.

4.5 *Influence of mean stresses*

The influence of mean stress or stress range can only be considered in exceptional cases according to EC 3-1-9 (Eurocode 3, 2005). Commonly, in welded structures, tension residual stresses are assumed, where the fatigue resistance is not depending on the mean stress, but only on the stress range. However, exterior compression stresses can have a positive influence, if they lead to a degradation of tension residual stresses. (Gurney, 1979) Tests on the influence of mean stress have shown, that the positive effect of compression stresses is worthwhile to consider.

This positive effect of compression stresses has been confirmed by the results of series S1, where three different stress ratios 0.5, 0 and -1 have been investigated.

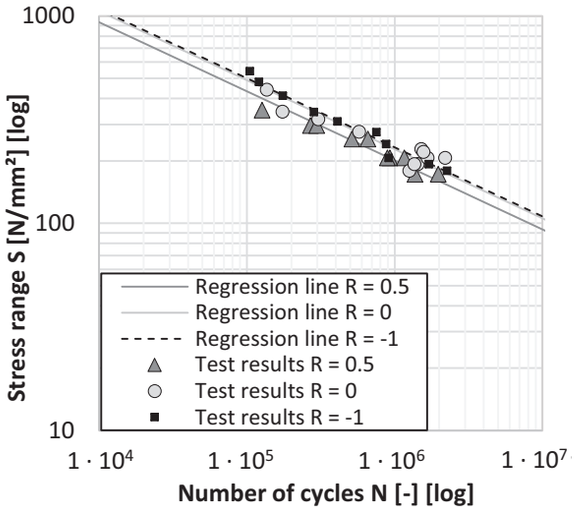


Figure 4. Depiction of S1 fatigue data in dependence of stress ratio (Reemsnyder, 1963).

As exemplary seen in Figure 4, fatigue tests with a tension compression alternating loading, R = -1 exhibit a higher resistance than specimens tested under a tension alternating loading, R = 0.5. The evaluation in terms of the prediction interval method results to:

– R = -1: $\Delta\sigma_c$ = 162.7 N/mm^2
– R = 0: $\Delta\sigma_c$ = 145.6 N/mm^2
– R = 0.5: $\Delta\sigma_c$ = 139.8 N/mm^2

Regarding these evaluation results, the tests with a stress ratio of -1 exhibit a 16% higher fatigue resistance than the tests with a ratio of 0.5. However, it has to be noticed, that this is only an exemplary investigation on the basis of one single series and not a general statement.

4.6 *Influence of boundary conditions and sample size*

In most cases, in order to suggest a fatigue category, it is not sufficient to evaluate only one series. Several series containing different boundary conditions (laboratories, test machines, stress relations, etc.) as existing in the selected series, have to be taken into account. Apart from influencing criteria, also a weighting regarding the sample size plays a huge role for deriving a characteristic S-N curve, as the results are proved differently strong. As seen in the evaluation, the results in terms of fatigue resistance differ in to a great extent. For more detailed evaluations in the future, concepts treating relevant influencing characteristics will be developed based on existing test data.

5 FUTURE EXPERIMENTAL TESTS

5.1 *Concept of experimental tests*

The presented fatigue evaluation process includes only test series of existing fatigue data collections for now. As seen in the above performed example, there is a huge lack of information on experimental data of several details. Regarding again for instance table 8.2 of EC 3-1-9 (Eurocode 3, 2005), eight of 15 details (including subcategories) are not based on experimental data, as far as known and the documentation of existing test data mostly has insufficient quality for present intentions.

More recent investigations regarding fatigue behavior of some details exist, but have not been included into the actual data base until now. However, there still are high demands for future experimental testing. Furthermore, some details of EC 3-1-9 (Eurocode 3, 2005) require extensive numerical analyses, aggravating a straightforward design procedure.

One example for a detail worth to be analyzed by future experimental investigations is the T-joint of detail 2 and 3 of table 8.5 (Eurocode 3, 2005), where modified nominal stress values have to be determined by sophisticated finite element (FE) investigations. An additional problem occurs in the design procedure of prestressed bolt connections. The detail category tables require knowledge of the actual bolt force, which however underlies additional loads due to support and loss of prestress effects, depending on the geometry of the connection. In order to determine the actual bolt force due to external loading, again expensive numerical investigations are necessary. In order to take into account these two issues, experimental investigations on end plate connections containing prestressed bolts are planned.

As a first step, large-scale tests on rolled sections with different endplate connections, cf. left hand side of Figure 5, will be conducted. Additionally, small scale T- or L-joint specimens depicting sections of the end plate connections will be tested afterwards.

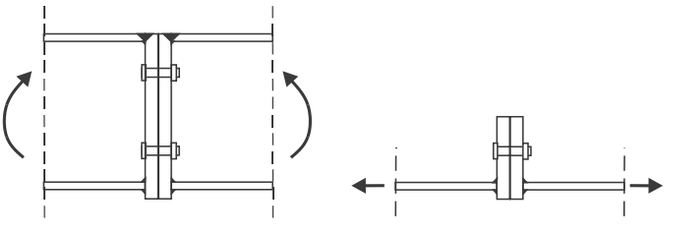


Figure 5. Depiction of planed tests: large- (left) and small-scale specimens (right).

During the experimental investigations, the stress distribution of large and small scale tests and their transferability shall be determined. The tests are planned to be recalculated numerically. After verification of the FE models, a parametric study in order to investigate influences of the thickness of bolts, accomplishment of welds and imperfections etc. will be conducted.

5.2 *Numerical investigations*

For planning of the experimental test, FE models have been created in order to investigate the stress distribution within the endplate connection. This section only concentrates on the beam tests. In order to create a constant bending moment and eliminating shear forces in the connection area, a four-point bending test is intended to be conducted. Consequently, also the FE models are loaded and supported at two points, respectively. The geometry of the connection is designed in a way that cracks will probably appear first in the welds. Nevertheless, the stress and stain behavior of the preloaded bolts will also be recorded.

In order to roughly estimate the number of cycles to failure during the tests, the approximately arising stress under a predefined bending moment has to be determined. The calculated lifespan according to the nominal stress approach of EC3-1-9 (Eurocode 3, 2005) has exemplary been compared to the probably more precise number of cycles determined by effective notch stresses according to IIW recommendations (Hobbacher, 2008).

The effective notch stress generally depicts the stress at the root of a notch. In order to apply the concept, the actual weld contour is replaced by an effective one, which means that the notch radius of weld root and toes has to be modelled. A radius of 1 mm and element sizes in the curved parts of less than 1/6 mm have to be satisfied to comply with the approach. (Hobbacher, 2008)

For preliminary investigations, an exemplary effective notch stress model has been created. In this case, fillet welds are assumed, which is why a gap of 0.5 mm thickness is modelled between section and end plate. Figure 6 depicts an excerpt of the global FE model, where also the most interesting part of the endplate connection is highlighted.

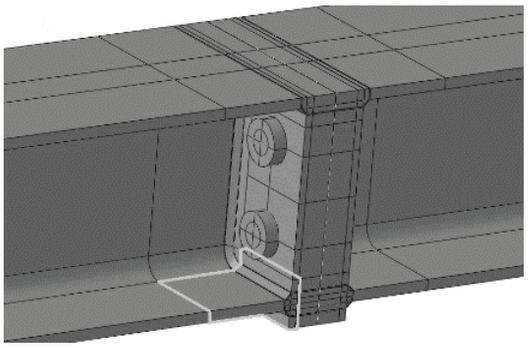


Figure 6. Global model and designation of sub model.

Because of the small element size and the accompanying high number of elements, only a small part of the model can be realized in accordance with the effective notch stress concept. As a first step, the simulation of the global model indicates the location of highest stresses. In a second step, a finely discretized sub model is created, which contains the location of most critical stresses. As resistance, one single S-N curve based on a reference stress of 225 N/mm^2 at 2 Million cycles with a slope of 3 is consulted. (Hobbacher, 2008).

Figure 7 illustrates a stress plot of the principle stresses in the sub model of the endplate connection. It can be observed, that the weld on the inside of the flange is more stressed than the outer one, due to the clamping action of the bolts inside the section.

The highest stresses of 389.8 N/mm^2 arise in the weld toe and the maximum stresses in the weld root amount to a similar value of 389.1 N/mm^2. Thus, according to the effective notch stress concept the crack initiation could start from the root of the weld or the weld toe with same probability.

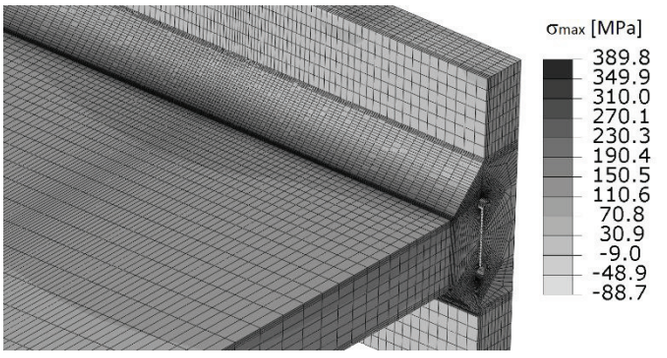


Figure 7. Maximum principle effective notch stresses.

The following section exemplary presents the lifespan estimation of the weld root. Table 4 depicts the comparison of lifespan of the weld root according to the nominal and the effective notch stress concept. Detail 3 of table 8.5 in EC3-1-9 (Eurocode 3, 2005) with a fatigue class of 36* has to be considered. Asterisked fatigue classes can be lifted one class higher, if the part of the S-N curve with a slope of 3 is extended until 10^7 cycles. Therefore, in the present investigations fatigue class 40 is taken into account. According to the nominal stress approach, the stress in the upper weld of the lower flange has been calculated to 121.7 N/mm^2. Regarding fatigue class 40, a lifespan of 70,929 cycles results.

Table 4. Lifespan according to nominal and effective notch stress approach.

Concept	Stress in weld root [N/mm^2]	Fatigue class	Number of cycles to failure
Nominal stress	121.7	(36*) 40	(51,707) 70,929
Effective notch stress	389.1	225	386,718

The effective notch stress concepts predicts a distinctly higher lifespan of 386,718 cycles to failure, taking into account the overall fatigue class 225.

It has to be mentioned, that a sensitivity analysis, especially in terms of discretization and assumption

of welding gap, has to be conducted for final FE models to create a validated foundation for the parametric study. Such investigations will be performed after a verification of FE models by means of experimental investigations.

Generally, the fatigue evaluation with effective notch stresses is deemed to be multiplicatively more precise than an estimation according to the nominal stress concept, leading to more economic results. (DVS, 2017) Still, also the effective notch stress fatigue curve is based on statistical evaluations in terms of the tolerance interval and therefore the true number of cycles to failure will probably be higher than predicted.

6 CONCLUSION

After explaining the basics on known fatigue test data and static methods to evaluate those, this paper presents and exemplary evaluation of fatigue strength of one detail in EC3-1-9 (Eurocode 3, 2005). Detail 3 of table 8.2 has been selected, which depicts automatic fillet or butt weld carried out from both sides and containing stop/start positions. The eight most expressive fatigue tests series have been evaluated taking into account two different statistical approaches. It has been shown that all series can doubtless be classified in the detail class 112 of EC3-1-9 (Eurocode 3, 2005). Additionally, depending on the statistical approach, six or seven of the eight selected series fall into the higher class 125. In conclusion, thought could be given to categories Detail 3 of table 8.2 into a higher fatigue class. However, more recent investigations on components with current characteristics (e.g. modern production methods, etc.) should be taken into account to confirm the presented evaluation results. Furthermore, a draft of future experimental investigations which intend to simplify the fatigue verification process of special details has been presented as an outlook. A forecast of the number of cycles to failure for one specimen has been presented, comparing results according to nominal and effective notch stress concepts.

7 ACKNOWLEDGEMENTS

The presented investigations have been conducted in the framework of the German research project “Re-evaluation and enhancement of the detail catalogue in Eurocode 3 for future oriented design of steel construction under high loading” (Enhancement detail catalouge, 2016). The financial contribution of the German Committee on Steel Construction (DASt) in cooperation with the Research Association for Steel Application (FOSTA) is greatly acknowledged. Additionally, the provision of fatigue test data from all kinds of institutions is hugely appreciated.

8 REFERENCES

Background Documentation Chapter 9, 1989. *Document 9.01, Eurocode No. 3, Design of Steel Structures, Part 1 - General Rules and Rules for Buildings*.

DVS, 2017. *Industrielle Anwendung des Kerbspannungskonzeptes für den Ermüdungsfestigkeitsnachweis von Schweißverbindungen*, Merkblatt DVS 0905.

EN ISO 2553, 2013. *Welding and allied processes – Symbolic representation on drawings – Welded joints*.

EN ISO 4063, 2010. *Welding and allied processes – Nomenclature of processes and reference numbers*.

EN ISO 6947, 2011. *Welding and allied processes – Welding positions*.

Enhancement detail catalogue, 2016. *Re-evaluation and enhancement of the detail catalogue in Eurocode 3 for future oriented design of steel construction under high loading - Proposal*.

Eurocode 3, 2005. *Design of steel structures - Part 1-9: Fatigue*.

Gurney, T. R., 1979. *Fatigue of welded structures*, Cambridge: Cambridge University Press.

Helms, R., Jaenicke, B., Wohler, H. & Bork, C.-P., 1989. *Zur Schwingfestigkeit großer geschweißter Stahlträger / Bundesanstalt für Materialforschung und -prüfung (BAM)*, Forschungsbericht 164.

Hobbacher, A., 2008. *Recommendations for fatigue design of welded joints and components - IIW-1823-07*.

ISO 12107, 2012. *Metallic materials -- Fatigue testing -- Statistical planning and analysis of data*.

Kosfeld, R., Eckey, H. F. & Türck, M., 2016. *Deskriptive Statistik*. 6 ed. Wiesbaden: Springer Gabler.

Minner, H. H., 1981. *Schwingfestigkeitserhöhung von Schweißverbindungen aus hochfesten Feinkornbaustählen StE 460 und StE 690 durch Einsatz des WIG-Nachbehandlungsverfahrens*, Darmstadt.

Olivier, R. & Ritter, W., 1981. *Einfluß von Poren aus Fertigungsbeschichtungen auf die Schwingfestigkeit längsbeanspruchter Kehlnähte*, Darmstadt: Bericht Nr. FB-160.

Reemsnyder, H. S., 1963. *Fatigue strength of longitudinal fillet weldments in USS "T-1" constructional alloy steel - Fritz Engineering Laboratory Report: No. 284.6*.

Schneider, C. R. A. & Maddox, J., 2003. *Best practice guide on statistical analysis of fatigue data - IIW-XIII-WG1-114 - 03*, Cambridge.

Sedlacek, G. et al., unpubl. *Commentary to Eurocode 3: EN 1993 - Part 1-9 - Fatigue*, Aachen.

Maintenance, Safety, Risk, Management and Life-Cycle Performance of Bridges – Powers, Frangopol, Al-Mahaidi & Caprani (Eds)
© 2018 Taylor & Francis Group, London, ISBN 978-1-138-73045-8

Recommended fatigue strengths of thick-walled circular K-joints and influence of weld root irregularities

S. Bove & M. Euler & U. Kuhlmann
Institute of Structural Design, University of Stuttgart, Germany

ABSTRACT: Welded tubular K-joints made of circular hollow sections under fatigue loading are widely used in civil, mechanical and plant engineering. Recently, more and more thick-walled structures with a low chord slenderness have been realized. Unfortunately, the existing design rules (e.g. CIDECT Design Guide 8 or EN 1993-1-9) cover only K-joint geometries with $\gamma = d_0 / (2 \cdot t_0) > 12$ or limit the wall thickness to t_0 and $t_1 \leq 8$ mm. There had been doubts due to a possible deteriorating size effect, if the fatigue strengths derived from the existing test data can also be recommended for tubular K-joints with low chord slendernesses, ranging between $3 \leq \gamma \leq 12$. The outcome of two German research projects is presented. In the first already finalized project the fatigue behavior of thick-walled tubular K-joints had been investigated. In the latter still running project the focus is laid on the influence of the weld quality on the fatigue strength of these joints.

1 INTRODUCTION

Welded tubular trusses under fatigue loading made of circular hollow sections (CHS) are widely used in civil, mechanical and plant engineering. Especially K-joints, where the braces and the chord form a lying K, are particularly frequent.

There are generally two possibilities to fabricate tubular K-joints. The truss members can be connected by means of cast steel elements which all truss members are welded on. Another possibility, being supposed to be focused on in this paper, is the fabrication by direct welding the braces to the chord members.

Recently, more and more welded thick-walled tubular K-joints with low chord slenderness $\gamma < 12$, Eq. (1) have been realized.

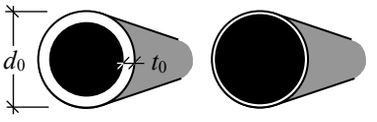
$$\gamma = \frac{d_0}{2 \cdot t_0} \tag{1}$$

d_0 … chord diameter
t_0 … chord wall thickness

However, the existing design recommendations cover only K-joints with relatively thin-walled chords and, consequently, high γ-values. For example the rules of CIDECT (Zhao et al. 2000) are only valid for $\gamma \geq 12$ and those of DNV (2010) for $\gamma \geq 8$.

The limitation of the chord slenderness γ can be attributed to the existing test database, lacking a statistically appropriate number of test results for tubular joints (including K-joints) with $\gamma < 12$.

Table 1. Definitions.

Wall thickness	**thick-walled**	**thin-walled**
absolute	$t_0 > t_{ref}$	$t_0 \leq t_{ref}$
relative, $\gamma = d_0 / (2\ t_0)$	$\gamma < 12$	$\gamma \geq 12$
Illustration		

There have been doubts due to a possible deteriorating size effect, if the fatigue strengths derived from the existing test data can also be recommended for tubular K-joints with low chord slendernesses ranging between $3 \leq \gamma \leq 12$. The size effect describes the size dependency of the fatigue strength due to statistical, technological or geometrical effects (Ørjasæter 1995).

For clarity, the chord of a CHS K-joint will be considered as absolutely thick-walled in this paper if its wall thickness t_0 exceeds the reference wall thickness t_{ref} of the detail category, for which no size effect has to be assumed. With respect to the limitation of the CIDECT design recommendations, the chord of a K-joint with $\gamma < 12$ is referred to as relatively thick-walled respectively, Table 1.

The paper derives a proposal for the fatigue strength (finite fatigue life regime, as-welded, in air) of uni- and multiplanar welded CHS K-joints whose chord slendernesses range between $3 \leq \gamma \leq 12$. The derivation of the proposal is based on the outcome of a German research project (Kuhlmann et al. 2014).

Another aspect being addressed in this paper is the influence of weld root irregularities of welded CHS K-joints on the fatigue strength. Frequently, welded hollow-section joints has been regarded as questionable because a reliable detection of internal weld irregularities by non-destructive testing (NDP) is nearly impossible. This is also one of the reasons why CHS joints were commonly fabricated by using cast steel elements. Hence, in order to increase the acceptance of directly welded CHS joints it is important to investigate and quantify the influence of the weld irregularities, such as incomplete fusion and weld root opening, on the fatigue strength. These aspects are addressed in a further still running German research project (Kuhlmann et al. 2017). The outcome of a numerical investigation and parameter study on the influence of varying weld root irregularities will be presented.

2 STATE OF THE ART

2.1 *Structural stress approach*

The fatigue evaluation of welded tubular joints including CHS K-joints is complicated due to the stress concentration at the member intersections that leads to an increase of the nominal stress at the joint region. The stress rising effect is caused by the structure of the joints (shift in overall geometry and stiffness) and the welding (local notch effects, residual stresses and material inhomogeneity induced by welding process).

The stress concentration varies around the member intersections and renders the definition of a meaningful nominal stress for tubular joints difficult. Therefore, the fatigue evaluation of tubular joints is usually based on structural stresses (also called hot-spot stresses) instead of nominal stresses.

2.2 *Fatigue strength from structural stresses*

The fatigue behavior in a finite fatigue life regime, in accordance with the structural stress approach for tubular joints, is described by particular *S-N* curves that relate the fatigue failure to structural stress range and number of stress cycles. The fatigue strength $\Delta\sigma_R$ of a joint with wall thickness, t, for a particular number of cycles, N, is defined by Equation (2). It includes three parameters: (i) the detail category expressed by the (theoretical) intercept A of the *S-N* curve with the log N axis, (ii) the slope m, and (iii) a proposal concerning the treatment of the size effect including the reference wall thickness t_{ref} and a corresponding exponent B.

$$\Delta\sigma_R = \underbrace{\sqrt[m]{\frac{10^A}{N}}}_{\text{detail category}} \cdot \underbrace{\left(\frac{t_{ref}}{t}\right)^B}_{\text{size effect}} \qquad (2)$$

Table 2 gives an overview of the parameters assumed by different common fatigue design recommendations. With exception of the recommendations of DNV, the design rules for the fatigue strength are similar. The recommendations of CIDECT are identical with those of IIW (Zhao & Packer 1999). The lower detail category of DNV can partly be explained by the higher reference wall thickness.

To characterize the detail category, a reference value $\Delta\sigma_C$ (structural stresses) is commonly used that represents the fatigue strength $\Delta\sigma_R$ of a tubular member with reference wall thickness t_{ref} for $N = 2$ million stress cycles.

The slope of the *S-N* curve for the reference wall thickness is fixed for all mentioned design recommendations to $m = 3$.

Table 2. Fatigue strength (structural stresses) in selected design recommendations.

	EC3	**DNV**	**API**	**CIDECT**
$\Delta\sigma_C$ [MPa] (air)	114 [a]	90 [b]	114 [c]	114
Intercept A [-]	12.476	12.164	12.476	12.476
Survival probability [%]	95 [a]	97.7	97 [c]	95
Failure criterion	through-crack	through-crack	through-crack [c]	through-crack [d]
Ref. wall thickness t_{ref} [mm]	16 [a]	32	16	16
Exponent B of size effect	–	0.25	0.25	0.06 log N
Positive effect for $t < t_{ref}$?	–	no	no	yes

[a] van Wingerde et al. (1997), p. 126 & 133
[b] curve T [c] API RP 2A-WSD, Sec. C5.2.5 & p. 58, 214
[d] Zhao & Packer (1999), p. 5

The size effect is usually expressed by a factor containing all influencing parameters. In Equation (2), only the failing wall thickness, t, is considered as a relevant influencing dimension. The existing formulation of fatigue strength $\Delta\sigma_R$ (structural stresses) in CIDECT is based on an extensive statistical evaluation of test data primarily recorded on thin-walled tubular joints ($\gamma \geq 12$) by van Wingerde et al. (1997). Herein the size effect is considered exclusively as a thickness effect, as in Equation (2) that depends on the number of stress cycles, N.

2.3 *Applicability of existing design rules*

For the fatigue design of thick-walled K-joints with $\gamma < 12$ the direct applicability of the existing definition of the fatigue strength had to be questioned. Therefore, a working hypothesis was formulated assuming that the separation in Equation (2) between the detail category on the one hand, and the size effect due to wall thicknesses $t \neq t_{ref}$ on the other hand, can be maintained for thick-walled K-joints.

If other parameters besides the wall thickness – especially the chord slenderness – had a significant influence on the fatigue strength, this influence should result in a lower detail category for thick-walled K-joints in a first step. In a second step it should be thought about if this influence should also be separated from the detail category by adding an additional factor.

To answer this question by experimental evidence, a first research project (Kuhlmann et al. 2014) was set up aiming to fill the gap of knowledge concerning the fatigue behavior of thick-walled welded K-joints and to enlarge the application range of this type of constructional detail.

2.4 *Influence of weld quality*

As the intersection region of welded hollow section joints is highly stressed, the influence of the weld shape (e.g. weld toe radius) and the weld quality (e. g. weld irregularities) on the fatigue strength is more pronounced. Several research projects were conducted focusing on weld irregularities and their influences on the fatigue behavior of the considered constructional detail.

For example, Scholte & Buisman (1988) investigated the influence of varying weld irregularities on the fatigue strength of CHS-to-CHS butt joints. It could be shown that an incomplete penetration can reduce the fatigue life by half and that defects at the weld root can lead to a crack initiation at this point.

Qian et al. (2013) investigated the influence of partially penetrated butt welds at the crown toe of CHS X-joints, see Figure 1(b). In contrast to the aforementioned butt joints they concluded that a partial penetration has a negligible influence on the fatigue strength of butt welds as long as the weld toes are not post-weld treated shifting the potential crack initiation point to the weld root.

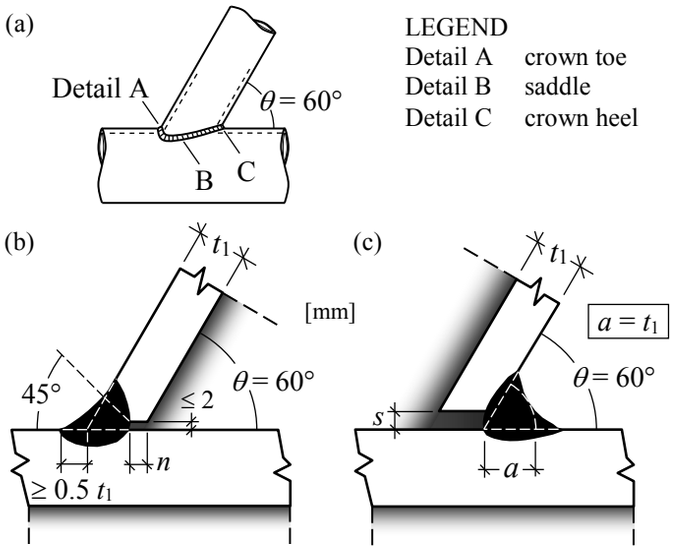


Figure 1. Weld root irregularities: (a) overview; (b) incomplete fusion, *n*, at detail A, (c) root opening, *s*, at detail C

To summarize, the influence of weld irregularities has to be differentiated depending on the type of joint. To quantify the influence of weld root irregularities on CHS K-joints is the aim of a further research project (Kuhlmann et al. 2017). In this project thick-walled CHS K-joints with artificial weld irregularities at the weld roots are investigated in order to develop a planning and fabrication guideline for designers as well as steel construction companies. In case of a discovered weld root irregularity, this guideline should help to determine if this defect has to be repaired or can be kept. The prerequisite is, however, that the presence and the size of an irregularity can be determined by NDP. Therefore, the investigation of the welds by means of ultrasonic examination is also part of this research project.

3 EXPERIMENTAL INVESTIGATIONS

3.1 *Overview*

In the first mentioned German research project No. P815/ IGF 325 ZBG of the "Forschungsvereinigung für Stahlanwendung (FOSTA) e. V." financed by the German Federal Ministry of Economic Affairs and Energy (BMWi), the fatigue behavior of welded uni- and multiplanar K-joints with thick-walled chords was investigated. The research project was carried out by four partners: (i) Stuttgart University, (ii) Munich University of Applied Sciences, (iii) Munich University of Armed Forces and (iv) Schweißtechnische Lehr- und Versuchsanstalt (SLV) Halle, and comprised a comprehensive test program and detailed numerical investigations.

The second German research project (FOSTA P1163 / IGF 18883 BG) was launched in order to investigate the fatigue strengths of thick-walled CHS K-joints with systematic weld irregularities at the crown heel and crown toe, see incomplete fusion, *n*, and weld root opening, *s*, in Figure 1. Additionally, two variations of the weld build-up including circumferential fillet welds and a sharper weld shape are investigated. This research project is carried out by (i) Stuttgart University, (ii) Munich University of Applied Sciences and (iii) Forschungszentrum Ultraschall (FzU) Halle.

3.2 *Test series*

The test program in Kuhlmann et al. (2014) contained in total more than 80 single-joint fatigue tests with constant stress amplitude that fell into eight test series, including a large-scale girder spanning about 11 m. Of these tests, 63 were performed on as-welded test specimens and are addressed in Table 3. The remaining 20 single-joint fatigue tests investigated the influence of a post-weld treatment on the fatigue strength and are not covered by this paper.

Table 3. Overview of test series in Kuhlmann et al. (2014).

Symbol	Series	Loading [a]	*R*	Joint	Chord	Brace	γ	Number
◇	1	Chord – IPB	> 0	K	177.8 × 20	88.9 × 5	4.45	5
○	1	Chord – AX	> 0	K	177.8 × 20	88.9 × 5	4.45	2
▽	1	Brace – IPB	– 1	K	177.8 × 20	88.9 × 5	4.45	3
□	1	Brace – AX	– 1	K	177.8 × 20	88.9 × 5	4.45	9
◇	2	Chord – IPB	> 0	K	177.8 × 20	88.9 × 12.5	4.45	5
○	2	Chord – AX	> 0	K	177.8 × 20	88.9 × 12.5	4.45	2
▽	2	Brace – IPB	– 1	K	177.8 × 20	88.9 × 12.5	4.45	2
□	2	Brace – AX	– 1	K	177.8 × 20	88.9 × 12.5	4.45	8
✦	3	Chord – IPB	> 0	K	273.0 × 40	139.7 × 10	3.41	5
✦	4	Chord – IPB	> 0	K	273.0 × 40	139.7 × 16	3.41	4
⊗	4	Chord – IPB	– 1	K	508.0 × 40	244.5 × 25	6.35	2
⊗	4	Chord – IPB	– 1	K	508.0 × 60	244.5 × 25	4.23	2
⊕	5	Chord – IPB	– 1	K	273.0 × 40	139.7 × 10	3.41	2
✡	6	Chord – IPB	> 0	KK	177.8 × 20	88.9 × 5	4.45	3
✡	6	Chord – AX	> 0	KK	177.8 × 20	88.9 × 5	4.45	1
✶	8	Combined	– 1	K	177.8 × 20	88.9 × 5	4.45	2
✶	8	Combined	– 1	K	177.8 × 20	88.9 × 12.5	4.45	2
●	Girder	Combined	0.1	K	193.7 × 25	88.9 × 12.5	3.87	–
▼	Girder	Combined	0.1	KK	193.7 × 25	88.9 × 12.5	3.87	–

[a] IPB: in-plane bending; AX: axial force

In order to isolate the deciding parameters on the fatigue strength and to identify the characteristics of the fatigue failure of thick-walled K-joints the specimens of single-joint tests were subjected to several elementary load cases, Figure 2. For further details see Kuhlmann et al. (2014).

In Kuhlmann et al. (2017) 30 single-joint fatigue tests will be performed in order to discover the influence of weld root irregularities, Table 4.

3.3 *Test specimen*

The cross-sectional dimensions and the varying parameters of the test specimens are given in Table 3. The brace angle was set to 60° for all specimens. Addressing the needs of practitioners, a combination of butt and fillet welds for the brace-to-chord intersection was realized. The weld starts as a full-penetration weld at the crown toe and turns into a fillet weld at the crown heel with a smooth transition, see Figure 1.

Only hot-finished circular hollow sections of steel grade S355J2H according to EN 10210-1 were used.

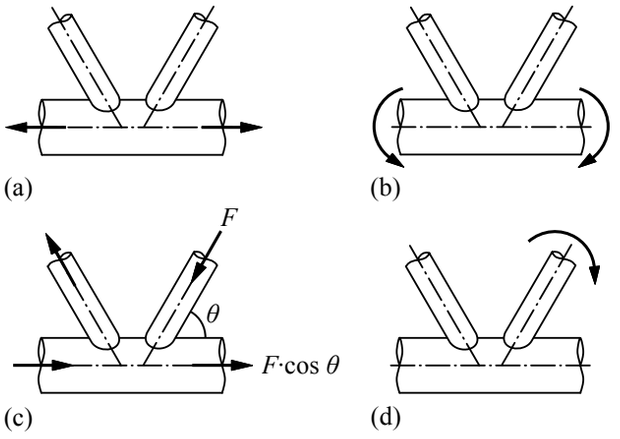


Figure 2. Investigated elementary load cases:
(a) chord axial force (Chord-AX), (b) chord bending (Chord-IPB), (c) brace axial force with compensating chord axial force (Brace-AX), (d) brace bending (Brace-IPB).

Table 4. Overview of test series in Kuhlmann et al. (2017).

Series	Loading [a]	*R*	Joint	Chord	Brace	γ	Number	Parameter
100	Brace – AX	– 1	K	177.8 × 20	88.9 × 12.5	4.45	3	as Kuhlmann et al. (2014)
101	Brace – AX	– 1	K	177.8 × 20	88.9 × 12.5	4.45	6	weld root opening s = 3 mm
102	Brace – AX	– 1	K	177.8 × 20	88.9 × 12.5	4.45	6	weld root opening s = 6 mm
103	Brace – AX	– 1	K	177.8 × 20	88.9 × 12.5	4.45	6	incomplete fusion n = 6 mm
200	Brace – AX	– 1	K	177.8 × 20	88.9 × 12.5	4.45	3	circumferential fillet weld
201	Brace – AX	– 1	K	177.8 × 20	88.9 × 12.5	4.45	3	sharper weld shape
300	Chord – IPB	– 1	K	660.0 × 60	406.4 × 12.5	5.5	3	large-scale tests

[a] IPB: in-plane bending; AX: axial force

3.4 *Failure criterion*

In accordance with the existing design recommendations, the first through-wall-thickness crack was considered as the relevant failure criterion, Table 2. To detect this through-crack reliably, the test specimens were set under a small overpressure after airproof closing their ends. As the overpressure was permanently recorded during the tests, a sudden pressure drop indicated the first through-crack.

In the case of the test girder this kind of crack detection was not possible. Here, the determination of the first through-crack was realized through beach marks on the fracture surface induced by variable-amplitude loading.

3.5 *Fatigue test results*

The outcome of the fatigue tests of Kuhlmann et al. (2014) is shown in Figure 4. For technical reasons, the fatigue tests had to be performed with different stress ratios, R, shown in Table 3. Furthermore, the failing member was different depending on the load case. Thus, the failing wall thickness was not the same in all tests. Therefore, to ensure compatibility of the test results the test data in Figure 4 have been modified (see details in Sec. 5).

For all as-welded test specimens the cracks were initiated at the weld toes of either the chord or the brace, Figure 3. Under chord loading the first through-crack was exclusively initiated at the weld toes of the chord either at the crown toe or at crown heel, No. 01 or 05 in Figure 3.

Under brace axial force the first through-cracks were detected in the gap region. For the test specimens with $t_1/t_0 = 0.25$ through-thickness cracking of the brace wall occurred, while for the test specimens with $t_1/t_0 = 0.63$ through-thickness cracking of the chord wall appeared. For specimens with a ratio of $t_1/t_0 = 0.25$ the cracks initiated at location No. 11, while for a ratio of $t_1/t_0 = 0.63$ location No. 01 in Figure 3 was the critical.

When brace bending was applied as a reverse loading with $R = -1$, cracks initiated at several locations (No.01, 05, 11 & 15 in Figure 3). The through-crack occurred either in the chord or the brace.

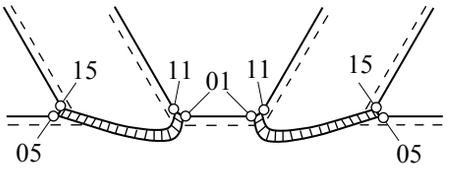


Figure 3. Possible positions of crack initiation.

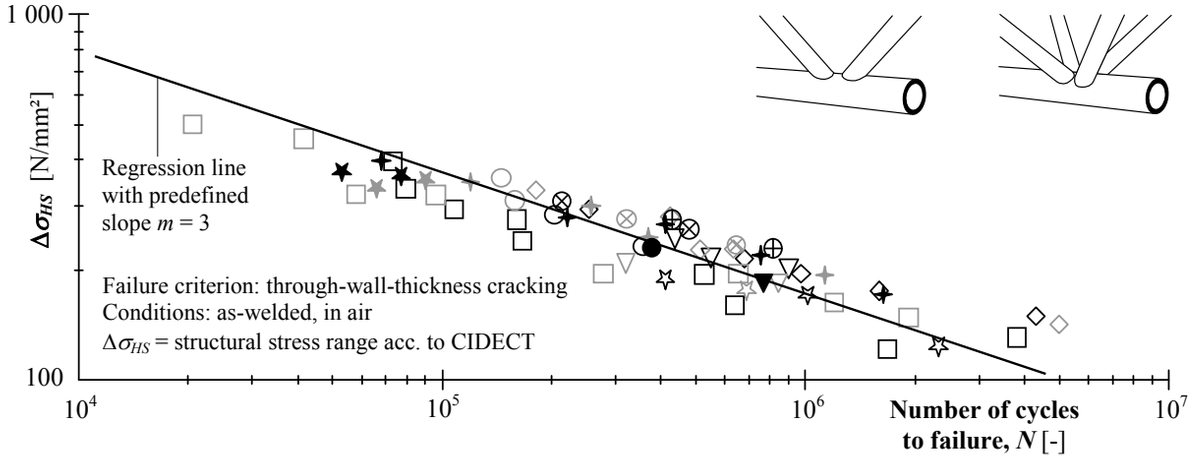


Figure 4. Test data of Kuhlmann et al. (2014) modified for failing wall thickness and stress ratio R according to Equations (3) & (4) (for symbols see Table 2)

4 NUMERICAL INVESTIGATIONS

In order to determine the structural stresses and stress ranges acting in the test specimens during the fatigue tests, a 3D parameterized Finite Element (FE) model with elastic material behavior was generated with ANSYS 14.0. 20-node-solid elements of type SOLID186 with reduced integration scheme 2×2×2 were used. The model was validated through strain measurements recorded before each fatigue test. As the test specimens differed in geometry and loading, they were grouped for the evaluation. The overall dimensions and the weld shape of all test specimens of one single group were measured and subsequently averaged, so that each group was represented by one mean geometry. The FE stress components perpendicular to the weld toe around the brace-to-chord intersections were determined. Based on these components a quadratic regression within the region next to the considered weld toe was performed. The stresses of the regression at the distances $L_{r,min}$ and $L_{r,max}$ were used for the linear extrapolation of the structural stresses at the weld toe. For further information, see Zhao & Packer (1999) and Kuhlmann et al. (2014).

5 STATISTICAL EVALUATION

5.1 *Modifications*

For the statistical evaluation the same thickness effect as for thin-walled tubular joints according to CIDECT (Zhao et al. 2000) with a reference wall thickness t_{ref} = 16 mm was assumed. For comparability, the results of the fatigue tests had to be adjusted to the reference wall thickness by Equation (3). For a test specimen that failed in a wall with $t < t_{ref}$ the structural stress range of the fatigue test was lowered by Equation (3) in order to account for the hypothetically shorter fatigue life of the same test specimen with $t = t_{ref}$, and vice versa.

$$\Delta\sigma^{t=16} = \Delta\sigma^{t\neq16} \cdot \left(\frac{16}{t}\right)^{-0.06 \log N} \quad (3)$$

To adjust all fatigue tests to the same stress ratio $R = 0$, the stress ranges of tests with $R = -1$ had to be modified by Equation (4), derived for an average of low and high residual stresses in Eurocode 3, Part 1-9, Sec. 7.2.1. For a stress ratio $R = -1$ the value f amounts to 1.125.

$$\Delta\sigma_{(R=0)} = \frac{\Delta\sigma_{(R=-1)}}{f} \quad (4)$$

For technical reasons the final rupture, instead of the first through-crack, was recorded as the failure criterion in five fatigue tests. For these tests the number of stress cycles to through-cracking was estimated at 67 % of the number of cycles to rupture. This relationship was found by van Wingerde et al. (1997) for thin-walled tubular joints.

5.2 *Discussion of results – Size effect*

The outcome of the statistical evaluation according to the procedure proposed by Brozzetti et al. (1989) is summarized in Table 5. The same procedure has been used by van Wingerde et al. (1997) for setting up the existing CIDECT detail category 114 for tubular joints (see Table 2).

Table 5. Characteristic reference value $\Delta\sigma_C$ [N/mm²] of fatigue strength (structural stresses) for 2 million stress cycles and reference wall thickness 16 mm; failure criterion: through-wall-thickness cracking; conditions: as-welded, in air; survival probability according to Eurocode 3 (Brozzetti et al. 1989).

Scope	***S-N* curve**		**Ref.**	**Sample size**
	***m* = 3**	***m* = var.**		
K/KK joints	104	116	‡	59
$\gamma < 12$	106	114	‡†	73
Tubular joints $\gamma \geq 12$	107	–	*	115

‡ = Kuhlmann et al. (2014)
† = Schumacher (2003), Borges (2008)
* = van Wingerde et al. (1997), p. 133

Actually, the CIDECT detail category 114 corresponds with complete loss of strength as a failure criterion. However, van Wingerde et al. (1997) could show that for the through-wall-thickness cracking, the corresponding detail category $\Delta\sigma_C$ = 107 N/mm² (Table 5) is only slightly decreased due to a lower scatter of test data for this criterion. Furthermore, the detail category 107 has to be considered still conservative because a steeper slope of m = 3 (instead of the real slope of test data) is assumed for the evaluation.

Interestingly, the computed reference value $\Delta\sigma_C$ = 104 N/mm² for thick-walled K-joints corresponds quite well with that for thin-walled tubular joints, $\Delta\sigma_C$ = 107 N/mm² in Table 5 for a fixed slope m = 3. Apparently, thick-walled K-joints with $\gamma < 12$ and tubular joints with $\gamma \geq 12$ belong to the same statistical population. Figure 5 illustrates this finding, plotting the structural stress ranges, $\Delta\sigma_{HS}$, against the achieved number of stress cycles to failure.

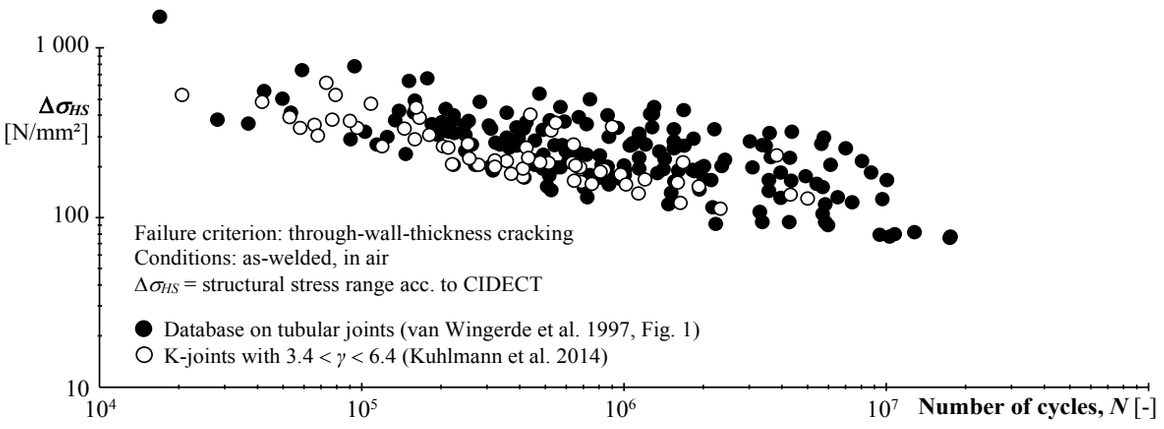


Figure 5. Test data of Kuhlmann et al. (2014) together with test database of van Wingerde et al. (1997) without any modification for failing wall thickness and stress ratio. Note: Test data of van Wingerde et al. are divided by 1.49 to account for the failure criterion.

It can be concluded that the size effect of thick-walled K-joints can mainly be attributed to the dependency on the absolute wall thickness. The influence of the chord slenderness γ (relative wall thickness) seems to be less pronounced.

6 WELD IRREGULARITIES – A FIRST NUMERICAL INVESTIGATION

6.1 *Introduction*

In order to increase the acceptance of directly welded CHS joints the influence of weld irregularities at the weld roots of CHS K-joints is investigated by Kuhlmann et al. (2017). A preliminary numerical study based on the notch stress approach according to Fricke (2008) identifies the effect of an incomplete fusion, s, of the crown toe's weld root and of a root opening, n, of the crown heel's weld root, see Figure 1. The notch factors k_f serve as reference.

6.2 *Global model*

In a first step a global numerical elastic model was generated with ANSYS 16.2 and built up of 20-node-solid elements of type SOLID186 with reduced integration scheme 2×2×2 with exception of the weld being modelled with 10-node-solid elements of type SOLID187. This model was validated by comparison with strain measurements recorded during the tests carried out at Kuhlmann et al. (2014) showing no significant weld irregularities s and n. Due to the boundary conditions of the test rig in Figure 6 (a), the K-joint of the global model has to be subjected to brace normal forces, N_1, and brace in-plane bending, M_1, Figure 6 (c). The same holds for the chord (not shown in Figure 6). Exclusively, CHS K-joints with chords of 177.8 mm in diameter and 20 mm in wall thickness were considered. The braces had diameters of 88.9 mm and a wall thickness of 12.5 mm.

6.3 *Submodel*

The notch factors k_f with respect to the nominal brace stress were determined by using the FE submodel technique. The elastic submodel consisted of of 20-node-solid elements of type SOLID186. For the crown toe and heel two 3D submodels (A and B) were created, Figure 6 (c). The displacements of the global model nodes corresponding with nodes of the submodel boundary areas were applied onto the submodel as loading. An effective notch radius of r_{ref} = 1 mm was assumed according to Fricke (2008).

The calculated notch factors k_f of three particular points of the weld at the crown toe for several values of incomplete fusion n are shown in Figure 7. It can be recognized that the weld toe at the chord (#1) remains still decisive when n increases. The notch factor of the weld root (#3) increases with greater n but stays beneath those of the weld toes (#1 and 2).

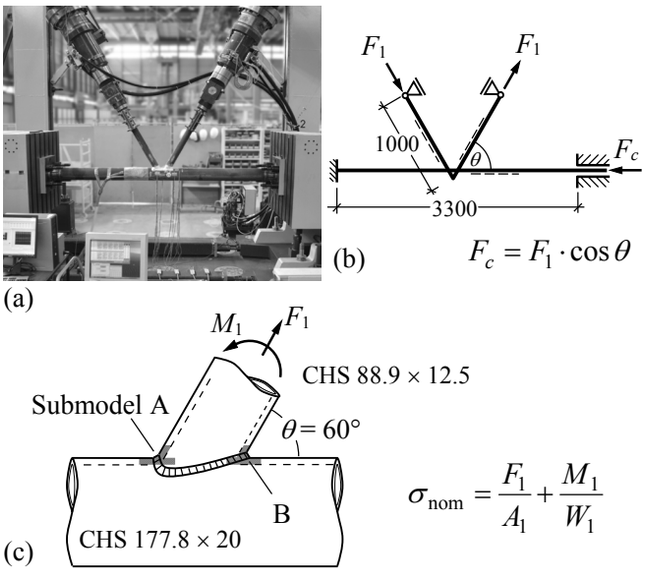


Figure 6. Global model: (a) test rig of Kuhlmann et al. (2014), (b) corresponding static system, (c) internal brace actions of global FE model due to brace loading with location of FE submodels and nominal stress definition

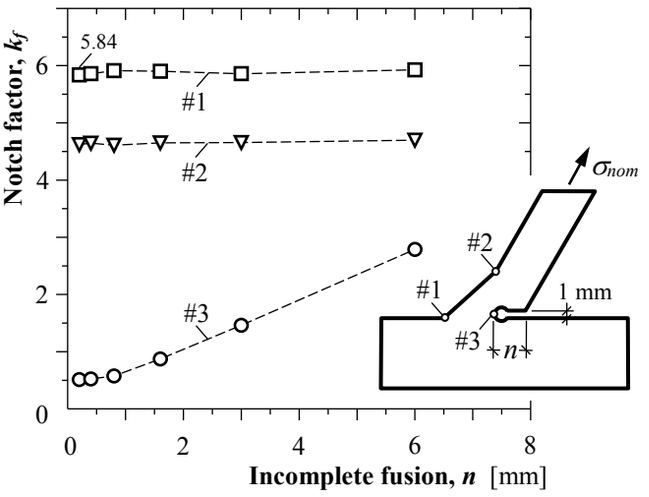


Figure 7. Notch factors k_f for varying incomplete fusion n at the crown toe (submodel A).

In Figure 8 the calculated notch factors k_f are plotted against the size of the weld root opening, s, at the crown heel. Notice that position #4 only appears for gap sizes larger than 2 mm. Otherwise #3 and #4 coincide.

Firstly, it can be stated that the weld toe of the brace (#2) remains decisive, and the effective notch stress of this point increases only slightly for higher values s. Secondly, the figure shows that with increasing weld root opening the notch factor of the weld root (#3) increases considerably but remains below the value of the weld toe (#2). Whether the crack is initiated at the crown heel or at the crown toe can be decided by comparing the notch factors calculated for #1 in Figure 7 and for #2 in Figure 8. Confirming the results from the conducted tests in

Kuhlmann et al. (2014) with no significant weld irregularities ($s \approx 0$, $n \approx 0$), the cracks initiate more likely at the crown toe with the higher $k_f = 5.84$.

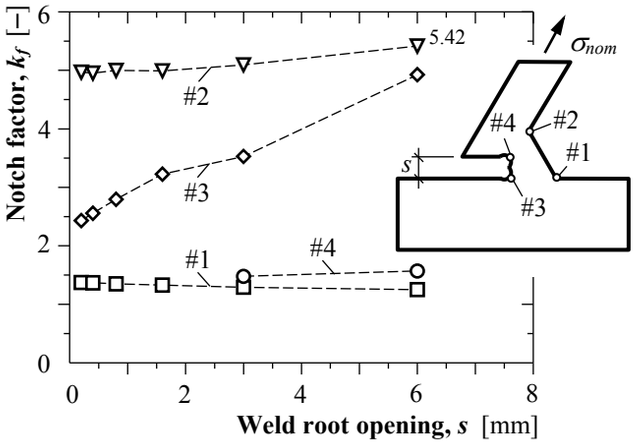


Figure 8. Notch factors k_f for varying gap sizes s between the brace and the chord at the crown heel (submodel B).

The incomplete fusion $n < 6$ mm at the crown toe does not seem to be critical for the considered joint geometry. The maximum notch factors occur at the weld toes. In terms of the weld root opening s at crown heel the notch factors of the weld root approaches that of the weld toe for values $s > 3$ mm. Nevertheless, the investigated range of s is not critical for the joint as the weld toes of the crown toe show higher notch factors assuming identical fatigue strengths of weld toe and weld root.

7 SUMMARY

Through experimental evidence it has been shown that the fatigue strength $\Delta\sigma_C$ (finite life regime, as-welded, in air, criterion: through-wall-thickness cracking) of uni- and multiplanar welded CHS K-joints with chord slendernesses $3 \leq \gamma \leq 12$ is comparable to that of tubular joints covered by the existing CIDECT detail category. For the tested specimens the size effect depended primarily on the failing wall thickness. The influence of the chord slenderness γ was not significant.

In a first numerical study it could be shown for a particular CHS K-joint geometry tested in Kuhlmann et al. (2014) that the effect of weld irregularities (incomplete fusion at crown toe, weld root opening at crown heel) on the fatigue strength is not significant. This finding has to be validated by fatigue tests being planned for the near future. Further numerical studies are supposed to enlarge the application range, additionally.

ACKNOWLEGDEMENT

The authors take this opportunity to express their profound gratitude to all supporters of their research. Special thanks to German Federal Ministry for Economic Affairs and Energy; Forschungsvereinigung Stahlanwendung (FOSTA) e. V.; Vallourec Deutschland GmbH, ZIS Industrietechnik GmbH, Meerane. Moreover, the authors would like to thank all project partners for their good and fruitfully cooperation.

8 REFERENCES

API RP 2A-WSD 2005. *Recommended practice for planning, designing and constructing fixed offshore platforms – working stress design*. American Petroleum Institute (API).

Borges, L.A.C. 2008. *Size effects in the fatigue behaviour of tubular bridge joints*. Dissertation, École Polytechnique Fédérale de Lausanne (EPFL), Switzerland.

Brozzetti, J.; Hirt, M.A.; Ryan, I.; Sedlacek, G. & Smith, I.F.C. 1989. *Background documentation 9.01: Background information on fatigue design rules – Statistical evaluation Chapter 9*. Eurocode 3 Editorial Group.

DNV-RP-C203 2010. *Fatigue design of offshore steel structures – Recommended practice*. Det Norske Veritas.

EN 1993-1-9: 2005 + AC: 2009. *Eurocode 3: Design of steel structures – Part 1-9: Fatigue*

Fricke, W. 2008. *Guideline for the Fatigue Assessment by Notch Stress Analysis for Welded Structures*. IIW-Doc. XIII-2240-08/XV-1289-08

Kuhlmann, U.; Bucak, Ö.; Mangerig, I.; Kranz, B.; Euler, M.; Hubmann, M.; Fischl, A.; Hess, A.; Hermann, J. & Zschech, R. 2014. *FOSTA P815 - Fatigue-resistant trusses of circular hollow sections with thick-walled chords* (in German). Düsseldorf: Forschungsvereinigung Stahlanwendung e. V.

Kuhlmann, U.; Dürr, A.; Steinhausen, R.; Bove, S.; Roth, J. & Pientschke, C. 2017. *FOSTA P1163 - Economical design of welded circular hollow sections joints under fatigue loading in consideration of the required weld quality (in German)*. In process. Düsseldorf: Forschungsvereinigung Stahlanwendung e. V.

Ørjasæter 1995. *Effect of plate thickness on fatigue of welded components*. IIW-Doc. XIII-1582-95.

Qian, X.; Petchdemaneengam, Y.; Swaddiwudhipong, S; Marshall, P.; Ou, Z. & Thang Nguyen, C. 2013. *Fatigue performance of tubular X-joints with PJP+ welds: I – Experimental study*. In: Journal of Constructional Steel Research 90, pp. 49 – 59

Scholte, H. G. & Buisman, B. C. 1988. *Fatigue behaviour of welded joints in offshore steel structures – Part 2: Tubular connections*. Final Report ECSC Convention 7210/KG/602.

Schumacher, A. 2003. *Fatigue behaviour of welded circular hollow sections joints in bridges*. Dissertation, École Polytechnique Fédérale de Lausanne (EPFL), Switzerland.

van Wingerde, A.M.; van Delft, D.R.; Wardenier, J. & Packer, J.A. 1997. *Scale effect on the fatigue behavior of tubular structures*. In Maddox, S. J. & Prager, M. (ed.), *Proc. of the International Conference on Performance of Dynamically Loaded Welded Structures, IIW 50th Annual Assembly Conference, San Francisco, 14-15 July 1997*: 123-135

Zhao, X.-L.; Herion, S.; Packer J.A.; Puthli, R.S.; Sedlacek, G.; Wardenier, J.; Weynand, K.; van Wingerde, A. M. & Yeomans, N. F. 2000: *CIDECT Design Guide for circular and rectangular hollow section welded joints under fatigue loading*. Köln: TÜV-Verlag.

Zhao, X.-L. & Packer, J.A. 1999. *Recommended Fatigue Design Procedure for Welded Hollow Section Joints*, IIW-Doc. XIII-1772-99/XV-1021-99

Maintenance, Safety, Risk, Management and Life-Cycle Performance of Bridges – Powers, Frangopol, Al-Mahaidi & Caprani (Eds)
© 2018 Taylor & Francis Group, London, ISBN 978-1-138-73045-8

Considering High Frequency Mechanical Impact Treatments in Design

S. Breunig & U. Kuhlmann
Institute of Structural Design, University Stuttgart, Germany

ABSTRACT: Regarding the revision of fatigue detail categories implemented in EN 1993-1-9, the discussion to integrate design approaches considering the beneficial application of innovative post-weld treatments, such as High Frequency Mechanical Impact (HFMI) treatment rises. Especially for fatigue loaded steel and composite bridges the potential of these technique enables to improve certain decisive welded details and shift the fatigue resistance to a higher level. In order to apply HFMI treatments for appropriate fatigue loaded steel structures in practice, rules have to be formulated in a code like manner.
Within this paper the work of the cooperative German DASt-AiF-Project "Development of a DASt-Guideline for High Frequency Mechanical Impact treatments" is presented, which aims at the implementation of a design concept in a German DASt-Guideline. The preceding work includes evaluation of existing knowledge and recommendations as well as analysis of collected and new test data with the aim to unify different applications into a homogenous and secured approach.

1 INTRODUCTION

1.1 *State of the Art*

The application of High Frequency Mechanical Impact (HFMI) treatment promises improved fatigue performance for selected welded details. Through the process of high frequent hammering with a hardened pin on the weld toe, a plastic deformation of its notch is achieved. This effect results in a reduction of the weld notch as well as the closure of micro cracks on the surface that could have led to points of crack initiations. Whereas the increase of fatigue resistance is mainly based on a change of residual stresses at the notch.

In order to be able to consider this improved fatigue strength in design, an official standard being approved by building authorities, is needed. Therefore it should be in accordance with Eurocode-design procedures. Efforts to quantify improvement factors for certain details, HFMI-techniques and influencing effects were made within several national and international projects.

Recently recommendations for the improvement quantification by HFMI for a wide range of details and conditions have been formulated by IIW. These IIW-Recommendations from Marquis & Barsoum (2016) are built up on the IIW-Guidelines of Hobbacher (2016), but have not been approved by a typical standardization process.

Thus the cooperative German DASt-AiF-Project "Development of a DASt-Guideline for High Frequency Mechanical Impact Treatments" (Kuhlmann et al. 2017) aims at the implementation of a design concept in a German DASt-Guideline, summarizing proved and secured application using the nominal stress concept according to EN 1993-1-9 (2005) and clearly giving application limits.

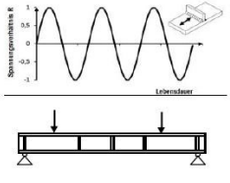
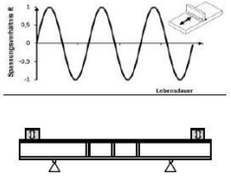
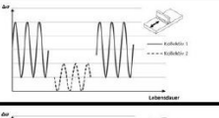
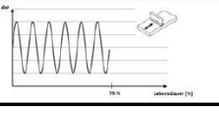
Tested Effect		Specimen Type	State	Amount
Component Effect		Small	aw	8
			HiFIT	6
			PIT	6
		Beam Series T2	aw	2
			HiFIT	8
			PIT	8
Mean stress		Small	aw	8
			HiFIT	6
			PIT	6
		Beam Series T1	aw	2
			HiFIT	3
			PIT	3
Multilevel Load		Small	aw	16
			HiFIT	12
			PIT	12
Preload		Beam	aw	8
			HiFIT	6
			PIT	6

Figure 1. Test program of DASt-AiF-project (Kuhlmann et al. 2017)

For that purpose, a test program of small scale and beam tests was realized to fill existing lack of knowledge, see Figure 1.

With the help of the test results, clear and secured rules should be defined that enable designers to take into account the beneficial usage of HFMI on new structures, depending on the specific conditions.

This paper summarizes the steps from the definition of tests and analyzing of current and existing test data up to the evaluation and modification of existing design approaches. Furthermore, additional gathered knowledge on influencing parameters such as mean stress effect and their impact on the revised approaches are shown. Finally, this knowledge is cumulated in a German DASt-Guideline on HFMI treatments, which is in accordance with EN 1993-1-9 and thus could be transferred into the future version of it.

1.2 *Design approaches and recommendations*

From 2007 on, when the first announcement of a design approach to consider Ultrasonic Impact Treatment (UIT) on unloaded transverse attachments in fatigue design was developed by Duerr (2007) (Kuhlmann et al. 2006), until now, there mainly exist three different design approaches based on the nominal stress concept built up on each other.

Based on knowledge of Duerr (2007) and own investigations on unloaded longitudinal attachments and transverse loaded butt welds, Weich (2009) (Ummenhofer et al. 2009) adapted and extended the design approach for these welded details and proved further boundary conditions.

Today the most recent design concept is the IIW-Recommendation of Marquis & Barsoum (2016). Its steadily development and thus improvement led to integration of several details and effects. Besides the nominal stress concept according to "IIW-Recommendation for fatigue design of welded joints and components" of Hobbacher (2016) it gives local approaches for the consideration of HFMI application. However the stepwise consideration of the improvement due to HFMI in the IIW-Guideline is not referring to EN 1993-1-9.

Berg (2016) has recently extended the approach based on the IIW-recommendations (Marquis & Barsoum 2016) and EN 1993-1-9 for ultra-high strength steels, namely from S960 to S1300 and additionally integrated cover plates in Stranghoener & Berg (2015).

2 MOTIVATION

2.1 *Claims for the DAS-Guideline*

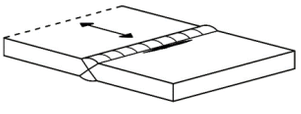
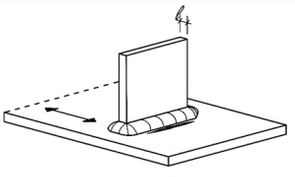
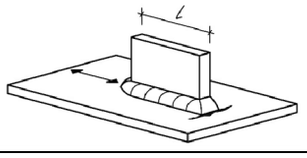
The intention of the DASt-Guideline is to enable designers of fatigue-loaded welded structures to consider the application of HFMI-treatment within the design using the nominal stress concept according to EN 1993-1-9 (2005).

In order to be approved by building authorities and used properly by designers there are several requirements for a guideline.

Obviously, the most important requirement for such a standard is to have sufficient secured results and understanding of the influencing effects for given statements and rules. This means that evaluated background information for several conditions and boundaries is needed. In case of gaps and lack of knowledge for certain conditions, they should be named and clearly excluded from the approach.

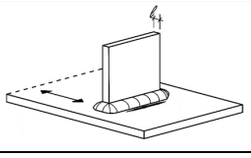
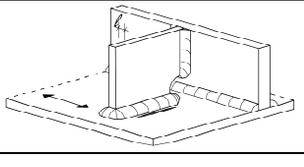
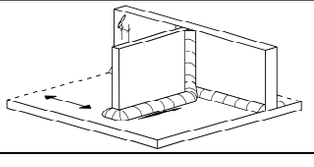
The second overarching objective of the DASt-Guideline is the user-friendliness. A certain level of simplification and thus unification of conditions can lead to an increased usage of HFMI. In order to meet acceptance of designers, the guideline should be practicable, easy to understand and reduced on the important and user-friendly form.

Table 2. Overview of investigated welded details.

Schematic view of detail	Description
	Transverse loaded butt weld acc. EN 1993-1-9 Tab.8.3
	Unloaded transversal attachment acc. EN 1993-1-9 Tab.8.4
	Unloaded longitudinal attachment acc. EN 1993-1-9 Tab.8.4

For both reasons the project partners decided to consider only three construction details and their variants. Especially the suitability for a successful treatment of the variants and the geometrical conditions of the details in Table 2 should be clearly de-

Table 1. Classification of appropriateness

appropriate	**not appropriate**	**appropriate**
		

fined within the DASt-Guideline.

As an example Table 1 shows appropriate and non-appropriate variants of the unloaded transverse stiffener.

2.2 *Conditions and test program of the project*

An extensive test program, consisting of 26 girder tests and 100 small specimen tests of S355 was developed to compensate deficiencies of the existing database and to answer open questions that need to be clarified. Figure 1 shows the test program. The decision of the main tested construction detail fell on the construction detail of the non-loaded transverse stiffener. Based on a large database of tests with different influencing factors that were investigated for unloaded transverse attachments in previous projects, this database can be used as a reliable reference basis so that comparisons to the planned series could be drawn. With the help of these specific test series the still open questions in terms of the design approach for HFMI will be clarified.

As the effectiveness of the HFMI treatments rises with the yield strength of the steel, the tests were conducted with S355J2 to be on the safe side for the draft of the guideline. Since the two most established techniques for Germany are the PIT technology and the HiFIT technology, those two different techniques were applied to the single series` specimen with their typically set parameters.

In the last ten years mainly two HFMI technologies have been established in Germany: the PIT (Pneumatic Impact Treatment) technique, that was further developed from the Ultrasonic Impact Treatment (UIT) by the German company Pitec GmbH, on the other hand the pneumatic actuated technology HiFIT (High Frequency Impact Treatment) developed by the German company Dynatec GmbH.

Besides a series of constant amplitude loading of small scale specimens and beam tests with a stress ratio of R = 0.1 representing tension-tension stresses, a series with an alternate loading of a stress ratio R = -1.0 could be tested. The aim was to be able to compare in regard of mean stress effects of HFMI-treated unloaded transverse stiffeners.

Another effect that was investigated experimentally is in how far the HFMI-treatment can prolong the lifetime of the welded detail, when the calculated service life of the as-welded state has already been reached. For that reason as-welded specimens have been loaded until 100% of their fatigue strength related to the respectively tested stress range level. Afterwards they have been HFMI-treated and tested until failure. This mainly represents the retrofitting potential due to HFMI-application on welds, that have had already reached their end of life-time.

For security reasons the impact of overloadings on the HFMI-treated welds is of increased interest. It could be that, due to higher loadings at the beginning of the lifetime of a treated weld, overloading could lead to destabilization of the introduced compressive residual stresses (see also Duerr (2007) and Weich (2009)). One aim of the project was to identify a critic level of load related to the yield strength in order to give a limitation or reduction factor in the guideline. Thus, a series of quasi-static tensioned and compressive overloadings has been developed within 40 specimens.

While the small scale tests were conducted at the KIT the 26 girder specimens were tested at the Materialprüfungsanstalt Universität Stuttgart. In this extract the focus lies on the girder test series T1 and T2 which will give information on the behavior of HFMI-treated girders depending on the mean stress.

3 BEAM TESTS ON THE MEAN STRESS EFFECT

3.1 *Test setup beam test series T1 (R = -1.0)*

The alternate loading of the beam tests with an unloaded transverse attachment in the mid span was realized with the help of resonance vibrations. This method has already been used in 1989 at BAM, (see Helms et al. 1989), since this is an advantageous testing method with regard to test duration and easy test setup. Therefore, external vibrators were fixed to the flanges in order to generate the desired bending line, which can be taken from Figure 2. With the help of measurement techniques, such as strain gages, applied on the beam flanges, load cycles could be counted and strains be measured.

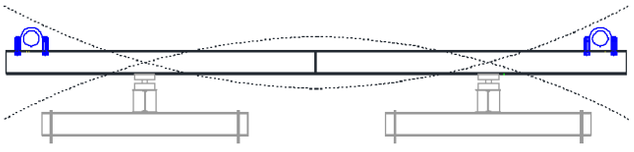


Figure 2. Sketch of bending line of test series T1

Defining the failure criterion to be a crack at the size of around 100 mm, the tests ran until that point. The difficulty was to detect the crack size while testing due to the high frequency of 33 to 35 Hz. Thus, strobe light was used to freeze the vibrating beam and detect the occurrence of cracks.

3.2 *Cracks and results beam test series T1 (R = -1.0)*

Due to the change of strains the crack initiation could be followed. Therefore, from time to time the external vibrators were stopped to document the time of crack initiation and crack propagation.

A typical crack on the weld toe connecting the bottom flange to the transverse stiffener can be seen in Figure 4. Two of the test beams were tested without a crack initiation until three million load cycles. Thus, they are characterized with an arrow and were neglected in the evaluation process. One of the six HFMI-treated girders failed from the flange without any impairment from welds.

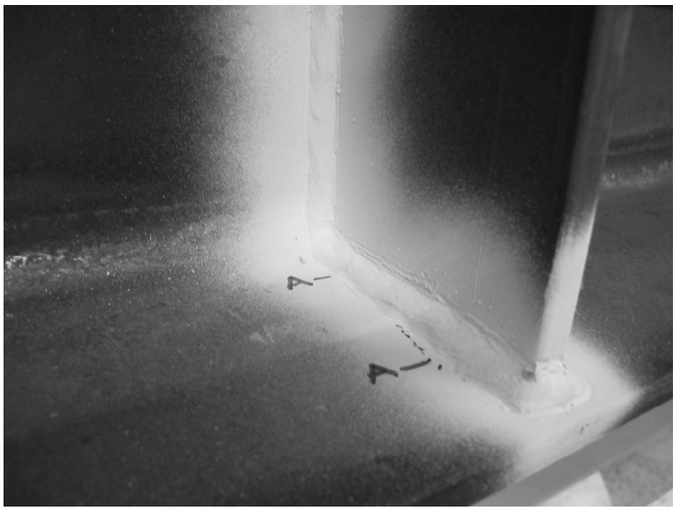


Figure 4. Typical crack at weld toe of transverse stiffener of beam test series T1

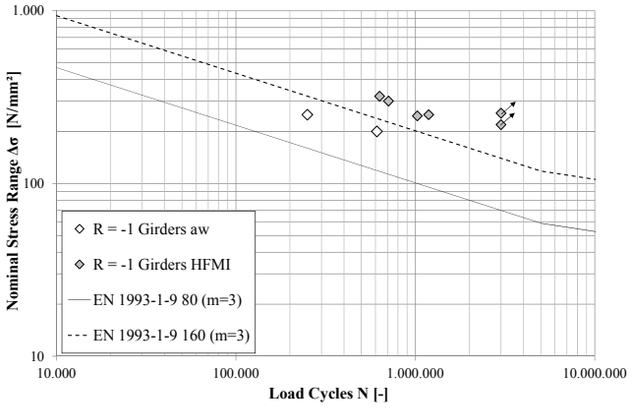


Figure 5. Results of beam test series T1 depending on the treatment-state compared to FAT-classes given in EN 1993-1-9

Figure 5 shows the single test results in a S-N-curve. The difference between HFMI-treated and as-welded series is clear. Whereas the difference between the two different HFMI-methods is not significant. In order to be able to compare to a non-treated state of standards, two fatigue categories, namely 80 MPa representing the as-welded transverse stiffener and 160 MPa, representing base material and

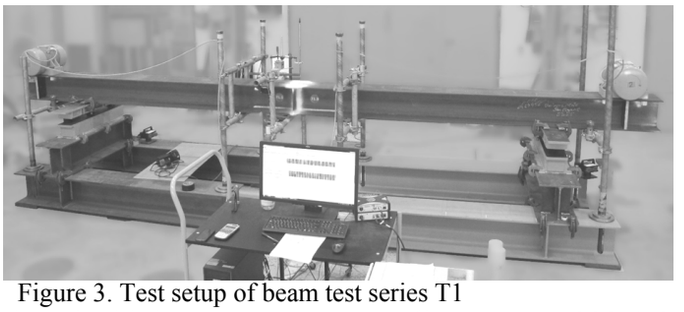


Figure 3. Test setup of beam test series T1

thus the highest category, according to EN 1993-1-9 (2005), are given. The potential of improvement due to HFMI-treatment is obvious, but also the as-welded state shows high potential in comparison to fatigue category 80 MPa.

3.3 *Test setup beam test series T2 (R = 0.1)*

In contrast to series T1, beam series T2 was regularly tested in a 4-point-bending test setup with two servo-hydraulic cylinders adapted to a testing portal. This setup enabled a testing speed of 0.8 to 2.5 Hz with a maximum dynamic loading of 800 kN per cylinder. In order to get secured results six transverse stiffeners were welded to the beam, so that some kind of redundancy was created.

3.4 *Cracks and results beam test series T2 (R = 0.1)*

Typical crack location can be seen in Figure 6. With the exception of one test specimen, all other beam tests cracked from the weld toe of the HFMI-treated weld connecting the transverse stiffener to the bottom flange. By opening the cracked cross section, it could be revealed, that the cracks usually started close to the area of the rounding off radius.

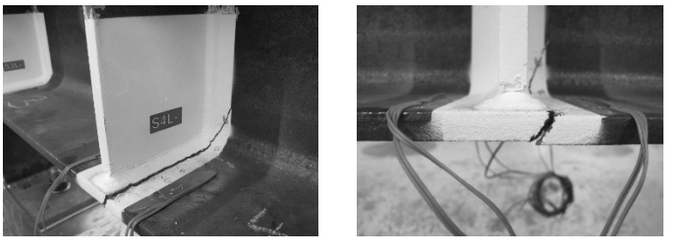


Figure 6. Typical failure mode of beam test series T2

The S-N-curve in Figure 7 shows the single test results, also compared to as-welded state of unloaded transverse attachment and base material category according to EN 1993-1-9 (2005). For the as-welded state it can be clearly seen, that comparatively high number of load cycles could be reached, which seems to be untypical for beam tests. On the other side the HFMI-treated girder test results scatter around fatigue category 160, clearly showing a higher slope than m = 3.

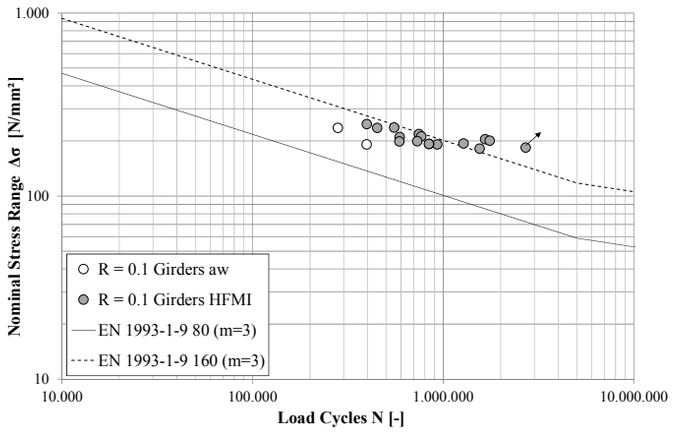


Figure 7. Results of beam test series T2 compared to FAT-classes given in EN 1993-1-9

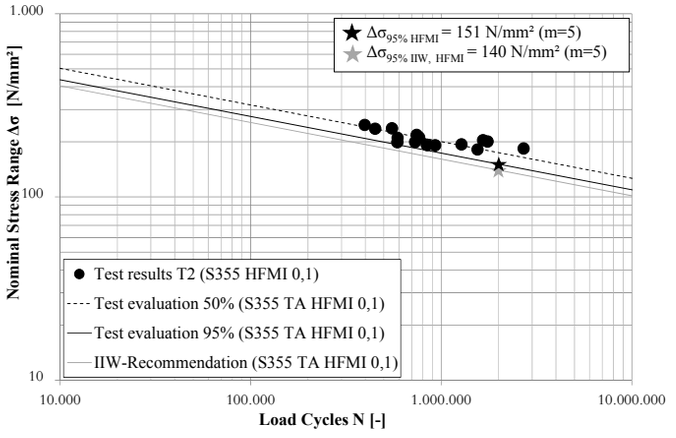


Figure 8. Evaluated results of HFMI-treated beam series T2 compared to IIW-Recommendations

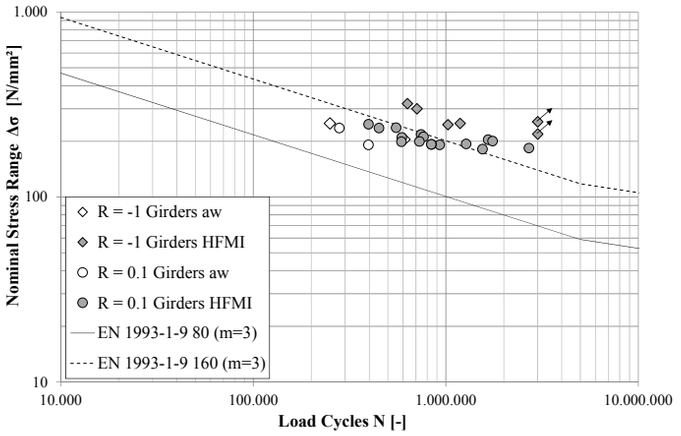


Figure 9. Results of beam test series T1 and T2 compared to FAT-classes given in EN 1993-1-9

3.5 *Evaluation and comparison of results concerning mean stress effects*

The evaluation has been conducted as a linear regression analysis according to Sedlacek et al. (2007) with a fix slope for HFMI-treatment of m = 5. Run-outs have been excluded from evaluation process.
Differences between the two applied HFMI methods are not significant, thus both methods can be evaluated together.

All four as-welded (aw) beam test results are clearly lower than HFMI-treated beams, but widely above 80 MPa.

Figure 8 shows the S-N-curve with the evaluation of HFMI-treated beam test series T2. For comparison reasons the IIW-Recommendation for stress range R = 0.1 and steel grade S355 is given. The evaluation leads to a reference value of fatigue strength at two million cycles of $\Delta\sigma_{c,\,HFMI,\,0.1,\,S355,\,BEAM} = 151$ N/mm² under the assumption of a fixed slope of m = 5. The assumption of a fixed slope of m = 5 is a bit advantageous in this case, but is necessary due to the low amount of test results. It can be concluded that even the beam test results, which are supposed to be worse than small scale test results, lie above the IIW-recommendation of $\Delta\sigma_{c,\,HFMI,\,0.1,\,S355} = 140$ N/mm².
Figure 9 shows the comparison of test results T1 and T2 regarding the mean stress effect. There is a visible difference between the HFMI-treated state, but the difference for the as-welded state is not clear. That might be owed to the low amount of as welded-girder tests.

4 EVALUATION OF MEAN STRESS EFFECT OF HFMI-TREATED WELDS

4.1 *General*

It is well known, that fatigue loadings with differing mean stress levels result in different fatigue performance for non-welded or stress-relieved welded construction details.
That is due to the superposition of residual and loading stresses. Whereas for welded construction details the residual stresses are almost equal to the yield strength, the quantity of loading stress is not of importance because the yield strength will easily be reached anyhow, so that no benefits due to compressive loading is assumed, see Gurney (1979).
EN 1993-1-9 takes this beneficial impact on the fatigue strength into account by reducing the value on the load side, namely the effective stress range $\Delta\sigma_{E,2}$, see equation (1).

$$\Delta\sigma = \left|\sigma_{max}\right| + 0.6 \cdot \left|\sigma_{min}\right| \quad (1)$$

Regarding HFMI treated welds, the question arises if the introduced compressive stresses lead to the same beneficial effects as in the non-welded or stress-relieved state.

4.2 *Collection of HFMI-treated data*

In order to be able to evaluate the huge amount of existing fatigue data on HFMI treated tests in the frame of the project a data base has been developed. Within this data base all accessible, existing and relevant test data of European and German test series have been collected and catalogued. All available relevant test data of both research partners were integrated with regard to the aim to filter the test data concerning influencing criteria and evaluate them. Thus it is possible to filter data, sorting them for example by stress ratios.

4.3 *Evaluation of HFMI-treated test data*

4.3.1 *Overview*

All single effects were evaluated in a group of data depending on the same conditions, but not necessarily of the same series. For example the mean stress effect was evaluated differing by construction detail and yield strength. So only different series with the same condition, were evaluated together in order to be independent of influencing parameters.

The evaluation has been conducted according to Sedlacek et al (2007) with a variable and a fixed slope for HFMI-treatment $m = 5$ and as-welded $m = 3$.

The mean stress effect of the HFMI treated test series is illustrated with the help of Haigh diagrams. If only the stress amplitude of test data would be influencing the fatigue behavior, one could draw a horizontal line connecting the points of different mean stress levels of each series. The evaluated stress ratios R are given with dashed lines.

4.3.2 *Transverse stiffener*

The results of the evaluated test data behave as expected for the stress ratios $R = 0.1$ and $R = -1.0$, namely $R = -1.0$ being beneficially higher than $R = 0.1$. Regarding the critical stress ratio $R = 0.5$ the results show less critical values than expected. It has to be mentioned that the evaluated series of $R = 0.5$ contain only few test data, but the tendency shows almost the same performance as for $R = 0.1$. It seems that there is no strong decrease of fatigue strength between the stress ratios $R = 0.1$ and 0.5 for the transverse stiffener.

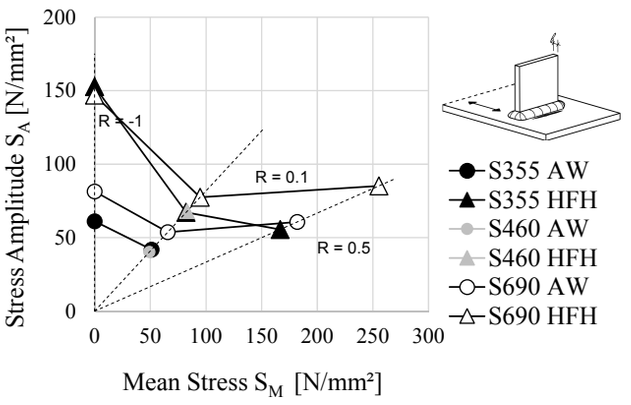


Figure 10. Haigh diagram showing mean stress effect of unloaded transverse attachment

4.3.3 *Loaded butt weld*

Regarding the evaluated test data of the transverse loaded butt weld differentiated by steel grades, the potential of alternate loading ($R = -1.0$) is obvious. In comparison to the transverse attachment, less test data could be found and thus evaluated, so that ensured statements can only be drawn for steel grade of S690. Similarities in unexpected positive behavior in comparison to the unloaded transverse attachment regarding the stress ratio $R = 0.5$ are given.

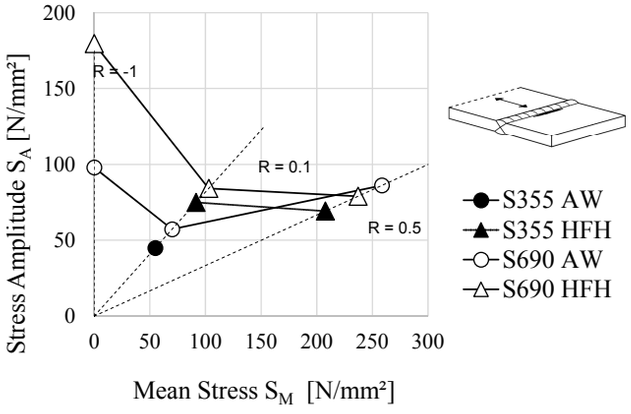


Figure 11. Haigh diagram showing mean stress effect of transverse loaded butt weld

4.3.4 *Unloaded longitudinal attachment*

By reason of a small data set covering other stress ratios than $R = 0.1$, it is difficult to draw conclusions on the mean stress effect for unloaded longitudinal attachments. The missing data are mainly due to problems during the testing execution on the longitudinal stiffener. It often occurs, that if the weld toe of the longitudinal attachment is improved due to HFMI-treatment, the crack is starting from the weld root.

Although there are only few data sets for unloaded longitudinal stiffener the tendency for the available data is identifiable. It can clearly be seen from Figure 12, that the influence of the mean stress tends to be milder for the HFMI-treated unloaded longitudinal attachment for the stress ratios $R = -1.0$ to

R = 0.1, than for the previous discussed details. This might result from the very sharp notch and thus the higher stress concentration for the frontal weld toe. Sonsino (1994) has verified a similar behavior of extreme sharp longitudinal notch within tests of stress relief heat treatment. This explains also the lower effectiveness of HFMI-treatment compared to the other investigated details.
It is known that the higher the notch intensity, the less the mean stress effects the fatigue strength of a detail.

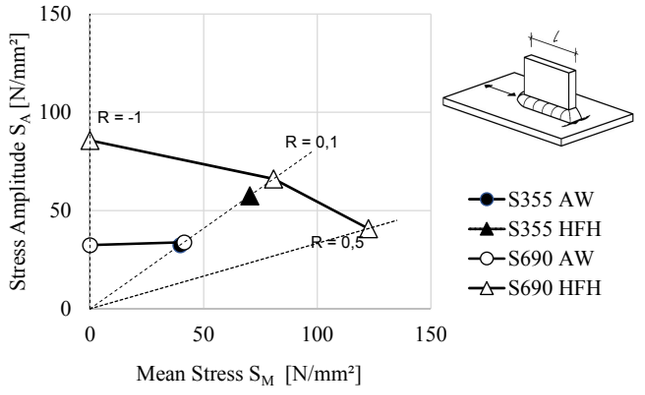


Figure 12. Haigh diagram showing mean stress effect of unloaded longitudinal attachment

4.3.5 *Conclusions*

The mean stress effects could be shown for the three investigated construction details. Whereas two of the details, the unloaded transverse stiffener and the transverse loaded butt welds showed a clear dependency from the quantity of the mean stress, the unloaded longitudinal stiffener showed milder behavior concerning the stress ratios R = -1.0 and R = 0.1. When formulating the DASt-Guideline on the design of HFMI-treated welds the different levels of sensitivity on effects depending on the type of construction detail will be integrated.

4.4 *Assessment of test data with regard to the IIW-recommendations*

As already mentioned in chapter 1.2 the recommendations of the IIW by Marquis & Barsoum (2016) are the most current and extensive ones. Thus, it is useful to evaluate their approach considering the latest findings of the mean stress influence on HFMI-treated welds.
In Marquis & Barsoum (2016) the improvement due to HFMI-treatment is considered by stepwise increase of fatigue classes (FAT-Class) depending on the type of steel grade, from 4 to 8 FAT classes.
In regard to the mean stress influence, the IIW-recommendations differ between four different stress ratios R. In order to consider a less favorable stress ratio level, a stepwise reduction is foreseen. As there is no data available for R = 0.52, that stress ratio gives the limitation.

Figure 13 shows the determination process for an unloaded transverse stiffener of S355 with a stress ratio of R = 0.1 as well as a stress ratio of R = -1.0. Finally, the determination of both stress ratios ends up at the same improved FAT-class, namely 140 MPa due to the missing differentiation. As could be shown in 4.3.2 the loading with a stress ratio of R = -1.0 is much more favourable and should be considered with its potential with further increase of fatigue strength.

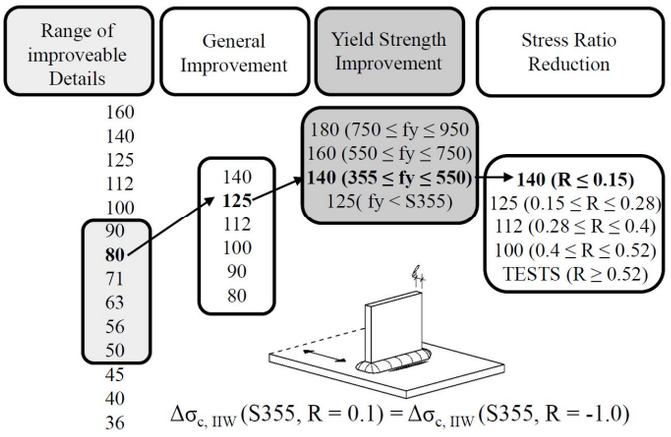


Figure 13. Example for determination of improved fatigue resistance for HFMI-treated transverse stiffener of S355 with R = 0.1 and R = -1.0 according to IIW-Recommendations

5 CONCLUSIONS AND OUTLOOK

Within this paper latest findings of the DASt-AiF project “Development of a DASt-Guideline for High Frequency Mechanical Impact treatments” were presented. In the beginning the aim of the project, namely to develop a German DASt-Guideline considering the effectiveness of HFMI treatment in the fatigue design process could be shown.

In order to complete gaps in knowledge on certain influencing effects on the HFMI-improved fatigue strength a large test program was motivated and presented. Out of this, latest results on the conducted beam test series T1 and T2 focusing on the mean stress effects in large structures were summarized and evaluated.

Additionally collected HFMI-fatigue test data concerning the mean stress influence were evaluated within the project and tendencies were shown for unloaded transverse attachments and transverse loaded butt welds. Thus, potential in formulating a design concept based on European standards was motivated regarding the mean stress effect out of several influencing factors.

It is obvious that implementing new techniques and rules into standards is a lengthy process, that has to be properly prepared with accurate and transparent background evaluation. But nonetheless, devel-

opment and adaption of standards is necessary work to be competitive to more modern construction techniques.

6 ACKNOWLEDGEMENT

The work presented has been carried out as part of a joint project “Development of a DASt-Guideline for high-frequency mechanical impact treatments”. This project of the research association DASt is financed over the AiF within the development program for industrial community research and development (IGF) from the Federal Ministry of Economic Affairs and Energy (BMWi) based on a decision of the German Bundestag.

This project is a cooperative research project with colleagues from the chair of Steel and Leightweight Structures of the Karlsruher Institute of Technology (KIT). The authors gratefully thank for their cooperation.

A special thank goes to the material providers “Stahlwerk Thüringen GmbH”, “Peiner Träger – Salzgitter Gruppe” and “voestalpine AG” for the donation of girders and plates.

Special acknowledgement is given to “EHS Engineering” formerly “Eiffel Deutschland Technology” for the fabrication of the test specimens.

Furthermore we gratefully thank “Pitec GmbH” and “DYNATEC GmbH” for their support by treating the specimens.

7 REFERENCES

Berg, J. 2016. Einfluss des Höherfrequenten Hämmerns auf die Ermüdungsfestigkeit geschweißter ultrahochfester Feinkornbaustähle, Dissertation, Universität Duisburg-Essen, 2016.

Duerr, A. 2007. Zur Ermüdungsfestigkeit von Schweißkonstruktionen aus höherfesten Baustählen bei Anwendung von UIT-Nachbehandlung. Dissertation, Institut für Konstruktion und Entwurf, Universität Stuttgart, 2007.

EN 1993-1-9: 2005 + AC: 2009. Eurocode 3: Design of steel structures – Part 1-9: Fatigue.

Gurney, T. R. 1979. Fatigue of welded structures, Cambridge University Press.

Helms, R. & Jaenicke, B. & Wohler, H. & Bork, C.-P. 1989. Zur Schwingfestigkeit großer geschweißter Stahlträger, Bundesanstalt für Materialforschung und -prüfung (BAM), Forschungsbericht 164.

Hobbacher, A. F. 2016. Recommendations for fatigue design of welded joints and components, Springer International Publishing, Switzerland.

Kuhlmann, U. & Bergmann, J. & Dürr, A. & Thumser, R. 2006. Effizienter Stahlbau aus höherfesten Stählen unter Ermüdungsbeanspruchung. AiF-Vorhaben Nr. 13866, P 620, Forschungsvereinigung Stahlanwendung e.V.

Kuhlmann, U. & Kudla, K. & Ummenhofer, T. & Weidner, P. 2013. Untersuchungen zur Anwendung höherfrequenter Hämmerverfahren im Stahlwasserbau, Final report. Bundesanstalt für Wasserbau (BAW).

Kuhlmann, U. & Breunig, S. & Ummenhofer, T. & Weidner, P. 2017. Entwicklung einer DASt-Richtlinie für höherfrequente Hämmerverfahren, Running research project, DASt/AiF IGF-Nr. 17886, Stuttgart.

Marquis, G. B. & Barsoum, Z. 2016. IIW Recommendations for the HFMI Treatment – For Improving the Fatigue Strength of Welded Joints, IIW Collection, Springer.

Puthli, R. & Herion, S. & Hrabowski, J. & Ummenhofer, T. & Weich, I. & Faber, T. & Lossin, M. & Huhn, H. & Uecker, J. 2008. Detaillösungen bei Ermüdungsfragen und dem Einsatz hochfester Stähle bei Offshore - Windenergieanlagen, Final report of research project, P633.

Sedlacek, G. & Hobbacher, A. & Nussbaumer, A. & Stoetzel, J. & Tschickardt, D. 2007. Commentary to Eurocode 3: EN 1993 – Part 1-9 – Fatigue. First Edition.

Sonsino, C. M. 1994. Über den Einfluss von Eigenspannungen, Nahtgeometrie und mehrachsiger Spannungszustände auf die Betriebsfestigkeit geschweißter Konstruktionen aus Baustählen. Mat.-wiss. u. Werkstofftech. 25, pp. 97 – 109.

Stranghöner, N. & Berg, J. 2015. Einfluss des höherfrequenten Hämmerns auf die Ermüdungsfestigkeit ultrahochfester Stähle der Festigkeitsklassen S960, S1100 und S1300 am Beispiel geschweißter Kerbdetails, Schlussbericht Projekt P938, Forschungsvereinigung Stahlanwendung e.V. FOSTA, Düsseldorf.

Ummenhofer, T. & Herion, S. & Hrabowski, J. & Rack, S. & Weich, I. & Telljohann, G. & Dannemeyer, S. & Strohbach, H. Eslami-Chalander, H. & Kern, A. & Pinkernell, S. & Smida, M. & Rahlf, U. & Senk, B. 2009: Lebensdauerverlängerung neuer und bestehender geschweißter Stahlkonstruktionen. REFRESH-Projekt, Final report.

Ummenhofer, T. & Weidner, P. & Kuhlmann, U. & Kudla, K. & Breunig, S. 2017: Entwicklung eines einfachen Qualitätssicherungstests für die Anwendung höherfrequenter Hämmerverfahren, FOSTA-Schlussbericht P872.

Weich, I. 2009. Ermüdungsverhalten mechanisch nachbehandelter Schweißverbindungen in Abhängigkeit des Randschichtzustands, Technische Universität Carolo-Wilhelmina zu Braunschweig, Dissertation.

Maintenance, Safety, Risk, Management and Life-Cycle Performance of Bridges – Powers, Frangopol, Al-Mahaidi & Caprani (Eds)
© 2018 Taylor & Francis Group, London, ISBN 978-1-138-73045-8

Statistical Analysis of Fatigue Test Data according to Eurocode 3

K. Drebenstedt & M. Euler
Institute of Structural Design, University of Stuttgart, Germany

ABSTRACT: The question how to correctly evaluate fatigue test data in order to establish the reference value $\Delta\sigma_C$ of the characteristic fatigue strength of steel structures according to the safety requirements of Eurocode 3 still leads to discussions. This paper is supposed to give an overview of the state-of-the-art on the statistical analysis of fatigue test data. Firstly, the classical methods to set up different types of two-sided statistical intervals such as confidence intervals, prediction intervals and tolerance intervals and their one-sided bounds are addressed. The different meanings of these intervals and bounds are pointed out. Secondly, the statistical method pursued by Eurocode 0 is described which partly differs from the classical approach. Finally, the formal requirements of Eurocode 0 and Eurocode 3 are summarized, and it is highlighted in how far the aforementioned methods meet these requirements. To illustrate the application of the aforementioned methods, a particular test data set is assessed with forced slope of the *S-N* curve in a worked example. The reference values $\Delta\sigma_C$ obtained by the different methods for the test data set are compared.

1 INTRODUCTION

The fatigue strength of constructional details in steel structures is described by its characteristic reference value $\Delta\sigma_C$ for $2 \cdot 10^6$ stress cycles according to Eurocode 3 with respect to their nominal stress range. In addition to random loading effects, the fatigue strength is mainly affected by *microgeometrical* influences, e. g. shape discontinuities of weld toes and roots, *macrogeometrical* influences, e. g. tolerances in form of misalignments and *metallurgical* inhomogeneities, e. g. differing material properties in weld and heat affected zone due to slight welding process discontinuities.

Due to small unavoidable sample-to-sample variations of the aforementioned influences, experimental test data always show a random scatter (sampling error) even under identical test conditions.

Facing the unknown sampling error, the test data should be evaluated according to the same and commonly agreed criteria at least. Although there has been the need for a standardized statistical analysis of fatigue test data to define reliable values $\Delta\sigma_C$ for decades, however, in practice these values are differently derived limiting their comparability.

In the following, the attempt is made to clarify the different used statistical methods as a basis for discussion in order to come to a common ground for determining comparable values $\Delta\sigma_C$.

2 STATISTICAL TERMS

2.1 *High cycle fatigue of steel structure*

For high cycle fatigue of steel structures, the applied stress range, S, and the corresponding number of stress cycles to failure, N, observed in fatigue tests obey an exponential law (Basquin 1910, p. 627):

$$N = a \cdot S^{-m} \tag{1}$$

On a log-log scale with decimal logarithm (base 10), the test data can generally be allocated to a straight line expressing a linear dependency of the number of stress cycles on the stress range (Fig. 1):

$$\log N = \log a - m \cdot \log S \tag{2}$$

The intercept a in Figure 1 describes the theoretical locus where the straight-line *S-N* relationship of the finite life region intersects the horizontal axis $S = 10^0 = 1$. The parameter m stands for the slope of the straight line; exactly speaking, it represents the negative inverse of the mathematical slope.

2.2 *Regression analysis*

In frame of fatigue, the regression analysis is an extracting technique to reveal the effects that S exerts on N. It tries to define a relationship in form of a mathematical function illustrated as *S-N* curve.

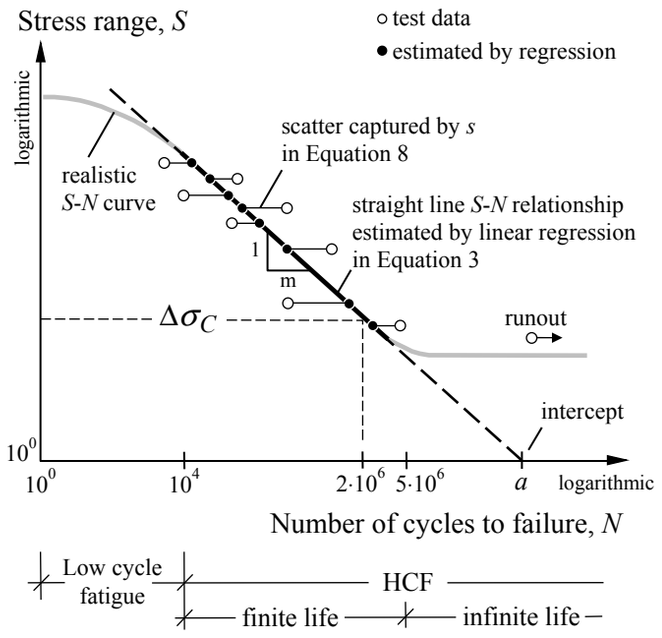


Figure 1. Regions of realistic *S-N* curve, finite life region of high cycle fatigue (HCF) described by linear regression

The stress range S is normally set to a desired value by the designer and, therefore, the independent variable within this functional relationship. Any deliberate change of S affects the number of stress cycles N as dependent response variable.

Generally, the real parameters a and m of the true *S-N* relationship (fatigue resistance model) in Equations 1 & 2 are unknown for a particular constructional detail as it is impossible to examine the whole population (all possible occurrences of S and N). Therefore, both parameters have to be substituted by the estimates $\hat{a}$ and $\hat{m}$ based on the information of a limited number of fatigue tests:

$$\log \hat{N} = \log \hat{a} - \hat{m} \cdot \log S \tag{3}$$

where $\hat{N}$ denotes the predicted number of stress cycles for a given stress range S when the linear regression function of Equation 3 is applied.

2.3 *Computation of linear regression function*

There are several methods for estimating $\hat{a}$ and $\hat{m}$ of the regression function of Equation 3 from which the Least Square Method is most common. It achieves the best fit with the test data through minimizing the sum of squares of deviations in Equation 4.

$$\sum {e_i}^2 \rightarrow \min \tag{4}$$

The so-called residual e_i in Equation 4 is the deviation of a measured number of stress cycles to failure, N_i, of the ith fatigue test from its corresponding value $\hat{N}_i$ obtained by use of the fitted linear regression function (Equation 3) as an estimate of the true *S-N* curve (Draper & Smith 1966, p. 14 and 86). It is defined by Equation 5 and represents the amount of the *S-N* relationship which the estimated regression function (Equation 3) fails to explain.

$$e_i = \log N_i - \log \hat{N}_i \tag{5}$$

The parameters $\hat{a}$ and $\hat{m}$ are obtained by setting the partial derivatives of Equation 4 with respect to $\hat{a}$ and $\hat{m}$ to zero leading to Equations 6 & 7:

$$\hat{m} = -\frac{n \cdot \sum (\log S_i \cdot \log N_i) - \sum \log S_i \cdot \sum \log N_i}{n \cdot \sum (\log S_i)^2 - (\sum \log S_i)^2} \tag{6}$$

$$\log \hat{a} = \frac{1}{n} \cdot \left(\sum \log N_i + \hat{m} \cdot \sum \log S_i \right) = \overline{N} + \hat{m} \cdot \overline{S} \tag{7}$$

where n is the sample size (number of fatigue test data), i is the index of the single fatigue test, and $\overline{N}$ and $\overline{S}$ are the mean values of the sample.

An important restriction of the Least Square Method is the exclusion of statistical outliers as all test data are equally weighted. An outlier is a data point that is far greater or smaller than the rest of the test data and lies three or four standard deviations or even further from the mean of the sample in Figure 1 (Draper & Smith 1966, p. 94). Particularly in fatigue, tests which have resisted $5 \cdot 10^6$ stress cycles and more and which had been terminated before failure, so-called runouts, cannot be accounted for when computing the linear regression function describing the finite life region of HCF.

2.4 *Precision of linear regression*

The linear regression function is derived on the basis of certain assumptions and normally suffers from a lack of fit. As the unknown parameters a and m of the true *S-N* curve are substituted by the estimates $\hat{a}$ and $\hat{m}$ indicating a statistical uncertainty (sampling error), it is only possible to determine the residuals e_i rather than errors (meaning the deviations between test data and true *S-N* curve).

Assuming that there is no bias error (meaning the model of regression function is correct), the residuals are random deviations and the residual mean square s^2 of the sample can be used as an estimate of the error variance σ^2 of the population (Draper & Smith 1966, p. 27). Thus, the estimate s of the standard deviation in terms of $\log N$ (see Figure 1) amounts to

$$s = \sqrt{\frac{\sum [\log N_i - (\log \hat{a} - \hat{m} \cdot \log S_i)]^2}{dof}} \tag{8}$$

where *dof* stands for the degrees of freedom.

Generally, the degrees of freedom in Equation 8 amount to the number of independent test data, n, minus the number of parameters of the regression function being estimated. For a given slope and intercept, $n-2$ of n test data can freely vary. The

knowledge of the $n-2$ test data allows to calculate what the $(n-1)$th and the nth test data must be in order to produce the given slope and intercept (Wood 2011). Following this reasoning, a linear regression with free slope and intercept exhibits $n-2$ degrees of freedom as all n test data are independent.

2.5 *Prior information*

Many constructional details of steel structures exhibit a similar fatigue behaviour. For example, the statistical analysis of hundreds of fatigue tests on welded joints in structural steels proved the validity to assume a uniform slope and scatter band of the *S-N* curves (Haibach et al. 1981, p. 33). Therefore, the slope of the *S-N* curves might be regarded as known due to prior information for welded constructional details (Haibach 2006, p. 527).

In cases where the slope m is forced to be of a certain value, Equation 6 can be skipped, and only estimate $\hat{a}$ has to be determined by Equation 7. Consequently, the estimate s of standard deviation according to Equation 8 comprises only $n-1$ degrees of freedom (Wood 2011).

2.6 *Design S-N curves*

The *S-N* curve of a particular constructional detail obtained by linear regression represents the mean fatigue resistance of the tested samples meaning that one half of additional samples of the same kind is expected to survive and the other half to fall below this curve (50%-survival). For design purpose such a low survival probability is unacceptable even if the *S-N* curve has been estimated from an infinitely large sample (no sampling error). In any case, a transformation of the mean *S-N* curve into a characteristic *S-N* curve with an appropriate survival probability (for example 95 %) is necessary. This requires the setup of statistical intervals and bounds.

3 STATISTICAL INTERVALS

3.1 *Preliminary remarks*

Because of their great importance for the fatigue design of steel structures, the explanations of the following sections are related to welded constructional details. As the slope m of the *S-N* curve of these details can be regarded as known due to prior knowledge, only the intercept a of the *S-N* curve is subject to statistical investigations.

In case of *S-N* curves with constrained slope, the lower and upper limits of all statistical intervals discussed in Section 3 are parallel. In the general case, statistical interval limits of the linear regression curve are hyperbolically shaped expressing that one might expect to make the "best" statistical statement in the "middle" of the investigated test range (Draper 1966, p. 22).

3.2 *Confidence interval / lower confidence bound*

In statistics, one differentiates between two-sided statistical intervals and one-sided statistical bounds (Hahn 1991, p. 31). In Figure 2a, a two-sided 95% confidence interval for the intercept of the *S-N* curve is depicted implying that the true value a of the whole population is expected to lie within this interval with 95% probability. The probability that the true intercept is either smaller than the lower or greater than upper interval limit amounts to 2.5%.

In case of fatigue, it is not necessary to confine the interval by an upper limit since overstrengths are not crucial. Here, a one-sided statistical lower bound is more appropriate representing a particular probability of survival. For example, the one-sided lower 95% confidence bound in Figure 2b claims that the true intercept of population lies above this limit with 95% probability. The probability of a lower intercept amounts to 5%. The lower confidence bound is computed by (Hahn & Meeker, Eq. 4.1):

$$\log \hat{a} - t_{1-\alpha,n-1} \cdot s \cdot \sqrt{\frac{1}{n}} \tag{9}$$

where t is the coefficient of Student's t distribution (Table A1), α is the significance level, $(1-\alpha)$ is the confidence level, $n-1$ stands for the degrees of freedom, n is the number of tests (sample size).

In general, a one-sided lower $100(1-\alpha)\%$ confidence bound is identical with the lower limit of a two-sided $100(1-2\alpha)\%$ confidence interval (Schneider & Maddox, p. 7). Therefore, the one-sided lower 95% bound in Figure 2b will coincide with the lower limit of a two-sided 90% interval.

In case of infinitely large sample size, the confidence interval diminishes as the estimated intercept obtained from the sample is identical with the true value of the population.

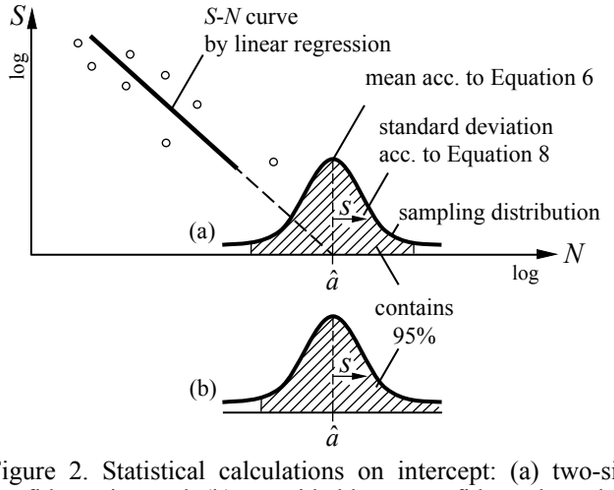


Figure 2. Statistical calculations on intercept: (a) two-sided confidence interval, (b) one-sided lower confidence bound

3.3 *Sampling distribution*

There is a tendency for errors that occur in many real situations to be normally distributed due to the Central Limit Theorem with mean zero and variance σ^2 (Draper & Smith 1966, p. 17). In case of no prior knowledge of the variance σ^2 of the population, this variance has to be estimated from the sample itself to describe the sampling distribution. Especially in case of decreasing sample size, the variance found from the sample becomes itself subject to an increasing error (Student 1908, p. 2) that requires in Equation 9 the usage of Student's t distribution rather than a normal (Gaussian) distribution (Fisher 1925, p. 42). See also Table A1.

3.4 *Prediction interval / lower prediction bound*

For design purpose the prediction interval and its lower bound is more important than the confidence interval as the latter only claims to include the true intercept of the *S-N* curve for past tests. The prediction interval is an estimate of an interval in which the mean of m future observations is expected to fall in with a certain probability. Similarly to Equation 9, the lower prediction bound for the intercept of the *S-N* curve is computed by (Hahn & Meeker 1991, Eq. 4.2):

$$\log \hat{a} - t_{1-\alpha,n-1} \cdot s \cdot \sqrt{\frac{1}{m} + \frac{1}{n}} \tag{10}$$

See Explanations of Equation 9.

In contrast to the confidence interval, the width of the prediction interval will not tend to zero in order to struggle with the uncertainty of future sampling even if the sample size becomes infinitely large.

An important special case arises when $m = 1$; this results in a prediction interval to contain a single future observation (Hahn & Meeker 1991, p. 61):

$$\log \hat{a} - t_{1-\alpha,n-1} \cdot s \cdot \sqrt{1 + \frac{1}{n}} \tag{11}$$

In fact, Equation 11 has been the most common way to derive the intercept of the characteristic *S-N* curve out of sampled data in the past (Brozetti et al. 1998, Sec. 5), (Gurney & Maddox 1973, p. 25).

3.5 *Tolerance interval / lower tolerance bound*

The tolerance interval describes an interval that is expected to enclose the intercept of a certain proportion, for example 95%, of the whole population. In (Holický 2005, p. A-23) the tolerance interval approach is also referred to as coverage method of fractile estimation. The lower tolerance bound is computed by (Hahn & Meeker 1991, p. 60):

$$\log \hat{a} - k_{1-\alpha,p,n} \cdot s \tag{12}$$

where $k_{1-\alpha,p,n}$ is the factor for an one-sided tolerance bound accounting for the covered proportion of the population, p, the confidence level $(1 - \alpha)$, and the sample size, n.

The coefficients $k_{1-\alpha,p,n}$ can be taken from Table A1 in connection with $n - 1$ degrees of freedom. According to Schneider & Maddox (2006, p. 17) coefficients for other degrees of freedom as they are necessary in case of linear regression with free slope are not really available.

Schneider & Maddox (2006) consider the usage of tolerance intervals/bounds as a fundamental change to previous practice leading to a risk of incompatibility with current design rules. Even so, they recommend their usage as a means of justifying design curves that are based on small samples, especially for critical applications, (p. 8).

Holický (2005, Fig. 4.3) demonstrates that the lower 95% tolerance bound with 75% confidence and the lower prediction bound for a single future test with 95% confidence are approximately equal, Figure 3. In maximum, the tolerance bound is more conservative (difference of coefficients ≤ 9%).

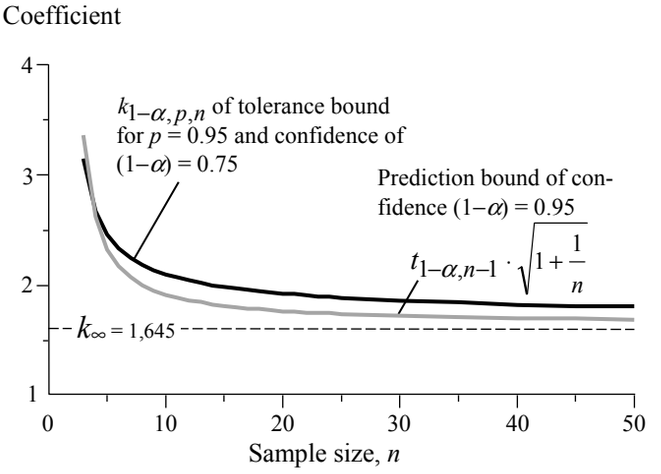


Figure 3. Coefficients of one-sided lower 95% tolerance bound and of lower prediction bound according (variance σ^2 unknown). See also Table A1.

4 STATISTICAL ANALYSIS ACCORDING TO EUROCODE 0

4.1 *Overview*

Eurocode 0 defines the reliability and safety concept of all European standards for structural design in civil engineering. The informative annex D contains rules for design assisted by testing.

In Section D.7 guidance on the statistical determination of a single property and in Section D.8 of a resistance model is given. In case of a *S-N* curve with constrained slope, the reference value $\Delta\sigma_C$ only requires a determination of a single property (meaning the intercept). The resistance model is basically known and only needs adjustment on the level of fatigue strength. In case of no prior information, the

value $\Delta\sigma_C$ requires the determination of all parameters of the *S-N* curve (resistance model).

4.2 *Statistical determination of a single property according to Eurocode 0*

The intercept of the *S-N* curve afflicted with a statistical uncertainty is assumed to be normally or lognormally distributed. As there is no prior knowledge about the mean, it is estimated by the average obtained from the sample. The variance σ^2 of the population is either known or unknown. In the latter case it is estimated by s^2 of the sample, see Equation 8.

The characteristic value of the intercept a_k is obtained by Eurocode 0 (2010, Equation D.1) using:

$$\log a_k = \log \hat{a} \cdot (1 - k_n \cdot V) \tag{13}$$

where $\hat{a}$ is the mean value according to Equation 7. Using s from Equation 8, the estimate for the coefficient of variation is explained as:

$$V = s / \log \hat{a} \tag{14}$$

The coefficient k_n is a factor to compute the 5% characteristic value (Table A1). It has following definition (Holický 2005, Tab. 4.4) for unknown variance σ^2:

$$k_n = t_{1-\alpha,n-1} \cdot \sqrt{1 + \frac{1}{n}} \tag{15}$$

Plugging Equation 14 into 13 gives Equation 11 and clarifies that the approach of Eurocode 0 for the determination of a single property basically leads to a lower prediction bound, compare Sec. 3.4.

4.3 *Statistical determination of resistance models*

4.3.1 *Probabilistic model of resistance*

A detailed description of the scientific background is given in (Holický, 2005). In the following, only some aspects of the calculation scheme are highlighted in terms of fatigue.

Generally, the mean *S-N* curve is considered as resistance model described by a function r_t identical with Equation 3 stating for any S_i:

$$r_{ti} = \log \hat{N}_i = \log \hat{a} - \hat{m} \cdot \log S_i \tag{16}$$

In the general case, the theoretical value r_{ti} predicted by the resistance function suffers from a lack of fit with the experimental value $r_{ei} = \log N_i$. By means of the so-called correction factor b, it is possible to adjust the resistance function r_t leading to the probabilistic model of resistance r_p afflicted by an error term δ representing the model uncertainty:

$$r_p = b \cdot r_t \cdot \delta \tag{17}$$

4.3.2 *Correction factor b*

To determine the fitting deviations, the experimental values r_{ei} are plotted against the predicted values r_{ti} obtained from Equation 16 in Figure 4. The factor b in Equation 17 is obtained by linear regression with zero intercept using the Least Square Method aiming at the same criterion as in Equation 4. Similar to Equation 6 that simplifies for zero intercept, the factor b is computed as:

$$b = \frac{\sum (r_{ei} \cdot r_{ti})}{\sum (r_{ti})^2} \tag{18}$$

It is understood that b equals 1 necessarily, if the average *S-N* curve (r_{ti}) is computed from the test data (r_{ei}) using the natural slope and intercept by linear regression. However for constrained slope, b differs from 1 if there is a difference between the natural and forced slope. In that case, the *S-N* curve obtained by linear regression does not fit the test data best. Nevertheless, the correction factor b seems to be close to 1 and, therefore, might be negligible in many practical cases.

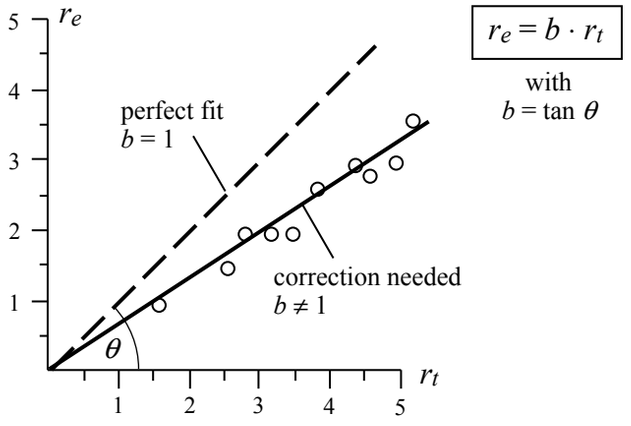


Figure 4. Comparison of experimental values r_e and theoretical values r_t of resistance in order to identify need of correction

4.3.3 *Coefficient of variation of "error" term*

The probabilistic model of resistance r_p is afflicted by a model uncertainty resulting in deviations between the predicted and experimental values. In absence of information this "error" has to be estimated assuming that $\delta > 0$ and that it is lognormally distributed. As the "error" term is multiplicative in Equation 17, the deviation δ_i is defined as:

$$\delta_i = \frac{r_{ei}}{r_{pi}} = \frac{r_{ei}}{b \cdot r_{ti}} \tag{19}$$

From probability theory it is known that the logarithm of a lognormally distributed random variable has a normal distribution. This dependency simplifies the estimation of the coefficient of variation V_δ if following transformation is performed:

$$\Delta_i = \ln(\delta_i) \tag{20}$$

The estimates of the mean $\overline{\Delta}$ and the variance s_Δ^2 can be computed by the known relations of normally distributed variables. Finally, it holds for the estimated coefficient of variation of the "error" term:

$$V_\delta = \sqrt{e^{s_\Delta^2} - 1} \tag{21}$$

4.3.4 *Coefficient of variation of probabilistic model*
In addition to V_δ, the coefficient of variation V_r of the probabilistic model depends on the coefficient $V_{rt} = V$ of the response variable N due to random changes in the basic variable S, see Equation 14. Thus, V_r sums up using the normal-lognormal relationship of probability theory:

$$V_r^2 = \left(1 + V_\delta^2\right)\left(1 + V_{rt}^2\right) - 1 \tag{22}$$

that simplifies in case of small variations as:

$$V_r^2 = V_\delta^2 + V_{rt}^2 \tag{23}$$

4.3.5 *Characteristic resistance function*
Finally, the characteristic resistance function is obtained introducing weighting factors α_{rt} and α_δ (Holický 2005, p. IV-15):

$$\log N_k = \log \hat{N} \cdot e^{-k_\infty \alpha_{rt} Q_{rt} - k_n \alpha_\delta Q_\delta - 0.5 Q^2} \tag{24}$$

where k_∞ is 1.64, k_n is computed according to Equation 15. See further explanations in Sec. 6.6.

5 FORMAL REQUIREMENTS OF EUROCODE 0 AND EUROCODE 3

Part 1-9 of Eurocode 3 (2010, Section 7.1) states how the available fatigue strengths of Eurocode had been derived if test data were available:

"Note 1 When test data were used to determine the appropriate detail category for a particular constructional detail, the value of the stress range $\Delta\sigma_C$ corresponding to a value of N_C = 2 million cycles were calculated for a 75% confidence level of 95% probability of survival for log N, taking into account the standard deviation and the sample size and residual stress effects. [...]"

As a logical consequence new test data should be evaluated in the same way. As this statement relates on survival, a one-sided lower statistical bound is supposed to be derived. Furthermore, two values of probability are specified. Thus, it is indirectly required to set up a lower tolerance bound of the mean *S-N* curve obtained by linear regression for 95% survival with 75% confidence.

6 WORKED EXAMPLES

6.1 *Overview*

A data set comprising n = 10 fatigue tests is statistically evaluated (Table 1). The slope of the *S-N* curve is forced to m = 3 based on prior knowledge.

Table 1. Data base for the statistical analysis

i	S_i [N/mm²]	N_i [–]	log S_i [–]	log N_i [–]
1	265	42,000	2.423	4.623
2	265	70,000	2.423	4.845
3	265	79,000	2.423	4.881
4	202	107,000	2.305	5.029
5	202	188,000	2.305	5.274
6	202	204,000	2.305	5.310
7	139	537,000	2.143	5.730
8	139	597,000	2.143	5.776
9	108	800,000	2.033	5.903
10	108	1,077,000	2.033	6.032
Σ			22.539	53.420

$$\log \hat{a} = 1/n \cdot \left(\sum \log N_i + m \cdot \sum \log S_i\right) \tag{7a}$$
$$= 1/10 \cdot \left(53.420 + 3 \cdot 22.539\right) = 12.104$$

Hence, the mean *S-N* curve is defined (Remark: Indeed, the natural slope is slightly greater with 3.102 resulting in an intercept of 12.334.):

$$\log \hat{N} = 12.104 - 3 \cdot \log S \tag{3a}$$

The standard deviation is estimated by

$$s = \sqrt{\frac{\sum \left[\log N_i - \left(\log \hat{a} - m \cdot \log S_i\right)\right]^2}{n-1}} = 0.1156 \tag{8a}$$

6.2 *Confidence interval of S-N curve's intercept*

The lower confidence bound from Equation 9 gives:

$$\log \hat{a} - t_{0.95,n-1} \cdot s \cdot \sqrt{1/n} \tag{9a}$$
$$= 12.104 - 1.833 \cdot 0.1156 \cdot \sqrt{1/10} = 12.04$$

where $t_{1-\alpha,n-1}$ is from Table A1 with $n = 10$ and $(1 - \alpha) = 0.95$.

6.3 *Prediction interval*

The lower prediction bound from Equation 11 gives:

$$\log \hat{a} - t_{0.95,n-1} \cdot s \cdot \sqrt{1 + \frac{1}{n}} \tag{11a}$$
$$= 12.104 - 1.833 \cdot 0.1156 \cdot \sqrt{1 + \frac{1}{10}} = 11.88$$

where $t_{1-\alpha,n-1}$ is taken from Table A1 with $n = 10$ and $(1 - \alpha) = 0.95$. Thus, the characteristic *S-N* curve is obtained as:

$$\log N_k = 11.88 - 3 \cdot \log S \quad (25)$$

The characteristic reference value $\Delta\sigma_C$ of the fatigue strength at $2 \cdot 10^6$ stress cycles amounts to

$$\log S_C = \frac{\log(2 \cdot 10^6) - 11{,}88}{-3} = 1.86 \quad (26)$$

$$S_C = \Delta\sigma_C = \mathbf{72.4}\ \text{N/mm}^2 \quad (27)$$

6.4 *Tolerance interval*

According to Section 5, Eurocode 3 Part 1-9 formally requires a one-side tolerance bound for the *S-N* curve's intercept computed by Equation 12:

$$\log \hat{a} - k_{1-\alpha,p,n} \cdot s \quad (12a)$$
$$= 12.104 - 2.103 \cdot 0.1156 = 11.86$$

where $t_{1-\alpha p,n}$ is taken form Table A1 with $n = 10$, $(1 - \alpha) = 0.75$, $p = 0.95$. Thus, the characteristic *S-N* curve can be written as:

$$\log N_k = 11.86 - 3 \cdot \log S \quad (28)$$

The characteristic reference value $\Delta\sigma_C$ of the fatigue strength at $2 \cdot 10^6$ stress cycles amounts to

$$\log S_C = \frac{\log(2 \cdot 10^6) - 11{,}86}{-3} = 1.853 \quad (29)$$

$$S_C = \Delta\sigma_C = \mathbf{71.3}\ \text{N/mm}^2 \quad (30)$$

6.5 *Statistical determination of a single property according to Eurocode 0*

The variance is computed according to Equation 14:

$$V = \frac{s}{\log \hat{a}} = \frac{0.1156}{12.104} = 0.00955 \quad (14a)$$

The characteristic value of intercept amounts to:

$$\log a_k = \log \hat{a} \cdot (1 - k_n \cdot V) \quad (13a)$$
$$= 12.104 \cdot (1 - 1.923 \cdot 0.00955) = 11.88$$

where k_n is taken from Table A1 with $n = 10$. Thus, the characteristic *S-N* curve can be written as:

$$\log N_k = 11.88 - 3 \cdot \log S \quad (31)$$

The characteristic reference value $\Delta\sigma_C$ of the fatigue strength at $2 \cdot 10^6$ stress cycles amounts to

$$\log S_C = \frac{\log(2 \cdot 10^6) - 11.88}{-3} = 1.86 \quad (32)$$

$$S_C = \Delta\sigma_C = \mathbf{72.4}\ \text{N/mm}^2 \quad (33)$$

6.6 *Statistical determination of a resistance model according to Eurocode 0*

Table 1 summarizes intermediate results necessary for the following calculations.

Table 1. Intermediate results

i	$r_{ei} = \log N_i$	$r_{ti} = \log \hat{N}_i$	$\delta_i = r_{ei}/r_{ti}$	$\Delta_i = \ln \delta_i$
1	4.623	4.834	0.956	-0.045
2	4.845	4.834	1.002	0.002
3	4.881	4.834	1.013	0.013
4	5.029	5.188	0.970	-0.031
5	5.274	5.188	1.017	0.017
6	5.310	5.188	1.024	0.023
7	5.730	5.675	1.010	0.010
8	5.776	5.675	1.018	0.018
9	5.903	6.003	0.983	-0.017
10	6.032	6.003	1.005	0.005
Σ	53.420	53.422		-0.005

$$b = \sum(r_{ei} \cdot r_{ti}) \Big/ \sum(r_{ti})^2 = 1.00023 \approx 1 \quad (18a)$$

$$\overline{\Delta} = \sum \Delta_i / n = -0.0005 = -0.0005 \quad (34)$$

$$s_\Delta^2 = \frac{\sum(\Delta_i - \overline{\Delta})^2}{n-1} = 5.164 \cdot 10^{-4} \quad (35)$$

$$V_\delta^2 = e^{s_\Delta^2} - 1 = 5.153 \cdot 10^{-4} \quad (21a)$$

$$V_{rt}^2 = V^2 = 0.00955^2 = 9.120 \cdot 10^{-5} \quad (36)$$

$$V_r^2 = V_\delta^2 + V_{rt}^2 = 6.078 \cdot 10^{-4} \quad (23a)$$

$$Q_{rt} = \sqrt{\ln(1 + V_{rt}^2)} = 0.00955 \quad (37)$$

$$Q_\delta = \sqrt{\ln(1 + V_\delta^2)} = 0.0227 \quad (38)$$

$$Q = \sqrt{\ln(1 + V_r^2)} = 0.0246 \quad (39)$$

$$\alpha_{rt} = Q_{rt} / Q = 0.387 \quad (40)$$

$$\alpha_\delta = Q_\delta / Q = 0.923 \quad (41)$$

Hence, the characteristic resistance function is:

$$\log N_k = \log \hat{N} \cdot e^{-k_\infty \alpha_{rt} Q_{rt} - k_n \alpha_\delta Q_\delta - 0.5 Q^2} \quad (24a)$$
$$= (12.104 - 3 \cdot \log S) \cdot 0.9545$$

where $k_\infty = 1.64$ and $k_n = 1.92$ are from Table A1 with $n = 10$. The characteristic reference value $\Delta\sigma_C$ of the fatigue strength at $2 \cdot 10^6$ stress cycles amounts to

$$\log S_C = \frac{\log(2 \cdot 10^6) / 0.9545 - 12.104}{-3} = 1.834 \quad (42)$$

$$S_C = \Delta\sigma_C = \mathbf{68.2}\ \text{N/mm}^2 \quad (43)$$

7 CONCLUSIONS

This paper compared the different methods to derive the reference value $\Delta\sigma_C$ of the fatigue strength at $2 \cdot 10^6$ stress cycles from test data. The main focus was laid on the statistical evaluation accounting for small sample sizes under the assumption of a constrained slope of the *S-N* curve based on prior knowledge.

Four methods were investigated: (i) prediction interval method, (ii) tolerance interval method, Eurocode 0 approaches for the determination (iii) of a single resistance property and (iv) of a resistance model.

The discussion of the safety requirements revealed that Eurocode 3 Part 1-9 formally requires a one-sided lower 95% tolerance bound with a 75% confidence for the determination of $\Delta\sigma_C$. Although such an interval cannot be produced by Annex D of Eurocode 0, it could be shown that a prediction interval with 95% confidence can serve as substitute.

To illustrate the difference of the aforementioned methods, a worked example was prepared. The most important findings are with respect to this example:

1 The Eurocode 0 approach for the statistical determination of a resistance model delivered the lowest reference value $\Delta\sigma_C = 68.2$ N/mm^2.
2 The prediction interval method being identical with the Eurocode 0 approach for the statistical determination of a single property provided the highest value $\Delta\sigma_C = 72.4$ N/mm^2.
3 The estimate of the tolerance interval approach was inbetween with $\Delta\sigma_C = 71.3$ N/mm^2.

To summarize, it is stated that the observed variations of $\Delta\sigma_C$ for the different methods are not very pronounced in terms of the worked example. Nevertheless, the outcome of the statistical evaluation of test data sets exhibiting a higher scatter and/or for cases with unconstrained slope might come to other conclusions.

The authors plan to expand their investigations for cases with an unforced slope of the *S-N* curve in near future.

8 REFERENCES

Basquin, O. H. 1910. The exponential law of endurance tests. *Amercan Society for Testing and Materials Proceedings*, Vol 10: 625-630.

Brozetti, J.; Hirt, M.A.; Ryan, I.; Sedlacek, G. & Smith, I.F.C. 1989. *Background information on fatigue design rules – Statistical evaluation – Chapter 9 – Document 9.01*, 1st draft. Eurocode 3 – Editorial Group.

Draper, N. R. & Smith, H. 1966. *Applied Regression Analysis*. New York: John Wiley.

EN 1990: 2002. Eurocode 0: Basis of structural design.

EN 1993-1-9: 2005. Eurocode 3: Design of steel structures – Part 1-9: Fatigue.

Gurney, T. R. & Maddox, S. J. 1973. A re-analysis of fatigue data for welded joints in steel. *Welded Research International* 3 (4).

Hahn, G. J. & Meeker, W. Q. 1991. *Statistical intervals – A Guide for Practitioners*. New York: Wiley.

Haibach, E.; Olivier, R. & Rinaldi, F. 1981. Statistical design and analysis of an interlaboratory program on the fatigue properties of welded joints in structural steels. *ASTM STP 744*: 24–54.

Haibach, E. 2006. *Betriebsfestigkeit – Verfahren und Daten zur Bauteilberechnung,* 3rd edition. Berlin: Springer.

Hobbacher, A. 1975. *On evaluation of fatigue test data*, IIW-Doc. XII-XV 15-75.

Holický, M. 2005. *Basic statistical concepts and technique – Implementation of Eurocodes Handbook 2 Reliability Backgrounds*, Leonardo da Vinci Pilot Project CZ/02/B/F/PP-134007.

Lieurade, H.-P.; Huther, M. & Maddox, S.J. 2005. *Recommendation on the fatigue testing of welded components*, Proposed ISO Technical Report, IIW-Doc. XII-2140-06.

Natrella, M.G. 1963 *Experimental statistics.* Washington: National Bureau of Standards.

Schneider, C.R.A. & Maddox, S.J. 2003. *Best practice guide on statistical analysis of fatigue data*, IIW-Doc. XII-WG1-114-03.

Wood, B. 2011. *Wiley-Blackwell Encyclopedia of Human Evolution*. Chichester: Wiley-Blackwell.

APPENDIX

Table A. Coefficients for Equations 9 to 13 (variance σ^2 unknown)

Sample size n	3	4	5	6	7	8	9	10	12	14	16	18	20	25	30	40	50	∞
Coefficent $t_{1-\alpha,n-1}$	with $(1-\alpha) = 0.95$										Ref.: Hahn & Meeker (1991, Tab. A.7)							
	2.920	2.353	2.132	2.015	1.943	1.895	1.860	1.833	1.796	1.771	1.753	1.740	1.729	1.711	1.699	1.685	1.677	1.645
Coefficent $k_{1-\alpha,p,n}$	with $(1-\alpha) = 0.75$ and $p = 0.95$										Ref.: Natrella (1962, Tab. A-7)							
	3.152	2.680	2.463	2.336	2.250	2.190	2.141	2.103	2.048	2.007	1.977	1.951	1.933	1.895	1.869	1.834	1.811	1.645
Coefficent k_n	with $(1-\alpha) = 0.95$ (compare Equation 15)										Ref.: Eurocode 0, Tab. D.1							
	3.372	2.631	2.335	2.177	2.077	2.010	1.960	1.923	1.869	1.833	1.807	1.787	1.772	1.745	1.727	1.706	1.693	1.645

Maintenance, Safety, Risk, Management and Life-Cycle Performance of Bridges – Powers, Frangopol, Al-Mahaidi & Caprani (Eds)
© 2018 Taylor & Francis Group, London, ISBN 978-1-138-73045-8

Quantifying Uncertainty in Visual Inspection Data

J. Bennetts
Department of Civil Engineering
University of Bristol, Bristol, United Kingdom

G. Webb, S. Denton
Civil, Bridge & Ground Engineering
WSP Ltd, London & Bristol, United Kingdom

P. J. Vardanega
Department of Civil Engineering
University of Bristol, Bristol, United Kingdom

N. Loudon
Safety, Engineering and Standards
Highways England, Bedford, United Kingdom

ABSTRACT: Visual inspection is the most common form of condition monitoring used by bridge owners. Information derived from visual inspection data is commonly used to indicate the performance of bridge stocks and inform bridge management decisions. However, several studies have highlighted that the inherently subjective nature of the methods used to record this data can result in uncertainty, due to differences between different inspectors' perceptions of the severity and extent of defects. It is important for asset managers to understand the nature of this uncertainty and the implications for decision making. This paper reports the results of a study which compared scoring of bridge defects by pairs of independent inspectors across 200 bridge structures on England's strategic road network. A sample of 200 structures was selected to be representative of Highways England's stock with regard to, inter alia, *age*, *condition* and *structural form*. Routine Principal Inspections for these sample structures, undertaken every six years by the relevant maintaining agents, were also attended by inspectors from WSP Ltd, with defects scored independently by each inspector. The results of these comparisons were used to derive an empirical profile of the uncertainty in different individual defect severity and extent scores. Statistical methods were then used to derive empirical probability density functions for the values of bridge and stock level condition metrics according to the widely adopted *Bridge Condition Indicator* system. The reported results highlight trends in the reliability of individual defect scores and the impact of uncertainty on commonly used performance metrics.

1 INTRODUCTION

1.1 *Introduction*

Visual Inspection is the primary form of condition monitoring that is currently operated by bridge owners in the UK (e.g. McRobbie et al. 2015, Bennetts et al. 2016) and can be considered as a form of 'Damage Detection' in the wider framework of structural health monitoring systems (Webb et al. 2015). However, studies of the reliability of visual inspection have shown that the recorded data can be subject to significant uncertainty due to human factors (e.g. Moore et al. 2001, Lea & Middleton 2002). Moore et al. (2001) compared data from 49 different inspectors across 10 inspection tasks, comprising routine inspection of seven bridges and in-depth inspection of three bridges on the disused Pennsylvania Turnpike highway in the USA. Moore et al. (2001) concluded that the experience and physical capabilities of inspectors, and the environment in which inspections were undertaken had significant influence on the reliability of the inspection data recorded.

The data collected during visual inspections is increasingly used to inform decision-making, both at an individual structure level and at a strategic, whole

stock level (e.g. British Standards Institution 2014, UK Roads Liaison Group 2016). It is important to understand the reliability of the underlying data and its implications for the reliability and utility of derived *Condition Performance Indicators*, on which strategic decisions may be based.

1.2 *Inspection Data*

The industry practice for visual inspection of UK highway bridges is for a cycle of 'General Inspections' every 2 years, with 'Principal Inspections' every 6 years (Highways Agency 2007). During these inspections any defects observed on the structure are noted and photographed and recorded digitally later on. These defects are assigned to individual components in the bridge inventory and, for each defect, the defect type is recorded along with a severity code (the options for which are set out in Table 1) and an extent code from *SA* to *SE* (Table 2). Severity codes are categorised into different severity types, according to the defect type (Table 3), and are suffixed with an *S* if they are considered to present an immediate safety concern. Defects observed during inspections of bridges on the Highways England network are entered into the Structures Management Information System (SMIS) database.

Table 1: Mapping of Severity Codes to Severity Scores

Severity Codes				Severity
D	P	A	X	Score
D1	P1	A1	X1, X2	1
		A2		1.1
D2	P2	A3	X3	2
D3	P3	A4	X4	3
D3S			X4S	3.1
D4	P4		X5	4
	P4S			4.1
D4S				4.2
D5	P5			5

1.3 *Condition Performance Indicators*

In order to monitor the overall condition of individual structures or stocks of bridges, it is necessary to derive a measure of 'condition' from recorded defect information and the structure inventory. The *Bridge Condition Indicator* was developed for this purpose by WS Atkins Ltd (Sterritt 2002) for the County Surveyors' Society (CSS, now the Association of Directors of Environment, Economy, Planning and Transport, ADEPT) in the UK, and is adopted as a metric to score the condition of a bridge asset, or a population of assets, by most highway bridge owners in the UK. An understanding of the way in which the *Bridge Condition Indicators*, BCI_{Ave} and BCI_{Crit} are calculated is critical to understand the implications of the results presented in this paper. The process that is used by Highways England in SMIS is slightly different from the original CSS process (Sterritt 2002) and is set out as follows:

Table 2: Mapping of Extent Codes to Extent Scores

Extent Code	SA	SB	SC	SD	SE
Extent Score	0	0	0.1	0.3	0.7

Table 3: Defect Severity Types

Defect Severity Type	Description
D	Damage causing defects
P	Paint coating and protective system defects
A	Appearance related defects
X	Defects affecting adjacent areas

1. Defects in SMIS are recorded against individual components. Each defect score comprises a severity code and an extent code. These codes are mapped to numerical scores as shown in Tables 1 and 2.

2. For each component the defect with the highest severity score is selected. If there are multiple defects with the same severity then the defect with the highest extent score is selected.

3. All other defects on that component are disregarded.

4. For each component type, only defects with the same severity as the most severe are included.

5. A weighted average extent score based on the total size of all the components of that type is calculated.

6. The extent and severity scores are added to calculate an Element Condition Score (ECS) for each component type, on a scale from 1 to 5.7.

7. The Element Consequence Factor (ECF) for each component type is calculated from the ECS and the component's importance as shown in Table 4.

Table 4: Mapping of Element Consequence Factor (ECF)

Component Importance	Element Consequence Factor (ECF)
Very High	0.0
High	$0.3 - [(ECS - 1) \times 0.3/4]$
Medium	$0.6 - [(ECS - 1) \times 0.6/4]$
Low	$1.2 - [(ECS - 1) \times 1.2/4]$

8. The Element Condition Index (ECI) is found by subtracting the ECF from the ECS. The ECI cannot take a value below 1.0.

Table 5: Mapping of Element Importance Factor (EIF)

Component Importance	Element Importance Factor (EIF)
Very High	2.0
High	1.5
Medium	1.2
Low	1.0

9. The Element Importance Factor (EIF) is determined based on the importance of the component type, as shown in Table 5.

10. The Average Bridge Condition Score BCS_{Ave} is calculated by averaging the ECI values, weighted by the EIF for each component type.

11. The Critical Bridge Condition Score BCS_{Crit} is found by taking the maximum ECS for all 'Very High' Importance components.

12. BCS_{Ave} and BCS_{Crit} are both scores between 1 (best condition) and 5 (worst condition). These are mapped using an assigned quadratic function to give Bridge Condition Indicators BCI_{Ave} and BCI_{Crit} between 0 (worst condition) and 100 (best condition). The mapping functions are shown in Equations 1 and 2.

$$BCI_{Ave} = 100 - 2[{BCS_{Ave}}^2 + 6.5BCS_{Ave} - 7.5] \quad (1)$$

$$BCI_{Crit} = 100 - 2[{BCS_{Crit}}^2 + 6.5BCS_{Crit} - 7.5] \quad (2)$$

To calculate stock level BCI scores these steps are repeated for all bridges in the stock and an average is taken, weighted by each structure's deck area.

2 METHODOLOGY

2.1 *Random Sample*

A stratified sample of 200 bridges was selected by the authors from Highways England's stock for inclusion in this research. This sample was selected to be representative of the whole bridge stock, taking into account the following attributes: *Condition; Deck Type; Construction Type; Road Class; Age Group; Structure Type; Maintenance Region*; and *Type of Tensioning*. For example, the proportion of bridges in the sample with post-tensioning was selected to be the same as the proportion of post-tensioned structures in Highways England's whole stock of bridges.

The sample was selected computationally by randomly choosing several thousand possible samples of 200 from the list of structures due to be inspected over the duration of the project, and then selecting the random sample which was the best fit for the whole stock. The quality of fit, Q_{sample}, was evaluated as the sum of the mean of the squares of the differences in the proportions of each attribute value in each attribute, with the lower numbers indicating a better fit as shown in Equation 3.

$$Q_{sample} = \sum_{attributes} \frac{\sum_{attribute\ values}[P_{stock} - P_{sample}]^2}{N_{attribute\ values}} \quad (3)$$

2.2 *Independent Scoring of Defects*

For each of the 200 bridges in the sample, a WSP bridge inspector attended the site to independently inspect and record a sample of the defects present on the structure. For the large majority of the bridges in the sample, this coincided with the Service Providers' Principal Inspection. However, for a small number of the sample bridges, the independent inspectors visited the structure during a separate shift. For each visit, the inspectors recorded independent defect type, severity and extent information for a subset of the defects on the structure. These were limited to those visible at close quarters on the structure using the available access. 1373 individual defects were independently recorded by WSP's inspectors, of which 988 could be directly compared to those entered by the Service Providers' inspectors.

3 DATA ANALYSIS

3.1 *Reliability of defect recording*

For 385 (28%) of the defects recorded by WSP's inspectors, it was not possible to identify an equivalent defect in the Service Providers' Principal Inspection reports. This indicates variability in the reliability of defect identification by inspectors during visual inspections. Across the 988 independently recorded defects that could be directly compared to those recorded by the Service Providers as part of their Principal Inspection, 21% agreed on the assigned defect type, defect severity and extent. Overall, for 58% of the compared defects there was agreement on the type (e.g. *Map cracking*) of defect assigned, and agreement on the overall class of defect (e.g. *Cracks in concrete or masonry*) for 78%.

The level of agreement of defect types varied between different classes of defects, as shown in Figure 1. Particularly low reliability of defect class assignment was found within the *Cracks in concrete or masonry* and *Loss of concrete or masonry* defect classes. Investigation into the causes of these inconsistencies suggests that the process allows too many options of defect type within these classes. Consequently accuracy has been compromised in exchange for the availability of greater precision in defect type assignment. Furthermore, it was noted that while some defect types can only be confirmed through laboratory testing, the codes for these defects could, and had been, applied based only on visual inspection.

Similar results were found for the probabilities of the two inspectors recording the same defect severity or extent, with agreement of defect severity assignment for 53% of the compared defects, and agreement on defect extent for 59%. The same defect severity and extent were applied by the two inspectors for 34% of defects compared.

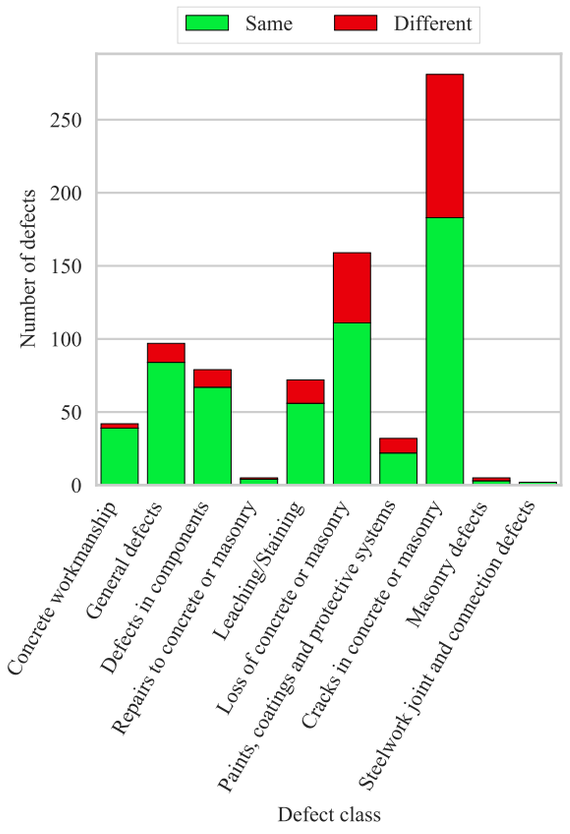


Figure 1: Comparison of defect type allocated by Service Provider inspector and WSP inspector for the defects included in this study, grouped by defect class

3.2 *Element Condition Scores*

For each recorded defect the extent and severity scores have been added to calculate an element condition score (ECS), giving a single measure to allow a comparison to be made between the two different inspectors (i.e. one each from WSP Ltd and Highways England's Service Provider for the maintenance area). These comparisons are presented in Figure 2, with each of the 988 comparisons represented as a blue marker. Due to the discrete nature of defect scores there are many overlapping markers. Red shading has therefore been added to indicate the density of markers at any point on the plot. Also shown, at the top and right of the plot, are histograms and gaussian kernel density estimations to provide an indication of the distribution of the scores from each inspector. While the two inspectors assigned the same, or a similar, defect severity and extent for many of the observed defects, there were substantial numbers of defects with a difference in ECS of more than 1. There were considerable discrepancies between the two inspectors' assessments of the severity of some defects, suggesting that the condition data for some structures could be markedly different, depending which individual inspector conducted the inspection.

3.3 *Trends in the reliability of defect scoring*

3.3.1 *Decision Trees*

Optimal decision trees allow presentation of the categorical factors that most influence a target variable (Quinlan 1986). To explore the factors affecting the reliability of defect scoring, a decision tree was generated to find the most informative multi-factor trends in the variation of defect score assignment (ECS) between two inspectors. For each compared defect the absolute difference between the ECS recorded by the WSP inspector and the Service Provider was calculated and banded into five groups as evenly as possible from those which were the same, to those which were the most different. Each pie chart in the decision tree has been drawn to represent the distribution of the ECS difference bandings within the sub-population below that point in the tree structure (Figure 3). The top *'All comparisons'* pie-chart represents the distribution of ECS difference in the full set of defect comparisons.

At each splitting point, the optimum attribute has been selected to partition the data in the way which provides the most information. The reduction in Shannon entropy (Shannon 1948) has been used to measure the information gained by a partition. For this measure, a perfect partition would be an attribute that perfectly split the structures into each of the ECS difference bands, whereas the worst possible partition would result in sub-populations that each had an even distribution of ECS difference within them. The size of each node's pie-chart has been drawn inversely proportional to its entropy and larger pie-charts have been plotted further from their parent node. This allows the most informative partitions to be readily identified. The following attributes were given to the algorithm from which it selected the optimum tree topology: *Component, WSP Class, WSP Extent, WSP Severity, Structure type, Construction type, Deck type, Structure use, Structure condition band, Distance from coast, Region, Age group*. Where:

WSP Class, WSP Extent & WSP Severity are the defect class, extent and severity, as recorded by the WSP inspector on site.

Age group splits the bridges into five bands from Youngest to Oldest with the same number of bridges in each band.

Structure condition band splits the bridges into five bands by their BCI_{Ave} condition score, from Best to Worse.

Nodes, and corresponding branches, have only been drawn if they represent at least 10 comparisons. The depth of the tree was limited to 3 partitions.

3.3.2 *Trends*

Figure 3 shows the most informative variables which affected the variation in ECS between two inspec-

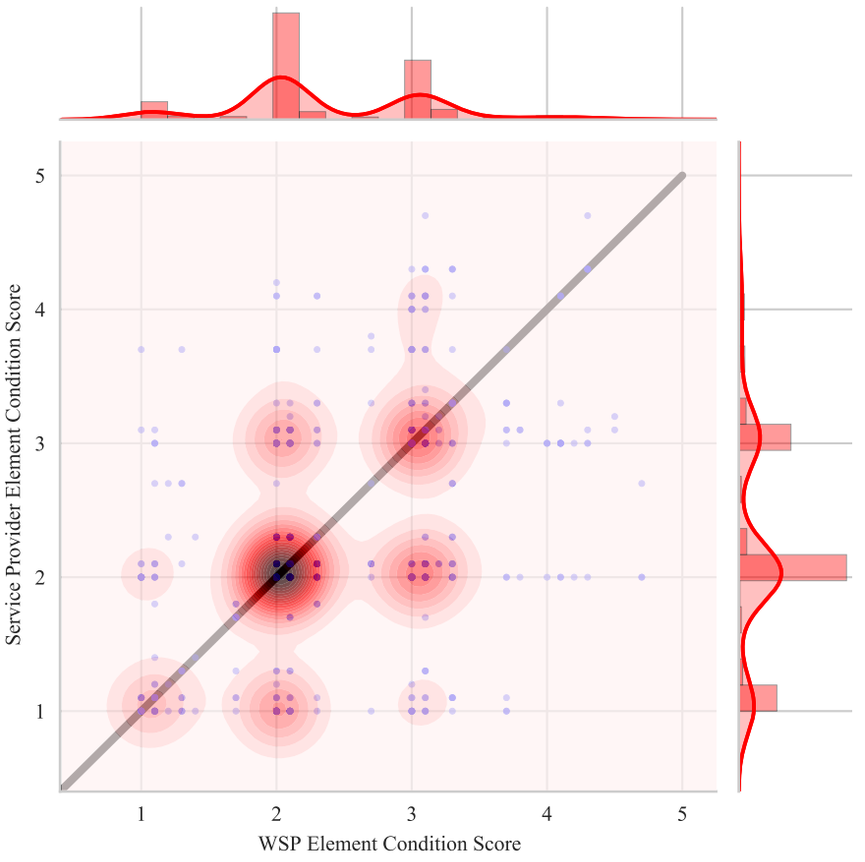


Figure 2: Comparison of element condition score allocated by Service Provider inspector and WSP inspector for the 988 defects included in the study. Red shading has been added to indicate the density of markers at any point on the plot.

tors. The *defect extent* had a significant influence. There was a much greater variation in ECS for defects with greater extent, than for those with lesser extents. This suggests that it is much harder to judge the severity of extensive defects. *Component type* was an important factor. Components such as *Road Vehicle Restraint Systems* and *Supports* were seen to exhibit much greater variation in scoring than components such as *Crossheads*, *Expansion joints* and *Wingwalls*. There was also a large degree of variation between different maintenance regions, suggesting that inspection guidance and practice are not consistent across the country. Structure details such as *age*, *structural form*, *construction material*, *road class*, and overall *structure condition* have a lesser influence on the reliability of defect scoring.

4 IMPLICATIONS OF DEFECT RATING VARIABILITY ON CONDITION METRICS

Given the variability of the visual inspection data collected by the owners of highway bridges, it is important to understand how this uncertainty affects derived metrics, which are used to inform strategy and decision making. The *Bridge Condition Indicator* calculation process is convoluted, and includes some non-linear steps, which means that it is difficult to derive directly the uncertainty in the resulting metrics from the uncertainty in the underlying data. Instead, Monte Carlo simulations have been used to derive this uncertainty empirically.

4.1 *Monte Carlo Simulations*

The 988 individual defect comparisons have been used to generate a table of probabilities mapping, for each extent code allocated by one inspector, the probabilities that a second inspector would allocate each of the possible extent codes. To avoid an implicit assumption that one inspector was 'correct', each observation was counted twice: once with the WSP inspector as Inspector 1 and once with the Service Provider's inspector as Inspector 1. This exercise was repeated for the severity scores. The resulting probabilities are presented in Table 6 and Table 7.

The probabilities have been derived from data from the sample of 200 structures only, however, since the structures were selected as a representative sample of the entire stock, it has been assumed that they are applicable to data from all structures in the stock. It is noted that no defects with a severity score of 4.1 or 5 were observed, by either inspector, on any of the structures in the sample. In the absence of additional information it has been assumed, for this analysis, that there was no variability in the scoring of defects with these severities. This will not significantly affect the results since defects with a severity score of 4.1 or 5 represented fewer than 1% of the approximately

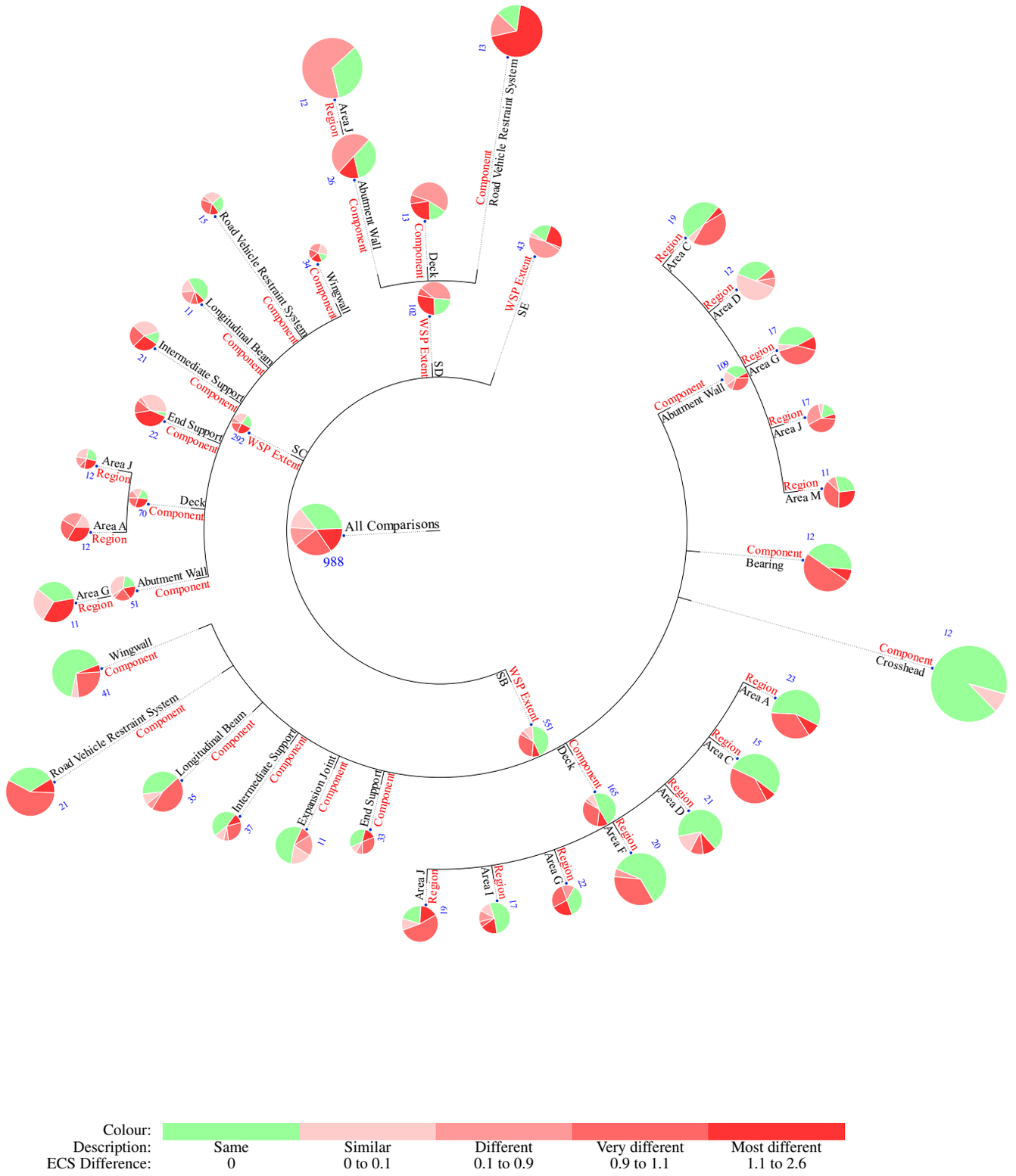


Figure 3: Decision Tree, showing the factors that most affect defect scoring agreement between inspectors.
(The blue number next to each pie chart denotes the number of comparisons that are included in that sub-population. The red text on each branch of the tree represents the attribute that the dataset has been partitioned by at that level, and the black text represents the value of the attribute.)

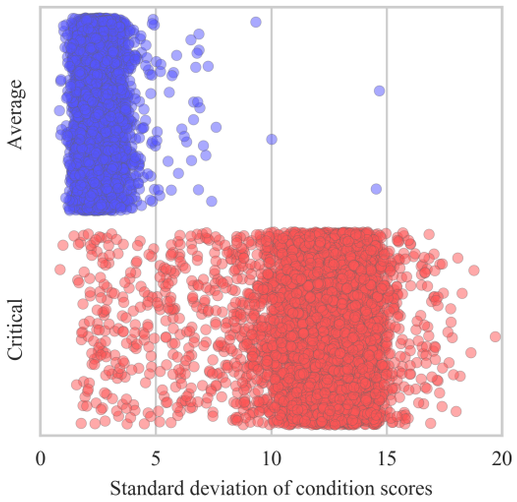


Figure 4: Standard deviation of condition scores obtained for each individual structure during Monte Carlo analysis

500,000 currently valid defects in the SMIS database.

The probability tables were used to vary the severity and extent scores for each of the currently valid defects in the SMIS database. These altered scores were then used to calculate new BCI_{Ave} and BCI_{Crit} scores for each bridge. This analysis was repeated for 1000 simulations.

Table 6: Probability table for defect extent codes

		Extent Code Allocated By Inspector 1			
		SB	SC	SD	SE
Probability of Inspector 2 Allocating Extent Code	SB	0.735	0.436	0.266	0.312
	SC	0.196	0.419	0.293	0.219
	SD	0.043	0.105	0.351	0.177
	SE	0.026	0.040	0.090	0.292

4.2 *Uncertainty in BCI scores for individual structures*

This analysis gives a set of plausible alternative values for the BCI scores for each individual structure. The level of uncertainty in BCI scores calculated by this method is dependent on a structure's inventory and defect assignments. It is therefore not possible to derive a definitive probability density function around a mean that would be valid for all structures. Instead, the standard deviations of each of these sets of alternative values have been plotted in Figure 4 for each of the approximately 7100 bridges on Highways England's network for which data was available. This shows that there is considerable uncertainty in the condition indicator scores for individual bridges; the BCI_{Ave} scores for most bridges have standard deviations of between 2 and 4 points, and the BCI_{Crit} scores for most bridges have standard deviations of between 10 and 15 points. The larger degree of uncertainty for BCI_{Crit} scores is due to them being governed by a very small number of defects on key structural components. In contrast, the BCI_{Ave} scores include defects from multiple component types and are therefore much less sensitive to variations in the scoring of individual defects.

In considering the implication of these results, it is useful to consider approximately what magnitude of change in a structure's condition score between consecutive inspections would be considered statistically significant. For a 95% confidence level, it is typically assumed that a change of two standard deviations would be required for the result to be considered significant. It follows that an apparent change in BCI_{Ave} score between inspections of less than about 6 points cannot be considered statistically significant. The larger uncertainty in BCI_{Crit} scores means that a change of around 25 points would be required to be significant.

A further consequence of this variation in individual structure BCI scores is that ranking structures by score (especially BCI_{Crit}) in order to prioritise maintenance would produce unreliable results. Thus, it would be undesirable to implement contractual conditions or targets that encourage prioritising interventions purely by structure condition scores.

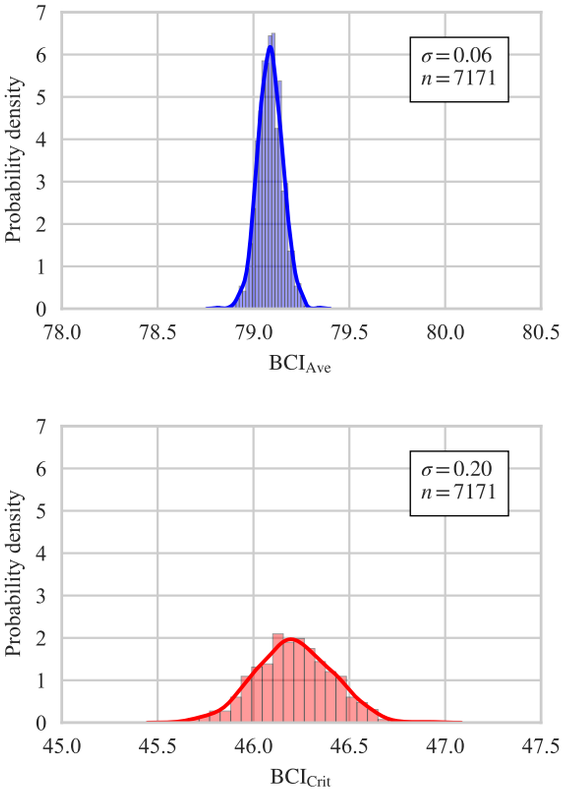


Figure 5: Empirical probability density function for the value of the BCI_{Ave} (top) and BCI_{Crit} (bottom) score for all structures in the stock

4.3 *Uncertainty in BCI scores for stocks of bridges*

Given that the computed variation in defect scores does not exhibit significant skew, convergence to the mean dictates that the uncertainty is reduced for metrics that include more data, as is the case for stock-

Table 7: Probability table for defect severity codes

		Severity score allocated by Inspector 1								
		1	1.1	2	3	3.1	4	4.1	4.2	5
Probability of Inspector 2 allocating Severity score	1	0.46	0.23	0.10	0.05	0.04	0.00	0.00	0.00	0.00
	1.1	0.03	0.31	0.01	0.01	0.00	0.00	0.00	0.00	0.00
	2	0.39	0.31	0.66	0.36	0.33	0.16	0.00	0.33	0.00
	3	0.11	0.15	0.20	0.50	0.25	0.53	0.00	0.33	0.00
	3.1	0.00	0.00	0.01	0.01	0.25	0.01	0.00	0.33	0.00
	4	0.00	0.00	0.01	0.06	0.04	0.29	0.00	0.00	0.00
	4.1	0.00	0.00	0.00	0.00	0.00	0.00	1.00	0.00	0.00
	4.2	0.00	0.00	0.00	0.00	0.08	0.00	0.00	0.00	0.00
	5	0.00	0.00	0.00	0.00	0.00	0.00	0.00	0.00	1.00

level BCI scores. The sets of plausible scores for each individual structure have been combined into a set of plausible stock level benchmarks by taking the mean of the structure values in each set, weighted by each structure's deck area. The results have been plotted in Figure 5. Despite the variation in individual defect scores, the average BCI_{Ave} and BCI_{Crit} scores for the entire stock of structures show very little deviation, with computed standard deviations of 0.06 and 0.20 respectively.

5 CONCLUSIONS

The following concluding remarks are made:

- Significant uncertainty was found in the classification and grading of individual defects during the visual inspection process.
- Defect classifications were particularly inaccurate for common concrete defects, where a large range of possible defect types is available.
- Defect grading by severity and extent was seen to be most unreliable for defects with high extents, and for component types such as *Vehicle Restraint Systems*.
- The degree of variation in defect grading between inspectors differed between different regional inspection teams, suggesting variation in practice.
- The industry standard *Bridge Condition Indicator* metric was shown to be sensitive to uncertainty in the underlying defect data, with the BCI_{Crit} metric particularly unreliable for comparing the performance of individual structures.
- Use of the *Bridge Condition Indicator* system at stock-level was shown to be considerably more reliable, with low levels of uncertainty.

DATA AVAILABILITY STATEMENT

The authors thank Highways England and Lockheed Martin for use of portions of the Structures Management Information System database as part of this research project. New experimental data collected during this study is owned by Highways England.

ACKNOWLEDGEMENTS

The authors would like to thank Highways England, Professor Colin Taylor and the Engineering and Physical Sciences Research Council (**Grant No. EP/G037353/1** Industrial Doctorate Centre: Systems).

REFERENCES

Bennetts, J., Vardanega, P. J., Taylor, C. A., & Denton, S. R. 2016. Bridge data - What do we collect and how do we use it? In Mair, R. J., et al. (Eds.), *Transforming the Future of Infrastructure through Smarter Information: Proceedings of the International Conference on Smart Infrastructure and Construction, 27-29 June 2016*, Cambridge, pp. 531–536. London, UK: ICE Publishing.

British Standards Institution 2014. *BS ISO 55000:2014 Asset management: Overview, principles and terminology*. London, UK: British Standards Institution.

Highways Agency 2007. BD 63/07 Inspection of Highway Structures. In *Design Manual for Roads and Bridges*, Volume 3. London, UK: HMSO.

Lea, F. & Middleton, C. 2002. Reliability of Visual Inspection of Highway Bridges, CUED/D-STRUCT/TR.201. Cambridge, UK: University of Cambridge - Department of Engineering.

McRobbie, S. G., Wright, M. A. & Chan, A. 2015. Can technology improve routine visual bridge inspections? *Proceedings of the Institution of Civil Engineers - Bridge Engineering 168*(3), 197–207.

Moore, M., Phares, B., Graybeal, B., Rolander, D., & Washer, G,. 2001. Reliability of Visual Inspection for Highway Bridges, Volume I: Final Report, FHWA-RD-01-020. Washington DC, USA: US DOT, Federal Highway Administration.

Quinlan, J. 1986. Induction of decision trees. *Machine learning 1*(1), 81–106.

Shannon, C. E. 1948. A mathematical theory of communication. *Bell System Technical Journal 27*(3), 379–423.

Sterritt, G. 2002. Bridge Condition Indicators, Volume 1. Technical report, WS Atkins for CSS Bridges Group, London, UK.

UK Roads Liaison Group 2016. *Well-Managed Highway Infrastructure: A Code Of Pracice*. London, UK: Department for Transport.

Webb, G. T., Vardanega, P. J. & Middleton, C. R. 2015. Categories of SHM Deployments: Technologies and Capabilities. *Journal of Bridge Engineering (ASCE) 20*(11), 04014118.

Maintenance, Safety, Risk, Management and Life-Cycle Performance of Bridges – Powers, Frangopol, Al-Mahaidi & Caprani (Eds)
© 2018 Taylor & Francis Group, London, ISBN 978-1-138-73045-8

BrIM bridge inspections in the context of Industry 4.0 trends

M. Salamak & M. Januszka
Silesian University of Technology, Gliwice, Poland

ABSTRACT: This paper describes two new technologies, Bridge Information Modelling (BrIM) and Augmented Reality (AR), which fit into the cyber-physical devices and cloud computing ideology of Industry 4.0. The rapid development of such technologies will have a significant impact on the design, construction, use, and management of transportation infrastructure, including bridges. This paper highlights difficulties in implementing BrIM technology for infrastructure projects and modelling of bridges. It also shows details of a new concept for inspection of bridges based on BrIM and AR.

1 INTRODUCTION

Large, ambitious projects in the field of infrastructure are being launched around the world. Often, their budgets exceed the capabilities of individual countries. The success of these projects primarily depends on improved management and the introduction of technological innovations. Three essential factors determine the nature of these projects: rapid growth of infrastructure investments, overruns of deadlines and costs, and low productivity of the entire construction industry (Changali et al., 2015). According to estimates, expenditures on mega infrastructure projects will double within fifteen years. Unfortunately, as these analyses indicate, almost 98% of these mega-projects are delayed and are in excess of their assumed budget. There are many causes for this situation, but one of the most important is low productivity in the construction industry. The cause of this is weak organisation and poor management of the entire process of investment and maintenance of existing infrastructure. Another cause is the lack of process, which has already been applied in product development processes (PDP) based on CAD/CAM systems. Digitisation and robotisation that revolutionised other industries (Teicholz, 2004). The design, realisation, and maintenance of buildings should be digitalised to transfer solutions from the manufacturing sector to the construction industry.

Our infrastructure will continue to develop. There will be more and more ageing bridges that need to be managed. The constant reduction in maintenance budgets will force extension of bridges' lifespan while still controlling their safety (Żarski et al., 2017). Two "Industry 4.0" digital technologies may help deal with this dilemma: Building Information Modelling (BIM) and Augmented Reality (AR).

2 DIGITAL TECHNOLOGIES IN BRIDGE MANAGEMENT SYSTEMS

2.1 *Industry 4.0 trends*

The industrial revolution and technologies such as the steam engine from the late seventeenth century teach us that each subsequent stage of industrial development is shorter. In 2011 in Germany, a development strategy called Industry 4.0 (German: Industrie 4.0) was announced. This was a combination of automation, processing of big data, and intelligent manufacturing techniques. There are also cyber-physical systems, such as the Internet of Things and cloud computing. The idea is to create a modern factory that will carry out nearly the entire production process with minimum human involvement. New production management systems that use the above-mentioned components will create an "intelligent" factory that will deliver tailored products according to individual's needs.

As already mentioned, the construction industry is delayed in implementing new, digital technologies,

such as automation and robotisation. However, development of digital technologies will eventually transform the construction industry. Many global corporations are interested in this industry as there are opportunities for profit by building faster and cheaper, as well as by lowering the cost of infrastructure maintenance and extending its lifespan.

However, BIM technology is the first step to make this possible and effective. Without three-dimensional models and their connection with digital information at the construction site, changes will not be made.

One of the key components of today's industrial revolution is so-called Cyber-Physical Systems (CPS). These are the mechanisms controlled or monitored by computer algorithms that are closely integrated with the internet and its users. Physical and software components in CPS are deeply interconnected with each other and operate in different time zones and at different scales. Examples of such systems include smart grids, autonomous vehicles, medical monitoring, process control systems, robotic systems, automatic avionics, and even Structural Health Monitoring (SHM).

Given the specifics of the construction industry and the fact development often occurs in open spaces, cyber-physical mobile systems with the ability to move and even work autonomously will be ever more important in this industry. Examples of such systems include mobile robotics, as well as electronic systems transported by humans or animals. The popularity of smartphones has increased the interest and potential of mobile CPS. These can be tablets and smartphones, but also smart watches, helmets, glasses, or contact lenses. Together these devices are called wearable devices. The most important requirements for wearable devices are:

- significant computational and storage resources with large processing capacities,
- sensory input and output devices such as touch screens, cameras, GPS modules, speakers, microphone, gyroscopes, light sensors, accelerometers, and proximity sensors,
- communication mechanisms such as WiFi, LTE, and Bluetooth for connecting devices to the internet or other devices,
- high-level programming languages for rapid development of mobile software and simple mechanisms for application distribution,
- durable and reliable battery performance.

In fact, nowadays, these requirements are met by a large group of commonly available smartphones, which can also be found at construction sites, although perhaps not always as a tool. Unfortunately, users of CPS such as smartphones do not have the ability to see and manipulate the information needed to make decisions about processes and their surroundings. They can use smartphone to download documentation and images can only be compared with drawings on the screen. In this way, errors arise from discrepancies between physical and cybernetic information.

2.2 *Augmented Reality*

The solution here may be use of Augmented Reality (AR). AR visualises cybernetic information against physical images and enables manipulation of cybernetic information by interaction with real and/or cybernetic objects (Azuma, 1997). AR can supplement and simultaneously use the BIM technology described above. AR, as an example of a computer technology that can assist a person in performing various tasks, is extremely promising. AR allows combining the computer-generated world (virtual) with the real world (where the user is) so that they form one synthesised environment (Abdullah and Thai, 2006). In contrast to the more popular Virtual Reality (Sherman and Craig, 2002), in which the user is completely immersed in the virtual world, AR gives one the freedom to work in the real world while enhancing human perception with virtual objects. Modern visualisation techniques such as AR allow representing the virtual world in an extremely intuitive way by 3D objects with the ability to view them from any perspective, with textures that are indistinguishable from the actual textures of real objects and at any scale (Fig. 1). Elements enriching reality using AR systems can also take forms beyond three-dimensional models, including subtitles, diagrams, photographs, films, and audio information (Bień et al., 2010), (Golparvar-Fard, 2012).



Figure 1. AR in the continuum of real and virtual worlds.

The increasingly popularity of AR technologies is due to the benefits they bring. First of all, it is possible to supplement reality with information from a database and/or knowledge. Instead of completely replacing the world surrounding a person with an artificial, virtual world (as is the case with VR), AR enriches the real world by adding only the information necessary to enhance one's reliability. This information can be delivered to the user of the system on demand (Januszka and Moczulski, 2013), (Moczulski et al., 2007). The more common practical use of AR technology is in special devices such as helmets or glasses. For example, when assembling or inspecting technical equipment, an installer "sees" animations and information superimposed on real images to help them complete their task correctly.

2.3 *BIM technology and bridges*

CAD programs have typically been used by designers as simply electronic 2D drawing boards. Neither the equipment nor the CAD program interface encouraged use of 3D tools. This began to change when 3D technology started to be used in the design of increasingly complex and sophisticated bridges. Development of these programs added more often contractual dimensions. The fourth dimension, time, can also be to create project animations as well as to prepare schedules and plans for supply of materials (Gołaszewska and Salamak, 2017). The fifth dimension introduces a cost factor and allows for a development of model estimates. The two subsequent dimensions are often combined and deal with management of finished projects. These capabilities allow use of BIM technology during inspection of bridges (Salamak and Januszka, 2015).

BIM technology is much better known in the construction industry (vertical BIM). It is used by architects, construction companies, and installers. Many public buildings are constructed with the use of this technology, such as hospitals, airports, office buildings, hotels, etc. BIM in infrastructure projects (linear BIM) is being implemented more slowly, for example in construction of roads, railway lines, bridges, tunnels, harbours, wharves, and dams. This delay may be due to the planning and realisation of infrastructure tasks.

The first fundamental issue is that the vast majority of infrastructure investments concerns the public procurement sector. Unfortunately, public institutions belong to organisations that are resistant to the implementation of new technologies and improvements in efficiency. Another difficulty that delays use of BIM technology in infrastructure projects is the slower development of BIM tools for infrastructure than for residential/commercial/industrial buildings. Finally, BIM itself still has problems, especially with regards to custom bridge geometries. This includes the overlapping of geometries in horizontal and vertical directions, transition curves, gradients, widening, and thickening (Jasiński et al., 2017). This is especially problematic for monolithic concrete bridges. The most popular CAD programs that are not part of the group of BIM products can cope with these challenges, but they do not have the ability to maintain the proper relationships between model objects without full parameterisation, which brings further burdens to storage and management of additional information. Taking into consideration all the specifics of bridges and the nomenclature of their components, we propose introducing BrIM, Bridge Information Modelling or Management.

2.4 *Future of Bridge Management Systems*

One of the most important elements of Bridge Management Systems (BMS) is the results of bridge inspections. These results are an essential source of information about the technical conditions and damages of a bridge (Thompson et al., 1998). In most countries they are obligatory and are performed based on a systematic strategy to control the condition of transportation infrastructure. Instructions for conducting inspections in each country are described in detail. These documents also define the scope and layout of inspection reports, which currently are paper documents. Classic tablets or smartphones are neither comfortable nor safe for inspectors, and even electronic documents do not provide comprehensive support. However, introducing a new type of inspection interface based on AR eliminates the disadvantages of current inspector aid devices.

Many publications (Abdullah and Thai, 2006), (Bień and Rawa, 2004), (Hu and Hammad, 2005), (Wang et al., 2010) have been written about the close connection of BMS with rapidly developing information technologies. These include use of artificial intelligence, virtual and augmented reality, monitoring systems, algorithms supporting decision making, etc.

Given current trends (Carlson, 2013), (Wang et al., 2013) and political decisions, it is increasingly likely that BIM technology in infrastructure, and in BMS, will rapidly develop in the coming decades. Advanced bridge modelling methods will be required as the efficiency of this technique in BMS will depend on the virtual model of the bridge being inspected. The BrIM bridge model will be the most important element of the BMS database (Fig. 2). Practical use of BIM models is currently limited to the design phase (3D and 4D BIM) and sometimes to the construction process (4D and 5D BIM).



Figure 2. Basic digital components of future Bridge Management Systems.

The use of BIM models for management and maintenance (6D and 7D BIM) occurs only in pilot projects and still requires research. This is particularly relevant to transportation infrastructure such as

roads and rail bridges. Therefore, it will be necessary to develop procedures for creating bridge models for use in inspections and BMS. For existing objects that do not yet have such models, other procedures for bridge inspections will need to be developed, such as laser scanning and BrIM models based on clouds of points. These procedures must take into account dominant span lengths and hard-to-reach areas such as high supports and pylons, where unmanned aerial vehicles (UAV) can assist.

3 SMART BRIDGE INSPECTOR SYSTEM CONCEPT

3.1 *Description of the system*

Currently, research on the development of computer-aided bridge management with the use of AR along with BrIM models are only conducted to a limited extent in a few countries around the world (mainly outside of Europe, e.g. in Canada, USA, Taiwan, Australia). More often similar systems are being developed for other facilities, such as buildings (Suyang et al., 2013), (Hammad et al., 2009). Certain functional assumptions and requirements for integration of BIM with AR were proposed in (Wang and Dunston, 2007). The authors proposed that visualisation of information, directly on the object, in real time, is necessary during inspection of the object.

During an inspection, a great deal of information must be collected about the current technical condition of the bridge. An inspector uses various tools to obtain this information. As a consequence, when using AR system during inspections, there is still the problem of the inspector having and transporting necessary equipment. In (Doppleb et al., 2004), the authors propose a wearable computer integrated with a localisation system and an AR display. However, this solution does not provide integration of additional equipment for the inspector, including measuring devices and sensors. Nor do the suggested solutions take into account users' safety (e.g. helmets).

Due to the lack of effective solutions, the authors present in this article an innovative solution for an intelligent system based on AR techniques to support bridge inspections. The system consists of several modules related to the three phases of bridge inspection (Fig. 3):

1. The preparation phase of the inspection during which the user, with the use of the simulator, plans the next inspection steps and familiarises themselves with the object.
2. The inspection phase during which the inspector uses the AR interface integrated with the decision-making and data acquisition system to collect and store up-to-date information about the condition of the object and/or to view information about its history.
3. The phase of report preparation during which a user supported by the system prepares a report about the object.

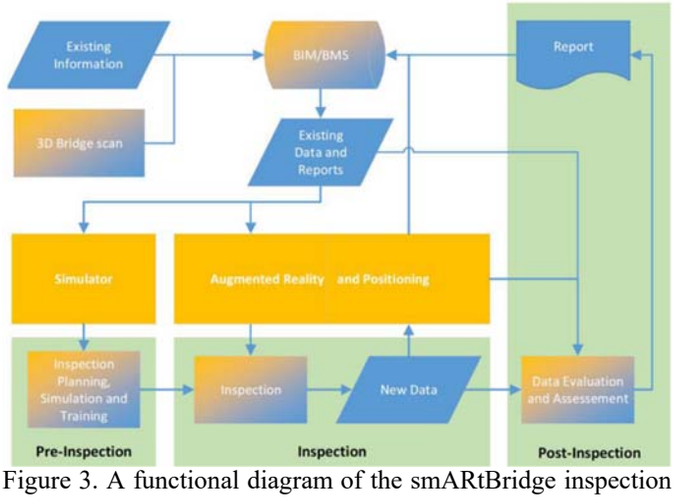


Figure 3. A functional diagram of the smARtBridge inspection system.

An important feature of the proposed AR-based system is its integration with BrIM and BMS. Integration allows updating information about object conditions and intuitive access to data on its construction and history at stages ranging from inspection preparation, through construction, to report preparation. During inspections, the system allows visualisation of selected - including those hidden or invisible to the inspector - structural elements of the bridge (e.g. reinforcement, tendons, bearings, etc.) and other elements of equipment and installations (e.g. drainage, electrical, and IT installations). These data come from BMS and BrIM models of the object.

The most important element of the proposed solution when preparing and planning an inspection is the simulator. The BrIM model and the collected object history data may be useful for the inspector to become acquainted with the bridge and with preliminary analysis. Prior to the inspection of the real object, the inspector, with use of the special simulator, has the ability to become familiar with the object using its virtual, but realistic, representation. This should make navigation on the bridge faster and more efficient. In addition, use of the simulator allows the user to plan future inspection steps, including locations that require special attention. In this way, during a virtual walk through the inspector may mark the most important locations on the bridge that should be checked during inspection of the real object. Then, when inspecting the real object, the AR-based system can point to the inspector locations that were previously marked in the simulator. The use of a simulator, in this case, is an innovative approach for inspection using BrIM, AR, and VR (Fig. 4).

During the inspection, the most important element of the system is the human-machine interface (HMI) with a graphical user interface (GUI) that uses AR techniques. The interface includes both hardware and software solutions. The AR-based system consists of

a wearable platform that integrates devices with displays (e.g. Microsoft HoloLens or Daqri Helmet) and data acquisition during inspections (e.g. a wearable smartphone). In addition, hardware platform integrates sensors (including non-destructive testing), tools (including measuring), and a location system.

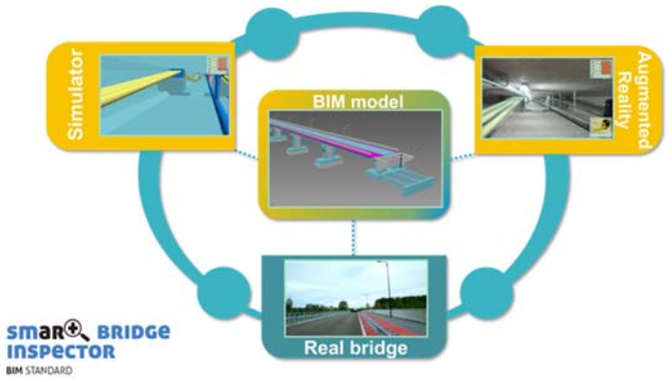


Figure 4. BrIM+AR+VR integration in the proposed system.

The hybrid location system is responsible for proper operation of the AR interface. In particular, presentation of the information during the inspection (including visualisation of elements and installations) directly on real object and acquisition of data and annotations in the BrIM model according to their actual location. The localisation system must work in open areas (outside) and inside bridges so that its operation can integrate with global location (satellite, e.g. GPS, Galileo) and mobile localisation systems (system installed on the object). Due to the accuracy in location, especially when assigning the location of the data being collected in the BrIM model, it should be possible to manually correct location of damage by the user.

Most of the information needed during the inspection is downloaded from the BMS system before the inspection and saved in the inspector's computer, which is a HMI hardware element (Fig. 5). Due to the enormous amount of information that can be stored in a BMS system, it is possible that some of the documentation, which may initially appear to be unnecessary and, therefore, were not downloaded to the device, will become necessary during the inspection. Then the use of advanced communication systems will enable wireless transmission of records from the BMS repository and vice versa. This transmission of data during the inspection will allow for quicker preparation of bridge inspection reports.



Figure 5. Wearable HMI system during a bridge inspection.

During work, the inspector has at his disposal a system supporting decision making. The user should enter the necessary data to the advisory system, which then instructs the engineer with further actions and enables classification of the observed damages (e.g. cracks, concrete defects). In this way, the inspector should be able to determine the class of damages that are then assigned to the virtual BrIM model at the location that corresponds to the location of the damage on the real object.

Using the sensory system integrated with AR interface the inspector measures critical parameters (e.g. measurements from non-destructive testing devices, the distance between two existing elements, the area of the defect, length of the crack, etc.), and then records the results in the BrIM model. All other inspector's annotations are saved in the same way, mainly in the form of photographic documentation, sketches, notes, and sound recordings. The collected data should be saved as layers on the BrIM model and integrated with the BMS. Any data collected by the inspector may be used at any time in the future, particularly at the time of report preparation and planning of the next inspection.

The last significant element of the system allows supporting the preparation of reports after inspection, based on collected information. The user's involvement at this stage should be limited to accepting particular sections of the report and conclusions from the expert system. Other tasks related to the preparation of the report should be done automatically.

The solution proposed by the authors and presented in this part of the article is in the early stage of research. The development of such a system requires a solution of numerous interdisciplinary problems that have not yet taken place anywhere in the world, or are ineffective and require improvement. The proposed system will improve the quality and reduce the cost of managing and maintaining bridges. In addition, integration of the system with BrIM models and BMS should contribute to a more efficient interpretation of information from assessment of the condition of bridges, and development of more detailed and accurate reports that may contribute to reducing the cost of maintenance and extending the lifespan of individual bridges.

The system can be used by inspectors (bridge engineers) and representatives of infrastructure manager. In the future, the system (particularly the simulator) could be used in institutions responsible for education and training of bridge inspectors applying for a license. Support of remote inspection and teleimmersion with the use of unmanned vehicles (UV), including autonomous mobile robots, would also be an innovative tool.

3.2 *Example of BrIM model*

The BrIM model of a road bridge was selected for inspection experiments on use of BrIM model in bridge management. It is a five-span bridge with a total

length of 216 m, which runs over railway lines in Gliwice, Poland (Fig. 6). It was constructed using the incremental launching technology in accordance with the traditional design documentation from 2013. In the cross-section, it is a concrete box-girder with external prestressing. The bridge can therefore be classified as a mid- to large-sized road bridge, whose inspection is typically time-intensive and important.



Figure 6. View of the bridge in Gliwice.

The BrIM model of the bridge (Fig. 7) was developed in accordance with two procedures: based on the design documentation, and based on the cloud of points obtained in laser scanning. Both models are currently being compared and merged for further research. The first contains a number of details and information that are not available for scanners. There are supports with reinforcement, box girder with tendons and reinforcement, internal installations, and equipment. Everything was assigned to the appropriate thematic layers and marked with specific colours. In this way, the user of the model will be able to select the displayed objects.

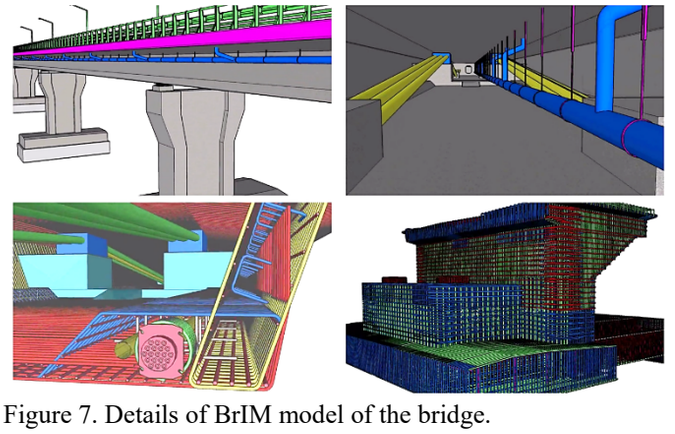


Figure 7. Details of BrIM model of the bridge.

3.3 *Bridge inspection with BrIM+AR devices*

The process of recording damage and saving in the BrIM model during inspection is very intuitive (Fig. 8). The inspector equipped with the proposed mobile devices goes to the site. When examining the object (e.g. inside the box-girder bridge), the inspector looks for possible irregularities by comparing the BrIM with the actual object. Once damage is found, qualitative and quantitative assessments are performed and data is archived in the BrIM model. A report from the inspection is generated automatic and goes to the administrator's database together with the damage observed. From this point on, the damage is stored in the BrIM model and can be imaged during the next inspection.

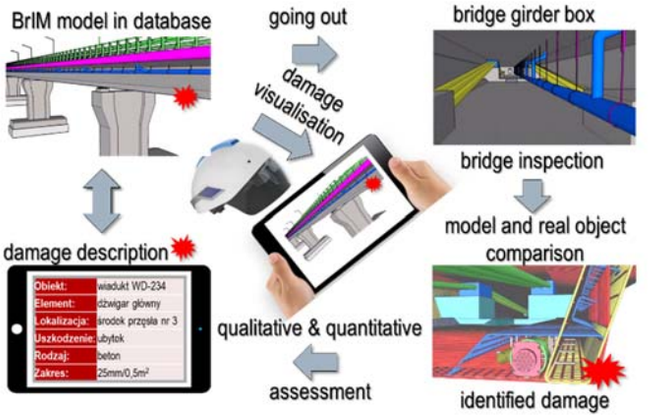


Figure 8. Storing of damage in the BrIM model.

AR technology has a key place in the process of inspection in the above scenario. The inspector registering the damage works with the tracking system as one of the AR subsystems. When collecting data on identified damage, the inspector uses a wearable mobile device to take photos and record videos with text description labels (e.g. text labels to indicate important locations in the picture), graphics (e.g. graphic elements to indicate important locations at the picture, e.g. arrows, lines, circles, etc.), and sound (e.g. voice recordings). In order to properly mark a location where the information was recorded or where the virtual object was imposed, it is necessary to use a tracking system. The location system allows saving recorded data in the BrIM model in the exact same location as on the real object.

In the described system two types of localisation are proposed: location based on a mobile device (accelerometer, gyroscope, compass) with SLAM support (simultaneous localisation and mapping) and GPS signal with hybrid location based on an independent localisation system (for localisation within objects).

Properly saved data may be displayed again in the future during inspection with the use of AR techniques. In this case, the user sees information regarding the current location (e.g. photos, text, sound information, sensory readings) which were saved during previous inspections and assigned to a specific location on the object on the helmet-mounted unit.

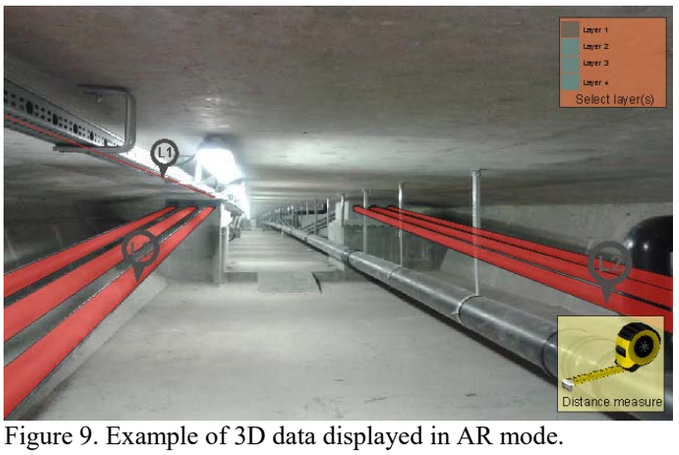


Figure 9. Example of 3D data displayed in AR mode.

In another application, once the mobile device is pointed at a specific place in the object and recognised the user's location and orientation, computer-generated 3D structural elements will be added to a real image. It is possible to display models of elements invisible to the naked eye. In both variants, the user selects the layer of information from the drop-down menu (according to the BrIM model such as installations, structural elements, etc.). In addition, it is possible to display information from multiple layers simultaneously (Fig. 9).

The latest use of AR techniques is integration with virtual instruments to measure identified damage. These tools are limited to simple instruments that allow measuring length (e.g. crack length) or surface area.

4 CONCLUSIONS

In the coming years, the industry of infrastructure construction including bridges awaits a revolution in design, construction, and maintenance of modern and demanding BIM technologies. Although this technology has already shown its advantages in building construction, there are still many difficulties and constraints for implementing it on a large scale for transportation infrastructure.

The cyber-physical system for bridge inspections presented here can be used not only by owners and administrators of infrastructure. In many countries, bridges inspections are carried out by small private entities which are gaining popularity in the public procurement market. On the basis of outsourcing, companies equipped with this type of equipment will be able to offer their services at a better value, which will also satisfy contracting authorities.

The authors hope that the information provided in the paper will be the basis for a meaningful discussion on the implementation of BIM and AR technologies in the design, construction, and maintenance of bridge structures. The infrastructure managers in those countries that choose to implement modernised BMS systems with intelligent tools for inspection will be able to use them to make more transparent and uniform investment decisions. This will improve the ability of prediction and planning of maintenance and replacement of elements of the transportation infrastructure networks.

REFERENCES

Abdullah, A., Thai, O.B., 2006. Personal digital assistants as a mobile inspection system at construction site, in: Proceedings of the 6th Asia-Pacific Structural Engineering and Construction Conference (APSEC 2006), 5 – 6 September 2006, Kuala Lumpur, Malaysia. pp. D28–D38.

Azuma, R.T., 1997. A Survey of Augmented Reality. Teleoperators Virtual Environ. 6,4(1997), 355–385.

Bień, J., Kużawa, M., Bień, B., 2010. To See is to Know: Visualization in Bridge Inspection and Management, in: 5th International Conference on Bridge Maintenance, Safety and Management. Philadelphia, pp. 567–574.

Bień, J., Rawa, P., 2004. Hybrid Knowledge Representation in BMS. Arch. Civ. Mech. Eng. Vol. IV, N, 41–54.

Carlson, W., 2013. A Critical History of Computer Graphics and Animation. Ohio State University, Ohio.

Changali, S., Mohammad, A., Nieuwland, M., 2015. The construction productivity imperative. How to build megaprojects better. McKinsey Q. July 2015.

Doppleb, J., Steinke, N., Meyer, N., Kulik, A., Petzold, F., Thurow, T., Bürgy, C., 2004. Wearable Computer for Building Surveying, in: 8th IEEE International Symposium on Wearable Computers (ISWC). Arlington, pp. 4–6.

Golparvar-Fard, M., 2012. D4AR. 4-Dimensional Augmented Reality. LiDAR Mag. Vol.2, No., 11–15.

Gołaszewska, M., Salamak, M., 2017. Challenges in takeoffs and cost estimating in the BIM technology, based on the example of a road bridge model. Tech. Trans. Civ. Eng. Vol. 4/201, 71–79.

Hammad, A., Wang, H., Mudu, S.P., 2009. Distributed augmented reality for visualizing collaborative construction tasks. ASCE J. Comput. Civ. Eng. Vol. 23, 2, 418–427.

Hu, Y., Hammad, A., 2005. Location-based Mobile Bridge Inspection Support System, in: 1st CSCE Specialty Conference on Infrastructure Technologies. Ontario, p. FR130.1-FR130.10.

Januszka, M., Moczulski, W., 2013. Acquisition and Knowledge Representation in the Product Development Process with the Use of Augmented Reality, in: J. Stjepandic et Al. (Eds.), Concurrent Engineering Ap-Proaches for Sustainable Product Development in a Multi-Disciplinary Environment. Springer-Verlag, London, pp. 315–326.

Jasiński, M., Płaszczyk, T., Salamak, M., 2017. Visual programming and BIM technology in parametric concrete bridge design, in: 12th Central European Congress on Concrete Engineering CCC2017. Tokaj, Hungary, pp. 130–138.

Moczulski, W., Panfil, W., Januszka, M., Mikulski, G., 2007. Applications of augmented reality in machinery design, maintenance and diagnostics, in: Recent Advances in Mechatronics. Springer-Verlag, Berlin Heidelberg.

Salamak, M., Januszka, M., 2015. BIM models and augmented reality for concrete bridge inspections, in: 11th Central European Congress on Concrete Engineering CCC2015. Hainburg, pp. 25–28.

Sherman, W.R., Craig, A.B., 2002. Understanding Virtual Reality: Interface, Application,and Design. Morgan Kaufmann Publishers Inc., San Francisco.

Suyang, D., Chen, F., Vineet, R.K., 2013. Sensitivity analysis of augmented reality-assisted building damage reconnaissance using virtual prototyping. Autom. Constr. 33, 24–36.
Teicholz, P., 2004. Labor Productivity Declines in the Construction Industry: Causes and Remedies. AECbytes Viewp.
Thompson, P.D., Small, E.P., Johnson, M., Marshall, A.R., 1998. The Pontis Bridge Management System. Struct. Eng. Int. Vol. 8, No, 303–308.
Wang, X., Dou, W., Chen, S., Ribarsky, W., Chang, R., 2010. An Interactive Visual Analytics System for Bridge Management. Comput. Graph. Forum Vol. 29 (3, 1033–1042.
Wang, X., Dunston, P., 2007. Design, strategies, and issues towards an augmented reality-based construction training platform. J. Inf. Technol. Constr. 12/2007, 363–380.
Wang, X., Love, P.E.D., Jeong Kim, M., Park, C., Sing, C., Hou, L., 2013. A conceptual framework for integrating building information modeling with augmented reality. Autom. Constr. 34/2013, 37–44.
Żarski, M., Płaszczyk, T., Salamak, M., 2017. Integrated lifecycle analysis of a concrete bridge, in: 12th Central European Congress on Concrete Engineering CCC2017. Tokaj, Hungary, pp. 140–148.

SS17: Smart bridge components: Monitoring and optimization of EJs, bearings and dampers

Organizer: K. Islami

Maintenance, Safety, Risk, Management and Life-Cycle Performance of Bridges – Powers, Frangopol, Al-Mahaidi & Caprani (Eds)
© 2018 Taylor & Francis Group, London, ISBN 978-1-138-73045-8

"Smart" bridge expansion joints enabling optimized decision-making at different life-cycle stages

P. Savioz
Mageba, Shanghai, P.R. China

K. Islami
Mageba SA, Bulach, Switzerland

V.V. Ghodke
Mageba, Sydney, Australia

ABSTRACT: The potential benefits of using structural health monitoring systems in measuring and recording bridge data have been established in many applications around the world, but the efficiency and effectiveness of such systems depends on how they are applied – for instance, in terms of sensor types and locations on the structure. Considering that the most important data required generally includes superstructure movements, which can easily be measured at the expansion joints, and the critical importance of the same expansion joints, which are less robust and therefore more susceptible to damage and deterioration than the main structure, it is often sensible to base the design of a monitoring system on data from the expansion joints. Developing technology now allows for the integration of appropriate sensors in a joint during fabrication, reducing effort and risk on site, and can enable a suitably configured system to automatically detect possible damage or deterioration based on vibrations only, marking the advent of "smart" expansion joints.

1 INTRODUCTION

A bridge's expansion joints are generally much less robust that the rest of the structure which supports them, but must facilitate deck movements and rotations while subjected to dynamic, fatigue-inducing loading from traffic. The expansion joints of a bridge that is crossed by 50,000 vehicles a day, for example, will be subjected to well over a billion axle loads, or mini dynamic impacts and rotations, during a 40-year or more service life. This enormous figure explains why the expansion joints of any bridge require proper maintenance throughout their lives, and why they will be likely to require replacement several times during the life of the main structure. It also illustrates well the importance of careful consideration, during selection and design of the bridge's expansion joints, of the complete life cycle of the main structure and of the joints themselves.

Decision-making during the life cycle of expansion joints can be greatly improved by Structural Health Monitoring (SHM). At an early stage of the life cycle, movements, rotations and dynamic load impacts (vibrations) can be measured on installed expansion joints for design verification purposes. During the expansion joint's service life, the same factors can be very useful in optimizing maintenance work and reducing the risk of damage escalation. And towards the end of the joint's service life, such information can be of great value in defining requirements for expansion joint replacement work.

2 LIFE-CYCLE COST CONSIDERATIONS OF BRIDGE EXPANSION JOINTS

The initial supply and installation cost of expansion joints typically represents less than 1% of the total bridge construction costs (Braun, 2011). It has also been concluded that these initial supply and installation costs for the structure's joints is "insignificant" in relation to the future costs of maintenance and replacement should the joints perform poorly (Dexter et al, 2002). The total life-cycle costs of expansion joints can be estimated to be 12 times the initial cost in the case of a high-quality product, and up to 47 times the initial cost in the case of a low-quality product that needs more repair and replacement (Savioz et al, 2014). It can thus be concluded that:

(1) The initial extra investment required to purchase a high-end expansion joint, as opposed to a low-tech one, is entirely insignificant compared to the enormous savings that can result over a period of several decades.
(2) In order to minimize the overall life-cycle costs of a bridge's expansion joints, it must be ensured that adequate resources are devoted to maximizing the suitability, durability and quality of the joints selected for use, and enabling them to perform as well as can be expected, for as long as can be expected, by ensuring the adequacy of subsequent inspection and maintenance activities.

3 THE USE OF MONITORING SYSTEMS TO MINIMIZE THE LIFE-CYCLE COSTS OF A BRIDGE'S EXPANSION JOINTS

Several strategies to minimize the total life-cycle costs of expansion joints are recommended by Savioz et al (2014). These include the use of SHM, which can provide very valuable support at any stage throughout the life cycle – including, in particular, at the design (verification) stage and during inspection and maintenance work.

3.1 *Design (verification) stage*

Due to the 'prototype nature' of many bridges, it is a challenge to clearly determine, during the design stage, the movements and rotations that the structure's expansion joints will have to accommodate. Often, the actual movements and rotations of a completed structure are not as expected. Loading can also vary significantly; while axial loads and dynamic amplification factors may be defined by design codes, load impacts may be significantly larger, e.g. due to overloaded trucks or bumpy road conditions. In either case, due to uncertain design input data, expansion joints may be under-designed, resulting in premature failure, or over-designed, resulting in unnecessarily high costs. It is therefore important for the involved parties – especially the bridge designer and the expansion joint supplier – to have a comprehensive understanding of the behavior of the various types of expansion joint available, in different applications and circumstances. Monitoring of installed expansion joints in different conditions can provide the necessary basis for such understanding. This knowledge can then be used in selecting the most appropriate type of expansion joint for a specific application, and to define detailed design features. As well as establishing the exact movements and rotations arising, data can also be provided relating to loading, water-tightness under extreme conditions, specification of noise reduction features, etc.

Such benefits are especially pronounced in the case of existing bridges that require their expansion joints to be replaced after years of service. In this case, movements, rotations, loading etc. can be recorded by a suitably designed SHM system, measuring expansion joint data (movements, loading, etc.) over a certain period of time prior to the replacement project. Typically, monitoring over a one-year period may be optimal as it can provide data from all seasons. If this amount of time is not available, a shorter period can be monitored and extrapolations can be made by means of further modelling. Such recording and modelling will enable design specifications to be developed which are very suitable for the real situation of the specific bridge.

Two case studies below will illustrate how structural monitoring was used to support decision making for an expansion joint replacement project (Section 4.1), and for the purpose of verification of design and behavior of installed expansion joints (Section 4.2).

3.2 *Inspection and maintenance stage*

Inspections, and the investigations associated with required remedial works, are no longer limited to purely manual efforts; great benefits, in terms of both ability and expense, may be offered by automated remote monitoring systems (Spuler et al, 2011). The formidable data measuring power of today's SHM technology can be used to measure and report on any chosen variables in the bridge's and/or expansion joints condition (saving manual inspection visits), or to precisely define a maintenance or repair challenge and thus refine and optimize the selected solution. Such systems can even be programmed to send alarm messages to the bridge engineer, by email or SMS, should any measured variable exceed a predefined boundary value – thus ensuring that any potential problem can be dealt with before it develops into a costly repair project.

Two further case studies below will illustrate how structural monitoring may be integrated into modular expansion joints during the supply stage, making them "smart". The first of these, presented in Section 4.3, focuses on movement and rotation measurements, including alarm settings, on a remote bridge in a seismically active zone. The second, presented in Section 4.4, illustrates a newly developed technology that, in addition to measuring typical movement and rotations, can also detect minor changes in the expansion joint's condition. The early identification of damage or deterioration that this makes possible can facilitate early intervention, avoiding further deterioration and increased risk.

4 CASE STUDIES

4.1 *Angus L. Macdonald and A. Murray MacKay twin suspension Bridges, Halifax, Canada*

The city of Halifax, capital of the Canadian province of Nova Scotia, relies heavily on two structures in particular - the Angus L. Macdonald Bridge (Fig. 1) and the A. Murray MacKay Bridge (Fig. 2), both of which connect the city across the sea inlet that divides it in two. Having been opened to traffic in 1955 and 1970 respectively, both structures have already provided several decades of service. The A. Murray MacKay Bridge was renovated in recent years, and similar renovation works, with similar changes to the bearing support of the bridge deck, were being planned for the Angus L. Macdonald Bridge. The bridge was proposed to receive an entire new deck, and FEM modeling of the deck, verified by measured data, was to play a key role in the design process.



Figure 1. The Angus L. Macdonald Bridge in Halifax.



Figure 2. The A. Murray Mackay Bridge in Halifax.

It was determined that an SHM system should be used to measure and record the movements and rotations of the deck of the Angus L. Macdonald Bridge at its expansion joints, providing the data needed by the finite element modeling. An example of some of the data provided by the system, for a specified period of time, is presented in Figure 3. This particular data enables rotations and displacements (both longitudinal and transverse) to be easily related to temperature, and to wind strength and direction.

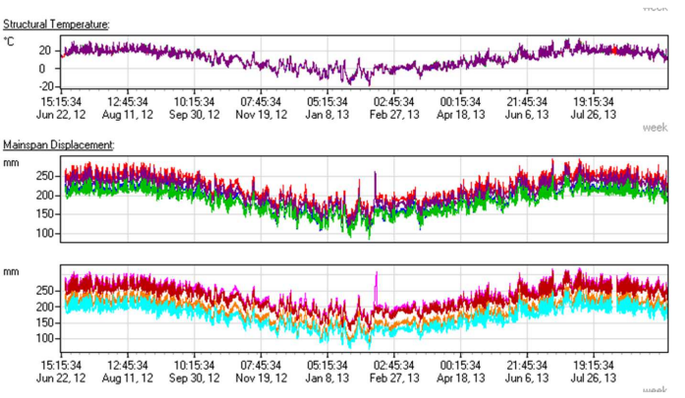


Figure 3. Example of data recorded during a one-year period.

The principal movements were correlated to temperature during the monitored period (Fig. 4). The plot shows a decreasing trend of displacement when temperature decreases. The same linear behavior must also be evidenced by the finite element model of the structure. To observe the distribution of movements, a very useful means is offered by histograms. Figure 5 shows on a histogram the number of times a value of measurement arose during one year of monitoring at a single sensor.

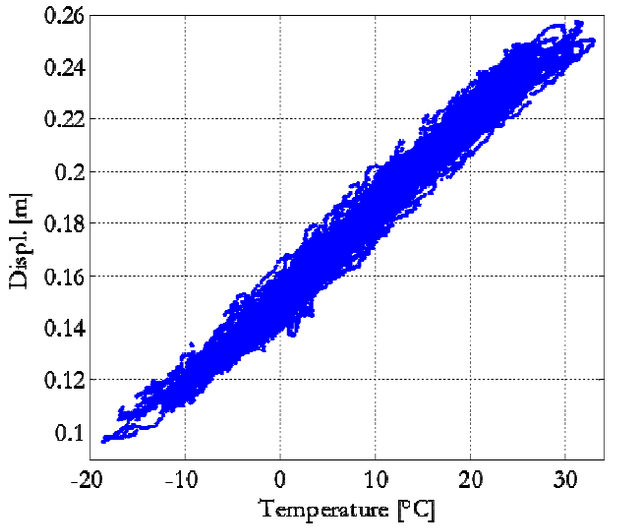


Figure 4. Temperature effects on displacement measurements.

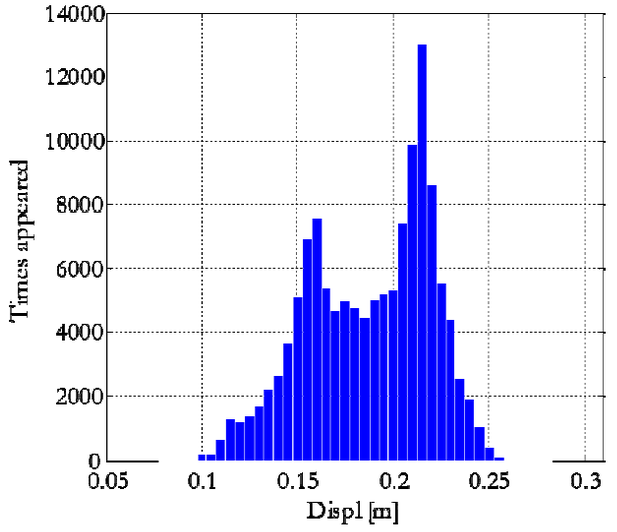


Figure 5. Histogram with distribution of displacement data.

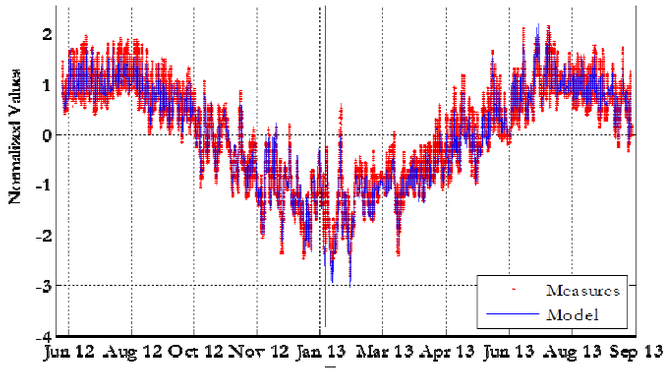


Figure 6. Comparison of measured and expected displacements.

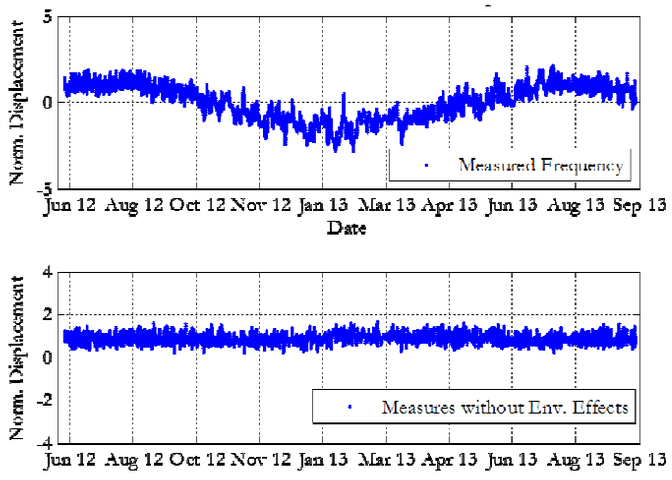


Figure 7. Regression model showing displacement data, before (above) and after (below) elimination of environmental effects.

To improve damage detection at a bridge's expansion joints, environmental effects can be eliminated using a regression model providing data such as that shown in Figures 6 and 7, generated from the correlation between temperature or humidity and the movements of the bridge. The resulting movements recorded by the system do not then include movements resulting from temperature or humidity, enabling abnormal influences (due to damage or other unexpected events) to be easily recognized. This is illustrated by Figure 7, which shows on the lower graph, with normalized values, the bridge movements that are due to traffic etc. and not due to temperature. Any abnormal shift on this graph would be immediately recognizable, enabling the need for repair or preventative action to be assessed.

A very interesting insight into the movements of the deck of the A. Murray Mackay Bridge was provided by the SHM system. It quickly established that the deck moves a great deal in the longitudinal direction, with accumulated movements of up to 2.5 km per month at a single expansion joint (Figure 8). Such enormous accumulated movements are extremely rare for such structures, and many times higher than the movements experienced by the decks of the great majority of long span bridges.

For comparison, the movements of the existing deck of the neighboring Angus L. Macdonald Bridge have been estimated by the same monitoring system to amount to less than 80 m per month at each joint (Figure 9). This provided a strong indication of how the movements of the new deck of the Angus L. Macdonald Bridge would increase if supported in the same way as the previously renovated deck of the A. Murray Mackay Bridge. The understanding of deck movements provided by the SHM system could thus play a crucial role in supporting the planning of renovation works of one deck and maintenance and possible adaptation works of the other. For instance, all mechanical parts of the bridge, such as its bearings and expansion joints, must be capable of accommodating and withstanding these extreme movements; and ways of controlling and minimizing the movements may also be considered – for example, through the use of hydraulic dampers. By recognizing and understanding the challenge, the responsible engineers are well equipped to plan and implement effective, durable solutions that reduce the life-cycle cost of the expansion joints.

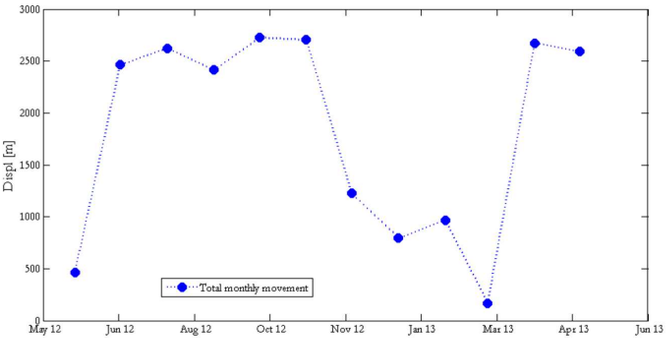


Figure 8. Accumulated movements (per month) on the A. Murray Mackay Bridge.

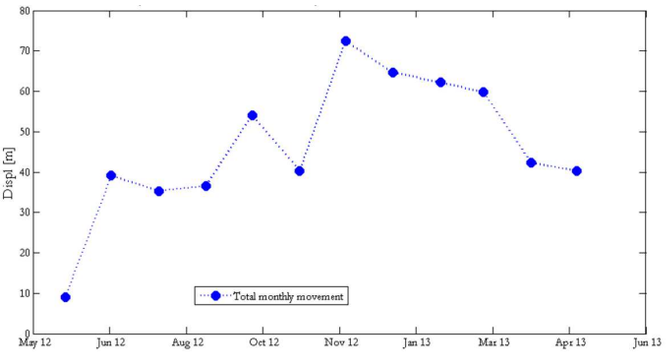


Figure 9. Accumulated movements (per month) on the Angus L. Macdonald Bridge.

4.2 *Hunter Expressway Viaducts, NSW, Australia*

The Hunter Expressway (Fig. 10) provides a much needed east-west link in the Hunter Valley, New South Wales, Australia. The Eastern Section from F3 to Kurri Kurri comprises three concrete box-girder viaducts through the Sugarloaf Range. The viaducts have a total length of 787 m and are up to 47 m in height above the ground.



Figure 10. A viaduct of the Hunter Expressway.

A temporary monitoring program was performed, with a series of controlled load test runs conducted on one of the installed modular expansion joints. The main aims of the tests were:

- To measure the static and dynamic strains for different vehicle speeds
- To assess the fatigue life of the modular joint
- To measure the fundamental natural modal characteristics of the joint
- To determine the maximum dynamic amplification factor (DAF)

Strain gauges and displacement transducers were installed on the expansion joint. A standardized test truck with different load configurations (allowable limit and overload) traversed the expansion joint at several speeds (from crawl speed to 90 km/h), which represent static and dynamic load scenarios. Data was recorded (see Figure 11 for a sample) with a high sampling frequency. A detailed description of the full monitoring program, instrumentation, data acquisition and various analysis and assessments was recorded by Ancich et al (2014).

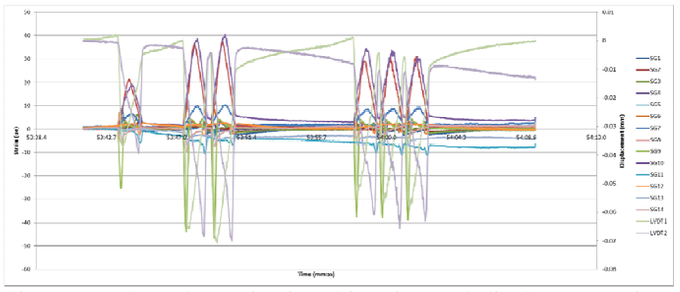


Figure 11. Sample strain time histories and displacement time histories for a slow roll on.

In summary, the main conclusions were:

- Static and dynamic strain levels are very low
- The fatigue life of all joint components assessed predicted to be unlimited with respect to all relevant expansion joint design codes
- The maximum dynamic amplification measured for the joint was a dynamic amplification factor of 1.4, i.e. very minimal amplification. The vertical stiffness of the joint was the highest yet measured in Australia.
- The fundamental vertical natural mode of the expansion joint was the highest yet measured in Australia, at 112 Hz. The first vertical bending mode of the centerbeams was the highest yet measured in Australia, at 183 Hz.

With this temporary monitoring program, the asset owner could convince himself of having expansion joints installed that meet the very demanding design standard in Australia, in particular with an unlimited fatigue life which reduces the life-cycle cost to a great extent.

4.3 *Longjiang Bridge*

The Long River Bridge, or Longjiang Bridge (Fig. 12) is a suspension bridge near Baoshan, Yunnan, China. The main span of the bridge is 1,196 m long, making it one of the longest ever built, and the longest of the world's very high bridges.

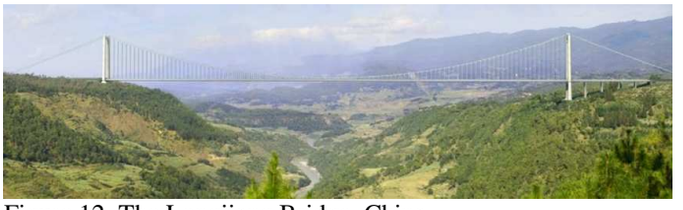


Figure 12. The Longjiang Bridge, China

Contrary to similar long-span high suspension bridges recently built in China, such as Siduhe, Balinghe, Lishuihe and Aizhai Bridges, which use traditional truss decks, this bridge has a thin steel box girder deck. This gives the deck less stiffness, resulting in the movements and rotations at the expansion joints becoming bigger, faster and more frequent. Furthermore, Yunnan is a seismically active zone, so ULS movements and rotations are expected to be significantly bigger than those occurring in service conditions. For example, longitudinal movements are expected to reach up 1,920 mm at expansion joint locations, with an additional movement of +/-350 mm in the case of an earthquake.

In order to avoid over-dimensioning the joints for seismic movements that might never arise, a specially designed and patented technology, based on a fuse element within the expansion joint, was used to enable the joint to survive such an earthquake without serious damage (Fig. 13). Likewise, due to the possible complex movements and rotations that may occur, a structural monitoring system was installed on the expansion joints (Fig. 14), in order to:

- Confirm design movements and rotations
- Generate movement and rotation statistics linked to temperature and other factors such as earthquakes
- Identify (by programmed alert system) irregularities at and possible damage to the expansion joints and thus, to be able to take immediate actions to prevent damage escalation

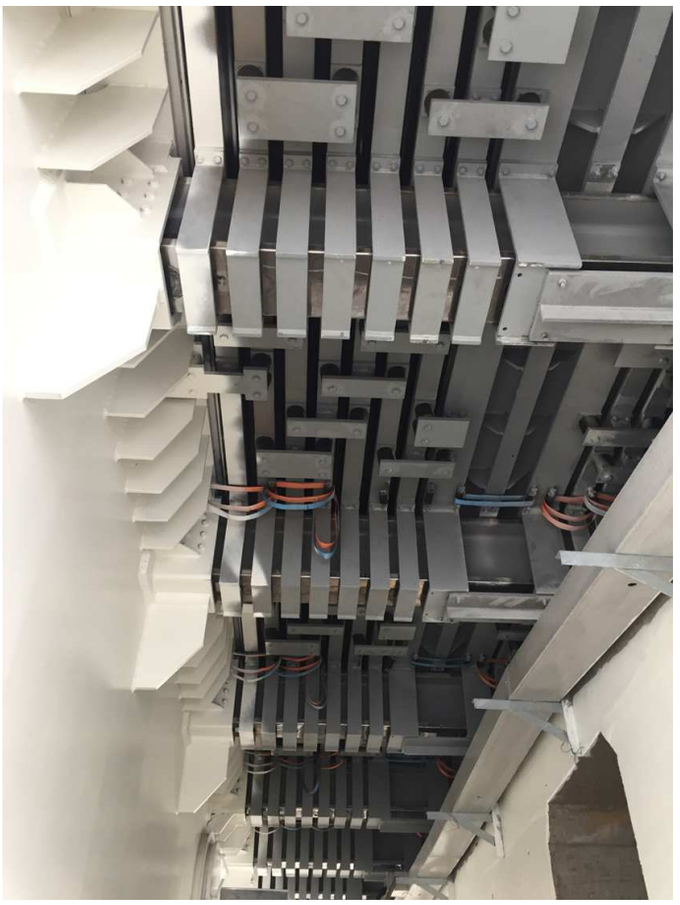


Figure 13. Modular joint with earthquake fuse element, viewed from below.



Figure 14. ROBO-CONTROL SHM data acquisition module.

A series of ultrasonic displacement sensors and temperature sensor have been installed at the expansion joints. Measurements are taken at both edges of the joints – measuring the entire gap between bridge and concrete support as well as rotations – and also at two centerbeam gaps in order to monitor the proper functioning of the expansion joint. A sample of the system's data output is presented in Figure 15.



Figure 15. Presentation of measured data (graph form) in the web interface. Correlation of movement and temperature can be observed, and irregularities and their impact on the expansion joint can be identified.

This monitoring provides the necessary information for decision-making during inspection and maintenance work, and in case of identified damage, can be used in planning repairs before further damage occurs. Life-cycle cost can thus be greatly reduced by well-timed interventions.

4.4 *Taizhou Bridge, Jiangsu Province, China*

The Taizhou Yangtze River Bridge (Figure 16), constructed at a cost of USD 400 million and opened in 2012, is the world's longest-span bridge of its type: The three-tower suspension bridge, with two main spans of 1,080 m each and side spans of 390 m, crosses the Yangtze River where it has a width of 2.1 km. The ambitious construction project represented the first attempt to create a long-span multi-tower suspension bridge.



Figure 16. The Taizhou Yangtze River Bridge.

This extraordinary bridge required some extraordinary key components such as the expansion joints which accommodate deck movements while providing a driving surface for traffic. Modular joints with 18 gaps each (able to facilitate 1440mm of longitudinal movement) were installed at each end of the deck (Figure 17).



Figure 17. One of the expansion joints of the Taizhou Yangtze River Bridge, viewed from below.

An SHM system was installed on the bridge to provide the type of data that is likely to be of interest to the owner of any exceptional structure. The basic system measures and records the movements and rotations of the deck at the expansion joints, and thus gives a valuable impression of the performance of the structure, enabling the need for maintenance or adaptation work to be quickly identified and planned. It also reports accumulated sliding movements over time – a key indicator in evaluating and predicting the condition of key mechanical components such as expansion joints and bearings.

Furthermore, pre-integrated sensors that allow high-frequency measurement of structure-borne vibrations, and a specially developed algorithm, were brought together on this project to create a new, first-of-its-kind SHM technology. This enables damage or deterioration to be clearly identified based on general testing and teaching of the system. As a result, unexpected damage can be immediately recognized and automatically notified, enabling the timing of replacement of components to be optimized and disruption to service to be minimized.

By recording movements, inclinations, temperature and structure-borne vibrations at a frequency of 25.6 kHz, even very tiny changes in the joint or its performance can be detected and visually represented by changes in a curve on a graph, enabling any sudden damage or deterioration to be immediately detected.

As a first step, many artificial failures were created simulating damages. This was done by temporarily removing stirrups which form sliding connections between the centerbeams at the joint's surface and the support bars beneath (see Figure 18). High-accuracy accelerometers and ultrasonic displacement sensors (Figure 19) were then used to evaluate the effects of these "failures" on the movements of specific elements, giving the system the data it needed to "learn" what data might be significant in terms of damage detection.

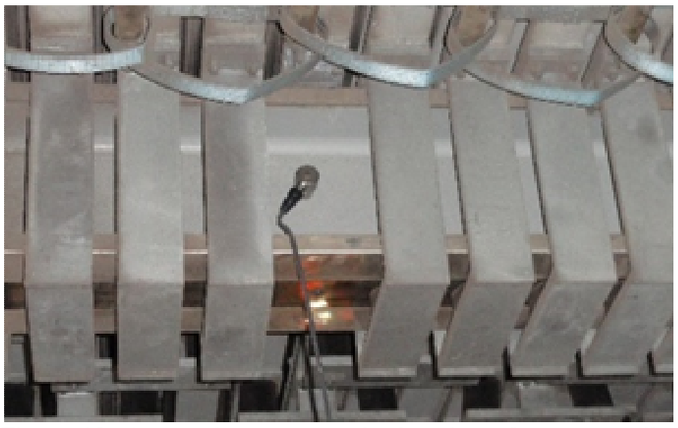


Figure 18. An accelerometer at the location of a temporarily removed stirrup during fault simulation and measurement of resulting vibrations and modal analysis.



Figure 19. An ultrasonic displacement sensor.

In service, the system sends data to a remote server, including daily records of vibrations due to heavy traffic together with the associated modal frequencies (see Figure 20). If established limits which might indicate the occurrence of damage are exceeded, an alarm notification is sent by email and also appears on the system's web interface, prompting a site inspection. As a result of the system's ability to automatically consider such information, therefore, planning of maintenance activities in general, and the timing of replacement of components in particular, can be optimized to reduce the life-cycle costs.

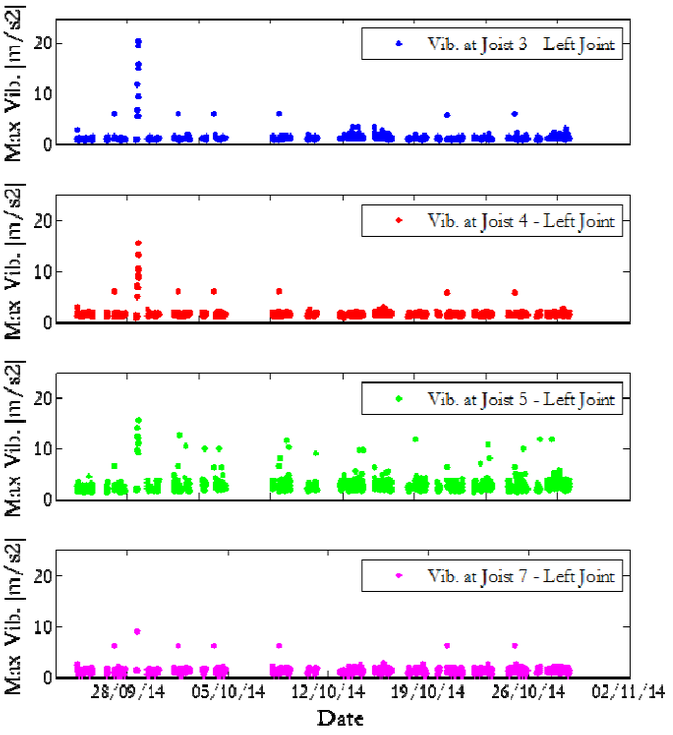


Figure 20. Example of one month of data from the smart expansion joint, at four positions.

5 CONCLUSIONS

The integration of sophisticated structural monitoring systems in the expansion joints of newly built and existing bridges can offer great benefits to their asset management programs. Such systems can efficiently provide data required for almost any purpose, at any stage of a structure's life cycle – e.g. to facilitate installation, inspection, maintenance or component replacement work, or assessment of unexpected events or planning of modifications.

Considering that the most important data required by a bridge monitoring system generally includes superstructure movements, which can easily be measured at the bridge's expansion joints, and considering also the critical importance of the same expansion joints, which are less robust and therefore more susceptible to damage and deterioration than the main structure, it is often sensible to base the design of a monitoring system on data from the expansion joints. Developing technology now allows for the integration of appropriate sensors in a joint during fabrication, reducing effort and risk on site, and can enable a suitably configured system to automatically detect possible damage or deterioration based on measurement and analysis of vibrations only, marking the advent of "smart" expansion joints.

REFERENCES

Ancich, E., Kessler, V., Brown, S., Duschlbauer, D. & Parker, A. 2014. Modular Expansion Joint testing for the Hunter Expressway. *Proc. 9th Austroads Bridge Conference*, Sydney, Australia.

Braun, C. 2011. Die Differentialbauweise in Brückenbau. *Brückenbau Construction & Engineering*, Issue 1 – 2011, Verlagsgruppe Wiederspahn, Wiesbaden, Germany.

Dexter, R. et al. 2002. Performance Testing for Modular Bridge Joint Systems. *NCHRP Report 467*, Transportation Research Board, Washington, USA.

Savioz, P., Spuler, T. & Moor, G. 2014. Life-cycle and total cost analysis of bridge expansion joints. *Proc. 7th International Conference on Bridge Maintenance, Safety and Management*, Shanghai, P.R. China.

Spuler, T., Moor, G. & Berger, R. 2011. Automated monitoring systems for bridge bearings and expansion joints. *Proc. 7th World Congress on Joints, Bearings and Seismic Systems for Concrete Structures*, Las Vegas, USA.

Maintenance, Safety, Risk, Management and Life-Cycle Performance of Bridges – Powers, Frangopol, Al-Mahaidi & Caprani (Eds)
© 2018 Taylor & Francis Group, London, ISBN 978-1-138-73045-8

Advances in materials and further improvements in bridge pot bearings

S.N. Kazi, V.V. Ghodke & C. Sarmiento
Mageba, Sydney, Australia

ABSTRACT: Bearings, which accommodate a bridge's multidirectional loads, movements and rotations, are among the most critical components of modern bridges. These connection devices are subjected to ever increasing challenges and opportunities due to constantly evolving design and material technologies. This is particularly true for pot bearings, have been widely used for decades but which have not always performed well – primarily due to inadequate design and execution of various solutions to the challenge of sealing the internal elastomeric pad, which, in the absence of an effective seal, can be extruded from the pot in which it is located when the piston it supports is loaded. Recently documented reports of premature failures of pot bearings in Australia due to elastomer extrusion have prompted detailed investigations into the root causes of the problem. This paper describes this problem and presents an already tried-and-trusted solution. The possible integration of monitoring system sensors into the bearing's design and fabrication, before installation, to enable such problems to be automatically identified and addressed before they develop, is also discussed.

1 INTRODUCTION

This paper presents results of investigation of some documented reports of underperforming pot bearings on bridges in Australia.

In recent years, it has repeatedly been reported that pot bearings are underperforming on rail bridges in particular. Asset owners became increasingly concerned about the early need to replace pot bearings (within ten years of installation in many cases, and within five years in some instances) – far earlier than expected considering the service life of 40 years specified by the Australian code AS5100. The reports were documented from cases in the Australian states of Western Australia, Queensland and New South Wales. The reports were not limited to a single manufacturer or supplier, but were limited to pot bearings that utilise a metallic internal seal to prevent extrusion of the elastomeric pad at the heart of the bearing (as described in Section 2 below).

In November 2015, Australian Rail Track Corporation (ARTC) engaged Lindsay Dynan, an engineering company specializing in Level 3 inspections and rehabilitation of structures, to investigate the observations of pot bearing failure on its railway bridges. The key findings of this report are discussed in this paper and recommendations based on state-of-the-art technology are presented to assist asset owners and engineers in their ongoing asset management work, helping minimise life-cycle costs.

2 THE POT BEARING AND ITS KEY COMPONENTS

Figure 1 shows a rendering (exploded view) of a pot bearing of the *free sliding* type. Figure 2 shows a typical cross section of a pot bearing of the *guided sliding* type, identifying its various components, which are described below with particular attention to the Australian context.

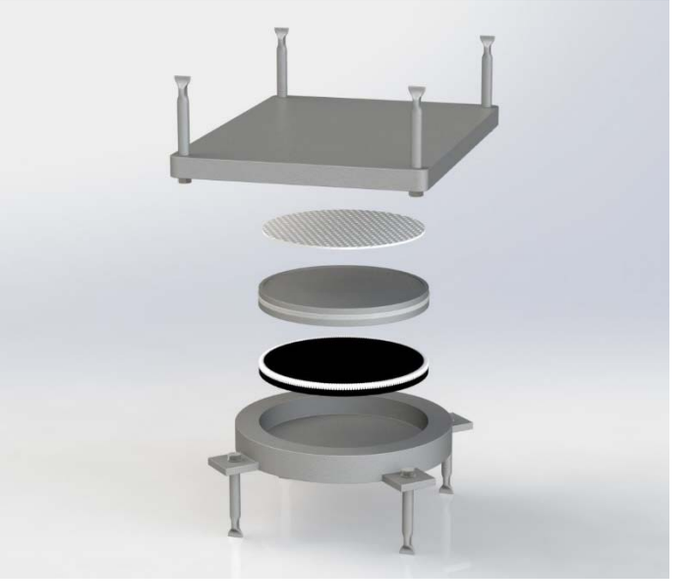


Figure 1. Rendering (exploded view) of a typical pot bearing of the free sliding type.

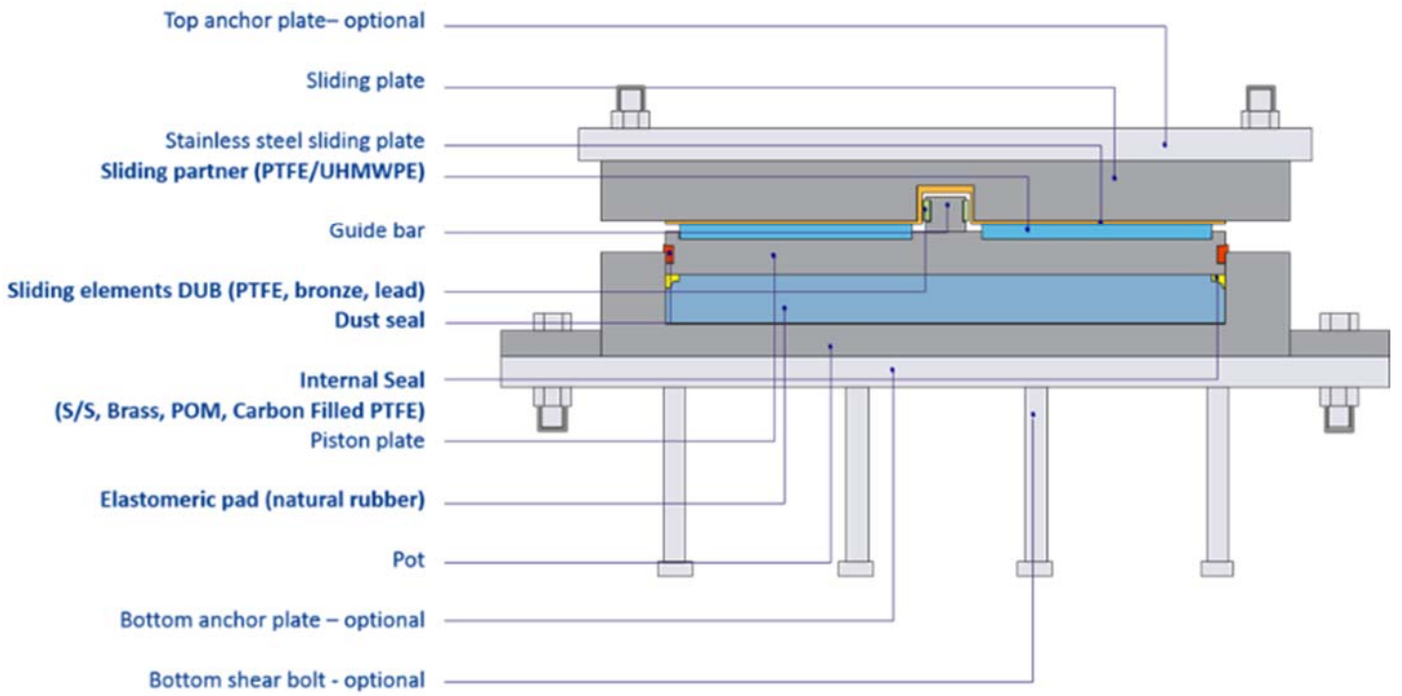


Figure 2. Cross section drawing of a typical guided sliding pot bearing (with internal guide bar) showing its key components.

2.1 *Pot and piston*

The pot and piston are generally manufactured from ferrous materials in accordance with AS3678 or the equivalent international standards. These components are typically machined out of solid steel blocks.

2.2 *Elastomeric pad*

The elastomeric pad at the heart of the pot bearing, which enables the bearing to accommodate rotations, is usually moulded from a rubber compound in accordance with AS5100.4 Table B3 (A).

2.3 *Internal Seal*

Under vertical load from the superstructure, the elastomeric pads, being confined by the internal walls of the pot, becomes semi-viscous and would be extruded from the pot if not prevented from doing so by an effective seal. Figures 3 to 6 show various sealing solutions that have found application in recent decades.



Figure 3. Internal seal for pot bearing: Stainless steel type.



Figure 4. Internal seal for pot bearing: Brass ring type.



Figure 5. Internal seal for pot bearing: Carbon-filled PTFE type.

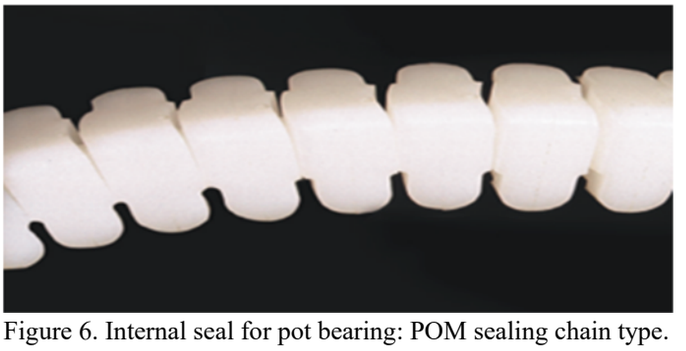


Figure 6. Internal seal for pot bearing: POM sealing chain type.

2.4 *Sliding Partners*

Three key materials are used as sliding partners to minimise friction between the upper and lower parts of the bearing.

2.4.1 *Stainless steel sheet*
Stainless steel sliding sheeting in accordance with AS 1419 or the equivalent international standard is attached to the bearing's upper sliding plate.

2.4.2 *PTFE / UHMWPE disc*
A dimpled PTFE or UHMWPE disc, recessed into the top surface of the piston, forms a non-metallic sliding partner for the stainless steel. Refer to Figure 7 for dimple pattern and Figure 8 for recess details.

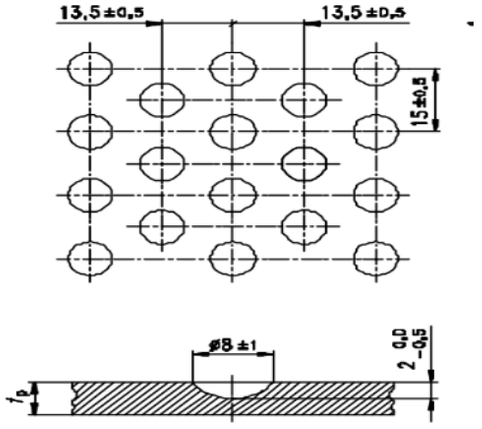


Figure 7. Dimple pattern in recessed PTFE / UHMWPE sheets.

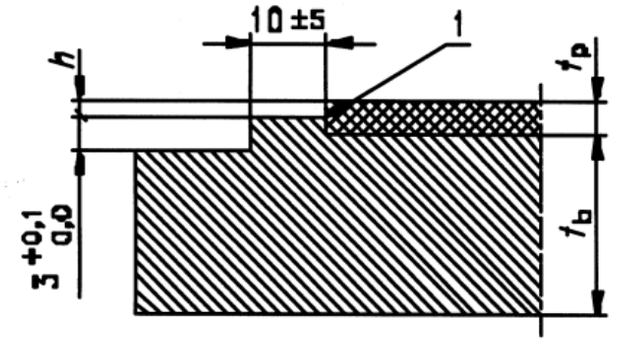


Figure 8. PTFE / UHMWPE recess details in steel base plate.

2.4.3 *Lubricant*
A long life, neutral and silicone-based lubricant is applied to the PTFE / UHMWPE disc, in a controlled environment, to minimise sliding friction.

3 DESIGN OF POT BEARINGS

Bearings must be designed to ensure safe transfer of applied vertical and horizontal loads between the superstructure and the substructure, and to accommodate any translational and rotational demands of the structure that may arise at this critical structural interface.

These performance requirements must be met with adequate reliability and durability, by adopting the design procedures specified by, for example, AS5100.4 (2017) or EN1337-5.

4 PREMATURE FAILURE OF POT BEARINGS

Pot bearings can be considered to have experienced failure in the following situations:

- Elastomer is extruded out of the pot
- PTFE is abraded to the bottom of dimples in the sheet or squeezed out from the recess
- The bearing is unable to accommodate required translation and/or rotation movements
- The pot, piston or any other structural part is cracked or significantly distorted/deformed

5 LATEST REPORTS OF PREMATURE POT BEARING FAILURE IN AUSTRALIA

Various asset owners/managers across Australia have reported premature failure of pot bearings due to either elastomer extrusion or movement/rotation capacity restriction. Many of these failures were investigated and causes documented, and ARTC and Lindsay Dynan have kindly made available the findings from the internal report prepared for ARTC, enabling a broader audience to benefit from the report's findings and recommendations. Figures 9 and 10 show, for example, pot bearings that failed within five to seven years of initial installation.



Figure 9. Failed pot bearing with elastomer extruded out.



Figure 10. Failed pot bearing with cracked steel pot.

6 DETAILS OF INVESTIGATIONS FROM KOORAGANG ISLAND BRIDGE AND RECOMMENDATIONS FOR ASSET OWNERS

The Kooragang Island Bridge consists of twin steel girder bridges, an 'arrivals' and a 'departures' bridge, crossing the Hunter River in Newcastle, Australia. The bridges provide the link between over 25 operating coal mines and the export terminals located on Kooragang Island, with in excess of 100 million tonnes of coal product being transported over the arrivals bridge each year. The arrivals bridge (Fig. 11) is subjected to fully loaded coal trains, and therefore experiences up to six times the magnitude of live load experienced by the departures bridge, which typically carries locomotives and empty wagons on return from the coal export terminal.

Figure 11. Kooragang Island Arrivals Bridge

6.1 *Bridge geometry and description*

The bridge has eight 30-metre spans, with the train track's continuously welded rails supported on timber transoms over twin 2.5m-deep steel girders. The steel girders are laterally braced with vertical and horizontal steel angle bracing. A cross-section of the bridge deck is shown in Figure 12.

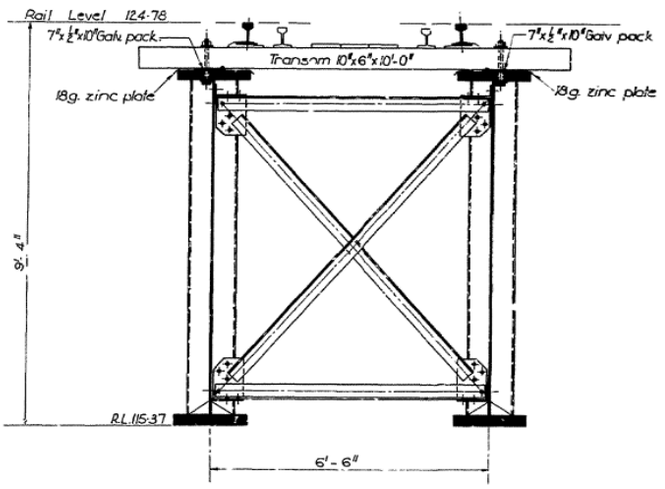


Figure 12. Cross-section of the Kooragang Arrivals Bridge deck.

The pot bearings are bolted to the bottom flange of the steel girders, and bear on a concrete grout pad formed on top of the concrete bridge piers. Through bolts attach the bottom anchor plate of the pot to the concrete piers, and the internal bearing arrangement is similar to that shown in Figure 2, with a stainless steel internal seal of the type shown in Figure 3. Each span has fixed pot bearings under each girder of the "country end", and guided sliding pot bearings under each girder of the "city end".

The arrivals bridge was constructed in 1968 and has undergone only minor modifications to the superstructure to date. The bearings have been replaced a number of times, with the most recent replacement occurring 13 years prior to the observed failure described herein.

6.2 *Bearing damage and observations*

Following observations of excessive lateral movement of the top of train wagons, an examination of the pot bearings was undertaken. It was observed that the elastomer had extruded from both the fixed and sliding bearings, and also that the steel piston plate of one sliding bearing had cracked substantially. The bolts connecting the uplift plates were observed to have sheared off. It was immediately obvious that the bearings were failing and as such, the bridge was closed to traffic whilst temporary repair works were carried out. The severely damaged bearings were completely removed and replaced at the next available opportunity.

During the removal and subsequent inspection of the damaged bearings, a clearer picture developed of the likely failure mechanism. It was evident that the internal stainless steel seal (see Section 2.3 above) had broken down and abraded/shredded the elastomer, causing the bearing to fail. The internal seal of a pot bearing is critically important for its proper functioning and durability, as recognised by Clause 13.1(e) of AS 5100.4 (2004). Figures 13 and 14 show the elastomeric pad within the upper housing, and fragments of the stainless steel seal can be seen sitting loose. Also apparent is the damage to the pad itself.



Figure 13. Damage to pot bearing's elastomeric pad and its metallic seal – Kooragang Arrivals Bridge.



Figure 14. Damage to pot bearing's elastomeric pad – Kooragang Arrivals Bridge.

6.3 *Assessment of Failure Mechanism*

Once the mechanism of bearing failure had been determined, attention shifted to understanding the underlying cause of the failure. The bearing assemblies were assessed for installation issues and for non-compliance with AS5100.2 and AS5100.4. No significant anomalies were noted in this regard.

After consideration of the bridge geometry and the observed damage, it was postulated that the internal stainless steel seal had failed due to excessive cyclic rotations under load. The magnitude of the difference between high-frequency live loads and dead load is much higher in rail bridges than in road bridges. Whilst these rotations can be accounted for in the bearing specification, it appears the internal seal is susceptible to abrasion-type damage under the high-magnitude cyclic live loading conditions. This loading caused the internal seal to fail and abrade/shred the elastomer, resulting in greater rotations and further damage to both the seal and the elastomer.

In the case of this rail bridge, the relatively lightweight superstructure (steel as opposed to concrete) increases the differential magnitude between dead and live loads. Additionally, the steel girders are deep, and due to the age and geometry of the structure, these are potentially subject to incidental lateral movements that may increase the net rotations experienced by the bearings under live loads.

6.4 *Conclusion*

It is the opinion of the authors that the above-mentioned factors have contributed to the early failure of the bearing due to excessive cyclic rotations and the poor design of the internal seal. The evidence suggests that pot bearings of the type used on the Kooragang Island Arrivals Bridge are not suitable for steel rail bridges, and similar suggestions have been noted in the American AREMA Manual for Railway Engineering (Part 5 - Bearing Design and Construction).

In the case of the Kooragang Arrivals Bridge, following temporary stabilization and repair works, the damaged pot bearings were replaced with spherical bearings which can accommodate much larger rotations and can be considerably more durable than pot bearings – resulting in significant savings in life-cycle costs.

For the future reference of bridge inspectors, the indicators of bearing distress in the Kooragang Island Bridge case were as follows:

- Excessive rotations / displacements of the bearings under load. In the case of the Arrivals Bridge, this was observed by rail authority staff on a routine inspection and was evident on closer inspection from the sheared bolts of the bearing uplift plates.
- Reduced gap between the top and bottom bearing parts (indicating loss of elastomer thickness).
- Extrusion of the elastomer from the bearing piston.

7 ROOT CAUSE OF THE PROBLEM

As discussed in Sections 5 and 6 above, the majority of pot bearing failures were found to be due to excessive abrasion of the internal seal around the perimeter of the elastomeric pad.

The European standard EN1337-5 provides comprehensive prescriptive guidance for selection of appropriate internal seal materials based on material abrasion resistance. The information presented in EN1337-5 is based on extensive independent testing and research and development work done by EUROCODE committees over the last several decades. AS5100.4 (2004) only mentioned metallic internal seals, which have been demonstrated to have the lowest possible abrasion resistance among the various types mentioned by EN1337-5. The revised AS5100.4 (2017) acknowledged the findings of EN1337-5 and included the materials in accordance with this norm for use on Australian structures.

8 TESTING OF INTERNAL SEAL DURABILITY

EN1337-5 prescribes internal seal systems with reference to the *Accumulated Sliding Path* achieved during testing. Testing was conducted in a laboratory environment by subjecting pot bearings with various internal seal designs to a vertical load increasing in steps of 0.5 N/mm^2 until the contact stresses on the elastomeric pads reach a maximum of 35 N/mm^2. An actuator with a frequency of $0.25\ \text{Hz} < f < 2.5\ \text{Hz}$ was utilised to induce rotations of between +0.0025 rad and -0.0025 rad in the bearing.

Acceptance criteria for these tests are as follows:

- There shall be no extrusion of cohesive elastomeric material.
- The compression deformation under the test load shall have not increased for at least 24 h.

Wear of the seal and discoloration of the lubricant is acceptable in these tests.

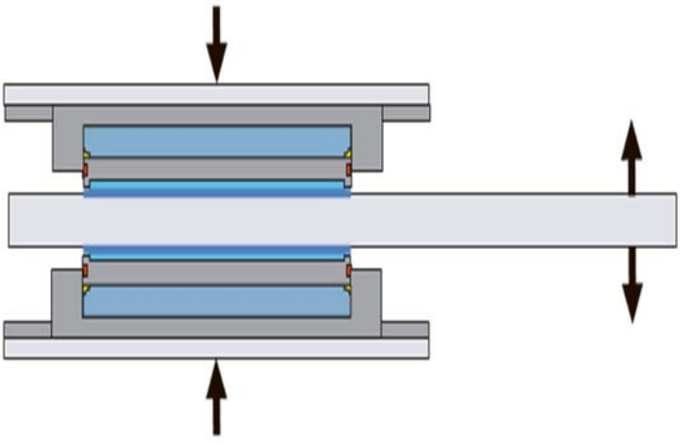


Figure 15. Test set-up for rotational testing per EN1337-5.

The sliding distance that each seal can withstand before failing under any of the above acceptance criteria is measured and taken as the "Accumulated Slide Path" of the seal. This can also be defined as the sum of the relative movements of the seal on the pot wall due to cycles of rotation of the bearing caused by external loading.

EN 1337-5 defines the Accumulated Slide Path for various materials as follows:

- Stainless Steel: 500m
- Brass: 1,000 m
- Carbon-filled PTFE: 2,000m
- POM chain: 2,000 m

8.1 *Accumulated slide path and service life of the pot bearing*

Accumulated Slide Path determined from the above tests can be translated into the service life of the bearing using Equations 1 and 2 below:

$$S_{A,D} = n_v \times \Delta\alpha_2 \times \frac{D}{2} \quad (1)$$

$$S_{A,D} \leq c \times S_T \quad (2)$$

where

$S_{A,D}$ Actual Accumulated Slide path required for the bearing internal seal due to characteristic traffic load on the bridge

n_v Number of heavy vehicles for the intended life of the bearing

c Correction factor (equal to 5) for the difference between the constant amplitude slide path used in the tests and the variable amplitude movements which actually occur due to loading on the structure

For example: Consider a bridge on a road with a traffic volume of 30,000 trucks per year (nv) for 100 years. Assuming a pot internal diameter (D) of 360 mm, based on vertical load carried, and a resultant rotation angle of 0.015 rads (Δα), then

$$S_{A,D} = (30000 \times 100) \times 0.0015 \times \frac{360}{2} = 8100m$$

Hence, to enable the pot bearings to survive the expected service life of the bridge, select pot bearings that have an internal seal with a verified accumulated slide path of 2,000m, so that the calculated slide path capacity (5 × 2,000 = 10,000 m) will exceed the actual sliding path of 8,100m.

9 BRIDGE BEARINGS AND AS5100.4 (2017)

Some significant changes have been made to the 2004 edition of AS5100.4 Clause 13.1 to enhance the performance of rail and road bridge bearings. The following are extracts from this clause:

- To prevent extrusion of the elastomer, the pot shall incorporate a seal around the top corner of the elastomeric disc. The internal seal shall be either a set of brass rings, a POM chain or a carbon-filled PTFE seal complying with the requirements of EN 1337-5.
- The maximum accumulated slide path (ASP) of the internal seals, defined as the sum of the relative movements of the seal on the pot wall due to cycles of rotation of the bearing caused by traffic loading shall be taken to be 2000 m for POM chain and carbon-filled PTFE seals, and 1000 m for brass rings.
- Due to the large number of loading cycles arising, only pot bearings with POM chain or carbon-filled PTFE seals shall be used on rail bridges and road bridges where the number of heavy vehicles per lane per day in the first year of service is predicted to exceed 1000, as defined by Clause 13.1(d) of AS 5100.2.

It is also worth noting that the performance of pot bearings is noted to significantly improve when the smoothness of the internal walls of the pot is increased. An existing European Technical Approval (Mageba ETA 13/0039) has shown that the POM seal's Accumulated Slide Path can be successfully increased up to a value of 3,200 m by suitably adapting the roughness coefficient of the pot's internal walls.

10 FURTHER POSSIBILITIES

To avoid the occurrence of problems of the type discussed in this paper, or mitigate such problems should they occur, the following possibilities are presented to indicate alternative or complementary solutions.

10.1 *High-quality pot bearings with well-proven sealing detail*

Of course, the simplest answer to the challenge / risk identified and discussed above is to only use a pot bearing type that has proven its quality and durability, particularly in relation to its sealing detail, on many bridge applications over a period of many years. One such pot bearing is the RESTON-POT bearing, different designs of which are illustrated in Figures 1 and 2 above, and which uses a POM sealing chain to seal the elastomeric pad against extrusion from the piston – a solution which has proven to be extremely effective and durable.

10.2 *Alternative bearing types*

To avoid the potential problem of rubber pad sealing entirely, an alternative type of bearing might be used. Spherical bearings can generally be used as an alternative, and so this type of bearing is described below.

10.2.1 *Spherical bearings*

Spherical bearings, such as the RESTON-SPHERICAL bearing illustrated in Figure 16 (which shows fixed, free sliding and guided sliding types, depending on the extent to which they accommodate horizontal superstructure movements), do not have a rubber pad at their core and are thus in principal stronger and more durable than pot bearings. They accommodate rotations, not by deformation of a compressible material, but by sliding rotation of a convex-shaped steel element in a concave-shaped recess. Due to their greater strength they can generally be designed to be smaller than an equivalent pot bearing (for the same design loading).

A comparison between key attributes of spherical bearings and pot bearings is provided in Table 1.



Fixed | Free sliding | Guided sliding (with external guide bars)

Figure 16. Exploded views of three types of spherical bearings.

Table 1. Comparison of pot and spherical bearings (based on RESTON-POT and RESTON-SPHERICAL).

Characteristic	**Pot bearing - typical**	**Spherical bearing - typical**
Sliding material	PTFE	Superior ROBO®SLIDE sliding material
Allowable pressure on sliding material	f_d = 64.3 N/mm^2 $f_{k,max}$ = 90.0 N/mm^2	f_d = 128.6 N/mm^2 $f_{k,max}$ = 180.0 N/mm2
Allowable pressure on elastomeric pad	f_d = 46.2 N/mm^2	No limitation since no elastomeric pad used
Resulting bearing size	Larger	Smaller
Resistance to wear of sliding material (in sliding types)	Limited to approximately 20,000 m accumulated sliding distance	Much higher (virtually no wear observed after 50,000 m of accumulated sliding distance)
Resulting service life of bearing	Shorter	Significantly longer
Rotational capacity	Restricted to 0.030 rad	Not restricted by standards
Temperature range	Can typically be used at temperatures down to –35 °C or –40 °C	Can typically be used at temperatures down to –45 °C to +50 °C

10.3 *Integrated monitoring system sensors*

Modern structural health monitoring (SHM) systems can serve many purposes in bridge construction, inspection, maintenance and renovation, by measuring key data such as movements and loading. Such data can often be optimally measured at the structure's bearings, and so it is often sensible to consider, on a structure which will have an SHM system, integrating load sensors into the bearings during their design and fabrication. This can enable loading data to be read via a data cable connection point as shown in Figure 17. With this cable connected to a suitably designed permanent SHM system, the loading on the bearing can be automatically monitored, all day and every day. Of course, if the seal of a pot bearing fails, and the elastomeric pad at its heart starts to be extruded, the load data from that bearing will change, indicating that a problem is developing and enabling the responsible engineers to take appropriate actions before the problem deteriorates. The ability to provide such peace of mind to asset managers is a key benefit offered by modern SHM systems.

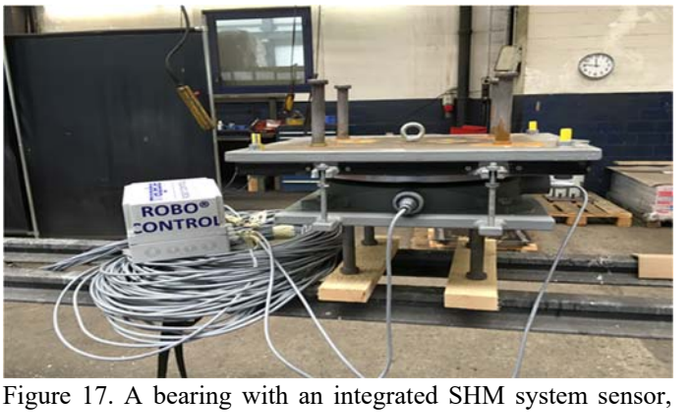


Figure 17. A bearing with an integrated SHM system sensor, with data cable connected for testing before installation.

ACKNOWLEDGEMENT

The authors would first like to thank the ARTC Chief Executive Officer and Managing Director, John Fullerton, National Bridges and Structures Engineer Peter Prasad, for their permission to publish this paper and Brenton Wakem and Dr. John Mullard from Lindsay Dynan for their valuable inputs and all of the asset owners and other professionals that assisted in composing this paper.

Maintenance, Safety, Risk, Management and Life-Cycle Performance of Bridges – Powers, Frangopol, Al-Mahaidi & Caprani (Eds)
© 2018 Taylor & Francis Group, London, ISBN 978-1-138-73045-8

Breaking the Asphalt code – Polyurethane flexible plug expansion joint

C. Sarmiento, G. Pope & S.N. Kazi
Mageba, Sydney, Australia

ABSTRACT: Typically, expansion-joints are installed between adjacent spans of a bridge deck or the bridge deck and the abutment. Their exposure to impact and vibration caused by traffic-loading, climatic-conditions and chemical agents' impact, causes them to deteriorate faster than other bridge components. This requires maintenance and replacement during the service life of a bridge.

An enhanced flexible-plug expansion-joint has been developed, with a polymeric surface, which offers a number of substantial advantages over the traditional bituminous type. The Polyflex®Advanced expansion joint offers all the benefits of the asphaltic plug joint, including smooth, safe, low-noise surface, great adaptability and easy installation. However, it overcomes numerous disadvantages and challenges that have always plagued asphaltic plug joints. Installation is also far easier and less prone to error, with the two-component compound being mixed at ambient temperatures. For these and other reasons, this joint should be considered for use in bridge-construction, in particular, in bridge-maintenance.

1 INTRODUCTION

Flexible plug expansion joints are generally used in road and railway bridges to bridge the structural gap and accommodate the movement between the bridge deck and abutments. This type of expansion joints are selected over other small movement expansion joint types because of their relative low cost, ease in handling, installation & maintenance and good waterproof properties. Furthermore flexible plug joints offer a smooth, neat and seamless joint surface that brings about the most desired benefits of driver comfort and huge noise reduction. In addition, they can be installed and replaced in varying deck plan geometry & profile and in sections which significantly minimise disruption to traffic.

Flexible plug expansion joints were traditionally made from bitumen-based material, a mixture of aggregates and plasticised polymer or bitumen. These traditional bitumen-based flexible plug expansion joints were popular for decades however they are prone to durability problems. They suffer from excessive softening during hot days and hardening during cold days. Continuous dynamic loading from vehicle wheels and poor material quality control during installation hasten their failure in the form of cracking, rutting, de-bonding, spalling, delamination, bleeding and loss of watertightness.

Extensive research then followed on how to overcome the durability problems and at the same time preserving the benefits of flexible plug expansion joints. This led to the development and introduction of Polyflex®Advanced flexible plug expansion joints which utilises a much more superior polyurethane-based flexible material and stronger support and connection details.

2 HISTORY AND BACKGROUND

The decision on the choice of the most appropriate type of bridge expansion joints rests on a number of factors which include service life and durability, functionality, code compliance, economics, quality, safety, maintainability, constructability, and environmental and ergonomic considerations.

The traditional bitumen-based flexible plug expansion joints (Figure 1) have been a popular choice where the overriding considerations are constructability, environmental and ergonimic. This is because they are relatively easy & quick to install, very quiet and do not generate undesirable level of noise, provide smooth neat riding surface and offer unsurpassed driver riding comfort. These traditional bitumen-based flexible joints however do not rate well on all other main considerations which had

restricted their use. There are numerous reported problems concerning durability, functionality and quality resulting in considerable reduction in service life , increased maintenance costs and reduction in efficacy in other areas like noise and comfort.

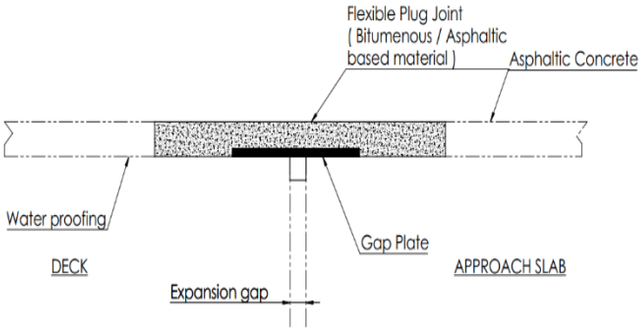


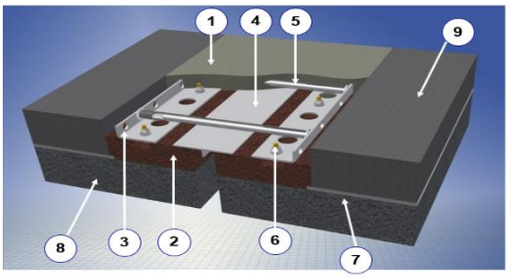
Figure 1. Bitumen-based flexible plug expansion joint

In NSW Australia, the Road and Maritime Service Authority (RMS – formerly RTA) had banned the use of bitumen-based flexible plug expansion joints on new bridges and are discouraged for use on maintenance and rehabilitation works except where noise issues are predominant and there is no suitable alternative (RMS 2008). This was based on reported softening of the bitumen-based material in hot weather and hardening & cracking in very cold weather. There were also noted failures like rutting & delamination when the joint is under heavy traffic loading.

In Switzerland, it was shown after investigations done in cooperation with the Swiss Federal Authorities for Material Science and Technology that the quality of the bitumen being used for these type of joints was very inconsistent which significantly affects functionality and durability. It was reported that small changes in the chemical composition of the raw materials led to big reductions in expansion joint quality (Gallai et al 2017 & Mageba SA 2016). This had led to increased concerns about the suitability for use of these bitumen-based flexible plug expansion joints.

In USA, Department of Transport Authorities (WSDOT & CDOT) no longer specify and do not recommend bitumen-based flexible plug expansion joints on highways with high traffic and roadways with heavy trucks. This is due to observed creep, poor expansion performance and bitumen binder migrating out of the block-outs (WSDOT Design Manual M23-50-17 2017 & CDOT Design Manual 2017).

Given the challenge of addressing and overcoming the aforementioned problems associated with bitumen-based flexible plug expansion joints while at the same time preserving the benefits, research and development efforts followed to optimise the design and come up with a superior flexible material and much improved quality. The result is the introduction of Polyflex®Advanced flexible plug expansion joint which had undergone extensive testing and has since been successfully installed in European countries, North America, parts of Asia and Australia and performing well without any reported problems usually associated with the old bitumen-based flexible plug expansion joint.



1 Special PU material
2 Polymer concrete base
3 Perforated angle
4 Bridging plate
5 Stabilizing element (for large movements)
6 Anchoring
7 Bridge water proofing
8 Substructure
9 Road surfacing

Figure 2 - Polyflex®Advanced Polyurethane (PU)-based flexible plug expansion joint

3 DESIGN & CHARACTERISTICS OF POLYURETHANE-BASED FLEXIBLE EXPANSION JOINT

The distinct features of the design is the use of polyurethane (PU) material instead of the traditional bituminous / asphaltic material. In addition it has side perforated steel supports and stabilisers if needed.

PU which has a long history of use as a waterproofing material in the building industry and as further improved over the years was adopted and proven to be a suitable material for flexible expansion joints. It has excellent elasticity having elongation test values of 650% before breaking (over 1.5x that of standard rubber 350-400%) which makes it ideal for use in expansion joints.

This special purpose PU offers large tear resistance capacity at 20 N/mm² and a tensile strength of 14 N/mm². It has a density of 1.05 g/cm³ and a "Shore A" hardness of approximately 65. It is highly resistant to wear and to the detrimental effects of exposure to chemicals and the environment, which gives it a long service life. Its service life is significantly longer than that of other roadway surface materials. The perforated steel supports allow the joint to withstand high traffic & dynamic loading including braking forces while also accommodating large movement and at extreme high & low temperature.

Total movements of up to 135 mm (See Figure 4) can be accommodated with this PU-based flexible expansion joint which is significantly larger than the

+/-20 mm for bitumen or asphaltic-based joint(Bridge Joint Association 2003).

Due to its stable characteristics at high and low temperature, this PU-based flexible expansion is fully functional in the operating structural temperature range of -50°C to +70°C, which is a big improvement over the bitumen-based joint.

The PU-based flexible joint can be installed or can fit into varying joint geometry like X-Shape and upstand shown in Figure 3.

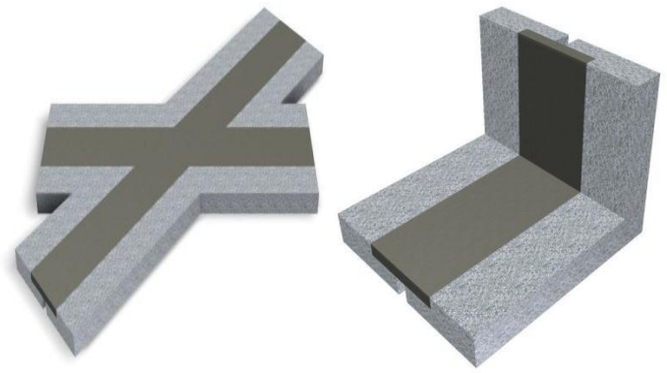


Figure 3 – X shape and upstand

Type	Total Movement mm	Movement Elongation mm	Movement Compression mm	Thickness of PU-layer mm	Width in starting position mm
PA 15	15	10	5	40	280
PA 30	30	20	10	50	350
PA 50	50	33	17	60	459
PA 60	60	40	20	60	500
PA 75	75	50	25	60	600
PA 90	90	60	30	60	750
PA 135	135	90	45	60	1100

- Table shows examples for general design, widths can be interpolated
- For individual cases, width and thickness are determined based on required movement
- All types are designed for a vertical displacement of ± 10 mm (± 0.39"), allowing for bearing replacements
- Movements are indicated in SLS, for ULS higher deformations are permitted

Figure 4 - Polyflex®Advanced Movement Capacity

4 INSTALLATION

New installation of PU-based flexible joint offers the huge benefit of ease of installation compared to other types of bridge joints including the bitumen-based flexible joint. There are no heavy joint metal components eliminating the need for lifting cranes. There is also no need for mixing plants and heaters. Unlike the tedious process ensuring the correct set out of metal components and anchorage bolts required for metal type joints (strip seal type, finger plate type), the PU material when poured, easily adapts to suit the shape & dimensions of the receiving joint block-out. The two-component PU material can be simply mixed from complete packing units at ambient temperature minimising the risk of substandard or non-compliant mixing. The processing of the PU material is possible at temperatures from +5°C to +35°C and irrespective of humidity conditions.

For rehabilitation works or replacement of other types of joints, the benefits of the PU-based flexible joint can even be more appreciated. The joint can be formed just within the depth of the bridge deck/ road surface, avoiding further invasive works like breaking of adjacent concrete. This minimal work on the existing structure combined with the short curing time translate into easy, quick, and economical installation and minimal impact on traffic. The joint can also be installed in sections or lane by lane which can further assist in minimising the impact on traffic. This is possible because the PU material from the previous section installed and already cured is chemically reactivated by the following fresh PU material which produces a strong homogeneous bond.

The following shows and describes the installation process:

- A block-out is prepared by machine cutting the road surfacing along markings of pre-determined width and depth. The road surface is cut down to a firm substructure (concrete or any stable sublayer) to which the polymer concrete can bond to. (Figure 5)
- The block-out is then cleaned and air-blasted to ensure PU joint materials will bond properly. (Figure 6)
- Where required, the bridge deck/road surface waterproofing membrane can be extended into the block-out (Figure 7)
- In the case of rehabilitation works where an old joint is removed and there is an absence of appropriate surface, formwork or a sheet of Styrofoam is then placed in the bridge gap to retain the polymer concrete base. (Figure 8)
- A suitable primer is then applied before the polymer concrete is poured. The polymer concrete cures naturally at ambient temperature. It cures in approximately 1 hour @ 15C. The perforated angles are then anchored on both sides and the bridge plate is placed over the joint gap. (Figure 9)
- After all the above works are done and verified to be in compliance with all requirements, the PU material is then poured, trowelled and levelled precisely to match the level of the connecting road surface. (Figure 10 & 11)



Figure 5 – Cutting of a Blockout



Figure 6 – Cleaning & Sand blasting of Block-out



Figure 7 – Waterproofing



Figure 8 – Forming polymer concrete base



Figure 9 – Perforated angles & Bridging Plate



Figure 10 – Pouring & Trowelling of PU material



Figure 11 – Precise levelling of road surface

5 TESTING – EUROPEAN TECHNICAL APPROVAL (ETA)

In the process of obtaining a European Technical Approval ETA-12/0260, and in accordance with ETAG 032 Part 3, an extensive testing program was implemented by the Federal Institute for Materials Research and Testing, BERLIN (BAM) and the "Inspection authority for road construction" of

Technical University of Munich (TUM) along with MAPAG Testing Institute Austria.

POLYFLEX®ADVANCED PU has successfully demonstrated to meet all the requirements laid down by ETAG 032 before the European technical approval was granted.

5.1 *Testing of bond strength of the PU material*

The tests included verifications of bond strength on various surfaces such as concrete, polymer concrete, steel and asphalt. The recorded values were much higher than the required 1.5N/mm2 required by ETA-12/0260. Even at low temperatures, excellent resistance to de-bonding and thus also excellent resistance to leaking could be demonstrated.

5.2 *Assessment of dynamic –mechanical behaviour, ageing and temperature characteristics of the PU material*

The ageing and temperature characteristics of the PU joint filling mixture were evaluated after ageing for 3030 hours at the BAM. The evaluation, based on ISO 4664, was carried out over a temperature range from -60°C to + 250°C. Both the complex modulus |G*| and the loss factor tan δ demonstrate very good performance for the declared temperature range of -40°C to +60°C. See Figure 12.

5.3 *Mechanical resistance testing*

At the TUM a full-scale assembled joint specimen in the maximum opening position was subjected to a test load of 150 kN via a pneumatic tyre. The contact pressure was 0.94 MPa, the temperature was +23°C and the specimen length was approximately 1 m. *The* test was carried out in accordance with the Austrian regulation RVS (2) and the appropriate European Technical Approval Guideline (ETAG 032, Part 3, Annex 3M Method a), and recorded deformation after loading and any subsequent recovery curve. In the test, deformations of max. 0.5 mm were recorded immediately after unloading. Within one hour of unloading a complete elastic recovery of the surface had occurred. No damages or other changes to the surface were detected. See Figure 13.

5.4 *Fatigue resistance testing – rollover testing*

A second full-scale joint specimen was subject to further testing in the same testing rig at the TUM. The test involved cyclic loading by a pneumatic trafficking simulator, at an elevated temperature in excess of 45°C, in accordance with draft ETAG 032, Part 3, Annex 3M Method b. The contact pressure of the pneumatic tyre was 1.0 MPa, and the number of overpasses was 3030, with 30 of these executed with an additional 10% of horizontal load to simulate braking forces. The test result was successful as neither de-bonding nor cracking was observed post testing.

On the basis of experience in Europe with the same testing procedure for asphaltic plug joints and various national regulations, this successful high-temperature testing justifies 15-year design service life categorization.

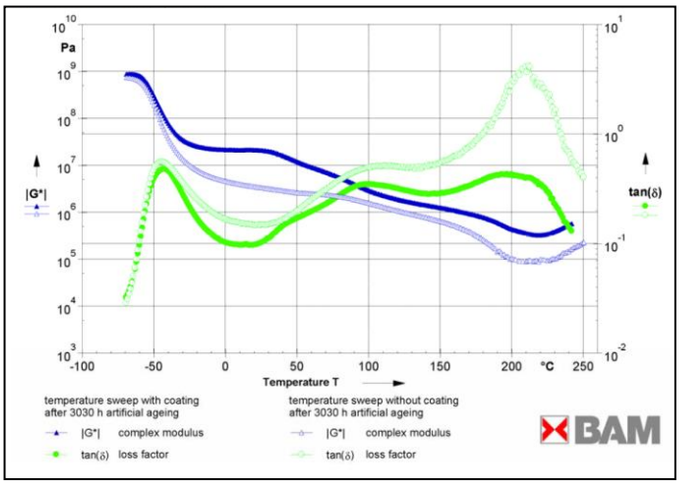


Figure 12 - Assessment of ageing and temperature characteristics



Figure 13 – Mechanical resistance testing

In addition, a standardized rutting test was carried out, at 60°C, in accordance with EN 12697-22. Figure 14 shows the enormous difference in performance between traditional asphaltic plug joint material and the POLYFLEX®ADVANCED PU material.



Figure 14 - Comparison of common asphaltic plug joint material and POLYFLEX®ADVANCED PU material after rutting test acc. to EN 12697-22 at 60°C (Top: Common asphalt plug material after 100 cycles at 60°C. Bottom: Polyflex®Advanced after 30,000 cycles at 60°C)

5.5 *Movement capacity testing*

To evaluate the movement capacity of the full-scale joint specimen, a test was performed at the BAM in accordance with draft ETAG 032, Part 3, Annex 3N. The complete declared movement range from maximum elongation to maximum compression at associated temperatures between -40°C and +60°C was subject of the test. During the test, reaction forces and deformations were recorded.

The specimen was horizontally extended by deforming it 1 mm for the duration of 7,500,000 sinusoidal cycles at ambient temperature and a frequency of 5 Hz. In addition, dynamic properties were voluntarily tested at -40°C. The dynamic behaviour of the material proved to be excellent, with the specimen showing no irregularities or signs of fatigue after the testing. See Figure 15

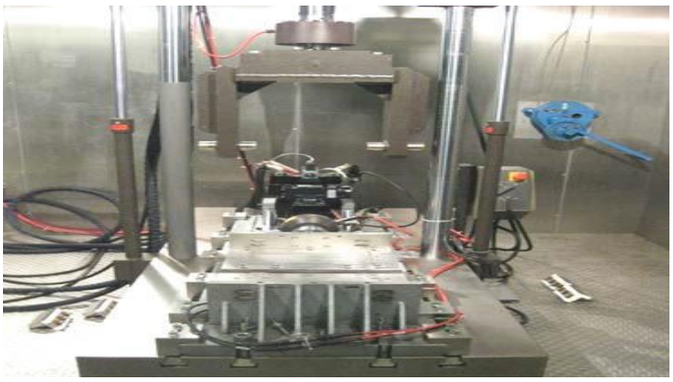


Figure 15 – Movement testing at-40C to +60C

5.6 *Watertightness testing*

After successfully passing the aforementioned movement testing, the full-scale specimen was subjected to a water tightness test at the BAM. At the maximum opening position of the joint, a full scale test specimen of 1m joint length was subjected to 30mm water head for six hours. After the test, no signs of leakage or moisture could be found under the specimen. The test was carried out in accordance with ETAG 032 Part 1, Annex L – Watertightness Test Method.



Figure 16 – Verification of watertightness at maximum opening position of joint following movement capacity test

5.7 *Measurement of level differences in the surface*

Level differences of the full-scale specimen was checked prior to any imposed horizontal deformations and in unloaded condition in accordance with the Austrian regulation RVS and the ETAG 032 Part 1- Section 4.1.4.1.2. The difference in the levels of the running surface of the joint from the ideal connection line between the two adjacent pavements in the traffic direction shall not be greater than 5 mm.

After loading, greater deviations are permitted, but these must not exceed 12 mm. Level differences were monitored during the fatigue and movement tests and upon their completion. The results were positive, with

a maximum level increase of +6 mm and a maximum level decrease of -5 mm being recorded.

5.8 *Skid resistance testing*

The full-scale specimen was subjected to skid resistance testing with a portable skid resistance pendulum tester as described in EN 13036-4, using the CEN rubber slider for carriageways and the 4S rubber slider for footpath areas.

5.9 *Further testing*

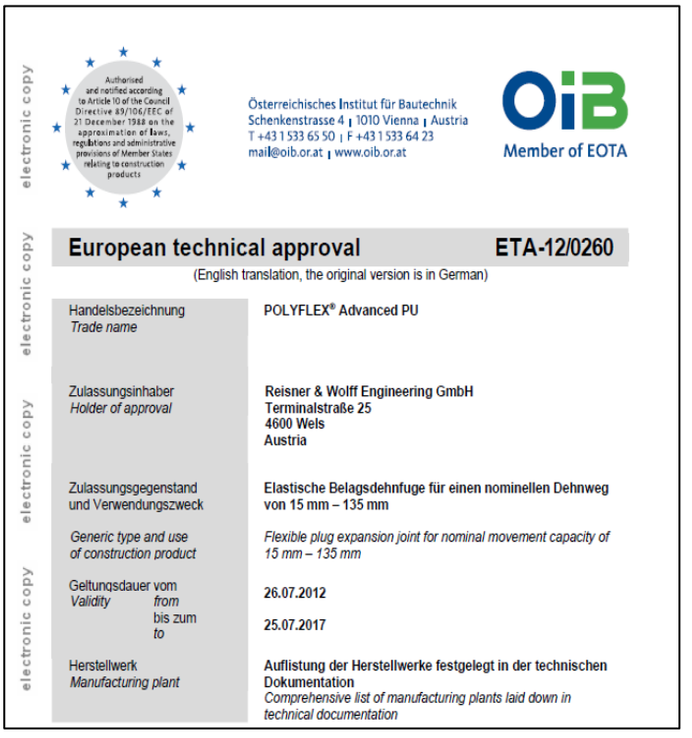
Testing was carried out on the joint's components to establish durability characteristics as follows and in accordance with ETAG 032 Part 1 requirements for Aspects of Durability verification methods:

- Resistance to chemicals, such as oil, fuel and de-icing agents, according to EN ISO 175
- Temperature-based ageing: Various tests according to EN 13687-2, EN 13687-3, EN 13687-5
- Ageing resulting from UV-radiation and weathering: Long-term tests (3030 hours) to TR010
- Ageing resulting from ozone: Test according to ISO 1431
- Freeze-thaw test (with thaw salt) according to EN 13687 Part 1

5.10 Resulting European Technical Approval (ETA)

As a result of this testing, the expansion joint has been awarded a European Technical Approval (ETA). This ETA covers joints of this type that accommodate longitudinal movements (SLS) of up to 135 mm (90 mm expansion and 45 mm compression), with a thickness of 60 mm and an initial width of 1100 mm. All types are designed for a vertical displacement of +/- 10 mm, permitting bridge bearing replacement work to be carried out without damaging the joint.

Further national approvals have also been awarded. For example, an approval issued by NEXCO (the West Japan Highway Administration) on the basis of specially completed testing according to Japanese regulations have validity right across Japan. The main focuses of the testing at the official Japanese testing institute at Fuji were verifications of resistance to rutting, abrasion, skid resistance and the ability to accommodate both slow and fast movements. The complete testing program was successfully completed in spring 2015.



electronic copy

Authorised and notified according to Article 10 of the Council Directive 89/106/EEC of 21 December 1988 on the approximation of laws, regulations and administrative provisions of Member States relating to construction products

Österreichisches Institut für Bautechnik
Schenkenstrasse 4 | 1010 Vienna | Austria
T +43 1 533 65 50 | F +43 1 533 64 23
mail@oib.or.at | www.oib.or.at

Member of EOTA

European technical approval **ETA-12/0260**

(English translation, the original version is in German)

Handelsbezeichnung *Trade name*	POLYFLEX® Advanced PU
Zulassungsinhaber *Holder of approval*	Reisner & Wolff Engineering GmbH Terminalstraße 25 4600 Wels Austria
Zulassungsgegenstand und Verwendungszweck *Generic type and use of construction product*	Elastische Belagsdehnfuge für einen nominellen Dehnweg von 15 mm – 135 mm *Flexible plug expansion joint for nominal movement capacity of 15 mm – 135 mm*
Geltungsdauer vom *Validity from* bis zum *to*	26.07.2012 25.07.2017
Herstellwerk *Manufacturing plant*	Auflistung der Herstellwerke festgelegt in der technischen Dokumentation *Comprehensive list of manufacturing plants laid down in technical documentation*

Figure 17 – ETA-12/060

6 AUSTRALIAN STANDARD COMPLIANCE

Extremes of shade air temperatures appropriate to structure locations in Australia are defined in Table 18.2(1) of AS5100.2. The maximum shade air temperature is 46°C which correlates to a maximum average bridge temperature of 50°C in accordance with AS5100.2, Table 18.2(2). For bridge superstructures consisting of a concrete deck on steel girders this temperature shall be increased by 10°C. This is deemed to be the highest temperature to be considered for this type of joint in accordance Australian Standards, and corresponds to the maximum tested temperatures.

AustRoads Guide to Pavement Technology, Part 2 and Main Roads WA Engineering Road Note 9 require the design tyre-pavement contact stress for pavement analysis to be taken no less than 0.75 MPa. The contact stress is related to the air pressure in the tyre in service. For highway traffic the contact stress is assumed to be in the range 500-1000 kPa. It was therefore concluded the ETA-12/0260 testing (refer to 5.3 and 5.4) for the pavement component of the POLYFLEX®ADVANCED PU expansion joint complies with Australian requirements.

7 REFERENCE PROJECT HISTORY

Since the first successful installation of Polyflex®Advanced flexible plug expansion joint in 2007, it has led to a rapid increase in orders each year in the following European countries including Australia:

- Germany
- Austria
- Hungary
- Italy
- Poland
- Belgium
- United Kingdom
- The Netherlands
- Switzerland
- Bosnia and Herzegovina
- Myanmar
- Croatia
- Sweden
- USA
- Canada
- Japan
- Denmark
- Norway
- Australia

In Australia, this joint was first installed successfully in May 2015 in Perth WA on the Judd Street Bridge. This was a rehabilitation project where the old Sliding Finger Type Joint had severe corrosion in the surface area of finger plate and in the counter bored holes affecting the anchorage integrity, compromising functionality which raised safety concerns. Figures 18 show the old replaced joint & Figure19 shows the new replacement Polyflex®Advanced flexible plug expansion joint. The new joint has given the benefits of a smooth surface resulting in huge noise reduction, better driver comfort, corrosion resistant while meeting functional and movement requirements.
Due to the success of the Judd Street project and the satisfaction of the asset owner (MRWA), succeeding orders followed including the South Western Highway Bridge, Bridge Over Warren River and Bridge Over Collie River.

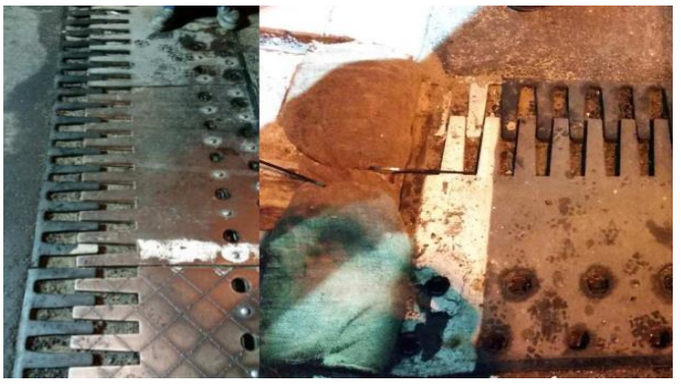


Figure 18 – Judd Street Bridge Old Sliding Finger Plate Joint



Figure 19 – Judd Street Bridge New Polyflex®Advanced flexible plug expansion joint

8 CONCLUSION

The Polyflex®Advanced flexible plug expansion joint offers all the benefits and at the same time overcomes the numerous disadvantages of the traditional bitumen asphaltic joint. This modern flexible plug type joint not only is a highly recommended replacement for the traditional bitumen asphaltic joint but also for other types of joints like the strip seal type and finger plate type which are prone to anchorage problems.

Summarised below are the benefits of this modern Polyflex®Advanced flexible plug expansion joint

- Exceptionally long working life, longer than adjacent surfaces
- Highest possible driving comfort
- No noise from traffic due to surface that is flush with adjacent road, i.e. no hitting by the wheels
- Fully watertight
- Maintenance-free (no cleaning, re-bolting, CP repair are required)
- Quickly installed lane-by-lane with minimal traffic impacts
- Installation within a wide temperature range (5°C to 35°C; installation at higher temperatures is also possible with some ventilation aids)
- Wear-resistant, no mechanical wear parts
- No rutting, high resistance to abrasion (e.g. from braking traffic)
- Damage to the joint can be easily repaired by reactivation of the PU material
- No recess for anchorage in structural concrete necessary

- Surfacing (asphalt or concrete) can be applied continuously before joint installation
- Any horizontal bend in the joint possible
- Any curb / sidewalk detail possible
- Low reaction forces
- Cold processing and easy handling with pre-set mixing ratio minimizes risk of mixing errors
- Resistant to environmental influences and acids, bases, chlorides, etc.
- Smooth surface ideal for pedestrian areas (e.g. in airports and railway stations)

9 ACKNOWLEDGEMENT

The authors wish to thank G Gallai and G Moor for allowing their published works at References 1 & 2 to be largely adopted in this paper.

10 REFERENCES

Gallai, G. et al, 2017. *Next Generation Flexible Expansion Joint material for Bridges, Austroads Bridge Conference 2017*

Moor, G. et al, 2016. *Flexible plug joints – Benefits of polyurethane vs bituminous*, *19th IABSE Congress Stockholm*

Bridge Joint Association 2003. *Standard for Asphaltic Plug Joints*, *BJA/S2/APJ*.

Mogawer, W. & Austerman, A. 2004. *Evaluation of Asphaltic Expansion Joints, NECTR 50*

Ghafoori, N. & Sharbaf, M. 2015. *Bridge Deck Asphalt Plug Joints - Problems & Solutions, DOI 10.1201/b18538-22*

RMS/RTA Bridge Circular, 2008. *Bridge Deck Joint Selection Design Installation & Maintenance, BTD 2008/10*

Austroads, 2012. *Design Rules for Bridge Bearings and Expansion Joints, AP-R405-12*

Mageba Manual, 2015. *Polyflex Advanced PU – flexible plug expansion joint*

European Organisation for Technical Approvals(EOTA), 2013. *ETAG n° 032 Guideline for European Technical Approvals of Expansion Joints for Road Bridges, Edition May 2013, Parts 1 -8, Brussels, Belgium*

Austrian Ministry for Traffic, 2011, Innovation and Infrastructure. *RVS 15.04.51, Design Regulations on Expansion Joints and RVS 15.04.52, Noise Evaluations of Expansion Joints, Vienna, Austria*

AustRoads Guide to Pavement Technology, 2008. *Part 2: Pavement Structural Design, Sydney, Australia, ISBN 978-1-921991-11-0*

Engineering Road Note 9, 2013,. *Procedure for the design of road pavements, Main Roads Western Australia*

Standards Association of Australia. *"AS5100 Bridge Design Standard (AS5100.2 and AS5100.4)"*

Spuler, T. et al , 2014, *Life-cycle considerations in the selection and use of bridge expansion joints, 7th IABMAS - International conference on Bridge Maintenance, Safety and Management, Shanghai, China*

European organisation for Technical Approval, 2012. *Part 1 – General and Part 3- Flexible Plug Expansion Joints*

ISO 175:2010, 2010 –*Plastics - Methods of test for the determination of the effects of immersion in liquid chemicals*

EN 13687-1:2002, 2002 –*Products and systems for the protection and repair of concrete structures. Test methods. Part 2, 3 and 5*

ISO 1431-1:2004, 2004 – *Rubber, vulcanized or thermoplastic -- Resistance to ozone cracking -- Part 1: Static and dynamic strain testing*

WSDOT Design Manual M23-50-17, 2017 – *Bearings & expansion Joints, Chapter 9*

CDOT Design Manual, 2017 – *Joints & bearings, Section 14*

Maintenance, Safety, Risk, Management and Life-Cycle Performance of Bridges – Powers, Frangopol, Al-Mahaidi & Caprani (Eds)
© 2018 Taylor & Francis Group, London, ISBN 978-1-138-73045-8

Critical factors in minimizing total life cycle costs of bridge expansion joints

G. Pope, J. Creighton & V.V. Ghodke
Mageba Aus, Sydney, Australia

ABSTRACT: Inadequate consideration to long term performance of the bridge expansion joint, and their exchangeability when finally end of service life approaches, could pose severe consequences to bridge owners or managers. A simple and low technology product selected predominantly based on lower initial product cost will almost always require premature replacement whereas a properly selected and engineered high quality joint may provide more than 40 years of uninterrupted service. Direct costs for maintenance and premature intervention or replacement and indirect costs of disruption to the commuters can be accumulated to many multiples of initial "savings" in product cost of low technology expansion joint. Understanding long term performance of expansion joints with the aid of engineering and testing of these joints can certainly help optimizing the life-cycle costs of the bridge expansion joint. This will benefit the bridge owners, commuters and society.

1 INTRODUCTION

Strong consideration for life-cycle costs is widely considered as an important part of responsible asset and project management. There have been numerous analyses into the impact of proper life-cycle cost consideration as well as advice on mitigating these costs. Despite showing a clear advantage to taking life-cycle costs into strong consideration, there has not yet been the shift toward responsible asset management in this regard which has been anticipated for some time.

This paper presents scenarios relating to the life-cycle costs of bridge expansion joints based on different philosophies. These are based on figures provided by owners and managers of bridges, as well as other related literature. Advice is offered for those creating strategies designed to reduce the total life-cycle cost of expansion joints through careful consideration of the key factors that affect the longevity of a joint.

Apart from direct life-cycle cost considerations above, there are indirect costs such as wasted material and time, noise pollution, and – significantly – economic effects due to congested traffic. Additionally, should a joint fail and cause damage to the main structure, this cost should also be considered as part of the total life cycle cost of a bridge expansion joint. Leaking joints can cause significant damage to a structure if left uncorrected.

These costs, direct and otherwise, are discussed below.

As bridge expansion joints is even more specialised a field than bridges themselves, the amount of literature regarding their life-cycle costs is quite limited. This paper aims to shed some light onto the various factors which will affect the long and short term costs both direct and indirect, of a given bridge expansion joint.



Figure 1. Large movement capacity of expansion joints of 1920mm on the Incheon Grand Bridge, South Korea

2 CHALLENGES OF BRIDGE EXPANSION JOINTS

Bridge expansion joints have some of the highest demands among bridge components (Moor et al. 2016). They are required to allow various movements

and rotations while resisting repeated impact and dynamic loading from passing traffic.
Over a 40 year service life, these load cycles total in the hundreds of millions or even billions and hence are subjected to fatigue stress. This is compounded by the fact that they are much lighter than the structure of which they are a part. Due to these conditions, maintenance is an inevitable part of the service life of a given joint.

Proper consideration of the total cost of the joint should be an important factor in the selection of a joint. As will be outlined in this paper, there are several factors contributing to the life-cycle and total cost of a bridge expansion joint. Among these are the costs associated with the wear and tear induced by fatigue and other processes.

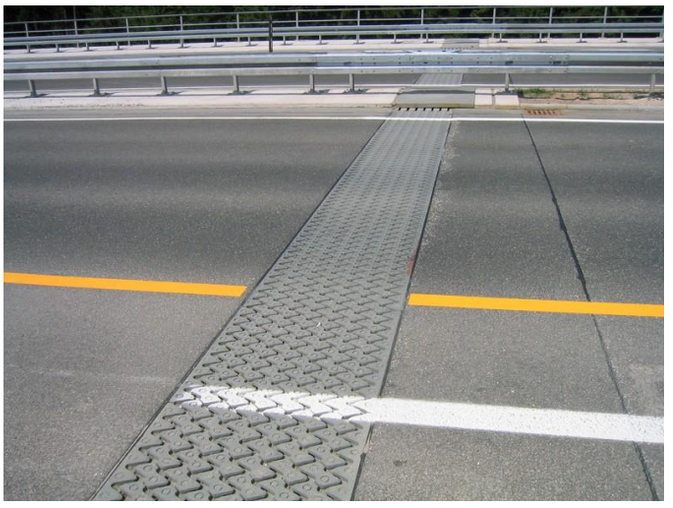


Figure 2. A 7-gap modular joint with noise reduction plates

3 BRIDGE EXPANSION JOINT TOTAL LIFE-CYCLE COST

3.1 *Definition*

Life-Cycle Cost (LCC) is "the sum of all costs anticipated during the service life" (Hawk et al. 2003). These costs are appropriately scaled to account for change in price and dollar value projections for the time period in which they are expected to occur. It is considered good practice to complete an LCC analysis to determine the best option, rather than simply the upfront cost.

3.2 *Components*

The LCC includes several components which summarise the various costs which can be expected for a given asset.

The LCC is the sum of Initial Supply Cost (ISC), Initial Installation Cost (IIC), Inspection and Maintenance Cost (IMC), Direct Replacement Cost (DRC) and Direct User Cost (DUC) over the service life of the bridge.

This is expressed using Equation 1 as below:

$$LCC = ISC + IIC + IMC + DRC + DUC \quad (1)$$

(Savioz, et al. 2014)

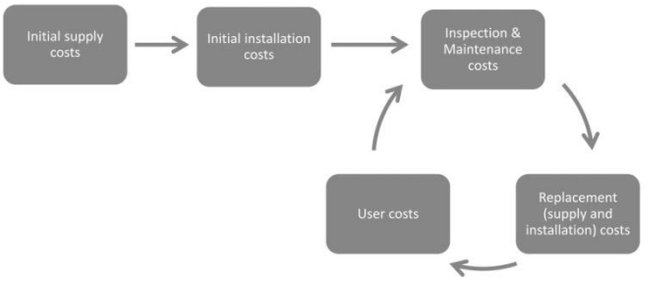


Figure 3. A flow chart of Life-cycle Cost (Savioz, et al. 2014)

3.3 *Consideration*

It is shown in Figure 3. that the life-cycle being considered in this analysis is that of the bridge itself, not the bridge expansion joint. This means that when a join has reached the end of its service life, it must be replaced. This process of replacement is expensive and recurs throughout the life of a bridge, as such, it contributes a major portion of the total Life-Cycle Cost.

Excluding the Direct User Cost, each of the other costs are taken up by the asset owner and so should be of direct concern when choosing a bridge expansion joint. There are, however, varying philosophies for the management of each of these costs.

Initial Supply Cost and Initial Installation Cost are the most obvious and traditionally of primary consideration to the decision maker. These costs are unavoidable, however, the reduction of these costs can lead to increases in other costs.

Direct Replacement Cost is directly affected by the service life of the previous joint and should be kept as minimal as possible.

Inspect and Maintenance Costs should be considered inevitable but also reducible through proper selection consideration.

All of the cost groups are connected and affect one another in different proportions. As an example, a large investment into a high quality joint and its maintenance will result in a longer service life, which in turn leads to less replacement cycles.

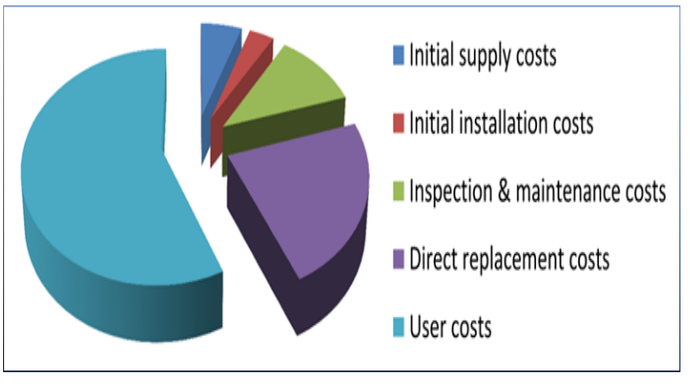


Figure 4. Distribution of life-cycle costs

Each cost group will be covered below in greater depth.

3.4 *Initial supply cost and initial instalment cost*

Initial supply and installation costs are generally unique from project to project. This is due to the widely varied expansion gaps and bridge widths, among other factors that contribute to the cost of a bridge and its joints.

It can generally be said that the cost of a bridge expansion joint will be in the range of 1% of the total construction cost of a bridge (Harper-Smith Kelly 2017). As such, it is a minor part of the total bridge construction cost, despite playing such a major role and having such demanding conditions.

The difference in initial supply and installation costs between a low and high quality product of similar parameters is approximately 60-80% increase in cost. This is significant, however, the increase in quality leads to reduction in other costs.

3.5 *Inspection and maintenance cost*

Asset owners often take one of two approaches to maintenance; proactive or reactive. A proactive strategy is most advisable as this allows early detection of potential failures followed by appropriate corrective action.

Reactive strategies are problematic as "failures are often a chain reaction (i.e., the failure of one component leads to the destruction of other components)" (Dexter et al. 2002). This is especially true for bridge expansion joints, as due to the dynamic movements and loadings which they carry, they are subject to particular deterioration. Additionally, when a bridge expansion joint fails, these loads and movements are transferred to other parts of the structure, which are not suited to these conditions, accelerating their own deterioration.

The chain reaction can result in damages and repair work costs that far exceed the cost of proactive inspection and maintenance.

Another benefit to proactive inspection and maintenance is that a joint which is deteriorating, if caught early, may be maintained and kept from failure for much longer than if left alone. This delays the replacement cycle of the expansion joint.

3.6 *Direct replacement cost*

Expansion joints, being highly dynamic moving parts, have a shorter service life than that of a bridge structure, as such, it is expected that it will require replacement at some point in the life of the bridge.

Replacement of a bridge expansion joint comes with many additional challenges than that of the initial installation, including work around traffic and the restrictions which that imposes. In conjunction with other bridge works, the replacement cost is anticipated to be approximately three times that of the initial installation cost, while when done independently of other works, this can be as high as six times the initial installation cost (Savioz, et al. 2014).



Figure 5. Failed aluminium joint in Jeddah, Saudi Arabia (Spuler et al. 2014)

This process therefore should be undertaken as few times as possible throughout the life of the bridge in order to minimise this cost. As seen in previous sections, the best strategy to extend the life of an expansion joint is to procure high quality products while using a proactive approach to inspection and maintenance.

3.7 *Direct user cost*

There is very little empirical data for direct user costs, and as such, estimates must be made based on expected outcomes and circumstances. Savioz et al. 2014 suggest that a reasonable estimation would be 10% of indirect user costs.

Direct user cost itself is the cost taken up by the bridge users resulting from improper performance of the joint. These cost are generally due to traffic disruption during replacement or maintenance works, though in some cases, they may be from damage caused by a joint which is damaged or not working correctly, as in Figure 5.

Aside from direct damage, there are considerations such as delay for commuters, additional fuel usage, detours which may be necessary and further impacts of any of these. As these are all very situation specific, it can be difficult to correctly calculate potential costs.

Example LCC calculation and comparison

Savioz et al. 2014 uses the example of a bridge expansion joint used on a European highway to illustrate the importance of using high quality products in order to reduce the total LCC. Taking the initial supply and installation costs as a combined EUR 200,000, the LCC was extrapolated using the figures in Figure 6.

Working Assumptions	High-End Product	Standard Product	Low-Tech Product
Lifetime (years)	40	25	10
Initial investment value	120%	**100%**	70%
Maintenance per year	2%	4%	6%
Direct replacement costs (DRC)	420%	400%	370%
User costs from traffic disruption (UC)	500%	500%	500%

Figure 6. Working assumptions of the cost intervals of high, standard and low quality products (Savioz, et al. 2014)

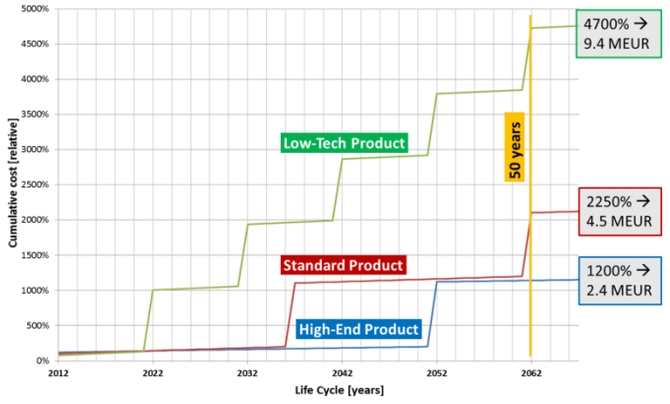


Figure 7. Typical Life-Cycle Cost progression of high, standard and low quality products (Savioz, et al. 2014)

Even discounting the user costs from this comparison, the difference is in the millions of Euros of additional cost to the asset owner over the life of the bridge. Along with the commentary provided in previous sections, this analysis shows the need to reduce the number of replacement cycles by extending the service life of a joint.

4 MINIMISATION OF A JOINT'S LCC

As seen above, the life-cycle cost of a bridge expansion joint can vary greatly and it is of great benefit to the asset owner to reduce this as much as possible. There are several components to an effective strategy which leads to a greatly reduced life-cycle cost of bridge expansion joints, these are outlined below.

4.1 *Suitability of the joint*

From the outset of a bridge design, a bridge expansion joint selection will be affected. The designer will be making considerations such as span length, affecting the joint movement capacity required among many others. As such, it is important to ensure that the type of joint specified is chosen with respect to the various factors that contribute to the required performance characteristics of a joint. Consultation with an experienced bridge expansion joint supplier is recommended in order to make sure the joint performance capabilities are properly considered in the design and joint selection.

It is then important to clearly and properly define all the characteristics which a joint will be required to fulfil. These include longitudinal movement, transverse movement, traffic loading and frequency, any other loading imposed on the joint itself, cumulative movement, rotations, any location or design specific conditions like earthquake conditions, among others.

All of the above factors must be integrated into the bridge expansion joint design and hence should not be left aside or underestimated or the joint will be prone to failure due to unsubstantial design parameters.

Once these factors have been determined, the type of joint which is selected is critical. There are several main categories of bridge expansion joint, each with advantages and disadvantages and differing capabilities. Again, consultation with an experienced bridge expansion joint supplier is recommended for this process to ensure the optimal option is chosen. From this point, the bridge designer must provide adequate blockout and other allowances to ensure that the selected joint is able to be installed correctly.

4.2 *Quality and durability of the joint*

It is important to strongly consider the quality of a bridge expansion joint as this can greatly impact on the service life of a joint.

4.2.1 *Material*

The material which is selected is of particular consequence. Primarily steel and aluminium are the materials used, each with their own advantages and disadvantages. Edwards & Yeung 2017 explain that while aluminium has superior corrosion protection to steel, it is less reliable in the long term due to fatigue effects which expansion joints experience over their service life. As can be seen in Figure 8. steel will reach a point ("endurance limit") where its integrity is maintained despite repeated loading cycle. Conversely aluminium continues to deteriorate over time as it is subjected to further load cycles. Load assumptions for bridge fatigue design are based on the nature of steel and its endurance limit. For aluminium joint, these assumptions may lead to an over estimation of the fatigue life. Therefore, it is recommended that in the case of using aluminium joints, extensive testing is recommended in order to assure that the joint design can withstand the fatigue effects.

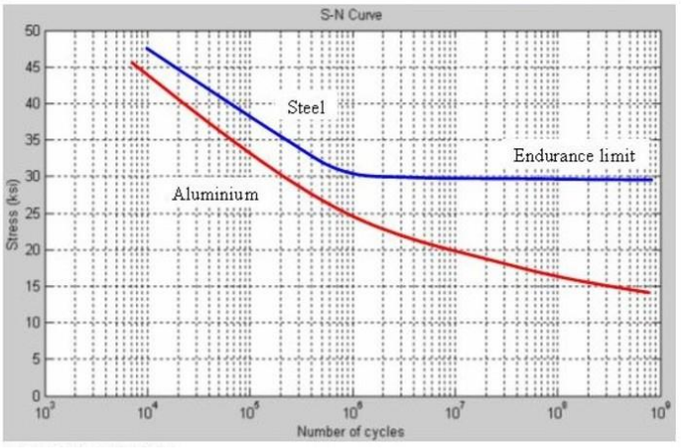


Figure 8. Comparison of aluminium and steel S-N curves

4.2.2 *Testing*

As above, aluminium joints in general are recommended to be tested against fatigue effects, however, this recommendation is extended to steel joints as well for proper joint design verification. Moor et al. 2016 note that the AASHTO specification for modular joint fatigue testing is the most demanding test requirement worldwide and that it should be used for verification that a joint "will provide good long-term performance".

While testing of bridge expansion joints may not yet be required in many local and global standards, it is one of the best ways to verify that a design will withstand the fatigue, movement, rotation and loadings which it will be subjected to throughout its service life. "The assurance that the testing can provide to the bridge owner that the delivered expansion joints will be fit for purpose can be of great significance, in particular if the supplier cannot demonstrate many years of successful experience" (Spuler et al. 2011). This verification, will then provide evidence to the bridge owner that the joint in question, with proper care, can be expected to have a long service life.

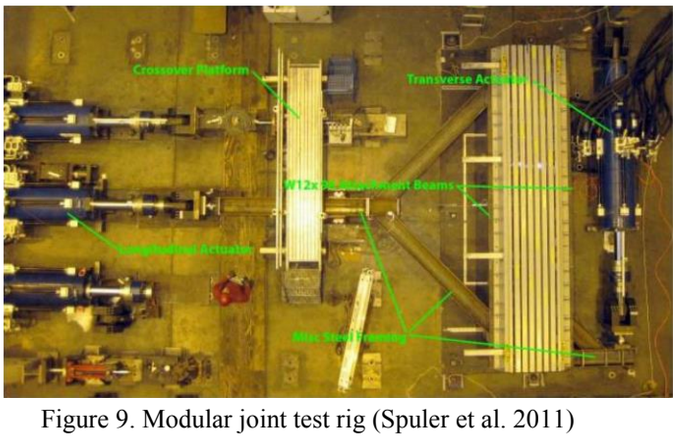


Figure 9. Modular joint test rig (Spuler et al. 2011)

4.2.3 *Corrosion protection*

Exposed steel should have adequate corrosion protection specified, applied and maintained in order to ensure the integrity of the joint. The bridge designer should specify the corrosion conditions so that the bridge expansion joint supplier can select the adequate corrosion protection system for the particular circumstance.

It should be considered that the use of hot-dip galvanisation may omit corrosion protection repair over the lifetime of a joint. A conservative approach to the expected lifetime is published in EN ISO14713.

Reapplication of painted corrosion protection should be considered part of the regular maintenance routine of the bridge to assure the joints integrity.

4.2.4 *Quality assurance*

The bridge expansion joint supplier and manufacturer should have comprehensive quality assurance, (generally according to ISO 9001) so that the product received is as specified and designed. This should preferably include third party verification as a means of ensuring this process is carried out correctly.

4.3 *Quality of the installation*

The installation of a joint is a critical part in determining its proper function. Dexter et al. 2002 identifies 10 common errors which lead to problems with the installation affecting the performance of the bridge expansion joint. For this reason, it is recommended to have an authorised person representing the bridge expansion joint supplier supervise and witness the installation. Most suppliers will also provide an installation guide which should be strictly adhered to.

The designs of the bridge and joint can also affect the installation quality, for example, a design which limits access and workability during installation can be problematic for the installation process.


Figure 10. Installation of a bridge expansion joint

4.4 *Adequate inspection and maintenance routine*

As noted previously, a proactive inspection and maintenance routine is a key component in ensuring the longevity of the bridge expansion joint along with other components. As with installation, the supplier will generally provide an inspection and maintenance manual which outlines the recommended practice and procedure for achieving the best service life for that joint.

Dexter et al. 2002 note that there are "three major factors inhibiting good inspection and maintenance practice", noting these as limited access, limited technical expertise among personnel, and expense factors.

Limited access is directly caused by design, and the designer of the structure should make efforts to avoid restricting the access to the expansion joints after construction.

Limited technical expertise can lead to issues being missed which would otherwise facilitate corrective action. For this reason, an inspection and maintenance manual is recommended to be followed by these personnel.



Figure 11. Excessive corrosion

Failing to carry out inspections and maintenance work to avoid the expense which they entail is strongly advised against. This practice can lead to missed opportunities for early corrective action, hence leading to expensive repair work, which are often far more expensive than the inspection and maintenance costs would have been (Savioz et al. 2014).

As seen in Figure 11. deterioration can become excessive if undetected due to either a lack of access to the area, or a poor inspection and maintenance routine.

A proper understanding of the importance of inspection and maintenance among decision makers will contribute to recommended practice, hence leading to longer expansion joint service life.

4.5 *Additional precautions to be considered*

There are several additional precautions which a bridge designer may choose to incorporate in order to improve the other aspects already discussed, primarily dampening mechanisms and structural heath monitoring.

4.5.1 *Dampening mechanisms*

Dampers, particularly hydraulic dampeners can reduce the effects of erratic movement which may cause undue detriment to the bridge expansion joint and structure as a whole. For example, these would be applicable for use in seismic areas to avoid potential deterioration from collision of elements due to unpredictable movements.



Figure 12. Hydraulic Damper

4.5.2 *Structural health monitoring*

Automated monitoring systems can greatly aid in the ongoing inspection and maintenance of the joint and bridge. They can provide metrics in real time such as movement frequency and magnitude directly to the bridge engineer. Having this system constantly monitoring the conditions of the bridge and its components can greatly reduce the manual effort of the inspection process. For example, it can be set up to flag or send a warning to the bridge engineer if a certain threshold is breached. This means that if it is approaching or exceeding limits which were defined, the engineer will not have to wait for the next inspection for this to be found, allowing for early intervention where required.

This system can therefore result in returning in savings many times the initial investment through early detection of problems which may lead to failure.



Figure 13. Structural heath monitoring system

5 TOTAL COST

The costs considered in the LCC method above are not the only costs associated with the life-cycle of a bridge expansion joint.

There are environmental costs from the production of the product as well as the type and quantity of material used, both at the initial supply and any replacement. There are numerous other factors contributing to the environmental cost of replacing a bridge expansion joint.

Ancich & Chirgwin 2006 estimate "community savings by avoiding replacement are estimated at a further $AU10 million" and Schulz & Mainka 2013 found that a full road closure for trucks on the A!-Rhine Bridge cost the economy between EUR 0.5-1.2 million per day of closure. This again, highlights the need to minimise closure time and reduce number of replacement cycles.

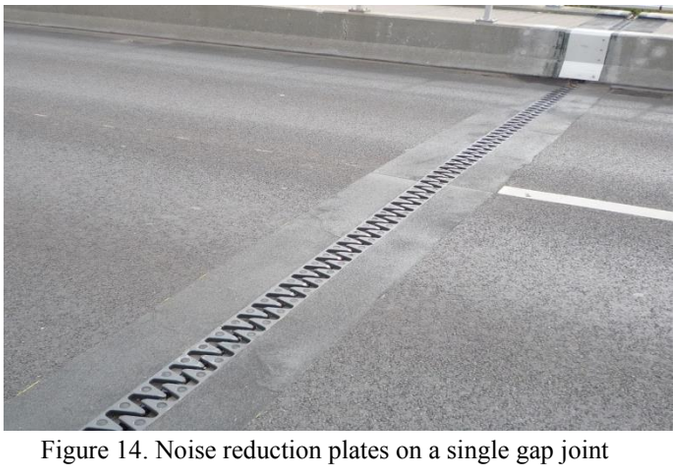


Figure 14. Noise reduction plates on a single gap joint

Additional to these costs of replacement is the noise pollution produced by traffic crossing the joint depending on the type of joint and the presence of noise reduction plates or lack thereof.

As alluded to previously, a faulty joint can have an impact on the main structure of the bridge. It is the role of many joints to catch and redirect water away from the structure, however if this function is failing, as is the case for a vast majority of bridges (Savioz et al. 2014), this will have detrimental effects to the structure itself, resulting in repair or maintenance costs that can far exceed the expansion joint's.

Aside from those costs outlined above there are others not covered.

The total expansion joint cost should be considered as the sum of its life-cycle cost, the indirect user costs, and any bridge maintenance costs resulting from expansion joint faults.

6 CONCLUSION

Proper consideration of the life-cycle cost of a bridge expansion joint over the life of a bridge shows that there are many elements worth taking into account beyond initial costs. Furthermore, a considered investment in a well-designed and well-made joint is very likely to generate savings well beyond the initial investment. High quality material, design and maintenance, although more expensive at the outset will minimise expensive repair and replacement costs.

The quality and appropriateness of a bridge expansion joint has great effects on the resulting service life, a high quality joint, selected properly for instance in which it is used, can last for 40 or more years before requiring replacement. Cheaper or poorly selected joints are likely to deteriorate and require repair or replacement much earlier.

Coupled with the initial quality of the joint, maintenance is a long term investment, which aids in the prevention of damages to the joint and the bridge structure itself where the joint has failed. These costs are minimal by comparison to the potential costs if proper inspection and maintenance is avoided.

The recognition of the investment in quality is yet to become wide scale practice, as it seems there is no incentive for construction companies to ensure the long term integrity of the asset once it has been completed. As the bridge expansion joint is such a small portion of the total initial expense, it is easy to see why construction companies might write it off as something to be procured for as little as possible, however, this attitude can lead to unnecessary increase in long term costs of maintaining the bridge.

Investigation into cause and effect of life-cycle costs also revealed the importance of technical advice from an experienced bridge expansion joint supplier throughout the design and construction process. This practice aids the designer, constructor and maintainer in their various roles contributing to the proper function and long and effective service life of a bridge expansion joint.

Aside from the financial benefits of a well-made, well-designed and well-maintained bridge expansion joint, there are also the social and environmental

benefits due to longer lasting joints which can be repaired and replaced less often and also easier than their cheaper counterparts.

High quality joints, verified through testing, using superior materials with proper maintenance is certainly worthy of investment for long term savings and social and environmental benefits.

7 REFERENCES

Ancich, E. & Chirgwin, G. 2006. Fatigue Proofing of an In-service Modular Bridge Expansion Joint. *In: Proc. 6th World Congress on Joints, Bearings & Seismic Systems for Concrete Structures*, Nova Scotia, Canada: Halifax

Dexter R.J. et al. 2002. Performance Testing for Modular Bridge Joint Systems, *In: NCHRP Report 467*, Washington, DC: Transportation Research Board.

Edwards, L. & Yeung, S. 2017. Bridge Deck Expansion Joints: A Comparison of Technical and Selection Requirements, Including Consideration of Life Cycle Costs and a Review of Commercially Available Products within Australia and New Zealand, *In: Proc. 10th Austroads Bridge Conference,* Melbourne, Australia: Austroads Inc.

Harper-Smith Kelly, A. L. 2017, *Life Cycle Cost Analysis for Joint Elimination Retrofits and Thermal Loading on Colorado Bridges*, Colorado State University.

Hawk, H. et al. 2003. Bridge life-cycle cost analysis, *In: NCHRP Report 483*, USA: Transportation Research Board.

Moor, G. et al. 2016. Testing of long-term performance of bridge expansion joints – a critical factor in minimizing life-cycle costs. In M.A.J. Williams & H. Faure (eds), *In: Proc. ICSBOC Halifax 2016*. Nova Scotia, Canada: Halifax.

Savioz, P. et al. 2014. Life-cycle and total cost analysis of bridge expansion joints. *In: Proc. 7th IABSE Conference*, Shanghai, China: IABSE.

Savioz, P. et al. 2015. Case Study: Refurbishment of Deteriorated Bridge Deck Expansion Joint in Suburban Area, *In: Proc. 7th Austroads Bridge Conference,* Melbourne, Australia: Austroads Inc.

Schulz W. H., Mainka M. 2013. *Gesamtwirtschaftliche Bewertung der Sperrung der A1-Rheinbrücke für den Lkw-Verkehr*, Pro Mobilität

Spuler, T. et al. 2011. Developments in modular expansion joint technology – codes and testing in Australia, America and Europe, *In: Proc. 8th Austroads Bridge Conference,* Haymarket, Australia: Austroads Inc.

Spuler, T. et al. 2012. Life-cycle considerations in the selection and use of bridge expansion joints. *In: Proc. 18th IABSE Congress*, Seoul, South Korea: IABSE.

Spuler, T. et al. 2014. Single Gap Expansion Joints – An Optimal Solution for Small Deck Movements, *In: Proc. 6th Small Bridges Conference,* Sydney, Australia: Leading Infrastructure Pty Ltd.

Maintenance, Safety, Risk, Management and Life-Cycle Performance of Bridges – Powers, Frangopol, Al-Mahaidi & Caprani (Eds)
© 2018 Taylor & Francis Group, London, ISBN 978-1-138-73045-8

Smart bridge components (expansion joints, bearings, seismic devices) for intelligent infrastructure

Kleidi Islami, Niculin Meng & Colm O'Suilleabhain
Mageba SA, Bulach, Switzerland

ABSTRACT: Modern automated structural health monitoring (SHM) systems have much to offer the responsible engineers in the construction, inspection, maintenance and renovation of structures in general, and of key structural components such as bridge bearings, expansion joints and seismic protection devices in particular. In the past, monitoring of such components generally involved the use of separate, independent sensors, connected not to the component but to the main structure and provided, to all intents and purposes, as an afterthought to the design and use of the components themselves. Improving technology is changing this, however, with "smart" components now available, with sensors pre-integrated in their design and fabrication before they leave the factory, and data analysis capabilities improving to include automatic identification of component damage based on general testing and teaching of the system.

1 INTRODUCTION

Recent technological developments in the field of structural health monitoring (SHM), particularly in relation to sensors and data logging, have greatly increased the potential of such technology to play a valuable role in civil and structural engineering – especially as it relates to critical infrastructure such as road and railway bridges. Continually progressing research work, and the innovations of suppliers, have resulted in the development of systems and solutions that can greatly increase the effectiveness and efficiency of bridge construction, inspection, maintenance and renovation work (Moor et al, 2014).

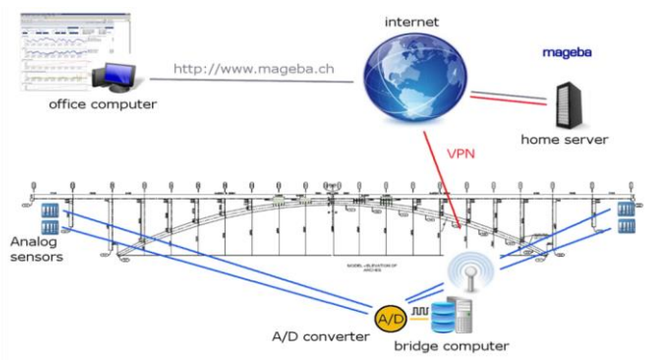


Figure 1. An SHM system with sensors integrated in key structural components can optimise inspection & maintenance work.

One such area of innovation relates to the key components which, if present, are generally critically important to a bridge's efficient design and proper functioning: its bearings, expansion joints and seismic protection devices such as dampers. This has led to the development of "smart" components, which feature pre-integrated SHM sensors already when fabricated, enabling bridge engineers to optimise the efficiency of their work as it relates to their structures' key components (Figure 1).

2 TYPICAL USES AND BENEFITS OF SHM IN CONSTRUCTION AND MAINTENANCE

Modern SHM systems can be used to provide reliable, precise data on virtually any variable of interest – e.g. forces, movements or rotations of any part of a structure. The data can be automatically measured and recorded around the clock, all year round, and at high frequency if required (e.g. to analyse vibrations), making the SHM much more capable, and also more efficient and cost effective, than traditional manual methods in many cases. By presenting the recorded data on a graph (for example, as shown in Figure 2), typically on a secure web interface, the effects of selected factors (e.g. temperature) on particular variables (e.g. structure movements, absolute or accumulated) can be easily analysed and understood.

Where specific concerns exist about a structure's safety or performance, an SHM system can be designed to provide notification, by email or SMS, to the responsible engineer of any exceeding of defined threshold values – for example, should movements of any part of the structure exceed expected values, or the width of a crack suddenly increase.

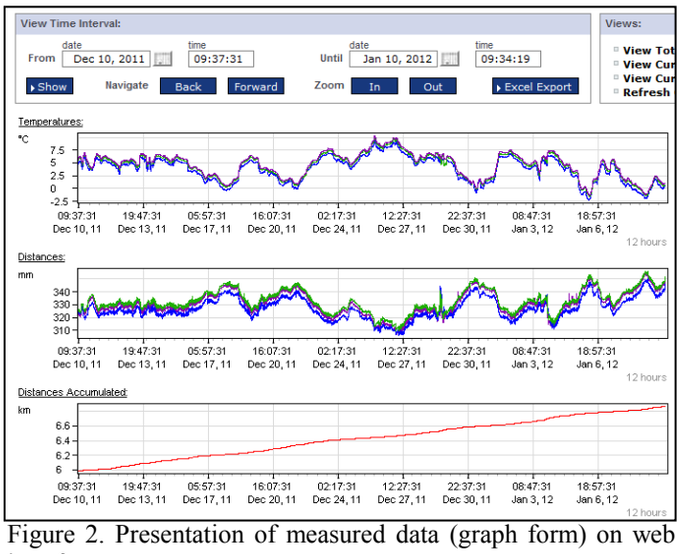


Figure 2. Presentation of measured data (graph form) on web interface.

Modern SHM systems can also be programmed to statistically analyse the data they record for easier evaluation. For example, histograms such as that shown in Figure 3 can be generated to visually present the frequency of occurrence of values in any given variable during a selected period of time, enabling anomalies to be readily identified.

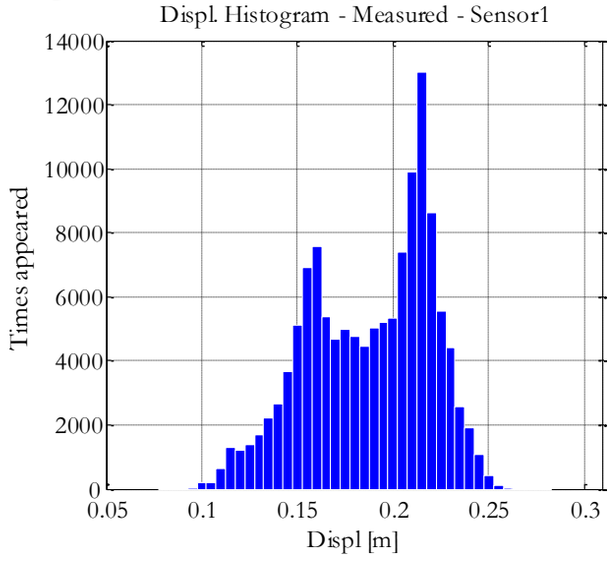


Figure 3. Example of a histogram presenting frequency of occurrence of all measured values.

Presentation of selected data on a single graph, e.g. as shown in Figure 4, can also enable correlations to be established and significant deviations to be identified.

It may also be helpful to be able to assess the static or dynamic behaviour of a structure due to certain influences but not others. By eliminating the influence of dominant, less relevant factors, small changes due to the factors of interest can be much more easily detected. For example, the effect of minor structural damage on a specific variable may remain unnoticed when clouded in data that includes the effects of temperature changes, but readily identifiable on a graph when the influence of temperature is excluded. Or the exclusion of temperature effects may enable the effect on deck displacements of other influences such as traffic to be more easily understood. Such analysis is made possible by the use of regression models as described by Islami & Modena (2013). The usefulness of this technique is illustrated by the graphs in Figure 5, which show how displacements at one point in a structure vary with time. The upper graph presents the measured data, unmodified, while the lower graph presents the data as modified to exclude the influences of environmental factors such as temperature but still showing the influence of traffic loading. As can be seen, the exclusion of particular data in this way makes analysis of the data far easier, with any irregular values being immediately recognizable, enabling the need for repair or preventative action to be assessed.

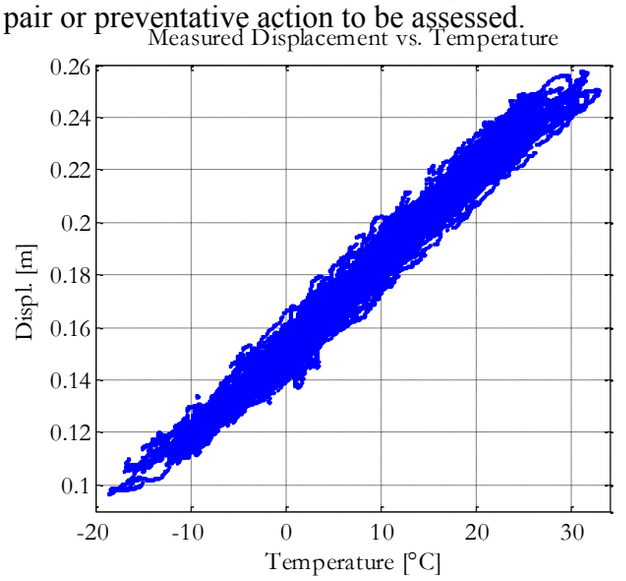


Figure 4. Example of a graph showing the correlation between an influence (temperature) and a measured effect (displacement).

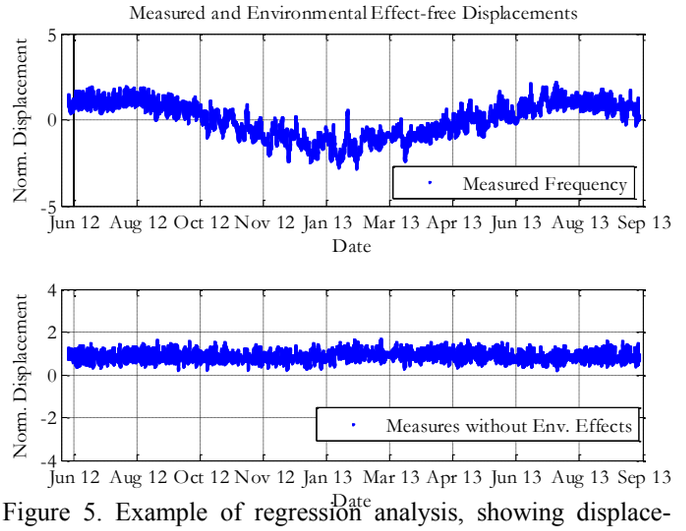


Figure 5. Example of regression analysis, showing displacement data, both before (above) and after (below) the elimination of environmental effects.

3 MONITORING OF BEARINGS

A structure's bearings are critically important for its proper long-term performance, and any loss of functionality can quickly develop into a serious problem for the structure. For example, if a bearing no longer enables a bridge deck to expand/contract or move as required by its design, enormous constraint forces can build up, potentially causing severe damage to the structure. It is therefore essential that the proper condition and functioning of a structure's bearings be adequately monitored, to ensure that any such loss of proper functioning, through deterioration, accidental damage or otherwise, is recognised in good time and appropriate actions taken to protect the structure. Where the condition of a structure's bearings has been found to be questionable or where further confidence in the ongoing performance of the bearings is required, the use of an SHM system is an attractive alternative to traditional manual inspections. Not only are automated SHM systems far more accurate and precise than manual measurements, they can be designed to operate 24 hours a day, 365 days per year, thus ensuring that any sudden deterioration or damage is immediately recognised and reported to the responsible authority. And if frequent visits to a bridge are required to perform manual inspections, the investment in an SHM system can be quickly paid off and easily justified.

3.1 *Case study: Spherical bearings of main junction of Qatar's new Orbital Highway*

Qatar's new Orbital Highway is currently under construction around the country's capital, Doha, and is expected to significantly reduce traffic congestion in the city while improving connections to other cities. At one of the highway's main intersections (Fig. 6), a spaghetti junction where it crosses the Dukhan Road, it was decided to install an SHM system to monitor the condition of the various structures. The recently installed system is based on measurement of data from the bearings that support the various superstructures – spherical bearings of the TENSA-SPHERICAL type. In all, 28 of these bearings are connected to 14 control boxes, as shown in Figure 8. The SHM system is designed to continuously monitor, in particular, the load acting on each monitored bearing – all day, every day. This will enable it to immediately identify any change in loading conditions – for example, should the load on any bearing increase or decrease due to structural damage/deterioration or ground settlement, either rapid or gradual. With so-called alarm values defined (above or below which the responsible engineers should be notified), risks to structure users can be minimized, and any structural damage or deterioration arising can be addressed before it develops into a bigger problem.

The bearings in question were specially designed to precisely measure the loads they are carrying at any time, with load cells integrated in their design – inserted beneath the sliding material at one side of each bearing's concave sliding surface. A short cable connects this sensor to the side of the bearing, where an external cable connection point enables the sensor to be integrated into the SHM system.



Figure 6. Construction of the new Orbital Highway in Qatar.



Figure 7. Testing of the load-measuring functionality and performance of a spherical bearing before installation.



Figure 8. One of the SHM system's 14 control boxes and its connection to the spherical bearing above it – with the cable connection point partially hidden by the bearing's rubber dust skirt.

4 MONITORING OF SEISMIC PROTECTION DEVICES SUCH AS DAMPERS AND SHOCK TRANSMISSION UNITS

Like bearings, structural protection devices such as dampers and shock transmission units (STUs) must also perform reliably when required by the structure's design, otherwise the consequences for the structure could be catastrophic – especially when used to protect the structure from seismic ground movements. Dampers must, as the name suggests, dampen large sudden forces or vibrations at a certain point in a structure, reducing the impact on the structure and enabling the structure to respond as designed or even to survive the event without damage. STUs, also known as lock-up devices (LUDs), protect a structure by transmitting sudden forces directly where they can be readily resisted without damage, thus reducing the impact on other, less robust parts of the structure. In order to provide confidence that these critical components remain ready to perform their vital function when the time comes, SHM systems can provide an efficient, cost-effective, round-the-clock solution – especially when the required sensors are pre-integrated in the devices during their fabrication.

4.1 *Case study: STUs of the Halogaland Bridge in Norway*

The Halogaland Bridge is currently being constructed in northern Norway, and will form part of the European Route E6 highway. The suspension bridge will have a main span of length 1.1 km, crossing one of Norway's many fjords. Its design required the installation of Shock Transmission Units (STU) at each of the bridge's towers.

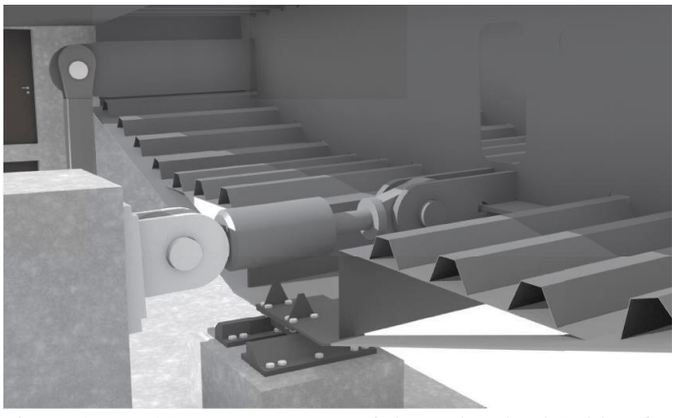


Figure 9. An STU at one tower of the Halogaland Bridge for control of deck movements.

The bridge is a good example of advanced structural engineering, and presented substantial design and construction challenges – and therefore also significant risks. To minimize these risks, it was decided to install an SHM system. Initially, the system is based on measurement of data from the RESTON-STU devices at the towers. A ROBO-CONTROL SHM system was designed to measure the longitudinal movements of the STUs, which have a stroke of +/- 450 mm, and to also measure pressure and temperature inside these hydraulic devices. Each STU is equipped with one sensor for measuring movements, two sensors for measuring oil pressure within the device, and one sensor for measuring internal temperature. All sensors were pre-integrated in the design and fabrication of the STUs before they left the factory, maximizing durability and ensuring reliability. The system measures the pressure inside the STUs at a frequency of 100 Hz, correlating the data against similarly monitored temperature and deck vibration data. This enables STU condition to be checked at any time, and for additional peace of mind, the system is also designed to provide immediate notification should pre-defined threshold values for movement or differential settlement be exceeded. And to enable the actual seismic performance of the STUs to be evaluated following an earthquake, the system also correlates the pressures inside the STUs against recorded seismic data.

The performance of these "smart" STUs is illustrated by the data available from a similar application as shown in Figures 10 and 11. This shows that the devices are sensitive, for example, to vehicles crossing the bridge on which they are installed. The graphs in these figures correlate pressures inside the STUs with deck accelerations during the passage of heavy vehicles. It is interesting to note how one can follow the progress of each vehicle as it crosses the bridge, from the first abutment (shown by STU pressure peaks) to mid-span (shown by acceleration/vibration peaks) and on to the second abutment (shown by further STU pressure peaks). This indicates that the system is working properly and that the STUs are contributing to protecting the structure against external excitations.

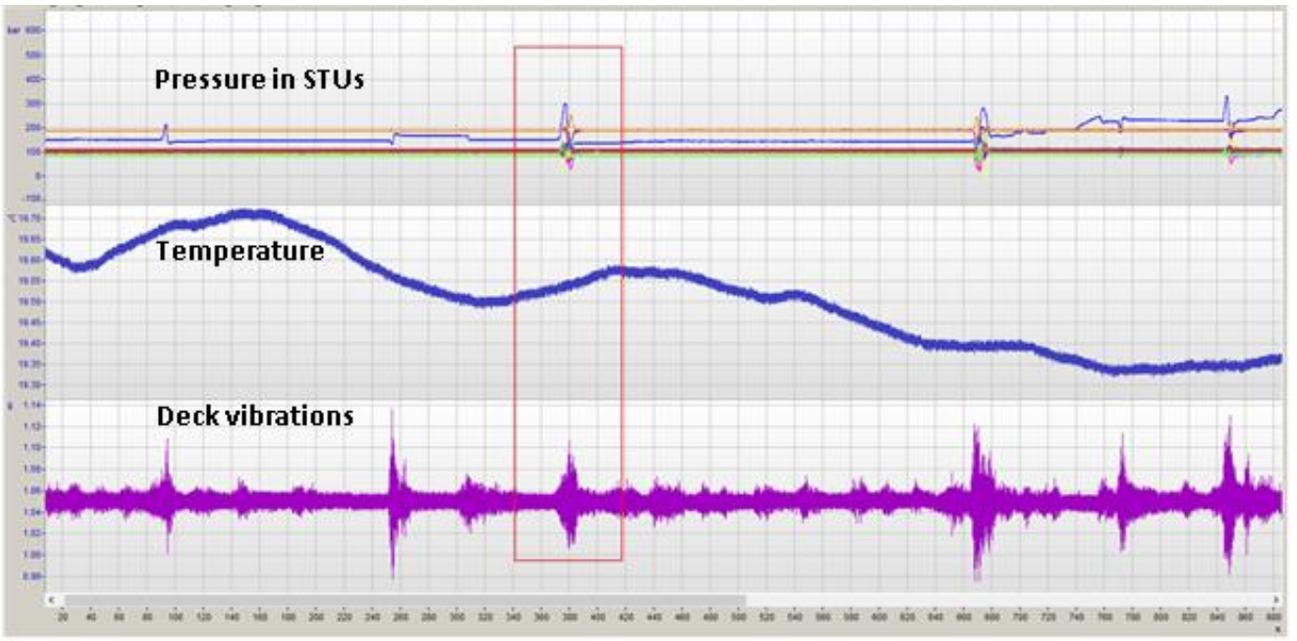


Figure 10. 100 Hz data measurements showing influence of traffic (indicated by deck vibrations) on STUs.

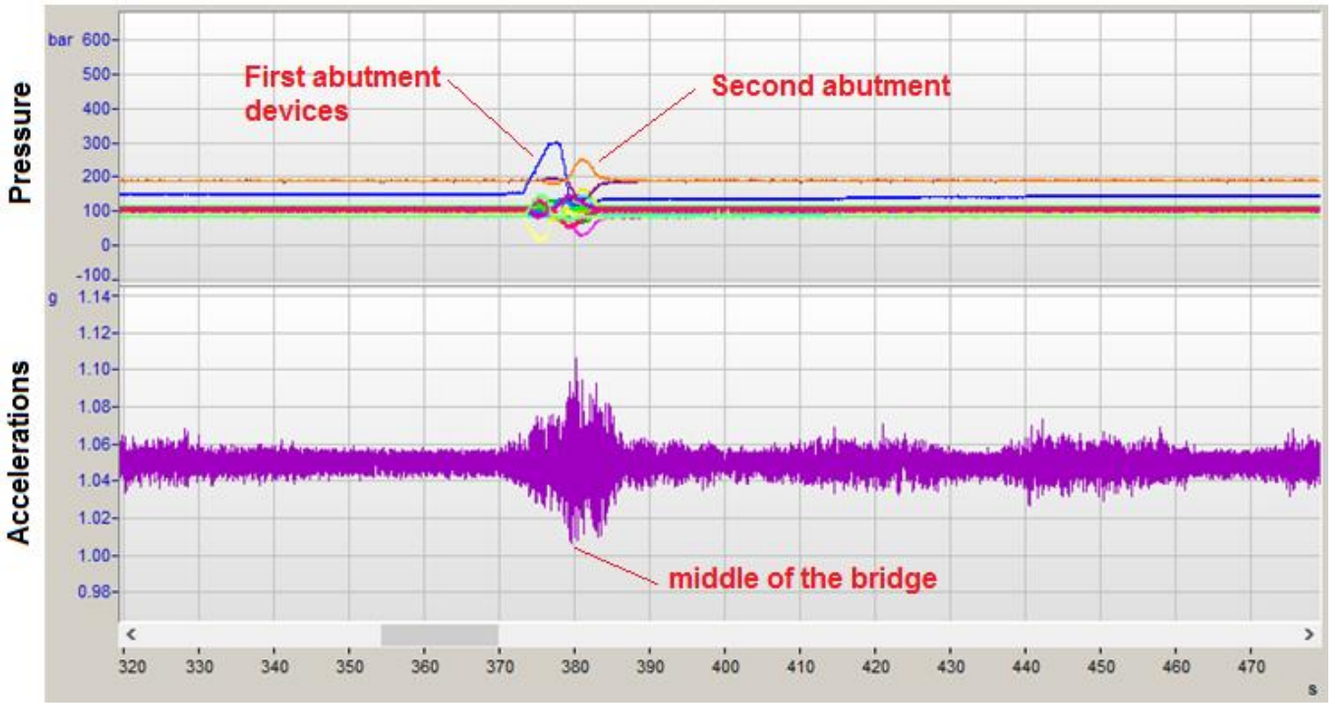


Figure 11. Close-up view of data (extract from Figure 10) showing the correlation of pressure and acceleration during the passage of a single truck.

5 MONITORING OF EXPANSION JOINTS

Although a bridge's expansion joints may not be as central to the structure's strength and stability as its bearings or dampers, the condition and performance of its expansion joints are critically important to a bridge's proper functioning as a transportation link. And given that expansion joints, very often mechanical devices with sliding interfaces, are typically subjected to direct impact loading from traffic millions of times a year, they are generally far more prone to wear and damage, and management of life-cycle costs can benefit enormously from the availability of good information relating to condition and performance (Spuler et al, 2012). Therefore, of all a bridge's key components, it is probably the expansion joints that can benefit most from the sensible use of SHM.

To maximize the benefit that can be gained from such technology, a worldwide supplier of both expansion joints and SHM systems has developed and combined the technologies, so that expansion joints can now be delivered with pre-integrated sensors for connection to a tailored SHM system. Not only that, the data analysis capabilities of the combined system have been greatly developed, based on the high-frequency measurement of structure-borne vibrations. This enables damage or deterioration to be clearly identified based on general testing and teaching of the system. As a result, unexpected damage can be immediately recognized and automatically notified, enabling the timing of replacement of components to be optimised and disruption to service to be minimized.

5.1 *Case study: Large-movement expansion joints of a new bridge*

The Taizhou Yangtze River Bridge (Figure 12), constructed at a cost of USD 400 million and opened in 2012, is the world's longest-span bridge of its type: The three-tower suspension bridge, with two main spans of 1,080 m each and side spans of 390 m, crosses the Yangtze River where it has a width of 2.1 km. The ambitious construction project represented the first attempt to create a long-span multi-tower suspension bridge.

This extraordinary bridge required some extraordinary key components such as the expansion joints which accommodate deck movements while providing a driving surface for traffic. Modular joints with 18 gaps each (able to facilitate 1440mm of longitudinal movement) were installed at each end of the deck (Figure 13).

An SHM system was installed on the bridge to provide the type of data that is likely to be of interest to the owner of any exceptional structure. The basic system measures and records the movements and rotations of the deck at the expansion joints, and thus gives a valuable impression of the performance of the structure, enabling the need for maintenance or adaptation work to be quickly identified and planned.



Figure 12. The Taizhou Yangtze River Bridge.



Figure 13. One of the Taizhou Yangtze River Bridge's enormous 18-gap modular expansion joints, viewed from below.

To maximize in particular the system's ability to monitor the condition and performance of the expansion joints, the above-mentioned newly developed technology was applied. By recording movements, inclinations, temperature and structure-borne vibrations at a frequency of 25.6 kHz, even very tiny changes in the joint or its performance can be detected and visually represented by changes in a curve on a graph. This will enable any sudden damage or deterioration to be immediately detected, based on testing and "teaching" of the system.

As a first step, many artificial failures were created simulating damages. This was done by temporarily removing stirrups which form sliding connections between the lamella beams at the joint's surface and the support bars beneath (see Figure 14). High-accuracy accelerometers and ultrasonic displacement sensors (Figure 15) were then used to evaluate the effects of these "failures" on the movements of specific elements, giving the system the data it needed to "learn" what data might be significant in terms of damage detection.



Figure 14. An accelerometer at the location of a temporarily removed stirrup during fault simulation and measurement of resulting vibrations and modal analysis.



Figure 15. An ultrasonic displacement sensor.

In service, the system sends data to a remote server, including daily records of vibrations due to heavy traffic together with the associated modal frequencies. If established limits which might indicate the occurrence of damage are exceeded, an alarm notification is sent by email and also appears on the system's web interface, prompting a site inspection. As a result of the system's ability to automatically consider such information, therefore, planning of maintenance activities in general, and the timing of replacement of components in particular, can be optimized.

The graphs presented in Figure 16 show acceleration data since the system was installed, with data from each of three selected joist beams (also known as support bars, which span the bridge movement gap, supporting the joint's steel surface beams). The graphs indicate a pre-defined limit of 20 m/s^2 (shown by red lines). Should a measured value exceed that limit, this could be a sign of a problem and so the SHM system is designed to send an alarm email to notify the responsible engineers. (The small number of data points above this limit were established to be no cause for concern, e.g. due to road works on the bridge.)

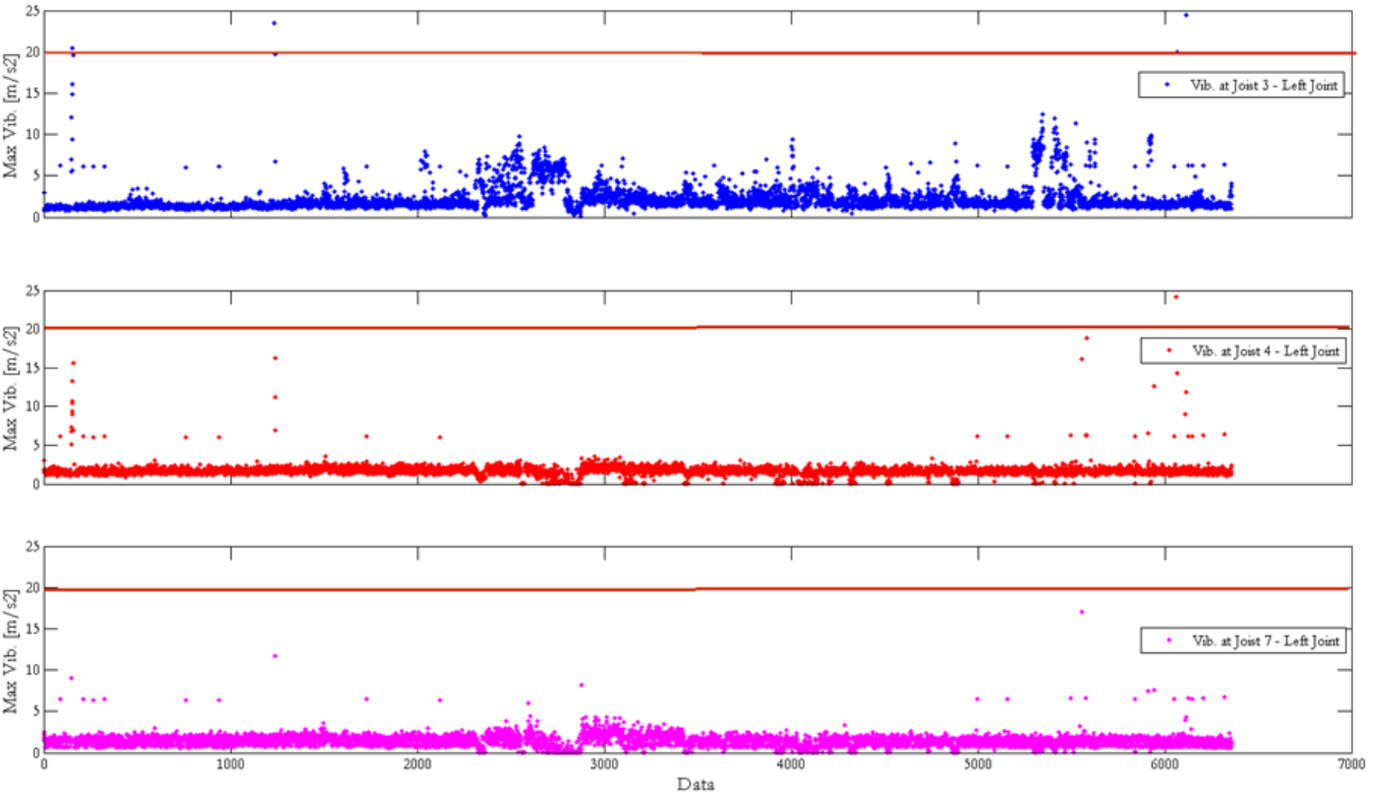


Figure 16. Acceleration data since the system was installed, with data from three of the expansion joint's joist beams. The graphs indicate a pre-defined limit of 20 m/s2 (shown by red lines), above which alarm messages are sent to the responsible emgineers.

6 CONCLUSIONS

The integration of SHM systems in key components (bearings, expansion joints and seismic protection devices) of bridges and other structures can offer great benefits to their asset management programs. Such systems can efficiently provide data required for almost any purpose, at any stage of a structure's life cycle.

In the case of expansion joints, in fact, the technology has already been brought another step forward, with the SHM system designed to clearly identify component damage based on general testing and teaching of the system. This enables any unexpected behaviour of the component (or the bridge) to be immediately recognised and notified, thus enabling the timing of component replacement, or other maintenance/repair work, to be optimised. With similar developments being planned for bearings and dampers, making them yet smarter and more efficient and useful in the construction, inspection, maintenance and renovation of structures, the potential benefits of the use of SHM technology in bridge asset management programmes continue to grow.

REFERENCES

Islami, K. & Modena, C. 2013. Life-cycle assessment by dynamic diagnosis and long term monitoring of old bridges in northeastern Italy. *Proc. 6th International Conference on Structural Health Monitoring of Intelligent Infrastructure (SHMII)*. Hong Kong.

Moor, G. Islami, K. & Meng, N. 2014. Construction and maintenance of bridges – the contribution of automated monitoring. *Proc. 9th International Conference on Short and Medium Span Bridges*, Calgary, Canada.

Spuler, T., Loehrer, R. & O'Suilleabhain, C. 2012. Life-cycle considerations in the selection and use of bridge expansion joints. *Proc. 18th IABSE Congress*, Seoul, South Korea.

SS18: Challenges for bridge technology implementation and management in developing countries

Organizers: T.N. Bittencourt, M.A. Valenzuela, F.C. Carrizo & M. Márquez

Maintenance, Safety, Risk, Management and Life-Cycle Performance of Bridges – Powers, Frangopol, Al-Mahaidi & Caprani (Eds)
© 2018 Taylor & Francis Group, London, ISBN 978-1-138-73045-8

Maintenance Plan Proposal on Cable-Stayed Bridge: Application to Yelcho Bridge

M. Márquez, J. Campusano, F. Hernández & J. Errazuriz
Ministerio de Obras Publicas, Santiago, Chile

M.A. Valenzuela
Pontificia Universidad Católica de Valparaíso, Valparaíso, Chile

ABSTRACT: The Yelcho Bridge is the only road cable-stayed bridge that has been built in Chile. The bridge is located in the mouth of the Yelcho Lake and it ensures the continuity of Route 7 (called Carretera Austral) in the Palena Province, Los Lagos Region, being a strategic point for the network road of Chile.
The bridge, in service since 1990, has a total length of 250 m with a central span of 150 m and two lateral spans of 50 m each one.
No maintenance programs have been conducted on the bridge since it became operational (27 years). However, it is estimated that the increase in its live load demand is causing a decrease in resistance due to fatigue.
The present paper provides studies conducted by the Roads Department, in order to structurally analyze the Bridge and assess its behavior related to the current design loads, including a study of its current state of stress, and visual inspections carried out.
The procedures of the study will be the basis for a maintenance plan proposal for cable-stayed bridges in Chile. The goal is to deliver a procedure to improve the management and maintenance of bridges, through preventive inspections focused on the detection of the main pathologies, and repair and reinforcement programs for this bridge typology.
The results of these activities will be included in the new version of the Road Manual–a code that provides guidelines for the design, construction and maintenance of bridges in Chile–as part of the philosophy of the life cycle of the structure.

1 INTRODUCTION

The Yelcho Bridge is the only cable-stayed bridge ever built in Chile (Figure 1). It is located in the Palena Province, Los Lagos Region, 47 km south of Chaiten. The structure is built over the outlet of Lake Yelcho, ensuring the continuity of Route 7 (also called the *Carretera Austral*).



Figure 1 - General overview of Yelcho Bridge (2016)

From the year it was built (1990), the bridge has been periodically visited for visual inspection. However, the Highways Manual of the National Roads Department, vol. 7, indicates that routine inspections must be conducted annually for singular bridges, such as cable-stayed bridges.

The Yelcho Bridge requires an assessment of its structure and its performance toward current design loads in regards to its current state of stress. This need arises from the elapsed time since the construction of the bridge construction, possible problems caused by an increase in the mechanical load demand due to increased weight of truck loads, and the reduction of resistance due to structural fatigue caused by the increased frequency of these loads, all of which affects the structural capacity of the bridge.

Compounding the issue, the National Roads Department is conducting a paving project for Route 7, which begins at one of the bridge access points. This means that once both of its access points are paved, the traffic speed on the bridge will go up, and thus increase the dynamic condition of the vehicular impact on the deck, including vibration and impact.

Furthermore, the environmental conditions at the bridge location are humid due to torrential rains and low temperatures during winter (freeze-thaw cycles are possible).

2 WORK DESCRIPTION

The bridge has a total length of 250 m, with a central span 150 m long and two side spans, each 50 m long.

The structure has two open-type abutments and two pylons. For their foundations, both the pylons and the abutments have pre-excavated, reinforced concrete, 1 m thick piles with anchor pier. Each abutment has eight piles, while each pylon has ten piles.

The deck is made of reinforced concrete and has a total width of 6.7 m, with a road 5 m wide, no walkways, and lateral ribs where the cables are anchored. The deck is longitudinally post-tensioned and braced by cables. There are steel barriers on both sides of the road.

The width of the road allows traffic to flow in only one direction at a time.

Near the abutment, the deck is transversally and vertically post-tensioned high elastic limit steel bars. This vertical mounting structurally compensates for the length difference of the side spans (50 m) in relation to the main span (150 m).

The cables are made of high-resistance, 36 mm thick, steel bars anchored to the top of two reinforced concrete pylons. In total, there are 112 cables (28x8) with a minimum breaking load of Fu= 10500 kg/cm2 and a yield limit of Fy = 8500 kg/cm2.

Protection of the cables achieved by injecting grout in the anchor area (in both the deck and the pylon) and painting the free extension (free length) of the anchors with three layers of epoxy paint.

To give the cables continuity, the bars are joined using mechanical couplers with an anticorrosion system made of thermo-retractile sleeves.

Near the deck, the steel bar cable is protected with a tamper-proof tube extending up to approximately 1.80 m over the level of the deck. The top is capped with an elastomeric seal cap, so as to protect the tube from water; past the seal, the cable is exposed for the rest of its free length, protected only by epoxy paint.

Near the pylon, the steel bars reach the upper anchor through a formwork metal tube.

The cables have a fan design, as they are similarly anchored to the upper crosspiece of the pylon (Figure 2).



Figure 2 - General overview of a pylon of Yelcho Bridge (2016)

The configuration of the lower zone of the cable is composed of the following elements:

- Formwork tube
- Grout pipe
- First support plate (embedded plate), welded to the formwork tube
- Second support plate (main plate), welded to the grout pipe
- Bar
- Ball nut
- Seal cap to protect the ball nut and grout injection

The pylons are 43 m high and made of reinforced concrete. They are composed of two legs in an H shape, braced together by two horizontal crosspieces: one is level with the underside of the deck and the other is at the top of the pylon. Additionally, there is a cross bracing at mid-height.

The pylons have post-tensioning bars in some sections.

Anchoring of the deck to the abutments is achieved through tensioning of high-strength steel bars. Each abutment has six bars for this purpose.

Each anchor has the following elements:

- High-strength bar with a diameter of 36 mm.
- Anchor plate and nut protected by an anti-corrosion seal at each end.
- Tube with a diameter of 80 mm, injected with an anticorrosion protection, to protect the anchor bar through the deck and in its last meter, in which the bar is embedded into the abutment.
- Tube with a diameter of 160 mm covering the 36 mm anchor bar to protect it from the support table of the abutment to one meter before the end of the lower anchor block (lower anchor plate and nut). The diameter of the tube allows horizontal movements relative to the deck and the abutment.

Each pylon is post-tensioned at the area of the upper crosspiece with high-strength 36 mm steel bars, both transversally and longitudinally. There are 11 transversal bars and 12 longitudinal bars.

The measurements of the abutment and pier supports differ from each other, as is shown below:

- Abutment vertical supports: 360x460x120 mm
- Pylon vertical supports: 350x460x90 mm
- Pylon and abutment longitudinal stops: 280x280x30 mm
- Pylon lateral supports: 280x280x30 mm

The finger joints provide the continuity between the abutment and the deck. No plans of this element exist.

Both riverbanks have protection gabions at each pylon. Likewise, the front of each abutment also has this type of element.

3 CURRENT SITUATION

To this date, very few records of the project (only some plan sheets) and the construction stage exist.

Gathered from assessing the visual inspection reports of the Yelcho Bridge from 2004, 2010 and 2016, the main observed pathologies of the elements of the structure are listed below:

3.1 *Concrete Elements*

Overall, the concrete throughout the structure shows no severe pathologies at first sight.

No important or large cracks or fissures, great loss of coating of the rebar, flaking, signs of corrosion on the rebar, or efflorescence were detected.

However, most of the concrete elements exposed to rainfall show large concentrations of moss, especially in extensive parts of the deck.

At certain places, concrete was found to be eroded by the constant flow of water in pylon crosspieces and abutments.

3.2 *Pylons*

Both legs of the pylon show more exposure to rainfall and wind on their upstream face. Due to the permanent humidity, moss was observed in all construction joints.

Many parts of the concrete show signs of erosion, particularly the lower crosspiece of the pylon, where the longitudinal stops and neoprene supports are located, due to the constant flow of rainwater.

3.3 *Abutments*

The area surrounding the abutments is partially covered by vegetation and dirt, hindering access to these elements and hampering their inspection (Figure 3). The concrete is covered by vegetation and moss.



Figure 3 - Abutment of Yelcho Bridge (2016).

The lack of elements meant to catch the water at the expansion joints causes all the rainwater that flows to the joints to run toward the support tables of the abutment or, in the case of the north abutment, to the back of the backwall.

3.4 *Deck*

Just as the rest of the structure, the deck is subjected to adverse climate conditions, especially high humidity (Figure 4). These conditions encourage the growth

of moss and vegetation along the deck, mainly on the sides next to the exit of the cables.

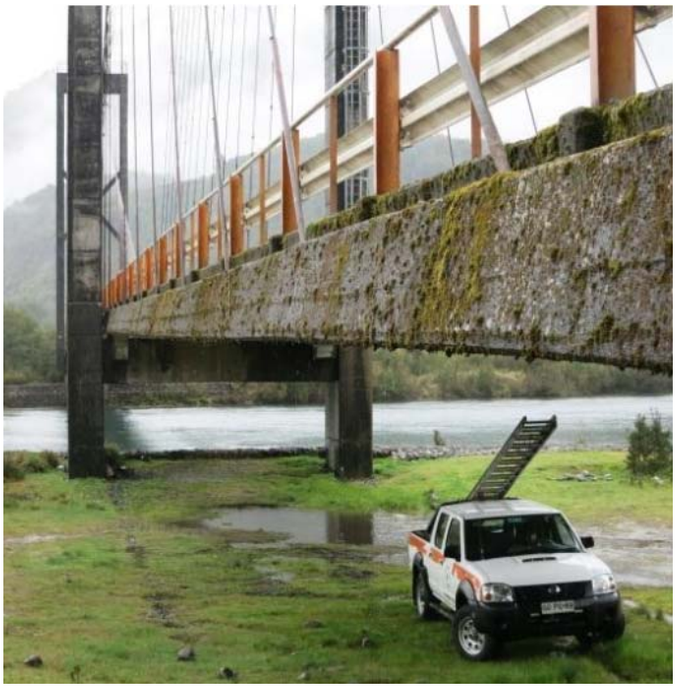


Figure 4 - Deck of Yelcho Bridge (2016).

Exposed rebar was observed, as well as corrosion on the elements that act as longitudinal stops.

A large amount of mud and dirt gathers on the road, obstructing the drainage holes and redirects the water to the expansion joints (because of the curved geometry of the deck). The drainage holes were found to be blocked.

On the underside of the deck, the localized damage was spotted in the areas where provisional anchors were installed as part of the construction method.

3.5 *Lower cable anchor*

Metal support plates were observed to have section loss, pitting in the steel, loss of anticorrosion protection, and rust on large part of the surface (Figure 5).



Figure 5 - Lower anchor of Yelcho Bridge (2016)

At one of the cables, the support plate is rotated.

Loss of anticorrosion protection was observed in both the injection cap and the overlength of the cable.

The wet areas of the plate show signs of advanced corrosion, loss of protection, and section loss in most cases (Figure 6).



Figure 6 - Lower anchor of Yelcho Bridge (2016)

3.6 *Cable recess tube*

On the tubes whose exit was not covered by vegetation, the seal was found to be damaged, letting water through.

3.7 *Cable tamper-proof tube*

The failure of the sealing system at the end of the tamper-proof tube (partial or total failure of the seal) allows water to flow freely into the tube, filling it (Figure 7).



Figure 7 – a Tamper-proof tube of Yelcho Bridge (2016).

Abnormal noises can be heard when the bars are manually shaken; however, these noises can also be caused by relative movements and/or bumping, none of which is ideal for the cables and can indicate a severe problem in the element.

The lack of a seal also enables the bar to move freely inside the tube. As the bars vibrate, they come into contact with the tube. This phenomenon might lead to a brittle rupture of the cable bars.

When it comes to the tube itself, all of them show a deterioration of their anti-corrosion protection. Several of the tubes were observed to have section loss in their upper end, due to the combined action of corrosion and constant bumping with the bar.

The anticorrosion bar protection system was originally composed of:

• Several layers of paint along the whole bar (estimated at three layers, which would be the standard for a steel protection paint system).
• Grout injection between the protection tube and the lower span of the bar.
• Injection cap to cover the spherical nut and part of the bar's over length. The exact makeup of the material injected is unknown, but reports at the time refer to it as concrete grout.

In the accessible part of the bars (from the end of the tamper-proof tube), many show signs of advanced degradation of their anticorrosion paint (Figure 8). The external pain layer has mostly flaked off, and the inner layers show damage as well, leaving the steel bars exposed–the steel already shows signs of surface corrosion. Around these areas, the paint seems to flake off, letting water bleed in between paint layers and the steel underneath.



Figure 8 - Loss of protection on the cables (2016).

The bar spans are directly exposed to rainwater, encouraging corrosion on the steel (which can already be observed) and threatening with possible section loss and strength reduction of the bars.

3.8 *Load on the cables*

When shaking the bars manually, several cables were found to be bearing a low load (low-frequency vibration and low damping). This can even be observed when heavy vehicles run through the bridge.

Important differences have been detected in the vibration frequency of the cables, predicting that some of the cables might be bearing a very low load (Figure 9).



Figure 9 - Cable arragement on Yelcho Bridge (2016).

Two of the cables were found to be particularly overloaded. This is confirmed by the deck profile, which shows an abnormal high point near the cables.

3.9 *Cable couplings*

In those cases, where the couplings can be visually inspected from the deck of the bridge, detachment at the ends of some thermo-retractile sleeves was observed.

3.10 *Neoprene Bearing Supports*

The structure has two neoprene vertical supports in each abutment and pylon. Furthermore, each pylon and abutment has two lateral stops and two longitudinal stops. The neoprene parts of the support systems generally appear to be in good condition.

At the abutment, the plates and part of the neoprene are covered by vegetation. The anticorrosion protection of the steel plates is in good condition. There are only some localized signs of early surface corrosion. Some deformation toward the center of the span can be observed, stemming from possible movements of the deck that were unforeseen during planning.

The lateral and longitudinal stops are simply vulcanized to a steel plate. This plate has four screws that anchor it to the concrete pylon. The screws and steel plate all show early signs of localized surface corrosion.

The lateral stops make contact with the deck through an embedded steel plate. As a consequence, they are no longer centered on the steel plates anchored to the deck (Figure 10). In the south pylon, the stops reached the edge of the plate without running off it, while the neoprene of the two lateral stops in the north pylon is approximately 2 cm off the steel plate, to the south (middle of the span).



Figure 10 - Lateral stops of Yelcho Bridge (2016).

The vertical supports of the deck are deformed toward the middle of the span, as a consequence of the rheological effects of the concrete of the deck.

3.11 *Abutment vertical bars*

The lower anchor of the abutment vertical bars is located in a caisson filled with a corrosion inhibitor.

However, the design might allow the water to penetrate into the lower anchor zone, behind the support plate. The quality of the sealing of the caisson containing the lower anchors is unknown.

This area is inaccessible, so it is not possible to ascertain the condition of the corrosion inhibitor or its type (petroleum derivate, concrete grout, etc.). In any case, the configuration of these bars and the movement they have suffered due to the rheological effects (movements observed in the supports) imply that the anticorrosion protection lost their adherence to their vertical bars, allowing water to seep into the space between both of them and into the caisson, encouraging corrosion.

It is also impossible to access the upper anchor of the bars, as they are encased under the pavement.

Chances are high that there is water in the formwork tubes and the lower caisson.

3.12 *Expansion Joints*

Both expansion joints -south and north- have no elements between the deck and the abutment to allow the drainage of rainwater.

In the south joint, gravel and asphalt can be found between the serrations of the joint.

In the north joint, dirt and vegetation buildup can be found in its ends. Water collects between the two modules of the joint (Figure 11). It runs to the open space behind the backwall of the abutment and from there, to the support table of the abutment, dragging detritus.



Figure 11 – Expansion joint condition (2016).

3.13 *Accessibility to the top of the pylons*

Access to the upper part of the pylons is granted by a cat ladder attached to the pylon (Figure 12).



Figure 12 - Access stairs to the top of the pylons (2016).

This ladder does not start at ground level, but rather at the same height as the deck of the bridge. In order to reach the ladder, an additional ladder is required, to be placed on the ground below. At the start of one of the ladders, some metal elements were noted to be loose. The current system (cat ladder) does not guarantee safe access, as there are some bolts missing from the safety cage.

From the deck, the safety rail guards installed on top of the pylons can be noted to be deficient, missing safety elements.

Because of this, access elements need improvement, as do the safety levels, to facilitate more in-depth future inspections and routine maintenance work.

4 DIAGNOSIS STUDY

Due to the current state of the Yelcho Bridge, the National Roads Department faces new challenges in relation to future work on structural maintenance.

With this in consideration, a study was conducted with the main objective of determining the structural capacity of the Yelcho Bridge. It seeks to determine its current state and the stresses in the main structural elements.

To this end, an assessment of the available records is conducted (plans, construction records, visual inspection reports) and additional information is gathered through detailed inspections. The information gathered is the base to conduct the structural assessment of the bridge and its elements, aiming to determine quantitatively and qualitatively its current situation.

4.1 *Description of the tasks to be conducted*

The diagnosis study consists of five stages. These have the final aim of determining the current situation of the structure and the future operations required to bring it up to better standards. Personnel trained in these types of structures and works is required to this end.

Stage 1 consists of the collection and assessment of the available records, including existing plans, relevant information on bridges of similar typologies, previous inspection reports, and field inspections. This is achieved by conducting visual reconnoitering of the structure in order to generate records of possible pathologies in the infrastructure and superstructure, taking into account relevant aspects of the materiality of the elements.

Stage 2 covers different levels of inspection, conducting general and detailed inspections with the required support tools. For this, complementary safety works must be generated in order to guarantee an optimal work on the structure. This activity covers the following areas: structural, road safety, and material engineering. Special studies are closely related to the different levels of inspection. Furthermore, after gath-

ering the information, a structural assessment is conducted to determine the original conditions of the bridge, considering the geometric and materiality characteristics of the elements. The axial forces on the cables in their initial construction condition are calculated, considering the weight of the bridge, the complementary dead loads and the tensile forces. This is then contrasted with the stresses calculated experimentally during stage 3.

Stage 3 has two main objectives: the first is to complement the available records from a geometric perspective through a topographic survey, respecting the technical dispositions given by the Highways Manual. After the information has been gathered, the second objective is to measure the stresses of the cables, for which non-destructive trials can be conducted by using hydraulic jacks, the vibrating string method, or a combination of both. The trials plan will be backed by bibliographic articles and the existing international experience on similar projects.

In stage 4, a structural model is generated through a finite-element program that is appropriate for cable-stayed bridges. The assessment is focused on determining the current conditions of the bridge, taking into account the geometric characteristics of the elements and the records gathered. For the initial stresses of the cables, the stresses experimentally calculated during stage 3 are used, as well as the available records, trials, and inspections conducted.

In stage 5, a final report is created, which summarizes the main milestones reached during the study, considering conclusions of the work conducted and suggestions regarding future operations on the structure.

5 CONCLUSIONS

Singular bridges, such as cable-stayed bridges, must receive constant inspections throughout their operational lifespan. The Highways Manual of the National Roads Department indicates that these inspections must be conducted once a year.

Modern Bridge Maintenance Management Systems, that include both traditional and singular bridges, are required. These must allow users to have access to a structure inventory and to record the whole life cycle of the bridge.

Singular bridges require that maintenance aspects be studied from their design onward, so as to allow the structure to be inspected completely and to easily replace its elements.

It is recommended that singular bridges include instrumentation tools to facilitate constant monitoring of the structure.

Chilean engineering does not have much experience in the design, construction, and maintenance of singular bridges. The previous implies that constant improvement and training of the specialized professionals is necessary at both public and private levels, in order to acquire the necessary knowledge.

The general inspection plan proposed to cable-stayed bridges has to include at least:

Concrete elements: check cracks and degradation

Pylon: inclination and cracks/corrosion

Abutments: cleaning area and support conditions

Expansion joints and bearing conditions

Cables: load capacity / stress, water accumulation, check lower anchor and drainage system. Verify the sealing system.

General Scheme: vibration and deformation.

A 3D model with a construction process is recommended carried out and also include the structure in a BIM system of the road network.

6 REFERENCES

Mondorf, P. (2010), Informe de visita al Puente Yelcho, Informe Técnico, Dirección de Vialidad, MOP, Puerto Montt, Chile.

Márquez, M. (2016), Informe de visita al Puente Yelcho, Informe Técnico, Dirección de Vialidad, MOP, Santiago, Chile.

Dirección de Vialidad (2017), Manual de Carreteras, Santiago, Chile.

Maintenance, Safety, Risk, Management and Life-Cycle Performance of Bridges – Powers, Frangopol, Al-Mahaidi & Caprani (Eds)
© 2018 Taylor & Francis Group, London, ISBN 978-1-138-73045-8

Management Systems for Inspection and Maintenance of Chilean Road Bridges

M. Márquez
Ministerio de Obras Públicas, Santiago, Chile

M.A. Valenzuela
Pontificia Universidad Católica de Valparaíso, Valparaíso, Chile

G. Arias & M. Pertierra
INES Ingenieros Consultores, Madrid, España

C. Sepulveda
Consorcio STRADALE-GAUSS, Santiago, Chile

ABSTRACT: Chile has a great heritage in road bridges, so it is necessary for the National Road Department to have a Management System for the maintenance of bridges, keeping up with best practices in developed countries.

Although there have been some regional initiatives in this area, in the vast majority of cases maintenance plans are based on professional experience, evaluating the performance of the bridges either through the Bridges Department or the Regional Road Departments. These plans mainly consider the maintenance of traditional bridges (composed of concrete - steel beams, concrete slab, concrete pillars, pillars and direct or deep foundations).

However, the development of bridge engineering in Chile has introduced new structural typologies such as cable-stayed bridges, suspension bridges, arch bridges, among others.

For that reason, the authorities of the National Road Department, aware of the importance of carrying out a diagnosis of their bridges, decide to implement at the national level a Management System for the Conservation of Bridges.

The article presents a proposal of this System for both traditional and singular bridges whose objective is to provide the National Road Department with a tool to improve the management and conservation of bridges through preventive inspections focused on the detection of major pathologies and on strengthening future maintenance programs, optimizing the behavior of bridges and the allocation of resources. The System allows the conduction of the inventory and condition inspection of the bridges, using then logical algorithms to obtain the severity index of the bridges,while it modernizes the data collection and its subsequent consultation and exploitation, using a web application to facilitate the access to information.

1 INTRODUCTION

Within the national road network, there are approximately 9,000 structures, of which 7,150 are bridges or grade-separated crossings; these are broadly distributed as follows:

Table 1 - Bridge typology distribution

Infrastructure	Girder	Slab	Bridges (#)	%
C	C	C	1800	25
C	S	C	1200	17
C	S	T	1300	18
C	T	T	1000	14
S	S	T	600	8
T	T	T	1250	17

* C: Concrete; S: Steel; T:Timber

Traditionally, bridge maintenance policy in Chile has had a reactive focus rather than a preventive one. Planning of maintenance and preservation activities are mostly aimed at repairing existing defects, and not so much at preventing their apparition. To date, there have been some initiatives within the Ministry of Public Works (MOP) that have sought to establish a Bridge Maintenance Management System, among which the following can be found:

- Manual for Maintenance Inspection of Bridges (1993), Cooperation Agreement between Japan International Cooperation Agency (JICA) and the National Roads Department [2].
- Manual for the Condition Inspection of Bridges and Structures (2007), Concession Unit of Public Works. [3]
- Manual for Survey and Diagnosis of Bridges (2012), Los Lagos Regional Roads Department. [4]
- Manual for Visual Inspection of Bridges (2013), Los Rios Regional Roads Department. [5]

According to this philosophy, bridge maintenance management in the country began with a cabinet study of the available technical records and with the identification of serious pathologies. By using some basic inspection guidelines and the particular knowledge of experts in the area, a report was created, describing the observed pathologies and the measures needed to correct them. Sometimes, when the geometric and functional characteristics of the bridge required it, inspections would be carried out supported by the Inspection Truck of the Bridge Department.

Once the technical evaluation of the observed damages and their classification according to severity was performed, the technical sheet provided in the Highways Manual was added to the national repair/rehabilitation priority program, setting the costs associated with these activities.

The National Roads Department has granted Stradale-Gauss Consortium Ltd. a contract to establish a Bridge Management System. The objective of this commission is to establish a well-organized system that focuses on preventive maintenance and anticipation of damages, in order to reduce the costs and risks associated to bridge maintenance, using databases with real and up-to-date information on the condition of structures along the national road network. To develop this project, the consortium hired INES Consultant Engineers. In order to complete this task, the team has performed an inventory survey and field visual inspection of 1,034 bridges, with total length over 30 meters and no structural timber components.

With this project, the National Roads Department seeks to automate, speed up and organize the information management, standardize inspection criteria, systematically update databases, and plan bridge conservation programs adequately; the expected result is to have a practical tool for maintenance management and future decision-making.

2 PRINCIPLES OF THE BRIDGE MANAGEMENT SYSTEM

The bridge management tool that the consultant developed for the National Roads Department of the Ministry of Public Works allows its users to manage all the information related to inventory, inspection, conservation, maintenance, and monitoring of bridges along the road network under the National Roads Department, achieving a agile and effective management of the conservation of these structures.

This tool is formally framed in the international standards for Asset Management, more precisely ISO 55000:2014, which is organized around five fundamental pillars: proper knowledge of the assets, consideration for the global organization and planning strategy, adaptation of the organizational and HR structure, close and bidirectional relations with stakeholders, and proper risk management during the whole lifecycle of the bridges.

The key objectives of Asset Management in general, and the Bridge Management System developed by the National Roads Department in particular, are as follow:

- Efficient management of historical and real information linked to each bridge.
- Global assessment of the bridge based on the damages observed during field inspections.
- Prioritization of the required maintenance interventions.
- Estimation of costs related to the maintenance interventions to be implemented.
- Short- and mid-term planning for repair and maintenance activities.
- Design of short-term maintenance strategies.

Below (Figure 1), the functional diagram developed for the Bridge Management System is presented:

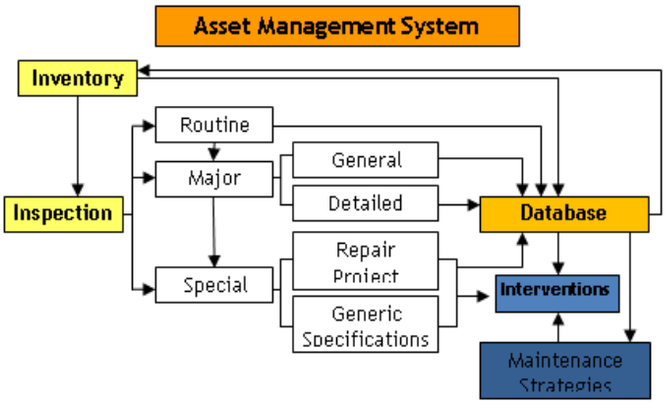


Figure 1 - Diagram of the Assets Management System ([18], 2015)

1

Every Asset Management System starts by having a proper knowledge of the assets. Management of the information associated with each asset, then, becomes the cornerstone of the system. On one hand, there is an attempt to collate and compile the available records, existing information, and historical data; and on the other hand, to collect and archive the inventory and current condition data into the system.

The first task is not free of challenges, as historical information tends to be scarce and scattered among different institutions (National Roads Department, Regional Departments, private companies involved in the corresponding projects, etc.). However, it is vital to understand the history of each bridge from its conception to the current date, so as to predict the evolution of its damages and to estimate its future maintenance needs. In this regard, the Management System developed is able to log all of the existing records to

make a perfectly structured and organized database that collects all related documents from the original plan of the structure to the subsequent reports of maintenance and conservation operations and completed inspections, records of plans and images linked to the structure, or any other information of any format that might be relevant. The Design Standards that have been used historically are also particularly relevant, as they can help estimate the design load used based onthe age of the bridges.

The second task to get a good knowledge base of the bridges to be managed is the implementation of a full inventory. The inventory survey begins with a cabinet phase, during which all descriptive data on the bridge—general, geometric and structure material data, obtained from existing plans and information—are entered into the Bridge Management System. Afterward, field campaigns are undertaken in order to contrast and update the information entered into the system. Lastly, and once the data on each bridge is confirmed in the field, the inventories are updated in the Management System through the cabinet (Figure 2).

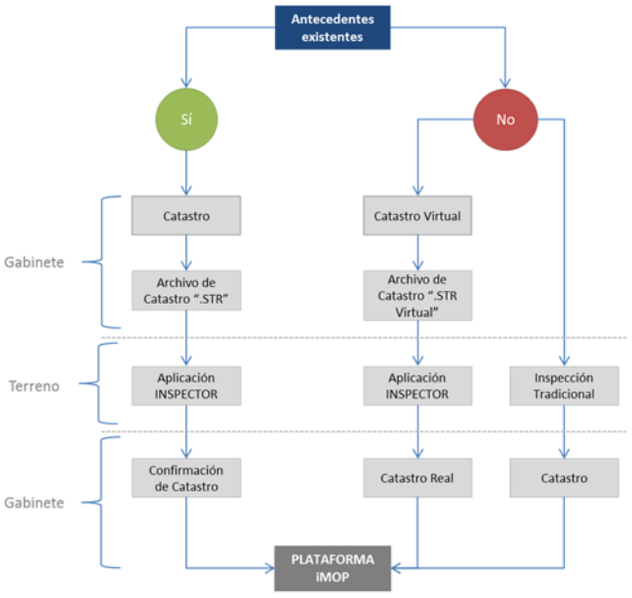


Figure 2 - Implementation of the inventory ([18], 2016)

Just as it will be explained in the following sections, the Bridge Management System that has been developed allows the inventory data to be recorded through a series of sheets to describe any element of the bridges, regardless of their typology. The aforementioned sheets collect anything from general data to functionality data, general structure description, and detailed inventory data.

In order to describe a bridge properly, the methodology that has been developed breaks down each bridge into the different elements that comprise it, according to a series of levels as shown in Figure 3. This outline is essential, as it then enables the user to associate the damages observed during field inspections to specific units of the bridge.

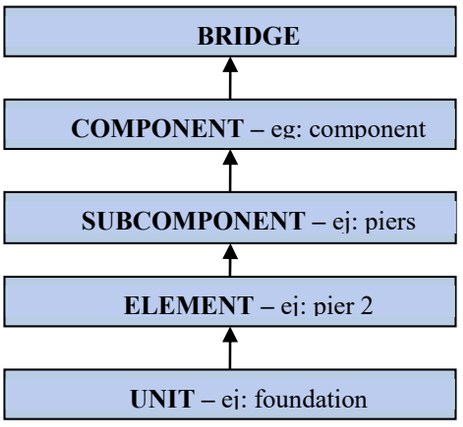


Figure 3 - Relational diagram of the parts of a bridge [19], 2016)2

The methodology developed establishes and collects in the corresponding manuals the criteria to identify the different parts of a bridge (Figure 4), so as to provide homogeneous criteria to the field teams developing the inventories.

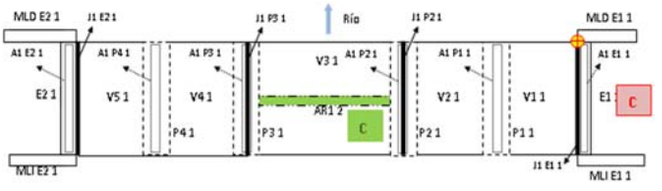


Figure 4 - Diagram of components/subcomponents of an Archtypology bridge (20, 2016)3

As shown in Figure 1, once assets have been inventoried or surveyed, an inspection campaign must be conducted to help determine their current conservation state. Regarding structure maintenance, three levels of inspection are broadly established: basic, major (itself divided into general or detailed, depending on whether auxiliary means of access are used or not), and special.

Basic Inspections are visual that can be conducted by non-specialist personnel are directed toward early detection of any damage that might require urgent intervention. Major Inspections are also visual, but they are conducted by specialist technical personnel, preferably knowledgeable in structural calculations and structural pathologies. Therefore, this kind of inspection is aimed at gathering information on every damage of the structure, specifying which bridge unit is affected by the damage, assigning a cause to each one, and indicating its extension and severity. Finally, Special Inspections are conducted by highly-trained technical personnel, who take additional steps (sam-

pling, trials, estimations, inspections conducted by divers or climbers, etc.) required to obtain all necessary information to assess the state of the structure and define the operations that must take place.

The methodology accompanying the Bridge Management System is based on the regular conduction of basic and major inspections, planned according to the maintenance strategy and whose frequency will be determined by the structure importance, which itself depends, among other factors, on the bridge typology and its conservation condition. Special inspections will be conducted only when it is impossible to assess the damages of a structure through major inspections.

To conduct visual inspections of the structures, the Bridge Management System developed sets some objective criteria so as to standardize the identification and assessment methodology of the existing damages.

Eliminating the inspectors' subjectivity and standardizing inspection results across the country is vital to gathering trustworthy data for the system to calculate the condition score of a structure; as based on the faults identified during inspection; the element it affects; and its extent, severity and cause, the system generates a score of the condition of the structure through an algorithm proposed by the consultant.

This score ranges between 0 and 100 points, as shown in Table 2 below, and it is the basis for the prioritization of the proposed maintenance intervention.

Table 2 - Global Condition Score range for the bridges (19, 2016)

Grade	Damage	Recommended time for the intervention	
80-100	Mild durable or functional damage	No need	No attention required
60-79	Medium durable or functional damage	Long-term	5 years
40-59	Mild resistant or durable or functional damage	Medium term	1 - 2 years
20-39	Medium resistant damage	Short term	Less than 1 year
0-19	Collapse or critical damage	Immediate	Immediate interventions

Currently, the main inventory and inspection campaign is underway, it involves over 1,034 bridges from every Region of the country and it is meant to calibrate the system to all climates, typologies, and particularities of the country's main bridges.

Based on the individual score of each bridge inspected, the Bridge Management System developed is capable of prioritizing rehabilitation/repair interventions, as well as plan future inspection campaigns and routine maintenance activities.

Furthermore, and considering that one of the main objectives of the project is to create a tool for assisting decision-making and planning the investment needs for the maintenance of the structures, the Bridge Management System has a budgeting module to generate a first cost estimate of the required interventions/maintenance activities.

This module is linked to a library of damage records associated to repair interventions as well as unit prices, custom-made for Chile and the National Roads Department. Based on the damages identified during the inspection, the system automatically assigns certain repair interventions and estimates the corresponding costs based off the unit prices, producing an illustrative budget which can be modified at a later time by the National Roads Department.

3 MANAGEMENT SYSTEM FUNCTIONALITY

The principles and functions presented in the previous section are particularized in a web application, accessible through any internet or intranet browser, and which operates in the cloud or a server owned by MOP, without requiring an executable file installed in the user's computer. The information collected in the application (the database that feeds the system) is located in a server owned by the Ministry, so as to guarantee data confidentiality and security.

The web application has four different modules, presented below:

When accessing the online platform, which requires a username and password, the user finds a home screen corresponding to the first module of the system: Location. Through this module, the user can access the complete list and browser of bridges entered into the Bridge Management System, which is itself linked to a cartographic database with the exact geographic location of the selected structures (Figures 5 and 6).

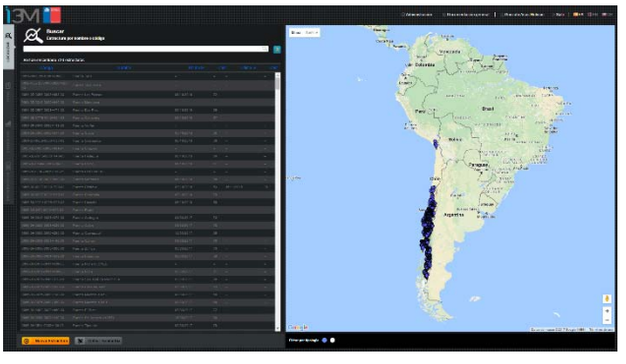


Figure 5 - Home screen (17, 2017)

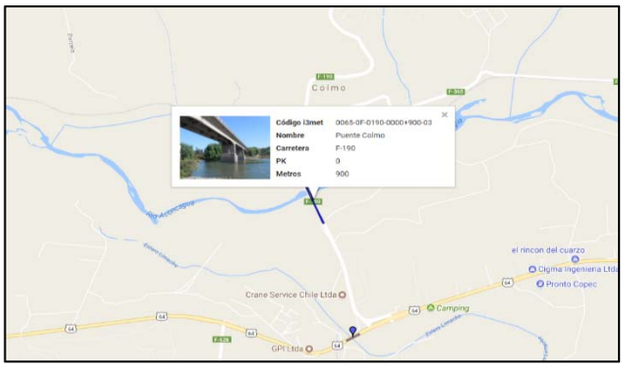


Figure 6 - Home screen ([17], 2017)

On the left side of the home screen, the user can find the access tabs for each of the other system's modules: File, Queries, and Budgeting.

The "File" module is connected to the system's database, and it presents all existing information related to each particular bridge. Through this module, the user can access all the general information of the bridge (Figures 7 and 8), existing documentation, photographs, inventory data, and inspections and interventions conducted. This is the key module of the system, from which the rest of the planning and cost estimation tools operate.

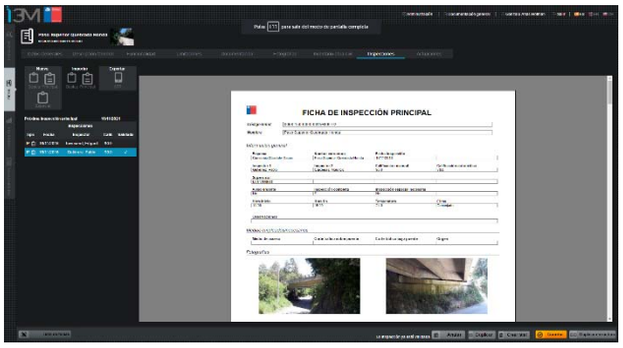


Figure 7 - General data screen, within the File module ([17], 2017)



Figure 8 - Main inspection screen, within the File module ([17], 2017)

Using the File module's database, the system's Query module allows the user to filter the alphanumeric data collected in both the inventory and field inspections and export them into Excel to use them for the maintenance planning and management.

To perform a query, a topic must first be selected, be it Inventory ('General data', 'Deck', 'ENR'), Inspection ('Inspections', 'Faults), or Repair ('Repairs'). Once a topic has been selected, the user can access different filtering and query options (Figures 9 and 10).

This module is particularly useful to make the most of the available database. The methodology proposed collects data from the assets at a high detail level, but this would be useless without a proper search tool to search and filter information from the data available.

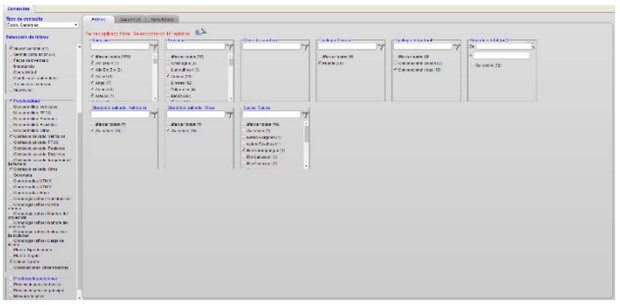


Figure 9 - Query module and Excel export ([17], 2017)



Figure 10 - Query module and Excel export ([17], 2017)

Lastly, the Bridge Management System has a Budgeting module (Figure 11) which allows the user to generate an estimated budget for the repair interventions of a bridge based on the damages recorded during the major inspection.

For this purpose, the system has a library of damages as well as a list of pre-defined interventions associated with a particular damage and cause, along with the material and unit of measurement. Likewise, the Bridge Management System has a database of the unit prices, developed particularly for this project, which will be linked to the Budgeting module.

Due to the fact that inspectors collect, besides the type of damage and affected element, the approximate quantities of the damages during major field inspections, the Budgeting module is able to assign a repair operation to each damage and calculate an estimated cost based on the field quantities.

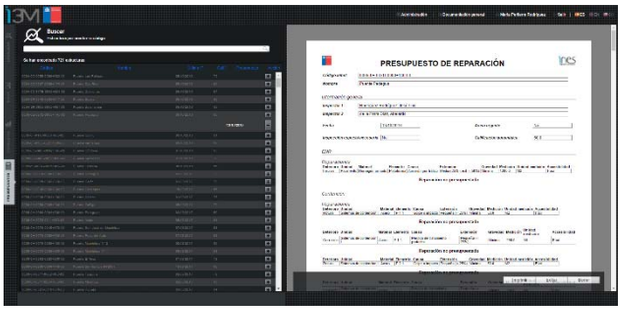


Figure 11 - Budgeting module, within the File module ([17], 2017)

The budgets generated are open and editable, so new repair interventions can be added to it, interventions that are decided not to be conducted can be deleted, quantities can be modified, and auxiliary means can be added if they are not included by default in the proposed budget.

4 CONTEMPLATED TYPOLOGIES

The methodology developed for this Bridge Management System applies to all existing structural typologies along Chile's road network (Figures 12 and 13), such as:

Beam bridges
Slab bridges
Truss bridges
Box girder bridges
Arch bridges
Cable-stayed bridges
Suspension bridges



Figure 12 - Example of suspension typology, represented in the General Carrera Bridge ([20], 2017)4

5 INSPECTION RATING

As the methodology is based in the breakdown of each bridge into lower level elements (as shown in Figure 3), each of which has a different weight in the condition scoring algorithm, any particular bridge — as long as all typological possibilities for its elements are included in the system— can be described and identified. Thus, when conducting the field inspection, the observed damages will be assigned to the specific bridge elements, so as to generate a condition score for the lower-level elements and compose the global condition scoring of the bridge through a weighed translation of the scores toward the higher-level elements.

For that purpose, the system runs a series of algorithms that firstly calculate the rating of each damage identified during a major inspection; secondly calculates the condition score of each specific bridge unit, subcomponent and component; and lastly calculates the general condition scoring of the bridge.

In relation to that first step, the calculation of the rating of each specific damage is obtained through the following formulation:

$$C_d = C_o \cdot P_d \cdot P_u \cdot P_c$$

Where:
C_d = damage rating
$C_o = [100 - ((V_{extension} + V_{severity}) \cdot 4)]/100$
P_d = damage weight factor
P_u = unit weight factor
P_c = cause weight factor

As shown above, each damage identified during the field inspection would be given a rating based on the type of damage (the more important the damage, the lower the P_d –i.e.the surface alteration of the concrete will have a P_d of 97 whereas the existence of cracks will have a P_d of 87-), the location of the damage (referred to the unit of the bridge that is affected by the damage –i.e. the P_u for the beams of a beam bridge has been established at 0.91, whereas the P_u for the slab has been established at 0.94), the cause of the damage (i.e. if the damage is caused by a torsional stress the P_c factor will be 0.80 while in the case of climatic actions it will go up to 0.98), its severity and its extension.

Once each of the existing damages has been rated, the system will calculate the condition score of the bridge units –as the minimum score of the damages located in that bridge unit- and the number of damages per unit. That number of damages will be calculated affecting the amount of damages by a factor that depends on the rating of those damages, in such way that the formulation penalizes the existence of damages of low rating.

The same methodology is applied for the bridge elements, calculating the minor condition score of the units of that bridge element and the total number of damages associated to that element.

The following step would be the calculation of the subcomponents' condition score. In order to do so, the system calculates the minimum condition score of the bridge elements that compose that subcomponent and the total number of bridge elements associated to that subcomponent. In order to get the condition score of the subcomponent, the system affects the minimum

score of the damages of the elements in that subcomponent by the number of damages and a factor related to the kind of subcomponent (pier, foundations, abutments…).
Similarly, the condition scoring of bridge components follows the same principle. The minor condition scoring of its subcomponents is taken and then reduced by the application of a corrective factor depending on the number of damages related to that specific component.
Finally, and in order to calculate the global bridge condition score, the minimum condition score of the load bearing components of the bridge is taken and then corrected by the minimum condition score of the non load bearing components, the number of total damages of the bridge, and the Truck Annual Average Daily Traffic (AADT).
Thanks to this formulation, the system obtains the value of the global condition scoring of the bridge and the total number of damages, which allows the user to characterize the state of conservation of the bridge, through the ranges established in Table 2.

Figure 13 - Example of cable-stayed typology, represented in the Yelcho Bridge ([20], 2017)5

6 CONCLUSIONS



Chile has a large number of bridges, which represent an important technical heritage.

Currently, the National Roads Department has no integrated Bridge Management System for the Conservation of Bridges. Nowadays, these tools are vital for decision-making regarding investment amounts dedicated to maintenance.

Any Bridge Management System should, at least, have the following features:

- Inspection techniques applied to bridges
- Inspection manuals
- Inspection protocols, including an inspection sheet
- Technical visits, defining the performance of destructive and non-destructive tests
- Proposal for monitoring, instrumentalization, and maintenance plan
- Constant training

The results of the new Bridge Management System are included in future versions of the Highways Manual of the National Roads Department, as part of the philosophy for the life cycle of the structures.

After the study of the implementation manuals existing to date, a proposal was made which is being adjusted as more results are being obtained through the field campaign. Currently, more than half of the planned campaign has been conducted, and the preliminary results point to a proper adaptation of the system to the typological variety of the existing bridges, as well as an adequate flexibility to be adapted to new structural elements.

7 REFERENCES

[1] AASHTO (1993).American Association of State Highway and Transportation Officials.AASHTO Guide for Design of Pavement Structures 1993. American Association of State Highway and Transportation Officials: Washington, DC.

[2] MOP. Guía de inspección para mantenimiento de puentes. Proyecto de rehabilitación y Conservación de Puentes en la República de Chile. Agencia de Cooperación Internacional de Japón. March 1993

[3] MOP. Instructivo para la revisión del estado de puentes y estructuras. Coordinación de Concesiones de Obras Públicas. División de Explotación. July 2007

[4] MOP. Instructivo para el catastro y diagnóstico de puentes. Departamento de Conservación. Dirección de Vialidad. Región de Los Lagos. June 2012

[5] MOP. Instructivo de inspección visual de puentes. Departamento de Conservación. Dirección de Vialidad. Región de Los Ríos. 2013

[6] MOP. Manual de Carreteras – Parte 7 (Mantenimiento vial). Dirección de Vialidad. June 2015

[7] AASHTO. Standard Specifications for Highway Bridges.2002

[8] AASHTO – LRFD Bridge. Bridge Design Specifications.2012

[9] FHWA.NBIS: National Bridge Inspection Standard. 2009

[10] AASHTO.Manual for Bridge Evaluation – 2nd Edition.2011

[11] FHWA. Bridge's Inspector Reference Manual. December 2012

[12] AASHTO.Manual for Bridge Element Inspection.2013

[13] FHWA.Evaluating Scour at Bridges (Report FHWA-HIF-12-003 HEC-18).Abril 2012

[14] FHWA.The Manual on Uniform Traffic Control Devices (MUTCD).2009

[15] FHWA.Recording and Coding Guide for the Structure Inventory and Appraisal of the Nation's Bridges (Report No.FHWA-PD-96-001). 1995

[16] Márquez, M. Valenzuela, M. Espinoza, J. & Campusano, J. 2016. Diagnóstico de Puentes e Implementación de Sistemas de Gestión para Conservación. 12° PROVIAL. August. Viña del Mar. Chile.

[17] Stradale-Gauss Consortium Ldt, INES Consulting Engineers. (2016). Manual Usuario i3met. Estudio diagnóstico de puentes e implementación de sistemas de gestión para conservación.

[18] Stradale-Gauss Consortium Ldt, INES Consulting Engineers. (2016). Manual para la realización de inspecciones principales en estructuras. Estudio diagnóstico de puentes e implementación de sistemas de gestión para conservación.

[19] Stradale-Gauss Consortium Ldt, INES Consulting Engineers. (2016). Manual para la obtención de la calificación de puentes. Estudio diagnóstico de puentes e implementación de sistemas de gestión para conservación

[20] Stradale-Gauss Consortium Ldt, INES Consulting Engineers. (2017). Manual de realización de catastro en estructuras. Estudio diagnóstico de puentes e implementación de sistemas de gestión para conservación.

Maintenance, Safety, Risk, Management and Life-Cycle Performance of Bridges – Powers, Frangopol, Al-Mahaidi & Caprani (Eds)
© 2018 Taylor & Francis Group, London, ISBN 978-1-138-73045-8

Dynamic analysis of a steel-concrete composite railway bridge considering vehicle-bridge interaction

L. R. Ticona Melo & T. N. Bittencourt
Structural Concrete Modeling Group, Polytechnic School, São Paulo University, São Paulo, Brazil

D. Ribeiro
CONSTRUCT-LESE, School of Engineering, Polytechnic of Porto, Porto, Portugal

R. Calçada
CONSTRUCT-LESE, Faculty of Engineering, University of Porto, Porto, Portugal

ABSTRACT: This study presents the calibration and validation of the numerical model of a steel-concrete composite railway bridge considering the vehicle-structure interaction. An ambient vibration test, based on limited experimental data, and a dynamic test under traffic actions, were performed, in order to estimate the modal parameters of the bridge and the dynamic responses for the passage of Alfa Pendular train, respectively. The numerical dynamic responses were obtained using ABAQUS software based on an iterative uncoupled method for vehicle-structure interaction which considerers the track irregularities. The calibration of the numerical model was based on the application of a genetic algorithm, minimizing the differences between numerical and experimental modal parameters. The experimental responses obtained from the dynamic test under railway traffic revealed a good agreement with the numerical responses.

1 INTRODUCTION

The worldwide implantation of the high-speed railways is requiring the construction of new lines, and inherently, a relevant effort of rehabilitation of existing structures, particularly bridges and viaducts.

The dynamic effects of trains running at high speeds can reach significant values, due essentially to the resonance phenomenon that generally occur at speeds higher than 200 km/h, which should be considered in evaluating existing bridges as well as in the designing of new bridges. Nowadays, the resonance effects are becoming important as a result of the increase of the traffic operating speeds and the improving of vehicles' characteristics, particularly the increase of axle loads.

These new demanding are requiring the implementation of structural heath monitoring systems on bridges in close articulation with the railways infrastructure managers.

In case temporary monitoring systems, like those that are used in static and dynamic tests, the infrastructure manager typically imposes restraints to the location of the sensors to be installed in bridges, due essentially to safety requirements.

In most situations the zones authorized for the installation of monitoring systems are located outside the rail traffic lanes, such as sidewalks and lower part of the deck, including supports and piers. Even in these locations, there are sometimes restrictions that difficult the installation of the monitoring systems, such as the presence of water courses, roadways and terrain with rugged topography.

This paper describes the calibration and experimental validation of the numerical model of a steel-concrete composite railway bridge based on dynamic tests performed with restrictions to sensors locations. An ambient vibration test allowed to identify the natural frequencies, vibration modes and damping coefficients of the bridge by applying a modal identification technique on frequency domain. The calibration of the numerical model was based on the application of a genetic algorithm, in order to minimize the deviations of the numerical and experimental modal parameters. The results of the calibration demonstrate a very good agreement between the numerical and experimental modal responses and a significant improvement of the numerical model before calibration. Finally, the comparison between the dynamic responses obtained from a dynamic test under traffic actions and a numerical simulation based on a train-structure interaction analysis revealed a good agreement.

2 ANTUÃ RAILWAY BRIDGE

The railway bridge over Antuã river is located at the Northern line of the Portuguese railways, at km + 286, 864, near the city of Aveiro (Fig. 1). The bridge has a total length of 44.4 m and consists in four simply supported spans with lengths equal to 10.27 m and 10.85 m, for the extreme spans, and 11.62 m, for intermediate spans.



Figure 1. General view of Antuã Bridge

The transversal section of the bridge has a total width of 12.3 m, and is composed by two half-symmetrical and independent decks separated by a longitudinal joint, as showed in Figure 2. Each half deck consists of two longitudinal steel beams (HEB700) spaced of 3.30 m, connected by four transversal steel beams (IPE500). The slab is composed by prefabricated panels with a variable thickness from 0.25 m to 0.37 m.

Figure 2 shows the dimensions and geometric properties of the cross section of the deck.

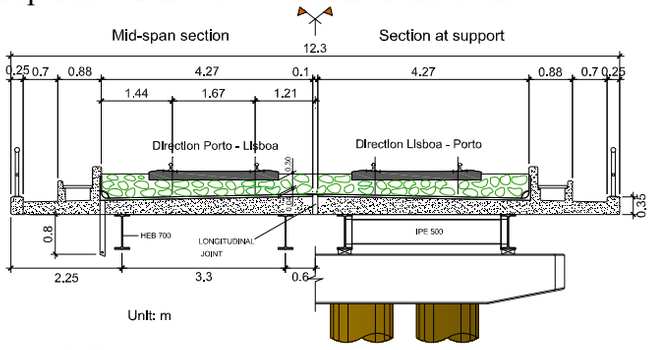


Figure 2. Cross-section of the deck.

Each individual deck is supported by four pot bearings: two fixed supports on one side, and two longitudinally guided supports on the other side.

The railway track over the bridge is formed by UIC60 rails rested on concrete sleepers, spaced every 0.60 m, and a layer of ballast with a thickness of 0.45 m, which is laterally restrained by concrete walls.

Figure 3a shows the geometric properties of the Antuã bridge.

3 DYNAMIC TESTING

3.1 *Ambient vibration test*

The ambient vibration test was focused on identifying the modal parameters of the second section of the bridge, including both decks, as well as the characterization of the track continuity effect.

This test involved the measurement of accelerations at 26 points, organized in 4 setups (Fig. 3b and Fig. 4). The location of sensors was restricted: from one side, due to limitations of accessing the track lane following the safety indications of REFER (infrastructure manager); from other side, due to limitations of the topography with respect to access the area under the deck.

The data acquisition was performed through National Instruments cDAQ-9172®, using 3 NI 9233® modules for IEPE accelerometers. The time series were acquired over 5 min periods, with a sampling frequency of 2000 Hz, posteriorly decimated for a frequency of 200 Hz.

The identification of natural frequencies, modal configurations and damping coefficients of the second section of the bridge was carried out using the Enhanced version of the Frequency Domain Decomposition Method (EFDD), available in ARTeMIS® software.

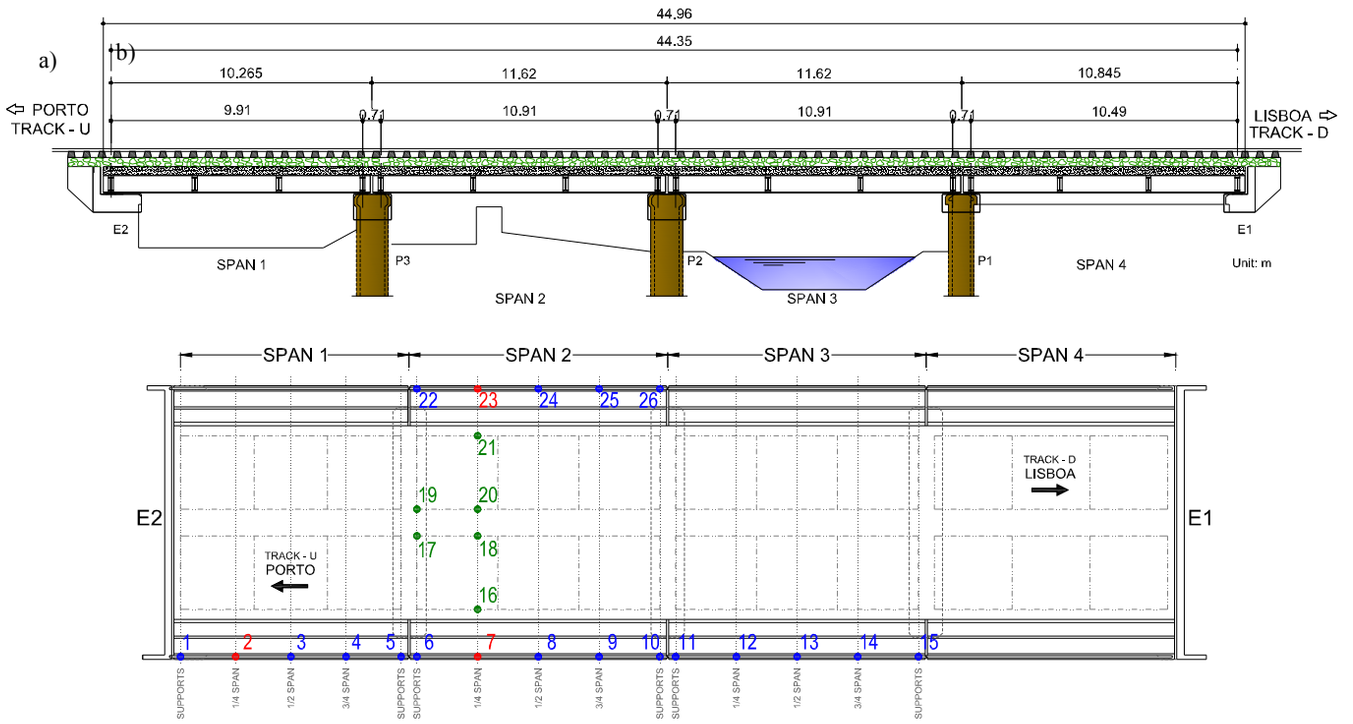


Figure 3. a) Elevation of Antuã bridge, b) Sensor positioning



Figure 4. Ambient vibration test experimental configurations and sensor positioning

Figure 5 shows the modal configurations of the six identified vibration modes, indicating the average values of the frequencies and damping coefficients.

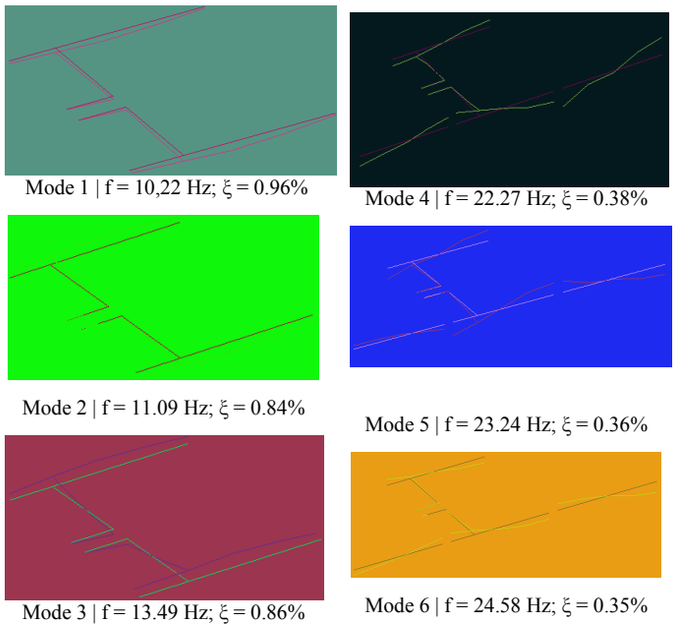


Figure 5. Experimental modal parameters.

The analysis of the modal configurations allowed to identify global modes associated to vertical bending (mode 1) and torsion (modes 2 and 3) of the deck with very good definition, and with natural frequencies equal to 10.22, 11.09 and 13.49 Hz, respectively. Modes 4, 5 and 6 are related to the 2nd mode of vertical bending, for which is clearly observable that the lack of experimental information conditioned an adequate modal representation.

3.2 *Dynamic test under traffic action*

The dynamic test under traffic action involved the measuring of displacements and accelerations at 3 points under the deck of the 2nd span of the bridge, on the ascending track (Lisbon - Porto direction), for the passage of Alfa Pendular train at speeds between 156 and 160 km/h.

The vertical displacements were measured using LVDTs, close to the support (D1) and under the main girder at 1/3 span (D2). The vertical acceleration was measured with an accelerometer installed at 1/3 span (A1).

Figure 6 shows the points instrumented in the second section of the bridge for the test under rail traffic.

4 NUMERICAL MODEL

The 3D finite element numerical model of the bridge was developed using ABAQUS program (Simulia, 2012). As the aim of this investigation is to study the 2nd section of the bridge, only three spans were modeled, allowing to adequately reproduce the structural continuity conferred by the track between the adjacent spans, and reducing the dimension of the numerical model.

The ballast, sleepers and rail pads were modeled using solid finite elements, while the rails and the main girders were modeled using beam finite elements.

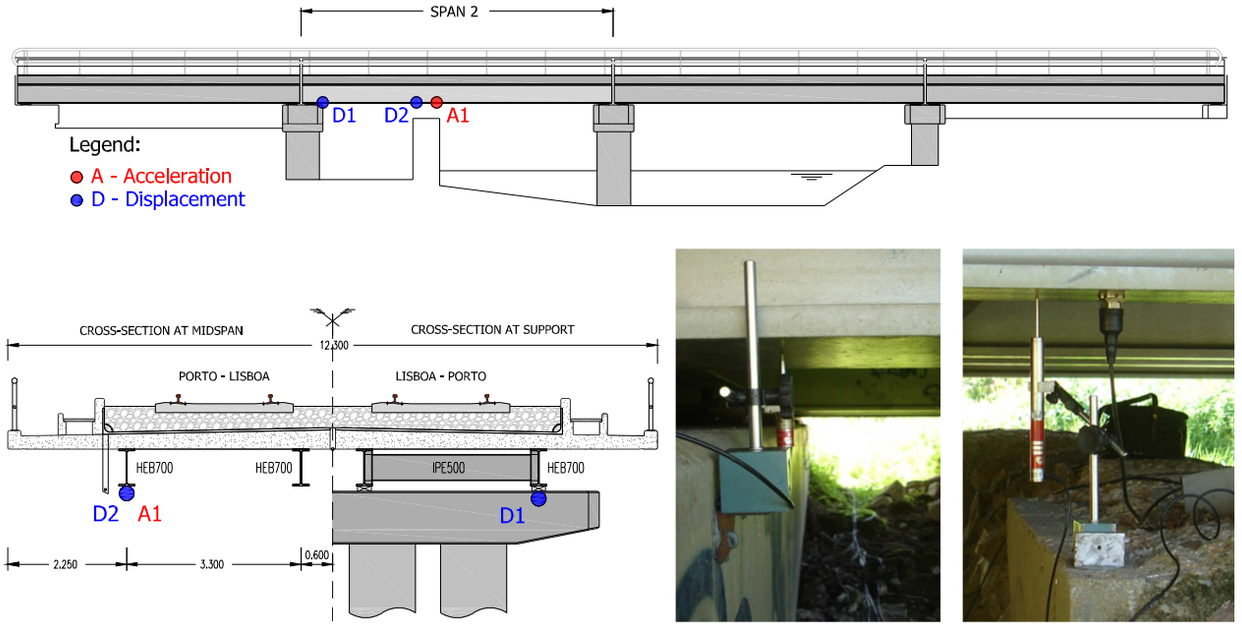


Figure 6. Dynamic test under traffic actions: instrumented points and sensors details.

Special attention was given to the continuity of the track ensured by the ballast layer between consecutive decks. In these regions the ballast layer tends to degrade its stiffness due to the passage of the railway traffic. The degradation of the ballast properties at the joints, particularly in the longitudinal joint (between two decks of the same section) and transversal joints (between decks of consecutive sections), were represented by means of elements with reduced modulus of elasticity. Figure 7 shows a general perspective of the numerical model developed.

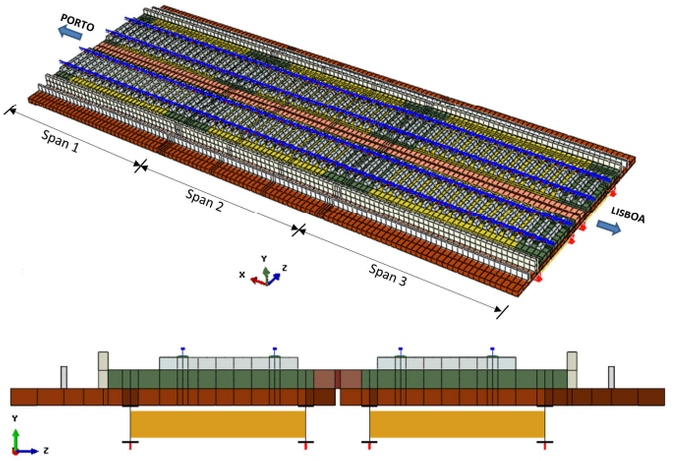


Figure 7. 3D model of bridge.

Table 1. Characterization of the numerical model parameters.

Parameter	Designation	Limits (lower/ upper)	Adopted value	Unit
ρ_c	Density concrete	2381.2 / 2715.6	2515.58	kg/m^3
E_c	Módulus deformability concrete	32.63 / 48.61	37.49	GPa
ν_c	Poisson ratio concrete	- / -	0.20	-
ρ_{bal}	Density ballast	- / -	1800	kg/m^3
E_{bal}	Módulus deformability ballast	130 / 208	145	MPa
$E_{bal,long1}$	Modulus deformability ballast (inner zone)	1 / 145	145	MPa
$E_{bal,long2}$	Modulus deformability ballast (outside zone)	1 / 145	145	MPa
$E_{bal,trans}$	Modulus deformability ballast between spans	1 / 145	145	MPa
ν_{bal}	Poisson ratio ballast	- / -	0.20	-
K_v	Vertical stiffness of the support	530 / 1047.4	788.7	MN/m
K_h	Horizontal stiffness of the support	0 / 100	0	MN/m
K_{palm}	Vertical stiffness of the rail pads	- / -	250	MN/m
ρ_s	Density steel	- / -	7850	kg/m^3
E_s	Modulus deformability steel	200 / 210	210	GPa
ν_s	Poisson ratio steel	- / -	0.30	-

Table 1 shows the mechanical and geometrical parameters considered in the numerical model of the bridge, including the adopted values and the corresponding units. Additionally, the lower and upper limits of the numerical parameters that will be used in the calibrations of the numerical model are also presented.

Figure 8 presents the numerical modal parameters in correspondence with the previously identified experimental ones.

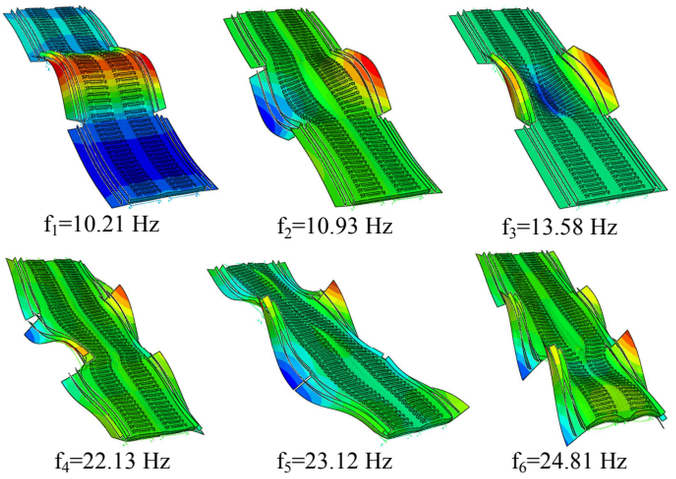


Figure 8. Numerical modal parameters.

5 MODEL CALIBRATION

The calibration of the numerical model involved 6 numerical parameters and 6 modal responses (3 frequencies and 3 nodal configurations). The objective function (*f*) involve two terms, one related to the residuals of the vibration frequencies, and other related to the residuals of the MAC values:

$$f = a \sum_{i=1}^{3} \frac{\left| f_i^{\exp} - f_i^{num} \right|}{f_i^{\exp}} + b \sum_{i=1}^{3} \left| 1 - MAC\left(\phi_i^{\exp}, \phi_i^{num} \right) \right| \quad (1)$$

where f_i^{num} is the numerical vibration frequency of the mode *i* and $f_i^{\exp}$ is the experimental vibration frequency. $\phi_i^{\exp}$, ϕ_i^{num} are the experimental and numerical modal configurations of the mode *i*.

For the pairing between numerical and experimental modes of vibration the EMAC parameter was used (Brehm et al., 2010).

In the optimization process a genetic algorithm based on an initial population of 30 individuals, randomly generated using Hypercube Latin method, was used. The stop criterion was a number of generations equal to 150 generations, in a total of 4500 individuals. The crossing rate was considered equal to 50% and the mutation rate was set equal to 15%, with a variable standard deviation between 0.10 to 0.01.

In the present study four independent optimization runs (GA1 to GA4) were performed, aiming to obtain an optimal solution due the stochastic nature of the genetic algorithms.

Table 2 presents the optimized values of each numerical parameter obtained for the four optimization runs (GA1 to GA4). The values of run GA1 were

adopted for the calibrated model because presented the lowest residual of the objective function.

Table 2. Parameters of the calibrated numerical model

Parameter	Unit	Initial value	GA1	GA2	GA3	GA4
ρ_c	kg/m^3	2548.4	2452.1	2443.6	2509.4	2519.4
E_c	GPa	40.62	33.8	34.7	33.9	35.6
$E_{las,long1}$	MPa	145	9.73	7.6	16.34	13.33
$E_{las,trans}$	MPa	145	136.2	140.2	140	137.9
K_V	MN/m	788.7	1047	1047	1047	1047
K_L	MN/m	0	20	40	50	50

Figure 9 shows the comparison of modal configurations of the second section of the bridge obtained experimentally and numerically after calibration.

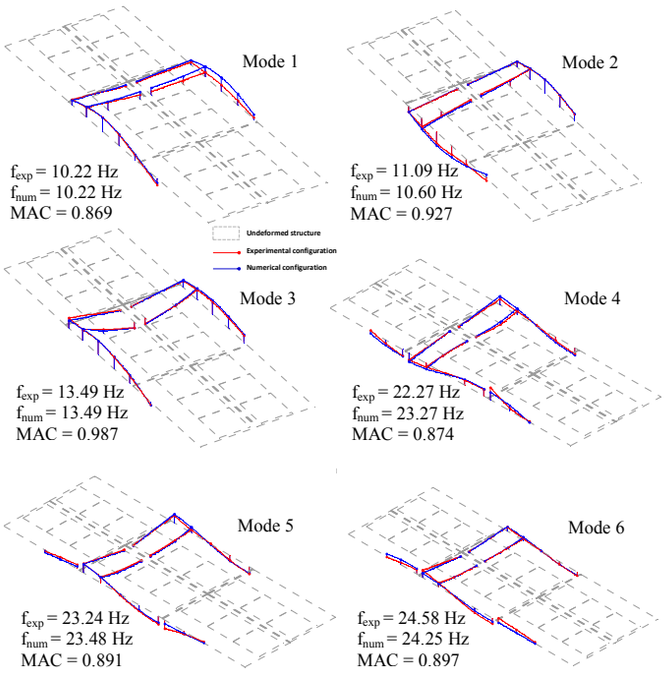


Figure 9. Comparison of numerical and experimental modal configurations after calibration.

The last comparison demonstrate that although the experimental information is limited in sections 1 and 3 of the bridge, the results after calibration are notoriously satisfactory, revealing the consistency of the results obtained in the calibration process of the numerical model.

6 VALIDATION OF THE NUMERICAL MODEL

6.1 *Methodology*

The numerical responses were obtained based on a dynamic analysis considering vehicle-structure interaction, including the track irregularities, performed by AIVE software (Ticona Melo, 2016). The software uses the modal superposition method for solving the dynamic equilibrium equations of the bridge, and an implicit direct integration method for solving the dynamic equilibrium equations of the train. The time increment adopted was equal to 0.001s.

The Alfa Pendular train was modeled based on a simplified model developed by Meixedo et al. (2014). This simplified model of the train was calibrated based on experimental modal parameters obtained by Ribeiro et al. (2013).

In this model the carbody and bogies were modeled as rigid beams arranged in the center of gravity of each component. The masses of the bogies and carbody were simulated by mass elements, including their translational and rotational inertial properties, and concentrated in the midpoint of the rigid elements. The suspension systems were modeled by spring-dashpots assemblies. Figure 10 shows the simplified numerical model of one of the vehicles of the train, in this case the BBN vehicle.

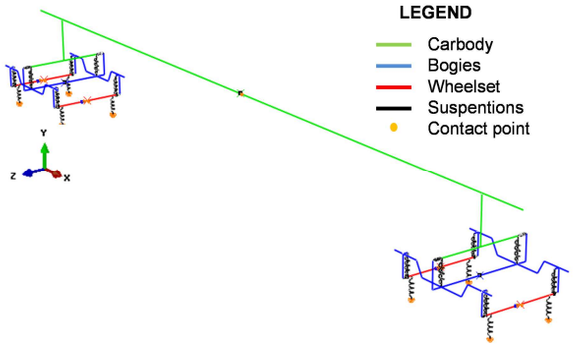


Figure 10. BBN vehicle numerical model.

The damping coefficients adopted for dynamic analysis of the bridge were experimentally estimated based on the ambient vibration test, using the EFDD method, and based on the dynamic test under traffic actions, by the application of the logarithmic decrement method (DL) to the free vibration acceleration responses after the train passage.

Table 3 presents a summary of the damping coefficients estimated from experimental tests.

Table 3. Experimental damping coefficients.

Mode	Type	Frequency (Hz)	Damping ξ(%) EFDD	Damping ξ(%) DL
1	1° vertical bending	10.22	0.96	6.95
2	1° torsion	11.09	0.84	6.10
3	2° torsion	13.49	0.86	6.33
4	bending	22.27	0.38	-
5	bending- torsion	23.24	0.36	-
6	bending	24.58	0.35	-

The track irregularities were provided by the track inspection vehicle EM120 from REFER. Figure 11a shows the longitudinal profiles, for the left and right rails, from km 286+700 to 287+300, including the bridge. The track irregularities were measured every 0.25 m and includes wavelength between 3 m and 70 m. Figure 11b presents the power spectra of the ir-

regularities as a function of the wave number (1/λ). It is possible to derive that the track irregularities with wavelengths between 25 m and 64 m presents the greatest amplitudes.

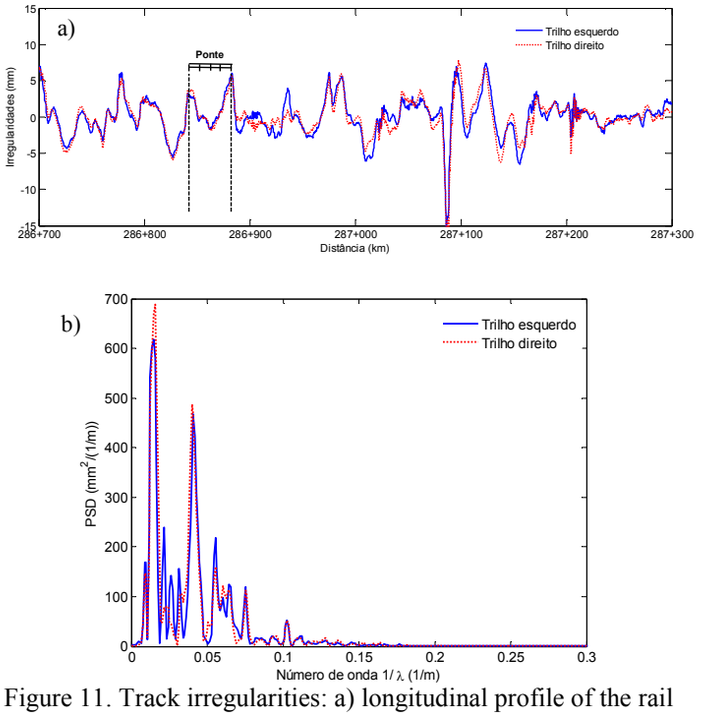


Figure 11. Track irregularities: a) longitudinal profile of the rail and b) power spectral density functions.

6.2 *Comparison between numerical and experimental results*

Figure 12 shows a comparison of the time records of the displacements close to support (D1), and 1/3 span (D2) obtained experimentally and numerically, after updating, for the passage of the Alfa Pendular train at a speed of 156 km/h.

In both comparisons it can be observed a very good agreement between the experimental and numerical after calibration records. The main differences were observed at the maximum displacements caused by the passage of the group of axles (bogies) corresponding to the 4th and 5th vehicles, at instants t = 3.48 s and t = 4.10 s.

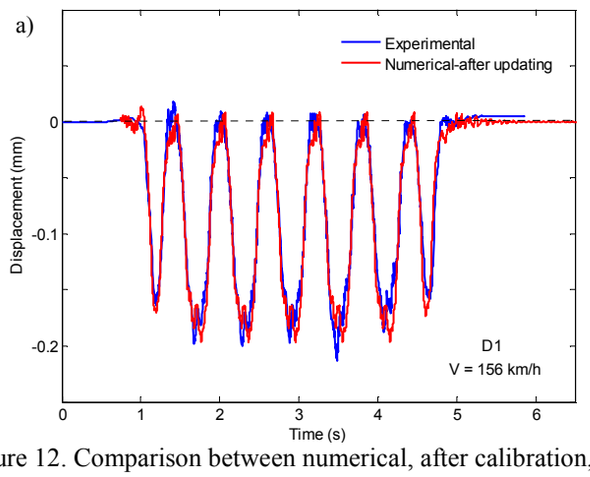


Figure 12. Comparison between numerical, after calibration, and experimental displacement records at position: a) D1; b) D2.

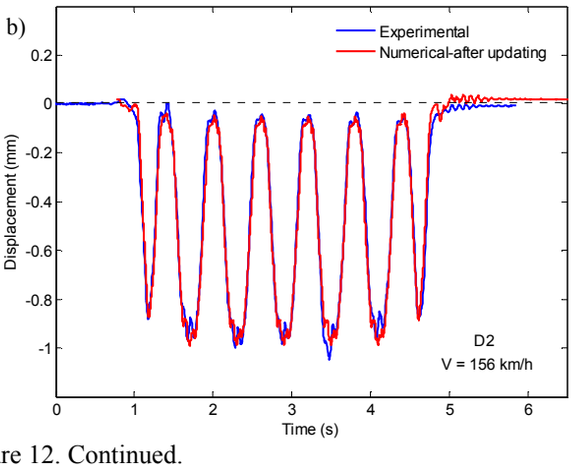


Figure 12. Continued.

Figure 13 presents a comparison between numerical after calibration and experimental acceleration records, for the passage of Alfa Pendular train at a speed of 156 km/h, at 1/3 of span 2 (position A1). The numerical responses were calculated considering the damping obtained by EFDD and DL methods, in order to determine which guarantees the best fit to the experimental responses. In both comparisons it is observed that the dynamic behavior of the bridge is very influenced by the damping. The decrease of the damping generates an amplifications of the dynamic responses.

The consideration of the damping coefficients obtained from EFDD method (Fig. 13a) led to accelerations values higher than the experimental values, particularly in terms of the maximum and minimum peaks of the response. On the other hand, the accelerations determined in the numerical model considering the damping from the DL method reveal to have a higher agreement with the experimental responses (Fig. 13b).

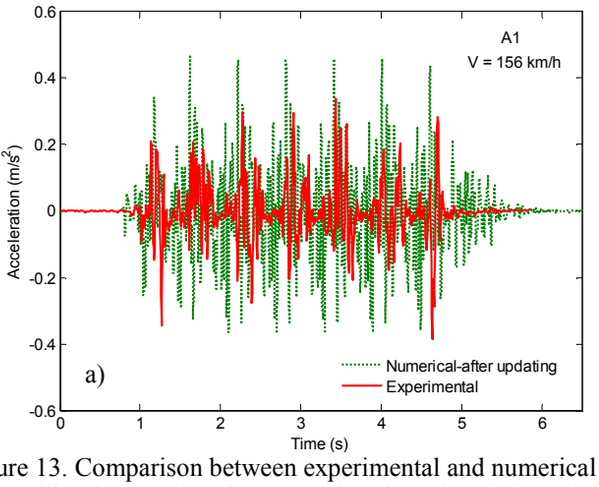


Figure 13. Comparison between experimental and numerical after calibration accelerations records using: a) EFDD method; b) DL method.

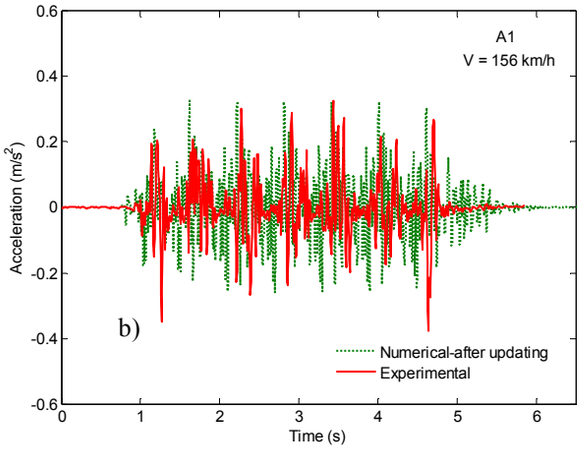


Figure 13. Continued.

Figure 14 shows the auto-spectra of the experimental and numerical after calibration accelerations obtained for the passage of the Alfa Pendular train at a speed of 156 km/h.

In the figure, it can be seen that the numerical model was able to reproduce some of the frequencies experimentally identified, particularly the contributions of vibrations modes with frequencies of 10.01 Hz and 13.43 Hz, as well as the frequencies associated with the passage of the regularly spaced group of axles of the train, at frequencies of 1.71 Hz, 5.01 Hz, 11.60 Hz and 13.43 Hz. Other frequencies displayed are probably related to the contributes of the track irregularities with wavelength lower than 3 m and wheels defects.

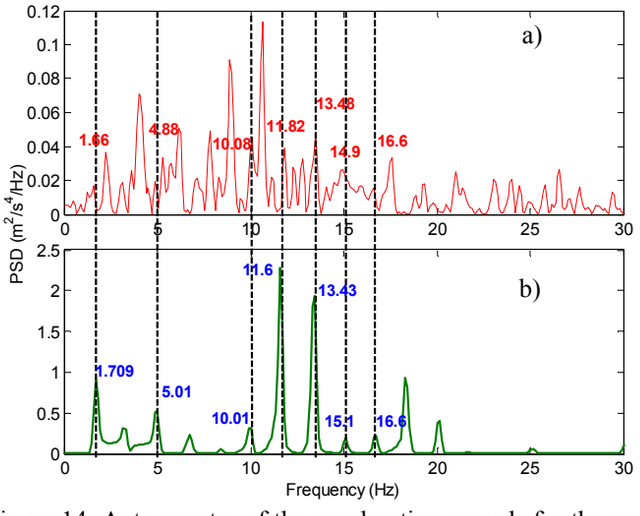


Figure 14. Auto-spectra of the acceleration records for the passage of Alfa Pendular train at a speed of 156 km/h: a) experimental, b) numerical.

7 CONCLUSIONS

The following conclusions can be drawn up from this research:

- The responses obtained after the calibration of the numerical model of the bridge showed a good approximation with those experimentally identified.
- The calibration process of the numerical model confirmed that the ballast layer between consecutive decks presents degradations particularly in the longitudinal joints and transversal joints.
- The dynamic analysis taking into account the experimentally measured irregularities, with wavelength between 3 and 25 m, showed that the contribution of modes up to 30 Hz were appropriate to characterize the dynamic behavior of the bridge.
- The calibration process improved very satisfactorily the agreement between the experimental and numerical records, due essentially to the decrease of values of the elasticity modulus of the ballast, that decrease the frequencies of vibration of the modes that contribute to the dynamic response of the bridge.
- The dynamic behavior of the bridge is extremely influenced by the damping, which was proved by the dynamic amplification observed in the accelerations response when reducing the structural damping. The method that allows a better adjustment of the numerical responses of the accelerations with the experimental measurements was the logarithmic decrement method (DL).

ACKNOWLEDGEMENTS

The first author PhD researcher expresses his gratitude to the CNPq for the financial support through the Postdoctoral Process 167555/2017-0.

REFERENCES

Meixedo A. Ribeiro D. 2014. Global and Local Dynamic Effects on a Railway Viaduct with Precast Deck in *Proceedings Conference on Railway Technology, Scotland*.

Ribeiro D, Calçada R., Delgado R., Brehm M. and Zabel V. 2012. Finite element model updating of a bowstring-arch railway bridge based on experimental modal parameters in *International Journal Engineering Structures*. v. 40, pp. 413-435.

Ribeiro D, Calçada R., Delgado R. 2013. Finite-element model calibration of a railway vehicle based on experimental modal parameters in *Vehicle System Dynamics,* Taylor & Francis, v. 51, Issue 6, pp. 821-856.

SIMULIA, DASSAULT SYSTÈMES 2012. Abaqus 6.12 Analysis User's ManualProvidence, RI, USA, 2012.

Zabel, V. and Brehm, M. 2009. System identification of high-speed railway bridges. In: Weimar Optimization and Stochastic Days 5.0, Dynardo Gmbh. Weimar, Germany.

Brehm M. Vibration-based model upating: Reduction and quantification of uncertainties. Weimar, Germany: Bauhaus-Universitat Weimar; 2011.

ARTeMIS. ARTeMIS Extractor Pro - Academic Licence. User's Manual. In: ApS SVS, editor. Aalborg, Denmark 2009.

Brehm M, Zabel V, Bucher C. An automatic mode pairing strategy using an enhanced modal assurance criterion based on modal strain energies. Journal of Sound and Vibration. 2010;329:5375-92.

Ticona Melo, L. R.; Silva, R. ; Bittencourt, T. N.; Bezerra, L.;. Identification of modal parameters in a scale model of a

railway bridge. International Journal of Structural Stability and Dynamics. v. 16, No. 09, p. 1550059-1550081, 2015.
Ticona Melo, L.R., Study of the dynamic effects of railway bridges considering vehicle-structure interaction, Ph.D. Thesis, University of Sao Paulo (2016), p. 271 (in Portuguese).
EN1991-2, Eurocode 1: Actions on structures - Part 2: Traffic loads on bridges, CEN (2003).
Y. L. Xu, Q. Li, D. J. Wu and Z. W. Chen, Stress and acceleration analysis of coupled vehicle and long-span bridge systems using the mode superposition method, Int. J. Comput. Struct. 32 (2010) 1356–1368.

Maintenance, Safety, Risk, Management and Life-Cycle Performance of Bridges – Powers, Frangopol, Al-Mahaidi & Caprani (Eds)
© 2018 Taylor & Francis Group, London, ISBN 978-1-138-73045-8

Management System for Natural Risk Disaster on Infrastructure: A Regional Approach

M.A. Valenzuela, N. Valenzuela, A. Peña-Fritz
Pontificia Universidad Católica de Valparaíso, Valparaíso, Chile

R. Romo
Pontificia Universidad Católica Chile, Santiago, Chile

ABSTRACT:

A problem that has been studied at national level is the prevention of risks that affect structures due to the large number of extreme natural events. This situation is worsened by the lack of systematic evaluation of current infrastructures. It is for this reason that the COSIPLAN - IIRSA platform, together with the Chilean Ministry of Public Works, is working on the development of a solution for adequately assessing infrastructure and preventing future risks. Large losses caused by disasters have increased in recent years, directly affecting human lives, finances, and particularly road network infrastructure. The South American region has been affected by diverse events such as earthquakes, floods, volcanic eruptions, among others. In the past 35 years there has been infrastructure losses of close to US$88,000 million (South American Council of Infrastructure and Planning [COSIPLAN], 2016). This context has led to COSIPLAN/IIRSA and its member countries to implement the methodology called Disaster Risk Management at Regional Level (GRDR in Spanish) with the purpose of reducing the effects of natural and anthropogenic disasters in the country's infrastructure. The present paper presents the theoretical guidelines for the implementation of the GRDR and a proposal for implementing it in Chile over the next few years, with special attention to transoceanic network structures in South America.

1 INTRODUCTION

1.1 *The Risk of Disaster*

The term disaster is defined as a variation caused by a natural phenomenon or a human action that directly interrupts the functioning of a society, resulting in loss of life, social, material or serious environmental damage, surpassing the affected society's capacity for resolving this situation using its own resources.

Disasters are not sudden, isolated events in the 'normal' life of the communities. Disasters must be interpreted in the context of the territory and the development processes through which the affected community interacts with the ecosystems it occupies, or on which it intervenes (UNESCO, 2011).

1.1.1 *Components of Disaster Risk*

Vulnerability: Vulnerability is one of the variables in the INDECI (2010) risk formula, and is defined as the degree of resistance and/or exposure of a structure or its components to a threat. This definition is supported by what UNISDR (2009) has described as "the characteristics and circumstances of a community, system, or asset that makes them susceptible to the harmful effects of a threat."

A vulnerability may decrease as long as the communities enlarge the capabilities they use to reduce exposure to disaster risk, being these understood as the combination of strengths available within an organization and/or community.

This front of resistance, formed by the community's strengths, is called resilience. Resilience is defined as the capacity of a society to cope with the negative impact of an adverse event and to recover from its effects in a timely fashion, restoring basic operating functions.

Threat: Threat is the probability of occurrence of a natural and/or anthropogenic phenomenon which presents a potential harm for a specific time period in a known area.

Threats are classified by their origin according to UNESCO (2011). They can be of natural origin, generated by the planet's dynamic processes, or induced by human action. This classification is represented in the following illustration, in which threats are described according to their origin.

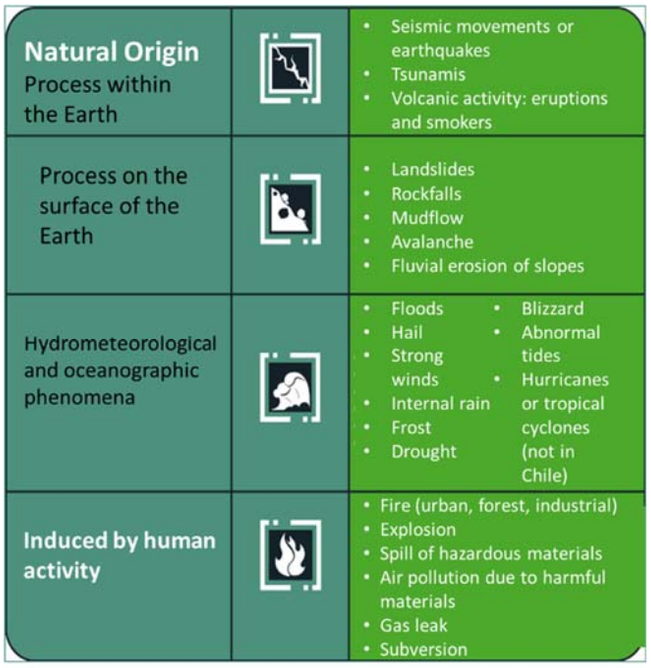


Figure 1. Origin of Threats
Source: Author compilation.

Risk: The UNISDR (2009) defines risk as "the combination of the probability of occurrence of an event and its negative consequences". This definition is complemented by INDECI (2010) as the sum of the likely losses that could arise from a disaster.

The risk is directly proportional to the threat and vulnerability. This means that the risk is dynamic, it can increase or decrease each time the other two factors vary, either separately or together.

The International Research Center on El Niño (CIIFEN) defines the following formula for risk calculation.



Figure 2. Risk Formula
Source: Author compilation based on CIIFEN (n.d.).

2 DISASTER RISK MANAGEMENT (UNESCO, 2011)

Disaster Risk Management is the methodological process in which various administrative guidelines, organizations, operational skills, and capacities are used, materializing public policies and strengthening coping abilities with the purpose of reducing the adverse impact of threats and the possibility of occurrence of a disaster (UNISDR, 2009; UNESCO, 2011).

The purpose of Disaster Risk Management is to prevent, reduce or transfer the adverse consequences of threats through various methodologies that seek prevention and mitigation.

2.1 *Intrinsic Processes of Disaster Risk Management (UNISDR, 2009; UNESCO, 2011)*

Disaster risk management is composed of four processes which are essential at the time of executing the methodology pertaining to this topic.

Risk estimation: Corresponds to the process in which the risk is identified and appreciated, obtaining the global perspective of the exposure that a particular community can have.
This perspective is obtained through the analysis of methodological information and the use of threat, vulnerabilities and capacities identification. This determines the probability of occurrence of damaging events.

Risk prevention and reduction: These are the various activities focused on the avoidance of new risks that may affect a society in addition to the reduction of vulnerabilities by means of actions materialized in advance. At this point the aim is to leave reactivity aside, generating proactive actions.

Preparedness, Response, and Rehabilitation: These consider the events with the aim of ensuring an optimal response tool for society in adverse situations such as disasters. This should ensure a correct response considering care for injured people, refitting basic services, and organizing activities in the affected region.

Reconstruction: These are the various actions undertaken for social, economic and physical recovery of the affected areasafter a harmful event such as a catastrophe.

3 DISASTER RISK MANAGEMENT IN INFRASTRUCTURE ACCORDING TO COSIPLAN.

The Method on Disaster Risk Management in Infrastructure (G.R.D) arises from the South American Council of Infrastructure and Planning (COSIPLAN),

which in turn was established by the heads of State of the members of the Union of South American Nations (UNASUR) in the year 2009. The statutes establishing COSIPLAN lay down a series of functions and responsibilities for the different support guidelines of this Council, among which stands out the Regional Infrastructure Integration Initiative (IIRSA) (COSIPLAN. n.d.).
The COSIPLAN/IIRSA's Plan of Action 2012-2022defines six areas of work in relation to planning methodologies, with a methodology of disaster risk management in infrastructure standing out among many other measures. The methodology was created with the purpose that the Council's member countries count with defined procedures to prevent, reduce or transfer the consequences of disasters such as earthquakes, volcanic eruptions, landslides, floods, among others, in infrastructure and finally put in place action plans for the development of resilient infrastructure for countries that implement it (COSIPLAN,n.d.).

The G.R.D. methodology's implementation philosophy includes different phases of development of projects ranging from the design phase of the infrastructure to the exploitation phase, also addressing requirements of expansion, rehabilitation, or improvement of existing projects. It is important to consider the internal regulations of each country in the context of design and construction for those projects that are analyzed by this methodology and are currently in the design and planning phase. Many of these design regulations address the threat and risk reductions analysis but only in the design stage. (Osorio, 2014; Valenzuela, 2016)

The G.R.D. is divided into three phases which allow for subdividing the objectives according to the methodological approaches required for each phase, as defined below.

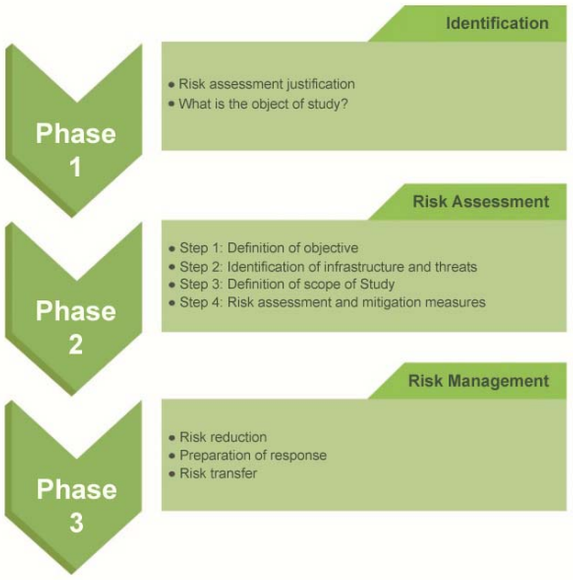


Figure 3. Phases of the G.R.D methodology according to COSIPLAN
Source: Author compilation based on Osorio (2014).

Phase 1: Identification. At this stage the object of assessment is defined, determining in advance the infrastructure and threats that will be analyzed in the application of the methodology.

The following figure shows the various forms that this methodology sets out for threat identification, as well as the infrastructure to analyze.

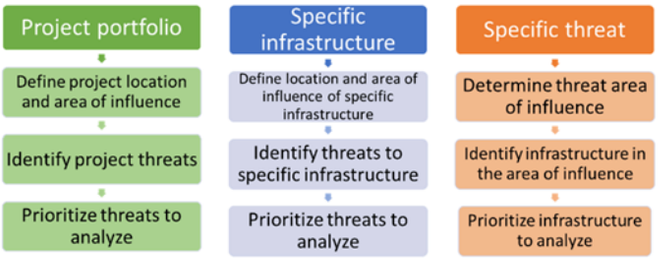


Figure 4. Methodologies for the Prioritization of Infrastructure.
Source: Author compilation based on Osorio (2014).

As Figure 4 shows, the methodology may be influenced by various motivations according to the risk under study, invariably resulting in the identification of threats as well as the infrastructure considered in the analysis.

Some of the reasons for the selection of project portfolio, specific infrastructure and threats, are described below. (Osorio, 2014; COSIPLAN, 2016)

a) Reasons for the selection of a project portfolio

- The infrastructure must ensure the continuous flow of international trade.
- Policy changes in structure design.
- Need to determine the risk of a specific road.
- Need to secure a specific infrastructure.

b) Reasons for the selection of a specific infrastructure.

- Specific infrastructure damage due to disasters of different nature.
- Policy changes in structure design.
- Presence of singular structures.

c) Reasons for the selection of a specific threat

- Record of disasters that caused damage, which is motivation for study and analysis.
- Evidence of any trace of natural or anthropogenic threat which motivates a detailed analysis. E.g.: volcanic eruptions.

Phase 1 of the GRD methodology is characterized by a basic analysis of the information available of both infrastructure as well as threats selected for study; this is a general characterization because only existing information is used.

Depending on the availability of resources, the risk analysis can be performed only in some components of the infrastructure, having to prioritize by importance according to the exposure to the threat. This analysis should be supplemented in Phase 2 of this methodology. (COSIPLAN, 2016)

Phase 2: Risk analysis. The objectives of performance which will be evaluated are defined, along with the characteristics of the threats and exposed infrastructure, thus defining the scope for risk analysis. At this stage, the analysis of the different measures of risk reduction is also considered.

This phase must usually consider the support of entities with expertise in the area, coordinated directly with the institution in charge of the methodology's analysis.

In the following diagram, the various steps needed to develop this phase are explained. The institution in charge of the analysis must be responsible for making decisions about the results achieved during the implementation of each of the steps in the diagram, ensuring that the results obtained may be useful for the correct development of the research (Osorio, 2014).



Figure 5. Methodologies for prioritization of infrastructure. Source: Author compilation based on Osorio (2014).

Step 1: Corresponds to the definition of performance indicators. At this point, the team in charge of project development should define what is the "acceptable risk" for the selected infrastructure against threats considered in Phase 1.

To define the structure's performance indicators and indexes the rules corresponding to the design and functionality of the structure studied must be known. Other important aspects are the considerations on the behavior of the structure with the purpose of:

- Prevention of damage caused to the environment.
- Prevention of economic losses.
- Maintenance of structure reliability.
- Prevention of damage to the communities and their assets.
- Prevention of damage to people's safety.

Step 2: In this step, the team responsible for the implementation of the methodology must perform, with the available information, a basic characterization of threats and infrastructure exposed. Such characterization can be delegated to expert institutions in the subject, facilitating the collection and analysis of the required data.

At this point the area of influence of the application of the methodology should also be defined prioritizing infrastructure exposed to threats, achieving the performance goals described in the first step of this phase.

- Threat characterization: It consists of the search of available information which allows for the characterization of the threats identified in Phase 1. The result of this stage is obtaining the characterization parameters of the threats used in the analysis.
- Infrastructure characterization: It is based on the essential information that should be collected to perform a correct analysis of vulnerability such as components, equipment, materials, pathologies, regulations, and design criteria, among others. As a result, the full characterization of the structure analyzed must be obtained.

Step 3: It consists of determining the depth level of risk analysis for the selected infrastructure. For this step the methodology defines three levels of risk analysis, which are defined below:

- Level 1 "Qualitative level": This level is characterized by simplified information delivery of both the threat and the selected infrastructure. The result of

this level of analysis can be obtained in the short term with the use of technical staff.

- Level 2 "Deterministic level": Quantitative analysis with the use of statistical and historical information for threat and infrastructure characterization. This level considers collecting and validating information in the field. This analysis can be done by technical professionals with knowledge of the structures defined in Phase 1, in addition to the collaboration of specialists in threat characterization and modeling.
- Level 3 "Probabilistic level": At this level, detailed results are obtained, supported by information and precise tools, and complemented by a probabilistic analysis. At this point advanced analysis methodologies must be used, requiring the intervention of experts in addition to instrumentation, exhaustive in-field analysis, and laboratory testing.

The level of risk analysis to select will depend specifically on the type of information available, financial resources, available time and professionals, among others.

Step 4: This step refers to the risk analysis. It is usually developed by experts in the subject matter based on the levels of depth of analysis described in the previous steps. Regardless of the level of risk analysis, the results must include the different risk reduction measures for further analysis and decision-making in Phase 4 of the methodology. In this step, it is important to have clarity about risk analysis, which should not only focus on compliance with regulations but also on knowing if the performance adapts to the performance described in step 1.

Phase 3: Risk Management Following the results obtained in the implementation of Phases 1 and 2, the different solutions for the implementation in the field of risk management are defined with the aim of generating a response with resilience towards the analyzed infrastructures. Within this phase, there are several alternatives that the entity responsible for the coordination of the analysis can use to increase resilience in the event of a threat: Scenarios for the planning of response to threats, risk reduction actions, and transfer of risk.

The team in charge of the coordination of the application of this methodology will be responsible for defining the actions for risk management of the infrastructure. These actions will be conditioned by the available resources and the type of action to be implemented, the measures may be for immediate or long-term implementation.

4 DISASTER RISK MANAGEMENT METHODOLOGY IN REGIONAL INFRASTRUCTURE GRDR (VALENZUELA & VALENZUELA, 2016)

In order to supplement the work done by COSIPLAN/IIRSA in the probabilistic risk analysis, a methodology called Disaster Risk Management in Regional Infrastructure (GRDR) has been proposed at the national level, coordinated directly by the Ministry of Public Works.

This method acts at phase 2 of COSIPLAN methodology, and has an impact on the actions to be implemented on Phase 3 for a resilient optimized response, and taking into consideration the country's context (Valenzuela & Valenzuela, 2016; Valenzuela, 2016)

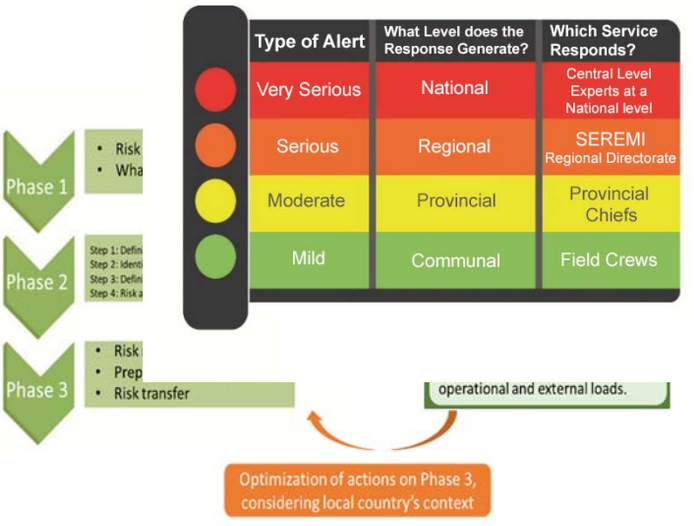


Figure 6. Chile's proposal for COSIPLAN methodology
Source: Author compilation.

The purpose of the methodology proposed by the Ministry of Public Works is the integration of aspects of decentralization through the regional management of the infrastructure. This implies that each region

must be able to carry out surveys of their infrastructure, providing information through technical entities, allowing for the generation of early warnings, and identifying and updating the damage indexes of the structures. This translates into Risk Management at the Regional Infrastructure (Valenzuela & Valenzuela, 2016; Valenzuela, 2016). The following illustration shows this decentralized approach through the incorporation of information by means of the regional technical team, allowing for the management of infrastructure at regional levels, enabling to act within the region's budgetary framework.

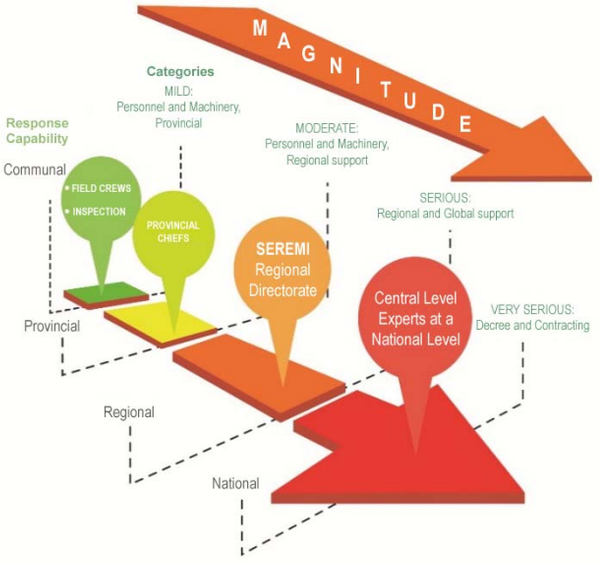


Figure 7a. GRDR Methodology Alert Levels
Source: Author compilation.
.

Figure 7b. GRDR Methodology Alert Levels
Source: Author compilation.

Some of the benefits associated with the management of infrastructure at the regional level results in lower costs associated with the information gathering stage, greater knowledge of the needs of the inhabitants, and better knowledge of the structure's geographical context.

4.1 *Phases of the G.R.D.R. methodology (Valenzuela & Valenzuela, 2016)*

The GRDR. methodology is comprised of four phases which help determine structures' pathologies and vulnerabilities to operating loads and external sources of stress. The methodology's phases are the following:

Phase 1: During this phase, pathologies are identified in the elements constituting the selected structures in a road network, taking into consideration the operational burdens of the structure as well. This must be achieved in field inspections of the structure through the use of inspection sheets.

Phase 2: Once the structure has been assessed through the pathologies of its elements and the operational burdens, it is assessed overall, taking operational burdens into consideration; this survey, as in the previous phase, is achieved through the use of inspection sheets.

Phase 3: Once the structure's pathologies and operational burdens have been assessed, the exceptional loads (seismic activities, floods, volcanic eruptions, landslides, etc.) must be identified. When acting each on its own, a vulnerability index is generated for the structure.

In this phase, it is important that public institutions provide documentation and input from their own databases of local threats.

Phase 4: During this phase, the structure is assessed through a single external stress, as well as in the event of more than one external stress (e.g.: an earthquake and tsunami, or a volcanic eruption and landslides).

The materialization of this methodology proposed by the MOP is carried out by professionals at the local units responsible for the maintenance and supervision of the national road network. These professionals must be trained by specialists in this methodology, so they can then survey the structures and provide an explanation for each pathology within each structure as well as guidance.

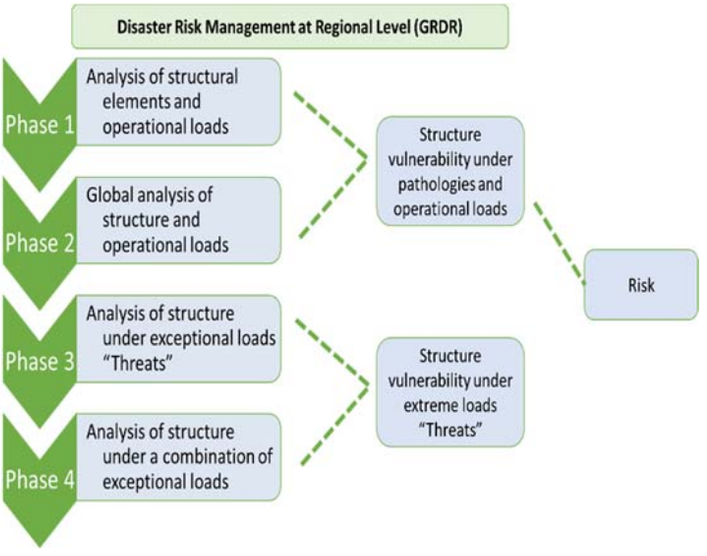


Figure 8. Phases of the G.R.D.R methodology
Source: Author compilation.

5 CONCLUSIONS

In the last two decades there several public policies have been put in place to increase the road network, especially in areas that have been highly fragile due to unfavorable morphological conditions.

The increase in natural disasters is directly related to the changes in the population's demographic and economic models, generating an overcrowding in the country's larger regions, leaving the ends of the territory sparsely populated. This distribution is highly vulnerable due to two important conditions.

Due to the context of the demographic and geographical environments, the latter in particular, during the course of the whole history of road development in Chile the logic of development of the current road network has been constant, based on longitudinal routes that link the country from north to south, which in turn are interconnected with side routes that connect the coastal edge and mountain range, forming a sort of "fishbone" structure (Chamorro, 2016). This results in an increased vulnerability in the national road network against threats of varied nature such as earthquakes, floods, landslides, volcanic eruptions, and fires, among others.

The GRD (Risk Management) Method is a tool for the UNASUR member countries which helps to have defined procedures for prevention and reduction of catastrophic events (tsunamis, floods, volcanic eruptions, among others) that affect each country's infrastructure and to establish plans for the recovery of connectivity and resilience of public infrastructure, designing methodologies for disaster management (Osorio, 2013).

In this geomorphological context, there is a remarkable need to implement the methodology for Management of Risk Disaster at Regional Level (GRDR) with the objective that technical units that inspect state-owned structures take this geographical context into account at the time of inspection. These technical units, such as the Ministry of Public Works (MOP) and the Housing and Urban Development Service (SERVIU) are the ones responsible for the development, implementation, and maintenance of public infrastructure in Chile. In addition, it is very important to take into consideration this methodology at the time of executing any intervention in the road infrastructure and when projecting future works within a road, in order to reduce the risk of disaster.

A new model (GRDR) was proposed in Chile with respect to the initial methodological model proposed by COSIPLAN. In this aspect and due to the country's geography, centralized work generates high costs for the Treasury. It is for this reason that the method proposed by Chile works at the regional level, decentralizing the tool with the objective of reducing costs associated with its application.

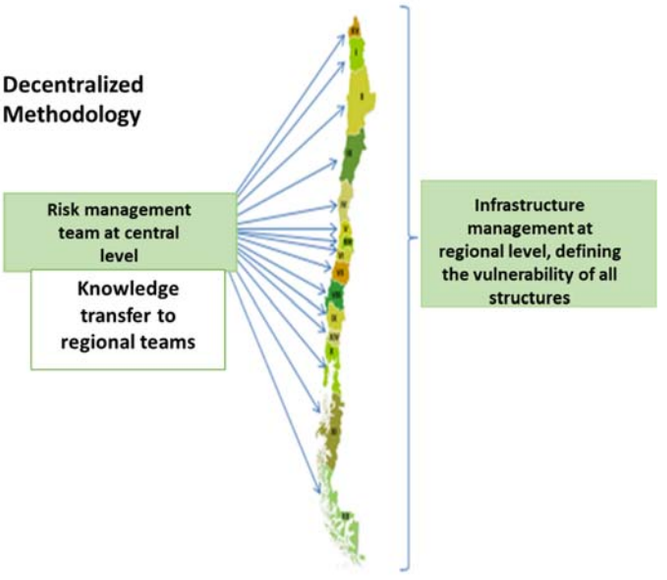


Figure 9. GRD Decentralized Methodology.
Source: Valenzuela (2017).

The application of the GRDR methodology provides a real and clearer perspective of the national road infrastructure, allowing for in-depth analysis of the most fragile areas of the network, supporting the decision-making process in the context of each structure studied, enabling finally a change in the current philosophy of the development of the national road network. COSIPLAN/IIRSA is fostering the application of this methodology in South America and in all its member countries, being Chile one of the pioneers in the application of this method.

The GRDR. method is based both on the road infrastructure as well as the climatological and morphological context where the structure is located, which means that the threats will take an important role at the time to inspect, repair and plan infrastructure belonging to the national road network. This method is focused on reducing the vulnerability of infrastructure while reducing the risk of social and

economic loss in the country in order to obtain a resilient road network.

By 2017 4 GRDR. pilot plans have been successfully carried out in Chile in the following regions: Arica - Parinacota, Aysen, Valparaiso, and Atacama. These plans have identified threats and vulnerabilities in bridges, roads, ports, and tunnels, considering the wide variety of climate conditions and threats from the northern desert to the Patagonian south of Chile.

6 REFERENCES

COSIPLAN (2016). La Gestion de Riesgos de Desastres en COSIPLAN: Metodología y aplicación en infraestructura de Chile y Perú. Buenos Aires, Argentina

Chamorro. A (2016). Investigación y desarrollo de modelos para cuantificar y mitigar el riesgo de eventos naturales en la red vial nacional. Paper presented at the Primer Seminario Desafíos para una Red Vial Resiliente, Santiago, Chile.

Bordas Coddou, A. (2006). Políticas Públicas para Enfrentar los Desastres Naturales en Chile. (Master's Thesis, University of Chile, Santiago, Chile). Retrieved from Http://repositorio.uchile.cl/handle/2250/102822

COSIPLAN. (S.f.). Metodología para la Incorporación de Gestión de Riesgos de Desastres en Infraestructura. Retrieved from: http://iirsa.org/Page/Detail?menuItemId=77#

Osorio, C. (2014). Manual de Usuario-Orientaciones para emprender análisis de riesgo. Paper presented at Grupo Técnico Ejecutivo (GTE) sobre la Metodología de Gestión y Prevención de Riesgos y Catástrofes en la Infraestructura Suramericana de Integración, Buenos Aires, Argentina.

Osorio, C. (2013). Metodología de prevención y gestión de riesgos y catástrofes en la infraestructura COSIPLAN/IIRSA. Paper presented at Grupo Técnico Ejecutivo (GTE) sobre la Metodología de Gestión y Prevención de Riesgos y Catástrofes en la Infraestructura Suramericana de Integración, Santiago, Chile.

Valenzuela, M (2016). Avances en la Nueva Metodología Regional Determinística de Prevención de Riesgo. Paper presented at Reunión GTE sobre Gestión de Riesgos de Desastres., Lima, Perú

Valenzuela, M. & Valenzuela, N. (2016). Metodología DFS-Orientado al análisis de riesgo: Innovación en análisis avanzado. Paper presented at Reunión GTE sobre Gestión de Riesgos de Desastres., Lima, Perú

UNISDR (2009). Terminología sobre Reducción del Riesgo de Desastres. Retrieved from http://www.unisdr.org/files/7817_UNISDRTerminologySpanish.pdf

INDECI (2010). Terminología de Defensa Civil. Instituto Nacional de Defensa Civil, 2010.

CIIFEN. (s.f). Aproximación para el cálculo del riesgo. Retrieved from http://www.ciifen.org/index.php?option=com_content&view=category&layout=blog&id=84&Itemid=336&lang=es

UNESCO (2011). Manual de gestión de riego de desastre para comunicadores sociales. Retrieved from Http://unesdoc.unesco.org/images/0021/002191/219184s.pdf.

Valenzuela, M. (2017). Risk Management System for Natural Disaster On Infrastructure: Regional Approach (GRDR) 11th International Bridge and Structure Management Conference. Table, USA.

Maintenance, Safety, Risk, Management and Life-Cycle Performance of Bridges – Powers, Frangopol, Al-Mahaidi & Caprani (Eds)
© 2018 Taylor & Francis Group, London, ISBN 978-1-138-73045-8

Strengthened Chilean bridges using carbon fiber: State of Knowledge

M. Márquez
Ministerio de Obras Publicas, Santiago, Chile

M.A. Valenzuela & H. Pinto
Pontificia Universidad Católica de Valparaíso, Valparaíso, Chile

ABSTRACT: Strengthening projects using carbon fiber have been implemented in several structures in Chile, such as buildings, stadiums, hospitals, and—very successfully—bridges. This document introduces the techniques implemented for the superstructure and infrastructure of bridges that are under threat of operational load, seismic activity or collapse. For infrastructure in particular, the application of carbon fibers in Lautaro Bridge, Maule Region, Chile, is presented. This structure was affected by the earthquake of February 27, 2010; it sustained damage on some of its piers. This paper shows the application of carbon fiber to concrete piers as a solution to the aforementioned threats. It also looks into the strengthening technique using carbon fiber applied to the Alhue Bridge, located in the O'Higgins Region. The strengthening of this structure is a response to problems related to an increase of load demand, modification of standards and regulation requirements, as well as a repair and prevention measure against damage or defects caused by seismic activity. In the case of the Alhue Bridge, an important increase of load demand was registered at the end of the 20th and start of the 21st centuries, which damaged the structural system of the deck, making the bridge vulnerable to exceeding heavy loads. Through this investigation, it is possible to extend the application of carbon fiber on slabs as a solution to the aforementioned threats, referencing its construction process through strengthening projects carried out in the country.

1 INTRODUCTION

The design, construction, and maintenance of bridges are guided mainly by the recommendations given by the Highways Manual of the National Roads Department of the Ministry of Public Works, complemented by the guidelines established in the AASHTO standards.

Most of the bridges designed in Chile are structures known as traditional bridges, which are made up of a girder superstructure (made of steel or prestressed concrete) with reinforced concrete slab, and an infrastructure of abutments and piers on footing or pile foundations.

The seismic conditions of the country have forced the design, construction, and maintenance of bridges to consider countermeasures against this phenomenon, leading to some existing bridges being strengthened to avoid collapse caused by seismic activity.

An example of this threat occurred on February 27th, 2010, when Chile was struck by an earthquake that reached a magnitude of 8.8 Mw, and the tsunami that followed. The territory affected by this disaster encompasses the area between the Arauco Peninsula (Araucania Region) and north of Pichilemu (O'Higgins Region), approximately 450 km long and 150 km wide. The hypocenter was located at an estimated depth of 30 km.

The aggressive action of seismic activities is part of the permanent threats to bridges built in this country, so it is necessary to keep an up-to-date record of the repair and strengthening techniques used as solutions to the different pathologies that affect these structures; this record is complemented by the Bridge Maintenance Management System, currently developed by the National Roads Department.

The Lautaro Bridge case study, located in the influence zone of the 2010 Chile earthquake, can be found in this context. It shows the rehabilitation and strengthening technique implemented to solve the detected pathologies in a way that makes it an alternative to general strengthening procedures used on traditional bridges in Chile.

2 SEISMIC CASE STUDY

The case study presented is based on the Lautaro Bridge, which uses carbon fiber as a strengthening method.

Lautaro Bridge

The Lautaro Bridge (formerly, Mataquito Bridge) was built in 1985 and is located near Curepto, at km 81.20 of Route J-60-k, Talca Province, Maule Region (Figure 1).



Figure 1 - Map showing the location of the Lautaro Bridge (black circle) (MOP, 2016)

The bridge is 280 m wide, with eight 35 m sections. The total width of the bridge is 7.5 m, with a road that is 6.1 m wide and a 0.7 m wide walkway on either side.

The superstructure is composed of three post-tensioned concrete girders resting on 450x300x40 mm elastomeric support bearings in each section. At the piers and abutments, the girders are braced by reinforced concrete crosspieces. The bridge also has a 20-cm reinforced concrete slab, topped with the roller-compacted concrete roadway.

The infrastructure is composed of the following elements:

2 abutments consisting of an in-fill headwall with wing-walls, both made of reinforced concrete, with pre-excavated reinforced concrete pile foundations.

7 in-fill wall-type piers with pre-excavated pile foundations as well.

Figures 2 and 3 show an overview of Lautaro Bridge.



Figure 2 - Overview of Lautaro Bridge (MOP, 2016)

2.1.1 *Earthquake damage*

After the 2010 earthquake, the main pathology detected in relation to the seismic event was problems in some of the bridge piers (Figures 4 and 5). The observed damage caused to piers No. 4 and No. 5 is listed below:

- Cracking located roughly at mid-height on the pier
- Deformation of the steel strengthening at the base of the piers
- Exposed rebar frame of the piers
- Flaking of the piers

Furthermore, side shifting was observed in some of the sections of the bridge, which thus damaged the lateral stops of the piers (Figures 3). Damage to the post-tensioned girder supports was also observed.



Figure 3 – Pier damage in Lautaro Bridge (MOP, 2017)

2.1.2 *Pier strengthening project*

The bridge strengthening project considers the application of carbon fiber bands at mid-height on piers No. 4 and No. 5 in order to repair the damage that was found and to improve the load capacity of the structure.

The project covers the following technical specifications, among others:

- Materials:
- High-strength mortar
- Strengthening rebar: A 63 - 42 H, Diameter18 mm

The construction sequence used (Figure 4) also considers the incorporation of carbon fiber to the strengthening of the piers with strengthening steel.



Figure 4 - Logic sequence of application of carbon fiber on piers (author compilation)

Each of the construction stages carried out is explained below:

Stage 1: Strengthening of the pier (Figure 5)

1. Straighten existing strengthening steel that shows deformations back into their original vertical position.
2. Place rebar (18mm diameter) joined to existing rebar.
3. Place repair mortar in a 3 m height, as this is the height that requires the rebar strengthening.

Stage 2: Implementation of carbon fiber band (Figure 6)

Reinforce external part of the piers with two layers of type TYFO SHC - 41 using TYFO S epoxy and a TYFO or polyurethane paint. The fiber circles around the outline of the pier, connecting on both frontal faces (the height of the carbon fiber strengthening is 4.2 m at mid-height on the pier).

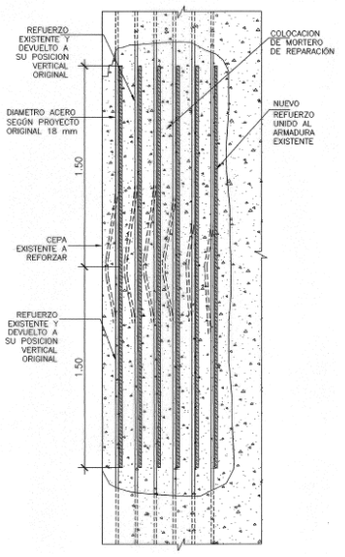


Figure 5 - Repairs and strengthening of the pier
Source: Plans for the Lautaro Bridge project. Contains "Strengthening of No. 4 and No. 5 piers with carbon fiber"

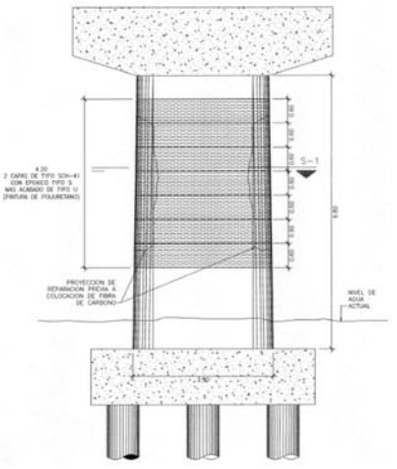


Figure 6 - Implementation of the carbon fiber
Source: Plans for the Lautaro Bridge project. Contains "Strengthening of No. 4 and No. 5 piers with carbon fiber"

2.1.3 *Strengthening solutions using carbon fiber*

The strengthening project using carbon fiber bands is implemented with the objective of reinforcing the structure, thus increasing the operational lifespan of the Lautaro Bridge. The durability of this structure is constantly threatened by seismic activity as well as load demand over the design limit, which then cause different pathologies to the bridge components.

In this case, the decision was made to apply carbon fiber strengthening where work was considered previously to provide optimal conditions for the application of the fiber and the improvement of the current state of the damaged elements. The work on Lautaro Bridge covers the repair and strengthening of the damaged piers.

The use of carbon fiber provides a solution to the aforementioned damage sustained by components of the infrastructure.

3 OVERLOAD CASE STUDY

There has been an increase of the load demand on Route 66 (the Fruit Road) which connects the port city of San Antonio in the Valparaiso Region to Route 5 South near the town of Pelequen in the O'Higgins Region; this road is also laid through part of the Metropolitan Region.

According to studies of this route (MOP), its characteristic vehicle flow shows a high volume of truck traffic, particularly at the access to the Port of San Antonio, which allows an effective connection to international trade. In this context, an important tonnage has been transported to and from the seaport through its access routes, one of which is Route 66 as its main communication road with Route 5. According to MOP, the tonnage projections for the Port of San Antonio (Figure 2) are the main factor that caused an increase of load demand on the bridges along the Fruit Road.[1]

The aggressive action of seismic activities and the extreme load increases are part of the permanent threats to bridges built in this country, so it is necessary to keep an up-to-date registry of the repair and strengthening techniques used as solutions to the different pathologies that affect these structures.

In this context, a study has been developed of one of the techniques used as bridge strengthening based on the incorporation of carbon fiber bands to the superstructure of bridges, with the purpose of counting with the general strengthening procedures applied to traditional bridges in Chile. For this, the case study of the Alhue Bridge (located in Central Chile) is used as a reference, which has been subjected to strengthening projects using this technique.

3.1.Alhue Bridge

The Alhue Bridge is located in the sector of Las Cabras, at Km 67.61 of Route 66—the Fruit Road, Cachapoal Province, Libertador General Bernardo O'Higgins Region, Chile (Figure 7).

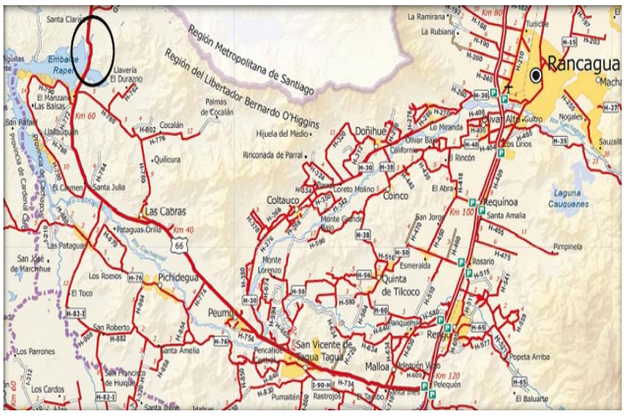


Figure 7 - Map showing the location of the Alhue Bridge (black circle) (MOP, 2015)

The original bridge is composed of two end sections, each approximately 12.50 m long, as well as a central section 15.40 m long, making the structure 40.20 m long from one end to the other. Its total width is 10.20 m, consisting of a road that is 8.00 m wide and a 1.10 m wide walkway on either side.

The superstructure is composed of two 1240x250 mm IN profile metal beams in each of the end sections and two 1240x350 mm IN profile steel beams in the central section; in both cases, the beams are separated 6.80 m and transfer the loads to the infrastructure through support steel plates. The beams are braced at the piers and the middle of their section by metal profiles, while no bracing or crosspieces can be found in the abutments.

Furthermore, the bridge has a reinforced concrete composite deck and 27 pre-tensioned concrete slabs that cover the entirety of the structure. The size of the slabs is 6.60x1.50x0.16 m, which means their effective support on each beam is 7.50 cm.

The infrastructure is composed of the following elements:

[1] The port of San Antonio had a 48 % share in the regional market in 2007 (MOP)

- 2 abutments consisting of an in-fill headwall with wing-walls, both made of reinforced concrete, with direct foundations.
- 2 piers consisting of columns with cap beam and direct foundations.

Currently, the Alhue Bridge (Figure 8) has similar characteristics to the original, since the interventions executed on it have not had much impact on its original structure.



Figure 8 - Overview of Alhue Bridge, 2015 (MOP, 2015)

3.1.1 *Damage caused by increased load demand*

The main pathology observed—the reason behind the strengthening project—is problems with the bridge deck; this has caused significant damage to 5 of the 27 pre-tensioned concrete slabs. The load demand on the bridge has been increasing, so it was decided that a strengthening project on the slabs would be carried out by means of incorporating carbon fiber bands so that the bridge remains operational.

3.1.2 *Strengthening project*

The strengthening project on the bridge carried out in 2007 considered the application of carbon fiber bands on the underside of the pre-tensioned concrete slabs, with the intention of improving the load capacity of the structure.

The strengthening project covered some technical considerations or techniques which must be taken into account for its proper execution so that it complies with the required quality standards.

Materials:

- Prefabricated slab concrete (H-50)
- Topping slab concrete (H-45):
  Characteristic cylindrical resistance in transfer: f'ci ≥ 400 [Kg/cm2]
  Characteristic cylindrical resistance after 28 days: f'c ≥ 400 [Kg/cm2]
  Maximum aggregates size = 2.0 cm
- Non-pre-tensioned steel:
  A 63 - 42 H with ledges
  Minimum anchor and overlap lengths according to AASHTO'96
  3.8 cm lining
- Pre-tensioned steel:
  Ø3/8" cables, grade 270 (low relaxation) must comply with the following standards:
  High-strength wires: ASTM A 421 – 80
  7-wire cable ASTM A 416 – 80
  3.8 cm lining
  Tensioning:
- Preload= 2.3 ton
- Tensioning strength 6.92 ton
- Elongation Max. 931 mm
  Min. 842 mm
  Others:

- HS 20 – 44 AASHTO 1996 standard truck
- This strengthening project considers that the depth of the cracks if there are any, should not be over 20 mm, which will be determined during work.
- The General Technical Specifications for Construction, vol. 5 of the Highways Manual, apply
- The planner must provide counseling, as this repair is being carried out without the construction plans
- This is a provisional repair meant to extend the operational lifespan of the bridge by at least five years.

Besides the incorporation of carbon fiber, the construction sequence that was used (Figure 9) considers the replacement of the slabs where damage and defects were observed.

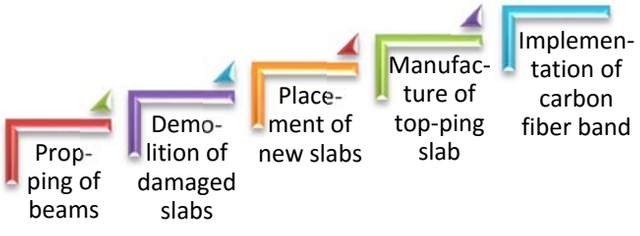


Figure 9 - Logical sequence of the application of carbon fiber to the slabs of Alhue Bridge (author compilation).

Each of the construction stages carried out is explained below:

Stage 1: Propping of the beams

1. Place props (provisional structures) under the beam, around the existing piers (Figures 10 and 11)
2. Place load stiffeners or wooden pieces in the propping spots

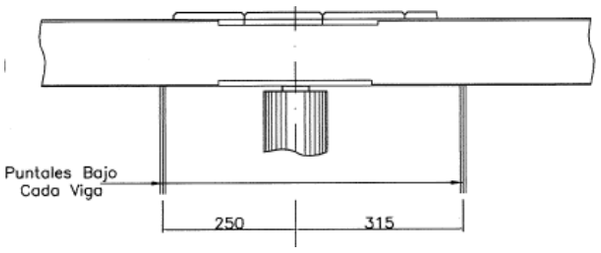


Figure 10 - Disposition of the load stiffeners under the beams Source: Plans for the Alhue Bridge project (Repairs). Contains "slab type section"



Figure 11 - Disposition of the load stiffeners under the beams

The foundation seal of the propping (provisional auxiliary structures) must be received by the construction manager and the planner in order to avoid subsidence.

Stage 2: Demolition of damaged slabs

1. Demolish damaged slabs (existing 1.5 m wide slabs) leaving the reinforced concrete slab rebar. In general, the demolition of five slabs is considered (Figure 12): two in the north support (Las Cabras pier) and three in the south support (Melipilla pier).

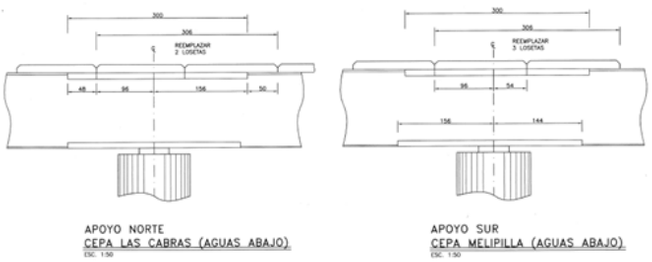


Figure 12 – Las Cabras and Melipilla Piers

Stage 3: Placement of new pre-tensioned concrete slabs according to project

1. Manufacture the 1.50x6.60 m pre-tensioned concrete slabs (Figure 13) according to technical specifications. For the manufacture of the slabs, the use of a stress layer is considered, with a distance of 194.70 m between wedges.
2. Position the new slabs in place of the ones that were demolished. The slabs will be lifted only from the hoisting points provided, keeping it horizontal at all times. Four hoisting hooks are considered, each 30 cm from the edge of the slab.

Stage 4: In-situ manufacture of the reinforced concrete topping slab

Stage 5: Implementation of the carbon fiber band

1. Clean, polish, and even out the underside of the prefabricated slabs
2. Reinforce the underside of the slabs with type SIKA WRAP 300C carbon fiber band. One 0.170 mm layer will be used, impregnated with SIKADUR 306 resin. The fiber must be placed in a transverse direction to the axes of the superstructure beam (Figure 13)



Figure 13 - Carbon fiber applied under the pre-tensioned slabs. Source: Documents provided by BDL Engineering, Diagnostic, Structural Review1

3.1.3 *Strengthening solutions using carbon fiber*

The main backgrounds provided in this paper refer to the analysis of one strengthening project using carbon fiber bands to increase the operational lifespan of the Alhue Bridge. The durability of this structure is constantly threatened by seismic activity and load demand over the design limit, which then cause different pathologies to the bridge components.

In this case, the decision was made to apply carbon fiber strengthening where work was considered previously to provide optimal conditions for the application of the fiber and the improvement of the current state of the damaged elements. Alhue Bridge requires some of its slabs and its topping slab to be repaired.

It is possible to propose the use of carbon fiber as a solution to the aforementioned damage sustained by components of the infrastructure (Figure 14).

4 CONCLUSIONS

Considering external threats, the effects of seismic activity are among the main pathologies that affect traditional bridges in Chile.

Case studies like Lautaro Bridge are routine in repair and strengthening projects to tackle these pathologies.

The strengthening of bridges using carbon fiber is a solution which offers technical and economic advantages compared to other alternatives.

The use of this strengthening technique is not common in Chile; however, following the development of the current Bridge Maintenance Management System of the National Roads Department, it should be considered a valid strengthening alternative.

Bridge professionals are required to specialize in this strengthening typology.

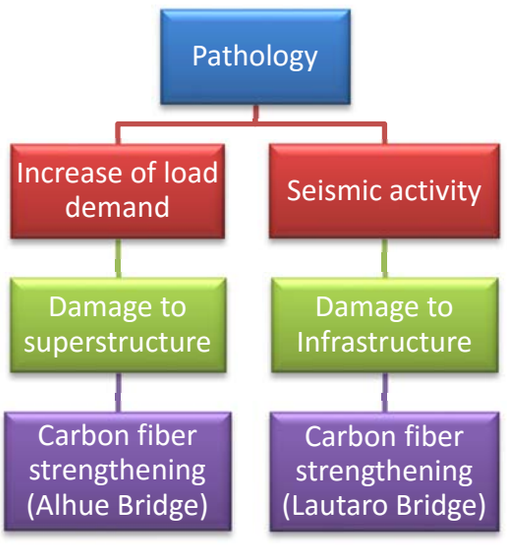


Figure 14 - Strengthening techniques using carbon fiber (Author compilation).2

Among the main pathologies that affect traditional bridges in Chile, external threats are included, such as the effects of seismic activities and an increase of the load demand on the structure, produced by the arrival of vehicles carrying loads greater than those considered in the original design.

Particular cases, such as the Alhue Bridge, enable identifying the techniques currently used in the country, as well as solving these pathologies.

In the case of the Alhue Bridge, the structure showed problems on the deck produced by the increase of loads that traveled through Route 66 (the Fruit Road), which communicates the port of San Antonio to Route 5 South.

5 REFERENCES

Valenzuela, M & Marquez, M. 2016. Procedimiento de refuerzo de puentes tradicionales chilenos: Socavación y Sismo. CINPAR. Octubre. Porto. Portugal.

Dirección de Vialidad -MOP. 2016. Informe de inspección visual con camión de inspección VII región del Maule.

Dirección de Vialidad - MOP. 2017. Manuales de Carretera.

MOP. (s.f.). Ruta 66 - Camino de la Fruta. Santiago: Cordinación de Concesiones de Obras Públicas.

Maintenance, Safety, Risk, Management and Life-Cycle Performance of Bridges – Powers, Frangopol, Al-Mahaidi & Caprani (Eds)
© 2018 Taylor & Francis Group, London, ISBN 978-1-138-73045-8

UAV: First Chilean Proposal of use on Road Bridge Inspections

M.A. Valenzuela, N. Valenzuela & A. Peña-Fritz
Pontificia Universidad Católica de Valparaíso, Valparaíso, Chile

D. Torres & M. Márquez
Ministerio de Obras Publicas, Santiago, Chile

ABSTRACT: Routine inspections of traditional bridges in Chile use the Maintenance Management and GRDR programs for their conservation and risk assessment, respectively. In order to do this, visual inspections or nondestructive tests are done by professionals, supported by survey trucks if the inspection zone has a difficult access. With the development of new technologies, UAV (unmanned aerial vehicle) utilization has been proposed for the inspection of bridges in Chile, which is already being used in the mining industry and the inspection of roads and hydraulic works. This document explains the current regulations, advantages, and requirements for the use of UAVs in Chile, focusing on their implementation in the inspections of bridges in Chile. This study presents the first experiences in the use of this technology following maintenance and risk analysis programs, and offers a comprehensive protocol for the standardization in the use of this technology.

1 INTRODUCTION

Most of the bridges that are in Chile are managed by the Roads Department of the Ministry of Public Works.

There is mainly one type of bridge that is constructed in Chile, which considers isostatic beams in the superstructure. These beams can be of concrete, pre-stressed and post-stressed, or steel, with a maximum span of 50 m. (Valenzuela M. et al, 2015)

These types of beam bridges are cheaper and faster to build, making them the most used typology due to favorable geographical conditions in the north and center south of the country, where there is no need to cross deep (eg. Amolanas Bridge) and large valleys (eg. Juan Pablo II Bridge).

The Amolanas Bridge is the highest road bridge in Chile and is located on the La Serena stretch - Los Vilos, Route 5 North in the Coquimbo Region. It has a length of 268 m and a height of 101.3 m. This bridge has its own characteristics for seismic protection, such as slide bearings on piers and visco-elastic dampers in abutments acting longitudinally. (Moroni, O., et al. 2004)

Juan Pablo II Bridge crosses the Biobío River in the city of Concepción. Currently, it is the longest bridge in the country (Fig. 2). It is 2430 m and is structured in 75 spans of 32.4 m each, with piers-piles and pre-stressed beams. (Morales, C., 2014)

Since 1995, the typology of bridges expands from simply supported beams (with expansion joints in the abutments for beams) to continuous beams and slab bridges, reducing points of failure by eliminating expansion joints to improve their seismic behavior and reduce maintenance cost. From 2002 to 2012, the continuous beam bridges were built with seismic isolation (eg: Marga Marga Bridge), and continuous slab on piers and abutments with a maximum span of 60 m. The seismic isolation is performed through elastomeric plates in the support beams, which, by the elastic behavior of the material, the superstructure has a degree of independence from infrastructure, reducing damage during an earthquake. (Campos, R., 2012)

The new tendency in bridges is to design it without expansion joints (jointless bridges), being implemented by the Road Department, highways and bridges in developed countries such as the United States and currently recommended in new Seismic Criteria Chilean. The benefits obtained from these structures are cheaper and safer, functionality and performance are improved in relation to disaster response, especially in cases of earthquakes (Campos, R., 2012).

Table N° 1 shows the main structural elements and their types, of a traditional Chilean bridge (Valenzuela M. et al, 2015), (Vallejo I, 2014).

Element	Type 1	Type 2	Type 3	Materiality
Piers	Wall	Pier-piles	Pile	Reinforced concrete
Abutments	Wall	Pier-piles	Spill-through	Reinforced concrete
Deck	Beam	Slab		1 – Reinforced concrete 2 – Steel

The following illustration shows the main elements of a traditional Chilean bridge.

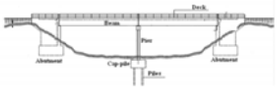


Figure 1. Main elements of a traditional Chilean bridge (Highway Manual, Volume 3, Road Department, 2013)

The Bridge Department has led to a proposal for the implementation of a Management System for the Maintenance of Bridges.

A management system for bridges must contain at least:

(a) Inspection techniques applied to bridges;
(b) Inspection protocols, including sheet inspection;
(c) Technical visits, defining, in corresponding technical reports, the implementation of destructive and nondestructive testing;
(d) Proposal for monitoring plan, instrumentation, and maintenance

The results of the new system of management are included in future versions of the Roads Manual as related to the Bridge Department, with code applied to the design, construction, and maintenance of bridges in Chile, as part of the philosophy for the life cycle of the structures.

Currently, inspections are carried out by survey trucks with telescopic walkways that are extended under the deck of the bridge; by visual inspections done by personnel; or by tests with simpler equipment, such as ladders and photographic cameras, among others, which are easy to use and implement in Chilean traditional bridges.

The biggest problem with this approach is its high cost, since traffic has to be closed for one lane; work or car accidents may occur; bridge length is variable and the approach does not work for all types of bridges, as it happens with singular bridges in Chile (such as cable-stayed, suspension or cantilever bridges). For this reason, with the help of the Ministry of Public Works (MOP), Chile is beginning to use aerial inspections with the **Remotely Piloted Aircraft System (RPA)**, with a focus on bridge inspection. This study offers the first protocol for the use of UAVs in the inspection of bridges in Chile, which was implemented in the inspections of the Maintenance Management (Marquez, M. et al. 2016) and Regional Disaster Risk Management programs, promoted by the MOP and Pontificia Universidad Católica de Valparaíso (Valenzuela, M. et al 2017).

2 GENERAL ASPECTS ABOUT UAVS:

The flight system can be referred to as UAV (Unmanned Aerial Vehicle), UAS (Unmanned Aerial System), RPA (Remotely Piloted Aircraft), o RPAS (Remotely Piloted Aircraft System). The term RPA is used for bridge inspections because the terms UAV and UAV are used for military aircraft, while the terms RPA and RPAS are used for civilian aircraft. For this reason, the term RPAS aircraft will be used, following term guidelines from the Directorate General of Civil Aviation (DGAC).

Applicable Chilean regulations:

-Instructions from the DGAC,
- DAN91: Aviation regulation, Rules of the Air
- DAN151: Aviation regulation, remotely operated aircraft operations (UAV) in events of public interest, carried out over populated areas.

Application of regulation DAN91:

The regulation is applied to each flight with RPAS, in situations where the area is not populated (see the definition in the regulation).

In order to fly under this regulation, an authorization from the DGAC is needed, which requires the following:

- RPAS operator license
- RPAS register
- Authorization from the DGAC, a filled sheet for flight plan authorization, etc. (Annex DAN91).
- Third party liability insurance

Application of regulation DAN151:

The regulation is applicable for public interest events in populated areas, such as events covered by the media, natural disasters, sports events, etc. This regulation does not apply to the use of RPA in bridge inspections.

In both cases, third party liability insurance is required.

Prior to the inspection, no-fly zones must be checked.

DJI's no-fly zones do not supersede local authorities' regulations or common sense.

Avoid flying in areas where rescue teams are actively using the airspace.

Not following these requirements can lead to fines by any affected third party in case of an accident.

Minimum technical requirements for the use of RPAS

Five minimum technical requirements must be considered for the inspection of bridges:

- A camera and video recorder with stabilizer and HD quality
- A monitor with a minimum range of 500 meters.
- Four smart batteries with an estimated duration of 20 minutes each.
- 100 GB storage
- A computer with an i7 processor, 32 GB of RAM, and between 500 GB and 1 TB storage.



Figure 2. RPA used for inspections

Environmental considerations

The following eight environmental requirements or conditions are needed to carry out a bridge inspection flight:

- Flight must take place in areas distant to structures adjacent to the bridge. This also applies to minimum distances to the inspected structure, so as to avoid any type of obstacle.
- Inspections must not take place near or over large crowds of people.
- Flight over 120 m of altitude must be avoided. This also applies to the inspection of the area surrounding the bridge.
- Extreme caution must be taken when the flight is carried out in areas over 6000 m above sea level.
- It is recommended that flight takes place in mild weather, with temperatures from 0 to 40 degrees Celsius.
- Special care should be taken when flying indoors, since the stabilization functions may be subject to interference. This also applies to inspection of box girder decks and even decks with metal girders with little spacing in between (less than 3 meters).
- Inspections must not be carried out during adverse weather conditions. These include wind speeds over 10 m/s, snow, rain, fog, strong winds, hail, lightning storms, tornadoes or hurricanes.

Maintenance and care

Maintenance of the RPA requires an inspection of the propellers before its use. If the propellers are worn, chipped or broken, its use should be avoided.

Equipment should be stored in places with temperatures between 22 and 28 degrees Celsius.

3 RPAS FLIGHT PROCEDURE CYCLE FOR THE INSPECTION OF BRIDGES

The next figure shows the UAV flight procedure cycle for the inspection of bridges.



Figure 3. Flight cycle procedure for the inspection of bridges.

Mission or inspection planning

For an adequate inspection planning and technical visit, the cycle described in each stage must be followed, starting with the identification of the place of inspection and its scope, that is, whether it is a detailed or emergency inspection.

Each of the inspection stages is explained in detail in the following section.

Office preparation

The following four items must be checked before the bridge inspection:

- Check the pilot's license and area of inspection. This is done by obtaining information about the plans and previous inspections.

- Check the RPA's batteries, camera, propellers, sensors, configuration, etc.

- For each flight, an authorization from the DGAC is recommended. This authorization must be obtained when the inspected structure is located near airfields or airports.

- In order to guarantee the safety of the UAV's flight maneuvers during the bridge inspection, the operator should be a DGAC authorized pilot (with a UAV's license and RPA inscription register), which ensures that the pilot is aware of the rules of the air.

Inspection of the area

An evaluation of the flight area is recommended in order to determine the type of regulation that must be applied. For singular bridges, a routine inspection is recommended in order to identify the RPA's basic flight parameters.



Figure 4. Inspection of the bridge location.

Furthermore, air traffic, obstacles and limits, take-off and landing zones, ground traffic, and weather conditions have to be checked. Singularities that will be inspected by the RPA also have to be identified.

Flight planning

Flight planning is important to study the viability of the use of the UAV, optimize flight time, and identify the best-suited areas to use the equipment, considering the limitations of a truck or visual inspections. In order to do this, wind direction, obstacles and distance, take-off and landing height offset must be calculated through a previous technical visit.

When the RPA viability is determined, a checklist for the RPA's image collection must be completed. This checklist will complement previous routine inspections and help in the analysis of performance indexes, according to the Maintenance Management or GRDR programs.

We present a list of minimum elements to be inspected with a UAV if the flight is feasible.

The list can be divided into three categories:

- General aspects of the structure. In this case, the UAV is used to study the conditions of the side of the bridge, with a focus on vehicle traffic, adjacent structures, hydraulic system, and longitudinal and horizontal projection overviews. The following figures are examples of the procedure on traditional Chilean bridges.



Figure 5. Aerial view of Limache bridge.



Figure 6. Las Gaviotas Bridge. River bank or vegetation environment.

- Superstructure. An inspection and image recording of the bridge's deck is performed, considering a flight above the roadway (of

four meters), with the objective of identifying the state of the pavement, expansion joints, and bridge accesses. Barriers, railings, and street lighting must be carefully analyzed. Furthermore, a flight must be performed in order to study the state of the girders and cap. This procedure requires the assistance of a professional and it is recommended that the operator is located below the deck, as long as it is safe.



Figure 7. Colmo Bridge. Longitudinal girder with a Gerber support system.

- Infrastructure. Piers and abutments elevation, including bridgeheads and connection elements with the superstructure, are considered for inspection. Support elements, hold-downs, and stoppers are inspected. The operator should be positioned under the bridge's deck, with an assistant to help with operations under the deck. Special care should be taken with bridges with steel girder decks and steel decks, as the GPS signal may be lost.



Figure 8. La Fabrica Bridge. Piers inspection.

In addition, the flight plan must consider:

A flight plan can be plotted in order to produce planimetrics, a 3D model, or an orthophoto of the area where the bridge is located, which can be opened on Google Earth. In that case, it is necessary to have aerial images of the area's planimetric and the images need to be overlapped at 80%.

Knowing the highest and the lowest heights in the area to be surveyed in order to avoid the RPA from crashing into any surface.

Determining the points of interest where pictures are to be taken. These points shall be areas that cannot be accessed by land since flight time is limited.

Pre-flight checks

These checks can be divided into two categories: RPA-specific requirements and bridge inspection requirements.

a) RPA requirements

There are minimum and general aspects to be considered for any inspection. The following should be noted:

The RPA should be in good conditions; that is, that the propellers are in good condition and are properly attached to the RPA before every flight, that the motors start and work normally, and that there is nothing obstructing the motors. In addition, the compass should be calibrated, the camera should be clean, and the lens should be free of smudges. Touching the sensors should be avoided since covering or interfering with them will affect the RPA's stability.

The RPA's software must be updated and properly installed.

In addition, all batteries should have enough power for the flight plan and inspection, including batteries from the remote control, smart flight battery, or any other mobile device. Likewise, there should be enough space on the memory card for taking pictures and recording videos according to the surveying plan.

Regarding responsibility, local regulations and those of authorities must be followed and flight conditions must be adequate, including weather, RPA, and pilot conditions (the effects of alcohol, drugs, or any substance that might affect the pilot's cognitive skills should be avoided).

b) Inspection requirements

Regarding bridge inspections, the following aspects should be noted:

Battery levels for the RPA, remote control, and monitor should be checked; sensors should be connected, the compass should be calibrated, and the fly to home configuration should be above the highest obstacle in the surveying area. Thus, a 50 meters height is recommended.

The operator should have a clear view of the RPA at all times or the signal should be good enough to watch the remote control's monitor without interrup-

tions. This is particularly important for inspections under the bridge's deck or when the structure has cables or other small obstacles.

In order to take pictures in hard-to-reach locations, such as shores, girders, piers, abutments, etc., there must be a second viewer located perpendicularly to the RPA, in order to have a proper depth of view and avoid accidents or crashes with obstacles, such as branches, rocks, walls, etc. The second viewer can carry a radio to inform the operator about movements of the RPA in that direction.



Figure 9. Pilot with a second viewer

Surveying plans must be checked and all flights should follow instructions from the engineer in charge of the inspection, especially regarding the identification of girders, piers, and abutments.

Flight

The flight takes off at point H (where the monitor is located) and it should be noted that there is a five-meter margin of error from point H at landing. In addition, the RPA's flight time will depend on wind conditions; that is, when wind resistance is higher, the battery lasts less time. Our experience shows that it has between 15 and 30 minutes of flight time. For inspections, at least three takeoff/landing areas are recommended for the proper inspection of the bridge, namely: bridge deck for inspecting the superstructure and in both shores, upstream and downstream, respectively. This will allow for an adequate visibility for inspecting the infrastructure. In case of inspections under the bridge, GPS connectivity and calibration must be checked. A clear landing area is recommended, and it should have a radius of at least five to seven meters from the fly to the home point (H). This aspect is important to consider for bridges are built on steep shores, since those areas might not be suitable.

Flights should last at least 10 minutes per bridge, divided into the three inspection categories. Video recording is recommended. In case of specific pathologies, photographs can be taken. Photographs must be taken according to the pathology or structure, as indicated by the engineer in charge. Pannings must be slow and last at least five seconds in each inspected location, in order to avoid distortions in the images.

Ideally, at the moment of recording or taking pictures of the structure, the pilot should be accompanied by the engineer in charge of the inspection or a qualified technician, so that information can be coordinated with the visual inspection software or programmed NDTs.

In the presence of cables interfering lengthwise or crosswise, working on the opposite shore is recommended in order to reach the elements, or at more than 20 meters from the power line.

Never record under the cap if the bridge is less than seven meters above the land or surface being surveyed, because of the strong likelihood of crashes and loss of signal.

RPA systems recommend against flying over reflective surfaces, such as water or snow because they affect the visual positioning systems. For this reason, bridge inspections should be performed at times when the river's reflections are lowest.

Height can be adjusted when the RPA is returning to the point of origin in order to avoid obstacles. For this reason, improvisations should be avoided during inspections; that is, in case of finding unexpected pathologies, the following steps are recommended: recording the event, finishing the flight plan, and preparing a new inspection. If the battery reaches 20% or point of no return feature activates the RTH function, the RPA should be landed in a safe location. If the battery reaches 10%, the RPA should be landed on a safe location with the camera aiming at the landing point, in order to control descent. In addition, the left stick should be aimed upwards in order to decrease the speed of descent of the RPAS and find a safe landing place for the RPA.

After landing, the motor should be turned off first, then the Smart Flight Battery, and then the remote control.

Post-flight check and information processing

Once inspection flight is finished, data must be extracted from the Micro SD card in order to be processed in the field computer. This process must be performed under the supervision of the professionals in charge of the inspection to determine the order of the gathered data and whether it is enough to be analyzed and interpreted.

In case of insufficient data, inspection and flight should be repeated to gather enough information.
For the processing of data, inspectors can see the pilot's monitor in real time or through the live streaming app in order to verify the surveying plan is being followed. Otherwise, data should be processed according to the Maintenance Management program's inspection templates (Marquez, M. et al. 2016) or the GRDR methodology (Valenzuela, M. et al 2017), dividing information into infrastructure inspection and possible environmental threats.

In this case, it is recommended that data comprises both photographs and videos in order to have a general picture of the area and details of the pathologies found, which would allow for a more precise evaluation of performance indexes of the structure.

If monitoring equipment is available at the bridge, inspection data gathered with the RPA must be integrated. Likewise, if BIM methodology has been implemented, RPA inspection must be added to the bridge's record.

4 CONCLUSIONS AND PROTOCOL PROPOSALS

According to the experience and implementation of inspections using the RPA system in Chile, general guidelines to be implemented in Chile's Manual for Roads are listed below:

Duties and obligations of the surveying person or persons before the inspection.

The flight plan should include at least:

- Name of operator and assistant (if applicable).
- Date of inspection and estimated duration.
- A short description of the flight's purpose.
- RPA's model.
- Geographic coordinates of the area to be surveyed.
- The dimension of the flight area.
- Length of the flight.
- Expected flight altitude ranges.
- Map with the corresponding flight route. Clearly marked north.
- Image recording type. It can be expressed verbally or through supporting images.
    - For specific images, specify the amount and distance between points.
    - For videos, specify amount and direction of the shoot.
- Flight authorization over the flight plan's specified area should be requested to the corresponding authorities. The flight plan should be attached to the request for its approval.
- Equipment should be checked for proper functioning and battery.
- Weather should be checked for the day of inspection in order to make sure wind and rain conditions are appropriate.

Duties and obligations of the surveying person or persons during the inspection.

- The inspection shall not begin unless the necessary traffic management measures are taken, whether it be detours, traffic interruption of one or several lanes, or road closures. If authorized, inspection can be performed without interrupting traffic, as long as conditions allow for the rest of the guidelines to be completely followed.
- Wind conditions must be checked before starting. In case of winds out of the range that is acceptable for the device, the inspection shall be suspended until conditions are acceptable. If wind conditions do not improve for a long period of time, the inspection shall be canceled and reprogrammed.
- The device should be checked to guarantee it has been assembled properly and that it works normally before take-off.
- At take-off, the operator shall be located in a place with a direct line of sight of the device at all times. If this is not possible, an inspection assistant equipped with a radio shall be required, so at least one person maintains a line of sight of the RPA at all times.
- The operator shall not fly outside of the authorized area, nor aim the device's camera to unauthorized areas.
- If weather conditions get worse and are not acceptable during flight, the inspection shall be suspended until they improve.

Duties and obligations of the surveying person or persons after the inspection.

- -Once the inspection is finished, the RPA shall be landed in a place that is safe for all participants.
- -Traffic will be resumed once all participants have left the surveying area.
- -Inspection results shall be properly organized and delivered to the bridge's or viaduct's administrator, along with recommendations for maintenance and/or repair.

Operator

- -The operator shall have a RPA certification according to their specialty.
- -The operator shall have at least 2 previous flight experiences (4 experiences for populated areas). These experiences shall be acquired through field assistance to certified operators in previous inspections.

Minimum points of inspection for bridges or viaducts.

- -RPA inspection shall cover the following minimum points for bridges or viaducts.
- -Aerial longitudinal view;
- -View of accesses;
- -General view of the surrounding area;
- -Lateral view of infrastructure;
- -View of infrastructure in detail;
    - o View of Pylons;
    - o View of Abutments;
    - o Lower view (with help of assistant);
    - o View of supports in detail.

5 REFERENCES

Vallejo, I; Valenzuela M.A & Márquez M. (2015) Design Parameters of Suspension Bridges: Updates of State of Art and its Application on Multi-span Typology, MultiSpan Porto'15 Conference, Porto, Portugal.

Valenzuela M.A., Márquez M. & Vallejo I (2015) Multi-span Bridges: The First Chilean Experience and Future Challenges, MultiSpan Porto'15 Conference, Porto, Protugal.

Valenzuela M.A (2016) "State of Art of Bridges Maintenance Programs in South America. Experience on seismic hazards and scour", TU COST meeting Belgrade – Serbia

Valenzuela, M.; Valenzuela, N.; Romo, R. (2017).Management System for Natural Risk Disaster on Infrastructure Regional approach (GRDR). 11th International Bridge & Structure Management Conference, Mesa, USA

Campos, R. & RCQ Engineering (2012). "Design of Bridges and Viaducts". The Engineering that coming, V Congress AICE (ed.). November 10, 2012, Santiago.

Morales, C. (2014). "Seismic isolation system for the viaduct Las Cruces, Route 160". AICE - Association of Structural Civil Engineers (ed), III Conference: Structural Engineering Sample, June, 2014, Santiago, Chile.

Moroni, O., Sarrazin, M., Benavides, C., & Dìaz, A. (2004). "Dynamic characteristics of Chilean bridges with seismic protection" in RevistaSul-Americana de EngenhariaEstrutural, V. 1, n. 2, p. 31-54, 2004.

Vallejo, I. (2014). Suspension Bridges of large span: Design and Construction applied to Chile. Memory for the degree of Civil Engineering, University of Los Andes, Santiago, Chile.

Márquez, M. Valenzuela, M. Espinoza, J. & Campusano, J. 2016. Diagnóstico de Puentes e Implementación de Sistemas de Gestión para Conservación. 12° PROVIAL. Agosto. Viña del Mar. Chile.

SS19: Bridge deterioration modeling and probabilistic bridge maintenance needs forecasting

Organizers: R. Goyal, M. Whelan & T. Cavalline

Maintenance, Safety, Risk, Management and Life-Cycle Performance of Bridges –
Powers, Frangopol, Al-Mahaidi & Caprani (Eds)
© 2018 Taylor & Francis Group, London, ISBN 978-1-138-73045-8

Predictive fidelity of bridge deterioration models: probabilistic vs deterministic

R. Goyal, M. Whelan, & T. L. Cavalline
University of North Carolina at Charlotte, North Carolina, United States

ABSTRACT: North Carolina was one of the original states to develop and implement a bridge management system (BMS) shortly after formal bridge inspections were mandated by federal legislation in the United States. However, the general form of the deterioration models currently in use by the North Carolina Department of Transportation to predict future changes in condition ratings of bridges has remained unchanged since original development. These models are deterministic in nature, piecewise-linear, are based on average condition rating durations calculated from historical bridge inspection records, and have relied on pre-classification to account for the effects of explanatory factors on deterioration rates. To overcome limitations in the predictive fidelity of these legacy models, a proportional hazards-based probabilistic deterioration model was developed and implemented on the historical database of over 35 years of deck, superstructure, and substructure condition ratings for the North Carolina state bridge inventory. These probabilistic models are multivariable, duration-based, and non-stationary with a non-homogeneous Markov chain prediction process. A simplified stationary approach was also developed for use within a conventional homogeneous Markov chain. This paper presents a comparative analysis of the predictive fidelity of updated deterministic models and the newly developed probabilistic models. In the absence of future response data, a methodology developed for a quantitative assessment of the predictive fidelity based on existing bridge records is described. The analysis includes over 6000 concrete deck records and a prediction period of 15 years. Probability distributions of prediction errors demonstrate that both the nonstationary and stationary implementations of the probabilistic models achieve a much higher degree of accuracy and precision in predicting bridge condition ratings than the deterministic models. Reasons for the improved predictive fidelity of these probabilistic models are discussed briefly while making a case for adoption of these models in place of deterministic models.

1 INTRODUCTION

Bridge deterioration models are predictive relationships developed on the basis of observable deterioration defects quantified in terms of inspector-assigned condition ratings and various contributory factors associated with deterioration such as age, environment, and traffic conditions in order to estimate future deterioration behavior. The aim is to facilitate appropriate budget allocation decisions towards ensuring the health of the bridge inventory and preventing costly failures. The United States (U.S.) National Bridge Inventory (NBI) contains bridge inspection data from the 1970's when legislation was first implemented to ensure mandatory binennial inspections for all bridge deck, superstructure, and substructure components, which are assigned condition ratings on a 9-0 ordinal scale. Availability of the NBI condition rating database facilitated the data-driven development of bridge deterioration models that have since evolved significantly over the past three decades.

The primary objective of deterioration modeling is to predict future condition ratings of bridge components, which are a critical input to the bridge management system (BMS) network analysis tools for accurate identification of maintenance, repair and replacement (MR&R) projects for data-driven transportation planning. However, few studies are available that evaluate the quantitative differences between the predictive capabilities of various deterioration models. Such an assessment is especially important because the latest BMS optimization tools are highly sensitive to any changes in deterioration inputs and even minor improvements in predictive accuracy can lead to economic benefits and potential network level improvements in the health of our bridge inventories. This paper presents a methodology developed for quantitative assessment of the predictive fidelity achieved

by various bridge deterioration models relative to the observed condition ratings. The methodology was applied to assess the deterioration models developed for the North Carolina (NC) bridge database. State-of-the-art multivariable duration-based probabilistic deterioration models, using proportional hazards regression and non-homogeneous Markov chain theory, were recently developed for the North Carolina bridge database (Goyal 2015). As part of this study, the deterministic deterioration models, originally adopted by the North Carolina Department of Transportation (NCDOT) in 2002 (Duncan and Johnston 2002) were also updated to include inspection data from the past twelve years (Cavalline et al. 2015). A brief background and description of both the deterministic and probabilistic models developed for the North Carolina BMS is provided followed by a comparison of the predictive fidelity of the two model types using the developed methodology.

2 DETERMINISTIC MODELS

The earliest bridge deterioration models were based on deterministic principles of predicting future bridge condition ratings based on simple measures like mean and standard deviation and linear or nonlinear regression. During the 1980's and early 1990's, deterministic deterioration modeling studies were carried out using National Bridge Inventory (NBI) data for the whole nation as well as for individual states, including North Carolina (Hyman and Hughes 1983, Chen and Johnston 1987, West et al. 1989, Veshosky et al. 1994). These studies ignored the random errors inherent in statistical prediction and therefore all of these models are classified as deterministic models.

2.1 *NCDOT deterministic models*

The functional form of the deterministic deterioration models for decks, superstructures, and substructures currently being used in the NCDOT BMS was first developed in 2002 (Duncan and Johnston) and is based on the average number of years spent in each condition rating. These models followed the heuristic pre-classification of bridge components originally adopted when developing North Carolina's first bridge deterioration models (Chen and Johnston 1987). In this heuristic classification, all of the three primary bridge components analyzed (deck, superstructure, and substructure) were initially grouped by primary material type. Bridge decks were further sub-classified into five categories by average daily traffic (ADT), superstructures were sub-classified by both structural design type and highway functional classification, and substructures were sub-classified by geographical region. The deterioration models were developed through a methodology to compute the expected duration spent in individual condition ratings by calculating the average of estimates generated from two analysis routines. The first routine extracts periods within individual bridge records where the condition rating remains continuously unchanged and calculates the average of this continuously observed duration for all bridges within the deterioration model. The second routine analyzes the entire bridge record for each structure and then sums the total number of years that each condition rating is observed, regardless of whether the rating is continuous or not. In both of the routines, any bridges that yield a total duration of less than two years are removed prior to obtaining the average across all bridges to minimize the effect of data anomalies resulting from incorrectly coded data since the inspection cycle is biennial.

Table 1: Updated concrete deck deterministic deterioration models for the North Carolina bridge inventory

Average Daily	Years In Rating						Total
Traffic (ADT)	9	8	7	6	5	4	Years
$0-200$	3.9	10.3	9.7	9.5	7.8	9.4	50.6
$201-800$	4.0	10.0	9.8	10.7	8.4	7.9	50.8
$801-2000$	3.8	9.2	9.6	11.1	8.3	8.0	50.0
$2001-4000$	3.3	8.4	9.7	10.5	8.3	6.9	47.1
>4000	4.0	7.2	9.1	10.3	7.7	8.3	46.6

In the current study (Goyal 2015, Cavalline et al. 2015), MATLAB software routines were first developed to update these NCDOT legacy models for the twelve years of additional data now available in the NBI database. In developing these routines, the procedures originally established by prior researchers were followed as closely as possible to ensure consistent updating. The updated deterministic deterioration models for concrete bridge decks computed from 1981-2015 historical condition rating data are provided in Table 1. The cumulative duration is plotted against each consecutive condition rating for the predicted concrete deck deterioration over its lifecycle to obtain a piece-wise linear deterministic model. Concrete deck deterioration models obtained in this way for all ADT categories are presented in Figure 1.

3 PROBABILISTIC MODELS

Deterioration model predictions were found to make a significant impact on the effectiveness of bridge management systems (BMS) and several new approaches, particularly probabilistic methodologies, were developed to overcome the limitations of deterministic models in handling the stochastic nature of deterioration (Frangopol et al. 2004). The most common among these is the Markovian state-based approach, which was incorporated in the two National bridge management systems in the United States, AASHTOWare BrM (earlier called Pontis) and Bridgit, both of which require the use of element level condition rating data. Since most states did not have sufficient element-level bridge condition rating data for their

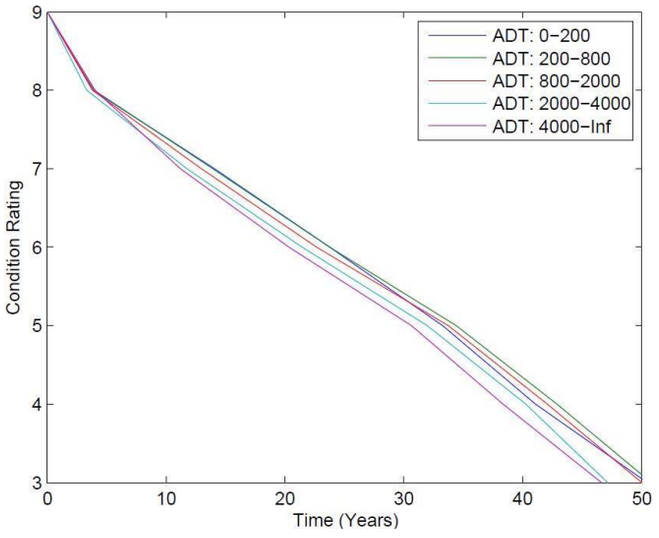


Figure 1: Updated concrete deck deterministic deterioration models for the North Carolina bridge inventory

bridge inventories when they implemented Pontis, Pontis provides for development of the initial transition probability matrix using subjective judgment-based estimates of bridge element transition probabilities obtained from transportation engineers, which are updated in a Bayesian context to provide more accurate results over time (Golabi and Shepard 1997). Among several limitations that have been identified in these models is the assumption of time independence in the traditional homogeneous Markov chain model, which is contrary to the time dependence of the deterioration process. The common approach of using linear regression to calculate transition probabilities is also considered inappropriate because the dependent variable is the condition rating, which is discrete and ordinal, and not continuous as presumed under linear regression (Madanat et al. 1995, Bulusu and Sinha 1997).

The most recent developments in probabilistic models are based on duration based analysis, which takes into account the aspect of time dependence of deterioration and also the impact of censoring (Mauch and Madanat 2001, Mishalani and Madanat 2002, Agrawal et al. 2010, Sobanjo 2011, Goyal 2015). 'Censoring' refers to instances of incomplete observation of an event, and is commonly encountered in duration data. Bridge condition rating data has a large number of censored observations, since discrete time measurements are made during the continuously ongoing deterioration process. Although accepted as superior, the suitability of duration based analysis is subject to the availability of at least 20 years length of inspection data. Since element level databases of most states are not developed for this duration, duration based studies have naturally relied on the original NBI database that offers several decades of consistently recorded condition rating data.

Similar to NCDOT deterministic models, most other deterioration models, including the probabilistic models in AASHTOWare BrM, do not model the effects of various explanatory variables, and therefore, have to rely on pre-defined segmentation of the bridge population into homogeneous categories for meaningful statistical analysis. The categorization is usually based on subjective assessment of factors influencing deterioration carried out during initial model development, which may not stand up to statistical scrutiny. This challenge of *a priori* classification is illustrated by the NCDOT concrete deck models presented in Figure 1, in which the use of ADT as a preclassifier results in insignificant differentiation between the models for different ADT categories. Moreover, increase in the number of categories or element types in these prior models was found to result in corresponding reduction in the number of bridges associated with each category, ultimately compromising the reliability and applicability of the statistical models.

3.1 *North Carolina's PHM probabilistic models*

The previously mentioned limitations of earlier models were taken into account in developing North Carolina's first probabilistic deterioration models in the current study (Goyal 2015, Cavalline et al. 2015). The researchers used multivariable duration analysis in the form of proportional hazards regression to avoid the segregation of condition rating data. The methodology not only identified the most significant factors influencing the deterioration rate of a bridge component, but also quantified the influence of these factors relative to specified baseline values in terms of proportional hazards model (PHM) hazard ratios at individual condition ratings during the component's lifecycle (Goyal et al. 2016).

Although survival analysis had been previously applied to quantify deterioration rates at individual condition ratings, the current study effectively extended it to develop the first non-homogeneous Markov chain bridge deterioration model with transition probabilities derived from the PHM survival analysis. The research also developed the first strategy for efficiently incorporating the proportional hazards effects within the transition probability matrix to facilitate ease of implementation of this advanced PHM model. The final model and its working is described here briefly, but details of development of the model inputs, statistical regression methodology, and Markov chain theory with rigorous treatment of both theoretical and applied aspects of the modeling approach are presented in the Ph.D. dissertation that stemmed from this research project (Goyal 2015).

In its simplest form, the probabilistic PHM deterioration model yielded by the developed methodology consists of two primary inputs: 1) A set of hazard ratios associated with individual factors deemed to be significant to the predictive accuracy of the model at each condition rating, and 2) A set of stay-the-same transition probabilities, P_{kk}, for all condition ratings, k, associated with every year of the prediction period

for baseline values of explanatory factors. These two inputs are used to produce a structure-specific transition probability matrix, P_i, associated with each year, i, of the prediction period as given below.

$$P_i = \begin{bmatrix} P_{99}^{(HR_9)} & 1-P_{99}^{(HR_9)} & \dots & 0 & 0 & 0 & 0 \\ 0 & P_{88}^{(HR_8)} & \dots & 0 & 0 & 0 & 0 \\ 0 & 0 & \dots & 0 & 0 & 0 & 0 \\ 0 & 0 & \dots & 0 & 0 & 0 & 0 \\ 0 & 0 & \dots & 1-P_{55}^{(HR_5)} & 0 & 0 & 0 \\ 0 & 0 & \dots & P_{44}^{(HR_4)} & 1-P_{44}^{(HR_4)} & 0 & 0 \\ 0 & 0 & \dots & 0 & 0.85 & 0.15 & 0 \\ 0 & 0 & \dots & 0 & 0 & 0.85 & 0.15 \\ 0 & 0 & \dots & 0 & 0 & 0 & 1 \end{bmatrix} \quad (1)$$

In this matrix, HR_k is the structure-specific hazard ratio for condition rating, k, and is obtained by multiplying the hazard ratios for those factors at each condition rating that are associated with the specific bridge under evaluation. The best subset factors included in the PHM model for concrete deck deterioration at each condition rating are presented in Table 2 alongwith their baseline categories and associated hazard ratios. It is clear that the hazard ratios from this table included in the structure-specific HR of a particular concrete bridge deck would be those associated with that particular bridge and taking a value of other than 1. If the bridge has only the baseline features, then the hazard ratio would be 1 and the baseline model will apply.

Further, if the initial state vector of condition rating probabilities, Z_0, is known, the PHM non-stationary transition probability matrices are applied as follows to obtain the future state vector

$$Z_n = Z_0 \Pi_{i=1}^{n} P_i. \quad (2)$$

Z_n contains the probabilities of a bridge component being in each of the possible condition ratings at any time n years in the future. The probabilities may be easily reduced to a single numerical expected condition rating value using

$$E = Z_n \cdot R \quad (3)$$

where R is a column vector of condition ratings used in the inspection program, which in this case is given by

$$R = [9\ 8\ 7\ 6\ 5\ 4\ 3\ 2\ 1]^T. \quad (4)$$

Although, the non-stationary implementation of the PHM model described above provides the best predictive outcomes, a stationary implementation was also proposed in this study (Goyal 2015). For the stationary PHM model, a set of stationary or constant transition probabilities is obtained by averaging the PHM non-stationary probabilities over the duration of the PHM survival function for each condition rating. Condition rating forecasting with the PHM stationary model is similar to that of the traditional Markovian models, however, it is noted that the PHM stationary transition probabilities are derived from the PHM survival analysis unlike the transition probabilities of the traditional Markovian models which were calculated using expert elicitation or linear regression based approaches. Moreover, the unique PHM multivariable advantage developed in this study of incorporating the effect of external factors through structure-specific hazard ratios is also available in the PHM stationary model.

In developing transition probabilities for the PHM model, it was observed that very few bridges in the North Carolina bridge inventory are permitted to deteriorate to condition rating 3 or lower. Since survival analysis was not possible due to insufficient data at these ratings, transition probabilities at condition ratings 3 and 2 were prescribed as 0.85 in this study to avoid an abrupt convergence of the deterioration models after condition rating 4. Condition rating 1 was considered as the absorbing state with a transition probability of 1. The stationary baseline transition probabilities obtained by implementation of the PHM model on the concrete deck subset of the North Carolina bridge inventory are presented in Table 3.

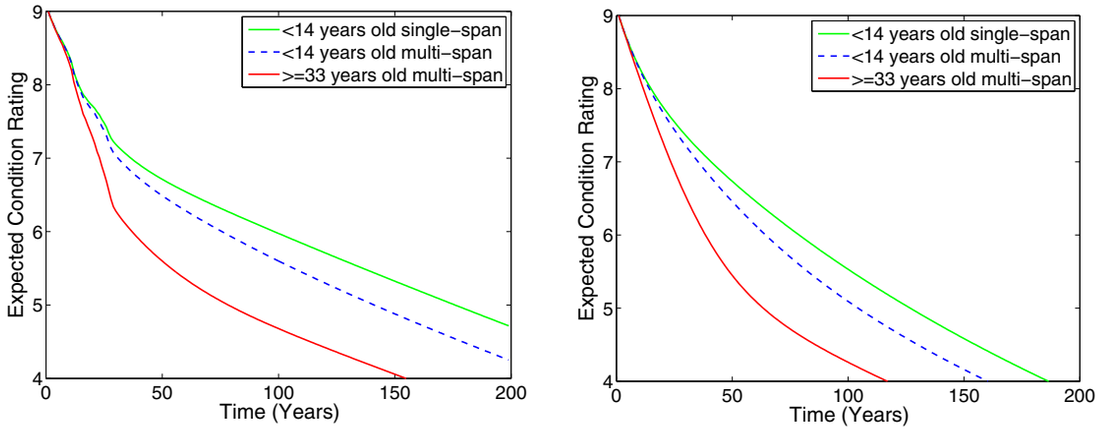
PHM deterioration models developed using the non-stationary as well as stationary forecasting approaches for multi-span and single-span bridges and belonging to various age categories, but associated with baseline assignments for the remaining best subset factors in Table 2, are presented in Figures 2(a) and 2(b). The figures illustrate the depth of information revealed by the models developed in this study using the same databases used for developing the deterministic deck models (Figure 1), which were classified using ADT and expressed far less variable-dependent behavior in comparison. Furthermore, it can be observed that the deterministic models offer far more conservative predictions of future condition rating than the PHM probabilistic models. While the deterministic models predict that all concrete decks would deteriorate to condition rating 4 in less than 50 years, the PHM model predictions for concrete decks with the specified covariate assignments are far more optimistic with a service life prediction of over 100 years by both the stationary and non-stationary models before the concrete deck deteriorates to condition rating 4. It is noted, however, that the models are based on underlying data that includes routine maintenance practices, so these models do not forecast such long service life without intervention.

4 METHODOLOGY TO ASSESS PREDICTIVE FIDELITY OF MODELS

A methodology to assess the predictive fidelity of deterioration models was developed in order to compare and contrast the accuracy and precision of the dete-

Table 2: PHM hazard ratios for the most significant factors associated with the deterioration of concrete deck over its lifecycle

Best subset	Baseline	Hazard ratios at condition rating					
factor	category	9	8	7	6	5	4
StateSystem2(Secondary)	StateSystem1(Primary/Interstate)	1	1	1	1.104	0.790	1
Reconstructed	Original/Rebuilt	1	1	1	1.146	1	1
Piedmont	Coastal region	1	1	0.917	0.766	1.423	1
Mountain	Coastal region	1	1	0.697	0.818	1	1
ADT4($\geq$ 9090)	ADT(0-878)	1	1	1	1	1	1.592
ADTT4($\geq$ 941)	ADTT(0-57)	1	1	1	1.180	1	1
MaxSpan2(4m-6m)	MaxSpan(0-4m)	1	1.509	0.854	1	1	1
MaxSpan3($\geq$ 6m)	MaxSpan(0-4m)	1	2.107	1	1.389	1	1
Multiple Spans	Single span	1	1.178	1.442	1.323	1	1
Age2(14-23 years)	Age($<$ 14years)	1.980	1.467	1.142	1.237	1	0.253
Age3(23-33years)	Age($<$ 14years)	1	1.936	1.467	1.446	1.325	1
Age4($\geq$ 33years)	Age($<$ 14years)	1	1.929	2.393	2.250	1	1



(a) Non-stationary PHM

(b) Stationary PHM

Figure 2: PHM deterioration models showing the effect of age and number of spans on deterioration rates through the lifecycle of concrete decks.

Table 3: Baseline stay-the-same transition probabilities for concrete deck PHM stationary model

Condition Rating	Stay-the-Same Probability
9	0.9034
8	0.9570
7	0.9780
6	0.9662
5	0.9860
4	0.9933
3	0.85*
2	0.85*
1	1.0*

$*$Assumed values due to insufficient data for survival analysis at these ratings

rioration models developed in this research program (Goyal 2015, Cavalline et al. 2015). Such assessment is challenging in the case of bridge deterioration models since a biennial collection rate of inspection data permits no possibility of developing future response data to verify current predictions for several years at the minimum. Therefore model assessment has to be necessarily carried out using past data on the basis of which the statistical models were developed. In this study model assessment was performed using select time periods ranging from 5 to 20 years of condition rating data extracted from the NCDOT historical bridge management database. The results presented in this paper are for concrete deck condition rating records corresponding to a 15 year time period from 2000 to 2015. Bridges with concrete decks represent a large percentage of the statewide inventory, and the results and conclusions drawn from model assessment using data from other bridge components and material types were found to be consistent with those reflected in the following concrete deck analysis.

The individual condition rating databases were first parsed to extract records for which condition ratings were recorded continuously for a 15 year duration. A pre-filtering algorithm was then applied to the extracted data to exclude those records that showed an improvement by more than one rating between consecutive years. This pre-processing was necessary to remove obvious cases where maintenance actions or reconstruction might have interrupted the natural de-

terioration process. In this way, the dataset used for model assessment was reduced to only those structures exhibiting typical deterioration under either natural conditions or routine maintenance actions that do not significantly improve the condition ratings. For each of the continuously observed condition rating records satisfying the filtering criteria, covariate assignments for each record consistent with the classification scheme prescribed for the deterministic deterioration models and the PHM probabilistic models were developed from the descriptive data in the bridge record to enable selection of the corresponding deterministic or probabilistic model applicable to each individual bridge component. In performing the model assessment, the initial condition ratings at the beginning of the 15 year prediction period were input to the deterioration models along with the duration already spent by the bridge component at that condition rating in order to incorporate the pre-existing duration into the predictions generated by each of the respective deterioration models. Through this measure, the fact that a bridge that has already spent 10 years in a particular condition rating is more likely to deteriorate to a lower rating than one that has only spent a single year is incorporated into the model forecasting.

A total of 6017 bridge records for concrete decks were obtained from application of the pre-filtering algorithm to the extracted 2000-2015 condition rating data. Statistics of this data, including the initial deck condition rating at the beginning of the 15-year prediction period, the change in condition rating over the 15 year period, and the pre-existing durations that the decks had already experienced at the initial condition rating are presented in Figure 3. It is observed that the initial condition ratings are fairly normally distributed between ratings 4 through 9 with the majority of decks rated either 6 or 7. By the end of the 15 year observation period, roughly 42% of the records experienced no net deterioration in condition rating, 40% decreased by 1 rating, 15% decreased by 2 ratings, and less than 3% decreased by 3 ratings.

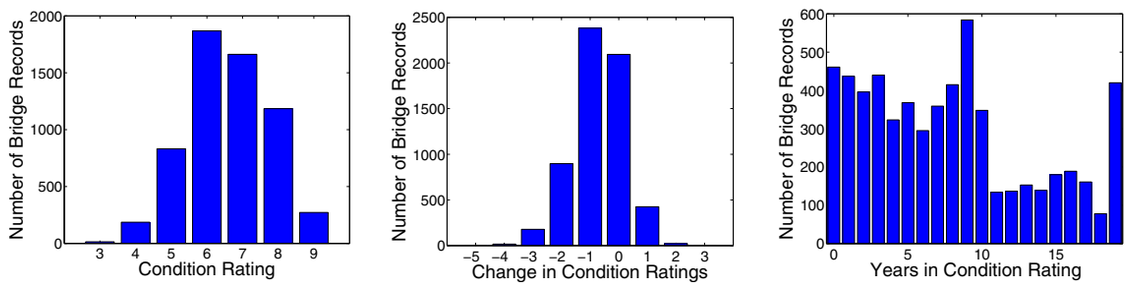
5 COMPARISON BETWEEN PROBABILISTIC AND DETERMINISTIC MODELS

Assessment of the predictive accuracy of the deterministic deterioration models and the non-stationary as well as stationary proportional hazards-based probabilistic deterioration models developed in this study was performed. For each model, the initial condition rating and pre-existing duration at the beginning of the 15-year prediction period for each of the 6017 concrete deck records were passed to the deterioration model with the bridge characteristics required for preclassification and the predicted condition rating after 15 years was compared to the actual recorded condition rating from the NCDOT BMS database.

Histograms of the prediction errors obtained from each model are presented in Figure 4. These results confirm the earlier observation that the deterministic deterioration models provide relatively conservative estimates of deterioration. For the concrete decks under assessment, the updated deterministic deterioration models over-predict the deterioration in condition by 1.82 condition ratings on average over the 15 year period. On the other hand, both the non-stationary as well as stationary PHM probabilistic deterioration models developed in this research project, exhibit markedly improved prediction accuracy in comparison to the deterministic models. The average prediction error for the non-stationary PHM model is reduced to a nominal 0.02 condition ratings. This mean error is especially inconsequential considering the +/- 1 integer precision of the condition rating scale. Even the stationary PHM model exhibits a mean error of only -0.36 condition ratings, which is also below the precision afforded by the condition rating scale. Furthermore, as reflected in the dispersion of the prediction errors and standard deviations presented across the three models, the probabilistic models yield significantly improved precision, as the spread in prediction errors around the mean is much smaller for these models.

To further qualify the improvement offered by the probabilistic deterioration models over the deterministic approach, empirical cumulative distribution functions were developed for the prediction errors developed with each model, as presented in Figure 5. The cumulative distribution functions can be used to characterize the performance of different deterioration models since they allow for determination of the probability of each model producing a prediction within a prescribed tolerance on the actual rating. For example, the empirical cumulative distribution function for the deterministic deterioration model reveals that this model will only produce a prediction within +/-1 of the actual concrete deck condition rating about 21% of the time after 15 years. In contrast, the probabilistic deterioration model is able to achieve a prediction within +/-1 condition rating of the actual about 70% of the time for the stationary model and as much as about 80% of the time for the non-stationary model. It is evident that the probabilistic models significantly out-perform the deterministic models demonstrating remarkable improvements in prediction accuracy and precision.

The reasons for the improved performance of the probabilistic deterioration models relative to the deterministic deterioration models are the ability to account for the large degree of censoring in the condition rating data and the better statistical performance on non-normally distributed duration data. The semi-parametric PHM survival function and the non-stationary Markov chain theory together provide a powerful combination for modeling the variability and stochasticity of the deterioration process, which is distinctly visible in the model assessment results. Moreover, the proportional hazards-based probabilis-

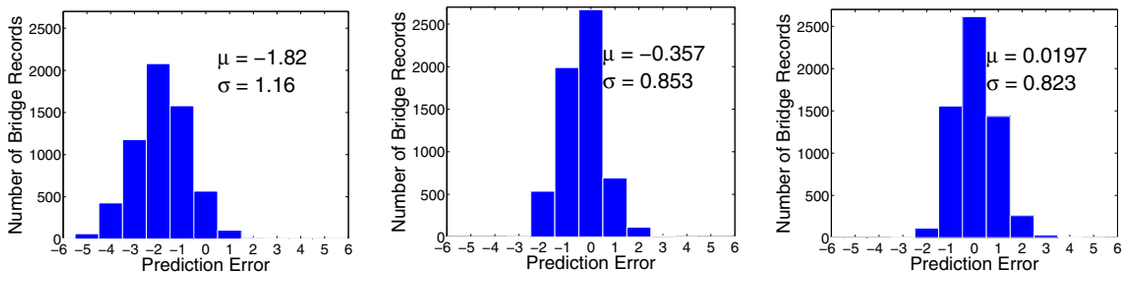


(a) Observed Initial Condition Ratings

(b) Change in Condition Ratings

(c) Pre-Existing Duration at Initial Observation

Figure 3: Histograms of concrete deck condition rating data in observation period.

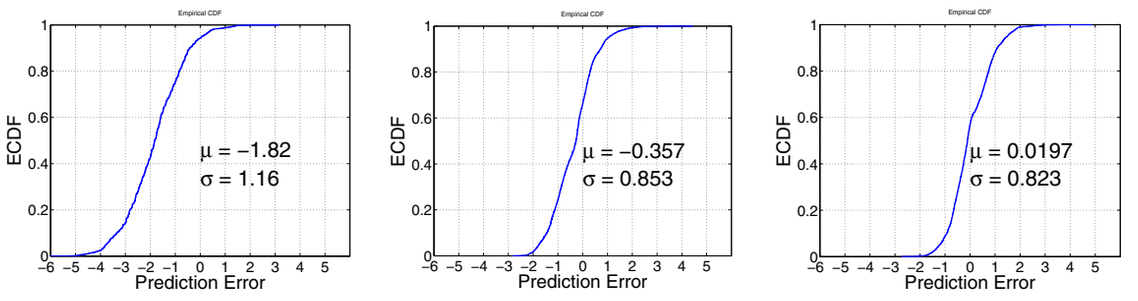


(a) Deterministic

(b) Stationary PHM

(c) Non-Stationary PHM

Figure 4: Histograms of prediction errors of deterministic and PHM probabilistic models applied to concrete deck condition rating data for a 15-year forecasting period.



(a) Deterministic

(b) Stationary PHM

(c) Non-Stationary PHM

Figure 5: Empirical cumulative distribution functions (ECDF) of prediction errors of deterministic and PHM probabilistic models applied to concrete deck condition rating data for a 15-year forecasting period.

tic models incorporate the effects of many more external factors than provided by the limited tiers of classifiers used in the deterministic models.

6 CONCLUSIONS

The updated deterministic models currently in use within the North Carolina bridge management system, and the new proportional hazards-based probabilistic models developed in a recent research project of the North Carolina Department of Transportation are described and compared in this paper. A model assessment methodology also developed through this research is presented and implemented on the concrete deck dataset of the North Carolina bridge inventory to quantify and compare the predictive fidelity of the deterministic and probabilistic models over a prediction period of 15 years. Statistical distributions of prediction errors obtained from the deterministic models and the PHM stationary and non-stationary probabilistic models reveal the distinctly superior predictive abilities of the probabilistic models. The quantitative model assessment results present a strong case to support the implementation of probabilistic models over deterministic deterioration models in the interest of significantly improved accuracy and precision in condition rating forecasting with important implications for more efficient management of the complete bridge inventory.

7 ACKNOWLEDGMENTS

Most of the research presented in this paper was conducted as part of the research project RP 2014-07 sponsored by the North Carolina Department of Transportation. The financial support provided by this grant is greatly appreciated. The contents of this paper reflect the views of the authors and not necessarily the views of the NCDOT. The authors are responsible for the accuracy of the data presented herein. Additionally, this paper does not constitute a standard, specification, or regulation and does not necessarily reflect official policies of NCDOT. In particular, the authors appreciate the guidance and technical support provided by Cary Clemmons.

REFERENCES

Agrawal, A. K., A. Kawaguchi, & Z. Chen (2010). Deterioration Rates of Typical Bridge Elements in New York. *Journal of Bridge Engineering 15*(4), 419–429.

Bulusu, S. & K. C. Sinha (1997). Comparison of Methodologies to Predict Bridge Deterioration. *Transportation Research Record 1597*, 34–42.

Cavalline, T., M. Whelan, B. Tempest, R. Goyal, & J. Ramsey (2015). Determination of Bridge Deterioration Models and Bridge User Costs for the NCDOT Bridge Management System. Final Report FHWA/NC/2014-07, University of North Carolina at Charlotte, Charlotte, North Carolina.

Chen, C. & D. W. Johnston (1987). Bridge Management Under a Level of Service Concept Providing Optimum Improvment Action, Time, and Budget Prediction. Final Report FHWA/NC/88-004, Center for Transportation Engineering Studies, North Carolina State University, Raleigh, North Carolina.

Duncan, S. A. & D. W. Johnston (2002). Bridge Management System Update. Final Report FHWA/NC/2005-06, Department of Civil Engineering, North Carolina State University, Raleigh, North Carolina.

Frangopol, D. M., M.-J. Kallen, & J. M. Noortwijk (2004). Probabilistic models for life-cycle performance of deteriorating structures: review and future directions. *Progress in Structural Engineering and Materials 6*, 197–212.

Golabi, K. & R. Shepard (1997). Pontis: A System for Maintenance Optimization and Improvement of US Bridge Networks. *Interfaces 27*(1), 71–88.

Goyal, R. (2015). Development of a Survival Based Framework for Bridge Deterioration Modeling with Large-scale Application to the North Carolina Bridge Management System. PhD Dissertation, University of North Carolina at Charlotte, Charlotte, North Carolina.

Goyal, R., M. Whelan, & T. Cavalline (2016). Characterizing the effect of external factors on deterioration rates of bridge components using multivariable proportional hazards regression. *Structure and Infrastructure Engineering 13*(7), 894–905.

Hyman, W. A. & D. J. Hughes (1983). Computer Model for Life-Cycle Cost Analysis of Statewide Bridge Repair and Replacement Needs. *Transportation Research Record 899 : Bridge Inspection and Rehabilitation*, 52–61.

Madanat, S., R. Mishalani, & W. H. W. Ibrahim (1995). Estimation of Infrastructure Transition Probabilities from Condition Rating Data. *Journal of Infrastructure Systems 1*(2), 120–125.

Mauch, M. & S. Madanat (2001). Semiparametric Hazard Rate Models of Reinforced Concrete Bridge Deck Deterioration. *Journal of Infrastructure Systems 7*(2), 49–57.

Mishalani, R. G. & S. M. Madanat (2002). Computation of Infrastructure Transition Probabilities Using Stochastic Duration Models. *Journal of Infrastructure Systems 8*(4), 139–148.

Sobanjo, J. O. (2011). State Transition Probabilities in Bridge Deterioration based on Weibull Sojourn Times. *Structure and Infrastructure Engineering: Maintenance, Management, Life-Cycle Design and Performance 7*(10), 747–764.

Veshosky, D., C. R. Beidleman, G. W. Buetow, & M. Demir (1994). Comparative Analysis of Bridge Superstructure Deterioration. *Journal of Structural Engineering 120*(7), 2123–2136.

West, H. H., R. M. McClure, E. J. Gannon, H. L. Riad, & B. E. Silverling (1989). A Nonlinear Deterioration Model for the Estimation of Bridge Design Life. Final Report FHWA-PA-89-016+86-07, The Pennsylvania Transportation Institute, The Pennsylvania State University, Pennsylvania.

Maintenance, Safety, Risk, Management and Life-Cycle Performance of Bridges – Powers, Frangopol, Al-Mahaidi & Caprani (Eds)
© 2018 Taylor & Francis Group, London, ISBN 978-1-138-73045-8

Life Cycle Assessment for Civil Engineering Structures of Railway Bridges

G. Lener & J. Schmid
University of Innsbruck, Unit of Steel Construction and Mixed Building Technology, Innsbruck, Austria

A. Strauss
Department of Civil Engineering and Natural Hazards, University of Natural Resources and Life Science, Vienna, Austria

ABSTRACT: This contribution presents the WEB based prognosis tool "LeCIE" (Life Cycle Assessment for Civil Engineering of Railway Bridges). LeCIE aims to develop a concept for the predictable life cycle management of engineering structures in the rail sector. In order to achieve this objective, inspection results regarding damage and damage processes are combined with probabilistic degradation predictions, forecasting procedures, monitoring and assessment methods. This includes the development of a framework for the life cycle's management system which takes into consideration structural components and singular as well as combined damage in the context of the overall structure of concrete-steel, steel and composite bridges. At the current stage of investigation, the focus of this tool is on railway bridges as this project has been financed by the Austrian Federal Railways company ÖBB. excluding the loading data, the method is general and could adopted for road bridges in the future.

1 INTRODUCTION

1.1 *General*

The project 'LeCIE (Life Cycle Assessment for Civil Engineering of Railway Constructions – Strategies and Methods') aims to develop a wide-ranging concept for a predictable life cycle management of engineering structures in the rail sector. In order to reach this objective, inspection results regarding damage and damage processes are combined with probabilistic degradation predictions and forecasting procedures as well as with monitoring and assessment methods. The next step is then to develop a framework for the life cycle management system to be adopted when considering singular as well as combined damage, structural components as well as the overall structure of concrete-steel bridges, steel bridges and composite ones. The development of this project is collaboratively divided between the University of Natural Resources and Life Science, Vienna (BOKU) and the University of Innsbruck (UIBK). The remit of the UIBK is the treatment of the stated objective when dealing with steel as well as composite bridges, whereas the BOKU group places its focus on concrete bridges.

1.2 *Aims of the Project*

The following aims have been defined for this project:

1. Evaluation of the results derived from the bridge inspections
2. Development of a WEB-based, general life cycle management framework for steel as well as composite bridges
3. Definition of relevant/significant processes of degradation
4. Identification of relevant/significant influencing factors
5. Development of models of degradation

2 DEFINITION OF RELEVANT PROCESSES OF DEGENERATION

2.1 *General overview*

An important foundation for the development of life cycle management tools is the best possible knowledge of the functional degradation processes of support structures, only once this is established is it possible to realistically integrate business-oriented considerations. To this aim, while taking into consideration the technical regulations, an extensive literature study on the relevant science has also taken place. At the same time, a sensitivity analysis of the known frequent degradation processes has been car-

ried out by evaluating the inspection results of the last project year. As a result of the knowledge acquired in the aforementioned steps and after having gathered an extended database, it has been possible to implement a concept study for a new procedure in order to deduce degradation functions. The process and the resulting outputs are explained in the following paragraphs.

2.2 *Evaluation of bridge inspections*

Various types of damage have been defined in order to assess the inspected objects, the results have been evaluated component-by-component similarly to the Austrian school grade system (Schmid, J. Lener, G. 2016). Subsequently, the data has been studied in order to identify, by means of statistical methods, clear and verifiable relations between individual categories such as the age of the structure or its level of corrosion. Firstly, the methods of the linear regression have been applied. This application delivered no significant output and was therefore classified as insufficient for the definition of degradation processes. The reasoning behind this conclusion was primarily that the available sample size was too low and hence impossible in being representative. Nevertheless, the results have been very suitable for the definition of relevant influencing parameters referring to the complete degradation.

On this matter, it is important to note the corrosion and fatigue effects on steel structures wherein fatigue ought to be seen as an overall process with secondary effects. In addition to statistical methods, the support structures and their signs of aging have been analyzed taking into consideration constructive designs and static mechanical observations.

It has thereby been ascertained that support structures of high quality constructional workmanship present a significantly slower degradation process. Moreover, it has been determined that in many cases fatigue problems are caused by issues concerning the measurement of support structures. A few years ago measurements would have been mostly conducted by using framework models and significantly less impact factors would have been considered. In this way local concentrated tension peaks at the stiffness cracks and in transverse connections were regularly determined to an insufficient level. Those areas are however exactly where fatigue damage begins to occur, especially when, in addition, corrosion protection has been poorly performed.

A part of this quickly developing damage process could potentially be prevented by the adoption of measurement methods and verification concepts based on spatial simulation models.

2.3 *Literary works and regulations*

With the acquisition of knowledge from bridge inspections and from general literature on steel structure degradation, the next step has been to gather insight into the topics of corrosion processes and fatigue. The basic literary works on fatigue to be mentioned are those by Radaj and Vormwald (Radaj D., Vormwald M., 1985), (Radaj D., Vormwald M., 2007) as well as the measurement standards of the Eurocode package (Österreichisches Normungsinstitut, ÖNORM EN 1991-2, 2012), the ÖBB Infrastructure guideline B45 (ÖBB Infrastruktur, 2011) and the IIW recommendations (Hobbacher A., 2014). Information on corrosion, environmental classes and corrosion protection systems is to be found in ISO standards. The depiction of fatigue is a multiple parameter problem without an analytical solution. The determination of fatigue resistance is concept-based on statistically evaluated test results. There are various possibilities which allow the consideration of impacts and their influence to be analyzed as well as the influence of traffic volume and traffic intensity. These last two aspects are not taken sufficiently into account in the presently used normative design rules according to the Eurocodes, despite this they ought to be handled as relevant influence parameters.

Clear deterministic models are available which illustrate corrosion and describe corrosion rates for different climates. However, the assignment to the individual climates for bridge details proves to be problematic. The classification of individual climates as input variables could only to be identified by means of elaborate measurements. Generally, the micro climate is taken into consideration, which is usually not deducible from the regional climate of the area in which the bridge is situated. Equally questionable is the ability to describe the degradation of the corrosion protection as very few data sources are available or could be found in literature, an issue which leads to high uncertainties (Petraschek, 2015).

3 DEVELOPMENT OF DEGRADATION MODELS

3.1 *General overview*

After having acquired the knowledge of the relevant degradation processes and their input variables, a general life cycle management framework has been developed. This was possible thanks to the cooperative conceptualization and organizational planning

between the UIBK and the BOKU. The present results are not to be considered as the final solution. This collaboration defined the relations between individual components, although their quantitative content would still require completion. A concept for the degradation model has also been developed. This model enables the connection of any axle load measurement data as well as the evolution of traffic on the load side with the component resistance of the different types of construction and support parameters.

3.2 *General life cycle management framework*

The general life cycle management framework combines the individual degradation models into a complete model, being able to take into account precaution and maintenance measures as well as cost figures. These measures, however, cannot be generally defined and therefore depend upon many parameters. In particular, it is important to mention the type of construction and material which reveal different degradation functions. It makes therefore sense to gather degradation models, degradation functions and the temporal propagation of processes together in a database and to evaluate and/or adjust (postprocessor) them in the life cycle management tool according to the information gathered from the master data sheet of the bridges and from possible additional available input variables of each individual object. The data taken as a b asis are internal curves of degradation of the ÖBB for the component of corrosion and the extensive axle load measurement data for the component of fatigue. Those are subsequently defined in a manner which presents and gives access to damage rates of different kinds of support systems and/or structural details in relation to different traffic configurations and traffic volumes.

3.3 *Models of degradation for steel*

Based on literary research, inspections of supporting structures and axle load measurement data, relevant degradation processes of steel and composite bridges have been defined. During this procedure, attention has been paid to certain approaches due to the impossibility to describe some of the processes in a deterministic way. The model design has been produced based upon the statistical analysis of prepared questionnaires about the maintained condition of various bridge structures and the assessment of the axle load measurement data of nine measurement points. The evaluation of this data has allowed the conveyance into a process model. Simultaneously, a deterministic process model has been developed. Previously conducted studies have shown that material fatigue and corrosion are the relevant life cycle processes in the case of steel and composite bridges. Thanks to these studies it has however come to light, that the current methods of fatigue strength determination, because of the various forms of support structures and their loads, are not suitable for a common life cycle management tool. As a result, concepts have been produced in order to calculate relations and simplify the different input parameters that allow the deduction of a common degradation function for material fatigue taking into account corrosion. Two models have been generated: one semi probabilistic and deterministic model and one model solely based upon probabilistic approaches.

Fatigue strength has been determined by applying calculations of train-crossing in combination with with evaluations of extensive axle load measurement data as impact factor and by subsequently deducing damage equivalence factors, forecast models and possible modification factors. With the use of an appropriate signal analysis, the resulting tension's time signal can thus be divided into parts and the damage calculated with the specification of a S-N curve. The Rainflow procedure has been used in this process (Rychlik, I. 1987), damage of single train crossings have been calculated by means of linear damage accumulation. The methods, which have been developed, use the load model 71 as their referential model. Figure 1 shows the axle load measurement data of nine measurement points which have been taken into account for the year 2014. These nine measurement points are distributed over the entire railway network in Austria.

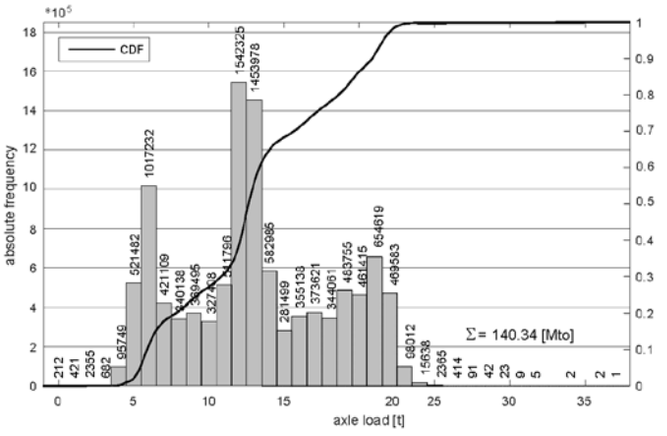


Figure 1. Considered axle load measurement data (Schmid, 2017).

The results from both models are to be demonstrated by using as example a railway bridge build in the year 1955, with single span girders of a range of 15 m and an arc radius of 1700 m.

The semi probabilistic deterministic model produces as a result the development in time of the amount of damage *D(T)*. In this model, corrosion is dealt with in a deterministic way. The extensive internal knowledge of the ÖBB as well as data from

Det Norske Veritas Classification Notes No. 30.7 (Det Norsk Veritas, 2003) are used referentially. The condition of the corrosion protection *K(T)* is to be divided into various parts. *K(T) = 1* signifies that at the time *T* the condition of corrosion protection is with 95% of probability barely still intact in all its layers. At *1 > K(T) > 0*, the condition starts to rapidly worsen, despite the fact that the protective effect on the base material remains intact. Only once the condition limit is reached. *K(T) = 0*, is there no protective effect and the base material is exposed to the outside weathering. After 5 years of exposure to the weather conditions, the damage rate of fatigue increases significantly per stress cycle, as on one hand, every stress range is effective (Miner elementar) and on the other, only a small damage sum is tolerated. With a timely renewal of corrosion protection, this damage rate increase can be hindered.

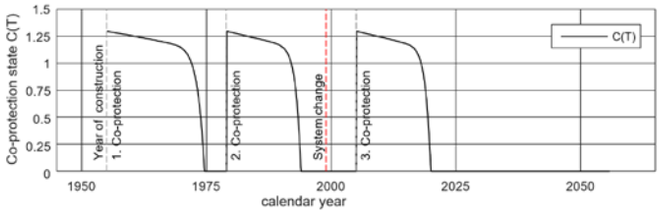


Figure 2. Development of corrosion protection state – main girder (Schmid, 2017).

The damage *D(T)* is obtain from the following expression:

$$D(T) = \int \dot{D}(T)dT =$$

$$= \int \left[\dot{D}(T - T_0) \cdot \left(1 + (\kappa - 1) \cdot \mathrm{H}(T - T_{ds})\right) \cdot \left(\frac{\Delta\sigma_E(T)}{\Delta\sigma_E(T_0)} \right)^{m_1} \right] \cdot \mathrm{H}(T - T_0) \cdot dT$$

with

$D(T)$	damage at time T
κ	factor considering corrosion effects
$\Delta\sigma_E$	equivalent constant amplitude stress range
H	Heaviside function
m_1	starting slope of fatigue strength curve
T_{ds}	irreversible timing of system change of fatigue behavior due to corrosion

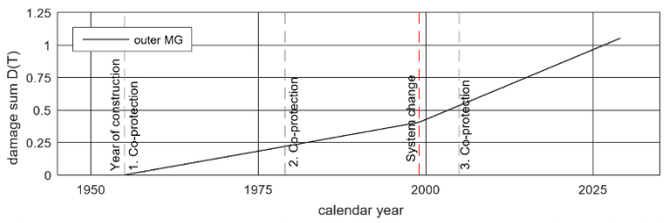


Figure 3. Damage D(T) of main girder at outer track (Schmid, 2017).

The probabilistic model takes into consideration the statistical range of the input variables based on data form (Geißler, K., Krohn, S., 2016), (Sedlacek, G., 2007) and produces as a result the time-dependent increase of the failure probability p_f and thereby the relation to the reliability index ß. The evaluation of p_f has been done by the use of Monte Carlo Simulations.

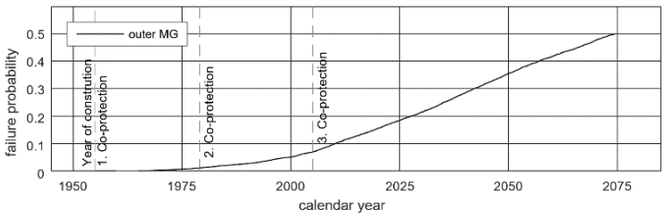


Figure 4. Probability of failure p_f of the main girder related to fatigue (Schmid 2017).

3.4 *Degradation model for reinforced concrete*

For a realistic application of the degradation model in LeCIE, it was necessary to calibrate the mathematical model for the transport processes of chloride and carbon as in bulletin 34 and the model code for the Service-Life-Design (Schiessl et al., 2006). According to RVS 13.05.11 (FSV, 2017), railway bridges are expected to have a life cycle of 120 years. In line with empirical values of the ÖBB experts, these requirements are fulfilled when applying the design in accordance with the regulations, in using a concrete of good quality and in ensuring high quality in the building of rail bridges. It is, however, necessary to adjust/calibrate the model parameter of the transport process in order to concord with these regulatory requirements.

On the basis of literature review and reports, the load models as well as the environmental conditions for this calibration have been defined together with the ÖBB experts for predefined, frequent situations. The primary aim of the aforementioned definition was to describe and consider the long term behavior of the reinforced concrete structures by taking into account the life cycle in case of chloride and carbon penetration.

These investigations have been concentrated on analyzing structures with concrete consisting of common cement types with different predefined environmental classes and various qualities of workmanship in the construction.

The aim in this section has been to characterize the parameters for the transport processes of historical concrete types, which have been used over the years by the ÖBB.

Among various model approaches, for the LeCIE Tool, the following has been selected in order to describe the penetration development of chloride (Schiessl et al., 2006)

$$C(x,t) = C_0 + \left(C_{S,\Delta x} - C_0\right) \cdot \left[1 - erf \frac{x - \Delta x}{2 \cdot \sqrt{D_{app}(t) \cdot t}}\right]$$

with

C_0 initial chloride content [weight -%/c]

$C_{S,\Delta x}$ chloride content of the predominant environmental impact in [weight -%/c]

Δx depth of the convection zone (concrete crust near to the surface), in which the process does not behave in conformity with the penetration resistance against chloride of Fick's second law of diffusion [m]

x depth with the appropriate chloride content C(x,t) [m]

t time [s]

D_{app} clear chloride diffusion coefficient [m²/s]

erf Gauss' error function

This equation is based on the Fick's second law which describes the diffusion in its one dimensional form. Although other kinds of transport mechanisms for chloride, which acts on concrete surfaces, appear to be more suitable in order to specifically illustrate the capillarity, absorption and penetration, Fick's second law is considered as the most generally effective and widely adopted law (Gehlen et al., 2015). A higher chloride content in concrete can lead to pitting corrosion and to sudden failure of the structure.

In order to describe the carbonation's construction, among the various model approaches, an adopted model from *fib* Model Code for Concrete Structures 2010 (Schiessl et al., 2006) has been integrated in the LeCIE Tool.

Carbon causes a reduction of the concrete's pH-value and therefore a depassivation of the reinforcing steel resulting in corrosion. The following equation describes the time-dependent carbon process:

$$x_{c,d}(t) = \gamma_f \cdot k_{NAC} \cdot \sqrt{k_e \cdot k_c \cdot k_a} \cdot \sqrt{t} \cdot W(t)$$

with

k_{NAC} rate [mm/year$^{0.5}$] by $W(t)=1$, $k_e=1$, $k_c=1$, $k_a=1$, relative air humidity 65±5%, temperature 20±2°C, CO_2 concentration 0.04±0.005 volume% by atmospheric pressure

k_e=1 factor as well as function to describe the environmental influence of the relative humidity (RHa) on the basis of the effective inverse carbonation's construction resistance [-]

$k_c=1$ factor as well as function to describe the effects of CO_2 concentration in the neighboring area's air [-]

$W(t)$ factor as well as function to describe the humidity rates [-] which prevent the penetration of CO_2. NOTE: W(t) gains in relevance with increasing depth into the carbonation's construction and also over extended time periods.

4 LECIE DATABASE & WEB BASED PROGNOSIS TOOL

The WEB based prognosis tool "LeCIE" allows to create, edit (making correction or complete) and to delete new and existing bridges in a free input format. The bridge objects are classified according to the internal ÖBB line number system and can be clearly identified on basis of the line number and kilometer distance. The analysis of the above mentioned processes (degradation analysis as well as life cycle assessments) can be done for the whole bridge object, groups of structural elements of the bridge or for each individual defined bridge element.

Figure 5 shows as example the cost-optimized chloride performance group evaluation, in this case the abutment A of the bridge object 1062 on the line 33.003, for two different maintenance strategies (strategy I "process delay due to coating" and strategy II "concrete replacement". From figure 5 it can be seen that an intervention is required for the abutment wall only and not for the abutment wing wall. The LeCIE WEB tool also allows the combination between the processes. Based on this capability, the most cost-effective intervention strategy can be determined.

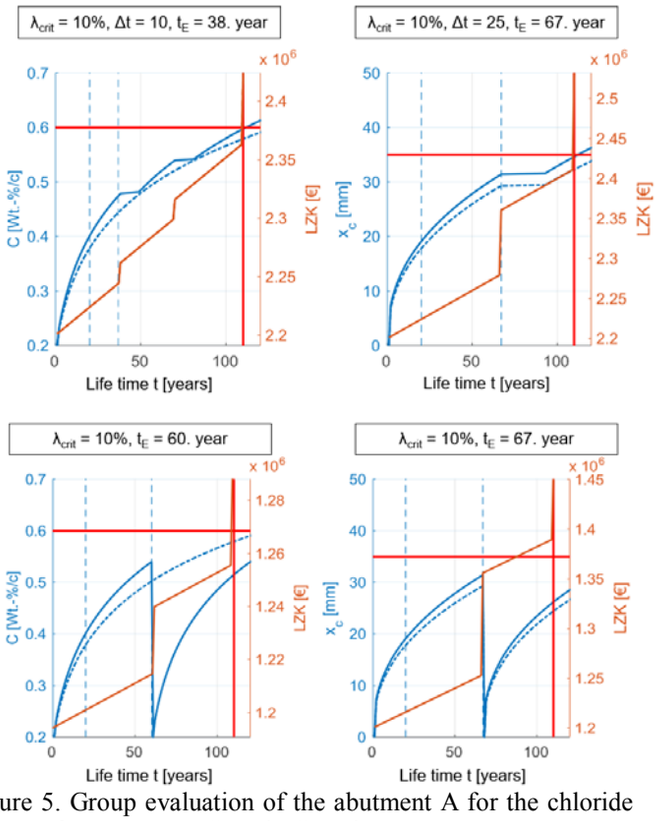


Figure 5. Group evaluation of the abutment A for the chloride process for strategy I "coating" and strategy II "concrete replacement".

5 SUMMARY AND OUTLOOK

A common Life-Cycle-Management-Framework could be provided including the evaluation of bridge inspection reports of the past year. In addition, the relevant impact parameters for the procedures to analyze the degradation processes, which are significant for steel support structures, have been identified and degradation models subsequently developed.

Noticeable progress was made regarding the component of fatigue and significant correlations were recorded. By using the developed WEB tool, results can be obtained numerically with acceptable time expenditure.

The major parameter for fatigue, the real impact due to loading, is solved by the evaluation of axle load measurement data. The only aspect, which refers to this point which remains open, is that of the definition of the traffic development on a long term basis.

Taking into account the component of corrosion, it has been possible to successfully conclude the concept study regarding the production of a new method which would deduce the function of degradation.

The next step will be to conduct further parameter studies for the component of fatigue which will bring a reduction in the problems to be solved, in doing so it will allow a final verification of the procedures featured here. In addition, the components of traffic prognosis and structural part resistance are to be investigated in more depth. The permitted damage sum as well as necessary factor modifications are to be quantified.

Furthermore, a transfer into a probabilistic method is necessary in order to represent the impact values of the reliability index. As far as the component of corrosion is concerned, the illustrated model approaches are to be refined as soon as a sufficient amount of data becomes available.

Subsequently, the resulting degradation functions are to be deduced and together with fatigue impacts are to be condensed into one complete model.

At the current stage of investigation, the focus of this tool is railway bridges as the Austrian Federal Railway Company ÖBB has financed this research project. Excluding the loading data, the presented method is general and could be adopted for road bridges in the future.

6 PREFERENCES

Schmid, J. Lener, G.: ÖBB Infra, LECIE, Lebenszyklusbewertung für Ingenieurbauwerke des Eisenbahnbaues – Strategien und Methoden, Projekt No. P8464-027-0445, Jahresbericht 2015.

Det Norske Veritas Classification Notes No. 30.7: Fatigue Assessment of Ship Structures, 2003.

Fib Model Code for Concrete Structures: Ernst & Sohn, 2010

Gehlen C., Greve-Dierfeld, S. v., Gulikers, J., Helland, S., Rahimi, A. et al.: fib Bulletin 76: Benchmarking of Deemed-to-Satisfy Provisions in Standards – Durability of Reinforced Concrete Structures Exposed to Chlorides – State-of-the-art report, Fédération internationale du béton (fib), 2015.

Hobbacher A.: IIW Recommendations for Fatigue Design of Welded Joints and Components: doc. XIII-2460-13/XV-1440-13, Paris: International Institute of Welding, 2014.

Radaj D. Vormwald M.: Fachbuchreihe Schweisstechnik: Bd 82: Gestaltung und Berechnung von Schweisskonstrukutionen, Düsseldorf: Deutscher Verlag für Schweisstechnik, 1985.

Radaj D., Vormwald M.: Ermüdungsfestigkeit: Grundlagen für Ingenieure. 3. neubearbeitete und erweiterte Auflage, Berlin: Springer-Verlag, 2007.

ÖBB Infrastruktur, B45: Technische Richtlinie für Eisenbahnbrücken und sonstige konstruktive Ingenieurbauwerke, Wien: ÖBB Infrastruktur, 2011.

Österreichisches Normungsinstitut, ÖNORM EN 1991-2: Eurocode 1: Einwirkungen auf Tragwerke: Teil 2: Verkehrslasten auf Brücken, Wien, 01.03.2012.

Petraschek T.: „Bedarfsgerechte Instandsetzung der Korrosionsschutzbeschichtung," Stahlbau, Bd. 84, Nr. 6, pp. 402-409, 2015.

Schiessl et al.: fib 34 - Model Code for Service Life Design, Fédération internationale du béton (fib), 2006.

Schmid J.: Neue Ansätze zur Bestimmung des Restlebensdauer von Eisenbahnbrücken aus Stahl, Dissertation in Arbeit, Innsbruck, 2017.

Rychlik, I.: A new definition of the rainflow cycle counting method, International Journal of Fatigue 9, No. 2, p 119-121, 1987.

Österreichische Forschungsgesellschaft Straße, Schiene, Verkehr: RVS 13.05.11: Lebenszykluskostenermittlung für Brücken, 2107.

Geißler, K., Krohn, S.: Nachrechnung bestehender Stahl- und Verbundbrücken – Restnutzung; Bericht der Bundesanstalt für Straßenwesen BASt, Heft 123, 2016.

Sedlacek, G.; Hobbacher, A.; Nussbaumer, A.; Stoetzel, J.; Tschickardt, D.: Commentary to Eurocode 3 EN 1993 - Part 1-9 – Fatigue, 2007.

Acknowledgment:

The support of the research project "LeCIE: Lifecycle assessment for railway constructions – strategies and methods" and the Austrian Federal Railways, particularly ÖBB-Infrastruktur AG, has been greatly appreciated. The invaluable contributions to the research made by many interdisciplinary colleagues at the Institute of Structural Engineering, Department of Natural Hazards and Life Sciences, BOKU, must also be acknowledged.

Maintenance, Safety, Risk, Management and Life-Cycle Performance of Bridges – Powers, Frangopol, Al-Mahaidi & Caprani (Eds)
© 2018 Taylor & Francis Group, London, ISBN 978-1-138-73045-8

National-scale bridge element deterioration model for the USA

P.D. Thompson
Consultant

ABSTRACT: The Federal Highway Administration of the United States uses its National Bridge Investment Analysis System (NBIAS) to develop needs estimates and report on the conditions and performance of the nation's 600,000 bridges and culverts. The system's deterioration model was recently updated to be consistent with the most recent bridge element inspection standards. A data set containing nearly 3 million element inspection records was stratified into nine climate zones according to average temperatures and moisture in each county of the United States. Algebraic methods developed in research for Florida and Virginia were used to process the element inspection data into transition probability matrices. The resulting models were then transformed for compatibility with the latest inspection manuals used in federal bridge condition reporting requirements. The product represents the first time there has been a true nationwide element level deterioration model for bridges in the United States.

1 INRODUCTION

The US Federal Highway Administration uses its National Bridge Investment Analysis System (NBIAS) to develop needs estimates and contribute data to a periodic report on the conditions and performance of the nation's highway and transit infrastructure, including more than 600,000 bridges and culverts (FHWA 2016). NBIAS performs a network-level life cycle cost analysis representing future deterioration and costs at the element level, to estimate the amount of investment in bridge preservation activities that is likely to keep long-term costs to a minimum.

Since the 1970s, states have been required to gather a standardized data set of bridge inventory and biennial inspection data, for submittal to FHWA each April. These are compiled into a National Bridge Inventory (NBI) (FHWA 1995) which provides the source data for the Conditions and Performance Report. Until recently, the NBI had only four data items describing bridge condition:

58 – Deck condition rating
59 – Superstructure condition rating
60 – Substructure condition rating
62 – Culvert condition rating

These four items represent separate parts of a structure, with a focus on the primary load-bearing components. Since the NBI Coding Guide is focused on safety rather than on maintenance needs, certain components having significant maintenance costs (such as expansion joints and paint) receive little or no consideration when assigning a condition rating. Each item is recorded using a coding scheme where 9 is excellent condition and 0 is failed and beyond corrective action. When any of the NBI condition ratings is 4 or below, the bridge is considered "structurally deficient".

Although the FHWA Coding Guide is still mandatory, bridge owners have found that the four condition ratings are insufficient for asset management purposes. They do not provide enough information on the cause of deterioration, to forecast future condition or select appropriate maintenance actions, and they do not provide enough information on the extent of deterioration for cost estimation.

As a result, nearly all bridge management systems worldwide use a more extensive condition description organized according to elements and condition states (Mirzaei et al 2014). In the United States, most of these systems have, until recently, been based on the AASHTO Commonly-Recognized (CoRe) Element Guide (AASHTO 1998). The guide defines 106 common structural elements and provides objective visual language for recognizing 3-5 condition states for each

element. Inspectors record the quantity or percentage of each element found to be in each condition state.

Previous versions of NBIAS used 72 of the 106 elements, focusing on the ones believed by FHWA to have some relationship to the criteria used in assessing the four NBI condition ratings. Since the collection of element-level data was optional at the time of NBIAS development, and because there was no process for states to submit such data to FHWA, it was necessary to develop a model to synthesize element data from NBI data. Only the 72 elements were capable of being imputed in this way.

One of the criticisms of the AASHTO CoRe Elements was the lack of detail on bridge decks, and the fact that deterioration processes were often commingled. It was difficult, for example, to separate deterioration of paint systems from deterioration of the underlying steel, or cracking from corrosion. As a result, the AASHTO manual moved toward a standard that makes a separate assessment of each major deterioration process, in order to provide the clearest and most relevant possible distinctions among condition states. This practice was formalized in the 2013 AASHTO Manual for Bridge Element Inspection (AASHTO 2013). Federal rules now mandate the collection and reporting of a subset of the elements defined in the new manual. Designated "NBI Elements," these are shown in Table 1 (FHWA 2014).

In order to prepare the next edition of the Conditions and Performance Report, FHWA wanted to base its analysis on the new catalog of 100 NBI Elements as submitted by the states. To do this, it would be necessary to develop a new bridge element deterioration model compatible with the new data set.

2 SOURCES OF DATA

A major challenge in this effort was the fact that the definitions of NBI elements and condition states was new, so very few studies had yet been undertaken to develop compatible deterioration models. At the time the work was done, only the Florida Department of Transportation had yet completed such models (Sobanjo and Thompson 2016). However, many of the states had long histories, some going as far back as 1995, of bridge inspection using the older CoRe Element manual, and some had developed deterioration models using the older format. These provided some potential sources of data.

2.1 *Model used in earlier NBIAS versions*

A 50-state survey conducted in 2005 identified 15 state Departments of Transportation that had developed bridge element deterioration models and were willing to share them for FHWA use. Most of these models were based on expert judgment, although some of the agencies had used the linear regression procedure within AASHTO's Pontis software to update their judgment-based models to incorporate bridge inspection data.

Table 1. National Bridge Inventory (NBI) Elements

12	Reinforced Conc (R/C) Deck	207	Steel Tower
13	Prestressed (PS) Conc. Deck	208	Timber Trestle
15	PS Concrete Top Flange	210	R/C Pier Wall
16	R/C Top Flange	211	Other Pier Wall
28	Steel Deck - Open Grid	212	Timber Pier Wall
29	Steel Deck - Filled Grid	213	Masonry Pier Wall
30	Steel Deck - Orthotropic	215	R/C Abutment
31	Timber Deck	216	Timber Abutment
38	R/C Slab	217	Masonry Abutment
54	Timber Slab	218	Other Abutments
60	Other Deck	219	Steel Abutment
65	Other Slab	220	R/C Sub Pile Cap
102	Steel Box Girder	225	Steel Pile
104	PS Box Girder	226	PS Concrete Pile
105	R/C Box Girder	227	R/C Pile
106	Other Box Girder	228	Timber Pile
107	Steel Open Girder/Beam	229	Other Pile
109	PS Open Girder/Beam	231	Steel Pier Cap
110	R/C Open Girder/Beam	233	PS Concrete Cap
111	Timber Open Girder	234	R/C Pier Cap
112	Other Girder/Beam	235	Timber Pier Cap
113	Steel Stringer	236	Other Pier Cap
115	PS Concrete Stringer	240	Steel Culvert
116	R/C Stringer	241	R/C Culvert
117	Timber Stringer	242	Timber Culvert
118	Other Stringer	243	Other Culvert
120	Steel Truss	244	Masonry Culvert
135	Timber Truss	245	PS Concrete Culvert
136	Other Truss	300	Strip seal joint
141	Steel Arch	301	Pourable joint
142	Other Arch	302	Compression joint
143	PS Concrete Arch	303	Assy. joint w/ seal
144	R/C Arch	304	Open joint
145	Masonry Arch	305	Assy. joint no seal
146	Timber Arch	306	Other joint
147	Steel Main Cables	310	Elastomeric Bearing
148	Sec Steel Cables	311	Moveable Bearing
149	Other Secondary Cable	312	Enclosed Bearing
152	Steel Floor Beam	313	Fixed Bearing
154	PS Floor Beam	314	Pot Bearing
155	R/C Floor Beam	315	Disk Bearing
156	Timber Floor Beam	316	Other Bearing
157	Other Floor Beam	330	Metal Railing
161	Steel Pin & Hanger	331	R/C Railing
162	Steel Gusset Plate	332	Timber Railing
202	Steel Column	333	Other Railing
203	Other Column	334	Masonry railing
204	PS Concrete Column	510	Wearing surfaces
205	R/C Column	515	Steel coating
206	Timber Column	521	Concrete coating

Each of the 15 states had up to four separate deterioration models representing categories of environmental and operating conditions within their states, in most cases reflecting the use of deicing chemicals and the presence of marine environments. The NBIAS models were organized into nine climate zones, based on rainfall and freeze-thaw experience, using conventions established in the Highway Performance Monitoring System. Each of the more than 3000 counties in the USA is classified into one climate zone. So the

researcher developed a correspondence, based on judgment, between geographic states and environments on one hand, and NBIAS climate zones on the other hand.

In this way, a deterioration model was selected for each element and climate zone to populate the NBIAS models starting in 2007. These models have been unchanged in NBIAS since then.

2.2 *Florida and Virginia research*

In 2010 to 2012, the Departments of Transportation of Florida and Virginia developed bridge element deterioration models using large databases of CoRe Element inspections over 12 years or more. The methodology, summarized later in this paper, was developed initially for Florida DOT (Thompson and Sobanjo 2010). These states addressed only three of the nine climate zones, and only the Florida model, at the time, had been migrated to fit the 2013 AASHTO elements. Nonetheless, the earlier studies provided some important lessons:

- There can be important differences between agencies in how the condition state language of the CoRe elements is interpreted. It was found, for example, that Virginia inspectors were reluctant to use the worst defined condition state of each element because they understood this to imply a requirement for a structural analysis. The Florida inspectors did not share that view and were more willing to use all of the defined condition states.
- The Florida research compared the models based on inspection history against earlier models based only on expert judgment. They found that expert judgment was not very accurate, that transition times were under-estimated by a factor of about 2 (Thompson and Sobanjo 2010).

For the current effort, these lessons implied that it would be desirable to base each model on more than one agency's data, and actual inspection history should be relied upon as much as possible, in preference to expert judgment.

2.3 *Collected Pontis data*

Between 2008 and 2015, the FHWA Long-Term Bridge Performance Program (LTBP) gathered Pontis data sets from 23 state DOTs, to help the program with its deterioration research. While the LTBP had not developed a national deterioration model of its own, it was willing to share its data set with the NBIAS project for that purpose. On further analysis it was found that 15 of the data sets could be made compatible with the present study, so a combined database was created from these 15 agencies. The new database contained 66,025 bridge records, 492,661 inspection events, and 2,868,505 element inspection records.

Although this database was apparently of sufficient size for useful analysis, it did not provide uniform coverage of all of the climate zones across the country. In the end, it was necessary to incorporate the earlier Florida and Virginia research, in order to avoid bias against the climate characteristics of the southeast United States. Certain results from the earlier NBIAS models were also used in order to provide reasonable variation in the effect of temperature on deterioration rates, as part of the climate zone model. Figure 1 shows the national coverage of the 50 states from the combination of all three data sources.

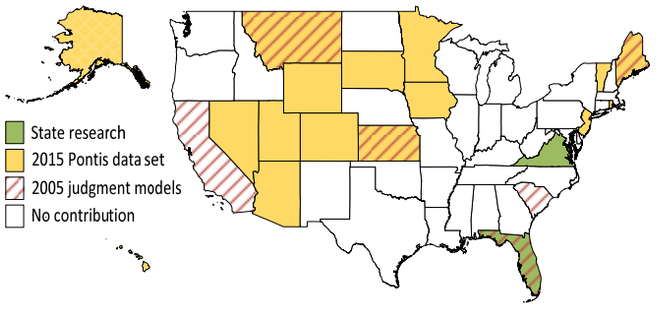


Figure 1. Sources of data

3 MODEL DEVELOPMENT PROCESS

A multi-step process, described in the following sections and summarized in Figure 2, was used to reduce and process the data set, to estimate transition times, to expand the result to nine climate zones, and to make the results compatible with the 2013 AASHTO Manual for Bridge Element Inspection.

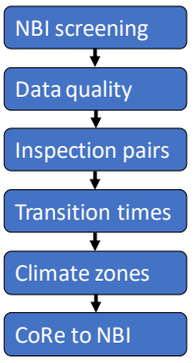


Figure 2. Model development process

3.1 *NBI screening*

The state DOTs have often used their Pontis databases for more than just federally-recognized bridges. As just one example, a recent examination of Florida's database found 36,889 structures, of which fewer than 9,000 are bridges that appear in the National Bridge Inventory. The rest are drainage culverts, sign structures, high-mast light poles, and traffic signal mast arms. For the purpose of the NBIAS analysis, it was necessary to remove certain objects:

- All bridges and culverts less than 20 feet in clear span length along the roadway centerline, and all other structures that do not qualify for the National Bridge Inventory.
- All agency-defined and customized elements.
- Approach slabs, slope protection elements, and any other elements not found in the list of 100 NBI Bridge Elements (FHWA 2014).
- All bridge deck elements that used the temporary 2001 interim revisions to the AASHTO CoRe Elements.

These redactions ensured that the deterioration models would faithfully represent the structures that are addressed in the NBIAS analysis.

3.2 *Data quality checking*

Analysis of the data set found that agencies varied considerably in their ability to maintain uniform quality control on element data. In particular, the first element inspection cycle attempted by each agency, usually in the mid-1990s, was often treated as a practice run for inspectors in training and for field manuals under development, and was not considered reliable by many of the agencies. The first inspection on each bridge was therefore deleted from the data set.

In addition, the first and last years of inspections often covered only a part of the inventory: the first year usually covered one or more pilot districts within the state, and the final year was typically still underway and partially complete at the time the database was obtained from the agency. Since these partial cycles were not likely to be random samples of the inventory, they were deleted.

For element inspections remaining, a variety of quality assurance tests were performed, which resulted in additional deletions. For example, it was required that the quantities of each element inspection in each condition state sum, over all condition states, to the total quantity indicated for the element.

3.3 *Creation of inspection pairs*

A Structured Query Language (SQL) command was used to process all of the remaining element inspections to create a table of inspection pairs. Each inspection pair consisted of two element inspections spaced 2 years apart (plus or minus 6 months). To form a pair, two inspections must match in their element number, environment code, and quantity.

At this stage it is desirable to omit any inspection pairs that have experienced preservation or replacement activity modeled by NBIAS, since the purpose of the analysis is to quantify pure uninterrupted deterioration. Unfortunately, the 15 agencies differed dramatically in their ability to collect work accomplishment data, and few had significant data sets to offer. As a result, the table of inspection pairs was reduced by omitting any bridge inspections where any elements showed an improvement in condition. This is a very imperfect solution, for at least three reasons:

- Preservation actions may have been applied, that did not change the condition state of any of the elements but may have postponed further deterioration of the bridge.
- Even if preservation occurred on some of the elements, the untreated elements should still be useful for deterioration modeling. For example, agencies often perform bridge deck work that does not affect the superstructure or substructure.
- Sometimes conditions appear to improve due to random error, or difference of opinion among inspectors. Filtering out only one direction of random error introduces a statistical bias.

These considerations are likely to affect the accuracy of the resulting models, but no research has been done to quantify the magnitude or direction of the bias. This would be a valuable topic for future research, and is also a factor arguing in favor of improved agency databases and procedures, including contractual requirements, for recording work accomplishments at a sufficient level of detail to identify at least the bridge and elements that were treated.

After creation of inspection pairs, the populations of individual element types in each climate zone were evaluated. It was found that many of the elements were not sufficiently common to produce the 500 inspection pairs that earlier research had found were necessary for a stable model (Thompson and Sobanjo 2010). For each model, it was also necessary to set aside a random sample for validation purposes, further increasing the population requirement. As a result, elements were clustered in order to increase the model populations. This clustering was done by judgment, grouping each uncommon element with a more common element believed to experience the same deterioration rates. This resulted in 30 element groups.

3.4 *Estimation of transition times*

The estimation procedure uses the data set of inspection pairs and the one-step algebraic procedure described in Thompson and Sobanjo (2010).

To set up the estimation of a one-step matrix, the prediction equation is defined as follows:

$$\begin{bmatrix} y_1 \\ y_2 \\ y_3 \\ y_4 \end{bmatrix} = \begin{bmatrix} p_{11} & p_{12} & 0 & 0 \\ & p_{22} & p_{23} & 0 \\ & & p_{33} & p_{34} \\ & & & p_{44} \end{bmatrix}^2 \begin{bmatrix} x_1 \\ x_2 \\ x_3 \\ x_4 \end{bmatrix} \quad (1)$$

The element inspection vectors [Y] and [X] are spaced two years apart, but the transition probability matrix [P] is expressed for a one-year transition. Hence, it is applied twice. Writing out the individual equations necessary to calculate [Y] results in:

$$y_1 = x_1 p_{11} p_{11} \tag{2}$$

$$y_2 = x_1 p_{11} p_{12} + x_1 p_{12} p_{22} + x_2 p_{22} p_{22}$$

$$y_3 = x_1 p_{12} p_{23} + x_2 p_{22} p_{23} + x_2 p_{23} p_{33} + x_3 p_{33} p_{33}$$

$$y_4 = x_2 p_{23} p_{34} + x_3 p_{33} p_{34} + x_3 p_{34} p_{44} + x_4 p_{44} p_{44}$$

Since the sum of each row in [*P*] must be 1.0, the following additional equations apply:

$$p_{12} = 1 - p_{11}; \quad p_{23} = 1 - p_{22}; \quad p_{34} = 1 - p_{33} \tag{3}$$

The vectors [*X*] and [*Y*] can be computed from the database of inspection pairs to describe the combined condition of the element before and after. So these quantities are known. Thus the system of seven equations and seven unknowns can be solved algebraically for the elements of [*P*]. First find p_{11} from equation 2, then find p_{12} from equation 3, then p_{22} and p_{23}, and so on in a simple sequence.

A complication arises because the equations are second-order polynomials in p_{ii}, so it is necessary to use the quadratic equation to find the roots. For example, the equation for p_{33} is:

$$p_{33} = \frac{-b \pm \sqrt{b^2 - 4ac}}{2a} \tag{4}$$

$$a = x_3; \quad b = x_2 p_{23}; \quad c = x_1 p_{12} p_{23} + x_2 p_{22} p_{23} - y_3$$

The same pattern of equations and solution methods apply to elements having 3 or 5 condition states as well. Each same-state transition probability p_{ii} is constrained to be in the range from 0 to 1 exclusive. Even though the quadratic equation finds two roots, in practice only one root was in the necessary range. The final transition time is computed from:

$$t = \frac{\log(0.5)}{\log(p_{jj})} \tag{5}$$

The model estimation and evaluation process was automated using Microsoft Excel.

3.5 *Climate zone factors*

NBIAS classifies the more than 3000 counties of the USA into nine climate zones according to moisture and temperature, using the same definitions as the Highway Performance Monitoring System (FHWA 2014) and the existing NBIAS data set. Even though the estimation data set was very large, the analysis found that population sizes were insufficient for the climate zones in the southeastern USA.

Another finding on detailed analysis of the results was that, even though each climate zone was internally consistent, the differences in models from one zone to another, for certain individual element groups, were not always consistent or intuitive. Even though the inconsistencies were statistically significant and based on factual data, the potential use of the model for resource allocation meant that a higher level of consistency was required.

As a result, it was decided to develop two separate but intersecting models: a model giving typical transition times for each element group across all zones, and a separate model for climate zone adjustment factors based on each bridge's location. This had the effect of smoothing the model so that it was always intuitive and consistent, and had the added benefit of boosting the element group populations.

In the end, the element group model was developed entirely from the 15-state data set, supplemented by the Florida and Virginia data. The climate zone factors were also developed from the large data set (not including the Florida and Virginia models), but supplemented by the climate zone factors used in the original NBIAS models. Table 2 shows the final climate zone factors.

Table 2. Climate zone factors

Zone	Moisture	Temperature	Factor
1	Wet	Freeze	0.64
2	Wet	Thaw	0.58
3	Wet	Warm	0.92
4	Damp	Freeze	0.84
5	Damp	Thaw	0.75
6	Damp	Warm	1.20
7	Dry	Freeze	0.94
8	Dry	Thaw	0.84
9	Dry	Warm	1.34

3.6 *Migration of element definitions*

The models developed to this point are all based on AASHTO CoRe elements, using the older element definitions that have 3 to 5 condition states defined for each element. A final step is necessary, therefore, to convert the results to be compatible with the NBI element definitions.

This transformation was accomplished using a migration probability matrix, a probabilistic mapping of each new element condition state to one or more of the old condition states. This mapping was prepared in Florida research using expert judgment, informed by the differences in element condition state language between the old manual and the new one (Sobanjo and Thompson 2016).

In many cases, such as railings, the new manual had exactly the same definitions as the old one, so no change was necessary. Changes were minimal for most concrete elements, because the only change in condition state language was the exposure of reinforcing steel in condition state 2. Other elements had more significant differences. Steel elements, for example, were divided into a substrate element and a coating element. Deck elements also had major changes. The full migration probability matrix and

the rationale for each allocation of condition states can be found in Sobanjo and Thompson (2016).

4 FINAL MODEL

Table 3 shows the final model of element group transition times developed in the study. To determine the transition times for a specific element on a given bridge, first determine the corresponding element group for that element, and the specific climate zone for the county in which the bridge is located. The element group determines the transition times to be extracted from Table 3. This is then multiplied by the climate zone factor from Table 2 to yield a final transition time estimate for each condition state.

NBIAS uses these transition times to generate a Markov transition probability matrix as a part of its life cycle cost analysis. The rightmost column in Table 3 shows the median number of years from state 1 to state 4 resulting from the Markov chain calculation.

Table 3. Final element group transition times (years)

Element group	State 1 to State 2	State 2 to State 3	State 3 to State 4	State 1 to State 4
A1 Concrete deck	12	24	24	79
A2 Concrete slab	9	30	17	72
A4 Steel deck	14	8	9	41
A5 Timber deck/slab	10	10	21	53
B1 Strip Seal expansion joint	28	10	10	59
B2 Pourable joint seal	12	6	6	32
B3 Compression joint seal	13	10	10	42
B4 Assembly joint/seal	24	15	15	70
B5 Open expansion joint	22	16	16	70
C1 Uncoated metal rail	18	27	56	127
C2 Coated metal rail	32	22	20	96
C3 Reinforced concrete railing	44	36	28	140
C4 Timber railing	31	9	9	62
C5 Other railing	36	13	13	77
D1 Unpainted steel super/substructure	23	40	40	132
D2 Painted steel superstructure	23	35	12	90
D6 Prestressed concrete superstr	68	40	15	152
D7 Reinforced concrete superstructure	24	40	24	113
D8 Timber superstructure	41	24	13	100
E1 Elastomeric bearings	94	18	18	152
E2 Metal bearings	28	34	34	123
F1 Painted steel substructure	19	30	11	77
F3 Concrete column/pile	38	34	36	140
F5 Concrete abutment	50	57	30	176
F6 Concrete cap	70	73	34	225
F8 Timber substructure	18	31	16	85
G1 Reinforced concrete culverts	37	42	53	170
G2 Metal and other culverts	12	18	31	78
P1 Deck wearing surface	11	32	19	79
P2 Protective coating	17	12	9	50

Median number of years to make the indicated transition

5 CONCLUSIONS

By drawing on the research and data sets of 19 state DOTs, the study was able to produce a nation-wide bridge element deterioration model for the National Bridge Investment Analysis System. Based on historical inspection data, the model avoids some of the problems that have been noted with earlier judgment-based models, particularly under-estimation of transition times noted in Sobanjo and Thompson (2013).

In addition to its use in NBIAS, the model is potentially useful to agencies that are getting started with bridge management and have not yet developed their own models. It may also be useful to researchers who need a national-scale model for life cycle cost analysis or investment analysis, but might not have the resources to develop one of their own.

REFERENCES

AASHTO 1998. *AASHTO Guide for Commonly Recognized Structural Elements with 2002 and 2010 Interim Revisions.* Washington: American Association of State Highway and Transportation Officials.

AASHTO 2013. *AASHTO Manual for Bridge Element Inspection.* Washington: American Association of State Highway and Transportation Officials.

FHWA 1995. *Recording and Coding Guide for the Structure Inventory and Appraisal of the Nation's Bridges.* Washington: US Federal Highway Administration. Report FHWA-PD-96-001.

FHWA 2014. *Specification for the National Bridge Inventory Bridge Elements*. Washington: Federal Highway Administration.

FHWA 2014. *Highway Performance Monitoring System: Field Manual*. Washington: US Federal Highway Administration. OMB Control No. 2125-0028.

FHWA 2016. *Status of the Nation's Highways, Bridges, and Transit: Conditions and Performance*. Washington: US Federal Highway Administration.

Mirzaei, Z., B.T. Adey, L. Klatter, and P.D. Thompson 2014. *Overview of Existing Bridge Management Systems*. International Association of Bridge Maintenance and Safety, Bridge Management Committee.

Sobanjo, J.O. and P.D. Thompson 2016. *Implementation of the 2013 AASHTO Manual for Bridge Element Inspection: Final Report*. Tallahassee: Florida Department of Transportation. Contract BDK30-977-07.

Thompson, Paul D., and John O Sobanjo. 2010. Estimation of enhanced Pontis deterioration models in Florida. *Proceedings of IABMAS 2010: The Fifth International Conference on Bridge Maintenance, Safety, and Management, Philadelphia.* Rotterdam: Balkema.

Maintenance, Safety, Risk, Management and Life-Cycle Performance of Bridges – Powers, Frangopol, Al-Mahaidi & Caprani (Eds)
© 2018 Taylor & Francis Group, London, ISBN 978-1-138-73045-8

Damage location in experimental/numerical models by acceleration amplitude change

R. L. Silva, L. M. Trautwein, L. C. Almeida & G. H. Siqueira
FEC - UNICAMP, Campinas - SP, Brasil

C. S. Barbosa
POLI - USP, São Paulo - SP, Brasil

ABSTRACT: This paper presents a technique to identify and locate a single fault at any point along the bridge span by vibration data analysis. In order to demonstrate this method, numerical and experimental models were developed and a simply supported single-span bridge was simulated. The experimental model is a slab with 150 cm of span, 5 cm of thickness, made with reinforced concrete and supported on rubber bearing. The finite element model was developed by using SAP2000® [1] software with the same geometric and materials properties from the experimental model. The first step was to create a vibration baseline data from undamaged models (experimental and numerical) by vibration test and computer simulation. Afterwards, a transversal cut of approximately 2 cm depth was performed to simulate structural damage and the vibration test was performed again. The vibration tests were performed with controlled impacts in the middle of the span and were monitored using capacitive accelerometers fixed along the span. At last, the damage location was obtained by comparing the sum absolute of acceleration data, from a specific time interval, between intact and damaged models. Therefore, the damage location coincides with the greater variation of the sum absolute sum of acceleration.

1 INTRODUCTION

Large structures such as bridges, dams, stadiums, etc. are subjected to severe loads over its service life. These actions can damage the structure, compromising its durability, bearing capacity and, in extreme cases, the structural collapse. The existence of damages causes changes on the structural dynamic characteristics, such as natural frequencies, amplitude of accelerations and displacements, modal shape and damping, that can be obtained through the dynamic monitoring.

The interest in the ability of monitoring a structure and detecting damage as soon as possible has permeated the aerospace, civil and mechanical engineering community (FARRAR 2001 [2]).

According to NOBREGA 2004 [3], the dynamic test is an adequate procedure because of its non-destructive character, which allows the collection of generalized information on the stiffness and structural damping, because of its comparability to a computer numerical model, and because it can be repeated and compared over time.

RYTTER 1993 [4] propose a classification system with four levels for damage identification methods:

- • *Level 1 (Detection): Indication that damage might be present in the structure;*
- • *Level 2 (Localization): Information about the probable position of the damage;*
- • *Level 3 (Classification): Quantification of the severity of the damage;*
- • *Level 4 (Assessment): Prediction of the remaining service life of the structure.*

OWOLABI 2003 [5] present a method for identifying a crack location based on the frequency and amplitude changes. The crack location is linked to changes in natural frequencies and acceleration amplitudes, expressed in frequency domain by a frequency response function (FRF).

In order to reach the level 2 of damage identification (RYTTER 1993 [4]), based on the studies presented by OWOLABI 2003 [5], an empirical formulation was developed, based on comparison of the sum absolute of acceleration data, from a specific time interval, between intact and damage models.

2 OBJECTIVE

The objective of this work is to present a technique of identification and localization of structural damages, able to locate a single damage at any point along the bridge span, from an empirical formula based on the changes of the acceleration amplitude, obtained from the dynamic monitoring. To reach the main objective, the following activities were performed:

- *preparation of a three-dimensional numerical model with the aid of software finite element;*
- *determination of the empirical formula by simulations with the numerical model;*
- *application of the damage localization technique in the numerical model for damages at different points in the span;*
- *construction of an experimental model;*
- *dynamic monitoring of the experimental models, intact and damaged;*
- *application of the empirical formula to locate a damage into experimental model.*

3 MODELS

Two models, numerical and experimental, were developed to simulate a simply supported single-span bridge. In the numerical model several simulations were made, varying the damage location, to support the determination of the empirical formula of damage location. Afterwards, the experimental model was used to demonstrate the developed method.

3.1 *Numerical model*

A representative three-dimensional numerical model of the structure was built using the SAP2000 software [1], with the same dimensions and mechanical properties of the materials from experimental model.
The numerical model is a rectangular slab with 150 cm of span and 5 cm of thickness, made with concrete and supported at the ends on rubber bearing (rubber dimensions: 500 x 50 x 18 mm). The properties of concrete and rubber bearing, experimentally determined, were shown in the Table 1.

Table 1. Properties of materials.

Concrete	f_{ck} (MPa)	24,9
	E (MPa)	33301*
	ν	0,2
Rubber bearings	E (MPa)	25
	ν	0,2

*It is considered the dynamic modulus of elasticity being 20% higher than the static modulus of elasticity

The model was discretized into solids elements, including rubber bearing, with the pinned support applied in all bottom face joints. The Figure 1 shows the numerical finite element model.

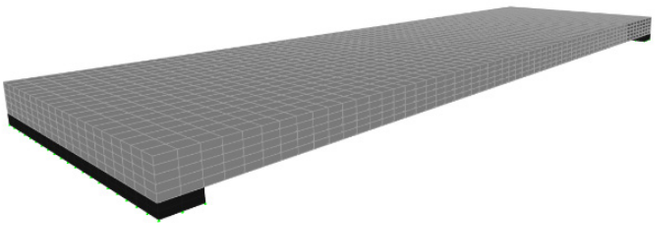


Figure 1. 3D view of the intact numerical model.

To simulate damages at different points of the structure, the intact model was replicated and the solid elements, located in the region of the hypothetical damage with 2 cm of depth, were removed. The damages were separately simulated in 8 points, distributed every 10 cm, from the middle span to the support - A. Figure 2 presents one of the damage models used in the simulations.

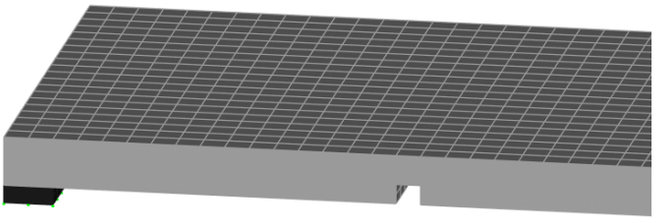


Figure 2. 3D view of the numerical model with a damage at 45 cm, from the support-A.

The dynamic tests of the models were performed by time-history impulsive load (fmax = 1 kN), applied in the middle spam. Then, the output acceleration data was extracted at 30 points along the span, with steps of 0.001 seconds, equivalent to the acquisition rate of 1000 Hz.

3.2 *Experimental model*

As discussed earlier, the experimental and numerical models were made with the same geometry and materials mechanical properties. The differences between models are: 1) experimental model was reinforced with a light weight steel wire mesh (CA-60); 2) the rubber bearings were fixed to the concrete with contact adhesive, in order to simulate a pinned support.
The dynamic tests were divide in two steps: 1 -vibration test of intact model, to create a vibration baseline; 2 – vibration test of the damage model. To collect the acceleration data was monitored 24 points. The monitoring was performed in three stages, each with eight sensors positioned vertically, distributed along the span (Figure 3). The Figure 4 shows the experimental model used with the set of acceleration transducers.

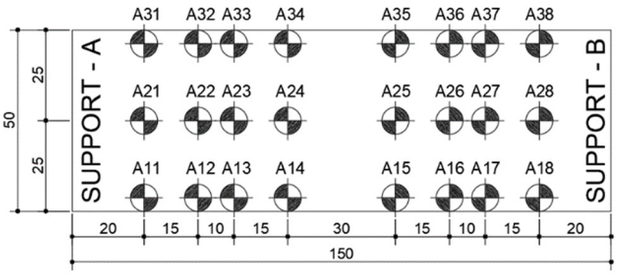


Figure 3. Positioning of the acceleration transducers.

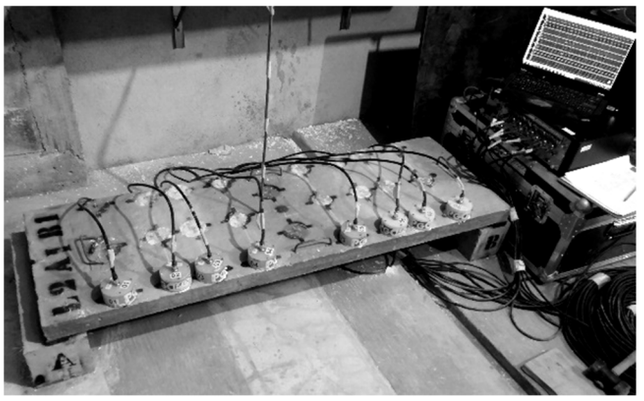


Figure 4. Experimental model.

Acceleration transducers capacitive type model 2210-002 Silicon Designs, Inc. conducted the dynamic monitoring. This instrument operates in a frequency range from zero to 300 Hz and has a sensitivity of 2000 mV/g. The range of the transducer for measuring acceleration varies from -19.6 m/s to 19.6 m/s².
Lynx Technology model ADS2002 system with AI2164 expansion module captured the data. This acquisition system has a power between 5 and 15 VDC, signal conditioning, A/D converter of 16 bits with a 12.5 μs / channel conversion time. The sensor data were recorded simultaneously using laptop with AqDados 7 software from Lynx Technology Company.
The vibration of the structure was performed by the free fall of a rubber ball in the middle of model, released from rest at a height 65.0 cm (Figure 5). The impact of the ball induces vibrations in the structure capable of mobilizing its main natural frequencies. The Figure 6 shows an example of induced vibration captured by the acceleration transducer.



Figure 5. Rubber ball falling in the middle of model.

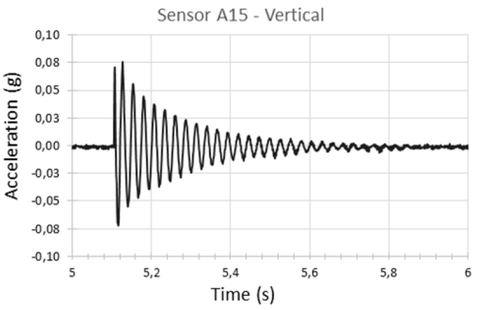


Figure 6. Acceleration captured by the sensor during the impact of the rubber ball.

After the vibration tests in the intact model, a transversal cut of approximately 2 cm depth (Figure 7) was performed to simulate structural damage and the vibration test was taken again. The Figure 8 show a close of the damage made with a diamond cutting disc.

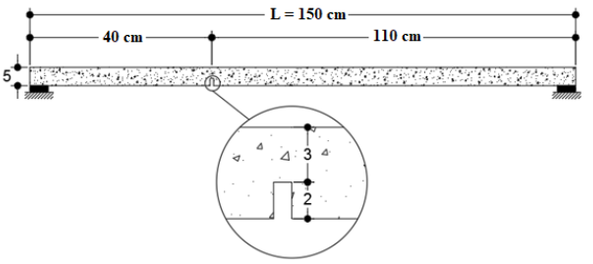


Figure 7. Position of the transversal cut on the experimental damage model.

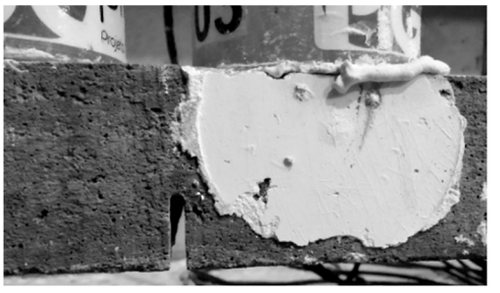


Figure 8. Transversal cut made with diamond cutting disc.

4 RESULTS

The results of the numerical analysis, with the determination and application of the empirical formula for the localization of damages, and the results of the application of the method to locate damages in the experimental model, will be presented in this section.

4.1 *Numerical model results*

The determination of a method that allow to find a single damage, at any point along the span of a simply support structure, was reached after several attempts. Among the hypothesis raised, the one that presented the most relevant results was the acceleration summation difference between intact and damage models.

This method consists in the difference of the acceleration amplitudes, obtained from the dynamic response of the structures for a determined excitation.
In order to perform the comparison between the intact and the damaged model, the absolute sum of the accelerations was used, in a determined time interval, starting the sum from the first peak of the impulse signal.
This allowed the accumulation of all acceleration data over time in a parameter, representative of the acceleration changes of each model. Figure 9 shows the behavior of this parameter along the span, for the acceleration data of the intact and damage models.

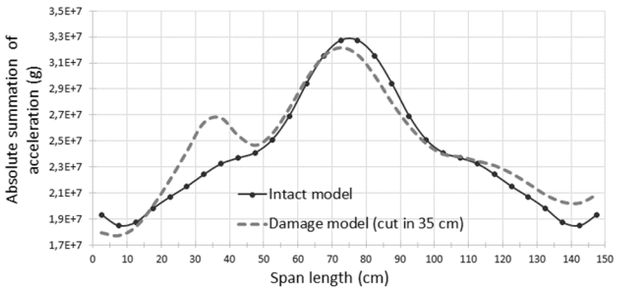


Figure 9. Absolute summation of acceleration (intact model x damage model).

In order to improve the graphical representation of the location of the damage, the acceleration summation difference was squared, making positive all values in the graph scale and increasing the amplitude of the damage indicator. As result, the following empirical formula was found:

$$\boldsymbol{ASD}_{(j)} = \left(\sum_{t_i}^{t_f} \left|\boldsymbol{a}_{j-int}\right| - \sum_{t_i}^{t_f} \left|\boldsymbol{a}_{j-dan}\right| \right)^2 \qquad (1)$$

Were:

$\boldsymbol{ASD}_{(j)}$ – squared of the Acceleration Summation Difference in the j-th point;

$\left|\boldsymbol{a}_{j-int}\right|$ – absolute acceleration values from the intact model in the j- th point;

$\left|\boldsymbol{a}_{j-dan}\right|$ – absolute acceleration values from the damage model in the j- th point;

$\boldsymbol{t_i}$ – initial time, considered from the peak of acceleration;

$\boldsymbol{t_f}$ – final time with the same interval in all analyzes, in this case $\boldsymbol{\Delta t} = 0{,}3\ seconds$.

Then, the ASD method was applied to the numerical models with damage, to evaluate the performance of the method in locating damages along the span.
The Figure 10 shows the results of the application of the ASD method in locating damage into numeric models with a single damage. It is observed that the amplitude of the peak that indicates the position of the damage, for damages with the same intensity, varies along the span. Figure 11 shows the amplitude variation along the span.

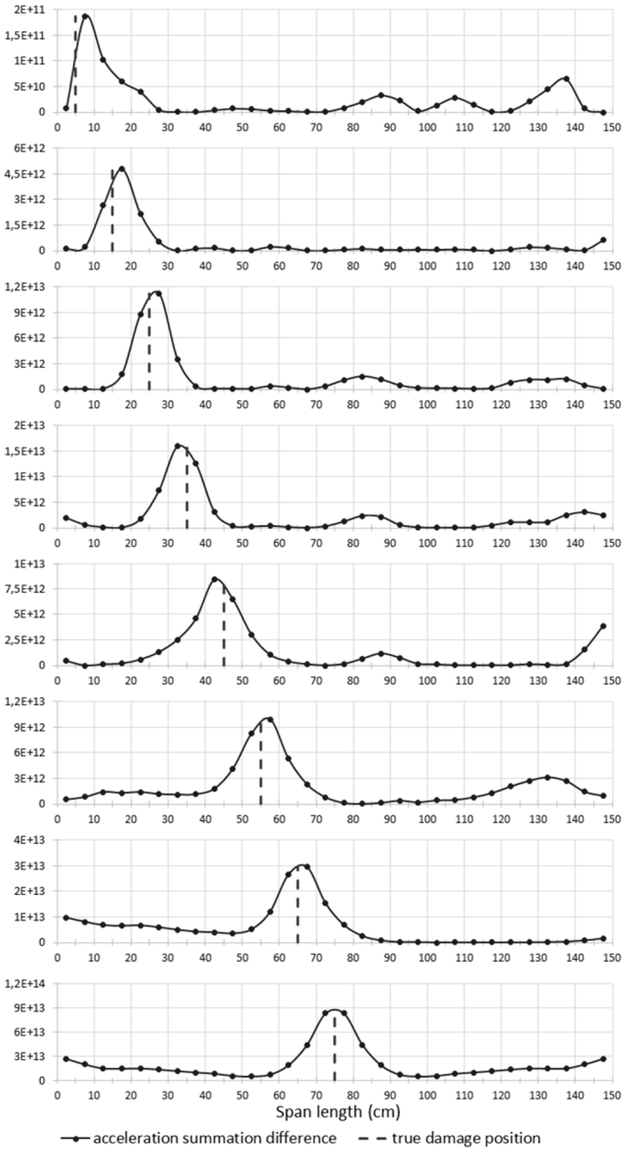


Figure 10. Identification of a single damage with ASD method.

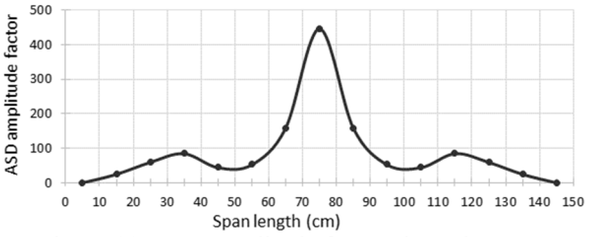


Figure 11. ASD amplitude factor along the span.

Despite the variation of the response along the span, it can be said that the ASD method was able to identify a single damage at any point in the span of a simply supported numerical model.

4.2 *Results of the experimental model*

To evaluate the ability of the ASD method to locate damages in real structures, the empirical formula was applied to the results of the experimental models. Figure 12 shows the results of the application of the ASD method in the location of damage at experimental

models with only one damage (damage at 40 cm of support A).

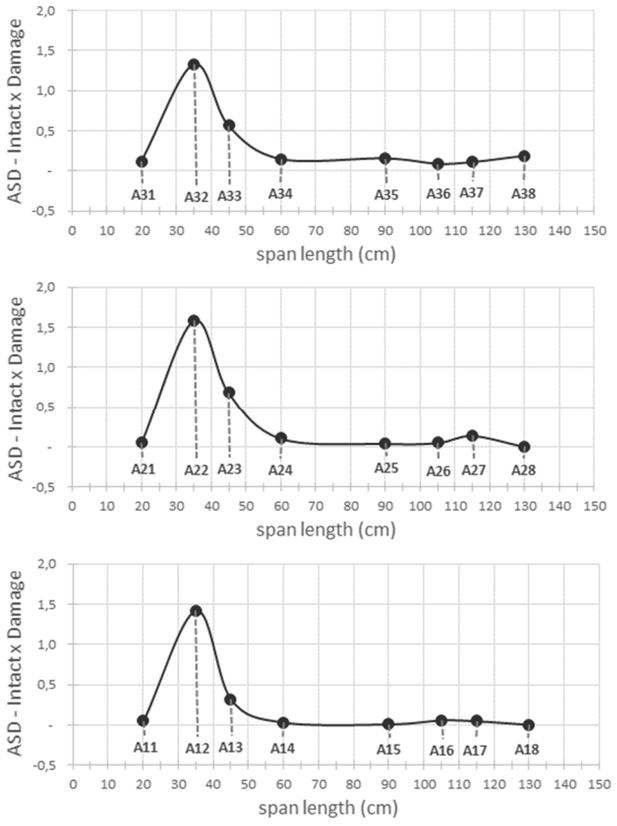


Figure 12. Application of ASD method on experimental model.

It is observed that the probable location of damage, obtained by the ASD method, is at 35 cm from the support-A, but the true position is at 40 cm. This occurs because the damage location, obtained with ASD method, is related to the position of the sensors, indicating that the damage is close to the sensors A12, A22 and A32. In order to synthesize the results found in Figure 12, a surface graph was elaborated for a plan view of the damage location (Figure 13).

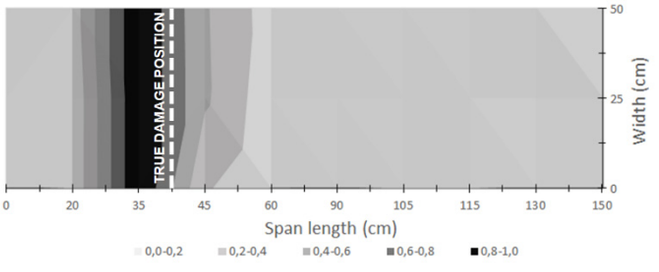


Figure 13. Surface graph of ASD results.

From the results presented, it can be said that the ASD method was able to find the approximate location of a single damage in a simply supported experimental model. It is important to highlight that the precision of the method is related to the positioning of the sensors. Therefore, the smaller the spacing between the sensors, the better the determination of the location of the damage.

5 CONCLUSION

In this work was presented the determination of an empirical formula, through simulations in numerical models, able to locate a single damage in simply supported structures. The method called Acceleration Summation Difference (ASD) was based on the difference of acceleration amplitudes between intact and damage structures.

The ASD method was applied to locate a single damage in numerical models. For this, damages were simulated at some points along the span. Despite the variation of the response along the span, it can be said that the ASD method was able to identify a single damage at any point in the span of a simply supported model.

Then, the ASD method was applied to the damage location in a reinforced concrete experimental model. The probable location of the damage was at 35 cm from the support - A, while the true location was 40 cm. It is important to highlight that the method precision is related to the position of the sensors. Therefore, it can be said that the ASD method was able to locate a single damage into experimental models.

The disadvantages observed in the ASD method were: the need for a baseline from the intact structure and the variation of the ASD along the span, for damages of the same intensity.

For future studies, it is intended to perform tests on structures with multiple damages and the adjustment of the empirical formulation, to homogenize the DSA response along the span.

6 REFERENCES

[1] CSI – Computers and Structures, Inc. – SAP2000 – Product Description. Website: <https://wiki.csiamerica.com/display/sap2000/Home>. Accessed in: Nov. 10 2017.

[2] FARRAR, C. R. Grand challenges for structural dynamics. In: EWINS, D.J.; INMAN, D.J., ed. Structural Dynamic @ 2000: current status and future directions. RSP, 2001.

[3] NOBREGA, P. G. B. Análise dinâmica de estruturas de concreto: estudo experimental e numérico das condições de contorno de estruturas pré-moldadas – São Carlos, 2004.

[4] RYTTER, A. 1993 Vibration Based Inspection of Civil Engineering Structures. PhD thesis, Department of Building Technology and Structural Engineering, Aalborg University, Denmark, 1993.

[5] G.M. OWOLABI, A.S.J Swamidas and R Seshadri (2003). Crack Detection in Beams using Changes in Amplitudes and Frequencies of Frequency Response. Journal of Sound and Vibration, 265(1), 1-22.

Maintenance, Safety, Risk, Management and Life-Cycle Performance of Bridges – Powers, Frangopol, Al-Mahaidi & Caprani (Eds)
© 2018 Taylor & Francis Group, London, ISBN 978-1-138-73045-8

Early detection of reinforcing-bar corrosion with Linearized Inverse Scattering Method

T. Tsunoda & K. Suzuki
University of Fukui, Fukui, Japan

ABSTRACT: This study proposes a visualization method for a cross section of RC structure in which condition of the reinforced bar (rebar) is healthily composite to the concrete or corrosively exfoliated from that. Visualization is based on Kirchhoff linearized inverse scattering method (K-LISM), and the rebar condition is emphasized by parasitic discrete wavelet transform (P-DWT) in its imaging process. An original filter included in P-DWT is developed and oriented to extract the information of rebar condition. Scattered waves from the rebar-concrete interface are obtained by UT the pitch-catch mode from the top surface of the concrete specimen. Scattered waves are filtered by P-DWT developed from the waveform measured from the exfoliated rebar; then, they are processed with K-LISM. The reconstructed images enable to differentiate between corrosively exfoliated rebar and healthy rebar.

1 INTRODUCTION

Corrosion of reinforcing bars induces cracks in concrete with its expansion process. Consequently, the cover concrete would be peeled off and the section loss would occur. Visual inspection can grasp the damage occurrence after the crack or the rusty water appears at the concrete surface. In order to carry out preventive maintenance works, corrosive damage in the early stage or healthy condition of rebar should be diagnosed with an accurate judging method before the crack appears at the surface.

When a rebar has corrosive damage, the condition of steel-concrete interface is different from that of healthy one. In addition, the interface may exfoliate if the corrosion progresses. In this study, we focus on the difference in acoustic impedance at the interface and consider a method to visually grasp the state of the steel-concrete interface by UT.

In recent years, great research results have been reported on a method of applying linearized inverse scattering methods (LISM) to the data of UT and detailed imaging of the defect shape. Application LISM for using concrete specimens have also been reported; therefore, the LISM is widely accepted as an effective processing method for visualizing defects in concrete medium.

This study focuses on the LISM based on Kirchhoff approximation, and attempt to visualize the state of rebar boundary in concrete. Kirchhoff LISM is known as a better method to visualize the interface of the medium compared with Born LISM.

Also Parasitic Discrete Wavelet Transform (P-DWT) is applied to filter the scattered waves to extract the frequency characteristics oriented for the defect information. Following chapters discuss the K-LISM and then, wave processing with P-DWT, the data processing is validated by experiments of 200kHz-UT pitch catch tests.

2 LINEARIZED INVERSE SCATTERING METHOD

2.1 *Kirchhoff inversion (K-LISM)*

Now consider the cavity defect D_c exists in homogeneous isotropic two dimensional infinite elastic material (Figure 1). It is assumed that the position of the defect can be estimated roughly, incident wave is transmitted towards target point *O* from point *y* on the measurement boundary S^{far} where is far from D_c.

It is supposed that a pulse echo mode for receiving the scattered wave u^{sc} from the cavity defect D_c at the point *y*.

$$u_m^{sc}(y) = A_m(k_L,\ \hat{y})D(k_L|y|) + B_m(k_T,\ \hat{y})D(k_T|y|) \quad (1)$$

where, k_L and k_T are wave number of longitudinal(L) and transverse(T) waves, $\hat{y}$ is the unit vector pointing to the measurement point y, $D(z) =$

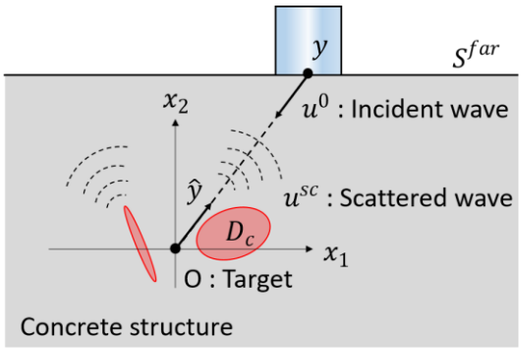


Figure 1. Configuration of inverse scattering analysis

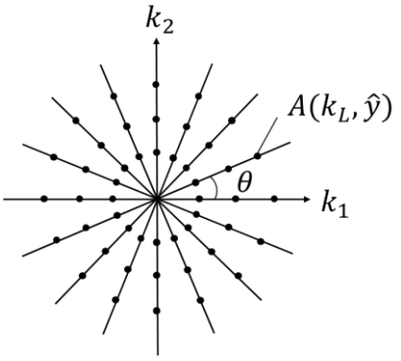


Figure 2. Two-dimensional plot of $A(k_L, \hat{y})$

$\sqrt{2/(\pi z)}e^{i(z-\pi/4)}$ is the cylindrical wave measured at the point y. A_m and B_m are the scattering amplitudes of longitudinal and transverse. These are used for reconstruction of the flaw shape. In this study, we only focus on the longitudinal scattering amplitude because of using the longitudinal wave transducer.

The boundary type for longitudinal amplitude A_m is defined by

$$A_m(k_L, \hat{y}) = \frac{i}{4\mu}\kappa^2 \hat{y}_i \hat{y}_m \int_D -\gamma(x) C_{ijkl}\{n_j(x)u_{k,l}(x) - n_j(x)u_k(x)\partial/\partial x_j\}e^{-ik_L \hat{y}\cdot x} dV \quad (2)$$

where $\gamma(x)$ is the singular function defined to represent the flaw boundary.

$$\int_D \gamma \, dV = \int_S dS \quad (3)$$

And in Equation 2, $\kappa = k_L/k_T$, n is the unit normal vector toward the base material on the flaw boundary S.

The scattering amplitude A_m and the singular function γ are nonlinear relation since this integral expression contains the unknown displacement field u.

The Kirchhoff approximation is introduced to the scattering amplitude of Equation 2 to replace the unknown displacement field u with the summation of the incident and reflected wave. After that, it is possible to reconstruct the shape and size of flaw with solving for the singular function γ.

The linearized expression of scattering amplitude A_m applied the Kirchhoff approximation is given by

$$A(k_L, \hat{y}) \cdot \hat{y} = -\frac{u^0 k_L}{2} \int_D \gamma(x) e^{-2ik_L \hat{y}\cdot x} dV \quad (4)$$

The final form of the scattering amplitude has the structure of the spatial Fourier transform in terms of x. Therefore, the singular function $\gamma(x)$ is obtained by the inverse Fourier transform as follows:

$$\gamma(x) = \frac{-1}{\pi^2} \int_0^{2\pi} \int_0^{\infty} \frac{2}{u^0 k_L} A(k_L, \hat{y}) e^{2ik_L \hat{y}\cdot x} k_L dk_L d\hat{y} \quad (5)$$

Since this inverse algorithm is based on Fourier transform, applying the fast Fourier transform (FFT) enables to process high speed.

2.2 *Fast processing method with FFT*

In the K-space (k_1, k_2) and the real image space (x_1, x_2) which are finite discrete spaces, Equation 5 is expressed by the following Equation 6.

$$\gamma(x) = \frac{1}{\pi^2} \int\int \frac{-2}{u^0 \sqrt{k_1^2 + k_2^2}} A(k_1, k_2) \, e^{2i(k_1 x_1 + k_2 x_2)} dk_1 dk_2 \quad (6)$$

The discrete data $A(k_1, k_2)$ in a finite range at the rectangular coordinate is required in order to apply 2D-FFT. The scattering amplitude data $A(k_L, \hat{y})$ obtained in the observation direction $\hat{y}$ is plotted at the discrete point of the polar coordinate $(k_L, \hat{y})$ shown in Figure 2. The grid point data $A(k_1, k_2)$ necessary for 2D-FFT is acquired by the interpolation of the scattering amplitude $A(k_L, \hat{y})$.

3 WAVEFORM PROCESSING

3.1 *Discrete wavelet transform (DWT)*

Discrete wavelet transform (DWT) is one of the frequency analysis effective for signals having nonlinearity and localized in the time domain. DWT is the method of expressing a signal to each frequency band level by linearly combining with base functions (mother wavelet) consisting of scaling function and wavelet function. The scaling function has characteristic of a low-pass filter and the wavelet function has characteristic of a high-pass one. As shown in Figure

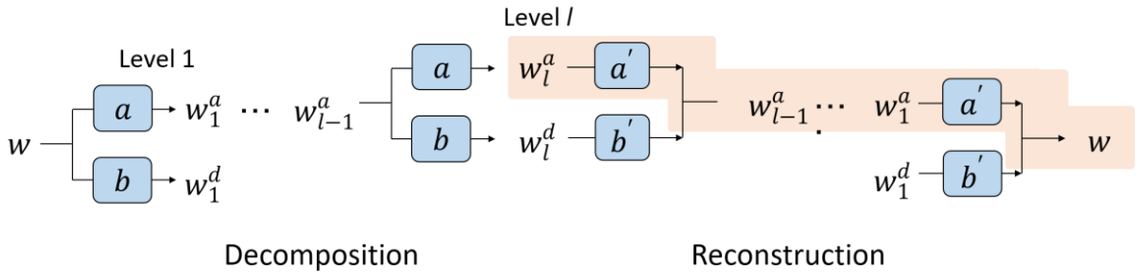


Figure 3. Calculation flow of DWT

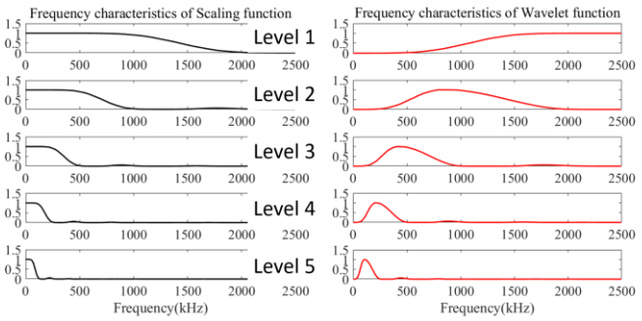


Figure 4. Frequency characteristics of 'Daubechies 5'

3, the signal is decomposed and reconstructed into low frequency components (Approximation) and high frequency components (Detail) for each frequency band level. In Figure 3, "w" is the target signal, a and b are decomposition sequence corresponding to scaling function and wavelet function, and a', b' are reconstruction sequence. As an example, Figure 4 illustrates the frequency filter characteristics of the scaling function and wavelet function of mother wavelet 'Daubechies 5' for each frequency band level up to level 5.

It has been reported that low frequency components greatly contribute to the imaging by LISM. Therefore, the signals of the approximation are used for the input data of inverse scattering method.

The following two-scale relationship is held for the scaling function $\phi(x)$ of the mother wavelet used for DWT shown in Figure 3.

$$\phi(x) = \sum_{k \in Z} p_k \phi(2x - k) \tag{7}$$

In addition, the following relationship establishes between wavelet function and scaling function.

$$\psi(x) = \sum_{k \in Z} q_k \phi(2x - k) \tag{8}$$

p_k is two-scale sequence, and the following relationship consists between the sequence p_k and q_k.

$$q_n = (-1)^{1-n} p_{1-n} \tag{9}$$

p_k determines the shape of the mother wavelet, and several famous ones which have been developed by researchers.

p_k has a characteristic of low-pass filter, and q_k has a characteristic of high-pass filter.

The decomposition sequence a_k, b_k required for calculation of DWT shown in Figure 3 is given by

$$a_k = \frac{1}{\sqrt{2}} p_{-k} \tag{10}$$

$$b_k = \frac{1}{\sqrt{2}} q_{-k} \tag{11}$$

The decomposition calculation of the target signal by DWT is repeated until the target level by following Equations 12 and 13.

$$w^a_{l,n} = \sum_{k \in Z} a_{2n-k} \, w^a_{l-1,k} \tag{12}$$

$$w^d_{l,n} = \sum_{k \in Z} b_{2n-k} \, w^a_{l-1,k} \tag{13}$$

w^a_l and w^d_l are scaling and wavelet coefficients obtained at level l.

The reconstruction calculation is performed recursively by the following Equation 14.

$$w^a_{l-1,n} = \sum_{k \in Z} a'_{n-2k} \, w^a_{l,k} + \sum_{k \in Z} b'_{n-2k} \, w^d_{l,k} \tag{14}$$

where, the following relationship holds between the reconstruction sequence a'_k and b'_k and the decomposition sequence.

$$a'_k = a_{-k} \tag{15}$$

$$b'_k = b_{-k} \tag{16}$$

Approximation data are calculated by reconstruction using only the scaling coefficients as shown in the colored flow in Figure 3.

3.2 *Parasitic Discrete Wavelet Transform (P-DWT)*

Parasitic discrete wavelet transform is a method to detect the target signal by adding an original filter in the frequency domain created by decomposing the

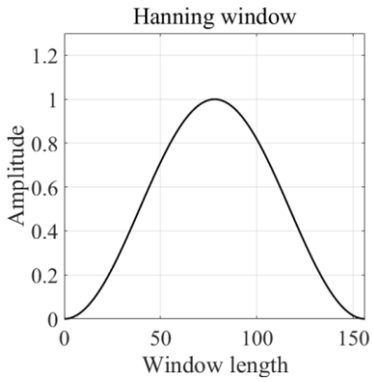


Figure 5. Hannig window

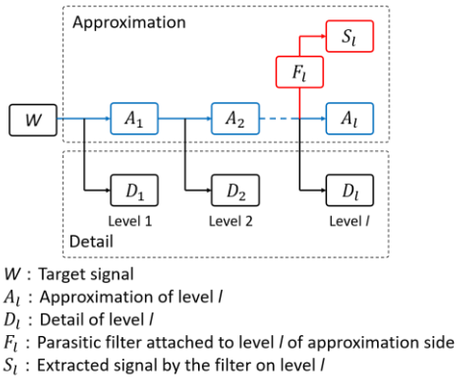


Figure 6. Calculation flow of P-DWT

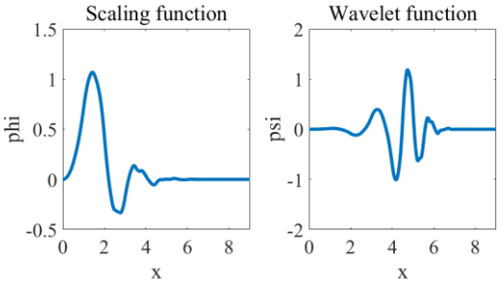


Figure 7. Daubechies 5

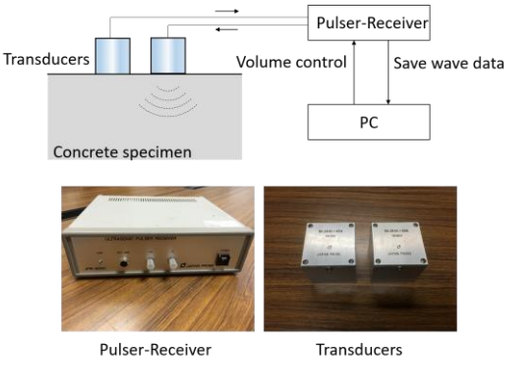


Figure 8. Measurement equipment of UT

waveform with real signal mother wavelet (RMW). The important point is that the waveform used for the filter is obtained from the similar shaped defect to the target one. Since the conventional DWT and FFT are used for calculation, high-speed processing is possible.

3.2.1 *Constructing RMW*

The design method of real type RMW ψ^R is as follows:

1) The window function is applied to the base wave to let the wave value zero at both ends. In this study, Hanning window (Fig. 5) is adopted because it has better resolution on time domain and frequency one.
2) Real type RMW ψ^R is constructed by performing normalization to set the norm to 1. The normalization formula is expressed as

$$\|\psi^R\| = \left[\int_{-\infty}^{\infty} \psi^R(t)^2 dt\right]^{\frac{1}{2}} = 1. \quad (17)$$

3.2.2 *P-DWT*

The mother wavelet used for DWT needs to satisfy the orthogonality condition between $\psi(x-k)$ and $\psi(x-l)$ $(k \neq l\ k, l \in z)$, however it is actually impossible to impose this condition on the real signal. Therefore, RMW composed of the real signal cannot be directly used for DWT.

P-DWT, which extracts a target signal, is constricted by adding an originally developed parasitic filter in the frequency domain. The parasitic filter $F_l(f)$ contains frequency characteristics of RMW.

The procedure (Figure 6) of creating and adding the parasitic filter $F_l(f)$ of the approximation side is described as follows:

1) RMW is decomposed to the level to which the filter is added with the base mother wavelet. The obtained time domain waveform data of the approximation are transformed into frequency domain data by FFT. In this study, 'Daubechies 5' (Fig 7) is used as the base mother wavelet. The acquired frequency domain data F_l^R, F_l^I of the real and imaginary part are the approximation side of parasitic filters.
2) The target signal is decomposed with the base mother wavelet by DWT up to the level -1 at which the filter is added. The obtained time domain approximation data are transformed to frequency domain ones by FFT, and parasitic filter is applied to each of the real and imaginary part respectively.
3) The filtered frequency domain data are converted to time domain ones by inverse Fourier transform.

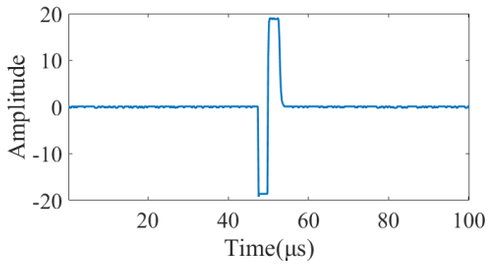


Figure 9. Incident wave

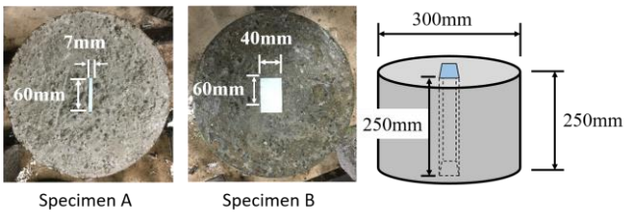


Figure 10-1. Specimens

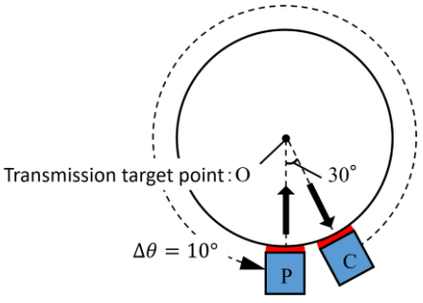


Figure 10-2. Measurement method

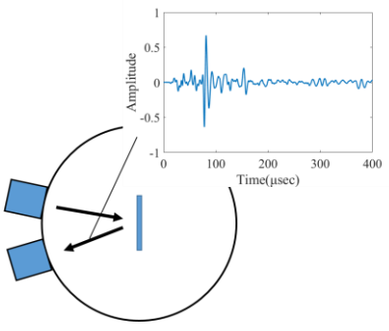


Figure 11. Calculation of wave velocity

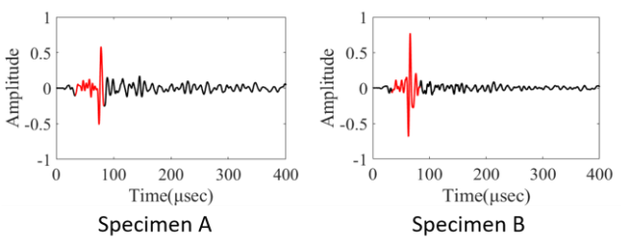


Figure 12. Extracting scattered wave

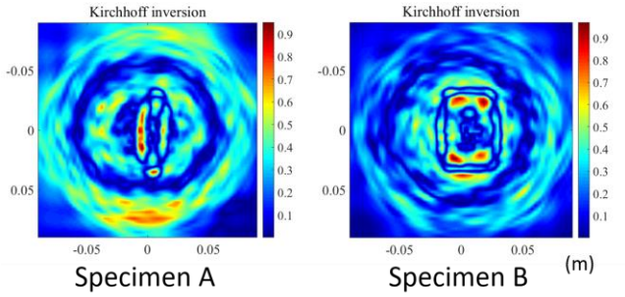


Figure 13. Results of K-LISM

4 PRE-EXPERIMENT

We conducted a pre-experiment for applying K-LISM and P-DWT to check the performance of the proposed process.

4.1 *Specimens and experiment*

The experiment is conducted with the equipment configuration shown in Figure 8. The transducers are the broadband type, the center frequency of which is 200kHz. Voltage control is carried out using the pulser-receiver, and obtained data are saved in a computer through the same device. The incident wave (Fig 9) used for LISM is recorded by the digital oscilloscope connected the pulser-receiver.

The outline of the specimen used in the pre-experiment is illustrated in Figures 10-1. In order to simulate the rectangular cavity, Styrofoam cut into 7mm ×60mm and 40mm×60mm is placed at the center of each specimen. The maximum size of coarse aggregate is 13mm in the concrete. As shown in Figure 10-2, the wave data are obtained from all directions from the specimen periphery at 10 degrees interval with a pair of transducers fixed at the 30 degrees angle.

Prior to the experiment, the wave velocity in the concrete is experimentally obtained using the specimen A. As shown in Figure 11, the incident wave is transmitted to the long side of the slit or cavity, and wave velocity is calculated from the measured time of the acquired reflected wave and the propagation distance. The velocity was 3600m/s.

4.2 *Applying K-LISM*

In the LISM, it is supposed that the cavity is located in the infinite elastic material. Waveforms at the range suspected of existence of a cavity are used. Therefore, we need to predict that there is a defect in the time domain occurring a large response on the A-scan, and extract the target time range; then, use it for inversion. Specifically, as shown in Figure 12, waveforms of 33.2*μsec* to 83.2*μsec* were extracted for the

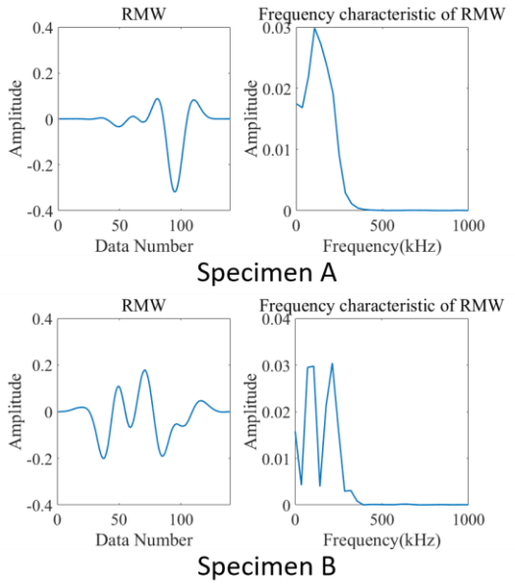


Figure 14. RMW corresponding of each specimens

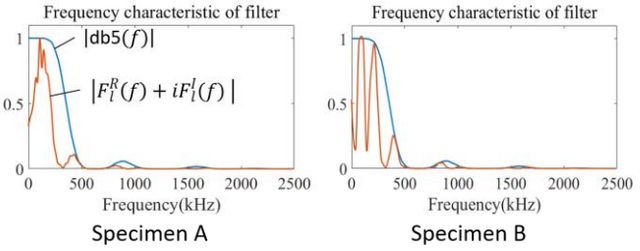


Figure 15. Frequency characteristics of P-DWT filter

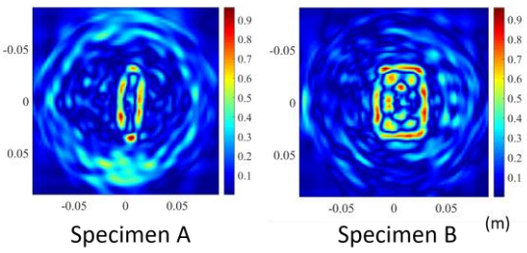
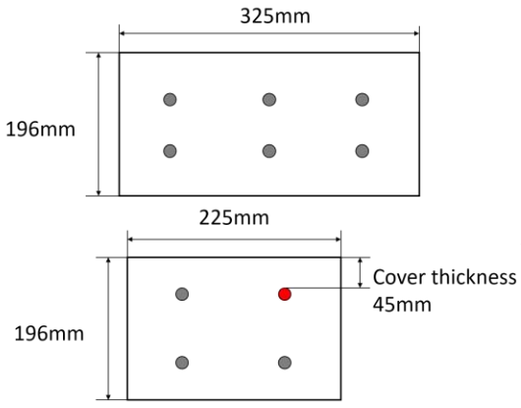


Figure 16. Applying P-DWT



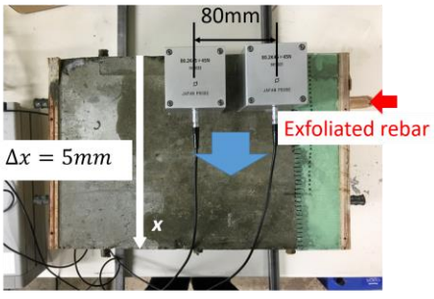


Table 1. Concrete formulation

Cement	366
Water	168
Fine aggregate	880
Coarse aggregate	906
Chemical mixture	2.35

(kg/m^3)

Figure 17. Specimen with the exfoliated rebar and measurement method

both specimens. Frequency data less than 320kHz was used for analysis.

The processing result of K-LISM without P-DWT is shown in Figure 13. The rough shape could be reconstructed, however defect shape was blurred compared to the noise.

4.3 *Image sharping with P-DWT*

We attempted to sharpen the defect shape image by applying the K-LISM with parasitic filter.

As shown in Figure 14, RMW is created from the extracted waveform from the defect of each specimen. Same as the prior case, waveforms of 33.2μsec to 83.2μsec were extracted.

Level 3 parasitic filter created from each RMW is shown in Figure 15. For comparison, the frequency characteristic db5(f) of Daubechies 5 corresponding to level 3 is also shown.

It is possible to extract the feature of frequency component for the target defect. Two reasons support it. First, the frequency range of db5(f) and the created parasitic filter $F_l(f)$ substantially agree with each other. Second, a dominant frequency spectrum becomes more prominent while frequency characteristics of 'Daubechies5' remain.

Figure 16 shows the result of sharpening by P-DWT. As a result, the flaw image became more clearly sharpened.

5 EXPERIMENT FOR EXFAOLIATED REBAR

5.1 *Specimen and experiment*

The specimen outline and the measurement method are shown in Figure 17. The specimen is cuboid made of the concrete (Tab. 1) the dimensions of which are W225 × D325 × H196. Concrete cover

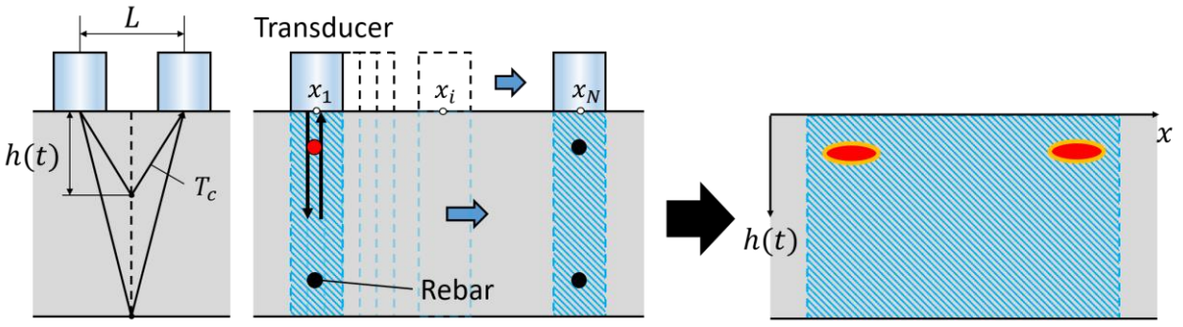


Figure 18. B-scan

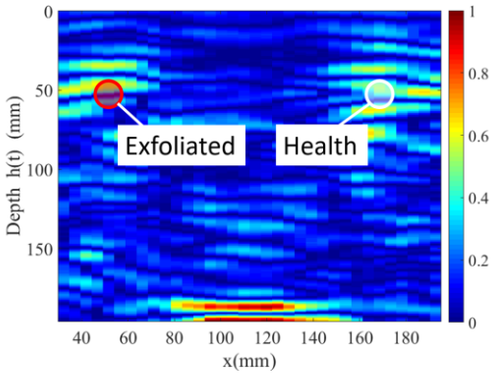


Figure 19. Result of B-scan

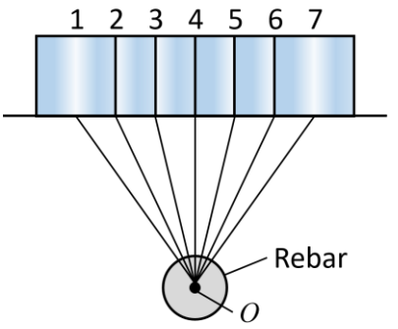


Figure 20. Configuration of target point *O*

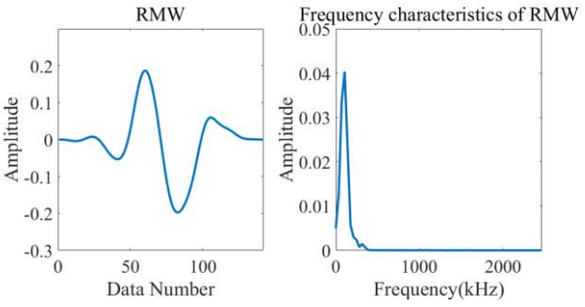


Figure 21. RMW of exfoliated rebar

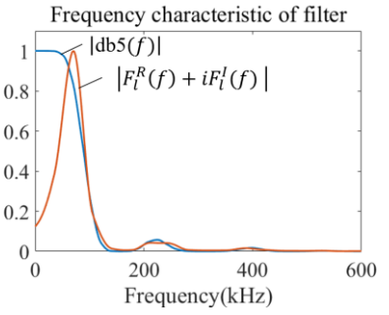


Figure 22. Frequency characteristics of parasitic filter

thickness from the rebar is 45mm, and the exfoliated state of the rebar is made by putting a wrapping film.

The experiment is conducted with the same equipment configuration of the pre-experiment. As shown in Figure 17, the wave data acquisition is performed every 5mm in the x direction by the pitch-catch mode from the top surface of the specimen. The distance between both transducers is fixed at 80mm.

For applying K-LISM, it is assumed that the approximate position of the target can be estimated. We applied K-LISM after grasping the rough position of the rebar by B-scan.

5.2 *Imaging of rebar inside the concrete*

5.2.1 *Grasping the position of rebar with B-scan*

B-scan is a technique to visualize the target cross-section by arranging the results of A-scan obtained by the experiment for each measurement position as shown in Figure 18.

Figure 19 shows the result of B-scan with the wave data acquired by experiment. The horizontal axis is the x direction shown in Figure 17, the vertical axis is depth direction $h(t)$.

As a result, it was possible to grasp the rough position of the rebar, however the shape and condition was unclear.

5.2.2 *Applying K-LISM and P-DWT*

As shown in Figure 20, the waveforms obtained at 7 points above the rebar are used for K-LISM. The center of rebar is set as transmission target point O, and the waveforms are extracted from the target point O. Frequency data less than 315kHz was used for analysis.

The measured wave data just above the exfoliated rebar is used for parasitic filter. The waveform of 20mm before and after the center point of the rebar is extracted from the measured wave data based on wave velocity. The time range used hear was 22μsec

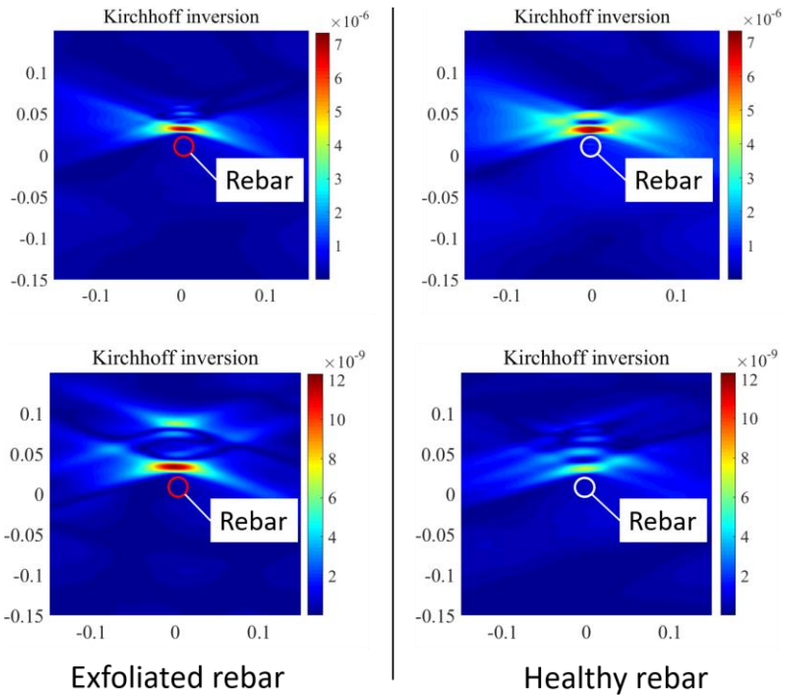


Figure 23. Results of K-LISM

set to 50.2μsec. The RMW constructed from this waveform is shown in Figure 21.

Parasitic filter is added in level 5. As shown in Figure 22, the frequency range of db5(f) and the created parasitic filter $F_l(f)$ substantially agree with each other.

The upper part of figure 23 shows the result of applying K-LISM without P-DWT. In this case, it could not be distinguished whether the rebar is health or exfoliated. The lower part of figure 23 illustrates the result of applying K-LISM with P-WDT. This result, in contrast, showed clear between exfoliated and healthy part of one surface of the rebar.

6 CONCLUSIONS

In this paper, image-based evaluation in terms of the rebar inside the concrete with a combination of wave processing by parasitic wavelet transform (P-DWT) and Kirchhoff inverse scattering method (K-LISM) was discussed.

The conclusions are summarized as follows:

1) P-DWT with the approximation side parasitic filter based on the waveform from defect enables to sharpen the image.
2) It is possible to differentiate between exfoliated and health part of the rebar by K-LISM with the parasitic filter created from the waveform obtained from the exfoliated rebar.

7 REFERENCES

Hirose, S., Nabeno, H. & Ohtomo, Y. 1997. Inverse scattering for reconstruction of cavities. *Journal of structural engineering* 43A: 453-460.

I, Daubechies. 1992. *Ten lectures on wavelets*. Philadelphia: Society for industrial and applied mathematics.

Kitahara, M., Nakahata, K & Hirose, S. 1998. Geometrical resolution of defects in linearized inverse scattering methods. *Journal of applied mechanics* 1: 167-174.

Nakahata, K. & Kitahara, M. 2000. Shape reconstruction of defects and effect of frequency range in measurement. *Journal of applied mechanics* 3: 91-98.

Nakahata, K., Onishi, M. & Kitahara, M. 2002. A fast method of linearized inverse scattering analysis and its application to shape reconstruction. *Journal of applied mechanics* 5: 67-74.

Nakahata, K. & Kitahara, M. 2003. A flaw reconstruction method in infrastructures with low frequency ultrasonic waves. *Journal of applied mechanics* 6: 1073-1080.

Nakahata, K., Saitoh, T. & Hirose, S. 2006. 3-D flaw imaging by inverse scattering analysis using ultrasonic array transducer. *34th Annual Review of Progress in Quantitative Nondestructive Evaluation*: 717-724.

Rose, J.H. 1989. Elastic wave inverse scattering in non-destructive evaluation. *Pure Appl. Geophy* 131: 715-739.

Tsunoda. T. & Suzuki, K. 2017. An attempt to visualize steel-concrete interface. *Journal of structural engineering* 63A: 581-587.

Yamada, M., Onishi, M. & Kitahara, M. 2004. Shape reconstruction of flaws in an inhomogeneous material by linearized inverse scattering methods. *Journal of applied mechanics* 7: 83-90.

Zhang, Z., Ikeuchi, H., Saiki, N., Imamura, T., Ishii, H., Toda, H & Miyake, T. 2009. Parasitic discrete wavelet transform and its application on abnormal signal detection. *Transactions of the Japan society of mechanical engineering* series C 71 No.757: 2529-2536.

Zhang, Z., Ohtaki, J., Toda, H., Miyake, T & Ishikawa, Y. 2015. A new discrete wavelet transform using variable band filters (Fetal ECG extraction using new discrete wavelet transform). *Transactions of the JSME (in Japanese)* 81 No.822: 14-00223.

Maintenance, Safety, Risk, Management and Life-Cycle Performance of Bridges – Powers, Frangopol, Al-Mahaidi & Caprani (Eds)
© 2018 Taylor & Francis Group, London, ISBN 978-1-138-73045-8

Fragility Curves for concrete girder bridges under flood hazard.

F. Kalendher, S. Setunge, D. Robert, H. Mohaseni

RMIT University, Melbourne, Australia

ABSTRACT: Fragility curves are developed for the reinforced concrete girder bridges under flood hazard in Lockyer Valley Region in Queensland, Australia. A failed bridge structure during 2011 severe flood event has been case studied in this paper. Uncertain nature of flood intensity for a given catchment area that causes random flood induced forces to the bridge structure and the variability of its geometry and concrete material strength are all taken into consideration in deriving these fragility curves. The fragility curves show that the probability of damage on bridges is much higher when it is subjected to urban flooding associated with log impact loading than that of being under a rural flooding. The results verify the AS5100 code provision for flood loading on to the bridges.

1 INTRODUCTION

Every year in Australia, floods cause millions of dollars damage to buildings and critical infrastructure, such as roads and railways as well as to agricultural land and crops. They also disrupt business and can affect the health of communities. Between 1967 and 2005, the average direct annual cost of flooding has been estimated at A$377 million(Department of Infrastructure and Regional Developmemnt, 2008)

Bridge collapse has tremendous consequences in every nation's transportation system. The recent flood events in Queensland, Australia between April 2010 and January 2013 had adverse effects on the bridge network of Queensland. Queensland state controlled road network included 3337km of roads and 6500 bridges and culverts (IBISWORLD, 2011)

It's reported in the recent literature that due to climate change, frequency of flood events has increased as well as they have become more intense. Queensland local governments are planning for with 5% increase in rainfall intensity per degree of global warming as the climate change factor to be incorporated in the flood studies (QueenslandGovernment, 2010). Climate change will not have a huge impact on the infrastructure as the effect due to short-term impact loads are built into the safety factors in the design process (Kong et al., 2013). However, extreme natural disasters will have an impact on the vulnerability as the infrastructure may not be designed for such a long-term intense event.

2 SIGNIFICANCE

Analysis of the performance of bridges under 2011/2013 flood in Lockyer Valley Region, Queensland, covered in (Farook et al., 2014) indicates that the bridge deck is the most commonly affected component followed by the bridge approach, pier/abutment scouring, cracks in the abutment wing walls and misalignment of abutment headstock connections to piles. Reinforced or pre-stressed concrete girder bridges are a common design configuration used in Australia. During the Lockyer Valley floods in 2013, vulnerability of girder bridges was observed by significant damage to these structures.

Bridge structures have a major impact on resilience of road infrastructure and the damage to bridges could increase the vulnerability of the community served by the road infrastructure significantly. A systematic method of quantifying vulnerability of bridge structures under varying flood loading is currently a significant gap in knowledge.

Using the concrete girder bridges as case studies, the methodology to derive structural vulnerability models for bridge structures and determine vulnerable structures in the road network have been proposed.

3 FRAGILITY ANALYSIS OF BRIDGES

Defined as the relationship between hazard intensity and the probability that a bridge is damaged exceeding a certain level, bridge fragility curves have been widely used to express the structural vulnerability of a bridge subject to a variety of natural hazards. However, previous studies have mainly focused on the fragility curve derivation for bridges under earthquakes. For example, Basoz et al. (1999) and Shinozuka et al. (2000) developed empirical fragility curves using a data set of bridge damages resulting from the 1994 Northridge earthquake and the 1995 Kobe

earthquake, respectively. Alternatively, Karim and Yamazaki (2001) generated analytical fragility curves of the highway bridge piers utilizing a numerical simulation based on the 1995 Kobe earthquake data.

Decò and Frangopol (2011) generated the fragility curves of highway bridges under multiple hazards including earthquake, scour, traffic load, and environmental attack. With a similar approach, Dong et al. (2013) derived seismic fragility curves of bridges considering the effects of scour and corrosion. In addition, Dawson et al. (2005) assessed the flood risk vulnerability of a fluvial dike system, and Witzany and Cejka (2007) performed a numerical analysis of flood fragility of a stone vault bridge structure. However, these studies mainly focused on the derivation of seismic fragility curves, while flood-related risk factors such as scour and corrosion were considered as an alternative cause of bridge failure in addition to earthquakes. As such, there have been few studies on the flood fragility estimation of bridges. However, various flood-related factors such as water stream pressure, debris accumulation, corrosion, and scour are reported as the most common causes of bridge failure (Wardhana and Hadipriono, 2003); (Cook, 2014). In reality, a flood often generates a rapid water flow with accumulated debris, which yields a combined loading impact on bridges via the service loads and may bring about structural damage or collapse. Furthermore, if the structural integrity of a bridge is significantly degraded by the corrosion of steel reinforcements in addition to the scour-induced removal of soil resistances, the failure risk of bridges under flood events increases and their failure modes can become more complex.

4 ANALYSIS OF CASE STUDY.

The case study approach adopted in this research examined the actual bridge inspection report compiled in the aftermath of 2011/2013 severe flooding incident in Queensland[(Pritchard, 2013);(QueenslandGovernment, 2012)] to understand the major failure mechanisms of the bridges. The study on this report indicated that the damage to bridge structures are complex and requires a detailed knowledge of underlying design principles, current classification of roads/bridges as well as construction methods adopted during different periods of design and construction. It was found that the impact load of the huge rocks, ship containers, vehicles and the other unexpected debris that were carried along the flood water with high velocity was the primary cause of damage to bridge superstructure, abutments, wing walls and piers.

Lockyer Valley Region of Queensland has been selected as a case study for this research. 2011/2013 floods had severely affected road and bridge infrastructure which enormously impacted on the community in the Lockyer Valley region. This case study aimed at identifying all possible components of bridges contributing to failure such as bridge superstructure with girders, bridge approaches, bridge substructure with piers, waterway etc. It further analyzed the failure criteria/ mode of failure of different types of bridges.

This paper investigated the impact of a floating container on Kapernicks Bridge in the case study area together with other flood induced forces.

Kapernicks Bridge is a three span, two lanes concrete Girder bridge located on Flagstone Creek Road in the case study area. The superstructure consists of a steel Bridge Barrier with cast-in-situ Kerbs on the left hand side and right hand side and a cast-in-situ concrete wearing surface topping four precast concrete Girders that are supported by elastomeric bearings at the abutments and piers. The substructure consists of two cast-in-situ abutments and two piers with a cast-in-situ headstock and two cast-in-situ piles. Abutment one is deemed to be the southern end (closest to Carpendale Road). The Approaches are bitumen sealed. There is room for vehicular parking on the right hand side of approach two. Upstream is on the right hand side of the structure. Figure 1 depicts the details of the Kapernicks Bridge (section view).

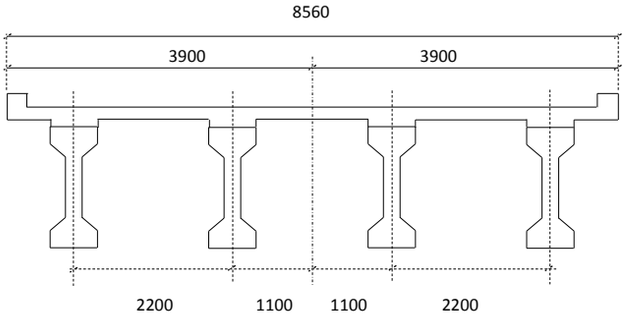


Figure 1: Section view of Kapernicks Bridge

5 FORCES ON BRIDGE RESULTING FROM FLOOD EVENT

AS 5100 Bridge Design code (Section 15 of AS 5100.2-2004) gives relevant equations to calculate the flood induced forces on bridge resulting from

water flow, debris and log impact (Australian Standard, 2004)

5.1 Forces on superstructure due to water flow

When the bridge superstructure is partially or fully inundated in a flood, it is subjected to a horizontal drag force (F_d) normal to its longitudinal axis and a vertical lift force (F_l) as given in AS 5100.

$$F_d(\text{kN}) = 0.5 C_d V^2 A_s$$

Equation (1)

Where C_d = drag coefficient read from the chart given in the code
V = mean velocity of water flow (flood) (m/s).
A_s = wetted area of the superstructure, including any railings or parapets, projected on a plane normal to the water flow (m^2).

$$F_l(kN) = 0.5 C_l V^2 A_l$$

Equation (2)

Where C_l = lift coefficient read from the chart given in the code
V = mean velocity of water flow (flood) (m/s)
A_l = Plan deck area of the superstructure (m^2).

5.2 Forces due to debris

Debris load acting on superstructures is given by the code as,

$$F_{deb}(kN) = 0.5 C_d V^2 A_{deb}$$

Equation (3)

Where C_d = drag coefficient read from the chart given in the code
V = mean velocity of water flow (flood) (m/s)
A_{deb} = Projected area of the debris mat described in the code (m^2).

5.3 Forces due to log impact

Where floating logs are a possible hazard, the drag forces exerted by such logs directly hitting bridge girder (superstructure) superstructure shall be calculated on the assumptions that a log with a minimum mass of 2t will be stopped in a distance of 75mm for such solid girder (superstructure). However for the bridge in question, this mass was taken equivalent to a mass of a shipping container to simulate the actual condition.

F(log) shall thus be given by the following equation

$$F_{log}(N) = \frac{mV^2}{2d}$$

Equation (4)

Where m= mass of a shipping container (kg)

d= stopping distance (m) and V= flood velocity (m/s)

6 DERIVING DAMAGE INDICES

In this research, the structural damage to the bridge girder is measured using Damage Index (DI) that is defined as the ratio between the moment induced by flood loading on the bridge girder (M*) and the residual moment capacity of the bridge girder (ϕMu) as given in Equation 5.

$$DI = \frac{M^*}{\emptyset M_u}$$

Equation (5)

Damage Indices are first derived to generate vulnerability curves for the Bridges under different flood exposure conditions. The effects of flood flow, debris and the log impact on the bridge girder have been considered to derive the damage indices. The damage index can also be defined using the costs associated with retrofitting/repairing the bridge under flood.

It is noted here that the definition of failure using $\frac{M^*}{\phi M_u}$ only consider flexural failure. Shear failure can also be critical in the case of short span structures which are not considered in this study because most of the bridges reported are long span bridges.

6.1 Estimating flood induced bending moment (M*)

In order to estimate flood induced bending moment on the bridge girder, general purpose finite element software, ABAQUS was used to model the Kapernicks Bridge deck and the girders. The bridge is 65.50 m long and about 8.56 m wide and

is supported by 4 numbers of 22 m long concrete girders over the mid-span and another 8 concrete 21.75 m long girders over the end spans. The girders are supported by two abutments and two headstocks. The middle span of bridge structure was analysed. All four girders were assumed simply supported and rest on the headstock of the piers. Self-weight of the bridge, the drag and the lift force due to water flow, debris force and the log impact force were considered in the analysis. Uncertain nature of flood velocity experienced by the case study region was considered in the analysis and corresponding M^* values for those velocities were obtained through a parametric study in ABAQUS. An ABAQUS script written in Python programming language was necessary to perform the recurring tasks of calculating these M^* values. Figure 2 depicts the bridge deck model used in the analysis.

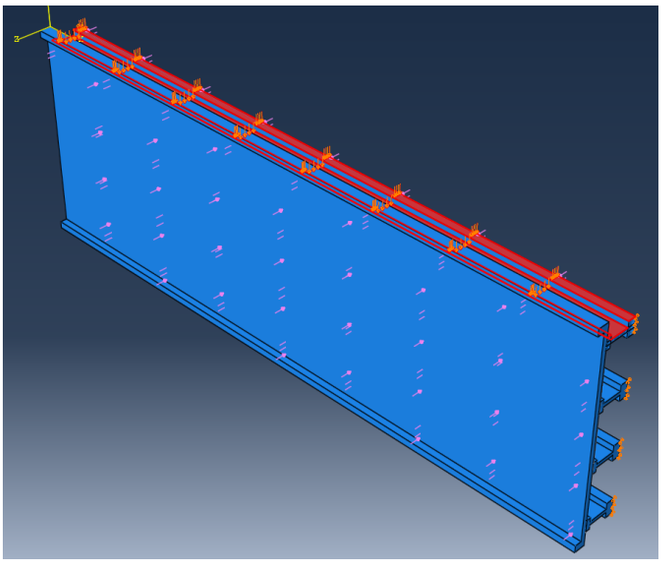


Figure 2: Model development of bridge and deck in ABAQUS

6.1.1 Analysis of actual flood data

Flood data required for this research has been sourced through water monitoring committee of Queensland Government. This web based data set (Figure 3) provided the flood discharge, flood height and the creek river profile data for all rainfall monitoring stations across the state. Figure 4 indicates the River profile of Lockyer Creek at Helidon Number 3 which is the closest monitoring station of the case study bridge in this research. The recorded data are available from as old as 1987 to date. Simple open channel flow equation (Equation 6) was used to derive the required flood velocity.

$$V = \frac{Q}{A} \qquad \text{Equation (6)}$$

Where V= Flood velocity

Q= Flood discharge

A= Creek cross sectional area at the given flood height

An Excel formula was devised for calculating cross sectional area of the river for different stream water level. Corresponding flood velocity was then calculated using stream discharge and the river cross section area.

Time	143203C		143203C		143203C			
and	10		100		140			
Date	Rainfall (mm)		Level (Metres)		Discharge (Cumecs)			
	Point	Qual	Point	Qual	Point	Qual		
19/11/1987 11:40			0.54	9	0.028	20	Sites:	
19/11/1987 12:33			0.55	9	0.037	20	143203C -	
19/11/1987 12:41			0.56	9	0.048	20		
19/11/1987 12:48			0.56	9	0.048	20	Variables:	
19/11/1987 13:02			0.57	9	0.061	20	10 - Rainfall (millimetres)	
19/11/1987 13:53			0.56	9	0.048	20	100 - Stream Water Level (Metres)	
19/11/1987 14:03			0.55	9	0.037	20	140 - Stream Discharge (Cumecs)	
19/11/1987 14:14			0.55	9	0.037	20		
19/11/1987 15:40			0.55	9	0.037	20	Qualities:	
19/11/1987 16:41			0.55	9	0.037	20	1 - Good (actual)	
19/11/1987 17:43			0.54	9	0.028	20	9 - CITEC - Normal Reading	
19/11/1987 21:47			0.54	9	0.028	20	10 - Good	
20/11/1987 7:19			0.54	9	0.028	20	15 - Water level below threshold (no flow)	
20/11/1987 12:57			0.55	9	0.037	20	20 - Fair	
20/11/1987 13:40			0.56	9	0.048	20	30 - Poor	
20/11/1987 14:44			0.56	9	0.048	20	59 - CITEC - Derived Height	
20/11/1987 16:18			0.56	9	0.048	20	60 - Estimate	
20/11/1987 22:53			0.57	9	0.061	20	83 - Non standard rainfall	
21/11/1987 9:08			0.57	9	0.061	20	130 - Not coded value	
21/11/1987 9:22			0.57	9	0.061	20	151 - Data not yet available	
21/11/1987 9:51			0.56	9	0.048	20	160 - Suspect	
21/11/1987 10:38			0.55	9	0.037	20	200 - Water level below threshold	
21/11/1987 12:11			0.55	9	0.037	20	255 - No data exists	
21/11/1987 16:09			0.54	9	0.028	20		
21/11/1987 20:20			0.54	9	0.028	20		

Figure 3: Extraction of as given data from water monitoring committee of QLD government (Station: Helidon No.3)



Figure 4: River profile of Lockyer Creek at Helidon Number 3

Distributive nature of the flood velocity for the period between 1987 and 2016 was obtained using @Risk software simulation techniques. It is worth to note that Lockyer Valley Region had experienced severe rain between beginning of December 2010 and end of January 2011 and in particularly on 7, 8, 9 and 10th of January 2011. Figure 5 shows the flood velocity distribution obtained for this analysis.

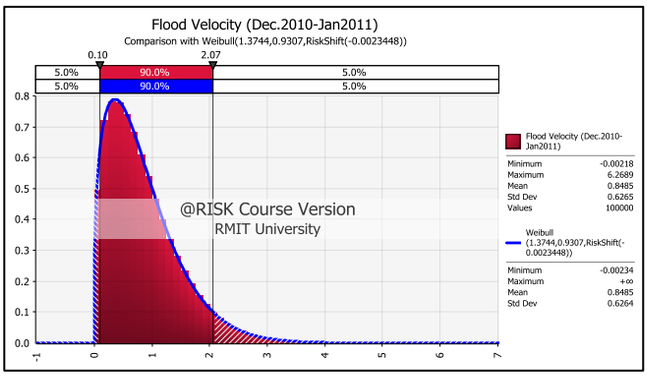


Figure 5: Flood Velocity Distribution (Dec.2010 – Jan 2011)

Type of fit: Pearson 5

Mean velocity: 1.53 m/s

Std. deviation: 0.78 m/s

From the above analysis, 100 random velocity values were generated using @Risk for parametric study as shown in Table 1 (below)

Table 1: Flood Velocity values used in the parametric study

2.172	1.745	1.635	1.694	2.002
1.745	1.828	2.608	2.015	1.881
2.469	1.649	1.635	1.912	1.628
1.707	2.146	1.934	2.538	2.305
2.118	1.727	2.643	1.733	2.012
2.329	1.708	1.683	1.831	1.659
1.988	1.734	1.716	2.203	1.779
1.772	1.894	2.427	1.744	1.609
1.88	1.895	2.376	1.921	2.597
1.94	2.177	2.263	1.618	3.175
2.843	2.084	1.69	1.558	2.318
1.666	1.793	2.399	3.653	1.698
2.078	1.994	1.621	1.76	2.799
2.028	1.604	1.954	2.766	2.369
1.78	1.626	1.566	1.729	1.746
1.679	2.146	1.804	1.846	2.019
1.65	1.785	1.878	2.783	1.784
1.669	1.728	2.026	1.572	1.634
2.176	1.682	2.908	1.868	1.552
1.659	2.075	1.798	1.68	1.599

6.2 Estimating residual moment capacity of bridge girder (ϕM_u)

In accordance with the Australian codes of practice for structural design, the capacity analysis methods contained in this section are based on ultimate limit-state philosophy. This ensures that a member will not become unfit for its intended use. This approach sets acceptable levels of safety against the occurrence of all possible failure situations. The nominal strength of a member is assessed based on the possible failure modes and subsequent strains and stresses in each material.

A typical beam section of the headstock is shown in Figure 1. The positive and negative flexural and shear capacities of the section were calculated in accordance with Australian standards (AS3600, 1988). The nominal steel reinforcing bars areas; nominal steel yield strength of 400 MPa for longitudinal reinforcement and 240 MPa for shear reinforcement and nominal concrete compressive strength of 20 MPa were used in the section capacity analysis. The degradation due to corrosion of the steel and creep and shrinkage of the concrete were ignored.

Moment capacity of reinforced concrete girders which is a function of girder cross section and the reinforcement configuration is influenced by several variables. The compressive strength of the concrete, the steel component area and the yield strength are the most influential. The geometry of the concrete girder is also an important factor that influences the compressive moment capacity of the bridge girder. Table 2Table 2 below shows the parameters used in the Monte Carlo simulation for generating suitable distributions of the nominal moment capacity i.e. the resistance in the Equation 7.

To capture the influences of uncertain factors on the property of the concrete material and the geometry of the bridge, the associated random variables were defined using distributions found in the literature as shown in table 2. Fundamental Beam section analysis was carried out to the bridge I- Girder section. Neutral Axis depth for the section was established when the total tensile and the compressive forces added up to zero. Moment Capacity was then calculated as shown in Equation 7 by taking moments about this neutral axis to the section. Figure 6 shows the geometry of the I Girder. Relevant random variable terms in this equation were simulated using @Risk software.

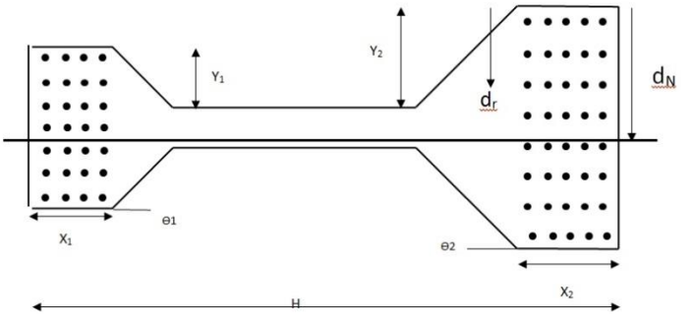


Figure 6: Geometry of the I girder

$$M_u = E_s \frac{\epsilon_c}{d_n} \sum_1^n a_r (d_n - d_r)^2 + 0.85 f_c' \left[x_1 y_1 \left(\lambda + \frac{y_1}{2} \right) + \frac{y_1^2}{2tan\theta_1} \left(\lambda + \frac{y_1}{3} \right) + x_2 y_2 \left(\lambda + \frac{y_2}{2} \right) + \frac{y_2^2}{2tan\theta_2} \left(\lambda + \right. \right.$$

$\frac{y_2}{3}\Big) + \frac{H}{2}\lambda^2\ \Big]$

Equation (7)

where

$\lambda = (0.9d_n - y_2)$

E_s = Elasticity of Steel

ϵ_c = Concrete yield strain

d_n = Neutral Axis Depth

f_c' = concrete compressive stress

d_r = depth to r^{th} layer of the steel.

a_r = rebar cross section areas at the r^{th} layer

H = Height of the concrete I Girder

M_u = Moment capacity

$X_1, X_2, Y_1, Y_2, \theta_1, \theta_2$ = Dimensions as shown in the Figure 6. (above)

Table 2: Random variable parameters (Adopted from Tavares (2011))

Variable	Mean	COV	Distribution	Std. Dev
Es-MPa	200000	0.1	Normal	20000
ε	0.0035	deterministic		
fc'-MPa	20	0.1	Normal	2
x1(mm)	152	0.015	Normal	2.28
y1(mm)	165.5	0.018	Normal	2.979
x2(mm)	180	0.015	Normal	2.7
y2(mm)	241.5	0.018	Normal	4.347
H(mm)	1372	0.015	Normal	20.58

7 GENERATION OF FRAGILITY CURVES

Failure of the bridge against flood is measured through Damage Index ($DI = \frac{M^*}{\emptyset M_u}$) that is defined as the ratio between the flood induced bending moment (M^*) on the girder and the residual moment capacity ($\emptyset M_u$). When the limiting value of the Damage is equal to greater than 1.0, the bridge is considered failed. Using @Risk software, the Damage Index value was simulated and the corresponding probability curves (the "S" curves) or fragility curves were obtained for Kapernicks Bridge considering different flood scenarios such as flood only and flood with log impacts etc. as shown in Figure 7.

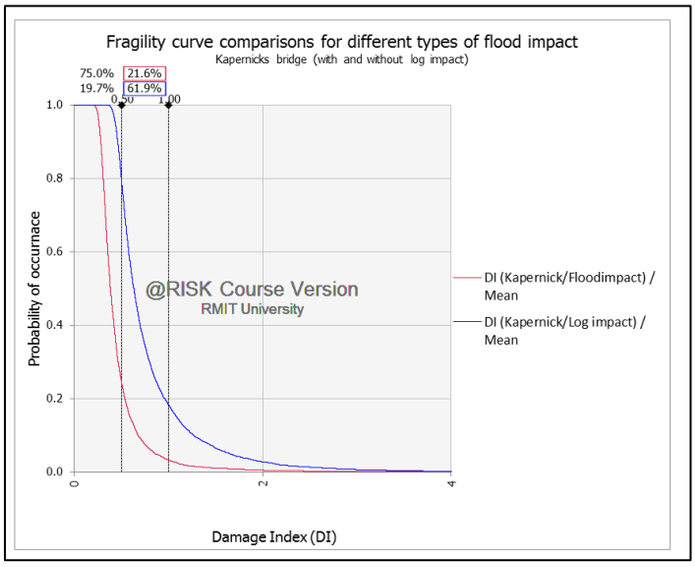


Figure 7: Fragility curve comparison for Kapernicks Bridge under flood and log impact

Table 3: Comparison of failure probability for different types of flood impact (Kapernicks Bridge)

Types of flood impact	Probability of failure (when DI=1.0)
Plain flood	3.3%
Flood with log impact	18.4%

8 CONCLUSION

In order to incorporate the uncertain nature of the flood intensity (flood velocity) and the structural capacity of the bridge structure due to deterioration, a probabilistic fragility modelling method was adopted to establish the probability of failure of the bridge structure under flood hazard.

A comprehensive method to establish relevant flood velocity values for use in this research was devised using simple open channel flow equations. The bridge examined here showed that it had the probability of failure of less than 5.0% as per the provision allowed in all the bridge design codes worldwide. However, it showed a higher probability of failure when it was under the influence of unusual debris such as containers, vehicles and leisure crafts.

REFERENCES

AUSTRALIAN STANDARD, A. 2004. 5100: Bridge Design. *Standards Australia International (SAI): Sydney*.

BASOZ, N. I., KIREMIDJIAN, A. S., KING, S. A. & LAW, K. H. 1999. Statistical analysis of bridge damage data from the 1994 Northridge, CA, earthquake. *Earthquake Spectra,* 15**,** 25-54.

COOK, W. 2014. Bridge Failure Rates, Consequences, and Predictive Trends.

DAWSON, R., HALL, J., SAYERS, P., BATES, P. & ROSU, C. 2005. Sampling-based flood risk analysis for fluvial dike systems. *Stochastic Environmental Research and Risk Assessment,* 19**,** 388-402.

DECÒ, A. & FRANGOPOL, D. M. 2011. Risk assessment of highway bridges under multiple hazards. *Journal of Risk Research,* 14**,** 1057-1089.

DEPARTMENT OF INFRASTRUCTURE AND REGIONAL DEVELOPMEMNT, A. G. 2008. *About Australia's Regions 2008* [Online]. Available: https://bitre.gov.au/publications/2008/other_005.aspx [Accessed 12.12.2013 2013].

DONG, Y., FRANGOPOL, D. M. & SAYDAM, D. 2013. Time-variant sustainability assessment of seismically vulnerable bridges subjected to multiple hazards. *Earthquake Engineering & Structural Dynamics,* 42**,** 1451-1467.

FAROOK, K., LOKUGE, W., SETUNGE, S. & ZHANG, K. Failure mechanisms of bridge infrastructure in an extreme flood event. Proceedings of the 1st International Conference on Infrastructure Failures and Consequences (ICFC 2014), 2014. RMIT Publishing, 124-132.

IBISWORLD. 2011. *Queensland floods: The economic impact Special Report* [Online]. Available: http://www.ibisworld.com.au/common/pdf/QLD%20floods%20special%20report.pdf [Accessed 23 May 2013].

KARIM, K. R. & YAMAZAKI, F. 2001. Effect of earthquake ground motions on fragility curves of highway bridge piers based on numerical simulation. *Earthquake engineering & structural dynamics,* 30**,** 1839-1856.

KONG, D., SETUNGE, S., MOLYNEAUX, T., ZHANG, G. & LAW, D. 2013. Structural resilience of core port infrastructure in a changing climate.

PRITCHARD, R. W. 2013. 2011 to 2012 Queensland floods and cyclone events: Lessons learnt for bridge transport infrastructure. *Australian Journal of Structural Engineering,* 14**,** 167-176.

QUEENSLANDGOVERNMENT. 2010. *Increasing Queensland's resilience to inland fl ooding in a changing climate:* [Online]. Available: http://www.ehp.qld.gov.au/climatechange/pdf/inland-flood-study.pdf [Accessed 30 April 2014].

QUEENSLANDGOVERNMENT. 2012. *Rebuilding a stronger,more resilient Queensland* [Online]. Available: http://www.qldreconstruction.org.au/u/lib/cms2/rebuilding-resilient-qld-full.pdf [Accessed 12 October 2013].

SHINOZUKA, M., FENG, M. Q., KIM, H.-K. & KIM, S.-H. 2000. Nonlinear static procedure for fragility curve development. *Journal of engineering mechanics*.

TAVARES, D. 2011. *Seismic risk assessment for bridges in quebec using fragility curves.* PhD thesis. Sherbrooke (QC): Faculté de Génie, Département de Génie Civil, Université de Sherbrooke.

WARDHANA, K. & HADIPRIONO, F. C. 2003. Analysis of recent bridge failures in the United States. *Journal of performance of constructed facilities,* 17**,** 144-150.

WITZANY, J. & CEJKA, T. 2007. Reliability and failure resistance of the stone bridge structure of Charles Bridge during floods. *Journal of civil engineering and management,* 13**,** 227-236.

SS20: Monitoring and assessment of bridges using novel techniques

Organizers: A. Strauss, K. Bergmeister & D.M. Frangopol

Maintenance, Safety, Risk, Management and Life-Cycle Performance of Bridges – Powers, Frangopol, Al-Mahaidi & Caprani (Eds)
© 2018 Taylor & Francis Group, London, ISBN 978-1-138-73045-8

Performance analysis of distributed optical fiber bonding adhesives to concrete

António Barrias & Joan R. Casas
Technical University of Catalonia, UPC. Department of Civil and Environmental Engineering, c/ Jordi Girona 1-3, 08034 Barcelona, Spain

Sergi Villalba
Technical University of Catalonia, UPC. Department of Engineering and Construction Projects, c/ Colom 11, Ed. TR5, 08022 Terrassa (Barcelona), Spain

ABSTRACT: In this paper, the authors conducted an experiment where a reinforced concrete beam was instrumented with a single DOFS performing four equal segments externally bonded to the bottom surface of the element. Each segment was adhered to the concrete using a different adhesive. This beam was then loaded, producing expected equal levels of tension in each of the fiber segments for a more direct comparison of the different adhesives performance. The experimental data is subsequently compared with the data provided through more conventional electrical strain gauges that were also deployed in the beam. The effect of alternating the spatial resolution and sampling acquisition is also analyzed. The results provided here will shed a clearer light on how to proceed when applying this promising sensing technique to concrete structures, mainly on what the bonding materials and resolution are concerned.

1 INTRODUCTION

All civil engineering infrastructures are subject to natural hazardous and ordinary mechanical resistance decay and deterioration through its lifetime. In the global and connected world of today, the accessible and immediate maintenance of such infrastructures is of paramount importance for the economic competitiveness of every region.

Therefore, structural health monitoring (SHM) of these civil engineering infrastructures has become an important topic of study and research in the past decades. The early and correct detection of the damage in these infrastructures derives on great economical savings, a better structural maintenance and an improved assessment of the structural safety.

Within SHM applications, the use of optical fiber sensors (OFS) has been a popular topic of research and practice in the last two decades due to the inherent advantages presented by the use of these type of sensors. When comparing with the more conventionally used electrical sensors, OFS are immune to electromagnetic interference presenting in this way less noisy measurements. These sensors perform also well under a wide range of temperature variations and are free from corrosion. Finally, OFS are generally small and lightweight, which facilitates the transport and installation of such sensors in a wide range of application scenarios. The use of these sensors has been well documented and practiced particularly through the use of Fiber Bragg Grating sensors [1].

On the other hand, the use of distributed optical fiber sensors (DOFS) in civil engineering infrastructures SHM applications is still relatively recent. These sensors provide the same advantages of the other optical fiber sensors, with the additional advantage of being capable of acquiring strain and/or temperature information for longer extensions of the monitored structural components on which they are instrumented and with very low distance between measurements [2].

In the monitoring of concrete structures, this assumes an even greater advantage since the exact location of a possible crack formation is not known beforehand and in this way, might be missed with the use of point or discrete sensors if not positioned at that particular location.

Furthermore, with the use of DOFS a larger area of the structure may be monitored with the use of up to one single sensor, which only requires one connecting cable, enabling a simpler a more economical monitoring system.

Nonetheless, a more profound research of this technology is still necessary in order to enable a more systematic and regular use of these distributed sensors in concrete monitoring applications.

2 OPTICAL BACKSCATTERED REFLECTOMETER (OBR) SYSTEM

When using DOFS technology, the optical fiber cables can be bonded to the surface of the material or embedded inside the material. When strain and temperature variations occur, these changes are transferred from the monitored material to the sensor which variates the scattered signal being reflected inside the fiber.

This scattering is at the origin of distributed optical fiber sensing and is defined by the interaction between the light and the optical medium. Three different scattering processes may occur in DOFS, which are the Raman, Brillouin and Rayleigh scattering [2].

Brillouin scattering based DOFS have been the most studied and used DOFS systems in civil engineering SHM applications due to their large-scale capability, which can reach the kilometer range. However, it presents a relatively low spatial resolution of roughly one meter, which is not appropriate for crack detection and other applications.

The optical frequency domain reflectometry (OFDR) systems which are based in the Rayleigh scattering, on the other hand, offer a spatial resolution as high as one millimeter which makes it ideal for crack detection and localization although limited to a monitoring length of 70 m.

In this way, in the present study it is used the ODiSI A model from LUNA technologies which is an optical backscattered reflectometry (OBR) system based on the Rayleigh OFDR, Figure 1.

More detailed information of this technology can be consulted in [2].

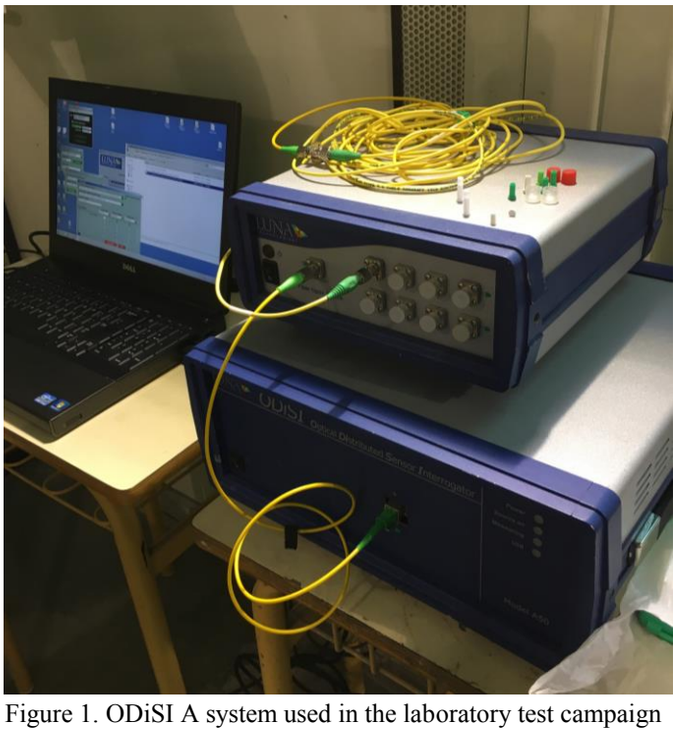


Figure 1. ODiSI A system used in the laboratory test campaign

3 DOFS ADHESIVE STUDY

Despite the significant increase in interest on the study and practice of SHM applications through the use of DOFS, an important lack of knowledge is still present regarding the choice of the best adhesive to use when mounting these sensors in reinforced concrete structures.

In order to obtain the optimal strain transfer between the sensor and the monitored material the topic of its deployment is of considerable importance. In addition to the removal of any grease or dust present in the surface of the host material and the smoothening of the surface, the decision on the adhesive to bond the optical fiber sensor to the surface has to be assessed. This is even, a more pressing issue when applying DOFS without any protective thick coating, such is the case of the deployed fiber in this research, Figure 2. The use of such fiber, is by itself, a way to reduce the influence of the sensor cladding material in the strain accuracy.

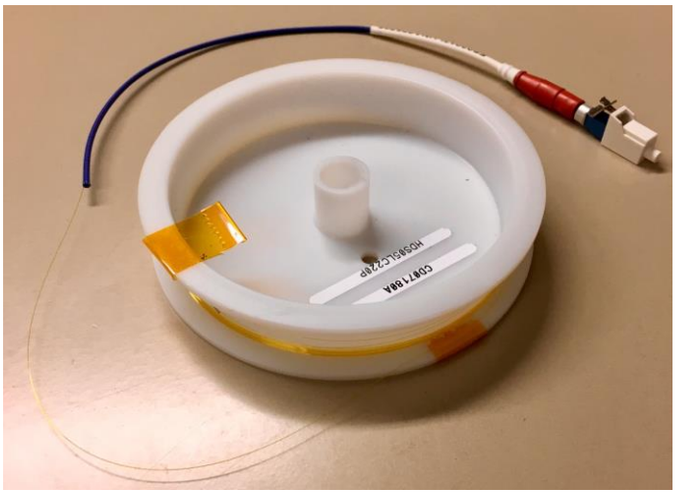


Figure 2. DOFS type deployed in this experimental campaign

Some studies have analyzed the coating influence on the strain transfer on point fiber optic sensors [3], the adhesive spread installation method [4] and the coating strain transfer impact in DOFS [5].

One study in specific [6],analyzed among many things the performance of the use of cyanoacrylate and epoxy adhesives together with both nylon and polyimide DOFS when attached to the surface of the concrete and when attached to the reinforcement of the same structural elements. The results showed a better performance of the polyimide fiber together with the cyanoacrylate adhesive when bonded to the reinforcement and the combination of nylon fiber with epoxy adhesive when bonded to the concrete.

In the present paper, a test is performed where a single 5 m polyimide DOFS is attached to the surface of a reinforced concrete beam using four different adhesives: epoxy, cyanoacrylate, polyester and neutral cure silicone, Figure 3.



Figure 3. Adhesives deployed in this experimental campaign, from left to right: Epoxy, Cyanoacrylate, Polyester, Neutral Cure Silicone

These adhesives were chosen based on the previous experience of the authors and through what was found during a literature review on this topic. Specifically the three first adhesives: epoxy, cyanoacrylate and polyester were ordered as advised by the TML strain gauges 2017 catalogue for concrete applications [7]. The used neutral cure silicone however, was a simple commercial one from Ceys brand for general construction applications including concrete. Furthermore, the silicone was used in this application as a true adhesive in opposition to what has been done in the past where it was used more as a sealant in order to provide better protection of the sensor.

4 EXPERIMENTAL TEST SETUP

As mentioned before, the main goal of this experimental campaign was to evaluate the performance of different adhesives for the bonding of DOFS to concrete elements during a three-point load test.

In this way, a 60x15x15 [cm] reinforced concrete beam, Figure 4, was produced. This element had two longitudinal ϕ12 and four ϕ6 S500 rebars.

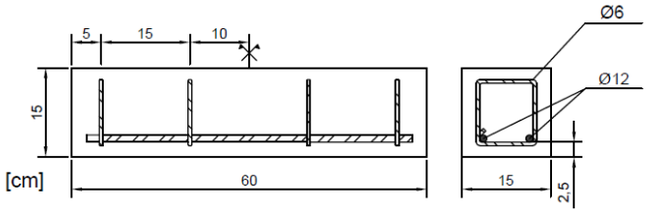


Figure 4. Tested beam definition

Consequently, a 5 m long DOFS was deployed to this concrete element in a way that performed four different equal segments on the bottom surface of the beam. During the conduction of a load test, these segments would be submitted to the same developing strains (in tension) and therefore they will be directly comparable.

Additionally, three 30 mm length strain gauges from the provider mentioned before (TML), were also sparsely bonded to the bottom surface of the concrete beam for comparison purposes with the data obtained by the DOFS, Figure 5.



Figure 5. Deployed strain gauges for comparison purposes

The deployment of the instrumented sensors on the reinforced concrete beam with the information of the adhesive used in each DOFS segment is presented in Figure 6.

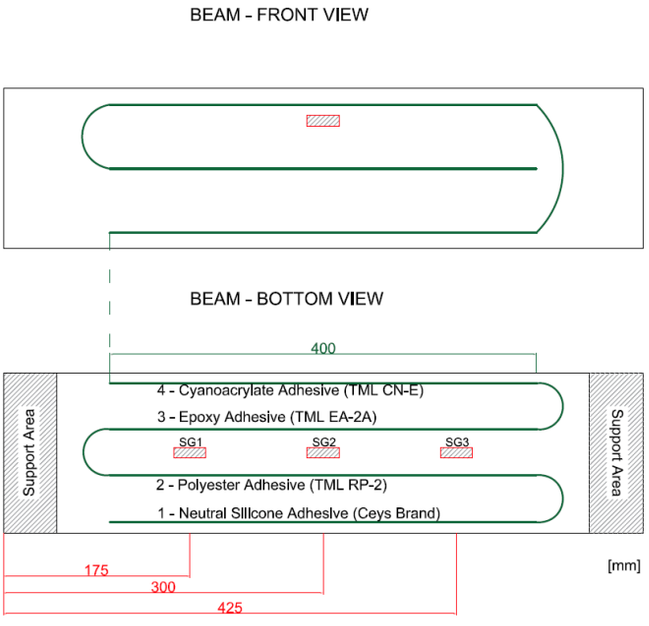


Figure 6. Plan of the reinforced concrete beam instrumented sensors

As seen from Figure 6, due to the 5 m length of the fiber, the remaining part of the DOFS was also adhered in three different segments in the front view surface of the beam. Nevertheless, the data from these segments is not analyzed here, as it is not relevant for the pursued objectives.

Hence, the setup of the three-point load test is as depicted in Figure 7 and 8.

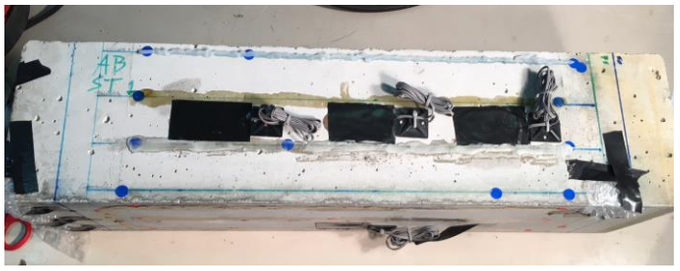


Figure 7. View of the sensors (DOFS and strain gauges) instrumented in the bottom surface of the tested beam

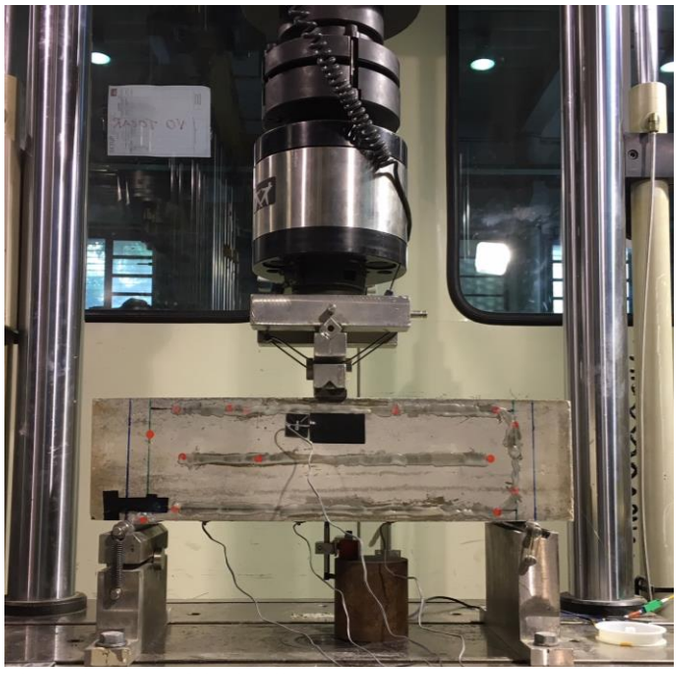


Figure 8. View of the loading arrangement

In order to obtain the material properties of the concrete of the tested specimen, different cylindrical samples were produced at the same time of the beam and tested. Consequently, the mean compressive strength, the mean tension strength and the mean Young modulus of the concrete was calculated as presented in Table 1.

Table 1. Concrete material properties

	f_{cm} [MPa]	f_{ctm} [MPa]	E [MPa]	ε_{ct} [με]
Specimen	48.027	3.944	37886.64	104.10

As an additional point of study, the spatial resolution of the DOFS on the measured results was also analyzed. Due to the heterogeneity of the concrete material and its aggregate sizes, this aspect is of interest for the application of DOFS based monitoring systems. Furthermore, it was intended also to analyze the influence the sampling acquisition frequencies of the DOFS data.

Therefore, it was decided to perform initially several load cycles with a maximum load of 11 kN (which wouldn't induce cracking in the specimen) where in each cycle, a different spatial resolution and sampling acquisition frequency were used.

Finally, a load test producing cracking and progressing up to failure of either the DOFS or the beam was conducted. The test sequence is described in Table 2. The load sequence along time is depicted in Figure 9 for test cycles 1 to 6 and Figure 10 for test cycle 7 up to failure.

Table 2. Test cycle description

Test cycle number	Inputted Spatial Resolution	Inputted Sampling Acquisition
1	1 cm	0.2 Hz
2	3 cm	0.2 Hz
3	1 mm	0.2 Hz
4	1 cm	1 Hz
5	3 cm	1 Hz
6	1 mm	1 Hz
7-rupture	1 cm	0.2 Hz

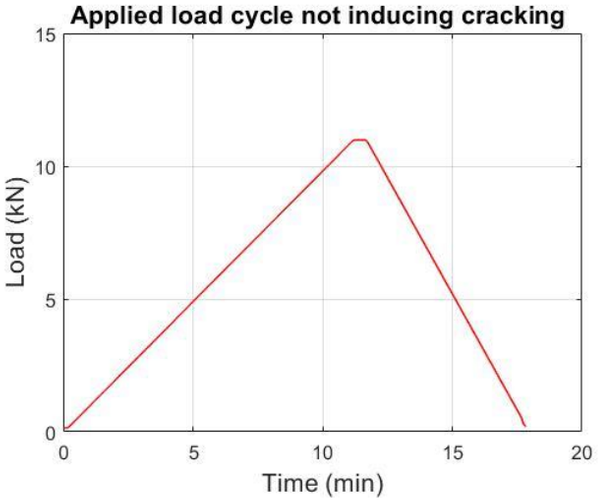


Figure 9. Load cycle applied for tests 1 to 6

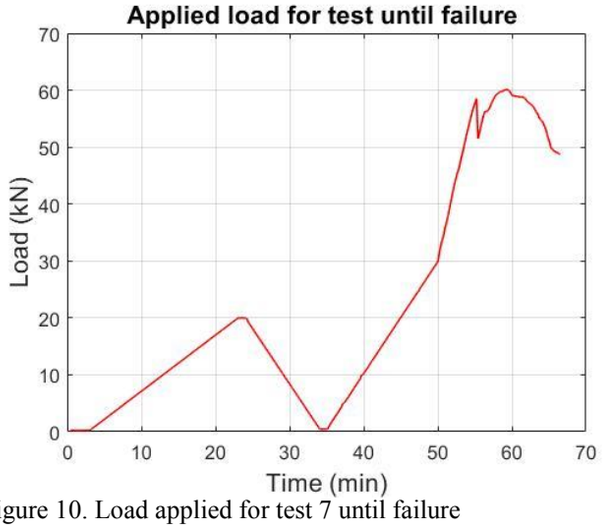


Figure 10. Load applied for test 7 until failure

5 RESULTS

Data from both the DOFS and the Strain Gauges was post processed and analyzed. In this step, it is important to mention that the *LUNA* software which post processes the optical fiber data provides the possibility of saving the measured values in the raw spectral shift form, the already converted strain and the spectral shift quality (SSQ) matrix.

It is also important to indicate that although it was intended to analyze the influence of different sampling acquisition frequencies, the test cycle numbers corresponding to these scenarios are not analyzed in this document. This is because the acquisition system was not able to obtain DOFS data at the target rate of 1 Hz.

5.1 *Comparison of spatial resolution input*

In this way, an initial comparison of the influence of the different spatial resolution parameters in the first three load cycle tests was carried out.

As mentioned in Table 2, three different spatial resolutions of the DOFS measurements were considered: 1 cm, 3 cm and 1 mm. These meant that, 520 points, 174 points and 5191 points were measured in the first, second and third load test cycle respectively.

As it is possible to see from Figure 11, the data measured with a spatial resolution of 1 mm presents a significantly high spatial variability. With the spatial resolution of 1cm, all adhesives present a noticeable variability except for the case of the neutral silicone.

Nevertheless, all segments present similar measurements as the instrumented strain gauges. Using a 3 cm spatial resolution (which is the same length of the deployed strain gauges) this spatial variability is, as expected, minimal.

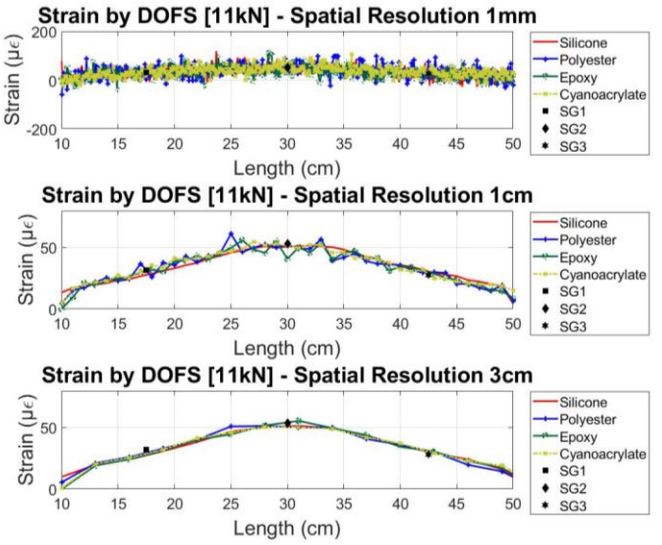


Figure 11. Data measured by DOFS with different spatial resolutions

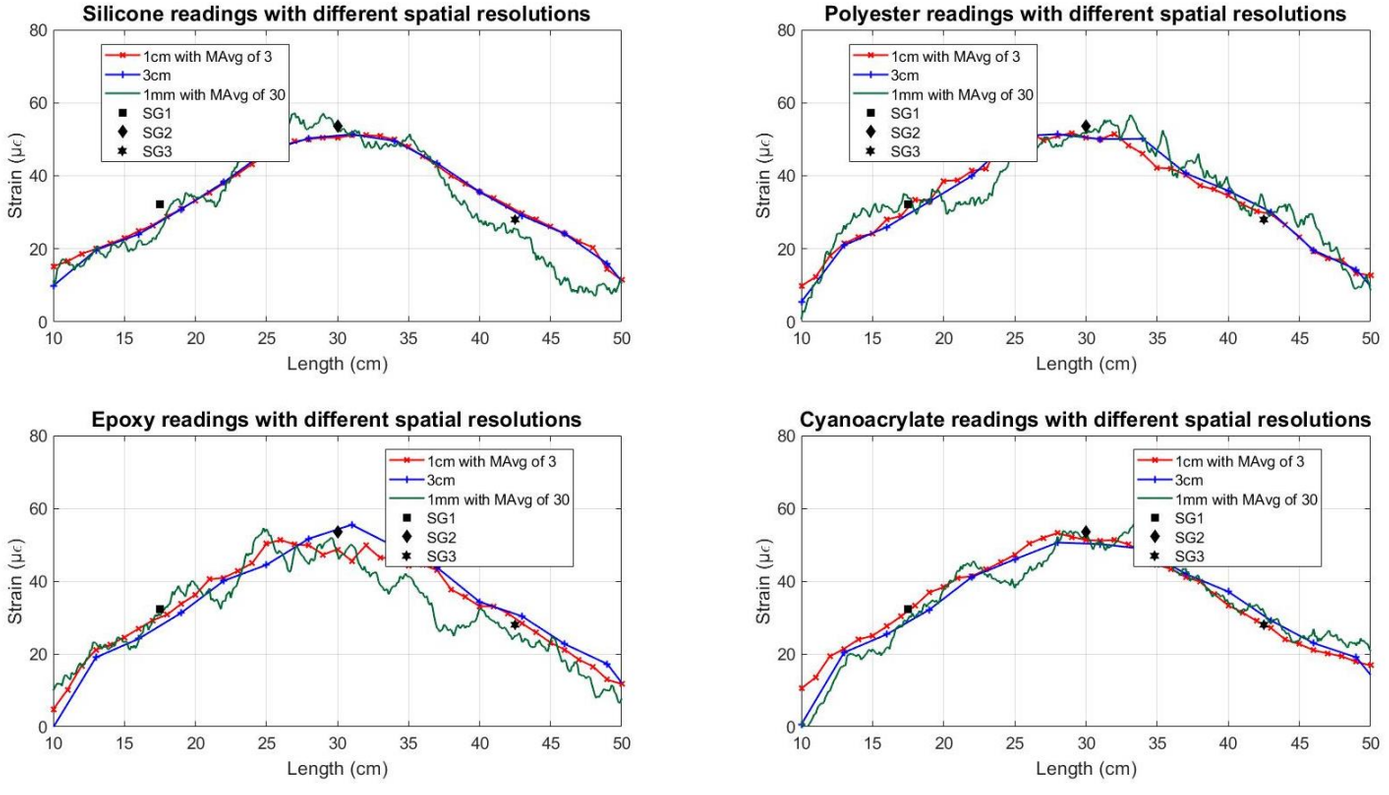


Figure 12. Data measured by each DOFS adhesive segment with different spatial resolutions while performing a moving average to the 1 mm and 1 cm data in order to directly compare it with the 3 cm spatial resolution data

In order to see if even using an initial high spatial resolution, it was possible to obtain better results, a moving average post-process was performed. A moving average with a window of 30, and another with a window of 3 was conducted on the values of the measurements with 1 mm and 1 cm respectively in order to directly compare it with the ones obtained with a 3 cm spatial resolution as seen in Figure 12.

Here, the averaged 1 mm data still presents an erratic spatial distribution when compared with the remaining data. However, the averaged 1 cm data generally presents a good fit with the 3 cm data except for the case of the segment bonded with the epoxy adhesive.

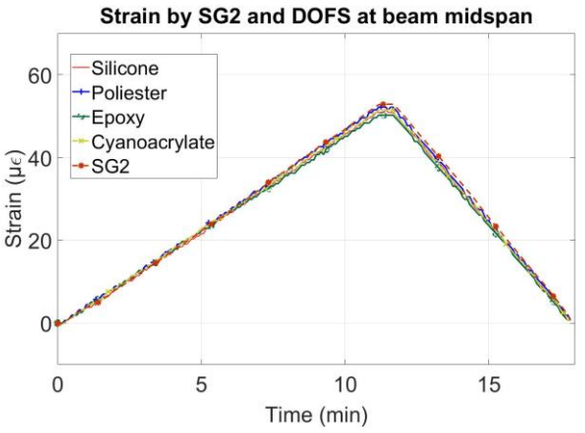


Figure 13. Strain evolution at the beam midspan as measured by the DOFS and Strain Gauge 2 (SG2).

5.2 *Comparison of different adhesives under elastic behavior*

Taking advantage of the load test cycles 1 to 6 performed on the elastic range of the instrumented beam, an initial comparison of the use of different adhesives for the bonding of the DOFS to concrete specimens is performed.

Figure 13 presents the comparison of the readings performed by the four DOFS segments at their midpoint with the data measured by strain gauge 2 (SG2) which is also located at the beam midspan, over the duration of this load cycle, with a maximum load of 11 kN. As it is possible to observe from this graph, all the adhered segments follow the measured data of the strain gauge with a satisfactory performance.

Nevertheless, by performing a surface plot of the measured strain on each DOFS segment over its length and the duration of the load cycle as depicted in Figure 14, it is possible to observe a slightly smoother and homogenous reading at the silicone segment when compared with the other adhesives. Here a clearer increase of the contour lines of its surface plot is detected.

This is especially true at the maximum measured strain, where a higher spacial variability in the data obtained at the Polyester, Epoxy and Cyanoacrylate bonded DOFS segments is observable.

Although it is also observable a good performance of the readings for the unload part of the cycle it would be interesting in further studies to perform a similar test for pure negative (compression) strains.

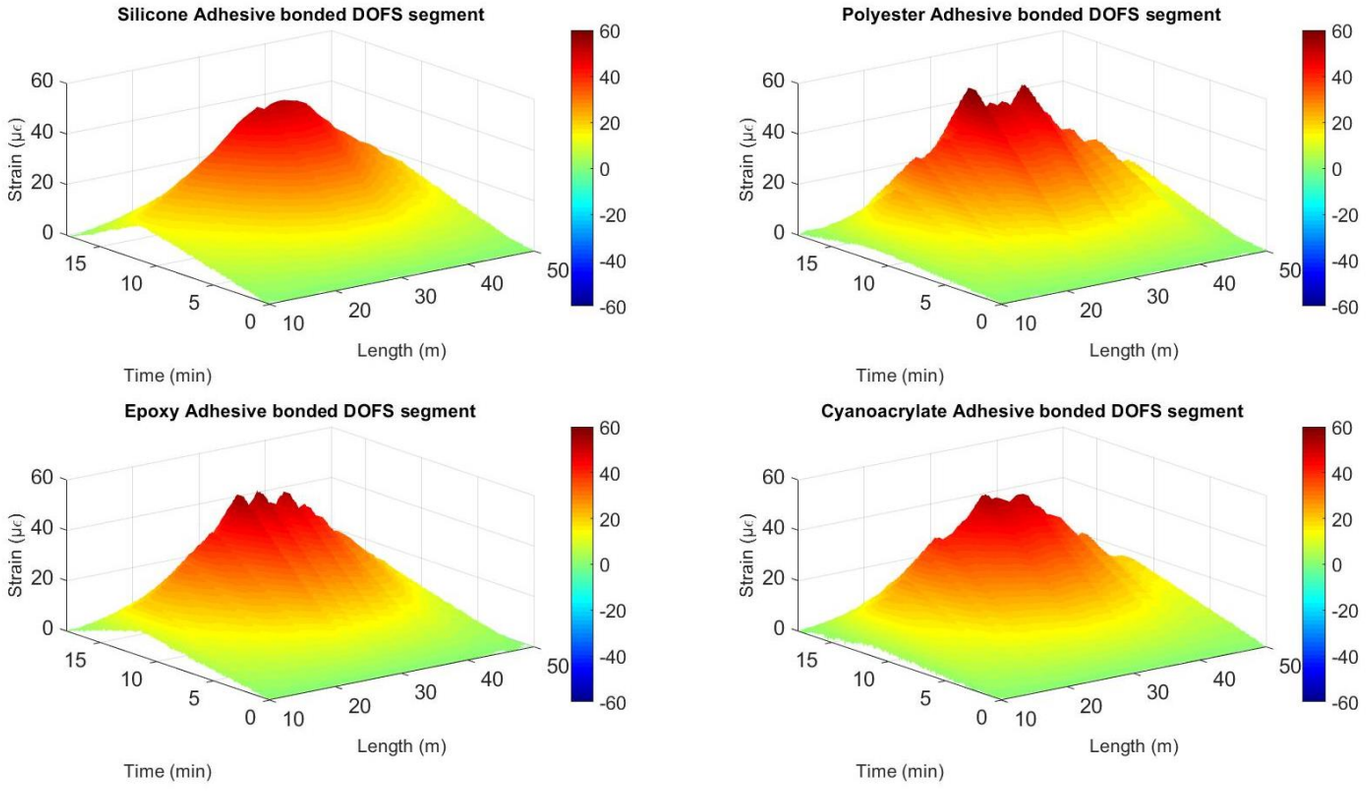


Figure 14. Strain measured for elastic load test cycle with different adhesive bonded DOFS segments

5.3 *Comparison of different adhesives for cracking detection*

After conducting the load test cycles under the elastic range behavior of the concrete beam, a load test cycle inducing cracking and continuing until the failure of either the beam or the DOFS was executed as illustrated in Figure 10.

According to the tests conducted to the cylindrical specimens and the calculated material properties, the load that would induce cracking was close to 18 kN. However, during the execution of the load cycle it was observed that, the resistance of the beam specimen was relatively higher and that the actual load which induced cracking was in fact a load of 23 kN.

By analyzing the information plotted in Figure 15, corresponding to a load level of 25 kN it is possible to observe that all segments detect and locate the occurrence of cracking as represented by a sudden peak in the measured strains. These peaks should present continually crescent positive strain with the increasingly applied load. However, as seen in Figure 15 also presents a negative peak for the polyester bonded DOFS adhesive. Note that none of the strain gauges detects the cracking.

Furthermore, by analyzing Figure 16, it is observable that when isolating the strain evolution in each segment by load steps, all adhesives with the exception of the silicone, present either positive or negative peaks in the crack location.

This is related with the value of the Spectral Shift Quality (SSQ) in the position of the produced damage after its occurrence.

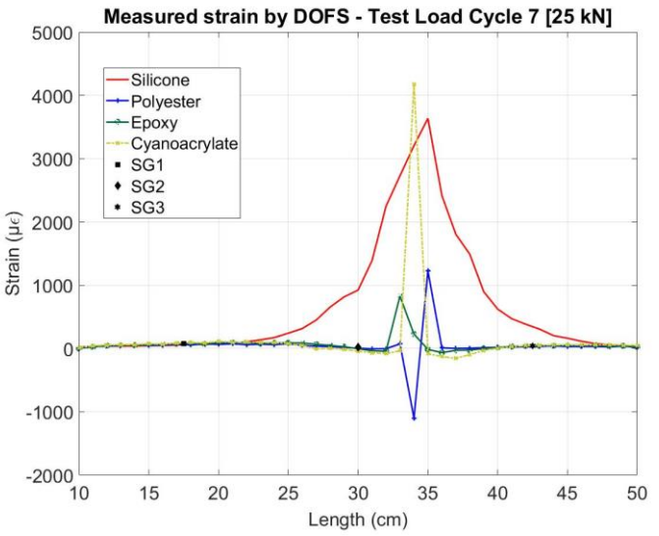


Figure 15. Detection and localization of cracking by the different adhesives bonded DOFS

When analyzing this data, it was observed that for the polyester, epoxy and cyanoacrylate segments the value of the SSQ in the location of the crack drops below 0.15, which indicates not reliable strain measurements at these points shortly after the development of the cracking.

However, it is also discernable the larger area of influence of the produced crack in the silicone segment when compared with the other ones which constitutes an obvious challenge for the pinpointing of additional cracking appearances in situations when they may occur and for the quantification of the crack width.

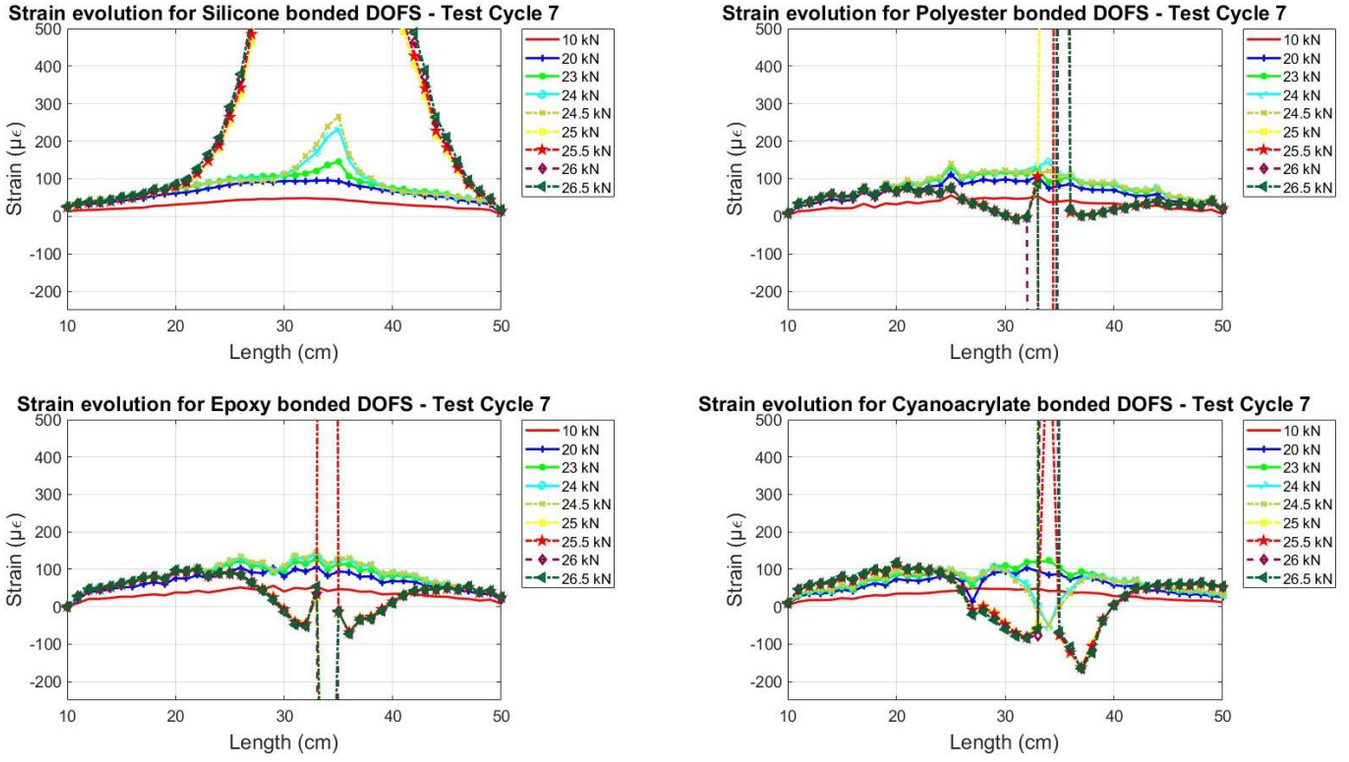


Figure 16. Measured strain at different load levels by the different adhesives bonded DOFS segment

6 CONCLUSIONS

In this paper, an experimental campaign to assess the performance of different bonding adhesives for distributed optical fiber sensors in concrete applications was presented. Moreover, as an additional point of study, the influence of different spatial resolutions was analyzed as well.

Through the conduction of load cycles under the elastic range of the concrete specimen, it was perceived how the use of a spatial resolution of 1 mm although theoretically better for an enhanced strain measurement resolution presents a highly spatial variability in its readings possibly related with the heterogeneity of the aggregates which constitute the concrete. This does not occur with a spatial resolution of 1 cm, which presented a good correlation with the data measured by the strain gauges, especially for the silicone bonded DOFS segment. The use of a 3 cm spatial resolution although presenting good correlation with the strain gauges did not present the expected advantage of generating smaller data files.

Furthermore, by performing a moving average of both the strain data acquired using a 1 mm and 1cm spatial resolution in order to directly compare it with the 3 cm measured strain, it was seen that with the use of 1 cm resolution very similar results were attainable. In this way, it is concluded that the use of a spatial resolution of 1cm is suitable for this type of applications.

Regarding the comparison of the different used bonding adhesives, it was observed that although all segments measured coherent strain data as also measured with the instrumented strain gauges, the silicone bonded segment presented a smoother and more uniform data than the other bonded segments.

When inducing strain higher than the concrete capacity and in this way generating cracking in the beam, all bonded segments were able to detect and locate the point where this damage was produced. Nevertheless, it was observable how quickly after the occurrence of cracking the points corresponding to this damage in the polyester, epoxy and cyanoacrylate bonded segments presented a low spectral shift quality (SSQ) which indicated not reliable measurements at those locations. However, the remaining length of these bonded segments continued to measure coherent strain information.

On the other hand, the silicone bonded DOFS segment continued to present acceptable SSQ values after the crack development but had a wider area of influence than the other segments, which is not advisable for the correct quantification of the damage (crack width) and the further strain monitoring in the remaining bonded areas.

It is important to mention as well, that this study contemplated the application of the mentioned adhesives in newly made small concrete specimens where it was easy to position the beam as best suitable for the adhesives application. In real and larger structural elements the viscosity and the time of curing of the adhesive contributes to an even greater uncertainty regarding the decision of the optimal adhesive in each application.

AKNOWLEDGMENTS

The authors want to acknowledge the financial support provided from the European Union's Horizon 2020 research and innovation programme under the Marie Sklodowska-Curie grant agreement No. 642453.

REFERENCES

[1] P. Ferdinand, "The Evolution of Optical Fiber Sensors Technologies During the 35 Last Years and Their Applications in Structure Health Monitoring," in *EWSHM-7th European Workshop on Structural Health Monitoring*.

[2] A. Barrias, J. Casas, and S. Villalba, "A Review of Distributed Optical Fiber Sensors for Civil Engineering Applications," *Sensors*, vol. 16, no. 5, p. 748, May 2016.

[3] F. Ansari and Y. Libo, "Mechanics of bond and interface shear transfer in optical fiber sensors," *J. Eng. Mech.*, vol. 124, no. 4, pp. 385–394, 1998.

[4] K. T. Wan, C. K. Y. Leung, and N. G. Olson, "Investigation of the strain transfer for surface-attached optical fiber strain sensors," *Smart Mater. Struct.*, vol. 17, no. 3, p. 35037, 2008.

[5] J. M. Henault *et al.*, "Analysis of the strain transfer mechanism between a truly distributed optical fiber sensor and the surrounding medium," in *Concrete Repair, Rehabilitation and Retrofitting III: 3rd International Conference on Concrete Repair, Rehabilitation and Retrofitting, ICCRRR-3, 3-5 September 2012, Cape Town, South Africa*, 2012, p. 266.

[6] R. Regier, "Application of fibre optics on reinforced concrete structures to develop a structural health monitoring technique," Canadian theses, 2013.

[7] TML, "TML STRAIN GAUGES 2017." Tokyo Sokki Kenkyujo Co., Ltd., 2017.

Maintenance, Safety, Risk, Management and Life-Cycle Performance of Bridges – Powers, Frangopol, Al-Mahaidi & Caprani (Eds)
© 2018 Taylor & Francis Group, London, ISBN 978-1-138-73045-8

Structural performance assessment using digital image correlation systems

Alfred Strauss & Roman Wendner
Institute of Structural Engineering
University of Natural Resources and Life Sciences, 1190 Vienna, Austria

Marco Marcon, Bernhard Krug, Pablo Castillo
Christian Doppler Laboratory LICROFAST, Institute of Structural Engineering
University of Natural Resources and Life Sciences, 1190 Vienna, Austria

Dan M. Frangopol
ATLSS Research Center
Lehigh University, Bethlehem, PA 18015-4729, USA

ABSTRACT: In engineering, quality control is related to systems development in order to ensure that products or services meet or exceed expectations and needs. Today, it is a challenge to manage civil infrastructure in an efficient manner. Thus, there is an increasing need to develop strategies to ensure asset quality with the aim of reducing the risk of unexpected costs. In order to assure the desired service quality with minimum interruptions, maintenance actions are taken when the risk of service impairment, interruption or life-cycle costs reach predefined levels. This risk depends on the establishment of performance goals for components, which when compared with performance indicators, obtained from visual inspection techniques, non-destructive tests or by monitoring systems, provide information regarding the assessed asset condition. The objective of this paper is to analyse a digital image correlation system and its ability to assess performance indicators, such as crack patterns, crack openings and vertical and horizontal deformations. The obtained values are then compared to goals so that structural performance assessment strategies can be implemented in an efficient and sustainable way.

1 INTRODUCTION

In engineering, quality control (QC) is related to systems development in order to ensure that products or services meet or exceed expectations and needs. Today, it is a challenge to manage civil infrastructure in an efficient manner. Thus, there is an increasing need to develop strategies to ensure asset quality with the aim of reducing the risk of unexpected costs. In order to assure the desired service quality, with minimum interruptions, maintenance actions are taken when the risk of service impairment, interruption or life-cycle costs reach predefined levels. This risk depends on the establishment of performance goals for components, which when compared with performance indicators, obtained from visual inspection techniques, non-destructive tests or by monitoring systems, provide information regarding the assessed condition.

Independently of the type of structural health monitoring system implemented, the general purpose is to efficiently monitor the structural performance such that proper maintenance actions may be identified and implemented in a timely fashion, with the aim of ensuring appropriate safety levels, maintaining the quality of the environment, as well as minimizing the asset life-cycle costs. In this paper, a digital image correlation system is used to assess performance indicators, such as crack patterns, crack openings and vertical and horizontal deformations. The obtained values are then compared to goals so that structural performance assessment strategies can be implemented in an efficient and sustainable way.

This research has been significantly affected by the objectives of COST TU1406 (2014) as well as the objectives of the COST TU 1402 (2013). The main objective of Cost Action TU1402 is to facilitate sustainable societal developments through improvements of resource efficiency, productivity, robustness, reliability and safety in the design and asset management for structures and infrastructure systems by optimized SHM systems. The Value of Information analysis quantifies this benefit relative to the costs of collecting the information. Hence, the identification of optimal SHM strategies is facilitated for both new and existing structures under a range of operating conditions and constraints. Hence, the objective of TU1402 is to quantify and assess the Value of Information collected by SHM in a life-cycle perspective prior to its implementation. Most often the beneficial value of SHM is only implicitly assumed, without considering how the information shall be utilized for improving the decision basis for

optimal life-cycle management of the structures. Information is only valuable if it deals with measurable and quantifiable parameters that may help decision making in asset management. Normally, the parameters/variables used in infrastructure management are defined as performance indicators.

Follow-up of the performance indicators along service life and their comparison with predefined target values according to desired performance goals will allow the definition of quality control plans. Therefore, the assessment of the value of information provided by the SHM techniques in regard to a set of predefined performance indicators is the key issue in a sustainable life-cycle assessment of civil infrastructure.

The shear-bearing capacity of reinforced concrete structures plays an important role concerning the sustainable life-cycle assessment of civil infrastructure. In the last decades, structural systems had been designed using different safety formats and levels, which in some cases do not comply completely with the current load models. Hence, the owners and operators of such civil infrastructure systems are highly interested in the assessment of the real existing shear load capacity and the still possible increase in the shear loading using advanced health monitoring or testing methods. For that kind of assessment of existing structures the value of health monitoring in structural performance assessment is obvious. The strength of reinforced concrete beams subjected to combined shear and flexure is affected by complex phenomena, such as existing multi-axial states of stresses, the anisotropy induced by the diagonal concrete cracking, the interaction between concrete and reinforcement and the brittleness of the failure mode. Trying to obtain valuable information about the shear transfer mechanisms, a large number of shear tests have been performed during the last 60 years, as summarized in Collins *et al*. (2008). Currently, both in the US and in Europe the shear design provisions are undergoing a revision. Open questions concern, among others, the existence and magnitude of the size-effect, see Yu *et al.* (2016), the influence of reinforcement degree, and the dependence on the axial stress state or pre-stress level, if applicable. Many different model formulations either mostly empirical, based on different physical mechanisms, see Mari *et al.* (2014), or supported by fracture mechanics have been proposed. Yet, clear evidence and quantification of the contribution of certain mechanisms can only indirectly be obtained by inverse statistical analysis.

This paper attempts to shed some light on the relevance of different mechanisms utilizing digital image correlation.

2 MECHANISM IN SHEAR MODELS

Refined theoretical models have been developed Bairán, J.M., & Marí, A.R. (2006) which are capable of tracing the non-linear response of these structures, but are too expensive and time consuming for daily engineering practice and design. Thus, simple semi empirically based equations have been also developed, some of which have been adopted by design codes European Committee for Standardization (CEN, 2002), although their applicability might be limited to the range of experiments used to derive them. Consequently, in some cases, the scatter of the predictions when compared with the experimental results is too large. Furthermore, recent studies, Sagaseta, J. & Vollum, R.L. (2011), reported that EC-2 overestimates or underestimates the shear strength, depending on the type of aggregate or the type of cross section, and neglects some key contributions. These facts suggest that there is still no universally accepted simplified mechanical model for shear design of reinforced concrete (RC) members, especially without shear reinforcement.

In addition, when assessing existing structures, they may falsely be considered unsafe. Recently, it was demonstrated how adequate filament non-linear models with shear capabilities are suitable for assessing this type of cases, Ferreira, D., Bairán, J. & Marí, A. (2013). Although adequate numerical models are a valuable assessment tool for existing structures, it is of paramount importance to develop rational mechanical models capable of reproducing as accurately as possible the physical behavior of concrete structures in order to safely and economically assess existing structures.

Furthermore, these models allow, after some simplifications, deriving simple equations which are suitable for code provisions or for their use in daily engineering practice. Among them are the Tooth model developed by Reineck, K. (1991), simplified models based on the Modified Compression Field Theory Vecchio, F.J. & Collins, M.P. (1986), the Critical Shear Crack theory Muttoni, A. & Ruiz, M.F. (2008), the Splitting Test Analogy Desai, S.B. (2004) and the theories based on the shear resisted by the uncracked compression chord Choi, K.K, Park, H.G. & Wight, J.K. (2007). On the other hand, methods based entirely on the theory of plasticity have also been applied with good results.

The above models were developed from different approaches, emphasizing the contribution of different shear transfer actions and proposing different expressions with different governing parameters. Nev-

ertheless, their strength predictions are similar and fit generally well with the experimental results.

3 EXPERIMENTAL DATA AND DOCUMENTATION

The proposed Digital Image Correlation (DIC) System for the classification of shear crack developments examined in this paper has been applied to a series of 16 laboratory tested beams. The test set up, the testing procedure, the classical monitoring set up and the material properties of the pre-stressed concrete small scale beams are documented in detail in Krug (2017). The length L of all laboratory tested beams was 5m and the effective span l_{eff} was 4,75m. The distance a between load point and support varied between 0,97m and 1,89m in order to have an appropriate shear span-to-depth ratio a/d to avoid unfavourable effects on the shear load transfer and bond shear failure. Typically, in shear tests the instrumentation is focusing first of all on the identification and monitoring of the compression field and the crack formation. Hence, the sensor arrangements include the application of strain gauges (SGs) glued externally along the sides of the concrete cross section, internal strain gauges fixed to the reinforcement and displacement transducers (e.g. LVDTs), see Krug (2016). In the present study, all these types of different electrical sensors were used. The external strain gauges were applied to the side surface of the web partly in a rosette-like arrangement in order to derive the principal strains and its inclination. Internal strain gauges were glued on additionally cast-in reinforcing bars with small diameters (φ_s = 6 mm). They were situated mainly at the same x/z-position like the outside ones in order to allow for later correlation studies between outside and inside recorded data. The LVDTs attached to the web are inclined perpendicular to the expected shear crack to make them more sensitive to shear crack openings but less to bending cracks, (Stoertzl 2015). In addition, LVDTs or laser sensors were used for vertical deflection measurements at the bottom of the beam. Moreover, visual inspections and manual crack recordings and crack width measurements by means of crack magnifiers were processed. Beams were tested under static loading in a three-point bending setup. To simulate shortly the life-cycle, first of all the specimens were subjected to a pre-loading phase consisting of 3 load cycles up to a representative SLS-load level estimated in advance.

When reaching the upper SLS load level, the crack propagation was recorded by the above mentioned visual inspection. Afterwards the load was increased displacement-controlled until failure, in between once again with single stops to do some crack recordings. Figure 1 depicts (a) the shear crack pattern at the load capacity, (b) the associated crack pattern of the optimized nonlinear Finite Element model, and (c) the modelled vs. experimental tested force-deflection curve.

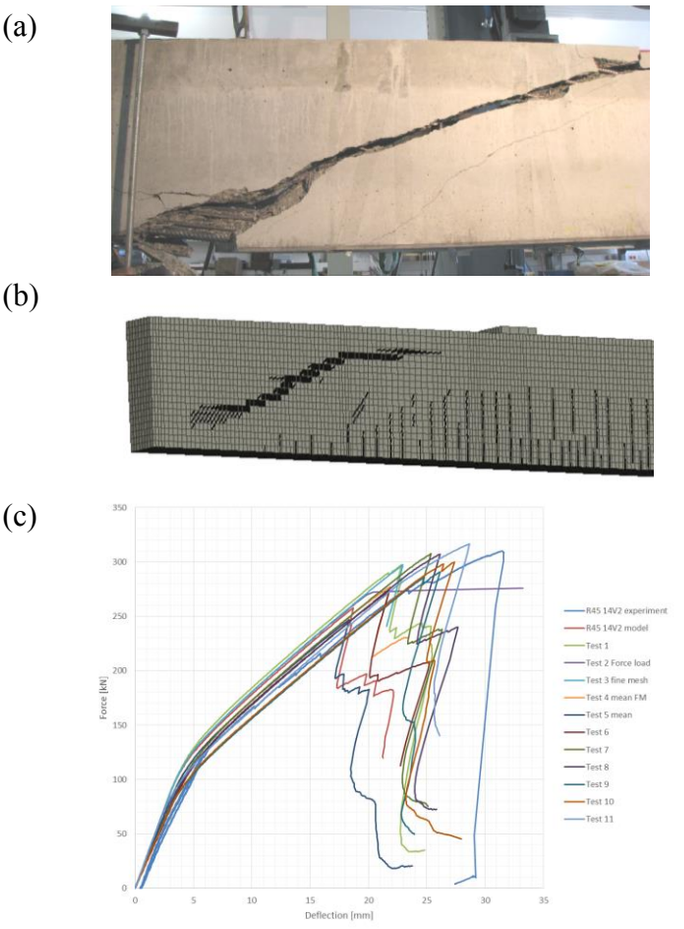


Figure 1. Experimental tested and modelled beams R30 (a) the shear crack pattern at the load capacity, (b) the associated crack pattern of the optimized nonlinear Finite Element model, and (c) the modelled vs. experimental tested force-deflection curve.

4 DIGITAL IMAGE CORRELATION

Digital Image Correlation is a non-contact optical technique used for measuring strain and displacement (Castillo et al. 2016). The system is based on grey scale value digital images. Using a stereoscopic sensor set-up each object point is projected on a specific pixel in the image plane of the respective sensor. Knowing the imaging parameter for each sensor and the orientation of the sensors with respect to each other the position of each object point in three dimensions can be calculated. In order to define the absolute size of the object a reference length is required and usually introduced curing the camera calibration.

Using a stochastic intensity pattern (speckle) on the object surface, the position of each object point in the two images can be identified by applying a correlation algorithm. The displacement and deformation of each point that compose the speckle allows the program to compute the displacement and the strain field. Applied to civil engineering problems, this technique allows the determination of deflections, the axial shortening of structural members and local strains, and crack patterns indicated by displacement jumps.

5 ADDED VALUE OF DIGITAL IMAGE CORRELATION FOR HEALTH MONITORING AND PERFORMANCE ASSESSMENT

As previously introduced, the beams are sustained by two supports and loaded eccentrically to ultimately cause shear failure. The accuracy and especially resolution of digital image correlation (DIC) is related to the pixel density of the camera, the size of the area of interest (AOI), and the quality of the speckle. A comprehensive discussion of the theoretical background and the applied algorithms can be found in Sutton *et al*. (2009). The latter is determined by the ratio between characteristic size of the stochastic pattern and pixel size. Taking into consideration the fact that the interesting zone is the one where the shear cracks will develop (Figs. 1(a) and (b)) the investigation is focused on this area. In the next phase the "ideal" camera setup has to be chosen. Variables are the distance between object and camera, depending on the lens and chip, the orientation of the cameras and the angle between the cameras of a stereo pair or the intentional choice to go for individual 2D single camera systems to cover a larger area of interest, see Fig.2. This choice is driven by the magnitude and type of the expected deformations as well as the likelihood of significant out-of-plane deformations. For the present problem, considering that four 9 Megapixel cameras were available, two options have been considered:

- The first option was using two 3D systems (each 3D system is composed of two cameras) set in such a way that a sufficient overlap between the two areas of interest is ensured, allowing both so far independent systems to be linked by coordinate transformation.
- The second option is to use separately the 4 cameras in order to make use of all the available resolution by moving the cameras closer to the beams and avoiding any overlap.

Both approaches have advantages and disadvantages. In this study four independent 2D systems (single camera) have been chosen for the following reason:

- The out of plane component is considered negligible compared to the in-plane components.
- Four independent 2D systems allow a substantially higher on specimen resolution which improves the ability to detect small cracks and quantify crack openings.
- The associated higher error due to lens distortion and out of plane deformations is considered acceptable in light of the goal to measure (a) global deformations such as deflections, and (b) perform a full field documentation of the crack development.
- The effect of out of plane deformations can be reduced by a perfectly level and centred setup of the cameras, as chosen for this study.

A crucial step is the specimen preparation, namely the creation of the stochastic pattern. In order to optimize the quality of the analysis it is important to ensure a "perfect" contrast in the images. This can be achieved by painting the beams white before applying the speckle in black. The speckle was applied with an airbrush in order to have the most repeatable and controlled speckle size. Furthermore, it is essential to avoid shadows and reflections by using non-gloss colour, covering all reflective surfaces and setting a number of light sources equipped with diffusors. Nevertheless, also the natural heterogeneity might suffice for certain measurement objectives. Thus, combined with a 2D system, reducing the monitoring effort significantly.

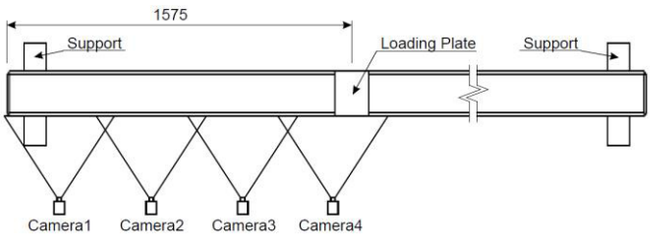


Figure 2. Sketch of DIC set-up

Correlating a set of images with the initial set provides information about the deformation state, and by derivation, about the strain field. The crack pattern then can be automatically determined based on the first principal strain field. The correlation analysis itself basically has only one parameter – the subset size. Like a moving average filter, a square correlation matrix is pushed over the image to mathematically express the local change between

two pictures related to deformations. Not unlike a finite element software, in case of a large subset size (element size) average strains with the smeared effect of cracks are determined. This approach is suitable for the measurement of global deformations, e.g. a bending line.

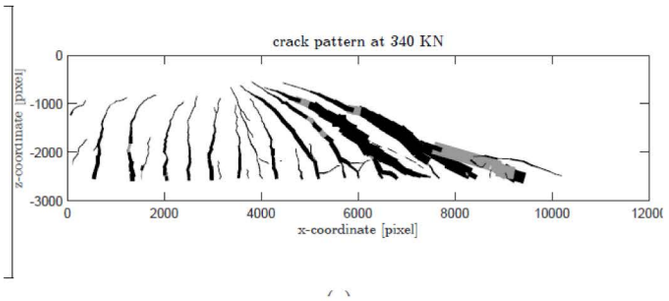


Figure 3. Crack pattern development

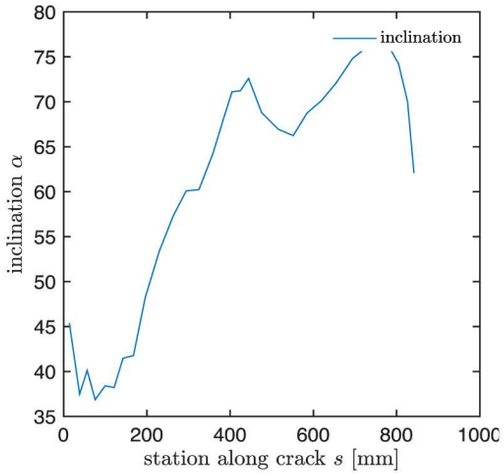


Figure 4. Crack inclination α along station s for a typical shear crack

Herein the task at hand is the determination of crack patterns and their evolution in time. Consequently, a small subset size is chosen allowing a good crack detection at the cost of higher noise in the output due to local variations in the speckle pattern, and, of course, significantly higher computational costs. Even though the first principal strain field is suitable to localize cracks it has to be noted that a strain field is a bad choice to quantify the crack opening. Depending on the subset size the actual crack is always smeared over a certain length resulting in ambiguous readings. Furthermore, if the crack opening exceeds a certain percentage of the subset size, correlation is locally lost, messing with automatic algorithms.

Thus, herein we propose a semi-automatic crack pattern survey with the following steps: (1) determine principal strain field with small subset size; (2) trace cracks based on fully developed crack pattern; (3) extract automatically the actual displacement jump along the traced lines for all time steps by e.g. Matlab script; (4) project the displacement jump onto the line segment to determine crack opening w_{90} and crack slip w_{00}. A further output is the crack inclination α measured between line segment and vertical axis, measured clockwise.

In Figure 3 a typical crack pattern for a load level of 340kN as obtained by the semi-automatic procedure is presented. The line width scales with the crack opening. Grey segments are interpolated for neighboring segments. A pixel corresponds to 0.18mm.

(a)

(b)

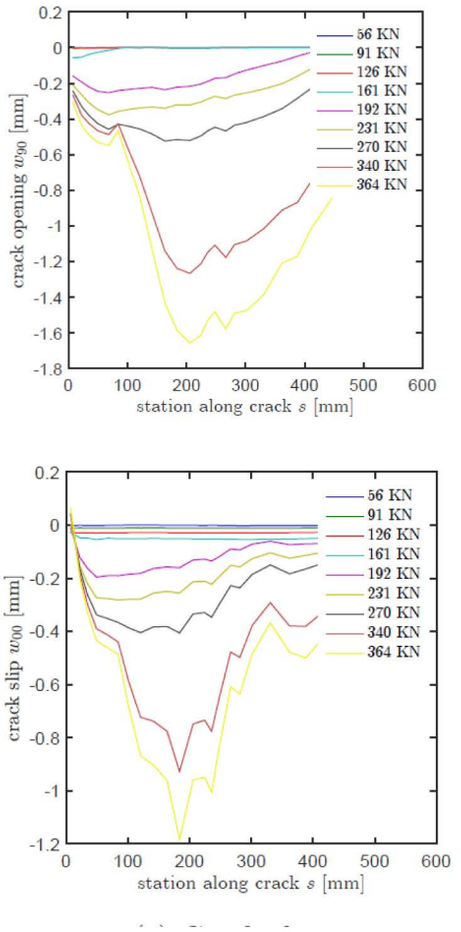


Figure 5. Crack pattern properties (a) opening, (b) slip

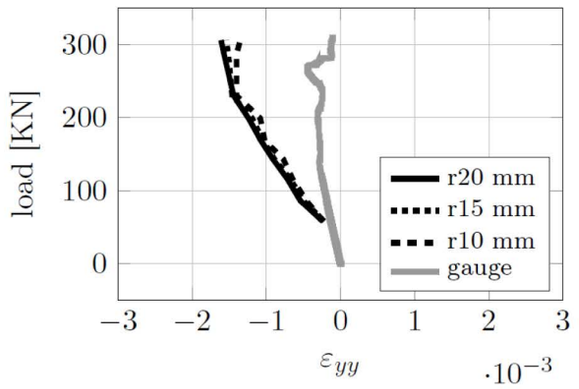
5.1 *Crack Movement*

For each of the line traces the geometrical information, i.e. the evolution of inclination, can be plotted against the station s along the crack, where s=0 represents the one end of the fully developed crack, for bending cracks equal to its initiation on the surface, see Figure 4. In Figure 5 the evolution of both components of the crack – opening and slip –with load level and depending on the position along the crack is presented. At 91 kN a small bending crack with a maximum opening of 0.05mm is present. This crack quickly grows into a shear crack. It is interest-

ing to note that the opening seems to be constrained until s=100mm, corresponding to the position of the tendon. Furthermore, a distinct shear slip is present in the range $0 < s < 300$ mm.

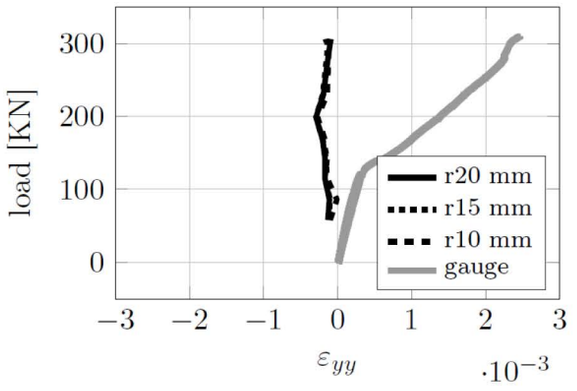
Fig. 6 presents the comparison between DIC strains and the corresponding electrical strain gauges on the reinforcing bars. In the shear zone of the 13 monitors of strain which deployed to Slowik et al. 2015. The graphs show that some of the strains derived from the DIC measurements on the surface of the beams show a good agreement with strains measured on the reinforcement (Fig. 6 (c)) and some are significant deviating (Figure 6 (a) and (b)) due to crack formation.

(a)



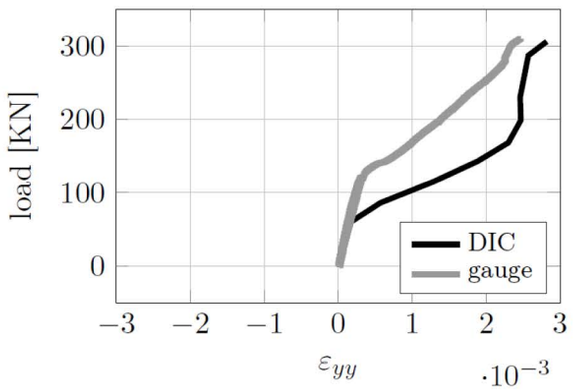
(a) T3D2

(b)



(e) T3D7

(c)



(f) T3D7 good correlation

Figure 6. Strain measurements horizontal ε_{xx}

6 CONCLUSIONS

The first studies on the digital image correlation systems demonstrate the capability of the method in the recording and interpretation of the crack pattern development in the shear field zone during the loading process up to the shear bearing capacity. The technology also shows a high potential for the understanding and interpretation of complex mechanical processes of the shear behaviour of reinforced concrete. A first comparison of the DIC recorded surface strains with the strains on the embedded reinforcement demonstrate partly a good agreement and hence the possibility to map surface measurements to the reinforcement layers. In addition, it could be shown that the DIC measurements have a high potential for optimizing processes in the arrangement of monitoring systems.

7 ACKNOWLEDGMENTS

The financial support by the Austrian Federal Ministry of Economy, Family and Youth and the National Foundation for Research, Technology and Development within the project OMZIN, the Czech Science Agency project No. 17-02862S ("PROMOSS"), as well as the HORIZON COST TU1402 and TU1406 activities are gratefully acknowledged. The opinions and conclusions presented in this paper are those of the writers, and do not necessarily reflect the views of the sponsoring organizations.

8 REFERENCES

Bairán, J.M., & Marí, A.R. (2006). Coupled model for the non-linear analysis of anisotropic sections subjected to general 3D loading. part 1: Theoretical formulation. *Computers and Structures*, 84, 2254–2263. doi:10.1016/j.compstruc.2006.08.036.

Castillo, P.; Jirovsky, L.; Marcon, M.; Wendner, R.; Strauss, A.: (2016): Investigation of shear fracture mechanism by digital image correlation systems. *The Fifth International Symposium on Life-Cycle Engineering* (IALCCE 2016), Delft, 16 - 20 October 2016.

Choi, K.K., Park, H.G., & Wight, J.K. (2007). Unified shear strength model for reinforced concrete beams - Part I: Development. *ACI Structural Journal*, 104, 142–152.

Collins, M.P., Bentz, E.C., & Sherwood, E.G. (2008). Where is shear reinforcement required? Review of research results and design procedures. *ACI Structural Journal*, 105, 590–600.

COST Action TU1402 MoU: European Cooperation in the field of Scientific and Technical Research – COST. (2013). Memorandum of Understanding for COST Action TU1402.

COST Action TU1406 MoU: European Cooperation in the field of Scientific and Technical Research – COST. (2014). Memorandum of Understanding for COST Action TU1406.

Desai, S.B. (2004). Influence of constituents of concrete on ist tensile strength and shear strength. *ACI Structural Journal*, 101, 29–38.

European Committee for Standardization (CEN). (2002). Eurocode 2: Design of concrete structures: Part 1: General rules and rules for buildings, Brussels, Belgium.

Ferreira, D., Bairán, J., & Marí, A. (2013). Numerical simulation of shear-strengthened RC beams. *Engineering Structures*, 46, 359–374. doi:10.1016/j.engstruct.2012.06.050.

Krug, B. 2017. Shear-normal force optimization of pre-stressed precast concrete components, Ph.D Thesis. Department of Civil Engineering and Natural Hazards, Institute of Structural Engineering, University of Natural Resources and Life Sciences.

Marí, A., Cladera, A., Oller, E., & Bairán, J. (2014). Shear design of FRP reinforced concrete beams without transverse reinforcement. Composites Part B: *Engineering*, 57, 228–241. doi:10.1016/j.compositesb.2013.10.005.

Muttoni, A., & Ruiz, M.F. (2008). Shear strength of members without transverse reinforcement as function of critical shear crack width. *ACI Structural Journal*, 105.

Reineck, K. (1991). Ultimate shear force of structural concrete members without transverse reinforcement derived from a mechanical model. *ACI Structural Journal*, 88, 592–602.

Sagaseta, J., & Vollum, R.L. (2011). Influence of beam cross-section, loading arrangement and aggregate type on shear strength. *Magazine of Concrete Research*, 63, 139–155. http://infoscience.epfl.ch/record/163648/files/Sagaseta11.pdf.

Slowik, O.; Novak, D.; Krug, B.; Strauss, A. (2015): Shear failure of pre-stressed concrete T-shaped girders: Experiment and nonlinear modeling. *IABSE Conference - Structural Engineering: Providing Solutions to Global Challenges*, Geneva , September 23 - 25,

Störzel, J.; Randl, N.; Strauss, A.: (2015): Monitoring shear-induced degradation of reinforced and pretensioned concrete members. *IABSE Conference - Structural Engineering: Providing Solutions to Global Challenges*, Geneva , September 23 - 25,

Strauss A., Mandić Ivanković A. (2016). Performance indicators for road bridges – categorization overview. *Paper prepared for WG meeting of COST action TU1406 Quality specifications for roadway bridges, standardization at a European level*, 30th March -1st April, 2016, Belgrade, Serbia,

Strauss A., Vidovic A, Zambon I., Dengg F., Tanasic N., Campos J.C. 2016. Performance indicators for roadway bridges. *Proceedings 8th international conference on Bridge Maintenance, Safety and Management, Foz do Iguaçu (Brazil), 26-30 June 2016.* London: Taylor and Francis.

Strauss, A. (2016) Numerical and monitoring based Markov Chain approaches for the fatigue life prediction of concrete structures Engineering Structures, 112, pp. 265-273.

Strauss, A., Bergmeister, K., Novák, D., Lehký, D. 2004. Probabilistic response identification and monitoring of concrete structures *Beton- und Stahlbetonbau*, 99 (12), pp. 967-974.

Strauss, A., Frangopol, D.M., Bergmeister, K. (2010) Assessment of existing structures based on identification Journal of Structural Engineering, 136 (1), pp. 86-97.

Strauss, A., Mordini, A., Bergmeister, K. (2006) Nonlinear finite element analysis of reinforced concrete corbels at both deterministic and probabilistic levels. *Computers and Concrete*, 3 (2-3), pp. 123-144.

Strauss, A., Wendner, R., Bergmeister, K., Reiterer, M., Horvatits, J. (2011) Monitoring and influence lines based performance indicators. Modellkorrekturfaktoren als "performance Indikatoren" für die Langzeitbewertung der integralen Marktwasserbrücke S33.24. *Beton- und Stahlbetonbau*, 106 (4), pp. 231-240.

Strauss, A., Wendner, R., Frangopol, D.M., 2012 Bergmeister, K. Influence line-model correction approach for the assessment of engineering structures using novel monitoring techniques. *Smart Structures and Systems*, 9 (1), pp. 1-20.

Strauss, A., Wendner, R., Frangopol, D.M., Bergmeister, K. (2012) Influence line-model correction approach for the assessment of engineering structures using novel monitoring techniques. *Smart Structures and Systems*, 9 (1), pp. 1-20.

Strauss, A., Zimmermann, T., Lehký, D., Novák, D., Keršner, Z. 2014. Stochastic fracture-mechanical parameters for the performance-based design of concrete structures. *Structural Concrete*, 15 (3), pp. 380-394.

Sutton, A. M., Orteu, J. J., and Schreier, H. W. (2009). *Image Correlation for Shape, Motion and Deformation Measurements*. Springer, New York.

Vecchio, F.J., & Collins, M.P. (1986). The modified compression- field theory for reinforced concrete elements

Yu, Q., & Baz˘ant, Z.P. (2011). Can stirrups suppress size effect on shear strength of RC beams? *Journal of Structural Engineering*, 137, 607–617. doi:10.1061/(ASCE)ST.1943-541X.0000295.

Zimmermann, T., Strauss, A., Bergmeister, K. 2010. Numerical investigation of historic masonry walls under normal and shear load. *Construction and Building Materials*, 24 (8), pp. 1385-1391.

Zimmermann, T., Strauss, A., Lehky, D., Novak, D., Kersner, Z (2014) Stochastic fracture-mechanical characteristics of concrete based on experiments and inverse analysis. *CONSTR BUILD MATER*. 2014; 73: 535-543.

Maintenance, Safety, Risk, Management and Life-Cycle Performance of Bridges – Powers, Frangopol, Al-Mahaidi & Caprani (Eds)
© 2018 Taylor & Francis Group, London, ISBN 978-1-138-73045-8

Development of Response-Based Load and Resistance Factor Rating (RB-LRFR) Methodology

M. Ghosn
The City College of New York/CUNY, New York, NY, USA

B. Sivakumar, E. Senturk
HNTB Corporation, New York, NY, USA

ABSTRACT: Based on current rating methods, about one in nine of the 607,380 US bridges are considered to be structurally deficient. However, not all these bridges are at risk of collapse as current code-specified analytical methods are generally conservative and may underestimate the true safety levels of existing bridges. For these reasons, there has been considerable interest in developing methods that combine field measured data with analytical models to obtain more accurate assessments of existing bridges.

This paper presents a Response-Based Load and Resistance Factor Rating (RB-LRFR) method that utilizes strain data to evaluate the safety of existing bridge members. Appropriate live load factors are calibrated to reflect the uncertainties associated with estimating the parameters and random variables needed to rate a bridge component using field data. The implementation of the proposed methodology is illustrated using a composite steel girder bridge as an example.

1 INTRODUCTION

1.1 *Background*

Bridge load rating is the determination of the live load carrying capacity of an existing bridge. Typically, load rating is determined by analytical methods based on information taken from the bridge plan and inspection reports. It is also common practice to supplement the rating process with field strain measurements that are primarily used for diagnostic purposes to confirm analysis results. Field test measurements are generally performed by running test trucks of known weights over instrumented bridges to obtain improved estimates of structural analysis results including the load distribution factors that may be directly used during the rating process or to calibrate finite element models of the bridge for more advanced analyses. Procedures have also been proposed to use truck Weigh-In-Motion (WIM) data to develop site specific load models for bridges subjected to traffic loads that may not be well represented by the generic code-specified nominal loads. Such piece-meal approaches require a combination of extensive finite element analysis and costly field measured data collection processes which often require bridge closures and controlled load tests.

1.2 *Objectives*

A method, herein named Response-Based Load and Resistance Factor Rating, RB-LRFR, is proposed to directly use strain measurements to load rate an existing bridge. The method measures the response of structural members under ambient traffic, instead of test trucks, to obtain more accurate rating factors that better reflect the true safety of the instrumented members. This proposed response-based approach will alleviate the expense and logistics of conducting a bridge controlled load test, the need to collect detailed WIM traffic data, and the development and execution of a calibrated finite element analysis. The proposed method uses properly calibrated live load factors which are consistent with current Load and Resistance Factor Rating, LRFR methodology (AASHTO, 2011).

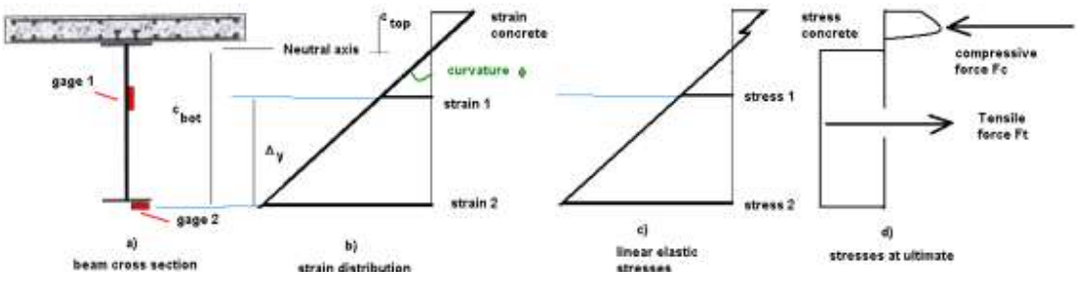


Figure 1. Distribution of Axial Strains and Stresses along the Depth of a Beam in Bending

2 BASIC CONCEPT

2.1 *Moment-Curvature Relationships*

The bridge rating process is concerned with evaluating the safety of particular bridge members to ensure that the effects of the applied loads are lower than the members´ load carrying capacities. In this paper, the focus is on moment effects on main members although a similar approach could eventually be implemented for shearing forces. In this context, axial strains measured on bridge beams are directly related to the internal moments induced by the crossings of trucks over the bridge. Utilizing measured strains directly to check member safety is not consistent with bridge rating methodology which is based on the ultimate capacity. Therefore, it is necessary to convert measured strains to moments.

As shown in Figure 1, axial strains measured at two different locations along the depth of a section can be used to obtain the curvature due to truck crossings, which in turn can be used to determine the applied truck moment. If the live load moment M_{LL} is obtained using the curvatures measured during truck crossings and the dead load moment M_{DL} is known, the load rating process can then proceed in the traditional manner by comparing the moment applied on the member to the calculated ultimate moment capacity of the member. This member-oriented response-based rating process involves a much lower level of uncertainty than the rating based on the nominal live load models specified in the AASHTO LRFR because by taking field measurements on particular members under ambient traffic, there is no need to perform a structural analysis nor is there a need to determine the load distribution factor or apply an arbitrary dynamic amplification.

In RB-LRFR the ambient traffic could include legal loads, illegal overloads or authorized overloads and the safety evaluation accounts for any random mix of these vehicles as they cross the bridge. As such, RB-LRFR ratings are reflective of bridge safety for these vehicles crossing the bridge individually or in combination. Thus, multiple-presence of vehicles on a bridge is automatically accounted for eliminating the need to use the conservative code-specified multiple presence factors.

As explained by Moses (2001), the bridge rating process considers the safety of bridge members subjected to the maximum expected load over a five-year rating cycle. Therefore, a statistical projection of the data collected over a limited period of strain measurements should be performed to obtain the maximum expected 5-year load effect. In this study, the approach developed by Ghosn et al. (2013) and Sivakumar et al. (2011) is used to execute the statistical projection.

2.2 *RB-LRFR Procedure*

The proposed RB-LRFR methodology follows the following steps:

1. Measure the strains ε_1 and ε_2 at two points along the depth of the section being evaluated.
2. Develop the complete moment-curvature relationship of the instrumented section by estimating the material properties and dimensions of the section being evaluated from design plans and inspection reports, as shown in Fig. 2.
3. Calculate the dead load moment M_{DL} on the section based on information taken from design plans and inspection reports.
4. Use the moment-curvature relationship to determine the curvature corresponding to the dead load moment, ϕ_{DL}.
5. Calculate the curvature due to the live load ϕ_{LL} using the measured strains and strength of materials principles, as $\phi_{LL} = (\varepsilon_2 - \varepsilon_1) / \Delta_y$, where Δ_y is the vertical distance between the two strain gages.
6. Add the dead load and live load curvatures to find the total curvature on the member, $\phi_{TL} = \phi_{LL} + \phi_{DL}$.
7. Use the moment-curvature relationship to find the total applied moment on the member, M_{TOTAL}.
8. Determine the live load moment by subtracting the dead load moment from the total applied moment, $M_{LL} = M_{TOTAL} - M_{DL}$.
9. Use the estimated values of the applied live load moments obtained based on the limited period of data collection (a minimum 3-month period is

recommended) to project the maximum load effect in the service period (5 years for load rating) using statistical methods.

10. Using the maximum live load effect over the rating period, the moment capacity and the dead load moment, obtain the LRFR Rating Factor. Rating Factor (*R.F.*) calculations will be based on specially calibrated live load factors as explained later in this paper.

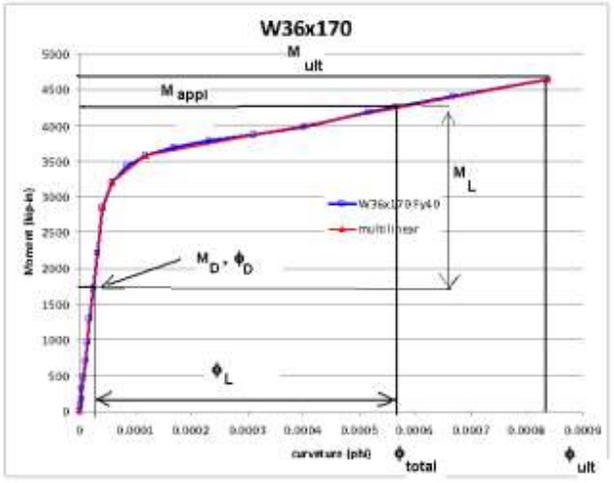


Figure 2. Example Moment-Curvature Diagram

2.3 *Load Rating*

The Rating Factor is used as the primary means for evaluating the load carrying capacity whereby a Rating Factor *R.F.* ≥ 1.0 indicates that the bridge has sufficient level of reliability to safely carry the live loads that are currently crossing the bridge.

The calculation of the Rating Factor, *R.F.*, can be executed using the usual Rating Equation given as:

$$R.F. = \frac{\phi R_n - \gamma_{DC}\left(D_{C1} + D_{c2}\right) - \gamma_{DW} D_W}{\gamma_{LL} LL_{\max}} \qquad (1)$$

where *R.F.* is the rating factor, ϕ is the resistance factor, γ_{DC} and γ_{DW} are the dead load factors, and γ_{LL} is the live load factor. R_n is the nominal resistance, D_{C1} is the dead load effect of pre-fabricated components, D_{C2} is the dead load effect of cast-in-place components and attachments, D_W is the nominal dead load effect for the wearing surface, LL_{max} is the maximum live load moment for the rating period as calculated using the measured curvature. The live load moment for each truck crossing is calculated from the section's moment curvature relationship. These live load moments are subsequently projected to estimate the maximum moment within a 5-year rating period.

The resistance and dead load factors in Eq. (1) can be obtained from AASHTO (2012). However, a new live load factor γ_{LL} needs to be calibrated to reflect the levels of uncertainties associated with estimating the maximum live load moment using the proposed method. Following widely accepted code calibration methods, the determination of the appropriate live load factor must be executed so that bridge sections that have a Rating Factor *R.F.* = 1.0 will exactly meet a target reliability index, β_T. The live load factors in the AASHTO LRFR (2001) were calibrated to produce a target β_T =2.5.

2.4 *Reliability Analysis*

To perform the reliability calibration of live load factors, bridge safety margin is expressed in terms of a function, *Z*, defined as:

$$Z = R - DL - LL \qquad (2)$$

where *R* is the actual resistance of the cross section being evaluated, *DL* and *LL* are respectively the dead and live load effects on the section. The reliability analysis studies the probability that the failure function *Z* is less than or equal to 0.0 and the reliability index, β, is defined such that $P_f = \Phi(-\beta)$ where Φ is the cumulative normal probability function that gives the probability that the normalized random variable is below a given value. The reliability analysis requires statistical models for all the random variables in Eq. (2). The statistical models for *R* and *DL* presented by Nowak (1999) are applicable for the purposes of this study. The focus is then on modeling the uncertainties in *LL*.

During the calibration of the AASHTO (2017) Specifications, the live load *LL* had the highest level of uncertainty expressed in terms of a Coefficient of Variation (COV) V_{LL}=20%. This value accounts for the overall variability in estimating the effect of the maximum load expected to be on the bridge during a 5-year rating period. These uncertainties include: a) variability within a site; b) site-to-site variability, and c) the effect of limitations in the data sample size, as well as the uncertainty in evaluating d) the dynamic amplification and e) the load distribution factor and other limitations in the structural analysis process. In the response-based rating process, many of the live load uncertainties, especially those related to site-to-site variability, load distribution and dynamic load amplification are reduced or completely eliminated because of the use of site-specific response data. Instead, the live load uncertainties are related to the following:

1. Variability in the measured strains compared to actual strains
2. Calculation of curvature
3. Moment curvature relationship

4. Finding the maximum live load moment in the 5-yr rating period
5. Sufficiency of data.

It is further noted that the uncertainties in evaluating the moment curvature relationship for extracting the live load moment are highly correlated to the uncertainties in estimating the resistance R because, as shown in Fig. 2, both use the same material property input and the same analysis principles.

2.4.1 *Strain Measurement Errors*

Strain measurement errors vary depending on the gages, their installation, electric circuitry, and signal conditioning including bridge completion resistors. A 2% error is usually estimated for properly calibrated signal conditioning systems with full bridge circuits with temperature compensation. Additional errors may be due to the type of gage used and the installation.

Installation errors are due to the placing of the gage in the right location and correct orientation. For a single gage, it is estimated that an error in the installation angle of about $\pm 10^{o}$ will produce an error in the strain reading on the order of $\pm 5\%$. The COV for the installation error is then taken as 5%.

To account for gage errors one should compare readings from different gages. An analysis of strain data collected during the course of this study showed that the standard error from the gages is less than 3.6 με. When the maximum strain reading is above 100 με, the standard error would be about 3.5% or less.

From this discussion, the errors in the recorded strains associated with the largest live loads can be conservatively represented by a COV of $6.5\% = \sqrt{(3.5\%)^2 + (5\%)^2 + (2\%)^2}$.

2.4.2 *Calculation of Curvature*

The curvature is the difference between the strains measured along the depth of one section divided by the distance between the two strain gages. This calculation is also related to the location of the Neutral Axis. Differences in determining the location of the neutral axis for different girders of the same bridge are found to be within $\pm 8\%$.

Overall, the uncertainties in estimating the curvature, ϕ_{LL}, are related to those of the strains (which are conservatively estimated to be 6.5%) and in estimating the location of the neutral axis (which are conservatively estimated to be 8%). Therefore, a very conservative estimate of the COV in estimating the curvature can be set as $V_{\phi} = \sqrt{(8\%)^2 + (6.5\%)^2} = 10.3\%$ or roughly 10.5%

2.4.3 *Moment Curvature Relationship*

The calculation of the live load moment, M_{LL}, from the curvature, ϕ_{LL}, depends on the moment-curvature relationship and the adjustment made to account for the dead load effect as described in Fig. 2. Developing the moment-curvature relationship and finding M_{total} for every value of curvature ϕ_{total} involves the same basic variables used to find the ultimate moment capacity $R=M_{ult}$. Therefore, M_{total} for a given curvature and the ultimate moment capacity $R=M_{ult}$ are highly correlated random variables. Nowak (1999) assumed that the mean value of R is related to the nominal value that one calculates using design code methods by a bias b_R=1.12 with a COV V_R=10%. These account for the material uncertainties, the manufacturing uncertainties, as well as the modeling uncertainties which evaluate the difference between the actual behavior of a beam as obtained from tests compared to the assumed behavior when using code-specified methods. If the ultimate moment capacity is found using realistic models for the stress-strain relationships of the constituent materials and using best estimates of the material strengths and moduli of elasticity, then the bias between the moment capacity obtained using code methods and the moment capacity calculated using advanced computer software such as SAP2000 is reduced to a value close to b_R=1.03. If the moment capacity uses the best estimates for the concrete strength but the nominal yielding stress of the steel, then the bias between the code calculated moment capacities and those of the actual behavior represented by the SAP2000 approach will have a total bias of close to b_R=1.08. The difference between the 1.12 bias used during the AASHTO LRFD calibration and the 1.08 bias mentioned herein is due to the difference between the specified concrete strength and the actual strength in the as-built conditions. The COV accounts for the modeling uncertainties which inherently include the uncertainties in estimating the effective width of a composite girder-slab beam and other basic modeling assumptions such as the assumption that plane sections remain plane. The material uncertainties account for the variations of the steel properties as well as the concrete strength from the values used in calculating the ultimate moment capacity, the manufacturing uncertainties account for the variability in the dimensions of the sections.

2.4.4 *Projection of Maximum Live Load Moment*

Previous analyses have shown that the calculation of the extreme value distribution of the maximum live load moment in the 5-yr rating period produces a COV V_{max} on the order of 4.5%. This value only reflects the variability in estimating the maximum live load moment from the histogram of live moments

extracted from the M-phi curve assuming that the histogram represents all the live loads that are crossing the bridge within the 5-yr period.

One method to check the sufficiency of data is to execute the projection of the maximum live load moment with data collected over increasing periods of time and verifying convergence. In this study, it has been observed that the estimated mean converges to a steady state value when data collected over four months are used to execute the statistical projection. The corresponding change in the expected 5-yr maximum live load is on the order of 2%.

2.4.5 *Summary*

In summary, a simplified model for accounting for the random nature of the calculated maximum live load moment M_{LL} can be presented as:

$$M_{LL} = (M_{total} - M_{DL})\lambda_{LL}\lambda_{\varepsilon}\lambda_{data} \quad (3)$$

where $\lambda_{LL}, \lambda_{\varepsilon}, \lambda_{data}$ are modeling variables that respectively account for the variability in the maximum live load moment, the variability in the measured strains including the calculation of the curvature and the insufficiency of the data and the accuracy of the fit of the live load moment cumulative histogram, M_{total} is the moment value on the M-phi plot which corresponds to the total curvature which is the sum of the live load and dead load curvatures, M_{DL} is the dead load moment.

The statistics for the random variables that model $M_{LL} = (M_{total} - M_{DL})$ are given in Table 1.

Table 1. Statistical Data for Live Load Moment Modeling

Variable	Mean	COV	Distribution type
M_{TOTAL}	$\overline{M}_{TOTAL} = \overline{M}_{LL\max} + \overline{M}_{DL}$	10%	Lognormal
M_{DL}	As built conditions	10%	Normal
λ_{LL}	1	4.5%	Gumbel
λ_{ε}	1	10.5%	Normal
λ_{data}	1	2%	Normal

The benefits of using the response-based LRFR are evident as the variability in estimating the intensity of the live load effect is represented by a COV $11.60\% = \sqrt{(4.5\%)^2 + (10.5\%)^2 + (2\%)^2}$. After adding a COV of 10% related to converting the intensity into a moment, the final COV value = $15.3\% = \sqrt{(11.6\%)^2 + (10\%)^2}$ is lower than the 20% used during the calibration of the AASHTO LRFD and LRFR. Furthermore, the correlation between the ultimate moment capacity and the live load moment leads to a reduction in the overall uncertainties associated with the safety margin Z of Eq. (2) used to perform the reliability analysis.

2.5 *Reliability Calibration of Live Load Factor for Response Based LRFR*

The live load factor that should be used in the RB-LRFR equation to evaluate the load carrying capacity of a bridge should be calibrated in such a way that when the rating factor is $R.F.$=1.0, the bridge member should achieve a target reliability index.

The target reliability is usually selected to match the reliability of bridges that have shown satisfactory performance. For the purposes of this study, we will assume the same target reliability index β_T=2.50 which was used during the calibration of the AASHTO LRFR for a 5-yr rating period.

To execute the calibration of the appropriate live load factor, a suite of bridges of different span lengths and member capacities and different permanent weights should be subjected to live load moments representing the effects of different traffic conditions on bridges with different numbers of beams and beam spacing and different dynamic amplification characteristics. Because such an extensive database of instrumented bridges is not available at this stage, we resort to creating a simulated database of composite steel bridges. For example, a random sample of hypothetical steel bridges is generated to have the following characteristics:

1. A range of members having nominal ultimate moment capacities between R_n=40,000 kN.m to 400 kN.m assumed to represent steel bridge members of various levels of deterioration for a large range of span lengths.
2. Dead load moments ranging between D_n=20,000 kN.m to 135 kN.m.
3. Mean live load moment ranges between $\overline{M}_{LL\max} = \overline{LL}_{\max}$=30,000 kN.m to 135 kN.m.

The failure function (safety margin equation) of Eq. (2) is expanded as follows:

$$Z = R - DL - LL = M_{ult} - M_{DL} - (M_{total} - M_{DL})\lambda_{LL}\lambda_{\varepsilon}\lambda_{data}$$

where $R=M_{ult}$ and M_{total} are correlated variables because they are both obtained from the moment-curvature relationship using the same input of section and material properties. Two cases are analyzed: a) full correlation with ρ=1.0 and b) partial correlation with ρ=0.5. The statistics of the random variables are given in Tables 1 and 2.

Table 2. Statistical Data for Moment Capacity and Dead Load Based on Nowak (1999)

Variable	Member	Bias	COV	Distribution
Resistance	Steel beams	1.12	10%	Lognormal
	Prestressed	1.05	7.5%	Lognormal
Dead Loads	Prefabricated	1.03	8%	Normal
	Cast in place	1.05	10%	Normal
	Wearing surface	1.00	25%	Normal

A total sample of 80,000 hypothetical bridge members is generated so that their capacity, dead load and live load ranges meet the characteristics set above. The reliability index β is calculated for each of the cases. The cases where the reliability index is found to be equal to β=2.50 (+/-0.01) are set to have a rating factor $R.F.$=1.0. The live load factor γ_L for the cases that met the target is calculated from:

$$\gamma_{LL} = \frac{\phi R_n - \gamma_{DC}(D_{C1} + D_{c2}) - \gamma_{DW} D_W}{R.F. \times LL_{\max}} \qquad (5)$$

The reliability calculations were performed assuming that each point on the moment-curvature plot M_{total} which gives the moment on the M-phi curve corresponding to the measured curvature is partially correlated to the ultimate moment capacity M_{ult} with $\rho_{M_{total}, M_{ult}} = 0.5$.

The live load factor γ_{LL} calculated from Eq. (5) is plotted against the dead load to resistance ratio D_n/R_n as shown in Fig. 3. The plot shows that a conservative live load γ_L=1.45 will provide an upper bound to the live load factors leading to a reliability index β equal to the target β_T=2.5 for all the cases for which D_n/R_n is less than 0.50. Therefore, the live load factor that should be used with the Response-Based LRFR of composite steel bridges is set at γ_{LL}=1.45. It is noted that as D_n/R_n exceeds 50%, the effect of the dead load becomes dominant and a dead load factor higher than 1.45 should be used. In fact, the AASHTO LRFD uses a dead load factor γ_{DC}=1.50 for the cases where the dead load is dominant.

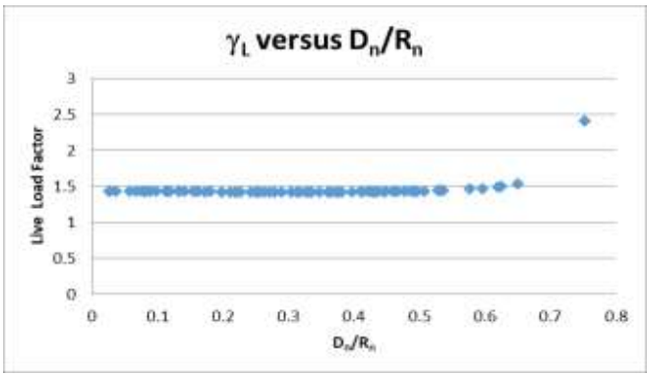


Figure 3. Live load factor versus D_n/R_n for partial correlation

3 IMPLEMENTATION

3.1 *Response-Based Rating of Composite Steel Bridge*

A numerical example is presented to describe the proposed Response-Based Load and Resistance Factor Rating methodology. The simple span 26-m long composite steel bridge on Interstate-195 over Sharon Station Road was instrumented to capture strain data resulting from ambient traffic. The bridge that carries two traffic lanes in one direction has six 36WF230 steel rolled beams supporting a 200-mm thick concrete deck with a 50-mm thick asphalt wearing surface. Four of the six girders were instrumented at midspan with two strain gages, one placed at the bottom flange level, and the other at the web, 305-mm away from the bottom flange gage.

The strain data collected in the field for three months are scanned to catch the peak strain values corresponding to sequential 15 minute intervals for each girder. Girder 2 of the NJ Pilot Bridge was found to experience the highest values of strain and was chosen for analysis. Section properties were extracted from the as-built plans. The girder has a 1380 mm x 32 mm cover plate welded to the bottom flange.

The concrete strength is found by ensuring that the calculated location of the neutral axis corresponds to that measured in the field from the two strains readings taken during truck crossings. The modular ratio, n, was determined to be n=4.13

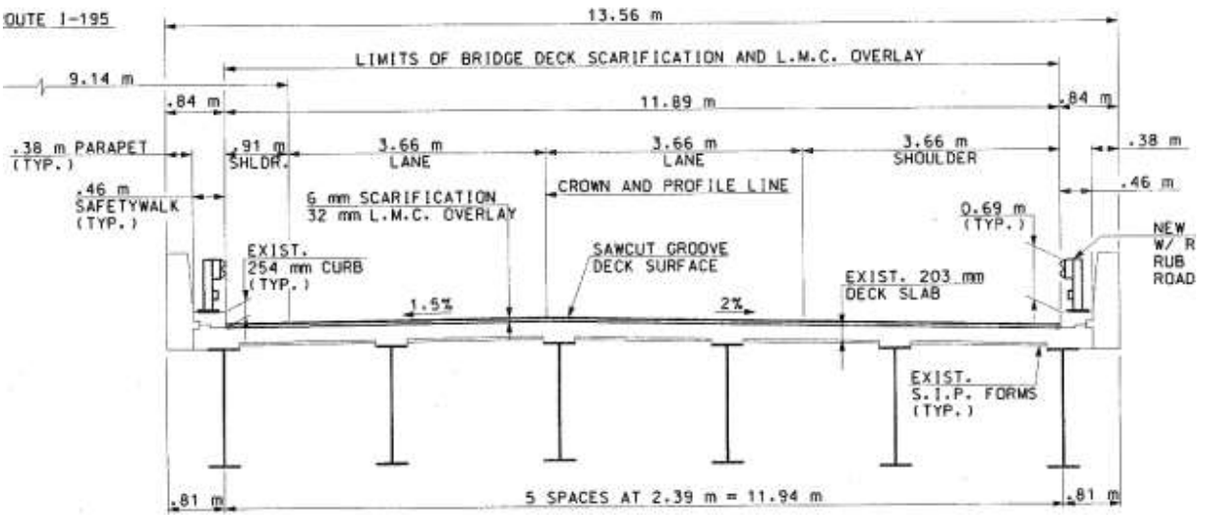


Figure 4. Cross Section of Bridge on Interstate-195 over Sharon Station Road.

The uniform dead load of the components and that for the wearing surface on Girder 2 were determined to be respectively $w_{DC} = 21\ kN/m$ and $w_{DW} = 2.7\ kN/m$. The corresponding total dead load moment is calculated to be M_{DL}=2000 kN.m.

For each peak strain the live load curvature is:

$$\phi_{LL} = \frac{\varepsilon_2 - \varepsilon_1}{\Delta_y} \qquad (6)$$

where Δ_y is the vertical distance between the two strain gages, ε_2 and ε_1 are the measured flange and web strains. The maximum 15-minute live load moment is extracted from the M-phi curve as described in Fig. 6.

The maximum load effect for the 5-year service period is determined using the upper 5% of the live load moment data by plotting the 15-minute maximum live load moments on a normal probability graph as shown in Figure 7. The corresponding mean and standard deviation are extracted as μ_{event}= 270 kN.m and σ_{event}=160 kN.m. Having the properties of the tail end of the maximum 15-minute live load moment distribution, the statistical properties of the maximum live load moment in the 5-year rating period can be obtained given that in a 5-year period, the total number of events is equal to N = 175,200 readings of the maximum 15-minute value. Given the large value of N, the maximum 5-year live load moment asymptotically approaches that of an Extreme Value Type I (Gumbel) distribution with an inverse measure of the dispersion α_N determined as:

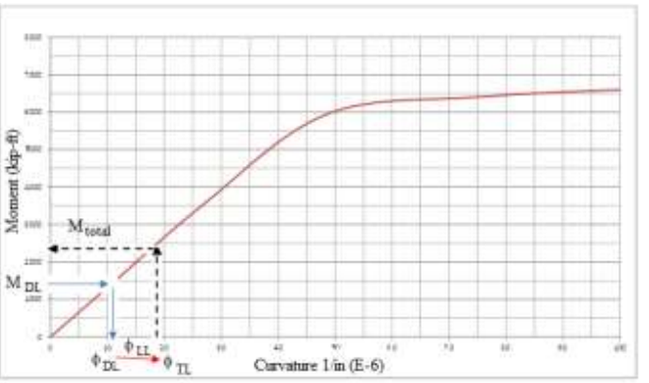


Figure 6. Determination of Live Load Moment from M-ϕ Curve

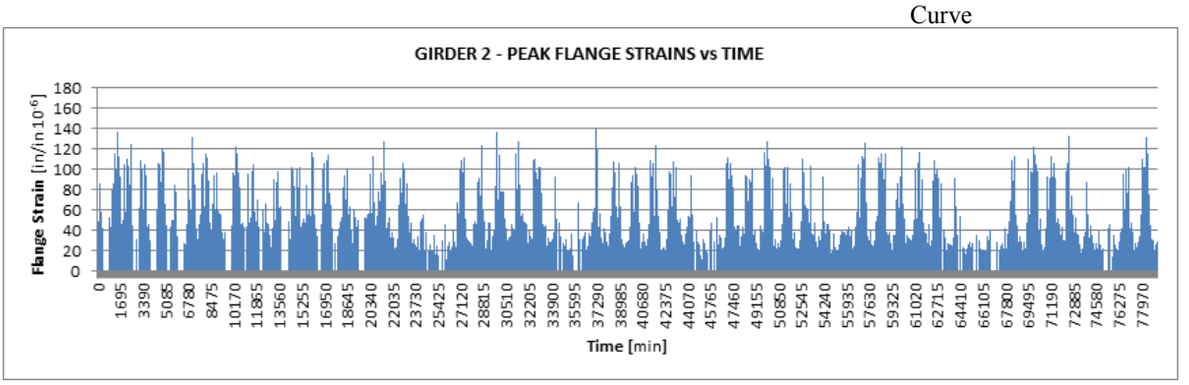


Figure 5. Sample of 15-minute Maximum Strains Collected on Composite Steel Bridge.

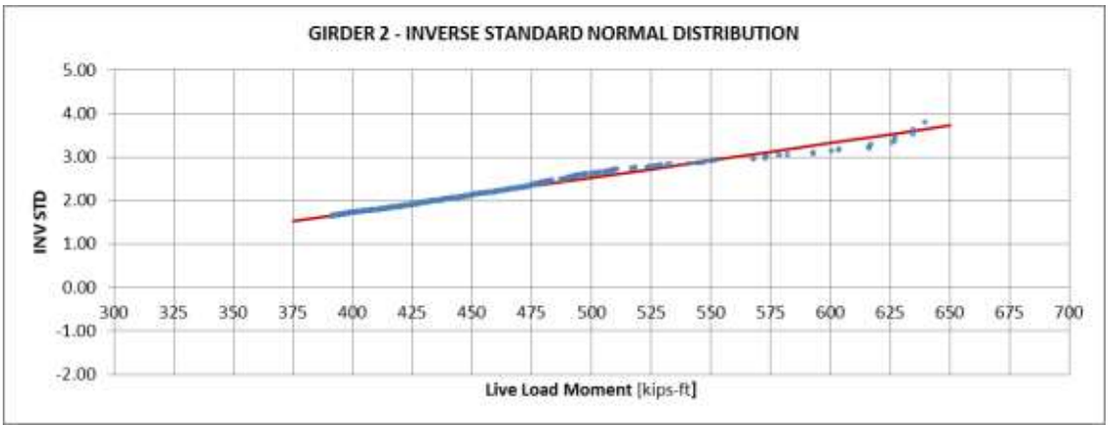


Figure 7. Normal Graph of Top 5% Moments for Girder 2

$$\alpha_N = \frac{\sqrt{2\ln(N)}}{\sigma_{event}} = \frac{\sqrt{2\ln(175200)}}{160} = 0.0307 \quad (7)$$

The most probable value u_N is calculated as:

$$u_N = \mu_{event} + \sigma_{event}\left(\sqrt{2\ln(N)} - \frac{\ln(\ln(N)) + \ln(4\pi)}{2\sqrt{2\ln(N)}}\right) = 970\ kN.m$$

The mean of the maximum load effect, LL_{max}, is:

$$LL_{\max} = u_N + \frac{0.577216}{\alpha_N} = 988\ kN.m \quad (9)$$

Based on the rating Equation (1), and the maximum live load moment for a 5-year period, the rating factor for Girder 2 can be computed as:

$$R.F. = \frac{0.9 \times 10680 - 1.25 \times 1770 - 1.50 \times 224}{1.45 \times 988} = 4.93$$

For comparison purposes, the bridge was also rated using analytical LRFR methods for design and both routine and SHV legal loads. The results are summarized in Table 3.

Table 3. RB-LRFR and MBE Design and Legal Load Ratings

Type of Rating	M_{LL} [kn.m]	R.F.
Response-Based	988 (includes DF and Dynamics)	4.93
HL-93 INVENTORY	1700 (Truck) 784 (Lane)	1.328
HL-93 OPERATING	1700 (Truck) 784 (Lane)	1.721
TYPE 3	1224	2.991
TYPE 3S2	1441	2.541
TYPE 3-3	1410	2.597
SU4	1375	2.665
SU5	1529	2.396
SU6	1707	2.145
SU7	1872	1.955

4 CONCLUSIONS

This paper presents a Response-Based Load Rating (RB-LRFR) method which uses the bridge response directly in the rating process to reduce many sources of uncertainty inherent in assessing bridge safety.

The proposed RB-LRFR combines the benefits of a static load test and site-specific truck Weigh-In-Motion analysis. It offers a non-intrusive method that uses the actual bridge as the evaluation model and actual traffic for modeling the live load.

The procedure follows statistically sound methods that maintain the same reliability goals as current load rating methods.

The proposed method is implemented for the analysis of an existing composite steel girder bridge and was found to improve the rating obtained from current methods by a large factor.

5 REFERENCES

AASHTO (2017), *Load & Resistance Factor Design (LRFD) Bridge Design Specifications*. 6th edition, American Association of State and Highway Transportation Officials, Washington, DC.

AASHTO MBE-2-M (2011), *Manual for Bridge Evaluation,* 2nd Edition, American Association of State and Highway Transportation Officials, Washington, DC.

Ghosn, M., Sivakumar, B., and Miao, F. (2013). "Development of State-Specific Load and Resistance Factor Rating Method." J. Bridge Eng., 18(5), 351–361.

Nowak AS (1999). *Calibration of LRFD Bridge Design Code,* NCHRP Report 368. Washington (DC), National Academy Press.

Sivakumar, B., Ghosn, M. and Moses, F. (2011) *"Protocols for Collecting and Using Traffic Data in Bridge Design",* NCHRP Report 683, Washington (DC), National Academy Press.

Maintenance, Safety, Risk, Management and Life-Cycle Performance of Bridges – Powers, Frangopol, Al-Mahaidi & Caprani (Eds)
© 2018 Taylor & Francis Group, London, ISBN 978-1-138-73045-8

Monitoring-based quantification of input parameters for chloride ion ingress models

M. Šomodíková & B. Teplý
Faculty of Civil Engineering
Brno University of Technology, Brno, Czech Republic

A. Strauss & I. Zambon
Institute of Structural Engineering
University of Natural Resources and Life Sciences, Vienna, Austria

ABSTRACT: Within structure management, the non-formal assessment where the structural condition is evaluated on the base of visual inspections takes place at most. The objective of the structural condition assessment is to determine its current state and to assume the future performance of a structure with a maximum of accuracy and a minimum of effort. Therefore, advanced methodologies and deterioration predictive models for the assessment of structure/structural element over time are needed. Data collected during visual inspection should mainly provide the information about the most serious problems and suggest most suitable scheme of extension the inspection by monitoring, additional on-site measurements and/or laboratory tests. These should provide more realistic information about the input parameter values, when using modeling of degradation processes for prediction of future condition of the structure. The aim of this contribution is to describe the process of possible calibration of input parameters for prediction of deterioration due to chloride ion ingress into concrete with the emphasis on model based assessment.

1 INTRODUCTION

Degradation processes of structural materials, such as chloride ion ingress, concrete carbonation or subsequent corrosion of reinforcement, are limiting factors for the service life of reinforced concrete structures and/or structural elements. Since the proper safety level of the structure needs to be ensured during the whole service life, owners and operators of existing structures face complex decisions making regarding maintenance and repair strategies and/or possible replacement (Neves et al. 2006, Strauss et al. 2013). Further, minimizing the overall cost by optimizing inspection, maintenance and repair work is a main task within this decision making process.

According to Rücker et al. (2006), assessment procedures can be classified into three groups: (i) Non–formal assessment; (ii) Model based assessment; and (iii) Measurement based assessment. Since they vary in sophistication, these procedures can be divided into several assessment levels, where experience based non-formal assessment presents the lowest level and conversely fully probabilistic approach the highest one. Generally structural assessment is carried out using limit state principles with characteristic values and partial safety factors. However, only the fully probabilistic approach provides quantitative information about safety level and hence it is increasingly supported. Its utilization is advocated also in *fib* Model Code 2010 (2012).

Within structure management, the non-formal assessment where the structural condition is evaluated on the base of visual inspections takes place at most. The objective of the structural condition assessment is to determine its current state and to assume the future performance of a structure with a maximum of accuracy and a minimum of effort. Therefore, advanced methodologies and deterioration predictive models for the assessment of structure/structural element over time are needed. Data collected during visual inspection should mainly provide the information about the most serious problems and suggest most suitable scheme of extension the inspection by monitoring, additional on-site measurements and/or laboratory tests. These should provide more realistic information about the input parameter values, when using modeling of degradation processes for prediction of future condition of the structure.

The aim of this contribution is to describe the process of possible calibration of parameters for prediction of deterioration due to chloride ion ingress into concrete with the emphasis on model based assessment. It is intended to explain the principles of structural evaluation and to feature the several levels of structural assessment, starting with simple but conservative methods and progressing to more sophisticated ones. The 'guideline' is to be aimed especially at existing concrete/reinforced concrete structures, such as bridges, located in mild European climate with deicing salt application.

2 CHLORIDE ION INGRESS MODELING

Reinforcement corrosion due to chloride ingress into reinforced concrete is one major process that is limiting the service life of reinforced concrete structures. Different approaches exist for description of the time-dependent process of chloride ingress into concrete (see e.g. Teplý et al. 2008). Due to inherent uncertainties in material, technological and environmental characteristics, stochastic models, dealing with probabilistic approaches and presenting the performance-related design of structures for durability, are recommended creating an effective tool for the assessment and prediction of time-dependent degradation processes; see *fib* Model Code 2010 (2012) and ISO 16204 (2012).

Chloride profiles can be modeled with relatively good approximation in many cases using Fick's second law of diffusion, describing a non-stationary diffusion process (Nilsson et al. 1996) and believing that the transport of chlorides into concrete is mainly diffusion-controlled (Hunkeler 2005). The widely used analytical models are based on the error function (Collepardi et al. 1972). In this contribution the focus is on the widely accepted model incorporated into the *fib* Model Code 2010 (2012) and fully probabilistic approach.

According to *fib* Bulletin 34 (2006), the Cl^- concentration at the depth x [mm] (the depth of concrete cover a [mm] is usually used) at time t [years], $C(x,t)$ [wt.-%/c] is calculated as:

$$C(x,t) = C_0 + (C_{S,\Delta x} - C_0) \cdot E$$
$$\text{with} \quad E = \left[1 - \text{erf}\frac{x - \Delta x}{2\sqrt{D_{app}(t) \cdot t}}\right], \tag{1}$$

where C_0 [wt.-%/c] is the initial Cl^- content in concrete, $D_{app}(t)$ [mm^2/years] is the time-dependent migration coefficient, 'erf' is the error function and $C_{S,\Delta x}$ [wt.-%/c] is the substitute surface Cl^- content in depth of convection zone Δx [mm]. Here, it should be noted that in a spray environment, the concrete close to the surface is often exposed to a frequent change of wetting and subsequent evaporation (so called splash conditions); this very zone is usually referred to as the 'convection zone'. As the transport mechanisms inside this convection zone are not mainly diffusion controlled, the approach of Fick's second law of diffusion yields no satisfactory approximation for chloride penetration inside the convection zone. In order to still describe the penetration of chlorides for an intermittent load using Fick's second law of diffusion, the data from the convection zone, which may deviate considerably from ideal diffusion behaviour, is ignored and Fick's second law of diffusion is applied starting at a depth of Δx with a substitute surface concentration of $C_{S,\Delta x}$ (Δx marks the depth of the convection zone). With this simplification, Fick's second law of diffusion yields a very good approximation of chloride distribution at a depth of $x \geq \Delta x$. At a distance to the road surface larger than 1.5 m (spray zone), the formation of a convection zone cannot be detected any more and the substitute surface concentration of $C_{S,\Delta x}$ is substituted for surface Cl^- content $C_{S,0}$ ($\Delta x = 0$ mm).

According to *fib* Bulletin 76 (2015), $D_{app}(t)$ can be determined based on the field data through chloride profiling method and subsequently, an ageing exponent is determined using two approaches:

$$D_{app}(t) = k_e \cdot D_{app}(t_0) \cdot \left(\frac{t_0}{t}\right)^{\alpha_A} \quad \text{or}$$
$$D_{app}(t) = k_e \cdot D_{RCM}(t_0) \cdot \left(\frac{t_0}{t}\right)^{\alpha_B}, \tag{2}$$

where α [-] is the ageing exponent assessed using approach A or B, t_0 [years] is the reference point of time, $D_{RCM}(t_0)$ [mm^2/years] is the migration coefficient based on the Rapid Chloride Migration (RCM) test method, and $D_{app}(t_0)$ [mm^2/years] is the effective diffusion coefficient at the reference point of time t_0 (different from time t) based on the field data through chloride profiling method. The environmental variable k_e [-] that takes into consideration the effect of temperature on chloride ingress into concrete is described in a simplified way by using the Arrhenius equation, in line with the temperature-dependent descriptions of the rate of corrosion and electrolytic resistance of concrete (Page et al. 1981, Raupach 1992):

$$k_e = \exp\left[b_e\left(\frac{1}{T_{ref}} - \frac{1}{T_{real}}\right)\right], \tag{3}$$

where b_e [K] is the temperature coefficient (proportional to activation energy), and T_{ref} [K] and T_{real} [K] are the reference temperature and the temperature of the structural element or the ambient air, respectively.

3 LEVELS OF ASSESSMENT

The values of input parameters for modeling of chloride ion ingress (see Table 1) can be assessed in different levels based on the input value precision and

accompanying uncertainties. The process is graphed using the flowchart in Figure 1 and can be itemized as follows:

1. As a starting position, a bridge structure or structural component can be assessed. In the case of new bridges, current standards are used with important information about concrete composition. For accurate prediction of structural deterioration due to chloride ingress, additional tests can be carried out to determine the diffusion characteristics of in common use or new material composition.

2. In the case of existing structure, the question 'What data are available?' arises. The assessment is carried out using the ISO and EN standards. Based on the data availability, three levels can be divided:

   (i) ***Level 1*** *– no inspection of the bridge was carried out and only information about material, load and environment from codes and other literature sources are available.*

   Structural requirements and recommended values of input parameters can be used according to European standards or other literature. These are based on former measurements and/or experience. For many of input parameters, using these values may not be quite accurate and realistic, consequently it may lead to very uncertain (sometimes even unsafe) results in modeling; see e.g. (Papworth and Gehlen 2016, Lollini et al. 2015, Pradelle et al. 2014) where the reliability level is assessed with different mean values for key variables;

   (ii) ***Level 2*** *– the design documentation (or birth certificate) is available and/or visual inspection of the bridge was carried out.*

   From design documentation, specific details on parameters important to the durability and service life of the structure concerned (e.g. age of the bridge, cover to reinforcement, cement type, water to cement/binder ratio, permeability, chloride diffusion properties of concrete, environmental conditions, quality of workmanship achieved, etc.) are available in order to define some of the input parameters properly. However, in prevailing number of cases, only basic input parameter, such as age of the bridge, is documented. On the contrary, if well documented (e.g. in the case of new bridge) and/or if some analysis were carried out for the material composition before its usage (e.g. in the case of new material composition), very important and more precise information about concrete composition and other material properties can be obtained. If unknown from design documentation, visual inspection is needed. Visual inspection will only detect visible damage of the structure. However, it might detect e.g. the development of structural deterioration and can be undertaken relatively cheaply over the whole structure at frequent time intervals. Results from a single visual inspection may be used to estimate the remaining service life, from which the timing of future inspection/maintenance can be determined based on the actual risk, and to identify what other tests should be undertaken in different areas. The conservation strategies and measures as well as condition survey and monitoring activities are also described in *fib* Model Code 2010 (2012);

   (iii) ***Level 3*** *– updated or realistic input values are available from on-site measurements (**Level 3a**) and/or supplementary laboratory tests (**Level 3b**).*

   If reliable data are not known from design documentation or visual inspection, additional on-site measurements and/or laboratory tests should be carried out. Tests may be carried out directly on the structure itself (in-situ testing) or on test specimens made in the laboratory or taken from the structure. Core samples may be taken to carry out detailed laboratory testing. Here, relevant ISO and EN standards; e.g. ISO 13822 (2010), EN 12504-1 (2009) and EN 12390-1 (2012) should be used. Non-destructive test methods and methods of sample analysis can be employed at intervals during the structure's life. Sampling for petrographic examination or wet chemical analysis might be called for where chemical attack is of concern due to the deterioration risk or due to low apparent surface strengths identified. Where the rate of chloride ingress is required (e.g. chloride profiles) to give the depth of corrosion activation front, test results can be used in conjunction with cover distributions established during construction to calculate the residual life; for more details see Concrete Institute of Australia (CIA) 2009.

Definitions of input parameters for modeling of chloride ingress using appropriate statistical characteristics, such as probability density function (PDF), mean value (μ), coefficient of variation (CoV) and limits (if needed) according to *fib* Bulletin 76 (2015), are summarized in Table 1. Test method is also mentioned for cases when parameter quantification is performed using on-site measurements and/or laboratory testing.

Table 1: List of input parameters for modeling of chloride ion ingress

Variable	Unit	PDF*	μ	CoV	Limits	Level	Method
Material parameters:							
CEM I–V	-	-	-	-	-	(1), 2, 3b	Petrographic analysis
w/c (w/b)	-					(1), 2, 3b	Petrographic analysis
C_0	wt.-%/c	D	0.1–0.4 (0)	-		1, 2, 3b	Chemical analysis
$D(t_0)^{**}$	m^2/s	N		0.20		1, 2, 3b	Chloride diffusion tests
α	-	B			(0; 1)	1, 3b	Chloride profiling method/Diffusion tests
Environmental parameters:							
T_{ref}	K	D (N)	293	-		1, 3a	On-site measurements/Nearest weather station
T_{real}	K	N				1, 3a	On-site measurements/Nearest weather station
b_{e}	K	N	4800	0.15		1, 3b	Chloride profiling method/Diffusion tests
Δx	mm	B (D)	10 (0)	0.50 (-)	(0; 50)	1, 3b	Chloride profiling method
$C_{\text{S},0}/C_{\text{S},\Delta x}$	wt.-%/c	LN		0.75		1, 3b	Chloride profiling method
Other parameters:							
t_0	years	D	0.0767	-		1, 2	
t	years	D		-		1, 2	
a	mm	N				1, 2, 3a	On-site non-destructive methods

Note: statistical definition is based on *fib* Bulletin 76 (2015)
*PDF = probability density function (B = Beta; D = Deterministic; LN = Log-normal; N = Normal)
** $D_{\text{RCM}}(t_0)$ or $D_{\text{app}}(t_0)$ can be used

When using recommended, i.e. uncertain values of input parameters for the estimation of chloride ion ingress over time, a noticeable improvement is possible if a prior (statistical) information gained by measurements taken from a real structure at a certain age is available. For this purpose Bayesian updating can be used. On-site measurements (chloride profiles in this case) are used to improve the estimations of chloride concentration over time as well as the reliability level of the structure. Starting from a-priori probabilities (estimated, or drawn from experience as well) additional information may be incorporated using Bayes' theorem thus arriving at a-posteriori probabilities that are proposed to be better estimates (Schneider 1997). Using Bayesian updating usually leads to lower variability of estimated results, thus the estimation of chloride concentration over time may be more realistic using this procedure.

4 CALIBRATION OF DIFFUSION PARAMETERS – CASE STUDY

Some of parameters can be obtained with sufficient accuracy only using more detailed laboratory tests and/or calibration processes. With utilization of chloride profiling method together with chemical analysis and chloride diffusion tests, chloride migration/diffusion coefficient at time, $D_{\text{RCM}}(t)/D_{\text{app}}(t)$, initial chloride content in concrete, C_0, surface chloride content, $C_{\text{S},0}$, eventually even substitute surface chloride content in depth of convection zone, $C_{\text{S},\Delta x}$, and the depth of convection zone, Δx, can be assessed. An ageing factor, α, which introduces the decrease of the chloride diffusion coefficient $D_{\text{app}}(t)$ in time, can be calibrated based on the above mentioned parameters.

The ageing exponent is dependent on both material

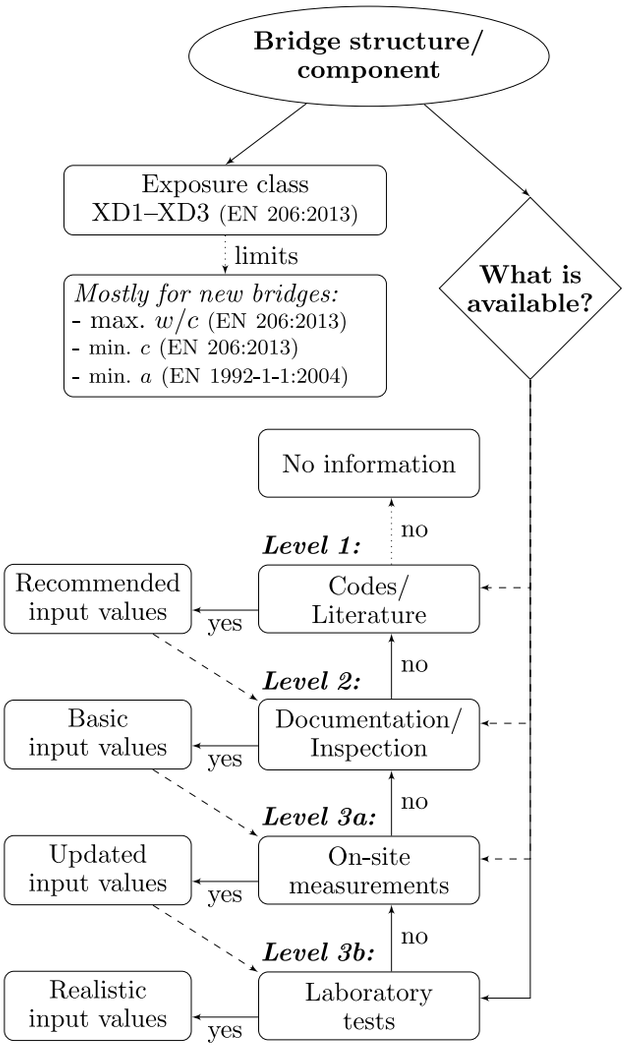


Figure 1: Levels of quantification of input parameters for modeling of chloride ion ingress

and exposure. In order to determine the ageing exponent, the long-term behavior of $D_{\text{app}}(t)$ of existing structures has to be considered by analyzing the development of chloride profiles over time. The process of quantification can be itemized as follows considering two possible approaches:

(i) *Approach A* can be used to determine the ageing exponent α_{A} by means of $D_{\text{app}}(t_0)$ and $D_{\text{app}}(t)$ from field data. In order to be able to quantify the ageing exponent, α_{A}, the values of $D_{\text{app}}(t)$ in at least two different points in time are required.

Effective diffusion coefficients, $D_{\text{app}}(t_0)$ and $D_{\text{app}}(t)$, and surface total chloride contents, C_{S}, are calculated based on the best fit of Fick's second law of diffusion; see Equation (1). Ageing exponent, α_{A}, is then quantified by a regression analysis using Equation (2).

(ii) *Approach B* can be applied in cases where a considerable amount of field data of concrete comparable to the design concrete is available. The ageing exponent α_{B} has to be determined by combining $D_{\text{app}}(t)$ obtained from the field data, and $D_{\text{RCM}}(t_0)$ of the design concrete from laboratory rapid chloride migration (RCM) test, i.e. $D_{\text{RCM}}(t_0)$ value has to be known.

It is assumed that chloride migration coefficient, $D_{\text{RCM}}(t_0)$, was simply determined by the RCM test method (see NT BUILD 492 1999) and substitutes the parameter $D_{\text{app}}(t_0)$ in Approach A. However, field data from real structures are needed to determine the ageing exponent, α_{B}. Effective diffusion coefficient, $D_{\text{app}}(t)$, and surface total chloride content, C_{S}, are then calculated in the same way as in Approach A.

As an example of calibration diffusion parameters using data from real structures, the railway bridge No. 4005026 from Gänserndorf to Marchegg in Austria was analyzed as a case study. The bridge was built in 1967 near Weikendorf as a one span reinforced concrete structure. The design documentation as well as the calculation from 1967 were available, hence the input variables could be defined in a realistic way. Furthermore, on-site measurements and/or laboratory tests were carried out within the inspection of the bridge in 2013, therefore some of parameters could be updated.

At first, only design documents and code recommendations (Levels 1 and 2 in Figure 1) were used for initial estimation of chloride content at reinforcement $C(a,t)$ over the design life, i.e. $t = 0$–100 years. The CEM II cement type was assumed as the most common cement used in Austria in the year of build (i.e. 1967) according to ÖNORM B3310 (1963). The water to cement ratio, w/c, was estimated for the concrete classes of abutments and supporting structure, i.e. B 225 and B 400 (corresponds to C16/20 and C30/37), based on the design documentation of the bridge. Since the information about type and quantity of additives was not available, material parameters $D_{\text{RCM}}(t_0)$ and α were quantified so that the values correspond with the values for CEM II/A-S type and prescribed w/c value (although the very detailed bridge design documentation was available, neither cement type nor w/c value were known in this case). The average annual temperature, T_{real}, was defined as the average temperature prevailing at a location over the 30-year period of time, i.e. 1981–2010. The average was calculated for Vienna, the nearest station to the location of the bridge using data from World Meteorological Organization (2017). Statistical definition of all input parameters is summarized in Table 2. Here, it should be noted that the XD3 exposure class was assumed, which means splash conditions and elements of bridge closer than 1.5 m from the road (e.g. abutments).



Figure 2: Analyzed bridge

In the second step, the data from measurements and laboratory tests carried out within the inspection in 2013 (Levels 3a and 3b in Figure 1) were used for model updating to gain more accurate results. Definition of input parameters is summarized in Table 3 where updated/changed values are highlighted in grey color. The updated estimation of chloride content was performed in the same way as in the case of initial estimation for the remaining life time of the bridge, i.e. $t = 46$–100 years.

Since the petrographical analysis of concrete was not carried out, the CEM II/A-S with $w/c = 0.45$ was kept without changes. Based on the cement type the $D_{\text{RCM}}(t_0)$ value was specified as in the case of initial estimation. The concrete cover a was specified based on the Ferroscan reinforcement detection analysis. Other updated parameters, namely the $D_{\text{app}}(t)$, Δx, $C_{\text{S},\Delta x}/C_{\text{S},0}$ and α, were defined based on the chloride concentration analysis. Eight chloride profiles from the bridge abutments (see left part of Figure 3) were used for quantification of the parameters using fitting of Equations (1)–(2). The 'mean' chloride profile was used for quantification of parameters $D_{\text{app}}(t)$, $C_{\text{S},\Delta x}$, Δx and α. Mean value and standard deviation of measured chloride concentrations in the depth of reinforcement ($a = 30$–45 mm) were $\mu = 0.65$ wt.-%/c, $\sigma = 0.9$ wt.-%/c. As in the case of initial estimation, splash conditions were assumed.

Table 2: Definition of input parameters for the initial estimation of $C(a,t)$ over time

Variable	Unit	PDF*	μ	CoV	Limits/Note	Source
Material parameters:						
CEM II/A-S	-	-	-	-	assumed	ÖNORM B3310 (1963)
w/c (w/b)	-	-	0.45	-	assumed	EN 206 (2013), VÖZ (1985)
C_0	wt.-%/c	D	0.1	-		EN 206-1 (2000), *fib* Bulletin 76 (2015)
$D_{\text{RCM}}(t_0)$	m^2/s	N	$8{\cdot}10^{-12}$	0.20		*fib* Bulletin 76 (2015), Lay & Schießl (2003)
α	-	B	0.35	0.45	(0; 1)	*fib* Bulletin 76 (2015), Lay & Schießl (2003)
Environmental parameters:						
T_{ref}	°C	D	20	-		*fib* Bulletin 76 (2015)
T_{real}	°C	N	10.65	0.79		World Meteorological Organization (2017)
b_e	°C	N	4526.85	0.15		*fib* Bulletin 76 (2015), Gehlen (2000)
Δx	mm	B	10	0.50	(0; 50)	*fib* Bulletin 76 (2015)
$C_{\text{S},\Delta x}$	wt.-%/c	LN	3	0.75		*fib* Bulletin 76 (2015), DARTS (2004)
Other parameters:						
t_0	years	D	0.0767	-		*fib* Bulletin 76 (2015)
t	years	D	0–100	-		
a	mm	N	35	0.20	min. 0	*fib* Bulletin 76 (2015), EN 1992-1-1 (2004)

*PDF = probability density function (B = Beta; D = Deterministic; LN = Log-normal; N = Normal)

Table 3: Definition of input parameters for the updated estimation of $C(a,t)$ over time

Variable	Unit	PDF*	μ	CoV	Limits/Note	Source
Material parameters:						
CEM II/A-S	-	-	-	-	assumed	
w/c (w/b)	-	-	0.45	-	assumed	
C_0	wt.-%/c	D	0.1			EN 206-1 (2000), *fib* Bulletin 76 (2015)
$D_{\text{RCM}}(t_0)$	m^2/s	N	$8{\cdot}10^{-12}$	0.20		Lay & Schießl (2003)
$D_{\text{app}}(t)$	m^2/s	N	$0.65{\cdot}10^{-12}$	0.20		fitting Equation (1)
α	-	B	0.30	0.31	(0; 1)	fitting Equation (2)
Environmental parameters:						
T_{ref}	°C	D	20	-		*fib* Bulletin 76 (2015)
T_{real}	°C	N	10.65	0.79		World Meteorological Organization (2017)
b_e	°C	N	4526.85	0.15		*fib* Bulletin 76 (2015), Gehlen (2000)
Δx	mm	B	10	0.50	(0; 50)	Cl^- profiles
$C_{\text{S},\Delta x}$	wt.-%/c	LN	1.2	0.75		fitting Equation (1)
Other parameters:						
t_0	years	D	0.0767	-		*fib* Bulletin 76 (2015)
t	years	D	46–100	-		
a	mm	N	35	0.15	min. 0	Hilti Ferroscan

*PDF = probability density function (B = Beta; D = Deterministic; LN = Log-normal; N = Normal)

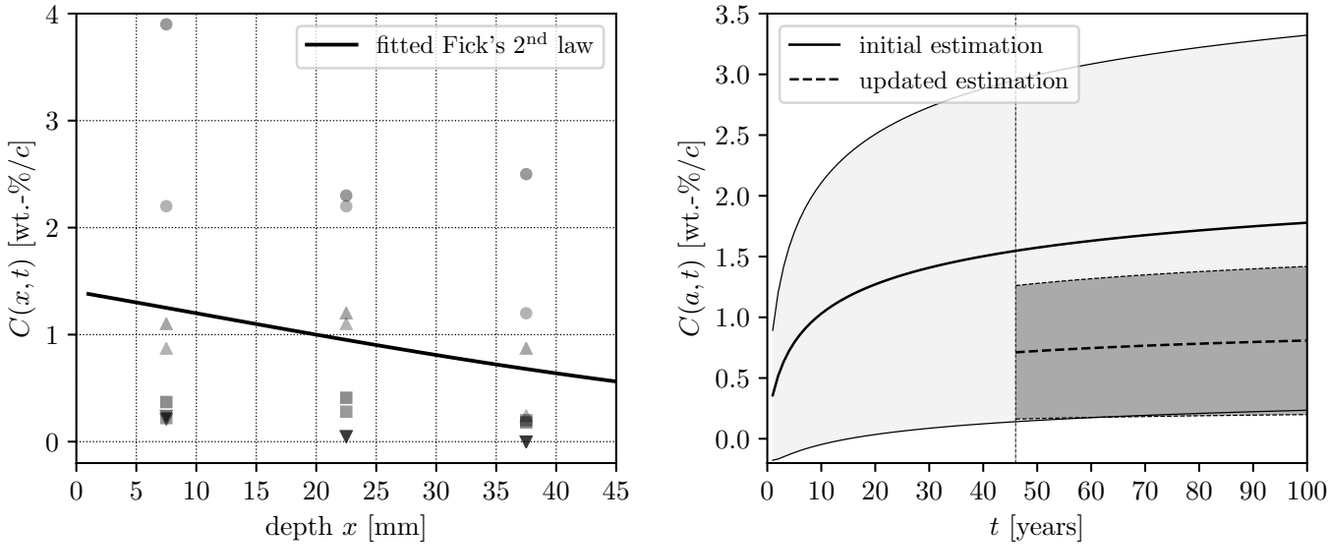


Figure 3: 'Mean' Cl^- profile obtained from Cl^- profiles of analyzed bridge abutments (left); Development of mean value and standard deviation of chloride concentration $C(a,t)$ of analyzed bridge over time t (right)

A fully probabilistic approach was used for estimations of chloride content over time. A thousand random realizations of input basic variables were simulated using the stratified Latin Hypercube Sampling method. The calculations of $C(a,t)$ over time were performed according to Equations (1)–(3) repeatedly for an individual vector of realizations of input random variables and then statistically analyzed to obtain the mean value and the coefficient of variation of $C(a,t)$. The development of mean value and standard deviation of $C(a,t)$ over time t is displayed in Figure 3 (right) using solid lines for initial estimation and dashed lines for estimation with updated values of input parameters.

As obvious from Figure 3 (right), there is a high variability of results when chloride concentration at reinforcement is estimated based on the literature recommendations only. Even information from detailed bridge documentation didn't help in this case since the most important information about concrete composition were missing. Using data from measurements and/or laboratory tests leads to more accurate results, following the current state of the analyzed structure (or its part) and environmental factors.

Using 'mean' chloride concentration obtained from analyzed chloride profiles led to realistic estimation of chloride concenration with much lower variability in results. However, more accurate estimation of chloride concentration can be predicted when the distance of chloride profiles to the road surface is taken into account. Chloride profiles can be classified into two groups based on the location on the abutments and values of $D_{\text{app}}(t)$ and $C_{\text{S},\Delta x}/C_{\text{S},0}$ can be defined based on the best fit of Equation (1) separately for profiles under splash and spray conditions, respectively. Here, results based on the 'mean' profile can be rather underestimated/unsafe for locations in the splash zone (i.e. the distance to the road less than 1.5 m). On the other hand, for locations in the spray zone, results assessed based on the 'mean' profile can lead to uneconomic treatment within the life cycle management of structures in this case.

5 CONCLUSIONS

Different levels for the efficient determination of the input parameters for the modeling of chloride ion ingress into concrete were described. Based on the data availability and the input value precision and accompanying uncertainties, three levels for the quantification of input parameters can be distinguished:

(i) Level 1 – no inspection is carried out and only information about material, load and environment are available. Values of input parameters can be used according to European standards;

(ii) Level 2 – the design documentation is available and/or visual inspection is carried out. From design documentation, specific details on parameters (e.g. cover to reinforcement, cement type, water to cement/binder ratio, permeability, chloride diffusion properties of concrete, environmental conditions, quality of workmanship achieved, etc.) are available in order to define some of the input parameters properly;

(iii) Level 3 – updated or realistic input values are available from on-site measurements and/or supplementary laboratory tests. The most suitable scheme of extension the inspection by monitoring, additional on-site measurements and/or laboratory tests should be suggested during visual inspection.

Regarding realistic estimation of the deterioration level of the structure, the calibration of diffusion parameters for prediction of deterioration due to chloride ion ingress into concrete with the emphasis on model based assessment was the aim of this contribution. Two possible approaches for the calibration of ageing factor based on the diffusion characteristics of concrete were described. Approach B was used in the case of reinforced concrete railway bridge in Austria.

It has been proven, that an improvement is possible if the statistical information regarding behavior gained by the analysis is combined with prior statistical information gained by measurements taken from a real structure at a certain age. For this purpose chloride profiles at the age of 46 years were used to improve the estimation of chloride content over time. Using data from laboratory tests led to more accurate results, following the current state of the analyzed structure and environmental factors. Data collected during visual inspection and results of supplementary laboratory tests (Level 3) provided more detailed information about the chloride concentrations. Based on the chloride profiles, diffusion parameters were updated. The chloride concentration at reinforcement was predicted over time and compared with the one assessed based on input parameter values according to design documentation and code recommendations only (Levels 1 and 2).

ACKNOWLEDGMENT

This work has been supported by research project 'Life-Cycle Assessment for Railway-Structures (LeCIE)', funded by Austrian ÖBB-Infrastruktur Bau AG, project No. LO1408 'AdMaS UP – Advanced Materials, Structures and Technologies', supported by the Ministry of Education, Youth and Sports of the Czech Republic under 'National Sustainability Programme I', and project COST Action TU1406 'Qualitätsspezifikationen für Straßenbrücken, Standardisierung auf europäischer Ebene (BridgeSpec)', supported by the COST (European Cooperation in Science and Technology). This support is gratefully acknowledged.

REFERENCES

Austrian Standards Institute (1963). *ÖNORM B 3310:1963 09 01: Portland cement, portland slag cement and blast furnace cement*. Wien: Austrian Standards Institute. Austrian Standard.

Austrian Standards Institute (2009). *ÖNORM EN 12504-1:2009: Testing concrete in structures – Part 1: Cored specimens – Taking, examining and testing in compression*. Wien: Austrian Standards Institute. European Standard.

Austrian Standards Institute (2012). *ÖNORM EN 12390-1:2012: Testing hardened concrete – Part 1: Shape, dimensions and other requirements for specimens and moulds*. Wien: Austrian Standards Institute. European Standard.

Collepardi, M., A. Marcialis, & R. Turriziani (1972). Penetration of chloride ions into cement pastes and concretes. *Journal of the American Ceramic Society 55*(10), 534–535.

Concrete Institute of Australia (CIA) (2009). *Concrete Durability Series: Z7/07 Performance Tests to Assess Concrete Durability*. Sydney, Australia: Concrete Institute of Australia (CIA).

DARTS (2004). *DARTS – Durable and reliable tunnel structures*. GROWTH 2000 Project GRDI-25633.

European Committee for Standardization (CEN) (2000). *EN 206-1:2010: Concrete – Part 1: Specification, performance, production and conformity*. Brussels: European Committee for Standardization (CEN). European Standard.

European Committee for Standardization (CEN) (2004). *EN 1992-1-1:2004: Eurocode 2: Design of concrete structures – Part 1-1: General rules and rules for buildings*. Brussels: European Committee for Standardization (CEN). European Standard.

European Committee for Standardization (CEN) (2013). *EN 206:2013: Concrete – Specification, performance, production and conformity*. Brussels: European Committee for Standardization (CEN). European Standard.

Gehlen, C. (2000, 06). *Probabilistische Lebensdauerbemessung von Stahlbetonbauwerken – Zuverlässigkeitsbetrachtungen zur wirksamen Vermeidung von Bewehrungskorrosion*.

Hunkeler, F. (2005). Corrosion in reinforced concrete: processes and mechanisms. In H. Böhni (Ed.), *Corrosion in Reinforced Concrete Structures*, Woodhead Publishing Series in Civil and Structural Engineering. Woodhead Publishing.

International Federation for Structural Concrete (*fib*) (2006). *fib Bulletin No. 34: Model Code for Service Life Design*. Lausanne, Switzerland: International Federation for Structural Concrete (*fib*).

International Federation for Structural Concrete (*fib*) (2012). *fib Bulletins Nos. 65 and 66: Model Code 2010 – Final draft, Volume 1 and 2*. Lausanne, Switzerland: International Federation for Structural Concrete (*fib*).

International Federation for Structural Concrete (*fib*) (2015). *fib Bulletin No. 76: Benchmarking of deemed-to-satisfy provisions in standards – Durability of reinforced concrete structures exposed to chlorides*. Lausanne, Switzerland: International Federation for Structural Concrete (*fib*).

International Organization for Standardization (2010). *ISO 13822:2010: Bases for design of structures – Assessment of existing structures*. Geneva, Switzerland: International Organization for Standardization. International Standard.

International Organization for Standardization (2012). *ISO 16204:2012 Durability – Service life design of concrete structures*. Geneva, Switzerland: International Organization for Standardization.

Lay, S. & P. Schießl (2003). *LIFECON DELIVERABLE D 3.2 Service Life Models*. Technische Universität München. EU-Project (5th FP GROWTH) G1RD-CT-2000-00378.

Lollini, F., M. Carsana, M. Gastaldi, E. Redaelli, & L. Bertolini (2015). The challenge of the performance-based approach for the design of reinforced concrete structures in chloride bearing environment. *Construction and Building Materials 79*(Supplement C), 245–254.

Neves, L. A. C., D. M. Frangopol, & A. Petcherdchoo (2006). Probabilistic lifetime-oriented multiobjective optimization of bridge maintenance: Combination of maintenance types. *Journal of Structural Engineering 132*(11), 1821–1834.

Nilsson, L.-O., E. Poulsen, P. Sandberg, H. E. Sørensen, & O. Klinghoffer (1996). *HETEK, Chloride Penetration Into Concrete State-of-the-art: Transport Processes, Corrosion Initiation, Test Methods and Prediction Models*. Danish Road Directorate. Report No. 53.

Nordtest (1999). *NT BUILD 492 Concrete, Mortar and Cement-Based Repair Materials: Chloride Migration Coefficient from Non-Steady State Migration Experiments*. Finland: Nordtest. Nordtest Method.

Page, C., N. Short, & A. E. Tarras (1981). Diffusion of chloride ions in hardened cement pastes. *Cement and Concrete Research 11*(3), 395–406.

Papworth, F. & C. Gehlen (2016). National and international code based deterministic and full probabilistic modelling to describe reliability of various australasian marine structures. In *Performance-based approaches for concrete structures – Proceedings of fib Symposium 2016, Cape Town, South Africa, 1–23 November 2016*.

Pradelle, S., M. Thiery, & V. Baroghel-Bouny (2014). Statistical study of existing chloride ingress models in immersed concretes. In *ConMod2014: Symposium on Concrete Modelling – Proceedings of RILEM International Symposium on Concrete Modelling, 12–14 October 2014, Beijing, China*, pp. 386–397.

Raupach, M. (Ed.) (1992). *Zur chloridinduzierten Makroelementkorrosion von Stahl in Beton*.

Rücker, W., F. Hille, & R. Rohrmann (2006). *F08a Guideline for the Assessment of Existing Structures*. Berlin, Germany: Federal Institute of Materials Research and Testing (BAM), Division VII.2 Buildings and Structures. SAMCO Final Report 2006.

Schneider, J. (1997). *Introduction to Safety and Reliability of Structures*. IABSE.

Strauss, A., R. Wendner, K. Bergmeister, & C. Costa (2013). Numerically and experimentally based reliability assessment of a concrete bridge subjected to chloride-induced deterioration. *Journal of Infrastructure Systems 19*(2), 166–175.

Teplý, B., M. Chromá, D. Voøechovská, & P. Rovnaník (2008). *FReET-D Deterioration Module Program Documentation, Part 1: Theory*. Prague, Czech Republic: Brno/Cervenka Consulting. `http://freet.cz/`.

VÖZ (1985). *Vereinigung der Österreichischen Zementindustrie: Zement und Beton [Cement and Concrete]*. Vienna: Bauberatungsstelle des Vereins der Österreichischen Zementfabrikanten und des Österreichischen Betonvereins.

World Meteorological Organization (2017). `https://public.wmo.int/en`. (accessed September 14, 2017).

Maintenance, Safety, Risk, Management and Life-Cycle Performance of Bridges – Powers, Frangopol, Al-Mahaidi & Caprani (Eds)
© 2018 Taylor & Francis Group, London, ISBN 978-1-138-73045-8

In-service stress and strain behavior of Missouri Bridge A7957

H.H. Alghazali & J.J. Myers
Missouri University of Science and Technology, Rolla, MO, USA

ABSTRACT: In this contest, bridge A7957 was designed and erected on HWY 50, Missouri State, USA, for in situ investigative studies to evaluate strains and stresses over different stages taken into account the effect of prestress losses. The bridge was designed with a concrete mixture of different mechanical and rheological properties. High strength concrete, high strength-self consolidating concrete and normal strength-self consolidating concrete were used to construct bridge girders. The bridge girders were instrumented with vibration wire strain gages to monitor the strains from concrete casting stage to the service life. The measured stresses (from strain readings) were compared to design limitation adopted by ACI 318-14. Based on the analysis of the test results, the measured compressive stresses at mid-span bottom fiber are higher than design compressive stresses for all the beams at release stage. Also, there are no substantial changes in the compressive strain level after 300 days.

1 INTRODUCTION

Monitoring the stresses within a concrete structure is absolutely necessary for sound design, especially when new concrete [self-consolidating concrete (Daczko (2012), ACI Committee 237R (2007))] is used in the construction. In prestressed concrete girders, stress and strain subject to change over a period of time, during which creep and shrinkage of concrete and relaxation of steel develop gradually. In sequence, concrete modulus of elasticity increases also with its age (Shahawy and Arockiasamy (1996)). Due to the progressive increase of concrete strains with time, considerations should be taken during design members with a new type of concrete.

A limited number of full-scale studies have been conducted to monitor the strain and stress time history of prestressed HS-SCC beams. In a recent study by Myers and Block (2010) at Missouri University Science and Technology, two precast prestressed high-strength concrete (HSC) and HS-SCC bridges were instrumented. The researchers found that the HSC bottom fiber compressive strains at release tended to be about 27% higher than predicted, and the bottom fiber HS-SCC compressive strains at release tended to be about 14% higher than predicted. During erection, they reported that the HSC had an average percentage difference of 60% and the HS-SCC 50% between actual and theoretical strain data (Myers and Block (2010)).

In this study, concrete stresses were not measured directly. Stresses were determined by multiplying measured strains by the measured modulus of elasticity. The objective of this study is to evaluate the strains and stresses developed in the girders with emphasis on types of measurements related to design calculations, as well as measurements that have a significant influence on the overall structural behavior of the bridges and their components. Obviously, strain measurements prior to the release of prestressing strands, immediately after the release of prestressing strand, erection, and service were considered as key stages for this study.

2 BRIDGE DESCRIPTION

A three spans bridge (A7957) with PC/PS concrete girders was utilized in this study. The A7957 Bridge on Highway 50 is located in Osage County, Missouri was designed to be simply supported for dead load and continuous for live load via a CIP deck. The two exterior spans are 30.5 m long and one interior is 36.6 m long. The target 28-day compressive strength of HSC and NS-SCC was 55.2 MPa and the specified release strength was 44.8 MPa. However, HS-SCC had 68.95 MPa target 28-day compressive strength and a release compressive strength of 55.2 MPa. The mixture proportions of each type of concrete are presented in Table 1.

Table 1. Concrete mixture proportions.

Material	Quantity		
	HSC	HS-SCC	NS-SCC
Portland Cement – Type I, (kg/m^3)	475	504	445
Water, (kg/m^3)	152	166	155
19 mm Crushed Stone, Coarse Aggregate (kg/m^3)	1056	---	---
12 mm Crushed Stone, Coarse Aggregate (kg/m^3)	---	795	876
River Sand, (kg/m^3)	644	850	850
Air Entraining Agent, (ml/m^3)	309	658	658
Type D Water Reducer and Retard, (ml/m^3)	356	2959	2611
Type F High Range Water Reducer, (ml/m^3)	665	986	986

3 MONITORING SYSTEM AND STRAIN MEASUREMENTS

HSC, HS-SCC, and NS-SCC girders were produced for spans 1, 2, and 3 of the A7957 Bridge, respectively. They were instrumented to obtain data for the measured strain and temperature. Instrumented girders are named as following: S1-G3, S1-G4, S2-G3, S2-G4, S3-G3, and S3-G4. A total of 86 vibrating wire strain gauges with built-in thermistors (type EM-5) were utilized to measure the strain and temperature for the PC/PS girders. The standard pattern in the mid-span consisted of five gauges over the height of the girder and two more in the slab above the girder. The data from the VWSGs were recorded by a data acquisition system (DAS). The DAS used was Campbell Scientific CR800 box which works wirelessly. Measurements were taken at five-minute intervals. The measuring strain was corrected due to the thermal effect.

4 MATERIAL PROPERTIES

Material property tests were performed on specimens collected from the same batch of concrete girders to have adequate predictions for the stresses. All the tests follow standard ASTM guidelines. A summary of the tests, test methods, and results are presented in Table 2.

5 RESULTS AND DISCUSSIONS

The VWSGs embedded in the concrete girder were utilized to measure strains in all the stages below. Strains are monitored with the temperature at the same locations. Strains are relative to baseline strain reading taken right after placement of concrete. Compressive strains are defined negative while tensile strains are defined as positive in this study. Since only compressive strains were observed in this paper, the maximum compressive strains at bottom fiber mid-span were discussed and compared with theoretical values and ACI Code limits.

5.1 *Concrete Strains after Release of Prestress*

The concrete strength is relatively low at this stage and checking the stresses is essential in design. Strain readings were recorded before and after the release of the prestress tendons. The stress values were estimated by multiplying the strain values with the mixture's measured modulus of elasticity and compared to the predicted stress (σ design) values demonstrated in Eq. (1). Figure 1 through Figure 3 illustrate strain data points at mid-span of the HSC, HS-SCC, and NS-SCC beams, respectively. A regression line was fit to the measured release strains for each beam. All HSC, HS-SCC and NS-SCC beams had an R2 range from 0.96 to 0.99. The values are relatively close to 1 indicated that plane section of the beam remained plane. The average curvature caused by prestressing release at mid-span in the HSC, HS-SCC, and NS-SCC beams were 0.53 με/mm, 0.41 με/mm, and 0.52 με/mm, respectively. It is apparent that both HSC and NS-SCC beams exhibited higher curvature than HS-SCC.

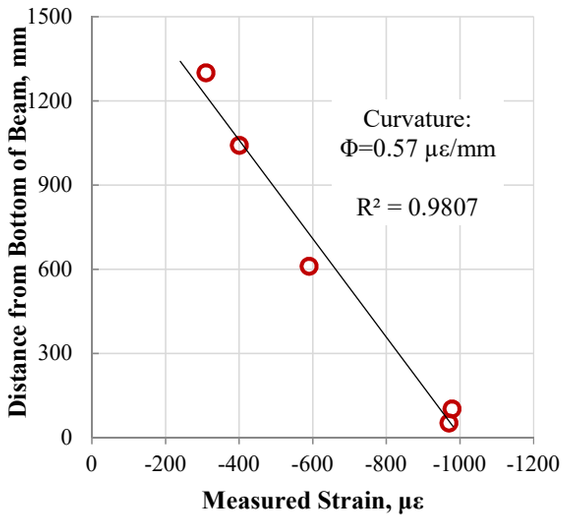
$$\sigma_{design} = -\frac{P}{A} \mp \frac{P.e.y}{I} \pm \frac{M_{self}.y}{I} \quad (1)$$

Where P is prestressing force, A is the cross-sectional area, I is the moment of inertia, e is the eccentricity, y is the distance from bottom or top to the centroid, and M is the moment applied due to self-weight or external load. In addition, ninety percentage of the original load at release was assumed for the prestressing force (Nawy (2009)).

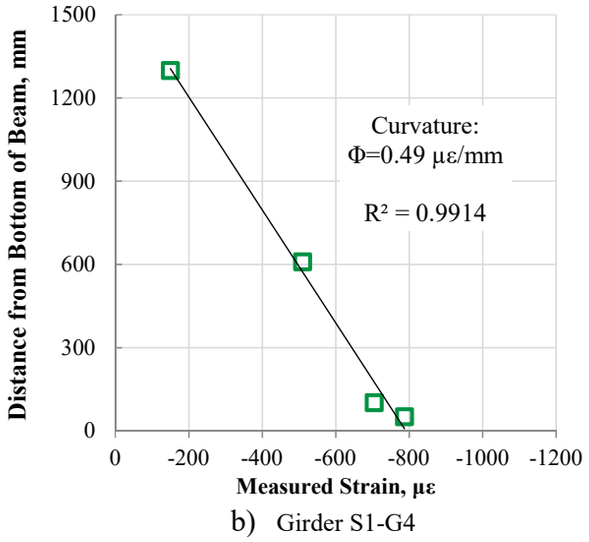
Comparison between measured stresses determined from linear regression with design and allowable stresses limited in ACI code (ACI Committee 318 (2014)) is presented in Figure 5. For all beams, measured compressive stresses at mid-span bottom fiber are higher than design compressive stresses. The differences range between 11-49%. However, when comparing with allowable stresses level, the compressive stresses at mid-span bottom fiber meet requirement for most beams expect beams S1-G3 and S3-G3. The measured compressive stresses for S1-G3 and S3-G3 were 7% and 20% higher than allowable stresses, respectively.

Table 2. Summary of fresh and hardened properties tests and results.

Tests	Member (Span-Girder)					
	S1-G3	S1-G4	S2-G3	S2-G4	S3-G3	S3-G4
Air Content, %	6.9	6.9	7.5	7.6	6	8.3
Slump or Slump Flow, mm	229	229	686	660	673	673
J-ring, mm	n.a.	n.a.	673	635	648	648
Segregation Column, S (%)	n.a.	n.a.	0	0.56	n/a	0
Compressive Strength, MPa	74	67	77	72	69	63
Modulus of Elasticity, GPa	36	35	39	36	36	33
Coefficient of thermal Expansion, με/°C	8.95		9.92		11.3	

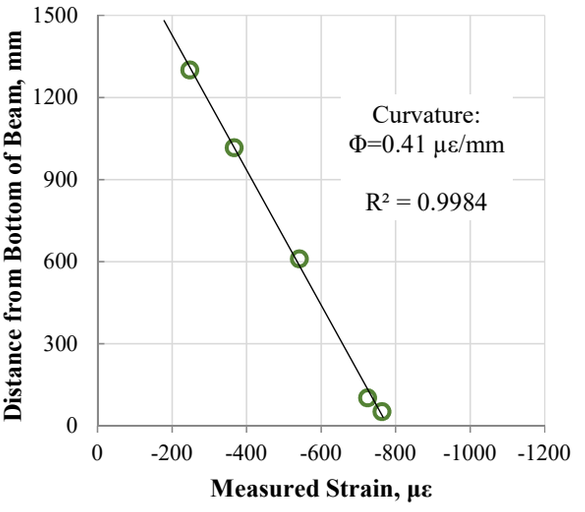


a) Girder S1-G3



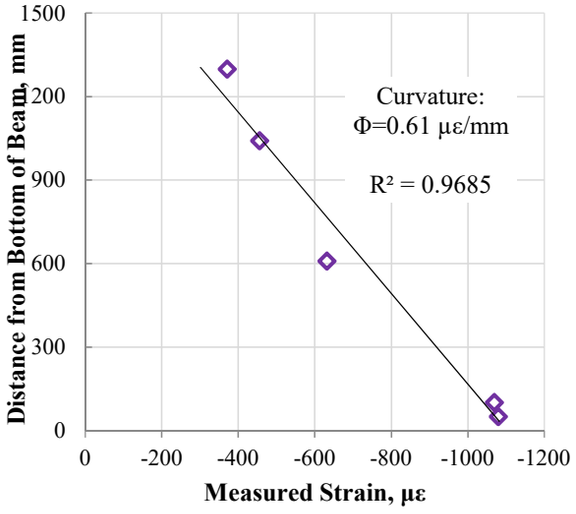
b) Girder S1-G4

Figure 1. Measured strains at mid-span of HSC girders at release.

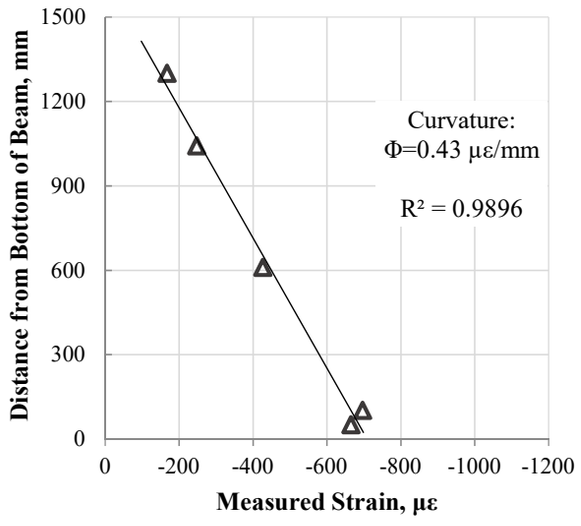


* Initial reading for S2-G3 girder was not recorded

Figure 2. Measured strains at mid-span of HS-SCC (S2-G4) girder at release*.



a) Girder S3-G3



b) Girder S3-G4

Figure 3. Measured strains at mid-span of NS-SCC girders at release.

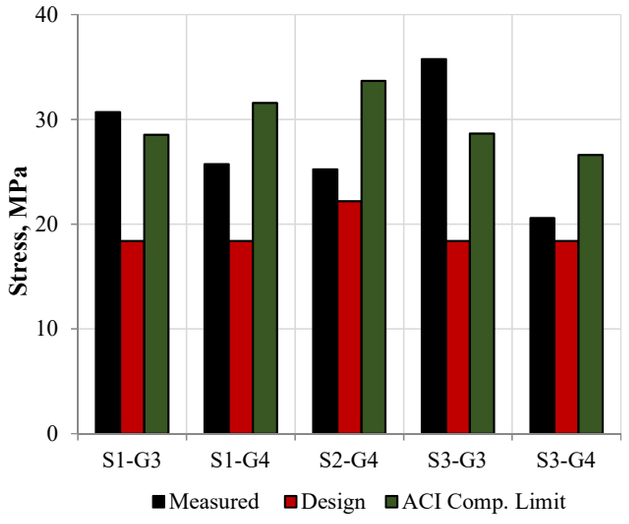


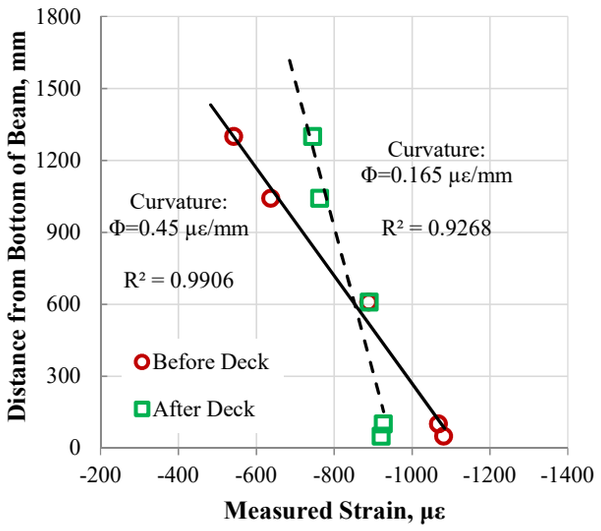
Figure 4. Comparison of stresses at release for bottom fiber mid-span.

5.2 *Concrete Strains before and after Deck Placement*

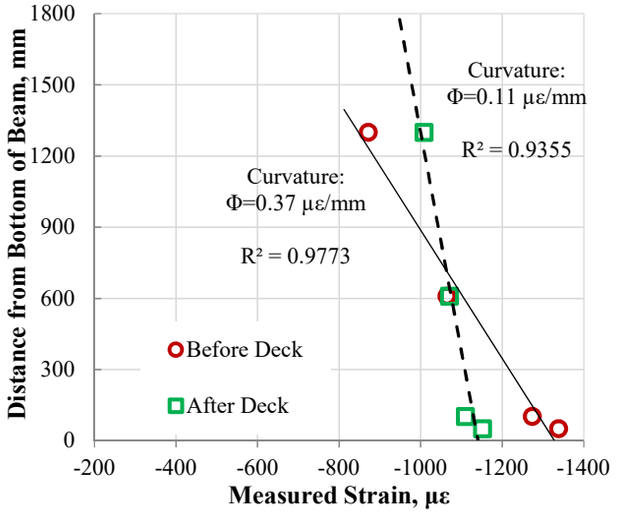
Due to time-dependent effects, prestressed concrete girders continue to deform after strand release (Alghazali and Myers (2015), Alghazali and Myers (2015)). The time-dependent losses included creep, shrinkage, and relaxation losses. Concrete strains were measured before and after deck placement using vibration wire strain gauges and the readings were corrected for thermal effect.

The time-dependent strains behaviors at mid-span section for all monitored girders are shown in Figure 5 through Figure 7. It is clear that from the strain profiles there is a significant decrease in the compressive strains for all girders after deck placement. Also, it can be inferred from strains profiles that HSC experienced more curvature growth than HS-SCC and NS-SCC after release and before deck placement.

The casting of the bridge deck and placement of precast deck panels are applied additional load to prestressed concrete beams (Myers and Yang (2005)). Measuring the stresses in this stage is essential for the design of highway bridges under service loads, which it is generally desired to prevent cracking (Gross (1999)). As shown in Figure 5 through Figure 7, the plane sections remained plane in all beams. HS-SCC beams exhibit significant curvature change than HSC and NS-SCC beams because the HS-SCC beam has a length 20% longer than HSC and NS-SCC beams.



a) Girder S1-G3



b) Girder S1-G4

Figure 5. Strain profiles before and after deck placement HSC girders.

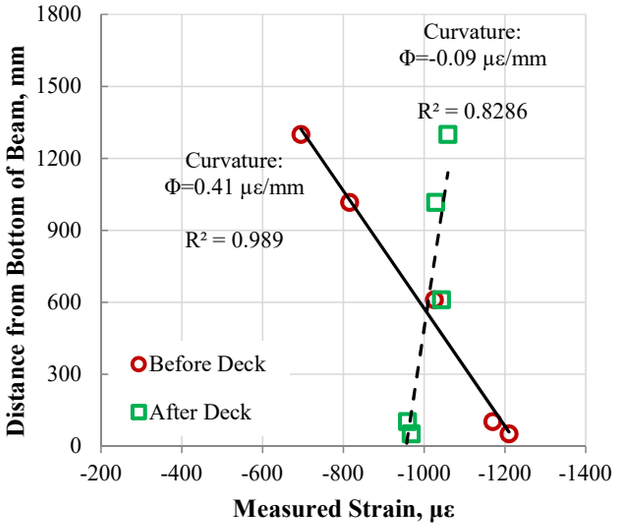
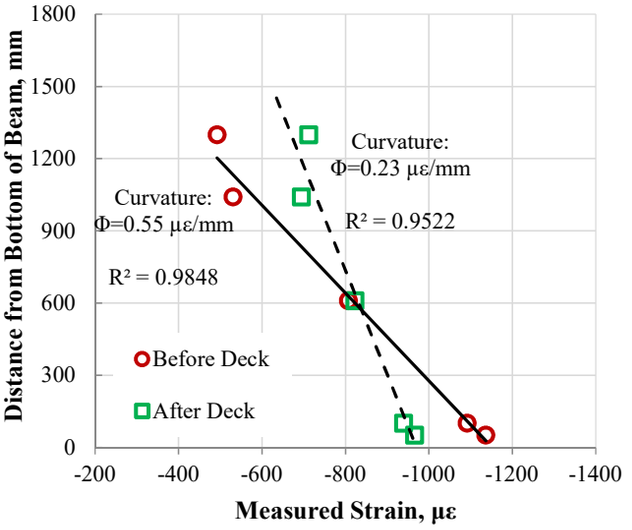
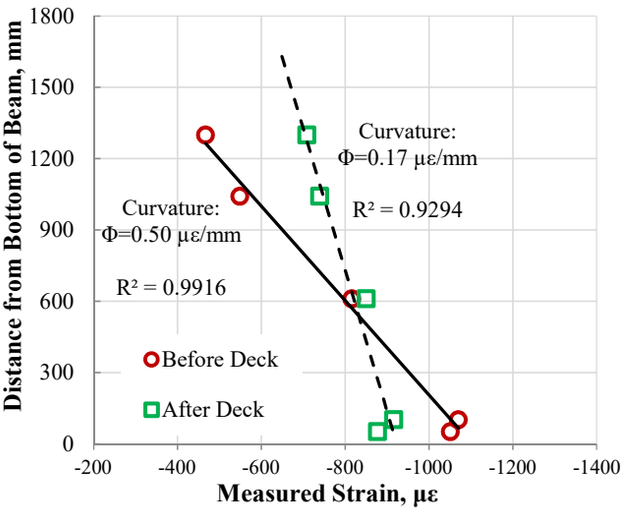


Figure 6. Strain profile before and after deck placement HS-SCC (S2-G4) girder.



a) Girder S3-G3



b) Girder S3-G4

Figure 7. Strain profiles before and after deck placement NS-SCC girders.

5.3 *Concrete Strains during Service*

Concrete strain history of the bridge girders is illustrated in Figure 10. Since monitoring of the bridge is ongoing, two ages were picked up to evaluate the concrete strain in service life (after 300 days and 900 days) to see the effect of long-term losses on strain change. As shown in Figure 8, there is an increase in compressive strain for all beams due to the creep effect. HSC and NS-SCC beams exhibited higher strains increase than HS-SCC. The stress increase for all beams ranges between 10 to 25%. Obviously, there are no substantial changes in the strain levels after 300 days.

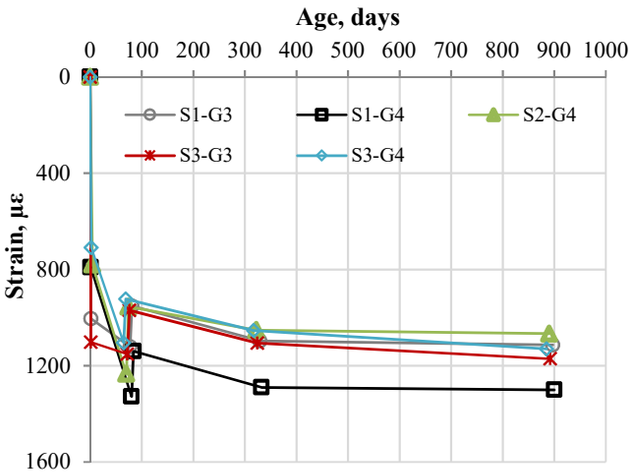


Figure 8. Strains versus time in the concrete in prestressed concrete girders.

6 CONCLUSION

This full-scale study was conducted to monitor strain behavior of prestressed concrete beams constructed with different concrete type. Based on this research, the following conclusions can be drawn:

1. Monitoring system is successfully recording the strains and temperatures in the girders of bridge A7957;
2. Measured strains due to release were fitted linearly. The R^2 values range from 0.96 to 0.99, which exhibits plane sections prior to the release of prestressing remain plane after release;
3. At release, measured compressive stresses at mid-span bottom fiber are higher than design compressive stresses for all the beams. The differences range between 11-49%;
4. HSC beams experienced more curvature growth than HS-SCC and NS-SCC beams after release and before deck placement;
5. In general, there are no substantial changes in the strain levels after 300 days.

7 ACKNOWLEDGEMENT

The writer would like to acknowledge the financial support provided by Missouri Department of Transportation (MoDOT) and the National University Transportation Center (NUTC) at the Missouri University of Science and Technology (Missouri S&T). The support received from the Department of Civil, Architectural, and Environmental Engineering and the Center for Infrastructure Engineering Studies at Missouri S&T are also highly appreciated.

8 REFERENCES

ACI Committee 237R-07, *Self-Consolidating Concrete*. American Concrete Institute, Detroit, Michigan, 2007.

ACI Committee 318, 2014, *Building Code Requirements for Structural Concrete*, American Concrete Institute; Detroit, Michigan.

ACI Committee 363, 2010, *State of the Art Report on High Strength Concrete*, American Concrete Institute, Farmington Hills, Michigan.

Alghazali H.H. and Myers J.J. 2015, *High Strength Self-Consolidating Concrete Prestress Losses of* Bridge A7957, MO, USA Compared to Code Models, Proceedings of Fifteen ConMat'15Conference, Vancouver, BC Canada, 2015.

Alghazali H.H. and Myers J.J., 2015, *Creep and Shrinkage of Ecological Self-Consolidating Concrete*, Proceedings of Fifth PLSE2015 Conference, Brisbane, Australia.

Daczko J.A, 2012, *Self -Consolidation Concrete, Appling What We Know*, *1st Edition*, Spon Press, Abingdon, Oxon.

Gross, S.P., 1999, *Field performance of prestressed high performance concrete highway bridges in Texas,* University of Texas at Austin, Ph.D. Dissertation.

Myers, J.J. and Bloch, K.E., 2012, Innovative concrete bridging systems for pedestrian bridges: implementation and monitoring. *Missouri University of Science and Technology, National University Transportation Center (NUTC) Report R250*.

Myers, J.J. and Yang, Y., 2005, High performance concrete for bridge A6130-Route 412 Pemiscot County, MO, *UTC R39*.

Nawy, E.G., 2009 *Prestressed Concrete: A Fundamental Approach Fifth Edition*, Upper Saddle River, New Jersey.

Shahawy, MA and Arockiasamy M. 1996, Analytical and Measured Strains in Sunshine Skyway Bridge. II, *Journal of bridge engineering*, pp. 87-97.

GENERAL SESSIONS

Maintenance, Safety, Risk, Management and Life-Cycle Performance of Bridges – Powers, Frangopol, Al-Mahaidi & Caprani (Eds)
© 2018 Taylor & Francis Group, London, ISBN 978-1-138-73045-8

Numerical assessment of the load-carrying capacity of a masonry bridge

R. Silva
CONSTRUCT-LESE, Faculty of Engineering (FEUP), University of Porto, 4200-465 Porto, Portugal

C. Costa
Engineering Department, Polytechnic Institute of Tomar, 2300-313 Tomar, Portugal
CONSTRUCT-LESE, Faculty of Engineering (FEUP), University of Porto, 4200-465 Porto, Portugal

A. Arêde
CONSTRUCT-LESE, Faculty of Engineering (FEUP), University of Porto, 4200-465 Porto, Portugal

ABSTRACT: This paper focuses on the numerical assessment of the load-carrying capacity of a stone arch railway bridge. The nonlinear analysis is based on 3D finite element models of the bridge under incremental static loading representing the railway traffic with appropriate configurations on the bridge deck. The numerical model of the constitutive material behaviour is defined based on the results of an experimental campaign covering material testing for characterization of masonry and infill components of this type of bridges.

1 INTRODUCTION

Numerical modelling strategies to evaluate the structural response of stone arch bridges with realistic service and limit loading conditions, settlements, material and structural composition can provide better understanding of the structural behaviour and contribute to help on implementing suitable management plans for this type of bridges.

The simulation of the structural behaviour of masonry bridges can usually be achieved by means of computational resources based on the Finite Element Method (FEM). These modelling technique allow evaluating the load capacity of stone arch bridges by incrementing the traffic loads included in the structural modelling and taking into account the nonlinear behaviour of bridge materials and suitable conditions for the geometrical discretization. Computational methods resorting to the Distinct Element Method (DEM) and the rigid blocks and limit analysis are also frequent for simulating the load-carrying capacity of stone masonry arch bridges.

The interaction between the structural elements of the bridge and its material behaviour is the main aspect to be represented by structural modelling. Therefore, suitable constitutive models of the bridge materials defined and supported by experimental results is as crucial contribution for the validation of the structural numerical models.

The FE modelling strategies representing the mechanical behaviour of the masonry components can be based on detailed strategies, also called simplified micro-models and continuous homogeneous models. In the first type of models, the blocks are modelled as homogeneous sub-regions using conventional solid elements and the contacts between blocks are simulated by interface elements. Usually, the nonlinearity of masonry mechanical behaviour is concentrated in the joint elements and the material of the blocks is considered with linear elastic behaviour. For highly-refined finite element meshes these micro-models allow detailed analyses with particular interest in zones where the stress field is strongly heterogeneous. Regarding the continuous models, an equivalent continuum is defined with characteristics that allow the description of the global behaviour of masonry as a composite material. In general, the material behaviour is considered isotropic; however modelling strategies including the anisotropy can also be found in the literature. The constitutive laws are established in terms of stresses and strains, and there are several different ways to formulate the problem such as the plastic models or damage models. These modelling strategies are particularly suitable for coarser finite element mesh allowing global analyses of the whole structure (or of a part of it). Continuous homogeneous models can also be used to represent the infill material. In this case, the FE mesh is composed of solid elements supporting a continuous model representative of the infill.

2 BRIDGE MODEL

2.1 *Brief description of the bridge*

The Côa bridge dates back to the late 1940s and has a structural system made of granite masonry arches as shown in Figure 1. The bridge is located in Beira Alta line which constitutes a rail link between the Portuguese main railway track (Norte line) near Coimbra and the border with Spain in Vilar

Formoso. The bridge consists of eight arches, one with 38 m span and seven with 20 m, which are supported onto seven piers and two abutments. The total length of the deck is about 238 m with a longitudinal rectilinear profile and 4.8 m width which supports one single-track. The maximum gap between the bridge ground level and the railroad is approximately 56 m high.



(a) (b)

Figure 1. Côa railway bridge: (a) general view and (b) freight traffic.

2.2 *FE bridge model*

The numerical model of the bridge, illustrated in Figure 2, consists of a 3D finite element discretization developed in ANSYS software, based in a previous work published in Jorge *et al.* (2016). This model was calibrated based on the identification of the bridge modal characteristics from measurements obtained in ambient vibration test complemented with sensitivity analyses and an optimization process, also referred to in a companion paper submitted to this conference by the authors.

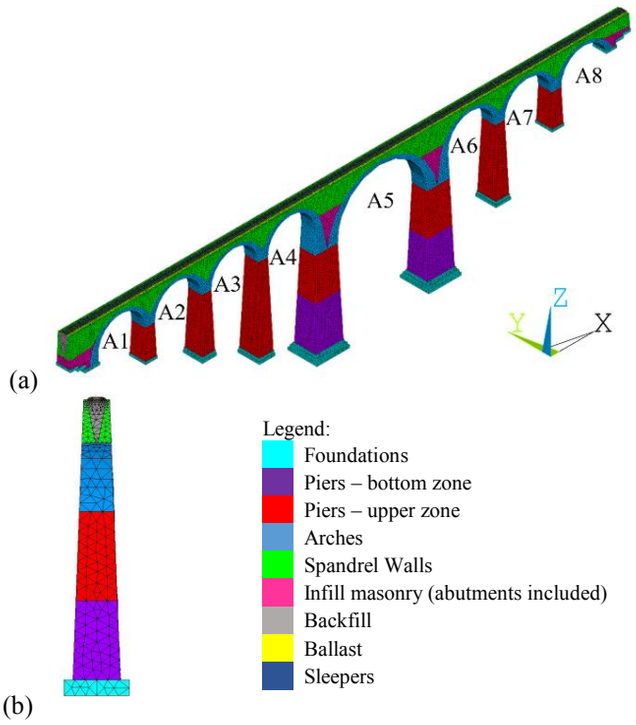


Figure 2. FE model of Côa Bridge: (a) perspective view and (b) cross section.

The bridge structural elements are modelled using tetrahedral finite elements with ten nodes and three degrees of freedom at each node (Solid 92) available in ANSYS elements' library. The rails are modelled by beam finite elements. In total the model has 442175 elements.

The initial boundary conditions were set using rigid supports to fix the displacement x, y and z of the mesh nodes located at the base of the foundations and embankments.

The masonry elements were modelled using a homogeneous composite material with equivalent mechanical properties so as to reproduce the properties of the assembly formed by stone blocks and mortar. The materials' nonlinear behaviour was simulated using the Drucker-Prager model implemented in ANSYS software. The mechanical properties were defined to represent a hypothetical scenario, where the bridge materials have some level of degradation as detailed later in Section 3.

2.3 *Load modelling*

The bridge structural response was evaluated under the influence of its self-weight and incremental static loading representing a standard train distributed along the bridge deck.

The static loading scheme used in the bridge analysis is represented by the load model LM71 proposed by UIC to simulate the envelope of several types of trains. The load configuration of the LM71 model is also used as a design load for railway bridges according to Eurocodes (EN1991-2, 2003) with the characteristic values shown in Figure 3 for bridges in rail tracks with normal traffic.

In railway lines with heavier or lighter traffic than the normal one, the characteristic values of LM71 loads are multiplied by a factor α. When multiplied by this factor, the loads are also called "classified vertical loads". The factor α ranges between 0.75 and 0.91 for rail tracks with lighter traffic and between 1.10 and 1.46 for the case of heavier rail traffic. In the analysis of Côa bridge the factor α was considered equal to 1.46, to account for its location in an international line (Beira Alta line) with heavy traffic of freight trains.

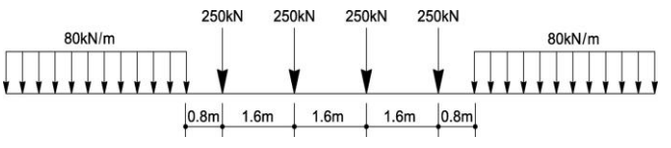


Figure 3. Load model of LM71 (EN1991-2, 2003).

The vehicle load position (see Figure 4) was defined from the most unfavourable position for the principal arch (A5) identified in a previous work from the analysis of the bridge under moving loads (Jorge *et al.*, 2016). For maximizing the defor-

mations in the principal arch, the uniform load of the LM71 model was not considered.

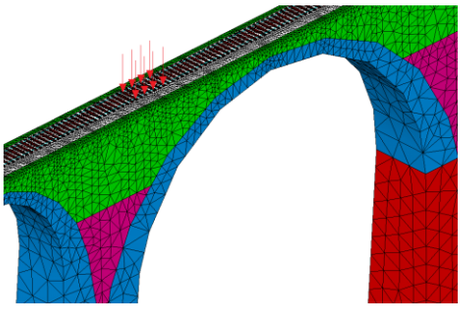


Figure 4. LM71 point loads applied in the zone of arch A5.

The static response of the bridge was therefore evaluated with the numerical model presented previously considering incremental levels of intensity of the vehicle load placed on the rail beam element near the ¼ span of the principal arch. The loading history includes an initial phase of equilibrium of the dead load which was applied incrementally. After the first phase, the vehicle loading was applied considering incremental levels of intensity.

3 HOMOGENIZED MATERIAL PARAMETERS

The assessment of the load-carrying capacity resorting to FE global models requires the definition of material models which should be able to represent adequately the material behaviour in the plastic domain. For that purpose a detailed characterization of the bridge materials by performing suitable material testing is a valuable mean to achieve this goal.

Since no experimental testing was performed for mechanical characterization of the Côa bridge materials, it was defined a hypothetical scenario for material modelling based on the parameters of another masonry bridge, the PK124 bridge, where a detailed experimental campaign was performed for material characterization. The details of this campaign and the obtained results can be found in another paper published by the same authors (Arêde *et al.*, 2017). Although this hypothetic scenario set up a more severe condition of material degradation, it also can be compared with the real one.

3.1 *Experimental characterization of materials*

The PK124 railway bridge illustrated in Figure 5a, is a culvert type bridge constructed in 1879, located in Minho line of the Portuguese railways. It is a short masonry bridge, consisting in only one single arch with 11 m length. PK124 bridge is 60 years older than Côa bridge, and its masonry is in a different weathered condition than Côa bridge, with a more deteriorated masonry.

The experimental campaign carried out in PK124 bridge involved laboratory tests for mechanical characterization of the stone and masonry joints. The i*n situ* material characterization comprised core extraction of masonry and stone samples from the bridge, two Ménard Pressuremeter Tests (PMT) in the infill material and double flat-jack tests in the masonry component. The *in situ* masonry stress and deformability properties were estimated from single and double flat-jack tests, respectively. These tests were performed in the masonry of the abutment zone (see Figure 5b).



(a) (b)

Figure 5. PK124 railway bridge: (a) general view of the bridge intrados, (b) pressiometer and (c) flat-jack *in situ* tests.

The infill material found in PK124 bridge is more similar to rock than soil, consisting of a mixture of mortar with variable size granite pieces. Therefore, the pressuremeter tests performed in the bridge never reached pressures capable of yielding that material, resting well below the threshold values for plastic deformation (Arêde *et al.*, 2017). However, based on the result curves obtained in these tests, it was possible to obtain deformability parameters, the pressuremeter deformation modulus (G_{PMT}) and the pressuremeter modulus (E_{PMT}). These values were useful for estimating the infill deformability modulus (E) for use in numerical simulations.

The lab tests allowed the physical and mechanical characterisation of the granite stone collected from the bridge and the characterisation of the joints behaviour, by the definition of strength and deformability parameters obtained from shear and compressive tests. Data collected from these tests was used to define the properties used for the Côa bridge analysis.

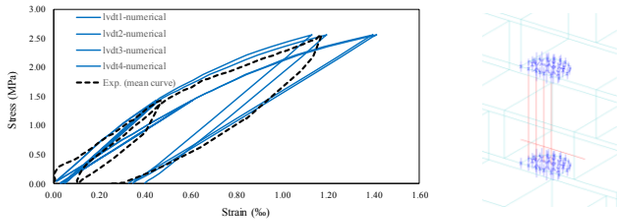
3.2 *Homogeneous material proprieties*

3.2.1 *Methodology*

Aiming at calibrating and validating the material parameters to be adopted in the bridge nonlinear model, a methodology resorting to the simulation of the double flat-jack tests was developed based on previous work (Costa *et al.*, 2017). With the same objective, the simulation of pressuremeter tests was also performed.

For this purpose, a nonlinear model of the double flat-jack test was defined using modelling strategies similar to those used in the bridge model (see test scheme in Figure 6b), therefore resorting to 3D FE

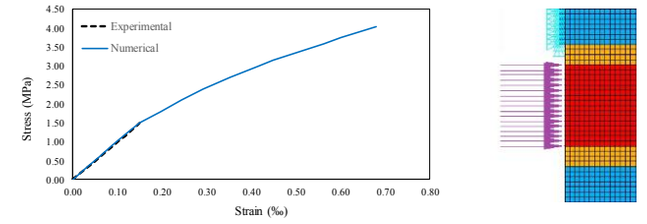
global models using the Drucker-Prager model to represent the constitutive behaviour of masonry. The material parameters assigned for the flat-jack model were then adjusted to obtain good agreement between the experimental parameters recorded with the flat-jack test and the corresponding parameters obtained by numerical simulation. Figure 6a shows a plot of the response obtained in the flat-jack tests in terms of the evolution of LVDTs deformation with the pressure applied by the flat-jacks, allowing to verity a good agreement between experimental and numerical results.



(a) (b)

Figure 6. Stress *vs.* strain of flat-jack tests: (a) numerical results in blue and experimental results in black, (b) test scheme.

The numerical modelling of the pressuremeter tests were based on a 2D axisymmetric FE model, also using the Ducker-Prager model for defining the material constitutive behaviour (see Figure 7b). The results shown in Figure 7a in terms of the evolution of the deformation with the pressure applied in the measurement zone, allow to compare the numerical and experimental results in the pseudo-elastic phase of the test (Arêde *et al.*, 2017) where good agreement is found.



(a) (b)

Figure 7. Stress *vs.* strain of pressuremeter tests: (a) numerical results in blue and experimental results in black, (b) test scheme.

3.2.2 *Material proprieties*

As a result of the strategy described in previous paragraphs, the elastic material properties of masonry in the bridge zones of foundations, piers, arches and spandrel walls are characterized by the elastic modulus, Poisson's ratio and unit weight listed in Table 1. The elastic characteristics of the infill material in the backfill zones estimated by the pressuremeter tests are also summarized also in Table 1.

Table 1. Elastic parameters of masonry and infill materials.

Parameter	Material	Adopted value	Unit
Elastic modulus	Masonry	2.0	GPa
	Infill	0.32	GPa
Poisson's ratio	Masonry and infill	0.2	-
Unit weight	Masonry	24.5	kN/m^3
	Infill	21.5	kN/m^3

For nonlinear behaviour of masonry, in the arches, spandrel walls and piers and in the infill material, in the backfill zones, the Drucker-Prager model was defined considering elastic-plastic behaviour with no dilatancy and the values of the friction angle and cohesion summarized in Table 2. Which definition consisted in the experimental characterization referred in section 3.1, and supported in numerical simulations of the flat-jack and the pressuremeter tests referred in section 3.2.1.

Table 2. Drucker-Prager parameters for masonry and infill.

Parameter	Material	Adopted value	Unit
Cohesion	Masonry	450	kPa
	Infill	900	kPa
Friction Angle	Masonry	35.5	º
	Infill	35.5	º

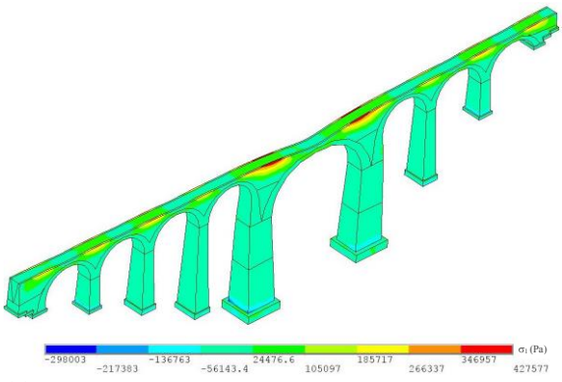
4 ANALYSIS OF THE BRIDGE RESPONSE

This section focuses in the bridge response considering the nonlinear behaviour of the bridge and intensity load levels (multipliers) of a nominal train load. The evolution of the structural response of the FE model concerning the effect of the dead load and the vehicle load are presented and discussed for six levels of incremental intensity of the vehicle load, ranging from 0 to 14, the latter being the maximum multiplier that was possible to be applied.

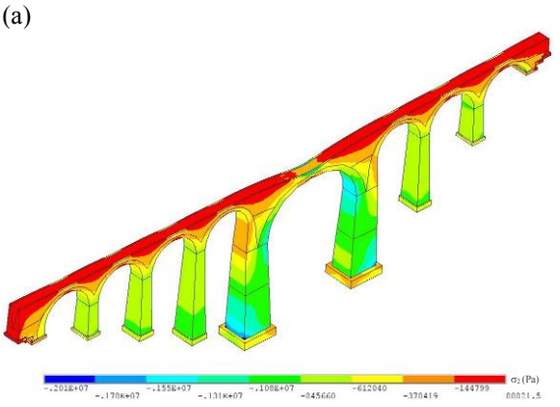
The numerical simulation is performed considering the action of the incremental static loading simulating the LM71 model. For this purpose, eight point loads with 182 kN each, representing four vertical axels spaced of 1.6 m, are considered as described in section 2.3.

4.1 *Results of service loading. DL+1P*

The response parameters of the numerical model is shown in Figure 8 in terms of the results of the maximum principal stresses (mainly tensile) and minimum principal stresses (mainly compressive) for the load level of the bridge weight and the vehicle with intensity of 1P, where P represents the nominal vehicle load. The results reflect the level of stress under service loads (reference loading). The maximum tensile stress occurs in the spandrel wall with a value of 0.43 MPa and the maximum compressive stress occurs in the base of the central pier with 2 MPa.



(a)



(b)

Figure 8. Stress level in the bridge deformed configuration under service conditions (DL+1P): (a) maximum principal stresses and (b) minimum principal stresses.

The results shown in Table 3 summarize the bridge numerical response for the dead load and for 1P intensity level of the vehicle loading, in terms of the vertical displacement registered in the principal arch, and the maximum and minimum principal stress found in the arch and in the spandrel walls.

Table 3. Response parameters in the arch and spandrel walls: displacements and principal stresses.

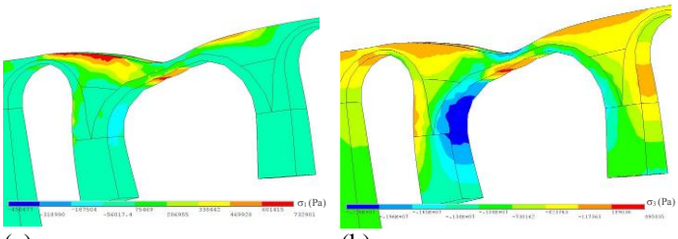
Intensity level	Element	dv mm	σ_1^+ MPa	σ_3^- MPa
DL	Spandrel	-	0.40	-1.38
	Arch	44.06	0.36	-1.41
DL+1P	Spandrel	-	0.43	-1.43
	Arch	45.60	0.36	-1.50

For this load level it was verified that the bridge response is still in the elastic domain (no plastic deformation was achieved in this step of analysis), with additional maximum displacements of 1.5 mm in the crown zone of the principal arch. Also, the intensity of the live load is small, so the additional stresses induced in the arch and spandrel walls are very low.

4.2 *Results of plastic evolution and maximum loading. DL+14P*

The structural response of the bridge model for the load level of the bridge weight and the vehicle with intensity of 14P (the maximum force applied) is shown in Figure 9. The results show the deformed configuration and the level of stress, in terms of maximum principal stresses and minimum principal stresses, for this step of loading, zooming the bridge area of the main arch, where the load is applied.

Table 4 summarizes the corresponding response values of the bridge model when the maximum intensity level was applied, 14P. Aiming for comparison, the results of intensity levels 5P and 10P are also included in Table 4.



(a) (b)

Figure 9. Stress level in the bridge deformed configuration for the final loading step (DL+14P): (a) maximum principal stresses and (b) minimum principal stresses.

The maximum displacement in the crown of the arch is around 80 mm. Both maximum and minimum principal stresses occur in the arch with values of 0.73 MPa and -2.26 MPa, respectively. For this intensity load level the response of masonry of the arch and the spandrel walls exhibit nonlinearity, as detailed in following paragraphs by the analysis of the plastic strain evolution.

Table 4. Response parameters in the arch and spandrel walls: displacements and principal stresses.

Level of intensity	Element	dv mm	σ_1^+ MPa	σ_3^- MPa
DL+5P	Spandrel	-	0.61	-1.65
	Arch	53.83	0.42	-1.84
DL+10P	Spandrel	-	0.61	-1.91
	Arch	65.34	0.59	-2.14
DL+14P	Spandrel	-	0.62	-1.95
	Arch	79.81	0.73	-2.26

Figure 10 and Figure 11 show the state of plasticity in terms of its principal components in the bridge central zone of the main arch. The figures allow observing the plasticity evolution for the intensity levels of 5P, 10P, 12P and 14P.

Table 5 summarizes the corresponding values for the plastic strains in maximum and minimum principal directions obtained for the same five different intensity levels considered in the bridge analysis.

The results allowed to verify that the plasticity in the main arch starts around the intensity level of load of 5P; and for the maximum applied force, DL+14P, the maximum principal plastic strain (0.694‰) is located in the extrados of arch, near the crown under the loading zone, and the minimum principal plastic

strain (-0.548‰) is in the base of the arch, also in the extrados.

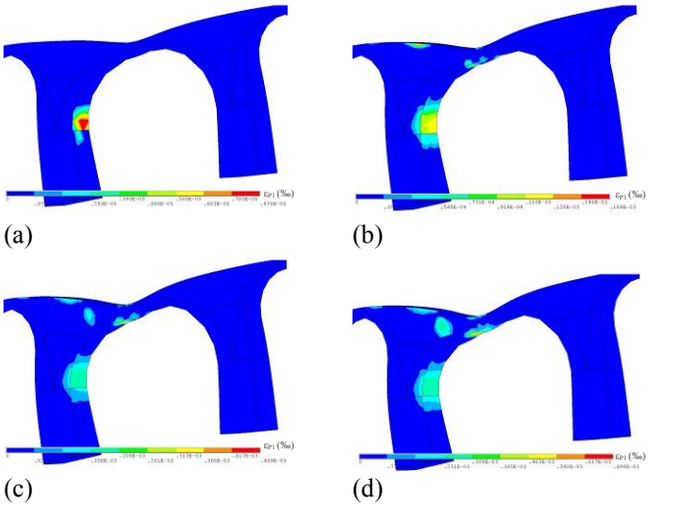


Figure 10. Principal maximum plastic strains in the bridge deformed configuration for intensity load levels of (a) 5P, (b) 10P, (c) 12P and (d) 14P.

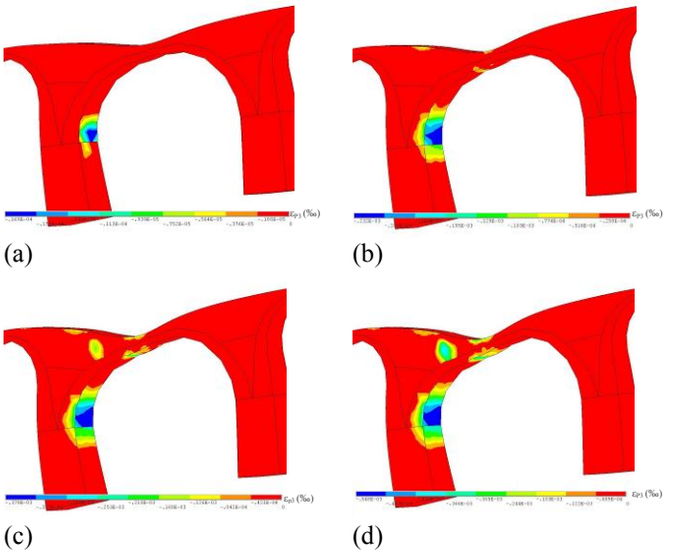


Figure 11. Principal minimum plastic strains in the bridge deformed configuration for intensity load levels of (a) 5P, (b) 10P, (c) 12P and (d) 14P.

For this final intensity level it is possible to identify the formation of two hinges in the arch (near the crown and in the arch springing) in the zones of the maximum (positive) and minimum (negative) plastic strains. Although the ultimate bridge response does not present a conventional arch hinge mechanism, it is also noted that in the spandrel walls, near the loading zone (both in vertical faces and in the horizontal top), the plastic strains reach high values the in compressive and tensile domains (-0.445‰ and 0.374‰), as well as the principal stresses as shown in Figure 9 (and in Table 4), thus evidencing its influence in the bridge strength mechanisms.

Table 5. Principal plastic strains for the arch A5 and spandrel wall.

Level of intensity	Element	dv	ε_{p1}^{+}	ε_{p3}^{-}
		mm	‰	‰
DL+1P	Spandrel	-	0.000	0.000
	Arch	45.60	0.000	0.000
DL+5P	Spandrel	-	0.003	-0.002
	Arch	52.83	0.008	-0.017
DL+10P	Spandrel	-	0.164	-0.123
	Arch	65.34	0.142	-0.232
DL+12P	Spandrel	-	0.248	-0.248
	Arch	72.40	0.469	-0.379
DL+14P	Spandrel	-	0.374	-0.445
	Arch	79.81	0.694	-0.548

In fact, the results of the plastic deformation in y-direction (transverse direction of the bridge), shown in Figure 12a, also allow to verify that the spandrel walls are influenced by transversal movements, with both spandrel walls in opposite directions, and the corresponding plastic deformation (ε_{py}), near the loading zone, also in opposite direction. This evidence allows pointing out that the plasticity occurs also due to the transmission of the horizontal impulses associated to the bridge behaviour in the transverse direction.

In z-direction the plastic deformation (ε_{pz}) shown in Figure 12b has the maximum values in the arch springing (base).

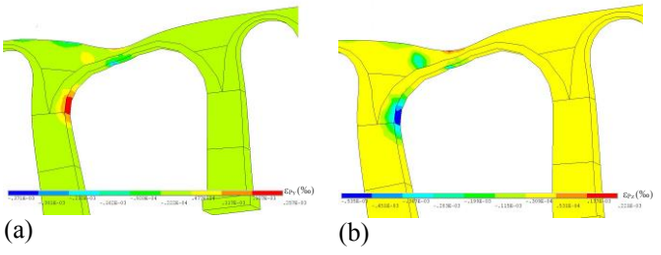


Figure 12. Plastic strains with deformed shape for the dead load and maximum load applied (DL+14P): (a) y direction, (b) z direction.

4.3 *Discussion*

The analysis of the bridge response allowed to recognize two vulnerable zones influenced by both basic failure modes of stone arch bridges: the hinges mechanism in the arch and out of plan of the spandrels.

For the maximum applied force it is possible to identify the formation of two plastic hinges in the principal arch and plastic deformation in the spandrel wall. No plastic deformation was found in the backfill zones. The values for the displacements reached in the crown of the principal arch are relatively high, approximately 80 mm (1/475 of the span arch).

Although the bridge response does not represent a conventional hinges mechanism for the maximum

applied force it was possible to evaluate the bridge response with reasonably high values of the multipliers, as expected for this type of bridge.

The study also points out specific difficulties when computing the bridge numerical response for intensity levels higher than 14, due to excessive deformation of the finite elements in the arch. Looking in detail the mesh in the arch it is possible to see that in some parts there exist only one element in height, which is very low given the large plastic deformations verified for such intensity levels of load applied. Therefore, it is deemed quite important to have several elements in height in the arch crown. For solving this problem one solution is to reshape the numerical model in order to have a denser mesh in the arch and spandrel in the bridge central zone where the load is applied.

5 CONCLUSIONS

This work provides a hypothetical scenario of a more severe condition of material deterioration to a bridge in a good state of conservation, and its assessment of the load-carrying capacity based on a 3D FEM numerical model. This preliminary work is based on the assumption of a damaged material scenario for the Côa bridge, using material properties of another bridge (older and in a more deteriorated state of conservation), where experimental characterization of the materials was performed.

The adopted modelling strategies provided means for comparing the numerical responses of the bridge under dead-load and incremental vertical forces to represent the static loading of a standard vehicle. This procedure allowed to simulate the formation of plastic hinges in the principal arch of the bridge and to identify the corresponding vehicle vertical loading.

Additional work, to refine the model to have a denser mesh in the arch and spandrel in the principal arch, will be required for a better representation of the arch bridge behaviour.

Also, sensitivity analyses for the material parameters adopted could be done in order to study different levels of damage in the masonry of the bridge.

ACKNOWLEDGEMENTS

Part of this work reports to research financially supported by Project POCI-01-0145-FEDER-007457—CONSTRUCT—Institute of R&D in Structures and Construction, funded by FEDER funds through COMPETE2020—Programa Operacional Competitividade e Internacionalização (POCI) and by national funds through Fundação para a Ciência e a Tecnologia (FCT). It also includes research supported by the FCT project PTDC/ECM-EST_1691/2012 – Experimental and Numerical Characterization of Structural Behaviour of Stone Masonry Arch Bridges under Railway Traffic Loading, Application to Existing Portuguese Bridges. The authors thank Rui Calçada, Diogo Ribeiro and Pedro Jorge from FEUP, for collaboration in the bridge model.

REFERENCES

ANSYS, I. ANSYS® Academic Research, Release 18.1, Help System.

Arêde, A., Costa, C., Gomes, A. T., Menezes, J.E., Silva, R., Morais, M., Gonçalves, R. 2017. Experimental characterization of the mechanical behaviour of components and materials of stone masonry railway bridges, in *Construction and Building Materials*, Vol. 153, Pages 663-681. doi:10.1016/j.conbuildmat.2017.07.069

Costa, C., Arêde, A., Morais, M., Costa, A. 2015 Detailed FE and DE modelling of stone masonry arch bridges for the assessment of load carrying capacity, Procedia Engineering, 114, p.854-861. doi: 10.1016/j.proeng.2015.08.039

Costa, C., Ribeiro, D., Jorge, P., Silva, R., Calçada, R., Arêde, A. 2015. Calibration of the numerical model of a short-span masonry railway bridge based on experimental modal parameters, Procedia Engineering, 114, p.846-853. doi: 10.1016/j.proeng.2015.08.038

Costa, C., Silva, R., Arêde, A. 2017. Mechanical Characteristics of Stone Masonry Bridges: Experimental Evaluation and Numerical Simulations, in 3rd International Conference on Protection of Historical Constructions, Lisbon, Portugal.

EN 1991-2 2013. Eurocode 1 Part 2: Traffic loads on bridges, Brussels, Belgium, European Committee for Standardization (CEN).

Jorge, P., Ribeiro, D., Costa, C., Arêde, A., Calçada, R. 2016. Train-bridge dynamic interaction on a stone masonry railway bridge in, 8º International Conference on Bridge Maintenance, Safety and Management, IABMAS 17, Foz Iguaçu, Brazil.

LimitState 2007. Ring 2.0. Theory & Modelling Guide. Sheffield, UK. (Available at: http://www.limitstate.com/ring).

Oliveira, C. 2015 Calibração do Modelo Numérico da Ponte Ferroviária do Côa, MSc Thesis, Polythecnic Institute of Tomar. (in Portuguese)

Maintenance, Safety, Risk, Management and Life-Cycle Performance of Bridges – Powers, Frangopol, Al-Mahaidi & Caprani (Eds)
© 2018 Taylor & Francis Group, London, ISBN 978-1-138-73045-8

Fatigue performance of diaphragm cutouts in steel box girder

C. X. Li & L. Ke & Z. Y. Chen
Key Laboratory of Bridge Engineering Safety Control by Department of Education, Changsha University of Science & Technology, Changsha, China
Y. M. Xiong & Z. Hu
School of Civil Engineering, Changsha University of Science & Technology, Changsha, China

ABSTRACT: In order to investigate the fatigue performance of cutouts in the diaphragm of steel box girder and decide the optimal structure of the cutout, finite element models of block-shell mixed elements were established to calculate the fatigue stresses of several fatigue vulnerable details. The fatigue lives were calculated based on Palmgren-Miner linear damage accumulation criteria and the S-N curves in Eurocode 3. And the comparison of fatigue performance and design optimization of several typical cutouts at home and abroad were carried out. The results show that obvious compressive and tensile stress concentration zones (Zone A and B, respectively) exist at the cutout under local wheel loads. Fatigue cracks usually initiate at Zone A, and the direction of crack propagation is almost perpendicular to the direction of the principal stress. The shapes of the cutouts have significant influences on the fatigue performance of vulnerable details, especially on that of Zone A. The shape of arc-straight line (Cutout 4) is the best shape for the rigid diaphragms among the commonly used cutouts at home and abroad. The fatigue life of the cutout will be improved by appropriately increasing the radius of the cutout and the thickness of diaphragm, but the effect of increasing the radius of the cutout is better than increasing the thickness of diaphragm.

1 INTRODUCTION

Orthotropic steel decks (OSDs) are usually used in steel box girder bridges around the world. The Network Monitoring and Emergency Treatment Center of China investigated 19 suspension bridges with orthotropic steel decks during 2011~2016, of which 15 bridges somewhat fatigue damaged in the OSDs, accounting for 78.9% of the total number of the inspected bridges. OSDs are susceptible to fatigue failure due to its small vertical stiffness, complicated structure, and the complex fatigue stresses under the direct action of wheel loads (Yokozeki and Miki 2016; Tang et al. 2014). The investigation results of 2 expressways in Japan showed that the fatigue cracks at the intersection of the U rib and the diaphragm occupied 56.3% of the total number of cracks in the two bridges. Thus, the fatigue cracking at the connection of U rib and diaphragm is one of the main diseases of OSDs.

Earlier studies (Shao et al. 2013; Shan 2010) showed that the ultra-high-performance concrete (UHPC) bridge deck and steel-elastomer sandwich bridge deck can effectively reduce the fatigue stress of U rib-deck details under wheel loads, avoiding the risk of fatigue cracking, but it can not solve the cracking problem of diaphragms. The shape of the arc-shaped cutouts, the spacing and thickness of the diaphragms are the principal factors affecting the fatigue performance of the diaphragm (Li et al. 2012; Tang et al. 2011). The comprehensive influence of various factors should be considered in the design of steel box girder. Reducing the spacing between the diaphragms or increasing the thickness of the diaphragms will increase the structural self-weight, and changing the design of other components only to improve the stress state at the cutout is clearly not the best solution. Researchers (Wang et al. 2012; Li et al. 2012) recommended a better structure of diaphragm cutouts, but the effect of the overall stress pattern of the diaphragm is not considered and the results are quite different.

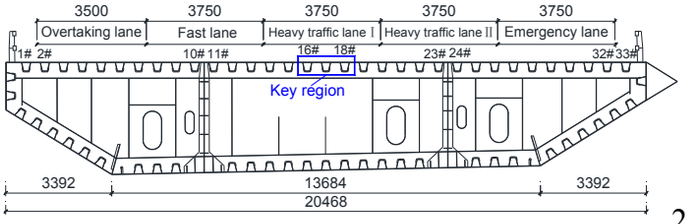
In Japan, Europe, and the USA, truss floor beams or low transverse diaphragms (the heights usually do not exceed 75 cm) are often used in steel box girder bridges, cutout design in these countries have been developed specifically for such flexible floor beams (called "floor beam" later in this paper). Studies (Song et al. 2014; Tang et al. 2011) have shown that the stress states in the cutouts of flexible floor beams under the wheel loads are affected greatly by the overall bending moment, but the stress states in the cutouts of commonly used full-high transverse diaphragm (rigid, called "diaphragm" later in this paper) are mainly induced by "local effect" of the

wheel loads, there are big differences in both fatigue stress state and fatigue mechanism. In this paper, the fatigue performance of the diaphragm cutouts in steel box girder is studied, and the fatigue behavior of six typical arc-shaped cutouts in Europe, America, Japan and China is compared, the influence of cutout radius and diaphragm thickness on the fatigue performance are analyzed, which can offer references for the detailed design of the anti-fatigue design of steel box girder.

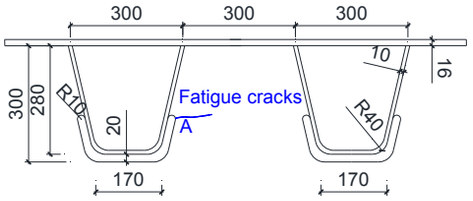
2 BACKGROUND ENGINEERING AND FE MODEL

2.1 *Bridge outline*

The main span of the suspension bridge is 350 m. The standard section of the main span steel box girder and structure of U rib-to-diaphragm connection is shown in Figure 1. The standard section is 3.5 m high, 20.468 m width excluding the wind fairing. The deck plate is 16 mm thick, the bottom plate is 14 mm thick, and the web is 16 mm thick. The U ribs are 10 mm thick and 280 mm high, 300 mm wide on the top, 170 mm wide on the bottom, the distance between centers of adjacent U ribs is 600 mm. The spacing of adjacent transverse diaphragms is 3.0 m longitudinally, and the spacing between adjacent suspenders is 12 m. The thick of transverse diaphragms without slings is 10 mm, and 12 mm with slings. A total of 121 cracks (see Figure 2) were observed in the arc-shaped cutouts of the diaphragms after operation for 9 years, accounting for 77% of the total number of diseases that have been found.



(a) Standard section



(b) Structure of U rib-to-diaphragm connection

Figure 1. Standard section of steel box girder and structure of U rib-to-diaphragm connection

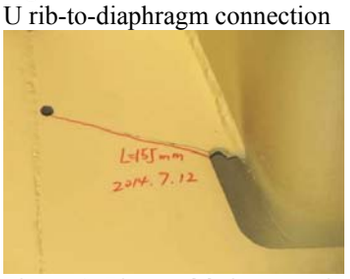


Figure 2. Photo of fatigue crack at the cutout of diaphragm

2.2 *FE modeling*

The fatigue stress of OSD is closely related to the effect of local wheel loads, but not affected much by the integral forced status of a bridge (Shao et al. 2013), thus a segment of the steel box girder was modeled to minimize the calculation scale. The FE model was established based on the following assumptions: 1) The structures behaves in elastic range, without considering material and geometrical nonlinearity; 2) Bearings of suspenders for steel box girder are considered as rigid supports, regardless of the sagging effect of main cable or the influence of the elastic stretching of suspenders.

A 3D finite element model of 15 m long, 3.5 m-high and 20.47 m-wide steel box girder was established using software Abaqus 6.14-3, as shown in Figure 3. The three translational degrees of freedom of nodes at the deck, bottom and web plates at end I are constrained, but nodes at the end J are constrained by the rigid vertical support. According to St-venenat's principle, little influence will be induced in the calculated stresses of structural details far away from the restraint boundaries. The model was built using "sub-model technology", most of the structure was modeled using 4-node shell elements, S4, except the key region that was modeled using 10-node block elements, C3D10. The model was meshed into 15 cm on the whole, except the key region that was meshed into 1 mm.

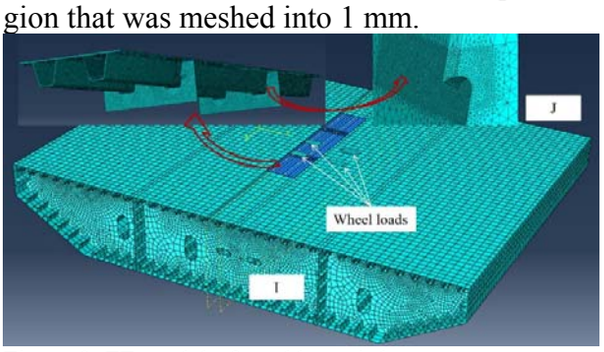


Figure 3. FE model of steel box girder

2.3 *Loading modes*

The load mode considered for the FE model is the vehicle load model III in Specifications for Design of Highway Steel Bridge (SDHSB) (2015), as shown in Figure 4, almost the same as the model III in Eurocode 3 (EC 3) (2005). Because no coupling effect was found between the two rear axles and the two front axes according to the FE analysis, the deck was considered undertaking double shafts 120 kN + 120 kN of the rear axles. The wheel loads were simulated by a uniformly distributed pressure with an area of 0.3 m × 0.7 m considering the dispersal effect of the asphalt pavement.

The left front one of the four wheels is taken as the reference wheel, the other wheel load positions were arranged according to the actual wheel track and wheelbase. To investigate the most adverse situ-

ation of the bridge deck under wheel loads, the reference wheel was moved transversely from above the concerned U rib to the right with a spacing of 10 cm, thus four transverse loading conditions (T1~T4) were considered. And the reference wheel was moved forward along the driving direction from the transverse diaphragm for 4 times with a spacing of 15 cm, and 4 times with a spacing of 30 cm, thus nine longitudinal loading conditions (L1~L9) were considered. The longitudinal wheel load positions illustrated in figure 7(b) corresponds to the transverse position T1 illustrated in figure 7(a), the most crucial longitudinal case was achieved, and then the most crucial case was achieved by offsetting the wheel loads transversely. The loading mode of the wheels is shown in Figure 5.

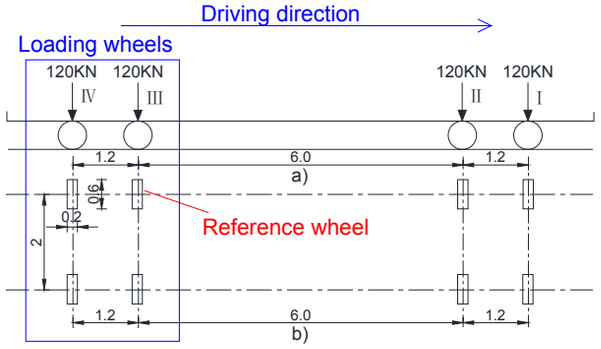
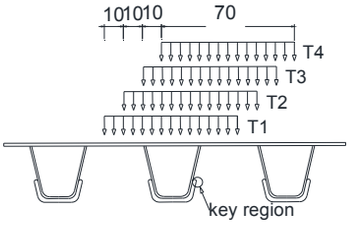
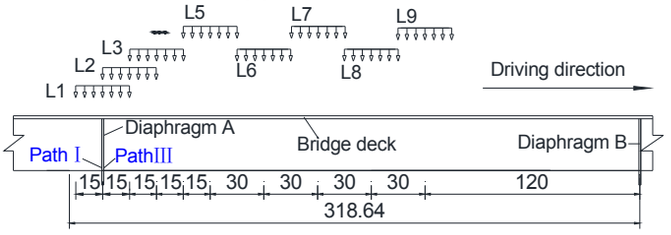


Figure 4. The model Ⅲ of fatigue load in SDHSB (unit: m)



（a）Transverse loading positions



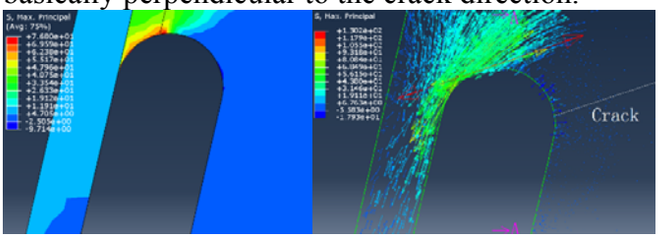
（b）Longitudinal loading positions

Figure 5. Loading mode of the reference wheel (unit: cm)

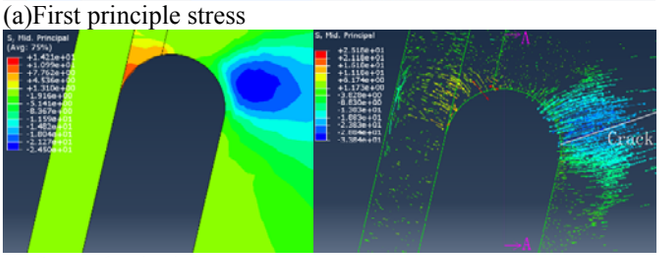
3 FATIGUE PERFORMANCE OF DIAPHRAGM CUTOUTS

3.1 *Fatigue Stress Analysis*

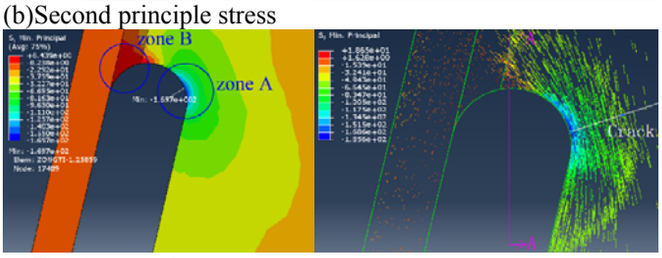
The structure effect is calculated under different loading conditions. According to the calculation results, the most adverse of the principal stress of the cutout is T2- L5, the nephograms and vectorgraphs of principal stress distribution of the cutout are shown in Figure 6. The results show that there are obvious compressive stress concentration zones (zone A) and tensile stress concentration zones (zone B, at the end of weld seam) around the cutout in the most adverse loading condition. The stress concentration in zone A and zone B is intense, and the stress at a small distance from the peak point of stress drops sharply to a very low level. The direction of the main compressive stress in the A zone is basically perpendicular to the crack direction.



(a)First principle stress



(b)Second principle stress



(c)Third principle stress

Figure 6. Nephogram and vectorgraph of principal stress distribution of the cutout (unit: MPa)

The weld toe on the surface of U rib at the intersection of U rib and diaphragm is one another hot spot prone to fatigue, which is defined as the “Zone C”, the location of Zone C and the extrapolation path of the hot spot stress are shown in Figure 7.

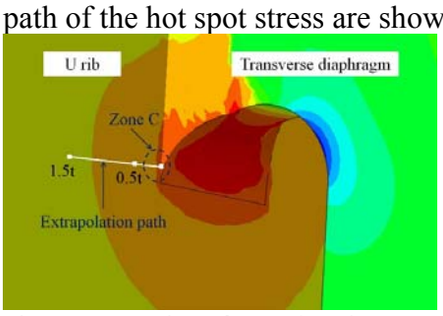


Figure 7. Location of zone C and extrapolation path of hot spot stress

As Zone A is located at the base metal of the diaphragm which is a non-welded area, the principal stress is taken as the fatigue control parameter. However, the fatigue of Zone B and Zone C should be regarded as the fatigue of welded joints, the hot stresses should be taken as the fatigue control parameter, the related calculation method has been reported (Aygül et al. 2012; Kim et al. 2009; Wang 2015). Zone B is located at the end of the attached plate, a path along the free edge of the cutout is taken as the extrapolation path, and the stress at the

point 5 mm away from the weld toe is taken as the hot spot stress.

The peak value of the compressive stress at zone A is -169.7 MPa, the hot spot stresses at Zone B and Zone C are -43.3 MPa and 44.4 MPa, respectively. According to EC 3 and SDHSB, the reduction factor of 0.6 should be considered for compressive stress, and the influence of transverse distribution of wheels should also be considered. The probability model of the transverse distribution of the wheels in China has been reported (Bu et al. 2015), the influence coefficient of transverse distribution of wheels are taken according to the literature of Bu (2015), that is, the influence coefficients of 0.76, 0.80, and 0.80 are taken for Zone A ~ Zone C, respectively. Considering these influence coefficients, the fatigue stress ranges for Zone A ~ Zone C are 77.4 MPa, 34.6 MPa and 35.5 MPa.

3.2 *Fatigue life prediction*

The fatigue life is calculated by the Palmgren-Miner linear damage accumulation criteria (P-M criteria) and the S-N fatigue curve in EC 3:

When $\Delta\sigma_i \geq \Delta\sigma_D$,

$$D_i = \frac{n_i}{N_i} = \frac{n_i}{10^7}\left(\frac{\Delta\sigma_i}{\Delta\sigma_D}\right)^m \quad (1)$$

When $\Delta\sigma_L \leq \Delta\sigma_i < \Delta\sigma_D$,

$$D_i = \frac{n_i}{N_i} = \frac{n_i}{10^7}\left(\frac{\Delta\sigma_i}{\Delta\sigma_D}\right)^{m+2} \quad (2)$$

When $\Delta\sigma_i \leq \Delta\sigma_L$,

$$D_i = 0 \quad (3)$$

The fatigue life:

$$Y = 1/\sum D_i = 1/\sum_{i=1}^{k}\frac{n_i}{N_i} \quad (4)$$

Where, D_i is the fatigue damage, n_i is the cycles of stress range $\Delta\sigma_i$, $\Delta\sigma_D$ is the constant fatigue limit in the S-N curves (the fatigue strength corresponding to 5×10^6 cycles), N_i is the cycles corresponding to the constant fatigue limit in the S-N curves (ie. 5×10^6 cycles), and $\Delta\sigma_L$ is the fatigue cut-off limit, m is the material coefficient which is taken as 3.

The fatigue lives of Zone A are calculated according to S-N curve of Category 71 specified in EC 3. The study shows that the fatigue lives of vulnerable details at welded seams such as zone B can be calculated using the S-N curve of FAT90 (the fatigue strength corresponding to 2×10^6 cycles is 90 MPa) in EC 3.

Considering the effect of compressive stress reduction and lateral load coefficient, the fatigue stress range of zone A is 130.0 MPa, the stress amplitude in zone B is 34.6 MPa. The fatigue lives of Zone A and Zone B are 2.91 million cycles and 11.9 million cycles, respectively. It should be noted that, even under pressure-zero cycles, cracks may still initiate at Zone A, because the thermal cutting process may produce large residual stresses that are even close to the yield strength of the steel, the fatigue performance is mainly related to the fatigue stress ranges, previous studies (Vasudevan and Sadananda 2001; Zhang et al. 2010) have confirmed the existence of such fatigue cracks.

4 STRUCTURAL OPTIMIZATION OF CUTOUTS BASED ON FATIGUE PERFORMANCE

To determine the optimal structure of diaphragm cutouts, a comparison of six typical kinds of diaphragm cutouts at home and abroad (see Figure 5) was carried out. As is shown in Figure 5, the shapes of the cutouts from Cutout 1 to Cutout 6 are the shapes of European standard/BS EN (2005) recommended highway-bridge cutouts, American standard/AASHTO LRFD (2007) recommended cutouts, Japanese standard/Steel Road Bridge Fatigue Design Pointer (2002) recommended all-bridge cutouts, Chinese highway-bridge commonly used cutouts ("straight + arc"), European standard/BS EN (2005) recommended railway-bridge cutouts and Chinese railway-bridge commonly used cutouts (large curvature circular arc), respectively. Given various cutouts in the diaphragms with different shapes and sizes in the FE models, fatigue stresses of the structural details near the cutouts are calculated.

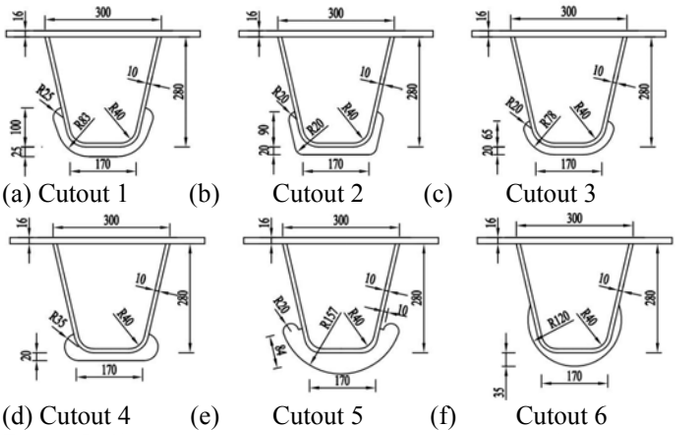
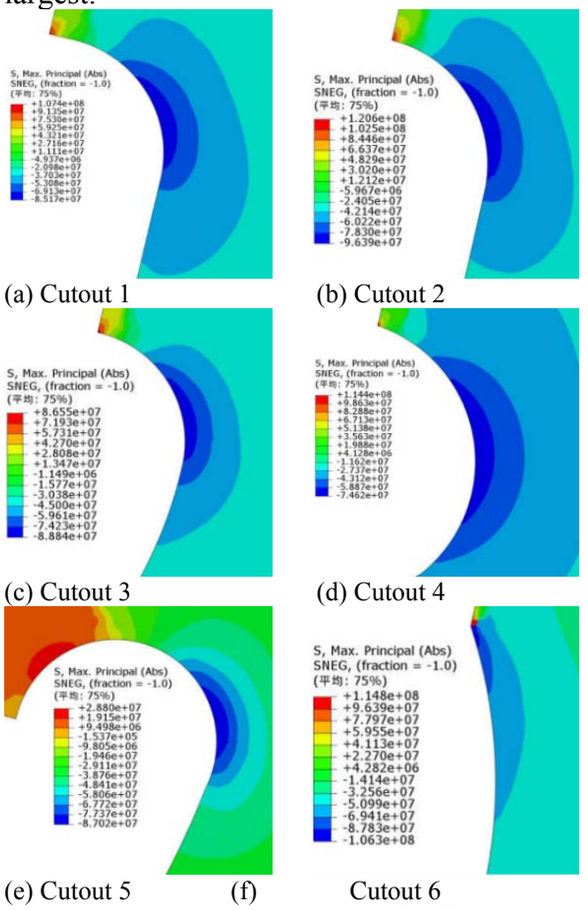


Figure 5. Six typical cutouts at home and abroad (unit: mm)

4.1 *Comparison of fatigue stresses of typical cutouts*

The original form of the cutout in the background engineering is defined as Cutout 7. Stress distribution of different cutouts under local wheel loads are shown in Figure 7. The com parison of fatigue stress of vulnerable details with different cutouts is shown in Figure 8. The stresses for Zone A 、Zone B and Zone C in Figure 8 represent the calculated principal stresses, hot spot stresses extrapolated along curve paths and hot spot stresses linearly extrapolated using stresses at 0.5 t and 1.5 t (t is the thickness of U rib) , and the stress in the table does not take into account any reduction. It can be seen that the fatigue stresses at Zone A of di fferent cutouts under the same working conditions are quite different. The fatigue stress of cutout 7 is significantly higher than of the other six cutouts, and the fatigue stress of cutout 4 is the lowest (-74.6 MPa). The hot spot stresses at Zone B are also greatly affected by the cutout shapes, some of the hot spot stresses are calculated as tensile stress and others are com pressive stresses, and the absolute values are quite different. Hot spot stresses at Zone C of Cu touts 1-5 are relatively smaller, while the hot spot stress of Cutout 7 is the largest.



(a) Cutout 1 (b) Cutout 2

(c) Cutout 3 (d) Cutout 4

(e) Cutout 5 (f) Cutout 6

Figure 7. Fatigue stress distribution of different cutouts

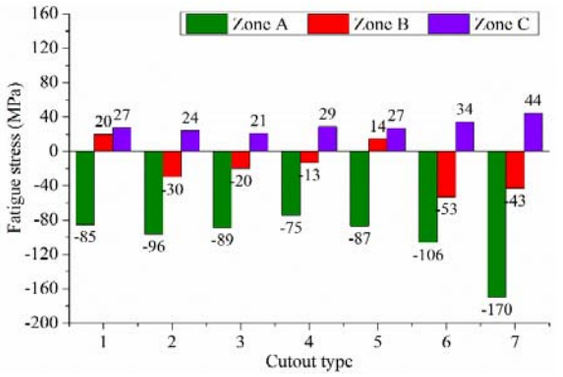


Figure 8. Conparison of fatigue stress of vulnerable details in different cutouts

4.2 *Comparison of fatigue lives of typical cutouts*

The predicted fatigue lives of fatigue prone details (Zone A ~Zone C) of differe nt cutouts are depicted in Figure 9. The results show that the fatigue life of 3 vulnerable areas of all cutouts exceed 1 $\times 10^7$ cycles except for the Zone A of Cutout 7. As to the Zone A, Cutout 4 has th e highest fatigue life of about 28.7 times that of Cutout 7, which is due to the fact that the fatigue life is related to the third power of fatigue stress range. Th e Zone B and Zone C of all cutouts, except the Zone B in Cutout 6 or Zone C in Cutout 7, will never f atigue in theory. That is to say, Zone B and Zone C have no fatigue risk for the majority of Cutouts, Zone A is the control area f or anti-fatigue design.

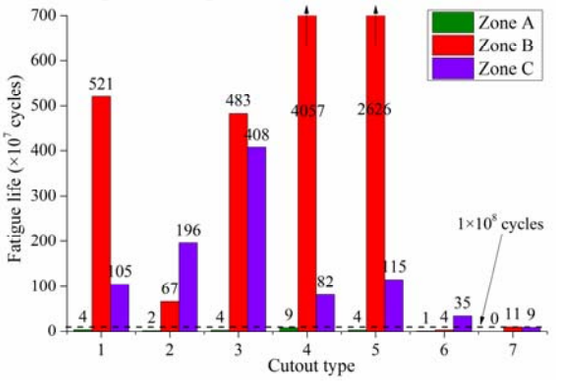


Figure 9. Predicted fatigue lives of Zone A~ Zone C of different cutouts

In general, it is of great significance to optim ize the diaphragm to improve the fatigue life of this area. According to the above analysis, the stress level at Zone A and Zone B of Cutout 4 are the lowest, and the fatigue stress at Zone C is also lower than the fatigue cut-off limit, which is the preferred shape of the diaphragm cutout.

4.3 *Structural optimization of Cutout 4*

The vulnerable detail at the weld toe at the intersection of U-rib, diaphragm and roof weld seam is set as Zone D, as shown in Figure 10. Based on the Cutout 4, the radius of th e free edge is taken as 35 mm, 45 m m and 55 m m, and the diaphragm thickness is taken as 10 m m, 12 mm and 14 m m, respec-

tively. The fatigue stresses of vulnerable details (Zone A, Zone B and Zone D) are calculated and compared, to determine the influence of cutout radius and diaphragm thickness on the fatigue properties of above vulnerable details.

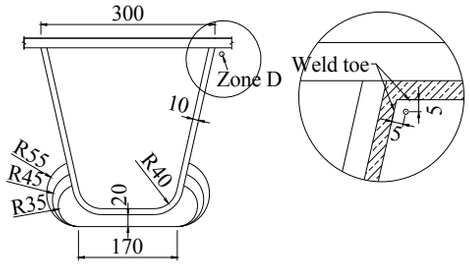


Figure 10. The changes of cutout radius and location of Zone D

The influence of cutout radius and diaphragm thickness on fatigue stress at Zone A, Zone B and Zone D is shown in Figure 11. The results show that: ① The fatigue stress at Zone A decreases with the increase of the radius of cutout free edge. The fatigue stress is reduced by 12 ~ 17 MPa as the radius increased from 35 mm to 45 mm, while it is reduced by only 3.2~4.0 MPa as the radius increased from 45 mm to 55 mm, the amelioration of stress tends to converge. ② The hot spot stresses at Zone B and Zone D are reduced little with the increase of the radius, but anyway they are less than the fatigue cut-off limit of FAT 90, thus cracks will not initiate at Zone B and Zone D in theory. ③ With the increase of the thickness of diaphragm, the principal stress at Zone A decreases greatly, the fatigue stress at Zone D decreases in some degree, and fatigue stress of Zone B changes little, so increasing the thickness of diaphragm will only actually affect the fatigue performance of Zone A. Increasing the radius of cutout free edge is conducive to improving the fatigue resistance of Zone A, by contrast, the fatigue property of Zone A is also improved by increasing the thickness of diaphragm, but the effect is not so good.

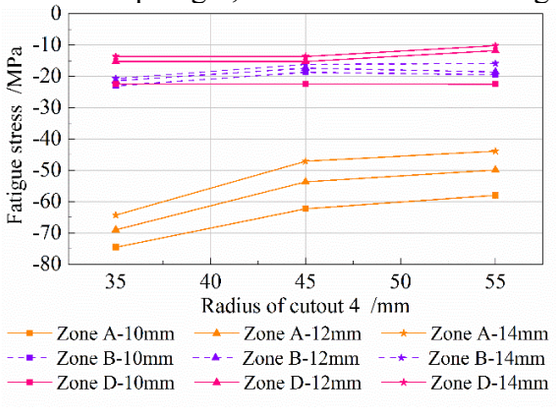


Figure 11. Influence of cutout radius and diaphragm thickness on fatigue stresses

5 CONCLUSION

Obvious compressive stress concentration zone (Zone A) and tensile stress concentration zone (Zone B) exists at the arc-shaped cutout in transverse diaphragm of steel box girder under the effect of local wheel loads. Fatigue cracks mostly occur at Zone A where the principal stress is almost perpendicular to crack propagation direction. The calculated fatigue stress range at Zone A is 77.4 MPa considering all influence coefficients, which exceeds the threshold value if fatigue initiation and leads to the fatigue cracking.

The fatigue stresses and fatigue lives of Zone A ~ Zone C at the intersection of U rib and diaphragm are significantly affected by the shapes of the cutouts. Among the seven kinds of typical shapes, the fatigue life of the cutout shape applied in the background engineering is the lowest, while the shape of arc+ straight line (Cutout 4) shows up the best anti-fatigue performance.

The increase of radius of Cutout 4 is conducive to improving the fatigue performance of Zone A, and it will not significantly affect the fatigue stresses of other vulnerable details. The increase of the thickness of transverse diaphragm is also conducive to improving the fatigue property of Zone A, but less effective than the increase of the cutout radius.

6 ACKNOWLEDGEMENTS

This research was supported by a project from the National Program on Key Basic Research Project of China (973 Program) (No. 2015CB057701), the National Natural Science Foundation of China (NSFC) (No. 51778069) and Hunan Provincial Innovation Foundation for Postgraduate.

REFERENCES

Aygül, M., Al-Emrani, M. and Urushadze, S. 2012. Modelling and fatigue life assessment of orthotropic bridge deck details using FEM. *International Journal of Fatigue*, 40, 129-142.

AASHTO. 2007. AASHTO LRFD Bridge Design Specifications, 4th Ed., AASHTO, Washington, DC.

BS EN 1993-1-9. Eurocode 3 Design of Steel Structures Part 1-9: Fatigue.

Bu Y, Yang S. L., Cui C., et al. 2015. Influence of wheel trace transverse distribution on fatigue stress ranges of steel deck. *Bridge Construction*, 45(2):39-45. in Chinese

JTG D64 -2015. Specifications for Design of Highway Steel Bridge. MOT, Beijing.

Kim, M. H., Kim, S. M., Kim, Y. N., Kim, S. G., Lee, K. E., and Kim, G. R. 2009. A comparative study for the fatigue assessment of a ship structure by use of hot spot stress and structural stress approaches. *Ocean Engineering*, 36(14), 1067-1072.

Li L. F., Zhang D. B ., Yuan Z. Y., et al. 2012. Stress analysis of arc-shaped cutouts in steel orthotropic deck plates. *Jour-*

nal of Highway and Transportation Research and Development, 29(4):55-61. in Chinese

Shao, X., Yi, D., Huang, Z., Zhao, H., Chen, B., and Liu, M. 2013. Basic performance of the composite deck system composed of orthotropic steel deck and ultrathin RPC layer. *Journal of Bridge Engineering*, 18(5), 417-428.

Shan C. L. 2010. Analysis of the mechanical property of orthotropic bridge deck with steel-elastomer sandwich structure. *Journal of Hunan University (Natural Sciences),* 37 (12):18-23. in Chinese

Song G. J., Hua L. H. 2014. Analysis and strengthening method research for cracks in diaphragms of steel box girder of a cable-stayed bridge. *Bridge Construction*, 44(4):107-111. in Chinese

Tang L., Huang L. J., Liu G., et al. 2014. Fatigue experimental study of a full-scale steel orthotropic deck model. *Journal of Civil Engineering,* 47(3):112-122. in Chinese

Tang L., Huang L. J., Liu G. 2011. FEA of stress along cope hole edge of crossbeam in orthotropic steel deck. *Journal of Highway and Transportation Research and Development*, 28(6):83-90. in Chinese

Vasudevan, A. K., and Sadananda, K. 2001. Analysis of fatigue crack growth under compression–compression loading. International Journal of Fatigue, 23, Supplement 1, 365-374.

Wang, B. 2015. Fatigue Assessment of the Diaphragm-to-Rib Welded Connection in Orthotropic Steel Deck Using Effective Notch Stress Approach. *Journal of Failure Analysis and Prevention*, 15(1), 65-73.

Wang C. S., Fu B. N., Zhang Q., et al. 2012. Floor-beam web cutout shape analysis in orthotropic steel bridge deck. *Journal of Chang'an University (Natural Science Edition)*, 32(2): 58-64. in Chinese

Yokozeki, K., and Miki, C. 2016. Fatigue evaluation for longitudinal-to-transverse rib connection of orthotropic steel deck by using structural hot spot stress. *Welding in the World*, 60(1), 83-92.

Zhang, J., He, X. D., Sha, Y., and Du, S. Y. 2010. The compressive stress effect on fatigue crack growth under tension–compression loading. *International Journal of Fatigue*, 32(2), 361-367.

Maintenance, Safety, Risk, Management and Life-Cycle Performance of Bridges – Powers, Frangopol, Al-Mahaidi & Caprani (Eds)
© 2018 Taylor & Francis Group, London, ISBN 978-1-138-73045-8

Assessment of Shear Lag in Pultruded GFRP Bridge Decks

S. Zhang & C. Caprani

Faculty of Engineering, Department of Civil Engineering, Monash University, Melbourne, Australia.

ABSTRACT: Pultruded Glass fiber-reinforced polymer (GFRP) composite is increasingly applied in civil engineering due to the cost-effective ease of manufacturing and excellent material properties. GFRP bridge decks are a good alternative to traditional decks to eliminate deterioration and improve durability. However, considering the low in-plane shear modulus of pultruded GFRP, shear lag of GFRP cross sections could be a significant design issue. This paper presents a Finite Element (FE) parametric study on the influence of shear lag on pultruded GFRP bridge decks. A simply-supported GFRP bridge with different span lengths and bridge configurations are modelled under representative loading conditions. The effective width of the GFRP bridge decks are then obtained. Additionally, steel bridges with the same configurations are examined as comparisons of effective width. The results of this paper indicate the importance of considering that in the design of orthotropic-deck pultruded GFRP bridges, shear lag is comparable with traditional forms of construction.

1 INTRODUCTION

1.1 *General background*

Fibre-reinforced polymer (FRP) has relatively high stiffness, strength to weight ratio, and good corrosion resistance. These benefits make it become attractive to meet the increasing demand of high-performance durable materials in civil engineering. To manufacture FRP profiles, a highly automated and continuous manufacturing process known as pultrusion, is considered as the most cost-effective method (Bank 2006). Normally, glass fibres embedded with polyester or vinyl ester resin are used in pultrusion. So far, GFRP has been widely used to as a reinforcing material with concrete and steel to reduce corrosion. In bridge engineering, GFRP hybrid bridge decks or pultruded GFRP sandwich bridge decks have been designed and built for many years. It has been reported by O'Connor and Hooks (2004) that around 83 bridges in United States have been constructed or rehabilitated using GFRP decks. Also, GFRP cable-stayed footbridges were constructed in Scotland and Kolding, Denmark, respectively (Bakis et al. 2002). Furthermore, FRP bridge decks with steel girders have been used on main highway bridge in Netherland (van Ijselmuijden and Tromp 2013).

Due to the low in-pane shear stiffness of GFRP composites, the stress distribution in the transverse direction becomes non-uniform, showing a decrease from the junction with girders to the edge—an example is shown in Figure 1. This non-uniformity is known as shear lag. Of course, shear lag occurs for all materials, but the peculiarity of GFRP is that its high longitudinal strength and stiffness is comparable to steel and concrete (respectively), but its shear modulus is more like some timbers.

For bridges, Hambly (1991) suggested that shear lag can be negligible only for collapse conditions; otherwise, it may generate an over-stiff problem for the bridge deck. Therefore, to account for shear lag of the bridge deck, the effective width is used for beam flanges in the analysis to allow the continued assumption of simple beam theory, having a uniform stress distribution across the flange width.

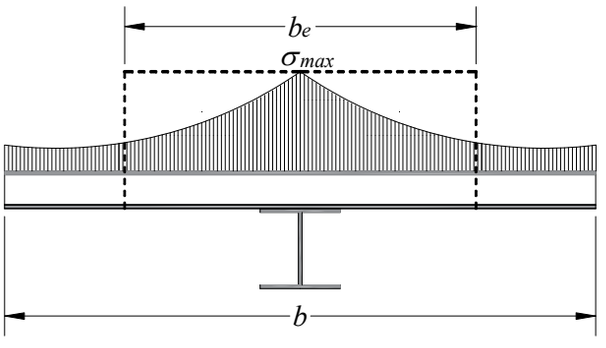


Figure 1: Transverse stress distribution due to shear lag, and the approximation of effective width, b_e, for simple beam theory.

1.2 *Study Objective*

Some research has been conducted on the influence of shear lag on composite bridge. Most studies focus on partial composite bridges, such as FRP bridge deck with steel girders or hybrid bridge deck (concrete with FRP) with steel girders (e.g. Keelor et al. (2004), Zou et al. (2011), and He (2011)). Generally, it has been shown that shear lag is highly dependent on the variations of span to width ratio, girder spacing, loading and support conditions (Sedlacek and Bild (1993) and Gara et al. (2011)). Cheung and Chan (1978) and Tenchev (1996) found that the effective width due to shear lag is independent of cross-section type and variations of material properties of the flange and web. A similar conclusion was found by Nagaraj and GangaRao (1997) after investigating the non-uniform distribution of bending strain of a pultruded GFRP I-section beam and box section in three-point bending tests. In addition, for partial composite bridge (FRP bridge deck supported by steel girders), the effective width was found to increase with the increase of span-to-width ratio, but decrease with girder spacing-to-span ratio (Moses et al. 2006). Also, the identified effective widths of FRP bridge decks are less than that of concrete decks obtained using AASHTO (Moses et al. (2006) and Alnahhal et al. (2008)). Moreover, it has been shown that a partial degree of composite action is achieved by hybrid FRP bridge deck with steel girders, which also affects the effective width of FRP bridge deck flanges (Alnahhal et al. (2008) and Zou et al. (2011)). However, despite all findings on partial composite bridges, the existing studies do not investigate shear lag for FRP sandwich bridge decks. Consequently, there are no recommendations to determine the effective width of such structures. This paper is a first step towards addressing this knowledge gap for GFRP sandwich bridge decks.

1.3 *Methodology*

This paper presents a parametric study using finite element (FE) analysis to investigate shear lag of pultruded GFRP composite bridges. A sandwich panel bridge deck is modelled consisting of flat plates and box-profiles in both longitudinal and transverse directions (Figure 2). Considering the influence of span-to-width ratio on the effective width of the beams, three bridge configurations are analyzed for different span lengths. All bridge models are established as simply-supported bridges under four-point bending loads. Moreover, the shear lag factor and effective width of fully-composite GFRP bridges and a non-composite steel bridge are calculated respectively to identify the relative influence of shear lag on bridges of different materials. This work should assist in improving the design and assessment of pultruded GFRP composite bridge structures.

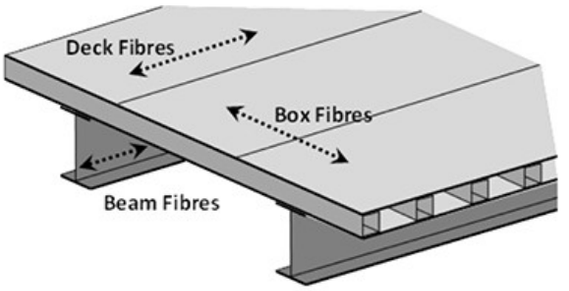


Figure 2: Fibre orientations for a GFRP sandwich panel deck and beams (Caprani et al. 2017).

2 MATERIAL INVESTIGATION

Pultruded glass fiber reinforced polymer (GFRP), supplied by Exel Composites, Australia, is used in this study. All pultruded profiles consist of E-glass fiber (major reinforcement) and polyester resin (matrix). The section thickness varies for different profiles: 6.21 mm for flat plates; 9.5 mm for box sections; and 9.5 mm for I-girders. Material properties of pultruded profiles with different thickness are shown in Table 1, which have been determined from extensive testing carried out at Monash University (Zhang et al. (2016). Each property is given as an average of 10 specimens.

According to the theory of elasticity (Timoshenko and Goodier 1969), pultruded GFRP is regarded as tetragonal material, which assumes the material properties in the thickness direction is the same as other directions (Bisplinghoff et al. (1965) and Bank (2006)).

Table 1: Material properties of pultruded GFRP.

Property	Unit	Thickness (mm)	
		6.21	9.5
Fibre volume fraction (FVF)	%	42.1	42.1
Density	kg/m3	1800	1800
Longitudinal modulus	GPa	22.99	24.63
Transverse modulus	GPa	10.32	10.43
In-plane shear modulus	GPa	3.35	3.5
Major Poisson's ratio	-	0.30	0.30

3 FINITE ELEMENT MODELING

An FE bridge model is developed for both GFRP and steel bridges. Four-node shell elements are selected, and there are six degrees of freedom at each node to account for the orthotropic nature of pultruded GFRP, while this is ignored for the isotropic steel bridge model. The sandwich bridge deck consists of two 6.21 mm-thick pultruded GFRP flat plates (top and bottom) bonded with pultruded GFRP box-profiles (9.5 mm) in-between (as shown in Figure 3).

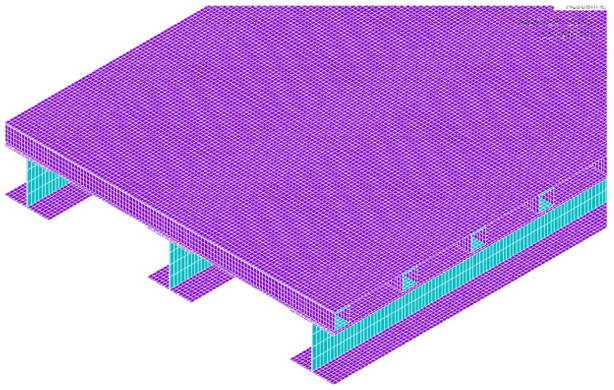


Figure 3: Finite element model of pultruded GFRP bridge deck with sandwich panel construction.

As noted previously, the span-to-width ratio presents a significant influence on shear lag of non-composite or partial composite bridges. Therefore, in this study, the width of the bridge deck is 1.5 m and the span length (L) varies as 9 m, 18 m and 27 m. Three bridge configurations including single girder, two girders and three girders are analyzed for each span length. The developed bridge models are summarized in Table 2 and bridge cross sections are shown in Figure 4.

Table 2: Summary of the analysed bridge models.

Bridge configuration	Cross-section (CS)	
	CS-1	CS-2
Single-girder bridge (SIGB)	9 m	9 m
	18 m	18 m
	27 m	27 m
Two-girder bridge (DIGB)	9 m	9 m
	18 m	18 m
	27 m	27 m
Three-girder bridge (TIGB)	9 m	9 m
	18 m	18 m
	27 m	27 m

The bridge model is simply-supported with pin constraints for both ends. Four-point bending loads are applied as two line-loads at one-third span distances from supports (as shown in Figure 5). Consequently, the shear region of this bridge model is located between the support and position of loading. Therefore, the results are taken from two cross sections: CS-1 in the shear region and CS-2 at the mid-span of bridge. For each cross section, nodes defined on the top panel of sandwich bridge deck (in the y-direction) are selected to generate stress results. Furthermore, it should be noted that full composite action is assumed for all bridge configurations.

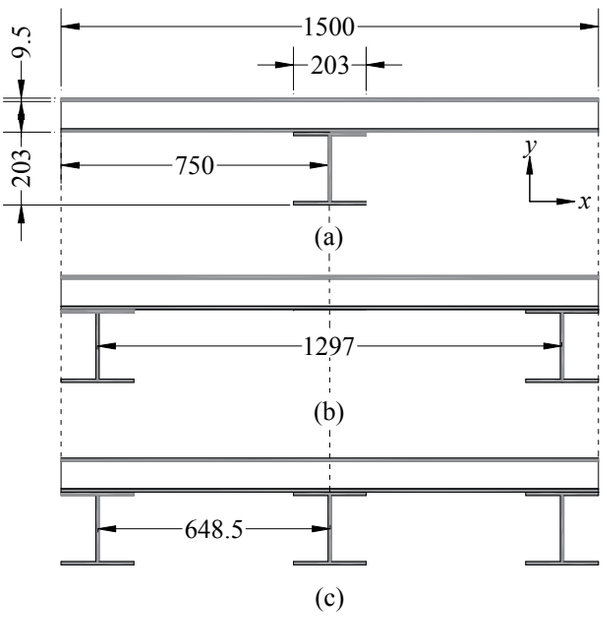


Figure 4: Bridge configurations: a) Single girder bridge (SIGB); b) Two girders bridge (DIGB); c) Three girders bridge (TIGB) (unit: mm).

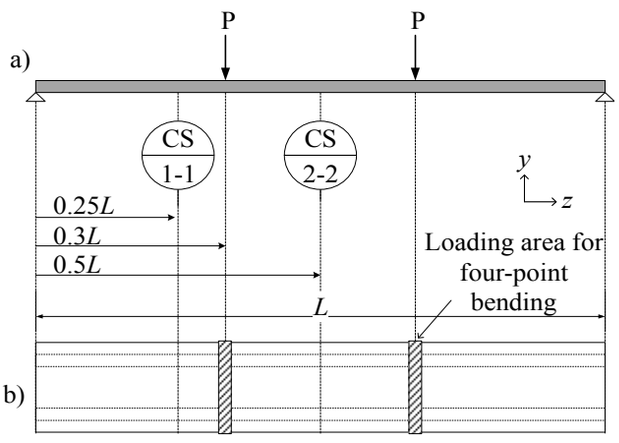


Figure 5: Positions of loading and typical cross-sections (unit: mm).

3.1 *Example Results*

The approach used to analyse the FE model outputs is explained using a sample set of results. The same steps are applied throughout. At the cross section of interest, the FE model nodes on the top surface of the deck are selected across the width of bridge (in the x-direction), and the longitudinal stresses (in the z-direction) at these nodes are extracted.

The stresses due to the different span lengths are considerably different in magnitude. Therefore, to compare transverse changes of longitudinal stress distributions obtained at different span lengths, normalized stresses are used, defined as:

$$\sigma_{norm} = \frac{\sigma_z}{\sigma_{\max}} \tag{1}$$

where, σ_{norm} is the normalized longitudinal stress; σ_z is the longitudinal stress along the cross-section; and σ_{max} is the maximum longitudinal stress at the junction of beam and girder (x = 0.75 m).

Longitudinal stresses taken from the 9 m single-girder bridge (Figure 6a and 6b) are shown as an example. Figure 6c shows the stress contour of single-girder bridge with nodes selected at CS-1 (2.25 m) and the corresponding extracted longitudinal stresses are shown in Figure 7. Therefore, the σ_{max} is 179.86 kPa for single-girder bridge with 9 m span at CS-1 and the corresponding normalized stress distribution is shown in Figure 8.

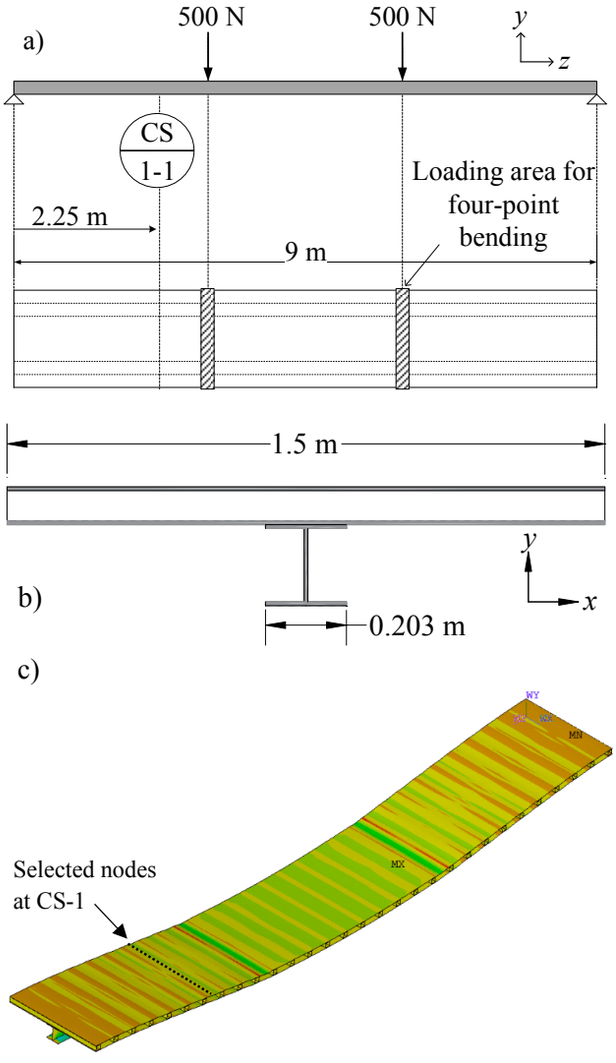


Figure 6: a) Location of CS-1 on 9 m single-girder bridge; b) cross-section; c) Longitudinal stress (σ_z) contours.

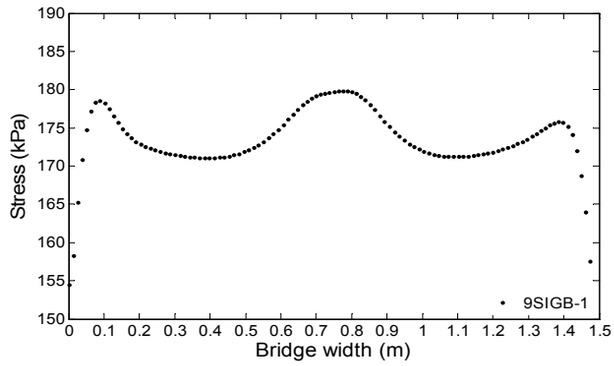


Figure 7: Longitudinal stress distribution of single-girder bridge with 9 m span at CS-1.

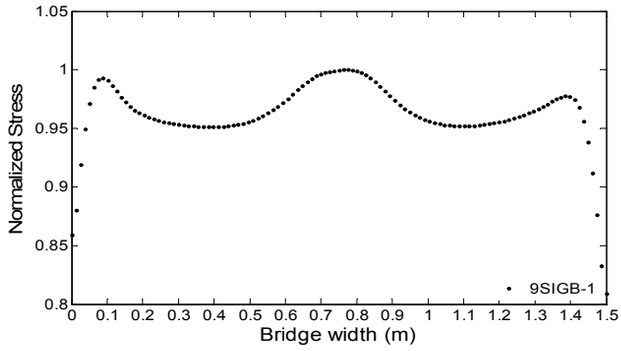


Figure 8: Normalized stress of single-girder bridge with 9 m span at CS-1.

4 RESULTS AND DISCUSSION

4.1 *Methodology*

Shear lag is expressed using the superposition of normal stress along the width of bridge. To allow the use of simple beam theory while accounting for the shear lag, an effective width of the flange is used, such that the maximum stresses and total flange force are equal (Hambly 1991)—see Figure 1. Therefore, it can be calculated by the integral of normal stress (Tenchev (1996) and Zou et al. (2011)):

$$b_e = \frac{\int_{-b/2}^{b/2} \sigma_z dx}{\sigma_{\max}} = \frac{2\int_{0}^{b/2} \sigma_z dx}{\sigma_{\max}} \tag{3}$$

where b_e is the effective width; b is the bridge width (1.5 m throughout this work); σ_z is the longitudinal stress along the cross-section; σ_{max} is the maximum longitudinal stress at the junction of beam and girder. A shear lag factor can be employed to evaluate the influence of shear lag on the beam behaviour:

$$\lambda = \frac{b_e}{b} \tag{4}$$

Values of the shear lag factor much less than 1 illustrate a strong influence of shear lag on the beam behaviour. Due to the symmetry of bridge, the value of

b is taken as the full width (1.5 m) for single-girder bridges and half width (0.75 m) for multiple-girder bridges. Furthermore, both the effective width and shear lag factor are based on the stress measured from the top panel of sandwich bridge deck.

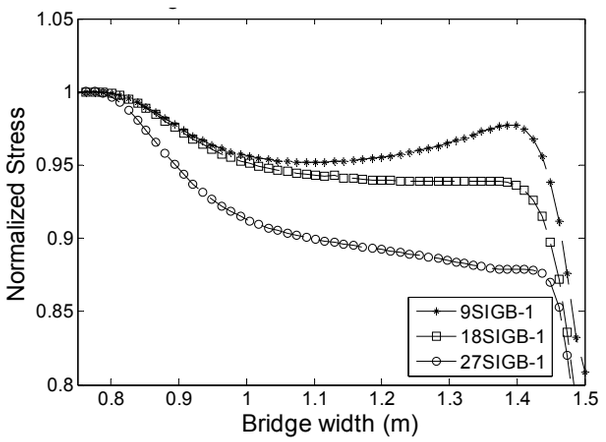


Figure 9: Normalized longitudinal stress distribution of single-girder bridge at CS-1 (quarter-span).

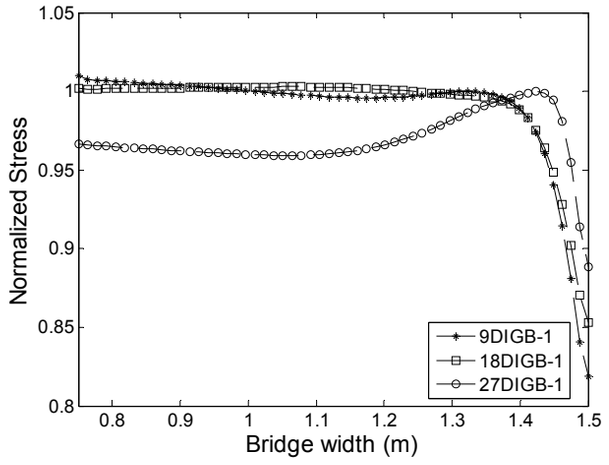


Figure 10: Normalized longitudinal stress distribution of two-girder bridge at CS-1 (quarter-span).

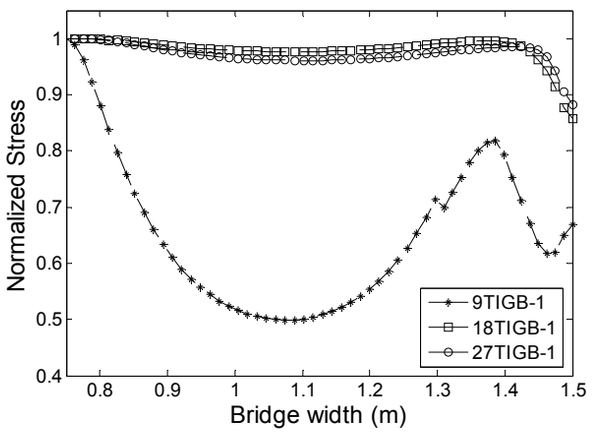


Figure 11: Normalized longitudinal stress distribution of three-girder bridge at CS-1 (quarter-span).

4.2 *Longitudinal stress distribution results*

Figures 9-14 show normalized longitudinal stress distributions (equation (1)) for the studied bridge configurations at CS-1 and CS-2, respectively Also, due to the symmetry of the cross section, stresses are only shown for one half-width in each figure.

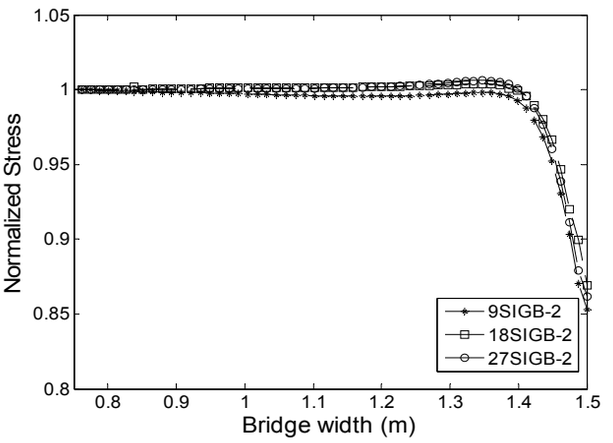


Figure 12: Normalized longitudinal stress distribution of single-girder bridge at CS-2 (mid-span).

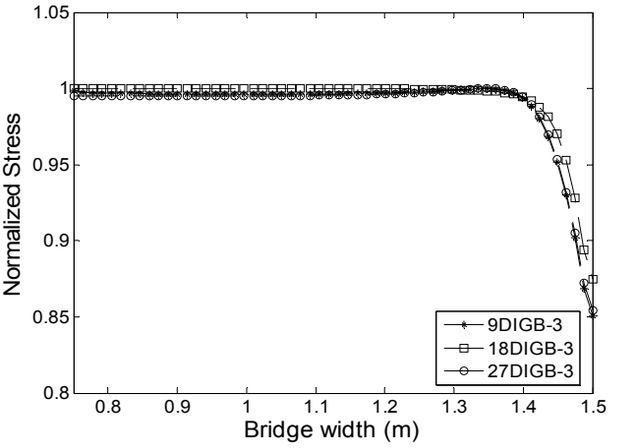


Figure 13: Normalized longitudinal stress distribution of two-girder bridge at CS-2 (mid-span).

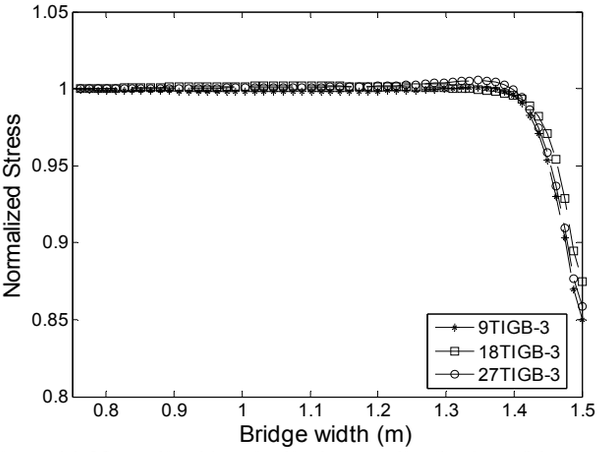


Figure 14: Normalized longitudinal stress distribution of three-girder bridge at CS-2 (mid-span).

Generally, the distributions of longitudinal stresses of pultruded GFRP bridge are more uniform at mid-span (CS-2) than those in the shear region (CS-1), regardless of variations of span length and bridge configuration. This finding indicates that pure bending occurs at the mid-span (CS-2). In turn, this means that the sandwich bridge deck with bi-directional profiles can efficiently share longitudinal stresses transversely. For longitudinal stresses at CS-1, the normalized stresses are approximately ranging from 0.9 to 1 for the 18 m and 27 m bridge cross sections, respectively. However, noticeable difference of normalized stresses occur for the short span bridge (9 m) at CS-1, especially for bridge with three girders, which ranges from 0.5 to 1. All these differences indicate that shear lag is highly dependent on span length. Interestingly, a similar conclusion has been drawn by Zou et al. (2011) for a partial composite bridge. Moreover, the non-uniform distributions are mainly at the positions of I-girders, leading to clear shear lag. This variation is also shown for stress distribution at CS-2. Interestingly, for the bridge model with three equal-spaced girders, the most non-uniform distribution occurs at the interior girder rather than the exterior girders.

4.3 *Effective width and shear lag factor*

For comparison with the GFRP bridges, the effective widths of steel bridges are also calculated for the same bridge configuration and loading condition. Table 3-5 presents the effective width and shear lag factors obtained from the two types of bridges. Considering the most non-uniform distribution appears at the interior girder for the three-girder bridge configuration, the effective width evaluated from interior girder is shown in the tables.

From the results given, it is clear that shear lag presents relatively similar influence on GFRP and steel bridges (Figure 15). The differences between effective widths for all configurations are less than 2%. At either CS-1 or CS-2, the slight difference between the shear lag factor obtained from both bridges are negligible, as the ratios between shear lag factors ($\lambda_{GFRP}/\lambda_{Steel}$) are in the range of 0.965 to 1 (Figure 16). Even though, bridges with multiple-girders have more varied ratios between the pultruded GFRP and steel shear lag factors than single-girder bridges.

Table 3: Effective width and shear lag factor of one-girder bridge.

Cross-section	Span (m)	b_e (m)		λ	
		GFRP	Steel	GFRP	Steel
CS-1	9	1.08	1.08	0.72	0.72
	18	1.10	1.11	0.73	0.74
	27	1.10	1.14	0.74	0.76
CS-2	9	1.12	1.12	0.74	0.75
	18	1.12	1.14	0.75	0.76
	27	1.15	1.17	0.76	0.78

Table 4: Effective width and shear lag factor for two-girder bridge.

Cross-section	Span (m)	b_e (m)		λ	
		GFRP	Steel	GFRP	Steel
CS-1	9	0.51	0.51	0.68	0.68
	18	0.53	0.53	0.71	0.71
	27	0.58	0.59	0.78	0.78
CS-2	9	0.59	0.59	0.78	0.79
	18	0.59	0.60	0.78	0.80
	27	0.61	0.62	0.82	0.83

Table 5: Effective width and shear lag factor of three-girder bridge.

Cross-section	Span (m)	b_e (m)		λ	
		GFRP	Steel	GFRP	Steel
CS-1	9	0.53	0.54	0.67	0.72
	18	0.59	0.59	0.78	0.79
	27	0.61	0.63	0.81	0.84
CS-2	9	0.62	0.62	0.83	0.83
	18	0.65	0.67	0.86	0.89
	27	0.68	0.70	0.90	0.93

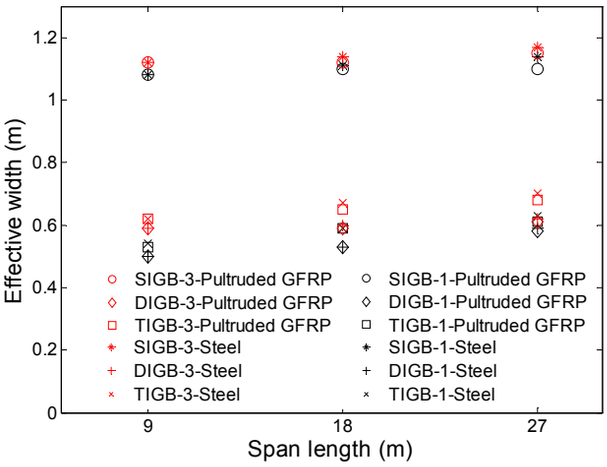


Figure 15: Summary of effective widths (1 and 2 are corresponding to CS-1 and CS-2, respectively).

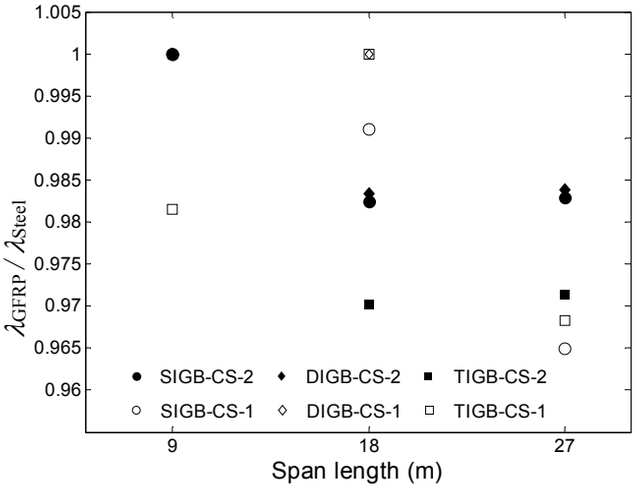


Figure 16: Ratios between pultruded GFRP and steel shear lag factors.

For both composite and non-composite material bridges, it is apparent that with the same bridge configuration, the effective width increases with the increase of span length regardless of the considered cross-section. Also, for all bridge configurations, the effective width is higher in the shear region (CS-1) than that at middle span (CS-2), which leads to a higher shear lag factor at mid-span. Furthermore, it has been found that the effective width of the interior girder in the three-girder configuration is relatively close to its girder spacing, at approximately 90% of half width.

5 SUMMARY & CONCLUSIONS

This paper investigates the shear lag on pultruded GFRP bridge by conducting a parametric study. Sandwich bridge deck are used and supported by two pultruded GFRP I-beams to achieve full composite action. Three bridge configurations are constructed at different span length varying from 9 m to 27 m. All proposed bridge models are tested under four-point bending loads.

Some conclusions from the research are summarized below:

- The sandwich bridge deck with fiber reinforcement in longitudinal and transverse directions can effectively prevent local shear deformation of the bridge deck.
- The transverse distribution of longitudinal stress depends on bridge length. Significant non-uniform distribution occurs for a 9 m span, while they are more uniform at 18 m or 27 m span.
- The effective widths are very similar for the studied pultruded GFRP bridge and steel bridges with the same geometry and configuration.
- Generally, with the same bridge configuration, the effective width increases with the increase of span length for full-composite and non-composite bridge.
- Although there is no specific standard for GFRP bridge deck, the effective width of pultruded GFRP bridge is lower than that obtained according to AASHTO.

Overall, based on the results of this study, it can be emphasized that pultruded GFRP bridges with orthotropic sandwich decks can be used in the replacement of non-composite steel bridge with similar configurations without changed considerations of shear lag.

REFERENCES

Alnahhal, W., Aref, A., and Alampalli, S. (2008). "Composite behavior of hybrid FRP-concrete bridge decks on steel girders." *Composite Structures*, 84(1), 29-43.

Bakis, C., Bank, L. C., Brown, V., Cosenza, E., Davalos, J., Lesko, J., Machida, A., Rizkalla, S., and Triantafillou, T. (2002). "Fiber-reinforced polymer composites for construction-state-of-the-art review." *Journal of Composites for Construction*, 6(2), 73-87.

Bank, L. C. (2006). *Composites for construction: structural design with FRP materials*, John Wiley & Sons.

Bisplinghoff, R. L., Mar, J. W., and Pian, T. H. (1965). *Statics of deformable solids*, Courier Corporation.

Caprani, C., Satasivam, S., Ahmadi, E., Ngan, J. W., Zhang, S. h., and Bai, Y. (2017). "Static and dynamic performance of an orthotropic-deck pultruded fibre-reinforced polymer footbridge." *39th IABSE Symposium*.

Cheung, M. S., and Chan, M. (1978). "Finite strip evaluation of effective flange width of bridge girders." *Canadian Journal of Civil Engineering*, 5(2), 174-185.

Gara, F., Ranzi, G., and Leoni, G. (2011). "Simplified method of analysis accounting for shear-lag effects in composite bridge decks." *Journal of Constructional Steel Research*, 67(10), 1684-1697.

Hambly, E. C. (1991). *Bridge deck behaviour*, CRC Press.

He, C. "Model experimental study of shear lag effect on the girder of a cable-stayed bridge." *Proc., Electric Technology and Civil Engineering (ICETCE), 2011 International Conference on*, IEEE, 2367-2369.

Keelor, D., Luo, Y., Earls, C., and Yulismana, W. (2004). "Service load effective compression flange width in fiber reinforced polymer deck systems acting compositely with steel stringers." *Journal of Composites for Construction*, 8(4), 289-297.

Moses, J. P., Harries, K. A., Earls, C. J., and Yulismana, W. (2006). "Evaluation of effective width and distribution factors for GFRP bridge decks supported on steel girders." *Journal of Bridge Engineering*, 11(4), 401-409.

Nagaraj, V., and GangaRao, H. V. (1997). "Static behavior of pultruded GFRP beams." *Journal of Composites for Construction*, 1(3), 120-129.

O'Connor, J., and Hooks, J. (2004). "A summary of six years experience using FRP composites for bridge decks."

Sedlacek, G., and Bild, S. (1993). "A simplified method for the determination of the effective width due to shear lag effects." *Journal of Constructional Steel Research*, 24(3), 155-182.

Tenchev, R. (1996). "Shear lag in orthotropic beam flanges and plates with stiffeners." *International journal of solids and structures*, 33(9), 1317-1334.

Timoshenko, S. P., and Goodier, J. N. (1969). *Theory of elasticity* McGraw-Hill, New York.

van Ijselmuijden, K., and Tromp, L. "Fibre-Reinforced Plastic (FRP) deck substitution of a fatigue damaged steel deck." *Proc., IABSE Symposium Report*, International Association for Bridge and Structural Engineering, 191-198.

Zhang, S., Caprani, C., Satasivam, S., and Bai, Y. (2016). "Static performance assessment of a novel pultruded fibre-reinforced polymer footbridge." *Mechanics of Structures and Materials: Advancements and Challenges*, CRC Press, 1529-1534.

Zou, B., Chen, A., Davalos, J. F., and Salim, H. A. (2011). "Evaluation of effective flange width by shear lag model for orthotropic FRP bridge decks." *Composite Structures*, 93(2), 474-482.

Maintenance, Safety, Risk, Management and Life-Cycle Performance of Bridges – Powers, Frangopol, Al-Mahaidi & Caprani (Eds)
© 2018 Taylor & Francis Group, London, ISBN 978-1-138-73045-8

Dynamic response analysis of widening bridge due to moving vehicles

Yan Li, Tingting Yang, Zhao Li, Lipeng Liu

School of Transportation Science and Engineering, Harbin Institute of Technology, Harbin, China. 150090

ABSTRACT: Rapid economic growth has led to a sharp increase in the highway traffic volume in China, and then more and more bridges widening projects are carried out to reply the situation. When a bridge is widened by constructing a new deck and casting a concrete stitch between the existing deck and the new deck, it is often required to maintain traffic without interruption and as a result the curing concrete stitch would be subjected to traffic induced vibration. The possible damaging effects of traffic vibration on curing concrete stitch have attracted concern from researchers and engineers. Therefore, it is very meaningful for the widening bridges to propose a detailed traffic restrictions or mitigation measures to avoid the adverse effect on the curing concrete stitch. Based on theoretical and experimental research results for concrete stitch of widening bridge, the vibration response threshold value causing crack damage induced by moving traffic load can be determined. The critical index of dynamic response value for a widening bridge is proposed, and its theoretical derivation process is explained in detail. Taking several typical PC simple supported T girder bridges as examples, the dynamic response of widening bridges under various vehicles loading cases are computed by the vehicle and bridge coupled vibration analyses program developed by authors. Some typical trucks and tested data for highway in China are applied on the research. Based on the analysis result, some advices about traffic control measures including limiting load, speed limit and lane limit etc. are presented to reduce or avoid the disadvantage influence of traffic vibration on curing concrete stitch for widening bridges. In addition, the reasonable construction technology is put forward, which provides a reference for the traffic control during constructing widening bridges.

1 INTRODUCTION

The rapid economic growth has contributed to the sharp increase of highway traffic volume in China. A large number of existing highway projects need to be expanded. Generally, a widened bridge makes its overall force by pouring a certain width of concrete joints between the old and new Bridges, to connect the upper structure of the new old bridge. The engineering practice shows that the joints between new and old part is one of the weakest parts of the bridge. It is one of the key criteria to measure the construction of widened bridge by ensuring that the construction maintenance of the concrete joints and not too much deformation and cracking in the later operation. The field test and laboratory model study showed that, traffic load adversely impact the concrete joints between new and old bridge mainly by the different vertical deflection between new and old bridge panel. When the difference exceeds a certain limit, the concrete joint cracks, and this will influence the development of concrete joint strength, integrity, the cohesive force between steel and concrete, and the flexural and shear capacity of concrete joints.

The bridge involved in the reconstruction project of the highway has a lot of traffic. In consideration of the social and economic cost and other aspects, traffic can't be closed in the process of casting the joint concrete. In order to effectively reduce the damage caused by traffic load vibration, some research work has been carried out at home and abroad. And various countermeasures have been put forward, including reasonable traffic control measures, temporary shear frame between the old and new bridge panel, temporary support under the old bridge, and casting the joint concrete piecewise. In the above measures, reasonable traffic control, if it can meet the requirements, is undoubtedly the most economical and convenient method. In the engineering practice and relevant research, analysis of the effectiveness of traffic control measures was carry out mainly accords to the typical load working condition of standard car lane load, so as to determine the effectiveness of traffic control and optimal control model.

In the analysis of the traffic control mode in the construction process of new and old bridge concrete joints, the existing research has not considered the impact of actual traffic composition and the characteristics of automobile dynamic load. At the same time, the process of car across the bridge, in essence, is a vehicle and bridge coupling vibration problems. It will be more targeted when study the bridge vibra-

tion under the vehicle load and put forward the reasonable traffic control measures on the dynamic level. It's beneficial to put forward the optimization of traffic control technology solutions.

For this purpose, based on the actual project of expansion, this paper relies on the relevant research results of highway vehicle load test data and typical vehicle model parameters. Using the self-braided bridge vibration analysis program, the dynamic response analysis of different heavy vehicle types and their combined working conditions is carried out. The effects of control measures such as limiting load, speed limit and restricted lane are studied to reduce the vibration amplitude of the joint slot. The critical index of the vibration control of the existing reinforced concrete slab is summarized and analyzed. The critical index determination method to control the vibration of the widened bridge is reached. The paper summarizes the process and strategy of traffic control technology for the construction of the widened bridge project.

2 INFLUENCE OF VEHICLE INDUCED VIBRATION ON THE CONCRETE OF THE CURRENT CAST-IN-PLACE JOINTS

2.1 *The characteristics of the concrete stress of the cast-in-place joint*

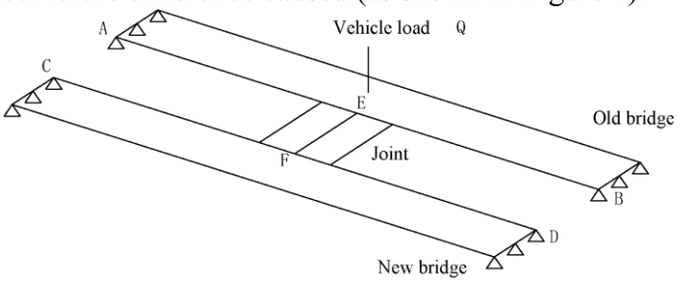
For bridge expansion projects, even in the construction and maintenance stage of the cast-in-place joint, it is generally necessary to keep the old bridges open. The vibration caused by traffic loads may cause cracks in the joint structure. The stress characteristics of the current cast-in-place joint structure during the phase of the traffic load are as follows:

(1) When the concrete has been cast, only the original bridge panel is bent under the traffic load, resulting in the deflection difference between the new and old bridge.

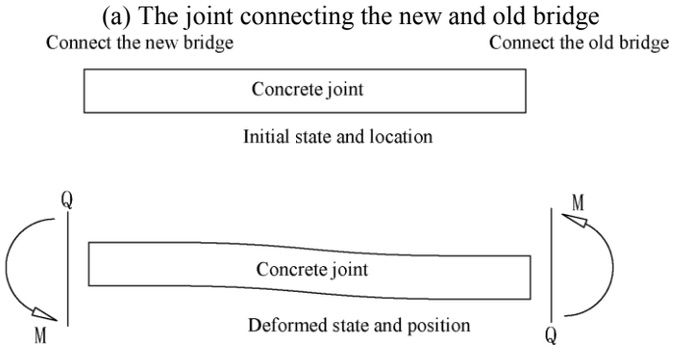
(2) When the concrete is gradually formed, the new bridge panel will be deformed with the original bridge panel, i.e. the old bridge traffic load is transferred to the bridge panel of the new bridge through the concrete joint plate;

(3) With the gradual hardening progress of the joints, the strength of the joints gradually increases, the deformation decreases under the constant traffic load, the shear strength increases, and the deflection difference between the new and old bridge decreases gradually.

(4) The adverse effects of traffic load on the joints between the new and old bridge are mainly caused by the difference of vertical deflection between the new and old bridge panels, resulting in the backward curvature difference caused (as shown in Figure 1).



(a) The joint connecting the new and old bridge



(b) The deformation drawing of the connecting joint with vehicles interaction on the old bridge

Figure 1. The deformation drawing of the connecting joint under the dynamic impact of moving vehicles

2.2 *Evaluation index of impact of traffic load on joint*

There are studies show that, the adverse effects of traffic load on the concrete joints between the new and old bridge panels are mainly caused by the difference of vertical deflection between the new and old bridge panels, resulting in the backward curvature difference caused (the deformation is shown in Figure 1).

According to the literature, the critical curvature formula obtained by Ng is:

$$\phi_{cr} = 2\left(\frac{1}{d}\right)\varepsilon_{cr} \tag{1}$$

In the formula, ε_{cr} is the ultimate tensile strain of the joint concrete; d is the thickness of the joint concrete slab.

In addition, the relationship between the reverse curvature ϕ and vertical deflection Δ is:

$$\phi = \frac{6\Delta}{L^2} \tag{2}$$

The L is the width of the joint concrete slab.

In the first two equations, the formula of vertical critical deflection between the new and old bridge joints can be obtained to reflect the deformation and damage of the joints. The critical deflection formula is:

$$\Delta_{cr} = \frac{1}{3}\left(\frac{L^2}{d}\right)\varepsilon_{cr} \tag{3}$$

Combined with K.H.Kwan et al., the critical curvature of the concrete slab in 200mm thick is used as the standard. Through the study of the model experiment to the concrete joint of the widened bridge, the

relationship between the initial curvature threshold and the degree of the joints cracks was obtained by the vehicle vibration simulation test: $18\times10^{-3}m^{-1}$, $27\times10^{-3}m^{-1}$, $36\times10^{-3}m^{-1}$, and $45\times10^{-3}m^{-1}$, corresponding cracks appeared, slightly cracking (0.1mm in width), medium cracking (0.2mm in width) and severe cracking (>=0.3mm in width). At the same time, the vibration curvature threshold which can lead to a significant reduction in the bond strength of the reinforced concrete is about $81\times10^{-3}m^{-1}$, far greater than the vibration threshold corresponding to concrete cracking, and it can be used as the absolute limit of vibration control of the bridge vehicle.

In this paper, the width of the cast-in-place joint is 50cm and 160mm thick. According to the above calculation formula, the corresponding vertical deflection value is 1.4mm. It is a critical evaluation index for the cracking of joints under the vibration of the bridge.

3 PRINCIPLE OF VIBRATION ANALYSIS OF VEHICLES AND BRIDGES

In the present study, the modal superposition and coupled method is used in solving VBCV problem. Since the dynamic responses of bridge are usually determined by the lower order modal shapes, the method is widely used to increase the computation efficiency (Calcada et al. 2005; Xu et al. 2010).

3.1 *Equation of motion of the vehicle*

The equation of motion for a vehicle can be expressed as follows:

$$[M_v]\{\ddot{X}_v\}+[C_v]\{\dot{X}_v\}+[K_v]\{X_v\}=\{F_v\} \qquad (4)$$

where $[M_v]$, $[C_v]$, $[M_v]$, and $[M_v]$, $[K_v]$ are the mass, damping, and stiffness matrices of the vehicle, respectively; $\{X_v\}$ and $\{F_v\}$ are the displacement vector of the vehicle and the vector of the wheel-road contact forces acting on the vehicle, respectively.

3.2 *Equation of motion of the bridge*

The equation of motion for a bridge under moving vehicle load can be written as:

$$[M_b]\{\ddot{X}_b\} + [C_b]\{\dot{X}_b\} + [K_b]\{X_b\} = \{F_b\} \qquad (5)$$

where $[M_b]$, $[C_b]$ and $[K_b]$ are the mass, damping, and stiffness matrices of the bridge, respectively; $\{X_b\}$ is the node displacement vector for all DOFs of the bridge, and $\{F_b\}$ is the force vector acting on the bridge through the vehicle's wheels.

3.3 *Road surface condition*

The road surface condition (RSC) is a very important factor that affects the dynamic responses of both the bridge and vehicles. The RSC is usually assumed to be a zero-mean stationary Gaussian random process and can be generated by an inverse Fourier transformation based on a power spectral density (PSD) function as:

$$r(x)=\sum_{k=1}^{N}\sqrt{2\varphi(n_k)\Delta n}\cos(2\pi n_k x+\theta_k) \qquad (6)$$

where θ_k is the random phase angle uniformly distributed from 0 to 2π, $\varphi()$ is the PSD function (m3/cycle) for the road surface elevation, and n_k is the wave number (cycle/m). The PSD functions for road surface roughness were developed by Dodds and Robson (1973), and the PSD function was simplified by Huang and Wang (1992) as:

$$\varphi(n)=\varphi(n_0)\left(\frac{n}{n_0}\right)^{-2} \qquad (n_1<n<n_2) \qquad (7)$$

where n is the spatial frequency (cycle/m); n_0 is the discontinuity frequency of $1/2\pi$ (cycle/m); $\varphi(n_0)$ is the roughness coefficient (m^3/cycle) which is related to the road surface condition; and n_1 and n_2 are the lower and upper cut-off frequencies, respectively.

The International Organization for Standardization proposed a road roughness classification index from A (very good) to H (very poor) according to different values of $\varphi(n_0)$. In the present study, the ISO road roughness classification is used.

3.4 *Assembling the vehicle-bridge coupled system*

Based on the displacement relationship and interaction force relationship at the contact points, the vehicle-bridge coupled system can be established by combining the equations of motion of both the bridge and vehicle as follows:

$$\begin{bmatrix} M_v & 0 \\ 0 & M_b \end{bmatrix}\begin{Bmatrix} \ddot{X}_v \\ \ddot{X}_b \end{Bmatrix}+\begin{bmatrix} C_v & C_v \\ C_{bv} & C_b \end{bmatrix}\begin{Bmatrix} \dot{X}_v \\ \dot{X}_b \end{Bmatrix} +\begin{bmatrix} K_v & K_{vb} \\ K_{bv} & K_b \end{bmatrix}\begin{Bmatrix} X_v \\ X_b \end{Bmatrix}=\begin{Bmatrix} F_v^b \\ F_b^v \end{Bmatrix} \qquad (8)$$

where C_{bv}, C_{vb}, C_b, K_{bv}, K_{vb}, K_b, F_v^b and F_b^v are the results of the wheel-road contact forces and time-dependent terms.

To simplify the bridge model and therefore save computational effort, the modal superposition technique can be used, and Eq. (8) can be simplified into the following:

$$\begin{bmatrix} M_v & 0 \\ 0 & M_B \end{bmatrix}\begin{Bmatrix} \ddot{X}_v \\ \ddot{q}_B \end{Bmatrix}+\begin{bmatrix} C_v & C_{vB} \\ C_{Bv} & C_B+C_B^v \end{bmatrix}\begin{Bmatrix} \dot{X}_v \\ \dot{q}_B \end{Bmatrix} +\begin{bmatrix} K_v & K_{vB} \\ K_{Bv} & K_B+K_B^v \end{bmatrix}\begin{Bmatrix} X_v \\ q_B \end{Bmatrix}=\begin{Bmatrix} F_v^r \\ F_B^{rG} \end{Bmatrix} \tag{9}$$

where subscripts "B" and "v" represent the bridge and vehicle, respectively; superscript "v" in the stiffness (K) and damping (C) terms refers to the contributions due to vehicles; subscripts "Bv" and "vB" refer to the vehicle and bridge coupled terms; superscripts "r" and "G" represent the acting force due to road roughness and gravity force of the vehicles, respectively.

The VBCV system in Eq. (9) contains only the modal properties of the bridge and the physical parameters of the vehicles. As a result, the complexity of solving the vehicle-bridge coupled equations is greatly reduced. Based on the methodology discussed above, a Matlab program is developed to automatically assemble the coupled equations of motion of the VBCV system and solve them in the time domain by the Newmark-β method. More details for the bridge-vehicle coupled system and solving process can be found in Li and Cai (2016).

4 DYNAMIC BEHAVIOR ANALYSIS OF WIDENED BRIDGE JOINTS UNDER TRAFFIC LOAD

4.1 *Engineering background*

This paper relies on a prestressed concrete simple branch T beam bridge single side extension reconstruction project involved in a highway reconstruction project from Shenyang (Wangjiagou) to Tieling (Xingshan). In the design scheme, the lower structure is separated and the upper structure is connected to the original bridge. The size of the new bridge T beam and the old bridge T beam are basically the same. For the example of a simple beam bridge with single hole span 20m, its typical cross-section is shown in figure 2. The beam is 150cm high and 170cm wide and the upper flange is 16cm thick. The 6th beam of new bridge is semi-rigid connected to the 5th beam of old bridge by concrete joints. As is shown in Figure 3, the joints' width is 50cm and the thickness is 16cm. Based on the relevant research results of highway vehicle load test data and typical vehicle model parameters. Using the self-braided bridge vibration analysis program, the dynamic response analysis of different heavy vehicle types and their combined working conditions is carried out. The pre-stressed concrete simple branch T beam bridge was analyzed with the span of 20m, 25m, 30m, 35m and 40m. After analyzing the influence of speed, lane position and vehicle weight on the dynamic response of the expansion bridge joints, it put forward some traffic control measures such as load limit, speed limit and lane limit.

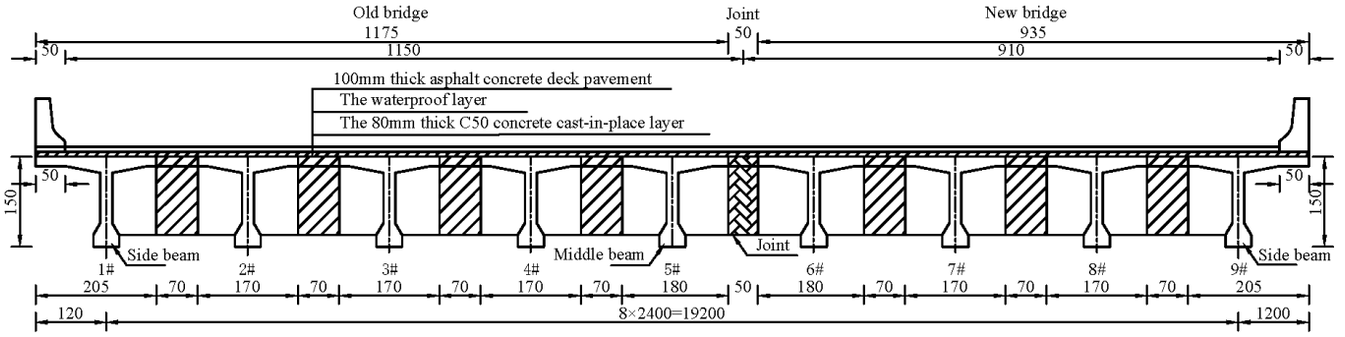


Figure 2. The typical section of the bridge (unit: cm)

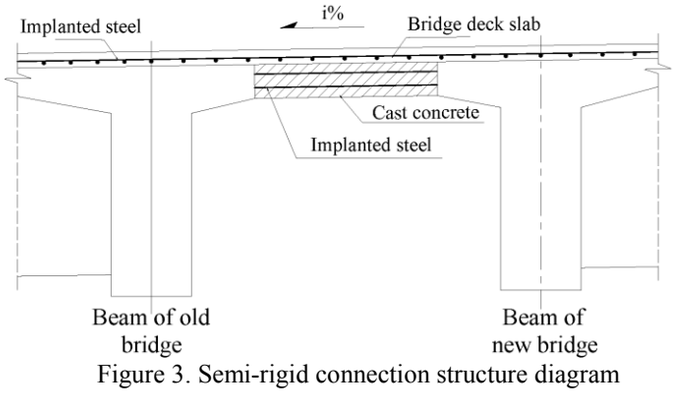


Figure 3. Semi-rigid connection structure diagram

4.2 *Widened bridge calculation and analysis model*

In order to analyze the stress state of key parts of the bridge, the spatial finite element model was established by ANSYS under the structure of semi-rigid transverse connection. The main beam and the connection of the new and old bridge is simulated by SOLID65 entity unit. The deck pavement adopts SHELL63 shell unit. The support is established with a COMBINE14 spring unit. Take the above 20m span bridge as the representative, its computational model is shown in Figure 4. In this paper, based on

the results of the existing experimental study, the critical value index of vertical deflection of the joint joints is proposed, and the vibration test is carried out in 1d of concrete pouring. For this reason, the parameters of the joint concrete in the bridge model are determined according to the age of 1d. And according to the results of the study of the mechanical properties of early stage concrete by Xuzhongqing, the elastic modulus is 1.72×10^4MPa.

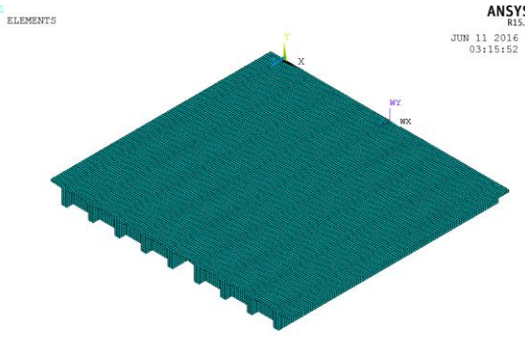
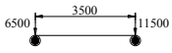
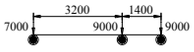
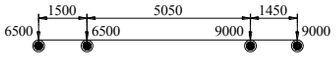
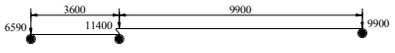
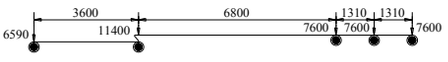
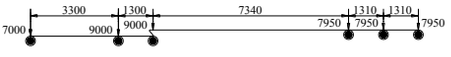


Figure 4. The finite element model of the bridge

4.3 *Characteristics of highway traffic load*

The traffic control analysis in the construction of the widening bridge is mostly based on the design lane load, and the difference of the effect of the actual bridge traffic load and the design load on the existing bridges are less considered. It is necessary to carry out detailed investigation and analysis of the traffic load characteristics (model, vehicle weight and overloading ratio, etc.) for the traffic control measures during the construction of specific bridges. When the data is not available, the traffic load conditions of similar roads in the area can be referenced. Based on a large number of road traffic survey, dynamic weighing data nationwide and existing relevant research results, the most common heavy-duty models in highway in China can be reduced to 7 types (see table 1). The related parameters of various types of models refer to the research results of Hanwanshui, Zhangxiang and other related research on vehicle and traffic investigation. The spatial dynamic analysis model of each model is detailed in the literature.

Table 1 Vehicle types and characteristics

No.	Types	Axle number	Graphic （wheel base: mm; Axle load: kg）
V1	Trucks	2	
V2	Trucks	3	
V3	Trucks	4	
V4	Trailer	3	
V5	Trailer	4	
V6	Trailer	5	
V7	Trailer	6	

Note: the V1 model is a two-axis vehicle, the V2 model is a three-axis vehicle, and the V3 model is a four-axis vehicle. The V4 model is a three-axle trailer, the V5 model is a four-axle trailer, and the V6 model is a five-axle trailer. The V7 is a six-axle trailer. The same below.

4.4 *The analysis cases*

The vibration response of the widening bridge is mainly affected by the following factors, including the vehicles type, load, speed, the position of the lane and the arrangement of vehicles. Besides, bridge surface roughness is also an important factor affecting the vehicle impact. The International Organization for Standardization (ISO, 1995) divides bridge surface roughness into 5 grades from "good" to "very poor". Considering the actual bridge surface roughness of the new bridge part which is widened and reconstructed, the roughness grade is taken as "good"". According to the actual situation of highway traffic in China, and considering the influence factors above, the relevant parameters of the analysis cases are determined as follows.

(1) Vehicle load condition

Based on the existing research with massive highway vehicle data and relevant vehicle dynamic model in China, seven typical truck models (as shown in Table 1) are selected for the subsequent analysis.

The standard of full load for various vehicles is determined by related department in China, which limits that each axle weight is under 10t, while the total weight is under 10t × axle number. Referred to the highway traffic load data in China, the load situation of the above 7 typical models is divided into three cases: full load, overload 50% and 100%, which provides the load limiting index for bridge widening and reconstruction with open traffic.

(2) Vehicle speed

Considering that the speed ranges from 20 to 100km/h, the vibration response of joint is calculated and analyzed, which provides the speed limit index of heavy vehicle during the widening bridge joint construction process.

(3) Vehicle lane

The old bridge part of the widening bridge is one-way street with two lanes. The position of the old

bridge lane is shown in figure 5. In the following analysis of vehicle-bridge coupled vibration, the single vehicle condition is considered. To be specific, the aforementioned 7 various vehicles pass the bridge, respectively, in Lane 1 (far from the seam side of the lane) and Lane 2 (near the side of the joint side of the lane) bridge at different speeds.

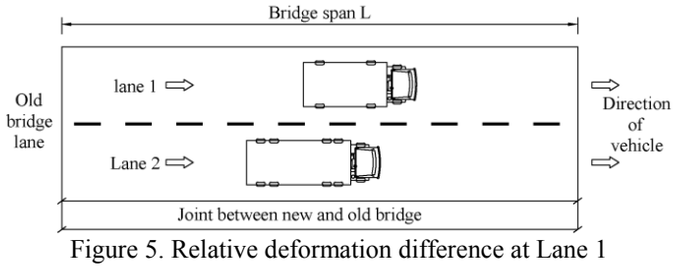


Figure 5. Relative deformation difference at Lane 1

4.5 *Dynamic response analysis of joints of widening bridge under single vehicle*

4.5.1 *A widening example of 20 m simply supported bridge*

(1) Vehicle load condition

Based on the analysis program of vehicle-bridge coupling vibration, the 7 types of vehicles pass Lane 2 at different speeds (as shown in Figure 5) respectively with full load, overload 50% and 100%. The maximum relative deformation difference of the cast-in-place joints between the new and old bridge is calculated as shown in Figure 6.

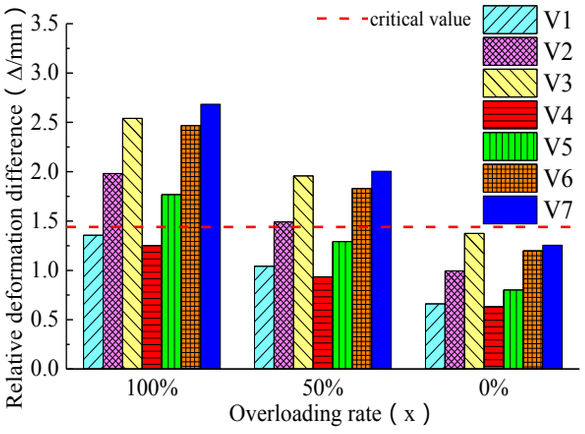


Figure 6. The maximum relative deformation difference under the action of various types of vehicles

According to the bridge vibration critical value mentioned above, when the vehicles are overloaded by 50% or 100%, the relative deformation difference induced by various vehicles all exceed 1.4mm; when the vehicles are full-loaded, the relative deformation difference is within the limit. The results show that, in this example, if all kinds of vehicles are not overloaded, there is no need for extra traffic control during the construction of bridge widening.

(2) Vehicle speed

The conditions of 5 types of vehicle overloaded by 100% on Lane 2 are selected for further analysis about the impact to the joint with vehicle speed ranging from 20 to 100 km/h. As shown in Figure 7, the vehicle speed has little effect on the relative deformation. The relative deformation difference exceeds 1.4mm under all speed conditions. Therefore, there is no speed limit condition for all type of vehicles. Similarly, the conditions of 5 types of vehicle overloaded by 100% on Lane 2 can induce the same results.

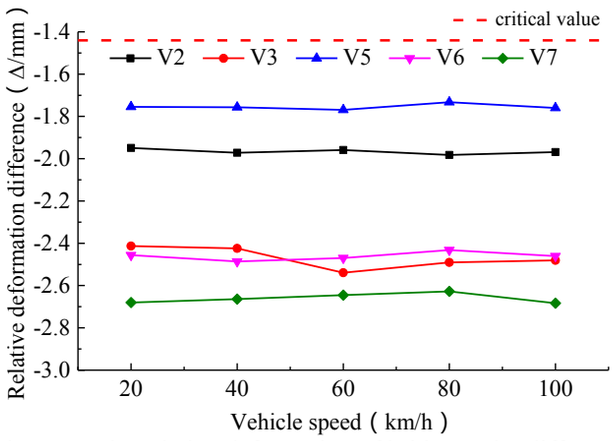


Figure 7. The relative deformation of bridge under different speed

(3) Vehicle lane

Changing the vehicle overloaded by 100% from Lane 2 to Lane 1, the distribution law of relative deformation difference along the longitudinal direction of the bridge can be calculated, as shown in Figure 8. The results of various vehicles are less than 1.4mm. It shows the measure that limiting the heavy vehicle traffic of Lane 2 can eliminate the adverse effects of the vehicle bridge vibration.

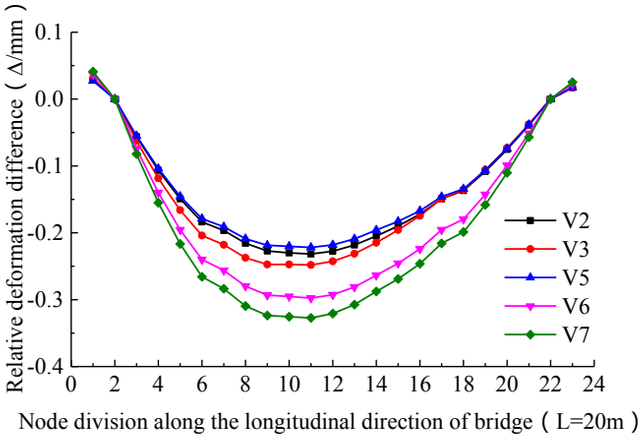


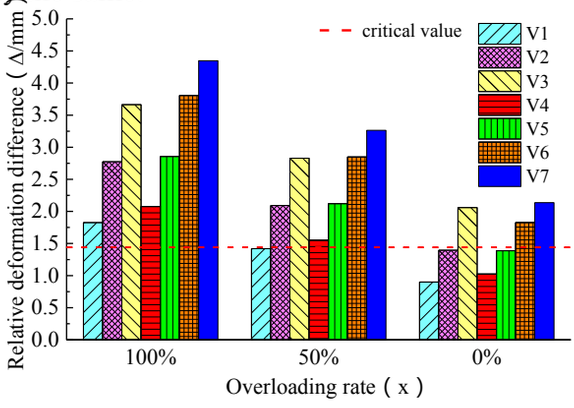
Figure 8. Relative deformation difference at Lane 1

4.5.2 *Examples with other spans*

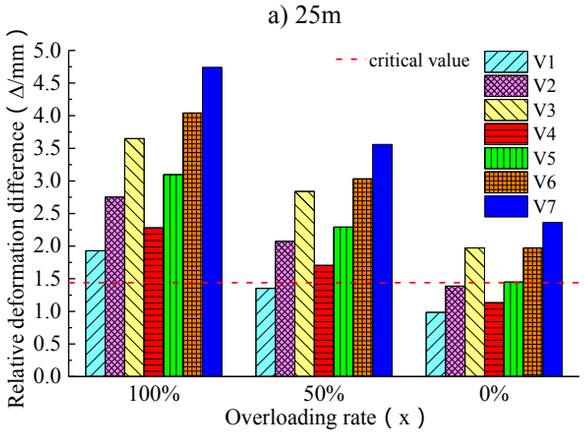
(1) Vehicle load condition

Considering 7 types of vehicles passing Lane 2 at different speeds respectively with full load, overload 50% and 100%, the maximum deformation differences with different span of 20, 30 and 40 m is calculated as shown in Figure 9. It can be seen the relative deformation of the different span increases that with the increase of the load. Compared with Figure 6, the relative deformation difference of widening bridge with 25 m span increases greatly. When the

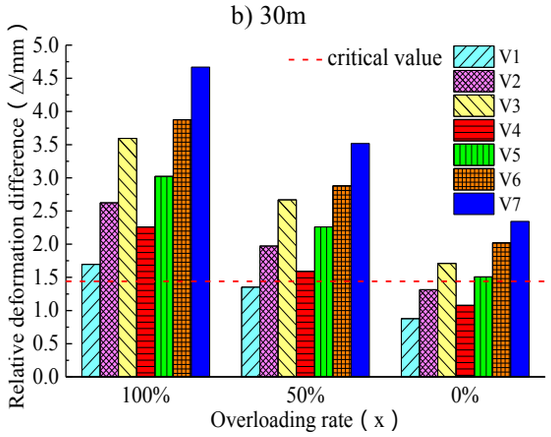
span exceeds 25m, the variation laws of the overload rate and the relative deformation difference are basically the same.



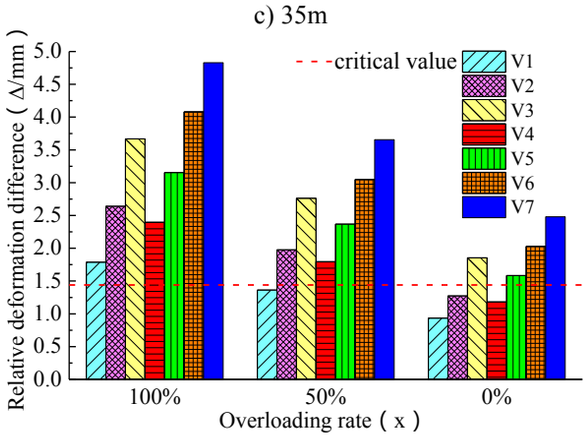
a) 25m



b) 30m



c) 35m



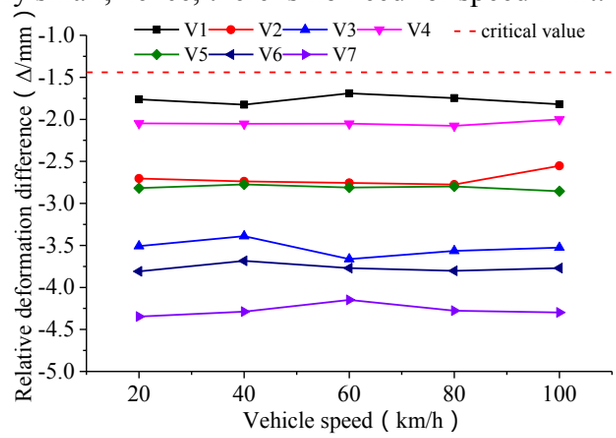
d) 40m

Figure 9. The maximum relative deformation difference under the action of various types of vehicles

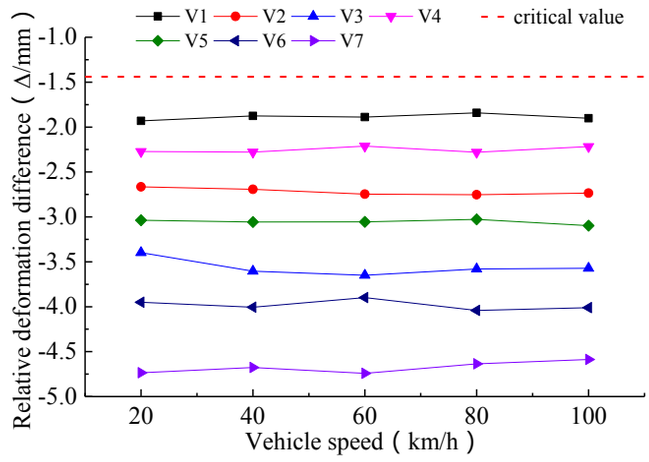
According to the bridge vibration critical value accounted above, as shown in Figure 9, when the vehicles are overloaded by 100%, the relative deformation differences of all 7 vehicles are greater than 1.4mm; when the vehicles are overloaded by 50%, only the result of 2 axle vehicle(V1) is under 1.4 mm; when the vehicles are full-loaded, the relative deformation differences induced by 4 axle vehicle (V3), 5 axle trailer (V6) and 6 axle trailer (V7) with all spans exceed 1.4mm. Besides, for 35m, 40m widening bridge, the relative deformation difference induced by 4 axle trailer (V5) is also more than 1.4mm.

(2) Vehicle speed

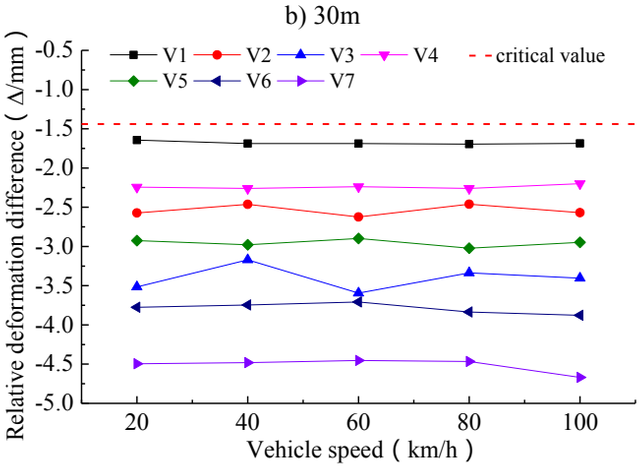
For the conditions of vehicle overloaded on Lane 2, the effect of velocity on the relative deformation difference with different spans is shown in Figure 10. The influence of speed on relative deformation is very small, hence, there is no need for speed limit.



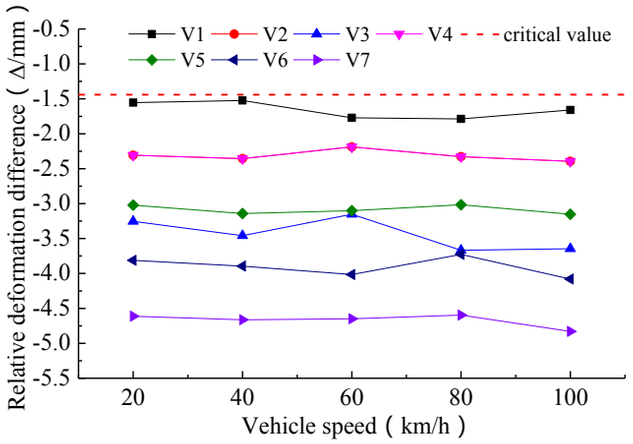
a) 25m



b) 30m



c) 35m

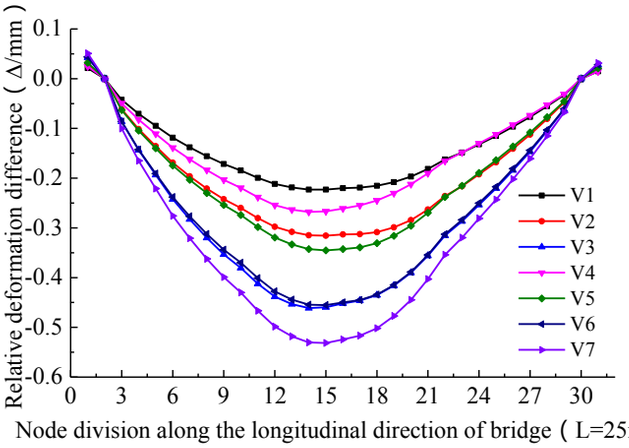


d) 40m

Figure 10. The relative deformation of the different span widening bridges under different vehicle speeds (Overload by 100%)

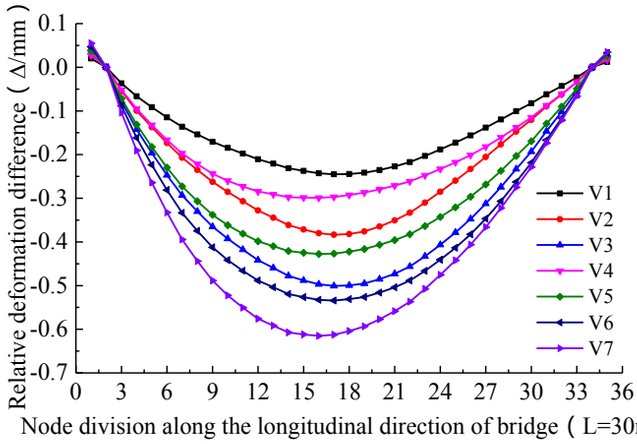
(3) Vehicle lane

The condition of the 7 types of vehicles overloaded by 100% are acted on Lane 1, the distribution law of relative deformation difference of the different spans bridge along the longitudinal direction is calculated, as shown in Figure 11. The maximum value appears near the mid-span of the widened bridge, and the value grows larger with the increase of the span, and it is still within the critical vibration index （$\Delta = 1.4$ mm）. Therefore, the traffic restriction measures can effectively reduce the deformation difference and eliminate the disturbance effect of the vehicle bridge vibration.



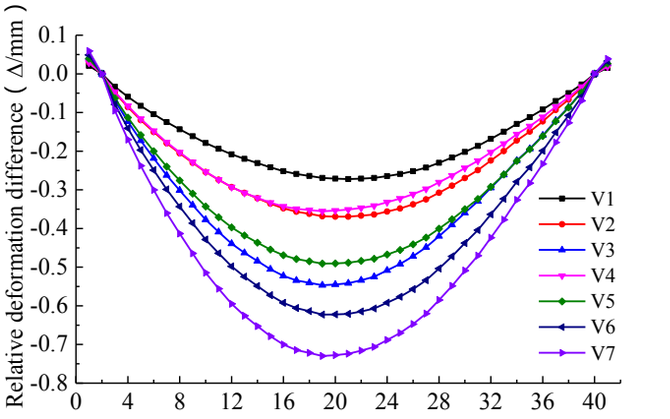
Node division along the longitudinal direction of bridge (L=25m)

a) 25m



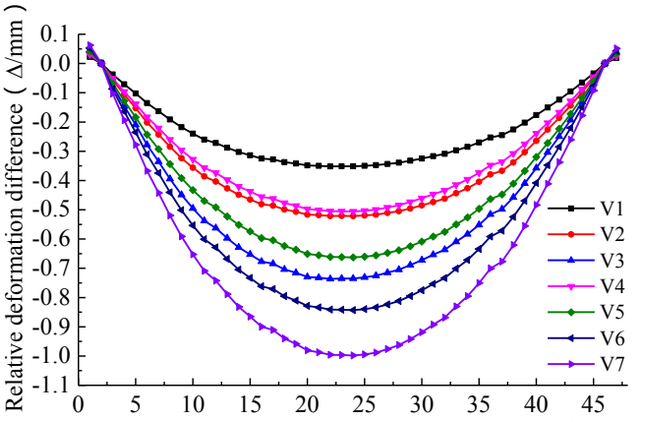
Node division along the longitudinal direction of bridge (L=30m)

b) 30m



Node division along the longitudinal direction of bridge (L=35m)

c) 35m



Node division along the longitudinal direction of bridge (L=40m)

d) 40m

Figure 11. The relative deformation of the different span widening bridges with vehicles load on the Lane 1 (Overload by 100%)

5 CONCLUSION

(1) In this paper, combining existing research results, the vibration evaluation index and the determination method of widened bridge joints under the traffic load are put forward, which can provide reference for the traffic control analysis of similar engineering construction process.

(2) The results of the vibration analysis of the bridge by the concrete simple supported T beam under typical automobile load are shown as follows: Under the same vehicle, the speed of the car has little influence on the relative deformation of the joints and can be ignored. As the bridge span increases, the relative deformation growth is not obvious. The relative deformation value increases linearly with the weight of the car. The main control factors of the relative deformation peak of the vehicle weight and the vehicle model need to be considered in the development of traffic control measures.

(3) In this paper, the analysis results of each bridge show that, for the model of the three-axle vehicle (V2), four-axle vehicle (V3), four-axle trailer (V5), five-axle trailer (V6) and six-axle trailer (V7), the relative deformation of the 25m~40m bridge has ex-

ceeded the critical vibration value in the full load. Among them, the six-axle trailer (V7) has a deformation difference of 2.5mm for the span of 40m bridge, exceeding the threshold of more than 72%. Therefore, these models should be controlled.

(4) In this paper, the analysis results of each bridge show that, the position of the vehicle action lane is most sensitive to the relative deformation of the cast-in-place joints. Keeping the car away from the stitching side lane of single span, vehicle loads can be unrestricted. Without lane control when vehicles cross the bridge, for the span of 20m: no traffic control need to be adopted for all kinds of fully loaded vehicles. For the span of 25m~ 40m: the three-axle vehicle (V2), four-axle vehicle (V3), four-axle trailer (V5), five-axle trailer (V6) and six-axle trailer (V7) require traffic control measures.

6 REFERENCES

FURR, H. L. & Fouad, F. H. 1981. Bridge slab concrete placed adjacent to moving live loads. *Concrete* 131.

FURR, H. L. & FOUAD, F. H. 1982. Effect of moving traffic on fresh concrete during bridge-deck widening. *Transportation Research Record* 860: 28-36.

HILSDORF, H. K. & LOTT, J. L. 1969. Revibration of retarded concrete for continuous bridge decks.

ISSA MA. 1999. Investigation of cracking in concrete bridge decks at early ages. *Journal of Bridge Engineering* 4(2): 116-24.

HARSH, S. & Darwin, D. 1986. Traffic-induced vibrations and bridge deck repairs. *Concrete International* 8(5).

ZHAO, X. 2009. Settlement prediction in whole process of high embankment broadening on soft soil foundation. *Road Machinery & Construction Mechanization* 26(9):40-42.

ANSELL, A. & SILFWERBRAND J. 2003. The vibration resistance of young and early-age concrete. *Structural Concrete* 4(3).

SHEN, P.S., FANG H. XIA X.H. & GONG H.G. 2006. Simplified analysis for frame structure considering construction process, shrinkage and creep. *Journal of Architecture and Civil Engineering* 23(2):41-45.

Li, M.X. 2008. Analysis of highway's extension and settlement. *Road Machinery & Construction Mechanization* 25(4):58-60.

HUBER, H. 2000. Rehabilitation of the devil's bridge over schollenen gorge. *Structural Engineering International* 10(1):23-25.

Montero, AC. 1980. Effect of maintaining traffic during widening of bridge decks (a case study). *M. SC. thesis. Columbus (USA): Ohio State University* 78.

KWAN, A. K. H. & Ng, P. L. 2006. Reducing damage to concrete stitches in bridge decks *Bridge Engineering* 159(2): 53-62.

KWAN, A. K. H. & NG, P. L. 2007. Effects of traffic vibration on curing concrete stitch: part i — test method and control program. *Engineering Structures* 29(11): 2871-2880.

NG, P. L. & KWAN, A. K. H. 2007. Effects of traffic vibration on curing concrete stitch: part ii—cracking, debonding and strength reduction. *Engineering Structures* 29(11): 2881-2892.

DU, J.S., ZHAO, G., ZHAO Y.G. & HUI, X.C. 2011. Control of deflection difference between existing and new decks during bridge widening. *Journal of Chang' an University. (Natural Science Edition)* 04:58-62+76.

NIE, J.G., WANG Y.H., FAN J.S. & ZHANG X.G. 2012. Mechanical behavior of the interface of composite cross beam in old concrete bridges widened with steel-concrete composite beam. *China civil engineering journal* 03:99-109.

Ng, P. L. & Kwan, A. K. H. 2004. Structural failure of concrete stitch in bridge widening and its mitigation. *International Conference on Structural and Foundation Failures* 113-122.

XU, Z.Q., YUAN, Q., YANG, Z.K. &WANG, M.M. 2015. Mechanical property experiment and uniaxial constitutive model for concrete at early age. *Journal of Shenyang University of Technology* 01:92-96.

WANG, T., HAN, W.S., & HANG, P.M. 2012. Statistic analysis for dynamic response of an expressway bridge under traffic loading. *Journal of vibration and shock* 31(20):116-120.

YAN, J.Y. 2013. Analysis of response and vehicle weight limit of fabricated box girder bridge based on monitoring data. *Chang' an University.*

Maintenance, Safety, Risk, Management and Life-Cycle Performance of Bridges – Powers, Frangopol, Al-Mahaidi & Caprani (Eds)
© 2018 Taylor & Francis Group, London, ISBN 978-1-138-73045-8

A Preventive Strengthening Strategy for Aged Steel Columns

W. Lin
Waseda University, Tokyo, Japan

N. Taniguchi
Maebashi Institute of Technology, Gunma, Japan

T. Yoda
Waseda University, Tokyo, Japan

S. Satake
Taiheiyo Materials Corporation, Chiba, Japan

ABSTRACT: Steel columns are widely used in buildings, bridge piers, and railway platform roofs etc. With aging, those steel columns are vulnerable to corrosion and fatigue, and can deteriorate for a variety of reasons, especially in great earthquakes. In order to avoid the unrecoverable damage of existing steel columns, the high cost of the structure owners and the great impact on the public use, effective preventive maintenance methods on the aged steel piers are necessary. On this background, a strengthening method for aged steel columns by using new construction materials such as glass fiber reinforced polymer (GFRP) plates, rapid hardening concrete, rubber-latex mortar, and reinforcing bars, is introduced in this study. Depending on possible applied load directions and corrosion conditions, two specimens were used in the loading tests. Static loading tests were performed on steel columns with and without strengthening. Applied load and deflection relationship and strain distribution on original and strengthened columns were measured and compared. Moreover, three-dimensional FE models were built, and the numerical results were compared with the test results. Both experimental and numerical results indicate that the present strengthening method can significantly enhance both rigidity and ultimate load carrying capacity of aged steel columns.

1 INTRODUCTION

Steel column structures are used in buildings, bridges, railway platforms and other civil engineering structures around the world, due to their simpleness in both design and construction. An example of column structures used in a railway platform is shown in Figure 1. In recent years, however, severe damages of aged steel columns were observed in earthquakes. For instance, a large amount of steel bridge piers damaged in the 1995 Hyogoken-Nanbu earthquake mainly because of either local buckling or rupture of welded corners (Chu, 2011). During the 2011 Tōhoku earthquake, severe damage was caused to electrification poles on viaducts of Tōhoku Shinkansen. Based on the existing experience, Japanese design specifications have been revised and updated a lot, but they are mainly used for designing new columns. For aged steel piers constructed with old design methods, they are generally not satisfied to new design codes, thus they should be strengthened appropriately. On this background, seismic retrofit on existing steel column structures has become a major concern.

With the purpose of improving the seismic performance of existing steel columns, a preventive seismic retrofit method for existing steel column structures is proposed in this paper. Both static loading tests and numerical simulations were conducted to investigate the real effectiveness of the present strengthening method and its improvement on the seismic performance of existing column structures.



Figure 1. Column structures in Japanese railway platforms.

2 STRENGTHENING STRATEGY

In this study, a strengthening method using GFRP plates, rubber-latex mortar, rapid hardening concrete, and reinforcing bars is proposed to strengthen the existing column structures. Rubber-latex mortar shows various abilities especially in adhesion bonding, waterproofing, shock absorption and abrasion resistance (Lin et al., 2013, 2014a), and significant contribution of rubber-latex mortar in enhancing bonding strength on steel-concrete interface was confirmed in previously performed bonding tests, as shown in Figure 2. In this method, the rubber-latex mortar is mainly used to enhance the integrity between aged structural steel and newly added surrounding concrete. Rapid hardening concrete is used for resisting the external loads together with the existing steel column, thereby increasing the rigidity and load carrying capacity. FRP plates are used as the formwork for concrete casting, and its contribution in the load carrying capacity is not considered in the design. Similar to other RC structures, reinforcements are used for controlling the crack width after concrete cracking.

As shown in Figure 3, the retrofitting sequence can be divided into surface preparation, spraying of rubber-latex mortar, set-up of the reinforcement and GFRP plates, and finally casting of rapid hardening concrete etc. Images of a steel pier during strengthening by using the method proposed in this study are shown in Figure 4. This method was originally proposed by authors of this paper for strengthening superstructures of aged short-span railway bridges, and both laboratory loading tests and field loading tests were performed by authors' group (Lin et al., 2014b, 2014c, 2017, and Taniguchi, 2016). Considering it outstanding effects in improving the structural performance of bridge superstructures, this study was performed to investigate its possibility in strengthening existing column structures.



Figure 2. Bonding test on steel-rubber latex mortar interface.

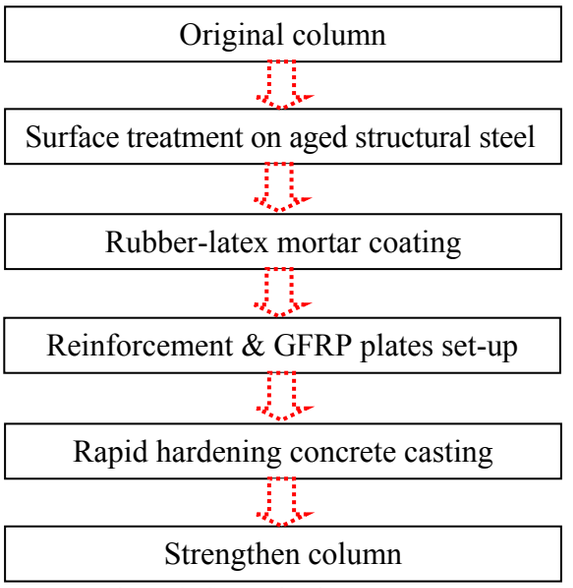


Figure 3. Strengthening process.

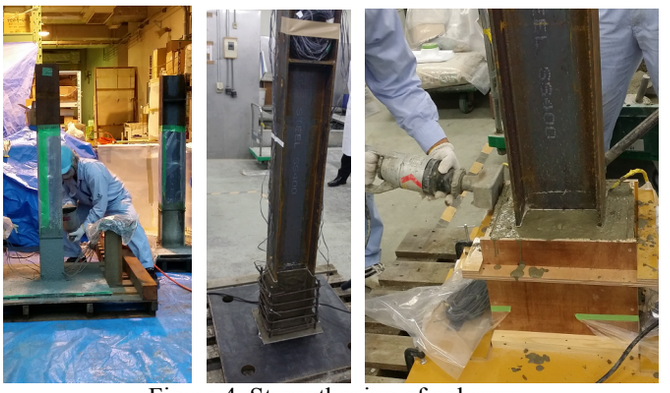


Figure 4. Strengthening of columns.

3 EXPERIMENTAL PROGRAMME

3.1 *Test Specimens*

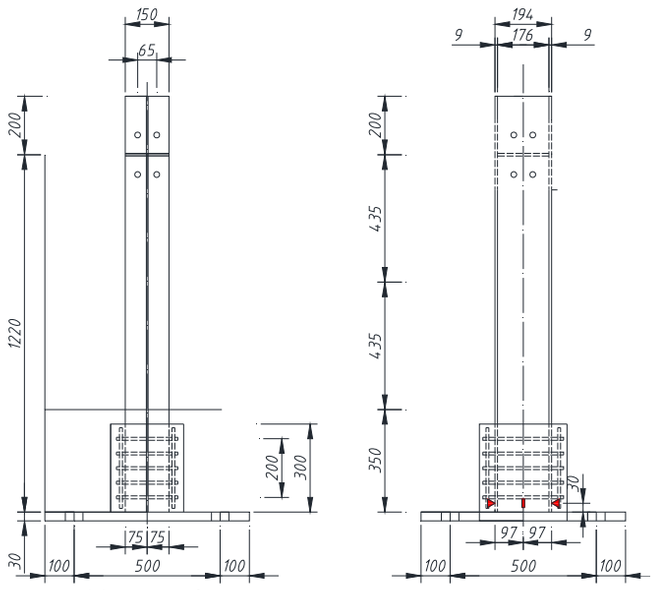
Two steel columns with same cross-section (an H-shape section of 194×150×6×9) were designed. Each of the specimens was 1.42m in height and the loading point was decided at the height of 1.2m. Stiffeners were welded at the loading point to prevent buckling and crippling of the web before flexural failure. A 700mm square steel plate with thickness of 30 mm was used as the base plate and connected with the steel column by welding. To strengthen the original steel column, the rubber-latex mortar with the thickness of 5mm was used on the surface of the aged structural steel. Reinforcement with a nominal diameter of 10mm for longitudinal reinforcement and 6mm for stirrups were used. Finally, rapid hardening concrete was casted. Mix proportions of rubber-latex mortar and rapid hardening concrete are shown in Table 1 and Table 2, respectively. The test specimens were fixed through connecting the base plate with the ground by using 4 bolts with a circular diameter of 60mm.The geometry dimension of the test specimen is shown in Figure 5.

Table 1. Mix proportion of rubber-latex mortar.

W/C (%)	P/C (%)	S/C	Mixture of rubber-latex	Rubber-latex coating powder
26.6	17.7	1.75	25kg	4.0kg

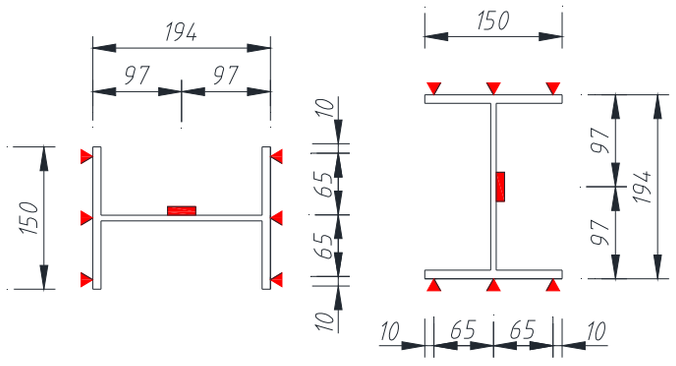
Table 2. Mix proportion of concrete.

W/C (%)	S/C (%)	Unit amount (kg/m^3)					
		Water	Early strength cement	Coarse aggregate	Fine aggregate	No.70	303A
50	46	165	330	814	971	2.97	0.66



(a) Front view (b) Side view

Figure 5. Size dimensions of test specimen (unit: mm).



(a) Strong axis (b) Weak axis

Figure 6. Strain gauge locations (unit: mm).

3.2 *Static Loading Test Set-up*

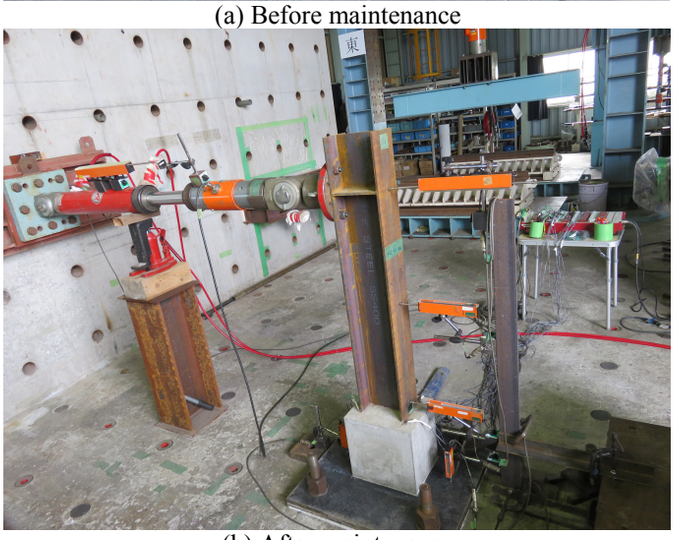
The load is applied by a jack in horizontal direction to simulate the earthquake load. For columns like electrification poles or columns in railway platform roofs, the axial force can be ignored in the design due to their negligible dead-weight. In terms of steel pier in bridge structures, the axial force is generally designed as no larger than 20% of its yield load. Therefore, the axial force in the column is not considered in order to simplify the loading test. However, the influence of the axial force on mechanical behavior of steel columns will also be investigated in this study, by using the numerical results.

As shown in Figure 6, there are strong axis and weak axis in a typical column with an H-shape cross-section. In order to investigate the effects of the proposed method in two different directions, the horizontal load was applied in both strong and weak axis directions, respectively. For this reason, two specimens were used in this study. Before strengthening, static loading tests were performed on the two original steel columns, including SC-S-1 (original steel column under load in strong axis direction) and SC-W-1 (original steel column under load in weak axis direction). The applied load was controlled in a low level to avoid any possible damage on columns. After strengthening, SC-S-2 (strengthened steel column under load in strong axis direction) and SC-W-2 (strengthened steel column under load in weak axis direction) were tested again to compare with the original steel columns without strengthening.

In order to confirm the sectional strain distribution, 7 strain gauges were used to measure the normal strain in the web and steel flanges near the bottom section, as shown in Figure 6. LVDTs were also used to measure the horizontal displacement at the loading section and two sections. The static loading test set-up for both original and strengthened columns was shown in Fig.7.



(a) Before maintenance

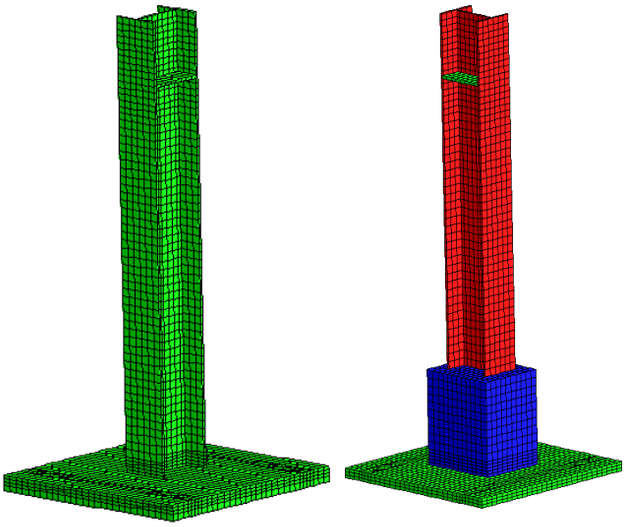


(b) After maintenance

Figure 7. Loading test set-up.

4 NUMERICAL MODELLING

The simulation of test specimen was carried out using the finite-element method and *DIANA* software. Solid elements were used to simulate the concrete, and shell elements were employed to model the steel column. Numerical models of steel column before and after strengthening were shown in Figure 8. To simulate the bond connection between the steel column and surrounding concrete, and the connection between the ground and the base plate, interface elements used in the numerical analysis, as shown in Figure 9. Re-bar elements were used for modeling the reinforcement, as shown in Figure 10.



(a) Before strengthening (b) Strengthened column
Figure 8. Numerical models for columns.

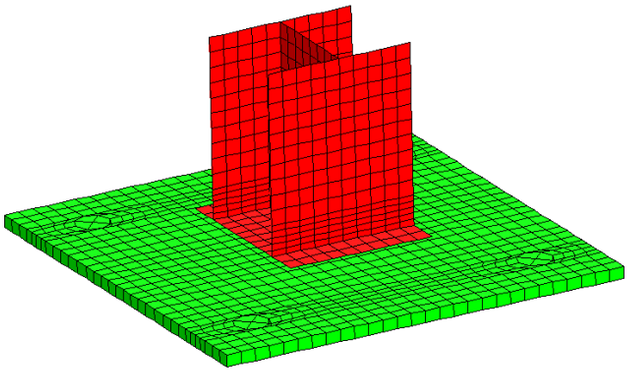


Figure 9. Simulation of interface.

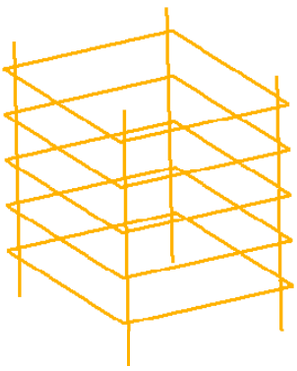


Figure 10. Simulation of reinforcement.

Material tests were performed, and the nominal compressive strengths of concrete achieved after 7 days and 11 days (test day) were 36.2 N/mm^2 and 39.3 N/mm^2, respectively. Experimental tensile stress-strain curve proposed by Nakasu et al. (1996) was used to simulate the tension softening behavior of concrete. The compression behavior of concrete was referred to JSCE (2002). The stress-strain curve considering the strain hardening was used to simulate the structural and reinforcing bars (JSCE, 2002). The yield strength of the H-shape column was 309 N/mm^2 according to the material test report. The yield strength of reinforcement was yield strength: 295 N/mm^2. The simplified interface model developed from Dörr's bond-slip model is used to model the steel-concrete interface (Dörr, 1980).

5 RESULTS AND DISCUSSION

5.1 *Applied Load in the Strong Axis Direction*

When the steel column is subjected to a load in the strong axis direction (SC-S), the load-displacement curve obtained from the numerical analyses is compared to the experimental results as shown in Figure 11. For retrofitting of aged steel columns, increase of rigidities in service state and increase of load carry capacity in the ultimate state are major concerns for engineers. On the basis of the obtained results, both experimental and numerical results demonstrate increase of the column stiffness after strengthening. Taking the horizontal deflection of 6.3mm (the maximum displacement in loading test for SC-S-1) as an example, the test load changed from 24.9kN in SC-S-1 to 31.4kN in SC-S-2, increased by 26%. For the strengthened column, the numerical model was stronger than the test model, which might be due to the ignored residual stress at the welded section in the numerical analyses. The comparison between the numerical results also indicates that the ultimate load carrying capacity of the column has increased obviously after strengthening. Taking the horizontal displacement of 61mm as an example, the corresponding load increased from 79.8 kN in SC-S-1 to 98kN in SC-S-2, thus 22.8% increase was confirmed.

In addition, the flexural strain measured at S2 and S5 were recorded and given in Figure 12 and Figure 13. The strain results at S2 and S5 indicate that the numerical values agree well with the experimental results during the elastic loading stage, and the significant reduction of flexural strain was confirmed in the strengthened column in comparison with the original column. Taking the applied of 24.9kN (maximum load applied in static loading test for SC-S-1) as an example, the corresponding strain at S2 reduced from -445μ in SC-S-1 to -110μ in SC-S-2, indicating 75% reduction in strain. On the other

hand, corresponding strain at S5 reduced from 301μ in SC-S-1 to 248μ in SC-S-2, indicating 17% reduction in strain. The different strain reduction ratio at S2 and S5 might be due to the residual stress at the welded section. Therefore, great improvement of seismic performance during an earthquake is expected.

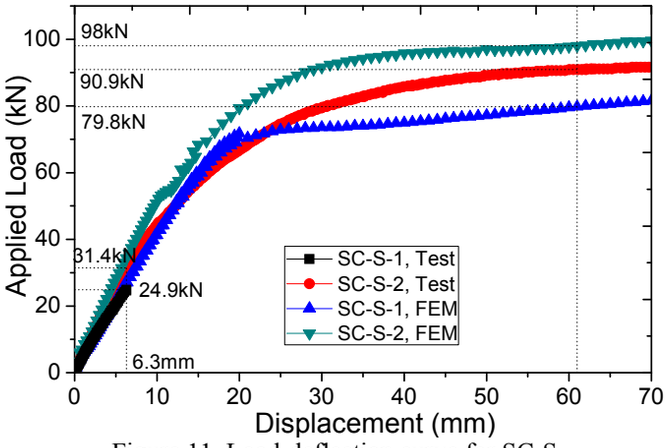


Figure 11. Load-deflection curve for SC-S.

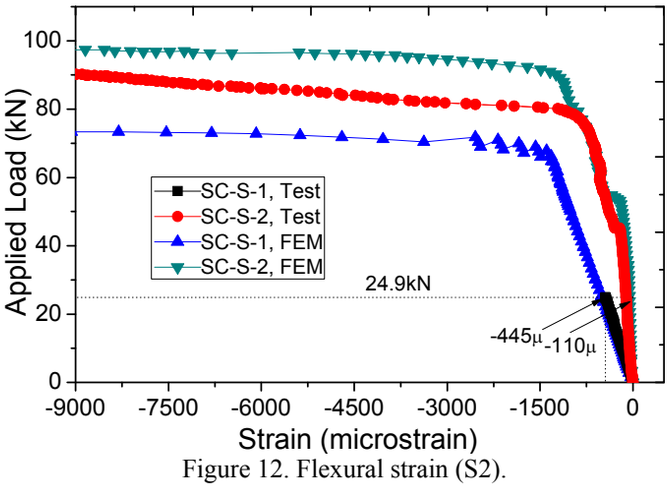


Figure 12. Flexural strain (S2).

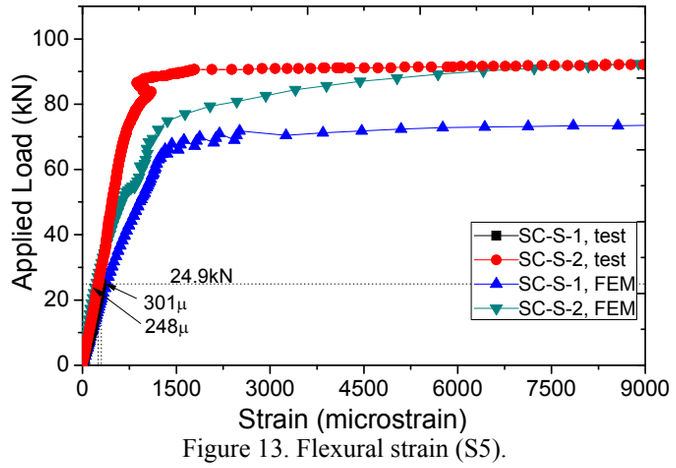


Figure 13. Flexural strain (S5).

5.2 *Applied Load in the Weak Axis Direction*

For the steel column under load in the weak axis direction (SC-W), the applied load and deflection relationship was given in Figure 14. According to the comparison, significant increase of the column stiffness and ultimate load carrying capacity in the weak axis direction were also confirmed. Taking the horizontal deflection of 6.9mm (the maximum displacement in loading test for SC-W-1) as an example, the test load changed from 9.5kN in SC-W-1 to 14.3kN in SC-W-2, increased by 51%. The ultimate load was increased from 26.4kN in SC-W-1 to 36.4kN in SC-W-2, thus 38% increase can be confirmed. The significant increase of the rigidity and load carrying capacity demonstrate the improvement of the seismic performance during earthquakes. Also, the comparison indicates that the numerical results agree well with the test results, indicating the validity of the numerical models used in this study.

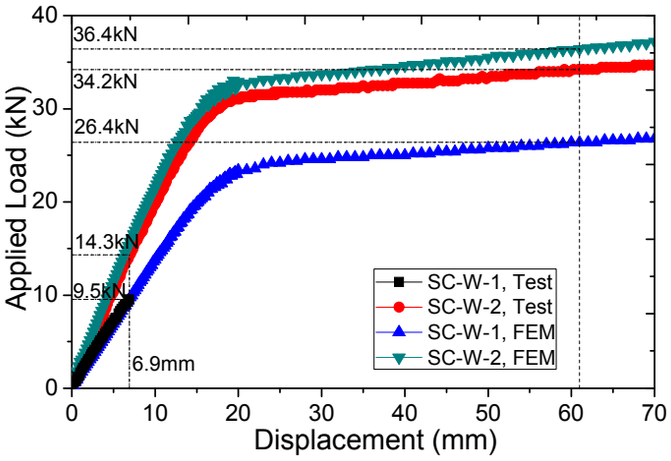


Figure 14. Load-deflection curve for SC-W.

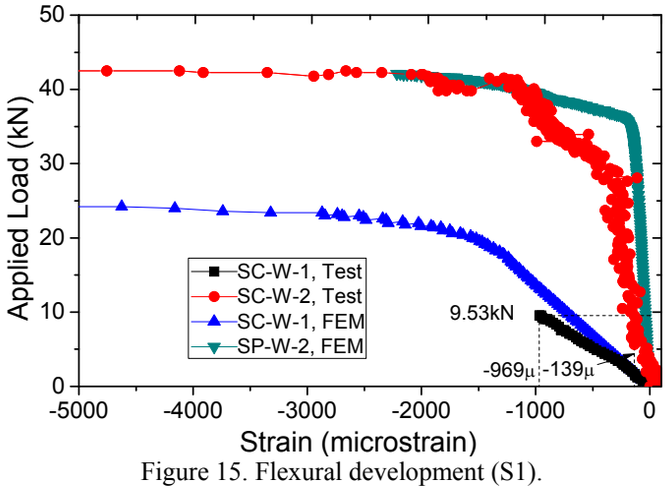


Figure 15. Flexural development (S1).

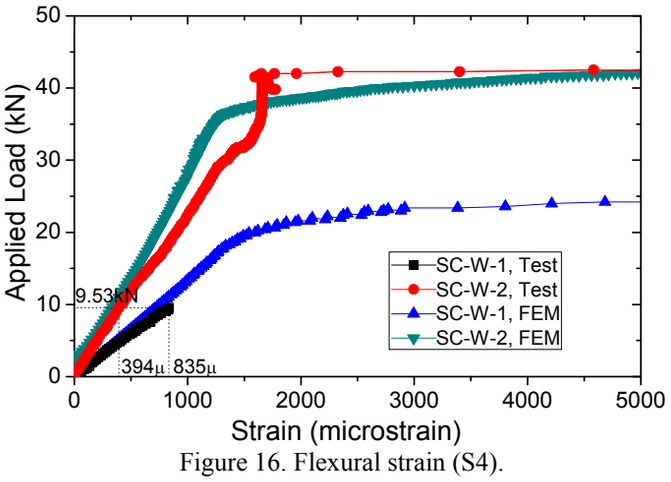


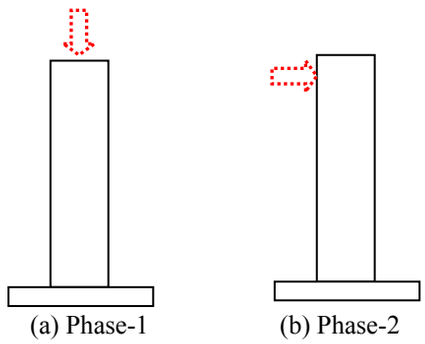
Figure 16. Flexural strain (S4).

In addition, the flexural strain results of S1, S3, S4 and S6 were also measured in the loading tests. Due to the symmetry positions, the flexural strains at S1 and S3 in the original and strengthened columns were given to make a comparison, as shown in Figure 15 and Figure 16 respectively. The numerical results were also provided. The comparison in Figure 15 and Figure 16 indicate significant reduction of the flexural strains in the strengthened column. Taking the applied of 9.53kN (maximum load applied in static loading test for SC-W-1) as an example, the corresponding strain at S1 reduced from -969μ in SC-W-1 to -139μ in SC-W-2, indicating 86% reduction in strain. On the other hand, corresponding strain at S3 reduced from 835μ in SC-W-1 to 394μ in SC-W-2, indicating 53% reduction in strain. Therefore, extension of residual fatigue life in service stage and improvement of seismic performance during an earthquake for the column subjected to loads in the weak axis direction are also expected. In addition, relatively good agreement was observed between the numerical results and the test results.

5.3 *Effects of Axial Force*

In this study, the axial force for columns was ignored in order to simplify the loading tests and numerical analyses. This assumption will not affect the behavior for steel columns with negligible axial force, e.g. electrification poles or columns in railway platforms. For other columns subjects to unneglectable axial forces, e.g. steel piers, the effect of due axial force on the structural behavior of column structure is still known and needs to be investigated.

Phase analyses (two steps) were performed in the numerical analyses. In phase-1, the axial force considering the loads due to a bridge superstructure was applied at the top of the column, as shown in Figure 17 (a). The axial force was taken as 20% of its yield load, according to the existing studies in Japan. Thereafter, the horizontal load was applied in phase-2 until the ultimate state of the column models.

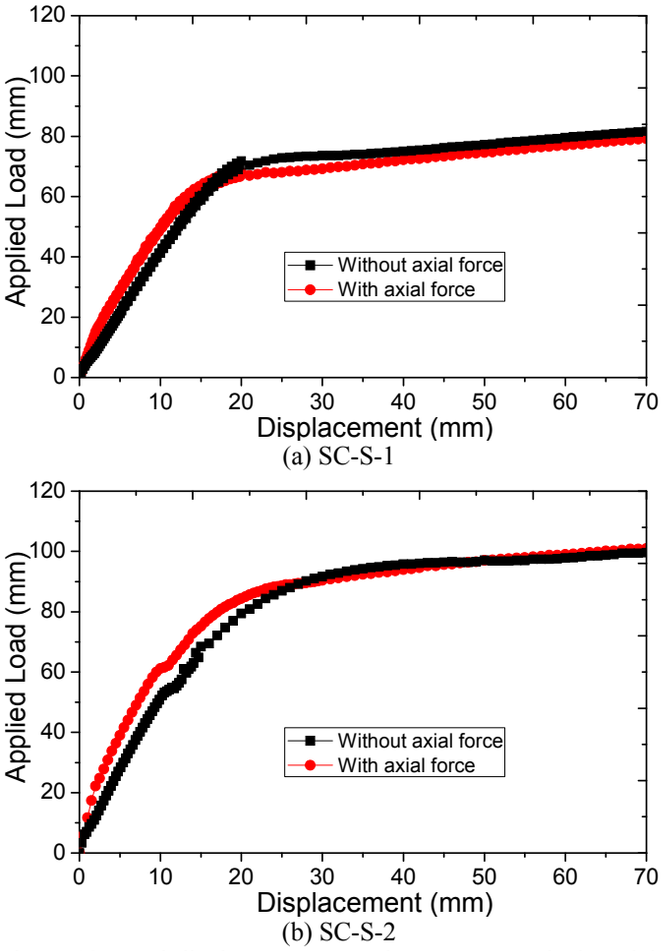


(a) Phase-1 (b) Phase-2

Figure 17. Phase analyses for considering the axial load.

For a column subjected to a horizontal load applied in strong axis, the load-displacement curves of both original and strengthened columns with and without considering axial force were shown in Figure 18 (a) and Figure 18 (b), respectively.

It is found that if the axial force was considered, the rigidities of columns (both original and strengthened columns) were increased slightly. However, no matter the axial force is taken into account or not, the effects of the proposed strengthening method can be confirmed. In addition, the ultimate load was affected little by the applied axial force. Therefore, it can be concluded that the present strengthening method is still effective even if a certain level (≤ 20%) of axial load is considered. Thus, this method can also be used for strengthening steel columns with axial force, like steel piers.



(a) SC-S-1

(b) SC-S-2

Figure 18. Load-displacement curve between numerical models with and without axial force.

6 CONCLUSIONS

A strengthening method for existing steel columns was introduced in this paper. In order to confirm the effect of this method, static loading tests were performed on two original steel columns and columns strengthened with rubber-latex mortar, rapid hardening concrete, and reinforcing bars. Detailed load-deformation response, and strain distribution on the steel columns were reported in this paper. Easily obtained construction materials and simple operated construction methods make this method competitive

in comparison with other repairing methods. Static loading tests were performed to confirm the effects of the present strengthening method. On the basis of the test results, the present strengthening method was proved to be effective for increasing both rigidity and load carrying capacity of the aged steel columns, resulting in improvement of seismic performance of aged steel columns.

A 3-D nonlinear finite element model was established for simulating the present test specimens. The ultimate load carrying capacity, load-displacement curves and strain development process predicted by FE models agree well with those obtained from the experiments, which demonstrates the accuracy and efficiency of proposed FE models. In addition, the influence of axial force in steel columns was investigated in the numerical analyses. For a column subjected to an axial force in service condition (where the axial force is relatively small compared with its yield strength), the proposed strengthening method is still effective.

7 ACKNOWLEDGEMENT

The loading tests performed in this study were sponsored by the Japan Iron and Steel Federation. This financial support is gratefully acknowledged.

REFERENCES

Chu, K., 2011. Study on Seismic Retrofitting Method for Existing Thin Steel Members. Doctoral thesis.

DÖRR, K., 1980. *Ein Beitrag zur Berechnung von* Stahlbetonscheiben *unter besonderer Berücksichtigung des Verbundverhaltens*. PhD thesis, University of Darmstadt, 1980.

Japan Society of Civil Engineers, 2002. *Standard specification for concrete structures-2002*.

Japan Society of Civil Engineers, 2007. *Standard* specifications *for steel and composite structures* (First Edition).

Lin, W., Yoda, T., 2013. Experimental and Numerical Study on Mechanical Behavior of Composite Girders under Hogging Moment. International Journal of Advanced Steel Construction, 9(4), 309-333.

Lin, W., Yoda, T., Taniguchi, N., Kasano, H., and He, J., 2014a. Mechanical Performance of Steel-Concrete Composite Beams Subjected to a Hogging Moment. Journal of Structural Engineering, ASCE. 140(1), 04013031.

Lin, W., Yoda, T., Taniguchi, N., 2014b. Rehabilitation and Restoration of Old Steel Railway Bridges: Laboratory Experiment and Field Test. Journal of Bridge Engineering, ASCE. 19(5), 04014004.

Lin, W., Yoda, T., Taniguchi, N., Satake, S., Kasano, K., 2014c. Preventive Maintenance on Welded Connection Joints in Aged Steel Railway Bridges. Journal of Constructional Steel Research, 92, 46-54.

Lin, W., Yoda, T., Taniguchi, N., Hansaka, M., Satake, S., and Sugino, Y., 2017. Renovation of Existing Steel Railway Bridges: Field Test and Numerical Simulation. Advances in Structural Engineering, 1-15.

Nakasu, M., and Iwatate, J., 1996. Fatigue experiment on bond between concrete and reinforcement, *Transaction of JSCE*, 426, 852-853.

Taniguchi, N., Fujiwara, Y., Lin, W., Yoda, T., Matsuo, H., Kubo, T., 2016. On the Evaluation of Actual Stiffness of a Railway Composite Bridge with the Help of FE Analysis, Journal of Japan Society of Civil Engineers, Ser. A2 (Applied Mechanics), JSCE, 71(2), 785-793.

Maintenance, Safety, Risk, Management and Life-Cycle Performance of Bridges – Powers, Frangopol, Al-Mahaidi & Caprani (Eds)
© 2018 Taylor & Francis Group, London, ISBN 978-1-138-73045-8

Generalized Pareto Distribution for reliability of bridges exposed to fatigue

M. Nesterova
Université Paris-Est, SDOA, MAST, IFSTTAR, Marne-la-Vallée, France

F. Schmidt
Université Paris-Est, SDOA, MAST, IFSTTAR, Marne-la-Vallée, France

E. Brühwiler
MCS, EPFL, Lausanne, Switzerland

C. Soize
Université Paris-Est, MSME UMR 8208, Marne-la-Vallée, France

ABSTRACT: To assess the reliability of existing bridges, in general, extreme effects on a structure are analyzed, which allows predicting their behavior. In particular cases of small bridges, effects caused by fatigue due to the cyclic traffic loading might be significant. The main interest of the current paper is the possibility of applying the extreme value analysis to dissimilar bridges using data from different types of monitoring. Research in this area is carried out on the Anneau bridge in Switzerland and on the Millau viaduct, France, in order to compare the fatigue behavior based on signals from strain gauges in one case and on the WIM data in the other. The estimation of the fatigue life is based on the Extreme Value Theory and, in particular, the Generalized Pareto Distribution. The results aid to derive the efficiency of the method for the predictions of the high cycle fatigue action.

1 INTRODUCTION

The complexity of predicting the behavior of such structures as bridges at the end of their design life is an important topic for modern research. Due to the fact that many European bridges, as well as bridges all over the world, are coming to the end of their design life, the question of the extension of their operational life is vital. Moreover, the study of such objects allows improving design rules for future structures and possibly some profit from an economic point of view.

Usually, in bridge engineering, for the forecasting of the return levels of actions within the time period of the interest, the Extreme Value Theory (EVT) is used (Coles et al. 2001) such as for background works on Eurocodes (Sedlacek et al., 2008). One of the most efficient approaches to be used is the Peaks Over Threshold (POT), which proved to work well in diverse fields: wind engineering (Agarwal & Lance, 2009), precipitation predictions with non-stationary data (Roth et al. 2014), electricity demand estimation with a time-varying threshold (Sigauke & Bere, 2017) and others.

Concerning bridges, the mentioned method is successfully used to envision the forthcoming situation with an object (Zhou, 2013, Treacy, 2014), based on the long-term monitoring of traffic actions. For the proper use of the EVT, usually only extreme, meaning the highest, actions are considered. For instance, heavy (even overweighted) trucks are taken into account without paying attention to light cars. Since the number of light duty vehicles in most cases is quite large, they may cause fatigue of certain elements of a bridge. An interesting question is if this case can significantly affect the structure and how to anticipate it. Therefore, the focus of the current paper is mainly on the fatigue loading.

The interest of this study lays in fitting the generalized Pareto distribution (GPD), as a principal distribution of the POT approach, to the distribution of the number of fatigue cycles caused by different vehicles and axles of trucks. There were several similar studies carried out in various areas. For instance, in the area of composites, the stiffness-based model is introduced by (Shiri et al. 2016) for fatigue damage and life prediction or (Adasooriya, 2016) compares a new probabilistic fatigue assessment approach with a deterministic approach for railway bridges.

As it was recently proposed (Cetin, 2013), the different aspects of material fatigue may be considered as an extreme value dependent process. For a certain observed object, it is important to understand which case is the most unfavorable for a bridge: high amplitude stresses caused by rare extreme events or small stresses by a high number of cycles.

2 METHODOLOGY

2.1 *General procedure*

In general, to estimate the probability of occurrence of certain load effects (return level) within specified

periods of time (return period), the EVT might be applied to structures or structural elements.

First of all, it is necessary to choose an element in the studied structure that is exposed to the most unfavorable action or combination of actions. For example, in a case of bridges, it can be an element in the middle of a long span, where the bending moment is high. For reinforced concrete bridges, the main interest would be in those rebars with higher tensile stresses; for steel bridges, it might be the bottom flange of the girder, in details, welded parts.

Then, recorded data are needed to make predictions of the future behavior of a structure. One of the possibilities is measurements by strain gauges installed on the surfaces of the observed elements. Several gauges installed at different levels can help to get the stress redistribution in a cross-section. The frequency of measurements is important to obtain correct values of stresses from the measured strain. For instance, in bridges, to detect passing cars, the frequency of 50 Hz can be sufficient. The length of monitoring is not recommended to be less than 3 months in a case of traffic loads (Treacy, 2014) due to the instability of predictions.

Usually, such measurements are used to apply EVT based on block maxima or threshold models (Coles, 2001), where only extreme effects are considered. Data are fitted, respectively, to generalized extreme value distribution (GEVD) or GPD with certain parameters. These parameters are used to estimate return levels. To identify extreme values of load effects (LEs) represented, in this case, by fatigue cycles, the POT method is used as it is briefly shown in Figure 1.

2.2 *Common use of GPD*

It has been recently adopted for predictions of extreme traffic actions (Zhou, 2013, Zhou et al. 2016). Peak values of LEs X_i that lay above a certain threshold u are fitted to the GPD. The conditional distribution function can be expressed as:

$$F_u(y) = P[Y \le y | X > u] = \frac{F(y+u) - F(u)}{1 - F(u)}$$

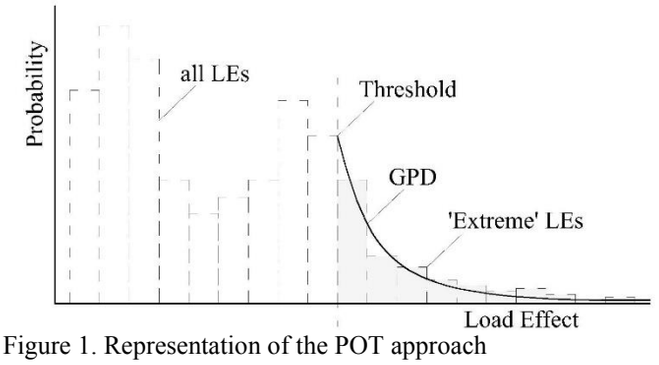


Figure 1. Representation of the POT approach

where $Y = X - u$ is a vector of (positive) threshold excesses Y_i, so that $Y_i = X_i - u$ and $F(u)$ is the cumulative distribution function of random variable X.

The main principe of the POT approach is based on the method described by (Pickands, 1975) and applied later for traffic loads: $F_u(y)$, under mentioned assumptions and conditions: $y = x - u,\ y \ge 0,\ \sigma > 0$ and $x \ge u$ for $\xi \ge 0,\ u \le x \le u - \sigma/\xi$ for $\xi < 0$; tends to the upper tail of a GPD:

$$G(x;\xi;\sigma;u) = \begin{cases} 1 - \left[1 + \xi\left(\frac{x-u}{\sigma}\right)\right]^{-\frac{1}{\xi}}, & \xi \ne 0 \\ 1 - \exp\left(-\frac{x-u}{\sigma}\right), & \xi = 0 \end{cases}$$

Conditions for the application of the EVT are the following:
- identical distribution of random variables X_i,
- random variables X_i are independent,
- threshold u is necessarily high.

For a long period, observations can be based on the cumulative distribution function of extreme values over a shorter period (Crespo-Minguillon & Casas, 1997).

Provided by (Coles et al. 2001), for the probability $P[X \le x | X > u]$ with $\zeta_u = P\{X > u\}$, the solution to the function is:

$$R_L(\mathrm{p}) = \begin{cases} u + \frac{\sigma}{\xi}[(p\zeta_u)^{\xi} - 1], & \xi \ne 0 \\ u + \sigma \log(p\zeta_u), & \xi = 0 \end{cases}$$

where $R_L(\mathrm{p})$ is p-observation return level – a quantile that exceeds once every p observations with large enough p to provide $R_L(\mathrm{p}) > u$.

The POT approach has also its difficulties such as selecting of an optimized threshold. On one side, it should be reasonably high, so, that extreme event types are not mixed, in order to avoid their convergence. On the other side, the threshold must be low enough to provide a necessary number of peaks for obtaining reliable results. The correct choice of parameter estimators σ, ξ for the GPD is also a drawback of the approach.

2.3 *Case of fatigue cycles*

In order to prove that there is no fatigue in an existing structure, European norms (EN 1993-1-1) provide S-N curves for diverse steel details or elements, and it is stated that there is no any danger under the value of five millions cycles of constant fatigue loading. Recent simulations bring the endurance limit in certain cases up to ten millions cycles (Baptisa, 2017).

Traffic actions on bridges are not constant as small frequent cycles are followed by high amplitude cycles rather randomly. There were

several recent studies focused on the fatigue simulation on bridges based on measurements. (Donghuang, 2017, Echard, 2013).
In the current study, the following suggestion is made: fitting of the GPD to a distribution of fatigue cycles, caused by vehicles or axles of different weights (Fig. 3). In certain cases, the proposed method takes into account all traffic actions on a bridge, though, the threshold u from the described previously approach is simply equal to zero.

The main idea is to verify the possibility and the efficiency of applying such method to predict the level of the fatigue of bridges (or their structural elements) due to high cycle fatigue load. Here, the term 'high cycle fatigue' is used to determine the cycles from frequent light vehicles.

The use of the GPD with its shape and scale parameters makes it be possible to assess values of return levels of fatigue cycles for different levels of loading. Taking into account that $u = 0$, the formula of the return level takes the following format:

$$R_L(\mathrm{p}) = \begin{cases} \frac{\sigma}{\xi}[(p\zeta)^{\xi} - 1], & \xi \neq 0 \\ \sigma \log(p\zeta), & \xi = 0 \end{cases}$$

where $\zeta = P\{X > 0\}$ is the probability of a positive X which is valid for all ELs in this case as number of cycles is always a positive value.

Normally, the value of ζ_u can be found as a ratio between all 'extreme' LEs – values that lay over a threshold u – and all LEs. Considering that all cycles are taken into account, this probability should be $\zeta = 1$ which would give the return level of a maximum number of cycles N_{tot}. On the other hand, knowing the probability of a number of cycles N_i for each range Δ_i of LEs $\zeta_i = N_i/N_{tot}$, $\sum \zeta_i = 1$, return levels are estimated for each Δ_i that gives the prediction of the distribution of cycles at the return period of the interest. So, the procedure consists of a few steps shown in Figure 2. The proposed algorithm is applied to monitoring data from two European bridges of totally different geometry and usage.

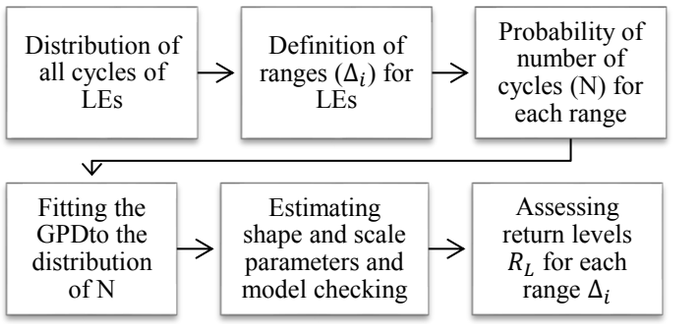


Figure 2. The algorithm of the proposed method

3 CASE STUDIES

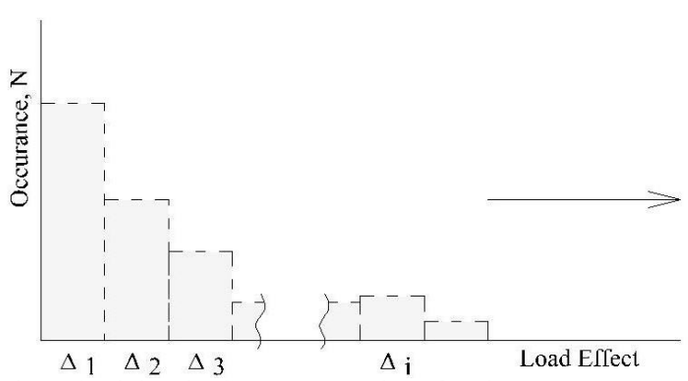
Results of the study of the following bridges are shown in the current paper:
– Millau Viaduct, France,
– Anneau viaduct, Switzerland.

Each bridge has the specific equipment, as well, a particular geometry, materials and loading levels. In addition, a different type of monitoring was used in each country: Weight-In-Motion (WIM) system in France, strain gauges – in Switzerland.

3.1 *Millau Viaduct*

The viaduct itself is a large structure of 2460 m long with pylons of 77 to 245 m high with the height of towers of almost 90 m (Fig. 2). Its orthotropic steel deck suspended by cables is stiff and provided with joints that permit openings up to 80 cm in horizontal directions. Each span of 245 m is composed of six meters long elements, each of them works almost as a simply supported beam. That allows assessing local effects in the complex structure of the bridge.

The final period of 180 days of data was obtained from the WIM system. Recordings were made between October 2016 and July 2017 with a few interruptions.



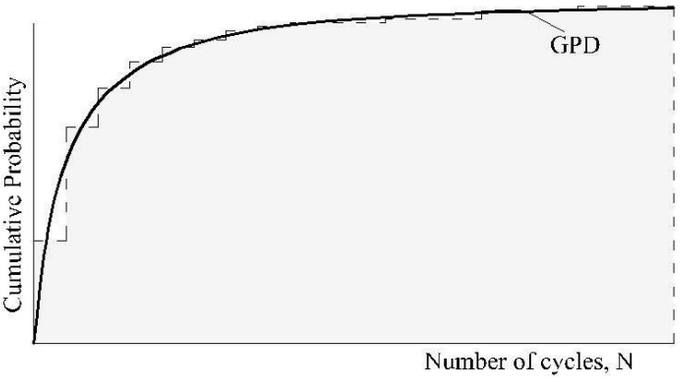


Figure 3. Fitting the GPD to N, number of cycles

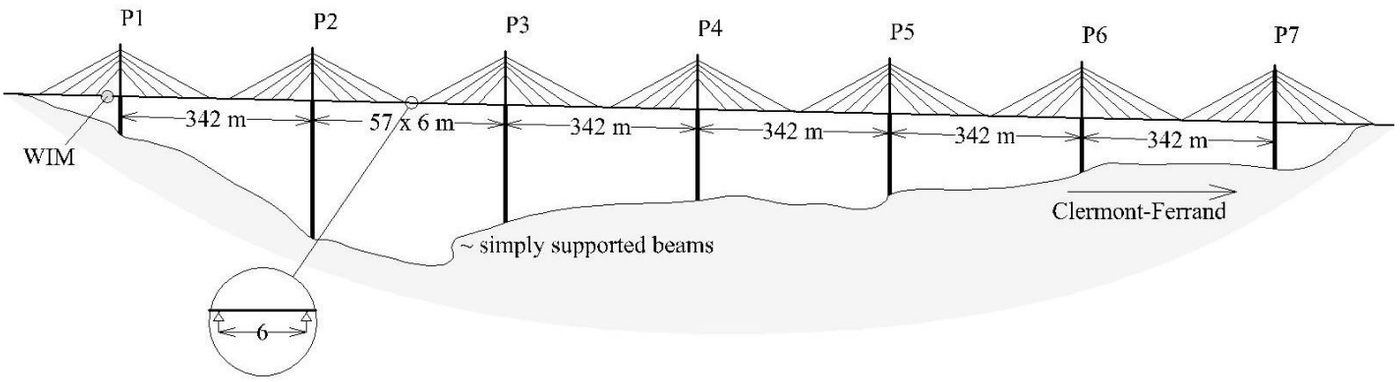


Figure 4. Millau Viaduct

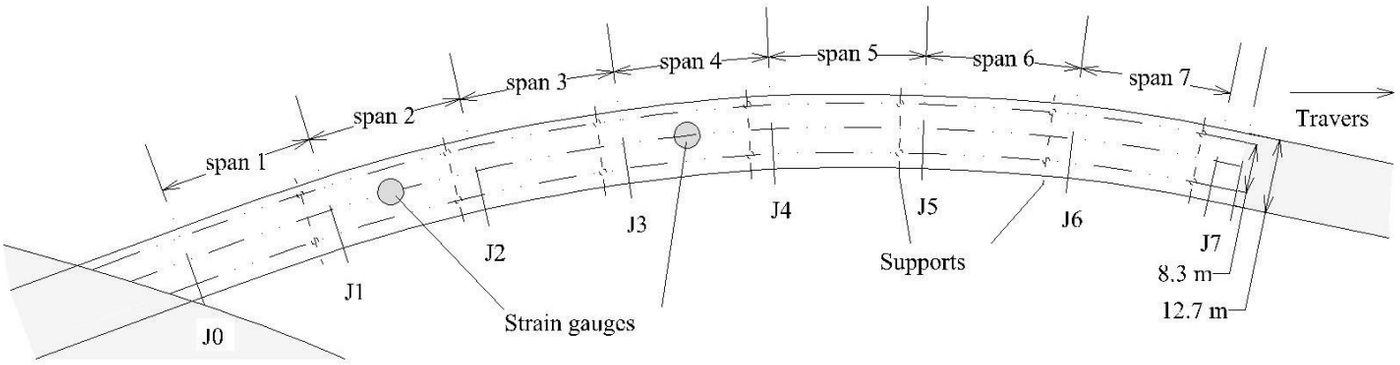


Figure 5. Anneau bridge

The system itself was located in the middle of the first span of the viaduct and recorded all trucks passing the bridge: their weights, speeds, dimensions. The deck of the bridge has two lanes in each direction – normal and high-speed. Monitoring was done only in one, more heavily loaded direction, which does not allow precise evaluating of effects on the viaduct, however, permits to use recorded data for the mathematical model and to make theoretical predictions in terms of LEs given by bending moments.

Table 1. Example of vehicles types

N	Vehicle type	Number of axles	Distance between axles, m			
			1 and 2	2 and 3	3 and 4	4 and 5
1	113	5	3.64	5.50	1.27	1.23
2	40	2	5.27	-	-	-
3	61	4	3.69	6.73	1.31	-
4	100	3	8.7	3.61	5.1	-
5	56	3	6.8	1.46	-	-

Table 2. Axle weights

N	Group of axles	Weight of each axles, kN				
		1	2	3	4	5
1	113	15	22	17	17	17
2	11	41	119			
3	112	32	139	34	34	-
4	111	46	65	5	-	-
5	12	78	142	142	-	-

Figure 4 shows the scheme of the viaduct with the place of the installed WIM system. Tables 1 & 2 give categories of vehicles recorded on the bridge with an example of recordings.

3.2 *Anneau bridge*

The viaduct consists of seven composite steel-concrete spans of 25.6 m (two steel box girders and a reinforced concrete deck slab). There are only two lanes – one in each direction. Strain gauges were installed directly on the reinforcement bars in transversal and longitudinal directions of the deck slab in the middle of the second and the forth spans (Fig. 5), as well as at the top and the bottom of a steel girder.

For each case, a pair of strain gauges was installed to record signals under the central line of the bridge and close to the middle of the lane. The highest values of stresses were obtained in the transversal reinforcement bars of the span 2, which makes this exact detail an object for the study.

Measurements of the strain have been done for one year (August 2016 to July 2017) with only short interruptions which provides almost one full year of monitoring. Moreover, strain gauges allow assessing load effects (stresses) directly, see Section 4.2.

4 APPLICATION OF THE GPD TO THE MONITORING DATA

4.1 *Millau Viaduct*

First, speaking about fatigue of a bridge, stresses and number of cycles for each stress range are needed. Therefore, critical elements subjected to fatigue loading have to be chosen. In the case of the Millau bridge, values of stresses in the deck are not measured directly. Therefore, it is impossible to observe the presence of dynamic effects; however, the estimation of fatigue is still achievable by using the results of WIM measurements. The system provides not only total weights of each vehicle but also the weight of each axle and distances between them.

Using long-term WIM data for evaluation of fatigue is possible even though it does not give stress cycles directly. Since the system provides forces from each axle of every passing truck that gives stress cycles in elements of the deck. Knowing the exact action applied to the bridge stress in the whole cross-section might be evaluated, in this study, cycles are defined in terms of actions.

There are different combinations of axles possible: some of them are grouped by two or three, as it was demonstrated in Table 1. Assuming that the average distance between axles in a group is $dx < 3m$, and using the recorded distances dx between each pair of axles, all recorded types of vehicles are counted and shown on the pie chart (Fig. 6). As it can be observed from the chart, the most frequent vehicle type is the one with five axles where three last are grouped together.

The value of the stress given by a group of axles is usually higher than the one caused by each axle separately and lower than their sum. So, in this case, to calculate cycles, the common action of three axles have to be considered. Also for the types 112, 12, 122 and 1211, the group of two axles should be taken into account.

As it can be found on Figure 7, P1, P2 and P3 are point loads from each axle of the group of three axles, and P1*, P2* and P3* are moments that can be obtained theoretically if each axle would pass the span individually. So, it is necessary to take into account that for the response of the structure, there is an influence between axles in groups of two or three. It could be performed theoretically as two or three point loads, presenting on the 6-meters span at the same time.

As it was mentioned in the Section 3.1, the current study is focused on local effects, therefore, 6-meters elements of the first span of the deck are considered. For simplicity, influence lines are obtained as the ones for the simply supported beam (Fig. 7).

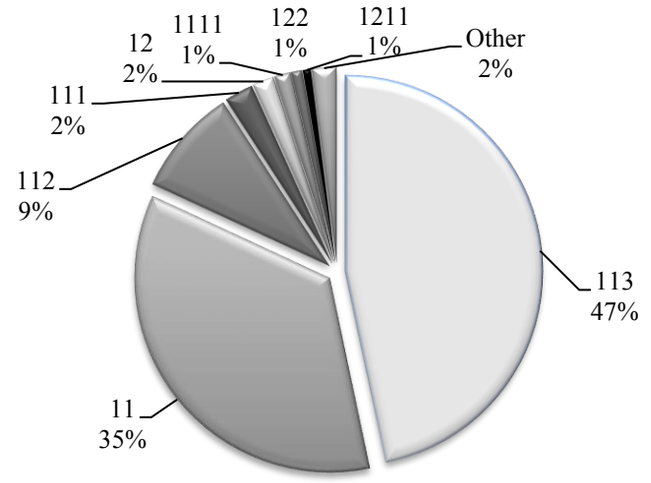


Figure 6. Main types of axles groups

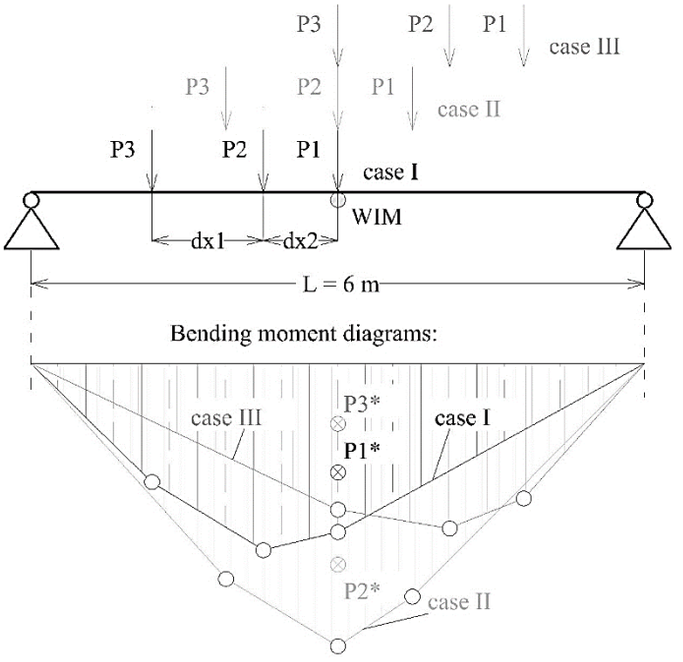


Figure 7. Bending moment from a 3-axles group

This gives the absence of the bending moment (or the values are neglectable) at "supports" – connections between each span. So, for large distances between single axles of vehicles, a weight of each axle can be taken separately as there is almost no influence in terms of stresses. However, for the groups of axles, different values of bending moments are considered as for two or three point loads.

Due to the absence of direct measurements of stresses in any part of the deck, cycles for fatigue are proposed by values of bending moments in the middle of the 6-meters-span, where WIM system was installed. Influence lines for a whole structure can be applied in order to assess bending moments in other parts of the bridge if needed. As well, stresses can be evaluated in the whole cross-section. Here, for simplicity, only measured actions (bending moments) are studied.

As the most frequent vehicles are 113, 11 and 112, bending moments in the midspan are calculated only for single, double and triple axles, as following:

- Single point load P_I is considered if the distance between axle I and other axles is larger than $L_{span}/2 = 3m$,
- Double axles are presented by two point loads P_{II}, when the distance between them is smaller than $3m$; the maximum moment is obtained from both positions: either P_{II-1} or P_{II-2}above the center,
- Triple axle load is given by three point loads P_{III} with three possible positions – each of them at the midspan one by one.

The exceptional combinations of axles removed from the calculations as not reliable. The main point here is to assess fatigue from frequent vehicles, therefore, rare trucks with more than 5 axles are removed from the initial data.

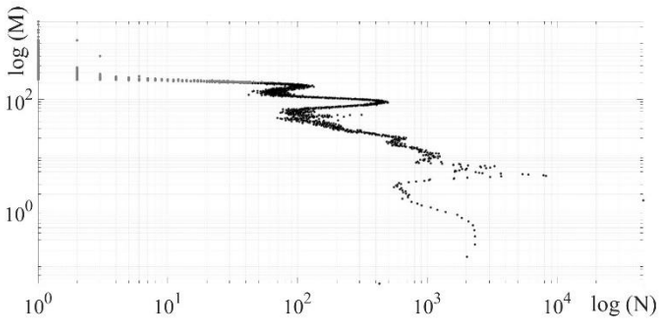


Figure 8. Bending moments, M, as a function of N, log-scale

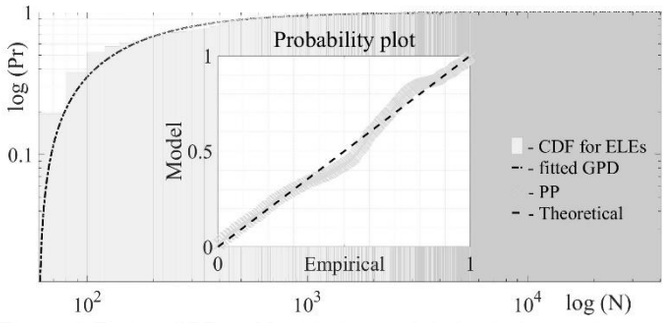


Figure 9.Fitting GPD to N with the model check, log-scale

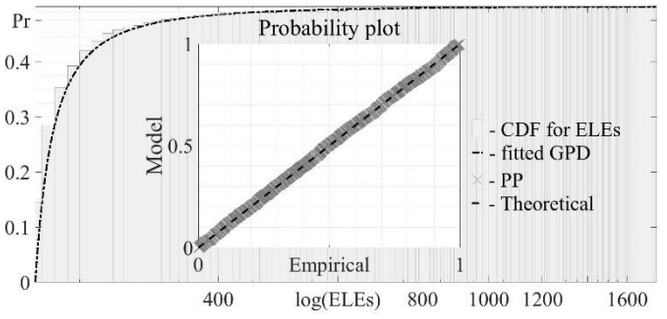


Figure 10. Fitting GPD to high amplitude LEs, with the model check, log-scale

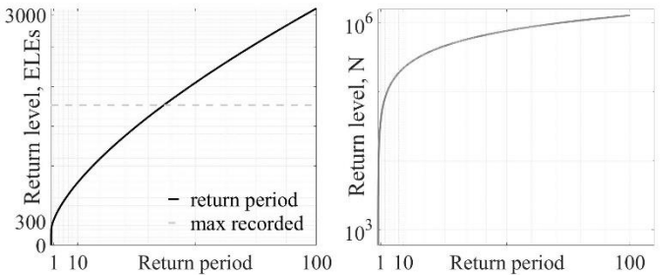


Figure 11. Return levels: for 'high amplitudes', M, kNm (left), for 'high cycles', N (right)

The distribution of all LEs is given in Figure 8. There are high amplitudes of LEs (in grey) that are treated by EVT and the approach explained in Section 2.2, the distribution of ELEs with the $TH = 215\ kNm$ and the model check is shown on the figure 10, the estimated return period – in Figure 11. Compared with the fitting the GPD to N, it can be concluded that the approach is working the same way for different types of LEs: bending moments or number of cycles.

4.2 *Anneau bridge*

Overall, 303 days of monitoring were completed between August 2016 and July 2017. After the detailed analysis of received data, it was detected that the highest values of stresses appeared in the transversal rebar of the span 2. Therefore, this exact rebar is studied for the current paper. Here, the monitored data are represented by measured strain $(\varepsilon, \mu m/m)$ directly in rebars, which allows assessing stresses easily knowing Young's modulus of steel $E = 210000\ N/mm^2 = 0{,}21\ N/\mu m^2$ (EN 1993-1-1, 2005):

$$\sigma = E \cdot \varepsilon, \qquad [MPa]$$

Fatigue cycles are counted using the "rainflow" method (ASTM E1049-85) that provides numbers of cycles for each stress amplitude (Fig. 12). To avoid the "noise" of the signal, all amplitudes under 1 MPa were removed from calculations and the histogram of stress amplitudes of different ranges is shown in Figure 15.

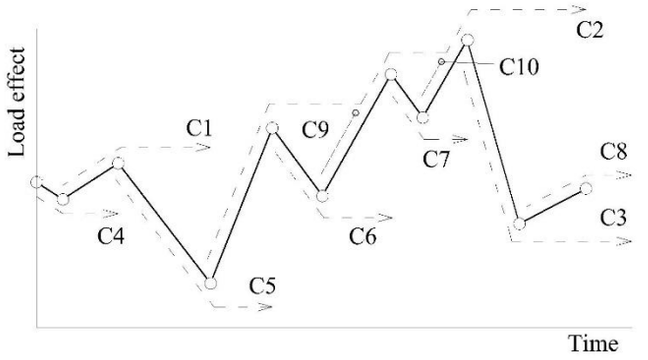


Figure 12. 'rainflow' counting

Again, there are two possible cases: a large amount of cycles of small amplitude ($< 10\,MPa$) and relatively rare high stresses ($> 50\,MPa$).

The case of high stresses and their extrapolation in time is a question of the EVT and its classical application. As it was shown in the previous section, for the case of Millau. The GPD is fitted to all LEs (given here by stress cycles) as it was described in Section 2.4, fitting with the model check is shown in Figure 13.

Stress amplitudes that are smaller than 1 MPa are removed from the distribution, assuming that such stress as the noise of the system. However, stresses over 1 MPa represent cars passing or light trucks passing not exactly above the installed strain gauge. The high amplitude cycles, over 50 MPa, should be fitted to a different GPD since a number of cycles produced by them is too small (Fig. 14)

Assuming that the fitting is successful (according to the model check, Figure 13), parameters of the GPD can be normally used further for the estimation of return levels. However, in this case, the ratio between 'exceedances' and all effects is equal to one due to the absence of any threshold. What is interesting in the case of fatigue, the estimation of cycles at each range of stress amplitudes – Figure 15.

Though, the probability of occurrence of each range of 5 MPa is found for the amount of data measured for 303 days (Fig. 16). Inserting these values into the formula, return levels are calculated for several values of the return period.

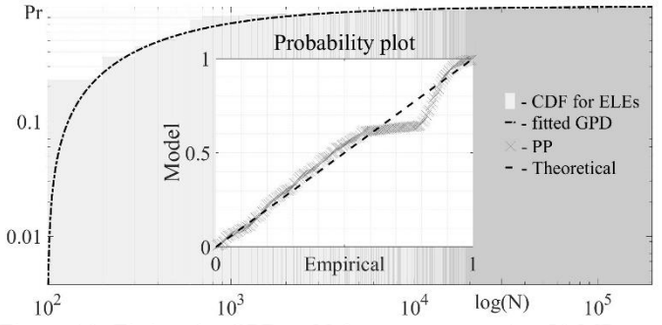


Figure 13. Fitting the GPD to N for stress range 1…50 MPa

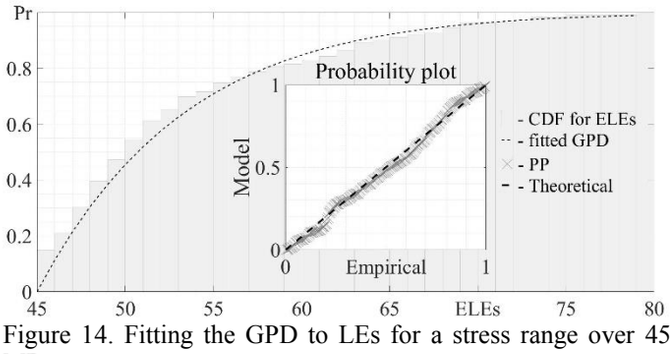


Figure 14. Fitting the GPD to LEs for a stress range over 45 MPa

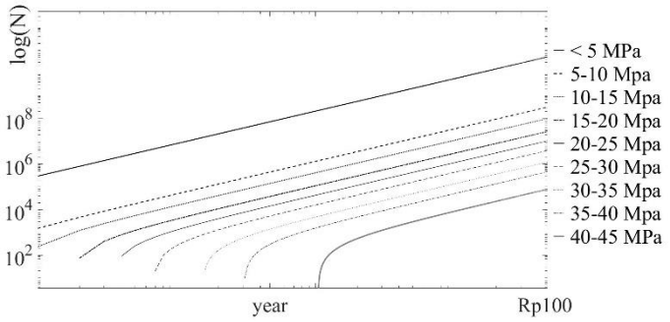


Figure 15. Return levels for different stress ranges, log-scale

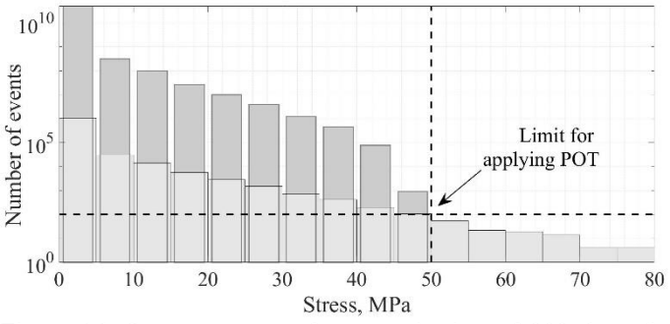


Figure 16. Stress spectrum from monitoring of 303 days (in grey), predictions in 100 years (in white)

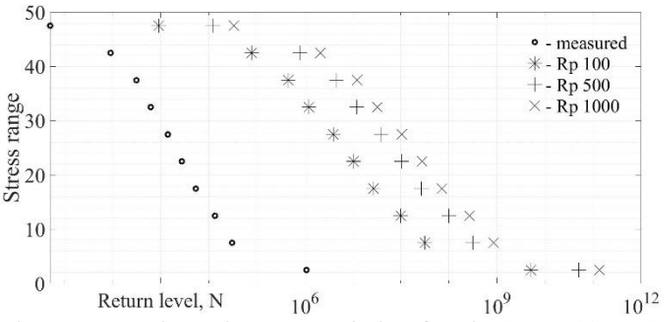


Figure 17. Estimated return periods of N in 100, 500, 1000 years, for each stress range

The method proposed in Section 2.4 is applied to the distribution of stress cycles with ranges each 5 MPa. The results for return periods of 100, 500 and 1000 years are shown in the Figure 17.

Knowing that in this particular case, all observed stresses lay under the cut-off limit (EN 1993-1-9, 2005) of the S-N curve for steel reinforcement bars, the applied algorithm only provides the estimated numbers of cycles over certain return periods (Fig. 17). Studied stresses caused by traffic actions are not high enough to cause any fatigue danger even in 1000 years.

5 CONCLUSIONS

The algorithm of application of the Generalized Pareto Distribution to fatigue cycles is proposed in the current paper. Results of two studied examples of monitored objects (the Anneau bridge, Switzerland,

and the Millau viaduct, France) permit the following summary:

- Monitoring data are required for long-term predictions of fatigue life. Moreover, demonstrated in the section 4.2 results for the Anneau bridge allow the following conclusion: measurements by strain gauges significantly simplify the study due to the direct access to stress ranges distribution.
- Estimation of return levels of N (number of cycles) at given period of time is possible using EVT and in particular, GPD with its parameters, however, more study of various objects is necessary to make more solid conclusions.
- The proposed algorithm works in described specific cases (one year of monitored stresses in the deck of the Anneau bridge and a half a year of recorded vehicles weights on the Millau viaduct), however, it does not show fatigue danger in perspective. Although, it might be applied to other structures with larger traffic volume.

Predicting the number of fatigue cycles in bridges is an actual topic of the modern research. Extending the service duration of existing bridges gives the motivation for novice theoretical approaches that are being proposed nowadays. The experimental part such as monitoring of real objects is undoubtedly useful for the developing of new mathematical models. It leads to the possibility of the application of the EVT for fatigue predictions. Since the traffic growth was not taken into account in the described method, as well, it requires further model uncertainties verification, the current study is being continued by authors.

6 ACKNOWLEDGEMENT

This project has received funding from the European Union's Horizon 2020 research and innovation programme under the Marie Sklodowska-Curie grant agreement No 676139. The grant is gratefully acknowledged.

The WIM measurements for the Millau viaduct were provided by EIFFAGE, France, and the data from monitoring of the Anneau bridge – by EPFL, Switzerland, which is highly appreciated.

7 REFERENCES

Adasooriya, 2016. Fatigue reliability assessment of ageing railway truss bridges: Rationality of probabilistic stress-life approach. *Case Studies in Structural Engineering 6,* pp. 1-10.

Agarwal, P. & Lance, M., 2009. Simulation of offshore wind turbine response for long-term extreme load prediction. *Engineering Structures 31,* pp. 2236 - 2246.

Baptista, R. N., 2017. Probabilistic S-N curves for constant and variable amplitude. *International Journal of Fatigue 00,* pp. 1-19.

Cetin, Naess & Härkegård, 2012. A physically based extreme value characterization of material fatigue. *International Journal of Fatigue 47,* pp. 216-221.

Coles, S., Bawa, J., Trenner, L. & Dorazio, P., 2001. *An introduction to statistical modeling of extreme values.* s.l.:Springer.

Crespo-Minguillón, C. & Casas, J. R., 1997. A comprehensive traffic load model for bridge safety checking. *Structural Safety 19,* pp. 339 - 359.

E1049-1985, A., 2005. *Standard Practices for Cycle Counting in Fatigue Analysis.* s.l.:s.n.

Echard, Gayton & Bignonnet, 2013. A reliability analysis method for fatigue design. *International Journal of Fatigue,* pp. 292-300.

Pickands, J. I., 1975. Statistical inference using extreme order statistics. *The Annals of Statistics 1,* pp. 119-131.

Roth, M. et al., 2014. Projections of precipitation extremes based on a regional, non-stationary peaks-over-threshold approach: A case study for the Netherlands and north-western Germany. *Weather and Climate Extremes 4,* pp. 1-10.

Sedlacek, Merzenich & Paschen, 2008. *Background document to EN 1991- Part 2 - Traffic loads for road bridges - and consequences for the design,* s.l.: JRC Scientific and Technical Reports.

Shiri, S., Pourgol-Mohammad, M. & Yazdani, M., 2016. Prediction of Remaining Fatigue Cycles in Composite Materials Under Uncertainty. *Journal of Risk and Uncertainty in Engineering Systems Part B: Mechanical Engineering.*

Sigauke, C. & Bere, A., 2017. Modelling non-stationary time series using a peaks over threshold distribution with time varying covariates and threshold: An application to peak electricity demand. *Energy 119,* pp. 152-166.

Treacy, M. A., 2014. *The use of monitored data in the verification of structural and fatigue safety of existing post-tensioned concrete highway bridges.* Lausanne: EPFL.

Yan, et al., 2017. Fatigue stress spectra and reliability evaluation of short- to medium-span bridges under stochastic and dynamic traffic loads. *Bridge Engineering 22.*

Zhou, X.-Y., Schmidt, F., Toutlemonde, F. & Jacob, B., 2016. A mixture peaks over threshold approach for predicting extreme bridge traffic load effects. *Probabilistic Engineering Mechanics 43,* pp. 121 - 131.

Zhou, X. Y., 2013. *PhD Thesis. Statistical analysis of traffic loads and their effects on bridges.* Paris: Université Paris-Est.

Maintenance, Safety, Risk, Management and Life-Cycle Performance of Bridges – Powers, Frangopol, Al-Mahaidi & Caprani (Eds)
© 2018 Taylor & Francis Group, London, ISBN 978-1-138-73045-8

Numerical Model Updating of Cable-Stayed Bridge Based on Experimental Data

I. C. Santos
National Department of Transportation Infrastructure, Brasília, Brazil

J. L. V. Brito
University of Brasilia, Brasília, Brazil

E. S. Caetano
Faculty of Engineering of the University of Porto, Porto, Portugal

ABSTRACT: The development of numerical models and the evaluation by techniques of dynamic analysis has gained significant importance and it is able to provide accurate information to analyze structural integrity, durability and reliability along the life cycle and optimize the operational activities and maintenance. The updated numerical model is a procedure to determine the parameters of uncertainty of the initial model, based on experimental results, and to achieve more appropriate upgraded model. This paper describes the application of the modal updating techniques implemented in commercially available software packages to the identification of the global behavior of a cable-stayed bridge. The updated numerical model can be used to evaluate the structural integrity, durability, and reliability along the life cycle and to optimize operational and maintenance activities.

KEYWORDS: *Cable-stayed bridge, finite element model, model updating, optimization.*

1. INTRODUCTION

In recent years, cable-stayed bridges have developed larges spans and more lightweight structures. This has been possible by modern technologies and more resistant materials. These factors, combined with the significant increase in the dimensions of the structures and computational advances, have provided engineers with the freedom to create increasingly slender structures. However, with an increase in slenderness and decrease of weight, more attention must be paid to the possibility of vibratory phenomena.

The development of numerical models and the techniques of dynamic analysis have provided accurate information that allow the analysis of structural integrity, durability, and reliability throughout the life cycle, optimization of operational activities and maintenance. An accurate representation of a structure is therefore essential to study its dynamic behavior.

The numerical model represented by the Finite Element Method (FEM) has a great level of detail in terms of the structure; however, it cannot be trusted if the results obtained diverge from experimental data. The updating of a numerical model is a technique whereby determination of uncertainties in parameters (based on experimental results) allows an increase in accuracy of the original model. Nevertheless, the successful application of the updating procedure depends on the numerical model of the target structure, a well-conceived, and controlled test and on the capacity to integrate both aspects in the model. There are a variety of techniques available for model updating and these employ dynamic and static measurements of the behavior of the structure. This investigation focuses on model updating techniques using the modal response of a structure.

For numerical models, the choice of the optimization function as well as the optimization approach, has been the subject of much research as illustrated by the precursors McCulloch et al. (1990), Farhat and Hemez (1993), Mottershead and Friswell (1993), Friswell and Mottershead (1995) and Friswell, et al. (1998).

Several authors have investigated methods for updating numerical models in structural dynamics. Important examples include Greening (1999) who analyzed the application of updating techniques in structures in which the dynamic performance was affected by the static loads, Santos (2009) who performed a FEM model updating based on EMA data from a footbridge in Brazil and Xia and Roeck (2014) who completed updating the numerical model of Jalon Viaduct, along the high-speed rail between Madrid and Barcelona, based on EMA.

2. METHODOLOGY

The aim of this research is to perform model tuning on a full-scale cable-stayed bridge by updating a model to closely match on-site conditions of two distinct experimental tests data, a first from dynamic tests dating from 1991, at the end of the construction of the bridge, and data from the second test conducted in 2006. This investigation describes modal updating

techniques implemented in commercially available software with the aim of identifying the global behavior of a cable-stayed bridge. To this end, a finite element model was created based on the design calculations and drawings of the structure. Results obtained from this simulation were then compared with measured modal test data.

The updating process has two distinct phases namely, manual, and automatic updating phases. The basic principle of both processes is the same, that is, they aim at adjusting the numerical model to obtain a new model which produces results approaching these of the experimental test. The difference between the two processes is that one changes the model manually and the other employs methods of optimization.

The manual updating process aims at refining the numerical model and this step changes model parameters that describe geometry and material. The method considers non-quantitative errors, such as element types and boundary conditions, which cannot be considered as design variables. Automatic updating is done in an iterative manner where the quantitative parameters of the system are iteratively modified. The errors in geometry, materials, stiffness etc. are evaluated and the convergence decision is automatic and depends on the tolerance of the objective function defined in pre-processing.

The automatic updating consists of two processes: pre-processing (or sensitivity analysis) where the parameters to be updated are defined, and the automatic updating process where the computational routine iteratively refines the parameters.

The numerical model was developed using the finite element software, ANSYS Academic Version 15. Automatic updating was performed by the FEMTools academic version software using the available sensitivity analysis and optimization processes.

2.1. *Case Study: Bridge over the Arade River*

The bridge over the Arade River located on National Road 125 at Portimão, Portugal is the case study analyzed in this investigation. Figure 1 shows details of the bridge geometry.

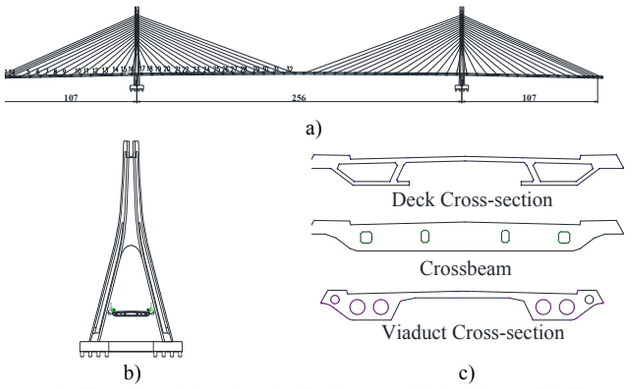


Figure 1: Details of the Arade Bridge: a) Side View; B) Tower; c) Deck Cross-section

The bridge is 850 meters long with three continuous spans of 107, 256, and 107 m and 2 viaducts. The bridge is totally suspended by 128 cables spaced at 8 meters along the deck, for two towers of reinforced concrete in the form of an inverted Y with 62 meters high. In the tower, the shorter cables are independently anchored, while the remaining cables pass over a saddle. The bridge cables are arranged in a half-harp system and are formed by bundles of parallel 14 to 35 closely-packed galvanized steel wire strands with varying lengths between 21 and 127 m.

2.2. *Experimental Data*

Reference data for the characterization of the dynamic behavior of the bridge was taken from the Report of Evaluation of Dynamic Characteristics of the Bridge over the Arade River performed by the Laboratory of Vibration and Structural Monitoring (ViBest) based at the Faculty of Engineering of the University of Porto (FEUP), in November 2006, (Caetano, et al. 2007), and Correa and Campos (1992), performed by the National Civil Engineering Laboratory (LNEC, 1991), in August 1991, before opening to traffic, shown in Tab. 1.

Table 1: Natural frequency and mode shapes. Font: (Caetano, et al., 2007) (Corrêa and Campos, 1992)

Mode	Frequencies (Hz) / Mode Shape	
	1991	**2006**
1	0.249	0.269
2	0.360	0.364
3	0.502	0.515
4		0.692
5	0.751	0.766
6	0.868	0.884
7	0.944	0.956
8	1.034	1.009
9		1.150
10	1.401	1.442
11	1.56 - 1.60	1.603

2.3. *Numerical Model Updating*

Updating is the process of modification of numerical models based on experimental data and aims to minimize errors and inaccuracies in modeling. The success of updating depends on the numerical model design, on a well-conceived and controlled test, and on the good integration of numerical and experimental

data. Figure 2 illustrates the flowchart of the model updating method. In this Figure, the quantities λ_{NUM}, ϕ_{NUM}, λ_{EXP} and ϕ_{EXP} are the numerical and experimental frequency and mode shape and M, K, M_{New} and K_{New} are the matrices of mass and stiffness of the primary and updated model.

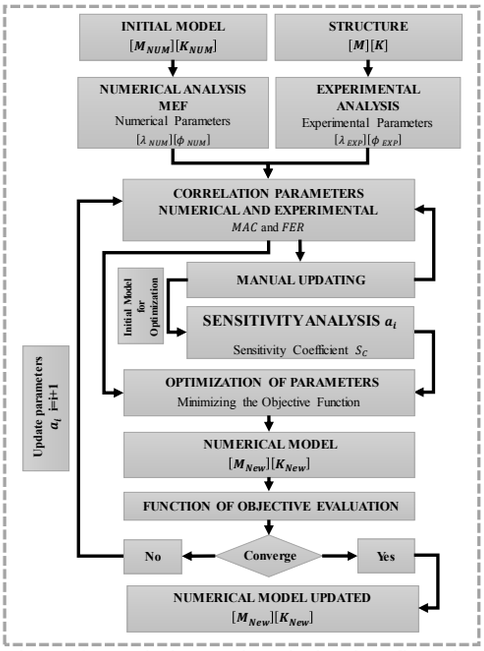


Figure 2: Updating and optimization flowchart.

2.3.1. Correlation Parameters

The Modal Assurance Criterion MAC proposed by Allemang and Brown (1982) apud. Allemang (2003), for comparison of mode shapes and the percentage of variation in the frequency FER, was used to calculate correlation parameters between numerical and experimental data.

MAC is a quantity that uses the amplitudes of experimental and numeric mode shapes at the points where they are located corresponding to the sensors in the experiment. The MAC is defined as shown in Eq.1:

$$MAC_{gh} = \frac{|\phi_g^T \phi_h|^2}{(\phi_h^T \phi_h)(\phi_g^T \phi_g)} \quad (1)$$

where ϕ_h is the vector of mode shape h obtained numerically and ϕ_g is the vector of the mode shape g obtained experimentally. The MAC value varies from 0.0 to 1.0. A value of 1 indicates complete correlation between the two modes and a value of 0 indicates that one mode is completely independent of the other.

FER is the correlation between the natural frequencies. The index FER is defined as shown in Eq.2:

$$FER_{gh} = \frac{\lambda_h - \lambda_g}{\lambda_g} \quad (2)$$

where λ_h is the natural frequency of numeric mode h and λ_g is the natural frequency of experimental mode g.

After calculating MAC_{gh} and FER_{gh}, the analysis selects among all numeric modes h those that are correlated with experimental modes g, whereas h > g. Firstly, the selection of the numerical–experimental sets between all numeric modes h with the highest values of MAC_{gh} compared to experimental modes g is completed and the smallest value of FER_{gh} is chosen. The result is the numeric mode shape ϕ_h and associated natural frequencies λ_h correlated with experimental data.

2.3.2. Optimization Process

The aim of optimization is to determine the optimal values of design variables to maximize or minimize an objective function, while the constraints or restrictions are satisfied. The formulation of an optimization problem involves the definition of the design variables, objective function, and constraints and this depends on the definition of a set of parameters that describe the model.

This study aims at expanding the method of optimization for the cable-stayed bridge model and lead to an optimal solution of the problem. In this case it is defined as the improvement of the correlation between dynamic parameters of the numerical model and the experimental test. Optimization can be divided in three steps: The first step aims at identifying the design variables by Sensitivity Analysis; The second step defines the objective function; and the last step involves the development of mathematical expressions responsible for the definition of constraints.

The objectives functions implemented in this paper are available in the FEMtools® software. The contributions of the various responses are weighted using the response confidence C_{R_i}. The following correlation functions were used in the optimization process:

- Weighted absolute relative difference (CC_{ABS}) between frequencies:

$$CC_{ABS} = \frac{1}{C_R}\sum_{i=1}^{N} C_{R_i} \frac{\Delta\lambda_i}{\lambda_i}; C_R = \sum_{i=1}^{N} C_{R_i} \quad (3)$$

where N is the number of frequencies.

- Average MAC values (CC_{MAC}):

$$CC_{MAC} = 1 - \frac{1}{C_R}\sum_{i=1}^{N} C_{R_i} \,.\, MAC_i; C_R = \sum_{i=1}^{N} C_{R_i} \quad (4)$$

where N is the number of MAC responses

- Weighted absolute difference between modal displacements (CC_{MDISP}):

$$CC_{MDISP} = \frac{1}{C_R}\sum_{i=1}^{N} C_{R_i} \,.\, \frac{|\Delta\Phi_i|}{\Phi_i}; C_R = \sum_{i=1}^{N} C_{R_i} \quad (5)$$

where N is the number of active displacement responses.

- Weighted absolute difference between the mass participation (CC_{MASS}):

$$CC_{MASS} = \frac{1}{C_R}\sum_{i=1}^{N} C_{R_i} \cdot \frac{|\Delta m_i|}{m_i}; C_R = \sum_{i=1}^{N} C_{R_i} \quad (6)$$

where N is the number of active masses, center-of-gravity and inertia properties.

The objective function was defined as Total Weighted Relative Differences (CC_{TOTAL}) Eq.7.

$$CC_{TOTAL} = CC_{ABS} + CC_{MAC} + CC_{MDISP} + CC_{MASS} \quad (7)$$

During optimization, the criterion used for convergence depends on the type of data used and it is described in more detail in the following sheets.

2.3.3. Convergence Criterion

In model updating, the correlation coefficients are interpreted as measures of the quality of the objective function minimization of each iteration loop the values of the correlation coefficients will be verified to check if a convergence criterion is satisfied. The value of the reference correlation coefficient CC_t should be less than an imposed margin ε.

$$CC_t < \varepsilon \quad (8)$$

2.3.4. Sensitivity Analysis

Sensitivity analysis is a technique that aims at determining how structural responses are influenced by properties such as material, stiffness, and geometry. The Sensitivity Coefficient S_C is defined as the derivative of the state variables or objective function in relation to the design variables or update parameters, as shown in Eq. 9 and 10:

$$\delta_z = S_C . \delta_A \quad (9)$$

$$S_C = \frac{\delta_Z}{\delta_A} = \frac{Z_m - Z}{A_m - A} \quad (10)$$

where, $\delta_A = A_m - A$ is the variation of update parameters and $\delta_Z = Z_m - Z$ is the variation in the state variables or objective function.

3. NUMERICAL MODELS

There are many considerations in the development of a numerical model for a cable-stayed bridge. In this study, the numerical model was performed using the academic version of Software ANSYS version R15. This software was employed to account for geometric nonlinearities in the simulation.

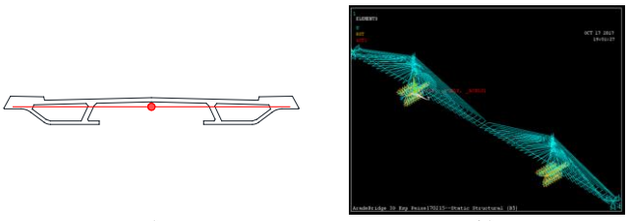
In this investigation, the numerical models developed namely *Fishbone*, the material properties and dimensions employed are taken from design (Rito, 1987). The main section of the bridge deck was modeled as an equivalent beam in the centroid of the cross-section along the longitudinal direction of the bridge axis together with two rigid crossbeams that connect the cable anchor points on the deck to the main beam. This scenario is shown in Figure 3 a) and the full model is shown in Figure 3 b).

The most complex part in the development of this model was the definition of stiffness of the crossbeam member. Equations 11 and 12 as proposed by Hambly (1991) were used to define the area a_s and inertia i_{trans} of the equivalent section per meter of width of deck.

$$a_s = \left(\frac{E}{G}\right)\left(\frac{d_w^3(d_t^3+d_b^3)}{l_1 h_1 (d_t^3+d_b^3)+l^2 d_w^3}\right) \quad (11)$$

$$i_{trans} = \frac{d_t^3}{12} + d_t\left(\frac{h_1}{2}\right)^2 + \frac{d_b^3}{12} + d_b\left(\frac{h_1}{2}\right)^2 \quad (12)$$

where d_b and d_t are the thicknesses of the lower and upper slabs, d_w is the width of the crossbeam l_1 and h_1 is the distance measured in transversal direction between the centroid of the slabs and they of the crossbeam.



a) b)

Figure 3: Fishbone Model a) Cross-section of the bridge deck (Black) and equivalent beam (Red); and b) full model

In the development of the Finite Element Model for the deck, towers and cables was used the element of BEAM188. The tower has a variable cross-section along the height, and was discretized using 6 different sections. The cables were modeled as beams to include the effect of bending in nonlinear numerical analyses for large displacements.

4. RESULTS AND DISCUSSION

The main aim of this investigation was to identify the efficiency of a FE model updating of a full-scale cable-stayed bridge based on the modal parameters. The results are presented in three steps, namely, static behavior, dynamic behavior, and model updating using modal test data sets.

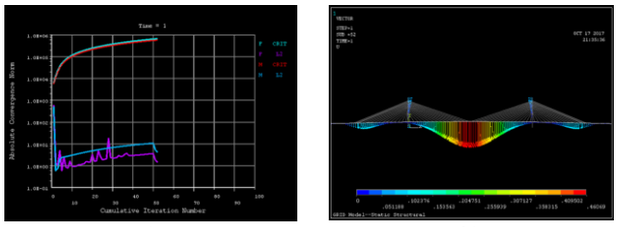
4.1. *Static Behavior*

The first step in the development of the model consisted on the static analysis considering the geometric nonlinearities and the stress in the cables, according to the report of Freyssinet S. A (2005).

For the analysis of the ideal tensile strength, retro-analysis of the project was implemented from the final phase to the beginning. This was done by trying to simulate the distribution of the forces according to the construction process, as proposed by Walther et al. (1999) and Walther et al. (1985).

In the numerical model, actions were therefore appropriately scaled. In the first phase, a portion of the load was applied to the cables and in the second phase, the final loads were added. So that the final stress state was achieved. The nonlinear analysis was performed by an iterative series of linear approximations in the ANSYS software. This simulation employs the iterative Newton-Raphson Method. At each

iteration the equilibrium forces, measured by the difference between the internal and external forces, are found. Figure 4 a) shows iterations of the forces during the convergence process and Figure 4 b) illustrates the final deformation obtained after the nonlinear analysis of the Bridge.



a) b)

Figure 4: Static Analysis: a) Force convergence; b) Total Deformation under statics loads

The force equilibrium on the structure at each iteration is archived until the residue becomes smaller than the convergence criterion. The solution is then considered convergent. Based on the final deformation state obtained in the static analysis, subsequently conducted dynamic analysis.

4.2. *Dynamic Behavior*

The starting point for the modal analysis was the deformed configuration of the bridge obtained in the static analysis. Based on stiffness matrices evaluated and the deformed configuration under statics loads, frequencies and mode shapes were obtained which are shown in Tables 2.

Table 2: Mode Shapes and Natural Frequencies: Vertical (V), Lateral (L) and Torsion (T)

N	Frequency (Hz)		Mode
	Num.	Exp.	
1L	0.268	0.269	
1V	0.363	0,364	
2V	0.491	0,515	
3V	0.728	0,766	
2L	0.744	0.692	
4V	0.781	0,884	
5V	0.871	0,954	
1T	1.036	1.009	
6V	1.017	1,15	
7V	1.321	1,442	
2T	1.556	1.603	

4.3. *Finite Element Model Updating*

This section presents the initial and final values of the response parameters, the sensitivity analysis performed for the definition of the design variables and the updated final model.

4.3.1. Experimental Data 1991

The Figure 5 shows the correlation between the experimental and numeric models for the nodes measured in the modal test.

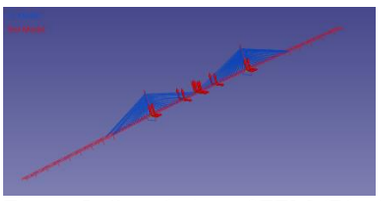


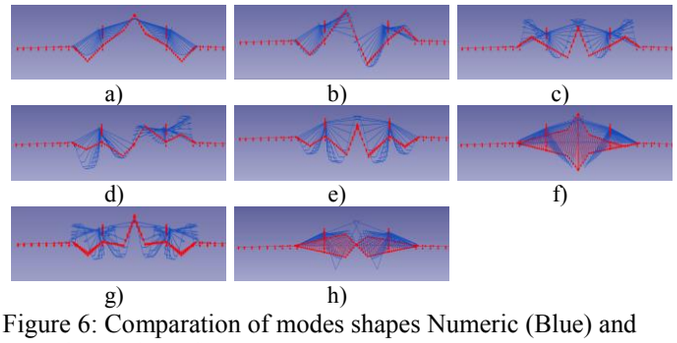
Figure 5: Correlation of FEM (Blue) and Modal Test (Red)

Table 3 shows the values of the numerical and experimental frequencies, correlation among the frequencies, FER, and the MAC index.

Table 3: Primary Frequencies, FER, and MAC index

Mode	Num. Freq. (Hz)	Exp. Freq. (Hz)	FER (%)	MAC
1 V	0,363	0,360	0,80	94,50
2 V	0,491	0,510	-3,79	93,10
3 V	0,728	0,750	-2,89	47,40
4 V	0,781	0,860	-9,14	73,50
5 V	0,871	0,940	-7,30	66,20
1 T	1,036	1,030	0,59	83,00
6 V	1,219	1,400	-12,93	37,40
2 T	1,556	1,600	-2,75	64,70

The numerical and experimental mode shapes show a good correlation, with MAC values ranging from 47.4 to 94.5 and with a mean value of 69.98. The numerical frequencies result a mean FER index of 5.03%. In Figure 6 and 7, comparison of the numerical and experimental mode shapes and the matrix of the MAC index, are presented.



a) b) c)

d) e) f)

g) h)

Figure 6: Comparation of modes shapes Numeric (Blue) and Experimental (Red)

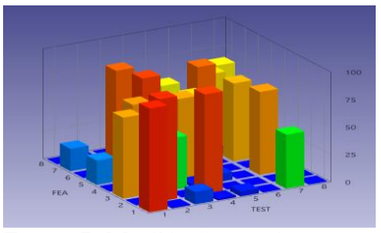


Figure 7: MAC before updating

Sensitivity analysis was used to evaluate the correlations between the parameters Young's modulus (1 to 9), mass density (10 to 18), area (19 to 27), inertia about X (28 to 36), Y (37 to 45), Z (46 to 54) and Poisson's ratio (55 to 63) of the main beam, viaduct beam, cables, crossbeams, and towers, with the response parameters frequencies (1 to 11) and the MAC

(12 to 22). Figure 8 shows the normalized sensitivity coefficient.

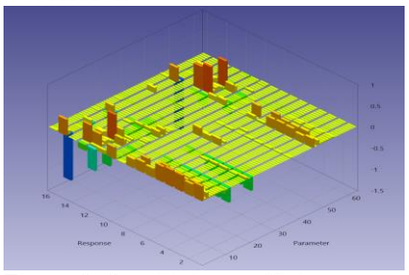


Figure 8: Sensitivity coefficient

Based on the sensitivity analyses decided to consider the 17 parameters that showed the highest absolute values of sensitivity namely, Young's modulus of the crossbeam (1), cables (2), main beam (3) and viaducts beam (4) and (5), mass density of the crossbeam (6), main beam (7) and tower (8 to 11), area of the cables (12), inertia about X of crossbeam (13), inertia about Z of the crossbeam (14), main beam (15) and viaduct beams (16) and (17). These parameters, their limits admissible are shown in Table 4.

Table 4: Parameter of Updating

Item	Type	Element	Limits (%)		Initial Values
			Lower	Upper	
1	Yung's Modulus (Pa)	Crossbeam	-150	150	3,68E+10
2		Cables	-15	15	2,00E+11
3		Main beam	-150	150	3,68E+10
4		Viaducts beam	-150	150	3,68E+10
5		Viaducts beam	-150	150	3,68E+10
6	Mass Density (Kg/m³)	Crossbeam	-15	15	2.600,00
7		Main beam	-15	15	2.600,00
8		Tower	-30	30	2.600,00
9		Tower	-30	30	2.600,00
10		Tower	-30	30	2.600,00
11		Tower	-30	30	2.600,00
12	Area (m²)	Cables	-50	50	0,0201
13	Inertia X (m⁴)	Crossbeam	-150	150	0,1099
14	Inertia Z (m⁴)	Crossbeam	-150	150	0,0400
15		Main beam	-150	150	2,4484
16		Viaducts beam	-150	150	2,4484
17		Viaducts beam	-150	150	2,4484

Considering that the modal test conducted in 1991 was based on the measured of the dynamic responses of 8 points on the deck, it was decided that simulations should employ a greater tolerance for the MAC. Thus, the stop criteria of objective function was consider the $\boldsymbol{CC_{TOTAL}} = 1\%$, and during the iterations the $MAC \geq 30$ and $FER \leq 15$ were adopted to correlate the modes. The model was updated, and the final values of the parameters are presented in Table 5. The parameters showed a mean variation of 6.45% in relation to the initial data.

The updating process resulted in a model that represents experimental observations more accurately as shown in Table 6.

On completion of the update, the FER index had an absolute average value of 2.45% and the MAC value had a mean of 78.58. The correlation criterion CC_{TOTAL} showed an increase from 31.74 to the final value of 23.60. This indicates an improvement in the correlation of mode shapes and frequencies as presented in Tab.7.

Table 5: Final values of the parameters updating

Item	Type	Element	Values		Diff. (%)
			Initial	Final	
1	Yung's Modulus (Pa)	Crossbeam	3,68E+10	3,05E+10	17,03
2		Cables	2,00E+11	1,70E+11	14,85
3		Main beam	3,68E+10	2,58E+10	29,98
4		Viaducts beam	3,68E+10	3,03E+10	17,61
5		Viaducts beam	3,68E+10	3,11E+10	15,54
6	Mass Density (Kg/m³)	Crossbeam	2.600,00	2.990,00	-15,00
7		Main beam	2.600,00	2.620,11	-0,77
8		Tower	2.600,00	1.820,00	30,00
9		Tower	2.600,00	2.350,55	9,59
10		Tower	2.600,00	2.328,03	10,46
11		Tower	2.600,00	1.820,00	30,00
12	Area (m²)	Cables	0,0201	0,0302	-50,00
13	Inertia X (m⁴)	Crossbeam	0,1099	0,1234	-12,31
14	Inertia Z (m⁴)	Crossbeam	0,0400	0,0939	-134,69
15		Main beam	2,4484	2,2108	9,71
16		Viaducts beam	2,4484	4,8918	-99,79
17		Viaducts beam	2,4484	2,0020	18,23

Table 6: Final Frequencies, FER, and MAC index

Mode	Num. Freq. (Hz)	Exp. Freq. (Hz)	FER (%)	MAC
1 V	0,3701	0,3600	2,81	95,90
2 V	0,4916	0,5100	-3,61	95,30
3 V	0,7699	0,7500	2,66	70,00
4 V	0,8499	0,8600	-1,17	81,90
5 V	0,9281	0,9400	-1,27	82,50
1 T	1,0372	1,0300	0,70	80,40
6 V	1,4402	1,4000	2,87	56,70
2 T	1,6718	1,6000	4,49	66,00

Table 7: Initial and final values of the criteria

Iteration	CC_{ABS}	CC_{MAC}	CC_{TOTAL}
0	5.32	26.43	31.74
15	2.19	21.40	23.60

The updated model shows satisfactory correlation with observations through an improvement in the correlation of mode shapes and frequencies in relation to the experimental data.

4.3.2. Experimental Data 2006

The Figure 9 shows the correlation between the experimental and numeric models for the nodes measured in the modal test.

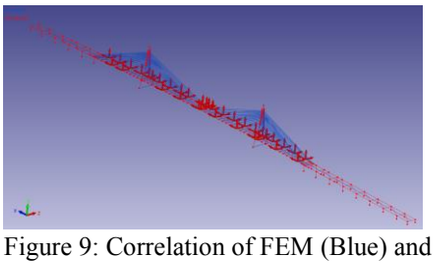


Figure 9: Correlation of FEM (Blue) and Modal Test (Red)

Table 8 shows the values of the numerical and experimental frequencies, correlation among the frequencies, FER, and the MAC index. The numerical and experimental mode shapes show a good correlation, with MAC values ranging from 52.00 to 97.20 and

with a mean value of 78.10. The numerical frequencies result a mean FER index of 5.83%.

Table 8: Primary Frequencies, FER, and MAC index

Mode	Num. Freq. (Hz)	Exp. Freq. (Hz)	FER (%)	MAC
1 L	0,26807	0,26938	-0,49	97,20
1 V	0,36288	0,36419	-0,36	96,80
2 V	0,49066	0,51547	-4,81	92,50
3 V	0,72835	0,76632	-4,95	75,30
2 L	0,74383	0,69231	7,44	90,80
4 V	0,78139	0,88420	-11,63	77,00
5 V	0,87137	0,95618	-8,87	65,90
1 T	1,0361	1,0091	2,67	85,30
6 V	1,0166	1,1500	-11,52	66,90
7 V	1,3212	1,4417	-8,36	59,40
2 T	1,5562	1,6030	-2,92	52,00

Sensitivity analysis was used to evaluate the correlations between the parameters with the response parameters frequencies and the MAC. Fig. 12 shows the sensitivity coefficient.

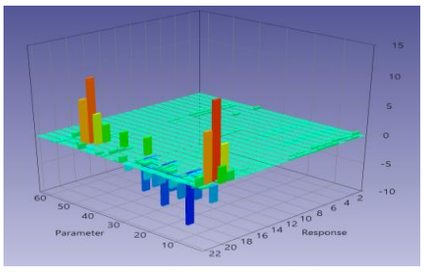


Figure 12: Sensitivity coefficient

Based on the sensitivity analyses, decided to consider the same 17 parameters that showed the highest absolute values of sensitivity namely, Young's modulus of the crossbeam (1), cables (2), main beam (3) and viaducts beam (4) and (5), mass density of the crossbeam (6), main beam (7) and tower (8 to 11), area of the cables (12), inertia about X of crossbeam (13), inertia about Z of the crossbeam (14), main beam (15) and viaduct beams (16) and (17).

Considering that the modal test conducted in 2006 was based on the measured of the dynamic responses of 31 points on the deck, it was decided that simulations should employ a smaller tolerance for the MAC. Thus, the stop criteria of objective function was consider the $\boldsymbol{CC_{TOTAL}} = 1\%$, and during the iterations the $MAC \geq 50$ and $FER \leq 15$ were adopted to correlate the modes. The model was updated, and the final values of the parameters are presented in Table 9.

The parameters showed a mean variation of 1.9% in relation to the initial data. The updating process resulted in a model that represents experimental observations more accurately as shown in Table 10. On completion of the update, the FER index had an absolute average value of 3.92% and the MAC value had a mean of 82.36. However, a greater difference in the first lateral frequency and the second torsional frequency was archived.

The correlation criterion CC_{TOTAL} showed an increase from 28.55 to the final value of 21.55. This indicates an improvement in the correlation of mode shapes and frequencies as presented in Table 11. The new MAC Matrix calculated from the updated model is shown in Figure 13.

Table 9: Final values of the parameters updating

Item	Type	Element	Values		Diff. (%)
			Initial	Final	
1	Yung's Modulus (Pa)	Crossbeam	3,68E+10	4,52E+10	-22,73
2		Cables	2,00E+11	1,99E+11	0,26
3		Main beam	3,68E+10	3,10E+10	15,86
4		Viaducts beam	3,68E+10	3,25E+10	11,76
5		Viaducts beam	3,68E+10	4,48E+10	-21,83
6	Mass Density (Kg/m³)	Crossbeam	2.600,00	2.540,11	2,30
7		Main beam	2.600,00	2.437,56	6,25
8		Tower	2.600,00	2.721,79	-4,68
9		Tower	2.600,00	2.565,01	1,35
10		Tower	2.600,00	2.578,93	0,81
11		Tower	2.600,00	2.714,82	-4,42
12	Area (m²)	Cables	0,0201	0,0216	-7,29
13	Inertia X (m⁴)	Crossbeam	0,1099	0,1091	0,69
14	Inertia Z (m⁴)	Crossbeam	0,0400	0,0470	-17,56
15		Main beam	2,4484	2,2544	7,92
16		Viaducts beam	2,4484	2,4378	0,43
17		Viaducts beam	2,4484	2,4824	-1,39

Table 10: Final Frequencies, FER, and MAC index

Mode	Num. Freq. (Hz)	Exp. Freq. (Hz)	FER (%)	MAC
1 L	0,2422	0,26938	-10,10	97,60
1 V	0,3633	0,36419	-0,24	97,40
2 V	0,4966	0,51547	-3,66	93,90
3 V	0,6973	0,76632	0,72	87,20
2 L	0,7698	0,69231	0,46	81,80
4 V	0,8486	0,88420	-4,02	80,00
5 V	0,9318	0,95618	-2,55	73,60
1 T	1,0818	1,0091	7,20	86,50
6 V	1,1498	1,1500	0,07	71,40
7 V	1,4003	1,4417	-2,87	73,80
2 T	1,7839	1,6030	11,29	62,80

Table 11: Initial and final values of the criteria

Iteration	CC_{ABS}	CC_{MAC}	CC_{TOTAL}
0	6.83	21.72	28.55
22	3.92	17.63	21.55

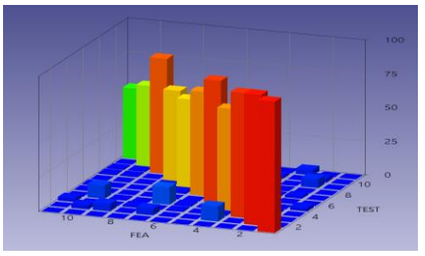


Figure 13: Final MAC

So, in the same line, the updated showed satisfactory correlation with observations through an improvement in the correlation of mode shapes and frequencies in relation to the experimental data.

5. CONCLUSIONS

The model was updated based on two experimental tests, the first test performed at the end of construction in 1991, and a second test performed in 2006.

The sensitivity analysis identified the influence of the variation of the design parameters on the responses. In general, could be observed that the modulus of elasticity, specific mass, and inertia of the main elements such as beams, transverse, mast, cables and slabs were the most influential in the dependent variables, frequencies and modes shapes. In this way, the most sensitive parameters can be identified as candidates for the updating process.

Regarding to the experimental data of 1991, the Fishbone model showed a reduction in FER of 2.59% and an increase the MAC correlation in 8.61 with the update process, showing at the end of the process a FER mean of 2.45% and MAC of 78.59. Concerning the experimental data of 2006, the model presented an improvement in the FER index of 1.91% and in the MAC index of 4.26, presenting at the end of the update process a FER of 3.92% and a MAC of 82.36.

By comparing the structural behavior predicted in the model and the experimental data, we can obtain some insights about the probable sources of errors. However, the differences between the final models updated with the different experimental data showed that the uncertainties in the models originate not only from modeling errors, resulting from simplifying hypotheses made in complex structures, but also incompatibility of the number of degrees of freedom between the data of FEM models and Experimental Modal Analysis (EMA) and inconsistency, when the number of natural frequencies identified, according to McCulloch et al. (1990).

Concerning the methodology, it was observed that the model can represent the structure with a level of detail considered satisfactory and accurate. Regarding the response parameters used, the increase in the number of response parameters promotes an overall increase in the quality of the available data, lead to a better correlation with the experimental data, which can be noted in the 2006 experimental data, where more data were available.

Finally, the FE model was successfully calibrated using multi-responses from the modal test data. The updated numerical models can therefore be used with confidence in analysis related to structures such as damage simulations or in the assessment and monitoring of structures by comparing the evolution of the dynamic properties.

ACKNOWLEDGMENTS

The authors would like to acknowledgement the support provided by the following institutions:

- National Department of Transportation Infrastructure (DNIT);
- University of Brasilia (UnB);
- Faculty of Engineering of the University of Porto (FEUP) and Laboratory of Vibrations and Structural Monitoring (ViBest); and
- FEMTools Academic License.

REFERENCES

ALLEMANG, R. J., 2003. The Modal Assurance Criterion Twenty Years of Use and Abuse. Sound and Vibration Magazine, pp. 14-21.

ANSYS®, 2015, Academic Student Version, Release 15.

CAETANO, E., MAGALHÃES, F. & CUNHA, Á., 2007. Ponte sobre o Rio Arade Estudo para Avaliação das Características Dinâmicas. Faculdade de Engenharia da Universidade do Porto (FEUP), Laboratório de Vibrações e Monitorização de Estruturas (VIBEST).

CORRÊA, M. R., & CAMPOS, C. A. (1992). Ensaios Dinâmicos da Ponte sobre o Rio Arade. Lisboa: Pontes Atirantadas do Guadiana e do Arade ed. LNEC.

FARHAT, C.; HEMEZ, F. M. 1993. Updating finite element dynamic models using an element-by-element sensitivity methodology. AIAA Journal of American Institute of Aeronautics and Astronautics, v. 31, n. 9, p. 1702-1711.

FEMTOOLS 3.8.1 ®.2015. FEMtools 3.8.1 Release Notes. Dynamic Design Solutions (DDS). Leuven – Belgium. 2015. Version 3.8.1

FREYSSINET S.A. 2005 Ponte sobre o Rio Arade Resultado de la Medicíon de Fuerza en los Tirantes Mediante el Método de la Cuerda Vibrante. Freyssinet.

FRISWELL, M. I.; MOTTERSHEAD, J. E. Finite Element Model Updating in Structural Dynamics. 2. ed. Swansea: Springer Science & Business Media, v. 38, 1995.

FRISWELL, M. I.; MOTTERSHEAD, J. E.; AHMADIAN, H. 1998. Combining Subset Selection and Parameter Constraints in Model Updating. Journal of Vibration and Acoustics, v. 120, n. 4, p. 854-859

GREENING, P. D. 1999. Dynamic Finite Element Modelling and Updating of Loaded Structures. University of Bristol. Bristol.

HAMBLY, E. C. (1991). Bridge Deck Behaviour (2 ed.). CRC Press.

LNEC. (1991, Agosto). Ensaio Dinâmico da Ponte sobre o Rio Arade. LNEC, Laboratório Nacional de Engenharia Civil, Lisboa.

MCCULLOCH, C. F.; VANHONACKER, P.; DASCOTTE, E. 1990. Validating and updating finite element models using experimental measurements of dynamics. Proceedings of the Institution of Mechanical Engineers, Journal of Aerospace Engineering, v.204, n.1, p.45-50.

MOTTERSHEAD, J. E.; FRISWELL, M. I. 1993. Model Updating in Structural Dynamics: A Survey. Journal of Sound and Vibration, v. 167, n. 2, p. 347-375, 21

RITO, A. A. M. 1987 Projeto de Execução Ponte sobre o Rio Arade. Ministério das Obras Públicas, Transportes e Comunicações (MOPTC). Lisboa.

SANTOS, I. C., 2009. Atualização do modelo numérico em elementos finitos de uma passarela de pedestres com base em dados experimentais. Universidade de Brasília.

WALTHER, R. et al. 1995. Ponts Haubané. França: Lausanne Presses Polytechniques Romandes.

WALTHER, R. et al. 1999 Cable Stayed Bridges. 2nd. ed. Londres: Thomas Telford.

XIA, C.; ROECK, G. D. 2014. Modal analysis of the Jalon Viaduct using FE updating. Proceedings of the 9th International Conference on Structural Dynamics.

Maintenance, Safety, Risk, Management and Life-Cycle Performance of Bridges – Powers, Frangopol, Al-Mahaidi & Caprani (Eds)
© 2018 Taylor & Francis Group, London, ISBN 978-1-138-73045-8

Rotational stiffness between vertical and horizontal members of system supports

J.H. Won & H.D. Lee & A.R. Oh & N.K. Jang
Chungbuk National University, Cheongju, Korea

ABSTRACT: This study examined the rotational stiffness of joints between vertical and horizontal members in system supports used in the construction of rahmen-type bridge. While the system supports were commonly used to support the concrete weight during casting concrete, the collapse of system supports was frequently reported. In order to prevent repeated collapse of system supports, it is important to examine the accurate behavior of system supports. The structural behaviors of system support were affected by the large variations of geometric and mechanical parameters, notably joint stiffness, initial geometric imperfections, yield stress and load eccentricity. Among various factors affecting the complex behavior of system supports, this study focused on the stiffness of joints between vertical and horizontal members. Experimental tests were performed to estimate the rotational stiffness of joints between vertical and horizontal members. The considered joint type was wedge type which is generally used in Korea. Results showed that the initial rotational stiffness was between 16 kNm/rad and 34 kNm/rad which is similar to other researches.

1 INSTRUCTIONS

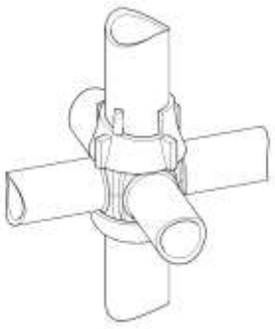
When concrete structures are built, a system support of temporary equipment is adopted to support various loads in the short term. Unfortunately, the improper design and installation of system supports have caused continuous accidents including collapse of system supports (Kim et al. 2017). In many countries, the safety of system supports is analyzed in terms of various structural aspects. These structural aspects take into account various factors such as initial geometric defects, number of structure floors, and stiffness of connection parts. In order to identify the geometrical defects such as impact or construction error during pouring of concrete on the system support, Chan et al. (2005) studied the behavior of the system support by applying the P-delta effect, the eigen-buckling mode approach (EBM), the notional horizontal force approach (NHF), and the initial geometric imperfection approach (IGI). Yu et al. (2004) analyzed the changing behavior based upon the number of floors in order to study the relationship of decreasing load carrying capacities to the increase in number of floors.

In addition, many researches have studied the rotational stiffness of connection parts between vertical and horizontal members according to the connection shape. It was found that the values of rotational stiffness were varied with the change of the shapes of connection, the number of members connected to the connection parts, and the direction of rotational axis (Chandrangsu & Rasmussen 2011, Prabhakaran et al. 2011, Liu et al. 2010). Overseas researchers have continuously experimented and analyzed various system perspectives to predict the behavior of system support. However, in Korea, the load-resistant capacity of system supports is simply calculated based on the experiments utilizing a single member. Furthermore, the connection condition between vertical and horizontal members is simply assumed to be a simple hinge in the design stage (MOLIT 2016). This assumption focuses on the elastic behavior of all structural members. As such, there is a limitation in the analysis of the ultimate load of system support and its behavior when it collapses. Actually, the connection has a rotational stiffness according to other researches. Therefore, this study investigates the rotational stiffness of connection parts between vertical and horizontal members in the system support in order to obtain to simulate actual behaviors of system supports. It also analyzes its changing behavior when the actual rotational stiffness value is applied through finite element analysis.

2 FACTORS AFFECTING STRUCTURAL BEHAVIOR OF SYSTEM SUPPORTS

2.1 *Types of connection part*

The system support consists of vertical, horizontal, and bracing members. The connective parts of vertical and horizontal members can be classified into the cuplok joint, wedge type, and clamp as shown in figure 1. Previous research argued that the type of connection affects the stiffness, and the range of stiffness is broad. One of the various shapes, the cuplok joint, has been shown to have the greatest rotational stiffness (Chandrangsu & Rasmussen 2009).



(a) Cuplok joint



(b) Clamp joint



(c) Wedge joint

Figure 1. Connection type of system support

2.2 *Eccentric loading*

The eccentricity of load can be occurred because the center lines of bearers and U-heads of the system support do not always coincide with each other. A general method for considering the eccentric load effect is to apply the vertical load at an eccentric distance from the bearer and connect it to a rigid link. In this case, the rigid link behaves as a short, stiff, cantilever that introduces vertical force and additional moment into the jack (Chandrangsu & Rasmussen 2009).

2.3 *Geometric imperfection*

The EBM, the NHF, and the IGI method have been used to model geometric imperfection of the initial shape of system support. In Korea, the temporary structure construction standard typically uses the horizontal load method (NHF) to consider potential imperfection during construction as well as identify possible impacts caused by concrete pouring. More specifically, it requires applying the bigger value between 2% of the vertical load and 1.5 kN/m per horizontal length unit to the top of the system support (MLTM. 2007).

2.4 *Rotational stiffness of connection part*

The rotational stiffness of various connection types has been studied. Parabhakaran et al. (2011) studied the rotational stiffness of a clamp connection part. In a cantilever experiment, loading and unloading were repeatedly applied in the upward direction and the results were compared with other rotational stiffness estimation methods of various models. The results of the Federation Europeene de la Manutention approach (FEM) were considered as a simple and reliable method. The rotational stiffness of the clamp connection is described in Table 1, and 10.65 kNm/rad can be applied as the initial stiffness.

Table 1. Rotational stiffness of clamp type according to FEM approach (Parabhakaran et al. 2011)

Equations	Rotation(radians)	Moment(kNm)
$M=10.65\theta_r$	$0 \le \theta \le 0.091$	$0 \le M \le 0.97$
$M=0.97$	$0.091 \le \theta_r$	$M=0.97$

Peng et al. (2013) studied the behavior of system support according to the number of floors of a wedge type connection by considering the existence of bracing and stiffness of connections. From the full-scale experiments (figure 2), rotational stiffness of 58.86 kNm/rad was applied to the spigot joint between vertical members. In addition, for the rotational stiffness of the connection of vertical and horizontal members, 34.34 kNm/rad was applied, 0 for the connection of vertical and inclined bracing members, and 34.34 kNm/rad for the bottom screw jack.

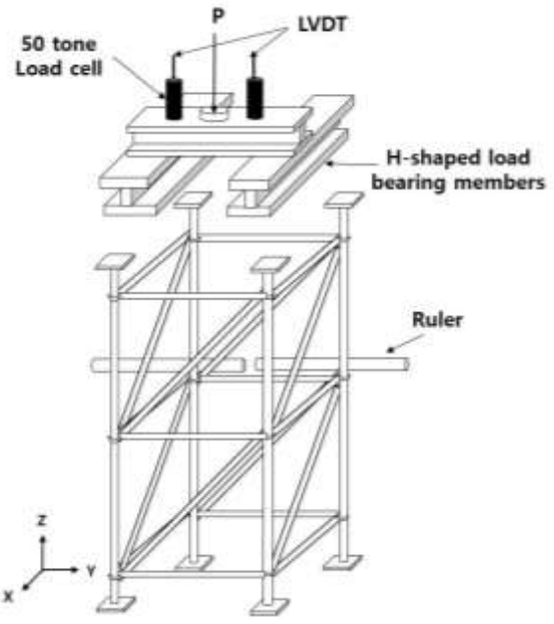


Figure 2 Test setup of system scaffolds under loading (Peng et al. 2013)

Chandrangsu and Rasmussen (2011) studied the changing stiffness of the system supports built with cuplok joints considering four directions (up, down, left, and right). As shown in figure 3, this experiment was conducted as a cantilever test. The vertical members were 48 mm in diameter, 4 mm thick, with a yield stress of 450 MPa. The horizontal members were 48 mm in diameter, 3.2 mm thick, with a yield stress of 350 MPa. As outlined in Table 2, the stiffness of the connections was largest when the load was applied in the upward direction. The value of stiffness increased as the number of horizontal members connected to the connecting part increased.

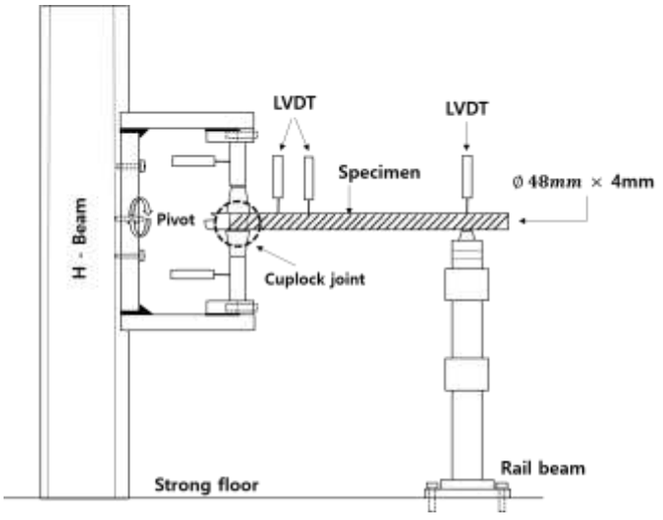


Figure 3. Schematic of typical cuplok joint test setup (Chandrangsu and Rasmussen 2011).

3 ROTATIONAL STIFFNESS AND FINITE ELEMENT ANALYSIS

3.1 *Determination of rotational stiffness*

Author's previous research (Kim et al. 2017) studied the rotational stiffness of the connections of the wedge type system support (figure 4), which is used predominately in Korea. The diameter and thickness of vertical members were 60.5 mm and 2.6 mm, respectively, while the diameter and thickness of the horizontal members were 42.7 mm and 2.3 mm, respectively. The steel grade was SS400.



Figure 4. Test setup of connection part with wedge type (Kim et al. 2017).

By comparing the experimental and analytical values, it can be confirmed that the rotational stiffness is nonlinear. The experimental results are compared with those obtained by applying 10%, 17%, 18%, and 20% of the flexural stiffness of the horizontal member to the rotational stiffness. The results showed that the rotational stiffness is different from the initial stiffness of the test, but it is found that 17 ~ 18% of the flexural stiffness of horizontal members is comparable to the overall tendency (figure 5). In addition, for the case of estimating a stiffness value that gives similar results to the experimental results, the rotational stiffness of the joint was estimated to be 12 kNm/rad ~ 13 kNm/rad (figure 6).

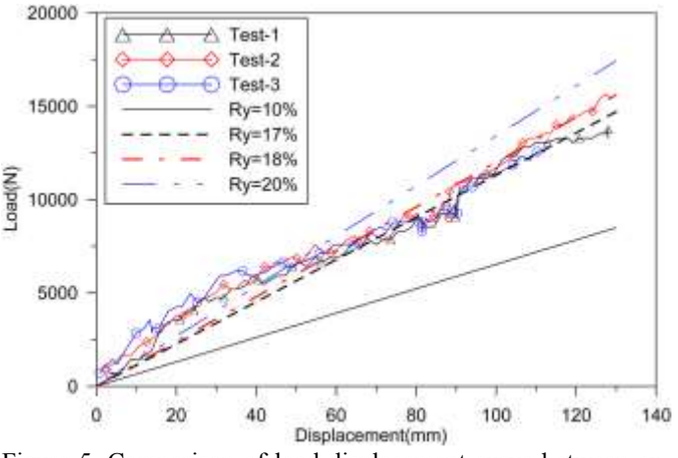


Figure 5. Comparison of load-displacement curve between experiment and analysis (ratio for flexural stiffness of horizontal members, R_y).

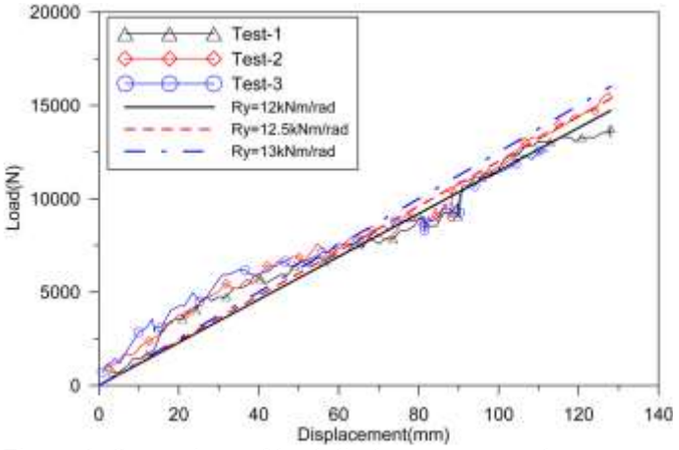


Figure 6. Comparison of load-displacement curve between experiment and analysis (rotational stiffness).

In order to determine the rotational stiffness of connection between vertical and horizontal members to be applied to the finite element analysis of the system support, the values derived from experiments conducted in Korea and other countries were compared and analyzed. As shown in Table 2, Kim et al. (2017) evaluated the rotational stiffness of the wedge type connection to be 12~13 kNm/rad. Peng et al. (2013) estimated the rotational stiffness to be 34.34 kNm/rad. Chandrangsu and Rasmussen (2011) studied the rotational stiffness of cuplok connection and yielded 96.23 kNm/rad for 4-way, 87.97 kNm/rad for 3-way, and 71.62 kNm/rad for 2-way. Parabhakaran et al. (2011) estimated the rotational stiffness of the clamp joint to be 10.65 kNm/rad.

Table 2. Comparison of rotational stiffness in various researches

Research	Joint type	Rotational stiffness (kNm/rad)
Kim et al. (2017)	Wedge	12.0~13.0
Peng et al. (2013)	Wedge	34.34
Chandrangsu and Rasmussen (2011)	Cuplok	96.23 (4-way) 87.97 (3-way) 71.62 (2-way)
Parabhakaran et al. (2011)	clamp	10.65

According to previous researches on the rotational stiffness of connections, there are big differences depending on type, manufacturer, and connection direction. Therefore, because the range of rotational stiffness is situationally dependent, the rotation stiffness value of the wedge type connection, which is mostly used in Korea, was determined. In this study, 12.5 kNm/rad was set for the rotational stiffness of the connection between vertical and horizontal members.

3.2 *Finite element model*

To understand the behavior of the system support considering the rotational stiffness values, the commercial finite element analysis program was used (figure 7). The system support is 6.2 m high, the vertical members are 0.9 m apart in longitudinal direction, and the horizontal members are 1.2 m apart in horizontal direction as outlined in Table 3. The steel grade of vertical, horizontal, and sloped members is STK400. The diameter and thickness of vertical members are 60.5 mm and 3.2 mm, respectively while the diameter and thickness of horizontal members are 42.7 mm and 2.3 mm, respectively. The diameter of the U-head jack base is 48.6 mm and its thickness is 2.3 mm as shown in Table 4.

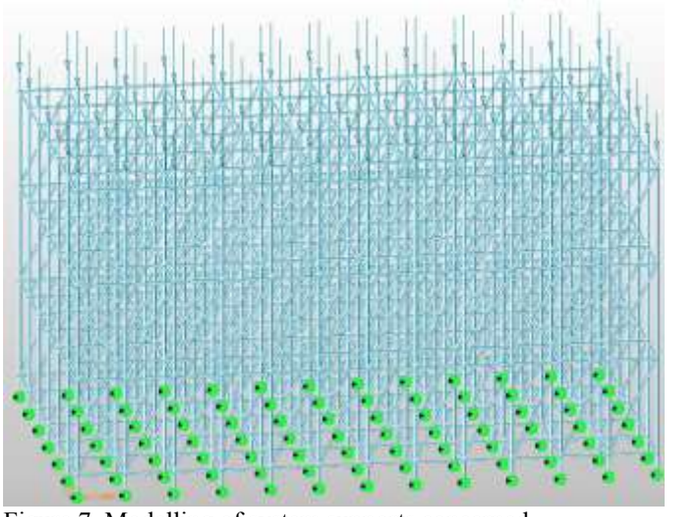

Figure 7. Modelling of system supports concerned

Table 3. Description of considered system support

Category	Specification and spacing
Height of system support	6.2m
Vertical member spacing	0.9m
Horizontal member spacing	1.2m

Table 4. Description of material of system support

Member	Specification	Steel grade
Vertical member	⌀ 60.5 mm×3.2 mm	STK400
Horizontal-Diagonal member	⌀ 42.7 mm×2.3 mm	STK400
U-head-Jack base member	⌀ 48.6 mm×6.0 mm	STK400

The boundary conditions applied to the target system support are the hinge at the bottom of vertical members, the continuous members at the connecting parts of the vertical members, the hinge at the connecting parts of the vertical and inclined bracing members, and the hinge at the connecting part between horizontal and bracing members. To analyze the changes considering the rotational stiffness, the connection of horizontal and vertical members was assumed to separately adopt the simple hinge and 12.5 kNm/rad of rotational stiffness. The slab weight was 24 kN/m^3, and the mold weight was 0.4 kN/m^2 while the live load was 3.75 kN/m^2. Considering the impacts of concrete pouring or construction errors,

the minimum horizontal load applied was heavier between the upper 2% of the dead load and 1.5 kN/m per horizontal length unit to the upper part of each floor.

4 INFLUENCE CONSIDERING ROTATIONAL STIFFNESS OF CONNECTION PART

To analyze the structural safety of the system support, considering the rotational stiffness of the connection of vertical and horizontal members, the first mode eigenvalue, the critical load, and the maximum combined stress ratio were analyzed. With the consideration of rotational stiffness, the eigenvalue and the critical load increased while the critical buckling load ratio of the application to the non-application of the rotational stiffness was 3.531 (Table 5).

Table 5. Comparison of critical load

	Without rotational stiffness(a)	With rotational stiffness(b)	b/a
Eigenvalue	0.131	0.466	3.531
Critical load (kN/m)	4.077	14.395	3.531

The maximum combined stress ratio was investigated with and without rotational stiffness. The combined stress ratio, determined by the design standard, is as follows:

$$\frac{f_c}{f_{caz}} + \frac{f_{bcy}}{f_{bagy}(1-\frac{f_c}{f_{Ey}})} + \frac{f_{bcz}}{f_{bao}(1-\frac{f_c}{f_{Ez}})} \le 1 \quad (1)$$

where fc = the compressive stress (MPa) generated by the axial force; f_{bcy} and f_{bcz} = the bending compressive stresses (MPa) at y-axis and x-axis; f_{caz} = the compressive stress (MPa) in the direction of the permissible axis of the weak axis reflecting the local buckling; f_{bagy} = the allowable bending compressive stress (MPa) of the circumference of the strong axis (y-axis) without considering local buckling; f_{bao} = the upper value (MPa) of the allowable bending compressive stress without considering local buckling; f_{Ey} and f_{Ez} = allowable Euler buckling stress (MPa) of the circumference of the strong axis (y-axis) and the weak axis (z-axis).

Table 6 represents the combined stress ratio along with the changing rotational stiffness. This connection is at the position generating the maximum combined stress ratio. Every maximum combined stress ratio was found in the vertical members. With and without considering rotational stiffness, the ratios ranged from 0.934~0.968. The analysis demonstrated that the maximum combined stress ratio, when considering the rotational stiffness, was 5-6% smaller than without considering the rotational stiffness.

Table 6. The maximum combined stress ratio according to vertical member location

Element number	424	573	722	729
Without rotational stiffness	0.764	0.765	0.764	0.699
With rotational stiffness	0.714	0.714	0.714	0.677
With rotational stiffness / Without rotational stiffness	0.968	0.934	0.934	0.938

5 CONCLUSION

This study analyzed the behavior and structural safety of the system support when the rotational stiffness is applied to the connection of the vertical and horizontal members. Based on the results of applying the actual rotational stiffness value to the connection parts, the following conclusions were obtained.

1. The rotation stiffness value of the wedge type connection, which is mostly used in Korea, was determined to be 12.5 kNm/rad by comparing the experimental and analytical values.

2. As a result of the buckling analysis using the vertical member of the system and the rotational stiffness of the horizontal joint, the critical buckling load increases with the consideration of the connection stiffness. When the concrete load is placed on the whole slab of the target system, the critical buckling load is 3.5 times larger than the hinge considering the rotational stiffness of the joint.

3. Considering the rotational stiffness of the vertical and horizontal joints, the maximum combined stress ratio of the vertical members was estimated to be 5 ~ 6% smaller than that of the hinge alone. Therefore, it is considered that the present design method considering the vertical and horizontal joints as hinges is conservative in evaluating the generated stress slightly higher than the actual stress.

According to the previous study on the rotational stiffness of the joint, the rotational stiffness of the joint can be changed according to the shape of the joint, the manufacturer, and the direction of the joint. The rotational stiffness of the connection used in this study is limited to the connection type and 1-way connection used in the experiment. Further study on the manufacturer, connection type, and various connection directions should be performed in the future.

6 REFERENCES

Chan, S. L. & Huang, H. Y. & Fang, L. X. 2005. Advanced analysis of imperfect portal frames with semirigid base con-

nections. *Journal of the Engineering Mechanics* 131: 633-640.
Chandrangsu, T & Rasmussen, K. J. R. 2011. Investigation of Geometric Imperfections and Joint Stiffness of Support Scaffold Systems. *Journal of Constructional Steel Research* 67: 576-584.
Kim, G. Y. & Won, J. H. Won & Kim, S. H. 2017. Structural behavior analysis of system supports according to boundary condition of joints between vertical and horizontal members. *Journal of the Korean Society of Safety* 32(3): 60-65.
Liu, H. & Zhao, Q. & Wang, X. & Zhou, T. & Wang, D. & Liu, J. & Chen, Z. 2010. Experimental and analytical studies on the stability of structural steel tube and coupler scaffolds without X-bracing, *Engineering Structures* 32: 1003-1015.
MLTM. 2007. *Guide to Installation of Shores for a Concrete Bridge*.
MOLIT. 2016. *Standard Specification in Temporary Construction*.
Peng, J. L. & Wu, C. W. & Chan, S. L. & Huang, C. H. 2013. Experimental and numerical studies of practical system scaffolds, *Journal of Constructional Steel Research* 91: 64-75.
Prabhakaran, U. & Beale, R. G. & Godley, M. H. R. 2011. Analysis of scaffolds with connections containing looseness, *Computer and Structures* 89: 1994-1955.
T. Chandrangsu and K. J. R. Rasmussen, "Structural Modelling of Support Scaffold Systems", School of Civil Engineering, Research Report R896, 2009.
Yu, W. K. & Chung, K. F. & Chan, S. L. 2004. Structural instability of multi-storey door-type modular steel scaffolds. *Engineering Structures* 26: 867-881.

Maintenance, Safety, Risk, Management and Life-Cycle Performance of Bridges – Powers, Frangopol, Al-Mahaidi & Caprani (Eds)
© 2018 Taylor & Francis Group, London, ISBN 978-1-138-73045-8

Research on Transverse Mechanical Property of Widened Box Girder Bridge

W.Q. Wu & H. Zhang
School of Transportation, South East Univ., Nanjing, China

Z.X. Tang
China Design Group Co., Ltd., Nanjing, China

ABSTRACT: In order to investigate the possible structural diseases brought to the deck of the existing prestressed concrete box girder bridge, the stress state of the existing box girder before and after widening were analyzed using finite element method in this paper. The possible structural diseases and their mechanisms that were brought to the upper plate and flange plate of the existing box girder were studied. The main parameters considered include the shrinkage and creep effect of the new concrete bridge, the uneven settlement difference between the old and the new box girder, the temperature gradient and the vehicle live load on the whole widened box bridge. Results showed that the inner flange of the old box girder were generally in the state of large tensile stress, the main reason for which was the shrinkage and creep effect difference and the uneven settlement difference of the new and old bridge. And the tensile stress was larger than tensile strength of C50 concrete, which would most likely cause crack in the deck plate of box girder. Hence, reinforcement measures are needed to be designed carefully. Meanwhile, the transverse deformation of structure had exceeded the distance between the anti-seismic block and the web of box girder at the end cross section, which would most likely squeeze anti-seismic block. Therefore, it is necessary to limit the length of continuous bridge that needs a widening work.

1 INTRODUCTION

At present, the technical needs of China's bridge widening mainly come from two aspects: one is the substantial increase in the volume of existing road traffic, which has exceeded the existing road capacity. The expansion of the expressway is indeed a quick and effective solution to this issue (Wu et al. 2007, Shushkewich 2005). On the other hand, the carrying capacity of existing bridges can be enhanced after widening according to some literatures (Zhang et al. 2006, Lu et al. 2013, Zhao & Zhang 2004). This is mainly because the structural stiffness of the new bridge can be changed to meet the bearing requirements of existing bridges.

Most of the current literatures focus on structural reinforcement measures to improve the carrying capacity of the original structure (Choi & Oh 2013, Zaid & Collings 2017), while there is little research on the performance indicators of widened bridge in the serviceability limit states under the interaction between the new and old bridge. Especially, the study on transverse stress and deformation is still insufficient due to the additional shrinkage and creep effect of the new concrete bridge and the uneven settlement difference between the old and the new girder, resulting in many structural diseases (Wang 2011, Ru & Liu 2016, Wen & Ye 2006, Jing & Wen 2014). For example, after the widening of a highway bridge, because the large lateral displacement appeared in the end section of large-span concrete box girder, the transverse anti-seismic block on the cover beam was squeezed seriously.

Different from the conventional design of box girder bridge, it is necessary for bridge joint widening design to consider the interaction between the new and old box girder bridge due to time-dependent effects. At the same time, the widened bridge has an obvious spatial effect of wide bridge due to the larger width–span ratio, compared with the original box bridge. Therefore in order to ensure the normal use performance and durability of the bridge after widening, it is necessary to focus on the analysis of the transverse stress state in the deck of the existing box girder bridge and the possible potential structural diseases, then to add rational strengthening measures to the existed bridge .

Taking a variable cross-section continuous box girder bridge that needs to be widened as the research background, the transverse mechanical property of the widened box girder bridge were analyzed by the finite element method in this paper, to clarify the influence of widening on the transverse force of the old bridge, especially on the bridge deck. Finally,

reinforcement measure for the old bridge was put forward accordingly.

2 PROJECT AND MODEL OVERVIEW

2.1 *Background of Project*

This is a (40+2×67+40) m prestressed concrete continuous box girder bridge with two single-box single-chamber box girder, constructed with C50 concrete and 1860MPa longitudinal prestressed steel strand. Full width of box girders is 13.5m, and the cantilever length of the flange plate is 3.5m with 0.15m thickness at cantilever end and 0.60m thickness at the root. The thickness of the floor and the beam height vary in accordance with 1.8 order parabola. The continuous prestressed concrete bridge was constructed with cantilever construction method. The design load for the old bridge is Automobile Ultra-20, trailer-120. The bridge elevation and cross-section diagram are shown in Figure 1 to Figure 2.

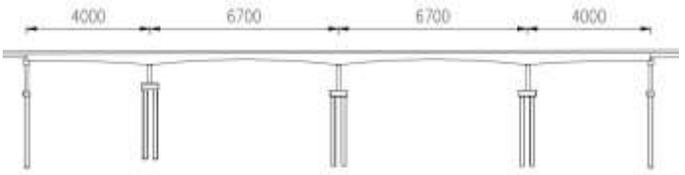


Figure 1. Bridge Elevation (Unit: cm)

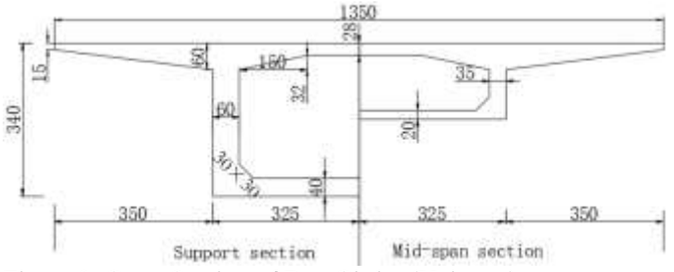


Figure 2. Cross Section of Box Girder (Unit: cm)

Taking various factors into consideration, the new bridge adopted the same structural form and span arrangement as the old bridge. And the superstructure was connected while the substructure remained separated. After widening the design load is highway level-I. The flange plate of the old and new bridge were spliced in a hinged manner without diaphragm for lateral connection. During construction, the part of 0.75m inner flange of the old box girder should be excised firstly to be easy for planting bar up in the flange plate. And then the buried bars in flange of the old box girder and embedded bars in the new were welded together. The last step is pouring concrete into the splicing seam, forming a hinged connection structure. The illustration of transverse splicing of box girder is shown in Figure 3.

2.2 *Finite element model*

The three-dimensional finite element model of the full–bridge was built according to design drawings. Hexahedral elements were used in the model and the element grid was encrypted at the seam. The transverse meshing was shown in Figure 4. A total of 10 control sections were selected to calculate the internal force and in order to characterize the stress changes along the height of each control section, 30 stress control points were selected in each control section, as shown in Figure 5 and Figure 6. The bearing constraints are shown in Figure 7 and Table 1. The definition of coordinated system is determined as follows, the direction along the bridge is X axis, the right direction is positive, direction transverse to the bridge is Y axis, the old bridge direction is positive, Z axis is vertical, the upward is positive and the downward is negative. In general, the full bridge model is divided into 636,336 elements and 852,527 node.

The working conditions considered by finite element model in this paper were defined as follows:

Stage 1–the additional shrinkage and creep effect;
Stage 2–the uneven settlement difference;
Stage 3–the vehicle live load;
Stage 4–the temperature gradient;
Stage 5–comprehensive conditions.

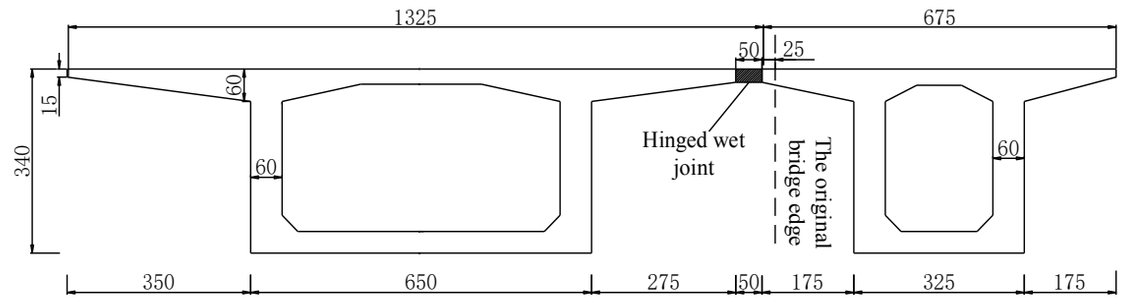


Figure 3. Transverse Splicing of Box Girder (Unit: cm)



Figure 4. Transverse Meshing

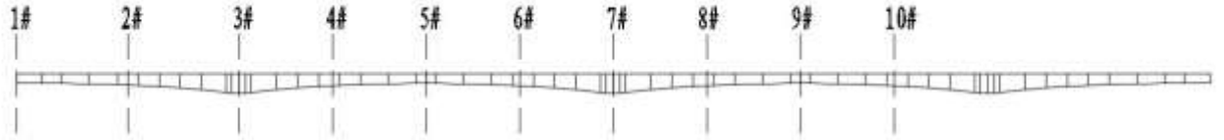


Figure 5. The Overall Bridge Elevation Model

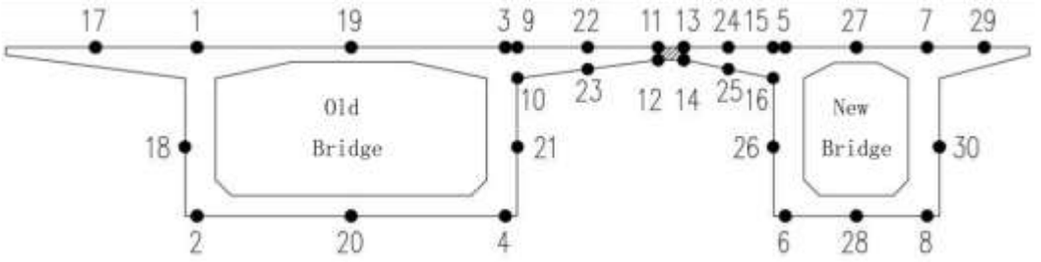


Figure 6. Sketch Map of Section Control Point

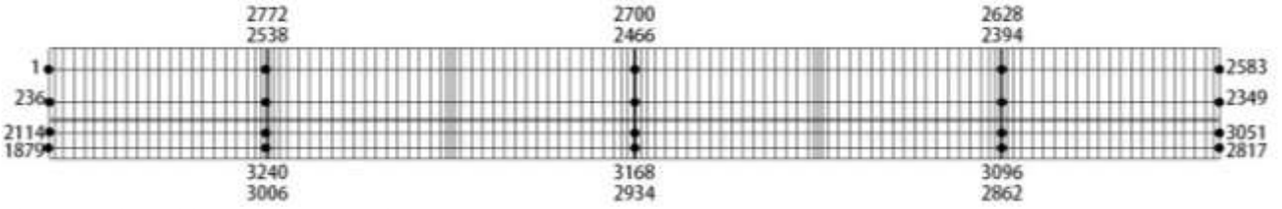


Figure 7. The Bridge Support Restraint

Table 1. Boundary conditions of the section of support point

Position	Node number	Longitudinal (X)	Transverse (Y)	Vertical (Z)
1#pier	1,236	free	free	constrained
	2114,1879	free	free	constrained
2#pier	2772,2538	free	free	constrained
	3240,3006	free	free	constrained
3#pier	2700,3168	constrained	free	constrained
	2466,2934	constrained	constrained	constrained
4#pier	2628,2394	free	free	constrained
	3096,2862	free	free	constrained
5#pier	2583,2349	free	free	constrained
	3051,2817	free	free	constrained

3 ANALYSIS OF TRANSVERSE MECHANICAL PROPERTY OF WIDENING STRUCTURE

3.1 *Influence of shrinkage and creep effect difference on old bridge flange after widening*

It is assumed that the shrinkage and creep effect of the old bridge concrete has been completed, while that of the new bridge just start after transverse splicing. In order to analyze the influence of the shrinkage and creep difference of the old and new bridge concrete on the force and deformation of the whole box girder structure, the construction process was divided into six stages, as shown in Table 2.

Table 2. Construction stages

Construction stage number	Construction content
1	Cantilever pouring construction and bridge deck pavement of the old bridge
2	After ten years(3650 d) of operation for old bridge
3	Cantilever pouring construction and bridge deck pavement of the new bridge
4	After six months of waiting period (180 d) for the new bridge
5	Construction of joint widening
6	Co-operation of new and old bridge for three years (1095 d)

3.1.1 *Analysis of transverse displacement*

In order to visually see the trend of transverse displacement, Figure 8 depicts the transverse deformation of each control section due to the shrinkage creep of the new cast concrete after transverse splicing. It can be seen from Figure 8 that the transverse displacement at the end of box girder was 68mm, which was about 1/3147 of the total bridge length. While the distance between anti-seismic block and the girder web was 50mm, if no effective measures were taken to suppress the transverse displacement,

the anti-seismic block was most likely to be squeezed severely, as shown in Figure 9.

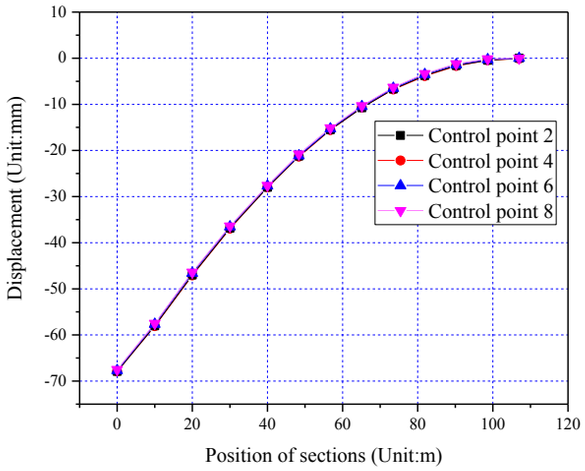


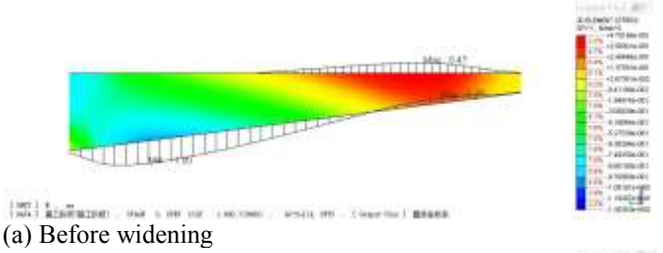
Figure 8. The Transverse Displacement Curve after Widening Due to Shrinkage and Creep



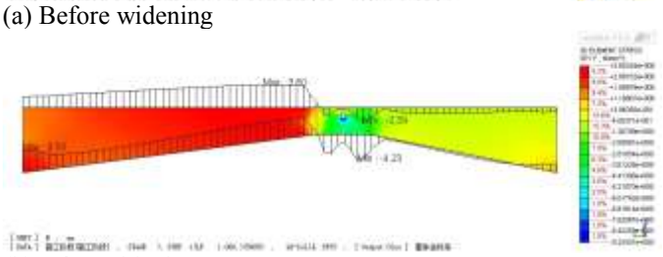
Figure 9. The Squeezed Anti-seismic Block

3.1.2 *Analysis of transverse stress*

As the maximum transverse displacement occurred at the beam end section (1#), Figure 10 shows the trend of transverse normal stress at the top and bottom of the flange plate of the old bridge in 1# cross section, and the stress above the base line indicated the tensile stress, while that below the base line indicated the compressive stress.



(a) Before widening



(b) After widening

Figure 10. The Overall Transverse Stress Changes of 1# Control Cross Section for the Old Bridge (Unit: MPa)

It can be seen from the above figure that the transverse stress of the inner side of old bridge flange was greatly changed. In order to clarify the stress distribution characteristics, Table 3 lists the stress values of the control points for the old bridge, among them tensile stress was positive while compressive stress was negative.

Table 3. Transverse normal stress value of control points in 1 # section

Control points	9	10	22	23	11	12
Ten years' operation for old bridge	-0.94	-0.05	-0.01	-0.72	0.47	0.23
After joint widening	-0.46	0.63	0.42	0.03	0.02	0.21
Co-operation for three years	1.65	2.35	3.00	2.32	0.84	0.20

As shown in Table 3 and Figure 10, there were large tensile stresses both on the upper and lower zone of the inner flange near the end section of the old girder, that is, the inner flange near the end section for the old bridge was in a transversely integral pull state. The mechanism of this stress state is that when longitudinal shrinkage and creep deformation occurred in the new whole bridge, the new bridge would exert a transverse tension effect on the old bridge due to the integral transverse deformation of the whole widened bridges in the end section. Therefore, when the inner flange of the old box girder is subjected to eccentric compression longitudinally, it was in an integral tension state transversely. This transverse tension effect will increase with the total length of the widened bridge, so reinforcement measures are needed for the inner flange of the old box girder near the end section.

3.2 *Influence of uneven settlement difference on old bridge flange after widening*

The uneven settlement difference between the old and the new box girder, which is also called settlement difference after construction, has a very important effect on the deformation and internal forces of the inner flange plate of the old and new box girders. In the model, the settlement difference was imposed according to the conclusion of Wu et al. (2008) that the settlement difference after construction should not be greater than 10mm for orthogonal bridges, while the value should not be greater than 5mm if putting skewed bridge orthogonally. As this bridge conformed to the latter case, therefore, in this paper the allowable settlement difference in the section of support point was identified as the value 5mm.

Figure 11 shows the distribution of the transverse stress of the whole widened structure under the effect of foundation settlement difference. It can be seen from Figure 11 that the transverse stress was small in most areas except in the section of support point. Taken 1# cross section as an example, the

trend of the lateral normal stress of the inner flange plate was shown in Figure 12, and the stress above the base line indicated the tensile stress, while that below the base line indicated the compressive stress. The specific lateral stress values on the upper and lower edge of the flange plate can be viewed in Table 4.

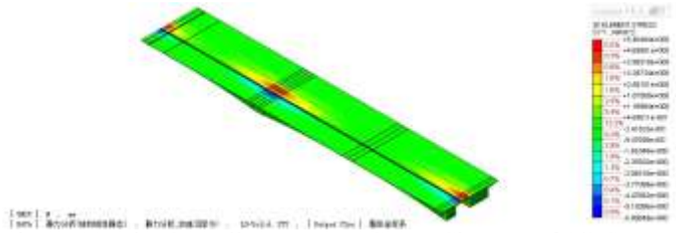


Figure 11. The Overall Transverse Stress Changes of 1/2 Span Bridge Structure

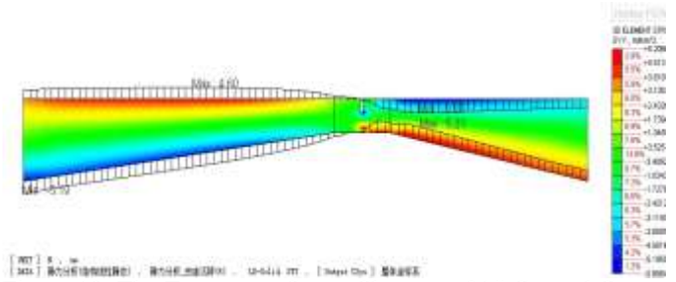


Figure 12. The Transverse Stress Changes of 1# Control Cross Section (Unit: MPa)

Table 4. Settlement-induced transverse normal stress of key points in 1 # section

Control points	9	10	22	23	11	12
Transverse stress	3.4	-3.41	4.6	-5.0	1.3	-1.62
Reduced stress	1.5	-1.53	2.1	-2.3	0.6	-0.73

In Table 4, the transverse stress caused by forced displacement was reduced because the effect of foundation settlement on the internal forces of transverse widened structures performs as a long-term process. Therefore, the stress relaxation effect of concrete should be considered in the stress calculation. With reference to the research results of previous literatures (Mohseni & Rashid 2013, Han et al. 2003, Wen et al. 2011), the reduction factor was recommended as 0.45 in this paper. However the value of tensile stress on upper flange was still threatening.

3.3 *Influence of vehicle live load on the flange of old bridge after widening*

The bridge was arranged horizontally with 5 lanes after widening. The lateral distribution of lane load mainly considered three kinds of working conditions such as load biased on the old bridge side, symmetrical load and load biased on the new bridge side, as was shown in Figure 13.

Figure 14 shows the transverse normal stress nephogram of the third mid-span section (9#) under the three kinds of working conditions and the specific transverse normal stress values can be viewed in Table 5, among them the tensile stress was of positive while compressive stress was of negative.

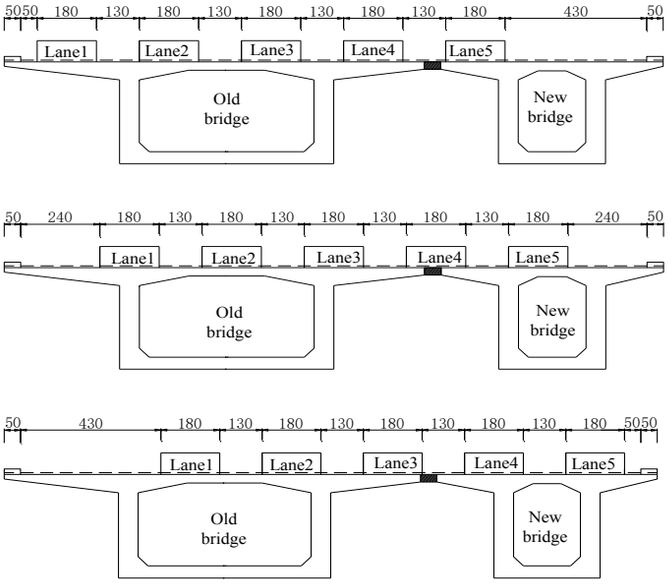


Figure 13. The Schematic Diagram of Transverse Load Distribution (Unit: cm)

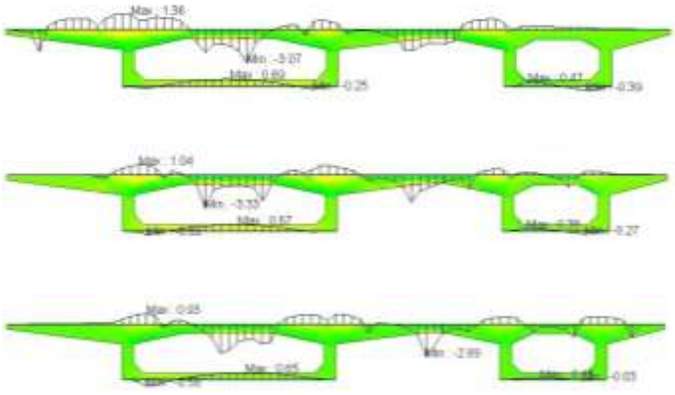


Figure 14. Transverse Stress Changes of 9# Control Cross Section (Unit: MPa)

Table 5. Transverse normal stress value of control points in 9 # section

Control points	9	10	22	23	11	12
Case 1	0.50	-0.20	-0.39	0.18	-1.26	0.69
Case 2	0.81	-0.63	-0.33	0.13	-1.31	0.76
Case 3	0.92	-0.73	0.09	-0.26	-2.90	1.72

It can be seen from the above finite element model analysis results: The stress distribution on the deck of the box girder was very similar except for some numerical changes, no matter under what kind of working conditions, which indicating good force collaboration between the new and old box girder. In addition, the splicing part between the new and old deck was generally in a good stress state, only the tensile stress of 1.72 MPa occurred at the individual control point 12 , which indicating that the structure showed good performance under the action of vehicle load, so the vehicle load is not the control factor to the transverse splicing site.

3.4 *Influence of temperature gradient on old bridge flange after widening*

The temperature gradient pattern is applied in accordance with the relevant provisions of the specification, as shown in Figure 15. The maximum temperature of the surface of the bridge deck T_1 is 14 degrees Celsius and T_2 is 5.5 degrees Celsius when calculating the positive temperature difference. When calculating the anti-temperature difference, multiply the former by -0.5 according to the specification.

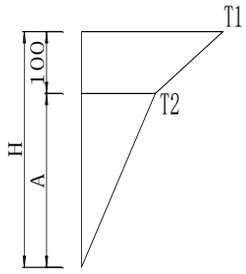
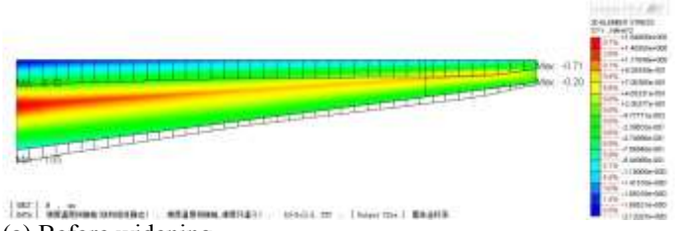
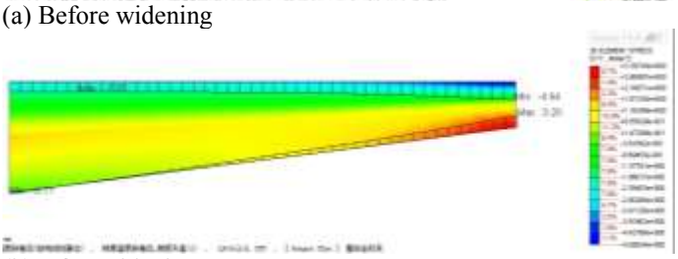


Figure 15. Vertical Temperature Gradient Curve (Unit: cm)

Figure 16 depicts the transverse stress nephogram of old bridge flange plate at the middle cross-section (2#) in side span under the positive temperature gradient, the stress above the base line indicated the tensile stress, while that below the base line indicated the compressive stress. The specific lateral stress values on the upper and lower edge of the flange plate can be viewed in Table 6. Among them tensile stress was positive while compressive stress was negative.



(a) Before widening



(b) After widening

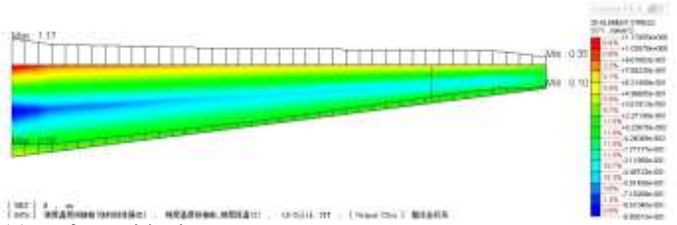
Figure 16. The Transverse Stress under Positive Temperature Gradient (Unit: MPa)

Table 6. Transverse normal stress value of control points in 2 # section

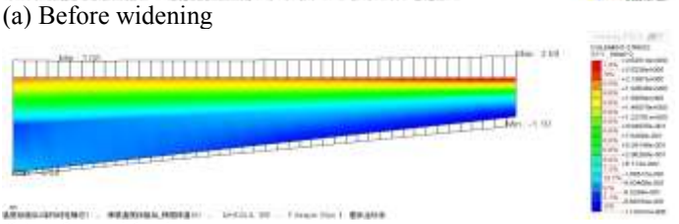
Control points	9	10	22	23	11	12
Before widened	-2.16	-0.72	-1.53	-0.50	-1.36	-0.55
After widened	-2.80	-0.10	-2.97	0.93	-4.77	3.02

As can be seen from Figure 16 and Table 6, there was a significant increase in the compressive stress values at the upper edge of the old bridge flange plate, under the positive temperature gradient, while transverse stress on the lower edge of the flange plate changed from compression to tension. The closer the position was to the splicing section, the greater the tensile stress was. The maximum stress value of 3.0MPa occurred at the splice section, which would exert adverse effect on the lower edge of the inner flange plate of the old bridge and the splicing section.

On the contrary, under the effect of negative temperature gradient, the tensile stress values at the upper edge of the old bridge flange plate increased obviously even up to 2.63MPa, resulting in high possibility of concrete cracking on the upper flange, as shown in Figure 17 .



(a) Before widening



(b) After widening

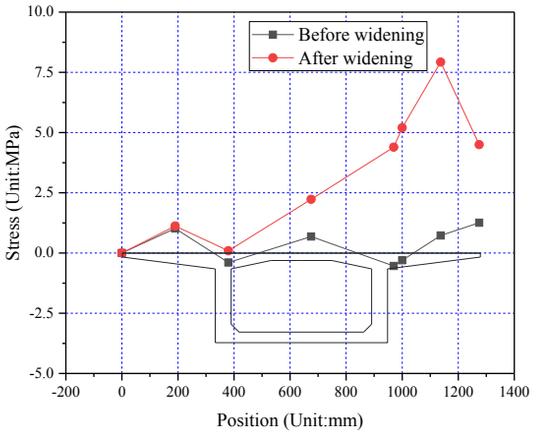
Figure 17. The Transverse Stress under Positive Temperature Gradient (Unit: MPa)

3.5 *Transverse stress state of the deck of old bridge under comprehensive conditions*

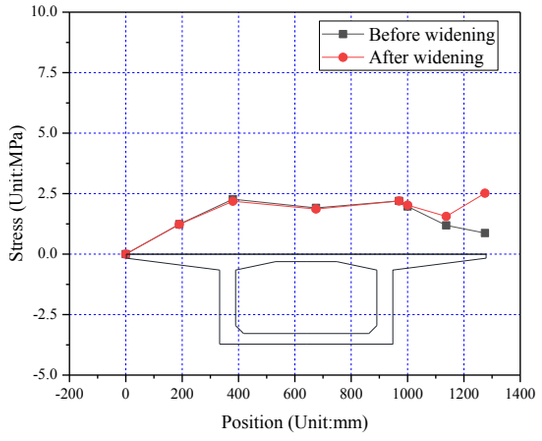
In order to fully consider the influence of self-weight, prestress, shrinkage and creep, foundation settlement difference, vehicle live load and temperature gradient on old bridge after widening, the stresses in above load conditions were combined, to study possible structural diseases on bridge deck that caused by a joint widening of prestressed concrete box girder bridge. Figure 18 shows the maximum transverse stress values of control points on several typical sections under comprehensive conditions.

The joint widening performed with a great influence on the stress state of the deck of old box girder at the section of support point, especially in the end section, while a little influence at the mid-span section relatively. Part of the upper plate and the inner flange plate of the old box girder were generally in the state of large tensile stress, for example the tensile stress reached 2.2-7.9 MPa in beam end section, which had exceeded the tensile strength of C50 concrete, and then the flange plate actually cracked or

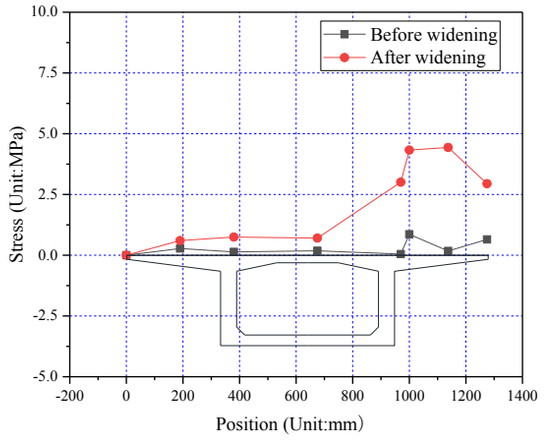
had a high possibility of cracking. Therefore, reinforcement measures ought to be taken to prevent serious cracking of concrete.



(a) 1# cross section



(b) 2# cross section



(c) 3# cross section

Figure 18. The Transverse Stress under Comprehensive Conditions (Unit: MPa)

3.6 *Suggested strengthening measure for the flange plate of the old bridge*

In view of the above finite element analysis results , it's obvious that after widening, the flange plate of the old bridge would face an unfavorable stress state under the effect of shrinkage and creep effect of the new concrete bridge, the uneven settlement difference between the old and the new box girder, the temperature gradient etc. Therefore, the top and bottom zone of the inner flange plate of the old bridge are to be reinforced and then the following methods that Nie et al.(2005) suggested can be proposed, that applying the lateral external prestressing to make the old bridge flange plate (after cutting 0.75m flange) in the preloading state. Taking into account the convenience of construction on old bridge, the transverse prestressing strands could be arranged on the upper edge of the old bridge flange, as shown in Figure 19. Reinforcement materials include high-strength stainless steel wire mesh and strongly permeable mortar. The specific reinforcement configuration data can be calculated according to the external prestressing structure, and the reinforcement range can be carried out in the whole bridge to improve the crack resistance of the structure. Compared with traditional strengthening method, this technology has many advantages such as prestressing effect, fire resistance, corrosion resistance, aging resistance, good quality, less damage to the deck of the main beam, convenience to construct, etc.

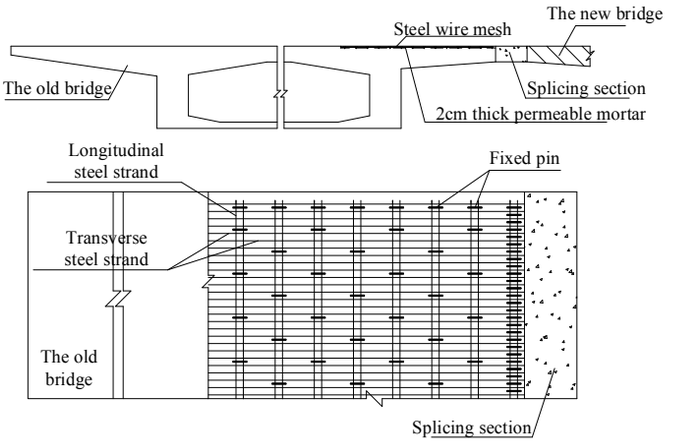


Figure 19. Layout of Steel Strand Mesh on the Flange Plate of the Old Bridge

To handle creep-shrinkage deformation of the added box girder fundamentally, other than accommodating the resulting stresses, one possible way is to limit the total length of continuous box girder bridge that needs to be widened and the application of shrinkage-compensating concrete can be another approach, which are all directions that can be studied in depth in the future.

4 CONCLUSION

Based on the results of solid finite element, the following conclusions and recommendations were summarized:

(1) The transverse deformation of the box girder structure resulting from shrinkage and creep effect of the new concrete bridge was very significant, especially in the end section of the widened bridge,

which was even possible to severely squeeze anti-seismic block.

(2) The shrinkage and creep effect of the new concrete bridge would cause greater tensile stress in the flange of old box girder at the end section, which should be carefully considered.

(3) The uneven settlement-induced tensile stresses were greater on the upper edge of the old bridge flange plate and the lower edge of the new in the section of support point.

(4) Under the action of vehicle load, the old and new box girders were able to work together as a whole structure and showed good bearing performance.

(5) The upper flange of the old bridge showed greater tensile stress under the effect of negative temperature gradient, needing reinforcement treatment.

(6) In summary, the upper plate and inner flange of the old bridge were generally in the state with a large tensile stress, and the main reason for which was the shrinkage and creep effect of the new concrete bridge and the uneven settlement difference between the old and the new box girder. There was a high probability of cracking in most zone of the widened bridge deck.

(7) In order to solve the problems above, a transverse external prestressing method could be introduced to reinforce the upper plate and lower plate of old bridges after joint widening in this paper.

REFERENCE

Choi, Y.C. & Oh, B.H. 2013. Transverse modelling of concrete box girder bridges for prediction of deck slab ultimate load capacity. *ASCE Journal of Bridge Engineering* 18 (12): 1373-1382.

Han, C.Q., Feng, J. & Lu, Z.T. 2003. Method of creep stress reduction coefficient for thermal stress analysis of large-area concrete beam-slab structures. *Engineering Mechanics* 20(1):7-14.

Jing, H.W. & Wen, Q.J. 2014. Numerical simulation of creep and shrinkage in widened concrete bridges. *Magazine of Concrete Research* 66(13):661-673

JTG D60-2015, General Code for Design of Highway Bridges and Culverts. Beijing: China Communications Press.

Lu, S.Q., Tang, M. & Xu, X. 2013. Effect of splicing on mechanical properties of PC continuous rigid frame bridge. *Journal of Railway Science and Engineering* 10(6):33-39.

Mohseni, I. & Rashid, A.K. 2013. Transverse load distribution of skew cast-in-place concrete multi cell box girder bridges subjected to traffic condition. *Latin American Journal of Solids & Structures* 10(2):247-262.

Nie, J.G., Wang, H.B. & Zhang, T.S. et al. 2005. Experimental study on flexural reinforcement of permeable polymer mortar. *Journal of Building Structures* (02):1-9.

Ru, Y. & Liu, Q.W. 2016. Research on the mechanical properties of bridge widening connection section of concrete continuous box girder due to the effect of shrinkage and creep. *Journal of China & Foreign Highway* (2): 196-200.

Shushkewich, K.W. 2005. Design of prestressed concrete bridges to accommodate future widening. *PCI Journal* 50(3):74-89.

Shi, X., Li, X. & Ruan, X. et al. 2008. Analysis of structural behavior in widened concrete box girder bridges. *Structural Engineering International* 18(4):351- 355.

Wollmann, G. P., Anderson, R. B. & Roberts-Wollmann, C. L. 2003. Creep and shrinkage effects in spliced prestressed concrete girder bridges. *PCI Journal* 48(6):92-105.

Wen, Q.J. & Ye, J.S. 2006. Analysis of shrinkage and creep effect on transverse stitching of old and new reinforced concrete beams. *Journal of Southeast University (Natural Science Edition)* 36(4):596-600.

Wu, W.Q., Ye, J.S. & Ju, J.Y. et al. 2007. Present situation and scheme analysis of bridge widening in expressway extension. *Journal of China & Foreign Highway* 27(6):100-104.

Wu, W.Q., Ye, J.S. & Hua, B.et al. 2008. Study on key technology of bridge expansion in Shanghai-Nanjing highway. *Proceedings of the National Symposium on Reinforcement, Renovation and Evaluation of Bridges.*

Wang, X.P. 2011. Study on the common defects and reinforcement technique of the widened prefabricated bridge. Chang'an University. Xi'an. China.

Wen, Q.J., Zhu, Y.X. & Wang, D.Q. 2011. Study of additional forces induced by differential settlement of widened box girder bridges. *Journal of China University of Mining and Technology* 40 (3): 351- 356.

Zhao, Y. & Zhang, K. 2004. Load carrying capacity of broadened existing bridge. *Journal of Chang'an University (Natural Science Edition)* 23(1): 51-53.

Zhang, L.F., Guo, T. & Wu, W.Q. et al. 2006. Analysis of the influence of connecting method on old bridge performance in widening bridge. *Journal of Highway and Transportation Research and Development* 23(2):102-104.

Zaid, A. & Collings, D. 2017. Transverse assessment of a concrete box girder bridge. *Proceedings of the Institution of Civil Engineers-Bridge Engineering* 170(1):14-27.

Maintenance, Safety, Risk, Management and Life-Cycle Performance of Bridges – Powers, Frangopol, Al-Mahaidi & Caprani (Eds)
© 2018 Taylor & Francis Group, London, ISBN 978-1-138-73045-8

Sensitivity and Reliability Analysis of long span Cable stayed Bridge

Xiaoming Wang , Wentao Wu, Juyou Zhang, Yu Cai
Institute of Bridge Engineering, College of Highways, Chang'an University, Xi'an, Shaanxi Province, China
Key Laboratory of Bridge Detection Reinforcement Technology Ministry of Transport(Xi'an)

ABSTRACT: This paper proposes a method of structural sensitivity and reliability analysis based on the reliability calculation method by using integration of Latin hypercube sampling(LHS) and one-order second-moment method, then a cable-stayed bridge with multi-cable system is analyzed by using the method. (1) The number and type of the random variables used in the reliability analysis are determined by reliability analysis and sensitivity analysis. (2) The analysis model is established to analyze the sensitivity and reliability of the parameters. (3) The reliability analysis results are compared to verify the correctness of the method. The feasibility of this method is proved by analyzing a 12-story frame structure, the method is applied to sensitivity and reliability analysis of a cable-stayed Bridge. The influence of materials and external factors is considered and the initial tensioning cable force is seen as random variable to carry out the analysis, that have a significant meaning on cable tensioning scheme optimization of cable-stayed bridge.

1 INTRODUCTION

Cable-stayed bridge is widely built because of larger stiffness of the main beam, convenience of cantilever construction and larger construction span. The optimization of the cable force of the cable-stayed bridge has been a hot topic in the field of structural optimization. But most of the studies are based on structural assumptions that are fully deterministic, also known as deterministic analysis. However, in practical engineering applications, the cable-stayed bridge itself is very sensitive to the influence of uncertain factors such as geometry, bearing displacement, material properties, external load and construction. Therefore, the deterministic analysis cannot provide a complete assessment of the cable-stayed bridge. So far, a large number of scholars have done a lot of optimization research of cable force of cable-stayed bridge. these methods, from the perspective of displacement and internal forces to optimize the cable force, are deterministic analysis. There is little research on the sensitivity and reliability analysis of the cable-stayed bridge structure. Therefore, in order to make a complete evaluation of the cable-stayed bridge, the material and other factors of the cable-stayed bridge are analyzed to calculate the reliability and sensitivity, and it is particularly important for complete evaluation of cable stayed bridge.

The Monte Carlo method (MC) is a numerical method for solving the reliability by stochastic simulation and statistical experiments. For some structures, when the function is implicit or difficult to obtain, the sample of the variable cannot be taken directly to calculate. But by using the finite element analysis software, the variables can be directly substituted into the finite element model, and the response results of the structures can be obtained by analysis, and the failure probability and reliability index of the structures can be calculated. The Monte Carlo method provides an important general method, but due to computational cost constraints, it has not been overwhelmingly applied. The one-order second-moment response surface method (RSM) is a widely-used method in structural reliability analysis. The response surface method uses the statistical sampling technique and the regression fitting technique in statistics to convert the function which is difficult to express to simple fitting function, and finally the reliability analysis method is used to analyze the structural reliability. In this paper, we introduce a new hybrid method and apply it to the sensitivity and reliability analysis of the cable-stayed bridge when we use the random response data to fit the whole sample space. Firstly, this method is proved by the analysis of the twelve-story rigid frame, and then the method is applied to the analysis of the sensitivity and reliability of the double-tower three-span cable-stayed bridge. The sensitivity of the random variables of the cable - stayed bridge is determined by the sensitivity analysis, and the results of reliability analysis which are calculated by using

partial variables and all variables are compared to describe the feasibility of this approach.

2 PROPOSED METHOD

The method is designed to integrate Latin hypercube sampling (LHS), artificial neural network response surface method(ANN), first-order Second-moment(FOSM) reliability analysis method and Monte Carlo(MC) method based on important sampling method without sacrificing accuracy to improve the reliability analysis efficiency.

2.1 *Latin hypercube Sample Technic*

Latin hypercube sampling (LHS) is the progress of sampling technology innovation. Compared with traditional direct random sampling, it is designed as a sampling method which can reflect the whole distribution of variables through fewer samples. Its basic principles are as follows:

(1) Each dimension has been divided into *m* non-overlapping regions so that each region has the same probability, that is, dividing by equal probability;

(2) A sample point has been randomly selected in each dimension;

(3) Then the data in (2) are randomly combined according to the one-to-one correspondence principle.

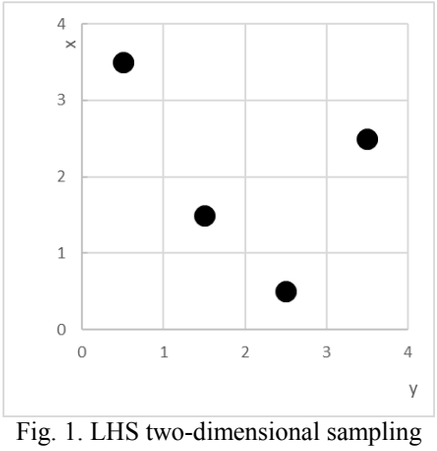


Fig. 1. LHS two-dimensional sampling

In the traditional sampling calculation, all the variables are selected randomly, this method is difficult to ensure that the selected variables can cover the entire range of variables. It also cannot be a good reflection of the overall variation of the variable. The Latin hypercube sampling (LHS), as shown in Fig.1, effectively avoids the repetitive combination of multidimensional combinations. And the equal probability division can effectively use the distribution of a small number of sample to reflect the whole distribution.

It should be noted that the Latin hypercube sampling is not for evenly distributed [0,1] samples, but according to the distribution of random variables to divide the variable which has the equal probability interval division.

2.2 *Back Propagation Artificial Neural Network*

BP artificial neural network (BPANN) is a one-way propagation of multi-layer feedforward network structure, which is currently the most widely used a network structure. A complete BP neural network structure consists of three layers: the input layer, the output layer, and the hidden layer, as shown in Fig 2. Hidden layer layers can be monolayer or multilayer, and there is no association between neurons in the same layer. The signal is input from the input layer, reaches the hidden layer, and finally outputs the result from the output layer. Only the two adjacent layers are signaled and the signal can only be transmitted unidirectionally to the next layer. This is also known as a multi-layer feedforward network.

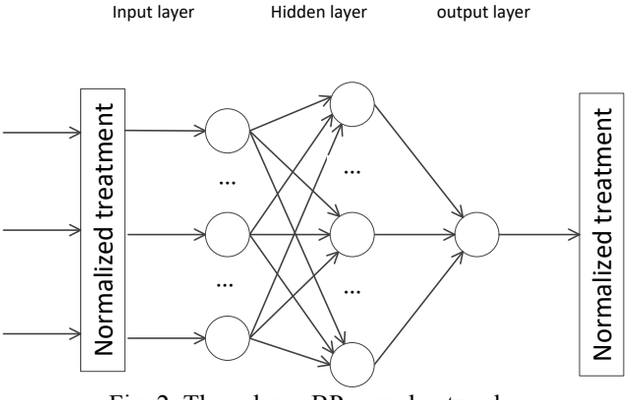


Fig. 2. Three-layer BP neural network

The transfer function of the hidden neurons in the BP neural network is usually a Sigmoid function. As shown in Fig.2, in a three-layer BP neural network, we assume that the number of nodes in the input layer is *n*, the number of nodes in the neurons of each hidden layer is *p* and the output neurons are 1. *N* sample points are obtained by sampling, and the sample points are brought into the finite element model for numerical simulation. *N* real output values corresponding to the *N* sample points are obtained, and the sample points are brought into the BP neural network to obtain the *N* output layer values. The network connection weight between the *j*th neuron node and the output layer of the input layer is w_{ij}, and the network connection weight between the *j*th neuron node and the output layer of the hidden layer is v_{ij}.

Assume that the structural functional function is:

$$Z = G(X) \tag{1}$$

Then there is a mapping relationship between the input sample point x^l and the true output value z^l:

$$z^l = G\left(x^l\right)\left(l = 1, 2, \cdots, N\right) \tag{2}$$

By studying the geometry of the sample, as shown in Fig 2, the BP neural network is going to determine a set of weights makes the actual output of the neural network the best approximation of the true output

value. The fitted response surface function can be expressed as:

$$\begin{aligned}\bar{Z} &= \bar{G}(X) = f_2\left(V^T f_1\left(W^T X-\theta\right)-\theta'\right) \\ &= f_2\left(\sum_{j=1}^{p} v_{j1} f_1\left(\sum_{i=1}^{n} w_{ij} x_i-\theta_j\right)-\theta'\right)\end{aligned} \tag{3}$$

Where f_1 and f_2 are the transfer functions between the hidden layer and the output layer, respectively, θ and θ' are the thresholds between the hidden layer and the output layer. The general hidden layer function selects the Tan-Sigmoid function (equation 4), and the output layer selects the linear function (equation 5):

$$f_1(x) = \frac{2}{1+\exp(-2x)} - 1 \tag{4}$$

$$f_2(x) = x \tag{5}$$

2.3 *First-order Second-moment method*

First-order Second-moment method(FOSM) uses the first-order moments (mean) and second-order moments (variance) of the data in the statistical information to calculate the structural reliability. Using Taylor series to expand the complex functional function into a polynomial is the main content of this method, and then through the mathematical statistics directly calculate the structural reliability.

There are two ways to expand the function. One is expanding at the mean of the variable, called central point method. One is expanding at the design verification point, called design verification point method. A checkpoint is the point at which the limit state surface is closest to the origin. This is improved second-order moment method. As the central point method is more sensitive to the functional function of the structure and the distribution of the variables, the improved first-order second-order moment method is generally used in the engineering practice.

The method will be expanded on the failure surface, taking into account the actual distribution of the basic random variables.

Let the limit state equation of the structure be:

$$Z = G(X) \tag{6}$$

Let $x^* = (x_1^*, x_2^*, \cdots, x_n^*)^T$ be the limit state point, that is: $G(x^*) = 0$.

The limit state function is expanded by Taylor series at x^* and taken to the first term:

$$Z_L = G(x^*) + \sum_{i=1}^{n} \frac{\partial G(x^*)}{\partial X_i}(X_i - x_i^*) \tag{7}$$

Reliability index:

$$\beta = \frac{\mu_{Z_L}}{\sigma_{Z_L}} = \frac{G(x^*) + \sum_{i=1}^{n} \frac{\partial G(x^*)}{\partial X_i}(\mu_{x_i} - x_i^*)}{\sqrt{\sum_{i=1}^{n} [\frac{\partial G(x^*)}{\partial X_i}]^2 \sigma_{X_i}^2}} \tag{8}$$

Define the sensitivity coefficient of variable X_i and use $Y_i = (X_i - \mu_{X_i})/\sigma_{X_i}$ to rewrite to get the normal hyperplane equation:

$$\sum_{i=1}^{n} \cos\theta_{Y_i} Y_i - \beta = 0 \tag{9}$$

The point P^* on the corresponding limit state is called the design verification point, The sensitivity coefficient is:

$$\alpha_{X_i} = \cos\theta_{X_i} = \cos\theta_{Y_i} = -\frac{\frac{\partial G(x^*)}{\partial X_i}\sigma_{X_i}}{\sqrt{\sum_{i=1}^{n} [\frac{\partial G(x^*)}{\partial X_i}]^2 \sigma_{X_i}^2}}$$

The sensitivity calculation formula is:

$$S_i = \frac{\left.\frac{\partial G}{\partial x_i}\right|_{X^*} \left(x_i^* - \mu_i\right)}{2\sum_{k=1}^{n} \left.\frac{\partial G}{\partial x_k}\right|_{X^*} \left(x_k^* - \mu_k\right)} \tag{10}$$

When the variable does not obey the normal distribution, use the equivalent normalization to calculate.

2.4 *Monte Carlo Simulation*

Monte Carlo sampling (MC) is a simple random sampling within the specified sampling range. The basic idea is to know the probability distribution of the random variable and the limit state equation of the problem. According to the distribution of each random variable, the method produces N sets of random data and then passes the data into the limit state equation (Same as Equation 1) to get failure probability. Sometimes we do not know the limit state equation, but with the development of computer technology and the popularity of finite element procedures, in many cases, we can use finite element(FE) technology to get a series of results and then calculate failure probability:

$$p_f = M / N \tag{11}$$

Where M is the number of sample groups which make $Z<0$(M is the number of the failure point when we use FE model).

Monte Carlo method is suitable for a wide range because of its simple principles. But in order to get relatively accurate results, the sample size should be large enough. However, in practical engineering, whether through functional or finite element models, to meet the needs of the project, you need a lot of sample support, so that the use of this method is limited. In order to reduce the computational cost of Monte Carlo, some scholars have used the above-mentioned Latin hypercube sampling to greatly reduce the number of samples required. But it still cannot fundamentally solve the problem of Monte Carlo method with large calculation.

3 PROCEDURE OF PROPOSED METHOD

In order to combine the advantages of Latin hypercube sampling with the first-order moment calculation reliability method, this paper presents a set of solutions. The following procedure of solution is the integration of the aforementioned method, the solution flowchart is at Fig.3:

(1) Determine the random variables and their distribution, use Latin hypercube sampling method to select the sample;

(2) Input the sample data into structure finite element model to obtain the structural response value;

(3) The artificial neural network model is established and the ANN model is tested by random variable sample value and structural response value.

(4) Use the fitting function to determine the function between the variable and the reliability of the equation;

(5) Analyze the reliability of the structure and the sensitivity of the variable.

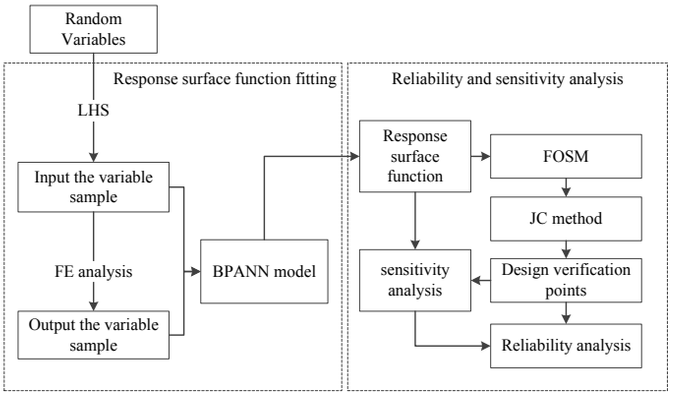


Fig. 3. Flowchart of analysis procedure

4 APPLICATION TO A FRAME STRUCTURE

A rigid frame model, as shown in Fig. 4, which is a 12-story rigid frame structure includes 84 constructs and 104 degrees of freedom is analyzed by using the preceding method.

In the figure, the horizontal displacement of point A is chosen as the object to be studied. The numbers 1 to 5 in the figure indicate the specifications of the corresponding bar, and the same number indicates that the rods adopt the same size cross-sectional area.

Table 1 selects six random influencing factors and their distribution functions (LN is Logarithmic normal distribution), which represent the cross-sectional area of the rods of the ith specification, P represents a static wind load acting on the structure, and the load is equivalent to the node at the frame. The load value of each node is P. Assuming that the above random variables are not related to each other and all of the constructed Young's modulus is a constant value to make the question easier. The relationship between the cross-sectional area of all bars and the moment of bending moment is expressed as $I_i=\alpha_i A_i^2$.

According to the method proposed in this paper, the analysis is divided into two parts: the first part is fitting response surface function. The initial variable sample is generated by using the LHS sampling method described in this paper, and the generated value is substituted into the finite element model to calculate corresponding response value. BP neural network method is used to fit the response surface function by using the sample and response value. The second part is the reliability and sensitivity analysis of the structure. The structural reliability is calculated by using first-order second-moment reliability calculation method.

Use the proposed method to analyze the sensitivity and reliability. The BP neural network method is used to fit the functional function, and the weights and thresholds of the neural network method when the six variables are obtained are shown as follow:

$$G_{BP}(X)=0.096-N_{R0}^{-1}\left(f_2\left(\sum_{h=1}^{3}v_h^{R0}f_1\left(\sum_{i=1}^{5}w_{hi}^{R0}N_{A_i}(A_i)+w_{h6}^{R0}N_P(P)-\theta_h^{R0}\right)-\theta^{R0'}\right)\right)$$

Where the value of parameters is shown as follows and f_1 andf_2 are shown at equation 4 and equation5.

$$W^{R0}=\begin{bmatrix}-0.080 & -0.050 & -0.066 & -0.140 & -0.055 & -0.413\\ 0.218 & 0.020 & 1.451 & 0.239 & -0.400 & -0.598\\ -0.003 & 0.019 & 0.060 & 0.646 & 0.176 & -0.425\\ 0.398 & 0.076 & 0.047 & -0.010 & 0.068 & -0.283\\ 0.047 & 0.028 & 0.049 & 0.107 & 0.036 & -0.278\end{bmatrix}$$

$$\theta^{R0}=[-1.014 \quad 0.809 \quad 1.304 \quad 1.384 \quad 0.052]$$

$$V^{R0}=[0.853 \quad 0.064 \quad 0.554 \quad 0.890 \quad 1.496]$$

$$\theta^{R0'}=-0.554$$

Analyze the sensitivity of each variable and the analysis results are shown in Fig.5. Variable sensitivity values are shown in the table 2. It can be seen that the sensitivity of the random variables A1, A4 and P is higher than that of A2, A3 and A5, and the

sensitivity of the random variable P is the highest, which indicates the reliability index of the random variables A1, A4 and P, the effect is more significant, in which the horizontal load P is the main influencing factor.

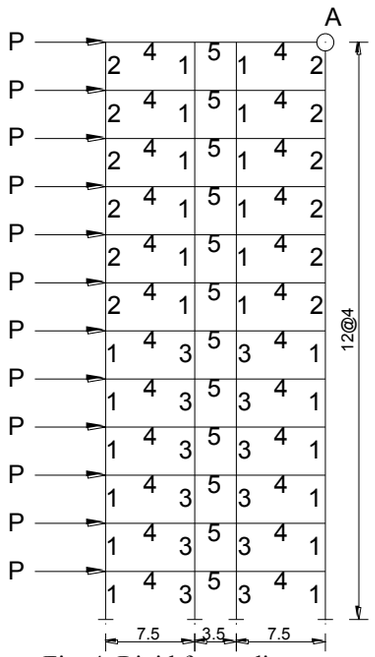


Fig. 4. Rigid frame diagram

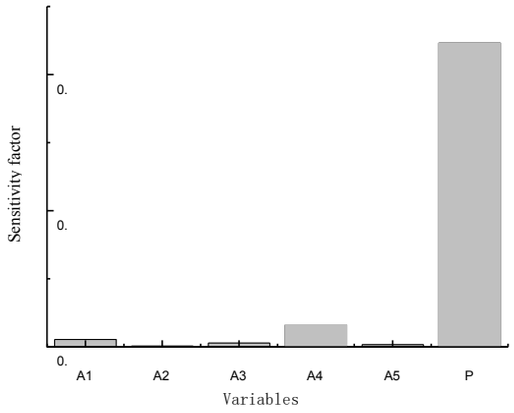


Fig. 5. Random variable sensitivity

Table 1 Random variable parameters

variables	mean	standard deviation	distribution	α_i
A1	0.25m^2	0.025m^2	LN	0.0833
A2	0.16m^2	0.016m^2	LN	0.0833
A3	0.36m^2	0.036m^2	LN	0.0833
A4	0.20m^2	0.020m^2	LN	0.2667
A5	0.15m^2	0.015m^2	LN	0.2000
P	30KN	7.5KN	GumbelI	

Table 2 Random variable sensitivity

Variables	A1	A2	A3	A4	A5	P
Sensitivity factor	0.011	0.001	0.006	0.032	0.003	0.446

Table 3 Reliability analysis results

Number of variables	Reliability index	Failure probability
6	1.43(BP)	7.67%
6	1.45(MC)	7.35%
3	1.47(BP)	7.09%
3	1.37(MC)	8.53%

Sensitivity of A2, A3 and A5 is very low, so that we can consider that A2, A3 and A5 cannot affect the reliability of the results of point A analysis. According to the variable sensitivity screening condition, we can ignore the influence of A2, A3 and A5 on the horizontal displacement reliability index of point A, and regard it as deterministic variable. In summary, select the random variables A1, A4, P on the structure of the reliability analysis. The reliability results are shown in the Table 3.

The results by using six random variables and three random variables on the structure of the reliability analysis are basically the same.

According to the above example, it can be seen that the structure has the same failure mode under the influence of three random variables and six random variables. Therefore, the reliability and sensitivity analysis method proposed in this paper can be applied to the actual structure.

5 APPLICATION TO A CABLE-STAYED BRIDGE

5.1 *Bridge description*

The cable-stayed bridge has a span of 193+332+113 m, a concrete high and low tower, a double-cable surface, a symmetrical fan-shaped arrangement, and a double-split-side cross-section main beam. Tower beam separation, semi-floating architecture. The main bridge tower is double column variable cross section "H" shaped tower, tower column and beam are hollow thin section. Its dimensions such as Fig.6 The cable-stayed bridge is a dense cable system with a multi-cable structure and an asymmetric structure. Its cable force has a great impact on the displacement of main span.

5.2 *Finite-Element Model*

The finite element model is built to simulate the actual force state of the bridge. The main tower and the main beam are simulated by the beam element. The truss element is used for the cable. The finite element model is shown in Fig.7. 160 truss element are used to simulate the cable. The initial tension of the cable is 1, and then use the coefficient to express the cable force in the load combination.

5.3 *Random Variables*

In this paper, cable force is considered as uncertain factor, so the initial tension force of the cable is chosen as the research variable, and the lower bending value of the 241 node is taken as the dependent variable. The reliability of the structure is analyzed. The finite element model obtained the initial cable

force as the mean value, according to the cable force error limit of less than 5%, according to 3σ criterion to determine the standard deviation. Variables are normal distribution, parameters are shown as table 4. Without enough data, it is difficult to determine the relevance of random variables. Thus, in this study it is assumed that all random variables in Table 4 are independent of each other to simplify sensitivity and reliability analysis.

5.4 *Sensitivity and Reliability analysis*

According to the selected variables, the LHS samples are sampled by the above method, and random samples are obtained. Then, the corresponding functions are obtained by fitting the functional function by using BPANN. According to the specification limit value which is specific under the action of the moving load that the biggest flexion value does not exceed 1/500 of the main span, that is, 664mm.

Then the limit state equation is:

$$G(\mathrm{X}) = 0.664 - g(\mathrm{x})$$

The BP neural network is divided into three layers, the first layer is the input layer, 80 neurons corresponding to 80 random variables, the second layer is the hidden layer, select 15 neurons as hidden layer due to the complexity of the cable-stayed bridge. Select the equation 4 as hidden layer function, the third layer for the output layer, the equation 5 as the output layer function.

The reliability and sensitivity of the structure are analyzed according to the fitting function. This paper uses proposed method to analyze the sensitivity of each variable, the analysis results shown in Fig.8. We can easily get the effect of the initial tension of the cables on the deflection is the most significant. This is mainly due to the reduction of cable force of the mid-span can lead to the reduction of deflection. According to the variable screening conditions, the variables whose sensitivity is less than 0.015 will be regarded as a determined value, the sensitivity of more than 0.015 of 10 variables are used for reliability analysis. The result is shown as Table 5.

Table 5 Reliability analysis results

Number of variables	Reliability index	Failure probability
80	2.7255 (BP)	0.321%
80	2.7045 (MC)	0.342%
10	2.7104 (BP)	0.336%
10	2.7338 (MC)	0.313%

According to the results of the reliability calculation, it can be seen that the obtained reliability values of all variables are basically the same when the rest of the cable force is determined.

Table 4 Reliability analysis results

Num	Mean	SD	Num	Mean	SD	Num	Mean	SD	Num	Mean	SD
1	5890.89	49.09	21	3098.90	25.82	41	5550.56	46.25	61	3685.34	30.71
2	5956.56	49.64	22	2787.94	23.32	42	5567.24	46.39	62	3144.99	26.21
3	5959.50	49.66	23	2501.68	20.85	43	5542.72	46.19	63	3226.56	26.89
4	5905.56	49.21	24	3048.67	25.41	44	5532.91	46.11	64	3190.10	26.58
5	5729.04	47.74	25	3051.74	25.43	45	5484.86	45.71	65	3145.43	26.21
6	5549.23	46.24	26	2490.89	20.76	46	5424.06	45.20	66	2745.86	22.88
7	5375.02	44.79	27	2766.46	23.05	47	5355.41	44.63	67	3118.51	25.99
8	4893.52	40.78	28	3050.85	25.42	48	5364.56	44.70	68	3601.00	30.01
9	4810.16	40.08	29	3384.27	28.20	49	5323.05	44.36	69	3841.26	32.01
10	4783.68	39.86	30	3631.40	30.26	50	5433.86	45.28	70	4077.61	33.98
11	4749.36	39.58	31	3861.86	32.18	51	5471.13	45.59	71	4212.94	35.11
12	4677.77	38.98	32	4159.00	34.66	52	5461.32	45.51	72	4419.86	36.83
13	4615.01	38.46	33	4346.31	36.22	53	5459.36	45.49	73	4538.52	37.82
14	4513.02	37.61	34	4525.77	37.71	54	5394.64	44.96	74	4663.06	38.86
15	4461.63	36.93	35	4697.39	39.14	55	5353.45	44.61	75	4725.82	39.38
16	4242.36	35.35	36	5066.12	42.22	56	5225.96	43.55	76	5889.87	49.08
17	4105.06	34.21	37	5205.37	43.38	57	4855.27	40.46	77	5981.08	49.84
18	3918.74	32.66	38	5348.55	44.57	58	4649.33	38.74	78	5999.71	50.00
19	3703.97	30.87	39	5433.86	45.28	59	4413.97	36.78	79	5982.06	49.85
20	3457.82	28.82	40	5492.70	45.77	60	3995.23	33.29	80	5976.91	49.81

Note: The cable is numbered from left span to right span; SD=Standard deviation; The unit of cable data in the table is KN; All variables are subject to normal distribution.

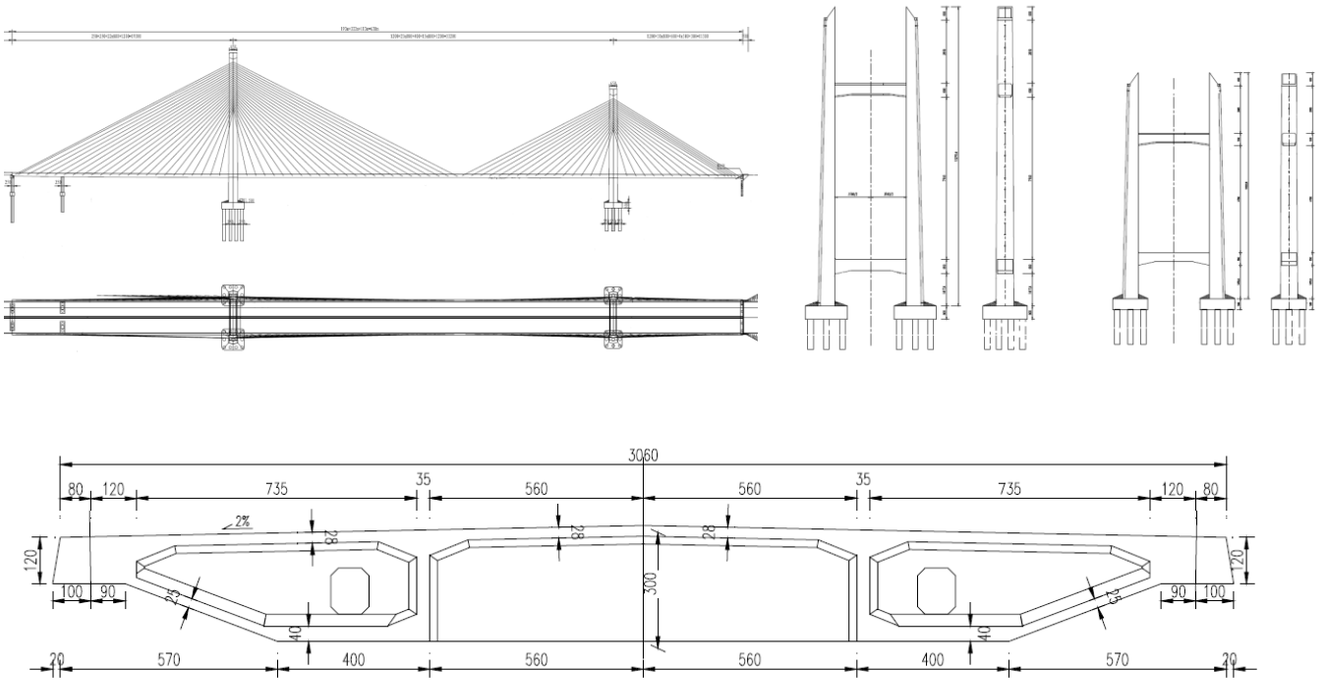


Fig. 6 Structure dimensions of the bridge(unit:cm)

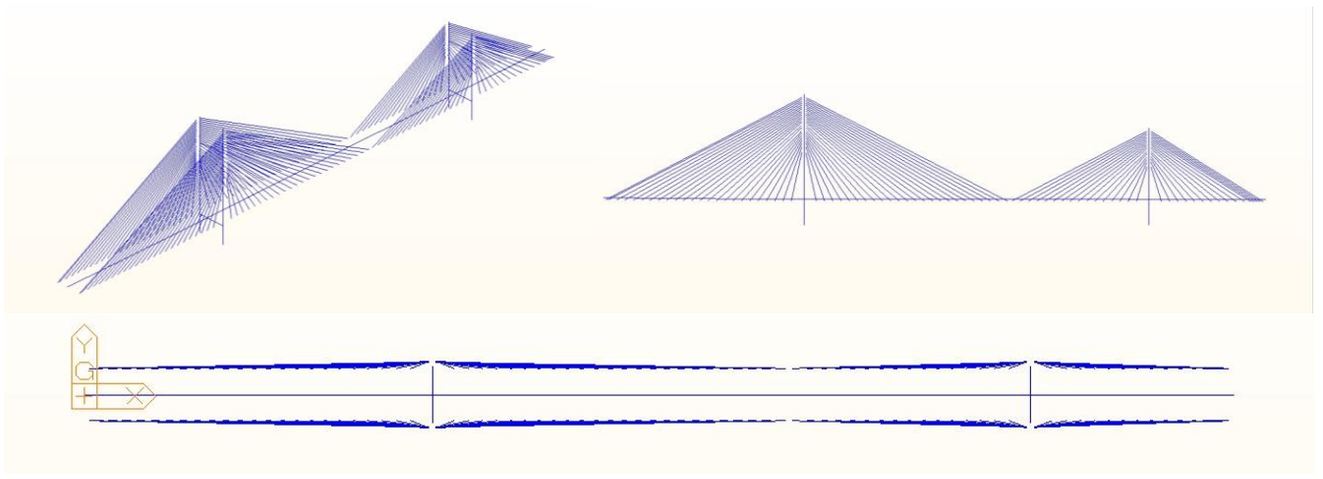


Fig. 7. Finite-Element model of the bridge

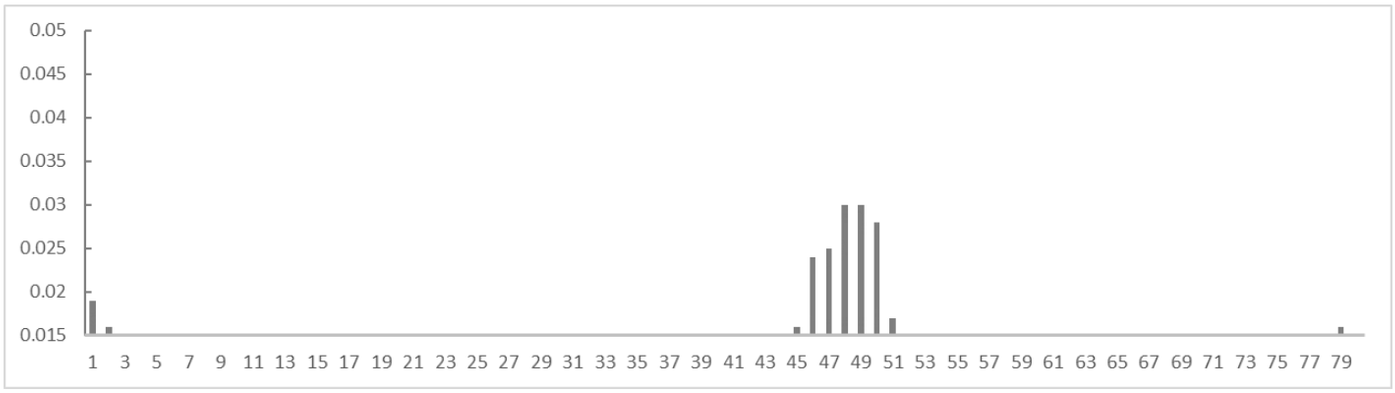


Fig. 8. Random variable sensitivity

It is necessary to note that there is not enough data to determine the correlation and variation of random variables. However, this method of sensitivity and reliability analysis still has some guiding significance in engineering. Through this sensitivity analysis, we can determine the optimization scheme of the structure and guide the operation of construction and structure.

6 CONCLUSION

The sensitivity and reliability analysis method presented in this paper has greatly reduced the sample capacity by using LHS sampling technique. By combining the sample with the finite element program, the structure response can be obtained accurately and the computational efficiency can be improved effectively. BP neural network method is used to fit the structural failure equation of the structural response value, and then using the first-order second-moment method for reliability and sensitivity analysis. The applicability of this method is validated by the comparison of the results obtained by Monte Carlo method.

Using this method to analyze the structure of a cable-stayed bridge, we can get that the influence of the cable force on the mid-span and the cross-section anchorage and the auxiliary pier has a great influence on the mid-span deflection. This is consistent with our actual construction experience. The sensitivity analysis of the initial tension of the cable can provide guidance for the structural optimization and the selection of the construction scheme. So this kind of analytic method has a very important research significance to the engineering field.

REFERENCE

China Communication Construction Company (CCCC). (2015). "General code for design of highway bridge and culverts." JTG D60-2015, China Communication Press, Beijing.

China Merchants Chongqing Communications Technology research & design institute CO.LTO(CMCT). (2007). "Guidelines for Design of Highway Cable-stayed Bridge." JTG/T D65-01-2007, Communication Press, Beijing.

Demuth, H., and Beale, M. (2000). "Neural network toolbox user's guide, MathWorks, Natick, MA"

Hirose, Y., Yamashita, K., and Hijiya, S. (1991). "Back-propagation algorithm which varies the number of hidden units." Neural Netw., 4(1), 61–66.

Hurtado, J. E., and Alvarez, D. A. (2001). "Neural-network-based reliability analysis: a comparative study." Comput. Methods Appl. Mech. Eng., 191(1–2), 113–132.

Jian, D. (2006). "Structural reliability analysis for implicit performance function using radial basis function network." Int. J. Solids Struct., 43(11–12), 3255–3291.

Li, Y. H., and Bao, W. G. (1997). Reliability and probabilistic limit state design for Highway Bridge structures, Communications Press, Beijing (in Chinese).

Li, J., & Li, A. (2013). "Sensitivity and Reliability Analysis of a Self-Anchored Suspension Bridge." American Society of Civil Engineers, 703-711.

Ming chen. (2013). "The Principle and Case of Matlab Neural Network." Tsinghua University Press.

Peng Liang, Rucheng Xiao. (2002). "Practical Method of Optimization of Cable Tensions for Cable-stayed Bridge." ournal of Tongji University(Natural Science)(11), 1270-1274.

The Ministry of construction and housing in urban and rural areas of People's Republic of China (MOHURD). (2008). "Unified standard for reliability design of engineering structures." GB 50153-2008, China Architecture & Building Press, Beijing.

Xuhong Zhou, Peng Dai, (2007). "Optimization Analysis of Cable Tensions of Dead Load State fo Cable-stayed Bridge with Steel Box Girder." Journal of Architecture and Civil Engineering (02), 19-23.

Yanqiu Dong, and Jingbo Tian. (2010). "Structural Reliability Analysis of Monte Carlo Method." Journal of Heilongjiang Institute of Engineering (Natural Science Edition) (01), 27-29.

Maintenance, Safety, Risk, Management and Life-Cycle Performance of Bridges – Powers, Frangopol, Al-Mahaidi & Caprani (Eds)
© 2018 Taylor & Francis Group, London, ISBN 978-1-138-73045-8

The development of the reinforcement method for U-shaped rib on orthotropic steel decks to improve the fatigue durability from the lower side

H. Yatsumoto, A. Tabata & H. Kobayashi
Hanshin Expressway Company Limited, Osaka, Japan

S. Inokuchi
Yokogawa Bridge Holdings Corporation, Chiba, Japan

H. Matsushita
Hitachi Zosen Corporation, Osaka, Japan

ABSTRACT: Fatigue cracks in the longitudinal weld between deck plate and U-shaped rib have been increased in Hanshin Expressway company limited. Various kinds of methods to improve the fatigue durability were conducted such as using steel fiber reinforced concrete (SFRC) pavement on the steel deck. SFRC pavement is one of the effective methods for increasing the fatigue durability, but it has the disadvantage that it is necessary to carry out the traffic regulations. Hanshin Expressway Company Limited developed three countermeasures to improve the fatigue durability of U-shaped rib on orthotropic steel decks without the traffic regulation. All repair works of three methods are able to be completed under the deck plate. First method is adding thin steel plates in the vicinity of the welded joint, Second method is cutting the U-shaped ribs in the immediate vicinity of welded joint and connecting between the U-shaped rib and deck plate by L-shaped plates and studs bolts. Finally, the third method is filling the mortar into the inner space of U-shaped ribs. In this paper, outlines of three methods and results of the loading test at the actual bridge to evaluate their effect are reported.

1 INTRODUCTION

1.1 *Fatigue cracks on orthotropic steel decks*

The Hanshin Expressway Company Limited established as a highway authority in May, 1962 and privatized in October, 2005 constructs and operates an urban expressway network in Kansai Metropolitan Area in Japan. These are linking the major cities of Osaka, Kobe and Kyoto is an important transportation network (Figure 1). The Hanshin expressway currently consists of 15 routes, extending for a total of 260.5 km. An average traffic volume is about 750,000 per day. Approximately 90% of the total length of the Hanshin Expressway consists of viaduct and about 80% of this is steel girder and 20% is concrete girder. There are 1431 spans of orthotropic steel deck bridges among 6764 spans of steel girder bridges. From the latest periodic inspection result of fatigue crack are detected by 364 spans among 1,431 spans of the orthotropic steel decks current as of August 2017. The reason of such a fatigue cracks are considered to be remarkable increase of traffic volume and existence of overloaded vehicles. In addition, the factors of fatigue damages are contemplated the stress concentration attributed to the local deformation of the thin deck plate. Such fatigue cracks are classified according to the structure of the longitudinal rib of orthotropic steel decks and the type of a crack.

Fatigue cracks generated in trough ribs are classified into several types. Figure 2 shows the typical fatigue crack types. Type I crack is generated along the longitudinal welding line between deck plate and trough rib. Type II crack is generated in the longitudinal stiffener's splice joint. Type III crack is generated along the welding line between vertical stiffener and deck plate. Type IV crack is generated from the connection point between trough profiles and crossbeam. Type I cracks appears more often than other types and the occurrence is showing



Figure 1.The Hanshin Expressway network map

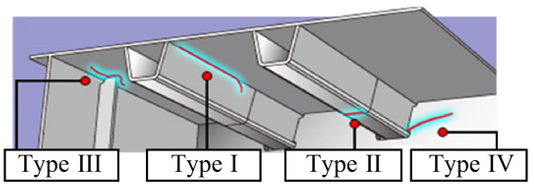


Figure 2. Typical fatigue cracks in U-shaped ribs

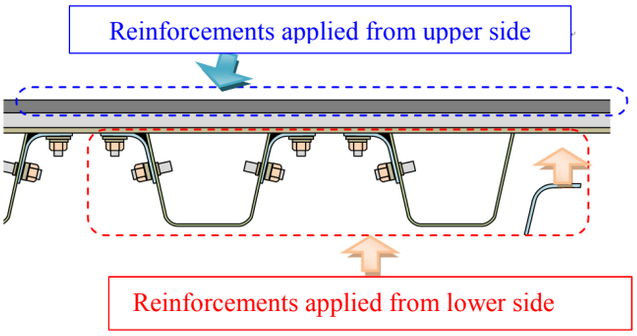


Figure 3. Concept of reinforcement method for orthotropic steel decks

an increasing tendency. The Hanshin Expressway Co. Ltd. have developed fundamental reinforcement solutions to prevent the further propagation of Type I cracks.

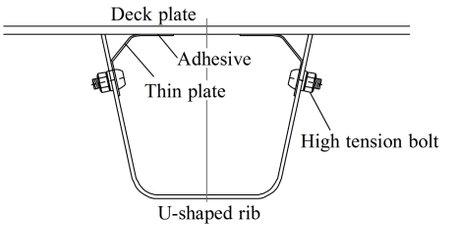
This paper describes about the outline of the newly developed reinforcement methods and the results of the field test conducted in order to evaluate the effects.

2 REINFORCED METHOD FOR U-SHPED RIB ON ORTHOTROPIC STEEL DECKS

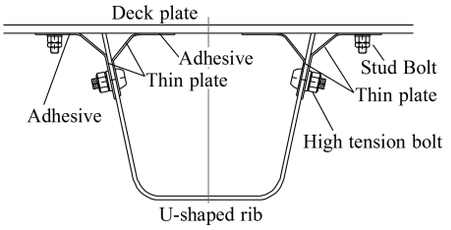
2.1 *Outline*

Steel Fiber Reinforced Concrete (SFRC) pavement has been developed as an effective countermeasure of Type I crack prevention and reinforcement. Though Hanshin Expressway has applied this method in some sections, its usage has some limitations because it is associated with long traffic regulation period due to works conducted from upper side of decks and it is often influenced by the weather. Therefore, it is urgently needed to develop a new reinforcement method against Type I cracks which can minimize the influence of traffic control and weather conditions.

The Hanshin Expressway Co., Ltd. has developed three reinforcement methods for trough ribs jointly with Yokogawa Bridge Holdings Corporation and Hitachi Zosen Corporation. As shown in Figure 3, those methods are applied from the deck's lower side so that traffic on the deck and any weather condition do not affect the work progress. The details of those methods are described in 2.2, 2.3 and 2.4.



(a) Inside reinforcement



(b) Both side reinforcement

Figure 4. Outline of the reinforced method (thin-plate)

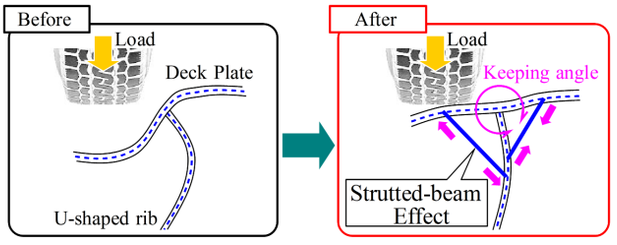


Figure 5. Concept of the thin-plate reinforced method

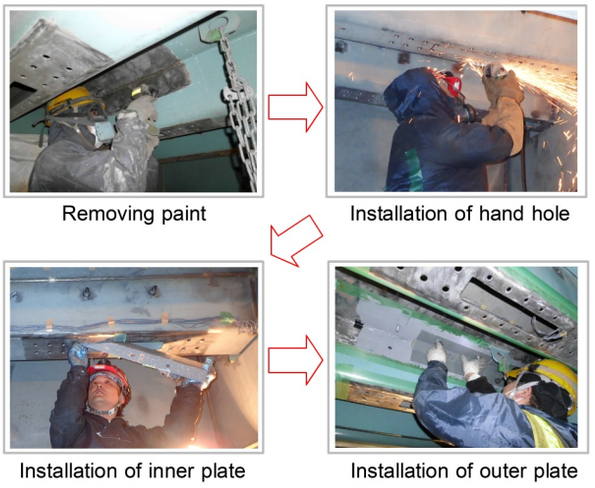


Figure 6. Outline of construction procedure (Both side reinforcement)

2.2 *Reinforced method (Thin-plate)*

In this reinforcing method as shown in Figure 4, thin and L-shaped steel plates for reinforcement are installed at the welding joint between U-shaped rib and deck plate. These plates do not reinforce welding joints firmly as usual methods and they are expected to provide "Strutted-beam Effect" in order to support deck plate by keeping the angle between U-shaped rib and deck plate when the load is located just above the welding joint (Figure 5). Because the reinforcing plates support in the vicinity of welded

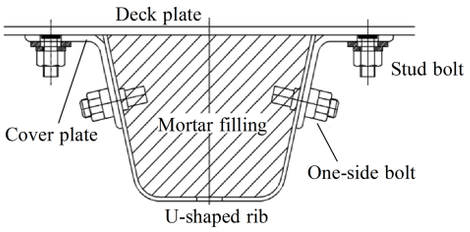


Figure 7. Outline of the reinforced method (filled with mortar)

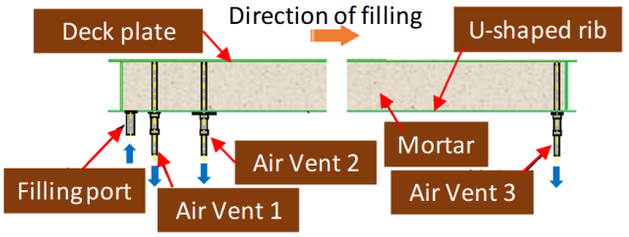


Figure 8. Filling of light weight mortar

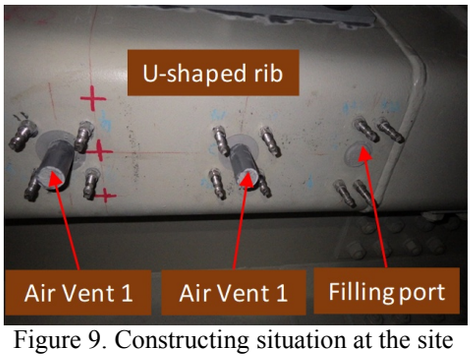


Figure 9. Constructing situation at the site

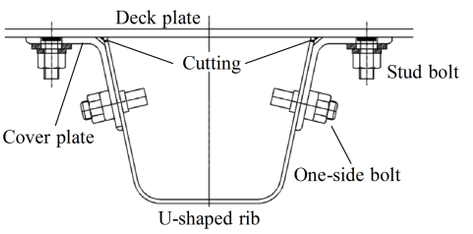


Figure 10. Outline of the reinforced method (stud with cover plate)

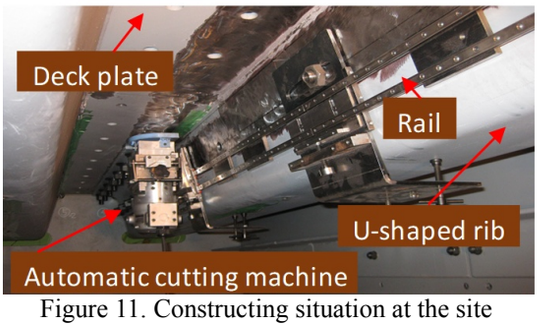


Figure 11. Constructing situation at the site

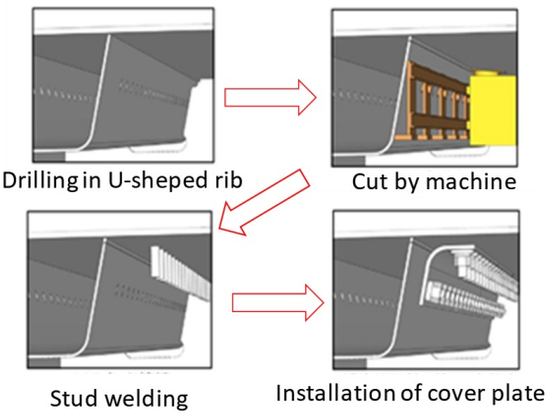


Figure 12. Outline of construction procedure

joints elastically and do not restrict behavior except welding joints, they are installed in the immediate vicinities of welding joints. Thickness of the reinforcing plate is 2.3mm and it was decided in consideration of reducing stress which generated on adhesive materials and also welding joints. In this method, the inside reinforcement where only inner plate is install inside of U-shaped rib and the both side reinforcement which the inner and outer plate are installed can be selected. Surely, the inside reinforcement has advantage in the point of cost. Although the high-tension bolts are also installed at the web of U-shaped rib in order to deicide the position of the steel plates during attaching process and to prevent from their falling in service, the reinforcing plates are attached to U-shaped rib and deck plate mainly using adhesive material of epoxy resin which has been newly developed for repair works of steel structures. The shape of reinforcing plates was optimized through the FE analysis and it was decided based on the results as shown in Figure 4.

Figure 6 shows the outline construction procedure of this reinforcement method. At first, paint around the welding joint without inside of the U-shaped rib.

The hand-holes are installed temporally at the bottom of the U-shaped rib at regular intervals in order to install the inner plates. The inner plates and outer plates are fixed by high tension bolts installed at the U-shaped rib web.

2.3 *Reinforced method (Filled with mortar)*

In this reinforcing method as shown in Figure 7, a lightweight mortar is filled in the U-shaped rib and a cover plate is installed outside the U-shaped rib. The local plate bending of the deck plate due to the wheel load considered to be the cause of the fatigue crack is prevented by the mortar filled in the U-shaped rib and the cover plate installed outside the U-shaped rib. the cover plate is connected by the stud bolts installed on the lower surface of the deck plate and the one-side bolts that can be connected from the outside of the U-shaped rib. Furthermore, filling of mortar into the U-shaped rib has been developed so that it could be applied from the bottom of U-shaped rib. As a result, it becomes

possible to reinforce from the underside of the deck plate.

In order to put this method into practical use, details of the structure that can reliably fill the U-shaped rib with mortar are clarified by the construction test and a method of confirming the filling property using the sensor was developed. Figure 8 shows the outline of this reinforcement method, Figure 9 shows the construction situation at the site.

2.4 *Reinforced method (Stud with cover plate)*

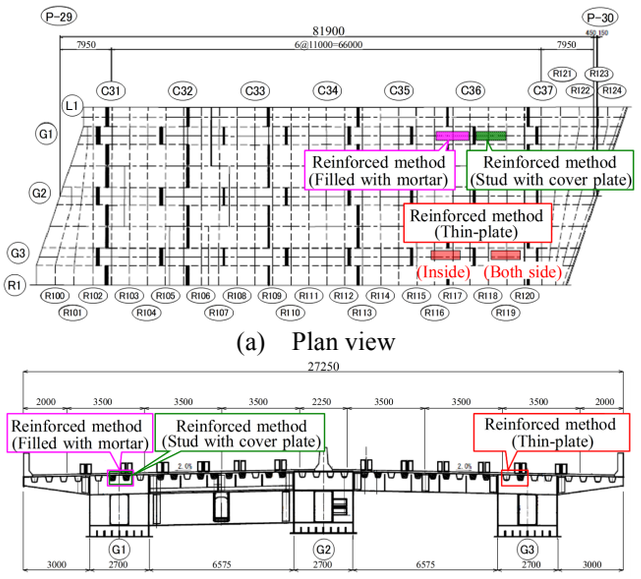
In this reinforcement method as shown in Figure 10 the U-shaped rib web is cut in the vicinity of the welding joints between the deck plate and the U-shaped rib. Instead of the welded joints, the bolted joint using a cover plate attached outside of U-shaped rib web is installed between the deck plate and the U-shaped rib. By changing connecting method from welded joint to bolted joint, there is an advantage that the stress concentration around the welded joint which may occur fatigue cracks can be reduced. In addition, because the cover plate is adopted same as the reinforcing method by mortar filling, it is possible to reinforce from the underside of the deck plate.

In order to put this method into practical use, we developed an automatic cutting machine with the aim of ensuring that the U-shaped rib web can be cut with securing the quality of the cut surface under traffic vibration. As shown in Figure 11, the automatic cutting machine cuts the U-shaped rib web along the predetermined position while traveling on a rail fixed to the U-shaped rib web using a rotating disk. Figure 12 shows the outline construction procedure of this reinforcement method.

3 THE FIELD TEST FOR VERIFYING THE EFFECT OF THE REINFORCED METHODS

3.1 *Outline of the field test*

The three reinforcement methods are actually applied to orthotropic steel bridges on "Wangan Route" of Hanshin expressway to examine the validity. Figure 13 shows the outline of the test bridge and the measurement arrangement. The bridge has 4-span continuous and three box girders whose length is 438m. The thickness of deck plate is 12mm and trough rib size is 320mm in width, 6mm in thickness and 240mm in height. The interval of trough rib arrangement is 2,750mm. For the fair and accurate comparison of three reinforcement methods,



(a) Plan view

(b) Sectional view

Figure 13. Outline of the test bridge and target for field measurement



Figure 14. Test truck

similar straight steel deck bridge is chosen to minimize the effects of different measurement location.

This paper also describes the results of dynamic loading test conducted on decks with three methods. The dump truck used for the test has the total weight of 196kN (front axle weight: 53.6kN, rear two-axle weight: 141.7kN) as shown in Figure 14. The truck runs at a low speed between 10 and 30km/h. The loading test for three methods was carried out on the same day.

3.2 *Reinforced method (thin plate)*

Figure 15 and Figure 16 shows the targets where strain gages were installed for the measurement. Targets of the deck plate is 5mm away from the inner corner of U-shaped rib. The target sections are located at the center of U-shaped rib span (target A) and the intersection between U-shaped rib and transverse rib (target B). All strain gages were installed in the transverse direction of the bridge axis. The loading position is represented as the distance (D_y) from the web of box girder.

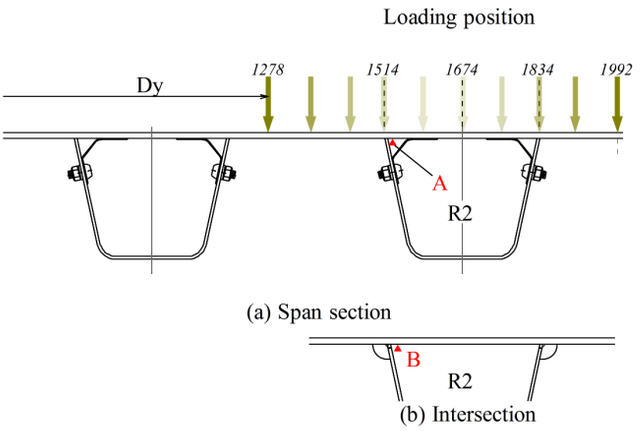


Figure 15. Loading positions and target points (Inside reinforcement)

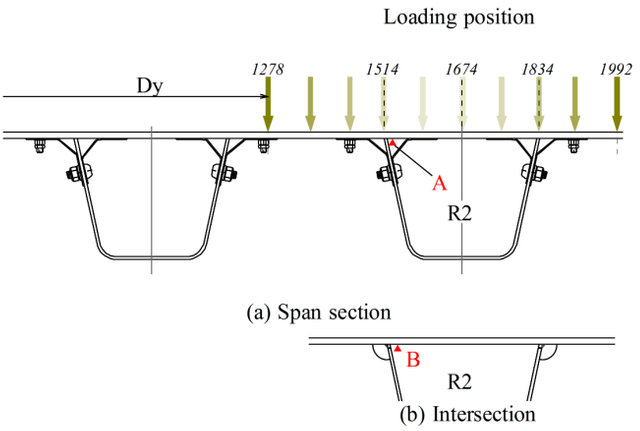
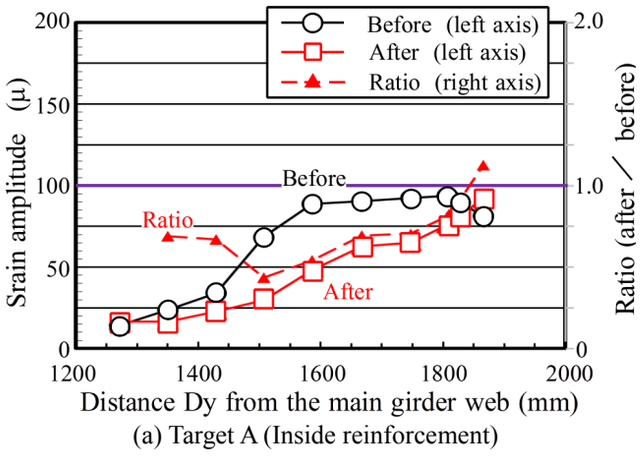
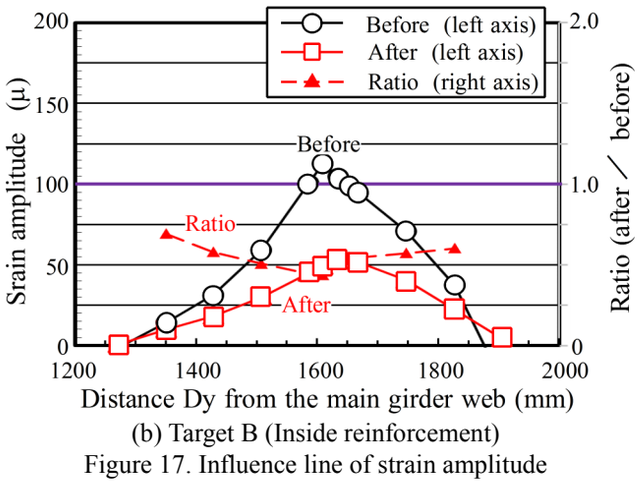


Figure 16. Loading positions and target points (Both side reinforcement)

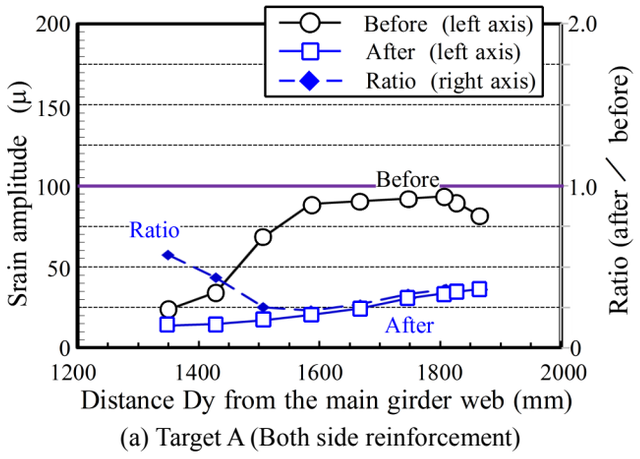


(a) Target A (Inside reinforcement)

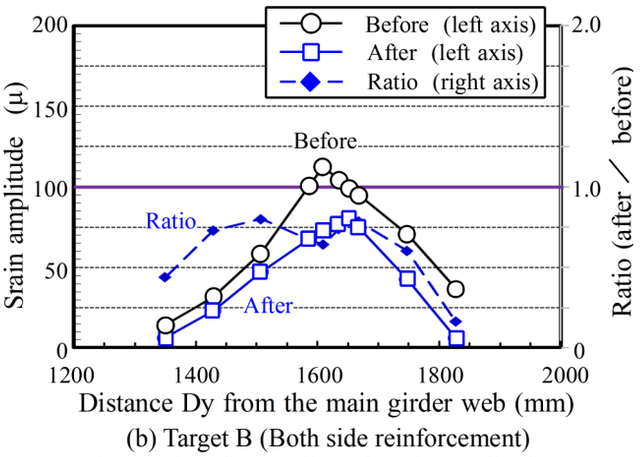


(b) Target B (Inside reinforcement)

Figure 17. Influence line of strain amplitude



(a) Target A (Both side reinforcement)



(b) Target B (Both side reinforcement)

Figure 18. Influence line of strain amplitude

Figure 17 and Figure 18 show the results of measurement. In these figures, the left vertical axis shows the strain amplitude and the horizontal axis shows the loading position in the transverse direction with D_y. The strain amplitude was calculated from the maximum and minimum strain values obtained by moving the wheel load in the longitudinal direction. For comparison, the ratio of the strain amplitude after reinforcement to before reinforcement is also shown in the figure on the right axis. Figure 17 shows the influence lines of strain amplitude occurred by single tire at the target A and B when reinforced by only the inner plates. When the single tire is located just above the U-shaped rib, relatively high strain occurs. On the other hands, Figure 18 shows the influence lines when reinforced by both side plates. At the center of U-shaped rib span, strain amplitude was reduced by using both side reinforcement more than the inside reinforcement.

In the case of inside reinforcement, the strain amplitude at the target A was reduced to about 40% to 80% before reinforcement except the loading case just above the opposite welded joint. At the target B,

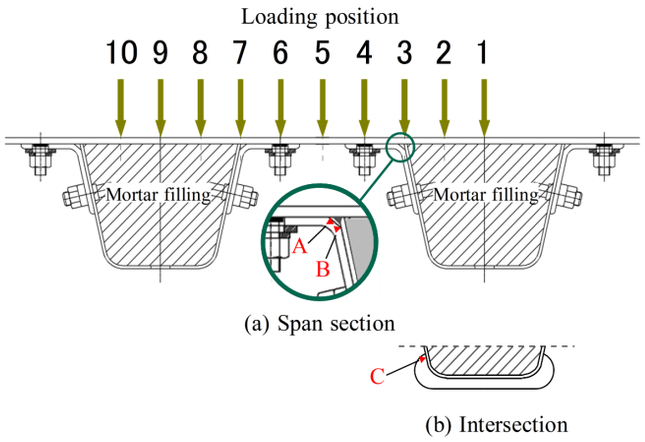


Figure 19. Loading positions and target points

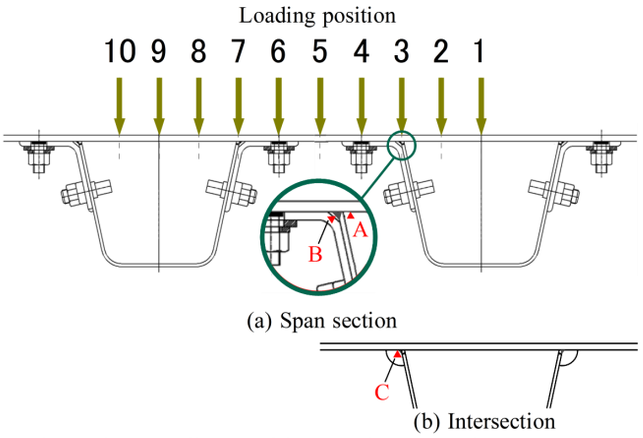
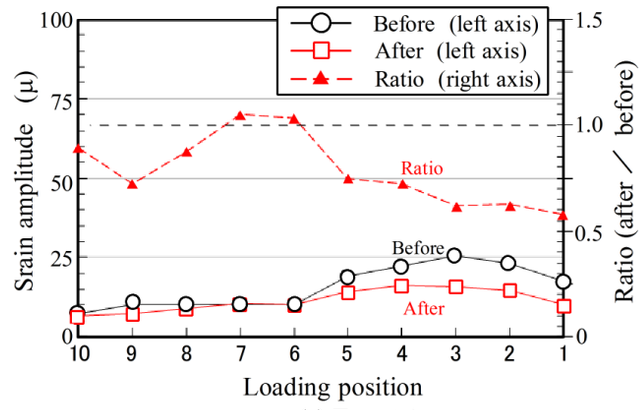
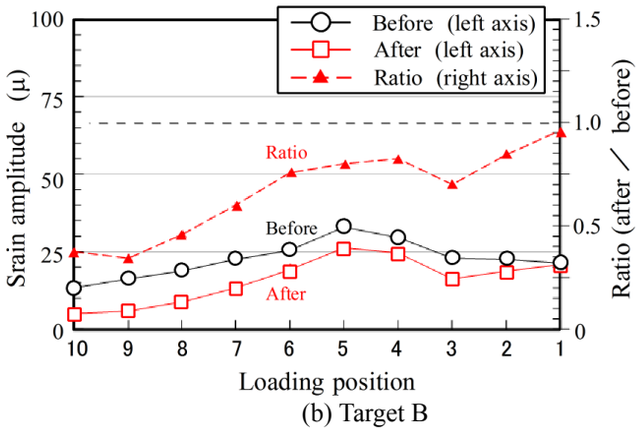


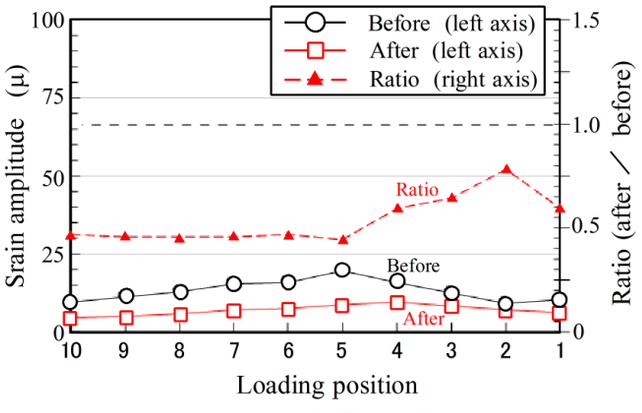
Figure 21. Loading positions and target points



(a) Target A

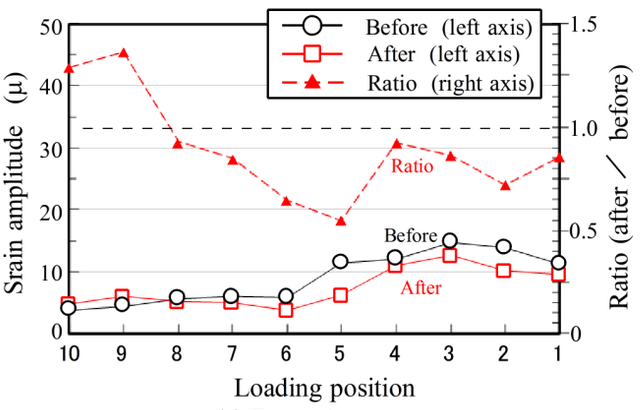


(b) Target B

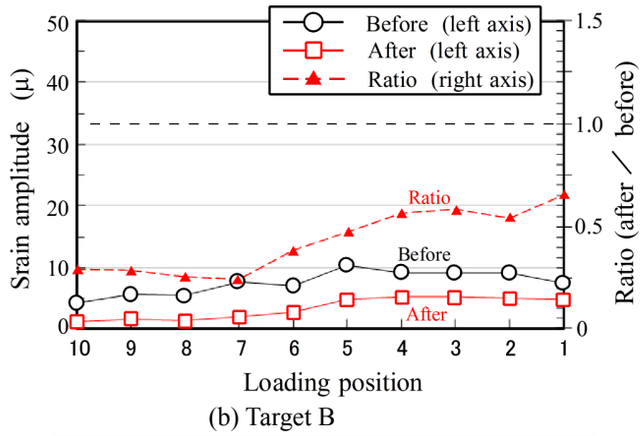


(C) Target C

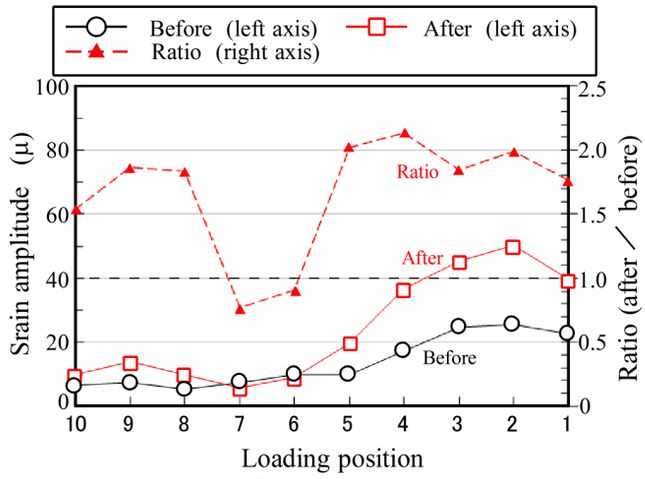
Figure 20. Influence line of strain amplitude



(a) Target A



(b) Target B



(C) Target C

Figure 22. Influence line of strain amplitude

the strain amplitude was reduced to about 40% to 70% before reinforcement (Fig. 17). In the case of both side reinforcement, the strain amplitude at the target A was reduced to about 25% to 60% before reinforcement. At the target B, the strain amplitude was reduced to about 10% to 80% before reinforcement (Fig. 18).

3.3 *Reinforced method (filled with mortar)*

Figure 19 shows the targets for the measurement. Target A is located at the lower side of the deck plate and Target B is located at the web side of U-shaped rib in the immediate vicinity of weld toe at the center of U-shaped rib span. Target C is located in the immediate vicinity of the turning weld toe at the lower scallop of intersection between the U-shaped rib and transverse rib. All strain gages were installed in the transverse direction of the bridge axis.

Figure 20 shows the strain amplitude occurred by double tire at the target A, B and C. As shown in Figure 20(a) and Figure 20(b), the strain amplitudes of the lower surface of the deck plate (target A) and the outer surface of the U-shaped rib web (target B), which are in the vicinity of the welded joint, are the maximum at the loading position 3 and 5. After reinforcement, the strain amplitude was reduced to 65% and 80% before reinforcement, respectively, and there was effect of reducing the strain amplitude by reinforcement. Even at the other loading positions, the strain amplitude is equal to or lower than before reinforcement.

Figure 20(c) shows the measurement results of the outer surface (target C). As shown in the figure, it is shown that the strain amplitude does not increase by reinforcement. However, the lower scallop will be reinforced by bolt-connecting method between the lower flange of the U-shaped rib and the transverse rib web with the L-shaped member.

3.4 *Reinforced method (stud with cover plate)*

Figure 21 shows the targets for the measurement. Target A is located at the lower side of the deck plate 5mm away from the inner corner of U-shaped rib and Target B is located at the surface of the weld bead at the center of U-shaped rib span. Target C is located in the immediate vicinity of weld toe at the intersection between the U-shaped rib and transverse rib. All strain gages were installed in the transverse direction of the bridge axis.

Figure 22 shows the strain amplitude occurred by double tire at the target A, B and C. As shown in Figure 22(a), the strain amplitude of the deck plate (target A) is maximum when the wheel load is located just above the target position. After reinforcement, the strain amplitude was reduced to 86% before reinforcement, respectively, which are equal to or slightly lower than before reinforcement. In other loading positions, the strain amplitude may increase compared to before reinforcement, but it is considered that there is no problem because the generated stress is small. Also, as shown in Figure 22(b), it can be seen that the strain amplitude was reduced to about half by the reinforcement at the weld bead (target B).

Figure 22(c) shows the measurement results of the inside of the scallop (target C) near the intersection between the U-shaped rib and transverse rib. As shown in the figure, there are positions where the strain amplitude increases after reinforcement, the countermeasure plans to be conducted in the future.

4 SUMMARY

The results of the experimental study about effect of three reinforced methods is described as below.

(Reinforcement method by thin plate)
- By the inside reinforcement, the strain amplitude in the vicinity of the welded joint was reduced to about 40% to 80% before reinforcement at the most load cases.
- The both side reinforcement can reduce the strain amplitude more than the inside reinforcement.

(Reinforcement method by filled with mortar)
- Because the strain amplitude in the vicinity of the welded joint at the span section was reduced to 62% or 80%, it is considered that there are strain reduction effect with the reinforcement method. Moreover the strain amplitude is equal to or lower than before reinforcement in other loading position.

(Reinforcement method by stud with cover plate)
- In the span section the strain amplitude was reduced to 86% before reinforcement at the deck plate and to about 50% at the surface of weld bead.
- The target position in the intersection where the strain amplitude increased after reinforcement will be improved in the future.

Although the magnitude of reinforced effect is different according to the location of targets, it was verified that all these reinforced methods can reduce the stress concentration in the vicinity of welded joints. It seems that their effect can never be evaluated perfectly but these methods can be adopted fully for reinforcement for fatigue cracks on the orthotropic steel decks.

5 REFERENCE

-Takada.Y, Aoki.Y and Sakano.M "Examination and review of fatigue cracks in orthotropic steel decks in Hanshin Expressway", Proceedings of 7th Japanese-German Joint Symposium on Steel and Composite Bridges, Osaka, Japan, 2007

Maintenance, Safety, Risk, Management and Life-Cycle Performance of Bridges – Powers, Frangopol, Al-Mahaidi & Caprani (Eds)
© 2018 Taylor & Francis Group, London, ISBN 978-1-138-73045-8

Effect of the shear deformation in the structural system identification methods

J.A. Lozano -Galant
University of Castilla-La mancha, Ciudad Rea, Spain

D. Tomás,
Nexeo Solutions, Spain

G. Ramos, J. Turmo
Universitat Politècnica de Catalunya, BarcelonaTECH, Barcelona, Spain

ABSTRACT: Despite its importance in some structures, shear deformation is systematically neglected by most static structural system identification methods. To fill this gap, this paper analyzes, for the first time in the literature, the effect of the shear deformation in the inverse analysis of structures. This study is focused on a parametric structural system identification method: the observability technique. As the majority of the methods, this technique is based on the Euler-Bernoulli beam theory. The method presented in the literature is unable to identify correctly the characteristics of a structure (such as flexural stiffness) when shear deformation is not negligible. In fact, in this method, the effects of shear deformation are close to those produced by measurement errors. To solve this problem, the observability procedure is updated according to the Timoshenko's beam theory. This formulation uses an algebraic approach combining both a symbolical and a numerical application. Thus, the updated observability formulation is able to obtain not only flexural stiffness but also shear stiffness. Besides this, for the first time in the literature, a parametric equation of the estimates is obtained. Some examples are presented to illustrate the validity of the new formulation.

1 INTRODUCTION

Damage in structures might produce changes in their mechanical properties. In order to quantify the magnitude of this damage Structural System Identification (SSI) might be used. This process is based on a subset of measured inputs and outputs (e.g. forces and/or displacements). The subset of measured inputs can be obtained by non-destructive tests that measure the structural response under a certain load case. According to the load nature, these tests can be classified as static (Sanayei et al. 1992, Sanayei & Saletnik 1996, Banan et al. 1994a, 1994b and Abdo 2012) or dynamics (Chao and Loh 2014, Noroozinejad et al. 2014, Lin et al. 201).

Matrix methods of structural analysis are universally accepted in structural design. These methods enable a rapid and accurate analysis of complex structures under both static and dynamic conditions. However, when applying matrix methods, the system must be modeled as a set of simple, idealized elements interconnected at the nodes. Matrix SSI methods are based on simplified models of structures too. These include axial and flexural deformation. Therefore, neglecting this deformation can be assumed as a modeling error which is a simplifying assumption well justified in most of the cases. However, in some cases for both direct and inverse analysis, this modelling error can lead to unjustified rough results.

The assumption of neglecting shear deformation is explained by the fact that, for most structures, this effect is usually much smaller than the flexural one. Nevertheless, shear deformation might play an important role in some structures, such as deep beams. Eurocode EN 1992-1-1:2004 defines deep beams as a beam for which the span is less than three times the overall section depth. ACI committee 318, defines these elements based on two criteria: beams with clear spans equal to or less than four times the overall member depth or beams with concentrated loads within twice the member depth from the face of the support. In these structures, neglecting the shear deformation may affect adversely the stiffnesses estimated by SSI methods. Shear deformation also might be an important factor to be considered in some structures, for example, in high-rise buildings (see Noroozinejad et al. 2014, Lin et al. 2016).

The literature review shows that the effect of shear deformation is mainly based on the structural response at the element level. The studies about structural system identification including this phenomenon are restricted to dynamic excitations and the effects on static tests are not studied. This is the case of the observability techniques (Lozano-Galant et al. 2013, 2014, 2015). As most of the static methods presented in the literature, it neglects the effect of the shear deformation into the structural system

identification analysis. This paper analyzes how sensitive observability techniques are to shear deformation effects. Moreover, in order to take these into account, a new formulation including the shear effects in observability simulation is proposed. All numerical simulations are based on measurement error free data obtained from numerical analyses. Paper will focus on evaluating the modeling error linked with shear effects, being numerical and measurement errors on structural system identification by observability treated elsewhere (Lei et al. 2016, 2017a, 2017b).

This article is organized as follows. In Section 2 the original observability method for structural system identification is briefly presented. This technique does not include the shear deformation. To illustrate the important role of this deformation in the identification of structures and to motivate the paper an example is analyzed. Section 3 introduces a new formulation to include the shear deformation into the observability analysis. Section 4 presents the application of the proposed algorithm for the structural system identification of a composite thin web bridge during its cantilevered construction. Finally, the conclusions obtained are summarized in Section 5.

2 OBSERVABILITY ANALYSIS WITHOUT SHEAR DEFORMATION

The stiffness matrix method is the most common implementation of the Finite Element Method (*FEM*) for structural analysis. The implementation of this method requires that the structure is modeled as a set of simple, idealized elements interconnected at the nodes. The material and stiffness properties of these elements are then compiled into a single matrix equation which governs the behavior of the entire idealized structure. In 2D, the traditional stiffness matrix *[K]* or a six degrees of freedom (two deflections (u and v) and one rotation (w) at the initial and final beam element nodes), beam element of length L and constant cross-section is:

$$[K]=\begin{bmatrix} \frac{EA}{L} & 0 & 0 & \frac{-EA}{L} & 0 & 0 \\ 0 & \frac{12EI}{L^3} & \frac{6EI}{L^2} & 0 & \frac{-12EI}{L^3} & \frac{-6EI}{L^2} \\ 0 & \frac{6EI}{L^2} & \frac{4EI}{L} & 0 & \frac{6EI}{L^2} & \frac{2EI}{L} \\ \frac{-EA}{L} & 0 & 0 & \frac{EA}{L} & 0 & 0 \\ 0 & \frac{-12EI}{L^3} & \frac{-6EI}{L^2} & 0 & \frac{12EI}{L^3} & \frac{-6EI}{L^2} \\ 0 & \frac{6EI}{L^2} & \frac{2EI}{L} & 0 & \frac{-6EI}{L^2} & \frac{4EI}{L} \end{bmatrix} \quad (1)$$

where E, A and I are Young modulus, area and inertia respectively.

In static structural analysis, a statement of the equilibrium conditions together with strength of materials theory leads to a relation between forces and displacements that has the form of a system of equations:

$$[K]\{\delta\}=\{f\} \quad (2)$$

Where $\{\delta\}$ and $\{f\}$ are the vectors of displacements and forces, respectively, in which the stiffness matrix is a singular matrix that leads to a system with infinite solutions. The direct solution of this system is carried out by any computer simulation software by assuming that all the terms in *[K]* are known.

Unfortunately, in real structures *[K]* might be known, as the flexural stiffness EI_j or axial stiffness EA_j of element j, may appear into the matrix *[K]* due to damage (e.g. by material degradation, such as carbonation or corrosion, or accidental actions, such as fires or impacts) or other uncertainties (e.g. lack of knowledge about the mechanical properties of the material). If the external forces applied to the structure in a non-destructive test are known and some displacements are measured, the observability method can be applied into the *SSI* to found the values of these unknown parameters.

Taking Eq. (2) where the matrix *[K]* is partially unknown and with the aim of determining the value of the unknown stiffnesses (EA_j and EI_j) a modified system of equations can be rewritten as:

$$[K^*]\{\delta^*\}=\{f\} \quad (3)$$

in which the products of unknowns are located in the modified vector of displacements $\{\delta^*\}$ and the modified stiffness matrix *[K*]* is a matrix of known coefficients with different dimensions than the initial stiffness matrix *[K]*. The new system leads to a non-linear problem due to the fact that unknown parameters, such as axial stiffness EA_j and flexural stiffness EI_j of the cross section are multiplied by unknown horizontal displacements (u_i) vertical displacements (v_i) and rotations at the *ith* node (w_i) of vector $\{\delta\}$. This fact implies that non-linear products of variables, such as EA_ju_i, EA_jv_i, EI_jv_i, EI_ju_i, and EI_jw_i might appear, leading to a polynomial system of equations. These kinds of problems usually appear in science and engineering fields, (see Castillo et al. 2016a, 2016b). Depending on the known information, the unknown variables of vector $\{\delta^*\}$ may be the non-linear products presented above, as well as other factors of single variables, such as EI_j or EA_j or nodal deflections and rotations.

Once the boundary conditions and the applied forces in the nodes have been defined, an inverse analysis can be performed to identify the unknown parameters. To do so, some deflections and rotations are measured in a known static test. This known in-

formation is clustered in a subset δ_1^* of $\{\delta^*\}$ and a subset f_1 of $\{f\}$, respectively. In this way, the remaining subset δ_0^* of $\{\delta^*\}$ and f_0 of $\{f\}$, are unknown. Hence, (3) can be written as follows:

$$[K^*]\{\delta^*\}=\begin{bmatrix}K_{00}^* & K_{01}^*\\ K_{10}^* & K_{11}^*\end{bmatrix}\cdot\begin{Bmatrix}\delta_0^*\\ \delta_1^*\end{Bmatrix}=\begin{Bmatrix}f_0\\ f_1\end{Bmatrix}=\{f\} \quad (4)$$

To join the unknowns, this system can be rewritten in the equivalent form:

$$[B]\{z\}=\begin{bmatrix}K_{10}^* & 0\\ K_{00}^* & -I\end{bmatrix}\cdot\begin{Bmatrix}\delta_0^*\\ f_0\end{Bmatrix}=\begin{Bmatrix}f_1-K_{11}^*\cdot\delta_1^*\\ -K_{01}^*\cdot\delta_1^*\end{Bmatrix}=\{D\} \quad (5)$$

where *0* and *I* are the null and the identity matrices, respectively. In this system, the vector of unknowns,*{z}*, appears on the left-hand side and the vector of observations, *{D},* on the right-hand side. Both vectors are related by a matrix of known coefficients *[B]*.

To evaluate if the system has a solution, it is sufficient to calculate the null space *[V]* of *[B]* and check that $[V]^T\cdot[D]=0$ $[V]^T\{D\}=0$. Note that the null space can be easily obtained from the singular value decomposition by using computer programs. If this holds, the system is compatible; otherwise, it has no solution [48]. The general solution (the set of all solutions) has the structure:

$$\begin{Bmatrix}\delta_0^*\\ f_0\end{Bmatrix}=\{z_p\}+[V]\{\rho\} \quad (6)$$

where $\{z_p\}$ is a particular solution of the system. This particular solution can be obtained by using two different subroutines in Matlab. The first one is the backslash function (\) that is able to find the parametric equations of the systems and therefore the symbolic and the numerical solution. The other one is the Moore-Penrose pseudoinverse function (*pinv*) with which only the numerical solution can be found.

$[V]\cdot\{\rho\}$ is the set of all solutions of the associated homogeneous system of equations (a linear space of solutions, where the column of *[V]* is a basis and the elements of the vector $\{\rho\}$ are arbitrary real values that represent the coefficients of all possible linear combinations). It is interesting to note that a variable has unique solution not only when matrix *[V]* has zero dimensions (it does not exist), but when the associated row in matrix *[V]*is null. Thus, examination of matrix *[V]* and identification of its null rows lead to identification of the observable variables (defined as the subset of variables with a unique solution) of vector *{z}*. By solving system (5), the numerical value of the observed parameters obtained by the particular solution of Equation (6) can be easily found. To obtain these numerical values of the observable parameters it is necessary to combine the symbolical and the numerical analysis as proposed by Nogal et al. (2015).

A recursive process is used to minimize the number of required deflections in measurement sets to obtain the unknown parameters. This process takes advantage of the connectivity of the beams in the stiffness matrix that is included in the partitioned matrices of *[K*]* in system (5). In this way, when in the initial observability analysis any deflection, force or structural parameter is observed, this information might help to observe new parameters in the adjacent elements through the recursive process. In this analysis, the observed information is successively introduced as input data in the observability analysis. .A new approach for the numerical solution of the system based on compatibility equations can be found in Lei et al. 2017a. In order to show the role of the shear deformation in the *SSI* by observability techniques an illustrative example is numerically analyzed in the following section.

2.1 *Example 1: Effect of the shear deformation in beams*

To motivate this paper, a sensitivity analysis is presented to evaluate the effect of the shear deformation on the *SSI* of a simply supported concrete beam loaded with a concentrated load *V* at mid span (Fig. 1). Young's modulus is E=27000MPa and Poisson's ratio is ν=0.25. The beam has a rectangular cross section 1 m deep (h=1m) and 0.1 m wide (b=1m), so its area is A=1m^2 and its inertia is I=0.00833m^4. Besides this, and according to [53], the shear coefficient, k, for rectangular cross-sections when width/depth ratio approaches zero is 5/6. With this shear factor, the shear area A_v is equal to 0.00833m^2.

Fig. 1.A shows the increment of deflections due to shear and bending deformability in a simply supported beam with a concentrate load *V* at mid span in terms of *L/h*. The shear deflection varies linearly with *L* while the bending deformability depends on L^3.

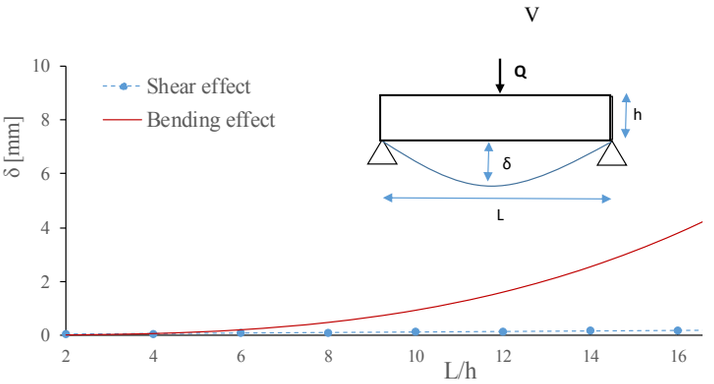


Figure 1. Example 1. Increment of deflection at mid span δ due to bending and shear

The analysis of Figure 1 shows that the closer the values of the height and the length of the beam, the higher the role that the shear deformation plays.

2.2 *Example 2: Effect of the shear deformation SSI by observability techniques*

To illustrate the problems of neglecting the shear deformation into the observability analysis, the simply supported beam described in Figure 2 is analyzed. This beam has a length of 6 meters and it is simulated with a *FEM* composed by 6 beam elements and 7 nodes. The length of each of these elements is 1m. The mechanical and geometrical properties of the analyzed example correspond with the beam presented in the preceding section. The boundary conditions of the structure are horizontal and vertical displacements restricted in node 1 and vertical displacement restricted in node 7 and the only external force applied is a concentrated vertical force in node 3 of -100kN. The beam was analyzed with Midas/Civil software with and without shear deformation.

The deformations will be used to estimate the flexural stiffnesses (EI_1 to EI_6) with and without considering the shear deformations. In order to do so, the measurement of at least 6 deflections or rotations that represent the flexural behavior of the beam are required. The selection of these measurements was analyzed by the observability trees method proposed in [41]. From the application of this procedure, it can be concluded that measuring the five vertical deflections of the inner nodes (v_2 to v_6), and the rotation of node 3 (w_3) will enable the estimation of all the unknown stiffnesses, or in other words, will provide full observability of the system.

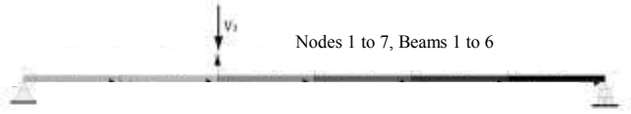


Figure 2. Example 2: Finite Element Model of the analyzed beam

Once the measurement set is selected, the observability method proposed by Nogal et al. (2015) is applied using the two following measurement sets: (1) Measurements without shear deformation, which is v_2 to v_6 and w_1. (2) Measurement with shear deformation, that is vs_2 to vs_6 and ws_1. The observable flexural stiffnesses obtained throughout the recursive process for both measurement sets are presented in Table 1 as percentage deviations.

Table 1: *Deviations of the EI estimated with and without considering the shear deformation*

Bending Stiffness	Without shear	With shear
EI_1	0.1%	149.9%
EI_2	0.0%	-35.7%
EI_3	0.0%	-5.5%
EI_4	0.0%	11.4
EI_5	0.1%	-16.8%
EI_6	0.1%	93.7%

The analysis of Table 1 shows no deviations when measurements without shear deformation are considered. Nevertheless, this is not the case when the shear deformation is included, as large errors are found. For example errors of -149.9% are found in the first beam element. This disproportionate error is explained by the fact that the used model does not consider shear effects. In fact, shear deformation is considered as a modeling error (Sanayei et al. (2012)) into the observability analysis.

The obtained results show that the role of shear deformation cannot be neglected in the *SSI* by observability techniques. Thus, it can be concluded that a reformulation of the observability algorithm is required to include the effect of the shear deformation. This new algorithm is presented in the following section.

3 INTRODUCING SHEAR DEFORMATION INTO THE STRUCTURAL SYSTEM IDENTIFICATION BY OBSERVABILITY TECHNIQUES

With the aim of including shear deformation into the *SSI* by observability analysis a new formulation of the stiffness matrix method is implemented. This formulation is based on the Timoshenko's beam theory.

3.1 *Shear formulation*

The stiffness matrix *[K]* for a beam element with uniform cross section with 3 degrees of freedom per node (u_i, v_i and w_i) is of order 6x6. The forces developed in the beam member when a unitary displacement is imposed along each degree of freedom holding all other displacements equal to zero leads to the finding of all the single elements of this stiffness matrix. According to the existing literature [54], the stiffness matrix *[Ks]* for a 2D analysis of a six degrees of freedom (two deflections (u and v) and one rotation (w) at the initial and final beam element nodes), beam element including the shear deformation is:

$$[K]=\begin{bmatrix} \frac{EA}{L} & 0 & 0 & \frac{-EA}{L} & 0 & 0 \\ 0 & \frac{12EI}{L^3(1+\phi)} & \frac{6EI}{L^2(1+\phi)} & 0 & \frac{-12EI}{L^3(1+\phi)} & \frac{-6EI}{L^2(1+\phi)} \\ 0 & \frac{6EI}{L^2(1+\phi)} & \frac{EI(4+\phi)}{L(1+\phi)} & 0 & \frac{6EI}{L^2(1+\phi)} & \frac{EI(2-\phi)}{L(1+\phi)} \\ \frac{-EA}{L} & 0 & 0 & \frac{EA}{L} & 0 & 0 \\ 0 & \frac{-12EI}{L^3(1+\phi)} & \frac{-6EI}{L^2(1+\phi)} & 0 & \frac{12EI}{L^3(1+\phi)} & \frac{-6EI}{L^2(1+\phi)} \\ 0 & \frac{6EI}{L^2(1+\phi)} & \frac{EI(2-\phi)}{L(1+\phi)} & 0 & \frac{-6EI}{L^2(1+\phi)} & \frac{EI(4+\phi)}{L(1+\phi)} \end{bmatrix} \quad (7)$$

A comparison with the traditional stiffness matrix presented in Equation (1) shows that differences appear in some terms in the form of a new coefficient. This coefficient is known as the shear parameter (ϕ) and can be expressed as:

$$\phi = \frac{12EI}{GA_v L^2} \tag{8}$$

where G is the shear modulus and can be calculated as:

$$G = \frac{E}{2(1+\nu)} \tag{9}$$

As it can be appreciated in Equation (7), the shear stiffness matrix has the same coefficients for the axial stiffness as the traditional stiffness matrix. This is because the shear and flexural stiffnesses are uncoupled from the axial stiffness. However, for the rest of the non-null elements of the matrix, shear and flexural stiffnesses are coupled.

When the beam is subjected to shear forces and associated moments, the vertical deflection is $v=v_b+v_s$ (where v_b is the deflection due to the flexural strains and v_s is the additional deflection due to shear strains). Analysis of Equation (7) shows that the shear parameter ϕ appears in both the numerator and the denominator of the matrix terms. Its location complicates significantly its estimation. In fact, the resulting system cannot be easily solved with observability techniques. To solve this problem a change of variable from ϕ to Q is proposed. This change simplifies the mathematical resolution of the system and enables the application of observability techniques as the new unknown parameter appears uniquely in the numerator of the matrix terms. The definition of parameter Q is as follows:

$$Q = \frac{\phi}{1+\phi} \tag{10}$$

Where Q is the so called observability shear parameter of the stiffness matrix *[Ks]*. It is to highlight that the value of this ranges from 0 to 1.

A detailed step by step application of the application of the *SSI* by observability techniques including shear deformations can be found in Tomás et al. (2017).

4 APPLICATION TO A BRIDGE

Accurate models to control construction of cantilever bridges are of uttermost importance. Deflection should be both controlled and forecast in order to give an adequate geometry to the segments. Hence, to calculate precamber, an accurate model upon which an analysis has to be performed is needed. As an example on how to use this technique to help model updating, a simplified model of the Yunbao Bridge over the Yellow River in China (see Fig. 3) is studied.

The span of the structure is 90m long. The model represents a simplification of an intermediate construction stage. This model includes two symmetric spans in cantilever supported by an intermediate pile. The length of the deck segments is 4.5m and the thickness of the pile 2.5m. The length of the analyzed construction stage is 13.5m.

The structural response at this stage is simulated numerically without considering actual site data. The creep and shrinkage effects in concrete were neglected.

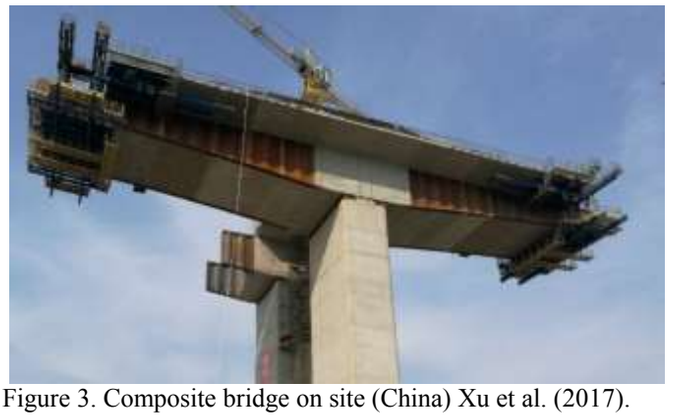


Figure 3. Composite bridge on site (China) Xu et al. (2017).

This structure is simulated by the mean of the simplified *FEM* presented in Fig. 4. This *FEM* includes 8 nodes and 7 beam elements. The cross section of the composite deck is presented in this figure and the mechanical and material properties are listed in Table 2. Whereas in the real bridge webs are corrugated, in the analyzed example they are considered 25mm thick steel sheets. The connection between concrete and steel is assumed as rigid, and the relative slip between both materials is neglected.

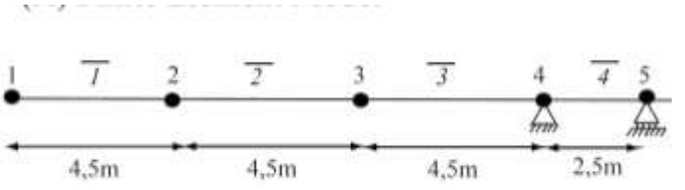


Figure 4. Finite Element model of analyzed bridge (symmetry section)

Table 2: *Properties of the Finite Element Model of the Bridge*

Area, m^2	12.59
Shear Area, m^2	9.83
Inertia, m^4	35.62
Steel Young's Modulus, GPa	210
Concrete Young's Modulus, GPa	35
Poissons' ratio, ν	0,3

The flexural and shear stiffnesses of all 7 beam elements (that is to say EI_1 to EI_7 and EAv_1 to EAv_7) are assumed as unknown.

4.1 *Static Load test*

EI6In order to identify the 14 unknown stiffnesses the measurement of 14 deflections and/or rotations in a static load case that excites the flexural mechanism is required. Observability will take into account the variation of deflections and rotations due to the movement of the form traveler. The load case used is presented in Fig. 5 in terms of the weight of the formwork Q=1041kN. In this paper, measurement errors are neglected. The effect of these unavoidable errors will be addressed by the authors in future works

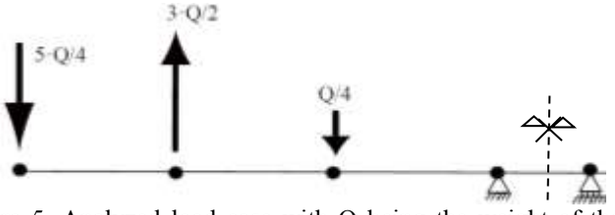


Figure 5. Analyzed load case with Q being the weight of the formwork (half structure).

The vertical deflections in the nodes of the structure were calculated with the software Midas/Civil both without including and including the shear deformation of the deck. The maximum deflection variations were located at the tips of the cantilevers. Shear deformation accounts for 0,1mm of the vertical displacement, which is not negligible as it represents the 7,6% of the total deformation. To get accurate measurements of the vertical deflections on site, different measuring devices can be used.

4.2 *SSI by observability techniques*

In this section the measured response of the structure is used to estimate the unknown stiffnesses. A flexural observability tree (Lozano-Galant et al. (2015)) has been used to select an adequate measurement set. When shear stiffness is neglected the measurement set consists on all the deflections (v_1, v_2, v_3, v_6, v_7, v_8) and one rotation (w_4). On the other hand, when shear stiffnesses is considered in the formulation the rest of rotations are also required.

Considering the shear stiffness, parametric equations can be obtained for the different elements. As an illustrative example, the estimated flexural stiffness for the first four element (EI_1 to EI_4) are presented:

$$EI_1 = \frac{-81 \cdot L^2 \cdot V_1}{8 \cdot (w_1 - w_2)} \tag{11}$$

$$EI_2 = \frac{-9L(-27L \cdot V_1 + 9LV_2)}{8 \cdot (w_2 - w_3)} \tag{12}$$

$$EI_3 = \frac{-9L(-45L \cdot V_1 - 27L \cdot V_2 + 9LV_3)}{8 \cdot (w_3 - w_4)} \tag{13}$$

$$EI_4 = \frac{-5L(27L \cdot V_1 + 18L \cdot V_2 + 9LV_3)}{8 \cdot (w_4 - w_5)} \tag{14}$$

These equations can be used to determine how sensitive the different estimates are to errors.

Table 3 presents a comparison of the percentual differences between the estimated flexural stiffnesses and the actual values in the seven elements of the beams with two observability procedures (with or without the shear effects into the stiffness matrix).

Table 3: *Deviations of the EI estimated with and without considering the shear deformation*

Bending Stiffness	Without shear	With shear
EI_1	0.0%	-65.5%
EI_2	0.0%	-26.7%
EI_3	0.0%	5.2%
EI_4	0.0%	-1.5%
EI_5	0.0%	5.2%
EI_6	0.0%	26.7%
EI_7	0.0%	-65.5%

This table shows that deviations when the shear formulation is included into the stiffness matrix and error-free measurements are considered are negligible. The reduced deviations obtained in this case can be explained by the fact numerical and non-actual site measurements are considered. It also illustrates that shear deformation cannot be neglected for the structural system identification of this structure. In fact, significant errors (e.g. -65,5 % in segments 1 and 7 or +26,7% in segments 2 and 6) appear when this phenomenon is not considered.

5 CONCLUSIONS

Most Structural System Identification (*SSI*) methods neglect shear deformation as this phenomenon is usually much less significant than the flexural one. Despite of the important role that this deformation might play especially in members with low span-to-depth ratio, no detailed study addressing the particular effects of this deformation in static *SSI* tests can be found in the literature. To fill this gap, this paper

presents the first study focused on the shear deformation effects in a structural system identification method: the observability technique. This is a parametric method based on static measurements.

An illustrative example shows how important the role of the shear deformation might be. To solve this modeling error, the formulation of the observability method is updated to include shear deformation. This new procedure enables, for the first time in the literature, the definition of parametric equations of the observability shear stiffness depending on the measured data for simple structures. The study of this equation might provide useful insight of the sensitivity to the estimation for each measurement. The proposed technique is also applied into a simply supported beam with six unknown parameters.

In order to show the applicability of the method on an actual thin web structure, an intermediate construction stage of a cantilever composite bridge in China is analyzed. The results of this structure illustrate how an adequate formulation can be used to reduce adequately the modeling errors without the need of optimization processes. This updated formulation enables also the calculation of parametric equations of the estimates that gives us information about their sensitivity to measurement errors.

6 ACKNOWLEDGEMENTS

The authors are indebted to the Spanish Ministry of Economy and Competitiveness for the funding provided through the research project BIA2013-47290-R, BIA2017-86811-C2-1-R and BIA2017-86811-C2-2-R, funded with FEDER funds.

7 REFERENCES

Sanayei, M., Onipede, O., & Babu, S.R. 1992 Selection of noisy measurement locations for error reduction in static parameter identification. *AIAA Journal*, 30, 2299–2309.

Sanayei, M. & Saletnik, M.J. 1996 Parameter estimation of structures from static strain measurements I: Formulation. *Journal of Structural Engineering*, 122, 555–562.

Banan, Mo.R., Banan, Ma.R., & Hjelmstad, K.D. 1994a Parameter estimation of structures from static response. I. Computational aspects. *Journal of Structural Engineering*, 120, 3243–3258.

Banan, Mo.R., Banan, Ma.R., & Hjelmstad. K.D. 1994b Parameter estimation of structures from static response. II: Numerical simulation studies. *Journal of Structural Engineering*, 120, 3259–3283.

Abdo, M.A. 2012 Parametric study of using only static response in structural damage detection. *Engineering Structures*, 34, 124–131.

Chao, S.H. & Loh, C.H. 2014 Application of singular spectrum analysis to structural monitoring and damage diagnosis of bridges. *Structure and Infrastructure Engineering*, 10 708–727.

Noroozinejad Farsangi, E., Melatdoust, H. & Bin Adnan, A 2014.A mathematical formulation to estimate the fundamental period of high-rise buildings including flexural-shear behavior and structural interaction. *Journal of Solid Mechanics*, 6, 122-134.

Lin, K.C., Hung, H.H. & Sung, Y.C. (2016) Seismic Performance of High Strength Reinforced Concrete Buildings Evaluated by Nonlinear Pushover and Dynamic Analyses. *International Journal of Structural Stability and Dynamics*. 16, 1-27.

EN 1992-1-1:*Eurocode 2: Design of concrete structures - Part 1-1: General rules and rules for buildings*. CEN, Brussels, 2002, Belgium.

ACI committee 318 *Building code requirements for structural concrete and commentary*. American Concrete Institute, Detroit, 2000, USA.

Lozano-Galant, J.A., Nogal, M., Paya-Zaforteza, I., & Turmo, J. 2014 Structural system identification of cable-stayed bridges with observability techniques. *Structure and Infrastructure Engineering*, 10 1331-1344.

Lozano-Galant, J.A., Nogal, M., Turmo, J., & Castillo, E. 2015 Selection of measurement sets in static structural identification of bridges using observability trees. *Computers and Concrete*, 15 771–794.

Lozano-Galant, J.A., Nogal, M., Castillo, E. & Turmo, J. 2013 Application of Observability Techniques to Structural System Identification. *Computer-Aided Civil and Infrastructure Engineering* 28, 434–450.

Lei, J., Lozano-Galant, J.A., Nogal, M., Xu, D., & Turmo, J. 2016 Analysis of measurement and simulation errors in structural system identification by observability techniques. *Structural Control and Health Monitoring*, doi: 10.1002/stc.1923.

Lei J, Lozano-Galant, J.A., Nogal, M., Xu, D., & Turmo, J. 2017a Constrained observability method in structural system identification, *Structural Control and Health Monitoring*, doi: 10.1002/stc.2040

Lei, J., Xu, D., & Turmo, J. 2017b Static structural system identification for beam-like structures using compatibility conditions Structural Control and Health Monitoring :e2062. https://doi.org/10.1002/stc.2062

Castillo, E., Lozano-Galant, J.A., Nogal, M. & Turmo, J. 2016a New tool to help decision making in civil engineering. *Journal of Civil Engineering and Management*, 21 689–697.

Castillo, E., Nogal, M., Lozano-Galant, J.A. & Turmo, J. 2016b Solving Some Special Cases of Monomial Ratio Equations Appearing Frequently in Physical and Engineering Problems. *Mathematical Problems in Engineering*, http://dx.doi.org/10.1155/2016/9764913

Nogal, M., Lozano-Galant, J.A., Turmo, J. & Castillo, E. 2015 Numerical damage identification of structures by observability techniques based on static loading tests, *Structure and Infrastructure Engineering*, 12 1216-1227.

Midas Civil [Computer software] Midas Information Technology Co.2015, Ltd. http://en.midasuser.com/product/

Sanayei, M., Phelps, J.E., Sipple, J.D., Bell, Erin S., Brenner & Brian R. 2012 Instrumentation, nondestructive testing, and finite-element model updating for bridge evaluation using strain measurements. *Journal of Bridge Engineering*, 17, 130–138.

Tomás, D., Lozano-Galant, J.A., Ramos, G., & Turmo, J. 2017 Structural System Identification of thin web bridges by observability techniques considering shear deformation. Thin-walled structuress

Dong, X. Zhao, L., Xu, Z., Du, S., Wang, S., Wang, X., & Jin, W. 2017 Construction of the Yunbao Bridge over the yellow river, EASEC-15, October 11-13, Xi'an, China.

Maintenance, Safety, Risk, Management and Life-Cycle Performance of Bridges – Powers, Frangopol, Al-Mahaidi & Caprani (Eds)
© 2018 Taylor & Francis Group, London, ISBN 978-1-138-73045-8

Optimizing rehabilitation strategies for bridge decks under performance-based contracting setting

M. Alsharqawi & T. Zayed
Dept. of Building, Civil and Environmental Engineering, Concordia University, Montréal, Québec, Canada
S. Abu Dabous
Dept. of Civil and Environmental Engineering, University of Sharjah, Sharjah, United Arab Emirates

ABSTRACT: The 2016 Canada infrastructure report alarmed that more than 26% of Canada's bridges are rated fair, poor, and very poor and an investment of $50 billion is required to replace all of these bridges. In the US, the situation is similar where the American Society of Civil Engineers (ASCE) report card graded bridges' condition in 2017 as "C+" which refers to a mediocre condition that requires immediate attention. There is an overwhelming amount of maintenance and rehabilitation works to be done and selecting a suitable maintenance, repair or replacement (MRR) strategy is one of the most challenging tasks for decision makers. Limited budget and resources are making the decision making process much more challenging. The growing needs and limited resources to maintain the transportation networks have resulted in motivating transportation agencies to expand the amount of contracting they do through long term performance-based maintenance contracts or what is called Performance-Based Contracting (PBC). The main objective of this research is to develop short and long term optimized rehabilitation plans for bridge decks under PBC setting. In order to achieve this goal, performance modeling is established to measure current performance and predict future deterioration and improvements rates; moreover, associated MRR costs are estimated. A key performance measure, named condition reliability, is defined as an indicator to the structural condition or performance of the bridge component. Furthermore, an associated level of service (LOS) threshold is proposed. The output of this research is a decision-making tool for optimizing rehabilitation strategies with the lowest cost while maintaining a specified performance LOS. The principles of the proposed tool are demonstrated through a real case study of a bridge located in Quebec, Canada. The result of the proposed decision support tool is an optimized work program that satisfies the identified performance LOS and budget constraints. The model is expected to support decision makers to maintain their bridges using the PBC method.

1 INTRODUCTION

Earlier practices for maintaining and managing transportation infrastructure were using separate contracts for each activity and with a labor rate or unit price. In recent years, there are innovative methods of procuring maintenance activities for all products and services under one contract and for a longer duration. These methods define and specify the desired end result which provides the contractor with more flexibility, innovation potential, and cost savings measures for the client organization (Pakkala 2002). In the traditional method-based contracts, the transportation agency specifies techniques, methods, materials, quantities, along with the time that the maintenance activities should be executed (Alyami and Tighe 2013). This causes a limitation on the use of new materials and innovative techniques and technologies while maintaining the infrastructure asset (Panthi et al. 2008). Moreover, this traditional way of contracting had failed in achieving the agencies' main goal of reducing maintenance expenditures and improving the transportation networks at an acceptable Level of Service (LOS) to the traveling public (Porter 2001; Piñero and de la Garza, Jesus M. 2004). The challenge of maintaining infrastructure to the highest possible condition while investing the minimal amount of money has promoted innovative contracting approaches. Contractors have better competencies of fulfilling required performance level through innovating in such new and unproven technologies (Panthi 2009). This can be achieved by extending the short maintenance period to a longer period so that the performance level can be satisfactorily measured over a longer duration. This type of agreement is called Performance-Based Contracting (PBC) which is a type of contract that pays a contractor based on the results achieved, not on the methods for performing the work. Such contracts allow the maintenance contractors to innovate and improve the efficiency of the services provided to the public (de la Garza et al. 2009).

PBC is defined as "a contracting method that provides incentives and/or disincentives to the maintenance contractor to achieve desired outcomes or results; in its purest form, PBC does not detail how, when, or where to do the work." (Hyman 2009). Therefore, payments for management and maintenance of assets in this type of contract are explicitly linked to the contractor successfully meeting or exceeding the specified performance LOS throughout the contract period. By paying contractors incentives and/or disincentives for predefined performance criteria and giving them the flexibility in choosing materials and methods in delivering maintenance services, contractors are encouraged to use new methods and mix quality which fosters innovation and improves the performance of the structure throughout its life. As in the case of PBC, the long-term planning provides the contractor with enough time horizon to deploy new technologies. Further, the contractors are encouraged to eliminate the future need to perform costly corrective maintenance actions by taking timely preventive maintenance ones (Gupta et al. 2011). Agencies that have converted to PBC claim cost saving between 10-50% over the traditional contracts (Stankevich et al. 2009). The agencies added that this price reduction took place in several areas from the non-technical, technical, and professional services (Office of Federal Procurement Policy (OFPP) 1998).

PBC can address different types of assets and operations including pavements, bridges, roadsides, traffic operations, traffic services, incident response, hazardous materials cleanup, and emergency repairs (Hyman 2009). Moreover, performance contracts are not limited to maintenance including preventive, routine, periodic, and demand-responsive maintenance as rehabilitation of roads and bridges has been part of many performance-based contracts (Hyman 2009). By looking into the literature, it is observed that many transportation agencies established PBC extensively for roads maintenance (Haas et al. 2009; Stankevich et al. 2009; Panthi 2009; Alyami and Tighe 2013). However, in the area of bridges management, there are very limited studies to assess this method and to integrate it into the decision-making process. The process of making appropriate maintenance, repair or replacement (MRR) decisions begins with performance assessment and rating based on condition survey. Current bridge assessment practices mainly depend on techniques to evaluate surface defects such as cracking and spalling. As a result, these practices are unable to precisely assess bridge elements with subsurface defects, such as corrosion of steel reinforcement. Predicting future performance is the next step where deterioration modeling and improvements resulting from different MRR strategies is modeled. Many researchers modeled deterioration stochastically to predict future condition of reinforced concrete bridge elements. Among them are Frangopol et al. (2004), Morcous (2006), Yang et al. (2009) and Li et al. (2016). Performance modeling is important to select appropriate MRR strategy that maintains the specified performance LOS. Finally, the process of selection of the combination of MRR actions is repeated to arrive at the optimum rehabilitation program within the available budget and over the planning time horizon.

2 SCOPE AND OBJECTIVE OF PAPER

The main objective of this research is to develop a decision support tool for concrete bridge MRR strategies while achieving the specified performance LOS during the intended contract period. To achieve this objective, the following sub-objectives are sought:

1. Assess bridge condition considering surface and subsurface defects to enhance the reliability of performance assessment.
2. Model deterioration and improvements to forecast bridge future performance rates.
3. Optimize selection of rehabilitation strategies under PBC setting over a predefined period.

Thus, this research proposes a mathematical optimization tool that provides a rehabilitation program for transportation agencies and maintenance contractors based on PBC arrangements.

3 METHODOLOGY AND MODEL DEVELOPMENT

The decision making support tool development process is illustrated in Fig. 1 and discussed in the following sections. The proposed models in this paper consider concrete bridge deck in particular because it deteriorates faster than other components due to its direct exposure to traffic in addition to the external environmental conditions. Initially, models for bridge deck management are adopted from previous research (Alsharqawi et al. 2016; Alsharqawi et al. 2017). The first model is a performance assessment model to rate current performance. The second is deterioration modeling to predict future ratings. And the third is a rehabilitation model to determine suitable MRR interventions. Then, the decision making support tool is developed based on an optimized selection of minimum total rehabilitation actions cost and maximum performance considering PBC setting of maintaining the specified performance LOS during the predefined duration.

3.1 *Bridge deck performance modeling*

Performance measures and performance LOS are the basis of a PBC which are expected to be achieved by the maintenance contractor (Alyami 2012). Measures

of performance are often expressed in terms of levels of service represented by specific rating scales corresponding to the condition of different assets. Many experts on performance measurement argue the benefit of using a few key performance measures instead of many because of the associated simplicity and manageability of those few performance measures (Hyman 2009). This research focuses on structural performance measures which are these attributes that indicate the condition or performance of the bridge component. In this context, these measures are the common bridge deck defect types, i.e., cracking, concrete disintegration, scaling and erosion, corrosion of steel reinforcements, delamination, spalling, deposits, expansion joints problems, and pop-outs. These assembled can represent the structural condition reliability which is a component's physical condition fitness or in other words an indicator of a component performance state. Reliability is the base measure for the bridge remaining service life, an indicator that is suggested by Haas et al. (2008; 2009).

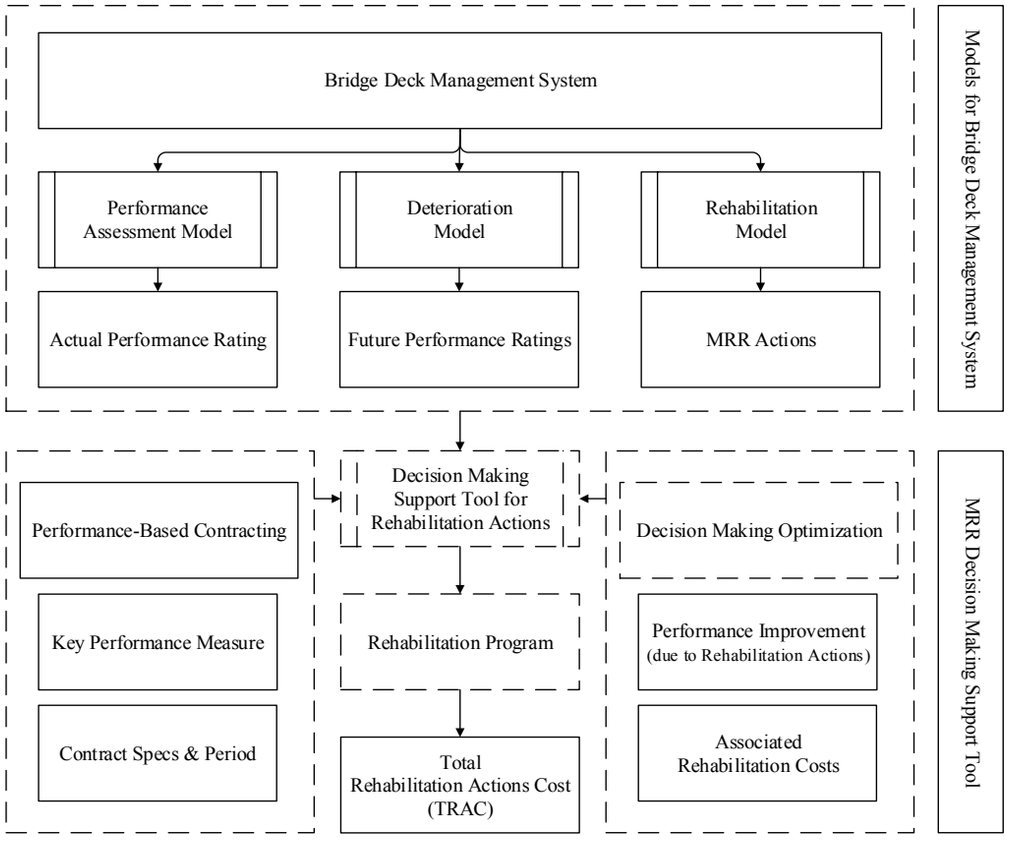


Figure 1. Schematic flow diagram of the proposed methodology

In order to assess bridge deck condition reliability, a Quality Function Deployment (QFD) condition assessment model is utilized. The QFD model can integrate surface defects detected by visual inspection and subsurface defects using NDE techniques in one framework (Alsharqawi et al. 2016). By applying the QFD model, a final crisp integrated condition value C_I is calculated representing the bridge deck overall condition using Eq. 1:

$$C_I = \frac{1\times Good + 3\times medium + 6\times Severe + 9\times V.Severe}{9} \quad (1)$$

where: C_I = integrated component condition; and $1, 3, 6, 9$ = numerical rating scale following a geometric progression where severity (condition ratings) is scored proportionally. Then, the reliability value is calculated which is one minus the component's overall condition and used as an input to the prediction model.

To model deterioration over time, a reliability-based Weibull Distribution Function (WDF) is employed to shape the bridge deck deterioration curve (Alsharqawi et al. 2017). The current research adopts the WDF to model bridge deterioration because of its particular advantages including i) the WDF has proven to be one of the best functions to represent concrete deterioration (Semaan 2011; Shami 2015); ii) Unlike the stochastic deterioration models, the Weibull function does not require large amount of historical inspection data to model deterioration; and iii) the Weibull reliability function parameters are calculated easily. An updated deterioration curve is created based on the last inspection condition survey for real representation of component deterioration over time using the Eq. 2 (Alsharqawi et al. 2017):

$$CR_I(t) = 1 \times e^{ln(CR_{Ii})(t/t_i)^s} \quad (2)$$

where: CR_t = component integrated condition reliability at time t; CR_{t_i} = integrated condition reliability at time t_i ; and t_i = inspection time.

3.2 *Development and optimization of maintenance, repair, and replacement strategies*

3.2.1 *Rehabilitation, improvement, and cost models formulation*

Rehabilitation modeling is the process of determining the suitable MRR actions. Improvement modeling is about predicting the conditions after performing MRR actions, and cost modeling is for estimating the associated costs of these actions. Based on the developed QFD condition assessment model, suitable MRR types are formulated and categorized into three types of rehabilitation. Table 1 proposes an interpretation of each MRR action corresponding to the performance of the bridge deck. For bridge decks under good performances, rehabilitation actions such as routine maintenance could be performed. Bridge decks with poor performances need repair actions such as strengthen the thickness of these bridge decks by doing local repairs to the concrete structure. For critical performance, the action would be full deck replacement.

Table 1. Performance assessment interpretation for bridge decks

Performance Assessment	Action
Excellent	No Action is needed.
Good	Bridge needs routine maintenance
Poor	Bridge needs repair
Critical	Bridge needs replacement

Modeling performance improvement and predicting the deterioration behavior of an asset after a rehabilitation action is necessary. This research classifies bridge rehabilitation actions into maintenance, repair or replacement (MRR) strategy. The improvement values by the three types of rehabilitation relied on a study that was performed by Seo (1994). Seo's estimated repair improvements according to FHWA condition rates. It is noticed from Seo's study that the rehabilitated action of replacing a new deck does not revert the condition to its best condition as of newly constructed bridges. Therefore, and in reference to the literature review, condition reliability is estimated to have an improvement of 20% when repair actions are implemented to the bridge deck. In the case of bridge deck replacement, the condition reliability is raised to be equal to 90%. For maintenance action, no improvement occurs, but this action reduces the deterioration of the bridge deck, i.e., bridge deck deteriorates at a slower rate.

Calculating a component's rehabilitation cost in Bridge Management Systems (BMSs) is often performed neither by assigning a fixed cost as a percentage of initial construction or replacement cost nor as a unit cost. The importance of defining the cost of the available repair options has been discussed by many researchers; however, the cost calculations were discussed without much detail. In practice, repair costs are associated with soliciting quotes to contractors/suppliers or by consulting published data references. As an example of percentage MRR costs, Seo (1994) proposed predefined estimates for the three types of rehabilitation. Abu Dabous and Alkass (2011) developed three unit cost models for each rehabilitation type. The unit cost of each rehabilitation action includes the direct cost, indirect cost and the markup added to cover the contractor's profit and contingency. Table 2 summarizes the rehabilitation actions costs as a percentage of initial construction (Seo 1994) and as a fixed unit cost (Abu Dabous and Alkass 2011). The unit costs are in Canadian dollars, adjusted for inflation and based on the 2017 dollar value.

Table 2. Rehabilitation strategies improvements and costs per type

Rehabilitation Action	Improvement	Rehabilitation Cost	
		% of initial construction	unit cost (C$/m^2)
Maintenance	0%	28.5%	$26.43
Repair	20%	65.0%	$789.40
Replacement	90%	100.0%	$1033.20

3.2.2 *Life-cycle costing and optimization model formulation*

Prediction models are the basis of life-cycle cost analysis. This is because the maintenance costs are dependent on the bridge performance which varies over the analysis period. The setting of a PBC is accomplished in the traditional life-cycle cost model through defining the desired performance threshold such that the LOS never exceeds the threshold limit. The calculations for Rehabilitation Actions Costs (RAC) costs are evaluated using net present value (NPV) and shown in the following equations:

$$RAC_{total} = \sum_{n=1}^{N} \sum_{m=1}^{M} \frac{1}{(1+i)^n} (RAC_m . X_{nm}) \quad (3)$$

$$\sum_{m=1}^{M} X_{nm} = 1 \ \forall \ n = 1, \dots, N \quad (4)$$

where: RAC_{total} = total rehabilitation actions costs; N = total number of contractual years (contract duration); i = discount rate; M = total number of MRR strategies m; RAC_m = rehabilitation action cost associated with the selected MRR strategy m; and $X_{nm} \in \{0,1\}$ binary constraint ensures that one MRR strategy is chosen at year n of the contract period. X_{nm} = 1 if MRR action m is applied, and 0 otherwise.

The outputs of the prediction model and life-cycle costing model are integrated as inputs to the optimization model in order to obtain a set of tradeoff lists of rehabilitation actions applied over the predefined period of the contracted bridge asset. The optimization model is developed to meet the needs that arise within a PBC setting. Thus, the objective functions and constraints are formed as:

Objective functions:

$$minimize\ RAC_{total} = \sum RAC_n \quad \forall n, 1 \leq n \leq N \quad (5)$$

$$maximize\ P = AVG\ P_n \quad \forall n, 1 \leq n \leq N \quad (6)$$

Subject to (constraints; *s.t.*):

$$TRAC \leq B \quad (7)$$

$$P_{limit} < P_n \leq P_{max} \quad (8)$$

where: RAC_n = rehabilitation actions cost in year n; B= budget constraint; P_{limit} = minimum allowable performance that could be reached even after applying disincentives (penalties); P_n = predicted performance after MRR action at year n; and P_{max} = maximum performance. In addition, the optimization model should account for the constraint of the contract specified LOS of the key performance measure, condition reliability. In other words, the condition reliability state should satisfy the specified LOS threshold of the performance measure:

$$P_{CR} > PM \quad (9)$$

where: P_{CR} is the condition reliability performance as a result of the latest rehabilitation action applied; and *PM* is the specified LOS (predefined threshold value) of the key performance measure. In case of failing to achieve the specified performance LOS, disincentives (penalties) will be applied. In contrary, if applicable, incentives defined in the contract are applied once the performance exceeds the target LOS. The transportation agency specifies these thresholds to be met or exceeded during the contract period. A threshold of 65% is suggested representing a good performance state. Further, the transportation agency can define performance targets or standards where a LOS rating of 80% for primary systems and 75% for the secondary systems is desired targets (Smith et al. 1997). The process of selection of the combination of rehabilitation actions that will maintain the specified LOS for the key performance measure is repeated to arrive at the optimum rehabilitation program. For assistance with the optimization process, a genetic algorithm (GA) code for optimization is developed using MATLAB® software.

4 CASE STUDY AND MODEL IMPLEMENTATION

4.1 *Description and assumptions*

The studied case is a concrete bridge in the municipality of Frelighsburg, Quebec. The bridge is located on the Chemin Richford, where it overpasses the creek, Selby. The bridge deck is 13.7 m in length, resting on four concrete girders with the roadway being approximately 10 m wide and about 30 cm thick. The bridge was built in 1960, and the deck was visually inspected and previously scanned using GPR tool (GSSI SIR-3000).

Based on results of the inspection that was performed in 2016, it can be noticed that the cracking existed with medium severity. The bridge deck suffered from steel reinforcement corrosion and delamination at various severity levels, and deposits were detected. These defect measurements are input into the QFD assessment model to produce an integrated condition assessment of the bridge deck. The obtained results of the considered case are summarized in Fig. 2. By applying Eq. 1, a rating value is calculated to be 36.01%, representing the integrated condition for the bridge deck in the year 2016. Then, the reliability value (one minus the integrated component condition) is calculated to plot the bridge deck deterioration curve.

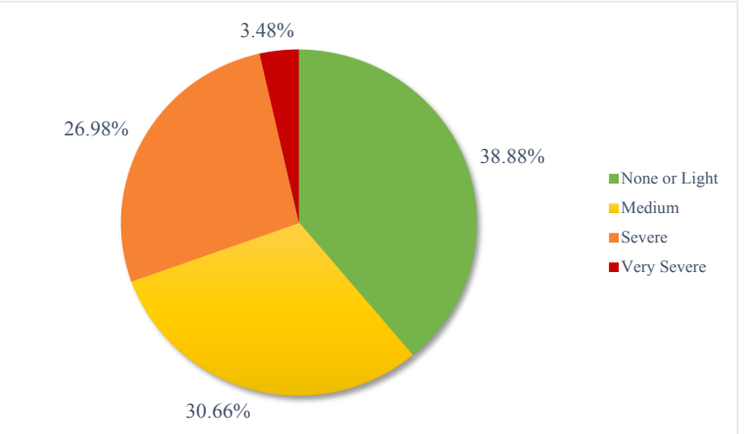


Figure 2. Assessment output for the case study based on 2016 inspection

Following the performance assessment, the WDF model is applied and the deterioration curve is mapped using Eq. 2. In this case, CR_{Ii} of 0.64 and t_i, year of inspection, of 56 are used based on data retrieved from the inspection survey conducted in 2016. Fig. 3 illustrates the performance curve without MRR interventions. As mentioned earlier, in PBC, the transportation agency specifies minimum performance measures to be met or exceeded in the contract specifications. Thus, the development of rehabilitation program is subjected to the specified performance measure and the associated LOS over the planning time horizon. In this research, the relia

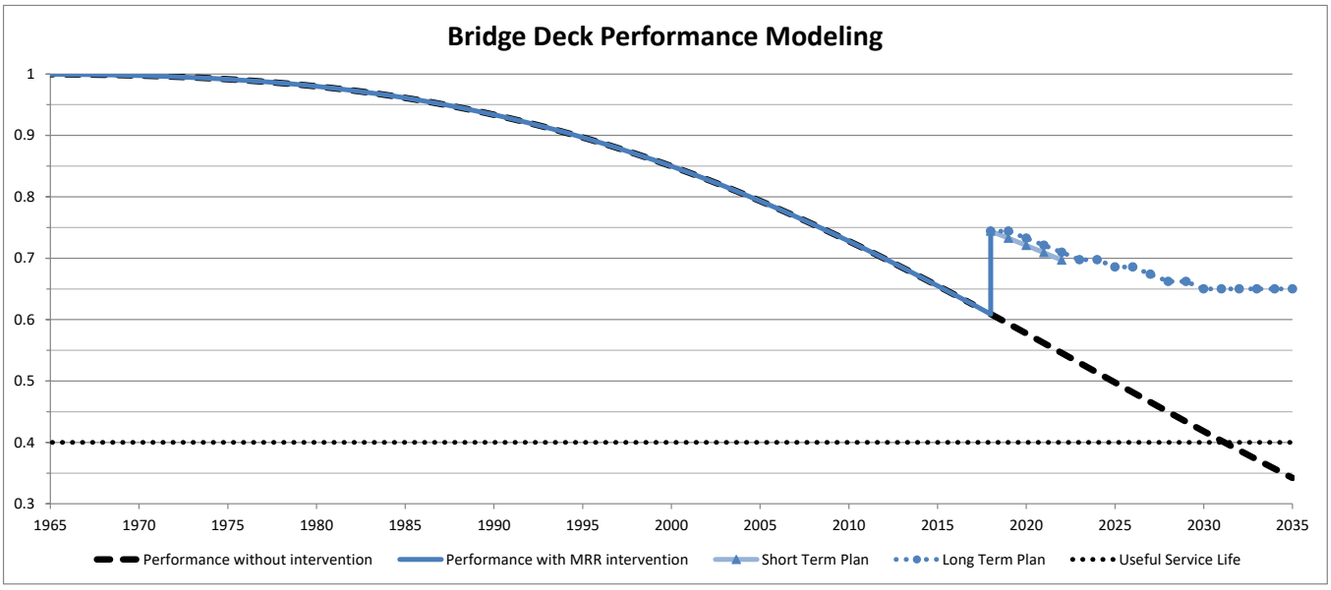


Figure 3. Performance curve without and with MRR interventions

bility of the bridge condition is adopted as a key performance indicator or measure to express the bridge's LOS.

In this paper, two optimization scenarios were developed, based on the following parameters: i) performance LOS threshold = 0.65; ii) discount rate i = 4%; iii) max number of iteration = 100,000; and iv) population size = 20. The first scenario was carried out over a 5 year predefined contract period and the second was carried out over the remaining life-cycle time of the contracted bridge asset. For the short term plan, a budget constraint B = \$160,000 allowing for a possibility to cover the cost of replacing the bridge deck. In the long term plan, a budget constraint B = \$320,000 is suggested to be allocated. A set of tradeoff lists of rehabilitation actions applied over the two scenarios will be discussed in the next section.

4.2 *Results and analysis*

The results obtained by implementing the QFD assessment model (Fig. 2) show that the medium condition state attained the second highest percentage of 30.66%. The severe condition state got a relatively high percentage of 26.98%. After implementing the Weibull deterioration model and based on the outcome from the 2016 inspection, the deterioration curve delivers an indication to the ministry of transportation to take an action no later than 2031 in order to maintain the minimum acceptable level (Performance = 0.40) that keeps the bridge functional and safe for users as forecasted in Fig. 3 (performance curve without MRR interventions).

The implementation of the optimization model presented earlier provides a variation of rehabilitation strategies applied at various years throughout the time horizon in the two described scenarios. Table 3 presents the program developed from implementing this model where the type of rehabilitation and corresponding performance for both scenarios are shown. The present worth of each scenario is also calculated. In scenario 1, the short term plan, the total rehabilitation actions costs RAC_{total} = \$115,373.28. While in scenario 2, the long term plan, the total rehabilitation actions costs RAC_{total} = \$138,209.56.

Table 3. Output of rehabilitation program

Year	Short Term Plan		Long Term Plan	
	Rehabilitation Strategy	Performance	Rehabilitation Strategy	Performance
0		0.624		0.62
1	Repair	0.744	Repair	0.744
2	No Action	0.733	Maintenance	0.744
3	No Action	0.721	No Action	0.733
4	No Action	0.709	No Action	0.721
5	No Action	0.697	No Action	0.710
6			No Action	0.698
7			Maintenance	0.698
8			No Action	0.686
9			Maintenance	0.686
10			No Action	0.674
11			No Action	0.662
12			Maintenance	0.662
13			No Action	0.650
14			Maintenance	0.650
15			Maintenance	0.650
16			Maintenance	0.650
17			Maintenance	0.650
18			Maintenance	0.650

By comparing the first five years in each plan, it is noticed that the long term plan has a better performance where the average performance P_{avg} is equal to 0.730 versus 0.721 in the short term plan. P_{avg} is equal to 0.684 over the whole period (18 years) in the long term plan. Regarding total rehabilitation actions costs, an increase of about 20% was encountered in the long term plan; yet this plan extends the study period by 13 additional years compared to the short term one. Although the allocated budget is doubled for the long term plan accounting for the increase in the time horizon, the developed optimization model minimized the budget consumption while maximizing the performance of the bridge deck.

5 CONCLUSIONS AND FUTURE RESEARCH RECOMMENDATIONS

There has been some movement over the past decade toward a performance-based contract model for maintaining and managing transportation infrastructure. However, there are limited computational tools to support optimal management and decision making under this innovative method of contracting. This research presents an overall methodology and introduces a decision support tool to optimize rehabilitation strategies under PBC setting. The availability of such tool will allow transportation agencies and maintenance contractors that are unfamiliar with PBC to make more informed decisions on their approach to better allocate the contractual risks. Implementing this tool can help contractors to establish optimum rehabilitation program with the lowest cost and appropriate time of MRR application to maintain the specified performance LOS along the contract period. Also, agencies can benefit from this tool to benchmark prices against bids during the bid evaluation process. Furthermore, it can be used in estimating the budget needed for contracted bridge assets. Performance models are presented in this research as they capture the asset current performance, deterioration, and improvements following to MRR actions.

While an extension of this research will be the topic of an extended paper, following are some of the authors ongoing research in this area: i) implementing the developed decision tool on other case studies and provide more detailed analysis and discussion of the rehabilitation program results; ii) establishing a PBC-based payment system that will estimate the cost to carry out MRR works (PBC contact cost) and define appropriate incentives, disincentives (penalties), or both; iii) conducting a sensitivity analysis of performance modeling and specified performance LOS threshold on the net present worth as a mean to quantify the accepted risk associated with this type of contract; and iv) design an evaluation criteria to assess the client agency selecting the best maintenance contractor, where the agency should check the contractors' capabilities prior to awarding the performance-based contract.

REFERENCES

Abu Dabous S, Alkass S. 2011. Managing Bridge Infrastructure under Budget Constraints: A Decision Support Methodology. Canadian Journal of Civil Engineering 38(11):1227-1237.

Alsharqawi M, Abu Dabous S, Zayed T. 2016. Quality Function Deployment Based Method for Condition Assessment of Concrete Bridges. Transportation Research Board 95th Annual Meeting. Washington, D.C., United States: Transportation Research Board of the National Academies.

Alsharqawi M, Abu Dabous S, Zayed T. 2017. Condition-Based Probabilistic Deterioration Model for Concrete Bridge Decks. Transportation Research Board 96th Annual Meeting. Washington, D.C., United States: Transportation Research Board of the National Academies.

Alyami Z. 2012. A Two-Phase Maintenance and Rehabilitation Framework for Pavement Assets under Performance Based Contracts [Master of Applied Science]. [Waterloo, Ontario, Canada]: University of Waterloo.

Alyami Z, Tighe S. 2013. Development of Maintenance and Rehabilitation Program: Pavement Assets Under Performance-Based Contracts. Transportation Research Record: Journal of the Transportation Research Board (2361):1-10.

de la Garza J, Piñero J, Ozbek M. 2009. A Framework for Monitoring Performance-Based Road Maintenance Contracts:433-441.

Frangopol DM, Kallen M, Van Noortwijk JM. 2004. Probabilistic Models for Life-Cycle Performance of Deteriorating Structures: Review and Future Directions. Progress in Structural Engineering and Materials 6(4):197-212.

Gupta D, Vedantam A, Azadivar J. 2011. Optimal Contract Mechanism Design for Performance-Based Contracts. Minnesota Department of Transportation Research Services Section. MN/RC 2011-18 No.

Haas R, Felio G, Lounis Z, Falls LC, editors. 2009. Measurable Performance Indicators for Roads: Canadian and International Practice. Annual Conference of the Transportation Association of Canada. Vancouver, British Colombia, Canada: Transportation Association of Canada.

Haas R, Tighe S, Yeaman J, Falls LC, editors. 2008. Long Term Warranty Provisions for Sustained Preservation of Pavement Networks. Annual Conference of the Transportation Association of Canada. Toronto, Ontario, Canada: Transportation Association of Canada.

Hyman WA. 2009. NCHRP Synthesis 389: Performance-Based Contracting for Maintenance. Washington, D.C., United States: National Cooperative Highway Research Program (NCHRP) Synthesis of Highway Practice.

Li L, Li F, Chen Z, Sun L, editors. 2016. Bridge Deterioration Prediction using Markov-Chain Model based on the Actual Repair Status in Shanghai. Transportation Research Board

95th Annual Meeting. Washington, D.C., United States: Transportation Research Board of the National Academies.
Morcous G. 2006. Performance Prediction of Bridge Deck Systems using Markov Chains. Journal of Performance of Constructed Facilities 20(2):146-155.
Office of Federal Procurement Policy (OFPP). 1998. Report on the Performance-Based Service Contracting Pilot Project. Washington, D.C., United States: Office of Federal Procurment Policy.
Pakkala P. 2002. Innovative Project Delivery Methods for Infrastructure. Helsinki, Finland: Finnish Road Enterprise.
Panthi K. 2009. A Methodological Framework for Modeling Pavement Maintenance Costs for Projects with Performance-Based Contracts [Doctor of Philosophy]. [Miami, Florida, United States]: Florida International University.
Panthi K, Farooqui RU, Ahmed SM, editors. 2008. Reliability-Based Model for Estimating Long Term Pavement Maintenance Contracts Under Performance Specifications. Proceedings of the First International Conference on Construction in Developing Countries (ICCIDC-I). Karachi, Pakistan. p. 456-463.
Piñero JC, de la Garza, Jesus M. 2004. Issues Related to the Assessment of Performance-Based Road Maintenance Contracts. American Society of Civil Engineers, Towards a Vision for Information Technology in Civil Engineering; p. 1-8.
Porter TM, editor. 2001. Trends in the Procurement Models for Highway Maintenance. Transportation Research Board 80th Annual Meeting. Washington, D.C., United States: Transportation Research Board of the National Academies.
Semaan N. 2011. Structural Performance Model for Subway Networks [Doctor of Philosophy]. [Montreal, Quebec, Canada]: Concordia University.
Seo JH. 1994. A Lagrangean Relaxation and Network Approach to Large-Scale Optimization for Bridge Management Systems [Doctor of Philosophy]. [Texas, United States]: Texas A&M University.
Shami A. 2015. Ground Penetrating Radar-based Deterioration Assessment of Bridge Decks [Master of Applied Science]. [Montreal, Quebec, Canada]: Concordia University.
Smith KL, Stivers M, Horner TE, Romaine AR. 1997. NCHRP Web Document 8: Highway Maintenance Quality Assurance. Washington, D.C., United States: Transportation Research Board, National Research Council.
Stankevich N, Qureshi N, and Queiroz C. 2009. Performance-based Contracting for Preservation and Improvement of Road Assets. The World Bank (Transport Note No. TN-27 September 2005 (updated August 2009)).
Yang Y, Pam H, Kumaraswamy M. 2009. Framework Development of Performance Prediction Models for Concrete Bridges. Journal of Transportation Engineering 135(8):545-554.

Maintenance, Safety, Risk, Management and Life-Cycle Performance of Bridges – Powers, Frangopol, Al-Mahaidi & Caprani (Eds)
© 2018 Taylor & Francis Group, London, ISBN 978-1-138-73045-8

Impacts of dynamic loads on the soil-steel bridges

D. Beben
Opole University of Technology, Opole, Poland

ABSTRACT: The paper presents an analysis of the impact of moving loads (road and railway) on the soil-steel bridges made from corrugated plates. Corrugated steel plate structures have been used for many years to construct culverts and small-to-medium bridges, as well as other engineering structures. The high popularity of these bridges results from advantageous technological properties, i.e. high carrying capacity, short construction time, ability to execute the works in the winter period, economic advantages (in comparison to traditional steel or concrete bridge structures), etc. The impact of moving loads was verified experimentally on a few bridges, especially by way of: (i) determining the impact of the road and railway service load on this type of bridges; (ii) determining the dynamic amplification factors and comparing the impact of the live load and analogous static load on the values of internal forces in the bridge; (iii) verifying the assumption regarding the non-inclusion of the dynamic impacts in bridges, which the soil cover thickness exceeds 1.0 m. The obtained results may be useful for professionals dealing with the soil-steel bridges and culverts.

1 INTRODUCTION

Live loads passing with certain, sometimes high speed through a bridge structure cause structural vibration induced, e.g. by diverse deflection of vehicle shock absorbers. Additionally, roadway or track irregularities cause an increase in the dynamic impacts on the structure (Fryba 1999, Paultre et al. 1992). The analysis of traditional steel or concrete bridges under live load is a known problem.

Corrugated steel plate structures (Fig. 1) have been used for many years to construct culverts and small-to-medium bridges, as well as other engineering structures (Janusz & Madaj 2009, Machelski 2008). The high popularity of these structures results from advantageous technological properties, i.e. high carrying capacity, short construction time, ability to execute the works in the winter period, economic advantages (in comparison to traditional steel or concrete bridge structures), etc. The testing of these structures in various load ranges has been conducted for many years (Bayoglu Flener 2009, Beben 2005, 2013a, Machelski 2008, Pettersson 2007, Vaslestad 1990). The testing mainly regarded the response of the bridge's structure to soil loads during construction works and static load placed in various configurations on the bridge. Based on the overview of worldwide literature, it was concluded that the recognition of the behavior of this type of structures under dynamic live load, especially service load, has not yet been discussed in detail. Some of the known works in this scope (Bayoglu Flener & Karoumi 2009, Beben 2013b, Beben & Manko 2010, Sezen et al. 2008) regards testing of soil-steel bridges under controlled dynamic load, i.e. recording the structure's response to the passage of a specific vehicle with planned speed.



Figure 1. Example of soil-steel bridge.

The paper presents the original aspects consisting of the dynamic loads influences on soil-steel bridges based on experimental testing. Dynamic amplification factors were also analyzed based on field testing on several soil-steel bridges. The obtained results can be helpful for designers.

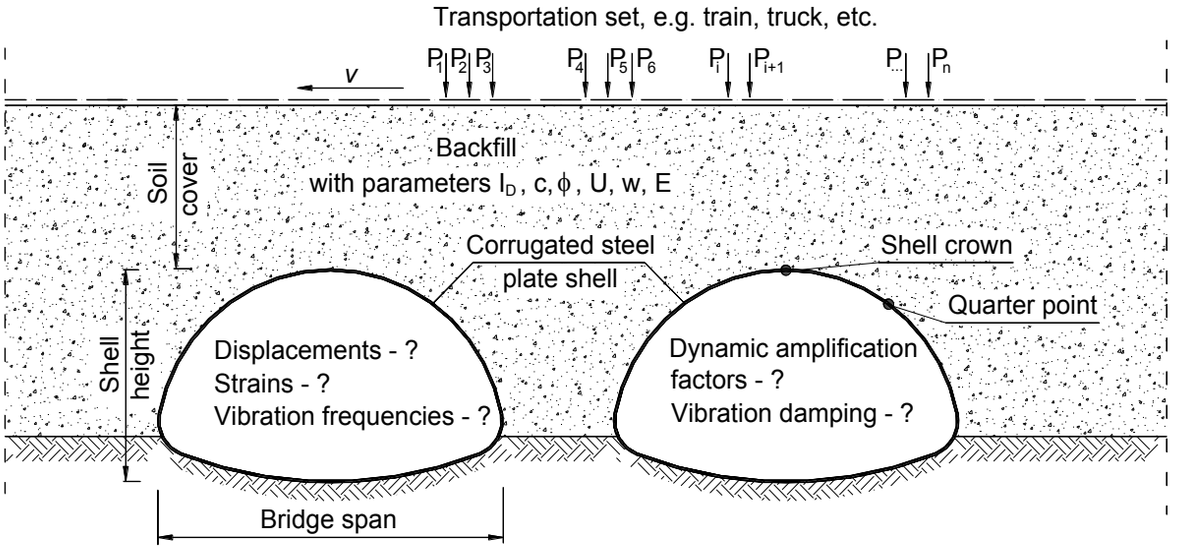


Figure 2. Schematic representation of the problem of live load impact on soil-steel bridges.

2 PROBLEM DESCRIPTION

The current studies (Bayoglu Flener & Karoumi 2009, Beben & Manko 2010, Sezen et al. 2008) have not included a detailed analysis of the impact of vehicle weight and speed, span and shape of shells and height of soil cover on the response of soil-steel bridges. No attempts have been made to determine in detail the displacements, strains, vibration frequencies and dynamic factors in these bridges or the impact of the backfill on vibration damping (Fig. 2). The analysis of these factors can contribute to the optimization of the selection of the minimum soil cover height and increase in the acceptable spans of soil-steel bridges. Additional effects may include a decrease in the execution costs of bridge infrastructure with the use of this type of bridges. Sezen et al. (2008) suggested that the response of soil-steel bridges is bigger from the static load than from the dynamic load. In addition, some researchers state (Janusz & Madaj 2009, McGrath et al. 2002) that in the case of bridges with a soil cover higher than 1.0 m, the dynamic impacts should not be taken into account, which is also reflected in relevant standards (AASHTO 2002, PN-85/S-10030 1985).

The article includes the analysis of the impact of road and railway live load on soil-steel bridges. The problem was verified experimentally, especially by way of: (i) determining the impact of the road and railway service load on this type of bridges; (ii)

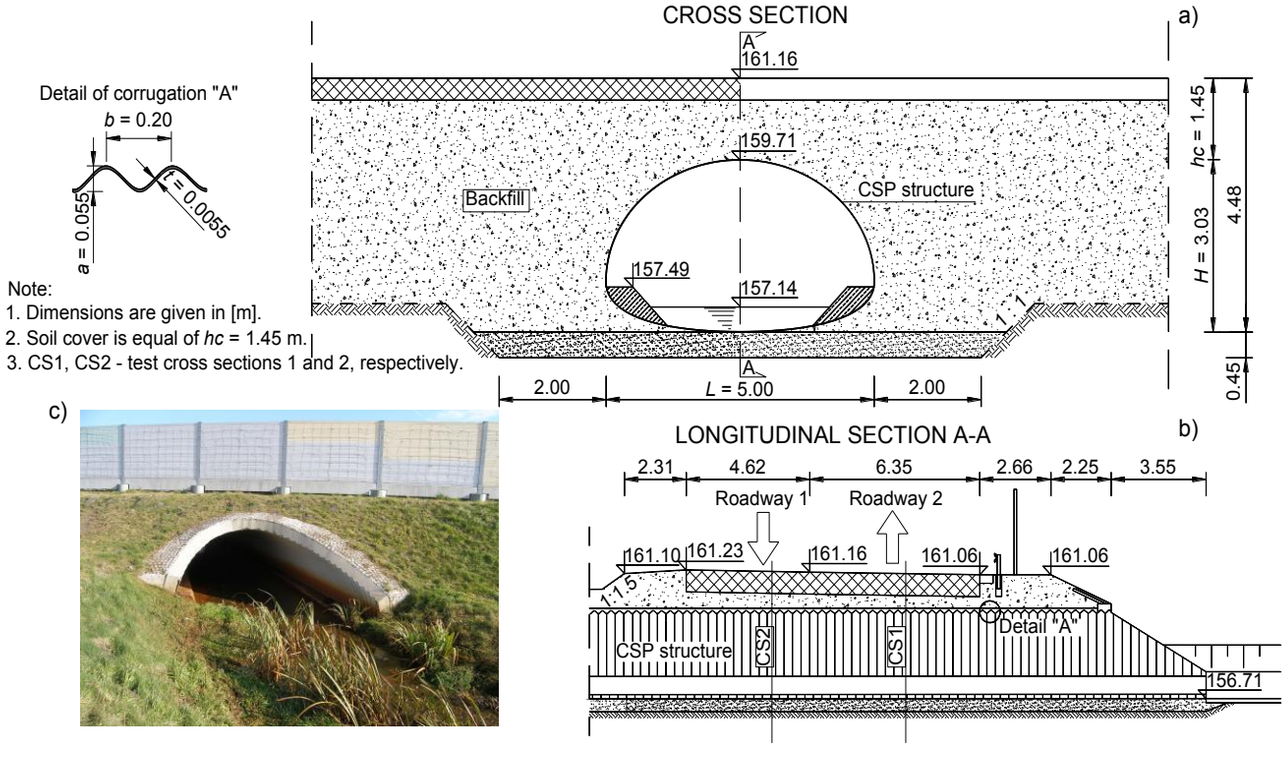


Figure 3. Road soil-steel bridge: a) cross-section, b) longitudinal section, and c) side view.

determining the dynamic amplification factors and comparing the impact of the live load and analogous static load on the values of internal forces in the bridge; (iii) verifying the assumption regarding the non-inclusion of the dynamic impacts in bridges, the soil cover thickness of which exceeds 1.0 m.

3 IMPACT OF THE ROAD AND RAILWAY SERVICE LOAD

3.1 *Road loads*

The study included testing of a road soil-steel bridges under service load (Fig. 3). The analysis of the results was conducted using the data concerning the vehicle traffic structure obtained from GDNRaM (General Directorate for National Roads and Motorways) and GIRT (General Inspectorate of Road Transport) as well as based on own video recordings. The displacements and strains in the selected bridge cross-sections were recorded in intervals, i.e. continuous measurement in eight half-hour intervals in different periods of the day. This allowed for obtaining a distribution of the maximum internal forces around the bridge's circumference from vehicle passage during the day.

The largest deformations, i.e. displacements amounting to 0.74 mm and strains with the value of 43×10^{-6}, were caused by the passage of a commercial vehicle with the weight of 46 t and speed of 70 km/h. The deformations occurred in the bridge's crown and in its quarter points. The distribution of the load along the bridge was determined by using the mutual correlation function for analyzing the sensor signals. It was observed that the impact of a vehicle passing over cross-section CS1 on test cross-section CS2, located within the distance of 5.0 m from the former, was smaller by 40%. A relatively small effort of the bridge was caused by the backfill at the crown h_c = 1.450 mm and the short time of load impact of 1 s. The FFT (Fast Fourier Transform) method was used during the analysis to determine the dominant bridge frequencies (Fig. 4) in the range of 0.2÷1.2 Hz

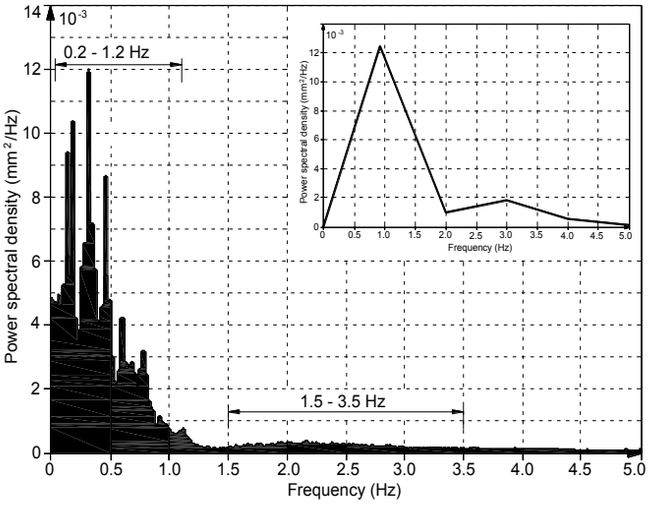


Figure 4. The power spectral density of the measured displacement.

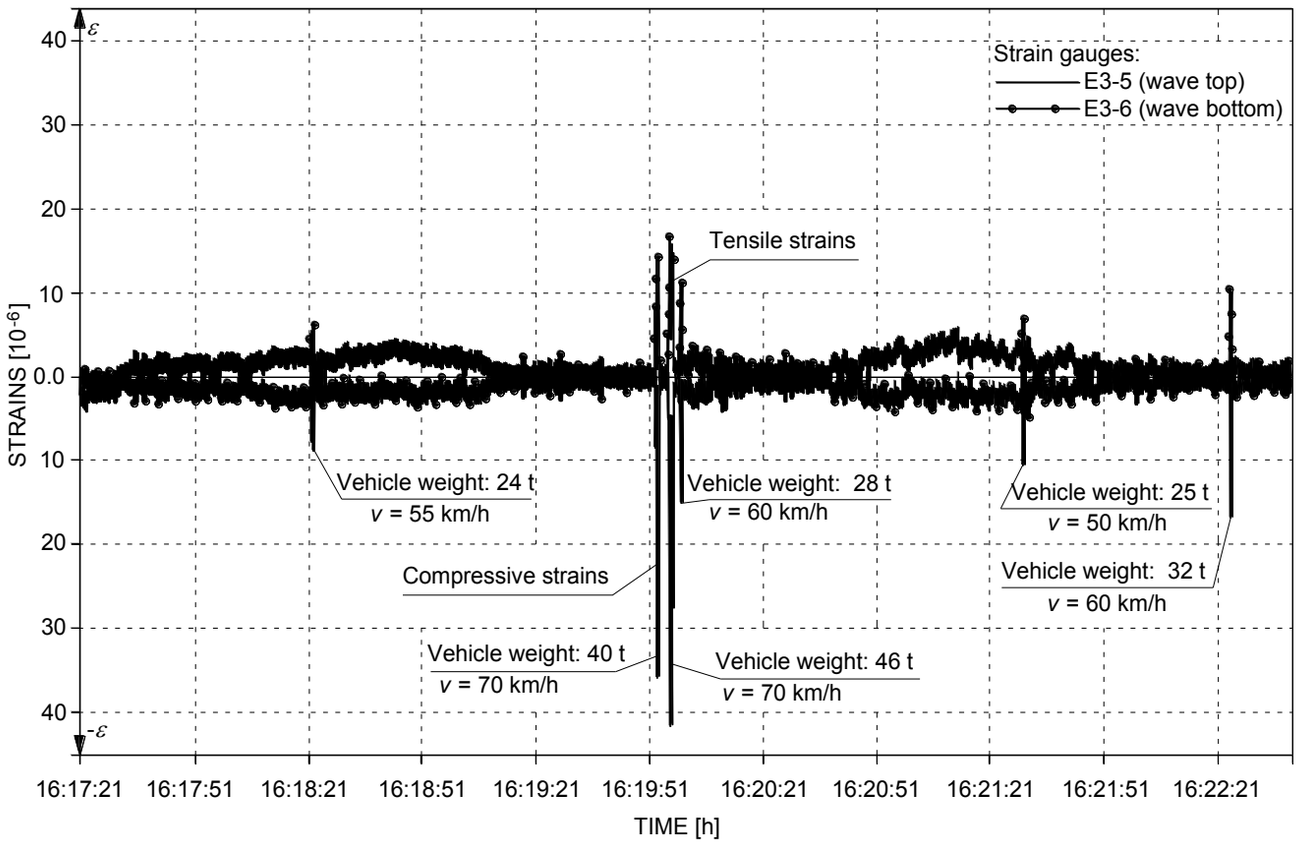


Figure 5. Graph of the compression and tension strains in the corrugated plate shell.

(angular frequencies ω = 1.26÷7.54 rad/s vibration period T = 0.83÷5.00 s). The less dominant frequencies were observed in the range of 1.5÷3.5 Hz (ω = 9.42÷21.99 rad/s and T = 0.28÷0.66 s). The small values of the soil-steel bridge frequencies confirm the positive impact of the backfill on damping the vibration caused by the passage of heavy vehicles.

It was also observed that the higher strain values (compression, sensor E3-5) occur at the peak of the wave (Fig. 5) and the smaller values – at the bottom of the wave (tension, sensor E3-6). This is related to the combined effect of axial forces and bending, as well as with the uneven distribution of the load around the shell's circumference (the shell's neutral axis is not located in the middle of the wave). The fact also affects the discrepancies in the results obtained acc. to the analytical methods and experimental studies.

The study also included the assessment and comparative analysis of the analytical methods (AASHTO LRFD 2010, CHBDC 2006, Pettersson & Sundquist 2014) used for estimating the internal forces in the bridges with the results of experimental studies. Axial thrusts calculated based on the CHBDC and Sundquist-Pettersson methods are closest to those obtained from the tests. However, in the case of the Sundquist-Pettersson method, a better agreement was obtained for higher values of live load, ca. 25%. Whereas, the biggest difference (ca. 60%) was recorded from the light loads, i.e., 60 kN. When the CHBDC method was used the biggest difference did not exceed 25%, but a better agreement was obtained for lower loads (< 340 kN). It was also observed that axial thrusts from the CHBDC method become convergent with the ones from the Sundquist-Pettersson method as the live load increased. Considering the whole range of live loads, the CHBDC method provides more reasonable thrust values than those from Sundquist-Pettersson method. The differences between the CHBDC and Sundquist-Pettersson methods can be related to the use of the Dynamic Amplification Factors (DAF), i.e., 1+DLA, by the CHBDC. These differences may also be caused by their approach to the load distribution through the soil cover and manner of determine the arching factor. The conservatism of these methods also derives from various loads and from additional safety factors used in the considered designing methods. Relatively high values of bending moments were obtained in the studies and estimations of the service loads. This confirms that the bending moments should not be ignored during the designing of arching and circular structures, which is suggested by the CHBDC (2006) and AASHTO LRFD (2010).

The test results were used in the estimation of the damping ratios ζ = 8.26÷21.02% and the logarithmic damping ratios LDD = 0.521÷1.351. Their values can be deemed as high in comparison to typical road

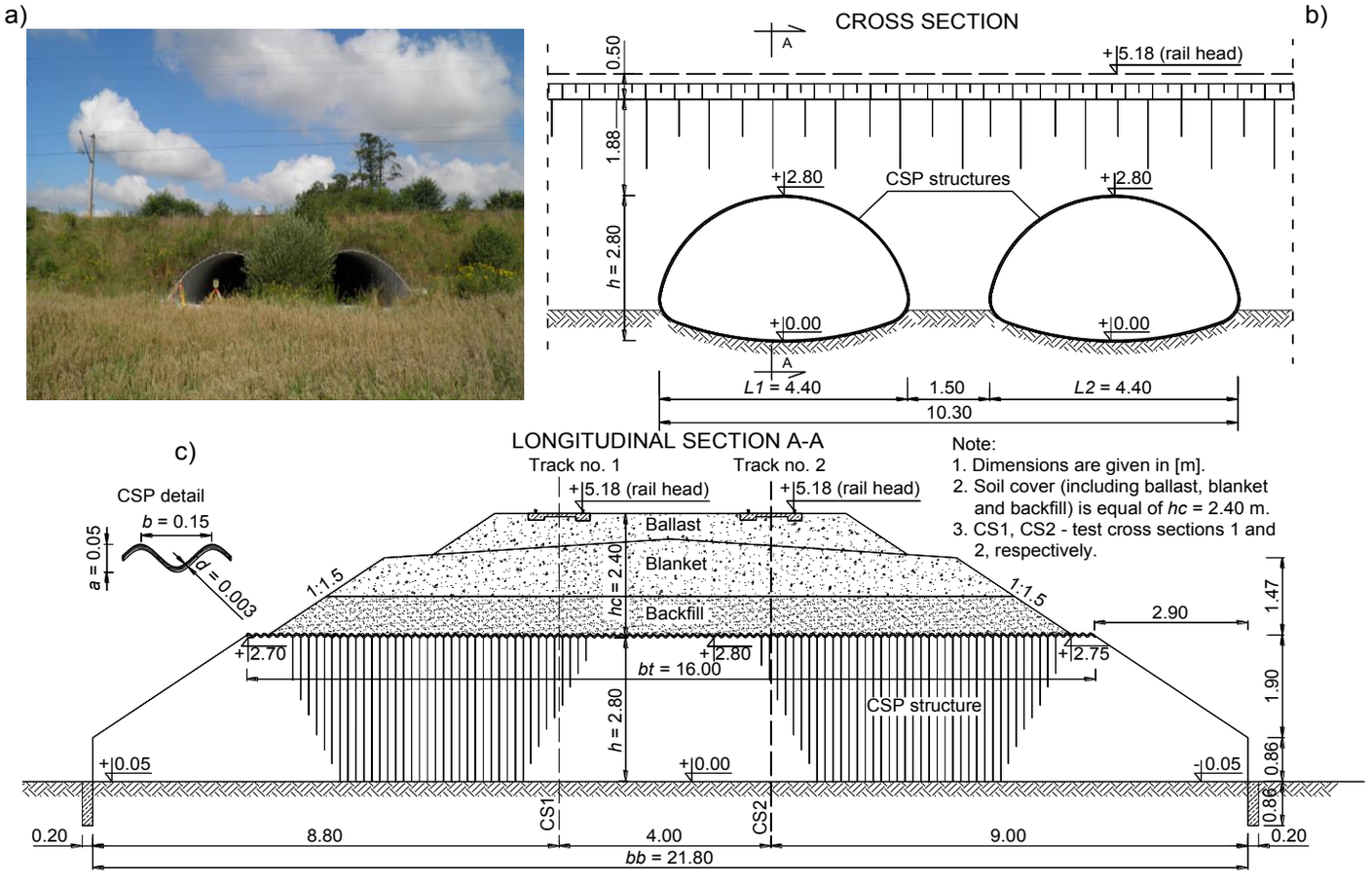


Figure 6. Railway soil-steel bridge: a) side view, b) cross-section, and c) longitudinal section.

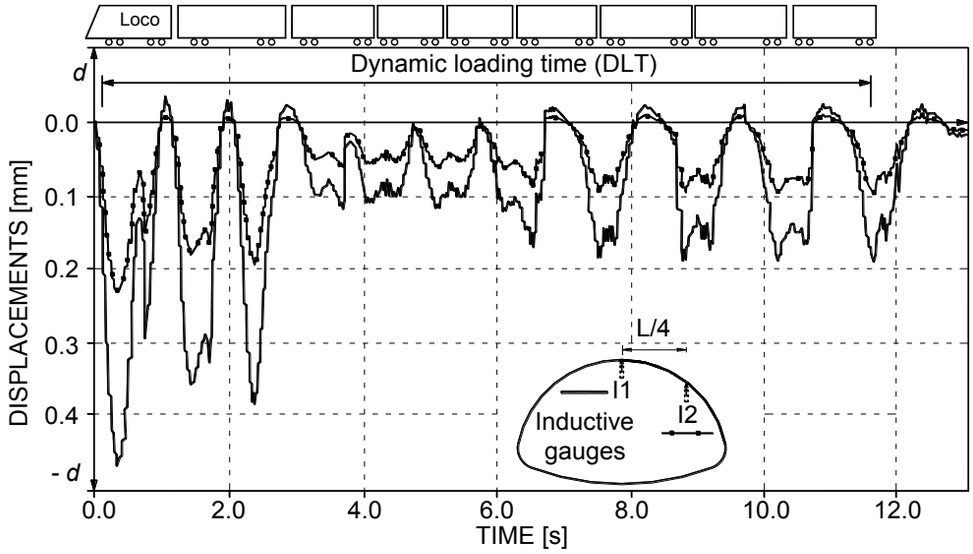


Figure 7. Bridge's crown and quarter point displacements during the passage of a freight train with the weight of 1,052.2 t and speed of 40 km/h.

and railway bridges. This results from the large height of the backfill in the crown, which in this case was damping the vibration and the energy dissipated within the backfill.

3.2 *Railway loads*

The main purpose of the railway soil-steel bridge (Fig. 6) testing was to obtain the responses to railway service load. The bridge's displacements and strains were measured in two cross-sections located under each of the railway lines. The maximum displacements have not exceeded 0.61 mm and strains – 54×10^{-6}, with the applied load of the train of approx. 1,700 t and speed of 35 km/h. The example of the bridge's displacement course is presented in Figure 7.

It was concluded that the backfill had a positive impact on the distribution of the load along the bridge, i.e. decrease in the displacements and strains by approx. 80%. This is related to the damping of vibration by the layers located above the bridge, i.e. backfill layers, gravel overburden, ballast and with the decreased rate of the waves in these layers. This means that the loads only affect the bridge near the track-way through which the train is passing. The highest displacements and strains were obtained at the bridge's crown and quarter points, respectively. The largest strains – compression was observed at the top of the wave and the lowest at the bottom – tension.

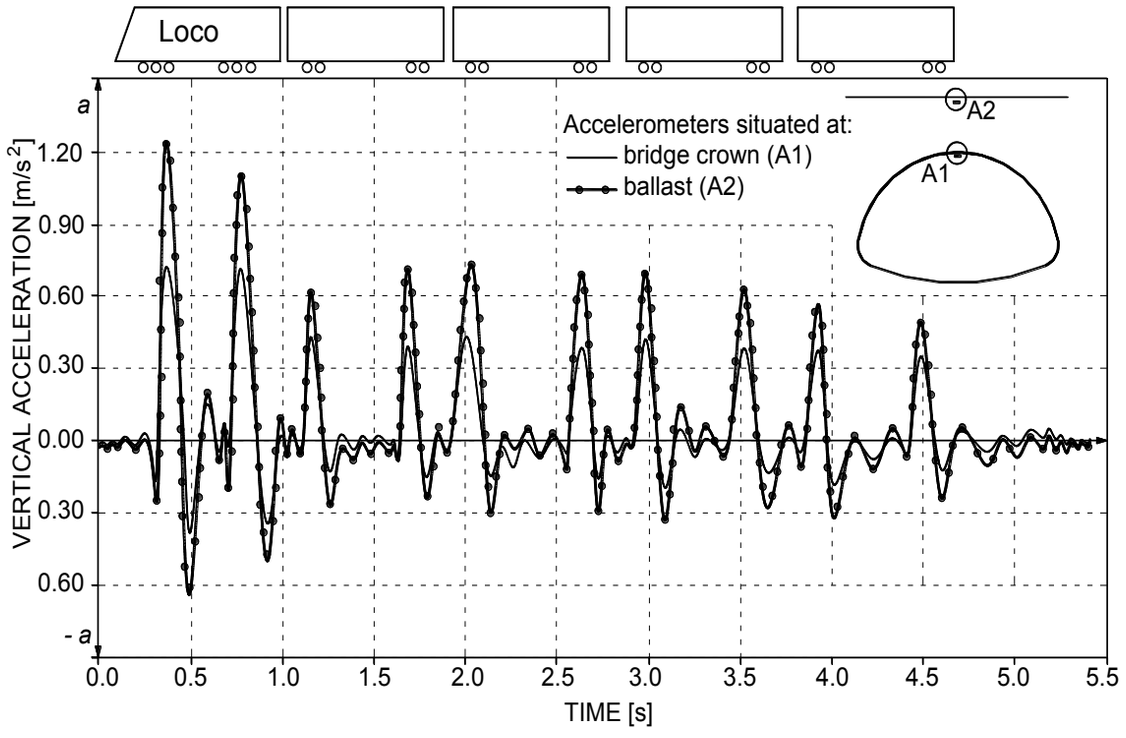


Figure 8. Bridge's crown and ballast vertical acceleration during the passage of an express train with the speed of 120 km/h.

The acceleration of the soil-steel bridge and railway ballast were smaller than the limit value of 3.5 m/s^2 according to Eurocode (2002). The acceleration at the bridge's crown (Fig. 8) was in every load case smaller than the ballast acceleration by approx. 45%. The decreased value of energy in the bridge's crown is caused by the reduction in the wave's velocity in the backfill and the substantial height of the soil in the crown. The test results also indicate that if the train speed increases, the bridge and ballast acceleration also increases.

Based on the measured displacements and using the DFT (Discrete Fourier Transform) method, it was possible to determine the bridge's dominant frequencies, which amounted to 0.1 or 0.2 and 1.2 Hz, which corresponds respectively to the circular frequencies ω = 0.63 or 1.26 and 7.54 rad/s and vibration periods T = 0.83 and 10 or 5 s. The highest bridge vibration frequencies were caused by the passage of trains with the speed of 70 to 120 km/h (irrespectively of their weight), while in the case of small train speeds amounting to $v < 40$ km/h, their weight had a larger impact on the bridge's frequencies. It can be stated that the bridge's frequencies are related to the weight of the passing trains. In the case of low speeds $v < 40$ km/h, there is an increase in the frequencies by approx. 69%, whereas in relation to higher speeds, the weight of the trains is not as important. Even trains with the weight of 135.3 t, passing through with the speed of 60÷75 km/h caused the same or higher frequencies than passages of heavy commercial trains, but with smaller speeds.

The bridge's natural vibration were also identified using the power spectral density for analyzing the displacements obtained from the so called ambient

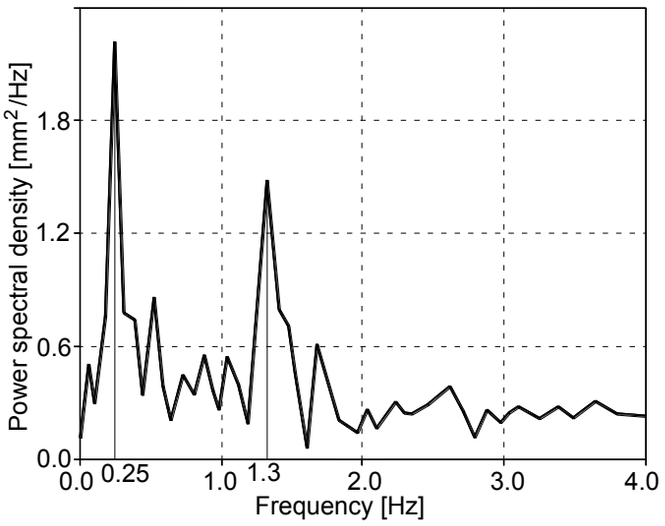


Figure 9. The power spectral density of the bridge's crown displacements after train passage.

vibration test. The first two natural frequencies of the bridge amounted to 0.25 and 1.3 Hz (Fig. 9), which corresponded in approximation to the dominant frequencies obtained from the primary tests under live loads (forced vibration test). The damping ratio determined using the Half Power Bandwidth method amounted to approx. 9% in the tests without a load and 50% in the case of tests with the use of passing trains. The large differences are caused by the impact of the activation of interaction between the steel shell and soil when the bridge is under load. The internal forces in the bridge, estimated according to the method specified by Pettersson and Sundquist (2014), were substantially higher than the values obtained during the experimental studies.

The available Australian (AS 3703.2-1989 1989.)

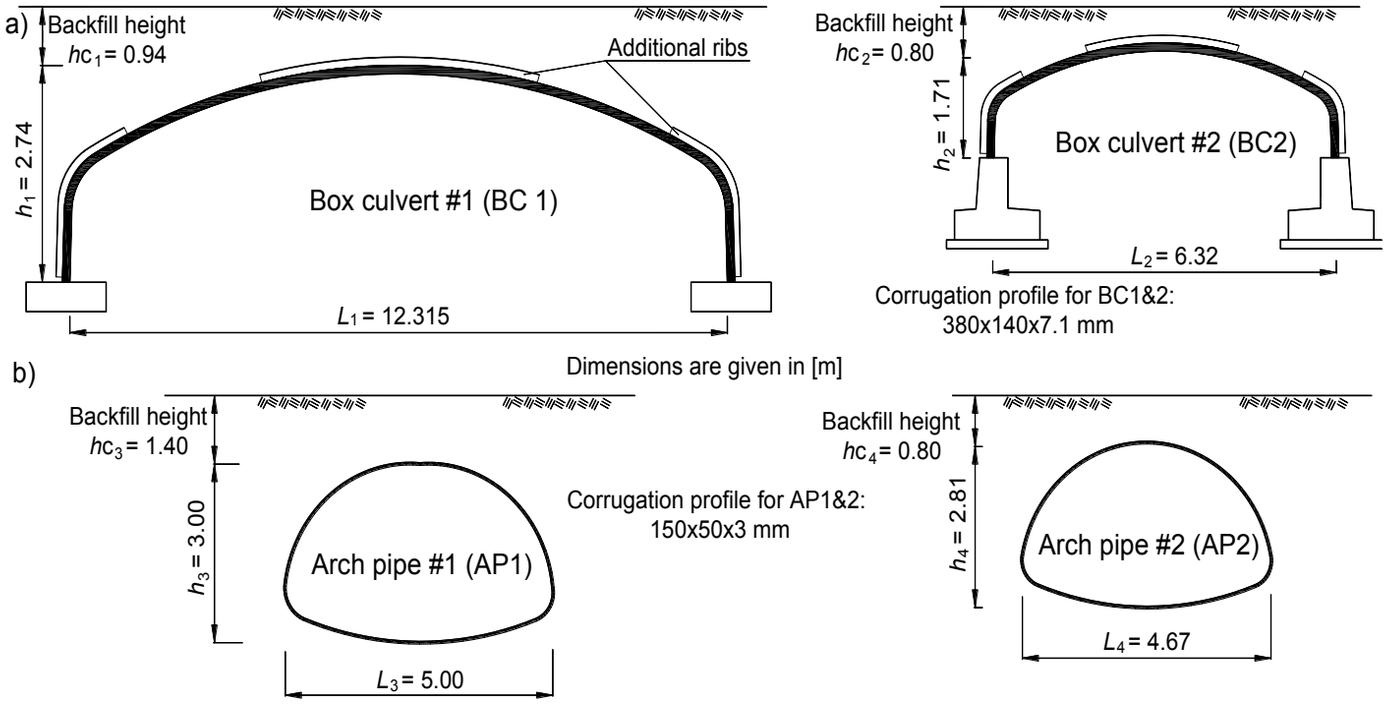


Figure 10. Cross-sections of the tested soil-steel bridges: a) box culverts (BC 1 and BC2), and b) arch pipes (AP1 and AP2).

and American (AREMA 2012) railway standards for this type of bridges recommend that the railway load should be adopted as uniform pressure at the level of the bridge's crown, which is contradictory to the obtained test results.

4 DYNAMIC AMPLIFICATION FACTORS IN SOIL-STEEL BRIDGES

The Dynamic Amplification Factors (DAF) in soil-steel bridges were analyzed on four structures with various spans and soil cover heights (Fig. 10). The impact of the live load was presented in comparison with a situation when the same load is located statically on the bridge, and the factors affecting the DAF were determined. According to Bakht & Pinjarkar (1989), the viable dynamic factors should be determined based on tests under the real load of vehicle traffic taking place at the given structure, i.e. service load. In this case however it is difficult to determine the response of the structure to the static load of each and every passing vehicle. The static value can be obtained by filtering the structure's dynamic response or by estimations, e.g. using FEM. In the case of typical steel or concrete bridges, the situation is advantageous enough that there are estimation methods that allow obtaining the structure's response with an adequate degree of accuracy. In contrast, in the case of soil-steel bridges, the use of the available estimation methods leads to excessive differences in the results in comparison to experimental studies. As of today, there is no fully adequate calculation model for the soil-steel bridges. For this reason, to obtain the static response, it was decided to use the filtration of the dynamic response of the considered bridges. It is necessary to note however that in the case of traditional steel or concrete bridges with the span of up to 15 m, the use of the dynamic response filtration results in errors in the dynamic amplification factors (Paultre et al. 1992). Therefore, an indirect effect of the conducted research was the determination whether the soil-steel bridges feature the danger of encountering errors during the designation of the DAFs using the dynamic response filtration.

It was determined that the dynamic impacts in the bridges should be taken into consideration during their designing, because the values of the DAFs estimated based on the measured displacements were in the range of 1.116÷1.260 and on strains - 1.105÷1.293 (Fig. 11). In bridge AP1 with a soil cover of over 1.0 m, the DAFs amounted to 1.116÷1.175 in relation to the displacements and 1.121÷1.205 in relation to the strains.

The DAFs in these bridges can also be used for assessing their actual carrying capacity – service capacity by estimating the dynamic impacts of the

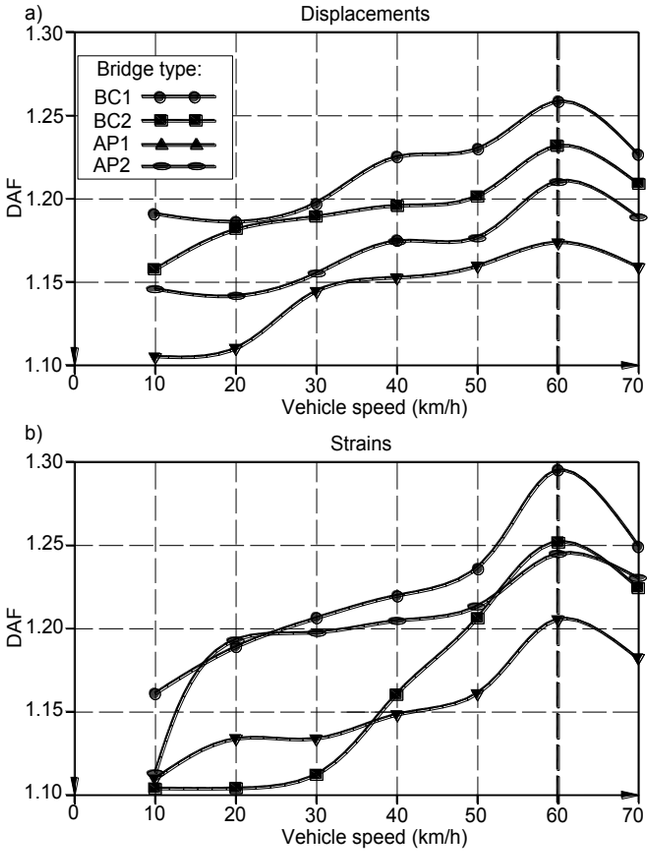


Figure 11. Dynamic amplification factors (DAF) determined based on: a) displacements, and b) strains.

live load. The tests have allowed for the assumption that the main factor affecting the value of the DAFs is the bridge's span. The DAFs increase along with the increase in the span. Other important factors affecting the DAFs include: height of the soil at the bridge's crown – the DAFs decrease along with the increase in the height; backfill height and bridge span ratio – if the ratio increases, the DAFs decrease; bridge crown radius and side radius ratio – if the ratio increases, the DAFs also increase. An increase in vehicle speeds also causes an increase in the DAFs (compare Fig. 11). The maximum DAFs were obtained in the case of the 60 km/h speed. This regarded all of the concerned bridges. At higher speeds, the DAFs had smaller values, which was related to the very short time of impact of the load on the bridge.

In the case of the railway bridge (Beben 2014), the DAFs obtained from the displacement measurements amounted to 1.11÷1.39 and from strains – 1.03÷1.54, which also confirms the necessity to consider them if the soil covers exceed 1.0 m.

In relation to traditional steel and concrete bridges with small and medium theoretical spans, the DAF increase along with the decrease in vehicle weight. For this reason, the results obtained during the passage of light vehicles should not be taken into consideration when determining the values of these factors. This dependency was not found in the case of soil-steel bridges. In the case of low train speeds

$v < 45$ km/h, the DAFs are more dependent on the weight than on the speed, because in the case of higher train speeds $v > 60$ km/h, the impact of the weight is smaller. In these cases, the DAF depend more on the speed, which is related to the higher impact of loads caused by trains moving with high speeds, i.e. emission of higher energy.

5 CONCLUSIONS

The most important effects of the conducted testing of various soil-steel bridges under dynamic loads include:

- demonstrating the necessity to take into consideration the dynamic amplification factor (DAF) when designing soil-steel bridges and culverts, even with the soil cover higher than 1.0 m;
- determining the impact of speed and weight of road and railway vehicles on the behavior of the soil-steel bridges, including determining the degree of deformation and vibration frequencies of steel shell structures;
- demonstrating the possibility of using the bridge dynamic response filtration to obtain the static value for determining the DAF (for bridges with the span of up to 15 m);
- verifying the current designing method (Pettersson & Sundquist method) and American (AASHTO LRFD) and Canadian (CHBDC) standards, regarding soil-steel bridges and culverts, which do not allow to correctly assess their carrying capacity, despite the fact that the obtained values are safe in relation to the structure.

It is necessary to conduct further testing and numerical analysis of soil-steel bridges and culverts, the results of which would include:

- development or modification of the designing guidelines and standards;
- determination of the actual acceptable service capacity of the bridges as a relation of the actual and designed carrying capacities;
- determination of the service strength and durability (life time);
- optimization of the selection of parameters, i.e. soil cover height, corrugated plate thickness, shell span;
- estimation of seismic effects in the soil-steel bridges, including the mining shocks.

REFERENCES

AASHTO. 2002. *Standard Specifications for Highway Bridges*. American Association of State Highway and Transportation Officials. 17th Ed., Washington D.C.

AASHTO LRFD. 2010. *LRFD Bridge Design Specifications*. American Association of State Highway and Transportation Officials. 5th Ed., Washington, D.C.

AREMA. 2012. *Manual for Railway Engineering*, *Chapter 1*. American Railway Engineering and Maintenance-of-Way Association. Washington D.C.

AS 3703.2-1989. 1989. *Long-span corrugated steel structures. Part 2: Design and installation*. Standards Association of Australian. Homebush, NSW.

Bakht, B. & Pinjarkar, S.G. 1989. *Review of dynamic testing of highway bridges*. Structural Research Report SRR-89-01. Ministry of Transportation of Ontario, Downsview, Ontario.

Bayoglu Flener, E. 2009. *Static and dynamic behavior of soil-steel composite bridges obtained by field testing*. Ph.D. thesis, Royal Institute of Technology, Stockholm, Sweden.

Bayoglu Flener, E. & Karoumi, R. 2009. Dynamic testing of a soil-steel composite railway bridge. *Engineering Structures* 31(12): 2803–2811.

Beben, D. 2005. *Interaction of soil and bridge made from corrugated steel plates*. PhD thesis. Faculty of Civil Engineering, Opole University of Technology, Opole, Poland.

Beben, D. 2013a. Field performance of corrugated steel plate road culvert under normal live load conditions. *Journal of Performance of Constructed Facilities* 27(6): 807–817.

Beben, D. 2013b. Dynamic amplification factors of corrugated steel plate culverts. *Engineering Structures* 46(January): 193–204.

Beben, D. 2014. Corrugated steel plate (CSP) culvert response to service train loads. *Journal of Performance of Constructed Facilities* 28(2): 376-390.

Beben, D. & Manko, Z. 2010. Dynamic testing of a soil-steel bridge. *Structural Engineering and Mechanics* 35(3): 301–314.

CEN, EN 1991-2. 2002. *Eurocode 1: Actions on Structures – Part 2: Traffic Loads on Bridges*. European Committee for Standardization, Brussels.

CHBDC. 2006. *Canadian Highway Bridge Design Code*. CAN/CSA-S6-06, Canadian Standards Association International, Mississauga, Ontario.

Fryba, L. 1999. *Vibrations of Solids and Structures under Moving Loads*. London: Thomas Telford House.

Janusz, L. & Madaj, A. 2009. *Engineering Structures from Corrugated Plates. Design and Construction.* Warsaw: Transport and Communication Publishers.

Machelski, Cz. 2008. *Modelling of Soil-Shell Bridge Structures*. Wroclaw: The Lower Silesian Educational Publishers.

McGrath, T.J., Moore, I.D., Selig, E.T., Webb, M.C. & Taleb B. 2002. *Recommended Specifications for Large-Span Culverts*. National Cooperative Highway Research Program, Transportation Research Board, Report 473. Washington D.C.

Paultre, P., Chaallal, O. & Proulx, J. 1992. Bridge dynamics and dynamics amplification factors – a review of analytical and experimental findings. *Canadian Journal of Civil Engineering* 19(2): 260–278.

Pettersson, L. 2007. *Full scale tests and structural evaluation of soil-steel flexible culverts with low height of cover*. Ph.D. thesis, Royal Institute of Technology, Stockholm, Sweden.

Pettersson, L. & Sundquist H. 2014. *Design of Soil-Steel Composite Bridges*. TRITA-BKN Rep. No. 112, Stockholm: Royal Institute of Technology.

PN-85/S-10030. 1985. *Bridge structures. Loads.* Polish Committee of Standardization, Warsaw, Poland.

Sezen, H., Yeau, K.Y. & Fox, P.J. 2008. In-situ load testing of corrugated steel pipe-arch culverts. *Journal of Performance of Constructed Facilities* 22(4): 245–252.

Vaslestad, J. 1990. *Soil structures interaction of buried culverts*. Ph.D. thesis, Norwegian Institute of Technology, Trondheim, Norway.

Maintenance, Safety, Risk, Management and Life-Cycle Performance of Bridges – Powers, Frangopol, Al-Mahaidi & Caprani (Eds)
© 2018 Taylor & Francis Group, London, ISBN 978-1-138-73045-8

Automated Steel Bridge Coating Inspection using Neural Network Trained Image Processing

Ahmed Elbeheri,
PhD Student, Department of Building, Civil & Environmental Engineering, Concordia University, Montréal, Québec, Canada.

Tarek Zayed,
Professor, Department of Building, Civil and Environmental Engineering, Concordia University, Montréal, Québec, Canada H3G 2W1

ABSTRACT
Steel bridges deterioration has been one of the problem in North America for the last years. Steel bridges deterioration mainly attributed to the difficult weather conditions however some solutions have been presented in the last years like weathered steel but there are still a large number of existing bridges that were built in other steel types other than weathered steel. Steel bridges suffer fatigue cracks and Corrosion, which necessitate immediate & regular inspection. Visual inspection is the common and traditional technique for steel bridges inspection but it depends on the inspector experience, conditions and work environment conditions. So many NDE models that have been developed use Non-destructive technologies to overcome these obstacles and be more reliable. Non-destructive techniques such as The Eddy Current Method, The Radiographic Method (RT), Ultra-Sonic Method (UT), Infra-red thermography and Laser technology have been used. Previous researchers had used Digital Image processing for rust detection as an Alternative for visual inspection. Different models had used grey-level and coloured digital image for processing. Coloured image Processing depend on the fact of using the colour of the rust, one of the rust unique characteristics to distinguish it from the different backgrounds. The detection of the rust is an important preliminary stage as it is the first warning for the corrosion and a sign of coating erosion. To decide which is the steel element to be repainted and how urgent it is the percentage of rust should be calculated and it can be always as indication of the corrosion level. In this paper, an image processing approach will be developed to detect corrosion and its severity. Two models were developed 1st to detect rust and 2nd to detect rust percentage. Machine learning was applied through neural network as it will be used to be trained to detect rust and calculate the percentage. The application of the neural network will ease the process of processing the inspection data. One of the great advantages of neural network that it can adapt to any new data it even helps as more data mean more training and better results.

Keywords: steel bridge; bridge inspection; steel corrosion; image processing; neural network.

1 INTRODUCTION

In North America, infrastructure condition is reported by a grade or percentage, like schooling system, which known as infrastructure report cards. In the United States, the American Society of Civil Engineers (ASCE) report card shows an overall rating for America's infrastructure is poor. Furthermore, the cost to improve infrastructures including but not limited to solid waste, drinking water, wastewater, roads, bridges, and rail is estimated as $3,635 billion *(1)*.

According to Infrastructure Canada Rating *(2)* the four asset categories show that a significant amount of municipal infrastructure ranks between fair and very poor, on average about 35%. The replacement cost of these assets alone totals $388 billion, nationally. Municipal roads require urgent attention. More than one third of the roads & bridges network fall below a rating of "good".

Historical figures indicate that 'transportation' sector forms the largest portion of the Canadian infrastructure industry value. Roads and bridges segments have the largest portion within the transport infrastructure representing the highest worth share according to the estimates by the Business Monitors International report on Canadian infrastructure *(3)*. However, large parts of these infrastructures were constructed during the 1960's and 1970's. Accordingly, they are facing an increasingly deteriorating problem *(4)*. Statistics Canada reports evaluate condition of infrastructure in terms of useful life expended by the infrastructure. ASCE report card also graded bridges' conditions as "C+" which refers to mediocre that requires attention *(1, 5)*. The growing problem of the bridges deterioration imposes challenges on ministries of transportation to maintain and preserve them. In 2011-2012 Quebec province alone spent more than $800 million for structural improvements, mainly for bridges *(6)*.

2 BACKGROUND

2.1 *Defects*

2.1.1 *Cracks*

Ductile failure, brittle fracture, and buckling/instability usually occur under static loading conditions wherein the applied load exceeds a critical load. In contrast, most structures are subjected to repeating loads of varying magnitude, which are most often below yield strength and design stress levels. Such repeated or fatigue loading occurs in bridges, buildings, etc. Fatigue failure is characterized by the initiation and growth of a cracks due to the repeated loading of the structure, which generates microscopic inelastic damage at regions of local stress concentration. If sufficient inelastic damage accumulates then a small crack develops, which then propagates through the structure. Failure occurs when the crack attains a critical size. Fortunately, fatigue is a progressive damage mechanism and is often identified before significant structural damage arises *(7)*.

2.1.2 Corrosion

Corrosion is one of the most important causes of deterioration of steel bridges. In the United States 40% of the bridges are built of steel. In some states, such as Michigan, the number exceeds 60% *(8)*. There is a need for rational criteria which can be used to determine the actual strength and remaining life of existing structures. The primary cause of corrosion is the accumulation of water and salt (marine environment or deicing media) on bridge steel. The source of water and salt is either from deck leakage or from the accumulation of road spray and condensation. The source of the moisture often determines the pattern of corrosion on a bridge. The rate of corrosion will depend upon the contaminants in the moisture and the ambient temperature.

2.1.3 *Creep*

(7) Described Creep as the damage accumulated from inelastic deformation of plain carbon and alloy steel under constant load even if the service stress is substantially below the yield strength because of thermal activation at elevated temperatures.

2.3 *Inspection techniques*

The traditional method Visual inspection proved to has some problem as inspector condition, inspection condition and non-applicable for subsurface defects. Image processing has great results for surface defects and overcome the condition for inspection and inspector mentioned in visual inspection but steel cannot detect subsurface defects. Eddy current technique used for detecting cracks without removing the coating but it is not efficient in detecting the surface defects. The radiographic method is able to detect cracks but even the process and the equipment is too complicated I.e. X-rays or it uses dangerous type or radiation i.e. gamma rays. Ultra-sonic method mainly used in thickness measurement to assess the corrosion loss in steel section either used to detecting cracks. It still questionable for the small size cracks However some advanced UT Technology such as (Phase Array Automatic Ultrasonic Testing (PA-AUT), Automated Ultrasonic Testing (AUT) etc...) have a promising Results regarding the accuracy. The other challenge that it needs a high skilled crew to guarantee the accuracy of the inspection especially in the advanced UT Technology. The IR thermography application shows the ability to detect different types of crack in steel bridges but not the surface defects. 3D laser technology was capable to detect any surface defects or any change in the structure from the original state but still it needs more application. In this paper Image processing is used to detect corrosion and the percentage of rust among the bridge steel elements. One of the advanced infrastructure inspection methods is the application of digital image processing. Digital image processing methods have been developed for steel bridge coating inspections for the past few years. The rust percentages on steel bridge coating surfaces can be reliably computed through the use of digital image processing methods. *(9)* developed a method works effectively with blue-paint-coated steel bridge images. However, this method didn't prove to work on other coating colors or in any other irregular conditions, such as coating images with background noise or different illumination patterns.

Shen et al. *(10)* developed an automated steel bridge coating rust defect recognition method based on color and texture feature. The methodology consists of two models, Fourier- transform-based steel bridge coating defect detection approach (FT-DEDA) and rust-colour-spectrum-based rust defect recognition method (RUDERM). The FT-DEDA approach used to detect any changes on the collected images. The used tools detect the rust and sharp edges but cannot discriminate rust so the RUDERM approach was used. The RUDERM approach used the color space to define the rust spots and discriminate it

from the background and other defects. With the comparison of Shen's model and Lee work Shen shows better results especially with the non -uniform illuminated images which simulate the some of the environmental condition as it was one of the Lee's drawback. The classification of the images gives defective and non-defective images and did not define the percentage of defect in each image which does not give an accurate result for the whole steel bridge coating.

2.3 *Machine learning*

Machine learning Machine learning teaches computers to do what comes naturally to humans and animals, learn from experience *(11)*. Machine learning algorithms find patterns in data that generate insight and help you make better decisions and predictions. Machine learning has become important for in areas like: Computational finance, for credit scoring; Image processing and computer vision, for face recognition, Voice recognition, and object detection; Computational biology, for tumor detection, drug discovery; Automotive, aerospace, and manufacturing, for predictive maintenance • Natural language processing*(11)*. According to the Figure 1 below, machine learning divide to two main categories, a) unsupervised b) supervised learning. Supervised learning, which trains a model on known input and output data so that it can predict future outputs, and unsupervised learning, which finds hidden patterns in input data.

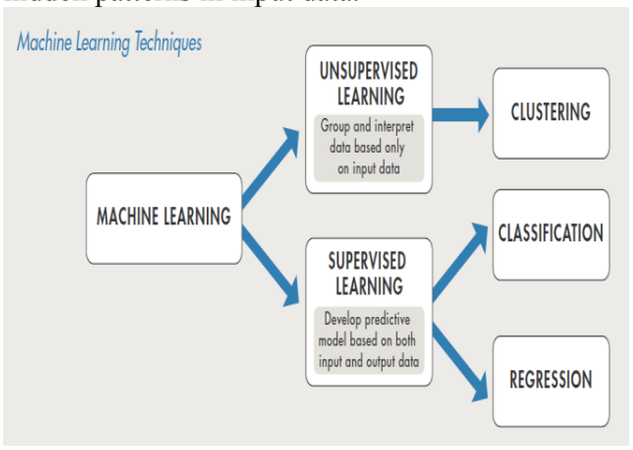


Figure 1. Machine learning types *(11)*

3 METHODOLOGY

The methodology consists of two models, 1) rust defect detection model which developed to detect the existence of corrosion, 2) rust severity detection model which used to determine the percentage of rust in bridge steel elements.

3.1 *Rust defect detection model*

The rust defect detection model steps are illustrated in fig 2. Step 1: data acquisition, in this step the images to be tested for detection will be the images of the steel bridge elements. In this research, these images obtained through literature review and from inspection reports from other research projects and municipality reports. Step 2: a standard size should be selected and unified for all the tested image to facilitate the next steps and for the training process as the neural networks needs the images to be the same size, Step 3: data reduction which has been done throw resizing the images. Step 4: image enhancement which has been done by histogram equalization process. Step 5: Data Compression, in this step Discrete Cosine Transformation (DCT) has been used as it proved its validity through different application on voice recognition and face detection. Step 6: training data, where we use neural Network algorism to train the system through the obtained images. At last the system detect the defective images and proceed to the second model.

The input of the NN is defined as the processed images samples for defective and not defective steel elements, while the output is the desired trained data that will help to discriminate between defective and non-defective images.

Therefore, NNs are required to train the data to the desired acceptable level by the user through nonlinear activation function, TANSIG. The nonlinear function has an 'S' shaped curve that limits the node's output. The network consists of two layers with a hidden layer connected to the output layer. Both layers have a non-linear transfer function to work with a feed-forward backpropagation training algorithm as shown in Figure 3. Using multi-layer neural network always combined with both complexity and efficiency and as complexity seems to be a drawback but in this case, it was not as the sample wasn't in a large population.

3.2 *Rust severity detection model*

The rust defect detection model steps are illustrated in fig 4. In this model, we add a step called image segmentation as more accuracy needed to distinguish rust from the image Step 1: data acquisition, the defective images produced from the first model will be the input in this stage. Step 2: a standard size should be selected and unified for all the tested image to facilitate the next steps and for the training process as the neural networks needs the images to be the same size, Step 3: data reduction which has been done throw resizing the images and converting the images to Grayscale. Step 4: image enhancement which has been done through histogram equalization to avoid any contrast concentration in some areas of the image. Step 5: image segmentation, in this step edge detection was used along with image binarization. Step 6: training data where we use neural Network algorism to train the system through the obtained images. At last the system was trained to calculate the percentage of rust.

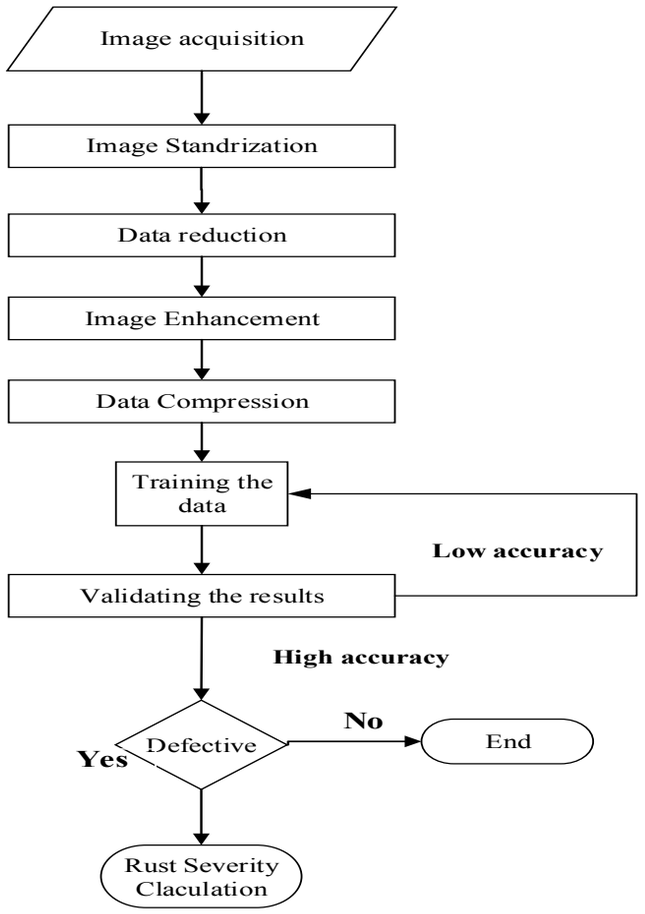


Figure 2. Rust defect detection model flow chart

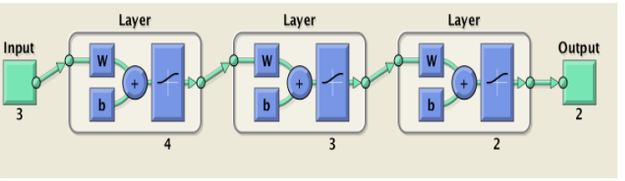


Figure 3. Multi-layer neural network example

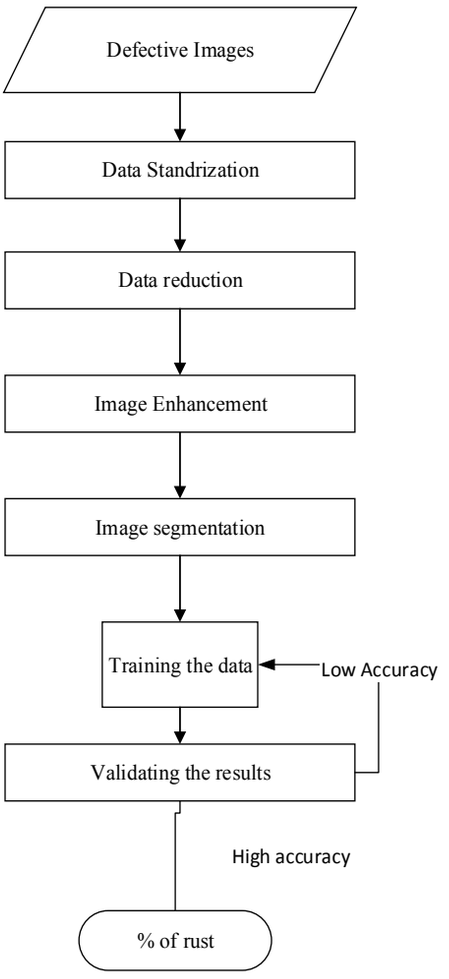


Figure 4. Rust severity detection model flow chart

4 MODEL IMPLEMENTATION & RESULTS

A set of twenty-eight images were collected from previous research consisting of twenty-two defective images and six non-defective images. First the data will be implemented in the first model for detection. All the images went through the image processing steps to be ready for the training process with the neural network. The training mechanism was

designed as follow: two types of data sets was developed, defective and non-defective. Two defective data set were entered together as data input and target to test the network. Then the same process was done for the non-defective.

After the network was trained, as validation three trial processes were planned, the first trial was entry of two defective data sets together, the correlation between the images in each set for the other set was measured to test if the network is working well or biased.

In this trial it was shown in table 1 that the correlation was maximum which is good as the two set was the same type as defective. The second trial was between 2 non-defective sets and as expected maximum correlation was obtained, the results shown in table 2. Finally, the main step to test with a mix of defective and non-defective images. It was found that the images of each set have the minimum correlation toward the opposite set as shown in table 3.

Table 1. Correlation results for the first trial

Image	Correlation to 1st Set	Correlation to 2nd set
1	0.499	0.500
2	0.500	0.500
3	0.500	0.500
4	0.499	0.500
5	0.499	0.500
6	0.499	0.500
7	0.500	0.500
8	0.500	0.500
9	0.499	0.500
10	0.499	0.500
11	0.499	0.500
12	0.499	0.500

Table 2. Correlation results for the second trial

Image	Correlation to 1st Set	Correlation to 2nd set
1	0.500	0.500
2	0.500	0.500
3	0.500	0.499
4	0.500	0.500
5	0.500	0.500
6	0.499	0.500
7	0.500	0.500
8	0.500	0.500
9	0.500	0.500
10	0.500	0.500
11	0.500	0.500
12	0.500	0.500

Table 3. Correlation results for the third trial

Image	Correlation to 1st Set	Correlation to 2nd set
1	0.905	0.008
2	0.850	0.200
3	0.939	0.097
4	0.980	0.046
5	0.905	0.076
6	0.096	0.022
7	0.183	0.853
8	0.067	0.930
9	0.051	0.951
10	0.028	0.910
11	0.040	0.952
12	0.120	0.872

After that the image was entered with the corresponding percentage of rust to train the neural network system to use them for learning and testing the system. The system proved its capability to predict the percentage of rust.



Figure 5. Original image



Figure 6. Grey level image

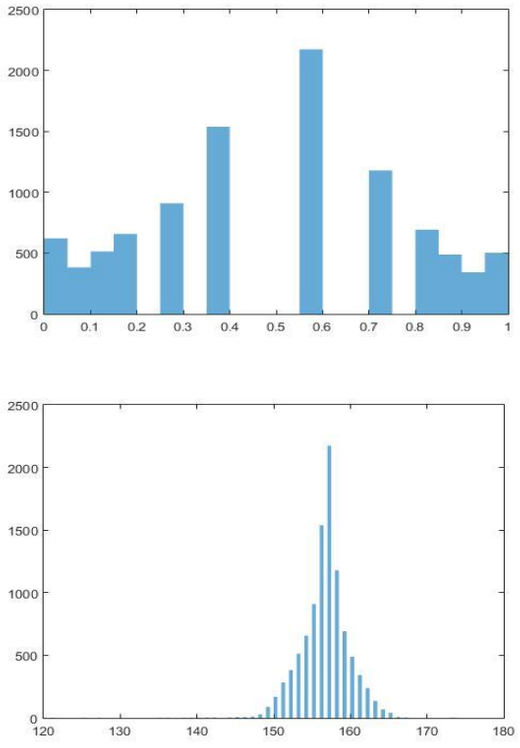


Figure 7. Image before (Top) and after (Bottom) histogram equalization



Figure 8. Image after black and white conversion

Table 4. Rust severity detection model results

Image	Rust %	Notes
1	0.05	
2	0.05	The example image used in model implementation part
3	99.95	High contrast back ground Error(Excluded)
4	10.67	
5	16.14	
6	8.82	
7	5.29	
8	12.22	
9	20.16	
10	99.95	High contrast back ground Error(Excluded)
11	39.95	
12	0.05	
13	0.04	
14	0.05	
15	38.02	
16	94.29	High contrast back ground Error(Excluded)
17	0.19	
18	0	
19	36.99	Used for Validation
20	18.73	Used for Validation
21	0.22	Used for Validation
22	80.44	Used for Validation

5 CONCLUSIONS

The proposed model approved its capabilities in rust detection and Percentage calculation. Neural network shows potential as a machine learning tool in construction application especially in infrastructure management. Bothe models needs improvements, the Rust detection model performance increases as we add more training data and include different coating sample in the training process. The model can be

further used in crack detection as well and it will be illustrated in further research. The model is adaptive which means it can be trained for different coating type even more, it can be trained for future different corrosion patterns.

The second model needs some improvement in the image processing stage. Advanced techniques should be used in image enhancement and image segmentation to solve high contrast background problem. Overall the system performance is acceptable and can be used for coating inspection.

6 REFERENCES

References

1. ASCE. *Report Card for America's Infrastructure.* 2015, American Society of Civil Engineers, http://www.infrastructurereportcard.org/, 2013.

2. Canadian infrastructure report card. *Canadian Infrastructure Report Card.* Canadian Society for Civil Engineering, 2016.

3. BMI. *Canada Infrastructure Report Q3.* Business Monitor International, 2013.

4. Dori, G., M. Wild, A. Borrmann, and O. Fischer. *A System Model Based Approach for Lifecycle Monitoring of Bridges.* Technische Universität München, Munich, Germany, 2011.

5. ASCE. *Report Card for America's Infrastructure.* American Society of Civil Engineers, http://www.infrastructurereportcard.org/, 2017.

6. MTQ. *Bilan De L'État Des Structures Du Réseau Routier Supérieur Québécois; Rapport Annuel De Gestion.* MTQ, Quebec, Canada, 2012.

7. Vecchio, R. S., and I. LPI. Condition Assessment of Steel Structures. In *Structures Congress 2006@ sStructural Engineering and Public Safety*, ASCE, 2006, pp. 1-11.

8. Kayser, J. R., and A. S. Nowak. Capacity Loss due to Corrosion in Steel-Girder Bridges. *Journal of Structural Engineering*, Vol. 115, No. 6, 1989, pp. 1525-1537.

9. Lee, S. Digital Image Processing Methods for Bridge Coating Management and their Limitations. *Journal of Civil Engineering and Architecture*, Vol. 5, No. 1, 2011.

10. Shen, H., P. Chen, and L. Chang. Automated Steel Bridge Coating Rust Defect Recognition Method Based on Color and Texture Feature. *Automation in Construction*, Vol. 31, 2013, pp. 338-356.

11. Math works & Simulink. Machine Learning-Section 3. , 2016, pp. 1.

Maintenance, Safety, Risk, Management and Life-Cycle Performance of Bridges – Powers, Frangopol, Al-Mahaidi & Caprani (Eds)
© 2018 Taylor & Francis Group, London, ISBN 978-1-138-73045-8

Inspection, Structural Health Monitoring and Maintenance of a Cable-Stayed Bridge in Vienna, Austria

P. Furtner
VCE Vienna Consulting Engineers ZT GmbH, Vienna, Austria

ABSTRACT: Donaustadtbrücke is a cable-stayed bridge over the Danube in Vienna, Austria. The bridge was erected as a road bridge for public buses in 1994. The inspection and maintenance concept included periodic visual inspection as well as periodic structural health monitoring activities like the measurement of the stay cable forces and of the dynamic characteristic of the bridge. In 2013 and 2014 remarkable stay cable vibrations were observed at the longest stays, which led to interruptions of the traffic of the bridge. Based on the measurement of the dynamic characteristic of the stays and the bridge deck, stay cable vibration measures were developed and installed. Additionally, a permanent monitoring system was installed. In 2015 damage was detected at the hinged columns at the south abutment. Measurements were carried out to assess the reasons for this damage. Furthermore a principal inspection of the bridge was done in 2015, followed by maintenance works.

1 INTRODUCTION

Donaustadtbrücke is a steel cable-stayed bridge built between 1995 and 1997 and connects the 2nd and 22nd district of Vienna. The bridge was opened to traffic in March 1997 and served as by-pass bridge during the lifting of the Prater bridge. In the period between 1998 and 2006 the bridge was only available for public bus traffic. After the extension of the underground railway line U2 from the station Stadion to the 22nd district the bridge has been used for underground railway operation since October 2010. In the course of reconstruction works for underground railway utilization the number of stay cables was doubled from 20 to 40 and the load at the existing stay cables was increased. During the works the forces in the stay cables were monitored.

In 2014 and 2015 considerable cable vibrations were observed at single cables. Immediately after each of the vibration events inspections, measurements and analyses were carried out in order to guarantee safe operation of the bridge. The measurements and analyses showed that the cable vibrations occurred under special weather conditions (rain-wind induced vibrations). The installation of so-called connection wires, which eliminate cable vibrations, was planned and realized as countermeasure.

In addition a permanent measuring system, which both monitors the vibrations of the bridge deck as well as the stay cables prone to vibration and records the weather conditions on site, was installed. Any cable vibrations are also recorded by means of a video system. All data are accessible via a web-user-interface.

In summer 2015 a main inspection of the bridge was performed. In the course of this inspection the corrosion protection was checked at the whole structure and defects were repaired. Selected stay cables were inspected with regard to wire failures and corrosion protection.

Furthermore damage at the southern hinged columns was identified. In addition to the comprehensive measurements calculations were carried out in order to detect the cause of the damage.

This contribution comprises all inspections, the results and conclusions as well as maintenance and repair measures.



Figure 1. Donaustadtbrücke

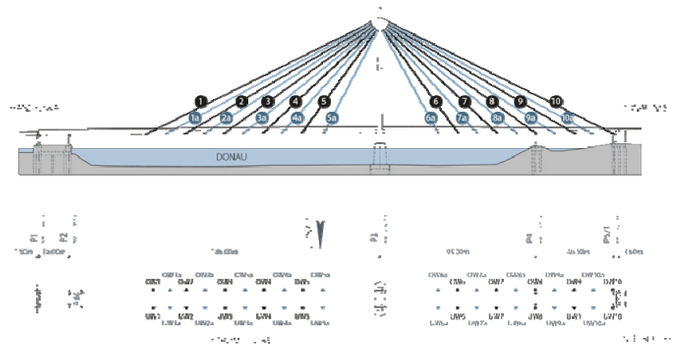


Figure 2. Stay Cable Layout

2 STAY CABLE MEASUREMENTS

Donaustadtbrücke was reconstructed for utilization by underground railway from 2008 to 2009. In this process the number of stay cables was doubled from 20 to 40 and the forces in the existing cables were changed. The force measurements at all stay cables were carried out in 2009 for the first time, follow-up measurements are performed every three years.

2.1 *Implementation of Measurements*

The measurements were carried out with the BRIMOS® Recorder 1000 developed by VCE. The external three-dimensional acceleration sensor of the recorder was fixed approximately 1.5 m above the deck at the cables. The measurements were performed separately, cable by cable. Two measurement files with 165 seconds and a scanning rate of 5 milli-seconds each were recorded per cable (this corre-sponds to 200 Hz). The measurement data were up-loaded on site and checked for plausibility.



Figure 3. Stay cable measurement

2.2 *Evaluation*

The evaluation was done with a software specially developed by VCE for cable measurements. The software has been used since January 2004 and offers the following advantages:

- Automatic offset adjustment and FFT (Fast-Fourier-Transformation) for the calculation of frequency spectra.
- Automatic peak-picking for the determination of the first 10 eigenfrequencies from the frequency spectrum; thus human failure is minimized and the accuracy of the evaluation is increased.
- Determination of f1 (1st eigenfrequency of the "ide-al" cable without bending stiffness) and the related cable stiffness ξ and the damping from the first 10 eigenfrequencies by means of a Gauss-Newton algorithm.
- Averaging of two measurement files per cable.

The cable eigenfrequencies are a function of the effective cable force N, the length l, the mass m of the cable per metre, the cable stiffness and the boundary conditions.

$$f_k = \frac{k}{2l} \cdot \sqrt{\frac{N}{m}} \cdot (1 + \frac{2}{\xi} + (4 + \frac{k^2 \pi^2}{2}) \cdot \frac{1}{\xi^2}) \qquad (1)$$

where f_k = eigenfrequency of the order k; N = cable force; m = cable mass per metre length; l = free length of the cable (length between the dampers and the clamping points respectively); and ξ = related bending stiffness.

2.3 *Results*

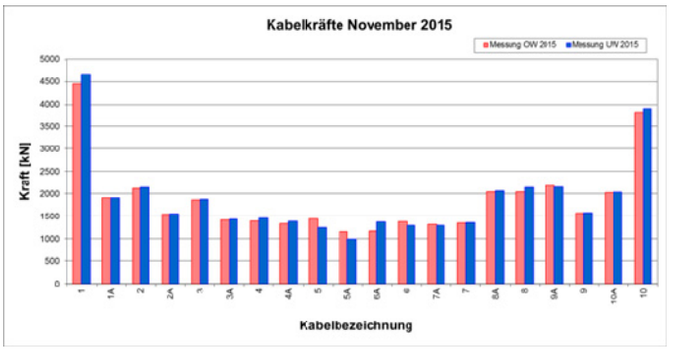


Figure 4. Stay cable forces determined

3 STAY CABLE VIBRATIONS

3.1 *Cable Vibrations Observed*

On 16 May 2014 and 23 October 2014 strong cable vibrations occurred at the stay cables of Donaustadtbrücke.

The stay cables concerned were those with the designations OW1 to OW2 and UW1 to UW2. Especially the stay cables OW1a, OW2, UW1a and UW2 (corresponding to the 2nd and 3rd stay cable of the upstream structure each) showed very intense vibrations. The cable vibrations observed were probably due to the current weather conditions (rain, wind force, wind direction).

In the course of the measurements at the stay cables vibration measurements at the bridge deck were performed to identify any resonance effects between the stay cables and the bridge deck. If the eigenfrequencies of a stay cable are very close to those of the bridge deck, mutual vibration excitation can occur. This phenomenon is called "parametric vibration excitation".

The vibration measurements on the deck are only measured with one sensor and are therefore afflicted with certain uncertainties. The following vertical eigenfrequencies were identified for the bridge deck and compared to the cable eigenfrequencies of the stay cables OW1a and OW2:

Table 1. Comparison of eigenfrequencies

Bridge deck [Hz]	Stay cable OW1a [Hz]	Stay cable OW2 [Hz]
0.60	**0.60**	
0.76		0.68
1.30	1.14	**1.31**
1.71	**1.71**	
1.89		
1.99	2.29	**1.96**
2.62		**2.63**
2.71		

The target is a minimum frequency distance of 10% between deck eigenfrequencies and cable eigenfrequencies to avoid resonances and parametric excitation. As illustrated in Table 3, this requirement is not met in case of Donaustadtbrücke.

3.2 *Assessment of Cable Vibrations*

The cable vibrations at Donaustadtbrücke observed on 16 May and 23 October are most probably due to the weather conditions prevailing at that period of time:

- Wind direction normal to the bridge axis
- Extensively constant wind speed of approx. 15-18 m/s
- Light rain

These weather conditions lead to the wind-rain-induced vibrations observed. In case of slightly lower or higher wind speeds even the neighbouring stay cables OW1 and UW1 as well as OW2a and UW2a can start to vibrate.

The vibration excitation of the stay cables is favoured and intensified by the phenomenon of "parametric vibration excitation", as the eigenfrequencies of the stay cables concerned correspond to the eigenfrequencies of the bridge deck.

3.3 *Installation of Connection Wires*

Due to the stay cable vibrations observed and the measurements and analyses it was decided to connect the 4 longest stay cables each on both bridge sides to so-called connection wires.

The strong cable vibrations observed concerned above all the 2nd eigenfrequency with a node in the centre of the cable. In addition vibrations in the 3rd eigenfrequency with two nodes were noticed.

Observation of similar cases at other cable-stayed bridges showed that perceptible cable vibrations typically occur in the eigenfrequencies 1 – 3. Therefore they were taken as a basis for subsequent assessment.

Connection wires are most effective in the maxima of the antinodes of the respective oscillation mode. If the connection wires are installed at the vibration nodes, there is a minimum effect. Naturally the antinodes of the individual oscillation modes are situated at different locations. The optimum mounting location shall be selected in such a way that all the basic oscillation modes for the assessment are damped.

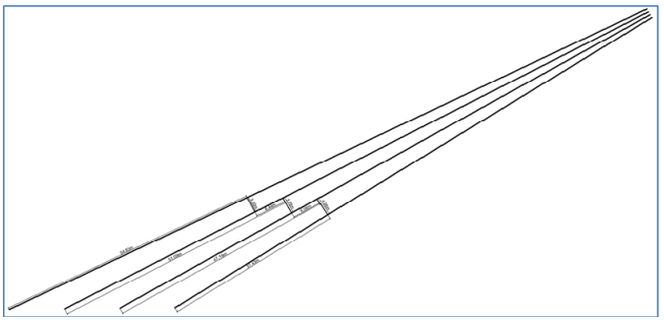


Figure 5. Positions of connection wires at stay cables

The following figure shows the layout of the connection wires and the fastening clamps.

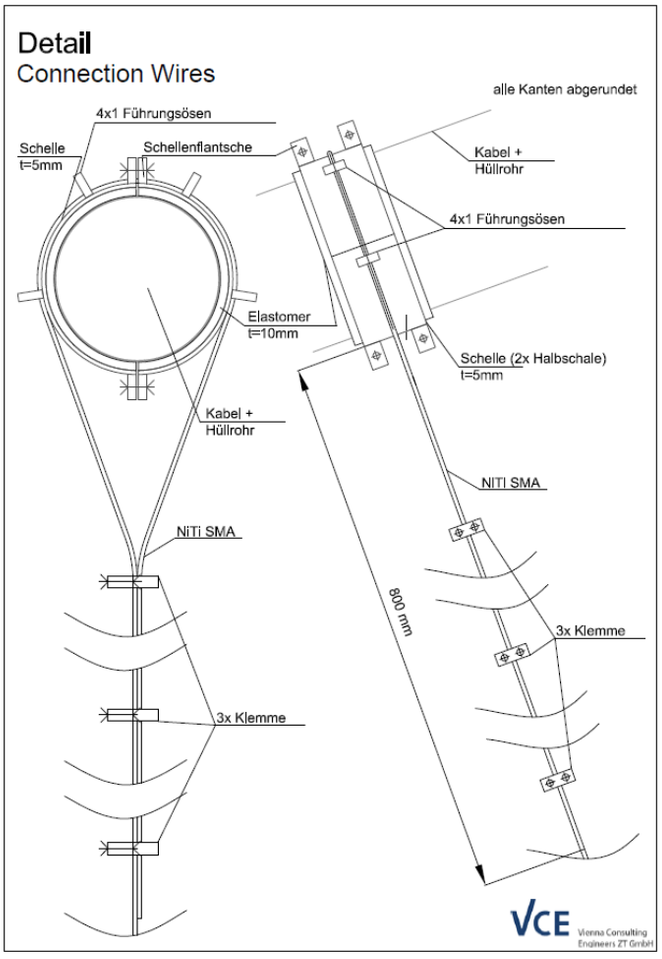


Figure 6. Design of connection wires

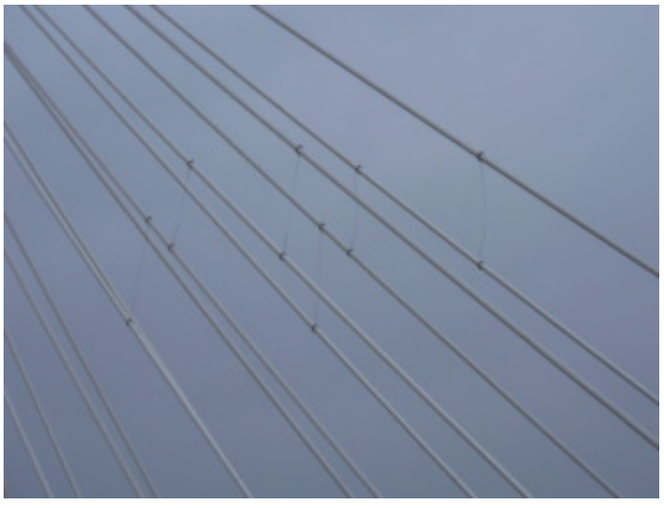


Figure 7. Installed connection wires

4 PERMANENT MONITORING

Furthermore the installation of a permanent monitoring system is recommended for the supervision of the vibration behaviour of the stay cables concerned and for the check of the success of the measures taken.

The monitoring system is assembled in the following way:

- 1 wind sensor ultrasound 3D, fixed approx. 3-5 metres above the deck at a measuring pole;
- 1 rain sensor, also mounted at the measuring pole;
- 1 3D-acceleration sensor, type Kistler, mounted at the stay cable OW2, fixed approx. 1-2 metres above the bridge deck
- 1 3D-acceleration sensor, type Kinemetrics, at the bridge deck close to the lower cable anchor of stay cable OW2;
- 1 video camera suitable for night operation with automatic recording in case of exceedance of vibration limits to be defined. The camera is placed in such a way that the stay cables can be observed and the vibration events can be recorded. The camera can be installed at the station building;
- 2 strain gauges at the upstream hinged column
- Measuring station (monitoring master station): The components (A/D converter, measurement computer, modem) are located in a measuring cabinet, which can be installed in the station building. All measurement data are saved on site;
- Double screened connecting cables between sensors and measurement station;
- Data remote transmission via mobile service and internet to the monitoring server in the VCE office. There the measurement data are archived in a database on the server;
- Visualization of the measurement data and results in the monitoring-web-user-interface: the latter is accessible via the internet with user name and password;
- Alarm thresholds are determined for all sensors;
- Start of video recording in case of exceeded thresholds;
- Alarm via automatically generated e-mails in case of exceeded thresholds.

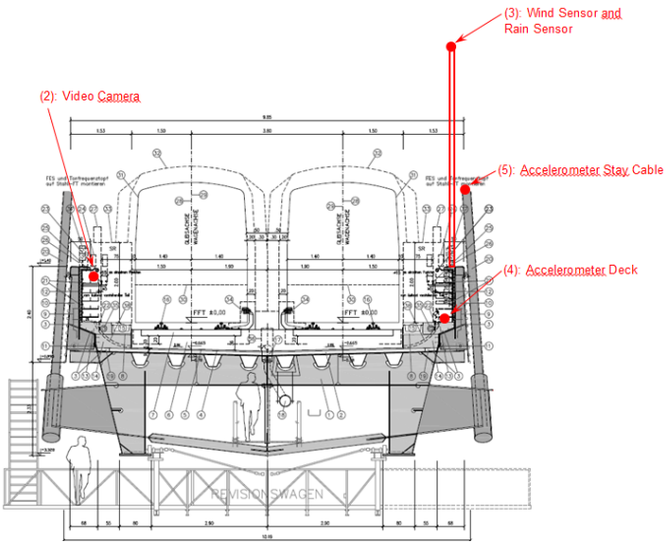


Figure 8. System sketch in cross section

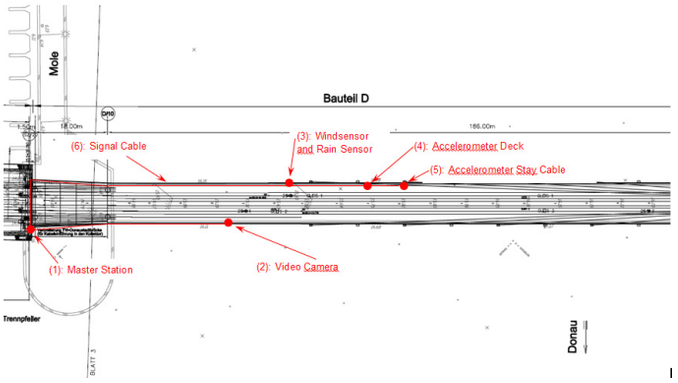


Figure 9. System sketch in plan view

5 MAIN INSPECTION

By order of the bridge owner, Wiener Linien GmbH & Co KG (Vienna's public transport operator), Donaustadtbrücke on the underground railway line U2 was subjected to a main inspection in July and August 2015.

Before the main inspection the bridge was cleaned by high-pressure water vapour with cleaning agents (Figure 1) as well as manually with fleece.

The inspection and maintenance works were carried out by means of movable scaffold networks. It was necessary to climb down from the pylon head by rope during the inspection of the pylon. The abutment walls and piers were examined from the ground and the cherry picker.

The inspection was predominantly executed within reach, not immediately accessible areas were subjected to a visual examination.

The following inspections were carried out in detail:

- Inspection within reach of all the surfaces of the soffit of the steel structure and the pylon as well as the abutment walls and columns, visual inspection of the noise barriers
- Coat thickness measurements were carried out at approx. 400 sites distributed over the whole structure.
- Additionally, weld inspections were performed on the basis of a previously prepared test concept. In this process sites which are especially susceptible to fatigue on the one hand and which are particularly important for the load-bearing capacity on the other hand as well as randomly chosen welded joints were selected.
- Bridge drainage was thoroughly rinsed and purged by means of high-pressure cleaners.
- On 3 Sept. 2015 the anchor cap was removed at two cable anchors and the cables were examined for wire failures and corrosion.
- In the time with no operation the trough area was visually inspected by means of test openings.

6 HINGED COLUMNS

6.1 *Failure Mode*

At the southern abutment the safety devices of the upper fastening bolts of the hinged columns were damaged. The screws of the safety discs were broken and the bolts had slightly slipped out. The bolts were temporarily secured with screwed steel plates. One bolt could be driven in for some millimetres.

Potential damage triggers are bridge vibrations, cable vibrations, temperature load cases, wind load cases, variable loads on the hinged column by crossing of underground railway trains.

Alternating loads of tension/pressure by train passages were assumed as most probable cause. Compressive load can lead to a slight, cyclic deflection of the hinged column, which exerts longitudinal forces on the bolt. This can result in the observed displacement of the bolts and subsequently lead to fatigue failure of the screws by cyclic load effects.



Figure 10. Hinged columns on southern bank

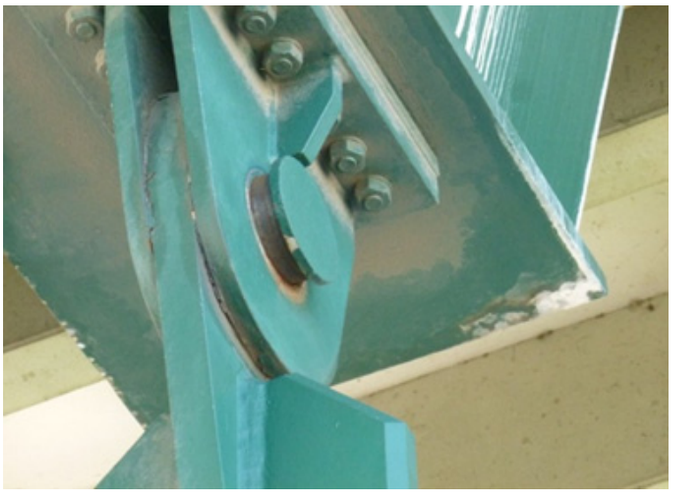


Figure 11. Damaged bolt

6.2 *Measurement Programme*

The following measurement concept was developed for the simultaneous measurement of both columns for the determination of the actual behaviour of the bridge deck, the two hinged columns and the bolts:

- Measurement of the horizontal and vertical relative movements of the steel deck to the abutment in case of train passages by means of high-precision displacement transducers (1 x 3 displacement transducers – only one hinged column axis)
- Measurement of the stress cycle in the hinged columns in case of train passage by means of strain gauges (2 x 2 strain gauges – both hinged columns)
- Measurement of the relative movement between hinged column and mounting straps by means of high-precision displacement transducers (2 x 1 displacement transducers – both hinged columns)
- Measurement of the horizontal deflections of the hinged column under compression load by means of train passage. For this purpose the deflection is measured at approx. half the height of the column in two directions by means of displacement transducers (2 x 2 displacement transducers – both hinged columns)
- Accompanying temperature measurement (1x)

6.3 *Results of the Analysis*

The measurements and analyses led to the following results:

1. The upstream hinged column is under tension in case of the unstressed bridge (no trains on the bridge).
2. During train passage, in case of train position in the main span of Donaustadtbrücke, tensile stress increases in the upstream hinged column.
3. In case of train position above the end of the structure and thus above the hinged column the upstream hinged column is under pressure.
4. The downstream hinged column is under pressure in case of the unstressed bridge (no trains on the bridge).
5. The compressive stresses in the downstream hinged column increase in case of train position above the end of the structure and thus above the hinged column.
6. During train passage, in case of train position in the main span of Donaustadtbrücke, the downstream hinged column is under tension.
7. The described load cycles can be clearly identified by means of the relative movements between bridge deck and hinged column (bolt tolerance) for both hinged columns. The vertical movement amounts up to approx. 2.5 mm at the downstream hinged column.
8. Deflections of the hinged column by compressive stresses were not measured.
9. The bridge deck performs slight movements into all directions in case of every train passage.

The measuring results of this analysis can be used for the calibration of the calculation model in the scope of verification.

7 SUMMARY

In the course of the maintenance works at the 20-year-old Donaustadtbrücke a main inspection as well as measurements at the stay cables, the bridge deck and at the hinged columns were carried out in 2015.

Cable vibrations observed at the longest upstream stay cables required the installation of connection wires.

Due to damage at the bolt safety devices of the hinged columns at the southern abutment a detailed measurement and analysis of the hinged columns was performed. The results will be incorporated in the verification of the structure.

Furthermore, the bridge was equipped with a monitoring system to enable permanent measurements at the longest stay cables and hinged columns.

The future maintenance programme provides follow-up measurements of the stay cable forces every three years in addition to the main inspections at an interval of five years.

REFERENCES

De Sá Caetano, E. 2007. Cable Vibrations in Cable-Stayed Bridges. Zürich Switzerland: IABSE-AIPC-IVBH.

Recommendations of French Interministerial Commission on Prestressing 2002. Cable Stays. Bagneux Cedex France: SETRA.

Wenzel, H. 2009. Health Monitoring of Bridges. Chichester England: Wiley and Sons Ltd.

Wenzel, H. & Pichler, D. 2005. Ambient Vibration Monitoring. Chichester England: Wiley and Sons Ltd.

Wenzel, H et al. 2013. IRIS - Industrial Safety and Life Cycle Engineering. Vienna Austria: VCE Vienna Consulting Engineers ZT GmbH.

Maintenance, Safety, Risk, Management and Life-Cycle Performance of Bridges – Powers, Frangopol, Al-Mahaidi & Caprani (Eds)
© 2018 Taylor & Francis Group, London, ISBN 978-1-138-73045-8

Determination of stay cable forces using highly mobile vibration measurement devices

G. Morgenthal, S. Rau, J. Taraben, T. Abbas & N. Hallermann
Chair of Modelling and Simulation of Structures, Institute of Structural Engineering, Bauhaus University Weimar, Weimar, Germany

ABSTRACT: Vibration measurements are an established method for determining the tension force of stay cables. The approach utilizes linearization of the vibration characteristics of stay cables that are structural members exhibiting significant geometrical nonlinearities. Based on measured natural frequencies the cable force can thus be identified. This paper presents measurements that have employed mobile measurement equipment, namely MEMS-based (microelectromechanical systems) acceleration sensors connected to battery-operated microcomputers as well as those integrated in smartphones, and studies the accuracy for tension force measurements. Software written for streamlined measurement processes is linked with nonlinear analyses for predicting the frequency-force relationship. In contrast to traditional monitoring systems that are composed of several individual hardware components, smartphones and tablets can integrate the recording, storage, processing, transfer and visualization of data within one single device. The proposed methodology and implementation is validated on cables of Queensferry Crossing during construction. The technology has shown potential to allow simple yet accurate tension force measurements.

1 INTRODUCTION

Cable-stayed bridges have proven themselves as structurally efficient and economically favorable system for a large range of bridge spans that today reach beyond 1000 m (Svensson 2012). The stay cables as tension elements are a main structural component for which different systems have been developed such as parallel wire, locked-coil and multi-strand layouts. Whilst these are all based on hi gh-strength steel wires, they differ in their composition and consequently the resulting weight and effective bending stiffness in relation to axial stiffness.

The distribution of the tension forces between individual stay cables is of significant importance for the bridge girder alignment and the stress distribution in all bridge components. During the construction of cable-stayed bridges, the cable forces are measured to ensure the bridge meets the design assumptions. In the in-service condition of the bridge tension measurements may also be required due to changes occurring in the structure over time. Different methods to evaluate the tension of a bridge cable are available. They can be broadly classified into two main categories:

- Direct measurements: Lift-off method, pre-installed load cells, strain gauges,
- Indirect measurements: vibration-based methods, other methods.

During construction, direct measurements are often used as these employ hydraulic jacks, which are used for the stressing of cables as part of the construction process. On a bridge in-service a lift-off test is particularly expensive and time-consuming and repeated tests may lead to damage in the sensitive wedge region.

As alternative, indirect measurements such as the vibration-based methods can be used to estimate the cable forces by exploiting the nonlinear relationship between cable force and natural frequencies of vibration. The stays are excited manually or by ambient sources and the acceleration time histories are recorded by sensors, typically accelerometers, mounted to the cable. Vibration characteristics can also be determined by contactless measurement. Natural frequencies can be obtained by transferring the measured signal into the frequency domain. This method is widely used in engineering practice due to its speediness and simplicity.

The estimation of cable forces on site requires simple and reliable methods that compromise the accuracy as little as possible. The lighter and more portable a measurement system is, the more simple the data acquisition and data processing become. This paper studies different modern vibration measurement systems based on mass-market components such as MEMS-based (microelectromechanical systems) acceleration sensors, microcomputers and

smartphones. Two possible configurations are presented and the properties and limitations of the technologies are studied.

Validation measurements performed on stay cables of Queensferry Crossing are described and evaluated. It is shown that such highly mobile and cost-effective systems have significant potential for stay cable applications if their limitations are considered.

2 STATE OF THE ART

2.1 *Condition Monitoring with Smartphones*

Modern smartphones and tablets are equipped with significant computational resources, large memory capacity and feature capable sensor components, which can be used for structural health monitoring purposes (Morgenthal & Höpfner 2012). These typically utilize the MEMS-based accelerometer of such systems to record structural vibrations in order to determine the dynamic system properties of the structure. In contrast to traditional monitoring systems that are composed of several individual hardware components, smartphones and tablets can integrate the recording, storage, processing, transfer and visualization of data within one single device.

Software implementations for measurements and data processing exist for most common operating systems (OS) such as Android (Gibbs et al. 2014) or iOS (Zhao et al. 2015, Yu et al. 2015). Since these software solutions are limited by the OS or the capabilities of the hardware components of the device, external sensors are additionally used for data acquisition. These external sensors can be connected directly to the smartphone or by means of a microcontroller, where the mobile device will solely act as central reader, processing and controller unit (Morgenthal 2012, Yu et al. 2015).

Fundamental characteristics of sensors integrated in smartphones, such as range, achievable resolution and maximum sampling rate were investigated in (Morgenthal & Hallermann 2013). Several of these studies found that the data obtained through smartphone applications may differ significantly from the sensor capabilities according to vendor datasheets as the OS exercises control over e.g. data rate and sensor operation modes. Therefrom, the motivation arises to connect external sensors to avoid these limitations.

The monitoring of infrastructures such as bridges has been promoted as a major application field of smartphone-based measurement systems. By utilizing a mobile measurement system Gibbs 2014 investigated the dynamic behavior of suspension bridges in developing countries. The internal cable force was determined by simplified formulae neglecting flexural rigidity and sag effects by vibration measurements on stay cables or hangers of suspension bridges (Yu et al. 2015, Zhao et al. 2015). By the same method, the tension of external tendons on a highway bridge was obtained (Morgenthal & Hallermann 2013).

With an increased adoption of mobile devices for vibration measurements there appears to be a genuine need to study the relationship between data quality obtained and the specific applications systematically. Devices such as smartphones use an enormous range of different sensors and a large spectrum of sensor properties results, imposing different kinds of limitations on accuracy of measurements.

2.2 *Vibration-Based Cable Force Measurement*

Several vibration measurements at cable-supported bridges have been conducted in the past. Cunha & Caetano 2001 reported an extensive dynamic test on the Vasco da Gama cable-stayed bridge. Vibration measurements also included the stay cables, where an accelerometer and a laser interferometry system were utilized. Smartphones were used in cable force determination for stays by Chen & Yan Chen 2013 to extract the tension force based on the fundamental frequency, thereby a good agreement to the results from a reference accelerometer with a relative error of less than 5% was achieved. An iOS application is introduced in Zhao et al. 2015, which was used to investigate the cable forces of the hanger of a suspension bridge.

3 MECHANICAL BEHAVIOR OF STAY CABLES

Vibration-based cable force determination is based on the relationship between force and frequencies which results from the cable's nonlinear mechanical behavior. The main methods to describe this behavior are presented here.

3.1 *Cable Properties*

Figure 1 shows an inclined cable stayed between the two anchorage points A and B. The horizontal and vertical distance between A and B defines the chord length L_c and the inclination of the undeformed cable α. Under the effect of mass m_c a sag due to the action of gravity d_v occurs. The effect of geometric nonlinearity of the cable ensures that even in the theoretical case of a cable with only axial stiffness EA (no bending stiffness EI) the member achieves an equilibrium through the axial force and the sag. Note that due to gravity the tension force T of an inclined cable is larger at the upper than at the lower anchorage $T_1 > T_2$. However, for short cables the anchorage forces might be affected by the end conditions (fixed or hinged).

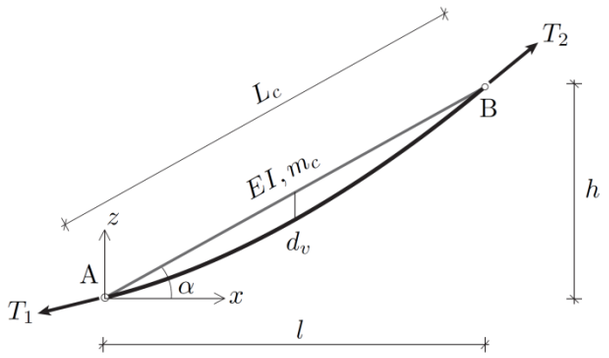


Figure 1. Inclined cable with the geometrical and mechanical properties.

Stay cables are prone to mechanical vibrations due to a very low bending stiffness and low inherent damping. The oscillations of the cables can be characterized in terms of their mode shapes and their corresponding natural frequencies.

3.2 *Simplified Taut String (TS)*

The linear theory of cable vibrations, which was first described in Irvine & Caughey1974, is based on three assumptions: (a) the cable is rigidly supported (b) the cable is shallow, i.e. the sag to span ratio d_v/L_c does not exceed 1/8 and (c) the cable deforms quasi-elastically.

The n-th natural frequency f_n for the in-plane vibration is based on the theory of a taut string, for which the relationship between cable force T and natural frequency f_n becomes

$$f_n = \frac{n}{2L_c}\sqrt{\frac{T}{m_c}} \qquad n = 1,2,3,\ldots \tag{1}$$

In literature different approaches considering the effects of sag and bending stiffness of a stay cable on the natural frequencies are presented. For a comprehensive review on the topic the reader is referred to Zui et al. 1996, Caetano 2007, Svensson 2004. The major challenge in the application of the above mentioned approaches is the definition of the bending stiffness EI. Besides the modulus of elasticity of the cable, the stiffness depends on the individual cable layout and composition, i.e. the cable system and its particular characteristics (Caetano 2007). The effective bending stiffness will depend on friction effects between individual cable components (wires and strands), which in turn may depend on the coating and the package density. The activated stiffness will depend on the curvature applied, i.e. the bending effect will be nonlinear and may differ between different cables of the same system. It is hence a property associated with relatively large uncertainty.

3.3 *Nonlinear Numerical Analysis of Cables (NL)*

The work in this paper is based on numerical simulations rather than any of the simplified approaches presented before. When the large-displacement geometrical nonlinearity of the cable under self-weight is taken into account and the vibration behavior computed on the basis of linearization at the static equilibrium, this yields accurate predictions of cable natural frequencies that can take all the relevant mechanical effects duly into account. Modal analysis is then performed using the effective linearized stiffness at the equilibrium condition. The static equilibrium is obtained from a geometrically nonlinear analysis, where the nonlinear relationship between load and displacements is considered by employing 3rd order theory (Clough & Penzien 1975).

Applying the finite-element method, a bending-stiff cable is modelled with beam elements without considering shear deformation. The cable system is then subjected to gravity load where the mass is considered to be lumped at each node. For such case, a tangent-stiffness approach may be utilized. The nonlinear part in the equilibrium equation can be determined by Newton-Raphson method (Bathe 1996). The updated stiffness is then used in the modal analysis for frequency determination.

4 MEASUREMENT CONCEPT

4.1 *Hardware and Measurement System*

The application of sensor technology in the context of condition monitoring of structures has seen an enormous increase in the past years which is primarily due to continuous improvements of hardware components in terms of performance and price. Of particular interest to this paper are hardware components employed for vibration measurements herein are smartphones and mass market MEMS accelerometers as well as credit card sized battery operated microcomputers.

Smartphones that are currently in the market vary drastically in terms of their hardware components as well as software systems. Thereby, the different built-in sensors lead to vastly different measurement properties. Differences in accelerometers and the sensor driver software configuration of the operating system lead to significant differences in the maximum possible sampling rate $f_{s,max}$, the measurement range R and the sensor resolution as well as the regularity of sampling points (equidistant sampling). Consequently, significant differences in the measurement quality will be obtained.

An investigation on the performance of several smartphones has been conducted by the authors. A comparison in terms of computational power, measurement range, sampling rate and resolution is given in Morgenthal et al. 2017. Modern smartphones offer sampling rates up to 200 Hz, resolve accelerations down to 1 – 4 mm/s² while possessing a range of ±2g to ±16g.

The specific sensor performance achieved by applications will be influenced by decisions that the smartphone developer makes at driver level and thus may vary drastically (towards lower performance) from the maximum performance of the sensor due to e.g. considerations for energy consumption. To remove the restriction imposed by the single built-in sensor and yet make use of the convenient form factor, powerful processing, storage and data communication as well as the rich and interactive user experiences possible on modern smartphones and tablets, a method for connecting external sensors has been developed. This is based on an Android application that communicates with an external single board computer called Raspberry Pi (RPi) to utilize external sensors connected to that. The connection, briefly described in the following section, ensures the transfer of data recordings from high quality sensors to the smartphone, where the data can be analysed and stored such that the smartphone remains the central control unit.

Besides the smartphone (4), the alternative measurement system, shown in Figure 2, comprises the RPi micro-computer (1), one or several external sensors (2), the sensor connection cable (3) and a battery power supply (5). For the attachment of the sensor at the stay cable, the external sensor is mounted to a U-shaped aluminum profile (2), which is then applied to the stay by means of a tension belt (6).

In general, different types of sensors can be integrated in the measurement system. However, for the system used herein a low-cost sensor is applied. The MPU6050 is a digital MEMS-based accelerometer with 16 bit signal conversion (Invensense 2013) and the smallest possible range R is set ($\pm$2g) to ensure the highest possible resolution.

4.2 *Smartphone Application*

To facilitate smartphone-based measurements, an Android application (App) was developed by the authors. The application provides a framework for the collection of building related information for inspection purposes. As such, besides the measurement tasks discussed here, it provides a database to store items of various data types such as photos, videos, images and notes (see Figure 3 left). All data is generated on the smartphone itself, utilizing the onboard hardware components.

For vibration measurements the sampling rate, sensing axes, duration can be configured. The recorded time histories are saved to the persistent internal storage of the device. Furthermore, the application features an extensive analysis tool including visualization of the signals and post-processing tools. For a selected axis and a user-defined time window, a Fast Fourier Transform (FFT) can be performed and the frequency content of the record is displayed (see Figure 3 right).

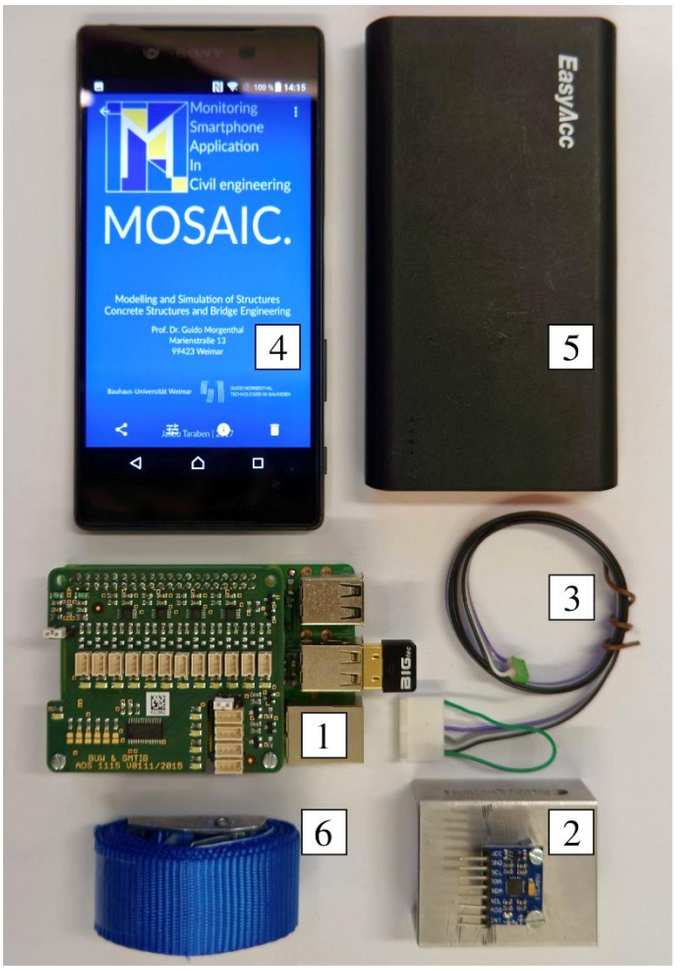


Figure 2: Hardware components of the smartphone-based measurement system.

Furthermore, an extension for the determination of cable forces is implemented. If the specific cable properties such as chord length L_c, mass per unit length m_c and angle α are provided either by data import or manually and a corresponding mode number is assigned to a prominent peak in the spectrum, the cable force is computed based on the simplified taut string approach. Any analysis steps are graphically supported, intuitive to use and fully suitable for processing on the smartphone to facilitate an effective in-situ evaluation.

The nonlinear numerical analyses discussed in this paper can be employed to save pre-calculated force-frequency relationships for each cable on the smartphone, which the App can then use to perform the tension force identification by interpolated lookup from this data.

The proposed approach and its implementation therefore constitutes an extension of previous studies such as (Yu 2015) which were limited to a spectral analysis of measured acceleration time histories and such as (Zhao 2015, Chen & Yan 2013) which were limited to a spectral analysis of measured acceleration time histories and such as (Zhao et al. 2015, Chen & Yan 2013) which were limited to simplified methods of cable force determination. The method presented here constitutes a complete framework for the sensor data acquisition and the advanced tension

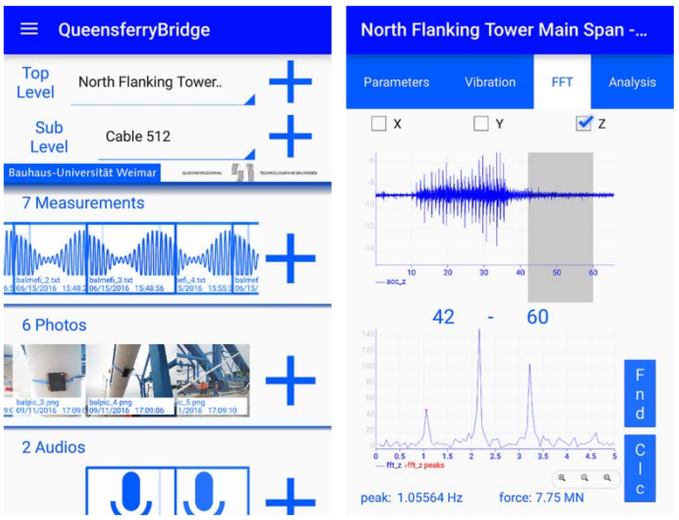


Figure 3. Screenshot of the user interface of the Android application. Various types of collected data (left) and visualization of the recorded time history and the frequency spectrum as computed for a selected time window (right).

force identification. The storage of cable properties including force-frequency relationships from nonlinear analysis allows for tension force identifications on the basis of the most advanced mechanical model available. The quality of such process is then only limited by the technical limitations of the sensors as will be studied in section 5.

4.3 *Interfaces of the Measurement System*

Within the App the user can establish a wireless network connection between smartphone and RPi, upon which the two devices will open a Websocket connection. The WebSocket protocol is commonly used for bidirectional network communication and data transfer.

A configuration file with the defined measurement settings for the sensor interface framework is sent to the RPi to trigger the measurement. After completing a measurement, the data is stored on the memory card of the RPi and is downloaded by the smartphone. The analysis tool of the App adapts data of external measurements in order to obtain further results immediately.

Further details about the hardware, the smartphone application developed and the interfaces used are provided in Morgenthal et al. 2017.

5 REFERENCE STUDY: QUEENSFERRY CROSSING CABLES

5.1 *Queensferry Crossing Project*

The Queensferry Crossing (QFC) is a new major bridge link over the Firth of Forth in the North of Edinburgh opened in august 2017. The three-tower cable-stayed bridge features two main spans of 650 m length each and side spans of 366 m total length on either side. There is a total of 144 stay cables in each of the two cable planes. A schematic of the cantilever construction stage of the bridge is shown in Figure 4.

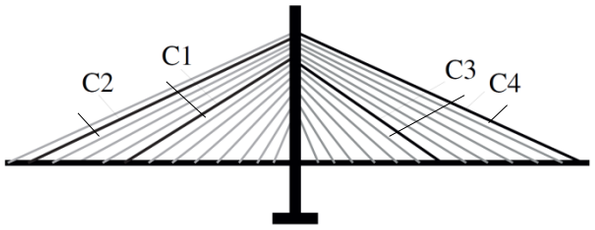


Figure 4. Schematic of the construction stage with indication of stay cables.

Table 1. Properties of the stay cables with corresponding reference cable force T_{ref}.

Stay cable		C1	C2	C3	C4
L_c	[m]	231.109	324.005	204.055	342.981
α	[°]	29.3	22.4	34.0	22.9
m_c	[kg/m]	131.6	134.2	112.5	116.4
EI_{min}	[kNm²]	55	56	48	49
EI_{max}	[kNm²]	14,452	14,760	7,589	7,867
T_{ref}	[MN]	8.11	12.22	6.50	9.63
Method		Lift-off	Vibration	Vibration	Lift-off

The measurements reported in this paper have been conducted on the bridge during its cable-stayed deck construction in summer 2016. Cable forces were available from different tests performed after stay cable installation to ensure the correct structural state. These reference forces are used to validate the cable forces determined by the presented measurement system. It is to be noted that lift-off tests were conducted at the upper stay anchorage and therefore cable forces studied here are reported for the upper end exclusively. Since the cable forces of inclined cable differ between the two ends, only nonlinear cable modelling can account for this effect.

5.2 *Vibration Measurements on Stay Cables*

In this section, the application of the alternative measurement system is described along with comparisons made to measurements from traditional setups. The cable forces had been measured by actual lift-off test and determined by natural frequencies obtained from vibration tests using standard high-quality sensor and data logger hardware. Two smartphones with different sensor characteristics are chosen for the on-site measurements, as shown in Table 2.

The built-in sensors coincide in their range R and differ in their smallest resolvable acceleration Δa and the maximum sampling rate $f_{s,max}$. The more recent Xperia Z5 enables a higher sampling rate than the Nexus 4, while the resolution of the acceleration is much lower. Further, the setup with RPi and the MPU6050 sensor is performed. All accelerometers

used sense motion in three axes. In comparison with the smartphone systems, the RPi setup offers more than double the sampling rate. The measurements of the smartphones were configured with a sampling rate f_s that is slightly smaller than the maximum sampling rate $f_{s,max}$ in order to assure a stable measurement. All measurements were triggered and evaluated using the presented Android application.

Table 2. Summary of sensor parameter for built-in and external accelerometer (External Sensor = MPU6050).

Device	R [g]	Δa [mm/s^2]	Noise (RMS) [mm/s^2]	$f_{s,max}$ [Hz]
Sony Xperia Z5	±2	4	40	225
Nexus 4	±2	1	35	200
External Sensor	±2	1	49	560

The vibration measurements were conducted on four different stay cables during erection of the bridge. The tested stay cables C1 to C4 are indicated in Figure 4 and Table 2 provides their geometrical and mechanical properties together with the reference cable force T_{ref} which was obtained by either lift-off or vibration method as indicated. Here, the minimum second moment of area I_{min} is computed as the sum of the second moments of area of the individual strands, which corresponds to a perfect slip possible between the individual strands and is the minimum stiffness physically possible. The maximum possible second moment of area I_{max} is calculated using an effective area of the cable which is based on the area of steel with respect to the total area of the section and thus assumes a full shear connection between all strands in the bundle. This represents an upper bound of the possible bending stiffness but is considered to be a strong overestimation of the actual bundle behavior due to slip effects between strands (Svensson 2012, Caetano 2007).

The smartphone and the external sensor were attached to the stay cable by means of a U-shaped aluminium profile and a tension belt. Both devices were placed close to the lower anchorage of the cable at a height of approximately 2.0 m from the deck. The distance of the attached devices from the cable anchorage was approximately 7 m, i.e. between 2 and 3.5% of the cable length. The cable was free to vibrate with no cable dampers or guide tube fixings installed.

5.3 *Test 1: Comparison of Sensor Systems*

In a first test the cable C1 was excited near the lower anchorage point by periodic manual pulling in order to excite the cable into significant vibrations. The measurements were conducted using one smartphone (Sony Xperia Z5) as well as the RPi with the external sensor (MPU6050). Only the accelerations after the excitation, i.e. with the cable in free vibration, were analysed. It should be noted that it proved difficult to excite the cable properly with the force introduced near the lower cable end.

Sample time histories of the measured accelerations of the built-in and the external sensor, obtained from two different excitations, are displayed in Figure 5 with the corresponding frequency spectra. The natural frequencies of the stay cables were determined by identifying the peaks in the frequency spectra, whereby the measurements with a duration of 20 and 60 seconds result in a frequency resolution of 0.05 Hz and 0.017 Hz, respectively.

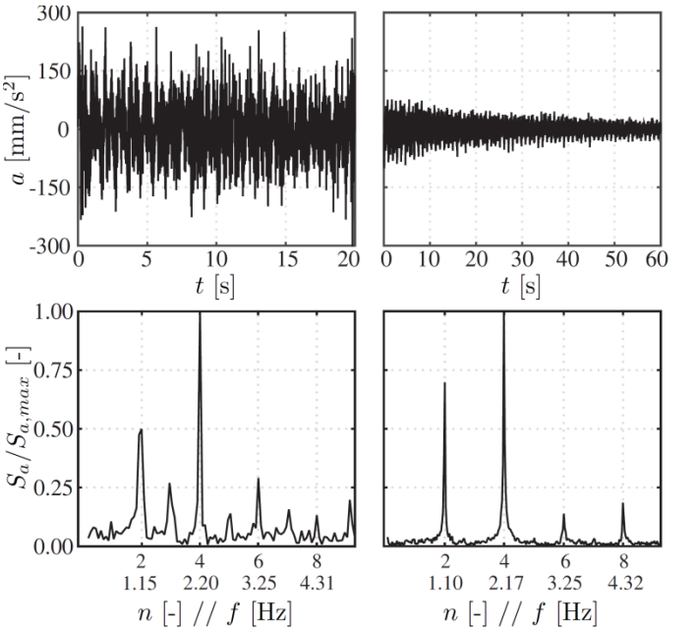


Figure 5. Sample time histories (top) and frequency spectra (bottom) for different manual excitations at cable C1: high excitation, smartphone Xperia Z5 (left); low excitation, external sensor MPU6050. (Note: Average sampling rates f_s^{SP} = 215 Hz, f_s^{MPU} = 550 Hz)

Table 3. Comparison of the identified natural frequencies obtained by measurement with smartphone (SP, high excitation) and external accelerometer (MPU, low excitation).

n		2	4	6	8
f_n^{SP}	[Hz]	1.15	2.20	3.25	4.31
f_n^{MPU}	[Hz]	1.10	2.17	3.25	4.32
f_n^{SP}/f_n^{MPU}	[-]	1.045	1.014	1.000	0.998

For both measurements the natural frequencies f_n identified are given in Table 3. The MPU6050 was tested for relatively small excitation amplitudes and it was found that these revealed only the anti-symmetric modes (n = 2, 4, ...) clearly. The smartphone was subjected to greater amplitudes and the data provided also the natural frequencies corresponding to symmetric modes. The superiority of the MPU sensor in terms of acceleration resolution Δa and noise can be seen in the spectrum with more distinct peaks and a much smaller noise floor. With manual excitations, typically the lower natural frequencies were found with the second to the fourth

mode being most prominent. The fundamental frequency was barely or not at all identifiable in both measurements, which can be attributed to the measurement location and the mode shape, i.e. the contribution of the first modes is relatively small near the anchorage point. The frequencies that could be identified in both systems agree very well with differences in higher modes typically being within 1%.

5.4 *Test 2: Influence of the Excitation*

Further measurements applying only a smartphone were conducted with and without manual excitation at cable C2. The Nexus 4 smartphone is utilized in order to achieve a higher signal quality as it possesses a higher resolution than the Sony Xperia Z5 (see Table 2). The influence of the excitation is investigated with manual excitations compared to ambient vibrations predominantly induced by wind. Thereby, it was seen that more natural frequencies were identified when excited manually, however also the frequencies determined under ambient vibration are in good agreement with reference values.

In a further step, the frequencies identified from the manually excited cable using the Nexus 4 smartphone, were converted into cable forces using a nonlinear numerical model. The cable properties from Table 1 were used to model the cable and determine the force-frequencies relationships for the minimum and maximum bending stiffness. This nonlinear function was then used to predict cable forces T_{meas} for each of the identified natural frequencies.

This procedure was also applied to the frequencies of the reference vibration measurement system and both compared in terms of the corresponding forces. The results, shown in Figure 6, underline the excellent agreement of the frequencies now in terms of the back-calculated tension forces. These are within 1% throughout and below 0.5% on average.

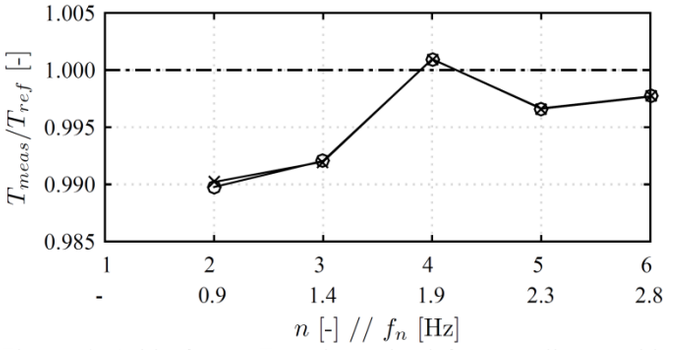


Figure 6. Cable forces T_{meas} determined from nonlinear cable modelling for frequencies of cable C2 measured with smartphone Nexus 4. Forces are shown relative to the cable force T_{ref} determined from reference vibration test.
—o— EI_{min}; —x— EI_{max}

5.5 *Test 3: Application Case of External Sensor under Ambient Vibrations*

A manual excitation of the cable represents an additional effort and only the best smartphones can detect ambient vibrations accurately. Therefore, the measurement setup with the smartphone as control unit and the external MPU sensor attached to the RPi as a measurement device is presented here as a robust and reliable test system, which features both: sufficiently high resolution and sampling rates for the validation under ambient vibrations.

Two different measurements were conducted, specifically on the shortest (C3) and longest cable (C4). The recordings are 30 seconds for cable C3 and 60 seconds for cable C4 which result in a frequency resolution of 0.033 Hz and 0.016 Hz, respectively. For both measurements, at least 10 natural frequencies have been identified. From the identified frequencies, the corresponding cable forces T_{meas} are computed based on the nonlinear numerical model for the assumed limits of the cable stiffness EI_{min} and EI_{max}. These cable forces are then compared with the reference cable forces T_{ref} from Table 1 in Figure 7.

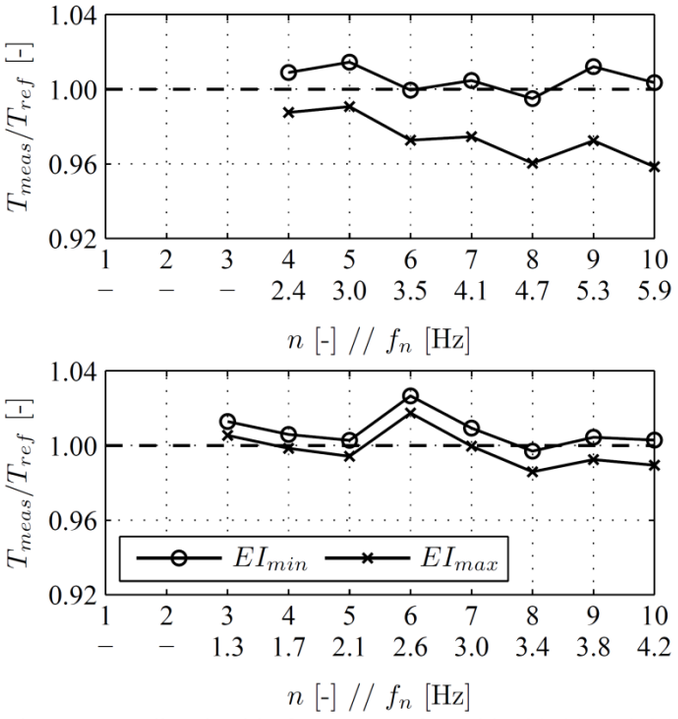


Figure 7. Predicted cable forces T_{meas} for cable C3 (a) and C4 (b) determined from measurements taken by external sensor MPU6050 under ambient vibrations.

The comparison for cable C3 needs to be interpreted considering the fact that the reference cable force had been supplied by a third party operating the standard vibration measurement system. It is not known to the authors how this force was computed from the (unknown) frequencies identified, but it is believed that it represents an average of the forces computed from applying the taut string relationship. As such, the comparison with the similar assumption of a low bending stiffness is very good and within

1% on average. The differences in prediction using the maximum bending stiffness successively increase by mode number. This represents the error introduced by assuming a bending stiffness too high.

The error of the maximum bending stiffness model can also be clearly seen for cable C4, where it is less pronounced because of the longer cable length. Again a very good agreement between the identified cable forces and the reference cable forces under consideration of the minimum bending stiffness can be seen while the mean error is around 1%.

When it is considered that this reference force in itself has a margin of possible error of 1% this shows that the sensor system proposed here can reliably measure cable forces. There is a tendency for the computed cable forces to be slightly on the high side, which may be the effect of using the minimum possible bending stiffness versus the real one. It is obvious that the real effective stiffness is impossible to quantify exactly because of many physical effects being at play, however it is slightly larger than EI_{min}.

6 CONCLUSIONS

This paper has investigated the application of mobile measurement systems to the determination of stay cable forces. The main aspects are the presentation of a coherent smartphone-based software framework, the incorporation of nonlinear Finite Element analyses into the identification process and studies into the effect that measurement data quality has on the identified forces.

Herein, the force-frequency relationship required for the cable force identification is based upon nonlinear Finite Element analyses for accurate representation of effects such as bending stiffness.

With the acceleration time-history characteristics being strongly dependent on properties of the individual systems, namely sensor type, hardware setup and limitations imposed by the smartphone OS, the paper systematically studies the data quality with respect to the identification of cable frequencies. It is found, that limitations of sensor resolution and the type of excitation are critical parameters determining the quality and reliability of the identification process. Reference measurements undertaken on cables of the Queensferry Crossing bridge could be used for force comparisons.

Whilst the microcontroller-based system and one specific smartphone system could identify frequencies sufficiently accurately even under ambient wind excitations, most smartphones require manual cable excitations for a robust identification. This is because the sensors attached near the lower cable end are subjected to small vibration amplitudes only. The external sensor connected to the microcontroller (RPi) and the smartphone acting as control unit provides reliable, highly accurate force measurements.

Beyond the smartphone or tablet the hardware costs are less than 100 USD and therefore the authors are convinced that such technology will find an important place in future simple measurement workflows. Further studies should be conducted into quantifying the statistical measurement uncertainties arising from sensor and system properties in order to be able to support hardware selection.

7 REFERENCES

Bathe, K.-J. 1996. *Finite element procedures*. Englewood Cliffs: Prentice Hall.

Caetano, E. d. S. 2007. Cable vibrations in cable-stayed bridges, *Vol. 9 of Structural engineering documents*. IABSE, Zurich, Switzerland.

Chen, S.-R. & Yan, Q.-S. 2013. A method of measuring the cable tension force with the application of smart phones. *Computer Modelling & New Technologies*, 17(5), 11-18.

Chopra, A. K. 4th ed. 2012. *Dynamics of structures: Theory and applications to earthquake engineering*. Upper Saddle River : Prentice Hall Pearson.

Clough, R. W. & Penzien, J. 1975. *Dynamics of structures*. New York: McGraw-Hill.

Cunha, A., Caetano, E., & Delgado, R. 2001. Dynamic Tests on Large Cable Stayed Bridge. *Journal of Bridge Engineering*, 6(1), 54-62.

Gibbs, M. et al. 2014. Dynamic Characteristics of Suspension Footbridges: A Novel Sensing Approach. *6th World Conference on Structural Control and Monitoring*.

InvenSense Inc. 2013. MPU-6000 and MPU-6050: Product Specification: datasheet PS-MPU-6000A-00 [08/19/2013].

Irvine, H. M. & Caughey, T. K. 1974. The Linear Theory of Free Vibrations of a Suspended Cable. *Proceedings of the Royal Society A: Mathematical, Physical and Engineering Sciences*, 341(1626), 299-315.

Morgenthal, G., Rau, S., Taraben, J., & Abbas, T. 2017. Determination of stay-cable forces using highly mobile vibration measurement devices. *ASCE Journal of Bridge Engineering* (in print).

Morgenthal, G. & Hallermann, N. 2013. Strukturidentifikation und Monitoring mit Smartphone-basierten Sensorsystemen [Structural identification and monitoring with smartphone-based sensor systems]. Ernst & Sohn Special: *Messtechnik im Bauwesen*, (4), 25-29.

Morgenthal, G. & Höpfner, H. 2012. The application of smartphones to measuring transient structural displacements. *Journal of Civil Structural Health Monitoring*, 2(3-4), 149-161.

Svensson, S. E. 2004. Vibration of Cable Stays. *Bygningsstatiske Meddelelser, Danish Society for Structural Science and Engineering*, (4), 79-106.

Svensson, H. 2012. *Cable-stayed Bridges*. Wiley.

Yu, Y. et al. 2015. Initial Validation of Mobile-Structural Health Monitoring Method Using Smartphones. *International Journal of Distributed Sensor Networks*, 2015, 1-14.

Zhao, X. et al. 2015. Cable force monitoring system of cable stayed bridges using accelerometers inside mobile smart phone. *Proceedings SPIE Smart Structures and Materials + Nondestructive Evaluation and Health Monitoring*, J. P. Lynch, ed., 94351H.

Zui, H., Shinke, T., & Namita, Y. 1996. Practical Formulas for Estimation of Cable Tension by Vibration Method. *Journal of Structural Engineering*, 122(6), 651-656.

Maintenance, Safety, Risk, Management and Life-Cycle Performance of Bridges – Powers, Frangopol, Al-Mahaidi & Caprani (Eds)
© 2018 Taylor & Francis Group, London, ISBN 978-1-138-73045-8

Estimation of bridge frequencies from a passing vehicle

N. Jin, T. S. Paraskeva & E. G. Dimitrakopoulos
Department of Civil and Environmental Engineering, Hong Kong University of Science and Technology, Hong Kong

ABSTRACT: Extracting the bridge dynamic properties from a moving vehicle is a promising solution to the ever-increasing demand for monitoring of bridges. A traversing vehicle excites the bridge, while the vibrating bridge affects the response of the vehicle. By processing the "monitored" vehicle response, the dynamic characteristics of the bridge can be efficiently extracted. In this paper, the stochastic subspace identification (SSI) method is applied to the vehicle response to estimate the frequencies of the bridge. Specifically, the present study assesses the accuracy and the effectiveness of the SSI method that is used to identify the frequencies of a straight reinforced concrete bridge, from the response of a passing vehicle. As a proof of concept, the response of the vehicle is first estimated from a vehicle-bridge interaction dynamic analysis. The bridge frequencies are then identified with the proposed SSI method assuming the dynamic characteristics of the vehicle and its motion are known. The results of the identification are validated against the theoretically correct values from the numerical analysis, and conclusions regarding the feasibility of the method are drawn.

1 INTRODUCTION

The frequency of vibration is one of the most important modal parameters of the bridge, and is frequently used as an index in the bridge health monitoring and the damage detection. Traditionally, the bridge frequencies are estimated by multiple sensors installed along the bridge. By processing the data obtained from the vibrating bridge, one can extract information regarding the dynamic properties of the bridge. Depending on the source of the excitation, the on-site experiments mainly include ambient vibration tests (Siringoringo & Fujino 2008), human excitation tests (Au et al 2005), impact excitation tests (Huang et al 1999), on-going traffic tests (Conner et al 1997), and tests that use the wind load as excitation for the bridge (Goi & Kim 2016) etc. However, the identification techniques based on the on-site instrumentation, can be very expensive, time-consuming, and sometimes dangerous, depending of the location and the type of the examined bridge (Yang et al 2004).

Recently, indirect techniques of extracting the bridge dynamic properties from the passing vehicles have attracted the interest of many researchers (Yang & Yang 2017). Compared with the traditional identification methods, this approach appears more cost-effective, portable, time-saving and easier for application. The idea is that since the vehicle and the bridge form a coupled system, when the vehicle crosses the bridge the response of the vehicle is dominated by the dynamic properties of both the vehicle and the bridge. Thus, by processing the response of the vehicle, and suppressing the effect of the vehicle characteristics, one can identify the bridge frequencies (Yang et al 2004).

Yang & Chen (2015) developed an alternative method for extracting the bridge frequencies from the response of the passing vehicles, using a modified Stochastic Subspace Identification (SSI) method. This paper, presents an application of the proposed approach in combination with a vehicle-bridge interaction (VBI) dynamic analysis, to extract the frequencies of a straight reinforced concrete bridge, using the vibration response of a passing "monitored" vehicle. As a proof of concept, the response of the vehicle is estimated from the VBI analysis, where the dynamic characteristics of the vehicle and its motion are known. The feasibility, the effectiveness and the accuracy of the modified SSI method is validated by comparing the results of the proposed identification method with the corresponding values obtained analytically from the modal analysis of the bridge.

2 METHODOLOGY

2.1 *Brief introduction to the Stochastic subspace identification method*

The Stochastic Subspace Identification (SSI) method is one of the most popular methods for identifying the dynamic properties of linear time-invariant (LTI) systems (Van Overschee & De Moor 1996, Katayama 2006).

A time-discrete LTI system with input and output signals and disturbance can be described by

$$\begin{aligned}\mathbf{X}_{k+1} &= \mathbf{A}\mathbf{X}_k + \mathbf{G}\mathbf{U}_k + \mathbf{w}_k \\ \mathbf{Y}_k &= \mathbf{C}\mathbf{X}_k + \mathbf{H}\mathbf{U}_k + \mathbf{v}_k\end{aligned} \quad (1)$$

where $\mathbf{X}_k$ is the state vector; $\mathbf{U}_k$ is the input vector; $\mathbf{Y}_k$ is the output vector; **A**, **C**, **G** and **H** denote the system matrices which are constant and time-invariant; $\mathbf{w}_k$ is the system noise; and $\mathbf{v}_k$ is the measurement noise. If there is not an input signal the system can be described as

$$\begin{aligned}\mathbf{X}_{k+1} &= \mathbf{A}\mathbf{X}_k + \mathbf{w}_k \\ \mathbf{Y}_k &= \mathbf{C}\mathbf{X}_k + \mathbf{v}_k\end{aligned} \quad (2)$$

This study uses Eq. (2) to describe the response of the coupled vehicle-bridge interaction system and applies the SSI to the response of a passing vehicle to estimate the bridge frequencies. A prerequisite for the proposed method is the transformation of the time-variant equations of the VBI system into discrete time-invariant state space format.

2.2 *Vehicle-bridge interaction model*

The present study examines a straight reinforced concrete bridge (Fig 1a) and uses a three-axle truck tractor with a trailer (Fig 1b) (Paraskeva et al 2017).

The equation of motion of the coupled VBI system is

$$\mathbf{M}\ddot{\mathbf{u}}(t) + \mathbf{K}\mathbf{u}(t) + \mathbf{C}\dot{\mathbf{u}}(t) - \mathbf{W}_N(t)\boldsymbol{\lambda}_N(t) = \mathbf{0} \quad (3)$$

where **M**, **K**, and **C** are the mass matrix, the stiffness matrix and the damping matrix, respectively, all created by assembling the pertinent matrices of the two individual subsystems (i.e. the vehicle subsystem and the bridge subsystem). Similarly, **u**(t) includes the displacements of the vehicle and the bridge. $\mathbf{W}_N(t)$ is the direction matrix of the contact forces between the vehicle and the bridge. $\boldsymbol{\lambda}_N(t)$ is the contact force vector, (Fig 1d), described as

$$\boldsymbol{\lambda}_N = \mathbf{K}_c\left(-\mathbf{W}_N(t)^T\mathbf{u}(t) + \mathbf{r}_c(t)\right) - \mathbf{C}_c\mathbf{W}_N(t)^T\dot{\mathbf{u}}(t) \quad (4)$$

where $\mathbf{K}_c$ and $\mathbf{C}_c$ are the tire stiffness and damping coefficients, respectively; $\mathbf{r}_c(t)$ denotes the road roughness condition which is assumed to be a zero-mean stationary Gaussian random process. Further information regarding the simulation of the coupled VBI system, as well as the VBI analysis conducted herein, can be found in detail, in Paraskeva et al (2017)

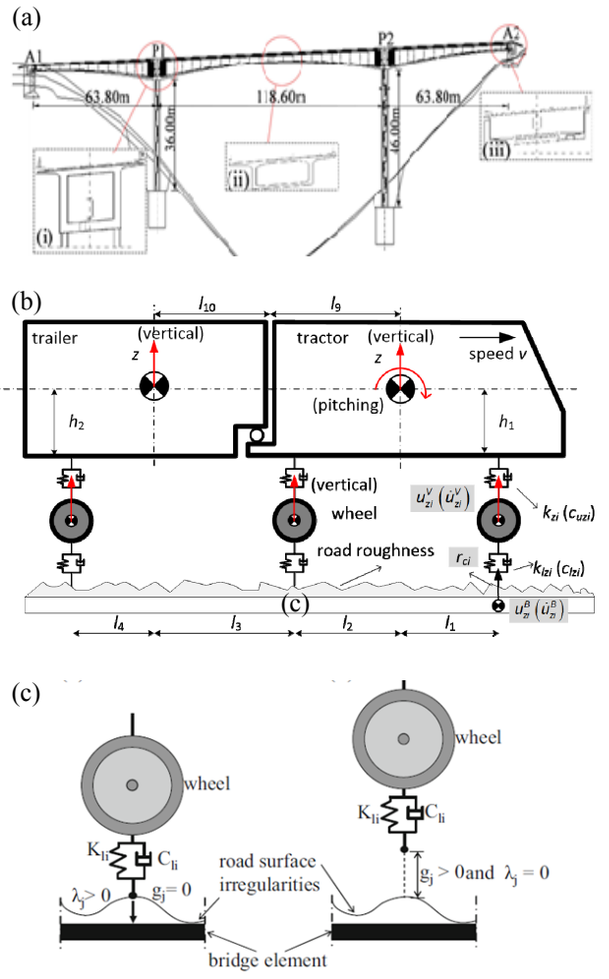


Figure 1. (a) The bridge model, (b) the vehicle model, (c) the contact model.

2.3 *Formulation of the VBI problem in discrete time-invariant state space form*

This section presents the transformation of the equations of motion of the coupled vehicle-bridge system, into (a) state space, and (b) a discrete time-invariant form.

The equation of motion for the bridge is

$$\mathbf{M}^B\ddot{\mathbf{u}}^B(t) + \mathbf{K}^B\mathbf{u}^B(t) + \mathbf{C}^B\dot{\mathbf{u}}^B(t) + \mathbf{W}_N^B(t)\boldsymbol{\lambda}_N(t) = \mathbf{0} \quad (5)$$

Substituting Eq.(4) to Eq.(5), the equation of motion for the bridge can be written in the state space as

$$\begin{aligned}\dot{\mathbf{X}}^B(t) = {} & \mathbf{N}_c^B\mathbf{X}^B(t) + \mathbf{N}^{BB}(t)\mathbf{X}^B(t) \\ & + \mathbf{N}^{BV}(t)\mathbf{X}^V(t) + \mathbf{N}^{RB}(t)\mathbf{R}(t)\end{aligned} \quad (6)$$

where

$$\mathbf{X}^{\mathrm{B}}(t)=\begin{Bmatrix}\mathbf{u}^{\mathrm{B}}(t)\\ \dot{\mathbf{u}}^{\mathrm{B}}(t)\end{Bmatrix}\in R^{2n\times 1} \tag{7}$$

$$\mathbf{X}^{\mathrm{V}}(t)=\begin{Bmatrix}\mathbf{u}^{\mathrm{V}}(t)\\ \dot{\mathbf{u}}^{\mathrm{V}}(t)\end{Bmatrix}\in R^{2m\times 1} \tag{8}$$

$$\mathbf{N}_c^{\mathrm{B}}=\begin{bmatrix}\mathbf{0} & \mathbf{I}\\ -\left(\mathbf{M}^{\mathrm{B}}\right)^{-1}\mathbf{K}^{\mathrm{B}} & -\left(\mathbf{M}^{\mathrm{B}}\right)^{-1}\mathbf{C}^{\mathrm{B}}\end{bmatrix}\in R^{2n\times 2n} \tag{9}$$

$$\mathbf{N}^{\mathrm{BB}}(t)=\begin{bmatrix}\mathbf{0} & \mathbf{I}\\ -\left(\mathbf{M}^{\mathrm{B}}\right)^{-1}\mathbf{L}_{\mathrm{K}}^{\mathrm{BB}}(t) & -\left(\mathbf{M}^{\mathrm{B}}\right)^{-1}\mathbf{L}_{\mathrm{C}}^{\mathrm{BB}}(t)\end{bmatrix}\in R^{2n\times 2n} \tag{10}$$

$$\mathbf{N}^{\mathrm{BV}}(t)=\begin{bmatrix}\mathbf{0} & \mathbf{0}\\ \left(\mathbf{M}^{\mathrm{B}}\right)^{-1}\mathbf{L}_{\mathrm{K}}^{\mathrm{BV}}(t) & \left(\mathbf{M}^{\mathrm{B}}\right)^{-1}\mathbf{L}_{\mathrm{C}}^{\mathrm{BV}}(t)\end{bmatrix}\in R^{2n\times 2\mathrm{m}} \tag{11}$$

$$\mathbf{N}^{\mathrm{RB}}(t)=\begin{bmatrix}\mathbf{0} & \mathbf{0}\\ -\left(\mathbf{M}^{\mathrm{B}}\right)^{-1}\mathbf{W}_{\mathrm{N}}^{\mathrm{B}}(t)\mathbf{K}_c & \mathbf{0}\end{bmatrix}\in R^{2n\times 2r} \tag{12}$$

$$\mathbf{R}(t)=\begin{Bmatrix}\mathbf{r}_c(t)\\ \dot{\mathbf{r}}_c(t)\end{Bmatrix}\in R^{2r\times 1} \tag{13}$$

n is the DOF of the bridge, m is the DOF of the vehicle, and r is the number of wheels; the superscripts "V" and "B" denote the vehicle and the bridge subsystems, respectively; $(\mathbf{L}_{\mathrm{K}}^{\mathrm{BB}}(t))_{ii}$ and $(\mathbf{L}_{\mathrm{C}}^{\mathrm{BB}}(t))_{ii}$ are diagonal matrices representing the stiffness and damping coefficients of the contact force applied on the i$^{\mathrm{th}}$ dof of the bridge, respectively; $\mathbf{L}_{\mathrm{K}}^{\mathrm{BV}}(t)$ and $\mathbf{L}_{\mathrm{C}}^{\mathrm{BV}}(t)$ denote the stiffness and damping coefficient of the contact force between the i$^{\mathrm{th}}$ dof of the bridge and j$^{\mathrm{th}}$ wheel axle of the vehicle, respectively. By definition, the matrix $\mathbf{N}_c^{\mathrm{B}}$ is the bridge system matrix in time-continuous form, which is time-invariant; $\mathbf{N}^{\mathrm{BB}}(t)$ and $\mathbf{N}^{\mathrm{BV}}(t)$ are related to the position and magnitude of the contact force between the wheels and the bridge; $\mathbf{N}^{\mathrm{RB}}(t)$ is related to the road roughness condition. Under the assumption that the external forces are considered as noise, they can be replaced by a stochastic process $\mathbf{w}(t)$. Therefore, Eq.(6) is written as

$$\dot{\mathbf{X}}^{\mathrm{B}}(t)=\mathbf{N}_c^{\mathrm{B}}\mathbf{X}^{\mathrm{B}}(t)+\mathbf{w}(t) \tag{14}$$

Similarly, the equation of motion for the vehicle in state space form is re written as

$$\begin{aligned}\dot{\mathbf{X}}^{\mathrm{V}}(t)=&\left(\mathbf{N}_c^{\mathrm{V}}+\mathbf{N}_c^{\mathrm{VV}}\right)\mathbf{X}^{\mathrm{V}}(t)\\ &+\mathbf{N}^{\mathrm{VB}}(t)\mathbf{X}^{\mathrm{B}}(t)+\mathbf{N}^{\mathrm{RV}}\mathbf{R}(t)\end{aligned} \tag{15}$$

where $\mathbf{N}_c^{\mathrm{V}}$ is the vehicle system matrix; $\mathbf{N}_c^{\mathrm{VV}}$ and $\mathbf{N}^{\mathrm{VB}}(t)$ are related to the contact forces between the wheels and the bridge; and $\mathbf{N}^{\mathrm{RV}}$ is the road roughness related term. Note that the matrices $\mathbf{N}_c^{\mathrm{V}}$, $\mathbf{N}_c^{\mathrm{VV}}$ and $\mathbf{N}^{\mathrm{RV}}$ are time-invariant.

The equation of the motion for the bridge can be converted to the time-discrete form by multiplying an exponential matrix $\exp(-\mathbf{N}_c^{\mathrm{B}}t)$ on each side of Eq.(14). Then the equation can be transformed as

$$\mathbf{X}_{k+1}^{\mathrm{B}}=\mathbf{N}^{\mathrm{B}}\mathbf{X}_k^{\mathrm{B}}+\mathbf{w}_k \tag{16}$$

where

$$\mathbf{N}^{\mathrm{B}}=\exp^{\mathbf{N}_c^{\mathrm{B}}\Delta t} \tag{17}$$

$$\mathbf{w}_k=\left(\mathbf{N}_{\mathrm{c}}^{\mathrm{B}}\right)^{-1}\left(\mathbf{N}^{\mathrm{B}}-\mathbf{I}\right)\mathbf{w}(k) \tag{18}$$

Applying the same procedure for the vehicle, Eq.(15) can be transformed to the time-discrete form as

$$\mathbf{X}_{k+1}^{\mathrm{V}}=\mathbf{N}^{\mathrm{V}}\mathbf{X}_k^{\mathrm{V}}+\mathbf{N}_k^{\mathrm{VB}}\mathbf{X}_k^{\mathrm{B}}+\mathbf{N}^{\mathrm{RV}}\mathbf{R}_k \tag{19}$$

where

$$\mathbf{N}^{\mathrm{V}}=\exp^{\left(\mathbf{N}_c^{\mathrm{V}}+\mathbf{N}_c^{\mathrm{VV}}\right)\Delta t} \tag{20}$$

$$\mathbf{N}_k^{\mathrm{VB}}=\left(\mathbf{N}_c^{\mathrm{V}}+\mathbf{N}_c^{\mathrm{VV}}\right)^{-1}\left(\mathbf{N}^{\mathrm{V}}-\mathbf{I}\right)\mathbf{N}^{\mathrm{VB}}(k) \tag{21}$$

$$\mathbf{N}^{\mathrm{RV}}=\left(\mathbf{N}_c^{\mathrm{V}}+\mathbf{N}_c^{\mathrm{VV}}\right)^{-1}\left(\mathbf{N}^{\mathrm{V}}-\mathbf{I}\right)\mathbf{N}^{\mathrm{RV}} \tag{22}$$

Since the response of the vehicle can be measured for all the time steps, Eq.(19) can be rewritten by separating the known parameters (i.e. those that are related to the vehicle properties) from the unknown parameters (i.e. those that are related to the bridge properties and road roughness condition) as

$$\mathbf{P}_k=\mathbf{N}_k^{\mathrm{VB}}\mathbf{X}_k^{\mathrm{B}}+\mathbf{N}^{\mathrm{RV}}\mathbf{R}_k \tag{23}$$

where

$$\mathbf{P}_k=\mathbf{X}_{k+1}^{\mathrm{V}}-\mathbf{N}^{\mathrm{V}}\mathbf{X}_k^{\mathrm{V}} \tag{24}$$

To apply the SSI method, the equations of the VBI system should be formulated in state space discrete time-invariant form (see Eq.(2)). It is obvious that Eq.(16) satisfies this requirement. However, in Eq.(23), even though the road roughness related term $\mathbf{N}^{\mathrm{RV}}\mathbf{R}_k$ can be regarded as noise, the matrix $\mathbf{N}_k^{\mathrm{VB}}$ is a time-variant matrix. To overcome this problem, we introduce the pseudoinverse matrix

$$\mathbf{M}^{\dagger}\mathbf{M}=\mathbf{I}\in R^{i\times j},\mathbf{M}\in R^{i\times j},i>j \tag{25}$$

Then the Eq.(23) is transformed to

$$\mathbf{Z}_k^{\mathrm{V}}=\mathbf{X}_k^{\mathrm{B}}+\mathbf{v}_k \tag{26}$$

where $\mathbf{Z}_k^{\mathrm{V}}$ is a known vector related to the vehicle response, and $\mathbf{v}_k$ is a random stochastic process.

$$\mathbf{Z}_k^{\mathrm{V}}=\left(\mathbf{N}_k^{\mathrm{VB}}\right)^{\dagger}\mathbf{P}_k \tag{27}$$

$$\mathbf{v}_k=\left(\mathbf{N}_k^{\mathrm{VB}}\right)^{\dagger}\mathbf{N}^{\mathrm{RV}}\mathbf{R}_k \tag{28}$$

Collectively, the equations of the coupled VBI system, in time-invariant state space form are

$$\begin{aligned}\mathbf{X}_{k+1}^{\mathrm{B}} &= \mathbf{N}^{\mathrm{B}}\mathbf{X}_{k}^{\mathrm{B}} + \mathbf{w}_k \\ \mathbf{Z}_{k}^{\mathrm{V}} &= \mathbf{X}_{k}^{\mathrm{B}} + \mathbf{v}_k\end{aligned} \tag{29}$$

which can be combined to the yield

$$\mathbf{Z}_{k}^{\mathrm{V}} = \left(\mathbf{N}^{\mathrm{B}}\right)^{k-1}\mathbf{X}_{1}^{\mathrm{B}} + \sum_{i=1}^{k-1}\left(\mathbf{N}^{\mathrm{B}}\right)^{k-i-1}\mathbf{w}_i + \mathbf{v}_k \tag{30}$$

2.4 *Stochastic subspace identification*

In discrete time, the response of the system can be represented by the data matrix

$$\mathbf{Z}^{\mathrm{V}} = \begin{bmatrix}\mathbf{Z}_1^{V} & \mathbf{Z}_2^{V} & \dots & \mathbf{Z}_q^{V}\end{bmatrix} \tag{31}$$

We define the block Hankel matrix $\mathbf{H}_{\mathbf{Z}}$ as

$$\mathbf{H}_{\mathbf{Z}} = \begin{bmatrix}\mathbf{Z}_1^{\mathrm{V}} & \cdots & \mathbf{Z}_j^{\mathrm{V}} \\ \vdots & \ddots & \vdots \\ \mathbf{Z}_{2s}^{\mathrm{V}} & \cdots & \mathbf{Z}_{2s+j-1}^{\mathrm{V}}\end{bmatrix} \in R^{4ns\times j} \tag{32}$$

where $2s$ is the number of the rows in the Hankel matrix; j is the number of the columns, and $q=2s+j-1$ is the total number of the data. To apply the SSI technique, the Hankel matrix $\mathbf{H}_Z$ is first divided into a "past" part $\mathbf{H}_{Z}^{p}$ and a "future" part $\mathbf{H}_{Z}^{f}$

$$\mathbf{H}_{\mathbf{Z}} = \begin{bmatrix}\mathbf{H}_{\mathbf{Z}}^{p} \\ \mathbf{H}_{\mathbf{Z}}^{f}\end{bmatrix} \tag{33}$$

where $\mathbf{\Gamma}_i$ is the observability matrix containing solely the bridge properties; $\bar{\mathbf{X}}^{p}$ and $\bar{\mathbf{X}}^{f}$ are the stochastic state vectors, composed of the bridge response; $\mathbf{\Psi}_i$ is the Toeplitz matrix, containing the bridge properties; $\mathbf{H}_{w}^{p}$, $\mathbf{H}_{w}^{f}$, $\mathbf{H}_{v}^{p}$ and $\mathbf{H}_{v}^{f}$ represent Hankel matrices generated by the random stochastic process.

By means of the LQ decomposition the Hankel matrix becomes

$$\mathbf{H}_{\mathbf{Z}} = \begin{bmatrix}\mathbf{H}_{\mathbf{Z}}^{p} \\ \mathbf{H}_{\mathbf{Z}}^{f}\end{bmatrix} = \begin{bmatrix}\mathbf{L}_{11} & \mathbf{0} \\ \mathbf{L}_{21} & \mathbf{L}_{22}\end{bmatrix}\begin{bmatrix}\mathbf{Q}_1^{T} \\ \mathbf{Q}_2^{T}\end{bmatrix} \in R^{4ns\times j} \tag{34}$$

where the submatrices $\mathbf{L}_{11}$, $\mathbf{L}_{21}$, $\mathbf{L}_{22} \in R^{2ns\mathrm{x}2ns}$ are those of the lower triangular, and the submatrices $\mathbf{Q}_1^{\mathrm{T}}$, $\mathbf{Q}_2^{\mathrm{T}} \in R^{2ns\mathrm{x}j}$ are both orthogonal matrices.

According to the orthogonal projection theorem, the projection of the "future" Hankel matrix $\mathbf{H}_{Z}^{f}$ onto the "past" Hankel matrix $\mathbf{H}_{Z}^{p}$ is (Katayama 2006)

$$\frac{\mathbf{H}_{\mathbf{Z}}^{f}}{\mathbf{H}_{\mathbf{Z}}^{p}} = \mathbf{L}_{21}\mathbf{Q}_1^{T} \tag{35}$$

Under the assumption that the vehicle-related terms are independent to each other, it can be concluded that only the bridge-related term is retained from the projection theorem. Thus,

$$\frac{\mathbf{H}_{\mathbf{Z}}^{f}}{\mathbf{H}_{\mathbf{Z}}^{p}} = \mathbf{\Gamma}_i\bar{\mathbf{X}} \tag{36}$$

where $\bar{\mathbf{X}}$ is the bridge-related stochastic state vector obtained after the projection of the Hankel matrices. Combining Eq.(35) and Eq.(36), one can obtain

$$\mathbf{L}_{21} = \mathbf{\Gamma}_i\bar{\mathbf{X}}\mathbf{Q}_1 \tag{37}$$

Then the singular value decomposition (SVD) yields the observability matrix $\mathbf{\Gamma}_i$,

$$\mathbf{L}_{21} = \begin{bmatrix}\mathbf{U}_1 & \mathbf{U}_2\end{bmatrix}\begin{bmatrix}\mathbf{\Sigma}_1 & 0 \\ 0 & \mathbf{\Sigma}_2\end{bmatrix}\begin{bmatrix}\mathbf{V}_1^{T} \\ \mathbf{V}_2^{T}\end{bmatrix} \in R^{2ns\times 2ns} \tag{38}$$

where $\mathbf{U}_1 \in R^{2ns\mathrm{x}2n}$, $\mathbf{U}_2 \in R^{2ns\mathrm{x}2n(s-1)}$, $\mathbf{V}_1 \in R^{2ns\mathrm{x}2n}$, $\mathbf{V}_2 \in R^{2ns\mathrm{x}2n(s-1)}$, and $\mathbf{\Sigma}_1 \in R^{2n\mathrm{x}2n}$ is a diagonal matrix containing $2n$ singular values related to the DOF of the bridge. Consequently, $\mathbf{L}_{21}$ is approximately

$$\mathbf{L}_{21} \approx \mathbf{U}_1\mathbf{\Sigma}_1\mathbf{V}_1^{T} \tag{39}$$

The diagonal matrix $\mathbf{\Sigma}_1$ is a proportional matrix separable into two square-root matrices (Katayama 2006). Based on this, one can obtain the observability matrix $\mathbf{\Gamma}_i$ and the state vector $\bar{\mathbf{X}}\mathbf{Q}_1$ as

$$\mathbf{\Gamma}_i = \mathbf{U}_1\mathbf{\Sigma}_1^{\frac{1}{2}} \tag{40}$$

$$\bar{\mathbf{X}}\mathbf{Q}_1 = \mathbf{\Sigma}_1^{\frac{1}{2}}\mathbf{V}_1^{T} \tag{41}$$

With the observability matrix available, the bridge system matrix $\mathbf{N}^{\mathrm{B}}$ can be obtained from the pseudoinverse calculation as

$$\mathbf{N}^{\mathrm{B}} = \underline{\mathbf{\Gamma}}_i^{\dagger}\overline{\mathbf{\Gamma}}_i \tag{42}$$

where $\underline{\mathbf{\Gamma}}_i \in R^{2n(s-1)\mathrm{x}2n}$ is the observability matrix $\mathbf{\Gamma}_i$ with the nethermost matrix $(\mathbf{N}^{\mathrm{B}})^{s-1} \in R^{2n\mathrm{x}2n}$ deleted; and $\overline{\mathbf{\Gamma}}_i \in R^{2n(s-1)\mathrm{x}2n}$ is the observability matrix $\mathbf{\Gamma}_i$ with the upmost unit matrix $\mathbf{I}_{2n} \in R^{2n\mathrm{x}2n}$ deleted.

The bridge system matrix $\mathbf{N}^{\mathrm{B}}$ is obtained from Eq.(42) in time-discrete form. It can be converted to the time-continuous form by taking the inverse operation of Eq.(17) as

$$\mathbf{N}_c^{\mathrm{B}} = \log\mathrm{m}\left(\mathbf{N}^{\mathrm{B}}\right)/\Delta t \tag{43}$$

where logm denotes the logarithmic matrix operation. The time-continuous bridge system matrix $\mathbf{N}_c^{\mathrm{B}}$ contains all the properties of the bridge. An eigenvalue decomposition of the system matrix $\mathbf{N}_c^{\mathrm{B}}$ returns the eigenvalues of the system

$$\mathbf{N}_c^{\mathrm{B}} = \mathbf{\Psi}\mathbf{\Lambda}\mathbf{\Psi}^{-1} \tag{44}$$

where $\mathbf{\Psi} \in R^{2n\mathrm{x}2n}$ contains the eigenvectors, $\mathbf{\Lambda} \in R^{2n\mathrm{x}2n}$ is a diagonal matrix containing the eigenvalues $\lambda_1, \lambda_1^{*}, \lambda_2, \lambda_2^{*}, \dots, \lambda_n^{*}$; where the symbol * denoting the complex conjugate.

3 RESULTS AND DISCUSSIONS

3.1 *Validation of proposed SSI method*

The frequencies of the examined bridge for the first five modes in the vertical direction are 1.99Hz, 5.52Hz, 7.73Hz, 7.71Hz and 7.91Hz, while the frequencies of the vehicle are 2.15Hz, 3.03Hz and 4.70Hz. These values are obtained from the modal analysis of the systems. The vehicle speed is assumed as constant of 5km/h and the bridge surface is smooth. Figure 2a shows the vertical acceleration of the truck tractor during the time that the vehicle is traveling on the bridge.

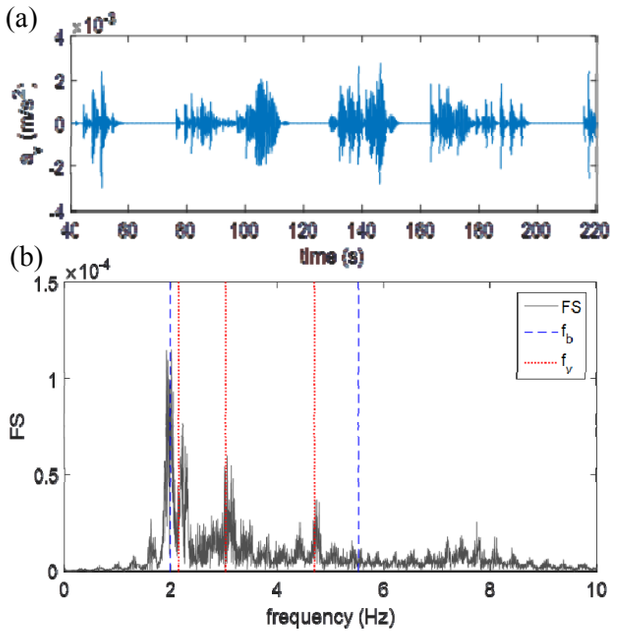


Figure 2. (a) Vertical acceleration of the tractor (b) Fourier spectrum for the vertical acceleration of the tractor.

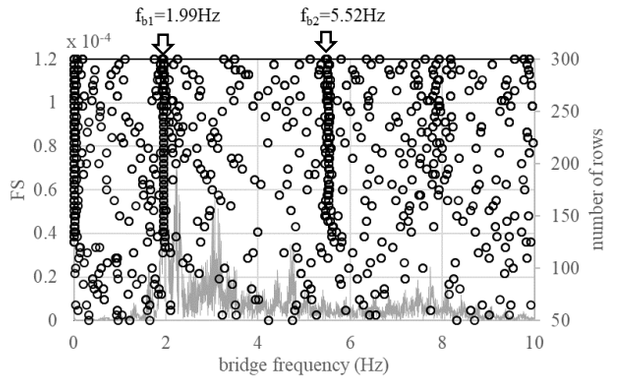


Figure 3. Identification of bridge frequencies by SSI method.

Figure 2b presents the corresponding Fourier spectrum. It is observed that both the frequencies of the vehicle, and the fundamental frequency of the bridge are visible in the Fourier spectrum. However, it is difficult to identify the second frequency of the bridge. In addition, a lot of disturbed peaks appear in the Fourier spectrum, which increases the difficulty of extracting the information of value.

In the following figures, the grey lines represent the Fourier spectra (FS) of the response of the truck tractor in the vertical direction, and the circles represent the bridge frequencies identified by the proposed SSI method, the bridge frequencies are considered to be successfully identified only if the circles create a line without much variation in value as the number of the rows (of the Hankel matrix) increases.

To estimate the bridge frequencies efficiently, the proposed SSI method is applied. The response of the vehicle is calculated by the VBI analysis and the dynamic properties of the vehicle are known.

Figure 3 shows the identification results obtained from the proposed SSI method, without considering the road roughness conditions. As the number of the rows in the Hankel matrix increases, the frequencies of the bridge stabilize gradually in lines. The two bridge frequencies can be efficiently identified from the figure. Meanwhile, the vehicle frequencies have been successfully suppressed.

3.2 *Effect of the road roughness condition*

It is known that the road roughness blurs the identification of the bridge frequencies from the vehicle response (Lin & Yang 2005). However, in reality, the irregularity on the bridge surface cannot be neglected. Thus, it is important to validate the efficiency of the proposed SSI method considering the road roughness condition. To this end, we define the road roughness profile of Figure 4 (Paraskeva et al 2017).

Figure 5 shows the results of the proposed SSI method, considering the road roughness conditions. Again, the first two bridge frequencies can be clearly identified. This example clearly demonstrates that the proposed SSI method has an advantage in practical applications.

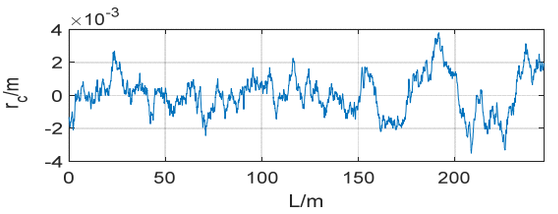


Figure 4. Road roughness profile on the bridge.

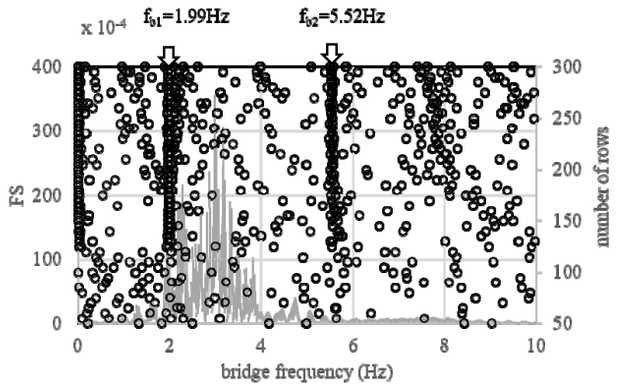


Figure 5. Identification of bridge frequencies by SSI method considering the road roughness.

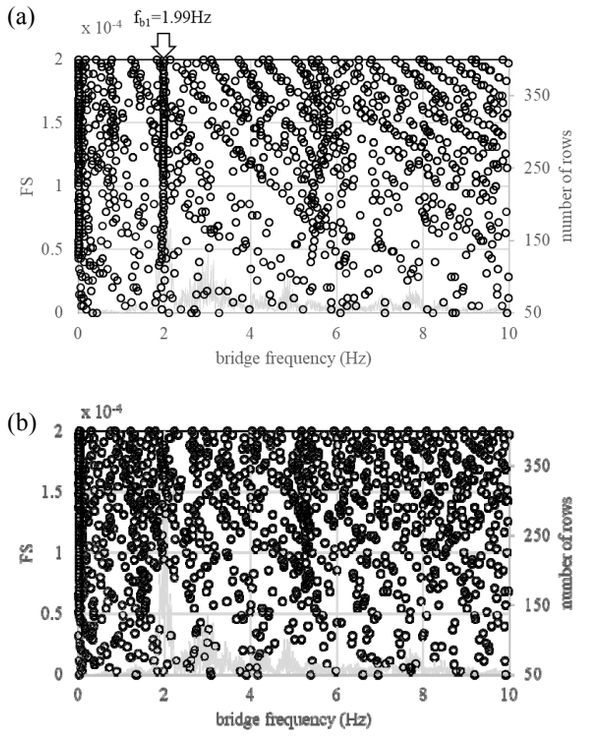


Figure 6. Identification of bridge frequencies by SSI method (a) V=10km/h (b) V=20km/h.

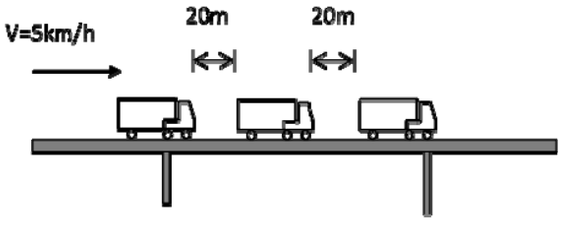


Figure 7. Configuration of the vehicle sequence on the bridge

3.3 *Effect of the driving speed*

This section examines the effect of the driving speed on the efficiency of the proposed SSI method. So far, a constant driving speed of 5km/h has been considered. In this section, we examine the effect of two more driving speeds (a) 10km/h and (b) 20km/h. The road surface is assumed to be smooth. Figure 6(a) shows the identification results by the proposed SSI method when the driving speed is 10km/h. Compared with the case that the driving speed is 5km/h, it is obvious that much more redundant circles appear in this figure, which increases the difficulty of distinguishing the bridge frequencies. As the driving speed increases to 20km/h (see Fig 6(b)), no concentrated lines can be identified, and the bridge frequencies cannot be extracted. Thus, a lower driving speed of the vehicle is beneficial to the accuracy of the proposed SSI method. These findings are in agreement with Yang & Chen (2015). The higher the speed of the vehicle is the shortest the duration of the vehicle on the bridge is which affects the identification procedure.

3.4 *Effect of on-going traffic*

This section examines the effect of the on-going traffic on the efficiency of the proposed SSI method. We use three vehicles running with a 20m relative distance, and speed 5km/h (Fig 7).

In Figure 8(a) all the vehicles have the same dynamic characteristics, and the 'monitored' vehicle is the second. Figure 8(b) repeats the analyses of Figure 8(a), considering the third vehicle as the 'monitored', i.e. it applies the proposed SSI method on the response of the last moving vehicle. The results show that in both cases, the concentrated line representing the fundamental frequency can be identified efficiently. However, the second frequency of the bridge is not that obvious.

In Figure 8(c), the first and the third vehicles have the same dynamic properties, while an additional mass of 26,113kg is added on the trailer of the middle vehicle. We use the response of the latest vehicle for the application of the proposed approach. Contrary to the previous results, we can now clearly identify the first three bridge frequencies. The comparison of Figures 8(a) to 8(c) indicates that the effect of the on-going traffic on the efficiency of the proposed approach is a very complicated phenomenon that merits further research.

4 CONCLUSIONS

The present study applies the SSI method combined with the vehicle-bridge interaction dynamic analysis, to extract the first eigenfrequencies of a straight re-

inforced concrete bridge, using the vibration response of a passing "monitored" vehicle. We examine the accuracy and the effectiveness of the proposed SSI method. The simulations show that the proposed stochastic subspace identification method can satisfactorily be applied for the identification of the bridge frequencies considering the road roughness conditions. This paper only offers a glimpse into the complex bridge system identification problem, and more research is needed to derive the decisive conclusions.

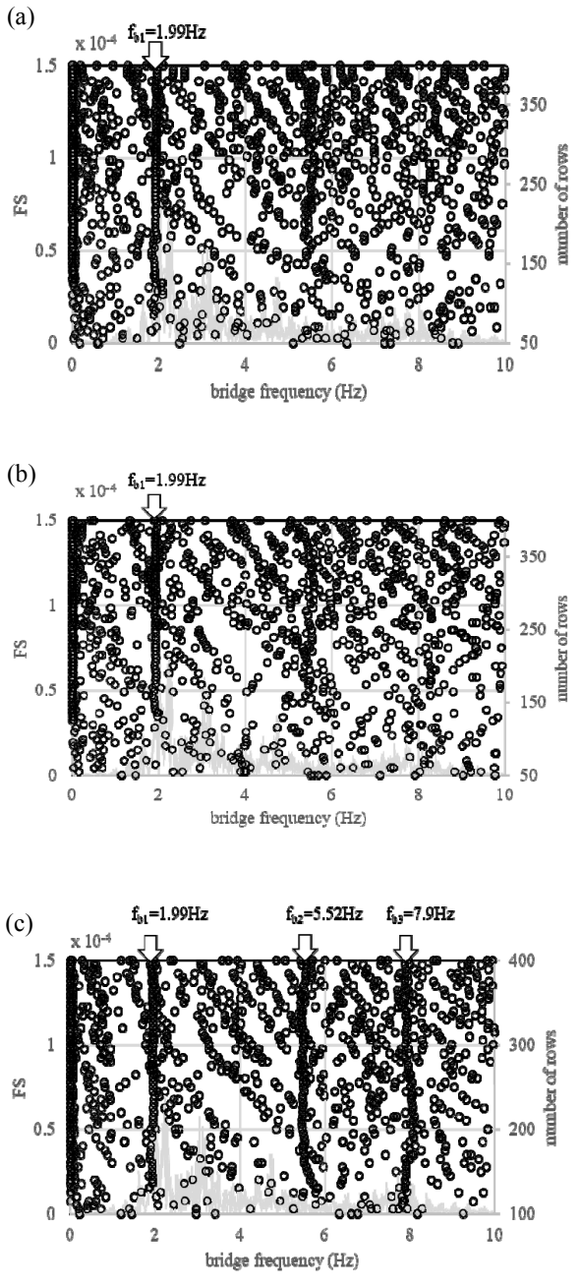


Figure 8. Identification of bridge frequencies by SSI method for the case (a) three same vehicles with the middle one measured (b) three same vehicles with the latest one measured (c) the middle vehicle is heavier, and the latest vehicle measured

5 REFERENCES

Au, S. K., Ng, C. T., Sien, H. W. & Chua, H. Y. 2005. Modal identification of a suspension footbridge using free vibration signatures. *Int. J. Appl. Math. Mech* 1(4): 55-73.

Conner, G., Stallings, J., McDuffie, T., Campbell, J., Fulton, R., Shelton, B. & Mullins, R. 1997. Steel bridge testing in Alabama. *Transportation Research Record: Journal of the Transportation Research Board* 1594: 134-139.

Huang, C. S., Yang, Y. B., Lu, L. Y. & Chen, C. H. 1999. Dynamic testing and system identification of a multi‐span highway bridge. *Earthquake engineering & structural dynamics* 28(8): 857-878.

Goi, Y., & Kim, C. W. 2016. Mode identifiability of a multi-span cable-stayed bridge utilizing stabilization diagram and singular values. *Smart Structures and Systems* 17(3): 391-411.

Katayama, T. 2006. *Subspace methods for system identification*. Springer Science & Business Media.

Paraskeva, T. S., Dimitrakopoulos, E. G. & Zeng, Q. 2017. Dynamic vehicle–bridge interaction under simultaneous vertical earthquake excitation. *Bulletin of Earthquake Engineering* 15(1): 71-95.

Siringoringo, D. M. & Fujino, Y. 2008. System identification of suspension bridge from ambient vibration response. *Engineering Structures* 30 (2):462-477.

Van Overschee, P. and De Moor, B. 1996. Continuous-time frequency domain subspace system identification. *Signal Processing*, 52(2): 179-194.

Yang, Y., Lin, C. & Yau, J. 2004. Extracting bridge frequencies from the dynamic response of a passing vehicle. *J. Sound Vibrat.* 272(3): 471-493.

Yang, Y. & Chen, W. 2015. Extraction of bridge frequencies from a moving test vehicle by stochastic subspace identification. *Journal of Bridge Engineering* 21(3): 04015053.

Yang, Y. B. & Yang, J. P. 2017. State-of-the-Art Review on Modal Identification and Damage Detection of Bridges by Moving Test Vehicles. *International Journal of Structural Stability and Dynamics* 18(2): 1850025

Maintenance, Safety, Risk, Management and Life-Cycle Performance of Bridges – Powers, Frangopol, Al-Mahaidi & Caprani (Eds)
© 2018 Taylor & Francis Group, London, ISBN 978-1-138-73045-8

Study on compressive strength of steel plates with a partial loss of cross-sectional area

Kohei SAITO
Graduate School at Ritsumeikan University, Shiga, Japan
Katsuyoshi NOZAKA
Ritsumeikan University, Shiga, Japan

ABSTRACT: Many bridges in Japan had been built from 1950 to 1995, indicating that most of them have been in service more than 50 years. Corrosion has one of the most deleterious effects on steel structures, and this makes maintenance of steel bridges seriously problematic. It is necessary to establish rational criteria in order to accurately predict the residual strength and remaining life of existing steel structures. The objective of this research is to propose a simple expression that can identify the residual strength of steel plate members in compression.

1 INTRODUCTION

Many steel bridges now in-service face problems including corrosion, cracking, and deterioration over time. At the same time, local governments have to inspect the present state of bridges they manage and make future maintenance plans for these bridges. In order to prevent not only serious accidents, such as a bridge falling, but also to prevent inconvenience to users resulting from sudden bridge closure, it is important to clarify the state of every bridge at the present time and take suitable countermeasures.

Research on the residual strength of steel members with partial loss of cross-sectional area caused by corrosion or with cracks has been performed (Ex. Yamasawa et al. 2013 & Nogami et al. 2001), and residual strength evaluation equations have been proposed. However, results were presented under limited conditions such as girder dimensions. In addition, without information about application range, it is difficult to use these equations for practical work. As a result, they have still not come into wide use in practical work, and there is room for further improvements.

In this study, aiming for formulae applicable to practical work, parametric analyses were performed in order to investigate the compressive strength of steel members and propose simple equations.

The partial loss of cross-sectional area considered in this study represents the flanges of I-girders and box girders, and plate edges, a part prone to corrosion are mainly discussed. Partial loss caused by corrosion is often first discovered by a close visual inspection and presumably, in many cases, such corrosion is pitting. So, this study assumes cases in which corrosion causes pitting, resulting in partial loss of cross-sectional area. Therefore, by focusing on the most dangerous damage, it is thought to be possible to use results from this study for screening during maintenance of existing bridges.

2 OUTLINE OF THE ANALYSIS

FEM analysis (Finite Element Analysis) was performed using MSC Marc (MSC Software Corporation 2015), which is a general purpose non-linear structural analysis program, and four-node shell elements were used.

2.1 *ANALYSIS MODEL*

A flange of an I-girder and the flange of a box girder as shown in Figure 1 and in Figure 2 (indicated as I-model and B-model in followings) were modeled. SM490Y steel was used in both the I-model and B-model. I-model represents the bottom flange of girders near the intermediate support, the top flange of a steel railway bridge, and secondary members such as an end cross girder. As the box cross-section, girder and members under axial compressive force were considered.

The yield strength of SM490Y was set to be σ_y=355N/mm^2, and Young's modulus and Poisson's ratio are E=200,000N/mm^2 and ν=0.3, respectively. The elements were ddivided at 5 mm both in X- and Y-axis direction. As initial deformation, in the length direction, for both the I-model and the B-model, sinusoidal waves with half wave of 100 mm were given, and in the width direction, linear change

was given in the I-model, and a sinusoidal wave with half wave was given in the B-model.

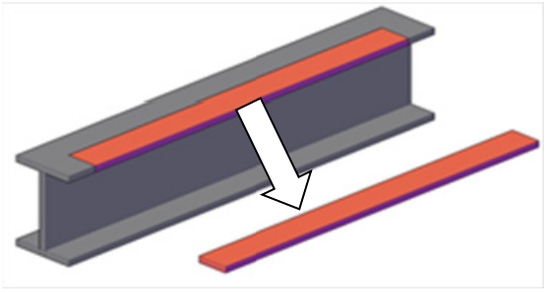


Figure 1. I-girder flange model (I-model)

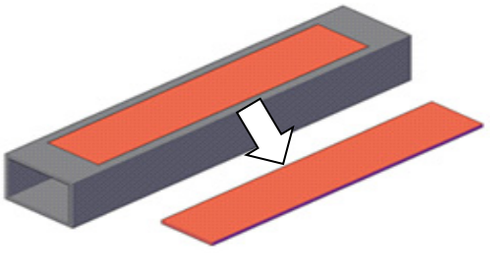


Figure 2. Box girder flange model (B-model)

Figure 3 shows the residual stress distribution used in the analysis. Regarding the I-girder cross-section model (I-model) shown in the top part of Figure 3, the residual stress distribution of only one side of the flange was used with reference to the residual stress distribution shown in Maeda et al. (2007). The bottom part of Figure 3 shows the one for box-girder cross section model (B-model), which assumed an idealized linear distribution shape with tensile residual stress of $1.0\sigma_y$ and compressive residual stress of $0.13\sigma_y$. This was defined by proportionally varying the residual stress distribution listed in Yamasawa et al. (2013).

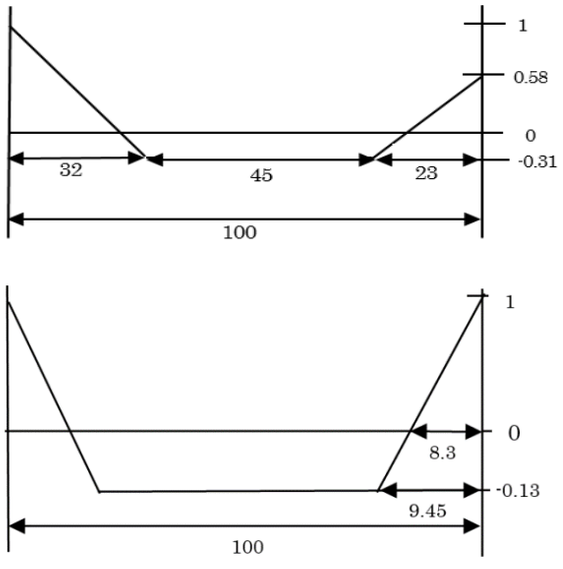


Figure 3. Residual stress distribution

2.2 *DETAILS OF I-MODEL*

The boundary conditions of the I-model were given as simple support on three sides and free on one side. Dimensions were set as 700 mm×100 mm, and the plate thicknesses (t) were the values shown in Table 1 to obtain the target width-thickness ratio parameter (R). The partial loss of cross-sectional area caused by corrosion was given as a partial loss of cross-sectional area of 10, 20, and 30% in the width and length direction respectively from the center of the edge (indicated as 10-10%, 20-20%, and 30-30% model in followings). In addition, in order to account for the effect of loss of cross-sectional area in the length direction so that the analysis was conducted expanding the partial loss in the sectional area to 20% and 30% (10-20%, 10-30%) only in the length direction while loss of cross-sectional area in width direction was fixed in 10%.

Table 1. Width-thickness ratio parameter and plate thickness (I-model)

R	1.2	1.0	0.9	0.8	0.7
t	5.5	6.6	7.4	8.3	9.5

2.3 *DETAILS OF B-MODEL*

The boundary conditions of the B-model were given as simple support on four sides. Its dimensions were set as three patterns: 500 mm×100 mm, 700 mm×100 mm, and 1,000 mm×100 mm. The plate thicknesses (t) and width-thickness ratio parameter (R) considered in this study were shown in Table 2. The partial loss of cross-sectional area caused by corrosion was given as 10, 20, and 30% in the width and length direction respectively from the center of the edge of the flange plate in Figure 2 (indicated as 10-10%, 20-20%, and 30-30% in followings). In addition, in order to account for the influence of partial loss of cross-sectional area caused by corrosion in the length direction, analysis was conducted expanding partial loss in the cross-sectional area to 20% and 30% (10-20%, 10-30%) only in the length direction, while loss of cross-sectional area was fixed as 10% in the width direction only for the 700 mm×100 mm model. The basic model without loss of cross-sectional area for B-model (0-0%) is shown in Figure 4, and the models with partial loss of sectional area of 10-10% and 10-30% are shown in Figure 5 and Figure 6 respectively.

Table 2. Width-thickness ratio parameter and the plate thickness (B-model)

R	1.2	1.0	0.9	0.8	0.7
t	1.8	2.2	2.5	2.8	3.2

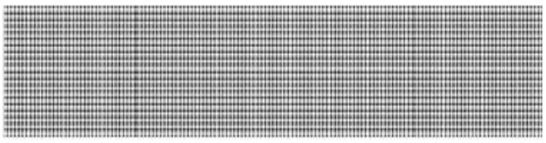


Figure 4. B-model:0-0%

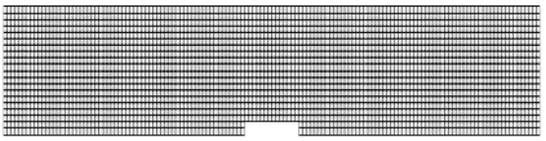


Figure 5. B-model:10-10%

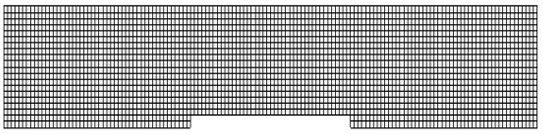


Figure 6. B-model:10-30%

3 RESULTS OF ANALYSIS

3.1 *I-MODEL*

Table 3 and Figure 7 shows the results of the I-model. In Figure 7, the vertical axis shows the value obtained by dividing the maximum stress of the analytical results by the yield strength (σ_u/σ_y), and the transverse axis shows the width-thickness ratio parameter. In addition, as reference, the dotted line represents $\sigma_u/\sigma_y = 0.5/R^2$, and the solid line represents $\sigma_u/\sigma_y = 1.0/R^2$. The maximum stress is the value obtained by dividing the maximum load obtained by the analysis by the cross-sectional area without loss.

Table 3. Results of analysis of the I-model

	σ_u / σ_y					
R	0-0%	10-10%	20-20%	30-30%	10-20%	10-30%
1.2	0.72	0.72	0.58	0.38	0.56	0.44
1.0	0.82	0.82	0.65	0.48	0.78	0.63
0.9	0.88	0.88	0.69	0.50	0.81	0.70
0.8	0.94	0.90	0.72	0.54	0.84	0.74
0.7	0.98	0.90	0.76	0.57	0.87	0.78

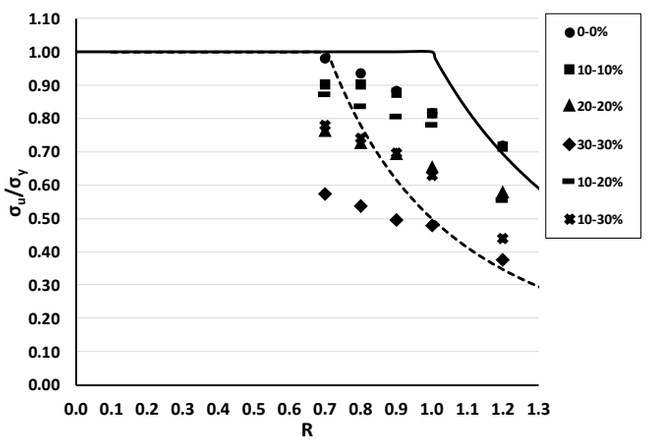


Figure 7. σ_u/σ_y -R relationship for the I-model

3.2 *B-MODEL*

The results of the B-model for 500mm×100mm, 700mm×100mm, and 1,000mm×100mm cases are shown in Table 4, Table 5, and Table 6 respectively. As in the case of the I-model, the results were organized based on the non-dimensional value (σ_u/σ_y) that was obtained by dividing the maximum stress of the analytical results by the yield strength. In following discussions, the lowest values among the cases for three aspect ratios is used, and these values are shown in Table 7 and Figure 8. In these figures, the transverse axis represents the width-thickness ratio parameter, and as reference, the dotted line represents $\sigma_u/\sigma_y = 0.5/R^2$ and the sold line represents $\sigma_u/\sigma_y = 1.0/R^2$. And the maximum stresses shown in Tables 4 to 7 and in Figure 8 were obtained by dividing the maximum load obtained by the analysis by the sectional area without loss.

Table 4. B-model (500mm × 100mm)

	σ_u / σ_y			
R	0-0%	10-10%	20-20%	30-30%
1.2	0.68	0.48	0.39	0.36
1.0	0.73	0.56	0.45	0.40
0.9	0.78	0.63	0.49	0.43
0.8	0.83	0.69	0.54	0.45
0.7	0.89	0.80	0.59	0.49

Table 5. B-model (700mm × 100mm)

	σ_u / σ_y					
R	0-0%	10-10%	20-20%	30-30%	10-20%	10-30%
1.2	0.68	0.45	0.38	0.36	0.39	0.39
1.0	0.74	0.51	0.43	0.40	0.45	0.44
0.9	0.78	0.58	0.46	0.42	0.49	0.47
0.8	0.83	0.64	0.50	0.45	0.54	0.50
0.7	0.89	0.74	0.55	0.47	0.59	0.55

Table 6. B-model (1000mm × 100mm)

	σ_u / σ_y			
R	0-0%	10-10%	20-20%	30-30%
1.2	0.68	0.37	0.38	0.35
1.0	0.74	0.56	0.42	0.39
0.9	0.78	0.62	0.46	0.42
0.8	0.83	0.68	0.50	0.44
0.7	0.89	0.75	0.55	0.47

Table 7. The lowest values among the B-model

	σ_u / σ_y					
R	0-0%	10-10%	20-20%	30-30%	10-20%	10-30%
1.2	0.68	0.45	0.38	0.35	0.39	0.39
1.0	0.73	0.51	0.42	0.39	0.45	0.44
0.9	0.78	0.58	0.46	0.42	0.49	0.47
0.8	0.83	0.64	0.50	0.44	0.54	0.50
0.7	0.89	0.74	0.55	0.47	0.59	0.55

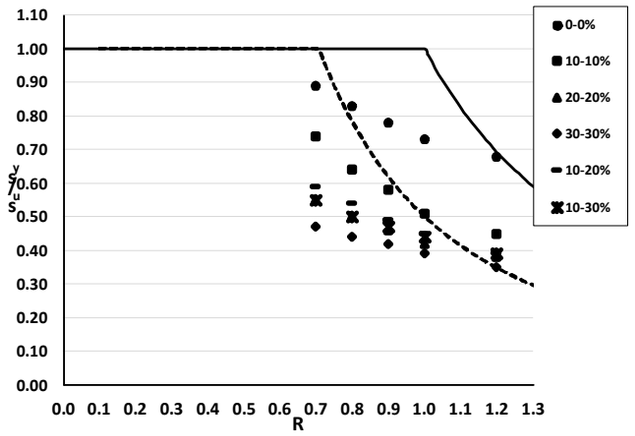


Figure 8. σ_u/σ_y -R relationship for the B-model

4 DISCUSSION AND PROPOSAL OF THE RESIDUAL STRENGTH EQUATIONS

The results of the analyses performed in this study are used to propose residual strength equations.

4.1 *I-MODEL*

First, for the case without loss of cross-sectional area (0-0% model), Figure 7 is used to estimate the compressive strength as in Equation 1.

$$\sigma_u/\sigma_y = 0.8R^{-0.6} \quad (1)$$

Next, the width-thickness ratio parameter R', focused on the corroded part, is obtained in order to propose the residual strength equation for a case with loss of cross-sectional area. As shown in Figure 9, b' of the white part left by the partial loss of cross-sectional area is used to calculate the width-thickness ratio parameter assuming a plate with simple support on three sides and one side free. The R' obtained are shown in Table 8. Figure 10 shows the relationships between the newly obtained R' in the transverse axis and the maximum stress/yield strength (σ_u/σ_y) in the vertical axis. The vertical axis in Figure 10 obtained by dividing the maximum load obtained from the analytical results by the cross-sectional area considering loss of cross-sectional area. In addition, in Figure 10, for the purpose of comparison, the nominal strength curve (Japan Road Association 2002) for a column obtained by Equation 2 and Equation 3 is shown. Figure 10 reveals that in the cases of partial loss of cross-sectional area of 10-10%, 20-20%, and 30-30%, the residual strength could be estimated by the nominal compressive strength curve for a column.

$$\sigma_u/\sigma_y = \begin{cases} 1.109-0.545R & (0.2<R\leqq 1.0) \quad (2) \\ 1.0/(0.733+R^2) & (1.0<R) \quad (3) \end{cases}$$

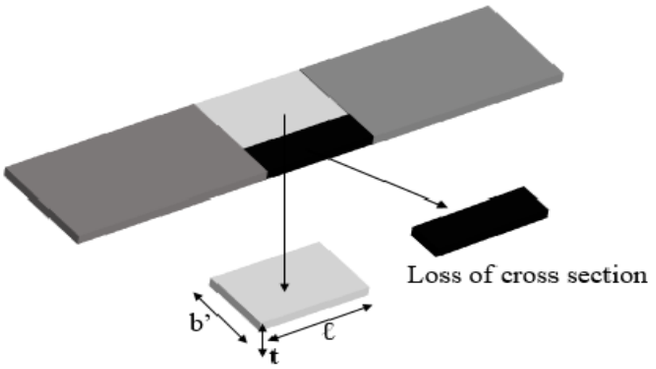


Figure 9. Derivation of width-thickness ratio parameter R'

Table 8. Width-thickness ratio parameter R'

		Width-thickness ratio parameter R'				
		1.2	1.0	0.9	0.8	0.7
Corroded (%)	10	0.59	0.48	0.44	0.39	0.34
	20	1.18	0.96	0.88	0.78	0.68
	30	1.77	1.48	1.32	1.18	1.03

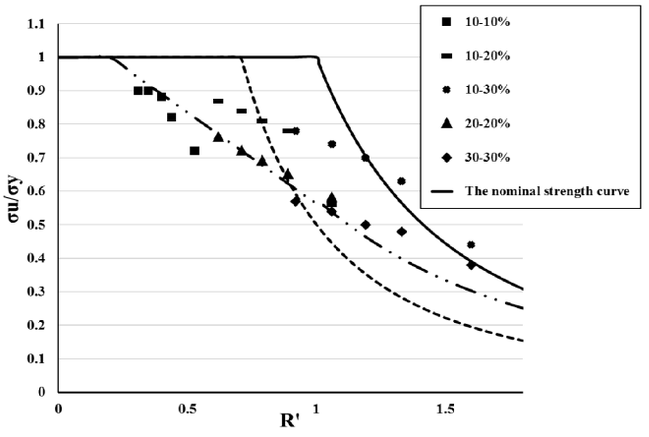


Figure 10. R'- σ_u/σ_y curve (I–model)

It can be stated that the buckling mode of the corroded part is similar to the buckling mode of a column and that the support condition—simple support on three sides and free on one side—is no longer effective. Figure 11 (10-10%, R=1.2) and Figure 12 (30-30%, R=1.2) show the buckling mode of the I-model. According to the buckling mode shown in Figure 12, it seems that the buckling coefficient can be calculated assuming that the effective buckling length (ℓ_k) is $\ell_k=0.9\ell$, considering the constraint conditions from the surroundings of corroded part. However, it is assumed that the value of σ_u/σ_y does not exceed that in the 0-0% case.

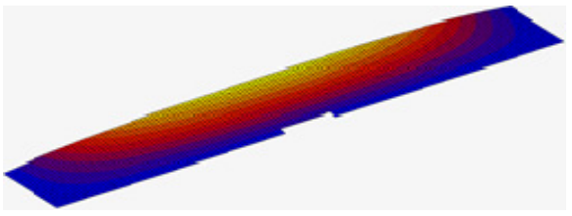


Figure 11. The buckling form of the I-model (10-10%, R=1.2)

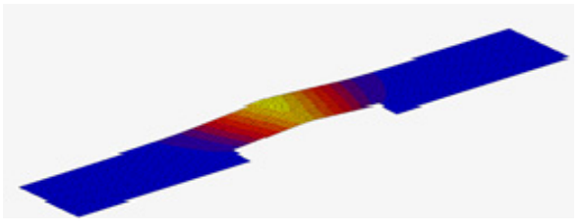


Figure 12. The buckling form of the I-model (30-30%, R=1.2)

Finally, in order to propose residual strength equations for cases, in which the partial loss of sectional area has expanded in the length direction (10-20%, 10-30%), a ratio of the partial loss of sectional area in the length direction is newly defined as β_l (%).

For the 10-20% and 10-30% cases in which the partial loss of cross-sectional area expanded in the length direction, the difference between σ_u/σ_y for 10-20% and 10-30% and σ_u/σ_y for 10-10%, in the case where the width-thickness ratio parameter R= 1.2 to 0.7, was calculated to obtain the respective average change (X). Table 9 shows these values, and Figure 13 shows the relationship between β_l and X. In the case where β_l=20 for example, the value of (σ_u/σ_y of 10-10%) - (σ_u/σ_y of 10-20%) for the five parameters of the width-thickness ratio parameter R=1.2 to 0.7 were calculated and the average values were obtained. Similarly, the value of β_l =30 are calculated, and the relationship of X=0.0054β_l was found by regression analysis as shown in Figure 13.

In brief, the residual strength equation for the cases where the partial loss of cross-sectional area expanded in the length direction (10-20%, 10-30%) is obtained using Equation 4 based on the value of 10-10% case.

$$\sigma_u/\sigma_y = (\sigma_u/\sigma_y \text{ of } 10\text{-}10\%) - (0.0054\beta_l) \qquad (4)$$

Table 9. β_l and average change

β_l	X
20	0.072
30	0.186

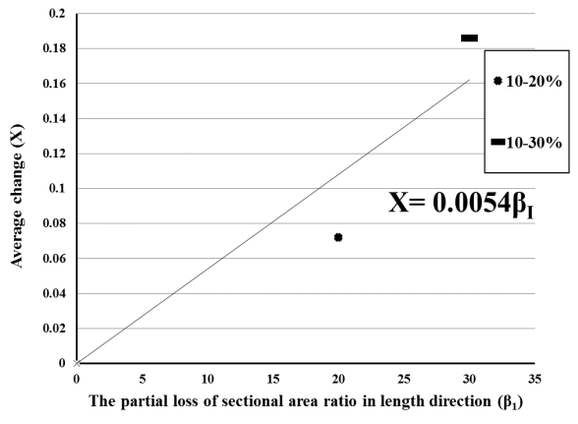


Figure 13. Estimation of relationship between X and β_l

Table 10. Predicted values by proposed equations

R	σ_u/σ_y 0-0%	10-10%	20-20%	30-30%	10-20%	10-30%
1.2	0.72	0.72	0.54	0.30	0.61	0.56
1.0	0.80	0.80	0.62	0.40	0.69	0.64
0.9	0.85	0.85	0.68	0.47	0.74	0.69
0.8	0.91	0.91	0.72	0.54	0.80	0.75
0.7	0.99	0.94	0.77	0.61	0.83	0.78

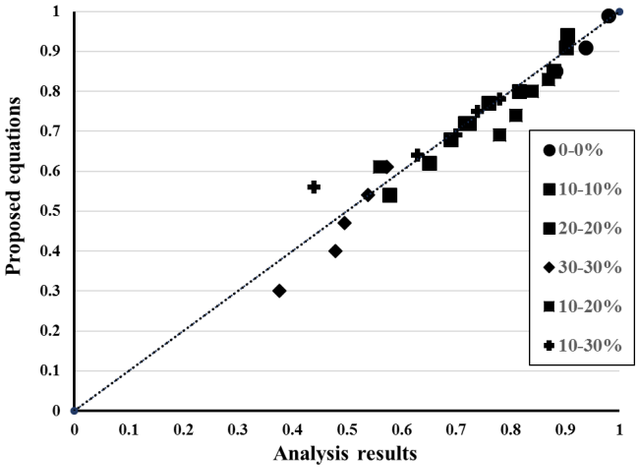


Figure 14. Comparison of estimated values and analytical results

The predicted values by the proposed equations, Equation 1 to Equation 4 are listed in Table 10. Figure 14 shows the comparison of estimated strength from the proposed equations on the vertical axis and the analytical results on the transverse axis.

Figure 14 reveals that there is a maximum error of 12% between the analysis values and values from the proposed equations, but it can be assumed that the analysis values can be roughly predicted. Therefore, it seems possible to use proposed equations to evaluate the compressive strength in a case with partial loss of cross-sectional area, assuming as a plate with simple supports on three sides and free on one side.

4.2 *B-MODEL*

First, in the case without loss of cross-sectional area (0-0%), the compressive strength is approximated by the Equation 5 based on Figure 8.

$$\sigma_u/\sigma_y = 0.75R^{-0.5} \qquad (5)$$

Next, as in I-model, the width-thickness ratio parameter R' focused on the corroded part is newly obtained in order to propose a residual strength equation. As shown in Figure 15, the width b' of the white part left by partial loss of cross-sectional area is used to calculate the width-thickness ratio parameter for a plate with simple supports on three sides and free on one side. Calculated value of R' are listed in Table 11. Figure 16 shows the relation-

ship R' that were newly obtained on the transverse axis and the maximum stress/yield strength value (σ_u/σ_y) on the vertical axis. Values in the vertical axis in Figure 16 were calculated by dividing the maximum load obtained from the analysis by the cross-sectional area considering loss of cross-sectional area. In addition, analytical results of a plate with simple supports on three sides and free on one side (700 mm×100 mm model) are plotted in Figure 16 for comparison purposes (legend in the figure is I-model 0-0%).

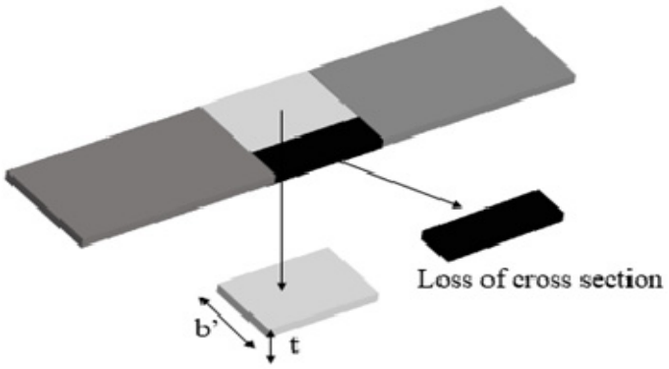


Figure 15. Derivation of width-thickness ratio parameter R'

Table 11. Width-thickness ratio parameter R'

		Width-thickness ratio parameter R'				
		1.2	1.0	0.9	0.8	0.7
Corroded (%)	10	3.40	2.78	2.45	2.18	1.91
	20	3.02	2.47	2.18	1.94	1.70
	30	2.64	2.16	1.90	1.70	1.49

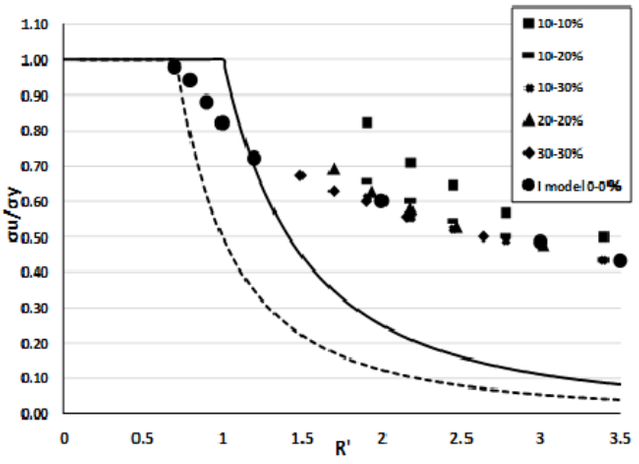


Figure 16. R'- σ_u/σ_y curve (B–model)

Figure 16 reveals that in the partial loss of cross-sectional area ratio of 20% or higher cases, the residual strength is superimposed on the results of I-model 0-0% case. It can be stated that the buckling mode of the remained part of the plate changes to one of a plate with the simple supports on three sides and free on one side, indicating that the support condition, simple supports on four sides, is no longer effective. However, in the case of partial loss of cross-sectional area ratio of 10-10%, a different trend is observed compared with that seen in I-model 0-0% case.

Therefore, for partial loss of cross-sectional area ratio of 10-10%, the residual strength is estimated by Equation 6 based on Figure 8, and for partial loss of cross-sectional area ratio of 20-20% or higher, residual strength is estimated by the strength curve for I-model 0-0% case, as shown in Equation 7.

$$\sigma_u/\sigma_y = 0.5R^{-1} \quad (6)$$

$$\sigma_u/\sigma_y = 0.8R'^{-0.5} \quad (7)$$

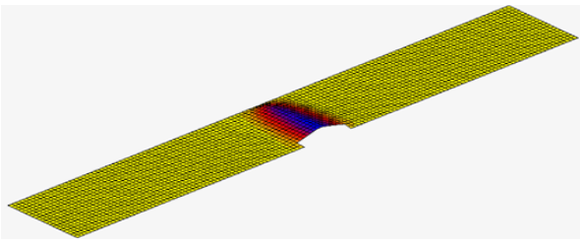


Figure 17. Buckling mode of the B-model (10-10%, R=1.2)

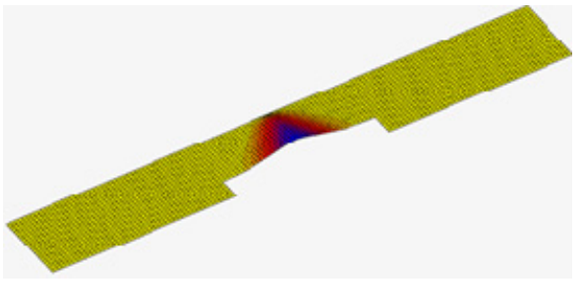


Figure 18. Buckling mode of the B-model (30-30%, R=1.2)

Figure 17 (10-10%, R=1.2) and Figure 18 (30-30%, R=1.2) show the buckling mode for B-model. Similar to I-model, in order to propose a residual strength equation for a case where the partial loss of sectional area expanded in the length direction (10-20%, 10-30%), the partial loss of sectional area ratio in the length direction is newly defined as β_B (%). In the 10-20% and 10-30% cases in which the partial loss of cross-sectional area expanded in the length direction, the difference between σ_u/σ_y for 10-20% and 10-30% and σ_u/σ_y for 10-10%, in all cases where the width-thickness ratio parameter R = 1.2 to 0.7, were calculated and the average change (X) was obtained. Table 12 shows these values, and Figure 19 shows the relationship between β_B and X.

Consequently, the residual strength equation for cases where the partial loss of cross-sectional area expanded in the length direction (10-20%, 10-30%) is proposed as Equation 8 with the value for 10-10% case as the standard.

$$\sigma_u/\sigma_y = (\sigma_u/\sigma_y \text{ of 10-10\%}) - (0.004\beta_B) \quad (8)$$

Table 12. β_B and average change

β_B	X
20	0.092
30	0.114

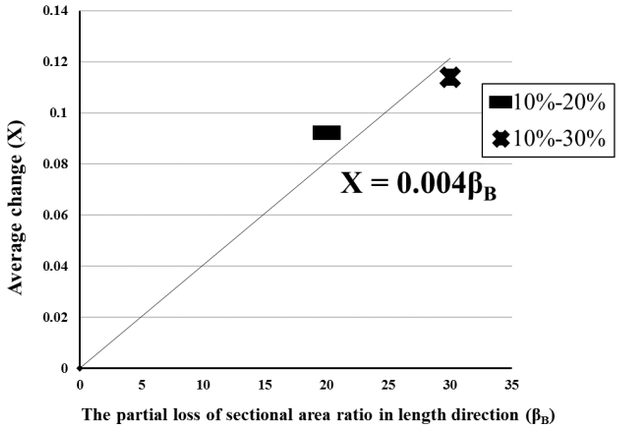


Figure 19. Estimation of relationship between X and β_B

Table 13. Predicted values by proposed equations

	σ_u / σ_y					
R	0-0%	10-10%	20-20%	30-30%	10-20%	10-30%
1.2	0.68	0.42	0.37	0.34	0.32	0.30
1.0	0.75	0.50	0.41	0.38	0.42	0.38
0.9	0.79	0.56	0.43	0.41	0.48	0.44
0.8	0.84	0.63	0.46	0.43	0.55	0.51
0.7	0.90	0.71	0.49	0.46	0.63	0.59

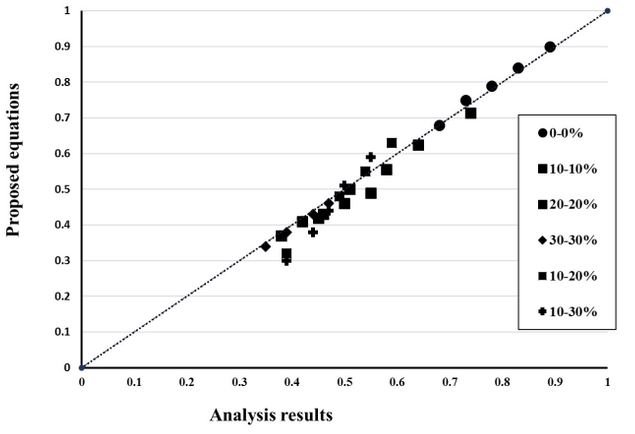


Figure 20. Comparison of estimated values and analytical results

Table 13 shows the predicted values by the proposed equations, and these are compared with the analytical results in Figure 20.

According to Figure 20, there is a maximum error of 9% for predicted values by the proposed equation; then, it is presumed to be possible to evaluate the compressive strength of a plate simply supported on four sides under partial loss of cross-sectional area considered in this study.

5 CONCLUSIONS

In this paper, compressive strength of plates with simple supports on three sides and one side free, and plates with simple supports on four sides having a partial loss of cross-sectional area caused by corrosion were investigated by performing FEM analysis combining a number of parameters. The results of analyses were used to propose compressive strength equations for a plate with a partial loss of cross-sectional area caused by corrosion.

The followings are major findings of this study:

[1] In a case where partial loss of cross-sectional area from the center of the edge of a plate with simple support on three sides and one side free was given, boundary conditions change, so that it is possible to evaluate the residual strength in partial loss of cross-sectional area of 10-10%, 20-20% and 30-30% as the standard strength curve of a column in a case where the residual part was considered to be a column.

[2] In the case where partial loss of cross-sectional area was given from the edge of a plate with support on four sides, if the loss is 20% or higher, the boundary conditions change, so it is possible to evaluate the residual strength as the standard strength curve in a case where the residual part is considered to be a plate with simple support on three sides and free on one side.

[3] From the above, equations that predict residual buckling strength, equations (1) to (4) for I-model and equations (5) to (8) for B-model, of a steel plate with partial loss of cross-sectional area caused by corrosion were proposed.

The analysis models in this study represented a part of a flange of a steel member subjected to compression. Therefore, it is necessary to carry out further study to find out if the proposed equation in this study can be used to evaluate the residual strength for members with partial loss of cross-sectional area (such as members subjected to flexure in particular).

6 REFEENCES

Japan Road Association. 2002. Road Bridge Guidelines, Commentary II, Steel Bridges.

Japan Society of Civil Engineers. 2005. Buckling Design Guideline, Second Revised Edition, Japan Society of Civil Engineers.

Kaita T, Fujii K & Nakamura H. 2004. A simple estimation method of compressive strength for corroded flange plates. Journal of the Civil Engineering, No.768/I-60, pp.59-71.

Kaita T, Fujii K, Hara T, Nakamura H & Uenoya, M. 2004. Strength and its rating method of corroded rectangular steel

plates subjected to shear force. Journal of Structural Engineering, Vol.50A, pp.121-130.

Kaita T, Fujii K, Miyashita M, Uenoya M & Nakamura H. 2005. An experimental study on remaining bending strength of corroded plate girder. Journal of Structural Engineering, Vol.51A, pp.139-148.

Maeda R, Nomura M, Nozaka K, Okumura M. & Ito M. 2007. Study on shear strength including tension field action for hybrid plate girders. Journal of Structural Engineering, Vol.53A, pp.97-108.

Mori T, Watanabe H & Masai S. 2003. A Study on the simulation of corroded steel plate surface and bending capacity of I-shaped girder with corrosion. Journal of Structural Engineering, Vol.49A, pp.675-686.

Mori T, Tachibana A, Nogami K & Yamazawa T. 2008. A Study on tensile strength evaluation method for corroded steel plate. Journal of the Civil Engineering A, Vol.64, No.1, pp.38-47.

MSC Software Corporation. 2015. MARC User documentation.

Muranaka A, Minata O & Fujii K. 1998. Estimation of residual strength and surface irregularity of the corroded steel plates. Journal of Structural Engineering, Vol.44A, pp.1063-1071.

Nogami S, Yamazawa T, Oguru Y & Kato M. 2001. Evaluation of capacity loss due to corrosion damages in composite girder and steel columns. Journal of Structural Engineering, Vol.47A, pp.93-102.

Vo Thanb Hung, Nagasawa H, Sasaki E, Ichikawa A & Natori T. 2002. An experimental and analytical study on bearing capacity of the supporting point in corroded steel bridge. Journal of the Civil Engineering, No.710/I-60, pp.141-151.

Vo thang Hung, Sasaki E, Ichikawa A & Miki C. 2002. Experimental and analytical study on shear capacity of artificially corroded steel girders. Journal of Structural Engineering, Vol.48A, pp.38.47.

Yamazawa T, Nogami K, Mori S & Tsukada S. 2006. Measurements of corrosion shape and bending experiments of steel corroded members. Journal of Structural Engineering, Vol.52A, pp.711-720.

Yamazawa T, Nogami K, Sonobe Y & Katakura K. 2009. Experimental study of steel column member on severe corroding environment. Journal of Structural Engineering, Vol.55A, pp.52-60.

Yamazawa T, Nogami K, Komine S, Yoda T, Kasano H, Murakoshi J, Toyama N, Sawada M., Arimura K & Guo L. 2013. Remaining compressive ultimate strength of diagonal members in steel truss bridge with imitated corrosions. Journal of Structural Engineering, Vol.59A, pp.143-155.

Maintenance, Safety, Risk, Management and Life-Cycle Performance of Bridges – Powers, Frangopol, Al-Mahaidi & Caprani (Eds)
© 2018 Taylor & Francis Group, London, ISBN 978-1-138-73045-8

Use of stochastic optimization in the analysis of weigh-in-motion data

F. El Hajj Chehade, R. Younes, H. Mroueh & F. Hage Chehade
Laboratory of Civil Engineering and geo-Environment (LGCgE) Lille 1 University, France
Modeling Center Doctoral School of Science and Technology, Lebanon
Lebanese University Faculty of Engineering, Lebanon

ABSTRACT: The calibration of traffic simulation models for bridge design or assessment is normally based on weigh-in-motion or WIM data, this implies the estimation of a large number of parameters related to load distribution and vehicle weights. In a similar stochastic problem, the use of genetic algorithm in the optimization process can greatly simplify the work by allowing the calculation of a very large number of parameters even with a small amount of data and conditions. This method is illustrated by an application example of genetic optimization to evaluate the correlation between the gross vehicle weight and its distribution on single vehicle axles.

1 INTRODUCTION

1.1 *Background*

The weigh-in-motion or WIM process is widely used all over the world, it consists in the estimation of total weight for a moving road vehicle and of the proportion carried per each axle by measuring the dynamic tire forces using specific sensors. Therefore the distribution of all axle weights can be provided directly from WIM data. Figure 1 present a redraw from Burnos & Rys (2017) for a pavement embedded WIM sensor.

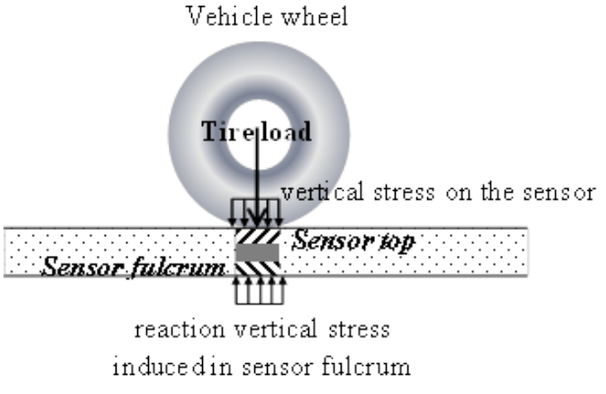


Figure 1. Schema of pavement embedded WIM sensor

The recorded WIM data on a multi-lane carriageway can then be used for the design or the assessment of highway bridges(O'Brien et al. 2006).

Bridge weigh-in-motion or BWIM systems constitute now an alternative way to the pavement-based weigh-in-motion systems and are considered more convenient and cost effective(Yu et al. 2016), these methods rely on measuring strains in some bridge components to estimate the vehicle weights; consequently, some algorithms have been developed to deduce axle loads especially Moses' algorithm.

1.2 *Approach*

The analysis of the recorded data from the real time traffic starts by fitting the histograms of measured data such as Gross Vehicle Weight (GVW), axle spacing, distribution of GVW, to a known probabilistic distribution which provides the basic parameters in the traffic simulation process.

The distribution of GVW between axles is used to illustrate the problem as it has a strong influence on the load effects especially on short to medium span bridges, from 10 to 35 m (Enright & O'Brien 2013)

Normally, the distribution of GVW should be performed for each axle in each vehicle class; it requires having the histograms of the distributions for each axle in all the vehicle classes, so a lot of data. In this paper we will try to do the same work based only on the global distribution of all axles.

The genetic algorithm is often used to interpret and analyze stochastic data from real world problem which cannot be assimilated to a well-defined mathematical function; weigh-in-motion data resulting from vehicle monitoring on highway have the same stochastic status. Genetic algorithm will be the basic

tool in this work.

2 GENETIC OPTIMIZATION

The most common type of stochastic optimization is represented by genetic algorithm (Holland, 1975) which constitutes a robust optimization tool mimicking the same process of natural selection (biological evolution). This algorithm is recommended when we have little analytical knowledge about the search domain and very large number of parameters, unlike the FMINS functions in Matlab which require the determination of an initial point that affects the optimization success, this random-search optimization algorithm is oriented by some genetic operators like selection, crossover and mutation which make its population more diverse and thus more immune to be trapped in a local optima and guarantee a global optima solution. The selection of an individual is based on how fit it is after a fitness evaluation process through a fitness function, also called objective function and the fittest ones have more chance to be inherited into the next generation, the strong tend to adapt and survive and the weak tend to die out, genetic algorithm uses the fitness function as Black Box and doesn't require any information about its structure or its mathematical model which isn't available in many real world problems, for example, axle weights data given from real time monitoring where it seems difficult to obtain explicit formula for the objective function with all constraints especially with variable and stochastic traffic loading , the general formulation of the fitness function to be minimized used in this optimization problem is mentioned in Equation 1:

$$\sum (y_1 - y_2)^2 \tag{1}$$

where y_1 is the data resulting from real time monitoring and y_2 the corresponding value resulting from genetic optimization, this function will be minimized by varying in each iteration the parameters described in Figure **5**, no matter if we have underweight or overweight, the goal is to reach a very small difference.

The main steps of genetic optimization can be summarized as follow:

1. Generate randomly initial population of individuals, each individual is assimilated to a chromosome and represents a set of the parameters which can be a feasible solution of the optimization problem;
2. Using the fitness function, calculate the fitness of each individual in the population;
3. Select the more fit individuals, those that give the minimum gap with the reference data, then cross over and mutate the remaining ones to form a new offspring while keeping the same initial population size or number of individuals;
4. Replace the current population with the transformed one;
5. Repeat steps 2, 3 and 4 until reaching the number of generations fixed at the beginning according to the problem circumstances.

This process is summarized in Figure 2.

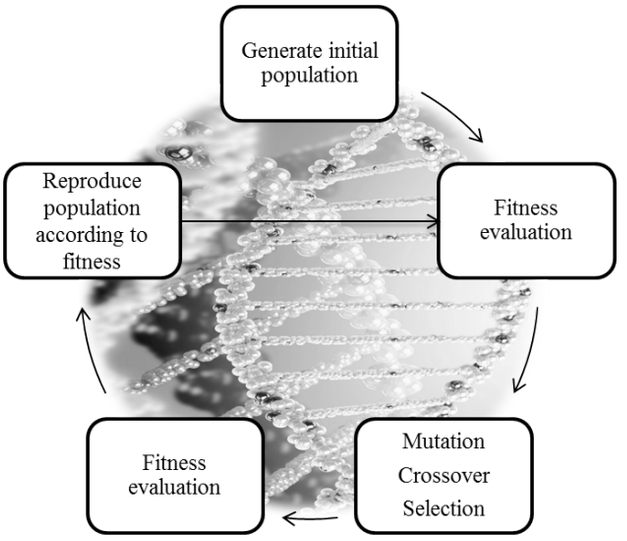


Figure 2. Schema of a simple genetic algorithm

3 MODELING DISTRIBUTION OF GVW BETWEEN AXLES

Normally vehicles can be simply classified according to their number of axles and axle layout, so the proportion of GVW carried per each individual axle is modeled for each vehicle class separately, this means that a very large number of parameters is to be estimated, for example Enright & O'Brien (2013) proposed a bimodal normal distribution for the proportion carried per each axle for each vehicle class, thus for the 6-axle vehicle class we should consider the histogram of the percentage of GVW for each axle separately in order to estimate the 6 parameters of the bimodal normal distribution, in total we need to estimate 36 parameters for the modeling of GVW distribution for only one vehicle class based on a complex analysis of the measured data in order to get the 6 histograms needed for the fitting process.Simon F. & Rolf(1999) proceeded in a similar way by considering bimodal beta distributions for modeling axle group loads for each vehicle class separately. In other cases, the proportion of GVW carried per axle is sometimes simply assumed as deterministic (GRAVE et al. 2000). Correlation be-

tween axle loads is also performed for each vehicle class in order to get the distribution of GVW among axles (Centre de recherche: ICOM EPF-Lausanne et al. 2006), for this purpose a complex work is established to deduce the correlation between axle loads for each axle on each vehicle class based on the correlation for every individual vehicle in this class. The latter case is chosen to prove the effectiveness of genetic optimization in the following paragraphs.

4 DESCRIPTION OF WIM DATABASE

The Swiss Federal Roads Office (FEDRO) has equipped the national road network in Switzerland with eight main weigh-in-motion monitoring stations(Treacy & Brühwiler 2011); the traffic data from the Mattstetten A1 motorway station are chosen to illustrate the proposed methodology in WIM analysis since they give a good representation of local or national traffic, these data are adopted as presented in the research work published by the FEDRO in 2006 (Centre de recherche: ICOM EPF-Lausanne et al. 2006) , all needed data are perfectly stripped in this report.

4.1 *Vehicle modeling*

According to the number of axles and axle layout, vehicles are classified in 12 classes with a known range of GVW for each vehicle class, the distributions of GVW for each vehicle class are also given and then fitted to bimodal beta distributions, since the proportion of each vehicle class from the total traffic is taken similar to that in the measured traffic, all GVW can be simulated using inverse-transform method as shown in Figure 3. Each class is designated by a series of characters which refer to the type and position of the axle, for example in case of *123a* class, all vehicles have one single axle, followed by a tandem then a tridem axle , the letter "a" means that vehicles in this class are articulated.The letter "r" refers to the vehicles with trailer. All vehicle class labels are summarized in Table 1.

Table 1. Labels of all vehicle classes

Vehicles alone	Vehicles with trailer	Articulated vehicles	Mixed vehicles
11	1111r	112a	111
12	112r	113a	122
22	1211r	122a	
	1112r		

After simulation of GVW, it should be distributed to the vehicle axles; as cited in the paragraph 3 , linear correlation between axle loads is performed for every axle in each vehicle class, for example to calculate the correlation between two loaded axles in a given class, we should plot for every measured vehicle, the load of the first axle as a function of the load of the GVW and so on, after that we can select the linear trend line that can describe the correlation function, an illustrative schema is used to explain the described procedure of calculating correlation coefficients (Figure 4), the general matrix of population used in the optimization process is presented in Figure 5.

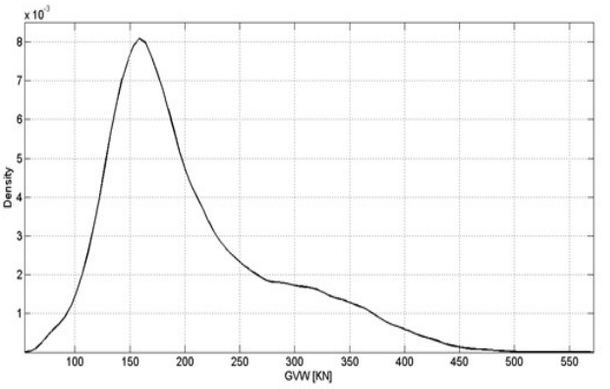


Figure 3. Distribution of GVW for all vehicles

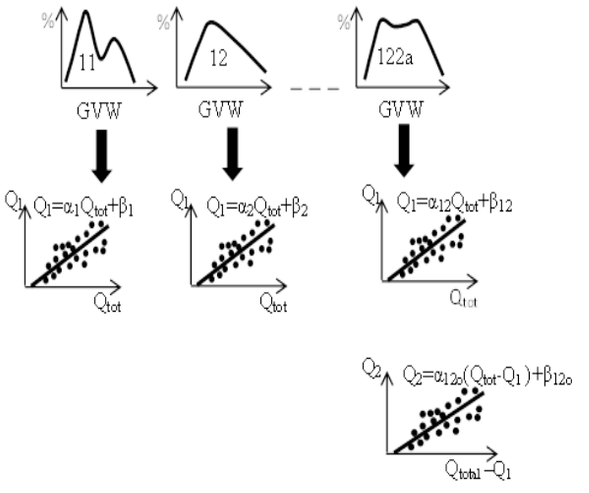


Figure 4. Calculation steps for correlation coefficients

4.2 *Filtering of WIM data*

The measured WIM data should be filtered to remove unreliable values, OBrien & Enright (2011) have well detailed the cleaning process, only vehicles more than 3.5 tones are retained , in our case, the following constraints will be considered to reject unreliable data:

1. Wheelbase > Vehicle length
2. Distance between two consecutive axles > 20 m
3. Distance between two consecutive axles <0.4 m
4. Sum of all axle loads > GVW
5. Axle load > 40 t
6. Axle load > 85% of GVW

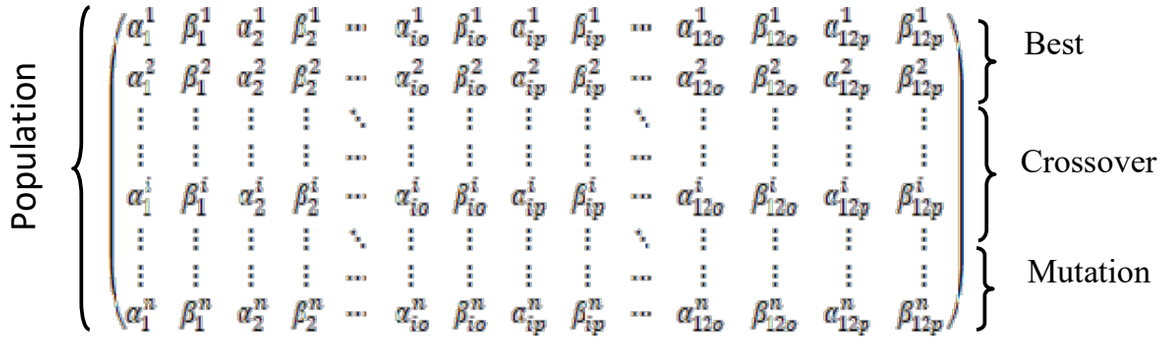


Figure 5. General matrix of population

Data cleaning constrains will be used to limit the search domain in the optimization process.

5 CALCULATION OF CORRELATION COEFFICIENTS

5.1 *General framework*

The proposed methodology will be summarized in the following flowchart:

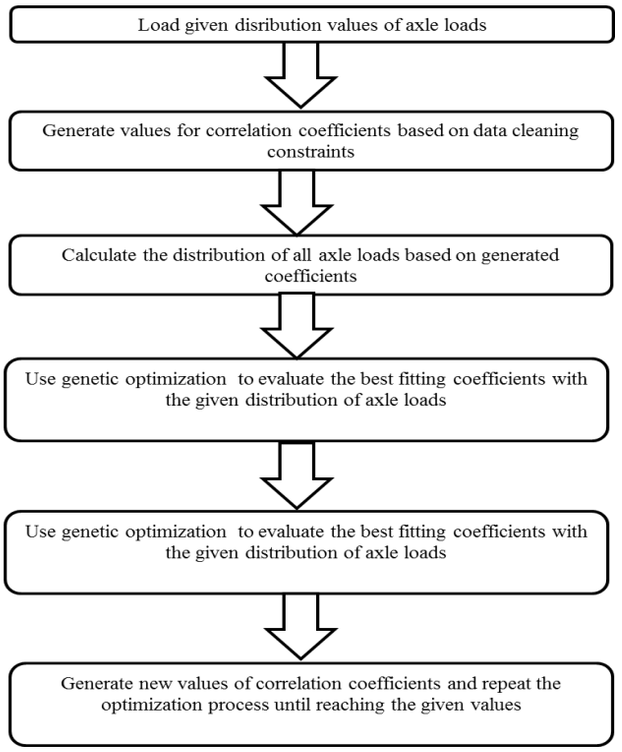


Figure 6. Flowchart of the proposed framework

5.2 *Illustrative example*

To better present the proposed methodology, more details will be explained for the vehicle class 22 (trucks with two tandem axles). Q_{tot}, Q_1 and Q_2 are respectively the total vehicle weight, the weight supported by the first tandem and the weight supported by the second tandem.

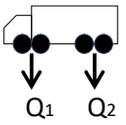
The correlation equations can be written as follow:

$$Q_2 = \alpha_3 Q_{tot} + \beta_3 \tag{2}$$

$$Q_1 = Q_{tot} - Q_2 \tag{3}$$

The search domain for α and β can be limited according to the following constraints:

1. The slope of the correlation line should be less than 1 ($0 < \alpha_3 < 1$);
2. Axle weight should be positive ($Q_i > 0$) ;
3. Single axle load should be less than 40t;
4. Single axle load should be less than 85% of GVW.



Therefore, the intervals of α and β will be:

- $0 < \alpha_3 < 1$
- $$\begin{cases} 0 < Q_2 < 0.85 Q_{tot} \\ \Rightarrow 0 < \alpha_3 Q_{tot} + \beta_3 < 0.85 Q_{tot} \\ \Rightarrow -\alpha_3 Q_{tot} < \beta_3 < (0.85 - \alpha_3) Q_{tot} \end{cases}$$

This should be valid for all Q_{tot} in the vehicle class 22, so we can choose the minimum Q_{tot} in this class to reduce the search interval.

The same work is done for all the vehicle classes, so we will have to calculate 48 parameters between the identified maximum and minimum limits. (Figure 5)

5.3 *Results*

After 15 generations of 30 populations of the 48 correlation coefficients, the best fitting coefficient val-

ues are used to calculate the distribution of all vehicle axles for one million vehicles.

The distribution of all vehicle axles based on the optimization results relative to the given distribution is shown in Figure 7.

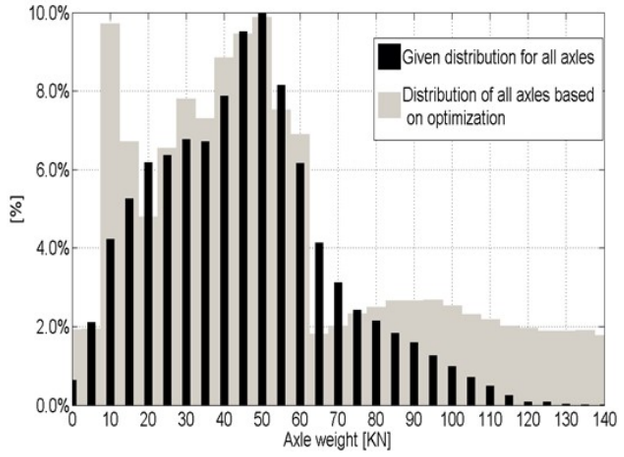


Figure 7. Given and simulated distributions of all vehicle axle loads

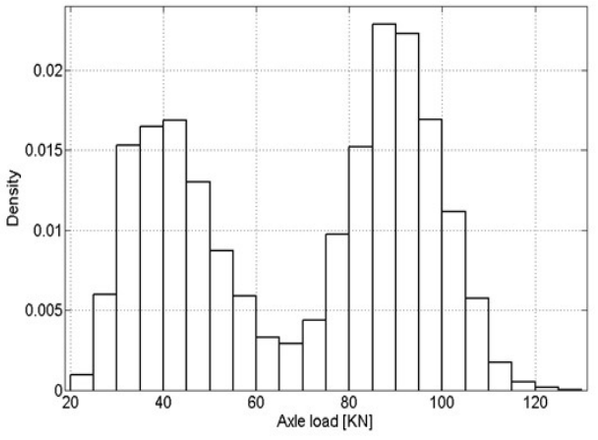


Figure 8. Distribution of Q_1 for vehicle class 22 based on calculated correlation coefficients

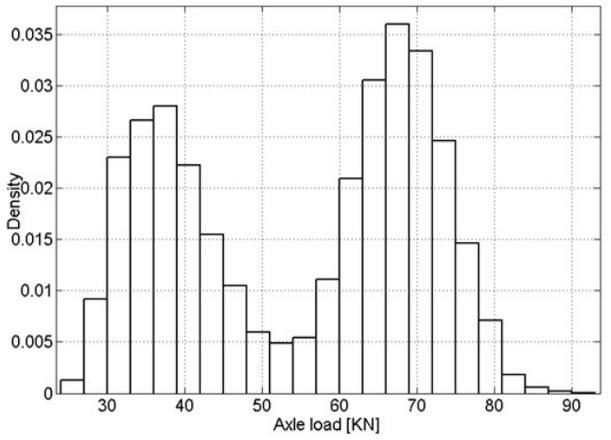


Figure 9. Distribution of Q_2 for vehicle class 22 based on calculated correlation coefficients; $Q_2=\alpha Q_{tot}+\beta$ /α=0.38, β=14.2

5.4 *Discussion*

The distribution of all vehicle axles based on the calculated correlation coefficients using genetic optimization is very consistent with the given distribution of all vehicle classes based on monitoring data (Figure 7). The distribution of every individual axle in each vehicle class can also be deduced, Figure 7-Figure **8** show the distributions of each axle for the vehicle class 22, in this case the values of correlation coefficients are also presented , α=0.38 and β=14.2, the distributions appear to be bimodal; it should be noted that, this is a sample from a set of 48 parameters calculated for 12 vehicle classes, this required a total of 15×30=450 iterations while improving the values of the searched coefficients in each new generation according to the minimum value of the objective function.

6 CONCLUSION

The proposed methodology allows calculating a large number of unknown parameters based only on a little amount of data and some constraints to limit the search domain.

In the same way, having the limitations for axle distances in each vehicle class and the general distribution of the axle distance, the probabilistic distribution for each distance in a given class can be detected directly from the general histogram and all the distribution parameters can be deduced using a global genetic optimization.

Genetic algorithm also constitutes a robust tool in the optimization process in BWIM techniques, it can be included in the Moses' algorithm in order to compute the GVW by minimizing the error between measured and theoretical response.

7 REFERENCES

Burnos, P., Rys, D., 2017. The Effect of Flexible Pavement Mechanics on the Accuracy of Axle Load Sensors in Vehicle Weigh-in-Motion Systems. *Sensors* 17, 2053.

Centre de recherche: ICOM EPF-Lausanne, Thierry Meystre, Manfred A. Hirt, Office fédéral des routes OFROU, 2006. Evaluation de ponts routiers existants avec un modèle de charge de trafic actualisé. Berne.

Enright, B., O'Brien, E.J., 2013. Monte Carlo simulation of extreme traffic loading on short and medium span bridges. *Struct. Infrastruct. Eng.* 9, 1267–1282. doi:10.1080/15732479.2012.688753

GRAVE, S.A.J., O'Brien, E.J., O'Connor, A.., 2000. The determination of site-specific imposed traffic loadings on existing bridges. *Bridge Manag.* 4M J Ryall G R Parke J E Harding Eds Thomas Telford Lond. 422–9.

John H.Holland, 1975. Adaptation in Natural and Artificial Systems. University of Michigan Press.

O'Brien, E.J., Caprani, C.C., O'Connell, G.J., 2006. Bridge assessment loading: a comparison of West and Central/East Europe. *Bridge Struct.* 2, 25–33.

OBrien, E.J., Enright, B., 2011. Modeling same-direction two-lane traffic for bridge loading. *Struct. Saf.* 33, 296–304.
Simon F., B., Rolf, B., 1999. Site specific probability distribution of extreme traffic action effects. *Probabilistic Eng. Mech.* 14, 19–26.
Treacy, M., Brühwiler, E., 2011. Fatigue loading estimation for road bridges using long term WIM monitoring. Presented at *the Advances in Safety, Reliability and Risk Management*, Taylor & Francis Group, London, pp. 1870–1875.
Yu, Y., Cai, C., Deng, L., 2016. State-of-the-art review on bridge weigh-in-motion technology. *Adv. Struct. Eng.* 19, 1514–1530.

Maintenance, Safety, Risk, Management and Life-Cycle Performance of Bridges – Powers, Frangopol, Al-Mahaidi & Caprani (Eds)
© 2018 Taylor & Francis Group, London, ISBN 978-1-138-73045-8

Parametric analysis of rib distortion in orthotropic steel decks

H. Fang & H. De Backer
Ghent University, Ghent, Belgium

ABSTRACT: In orthotropic steel decks, the trapezoidal section is one of the most widely adopted geometries for ribs. However, due to the existence of cut-outs in the crossbeams, the torsional rigidity of the ribs is fundamentally reduced by distortion, especially when the load was at mid-span and eccentric from the axis of the rib. The rib distortion causes high stress concentrations at the rib-to-crossbeam joint, which had become one of the most vulnerable details to fatigue. In this paper, the influence of 5 classical design parameters on the distortional behavior was analyzed based on finite element analysis. A refined finite element model of an orthotropic steel deck specimen (8.2 m × 4.1 m) was developed, adopting the sub-model analysis technique and the hot spot stress approach. Research results revealed that the distortional stress of rib-to-crossbeam joint was negatively correlated with the thickness of rib, positively correlated with the spacing of rib, the weld length of rib-to-crossbeam joint and the spacing of crossbeam. The height of crossbeam did not have obvious influence on distortional behavior. Approaches e.g. increasing the thickness of rib or decreasing the spacing of crossbeam would increase the stress of rib-to-deck joint while reducing the distortional stress.

1 INTRODUCTION

The orthotropic steel deck had been widely used in long-span bridges because of its light weight, high load carrying capacity, etc. Nevertheless, stress concentrations were easily caused because of the complex structure and the existence of numerous welds. Thus, fatigue damage had become the most severe problem when adopting orthotropic steel decks. Previous research revealed that typical fatigue cracks mainly appear at four locations, namely rib-to-deck joint, splice joint of the longitudinal rib, deck plate at the position of crossbeam and rib-to-crossbeam joint(De Jong, 2004). Relevant research about these fatigue-prone details had been reported(Kainuma, 2017, Nagy, in press) but the stress concentration at the rib-to-crossbeam joint caused by rib distortion was more or less ignored in previous research.

In orthotropic steel decks, the trapezoidal section was one of the most widely adopted geometries for ribs. However, due to the existence of cut-outs in the crossbeams, the torsional rigidity of the ribs was fundamentally reduced by distortion, especially when the load was at mid-span and eccentric from the axis of the rib(Connor, 2012). The rib distortion caused high stress concentrations at the rib-to-crossbeam joint. Moreover, when tension stress appeared on the outside of one stem of the rib, compression stress appeared on the outside of the other stem. Thus, the rib-to-crossbeam joint carried positive and negative stress alternately when vehicles passing by, which made the joint more vulnerable to fatigue damage. Nowadays, no explicit recommendations on relevant parameters with respect to the influence of rib distortion e.g. the weld length between rib and crossbeam, etc. were given in current major design codes.

This paper presented the influence of a number of classical design parameters on the distortional behavior, based on finite element analysis. Firstly, a refined finite element model of an orthotropic steel deck specimen was developed, adopting the sub-model analysis technique. The hot spot stress approach was also adopted to achieve a more accurate assessment of the stress ranges. Then, the influence of the considered parameters was calculated and analyzed, which will be the foundation for developing a simplified calculation method for the estimation of stress concentrations at the rib-to-crossbeam joint in further research.

2 PARAMETRIC STUDY OF RIB DISTORTION

2.1 *Finite element model*

In order to investigate the influence of classical design parameters on the distortional behavior, parametric analyses were performed using ANSYS. Initially, a standard orthotropic steel deck was designed, which was composed of 6 ribs, 3 crossbeams and 2 main girders. The longitudinal trapezoidal ribs were 300 mm high, 300 mm wide at the top and 125 mm wide at the lower soffit. Relevant geometries are shown in Figure 1.

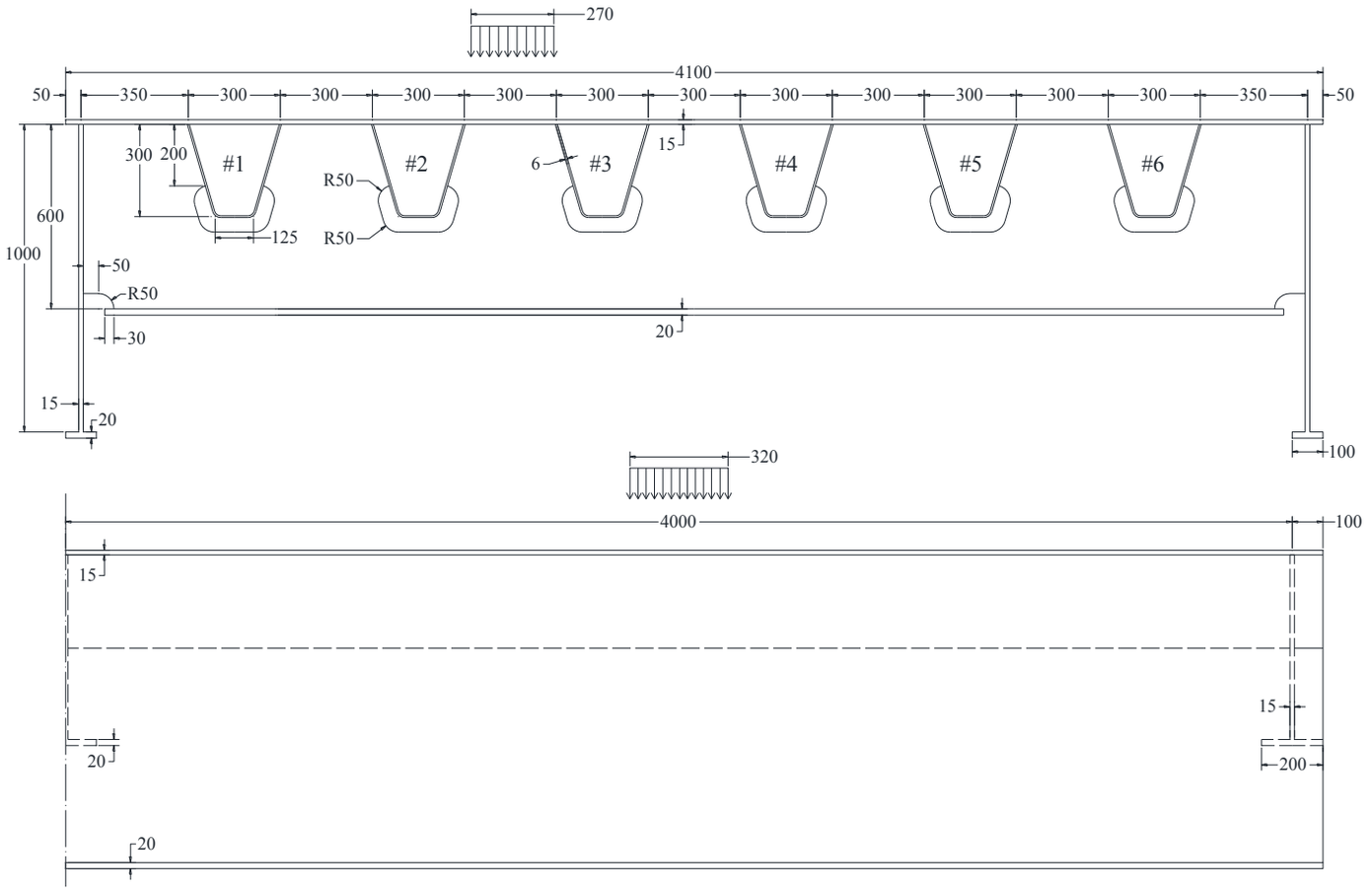
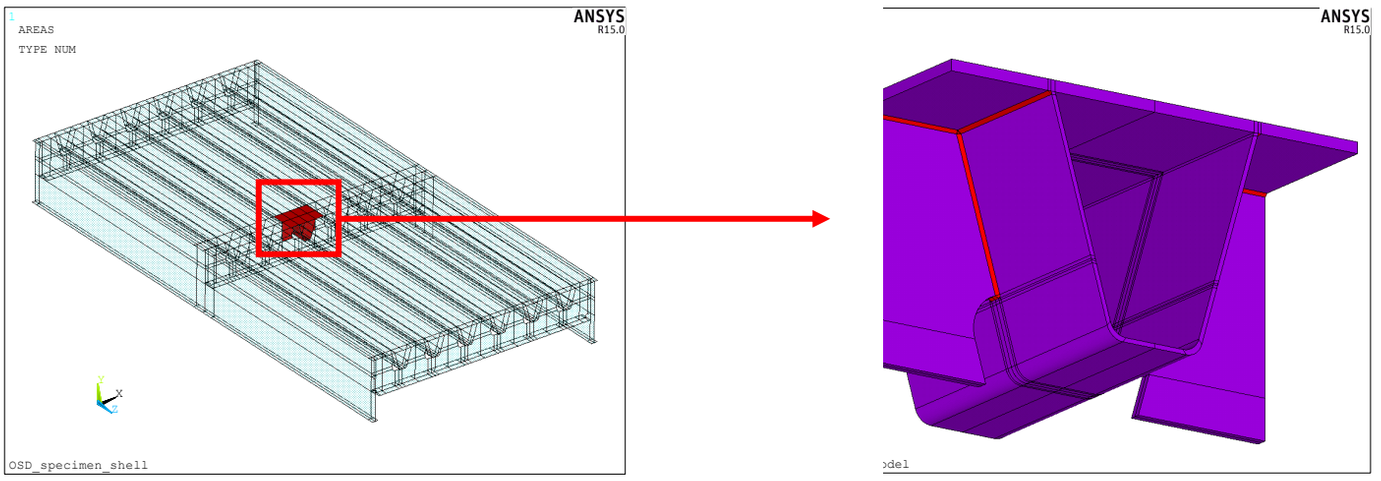


Fig. 1. Geometries of the standard orthotropic steel deck (unit: mm)

According to the design of the standard orthotropic steel deck, a global model was first built using shell element, as shown in Figure 2(a). In order to take the influence of welds into account and to get more accurate results of stress, a sub-model was built using solid element based on the global model. The sub-model was composed of segmental deck, rib, crossbeam and welds as shown in Figure 2(b). The location of the sub-model was at the middle crossbeam of the global model longitudinally and at the third rib (see Figure 1) transversally. Welds of the sub-model were modeled with a triangular profile. The weld throat thickness of 4 mm was used.



(a) global model (b) sub-model

Fig. 2. Finite element models of a standard orthotropic steel deck: (a) global model; (b) sub-model

Liner elastic properties of material were considered in both models. The modulus of elasticity 210 GPa and the Poisson's ratio in elastic stage 0.3 were adopted in analyses. According to previous research(Kolstein, 2007), the structural hot spot stress approach was more appropriate for this joint as well as the liner extrapolation method. Thus, based on the IIW recommendations (Hobbacher, 2015), two reference points were at a distance of 0.4 times and 1.0 times the thickness of the rib wall separately. The mesh size of elements close to the lower end of rib-to-crossbeam weld was controlled at 0.1 times the thickness of the rib wall to fulfill the IIW recommendations. The reference points and mesh nearby are shown in Figure 3.

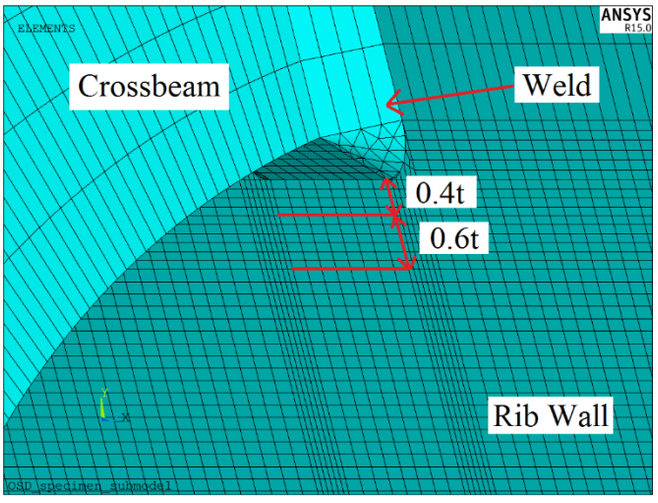


Fig. 3. Reference points and mesh

2.2 *Loadcase and boundary conditions*

According to Eurocode 1, the fatigue load model 2 was chosen since it was more appropriate to steel constructions. The axle load of 110 kN with wheel type C was adopted. The wheel contact area was 270 mm wide and 320 mm long. The dynamic amplification factor was 1.3. As mentioned before, the rib distortion was caused by eccentric load. Hence, one wheel load of 70 kN at mid-span and eccentric from the axis of the rib was adopted, as shown in Figure 1 and Figure 4. Because the real orthotropic steel deck specimen of this study was not covered by pavement, the dispersal of concentrated loads caused by the pavement was not considered in order to make contrast between the FEA results and the experimental results in the future.

The boundary condition of the global model was based on the support condition of the orthotropic steel deck specimen in reality. Six bearings were at the middle and two ends of two main girders separately, as shown in Figure 4. The contact area of a bearing was 80 mm × 80 mm. The boundary condition of the sub-model was extracted from the calculation results of the global model with corresponding geometries. The deformations of nodes along the cutting boundary between two models were placed on the sub-model as external loads. Since the cutting boundary was far away from the zone of stress concentration, final results were not affected.

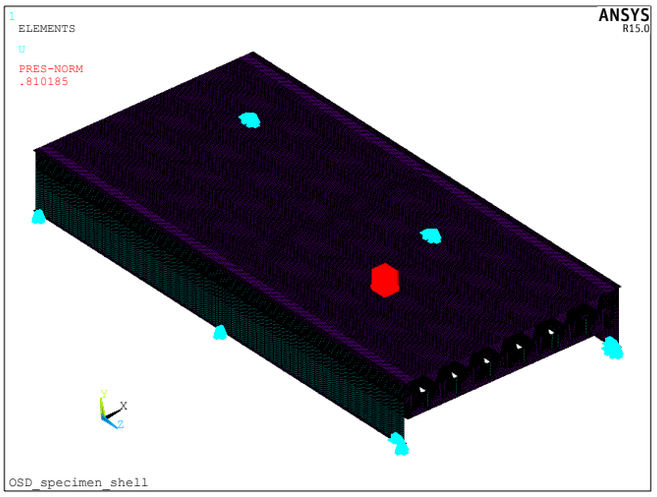


Fig. 4. Loadcase and boundary conditions

3 RESULTS AND DISCUSSION

In total 5 classical design parameters were considered, namely the thickness of rib, the transversal spacing of rib, the height of crossbeam, the longitudinal spacing of crossbeam and the weld length of rib-to-crossbeam joint. Among these parameters, the thickness of rib was determined by the stiffness of rib which was normally selected in accordance with the traffic category, etc. Thus, the second moment of area of ribs was treated as the constant reference when adjusting the thickness of rib. One rib and the deck plate of unit length, which was the upper width of rib plus the spacing of rib, were counted in the calculation. Relevant models with various parameters of this study are shown in Table 1.

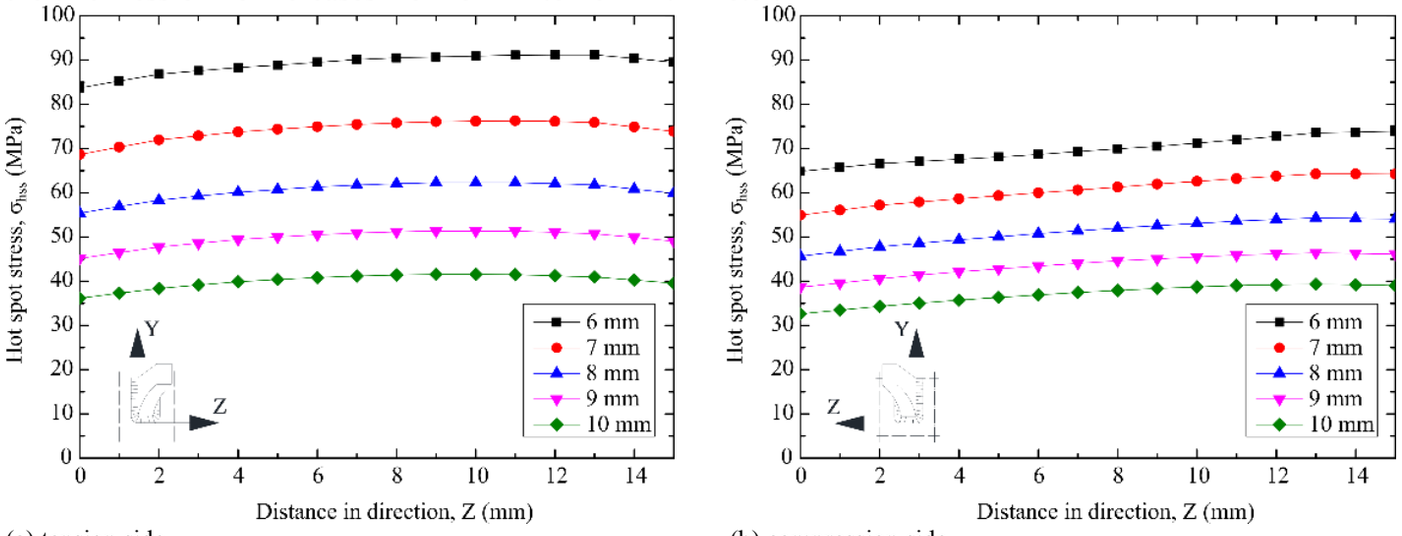
Table 1. Parameters of geometries

Model number	Height of rib	Upper width of rib	Bottom width of rib	Thickness of rib	Spacing of rib	Height of crossbeam	Spacing of crossbeam	Weld length of rib-to-crossbeam joint
0(standard)	300	300	125	6	300	600	4000	200
1	285	-	-	7	-	-	-	-
2	275	-	-	8	-	-	-	-
3	265	-	-	9	-	-	-	-
4	255	-	-	10	-	-	-	-

5	-	-	-	-	200	-	-	-
6	-	-	-	-	250	-	-	-
7	-	-	-	-	350	-	-	-
8	-	-	-	-	375	-	-	-
9	-	-	-	-	-	500	-	-
10	-	-	-	-	-	700	-	-
11	-	-	-	-	-	800	-	-
12	-	-	-	-	-	900	-	-
13	-	-	-	-	-	-	2500	-
14	-	-	-	-	-	-	3000	-
15	-	-	-	-	-	-	3500	-
16	-	-	-	-	-	-	5000	-
17	-	-	-	-	-	-	-	150
18	-	-	-	-	-	-	-	180
19	-	-	-	-	-	-	-	210
20	-	-	-	-	-	-	-	240

3.1 *Thickness of rib*

Figure 5 shows the influence of the thickness of rib on distortional stress. According to the figures, the distortional stress decreases as the thickness of rib increases. On the tension side, the average distortional stress decreases from 89.10 MPa to 40.09 MPa when the thickness of rib increases from 6 mm to 10 mm. On the compression side, the average distortional stress decreases from 69.72 MPa to 37.05 MPa as the thickness of rib increases. The decreasing amplitude is about fifty percent. The distributions of distortional stress on both sides are not influenced by this parameter.



(a) tension side (b) compression side

Fig. 5. Influence of the thickness of rib: (a) tension side; (b) compression side

The calculation result shows that when using a thicker rib, the stress of rib-to-deck joint increases at the same time. Figure 6 displays the calculation result of model 4 in Table 1, of which the thickness of rib is 10 mm. The stress peak appears at the rib-to-deck joint.

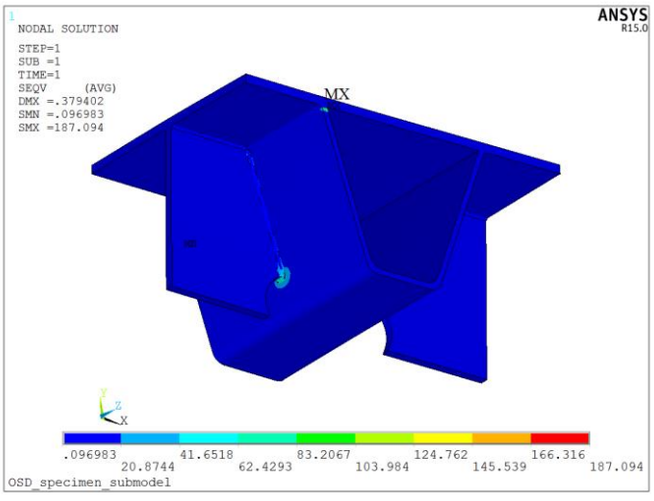
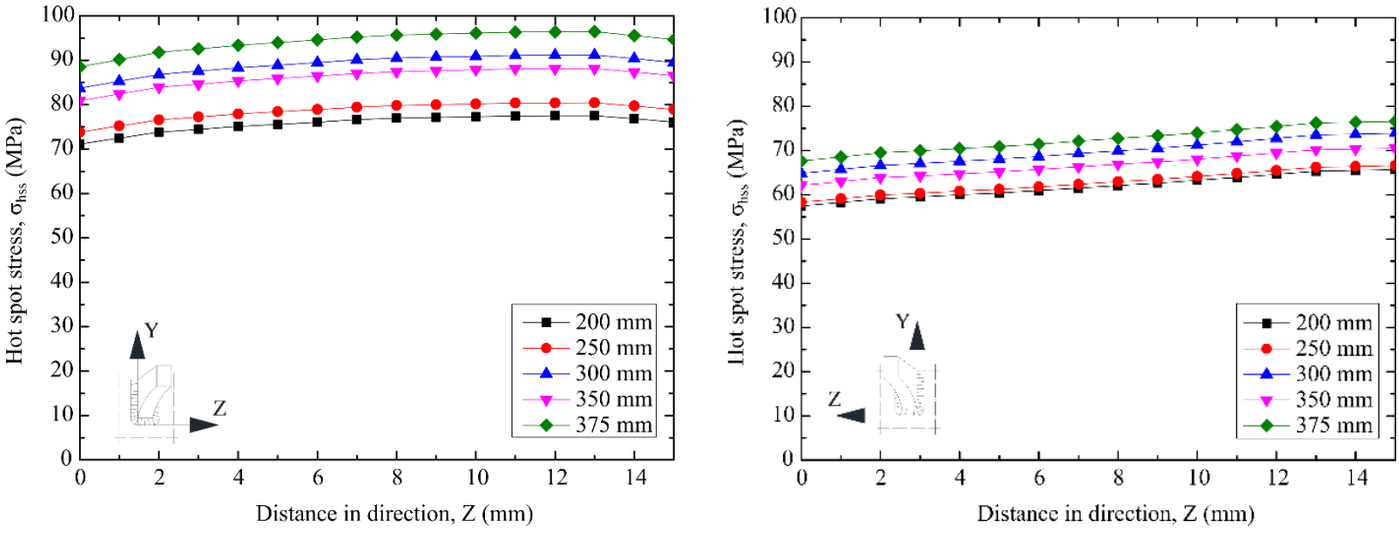


Fig. 6. Calculation result of model 4

3.2 *Spacing of rib*

Figure 7 presents the influence of the spacing of rib on distortional stress. The distortional stress and the spacing of rib are positively correlated. On the tension side, the average distortional stress increases from 75.76 MPa to 94.22 MPa as the spacing of rib increased from 200 mm to 375 mm. Meanwhile, the average distortional stress increases from 61.89 MPa to 72.51 MPa on the compression side. Similar to the

thickness of rib, the spacing of rib does not change the distribution of stress.

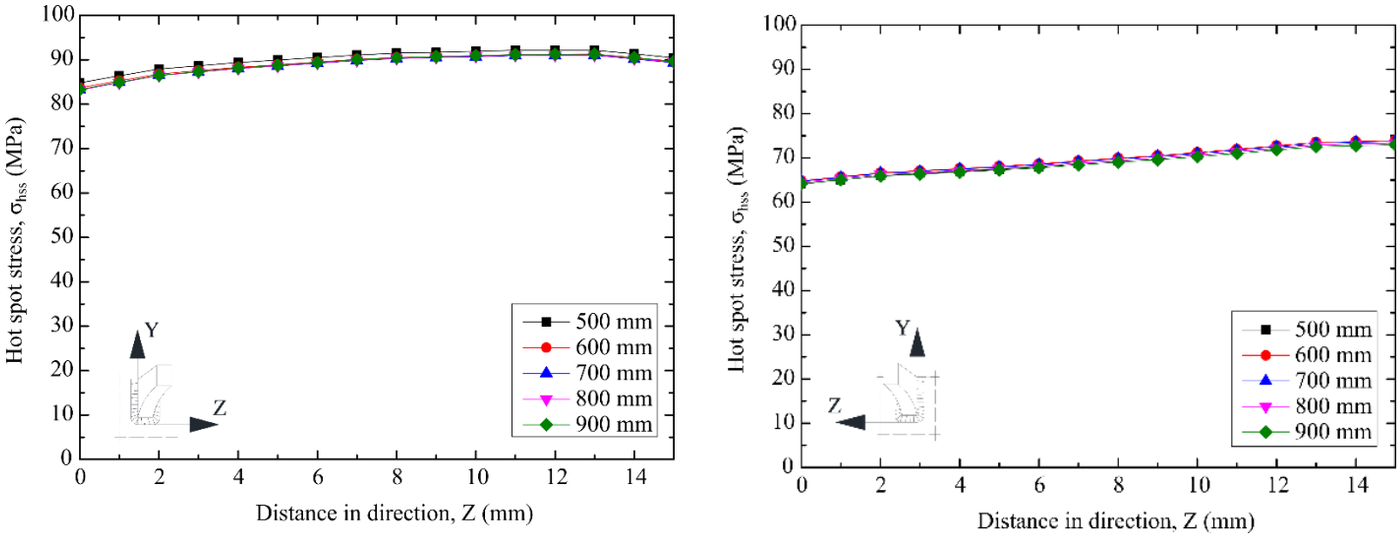


(a) tension side (b) compression side

Fig. 7. Influence of the spacing of rib: (a) tension side; (b) compression side

3.3 *Height of crossbeam*

Figure 8 displays the influence of the height of crossbeam on distortional stress. Compared to other parameters, the influence of the height of crossbeam is not obvious. On the tension side, the distortional stress decreases about 2.5 MPa as the height of crossbeam increases from 500 mm to 900 mm. On the compression side, the distortional stress remains the same as the height of crossbeam increases.

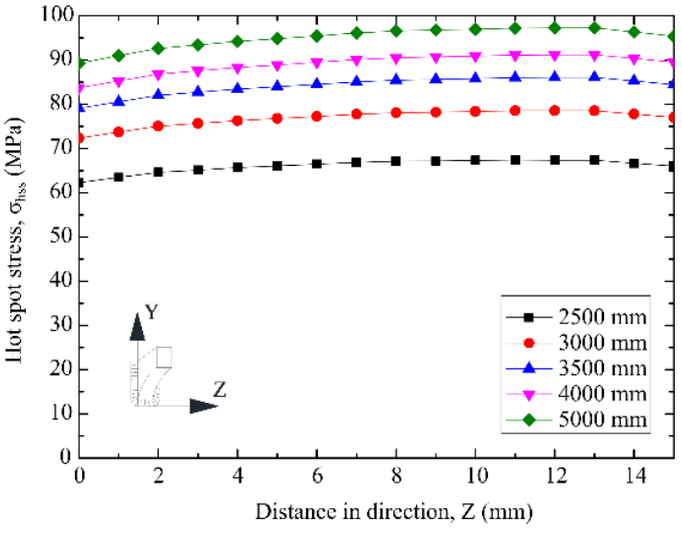


(a) tension side (b) compression side

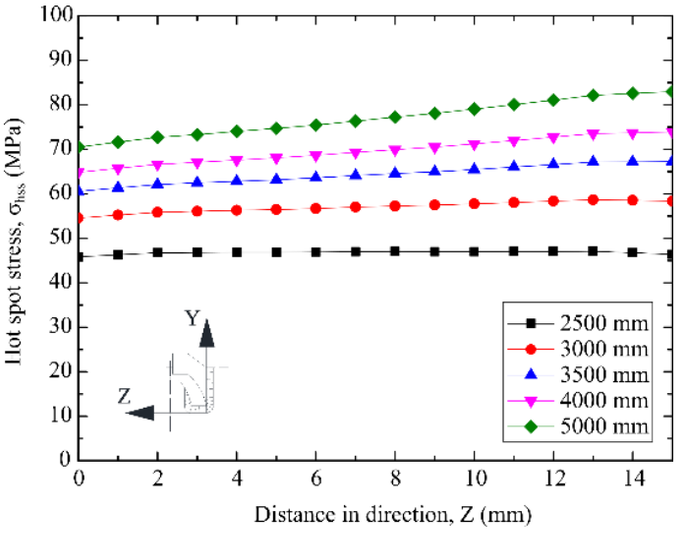
Fig. 8. Influence of the height of crossbeam: (a) tension side; (b) compression side

3.4 *Spacing of crossbeam*

Figure 9 shows the influence of the spacing of crossbeam on distortional stress. The distortional stress and the spacing of crossbeam are positively correlated. When the spacing of crossbeam decreases from 5000 mm to 2500 mm, the average distortional stress of the tension side decreases from 95.04 MPa to 66.06 MPa and the average distortional stress of the compression side decreases from 76.99 MPa to 46.78 MP. On the compression side, the distribution of distortional stress trends to be more uniform as the spacing of crossbeam decreases.



(a) tension side



(b) compression side

Fig. 9. Influence of the spacing of crossbeam: (a) tension side; (b) compression side

Similar to the influence of the thickness of rib, the stress of rib-to-deck joint increases when adopting a shorter span. Figure 10 displays the calculation result of the model 13 in Table 1, of which the spacing of crossbeam is 2500 mm. The maximum stress also appears at the rib-to-deck joint.

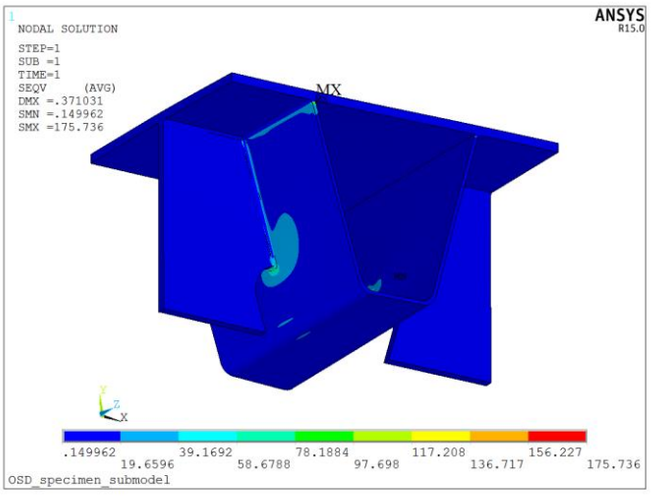
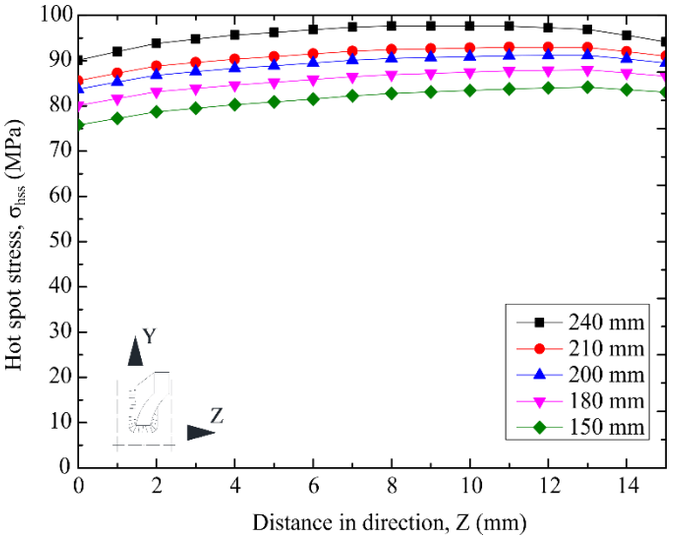


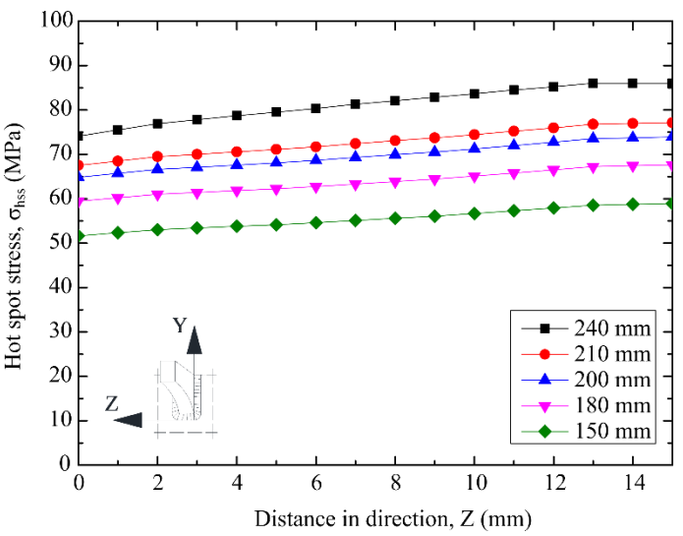
Fig. 10. Calculation result of model 13

3.5 *Weld length of rib-to-crossbeam joint*

Figure 11 presents the influence of the weld length of rib-to-crossbeam joint on distortional stress. The distortional stress and the weld length of rib-to-crossbeam joint are positively correlated. On the tension side, the average distortional stress increases from 81.50 MPa to 95.72 MPa as the weld length of rib-to-crossbeam joint increases from 150 mm to 240 mm. Meanwhile the position of the peak stress moves toward the middle position of crossbeam. On the compression side, this parameter appears relatively larger influence. The average distortional stress increases from 55.50 MPa to 81.28 MPa as the weld length increases but the distribution of stress does not change on this side.



(a) tension side



(b) compression side

Fig. 11. Influence of the weld length of rib-to-crossbeam joint: (a) tension side; (b) compression side

4 CONCLUSIONS

This paper investigated 5 classical design parameters on the distortional behavior of ribs in orthotropic steel deck. Based on the presented results, the following conclusions can be drawn:

- Among 5 classical design parameters, the distortional stress is negatively correlated with the thickness of rib, positively correlated with the spacing of rib, the weld length of rib-to-crossbeam joint and the spacing of crossbeam. The height of crossbeam dies not have obvious influence on distortional behavior.
- When designing an orthotropic steel deck, approaches e.g. increasing the thickness of rib and decreasing the spacing of crossbeam could reduce the distortional stress. However, on one hand, the stress of the rib-to-deck joint increases at the same time which made this joint easier prone to fatigue. On the other hand, thicker rib and shorter spacing of crossbeam would increase the overall weight of the orthotropic steel deck which would deteriorate merits of orthotropic steel deck. Thus, in order to reduce the distortion of rib and improve the fatigue performance, possible alternatives e.g. adding elements would be verified in further research.

5 REFERENCES

Kainuma, S. et al. 2017. Experimental investigation for structural parameter effects on fatigue behavior of rib-to-deck welded joints in orthotropic steel decks. *Engineering Failure Analysis* 79(2017): 520-537

Nagy, W., Wang, B., Culek, B. et al. 2017. Development of a fatigue experiment for the stiffener-to-deck plate connection in orthotropic steel decks. *International Journal of Steel Structures*. In press.

Connor, R., Fisher, J., Gatti, W. et al. 2012. *Manual for Design, Construction, and Maintenance of Orthotropic Steel Deck Bridges*. Pittsburgh: HDR Engineering Inc.

CEN/TC 250. 2004. EN 1991-2:2004/AC:2010 – *Actions on structures – Part 2: Traffic loads on bridges*. Brussels

Kolstein, M. H. 2007. *Fatigue classification of welded joints in orthotropic steel bridge decks*, PhD thesis, Delft University of technology, The Netherlands

Hobbacher, A. F. 2015. *Recommendations for Fatigue Design of Welded Joints and Components*. Switzerland: Springer International Publishing

De Jong, F. 2004. Overview fatigue phenomenon in orthotropic bridge decks in the Netherlands. *2004 Orthotropic Bridge Conference*, Vancouver

Maintenance, Safety, Risk, Management and Life-Cycle Performance of Bridges – Powers, Frangopol, Al-Mahaidi & Caprani (Eds)
© 2018 Taylor & Francis Group, London, ISBN 978-1-138-73045-8

Rehabilitation of the swing bridge from 1905, North of Spain

Collazos-Arias, F.
Departamento de Transportes y Tecnología de Proyectos y Procesos.Universidad de Cantabria, Spain

Garcia-Sánchez, D.
Infrastructures Area.Tecnalia Research and Innovation, Spain

Ruiz-Bedia, Maria L.
Departamento de Transportes y Tecnología de Proyectos y Procesos. Universidad de Cantabria, Spain

Ramos-Gutiérrez. O-R.
Bridge Director, International. Louis Berger, Spain

Delgado-Nuñez, M-A.
Technical Director at Tecyrsa, Spain

ABSTRACT: The bridge over the Asón estuary at Treto, is located in kilometer point (KP) 173,800 of the N-634 road, formerly known also E-70, in the North of Spain, and has been continuously inspected and studied in recent years because of its bad general condition and its importance in the regional transportation network road. This bridge presented significant problems and the structural condition level was critical previously to its intervention in 2015. The rehabilitation project including the restoration of the structural and functional safety level of the structure was deled after material studies and tests were performed. The new updated of the structure fromthe old nineteenth centuries to the newstandard codes was also performed. This paper analyzes the recent experience in the rehabilitation and retrofitting of a singular rotating steel bridge.
A part from the "green" and safe-security aspects, the intervention took in to account all the social requirements of the population in the area who recovered the pride in this emblematic and centenarian infrastructure and it is, itself, a successful intervention from the resilient point of view.

1. INTRODUCTION

Bridge on the N-634 on its way through Colindres (Cantabria) was put into service in 1905 and, since then, it is an emblematic infrastructure of high traffic and pedestrian intensity. In 2016 his rehabilitation was faced. This rehabilitation required the development of very specific works in an environment of great natural and landscape singularity.
The structural non-uniformity of the bridge and the heterogeneity of the materials conditioned a rehabilitation clearly differentiated by the typology of the units and materials. This differentiated rehabilitation required the development of very specific works in an extremely worthy environment. Some innovative actions to mitigate the different sources of risks during the works on site are also explained. One of the most singular mitigation actions was the placement of a movable scaffold wearing an ad hoc encapsulation system in order to comply with the condition of no discharge to the Asón estuary of any sand blasting treatment for the cleaning of the rust on the entire surface of the elements.

2. STORY OF THE BRIDGE

2.1. Historical, administrative and technical background

Although the construction of Treto Bridge (Cantabria, Spain) is framed between 1893 and 1905, it was designed to satisfya previous long term demand. Indeed, it was framed in a territorial conflict by the preponderance of an old trade route that communicated the fishermen towns in the North of Spain and that is why it was call to be a nexus of union between the most important provinces (Cantabria, Basque Country and Castilla y León).
Thus, the project of the puddled iron bridge with two fixed spans and one swing span is approved in April 1890.
Most of the work for thefixed spans was carried out in Spanish workshops and those corresponding to the swing section by the Angler-Tilleur workshops from Liège (Belgium) "Figure 1".

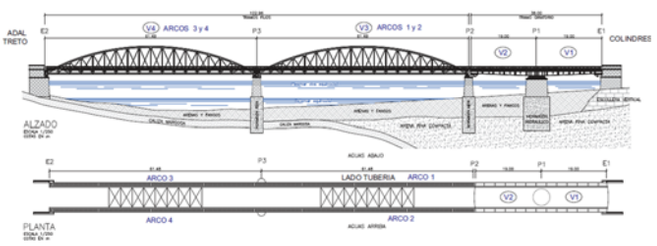


Figure 1. Elevation and plan view. Treto Bridge.

2.2. Bridge description

The total length of the bridge is of 161.74 m, each fixed (parabolic) section is 61.84 m and the swing section is 38.00 m long. The width lane "for carriages" was 9.90 m and had two pedestrian platforms 0.75 m wide in the fixed section and 1.42 m in the swing one. The width of the roadway was 5.50 m for both lanes.

It is a four-span puddled iron bridge composed of two fixed segments, isostatic, with a lower bow-string deck and a continuous swing segment, very different structurally from the previous ones. This superstructure is supported on piles and abutments made of masonry and hydraulic concrete cemented founded on the estuary.

The main structural elements of two fixed spans are the top chords that basically are arches with a variable height along the span according to a parabolic law of second degree that leads to the maximum use of the material. The arches are connected with transversal trusses limiting the vertical clearance. Thus, each fixed span defines a closed but permeable space through which the traffic circulates. The substructure is formed by abutments and masonry piers, two with an oval section and a third one with a circular one on which the swing unit connected with the deck thanks to a wheel mechanism made of an improved iron comparing with the fixed unit close to steel.

Originally and until the year 1940, the swing unit could rotate on the ring gear housed in the circular pile and be arranged perpendicular to the road, allowing the passage of boats, with a height of 3.37 m above the level of PMVE, measured from the underside of the board in fixed sections.

The swing was possible because the section was based on a circular pile of 6 m in diameter with a vertical axis of wrought puddled iron embedded in the center. To verify the movement, twelve conical casting wheels were arranged, on which the metal section was fixed by means of a circular wrought puddled iron disk of 2.40 m outside radius "Figure 2".

The pavement of the swing unit was designed and made of timber. In the other unit it was a bituminous pavement.



Figure 2: Mechanism for the swing span.

All structural elements are connected by rivets. According to the documentation related to the successive projects that gave rise to the Treto Bridge, the material used in it is wrought iron or puddled, 92.16%, which is one of the iron-derived materials that have been used successively in the construction of bridges, after the cast iron and before the steel.

The construction works of the bridge began in 1894, and it was inaugurated in 1905. In 1968, an intervention project was carried out as an emergency and in 1971. Since then, ordinary maintenance tasks have been carried out exclusively.

2.3. Inspections from the construction to 1960

There exist three reports that identified signs of oxidation, consequence of the insufficient protection of the metallic surfaces. They were solved with chopping and scraping of the rusted parts, and repainted with metallic paint based on silver glitter. In these reports is also described the blocking of the swing span, which had not been revolved since the first years of the post Spanish Civil war period.

2.4. Inspection in 1965

The inspection works carried out in 1965 analyzed for the first time the conditions of resistance and stability and looked for a solution to reactivate the turn of the swing section, although finally it was blocked.

In order to know the mechanical behavior of the bridge, a load test was carried out, and it was observed that in all the sections the vertical

displacements (3mm in the mobile and 12.5mm in the fixed ones) were recovered completely, from which it was deduced that the tensions were in the elastic range.

A chemical analysis of the steel of the bridge determined that the material was easily weldable by any procedure, and thus all the unions intervened, more than half, were repaired with this technique.

Finally, in 1966 a project was drafted in which a large number of actions were collected, among which were:

Table 1: List of relevant actions recommended

Relevant actions recommended in 1966
1. Union of the floor beams and bottom chords in the fixed units, which were in very bad conditions due to oxidation.
2. Stuffing of the bottom chords of a waterproofing material and lightweight to make them watertight, as they had insufficient drains and clogged. The proposed material was "termite concrete or similar" protected in its upper 5 cm with a lightweight concrete with aggregates.
3. The diagonals of the fixed units were not joined at the crossing points and they vibrated a lot when passing vehicles. To increase its stiffness, it was proposed to weld them to a sheet of 50x6 mm so that the cross section of each one was a T, and to join each pair of parallel diagonals together, in addition to welding them at the crossing point.
4. Repair of the metal formwork that constituted the resistant element of the forged of the parabolic sections. They were rusted due to seepage through the pavement and fill. Its repair was projected by sheet and welding and replacement of the filling by a rich concrete reinforced with a round mesh.
5. Replacement of timber sidewalks.

The consequences of this intervention has been observed and valued in the current intervention of 2016.

In 1986 the last rehabilitation project on the bridge was approved, which included only painting works. In summary, the bridge built in 1905 did not receive any type of intervention until 1965. Twenty years after these works, 1986, it was repainted and no works were carried out on the bridge until the approval of the rehabilitation project in 2016.

3. AIM OF THE REHABILITATION PROJECT IN 2016

The Ministry of Public Works in Cantabria (Spain) promoted an emergency project in 2015 to retrofit, protect and structurally rehabilitate a bridge that, from its origins, has been fundamental for the socioeconomic development of the area. The condition in which the bridge was 30 years after its last intervention was severe enough to drive a comprehensive rehabilitation project that would return the bridge to levels of structural security and service suited to the needs of the 21st century and, at the same time, conserving its essence.

4. INVENTORY OF MOST IMPORTANT DAMAGES

Corrosion, until the break, in many elements of the structure, highlighting the units between vertical and diagonal members, top and bottom chords, floor beams and bottom chords. It is a generalized damage caused by the deterioration and / or lack of protection, and it could beconsidered as a very risky damage because it endangers the safety of the pieces that are not easily accessible. Water accumulates easily, which intensifies corrosion, deteriorating the rivets and gussets and decreasing the strength of the union between structural elements.



Figure 3. Corrosion damage location. General condition.

The most relevant damages are included in the next Figure:

Table 2: General list of relevant damages.

Relevant damages
1. Instability of the diagonals to the compression efforts.
2. The bearing capacity of the lost puddled iron formwork elements has been exceeded.
3. Loss of section in bottom chords.
4. Unexpected displacement of the retaining walls in their encounter with the abutments.
5. Scour in abutments.
6. Damages caused in diagonals, vertical members and by the impact of vehicles
7. Deformations in diagonals and vertical members and struts caused by vehicle impacts.
8. Damages, unexpected deformations and displacements in masonry parapets of abutments.
9. Leakage

5. MILESTONES DURING REHABILITATION WORKS

It can be found below the solutions undertaken to restore the level of structural and functional saf ety of the structure, defined after the diagnosis study and after analyzing the pa thologies identified. The rehabilitation procedure is shown in Table 3.

Table 3: General list of rehabilitation procedures

Rehabilitation procedures during works
1. Blasting and cleaning of all truss members with sandblasting, grade Sa 2 ½. Initial primer of steel. Protection and greasing of bearing devices.
2. Calculation and evaluation of the remaining life of the bridge and definition of the retrofitting details to restore the resistant sections of steel, by means of the provision of new steel elements. Replacement of all lost, broken or loose rivets.
3. Replacement of the existing riveted unions by high resistance screws.
4. Reinforcement of all floor beam-bottom chord-vertical connections in fixed spans. The main connections of t he bridge.
5. Reinforcement of all top chord-vertical connections in fixed units.
6. Rectification of diagonals in arches.
7. Dismantling of in ternal truss according to original version. 8. Replacement of 18 portal struts and sway bracings in fix ed units. Elimination of the existing subgrades (44 cm thick) on the original lost formwork supported by floor beams and stringers.
9. Complete removal of the pavement. Execution of reinforced concrete slabs connected to floor beams by bolts in fixed units. Execution of a waterproofing system on the new slabs. Cleaning and unblocking of the existing scuppers.
10. Construction of new scuppers to provide the deck greater drainage capacity.
11. Rectification and/or replacement of some verticals.
12. Replacement of damaged verticals in fixed spans.
13. Replacement of expansion joints.
14. Stuffing of the bottom chords of a waterproofing material and lightweight to make them watertight, as they had insufficient drains and clogged.
15. Retrofitting of stringers and floor beams in swing unit.
16. Anchoring new a traffic barrier system in the swing unit.
17. Widening of sidewalks, from 0.80 m to 1.90 m by means of metal brackets housing the water pipeline.
18. The original bridge railing was reproduced.
19. Replacing of the existing water pipeline with a diameter of 500 mm, by another with a diameter of 600 mm below the new sidewalks.
20. Protection of all the truss members of the bridge with a protective coating resistant to marine environment, (280 and 400 microns thick).

6. REHABILITATION OF MAIN CONNECTIONS

It has been considered as m ain connections those ones between bottom chord, vertical and floor-beam.

The rehabilitation of m ain connections consists in the replacement of old dam aged gusset plates by new ones following an eight steps procedure.

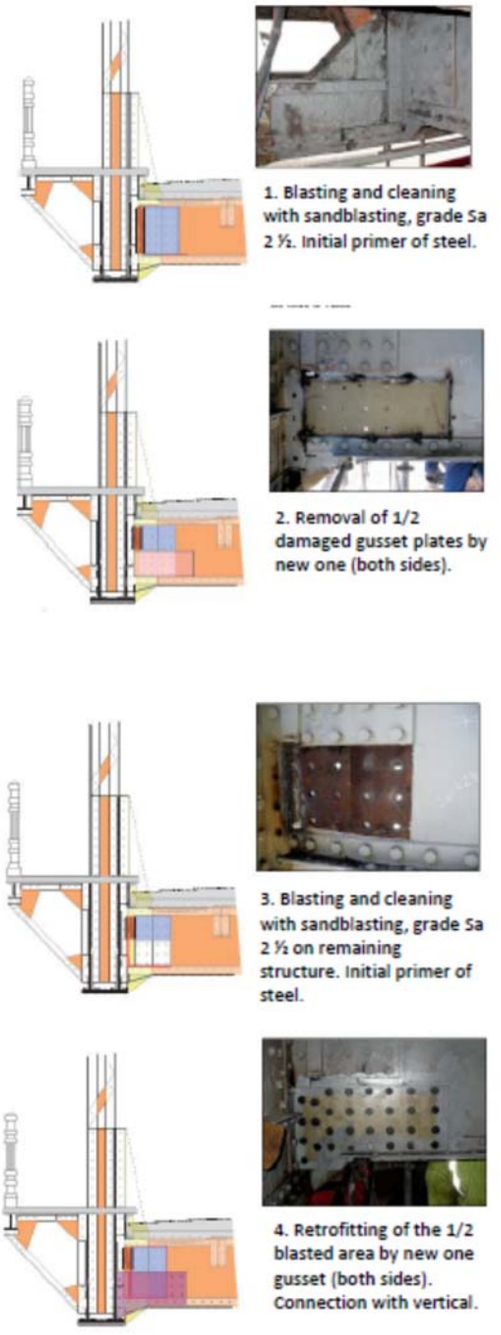
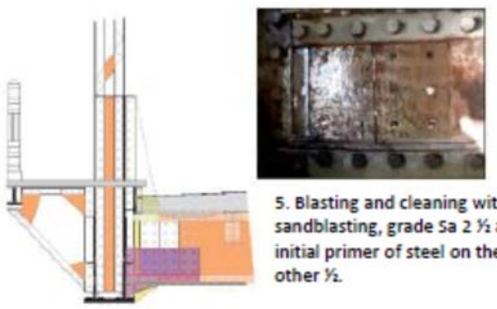
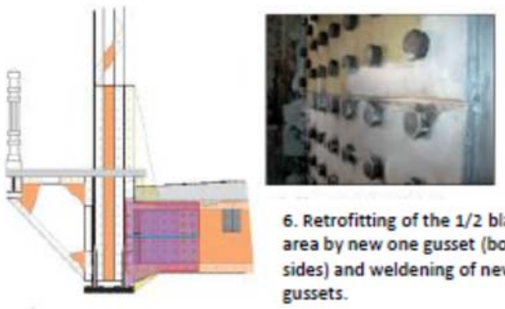


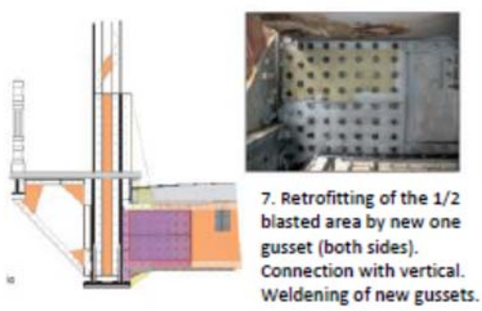
Figure 4: Rehabilitation of main connections.4 first steps.



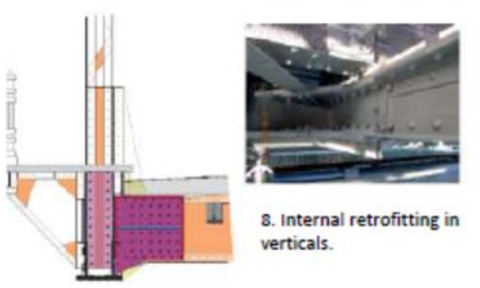
5. Blasting and cleaning with sandblasting, grade Sa 2 ½ and initial primer of steel on the other ½.



6. Retrofitting of the 1/2 blastedl area by new one gusset (both sides) and weldening of new gussets.



7. Retrofitting of the 1/2 blasted area by new one gusset (both sides). Connection with vertical. Weldening of new gussets.



8. Internal retrofitting in verticals.

Figure 5: Rehabilitation of main connections.4 last steps.

7. CONCLUSIONS

The complete analysis of Treto Bridge shows that it is a very advanced tec hnical and technological structure for its time. It is no t coincidental th at, despite the aggressive environm ent and the poor maintenance received since its construction, it has reached our days being a fundamental service for the users of the road and its neighbors and an iconic infrastructure for the region.

AKNOWLEDGEMENTS

José Francisco Sánchez Ci miano (Director of the Project), Marcos Pantale ón Prieto (Head of the Project, Louis Berger International Design Center) Miguel Angel Delg ado (Technical Director at Tecyr, S.A.).

REFERENCES

J. Páez Ma rtínez, J. 1996. Proyecto de rehabilitación del puente metálico de 1901,

Ruiz Bedia, M. L. 2010. Hitos y Mitos de la Ingeniería Civil en Cantabria. El puente de Treto. Ponencia Universidad de Cantabria.

Sánchez Cimiano, J. F. Pantaleón Prieto, M. J. 2016. Proyecto Modificado de rehabilitación del puente metálico de 1901.

Sánchez Cimiano, J. F. Delgado, M. A. 2016. Rehabilitación integral del puente metálico entre Treto y Colindres, Ctra N634.

Maintenance, Safety, Risk, Management and Life-Cycle Performance of Bridges – Powers, Frangopol, Al-Mahaidi & Caprani (Eds)
© 2018 Taylor & Francis Group, London, ISBN 978-1-138-73045-8

Management of Risk Disasters: Application in Aysen and Valparaiso, Chile

M.A. Valenzuela, N. Valenzuela & P. Moraga
Pontificia Universidad Católica de Valparaíso, Valparaíso, Chile

F. Pineda & M. Márquez
Ministerio de Obras Publicas, Santiago, Chile

R. Romo
Pontificia Universidad Católica de Chile, Santiago, Chile

ABSTRACT: In the last 35 years, the South American region has been affected by events of diverse nature such as earthquakes, floods, volcanic eruptions, landslides, and others, generating infrastructure losses close to US$88,000 million (South American Council of Infrastructure and Planning [COSIPLAN], 2016). This context has led to the implementation of the methodology called Disaster Risk Management (GRD.) by COSIPLAN/IIRSA (Initiative for the Integration of Regional Infrastructure in South America), in conjunction with the countries members of this council, created with the aim of reducing the effects of natural and anthropogenic disasters in the country's infrastructure.

In addition to the work on infrastructure management developed in South America, Chile, through the Ministry of Public Works, the Pontifical Catholic University of Valparaíso and the Pontifical Catholic University of Chile, has proposed a methodology called Management of Risk Disaster at Regional Level (GRDR in Spanish), which is applied in one of the phases of the COSIPLAN methodology.

The aim of this methodology is to incorporatedecentralized information by enabling the participation of technical teams or sub-departments at city level, allowing for the generation of preventive early warnings, identifying and updating the structural damage indexes (in addition to maintenance plans) and executing reduced budgets at early stages.

The present work describes the most relevant aspects of this methodology, presents the results obtained in field applications, and describes an implementation proposal for Route 115 CH.

1 INTRODUCTION

Chile is the longest country in the world, with approximately 4,300 kilometers from north to south in its South American continental territory. It presents a variety of conditions regarding both weather and morphology along its territory. The physical characteristics of the Chilean territory are defined by Bordas (2006) as "one of the most seismically active areas of the planet, with a large number of volcanoes, an extensive coastline exposed to the Pacific Ocean, a mountainous territory stark altitudinal differences, and an intense pluviometric regime".

In this geomorphological context, there is a remarkable need to implement the methodology for Management of Risk Disaster at Regional Level (GRDR) with the objective that technical units that inspect state-owned structures take this geographical context into account at the time of inspection. These technical units, such as the Ministry of Public Works (MOP) and the Housing and Urban Development Service (SERVIU) are the onesresponsible for the development, implementation, and maintenance of public infrastructure in Chile. In addition, it is very important to take into consideration this methodology at the time of executing any intervention in the road infrastructure and when projecting future works within a road, in order to reduce the risk of disaster.

The application of the GRDR methodology provides a real and clearer perspective of the national road infrastructure, allowing forin-depth analysis of the most fragile areas of the network, supporting the decision-making process in the context of each structure studied, enabling finally a change in the current philosophy of the development of the national road network. COSIPLAN/IIRSA is fostering the application of this methodology in South America and in all its member countries, being Chile one of the pioneers in the application of this method.

The GRDR. method is based both on the road infrastructure as well as the climatological and morphological context where the structure is located, which means that the threats will take an important role at the time to inspect, repair and plan infrastructure belonging to the national road network. This method is focused on reducing the vulnerability of

infrastructure while reducing the risk of social and economic loss in the country in order to obtain a resilient road network.

2 CHILE'S PROPOSAL ON THE METHODOLOGY FOR DISASTER RISK MANAGEMENT IN REGIONAL INFRASTRUCTURE (GRDR)

With the purpose of complementing what has been done by COSIPLAN/IIRSA, on the progress made in probabilistic risk analysis, it has been proposed at the national level a methodology called Management of Risk Disaster at Regional Level (G.R.D.R), coordinated directly by the Ministry of Public Works. This method is applied at phase 2 of the COSIPLAN methodology, having an impact on actions to be implemented in phase 3, thus enabling a resilient response optimized to thecontext of the country (Valenzuela & Valenzuela, 2016).

The purpose of the methodology proposed by the Ministry of Public Works (MOP) is the integration of aspects of decentralization through regional management of the infrastructure, which implies that each region should be able to carryout surveys of their infrastructure, providing information through technical entities, allowing for the generation of early warnings, identification and updating of the damage indexes of the structures, which results in the management of risks in the Regional Infrastructure (Valenzuela & Valenzuela, 2016). Figure 1 shows this decentralized approach that collects information from regional technical units, which allows for infrastructure management at thelocal level and within the region's budgetary framework.

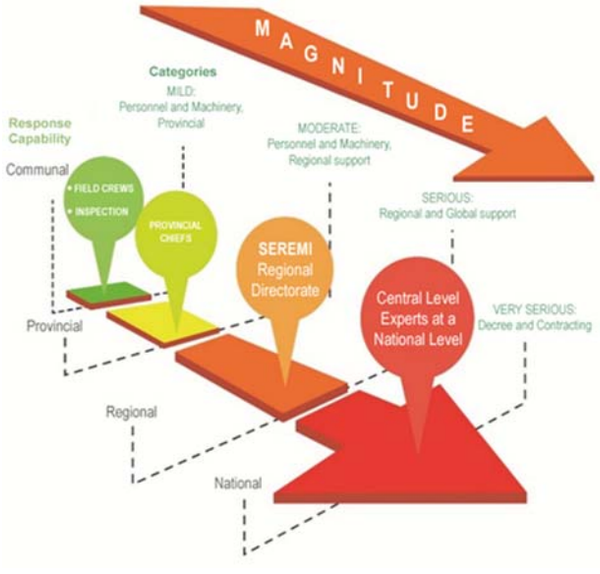


Figure 1. GRDR Methodology Alert Levels
Source: Author compilation.

Some of the benefits derived from the management of infrastructure at the regional level are the following: lower costs incurred at the stage of information collection, better knowledge of the "needs" of the region's communities, and better understanding of the structure's geographical context.

2.1 *Phases of the G.R.D.R methodology.*

The GRDR. methodology is comprised of four phases which help determine structures' pathologies and vulnerabilities to operating loads and external sources of stress. The methodology' s phases are the following:

Phase 1: During this phase, pathologies are identified in the elements constituting the selected structures in a road network, taking into consideration the operational burdens of the structure as well. Thismust be achieved in field inspections of the structure through the use of inspection sheets.

Phase 2: Once the structure has been assessed through the pathologies of its elements and the operational burdens, it is assessed overall, taking operational burdens into consideration; this survey, as in the previous phase, is achieved through the use of inspection sheets.

Phase 3: Once the structure's pathologies and operational burdens have been assessed, the exceptional loads (seismic activities, floods, volcanic eruptions, landslides, etc.) must be identified. When acting each on its own, a vulnerability index is generated for the structure.

In this phase, it is important that public institutions provide documentation and input from their own databases of local threats.

Phase 4: During this phase, the structure is assessed through a single external stress, as well as in the event of more than one external stress (e.g.: an earthquake and tsunami, or a volcanic eruption and landslides).

Phases 1 and 2 are activities commonly executed by the National Road Directorate for its road infrastructure. For bridges, the sheets contained within the Highways Manual, Vol. 7 are used most of the time.

The materialization of this methodology proposed by the MOP is carried out byprofessionals at the local units responsible for the maintenance and supervision of the national road network. These professionals must be trained by specialists in this methodology so

they can then survey the structures and provide an explanation for each pathology within each structure as well as guidance (Figure 2).



Figure 2. Training courses of GRDR Methodology.

3 PILOT PLAN ARICA Y PARINACOTA REGION

The first pilot plan to use this methodology consisted on the inspection oftraditional typology Poconchile and Chacabuco Bridges, located in the Arica and Parinacota Region, specifically along the 11 CH route, as well as a visit to the Sea Port Terminal of Arica. This is considered a bi-oceanic route, and so it is highly important to South America, as it connects countries such as Brazil to the Pacific Ocean.

The inspection program was developed with the aid of 20 professionals in charge of the inspections using the bridge sheet; they were divided into four groups of five inspectors each to get a correct assessment of the information obtained in the field, placing a great focus on the assessments of the sheets. This feedback from the professionals allows for the continuous improvement of these tools.

According to the assessment of the results gathered in the field (Valenzuela & Valenzuela, 2016), the groups perform as follows:

- **Group 1:** Through their comments on the sheet, this group failed to demonstrate their understanding of the inspection tool.

- **Group 2:** This group managed to correctly interpret the evaluation sheet, using the concepts provided to them. They generated comments regarding the position of the pathologies in the structure.

- **Group 3:** This group understood the location of the pathologies correctly, but failed to understand the application of the Risk Phase.

- **Group 4:** This group failed to correctly interpret the application of the sheet. They generated comments of a technical character, which are not considered within the scope of the sheets.

Some of the improvements considered for the implementation of these data sheets in future pilot plans focus on an improvement of the user guide, to fill the data sheets in a more orderly fashion in order to correctly guide the professionals and reduce the subjectivity of the data obtained. This is a relevant issue considering the subjectivity of the inspections carried out as part of this pilot plan.

4 PILOT PLAN LOS LAGOS REGION AND AYSEN REGION

The implementation of the tools developed within the framework of action of the GRDR methodology consists of a field test applied between kilometers 170 and 345 at Route 7 "Carretera Austral", corresponding to the second pilot plan for the above-mentioned methodology. This route is the main connection between these regions, becoming an important asset for Chile.

The main objective pursued in this process is to get validation and feedback from professionals with regard to the tools developed, particularly their applicability to the road network and its site context.

The pilot plan is based on the application of the visual inspection sheets developed by the GRDR team which is tested in different infrastructures and sectors vulnerable to threats, having their influence radius within the road network covered by the pilot plan. The procedure considers the participation of seven inspectors with different professional qualificationsin the structures, construction, and environment fields. These professionals are responsible for the field validation of the developed tools.

The inspection section of the selected pilot plan is considered as one of the sectors with the greatest fragility within Route 7 product of the morphological and climatical context of its environment, presenting multiple threats of varied nature. The latter, together with the presence of unique bridges (suspension and cable-stayed bridges), corresponds to the main motivations for the entity responsible for the administration of the GRDR methodology (Figure 3, 4 and 5).



Figure 3. Raya Bridge. Pier Damage.



Figure 4. Amarillo Bridge. Pier Damage.



Figure 5. Suspension bridge at Aysen region.

From the threats identified in the pilot plan, the entity in charge of coordination of the methodology and the multidisciplinary team that makes up the GRDR selected the following threats: volcanic activity, fire risk, landslide and flooding threats and river overflow (Figure 6).

These threats should be analyzed by the methodology, which corresponds in the first instance to an in-officecharacterization and ending with visual inspection in the field.



Figure 6. Landslide area on Route 7.

Generally, there is feedba ck from professionals, which is identified in all of the tools developed:

- The data sheets provide an easy-to-understand design for the user.
- Proposal of inspection protocols for the use of GRDR. data sheets
- The data sheets allow for having a historical and detailed record of the threat studied, in addition, to supplement it with ph otographic record. This registration is required in the inspection protocols, both for the m icro inspection of the structure as well as f or the m acro inspection of the threats.
- Incorporation of variables not provided for in the prior description: an example of this are the bonfires under the bridge structure.
- The possibility of using a tablet device to take photos and incorporate th em immediately into the report.



Figure 7. Inspection activities under GRDR Methodology.

The process for obtaining feedback indicated on each data sheet consists of the study of inspection instruments used in the field, complemented by the analysis of the videos corresponding to the technical meetings. These two sources of data provide important feedback for each one of the inspection data sheets. This process was carried out with each of the tools defined for the survey (Figure 7).

This allows for improving each of the data sheets, taking into account the observations obtained in thefield and by validating them with literature relevant to the topic.

5 RESULTS OBTAINED IN THE IMPLEMENTATION IN FIELD AND A PROPOSAL FOR IMPLEMENTATION IN ROUTE CH-115

The experience gained in the implementation of the pilot plans mentioned above, particularly in the one executed at Carretera Austral, as well as the identification and characterization of threats done in office demonstrate that some variables appear constantly in the events analyzed, being one of the most important the one corresponding to the morphological variables, in particular, the slope, which according to the studies carried out conditions all the events covered in the pilot plan of the Los Lagos Region and Aysen.

- **Volcanic threat "lahars":** The slopes directly affect the speed of the lahar, generating great drag of materials eroding works within the area of influence of this threat.

- **The threat of forest fires:** Because heat rises, the steepness of the slope is an important factor in the behavior of the fire and its spread. There is a danger associated with the slope percentage. Gradients below 15% are assumed as danger null, between 15 and 30% low danger, between 30 and 40% medium danger, 45 to 60% high risk and slopes of over 60% are considered extreme slopes (National Forest Corporation CONAF et al., 1999).

- **The threat of landslides:** Slope topography (its geomorphological features) condition the occurrence of landslides. These characteristics have a direct influence on the speed, energy, and volume of mass removals. Any alteration in the topographical features of the hillside can make it go from stable to unstable (Popescu, 2002).

  According to Hauser (1993), slopes with gradients greater than 25° in the headwaters of the drainage basins favor the formation of floods. In the case of slopes formed by rock, the slopes greater than 35° are those that generate a greater susceptibility to landslides.

It is of great importance that slopes are analyzed in all the tools developed in Phase 3 of the GRDR methodology, where the professionals responsible for the gathering of field information are able to analyze these variables and provide feedback in the best possible way through the inspection data sheets.

5.1 *Application of G.R.D.R. methodology to Route 115 CH*

With the objective of calibrating all procedures and products which are obtained by applying this methodology, it is necessary to have more pilot plans. All of the analyses developed in the pilot plans listed above can be interpolated to the context of Route 115 CH where there are threats that are reiterated with regard to the geomorphology present in the location of the route, such as forest fires, landslides and volcanic processes.
The existing threats in this route are:

Forest fire: fire outbreaks reported by CONAF along Route 115CH, where different fire outbreaks characterized mainly by low density can be appreciated. The density of forest fires exposed by CONAF depends on the number of forest fires per square kilometer that have occurred in the last five years: Low: from 1 to 5.; Medium: from 5 to 10, and High: more than 10.

Although there is a low density in the event analyzed, the present geomorphological context, the steep slopes, in particular, are determining factors for greater acceleration and ignition of forest fires, generating great risk in structures, especially to bridges built of a mixed structure of steel-concrete, which varies its supportive behavior.

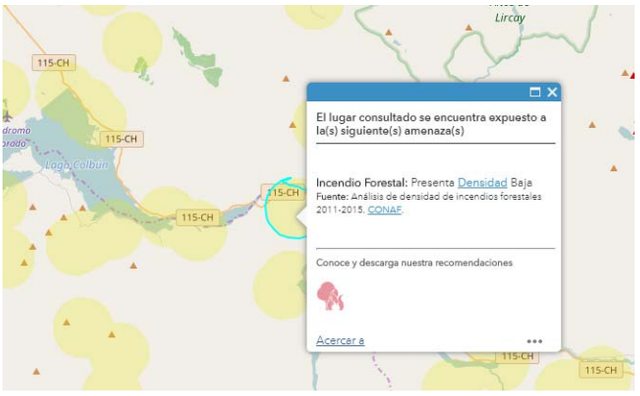


Figure 8. Threat of Forest Fires in Route 115 CH.

Landslides: in route 115 CH different landslides of rocks can be appreciated, such as the one that occurred in kilometer 128 of the road, Los Condores sector. This event is enhanced by the steep slopes in the high mountain road context.

Volcanic threat: on route 115 CH different levels of volcanic hazards are present according to the report carried out by the National Emergency Office ONEMI, where there are sectors on the route which are exposed to high volcanic hazards where its location includes the influence of the volcanic complex Laguna del Maule, Pedro-Pellado volcano, and Cerro Azul- Quizapu volcano.

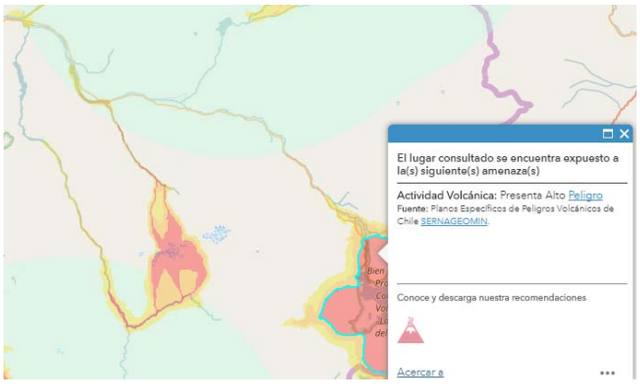


Figure 9. Volcanic Threat on Route 115 CH.

The geomorphological context present in Route 115 CH generates a significant risk to the structures present on this route, before which the implementation of the GRDR methodology is important, where the inspection of the structure considers a comprehensive analysis that takes into account the study of the structure, its location, and their interaction.

6 CONCLUSIONS

- The constant external threats to which the road infrastructure is constantly exposed make it the implementation of inspection methodologies necessary, both at the national and regional level, including all aspects described in this work.
- The current methodologies of inspection carried out by the Road Management Office (Dirección de Vialidad) and the data sheets contained in the Manual of Roads should be complemented to contain aspects relating to threats (external stress sources) that put at risk, in particular, the infrastructure of bridges.
- Continuous training of professionals involved in these tasks is required, with type data sheets and application manuals.
- The routes that have a high factor of importance, such as for example the bi-oceanic corridors, need to be constantly studied from the point of view of the threats that they are exposed to. The above should be complemented with routine and periodic inspections.
- With regard to the implementation of the pilot plan in the Carretera Austral, several zones which are influenced within the buffer of threats are shown, generating a great risk for infrastructure located in the route, generating the need to implement a methodology concerning risk management.
- The implementation of the G.R.D.R. methodology in the context of threats in Route 115CH can bring with it an improvement in the effectiveness of the road network in the area of analysis, providing tools to improve the management of the infrastructure at the regional level.

7 REFERENCES

Bordas Coddou, A. (2006). Políticas Públicas para Enfrentar los Desastres Naturales en Chile. (Master's Thesis, University of Chile, Santiago, Chile). Retrieved from Http://repositorio.uchile.cl/handle/2250/102822.

CONAF; CONAMA; BIRF. (1999). Proyecto Catastro y E valuación de Recursos Vegetacionales Nativos de Chile, Décima Región de Los La gos. Universidad Austral de C hile, Pontifical Catholic Universityof Chile; Temuco Catholic University. 138p. Includes update by monitoring changes to the 10th North Region.

COSIPLAN (2016). La Gestión de Riesgos de Desastres en COSIPLNA: Metodología y aplicación en infraestructura de Chile y Perú. Buenos Aires, Argentina.

Hauser, A. (1993). Remociones en masa en Chile. No. 45, p. 7-29. Servicio Nacional de Geología y Minería, Santiago.

Oficina Nacional de Emergencia (ONEMI). Visor de Chile preparado: http://www.onemi.cl/visor-chile-preparado/

Osorio, C. (2014). Manual de Usuario-Orientaciones para emprender análisis de ri esgo. Documento presentado en el Grupo Técnico Ejecutivo (GTE) sobre la Metodología de Gestión y Prevención de Riesgos y Catástrofes en la Infraestructura Suramericana de Integración, Buenos Aires, Argentina.

Popescu, M.E., (2002). Landslide Causal Factors and Landslide Remedial Options. Document shown at 3rd International Conference on Landslides, Slope Stability and Safety of Infra-Structures, Singapore, p. 61-81. http://www.geoengineer.org/Lanslides-Popescu.pdf.

Valenzuela, M.; Valenzuela, N. (2 016). Metodología DFS-Orientado al análisis de riesgo: Innovación en análisis avanzado. Paper presented at Reu nión GTE sobre Gestión de Riesgos de Desastres., Lima, Perú.

Valenzuela, M. (2017). Application methodology of local Risk Disaster Management on Chile (GRDR). Paper presented at RakennusTekniikka, Finland.p. 58-62.

Valenzuela, M.; Valenzuela, N.; Romo, R. (2017). Management System for Natural Risk Disaster on Infrastructure Regional approach (GRDR). Pape r presented at 11th International Bridge & Structure Management Conference, Mesa, USA

Maintenance, Safety, Risk, Management and Life-Cycle Performance of Bridges – Powers, Frangopol, Al-Mahaidi & Caprani (Eds)
© 2018 Taylor & Francis Group, London, ISBN 978-1-138-73045-8

Fatigue behavior of full-penetration inclined cruciform welded-joints with artificial pit corrosion

X. Wei
Southwest Jiaotong University, Chengdu, China
Z.Y. Jie
Ningbo University, Ningbo, China

ABSTRACT: To investigate the effect of corrosion pit on fatigue damage evolution of welded joints, specimens of full-penetration inclined cruciform (FIC) welded joints with artificial corrosion pits were designed and fatigue tests of three kinds of welded joints in different corrosion depth were carried out. Based on fracture mechanics theory and maximum circumferential tensile stress criterion, crack propagation rate formula of FIC welded joints were derived with different corrosion pit. Research results showed that fatigue lives obtained from crack propagation rate formula have a good agreement with test results.

1 INTRODUCTION

Local damage of steel structure is always induced by corrosion and fatigue. Accumulated damage cause performance deterioration of steel structure and eventually will lead to structural failure and decrease the service life of steel structure. Due to the reduction of plate thickness and the increase of stress concentration, corrosion has effects not only on the ultimate static strength but also on the fatigue strength of welded joints. It was found that large stress concentration with corrosion pit was the major cause of the decrease of fatigue strength. Over the past few years, fatigue performance of corroded steel material has been studied extensively. But for steel welded joint, it is less than satisfactory with the existing information. Only a few literatures can be found on the aspects of this problem. Garbatov & Soares (2014) studied fatigue strength of corroded welded steel specimens with prior corrosion. Nguyen et al. (2012) applied the effective notch stress method to the analysis of time-dependent stress distribution and fatigue damage of a corroded oil tanker. Huang et al. (2014) evaluated the fatigue reliability of a complicated welded structure subjected to simultaneous random non-uniform corrosion and fatigue loading.

In this paper, test specimens of full-penetration inclined cruciform (FIC) welded joints with artificial corrosion pits were designed and fatigue tests of three kinds of welded joints in different corrosion depth were carried out. Nominal stress S-N curves and fracture mechanics theory were used to predict the fatigue life of FIC welded joints including artificial corrosion pits.

2 FATIGUE TEST

2.1 *Test specimens*

Full-penetration inclined cruciform welded joints were investigated, which include two long plate members and one short plate member, as shown in Figure 1. The inclined angle θ is 45°.

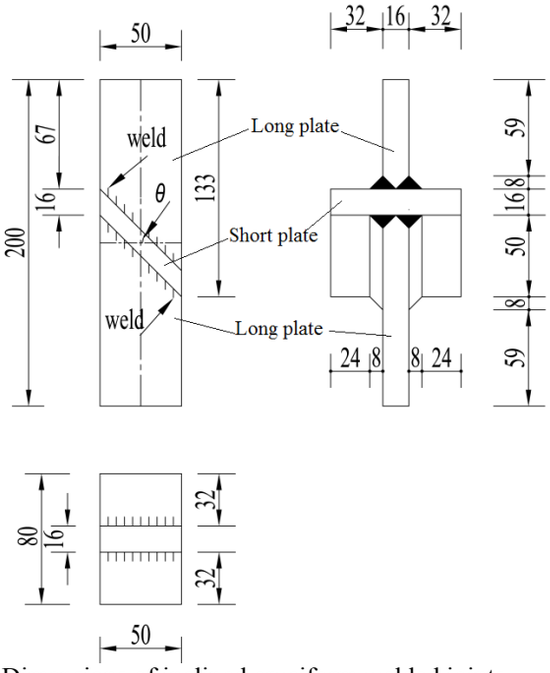


Fig.1 Dimensions of inclined cruciform welded joints

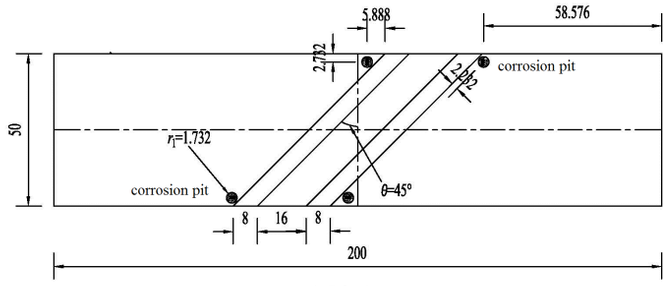
Three groups of test specimens were design for fatigue tests (list in Table 1). There are not corrosion

pits on specimens of group P0. Two kinds of artificial corrosion pits with spherical shape are considered in Group P1 and Group P2. The geometric parameters of the pits, including pit depth and pit radius, are listed in Table 1.

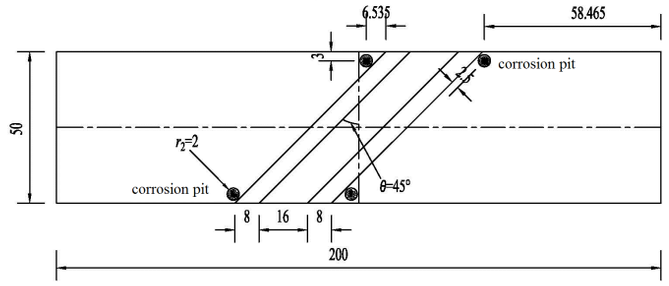
Table 1. Fatigue specimens

Group	No.	*depth* /mm	*radius* /mm	Δσ /MPa	P_{min} /kN	P_{max} /kN
P0	P0D1	0	0	140	12.4	124.4
	P0D2	0	0	160	14.2	142.0
	P0D3	0	0	180	16.0	160.0
P1	P1D1	1	2	140	12.4	124.4
	P1D2	1	2	160	14.2	142.0
	P1D3	1	2	180	16.0	160.0
P2	P2D1	2	2	140	12.4	124.4
	P2D2	2	2	160	14.2	142.0
	P2D3	2	2	180	16.0	160.0

Each specimen in group P1 and group P2 contains 8 artificial corrosion pits located on long members near the ends of welds (see Figure 2).



a) Pit 1



b) Pit 2

Figure2 location of corrosion pitting

The material of the FIC welded joints specimens is hot-rolled low alloy structural steel Q345qC, a typical structural steel for steel bridges in China.

Fatigue tests were performed under the axial tension loading condition. The test overview is shown in Fig.3. With force control and constant amplitude, sinusoid loading was employed for cyclic loading. The ratio between the minimum and maximum stresses was $R=\sigma_{min}/\sigma_{max}=0.1$. Based on the nominal stress method, 9 specimens were divided into three types with different stress range levels in every group. The peak value of fatigue loading was defined as P_{max}, whereas the minimum value was defined as P_{min}. The fatigue loading and stress range levels for each series of specimens are listed in Table 1.

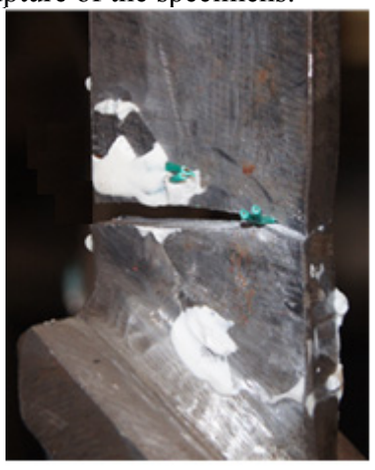


Figure3 Overview of Fatigue test

2.2 *Fatigue Test Results*

As shown in Figure4 (a), in all specimens without artificial corrosion pits the fatigue crack first occurred at the welded toe of the long plate member near short edge sides. Fatigue damage accumulated with increasing cycle number; cracks also penetrated the long plate thickness and propagated along the width of long plate. The fractured plate lost its carrying capacity with crack propagation, and the stress on the plate increased dramatically.

As shown in Figure4 (b), in most of specimens with artificial corrosion pits the fatigue crack first occurred at the corrosion pits of the long plate member near short edge sides. Fatigue crack propagated with increasing cycle number. Cracks decreased the effective area of the cross section of the specimens that carry the axial tension loading, thus leading to the final rupture of the specimens.



（a）No pits



（b）With pits

Figure4 Failure modes of inclined cruciform welded joints

Table 2. Fatigue test results

Group		Δσ /MPa	P_{min} /kN	P_{max} /kN	Cycle number
P0	P0D1	140	12.4	124.4	1.43E+06
	P0D2	160	14.2	142.0	9.77E+05
	P0D3	180	16.0	160.0	6.03E+05
P1	P1D1	140	12.4	124.4	9.55E+05
	P1D2	160	14.2	142.0	6.40E+05
	P1D3	180	16.0	160.0	5.36E+05
P2	P2D1	140	12.4	124.4	7.44E+05
	P2D2	160	14.2	142.0	4.15E+05
	P2D3	180	16.0	160.0	2.91E+05

3 NOMINAL STRESS S-N CURVE

Stress-based and fracture mechanics-based approaches are the two main approaches for fatigue life assessment of weld structure. By choosing different stress parameters, which are defined in Figure 5, the stress-based approaches can be divided into the nominal stress approach, the hot spot stress approach, and the notch stress approach.

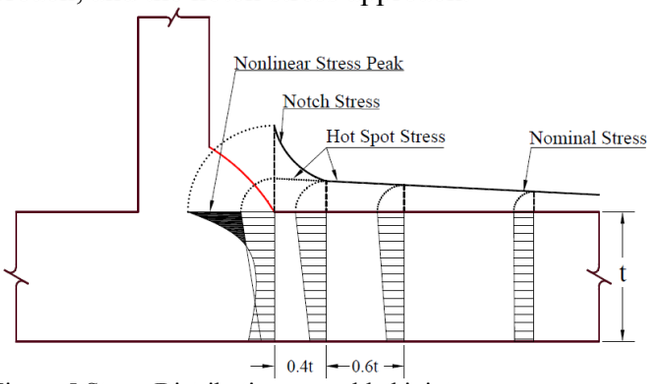


Figure 5 Stress Distribution on welded joint

Nominal stress does not include stress concentrations due to detail geometry, which is primarily determined based on the cross-section properties. Given the different S-N curves for common structural details, the effects of residual stresses, imperfections, welding procedures, and stress concentrations as a result of detail geometry are implicitly accounted for by the fatigue classification of typical details based on statistical evaluation of fatigue test data. The nominal stress range, number of loading cycles, crack location and the structural detail properties are the four main variables that control the fatigue performance of weld details. The nominal stress approach is easy to apply and is adopted in many fatigue design and fatigue life evaluation guidelines. However, its accuracy decreases for complex weld details.

To develop a general understanding of the fatigue performance of FIC welded joints with artificial corrosion pits, fatigue tests results of 9 groups were summarized in this study.

The fatigue test results of FIC welded joints are often plotted with the *S*-*N* curves. The relationship between *S* and *N* is:

$$\Delta\sigma^{m}N=C \tag{1}$$

or

$$\log N=\log C-m.\log\Delta\sigma \tag{2}$$

The fatigue design curves for welded joints have been proposed and adopted by many standards and recommendations, in which each curve is set at a constant slope of minus 3.0(m=3). Given that m=3, the least-squares method was utilized to obtain a linear fitted equation that generate a line of best fit from the data. The equation was based on the fatigue test data from Table 2.

For group P0, the relationship between *S* and *N* is:

$$\log N=12.58-3\log\Delta\sigma \tag{3}$$

Where, the standard deviation is 0.0175.

For group P1, the relationship between S and N is:

$$\log N=12.444-3\log\Delta\sigma \tag{4}$$

Where, the standard deviation is 0.0255.

For group P2, the relationship between S and N is:

$$\log N=12.257-3\log\Delta\sigma \tag{5}$$

Where, the standard deviation is 0.0266.

The aforementioned test results and three S–N curve equations are plotted in figure 6.

The design *S*-*N* curve is commonly selected at two standard deviations below the mean *S*-*N* curve, thus, the majority of the fatigue test data are above the lower-bound value. The fatigue life has a 97.7% possibility of survival with a 95.5% confidence level. The design *S*–*N* curve equation can be expressed as follows:

$$\lg N=\begin{cases}12.545-3\lg\Delta\sigma & Pit0\\ 12.394-3\lg\Delta\sigma & \text{Pit1}\\ 12.204-3\lg\Delta\sigma & Pit2\end{cases} \tag{6}$$

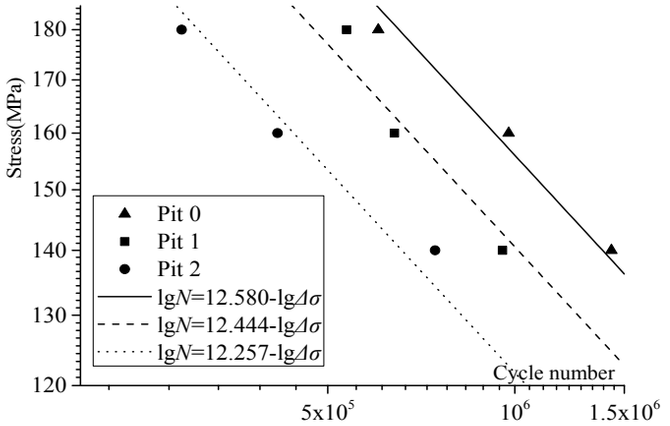


Figure 6 fatigue test results and fitted S-N curve

The test results and three S–N curves for design are plotted in figure 7.

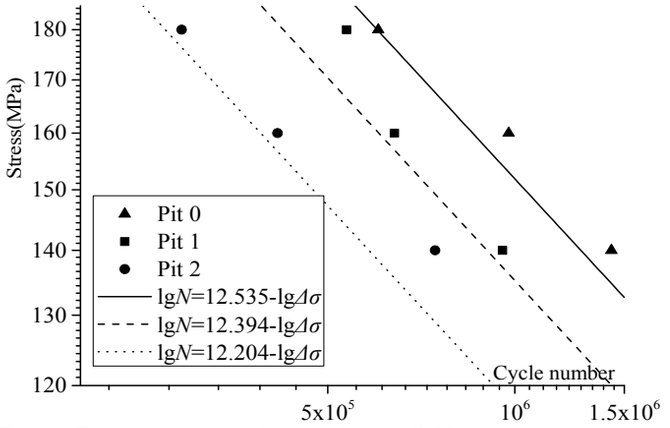


Figure 7 fatigue test results and design S-N curve

4 FRACTURE MECHANICS APPROACH

The fatigue fracture processes in FIC welded joints can be described from the point of view of fracture mechanics. The stress intensity factor (SIF) at the crack or slit tip is used as the basis of this approach. The process of fatigue failure of steel material is subdivided into the stages of crack initiation, stable crack propagation and unstable final fracture. the fatigue life of welded joints is exclusively propagation of very small cracks occurring in the mixed material zone of filler and parent materials at the toe and root of the weld seam, the propagation can be described on the basis of the crack intensity factor range, ΔK.
The fracture mechanics approach, independent of its degree of formalization, complements the nominal stress, structural stress, and notch stress assessments, which are the only basis for dimensioning and design of welded joints, by an assessment of failure safety and service life on the basis of detected actual defects or undetected assumed crack-like defects.
Under uniaxial stress field, there are three crack propagation modes, shown in Figure 8.
Crack mode I is opening mode (a tensile stress normal to the plane of the crack), crack mode II is sliding mode (a shear stress acting parallel to the plane of the crack and perpendicular to the crack front), and crack mode III is tearing mode (a shear stress acting parallel to the plane of the crack and parallel to the crack front)

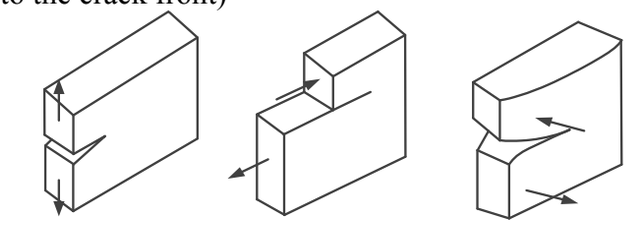


Figure 8 Crack mode in Fracture mechanics

For FIC welded joints, fatigue crack is propagating under tension-shear complex stress. Crack mode of FIC welded joints combines crack mode I and crack mode II. Mixed mode crack propagation criteria are needed to be investigate.
Generally, the mixed mode crack propagation and fatigue life are estimated via the following procedures: firstly, the direction and path of mixed mode crack propagation are determined by numerical methods (e.g. the finite element method (FEM) , boundary element method (BEM) and meshless methods); secondly, crack propagation rates are expressed by the effective stress intensity factor range; finally, fatigue life can be predicted by Paris law based on the effective stress intensity factor range.

4.1 *Mixed mode crack propagation criteria*

Spatial stress state of mixed mode crack front is shown in Fig. 1.

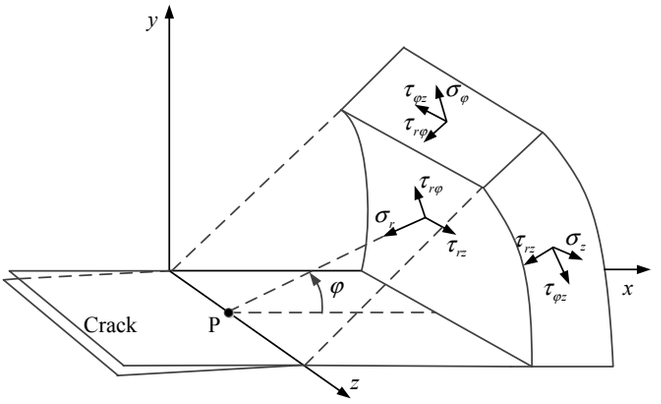


Figure 8. Spatial stress state of crack front

According to the superposition principle, stress components can be expressed in the cylinder coordinate system as:

$$\sigma_r = \frac{K_{\mathrm{I}}}{4\sqrt{2\pi r}}\left\{5\cos\left(\frac{\varphi}{2}\right)-\cos\left(\frac{3}{2}\varphi\right)\right\} - \frac{K_{\mathrm{II}}}{4\sqrt{2\pi r}}\left\{5\sin\left(\frac{\varphi}{2}\right)-3\sin\left(\frac{3}{2}\varphi\right)\right\} \quad (7)$$

$$\sigma_\varphi = \frac{K_\mathrm{I}}{4\sqrt{2\pi r}}\left\{3\cos\left(\frac{\varphi}{2}\right)+\cos\left(\frac{3}{2}\varphi\right)\right\} - \frac{K_\mathrm{II}}{4\sqrt{2\pi r}}\left\{3\sin\left(\frac{\varphi}{2}\right)+3\sin\left(\frac{3}{2}\varphi\right)\right\} \quad (8)$$

$$\tau_{r\varphi} = \frac{K_\mathrm{I}}{4\sqrt{2\pi r}}\left\{\sin\left(\frac{\varphi}{2}\right)+\sin\left(\frac{3\varphi}{2}\right)\right\} + \frac{K_\mathrm{II}}{4\sqrt{2\pi r}}\left\{\cos\left(\frac{\varphi}{2}\right)-3\cos\left(\frac{3\varphi}{2}\right)\right\} \quad (9)$$

$$\tau_{rz} = \frac{K_\mathrm{III}}{\sqrt{2\pi r}}\sin\left(\frac{\varphi}{2}\right) \quad (10)$$

$$\tau_{\varphi z} = \frac{K_\mathrm{III}}{\sqrt{2\pi r}}\cos\left(\frac{\varphi}{2}\right) \quad (11)$$

$$\sigma_z = \nu\left(\sigma_r+\sigma_\varphi\right) = \frac{8\nu}{4\sqrt{2\pi r}}\left\{K_\mathrm{I}\cos\left(\frac{\varphi}{2}\right)-K_\mathrm{II}\sin\left(\frac{\varphi}{2}\right)\right\} \quad \text{plane strain} \quad (12)$$

$\sigma_z = 0$ plane stress

where K_I, K_II,K_III are respectively the stress intensity factors of modes I, II and III, r, φ are polar coordinates at the crack tip, ν is Poisson's ratio, and σ_r, σ_φ, σ_z, $\tau_{r\varphi}$, τ_{rz} , $\tau_{\varphi z}$ are normal and shear stresses in the polar coordinate system.

Erdogan and Sih (1963) proposed the maximum circumferential stress criterion. The criterion adopts the following two basic assumptions: (1) crack will initiate in the direction of the maximum circumferential stress $\sigma_{\varphi,\max}$; (2) crack will grow when $\sigma_{\varphi,\max}$ reaches a critical value $\sigma_{\varphi,\mathrm{c}}$. According to assumption (1), the conditions that circumferential stress reaches the maximum are

$$\frac{\partial\sigma_\varphi}{\partial\varphi}=0 \quad \text{and} \quad \frac{\partial^2\sigma_\varphi}{\partial\varphi^2}<0 \quad (13)$$

Which yields

$$K_\mathrm{I}\sin\varphi+K_\mathrm{II}\left(3\cos\varphi-1\right)=0 \quad (14)$$

and

$$\varphi_0 = \pm\arccos\left\{\frac{3K_\mathrm{II}^2+K_\mathrm{I}\sqrt{K_\mathrm{I}^2+8K_\mathrm{II}^2}}{K_\mathrm{I}^2+9K_\mathrm{II}^2}\right\} \quad (15)$$

Where φ_0 is the crack initiation angle. The fracture criterion can be given as

$$\frac{1}{2}\cos\frac{\varphi_0}{2}\left[K_\mathrm{I}\left(1+\cos\varphi_0\right)-3K_\mathrm{II}\sin\varphi_0\right]=K_\mathrm{Ic} \quad (16)$$

Where K_Ic is the fracture toughness of the material under mode I loading condition.

According to the stress field of crack tip introduced in section 4.1, the effective stress intensity factor ranges, ΔK_{Ieff} ,$\Delta K_{\mathrm{II\,eff}}$ and $\Delta K_{\mathrm{IIIeff}}$, are expressed as:

$$\Delta K_{\mathrm{Ieff}} = \sigma_\varphi\sqrt{2\pi r} = \frac{1}{2}\cos\frac{\varphi}{2}\left[\Delta K_\mathrm{I}\left(1+\cos\varphi\right)-3\Delta K_\mathrm{II}\sin\varphi\right] \quad (17)$$

$$\Delta K_{\mathrm{IIeff}} = \tau_{r\varphi}\sqrt{2\pi r} = \frac{1}{2}\cos\frac{\varphi}{2}\left[\Delta K_\mathrm{I}\sin\varphi+\Delta K_\mathrm{II}\left(3\cos\varphi-1\right)\right] \quad (18)$$

$$\Delta K_{\mathrm{IIIeff}} = \tau_{z\varphi}\sqrt{2\pi r} = \Delta K_\mathrm{III}\cos\frac{\varphi}{2} \quad (19)$$

The effective stress intensity factor range ΔK_{eff} based on the maximum circumferential stress criterion is expressed as

$$\Delta K_{\mathrm{eff}}=\Delta K_{\mathrm{Ieff}} \quad (20)$$

Since the maximum circumferential stress criterion is relatively simple and easy to use in practical applications, and the criterion is validated by a large number of tests, the maximum circumferential stress criterion is recommended being used to predict the fatigue life of welded joints with mixed mode surface crack.

4.2 *Crack propagation equations*

The typical curve of the crack propagation rate da/dN (limes of the ratio of the increase of crack length, Δa, per number of cycles, ΔN) for metallic materials, measured in specimens with macrocrack, dependent on the (constant) stress intensity factor range, ΔK, at the crack tip subjected to pulsating tensile load.

Based on linear elastic fracture mechanics theory, according to the Paris laws, fatigue crack propagation rate of FIC welded joints is expressed as:

$$\frac{\mathrm{d}a}{\mathrm{d}N} = C\left(\Delta K_{eff}\right)^m \quad (7)$$

$$\Delta K_{eff} = Y\Delta\sigma_\varphi\sqrt{\pi a} \quad (8)$$

$$\int_{a_\mathrm{i}}^{a_\mathrm{c}}\frac{\mathrm{d}a}{C\left(Y\sqrt{\pi a}\right)^m} = \Delta\sigma_\varphi^m N \quad (9)$$

Where C, m are material constants, Y denotes the crack shape correction factor, $\Delta\sigma_\varphi$ denotes stress range, a denotes the crack size, N denotes the fatigue life, and a_i and a_c denotes the size of the initial crack and the critical crack, respectively. To simplify the calculation, crack shape correction factor Y is assumed to be a constant. Thus Eq. (9) can be rewritten as

$$\Delta\sigma_\varphi^m N = \frac{a_\mathrm{i}^{1-m/2}-a_\mathrm{c}^{1-m/2}}{CY^m\pi^{m/2}\left(m/2-1\right)} \quad (10)$$

The relation between stress range and fatigue life can be obtained from *S-N* curves defined by fatigue test, thus one can have

$$\Delta\sigma^m N = A \tag{11}$$

Where C is a material constant. The material constant C can be rewritten as

$$C = \frac{a_i^{1-m/2} - a_c^{1-m/2}}{AY^m \pi^{m/2}(m/2-1)} \tag{12}$$

Given Y =1, a_i =0.25 mm, a_c =16 mm, m=3, A=3.75×10^{12}, 2.74×10^{12} and 1.79×10^{12}, the fatigue crack propagation rate of the welded joint with no pit is expressed as

$$\frac{da}{dN} = 1.676\times10^{-13}(\Delta K)^3 \tag{13}$$

The fatigue crack propagation of welded joints with pit 1 is expressed as:

$$\frac{da}{dN} = 2.294\times10^{-13}(\Delta K)^3 \tag{14}$$

The fatigue crack propagation rate of welded joints with pit 2 is expressed as:

$$\frac{da}{dN} = 3.511\times10^{-13}(\Delta K)^3 \tag{15}$$

4.3 *Crack-shape factor*

Using FEM software Franc3D, numerical simulation of FIC welded joint were carried out. The numerical model of FIC welded joint is shown in Figure 9. Initial crack length is 0.25mm.

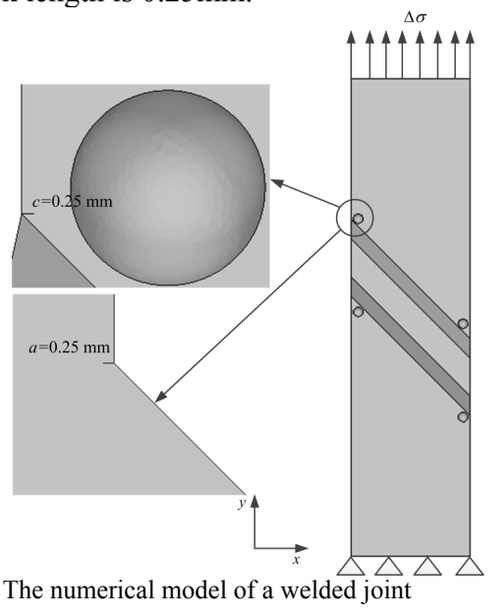


Figure 9. The numerical model of a welded joint

As shown in Figure 10, based on the maximum circumferential stress criterion, the relationship between crack-shape factor Y of the surface crack at the deepest point and crack depth ratio a/t of FIC welded joints with three different artificial corrosion pits were obtain

In Figure 10, it is observed that at the beginning crack-shape factor is in high value. With the increasing of a/t from 0.0 to 0.2, crack-shape factor is decreased from 1.9 to 0.8. With the increasing of a/t from 0.2 to 0.8, crack-shape factor have little fluctuation around 0.7. With the increasing of a/t from 0.8 to 1.0, crack-shape factor is increased from 0.8 to 1.3. When the crack depth ratio is about 0.5, crack-shape factor is in minimum value. The crack-shape factor rises with the increasing of pit depth. The effect of pit depth on the crack-shape factor becomes insignificant when a/t is greater than 0.3.

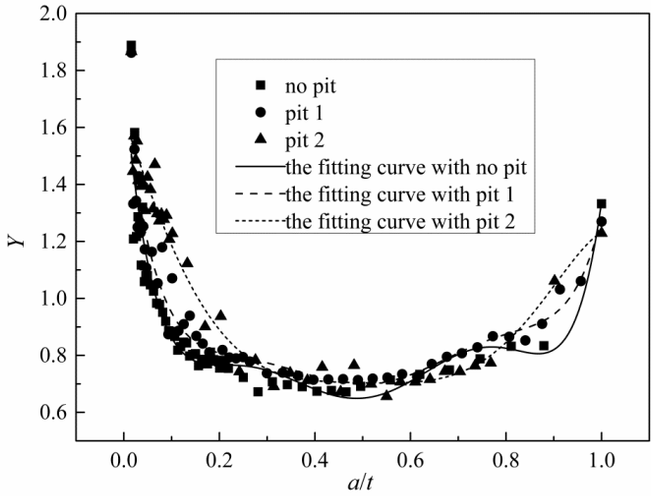


Figure 10 Curve of Y-a/t

Using a polynomial regression technique, crack-shape factor of FIC welded joints with no pit, pit 1 and pit 2 can be expressed as:

$$Y_1 = 1.619 - 16.039\frac{a}{t} + 111.606\left(\frac{a}{t}\right)^2 - 380.735\left(\frac{a}{t}\right)^3 + 666.512\left(\frac{a}{t}\right)^4 - 571.621\left(\frac{a}{t}\right)^5 + 190.199\left(\frac{a}{t}\right)^6 \tag{16}$$

$$Y_2 = 1.587 - 11.865\frac{a}{t} + 68.322\left(\frac{a}{t}\right)^2 - 200.171\left(\frac{a}{t}\right)^3 + 308.501\left(\frac{a}{t}\right)^4 - 237.090\left(\frac{a}{t}\right)^5 + 71.820\left(\frac{a}{t}\right)^6 \tag{17}$$

$$Y_3 = 1.609 - 5.978\frac{a}{t} + 14.663\left(\frac{a}{t}\right)^2 - 16.611\left(\frac{a}{t}\right)^3 + 9.143\left(\frac{a}{t}\right)^4 - 3.497\left(\frac{a}{t}\right)^5 + 1.944\left(\frac{a}{t}\right)^6 \tag{18}$$

4.4 *Fatigue life prediction*

Using equations (13)-(15), fatigue life of FIC welded joint with artificial corrosion pits can be predicted. In equations (13)-(15), the crack-shape factor is assumed to be 1, but it is a function of crack depth ratio in actual crack growth. In order to obtain more accurate fatigue life predictions, it makes sense to modify equations (13)-(15) based on formulas (16)-(18) and material constants of S-N curves. The modification of fatigue crack propagation rates based on the maximum circumferential stress criterion can be expressed as:

$$\frac{da}{dN} = 1.874\times10^{-13}\left(\Delta K_{\text{eff}}\right)^3, \text{ for no pit} \quad (19)$$

$$\frac{da}{dN} = 2.154\times10^{-13}\left(\Delta K_{\text{eff}}\right)^3, \text{ for pit 1} \quad (20)$$

$$\frac{da}{dN} = 2.632\times10^{-13}\left(\Delta K_{\text{eff}}\right)^3, \text{ for pit 2} \quad (21)$$

In terms of Equations (19)-(21), the fatigue crack propagation rates of welded joints with pit 1 and 2 are respectively 1.15 times and 1.40 times larger than that of the welded joint with no pit. The main reason is that the high stress field close to weld toe is affected by corrosion pits, and stress concentration factors of weld toes rise with the increase of pit depths.

Fatigue life prediction results are list in Table 3. Column (1) is the fatigue life prediction results calculated by equations (13)-(15); Column (2) is the fatigue life prediction results calculated by equations (19)-(21). Error between test result and column (1) are given in column (3) and maximum error is 30% ; Error between test result and column (2) are given in column (4), and maximum error is only 12.4%.

Obviously, fatigue prediction results from equations (19)-(21) are in good agreement with fatigue test results. Therefore, crack-shape factor obtained from the maximum circumferential stress criterion is recommended being used to predict fatigue life.

Table 3. Fatigue life prediction results

Group	Prediction×10^5		Test	Errors %	
	(1)	(2)	×10^5	(3)	(4)
P0S1	16.2	13.7	14.3	13.3	-4.2
P0S2	1.07	9.15	9.77	9.5	-6.3
P0S3	7.53	6.43	6.03	24.9	6.6
P1S1	9.82	9.98	9.55	2.8	4.5
P1S2	6.67	6.69	6.40	4.2	4.5
P1S3	4.85	4.70	5.36	-9.5	-12.3
P2S1	5.21	6.52	7.44	-30.0	-12.4
P2S2	3.38	4.37	4.15	-18.6	5.3
P2S3	2.40	3.07	2.91	-17.5	5.5

5 CONCLUSION

In this paper, combined fatigue test and fracture mechanics theory, fatigue behavior of full-penetration inclined cruciform welded-joints with artificial pit corrosion were investigated. the following conclusions can be drawn.

(1) Fatigue test results indicate that fatigue cracks initiate at the weld toes with the maximum stress.

(2)With the increasing of pit depth, constant parameter C is decreased in the relationship $\Delta\sigma^m N$=C in nominal stress approach. With the increasing of pit depth, fatigue crack propagation rate is increased in fracture mechanics approach.

(3) With the increase of crack depth ratio, the crack-shape factor falls at first and then rises.

(4)The maximum circumferential stress criterion is more suitable to predict fatigue growth behaviors of welded joints. Fatigue crack growth rates based on effective stress intensity factors are suitable for assessing fatigue life of welded joint with mixed mode cracks.

ACKNOWLEDGEMENT

The authors are supported by the National Natural Science Foundation of China (51378431). The support is gratefully acknowledged.

REFERENCES

Erdogan F, Sih GC(1963). On the crack extension in plates under plane loading and transverse shear. Journal of Fluids Engineering,85(4):519-525.

Garbatov Y, Soares CG, Parunov J (2014). Fatigue strength experiments of corroded small scale steel specimens. INT J FATIGUE,59:137-144.

Huang W, Garbatov Y, Guedes Soares C(2014). Fatigue reliability of a web frame subjected to random non-uniform corrosion wastage. STRUCT SAF,48:51-62.

Paris PC, Erdogan F(1963). A critical analysis of crack propagation laws. Journal of basic engineering ,85(4):528-533.

Rahgozar R, Sharifi Y. Remaining Fatigue Life of Corroded Steel Structural Members. ADV STRUCT ENG 2011, 14(5):881-890.

Radaj D.(1990) Design and Analysis of Fatigue Resistant Welded Structures [J]. Design & Analysis of Fatigue Resistant Welded Structures, Woodhead Publishing, London, UK:66–97.

Tran Nguyen K, Garbatov Y, Guedes Soares C (2012). Fatigue damage assessment of corroded oil tanker details based on global and local stress approaches. INT J FATIGUE ,43:197-206.

Jie Z.Y., Li Y.D. &Wei X.(2016). Analysis of the stress intensity factor of welded joints under prior corrosion and complex stress fields[J]. Journal of Modern Transportation, 24(4):1-7

Jie, Z. Y., Li, Y. D., & Wei, X. (2017). A study of fatigue crack growth from artificial corrosion pits at welded joints under complex stress fields. Fatigue & Fracture of Engineering Materials & Structures.40(9):1364-1377.

Xing Wei, Lin Xiao, Shiling Pei(2017).Fatigue assessment and stress analysis of cope-hole details in welded joints of steel truss bridge. International Journal of Fatigue,2017,100: 136-147.

Maintenance, Safety, Risk, Management and Life-Cycle Performance of Bridges – Powers, Frangopol, Al-Mahaidi & Caprani (Eds)
© 2018 Taylor & Francis Group, London, ISBN 978-1-138-73045-8

Stress-concentration effects due to weld root imperfections in orthotropic steel decks

H. De Backer, W. Nagy & A. Outtier
Ghent University, Ghent, Belgium

ABSTRACT: An orthotropic steel deck system consists of a steel plate supported by longitudinal stiffeners and transversal crossbeams. Orthotropic bridge decks are prone to fatigue cracking due to the complicated weld details and the direct action of traffic loads. Although the stiffener-to-deck plate detail is of high importance in these decks, this connection seems to be one of the most difficult welding details since it can only be welded from the outside. Therefore, the influence of the weld penetration ratio and the geometry of the weld root on the stresses in the stiffener-to-deck plate connection is investigated. In Siemens NX, detailed 3D models based on real stiffener-to-deck plate connections were modelled. These 3D models were then included in a reference model of an orthotropic bridge deck, which consists of 2D shell elements. A parametric study was executed varying the weld penetration ratio of each model and investigating the peak principal stresses. The results clearly indicated that the shape of the weld root imperfection has a high influence on the peak principal stresses. The smaller and sharper the shape of the weld root imperfection, the higher the stress concentrations. The parametric study also showed that the absolute value of the peak principal stress decreases for an increasing weld penetration ratio. This is in contradiction with most conclusions in literature. However, most studies calculated a general model, of which the translations and rotations occurring in the zone of interest were then transferred to a smaller 3D model. This is an important difference with the method used in this study, which allows redistribution of the stresses since the 3D model is included in the reference model.

1 INTRODUCTION

An orthotropic steel deck system consists of a steel plate supported by stiffeners in the longitudinal direction and by crossbeams in the transversal direction. One of the main advantages of an orthotropic steel deck bridge is its low dead weight. However, orthotropic steel deck bridges also have significant disadvantages. Fatigue cracking due to the complicated weld details and the direct action of traffic loads, which induces high stress variations, is an important problem.

In a weld, fatigue cracking can either start at the weld toe or at the weld root. While weld toe cracks are initially located in the weld toe line, weld root cracks will first penetrate through the weld material before appearing on the weld surface. Since weld root cracks can only be detected once they penetrated through the weld material and appear on the weld surface, they are often considered to be more dangerous than weld toe cracks.

In the orthotropic steel deck, the stiffener-to-deck plate detail is one of the most important welded joints. Unfortunately, this connection seems to be one of the most difficult welding details since it can only be welded from the outside. As a consequence, it is hard to control the weld quality with respect to weld penetration. Both a lack of penetration and an excessive weld penetration will cause additional stress concentrations, resulting in a reduced weld quality. Therefore, the influence of the weld penetration ratio and the geometry of the weld root on the stresses in the stiffener-to-deck plate connection is investigated.

2 EXPERIMENTAL EVALUATION OF REAL WELD GEOMETRIES

Several real welded stiffener-to-deck plate details were available (Figure 1), from these details test specimens were cut at well-chosen locations.

Three test specimens were cut from each welded stiffener-to-deck plate detail. Since these details were first tack welded before being completely welded using a fully automatic welding procedure, one of the three specimens of each detail was cut out in the area of the tack weld. In total 15 test specimens, from 5 different welded stiffener-to-deck plate details, are investigated. To study the weld irregular-

ities at the weld root, the test specimens were first grinded until a smooth surface was obtained, after which they were photographed using a microscopic camera. The pictures of each test specimen were then scaled to their real dimensions. The weld root imperfection of one of the test specimens is illustrated in Figure 2.



Figure 1. Real welded stiffener-to-deck plate detail

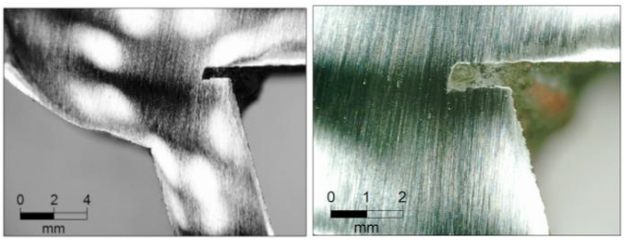


Figure 2. Scaled picture of the weld root of one of the models

The observations for the specimens containing a tack weld and those without a tack weld were compared. However, no clear relation seems to be present between the geometry of the weld root or the weld penetration ratio and the presence of a tack weld. An important observation that was made based on these pictures is the fact that only 7 out of the 15 test specimens has a weld penetration ratio that is higher than 66.7%, which is suggested by the Eurocode for a stiffener with a thickness of 6 mm. The requirements given by the Japan Road Association and the AASHTO LRFD Bridge Design Specifications, which are respectively a weld penetration ratio of 75% and 80%, are not even met by one of the test specimens.

3 FINITE ELEMENT MODELLING

The finite element software package Siemens NX 11 was used to model an orthotropic steel deck and a detailed model containing the real weld geometries.

3.1 *Reference model*

The reference model uses 2D shell elements to model part of an orthotropic bridge deck. It consists of two main beams, two transversal crossbeams, five longitudinal closed stiffeners and a deck plate. The deck plate and longitudinal stiffeners were assigned a shell thickness of 15 mm and 6 mm respectively. The structure was meshed using quadrilateral shell elements with an element size of 20 mm, which is sufficiently small for this global analysis model.

The entire deck has a steel grade S355 with a yield stress of 355 MPa and a mass density of 8750 kg/m³. With respect to the elastic material properties, a young's modulus of 210 GPa and a Poisson's ratio of 0.3 were assigned.

The boundary conditions were applied at the edges of the bottom flanges of the main beams. Four different bearings were used, which all allow rotation and prevent displacement in the vertical direction, but with respect to the displacements in the horizontal directions they are different. A schematic overview of the enabled horizontal displacements for each support, is given in Figure 3.



Figure 3. Boundary conditions of the bridge deck

Only one load case is used to determine the stresses in the weld root of the stiffener-to-deck plate detail. The detailed 3D model will be implemented at the connection of the second longitudinal stiffener from the right at mid-span, as depicted in Figure 4. Since the stresses will be determined in this detailed 3D model of the connection, a wheel load of 35 kN is applied in between the second and third stiffener from the right at mid span. In this way, tensile stresses will be generated in the stiffener near the weld root, which is devastating for fatigue. In addition, there will be no risk of any contact pressure due to the unwelded free surfaces of the deck plate and the stiffener. In such case, additional boundary conditions should be implemented on the finite element model to restrict faces from going through each other, which is physically not possible.

The surface area of this wheel load was determined according to wheel type A suggested in Eurocode EN 1991-2, being a rectangular area of 220 mm by 320 mm.

3.2 *3D model containing real weld geometries*

Based on the scaled microscopic pictures of the welded specimens, an AutoCAD model was drawn of the cross section of the 3D model. This AutoCAD drawing was then imported into the Siemens NX software, after which it was extruded over a length of 50 mm. It was then inserted into the 2D reference model of the orthotropic bridge deck on the left side of the second longitudinal stiffener from the right, at mid span. This is illustrated in Figure 4.

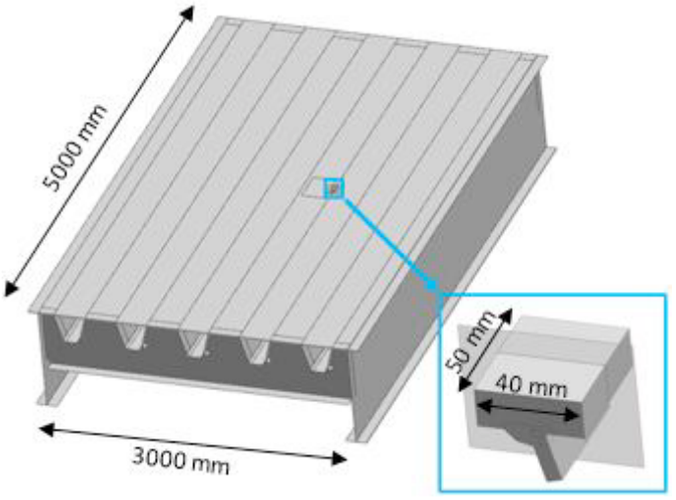


Figure 4. Boundary conditions of the bridge deck

The outside surfaces of the 3D model need to be connected to the matching edges of the 2D reference model, this was achieved by applying an edge-to-surface gluing constraint in Siemens NX.

The mesh of the 3D part was refined near the weld root imperfection. Stresses are eventually determined at the centre of the 3D part, in the plane that is indicated in Figure 4. The stresses at the outside edges of the 3D element are not considered since local stresses due to the transition from the 2D shell elements to the 3D elements arise at those locations. Therefore, the mesh size did not need to be very fine around those edges. It was only refined towards the weld root imperfection in the plane indicated in Figure 4.

Tetrahedral 3D elements were used to mesh the detailed model. Since namely the stresses around the weld root imperfection are of importance, the elements around this imperfection have 10 nodes (CTETRA 10). In the rest of the 3D model, tetrahedral elements with 4 nodes (CTETRA 4) are sufficient.

Eight of these models were modelled, four models based on the pictures of the test specimens (Model 1 to 4 in Table 1), one model with an 'ideal' rounded weld root, one model according to the effective notch stress method, one model with a 100% penetration ratio and one model with an excessive weld penetration. An overview of the weld root imperfections of these models is given in Table 1. The model according to the effective notch stress method is introduced because in literature, the influence of the weld penetration ratio is often determined based on this method. The effective notch stress method is discussed in the guidelines of the IIW, it includes replacing the actual weld root imperfection by an effective contour with a radius of 1 mm. The tip of that radius should coincide with the root of the real notch. The effective notch stress is then calculated based on the worst principal stress.

Table 1. Overview of the weld root imperfections of the 8 models that will be investigated.

	Cross-section of the model
Model 1	
Model 2	
Model 3	
Model 4	
Model with an 'ideal' rounded weld root	
Model according to the effective notch stress method	
Model with a 100% penetration ratio	
Model with an excessive weld penetration ratio	

Since some of the weld root imperfections of the models include relatively sharp angles, stress singularities can occur. At these stress singularity points the stress will not converge and it will in theory become infinite. In reality, the stress will have a finite value and therefore it is important to check if the

models contain such singularities or not. A convergence study was executed for all 3D models to ensure that no such stress singularity points occur. This is done by refining the mesh and making sure that the stresses around the weld root imperfection converge. The stresses in the models that are illustrated in Table 1, all converged and thus no singularities should be feared.

4 PARAMETRIC VARIATIONS

The influence of the weld root imperfection on the stress concentrations is investigated. A parametric study is done varying the weld penetration ratio of the models from Table 1. As already mentioned, the influence of the weld penetration ratio is often studied in literature based on the effective notch stress method. To make comparison with those studies possible, it was chosen to include a model in which the weld root is replaced by an effective notch.

The weld penetration ratio was varied from 52% to 90%. The reason for starting at 52% and not at 50%, is purely to avoid problems in the finite element model. If the weld root imperfection has a weld penetration ratio of 50%, the edge of the imperfection would coincide with the center line of the stiffener. This causes problems when connecting the tetrahedral elements to the 2D shell elements. Therefore, the lowest weld penetration ratio is 52%, after which it is increased to 60%, 70%, 80% and finally 90%. For each of the models, five different weld penetration ratios are thus studied. An example of the change in geometry for model 1 is illustrated by Figure 5.

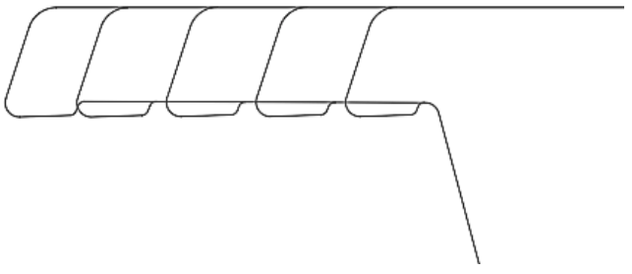


Figure 5. Varying weld penetration ratio for model 1

Once the finite element model has been calculated, it is important to select the most suitable stress output for evaluating the results. Although Von Mises stresses include the influence of shear stresses, it is chosen not to use these stresses since they do not distinguish compression and tensile stresses. Hence, principal stresses will be used

4.1 *Results*

The results provided by the Siemens NX software for a varying weld penetration ratio in case of model 1, are illustrated in Figure 6. A dark blue zone with high compression stresses is present at the upper left corner of the weld root imperfection. At the lower left edge of the imperfection a red zone with high tensile stresses is present. This is a consequence of the loading that was applied to the reference model, which causes tension near the weld root in the web of the longitudinal stiffener. The red tensile zone becomes smaller for an increasing weld penetration ratio, meaning that the principal stress is reduced for an increase of the weld penetration ratio. The location of this high compression and tension zone does not change relatively to the edge of the weld root imperfection.

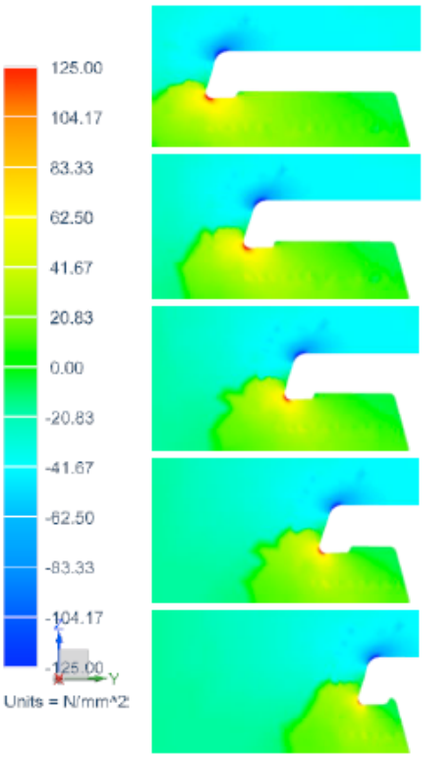


Figure 6. Evolution of the worst principal stresses in model 1 for a varying weld penetration ratio

Although Figure 6 clearly shows the location of the highest compressive and tensile stresses, it is difficult to compare the values of the peak stresses based on the color scale. Therefore, Figure 7 and Figure 8 show respectively the peak compressive and tensile principal stresses for each model in function of a varying weld penetration ratio.

The first observation that can be made is the fact that the shape of the weld root imperfection has a significant influence on the peak principal stresses. The smaller and sharper the shape of the weld root imperfection, the higher the stress concentrations. For both the compressive (Figure 7) and tensile (Figure 8) stresses, model 4 resulted in the highest values because of the small dimensions of its weld root imperfection. While for the compressive stresses model 3 showed the second highest values, the re-

sults for the tensile stresses indicated that model 2 has the second highest peak principal stress. This is due to the fact that model 3 has sharper edges at the upper side, at which the compressive stress peak is located, while model 2 shows a sharper geometry at the lower side, which is under tension.

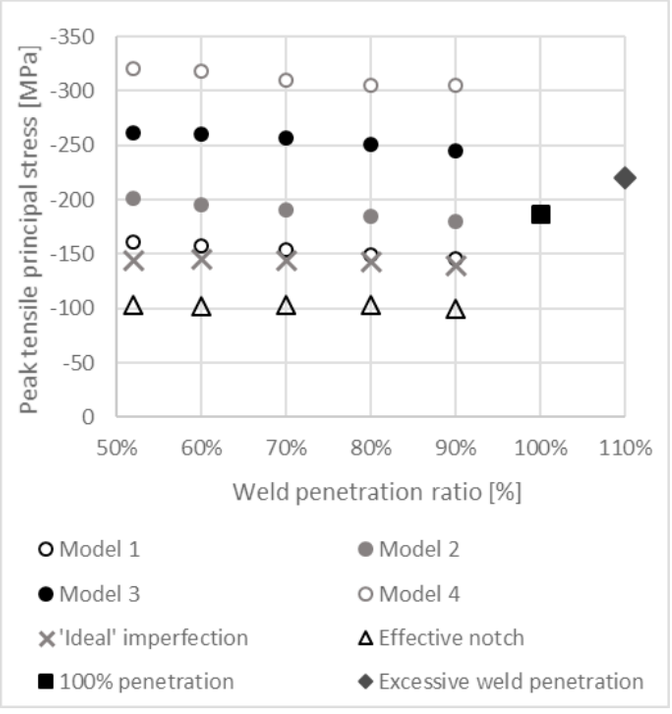


Figure 7. Overview of the peak compressive principal stresses in function of the weld penetration ratio

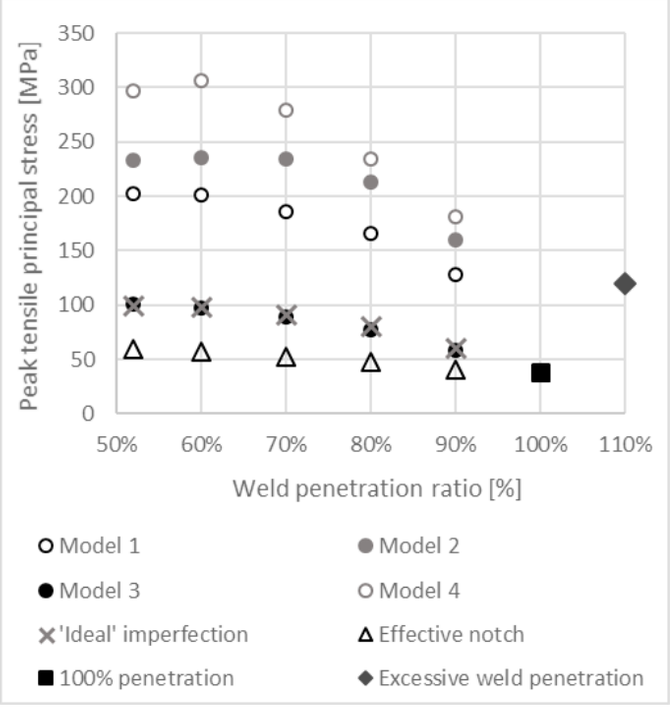


Figure 8. Overview of the peak tensile principal stresses in function of the weld penetration ratio

Based on the evolution of the values of the peak stresses, it can also be concluded that the absolute value of the principal stress decreases for an increasing value of the weld penetration ratio. The results of the models with a lack of penetration can also be compared to those of the models with a 100% penetration ratio and with an excessive weld penetration. In comparison with the other models, the model with a 100% weld penetration ratio does not show a high tensile stress peak. Since tensile stresses are the most devastating for fatigue, this would mean that for the load case that was tested in this study a 100% weld penetration ratio is beneficial for the fatigue resistance. However, obtaining a weld penetration ratio of 100% without having regular weld melt-through, is very difficult in practice, if not impossible. Therefore, the results of the model with an excessive weld penetration ratio are interesting. This model did show high stress peaks, but it is depending on the shape of the weld root imperfection if these stress peaks are higher or lower than those in the models with a lack of penetration.

For the load case that is tested in this case, the tensile stresses are more influenced by the weld penetration ratio than the compressive stresses. Since the tensile stresses are the most devastating for fatigue, the weld penetration ratio will thus significantly influence the fatigue resistance. This could be because the tensile stresses are located in the stiffener, of which the cross-section is smaller and more influenced by the weld penetration ratio compared to the deck plate, which is subjected to compressive stresses.

4.2 *Comparison with literature*

The results from the previous paragraph were first compared to the guidance rules with respect to the weld penetration ratio. The Eurocode suggests a maximum lack of penetration of 2 mm, which corresponds to a weld penetration ratio of 66.7% for a rib thickness of 6 mm. The Japan Road Association requires a weld penetration of 75% while the AASHTO LRFD Bridge Design Specifications suggests a weld penetration ratio of 80%. The 80% penetration limit seems to be a practical limit, since it is approximately the maximum penetration that could be achieved without regular weld melt-through.

The 70% to 80% weld penetration ratio that is suggested in several codes, does not result in the lowest principal stresses according to the results. An even higher weld penetration ratio of 90%, results for all models in a lower principal stress and thus a higher fatigue resistance. As already mentioned, the 80% limit is probably more a practical limit, since higher weld penetration ratios would result in regular weld melt-through.

Although the results in the previous paragraph clearly indicated that an increase in weld penetration ratio results in lower principal stresses, conclusions in literature do not confirm this. The studies of Sim, H.B. & Uang, C.M. 2012, Vu Dung, Sasaki, E., Tajima, K. & Suzuki, T. 2014 and De Backer, H. 2006

all conclude that an increasing in weld penetration ratio results in increasing stresses.

Sim, H.B. & Uang, C.M. 2012, Vu Dung, Sasaki, E., Tajima, K. & Suzuki, T. 2014 evaluated the influence of the weld penetration based on the Von Mises stresses in an effective notch model. The fact that the results in the previous paragraph were based on principal stresses does not justify the different conclusions, since the Von Mises stresses in these models also decrease for an increasing weld penetration ratio. The effective notch radius that is applied in the studies of Sim, H.B. & Uang, C.M. 2012 and Vu Dung, Sasaki, E., Tajima, K. & Suzuki, T. 2014 is 0.5 mm while the radius applied in the model of this study is 1 mm, according to the recommendations of the IIW. This will probably not justify the different conclusions either since all models in this study, independently of their size or shape, show the same relation: an increase in weld penetration ratio results in a lower principal stress.

A possible explanation for the contradiction could be the fact that none of these studies included the sub model in the global model. The nodal displacements of the global model were applied as boundary conditions on the sub model, not allowing a redistribution of the stresses. This is an important difference with the method used in this study, which includes a smaller 3D model into a large reference model and therefore does allow redistribution of the stresses. There is also the possibility that because of different loading cases, these studies included contact pressures between the unwelded free surfaces of the deck plate and the stiffener, which was not the case in this study.

5 FATIGUE BEHAVIOUR OF THE MEASURED WELD GEOMETRIES

5.1 *Stress concentration factors (SCF)*

The resistance to fatigue can be determined based on several methods that are suggested in literature. The nominal stress method evaluates the fatigue life based on the nominal stress range, local stress raising effects are thus not included. The hot-spot stress is determined by applying an extrapolation procedure using stresses in the vicinity of the weld. This method includes the stress-raising effects of the structural detail but excludes the stress concentration due to the local weld profile. Since these two methods eliminate the influence of the local weld profile, they are unsuitable for the purpose of this study. Finally, the effective notch stress method takes into account both the local stresses caused by the geometry of the structure and the stresses caused by the weld profile. This method consists of replacing the actual weld contour by an effective notch with a radius of 1 mm. Since most of the weld root imperfections that were modelled have dimensions smaller than 1 mm, this would again eliminate the influence of the shape of the weld root imperfection. Therefore, also the effective notch stress method is not suitable in this case.

Since these methods are unsuitable for comparing the fatigue behavior of the measured weld geometries, the comparison was done using a stress concentration factor. This factor is the ratio of the maximum stress in the weld root and the nominal stress. If the stress concentration factor of a structure is known, it should only be multiplied with the nominal stress in the detail to obtain the maximum stress occurring.

$$SCF = \frac{\sigma_{max}}{\sigma_{nom}} \tag{1}$$

For calculating the stress concentration factors of the models, the maximum stresses given in Figure 7 and Figure 8 are used. The nominal stress in the detail is determined based on the nominal stress in the reference model, which is equal to 30.6 MPa in the web of the stiffener near the weld root. Since the results are obtained by dividing all peak compressive or tensile stresses by the same factor, being the nominal stress, the conclusions regarding the influence of the weld root imperfection will be identical to those given in the previous sections.

Figure 9 compares the stress concentration factors of the different models to the stress concentration factor of the model with a 100% weld penetration ratio. This relative stress concentration factor ς is thus calculated according to equation (2), in which SCFx is the stress concentration factor for the model and weld penetration ratio under consideration and SCF100% is the stress concentration factor of the model with a 100% weld penetration ratio. The Eurocode suggests the fatigue life should be determined based on the bending moments and stresses in the stiffener. For this reason and since tensile stresses are the most devastating for fatigue, it is chosen to determine this relative stress concentration factor based on the tensile stresses in the models (Figure 8).

$$\varsigma = \frac{SCF_x}{SCF_{100\%}} = \frac{\sigma_{max,x}}{\sigma_{max,100\%}} \tag{1}$$

The assumption is made that the peak stress obtained from the model with a 100% weld penetration ratio is comparable to the nominal stress in the detail, meaning that this peak stress represents the stress in a stiffener-to-deck plate detail including the stress raising effects of the geometry and the weld. The latter is not included in the nominal stress. By determining the factors from Figure 9, the results of two 3D models are compared. This seems more accurate than comparing the results of the 3D models with the nominal stress of the reference model,

which consists out of shell elements. Since the stresses in the models can be up to 8 times higher than those in the model with a 100% weld penetration ratio, it would be safe to multiply the nominal stress in the reference model with this same factor. By increasing the nominal stress, which can then be used to determine the fatigue life of the detail, the weld root imperfections that can occur in the stiffener-to-deck plate connection could safely be taken into account.

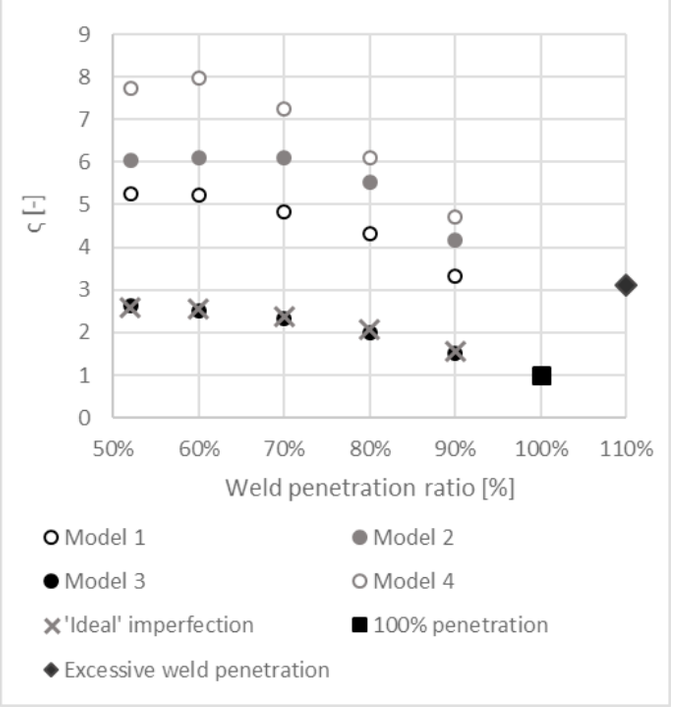


Figure 9. Relative stress concentration factor ς for a varying weld penetration ratio

5.2 *Estimated fatigue life*

As already explained, the guidance rules given by the Eurocode for calculating the fatigue resistance are not directly applicable in this case. In order to determine an estimation of the fatigue life, the guidance rules will thus need to be adapted. The nominal stress method suggests to determine the fatigue resistance based on the nominal stress in the stiffener and a fatigue curve, which has a fatigue class of 71 MPa for the stiffener-to-deck plate connection. It is proposed to multiply the nominal stress in the detail with the factors from Figure 9, which is the ratio of the stress concentration factor of the model under consideration and the stress concentration factor of the model with a 100% weld penetration ratio. Using this adapted nominal stress and the S-N curve with a fatigue class of 71 MPa, an estimation could then be made of the fatigue resistance of each model.

It is important to stress that determining the fatigue resistance in this way is not according to the recommendations of the Eurocode nor the IIW.

6 CONCLUSIONS

Each model showed a peak tensile stress at the lower side of the imperfection and a peak compressive stress at the upper side. The results clearly indicated that the shape of the weld root imperfection has a high influence on the peak principal stresses. The smaller and sharper the shape of the weld root imperfection, the higher the stress concentrations.

According to the results from the parametric study, the absolute value of the principal stress decreases for a decreasing lack of penetration. This is in contradiction with the conclusions in the studies of Sim, H.B. & Uang, C.M. 2012, Vu Dung, Sasaki, E., Tajima, K. & Suzuki, T. 2014 and De Backer, H. 2006. However, these studies all calculated a general model, of which the translations and rotations occurring in the zone of interest were then transferred to a smaller 3D model. This is an important difference with the method used in this study, which allows redistribution of the stresses since the 3D model is included in the reference model.

The results of the models with a lack of penetration were also compared to those of the models with a 100% penetration and with an excessive weld penetration. In comparison with the other models, the model with a 100% weld penetration did not show a high tensile stress peak. The model with an excessive weld penetration ratio did show high stress peaks, but it is depending on the shape of the weld root imperfection if these stress peaks are higher or lower than those in the models with a lack of penetration.

For the load case that was tested, the tensile stresses were more influenced by the weld penetration ratio than the compressive stresses. Since the tensile stresses are the most devastating for fatigue, the weld penetration ratio will thus significantly influence the fatigue resistance.

Finally, the guidance rules given by the Eurocode for calculating the fatigue resistance are not directly applicable. It is proposed to determine the fatigue resistance using the S-N curves with an adapted nominal stress, being the nominal stress multiplied with the ratio of the peak tensile stress in the model under consideration and the peak tensile stress in the model with a 100% weld penetration ratio.

7 REFERENCES

CEN, *EN 1991-2: 2006/AC: 2009 – Design of steel structures – Part 2: Steel bridges*, CEN.

CEN, *EN 1993-1-9: 2005/AC: 2009 – Design of steel structures – Part 1-9: Fatigue*, CEN.

Hobbacher 2014 *Recommendations for Fatigue Design of Welded Joints and Components*, International Institute of Welding.

AASHTO 2012. *AASHTO LRFD Bridge Design Specifications,* 6th. ed., Washington, DC: Highway and Transportation Officials.

Japan Road Association 2002, *Fatigue design guidelines for steel highway bridges (in Japanese)*, Tokyo.

Sim, H.-B. & Uang, C.-M. 2012 Stress Analyses and Parametric Study on Full-Scale Fatigue Tests of Rib-to-Deck Welded Joints in Steel Orthotropic Decks*, Journal of Bridge Engineering*, 17(5): 765-733.

Vu Dung, Sasaki, E., Tajima, K. & Suzuki, T. 2014. Investigations on the Effect of Weld Penetration on Fatigue Strength of Rib-to-Deck Welded Joints in Orthotropic Steel Decks. *International Journal of Steel Structures.* 15(2): 299-310.

De Backer, H. 2006. *Optimalisatie van het Vermoeiingsgedrag van het Orthotroop Brugdekconcept door Verbeterde Dispersie van de Verkeersbelasting (in Dutch)*, PhD Thesis, Ghent University.

Maintenance, Safety, Risk, Management and Life-Cycle Performance of Bridges – Powers, Frangopol, Al-Mahaidi & Caprani (Eds)
© 2018 Taylor & Francis Group, London, ISBN 978-1-138-73045-8

AS5100.2: 2017 changes to traffic-barrier loadings – a Victorian perspective

B.E.Gibbens
Principal- Bridges
BG&E, Melbourne, Australia

ABSTRACT: The Australian Bridge Design Code AS5100 was revised in April 2017, resulting in substantial changes to the design requirements for bridge traffic barriers. This paper proposes improved analysis approaches to achieve greater barrier capacity and improved barrier constructability, and cautions where some design and detailing approaches may inadvertently lead to unsafe traffic barriers.
This paper postulates the likelihood that Australian road authorities have – since the turn of this century – over-spent many-tens-of-million dollars constructing unnecessarily-strong traffic barriers. The author argues the industry should move away from its reliance on engineering calculations for traffic barriers – and towards the physical load-testing of standardized bridge barrier systems. It is suggested that this alternative approach may reduce the demands on the structural configurations of traffic barriers and their supporting elements, and perhaps save road authorities significant monies over the long-term.

1 INTRODUCTION

1.1 *Code changes*

The Australian Bridge Design Code AS5100 was revised in April 2017, resulting in substantial changes to the design requirements for bridge traffic barriers. Both the magnitudes and 'effective-heights' of all Performance Levels were increased.

Table 1. Changes in traffic-barrier characteristics.

Performance Level	AS5100: 2004		AS5100: 2017	
	kN	He (mm)	kN	He (mm)
Low	125	500	150	600
Regular	250	800	300	900
Medium	500	1100	600	1200
High	1000	1400	1200	1500

* Effective-height (He) above top of trafficable surface

Vicroads is the road authority of the Australian state Victoria. In the period 1997 to the issue of AS5100:2004 – traffic barriers on Victorian projects including Melbourne's CityLink toll-road (circa 1998) – were designed to the requirements of Vicroads' Bridge Technical Note No. 971001 *Design Requirements for Bridge Traffic Barriers* which included the same requirements for barrier designs as the later AS5100:2004.
Notwithstanding twenty years' of unvarying design requirements – the author believes that designers continue to grapple with the identification of efficiently-proportioned traffic-barrier systems. The author anticipates the increased design requirements of AS5100:2017 will present a 'step-change' in the difficulty of designing and constructing bridge traffic barriers – both on- and off-structure. This paper critiques analysis and detailing approaches which benefit safe and efficient traffic barrier designs.

This paper also postulates the likelihood that Australian road authorities have – since the turn of this century – over-spent many-tens-of-million dollars constructing unnecessarily-strong traffic barriers. The author believes this is likely to be the case particularly for the buried-footings of off-structure barriers – when designers rely on engineering calculations rather than on physically-crash-tested barriers – for which none may exist for most of the Performance Levels outlined in either AS5100:2004 or AS5100:2017. With the recent and substantial changes to codified traffic-barrier loadings – this paradigm is likely to become worsened, increasing the probable over-spend on projects.

1.2 *Scope*

In the remainder of this paper – traffic barriers are discussed in the context of a 'steel post-and-rail' system which is mounted on the top of a concrete barrier in order to achieve the full containment 'effective-height'. The reader may extend these discussions to barrier systems which are either wholly concrete, or are wholly 'steel-post-and-rail'.

2 VICTORIAN INDUSTRY-APPROACHES

Within Victoria (traffic-barrier-upgrade projects notwithstanding) – it is broadly-possible to date a bridge structure by the nature of the traffic barrier which is mounted on it. For the bridges constructed in the late 1970s and 1980s by the MMBW and RCA (precursor authorities to Vicroads) – the traffic barriers are substantially similar to the barriers shown in Figure 1.



Figure 1. Bridge barriers similar to those of the 1970s and 1980s (barriers in this photograph were constructed in 2009 as facsimiles of those existing elsewhere on the same structure)

Due to increasingly-onerous traffic-barrier design-requirements; the advent of the design-and-construction (D&C) approach to procurement; numerous privately-funded toll-roads; and the increasing architectural contribution towards urban design – traffic-barriers are increasingly varied in their appearance and configuration. Common Victorian traffic barriers since 2000 are illustrated below in Figure 2.



Figure 2. Traffic barrier circa 2013 (left) and 2014 (right).

2.1 *On-structure barriers*

Since circa 2000 – Victorian traffic-barrier types have included longitudinally-continuous concrete barriers which utilized full-thickness in-situ stitches to join together precast units (e.g. the 1000 mm-long stitches on the Rob Sergi Bridge, Geelong). Also longitudinally-continuous is the concrete barrier at Burnley Viaduct (Monash Freeway) where precast panels provided backing formwork for a full-height carriageway-side facing of in-situ concrete.

Much more common has been the approach to utilise precast barrier units (nominally) 3000 mm or 6000 mm long, for all of Regular-, Medium-, and High-Performance levels. When the precast barrier-units support a steel post-and-rail system – with posts at 3000 mm centres – the structural advantage of the 3000 mm-long barrier system is improved, whereas the advantage of the 6000 mm-long barrier system is lost (i.e. is no better than that of 3000 mm-long units).

Some experimentation with post-spacing of 1500 mm or smaller centres has been undertaken for High-Performance barriers, however the author does not support this approach: the close spacing of posts increases the vertical strength of the barrier system at the cost of the system's horizontal strength – a load-path which is opposite to an efficient design.

There have been attempts at providing dowelling between the precast panels: for example steel dowels were used on the Eastlink toll-road, and grout-dowels on Craigieburn Bypass. In the author's opinion the latter approach is almost useless, and the construction effort for the former approach is disproportionate to the greater efficiencies that can be achieved by concentrating the design effort elsewhere.

In all cases – traffic barriers are set out vertical. This contrasts to the (sometimes) overseas approach whereby cast-in-place barriers are set out normal to the transverse grade of the deckslab.

Precast traffic barrier units are stitched to the deckslab via a continuous 'kerb stitch' as shown in Figure 3. This stitch is subject to reflected-cracking at the joints between the precast panels, and a vertical crack-initiator is formed into the green concrete.



Figure 3. Longitudinal kerb-stitch (steel levelling bracket for precast barrier unit also shown).

2.2 *Off-structure barriers*

Off-structure barriers include those in freeway medians, and on the approach and departure sides to the bridge. Off-structure barriers are increasingly being used to protect street furniture including gantry legs.

2.2.1 *Fill-embankments*

The barriers on bridge approaches are usually Regular-, and Medium-Performance level. When wholly

above the level of rock, the prevailing approach is to utilize 6000 mm-long precast units supported by piles. The lateral load-resisting capacity of a pile is significantly reduced when adjacent to a cut-slope. When the barrier is located close to a vertical edge, the piles are then either offset from the edge via buried tie-beams, or a large L-shaped cast-in-place footing is used. For the latter – a large shear key and granular sub-base is almost invariably required to resist sliding.

2.2.2 *Reinforced-soil walls*

L-shaped footings are commonly used atop reinforced-soil walls when the barrier is located close to the edge of the wall. For narrow-width embankments – the L-shaped footings may be tied together by reinforcing bars or by joining the concrete footings.

2.3 *Vicroads' requirements*

Vicroads' requirements for the design and detailing of traffic barriers are outlined in Bridge Technical Notes, and in the Standard Specification for Roadworks and Bridgeworks.

While not current at the time of writing this paper, the author supports the following detailing requirements which were stipulated by Section 671DC at the time of Victoria's Eastlink Project in 2005.

Contraction joints in the cast-in-place sections of concrete barriers (i.e. kerb stitch-pours) *shall coincide with the joints between precast sections of barriers. Reinforcement in the cast-in-place sections shall terminate and have the specified cover each side of contraction joints* (i.e. v-notch crack-initiators).

Where the deck slab is de-bonded from the top flange of beams to provide continuity at pier locations, the cast-in-place section of barrier shall also be de-bonded from the deck slab.

In other words – the flexibility of linking slabs should not be reduced by building traffic barriers into them.

2.3.1 *Welded railing*

Vicroads requires horizontal steel railings to be welded to their supporting posts. This approach results in a more robust and durable connection than for the archaic method whereby the railings were bolted to the posts via steel angle-sections.

3 ARCHITECTURAL CONFLICTS WITH TECHNICAL REQUIREMENTS

With the advent of D&C influenced by urban design, traffic barriers have been seen as a ready opportunity for architectural embellishment. Common urban-design outcomes include: the outside-face-patterning of precast panels, and the use of (sometimes) inefficiently-shaped steel railings and posts. This paper argues that urban design inputs towards what is a critical safety element should be moderated strongly by the engineer early in the design process. The reasons for this and the possible adverse implications versus best-practice engineering approaches are outlined in this chapter.

3.1 *Industry-norms regarding barrier setting-out*

3.1.1 *Panel lengths*

Although degraded in the current D&C era – the author contends that the following detailing approaches have been in evidence since at least the early 1970s.

A gap between the precast barrier units is located at pier centrelines when the spans are 'simple'.

Unless barriers are proven to be substantially isolated from the flexural behavior of the supporting beams due to shear-lag – longitudinally-continuous concrete barriers should not be continuous over piers – even if the spans are also continuous (e.g. the Rob Sergi Bridge, Geelong demonstrates full-thickness vertical flexural-cracks in the barriers over the piers). Hence a barrier joint should occur over piers.

An integer number of barrier units is provided in each bridge span. Each barrier unit is nominally 3000 mm long (or 6000 mm). The spacing of posts in both cases is also nominally 3000 mm. It is interesting to note this approach yields barrier lengths 3000 mm (+/- 5%) in the span-range 30 m to 200 m, with the variation increasing to (+/-10%) in the range 20 m to 30 m. The lengths of barriers in opposing spans may be different, however this difference should not be noticeable to the observer (compared to the disparate barriers in Figure 4), or consequential to the design.

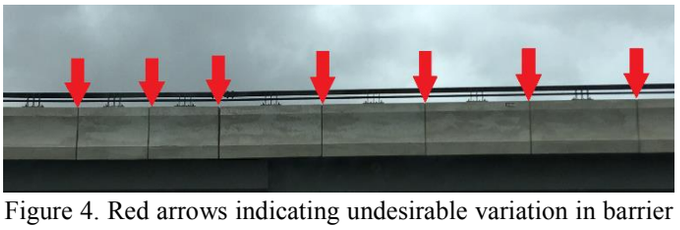


Figure 4. Red arrows indicating undesirable variation in barrier lengths.

3.1.2 *De-bonded deckslabs*

As argued earlier – traffic barriers should not be built into the linking slabs over the piers. Locating a barrier joint on the pier centerline divides the loss of deckslab connection between two barrier units. Interestingly – this approach is not evident in Figure 1.

3.1.3 *De-bonded structural footpaths*

For High-Performance barriers, especially – it is common for footpaths to be solid concrete, and for the traffic barriers to be built into both the footpath and the deckslab. In such cases – the imperative that linking slabs must flex without distress remains. This is achieved by de-bonding both the barrier and the footpath (or road median) from the linking slab, as shown in Figures 5 and 6, below.

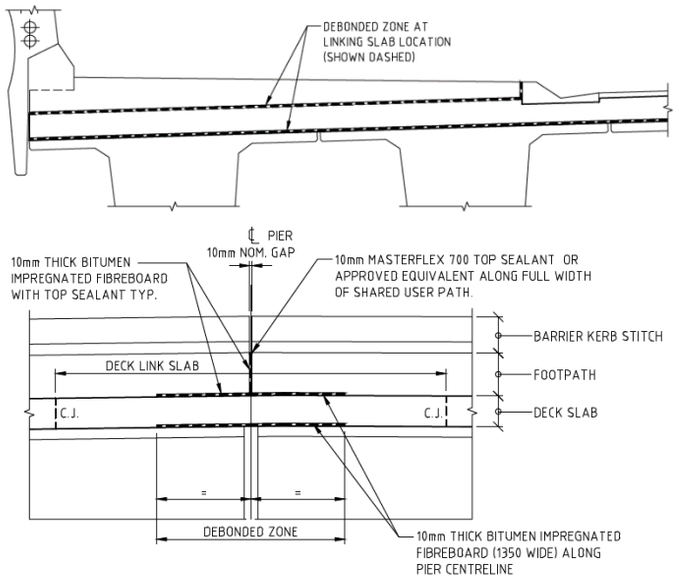


Figure 5. De-bonding of both footpath and linking slab.

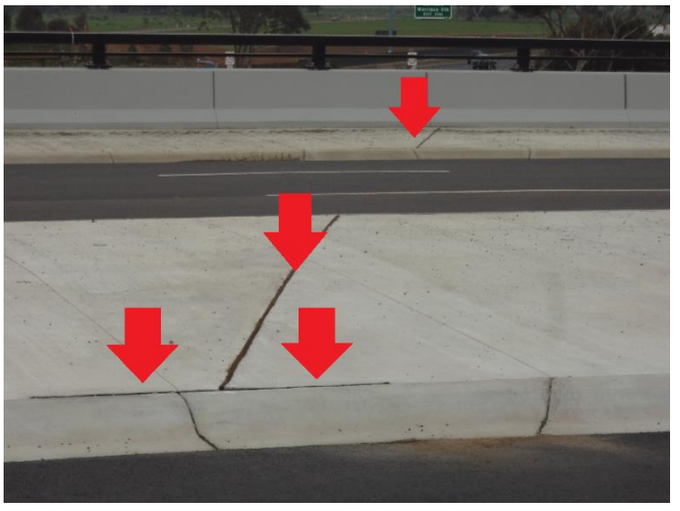


Figure 6. Locations of vertical jointing material at linking slab.

3.2 *Setting-out conflicts*

Industry norms towards the beneficial setting-out of traffic barriers were outlined in the forgoing text. The section below illustrates where urban-design inputs can run counter to these norms.

3.2.1 *Architectural patterning*

The selection and arrangement of barrier-unit lengths was outlined above. This arrangement is not affected by the decades-old Vicroads approach to utilize a pattern on the outside face of barriers which varies vertically, and not horizontally (Figure 7). When urban design mandates a patterned outside-face which varies horizontally – then many of the best-practice setting-out approaches illustrated above may be violated (Figures 8 and 9). In the case of Peninsula Link (Figure 9) – most bridges were two-span overpasses. The architectural pattern began on the centerline of the single pier – and extended outwards to opposite abutments on lengths of precast barrier units which matched the repeating pattern geometry. At expansion joints – the pattern merely 'ran out' of barrier. For bridges of greater number of spans than two – the barrier joints did not occur at pier centerlines – except in the unlikely cases where the span was exactly divisible by the length of the repeating pattern.



Figure 7. Pattern on barrier outside-face which varies vertically (Monash Freeway, Melbourne).



Figure 8. Pattern on barrier outside-face which varies horizontally (Charles Grimes Bridge, Melbourne)



Figure 9. Pattern on barrier outside-face with varies horizontally (Peninsula Link, Melbourne).

3.2.2 *Rail and post geometries*

Architectural input can also extend to the definition of the steel post-and-rail elements. For the reasons outlined later in this paper – the urban design input should be strongly moderated by the engineer, and ideally should be avoided.

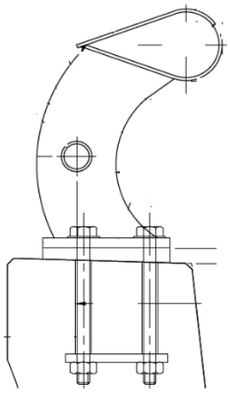


Figure 10. Architecturally-derived post and rail system (Geelong Bypass (2009), Princes Freeway interchange with Anglesea Road (2013), Baanip Boulevard (2015): all Victoria).

4 EFFICIENT TRAFFIC-BARRIER DESIGN

4.1 *Longitudinal and vertical strengths*

The most efficient way to design a traffic barrier is to mobilise the greatest length of foundations possible, while minimizing the nature of the foundations. This is achieved by maximizing the horizontal strength of the barrier system, and minimizing its vertical strength. As will be outlined later – it is possible for a barrier to be too strong in the vertical direction. To achieve a beneficial loadpath – a ductile system is usually required.

The vertical steel in the concrete component of the traffic barrier should be limited in recognition of the flow-on effect to the proportioning to the bridge deck-slab or off-structure-barrier footings. For full-height continuous-concrete barriers – the content of horizontal barrier reinforcement is usually great – in order to distribute the loading over as long a length of barrier as possible. When part-height concrete barriers support a steel post-and-rail – whether the concrete component is continuous is much less important – as most of the longitudinal distribution of load occurs at the level of the steel railing.

4.2 *Steel grades*

In order to maximize the longitudinal distribution of loading – high-yielding (e.g. 450 MPa) steel should be used for railing. Often it is preferable to use lower-yielding steel for the posts (e.g. 350 MPa). It is noted that locally-sourced circular rail-sections do not have a yield strength greater than 350 MPa.

4.3 *Barrier 'fusing'*

It is obvious that an efficiently-designed traffic barrier is not only a 'safety device' from the point-of-view of the road user – it must also act to protect the bridge from excessive damage. It may be unacceptable for particular elements in the load-path to be proportioned with greater strength than assumed for the distribution of load; greater strength is not always beneficial. For example – in order to maximise the longitudinal distribution of load – it is normally required that steel posts act (in the vertical sense) as load-limiting 'fuses'. If posts are stronger than necessary, or are spaced too closely together, then the vertical distribution of load may be amplified – possibly overloading a link in this unintended loadpath.

4.4 *Capacity-protection*

In exactly the same sense as is now required in AS5100.2:2017 for earthquake design – the capacity-protection of certain elements in the traffic-barrier load-path is mandated by AS5100. In particular the traffic-barrier-supporting element (e.g. deckslab) must be at least ten-percent stronger than the vertical strength of the barrier at the joint – in order than substantial in-elasticity or damage is restricted to occur within the (accessible) height of the barrier (Figure 11). This constitutes the capacity-protection of the supporting element by designing it to be stronger than the yield-capacity of the barrier (and accounting for the post-yield increase in reinforcement or steel stresses).

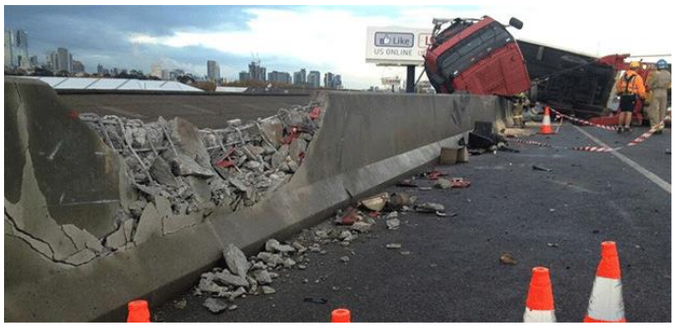


Figure 11. Incident on Bolte Bridge, Melbourne in 2013 (Grzebieta 2013).

5 ANALYSIS TECHNIQUES

5.1 *Yield-line*

The yield-line techniques of AASHTO (2007) and AS3845:2015 are implemented easily in the designs of both steel and concrete traffic-barriers. These codified approaches can be reproduced from first-principles by hand, and by non-linear computer analysis.

5.2 *Non-linear computer analysis*

Although the yield-line approach is an upper-bound solution – the lowest-energy solution may be improved upon if additional load-paths are introduced. For example – the addition of tension and torsion load-paths through the steel railing may be beneficial. Equally – and perhaps paradoxically – the omission of the torsional load-path under the yield-line approach may result in an unsafe design – for the reasons outlined in the next chapter.

6 POSSIBLE UNSAFE DESIGNS

6.1 *Buckling*

An efficient traffic-barrier design requires the barrier components to deform in a ductile manner. It follows that steel posts and railings must be 'compact', in order than buckling does not occur.

6.1.1 *Yield-line across barrier base*

The yield-line equations in AASHTO (2007), and AS3845:2015 assume the concrete barrier is continuous longitudinally. These codified methodologies do not acknowledge the possible vertical joints between precast barriers. The designer must always undertake the ancillary check of a horizontal yield-line across the base of the barrier. This simple yield-line is usually critical for 3000 mm- and 6000 mm-long precast traffic barriers. The vertical joints between precast barrier units essentially precludes the design from taking advantage of substantial horizontal load-distribution through the height of the concrete barrier – and relies most heavily on longitudinal distribution through the steel post-and-rail elements.

6.1.2 *Shear-moment interaction*

For a ductile (compact) steel post – the maximum shear force which develops in the post is a function of the plastic-section-capacity of the post, and the distribution of bending moment in the post. The interaction between shear and moment must be considered in the design, and when the applied moment is equal to the plastic-moment capacity – the shear strength is reduced significantly. It is for this reason, at least, that the author does not use column-section steelwork for posts, but prefers to utilize the twin webs of hollow sections.

6.1.3 *Double-curvature*

The standard yield-line approach assumes single-curvature in the steel traffic-barrier posts – whether single or double-railings are used. Whatever the number of railings used – when the torsional stiffness and torsional strength of railings is included in the analysis it is possible that double-curvature is induced in the posts – whether or not the moment in the post close to the railing is near the state of plastic-hinging. Double-curvature can increase the capacity of the traffic-barrier system. Under double-curvature the shear force in the post can be as great as twice the shear force in the post under the single-curvature condition i.e. under double-curvature, the post will be wont to 'fuse' at a higher level of loading, and will impart a greater load to the supporting elements. If not anticipated by the designer – the bolts may fracture, or the concrete barrier may become overloaded. In any case – if double-curvature is inadvertently overlooked, and the design assumes single-curvature, the element supporting the concrete barrier remains capacity-protected (i.e. the foundations / deckslab).

Post heights usually range from 250 to 550 mm tall. At the shorter end of this range – the presumption of double-curvature may even be invalid if the post acts as a rigid 'block' rather than as a flexible beam. In the former case it is questionable whether such a barrier can 'fuse' in a ductile manner. A three-dimensional 'shell-' or 'solid-element' finite-element analysis will confirm the true behavior of short posts.

6.1.4 *Too-strong posts and rails*

On Melbourne's Peninsula Link project – the traffic barriers were substantially configured by the urban designer, with only 'late' moderation by the engineer. The urban-design concept called for 273 mm-diameter circular-section railings (variously 9.2 mm and 12.7 mm thicknesses) supported by three-sided steel-box posts.



Figure 12. Traffic barriers on Peninsula Link, Melbourne.

The designer was faced with numerous challenges imposed on the project by the urban designer (PC 2017):

- Firstly the railing could only be procured in grade 350 MPa steel rather than grade 450 MPa.
- Secondly the (flexural) section modulus of the circular section was less than that of a smaller square hollow-section.

– Thirdly, advanced FEA analysis was required to demonstrate adequate shear-moment interaction of the railing – given that AS5100 did not assume that a circular hollow-section would ever be used as a 'beam'.
– And last, the three-sided box-post was found at first to be too strong. In other words the post was at first found to resist the impact load wholly at one location, without any beneficial longitudinal distribution through the railing – likely fracturing the supporting holding-down-bolt device and the traffic barrier, or both. The rear backing plate was necessary to eliminate local buckling of the thin-but-deep 'post side plates', however it was not until it was eliminated as a structural element by the inclusion of a thin horizontal slot immediately above the level of the baseplate – was the post (and its fixings) demonstrated to be a ductile element.

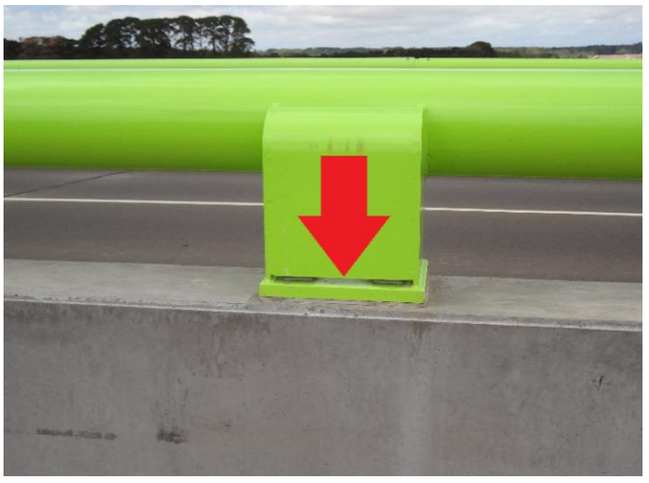


Figure 13. Slot at base of posts: Peninsula Link, Melbourne.

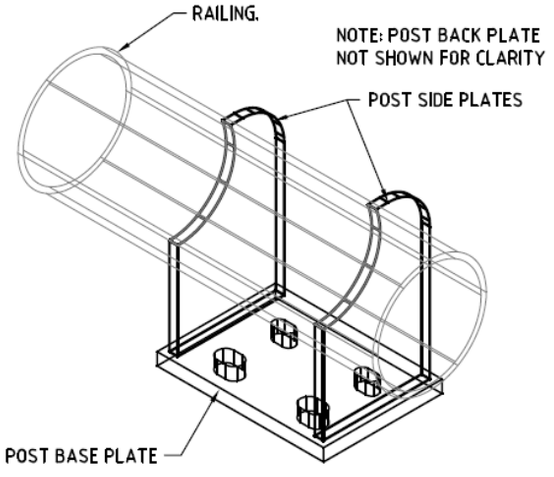


Figure 14. Isometric view of barriers: Peninsula Link, Vic.

In the preparation of this paper, the author reviewed a half-dozen Medium- and High-Performance traffic barriers constructed elsewhere in Melbourne over the last decade. Each of these barriers included a significantly-proportioned steel hollow-section railing. In the greatest case – the torsional strength of the railing was two-hundred percent the magnitude of the plastic-moment capacity of the post. This indicates the potential for a torsionally-continuous hollow-section railing to resist as much as four-times the plastic-moment capacity of the post, and supports the proposal that designers should be alert to the implications due to double-curvature – especially for bolt-group and concrete-barrier-unit designs.

7 POSSIBLE IMPROVEMENTS TO THE DESIGN APPROACH TO SUIT THE INCREASED AS5100:2017 LOADINGS

7.1 *Width of kerb-stitch*

Many designers continue to utilize a width of in-situ concrete kerb-stich of 280 – 300 mm, often resulting in poor constructability. The author has not (willingly) used a figure less than 350 mm for nearly twenty years. Increased barrier loading may require an even larger width of kerb – in order to relieve increased reinforcement contents.

7.2 *Kerb-stitch longitudinal reinforcement*

The author is unconvinced of the benefit of longitudinal reinforcement with the kerb stitch (Figure 3). Recent years have seen the use of un-tensioned 12.7 mm prestressing strand rather than 'black' reinforcement. The poor concrete-bond characteristic of un-tensioned strand is unlikely to benefit the crack-control of the kerb-stitch (due to differential shrinkage). The author is also unconvinced of the benefit of longitudinal kerb-stitch reinforcement towards the transfer of load between the overlapping reinforcement loops. As stated above – the critical barrier yield-line is normally a horizontal line across the barrier base – whereupon the kerb stitch is in a state of plane strain over the length of the yielding barrier-unit. Under these conditions – the compressive strength of the kerb concrete is increased greatly. It is interesting to note that for the case of the 'end-condition' where plane-strain does not exist (Araujo 2014) predicts that for closely-spaced overlapping loops – the concrete tensile strength is sufficient to tie the transfer of forces longitudinally, whereupon the crushing strength of the concrete compression struts becomes critical. The author is of the opinion that the deletion of longitudinal kerb stitch reinforcement, and its replacement with a steel-fibre concrete mix may benefit both the control of cracks due to differential shrinkage, and also benefit the transfer of load across the opposing loops. Steel fibres may be a useful method to restore constructability of this detail upon the likely increase in starter bar reinforcement content due to

increased loading. Steel fibres may also be an expeditious method to address vertical differential-shrinkage cracking of the detail.

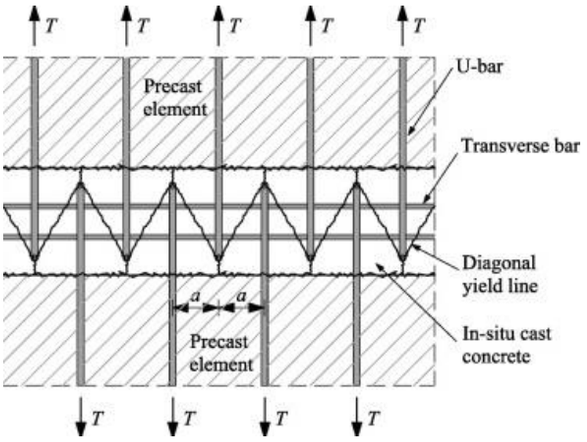


Figure 15. Schematic of load path for overlapping loops

7.3 *Continuous concrete barriers*

Increased barrier loading may see the increasing use of full-height concrete barriers which are also continuous longitudinally. Tall barriers may result in an experience akin to driving down a 'storm-water drain'.

7.4 *Thicker, longer, and heavier concrete barriers*

Increased barrier loadings may result in heavier barrier units. For many years the Victorian approach has been to use steel levelling-brackets as shown in Figure 3. For various reasons there have been bolt-punch-through failures of the C-shaped bracket. The engineer will need to reassess this detail for heavier barrier units. Additionally – the engineer should not utilize more than two levelling brackets, as has occurred in the state of Victoria. A greater number than two levelling brackets per barrier-unit results in an indeterminate support-system, for which the loading of the bolts/brackets cannot be controlled during erection – risking the overloading of one or more brackets. Indeed, a redundant levelling-support system can even jam and disallow adjustment.

7.5 *Analysis methods*

Increased barrier loading is likely to see the designer resort to finite element analysis as outlined above – in recognition of the advantage of post double-curvature towards increasing the load-capacity of the barrier system. Double-curvature in posts may reduce the sizes of the steel post and railing, however is likely to increase the sizes of holding-down bolts; the quantum of vertical barrier reinforcement; and also the deck-slab reinforcement content and thickness.

7.6 *Crash-tested barriers*

The author recommends that state road authorities undertake physical crash-testing of standardized traffic barrier systems – or at least undertake the physical load-testing to the codified static-design-loads. The author is of the opinion that such testing may be especially advantageous for off-structure barriers. The cost of load testing is likely to be orders of magnitude less than the likely deferred cost of conservative designs applied over the next decade's projects.

8 SUMMARY

Traffic barrier design to the former AS5100:2004 has proved complex to prepare and construct. For the last two decades at least – traffic barrier designs have proved problematic for new designs and traffic-barrier upgrade projects. The amendments of AS5100:2017 see the design requirements for traffic barriers increased substantially. Without clear precedent from local or international experience – the consequential effects on bridge design are anticipated to be onerous, and may be found on occasion to be prohibitive. The author postulates the industry should move away from its reliance on engineering calculations for traffic barriers – and towards the physical load-testing of standardized bridge barrier systems. It is hoped that this alternative approach may reduce the demands on the structural configurations of traffic barriers and their supporting elements, and perhaps save road authorities significant monies over the long-term.

9 REFERENCES

Standards Australia 2017. AS5100:2017 Bridge Design, Standards Australia, Sydney, NSW

Standards Australia 2015. AS3845:2015 Road Safety Barrier Systems, Standards Australia, Sydney, NSW

AASTHO 2007. LRFD Bridge Design Specifications 4th Ed. American Association of State Highway and Transportation Officials, Washington, D.C.

Araujo, D. Craveiro, M. Rodrigues, P. 2014. Loop connection with fibre-reinforced precast concrete components. *Engineering Structures 72 (2014):* 140-151

Grzebieta, R. Rechnitzer, G. (2013) Interface analysis and design: Improving heavy vehicle road safety barrier design. Proceedings of 2013 Australasian Road Safety Research, Policing & Education Conference, 28th- 30th August, Brisbane, Queensland.

PC 2017. Personal correspondence with designer.

Maintenance, Safety, Risk, Management and Life-Cycle Performance of Bridges – Powers, Frangopol, Al-Mahaidi & Caprani (Eds)
© 2018 Taylor & Francis Group, London, ISBN 978-1-138-73045-8

Displacement-based seismic design to AS5100.2: 2017 – simplified

B.E. Gibbens
Principal- Bridges
BG&E, Melbourne, Australia

ABSTRACT: The Australian code of practice AS5100 *Bridge Design* was revised in April 2017. Significant changes see the analysis methods for seismic design and also earthquake return-periods brought closer to those of major world codes. While retaining the response-spectrum and time-history analysis approaches of the former code as 'normative' (both representing dynamic 'force-based' methods) – the 'informative' Appendix B of the new code allows the optional use of 'displacement-based' earthquake design.

This paper describes the empirical basis for displacement-based design, and seeks to clarify the differences and advantages of this method from the older force-based methods when applied to both new and existing bridges. Simplified approaches, and practitioner techniques are illustrated – with the view to encouraging the adoption of this modern and often beneficial approach to seismic design.

1 INTRODUCTION:

This paper encourages Australian engineers to adopt the new displacement-based approach to seismic design. This paper identifies the empirical basis of the method, and compares the advantages of the method with older force-based design approaches.

This paper contrasts the outcomes of the force- and displacement-based design approaches for both existing and new structures.

The displacement-based design (DBD) approach represents the state of art in the most seismic regions of the world. It is represented in the design codes of the United States, Canada, Japan, and Eurocode, and is prescribed by Californian Department of Transportation and New Zealand Transport Agency.

The revised AS5100.2: 2017 also removes the inconsistencies in earthquake return-period which existed beforehand with the supporting Australian design code AS1170.4:2007 *Structural Design Actions – Earthquake.*

2 AS5100.2: 2017 METHODS

The revised bridge code allows the following force-based design methods: static or dynamic (elastic) response-spectrum, and elastic or inelastic dynamic time-history analysis. The recently-developed displacement-based design approach is also now permitted.

2.1 *Response-spectrum analysis*

Response-spectrum analysis (RSA) is a force-based design approach which infers that the actions which develop in a structure are proportional to the inertial effects (accelerations) induced in the structure.

In order that the main elastic periods of the structure can be determined, the RSA-approach requires the structure's elastic stiffness to be estimated at the start of the design, however the true elastic stiffness is not known at this stage. The RSA approach also relies on the original stiffness assumptions in order to distribute the total-calculated inertial effect between components. This results in stiffer elements being reinforced more heavily than more flexible ones.

Under the RSA-approach, the designer must also assume the level of plasticity which may develop in the structure on an averaged basis, via the use of a 'structural-response' factor; plasticity is not calculated explicitly. Furthermore – the RSA approach does not facilitate the progressive development of inelastic behavior to be differentiated between the different components of the structure.

Response-spectrum analysis combines the results of multiple modes of vibration using the 'square root of the sum of the squares' (SSRS) or 'complete quadratic equation' (QDC) techniques. These methods of vector-addition obscure both the sign and true magnitude of structural displacements under earthquake, as will be illustrated later in this paper for the case of expansion-joint design.

2.2 *Displacement-based analysis*

In contrast to force-based design, displacement-based design recognizes that the actions which develop in the structure under earthquake are consequential to the displacement of the structure, rather than being the cause of the structure's displacement.

In contrast to force-based approaches – the understanding of initial element-stiffness and the possible rate-of-change of element-stiffness is achieved with the use of moment-curvature or equivalent relationships which are known at the start of analysis.

For displacement-based design, the strength of the structure is less important than its ability to displace. The DBD-approach may allow the strengths of components to be reduced and rationalized; different-stiffness elements may be proportioned similarly. The potential benefit of DBD towards existing structures is obvious. For the reasons outlined later in this paper, the application of the DBD design approach towards both new and existing structures compares favourably with forced-based design approaches. When a 'push-over' model supports DBD calculations – both the progression and levels of inelasticity are calculated explicitly, and are differentiated between components.

2.3 *Rules of thumb*

Before the empirical basis of the DBD approach is outlined, it is useful to consider the 'rules-of-thumb' which illustrate the interpretation of the dissimilar force-based technique.

Figure 1 shows a typical acceleration-period response-spectrum curve. On account of their high primary-response-period – flexible structures are part-isolated from the peak ground acceleration (T = 0 seconds), and are not susceptible to the large amplification of ground motions which can occur for stiffer structures (e.g. $0 < T < 0.75$ seconds). This is the 'period-shift' effect. Similarly, the effect of increased damping can reduce the amplification of ground motions.

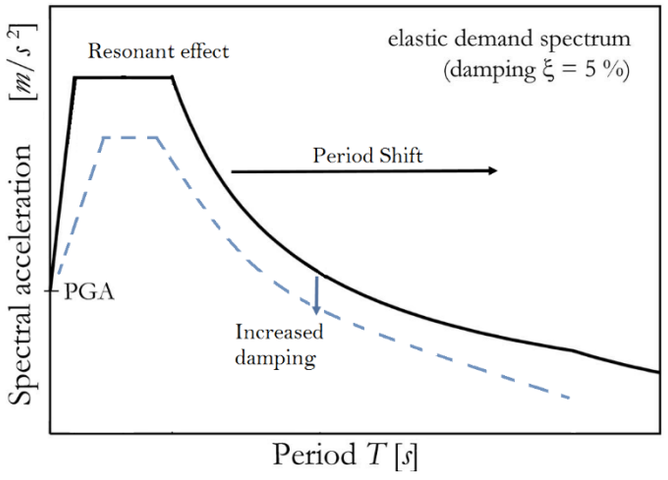


Figure 1. Graph of spectral acceleration versus structure period.

Under the DBA approach, these rules-of-thumb may be considered less-relevant, as outlined below.

2.4 *Equal-displacements rule*

The displacement-based design approach has been developed empirically. Physical experimental modelling predicts that a given structure which exhibits a predominantly single-degree-of-freedom response under earthquake loading – will displace a similar amount – whether this structure remains elastic, or develops an inelastic response (Fig. 2). Furthermore, this modelling predicts the earthquake-induced displacement would be: independent of the initial or final stiffness of the structure; independent of the level of plasticity which develops under the seismic action; and is independent of the strengths of components within the structure. This general result is indicated for structures with a fundamental period-of-vibration within the approximate range of ($0.7 < T < 3.0$ seconds), as indicated in Figure 2, below.

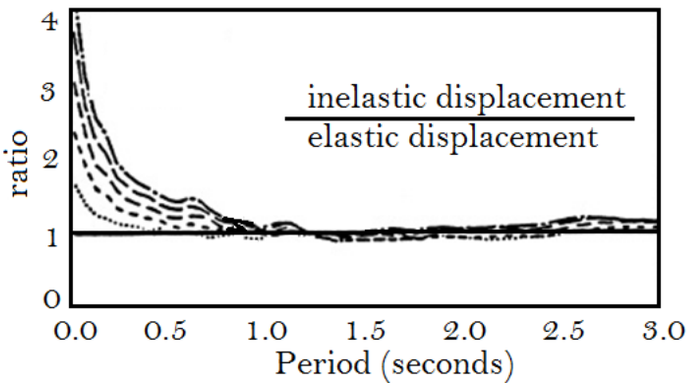


Figure 2. Variation of elastic and inelastic displacement-responses with fundamental period: single-degree-of-freedom oscillator (Pierino et al. 2003 & Miranda 2000 & ATC 1996).

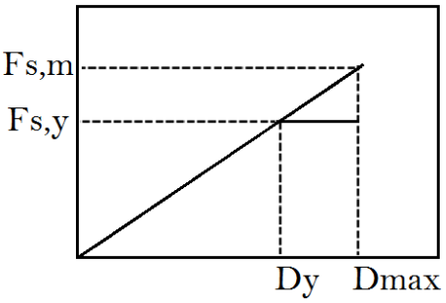


Figure 3. Equal-displacing elastic and inelastic responses (Priestley et al 2003).

For structures with a fundamental period in the range $0.7 < T < 3.0$ seconds: the elastic and inelastic responses (displacements) are not significantly different. In other words – whether the qualifying structure responds elastically, or in-elastically – the peak displacement is the same. Additionally, the maximum displacement is independent of the yield strength – ir-

respective of whether the response is elastic or inelastic. These outcomes constitute the 'equal-displacements' rule.

As inferred by Figure 3, the 'structural-response' factor is the ratio of the set of elastic actions divided by the set of inelastic actions – calculated for the same maximum displacement in the plastic range.

2.5 *Limits-of-validity*

In AS5100.2: 2017, the equal-displacements rule is held to remain true for structures with a primary mode of vibration in excess of the (second) 'elastic corner-period', which AS5100 takes as 1.5 seconds.
The Californian document ATC-32 provides design factors to extend the DBD approach to outside the limit-of-validity of the equal-displacements rule (ATC 1996).

3 SIMPLIFIED AS5100.2: 2017 APPROACH

Many of the Appendix B equations in the new Australian code may be daunting to the unfamiliar practitioner, who may undertake these calculations in the manner of following a 'cook-book', and without a clear appreciation of the technical basis of the design.

3.1 *Alternative DBD approaches*

Two alternative approaches to the DBD method are available under AS5100.2 Appendix B.

The first approach forms most of the AS5100.2 Appendix B, and requires hand calculations to be undertaken incrementally to define the displacement-capacity – which is then compared to the applicable 'displacement-spectrum' which defines the seismic displacement-demand.

The second approach uses a dynamic RSA analysis to define the seismic displacement-demand. An inelastic 'push-over' analysis is then used to demonstrate adequate displacement-capacity. It is this second approach which shall be the subject of the remainder of this paper.

3.1.1 *RSA versus 'push-over'*

In lieu of adopting of most of the Appendix B hand-calculations, the last paragraph of Clause B1 *General* permits a simplified DBD approach. For structures which qualify under the equal-displacements rule – the simplified approach allows an adequate seismic design to be demonstrated if the structure is proven capable to displace an amount at least as great as the displacement predicted by a linear response-spectrum analysis. In this case the response spectrum is of magnitude $1.5k_pZC_h(T)$. For safety – this design response-spectrum includes a 1.5 multiplier to the basic response-spectrum.

The simplified approach is undertaken in two stages. Firstly – the displacement-demand is predicted by a linear RSA analysis. Secondly – a non-linear 'push-over' analysis is undertaken to demonstrate the structure has sufficient ductility to displace at least as far as the displacement-demand.
The 'push-over' analysis will allow the states of stress and strain throughout the structure to be understood including the propensity for brittle-failure, and any susceptibility to P-Δ effects.

4 PUSH-OVER ANALYSIS

4.1 *Derivation of displacement-capacity spectrum*

Figure 4 outlines the generalized method to turn the force-displacement results from a non-linear push-over analysis into an acceleration-displacement 'displacement-capacity' diagram. The increasing base-shear versus structure-displacement is first plotted and then scaled versus the mass-coefficient and mode-participation factors (both of which are close-to-unity for 'single-degree-of-freedom' structures) in order to turn the base-shear in to pseudo-acceleration values.

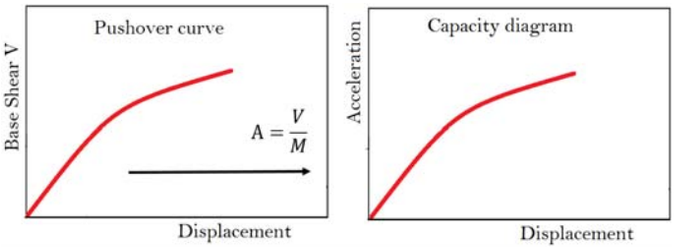


Figure 4. Derivation of displacement-capacity diagram.

4.2 *Derivation of displacement-demand spectrum*

Figure 5 outlines the generalized method to turn an acceleration-period (response-spectrum) curve into an acceleration-displacement 'seismic displacement-demand' diagram. In this case the following well-known single-degree-of-freedom dynamics equations are used, where ω_n = circular frequency; k = stiffness; M = mass; f_n = frequency; T = period; D = displacement, and where equations (1) and (2) are rearranged to equation (3).

$$f_n = \frac{\omega_n}{2\pi} \tag{1}$$

$$\omega_n = \sqrt{\frac{k}{M}} \tag{2}$$

$$D = \frac{AT^2}{4.\pi^2} \tag{3}$$

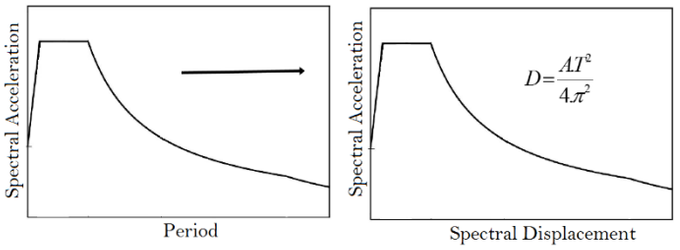


Figure 5. Derivation of displacement-demand diagram.

4.3 *Capacity-spectrum methodology*

Figure 6 overlays the 'displacement-capacity' and 'seismic displacement- demand' diagrams. Codified magnifiers notwithstanding, the earthquake design essentially reduces to confirming the bridge is capable to displace in excess of the displacement predictions of the elastic response-spectrum analysis. A structural member 'survives' the earthquake if the 'ductility-capacity' is greater than the 'ductility-demand'

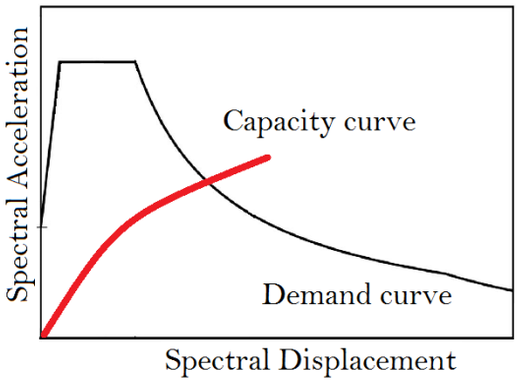


Figure 6. Super-position of displacement-capacity and displacement-demand diagrams. (Caltrans 2010 & Chopra 1999).

A pushover-analysis helps identify potential non-ductile or weak areas in the structure, and tracks the sequence of damages in each component in the structure. A pushover-analysis can show where the retrofitting is required, and the scope of retrofitting.

5 PREDICTING STRESS AND STRAIN

5.1 *Strength and stiffness interdependency*

Notwithstanding the necessary approximations of structure-materials and component-stiffnesses when using RSA modelling of displacement-demand, it must be recognized that the common design assumption that member stiffness is independent of strength is untrue. Instead – the curvature at first-yield is independent of strength – stiffness being directly proportional to flexural strength. In Figure 7: *M* is moment, φ is curvature, and φy and *My* are the states at first-yield of curvature and moment, respectively.

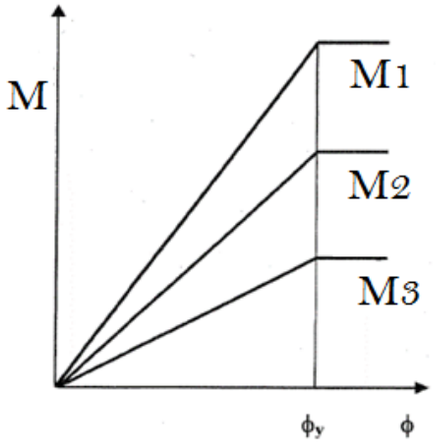


Figure 7. Yield-curvature is independent of moment capacity

5.2 *Ductility*

5.2.1 *Minor earthquake motion*

A 'ductile' design is one whereby the structure can deform in-elastically for several cycles without significant degradation of strength or stiffness. Not all bridges, or components of a bridge, will require a ductile earthquake design. Those bridge components which displace under the design displacement-demand an amount less than the yield-displacement-capacity of that component do not require detailing for a ductile earthquake design (i.e. the component responds in an elastic manner).

5.2.2 *Strong earthquake motion*

AS5100.2 Clause B17.1 contains the general and vague statement "*Potential plastic hinge locations in columns have to take into account the consequence of the possibility of the bridge being subject to excitation exceeding the design level".*

In order to ensure the dependable rotational-capacity at plastic hinges – Caltrans' Seismic Design Criteria (Caltrans 2010) requires each member to have a 'local' displacement-ductility capacity sufficient to achieve a total local-displacement in excess of three times the 'local' displacement at first-yield – irrespective of the magnitude of earthquake loading, and irrespective if global ductility is otherwise demonstrated.

5.3 *Capacity-protection and 'over-strength' design*

The objective of 'capacity design' is to confirm a structure may undertake controlled ductile-behaviour in order to avoid collapse in a design-level earthquake. This involves designing the structure to ensure ductile failure at key predictable locations within the structure and to prevent other failure types or damages occurring elsewhere in the structure.

The substantial in-elasticity which is allowed in columns can be used to 'protect' the superstructure

and the foundations from developing significant inelastic behavior. The plastic hinges in columns may be regarded as fuse-elements which limit the magnitudes of the actions developed in the structural components which are required to undertake essentially-elastic responses. It is essential, therefore, that this desirable fusing behavior can develop, and that brittle failure does not develop anywhere.

Additionally – most of the seismic displacement-capacity is achieved via the column plastic hinges. In order to assure the seismic displacement-capacity is achieved via the column hinges – the components of the structure which are to remain essentially-elastic in their responses – must be designed for the 'over-strength' properties of the column hinges.

For example – the shear force which develops in the columns at a high level of plasticity, and which must be resisted by the foundations and/or superstructure – is proportional to the post-yield stress in the column reinforcement, rather than the reinforcement stress at first yielding.

5.4 *Performance-based design*

Structural damage is strain-dependent, and can therefore be related to the displacement of the structure. The default performance criterion in AS5100.2: 2017 is for 'damage control' whereby the bridge shall maintain its structural integrity after the design earthquake. This contrasts to the requirements of other major codes which may also stipulate material-strain limits for earthquakes of lesser return-period – with the view to minimizing the repair effort, and the time a bridge may be out of service. The methodologies outlined in this paper are directly useful to assess material strains anywhere in the structure at any level of seismic loading.

5.5 *Buried elements*

The designer must understand the possible implications of strong columns on buried foundations. Whether column plastic-hinges 'capacity-protect' the pilecaps, or otherwise – substantial inelastic behavior in the columns may generate very large actions on foundations – especially shear force – as stress in the column reinforcement increases past nominal yield. The designer must consider the possibility of pile brittle-failure in any case, and also the level of pile 'damage' when a prescriptive 'performance-based' design is undertaken.

It is noted there that if the foundation is capacity-protected by hinging in the columns – then the foundation does not deflect beyond the level corresponding to plastic hinging of the columns.

6 DISPLACEMENT-BASED APPROACH

Figure 8 illustrates a bridge with columns of different height. Table 1 illustrates the merits of adopting the displacement-based seismic design approach in lieu of a force-based one.

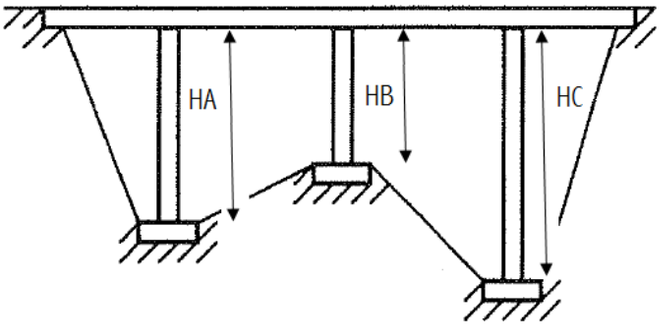


Figure 8. Multi-span bridge with different column heights

Table 1. Proportional-response to column height

	Force-based design	Displacement-based design
Stiffness	$1/H^3$	$1/H$
Shear force	$1/H^3$	$1/H$
Moment	$1/H^2$	similar
Reinforcement	$1/H^2$	similar
Ductility	similar	$1/H^2$

6.1 *Application of DBD to new structures*

The global ductility-demand is the ratio of total structure displacement to the structure displacement at the first point-of-yield, and varies depending on the type of structural system, and is analogous to the 'structural-response' factor used for force-based design. For new design, and when choosing framing, the designer should consider maximizing the inelastic response within the limits of the structural-response factors used for force-based design. This approach may maximize the use of a given tonnage of reinforcement, and lessen the demands of 'capacity-protection', if this is required. Performance-based limits to structural 'damage' should also be considered.

It has been the author's experience that an adequate seismic design of a new structure often follows (without revision) the prior proportioning and rationalization of reinforcement contents which is derived from non-seismic loadcases.

6.2 *Application of DBD to existing structures*

The explicit calculation of the states of stress and strain under the DBD-approach is useful for the review of existing structures which do not reflect modern reinforcement-detailing approaches, and which may not have been designed for seismic loading.

Archaic reinforcement detailing might be accepted if the DBD seismic design demonstrates that an existing structure can displace elastically in excess of the

seismic displacement-demand. Conversely – the DBD calculations may indicate that some structure-components exceed the yield-limit. If the original detailing is inadequate to assure ductility, then these components should be subject to a seismic retrofit.

6.3 *Example application to an existing structure*

DBD is particularly useful towards structures which were not originally designed for seismic loading. The author recently undertook a seismic assessment of the existing E.J. Whitten Bridge on the M80 Ring Road in Melbourne. This major bridge utilizes different-height concrete columns with almost-identical reinforcement contents. For this review – a force-based approach indicated the shorter and stiffer piers would become more-heavily loaded than the taller piers. An assessment using DBD indicated substantially improved results, especially for foundations.

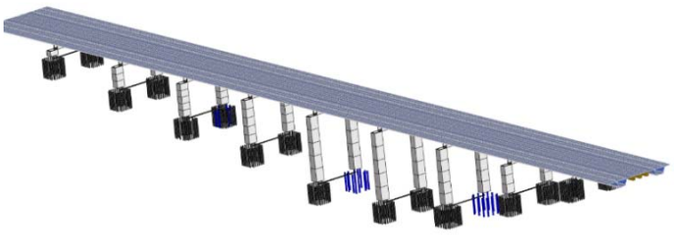


Figure 9. 3D bridge computer model (EJ Whitten Bridge)

7 PRACTITIONER TECHNIQUES

Useful modelling techniques which the author has used variously for new and existing structures are illustrated in this section.

7.1 *Response-spectrum model*

For concrete structures - linear-elastic RSA models usually assume 5% damping overall, although as much as 10% may be warranted for concrete structures with significant plastic-hinging (Caltrans 2010). The responses of foundations and superstructure are assumed to remain elastic, and a fifty-percent reduction of the column moment-of-inertia stiffness is normally adopted (AS5100.2: 2017 & Caltrans 2010). Foundation flexibility can contribute a significant proportion of the total structure displacement, and therefore should be modelled carefully. The axial stiffness of 'skin-friction-only' piles is often modelled as fifty-percent of that of end-bearing piles (AASHTO 2014).

7.2 *Finite-element 'push-over' models*

The author has developed and calibrated various push-over modelling techniques which can be used in conjunction with the finite-element package Strand7 or similar programs. These are outlined below.

7.2.1 *Non-linear column model*

In this model, beam elements which represent the column concrete are overlain by beam elements representing the column reinforcement (Fig. 10). The reinforcement is entered according to its true distribution in space using Strand7's user-defined 'BXS' section property. In order that Strand7's 'mesh-cleaning' function is not confused by overlapping elements which share the same end-nodes, the beam elements which represent the reinforcement connect to every-second node associated with the concrete-property beam elements.

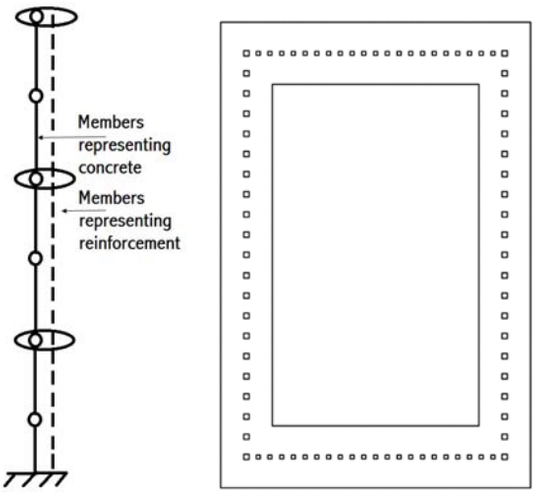


Figure 10. Beam-element model for non-linear column analysis

'Concrete elements' are programmed with the non-linear CEB-fip concrete-strength curve, including the characteristic of zero tension-capacity. Alternatively the Mander concrete-model (or similar) may be appropriate if earthquake detailing justifies the improved concrete strengths which result from substantial confinement. The 'reinforcement' beam-elements are programmed with a stress-strain curve which reflects the increase in reinforcement stress beyond the point of first yielding. The two connected elements constitute a 'composite' section from which a cracked-section analysis is derived (Fig. 11). A non-linear 'push-over' analysis will automatically calculate the true states of stress and strain – without the need to transform stresses. To avoid analytical non-convergence due to the abrupt loss of stiffness at zero-gradient locations on the material stress-strain curves – the author recommends that the 'push-over' is incremented as an imposed displacement, not an incremented (arbitrary) load.

The model described here is capable of describing the incremental change in cross-section stiffness and material strains at every stage through the imposed displacement. The locations throughout the structure which resist the seismic motions in-elastically (and which therefore must be ductile) are identified explicitly. In this approach, curvatures do not need to be calculated, however curvatures can be derived simply from the changes in deflected shape.

As a variation to this approach – if the designer prefers to utilize moment-curvature relationships in his non-linear push-over model, then these can be derived beforehand by the model in Figure 10.



Figure 11. Example Strand 7 output showing extent of cracking.

7.2.2 *Automated strut-and-tie models*

Figure 12 represents the model the author used to prove the capacity-protection of the superstructure of a major North-American balanced-cantilever bridge. In this example – the columns were built integrally into the pier table. In order to ensure the beneficial fusing of the plastic-hinge zones at both the top and bottom of the column – the pier table and foundations (including piles) were each designed for the 'over-strength' actions resulting from the plastic-hinging.

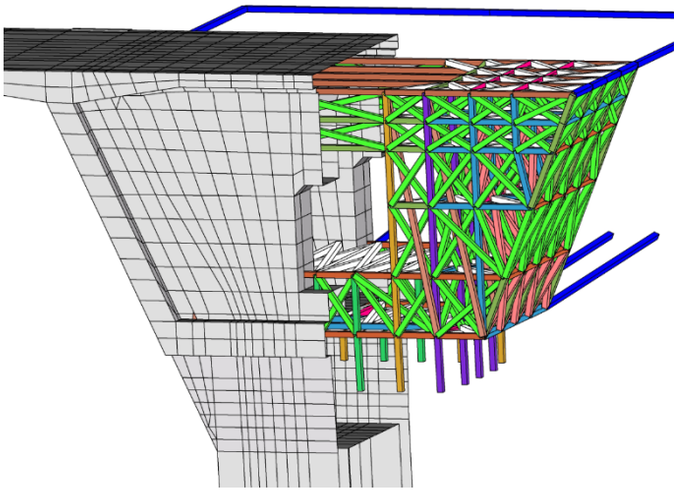


Figure 12. Isometric view of 3D strut-and-tie model: pier table.

Due to the difficulty in attributing a load-path within the diaphragm walls and webs of the pier table, while maintaining a sensible reinforcement pattern – the author undertook an automated non-linear strut-and-tie design – whereby the reinforcement was detailed before it was designed for earthquake. Next – the reinforcement crossing the location of the upper column hinge was assumed at the state of stress representing the steel's 'over-strength' properties. The load-path was derived automatically by the model, and vetted for its sensibility by the author.

For the E.J. Whitten Bridge review, the author applied a similar modelling approach towards automating the check of orthogonal reinforcement bands within the pilecaps (Fig. 13).

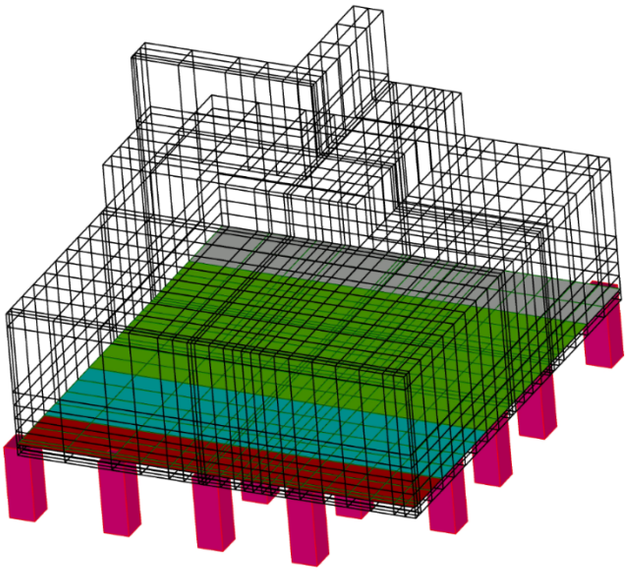


Figure 13. Automated non-linear strut-and-tie pilecap model.

In this model the reinforcement bands were represented in a 'smeared' sense by plate elements – for which non-linear steel properties were modelled. The concrete was modelled using 'brick elements', again with non-linear CEB-fib properties, and with the characteristic of zero tension-stress capacity. This model was combined with the non-linear push-over formulation outlined above, and also allowed the automated review of dozens of 'gravity-load' loadcases.

7.3 *Expansion joint design*

As illustrated beforehand, both of the RSA-method SRSS and CQC approaches to combining a multi-mode structural-response obscure the sign of bridge displacements. While unimportant for the design of abutment expansion-joints, the seismic movements which occur at expansion joints located within the length of bridge may be over-estimated by the RSA model – as the RSA results cannot differentiate between opening and closing movements, and whether the opposite sides of the expansion joint are moving in- or out-of-phase. The simple addition of a nominal beam-element across the expansion joint will allow the maximum expansion joint movement to be obtained from the beam-element's axial force. While this modelling trick solves the 'phase' question, the designer remains unclear whether this movement represents 'opening' or 'closing'. Only the resort to a n-linear time-history model may solve this remaining question. In any case – AS5100 does not require expansion joints to cater for seismic movements.

7.4 *Capacity-protection of knee joints*

When the plastic hinges which may develop in the columns are relied upon to achieve the seismic displacements – then the elements adjoining the hinges must be 'capacity-protected'. In such cases – pilecaps and pier crossheads must be capable to resist the actions which develop on account of the 'over-strength' properties at column hinges. For these elements – the complete loadpath must be demonstrated. Simply embedding the column reinforcement into a pilecap or into a column crosshead a 'development length', does not constitute an engineered outcome. Indeed – the act of merely adding bar cogs or 'bar heads' to the reinforcement, does not ensure a complete loadpath. As an alternative to first-principles calculations, the designer may engineer the capacity-protection of knee joints by referencing the empirical approaches of Caltrans (ATC 1996). As well as ensuring the capacity-protection of the knee joint, these empirical approaches often yield simpler reinforcement outcomes. For example the author's use of the empirical Caltrans method resulted in the deletion of all bar cogs on the triple-bar-bundle longitudinal reinforcement for the capacity-protected detail in Figure 14.

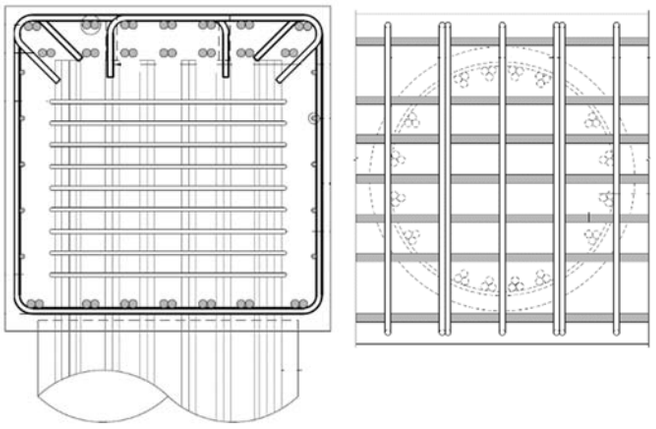


Figure 14. Capacity-protected knee-joint (empirical method).

7.5 *Distribution of reinforcement*

A detailing approach which can be used to alleviate reinforcement congestion recognises that the plastic capacity of a ductile reinforced-concrete section is essentially independent of the distribution of the reinforcement, as long as the layout is symmetrical about the plastic centroid (Fig. 15).

The capacity-protection of the Port Mann Bridge superstructure (Fig. 16) due to top and bottom column-hinges was achieved by distributing the reinforcement of the transverse tie-beams between the pier tables in the manner of Figure 15.

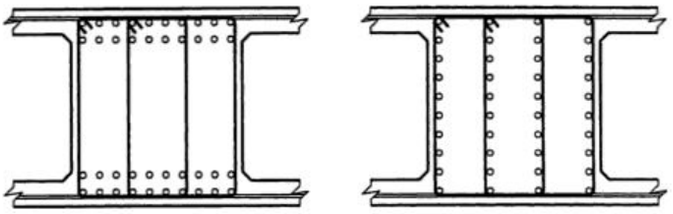


Figure 15. Similar-strength from different reinforcement layouts (both vertical and horizontal bending)



Figure 16. View of Port Mann Bridge pier table tie-beam.

8 CONCLUSIONS

This paper demonstrates the displacement-based approach to be a straightforward and beneficial method of assessing the seismic performance of new and existing bridges. In particular, the explicit calculation of material strains at any point in the structure allows the spatially-accurate identification of components which may require seismic-retrofit in order to achieve the appropriate level of component ductility.

9 REFERENCES

Pierino, L. Badoux, M. 2003. An experimental confirmation of the equal-displacement rule for RC structural walls. *Proceedings of the fib-symposium 2003.*

Miranda, E. 2000. Inelastic displacement ratios for structures on firm sites. *Journal of Structural Engineering 126.10*

Chopra, A. Goel, R.K. 1999. Capacity-demand-diagram methods based on inelastic design spectrum. *Earthquake Spectra: November 1999, Vol. 15, No. 4*: 637-656.

Priestley, M. J. N. Calvi, G. M. 2003. Direct displacement-based seismic design of concrete bridges. *Proceedings of the 5th ACI international conference of seismic bridge design and retrofit for earthquake resistance.*

Caltrans 2010, *Caltrans seismic design criteria version 1.6*, California Department of Transportation, Sacramento, California, pp.3.4, 4.1, 7.13-7.30.

ATC 1996. *Improved seismic design criteria for Californian bridges: resource document,* ATC-32-1, Applied Technology Council, Redwood City, California: 42.

Maintenance, Safety, Risk, Management and Life-Cycle Performance of Bridges – Powers, Frangopol, Al-Mahaidi & Caprani (Eds)
© 2018 Taylor & Francis Group, London, ISBN 978-1-138-73045-8

How did the future work out? The tale of E.J. Whitten Bridge

R.A. Percy & P.J. Robinson
COWI, United Kingdom

ABSTRACT: The E.J. Whitten Bridge is composed of twin multi-span concrete viaducts that carry the M80 freeway over the Maribyrnong River in Melbourne, Australia. Overall length is around 518m long. The bridge was completed in 1995 and it now carries 160,000 vehicles per day. In 2017 widening of the structure commenced through the addition of a new deck structure between the existing viaducts. Unusually for a bridge, provision for widening had been made in the original foundation and pier design, although increased highway loads and seismic requirements required an innovative design approach. Through this case study, the paper comments on how well this bridge has stood up to the comparatively recent future. From this, and knowledge from similar works on other bridges, lessons are then drawn for today's designers and those procuring bridges to enable bridges to better withstand the test of time and to lower the cost of future works.

1 INTRODUCTION

Modern transport demands on bridges continue to increase. By their very nature, bridges are often highly utilized structures placed at key locations in the transport network. There is rarely excess capacity or convenient alternative routes, and hence they become critical pieces of infrastructure that are depended upon to operate 24/7 throughout the year. Resulting available maintenance periods are short and consequences of over-running works severe in terms of disruption and financial penalties imposed.



Figure 1. E.J. Whitten, Bridge

Historically the design of bridges has not fully anticipated or catered for this level of high service demand, and where designers have not anticipated the future well the shortcomings can be ruthlessly exposed. This paper looks at a comparatively recent bridge to review how the bridge has been adapted to meet current demands and the innovation necessary to enable this. Lessons are then drawn on how designers and owners can better future-proof their bridges.

The structure considered here is the E J Whitten (formally named Maribyrnong Bridge) located on the M80 around Melbourne, Australia. It is a major viaduct structure currently being modified to carry additional lanes of traffic. Unusually for a bridge structure, some provision had been made at the time of original design for future widening. Nevertheless, exceedance of anticipated future loads and constraints within the existing structure have demanded innovation and alternative approaches to successfully realise the widened design.

2 EJ WHITTEN BRIDGE

2.1 *Location and description*

The existing E.J. Whitten Bridge is a twin post-tensioned prestressed concrete box girder viaduct that forms part of the M80 Ring Road around Melbourne, Australia. The viaducts cross the

Maribyrnong River Valley and are composed of ten spans with total viaduct length of 520 m.

In addition to longitudinal posttensioning of the girders, the concrete box girder decks are also transversely prestressed, with the tendons running from cantilever tip to cantilever tip, typically at 3.6m intervals.

2.2 *History*

During the original design and construction of the bridge in the early 1990s, provision was made for future widening of the structure through infilling the central reserve gap between the two viaduct structures. The concept envisaged was a third concrete box girder that would be supported on a concrete crosshead beam between existing piers (see Figure 2). The construction technique assumed was to cast insitu the cross head beam and launch the concrete box girder (similar to the original construction technique. The original designer included key elements to facilitate the future widening including;

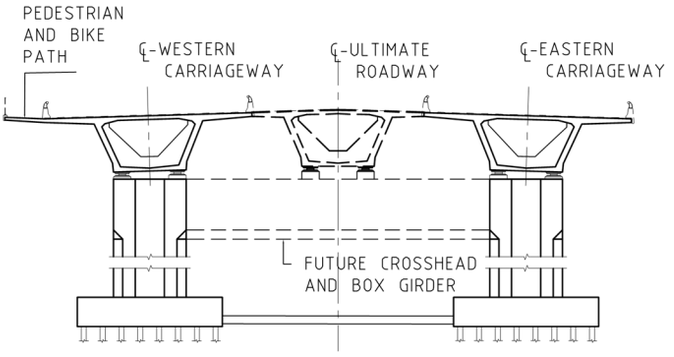


Figure 2. Image of the intended future widening concept (Noonan, 1994).

• Post Tensioning Ducts – 12 number (laid out in two rows of six) 105mm diameter ducts were provided across the top of the piers to allow for a post tensioned concrete crosshead beam to be installed.

• Foundations – the piers and foundations were designed for the loads from the future widened structure namely a third concrete box girder under T44 / L44 traffic loading. The original design also included a tie beam between pile caps to assist with any lateral forces from the portal frame action that would arise once the new crosshead beam is installed.

Aside from the provision of a new crosshead beam no new foundations or piers would be required for future widening except at the two bridge abutments.

• Deck Connection – the future concept anticipated an integral deck connection so top and bottom reinforcement was provided in the cantilever tip. When the widened structure is completed, under transverse load distribution, the inner cantilevers of the existing concrete box girders will be transformed from cantilever spans to continuous sections. This means the previous cantilever tip becomes an area of high sag moment. The original design accounted for this change in the behaviour of this element and provided sufficient reinforcement in both the top and bottom layers of bars to account for both the original and future behaviours of this section. The detail at the end of the cantilever ensured the transverse reinforcement extended beyond transverse tendon anchorages and cantilever tip u-bars so a connection between the new and existing reinforcement could be made.

• Articulation – bearings were provided with removable guide strips so the articulation could be changed in the widened condition. Main bridge abutments and expansion joints were aligned so that expansion joints in the widened structure could be made continuous over the full width.

2.3 *Widening*

In 2016, the widening of EJ Whitten Bridge was tendered by VicRoads as part of the Sunshine Avenue to Calder Freeway upgrade of the M80. With the Contract type being Design Contruct, the tenderers were free to propose alternatives to the reference scheme of a third concrete box. The winning tender design incorporated twin composite steel boxes with insitu concrete deck placed on precast concrete slabs. The superstructure was supported on new pierhead crossbeams, as the original design intended, and made integral with the existing deck. Advantage was taken of the presence of the existing structure to place the steel girders with a pair of gantry cranes running along the cantilevers of the original viaducts. The gantry cranes were also used to place the precast deck panels and the formwork for the pier crosshead beams.

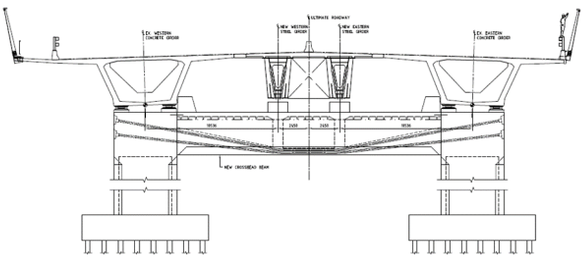


Figure 3. Typical section of actual widening scheme.

The final design solution is shown in Figures 3 and 4. A large major factor in adopting this design was the lighter weight of the superstructure elements

resulting in elimination of any strengthening requirements for the existing substructure. The form of the crosshead beams consists of insitu concrete sections built between existing pier columns to support the new bridge superstructure. Each end of the new crosshead beams was made integral to the existing pier columns. The post tensioning ducts provided within the existing piers were utilised for post tensioning as envisaged and were sufficient to provide the structural connection capacity between the existing pier and new crosshead.

The scope of works for the widening includes strengthening of the existing girders where necessary. As a design and construct contract it was necessary to determine the full extent of strengthening at tender stage through detailed analysis and assessment of the existing concrete girders. The design aimed to minimise strengthening and using steel girders helped this by achieving the necessary stiffness without weight. The steel girders were sized for stiffness, to limit bending of the slab from differential displacements between the new and existing girders. The girders also needed to satisfy height limits for transport and weight limits for the travelling gantry crane. This resulted in two 3.2m deep steel girders of 85 tonnes each (per 54m span).

The analysis was initially carried out using a 3D finite element grillage model, but was supplemented with a 3D shell model where greater accuracy was needed for the effects of distortion and slab bending. By using the shell model it was shown that strengthening was not required to the existing deck slab and the existing diaphragms.

Substantial benefit was taken from material testing of the existing concrete girders to avoid shear strengthening in the webs. The concrete was tested using 100mm diameter core samples and the results supported a cylinder strength of approximately 60MPa for assessment. This was a significant benefit compared to the design value of 45MPa, and showed the existing webs to be fully adequate without strengthening.

As part of the widening works some specific upgrades were specified by VicRoads. These included the addition of high anti-climb public safety barriers to the edges of each carriageway to provide enhanced safety, and the provision of high containment vehicle barriers.

The public safety barriers (PSB) were particularly problematic to fit as they were not considered in the original design, and hence there was a lack of viable attachment points. The provision of barriers over a long length requires a standardised post and panel system with repetitive components to achieve economy in not only production and installation, but also for future maintenance and repair where a standard panel can be swapped out. On the carriageway edge with the Shared User Path (SUP) for cyclists and pedestrians, there is a concrete fascia beam. However, this was not of sufficient size or well enough attached to the box girder cantilever to be able to form an anchorage for the significant post loads. Similarly, the cantilever tip was also lightly reinforced. This meant the post anchorage had to make use of the additional reinforcement provided locally to the original transverse deck prestressing anchorages to achieve satisfactory capacity. Although the additional reinforcement provides the capacity required, the post anchorages had to span the post tensioning anchors and be sufficient flexible in hold down bolt positions to avoid the congested reinforcement. On the other side of the carriageway there is no pedestrian path and the PSB posts were anchored on the rear face of the concrete vehicle parapets. This is also a fairly complex connection requiring the embedding of an anchorage plate under the inside face of the precast barriers.



Figure 4. Render of final widened configuration

The other user upgrade requirement that impacted the main bridge was the upgrade of the vehicle barriers to high containment level. With the capacity of the existing barrier limited by its connection to the deck, which in turn exceeds the cantilever's own capacity, the options for anchoring in a new higher containment barrier were limited. An alternative approach was used which replaced the barrier rails only and used a combination of rail continuity and tailored stiffness to achieve high containment performance. This was underwritten with finite element analysis including both vehicles and barrier modelling undertaken by a barrier impact simulation specialist.

A severe constraint on the design was the limitation on use of bonded dowelled in bars. Currently the use of bonded dowelled in bars is very restricted where a design is to be in compliance with VicRoads Technical Note BTN 2012/002. This means that the use of bonded dowelled in bars in tension was not used for any primary structural connections. This is a relatively severe constraint when strengthening and adapting an existing structure, particularly where many new elements are

to be made integral with the original structure. In the case of this structure, this affected the design of the stich between the new and existing decks; the connection of the pier connections to the crosshead beam and the integral connections between the new and existing abutment structures. In the case of the pier crosshead beam the problem was resolved by using the prestress to eliminate tension at the connection. For the deck stitch it constrained the solution to using existing reinforcement bars only, and making them work optimally. This resulted in having to achieve a high fatigue classification for the welded connection between the stitch reinforcement and the existing cantilever bars. For the abutments a shear only connection was sufficient however the problem of differential settlement between the existing and new abutments had to be catered for. Where differential settlement was predicted to be significant, dowelled bars in ducts were used, which were to be grouted when the full permanent load had been reached.

The integral nature of the final configuration meant that the original articulation would no longer suffice, as there would be two bearings with transverse restraint on the same pier axis. VicRoads also took the opportunity to specify the replacement of the existing bearings as part of the contact as these were over 20 years old. In addition, transverse seismic restraint blocks were required to be installed at each pier. The solution was to change the transverse restraint to occur at one of the new steel box girder bearings, whilst the longitudinal restraint remained at the three tall piers in the middle of the viaduct.

Future maintenance access and durability were important considerations in the design of the new structure and upgrades. Efforts were made to ensure that new steel elements such as the public safety barrier could largely be maintained either above deck or removed for off-site maintenance. With the new steel box girders being shielded by the concrete boxes either side they are in a relatively benign environment. Nevertheless, provision for future maintenance was made through four access hanging points per section being provided every 2m along the length of the structure. This will cater for a variety of access platforms formats and functions including local and whole bridge maintenance, and were therefore seen as a better option for the future, than designing a bespoke maintenance platform that itself requires maintenance and in time, refurbishment.

2.4 *Contract Form*

Contract forms such as Alliance, Early Constructor Involvement, or Design-Construct all permit the Designer to work with the Contractor from the early concept design stage to incorporate the constructors preferred construction methodology. This is highly advantageous particularly when working with existing structures. The design and construct contract created many challenges, such as the need to accurately determine strengthening requirements at tender stage. Several parts of the existing structure were found to be very near the limit where strengthening would be required. The difference between strengthening and not strengthening is a large cost and this required tender stage analysis to be very precise. This situation has the potential to impose substantial risk on the constructors and designers which could have been avoided through an alliance form of contract.

In this instance, the proposed use of gantry cranes to install the new steel box girders from the existing viaducts was a key decision which thereafter acted as a constraint on the remainder of the design. With the existing viaduct cantilevers having limited capacity, and to avoid needing to strengthen them, this constrained both the local wheel loads from the gantry and the weight of the new box girders. As the gantry cranes were also used to install the formwork for the pier crossbeams, much analysis effort was put into maximising construction flexibility whist respecting the weight limits the designers needed to operate within. Temporary cantilever props were required at each end of the bridge where the gantry crane wheel loads are not able to distribute loads into the cantilever in both directions

2.5 *Commentary on provision versus widening demands*

The new widening scheme has utilised all provisions made by the original designers, which makes the provisions a success. Access for construction and launching of the original envisaged scheme would have been difficult under the current constraints on traffic closures. Requirements to replace bearings under traffic load were not anticipated, and this required some local strengthening of the pier tops to be undertaken in advance. More generally, the higher traffic and seismic loading of current design standards was not anticipated.

Provision for future widening was less pronounced in the 130m concrete approach structure. In this case the concrete slab did not make direct provision for connection of the new deck and the expansion joints were not aligned, but a widening scheme was nonetheless achieved to match the existing structural form.

3 LESSONS FOR THE FUTURE

The case study provides an interesting example on how this structure has withstood the demands of time and upgrade work in order to cater for today's

transportation demands. Together with experience of maintenance and upgrade work from other bridge structures the authors have worked on there are some lessons we can propose for the future.

3.1 *Limitations of Code Compliant Design*

Whilst bridges are designed to the codes in force at the time, Code compliant design is not a guarantee that the bridge will see through its service life without problems. Unanticipated behaviour can still arise.

Codes and standards are through necessity a simplification to reduce a range of details and behaviours down to a level where they may be represented by rules and equations. Design innovation and constraint are increasingly necessary in modern design, but the research and testing behind the codes becomes more distant and inaccessible to the Engineer. This can permit the design of details, which were not adequately covered or were beyond the intent of the original research. Research and testing can also be dated and therefore may not adequately reflect the current transportation and environment conditions and current construction methodologies. Engineers should have greater access to this research to be able to make an informed decision on its adequacy.

Where the codes and research do not provide sufficient authority then Engineers need to acknowledge and promote the need to their Clients and Owners to undertake testing and research at design stage for novel and unusual features. Clients and Owners must recognise the value of this and allow sufficient time and funding. Prototypes, including full scale mock up modules can provide immense value to a project.

3.2 *Future provision versus retrofit*

In the case of EJ Whitten, the provision made for the future was largely successful - although only just given the increased demands of current loads. The lesson is to anticipate future demands and aim to build in sufficient reserve beyond that for the inevitable changes that will occur. Although it is not always possible to predict the future, trends are usually evident and provide a good basis. The most economical time to provide modest additional capacity is at the time of original construction.

Our experience of retrofitting is that it is often complex, and heavily constrained, and with a modest degree of additional foresight by the original owner and designer, would be made much easier and therefore more economic. Typically, access remains poor to many structures and often has to be upgraded in advance of the main works. Provision for replacement of bearings and movement joints also remains patchy even in comparatively recent structures. Restrictions on traffic closures required all bearing replacements on the existing girders to be done under full traffic load, but design requirements for many new structures (including the new parts of this structure) do not typically consider this. More focus needs to be placed on the adequacy and practicality of any provision made, as even if it is provided, it often insufficient and impacts unnecessarily on bridge operation. For example, movement joints, which inevitably require periodic replacement throughout the structure life, are typically concreted in, requiring major works to replace them; and bearings are rarely replaceable under full live load. Operation and maintenance need to be included as design input and design cases, and the operation and maintenance manual, at least at principles level, drafted prior to design.

Basic provisions for maintenance access are still often overlooked during design and yet basic provisions can improve the safety of the structure over its lifetime. As an example, the new steel girders for E J Whitten include multi-purpose drainage holes at regular intervals which can also function as hanging points for scaffold or future maintenance platforms. Such provisions are also likely to be used during construction for bolting platforms, or for ventilation of the girder confined space.

Additional provision for the future is also rarely economically feasible during strengthening as each further amount of reserve provided takes the structure further beyond its original design. Whilst more sophisticated analysis means new structures can be designed with greater optimisation (which itself will yield less future reserve) it can also be onerous for existing structures where the advent of computing power enables more exhaustive load conditions to be examined. This means that theoretical full utilisation of major components is comparatively common in existing structures even before upgrade works commence, and that the additional capacity yielded by upgrade is limited by extent of the structure requiring work.

3.3 *Analysis and investigation*

Analysis and investigative technology are able to investigate behaviour to a depth often not possible at the time of design, both through the power of modern analytical software and the use of instrumentation. The actual structure provides the best analytical model of behavior, and with ever increasing instrumentation options and decreasing cost it is possible to investigate behavior in some depth. This can often be used to mitigate the extent of intervention required and to manage problems which are predicted in service. The route itself can be instrumented for vehicle loading using weigh-in-

motion sensors, and used to inform a route or structure specific load model.

It is also apparent that the feedback loop from reality back to codes and standards is not strong. It is important that this is strengthened to ensure that mistakes or mis-judgements made in the past are not repeated. Design and construct contracts put increasing pressure on performance to the letter of the design codes, rather than permitting alternative approached based either on combinations of first principle approaches, supplementary evidence and research and reviewing the intent and application of the original code provisions

4 SUMMARY

Finally, whilst it is clear that future provision is best made at design stage, there is no standard guidance or approach, and asset owners or developers rarely see the incentive in doing so – despite the long-term cost to society. One key aspect of this is that even for today works Engineers are rarely able to close the highway for any significant length of time with the great economic cost to a wide range of stakeholders.

In the future full or even partial closures might be inconceivable.

5 ACKNOWLEDGEMENTS

The authors would like to acknowledge the other parties in the project who together with COWI jointly contributed to the successful outcome including co-designers ARUP and SMEC, the constructor Fulton Hogan, and the client VicRoads.

Maintenance, Safety, Risk, Management and Life-Cycle Performance of Bridges – Powers, Frangopol, Al-Mahaidi & Caprani (Eds)
© 2018 Taylor & Francis Group, London, ISBN 978-1-138-73045-8

How strong is your bridge? Optimising New Zealand's longest road bridge.

J. Waldin, B. McHaffie & V. Wong
Opus International Consultants, Christchurch, New Zealand

ABSTRACT: Many nations around the world have a significant proportion of their road bridges approaching end of life. As an example, over 25% of New Zealand's existing State Highway bridges were constructed over a 15 year period between 1926 and 1941, many of which are expected to require significant repairs or replacement within the next 10-15 years. In addition to an aging asset, vehicle load requirements are also continuing to increase with a strong demand for heavier vehicles on roads. In New Zealand, the introduction of high productivity motor vehicles (HPMV's) has significantly increased the demands on existing road infrastructure, causing loads in excess of the capacity of most road bridges constructed prior to the early 1940's. Therefore, it is becoming essential for asset owners to utilise modern optimisation techniques to extend the life of these structures to avoid having to replace or strengthen a large number of bridges over a short period of time.

This paper outlines a case study of how modern optimisation techniques have allowed the longest bridge in New Zealand, the Rakaia River Bridge, to support increased loading without the need for costly strengthening or replacement. Optimisation has involved a wide range of conventional and state-of-the-art techniques, including materials testing, verification of boundary conditions, advanced modelling calibrated with field testing, and calculation of a statistically appropriate load factor and bridge specific impact factor. By refining both the capacity of the structure and the load demand, a significant increase in the bridges theoretical capacity was achieved, saving the asset owner over $10 M in strengthening costs.

1 BACKGROUND

1.1 *Aging assets*

One of the largest challenges to modern society is the ongoing maintenance of aging assets. In particular, a significant proportion of road bridges in Western society are approaching the end of their theoretical design life of around 90-100 years. During the Great Depression (circa 1929 – 1941) many nations undertook significant infrastructure spending to reduce the effect of the economic downturn and provide employment. This resulted in a significant number of new road bridges being constructed in many nations over this period. As an example, over 25% of New Zealand's existing State Highway bridges were constructed over a 15-year period from 1926 – 1941. Given the lower design and construction standards at the time, these structures are estimated to have operating lives of 90-100 years. As such, a significant proportion of bridges constructed during this period are nearing their theoretical end of life and may require significant repairs or replacement within the next 10-15 years.

1.2 *Increasing load requirements*

As technology improves, there is a constant demand for heavier and heavier vehicles to be accommodated on roads. Not only do heavier vehicles provide more efficient movement of freight, they also have the potential to reduce the number of truck movements, improving road safety and efficiency and reducing environmental impact.

In New Zealand, the current Gross Mass limit for legally configured Class 1 trucks is 46 T. However, changes to the Vehicle Dimension and Mass Rule in 2010 allowed High Productivity Motor Vehicles (HPMV's) complying with certain criteria to obtain route specific permits for up to 62 T. Whilst the majority of road bridges constructed since 1960 are able to support these loads using modern load factors; load effects from HPMV's are well in excess of more historic design loadings, particularly for bridges designed prior to 1942 to Traction Engine design loading.

In addition to current loads exceeding historic design loadings; modern ultimate limit state (ULS) load factors are typically higher than the effective load factors from historic working stress design. These effects compound, resulting in the ULS live load capacity of bridges designed prior to 1942 being as low as 65% of current HPMV load effects.

Given aging infrastructure and increasing load demands, it is important for asset managers to optimise the assessment of bridges to extend their life and avoid a wave of bridge replacements.

1.3 *Load factors for heavy vehicle permitting*

The NZ Transport Agency Bridge Manual specifies a design live load factor of 2.25 for Highway Normal (HN) vehicle loading. The current HN-HO-72 design loading was adopted in 1972 as an adaption of the H20-S16-T16 design loading, with the HN element based on the HA loading in BS 153 (Chapman et al 1974). The design load factor of 2.25 was originally

adopted from the AASHTO design codes in the 1980's when ULS design principles were first being adopted for road bridges in New Zealand. When assessing existing bridges, this load factor is reduced to 1.90 reflecting an increased acceptance of risk for structures with limited remaining life. Another reason for the reduction in load factor is that the statistical risk of overloading is reduced for bridges with limited remaining life given the shorter time period.

The NZ Transport Agency Bridge Manual allows this load factor to be further reduced to 1.75 where the following criteria are met:

i. The restrictive bridge must be one of a small number of bridges on an important route.
ii. The deterioration factors for the bridge shall be accurately assessed.
iii. The engineer shall be satisfied that the structure has a ductile failure mode.
iv. The accuracy of the bridge structural data shall be confirmed.
v. The bridge shall be inspected at no more than six-monthly intervals to observe any structural deterioration.
vi. The engineer shall be satisfied that early replacement or strengthening is feasible.

This criteria reflects an increased acceptance of risk where the consequence of damage is lower.

There is a formal vehicle permitting system in New Zealand to allow for the movement of vehicles heavier than legal Class 1 loading, while protecting road bridges from damage. Overweight vehicles with indivisible loads that cannot be readily reduced in weight are able to obtain Overweight Vehicle Permits over specific routes as well as area-wide permits for up to two years. Given the payload on these vehicles are known and indivisible, the risk of overloading is considerably lower than for normal freight vehicles. As such, Overweight vehicles are assessed using a live load factor of 1.49 compared with posting load factors of 1.90 for normal Class 1 vehicles in the NZ Transport Agency Bridge Manual.

Since 2010, High Productivity Motor Vehicles (HPMV's) with divisible loads have also been able to obtain HPMV permits on specific routes for up to two years. Given the increased risk of overloading of these general freight vehicles, they are assessed in the same way as legal Class 1 vehicles using a live load factor of 1.90.

2 RAKAIA RIVER BRIDGE

2.1 *Structural form*

The Rakaia River Bridge is located on State Highway 1S (SH1S) within the South Island of New Zealand just north of the Rakaia township. The bridge was constructed circa 1939, and comprises a two lane reinforced concrete T-beam superstructure, supported on reinforced concrete columns and pile caps, founded on driven reinforced concrete piles, as illustrated in Figure 1 below.



Figure 1. View of Rakaia River Bridge showing structural form

At 1.76 km long, the Rakaia River Bridge is the longest bridge in New Zealand, and consists of 144, 40 foot (12.2 m) spans. The bridge has expansion joints in the form of split piers generally every 5 spans. The bridge is currently managed by Opus International Consultants Ltd (Opus) as part of the Canterbury and West Coast Bridge Management Contract.

2.2 *Capacity*

Previous assessments of the Rakaia River Bridge indicated that it was under-capacity for supporting Full HPMV loading. Given the length of the Rakaia River Bridge, the cost of strengthening the bridge to support HPMV loading was estimated at over $10 M (NZD). Therefore, the NZ Transport Agency and Opus proposed allowing the bridge to operate at slightly higher stresses, as allowed for within Section 7.4.3 of NZ Transport Agency Bridge Manual (the Bridge Manual). Due to the size and value of this bridge, Opus developed a Structural Response Monitoring (SRM) system to give further confidence that the bridge could sustain the increased loads, and provide an early warning system to protect the bridge from progressive damage. This included a range of conventional bridge monitoring and testing techniques, such as visual inspections, material testing, crack monitoring and survey levelling; as well as more advanced monitoring systems using accelerometers, displacement transducers, vehicle weigh-in-motion testing, advanced bridge model calibration, and concrete condition assessment. Details of the development of this SRM system have been the subject of past papers (Waldin et al 2017, 2015) and hence will not be covered in detail within this paper.

3 OPTIMISATION TECHNIQUES

3.1 *General*

Given the ongoing increase in live loads on New Zealand roads and the desire to extend the life of structures to avoid major replacement costs; there is a strong desire to utilise modern techniques to optimise the assessed load capacity of bridges to avoid conservatively restricting vehicle movements or requiring replacement of structures. Many reinforced concrete T-beam structures built prior to 1942 are still in reasonable condition, as is the case for the Rakaia River Bridge. These structures have also been shown to have very low fatigue risk given their detailing and the relatively low traffic volumes on most New Zealand Highways. As such, serviceability limits are often not deemed to be critical for this form of structure, and ULS assessment becomes the limiting criteria. As such, this paper focusses solely on the ULS capacity of reinforced concrete T-beam bridges.

The NZ Transport Agency Bridge Manual requires the calculation of a GROSS live load assessment of critical members to determine whether a bridge can support normal highway loads, as outlined in equation 1.

$$GROSS = \frac{\phi Mn - \gamma_D \times M_{DL} - \Sigma\left(\gamma\left(OtherEffects\right)\right)}{\gamma_L \times M\left(PostingLoadEffect\right) \times I} \qquad (1)$$

To avoid conservatism and ensure the optimal capacity of a bridge is achieved, each factor of this formula can be reviewed and assessed in detail. This includes review of material strengths and member capacities (ϕMn); load factors for dead and live loads (γ_D and γ_L); dead load demand (M_{DL}); live load demands ($M_{Posting\ Load\ Effect}$); impact loading ($I$); and analysis techniques used to calculate the distribution of loads into critical members.

3.2 *Material Strength*

The strength of key materials such as reinforcing steel and concrete are typically taken as the lower 5th percentile based on material testing. Material strengths used for assessment are usually taken from figures specified on design drawings, or conservative values based on the era that a bridge was constructed. Testing of actual materials in a structure can result increases in strength, improving the assessed capacity of a structure. To further reduce the statistical variation of tested samples, the standard error of a group of bars or members can be considered where these act together in a structure (see Addendum 7A of the Bridge Manual for further details).

For the Rakaia River Bridge, Opus Research undertook non-destructive steel leeb hardness testing on 18 samples to derive the yield strength of the reinforcing steel. The average yield stress of the reinforcement was calculated as 288 MPa, compared with a previously assumed value of 250 MPa. Statistical assessment indicated that the lower 5th percentile yield strength for the whole sample set was 263 MPa for a single bar, and 280 MPa for a group of 12 reinforcing bars at the mid-span of the beams.

Concrete core samples were also taken and crushed to determine the material properties of the concrete. Concrete compressive strength results for the Rakaia River Bridge were highly variable, ranging from 17.0 – 62.0 MPa with an average of 35.7 MPa. This was likely due to the variability in the quality of materials and the quality of construction and compaction of the concrete. Samples with rounded greywacke aggregate were identified in three of the sample spans, and exhibited lower strengths. Samples with crushed greywacke aggregate were identified in the other two sample spans, and exhibited considerably higher strengths. Statistical assessment of the sample set in accordance with Section 7 of the NZ Transport Agency Bridge Manual was not considered appropriate as this yielded lower 5th percentile capacities below zero MPa. This is due to the concrete strength not being normally distributed. As such, the lowest tested capacity of 17MPa was considered an acceptable lower bound capacity for assessment purposes. In future, consideration should be given to altering the statistical figures in the NZ Transport Agency Bridge Manual to reflect that materials are typically more accurately represented by log-normal distributions rather than the current normal distribution figures shown.

3.3 *Member Capacities*

Modern analysis techniques generally provide very accurate assessment of the capacity of structural members. However, assumptions are often made to simplify assessments such as ignoring the effects of kerbs or upper reinforcing steel in the capacity assessment of reinforced concrete beams. By including these in the structural assessment, small gains in the assessed capacity can be achieved.

For the Rakaia River Bridge, the contribution of upper reinforcement was ignored, as recommended by the NZ Transport Agency Bridge Manual. However, a contribution from 50% of the kerbs was incorporated in the capacity assessment, as allowed for in the Bridge Manual. This increased the overall mid-span moment capacity of the superstructure by 10%.

3.4 *Boundary Conditions*

Boundary conditions at the end of members can play a significant part in the assessment of capacity. In particular, fixity at the end of spans will significantly reduce the mid-span bending moments. However, this can have a detrimental effect with additional hogging load occurring at beam ends.

For the Rakaia River Bridge, load testing indicated that the beams were exhibiting significant continuity over the spans, despite being designed to act simply supported with no steel continuity across the piers. This was due to monolithically placed concrete causing a propping force at the base of the beams. This has a significant effect on the bridges performance under service loads, with mid-span bending moments being only around half of those expected from simply supported beams. However, it is unknown whether these boundary conditions would continue under ULS loads, as excessive stresses at the base of the beams may result in failure of concrete sections, with the beams reverting to behaving simply supported. As such, the beams have been assessed to act simply supported under ULS loads, with an advanced monitoring system installed to provide a trigger for damage at the beam supports as an early warning system. The details of this system are provided in previous papers on this subject (Waldin et al 2017, 2015).

3.5 *Dead Load Demand and Load Factor*

Dead load demand is typically calculated using member and surfacing dimensions from as-built or construction drawings and typical material densities. In New Zealand, the density of reinforced concrete is commonly assumed to be 2400 kg/m3, however this can increase where the steel reinforcement ratio is high and reduce for lightweight concrete. Steel density is commonly assumed to be 7850 kg/m3 and surfacing is commonly assumed to weigh 2000 kg/m^3.

Site measurements, sampling and density testing can be undertaken to further refine the dead load demand. Section 7 of the NZ Transport Agency Bridge Manual also allows the ULS dead load factor to be reduced to as low as 1.10 where member dimensions are measured on site and density is verified. The Bridge Manual does limit the total load factor on all gravity effects to no lower than 1.25. However, if a statistical assessment of the variability of dead load is undertaken, this load factor could potentially be reduced below this value.

For the Rakaia River Bridge, no detailed measure up or density testing was undertaken as the cost of this was relatively high given the small gains in assessed capacity that may be achieved.

3.6 *Live Load Demand*

Load demand assumptions are typically based on a simplified load model which is used to represent a stream of legal vehicles. As these are based on averages used to represent a wide range of spans and structural forms; these will be inherently conservative and unconservative for some structures. As such, more accurate load demand models can be developed based on a stream of legal loads run across a particular bridge.

In New Zealand, the NZ Transport Agency Bridge Manual represents a stream of legally configured Class 1 vehicles as 85% of the Highway Normal (HN-72) design loading. HPMV's are represented by 90% of the HN-72 envelope for spans less than 25 m and 95% HN-72 for spans greater than 25 m. This is known to be unconservative for certain span ranges, particularly for shear effects in longer span bridges. However, statistical analysis has shown that when combined with the high design live load factors in the Bridge Manual, these load models provide an appropriate reliability index (Goodall & Hobman 2011). For span lengths less than 7 m, these load assumptions are generally conservative and over-estimate effects from legally configured vehicles.

For the 12.2 m spans of the Rakaia River Bridge, the critical mid-span moment effects from a stream of High Productivity Motor Vehicles is equivalent to 91% HN-72. Shear effects from HPMV's are equivalent to 89% HN-72. Therefore, the 90% HN-72 representation adopted in the Bridge Manual is very appropriate for this span range.

3.7 *Live Load Factor*

Live load factors used in modern design codes are typically generated through statistical reliability analysis. These utilize reliability factors, often termed beta factors (β), to calculate the probability of failure of an element over the design lifetime of a structure. β can be thought of as representing the number of standard deviations from the mean for a normally distributed data set, and takes into account variability in member capacity as well as load effects from streams of heavy vehicles. Member capacity is typically symbolized by R for resistance, with load effects symbolized by Q, as illustrated in Figure 2.

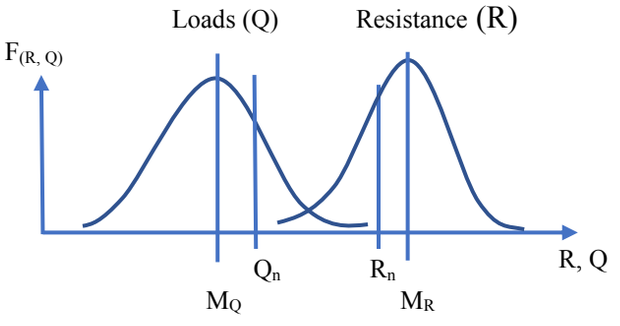


Figure 2. Distribution of load and resistance of a structure

M_Q and M_R represent the mean of the load effects and resistance, with Q_n and R_n showing the nominal load and resistance used for design. The failure point is located at the intersection between the load and resistance curves, with load factors set at an appropriate level to ensure the probability of failure is reliably low.

The statistical distribution of the difference between the resistance and capacity is shown in Figure

3. M_{R-Q} represents the mean of the difference between the resistance and load effects, with β representing the number of standard deviations from the mean to the point of failure where the load effects exceed the resistance of a critical member.

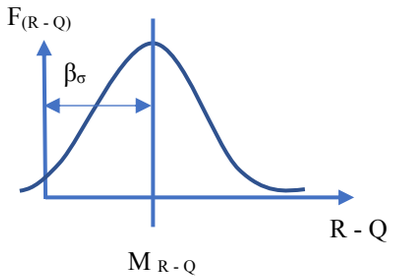


Figure 3. Distribution of difference between resistance and load on a structure.

Equation 2 indicates how beta factors are calculated with m_R and m_Q representing the mean of the resistance and maximum load effects, and σ_R and σ_Q representing the standard deviation of the resistance and the maximum load effects respectively.

$$\beta = \frac{m_R - m_Q}{\sqrt{{\sigma_R}^2 + {\sigma_Q}^2}} \quad (2)$$

Equation 3 shows the full beta factor calculation utilising the mean and standard deviation of various vehicle and material parameters. Further details on this formula can be found in the National Cooperative Highway Research Program report NCHRP 20-7/186 (Kulicki et al 2007), commissioned by the American Association of State Highway and Transportation Officials (AASHTO).

$$\beta = \frac{R_n \times \lambda_R \times (1 - k \times V_R) \times [1 - \ln(1 - k \times V_R)] - m_Q}{\sqrt{[R_n \times V_R \times \lambda_R \times (1 - k \times V_R)]^2 + {\sigma_Q}^2}} \quad (3)$$

Design load factors used in the NZ Transport Agency Bridge Manual have been checked against a desirable beta factor (β) greater than or equal to 3.5 (Goodall & Hobman 2011) assuming a design life of 100 years. A target β of 3.5 aligns with AASHTO's Load Resistance Factor Rating (LRFR) Bridge Design Specifications (Kulicki et al 2007)) and represents a probability of failure of 0.00023 over the design life, which is assumed to be 75 years in the AASHTO LRFD load factor calculations. This equates to a likelihood of failure of 1 in 4350 over the life of a structure.

Various international design codes also reference a minimum beta factor of β = 2.5 being acceptable for the assessment of structures in operation where risk is appropriately addressed through inspection and confirmation of a ductile failure mechanism or redundant load path. A beta factor of 2.5 represents a probability of failure of 0.0064 or a likelihood of 1 in 160 over the life of a structure. This is considered appropriate given existing bridges have more well defined live load effects than is the case at the outset of the design of a new bridge. Also, the incremental cost of a higher beta factor and higher load factors is relatively low for new bridges. However, the cost associated with conservatism in load factors for an older structure can be very high if it requires major strengthening works to take place. Beta factors of 2.5 also roughly align with the reliability factor for many existing bridges designed using the old Load Factor Rating (LFR) assessments prior to the adoption of Load Resistance Factor Rating (LRFR).

Table 1 outlines the live load factors specified in various bridge design codes for normal highway loading. As shown, the design and assessment live load factors used in the New Zealand Transport Agency Bridge Manual are relatively high compared with international bridge design and assessment codes.

Table 1. Distribution of difference between resistance and load on a structure.

Country and Code	Phase	Live Load Factor	Comments
New Zealand (NZTA Bridge Manual SP/M/022 3rd Ed. 2013 incl. 2016 amendments)	Design	1.84 – 2.25	Reduced from 2.25 for lightly trafficked rural roads.
	Assessment	1.75 – 1.90	Reduced from 1.90 for single restrictive bridges on key routes with ductile failure mechanisms.
Australia (AS 5100 2017)	Design	1.80	
	Assessment	1.60 – 2.00	Varies based on vehicle type.
Canada (CSA S6-2014 incl. 2017 amendments)	Design	1.70	
	Assessment	1.35 – 1.70	Varies with ductility, redundancy and inspection type.
United States of America (AASHTO LRFD; AASHTO annual for Bridge Evaluation)	Design	1.80 – 2.43	Varies with ductility, redundancy, importance and traffic volume.
	Assessment	1.40 – 1.80	Varies with traffic volume.
United Kingdom (BD 37/01; BD 21/01)	Design	1.65	Includes 1.10 factor for assessment inaccuracies.
	Assessment	1.65	Includes 1.10 factor for assessment inaccuracies.

Although the Bridge Manual does not specifically provide guidance around further reduction in load factors due to statistical assessment, reliability analysis and risk of failure; guidance from the Canadian and American design standards (CSA S6-2014 and AASHTO LRFD) could be considered where appropriate.

AASHTO's LRFD utilizes lower load factors for bridges with lower Annual Average Daily Traffic (AADT) given their statistical risk of overload is lower. This approach has not been adopted in New Zealand as lower volume roads are considered to have a higher risk of vehicle overloading given their more remote locations and reduced presence of enforcement and weigh stations. However, lower live load factors for assessment could be considered as a structure approaches end of life given the reduced likelihood of an extreme overload event. At present, this approach is not generally adopted within international bridge assessment codes, probably because reduced remaining life only has a relatively small probabilistic effect on load factors.

The Opus Report "Development of Bridge Design Loading for HPMV's" (Goodall and Hobman 2011) indicated that although moment and shear effects from HPMV's can exceed the theoretical 0.90 and 0.95 HN-72 design load envelopes; the design live load factor of 2.25 in the Bridge Manual was sufficiently large to ensure beta factors greater than 3.5 were still achieved for all typical bridge span ranges. For simply supported bridge spans less than 35 m, HPMV load effects were well modelled by the 0.90 and 0.95 HN-72 load envelopes and beta factors are generally well in excess of 3.5. This indicates that the current design live load factor of 2.25 used in the NZ Transport Agency Bridge Manual could potentially be reduced for simply supported bridge spans less than 35 m long.

3.8 *Bridge Specific Live Load Factor*

By using the Weigh-in-Motion data from the Rakaia River Bridge, a bridge specific live load factor was able to be developed. This was done using similar methods to the Opus Report "Development of Bridge Design Loading for HPMV's" (Goodall and Hobman 2011) and AASHTO's LRFD. Vehicles heavier than legal Class 1 loading were classified as either HPMV's or overweight vehicles based on their axle mass and configurations. The ratio of their load effects over the 12.2 m simply supported spans on the Rakaia River Bridge was then compared to the maximum load effects from legally configured Class 1 vehicles. These load effects were calculated from 12 months of Weigh-in-Motion data and plotted on a log-normal graph shown in Figure 4.

The data was then statistically extrapolated from 12 months to estimate the expected maximum load effects over a 20 year and 100 year period assuming 2.5% annual growth of heavy vehicles over this route. For more background on this extrapolation process, see NCHRP report 20-7/186 (Kulicki et al 2007). This statistical extrapolation is considered highly accurate compared with other international studies that have typically only used a few weeks of heavy truck data to extrapolate maximum predicted load effects over a 75 – 100 year design life.

Figure 4 indicates that the average (mean) maximum load effects over the 12.2m simply supported spans on the Rakaia River Bridge are expected to be 152% of the legal Class 1 load effects over a 100 year period. This is equivalent to 142% of HPMV load effects. The standard deviation of this 100 year maximum is estimated to be 0.167 based on the slope of the CDF curve. The mean maximum load effect over the estimated 20 year remaining life of the bridge are 140% of Class 1 effects and 131% of HPMV Effects.

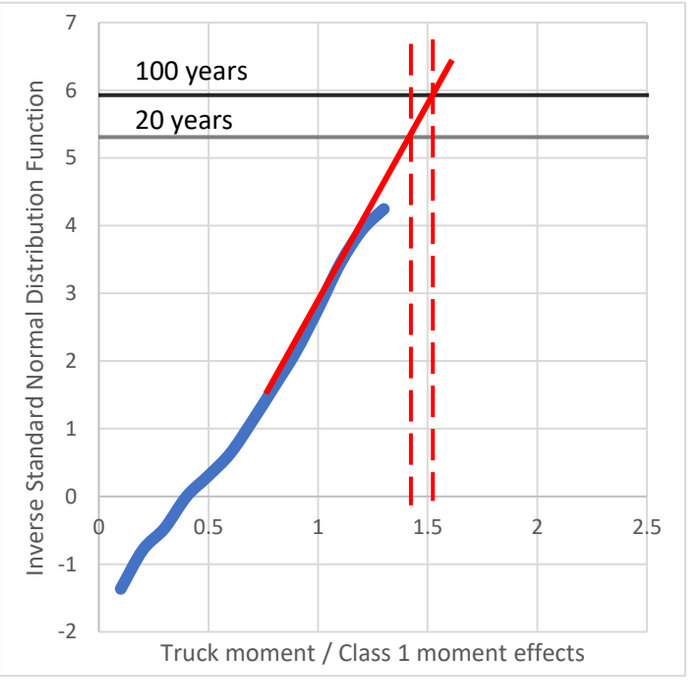


Figure 4. Extrapolated Cumulative Distribution Function of simply supported moment for trucks from Rakaia Weigh-in-Motion data from August 2016 – 2017.

Statistical analysis of permitted overweight vehicles provided a slightly higher mean maximum load effect of 175% of Class 1 load effects extrapolated over a 100 year period. However, overweight vehicles are well defined, indivisible loads with route specific permits. These are permitted using reduced load factors of 1.49 due to the significantly reduced risk of overloading. Over the Rakaia River Bridge, permitted overweight vehicles can reach load effects up to 120% of Class 1 load effects in their own lane, or over 200% Class 1 load effects for central travel at reduced speed. There is no definitive indication of any level of overloading of permitted overweight vehicles from the WiM data. As such, permitted overweight data has been removed from the WiM data to avoid skewing the data.

Parameters for the variability in material strengths in reinforced concrete bridges were calculated based on the material testing results from the Rakaia River Bridge. Table 2 indicates these parameters in comparison to the figures from NCHRP report 20-7/186 (Kulicki et al 2007). This indicates the material variability of the Rakaia River Bridge was similar, but slightly less than the average data sets used in NCHRP report 20-7/186. λ represents the bias between the nominal capacity and the mean and V represents the coefficient of variation.

Table 2. Bias and coefficient of variation for materials, fabrication and overall resistance of reinforced concrete bridges.

	Material and Fabrication Factors, F M		Professional Factor, P		Total Resistance, R	
Case Study	λ	V	λ	V	λ	V
NCHRP Report 20-7/186 Data for RC Bridges	1.12	0.12	1.02	0.06	1.14	0.13
SH1S Rakaia River Bridge	1.08	0.08	1.02	0.06	1.10	0.10

If a suitable beta factor is selected, the value of the resistance (Rn) and an appropriate live load factor can be calculated using Equation 3. Table 3 shows bridge specific live load factors for various design and assessment scenarios. The material capacity reduction factor (ϕ) could also be removed from the expected member resistance, further reducing the calculated live load factor. However, for the 144 span Rakaia River Bridge, this was still used given the number of spans increases the statistical risk of a weaker span reaching yield due to being overloaded.

Table 3. Bridge specific live load factors based on Weigh-in-Motion and material data from the Rakaia River Bridge.

Phase	**Remaining Life**	**Assumed Beta Factor**	**Calculated Live Load Factor**
Design	100 years	3.50	2.11
Assessment	100 years	2.50	1.84
Assessment	20 years	2.50	1.72

3.9 *Impact Factor*

The NZ Transport Agency Bridge Manual defines impact as outlined in Equation 4.

$$I = 1 + \frac{15}{L + 38} \tag{4}$$

Equation 4 applies to moment effects in simple or continuous spans and is capped at a maximum of 1.30. Moment in cantilevers, deck slabs, and shear effects are set at a constant value of 1.30. The Bridge Manual uses this same design impact factor for assessment. Given it is intended to represent an upper 5th percentile of impact loads, it may be considered conservative for certain structural forms.

For the Rakaia River Bridge, test loading of the bridge spans using a known load at various speeds indicated a maximum impact factor of 1.18. The fundamental frequency of the bridge beams was also measured and indicated that typical heavy vehicle speeds would need to be in excess of 130 km/hour to initiate resonance in the spans, and this is considered highly unlikely for heavy vehicles on this narrow bridge. This therefore reduces the likelihood of impact factors reaching the level of 1.3 specified in the Bridge Manual.

Considerably more vehicle runs are still required to give the test results more statistical accuracy. However, initial results indicate that the impact load factor in the Bridge Manual is likely to be conservative for this bridge form, and an impact factor of around 1.20 is likely to be more appropriate for this bridge.

3.10 *Structural Analysis*

Reinforced concrete T-beams were typically designed using simple load distribution models such as Courbon's method. The distribution of load within beams can now be more accurately assessed using the more sophisticated empirical methods in the latest AASHTO LRFD Design Code, or through a grillage or Finite Element model.

Assessment of the Rakaia River Bridge was undertaken using a grillage model in Microstran. This model was calibrated based on material testing and measurement of actual span behavior under loading, allowing it to be more accurately calibrated. This provided improvements in the assessed load spread through the superstructure resulting in an increase in the assessed load capacity of around 10%.

4 OPTIMISED CAPACITY

As outlined in Section 3, by refining both the capacity and the load demand on a structure, a significant increase in a bridge's assessed capacity can be achieved. Table 4 shows the effect that more detailed analysis of these parameters had on the assessed capacity of the Rakaia River Bridge, with the overall assessed capacity increasing from 65% Class 1 to 110% Class 1. Along with a sophisticated real-time monitoring system, this allowed the bridge to be opened to HPMV loading without the need for costly strengthening, saving the asset owner over $10 M in strengthening costs.

As well as the outcomes for the Rakaia River Bridge, a parametric study of 30 other reinforced concrete T-beams in New Zealand was undertaken. This study was used to provide information on the typical

range of improvements that can result from review of various capacity and loading inputs. The results of this study are also shown in Table 4.

Table 4. Typical variation in resistance and load parameters for reinforced concrete T-beam bridges following more detailed assessment and testing.

Parameter	Change after Rakaia Assessment	Effect on Rakaia GROSS Capacity	Typical Effect on GROSS Capacity of RC T-Beams
Steel Strength (fy)	+12%	+18%	0 – +20%
Concrete strength (f'c)	0% (no change)	0% (no change)	0 – +5%
Upper reinforcement	-	-	+2 – +4%
Integral kerbs	-	+10%	+5 – +15%
Boundary Conditions	*	*	*
Dead Load Demand (M_{DL})	0% (no change)	0% (no change)	0 – +5%
Dead Load Factor (γ_{DL})	0% (no change)	0% (no change)	0 – -15%
Live Load Demand (M_{LL})	-1%	-1%	-5% - +10%
Live Load Factor (γ_{LL})	+10%	+10%	-5% - +35%
Impact Loading (I)	-8%	+8%	0 – +20%
Structural Analysis	+10%	+10%	0 – +15%

* Although boundary conditions can play a significant part in assessed capacity, it is often difficult to prove that an assessed condition will remain when subject to ULS loads.

As outlined in Table 4, the most significant increases in assessed live load capacity of older reinforced concrete bridges can generally be achieved through testing of the steel reinforcement, incorporation of previously ignored structural components such as integral kerbs and upper reinforcing steel, refinement of the dead and live load factors, and more detailed structural analysis. Where the assessed ULS capacity of a bridge is still limiting the movement of heavy vehicles, review of other parameters can be undertaken to further refine the accuracy of an assessment. Although detailed truck data is often not available for a bridge, the beta and live load factor information in Section 14 of the Canadian Bridge Design Code (CSA-S16-2014) provides good guidance around reducing assessment load factors based on risk of failure. A similar approach could be considered for New Zealand road bridges. Alternatively, the Rakaia River Bridge assessment indicates that a live load factor of 1.75 could be considered for the assessment of all existing New Zealand bridges provided certain risk criteria are met.

5 CONCLUSIONS

In conclusion, the rate of significant bridge strengthening and replacements are predicted to increase significantly over the next 10-15 years. To ensure the rate of replacement and improvements is manageable, it is important for asset managers to optimise the assessment of bridges.

A detailed analysis of various capacity and load parameters was undertaken for the Rakaia River Bridge to optimise the bridges assessed live load capacity. The most significant gains in capacity were achieved through steel reinforcement testing, more detailed structural analysis calibrated with field testing, and the development of a bridge specific live load factor and impact factor. In particular, the design and assessment live load factors used in the NZ Transport Agency Bridge Manual have been shown to be relatively high compared to other international standards. This provides an opportunity for reduction in the load factor where it can be shown that the risks are effectively managed and at a level that is acceptable to the asset owner.

By refining both the capacity and the load demand of the Rakaia River Bridge, the bridges theoretical capacity was increased from 65% to 110% Class 1. Along with a sophisticated real-time monitoring system, this allowed the bridge to be opened to HPMV loading, saving the asset owner over $10 M in strengthening costs.

6 REFERENCES

Goodall, D. & Hobman, H. 2011. Vehicle Dimension and Mass Rule Change: Development of Bridge Design Loading for HPMVs. *Opus Report 5-C1924.00*

Kulicki, J., Prucz, Z., Clancy, C., Mertz, D. & Nowak, A. 2007. Updating the Calibration Report for AASHTO LRFD Code, *National Cooperative Highway Research Program (NCHRP) Report 20-7/18*

Waldin, J., Cowan M. & Kean R. 2017. How is your Bridge Behaving? Advanced Monitoring of New Zealand's Longest Bridges, *Austroads Bridge Conference April 2017.* Melbourne, Australia

Waldin, J., McKenzie, C., Jennings, J., & Kean, R. 2015. Structural Response Monitoring of New Zealand Bridges, *Performance-based and Lifecycle Engineering (PLSE) Conference 2015.* Brisbane, Australia

Maintenance, Safety, Risk, Management and Life-Cycle Performance of Bridges – Powers, Frangopol, Al-Mahaidi & Caprani (Eds)
© 2018 Taylor & Francis Group, London, ISBN 978-1-138-73045-8

Performance of prestressed concrete girder in ultimate bending for AS5100:2004 and AS5100:2017

M.M. Melhem & C. Caprani
Department of Civil Engineering, Monash University, Victoria, Australia

M.G. Stewart
Centre for Infrastructure Performance and Reliability, University of Newcastle, New South Wales, Australia

ABSTRACT: In 2017, AS5100, the Australian standard for bridge design and assessment, underwent significant updates from the previous 2004 edition. While the assessment methods remain similar, the design methods for prestressed concrete bridge components, which are required for their assessment, have significantly changed. It is then of interest to determine the implications of the changes. To do this, the performance of an already-constructed Super-T girder is assessed for ultimate strength in bending. Using the deterministic method prescribed by the code, the performance requirement is not met using the current code, whereas it is met using the 2004 superseded code (the code used for its design). From this, it is apparent that reliability analysis could play a very useful role in assessing such bridges. Consequently, a reliability analysis is conducted and it is found that both codes give indices significantly higher than an accepted target reliability index. It is concluded that the level of conservatism of AS5100 should be further investigated.

1 INTRODUCTION

1.1 *Measuring Structural Performance*

Structural performance is commonly described as the ability for a structure to fulfil certain criteria (Cremona, 2013). Often, structural performance and structural safety are thought as the same measure. Indeed, this is the case if the criteria considered is the structural integrity. However, for bridge structures other requirements exist such as limits on deflection and prevention of concrete cracking. Hence, measurement of the performance of bridge structural components is more generally appropriate.

Traditionally, the performance assessment of bridge components is based on a combination of field test data and expert opinion (Akgul & Frangopol, 2003). Bridge ratings provide a quick, efficient and thus economical measure of bridge performance. However, ratings contain uncertainty as input parameters are subject to randomness and so may not reveal the true performance level. The use of a probabilistic approach can consider these uncertainties. Nowadays, bridge standards such as the American, Canadian, Danish, Swiss and British codes have moved away from traditional deterministic load rating processes and also allow the use of reliability analysis for bridge performance assessments (Wisniewski *et al.*, 2012). One international standard that is yet to adopt this change is the Australian bridge standards (AS5100).

1.2 *Australian Bridge Standards (AS5100)*

AS5100 is the Australian standard for the design of new bridges and assessment of existing bridges. In the 2004 edition, the code comprised of seven parts. Part 1 outlines the scope and design life of 100 years. Part 2 details the design load models and associated factors. Part 5 and Part 6 are used for the design of concrete and steel components, respectively. Part 7 details the procedures for the assessment of existing bridges.

In early 2017, the entire code underwent a significant revision. The latest revision included updated Parts 1 to 7, and the inclusion of new parts; Part 8 for rehabilitation and strengthening of existing structures, and Part 9 for new timber bridges (Pritchard, 2017a).

Although AS5100.7 (Bridge Assessment) has been considerably revised, the fundamental process remains the same as the superseded 2004 code (Pritchard, 2017b). Both codes infer the use of bridge ratings as the first-basis performance measure for capacity. Unlike the other international design codes, the use of reliability analysis for performance assessment of bridge components is not facilitated.

Both superseded and current codes indicate that the structural capacity of existing components is to be determined using the relevant design standards. For prestressed concrete (PSC) components, the applicable standard is AS5100.5 for concrete bridges.

Some significant changes between AS5100.5:2004 and AS5100.5:2017 exist (Hilton, 2017). Notably, in AS5100.5:2017 modified compression field theory is adopted for the shear and torsion design. Additionally, models for quantifying prestress losses are updated to better consider higher concrete grades. More minor updates include those of material properties for concrete, steel reinforcement, and strands, and the parameters for the simplified concrete stress block under ultimate strength in bending. Many updates are such that they match those found in the concrete code for building structures (AS3600:2009).

1.3 *Motivation*

There is no indication that the 2017 updates to AS5100 were made with any reliability basis or calibration. Consequently, the performance assessment of existing PSC bridge components designed to the superseded code may be different if assessed under the current code. If this is the case, then the performance levels of bridges designed and built under the 2004 code will differ from those to be designed and built from 2017. This could have implications for future management of these structures.

To investigate the code-implied performances, an already-constructed Super-T girder is assessed for flexural strength. Super-T girders are standard precast bridge girders used in Australian and New Zealand practice. The performance criteria (limit state) considered is ultimate strength in bending. The assessment is carried out two ways: applying the methods indicated by AS5100.7 (deterministic), and performing a reliability analysis (probabilistic). Both the 2004 and 2017 editions of the code are considered in this way. From these results, the AS5100 deterministic method of assessment is compared with probabilistic methods. Additionally, the implications of changing the AS5100.5 design rules, without changing the AS5100.7 assessment rules that rely on AS5100.5 can be inferred.

2 BRIDGE GIRDER DESIGN

The representative bridge girder in this study is one of five simply-supported PSC Super-T girders from a bridge deck spanning 33.5 m, previously studied in Caprani *et al.* (2017). The girder is 1500 mm deep (designation T4) and the outermost girder in the bridge deck, as this is the most heavily loaded. The design geometric properties and concrete properties of the girder are shown in Table 1.

The PSC girder is pretensioned with 56 No. 15.2 mm diameter 7-wire strands. The design requires each strand to be prestressed to 188 kN (P_j) and arranged within the girder as shown in Figure 1. The material properties for the strands in accordance to AS5100.5 (both editions) are shown in Table 2.

Table 1. Representative Girder Properties

Property	Symbol	
Compressive Strength (N/mm^2)	f'_c	65
Young's Modulus (kN/mm^2)	E_c	37.4
Gross Cross-Section Area ($\times 10^3$ mm^2)	A	934
Second Moment of Area ($\times 10^6$ mm^2)	I	348
Top fibre to section centroid (mm)	y_t	634

Table 2. Prestressing Strands Material Properties

Property	Symbol	
Strand cross-section area (mm^2)	A_p	143
Breaking strength (N/mm^2)	f_{pb}	1830
Young's Modulus (kN/mm^2)	E_p	195

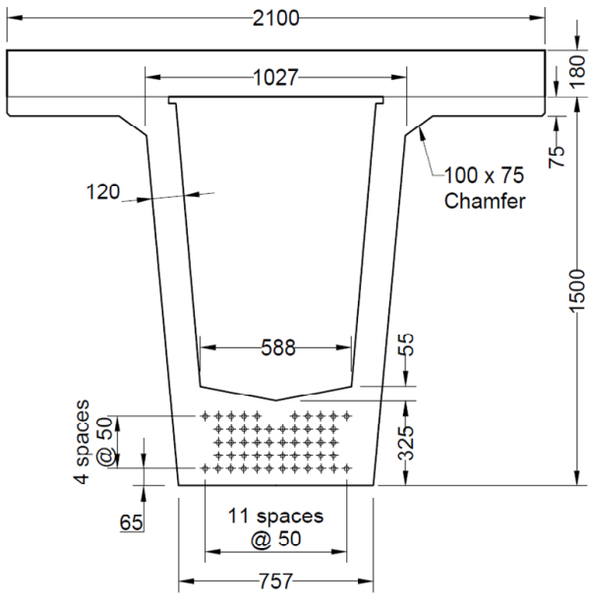


Figure 1. Strand arrangement of 56 No. 15.2 mm diameter 7-wire strands and dimension for representative girder including 180 mm *in-situ* overlay slab.

3 PERFORMANCE BY CODE

3.1 *Assessment Procedure*

In accordance to AS5100.7 (both years), the assessment of existing bridges involves determining the load rating factor (*RF*) for a given limit state, where the rating factor is expressed as:

$$RF = \frac{\text{Available capacity for traffic load effects}}{\text{Load effects of nominated rating vehicle}} \quad (1)$$

If the limit state considered is ultimate strength in bending, then the *RF* becomes:

$$RF = \frac{\phi M_R - M_D}{M^* - M_D} \quad (2)$$

where M_R is the nominal moment capacity; M^* the design moment (induced by non-traffic and the nominated rating vehicle, including all relevant factors); M_D is the design moment from all non-traffic loads (including relevant load factors); and ϕ is the capacity reduction factor. If $RF < 1$, then the bridge performance is deemed unsatisfactory.

3.2 *Loading Calculation*

Dead, superimposed dead, and traffic loads are considered for this work. The dead loads are the self-weight of the Super-T girder and a 180 mm *in-situ* concrete overlay slab. Asphalt surfacing and non-structural precast concrete edge barriers constitute the superimposed dead load (Caprani *et al.*, 2017). For traffic loads, the M1600 load model is critical and used in accordance with AS5100.2 (both years).

The bridge deck is modelled using a beam-and-slab grillage analysis, accounting for torsional stiffness of the elements. The design maximum ultimate bending moment (M^*) for the representative girder is obtained applying the relevant load factors, dynamic load allowance, and accompanying lane factors as specified in AS5100.2. As there are no differences in these factors between the 2004 and 2017 editions, M^* is the same for both codes. The design moment from all non-traffic loads (M_D) is also obtained for Equation 2. Maximum nominal values (load factors omitted) are obtained for later use in the reliability analysis. All these moment values are shown in Table 3 (Caprani *et al.*, 2017).

Table 3. Maximum bending moments for considered load components.

Load Component	Symbol	Moment (kNm)
Super-T Girder Self-Weight	M_i	2068
Girder + Overlay Slab	$M_i + M_{slab}$	3430
Superimposed Dead Load	M_{sdl}	869
Design Non-Traffic Load	M_D	5854
Traffic Load *	M_L	5154
Design ULS Load Combinations	M^*	14317

*includes dynamic load allowance and accompanying lane factors

3.3 *Capacity Calculation*

As indicated previously, the ultimate capacity of an existing concrete structure is to be estimated using AS5100.5. For ultimate strength in bending, both codes state to apply the following assumptions: (i) plane sections remain plane; (ii) concrete has no tensile strength; (iii) the distribution of compressive stress of the concrete is approximated by a rectangular stress block, and; (iv) the maximum compressive reinforcement strain does not exceed 0.003. These assumptions are depicted in Figure 2.

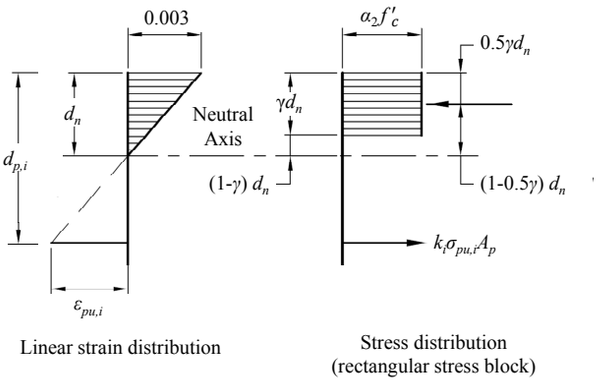


Figure 2. Strain and stress distribution assumption for ultimate bending for AS5100.5 (both editions). Concrete under compression and each row i of strands (out of n rows) are under tension. (Adapted from AS5100.5:2004).

Based on these assumption, the ultimate moment capacity (M_R) can be found from the sum of moments about the top fibre: the positive moment from the prestressed strands in tension (M_p) and a negative moment from the concrete in compression (M_c):

$$M_R = M_p - M_c \quad (3)$$

where:

$$M_p = \sum_{i=1}^{n} k_i \sigma_{pu,i} A_p d_{p,i} \quad (4)$$

in which k_i is the number of strands in row i of n rows and $d_{p,i}$ the depth from the top fibre to the centroid of the row of strands i. The ultimate stress of the strands in each row, $\sigma_{pu,i}$ is determined from strain compatibility. In general:

$$\sigma_{pu,i} = \min\left[f_{py}, \left(\varepsilon_{pe,i} + \varepsilon_{e,i} + \varepsilon_{u,i}\right) E_p \right] \quad (5)$$

where f_{py} is the yield stress of the strands, and the, prestress, decompression, and ultimate strains are:

$$\varepsilon_{pu,i} = \frac{P_j - \Delta P}{E_p A_p} \quad (6)$$

$$\varepsilon_{e,i} = \frac{k_i \left(P_j - \Delta P\right)}{E_c} \left(\frac{1}{A} + \frac{\left(d_{p,i} - y_t\right)^2}{I} \right) \quad (7)$$

$$\varepsilon_{u,i} = 0.003 \left(\frac{d_{p,i} - d_n}{d_n} \right) \quad (8)$$

Finally, the moment due to the compression block is:

$$M_c = \alpha_2 f'_c b \left(\frac{\gamma d_n^2}{2} \right) \quad (9)$$

where d_n is the depth from the top fibre to the neutral axis at ultimate, and b is the width of the top fibre.

In the parameters of the above equations there are three differences between AS5100:2004 and AS5100:2017 which are detailed next.

3.3.1 *Parameters for Rectangular Stress Block*

The parameters α_2 and γ for the rectangular stress block as shown in Figure 2 vary. For AS5100:2004, $\alpha_2 = 0.85$, and $\gamma = 0.85 - 0.007\ (f'_c - 28)$ with limits of 0.65 to 0.85. In AS5100:2017 these equations and limits were revised to better consider higher concrete grades; these are $\alpha_2 = 1 - 0.003 f'_c$ and $\gamma = 1.05 - 0.007\ f'_c$, where both parameters have limits of 0.67 to 0.85.

3.3.2 *Estimation of Yield Stress*

While the material properties for the strands may be provided by the manufacturer, AS5100.5 does provide some estimates for designers and assessors. For the yield stress of the strands (f_{py}), AS5100:2004 gives it as 85% of the breaking strength (f_{pb}), whereas for AS5100:2017, it is said to be 82% of f_{pb}.

3.3.3 *Estimation of Long-Term Prestress Losses*

A significant change from the 2004 edition of AS5100.5 are the methods for estimating long-term prestress losses (ΔP) in PSC members, particularly for time-dependent losses of concrete shrinkage and creep. AS5100.5:2004 estimates losses based on experimentally derived shrinkage and creep strains multiplied by k-coefficients to consider the environment, exposed dimensions, age of first loading, and commencement of drying of the member. Additional factors are included if any steel reinforcement in present (Gilbert *et al.*, 2015).

In AS5100:2017, the equations for the k-coefficients were revised and new coefficients were introduced to better consider higher concrete grades (Gilbert, 2002). Moreover, a new 0.8 factor for creep losses estimates was included to account for a reduction due to steel reinforcement present in the member. The shrinkage strain now includes the strain due to chemical reaction of hydration (autogeneous strain) as well as the drying strain that was previously only considered in AS5100:2004. In addition, different basic shrinkage strains are now present in AS5100:2017 to better reflect the difference in aggregates types around Australia.

The representative bridge is located in a temperate inland environment (such as near Melbourne). The long-term prestress losses (immediate and time-dependent losses 30 years after transfer) are calculated using the methods in AS5100:2004 and 2017 and are expressed as a percentage of the jacking force in Table 4. It is found that the 2004 code indicates substantially greater prestress losses, compared to the 2017 edition.

Table 4. Moment capacity calculation according to AS5100:2004 and 2017.

Description	Symbol	AS5100	
		2004	2017
Stress Block Parameters	α_2	0.85	0.805
	γ	0.65	0.67
Prestress Losses (% of P_j)	ΔP	26	20
Yield Stress (N/mm^2)	f_{py}	1500	1555
Moment Capacity (kNm)	M_R	18203	17548

3.4 *Rating Factor Performance*

The calculated girder moment capacities from the two codes are shown in Table 4. It can be seen that AS5100:2004 provides a greater design capacity than AS5100:2017. Notably, this is attributed to the higher estimation of the yield stress for the strands. For both codes, the Super-T is deep enough that all strands yield at the ultimate stage, thus a ductile failure mode results. Given these large ultimate strains, the prestress losses have no effect on moment capacity.

The *RF*s calculated for the two codes are shown in Table 5. For both codes, the capacity reduction factor for ultimate strength in bending is 0.8. It is expected that $RF > 1$ for the 2004 code because the girder was designed to this code. However, for the 2017 code, $RF < 1$, suggesting if the bridge is assessed today for the M1600 load model, the bridge performance is not satisfactory and additional investigations may be required.

Table 5. Rating factor (*RF*) performance of considered PSC girder for AS5100:2004 and 2017.

	AS5100	
	2004	2017
ϕ	0.8	
M_R (kNm)	18203	17548
M_D (kNm)	5854	
M^* (kNm)	14317	
RF	1.03	0.97

4 PERFORMANCE BY RELIABILITY

4.1 *Assessment Procedure*

The rating factor measure of performance used above as stipulated by AS5100.7 is deterministic. In reality, the material, geometric and load effects are

random in nature and can be described through probability distributions. The performance measure can be then expressed as the probability of satisfactorily performing a certain criteria over the design life. A reliability analysis provides the probability of this happening through a reliability index (Nowak & Collins, 2013):

$$\beta \approx \Phi^{-1}\left(1-p_f\right) \tag{10}$$

where Φ^{-1} is the inverse standard normal distribution function and p_f is the probability of failure. If $\beta < \beta_T$, where β_T is the target reliability index, then the bridge performance is deemed unsatisfactory.

Target reliability indices are the acceptable level of performance of the structure. The selection of a suitable target reliability index varies widely in literature, and depend on a many factors such as the criteria considered, the associated costs should the performance not be satisfactory, and the costs for improving performance (Stewart *et al.*, 2016). AS5104 (2017), recommends an annual $\beta_T = 4.4$ for ultimate limit states with a relative low costs for performance measures and major bridge structures. However, the design life for AS5100 is 100 years, hence when converted, $\beta_T = 3.7$ and thus is used for this assessment

4.2 *Limit State Function*

Limit state functions, $g(\cdot)$, describe the boundary between acceptable and unacceptable performance of the structure (Nowak & Collins, 2013). For this assessment, the limit state function is:

$$g = R - Q \tag{11}$$

where,

$$R = \varpi M_R \quad , \quad Q = M_i + M_{slab} + M_{sdl} + M_L$$

in which M_R is the moment capacity; ϖ is the model error; M_i is the moment induced from self-weight; M_{slab}, the moment induced from in-situ slab; M_{sdl}, the moment induced from superimposed dead loads, and; M_L, the moment induced from traffic load. All variables are now considered random in nature and independent to each other.

4.3 *Random Variable Distributions*

Distributions of random variables can be described using bias factors and the coefficients of variation (Nowak & Collins, 2013). The bias factor (λ) for a variable is the ratio of the mean to the nominal value, and its coefficient of variation (V) is the ratio of its standard deviation to the mean. Some of these statistical parameters are widely published in the literature.

4.3.1 *Loading Distributions*

Table 6 lists the distribution type, λ, and V for the load effect random variables. As detailed in Caprani *et al.* (2017), the bias factor for traffic load effects depends on the probability of exceedance, p, for the design code load model and V:

$$\lambda_L = \frac{1+r\delta}{1+rs_p} \tag{12}$$

where, $\delta = 0.5772\ldots$ is the Euler-Mascheroni constant, $r = \left(\pi/V\sqrt{6} - \delta\right)^{-1}$, and $s_p = -\ln\left(-\ln\left(1-p\right)\right)$.

In accordance with AS5100.1, an ultimate design action has a 5% probability of exceedance during its design life of 100 years. This is the same for both editions of the code. Thus p = 0.05 and therefore $\lambda_L = 0.75$.

Table 6. Distributions for random variables in limit state function (Equation 11)

Variable	Type	λ	V	Reference
M_i	Normal	1.03	0.08	[1]
M_{slab}	Normal	1.05	0.10	[1]
M_{sdl}	Normal	1	0.25	[1]
M_L	Gumbel (Type 1)	0.75*	0.18	[2]
R	Log-Normal	1.11	0.06	[2]

* based on a design life (100 year) probability of exceedance
[1] (Rakoczy & Nowak, 2013)
[2] This study

4.3.2 *Resistance Distribution*

There exists a range of published values for the resistance in ultimate strength in bending of PSC members (Akgul & Frangopol, 2004; O'Connor & Enevoldsen, 2008; Rakoczy & Nowak, 2013; Foster *et al.*, 2016). However, none of these previous studies have investigated the resistance of Super-T girders. Hence, to determine the probability distribution of R for the 2004 and 2017 editions, simulation methods are used.

Based on a thorough search of literature, Table 7 list the variables in Equations 3 to 9 that are concluded to be random in nature, together with their respective published distribution type, λ, and V. Model error (ϖ) is ratio of experimental capacity to capacity calculated using the predictive model (Figure 2). Therefore, it must be included in the limit state function to better represent reality. The distribution of model error was obtained by Foster *et al.* (2016) from a database of experimentally tested concrete members detailed in Foster *et al.* (2015).

MCS is performed using Equations 3 to 9 to obtain the final distribution type and parameters for ϖM_R as a random variable of both editions of AS5100.5, where the number of simulations (N) was 10^7. Using the maximum likelihood estimator, a log-normal distribution is found to be a suitable fit for

the resistance distribution—its statistical parameters are shown in Table 6. Although the nominal value, mean, and standard deviation varies between the two codes, their bias factors and coefficients of variation are approximately equal.

Table 7. Distributions for random variables in moment capacity (Equations 3 to 9).

Variable	Type	λ	V	Reference
f'_c	Log-Normal	1.084	0.154	[1]
ΔP	Normal	1	0.3	[2]
A_p	Normal	1	0.015	[3]
f_{pb}	Normal	1	0.016	[1]
$d_{p,i}$	Normal	1	0.025	[3]
ϖ	Normal	1.06	0.05	[1]

[1] (Foster *et al.*, 2016)
[2] (Mathieu, 1991)
[3] (Nowak & Collins, 2013)

4.4 *Methods for Reliability Analysis*

In this study, the reliability index (β) is computed in two ways; the first-order reliability method (FORM) and MCS using importance sampling (or IS-MCS). Further details about FORM and IS-MCS can be found elsewhere in literature (Lemaire, 2009; Melchers, 1999; Nowak and Collins, 2013). Importance sampling MCS is used, rather than naïve MCS, because the probabilities of failure to be calculated are small, requiring the number of MCS to be very large ($>10^9$) for a robust result.

4.5 *Reliability Performance*

Table 8 shows the reliability indices obtained using FORM and IS-MCS, and the corresponding probability of failures (p_f) for AS5100:2004 and 2017 for the design life of the structure. The results obtained by FORM and IS-MCS are similar, giving some confidence to the results. With both methods, the reliability index is greater for 2004 code than the 2017 code. That is, the rules in AS5100:2004 indicate the girder is performing better, compared to the rules in AS5100:2007. This is a similar result to the deterministic analysis findings. However, in both cases, the reliability indices far surpass the adopted target reliability index of 3.7. Therefore, although the performances are different, they are clearly satisfactory on this measure. This is a markedly different result to the deterministic rating factor approach.

5 CONCLUSIONS

The results of this study suggest that the deterministic assessment rating factor method in AS5100 may unreasonably conclude that a structural component is unsatisfactory, if the updated code is used for estimating capacity. This may lead to unnecessary allocation of funds for higher-tier bridge assessments, or strengthening measures to ensure the performance target ($RF \geq 1$) is met. The reason for the lower RF for the 2017 code is because of the lower estimate of the yield stress of strands. Thus, it can be argued that with more precise data about these material properties and other problem variables, a more precise RF can be obtained.

Table 8. Reliability performance (β, p_f) of the girder for AS5100:2004 and 2017 for the design life of 100 years.

Measure	Analysis	AS5100	
		2004	2017
β	FORM	5.95	5.75
	IS-MCS	5.93	5.74
p_f	FORM	1.4×10^{-9}	4.6×10^{-9}
	IS-MCS	1.5×10^{-9}	4.8×10^{-9}

But what if precise material data cannot be obtained? In this case a reliability analysis can be very useful as a direct calculation of level of safety or performance. Reliability analysis considers the uncertainty present in the relevant parameters to better determine the performance of the structure. When comparing β in Table 8 to a typical acceptable level of performance ($\beta_T = 3.7$) the results show the girder far surpasses this level. With probability of failure in the order of 10^{-9}, it suggests the performance for the girder is well beyond what are considered satisfactory limits internationally. Thus, when the uncertainty and randomness of the problem variables (including model error) are considered, otherwise unsatisfactory bridge girders can be shown to be satisfactory.

The amount by which the girder passes a reasonable performance level suggests that Australian bridge components may be performing too well. Unlike other international codes, there is no indication that the 2017 update to AS5100 was calibrated to a specific target reliability. A calibrated bridge design code is especially important when the capacity estimation for assessment is based on the bridge design rules. This Australian practice is different to other international design codes where different rules apply for the assessment of existing and the design of new bridge components, e.g. Canada.

As a relative comparison between the two code editions, the reliability index is found to be greater in the superseded code. This suggests that the 2017 revisions will lead to the design of new bridge components which perform marginally less well than those designed to the 2004 edition. This unusual result could perhaps have been avoided if a reliability basis had been adopted for the 2017 edition.

The use of probabilistic methods for bridge assessment in Australia is not facilitated in the 2017 version of AS5100.7. While the 2004 edition simply focused on the use of rating factors for performance

assessment, the 2017 edition encourages the use of higher-tier assessments. However, details on what constitutes higher-tier assessments is limited. The Austroads Project TP1952 is currently investigating appropriate methods that can be used (Ng *et al.,* 2017). The early stages of this project have suggested that probabilistic methods are one feasible approach. Indeed, this study has demonstrated the potential benefits of this approach. Moreover, a Danish study has compared the cost savings probability-based bridge assessment methods have over deterministic approaches (O'Connor & Enevolden, 2007).

Whether FORM, IS-MCS, or another method is applied, use of the reliability index for assessment of structural performance is shown in this study to be a valuable alternative to bridge ratings. Although such bridge ratings may be cheap to perform, the costs associated with decisions based on these outputs can be unnecessary. Hence, it is recommended that the next revision of AS5100 should facilitate probability-based bridge assessment, most easily by specifying a target reliability index to be achieved.

ACKNOWLEDGEMENT

The authors wish to thank Mr S. Mohanakumar and Mr G. Guo for development of coding for reliability analysis, and Mr T.M.T. Lui for his grillage analysis model. This research work was completed under a Noel Murray Scholarship at Monash University and supported by the Australian Government Research Training Program Scholarship.

REFERENCES

Akgül, F. & Frangopol, D.M., 2004. Lifetime performance analysis of existing prestressed concrete bridge superstructures. Journal of Structural Engineering, 130(12), pp.1889–1903.

Akgül, F. & Frangopol, D.M., 2003. Rating and reliability of existing bridges in a network. Journal of Bridge Engineering, 8(6), pp.383–393.

Caprani, C.C., Melhem, M.M. & Siamphukdee K, 2017. Reliability Analysis of a Super-T Prestressed Concrete Girder at Serviceability Limit State to AS 5100:2017. Australian Journal of Structural Engineering, 18(2), pp.60–72.

Cremona, C., 2013. Structural Performance, London: John Wiley & Sons.

Foster, S.J. et al., 2016. Calibration of reinforced concrete structures Standard AS3600 Part I : Statistical analysis of material properties and model error. Australian Journal of Structural Engineering, 14(4), pp.242–253.

Foster, S.J. et al., 2015. UNICIV Report R-464: A Re-evaluation of the Safety and Reliability Indicies for Reinforced Concrete Structures Designed to AS3600, UNSW, Australia.

Gilbert, R.I., Mickleborough, N.. & Ranzi, G., 2015. Design of Prestressed Concrete to AS3600-2009, Boca Raton: CRC Press.

Gilbert, R.I., 2002. Creep and shrinkage models for high strength concrete – proposals for inclusion in AS3600. Australian Journal of Structural Engineering, 4(2), pp.95–106.

Hilton, J., 2017. The New AS 5100.5. In Austroads Bridge Conference.

Lemaire, M., 2009. Structural Reliability, Hoboken: John Wiley & Sons.

Mathieu, H., 1991. Reliability Problems Associated with Prestress. In Reliability of Concrete Structures. Lausanne: Comite Euro-International Du Beton (CEB), pp. 99–163.

Melchers, R.E., 1999. Structural Reliability Analysis and Prediction, Chichester: John Wiley & Sons.

Ng, A., Rooke, A. & Pape, T., 2017. Austroads Project TP1952 – Higher order assessments for existing bridges. In Austroads Bridge Conference.

Nowak, A.S. & Collins, K.R., 2013. Reliability of Structures 2nd ed., Boca Raton: CRC Press.

O'Connor, A. & Enevoldsen, I., 2008. Probability based modelling and assessment of an existing post-tensioned concrete slab bridge. Engineering Structures, 30, pp.1408–1416.

O'Connor, A. & Enevoldsen, I., 2007. Probability-based bridge assessment. Bridge Engineering, 160(BE3), pp.129–137.

Pritchard, R., 2017a. 2017 Revision of Australian Standard AS 5100 Part 1 – Scope and General. In Austroads Bridge Conference.

Pritchard, R., 2017b. Revision of Australian Standard AS 5100 Part 7 : Bridge Assessment. In Austroads Bridge Conference.

Standards Australia, 2009. AS 3600-2009: Concrete structures, Sydney: Standards Australia.

Standards Australia, 2017a. AS 5100.1-2017: Bridge design - Scope and general principles, Sydney: Standards Australia.

Standards Australia, 2017b. AS 5100.2-2017: Bridge design - Design loads, Sydney: Standards Australia.

Standards Australia, 2004a. AS 5100.5-2004: Bridge design - Concrete, Sydney: Standards Australia.

Standards Australia, 2017c. AS 5100.5-2017: Bridge design - Concrete, Sydney: Standards Australia.

Standards Australia, 2004b. AS 5100.7-2004: Bridge design - Rating of existing bridges, Sydney: Standards Australia.

Standards Australia, 2017d. AS 5100.7-2017: Bridge design - Bridge assessment, Sydney: Standards Australia.

Standards Australia, 2017e. AS 5104: General Principles on Reliability for Structures, Sydney: Standards Australia.

Stewart, M.G. et al., 2016. Calibration of Australian Standard AS3600 concrete structures part II: reliability indices and changes to capacity reduction factors. Australian Journal of Structural Engineering, 17(4), pp.254–266.

Wiśniewski, D.F., Casas, J.R. & Ghosn, M., 2012. Codes for Safety Assessment of Existing Bridges — Current State and Further Development. Structural Engineering International, 4, pp.552–561.

Maintenance, Safety, Risk, Management and Life-Cycle Performance of Bridges – Powers, Frangopol, Al-Mahaidi & Caprani (Eds)
© 2018 Taylor & Francis Group, London, ISBN 978-1-138-73045-8

Coupling finite elements to model steel to concrete bond

R.J. Gravina
School of Engineering, RMIT University, Melbourne, Australia
L.A.G Bitencourt Jr. & L.C. Meneghetti
Polytechnic School at the University of Sao Paulo, São Paulo, Brazil

ABSTRACT: There are several bond performance tests that are commonly used for steel reinforcement in concrete namely, bar pull-out test, beam bond test, beam end bond test. Experimental testing can be time consuming and material consumption is high, hence numerical models of the bond behavior of steel bar to concrete have been developed that can provide opportunity to simulate multiple parameters efficiently and cost effectively. The numerical analysis allows for the local bond stress and slip characteristics to be determined. Local bond stress versus slip relationships are needed to be able to simulate the behavior and deformations of concrete infrastructure, such as bridges under various loading conditions and environments using finite element analysis techniques. This paper presents a numerical model that adopts coupling finite elements to represent the contact behavior of steel to concrete. The ability of the numerical model to simulate the bond is compared to experimental results from a series of beam bending bond tests.

1 INTRODUCTION

The bond between concrete and its reinforcement is highly dependent on several major factors (*fib* bulletin 10, 2000; ACI 408R-03, 2003): i) chemical adhesion between the bars and the concrete – the chemical adhesion is provided by the cement and is created during the hydration process; ii) mechanical interlock involves the transfer of load between concrete and its reinforcement by means of a bearing interlock of the ribs against the concrete surface; iii) surface friction that is created from the roughness of the interface - is the force that resists motion, or more accurately, slip of the bar under loading conditions. Another aspect that highly influences the performance of reinforced concrete is the length of the bonded region of the reinforcing bar within the concrete element. Providing insufficient bond lengths will restrict the section in achieving its maximum debonding resistance.

Generally, bond failure of a steel reinforced concrete occurs over three stages. Firstly, the reinforced concrete element sustains a particular level of bond stress which is primarily attributed to the adhesive component of the bond. Once the peak bond stress has been obtained and cracking of the concrete has started, the adhesive component of bond has been overcome and mechanical interlock between the deformations of the bar and the surrounding concrete commences. This mechanical interlock continues until excessive local slip occurs such that the concrete between the bar deformations has sheared off. At this stage, only frictional component of bond remains until complete bond failure occurs (Haskett et al., 2008). In addition, with the primary cause of failure in structural applications related to splitting cracks, it follows that the concrete tensile strength would be one of governing factors related to the bond strength (Jones & Ramirez, 2016).

In addition to the major factors discussed above, the bond of steel reinforcement is also dependent on the compressive strength, the geometry of the concrete member and the bar placement in the member cross-section. However, fully anchored steel reinforcing bars are much more likely to yield before debonding.

The bond tests available in the literature can be divided according to the type of test: beam tests and pull-out tests. Pull-out tests are simple and have a good accuracy, since some care must be taken for the usual parameters (development length, concrete cover and bar diameter) for a correct evaluation of the real case (Almeida Filho et al., 2008). However, in the beam test, the concrete around the bar is also in tension, better simulating the real stress conditions of the flexure elements.

In this paper, a numerical model that adopts coupling finite elements developed by Bitencourt Jr. et al. (2015) to represent the contact behavior of steel to concrete is presented. The ability of the numerical model to simulate the bond is compared to experimental results from a series of beam bending bond tests.

2 NUMERICAL MODEL

In this section, the numerical model to describe the interaction between the steel bars and concrete based on the use of coupling finite elements (CFEs) is presented.

The procedure to describe the numerical model is depicted in Figure 1. Initially, concrete and steel bars are discretized in finite elements in a totally independent way (non-conforming meshes). Herein, three-node triangular finite elements and two-node truss finite elements were employed to represent concrete and steel bars. Then, CFEs are inserted in order to couple the initially independent meshes (see Figure 1(c)).

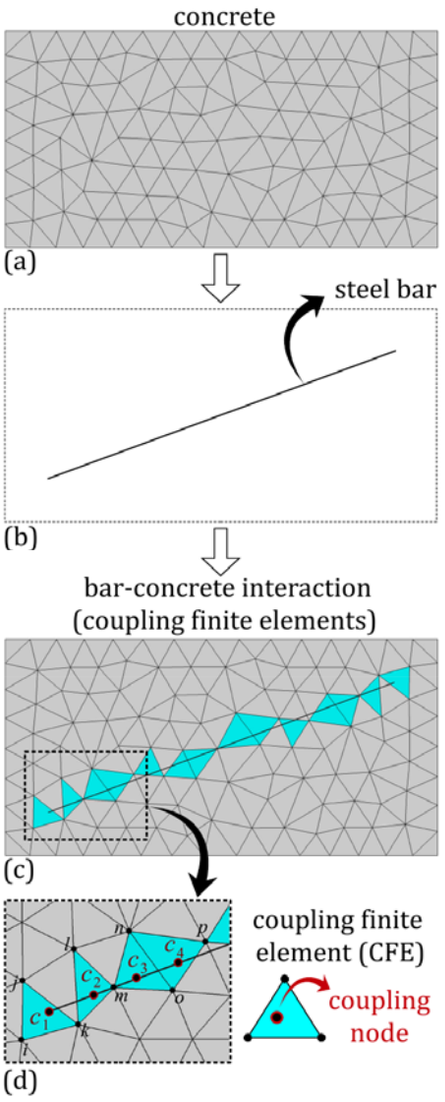


Figure 1. Coupling procedure for non-matching finite element meshes: (a) discretization of the concrete in FEs; (b) generation and discretization of the steel bar; (c) creation and insertion of the CFEs; (d) detail of the coupling in overlapping meshes.

As can be seen in Figure 1 (d), each CFE has the same nodes of a underlying finite element of the existing mesh and an extra node, coinciding with the loose node (this node is called the coupling node) that belongs to its domain. As a consequence, the CFEs overlap the finite elements of the original mesh around the coupling nodes "c_i". Note that for each loose node, one coupling finite element is required, as for example, $CFE_1=\{i,j,k,c_1\}$; where c_1 is the coupling node 1.

After the application of the coupling procedure (Figure 1 (c)), the global internal force vector and the stiffness matrix can be written as:

$$\mathbf{F}^{\text{int}} = \mathrm{A}_{e=1}^{\text{nel}\,\Omega_C}\left(\mathbf{F}_e^{\text{int}}\right)_{\Omega_C} + \mathrm{L} + \mathrm{A}_{e=1}^{\text{nel}\,\Omega_{SF}}\left(\mathbf{F}_e^{\text{int}}\right)_{\Omega_{SF}} + \mathrm{A}_{e=1}^{\text{nel}\,CFE}\left(\mathbf{F}_e^{\text{int}}\right)_{\Omega_{CFE}} \quad (1)$$

$$\mathbf{K} = A_{e=1}^{nel\,\Omega C}\left(\mathbf{B}_e^T\right)_{\Omega_C}\left(\mathbf{C}_{tg}\right)_{\Omega C}\left(\mathbf{B}_e\right)_{\Omega_C} + \mathrm{L} + A_{e=1}^{nel\,\Omega SF}\left(\mathbf{B}_e^T\right)_{\Omega_{SF}}\left(\mathbf{C}_{tg}\right)_{\Omega_{SF}}\left(\mathbf{B}_e\right)_{\Omega_{SF}} + A_{e=1}^{nel\,\Omega CFE}\left(\mathbf{B}_e^T\right)_{\Omega_{CFE}}\left(\mathbf{C}_{tg}\right)_{\Omega_{CFE}}\left(\mathbf{B}_e\right)_{\Omega_{CFE}} \quad (2)$$

2.1 *Steel bar/concrete interaction*

Consider the 4-node triangular coupling finite element (see Figure 2) constructed by the standard three-node triangular finite element and an additional bar node that belongs to its domain.

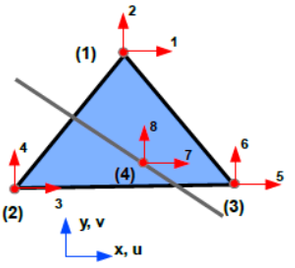


Figure 1. Steel bar/concrete interaction using 4-node coupling finite element.

The relative displacement $\left([[\mathbf{U}]]\right)$ can be defined as the difference between the displacement of the coupling node (C_{node}) and the displacement of the material point at the same position of the bar node $\left(\mathbf{X}_{C_4}\right)$:

$$\begin{aligned}\left[\left[\mathbf{U}\right]\right] &= \mathbf{D}_4 - \bar{\mathbf{U}}\left(\mathbf{X}_{C_4}\right) \\ &= \mathbf{D}_4 - \sum_i^3 \bar{N}_i\left(\mathbf{X}_{C_4}\right)\mathbf{D}_i = \mathbf{B}_e\mathbf{D}_e\end{aligned} \tag{3}$$

where, $\mathbf{D}_4$ stores the displacement components of the bar node, $\bar{N}_i\left(\mathbf{X}_{C_4}\right)$ $(i=1,3)$ are the shape functions of the underlying finite element (concrete), evaluated at point $\mathbf{X}_{C_4}$, and $\mathbf{D}_e$ stores the displacement components of the CFE.

Assuming a linear elastic model to describe steel bar/concrete interaction, the relation between the reaction force ($\mathbf{F}\left(\left[\left[\mathbf{U}\right]\right]\right)$) (owing to the relative displacement ($\left[\left[\mathbf{U}\right]\right]$) and the relative displacement is given by:

$$\mathbf{F}\left(\left[\left[\mathbf{U}\right]\right]\right) = \mathbf{C}\left[\left[\mathbf{U}\right]\right] = \mathbf{C}\mathbf{B}_e\mathbf{D}_e \tag{4}$$

where $\mathbf{C}$ is the matrix of elastic constants that assume very high values when perfect adherence is considered.

$$\mathbf{C} = \begin{bmatrix} C & 0 \\ 0 & C \end{bmatrix} \tag{5}$$

Since the relative movement of the reinforcement with respect to the concrete matrix is in essence a sliding in the direction of the reinforcement axis, it is necessary to use a local coordinate system (**n**,**s**), oriented such that the axis **n** coincides with the reinforcement axial orientation.
Thus, the relative displacement and its corresponding reaction force can be expressed as $\left[\left[\mathbf{u}\right]\right] = \mathbf{R}\left[\left[\mathbf{U}\right]\right]$ and, respectively $\mathbf{f} = \mathbf{R}\mathbf{F}$, where is the orthogonal rotation matrix between the local and global reference systems. The loss of adherence model can be easily represented by assuming an elastic constitutive model with distinct elastic constants, according to the local coordinate system:

$$\mathbf{C} = \begin{bmatrix} c_n & 0 \\ 0 & c_s \end{bmatrix} = \begin{bmatrix} c_n & 0 \\ 0 & C \end{bmatrix}, \quad c_n << C \tag{6}$$

The interaction force between the concrete matrix and the steel reinforcement, at coupling node, one may consider that this force results from the bond (shear) stress, τ, on the bond area (reinforcement-matrix interface) in the vicinity of the coupling node. Therefore, by assuming that the bond (shear) stress is constant in the vicinity of the node and that the size of the vicinity (influence length) that contributes to the resultant force in a specific node corresponds to the average of the half distances between the node "i" and its adjacent nodes of the reinforcement "j" and "k", the interaction force may be expressed as:

$$f_n = \tau(\left[\left[u_n\right]\right])PL \tag{7}$$

where $L = (L_{ij} + L_{jk})/2$ is the influence length and P is the perimeter of the reinforcement cross-section. Note that the slip, s, is given by the relative displacement in direction **n**, i.e., $s = \left[\left[u_n\right]\right]$. The remaining transverse component of the resultant force can be expressed as:

$$f_s = \beta(\left[\left[u_s\right]\right])PL \tag{8}$$

Finally, a constitutive model based on the continuum damage theory may be used to describe the constitutive relationship between the shear stress (adherence stress) and the relative sliding. Thus, the damage model can be described by the following equations:

$$\begin{aligned}
&\tau = (1-d)\bar{\tau} && \text{(constitutive relation)} \\
&\bar{\tau} = c_n\left[\left[\mathbf{u}\right]\right] && \text{(effective shear stress)} \\
&\phi = \|\tau\| - r \le 0 && \text{(damage criterion)} \\
&r = \max[\tau] && \text{(evolution law of the internal variable)} \\
&d = 1 - \frac{q(r)}{r} && \text{(evolution of the damage variable)}
\end{aligned} \tag{9}$$

where c_n is the elastic stiffness constant (unit of stress per unit of length), $d \in [0,1]$ is the scalar damage variable, $\bar{\tau}$ is the effective shear stress, and r is the strain-like internal variable that assumes the maximum value reached by $\bar{\tau}$ during the load process. The function $q(r)$ represents the hardening/softening law of the constitutive model, and it may be adjusted to fit any bond slip model of type $\tau(s)$, considering the relationship $q(r) = \tau(r/c_n)$.
Taking as an example the bond-slip relationship proposed by the CEB *fib* Model Code, depicted in Figure 3 and described by the equations:

$$\tau(s)=\begin{cases}\tau_{\max}\left(\dfrac{s}{s_1}\right)^{\alpha} & \text{if} \quad s\le s_1\\ \tau_{\max} & \text{if} \quad s_1<s\le s_2\\ \tau_{\max}-\dfrac{(\tau_{\max}-\tau_f)(s-s_2)}{s_3-s_2} & \text{if} \quad s_2<s\le s_3\\ \tau_f & \text{if} \quad s>s_3\end{cases}, \tag{10}$$

the corresponding hardening/softening law is defined in terms of the stress- and strain-like internal variable as:

$$q(r)=\begin{cases}\tau_{\max}\left(\dfrac{r/c_n}{s_1}\right)^{\alpha} & \text{if} \quad r/c_n\le s_1\\ \tau_{\max} & \text{if} \quad s_1<r/c_n\le s_2\\ \tau_{\max}-\dfrac{(\tau_{\max}-\tau_f)(r/c_n-r_2)}{s_3-s_2} & \text{if} \quad s_2<r/c_n\le s_3\\ \tau_f & \text{if} \quad r/c_n>s_3\end{cases}, \tag{3}$$

where α, $\tau_{\max}$, τ_f and $s(i=1=1,2,3)$ are the parameters of the model, which depend on the concrete strength f_{ck}, the bar geometry (ribbed or smooth), the confining situation (confined or unconfined) and bond condition (good or poor), according to the CEB *fib* Model Code.

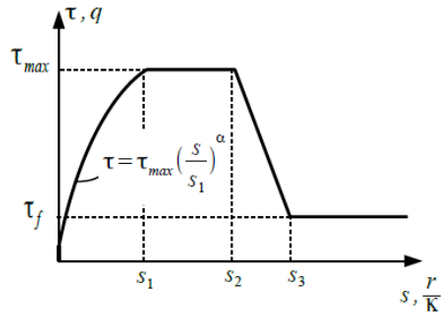
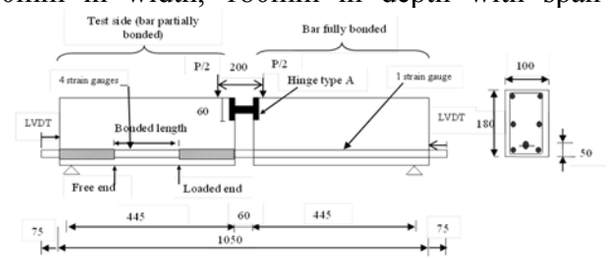


Figure 2. Interface stress bond-slip relationship (monotonic loading) proposed by CEB fib Model Code.

3 EXPERIMENTAL PROGRAM

3.1 *Test beam design and fabrication*

Beam bond tests specimens were reinforced concrete beams vertically loaded with a steel hinge at the top and the specimen separated at mid span to allow control of the internal force distribution (see Figure 4). Strain gauges were placed along the steel bar in the bonded region, which were used to determine strain and calculate slip at locations along the bar. Transducers were placed at the end of the bar to measure free-end slip. Two beam types were tested, for type B1 one side of the beam was be the test region and the other side was be fully bonded to ensure that bond failure occurs in the instrumented region. For beam type B1' there were two test sides where the bar was only partially bonded. The dimensions of both beams were 100mm in width, 180mm in depth with span of



1050mm. The target concrete compressive strength for the mix design was 35MPa. Deformed steel reinforcement as main tensile reinforcement of bar diameter 16mm and characteristic yield strength of 450MPa was used.

Figure 3. Beam B1 specimen details

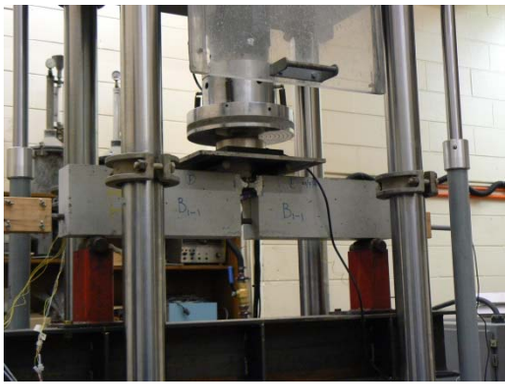


Figure 5. Beam B1 specimen

4 NUMERICAL ANALYSIS

In this section, the numerical model developed to simulate the behavior of the bending bond tests is presented. The results are also compared with those obtained in the experimental tests performed at the RMIT University.

4.1 *Description of the numerical model*

The tests involves two half-beams with a cross-section of 100x180mm², connected at the top by a steel hinge and at the bottom by the tested reinforcing bar with a diameter of 16mm embedded in concrete.

The concrete is assumed to be linearly elastic with Young's modulus of 34GPa and Poisson' ratio of 0.2. The steel bar is elastic perfectly plastic, with Young's modulus of 200GPa and yield stress of 450MPa. In the

region where bonded is considered a no n-rigid coupling procedure is applied to described the bond-slip behavior between the concrete and rebar with a continuum damage model adjusted to the CEB-FIP model code for good bond conditions (f_c=32MPa). Based on this strategy, the properties of the interface material adopted were: τ_{max}=9.0MPa; τ_f =0.4; s_1=0.6; s_2=0.6; s_3=6.0.

4.2 *Numerical Simulation of the bending bond tests*

Figures 6 and 7 display the discretized mesh and coupling finite elements adopted in the numerical analysis.

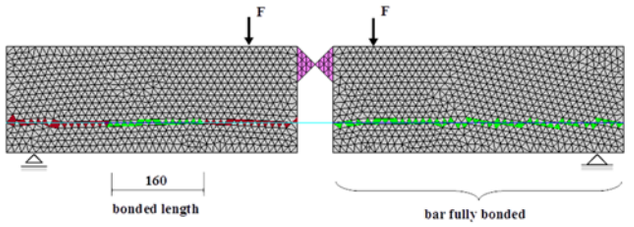


Figure 6. Beam B1

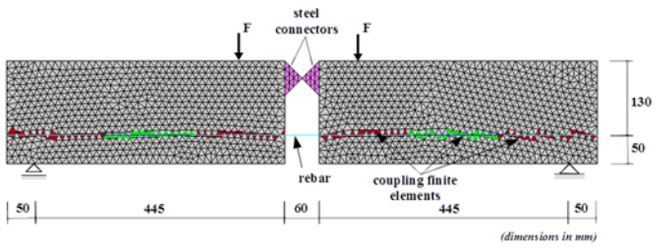


Figure 7. Beam B1'

The following graphs represent the ability of the numerical model to simulate the bond behaviour response by comparing the numerical results with results obtained in the experimental tests performed at the RMIT University. Figures 8 and 9 show the applied load vs mid span deflection, Figures 10 and 11 load vs bar end slip, and Figures 12 and 13 left slip vs tensile bar strain, and load vs tensile bar strain at strain gauge positions 1, 2 and 3, respectively in the bonded steel bar region comparisons. The numerical model has the capability to simulate the bond behaviour between steel bars and concrete with reasonable accuracy.

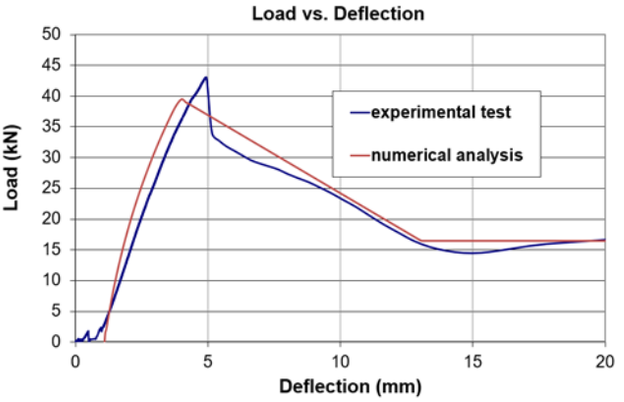


Figure 8. Load vs mid span deflection Beam B1

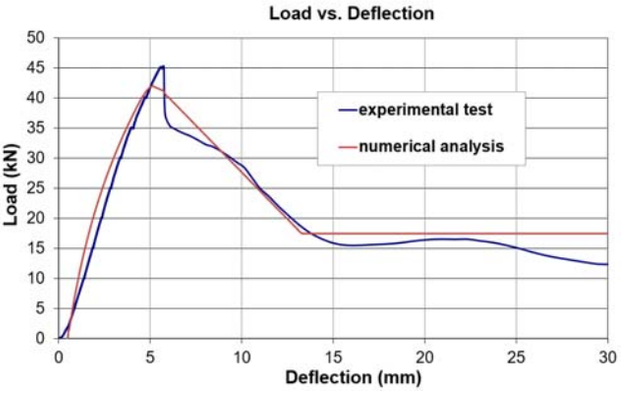


Figure 9. Load vs mid span deflection Beam B1'

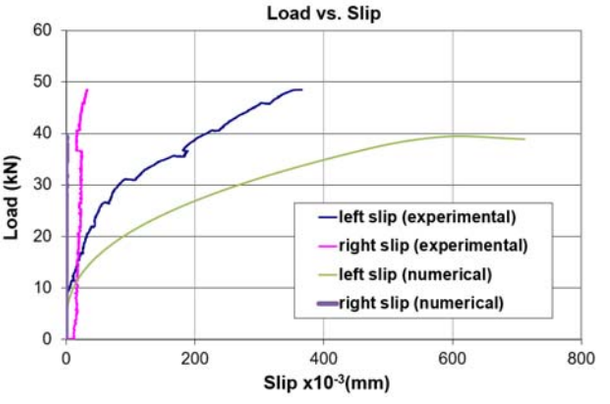


Figure 10. Load vs bar end slip Beam B1

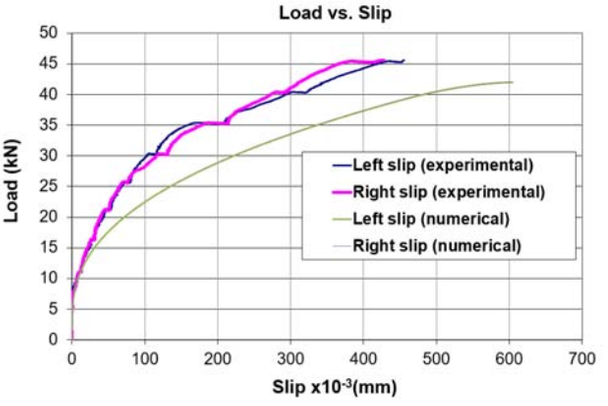


Figure 11. Load vs bar end slip Beam B1'

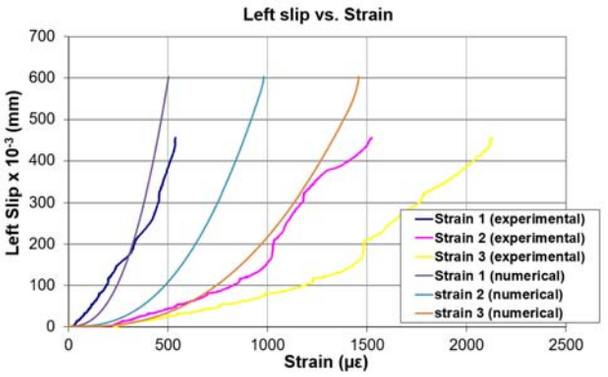


Figure 12. Left slip vs tensile bar strain Beam B1'

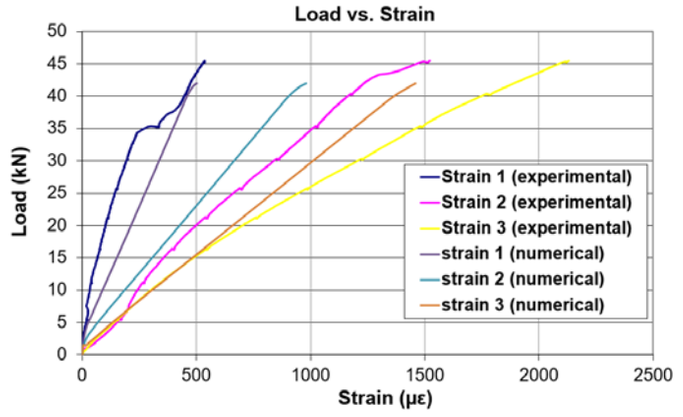


Figure 13. Load vs tensile bar strain Beam B1'

5 CONCLUSIONS

This paper presents a numerical model that adopts coupling finite elements to represent the contact behavior of steel to concrete. The ability of the numerical model to simulate the bond is compared to experimental results from a series of beam bending bond tests.

6 REFERENCES

Almeida Filho et al. 2007. Bond-slip behavior of self-compacting concrete and vibrated concrete using pull-out and beam tests. *Materials and Structures* 41: 1073-1089.

American Concrete Institute. 2012. Bond and development of straight reinforcing bars in tension, ACI 408R-03. Michigan, American Concrete Institute.

Bazant, Z.P. 1986. Mechanic of distributed cracking. Applied Mechanics Review, v.39, n.5, p.675-705.

Bitencourt Jr. et al. 2015. A coupling technique for non-matching finite element meshes. Computer Methods in Applied Mechanics and Engineering, 290:19-44.

Comite Euro-International du Beton. 2000. Bond of reinforcement in concrete. Boletim nº 10. Lausanne: Comite Euro-International du Beton.

Comite Euro-International du Beton. 2013. Model code for concrete structures 2010. MC2010. Lausanne: Comite Euro-International du Beton.

Haskett et al. 2008. Local and global bond characteristics of steel reinforcing bars. *Engineering Structures* 30: 376-383.

Jones & Ramirez. 2016. Bond of reinforcement in high-strength concrete. *ACI Structural Journal* 113(6): 549-556.

Maintenance, Safety, Risk, Management and Life-Cycle Performance of Bridges – Powers, Frangopol, Al-Mahaidi & Caprani (Eds)
© 2018 Taylor & Francis Group, London, ISBN 978-1-138-73045-8

Shear and Torsion Design Review – Australian and International Standards

T. Hossain; S. Mikhael; A. Chaudry & S. Mohanakumar
ARCADIS, Melbourne, Australia

ABSTRACT: The shear and torsion design provision of the Australian Bridge Design Standard AS5100.5 has been revised significantly in 2017 and is now based on the Modified Compression Field Theory (MCFT). The MCFT approach is based on the equilibrium, compatibility and stress-strain characteristics of cracked concrete. The previous Australian Standard provisions, based on the parallel-chord truss model, considered the design effects of shear and torsion separately and are added later for reinforcement calculations. The cracked concrete capacity is also ignored under high shear and torsion. This is inconsistent to the true beam behavior and could lead to unsafe results for certain beams or underestimated capacity in other cases.
The Australian bridge stock includes bridges designed or strengthened to previous national design Standards including, apart from the recently replaced AS5100-2004, the Australian Bridge Design Code ABDC 1992 and the National Association of Australian State Road Authorities NAASRA 1976 Standard. The question that arises at this moment is where do these bridges stand as to their shear strength compared to a more consistent and accurate Standard provision and does the new Australian Standards' shear provision really indicate any strength issue that needs to be addressed? A review of the main areas of differences with the previous Standards provisions is presented in this paper with a comparison with those of other international Standards, mainly the AASHTO and the Canadian Standards. Comparison is also made with tested capacities of a limited number of published test results. Areas of major differences with the previous Standards that may affect the existing bridge stock are highlighted and a conclusion is drawn.

1 INTRODUCTION

Over the last few decades, great progress has been made in the analytical solution for shear and torsion design rules in concrete bridges. However, most of these highly sophisticated tools require considerable simplification to make them suitable for codes of practice. In addition, high-strength concrete has been increasingly used in the construction industry during the last few years, and any shear and torsion design procedure should be applicable across the wide range of concrete grades.

Many structural components in bridges are subjected to significant torsion in combination with shear that are critical in design. The previous Australian Code (AS5100-2004) was based on semi-empirical equations chosen to fit the available experimental data. On the other hand, the current Australian bridge standard (AS5100-2017), American bridge code (AASHTO LRFD 2012) and Canadian Standards (CSA 2014) offer two alternative design methods for shear and torsion. The first approach, referred to as the "simplified method", is based on the traditional semi-empirical models. The second approach, referred to as the "General Method", is a simplification of a more rational model named the Modified Compression Field Theory (MCFT). The MCFT is a powerful rational model capable of calculating the full response of sections subjected to shear, axial load, bending and torsional moments (Vecchio and Collins 1986, 1988, Collins and Mitchell 1991). It is noted that the above-mentioned specifications often give significantly different values of calculated ultimate shear strengths.

The objective of this study is to investigate the differences between the AS5100, AASHTO and CSA approaches for shear and torsion design provisions of concrete beams and to evaluate how well they represent the actual beam behavior through a series of statistical comparisons. The studies are made to compare the predicted strengths by using the national and international code approaches with nine (6) physical test results of reinforced concrete beams available from published experimental research.

2 REVIEW OF MCFT

The Modified Compression Field Theory, MCFT, is a shear model developed by Vecchio and Collins (1986), which is based on a variable angle truss model. The MCFT is a behavioral model that can be used to predict the shear stress and shear-strain response of an element subjected to in-plane shear and membrane forces. The formulation of MCFT includes equilibrium, strain compatibility, and a constitutive relationship for diagonally cracked concrete that enable determination of the state of stress (f_x, f_y, v_{xy}) in structural concrete corresponding to a specific state of strain (ε_x, ε_y, γ_{xy}). Using these principles, the MCFT accounts not only for Vs, but also the combined effect of the complex

shear resistance mechanisms that contribute to V_c without having to consider each mechanism individually. The theory considers cracked concrete as a material with its own stress-strain characteristics and accounts for tensile stresses in the concrete between cracks from the aggregate interlock mechanisms.

This method requires the calculation of the actual angle θ, and the crushing strength of the concrete struts. The crushing strength is a function of the tensile strain perpendicular to the strut. As with plasticity analyses, the MCFT predicts that a variable angle strut model will provide conservative estimates of shear strength over a relatively wide range of angles. For a particular design shear stress, a lower limit on θ is set to avoid crushing of the concrete in diagonal compression, while the upper limit on θ ensures yielding of the links. As the shear stress levels increase, the feasible range of angles becomes smaller.

All equations presented in this paper are in SI unit.

3 DISCUSSION OF CODE PROVISIONS

The authors reviewed several widely used shear-design methods, and the basis of these methods, for the purpose of identifying differences among these methods as well as positive attributes to be considered for incorporation into the AASHTO LRFD specifications' new simplified shear-design provisions. The reviewed methods were those in 2012 2012 AASHTO standard specifications, Canadian Standards Association's (CSA's) Design of Concrete Structures (CSA A23.3-94) and Australian Standard, both the previous 2004 and the latest 2017 revision.

3.1 *AASHTO LRFD 2012*

The general procedure of the AASHTO LRFD specifications is based on the Sectional Design Method (SDM) that provides a hand-based shear design procedure derived from MCFT in a simplified manner. In this procedure, the nominal longitudinal strain in the web ε_s and the shear stress are calculated. The shear strength is a function of 2 parameters θ the diagonal shear crack angle, and β that depend on longitudinal strain ε_s at the cross-section of interest and are illustrated in Equation 1 and 2 below:

θ = diagonal shear crack angle
$= 29 + 3500\ \varepsilon_s$
(1)

β = factor to measure the ability of cracked concrete to transmit shear stress across crack,

$$= \left(\frac{0.4}{1+750\varepsilon_s}\right)\left(\frac{1300}{1000+s_{xe}}\right) \quad (2)$$

where the first term models the strain effect and the second term models the size effect. This equation primarily derives from the aggregate interlock relationship. The effective crack spacing in the size effect term, s_{xe}, which accounts for the influence of aggregate size, a_g, is:

$$S_{xe} = S_x\left(\frac{35}{a_g+16}\right) \quad (3)$$

where s_x = crack-spacing parameter, the lesser of either d_v or the maximum distance between layers of longitudinal crack-control reinforcement.

AASHTO simplifies the MCFT by direct use of ε_s, the strain in the section at the level of the longitudinal tensile reinforcement, in the above equations instead of the strain at mid-depth ($\varepsilon_x = \varepsilon_s/2$) as is in the original MCFT. The strain in the ε_s for sections with prestressing tendons is computed by Equation 4:

$$\varepsilon_s = \frac{\frac{|M_u|}{d_v} + 0.5N_u + |V_u| - A_{ps}f_{po}}{E_sA_s + E_pA_{ps}} \quad (4)$$

Where M_u, V_u, and N_u are the factored moment and shear and the axial force (tension positive) at the section of interest. While V_p is the component of prestress force in the direction of shear and As, Es, Ap, Ep are the areas and Young's moduli of the regular and bonded prestressed reinforcement respectively. The term f_{po} is the stress in the prestressing reinforcement when loaded to an extent that the strain in the surrounding concrete is equal to zero. If the value of ε_s calculated is negative, account for the compressive stiffness of the concrete in the flexural tension flange is taken by adding the term E_cA_c to the reinforcement stiffness in the denominator.

The concrete contribution V_c to the shear capacity is controlled by the value of the coefficient β as illustrated by Equation 5 below:

$$V_c = 0.083\beta\sqrt{f'_c}\,b_v\,d_v \quad (5)$$

where f'_c = concrete compressive strength; b_v = effective web width; d_v = effective shear depth measured perpendicular to the neutral axis between the resultants of tensile and compressive forces due to flexure and ≥ greater of 0.9 x effective depth (d_e)or 0.72 x total depth (h).

3.2 *CSA 2014*

The CSA shear-design provisions are essentially the same as the AASHTO LRFD specifications except one significant difference of using longitudinal strain at mid-depth $\varepsilon_x = \varepsilon_s/2$ in the equations. The transverse shear reinforcement helps a member evenly distribute the shear stresses in cracked concrete; therefore, calculating strain at the level of the longitudinal reinforcement as in AASHTO is conservative. For members with transverse reinforcement, the CSA code suggests the factor controlling the contribution of the concrete β and θ as below:

$$\beta = \left(\frac{0.4}{1+1500\varepsilon_x}\right)\left(\frac{1300}{1000+s_{xe}}\right) \quad (6)$$

$$\theta = (29 + 7000\ \varepsilon_x)\ (0.88 + s_{xe}/2500) \quad (7)$$

The longitudinal strain ε_x at mid-depth is computed by Equation 8:

$$\varepsilon_x = \frac{\frac{|M_u|}{d_v} + 0.5N_u + |V_u| - A_{ps}f_{po}}{2(E_s A_s + E_p A_{ps})} \quad (8)$$

The concrete contribution V_c in CSA code is illustrated by Equation 9.

$$V_c = 2.5\beta f_{cr} b_v d_v \quad (9)$$

where $f_{cr} = 0.4\sqrt{f'_c}$ is the cracking strength of normal-strength concrete.

3.3 *AS5100.5-2004*

The empirical shear design provisions based on variable angle truss model in 2004 Australian Standard had their roots in the 45° parallel-chord truss model proposed by Ritter and Mörsch and was applicable for normal-strength concrete up to 65MPa compressive strength. The concrete contribution is a function of the type of shear cracking that controls (flexure-shear or web-shear) at a given cross-section. It also accounts for the axial compressive or tensile force in the section.

The 2004 standard considered the effects of shear and torsion separately with the effects additive which was somewhat incongruous to the beam behavior leading to unusual results particularly beam with high torsion loads. The concrete contribution to shear was based on empirical equation assuming shear stress remains constant over the depth of the web.

3.4 *AS5100.5-2017*

The basic expression used in the AS5100 at 2017 revision is similar to the CSA based on the MCFT where the distribution of shear stresses is assumed at mid depth of the effective shear section of interest. The only difference is with respect to the diagonal shear crack angle θ, which is a function of the longitudinal strain ε_x only unlike the CSA provision. Due to the smoother crack faces where cracks pass through, rather than around aggregate particles, and the resulting larger variability in the shear resistance of members with higher strength concrete, both AS5100 and CSA limits the concrete compressive strength f'_c to maximum of 65 MPa.

In the 2017 edition, for sections subject to combined actions of shear and torsion, torsion is accounted for by adjusting the value of shear stress and β and θ selected and ε_x calculated using the increased shear stress values. This approach is similar to what specified in the latest CSA and AASHTO standards. The reinforcement required for torsion is calculated separately, with θ selected using values of shear force and shear stress adjusted for torsion, and added to the reinforcement required for shear. It seems illogical that 2 different values of θ are used for sections subject to shear and torsion.

4 REVIEW OF PREVIOUS EXPERIMENTAL STUDY IN SHEAR & TORSION

In order to evaluate the accuracy of AS5100-2004, AS5100-2017, AASHTO and CSA it is imperative that the calculated results are compared against highly acclaimed experimental results. There were 2 particular test series that were adopted in this comparison: the first test series was performed by Arbesman which simulated two beam specimens (SA3 and SA4) (Gregori et al. 2007). These specimens were RC rectangular hollow sections and were tested under pure shear. The second test series was performed by Rahal and Collins, which simulated four beam specimens (RC2-2, RC2-4, RC2-1 and RC2-3) (Rahal & Collins 2003). These specimens were RC rectangular solid sections and were tested under combined shear and torsion. The RC2 specimens were part of a grid of beams. The central longitudinal beam was 6 m in length, with two transverse beams of 3 m length with the same section dimensions (as shown in Table 1). The test region was the region between the two transverse beams and was 2 m in length. The test beam was loaded with three actuators, supported on three spherical bearings with two actuators inducing torsional action and one inducing shear action.

The relevant material properties and section dimensions of the above-mentioned sections are listed in Table 1:

Table 1: Experimental Sections

	f'_c	f_y (ligs)	Total Width/Internal Width	Total Depth/Internal Depth
	MPa	MPa	mm	mm
SA3[1]	40	373	305/149	610/406
SA4[1]	40	373	305/149	610/406
RC2-2	38	466	340	640
RC2-4	49	466	340	640
RC2-1	54	466	340	640
RC2-3	42	466	340	640

[1]Hollow Section

The tested results, code comparisons and parametric comparisons are shown in Table 2 and 3 in Section 4 of this paper. The cross-section for test specimens (1), (2) and (3) are shown in Figures 1, 2 and 3 respectively.

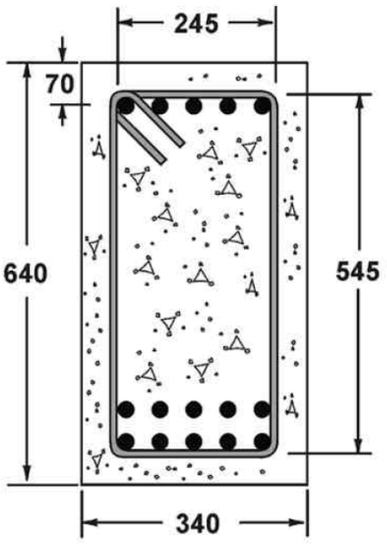


Figure 2: Rahal and Collins test specimen (2)

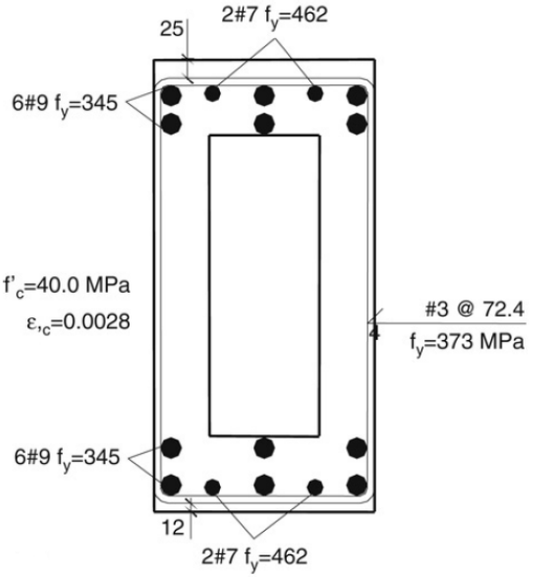


Figure 1: Arbesman test specimen (1)

5 CODE COMPARISON AND PARAMETRIC STUDY

Each sample was evaluated for its shear capacity using the various codes discussed in Section 3 of this paper. The resultant values were compared with the experimental values to ascertain which code provided the closest results to the experimental values and which code was most conservative. This comparison is shown in Table 2. In the scenario where shear and torsion were applied together, the requirement of transverse steel for torsion was calculated first and then subtracted from the amount of transverse steel provided in the section to assess the V_{us} component contribution to the section shear capacity. The angle of inclination of the concrete compression strut and the longitudinal axis of the member, θ, is varied between 30° and 45° as shown in Table 3. The purpose of which is to demonstrate the magnitude of change in shear capacity between codes. Table 4 presents the factored shear capacity for each respective code. Figure 4 and Figure 5 show column graphs depicting the direct comparison of unfactored shear capacity and factored shear capacity as shown in Table 2.

Table 2: Code Comparison

Specimen	Experimental Value		AS5100-2004		AS5100-2017			AASHTO-2012			CAN-2014		
	Texp kNm	Vexp kN	θ deg	Vu kN	θ deg	kv	Vu kN	θ deg	β	Vu kN	θ deg	β	Vu kN
SA3	0	730	45.0	338	31.7	0.228	763	31.8	3.015	673	31.7	0.253	727
SA4	0	534	45.0	338	30.9	0.124	794	31.0	3.341	692	30.9	0.281	756
RC2-2	0	796	40.0	420	31.8	0.226	688	31.8	2.983	509	31.8	0.249	711
RC2-4	55	715	36.0	470	32.1	0.217	508	31.9	2.980	371	31.9	0.248	620
RC2-1	83	535	33.0	504	32.4	0.212	517	31.7	3.030	304	31.7	0.253	562
RC2-3	135	111	30.0	521	33.5	0.185	321	32.2	2.85	162	32.2	0.237	400

Table 3: Code Comparison with variation in θ

	AS5100-2004		AS5100-2017			AASHTO-2012			CAN-2014		
	θ deg	Vu kN	θ deg	kv	Vu kN	θ deg	β	Vu kN	θ deg	β	Vu kN
SA3/SA4	30	508	30	0.295	840	30	3.918	721	30	0.326	797
	36	426	36	0.144	624	36	1.920	573	36	0.160	599
	45	338	45	0.081	441	45	1.080	232	45	0.090	425
RC2-2	30	514	30	0.297	749	30	3.918	562	30	0.326	824
	36	453	36	0.145	540	36	1.920	109	36	0.160	341
	45	389	45	0.082	368	45	1.080	321	45	0.090	376
RC2-4	30	533	30	0.297	710	30	3.918	411	30	0.326	744
	36	472	36	0.145	434	36	1.920	295	36	0.160	452
	45	408	45	0.082	254	45	1.080	175	45	0.090	267
RC2-1	30	541	30	0.297	663	30	3.918	342	30	0.326	700
	36	480	36	0.145	379	36	1.920	225	36	0.160	397
	45	416	45	0.082	195	45	1.080	104	45	0.090	205
RC2-3	30	521	30	0.297	503	30	3.918	210	30	0.326	534
	36	460	36	0.145	240	36	1.920	94	36	0.160	256
	45	396	45	0.082	88	45	1.080	4	45	0.090	96

Table 4: Code Comparison (including capacity reduction factor)

Specimen	AS5100-2004	AS5100-2017	AASHTO-2012	CAN-2014
	ϕVu (ϕ = 0.7)	ϕVu (ϕ = 0.7)	ϕVu (ϕ = 0.9)	ϕVu (ϕc = 0.75; ϕs = 0.9)
SA3	237	534	606	664
SA4	237	556	623	690
RC2-2	294	482	458	602
RC2-4	329	406	334	515
RC2-1	353	362	274	460
RC2-3	365	225	146	321

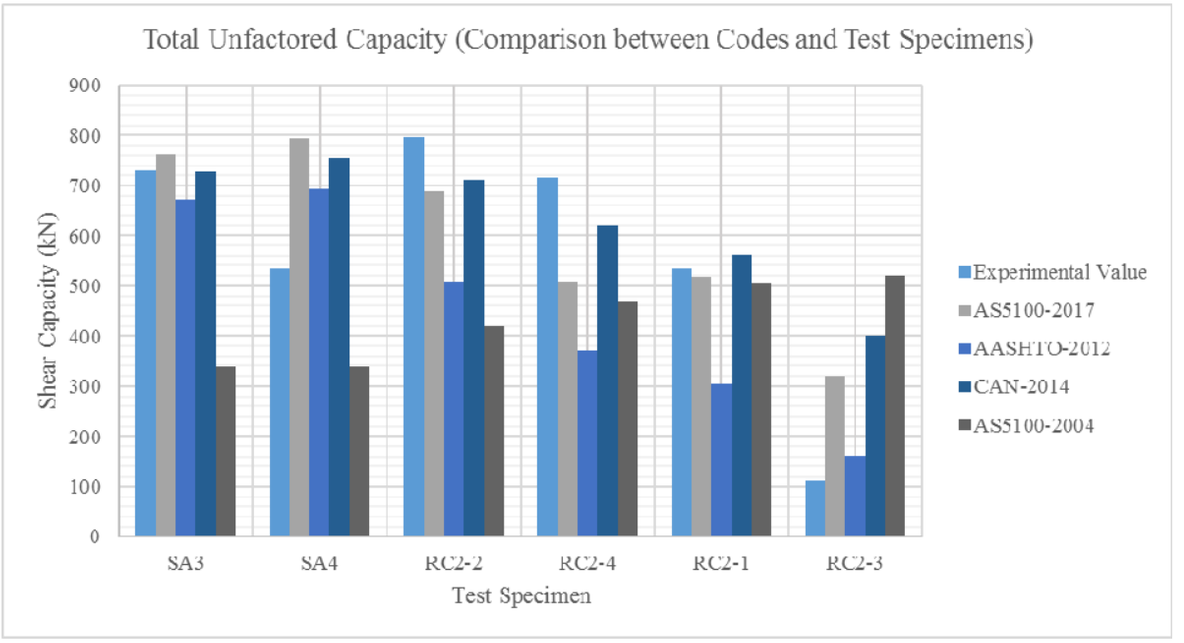


Figure 3: Total Unfactored shear capacity comparison between codes and test specimens

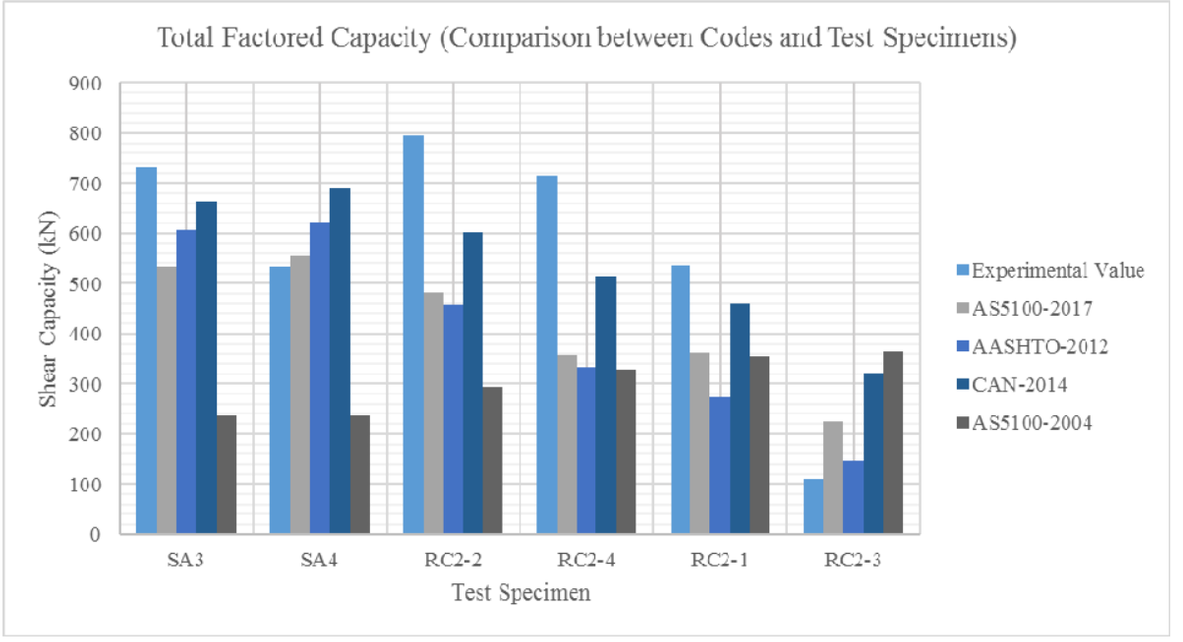


Figure 4: Total Factored shear capacity comparison between codes and test specimens

From the results presented in Figure 4, the following observations were made with respect to the unfactored shear capacity:

- AS5100-2017 provides the most efficient estimate of shear capacity of hollow section members in the database, followed by CSA-2014, AASHTO and AS5100-2004 respectively.
- For solid section members, CSA-2014 predominantly provides the most efficient estimate of the shear capacity, followed by AS5100-2017, AS5100-2004 and AASHTO respectively.

From the results presented in Figure 5, the following observations were made with respect to the factored shear capacity:

- For hollow section members considered in the database, CSA-2014 provides the most efficient estimate of shear capacity, followed by AASHTO, AS5100-2017 and AS5100-2004 respectively.
- For solid sections, CSA-2014 provides the most efficient estimate of the shear capacity, followed by AS5100-2017, AASHTO and AS5100-2004 respectively.
- The question that arises in this instance is that while AS5100-2017 has been modified to simulate a better estimate of shear resistance in concrete sections, why hasn't the capacity reduction factor been revised? The 0.7 reduction factor has been brought forward from the previous revision. The implication therefore is that there still remains a high level of uncertainty in the concrete code with respect to shear and torsion.

It is clear from the results that AS5100-2017 provides vastly different results to AS5100-2004 and one that is much closer to its international counterparts, particularly CSA-2014, although falling just short of the efficiency achieved by CSA in considering the total factored shear capacity.

6 CONCLUSION AND RECOMMENDATION

Understanding the behavior of reinforced concrete beams subjected to shear and torsion was always challenging. Despite many years of research, a unique design agreement on the best design model for shear and torsion design has not yet been reached. However, almost all the major code specifications around the world used to estimate shear and torsion capacity are now based on MCFT either in the originally developed model or in the further simplified method based on local national research. It is evident that the variation in the calculated shear and torsion capacity from different design codes can be high.

The CSA Standard shear provisions are most efficient for predicting the capacity of existing members because they are closest to the actual experimental loads achieved compared to those capacities estimated by AS5100-2017 and AASHTO-2012.

The recommendations of this paper are the following:

- Further testing on reinforced concrete and prestressed concrete beams should be undertaken in Australia to Australian construction standards and requirements to truly determine the accuracy of AS5100.5-2017 shear and torsion provisions.
- Further research to be undertaken to determine a suitable capacity reduction factor for shear and torsion in light of the new changes to the shear and torsion design provisions.

7 ACKNOWLEDGEMENTS

We would like to acknowledge Dr Amin Heidarpour, Head of Structures Group at Monash University for his assistance in providing relevant test papers from around the globe to make this analysis and discussion possible.

8 REFERENCES

[1] American Association of State Highway and Transportation Officials, *AASHTO LRFD Bridge Design Specifications - 2012*, Washington, 2012.

[2] Bentz, E.C., Vecchio, F.J., and Collins, M.P., *Simplified Modified Compression Field Theory for Calculating Shear Strength of Reinforced Concrete Elements,* ACI Structural Journal Vol. 103-S65, 2006, pp. 614-624.

[3] CSA Standards, *Canadian Highway Bridge Design Code – CAN/CSA-S6-14,* Ontario, 2014.

[4] Gregori, J.N. et al., *A 3D numerical model for reinforced and prestressed concrete elements subjected to combined axial, bending, shear and torsion loading,* Engineering Structures Vol. 29, 2007, pp. 3404-3419.

[5] Rahal, K.N., and Collins, M.P., *Experimental Evaluation of ACI and AASHTO-LRFD Design Provisions for Combined Shear and Torsion,* ACI Structural Journal Vol. 1000-S29, 2003, pp. 614-624.

[6] Stefanou, G.D., and Regan, P., *Torsional Resistance of Prestressed Concrete Beams with Rectangular Section,* Engineering Fracture Mechanics Vol. 40, 1991, pp. 211-225.

[7] Standards Australia, *AS5100.5-2004: Bridge design – Concrete*. Sydney: Standards Australia, 2010.

[8] Standards Australia, *AS5100.5-2017: Bridge design – Concrete*. Sydney: Standards Australia, 2017.

Maintenance, Safety, Risk, Management and Life-Cycle Performance of Bridges – Powers, Frangopol, Al-Mahaidi & Caprani (Eds)
© 2018 Taylor & Francis Group, London, ISBN 978-1-138-73045-8

Intermodal research to increase the reliability of transport infrastructures

R. Holst
Federal Highway Research Institute (BASt), Germany

ABSTRACT: The transport infrastructures (rail, road, waterways) in Germany are ageing and a considerable proportion of them need to be repaired and upgraded. As the civil engineering structures for these modes of transport have much in common regarding their design and damage, and because it is necessary to find sustainable solutions for the future quickly, it makes sense to work together in this area. This takes place within the BMVI network of experts.

Due to the complexity and interdependencies between various aspects of the subject of "maintenance", it has also proved useful to conduct the joint activities in four key areas in parallel. There are "Condition Assessment/Monitoring", "Reliability", "Measures/Forecast/Vulnerability (Resilience)" and "Construction during road use".

All of this work is important to achieve technically expedient, environmentally friendly, long-lasting and economical construction projects on site. Here too, there is need for substantial optimisation to minimise interference with transport and the environment while nevertheless carrying out construction work of high quality.

Familiar processes and methods are explored, adapted and expanded, subjected to practical tests on an individual object and in pilot areas, and the findings obtained shared internally and with external actors.

Only in this way is it possible to take reasonable account of the challenges of ever faster changes to marginal conditions and amass a joint body of expert knowledge.

1 BACKGROUND/REQUIREMENTS

The rail, road and waterways transport infrastructures represent the backbone of economic prosperity, and form the foundation for future development in Germany. Many of these infrastructures, and especially civil engineering structures such as bridges, tunnels, sluices and weir systems, have now reached or even exceeded much of their planned service life. What is more, the impact has changed greatly compared to the planned impact, and in some cases even amounts to a change of use. A joint effort by all concerned is needed so that these infrastructures can continue to perform their set tasks, as the growing speed of economic change dictates that essential modifications are made quickly. The order of the day is therefore to systematically develop and pool the knowledge and experience from the various modes of transport, and to learn from each other.

2 BMVI NETWORK OF EXPERTS

2.1 *Network of experts*

For this reason, at the instigation of the Federal Ministry of Transport and Digital Infrastructure (BMVI), seven of the subordinated authorities that report to it have joined together to form a BMVI network of experts to manage the tasks ahead [1].

The BMVI network of experts is a new research format for departmental research. Its guiding theme of "Knowledge – Ability – Action" represents the most important levels of action and identifies the requirement to deliver results that are of practical relevance.

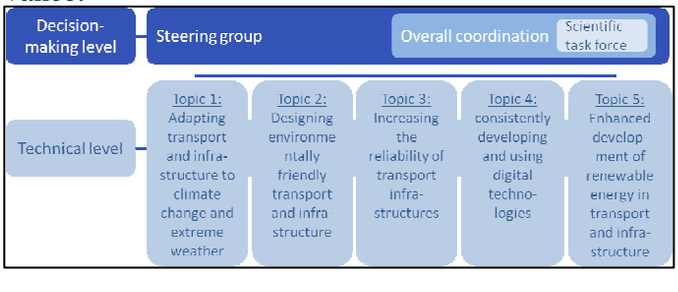


Figure 1: Structure of the network of experts [1]

Their objective is to address urgent transport questions of the future through innovations in the areas of adapting to climate change, environmental protection and risk management. In doing so, the network of experts builds directly on the principles of the Federal Government and its high-tech and sustainability strategy.

2.2 *Topics*

The Federal Highway Research Institute (BASt), Federal Institute of Hydrology (BfG), Federal Waterways Engineering and Research Institute (BAW), German Meteorological Service (DWD), Federal Office for Goods Transport (BAG), Federal Maritime and Hydrographic Agency (BSH) and Federal Railway Authority (EBA) all collaborate in the BMVI network of experts. Their competences and resources are initially being pooled in five topics:
1. Adapting transport and infrastructure to climate change and extreme weather events;
2. Designing environmentally friendly transport and infrastructure;
3. Increase the reliability of transport infrastructures.
4. Consistently developing and using digital technologies and
5. Stepping up the development of potential uses for renewables in transport and infrastructure.

3 TOPIC 3

3.1 *Tasks and objectives [2]*

The growing age of structures, the changing impacts and design weaknesses have an influence on the load-bearing capacity and stability of these structures and on their fitness for purpose. It is reasonable to assume that it will not be possible to safely accommodate the forecast volume of goods traffic unless there are targeted upgrading and replacement measures. In turn, this could lead to the inability to continue to guarantee unrestricted operational and transport related reliability in the form of the availability of transport routes. Suitable measures must be introduced to counter this issue.

Tasks were therefore divided into four key areas (SPT), because it will only be possible to maintain or improve reliability as a whole if all important aspects are dealt with together.

The strength of this new approach to research is that the institutions involved are able to directly bring their different approaches and thus strengths to the table, and that there is a continuous exchange between project team members. The BAW, for example, has large test facilities for directly simulating issues related to waterways. For decades, through its experience of contract research, BASt has very close ties to other research facilities and universities, ensuring that knowledge is not merely exchanged within the network of experts, but also with external actors, for example by means of workshops, milestone conferences and the website (www.bmvi-expertennetzwerk.de). Support groups staffed by members of the authorities involved are set up, particularly in connection with research projects that are being processed externally. Practical relevance and reference to potential users of the research results is guaranteed by the fact that employees of the waterways administration, of Deutsche Bahn AG and of road authorities in the Federal States are directly involved even during the processing phases.

This course of action replaces the classic approach of developing, presenting and practically implementing section by section with a combined approach. This demands transparent and flexible working practices on the part of all institutions and individuals involved.

The projects are processed in the following four key areas:

- SPT 301 (monitoring/assessment of condition);

- SPT 302 (reliability);

- SPT 303 (measures/forecast/vulnerability);

- SPT 304 (construction during road use).

Figure 2 shows the four key areas (SPTs), their content and interaction.

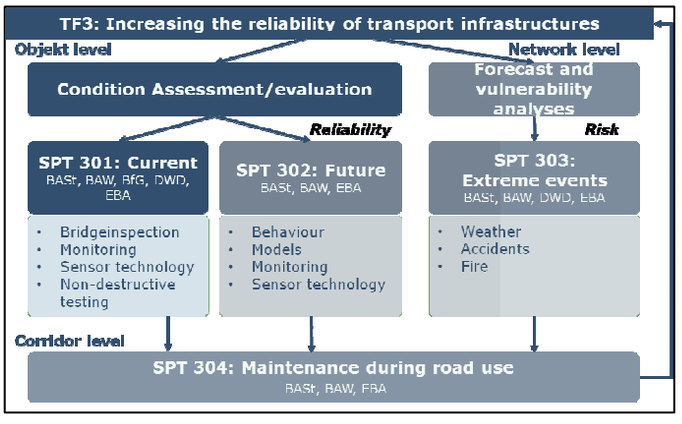


Figure 2: Interaction between the key areas

Figure 3 depicts the interaction between the institutions concerned and therefore the 3 modes of transport with their specialist topics.

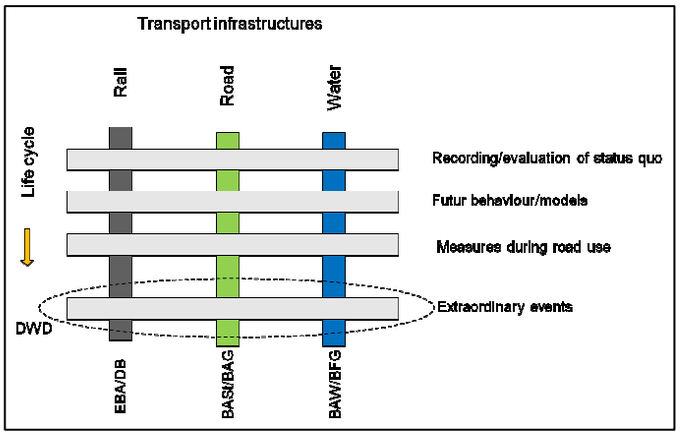


Figure 3: Links between key areas and authorities

3.2 *SPT 301 (condition)*

Recording the current and forecasting the future condition of civil engineering structures is the best foundation for technically practical, timely and economical construction work on these structures. The aim here is to purposefully supplement existing procedures with new technologies and succeed in providing additional information for following phases.

Imaging with the help of unmanned aerial vehicles (UAV) or unmanned aerial systems (UAS) has advanced in recent years to the extent that such equipment can be viewed to be completely practicable. For this reason, these devices are components in projects for all three modes of transport, and are designed to obtain additional and better information about structures and improve accessibility. The objective of the network of experts is to make the information and experience obtained available to all involved so that it can be consciously adapted to suit the needs of the respective mode of transport and introduced to practical use. This approach reduces the cost of research activities, both in financial and particularly also in temporal terms.

The purpose of a sub-project conducted by the Federal Institute of Hydrology (BfG) is to answer questions based on geodetic monitoring. One task here is to record measurement data from a combined sluice and weir system using a UAS. With the help of these results, the direct environment of the structure can be scanned, portrayed in a 3D format and the changes documented at defined intervals. This task should be performed both technically and economically with an eye to the future [3], enabling relevant changes to be detected at an early stage and requisite measures taken in good time.

As well as this aspect of documenting the position, the matter of partial or fully automated detection of damage to structures also plays an important role. The cost of recording and documenting the damage to structures in the course of the regular, usually nearby, structural tests is considerable and requires a high degree of preparation and follow-up work. Modern methods can provide very important support here. A UAS can reach all parts of the structures very quickly and take high quality digital images of them. It has been demonstrated, for example, that a surface image can be taken of pillars on a viaduct at a height of up to 100 m in less than 1 hour, including preparation time. The usually required deployment of an inspection device underneath the bridge with attached inspection platform takes several hours of operating time with at least 2 members of inspection staff.

Because data are fully digital, it is possible to very quickly create different images of diverse measuring campaigns. These clearly demonstrate the changes that have occurred since the last image was taken, and form an accurate basis - focussed on the essentials - for making a decision about possible courses of action.

During a test application on a retaining wall some years ago with cyclopean masonry (300 m long, 15 m high), artificial false edges in the range of a few centimetres could be repeatedly detected. The preparation of the necessary 3D model took several hours. These periods will be substantially reduced in future as Building Information Modelling (BIM) is developed. Experience based on sonar data from underwater components has recently shown that initial 3D presentations are possible directly on site in a few minutes.



Figure 4: Example of a UAV/UAS

Numerous images are created while flying over large structures, and until now these have had to be visually evaluated and assessed by trained staff. This task is very time-consuming and tiring for the staff involved.

It therefore makes sense to deploy existing techniques or develop new techniques to do this.

The Federal Railway Authority (EBA) [4] and the Federal Highway Research Institute (BASt) [5] are engaged in two projects dealing with this subject,

and both organisations are examining the problem from different perspectives.

The project [4] starts with a description of the damage which is necessary to permit simple classification on the basis of shape, progression and size. The evaluation logic is developed on the basis of this, defining which information the sensor system must be able to deliver for a meaningful analysis. The support system with which the sensor can be used should only be selected in the final step.

Parallel to this, a research project will investigate how partially or fully automated processes can be used to help detect damage, e.g. cracks. This is intended to reduce the work of those engaged in inspecting structures, who will then only need to take a close look at those areas of the structures that have been revealed by the algorithm to be suspect.

Finally, the results of both approaches will be evaluated and a decision taken in collaboration with end users about which approaches are beneficial for which areas and should be used in practice.

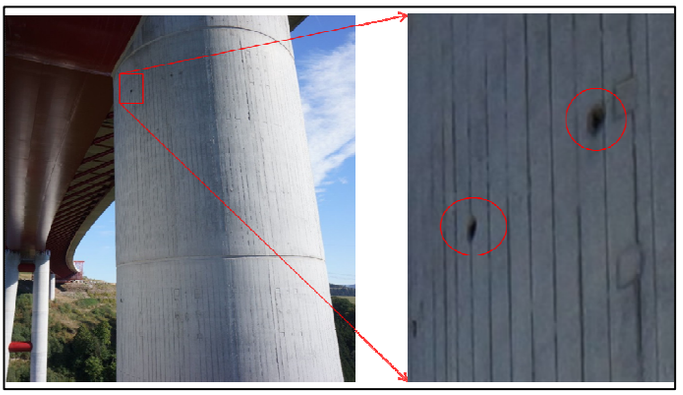


Figure 5: Close-up of damage detection

3.3 *SPT 302 (Reliability)*

Previous assessment procedures for evaluating the condition of civil engineering structures have been deterministic in nature. No consideration is taken of whether and with which likelihood damage is to be expected in as yet undamaged areas today and in the future, and how the damaged areas will behave in future. For this reason, different procedures will be examined or developed to incorporate reliability when assessing civil engineering structures for the specific issues of the different modes of transport. The results of the procedures are then to be evaluated and jointly appraised. In this way, the approach of working in parallel will allow qualified statements to be made about different reliability methods on comparable structures in a short amount of time.

Research facilities can then provide public authorities with an even more knowledgeable consultancy service, while simultaneously reducing the expense in their own organisation.

The following methods will be examined:

For structures on waterways such as sluices, weir systems and bridges, a risk classification will be performed for navigable waterway constructions. Classification of the risk of the structures will be based on meaningful operating data [6], whereby the load-bearing capacity is to be taken into consideration in addition to the condition-related rating system. This system is to be applied to all types of structure [7].

As well as this, the problem of surveying the revetments on the banks of rivers and canals will be considered. Based on interviews with experts, pilot trials will be conducted by the Federal Waterways Engineering and Research Institute and field measurements taken, and a calculation model developed. This will be based on reliability-based procedures such as the cohort survival model, Markov chains or Bayesian networks. A precise specification will emerge following the three basic evaluation steps [8].

Bayesian networks will specifically be used for road bridges. A suitable concept has been developed that estimates the reliability of road bridges on the basis of the structural data from the regularly performed structural inspections under DIN 1076 and the associated construction and damage data stored in the “SIB structures” program system.

The objective is to estimate a reliability index (= probability of failures, POF) by comparing the resistances or the limits of use with the effects of traffic loads [9].

The prerequisite for this is that the resistance in an undamaged state is produced from the measurement data of the resistance standards for the year of construction on a simplified static system. Damage detected by the structural inspection can be incorporated by reducing the resistance or the limits of use. This reduction is subject to many uncertainties, something that must also be taken into consideration. A simplified Bayesian network is used to enable a risk assessment to be performed with the scant information available at the beginning. With additional information, it is possible to improve these results with the help of the same Bayesian networks.

The impact for bridges is largely made up of traffic, and in particular heavy goods traffic. The necessary input variables can be found in current rules and standards and the corresponding national application documents.

3.4 *SPT 303 (Forecasts/vulnerability analyses)*

The structures in traffic infrastructure have been assessed with respect to planned impact such as traffic, wind and temperature. Developments over recent years, in particular in conjunction with climate change, have demonstrated, however, that extraordinary events increasingly exert a substantial influence on the safety and functionality, and thus the availability, of the structures. It is important, therefore, to

systematically record the events, e.g. as a result of heavy rainfall, flooding, phases of low water or hot spells, and to examine their impact on transport infrastructures.

It's a big advantage that the German Meteorological service (DWD) is likewise a partner in the network of experts and that an investigation into the impact of climate change on transport infrastructures is also covered under Topic 1.

With this approach, it's possible to take both short-term, localised events (local heavy rainfall) and more generalised and prolonged events or changes (heavy rain over a larger area and for a longer period, longer periods of hot weather and drought, climate changes) into account and to focus on obtaining the input variables required for the respective question.

One concrete requirement from experience is the development of an automated procedure which enables the barrage controls for the area of barrage-regulated, navigable waterways to be put in place quickly so that these waterways remain open to inland shipping on as many days as possible each year. This is also important in view of keeping the environmentally friendly waterways attractive for users, thereby making an important contribution to the sustainability of transport infrastructures.

The matter of "resilience" also plays a very important role in addition to sustainability, and simultaneously constitutes one of the two guiding themes of the network of experts.

Resilience is understood as shown in the cycle for Topic 3 in Fig. 6.

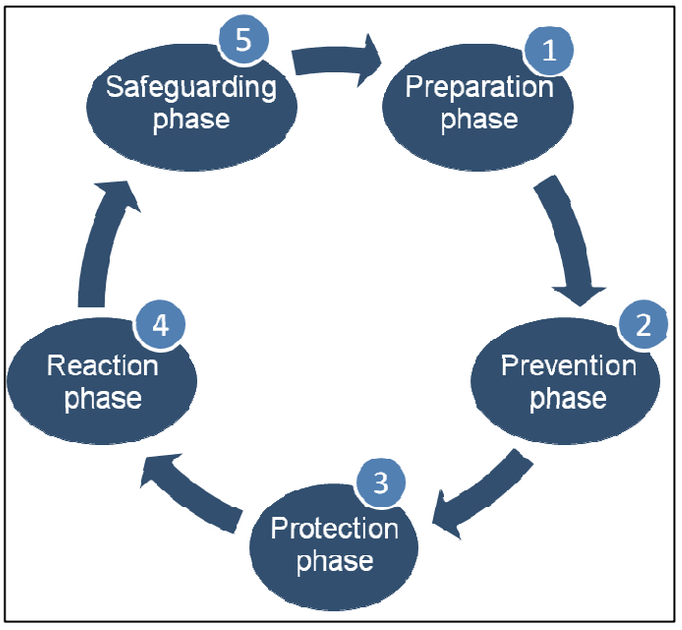


Figure 6: Resilience cycle

The objective is to guarantee the availability and safety of the road infrastructure in Germany even during extraordinary events. An approach to quantify availability and safety has been developed to this end.

3.5 *SPT 304 (Construction during road use)*

Due to the age and condition of structures, the availability of transport infrastructures can only be guaranteed in future if a considerable amount of work is conducted on maintenance and new building projects. The results of the preceding main topics provide important input variables, e.g. the current and forecast conditions and conduct under scheduled and extraordinary loads. The type, time and scope of necessary construction measures can then be calculated. The greatest challenge in connection with this is "construction during road use". Whereas new building projects are generally carried out on "greenfield sites", work on existing structures must focus on the safe and smooth flow of traffic and on environmental concerns.

The following aspects are dealt with in the network of experts:

- Maximisation of availability;
- Adaptation to changed conditions of use;
- Smart repair;
- Standardised flyovers.

Furthermore, Topic 2 examines the impact of material input from structures on the environment, in order to achieve the minimisation of damaging substances here in the future.

"Construction during road use" is characterised by the prime objective of keeping the influence on flowing traffic and the environment to a minimum while nevertheless ensuring that the quality of structures corresponds at least to that on green field sites.

This can be achieved as follows:

- By selecting construction methods that permit traffic to flow without reducing the number of lanes but with width restrictions;
- By selecting types of structures that need as little maintenance and repair work as possible;
- By optimising building processes to reduce work periods during road use;
- By the quality of structures at least equalling that of new builds and having the longest possible service lives.

Work on these different aspects will take place in parallel over the course of several projects. The first such project is concerned with designing draft structures which will only require minor structural adjustments during subsequent work to prepare the structure in accordance with new requirements. This method only makes economic sense for structures as from a certain size ($L > 100$ m), because the ratio between the original structure and the expense of subsequent changes (e.g. built-in components) would not otherwise be proportionate. This has produced

the following possibilities for reinforced and prestressed concrete structures:

- Anchor plates for the subsequent installation of struts on the cantilever;
- "Tube-In-Tube" or hollow box sections that are reinforced by an inserted box girder;
- Additional ducts for subsequently inserting further tendons;
- Unbonded tendons for the subsequent replacement of tendons;
- Adaptive systems, e.g. in the form of self-tensioning tendons.

This list is currently being supplemented by the possibilities for steel bridges.

In addition to these methods for new builds, others are also needed for work on existing structures.

The condition of structures in Germany has today already led to a growing tendency for the existence of restrictions, e.g. weight or speed restrictions on bridges, which can only be cancelled once the necessary construction work has been completed. This means it is necessary not only to optimise the construction work itself, but also to keep the lead times as short as possible. From the point of view of technicians, there is little leeway to influence legal requirements, e.g. to conduct a planning approval process in the case of construction work aimed at boosting capacity.

So that these periods don't go unused, it also makes sense to reduce construction times during road use by taking advantage of standardisation. Deutsche Bahn AG and the EBA have had calculations performed for standardised framework structures up to 16 metres long [10]. These affect around 80% of underpasses for Deutschen Bahn AG. Due to the high number of rail structures that will need replacing in coming years, this is a very big advantage. This is also the case in view of the fact that possible disruptions and closures on the railways are very limited, and that alternative routes or temporary structures are only available or usable to a limited extent.

Comparable investigations have been conducted for the road area. One possibility is the so-called "LEGO" bridge (bridge made completely from prefabricated parts). In 2016, it was decided following a competition that a bridge over the A46 near the city of Hagen should be erected using this method as a pilot project [11]. The expectation is that the planned construction time of 220 days can be reduced to 100 days. The construction work is scheduled for 2018. Following this, experience will be gathered and evaluated, regarding both the construction and the practicability in real use. Construction using prefabricated parts has advantages during prefabrication and erection, but produces very many more joints which, during operation, may prove to be areas that are penetrated by de-icing salts, thereby causing greater corrosion.

In addition to the examples set out here, there are also other ways of optimising "construction during road use" [12], e.g.:

- Integral construction;
- Use of shunting and lifting technologies;
- The structural addition of further lanes.

There are advantages and disadvantages as well as application limits regarding all of these variants, and it's always necessary to look at which variant offers the most expedient solution for the case in hand. Despite uniform rules and standards and potential solutions regarding implementation details – known as guideline drawings - bridge structures in Germany are always a unique specimen. This enables them to be adapted to the conditions on site. However, in view of the extent of upcoming construction work on bridges in future, all possibilities must be examined and incorporated so as to save time and money and to protect the environment. Only in this way will it be possible to reliably guarantee the availability of transport infrastructures in an environmentally friendly way in the future.

4 SUMMARY

The transport infrastructures in Germany are ageing and a considerable proportion of them need to be repaired and upgraded. This especially affects the rail, road and waterways modes of transport. As the civil engineering structures for these modes of transport have much in common regarding their design and damage, and because it is necessary to find sustainable solutions for the future quickly, it makes sense to work together in this area. This takes place within the BMVI network of experts.

Due to the complexity and interdependencies between various aspects of the subject of "maintenance", it has also proved useful to conduct the joint activities in four key areas in parallel. In this way, methods and processes to monitor and assess the condition of structures are being examined and further developed. As well as the improved documentation of the actual conditions, the future conduct of the structures with respect to reliability is also of great significance when moving in future from a reactive approach to a proactive approach that avoids undesirable states, i.e. to guarantee the availability of the transport routes. As a result of climate change and other factors, in future it will not be sufficient merely to consider the response of structures to planned impact, but also to unplanned impact. The topic of resilience plays a very crucial role, acting before, during and after events in a way that restores availability in the shortest possible time.

All of this work is important to achieve technically expedient, environmentally friendly, long-lasting and economical construction projects on site. Here too, there is need for substantial optimisation to minimise interference with transport and the environment while nevertheless carrying out construction work of high quality.

The authorities in the network of experts collaborate internally, but also with the contribution of external expertise. Familiar processes and methods are explored, adapted and expanded, subjected to practical tests on an individual object and in pilot areas, and the findings obtained shared internally and with external actors.

Only in this way is it possible to take reasonable account of the challenges of ever-faster changes to marginal conditions and amass a joint body of expert knowledge.

5 OUTLOOK

The first phase of the BMVI network of experts runs from 2016 to the end of 2019, and represents the identification phase. During this phase, the foundations will be laid for further action. The strategic plan envisages a further phase from 2020 – 2025, which will be the integration phase. During this phase, the findings obtained will be further developed for practical use.

An implementation phase up to 2030 is finally planned, during which results are to be realised in practice.

This plan should ensure that the transport system in Germany is resilient and environmentally friendly. Promoting and using new technologies and innovations for infrastructure and sustainable mobility are key points of the strategy.

This plan is not static, but is open to adjustments to planned aspects and the incorporation of new topics. The diversity of the experts involved offers the ideal basis for this.

6 REFERENCES

[1] 2017, BMVI Network of Experts “Knowledge – Ability – Action”, at www.bmvi-expertennetzwerk.de ,

[2] Holst, R., “Verlässichkeit der Verkehrsinfrastrukturen erhöhen; Feinkonzept des Themenfeldes 3 im BMVI-Expertennetzwerk Wissen – Können – Handeln”, 2017, www.bmvi-expertennetzwerk.de,

[3] Brockmann, H., Fedan, F., 2017, milestone report on “effizientes ingenieurgeodätisches Monitoring der Verkehrsbauwerke”, Koblenz, (unpublished)

[4] Reinhardt, M., 2017, milestone report on “automatisierte Bilderfassungsverfahren als Ergänzung zur handnahen Inspektion”, Bonn, (unpublished)

[5] Gößmann, R, Sperber, M., 2017, Unterstützung der Bauwerksprüfung durch innovative digitale Bildauswertung – Pilotstudie, Volume B139 of the series of publications by the Federal Highway Research Institute, NW-Verlag, Bremerhaven

[6] Schmidt-Bäumler, H., 2017 milestone report on “Methode zur Risikoklassifizierung für Verkehrswasserbauwerke” Schmidt-Bäumler, Karlsruhe, (unpublished)

[7] Panenka, A., 2017, milestone report on “Tragfähigkeitskennzahlen für bestehende Konstruktionen“”, Karlsruhe, (unpublished)

[8] Sorgatz, J., 2017 milestone report on “Zuverlässigkeitsbasierte Deckwerksbemessung”, Karlsruhe, (unpublished)

[9] Hajdin, R., Novak, B., 2017, interim report on „Zuverlässigkeitsbasierte Bauwerksprüfung – Konzeption und fachliche Lösungen“, FE 15.628/20016/LRB, Zürich/Bergisch Gladbach (unpublished)

[10] Raischl, A, Hennecke, M, “Standardisierung von Rahmenbauwerken (Spannweite 10 bis 15 m)“, München/Bonn, (unpublished)

[11] Lego-Brücke, 2017, www.strassen.nrw.de/presse/meldungen/2017/pi2017-2-1631.html

[12] Lederhofer, E., et al., 2013, “Machbarkeitsstudie zum nachhaltigen Ersatzneubau von Brücken “Die innovative Brücke””, 2013, Final report for FE-No. 15.0551/2012/NRB, Bergisch Gladbach, (unpublished)

Maintenance, Safety, Risk, Management and Life-Cycle Performance of Bridges – Powers, Frangopol, Al-Mahaidi & Caprani (Eds)
© 2018 Taylor & Francis Group, London, ISBN 978-1-138-73045-8

Traffic safety and passenger comfort for steel railway bridges

E.-S. Hwang & D.-Y. Kim
Kyung Hee University, Yongin, Korea

ABSTRACT: Recently rapid-transit railway systems have been constructed in many developing countries due to its advantages in congestions and environmental problems. Railway bridges show many different aspects compared to road bridges and passenger comfort and traffic safety are one of them. In particular, deflection and acceleration due to repeated vibration characteristics have a structural weakness that can cause undesirable response. Especially steel railway bridges have been known to have weaknesses due to its relatively light weights compared to concrete bridges. The purpose of this study is to analyze the dynamic response of steel box girder bridges due to passing trains then propose the appropriate method to mitigate the level of vibration in terms of accelerations. Three steel railway bridges are tested and the theoretical model to analyze the dynamic response of the bridge by passing train are developed. For the verification of the model, the natural frequency extracted using the acceleration data measured in the bridge is compared with the natural frequency of the theoretical model. To mitigate the acceleration level of the bridge, parametric studies are performed to find the effectiveness of the method. Based on the analysis, the appropriate method is proposed for decreasing the acceleration of the bridge for passenger comfort and traffic safety.

1 INTRODUCTION

In Korea, transportation network has been developed mainly on the road, but recently, the perception of railway system is changing due to traffic congestion, environment, and safety issues. Due to the geographical feature of Korea, which has a lot of mountains and rivers, there are many bridges and tunnels. The total length of the railway line is 2,185,312 km, of which the bridge is 429,184 km, accounting for 20% of the total. In the case of railway bridges, the size and characteristics of loads are different from those of highway bridges, and traffic safety and the passenger comfort due to the vibration caused by the wheel load when the train passes through the bridge at high speed should be considered. In order to ensure the serviceability such as the traffic safety and passenger comfort of the train, the deflection and acceleration of the bridge should be examined. The purpose of this study is to investigate and evaluate the criteria for passenger comfort and traffic safety of railway bridges. The deflection and acceleration data are measured in the steel box girder bridges for about a month. Effects by axle weights, types of trains were analyzed. And traffic safety and passenger comfort has been checked by analyzing vertical acceleration and deflection of the bridges. The results are compared with international design criteria including UIC and Eurocode. Also numerical and measured values were compared through dynamic analysis.

2 DESIGN CRITERIA

In the design of railway bridges, most design codes specify the traffic safety and passenger comfort criteria as the serviceability check of the bridge. For the traffic safety, vertical acceleration and vertical deflection of the deck and deck twist are considered. For the passenger comfort, vertical deflection of the bridge is considered (BSI, 2005) (UIC, 2006).

2.1 *Traffic Safety*

According to Eurocode (CEN 2005), the maximum peak acceleration of the deck due to rail traffic should not exceed 3.5 m/s^2 for ballasted tracks and 5 m/s^2 for

slab tracks. This requires the dynamic analysis of the real train loaded on one track. Accelerations should be considered for frequencies up to the greater of 30 Hz, 1.5 times of the first mode natural frequency or the frequency of the third mode of vibration of the structure.

The vertical deformation of the deck is another criterion for the traffic safety. It includes vertical deflection along the track, rotation of ballasted bridge deck ends, angular rotations at the end of decks, and vertical displacement of bridge deck ends beyond bearings. The maximum total vertical deflection measured along any track due to rail traffic (LM71 Model) should not exceed L/600.

The twist of the deck is also important for the safety of the train. The criteria are for the twist of the deck to limit that four wheels of one bogie do not deviate one plane as shown in Figure 1. Limiting values of the deck twist are described in Table 1. UIC code has the similar criterion.

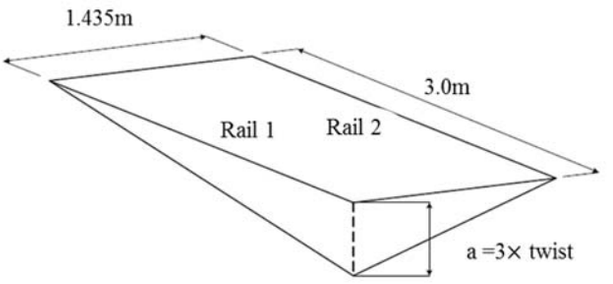


Figure 1. Definition of deck twist

Table 1. Limiting values of deck twist

Speed range V (km/h)	Maximum twist t (mm/3m)
$V \leq 120$	$t \leq 4.5$
$120 < V \leq 200$	$t \leq 3.0$
$V > 200$	$t \leq 1.5$

2.2 *Passenger Comfort*

Passenger comfort is determined by the vertical acceleration b_v inside the coach when train is passing the bridge. The limit values of the vertical acceleration b_v are depending on the level of comfort and shown in Table 2. However, design codes specify the vertical deflection along the center line of the track of the bridge instead of the acceleration of the cabin. Figure 2 shows maximum permissible vertical deflection δ for railway bridges with 3 or more decks corresponding to a permissible vertical acceleration of b_v = 1.0 m/s² which is taken by providing a "very good" level of comfort in a coach for speed V [km/h]. For a bridge composed of either a single span or two simply supported beams or two continuous spans, the values of L/ δ given in Figure 2 should be multiplied by 0.7. In case of continuous beams with three or more spans should be multiplied by 0.9. Table 3 shows the deflection limit for passenger comfort δ considering the very good level in case of speed V=350km/h, which represents the limiting values one of the test bridge in this study. In other levels of comfort, L/ δ is divided by b_v which is acceptable or good so that deflection can be easily calculated. In the case of bridges with double or more tracks, only one track is loaded for the calculation of the deflection.

Table 2. Recommended levels of comfort (Eurocode)

Level of comfort	Vertical acceleration b_v (m/s²)
Very good	1.0
Good	1.3
Acceptable	2.0

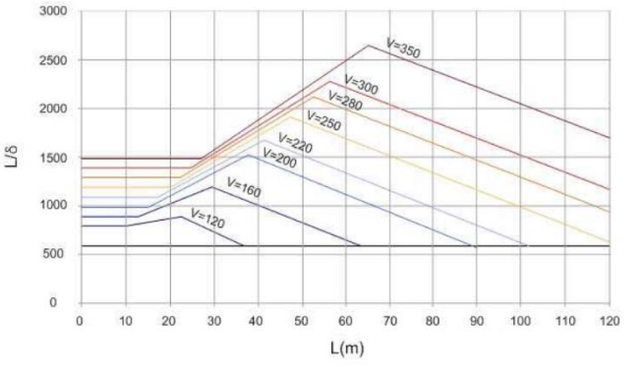


Figure 2. Maximum permissible vertical deflection for railway bridges (b_v =1m/s²)

Table 3. Limitation of maximum vertical deflection (b_v =1m/s²)

	Span length L(m)				
1 or 2 simple supported beams or 2 continuous spans	10	20	30	40	50
	L/1100		L/1200	L/1400	L/1600
	60	65	70	80	90
	L/1800	L/1900	L/1800	L/1700	L/1600
	100	110	120		
	L/1500	L/1400	L/1200		

3 FIELD TEST

3.1 *Test Bridges*

To collect the data for deflections and accelerations, sensors were installed at midspan of the bridge. Test bridges are steel box girder bridges as shown in Table 4. It was measured at the moment the train passed, and the period is over 40 days (Table 5).

3.2 *Measurement Results*

Figure 3 shows the typical cases of deflection and acceleration measurement results for A bridge. Addition to deflection and acceleration of the bridge, axle weights are mesured before the train enter the bridge by other weighing system. The measured axle weights are shown in Table 6. Results show the C.O.V. of about 15~19%.

Measured deflection and accelerations are summarized in Table 7. Maximum deflection and acceleration of A bridge are 5.384 mm and 0.453 g, respectively. B bridge are 3.056 mm and 0.24g and C bridge are 8.392 mm, 0.327 g, respectively. The deflection shows 20~27% C.O.V. On the other hand, the acceleration shows 35~89% C.O.V., larger than deflections.

Table 4. Test bridges

	Line	Type	Span length	Track
A	Jungang	Steel Box	35 m	Ballsted
B	Jungang	Steel Box	25 m	Ballsted
C	Kyungbu	Steel Box	40 m	Ballsted

Table 5. Measurement Overview

	A	B	C
Period	Sep 24, 2016 ~ Nov 03, 2016 (41 days)	Sep 10, 2016 ~ Dec 22, 2016 (43 days)	Apr 12, 2016 ~ Jun 02, 2016 (52 days)
Events	720	890	2635

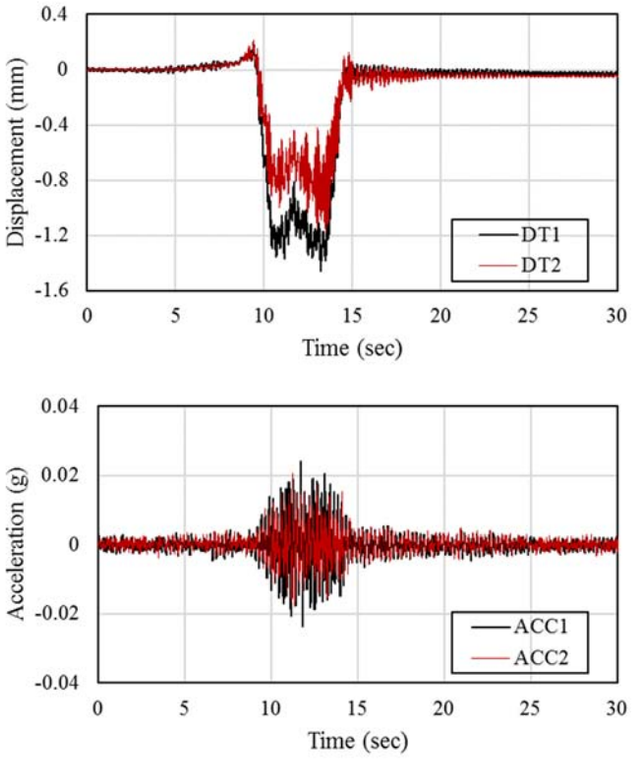


Figure 3. Typical cases of deflection and acceleration of the bridges A

Figure 4 shows maximum deflection and acceleration of each event by velocity and wheel load in bridge A. It shows that displacements are not affected by the velocity. It also shows that displacements are larger for DT1 side (train runs on this side) than for DT2 side but for acceleration both side show almost the same values

Table 6. Axle weight and velocity

		A	B	C
Velocity (km/h)	Min.	23.6	14.3	46.8
	Ave.	98.7	79.0	108.7
	Max.	148.0	112.0	137.0
Axle load (kN)	Min.	127.5	117.9	93.3
	Ave.	254.1	257.2	184.1
	Max.	455.9	528.9	570.9
	C.O.V	0.159	0.170	0.190

Table 7. Deflection and acceleration

		DT1 (mm)	DT2 (mm)	ACC1 (g)	ACC2 (g)
A	Min.	1.454	0.655	0.016	0.014
	Ave.	3.615	2.583	0.067	0.045
	Max.	5.247	5.384	0.446	0.453
	C.O.V.	0.234	0.247	0.523	0.478
B	Min.	0.811	0.435	0.007	0.007
	Ave.	2.199	1.351	0.105	0.062
	Max.	3.056	2.844	0.607	0.911
	C.O.V.	0.207	0.271	0.892	0.769
C	Min.	1.334	0.227	0.022	0.020
	Ave.	4.450	3.699	0.052	0.048
	Max.	8.392	8.294	0.307	0.327
	C.O.V.	0.244	0.249	0.354	0.453

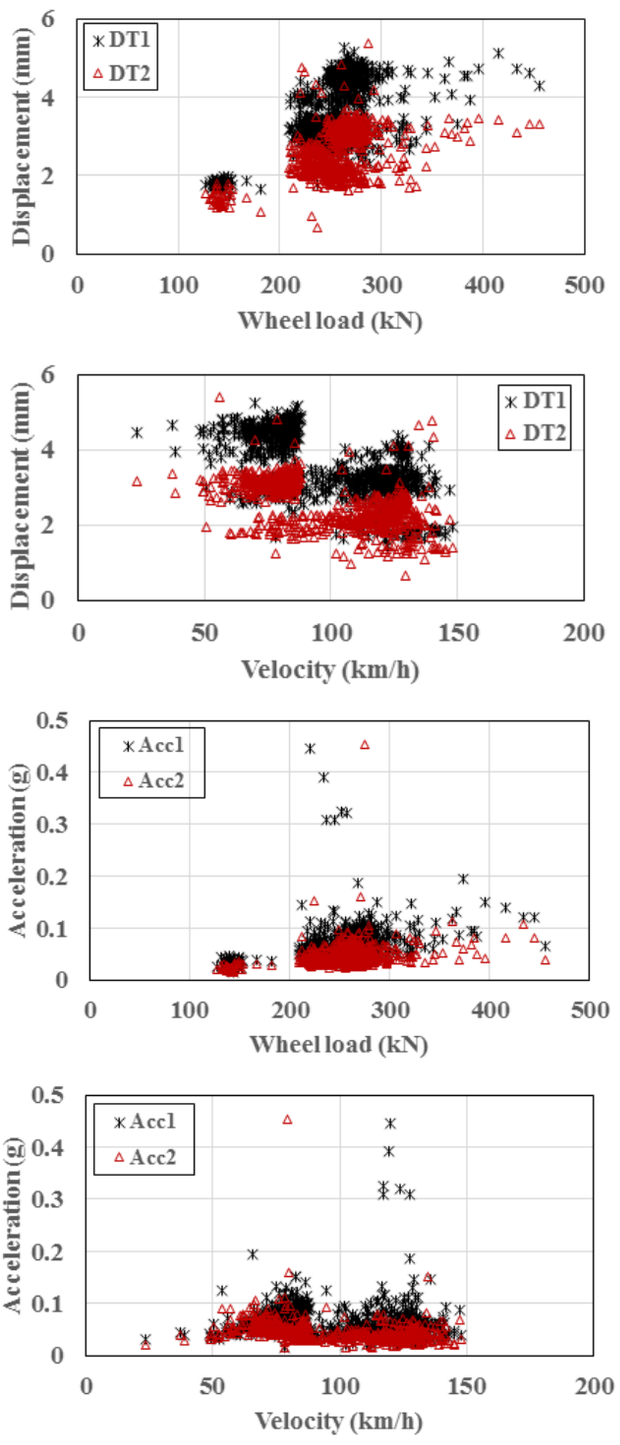


Figure 4. Displacement and Acceleration by Wheel load and Velocity (A bridge)

3.3 *Comparison with Design Criteria*

Table 8 shows the comparison of measured values with design criteria. Tthe limiting vlaues for traffic safety are L/600, and 58.33 mm, 41.67 mm, 21.05 mm for the A, B, and C bridges, respectively. And the passenger comfort are 20 mm (=L/1750) for A bridge, 16.67 mm (=L/1500) for B bridge and 21.05 mm (=L/1900) for C bridge. In case of deflection, three bridges are far less than design criteria. However, in case of acceleration, both of the bridges on the Jungang-line exceeded the design criteria by 127% and 173%, and the C bridge was also close to the reference value by 87.7%.

4 THEORETICAL ANALYSIS

4.1 *Verification of modeling*

In this study, each bridge is modeled using a commercial program (Midas 2005) to analyze dynamic behavior of steel box girder railway bridges (Figure 5). Plate and beam elements are used for steel box and slab and cross beam, respectively. In order to improve the accuracy of the dynamic analysis, a secondary static load of gravel track, railroad tie, and rails were added.

The load was used to generate the train load by using the actual measured wheel load and wheel spacing for comparison with the measurement results.

Unlike high-speed railway lines, test bridges are located on the general railway line, so various types of trains are passing. In this study, three types of trains with high frequency of passing were selected. In the case of A and B bridge on the Jungang-line, 28 axles, 32 axles, and 86 axles trains were selected. And the C bridge, which is the Kyungbu-line, selected 24 axles, 38 axles, and 54 axles trains.

The time history analysis using the mode superposition method is based on the eigenvalue analysis, so the eigenvalue analysis must be performed. From the measured acceleration after the truck leaves the bridge, the natural frequency of the bridge is calculated using FFT process. Acceleration data are filtered at 30 Hz to minimize the noise. The results are shown in Figure 6 and summarized in Table 9. The natural frequencies of the bridges are also calculated from the numerical model. Both frequencies are in Table 9 and it shows similar values.

4.2 *Comparison with test results*

The measured values and the analytical values of each bridge are compared with respect to typical trains. Selected trains are shown in Table 10. Comparisons are shown in Table 11 and Figure 7 to 12.

For A bridge (Figure 7 and 8), in case of deflection, measured values and analytical value (using average axle weights) show similar values. However, acceleration values of the 28-axles and the 32-axles shows very large values than those of the analytical results. This may be due to the resonance of the train and the bridge. The resonance occurs when the effective beating interval of the train coincide with the natural frequency and the resonance speed can be calculated using following equation.

$$V_{cr} = \omega_1 \times S_{eff} \quad (1)$$

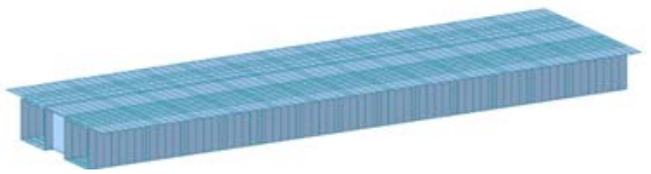
where, ω_1 is the natural frequency of the bridge and S_{eff} is effective beating interval.

For B bridge (Figure 9 and 10), the responses of 28 and 86 axle trains are compared. Deflections from experimental study are far less than the analytical study but accelerations show similar values and trends. As the velocity of the train increases, the acceleration tends to increase. However, the acceleration values are within the design code limits in the range of normal train speed.

In case of C bridge, the general results show the same trends and values as B bridge.

Table 8. Comparison with design criteria

		A	B	C
Traffic safety	Measurement (mm)	5.247	3.056	8.392
	%	9.00	7.33	12.59
	Deflection L/600 (mm)	58.33	41.67	66.67
	Measurement (g)	0.446	0.607	0.307
	%	127.43	173.33	87.71
	Acceleration (g)	0.35	0.35	0.35
Passenger comfort	Measurement (mm)	5.247	3.056	8.392
	%	26.24	18.34	39.87
	Deflection (mm)	20.00 =L/1750	16.67 =L/1500	21.05 =L/1900



(a) A bridge



(b) B bridge



(c) C bridge

Figure 5. Modeling of A, B, C bridges (by Midas Civil)

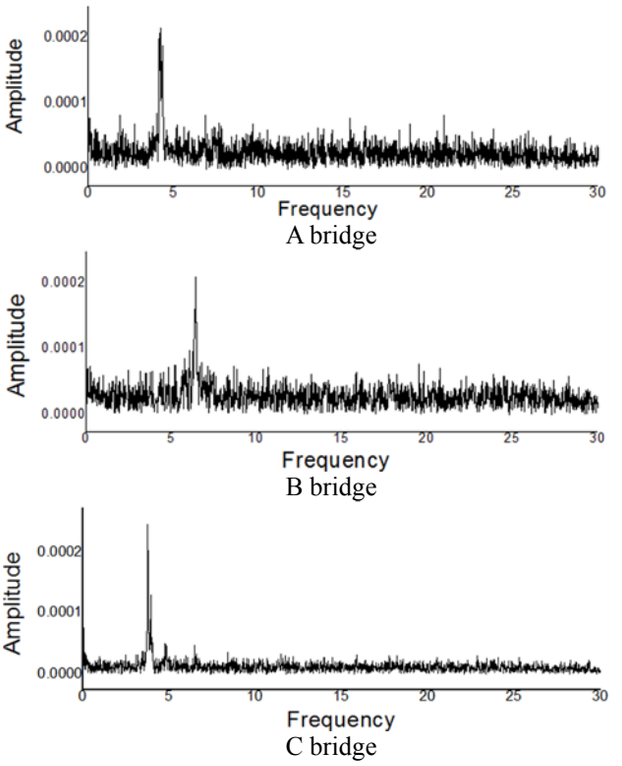


Figure 6. Natural frequencies of the bridges.

Table 9. Comparison of frequencies from experimental and analytic studies.

Bridge	Frequency (FFT)	Frequency (Analysis)	Response ratio
A	4.229	4.379	0.97
B	6.150	5.440	1.13
C	3.845	3.472	1.11

Table 10. Parameters of train

Train Parameters			
Number of Axles		Max. Axle Weight (kN)	Average Speed (km/h)
A bridge	28	248.87	114.16
	32	255.38	109.98
	86	277.94	76.670
B bridge	28	268.00	87.04
	32	270.26	93.44
	86	261.12	70.16
C bridge	24	136.69	128.71
	38	182.97	119.13
	54	202.51	86.406

Table 11. Comparison of the measured and analytic value

		Measured Value		Analytic Value	
		DT (mm)	ACC (g)	DT (mm)	ACC (g)
A bridge	28	3.097	0.0580	4.294	1.138
	32	3.036	0.0611	4.813	0.290
	86	4.481	0.0788	7.355	0.468
B bridge	28	1.868	0.0820	3.744	0.569
	32	1.874	0.2071	7.809	1.358
	86	2.604	0.0766	5.545	0.270
C bridge	24	2.334	0.0331	5.291	0.098
	38	4.901	0.0536	8.747	0.100
	54	5.198	0.0531	8.532	0.093

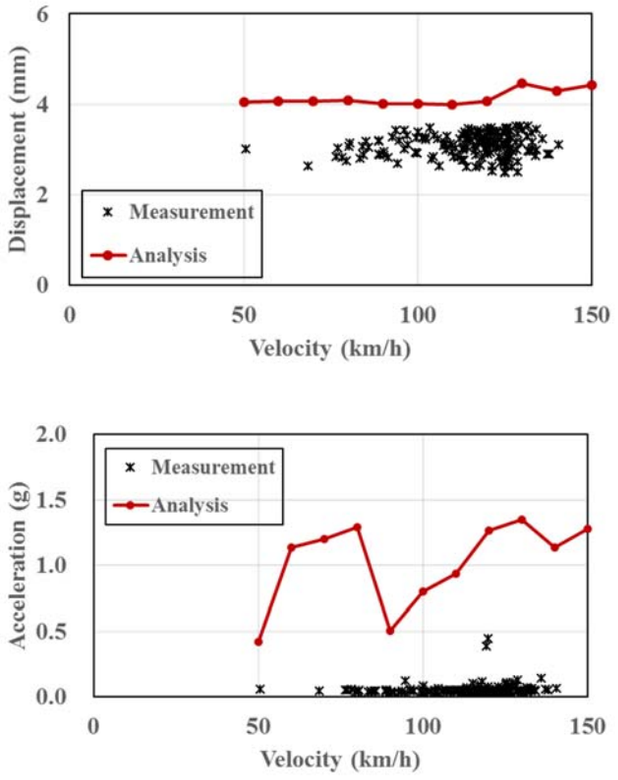


Figure 7. Comparison of measured and analytical values by velocity (A bridge, 28-axles train)

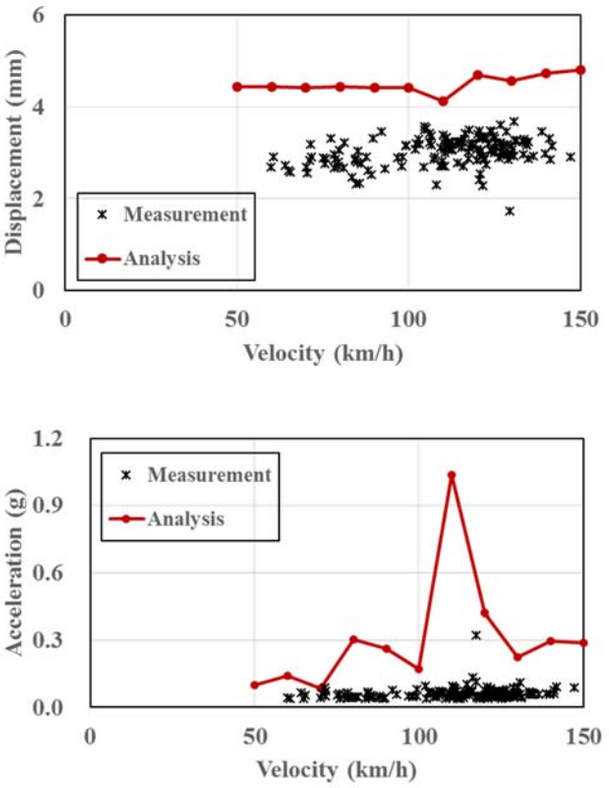


Figure 8. Comparison of measured and analytical values by velocity (A bridge, 32-axles train)

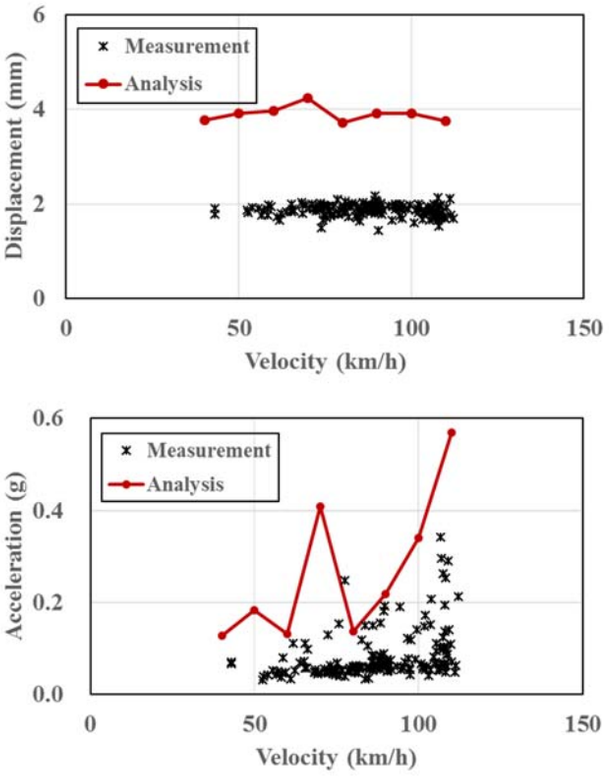


Figure 9. Comparison of measured and analytical values by velocity (B bridge, 28-axles train)

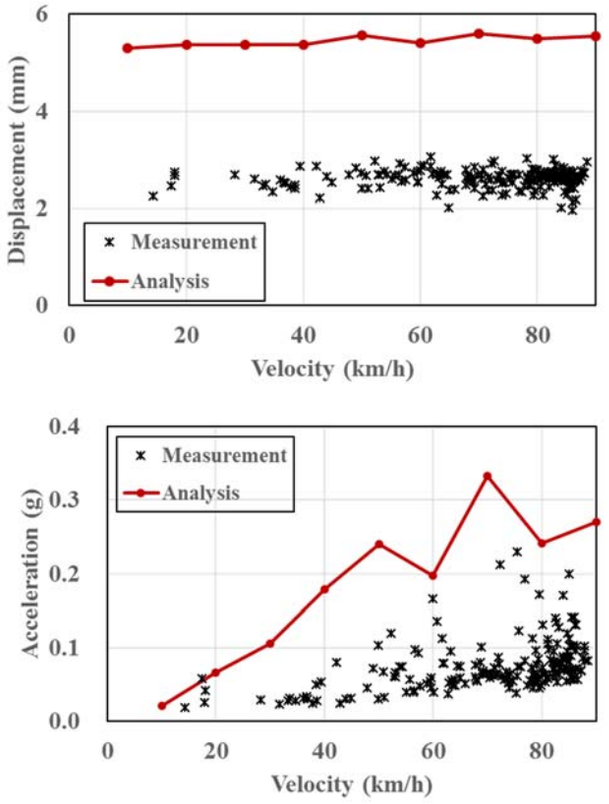


Figure 10. Comparison of measured and analytical values by velocity (B bridge, 86-axles train)

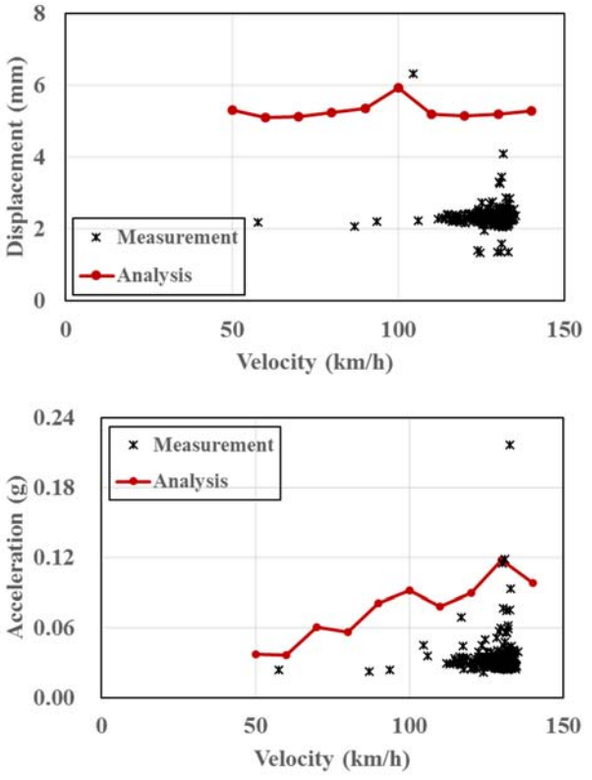


Figure 11. Comparison of measured and analytical values by velocity (C bridge, 24-axles train)

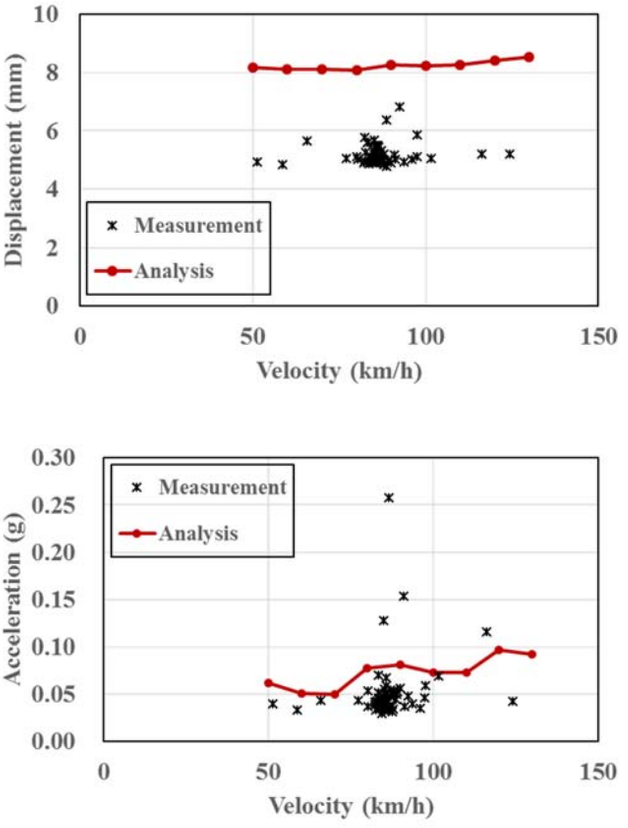


Figure 12. Comparison of measured and analytical values by velocity (C bridge, 54-axles train)

5 CONCLUSIONS

This paper investigates and evaluates the deflection and acceleration criteria for traffic safety and passenger comfort of the steel box girder railway bridge by experimental and analytical study. Tests have been performed over 40 days on three steel box girder bridges. Structural analysis of bridges by moving trains was performed to compare measured values with analytical values.

Following conclusions may be drawn from this study;

1. In case of measured deflection, results of this study fully satisfy design criteria in terms of passenger comfort and traffic safety.
2. In case of acceleration, some test values exceed the design limit in some bridges. Analytical values generally show the same trends as test values.
3. Displacements of the bridges at midspan are proportional with the number of train axes.

As a further study, both experimental and analytical studies should be carried out in order to reduce the vibration of steel bridges.

ACKNOWLEDGEMENTS

This research was supported by a grant(17RTRP-B067919-05) from Railroad Technology Research Program funded by Ministry of Land, Infrastructure and Transport of Korean government. The authors wish to express their gratitude for the financial support.

REFERENCES

CEN(2005) Eurocode 0, Basis of structural design, EN 1990:2002(E), pp. 74~83.

Hwang, E. S., Kim, D. Y., Yeo, I. H. (2016) Probabilistic Analysis on Dynamic Response of Steel Box Girder Bridge by Actual Passing Trains, Journal of Korean Society of Steel Construction, KSSC, Vol.28, No.3, pp.163-171. (in Korean)

Kim, S. I., Kwak, J. W., (2012) Traffic Safety and Passenger Comforts of Railway Bridges, KSSC Jun. 2012, Korea Society Steel Construction, pp. 39~46.

KOREA RAIL NETWORK AUTHORITY (2013) Rail Design Standard (Roadbed), MOLIT, pp. 8-80~8-88.

Kyung, K. S., Lee, S. J., Park, J. E., Cha, C. J., (2012) A Study on Repair/ Retrofit for Deteriorations of Steel Bridge -Behavior Characteristics of Welded Joint Part of Flange and Repair/Retrofit of Fatigue Crack in Railway Steel Bridge-, Journal of Korean Society of Steel Construction, KSSC, Vol.24, No.6, pp.613-625. (in Korean)

MIDAS(2005), Structural Analysis by Midas Civil.

Park, Y. M., Kim, D. H., KIM, H. S., Park, J. B. (2014) Evaluation of Impact Factor in Suspension Bridges under A Series of Moving Vehicles, Journal of Korean Society of Steel Construction, KSSC, Vol.26, No.5, pp.486-498. (in Korean)

Park, J. B., Park, Y. M., Kim, D. H., Lee, J. H. (2013) Evaluation of Impact Factor in Composite Cable-Stayed Bridges under Reliability-based Live Load Model, Journal of Korean Society of Steel Construction, KSSC, Vol.25, No.4, pp.335-346. (in Korean)

UIC 776-2(2009) Design requirements for rail-bridges based on interaction phenomena between train, track and bridge, pp. 7~15.

Maintenance, Safety, Risk, Management and Life-Cycle Performance of Bridges – Powers, Frangopol, Al-Mahaidi & Caprani (Eds)
© 2018 Taylor & Francis Group, London, ISBN 978-1-138-73045-8

The Ultimate Limit State vs. Limit Analysis of masonry arch bridges

T. Kamiński
Wrocław University of Technology, Wrocław, Poland

ABSTRACT: The paper presents features of procedures dedicated to assessment of masonry arch bridges (MAB). Two essentially different approaches, i.e. based on the Ultimate Limit State and the Limit Analysis, commonly used in load carrying capacity evaluation of various structural systems are described and their potential and effectiveness in application to MAB are discussed. Various formulations of the methods are presented depicting fundamental differences between them. Basic features of the methods are explained in relation to characteristic structural behaviour of masonry arch barrel determined mainly by its non-tensile-resistant material. Limit criteria governing the methods are defined and commented. The margin of safety that is provided by means of safety factors (partial or global ones) within the corresponding methods is presented and used to show essential differences between the approaches. The theoretical considerations are supplemented with several case studies of advanced numerical analysis of bridges with different geometry realistically simulating behaviour of the structures at the ultimate loading. Carried out analyses are based on finite element models taking into account all crucial features of the bridges including nonlinear material properties as well as geometrical nonlinearities related e.g. to contact problem between structural components. Results of the simulations are referred to criteria of the theoretical assessment methods revealing their advantages and drawbacks in case of such structures. The work is summarised with conclusions giving basis for determination of general assessment procedures that could be included in still missing modern codes for evaluation of existing masonry arch bridges.

1 INTRODUCTION

Assessment of masonry arch bridges has been a research topic as well as a subject or engineering work for a long time. Therefore there is a large number of different approaches to the problem including both analytical and numerical methods. Application of each of the procedures needs deep understanding of its consequences in terms of the obtained results and possibilities of their further use.

Two essentially different approaches, i.e. based on the Ultimate Limit State (ULS) and the limit analysis (LA), commonly used in load carrying capacity evaluation of various structural systems are described and their potential and effectiveness in application to masonry arch bridges are discussed. Basic features of the methods are explained in relation to characteristic structural behaviour of masonry arch barrel determined mainly by its non-tensile-resistant material. Limit criteria governing the methods are defined and commented. Finally the margin of safety that can be reached by means of safety factors (partial or global ones) within the corresponding approaches are presented and further used to show essential differences between the approaches as well as to indicate the most appropriate way of analysis of masonry arch bridges.

2 THE ULTIMATE LIMIT STATE OF MAB

Analysis based on the Ultimate Limit State (ULS) is a common element of procedures dedicated to load carrying capacity evaluation of various structural systems. It is precisely determined by many standards (like Eurocodes) for designing of different structures including masonry walls, however in case of masonry arches the existing codes are not directly applicable.

Anyway, the idea of checking the ULS may be applied in analysis of MAB however it needs proper selection of the limit criteria and right understanding of

the results possible to get by means of such a verification.

The basic feature of the procedure in application to MAB is checking of a given limit criteria in a critical section of the arch barrel. The considered section is chosen as that one where the extreme values of a given criteria are exceeding the limit value first during increasing of the applied loads. Thus, the check is limited to a single section what is very conservative approach in case of masonry arch barrel regarded as a triple statically indeterminate element. It means that failure of a single section related to formation of a so-called plastic hinge do not threaten the global stability and safety of the whole arch. Only four hinges at least are needed to provoke the bridge collapse.

The limit criteria which one can formulate are corresponding to the level of:

1. tensile strength (f_t)
2. cracking depth (δ),
3. compressive strength (f_c)
4. shear strength (f_v)

The given order of the criteria is representing subsequent steps of real section gradual destruction with increasing load level. In the first step, the whole arch barrel is under compression what means that the thrust line is contained within the middle third of the arch profile i.e. the resultant force in each section of the arch lays within the section core.

Criterion 1. is related to control of cracking occurrence which takes place at the lowest level of loads (see e.g. Fig. 3). UIC Code 778-3R recommends value of $f_t = 0.5$ MPa. Practically the tensile strength should be assumed even lower: $f_t = 0.05 \div 0.10$ MPa what takes into account typical technical condition of MAB suffering from material degradation and overall cracked structure. It is a very conservative criterion as it corresponds to the first appearance of a crack at the edge fibres of the single section, what means that the most part of this section as well as all other sections are under compression.

Criterion 2. is more important than the previous one since it measures the resultant compressive force eccentricity acting in the section. It is expressed usually in a relationship to the arch thickness, i.e. $\delta = d_c/D$ where d_c is the cracking depth and D is the arch thickness. The limit value of δ is usually assumed equal to 0.7-0.8. UIC Code 778-3R recommends value of $\delta = 0.75$. Deeper cracking influences the arch durability because an intensive opening and closing of the crack may accelerate the material degradation.

Criterion 3. seems to be the most useful as it may indicate some real threat to the arch barrel stability. Exceeding the compressive strength leads to crushing of the material at the edge of the section and further to redistribution of internal forces. In extreme case it is related to significant deformation of the compressed part of the section, formation of a plastic hinge or even to punching-through of the arch in this area.

Criterion 4. is the least important condition since sufficiently large transverse forces to threaten the arch shear strength occurs very rarely. It may happen only in specific combinations of arch geometry (with low rise-to-span ratio) and loading conditions (distributed over wider area to eliminate hinge formation occurring before). This criterion will be therefore ignored further within this study.

The order of reaching the criteria 2. to 4. by corresponding static effects in a section may be changed in some unusual cases or some of them (mainly 2. and 3.) may be reached at the same time.

An important element of ULS analysis are partial safety factors. They are applied to loads (usually increasing their values) as well as to the material resistance (as reducing factors). This essential idea of the load and resistance factor separation is found to provide the largest level of the structure safety, however its usefulness to MAB will discussed further.

Linear or non-linear material models may be applied in ULS analysis but the linear models are appropriate at the level of criterion 1. only. The limit values to check the other criteria are possible to be calculated in linear models, however to perform reasonable verification the nonlinear models are indispensable.

There are many practical implementations for checking the presented limit criteria which are utilising both numerical, like FEM, and analytical solutions, based e.g. on the thrust lines (Heyman, 1982 or Harvey 1988) or interaction envelopes. Various formulations of the interaction envelopes were proposed by many authors including for instance *N-M* (Boothby, 2001) or *N-M-V* (Martín-Caro et al, 2001) envelopes.

3 THE LIMIT ANALYSIS OF MAB

Limit Analysis (LA) contrary to ULS concentrates on the real collapse load of a given structure only. Its application to MAB is very useful since it provides information on behaviour of the whole structure at extreme loads and on associated failure mode. It was elaborated by Heyman (1982). The main advantage of the LA is simultaneous consideration of all sections of the arch barrel. The limit criterion is the loss of the global stability of the structure which corresponds to the failure (ultimate) load value of a given loading scenario (usually a single axle load located over a quarter of the span). All input data to carry out the limit analysis defining both the loads as well as material properties should have characteristic (unfactored) values. By means of such analysis one can find out how far is any exploitation real load value from that one leading to collapse and in this way a realistic margin of safety may be determined. Following this concept, a global safety factor γ_{fL} may be applied to the collapse load value to determine the admissible load

for the given structure and loading scenario. According to British recommendations (Department of Transport, 2001) the safety factor should be $\gamma_{fL} = 3.4$.

As the result of limit analysis also the collapse mode corresponding to the ultimate load scenario is being found. It is mainly based on a four-hinge mechanism which is the critical (the most easily reachable) for definite majority of MAB topologies. Although other mechanisms are also possible theoretically, they usually correspond to load scenarios which are not the most unfavourable for the structure (e.g. a five-hinge mechanism in case of a concentrated force located in the mid-span).

In specific cases some difficulties with triggering of the structure failure (the mechanism of collapse) may occur, especially considering more complex load scenarios (like multi-axle vehicles). One can also encounter some problems analysing massive structures with thick arch and its low rise-to-span ratio or with large height of the backfill over the arch. Than so-called geometrical blocking of the arch may appear or failure of the soil itself may dominate limiting development of typical collapse mechanism of the arch. However, it does not show any general weakness of the LA but indicates limitation of its applied formulation simply not covering the actual mechanism governing the collapse in the given case. That kind of difficulties are related to general feature of MAB defined by large capacity and geometrical stability for which the only possible collapse mechanism requires sometimes consideration of extensive material crushing or structural system general reconfiguration including e.g. support movements.

Among the available solution methods applied in LA especially those based on upper bound theorems and discontinuous models, like Kinematic Method (Kamiński & Bień 2013), Rigid Block (RB) analysis (Gilbert & Melbourne 1994) or Discrete Element Method (DEM) (Costa & Kamiński 2016), are the most useful and efficient in determination of the ultimate load and failure mode of MAB. The continuous models of masonry, like those based on macro- modelling within Finite Element Method (FEM), are less effective in the expected failure simulation mainly due to strain localization problem. However, using e.g. a specific masonry discretization technique called meso-modelling (Kamiński 2008) may solve this problem and allow to search the ultimate load also within FEM as a lower bound approach.

4 SELECTION OF APPROACH

Selection of the most appropriate approach from among ULS and LA to solve a studied problem is dependent on the actual purpose of analysis i.e. whether it is an element of a designing process of a new structure or a check of an existing bridge. Thus, the ULS is the standard approach in the first case while the LA may be more convenient in the second one. Anyway, consideration of complex design load models is practically reachable in ULS only due to aforementioned problems.

Final choice of the procedure should consider also better control over the safety margin possible to get within the chosen approach. As it is shown in one of the next chapters with some representative case studies, this selection may be dependent on the analysed bridge geometry. Also fragility of results to inaccuracy of the problem formulation (related e.g. to wrong input data assumption or improper structure representation) should be also the matter of consideration.

To simplify the choice the basic feature of ULS analysis vs. Limit Analysis in application to masonry arch bridges is summarised in Table 1.

Table 1. Basic feature of ULS analysis vs. Limit Analysis of masonry arch bridges

Considered feature	Ultimate Limit State Analysis	Limit Analysis
Checked member/section	arch barrel single section	all sections of the arch barrel
Limit criteria	1. tensile strength (f_t) 2. crack depth (δ) 3. compressive strength (f_c) 4. shear strength (f_v)	global stability
Safety factors	partial safety factors (material & load factors)	global safety factor
Nature of parameter values	design	characteristic
Available solution methods	static method, FEM, thrust line method, interaction envelopes	Rigid Block Analysis, kinematic method, DEM, FEM, thrust line method
Model linearity	linear of non-linear models	non-linear models only
Load scenarios	any	single axle load mainly
Consideration of support settlement	available	not directly covered

Extent of load value increase (analysis duration time)	carried out until the first section failure	carried out until getting of the global collapse

5 THE APPLIED MODEL

5.1 *General description*

The aim of the computations is to determine the ultimate load bearing capacity considering the two approaches: based on ULS and LA. Plane two-dimensional Finite Element models of masonry bridges representing: the arch barrel, the soil above the arch barrel and in the access zones, pavement layer and a loading element are adopted in the analyses, see Figure 1. The model is defined as a plane-strain problem and it represents a unit width of the bridge structure what is a standard procedure validated by means of numerous laboratory and field tests (Kamiński 2010, Hojdys et al 2013 or Kamiński & Machelski 2016). The bridge is subjected to an external loading simulating a single axle pressure coming from a vehicle against which the load bearing capacity is being evaluated.

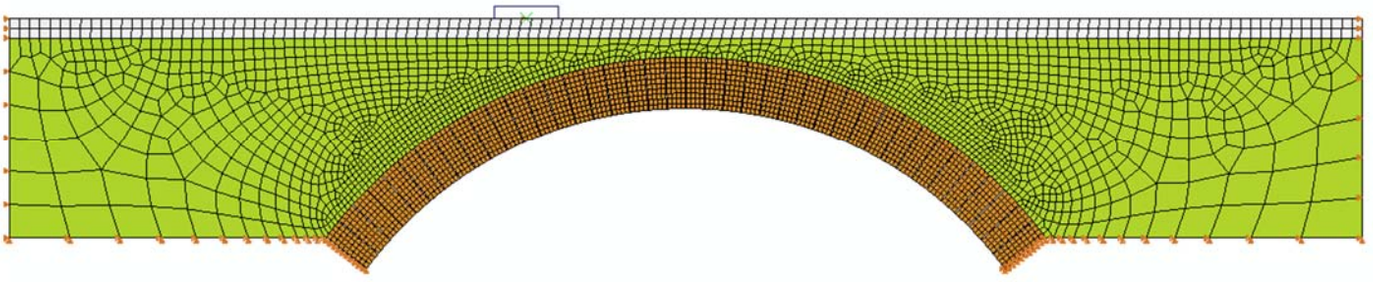


Figure 1. 2D FE model of a masonry arch bridge.

5.2 *Details of the numerical model*

The arch barrel is modelled as a continuous area, however an original modelling technique developed by author (Kamiński 2007, 2008), called meso-modelling, was used to discretise the masonry arch. The distinguishing feature of this modelling technique is division of the arch area into the so-called masonry segments, comprising groups of several masonry blocks together with the joints between them, and into layers of radial joints between the segments. The masonry segments are defined by an orthotropic material model with the mechanical characteristics defined using the a two-stage laminar material homogenization XY (according to Lourenço 1996). Since the selected radial joints (between the masonry segments) are the areas where the arch barrel cracking occurs forming the typical failure mode, they are modelled with special care. The material of joints defined as a plastic-damage model (proposed by Lubliner et al. 1989 and Lee & Fenves 1998) corresponds to the constitutive model of concrete. A simplified representation of σ-ε relationship for uniaxial behaviour of the mortar material is presented in Figure 2.

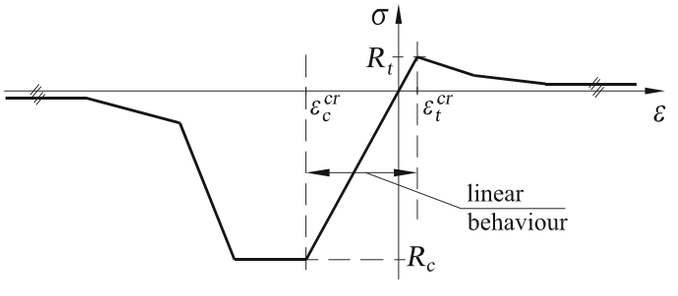


Figure 2. σ-ε relationship for uniaxial behaviour defining concrete-like material model of mortar.

The branches covering compression and tension outside the linear elastic range of σ-ε relationship are precise determined by means of strain hardening/softening curves. The initial yielding stresses at tension and compression are equal to: f_t = 0.10 MPa and f_c = 4 MPa correspondingly, while they are being reduced to one order lower values at extremities of the diagram in Figure 2.

Other main and common material properties of the bridges assumed in analyses are shown in Table 2 where: $\gamma_{M/pav}$,γ_f = unit weights of masonry/pavement and backfill; E_m, E_b, E_f, E_p = modulus of elasticity of mortar, bricks, backfill and pavement; c = cohesion of the backfill; ϕ = angle of internal friction of the backfill, μ = coefficient of friction between arch barrel and the soil.

Table 2. Material properties of the analysed bridges.

Parameter	$\gamma_{m/pav}$	γ_f	E_b	E_m	E_f	E_p	ϕ	c	μ
	kg/m^3	kg/m^3	GPa	GPa	MPa	MPa	deg	-	-
Value	2000	1850	10	1.0	50	100	45	10	0.4

The applied modelling technique significantly simplifies the mesh and reduces the number of required finite elements. At the same time it simplifies simulation of the arch failure and reaching the actual ultimate load of the structure which is usually impossible with application of typical continuous models like those based on macro-modelling technique. In many non-linear analyses presented in literature the

first problems related to numerical convergence are interpreted as the moment of getting the limit load level which in fact is much before the actual ultimate load of the analysed structure.

At the boundary between the backfill and the arch the contact elements are defined. They represent interaction between the contacting bodies by means of compressive and shear forces but without transfer of the tension.

The live load is applied by means of a rigid block acting through a contact line on the upper edge of the pavement covering the soil from the top (see Figure 1). Such a solution enables one to apply conveniently the load in any position without limiting the transverse displacements of the soil under the loading block. In the presented analyses the load is located at the quarter of the span. The boundary conditions limit the horizontal translation of the rigid body.

5.3 *Analysis procedure*

The solution is carried out incrementally in two consecutive steps: in the first one self-weight of all structural components is applied, in the second one the live load acting through the rigid block is added. The incremental application of the live load is controlled by means of the vertical displacement of the loading block. Such a solution gives a better control over the development of the global failure of the structure and enables one to reach and exceed the limit state which is the goal of the analysis. The ultimate (collapse) load P_{ult} is defined by the highest value of the load taken from the relationship between the vertical displacement u of the loading block and the applied concentrated force P equal to the reaction on the block. In the analysed cases a sufficient displacement u to reach the limit state is equal to a few centimetres. In most of the cases the number of increments was about 20 for the first step and at least 300 for the second step.

6 CASE STUDIES

6.1 *Considered bridge parameters*

The basic geometrical parameters of the analysed bridges are presented in Table 3, where L = arch clear span; r/L = rise-to-span ratio; D = arch thickness; h = backfill height over the crown; w = length of loading block. In total 8 various cases are considered varying in arch rise and thickness.

Table 3. Geometrical parameters of the case studies.

Parameter	L	r/L	D	h	w
	m	m	m	m	m
Values	5.0	1/2; 1/4; 1/6; 1/8	0.25;0,40	0.3	0.5

The material properties given in Table 2 are prescribed to the model components with their characteristic values. Although for ULS analysis the material self-weights should be factored, in fact diverse effect of different regions of the structure on the considered limit criteria influenced the decision to leave the masses of the materials unfactored.

6.2 *Results of analyses*

The main result of analyses are included in Table 4 corresponding to considered arch geometries in consecutive rows. In the central columns of the table various limit criteria defined on the basis of those presented in chapters 2 and 3 are indicated which are:

1. tensile strength of mortar (f_t)
2. cracking depth of a mortar joint (δ)
3. design value of the mortar compressive strength (f_{cd})
4. characteristic value of the mortar compressive strength (f_{ck})
5. the ultimate compressive stress value within the mortar (σ_{cu})
6. the ultimate load (P_{ult})

The design value of the mortar compressive strength (f_{cd}) is calculate on the basis of its characteristic value (f_{ck}) using a material safety factor $\gamma_m = 2.0$ (according to Eurocode 6, 2005).

For each case study the external load values P_c accompanying the moments of reaching the given failure criteria by the analysed static effects in the critical section are presented in the form of absolute value as well as a percentage of the ultimate load P_{ult}. As the critical section is taken that one where the static effects get the limit criteria first within the arch during the process of increasing the load. In all considered bridges the critical section of the arch has been localized directly under the live load. Also the limit criteria values governing each case are given in Table 4 differing in the values of δ and σ_{cu}. The other limit criteria values are assumed the same for all cases.

The criterion 3. (f_{cd}) is directly utilized in ULS analysis while the criterion 6. (P_{ult}) – in LA to calculate the admissible load values for the external loading according to the following equations 1 & 2 (for each approach correspondingly):

$$P_{adm.d} = \frac{P\left(f_{cd}\right)}{\gamma_f} \tag{1}$$

$$P_{adm.k} = \frac{P_{ult}}{\gamma_{fL}} \tag{2}$$

where $P_{adm,d}$ = admissible load calculated on the basis of ULS analysis; $P_{adm,k}$ = admissible load calculated on the basis of LA; γ_f = live load safety factor equal to 1.35 (according to Eurocode 1); γ_{fL} = global safety

factor equal to 3.4 (according to Department of Transport, 2001).

Table 4. Results of analyses

Geometry			Load levels at given criteria [kN]							Admissible loads [kN]	
L_0 [m]	r [m]	D [m]	Criterion	f_t	δ	f_{cd}	f_{ck}	σ_{cu}	P_{ult}	$P_{adm,d}$	$P_{adm,k}$
			criterion value	100 kPa	0.8	2 MPa	4 MPa*	3.7 MPa**			
5.0	2.50	0.40	load value	30	69	91	199	218	219	67	64
			% of $P_{ult/adm,k}$	13	32	42	91	100		105	
			criterion value	100 kPa	0.8	2 MPa	4 MPa	4.5 MPa			
5.0	1.25	0.40	load value	32	113	112	175	215	217	83	64
			% of $P_{ult/adm,k}$	15	52	52	81	99		130	
			criterion value	100 kPa	0.8	2 MPa	4 MPa	5.2 MPa			
5.0	0.833	0.40	load value	34	235	127	224	297	300	94	88
			% of $P_{ult/adm,k}$	11	78	42	75	99		106	
			criterion value	100 kPa	0.7	2 MPa	4 MPa	5.2 MPa			
5.0	0.625	0.40	load value	35	- ***	125	247	363	388	92	114
			% of $P_{ult/adm,k}$	9	-	32	64	94		81	
			criterion value	100 kPa	0.8	2 MPa	4 MPa*	3.5 MPa**			
5.0	2.50	0.25	load value	21	51	55	102	103	104	41	31
			% of $P_{ult/adm,k}$	20	49	53	97	99		133	
			criterion value	100 kPa	0.8	2 MPa	4 MPa	4.4 MPa			
5.0	1.25	0.25	load value	22	62	58	91	103	103	43	30
			% of $P_{ult/adm,k}$	22	60	56	88	100		141	
			criterion value	100 kPa	0.8	2 MPa	4 MPa	5.2 MPa			
5.0	0.833	0.25	load value	23	88	62	94	110	110	46	32
			% of $P_{ult/adm,k}$	21	80	56	86	100		141	
			criterion value	100 kPa	0.7	2 MPa	4 MPa	4.7 MPa			
5.0	0.625	0.25	load value	23	87	66	113	135	135	49	40
			% of $P_{ult/adm,k}$	17	64	49	84	100		124	
			$\overline{\%\text{ of } P_{ult/adm,k}}$	16	59	48	83	99		120	

* stress equal to f_{ck} reached in another than the critical section
** ultimate compressive stress in the critical section lower than f_{ck}
*** cracking do not reach limit criteria δ

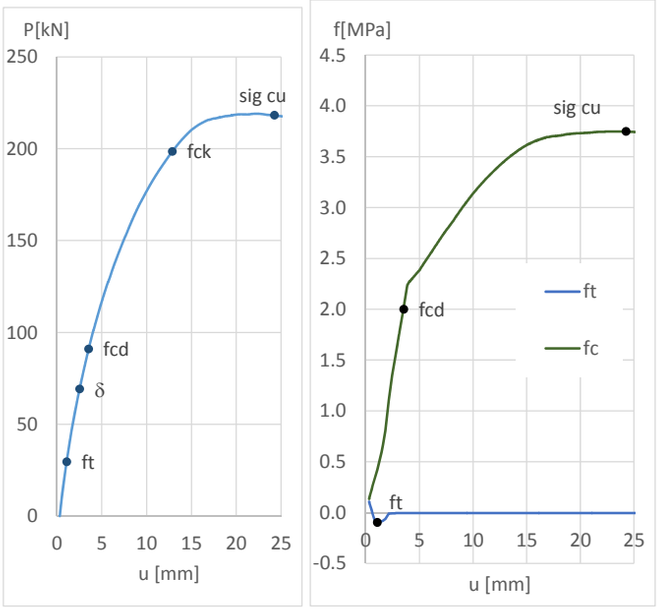


Figure 3. Obtained relationships for the bridge with r = 2.5 m and D = 0.40 m with marked points of reaching the limit criteria: a) load-displacement P-u, b) stress-displacement f-u

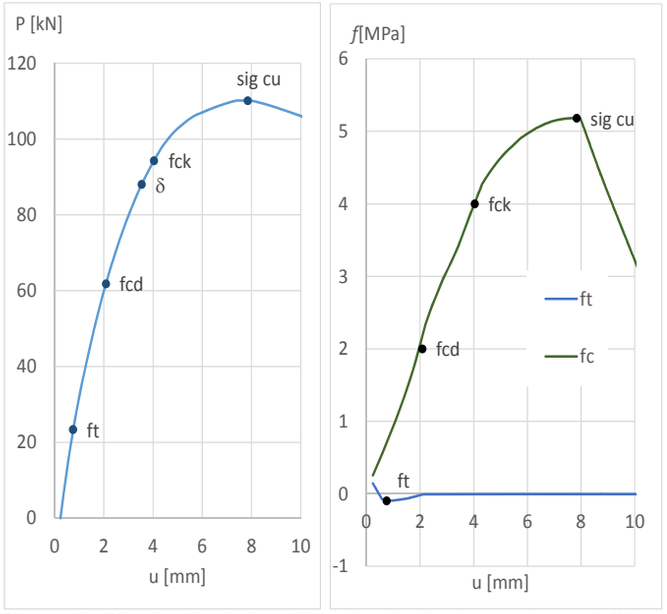


Figure 4. Obtained relationships for the bridge with r = 0.83 m and D = 0.25 m with marked points of reaching the limit criteria: a) load-displacement P-u, b) stress-displacement f-u

The calculated values of the admissible loads $P_{adm,d}$ and $P_{adm,k}$ are presented for each case study in the last two columns of the Table 4. Additionally the ratios of $P_{adm,d}$ to $P_{adm,k}$ are given at the bottom of each row on the percentage basis. At the bottom of the table average values of the ratios P_c/P_{ult} and $P_{adm,d}/P_{adm,k}$ expressed on the percentage basis are provided.

The relationships between applied force P and displacement u as well as between compressive/tensile stresses and displacement u for two representative cases of bridges: with r = 2.5 m, D = 0.40 m and r = 0.83 m, D = 0.25 m are shown in Figures 3 & 4, correspondingly. It the diagrams the characteristic points showing the moments of reaching the limit criteria by the controlled static effects are shown.

6.3 *Discussion of the results*

Obtained fundamental results including P_c/P_{ult} and $P_{adm,d}/P_{adm,k}$ ratios are generally quite similar for most of the considered cases. The order of criteria being reached by the controlled static effects along with the increase of the load P is similar for arches of a given r/L ratio. For deep arches they are ordered according to the list: f_t, δ, f_{cd}, f_{ck}, σ_{cu}, P_{ult}. However for shallow arches (with $r/L \leq 1/4$) the limit criterion δ is reached after f_{cd} (or even never). In some cases representing deep arches (with r/L = 1/2) f_{ck} is not reached in the critical section before P_{ult}. In such cases (which should be separately and more precisely studied) the ultimate compressive stress within the mortar of the critical section gets value $\sigma_{cu} < f_{ck}$ while f_{ck} is reached in another section.

Criterion f_t is satisfied at very low values of P not exceeding 22% (16% on average) of P_{ult} and thus it is not useful nor representative for the load bearing capacity evaluation of MAB.

Criterion δ equal to 0.7-0.8 is mostly reached by the critical section cracking but for specific structural system configurations it may be even more extensive in other sections after reaching σ_{cu} in the critical section. In one case of a flat thick arch it did not reach even 0.7. A separate careful study of δ development within the whole arch is planned as a subject of further works.

f_{cd} directly represents the fundamental limit criterion being checked within ULS procedures predicted e.g. by Eurocodes. It is reached for the considered typical structures at levels of P equal on average to 48% of P_{ult}.

f_{ck} is directly related to actual yielding of material in uniaxial compression, thus the level of P referring to this criterion should be of crucial importance. It is reached at P values close to 80% of P_{ult} on average.

σ_{cu} is presented as supplementary information to pay attention to the fact that material of the masonry arch is undergoing two- or three-axial compression what leads to the effect of reaching by the stresses values higher than f_{ck} (by even up to 30%). The ultimate stresses are reached on average at 99% of P_{ult} what is usually related to actual collapse of the structure.

The admissible load values P_{adm} calculated by means of both approaches are quite similar, however higher values are mostly obtained within ULS analysis. The opposite situation was encounter for only a single structures from the considered case studies representing a thick and shallow arch.

7 CONCLUSIONS

Comparison of two basic approaches to assessment of MAB in terms of their applicability, effectiveness and consequences of application has been presented. The essential results in the form of admissible load values P_{adm} calculated by means of the both methods are found to be generally similar with more conservative values obtained by means of Limit Analysis. Valuable information may be gathered following development of considered static effects (extreme stresses and cracking) within the critical section in the domain of load P revealing the gradual process of the structure destruction along with the increase of the applied loading.

Values of the applied load P_c corresponding to reaching by the static effects the successive limit criteria (f_t, δ, f_{cd}, f_{ck}, σ_{cu}) referred to the ultimate load value P_{ult} allow to answer the following general questions related to analysis MAB:

- what is the typical order of limit criteria which are consecutively satisfied along with the increase of the external load P, and

- how far from the ultimate load P_{ult} are the load levels P_c corresponding to reaching the limit criteria.

All these conclusions may be useful for defining the safe ranges of the MAB loading and establishing the safety factor for corresponding approaches. The presented work could be also a basis for selection of the crucial limit criteria to be included in modern procedures of ULS analysis of MAB. Such analysis should be a part of general procedures for condition evaluation of MAB (Helmerich et al. 2012, Kamiński & Bień 2015).

REFERENCES

Boothby T.E., 2001. Load Rating of Masonry Arch Bridges, *Journal of Bridge Engineering ASCE* (6): 79–86.

Costa C. & Kamiński T. 2016. Comparison of various modelling techniques applied in analysis of masonry arch bridges, *8th International Conference on Arch Bridges, Wrocław, Poland, October 5-7, 2016*: 835-842.

Department of Transport, 2001. *BA 16/97 The Assessment of Highway Bridges and Structures.* Design Manual for Roads and Bridges: Volume 3. Section 4. Part 4.

Eurocode 1. 2003. EN 1991-2: Actions on structures. Part 2: Traffic loads on bridges.

Eurocode 6. 2005. EN 1996-1-1: Design of masonry structures. Part 1-1: General rules for reinforced and unreinforced masonry structures.

Gilbert M. & Melbourne, C., 1994. Rigid-block analysis of masonry structures, *The Structural Engineer* (72) 21: 356-361.

Harvey, W.E.J., 1988. Application of the mechanism analysis to masonry arches, The Structural Engineer (66): 77-84.

Helmerich, R., Niederleithinger, E., Trela, C., Bień, J., Kamiński, T. & Bernardini, G. 2012. Multi-tool inspection and numerical analysis of an old masonry arch bridge. *Structure and Infrastructure Engineering*, 8(1): 27-39.

Heyman, J., 1982. *The Masonry Arch*, Ellis Horwood,

Hojdys, Ł., Kamiński, T. & Krajewski, P. 2013. Experimental and numerical simulations of collapse of masonry arches. In *7th International Conference on Arch Bridges, Trogir-Split, Croatia*: 715-722.

Kamiński T., 2007. Three-dimensional modelling of masonry arch bridges based on predetermined planes of weakness, *5th International Conference on Arch Bridges, Funchal*: 525-533.

Kamiński, T. 2008. Mesomodelling of masonry arches. In 6th International Conference *AMCM'2008 – Analytical Models and New Concepts in Concrete and Masonry Structures Łódź, Poland, 9-11 June, 2008*: 359-360.

Kamiński, T. 2010. Tests to collapse of masonry arch bridges simulated by means of FEM, *5th International Conference on Bridge Maintenance, Safety, Management and Life-Cycle Optimization (IABMAS 2010)*: 1420-1427, Philadelphia, USA.

Kamiński T. & Bień J. 2013. Application of Kinematic Method and FEM in Analysis of Ultimate Load Bearing Capacity of Damaged Masonry Arch Bridges, *Procedia Engineering* (57): 524–532.

Kamiński T. & Bień J. 2015. Condition assessment of masonry bridges in Poland, *National Conference on Bridge Maintenance and Safety of Bridges (ASCP'2015), June 25-26, 2015:* 126-135. Lisbon, Portugal.

Kamiński T. & Machelski Cz. 2016. Experimental and numerical study on displacements of masonry bridges under live loads, *8th International Conference on Arch Bridges, Wrocław, October 5-7, 2016*: 1019-1028.

Lee, J.S., Fenves, G.L., 1998. Plastic-Damage Model for Cyclic Loading of Concrete Structures, *Journal of Engineering Mechanics* 124(8): 892-900.

Lourenço, P.B., 1996. Computational strategies for masonry structures, PhD Thesis, Delft University Press, The Netherlands.

Lubliner, J., Oliver, J., Oller, S. & Oñate, E., 1989. A Plastic-Damage Model for Concrete, *International Journal of Solids and Structures* 25(3): 229-326.

Martín-Caro J.A., Martínez J.L., León J. & Lopez L., 2001. A Methodology for the Assessment of Masonry Arch Bridges, *3rd International Conference on Arch Bridges, Paris, September 19-21.*

UIC Code 778-3R. 1995. Recommendations for the assessment of the load carrying capacity of existing masonry and mass-concrete arch bridges.

Maintenance, Safety, Risk, Management and Life-Cycle Performance of Bridges – Powers, Frangopol, Al-Mahaidi & Caprani (Eds)
© 2018 Taylor & Francis Group, London, ISBN 978-1-138-73045-8

Importance of Simulation in the Design of Experimental Tests

M. Karalar
Bulent Ecevıt Universıty, Department of Cıvıl Engineering, TURKEY
M. Dicleli
Middle East Technical University, Department of Engineering Sciences, TURKEY

ABSTRACT: Linear and Nonlinear finite element (FE) models of the steel H-pile specimens used in the experimental test set up are developed using the computer program ANSYS to identify potential problems that may be encountered during testing and to improve the test apparatus. First, linear FE models of the steel H-pile specimens are built to determine maximum stress concentrations occurring in the HP sections and the steel base fixture used for fixing the pile to the testing frame. From these linear analyses results; the locations of stress concentrations in the HP sections are identified. Using these results, the test set up is modified to decrease the stress concentrations. Then, nonlinear FE analyses of the steel H-pile specimens are repeated on the modified specimen model to observe the distribution of stresses and strains in the steel HP sections and the steel base fixture. Then, low cycle fatigue tests are conducted to investigate the fatigue life of steel H-piles subjected to thermal induced cyclic strains/displacements. In the experimental part, HP220x57 pile specimens are tested to estimate the low cycle fatigue life of steel H-piles as a function of large flexural strain cycles with various amplitudes. Using the FEM, comparisons between FE model predictions and experimental test results are made in terms of fatigue life in the steel H-pile specimens. Consequently, it is shown that nonlinear FEMs of the steel H-pile used in the experimental part should be used to identify potential problems that may be encountered during testing and to improve the test apparatus if necessary.

1 GENERAL INSTRUCTIONS

Traditionally, engineers have used laboratory testing to investigate the structural behaviour of bridge, steel building products and systems subject to the expected wind loads, live loads, earthquake loads and the temperature-induced lateral displacements and to develop appropriate design rules. Laboratory testing is also used to develop new building products and systems. However, time-consuming and too expensive laboratory tests have delayed progress in this area. Thus, the product manufacturers and designers often decided on traditional designs to avoid expensive and time-consuming laboratory testing. However, advances in the field of computer aided engineering during the last two decades have changed this situation significantly in many engineering industries, especially in the field of structural and bridge engineering. In the bridge and steel building industry, the use of advanced FE tools has not only allowed the introduction of innovative and efficient building products, but also the development of accurate design methods.

Bridge structural and loading conditions can change over the life of the bridge. Especially, due to seasonal temperature changes, the abutments are pushed against the approach fill and then pulled away, causing lateral displacements at the top of the piles that support the abutments as shown in Fig.1. This may result in the reduction of their service life due to low-cycle fatigue effects. Although bridge engineers (Dicleli,2000, French et al., 2004, and Razmi 2013) have already predicted that low cycle fatigue may occur in the steel H piles of integral bridges due to thermal effects, only a few research studies and experimental test results have been found on this topic in the literature.

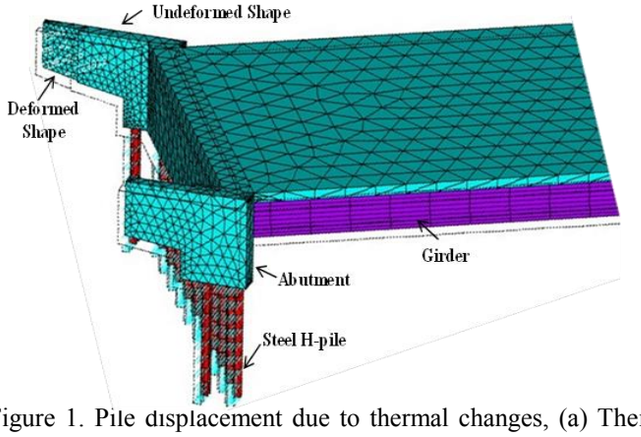


Figure 1. Pıle dısplacement due to thermal changes, (a) Thermal Expansion, (b) Thermal contraction

The main design resource for civil engineers, the American Association of State Highway and Transportation Officials (AASHTO), explains the importance of the fatigue issue in structures only (Wish, 2002), but does not provide any guidelines for fatigue design and its consideration in the steel pile of integral bridges. As the length of integral bridges increases, the temperature-induced lateral cyclic displacements in the steel H-piles at the abutments become larger as well. As a result, the piles may experience cyclic plastic deformations. This may result in the reduction of their service life due to low-cycle fatigue effects. Thus, it is necessary to exactly understand the behavior of piles under cyclic lateral loads. Thus, experimental measurement is needed. However, experimental measurements are often too expensive and time-consuming especially when integral bridge components (abutment, pile, etc.) are subjected to long arbitrary multi-axial cyclic loading histories in service life and also in some cases, experimental measurements can not be performed successfully as shown in Fig.2.

To avoid the huge cost and testing time required for conducting experimental tests, researchers often use some forms of FE analysis to carry out their research. FE analysis predictions have been widely used to evaluate the different models.

The main objective of this research study is to identify potential problems that may be encountered during testing as shown in Fig.2 and to improve the test apparatus for all bridge engineering structure as simulating the low cycle fatigue performance of steel H-piles via FE approach. Using FEMs of the steel H-pile specimens it will be possible to simulate cyclic behavior of steel H-piles under thermal effects in integral bridges, as in actual experimental test set up. Thus, FE models may be used to avoid the huge cost and testing time required for conducting experimental tests.

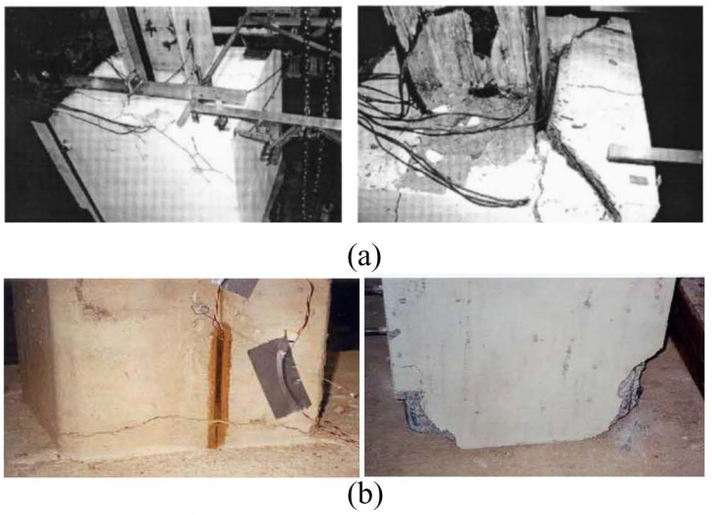


Figure 2. Potential problems that may be encountered during tests, (a) Arsoy ve diğerleri, 1999, (b) Xiao ve diğerleri, 2006

2. LINEAR FINITE ELEMENT ANALYSES

The main objective of the linear finite element analyses is to determine stress concentrations occurring in the HP sections and the steel base fixture. First, linear finite element models of the steel H-pile specimens are developed using the computer program ANSYS. Figure 3 shows the linear finite element model for the HP220x57 section. The HP220x57 section for bending about the strong axis is modeled. The steel base fixture is attached to the testing frame using 30 mm diameter bolts. The steel base fixture-pile interaction is modeled using the frictionless contact algorithm in ANSYS. In the FEM, the HP220x57 section is meshed using ANSYS's automatic mesh generation feature. However, the automatically generated mesh sizes are modified manually in ANSYS to obtain a more accurate simulation of the stress distribution (the mesh size is taken as 25 mm within contact regions and 50 mm within the rest of the model). The model consists of 63,897 tetrahedron elements and 20,657 nodes. Further details on the linear FEM of the test specimen are presented in the following subsections.

2.1 *Element Types*

In the FEM, a structure is divided into small and simple elements. The finite elements used in the model are composed of 10-node high-order tetrahedron elements. Every node has three degrees of freedom: translations in the nodal x, y and z directions. The element has a quadratic displacement behavior and is well suited to modeling irregular meshes (Yazdizadeh, 2010). Further, the contact algorithm of FEM requires definition of contacting surface. To define a contact pair completely, contact and target element have to be referred to same characteristic parameters (Kamil et al. 2011). For the contact elements, CONTA174 is used to represent contact and sliding between 3-D “target” surfaces and a deformable surface. For the target elements, TARGE170 is used to represent various 3-D “target” surfaces for the associated contact elements (Kadhim, 2012). The contact element 174 and target 170 are used as a contact surface-to-surface as shown in Fig.3.

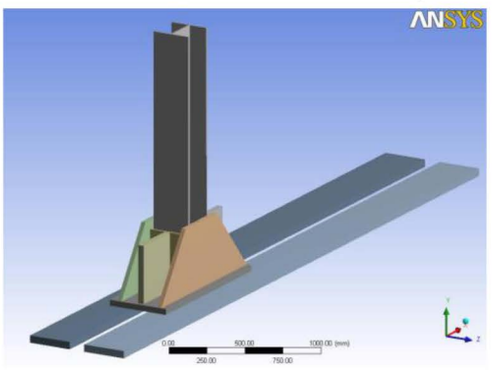


Figure 3. Finite element model for the HP 220x57 section.

2.2 *Contact modeling*

Contact mechanics is the study of the deformation caused by solid bodies that touch each other at one or more points (Popov, 2010). In this study, contact between the HP section and the connection plates is defined as surface-to-surface contact type. This contact type is established when a surface of one body comes in contact with the surface of another body. This contact type is commonly used for arbitrary bodies that have large contact areas (Thomas et al. 2006, Al-Mughairi et al. 2010). In this study, frictionless contact is chosen between the HP section and connection plates as gaps form in the model between contacting bodies. For the remainder of the model, bonded contact is chosen (for the contact with the side plates of the steel base fixture as shown in Fig.4).

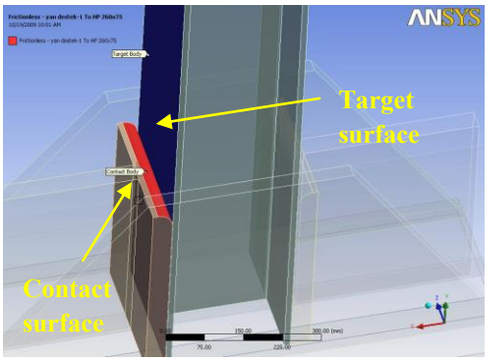


Figure 4. Details of contact surfaces

2.3 *Meshing*

To confirm mesh density used in the FEM, case studies with different mesh sizes on the HP section and connection plates are carried out. Mesh size and type are important for accurate stress values. Thus, four meshing options are tested and compared in the FEM: Automatic, Tetrahedrons, Hex Dominant and Sweep meshing options as shown in Fig.5. The first option, automatically-generated mesh, consists of 13,626 elements and 40,826 nodes. Tetrahedrons mesh consists of 62,303 elements and 20,207 nodes. The other mesh properties are shown in Table 1. In ANSYS, the number of the nodes leads to excessive computation time. Based on these mesh properties, Tetrahedrons meshing option is chosen because the obtained mesh has a better size distribution across the model and the number of the nodes. Then, the selected meshing type, the tetrahedron mesh, is tested using various sizing mesh starting with 250 mm and reducing the mesh size until the results become stable. When the stress values are stable, this mesh sizing can be applicable for FEM analysis. As shown in Fig.6, the maximum stress value in the HP section remains nearly constant for both 50 mm and 25 mm mesh sizes (526 MPa and 529MPa, respectively). Thus, the mesh sizes are input manually and taken as 25 mm within contact regions and 50 mm within the rest of the model.

2.4 *Material Model and Boundary Conditions*

In the nonlinear FEM, the main material model used in this structure is steel. Nonlinear material model is used for steel HP sections with Young's modulus of 200,000 MPa, Poisson's ratio 0.3, tensile yield stress 306 MPa and tensile ultimate stress 421 MPa for the HP220x57 steel section.

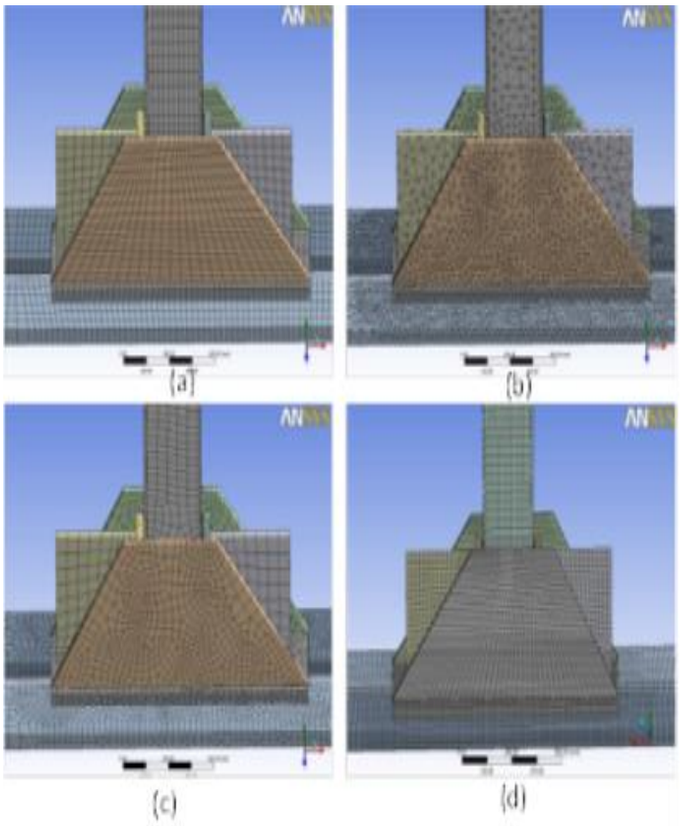


Figure 5. Mesh options, (a) Automatic Mesh generation, (b)Tetrahedrons Mesh, (c) Hex Dominant Mesh, (d) Sweep Mesh.

In addition to material model, correct definition of boundary conditions is of great importance in the FE analysis and, depending on the structure, can greatly affect the behavior. Thus, fixed support means that any movement of the body is restrained, is defined below surfaces of the structure as the boundary conditions. To compare between FE model predictions and experimental test results in terms of fatigue life in the steel H-pile specimens for various lateral and axial load values, fatigue damage model are defined in ANSYS as strain-based model.

Table 1.Numbers of Nodes and Elements for different mesh type.

Mesh Type	Number of Nodes	Number of Elements
Tetrahedrons	20207	62303
Automatic	40826	13626
Hex Dominant	47052	16026
Sweep	43922	14658

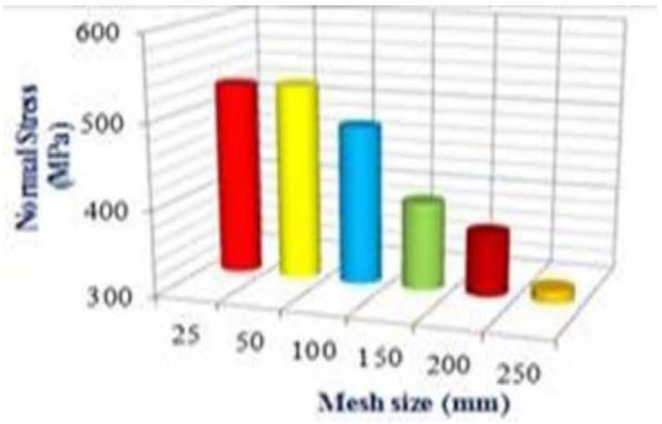
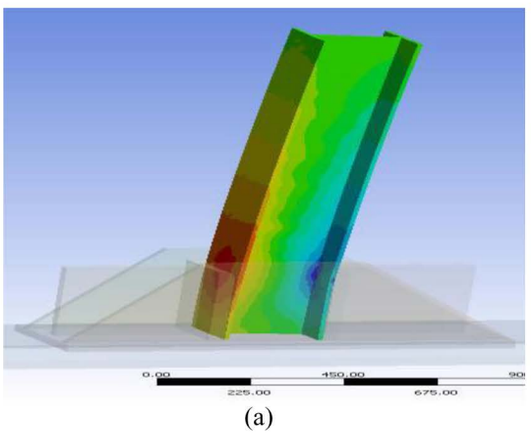


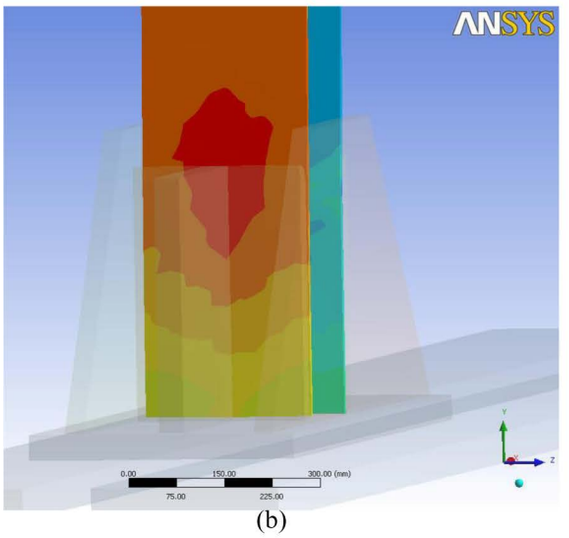
Figure 6. Stress value for different mesh size

3. FINITE ELEMENT MODEL RESULTS

The results obtained from the linear three dimensional FE analyses are evaluated for the HP220x57 sections. The distributions of the axial stresses are shown in Fig.7 for the HP220x75 section. The analyses results revealed that high axial stress concentrations exist around the connections of the HP 220x57 section and the 400 mm-high plate of the steel base fixture. The magnitude of these stresses is very high on HP section as noted from the 589 MPa stress value. This is indicative of local damage to HP section. Such local damage may be amplified under cyclic loading. To prevent these local damage (which do not occur in the case of steel H-piles embedded in concrete abutment), steel blocks are used between flanges of the HP section within the steel base fixture and the FEM is modified accordingly. In the case of the modified FEM, the presence of the steel blocks between the flanges of the HP section within the steel base fixture results in a more even distribution of stresses as shown in Fig.8. This results in a more uniform stress distribution over the flanges of the steel HP sections (e.g. the stress is reduced from from 676 to 338 MPa for the HP220x57 section as shown in Fig.8). Consequently, it is expected that the modified-test set up with steel blocks between flanges of the HP section will offer a better experimental set up for the HP220x57 sections. Stress distributions for these sections are shown in Fig.9 and 10.

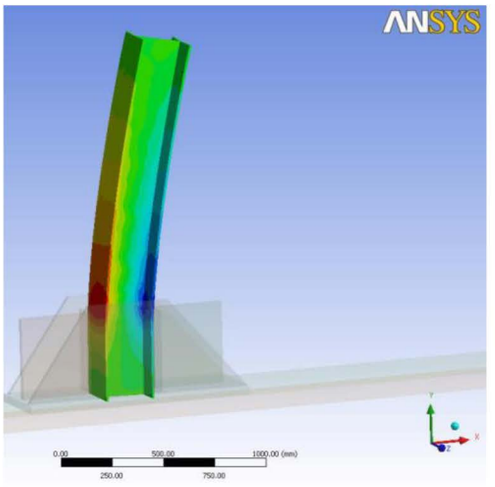


(a)

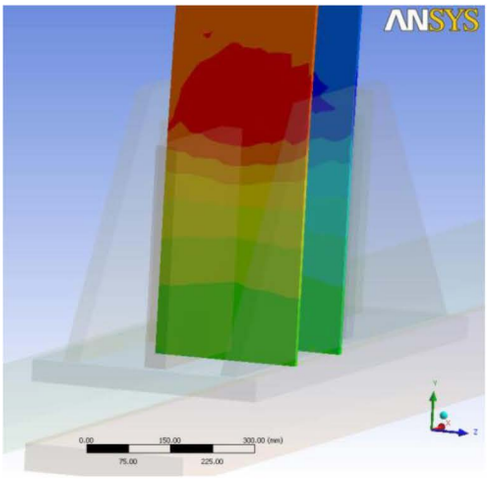


(b)

Figure 7. Axial stresses on HP 220x57 section without blocks at the location of the connection with a maximum stress of 589 Mpa; (a) side view, (b) front view.

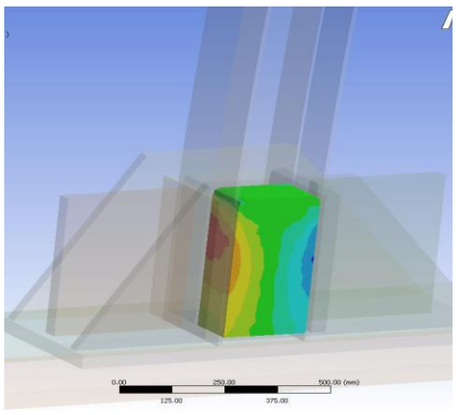


(a)

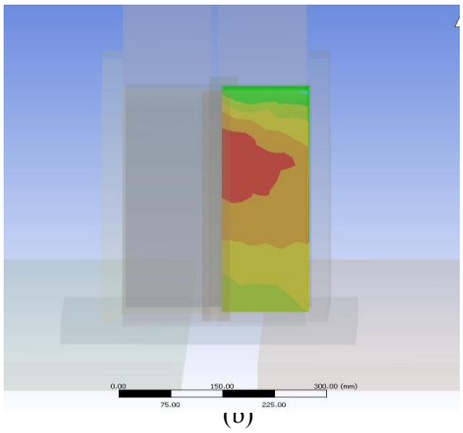


(b)

Figure 8.Axial stresses on HP 220x57 section with block, (a) side view, (b) front view.

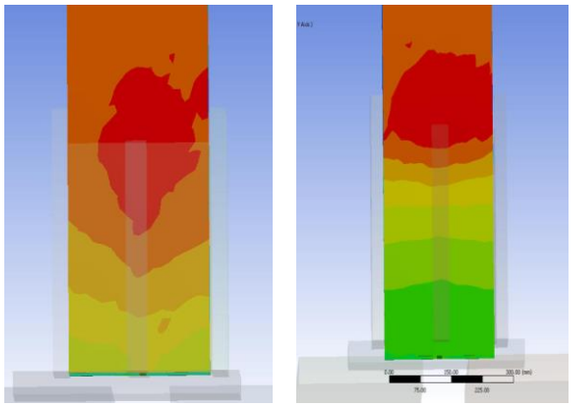


(a)



(b)

Figure 9. Axial stresses on block at the between flanges for HP 220x57; (a) side view, (b) front view.



(a) (b)

Figure 10. Comparison of the axial stresses; (a) HP section without block, (b) HP section with block.

4 FINITE ELEMENT MODEL RESULTS

4.1 *Specimen#1: A Maximum Strain of $\varepsilon_a=\pm 5\varepsilon_y$ in Bending about Strong Axis with No Axial Load*

FEM is constructed similarly according to actual HP220x57 steel in the test set up. For this reason, a lateral pressure is implemented over the entire top surface of the HP220x57 steel section in the ANSYS software to reach a flexural strain equal to five times the yield strain ($\varepsilon_a=5\varepsilon_y$) developed in the outermost fibers of the flanges. Then, FEM is solved based on above procedure explained in detail. Based on the FE analysis results, strain values for HP 220x57 steel sections are obtained as seen in Fig.11. Finite element analysis results show that maximum strain in the piles occurs in the flange of the HP 220x57 steel specimen right above the 465 mm-high steel base fixture.

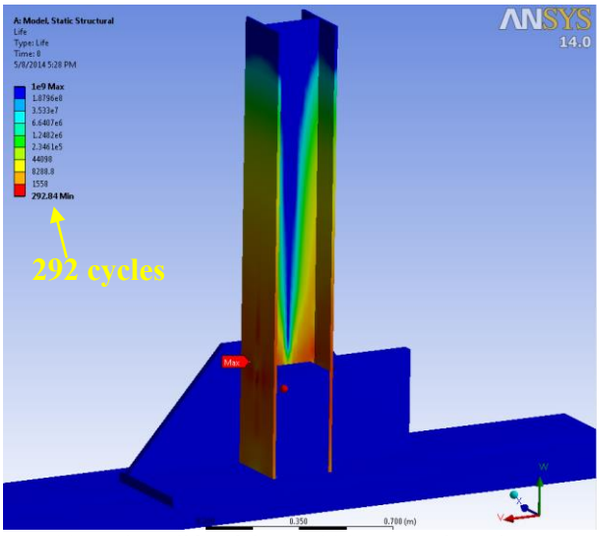


Figure 11. Fatigue life of the HP220x57 steel section on FEM

Using the FEM, fatigue life of HP220x57 steel specimen is investigated. In the FEM, the fatigue life of the HP220x57 steel specimen is obtained 292 cycles as seen in Fig.11.

4.2 *Specimen#2: A Maximum Strain of $\varepsilon_a=\pm 5\varepsilon_y$ in ending about Strong Axis with Axial Load*

A lateral pressure is implemented over the en-tire top surface of the HP220x57 steel section in the ANSYS software to obtain a flexural strain equal to five times the yield strain ($\varepsilon_a=5\varepsilon_y$) developed in the outermost fibers of the flanges as applied in test set up. To do so, ±64 mm lateral displacements are applied in the FEM as in the experiment test set up. Additionally, an axial load is also applied over the entire top surface of the HP220x57 steel section in the ANSYS software as seen in Fig.12. Average value of axial load is applied as 250 kN ($P=0.11P_y$) for the FEM. it is seems that local buckling takes place accurately above the 425 mm-high steel base fixture in FEM as seen in Fig.13. Finally, in the FEM, low cycle fatigue takes place when steel HP220x57 section is reached to the 585 cycles.

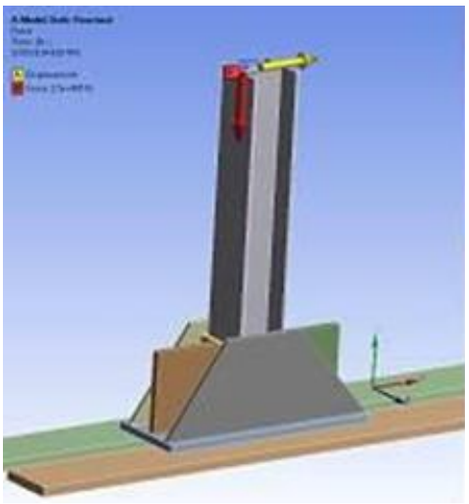


Figure 12. (a) Applied axial and lateral load in FEM,

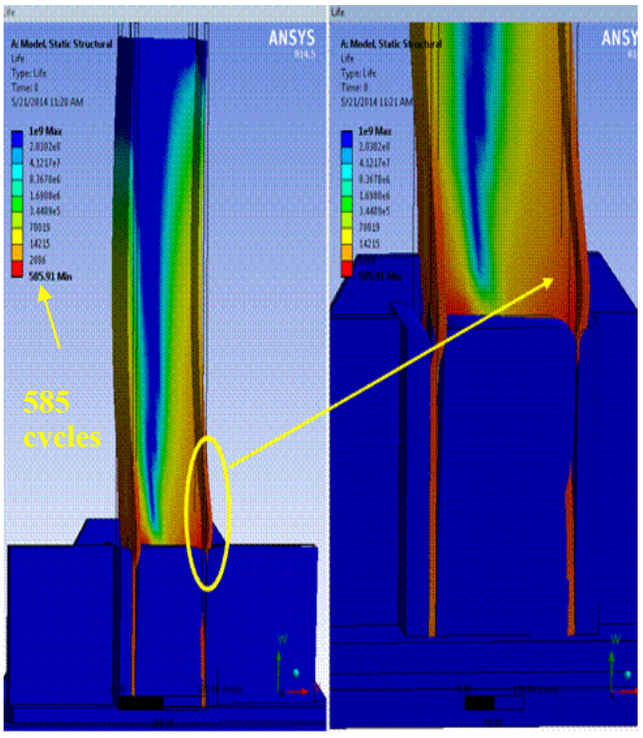


Figure 13. Local buckling due to low cycle fatigue in FEM

5 EXPERIMENTAL TEST SET UP

In this study, steel HP220x57 pile specimens are tested to investigate the effect of low cycle fatigue life of steel H piles at the abutments of integral bridges. For this purpose, constant amplitude reversed cyclic displacements are applied to the top of the cantilever HP220x57 piles using a servo-controlled hydraulic actuator operated in displacement control where a sinusoidal cyclic displacement waveform signal with a frequency of 0.5Hz is employed for displacement control at room temperature. Axial load is applied on the pile specimen due to the limitations of the test setup and lateral load is applied only in the strong axis direction. Detailed discussion of the experimental tests and test results are given in the following subsections.

5.1 *Test set up*

A cantilever steel HP220x57 section is tested to simulate the inelastic cyclic behavior of steel H-piles under thermal effects in integral bridges. The cantilever system has an upside down geometry of the pile-abutment system of an integral bridge as shown in Fig. 14. A steel fixture is designed to simulate the fixity condition of the pile to the integral abutment. A reinforced concrete fixture simulating the integral bridge abutment is not used in the tests due to possible damage and cracking of the reinforced concrete abutment upon cyclic loading that may result in loosening of the pile-abutment connection. This may then render the correct measurement of inelastic pile strains ineffective. Accordingly, as the focus of the research is to assess the low cycle fatigue life of steel H-piles, a steel fixture becomes more appropriate. The steel fixture is connected to the rigid test frame and the cyclic displacement is applied to the top of the cantilever HP steel section. The cantilever length is chosen to approximately correspond to the length of the pile effective in resisting the lateral movement due to temperature fluctuations (equivalent cantilever length). The equivalent cantilever length of the pile is calculated as the length from the top of the pile (where the maximum moment occurs) to the point of contra-flexure. For this purpose, a total of 128 static pushover analyses of typical integral bridges are conducted to determine the equivalent cantilever length of the steel H-piles that are used in the experimental part of this research study. Based on the pushover analyses results, the average equivalent length of a pile made of HP steel section is determined as 1.35 m. Accordingly, HP220x57 steel members are cut in 1.90 m length where the 0.4 m part is encased in the steel base fixture to provide fixity and the load is applied at approximately 0.15 m from the top of the pile (the centerline of the load is at 0.15 m from the pile top).

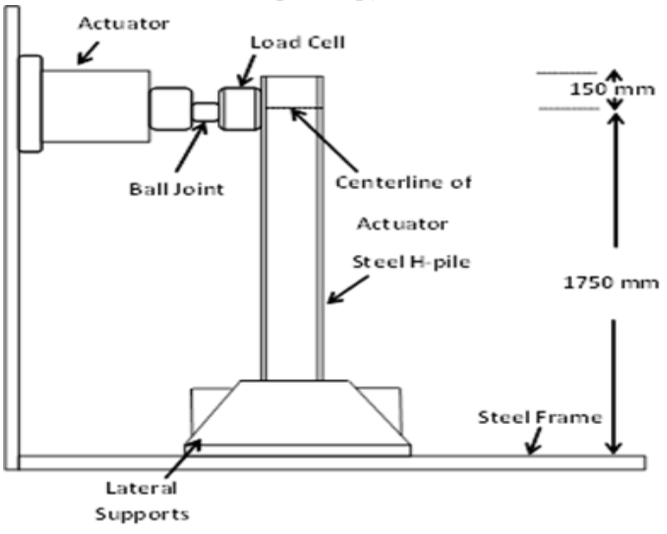


Figure 14. The equivalent pile system

5.2 *Instrumentation*

Three types of measuring devices are used to instrument the steel H-piles. These are, (i) electrical resistant strain gauges for measuring strains on the steel H–piles. (ii) Load cell for measuring the lateral load level, (iii) LVDT (displacement transducer) for measuring the lateral displacement. The test setup is shown in Fig.14. The HP steel section is vertically erected and fitted to the base fixture and the base fixture is bolted to the bottom of the test frame. The pile is instrumented with twelve strain gauges and three displacement transducers. The plan view of the configuration of the strain gauges on the pile cross-section is also shown in Fig.15. Strain measurements are required to correlate fatigue life of HP steel section with the cyclic strain amplitudes. Therefore, strain measurement is performed at the critical locations where fatigue failure occurs. Displacements, strains and lateral loads are measured and recorded using a data-logger (TDG-Ai8b). Furthermore, in the test set up, a displacement controlled hydraulic actuator capable of applying ±500 KN of load and a stroke of ± 125 mm is used to impose lateral cyclic displacements.

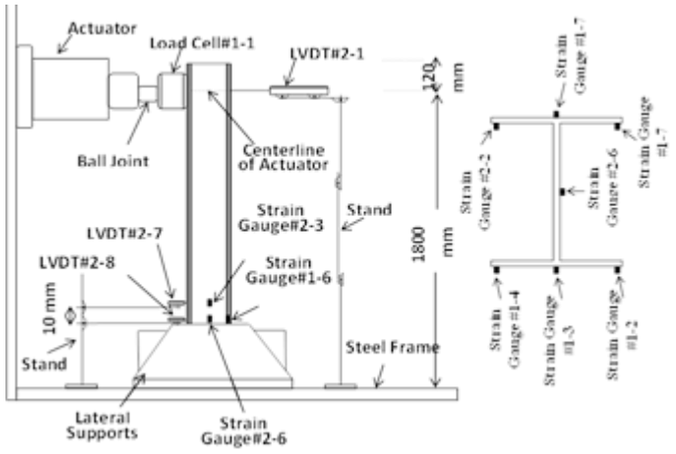


Figure 15. Experimental set-up: location of the strain gauges and LVDT.

6. EXPERIMENTAL TEST

6.1. Low Cycle Fatigue Test results of Specimen#1

The low cycle fatigue tests of Specimen #1 are conducted by applying only large amplitude strain cycles to the specimens. The amount of cyclic displacement at the top of the piles is controlled such that a flexural strain equal to five times the yield strain ($\varepsilon_a=5\varepsilon_y$) is developed in the outermost fibers of the flanges. This required the application of a cyclic lateral displacement of ±64 mm at the pile top. Fig.16 shows a typical HP220x57 pile specimen under cyclic lateral displacement. During the experimental testing of the piles under constant amplitude cyclic displacements/strains, the fatigue-induced cracks firstly developed in the intersection of the flanges and the web. The cracks then expanded towards the tips of the flanges under further cycling as shown in Fig.17. In the case of this test, the specimens fractured due to low cycle fatigue when the average number of cycles from the test reached 241.

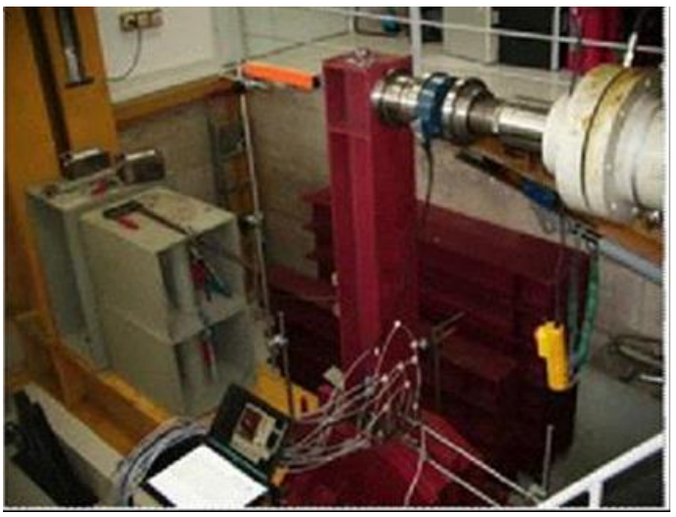


Figure 16. Specimen-1 under cyclic lateral load normal to its strong axis.



Figure 17. Front and side views of fatigue induced steel pile fracture right above the steel base fixture

6.2 Low Cycle Fatigue Test results of Specimen#2

In this phase of the research study, in addition to lateral load, axial load is also applied to the pile specimens made of a HP220x57 section (identical to that of Specimen #1) to explore the effect of axial load on the low cycle fatigue life of steel H piles at the abutments of integral bridges. The cyclic displacements applied to the top of the pile specimens are shown in Fig.18. To achieve the same large amplitude flexural strain level as in the case of Specimen #1 (five times the yield strain ($\varepsilon_a=5\varepsilon_y$)), the piles are subjected to a displacement of 64 mm at the top. In addition, axial loads are also applied as 360 kN, 156 kN and 280 kN during the push, normal and pull direction together with the lateral loads as shown in Fig.19. Average value of axial load is determined as 250 kN ($P=0.11P_y$).



Figure 18. Specimen-2 under cyclic lateral load and axial load.



Figure 19. (a) Push direction, (b) Mid-position, (c) Pull direction.

The results obtained from experimental test on HP220x57 section demonstrate that first fracture begins 341 cycles as shown in Fig.20-a. After 341 cycles, fracture starts to expand as shown in Fig.20-b. Finally, low cycle fatigue occurs when steel HP220x57 section is reached to the 508 cycles as shown in Fig.20-c. The result obtained from experimental test on HP220x57 section reveals that local buckling occurs exactly above the 400 mm-high steel base fixture as shown in Fig.20-d.



Figure 20. (a) First fracture occurs 341 cycles, (b) First fracture begins expansion after 341 cycles, (c) Front view of fracture occurs exactly above the 400 mm-high steel base fixture, (d) Local Buckling.

7 CONCLUSIONS

Followings are the conclusions deduced from this research study. In light of the data obtained from FE models of the steel H-pile specimens used in the experimental test set up, it is observed that high axial stress concentrations exist around the connections of the HP steel section and the 400 mm-high plate of the steel base fixture. It is observed that the magnitude of these stresses is very high on HP section. Due to the fact that this is indicative of local damage to HP section, FE model should be simulated to prevent these local damage before experimental tests are performed. At the large strain amplitude, due to local buckling of the flange, the reduction in fatigue life is observed. In light of the data obtained from FEM predictions, these local buckling can be predicted and prevented before experimental tests are performed. Further, it is observed that FE analysis predictions can be used to avoid the huge cost and testing time required for conducting experimental tests.

Comparing the FEM results and experimental test results of HP220x57 specimens, it is observed the observations from this numerical study are also verified experimentally. Thus, it may be possible to make a correlation and calibration between FEMs and experimental test results of the thermal induced cyclic displacements/strains on the low cycle fatigue performance of steel H-piles at the abutments of integral bridges. FEM predictions can be an excellent alternative of destructive laboratory test with an acceptable variation of results.

8 REFERENCES

ANSYS R14.0. Swanson Analyses System. 2014.

Dicleli M., A Rational Design Approach for Prestressed-Concrete-Girder Integral Bridges, Engineering Structures; 22 (3):230-45,2000.

French C., Huang J., Shield C., Final Report, Behavior of Concrete Integral Abutment Bridges, 2004.

Razmi J., Ladani L., Aggour M.S. Fatigue Crack Initiation and Propagation in Piles of Integral Abutment Bridges. Computer-Aided Civil and Infrastructure Engineering 2013

Khodair Y.and Hassiotis S , Numerical and experimental analyses of an integral bridge ,2013-14

Popov V.L,Contact Mechanics and Frictio:Physical Principles and Applications, 2010

Wiss, J., Synthesis of Technical Information for Jointless Bridge Construction, Technical Report, Elstner Associates, Inc., State of Vermont Agency of Transportation, pp. 25-36, June 2002

Maintenance, Safety, Risk, Management and Life-Cycle Performance of Bridges – Powers, Frangopol, Al-Mahaidi & Caprani (Eds)
© 2018 Taylor & Francis Group, London, ISBN 978-1-138-73045-8

Experimental Investigation on the Low Cycle Fatigue Life of Piles

M. Karalar
Bulent Ecevıt Universıty, Department of Cıvıl Engineering, TURKEY
M. Dicleli
Middle East Technical University, Department of Engineering Sciences, TURKEY

ABSTRACT: In this study, the low cycle fatigue tests are conducted to investigate the fatigue life of steel H–piles subjected to thermal induced cyclic strains/displacements. Review of literature revealed that there are few experimental research data on the low cycle fatigue performance of integral bridge steel H-piles. For this purpose, experimental studies on full scale steel H-pile specimens are conducted to simulate cyclic behavior of steel H-piles under thermal effects in integral bridges by considering the effect of axial load combined with large amplitude strain cycles with various amplitude levels. Using experimental test results, the effect of axial load level is investigated on the low cycle fatigue performance of integral bridge steel H–piles. It is observed that the effect of axial load on the low cycle fatigue performance of integral bridge steel H-piles are so important to reduce the bending stresses in the steel H-piles and also increase the low-cycle fatigue performance of steel H-piles at the abutments of integral bridges at the moderate strain amplitudes. Moreover, it is observed that at large strain amplitudes the effect of local buckling should be considered more than the effect of axial load on the low cycle fatigue life of steel H piles at the abutments of integral bridges.

1 GENERAL INSTRUCTIONS

Integral bridges are jointless bridges where the superstructure is connected monolithically with relatively thin, stub abutments supported on a single row of piles that provide the required flexibility to allow for longitudinal movement of the bridge under thermal effects. A typical two-span, prestressed-concrete girder, integral bridge is shown in Fig.1. The most common type of piles used at the abutments of integral bridges is steel H-piles. The daily and seasonal temperature changes result in imposition of cyclic horizontal displacements on the continuous bridge deck of integral bridges and thus on the abutments, backfill soil, steel H-piles, and cycle control joints at the ends of the approach slabs. Consequently, the abutments are pushed against the approach fill and then pulled away, causing lateral deflections at the tops of the piles that support the abutments of the bridge.

As the length of integral bridges increases, the temperature-induced lateral cyclic displacements in the steel H-piles at the abutments become larger as well. As a result, the piles may experience cyclic plastic deformations. This may result in the reduction of their service life due to low-cycle fatigue effects. The number and amplitude of thermal-induced cyclic flexural strains in integral bridge steel H-piles are important parameters that effect their low cycle fatigue life. Close examination of the existing field measurement data for integral bridges revealed that the measured thermal-induced cyclic flexural strains in steel H-piles at the abutments consist of large amplitude, primary small amplitude and secondary small amplitude cycles (Dicleli & Albhaisi 2004). Although a few research studies on low cycle fatigue effects in the steel H-piles of integral bridges at the abutments are found in the literature (Arsoy et al.1999, Abendroth&Greimann 2005, Dicleli&A lbhaisi 2004, French et al. 2004, Razmi et al. 2013, Khodoir&Hassiatis 2013, Hallmark 2006], none of these research studies provide analytical and experimental results on the effect of the flexural strain cycles on the low cycle fatigue life of steel H-piles at the abutments of integral bridges until recently. However, in recent years, Karalar &Dicleli (2010) only studied the effect of the primary and secondary small amplitude flexural strain cycles on the low cycle fatigue life of steel H-piles at the abutments of integral bridges analytically using steel H pile cyclic strain data from the field measurements of several integral bridges in North America. Further, Karalar and Dicleli (2010) also conducted some experimental studies on full scale steel H-pile specimens to verify these analytical results. In this research study, the effect of strain cycles with various amplitude

levels on the low cycle fatigue life of steel H piles at the abutments of integral bridges is studied experimentally. The results from this research study are used to evaluate the thermal-induced low cycle fatigue life of steel H-piles. The observation regarding the experimental results of the low cycle fatigue life of steel H piles at the abutments become important as it provides evidence about the adequacy of the current design methods in relation to the low cycle fatigue life of steel H-piles at the abutments. The outcome of such a research study may also be used to develop design guidelines that may be used to design steel H-piles to endure low cycle fatigue effects throughout the service life of the bridge.

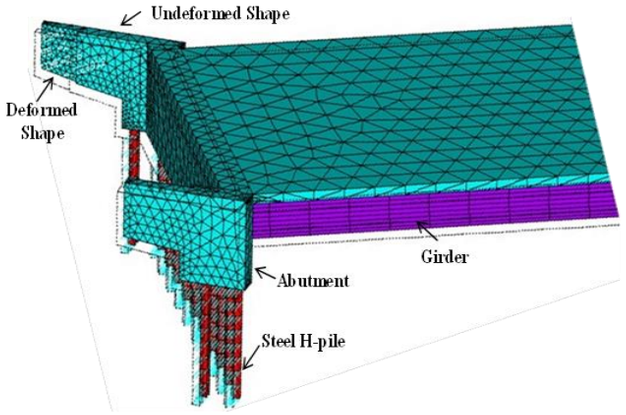


Figure 1. Pile displacement due to thermal changes, (a) Thermal Expansion, (b) Thermal contraction

2 EXPERIMENTAL TEST SET UP

In this study, steel HP220x57 pile specimens are tested to investigate the effect of low cycle fatigue life of steel H piles at the abutments of integral bridges. For this purpose, constant amplitude reversed cyclic displacements are applied to the top of the cantilever HP220x57 piles using a servo-controlled hydraulic actuator operated in displacement control where a sinusoidal cyclic displacement waveform signal with a frequency of 0.5Hz is employed for displacement control at room temperature. Axial load is applied on the pile specimen due to the limitations of the test setup and lateral load is applied only in the strong axis direction. Detailed discussion of the experimental tests and test results are given in the following subsections.

2.1 *Test set up*

A cantilever steel HP220x57 section is tested to simulate the inelastic cyclic behavior of steel H-piles under thermal effects in integral bridges. The cantilever system has an upside down geometry of the pile-abutment system of an integral bridge as shown in Fig. 2. A steel fixture is designed to simulate the fixity condition of the pile to the integral abutment. A reinforced concrete fixture simulating the integral bridge abutment is not used in the tests due to possible damage and cracking of the reinforced concrete abutment upon cyclic loading that may result in loosening of the pile-abutment connection. This may then render the correct measurement of inelastic pile strains ineffective. Accordingly, as the focus of the research is to assess the low cycle fatigue life of steel H-piles, a steel fixture becomes more appropriate. The steel fixture is connected to the rigid test frame and the cyclic displacement is applied to the top of the cantilever HP steel section. The cantilever length is chosen to approximately correspond to the length of the pile effective in resisting the lateral movement due to temperature fluctuations (equivalent cantilever length). The equivalent cantilever length of the pile is calculated as the length from the top of the pile (where the maximum moment occurs) to the point of contra-flexure. For this purpose, a total of 128 static pushover analyses of typical integral bridges are conducted to determine the equivalent cantilever length of the steel H-piles that are used in the experimental part of this research study. Based on the pushover analyses results, the average equivalent length of a pile made of HP steel section is determined as 1.35 m. Accordingly, HP220x57 steel members are cut in 1.90 m length where the 0.4 m part is encased in the steel base fixture to provide fixity and the load is applied at approximately 0.15 m from the top of the pile (the centerline of the load is at 0.15 m from the pile top).

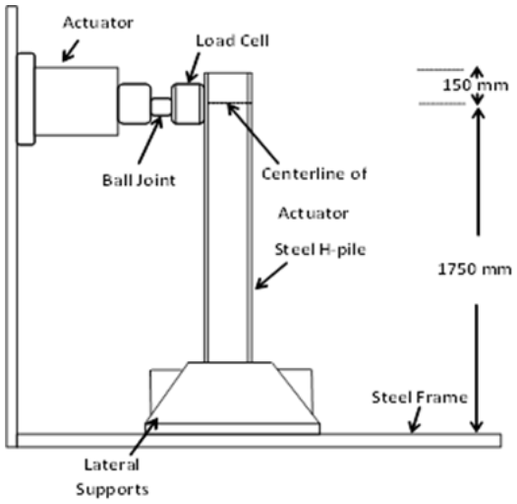


Figure 2. The equivalent pile system used in the experimental set-up

2.2 *Instrumentation*

Three types of measuring devices are used to instrument the steel H-piles. These are, (i) electrical resistant strain gauges for measuring strains on the steel H–piles. (ii) Load cell for measuring the lateral load level, (iii) LVDT (displacement transducer) for measuring the lateral displacement. The test setup is shown in Fig.3. The HP steel section is vertically erected and fitted to the base fixture and the base fix-

ture is bolted to the bottom of the test frame. The pile is instrumented with twelve strain gauges and three displacement transducers. The plan view of the configuration of the strain gauges on the pile cross-section is also shown in Fig.3. Strain measurements are required to correlate fatigue life of HP steel section with the cyclic strain amplitudes. Therefore, strain measurement is performed at the critical locations where fatigue failure occurs. Displacements, strains and lateral loads are measured and recorded using a data-logger (TDG-Ai8b). Furthermore, in the test set up, a displacement controlled hydraulic actuator capable of applying ±500 KN of load and a stroke of ± 125 mm is used to impose lateral cyclic displacements.

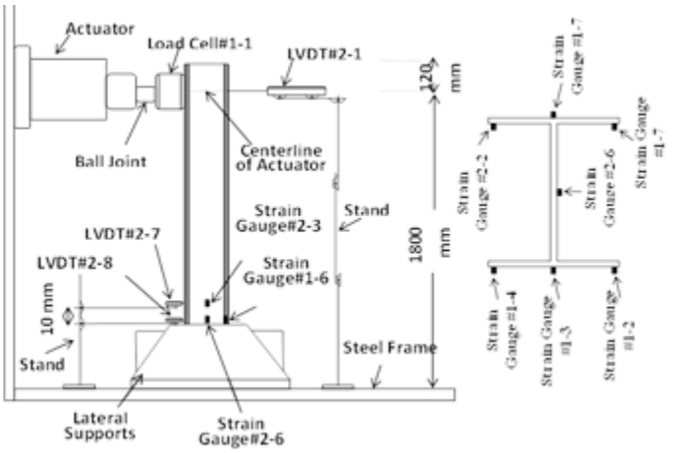


Figure 3. Experimental set-up: location of the strain gauges and LVDT.

3. EXPERIMENTAL TEST

3.1. Low Cycle Fatigue Test results of Specimen#1

The low cycle fatigue tests of Specimen #1 are conducted by applying only large amplitude strain cycles to the specimens. The amount of cyclic displacement at the top of the piles is controlled such that a flexural strain equal to two half five times the yield strain ($\varepsilon_a=2.5\varepsilon_y$) is developed in the outermost fibers of the flanges. This required the application of a cyclic lateral displacement of ±44 mm at the pile top. Fig.4 shows a typical HP220x57 pile specimen under cyclic lateral displacement. During the experimental testing of the piles under constant amplitude cyclic displacements/strains, the fatigue-induced cracks firstly developed in the intersection of the flanges and the web. The cracks then expanded towards the tips of the flanges under further cycling as shown in Fig.5. In the case of this test, the specimens fractured due to low cycle fatigue when the average number of cycles from the test reached 2134 cycles.

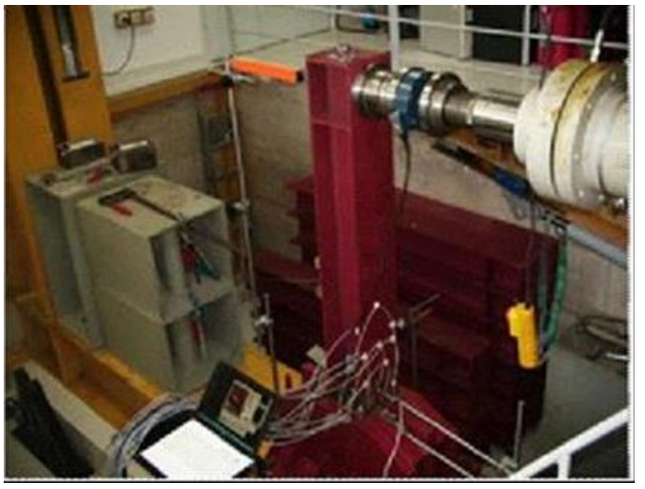


Figure 4. Specimen-1 under cyclic lateral load normal to its strong axis.



Figure 5. Front view of fatigue induced steel pile fracture right above the steel base fixture

3.2. Low Cycle Fatigue Test results of Specimen#2

The low cycle fatigue tests of Specimen #2 are conducted by applying only large amplitude strain cycles to the specimens. The amount of cyclic displacement at the top of the piles is controlled such that a flexural strain equal to five times the yield strain ($\varepsilon_a=5\varepsilon_y$) is developed in the outermost fibers of the flanges. This required the application of a cyclic lateral displacement of ±64 mm at the pile top. Fig.6 shows a typical HP220x57 pile specimen under cyclic lateral displacement. HP220x57 pile specimen Lateral Load-Micro strain Relationship for Specimen#2 is shown in Fig.7 (b). During the experimental testing of the piles under constant amplitude cyclic displacements/strains, the fatigue-induced cracks firstly developed in the intersection of the flanges and the web. The cracks then expanded towards the tips of the flanges under further cycling as shown in Fig.7. In the case of this test, the specimens fractured due to low cycle fatigue when the average number of cycles from the test reached 241.

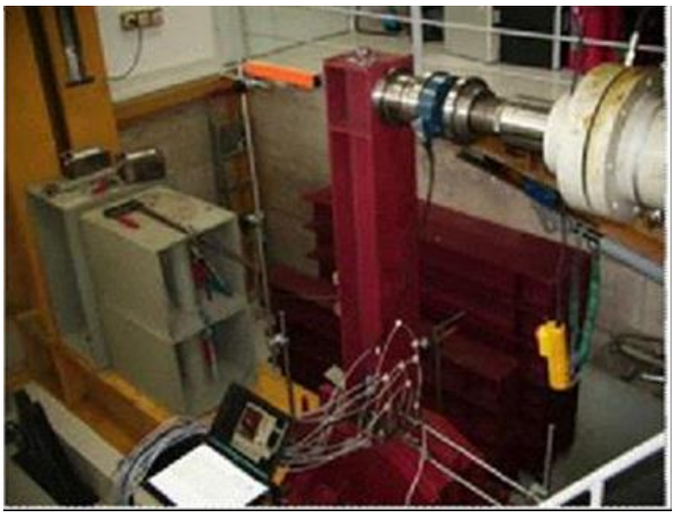
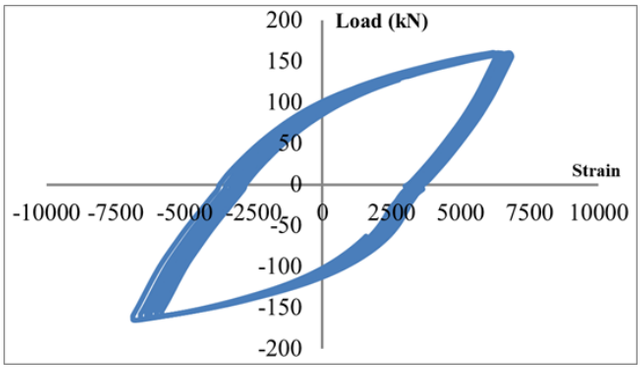


Figure6. Specimen-1 under cyclic lateral load normal to its strong axis.



(a)



(b)

Figure 7. (a) Front and side views of fatigue induced steel pile fracture right above the steel base fixture, (b) HP220x57 pile specimen Lateral Load-Micro strain Relationship for Specimen#2.

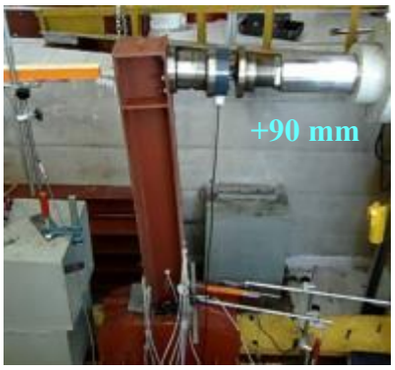
3.3 Low Cycle Fatigue Test results of Specimen#3

The low cycle fatigue tests of Specimen #3 are conducted by applying only large amplitude strain cycles to the specimens. The amount of cyclic displacement at the top of the piles is controlled such that a flexural strain equal to ten times the yield strain ($\varepsilon_a=10\varepsilon_y$) is developed in the outermost fibers of the flanges. This required the application of a cyclic lateral displacement of ±90 mm at the pile top as shown in Fig.8. During the experimental testing of the piles under constant amplitude cyclic displacements/strains, the fatigue-induced cracks firstly developed in the intersection of the flanges and the web. The cracks then expanded towards the tips of the flanges under further cycling as shown in Fig.8. In the case of this test, the specimens fractured due to low cycle fatigue when the average number of cycles from the test reached 154.

Comparing the test results, it is observed as expected that the average number of large amplitude strain cycles to failure reduced when the yield strains level increased from the five times yield strain ($\varepsilon_a=5\varepsilon_y$) to ten times yield strain ($\varepsilon_a=10\varepsilon_y$) in the tests as shown in Fig.9.

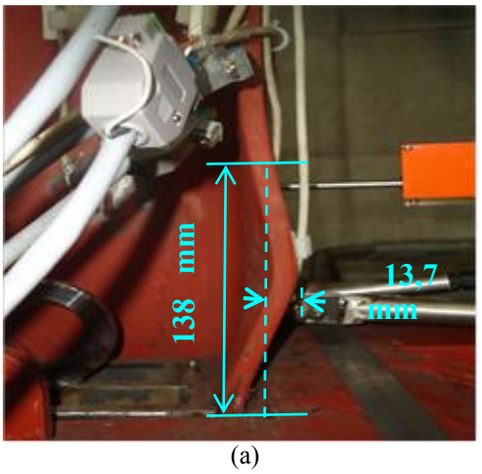


(a)

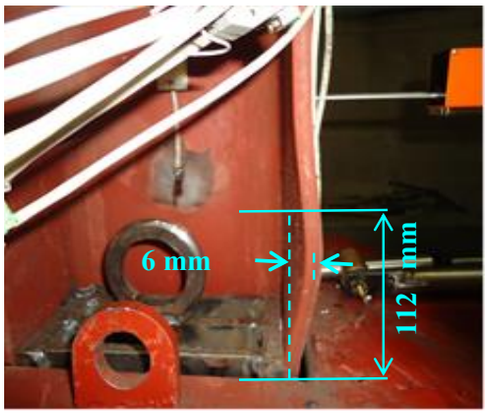


(b)

Figure 8. (a) The application of a cyclic lateral displacement of -90 mm at the pile top, (b) the application of a cyclic lateral displacement of +90 mm at the pile top.



(a)



(b)

Figure 9. Local buckling of HP220x57 section for large FS cycles of (a) $\varepsilon_a=10\varepsilon_y$, (b) $\varepsilon_a=5\varepsilon_y$

3.4 Low Cycle Fatigue Test results of Specimen#4

In this phase of the research study, in addition to lateral load, axial load is also applied to the pile specimens made of a HP220x57 section (identical to that of Specimen #2) to explore the effect of axial load on the low cycle fatigue life of steel H piles at the abutments of integral bridges. The cyclic displacements applied to the top of the pile specimens are shown in Fig.10. To achieve the same large amplitude flexural strain level as in the case of Specimen #2 (five times the yield strain ($\varepsilon_a=5\varepsilon_y$)), the piles are subjected to a displacement of 64 mm at the top. In addition, axial loads are also applied as 360 kN, 156 kN and 280 kN during the push, normal and pull direction together with the lateral loads as shown in Fig.11. Average value of axial load is determined as 250 kN ($P=0.11P_y$).



Figure 10. Specimen-4 under cyclic lateral load and axial load.



Figure 11. (a) Push direction, (b) Mid-position, (c) Pull direction.

The results obtained from experimental test on HP220x57 section demonstrate that first fracture begins 341 cycles as shown in Fig.12-a. After 341 cycles, fracture starts to expand as shown in Fig.12-b. Finally, low cycle fatigue occurs when steel HP220x57 section is reached to the 508 cycles as shown in Fig.12-c. The result obtained from experimental test on HP220x57 section reveals that local buckling occurs exactly above the 400 mm-high steel base fixture as shown in Fig.12-d.



Figure 12. (a) First fracture occurs 341 cycles, (b) First fracture begins expansion after 341 cycles, (c) Front view of fracture occurs exactly above the 400 mm-high steel base fixture, (d) Local Buckling.

3.5 Low Cycle Fatigue Test results of Specimen#5

In this phase of the research study, in addition to large amplitude strain cycles, axial load is also applied to the pile specimens to investigate the effect of axial load level combined with large amplitude strain cycles with various amplitude levels on the low cycle fatigue life of steel H piles at the abutments of integral bridges. To achieve the same large amplitude flexural strain level as in the case of Specimen#3 (ten times the yield strain ($\varepsilon_a=10\varepsilon_y$)), the piles are subjected to a displacement of ±90 mm at the top. In the tests, average value of axial load is determined as 170 kN ($P=0.075P_y$). Fig.13 shows a typical HP220x57 pile specimen under cyclic lateral and axial load.



Figure 13. Step-by-step spread of local buckling and fracture throughout the pile flange.

4 CONCLUSIONS

The following discussion is aiming to qualitatively describe the effect of strain cycles with various amplitude levels due to daily and/or weekly temperature fluctuations. All the results are based on the assumption that the steel H piles of integral bridges response is primarily correlated to daily and/or weekly temperature fluctuations. Comparing the test results, it is observed that, as expected, number of cycles to failure is inversely proportional to the strain amplitude. The reduction in fatigue life is observed to range between 40% and 50% when the pile is subjected to larger strain amplitudes (10 times the yield strain). This is mainly due to local buckling of the flange under the effect of compressive stresses from the high compressive strains due to the effect of bending. Local buckling increases the local curvature and strains. This locally accelerates the cracking of the material. As a result of this large lateral buckling, fracture starts earlier and also low cycle fatigue in steel HP sections takes place at smaller cycles. Additionally, in the test, the effect of the axial load on small amplitude cycle is also investigated. It is observed that the effect of axial load on small amplitude cycle have a significant effect on the low cycle fatigue performance of steel H-piles in two ways: (i) when the pile is subjected to moderate strain amplitudes (five times the yield strain), the presence of axial load is observed to enhance the low cycle fatigue life of the pile. This mainly due to the fact that, the presence of axial load decreases the amplitude of the tensile strain that results in cracking of the material (it delays the initiation of the crack), (ii) when the pile is subjected to larger strain amplitudes (10 times the yield strain), the presence of axial load is observed to decrease the low cycle fatigue life of the pile. This is mainly due to local buckling of the flange under the effect of compressive stresses from the axial load and high compressive strains due to the effect of bending. Local buckling increases the local curvature and strains. Thus, it should be found an effective way to delay the local buckling to enhance the fatigue life of steel H-piles.

5 REFERENCES

Arsoy S., Barker R.M., and Duncan J.M. 1999. The Behavior of Integral Abutment Bridges, *Final Contract Report*, VTRC 00-CR3.

Abendroth R.E., Greimann L.F. 2005. Field Testing of Integral Abutments, *Iowa DOT Project HR-399*, Iowa State University and Iowa Department of Transportation.

Dicleli M, Albhaisi SM. 2004. Effect of Cyclic Thermal Loading on the Performance of Steel H-Piles in Integral Bridges with Stub-Abutments, *Journal of Constructional Steel Research*; 60(2):161-182.

Dicleli M. 2000. A Rational Design Approach for Prestressed-Concrete-Girder Integral Bridges, *Engineering Structures* 22 (3):230-45.

French C., Huang J., Shield C. 2006. Behavior of Concrete Integral Abutment Bridges, *Final Report*.

Hällmark R.2006. Low Cycle Fatigue of Steel Piles in Integral Abutment Bridges, *Master Thesis*.

Karalar M. and Dicleli M.2016. Effect of Thermal Induced Flexural Strain Cycles on the Low Cycle Fatigue Performance of Integral Bridge Steel H-Piles, *Engineering Structures*, 124:388-404.

Khodair Y.and Hassiotis S.2013. Numerical and experimental analyses of an integral bridge, *International Journal of Advanced Structural Engineering*,5:14.

Razmi J., Ladani L., Aggour M.S.2013. Fatigue Crack Initiation and Propagation in Piles of Integral Abutment Bridges, *Computer-Aided Civil and Infrastructure Engineering* 28(5): 389-402

Maintenance, Safety, Risk, Management and Life-Cycle Performance of Bridges – Powers, Frangopol, Al-Mahaidi & Caprani (Eds)
© 2018 Taylor & Francis Group, London, ISBN 978-1-138-73045-8

Investigation on the Closed Longitudinal U-ribs Corrosion of Cable Stayed Bridge with Steel Plate Deck

Kang Yeon Lee & Sang Ho Jin
Assistant Manager , Korea Infrastructure Safety & Technology Co, Mokpo, South Korea

Dal Soo Oh
Deputy General Manager, Korea Infrastructure Safety & Technology Co, Mokpo, South Korea

Hyeong Seok Joo
Department General Manager, Korea Infrastructure Safety & Technology Co, Mokpo, South Korea

Do Kyoun Kim
Office Chief, Korea Infrastructure Safety & Technology Co, Mokpo, South Korea

ABSTRACT: In this paper, we present the closed U-ribs deteriorated case with steel plate deck of bridge in service. In the investigation, we carried out a desk study of the deck to through details and to identify if there are any details that have a track record of causing problems on other bridges. Defect identification, detailed inspection, finding causes and evaluation were also conducted. This case will contribute to prevent similar case in the future and the ongoing development of operational and maintenance procedures for the life of the bridge.

1 GENERAL INSTRUCTIONS

1.1 *Research background*

Construction of facilities in Korea have leaned heavily toward quantitative aspects that emphasized "low construction costs" and "fast-track construction" during the period of rapid economic growth since 1970s. This resulted in weakness in qualitative aspects compared with leading countries, and the situation was aggravated by the lack of institutional initiatives for proper maintenance and investments in relevant fields.

The social perception of facilities are concentrated in expanding new facilities but paying no attention to the investment for maintenance, with arbitrary decision of the maintenance managements. The systematic maintenance managements had not been done due to the absence of the safety management relation laws in Korea until 1995s that had resulted in tragic disaster like the collapse of Songsu bridge in Seoul.

After that, The "Special Act for the safety Control of public facilities and multi-use facilities were finally initiated, which enhance the convenience of people who use public facilities and to ensure public safety and welfare.

The safety and maintenance management is sorted into two system, one is precautionary measures to prevent disaster of facilities which is called as "Construction Technology Management Act" and another is the restoration measures of facilities after accident which is called "Special Act for the safety Control of public facilities and multi-use facilities", "Framework Act on the Management of Disasters and Safety".

The facilities graded 1 and graded 2 among the important facilities classified by Korea government can be conceptualized according to Table 1. In-depth inspection in Korea, which should be done to facility graded 1 above mentioned within 1year every 5years after 10years has been completed, is carried out after a safety check for prevention of disasters and facility safety.

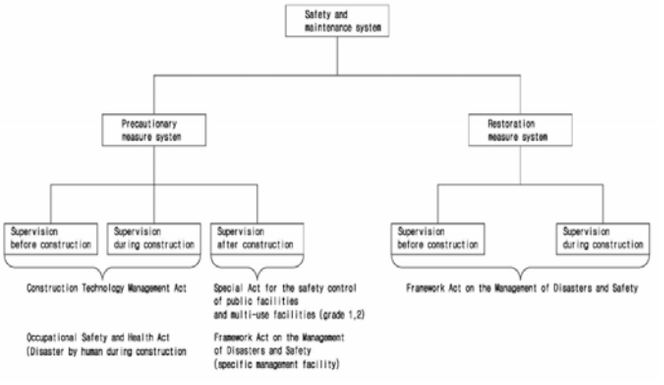


Figure 1 Act system on safety and maintenance of Korea facilities

In-depth inspection above is defined as the behavior to propose the possible solution including repair and reinforcement for facility having physical and functional defect investigated by field investigation and test for structural stability. Each representative bridge of different form , which is Suspension bridge, cable stayed bridge, arch bridge and truss bridge among facilities graded 1, are shown in Figure 2 and the completion year and condition grade of the facility graded 1 and 2 are shown in Figure 3 and 4.

Table 1 Facility graded

grade	Contents
Facility graded 1	・Bridge having form of superstructure such as suspension bridge, cable-stayed bridge, arch bridge, truss bridge ・Bridge having maximum span of 50m (except for one span bridge) ・Bridge over length 500m
Facility graded 2	・Bridge having maximum span of 50m ・Bridge over length 100m except for Facility graded 1



(a) Suspension Bridge- Gwangan Bridge(8,428m)



(b) cable-stayed bridge-Suhae Bridge(7,310m)



(c) Arch Bridge-Hangang Bridge (840m)



(d) Truss Bridge-Hangang railroad Bridge(1,113m)

Figure 2 Representative bridges of Grade 1 in Korea

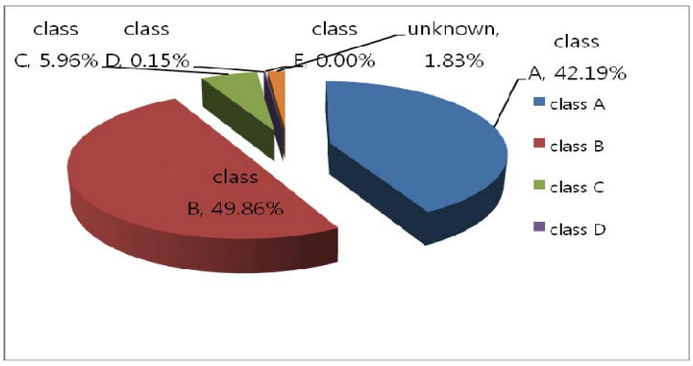


Figure 3 Condition class on Bridge of grade1,2

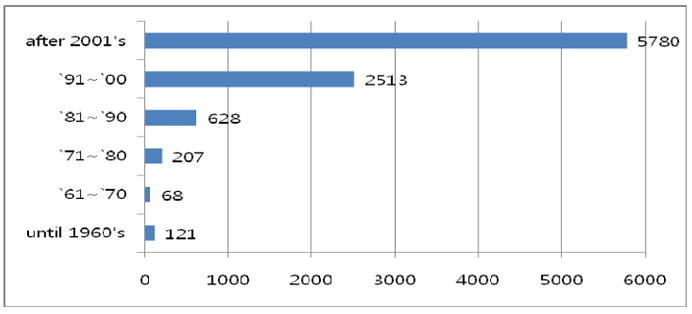


Figure 4 Completion year on Bridge of grade1,2

1.2 *INTRODUCTION OF LONG SPAN BRIDGE MANAGEMENT CENTER(LOBMAC)*

KISTEC(Korea Infrastructure Safety & Technology Co. is running Long Span Bridge Management Center(LOBMAC) to improve maintenance works based on unified remote monitoring system of long span bridges on national highway in Korea.

LOBMAC has 5 main missions as follows. LOBMAC consists of 3 divisions as shown on Figure 5. There are 26 Bridges under management of LOBMAC as of 2017 such as Table 2

1. Regular, and in-depth inspection(including of management facilities such as a trolley, elevator and dehumidifier)
2. Operation of the unified monitoring system
3. Real-time monitoring of the bridges in service life
4. Building and analyzing the database for monitoring data using FEA model
5. Consulting of monitoring system for long span bridges under construction

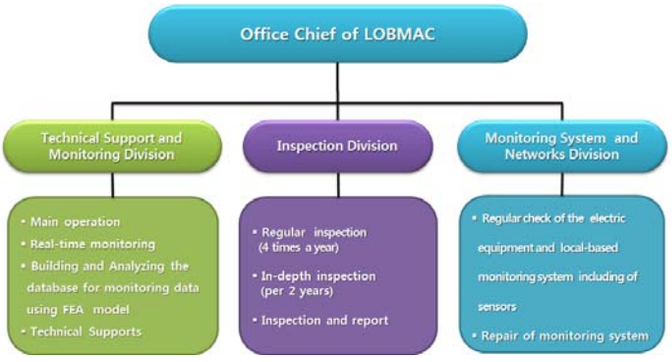


Figure 5 Organization of LOBMAC

Table 2 Bridges under management of LOBMAC

Management entity	No.	Bridge Name	Type	Length (m)	Completion
Ministry of Land, Infrastructure and transport	1	Jindo Br.	CS	484	1984.10
	2	Jindo Br.(2nd)	CS	484	2006.04
	3	Aphae Br.	AR	1,420	2009.01
	4	Wando Br.	CS	500	2012.12
	5	Mokpo Br.	CS	3,060	2013.01
	6	Yeonggwang Br.	CS	590	2016.03
	7	Gogunsan Br,	SU	757	2016.06
	8	Jeonjuchun Br.	CS	495	2016.11
	9	Samdo Br.	CS	550	2017.06
	10	Jangbogo Br.	CS	1	2017.11
	11	Jangja Br.	CS	305	2017.12
	12	Dolsan Br.	CS	450	1984.12
	13	Baekya Br.	AR	325	2005.03
	14	Sorok Br.	SU	1,160	2009.01
	15	Geoguem Br.	CS	2,028	2012.04

Table 2 Bridges under management of LOBMAC (resumed)

Management entity	No.	Bridge Name	Type	Length (m)	Completion
Ministry of Land, Infrastructure and transport	16	Geobuksun Br.	CS	744	2012.06
	17	Hwatae Br.	CS	1,345	2016.03
	18	Pallyeong Br.	SU	1,340	2016.12
	19	Namhae Br.	SU	660	1973.06
	20	Sinkeojae Br.	STB	940	2000.07
	21	Chang-sunBr.	AR	340	2003.05
	22	Seoandong	CS	595	2015.12
	23	Donggang	CS	460	2009.07
	24	Dongyi Br.	CS	576	2016.01
Local Government	25	Sam-cheonpo Br.	CS	436	2003.05
	26	Choyang Br.	AR	317	2003.05

CS: Cable Stayed, AR: Arch, SU: Suspension, STB: Steel Box

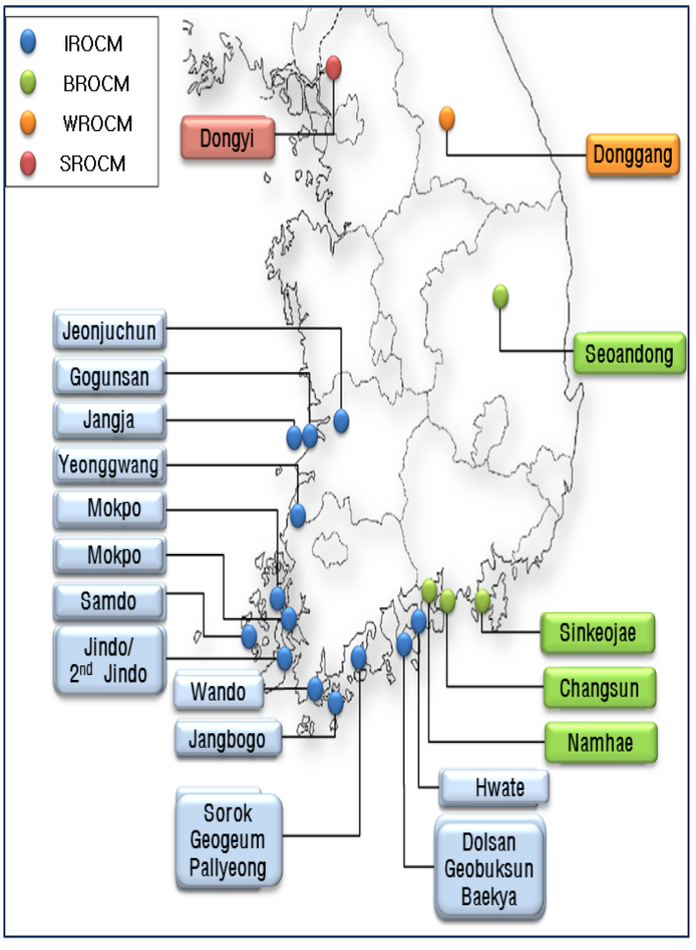


Figure 6 Bridges under management of LOBMAC

2 BRIDGE IN THIS PAPER

2.1 *Bridge Specification*

The bridge in this paper is one of the bridge under management of LOBMAC which is first constructed cable stayed bridge in the 1980s. The public service period has been aged for more than 30 years and design live load was improved from DB-18 to DB-24 through the performance improvement construction recently.

It has 484m total length involving 344m main span length, superstructure 3span of continuous stiffening girder. The deck plate is consist of 18 longitudinal U-ribs in the upper flange.[Figure 8]

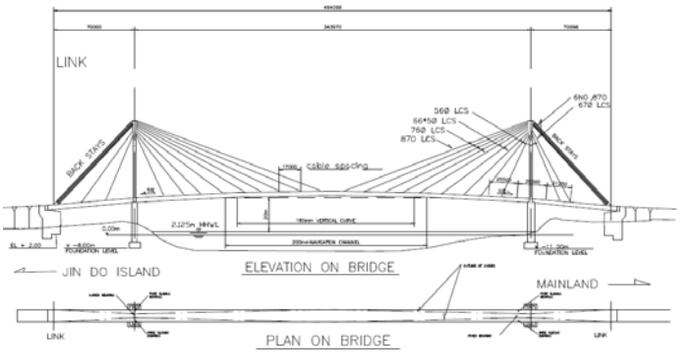


Figure 7 Longitudinal Drawing

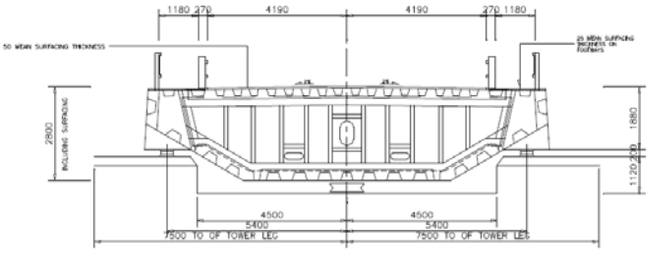


Figure 8 Cross-sectional drawing

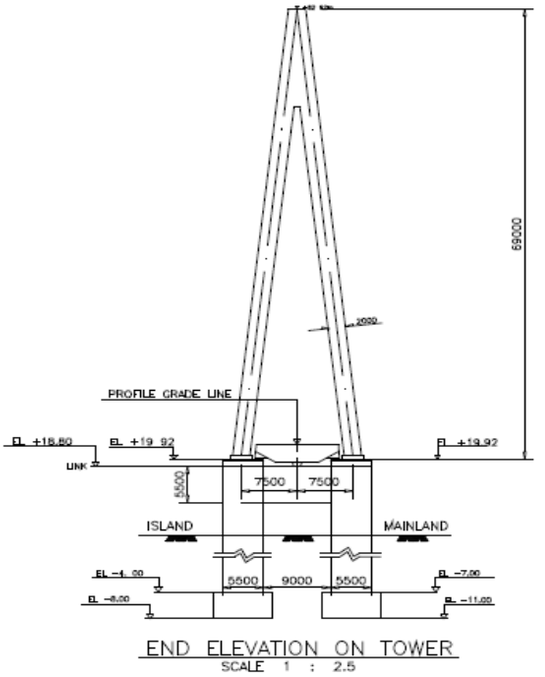


Figure 9 End elevation on pylon

2.2 *Maintenance and reinforcement history*

There were 7 tim es of Precision safety inspection(including urgent) & 2 tim es repavement were conducted during 30 years above. The dehum idification facility was installed in the stif fening girder in 1990's.

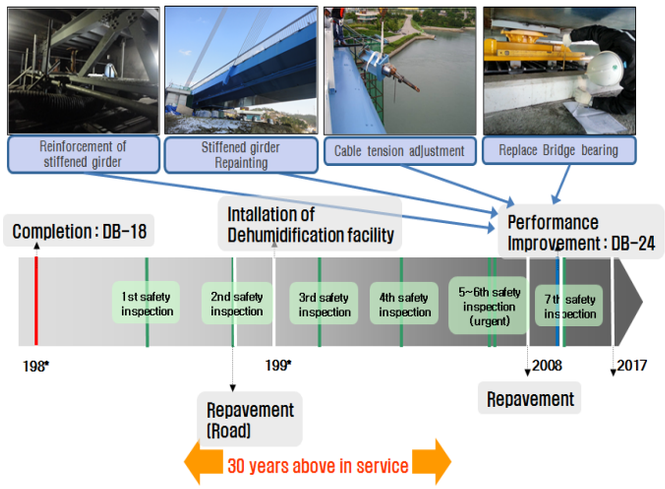


Figure 10 Maintenance history of the bridge

The maintenance history about painting and pavement what the particular factor to find causes of corrosion was summarized in Table 3 & 4.

Table 3 Maintenance history of painting

Construction	Unit	Quantity	Year	Remark
Repainting of Stiffening Girder(partial)	m^2	55	1995	External
	m^2	4,150	1998	Internal
	m^2	1,115	1998	External
	m^2	6,259	1999	External
Repainting of Pylon(partial)	m^2	645	1998	Internal
	m^2	2,383	1999	External
	m^2	3,430	2000	Internal
Repainting of Stiffening Girder(whole)	m^2	14,366	2001	Internal
	m^2	12,190	2002	
Repainting of Stiffening Girder(partial)	m^2	1,268	2007	External
Repainting of Stiffening Girder(whole)	m^2	13,668	2013	External
Repainting of Pylon(whole)	m^2	2,338	2014	External

Table 4 Maintenance history of pavement

Construction	Unit	Quantity	Year	Remark
Repavement (Latex)	m^2	4,066	1996	Whole
Crack repair (Patching)	m	742	2001	
Repavement (Epoxy mortar)	m^2	1,597	2002	Sidewalk
Crack repair (Road seal)	m	920	2003	
Repavement (Guss40mm + Polymer modified 30mm	m^2	4,060	2009	Whole (Road)
Repavement (Urethane)	m^2	1,161	2009	Sidewalk
Repavement (Elastic Pavement)	m^2	1,455	2014	

3 DEFECT IDENTIFICATION

A cable stayed bridge deck is a vital part of the load carrying system of the bridge. Unlike a suspension bridge where the deck is simply a suspended stiffening element where local failures do not imperil the overall stability of the bridge, a cable stayed bridge deck is a primary load carrying element that carries the compression load generated by the horizontal component of the cable stayed forces. If the deck capacity is reduced then there is the outside risk that the deck could buckle locally which would be catastrophic for the bridge structure. Thus, deterioration of the bridge deck through corrosion could lead to a very serious problem if not rectified.

It has been noted by the inspectors that it is suspected that the water flow in the longitudinal U-ribs emanates from the top surface, implying that either surface could be cracked or have extraneous construction holes which are letting water through the surfacing.

There were two immediate issues to be resolved for this bridge and the problem of the influx of water into the U-ribs and the subsequent corrosion.

The first was to identify the source of ingress of the water and to stop it, thereby removing the potential for corrosion.

The second was to identify the extent of the corrosion and to assess its impact on the integrity of the bridge.

3.1 *Corrosion extent*

Corrosion was identified in 4 ribs in the upper flange of the total 18 ribs in the form of its painting heaving like an air pocket on external surface of the longitudinal U-ribs. It was corroded about 80m along the longitudinal direction after removal of heaved painting.[Figure 2]



Figure 11 Corrosion of Longitudinal U-ribs

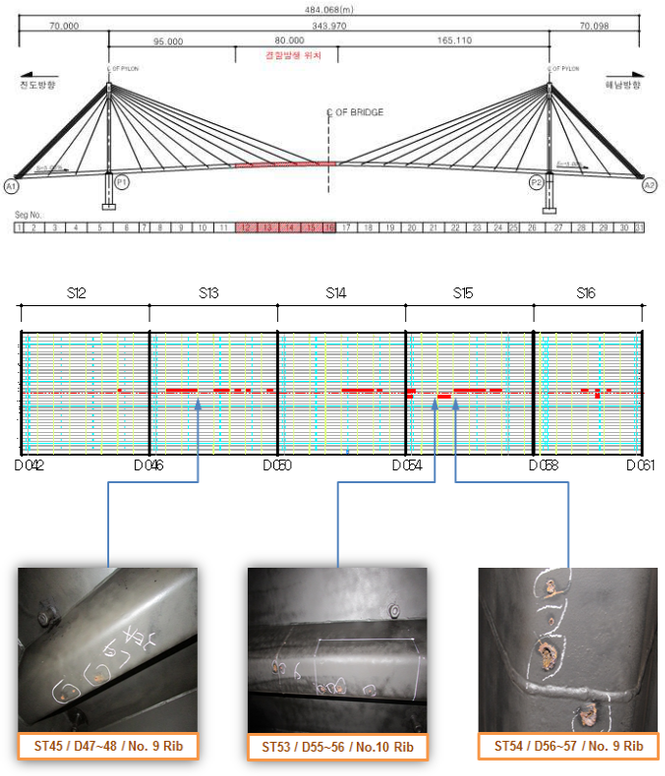


Figure 12 Location of corrosion by visual inspection

Table 5 Corrosion extent

Longitudinal rib No.	Location			Remark
	Segment	Diaphragm	Point(EA)	
9	S12~16	D45~61	71	
10	S15~16	D54~56 D59~60	10	

3.2 *Causes of corrosion*

The first step would be to investigate the extent of the ingress of water whic h will enable us to understand the extent of potential corrosion dam age and the likely sources of ingress into the deck.

It would be vitally im portant to identify the areas of ingress so that repairs may be made to the U-ribs.

The first stage would be to carry out a desk study of the deck to trough details and to identify if there are any details that have a track record of causing problems on other bridges. W e understood that at this stage the source of wa ter ingress has been identified as being at the location of the deck splices f or the make-up piece of the box section where bolted joints are present across the flange which were installed for the tem porary shear key. These joints are now redundant it would be expected that the holes were plugged by a suitable tapped thread so that the head did not project into the surfacing layer. It was not clear from video foot age taken of the troughs whether there are heads or nuts on these studs.

The four U-ribs that are affected were for the centermost. In each instant it would appear that the sealing protection of the bolts or threads has failed in every case and that a new detail would be required to reseal these holes.

A. As-built drawing & construction record

A total of 56 bolt holes were installed for shear key, a temporary fixture for transverse restraint on the upper part of the reinforced girder. And 16 of them were located within internal U-ribs.[Figure 13]

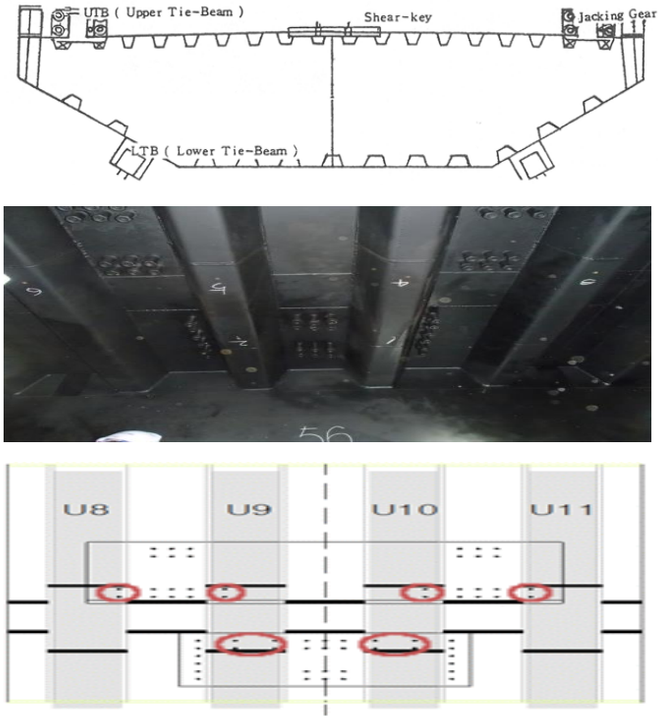


Figure 13 Deck details around the bolted tem porary works

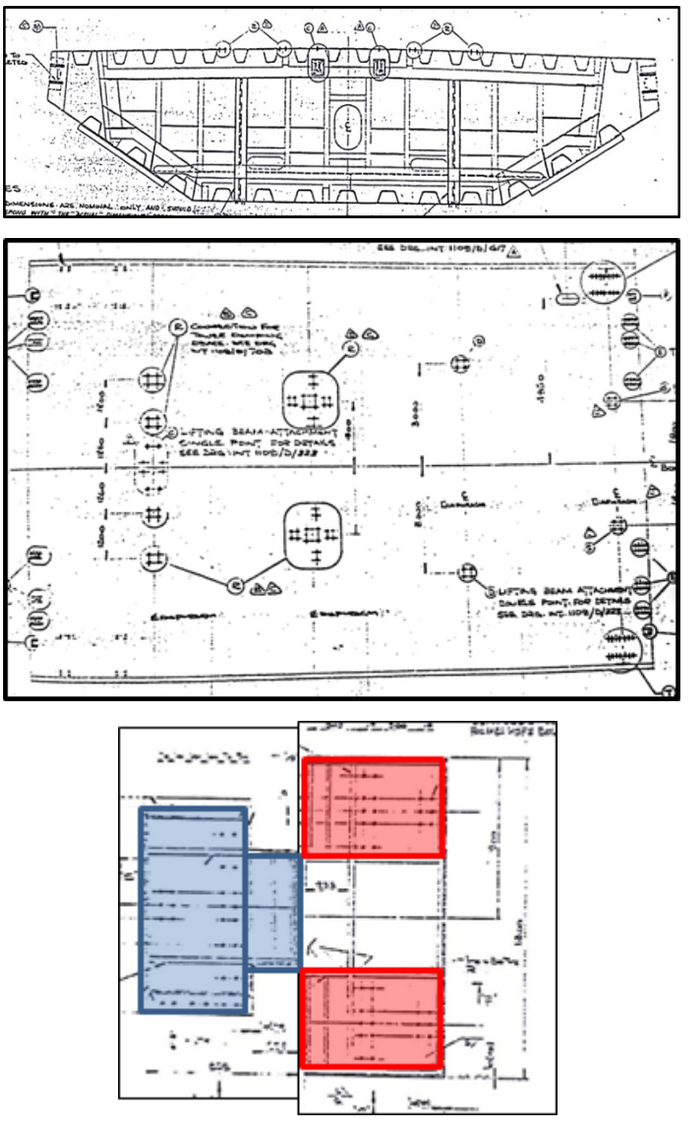


Figure 14 Location of Bolt holes & shear key details on as-built drawing

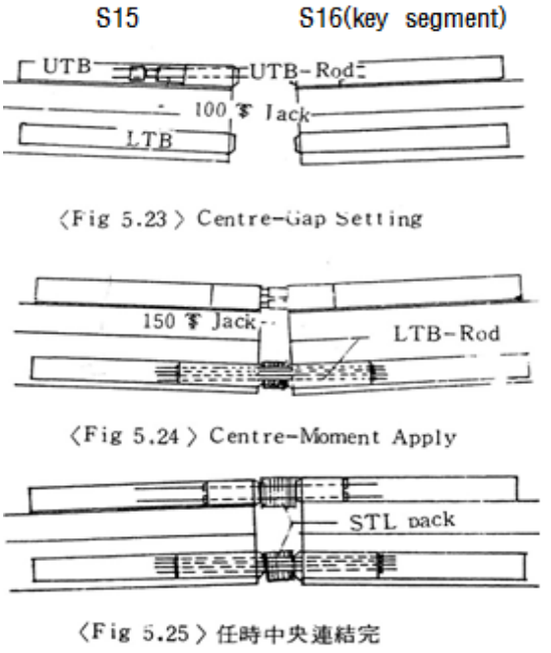


Figure 15 Closure Procedures of key segment

B. Maintenance and reinforcement history

As a result of analysis, it was found that the bolt holes drilled into the upper deck for tem porary works were not fully sealed. According to the record of whole repaving in 2008, bolt fracture & slip on the exposed part were checked.[Figure 7]



Figure 16 Bolts fracture & slip in perform ance improvement construction record

C. Previous inspection report

We checked out continuous water leak through a bolt holes from the top surface safety after reviewing inspection report.



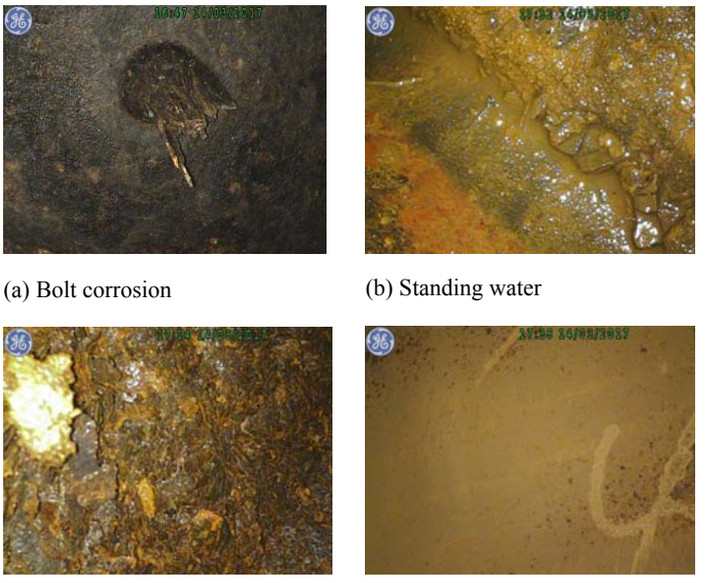
(a) 3rd safety inspection (b) 4th safety inspection

(c) 4th safety inspection (d) 7th safety inspection

Figure 17 W ater leak though a bolt holes(Previous safety inspection report)

D. Borescope inspection

Borescope inspection conducted corroded zone & not-damaged zone separately to determ ine the detailed internal corrosion status. W e also identif ied existing bolt holes & water inf lux into the longitudinal U-ribs after detailed inspection by the borescope.[Figure 18]



(a) Bolt corrosion (b) Standing water

(c) Corrosion & debris (d) Health condition not damaged

Figure 18 Corroded internal U-rib by borescope inspection

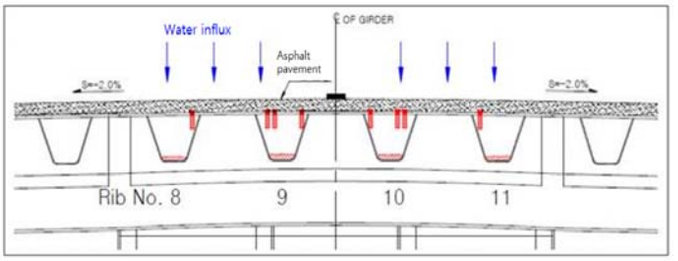


Figure 19 Estimated path of water inflow

4 FUTHER INVESTIGATIONS

Further investigations are scheduled as follows.

4.1 *Detail internal inspection using inspection robot*

Work has been carried out to date on som e limited borescope video studies. These show that there is a build-up of corrosion products on the bottom flange of the U-Ribs.

It would be required to ascertain how m uch damage had taken place from the corrosion of the steelwork. The extent of this build-up of deleterious m aterial was not clear from the borescope and the nature and extent of the m aterial should be investigated. Production of inspection robot is in progress to identify the exact extent of corrosion.

4.2 *Finite element analysis*

Finite element analysis is in progress to determ ine the penetrating location of inspection robot about

longitudinal & transverse directions, analytically. In the finite element analysis, MIDAS FEA, which is general purpose structural analysis software, was used. And the plate element was used in modeling of stiffening girder.

4.3 *Measurement of steel & coating thickness*

Ultrasonic testing to measure the thickness loss of the steel section of the U-ribs is scheduled.

4.4 *Repair & rehabilitation design*

The extent of the repair and rehabilitation design will depend upon the findings from the earlier investigations. It is anticipated that the design will need to provide a new means of sealing the bolt holes within the U-Ribs that can be demonstrated to be completely watertight, as well as establishing what if any repairs are required to replace material lost to corrosion within the troughs.

The development of a bold sealing design will be dependent on access to the top deck and the means by which resurfacing of the bridge deck is carried out. The design of the bolt sealing will need to be sufficiently robust so that it can withstand the rigours of removal of the deck surfacing by mechanical means. It is suspected that this may have played a part in the failure prior to this, but this is speculation at this point.

The rehabilitation design of the troughs will be developed based upon an assessment of the traffic loading requirements on the bridge deck to determine the minimum structural capacity of the U-Ribs. Clearly it would be needed to minimize the amount of strengthening and therefore if it can be shown that the loss of section is still sufficient for the current traffic loading on the bridge then strengthening may be avoided. However, this presupposes that we would carry out a specific live loading assessment.

The video footage taken from the borescope shows considerable debris within the troughs that would appear to be material that has parted company with the parent metal of the trough. If this is the case then there is likely to be significant loss of section, even though that is not appear to be any evidence of complete loss of section. It is expected to be proper that effective strengthening would be to cut out the existing trough and to re-weld a new segment in place.

Detailed inspections & record is required on the top surface of the exposed deck when the next whole repaving to prevent repetition case.

5 CONCLUSION

The bridge in this paper is one of the bridge under management of LOBMAC which is first constructed cable stayed bridge in the 1980s.

It has been noted by the inspectors that it is suspected that the water flow in the longitudinal U-ribs emanates from the top surface, implying that either surface could be cracked or have extraneous construction holes which are letting water through the surfacing.

Corrosion was identified in 4 ribs in the upper flange of the total 18 ribs by its painting heaving like an air pocket on external surface of the longitudinal U-ribs.

We carried out a desk study of the deck to through details and to identify if there are any details that have a track record of causing problems on other bridges. Defect identification, detailed inspection, finding causes and evaluation were conducted.

In this paper, we present only the part of research results obtained in the on-going research. Further investigations relating to be resolved of this bridge are scheduled.

This case will contribute to prevent similar case in the future and the ongoing development of operational and maintenance procedures for the life of the bridge.

REFERENCE

[1] Do Kyoun Kim , Jae Uk Lee, "The Study on stability of Bridge on which Heavy Military Vehicle passes" (2012)

[2] Korea Infrastructure Safety and Technology Corporation, "Precision Safety inspection Report of A Bridge." (2014)

[3] COWI, “Proposal for Deck Repairs to the A bridge” (2017)

Maintenance, Safety, Risk, Management and Life-Cycle Performance of Bridges – Powers, Frangopol, Al-Mahaidi & Caprani (Eds)
© 2018 Taylor & Francis Group, London, ISBN 978-1-138-73045-8

Experimental and analytical investigation of bridge deck under restrained shrinkage

M. Rahman, Y. Chen and R. Hindi
Saint Louis University, St. Louis, MO, United States

A. Ibrahim
University of Idaho, Moscow, ID, United States

W. Lindquist
William Jewell College, Liberty, MO, United States

ABSTRACT: Early-age cracking on concrete bridge decks is a major concern because it leads to premature deterioration of bridges. Most of the cracks formed during the curing stage of concrete are due to the drying shrinkage. This paper presents the experimental and analytical investigation of shrinkage-induced stresses and strains within large-scale bridge prototype. Three large-scale bridge decks of 7 x 10 ft were built using three different types of concrete mixtures: (1) a mixture containing 100% Portland cement, (2) a mixture incorporate Type-K cement and (3) a mixture containing partially saturated fine lightweight aggregate (LWA) to promote internal curing. The results show that the LWA concrete mixture induced the least amount of stresses within the deck while the Type-K developed the largest stresses at the end of six-month shrinkage period. The finite element simulation was used to predict the shrinkage of concrete decks with a reasonable accuracy.

1 INTRODUCTION

Cracks in concrete bridge decks are detrimental as it allows harmful substances to reach the reinforcing steel and initiate corrosion and compromise the integrity of the deck. Bridge decks are especially vulnerable to cracking due to their large surface-to-volume ratios, which exposes the concrete to a high-water evaporation rate.

Concrete shrinks due to moisture loss, temperature reduction or hydration reactions. When these volume changes are restrained, tensile stress develops in concrete which may cause cracking. Cracking often occurs in concrete bridge decks due to restrained shrinkage of concrete. Numerous research studies have been conducted to evaluate the causes of crack-ing in bridge decks through experimental and field investigations (Cheng and Johnston, 1985, Darwin et al., 2004, French et al., 1999, Horn et al., 1975, Neville, 1995). This includes altering the concrete mixture design (Streeter, 1996, Lawler et al., 2006, Brown et al., 2007), incorporating steel or polymer fibers or other additives (Altoubat and Lange, 2001, Naik et al., 2006, Subramaniam et al., 2005), and adjusting construction practices in terms of placing sequence, curing time and weather requirements (Issa, 1999, Krauss and Rogalla, 1996, Schmitt and Darwin, 1995).

In addition, studies have examined optimizing the structural design of bridge superstructures including changing the number of shear studs or the spacing between reinforcement (French et al., 1999, Frosch et al., 2002, Schmitt and Darwin, 1995). Some studies have also found that lowering the amount of restraint inside the concrete deck can help reduce crack formation as well. Another study modeled bridge deck shrinkage and found that the reinforcement within the deck leads to high tensile stresses in the concrete deck (Nagataki and Gomi, 1998).

Three types of concrete mixtures were studied in this research: (1) a deck containing 100% portland cement, (2) a deck incorporating Type-K cement (a shrinkage compensating cement), and (3) a deck containing partially saturated fine lightweight aggregate (LWA) to promote internal curing. Type-K cement is shrinkage compensating cement which, unlike portland cement, compensates for drying shrinkage by initially expanding during the early stages of hydration (Chaunsali et al., 2013, Gruner and Plain, 1993, Klein et al., 1961, Nagataki and Gomi, 1998, Pittman et al., 1999, Richardson et al., 2014). The mechanism of expansion in the Type-K cement concrete is a result of the early formation and stability of ettringite. The ettringite crystals need water to expand; therefore, moist curing must

be used or minimal expansion will occur. Numerous studies have concluded that the use of pre-wetted lightweight aggregate can minimize the development of autogenous and drying shrinkage through improved curing (Bentur et al., 2001, Bentz and Weiss, 2011, Wei and Hansen, 2008, Henkensiefken et al., 2009, Browning et al., 2011, Guthrie and Yaede, 2013). The pre-wetted fine aggregate extends the curing period by releasing absorbed water.

Cracking due to restrained shrinkage is a major concern for both serviceability and durability of concrete, but only limited research has sought to model the shrinkage of concrete by finite element (FE) analysis. Ngo and Scordelis (1967) presented the first finite element analysis of reinforced concrete that included the effect of cracking. In order to simulate the shrinkage phenomenon of concrete, some researcher converted the total shrinkage into thermal shrinkage by means of the method of Equivalent Temperature Difference (Attiyah et al., 2014, Kianoush et al., 2008, Ma and Gao, 2008). In this study shrinkage behavior was presented by converting the shrinkage induced strain into an equivalent temperature to simulate the cracking tendency of concrete.

This study strives to investigate shrinkage cracking through a combination of laboratory experimentation and finite element modeling. A specific objective of this research included the development of a finite element model that could correctly evaluate and predict the shrinkage induced stresses within a bridge deck. Three-dimensional FE models using ABAQUS were developed to determine the overall structural response due to shrinkage. The developed FE models were verified using experimental results from large scaled bridge decks. Three 7 x 10 ft concrete bridge bays were used for the verification of the FE models. The reinforcement and bay design details will be discussed in details in the finite element modeling section. Finite element model was used to monitor the stress and strain change within the concrete deck to predict the potential of cracking.

2 FINITE ELEMENT MODELING

The objective of the finite element (FE) analysis is the development of a model that predicts the stress-strain behavior of a bridge resulting from concrete shrinkage. The FE simulation conducted in the study was carried out using ABAQUS finite element software. To study the effects of shrinkage, as well as to better replicate full-scale bridges, large-scale bridge prototypes (also called bridge bays) measuring 7 × 10 ft with an 8 in thick slab were created using ABAQUS, as shown in Fig. 1. The size and shape of the bridge deck was scaled based on Illinois Department of Transportation standard design (Ardeshirilajimi et al., 2016, Chaunsali et al., 2013). The deck was surrounded by four C10×15.3 steel channels on the outside perimeter to simulate the continuity of an actual concrete deck. Two layers of epoxy coated reinforcement were placed within the deck with a top and bottom clear cover of 2 in and 1.75 in, respectively. The girders were spaced at m 5 ft. and were constrained by two C6×8.2 steel channels to prevent the girders from twisting.

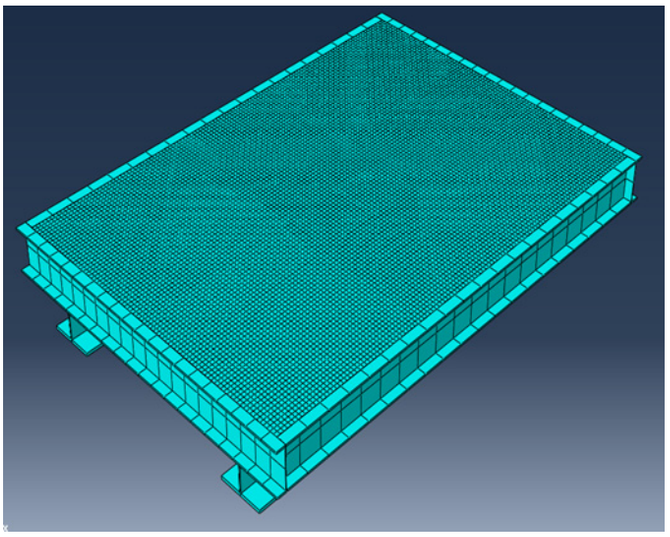


Figure 1. ABAQUS model of experimental deck.

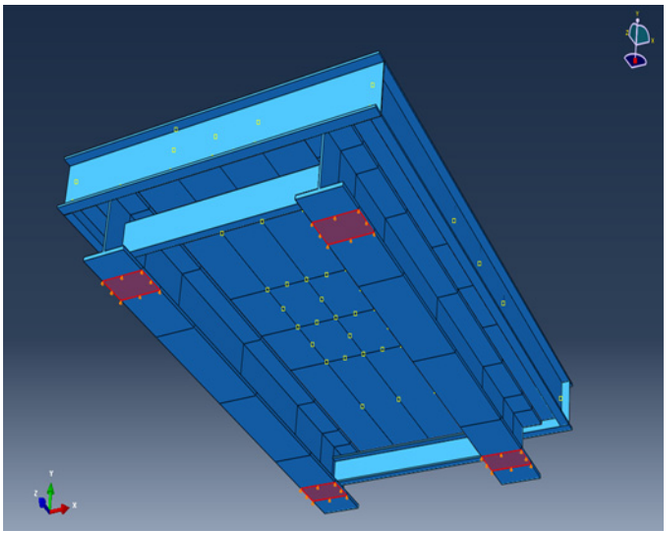


Figure 2. Boundary conditions; fixed in y direction (gravity direction) at the red marks.

The reinforcement was idealized using 2-node linear truss elements that consider only axial strain along the reinforcement length (T3D2 elements). The experimental deck, supporting girders and perimeter channels were modeled with 8-node linear brick elements (C3D8R continuum solid elements). Each node had three translational degrees of freedom in the x, y and z directions. The brick elements utilize reduce integration used to limit the number of integration points and reduce the running time with-out an unreasonable sacrifice of accuracy (ABAQUS, 2014).

The focus of the FE analysis is to model the shrinkage-induced strain before first cracking of the

deck with the entire analysis conducted in the linear elastic range. The concrete and steel material properties used for FE modeling are listed in Table 1. A different elastic modulus and weight-per-unit volume were used for the different types of concrete according to the measured mixture properties. An elastic modulus value consistent with a 28-day unconfined compressive strength and a Poisson's ratio of 0.2 was selected for all concrete materials. The thermal coefficient of concrete usually varies be-tween 3 to 8×10^{-6}/°F for normal-weight concrete (ABAQUS 2014). A thermal coefficient of 5.5×10^{-6}/°F was used for all types of concrete in this study.

Full bond is assumed between the steel and the concrete by sharing nodes at their intersection points. All the elements in the large-scale model are bound by applying tied constraints, except for the reinforcement that was embedded inside the concrete deck, which allowed the concrete and reinforcement to act together when the concrete is expanding or shrinking. The entire experimental deck was fixed in the gravity direction at the supports located at the bottom of the girders (Fig. 2).

Table 1. Mixture Properties

	Control	Type-K	LWA	Steel
Weight per unit volume (lb/ft^3)	142	141	136	490
Modulus of elasticity (ksi)	3770	3668	4380	29000
Poisson's ratio	0.2	0.2	0.2	0.3
Thermal coefficient of expansion (10^{-6}/°F)	5.5	5.5	5.5	6.5

3 EXPERIMENTAL BRIDGE BAY DESIGN

Experimental bridge "cut-outs" built with three different concrete mixtures was constructed using the dimensions described FE modeling section (Fig. 3). All the scaled concrete decks were constructed using the same steel sections, reinforcement size and type, and were placed at the same time of the year by the end of September to minimize variation in results due to environmental effects.

Multiple strain and temperature gages were installed within and on the surfaces of the concrete deck panels. To minimize interference from perimeter C-channels and supporting steel girders, all of the gages were installed towards the center of the deck, as shown in Fig. 4 and 5. Twenty strain gages were interspersed throughout the top and bottom reinforcement layers in both the longitudinal and transverse directions and was monitored for a period of six months. More gages were placed on the top layer of reinforcement, as this is generally where the greater amount of cracking is found and is of greater interest for this study.

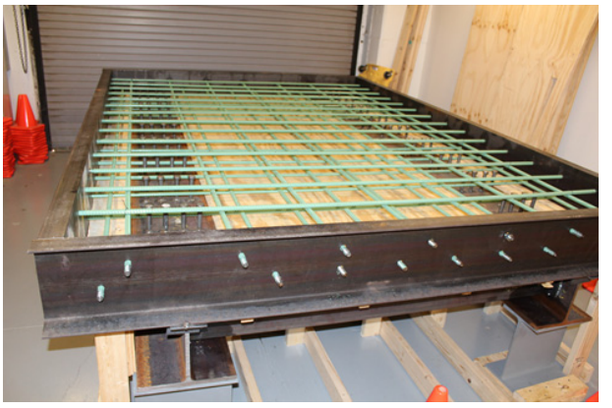


Figure 3. Experimental deck.

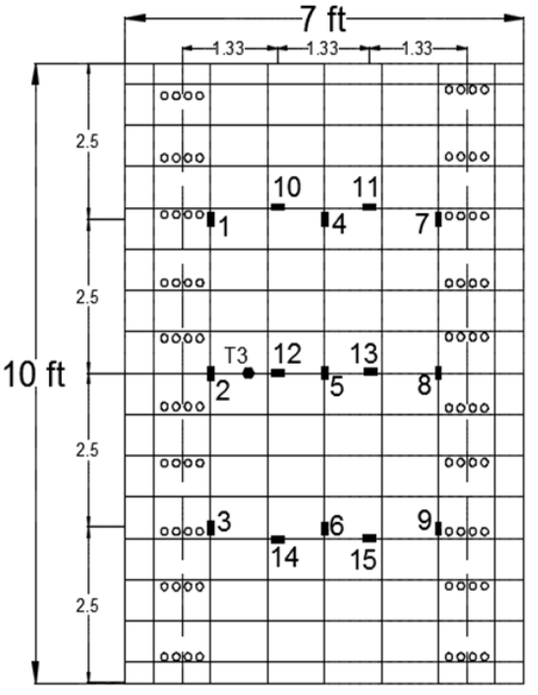


Figure 4. Strain gage location on top reinforcement.

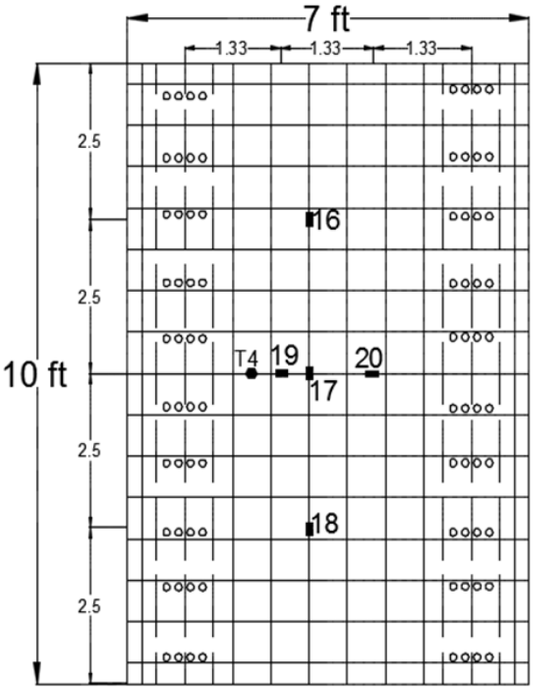


Figure 5. Strain gage location on bottom reinforcement.

A total of 15 strain gages were attached to the top layer of reinforcement, nine on the longitudinal reinforcement and six on the transverse reinforcement for each concrete deck (Fig. 4). Another five gages were installed on the bottom layer of the reinforcement including three on the longitudinal and two on the transverse reinforcement (Fig. 5). All foil gages were given a protective coating in accordance with manufacturer recommendations.

4 COMPARISON BETWEEN FE AND EXPERIMENTAL RESULTS

Strains measured in the longitudinal reinforcement are chosen to be the primary focus for this research because they represent the mechanism by which transverse cracking is initiated in actual bridge decks. Concrete initially expands during the 7-day curing period followed by shrinkage upon initiation of drying (in this case after 7 days). Strain data were recorded for a period of six months and the negative strain indicates shrinkage. Modeling of drying shrinkage strain directly using the FE method is not possible in ABAQUS, and as a result, an equivalent temperature load was used to model the shrinkage behavior of the concrete. After comparing all data collected from the experiments, it was obvious that the strain data collected from different locations within the experimental deck showed no obvious trend (Ardeshirilajimi et al., 2016); therefore, an average longitudinal total shrinkage strain (shown in Fig. 6) was used to determine the equivalent temperature load. The temperature load applied was uniform throughout the deck and was determined using the equation $\varepsilon = \alpha\Delta T$. The strain ($\varepsilon$, from the average longitudinal total shrinkage strain collected from the experimental data) divided by the concrete thermal coefficient of expansion ($\alpha = 0.5\times10^{-6}$/°F) yields the temperature load applied to the concrete deck in the FE model. Figure 7 shows the temperature load applied to each type of concrete. These temperature loads permit shrinkage strains to be mimicked using ABAQUS and the results from the comparison between the FE models and the experimental data are shown in Fig. 8 through Fig. 10.

As shown in Fig. 8 and Fig. 9, the strain results (ABAQUS compared with experiments) for the control and Type-K deck were very comparable until day 30, but by the end of 6 months, there was a deviation of about 50 με. However, the result for the LWA (Fig. 10) was almost identical. Overall, the temperature load that was applied to the three types of FE models, predicted results in good agreement with the data collected from the tested concrete decks.

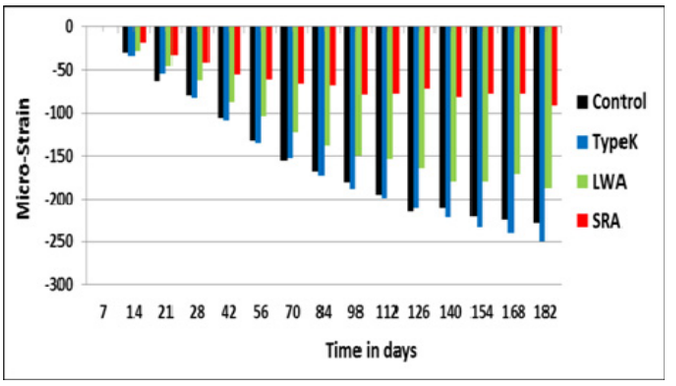


Figure 6. Average longitudinal total shrinkage of experimental deck.

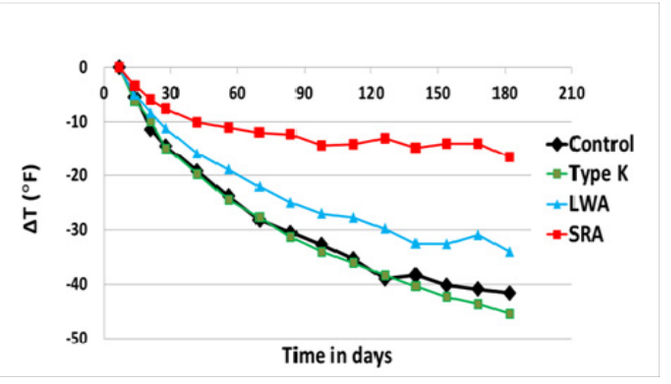


Figure 7. Temperature load applied to the FE model, in °F.

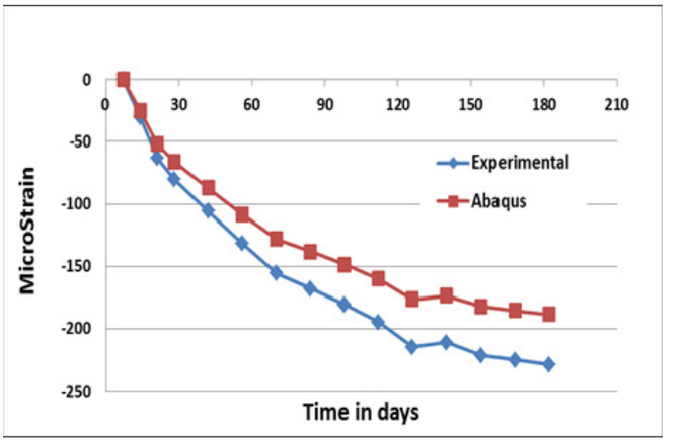


Figure 8. Control concrete deck.

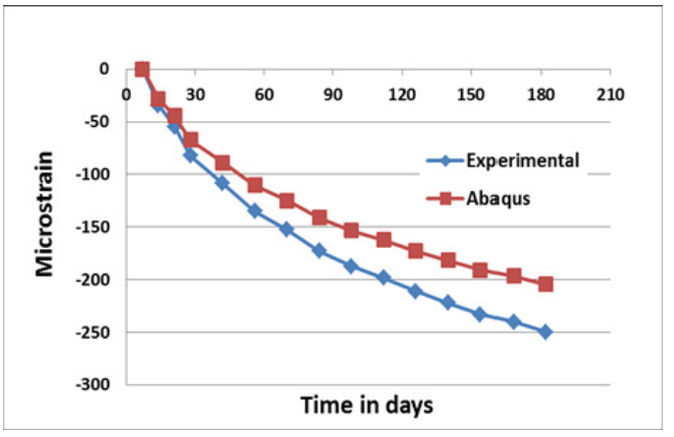


Figure 9. Type-K concrete deck.

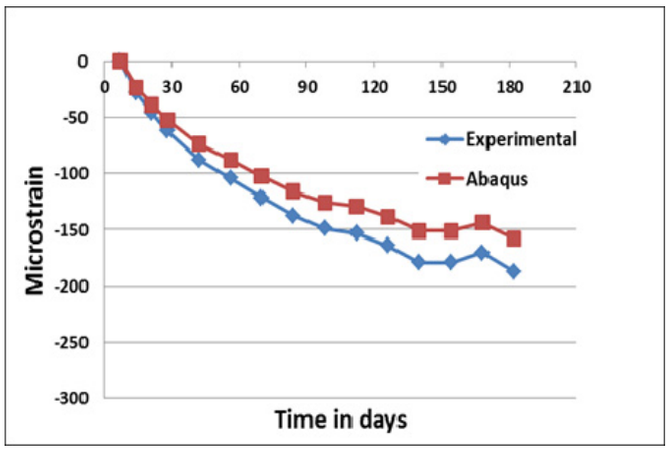


Figure 10. LWA concrete deck.

Longitudinal stress contours at the bottom layer of reinforcement inside the concrete deck for the three different types of concrete are shown in Fig. 11 to 13. Concrete containing internally cured lightweight aggregate (LWA) has a similar stress contour compared with the control mixture with a lower calculated stress at the center of the deck (279 psi and 236 psi for the control and LWA decks, respectively). On the other hand, the Type-K deck has a higher stress concentration around the supporting girders with a stress of 287 psi at the center of the deck.

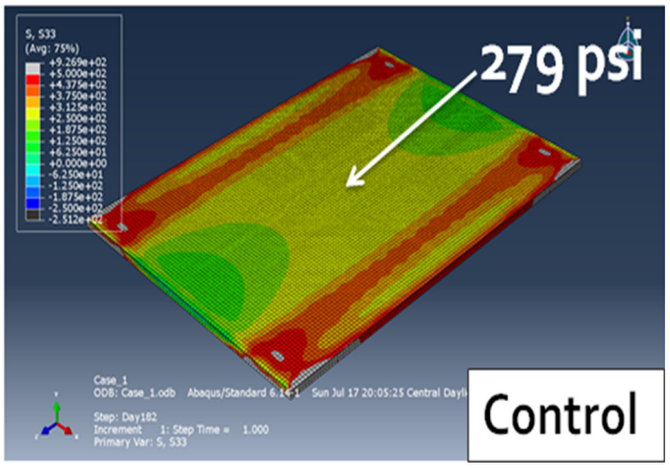


Figure 11. Control deck stress contours in longitudinal direction.

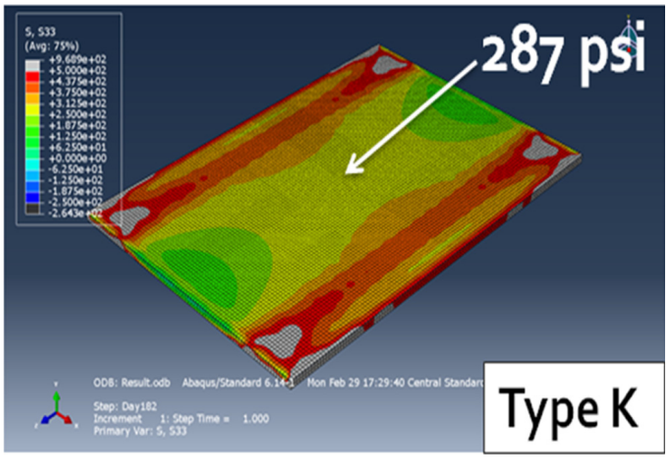


Figure 12. Type-K deck stress contours in longitudinal direction.

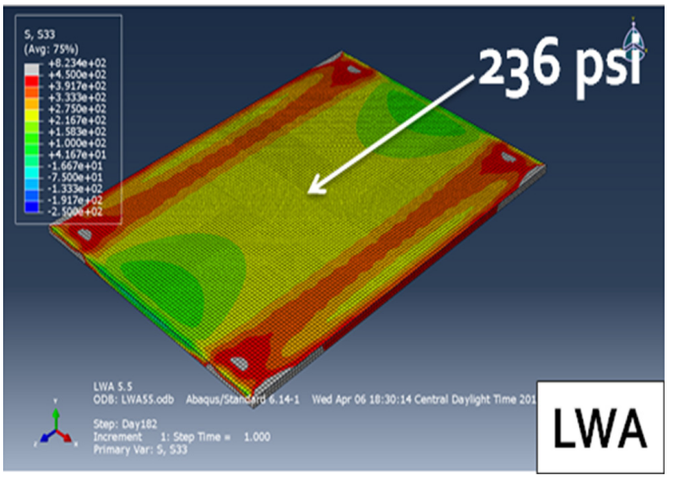


Figure 13. LWA deck stress contours in longitudinal direction.

The objective of this simulation is to evaluate the effect of drying shrinkage-induced strains on developing stress that cause cracking in concrete decks. It is possible that at early age tensile stress introduced by shrinkage strain exceed the tensile strength of concrete which may initiate cracking in bridge decks. Reduction in stress turns less chance of cracking inside the concrete deck which supports that LWA has the least amount of shrinkage among the three different types of concrete.

5 SUMMARY AND CONCLUSION

Cracks reduce the service life of concrete decks and it is a major safety concern for the bridge decks. Significant research has been conducted in the past on assessment of cracking in bridge decks through field investigation, but only limited research has sought to model the shrinkage of concrete by finite element (FE) analysis. In this study shrinkage of concrete in bridge decks is modeled using the finite element (FE) software ABAQUS. Through the application of a uniform equivalent temperature load, the shrinkage of concrete can be closely simulated in all experimental decks. The main focus of the FE modeling is to study the stress and strain induced by concrete shrinkage in generating early age cracking in bridge decks. The following conclusions are based on the experimental and analytical work presented in this paper:

- Shrinkage of the concrete deck can be predicted analytically with reasonable accuracy using finite element (FE) model.
- Finite element models can be used to predict the stress and strain within the concrete deck and as well as to predict the potential of cracking.
- LWA concrete mixture induced the least amount of stresses within the deck compared to control mixture.

- Type-K developed the largest stresses within the deck at the end of six-month shrinkage period.

ACKNOWLEDGEMENT

This work was supported by the Illinois Department of Transportation (IDOT) through the Illinois Center of Transportation (ICT). This publication is based on the results of ICT-R27-88 and ICT-R27-139, Bridge Decks: Mitigation of Cracking and Increased Durability. This research was conducted in cooperation with the Illinois Center for Transportation; the Illinois Department of Transportation, Office of Program Development; and the US Department of Transportation, Federal Highway Administration. This support is gratefully acknowledged. Acknowledgements are also in order for Saint Louis University (SLU) for internal financial support. The opinions and findings of this paper are those of the authors and not necessarily those of the sponsors.

REFERENCE

ABAQUS 2014. ABAQUS 6.14 Analysis User's Manual.

ALTOUBAT, S. A. & LANGE, D. A. 2001. Creep, Shrinkage, and Cracking of Restrained Concrete at Early Age. *ACI Materials Journal,* 98**,** 323-331.

ARDESHIRILAJIMI, A., WU, D., CHAUNSALI, P., MONDAL, P., CHEN, Y. T., RAHMAN, M. M., IBRAHIM, A., LINDQUIST, W. & HINDI, R. 2016. Bridge Decks: Mitigation of Cracking and Increased Durability. Illinois Center for Transportation, IL.

ATTIYAH, A. N., GESUND, H. & RASOOL, M. H. 2014. FINITE ELEMENT MODELLING OF CONCRETE SHRINKAGE CRACKING IN WALLS. *Kufa journal of Engineering,* 5.

BENTUR, A., IGARASHI, S.-I. & KOVLER, K. 2001. Prevention of autogenous shrinkage in high-strength concrete by internal curing using wet lightweight aggregates. *Cement and concrete research,* 31**,** 1587-1591.

BENTZ, D. P. & WEISS, W. J. 2011. *Internal curing: a 2010 state-of-the-art review*, US Department of Commerce, National Institute of Standards and Technology.

BROWN, M. D., SMITH, C. A., GREG SELLERS, J., FOLLIARD, K. J. & BREEN, J. E. 2007. Use of alternative materials to reduce shrinkage cracking in bridge decks. *ACI Materials Journal,* 104**,** 629-637.

BROWNING, J., DARWIN, D., REYNOLDS, D. & PENDERGRASS, B. 2011. Lightweight aggregate as internal curing agent to limit concrete shrinkage. *ACI Materials Journal,* 108**,** 638-644.

CHAUNSALI, P., LIM, S., MONDAL, P., FOUTCH, D. A., RICHARDSON, D., TUNG, Y. & HINDI, R. 2013. Bridge Decks: Mitigation of Cracking and Increased Durability. Illinois Center for Transportation, IL.

CHENG, T. & JOHNSTON, D. 1985. Incidence Assessment of Transverse Cracking in Concrete Bridge Decks: Construction and Material Considerations. North Carolina State University Department of Civil Engineering, Raleigh, N.C.

DARWIN, D., BROWNING, J. & LINDQUIST, W. D. 2004. Control of cracking in bridge decks: observations from the field. *Cement, Concrete and Aggregates,* 26**,** 148-154.

FRENCH, C., EPPERS, L., LE, Q. & HAJJAR, J. 1999. Transverse cracking in concrete bridge decks. Washington, D.C.: Transportation Research Record 1688.

FROSCH, R. J., BLACKMAN, D. T. & RADABAUGH, R. D. 2002. Investigation of bridge deck cracking in various bridge superstructure systems. West Lafayette, Indiana: Join Transportation Research Program Technical Report.

GRUNER, P. & PLAIN, G. 1993. Type K shrinkage-compensating cement in bridge deck concrete. *Concrete International,* 15.

GUTHRIE, W. & YAEDE, J. 2013. Internal curing of concrete bridge decks in Utah: preliminary evaluation. *Transportation Research Record: Journal of the Transportation Research Board***,** 121-128.

HENKENSIEFKEN, R., BENTZ, D., NANTUNG, T. & WEISS, J. 2009. Volume change and cracking in internally cured mixtures made with saturated lightweight aggregate under sealed and unsealed conditions. *Cement and Concrete Composites,* 31**,** 427-437.

HORN, M., STEWART, C. F. & BOULWARE, R. 1975. Factors Affecting the Durability of Concrete Bridge Decks: Construction Practices. Bridge Department California Division of Highways.

ISSA, M. A. 1999. Investigation of cracking in concrete bridge decks at early ages. *Journal of Bridge Engineering,* 4**,** 116-124.

KIANOUSH, M., ACARCAN, M. & ZIARI, A. 2008. Behavior of base restrained reinforced concrete walls under volumetric change. *Engineering Structures,* 30**,** 1526-1534.

KLEIN, A., KARBY, T. & POLIVKA, M. Properties of an expansive cement for chemical prestressing. Journal Proceedings, 1961. 59-62.

KRAUSS, P. D. & ROGALLA, E. A. 1996. Transverse cracking in newly constructed bridge decks. Washington, D.C.: NCHRP.

LAWLER, J., KRAUSS, P. & ABERNATHY, C. 2006. HPC Mixture Development for Montana Using Local Material. *HPC Bridge Views,* 43**,** 4.

MA, B.-G. & GAO, Y.-L. 2008. Finite Element Analysis for shrinkage in the Interface of Functionally Graded Concrete Segment Used in Shield Tunneling.

NAGATAKI, S. & GOMI, H. 1998. Expansive admixtures (mainly ettringite). *Cement and concrete composites,* 20**,** 163-170.

NAIK, T. R., CHUN, Y.-M. & KRAUS, R. N. 2006. Reducing shrinkage cracking of structural concrete through the use of admixtures. Wisconsin Highway Research Program.

NEVILLE, A. M. 1995. *Properties of concrete*.

NGO, D. & SCORDELIS, A. Finite element analysis of reinforced concrete beams. Journal Proceedings, 1967. 152-163.

PITTMAN, D. W., RAMEY, G. E., WEBSTER, G. & CARDEN, A. 1999. Laboratory evaluation of concrete mixture designs employing type I and type K cement. *Journal of materials in civil engineering,* 11**,** 144-150.

RICHARDSON, D., TUNG, Y., TOBIAS, D. & HINDI, R. 2014. An experimental study of bridge deck cracking using type K-cement. *Construction and Building Materials,* 52**,** 366-374.

SCHMITT, T. R. & DARWIN, D. 1995. Cracking in concrete bridge decks. University of Kansas Center for Research, Inc.

STREETER, D. 1996. Developing high-performance concrete mix for New York State bridge decks. *Transportation Research Record: Journal of the Transportation Research Board***,** 60-65.

SUBRAMANIAM, K. V., GROMOTKA, R., SHAH, S. P., OBLA, K. & HILL, R. 2005. Influence of ultrafine fly ash on the early age response and the shrinkage cracking potential of concrete. *Journal of materials in civil engineering,* 17**,** 45-53.

WEI, Y. & HANSEN, W. 2008. Pre-soaked lightweight fine aggregates as additives for internal curing in concrete. *Special Publication, American Concrete Institute,* 256**,** 35-44.

Maintenance, Safety, Risk, Management and Life-Cycle Performance of Bridges – Powers, Frangopol, Al-Mahaidi & Caprani (Eds)
© 2018 Taylor & Francis Group, London, ISBN 978-1-138-73045-8

Methods for fast and reliable determination of damping and tension force of stay cables

Thomas Mack
Schimetta Consult, Department Monitoring and R&D, Linz, Austria
Roman Geier
Schimetta Consult, CEO, Vienna, Austria

ABSTRACT: After the construction of cable-stayed bridges it is always necessary in the framework of bridge inspections and special investigations to determine the static and dynamic parameters like cable force and the damping of the stay cable. Methods employed so far have often been too cost-intensive and time-consuming whereas the results have indicated in terms of the cable force deviations of up to ± 10%, which often proved to be insufficient for engineers and operators. In the framework of several research projects measurement and evaluation methods have been developed for both parameters and which can be applied faster and easier and at the same time improve the accuracy of the cable force determination to ± 1%. As concerns the damping parameter, an evaluation method has been developed which satisfies the constructive requirements and leads to reliable and reproducible damping values.

1 INTRODUCTION

Stay cables are decisive bearing elements of a cable-stayed bridge and are essential for the system stiffness and system damping. Today mainly prefabricated cables are used which are provided with a final or temporary corrosion protection. The laid ropes as well as parallel wire ropes usually consist of single wires with a diameter of 5-7 mm. These steel wires have a considerably higher carbon share than structural steel and correspondingly a higher stability. This, however, leads to a considerably lower ductility which manifests itself in a respective ultimate elongation.

Dynamic analysis is very important for cable-stayed bridges as well as suspension bridges in the project stage. In general vibrations of a structure can be stimulated by the effects of wind, traffic and earthquakes. The safety of a cable-stayed bridge is considerably determined by the aerodynamic behaviour. So far example dynamic instabilities were the reason for collapses of some early suspension bridges (Tacoma Narrows Bridge). Vibrations can clearly affect or reduce the load-bearing capacity, the durability (fatigue) as well as the serviceability limit strength (effects on the user).

Up to today the development of bridge construction has continued, constantly new materials and technologies have been used – the limits of technological feasibility have continuously shifted into the extreme range. Whereas increasingly wide spans have been successfully bridged, numerous structural problems have emerged which have to be considered during planning. The dynamic properties of the respective structure have assumed a special importance in this connection. As early as in the 19th century, after the disaster in the Tay Bay, dynamic load cases were considered important factors during the planning of structures.

In the course of history of bridge construction dynamic loads on bridges were to provide for big surprises frequently. In the 20th century in particular the spectacular collapse of the Tacoma Narrows suspension bridge in the US state of Washington on 7 November 1940 has to be emphasized in this connection, where fortunately no human-being was harmed. The catastrophic collapse of the Tay Bridge as well as the spectacular failure of the Tacoma Narrows Bridge in the USA in 1940 made the responsible engineers as well as the general public aware of the significance of dynamic effects in the building trade. World-wide the research activities in the field of dynamics were intensified.

Today the practical and easy availability of dynamic investigation methods has been reached by means of the possibilities of modern measuring and analysis techniques. Not only in the last few decades and centuries were engineers confronted with vibration problems at structures. Also during the last few years, despite sufficient knowledge of dynamic effects as well as the decisive structural parameters, vibration problems have continued to emerge in building, above all in bridge construction. Here above all the "Erasmus-Bridge" in Rotterdam opened to traffic in 1996 as well as the "Millennium

Bridge" in London opened on 10 June 2001 have to be mentioned.

From the shortly mentioned early as well as current vibration problems at bridges it is clearly recognizable that there is still extensive demand for research in the field of structural dynamics. Whereas for some problems respective solutions or assessment methods are already existing, there are still numerous fields where practical approaches and investigation methods are lacking. This publication shall provide the essential findings of the last few years with regard to the investigation and assessment of tension bars of stayed structures, especially the easy, secured and reproducible determination of the cable force and the damping of stay cables.

2 STATE OF THE ART

2.1 *Stay Cable Forces*

Bridges but also many other buildings have an individually developed vibration behaviour which may be addressed as vibration characteristic. This dynamic behaviour typical for a structure can be registered by appropriate measurements and be used for the assessment of the condition of the load-bearing structure and the determination of damages after respective evaluation. This structural response can be well described by the modal parameters eigenfrequencies, mode shapes as well as the respective damping values.

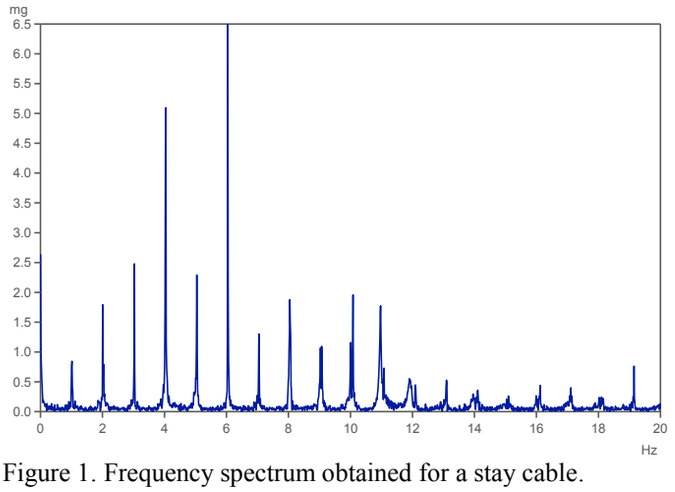


Figure 1. Frequency spectrum obtained for a stay cable.

The arrangement of the cables represents one of the decisive design criteria for cable-stayed bridges. The load-bearing behaviour, the construction procedure and the economic efficiency is substantially determined by the cable geometry. This is decisive above all for big spans. The spans of cable-stayed bridges have continuously grown since the development of this design type. The dynamic behaviour of the big bridges planned in the last few years therefore moved more and more into the centre of interest of the responsible engineers. Today no bridge is built anymore without performing wind tunnel and dynamic tests first where the behaviour of the total system as well as of the individual elements (cables) is investigated in detail (Geier 2004).

Dynamic analysis is very important for cable-stayed bridges as well as suspension bridges in the project stage. In general vibrations of a structure can be stimulated by the effects of wind, traffic and earthquakes. Vibrations can clearly affect or reduce the load-bearing capacity, the durability (fatigue) as well as the serviceability limit strength (effects on the user). The estimation of the fundamental modes is very important for planning and subsequent assessment. Whereas the natural vibrations can be very accurately determined by means of dynamic measurements, rules-of-thumb are an advantage for being able to roughly determine a frequency range on site or in the framework of planning. A connection between main span L as well as the first vertical bending eigenfrequency f of all bridges investigated by the authors (more than 100 structures) is shown in figure 2.

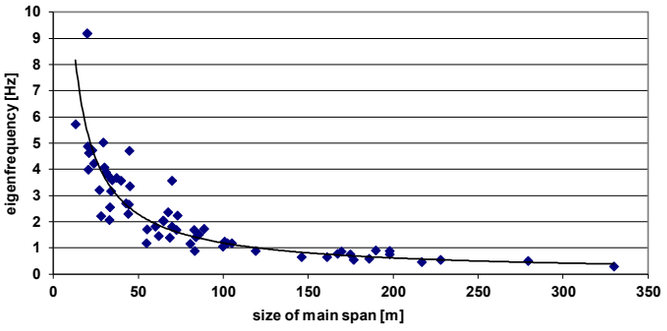


Figure 2. Relation between first vertical bending frequency and main span of the structure.

The function for the first vertical bending eigenfrequency derived from the measured frequency values exclusively for cable-stayed bridges is:

$$f = 84{,}309 \cdot L^{-0{,}9586} \approx \frac{100}{L} \qquad (1)$$

2.2 *Damping of stay cables*

An essential dynamic parameter which needs to be determined with cable-stayed bridges is the damping of the stay cables. Despite the most recent methods of calculation for modern bridge structures, as well as FE-modelling and wind tunnel tests damping continues to be a difficult parameter to determine and has to be determined on-site.

Given that the stay cables are a structural element very much prone to resonance due to wind and traffic, in the project phase vibration reducing external dampers are often designed which are configured for theoretical frequencies and damping values. For the reception of these structural elements nowadays it is

customarily necessary to determine the inherent damping of the cables and the damping with installed external dampers in order to check the design values and to prove the action mode of the external dampers.

For these measurements, according to the state of the art, acceleration sensors are installed and then ambient measurements or measurements with targeted excitation are performed. Based on the measured data the damping is determined through the reduction or distribution of energy. This can be achieved either in the time or frequency domain.

In the time domain the logarithmic decrement Λ can simply be determined. It describes the range of energy dissipation from amplitude to amplitude of a vibration. In nature the physical behaviour of a fading vibration is often times closest to a natural logarithm which accounts for its definition as the quotient of two successive vibration maximums and is described in the following formula:

$$\Lambda = \frac{1}{n} \ln \frac{y_0}{y_n} \tag{2}$$

Another evaluation method is the broad band method which is employed in the frequency domain. The determination is based on the idea that increasing damping causes faster energy reduction which leads to a compression of the frequency peaks in the spectrum and hence to an increase in broadness. The maximum energy peak in the frequency spectrum is divided through $\sqrt{2}$ and the energy level thus determined is cut with the frequency line. Both frequencies thus determined f_1 and f_2 are then used for the determination of damping according with the following formula:

$$\zeta = \frac{f_2 - f_1}{f_2 + f_1} \tag{3}$$

For both evaluation methods automated software packages have been already developed which implemented these formulas and which compare the measurement signal with the known functions of known damping (Mack 2017).

3 DEFINITION OF PROBLEM

3.1 *Stay Cable Forces*

In the framework of planning as well as the subsequently required maintenance of bridge structures engineers are increasingly confronted with stay cables and external tendons. On the one hand because cable-stayed bridges are increasingly designed and built due to their aesthetic appearance, on the other hand because in the framework of rehabilitations of old structures as well as in case of new designs external prestressing is more and more frequently used. In case of the complex cable-stayed bridges there is the additional problem that the condition as well as the current load-bearing capacity of the most sensitive load-bearing elements of such structures –cables and ropes – can only be checked with difficulty.

The main objective of the current research activities is the development of accurate, non-destructive methods for the determination of the tensile force effective in the cable on the basis of vibration measurements. Methods used up to now are either very time-consuming and expensive (for example by lift-off tests with a repeated application of the prestressing jack) or can cause damages in the cable itself, the anchoring structure or the input area of the cable forces. Principally up to now also vibration measurement methods were used for the determination of the effective cable force, the accuracy achieved in this process was, however, not satisfactory. Above all in case of high cable forces and short cables sometimes errors of up to ± 10% of the actual cable force could be determined.

A further ambitious goal of the research activities is the derivation of assessment parameters which enable the determination of the current condition of a tendon. Quantifiable and therefore comparable decision criteria have to be developed with which an objective assessment of the cable can be carried out. It is the aim to identify damaged and critical cables from the whole entity of stay cables by means of the evaluation of certain parameters on the basis of dynamic measurements. Consequently an efficient instrument for assessment is available on which rehabilitation measures or monitoring concepts can be based (Geier 2004).

3.2 *Damping of stay cables*

Stay cables have a theretically infinite number of natural vibration forms. Whereas with other structural elements the natural frequencies can be looked at and analyzed individually, with stay cables the vibration forms always overlap, given that they depend on each other. The harmonic content is always about several times the basic vibration.

In recent laboratory tests it was proven that despite excitation of a natural frequency with a shaker all the other natural frequencies are always present in the frequency spectrum. When the shaker excitation is stopped, the amount of energy created overlaps with the energies transferred to the neighbouring frequencies.

In detailed studies dedicated to the determination of damping in stay cables, superpositions of a large number of vibrations were ascertained in a large number of cases. The result of filtering for only one natural vibration form has also been indicative of significant overlapping and beat frequencies in the

measurement result. Figure 3 displays a typical image of a filtered result of a decay process. Several frequencies laying close together and which cannot be separated through filtering methods lead to these well-known time signals in stay cables based on which the determination of damping is extremely difficult.

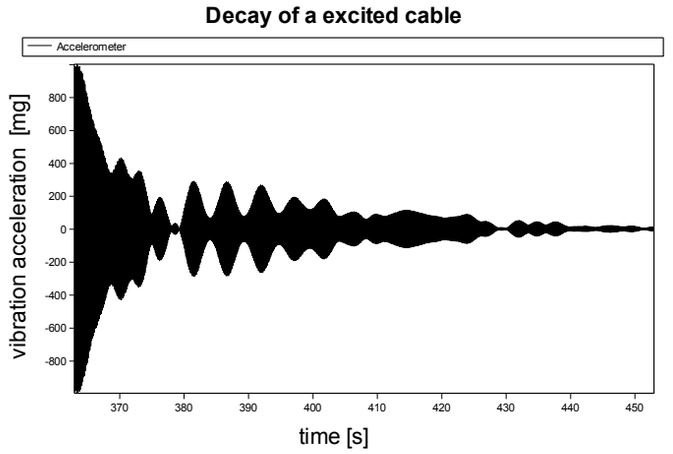


Figure 3. Filtered decay process with overlapping and beat frequencies.

The difficulty in terms of damping determination is the correct application of the evaluation methods known. With the broad band method the frequency peak is decisive which fails with beat frequencies given that we have several peaks laying next to each other. For the determination of the logarithmic decrement in time signal the peak-picking method is used, which has proven to be, given the beat frequency (apparent reduction of an energy which subsequently increases again) and the arbitrary use of peaks, difficult as well, considering that the results are often not reproducible through new evaluation staff. Given that automatisation in software programmes employs these methods, the results are also not secure and reproducible.

In order to be able to avoid these uncertainties and still to have a fast evaluation method, a combination of methods and a correspondingly new approach in terms of measurement, evaluation and representation of damping was elaborated in order to obtain secure and reproducible results (Mack 2017).

4 NEW DETERMINATION APPROACH

4.1 *System Identification and Stay Cable Forces*

In the scope of this work a practice oriented method was developed which enables the determination of the effective cable force under the consideration of the real bending stiffness of a cable. The accuracy of the force determination is clearly higher than for methods used up to now and therefore fulfils the requirements of engineering. As a real cable, however, deviates from the ideal concept very clearly, an accurate calculation of the cable force is much more complicated. In particular the bending stiffness of the stay cables is significant because it can exert a decisive influence on the eigenfrequency in a high band width as seen in Figure 4.

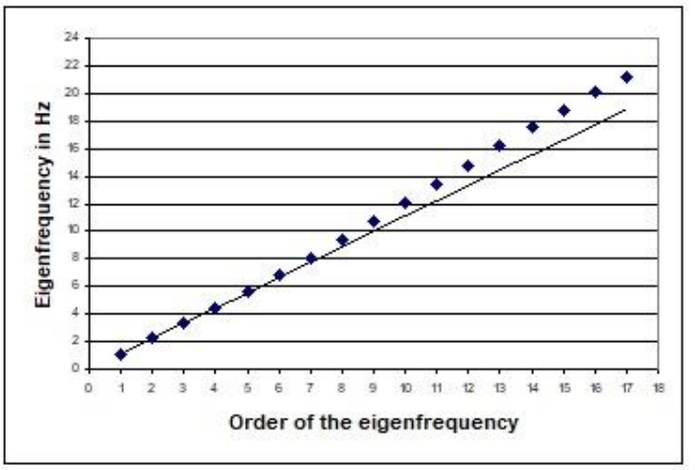


Figure 4. Shift of frequencies of a real cable.

If a complete flexibility of the stay cable (ideal concept of a tight wire) is assumed, the bending stiffness can be theoretically neglected. If the cable, however, deviates from this ideal concept (this is above all the case for thick and short cables), its bending stiffness is decisive for its behaviour. During the field measurements of stay cables it was realized that the harmonic succession of the eigenfrequencies (f_1, $f_2=2*f_1$, $f_3=3*f_1$,..., see Figure 5) valid for the tight wire is not valid for real bridge cables. A trend towards increasing frequency differences in the high bandwidth is recognizable. If the measured eigenfrequencies are compared with the linear progress, the influence of the bending stiffness is clearly visible. Whereas between the first 5-10 eigenfrequencies and their order k there is a linear coherence, the higher eigenfrequencies clearly deviate from this linear (ideal) progress.

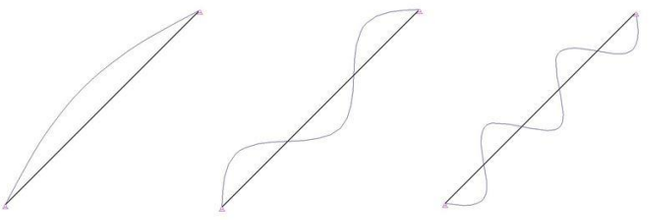


Figure 5. Basic mode as well as 3rd and 5th symmetric mode of a stay cable

The eigenfrequency of a cable is therefore dependent on the cable force and the bending stiffness, the fundamental modes ($\approx f_1$-f_5) of a cable being decisively determined by the cable force, the higher mode forms but also by the bending stiffness. The bending stiffness is of secondary importance to the dynamic behaviour due to the minor modal curvature of the fundamental mode during movement. The in-

fluence of the stiffness gains importance for a greater modal curvature of the cable in case of higher natural vibration modes. This effect is also plausible from the static point of view if a deformation of a bar equivalent to the vibration is produced by application of a static substitute load.

Of course technologies which are based on the analysis of the dynamic response of a cable under tension are very well known. Based upon ambient vibration testing quick and reliable evaluation of cable forces are possible. Numerous papers have been presented on this topic (Sa Caentano & Cunha 2003), (Peeters et al. 2002).

From stringed instruments the simple relationship between the measured natural frequency f_{ks} of order k and the cable force N is well known. In addition the free length of vibration L and the mass per unit length μ of the cable is required. This assumption is valid for frequency determination of the taut string:

$$f_{ks} = \frac{k}{2L} \cdot \sqrt{\frac{N}{\mu}} \tag{4}$$

In the beginning usually the first in-plane mode of the cable was used in practice, because the frequency was rather easy to obtain. But it turned out soon, that this approach did not fulfil the accuracy demands which have been defined for reliable testing. Consequently, during the last years the following two approaches usually have been employed:

(i) Consideration of the frequency of the first asymmetric vibration mode (which is the second frequency of the cable in the frequency response). The relationship according equation (4) is established consequently for the second mode described by k = 2.

(ii) Creating a mean value of the first 5 to 10 frequencies of the stay cable. When doing so, the first symmetric mode of vibration should be neglected before calculating the average.

Target of both methods is to determine a single, representative frequency which is used as input for equation (4). This procedure results in a more accurate estimation of the cable force. Although these two approaches seemed to fulfil the requirements of testing at the beginning, the demands with regard to non-destructive testing was continuously increasing.

Therefore the realistic dynamic behaviour of a stay cable is between the borderline cases of a hinged supported string represented by equation (4) and a massive beam with clamped boundary conditions and a certain bending stiffness EI. A solution with regard to the frequency was presented in (Morse & Ingard 1987):

$$f_k = \frac{k}{2L} \cdot \sqrt{\frac{N}{\mu}} \cdot \left(1 + 2 \cdot \sqrt{\frac{EI}{N \cdot L^2}} + \left(4 + \frac{k^2 \pi^2}{2}\right) \cdot \frac{EI}{N \cdot L^2}\right) \tag{5}$$

By considering these effects it is possible to determine an idealized frequency and a bending stiffness based on the measured basic and higher order modes. The application of this method was tested on several stay cables (Geier 2004) and the results have been compared to the design cable forces as well as to the basic identification method according equation (4). These tests have shown that the accuracy of determining the cable force is close to ± 1% of the real value.

4.2 *Combination of different Determination methods to evaluate the damping of stay cables*

The approach of damping in stay cables has been improved following the laboratory tests, verifications on existing bridges and control evaluations with existing measurement data which were conducted. For this purpose two evaluation methods were combined and demonstrated based on the possibility for reproduction of the measured vibration.

The damping depends as expected on the amplitude, but, given the beat frequencies, it cannot be directly opposed to the mere energy reduction. An envelope curve is generated instead, which corresponds to the logarithmic decrement, but considers the frequency of the main vibration, the starting energy value and the free oscillation time as decisive parameters. Based on the envelope curve and the peak-picking it is possible to determine the damping.

Through filtration the individual natural vibration forms are separated von each other and looked at individually. The beat frequencies and the super positions in each eigenfrequency cannot be separated any longer with the help of a filter, but through the determination of the individual responsible frequencies the decay process can be reversed through superposition of several harmonic vibrations and the damping can be thus determined iteratively whereas the reproduction is equated with the measurement signal.

In this way it is possible to determine the damping values of all natural vibration forms. Each eigenfrequency participates with the energy amount in the frequency spectrum pro quota to the total energy. Through transfer of these proportions to the individual damping values it is possible to determine the value of the vibration signal measured.

With other decay processes the determined values are slightly different as a result of the fact that through various excitation methods, but also various energy inputs and vibration directions different damping parameters are activated. In case of wind stimulation it is not clear which damping is activated and which remains inactive. This is why for the representation it is not an individual damping factor, but the indication of a „damping corridor“ like in figure 6 which is developed. Depending on the energy input the damping of the stay cable will be found in this corridor. For the evaluation of external dampers

the lower values are used, but one can also consider that with higher energy amount the inherent damping of the cable is also higher (Mack 2017).

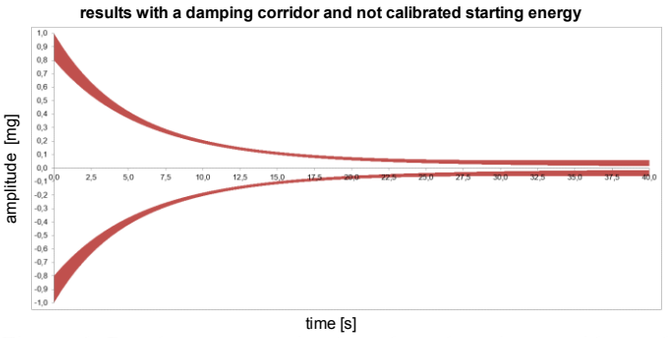


Figure 6. Result representation based on damping corridor and not calibrated start-up energy

5 APPLICATION EXAMPLES

5.1 *Force – Elbauenbridge, Schönebeck, Germany*

The determination of the stay cable has been recently conducted at the Elbauenbridge in Schönebeck. Die Elbauenbridge Schönebeck (Figure 7) is made up of two foreland bridges and the side sections of the river bridge, as well as the river area with the stay cables. The transverse section of the river bridge is made up of the trapezoidal hollow steel box with continuous cover plate and side steel consoles, as well as the overlying concrete pre-fabricated pieces and the carriage way concreted full width (Brand et al. 2013). In 18 m distance the transverse beams introducing the cables protrude and, together with the fan-shaped spreading of the 18 cable groups, create a new geometry on the superstructure, seen from the 75.30 m high pylon.

Stranded cables of the type DYNA Grip® manufactured by the company DYWIDAG-Systems International GmbH were used. The stranded stay cables are made up of seven galvanized, cold-drawn, plain individual wires with circular section. The stranded wires are surrounded by a corrosion protection wax and the entire fold is coated with a tight PE-jacket.

Ambient and stimulated measurements were conducted on this bridge. The acceleration sensor was fastened in the lower third of the pylon onto the stay cable. The stimulation was performed with the hand in order to introduce various amounts of energy and to activate various vibration and damping mechanisms, whereas the stimulation came either from the bridge deck or with the help of a riser.

Given the high-precision sensor technology and the evaluation method which took into consideration the bending stiffness, a short measurement period per cable was enough in order to be able to identify the eigenfrequencies of the first 10 natural vibration forms and to determine the cable forces reliably according with formula (5).

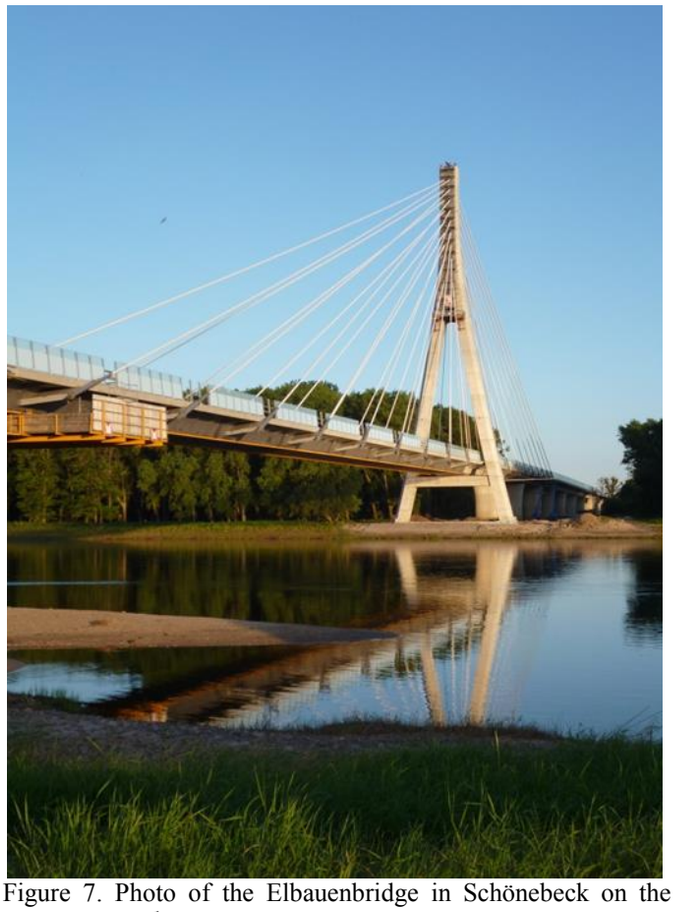


Figure 7. Photo of the Elbauenbridge in Schönebeck on the measurement day

5.2 *Damping – Abraham-Lincoln-Bridge, Louisville, Kentucky, USA*

The determination of damping and the development of methods were conducted when the vibration measurements were performed on the Abraham-Lincoln-Bridge in Louisville, Kentucky, USA. Here we have a cable-stayed bridge with 3 H-shaped pylons. The new structure has six traffic lanes for the traffic heading North.

The bridge is part of the Interstate 65 (I-65), has a total length of 761 m and the pylons are all located in Ohio River (Figure 8). The I-65 begins at the Interstate 10 in Mobile, Alabama, and leads to the Highways 12 and 20 in Gary, Indiana, a little South-East of Chicago, Illinois. The main pylon in the middle is somehow more massive and higher than the two neighbouring pylons. The structure is supported by a total of 88 stay cables. The stay cables were again provided and mounted by the company DYWIDAG-Systems International GmbH. Given that one could expect higher vibration paths for the cables as a result of the significant wind loads along the Ohio Valley, each cable was equipped with an external damper.

It was necessary to prove the function of the dampers and for this reason a vibration measurement was conducted for determination of the damping on a quarter of the cable (22 pieces). The measurements

were conducted one without the damper installed and once with the damper in operation.



Figure 8. Photo of Abraham-Lincoln-Bridge on the measurement day

Given the intensive vibrations caused by the construction works during the respective day, the measurements were conducted at night. Another time criterion was the asphalt paving. The weight of the asphalt influences the frequencies and thus the vibrations, so the measurements had to be conducted with or without asphalt.

An acceleration sensor and a position sensor were used for the performance of the measurements. The position sensor was mounted always on position L/8 where L represents the respective cable length in meters. The position sensor was mounted in the anchorage area where the vandalism protection tube ends in order to get the amplitudes near the damper, which was part of the protection tube. The steel tube itself is directly connected with the bridge deck and performs no swinging motion with the tube itself which made it possible to connect the damper with the tube. In order to get significant amplitudes as close to the damper as possible without entering the already closed envelope system the first point capable of vibration after the steel tube was used.

A static deflection and a dynamic stimulation in the middle of the cable were used as stimulation. For the static deflection a riser was used which moved the cable from its rest position with the help of a cord. The fork lift had the possibility to slowly perform the deflection by directing the fork upwards and finally releasing abruptly. In this way the cable was forced to die in its natural vibration form. For the dynamic stimulation a riser with arms was used by means of which a person located around the middle of the cable felt with his hand the strongest (usually the first) natural vibration form and then, using his hand, caused the cable to resonate.

The decay process was recorded by the sensors and a multitude of superpositions of vibrations resulted as indicated in Figure 9. Here it was possible to apply the new method which combines peak-picking and envelope curve in a fast and precise manner. With the determined parameters eigenfrequency, damping per eigenfrequency, energy level for each eigenfrequency and phase difference of the vibration, the superposition of all sine vibration was programmed, which reflects except a few deviations the actual recorded signal. The overlapping of these two signals is presented in Figure 9.

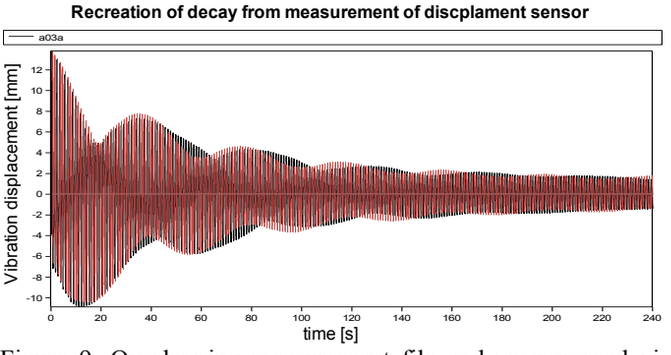


Figure 9. Overlapping measurement file and programmed vibration process with dynamic parameters determined

This application was repeated for all other cables and in this way it was possible to determine the damping which each cable reflects with each stimulation form. The values themselves were determined in a documented manner and based on the methods can be reproduced also by other evaluation staff.

By reproduction of the vibration in the software for the control of overlapping it was possible to document the damping with absolute certainty.

6 CONCLUSION

All known methods for cable force determination and damping determination in stay cables have been used for decades and are permanently in development with a view to determine the dynamic critical behaviour of structures and cable components. Often times difficulties were encountered given that stay cable determinations displayed deviations of ± 10% as compared to other measurement methods or the target force and the damping values obtained through other measurements and evaluation methods were not reproducible.

These newly developed methods have on the one hand the advantage of a higher exactness of ± 1% for the stay cable determination, but also for the damping in a large number of cases and, on the other hand, a fast and cost-efficient application. The measurements for the stay cable determination can be conducted in the lower anchorage area by using acceleration sensors and, taking into consideration the bending stiffness, it is possible, based on the determination of the first 10 eigenfrequencies, to reliably determine the cable force.

The mounting and stimulation at a higher place is more convenient for damping, given that otherwise the determination of secure values is not possible. Instead, the use of the combined methods and the reproduction of the vibration can be performed fast

and in a documented manner which is beneficial to the structure operator and designer. With the help of this application it is possible to obtain a damping corridor in which, in terms of the energy level, during resonance, the cable damping is located in this corridor, depending on the activated damping mechanisms In this way one can take into consideration all behavior patterns for simulations and verifications.

These applications render cost-intensive verifications conducted with the help of vibration generators and a large number of sensors unnecessary any longer whereas the values can be determined and verified any time in a reliable manner.

7 REFERENCES

BRAND, W.; ANISTOROAIEI, CH.; LANGER, S.; PULS, J.: „Elbebrücke Schönebeck - Schrägseilbrücke mit Litzenbündelseilen“, STAHLBAU 82 (2013), H. 3, S. 170–178.

GEIER, R.: „Brückendynamik – Schwingungsuntersuchungen von Schrägseilen“, Verlag BOD GmbH., ISBN 3-8334-1465-0, Norderstedt, Deutschland, 2004, 228 p.

MACK, T.: „Analysemethoden zur wirklichkeitsnahen Bestimmung der Dämpfungseigenschaften des Schwingverhaltens von Schrägseilen und Schrägkabeln“, Dissertation, BOKU Vienna, Austria, 2017

MORSE P., INGARD K., “Theoretical Acoustics”, First Princeton University Press, ISBN 0-691-08425, Copyright Mc Graw-Hill Inc, 1968, Princeton, New-Jersey, 1987, 949 pp.

PEETERS B., DE ROECK G., SA CAETANO E, “Dynamic Study of the Vasco da Gama Bridge”, Proceedings of ISMA 2002, pp. 545-554.

SA CAETANO E., CUNHA A., “Identification of parametric excitation at the International Guadiana Bridge”, 5th International Symposium on Cable Dynamics, 2003, pp. 525-532.

Maintenance, Safety, Risk, Management and Life-Cycle Performance of Bridges – Powers, Frangopol, Al-Mahaidi & Caprani (Eds)
© 2018 Taylor & Francis Group, London, ISBN 978-1-138-73045-8

Noise radiation from steel bridge structure - Old Årsta bridge Stockholm

A. Olsen
Vibratec Akustikprodukter ApS, Kvistgaard, Denmark

R.S. Lützen, S. Holmes
Lloyds Register, Copenhagen, Denmark

ABSTRACT: The 1929 Old Årsta bridge in central Stockholm (Sweden), owned and operated by the Swedish Transport Administration(Trafikverket), is a monumental structure of architectural value and infrastructural importance to the city. Following recent renovation work, an increase of train noise was observed. Hence, the Swedish Transport Administration decided to mitigate the noise. A multi-step project was defined to this end. The present paper presents the findings of the pre-study, the purpose of which was to investigate the noise radiation from the bridge. This involved vibro-acoustic modelling by Statistical Energy Analysis (SEA), laboratory testing of various Constrained Layer Damping (CLD) configurations at different temperatures, as well as similar CLD tests on a mock-up, noise and vibration measurements on the actual bridge, and acoustical beamforming measurements.

1 INTRODUCTION

Constructed in 1920 to 1929, the Old Årsta bridge is a monumental double track steel arch bridge with a steel deck and a main span of 151 m. It is located on one of the main railway lines of Stockholm (Sweden) and recently underwent refurbishment to upgrade bridge bearing capacity. This included a new bridge deck in terms of a full steel deck with welded longitudinal and transversal girders. The deck is connected to the supporting arch using hangers and columns. The track of the retrofitted deck is now based on a Pandrol VIPA rail fastening system. Following construction of the new bridge deck, increased noise from train passages was reported. The Swedish Transport Administration initiated a project with focus on noise reduction from the bridge, including the present pre-study. Given an around the clock average interval of only 6 minutes between trains, a non-intrusive execution was required. Hence, for the investigation no access was allowed to the top of the bridge deck. Similarly, any recommended mitigation means would have to be installed from below.

To the west of Old Årsta bridge, in parallel at approximately 45 m distance, runs a newer bridge, which proved to be a useful platform for measuring train passage noise. Furthermore, to the North a concrete bridge, having the original fasteners on ballasted track as the new bridge before retrofitting, is located on the same line as Old Årsta.

2 METHOD

Past noise control actions for Old Årsta bridge involved modifying the track from wooden sleepers to resilient rails fasteners (Cox 2007, Thompson 2009). Given the current restrictions on access, track modification was no longer a relevant option. Instead, focus was placed on the potential of targeting the bridge steel structure itself. Thompson (2009) lists several such examples, with varying results in terms of noise reduction. In the discussion, it is mentioned that the achieved reduction was limited in general by the amount of damping already present in the untreated structure. Furthermore, the balance between rolling noise and noise radiated by the bridge structure plays a limiting role.

In certain cases, structural damping may be added using vibration absorbers (Schrey & Veit 2017). This solution is, however, quoted as being suitable only for frequencies below 150 Hz.

In this study, which was undertaken on behalf of the main contractor Skanska by Vibratec and the consulting branch of Lloyd's Register (LR), the potential of Constrained Layer Damping (CLD) for noise reduction was investigated. A general challenge of CLD solutions is the inherent temperature dependence of the viscoelastic material. However, previous successful experience was found for an outdoor industrial application in mid-continent climate (Olsen et al. 2016). This was achieved using CLD patches with two viscoelastic materials, having different properties.

For Old Årsta Bridge an engineering approach was decided. An empirical investigation of noise and vibration of the existing, untreated bridge was combined with numerical simulations using SEA as well as laboratory measurements. The study outline was:

- Empirical investigation of noise, and corresponding vibration
- Identification of noise contributors, particularly train (rolling noise) vs. bridge contribution
- Establishment of prediction model
- Use of prediction model with CLD damping input from lab tests and SEA model
- Identification of the optimum CLD configuration and expected noise reduction

In the following, comments are given to the various measurements and modelling actions. The measurements were taken 5-7 April 2017 during wind speed 2-4 m/s mostly western wind and about 10°C.

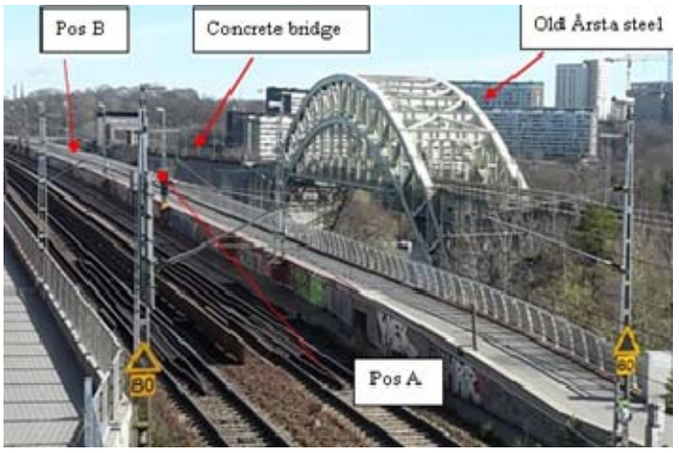


Figure 1. Measurement positions

2.1 *Noise and vibration measurements*

As the study focuses on Old Årsta steel bridge, it was necessary to find a means of identifying start and stop times for trains crossing the bridge. To that end, a "train detector" system was installed. This consisted of a 1 mV/(m/s^2) accelerometer on the underside of the deck, at each end of the bridge. The individual passage of every bogie, sometimes even every wheelset, was clearly distinguishable from the recorded time series. The train detector system furthermore enabled determination of the train speed. Of the considered passages, an average of 88 km/h was found, typically ranging from 80 to 95 km/h.

Using a multi-channel, 24 bit data acquisition system, the train detector accelerometers were recorded to a laptop in parallel with 5 accelerometers of sensitivity 1 mV/(m/s^2). Train passages were measured for accelerometer positions representing the main components of the bridge, collecting several passages per measurement position. Sample frequency was 6400 Hz.

Simultaneously, a separate measurement system for recording noise was placed opposite the steel bridge, at Pos A. This autonomous system was a sound level meter BK2270 with its microphone fitted in an outdoor microphone kit. The system continuously recorded time series with maximum useable frequency 3300 Hz, in 24 bit quality.

2.2 *Microphone array measurements*

At Pos B, a limited number of measurements were taken with LR's in-house developed 2D array consisting of 56 microphones, see Figure 2. A sample rate of 5000 Hz was used. These were taken at the end of the measurement campaign, when the train detector system had been disabled, hence, train speeds were unknown.



Figure 2. Array measurement setup

The spatial resolution from the applied position was insufficient for directly separating noise contributions from train, rails, and bridge using basic Delay and Sum algorithm. However, a few useful observations were indeed made. The array included a centred and calibrated camera, providing one still image per train passage.

2.3 *Structural dynamic measurements*

2.4 *Point mobility of bridge components*

Point mobility was measured of several components of the Old Årsta bridge, using an instrumented impact hammer of 0.26 mV/N and a magnet mounted accelerometer of sensitivity 100 mV/(m/s^2). An LR in-house tool was used for processing complex FRF spectra as an average of 5-10 hits per position, with no data window applied. These were input to industry standard modal analysis software BK PULSE Reflex Modal. The Rational Fraction Polynomial-Z algorithm was applied to extract natural frequencies and damping ratio for each measurement position, for the frequency range 50-1000 Hz.

2.4.1 *Test of temperature dependent CLD damping*
At LR's lab a climatic chamber was established to test the structural damping of an 18 mm x 70 mm x 1400 mm steel beam sample with several different CLD add-on treatments, designed and provided by Vibratec. The beam thickness corresponds to the deck and main girders of the Old Årsta bridge components. The width and length were selected to ensure bending modes starting at 50 Hz, to represent the bridge plating as well as possible. At temperatures, +20, +5, and -10 °C the resiliently suspended beam was excited by continuous white noise from a shaker with introduced force transducer. The vibration response was captured with 7 accelerometers. Post-processed FRF spectra were, as in Section 2.3, introduced to modal analysis software and analysed up to 1000 Hz. Analysis was performed with combinations of Rational Fraction Polynomial-Z, Alias-Free Polyreference, and Polyreference Time, depending on the properties of the test specimen. Mode shapes were used qualitatively to separate bending modes from torsion and lateral modes, as only bending modes were considered relevant for the noise control of Old Årsta bridge. This approach provided temperature and frequency damping ratio estimates, which should be regarded as engineering linear approximations of the non-linear viscoelastic behaviour.

2.5 *Large-plate mock-up test with different CLD configurations*

At Vibratec's workshop in Estonia, an indoor test at approximately 15°C was performed on an 18 mm x 1400 mm x 2000 mm steel plate elastically suspended from a crane. For 6 different CLD configurations, random impacting was performed with a hammer, and the vibration was recorded with two accelerometers. The resulting vibration time series were input to industry standard Operational Modal Analysis software ARTeMIS Modal and analysed using Stochastic Subspace Identification (SI) algorithms as well as Enhanced Frequency Domain Decomposition (EFDD).

2.6 *Numerical Statistical Energy Analysis model for insertion loss*

Commercial software VAOne for Statistical Energy Analysis (SEA) was used for establishing a numerical, vibro-acoustic model of the bridge without hangers and arches,

A line of distributed, vertical uncorrelated point forces placed in the centre line of one track. They were assigned white noise with 1 N amplitude each. With this excitation, the SEA model was used to calculate the un-calibrated resulting noise in a horizontal distance of 45 m, corresponding to the physical Pos A. This was first done with low-level structural damping assigned to all bridge elements, corresponding to the present stage of the untreated bridge. Subsequently, CLD configurations were investigated by assigning the lab test damping of Section 2.4.1 to individual bridge components and calculating the un-calibrated resulting noise. Subtraction from the noise of the untreated bridge thus provided an insertion loss corresponding to that particular CLD configuration. The SEA model output was presented in 1/3-octave bands from 160 to 2500 Hz.

2.7 *Combined prediction model*

A simple prediction model was established, describing the noise contribution at Pos A for each major bridge component (deck, longitudinal girders, flanges of longitudinal girders, etc.). The model combined statistically averaged vibration spectra with radiation index spectra. The resulting sound power spectra were propagated to the distance of Pos A using a simple spherical spreading law.

For prediction of the various CLD configurations, the measured input vibration spectra of the untreated bridge were first corrected for insertion losses. The latter were either calculated using the SEA model of Section 2.6, or using simple algebraic expressions proportional to the relative increase of damping ratio.

2.8 *Considered CLD configurations*

10 different CLD configurations were tested in the climatic chamber at LR. The CLD's varied from either simple single layer to multi-layer solutions. Previous experience (Olsen et al 2016) with CLD configurations in temperature dependent applications indicated that single layers only provide high performance in either high or low temperature environment, depending on the properties of the damping material. Therefore, the relevance of combining damping materials is essential and reported in the literature, for example (Jones 2001).
In this project, two different damping materials were used. Each material consisted of a 1.4 mm bitumen layer, with viscoelastic glue on each side with release liner. Only difference between the two types is the viscoelastic glue.

The damping materials are usually manufactured in sheets of 1000 mm x 1000 mm with release paper on each side, for easy mounting. The two basic damping material solutions used in this project are shown in Figure 3.

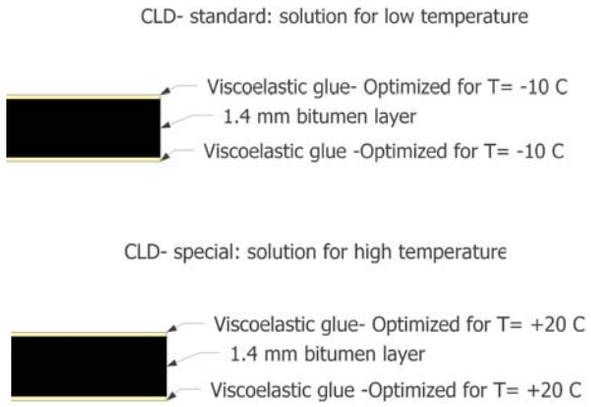


Figure 3. Basic viscoelastic materials and glue

Each type of material is normally considered as a single layer, however note that this is a 3-layer system, since glue as well as bitumen layer has viscoelastic behavior.

The two materials were used in the 10 CLD configurations that are shown in Table 1.

The following terms are used for simplicity:
A: Steel beam sample (18 mm thick)
B: CLD-Standard (app. 2 mm including glue)
C: CLD-Special (app. 2 mm including glue)
D: Sandwich steel bar (2 mm)
E: Sandwich steel bar (1 mm)
F: Constraining steel bar (3 mm)
G: Constraining steel bar (5 mm)

Table 1. CLD configurations

Sample ID	Layers	CLD patch thickness mm
1	A/B/G	7.0
2	A/C/G	7.0
3(shaker ref. A)	A/(B/C)/G	9.0
4	A/(2xB/C)/G	9.0
5	A/C/D/B/F	9.0
6	A/B/D/C/F	9.0
7	A/(2XB/C)/G	9.0
8	A/B/C/G	9.0
9(shaker ref. I)	A/C/B/G	9.0
10	A/(B/C)/E/(B/C)/G	9.0

In order to have the most realistic setup in relation to real world application, each of the CLD configurations were mounted on the 18 mm steel beam, using weld studs. This ensured that local de-bonding was minimized. A torque of 30-50 Nm was used for tightening of the lock bolts, depending on the manufacturing tolerance of the steel bars. For structural and practical reasons, the weight of the CLD systems are restricted to approx. 40-45 kg/m^2, which mean that the max. thickness of the constraining steel plate is app 5.0 mm. Generally, for CLD systems, increased thickness of the constraining plate leads to increased damping ratio.

Local de-bonding of damping layers will have an influence on the measurements and lower the damping ratio, due to non-contact zones. However, in real applications it is very difficult to completely avoid this. Weld studs are also used in real installation, as CLD patches are mounted vertical and below steel decks, which mean that gravity forces will influence the contact pressure.

No numerical or analytical estimates were performed for the composite damping ratio of the various configurations, as the general Ross, Kerwin and Ungar (RKU) equations (Jones 2001, Nashif 1984) are only valid for simple configurations such as sample IDs 1 and 2. Multi layers may be predicted with RKU equations but given the limited information of the viscoelastic glue damping properties, the theoretical and analytical approach is difficult. Understanding the viscoelastic glue better will require several measurements and extraction of the damping ratio as well as complex E-modulus of the glue.

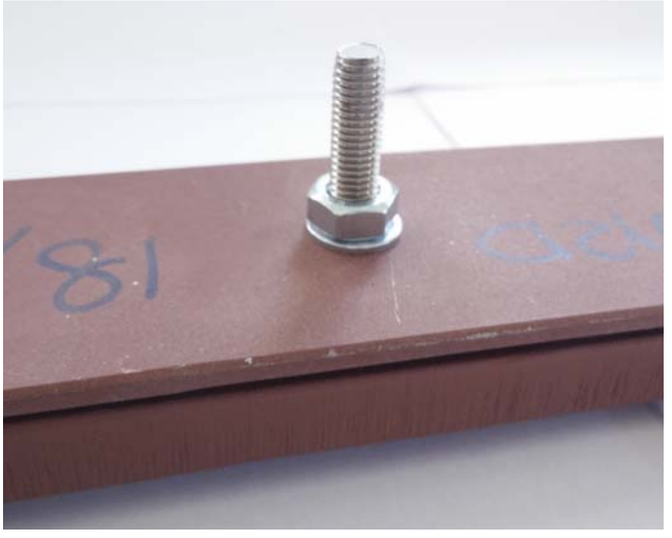


Figure 4. Steel beam with weld studs

3 RESULTS

3.1 *Findings noise & vibration at steel bridge*

Figure 5 shows passage noise spectra at Pos A, synchronised from the train detector system to precisely the passage of the steel bridge. Due to the intense traffic on both parallel bridges care had to be exercised to identify undisturbed passages with only one train at a time. A total of 8 undisturbed passages were identified. Based on time synchronization with the train detectors, 1/3-octave band spectra corresponding to the passage of the steel bridge were extracted, see Figure 5.

.

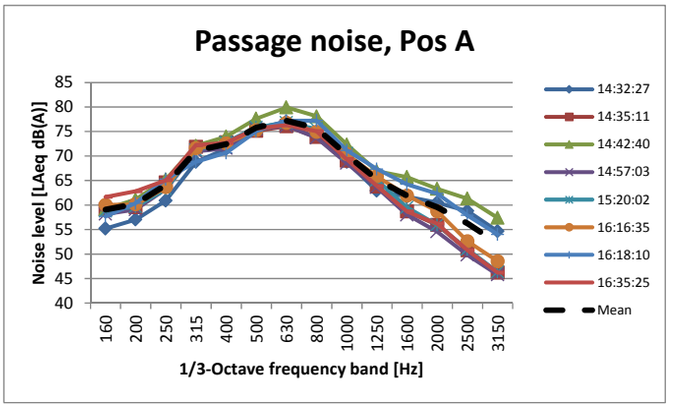


Figure 5. A-weighted 1/3-octave band spectra at Pos A (in front of steel bridge).

The passage time was typically about 6 s, and the average overall noise level was 83 dB(A), with a standard deviation of 1 dB. In Figure 5 it is seen that the noise is dominated by the 500-800 Hz range. It is seen that the range 250-800 Hz has relatively little spread, while the passages vary much more for higher frequencies. Realizing that train wheels typically become effective acoustic radiators above about 1 kHz, this might indicate that the noise contribution below 1 kHz is dominated by the bridge properties, while noise about 1 kHz is more strongly influenced by the individual vehicle.

At one point when the train detectors were not in operation, a handheld sound level meter BK2250 was used to measure at Pos B in front of the concrete bridge. For the same train passing the steel bridge, the corresponding spectrum was extracted from Pos A. One such example is shown in Figure 6.

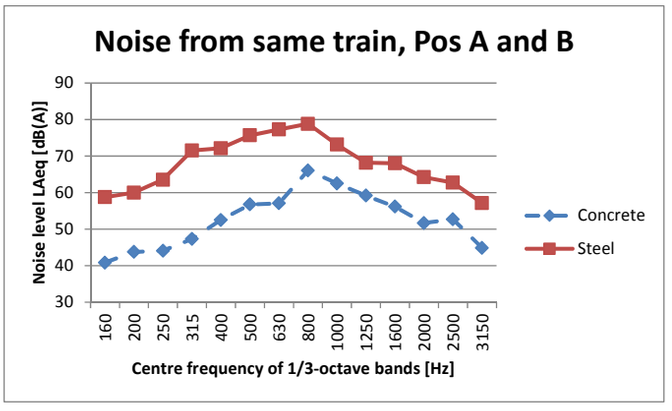


Figure 6. A-weighted 1/3-octave band spectra for same train, in front of concrete and steel bridges.

In Figure 6, the spectrum from the front of the steel bridge is clearly louder than in front of the concrete bridge. Overall levels here increased by 15 dB. Following the approach by Cox (2007) it is reasonable to assume that noise at Pos B is dominated by the train (actually, rolling noise) contribution, as the concrete bridge is unlikely to radiate significantly. Assuming that the 1-2 kHz range is dominated by the train contribution at both bridges, an increase of 10 dB in this range was determined as an average of 6 train passages. It is assumed that this is the increase in rolling noise caused by the different track and fastener types. This is in line with typical findings of 5-10 dB rolling noise increase (Thompson 2009). From this finding, the rolling noise on the steel bridge was predicted as the average spectrum at the concrete bridge (Pos B) plus 10 dB. The corresponding overall level was 78 dB(A).

By using the train detector system, vibration spectra of train passages were extracted for several bridge components. By means of example, the vibration spectra at deck underside positions are shown in Figure 7. For the deck, an average overall level L_v of 133 dB re. 10^{-9} m/s was found, with a standard deviation of approximately 1.5 dB.

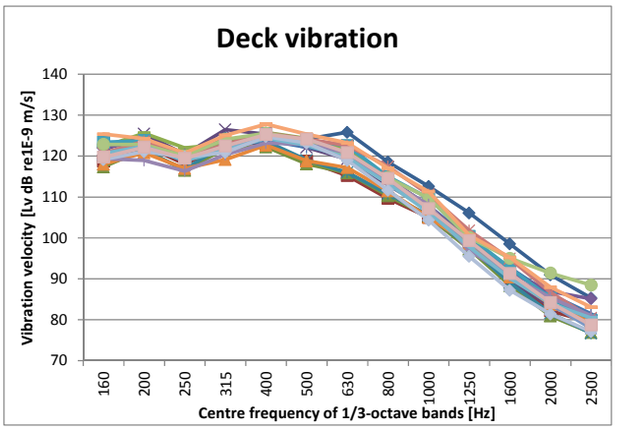


Figure 7. Measured vibration velocity spectra of deck underside, average of 22 passages.

3.2 *Findings from microphone array measurements*

An array example of 1.6 s of a train passage is shown in Figure 8, for frequency range 1 to 2 kHz. The spatial resolution obtained with the array was insufficient to separate the radiating components, mainly due to the large distance between measurement position and the bridge. The colours indicate the upper 6 dB of the measured noise level range. When inspecting a sequence of analyses corresponding to the train passages (not shown here) the various "hot spots" appear fairly concentrated (as in Figure 8) and travel with the train along the bridge. It seems likely that these spots relate to the rolling noise of the bogies. It is furthermore observed that the bridge arches do not appear to radiate significantly, as they do not "light up" in these plots.

For lower frequencies, e.g. 600-800 Hz (array plot not shown), the "hot spots" became unrealistically large due to the wavelength proportional spatial resolution. Though less clear than for the kilohertz range, the "hot spots" still mostly appear round/elongated and centred in the train/deck region.

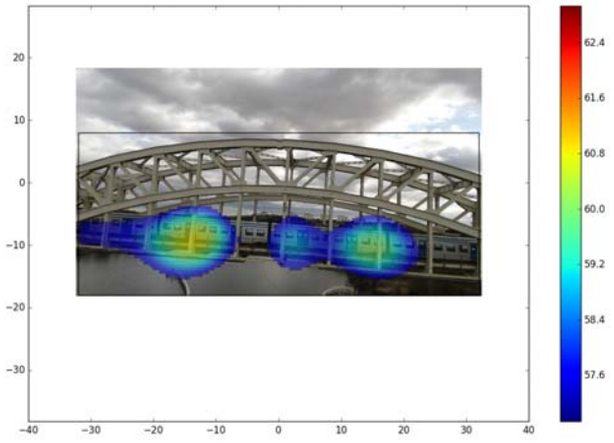


Figure 8. Microphone array analysis for frequency range 1-2 kHz, using Delay and Sum.

3.3 *Findings from structural dynamic measurements*

By means of example, Figure 9 shows a stability diagram (0-500 Hz range) of the modal analysis performed on point mobility input from a position on the longitudinal girder. Corresponding natural frequencies (0-1 kHz) and damping ratios are included. Generally, it was found for the bridge components that in the frequency range of interest the damping ratio was typically 0.5-1%. Furthermore, as in the case of the girder, lowest natural frequencies were found in the 50-100 Hz range. Both observations are positive as to the noise reduction potential of adding structural damping, as this requires many and at best low-damping, resonant modes.

From the lab climatic chamber damping tests, it was found that various CLD configurations demonstrated damping ratios up to about 14% at certain frequencies, see e.g. configuration I of Figure 10. However, as in the case of configuration I, the same CLD performed rather poorly at other temperatures. Other configuration provided more consistent damping across frequency and temperature, e.g. configuration 3 (Shaker ref. A) of Figure 11.

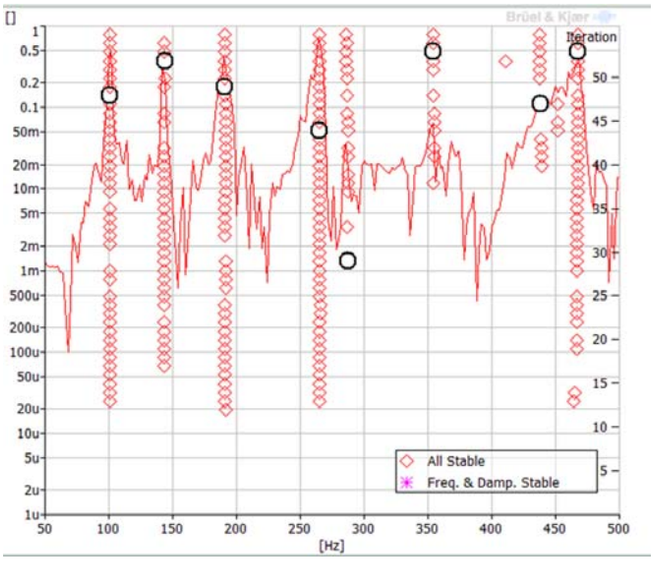


Figure 9. Example of mobility analysis results from longitudinal girder.

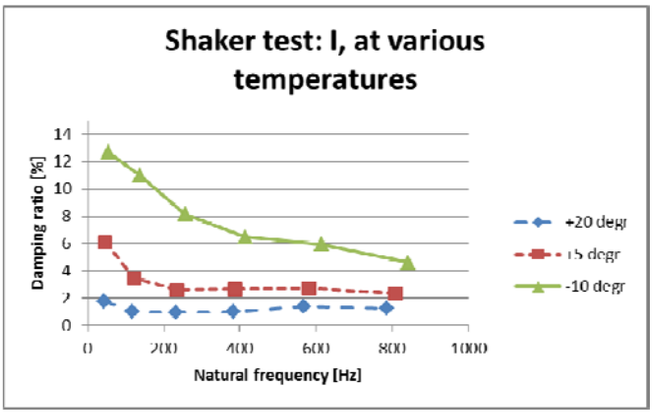


Figure 10. Lab damping test of CLD configuration I

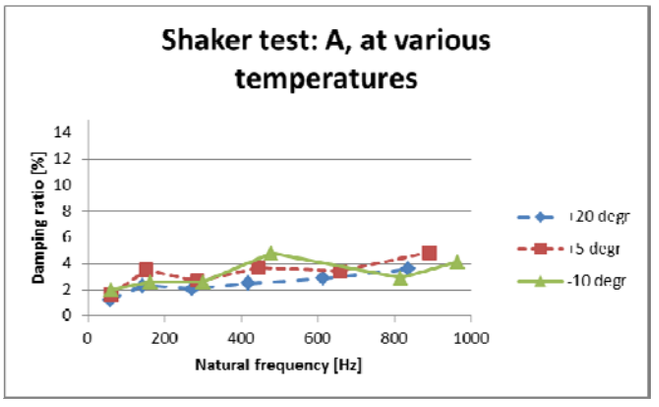


Figure 11. Lab damping test of CLD configuration 3 (shaker ref. A)

3.4 *Findings from SEA model*

Following a conservative approach, it was decided to assign a damping ratio of 1% to all bridge components in the untreated stage.

Figure 12 illustrates that noise insertion loss IL_p of the various bridge components are generally not the same, even in the shown configuration where all

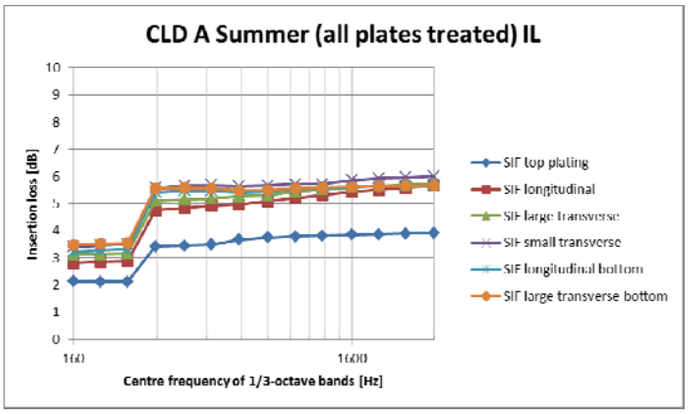


Figure 12. Example of SEA calculated insertion loss from CLD configuration 3, summer temperature

plates are assigned the same damping ratio. This is a consequence of the energy- wise closely coupled set of sub-systems, with forcing taking place on one system (the deck/top plating).

3.5 *Findings from prediction model*

In terms of overall values, the model predicted 84 dB(A), which is slightly higher than the measured 83 dB(A). Given the involved uncertainties, this seems an acceptable agreement. From Figure 13 it follows that the frequency range up to 800 Hz according to the prediction model is dominated by radiated "bridge noise", i.e. the noise produced by vibration of the bridge plating and girders. Above 800 Hz the "train", or rolling, noise takes over and dominates. This is in line with expectations from literature.

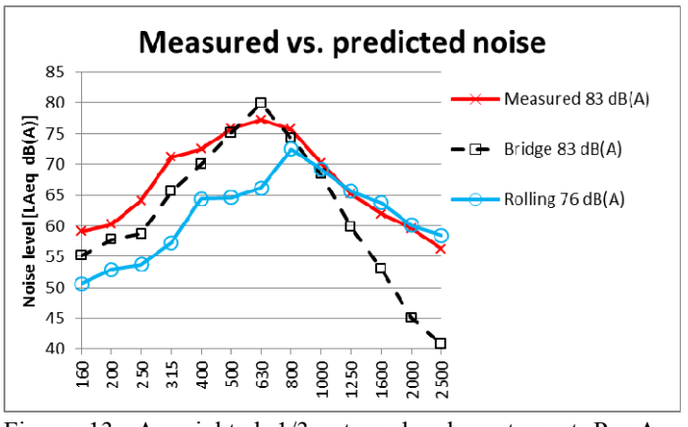


Figure 13. A-weighted 1/3-octave band spectra at Pos A, measured and predicted spectra

One step further, the prediction model shows the distribution and ranking of noise contributions from the different bridge components for the untreated bridge, see Figure 14. It follows that the most significant components are the deck, and longitudinal girders. From Figure 14 it can be assessed that the potential for noise reduction based entirely on reducing the bridge contribution is approximately 7 dB, in

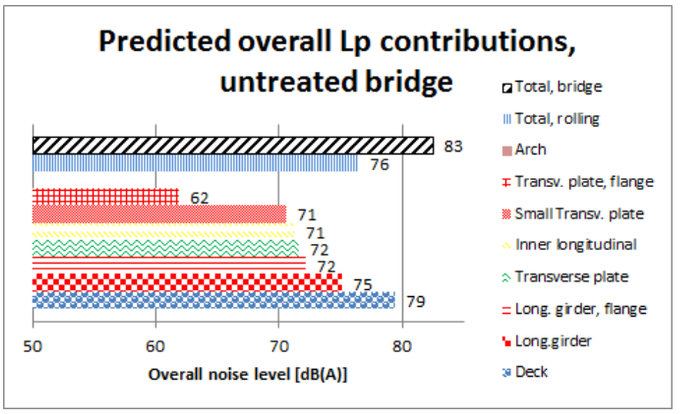


Figure 14 – Distribution of component related noise contributions for untreated bridge

the hypothetical case that the bridge radiated noise is reduced by about 20 dB or more.

With reference to the prediction results of the untreated bridge, the noise at Pos A for each of the CLD configurations was calculated using the prediction model. It was found that the bridge noise contribution could be reduced by up to 8 dB. The overall noise, when including train/rolling noise, could be reduced by up to 4 dB by several of the CLD configurations. As illustration, the predicted, detailed reduction corresponding to the use of Sample ID 3 (Shaker ref. A) is shown in Figure 15.

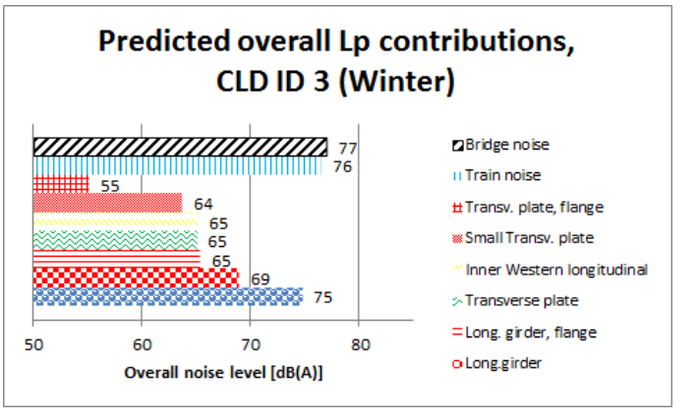


Figure 15. Example of predicted noise reduction for winter temperature using CLD ID 3 (shaker ref. A). Predicted overall level is 80 dB(A), corresponding to a reduction of 4 dB. Reduction of the bridge noise is 6 dB

4 CONCLUSION

Using a combination of different measurement techniques and numerical modelling, a simple prediction model was established for the train passage noise. Introduction of laboratory based damping data for various Constrained Layer Damping (CLD) solutions, allowed assessment of the potential for noise reduction by means of only treating the bridge components. A significant potential was found. Furthermore, it was found that CLDs based on specific combinations of two viscoelastic materials could provide relatively consistent noise reduction across frequency and temperature.

Based on the presented findings, the Swedish Transport Administration has started to implement the use of CLD treatment for the Old Årsta bridge.

ACKNOWLEDGEMENTS

This study was financed by the Swedish Transport Administration and SKANSKA, and the authors wish to express their gratitude to these organisations for constructive collaboration. In addition, thanks to the many colleagues at Vibratec and LR who helped with the project.

REFERENCES

Cox S., 2007. Railway noise: some case studies of different problems with different solutions. In: Proc AusRAIL PLUS 2007, *AusRAIL PLUS 2007*. Sydney, Australia, 4-6 December 2007.

Jones D.I.G., 2001. *Handbook of viscoelastic vibration damping*. Chichester, UK: Wiley & sons.

Nashif A., Jones D.I.G., Hendenson J., 1984. *Vibration damping*. Dayton Ohio: Wiley & sons; 1984.

Olsen A., Lützen R.S., 2016. Vibration Damping of air intake filter for gas engine, using constrained layer damping (CLD). In: Proceedings of Baltic-Nordic Acoustic Meeting (BNAM) 2016, *BNAM 2016*. Stockholm, Sweden, 20-22 June 2016.

Schrey & Veit GmbH, 2017. Railway steel bridges [online]. Schrey & Veit GmbH. Available at: http://www.sundv.de/en/steel-bridges.html [Accessed 5 May 2017].

Thompson D., 2009. *Railway Noise and Vibration*. Oxford, UK: Elsevier.

Maintenance, Safety, Risk, Management and Life-Cycle Performance of Bridges – Powers, Frangopol, Al-Mahaidi & Caprani (Eds)
© 2018 Taylor & Francis Group, London, ISBN 978-1-138-73045-8

Damping performance identification for large-scale dampers of a cable-stayed bridge

X.H. Hu & C.X. Ge
Department of Bridge Engineering, Tongji University, Shanghai, China

ABSTRACT: Hydraulic dampers were broadly used in the seismic design of structures, especially in those long span cable-stayed bridges. However, the practical performance of those dampers is quite difficult to acquire and predict. Aiming to understand the damping performance of dampers of Sutong bridge, an experimental method based on vibration testing was proposed in this paper. Firstly, dynamic response numerical simulation of a SDOF model under random excitation with lower frequency about 0.065Hz and higher damping property were carried out. A damping ratio identification method was proposed and verified based on simulated random acceleration output. Then, field testing was performed, and several acceleration gauges were mounted on the bridge. The longitudinal vibrations were gathered, and the damping ratio had been identified four times during the past two years. The results show that the overall damping ratio of those large-scale hydraulic dampers kept in the relatively constant level, which reveals that the performance of those dampers was in a relatively good condition.

1 GENERAL INSTRUCTIONS

With the construction material and technology continuing to improve, the main span of cable-stayed bridge rush to the 1km level in the reasonable structure system. The cable-stayed bridge system gradually developed as: floating system, semi-floating system and tower-beam consolidation system. In order to avoid several problems such as too large displacement of the tower due to the excessive displacement of the girder in the floating system, the unreleasable temperature load stress of girder and the excessive bending moment of tower by seismic load in the consolidation system, the semi-floating system with a certain constraint is the preferred proposal of long-span cable-stayed bridge. Domestic and foreign scholars have also developed an elastic connection device and viscous damper as the tower-beam connection. Kyu-Sik Park compared the damping effect on a standard cable-stayed bridge with different connections, namely, semi-active stiffness dampers, semi-active friction damper, passive dampers mixed connection in his article. Agrawal A.K. and Yang J.N. adopted the lead rubber bearing as the passive control element working together with the ideal hydraulic actuator as the active control element, and also obtained the ideal damping effect. Sutong Bridge, as a cable-stayed bridge with a main span of 1088 meters, also took three structure systems into consideration in the design process. By comparing the shear force and the bending moment at the bottom of tower, and the longitudinal displacement of the girder in the floating system and semi-floating system with viscous dampers or hydraulic buffers under the earthquake load, the large-scale viscous dampers is the final connection between tower and girder as a longitudinal constraint of girder. Four 67DP-17621-01 dampers produced by Taylor Company were installed in the vicinity of each tower respectively (Figure 1).

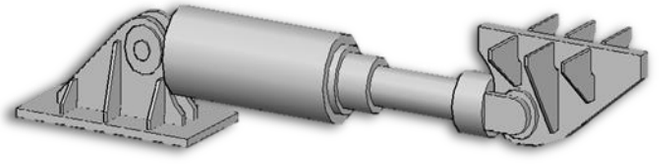


Figure 1 67DP-17621-01 dampers of Taylor company

Large damper is a long-term service component in the normal maintenance of the bridge during the operation. Because viscous dampers always bear very large pressure in each second, the requirements of materials and the manufacturing process are very strict. It is also common abroad that viscous dampers have to replace before the service life due to premature failure. Dampers of South Korea high-speed railway were all replaced soon after the installation because of oil spill. Greek peace and friendship

gymnasium large-scale dampers that only worked several years were also replaced in the 2004 Olympic renovation, which wasted a lot of manpower and material resources.

At present, most of the scholars focus on the study of the performance of the damper itself, and simulate the seismic performance under earthquake in the finite element model. The positive conclusions are got in the computer or lab. However, the damper conditions and effects in the real bridge lack of data support. In this paper, the assessment process of the damper performance, are mainly based on the field-measured data for further analysis and research.

The manual of Taylor dampers installed on the Sutong Bridge mentions that only a visual inspection is required for the 35-year life cycle without the need for maintenance or replacement. Since Sutong Bridge open to traffic, the maintenance and management of the tower-beam damper is also limited to the appearance inspection of whether the damper cylinder is leaking or not. Based on the field measurement data to analyze and study, we can further understand the Sutong Bridge tower-beam damper long-term performance without interrupting normal operation of the Sutong Bridge, to assess the bridge components and guide maintenance scientifically.

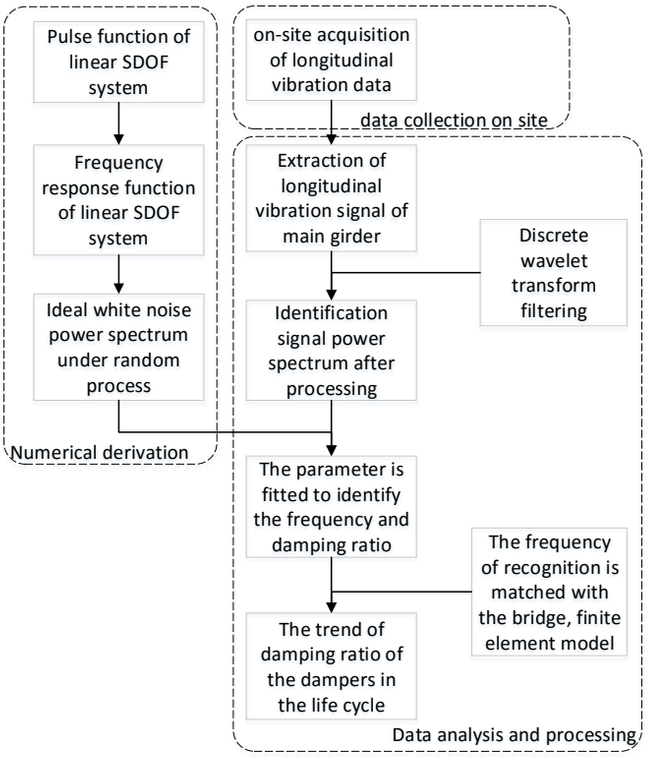


Figure 2 Technical route of this paper

In this paper, the cable-stayed bridge is simplified as a single-degree-of-freedom linear system, and the vibration power spectrum is deduced under random process with the ideal white noise excitation. Then, based on the field-measured data of damper, the longitudinal vibration data of the main beam are extracted by the wavelet transform filtering method, and then the recognition of vibration power spectrum is carried out. Finally, the power spectrum of the field recognition is fitted with the derived formula to obtain the approximate frequency and damping ratio of the longitudinal vibration. After repeated tests in a long period, the performance of the tower beam dampers is forecasted.

2 RANDOM RESPONSE OF SDOF LINEAR SYSTEM UNDER WHITE NOISE

The installation of viscous dampers at the tower-beam joints is a typical local damping nonlinear increasing problem to the long span cable - stayed bridge. In the study, the single-degree-of-freedom evaluation model of Soneji B.B. and Terenzi G. can be used to replace the nonlinear system with viscoelastic dampers by using the concept of additional damping ratio. The two systems have the same energy consumption in simulation.

Already simplifying the system to a linear system, according to the simplification method proposed by Li Guohao about first-order longitudinal mode shape of a single-degree-of-freedom model, the whole bridge is simplified to a system whose longitudinal stiffness is same as the pylon's thrust stiffness and the mass is equal to the girder mass plus with participated mass at the top of the tower. The random excitation of the environment to the main beam is similar to white noise excitation. We use the knowledge of structural dynamics to solve the frequency response function and power spectrum of the system, and gradually deduce the power spectrum of the SDOF system under white noise environment.

2.1 *Frequency response function of SDOF system*

Considering the SDOF linear vibration system, the motion equation is

$$m\ddot{Y}(t)+c\dot{Y}(t)+kY(t)=X(t), Y(0)=\dot{Y}(0)=0 \tag{1}$$

m is the equivalent mass, c is damping parameters, k is stiff of the system. Expression (1) can transform to no-dimensional form：

$$\ddot{h}(t)+2\xi\omega_0\dot{h}(t)+\omega_0^2 h(t)=\frac{1}{m}\delta(t) \tag{2}$$

where $\omega_0=\sqrt{\frac{k}{m}}$ is the system natural frequency; $\xi=c/2m\omega_0$ is damping ratio of system.

Suppose $Y(t)=H(\omega)e^{i\omega t}$, the motion equation can rewrite as follow:

$$[(i\omega)^2+2\xi\omega_0(i\omega)+\omega_0^2]H(\omega)e^{i\omega t}=e^{i\omega t}\cdot\frac{1}{m} \tag{3}$$

where $i=\sqrt{-1}$, the solution of equation (3) is:

$$H(\omega)=\frac{1}{m}\frac{1}{(\omega_0{}^2-\omega^2)+2i\xi\omega_0\omega} \tag{4}$$

$H(\omega)$ is a complex function whose amplitude (5) and phase (6) are as follow:

$$\left|H(\omega)\right|=\frac{1}{m}\frac{1}{\sqrt{(\omega_0{}^2-\omega^2)+(2\xi\omega_0\omega)^2}} \tag{5}$$

$$\psi=\tan^{-1}\left\{\frac{2\xi\omega/\omega_0}{1-(\omega/\omega_0)^2}\right\} \tag{6}$$

2.2 *Response power spectrum under ideal white noise*

The autocorrelation function $R_Y(\tau)$ of stationary random process $Y(t)$ under white noise is:

$$R_Y(\tau)=E[Y(t)Y(t+\tau)]$$

$$=\int_{-\infty}^{+\infty}h(u)\int_{-\infty}^{+\infty}h(v)R_X(\tau+u-v)\mathrm{d}u\mathrm{d}v \tag{7}$$

$$S_Y(\omega)=\frac{1}{2\pi}\int_{-\infty}^{+\infty}R_Y(\tau)e^{-i\omega\tau}\mathrm{d}\tau=H(-\omega)H(\omega)S_X(\omega) \tag{8}$$

Consider that $H(-\omega)$ and $H(\omega)$ are conjugate functions, so power spectrum can deduce further as below:

$$S_Y(\omega)=\left|H(\omega)\right|^2S_X(\omega)=\frac{S_0}{m^2[(\omega_0{}^2-\omega^2+4\xi^2\omega_0{}^2\omega^2]} \tag{9}$$

$$R_Y(\tau)=\frac{\pi S_0}{2m^2\xi\omega_0{}^3}e^{-\xi\omega_0|\tau|}(\cos p\tau+\frac{\xi\omega_0}{p}\sin p|\tau|) \tag{10}$$

$$\sigma_Y{}^2=\frac{\pi S_0}{2m^2\xi\omega_0{}^3}=\frac{\pi S_0}{ck} \tag{11}$$

The expression (9) can be written as a fitting function with a_1, b_1, c_1:

$$S_Y(\omega)=\frac{a_1}{(b_1{}^2-\omega^2)^2+4c_1{}^2b_1{}^2\omega^2} \tag{12}$$

$$S_{\ddot{Y}}(\omega)=\omega^2S_{\dot{Y}}(\omega)=\omega^4S_Y(\omega) \tag{13}$$

where $a_1=\frac{S_0}{m^2}$, $b_1=\omega_0=2\pi f_0$, $c_1=\xi$ are three fitting parameters needed. The damping ratios is obtained as well.

3 DISCRETE WAVELET TRANSFORM

The idea of wavelet transform is different from the Fourier transform which decomposes the signal into an infinite length of the sine, cosine function. It is defined as a finite length wavelet that transforms the signal over the entire time domain. Its essence is actually the convolution of different scales wavelet function with the signal:

$$\langle u,K\rangle=\int_{-\infty}^{\infty}u(t)K(t,a,b)\mathrm{d}t \tag{14}$$

$u(t)$ is a signal with finite energy which is expressed as follow:

$$E_u=\int_{-\infty}^{\infty}\left|u(t)\right|^2\mathrm{d}t<\infty \tag{15}$$

$K(t,a,b)$ is a scaled and shifted version of the complex conjugate of the wavelet $\psi(t)$. This wavelet $\psi(t)$ has a zero average：

$$\int_{-\infty}^{\infty}\psi(t)\mathrm{d}t=0 \tag{16}$$

and fulfills the following condition of admissibility.

$$\int_{-\infty}^{\infty}\frac{\left|\hat{\psi}(\omega)\right|^2}{|\omega|}\mathrm{d}\omega<\infty \tag{17}$$

Throughout this text, $\hat{(\bullet)}$ will be used to denote the Fourier transform. In addition, the wavelets is normalized $\|\psi\|=1$ and centered around $t=0$.

With the wavelet chosen, a set of functions is obtained by scaling the wavelet by a and shifting it by b . the resemblance between the signal and the scaled and shifted wavelet is given by means of inner product. To preserve the normalization of the wavelet at each scale, the wavelet is divided by $\sqrt{a}$.

$$T_\psi[u](a,b)=\frac{1}{\sqrt{a}}\int_{-\infty}^{\infty}u(t)\overline{\psi\left(\frac{b-t}{a}\right)}\mathrm{d}t \tag{18}$$

where $\bar{\bullet}$ denotes complex conjugation.

Compared with the continuous wavelet transform, the principle of discrete wavelet transform is almost the same. The scale parameters a and the shift parameters b in the continuous wavelet transform are continuous real numbers. Therefore, the computational complexity is huge and the redundancy of the data is greatly increased.

Discrete wavelet transform discretizes the scale a and the shift b, that is, only the partial scales and the shifts are picked out and calculated which makes that the analysis is very effective. What's more, after

the discrete wavelet transform, the effective information of the signal will not be lost, just because the wavelet basis function has orthogonality. The total length of the signal after the decomposition did not change by down sampling. The correlation redundancy between the two points in the wavelet space was eliminated.

The discrete wavelet with orthogonality has four filters, which can decompose the large and small scale information from the signal and reconstruct it in the next step. In the discrete wavelet analysis process, setting the threshold to the decomposition of the signal, the reconstruction of the signal can filter out part of the data. Decomposition filter can also continue break down into next layer followed the first layer to achieve frequency domain refinement by multi-layer decomposition. Taking the three-layer decomposition for instance, the interval of the frequency can be refined to the one eighth of total frequency range (see Figure 3).

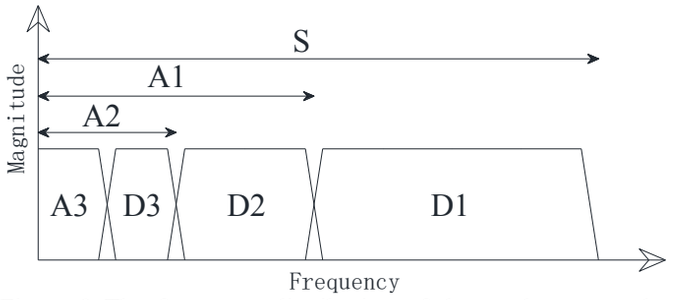
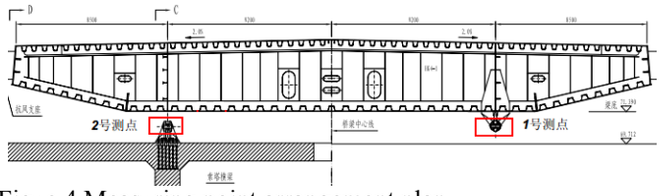


Figure 3 The frequency distribution of three - layer wavelet decomposition

4 FIELD DATA COLLECTED

The experiment was carried out under the condition of temperature of 15 ~ 20 Celsius degrees and wind speed of 3 ~ 4 m/s. The measuring points were located at the tower-beam damper on the north side of the north tower of Sutong Bridge. There were two measuring points in the experiment. No.1 point located downstream, while No. 2 point located upstream (Figure 4, Figure 5). The data of the longitudinal vibration of the main girder were collected by acceleration sensor installed on the tower-beam damper. This experiment employed the 3082T2 data acquisition instrument of china orient institute of noise and vibration and KD12000 acceleration sensor.



Figue 4 Measuring point arrangement plan

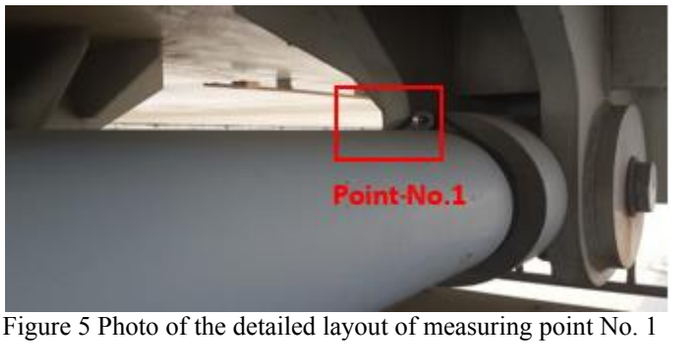
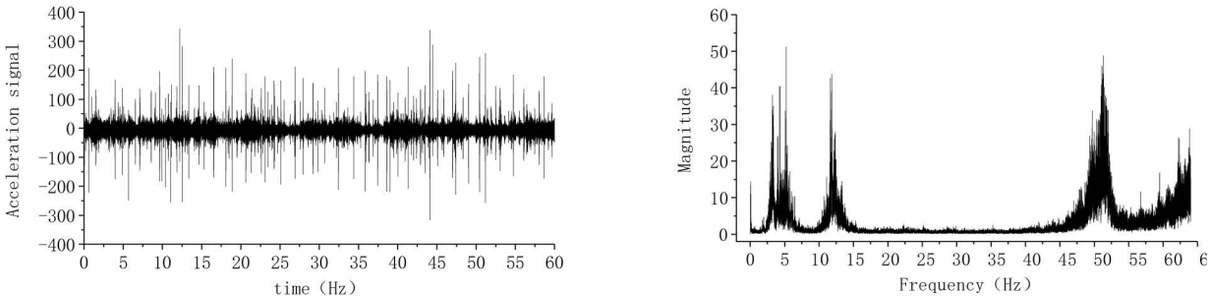


Figure 5 Photo of the detailed layout of measuring point No. 1

Having finished the installation of the sensor and the collector, we set the sampling frequency as 128Hz. And in order to ensure the results similar to the smooth process, the sampling time needed to extend to some degree and finally set as 3600 seconds. According to the experimental requirements, the experiment was repeated on April 17th, 2014, April 27th, 2015 and November 9th, 2016 respectively, to observe the system damping ratio trend over time.

5 DATA ANALYSIS

Firstly, the fluctuation of the original data in time domain and the power spectrum in the frequency domain are analyzed (Figure 6). From the perspective of the time domain, it can be seen that the vibration data are random. Meanwhile, the frequency domain reflects that there are several frequency peaks. The first frequency peak is near 0Hz, which is also the closest to the girder longitudinal vibration frequency and need to extract and further analysis. The peaks around 5Hz ~ 10Hz is mainly affected by the vibration of the vehicle passing by, different speed may lead to the main beam vibration frequency is different; and 45Hz frequency is not the structure of the vibration, and therefore not in the range of the study. In order to better perform the first-order longitudinal vibration of the main beam, it is necessary to use the reasonable method to carry on the preliminary processing to the data, and the signal close to the longitudinal frequency of the main beam is kept as complete as possible.



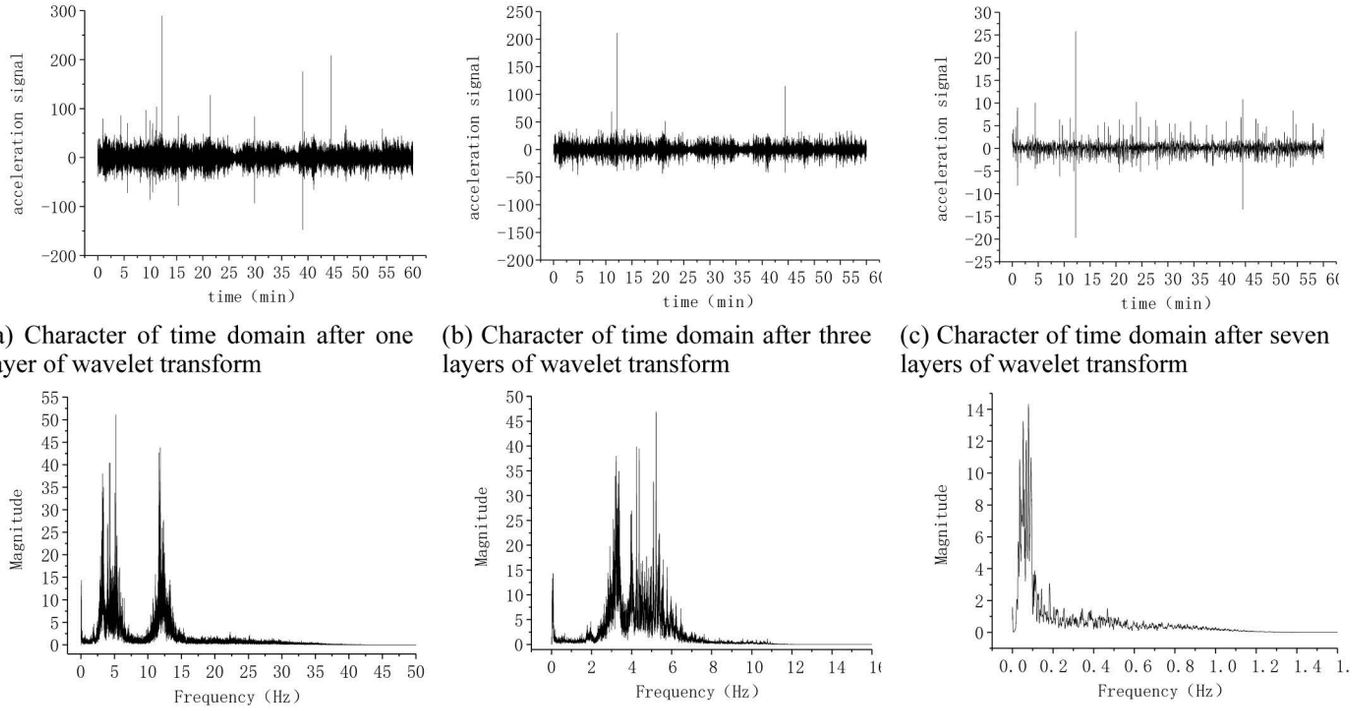
(a) Time characteristics of the original data for one hour (b) Frequency characteristics of the original data for one hour

Figure 4 Measured original data in the time domain (a) and frequency domain (b)

5.1 *Filtered by discrete wavelet transform*

The discrete wavelet is used to decompose the data into two components, namely high-frequency components and low-frequency components. The high-frequency components remove through threshold, and then reconstruct with the low-frequency components without any further processing. The low-frequency components are preserved after decomposing and reconstructing, thus achieving the purpose of low-pass filtering. In the process of analysis, Coiflet biorthogonal wavelet is selected. In addition to good ability of reconstruction, Coiflet wavelet has better symmetry, longer support length and higher disappearance moment. In the matlab software, the data were preliminarily decomposed by different layers (see Figure 7), and the changes in the time domain and frequency domain were observed by the increase of the number of wavelet layers.

It can be seen from Figure 7, with the gradual increase in the number of wavelet decomposition layer, some peaks of vibration signal removed in time domain. In view of frequency domain, the range of suppression high frequency gradually increase. After decomposing the first layer, the range of low-pass is 0 ~ 40Hz, and deeply decomposed into the third layer, the range is 0 ~ 12Hz, and finally to the seventh layer, the range of the low-pass is only 0 ~ 1.4Hz. During the process of decreasing the frequency range of the low pass filter, the power spectrum of the low frequency range does not change which means that the wavelet filtering method has better filtering effect on the signal. The desired frequency ranges only including longitudinal vibration has extracted successfully with the seven layers' decomposition and reconstruction of wavelets transform.



(a) Character of time domain after one layer of wavelet transform

(b) Character of time domain after three layers of wavelet transform

(c) Character of time domain after seven layers of wavelet transform

(d) Character of frequency domain after one layer of wavelet transform

(e) Character of frequency domain after three layers of wavelet transform

(f) Character of frequency domain after seven layers of wavelet transform

Figure 5 Characters of time and frequency domain after different layers of wavelet transform

5.2 *Identification of system damping ratio*

The power spectrum filtered by the seven-layer wavelet transform is fitted according to the formula (12) deduced in chapter 2.2. Least square method based on the given function are used to fit the three parameters a_1, b_1, c_1. The equivalent mass of the main beam is unchanged and the relationship of $a_1 = \frac{S_0}{m^2}$, so a_1 is mainly to reflect the power spectrum density of the white noise. The fitting value b_1 can converted to the first-order longitudinal frequency of the main beam with $f_0 = \frac{b_1}{2\pi}$. c_1 is the damping ratio of the longitudinal vibration.

Taking the measured data of point No. 1 (see Figure 8) in 2014 and the measured data of the point No. 1 in 2016 (see Figure 9) for examples, it can be seen that the fitted curve matched the power spectrum well.

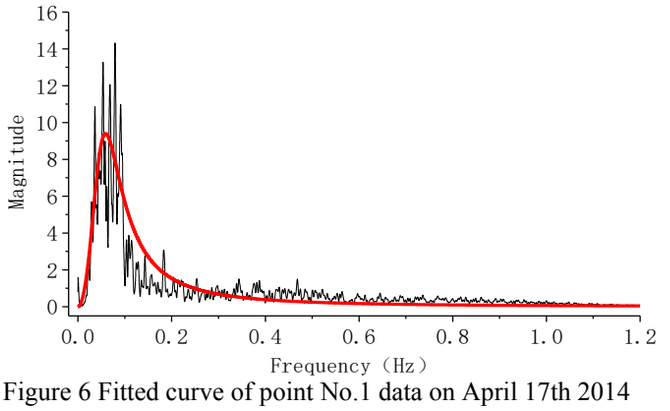


Figure 6 Fitted curve of point No.1 data on April 17th 2014

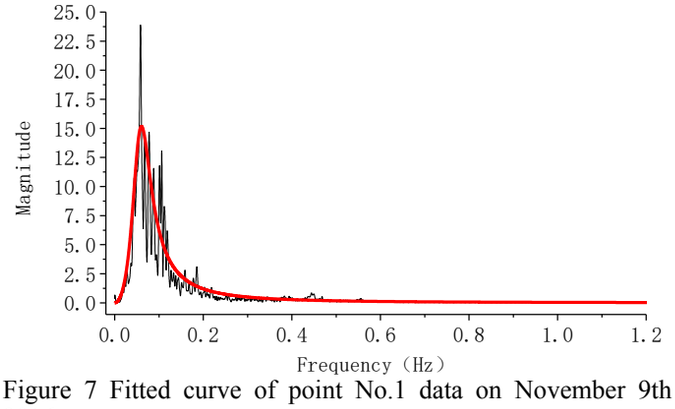


Figure 7 Fitted curve of point No.1 data on November 9th 2016

Table 1 Fitted recognition results of first-order longitudinal frequency and damping ratio

date	2014/04/17			2015/04/27			2016/11/09		
point	No.1	No.2	average	No.1	No.2	average	No.1	No.2	average
a_1	2.568	2.666	2.117	2.072	2.166	2.319	1.692	1.562	1.527
f_0	0.0595	0.0564	0.0580	0.0608	0.0614	0.0611	0.0596	0.0599	0.0601
c_1	0.5988	0.6112	0.605	0.5147	0.5614	0.5381	0.4403	0.4839	0.4621

To avoid the deviation of an experiment, we calculate the results of the two measured points and calculate the average in Table 1. Through the data in the Table 1, the white noise power of two points is relatively close in the same hour and slightly different for different periods. The identified first-order longitudinal vibration frequencies of the main beam in three experiments are very close. In addition, the first-order longitudinal vibration frequency of finished bridge(0.060 Hz) and the finite element model with the pile cap and pile foundation into consideration(0.0637 Hz) are also close to the identified result, which verifies the correctness of the measured data.

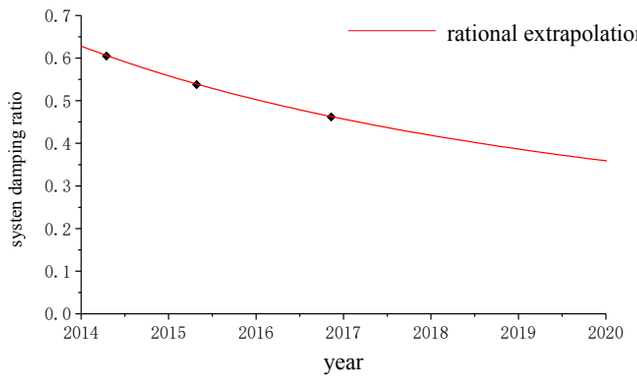


Figure 8 The extrapolation of system damping ratio trend

Time of the three experiments in accordance with horizontal axis, the system damping ratio as the vertical axis, we fit the damping ratio trend of the system. It is found that the damping decay rate gradually decreases with the passage of time (Figure 10), which also reflects the slow degradation of the performance of the damper.

Based on current data, the damping ratio of tower-beam damper will continue to decay in the future life cycle. This paper only selected three data in three years to compare and predict due to the time constraints. Whether the trend of the damping ratio is still like this need to collect more data to support in certain intervals for more accurate evaluation. This identification method can help the bridge maintenance team combine with the vibration data to assess the performance of large-scale damper based on a simple visual inspection. Even beyond the service life of the dampers, it is also a good basis to determine whether dampers need to be replaced, and result in more scientific management of the important components of the bridge.

6 CONCLUSIONS

In this paper, the formula of power spectrum of single degree of freedom system under random process is deduced, and the longitudinal vibration data of Sutong Bridge are collected and analyzed three times in three years. Filtered the measured signal by wavelet transform method, the damping ratio of large tower beam damper can be identified in the field experiment. The identification and prediction of damping ratio and performance can lead more and more scientific maintenance and management of the bridge damper.

Based on the analysis and elaboration of the experimental data in this paper, the following conclusions are obtained:

1. The longitudinal vibration of the Sutong Bridge is equivalent to a linear single-degree-of-freedom system, while the excitation of the environment is similar to the white noise excitation, which can effectively simplify the problem. The formula of power spectrum in random process can deduce in this condition and with the field measured data fitted with the formula, the system damping ratio can be identified without affecting the traffic.

2. With the number of layers of discrete wavelet transform increasing, the recognition resolution of the signal in frequency domain increases. Remove the specified decomposed signal through threshold, and then reconstruction signal can be the wanted signal to achieve low-pass, or band-pass, or high-pass filter. Meanwhile, the decomposition process did not affect the total length of the signal by down sampling, even neither the reconstructed data due to the orthogonal wavelet.

3. With the measured power spectrum fitting with the formula deduced, the system damping ratio can be obtained. The three-year system damping ratios in accordance with the chronological order, we can find that the damping performance of the tower beam damper is still in a good condition but also in a process of slow degradation. The extrapolation of the current data analysis results can predict the attenuation curve of the tower beam damper over time. In order to predict the curve of the damper performance better, it is necessary to repeat the experiment for more data and further analysis.

4. The only maintenance for the tower-beam dampers of Sutong Bridge is the visual inspection to determine whether they work normally. The method in this paper can better monitor the performance of the damper, which leads to repair and replace the damper in time when the tower-beam damper failed to consume energy. In addition, it can also provide a basis of whether we need to replace the tower-beam damper beyond its service life for ensuring the normal operation of the bridge.

REFERENCES

Georgakis C T, Gimsing N J. 2012 Cable supported bridges :concept and design. 3rd ed. Chichester, West Sussex, U.K.: J. Wiley,.

Park K S, Jung H J, Lee I W. 2003 Hybrid control strategy for seismic protection of a benchmark cable-stayed bridge. *Engineering Structures*., 25(4): 405-417.

Agrawal A K, Yang J N, He W L. 2003 Applications of some semiactive control systems to benchmark cable-stayed bridge. *Journal of Structural Engineering-Asce.*, 129(7): 884-894.

Taylor device inc 2007 Fluid viscous damper operation and maintenance manual(3.025 MN Fluid Viscous Damper With10 MN Spring).,.

Soneji B B, Jangid R S. 2007 Passive hybrid systems for earthquake protection of cable-stayed bridge. *Engineering Structures*., 29(1): 57-70.

Terenzi G. 1999 Dynamics of SDOF systems with nonlinear viscous damping. *Journal of Engineering Mechanics-Asce*., 125(8): 956-963.

Fugal D L. 2009. Conceptual wavelets in digital signal processing: an in-depth, practical approach for the non-mathematician. 1st ed.. San Diego, Calif.: Space & Signals Technical Pub.,

Mallat S G. 2009 A wavelet tour of signal processing: the sparse way. 3rd ed. Amsterdam: Elsevier/Academic Press

Maintenance, Safety, Risk, Management and Life-Cycle Performance of Bridges – Powers, Frangopol, Al-Mahaidi & Caprani (Eds)
© 2018 Taylor & Francis Group, London, ISBN 978-1-138-73045-8

Use of Comparative Vacuum Monitoring Sensors for Automated, Wireless Health Monitoring of Bridges and Infrastructure

Dennis Roach
Sandia National Laboratories, New Mexico, United States of America

ABSTRACT: Economic barriers to the replacement of bridges and other civil structures have created an aging infrastructure and placed greater demands on the deployment of effective and rapid health monitoring methods. To gain access for inspections, structure and sealant must be removed, disassembly processes must be completed and personnel must be transported to remote locations. Reliable Structural Health Monitoring (SHM) systems can automatically process data, assess structural condition, and signal the need for specific maintenance actions. They can reduce the costs associated with the increasing maintenance and surveillance needs of aging structures. The use of in-situ sensors, coupled with remote interrogation, can be employed to overcome a myriad of inspection impediments stemming from accessibility limitations, complex geometries, the location of hidden damage, and the isolated location of the structure. Furthermore, prevention of unexpected flaw growth and structural failure could be improved if on-board SHM systems were used to regularly, or even continuously, assess structural integrity. A research program was completed to develop and validate Comparative Vacuum Monitoring (CVM) sensors for crack detection. Sandia National Labs, in conjunction with private industry and the U.S. Department of Transportation, completed a series of CVM validation and certification programs aimed at establishing the overall viability of these sensors for monitoring bridge structures. Factors that affect SHM sensitivity include flaw size, shape, orientation and location relative to the sensors, along with operational environments. Statistical methods using one-sided tolerance intervals were employed to derive Probability of Flaw Detection (POD) levels for typical application scenarios. Complimentary, multi-year field tests were also conducted to study the deployment and long-term operation of CVM sensors on aircraft and bridges. This paper presents the quantitative crack detection capabilities of the CVM sensor, its performance in actual operating environments, and the prospects for structural health monitoring applications on a wide array of civil structures.

1 INTRODUCTION

Multi-site fatigue damage and hidden cracks in hard-to-reach locations are among the major flaws encountered in today's extensive array of aging structures and mechanical assemblies. The costs associated with the increasing maintenance and surveillance needs of aging structures are rising. The application of Structural Health Monitoring (SHM) systems using distributed sensor networks can reduce these costs by facilitating rapid and global assessments of structural integrity. These systems also allow for condition-based maintenance practices to be substituted for the current time- or cycle-based maintenance approaches thus optimizing maintenance labor [1]. Other advantages of on-board, distributed sensor systems are that they can eliminate costly, and potentially damaging, disassembly, improve sensitivity by producing optimum placement of sensors with minimized human factors concerns in deployment and decrease maintenance costs by eliminating more time-consuming manual inspections. Current structural maintenance operations require personnel entry into normally-inaccessible or hazardous areas to perform mandated, nondestructive inspections. These processes are not only time consuming but they provide the opportunity to induce damage to the structure. The use of in-situ sensors for monitoring the condition of structures and mechanisms, coupled with remote interrogation, can be employed to overcome inspection difficulties including the remote location and expansive distribution of critical structures such as railway bridges and rail cars. Prevention of unexpected flaw growth and structural failure could be improved if on-board health monitoring systems are used to more regularly assess structural integrity [2, 3]. The ease of monitoring an entire network of distributed sensors means that structural health assessments can occur more often, allowing operators to be even more vigilant with respect to flaw onset.

1.1 *Comparative Vacuum Monitoring*

Comparative Vacuum Monitoring (CVM) is a simple pneumatic sensor technology developed to detect the onset of cracks. CVM sensors are permanently installed to monitor critical regions of a structure. The CVM sensor is based on the principle that

a steady state vacuum, maintained within a small volume, is sensitive to any leakage [4]. A crack in the material beneath the sensor will allow leakage resulting in detection via a rise in the monitored pressure. Figure 1 shows top-view and side-view schematics of the self-adhesive, elastomeric sensors with fine channels etched on the adhesive face along with a sensor being tested in a lap joint panel. When the sensors are adhered to the structure under test, the fine channels and the structure itself form a manifold of galleries alternately at low vacuum and atmospheric pressure. Vacuum monitoring is applied to small galleries that are placed adjacent to the set of galleries maintained at atmospheric pressure. If a flaw is not present, the low vacuum remains stable at the base value. If a flaw develops, air will flow from the atmospheric galleries through the flaw to the vacuum galleries. When a crack develops, it forms a leakage path between the atmospheric and vacuum galleries, producing a measurable change in the vacuum level. This change is detected by the CVM monitoring system shown in Figure 2. It is important to note that the sensor detects surface breaking cracks once they interact with the vacuum galleries. Since the sensor physics is based on pressure measurements, there is no electrical excitation involved. These sensors can be attached to a structure in areas where crack growth is known to occur. On a pre-established engineering interval, a reading will be taken from an easily accessible point on the structure.

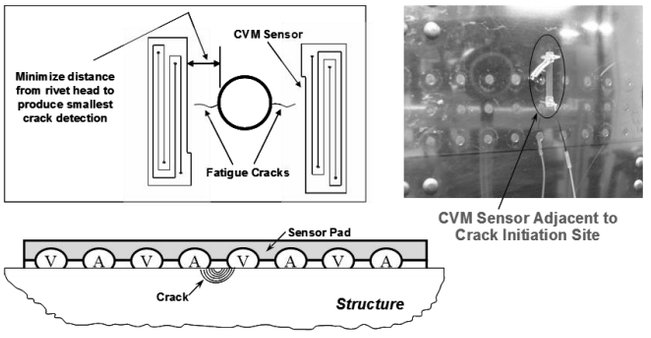


Figure 1. Schematics depicting operation of CVM sensor and polymer sensor mounted on the outer surface of a riveted lap joint.

2 APPLICATIONS FOR CRACK DETECTION USING CVM SENSORS

Recent events have demonstrated the need to address critical infrastructure surety needs [5]. The applications for CVM sensors can include such diverse structures as: buildings, bridges, trains and subway vehicles, mining structures, railroad cars, trucks and other heavy machinery, pressure vessels, oil recovery equipment, pipelines, steel transmission towers, ships, tanks and a wide array of military structures. Damage can arise from service loads as well as from external impact, off-design conditions or malevolent attacks.

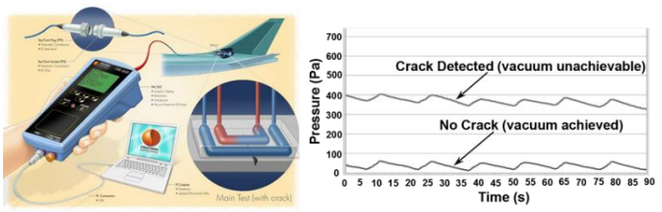


Figure 2. Crack detection monitoring with CVM system and pressure response used to indicate the presence of a crack.

In the matter of bridge refurbishment alone, the National Bridge Inventory Database (Fed. Highway Admin. 2003) indicates that 30% of the 600,000 bridges in the United States are "structurally deficient." In addition, a majority of the rail bridges in U.S. are operating beyond their initial design life. A bridge that is "structurally deficient" is still strong enough and stable enough for use; however, closer scrutiny of the bridge is required to ensure its continued, safe operation. In 2006, the American Society of Civil Engineers (ASCE) issued a report on the status of the U.S. infrastructure. It assessed everything from roads to hazardous waste systems and gave the country's infrastructure an overall grade of "D". Steel superstructure bridges built during the interstate construction boom of the 1950s and 1960s are reaching or surpassing their initial design lifetime. Depending on their level of maintenance, some bridges are showing visible signs of deterioration.

On September 30, 2006, part of an overpass collapsed in Montreal. On August 1, 2007, an Interstate 35 bridge crossing the Mississippi River in Minneapolis failed. The collapse of the Interstate 35 bridge prompted many questions regarding the health of similar structures around the world and their associated maintenance programs. Figure 3 shows three bridge failures – in Minneapolis, Montreal and Connecticut – and one bridge in Delaware with a large fatigue crack that was discovered and repaired prior to any catastrophic failure.

3 CVM PERFORMANCE ASSESSMENT USING ONE-SIDED TOLERANCE INTERVALS

The Federal Aviation Administration's Airworthiness Assurance Center at Sandia Labs, in conjunction with industry and airline partners, completed validation testing on the CVM system in an effort to adopt Comparative Vacuum Monitoring as a standard NDI practice [5-6]. Fatigue tests were completed on aircraft components to grow cracks in representative structure while the vacuum pressures within the various sensor galleries were simultaneously recorded. A fatigue crack was propagated until it engaged one of

the vacuum galleries such that crack detection was achieved and the sensor indicated the presence of a crack by its inability to maintain a vacuum. Probability of flaw detection assessments were coupled with on-aircraft flight tests to study the performance, deployment, and long-term operation of CVM sensors on aircraft. The result was a series of flaw detection curves that can be used to propose CVM sensors for aircraft crack detection. One set of test specimens were wing box fittings from the Boeing 737 which was the chosen CVM application from Delta Air Line's fleet. Figure 4 shows the details of one test series addressing a wing box fitting application along with installation of CVM sensors for the flight test program.

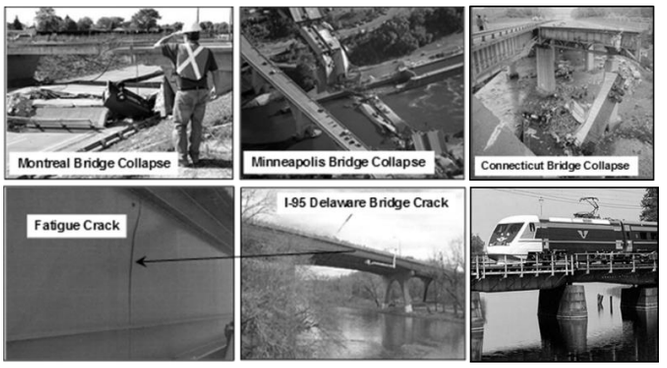


Figure 3. Applications for in-situ crack detection using CVM sensors.

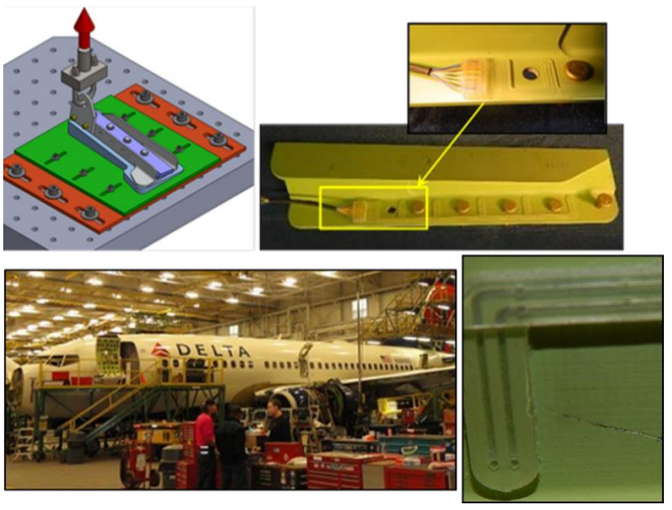


Figure 4. CVM testing on wing box fitting with close-up showing fatigue crack crossing into CVM sensor and installation of CVM sensors on Delta Air Lines aircraft for flight tests.

SHM reliability calculations will depend greatly on the complexity of the structure and geometry of the flaw profile. Since it is based on a sample of the entire population (n data points), the confidence is less than 100%. Thus, the One-Sided Tolerance Interval (OSTI) is greatly affected by two proportions: 1) the percent coverage which is the percent of the population that falls within the specified range (normally chosen as 90%), and 2) the degree of confidence desired (normally chosen as 95%). The data analyzed here consisted of fatigue cracks that were propagated in various metal specimens with the direction of growth aligned with the CVM mounted sensors. The data captured is that of the flaw length at the time for which the CVM provided sustainable detection. With these assumptions, there exists a distribution on the flaw lengths at which detection is first made. In this context, the probability of detection for a given flaw length is just the proportion of the flaws that have a detectable length less than that given length. That is, the reliability analysis becomes one of characterizing the distribution of flaw lengths and the cumulative distribution function is analogous to a Probability of Detection (POD) curve. Assuming that the distribution of flaws is such that the logarithm of the lengths has a Gaussian distribution, it is possible to calculate a one-sided tolerance bound for various percentile flaw sizes. To do this, it is necessary to find factors $K_{n,\gamma,\alpha}$ to determine the probability γ such that at least a proportion $(1-\alpha)$ of the distribution will be less than $X - K_{n,\gamma,\alpha}$ where X and S are estimators of the mean and the standard deviation computed from a random sample of size n. The data captured is the crack length at CVM detection. From the reliability analysis, a cumulative distribution function is produced to provide the maximum likelihood estimation (POD). This stems from the one-sided tolerance bound for the flaw of interest using the equation:

$$T_{POD(90,\,95)} = X + (K_{n,\gamma,\alpha})(S) \qquad (1)$$

where T = tolerance interval for crack length corresponding to 90% POD with a 95% confidence; X = mean of detection lengths; K = probability factor (~ sample size and confidence level desired); S = standard deviation of detection lengths; n = sample size; $1-\alpha$ = detection level; and γ = confidence level.

Because of physical, time or cost constraints, it is often impractical to inspect an entire population. Due to the limited number of data points, the reliability calculations induce a penalty by increasing the magnitude of the K (probability) factor. As the number of data points increases, the K value will decrease and the POD numbers could also decrease. The formula in equation (1) is set-up to produce the upper bound for the tolerance interval which represents the actual POD value. With the same parameters described above, the maximum likelihood estimate describing the optimal performance on the Probability of Detection for the OSTI approach can be calculated as:

$$\mathbf{POD} = \frac{1}{xS\sqrt{2\pi}} EXP\left(\frac{-(\ln(x)-X)^2}{2S^2}\right) \qquad (2)$$

As an example, the data acquired from CVM fatigue tests on 2.54" (0.1") thick 2024-T3 aluminum structure were used to calculate the 90% POD level for CVM crack detection. This POD curve, representing

the 95% confidence level, is plotted in Figure 5. The maximum likelihood estimated POD function, representing the optimum performance for CVM crack detection, was calculated from equation (2) and is plotted alongside the 95% confidence bound. The overall POD value (95% confidence level) for CVM crack detection in 2.54 mm thick aluminum skin was determined to be 0.58 mm (0.023”). In this particular instance, it was desired to achieve crack detection before the crack reached 0.1” in length so this goal was achieved. In over 200 fatigue tests conducted using CVM sensors there were no false calls produced by the sensors.

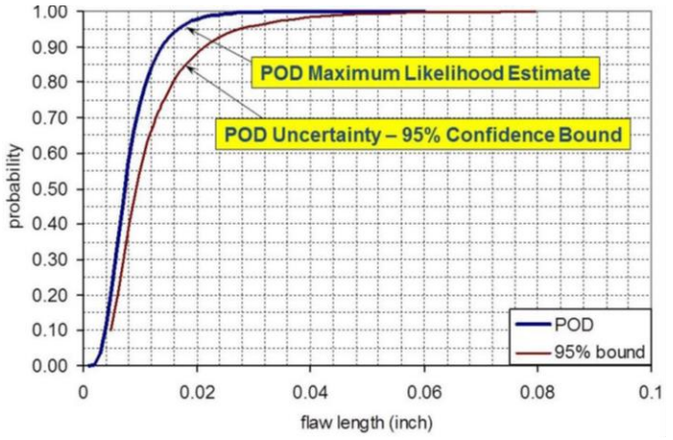


Figure 5. Probability of crack detection curves showing detectable flaw lengths for CVM sensors.

The results sited above are valuable for thin-walled structures such as those used in aircraft, automotive, and some pipeline construction. However, many civil structures use thick steel members. Earlier studies revealed that the thickness of the plate can affect CVM performance so additional performance tests studied CVM crack detection in thick-walled structures. Aircraft use thinner materials and have crack detection requirements of 1.27 mm to 2.54 mm in length. Civil structures contain thicker materials, have higher safety factors and can tolerate longer cracks such that their crack detection requirements are in the range of 12.7 mm to 25.4 mm in length. Additional tests studied CVM sensors monitoring cracks in 9.5mm thick steel. For the loaded structure, CVM crack detection occurred when the fatigue cracks ranged from 1.02 mm to 1.78 mm in length. For the unloaded condition, CVM crack detection occurred when the fatigue cracks ranged from 1.52 mm to 9.65 mm in length. However, regardless of whether the sensor monitoring is completed during a loaded or unloaded condition, the results indicate that CVM sensors could reliably detect fatigue cracks well before they reach 12.7 mm (0.5”) in length.

4 MULTI-CVM SWITCH-BASED SYSTEM FOR REMOTE BRIDGE MONITORING

A real-time monitoring system was developed for remotely interrogating a distributed array of CVM sensors on a transportation bridge structure. It uses a series of pressure switches that can continuously monitor structures remotely via a wireless transmitting device. Sensors were placed in known fatigue critical locations on the bridge structure. When a crack breaches a sensor, the pressure switch is opened and, in turn, triggers a message that is sent to a central maintenance center. Up to 50 switches can be powered by one vacuum pump. The CVM monitoring system, shown in Figure 6, was mounted at a centralized point on the structure of interest. Sensors can be made in almost any shape and out of a material to suit the required environment. Multiple sensors can be arranged to monitor the growth of a crack. It may be that there is a known crack and a sensor placed ahead of the crack will be triggered if the crack grows. Often there are known critical locations at joints or welds that require monitoring. The CVM monitoring system can continuously update web sites or send automated text messages or e-mails so that operators can quickly and remotely ascertain the condition of a structure and determine if maintenance action is required. Solar cells were used to recharge the onboard batteries so that the system can provide continuous, real-time monitoring for 3-4 years without maintenance. Multiple years of field operation has revealed excellent bridge health monitoring capabilities of such an SHM system.

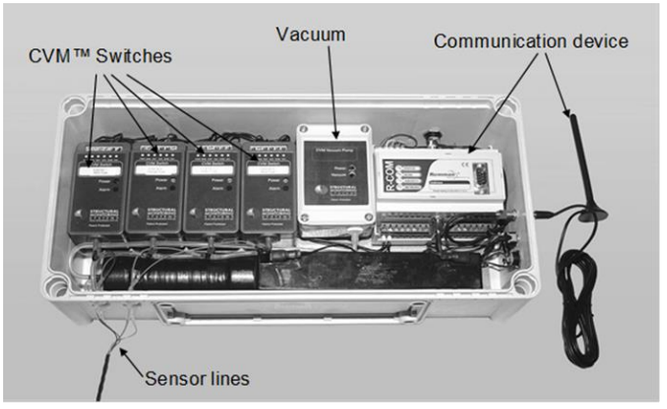


Figure 6. Real-time, remote monitoring system for a network of CVM sensors.

5 CONCLUSIONS

The effect of structural aging and the dangerous combination of fatigue and corrosion has produced a greater emphasis on the application of sophisticated health monitoring systems. Corrective repairs initiated by early detection of structural damage are more

cost effective since they reduce the need for subsequent major repairs and may avert a structural failure. Through the use of in-situ CVM sensors, it is possible to quickly, routinely, and remotely monitor the integrity of a structure in service and detect incipient damage before catastrophic failures occur. These sensors can be attached to a structure in areas where crack growth is known to occur. On a pre-established monitoring interval, a reading can be taken remotely or from an easily accessible point on the structure. Each time a reading is taken, the system performs a self-test. This inherent fail-safe property ensures the sensor is attached to the structure and working properly prior to any data acquisition. In several structural categories studied, the CVM sensors provided crack detection well before the crack propagated to the critical length determined by damage tolerance analyses. In addition, there were no false calls experienced in over 200 fatigue crack detection tests. The sensitivity, reliability, and cost effectiveness of the CVM sensor system was demonstrated in both laboratory and field test environments.

Global SHM, achieved through the use of sensor networks, can be used to assess overall performance (or deviations from optimum performance) of large structures such as bridges, pipelines, transport vehicles, and buildings. The ease of monitoring an entire network of distributed sensors means that structural health assessments can occur more often, allowing operators to be even more vigilant with respect to damage onset.

6 ACKNOWLEDGEMENTS

Sandia National Laboratories is a multi-mission laboratory managed and operated by National Technology and Engineering Solutions of Sandia, LLC, a wholly owned subsidiary of Honeywell International, Inc., for the U.S. Department of Energy's National Nuclear Security Administration under contract DE-NA0003525.

7 REFERENCES

Roach, D. (2006). Health monitoring of aircraft structures using distributed sensor systems. Proceedings of DoD/NASA/FAA Aging Aircraft Conference.

Beral, B. & H. Speckmann (2003). Structural health monitoring for aircraft structures: A challenge for system developers and aircraft manufacturers. Proceedings of International Workshop on Structural Health Monitoring.

Roach, D. (2004). Use of distributed sensor systems to monitor structural integrity in real-time," *Quality, Reliability, and Maintenance in Engineering*, Oxford, UK: Professional Engineering Publishing Ltd.

Roach, D, J. Kollgaard, & S. Emery (2006). Application and certification of comparative vacuum monitoring sensors for in-situ crack detection. Proceedings of Air Transport Assoc. Nondestructive Testing Forum.

U.S. White House document (2003). *National strategy for physical protection of critical infrastructures and key assets*.

Wheatley, G., J. Kollgaard, J. Register, & M. Zaidi (2003). Comparative vacuum monitoring as an alternate means of compliance. Proceedings of FAA/NASA/DOD Aging Aircraft Conference.

Roach, D., T. Rice, S. Neidigk, & D. Piotrowski (2015). Establishing the reliability of SHM systems through the extrapolation of NDI probability of detection principles," Proceedings of International Workshop on Structural Health Monitoring.

Maintenance, Safety, Risk, Management and Life-Cycle Performance of Bridges – Powers, Frangopol, Al-Mahaidi & Caprani (Eds)
© 2018 Taylor & Francis Group, London, ISBN 978-1-138-73045-8

Considerations for identification of moisture in building materials using Bluetooth®

R. Helmerich, L. Moldenhauer, G. Voigt, F. Adao
Bundesanstalt für Materialforschung und -prüfung

E. Köppe
SmartSensorik GmbH Michendorf, Germanys

ABSTRACT: The vulnerability of low-quality concrete of some bridges to ageing and deterioration while they are exposed to environmental conditions during their service life, influence of growing population and climate changes, is a well-known effect and requires survey. For survey, the development of a low cost, cost-efficient sensor network to be embedded for continuous or attached to the surface for periodic monitoring is essential. Changing ground water conditions, flood or even leakage in fresh or disposal of waste water can lead to increased moisture content in building materials and structural elements as walls or floors. Moisture allows the transport of other adverse chemicals that might reduce the durability of structures. The paper presents a feasibility study about the capability of microwave modules as Bluetooth® or ZigBee with frequency range at 2,4 GHz to create advanced Wireless Sensor Networks (WSN) for estimation and visualization of moisture distribution in infrastructure assets. It was found that the value of the received signal strength indication (RSSI) depends on the moisture content and can be the basis for the moisture distribution inside a massive structure. The microwave modules may be used to compose networks outside and inside of building materials or structural elements. The higher the number of connections between BLE modules, the more precise and the more distant information can be obtained from the network. Mesh networking was applied to increase the quantitative information.

1 INTRODUCTION

1.1 *Task to solve*

Bridge structures are ageing while they are exposed to changing environmental conditions as temperature or moisture, influence of growing population and climate changes during their service life. Changing ground water conditions, flood or even leakage in fresh or disposal of wastewater pipes can cause increased moisture content in building materials and structural elements as walls or floors. Moisture allows the transport of other adverse chemicals that are reducing the durability of structures. This is the reason, why early indication of moisture is required to immediately undertake preventive measures. Moisture allows adverse chemicals to penetrate the structure, Without moisture chemical processes as Alcali Silica Reaction (ASR) or Delayed Etringit Formation (DEF) that are reducing the service life of structural concrete, would not be possible.

1.2 *Idea to apply*

The propagation of electromagnetic waves in a medium depends on the character of the medium, e.g. air sand or concrete. This character changes, if the medium gets moist. Water is damping the signal strength of microwave signals. Aim of the project is to survey the changes of the signal strength due to changes in the medium in periodic or continuous measurements. The basic research was related to the feasibility and capability of a network of microwave modules to estimate the moisture distribution in massive structures of infrastructure assets (Helmerich, Voigt, Adao, Moldenhauer, & Köppe, 2018).
It is well known from heating food, that water absorbs energy at a frequency of 2,45 GHz, wavelength 122 mm, commonly used to heat food in a microwave. The same frequency range is used for data transfer by Bluetooth®, ZigBee and other protocols.
To reduce the number of influence parameters during the basic investigations, the influence of changing moisture in a medium on changes of microwave signal strength was considered, only. Other influence factors as salt, thickness, temperatures or cracks were not considered.

1.3 *Setup to use*

A network with optimum microwave modules will be proposed. The modules can be attached to both sides of a structure (existing structures, see Figure 1) or shall be embedded into specimen during the construction process of any new cast concrete structure (see Figure 2. Externally attached microwave-module networks have the advantage, that they can be reused in future.

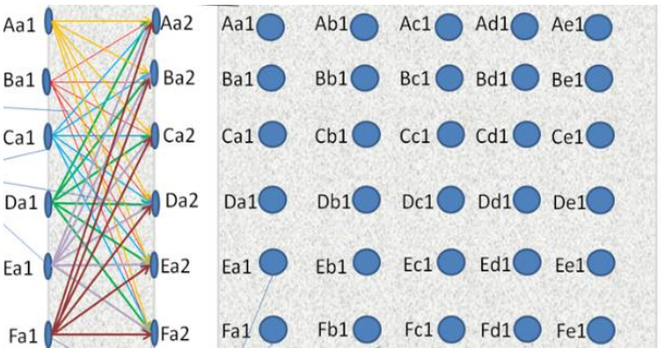


Figure 1. Symbolic measurement traces for monitoring set-up with modules (Blue) attached to the surface of an existing structure, side view and front view.

The network to develop includes making use of advanced Wireless Sensor Networks (WSN)
Inside of sand or other structural material, distributed microwave sensors will provide information about their signal strength and send the message about their signal strength to the adjoined microwave modules.

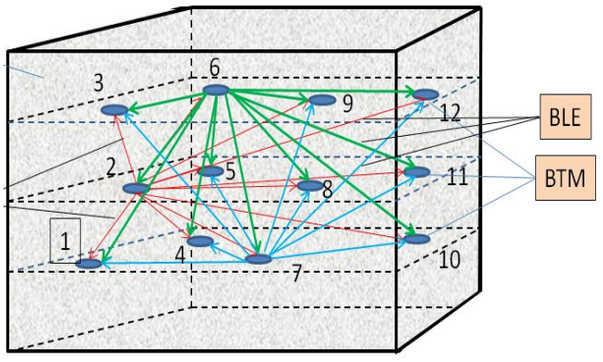


Figure 2. Symbolic measurement traces for monitoring set-up with modules (Blue) embedded in a cast concrete structure.

A fully meshed network of microwave sensors might be able to transfer data deep inside a structure. The reach of ZigBee, Bluetooth®, Bluetooth®Low energy and other specifications is up to 100 m (in air), in fully meshed networks even more.
The higher the number of connections between microwave modules, the more precise information can be obtained from the network. Finally, mesh networking can be applied to increase the quantitative information.

Further part of the project is a feasibility study about localization of distributed modules inside the concrete and signal strength and send the message about their signal strength to the neighboring microwave module.

2 TASKS AND TOOLS

2.1 *Project idea*

All mentioned methods cannot penetrate massive structures. The project idea was to create a meshed network consisting of microwave modules that are communicating in 2,45 GHz. The modules may be embedded in a new structure or externally bonded to an existing bridge structure. Measure for the moisture content is the different damping of the signals due to changing moisture content.
Increasing moisture content influences the damping and finally the RSSI. Consequently, the change of the microwave signals allows the application to estimation of the moisture content either from outside and/ or from an embedded set of modules (Köppe, Moldenhauer, Helmerich, Haamkens, & Wittmann, 2016). Finally, if the method is further developed, it will be applicable in bridge embankments, substructures, road ways or bridge main structures.

2.2 *State of the art of humidity measurements*

Drilling holes and estimating the moisture of the drilled powder is the most popular minor destructive technique to estimate moisture in practice. Another minor destructive technique is the microwave borehole method. Further quantitative non-destructive techniques use sensors attached to the surface. These methods are the time domain reflectometry or complex resistivity method. The complex resistivity method looks at resistivity magnitudes relative to a reference resistor. The frequency range is typically between 1 kHz to 1 MHz. Other methods use the electrical conductivity which is simply the reciprocal value of the electrical resistivity These methods provide information for the near surface area.
Commercial modules, e.g. produced by Texas Instruments, contain a microchip, e.g. Sensirion chip to measure local moisture. The data is transferred by Bluetooth®. If they were protected against water, it would be possible to embed them. Data transfer is only in one direction, from the local position to the reading unit in a smart phone or tablet (Moldenhauer & al, 2016).
Other researchers measure the local moisture with a microchip and transfer the data by Radio Frequency Identification (RFID) RFID can be active or passive. As the lifetime of the sensors depend on the energy supply, the passive solution is given the priority, as it

is more energy saving. In this case sensor is activated from a reading device passing over the surface. Disadvantage is the fact, that the RFID reader must be relatively close to the surface and the sensor should not be deep inside the structure (Stoppel & Fakhouri, 2014).

2.3 *Networks for moisture measurements and IoT*

The idea about a wireless network for the estimation of moisture distribution in a massive medium by means of microwave signal change analysis is not known to the developers.
In difference to past projects, the microwave signals as e.g. Bluetooth® or ZigBee were not used to transfer a signal measured by a digital microchip, but the signal change itself was the measure of the investigated parameters in the presented project.
As basic tasks for the feasibility of the idea, the following questions need answers:

- How does the damping due to moisture content generally influence the distance of the signal transfer in air and moist sand?
- What is the influence of polarization?
- What are the optimum module?
- What is the optimum set-up of the network?
- Is a connection to the IoT useful?

2.3.1 *Damping*

How does the damping due to moisture content generally influence the distance of the signal transfer in air and moist sand? In a vacuum, the electromagnetic signal would not change, in air only slightly. In concrete, the distribution of moisture is usually not homogeneous, as the curing starts from outside. The inner part cures as latest. In difference to concrete, in sand it is possible to distribute the moisture homogenously and estimate the content precisely. Therefore, the preliminary tests were carried out with sand to get an idea about the influence of the damping due to moisture on the transfer distance and the change of the Received Signal Strength Indicator (RSSI).

2.3.2 *Polarization*

What is the influence of the polarization? Electromagnetic waves radiate into a three-dimensional space. The microwave antenna has usually an antenna polarization. The antenna polarization must be known and has to be considered during the analysis of the measured damping.

2.3.3 *Selection of the optimum module*

A second series of tests was carried out with an LinTech-Module including a BLE chip BTM-800 (by Rayson) BLE sensor ((Adao, Helmerich, Voigt, Moldenhauer, & Neumann, 2017). The BLE-module was provided together with a sniffer.
The optimum module for a mesh network fulfilling the requirements of the project to receive and forward data packages was developed, composed and provided by our project partner LinTech GmbH.

2.4 *Optimum set up for a network*

2.4.1 *Choice of Network*

The high requirement for communication of each sensor with the twelve neighboring modules to obtain the maximum information about the damping between all modules, were the basis for the choice of a full mesh communication network. The concept was realized and the function was tested with 27 NC2400-modules embedded in fresh and curing concrete.
The number of measurements at a time is limited by the memory of the modules and the maximum size of one data package supported by the protocol of the meshed network. The important information in this case is the receiving node id number, the sending node id numbers and the corresponding RSSI value. This information will then be wrapped up into a data package (Voigt, Helmerich, & Rückschloss, 2017).
If data is transferred to a node close enough to the SmartHub (gateway) then the data is transmitted to the NC2400 in the SmartHub. Advantage of the full mesh network is, that in case one module would not survive any more, the package transfer would go automatically through other nodes.

2.4.2 *Connection to IoT*

The SmartHub (gateway) is equipped with a mobile cellular module in remote areas. This makes it possible to get access to the data via a server from the office or elsewhere, on site or when visiting the contractor.

2.4.3 *What is the optimum communication protocol*

The optimum microwave device passes data over a long distance with minimum need for energy. Usually the data is transferred via a mesh network. The maximum number of data transfers offers a full mesh network. Mesh networks- in difference to tree networks- allow the data transfer in two directions if needed.

2.5 *How can microwave modules serve as a sensor?*

Any electromagnetic source transmits the electromagnetic waves into a 3D space. Usually the electromagnetic wave is used for transmission of data. The transmitter therefor needs energy supply in the range of Milliwatts. Some of this transmitting energy gets lost on the way between transmitter and receiver through the medium as air, dry or moist building material (Voigt, Helmerich, & Rückschloss, 2017).
Due to the swinging of waterdipoles at a frequency of 2,4 GHz we expect a more significant change of signals on their way through the medium between transmitter and receiver. Water dipoles influence the

absorption of energy. A second advantage is the usage of modules in the frequency range of 2.4 GHz are introduced protocolls, e.g. for Bluetooth®, Bluetooth®Low energy or ZigBee, that the mayority of notebooks tablets or mobile phone could receive directly and wireless.

2.6 *What is the role of water dipoles?*

Damping of the electromagnetic signal in moist environment is much higher than in dry medium or even in air. The polar nature of water with the characteristic dipole moment is responsible for the electric properties of the moist material. At a frequency of 2,45 GHz water dipoles start to swing. Given the assumption that the distance and material between transmitter and receiver of two sensor nodes are known it is now possible to find a correlation between the RSSI value and the moisture content between these two sensors (Voigt, Helmerich, & Rückschloss, 2017).
As a first step, the influence of moisture on the Received Signal Strength Indicator (RSSI) between two modules was analyzed. The first module transmits a signal in the range of 2,45 GHz and the second module receives this signal. It is well known that the value of the received signal strength indication (RSSI) depends on the moisture content.
The higher the number of connections between any two modules, the more precise information can be obtained from the network. Finally, mesh networking can be applied to increase the quantitative information.

2.7 *Modelling the moisture damping coefficient*

The damping of the signal strength depends on the damping of an electromagnetic material in air (L_{FS}) and due to the material (L_M). Further influence parameters are the antenna gain of the transmitting ($G_{t\ dBm}$) and receiving antenna ($G_{r\ dBm}$). The losses on the transmitting ($L_{r\ dBm}$) and receiving ($L_{r\ dBm}$) sides as well as the losses during transfer ($-L_{FS}-L_M$) are considered The following equation expresses the resulting link budget (Moldenhauer, 2016):

$$P_{r\,dBm} = P_{t\,dBm} + G_{t\,dBm} - L_{t\,dBm} - L_{FS} - L_M + G_{r\,dBm} - L_{r\,dBm}$$

2.8 *What are the alternative modules*

Common modules, that are based on the highly available Bluetooth®Low Energy standard, emit electromagnetic waves, whose signal strength gets dampened by water molecules.
For first feasibility tests we applied the TI module in order to get the additional information about local moisture from the Sensirion microchip in sand, see



Figure 3. Commercial TI Module with included microchip to determine local moisture.

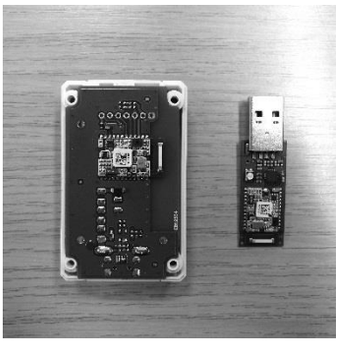


Figure 4. BLE-sensor provided for preliminary tests (provided by Lintech GmbH).

This effect serves as the basis on determining the moisture level in material. We will show how to apply this method in a meshed sensor network for online monitoring.
The BLE-standard does not allow that BLE Modules act as transmitter and receiver in a full-mesh network. Therefore, it was necessary to switch to a final module, produced by NeoCortec that is emitting microwaves in the 2.45 GHz range as well. The NC 2400 was used in the final LinTech-modules for communication and is also placed on the SmartHub.

2.9 *Modelling*

For the visualization of the preliminary RSSI measurements, the maximum likelihood expectation maximization (MLEM) algorithm (Adao, Helmerich, Voigt, Moldenhauer, & Neumann, 2017) was applied. MLEM, a grid was defined that was representative for the investigated area. The assumption was made that the loss of signal strength is linear along the distance between the transmitter and receiver.

3 NETWORK COMMUNICATION

3.1 *Components of the communication network*

For the design of the communication network we established the following requirements:
- Computing unit
- BLE-Interface and WLAN
- Mobil cellular module
- local memory
- NC2400 interface
- power supply
- water proof casing

The main point of the network is the wireless transfer of data. Along with the transmitted and received signal strength, the names of the transmitting and receiving module must be transmitted.

3.2 *SmartHub- the gateway*

To receive the data output of the modules, a gateway was designed. The computing module is an intel Edison, including Bluetooth Low energy and WiFi. The gateway, in our study, has wired connections to power supply and an USB- interface. For external gateways, a solar panel may provide energy together with a battery. A mobile cellular module and an SD-card enable the data transfer to the internet (Voigt, Helmerich, & Rückschloss, 2017).

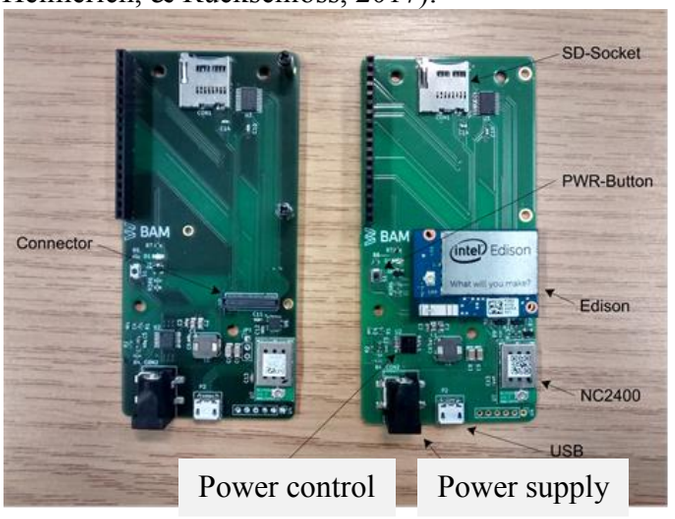


Figure 5. SmartHub (Gateway) carrying the data processing unit, power supply, NC 2400 module. A FONA 3G was added later.

From the SmartHub, the data could be stored in a cloud and accessed from elsewhere.

3.3 *Computing unit*

With the computing unit or platform, you want something fast, relatively easy to use and preferably bringing along as many interfaces as possible on the list. Given the tasks an operating system is necessary in any case. Thus, a popular choice would be a Raspberry Pi, Beagle Bone Black, C.H.I.P. Pro or the Intel Edison as a prototype platform. Basically, any will work fine, but when the choice was made only the Intel Edison already had WiFi and Bluetooth on board. It was also small scale and could be easily integrated into a custom circuit board, which would be necessary anyways since some modules like the mobile cellular module need to be connected externally on another board anyways. (Voigt, Helmerich, & Rückschloss, 2017).

3.4 *How to choose an optimum network setup*

The software architecture of the network is visible from Figure 6 (Helmerich, Voigt, Adao, Moldenhauer, & Köppe, 2018).

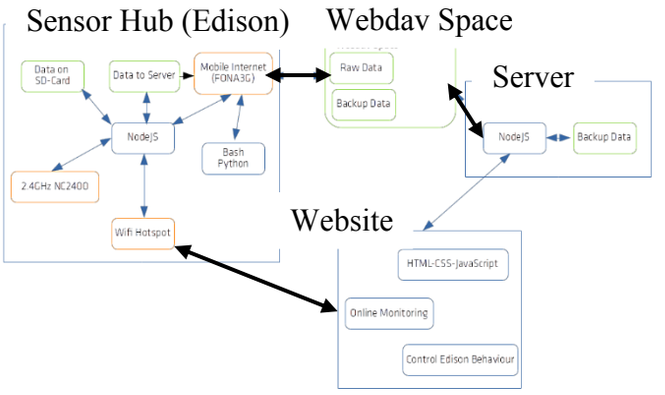


Figure 6. Flow chart of the network architecture.

4 EXPERIMENTAL STUDIES

4.1 *Modules embedded in sand*

Three experimental studies were carried out:

- Embedded modules to estimate the different signal transfer distance in moist sand with different moisture content
- Influence of antenna polarization regarding the wave path
- Influence of the location of the antenna
- Embedding sensors in a massive specimen
- Test of the function of the module network

4.1.1 *Influencing the signal transfer distance*

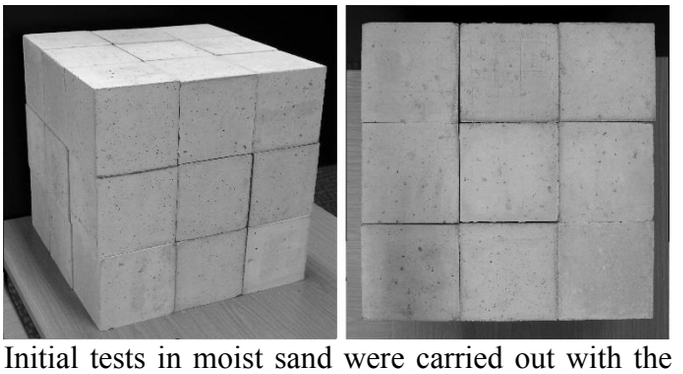


Figure 7. Set-up for preliminary tests with concrete cubes

Initial tests in moist sand were carried out with the module by TI. The advantage was the fact, that a microchip for local moisture measurement was included and the weight difference allowed the precise calibration of the moisture content. The module allowed basic investigation of the maximum reading distance from the embedded sensor depending on the distance between receiver. A mobile phone with the app provided by TI served as the receiver (Köppe, Moldenhauer, Helmerich, Haamkens, & Wittmann, 2016).

The first test series was carried out with a TI-module in sand, the TI-App on a mobile phone with enabled Bluetooth function served as receiver. The RSSI was

analyzed in moist sand. External B®LE-Nets may be reused.

4.1.2 *Visualization of a moist core*

A series of experiments with modules attached to the surface of a bigger cube 45 x 45 x 45 cm, composed of 27 concrete cubes 15 x 15 x 15 cm. Nine cubes were laid in each of the three layers. The middle cube was saturated with water, as seen in the visualization using the MLEM algorithm

4.2 *Experimental studies with externally attached sensors*

To be flexible, experiments were carried out with a series of concrete cubes. Thus, it was possible to compose walls or larger cube by means of the smaller cubes. Dry cubes were than replaced by water saturated cubes to check the ability to visualize the wet cube using processed RSSI data by MLEM, computed tomography.

4.2.1 *Influence of moisture content on the RSSI*

The influence of the moisture was simulated in measurements with one water-saturated cube inside a wall of eight further dry cubes, see Figure 7.

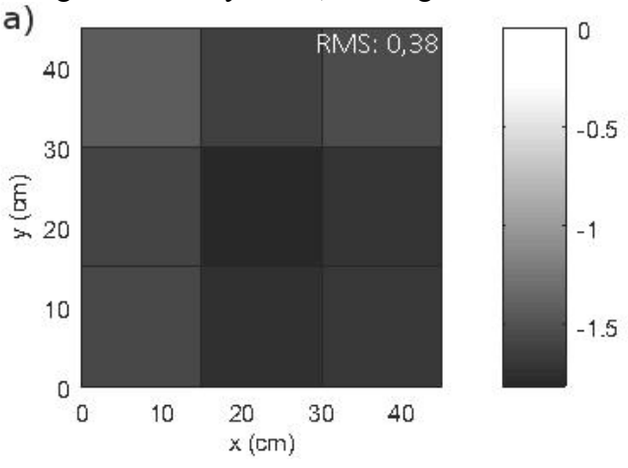
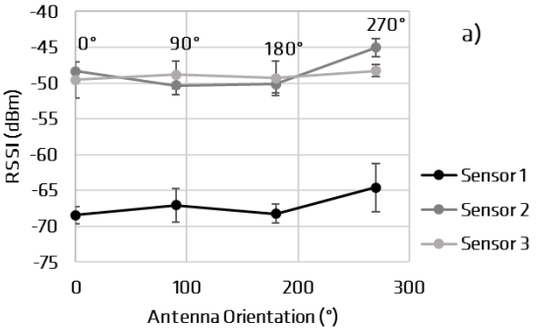


Figure 8. RSSI distribution map calculated with the MLEM algorithm, scale in dBm/m according to measurements on the cube in Figure 5.

The observed change of the moisture content was not directly proportional to the change in RSSI. The change in the RSSI was higher when moisture content was changing above 50% of its initial total weight. Below this level, the change in the RSSI was lower. This means that humidity monitoring with BLE sensors becomes increasingly challenging as water content lowers in concrete (Helmerich, Voigt, Adao, Moldenhauer, & Köppe, 2018).

4.2.2 *Influence of the polarization on the RSSI*

The polarization has an influence on the measured



RSSI, see . The RSSI differs up to 10 % (± 2.5 dBm) depending on the angle of the position of the receiving module. This means, that for all traces of microwaves the antenna orientation must be known and considered in the final analysis of the network. The results show, that the antenna polarization must be well known and needs deeper investigation. The knowledge about the characteristic of any microwave antenna and the correlation with the real moisture content is an important part of the calibration before data analysis.

Figure 9. Influence of the antenna orientation on the RSSI of a 15 cm thick specimen (diagram a).

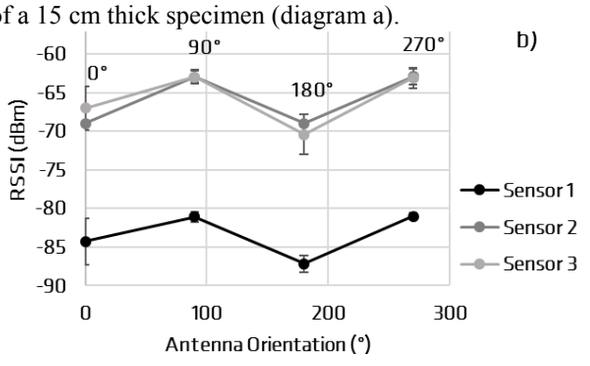


Figure 10. Influence of the antenna orientation on the RSSI of a 45 cm-thick specimen (diagram b).

4.3 *Experimental studies with embedded modules in concrete*

A watertight casing was constructed to safe the sensitive modules from moisture during the casting of concrete and curing. Different variations for embedding the modules into concrete were tested as shown in Figure 11.

For the first tests, the modules were attached to a grid made of a kind of stable fishing line as seen in Figure 12. The modules were fixed to fishing line in three levels with nine modules in each layer.

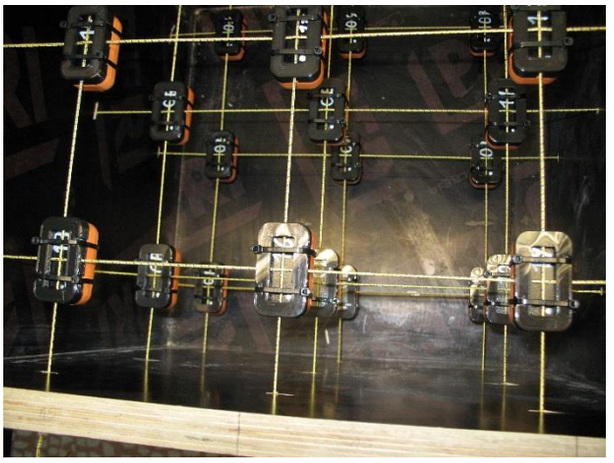


Figure 12. Encased sensors attached to a fishing line before casting the concrete.

4.4 *Localization of modules*

During the tests, as shown above, all modules had the same orientation related to the specimen´s external edges. If modules would be used in practice, it would be probably not economic to attach them to the reinforcement or fix the modules in a grid. The plan is to ad robust modules to the final concrete mixture to reduce the additional workload on construction sites. This procedure would require a localization of the modules after casting and getting additional information about their orientation after hardening of the concrete. In the current stage of research, the localization of microwave sensors is not possible. For preparation for this next step, a study was prepared about concepts for localization.
The localization and obtaining information about the final antenna orientation need adding inertial sensors to the microwave module, consisting of an 3D-accelerometers and 3D-magnetic field sensors.
None the less, ultrawideband (UWB) modules were attached for distance measurements and compared to distance measurements in air without concrete as feasibility measurements for the continuation of the current study.

4.5 *Specimen with embedded microwave modules*

In this basic research, all modules embedded in a specimen will have the same orientation and a regular distribution in three layers. Given, there are 27 microwave modules embedded in a massive structure. It was appointed in our concept that any sensor is transmitting the following information to their closest twelve neighbors: Name of the transmitting module, transmitted signal strength, the addressed module and then the received signal strength is added. In case the

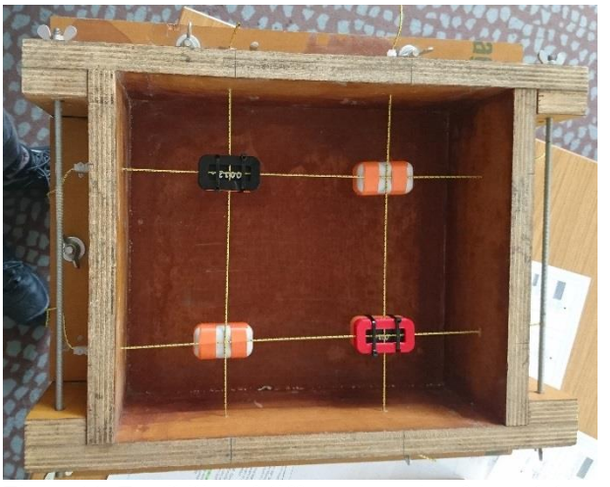


Figure 11. Feasibility of different encasing for modules.

module has received this information from other sensors, the next package will include the information from module x including the transmitted signal strength and the received signal strength from the receiving module y including its name.
As seen in Figure 13, the measurements were started before casting the concrete. The data acquisition worked reliable as described in chapter 3.



Figure 13. Continuous measurement starting before casting.

After casting, the monitoring continued during the curing period of the specimen. The data was made available via a server and could be accessed

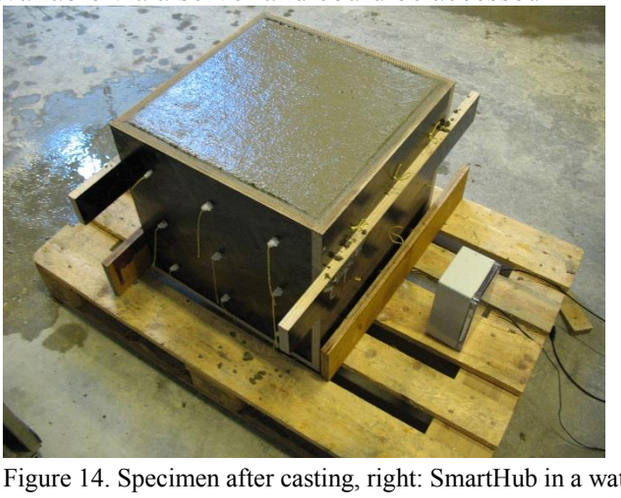


Figure 14. Specimen after casting, right: SmartHub in a water proof casing for data collection from modules inside the concrete specimen.

All measurements were accessible any time via internet. Depending on the potential hazard, the frequency of data acquisition may be adapted to the need. Less data acquisition means longer lifetime of the embedded sensors as the batterie lives longer.

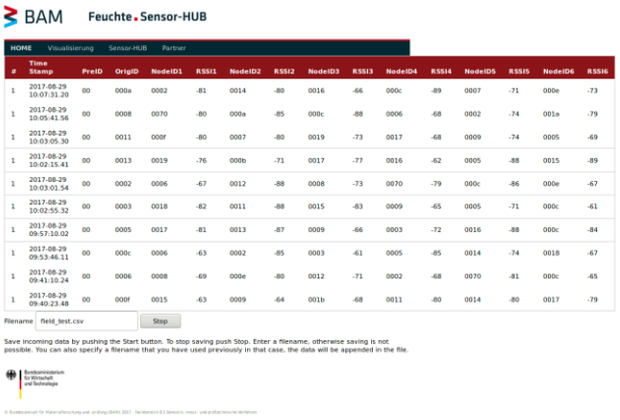


Figure 15. Web-based data access of the SmartHub.

5 FURTHER RESEARCH NEEDS AND OUTLOOK

The results of one year intensive testing and development are promising. So far, we have shown the basic principles on how Bluetooth Low Energy modules can be used to qualitatively show the distribution of moisture in a building material. An Explanation on the meshed sensor network used has been given and a straight forward selection of modules to set up such a network has been presented.

Besides microwave modules in the 2.45 GHz range, UWB modules will be added. The modules will be further equipped with 3D-accelerometers and 3D-magnetic field sensors to characterize the location and orientation of randomly distributed modules.

Next steps should focus on localization of the sensors and visualization of an embedded data set. Final goal is a set of randomly distributed microwave modules, which will communicate with their closest neighbors to provide information about their location and indication about the received signal strength.

As further step the number of modules and measured distances should be increased along with the number of cells in the MLEM-analysis to increase the resolution of the damping of signals distribution.

Ultimately, our goal will be to do a time -lapse of already calibrated distribution images, which can help us continuously monitor and visualize humidity changes. To do this we will need data time series that are long enough to observe humidity variation in concrete.

6 ACKNOWLEDGEMENT

The basic research was carried out together with the SME Lintech GmbH under the ZIM-KOOP program of the German Minister of Economic affairs and Energy (BMWI) supported by the German Society of Engineers (VDI) under contract number 16KN050827. We acknowledge the fruitful cooperation with the LinTech GmbH and the national funding provided by BMWI.

7 REFERENCES

Adao, F. J., Helmerich, R., Voigt, G., Moldenhauer, L., & Neumann, P., Humidity monitoring in concrete using Bluetooth Low Energy sensors *SMAR 2017- Forth Conference on Smart Monitoring, Assessment and Rehabilitation of Civil Structures*.

Helmerich, R., Voigt, G., Adao, F., Moldenhauer, L., & Köppe, E. (2018). *Final Report of the project BT-Feuchte, internal report.* Berlin.

Köppe, E., Moldenhauer, L., Helmerich, R., Haamkens, F., & Wittmann, J. (2016). Moisture measurements in building materials and other structures making use of Bluetooth Low Energy. *Bautechnik*, 747-751.

Moldenhauer, L., Helmerich, R., Köppe, E., & Wittmann, J. (in preparation). Experimental modelling approach for determining the moisture damping exponent of a Bluetooth Low energy signal in mois building material. *Materials today*.

Moldenhauer, L., Helmerich, R., Köppe, E., Haamkens, F., & Wittmann, J. (2017). Experimental feasibility study about moisture in building materials measured with Bluetooth. *Materials Today: Proceedings 4*, 5889-5892.

Shojaifar, A. (2015). Evaluation and Improvement of the RSSI based Localization algorithm, Received signal strengthe indication (RSSI). *Master of Science thesis*. Karlskrona, Sweden: Blekinge Institute of technology.

Stoppel, M., & Fakhouri, A. (2014). Einsatzfähigkeit von eingebetteten RFID-Sensoren für das Bauwerksmonitoring . *Fachtagung Bauwerksdiagnose*. Berlin: DGZfP.

Voigt, G., Helmerich, R., & Rückschloss, M. (September 2017). Determining Moisture in Materials and IOT. *SMAR 2017- Forth Conference on Smart Monitoring, Assessment and Rehabilitation of Civil Structures*.

Maintenance, Safety, Risk, Management and Life-Cycle Performance of Bridges – Powers, Frangopol, Al-Mahaidi & Caprani (Eds)
© 2018 Taylor & Francis Group, London, ISBN 978-1-138-73045-8

Quantifying increases in maintenance costs of prestressed reinforced concrete (PRC) bridges due to increasing fatigue from heavier traffic loads

M. Frizzarin, L. Mancassola, P. Franchetti
Franchetti Group, Rome, Italy

ABSTRACT: Over the life cycle of a road bridge, traffic flow over time can exceed initial predictions, sometimes due to new code allowances. This extra traffic can compromise bridge integrity over time and decrease its service life. The aim of this work is to quantify the extra funds necessary for maintenance interventions over a given time interval to preserve the original lifespan of prestressed reinforced concrete (PRC) bridges. The method begins with the evaluation of the reduction in bridge service life due to increasing fatigue loads. Subsequently, the total sufficiency rating (TSR) parameter is used to estimate the decay of bridge health over its lifespan. Those variables are then translated into an estimate of the funds required for further maintenance interventions over the time period considered. This method will be a useful tool for bridge maintenance managers for estimating maintenance costs.

1 INTRODUCTION

1.1 *Load increases over road bridge life cycles*

Road bridges are designed to resist fatigue induced by traffic passing over them. Design parameters are generally specified by construction rules and/or codes in force in the region where and at the time when a given bridge is built.

Over the last few decades, however, some countries have approved new legislation that increased the allowable weight limits for some types of multi-axle vehicles. Moreover, the number of vehicles circulating in recent years has increased beyond expected thresholds, and this holds also for the number of heavy vehicles in circulation. In many cases, design codes for new bridges have been updated to account for the transit of heavier vehicles.

As a consequence of these changes, however, older bridges are now loaded with heavier and more frequent loads than were anticipated when they were built, and are therefore more vulnerable to fatigue problems. They will therefore require more maintenance interventions than originally anticipated in order to stay in service over their planned lifespans.

1.2 *A method for maintenance cost estimation*

This paper introduces a method to estimate the extra maintenance costs necessary over a given time interval to preserve bridge integrity and counteract fatigue problems despite traffic load increases.

The procedure, valid for highway prestressed concrete bridges, can be summarized as follows:

1. Evaluate the variations in service life due to changes in traffic fatigue loads;

2. Estimate the evolution of bridge health degradation over time for two traffic load conditions, that is, the original theoretical load conditions and the actual load conditions;

3. Evaluate the increase in maintenance costs over the designated time period using the results of the previous assessments steps in order to ensure that the health conditions of the bridge over time remain the same as those expected at the beginning of the life cycle of the structure.

2 PRESTRESSED CONCRETE BRIDGE SERVICE LIFE ESTIMATION

The first step of the method is to assess the theoretical service life of the bridge when it is subject to variations in load conditions. The service life is calculated following Jin-song Zhu et al. (2015), taking cable corrosion and fatigue from traffic loads into account and assuming unchanging environmental conditions.

Cable stress inside the PRC beam due to traffic cyclic loads, $\Delta\sigma$, is first calculated for two load conditions, called scenario 1 (S1) and scenario 2 (S2). These scenarios represent the service load conditions before and after a change in the fatigue loads to which the bridge is subjected, respectively.

Service life estimations also require a measure of the frequency of the heavy loads traveling over the bridge, defined as the ADTT (Average Daily Truck Traffic volume) parameter.

The cumulative number of truck passages, N_f, for the bridge age t (years) is estimated as show in in Eq. (1):

$$N_f(t) = 365 \times ADTT \times \frac{(1+\alpha)^t - 1}{\ln(1+\alpha)} \quad (1)$$

where α is the annual rate of traffic increase.

The number of stress cycles, N, over the entire life cycle of the bridge can be calculated according to the S-N curve in Eq. (2):

$$\lg N = 8.08 - 3.5 \lg S \quad (2)$$

where S is the stress amplitude of the prestressing strand induced by one truck passage, taking into account corrosion and dynamic impact. It is given by Eq. (3):

$$S = \mu \times \lambda \times \Delta\sigma \quad (3)$$

where μ = impact factor and λ = stress concentration factors of prestressing strands induced by corrosion pits, as defined in Eq. (4):

$$\lambda \begin{cases} 1{,}045 + 0{,}00335(t_1 - t_0) & round\ \ pit \\ 1{,}039 + 0{,}00313(t_1 - t_0) & oval\ \ pit \\ 1{,}095 + 0{,}00234(t_1 - t_0) & triangular\ \ pit \end{cases} \quad (4)$$

where t_0 is the reinforcement corrosion period in years and t_1 is the life of the bridge in years.

When $N_f(t) = N$, the bridge life limit has been reached, and, therefore, the theoretical service life of the bridge, t_T, can be predicted by combining Eq. (1) and Eq. (2), as written in Eq. (5):

$$t_T = \frac{\ln\left\{\frac{10^{8.08} \times \ln(1+\alpha)}{365 \times ADTT \times [\mu \times \lambda \times \Delta\sigma]^{3.5}} + 1\right\}}{\ln(1+\alpha)} \quad (5)$$

Therefore, the residual life of the bridge is equal to t_T-t. This procedure is repeated for S1 and S2.

3 TSR AND BRIDGE LIFE EVOULTION

Restoration costs over the life of a bridge life strictly depend on the condition of the structure. An objective quantification of the condition of a bridge is not trivial, especially with respect to future needs. The total sufficiency rating (TSR) parameter method (Pellegrino et al. 2011, Zanini et al. 2016a, c) is therefore applied. This numerical parameter has been developed to give an objective indication of bridge health and the urgency of intervention. It takes into account several key characteristics of the bridge: bridge age, the importance of the structure in the traffic network, traffic intensity, road type, defects in structural and non-structural elements (obtained from bridge inspections), and the importance of those elements in the global functionality of the bridge. As discussed specifically below, knowing the trends in the TSR over time allows for the prediction of the costs of rehabilitating the bridge to a safe state over the various life phases of the structure. TSR values can range from 1 to 100, with the maximum value at the beginning of the life of a bridge. The TSR decreases over time with the decay of the health of the structure. Zanini et al. (2016c) stated that it is appropriate to consider a parabolic decrease trend for the TSR over time, as shown in Eq. (6):

$$TSR(t) = at^2 + bt + c \quad (6)$$

Using the method described in this paper, the goal is to obtain two TSR decay curves for the two different load cases so that they can be compared, i.e. parameters a_1, b_1, and c_1 for S1 and a_2, b_2, and c_2 for S2. They are evaluated with the following boundary conditions:

1. The TSR values for both curves must both start with the same value (the maximum) at the time the bridge came into use, i.e. $TSR_1(0) = TSR_2(0)$ and $c_1 = c_2$;

2. The TSR must go down to 1 at the end of the theoretical service life of the bridge (calculated as shown in the previous section);
3. The actual value of the TSR for S2 can be calculated by collecting data via visual inspection of the bridge elements. This is the third point in the calibration of the S2 life curve;
4. Changes in load conditions usually do not start at the beginning of the life of the bridge, but instead emerge over time. To model these changes, the same decay rate for the two curves is assumed for the first years of bridge life, and so the same first derivative is used for the two curves for $t = 0$ (i.e. $b1=b2$). This boundary condition is expressed in Eqs. (7), (8), and (9).

$$TSR_1'(0) = 2a_1 * 0 + b_1 \quad (7)$$

$$TSR_2'(0) = 2a_2 * 0 + b_2 \quad (8)$$

$$(TSR_1' = b_1) = (TSR_2' = b_2) \quad (9)$$

This last boundary condition allows the S1 life curve to be plotted as well. Figure 1 represents the generic application of the method. The significant points useful in the construction of the curves are indicated in the figure.

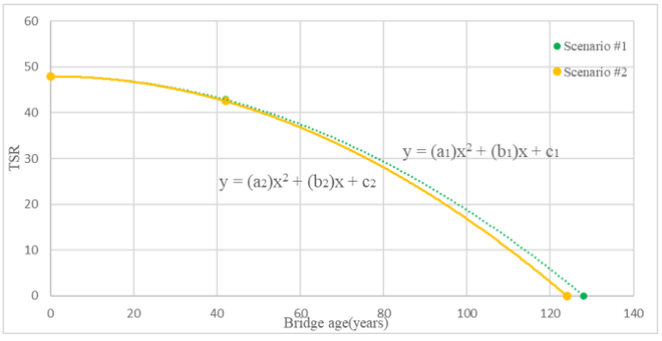


Figure 1. TSR life curves for scenarios 1 and 2.

A comparison of the two life curves of the two different load cases shows that, over any given time interval, the vertical difference (i.e. TSR variation) over time increases because, in the scenario with increased loads, the bridge deteriorates faster (Fig. 2). This incremental difference represents the deterioration of bridge health over the period analyzed due to the increased load increment.

For any given period (t_A-t_B) the loss is quantifiable as:

$$\Delta TSR = \Delta TSR_B - \Delta TSR_A = \left[TSR_2(t_B) - TSR_1(t_B)\right] - \left[TSR_2(t_A) - TSR_1(t_A)\right] \quad (10)$$

4 MAINTENANCE COSTS

The last target of the methodology is to translate the effects of the load increment on bridge health, as calculated with the procedure presented above using the TSR, into a monetary value representing additional retrofit costs.

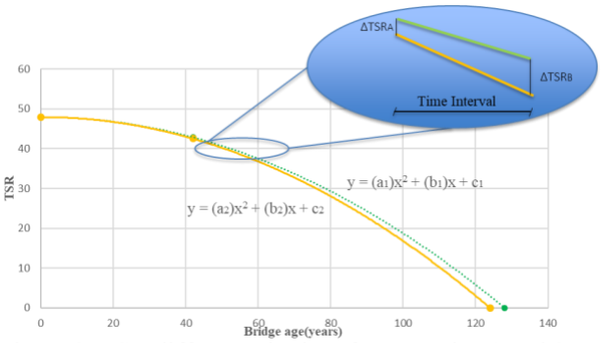


Figure 2. TSR difference in time for scenarios 1 and 2.

Zanini et al. (2016a, b) have examined a set of 150 existing bridges and calibrated a series of curves that correlate unitary maintenance costs (UMC) (€/m²) and the TSR.

For every bridge in the dataset, they evaluated the TSR, and derived unit costs from a comprehensive analysis of maintenance operations performed by the company responsible for the bridge over the last few years. This procedure allowed them to incorporate the maintenance protocols commonly adopted by the owners of the types of structure analyzed and their relative real costs into the BMSs (bridge management systems).

Cost estimates are inherently dependent on the local maintenance costs in effect at a given place and time. In Zanini et al. (2016a and b), the authors use Italian prices, estimations of which were validated by a review of Italian national (A.N.A.S. S.p.A, 2014) and local (Veneto Strade S.p.A, 2014) official unit price lists by assessing each element and CV (*Condition Values*) of each analyzed structure, as well as the unitary costs per square meter related to the sequence of possible maintenance sub-phase operations, and comparing them with information coming from the bridge owners.

Figure 3 represents the dataset used for UMC-TSR curve calibration.

The UMC-fitting equation for reinforced concrete and prestressed reinforced concrete bridges is shown in Eq. (11) below:

$$UMC = 3316.4 - 777.8 \times \ln(TSR) \quad (11)$$

With this equation, it is possible to convert the TSR differences between the two scenarios into monetary units, and quantify the extra maintenance costs due to the change in load scenarios.

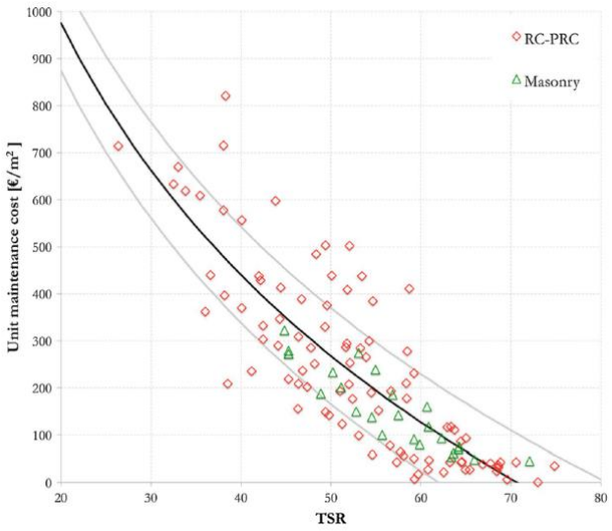


Figure 3. Unit maintenance cost vs. TSR value.

5 CASE STUDY

In the following case study, a prestressed concrete bridge with a simple supported span of 35 m is considered (Fig. 4). The span is composed of 8 prestressed concrete I beams shaped with a paraboloid variation of the height along the length (maximum in the middle, minimum at the bearings). The deck is completed with a cast-in-place concrete slab.



Figure 4. Bridge structure used in the case study.

Two different load conditions are examined. S1 considers a triaxial load with a distance between axes of 1.5 m and a load per axis equal to P = 115 kN. The total load is 345 kN. S2 uses the same configuration but with P = 120 kN (Fig. 5).

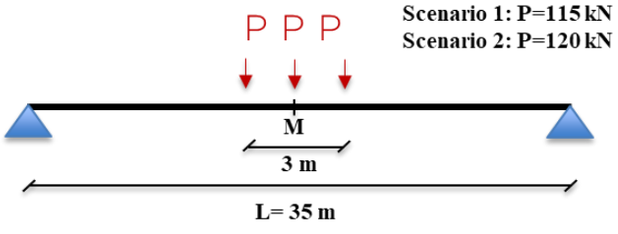
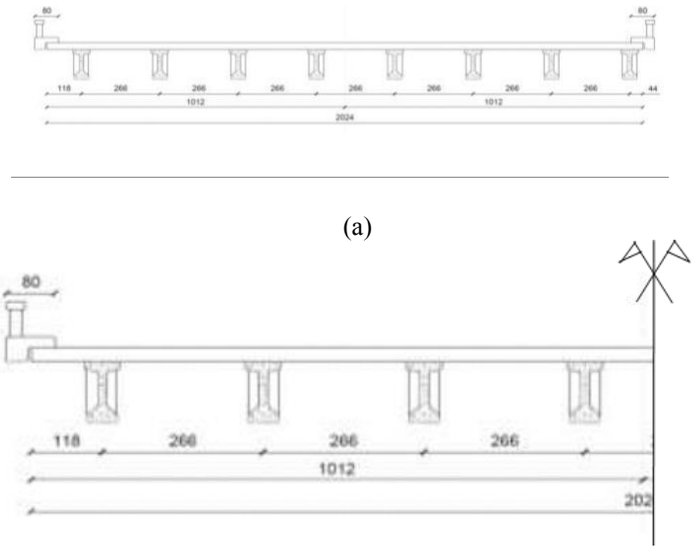


Figure 5. Scheme of bridge structure and load cases.

It is assumed that the two loads represent the service load condition before (S1) and after (S2) a variation in the construction code requirements.
The method considers an impact factor coefficient to amplify the static response to take into account the dynamic effects of traffic loads. In this specific example, and in the absence of specific dynamic tests, the dynamic effects are taken into account by multiplying the static load by a dynamic Factor (DF) defined by the national construction code in effect where the bridge is located:

$$DF = 1 + 1.06\left(\frac{20}{L+50}\right) = 1.2494 \qquad (12)$$

where L is the length of the span (m).



(a)

(b)

Figure 6. (a) bridge middle span section; (b) detail of half of the section.

By multiplying P by DF, the updated values of P become P = 143.7 kN for S1 and P = 149.9 kN for S2. The maximum bending moment in section M is then calculated, and the maximum stresses in the steel cables are derived according to section characteristics (Fig. 6).

For the described example, the maximum cable stress amplitudes in the middle span section are $\Delta\sigma$ = 3.14 MPa for S1 and $\Delta\sigma$= 3.56 MPa for S2.

In order to estimate service life, the frequency of the loads is also needed. This parameter can be estimated with, e.g., the use of weight-in-motion measurements. The frequency of the triaxial load is computed this way using the ADTT parameter mentioned above. In the case study, a 46-day experiment was run. The value of ADTT is calculated as follows:

$$ADTT = \frac{Total\#trucks}{\#days} = \frac{16.000}{46} = 348 \quad (13)$$

N_f for the bridge age t (years) is estimated as shown in Eq. (14):

$$N_f(t) = 365 \times ADTT \times \frac{(1+\alpha)^t - 1}{\ln(1+\alpha)} \quad (14)$$

where α is the annual rate of traffic increase, evaluated as 0.04 for the study case.

The number of stress cycles, N, over the entire life cycle of the bridge can be calculated using the S-N curve, as in Eq. (15):

$$\lg N = 8.08 - 3.5 \lg S \quad (15)$$

where S is given by Eq. (16):

$$S = \mu \times \lambda \times \Delta\sigma \quad (16)$$

with μ = the impact factor previously cited and accounted for through DF, and λ = stress concentration factors of prestressing strands induced by corrosion pits, as defined in Eq. (17):

$$\lambda \begin{cases} 1{,}045 + 0{,}00335(t_1 - t_0) & round \quad pit \\ 1{,}039 + 0{,}00313(t_1 - t_0) & oval \quad pit \\ 1{,}095 + 0{,}00234(t_1 - t_0) & triangular \quad pit \end{cases} \quad (17)$$

where t_0 is the reinforcement corrosion period in years and t_1 is the life of the bridge in years.

When $N_f(t)=N$, the bridge life limit has been reached, and therefore the theoretical service life of the bridge can be predicted by Eq. (18):

$$t_T = \frac{\ln\left\{\frac{10^{8.08} \times \ln(1+\alpha)}{365 \times ADTT \times [\mu \times \lambda \times \Delta\sigma]^{3.5}} + 1\right\}}{\ln(1+\alpha)} \quad (18)$$

In the case study, the same environmental conditions are considered for S1 and S2: round pits and $t_1=t_0$. The service life of the bridge in the two different load cases is estimated as t_T = 151 years for S1 and t_T = 147 years for S2. The incremental change in traffic is responsible for a theoretical bridge service life reduction of 4 years.

5.1 *TSR calculation*

The procedure starts with the calculation of the TSR of the structure at the present time, based on inspection reports available for the structure.

Visible elements of the bridge examined are beams, slabs, piers, pier top beams, bearings and joints. Non-visible/not-inspected elements are the pavement, safety barriers and the drainage system. Barely visible elements, e.g. pier foundations or waterproofing of the deck, are not considered in this method (i.e. their weight W is zero). The bridge is situated along a highway (RT = 0.80), with long deviations or unsuitable alternative roads (NBI = 0.96). It is a very busy roadway (TI = 0.90). The bridge is 43 years old (AF = 1). All other parameters necessary for the TSR calculation are listed in Tables 1 and 2 (*Condition Factor CF, Condition Value CV, Weight of the Element W*). Table 1 illustrates the main parameters for the TSR calculation for the bridge when it opened, and Table 2 refers to 2016, the year inspections were made.

Table 1. TSR method parameters for new bridge

Visible Elements	CF	CV	W
Beams	1	100	12
Piers	1	100	12
Pier top beams	1	100	10
Slabs	1	100	10
Bearings	1	100	10
Joints	1	100	6
Non-Visible Elements			
	CF	CV	W
Pavement	1	100	4
Drainage system	1	100	6
Safety barriers	1	100	4
Pier foundations	1	100	0

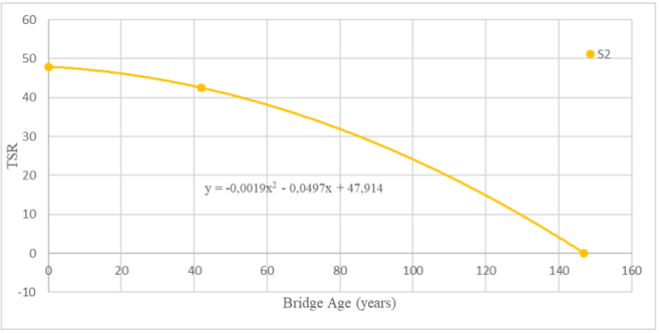
Table 2. TSR method parameters for bridge in 2016

Visible Elements			
	CF	CV	W
Beams	1	100	12
Piers	2	75	12
Pier top beams	1	100	10
Slabs	1	100	10
Bearings	2	75	10
Joints	1	100	6
Non-Visible Elements			
	CF	CV	W
Pavement	3	50	4
Drainage system	3	50	6
Safety barriers	3	50	4
Pier foundations	3	50	0

CV and CF for the various bridge elements are attributed based on the evidence from that inspection.

The TSR_0 value obtained is 47.914, while TSR_2 (2016) is 42.512. With those values, the parabolic

decay curve for S2 can be calibrated. It is shown in Figure 7.
b_1, c_1 and the service life of 151 years, as well as the



S1 curve can be calibrated, as shown in Fig. 8.

Figure 7. Life decay curve for scenario 2.

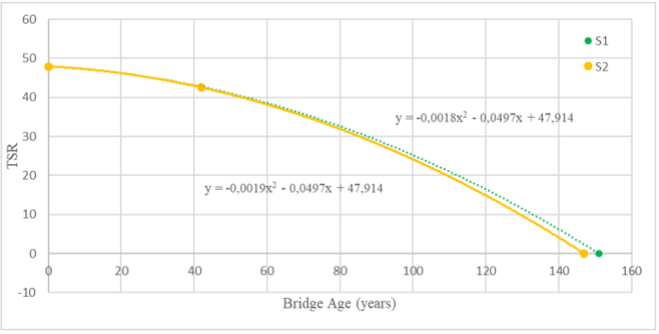


Figure 8. Life decay curve for scenarios 1 and 2.

The authors have taken into account the fact that service life calculations have been made for different loads over the whole life of the structure. However, decay is a non-linear phenomenon that hastens in the last few years of the life of a bridge (Zanini et al. 2016c). Because of this, if a change in load conditions happens in the first few decades of the life of a bridge and it is not a significant fraction of the load intensity/frequency itself, the procedure is basically insensitive to the effective starting time of the change in bridge loads. What matters is the variation in time of the TSR parameter, not its absolute value.

5.2 *TSR variations*

A period of 30 years, from t_A= 41 years (2015) to t_B = 70 years (2044), is considered and shown in Figure 9. The period corresponds to the concession period of the bridge.

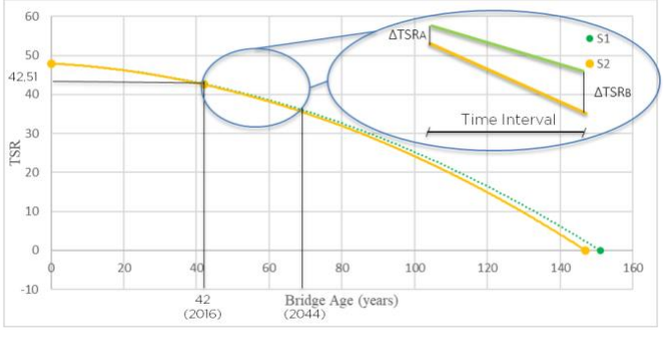


Figure 9. Bridge decay comparison between S1 and S2 over a 30-year period.

The equations of the two curves have been already calculated as previously explained, so their TSR values can be extrapolated for the desired time interval. Results are summarized in Table 3.
Over the 30 years of the grant, the load increment will cause a loss of 0.335 in the TSR parameter.

Table 3. TSR values and variations over the time interval considered.

	TSR	
	t_A	t_B
Scenario 1	42.701	35.751
Scenario 2	42.512	35.227
Difference ΔTSR_{1i-2i}	0.189	0.524
Global Diff. ΔTSR		0.335

5.3 *Cost estimates*

Using Equation (11), all TSR values are converted into monetary units. Results are shown in Table 4.

Table 4. UMC values corresponding to TSR values according to Eq. 12.

	UMC (€/m²)	
	t_A	t_B
Scenario 1	396.3	534.53
Scenario 2	399.81	546.32
Difference $(€/m^2)_{2i-1i}$	3.44	11.49
Additional maintenance cost (€/m²)		8.05

The additional maintenance budget required to cope with the extra traffic load increment is then quantified as 8.05 €/m². Since the bridge surface is 708.4 m² (20.24 m wide and 35 m long), the total amount is 5,702 €.

6 CONCLUSIONS

The method presented in this paper incorporates the results of recent research on the subject of bridge life-cycle analysis and the economic evaluation of bridge maintenance in order to yield an objective method of quantifying restoration costs so as to save bridges from additional damage and deterioration caused by increasing load conditions over their lifespans. The method is applicable to prestressed reinforced concrete bridges, and its precision is strictly correlated with the number and level of detail of the inspections performed during bridges' life cycles.

The proposed method could be a useful tool for bridge managers to use to estimate possible variations in the maintenance costs of bridges for which they are responsible during a given concession period.
This work could be expanded with the creation of databases of parametric costs to be applied in different countries all over the world. This additional data could enhance the calibration of the correlation curves used in this paper, which would allow the proposed method to become more standardized. The authors are also extending the method to steel structures, which suffer from well-known vulnerabilities to traffic cyclic loads.

7 REFERENCES

Pellegrino, C., Pipinato, A., Modena, C., 2011. A simplified management procedure for bridge network maintenance. Structure and Infrastructure Engineering, 7(5): 341-351.

Zanini, M.A., Faleschini, F., Pellegrino, C., 2016a. Cost analysis for maintenance and seismic retrofit of existing bridges. Structure and Infrastructure Engineering, January 2016.

Zanini, M.A., Hofer, L., Faleschini, F., Franchetti, P., Pellegrino, C., 2016b. Maintenance and seismic retrofit cost assessment of existing bridges. Maintenance, Monitoring, Safety, Risk and Resilience of Bridges and Bridge Networks. Bittencourt, Frangopol & Beck (Eds).

Zanini, M.A., Faleschini, F., Pellegrino, C., 2016c. Bridge residual service-life prediction through Bayesian visual inspection and data updating. Structure and Infrastructure Engineering, September 2016.

Zhu, J.S., Huang, F.M., Guo, T., Song, Y.H., 2015. Residual life evaluation of prestressed reinforced concrete highway bridges under coupled corrosion-fatigue actions. Advanced Steel Construction, 11(3): 372-382.

Maintenance, Safety, Risk, Management and Life-Cycle Performance of Bridges – Powers, Frangopol, Al-Mahaidi & Caprani (Eds)
© 2018 Taylor & Francis Group, London, ISBN 978-1-138-73045-8

Assessment of concrete pylon of cable stayed bridge with floating crane collision

Jae-Hoon Lee
Professor, Yeungnam University, Korea

Seong-Cheol Lee
Assistant Professor, Kyungpook National University, Korea

Ho-Young Kim
Ph. D Student, Yeungnam University, Korea

SungKyun Park
Specialist, COWI Korea, Korea

ABSTRACT: This paper introduces structural assessment and strengthening of a rein forced concrete pylon which experienced torsional deformation. The pylon with a hexagonal hollow section is the lower part of the cable-stayed bridge under construction. As a floating crane hit the cantilever end of the super-structure of the bridge constructed through cantilever erection method, torsional deformation of 1.2 degree occurred along the pylon. After the collision, torsional cracks were observed on the outer and inner surfaces of the hollow pylon. The structural assessment of the pylon was conducted with nonlinear finite element analysis to simulate structural behavior. The result showed that yields of transverse and longitudinal reinforcements were not significant when the floating crane collided. After the super-structure of the bridge was restored to the original position, there were residual strains in the reinforcements, but stresses almost returned to near the origin. Therefore, it could be concluded that there were no significant damage to the pylon. In spite of little deterioration on the structural capacity, the client decided to strengthen the pylon by wrapping it with GFRP sheets after repairing cracks.

1 INSTRUCTION

The steel-composite cable-stayed bridge with 1,305 m span experienced floating crane collision. Super-structure of the bridge consists of Edge-type and I-type of 2 steel-composite for the main girder, and H-type precast concrete structure for the deck. The cable was Multi Strand Cable with 2 side arrangement. For the foundation, cast-in-place concrete pile was applied.

The accident occurred when the super-structure of the bridge was collided with the floating crane which was working at the port in the construction site. As a result, the super-structure was deformed due to the lateral load. Meanwhile, the pylon was cracked due to torsional deformation. After the collision, the super-structure and pylon were restored to the original position. And then, it was observed that inner and outer surfaces of the lower part of the pylon were diagonally cracked due to the torsion. Because of the damage on the pylon, it was required to investigate safety of the bridge not only during the construction but also under the service. Therefore, this study focuses on the evaluation of the structural safety of the pylon damaged by the collision, at the present time as well as after the construction.

2 PYLON OF CABLE-STAYED BRIDGE

The pylon where the accident occurred was H-type reinforced concrete structure. Due to the torsion caused by the collision, cracks occurred from the bottom to 16 m height among the total height of 90.5m. The foundation of the pylon was 16, 24, and 4.5 m in the longitudinal, transverse, and height directions, respectively. Fig. 1 shows the dimension of the cross-section at the bottom of the pylon. As presented in the figure, the pylon had a hexagonal hollow section with a dimension of 5 and 10 m in the longitudinal and transverse directions, respectively, consisting of walls with a thickness of 1 m.

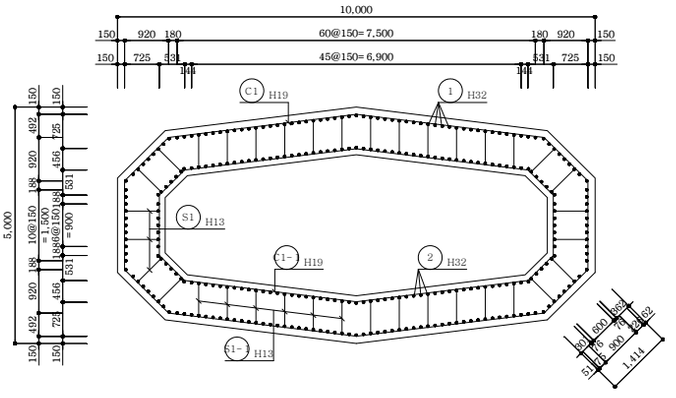


Figure 1. Dimension of the cross-section at the bottom of the pylon

3 DAMAGE STATUS

During the construction of the cable-stayed bridge, the floating crane collided with the super-structure as shown in Fig. 2. The collision occurred at the distance of 62 m from the pylon. Because of the accident, the lateral displacement of 1.75m occurred at the other end of the super-structures (① in Fig. 3) while deviation of 90 cm at the key-segment as presented in Fig 2(b), (c), and (d). In addition, lots of torsional cracks occurred at the lower part of the pylon (② in Fig. 3). After restoring the bridge to the original position, the maximum crack width was measured to 1.4 mm. Fortunately, no damage was found at the connection between the pylon and the super-structure.



(a) Floating crane(800ton)



(b) Super-structure displacement



(c) Deviation at the key-seg



(d) Deviation at the key-seg

Figure 2. Damage status after the crane collision

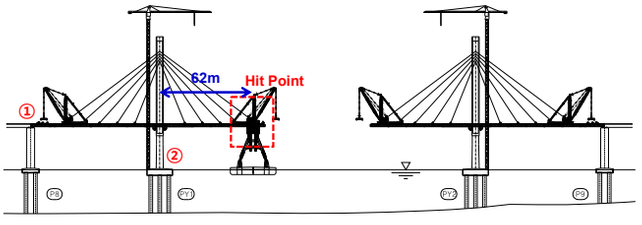


Figure 3. Schematic of the crane collision

4 FIELD INVESTIGATION OF THE STRUCTURE

4.1 *The pylon*

The pylon subjected to the collision was investigated in detail after setting temporary facilities on the inside and outside of the pylon.

(1) Lower part of the pylon

On the inner and outer surface of the pylon, many cracks with an inclination of about 45 degrees were observed because of torsion due to the collision of the floating crane. The crack width ranged from 0.1 mm to 1.4 mm.

(2) Leg part of the pylon

In the leg part of the pylon, the cable anchorage was generally in good condition with little damage; only several cracks less than 0.2 mm width were observed inside. It was inferred that the cracks were caused by concrete shrinkage. It has been decided to have appropriate maintenance.

4.2 *Bridge deck*

The top surface of the bridge deck was generally in good condition, but some cracks with 0.1 mm width were observed in some sections. In addition, breakage and peeling occurred on the top surface of right side deck of the pylon. It is considered that the cracks on the deck were caused by concrete shrinkage, not by the collision with the floating crane.

4.3 *Support*

At the time of the collision with the floating crane, the vertical support was deviated about 150 mm, which exceeded the allowable limit of 50 mm.

5 SAFETY EVALUATION OF THE PYLON

5.1 *Summary of the analysis*

3D nonlinear finite element analysis was conducted to simulate the structural behavior of the pylon. The analysis employed VecTor 3[(1)] which was a nonlinear analysis program using 8-nodes or 6 nodes solid elements. Since VecTor 3 is based on the Modified Compression Field Theory (MCFT), it is well known that nonlinear behavior of reinforced concrete structures is predicted in good accuracy. From the analysis results, the structural behavior such as loading capacity, deformation, and crack patterns can be investigated in detail.

In order to consider the effect of the collision on the structural behavior of the pylon, 3D nonlinear finite element analysis was conducted through three phases; 1) analysis for the torsion dueto the collision, 2) analysis for the restoration, and 3) analysis for the structural behavior under lateral load. In order to evaluate original structural capacity, analysis without any damage was conducted with lateral load as well.

5.2 *FE Model of the structure*

To model the pylon more, the cross-section was divided into rectangles and triangles as shown in Fig. 4. As presented in Fig. 5, the pylon was modelled with total 8 layers; each layer had a height of 2 m. Longitudinal and transverse reinforcements embedded in the pylon were modelled as smeared through the designated concrete elements. Since the foundation was considerably stiff, the bottom of the pylon was fixed in the model.

In addition to the pylon, the super-structure above the pylon was also modelled. Consequently, the actual

collision with the floating crane could be described through the displacement load applied at the location where the floating crane collided, as presented in Fig. 6 which was so similar to the actual situation as presented in Fig. 7.

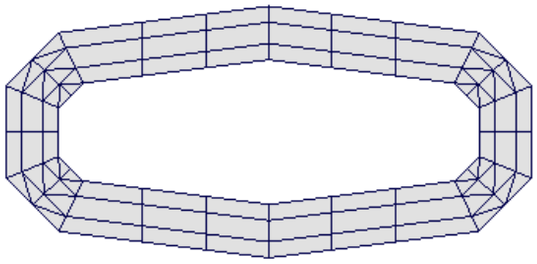


Figure 4. FE Model of the cross-section of the pylon

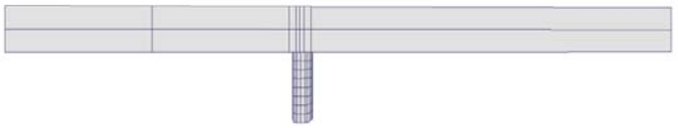


Figure 5. Front view of the FE model for the structure

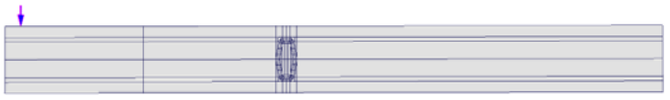


Figure 6. Plan view of the FE model for the structure

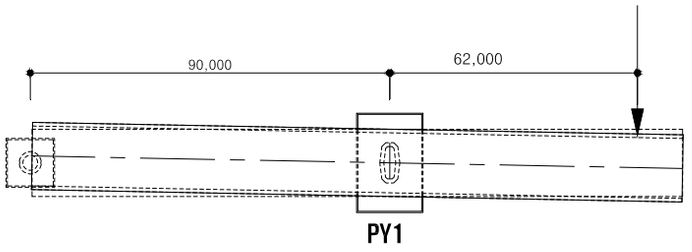


Figure 7. Location of the floating crane collision

5.3 *Analysis results*

(1) Torsional behavior of the pylon

Torsional behavior of the pylon predicted by the analysis has been presented in Fig. 8. As can be seen in the figure, the pylon had sufficient torsional stiffness before the initial cracking. Once the pylon was cracked due to the torsion, the torsional stiffness decreased and the torsional moment increased as the torsional angle increased. This is a kind of the typical torsional behavior of reinforced concrete members. It is noted that the torsional moment corresponding to the ultimate state in the design code was 239,493 kN-m. As can be seen in the figure, the torsional moment caused by the collision was evaluated to about 190,000 kN-m. Therefore, since the torsional moment caused by the collision was smaller than the torsional moment corresponding to the design criteria, it can be concluded that torsional failure was not reached by the collision.

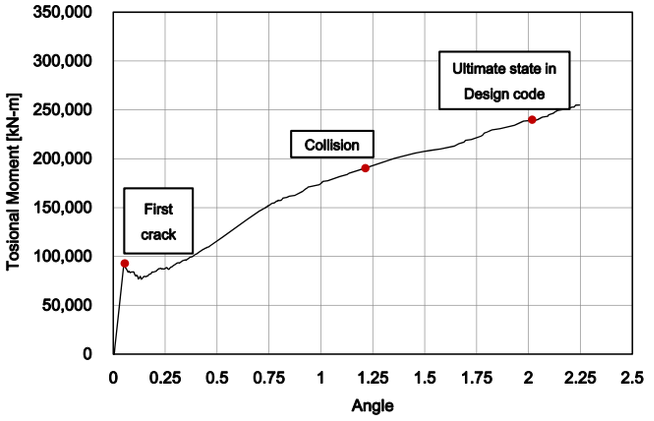
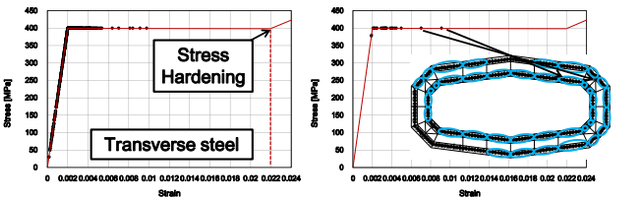


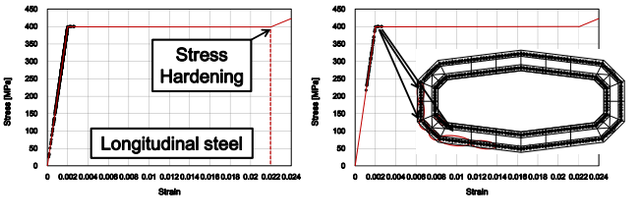
Figure 8. Torsional behavior of the pylon

(2) State of the reinforcing bars in the pylon

Figure 9 shows the stress and strains of the transverse and axial reinforcements immediately after the collision. Immediately after the collision, it was predicted that the maximum deformation of the reinforcing bars occurred at a height of 8 ~ 10 m from the bottom of the pylon. In this section, the strains reached up to 0.00977 and 0.00255 for transverse and axial reinforcements, respectively. Since the maximum strains were only 44% and 12% of the strains to initiate the strain hardening for SD400 reinforcing bars, it could be seen that damage on the reinforcements was not significant.



(a) Stress-strain(transverse) (b) Yielding point(transverse)

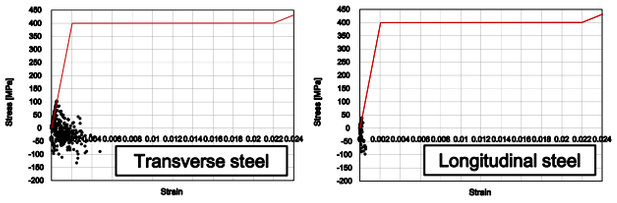


(c) Stress-strain(longitudinal) (d) Yielding point(longitudinal)

Figure 9. Stress-strain states of reinforcements upon the collision

Fig. 10 shows the stresses and strains in each reinforcing bar after the restoration of the pylon from the deformation due to the collision. As shown in the figure, the reinforcing bars which experienced yielding upon the collapse were restored to small residual stress and

strain after the restoration. However, some reinforcing bars showed relatively considerable residual stress and strain.



(a) Transverse steel (b) Longitudinal steel

Figure 10. Stress-strain states of reinforcements after the restoration

(3) Structural capacity against flexural moment

After the construction is completed, the torsional behavior of the pylon is not considerable any more. Instead, flexural and shear behaviors are main consideration. Therefore, it is important to investigate the structural behavior of the pylon under flexure and shear considering the damage caused by the collision. Fig. 11 shows the analysis results for the flexural moment-displacement responses of the pylon with or without the damage. As presented in the figure, the typical flexural behavior was predicted; a high stiffness before the initial cracking, followed by decrease in the stiffness due to flexural cracks, and increase in the flexural strength as the lateral displacement increases. The analysis also showed that the flexural strength of the pylon damaged by the collision was 470,625 kN-m, which was only 5% lower than that of the pylon with no damage. Therefore, it can be seen that the effect of the damage was not significant on the flexural strength of the pylon.

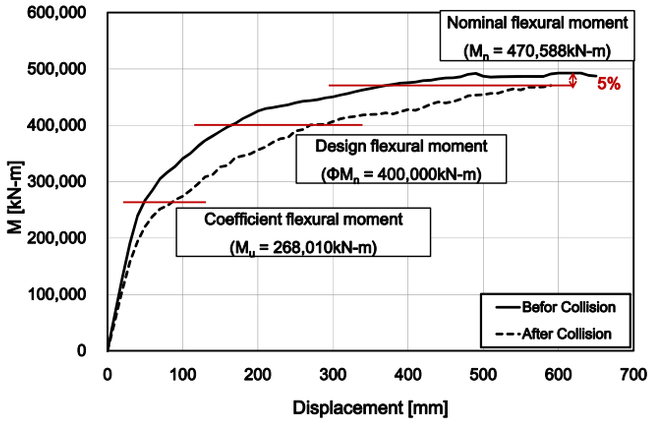


Figure 11. Flexural performance of pylon

In addition, the nominal bending strength calculated by simple theory according to the design code[2] is almost the same as 470,588kN-m, and the design nominal bending strength is about 1.18 times larger than 400,000kN-m and is about 1.76 times larger than the coefficient bending strength 268,010kN-m appear.

Therefore, although the pylon was damaged due to the torsional moment caused by the collision with the floating crane, it was evaluated that the flexural strength of the damaged pylon considering safety factor ($\emptyset M_n$) exceeds the design flexural moment with factored loads (M_u). Consequently, it can be concluded that there is no serious problem on the structural safety of the pylon in spite of the damage.

6 CONCLUSION

(1) Due to the torsion caused by the collision with the floating crane, it was analyzed that the transverse and axial reinforcements in the pylon experienced the yielding. However, since the maximum strain was much less than the strain to initiate the strain hardening, it can be concluded that structural safety of the pylon was not significantly deteriorated by the collision.

(2) The flexural strength of the pylon damaged by the collision was interpreted to be about 5% less than that of undamaged pylon. The flexural strength of the damaged pylon was evaluated to 1.8 times the design flexural moment due to factored loads.

(3) The maximum bending moment generated during the hypothesis is within the elastic range of the member and it is considered that there is no additional cracking of the member due to the progress of the process.

(4) As the pylon was cracked by the collision, it was decided to apply glass fiber-reinforced polymer sheets on the inner and outer surfaces of the pylon so that the durability and structural capacity of the pylon could be enhanced.

7 REFERENCE

(1) Vecchio, VecTor 3 analysis program, University of Toronto, Canada.

(2) Ministry of Land, Infrastructure and Transport, Korea Institute of Bridge and Structural Engineers, Korea Highway Bridge Design Code (LSD), 2015.

Maintenance, Safety, Risk, Management and Life-Cycle Performance of Bridges – Powers, Frangopol, Al-Mahaidi & Caprani (Eds)
© 2018 Taylor & Francis Group, London, ISBN 978-1-138-73045-8

Parametric analysis of dissipative rocking superstructures

Z. Chegini
WSP Opus Intl. Consultants, Christchurch, New Zealand
A. Palermo
University of Canterbury, Christchurch, New Zealand

ABSTRACT: A hybrid connection has been developed for prefabricated concrete bridge superstructures by combining unbonded longitudinal post-tensioning and axial mild steel dissipaters. The connection aims to increase energy dissipation, introduce self-centering and improve overall structural performance during seismic loading. It can be used as an alternative to seismic isolation, resulting in reduced maintenance costs. The connection was tested in a large-scale precast concrete bridge specimen at the University of Canterbury. The specimen exhibited a desirable flag-shape hysteretic response when subjected to transverse quasi-static cyclic loading. The experimental results were extrapolated to various bridge geometries and design target values through parametric analysis. The effects of superstructure beam type, length of bridge, number of spans and target ductility on the transverse force-displacement relationship of the superstructure configurations was investigated. The structures were designed using a direct displacement-based (DDBD) method and analyzed with a modified version of the revised monolithic beam analogy (rMBA). The results show that higher target ductility values decrease the superstructures' secant stiffness, increase their fundamental period and significantly reduce the base shear and necessary reinforcement ratio (for both mild steel dissipaters and post-tensioning). For low ductility levels (μ=1) greater superstructures lengths generally result in higher ratios of base shear demand to seismic weight due to their larger seismic mass. However, as target ductility levels increase, the secant stiffness of the structures decrease, and greater superstructure lengths result in a decrease in the ratio of base shear demand to seismic weight. Finally, an expression to find the equivalent viscous damping in dissipative rocking superstructures was found by calibrating results from the parametric analysis to theoretical values.

1 INTRODUCTION

Prefabrication of bridge superstructures is a popular method which offers several advantages such as reduced construction time, higher construction quality and improved work-zone safety. Traditionally, a concrete bridge superstructure is either designed to be monolithic with the cap beam and abutments through moment resisting connections or is simply supported on bearings. Numerous instances of failure of simply supported bridge superstructures subjected to seismic loading have been observed, including unseating of the superstructure (Kawashima & Unjoh 1997, Zhiqiang & Lee 2009, Buckle et al. 2012, Schanack et al. 2012, Palermo et al. 2012) and damage to the cap beam or abutment shear keys (Silva et al. 2009). Such forms of failure can be mitigated to a certain extent by increasing the seating length and connecting adjacent sections of the superstructure with steel linkages (Wood & Chapman 2013). However, these solutions do not eliminate the fundamental issue of residual displacements in simply supported superstructures under transverse seismic loading.

In this paper, a connection is proposed between simply supported superstructure spans which combines unbonded longitudinal post-tensioning and mild steel dissipaters to improve the behavior of simply supported superstructures under transverse seismic loading. The post-tensioning provides a self-centering capability by reducing the residual deformation of the superstructure, which in combination with the properties of the axial mild steel dissipaters, creates a hysteretic behavior characterized by flag-shaped loops in the connection (Figure 1). Such 'hybrid' connections were originally developed for use in precast concrete frames (Priestley et al. 1999) and later used in shear walls and bridge piers (Mander & Cheng 1997, Palermo et al. 2007, Marriott et al. 2009,

White et al. 2016). Unlike traditional monolithic moment-resisting connections, which are designed to provide ductility and dissipation through plastic hinging, hybrid connections allow for the inelastic demand to be accommodated outside the precast elements (in the mild steel or dissipative devices) while other parts of the seismic-resisting structure remain elastic and relatively intact. When used between spans of a simply supported bridge superstructure, hybrid connections can be used to reduce residual displacements, introduce dissipation, and in general improve the performance of the bridge under transverse seismic loading.

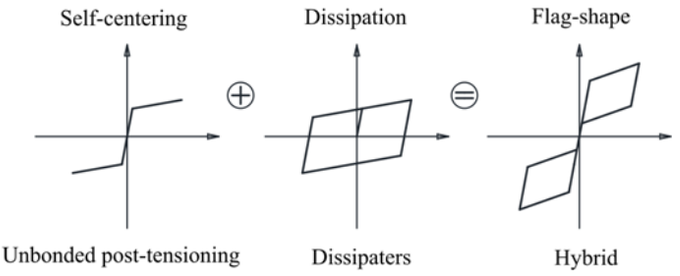


Figure 1. Flag-shape hysteresis loop of a hybrid connection

This paper presents results from quasi-static cyclic testing on a 1:3 scale, 2-span precast concrete bridge specimen featuring hybrid connections in the superstructure, followed by finding from a parametric analysis on several superstructure configurations which were performed to extrapolate the experimental results to various geometries.

2 EXPERIMENTAL TESTING

2.1 *Prototype bridge*

The prototype structure which the test specimen was based on was representative of a typical short-span concrete highway bridge in New Zealand (Figure 2). A span length of 13m and a width of 10.35m (one lane in each direction) was considered for this bridge. The superstructure beams comprised standard double hollow-core sections as described in the NZTA Research Report 364 (NZTA 2008), which are typically manufactured separately and assembled on-site using a combination of transverse post-tensioning and grout. The substructure consisted of two seat-type abutments and a central pier and cap combination. The center of mass of the super structure was located 7m above the base of the pier. The footings shown are for indicative purposes only.

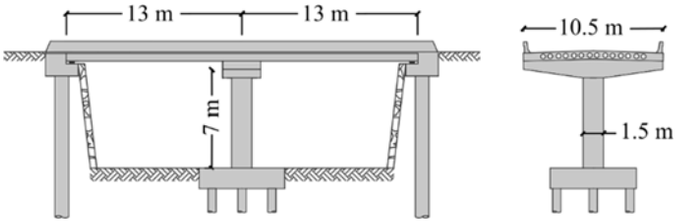


Figure 2. Prototype bridge on which the test specimen was based on

The prototype bridge was designed according to the New Zealand Standard (NZS 2004), and was assumed to be of a 'normal' importance level and located in Christchurch with a seismic zone factor of 0.3, soil type C and no near field effects. A target ductility of 3 and target drift of %2.7 was adopted for its design.

2.2 *Specimen details*

The test specimen was a 1:3 scaled model of the prototype bridge. It consisted of abutments supported on two square columns which represented the abutment piles, a foundation for the central pier, a central circular pier, a rectangular cap beam and two hollow core superstructure spans, all which were prefabricated off-site and assembled in the laboratory. In order to facilitate assembly of the superstructure the hollow-core slabs were cast as one piece rather than in smaller segments. PVC pipes were used to provide the hollow ducts (cores) in the slabs.

The abutment piles were supported by steel foundations, and connected to the abutments with grouted dowels. To decrease the tensile stresses in the concrete and increase the bending moment capacity of the piles, a 32mm MacAlloy bar was used to post-tension each pile to 150kN. The piles were braced using 25mm diameter Reidbraces in order to further increase the lateral stiffness of the abutment-pile combination.

The central pier, concrete foundation and cap beam were post-tensioned together to 700kN using a 40mm MacAlloy bar. Two 25mm grouted dowel bars connected the pier and cap beam to prevent their relative rotation. At the bottom of the pier four 25mm threaded bars mounted on brackets on the pier and grouted in the foundation provided a similar restraint.

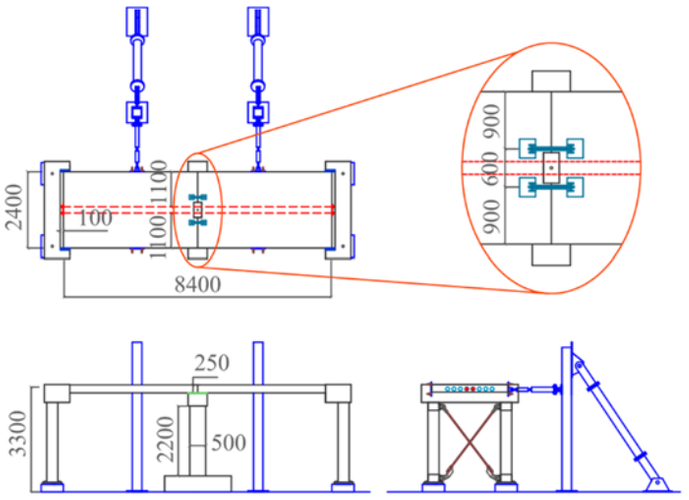


Figure 3. Details of test specimen

The superstructure was simply supported on the abutments and cap beam. The external shear keys on the abutments provided lateral restraint for the superstructure in the transverse direction. Elastomeric bearings of type IRHD60 with a thickness of 25mm were placed vertically between each superstructure segment and the abutment shear keys to prevent stress concentration and concrete damage. The corners of the superstructure spans were protected from similar effects with 6mm armoring plates installed before pouring and connected to the concrete using steel studs. Since the aim of testing was to study the response of the superstructure to transverse loading, the superstructure was isolated from the cap beam using 20mm ultra-high molecular weight polyethylene (UHWMPE) bearing plates which were in contact with the protective armoring steel of the superstructure.

The superstructure was post-tensioned longitudinally using two 15.2mm VSL post-tensioning tendons which passed through the two central ducts in the concrete section. A 100mm gap separated the end of each span from its adjacent abutment to allow rotation of the superstructure without engaging the abutments. In practice, this gap can be bridged using methods similar to those used in deck joints, such as engineered cementitious composite link slabs (Kim et al. 2004, Lepech & Li 2009), which can undergo considerable deformations with minimal damage.

The axial dissipaters were manufactured from G300 mild steel rods, and were reduced to a cruciform with a cross sectional area of 215mm^2. The dissipaters were confined in a steel tube strengthened with stiffeners to prevent buckling. Two dissipaters were used for testing, which were connected to the top surface of the superstructure using a combination of steel brackets and bolts.

Several tests were performed each using different values of post-tensioning force in the superstructure and specifications of axial dissipaters.

This paper presents the results of two tests, the first featuring axial dissipaters between the superstructure spans and second test lacking mild steel dissipative devices.



Figure 4. View of test specimen in the laboratory

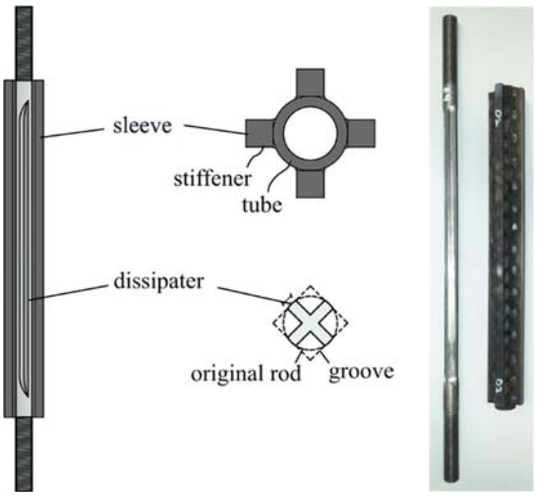


Figure 5. Axial dissipaters used in testing

The initial post-tensioning force in the superstructure in both tests was close to 150kN, however this value is slightly lower in the second test due to loss of post-tensioning

2.3 *Loading protocol*

A displacement-controlled cyclic loading protocol in accordance with ACI 2008 was used for testing, and is shown in Figure 6. Transverse loading was applied at the superstructure level using two actuators with a maximum capacity of 500kN which were mounted onto reaction frames. The force was applied to the center of the spans, imposing rotations in opposite directions.

Due to friction between the superstructure and UHWMPE bearing pads, supplementary gravity loading would have affected the results of the testing and increased the amount of transverse loading for a given displacement. However, the amount of increase in lateral force is dependent on the bearing properties and

superstructure weight and can be easily calculated and considered in the analytical modeling by addition of a Coulomb friction to the force-displacement diagrams. Therefore, no supplementary gravitational forces were applied to the test specimen.

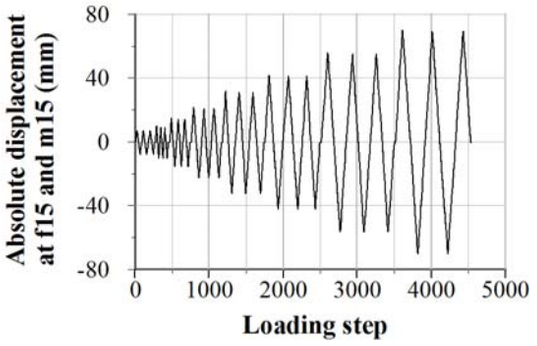


Figure 6. Loading protocol

2.4 *Analytical modeling*

The superstructure's response to transverse loading was modeled using the revised Monolithic Beam Analogy (rMBA), developed by Palermo (2004). The moment-rotation relationship of hybrid connections cannot be established using conventional section analysis methods. The rMBA finds a relationship between the concrete strain and depth of the neutral axis in a hybrid connection by comparing it to a monolithic plastic hinge. This method recognizes three stages of deformation in the connection; before decompression, after decompression and prior to yielding, and after yielding. The relationship between the concrete strain in the extreme compression fiber and the neutral axis depth during each of these stages can be found using Equation 1. The moment-rotation relationship of the connection is then found using an iterative approach which involves applying an incremental imposed displacement to the connection, assuming a neutral axis depth, finding the concrete strain in the extreme compression fiber, calculating the forces in the section and checking for equilibrium. If equilibrium is not met the procedure is iterated using a revised neutral axis depth. Finally, the bending moment at the imposed rotation is calculated and the rotation is increased and the process is repeated.

$$
\begin{aligned}
&\textit{if} \quad 0 < \theta_{imp} \le \phi_{dec} \frac{L_{tot}}{3}; \\
&\qquad \Delta_{imp} = \Delta_{eq} = \phi \frac{L_{tot}^2}{3} \\
&\textit{if} \quad \theta_{dec} < \theta_{imp} \le \left(\phi_y - \phi_{dec}\right) \frac{L_{tot}}{3}; \\
&\qquad \varepsilon_c = \left(\frac{3\theta_{imp}}{L_{cant}} + \phi_{dec} \right) \cdot c \\
&\textit{if} \quad \left(\phi_y - \phi_{dec}\right) \frac{L_{tot}}{3} < \theta_{imp} \\
&\qquad \varepsilon_c = \left(\frac{\dfrac{3\theta_{imp}}{L_{cant}} - \left(\phi_y - \phi_{dec}\right)}{\dfrac{3L_p}{L}\left(1 - \dfrac{L_p}{2L_{cant}}\right)} + \phi_y \right) \cdot c
\end{aligned}
\tag{1}
$$

Further details regarding the rMBA method can be found in Palermo (2004).

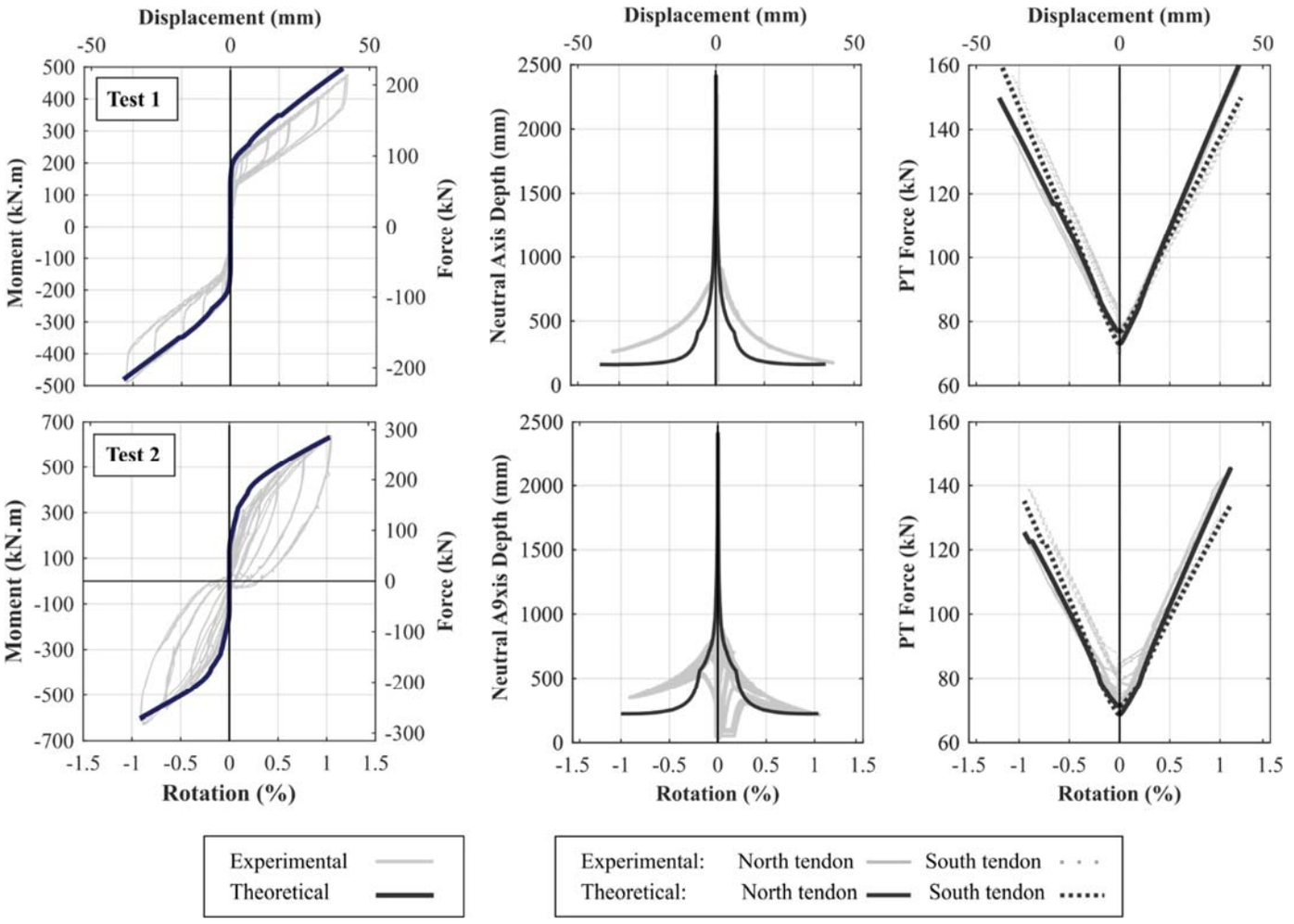


Figure 7. Comparison of experimental and analytical results for test setups with and without axial mild steel dissipaters

2.5 *Comparison of experimental and analytical results*

The experimental and analytical results of both tests are shown in Figure 7. The area encompassed by the moment-rotation plot in the first test is a result of Coulomb friction between the cap beam and superstructure. The moment-rotation plots of the second test show a promising flag shaped hysteresis loop which confirm the self-centering and energy dissipation properties of the hybrid superstructure. It is possible to achieve a higher self-centering to dissipation ratio by increasing the amount of post-tensioning in the tendons and also reducing the friction between the superstructure and cap beam.

The comparison shows that the rMBA method can be used to model the moment-rotation behavior of two-span precast concrete superstructures featuring a hybrid connection between the spans with remarkable accuracy.

3 PARAMETRIC ANALYSIS

3.1 *Superstructure configurations*

Various superstructure configurations were considered for the parametric analysis. First, three standard precast concrete superstructure beam types (NZTA 2008) with different cross sections (shown in Figure 8) and span lengths were selected. The number of spans in the superstructures ranged from 2 to 5, and the designs were performed with target ductility values ranging from 1 to 15. The span lengths were dependent on the beam type, being equal to 16, 20 and 30m for 650mm deep double hollow-core, 900mm deep double hollow-core and 1225m deep Super-T beams respectively. The superstructures were assumed to be supported on low-friction bearings and therefore unrestrained and independent from the piers in the transverse direction.

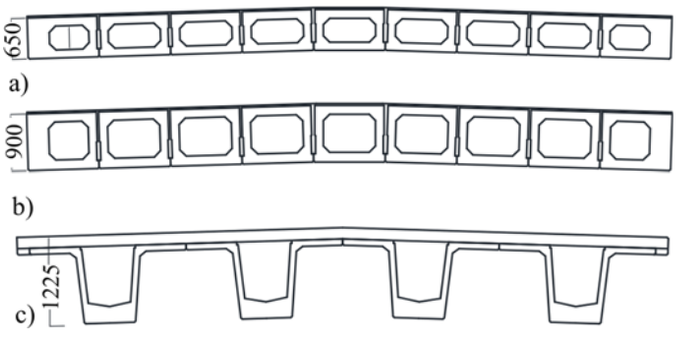


Figure 8. Superstructure beam types considered in the parametric analysis; a) 650mm deep double hollow-core, b) 900mm deep double hollow-core, 1225mm deep Super-T beams.

The post-tensioning tendons used in design of the superstructure configurations were 15mm VSL strands, which were assumed to be located at the center of the superstructure beam (bridge spine) to minimize excessive strains. The initial post-tensioning value of the tendons was taken as equal to 50% of yield strength (0.1% proof loading), to provide a sufficient safety margin from brittle failure of the tendons.

The dissipaters were assumed to be tension-compression steel devices manufacture from G300 mild steel, similar to those used in the experimental testing. The dissipaters were assumed to be installed at the edges of the superstructure beams to maximize their contribution to the resisting moment. This placement results in an increase in dissipater strain and a decrease in the yield displacement of the system.

3.2 *Design*

A direct displacement based procedure was used for designing the post-tensioning and dissipative devices in the superstructure connections. A parabolic displacement profile similar to that of a simply supported beam under uniform distributed loading was used for the superstructure, which is a profile traditionally used in the direct displacement based design of bridges with transverse load-resisting abutments (Priestley et al. 1996).

The seismic design parameters were chosen in accordance with NZS 2004, and were similar to those used in the experimental testing.

3.3 *Revised monolithic beam analogy for dissipative rocking superstructures*

The rMBA discussed in section 2.4 was modified for use in dissipative rocking superstructures, by comparing them to a simply supported beam with "weak joints', or regions of potential plastic hinging, and subjected to uniform distributed loading. The additional displacement of the dissipative rocking superstructure at its center, after decompression, was equated to that of the simply supported superstructure. Three stages of deformation were considered; prior to decompression (or gap opening) of the hybrid connections, after decompression and before nonlinearity, and after nonlinearity. The nonlinearity can be geometric or a result of yielding of the dissipaters, depending on the configuration.

$$\begin{aligned} &n_{spans}=2; && \kappa=1\\ &n_{spans}=3; && \kappa=2\\ &n_{spans}=4; && \kappa=4\\ &n_{spans}=5; && \kappa=6 \end{aligned} \tag{2}$$

The relationship between the concrete strain in the extreme compression fiber and the neutral axis depth during each of these stages can be found using Equation 3. The coefficient κ is dependent on the number of spans, and is given in Equation 2.

$$\begin{aligned} &if \quad 0<\theta_{imp}\le\phi_{dec}\frac{L_{tot}}{8};\\ &\qquad \Delta_{imp}=\Delta_{eq}=\phi\frac{L_{tot}^2}{8}\\ &if \quad \theta_{dec}<\theta_{imp}\le\left(\phi_y-\phi_{dec}\right)\frac{L_{tot}}{8};\\ &\qquad \varepsilon_c=\left[\kappa\theta_{imp}L\left(\frac{8}{L_{tot}^2}\right)+\phi_{dec}\right]\cdot c\\ &if \quad \left(\phi_y-\phi_{dec}\right)\frac{L_{tot}}{8}<\theta_{imp}\\ &\qquad \varepsilon_c=\left(\frac{\dfrac{8\theta_{imp}}{L}-\dfrac{n_{spans}^2\left(\phi_y-\phi_{dec}\right)}{\kappa}}{\dfrac{8L_p}{L}\left(1-\dfrac{L_p}{2L}\right)}+\phi_y\right)\cdot c \end{aligned} \tag{3}$$

The superstructure configurations considered for the parametric analysis were modelled using the developed rMBA method.

3.4 *Analysis results*

Results of the parametric analysis show the effects of superstructure length on base shear demand, and ratio of base shear demand to the seismic weight of the superstructure. Figure 9-a shows the overall relationship between these values and the superstructure length, based on ductility levels. It can be seen that in general, the value of base shear increases with increase in superstructure length (and mass), however as a general trend it decreases at higher ductility levels. Figure 9-b shows the base shear to superstructure weight ratio (V/W) as a function of superstructure length and target ductility. For low ductility levels (μ=1) a longer superstructure generally results in a higher V/W. However, as ductility levels increase, a greater superstructure length results in a lower V/W ratio. This can be attributed to the decreased stiffness and increased natural period of the structure at higher ductility levels. At the lower range of ductility, the period of the equivalent structure coincides with the equal acceleration or equal velocity section of the design spectra, leading to an increase in the ratio of base shear demand to superstructure weight.

The parametric analysis was also used to establish a relationship between equivalent viscous damping of the structure, ξ_{eq}, and ductility, μ. The equivalent viscous damping is composed of two components; the

initial elastic damping, ξ_0, and the hysteretic damping, ξ_{hyst}, as shown in Equation 4.

$$\xi_{eq} = \xi_0 + \xi_{hyst} \tag{4}$$

The equivalent hysteretic damping ratio can be calculated by comparing the energy dissipated by a viscous damper with the energy dissipated from nonlinear behavior in a stabilized steady-state response (Jacobsen 1960), as shown in Equation 5.

$$\xi_{hyst} = \frac{1}{4\pi} \cdot \frac{E_{Diss}}{E_{sto}} = \frac{1}{2\pi} \cdot \frac{A_{hyst}}{F_0 u_0} \tag{5}$$

Where A_{hyst} is the area encompassed by the flag-shape hysteresis loop, and F_0 and u_0 are the maximum force and displacement in the force-displacement plot respectively.

For structures with hybrid connections, the equivalent hysteretic damping should be modified by a function of the re-centering ratio of the hybrid connections (Equation 6). The re-centering ratio is equal to the bending moment contribution from the post-tensioning tendons divided by the bending moment provided by the dissipative devices (Equation 7).

$$\xi_{eq} = 5 + \frac{1}{1+\lambda} \cdot \xi_{hyst} \tag{6}$$

$$\lambda = \frac{M_{pt}}{M_{dis}} \tag{7}$$

Where M_{pt} and M_{dis} are the contributions of post-tensioning steel and dissipative devices to the resisting bending moment in the connections respectively.

The area encompassed by hysteresis loops in the force-deformation plots found from analysis of the superstructure configurations was calculated and used to find the corresponding hysteretic damping for each configuration, ξ_{hyst}. The resulting values were modified by the re-centering ratio, λ, also found from the analysis and added to the 5% assumed elastic damping to find the equivalent viscous damping, ξ_{eq} (Equation 7).

The results of these calculations are shown in Figure 10. The equivalent damping ratio for structures with hybrid connections was calculated using a method proposed by Priestley (2007) and has also been plotted in the same graph (Equation 8).

$$\xi_{eq} = 0.05 + R_\xi \left(\frac{\mu - 1}{\mu\pi} \right) \tag{8}$$

Where R_ξ depends on the properties of the hybrid connections and type of dissipative rocking system.

$$R_\xi = 0.435 \tag{9}$$

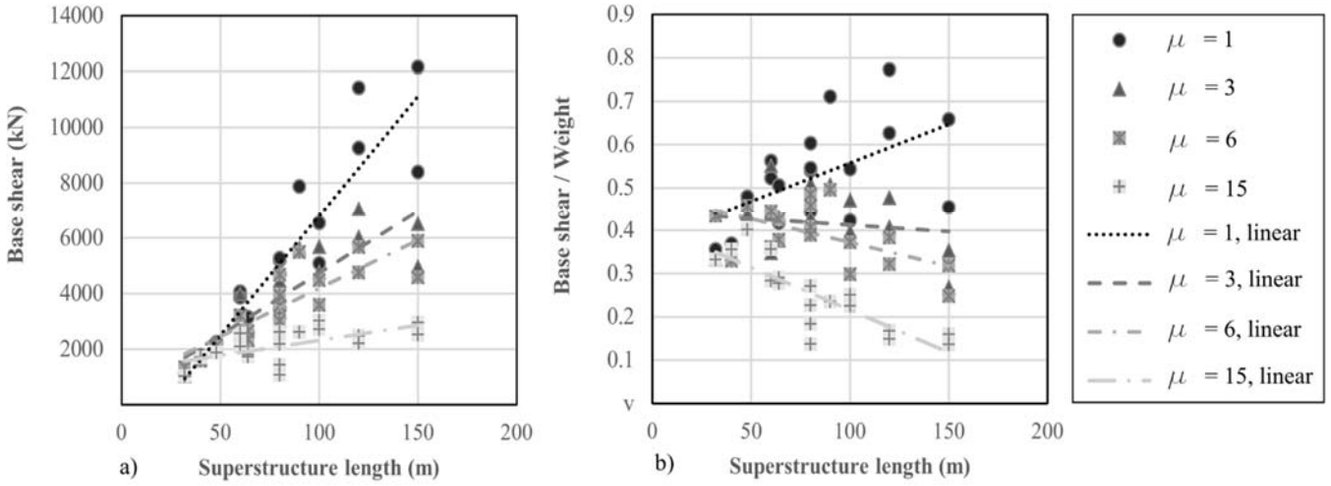


Figure 9. Relationship between base shear demand and superstructure length based on results from parametric analysis

The value of R_ξ for dissipative rocking superstructures was calculated to minimize the square root of the sum of squares between Priestley's method (Equation 8) and the mean value of the damping values found from the parametric analysis (Equation 5), and is given in Equation 9.

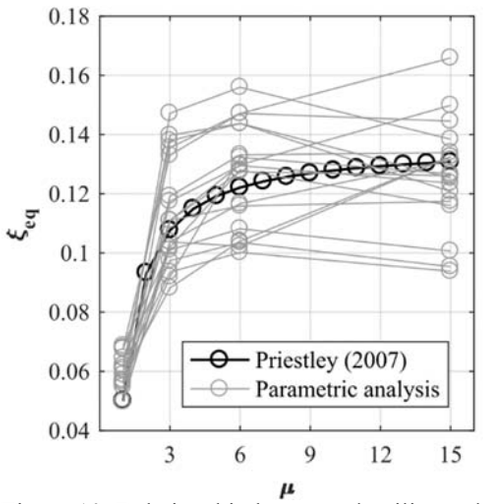


Figure 10. Relationship between ductility and equivalent damping

4 CONCLUSIONS

A hybrid connection was developed for prefabricated concrete bridge superstructures by combining unbonded longitudinal post-tensioning and axial mild steel dissipaters. The study comprised of experimental testing on a large-scale two-span precast concrete bridge and a parametric analysis to extrapolate the results of testing to various superstructure configurations.

The experimental testing was performed on a 1:3 scaled specimen typical of typical short-span bridges in New Zealand. The specimen was subjected to quasi-static transverse cyclic loading, and exhibited a desirable flag-shape hysteretic response when dissipative devices were installed between the two spans. The experimental results were extrapolated to various bridge geometries and design target values through parametric analysis. The structures were designed using a direct displacement-based (DDBD) method and analyzed with a modified version of the revised monolithic beam analogy (rMBA). The effects of superstructure beam type, length of bridge, number of spans and target ductility on the transverse force-displacement relationship of the superstructure configurations was investigated.

The results show that higher target ductility values decrease the superstructures' secant stiffness, increase their fundamental period and significantly reduce the base shear and necessary reinforcement ratios (for both mild steel dissipaters and post-tensioning). For low ductility levels, greater superstructure lengths generally result in higher ratios of base shear demand to seismic weight due to their larger seismic mass. However, as target ductility levels increase, the secant stiffness of the structures decrease, and greater superstructure lengths result in a decrease in the ratio of base shear demand to seismic weight. Finally, an expression to find the equivalent viscous damping in dissipative rocking superstructures was found by calibrating results from the parametric analysis to theoretical values.

REFERENCES

ACI Innovation Task Group 5, 2008. *Acceptance criteria for special unbonded post-tensioned precast structural walls based on validation testing and commentary: an ACI standard*. Farmington Hills: American Concrete Institute.

Buckle, I., Hube, M., Chen, G., Yen, W.H. & Arias, J. 2012. *Structural performance of bridges in the offshore Maule earthquake of 27 February 2010*. Earthquake Spectra, 28(SUPPL.1), S533–S552.

Jacobsen, L. S. 1960. Damping in composite structures. In *Proceedings of the 2nd world conference on earthquake engineering*. Vol. 2, pp. 1029–1044.

Kawashima, K. & Unjoh, S. 1997. The damage of highway bridges in the 1995 Hyogo-Ken Nanbu Earthquake and its impact on Japanese seismic design. *Journal of Earthquake Engineering*, *1*(3), 505–541.

Lepech, M. D. & Li, V. C. 2009. Application of ECC for bridge deck link slabs. *Materials and Structures/Materiaux et Constructions*, *42*(9), 1185–1195.

Mander, J. B., Priestley, M. J. N. & Park, S. W. 1988. Theoretical stress-strain model for confined concrete. *Journal of Structural Engineering*, 114(8), 1804–1826.

Mander, J. B. & Cheng, C.T. 1997. *Seismic resistance of bridge piers based on damage avoidance design*. *Technical Report NCEER-97-0014*. Buffalo: US National Center for Earthquake Engineering Research.

Marks, J. 2013. Engineered Cementitious Composites: Applications and Impact of High Tensile, Self-healing Concrete. *University of Pittsburgh - Swanson School of Engineering*, *A5*(3204), 1–8.

Marriott, D. J. 2009. *The development of high-performance post-tensioned rocking systems for the seismic design of structures*. PhD thesis. Christchurch: University of Canterbury.

NZ Transport Agency 2008. *NZ Transport Agency Research Report 364: Standard precast concrete bridge beams.* Wellington: New Zealand Transport Agency.

NZS 2004. *NZS 1170.5:2004 Structural design actions – Part 5: Earthquake actions – New Zealand.* Wellington: Standards New Zealand.

Palermo, A. (2004). *The Use of controlled rocking in the seismic design of bridges*. PhD Thesis. Milan: Technical university of Milan.

Palermo, A., Pampanin, S. & Marriott, D. 2007. Design, modeling, and experimental response of seismic resistant bridge piers with posttensioned dissipating connections. *Journal of Structural Engineering*, 133(11), 1648–1661.

Priestley, M. J. N., Seible, F., & Calvi, G. M. (1996). *Seismic design and retrofit of bridges*. New York: Wiley-Interscience.

Priestley, M. J. N., Sritharan, S. S., Conley, J. R. & Pampanin, S. 1999. Preliminary results and conclusions from the PRESSS five-story precast concrete test building. *PCI Journal*, *44*(6), 42–67.

Priestley, M. J. N., Calvi, G. M., & Kowalsky, M. J. (2007). *Displacement-based seismic design of structures*. IUSS Press, Pavia, Italy.

White, S. & Palermo, A. 2016. Quasi-Static testing of posttensioned nonemulative column-footing connections for bridge piers. *Journal of Bridge Engineering*, *21*(2011), 1–13.

Wood, J. H. & Chapman, H. E. 2013. Performance of linkage bars for restraint of bridge spans in earthquakes. *Bulletin of the New Zealand Society for Earthquake Engineering*, *46*(1), 25–39.

Schanack, F., Valdebenito, G. & Alvial, J. 2012. Seismic damage to bridges during the 27 February 2010 magnitude 8.8 Chile earthquake. *Earthquake Spectra*, *28*(1), 301–315.

Silva, P. F., Megally, S. & Seible, F. 2009. Seismic performance of sacrificial exterior shear keys in bridge abutments. *Earthquake Spectra*, *25*(3), 643–664.

Zhiqiang, W. & Lee, G. C. 2009. A comparative study of bridge damage due to the Wenchuan, Northridge, Loma Prieta and San Fernando earthquakes. *Earthquake Engineering and Engineering Vibration*, *8*(2), 251–261.

Maintenance, Safety, Risk, Management and Life-Cycle Performance of Bridges – Powers, Frangopol, Al-Mahaidi & Caprani (Eds)
© 2018 Taylor & Francis Group, London, ISBN 978-1-138-73045-8

Mechanical properties of alkali activated concrete based class C fly ash

Eslam Gomaa[1], Simon Sargon[1], Ahmed Gheni[2], and Mohamed A. ElGawady[3*]

[1]Graduate Research Assistance, Dept. of Civil, Architectural, and Environmental Engineering, Missouri University of Science and Technology, Rolla, MO. 65401; Email: eyg9qc@mst.edu
[1]Graduate Research Assistance, Dept. of Civil, Architectural, and Environmental Engineering, Missouri University of Science and Technology, Rolla, MO. 65401; Email: ssk36@mst.edu
[2] PhD Candidate, Dept. of Civil, Architectural, and Environmental Engineering, Missouri University of Science and Technology, Rolla, MO. 65401; Email: aagmr6@mst.edu
[4] Benavides Associate Professor, Dept. of Civil, Architectural, and Environmental Engineering, Missouri University of Science and Technology, Rolla, MO. 65401; Email: elgawadym@mst.edu
[*]Corresponding author

ABSTRACT: In this paper, the mechanical properties of alkali activated concrete (AAC) produced from three different fly ash sources were studied. Class C fly ashes (Sk, TH, and KC) were located in the State of Missouri, USA where used in this study. The three fly ashes had different chemical composition. The workability of the mixtures was assessed based on the slump value of each mixture. The mechanical properties including the compressive, splitting tensile, and flexure strengths were tested. The compressive strength was tested at different ages including 1, 7, 28 days. Elevated heat curing regime was applied on the three fly ashes in an electric oven. The temperature of the oven was constant at 70 ºC for 24 hours. The results revealed that the workability and the mechanical properties depended mainly on the calcium content of the fly ashes. The Sk fly ash that had lowest calcium content showed high slump value. With decreasing the calcium content in the fly ash, the mechanical properties were improved. The strength of all mechanical properties has a slightly or constant development with time. The compressive strength reached to 41.28, 39.85, and 36.43 Mpa for Sk, TH, KC that were ordered from the lowest to highest calcium content, respectively. The splitting tensile strength results showed a good match with AS 3600 code. However, the flexure strength results showed a good match with ACI 318. Proposed equations were suggested to predict the splitting tensile and flexure strengths of the AAC with R^2 higher than 0.90.

1 INTRODUCTION

Recently, the environmental concern has been developed and become a worldwide objective to reduce using the materials that cause environmental issues. The concrete has been widely used in the construction industries due to the low cost, high strength, low maintenance, and good durability [1]. Therefore, the demand of the concrete has been kept increasing significantly. However, the main binder of the conventional concrete is the ordinary Portland cement (OPC). Manufacturing the OPC has been associated with a serious environmental issue. Where, producing one ton of the OPC released approximately one ton of carbon dioxide (CO_2) emission into the atmosphere [2]. In addition, the industry of OPC is responsible for 5% of manmade CO_2 emissions [2]. Therefore, finding a replacement for the OPC became urgent.

It has been reported that the materials that rich in silica SiO_2 and alumina Al_2O_3 had the ability to react with alkali activators to form a new binder [3]. This process named as geopolymerization. This process starts with dissolving the silica and alumina species from the source material in presence of the alkali activators to form free SiO_4 and AlO_4 tetrahedral units [3]. With time, the tetrahedral units are connected to yield polymeric precursor and shared all oxygen atoms to form an amorphous polymer material (called: geopolymer) [4].

Fly ash (FA) was widely used as a source of the aluminosilicate due to its low cost and availability [5]. The ASTM requirements of the class C FA to have (SiO_2+Al_2O_3+F_2O_3) in between 70 % and 50 %, however that this classification is not based on the calcium content but usually class C FA is associated with high calcium content compared with class F FA. Due to the high calcium presence of calcium in class C FA, it interferes with the microstructure geopolymerizaition process and alter the microstructure [6]. In addition, it associated with a short setting time and low workability [7, 8].

One of the advantages of the alkali-activated system based class F FA that it can be cured for a short period at high temperature and gain a high strength at the early stages. On the other hand, using class C FA preferred in case of ambient temperature curing regime due to the formation of calcium silicate hydrate (CSH) and/or calcium aluminate silicate hydrate (CASH) [9, 10] which known as the hydration process. Studying the applicability of using the elevated heat curing regime in the precast plants was investigated in this study. Three different FAs con-

tain high calcium content which higher than 20 % were used to produce AAC. The mechanical properties included the compressive strength splitting tensile strength, and flexural strength was studied.

2 EXPERIMENTAL PROCEDURE

2.1 *Materials*

Commercially available dolomite used in this study as the coarse aggregate with a maximum size of 19 mm (3/4 in) and specific gravity of 2.76. Missouri river sand used as the fine aggregate in this study with the maximum specific gravity of 2.60. The coarse and fine aggregates were used in a saturated surface dry condition (SSD), where the water content and the total absorption were determined for both aggregate and the total absorption. So, the difference between them was taken into considerations during calculating the added water to the mixture to make the aggregate in SSD condition. Both coarse and fine aggregates passed the ASTM C33 [11] particles sizes limits.

Locally available fly ashes (FAs) were used in this study. Three different FAs were collected from Sikeston (Sk), Kansas City (KC), Thomas Hill (TH), Missouri State, USA. The mineral compositions of the FAs were given in Table 1. The mineral compositions were analyzed by X-ray fluorescence as described in ASTM D4326 [12]. As shown in Table 1, the three FAs have different mineral compositions and all of them have high calcium content higher than 20 %. According to ASTM C618 [13] requirements, the three FAs were classified as class C where the summation of SiO_2, Al_2O_3, and Fe_2O_3 was in between 70 % and 50% for all of them. The particles size distribution test was conducted on the four FAs using Microtrac S3500 series size analyzer. The diameters that at it 50% of the particles passed (D_{50}) were 12.81, 16.25, and 16.13 μm for Sk, KC, and TH, respectively.

The alkali activator solution was prepared by mixing sodium silicate (Na_2SiO_3) and sodium hydroxide (NaOH) solutions. The selected mixing ratio between the two solutions was 1.0 by weight based on a previous study [7]. The sodium silicate solution was brought in solution from PQ Corporation with a modulus ratio M_s (SiO_2/Na_2O) of 2.0, where SiO_2 = 29.4%, Na_2O = 14.7%, and H_2O = 55.9%. However, the sodium hydroxide was in pellets form with purity of 100%. The sodium hydroxide pellets were dissolved in distilled water to prepare alkaline solution 24 hours to let it cool down to the room temperature prior to use. The molarity of the sodium hydroxide was fixed at 10M.

Table 1. Chemical composition of the FAs by XRF.

Chemical composition	Sk (%)	KC (%)	TH (%)
SiO_2	43.91	42.25	40.43
Al_2O_3	20.12	17.91	17.53
Fe_2O3	4.96	4.73	4.72
CaO	21.24	25.86	24.07
MgO	4.29	4.74	9.39
Na_2O	2.87	1.58	1.17
K_2O	0.70	0.56	0.48
TiO_2	1.36	1.44	1.40
P_2O_5	0.51	0.89	0.79
MnO	0.05	0.04	0.02
LOI*	0.40	0.12	0.62
Sum(SiO_2 + Al_2O_3 + Fe_2O_3)	68.99	64.89	62.68

* Loss on ignition.

2.2 *Sample preparation*

Three mixtures were designed to represent the properties of high calcium FAs (Class C) AAC. The concrete details were summarized in Table 2. The volume of the limestone and sand in the mixture represented almost 65 % of the total volume. The water (W) content included the water that already existed in the alkali activators solutions and the extra added water to make the limestone and water under SSD condition. The alkali activator solution-to-fly ash (Alk/FA) ratio was 0.30. The water-to-fly ash ratio (W/FA) was 0.35 for KC FA and 0.34 for Sk and TH. The Alk/Fa ratio was selected according to a previous study and the W/FA ratio was design to reach a slump value in between 150 and 200 mm [7].

Table 2. Concrete mixture design.

Material	Sk (Kg/m^3)	KC (Kg/m^3)	TH (Kg/m^3)
Limestone	959	959	959
Sand	799	799	799
FA	450	450	450
SH	67.5	67.5	67.5
SS	67.5	67.5	67.5
W	78.3	82.8	78.3

The mixer that was used to mix the materials was a normal mixer. The mixing procedure started with mixing the limestone and sand in a dry condition in the mixer for 1 minute. Then the FA was added and mixed for more 1 minute. The W was added gradually to all dry materials for 2 minutes. The two alkali activators solution were mixed together prior to adding them to in the mixer gradually for 5 minutes. Then the mixture was left to be mixed for another 5 minutes.

The mixed AAC was cast into cylinders in two layers according to ASTM C192 [14]. Also, concrete beams 150 (height) x 150 (width) x 600 (length) mm was casted into steel molds. The mixing was done at the ambient temperature 23 ± 2 ºC in the laboratory room. Directly after casting, the molds were covered with a plastic oven bag to prevent moisture loss. The cylinders were placed in an electric oven and cured for 24 hours at 70 ºC. then the cylinders was demolded after getting them out of the oven and let-

ting them cool down at the room temperature until the test age.

2.3 *Sample testing*

The workability of the AAC was assessed by conducting the slump test. The slump test was done according to ASTM C143 [15].The compressive strength of the concrete cylinders was tested following the ASTM C39 [16]. Three samples were tested for each mixture and the reported data were the mean of the three results. The cylinders were tested at 1, 7, and 28 days. The splitting tensile strength of the concrete cylinders was tested following the ASTM C496 [17] and the flexure strength of concrete beams was tested according to ASTM C78 [18] at 7 and 28 days.

3 EXPERIMENTAL RESULTS AND DISCUSSION

3.1 *Slump of fresh concrete*

The slump of the three FAs fresh mixtures was shown in Figure 1. It can be seen that with increasing the calcium content of the TH FA, the slump value was reduced compared with Sk FA. Although the calcium content of KC FA was the highest one among the three FAs, it showed the higher slump value due to the higher water content in the KC FA mixture.

The decrease in the slump in SK FA comparing with TH FA was directly related to the particles size distribution of the FAs, where the SK FA has the lower particles size distribution (D_{50}) among the three FAs, which means more surface area, higher dissolution rate and lower workability.

3.2 *Mechanical properties*

The compressive strength development of AAC at 1, 7, 28 days was shown in Figure 2. It is clear that the curing regime had a significant influence on the compressive strength development with time. Unlike the conventional OPC concrete, there was not a significant development in the compressive strength with time, where the improvement in the compressive strength from 1 day to 28 days was less than 15% as summarized in Table 3. This was related to the type of curing regime. The curing at elevated temperature was substantial for inducing the geopolymerization process, thereafter forming the N-A-S-H gels. This concept was agreed with previous researchers [19-21]. The curing regime was in the oven at an elevated temperature for 24 hours, so the water that was existed in the sample was consumed during the curing period. Therefore, there was enough water to form calcium silicate hydrate (C-S-H) and/or calcium aluminate silicate hydrate (C-A-S-H) that can form under the ambient temperature without any need for elevated temperature due to existing high calcium content in the raw FAs.

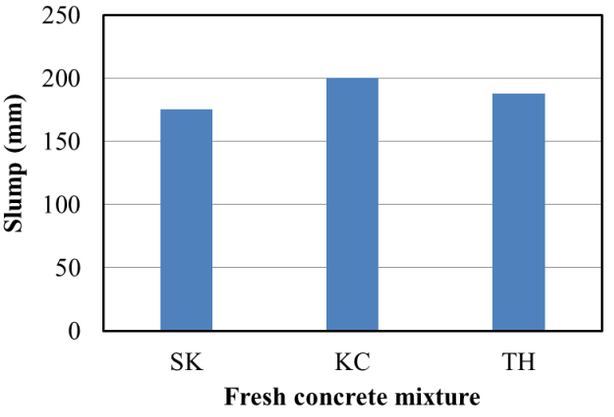


Figure 1. Slump of fresh AAC.

Comparing the compressive strength of the AAC based the three FAs, the FA that had lowest calcium content (Sk) showed the higher compressive strength among the three FAs. However, the FA that had highest calcium content showed the lowest compressive strength among the three FAs. This is mainly related to the geopolymerization process that relied on the silica and alumina content, in addition the alkali activators (SS and SH). So, the presence of the calcium in the geopolymerization process was considered as a contaminant and alter the microstructure of the aluminosilicate chains [6], which caused a decrease in the compressive strength of the AAC that cured under elevated temperature condition.

Table 3. Percentage of compressive strength development of AAC.

FA	Compressive strength (SD*) at 1 day (MPa)	Compressive strength (SD*) at 28 days (MPa)	Percentage of strength development (%)
Sk	37.83 (0.31)	41.28 (1.42)	9.12
KC	31.92 (0.80)	36.43 (1.00)	14.12
TH	37.08 (1.63)	39.85 (1.77)	4.74

* Standard deviation.

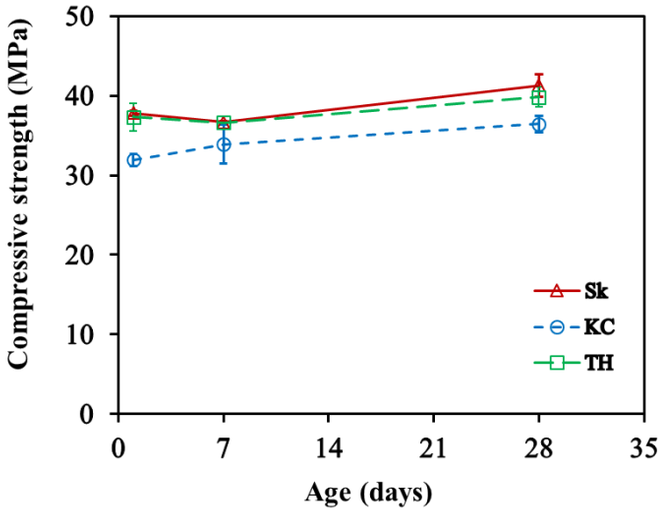


Figure 2. Compressive strength development of AAC.

The splitting tensile strength of the three AACs based the three FAs were shown in Figure 3. The results were presented the same trend as the compressive strength, whereas the FA that had the lowest calcium content (Sk), showed the higher splitting tensile strength among the other FAs. However, the splitting tensile strength was decreased with increasing the calcium content in the FAs. Moreover, the strength showed a slight increase from 1 day to 28 days.

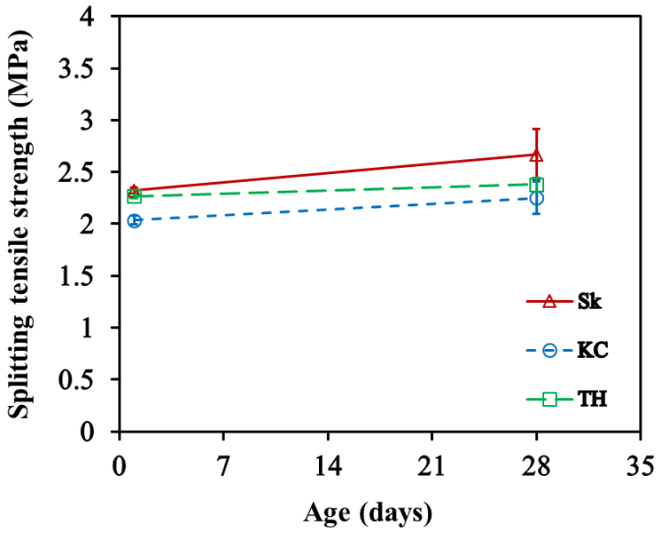


Figure 3. Splitting tensile strength development of AAC.

For design calculations, the ACI 318 [22] and AS 3600 [23] suggested equations that related the tensile strength with the compressive strength expressed in Equations 1 and 2, respectively. In addition, several researchers proposed different equations that adapted their results given in Equations 3 [24].

$$f_t = 0.56(f_c)^{0.5}, \text{ ACI 318 (2014)} \quad (1)$$

$$f_t = 0.40(f_c)^{0.5}, \text{ AS 3600 (2001)} \quad (2)$$

$$f_t = 0.17(f_c)^{0.75}, \text{ Ryu et al. (2013)} \quad (3)$$

Where f_t = splitting tensile strength; and f_c = compressive strength.

In Figure 4, the experimental results of this study were plotted along with the previous equations. As shown in Figure 4, the splitting tensile strength results in this study were generally lower than the strengths calculated using the ACI 318 equation, however, they were close to the AS 3600 and [24] equations. Accordingly, Equation 4 was proposed to model the relationship between the splitting tensile strength and compressive strength with a coefficient of determination of 0.986 of AAC based high calcium FA.

$$f_t = 0.38(f_c)^{0.5} \quad (4)$$

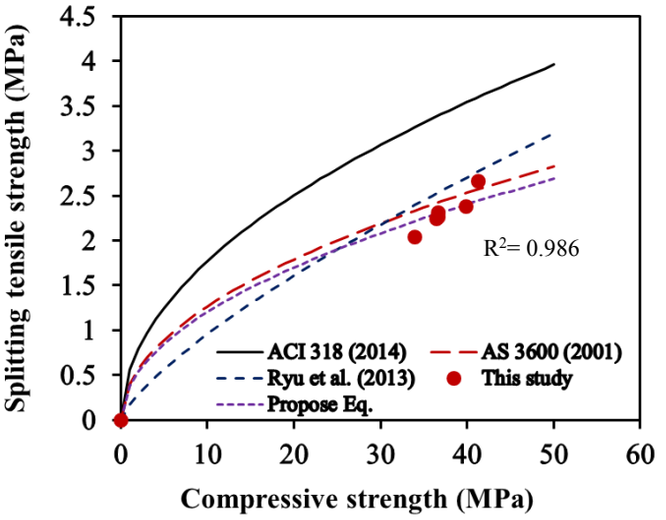


Figure 4. Relationship between splitting tensile strength and compressive strength of AAC.

The flexural strength of the three AACs based the three FAs were presented in Figure 5. The results were exhibited the same trend as the compressive strength, whereas the FA that had the lowest calcium content (Sk), showed the higher flexural strength among the other FAs. However, the flexural strength was decreased with increasing the calcium content in the FAs. The strength showed a slight increase from 1 day to 28 days for KC FA, however, the flexural were almost the same at 1 day and 28 days for Sk and TH.

Figure 6 shows the relationship between the flexural strength and the compressive strength of the AAC. In addition, the design codes equations, e.g. ACI 318 and AS 3600 along with a previously proposed equation [25], were plotted in Figure 6 and presented in Equations 5, 6, and 7, respectively. The results of this study showed a slightly higher flexural strength than the design codes equation, however, they were less than the proposed equation by Diaz. Therefore, a newly proposed equation has suggested the relationship between the flexural strength and

compressive strength with a coefficient of determination of 0.919 of AAC based high calcium FA and given in Equation 8.

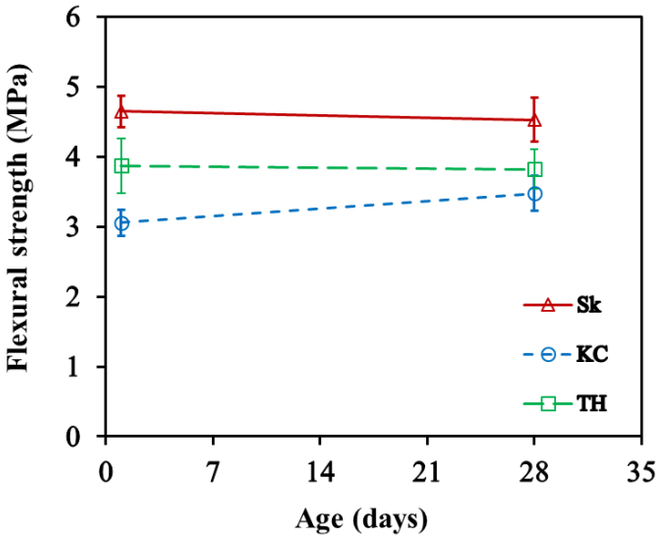


Figure 5. Flexural strength of AAC.

$$f_r = 0.62(f_c)^{0.5}$$, ACI 318 (2014) (5)

$$f_r = 0.60(f_c)^{0.5}$$, AS 3600 (2001) (6)

$$f_r = 0.69(f_c)^{0.5}$$, Diaz-Loya et al. (2011) (7)

$$f_r = 0.64(f_c)^{0.5}$$ (8)

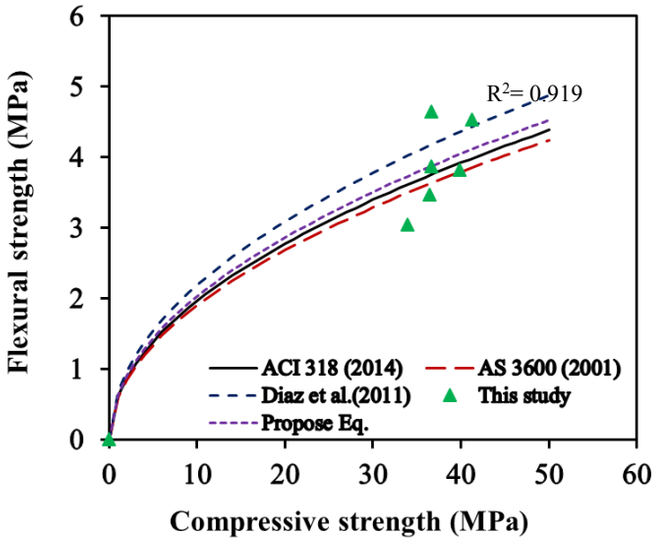


Figure 6. Relationship between splitting tensile strength and compressive strength of AAC.

4 CONCLUSION

The fresh and mechanical properties of the alkali-activated concrete (AAC) were investigated in this study. Class C FA was used to synthesize the AAC. The results revealed the following: with increasing the calcium content in the FA, the slump value was reduced and the mechanical properties including the compressive, splitting tensile, and flexure strengths were reduced in case of curing the concrete at an elevated temperature of 70 ^{o}C for 24 hours. The splitting tensile and flexure strengths of the AAC had a good correlation with the design codes (ACI 318 and AS 3600) that were developed mainly for the Ordinary Portland cement concrete.

5 ACKNOWLEDGMENT

This research was supported by the Missouri Department of Transportation (MoDOT) and Ameren Corporation. In kind contribution of the fly ash from Headwaters Resources is appreciated. However, any opinions, findings, conclusions, and recommendations presented in this paper are those of the authors and do not necessarily reflect the views of the sponsors.

6 REFERENCES

1. Behera, M., et al., *Recycled aggregate from C&D waste & its use in concrete – A breakthrough towards sustainability in construction sector: A review.* Construction and Building Materials, 2014. **68**(Supplement C): p. 501-516.
2. Temuujin, J., et al., *Utilization of radioactive high-calcium Mongolian flyash for the preparation of alkali-activated geopolymers for safe use as construction materials.* Ceramics International, 2014. **40**(10, Part B): p. 16475-16483.
3. Davidovits, J., *Geopolymer chemistry and application*, ed. t. Edition. 2015, Saint-Quentin, France: Geopolymer Institute.
4. Somna, K., et al., *NaOH-activated ground fly ash geopolymer cured at ambient temperature.* Fuel, 2011. **90**(6): p. 2118-2124.
5. Pattanapong, T.-N., C. Prinya, and S. Vanchai, *Setting Time, Strength, and Bond of High-Calcium Fly Ash Geopolymer Concrete.* Journal of Materials in Civil Engineering, 2015. **27**(7).
6. Temuujin, J., A. van Riessen, and R. Williams, *Influence of calcium compounds on the mechanical properties of fly ash geopolymer pastes.* Journal of Hazardous Materials, 2009. **167**(1–3): p. 82-88.
7. Gomaa, E., et al., *Fresh properties and compressive strength of high calcium alkali activated fly ash mortar.* Journal of King Saud University - Engineering Sciences, 2017.
8. Chindaprasirt, P., et al., *Effect of SiO2 and Al2O3 on the setting and hardening of high calcium fly ash-based geopolymer systems.*

Journal of Materials Science, 2012. **47**(12): p. 4876-4883.
9. Yip, C.K. and J.S.J. van Deventer, *Microanalysis of calcium silicate hydrate gel formed within a geopolymeric binder*. Journal of Materials Science, 2003. **38**(18): p. 3851-3860.
10. Guo, X., H. Shi, and W.A. Dick, *Compressive strength and microstructural characteristics of class C fly ash geopolymer*. Cement and Concrete Composites, 2010. **32**(2): p. 142-147.
11. *Standard Specification for Concrete Aggregates*. 2016, ASTM International.
12. *Standard Test Method for Major and Minor Elements in Coal and Coke Ash By X-Ray Fluorescence*. 2013, ASTM International.
13. *Standard Specification for Coal Fly Ash and Raw or Calcined Natural Pozzolan for Use in Concrete*. 2015, ASTM International.
14. *Standard Practice for Making and Curing Concrete Test Specimens in the Laboratory*. 2016, ASTM International.
15. *Standard Test Method for Slump of Hydraulic-Cement Concrete*. 2015, ASTM International.
16. *Standard Test Method for Compressive Strength of Cylindrical Concrete Specimens*. 2017, ASTM International.
17. *Standard Test Method for Splitting Tensile Strength of Cylindrical Concrete Specimens*. 2011, ASTM International.
18. *Standard Test Method for Flexural Strength of Concrete (Using Simple Beam with Third-Point Loading)*. 2016, ASTM International.
19. Zhang Hongen, J.F.W.Q.T.L. and X. Shi, *Influence of Cement on Properties of Fly-Ash-Based Concrete.* Materials Journal, 2017. **114**(05).
20. de Vargas, A.S., et al., *The effects of Na2O/SiO2molar ratio, curing temperature and age on compressive strength, morphology and microstructure of alkali-activated fly ash-based geopolymers.* Cement and Concrete Composites, 2011. **33**(6): p. 653-660.
21. Bakharev, T., *Geopolymeric materials prepared using Class F fly ash and elevated temperature curing.* Cement and Concrete Research, 2005. **35**(6): p. 1224-1232.
22. ACI, A., *318-14.* Building Code Requirements for Structural Concrete, American Concrete Institute, Farmington Hills, Michigan, 2014.
23. AS, A.S., *Concrete structures.* AS3600-2001. Sydney (Australia): Standards Australia, 2001.
24. Ryu, G.S., et al., *The mechanical properties of fly ash-based geopolymer concrete with alkaline activators.* Construction and Building Materials, 2013. **47**(Supplement C): p. 409-418.
25. Diaz-Loya, E.I., E.N. Allouche, and V. Saiprasad, *Mechanical Properties of Fly-Ash-Based Geopolymer Concrete.* Materials Journal, 2011. **108**(3).

Maintenance, Safety, Risk, Management and Life-Cycle Performance of Bridges – Powers, Frangopol, Al-Mahaidi & Caprani (Eds)
© 2018 Taylor & Francis Group, London, ISBN 978-1-138-73045-8

Bayesian integration of NDT with corrosion model for service-life predictions

S. A. Faroz & S. Ghosh
Structural Safety, Risk and Reliability Lab, Department of Civil Engineering
Indian Institute of Technology Bombay, Mumbai, India

ABSTRACT: Corrosion damages reinforced concrete (RC) bridges primarily through the loss of steel rebar volume. Theoretical corrosion growth models are usually employed to predict this loss of steel over the life of a RC structure. Typically, these models fail to provide realistic estimates of the actual corrosion observed in the field. Alternatively, non-destructive testing/evaluation (NDT/E) or monitoring is used to evaluate the current state of a structure. However, either of these two approaches, alone, fails to provide a comprehensive understanding of how a bridge is expected to deteriorate over its lifetime. In order to be able to manage a degrading bridge over its service-life, it will be beneficial to scientifically combine the predictive capability of the theoretical degradation model and the data obtained from NDT/E for assessing the residual life of a structure. In this paper, this is achieved through a sequential Bayesian updating to address the issue of uncertainty present in the (i) physical process of corrosion and in the (ii) corrosion growth model used for prediction. The parameters of the updated corrosion growth model are stochastic in nature. A robust estimation of the time-varying steel loss due to corrosion is obtained incorporating these parameter uncertainties. The updated model is further used for the reliability assessment of a corroding RC bridge slab. Based on the target reliability, service-life of a bridge is obtained considering flexural failure.

1 INTRODUCTION

Reinforced concrete (RC) highway and railway bridges, which form an integral part of the transportation infrastructure, degrade gradually over time, primarily due to environmental effects and possible overloading. Condition surveys in saline environment have indicated that reinforcement corrosion is the most critical cause of degradation (Almusallam et al. 1996).

As loss of steel due to corrosion can be linked to various damage states (Faroz et al. 2016), the primary interest of a maintenance/structural engineer is to track the steel loss due to corrosion (Faroz et al. 2014). As the rebars are embedded in concrete, they are unavailable for a visual inspection, unless the cover concrete is destroyed. A precise estimation of the residual steel area of rebars is possible through the destruction of cover concrete, however destruction of concrete may only lead to further acceleration of the deterioration process (besides, the destructive tests are costly). Therefore, it is not always practical to go for a destructive testing. To circumvent this situation, the linear polarisation resistance (LPR) technique is the most common non-destructive technique (NDT) (Andrade & Martínez 2005) used for the on-site evaluation of corrosion rate, which can be used to predict the loss of rebar diameter/cross-section area (IRC 2002).

However, such NDT inspections give only the instantaneous condition of the structure and cannot be used independently for predicting its future degradation. In order to be able to manage a degrading structure over its service-life, it will be beneficial to combine the predictive capability of the theoretical degradation model and the data obtained from inspections (Ghosh & Faroz 2016, Faroz 2017, Faroz & Ghosh 2017).

Engineers usually take the aid of mathematical models to predict the degradation. A common issue in this is the use of deterministic prediction models. For example, one finds considerable scatter in actual steel loss data as compared to predictions by a deterministic steel loss model (Malumbela et al. 2012), signifying that such models are incomplete. The use of deterministic models giving point estimates, thus, becomes inappropriate. Due to the (unavoidable) presence of uncertainties in a natural phenomenon like corrosion, it is necessary that structural performance be treated within a probabilistic framework (Ellingwood 2005). The basic idea here is that, in a probabilistic setting, such deterministic models can be "completed"

by introducing "correcting" random variables (RVs) (Ditlevsen 1982) into the model.

This motivates the present work in modifying the existing corrosion loss estimation models with limited monitored data using Bayesian updating (Faroz et al. 2017). The Bayesian approach facilitates the integration of prediction model and inspection data, towards an overall uncertainty quantification for the engineering system/phenomenon under consideration. This paper presents a methodology for a probabilistic evaluation of the time-dependent corrosion loss of rebars in a RC slab bridge. A generalised procedure for the Bayesian updating of a steel loss model, using measured "limited" instantaneous data, is presented. A numerical study is also carried out to illustrate the proposed procedure, using data adopted from existing literature. The service-life of the bridge is determined considering the probability of its flexural failure. The primary objective is to show how integrating the NDT/E information with some prior knowledge (i.e., mathematical degradation model) of the bridge leads to significantly better estimations and consequently better decision-making in the life-cycle bridge management.

1.1 *Illustrative RC slab bridge*

For the purpose of demonstration, we consider a simply-supported RC two-lane slab bridge of span 6.4 m and width of 10.5 m (including a kerb width of 0.55 m at each side). The overall depth is 550 mm and effective depth $d = 500$ mm. The slab is reinforced with Fe415 20 mm rebars at a centre-to-centre spacing of 180 mm (on the tension side only), and M25 grade of concrete is used. This bridge is designed for the limit state of collapse due to flexure considering self weight (25 kN/m^3), 60 mm thick wearing course (22 kN/m^3), and live load due to class AA tracked vehicle as per IRC (2014). The bridge is designed as per IRC (2011) specifications, for the load combination $1.35\text{DL}_s + 1.75\text{DL}_w + 1.5\text{LL}$, DL_s being the dead load due to self weight, DL_w being the dead load due to wearing course and LL the live load of class AA tracked vehicle. LL comprises of the vehicle static load and impact effect. The effective width method is adopted for the dispersion of live loads. For the purpose of analysis, a $b = 1000$ mm strip of the bridge slab is considered.

NDT inspections of corrosion rate are done biennially (IRC 2002) from the initiation of corrosion ($t = 0$) upto 20 years. It is assumed that all the subsequent inspections are performed using the same NDT instrument. These inspection are done at the mid-span of the simply supported slab under consideration.

2 PROBABILISTIC CORROSION MODEL

The rate of 'uniform' reduction of rebar diameter (δ) due to corrosion can be obtained using Faraday's law (Mangat & Elgarf 1999):

$$\frac{\mathrm{d}\delta}{\mathrm{d}t} = \frac{2A}{\rho z F} i_{corr}(t) \tag{1}$$

where, $F = 96494$ As (Faraday's constant), $A = 55.85$ g (atomic weight of Fe), $z = 2$ (valency of corrosion reaction), and $\rho = 7.85$ g/cm^3 (density of Fe). The corrosion rate, $i_{corr}(t)$, is measured in μA/cm^2 and time (t) in year. As F, A, z and ρ are universal constants, we assume the overall modeling discrepancy to be present in the model of $i_{corr}(t)$ only. By introducing the correcting random variable E into the estimation, the true model of i_{corr} is given as

$$I_T(t) = i_{corr}(t) e^E \tag{2}$$

where E is assumed to follow a zero mean Gaussian distribution: $E \sim \mathcal{N}(0, \sigma_E)$, and $I_T(t)$ describes the true value of the corrosion rate.

Usually the corrosion rate of a corroding structure is a function of time, typically due to seasonal variations. However, an annual average time-invariant rate of corrosion have been adopted in many studies focusing on the probabilistic assessment of corroding structures (Enright and Frangopol 1999, Val and Stewart 2003, Stewart 2004, Firodiya et al. 2015). Thus,

$$i_{corr}(t) = C \tag{3}$$

where C is the random variable representing the time-invariant corrosion rate. Combining Eq. (2) and Eq. (3) the corrosion model becomes

$$I_T = C e^E \tag{4}$$

and the reduction in the rebar diameter is

$$\delta(t) = \frac{2A}{\rho z F} \int_0^t I_T \mathrm{d}t = 0.02325 I_T t \quad \text{(mm)} \tag{5}$$

3 BAYESIAN MODEL UPDATING FOR CORROSION

It is sufficient to update the corrosion rate model with in-situ measurements of corrosion rate, whose parameters are $\boldsymbol{\xi} = [C \quad \sigma_E]^\top$. The NDT measurement of corrosion is taken as the actual corrosion rate and used for updating.

3.1 *Likelihood function*

The parameter $\boldsymbol{\xi}$ conditioned predictive distribution of corrosion rate based on Eq. (4) is

$$f(I_T|\boldsymbol{\xi}) = \frac{1}{I_T \sigma_E \sqrt{2\pi}} e^{\left[-\frac{(\ln I_T - \ln C)^2}{2\sigma_E^2}\right]} \tag{6}$$

Eq. (6) is used to form the likelihood function for a reading of I_T as $f(\hat{I}_{T_j}|\boldsymbol{\xi})$, where $\hat{I}_T$ is the measured

value of the corrosion rate. For m number of measurements of the corrosion rate, assuming each to be statistically independent of the other the overall likelihood function can be formed as

$$\mathcal{L}(\boldsymbol{\xi}) = \prod_{j=1}^{m} f(\hat{I}_{T_j}|\boldsymbol{\xi}) \tag{7}$$

3.2 *Prior distribution*

The parameters $\boldsymbol{\xi} = [C \quad \sigma_E]^\top$ can take only positive values. Therefore their prior distributions are modelled as a lognormal distributions. A prior estimate of corrosion rate may be obtained from $\frac{37.8(1-\text{w/c})^{-1.64}}{x}$ (Val & Stewart 2003). For water-cement ratio w/c $= 0.45$ and effective concrete cover $x = 50$ mm, a corrosion rate of 2.015 μA/cm^2 is obtained, which is taken as the mean of C. Its coefficient of variation (COV) is taken as 0.3 (Enright & Frangopol 1999) leading to the following prior:

$$\ln C \sim \mathcal{N}(0.6575, 0.2936) \tag{8}$$

Stewart (2009) reported that the COV of corrosion rate can vary from 0.25 to 0.6 for typical covers and concrete strengths. The corresponding lower standard deviation is adopted as the 0.5 percentile value and the upper standard deviation as the 99.5 percentile value to form the prior distribution of σ_E:

$$\ln \sigma_E \sim \mathcal{N}(-0.2479, 0.17) \tag{9}$$

The joint prior distribution is taken as the product of the densities of individual parameters, by assuming the parameters to be independent of each other:

$$f'(\boldsymbol{\xi}) = f(C)f(\sigma_E) \tag{10}$$

3.3 *Corrosion rate inspection data for model updating*

As suggested by IRC (2002) a prescriptive inspection may be done every two years. In this work, during such a biennial inspection the corrosion rate is measured using the LPR technique. Recently, Guo et al. (2014) have proposed a comprehensive model to predict the time-varying corrosion rate:

$$\begin{aligned} i_{corr}(t) = &\left[e^{-6000(M_c-0.75)^6}\right] \times \left[\frac{(1-\text{w/c})^{-1.64}}{x}\right] \\ &\times \left(\frac{C_{so}+C_{th}}{2C_{th}}\right) \times \left[e^{2283\left(\frac{1}{284.15}-\frac{1}{T_m}\right)}\right] \\ &\times \left\{\frac{(T_h-T_l)\sin[2\pi(t-a_s)]}{8.6(t-a_s)} + 7.6\right\} \end{aligned} \tag{11}$$

This model is complicated in the sense that it considers many environmental factor. In the present work, it is assumed that this model is exact and values are generated for corrosion rate and used for updating the assumed model. This model is used only to supplement the lack of actual corrosion rate measurements. In this relation, M_c is the moisture content, w/c is the water cement ratio, C_{so} and C_{th} are the water soluble and threshold chloride concentration (kg/m^3) at the steel level, respectively. T_m is the annual mean temperature (K) at the depth of steel, T_h is the average high temperature (K) and T_l is the average low temperature (K). a_s is corrosion initiation season factor.

Values of the parameters used in the above equation are adopted from Guo et al. (2014). The temperature values however are taken from Allampallewar & Srividya (2008) for Santacruz in Mumbai, India, with w/c $= 0.45$ and $x = 50$ mm. It is assumed that corrosion rate is measured biennially upto 20 years from corrosion initiation, after which no measurement is made. Fig. 1 shows biennial values of the measured corrosion rate, $\hat{I}_T$ obtained by introducing some randomness in Eq. (11). Since in real life, corrosion rate values may not follow a deterministic relation, the randomness is induced to simulate such uncertainty. This randomness is in the form of a multiplicative lognormal random variable with mean 1 and standard deviation 0.1. Using a lognormal RV ensures positivity of the quantity. The value obtained from Eq. (11) is multiplied by a sample value of this lognormal RV. These values are considered to be the readings taken by the LPR based NDT at the mid-span of the bridge at any inspection time. As a simplification, it is assumed that the "uniform" corrosion rate at any other location in the bridge remains the same.

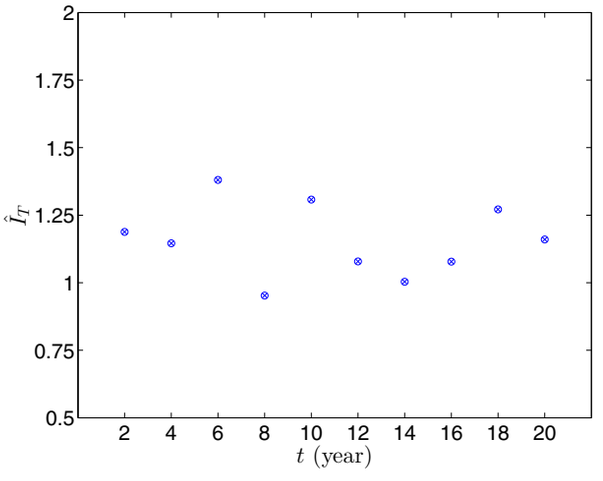


Figure 1: Biennial values of measured corrosion rate for updating

3.4 *Updating*

The model parameters are updated to the posterior $f''(\boldsymbol{\xi})$ using Bayesian inference

$$f''(\boldsymbol{\xi}) \propto \mathcal{L}(\boldsymbol{\xi})f'(\boldsymbol{\xi}) \tag{12}$$

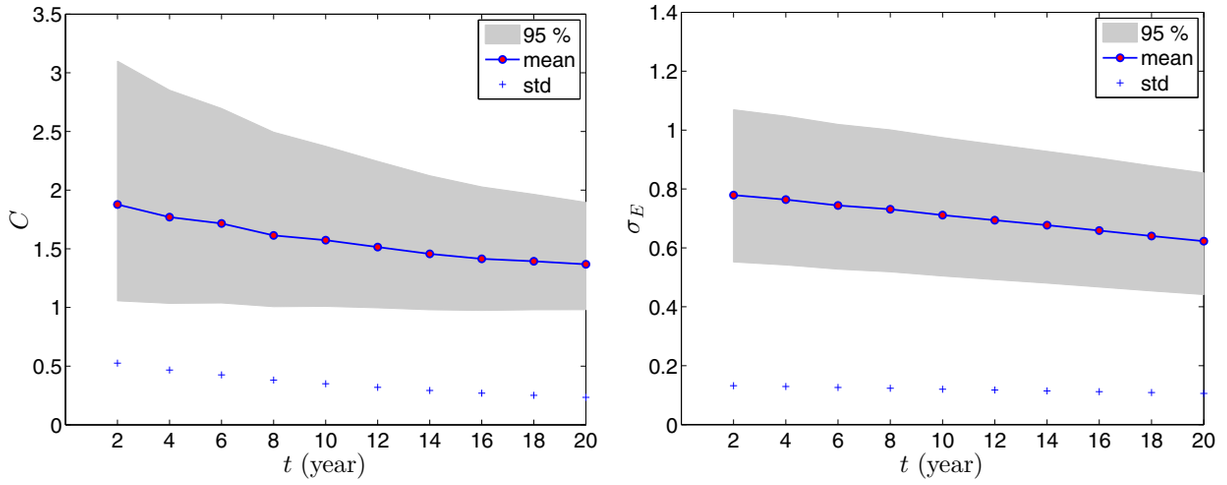


Figure 2: Mean and 95% bounds for the updated parameters, C and σ_E

through the Metropolis algorithm. In the Metropolis simulation, $N = 5,00,000$ samples are generated and used for inference after "thinning" at 10 samples and applying a suitable "burn-in". Fig. 2 shows the mean and 95% confidence interval of the parameters, updated at each new measurement in every two years. It is observed that the spread indicated by the 95% interval reduces as more inspection information are included for updating the corrosion rate model.

3.5 *Robust model prediction*

The (corrosion model parameters) $\boldsymbol{\xi}$-conditioned predictive distribution of the true corrosion rate (I_T) for any time t is as per Eq. (6). Once the corrosion rate model is updated, the parameters $\boldsymbol{\xi}$ are available in the form of sample values. In most of Bayesian inferences applied to model updating in engineering problems, either the sample mean or the sample median value is used for prediction (Faroz 2017). This ignores the parameter uncertainty. In the present work, a single parameter-unconditioned distribution of I_T, which includes the variability due to the random samples of $\boldsymbol{\xi}$, can be obtained using the total probability theorem for a robust predictive distribution for any time t:

$$f(I_T) = \int_{\boldsymbol{\Xi}} f(I_T|\boldsymbol{\xi}) f''(\boldsymbol{\xi}) \mathrm{d}\boldsymbol{\xi} \tag{13}$$

The above PDF can be approximated by using the N samples $\boldsymbol{\xi}^{(k)}$ from $f''(\boldsymbol{\xi})$:

$$f(I_T) \approx \frac{1}{N} \sum_{k=1}^{N} f(I_T|\boldsymbol{\xi}^{(k)}) \tag{14}$$

Samples of I_T from the above PDF can be obtained as (Sankararaman & Mahadevan 2013):

1. Generate $u \sim \mathcal{U}(0,1)$ and select one set of parameters $\boldsymbol{\xi}^{(k)}$ (obtained from updating)
2. Obtain I_{Tk} from $u = \int_0^{I_{Tk}} f(I_T|\boldsymbol{\xi}^{(k)}) \mathrm{d}I_T$
3. Repeat Steps 1-2 to obtain samples of $I_{Tk}, k = 1, \ldots, N$

4 DEGRADATION OF FLEXURAL CAPACITY

In the present work only the reduction in rebar cross-section is considered in determining the remaining flexural capacity of the bridge slab. Other effects of corrosion, such as reduction in rebar yield stress, loss of rebar ductility, loss of bond, etc., are ignored.

4.1 *Pitting corrosion*

Due to uniform reduction, the residual diameter at any instant t is

$$D(t) = D_0 - \delta(t) \tag{15}$$

where, D_0 is the diameter of the uncorroded bar. The assumption of uniform corrosion is an idealistic assumption, a realistic estimation of the failure of a structure due to corrosion needs to account for pitting effects (non-uniform corrosion). The pitting effect can be accounted through the application of an area spatial heterogeneity factor R (Zhang et al. 2014). R is characterised by a Gumbel distribution whose parameters, the scale (ν) and the location (κ), are expressed as functions of the mass loss ratio (η_t) at time t:

$$\eta_t = \frac{D_0^2 - D(t)^2}{D_0^2} \tag{16}$$

As suggested by Zhang et al. (2014), the statistics of R is defined for a rebar element length of 150 mm, the parameters of the Gumbel distribution for a 20 mm diameter rebar being

$$\nu = 0.454\eta_t + 1; \qquad \kappa = 0.329\eta_t \tag{17}$$

Assuming full correlation of steel loss between rebars at a given location at any time, the minimum residual steel area comprising of n_b rebars is calculated as

$$A_{\min}(t) = \frac{n_b \frac{\pi}{4} D(t)^2}{R(t)} \tag{18}$$

4.2 *Probabilistic flexural capacity estimation*

Following the specifications of the Indian Standard for RC design, the time-varying moment capacity of the singly-reinforced RC slab is calculated as (Faroz et al. 2016)

$$M_r(t) = f_y A_{\min}(t) \left[d - 0.77 \frac{f_y A_{\min}(t)}{b f_c} \right] \tag{19}$$

Here, b is the (effective) width of the slab, f_y is the yield strength of steel and f_c is the crushing strength of concrete. Variations in the geometric parameters such as d, b are neglected (Ranganathan & Deshpande 1987) and their nominal values are adopted as best estimates. The statistical properties for material parameters are given in Table 1 (Faroz et al. 2016).

Table 1: Statistics of material parameters

	Distribution	Mean	Standard deviation	Unit
f_y	Lognormal	461.9	41.57	N/mm^2
f_c	Normal	31.6	4	N/mm^2

To infer the probabilistic information of the time-varying moment capacity considering non-uniform corrosion, we propose the following sampling steps:

1. Draw samples of corrosion rate I_T at time t from $f(I_T)$ of Eq. (14).
2. Compute the reduction in diameter $\delta(t)$ from Eq. (5) and obtain the reduced diameter $D(t)$ using Eq. (15)
3. Evaluate η_t from Eq. (16) and the Gumbel parameters of R as in Eq. (17)
4. Sample R for the parameters obtained in Step 3. and obtain $A_{\min}$ using Eq. (18)
5. Sample f_y and f_c from their respective distributions
6. Compute the moment capacity M_r using Eq. (19)
7. Repeat above steps to obtain N samples of M_r

Note that all samples with $\delta > D_0$, $D_0 < 0$, $R < 1$, $f_c < 0$ or $M_r < 0$ are discarded.

5 ESTIMATION OF SERVICE LIFE BASED ON FLEXURE CAPACITY

Figure 3 shows load arrangement causing the maximum moment at the mid-span of the bridge for the Class AA tracked vehicle. The length (4.82 m) of the uniformly distributed load (UDL) is obtained based on the effective width method of load dispersion for

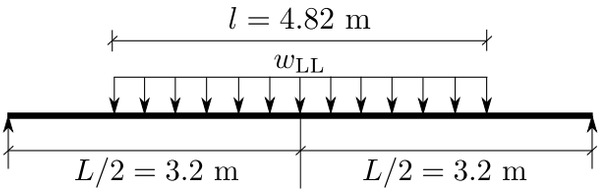


Figure 3: Sketch of bridge

the Class AA tracked vehicle. The value of this UDL with impact is $w_{\mathrm{LL}} = 25$ kN/m (unfactored). For a lack of information on the distributional nature of live load defined in the relevant Indian codes, the live load intensity on this bridge is considered known. The dead load intensity w_{DL} is also assumed to be deterministic. The external moment at the midspan is therefore

$$M_q = \frac{w_{\mathrm{DL}} L^2}{8} + \frac{w_{\mathrm{LL}} l(2L - l)}{8} \tag{20}$$

The limit state function for collapse against flexure at the mid-span can now be expressed as

$$G(t) = M_r(t) - M_q \tag{21}$$

In the limit state M_r is the only random variable. At any given time t, with the knowledge of the distribution of M_r the instantaneous probability of failure can be computed as

$$P_f(t) = F_{M_r}(M_q) \tag{22}$$

where $F_{M_r}(\cdot)$ is the cumulative distribution function (CDF) of $M_r(t)$. However in the present case, we have N sample values of M_r at time t, with which the probability of failure can be computed as

$$P_f(t) = \frac{1}{N} \sum_N \mathbb{I}(G(t) < 0) \tag{23}$$

where $\mathbb{I}(G(t) < 0) = 1$ for $G(t) \leq 0$ and 0 otherwise. The results are expressed in terms of the instantaneous reliability index ($\beta(t)$) which is related to the instantaneous failure probability estimate as

$$\beta(t) \approx -\Phi^{-1}[P_f(t)] \tag{24}$$

Here, $\Phi(\cdot)$ is the standard normal CDF operator.

To assess the service-life of the bridge, an acceptance criterion is required. In this work, this criterion is set at the minimum acceptable reliability or target reliability (β_T) for the structure. The service-life is considered terminated if the actual reliability, $\beta(t)$, falls below this value. The target reliability index for Consequence Class 2, considering repair is 3.3, and for closing down a structure is 2.5 (structure becoming unfit) (Steenbergen & Vrouwenvelder 2010).

Fig. 4 shows the reliability degradation over time, based on the sequential updating of the corrosion model. The thick continuous (blue) line shows the reliability plot based on sequential updating and predicted degradation for every biennial measurement

conducted. This line shows a sudden change on the predicted reliability value at every two years. This is because a new measurement is done biennially and the updating of the model causes this sudden shift. Considering this, a smoothed time-varying "reliability profile" is created for this structure. This profile can be compared with the two β_T lines, one for repair and one for closing down the structure. Based on this, the bridge reaches a repair requirement in 2.78 years from the initiation of corrosion. One should note that this decision is reached after updating the degradation process through only the first LPR measurement (at $t = 2$ years). From the reliability profile, closing down the structure is recommended at the tenth year of corrosion. However, if we take a look at the thick continuous line, this closing is predicted at 9.29 years based on the update available on the eighth year, that is when we take the previous measurement. Of course this estimate would be wrong and one should take a note of the trend visible in the "profile" plot and estimate accordingly. However, such trends will not be visible if the measurements are not repeated multiple times. The thin continuous (blue) lines show the predictions based on the updates stopping after the fourth and the sixth year. These two lines show a considerable difference in the service-life prediction based on closing down the bridge, with 8.25 years and 8.68 years of service-life predicted by the four-year and six-year updates, respectively.

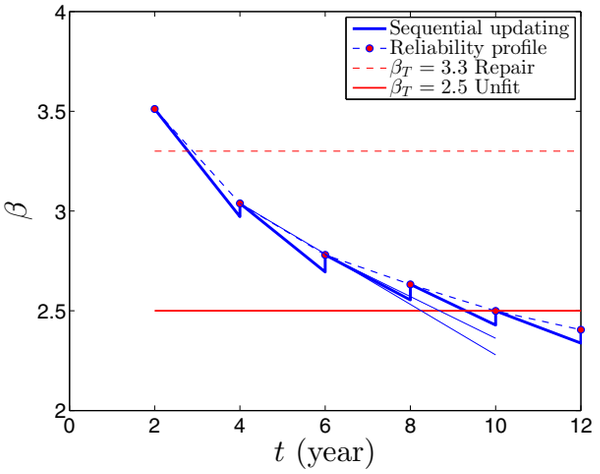


Figure 4: Degradation of reliability over time

6 CONCLUSIONS

Corrosion of rebars is the primary durability concern in RC structures. From a structural engineering point of view, loss of rebar area is the most significant aspect of corrosion because it may eventually lead to the possible collapse of a structure. The present study proposes a novel approach of Bayesian updating of an existing steel loss model based on monitored data. This paper presents the estimation of the service-life of a bridge in a probabilistic framework using sequential updating based on biennial LPR measurements of the corrosion rate. It also demonstrates the computation of this service-life for a RC slab bridge. The probabilistic framework has the advantage of including the uncertainty of the corrosion phenomenon, which can be easily incorporated into the time-varying reliability estimation for a degrading structure, and its service-life estimation. The results show the importance of obtaining a trend in the "true" degradation based on measurements taken at multiple time instants.

The proposed framework of corrosion reliability analysis can be further extended to include complexities, for example, (a) the corrosion initiation time, (b) the uncertainty in NDT measurements, (c) a probabilistic load model, (d) the spatial variability of corrosion, and at a larger scale, to come up with an ageing management system for corroding RC structures.

REFERENCES

Allampallewar, S. B. & A. Srividya (2008). Corrosion performance of reinforced concrete member along Indian coasts: Effect of temperature & relative humidity. *International Journal of Performability Engineering 4*(3), 285–292.

Almusallam, A. A., A. S. Al-Gahtani, A. R. Aziz, F. H. Dakhil, & Rasheeduzzafar (1996). Effect of reinforcement corrosion on flexural behavior of concrete slabs. *ASCE Journal of Materials in Civil Engineering 8*(3), 123–127.

Andrade, C. & I. Martínez (2005). Calibration by gravimetric losses of electrochemical corrosion rate measurement using modulated confinement of the current. *Materials and Structures 38*(283), 833–841.

Ditlevsen, O. (1982). Model uncertainty in structural reliability. *Structural Safety 1*(1), 73–86.

Ellingwood, B. R. (2005). Risk-informed condition assessment of civil infrastructure: State of practice and research issues. *Structure and Infrastructure Engineering 1*(1), 7–18.

Enright, M. P. & D. M. Frangopol (1999). Condition prediction of deteriorating concrete bridges using Bayesian updating. *ASCE Journal of Structural Engineering 125*(10), 1118–1125.

Faroz, S. A. (2017). *Assessment and Prognosis of Corroding Reinforced Concrete Structures through Bayesian Inference*. Ph. D. thesis, Indian Institute of Technology Bombay, Mumbai, India.

Faroz, S. A. & S. Ghosh (2017). Falling Short But Not Falling Down: Challenges and Solution for the Service-Life Estimation of Gradually Degrading Bridges. *The Masterbuilder 19*(7), 144–148.

Faroz, S. A., N. N. Pujari, & S. Ghosh (2014). A Bayesian Markov Chain Monte Carlo approach for the estimation of corrosion in reinforced concrete structures. In B. H. V. Topping and P. Iványi (Eds.), *Proceedings of the Twelfth International Conference on Computational Structures Technology*, Stirlingshire, UK. Civil-Comp Press. Paper 150.

Faroz, S. A., N. N. Pujari, & S. Ghosh (2016). Reliability of a corroded RC beam based on Bayesian updating of the corrosion model. *Engineering Structures 126*, 457–468.

Faroz, S. A., N. N. Pujari, R. Rastogi, & S. Ghosh (2017). Risk Analysis of Structural Engineering Systems Using Bayesian Inference. In P. Samui, S. Chakrabarty, and D. Kim (Eds.), *Modeling and Simulation Techniques in Structural Engineering*, Chapter 14, pp. 390–424. IGI Global.

Firodiya, P. K., A. K. Sengupta, & R. G. Pillai (2015). Evaluation of corrosion rates of reinforcing bars for probabilistic assessment of existing road bridge girders. *ASCE Journal of Performance of Constructed Facilities 29*(3).

Ghosh, S. & S. A. Faroz (2016). Integrating NDT measurements

and theoretical model for the failure assessment of a corroding girder. In *1st Biennial Conference On Bridge Management System (IBMS2016)*, New Delhi, India.

Guo, Y., D. Trejo, & S. Yim (2014). New model for estimating the time-variant seismic performance of corroding rc bridge columns. *ASCE Journal of Structural Engineering 141*(6).

IRC (2002). *An approach document for assessment of remaining life of concrete bridges*. IRC:SP:60-2002, Indian Roads Congress, New Delhi, India.

IRC (2011). *Code of Practice for Concrete Road Bridges*. IRC:112-2011, Indian Roads Congress, New Delhi, India.

IRC (2014). *Standard Specification and Code of Practice for Road Bridges-Section II Loads and Stresses*. IRC:6-2014, Indian Roads Congress, New Delhi, India.

Malumbela, G., P. Moyo, & M. Alexander (2012). A step towards standardising accelerated corrosion tests on laboratory reinforced concrete specimens. *Journal of the South African Institution of Civil Engineering 54*(2), 78–85.

Mangat, P. S. & M. S. Elgarf (1999). Flexural strength of concrete beams with corroding reinforcement. *ACI Structural Journal 96*(1), 149–158.

Ranganathan, R. & A. G. Deshpande (1987). Reliability analysis of reinforced concrete frames. *ASCE Journal of Structural Engineering 113*(6), 1315–1328.

Sankararaman, S. & S. Mahadevan (2013). Separating the contributions of variability and parameter uncertainty in probability distributions. *Reliability Engineering and System Safety 112*, 187–199.

Steenbergen, R. D. J. M. & A. C. W. M. Vrouwenvelder (2010). Safety philosophy for existing structures and partial factors for traffic loads on bridges. *Heron 55*(2), 123–140.

Stewart, M. G. (2004). Spatial variability of pitting corrosion and its influence on structural fragility and reliability of rc beams in flexure. *Structural Safety 26*(4), 453–470.

Stewart, M. G. (2009). Mechanical behaviour of pitting corrosion of flexural and shear reinforcement and its effect on structural reliability of corroding rc beams. *Structural Safety 31*(1), 19–30.

Val, D. V. & M. G. Stewart (2003). Life-cycle cost analysis of reinforced concrete structures in marine environments. *Structural Safety 25*(4), 343–362.

Zhang, W., B. Zhou, X. Gu, & H. Dai (2014). Probability distribution model for cross-sectional area of corroded reinforcing steel bars. *ASCE Journal of Materials in Civil Engineering 26*(5), 822–832.

Maintenance, Safety, Risk, Management and Life-Cycle Performance of Bridges – Powers, Frangopol, Al-Mahaidi & Caprani (Eds)
© 2018 Taylor & Francis Group, London, ISBN 978-1-138-73045-8

Brunei Temburong Link – Temburong Viaduct

Naeem Hussain
Arup Fellow, Director, Global Bridge Leader

Sammy Yip
Associate, Arup Hong Kong

John Cain
Senior Engineer, Arup Melbourne

ABSTRACT: Brunei Temburong Link is one of the largest infrastructure projects currently being constructed in South-East Asia. It is a 30km dual 2-lane road link which will connect the main Brunei districts of Muara, Tutong and Belait with the isolated district of Temburong which is separated by the Malaysian state of Sarawak. The link comprises of approximately 3km of tunnels, viaducts and at-grade road on land, 14km of marine viaduct across Brunei Bay, two navigation channel cable stay bridges and 12 km of swamp crossing viaduct. The paper will describe the feasibility study and detail design of the Link focussing on the unique construction of the swamp forest viaduct.

1 INTRODUCTION

1.1 *Location*

Brunei is located on the north coast of the island of Borneo in Southeast Asia.

Apart from its coastline with the South China Sea, it is completely surrounded by the state of Sarawak, Malaysia; and is separated into two parts by the Sarawak district of Limbang (Figure 1).

This physical separation of Temburong district from the majority of Brunei has significantly affected the economic development of the district and Brunei as a whole. Despite comprising 23% of the total land area of Brunei, Temburong only contains 2% of the population.



Figure 1 Map of Brunei

To travel to Temburong by land requires passing into and out of Sarawak through a long circuitous route typically involving significant waiting times at the borders which can result in a journey time of up to four hours between the central business district of Bandar Seri Bagwan and the main district town of Bangar (Figure 2). Alternatively it is possible to travel by speedboat across Brunei Bay and then up-river to Bangar. Neither of these alternatives offer 24 hours a day accessibility.

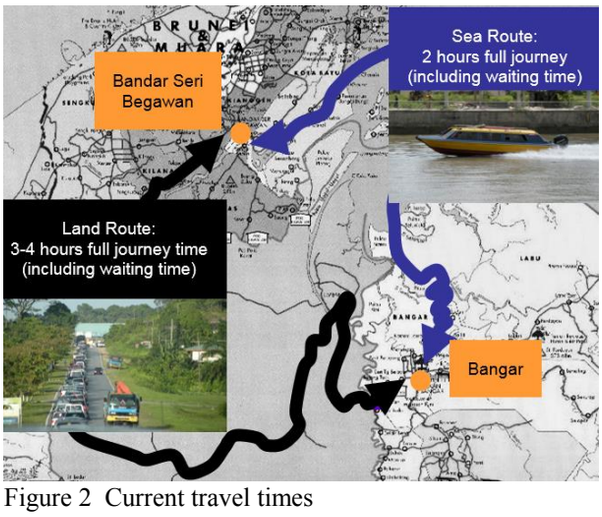


Figure 2 Current travel times

2 ROUTE SELECTION

2.1 *Optional Alignments*

A route selection exercise was carried out to determine the most favourable alignment across Brunei Bay as well as the optimum connection points in both Brunei-Muara and Temburong districts. In order to assess the route options, the goal achievement matrix technique was adopted considering the following criteria:

- Planning and Land Matters
- Environmental Issues

- Transport Planning
- Impact on Local Community
- Engineering
- Implementation Programme
- Cost

Within each of the criteria listed above, sub-criteria were investigated and scored. Sensitivity studies were carried out varying the weight assigned to each of the criteria in order to confirm the robustness of the route selection.

The above assessment considered information from various sources, including available master plans. Spatial data was overlaid and correlated using a Geographic Information Systems (GIS) model. This enables multiple layering of geographic data to ensure that all captured information is correlated and taken into account in the development of the alignment.

An example screenshot from the GIS model is shown in Figure 3. In this case the four different routes that were considered are overlaid on the growth areas in Temburong which were extracted from the masterplans. The existing road network, designated navigation channels, mangrove forests of high ecological value and national boundaries are also shown. These are just examples of the many layers of information which were included.

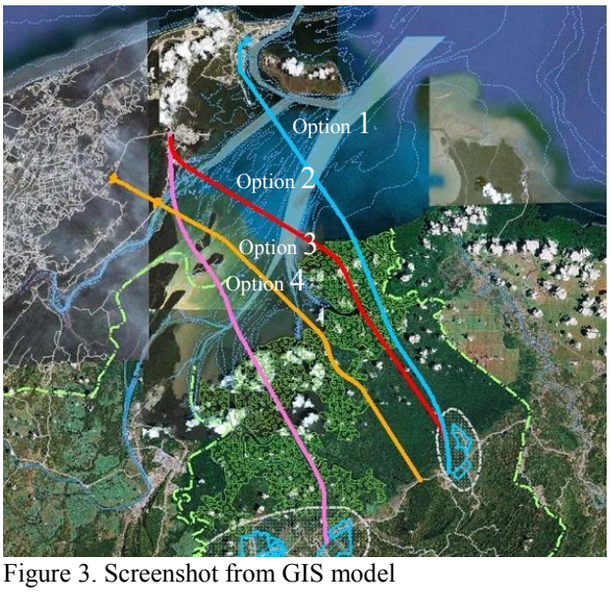


Figure 3. Screenshot from GIS model

2.2 *Chosen Alignment*

Option 3 (refer Figure 3) was selected as the preferred route with the highest score under a range of sensitivity tests. The advantages are summarised as:
Transport Planning: It provides the shortest travel distance and travel time between Brunei-Muara and Temburong.
Planning and Land Matters: It requires minimal private land acquisition and hence has the least land issues and anticipated to be more acceptable to the general public.
Environmental: It will avoid encroachment in conservation mangrove areas and minimise encroachment through production mangrove areas.
Stakeholder Opinion: It was the preferred alignment of the majority of stakeholders.

3 TEMBURONG SWAMP VIADUCT

3.1 *Location and Alignment*

Following completion of the Feasibility Study for the 30 km long Brunei Temburong Link, the project was divided into several construction packages. The location and alignment of the 12 km low height piled slab viaduct crossing the peat swamp forest in the Temburong District is shown in Figures 4 & 5

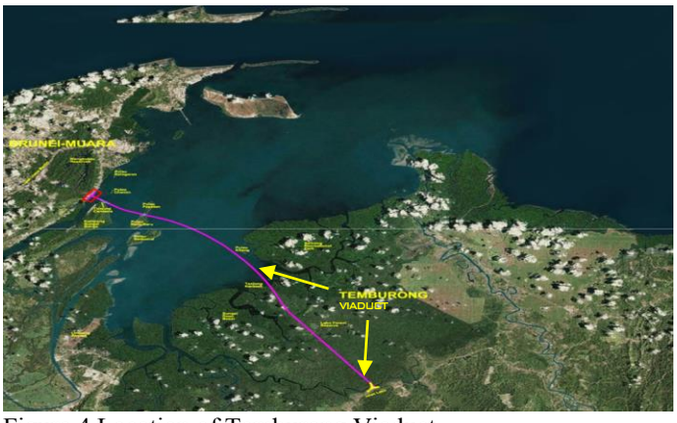


Figure 4 Location of Temburong Viaduct

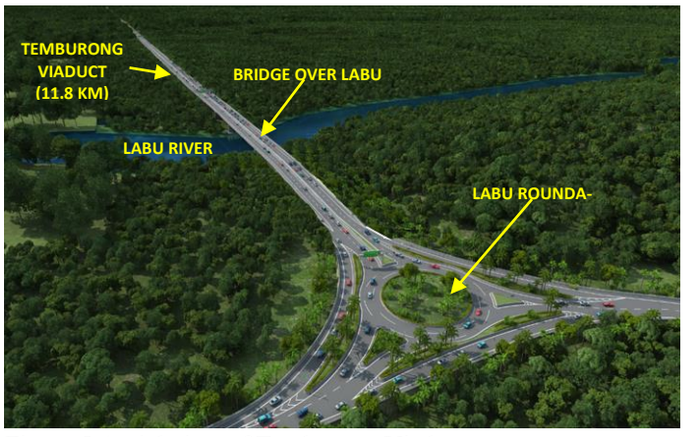


Figure 5 Aerial view of Temburong Viaduct

The peat swamp forest has unique and endangered flora and fauna. The soil conditions consist of soft peat overlying soft marine clay with depths exceeding 70m. Due to these challenging ground conditions and in order to safeguard the flora and fauna of the swamp forest, a top-down construction method has been developed, with all construction undertaken from deck level.

3.2 *Design Development*

The concept of using a series of short spans to cross a swamp is not new. Given the poor ground conditions, loadings from shorter spans are usually all the

soil can accommodate. This did pose quite a problem however as typically, for such a long viaduct, a larger span concept would be more desirable, to reduce the number of spans and foundations required.

3.3 *Key Considerations*

For this viaduct, the key considerations that have defined the design are:

- Programme and cost
- Ground conditions
- Environmental and site constraints
- Construction method

3.3.1 *Ground Conditions*

The ground profile comprises of a very soft peat layer of depths up to 4m and overlying soft marine clays at depths up to 70m. Water level is up to the ground level at high tides. The peat material has very little strength and is unable to support any large construction machinery or plant.



Figure 6 Typical site conditions

The soil has very little capacity in supporting load both axially and laterally. The minimal lateral resistance from the peat layer means that piles would be essentially unrestrained throughout the overlying peat layer. For the proposed design of 12m span length, the piles are being driven up to 80m for a large proportion of the alignment. Increasing the pile length will increase the risk of pile damage during the pile driving process.

3.3.2 *Environmental and site constarints*

The viaduct crosses the peat swamp forest which is in turn surrounded by mangrove forest, both of which are essentially untouched. To minimise the potential impact on the environment, the project Environmental Impact Assessment restricts the use of embankments. As shown in Figure 7, there are only three points of access to the alignment. Since temporary access roads by embankment are prohibited, there can only be a maximum of four working fronts. This further called for a design that could be constructed easily and quickly.

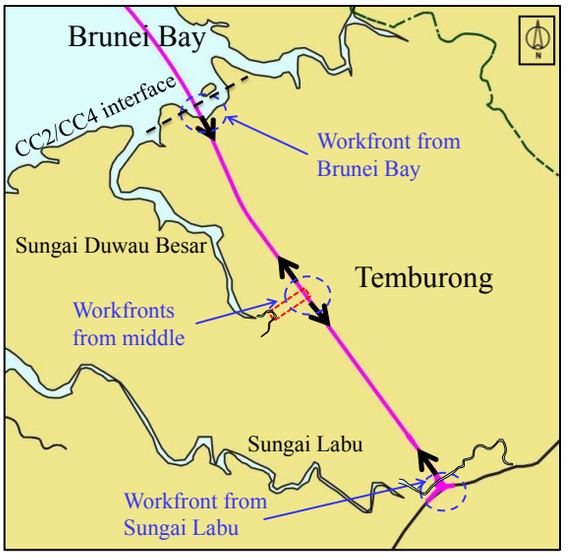


Figure 7 Work fronts

3.3.3 *Top-down construction*

The constraints required a design that could be constructed in a top-down manner, meaning material delivery, and installation of structural components (including piles, pile caps and superstructure) can be carried out from the viaduct deck already erected. Bridge scheme.With the key considerations in mind, evaluation of options was carried out and the following describes the key features of the scheme.

3.4 *Span length*

Determining the span length was an iterative process. The primary factor was the limited foundation capacity due to the poor ground conditions.

The span was chosen such that only a single row of piles are required at each pier, to minimise the size and weight of the precast pile cap.

With construction needing to take place at deck level and the carriageways only 10m wide, a shorter span length that would permit smaller structural components and equipment was preferred.

Consideration to the crane size and lever arm for installing the piles and pile caps was also given.

Considering the above, a 12m span was chosen.

3.5 *Viaduct Deck Structure*

The viaduct consists of almost 200 no. 120m long piled slab modules. Each module consists of 10 no. 12m spans. The design maximises the use of precast concrete elements and repetition, enabling construction to be undertaken in a fast track manner, a necessity to meet the completion date.

Each pier foundation consists of 4 no. 0.9m diameter concrete spun piles, with a precast pile cap. The piles and precast cap are connected via a cast in-situ pile plug at each pile.

The superstructure comprises of five precast double T beams per span, which are landed onto the precast pile caps.

Four deck slab stitch pours connect the double T beams together to form the deck slab, whilst an in-situ diaphragm pour connects the double T beams to the precast pile cap, completing the structure. Figures 8 and 9.

It was decided that the deck would be of monolithic design for two main reasons; to reduce the number of bearings required and to maximize the foundation efficiency.

Reducing the number of bearings reduces the amount of maintenance required over the structure's life. This is critical due to the remote location of the bridge and difficulty in accessing the deck soffit and to support machinery from ground level. An added advantage is that during construction, the number of bearing installation is minimised

A deck cast monolithically with the substructure also meant that the piles would experience double curvature in bending, reducing their effective buckling length. This was critical given the pile length and poor lateral capacity of the soil.

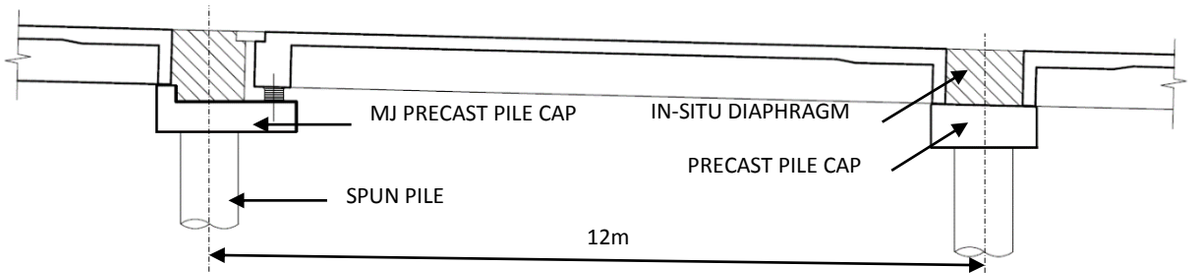


Figure 8. Typical elevation of the Piled Slab Viaduct (M.J included)

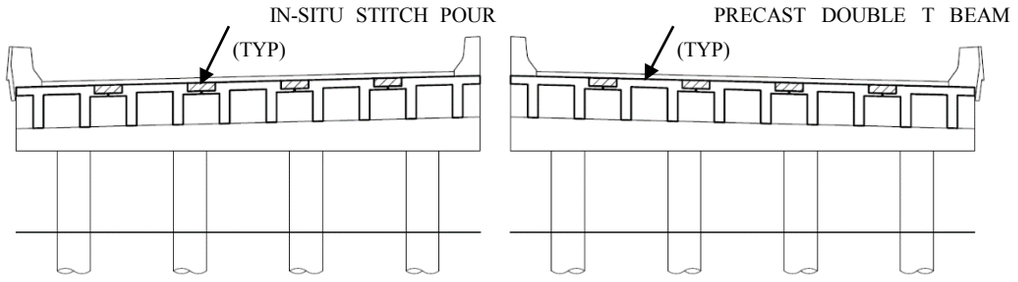


*Figure 9. Typical section of the Piled Slab Viaduct*Monolitic joints

3.6 *Foundations*

3.6.1 *Piling*

Prestressed precast spun piles were chosen primarily due to their cost relative to steel piles. Another reason was the concern of durability and corrosion of steel piles in the aggressive soil condition. The spun piles are being manufactured in lengths up to 30m and are welded together via steel plates located at each end. The prestressed strands within the piles, are welded to these plates to ensure continuity across the total pile, when lengths are connected.

3.6.2 *Precast pile cap*

The precast pile cap is a solid concrete element with voids to permit encasement of the piles.

The precast pile cap is of varying depth, such that when the double T beams are landed, the deck will be at the correct slope and grade.

Four steel I sections will be cast into each precast pile cap, each spanning across a pile void.

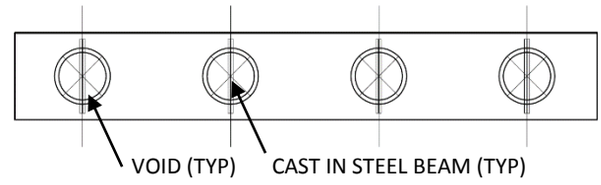


Figure 10 Plan of precast pilecap

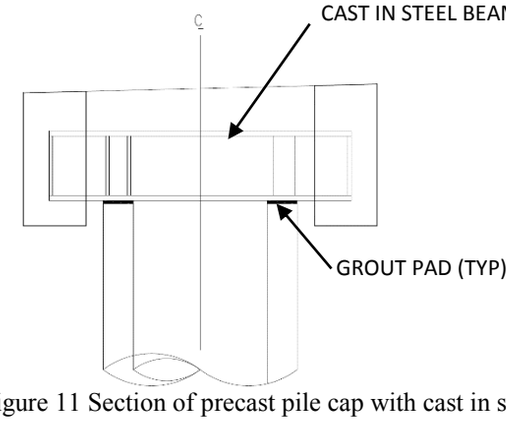


Figure 11 Section of precast pile cap with cast in steel beam

The steel beams are pivotal in both the construction and permanent cases. Firstly the beams are used as a means of temporary support when landing the precast pile cap on top of the piles. This arrangement (as opposed to having the cap soffit land

onto the pile) enables a void in the precast that is large enough to account for the pile tolerance. Furthermore the accuracy at which the pile must be cut at is reduced, as only two points per pile are in contact with the cut face.

The additional pile plug reinforcement is then installed and the in-situ pile plugs are cast. The pile cap self-weight now becomes "locked" into the steel beam. At this stage the steel beam detail has the advantage of providing a positive connection between the pile plug and the precast pile cap, without the need for excessive reinforcement being needed to be fixed on site. In addition the top of the spun pile becomes embedded within the pile plug pour. This protects the pile pre-stressed strand exposed during cutting from getting corroded.

Once the plug has been partially cured, the T-beams can be landed. At this stage the plug and steel beam act compositely and the self- weight of the precast double T beams is "locked" into the precast pile cap and composite pile plug connection.

3.6.3 *In-situ pile plug*

The in-situ pile plugs provide fixity between the spun piles and the precast pile cap. The critical consideration in designing the pile plug was ensuring there was sufficient space for the reinforcement for cases where the pile has been installed slightly away from the specified position

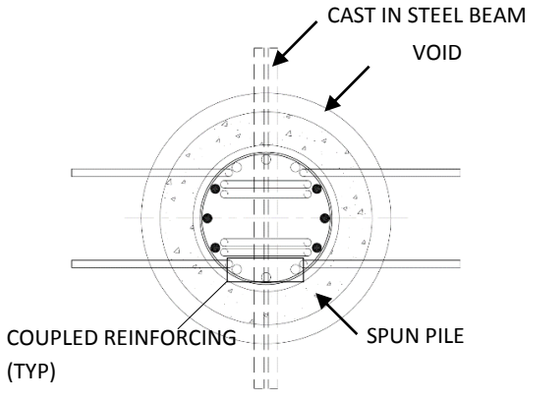


Figure 12 Plan of pile plug connection

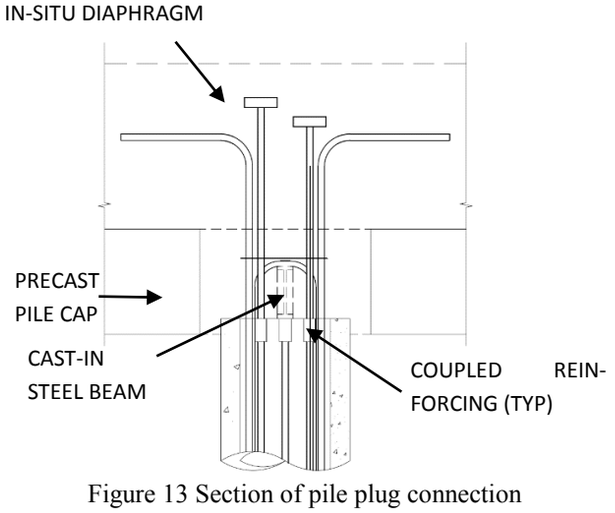


Figure 13 Section of pile plug connection

3.6.4 *In-situ diaphragm*

The in-situ diaphragm ties the precast double T beams to the precast pile cap substructure, ensuring a monolithic connection between the piles and the double T beams.

The in-situ diaphragm reinforcement comprises starter bars from the precast pile caps (to form the composite torsion element), pile plug and the precast deck beams on either side

When cured, the in-situ diaphragm works compositely with the precast pile cap. The combination of torsional and shear forces govern the design

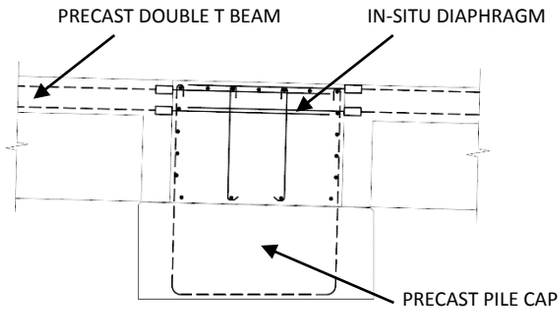


Figure 14 Section of cast in-situ diaphragm

4 CONSTRUCTION METHODOLOGY

Throughout the design process, the construction methodology and expected duration was critically scrutinised. As a result of design progression, two construction methods were devised; the standard method and fast track method. The fast-track method is being used

4.1 *Fast track construction method*

The construction is based on the use of tracked cranes and platforms working as a train. The platforms span between the row of piles.

The front part of the train comprises of three platforms for each carriageway with piling cranes sitting on the platforms. The guide for the piles is cantilevered from the platform.

Following the piling cranes there are other cranes that install temporary platforms, erection of precast pile caps and the T-beams. The combination of temporary platforms and completed deck structures allows delivery of insitu concrete, precast piles, pile caps and t-beams.

The sequence of construction is shown diagramatically in Figure 15 below, with the actual construction shown in Figure 16.

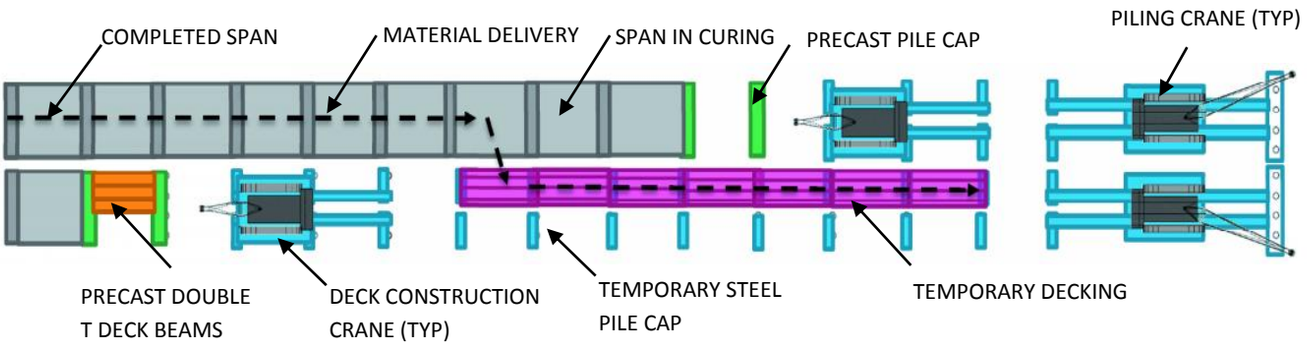


Figure 15 Fast track sequence of construction



Figure 16 Aerial views of construction

5 CONCLUSION

The Temburong swamp crossing design focused on simplifying the construction process and is enabling the construction to be carried out rapidly and entirely from deck level. The design reduces the amount of reinforcement fixing and in-situ concrete work required on site, ultimately to minimise the impacts to the surrounding forest and to maximise speed of construction.

6 ACKNOWLEDGEMENTS

This paper has been published with permission from Public Works Department, Ministry of Development, Brunei Darussalam.

7 REFERENCES

[1] Carter, M., Yip, S., Hussain, N., Chin, KK., Ding, LS., Lim, SY. "Temburong Bridge, Brunei – Feasibility Study". IABSE Conference 2015: Providing Solutions to Global Challenges, Geneva, September 2015.

[2] John Cain, Sammy Yip, Chi-Ho Poon, Paresh Vishnoi, Naeem Hussain "Temburong Bridge, Brunei, CC4 Swamp Crossing in Temburong District". IABSE Conference 2015: Providing Solutions to Global Challenges, Geneva, September 2015.

Maintenance, Safety, Risk, Management and Life-Cycle Performance of Bridges – Powers, Frangopol, Al-Mahaidi & Caprani (Eds)
© 2018 Taylor & Francis Group, London, ISBN 978-1-138-73045-8

Effect of cracks on air-tightness of vacuum tube bridge structures

P. Devkota & J. Park
Department of Civil and Environmental Engineering, Wonkwang University, Iksan, Republic of Korea.
E. Choi
Department of Civil Engineering, Hongik University, Seoul, Republic of Korea.

ABSTRACT: Air resistance is a very important consideration for any kinds of vehicles that travel at high speed. The vacuum tube transportation system is therefore considered as one of the most effective transportation system, which can maintain the high speed of the train by minimizing the air resistance. The air resistance can be minimized by reducing and maintaining air pressure inside the tube. For bridges with vacuum tube structures, the impact of externally applied loads on the air-tightness performance level should be taken into consideration. Therefore, the aim of this work is to study the effect of load-induced cracks on the air-tightness of concrete vacuum tube structures. To achieve this aim, a predictive model that describes the crack width is adopted and the cracking pattern on the vacuum tube structure is analyzed. The leakage rate of air through the cracks is then assessed and finally, the relationship between the crack behaviour and its effect on the air-tightness of vacuum tube structure is established.

1 INTRODUCTION

The development of fast, reliable and efficient transportation system is the prerequisite for the rapid development of the country. On the way of developing the transportation system as the fast, reliable and efficient system, the vacuum tube transportation system came into consideration. The vacuum tube transportation system is also known as the super speed tube train (SSTT) system, where the trains are expected to operate with the practical speed of 700km/h (Cassat et al. 2003, Lee et al. 2008). Therefore, this system is considered as the most effective transportation system that will be able to substitute the existing system in the sense of its operating speed.

The main idea for the development of vacuum tube transportation system (Figure 1) is to create the vacuum inside the concrete tube structure by maintaining the internal air pressure as low as possible so that the train operating inside the tube will undergo less air resistance, which ultimately increases its speed. The train, theoretically, can operate with the speed of 8000 km/h on the maglev lines through vacuum tubes but due to the great cost expected for its construction, operation, and maintenance, the system has never come into realization. Recent studies on the super speed tube train conducted by Cassat et al. (2003) and Lee et al. (2008) have aimed the operating speed of train up to 700km/h provided that the internal pressure of the tube is maintained as low as 0.1atm. Maintaining the air pressure of the tube at low level is a very challenging task. Several factors such as the material of the structure, discontinuities present in the structure such as construction joints, bolted regions, and load-induced cracks will have an effect on the air-tightness performance of the tube structure. Park et. al (2013) had studied the effect of material and discontinuities on the tube airtightness and concluded that the concrete material with high strength and the tube with less number of discontinuities is most appropriate for maintaining the airtightness of the tube. But that study lacks on consideration of the effect of cracks induced by external loads applied on the structure. Concrete structures are subject to cracks under service loads, which will cause great effect on the air-tightness due to potential air leakage.

This study describes the effect of load-induced cracks on airtightness of concrete vacuum tube structures. Under the application of external loadings, the cracks will be induced on the structure and air will inflow through the cracked portion, which is shown schematically in the figures 2 and 3. The induced cracks will show the effect on the airtightness performance of the structure. The cracks developed due to the application of external loads will increase the air inflow rate decreasing the air resisting capacity of the vacuum tube structure, which ultimately decreases the speed of the train inside the tube. The study on the effects of cracks is therefore essential to the description of the airtightness of concrete tube struc-

tures. For a study about the effect of crack on airtightness, the calculation of crack properties and the leakage rate are the important requirements.

The analytical crack model is developed from the mathematical expression proposed by Rizkalla for estimating and describing the effect of the air inflow through cracks developed due to the external loads. The crack length, width, and depth are defined as the damage indicators for the prediction of internal pressure change due to air flow. This study develops an analytical model that describes the air pressure behaviour in the vacuum tube structure and develops the relationship between load induced cracks and tube airtightness. The external load applied on the structure is assumed to be sufficient enough to form the crack in the tube structure, where the internal pressure is initially dropped down to ten percent of the atmospheric pressure. The formula for describing the internal pressure change or air inflow with time inside the tube structure is derived first based on Rizkalla formula. The pressure change inside the tube structure directly depends upon the air flow through the cracks. The results obtained from the analytical study of Rizkalla formula are calibrated with the results obtained from the experimental study.

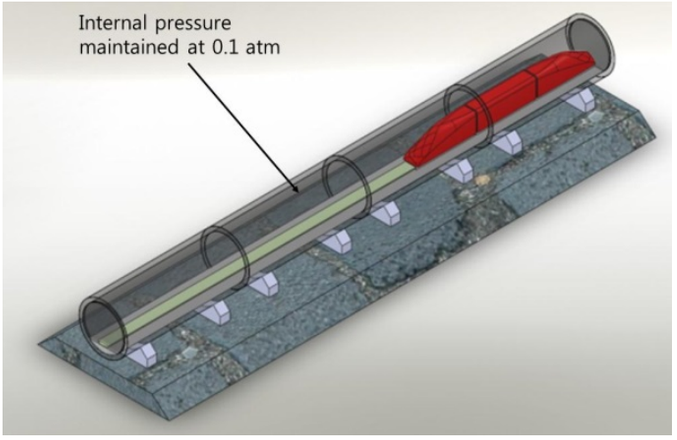


Figure 1. Vacuum tube transportation system (Park et al. 2013)

2 MODEL FOR AIR PRESSURE CHANGE DUE TO CRACKS:

Air tightness in any structure is the resistance to inward or outward air leakage through the possible leakage points. The pressure difference between inside and outside of the structure will propel for the air leakage through the cracks that are formed due to the application of external loads. The flexural cracks due to loadings would be developed on the structure as shown in figure 2. The rate of flow increases with the increase in number, width, and length of the cracks. From the design point of view, it is necessary to anticipate the amount of pressure change due to air inflow into the vacuum tube structure with time. Nam. (2010) & Park et al. (2013) had explained about the design variables like capacity and spacing of the vacuum pump along with their operating time and the operating speed of train with the consideration of airtightness of the structure. The change in pressure due to the flow of air can be determined by using various leakage rate formulas. The Bernoulli's equation was used by Choi et al. (2016) to determine the change in internal pressure along with time. Bernoulli's equation is expressed in equation (1), which relates the pressure change with some variables such as velocity, density and elevation difference between two points.

$$p_o + \frac{1}{2}\rho \cdot {v_o}^2 = p(t) + \frac{1}{2}\rho \cdot (v(t))^2 \qquad (1)$$

where p_o is the atmospheric pressure, v_o is the velocity of the air outside the structure, ρ is the density of the air, $p(t)$ is the internal pressure at time t, and $v(t)$ is the velocity of the air inflow measured inside the crack.

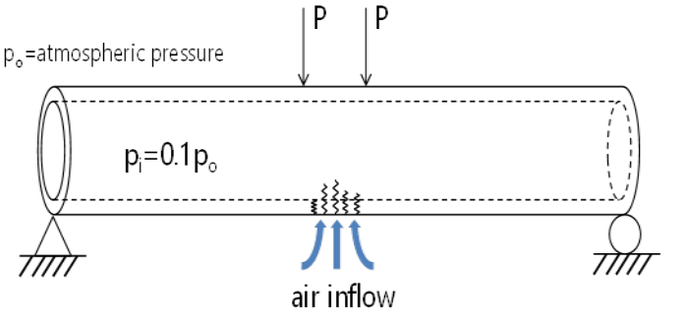


Figure 2. Loading on the tube structure (Choi et.al 2016)

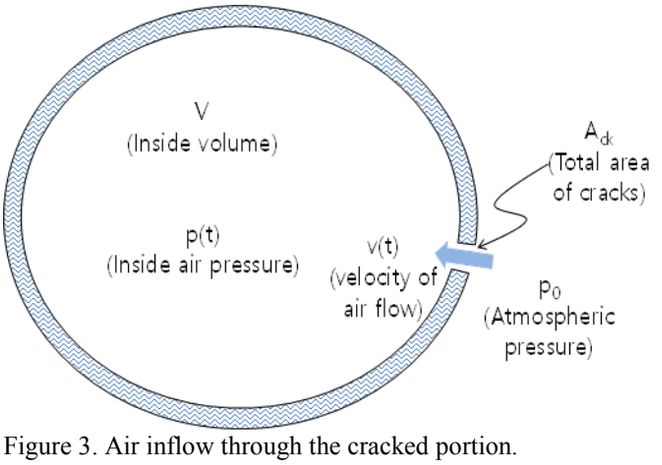


Figure 3. Air inflow through the cracked portion.

In fact, the change in pressure along with time in the concrete tube structure is affected by many other variables such as friction, viscosity, and temperature, which Bernoulli's formula does not account for.

According to Scoppe et al. (2012), the method by Rizkalla et al. (1984) provides the most reasonable and consistent result for the calculation of air leakage through cracks developed on a concrete structure. The effect of friction and viscosity of the air is explicitly

considered in the model. In this study, the Rizkalla formula is adopted for development of mathematical model for describing the internal pressure change due to cracks.

3 DERIVATION OF ANALYTICAL MODEL FOR PRESSURE CHANGE:

Rizkalla et al. (1984) developed the leakage rate formula through cracks by performing the experiment on eight reinforced wall specimens. This formula was formulated by modeling the idealized isothermal flow of air between two plates as shown in Figure 4, which is known as Poiseuille flow. The formula was developed by assuming a uniform crack width through the thickness of the wall and the flow is assumed as isothermal, steady and uniform.

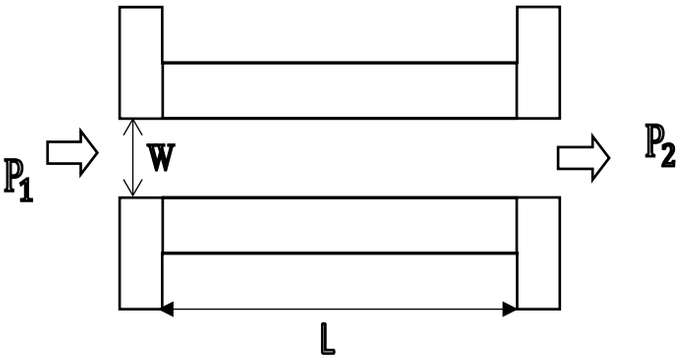


Figure 4. Flow between the plates

The flow formula developed by Rizkalla is:

$$\frac{P_1{}^2-P_2{}^2}{L}=\left(\frac{k^n}{2}\right)\left(\frac{\mu}{2}\right)^n (RT)^{n-1}\left|\frac{P_2Q}{B}\right|^{2-n}\frac{1}{1.42N*W_{avg}{}^3} \quad (2)$$

where, p_1 = Inflow pressure; p2 = outflow pressure; L = thickness of the wall; k = wall roughness coefficient; μ = Viscosity of the gas; *R* = Gas constant; *T* = Absolute temperature; *n* = Flow coefficient; *B* = Average measured crack length; *Q* = Total flow rate; *N* = Number of cracks; W_{avg} = Average crack width (input in feet).

Rizkalla had developed the formula for leakage rate by assuming the flow between the plates but our study deals with the flow of atmospheric air towards the concrete tube through the cracks formed. Initially, the internal pressure was maintained at ten percent of the atmospheric pressure but the change in pressure occurs due to the flow of air through cracks and internal pressure started to change. For determining the change in internal pressure with time, the differential equation is developed by using the Rizkalla formula.

$$\frac{P_1{}^2-P_2{}^2}{L}=C_1*\left|\frac{P_2Q}{B}\right|^{2-n} \quad (3)$$

where,

$$C_1=\left(\frac{k^n}{2}\right)\left(\frac{\mu}{2}\right)^n (RT)^{n-1}*\frac{1}{1.42N*W_{avg}{}^3}$$

$$n=\frac{0.195}{(N*W_{avg}{}^3)^{0.063}}$$

$$k=8.702\times10^6\left(N\cdot W_{avg}{}^3\right)^{0.367}$$

From the above equation (3),

$$Q=\frac{B}{P_2}\left(\frac{P_1{}^2-P_2{}^2}{C_1L}\right)^{\frac{1}{2-n}} \quad (4)$$

If, $C_2=\frac{B}{(C_1L)^{\frac{1}{2-n}}}$ then,

$$Q=\frac{C_2}{P_2}\left(P_1{}^2-P_2{}^2\right)^{\frac{1}{2-n}} \quad (5)$$

If the case of the vacuum tube, the atmospheric pressure corresponding to the outside/atmospheric pressure (P_1) can be considered as constant regardless of the flow time if the temperature and attitude are constant. If the air enters through the cracks in the tube, the outlet pressure that is the pressure inside the tube will rise with time. Thus, the pressure (P_2) will be the function of time and can be expressed as below:

$$Q(t)=\frac{C_2}{P_2(t)}\left(P_1{}^2-P_{2(t)}{}^2\right)^{\frac{1}{2-n}} \quad (6)$$

If the temperature inside and outside the tube are equal, the pressure rise inside the structure will be proportional to the air inflow; in other words,

$$P_1Q=\frac{dp_{2(t)}}{dt}V \quad (7)$$

Then, comparing above two equations (6) and (7),

$$\frac{P_1C_2}{V\cdot P_2(t)}\left(P_1{}^2-P_{2(t)}{}^2\right)^{\frac{1}{2-n}}=\frac{dp_{2(t)}}{dt} \quad (8)$$

If $C_3=\frac{P_1C_2}{V}$, $r=\frac{1}{2-n}$ then,

$$\frac{dp_{2(t)}}{dt} = \frac{C_3\left(P_1{}^2 - P_{2(t)}{}^2\right)^r}{P_2(t)} \quad (9)$$

Integrating both sides, we get the pressure inside the tube as:

$$P_2(t) = \sqrt{P_1{}^2 - [(2r-2)(C_3 t + C)]^{\frac{1}{1-r}}} \quad (10)$$

At the initial condition that the pressure inside the tube is 0.1 times the outside pressure, that is, $P_2(t)$ at $t = 0$, is $0.1P_1 = P_0$, then C will be as below:

$$C = \frac{\left(P_1{}^2 - P_0{}^2\right)^{1-r}}{2r-2} \quad (11)$$

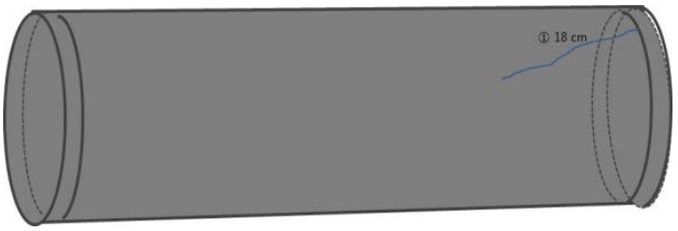
Therefore, if the number of cracks (N) and average crack width (W_{avg}) are known, the change in internal pressure in a vacuum tube structure with time could be anticipated mathematically by using the formula expressed above in equation (10).

4 EXPERIMENTAL STUDY:

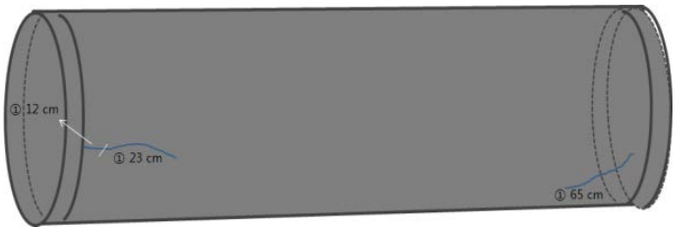
The experimental test was conducted to evaluate the cracking and air leakage behaviour of concrete vacuum tube structure. The concrete tube structure with radius 0.195m, length 2m and thickness 0.035m was modeled and constructed in the laboratory. A vertical point load of 35 kN is applied on the mid-span of the structure and the cracks are expected to develop in the structure with this loading condition. Under this loading condition the crack length, average width, and numbers are measured manually and found to be 1.18m, 0.1mm and 3, respectively as shown in figure 5. The figure displays the front and rear view of the tube structure with cracks developed on it.

5 COMPARISON OF EXPERIMENTAL AND ANALYTICAL RESULTS:

Based on the calculations made analytically by using Rizkalla formula for the change in internal pressure with time due to cracks, the analytical results are compared with that of the experiment. Detecting and measuring the cracks present on concrete is really a tough task and the measured data are subject to a great deal of errors. During the experiment, the measurement of crack length and numbers is quite easy as compared to crack width so we expect that we had extracted more accurate data for number and length of the cracks. For minimizing the error associated with crack width, it is necessary to refine it. The crack width data are refined by calibrating the experimental data with the analytical data, as shown in figure 6. The nonlinear regression analysis is done to find out the best-fit curve for both experimental and analytical results, which gives the refined data for the crack width. From the experiment, the crack width value was found to be 0.1mm whereas after refining value of crack width is found to be 0.04mm, which is 2.5 times lesser than that given by experiment. The numerical modeling can be done by using the nonlinear finite element program, Midas FEA (Midas I.T. 2016) which considers the total strain crack model (Ngekpe B.E. 2016) for the analysis. The data obtained from numerical modeling can be used for calibration in order to obtain the more refined model which could be part of the future study.



(a) Front view



(b) Rear view

Figure 5. Practical tube structure with cracks after loading.

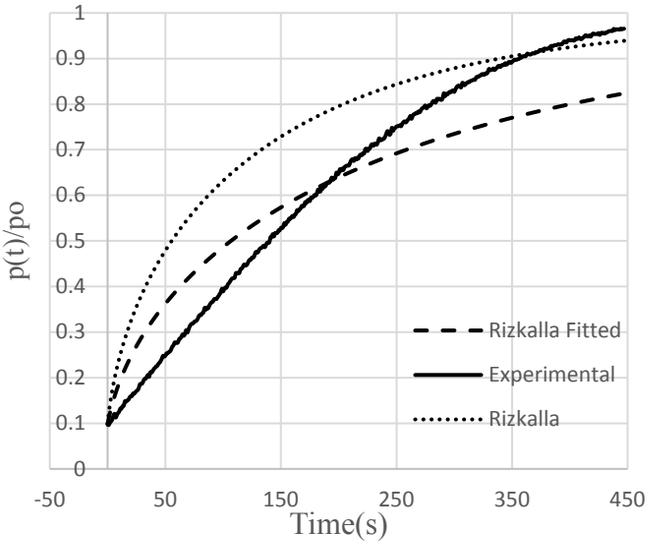


Figure 6: Comparison of experimental and analytical results.

6 NUMERICAL SIMULATION AND PARAMETRIC STUDY:

The actual dimension for the concrete tube structure has not been determined yet, so only a conceptual study is being conducted at present. The dimension of the tube structure can only be determined after finalizing the detailed design. Therefore, in this study, the tube structure with an inner diameter of 0.39m, length of 2m and thickness of 0.035m is assumed as the baseline dimension for an illustrative purpose. Crack is used as the damage indicator for studying the airtightness of the tube structure. The parameters of the crack, such as crack length, width and numbers are varied in order to identify the sensitivity of the crack with the airtightness of the system.

The change in internal pressure with time for different values of crack width, number and length are shown in figures 7, 8 and 9 respectively. For studying the change in internal pressure with time, crack width is varied from 0.01mm to 0.04mm keeping the crack length and number constant at 1m and 3 respectively, crack length is varied from 1m to 15m keeping the crack width and number constant at 0.002m and 3 respectively and crack number is varied from 1 to 15 keeping the crack width and length constant at 0.002m and 1m respectively. Initially, it was assumed that the internal pressure is dropped down to 10 percent of the atmospheric pressure. The pressure increases more rapidly when either crack width or crack length or both of them increases. Figures 10, 11 and 12 show that the time required for the internal pressure to reach the specified value decreases as width, numbers, and length of the crack increases. These trend analyses could be effectively used for determination of the limit states of cracks associated with the system airtightness.

It is necessary to assume that the vacuum pumps present in the tube structure reactivate when the internal pressure reaches a certain value, which is not more than initially maintained internal pressure. For this study, 50 percent of the atmospheric pressure is assumed to be the limit value of pressure. The analysis result shows that if the width of the crack is maintained below 0.02mm with the fixed crack length and number of 1m and 3, and length of the crack is maintained below 1m with a fixed width and number of 0.02mm and 3, then time for reactivating the pump will be longer than eight minutes. Eight minutes is a short period for reactivation of the pump, which shows that the airtightness performance of the tube is not satisfactory. Therefore, the crack widths lengths and numbers are needed to be maintained as low as possible for ensuring the better airtightness performance of the tube structure.

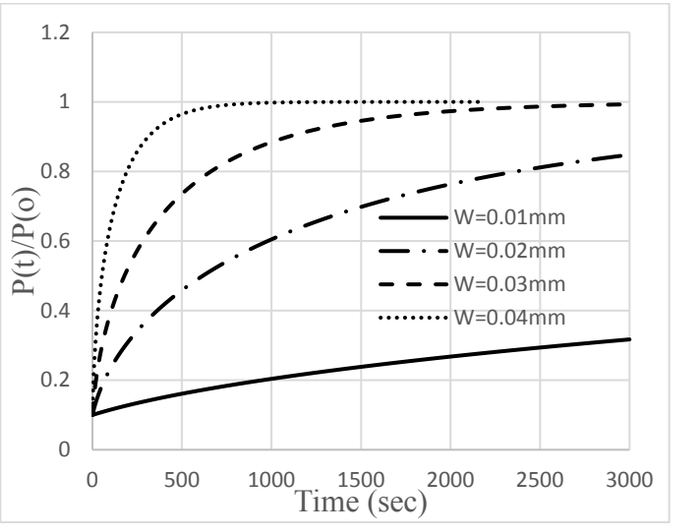


Figure 7. Pressure behavior with varying crack width.

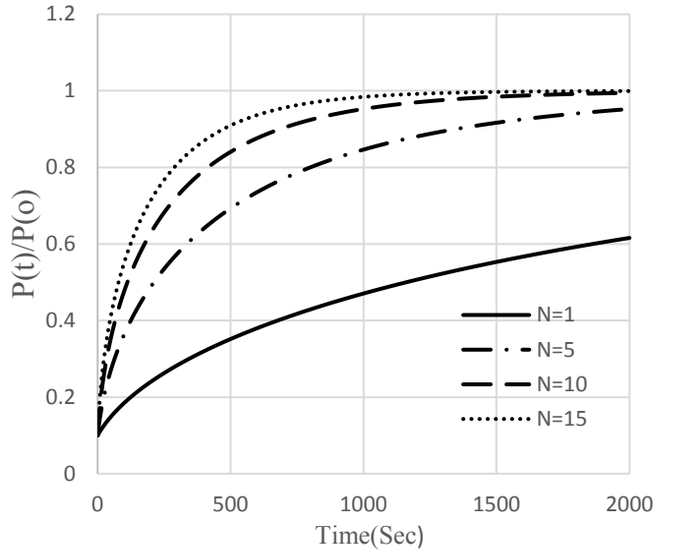


Figure 8. Pressure behavior with varying number of cracks.

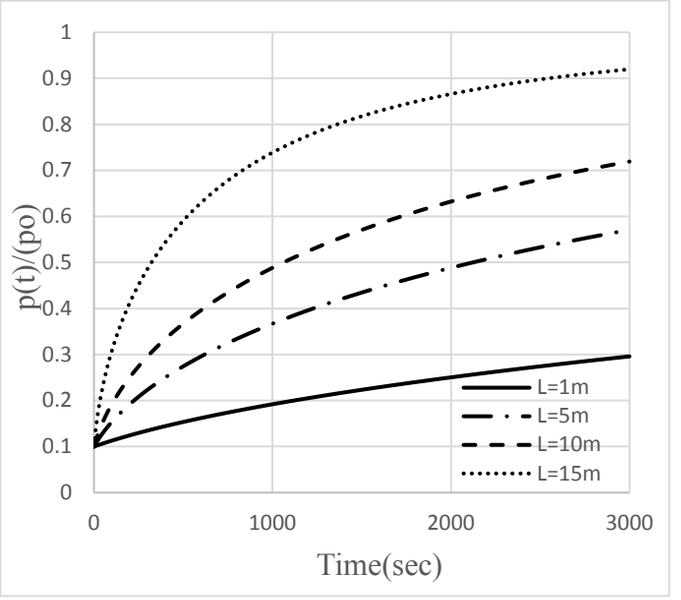


Figure 9. Pressure behavior with varying crack length.

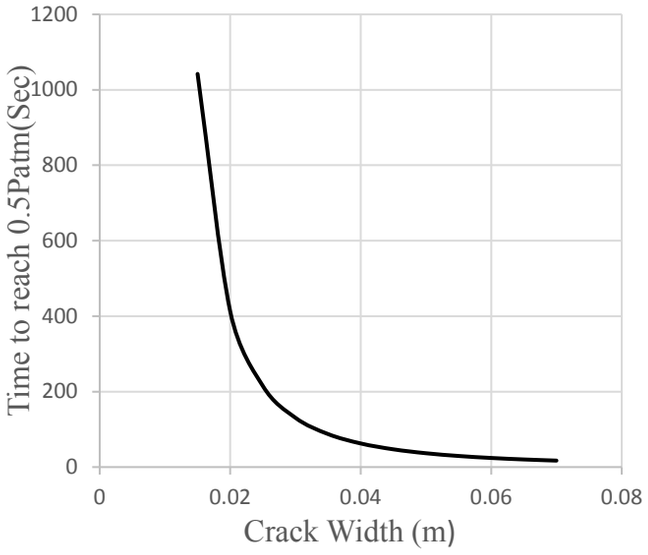


Figure 10. Time to reach $0.5P_{atm}$ for various crack width.

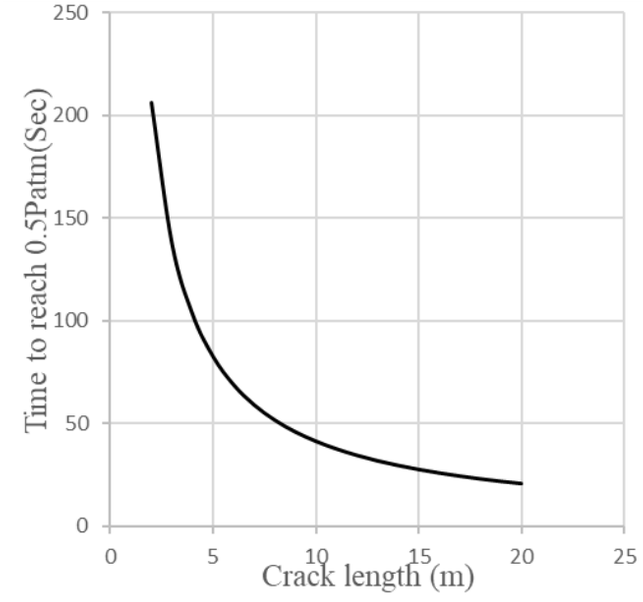


Figure 11. Time to reach $0.5P_{atm}$ for various crack length.

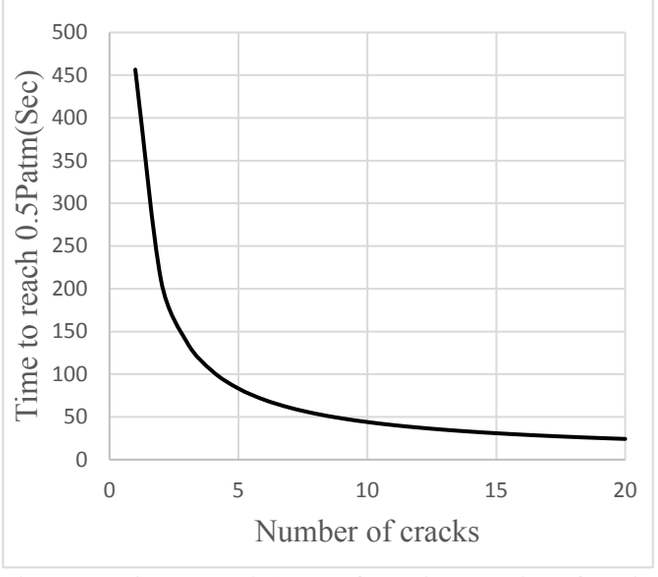


Figure 12. Time to reach $0.5P_{atm}$ for various number of cracks

7 CONCLUSION:

The experimental, as well as the analytical study is carried out to investigate the behavior of the load induced crack and its effect on airtightness of the concrete tube transportation system. The experiment is conducted to determine the crack properties and change in internal pressure due to crack. The analytical model describing the pressure change inside the tube structure due to cracks is developed by using Rizkalla formula. The nonlinear regression analysis between the analytical and experimental curves of change in internal pressure with time is done to obtain the best-fit curve describing the refined data of crack width. The numerical simulation of the data can effectively show the trend of the system airtightness due to the changes in selected control variables such as crack width, number and length. Time for the internal pressure to reach a pre-defined, pump-reactivating pressure was also monitored for changes in the control variables. These trend analyses could be effectively used for determination of the limit states of cracks associated with the system airtightness.

REFERENCES:

Cassat A., Bourquin V., Mossi M., Badoux M., Vernez D., Jufer M., Macabrey N., & Rossel P. 2003 SWISSMETRO - Project Development Status, *International Symposium on Speed-up and Service Technology for Railway and Maglev Systems 2003 (STECH '03)*, pp. 453-410, Tokyo, Japan.

Choi J, Han O, Park J. 2016. Development of Air Inflow Model for Airtightness Performance Evaluation of Concrete Tube Structures with Cracks. *Fourth International Conference on Sustainable Construction Materials and Technologies, 7-11 August 2016.* Las Vegas, USA.

Lee J, Kim K.S, Nam D, Kwon H & Kim J.Y. 2008. Performance requirement and economic efficiency for tube transportation system. *Journal of the Korean Society for Railway* 11(5), pp. 513-518. (In Korean)

Midas I.T. 2016. *Analysis & Algorithm*. Sungnam: Korea.

Nam S.W. 2010. Parametric study on the capacity of vacuum pump for tube structure, *Journal of the Korean Society for Railway*, 13(5), pp. 516-520. (In Korean)

Ngekpe B.E. 2016. Application of Total-Strain Crack Model in Finite Element Analysis for Punching Shear at Edge Connection, *International Journal of Research in Engineering and Social Sciences,* ISSN 2249-9485, 06(12), pp. 1-9.

Park J., Cho J., Park H-J. 2014. Probabilistic estimation of airtightness of performance of concrete vacuum tube structures, *10th International Symposium on High Performance Concrete – Innovation & Utilization, 16-18 September 2014.* Beijing, China

Park J., Kim L-H., Nam S-W., and Yeo I. 2013. Performance Evaluation of Airtightness in Concrete Tube Structures for Super-Speed Train Systems. *Magazine of Concrete Research*, 65(9), pp. 535-545.

Rizkalla S.H, Asce M, Lau B.L & Simmonds S.H. 1984. Air leakage characteristics in reinforced concrete. *ASCE Journal of.Structural.Engineering*, 110(5): Paper No.18809, pp. 1149-1162.

Scoppe T.E, Masce P.E & Masce T.C.H. 2012. Assessment of Gas Leakage Rates through Damaged Reinforced-Concrete Walls, *Journal of Materials in Civil Engineering,* 24(9), pp. 560-567.

Maintenance, Safety, Risk, Management and Life-Cycle Performance of Bridges – Powers, Frangopol, Al-Mahaidi & Caprani (Eds)
© 2018 Taylor & Francis Group, London, ISBN 978-1-138-73045-8

Moving Substrate in an Ephemeral Stream Revisited: A Continuing Case Study

George R. Herrmann, Ph.D., P.E., P.H., D.WRE. CFM
Instructor, Department of Civil, Environmental, and Construction Engineering
Texas Tech University, Lubbock, Texas, USA
Principal, Desert Sky Engineering and Hydrology
Lubbock, Texas, USA

Theodore G. Cleveland, Ph.D., P.E.
Associate Professor, Department of Civil, Environmental, and Construction Engineering
Texas Tech University, Lubbock, Texas, USA

ABSTRACT: A follow-on case study revisits the site of a small highway bridge crossing an ephemeral stream in an arid area of Texas with little hydrologic information. The bridge has presented chronic problems and maintenance issues for years because of stream instability. The bridge is at US Highway 62—180 where it crosses Guadalupe Arroyo in Culberson County. Texas.

Bed load sediment transport through the reach adjacent to the bridge appears inhibited. The authors originally concluded that the inhibition of bed load sediment movement through the bridge reach must be addressed for any solution to be effective; sediment accumulated since construction in 1959 must be allowed to disperse downstream, and sediment arriving at the site in the future must pass the reach without further accumulation upstream of the bridge. The authors conjectured engineered solutions that failed to address the inhibition of sediment movement through the reach by restoring stream geometry to a condition favorable to bed sediment movement would doom conventional approaches such as bank armoring to continued failure. Despite these recommendations, a construction project intended to stabilize the situation using only conventional bank armoring took place in 2009. This continued case study involves revisiting the site as it exists in 2017, and documenting the performance of those measures under conditions of extreme bed load sediment movement. The original case study was presented at the 7th TRB International Bridge Engineering Conference in San Antonio, Texas.

The authors find that this provides a unique opportunity to examine both the performance of bank armoring in areas of extreme bed sediment load, and document the stability state of the stream at another point in time, eight years after the original data was collected. A more complete understanding the interaction of roadway bridges with the geomorphic environment in which they exist is essential for their long-term performance and survival.

1 INTRODUCTION

Culberson County, Texas, is located in the far western part of the state (Figure 1). The region has rugged terrain, low mean annual rainfall (approximately 250 mm), sparse desert scrub vegetation, and is traversed by several mountain ranges including the Guadalupe Mountains, that extend North into New Mexico. The sparsely populated area has few improved roadways. United States Highways 62 and 180 (US 62-180) are co-aligned, crossing the bridge area from northeast to southwest, entering Texas from New Mexico and traversing the lower levels of the Guadalupe Mountains and Guadalupe Mountain National Park.

The subject bridge was constructed in 1959, and crosses an ephemeral stream known as Guadalupe Creek, or Guadalupe Arroyo. The stream adjacent to the bridge has exhibited stream instability, first coming to the attention of the Texas Department of Transportation (TxDOT) as lateral migration threatening the southwest abutment and embankment, and accompanied by aggradation of the stream bed adjacent to and within the bridge opening.

TxDOT planners were unaware of the connection

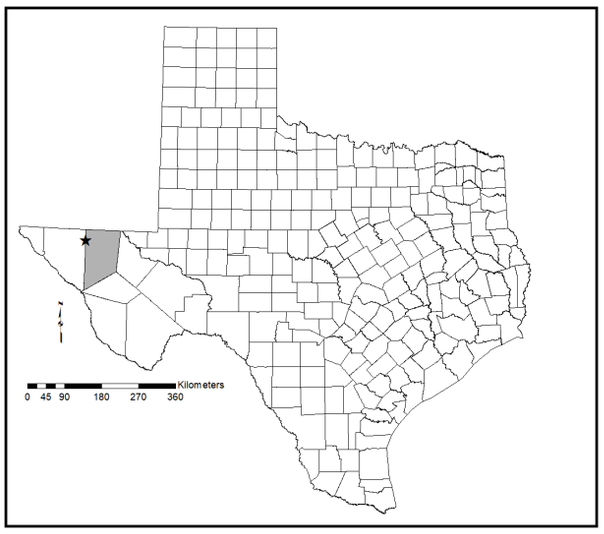


Figure 1: Culberson County, Texas (shaded) Star denotes the bridge location.

between lateral migration and aggradation in 2008 following the submission of a consulting engineering report that focused on erosion as the culprit. Upon reviewing the report, visiting the site, and reviewing historical overhead imagery the authors found was evidence that stream-bed aggradation on stream bed lateral migration played an important role that had been overlooked in the consultant report. A subsequent report on the issues, and recommended guidance for addressing them, was prepared for TxDOT in 2009 (Herrmann 2009). That report concluded that the natural hydraulic geometry of the stream had been obliterated, resulting in inhibited sediment transport through the bridge reach, and chronic aggradation. The recommendations in that report included restoration of the geometry necessary for transport, and allowing accumulated sediment to disperse downstream. The report specifically stated that addressing bank erosion solely by bank stabilization was unlikely to succeed, and noted that addressing the dominant problem would require work off of TxDOT right-of-way, necessitating easements onto private land.

At the 2010 TRB International Bridge Engineering Conference in San Antonio, Texas a case study of the bridge was presented (Herrmann & Cleveland 2010) (Herrmann 2013); in which the authors described the situation in detail. The case was thought to be of considerable interest to bridge engineers and managers in areas of similar climate and geology.

TxDOT funded a $561,375 USD project under the American Recovery and Reinvestment Act of 2009 (ARRA) constructed in 2009-2010, with a time frame too short to allow acquisition of the necessary easements; the project deployed revetment-type bank stabilization. This paper re-studies the site as it appears in 2017, approximately 7 years after the completion of the original project, to assesses the viability of bank stabilization revetments in similar cases, and the consequences of overlooking the role of hydraulic geometry and bed load sediment transport in stream stability.

2 WATERSHED DESCRIPTION

The watershed contributing to the bridge site is just over 100 sq. km. in area. The area is divided among two major and four minor subwatersheds, ranging in area from 0.31 to 48.2 sq. km. The longest flow path from the most remote point on the watershed to the bridge is approximately 22 km. In that distance, the elevation falls from 2667 m. on Guadalupe Peak to 1170 m. above MSL (NAD 1983); a fall of 1497 m. in 22 km. However, in the last 2.025 km. leading to the bridge, fall is 25 m., still quite steep, but gentler than on the mountain slopes.

The Guadalupe Mountains generate orographic rainfall on the mountain slopes themselves, but little of that rain falls in the surrounding desert. Much of the discharge that passes the bridge results from rainfall in the mountains, when rainfall at the site may be completely absent. There are no long-term stream gauges in the area, and rain data is anecdotal. Lack of rainfall statistics by which to model rainfall-runoff, and dissimilarity to other stream gauge sites, makes hydrologic estimation of discharge very difficult or impossible. Interestingly, Guadalupe Arroyo begins high and at extremely steep slopes, but empties into a dry ”salt flat” to the west. Gradient vanishes as it approaches the lake.

Figure 2 is a map of the watershed, with subwatershed boundaries, areas, and longest flow paths denoted. There exist two suitable sites along tributaries where access is readily available to measure hydraulic geometry.

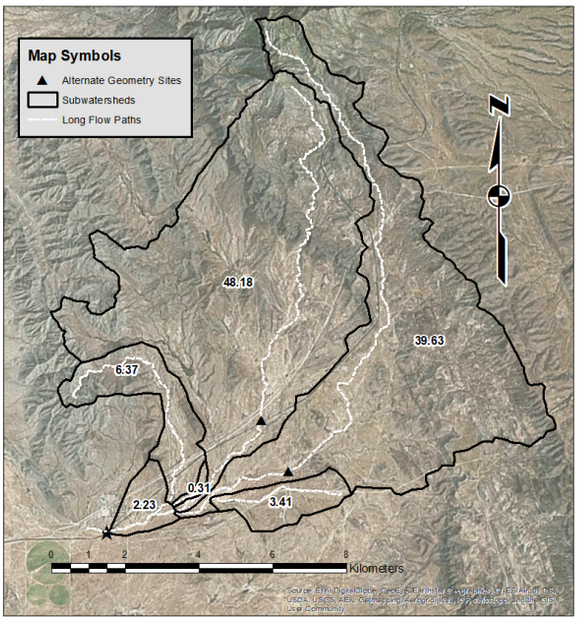


Figure 2: Guadalupe Arroyo Watershed and Subwatersheds. Star denotes the bridge location. Subwatershed areas are in square kilometers.

Watershed vegetation is predominantly upper Chihuahaun desert-type; sparse, drought-tolerant plants, cacti and succulents, pinon, juniper, and woody shrubs. There is substantial bare rock outcrop. Soils are thin and spotty on the slopes, composed of the products of mass wasting, and of thick alluvium adjacent to streams. Streams are all ephemeral- smaller streams may exhibit flow only a few times a year, or none in drought years.

3 STREAM AND SEDIMENT

Guadalupe Arroyo is atypical for the extreme elevation change and gradient change over its course, otherwise it resembles many desert streams. Sediment supply is substantial and exhibits a wide size distribution, ranging from silt to large boulders. Because it is ephemeral, 70-80 percent of the sediment transport is likely bed load, rather than suspended load. For the large particles to be transported regularly, hydraulic geometry must be favorable; bank full shape and dimensions are critical to that transport (Rosgen 1996). Figure 3 gives a visual assessment of the sediment in the immediate area of the bridge.

The previous case study concluded that the construction of the bridge had changed hydraulic geometry from natural to one that only considered water, and that sediment transport through the bridge reach had been inhibited. The authors estimated approximately 230 cu. m. of sediment per year had accumulated in the reach approximately 500 m. upstream of the bridge, in the 50 years between construction in 1959 and the study in 2009. The larger particles were preferentially retained, and the stream bed elevated as much as 2-3 meters, forcing lateral movement of the stream by erosion of the banks. Ground artifacts and overhead imagery indicated at least 5 previous attempts to address lateral movement by bank stabilizing revetments.



Figure 3: View of the bridge showing sediment size and distribution. Large particles are readily evident, and are preferentially retained in the bridge reach. (May, 2017 photograph)

4 2009-2010 PROJECT

In 2009, TxDOT funded a construction project intended to address the threat to the Southwest abutment of the bridge using flexible revetment treatments. The common TxDOT practice for addressing this type of issue is rigid concrete slope paving, which is ingrained in the institutional mindset despite a poor performance record. The Herrmann 2009 report recommended that slopes would be best treated with flexible treatments, but cautioned that restoring hydraulic geometry was also needed, and that without restoration of the hydraulic geometry slope treatment would be unlikely to succeed. Despite this specific recommendation, slopes received their armor but the channel restoration was not applied. Figure 4 shows the locations of the various revetments constructed in 2009-2010 and referred to subsequently in this paper.

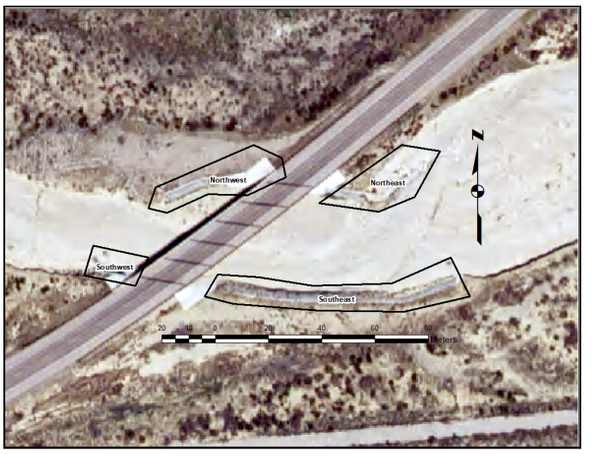
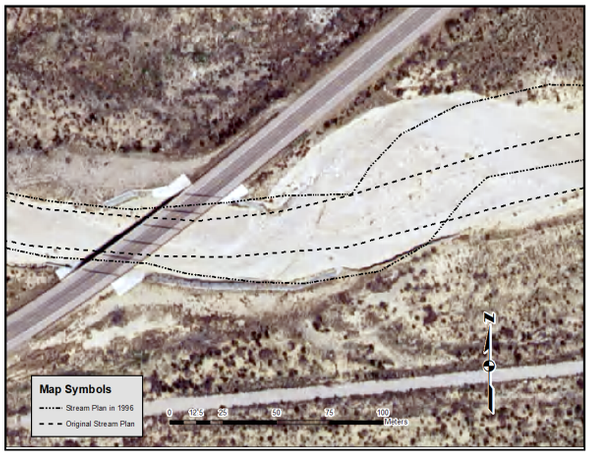


Figure 4: Location of revetments constructed in 2009—2010 with respect to the bridge. (2015 imagery)

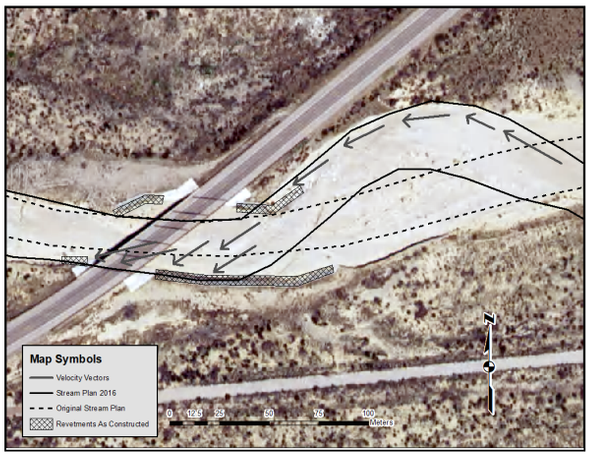
The top of Figure 5 shows the author's estimate of the natural condition stream bank plan view (dashed lines), as well as stream bank plan view circa 2009, both overlaid on 1996 imagery. The figure demonstrates that stream migration was already substantial by 1996 (37 years after construction of the bridge). A series of short-wavelength meanders was developing, indicating flattening of the streambed grade. No artifacts of the original stream geometry are visible in imagery from that time in the vicinity of the bridge, but upstream and downstream it appears natural.

The bottom of Figure 5 shows the natural condition along with the plan as existed in 2016. The meanders are continuing to develop, despite the construction in 2009-2010 of revetments. Velocity vectors of incoming flow are approximated. In two places, at the upper right and lower center, the meanders have resulted in velocity vectors directly impinging on highway embankments and abutments. This redirection of velocity is, in fact, the ultimate cause of problems at the site. Erosion of embankment and abutment material is the visible and immediate threat to the bridge; meander movement is the direct cause of the velocity redirection; aggradation of the stream bed is the cause

of the meander movement, and inhibition of sediment transport through the bridge reach by destruction of hydraulic geometry favorable for bed sediment movement is the cause of aggradation.



(a) Approximate original stream plan overlaid with plan as in 1996 imagery.



(b) Location of revetments constructed in 2009, and with flow velocity direction vectors.

Figure 5: Stream changes between 1996 and 2009, (2015 imagery)

Figure 6 shows two views of the revetments as constructed, shortly after the completion of the project. The top of the figure is taken from near the east end of the southeast revetment, and is looking west, through the bridge. The northwest and southwest revetments can be seen through the bridge opening. The near-bridge end of the northeast revetment can be seen in the same photograph. The bottom photograph looks west northwest from the same point, and shows the remainder of the northeast revetment. No resemblance to a natural stream geometry has been reestablished – the entire bridge opening is presented as area of flow. The practice of creating a geometry that appears to present greater conveyance of water is the activity that triggers instability in such ephemeral streams by creating a ”dead zone” with respect to stream power/sediment transport – essentially a sediment trap.



(a) Revetments viewed west through the bridge from the east.



(b) The northeast revetment viewed from the same point as above.

Figure 6: Post-project photographs from March, 2010.

5 SITE CONDITIONS IN 2017

In May, 2017, the authors revisited the site to assess the effectiveness of the previous project, after 7 years of service. At that time personnel and equipment were at the site to begin data collection for a future replacement project of $1 million USD. The necessity of a repair/replacement project was obvious; the revetments placed in 2009-2010 had failed completely in critical areas, re-exposing the embankments and abutments to severe erosion. Figure 7 show the northeast revetment, and Rigure 8 the southwest revetment. The impinging flow has undermined the revetments, which have collapsed. The stream bed elevation is still approximately what it was prior to construction, indicating bed movement under high flow conditions to considerable depth of sediment.



(a) Northeast revetments viewed in October, 2010 after the project.



(b) Northeast revetments viewed in May, 2017.

Figure 7: Northeast revetment after project and in 2017.



(a) Southwest revetments viewed in October, 2010 after the project.



(b) Southwest revetments viewed in May, 2017.

Figure 8: Southwest revetments after project and in 2017.



(a) Sagging southeast revetment in 2017.



(b) Relatively undamaged northwest revetment, 2017.

Figure 9: Project revetments as seen in May, 2017.

Figure 7 shows before and after views of the debris remaining from the northeast (top) and southwest (bottom) revetments. The remains of concrete footings are readily visible, as they have been uprooted completely. Impinging flow as indicated by flow vectors in Figure 5 ”flanked” the revetments and continued to erode the embankment behind, completely destroying the revetments.

The southeast and southwest revetments were intended to provide protection for the west abutment, undermining of which was the first problem recognized at this bridge. Figure 9 (top) shows the damaged southeast revetment. The undermining of the southeast revetment progressed beneath the bridge and caused a catastrophic failure of the southwest revetment. Direct impinging flow accompanied by extreme bed movement, presented forces that revetments could not withstand.

Of the four ”corners” of the bridge, only the northwest revetment remained unharmed, as shown in Figure 9 (bottom). Because of the geometry of flow, it stood in an area of relatively slack water with no impinging flow.

6 DISCUSSION

The study is an opportunity to observe the effects of human activities on a very fragile system, and how those activities can echo for decades. The preponderance of damage appears to have occurred in calendar year 2015. Rainfall depth in the area in 2015 was approximately 80th percentile of recorded rainfall, or roughly corresponding to a 5-year annual recurrence interval. Damage to the extent observed in seven years, with the largest rainfall in a single year of that frequent depth, and no single month showing an exceptionally large rainfall depth is unexpected, and may be said to be unacceptable.

The transportation branch of the civil engineering community has historically designed stream-crossing structures with consideration only for the passage of water. Streams convey at least two media – water and sediment.

In arid environments, the vast preponderance of streams only flow under conditions of recent rainfall. The inevitable movement of the products of mass wasting from geologic features can only occur during those flows. Bed load sediment transport is the principle mechanism of that movement. The consideration of large bed load movement, and the stream power to accomplish it, should be a part of the design and maintenance processes for transportation structures, in arid areas if not everywhere. Some knowledge of geologic processes, especially fluvial geomorphology, should be accessible to design engineers.

Stream instability such as meander migration, streambank lateral migration, avulsion, embankment erosion, and aggradation/degradation may be symptoms, rather than causes. As in health, treatment of the symptoms may do nothing to cure the underlying cause. In this case, the symptoms are lateral instability, meander development, and meander migration, resulting in threats to the bridge abutments and embankments. The cause is attributed to the destruction of the natural hydraulic geometry (as bankfull stream configuration) necessary for continued sediment throughput decades ago, when the bridge was constructed. Natural sediment movement was inhibited. The resulting accumulation of sediment has locally altered the stream bed gradient, which has resulted in a change in the planform in the reach occupied by the bridge. Several references on fluvial geomorphology exist, and can be of considerable use to the engineer performing designs in fragile streams. Examples are Leopold, Wolman, & Miller 1992, Leopold 1994, Leopold 1997, and Bull & Kirkby 2002.

Figure 10 shows a longitudinal profile (from a digital elevation model) of the stream, beginning approximately 400 m. downstream and progressing approximately 1000 m. upstream. The aggraded reach is clearly shown in this profile as a level section. Many cubic meters of material have accumulated in the upstream reach since 1959. Maintenance forces have

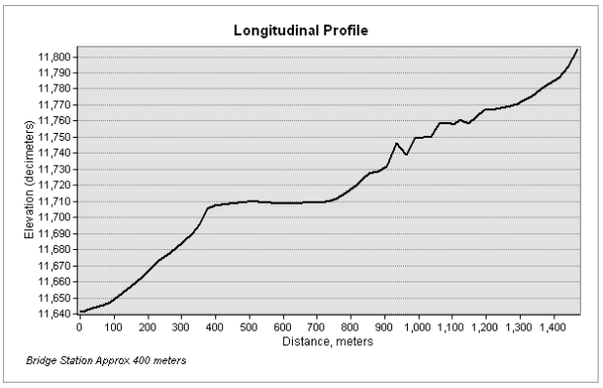


Figure 10: Guadalupe Arroyo Longitudinal Profile. The ”flat” reach beginning at 400 meters is the location of the existing bridge. Flat reaches are indicative of aggradation.



Figure 11: View of box culvert at the crossing of US 62/180 by one of the Guadalupe Arroyo tributaries. Note the accumulation of sediment.

found it necessary to remove large amounts from the bridge opening every year; imagery over time shows material being replaced in the eroding areas, to later be transported away by the erosive forces of water.

As mentioned earlier, four sites present themselves within the same watershed for examination (Figure 2). The measurement of geometry, specifically bankfull width and depth of the stream channel, allow the development of a ”watershed curve” relating those features to contributing area. This analysis would facilitate the calculation of appropriate dimensions for reestablishment in the bridge reach.

Two of the sites thought to be suitable from imagery proved unsuitable in field reconnaissance, the westernmost site proved to have no defined stream channel at all, while the next-westernmost proved to have been heavily impacted by aggradation itself; hydraulic geometry was divided among several braided channels. The box culvert at that location contained approximately 1 meter of sediment accumulation (Figure 11). The presence of this depth of sediment is indicative of impact to the tributary similar to that at the main bridge location.

The remaining two sites provided points for graphing three hydraulic variables- bankfull depth, width, and flow area versus base 10 log of contributing area (Rosgen 2008). Projecting upwards to the entire area contributing at the bridge results in an estimate of these dimensions needed at that location. Figure 12 is a plot of bankfull depth (left) and bankfull width (right) in meters, versus contributing area in hectares. Flow area is estimated as $2/3$ of the bankfull depth times width. Bankfull depth rounded to 1.5 meters, width of 18 meters, and flow area of 17.5 square meters, approximate the hydraulic dimensions needed at the bridge site.

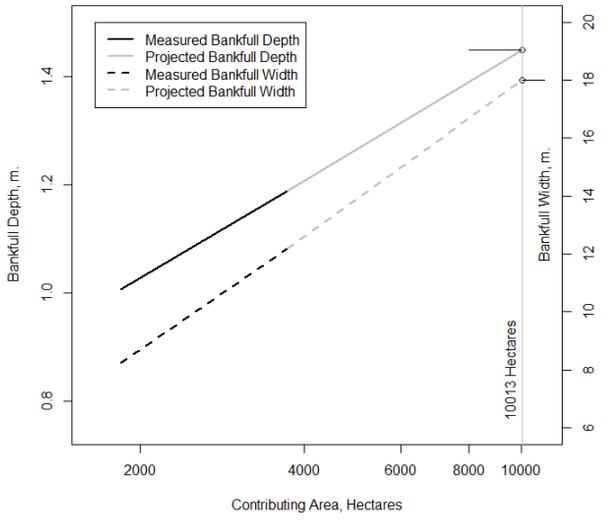


Figure 12: Guadalupe Arroyo bankfull dimensions. Black lines connect two measured site dimensions, while grey lines project from the contributing areas associated with those dimensions to the full watershed contributing area of 10013 hectares.

7 CONCLUSIONS

The examination of the Guadalupe Arroyo site over the period 2008-2017, and the critical examination of attempted treatment, provides several learning opportunities:

1. The visible symptoms of a problem may be misleading. Engineers should use the best science available to ascertain the true nature of a problem.

2. Failure to address the actual problem may result in early failure of expensive projects.

3. Ephemeral streams in arid areas may be extraordinarily fragile. Great care should be taken to avoid disturbing their natural geometry.

4. Moving bed sediment may well include particles much larger than are expected to move easily.

5. Large bed particles may be segregated at locations where stream power is reduced, creating large deposits.

6. Bed sediment may move to depths that exceed ordinary expectation, in areas with steep slopes and large bed material gradation range.

7. Commercially available revetments perform poorly under conditions of impinging flow and large bed sediment movement.

It is clear that the funds spent in 2009-2010 to address long-running stability problems at Guadalupe Arroyo were not well-spent. It appears to have been at least the sixth attempt since 1959 to address the situation with bank stabilizing revetments. The authors contend that further attempts at bank protection will continue to be unsuccessful; recognition that aggradation is the underlying driver, and restoration of favorable hydraulic geometry would be more likely to succeed.

The case under study here emphasizes the fragile nature of ephemeral streams in arid areas, and the ambiguity that may be present at problem sites. Engineers attempting to address problem sites have need of some knowledge of fluvial processes and sediment transport; brute force approaches may be futile. Unless favorable hydraulic geometry is restored to the stream for approximately 500 meters upstream of the bridge, the development of meanders in that reach will continue. In the absence of restoration of the hydraulic geometry, attempts to protect the bridge ends from damage by bank revetment have repeatedly proven futile in the past. There is no reason to believe that further attempts along those lines will meet with success.

In general, the emphasis placed on the design of drainage structures is to conduct only water. As stated earlier, streams invariably transport at least two media- water and sediment. Few engineers are trained or knowledgeable in stream stability and the role of bed load sediment transport. Bed load sediment transport is, even today, poorly understood from a theoretical standpoint. Neglecting the role of sediment in the function of bridges can lead to chronic, expensive bridge damage, as well as adverse impacts to the environmental state of streams.

REFERENCES

Bull, L. J. & E. Kirkby, M. J. (2002). *Dryland Rivers; Hydrology and Geomorphology of Semi-arid Channels*. Chichester, West Sussex, England: John Wiley and Sons, LTD.

Herrmann, G. R. (2009). Report of Observed Conditions and Scientific Conclusions with respect to the crossing of Guadalupe Arroyo by US 62/180.

Herrmann, G. R. (2013). Conceptual, Algorithmic, and Statistical Exploration of Relations Between Runoff Generation, Stream Geomorphology, and Watershed Topography in West Texas.

Herrmann, G. R. & T. G. Cleveland (2010). Moving Substrate in an Ephemeral Stream: A Case Study in Bridge Survival. *Transportation Research Record: Journal of the Transportation Research Board 2201*, 3–9.

Leopold, L. B. (1994). *A View of the River*. Cambridge, MA, USA: Harvard University Press.

Leopold, L. B. (1997). *Water, Rivers, and Creeks*. Sausalito, CA, USA: University Science Books.

Leopold, L. B., M. G. Wolman, & J. P. Miller (1992). *Fluvial Processes in Geomorphology*. New York, NY, USA: Dover.

Rosgen, D. (1996). *Applied River Morphology* (2 ed.). Pagosa Springs, Colorado: Wildland Hydrology.

Rosgen, D. (2008). *River Stability Forms and Worksheets*. Pagosa Springs, Colorado: Wildland Hydrology.

Maintenance, Safety, Risk, Management and Life-Cycle Performance of Bridges – Powers, Frangopol, Al-Mahaidi & Caprani (Eds)
© 2018 Taylor & Francis Group, London, ISBN 978-1-138-73045-8

Experimental study on the fatigue resistance of prestressing strands at low temperature

F. Bomholt
Structural Testing Laboratory of Ruhr-Universität, Bochum, Germany

H. Alawieh
Structural Testing Laboratory of Ruhr- Universität, Bochum, Germany

M. Knobloch
Chair of Steel, Lightweight and Composite Construction, Ruhr-Universität, Bochum, Germany

ABSTRACT: Cold-drawn high-strength steel for prestressing applications and stay cable bundles is suspected to have reduced fatigue resistance at low temperature between -20° and -50°C (Nürnberger 1981a, Kobrin 1974). For strands as tensile elements of a stay cable, high stress range results from combined low dead loads and high traffic loads and fatigue loading is decisive for the cable design (Svensson 2011). An experimental research project at Ruhr-Universität Bochum investigated the fatigue behavior of 7-wire strands (R_m = 1860 N/mm²) at low temperatures. In total 108 fatigue tests were carried out. The tests were equally distributed at room temperature and at low temperature [-30°C to -50°C]. The specimens were anchored particular in a laboratory anchorage which takes failure on the free length. Similar tests with equal fatigue parameters were carried out with a standard wedge anchorage to investigate the behavior in the anchorage region. In addition to 88 single-stage fatigue tests 20 multi-stage fatigue tests were carried out at room temperature and at low temperature. The multi-stage fatigue tests can be separate in structural durability program tests and in tests with a progressively increasing load range. Latter can be used for an alternative calculation of the endurance strength of strands (Prot 1948).
The single-stage fatigue tests at room temperature showed the expected differences between laboratory and wedge anchored strand specimens. Moreover the results showed a tendency to a reduced fatigue strength for laboratory anchored strands at low temperatures. The fatigue resistance decreased to the level of the anchorage zone at room temperature. A superimposed effect for the fatigue resistance of wedge anchored strands at low temperature was not found. The multi-stage fatigue tests confirmed the reduced fatigue resistance of laboratory anchored strands at low temperature. Moreover an underestimation of the material for the cumulative damage calculation with the linear miner rule can be observed.

1 INTRODUCTION

Stay cable bridges are often used for medium to long spans in different parts of the world and climatic regions. For these bridges, parallel strand bundles with 7-wire strands made of cold-drawn high-strength steel are used worldwide. The fatigue strength usually increases with decreasing temperatures (Suresh 2004). However, former investigations on the strand material show a serious reduction of the endurance strength. Modern strand material possesses higher fatigue resistance (Heeke 2016) in general, but it is unclear if a comparable reduction of the endurance strength at low temperature exists. A follow-up question concerns the usage of the standard wedge anchorage, which provokes micro-notches in the strand surface (Nürnberger 1981b). Normally a fatigue crack starts in the anchorage region at the strand surface by means of notching effects or fretting corrosion with the inner wedge profile. For notched steel specimens in general a higher reduction of the fatigue strength can be found with decreasing temperature (Stephens et al 2001). This leads to the suggestion of a superimposed effect of low temperatures on the endurance strength of prestressing strands.

A bridge bears different stress situations which can be counted to a load spectrum (i.e. rainflow method, reservoir-counting, etc.). By means of the cumulative damage calculation a load spectrum can be calculated to a single-stage fatigue loading. For this calculation different models are available. These models are based on different assumptions (i.e. sequence effects, linear or non-linear damage accumulation, micro damages below the endurance strength). The effect of low temperature on the endurance strength of multi-stage fatigue loading on strands, material and anchored specimens, is accordingly a practical issue and is experimentally analyzed in this paper.

2 TEST PROGRAM & RESULTS

2.1 *Single-stage fatigue tests*

Single stage fatigue tests at room temperature (RT) T_{RT} = 23°C ±5°C and at low temperature (sub-zero temperature = SZT) T_{SZT} = -40°C ±10°C constitute the basis of the test program. First, two test series were carried out on laboratory anchored (Lab) strands at both temperature regions. Second, two test series with specimens anchored by means of a standard wedge anchorage (System) were performed. All

test series were carried out in accordance with the Interactive Method which requires fatigue tests with a varying stress range from the endurance strength up to very high stress ranges with upper loads close to the yield limit. The tests are separated into blocks with four tests in the first block and further with five tests per block. In the first block the both first tests are carried out with high stress ranges, the last two tests are carried out above and below the currently calculated endurance limit. In the following blocks a similar procedure but with each three tests in the low cycle fatigue regime was conducted. Fig. 1 shows a typical schema of the Interactive Method. For all fatigue tests a constant lower load of 29% of the nominal tensile strength was chosen.

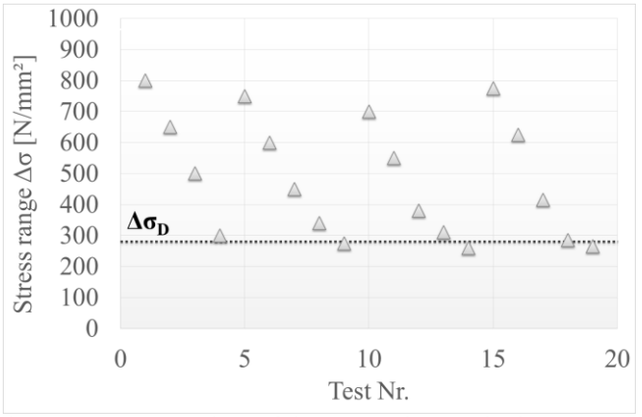


Figure 1. Test procedure of the Interactive Method

The fatigue test was stopped if either wire breakage occurred or 1.1×10^7 load cycles were completed without failure. In the isolated test setups for testing at SZT an increase in the stroke range was used for breakage detection. After test stop for a non-broken specimen a second fatigue loading far more intensive as the first loading was subjected to the specimen. All run-outs were broken in the second stage loading. Afterward the result was checked in comparison with the other test results. If no significant reduction of the fatigue strength was found, the first test was counted as run-out and the second loading was counted as a fully independent fatigue test.

Table 1. Single stage fatigue testing program

Anchorage	Temperature	n
Lab	RT	19+5
Lab	SZT	19+1
System	RT	19+3
System	SZT	19+3

In total 88 single-stage fatigue tests was carried out and are summarized in Table 1. Additionally the parameters of the wöhler functions are shown. Fig. 2 shows all test results and the four different wöhler curves for each test series in a double-log Δσ-N diagram. Three results from series System SZT were found as outliers and were ceased for the further analysis. For the calculation of the wöhler curve parameter all run-outs were recounted to 10^7 load cycles to ensure a conservative data analysis. The stress range can be calculated as a function of three parameters according to the following equation:

$$\Delta\sigma = \Delta\sigma_D + (R_m - \sigma_u - \Delta\sigma_D) \bullet a^{(\lg N)} \quad (1)$$

where R_m = nominal tensile strength; σ_u = lower load; $\Delta\sigma_D$ = endurance strength; N = load cycles; and a & b = positive dimensionless parameter.

Table 2. Single stage fatigue testing results

Series	$\Delta\sigma_D$	a	b
	[N/mm²]	[-]	[-]
Lab RT	341	0.9998	5.575
Lab SZT	247	0.9994	4.724
System RT	266	0.9972	4.143
System SZT	253	0.9982	4.395

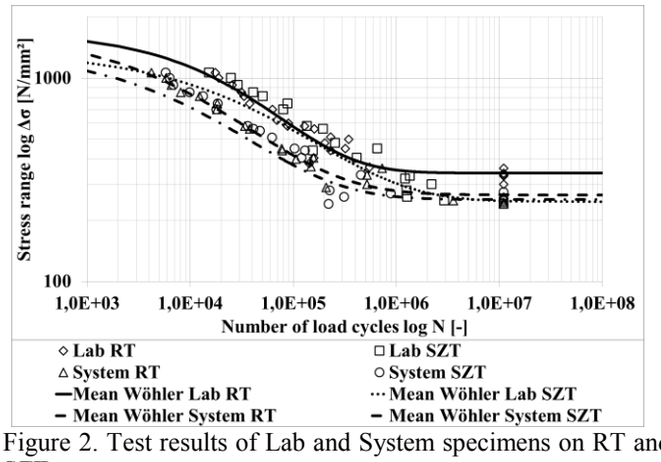


Figure 2. Test results of Lab and System specimens on RT and SZT

2.2 *Multi-stage fatigue tests*

Multi-stage fatigue tests were carried out to analyse the effect of low temperatures on the fatigue behavior of stay cables with common load scenarios. Fatigue tests with specimens with laboratory (Lab) and wedge anchorage (System) were again performed, both at room (RT) and low temperatures (SZT).
The multi-stage fatigue tests based on the purpose by Gasner et al. (1964) which determine operational stability program tests to investigate the fatigue strength of construction elements under a random load. The program tests were based on amplitude collectives who can be described as following:

$$\ln H_i = \left(1 - \frac{\Delta\sigma_{a,i}}{\Delta\sigma_{a,\max}}\right)^{\nu} \ln H_0 \quad (2)$$

where H_i is the cumulative load cycle number for a given stress amplitude $\sigma_{a,i}$; H_0 = block size; $\sigma_{a,max}$ = maximum value of the amplitude collective;

and ν = shape parameter of the collective. The steady function is transferred to a stair step curve with 8 steps which means 8 different stress amplitudes.
The tests were performed with a block size of H_0 = 400,000 load cycles to ensure a significant repetition of the load spectrum and ν = 2.0 which is a lower value for typical bridge traffic loading (Heuler et al. 2005). All tests were carried out with a fixed lower load level mentioned in Chapter 2.1. A test was stopped after 28 block repetitions (11,200,000 load cycles) or if a wire breakage occurred. For the case of a run-out an additional fatigue loading $\Delta\sigma_{add} = \Delta\sigma_{max}$ was performed on the concerning specimen.
All Lab RT specimens withstood the multi-stage fatigue loading and withstood an additional fatigue loading in the amount of an undamaged specimen, as shown in Table 3. Only in the first multi-stage fatigue test at low temperature (SZT) a run-out was found.

Table 3. Multi stage fatigue testing results

Series	$\Delta\sigma_{max}$	N_{br}	N_{add}
	[N/mm²]	[x 1000]	[x 1000]
Lab RT	500	-	344.0
	600	-	85.8
	700	-	58.7
Lab SZT	500	-	222.5
	600	4,817.1	
	700	4,501.0	
Sys. RT	500	-	51.0
	600	-	19.4
	700*	4,624.5	21.0
	700	1,048.6	
	700	-	14.4
Sys. SZT	500	7,468.4	
	600	5,139.3	
	700	3,724.6	

*Start of $\Delta\sigma_{add}$ after unplanned test stop

All tests with System at SZT failed during the multi-stage fatigue loading. In comparison for all specimen at RT with System run-outs occurred, but for $\Delta\sigma_{max}$ = 700 N/mm² two repetitions were made due to unplanned and unexpected breakages. While in the first test an unplanned stop occurred and $\Delta\sigma_{add}$ was applied to the specimen, in the second test the early breakage incited to a second test repetition. Nevertheless the high scatter of this results show the difficulties in fatigue especially with multi-stage loading.

2.3 *Progressive load increase fatigue tests*

In addition to the multi-stage fatigue tests, a fatigue test procedure for a faster determination of the endurance strength of specimens was used for all categories mentioned above. The procedure was developed by Prot (1948) and modified by Dengler & Harig (1980). A minimum of two specimens is needed and both started with a stress range below the assumed endurance strength. For both tests the stress range increased with every load cycle by means of a specific load increasing rate ω. For practical reasons the load increasing was carried out in blocks of a size of 10,000 load cycles. The increasing rates were $\omega_1 = 10^{-4}$ N/mm²/load cycle and $\omega_2 = 10^{-3}$ N/mm²/load cycle which resulted in 0.15 kN/block and 1.5 kN/block. For the calculation of the endurance strength the breakage stress range was noted and placed in a $\Delta\sigma$-ω^n diagram. The linear extrapolation of the connection line between the test results to the ordinate with ω = 0 shows the endurance strength of the specimen.
The results of the load increasing tests on strands with laboratory anchorage and system anchorage are presented in Table 4. All tests were carried out with a constant lower load as mentioned for the single-stage fatigue tests. Tests with a low load increasing rate reached higher load cycles due to a longer duration in the non-destructive fatigue regime below the endurance strength. Remarkable is the result of the first load increasing rate on room temperature compared to the same test on low temperature.

Table 4. Progressive load increase fatigue testing results

Series	$\Delta\sigma_0$	$\Delta\sigma_{br}$	N_{br}
	[N/mm²]	[N/mm²]	[x 1000]
Lab RT ω_1	320	522	2,026.0
Lab RT ω_2	320	550	235.1
Lab SZT ω_1	250	359	1,091.4
Lab SZT ω_2		530	281.3
Sys. RT ω_1		272	225.8
Sys. RT ω_1		293	431.7
Sys. RT ω_1		281	319.2
Sys. RT ω_2		370	126.5
Sys. RT ω_2		380	135.0
Sys. RT ω_2		380	122.5
Sys. SZT ω_1		287	371.2
Sys. SZT ω_2		370	124.5

3 ANALYSIS AND INTERPRETATION OF THE RESULTS

3.1 *Single-stage fatigue tests*

A statistical analysis for each series was carried out. In a first step, a non-constant standard deviation with n_{cum} = n/2 from low to high number of load cycles for the calculation of the standard variation was used. Afterwards the 5% quantil values were calculated:

$$\Delta\sigma_{p\%} = \Delta\sigma_m \pm k_n \bullet \Delta\sigma_s \quad (3)$$

where $\Delta\sigma_m$ = mean value of the fatigue strength for a given N, k_n = fractil factor for normal distribution, and $\Delta\sigma_s$ = standard deviation. A second regression

analysis using Eq. 1 was made for the determination of the 5% quantil curve. Next step was the transformation of the wöhler curve into a bilinear fatigue resistance curve which can be describes by the inclinations k1 and k2. For the transformation a limitation of the fatigue resistance curve by means of the yield limit and the lower load was made:

$$\Delta\sigma_{Lim,m} = R_{p,0.1,m} - \sigma_u \tag{4}$$

where $R_{p,0.1,m}$ = mean value of the actual yield limit with a permanent elongation of 0.1% (determined by five static tensile tests).
And in case of the 5% quantil:

$$\Delta\sigma_{Lim,5\%} = R_{p,0.1,5\%} - \sigma_u \tag{5}$$

where $R_{p,0.1,5\%}$ = 5% quantil value of the actual yield limit with a permanent elongation of 0.1%. The bilinear fatigue resistance curve starts at the limitation point and needs the knee point of the wöhler curve k1/k2. The knee point is made with the tangent on the wöhler curve with the fix point at the limitation point and the horizontal expression of the endurance limit. The intersection point marks the knee-point k1/k2, the inclination k1 can be calculated:

$$k1_m = \left(\log \frac{\Delta\sigma_{D,m}}{\Delta\sigma_{Lim,m}} \frac{N_{\lim}}{N_{k1/k2}} \right)^{-1} \tag{6}$$

And in case of the 5% quantil:

$$k1_{5\%} = \left(\log \frac{\Delta\sigma_{D,5\%}}{\Delta\sigma_{Lim,5\%}} \frac{N_{\lim}}{N_{k1/k2}} \right)^{-1} \tag{7}$$

With the inclination k1 the dependent inclination k2 can be calculated:

$$k2 = 2 \bullet k1 - 1 \tag{8}$$

The results of the analysis are summarized in Tables 5 and 6.

Table 5. Characteristics of the mean value function of the bilinear characteristic fatigue resistance

	$k1_m$	**$k2_m$**	**$k1/k2_m$**
	[-]	**[-]**	**[x 1000]**
Lab RT	3.25	5.51	531
Lab SZT	3.46	5.93	2480
Sys. RT	3.60	6.19	530
Sys. SZT	3.37	5.75	485

Table 6. Characteristics of the 5% quantil function of the bilinear characteristic fatigue resistance

	$k1_{5\%}$	**$k2_{5\%}$**	**$k1/k2_{5\%}$**
	[-]	**[-]**	**[x 1000]**
Lab RT	2.84	4.68	522
Lab SZT	3.13	5.27	2450
Sys. RT	3.33	5.65	620
Sys. SZT	3.00	5.00	600

In the end the analysis of the single stage fatigue test leads to the results summarized in Fig. 3 and Fig. 4, which shows the technical endurance strength for each series at different levels from $2x10^6$ load cycles to 10^8 load cycles. The values are given for the mean value curves and the associated 5% curves of the wöhler curve and the bilinear fatigue resistance curve.

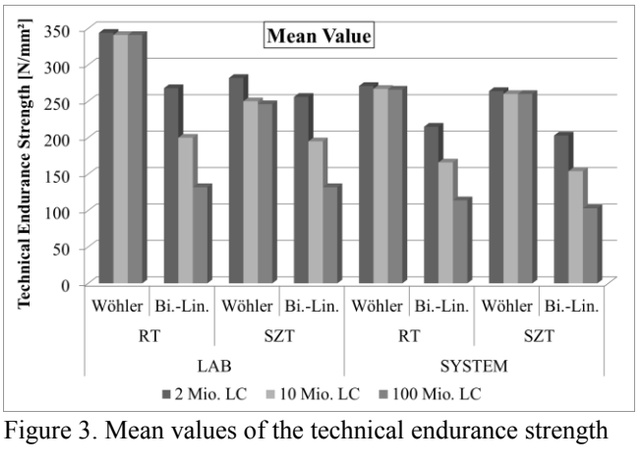


Figure 3. Mean values of the technical endurance strength

A clear trend can be seen with a high difference between room temperature and low temperature for laboratory anchored specimens. No significant difference can be found for wedge anchored specimens between room and low temperature. The decrease of the fatigue resistance from laboratory anchorage to wedge anchorage is in the same order as the reduct ion of the fatigue resistance by means of temperature decreasing for laboratory anchorage. This can be ob

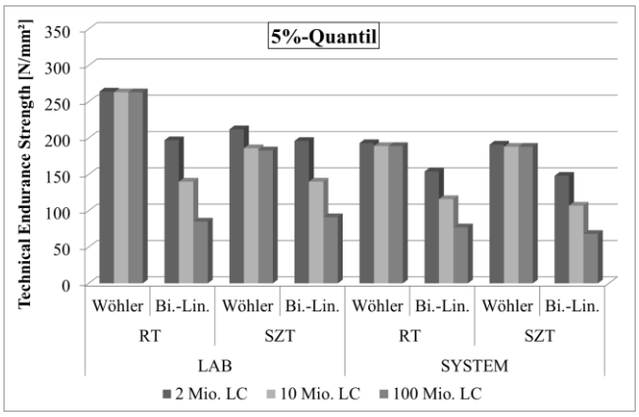


Figure 4. 5% quantil of the technical endurance strength

served in Fig. 5 which shows all mean value functions in a double log Δσ-N diagram. Additional a historical fatigue range shows the results of former fatigue tests, the reference curves of the international recommendations for stay cables from PTI and fib are additionally shown.

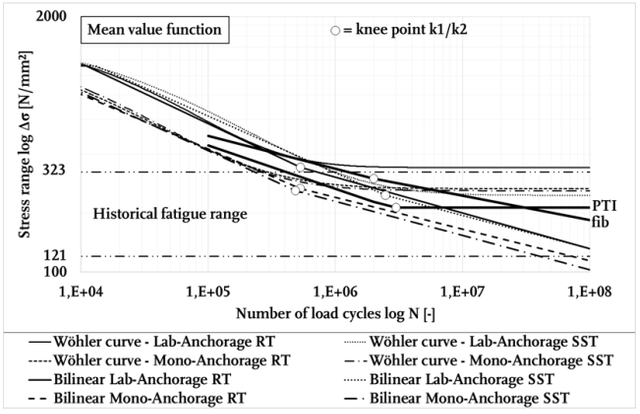


Figure 5. Summarized analysis results of the single-stage fatigue tests

3.2 *Multi-stage fatigue tests*

Linear and non-linear damage accumulation analysis was made. The following linear methods were applied: [1] the original wöhler curve (Palmgren 1924), [2] the elemental rule of Miner (1945) (k2 = k1), [3] the bilinear fatigue resistance curve by Haibach (2006) and [4] the modification of the bilinear resistance curve by Zenner & Liu (1992). The results of the established wöhler curves obtained from the single-stage fatigue tests were used to calculate the parameters of the different models.

The findings of the first two linear methods are shown in Table 7, besides the additional damage $d_{i,add}$ is shown here for Run-Outs.

Table 7. Damage D and $d_{i,add}$ found by linear damage analyis

	Origin Wöhler [1]		**Haibach [3]**	
	D	**$d_{i,add}$**	**D**	**$d_{i,add}$**
Lab RT				
500	2.20	2.17	3.35	2.25
600	1.19	0.94	3.89	1.02
700	2.89	1.01	7.02	1.15
Lab SZT				
500	1.35	0.96	2.20	1.04
600	0.72	-	1.08	-
700	1.64	-	1.89	-
System RT				
500	1.91	0.91	4.56	0.93
600	3.84	0.61	9.89	0.68
700_1	6.75	1.09	8.10	1.28
700_2	1.24	-	1.50	-
700_3	14.52	0.75	17.47	0.88
System SZT				
500	0.91	-	3.06	-
600	2.26	-	4.93	-
700	5.09	-	6.45	-

The linear damage accumulation leads to an overestimation of the calculated damage. Especially for Run-outs an additional damage $0.68 \leq d_{i,add} \leq 2.25$ can be found. Moreover the system anchored specimens shows the higher tendency to an overestimation of the calculated damage.

Table 8 presents the linear damage accumulation in accordance to the Miner Origin and the bilinear modification by Zenner & Liu (1992).

Table 8. Damage D and $d_{i,add}$ found by linear damage analyis

	Miner elem. [2]		**Zenner & Liu [4]**	
	D	**$d_{i,add}$**	**D**	**$d_{i,add}$**
Lab RT				
500	4.92	2.25	3.67	1.96
600	5.84	1.02	4.05	0.91
700	9.12	1.15	7.41	1.06
Lab SZT				
500	2.20	1.04	2.41	0.98
600	1.08	-	1.12	-
700	1.89	-	1.92	-
System RT				
500	6.49	0.93	5.63	0.93
600	11.40	0.68	11.38	0.68
700_1	8.95	1.28	8.94	1.28
700_2	1.69	-	1.69	-
700_3	19.54	0.88	19.51	0.88
System SZT				
500	4.56	-	3.16	-
600	5.74	-	4.86	-
700	7.31	-	6.30	-

Both methods do not use an endurance limit and hence the calculated damage increases in all tests.

Therefore the overestimation here is aggravated compared to [1] and [3].
The non-linear damage accumulation analysis was carried out in accordance to the methods of [5] Subramanyan (1976), [6] Hashin & Rotem (1978) and [7] Manson et al. (1967). All models were configured by means of the single-stage fatigue data. The results of the analysis are summarized in Table 9.

Table 9. Damage D found by non-linear damage analysis

	Subraman. [5]	**Hashin [6]**	**Manson [7]**
Lab RT			
500	2.17	2.21	2.17
600	0.97	1.22	1.06
700	4.80	2.73	112.6
Lab SZT			
500	1.06	1.40	1.12
600	1.16	0.77	0.92
700	1.67	1.67	1.61
System RT			
500	1,289	2.63	3.98
600	661	4.45	31.8
700_1	2.69E+7	6.94	830
700_2	1.74	1.73	1.68
700_3	9.70E+10	11.2	17,194
System SZT			
500	3.55	0.87	0.91
600	1.70	1.72	1.78
700	16.7	4.56	531.7

The analysis model by Subramanyan (1976) fail in the calculation of the System RT with the highest $\Delta\sigma_{max}$ if additional fatigue loading after the Run-out was carried out. In other cases especially for Lab SZT a good agreement can be seen. The calculation made by Hashin & Rotem (1978) shows in general the best agreement in all multi-stage fatigue tests while the calculation method in accordance to Manson et al. (1968) delivers some extraordinary overestimations due to the non-linear nature of the analysis. In general it is obviously that reduced fatigue strength in multi-stage fatigue tests can be observed at SZT directly and after the linear and non-linear damage accumulation analysis. These findings can be seen for Lab and System specimens.

3.3 *Progressive load increasing fatigue tests*

The findings of the progressive load increasing tests analysis depends on the load increasing rate ω and the exponent n. While ω is chosen before the test, n can be determined in different ways. In the origin form by Prot (1948) of the load increase tests n = 0.5, a modification was made by Dengel & Harig (1980) gives n = 1/(k1+1) which consider the inclination of the wöhler curve in the regime of the fatigue strength. Table 10 shows the results of the analysis and the comparison with the endurance strength $\Delta\sigma_{D,W}$ established by the single-stage fatigue tests. In three of four cases the accelerated method is in the vicinity of the Wöhler results for $\Delta\sigma_{D,P}$ (n=0,5). Only for Lab specimens at room temperature a high overestimation was observed. This overestimation remain nearly unchanged for $\Delta\sigma_{D,P}$ (n=1/(k1+1)), but here the other results shows a high underestimation.

Table 10. Endurance limits from progressive load increasing fatigue tests in comparison to the wöhler endurance limit

	$\Delta\sigma_{D,W}$	**$\Delta\sigma_{D,P}$ (n=0,5)**	**$\Delta\sigma_{D,P}$ (n=1/(k1+1))**
	[N/mm²]	**[N/mm²]**	**[N/mm²]**
Lab RT	341	509	483
Lab SZT	247	280	106
Sys. RT	266	230	153
Sys. SZT	253	249	167

Regarding the effect of SZT in comparison of RT a clearly tendency can be seen in the fatigue tests under progressive loading. The Lab specimens show a clear reduction in the fatigue strength while no significant difference for System specimens can be seen.

4 CONCLUSIONS

The effect of low temperature on the fatigue strength of cold-drawn high strength steel strands has been experimentally investigated. Four wöhler curves and bilinear fatigue resistance curves have been determined based on the results of 88 single-stage fatigue tests. A statistical analysis of the test data showed the different scatter of the wöhler and bilinear curves. In the low cycle fatigue regime the fatigue strength of Lab specimens increases if the temperature is decreased from RT to SZT.For these low temperatures, a significant reduction of the endurance limit was additionally verified. The reduction of the endurance limit by means of SZT has a comparable amount as the reduction by means of the harmful effects initiated by the wedge anchorage.
The results of multi-stage fatigue tests with a typical bridge load collective confirmed the decreasing effect of SZT on the fatigue strength of 7-wire strands. These results also indicated the tendency of slightly lower fatigue strength for wedge anchored strands. Common linear and non-linear analysis overestimates the accumulated damage compared to the multi-stage fatigue tests. The results of the progressively increasing load tests provide experimental evidence on the suitability of this test method for the determination of the endurance limit of system anchored strand specimens. For laboratory anchored strands, the test results a harmful effect under SZT compared to RT to the endurance limit.

REFERENCES

Dengel, D & Harig, H. 1980. Estimation of the fatigue limit by progressively-increasing load tests. Fatigue of Engineering Materials and Structures 3: 113-128.

Gaßner, E. et al. 1964. Ertragbare Spannungen und Lebensdauer einer Schweißverbindung aus ST37 bei verschiedenen Formen des Beanspruchungskollektivs. Archiv für das Eisenhüttenwesen 35 (3): 255-267.

Haibach, E. 2006. Betriebsfestigkeit. Berlin: Springer-Verlag

Hashin, Z & Rotem, A. 1978. A cumulative damage theory of fatigue materials. Materials Science and Engineering 34: 147-160.

Heeke, G. 2016. Untersuchungen zur Ermüdungsfestigkeit von Betonstahl und Spannstahl im Zeit- und Dauerfestigkeitsbereich mit sehr hohen Lastwechselzahlen. Dortmund: Technische Universität Dortmund - Schriftenreihe Betonbau - Prof. Dr.-Ing Maurer.

Heuler, P. et al. 2005. Standardised load-time histories – A contribution to durability issues under spectrum loading. Materialwissenschaft und Werkstofftechnik 36 (11): 669-677.

Kobrin, M. 1974. Fatigue resistance of high strength wire and wire cables for reinforced concrete structures at normal and low temperatures. Haifa: Faculty of Mechanical Engineering, Technion - Israel Institute of Technology.

Manson, S.S. et al. 1967. Application of a double linear damage rule to cumulative fatigue. American Society for Testing and Materials: 384-412.

Miner, M.A. 1945. Cumulative damage in fatigue. Journal of Applied Mechanics 12: 64-159.

Nürnberger, U. 1981a. Dauerschwingverhalten von Spannstählen. Bauingenieur 56: 311-319.

Nürnberger, U. 1981b. Verhalten von Spannstählen in Keilverankerungen unter statischer Belastung. Bauingenieur 56: 25-32.

Palmgren, A. 1924. Die Lebensdauer von Kugellagern. Zeitschrift des Vereins Deutscher Ingenieure 68 (14): 339-341

Prot, M. 1948. Fatigue testing under progressive loading; A new technique for testing materials, Rèvue de Metallurgie, XLV (12): 481.

Stephens R.I. et al. 2001. Metal Fatigue in Engineering.

Subramanyan, S. 1976. A cumulative damage rule based on the knee point of the S-N curve. Journal of Engineering Materials and Technology. 315-321.

Suresh, S. 2004. Fatigue of Materials. Cambridge: Cambridge University Press.

Svensson, H. 2011. Schrägkabelbrücken. 40 Jahre Erfahrung weltweit. Zeuthen: Ernst & Sohn GmbH & Co. KG.

Zenner, H. & Liu, J. 1992. Vorschlag zur Verbesserung der Lebensdauerschätzung nach dem Nennspannungskonzept. Konstruktion 44: 9-17.

Maintenance, Safety, Risk, Management and Life-Cycle Performance of Bridges – Powers, Frangopol, Al-Mahaidi & Caprani (Eds)
© 2018 Taylor & Francis Group, London, ISBN 978-1-138-73045-8

Multi-scale finite element model updating of highway bridge based on long-gauge strain response

Shizhi Chen & Gang Wu & Huile Li.
Key Laboratory of Concrete and Prestressed Concrete Structures of the Ministry of Education, Southeast Univ., Nanjing 210096, China.

ABSTRACT: The damages in the bridges severely endangered their lives. In order to ensure the safety and facilitate daily maintenance, the methods for detecting damages were needed. Conventional damage identification methods based on finite model updating achieved in precisely damage detection. However, their processes of finite element updating would cost a lot of computing time. Also, the finite element updating methods require multi-order modes of the bridges, which are difficult to obtain in actual scenes with regular traffic condition. Under such circumstances, this paper presented a bridge finite element updating method based on long-gauge strain response. This method utilizing long-gauge FBG sensors has two steps. The first step is to detect the location of the damage initially using a damage localizing method. Then in the second step, on the basis on step 1, the damage would be further determined through finite element updating through a multi scale element model to measure the location and extent of the damage more accurately. With the combination of step 1 and 2, the computation complex would be reduced greatly without harming the identification accuracy. In order to verify this method, an experiment was conducted in laboratory. In the experiment, the long-gauge strain response of the bridge models with a damage condition was extracted by the long-gauge FBG sensors mounted beneath them. Utilizing this method, the damage conditions can be successfully detected in the bridge model, which verified the potential of this method.

1 INTRODUCTION

Bridges, as one of the lifeline civil engineering structures, play an important role in the economic sphere and people's safety. The designed life expectancy of these bridges usually ranges from 50 to 100 years. During the service life of bridges, the performance will deteriorate when they are subjected to normal traffic load, occasional excessive load, and earthquake load. Moreover, because of the steady development of the global economy and national transportation industries, traffic loading has significantly increased in recent decades. This would further accelerate the deteriorating process of the bridges (Richardson & Jones 2014). Under this circumstance, it is essential to operate routine monitoring of bridges to prevent potential damages.

Nowadays, structural health monitoring is becoming more and more popular. Compared with conventional manual inspect, it is less time consuming and more efficient which could fulfill long-term damage monitoring of the bridge (Brownjohn 2007). In this field, there are many damage identification techniques, among which finite element (FE) model updating technique is an efficient way for damage location and extent identification (Teughels & De Roeck 2004, Brownjohn et al. 2001).

FE model updating techniques have been a viable approach to correcting an initial mathematical model based on monitored data. The objective of structural model updating is to reduce inherent modeling errors in FE models due to simplifications, idealized connections, and uncertainties of material properties. Updated FE models, which have less discrepancy with real structures, give more precise predictions of structural property for future analyses (Jaishi & Ren 2005). It can be an effective way for structural damage identification.

As mentioned above, the procedure of model updating aims to adjust the uncertain properties of the FE model by minimizing iteratively the differences between the measured reference index and the corresponding analytical predictions.

Currently, there are two kinds of model updating methods, direct model updating method and indirect model updating methods. Direct model updating techniques involve updating models using a single updating formula or series of formulas based upon modal parameters (Eskew & Jang 2017). Indirect model updating technique involves optimization of parameters in the model, such as stiffness, young's modulus based on discrepancies between model and monitored structural information. Compared with indirect model updating method, direct method does not ensure the connectivity and physical meaning of the model. Hence, most studies about model updating nowadays belong to indirect updating method.

For reference index to updating model, most methods usually choose natural frequencies and modal shapes of the structure. A lot of studies succeeded in utilizing these indexes for FE model updating. However, in actual engineering natural frequencies do not contain spatial information which is not sensitive to structural local damage and modal shapes are not easy to obtain, especially for high level modes which are usually more sensitive to local damage of the structure (Salawu 1997, Hong *et al.* 2014). All these difficulties made it very inconvenient for application in SHM systems. Some new indexes were proposed, such as mode shape curvatures, modal strain energy, and other modal based dynamic characteristics for model updating with better performances.

As for the process to adjust FE model parameter, it is a parameter optimization process, whose object function is to minimize the difference of reference index between FE model and actual engineering by optimizing the uncertain properties in FE model, such as element stiffness. Optimizing algorithm such as genetic algorithm, particle swarm algorithm need run FE model independently in every iteration, as a result of which the process would be time consuming and inefficient. To solve this problem, time needed for running FE model need to be reduced. Therefore, FE model need to be simplified as far as possible without harming the accuracy. Besides, response surface method was also an effective way for this problem.

Under such circumstance, in this article, based on monitored long-gauge strain signal, a two-step FE model updating method is initially proposed. A new reference index in time domain and a new corresponding object function is established. The feasibility of the method has been verified through a vehicle-bridge interaction simulation on the basis of an indoor model experiment.

2 THEORETICAL BACKGROUND

2.1 *Long-gauge FBG sensor*

The long-gauge FBG sensor was proposed by Li & Wu (2007). The basic structure of this sensor is presented in Figure 1. The long-gauge FBG sensor consists of two end anchor points with an FBG between them. The shield sleeve plays the role of protection and keeps the inner FBG free from structural deformation. With this structure, the sensor could measure the average strain between two anchor points unlike conventional sensors based on single-point measurement. In practical engineering, conventional point sensors are easily affected by discontinuous characteristics of structures, such as cracks and inclusions. In contrast, long-gauge FBG sensors are more robust to these characteristics owing to their structure (Kim *et al.*, 2016). One other advantage of this sensor is its multiplexing capacity. This capacity means that, to cover a certain region of a structure, many sensors can be installed with minimal wiring. For large structural engineering projects, such as bridges, its installation would be more convenient than that of conventional strain gages because each normal strain gage requires at least two lead wires, which would lead to a large number in total (Kang *et al.*, 2007; Moyo *et al.*, 2005). In addition, it still has the advantages of traditional FBG sensors, such as immunity to electromagnetic interference, light weight, and small size like Figure 2 shows.

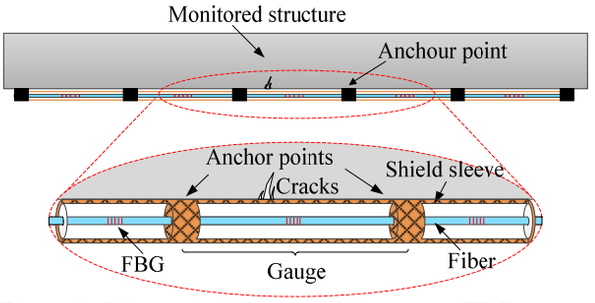


Figure 1. Schematic diagram of long-gauge FBG sensor.

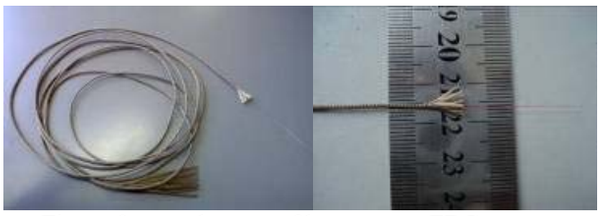


Figure 2. actual scene of long-gauge FBG sensor.

2.2 *Damage identification method*

The damage identification method is proposed by Chen *et al.* (2017) which utilized long-gauge strain influence line (SIL). For brevity, the method is simply introduced here and all the details of this method are thoroughly provided in Chen *et al.* (2017).

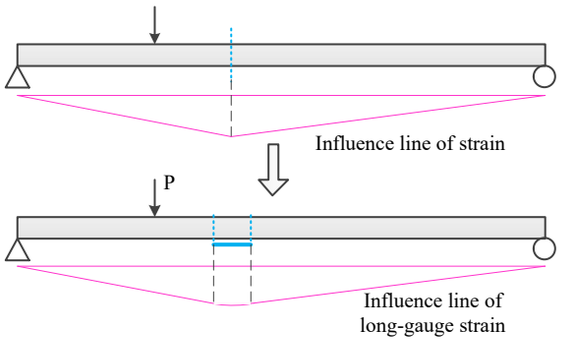


Figure 3. Comparison between traditional SIL with long-gauge SIL.

According to classic structural mechanics, the static long-gauge strain history of a single moving force is:

$$\varepsilon(x)=\begin{cases}\dfrac{(L-x_i)y}{(EI)_i L}x & x\in[0,x_i)\\ \dfrac{x_i y}{(EI)_i}\left(1-\dfrac{x}{L}\right) & x\in[x_i,L]\end{cases} \quad (1)$$

In the meantime, based on the definition of long-gauge strain, the relationship between conventional 'pointy' strain and long-gauge strain can be expressed in Equation 2.

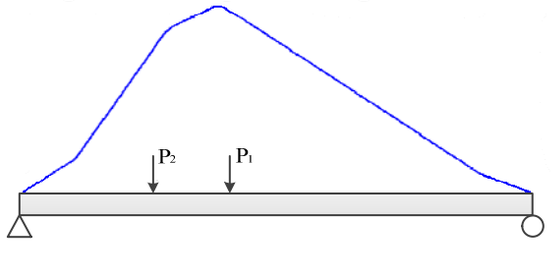
$$\bar{\varepsilon}_m(x)=\frac{1}{l_e}\int_{ml_e}^{(m+1)l_e}\varepsilon(x)\,dx \quad (2)$$

After substituting Equation 1 into Equation 2, the formulas of long-gauge SIL can be obtained. The specific expressions of long-gauge SIL are omitted here because of their complexity. The core of this damage identification is focused on one special property of long-gauge SIL. Long-gauge SIL is a two order function only when the load is within the range of the sensor, like Figure 3 shows.

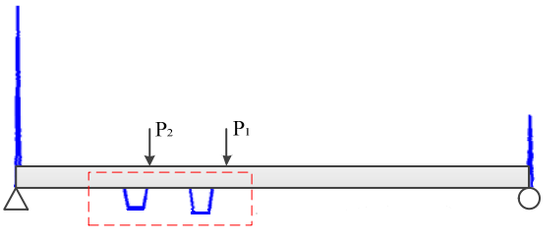
Beyond the range of the sensor, it is a linear function of t. Taking two order derivative of long-gauge SIL, Equation (3) can be deduced.

$$\frac{d^2\bar{\varepsilon}_m(t)}{dt^2}=\begin{cases}0 & t\in[0,ml_e/v)\\ -P\cdot v^2\cdot\dfrac{n\bar{y}_m}{(\overline{EI})_m} & t\in[ml_e/v,(m+1)l_e/v)\\ 0 & t\in[(m+1)l_e/v,L/v]\end{cases} \quad (3)$$

in which n is the total number of the gauge distributed along the entire span of the girder.



a. long-gauge strain influence line under a two-axle vehicle



b. two order derivative of long-gauge strain influence line

Figure 4. long-gauge strain influence line and its two order derivative.

Figure 6 displays the two order derivative of long-gauge SIL under two moving loads. According to Equation (3), it can be seen that the height of each rectangular part in Figure 4 is related to structural bending stiffness within each sensor. According to this relationship, the damage location can be initially located.

An index vector would be obtained by combining two order derivative (TOD) of SIL in each gauge which contains structural spatial information.

$$Index=\{TOD_1,TOD_2,\cdots,TOD_n\} \quad (4)$$

2.3 *Two-step FE model updating method*

The flow chart of this two-step model updating method is proposed in Figure 5. The first step is to locate the damage using the damage identification method introduced in the last section. Then in the second step, the FE model would be established in a multi-scale manner to reduce calculating time. The gauge where damage is located would be established using solid elements. For the other parts of the bridge, only beam element would be used. The disposal of the connection between different elements is displayed in Figure 6. The freedoms of solid elements are coupled with the node of beam element by several constraint equations.

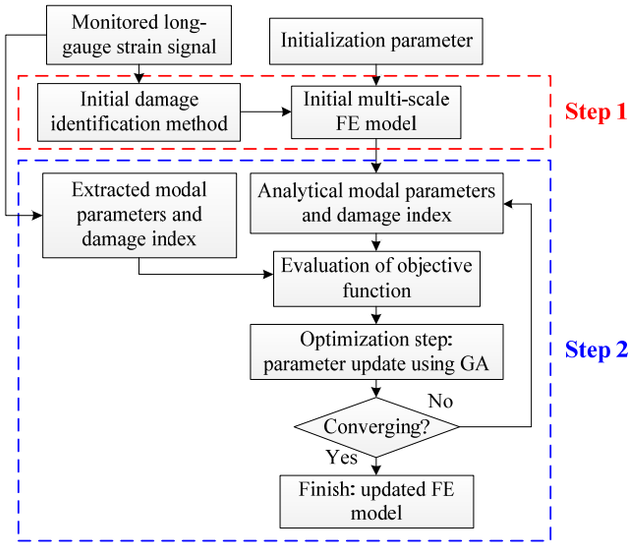


Figure 5. Flow chart of two-step model updating.

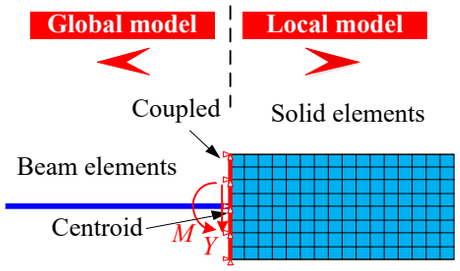


Figure 6. Connection between beam elements and solid elements.

As for the object function of this updating method, it is a combination of frequency and time domain index, which is shown in Equation (5).

$$\min f(x)=\alpha\cdot\frac{\left\|Index_s-Index_m\right\|}{\left\|Index_m\right\|}+\beta\cdot abs\left(\frac{f_s-f_m}{f_m}\right)+\gamma\cdot\left(E_s-E_0\right)^2 \tag{5}$$

where α, β, γ are optimization parameters and the last item of the function is for regulation in order to avoid solutions with no physical meanings. Subscript s, m represent the model simulated information and monitored information, respectively. In addition, index vector need to be normalized in advance in order to quantify the difference. E_0 is original elastic modulus.

The frequency of the monitored structural is obtained through Frequency domain decomposition (FDD) method.

The optimization genetic algorithm is utilized to solve this problem. Genetic algorithm (GA) is an excellent global optimization method inspired by the process of natural selection that belongs to the larger class of evolutionary algorithms. It has been verified to be an efficient method in application in structural engineering (Ye & Wu 2017).

3 VEHICLE BRIDGE COUPLING SIMULATION

In this section, a vehicle bridge coupling (VBC) system is developed to verify this model updating method. In-service bridges normally work within the linear-elastic range under routine traffic load; therefore, the following derivation was carried out under the assumption of elasticity.

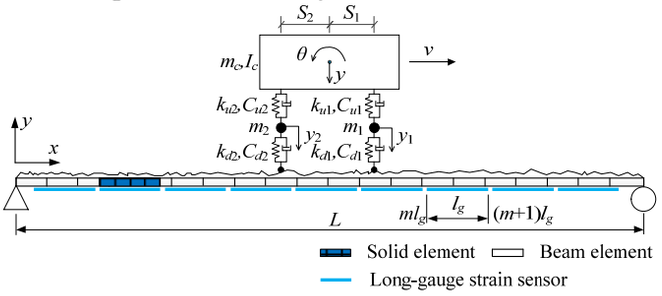


Figure 7. Model of the vehicle-bridge interaction system.

Figure 7 shows a four-degrees-of-freedom (DOFs) vehicle model moving at a uniform speed v over a simply supported bridge whose bottom surface is covered by long-gauge FBG sensors with l_g gauge length. Using the Lagrange formulation, the equation of motion of the vehicle model is derived as follows (Law & Zhu 2004, Wu & Law 2011):

$$\begin{bmatrix}\boldsymbol{M}_{c1}&0\\0&\boldsymbol{M}_{c2}\end{bmatrix}\ddot{\boldsymbol{Y}}+\begin{bmatrix}\boldsymbol{C}_{c11}&\boldsymbol{C}_{c12}\\\boldsymbol{C}_{c21}&\boldsymbol{C}_{c22}\end{bmatrix}\dot{\boldsymbol{Y}}+\begin{bmatrix}\boldsymbol{K}_{c11}&\boldsymbol{K}_{c12}\\\boldsymbol{K}_{c21}&\boldsymbol{K}_{c22}\end{bmatrix}\boldsymbol{Y}=-\begin{Bmatrix}0\\\boldsymbol{P}(t)\end{Bmatrix}+\begin{Bmatrix}0\\\boldsymbol{P}_0\end{Bmatrix} \tag{6}$$

in which $\boldsymbol{Y}$ is the response vector of the vehicle, which corresponds to four DOFs; $P(t)$ is the interaction force vector between the vehicle and bridge; and P_0 is the static axial weight of the vehicle. $\boldsymbol{M}_c$, $\boldsymbol{C}_c$, $\boldsymbol{K}_c$ are submatrices of the vehicle's mass, damping and stiffness matrices, respectively.

The intact bridge is assumed to be an Euler-Bernoulli beam. And damaged gauge is modeled using solid element for finer solution. The equation of motion of the bridge can be expressed as:

$$\boldsymbol{M}_b\ddot{\boldsymbol{R}}+\boldsymbol{C}_b\dot{\boldsymbol{R}}+\boldsymbol{K}_b\boldsymbol{R}=\boldsymbol{H}_l\boldsymbol{P} \tag{7}$$

where $\boldsymbol{M}_b$, $\boldsymbol{C}_b$ and $\boldsymbol{K}_b$ are the mass, damping and stiffness matrices of the bridge structures, respectively, $\boldsymbol{C}_b$ is obtained with the assumption of Rayleigh damping, $\boldsymbol{R}$ is the nodal displacement vector of the entire bridge, the point (.) above $\boldsymbol{R}$ represents derivation with respect to time, and $\boldsymbol{H}_l\boldsymbol{P}$ is the equivalent nodal load vector. $\boldsymbol{H}_l$ is the location matrix of each axial interaction force.

According to the equilibrium of the interaction force between the bridge and vehicle, the coupled equation of motion of the vehicle-bridge interaction system can be obtained by combining Equation (6) with Equation (7):

$$\boldsymbol{M}(t)\ddot{\boldsymbol{Z}}+\boldsymbol{C}(t)\dot{\boldsymbol{Z}}+\boldsymbol{K}(t)\boldsymbol{Z}=\boldsymbol{F}(t) \tag{8}$$

where $\boldsymbol{Z}=\{\boldsymbol{Y}^T\ \boldsymbol{R}^T\}^T$ is the total displacement vector of the vehicle-bridge interaction system; $\boldsymbol{M}(t)$, $\boldsymbol{C}(t)$ and $\boldsymbol{K}(t)$ are the mass, damping and stiffness matrices of the entire vehicle-bridge interaction system; and $\boldsymbol{F}(t)$ is the external force vector.

Equation (8) can be solved by the Newmark-β method. Then, the dynamic nodal response of the bridge under a moving vehicle can be obtained. Then coordinating with the arrangement of long-gauge FBG sensors, the dynamic long-gauge strain response can be extracted.

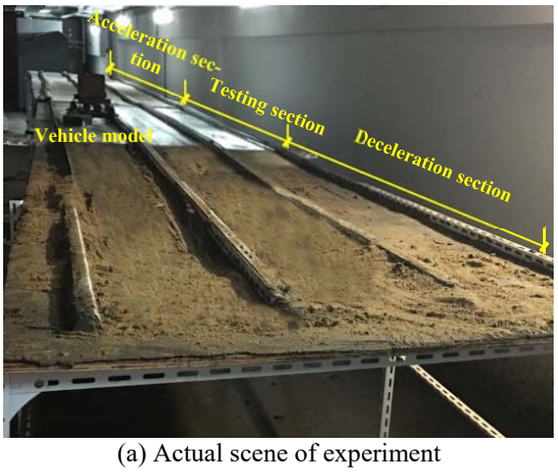
4 NUMERICAL VERIFICATION BASED ON EXPERIMENT

Based on the theory of last section, a VBC simulation was developed based on the results of Wu *et al.* (2017)'s indoor experiment. The actual scene of the model experiment is presented in Figure 8. The bridge model consists of five T-beams which are made of

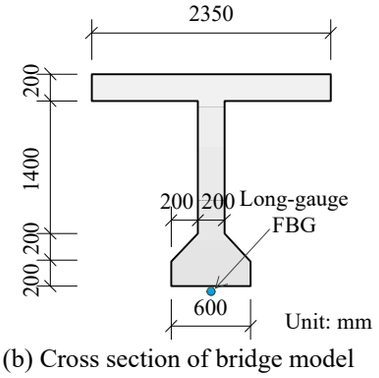
plexiglass. The detail of the model bridge cross-section is shown in Figure 8 (b). Whole model can be divided into three sections longitudinally, acceleration section, testing section and deceleration section, just as Figure 8 displays. The testing section is 3 m long. The model vehicle is a biaxial vehicle as shown in Figure 9. In order to monitor the long-gauge strain response caused by moving model vehicle, 9 long-gauge FBG sensors whose gauge length is 30mm were attached on the bottom surface of testing section.

Based on the arrangement of the experiment, a VBI system was established in ANSYS and Matlab software. The bridge model consists of 18 beam elements and 95 solid elements. 9 long-gauge strains under the bridge are extracted corresponding to 9 long-gauge FBG sensors in experiment. The FE model is presented in Figure 11. In order to mimic the experimental situation, white Gaussian noise is added to the original signal using the command 'awgn' in Matlab. The signal-to-noise ratio is set as 20 dB, because with this value, the simulation results are more close to the results obtained in Wu *et al.* (2017)'s experiment. The optimization process is achieved by MATLAB optimization tool box. In each iterative generation, population size is set as 50.

In experiment, the beam section within gauge 4 is cut in order to reduce 10% bending stiffness in gauge 4. The initial FE model is established using original designed parameters.



(a) Actual scene of experiment



(b) Cross section of bridge model

Figure 8. (Wu *et al.*, 2017)'s experimental arrangement.

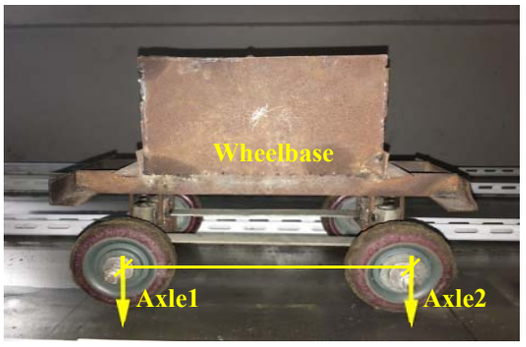


Figure 9. Vehicle model adopted in (Wu *et al.*, 2017)'s experiment.

Firstly, using method introduced in section 2.2, the damage location can be directly decided, as shows.

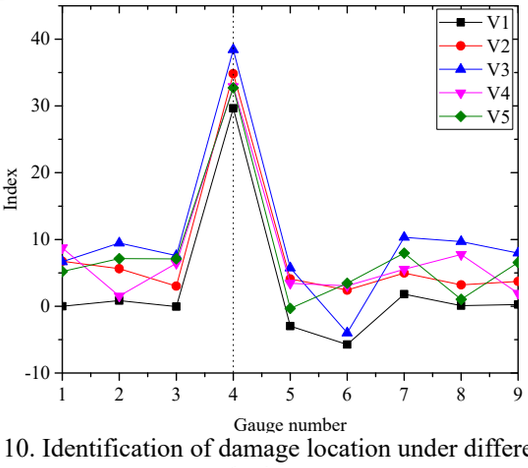


Figure 10. Identification of damage location under different velocity

Then the FE model's 4th gauge is modeled using solid elements. Choosing elastic modulus as optimizing parameter, after 50 generations' iteration in GA, the value of object function converged, just as Figure 12 shows. The blue circle represents the mean performance in each generation and the red point is the best individual in each generation. The whole optimization process seems to be successful. Meanwhile, the distribution of the beam before and after optimization is displayed in Figure 13, where object, initial and after optimization represent the actual one in experiment, initial value in FE model and the one updated using GA, respectively. It can be observed that after optimization, the bending stiffness error between actual structure and updated FE model is reduced dramatically.

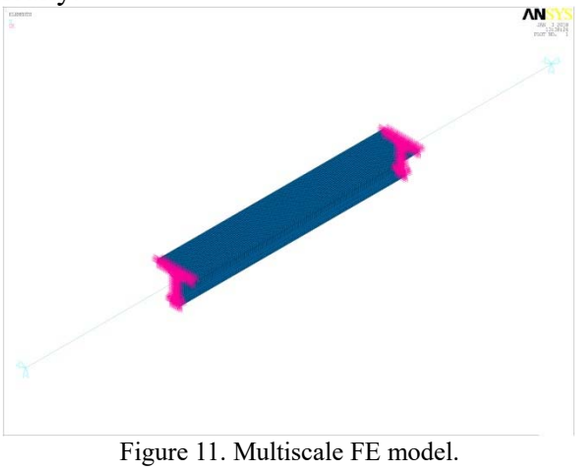


Figure 11. Multiscale FE model.

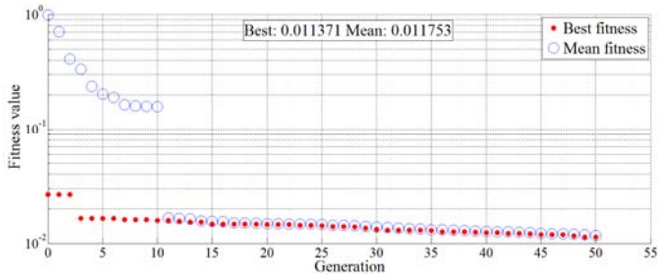


Figure 12. Object function value in each iteration.

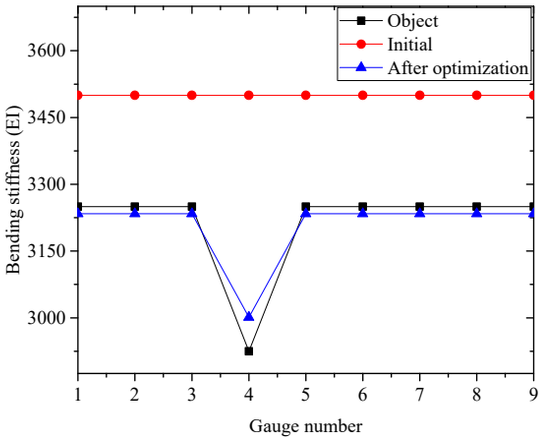
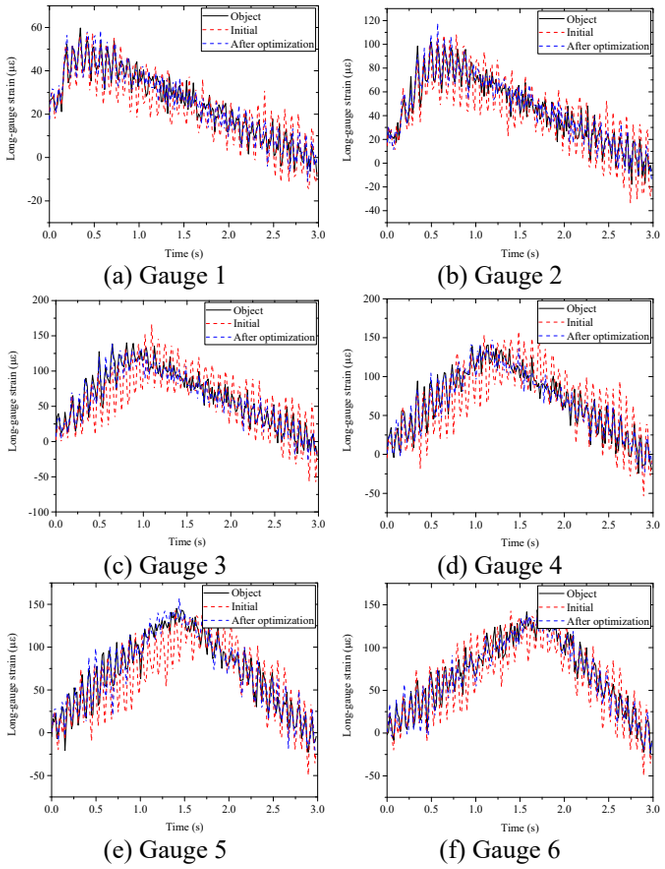


Figure 13. Identified bending stiffness distribution.

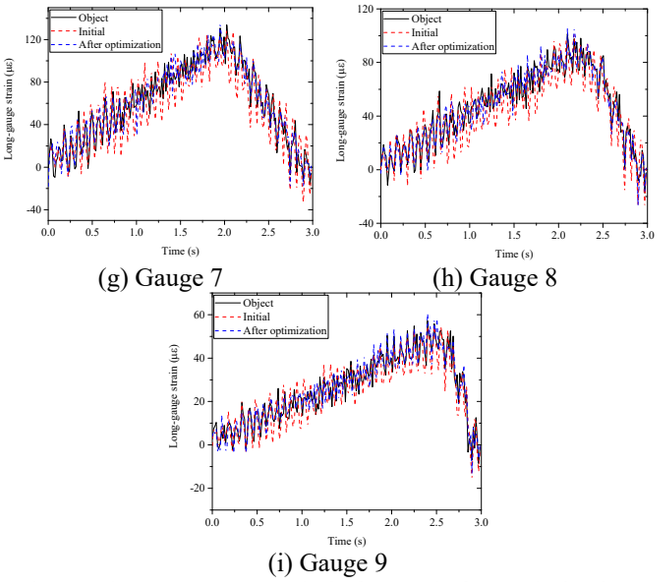
In order to further examine the updated model's performance, the long-gauge strain time history in each gauge is compared with actual monitored signal, displayed in Figure 14. The difference between initial model and updated model is obvious. The performance of updated model is much more similar to the actual monitored signal. The error of FE model has been successfully controlled at a low level.



(a) Gauge 1 (b) Gauge 2

(c) Gauge 3 (d) Gauge 4

(e) Gauge 5 (f) Gauge 6



(g) Gauge 7 (h) Gauge 8

(i) Gauge 9

Figure 14. Long-gauge strain before and after optimization.

5 CONCLUSIONS

In this article, a two-step multi-scale model updating method was initially proposed based on monitored long-gauge strain signal. Its feasibility is initially verified through numerical simulation combined with an indoor model experiment. It can be found that it has the potential to be utilized in actual application. Even though, the in-situ testing is needed in the future.

6 ACKNOWLEDGEMENTS

The authors would like to acknowledge financial support from the National Natural Science Foundation of China (No.51525801 and No.51708112), Chang Jiang Scholars Program, the Priority Academic Program Development of Jiangsu Higher Education Institutions (No.1105007002).

7 REFERENCE

Brownjohn, J.M.W. 2007. Structural health monitoring of civil infrastructure. *Philosophical Transactions of the Royal Society A: Mathematical, Physical and Engineering Sciences.* 365(1851): 589-622.

Brownjohn, J.M.W., Xia, P., Hao, H. & Xia, Y. 2001. Civil structure condition assessment by FE model updating: methodology and case studies. *Finite Elements in Analysis and Design.* 37(10): 761-776.

Chen, S.Z., Wu, G., & Wu, B.T. 2017. Simultaneous identification method of damage and vehicle parameters on bridges utilizing long-gauge strain influence line under moving vehicle loads. *Sensors and Smart Structures Technologies for Civil, Mechanical, and Aerospace Systems; Proc. SPIE 10168, Portland, 25-30 March 2017.*

Eskew, E.L. & Jang, S. 2017. Remaining stiffness estimation of buildings using incomplete measurements. *Structural Control and Health Monitoring.* 24: e1899.

Hong, W., Wu, Z.S., Yang, C.Q., Wu, G. & Zhang, Y. 2014.

Finite element model updating of flexural structures based on modal parameters extracted from dynamic distributed macro-strain responses. *Journal of Intelligent Material Systems and Structures*. 26(2): 201-218.
Jaishi, B. & Ren, W.X. 2005. Structural finite element model Updating using ambient vibration test results. *Journal of Structural Engineering*. 131(4): 617-628.
Kang, L., Kim, D. & Han, J. 2007. Estimation of dynamic structural displacements using fiber Bragg grating strain sensors. *Journal of Sound and Vibration.* 305(3): 534-542.
Kim, T.M., Kim, D.H., Kim, M.K. & Yun, M.L. 2016. Fiber Bragg grating-based long-gauge fiber optic sensor for monitoring of a 60 m full-scale prestressed concrete girder during lifting and loading. *Sensors & Actuators A: Physical.* 252: 134-145.
Law, S.S. & Zhu, X.Q. 2004. Dynamic behavior of damaged concrete bridge structures under moving vehicular loads. *Engineering Structures*. 26(9): 1279-1293.
Li, S.Z. & Wu, Z.S. 2007. Development of distributed long-gage fiber optic sensing system for structural health monitoring. *Structural Health Monitoring.* 6(2): 133-143.
Moyo, P., Brownjohn, J.M.W., Suresh, R. & Tjin, S.C. 2005. Development of fiber Bragg grating sensors for monitoring civil infrastructure. *Engineering Structures*. 27(12): 1828-1834.
Richardson, J. & Jones, S. 2014. On the use of bridge weigh-in-motion for overweight truck enforcement. *International Journal of Heavy Vehicle Systems*. 21(2): 83-104.
Salawu, O.S. 1997. Detection of Structural Damage Through Changes in Frequency: A Review. *Engineering Structures*.19(9): 718-723.
Teughels, A. & De Roeck, G. 2004. Structural damage identification of the highway bridge Z24 by FE model updating. *Journal of Sound & Vibration*. 278(3): 589-610.
Wu, B.T., Wu, G., Lu, H.X. & Feng, D.C. 2017. Stiffness monitoring and damage assessment of bridges under moving vehicular loads using spatially-distributed optical fiber sensors. *Smart Materials & Structures.* 26(3): 035058.
Wu, S.Q. & Law, S.S. 2011. Vehicle axle load identification on bridge deck with irregular road surface profile. *Engineering Structures*. 33(2): 591-601.
Ye, Z.H. & Wu, G. 2017. Optimal lateral aseismic performance analysis of mega-substructure system with modularized secondary structures. *The Structural Design of Tall and Special Buildings.* 26: e1387.

Maintenance, Safety, Risk, Management and Life-Cycle Performance of Bridges – Powers, Frangopol, Al-Mahaidi & Caprani (Eds)
© 2018 Taylor & Francis Group, London, ISBN 978-1-138-73045-8

Limit Analysis of an old and damaged R.C. grillage deck

E. Conti & P.G. Malerba
Departement of Civil and Environmental Engineering
Politecnico di Milano, Milan, Italy

M. Quagliaroli
Structural Engineer
Founder and Director at m^{2}Structures, Piacenza, Italy

A. Maffei
Structural Engineer

ABSTRACT: The paper concerns the analyses carried out on an old, severely damaged 34.70 m long and 9.20 m wide R.C. grillage deck, composed of four longitudinal beams and five cross-beams. The deck is part of a 28-spans viaduct, built in 1968, which exhibits a severe corrosion state, due mainly to salted water coming from the roadway platform. The study is aimed at assessing how the bearing capacity of the structure varies over time, depending on the progression of corrosion phenomena, and to searching for the corresponding collapse mechanisms. The work starts by presenting the hypotheses and algorithms at the base of the Limit Analysis procedure developed for the specific purpose of this study, followed by a brief recall of the damage model assumed to represent the deterioration in time of the mechanical properties. The most important conclusions highlight how the damage, represented according to different scenarios, determines not only a reduction of the local bearing capacity, but also an internal force redistribution towards the undamaged structural elements. The conclusions of the study were taken into account in the actual design of the deck repairing interventions. In fact, the design focussed not only on substituting/repairing the elements which had undergone the most damage, but also assessed the robustness of the deck in its entirety, verifying that the undamaged elements had sufficient bearing capacity to carry the increase of internal forces derived from the redistribution mechanism.

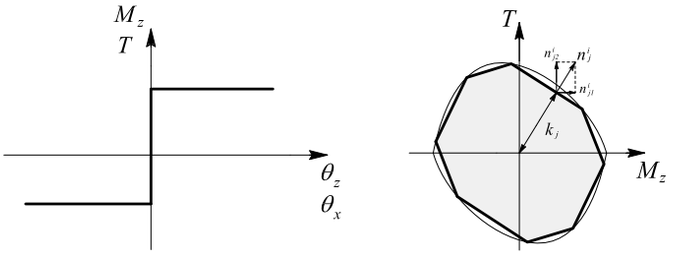
1 INTRODUCTION

As known, R.C. and P.C. bridges and viaducts with some decades of service life may exhibit severe damage states due to aggressive agents from environmental and service conditions. For this reason, many Road and Highway Administrations are faced with two typical problems: *(a)* in designing new bridges, estimate their bearing capacity after a certain amount of years from construction time under given environmental and service condition; *(b)* for existing bridges, assess their residual bearing capacity in the damaged state after a certain amount of years from construction time. Both these problems may be solved through a unique approach consisting in an analysis of the diffusion of the deterioration processes induced by aggressive agents, followed by the analysis of the damaged structure. This research is specialized to grillage decks made of beams and cross-beams. The deterioration process is supposed to be induced by chlorides diffusion and is investigated by means of the Cellular Automata technique. The structural assessment is carried out through Limit Analysis by considering the reinforcement reduction due to corrosion. With reference to the case of a grillage deck built in the 60s and severely damaged, the results of the analyses allow to evaluate how the damage reduces the bearing capacity of the most exposed elements at present and how the internal forces redistribute towards the undamaged structural element. For new bridges, the results of this methodology allow to assess the structural response at different times of their life.

2 LIMIT ANALYSIS FORMULATION

The Limit Analysis and its applicability to R.C. structures have been widely studied and discussed in the works by (Martinez y Cabrera, Biondini, Malerba, & Bontempi 1997), (Biondini & Frangopol 2008), (Conti, Malerba, & Quagliaroli 2017) and others. For

the purpose of this work, a force-based finite element for the Limit Analysis of three-dimensional R.C. framed structures is proposed. The hypotheses of small displacements and stable structure are assumed. Interacting internal generalized plastic forces are the bending moment M_z and the torque moment T. Shear effects are neglected. Stresses and correlative generalized plastic strains are related by a rigid perfectly-plastic constitutive law Fig. 1(a). In this way, the behavior of the discrete cross-sections where the plastic strains tend to develop, can be represented by a plastic hinge which makes this kinematic behaviour possible and, at the same time, fully transfers the corresponding plastic values of the bending moment and torsion. The ultimate values of M_z and T are correlated through a curve in the (M_z-T) plane, which bounds a convex domain containing the origin of the axis Fig. 1(b). Such a frontier can be idealized by a stepwise approximation, which, for safety's sake, is assumed inscribed within the effective curve. We assume that the formation of plastic hinges occurs at the ends of the elements. The resulting approximations can be overcome by increasing the number of the elements. The plastic collapse is reached when the set of generalized plastic hinges allows the activation of a kinematic mechanism, for which the equilibrium can no longer be satisfied. In the discretization, distributed loads are replaced by equivalent concentrated loads applied in an appropriate number of cross-sections.



(a) Rigid plastic behaviour. (b) T-M_z domain.

Figure 1: Limit Analysis hypotheses.

2.1 *Equilibrium and compatibility conditions*

For the generic *j-th* element of the structure, the equilibrium conditions are set in accordance to the force method. In the local coordinate system, by removing the rigid body motions, the internal forces $\mathbf{r}_i = [M_z, T]$ at the sections ($x = 0, l$) are expressed in function of the basic forces $\bar{\mathbf{Q}}_j$ at the end nodes n_1, n_2 (Fig. 2) from simple equilibrium equations $\mathbf{r}_i = \mathbf{h}_b \bar{\mathbf{Q}}_j$. In the same way, the end global forces $\mathbf{Q}_j$ are derived from $\bar{\mathbf{Q}}_j$ as $\mathbf{Q}_j = \mathbf{h}_l \bar{\mathbf{Q}}_j$. Through a coordinate transformation, the end global forces $\mathbf{Q}_j$ are rewritten in the global coordinate system as $\mathbf{Q}_{g,j} = \mathbf{T}_\alpha \mathbf{Q}_j = (\mathbf{T}_\alpha \mathbf{h}_l)\, \bar{\mathbf{Q}}_j = \mathbf{H}_{g,j} \bar{\mathbf{Q}}_j$, with $\mathbf{T}_\alpha$ the orthogonal transformation matrix and $\mathbf{H}_{g,j}$ the transformed equilibrium matrix for *j-th* the element.

By assembling over all the *ne* elements, we obtain the global equilibrium equations which correlate the vector $\mathbf{Q}_t$, containing all the element basic forces, to the external nodal forces vector $\mathbf{F}_e$, by means of the equilibrium matrix $\mathbf{H}$ of the whole structure.

$$\mathbf{F}_e = \sum_{j=1}^{ne} \mathscr{A}\left(\mathbf{Q}_{g,j}\right) = \sum_{j=1}^{ne} \mathscr{A}\left(\mathbf{H}_{g,j} \bar{\mathbf{Q}}_j\right) = \mathbf{H}\mathbf{Q}_t \qquad (1)$$

Compatibility conditions are derived through the Virtual Force Principle, by equating the virtual internal work $\delta W_i = \delta \mathbf{Q}_t^T \mathbf{q}_t$ to the external one $\delta W_e = \delta \mathbf{F}_e^T \mathbf{s}$.

From Eq. 1, we have $\delta \mathbf{F}_e = \mathbf{H} \delta \mathbf{Q}_t$ and stating $\delta W_e = \delta W_i$, we obtain $\delta \mathbf{Q}_t^T \mathbf{H}^T \mathbf{s} = \delta \mathbf{Q}_t^T \mathbf{q}_t$. Since such an equation is valid for any choice of $\delta \mathbf{Q}_t^T$, the compatibility equations are finally derived as:

$$\mathbf{q}_t = \mathbf{H}^T \mathbf{s} \qquad (2)$$

The compatibility matrix $\mathbf{H}^T$ is the transposed of the equilibrium matrix $\mathbf{H}$. In these correspondences, the vector of the forces $\mathbf{F}_e$ works for that of the displacements $\mathbf{s}$ in the global reference system, as the vector of the basic forces $\mathbf{Q}_t$ works for that of the basic displacements $\mathbf{q}_t$.

2.2 *Yield condition and flow rule*

The constitutive law for a *perfectly-plastic* material must include: *(i)* a *yielding criterion*, which defines the stress state corresponding to the starting of the plastic flow (the yield function curve is convex) and *(ii)* an *associated flow rule*, through which the increments of the plastic strains are correlated to the actual stress state. In the present case, where the only active generalized plastic stresses for the *i-th* critical

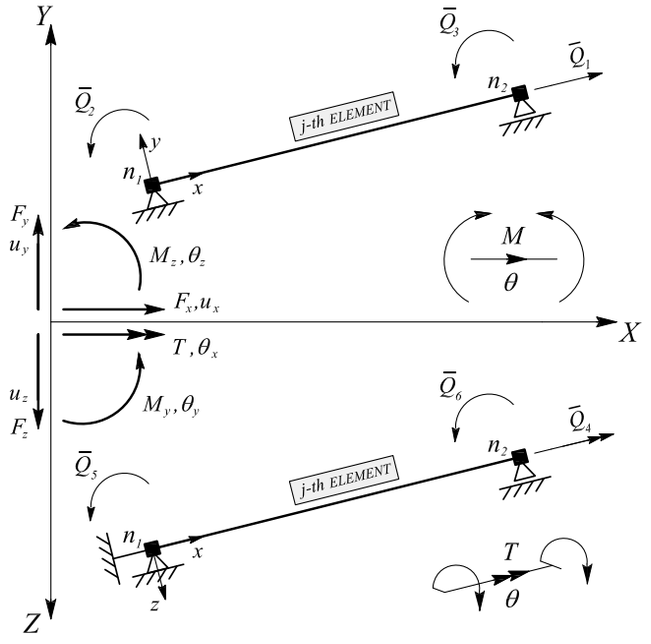


Figure 2: Static Field: reference system and *j-th* element without rigid body modes both in *x-y* and *x-z* plane.

cross-section are the bending moment M_z and torsion T, the yielding criterion has the shape shown in Fig. 1(b), which can be defined by the equation $f_i(M_{z,i}, T_i) = 0$. The stress state must verify the condition $f_i(M_{z,i}, T_i) \leq 0$. Having modelled the yielding criterion by a stepwise linearization with q sides for each *i-th* plastic domain, the yielding criterion for the *i-th* critical cross-section may be written in matrix form as $\mathbf{\Phi}_i = \mathbf{N}_i\mathbf{r}_i - \mathbf{k}_i \leq 0$ where $\mathbf{\Phi}_i = [\phi_1^i \quad \phi_2^i \quad \dots \quad \phi_{q_i}^i]^T$, $\mathbf{N}_i = [\mathbf{n}_1^i \quad \mathbf{n}_2^i \quad \dots \quad \mathbf{n}_{q_i}^i]$, $\mathbf{n}_j^i = [n_{j1}^i \; n_{j2}^i]$ and $\mathbf{k}_i = [k_1^i \; k_2^i \; \dots \; k_{q_i}^i]^T \geq \mathbf{0}$. For each element the yield criterion becomes $\mathbf{\Phi}_i = \mathbf{N}_i\bar{\mathbf{Q}}_i - \mathbf{k}_i \leq 0$ and assembling these conditions for the whole structure one has:

$$\mathbf{\Phi}_t = \sum_{j=1}^{ne} \mathscr{A}\left(\mathbf{\Phi}_j\right) = \mathbf{N}\mathbf{Q}_t - \mathbf{k} \leq 0 \tag{3}$$

The associated flow rule for the *i-th* critical cross-section is given by equations $\theta_{z,i} = \mu_i \partial f_i / \partial M_{z,i}$ and $\theta_{x,i} = \mu_i \partial f_i / \partial T_i$ where $\mu_i > 0$ is the multiplier that allows plastic flows only for the points lying on the yielding curve, for which the normal is oriented outside the domain, that is $\mu_i f_i(M_{z,i}, T_i) = 0$. For the linearized case with q sides, by introducing the vector $\boldsymbol{\mu}_i = [\mu_1^i \quad \mu_2^i \quad \dots \quad \mu_{q_i}^i]^T \geq \mathbf{0}$ and collecting the terms μ_i^j relative to each side of the linearized frontier, we finally have $\mathbf{d}_i = \mathbf{N}_i^T \cdot \boldsymbol{\mu}_i$ with $\mu_j^i \cdot \phi_j^i = 0$ $(j = 1, \cdots, q)$ and $\boldsymbol{\mu}_i \geq 0$. The flow rule can be written for the generic element by connecting the vector of plastic strain $\mathbf{d}_i$ with the vector of basic displacement $\bar{\mathbf{q}}_j$ by means of the compatibility equations $\bar{\mathbf{q}}_j = \mathbf{N}_i^T \; \boldsymbol{\mu}_i$. By assembling all the element contributions for the entire structure, the corresponding compatibility equations become:

$$\mathbf{q}_t = \sum_{j=1}^{ne} \mathscr{A}\left(\bar{\mathbf{q}}_j\right) = \mathbf{N}^T \cdot \boldsymbol{\mu} \tag{4}$$

with

$$\begin{cases} \mu_j^i \cdot \phi_j^i = 0 \qquad j = 1, \cdots, q \\ \boldsymbol{\mu} > 0 \end{cases}$$

2.3 *The static and the kinematic approach*

With reference to a generic structure, let $\mathbf{P}_0$ be a vector of constant loads and $\mathbf{P}$ a vector of loads whose intensity varies proportionally to a unique multiplier $\lambda \geq 0$. We assume that for $\lambda = 0$ equilibrium and compatibility are satisfied. We search for the multiplier λ_c associated to the collapse load. In mathematical terms, the *upper* (Eq. 5) and *lower* (Eq. 6) bound theorems of Limit Analysis are traduced in the following dual linear constrained optimization problems, solved here by means of the Simplex Method.

$$\lambda_c = max(\lambda) \begin{cases} \lambda\mathbf{P} - \mathbf{H}\mathbf{Q}_t = -\mathbf{P}_0 \\ \mathbf{N}\mathbf{Q}_t \leq \mathbf{k} \\ \lambda \geq 0 \end{cases} \tag{5}$$

$$\lambda_c = min(\mathbf{k}^T\boldsymbol{\mu} - \mathbf{P}_0^T\mathbf{s}) \begin{cases} \mathbf{N}^T\boldsymbol{\mu} - \mathbf{H}^T\mathbf{s} = \mathbf{0} \\ \mathbf{P}^T\mathbf{s} = 1 \\ \boldsymbol{\mu} \geq 0 \end{cases} \tag{6}$$

In this way, Eq.(5) requires finding a maximum multiplier, while Eq.(6) a minimum one. It must be underlined that in the second case, the minimum condition is related to the work done by the proportional loads $\mathbf{P}$ for the displacements $\mathbf{s}$ associated with the collapse mechanism. Since this mechanism is correlated to an arbitrary multiplier, it results univocally identified by the condition $\mathbf{P}^T\mathbf{s} = 1$. As known, the uniqueness of λ_c does not necessarily mean the uniqueness of the collapse mechanism, or that of the stress field at collapse.

2.4 *Time-variant Limit Analysis*

In the previous Limit Analysis, the cross-sectional performance is quantified by using fixed values of the quantities $\mathbf{N}$ and $\mathbf{k}$, which define the yielding criterion and the flow rule. However, due to the reinforcement deterioration corresponding to the damage state at certain time, such quantities, as well as the corresponding collapse multiplier λ_c, vary over time. In order to account for such a variability, a specific analysis of the deteriorating cross-sections is firstly required to build the modified frontiers $f(M_z, T) = 0$ and the functions $\mathbf{N} = \mathbf{N}(t)$ and $\mathbf{k} = \mathbf{k}(t)$. In this way, a time-variant Limit Analysis leading to the time evolution of the *complete solution* (collapse multiplier, collapse mechanism and internal stress distribution at the incipient collapse) is performed by solving the previous linear programs at different time instants.

3 DAMAGE MODELLING IN R.C. STRUCTURES

Concrete structures exposed to environmental aggressive agents, like sulphates and chlorides, are subjected to lifetime degradation which may lead to the deterioration of concrete and the corrosion of steel reinforcement (C.E.B. 1992). In this context, the attention is focussed only on chlorides induced corrosion of steel bars. In fact, when chlorides, which are critical in a marine environment or come from the application of de-icing salts on bridge platforms exceed a threshold value in carbonated concrete, they can cause a progressive deterioration of the mechanical properties of the materials. In addition, damage induced by mechanical loading interacts with the environmental factors and accelerates the deterioration process. For these reasons, the safety of reinforced concrete structures exposed to corrosion needs to be checked over time by means of a durability analysis able to account for both the diffusion process and the corresponding mechanical damage, as well as for the coupling effects between diffusion, damage and structural behaviour.

3.1 *Modelling of diffusion process*

The diffusion process is described by the Fick's law (Glicksman 2000):

$$D\nabla^2 C = \frac{\partial C}{\partial t} \tag{7}$$

where D is the diffusion coefficient, $C = C(\mathbf{x}, t)$ is the mass concentration of the aggressive agent at point $\mathbf{x} = (x, y, z)$ at t time, and $\nabla C = \mathbf{grad}C$. Based on the work of (Biondini, Bontempi, Frangopol, & Malerba 2004) and (Titi 2012), the analytical solution of the linear partial differential equation (7) is carried out by using a special class of evolutionary algorithms called *Cellular Automata*. This computational technique consists of a regular uniform grid of sites or *cells*, theoretically having an infinite extension, with a discrete variable in each cell, that can take on a finite number of states. During time, Cellular Automata evolve in discrete time steps according to a set of local evolutionary rules. For the diffusion problem in two-dimensions, the Fick's law can be accurately reproduced by the following evolutionary rule (Biondini, Bontempi, Frangopol, & Malerba 2004):

$$C_i^{k+1} = \phi_0 C_i^k + \frac{1-\phi_0}{4} \sum_{j=1}^{2} \left(C_{i-1,j}^k + C_{i+1,j}^k \right) \tag{8}$$

where the discrete variable $C_i^k = s_i^k = C(\mathbf{x}_i, t_k)$ represents the concentration of the aggressive agent at time t_k in the *i-th* cell of the automaton located at point $\mathbf{x}_i = (y_i, z_i)$ of the cross-section, $C_{i\pm1,j}^k$ is the concentration in the adjacent cells $i \pm 1$ in the direction $j = 1, 2$ and ϕ_0 is a suitable evolutionary coefficient related to the rate of mass diffusion. Additionally, the diffusion process can be regulated according to a given value of the diffusion coefficient D by relating the grid dimension Δx and the time step Δt through the relationship:

$$D = \frac{1-\phi_0}{4} \frac{\Delta x^2}{\Delta t} \tag{9}$$

Finally, in case of constant diffusivity, the value of the central evolutionary coefficient $\phi_0 = 1/2$ usually ensures a good accuracy of the automaton.

3.2 *Modelling of mechanical damage*

The structural damage can be introduced as a degradation of the law of the effective resistant areas for steel bars. This degradation is effectively evaluated by means of a dimensionless damage index $\delta_s = \delta_s(t)$ which gives a direct measure of the damage within the range [0;1].

$$A_s(t) = [1 - \delta_s(t)]\, A_{s0} \tag{10}$$

where $A_{s0} = \pi\, D_0^2/4$ is the area of the undamaged bar at the initial time $t = t_0$. The damage rate of the material depends on the mass concentration $C = C(\mathbf{x}, t)$ of the aggressive agent at a point $\mathbf{x} = (y_i, z_i)$ of the cross-section. Based on available data for corrosion rate under chloride attack, a linear relationship between the damage rate and the mass concentration is assumed:

$$\frac{\partial \delta_s(\mathbf{x}, t)}{\partial t} = \frac{C(\mathbf{x}, t)}{C_s \Delta t_s} = \rho C(\mathbf{x}, t) \tag{11}$$

where C_s represents the value of constant concentration $C(\mathbf{x}, t)$ in a certain position and at a specified time instant, which leads to a complete damage of the steel bar after the time period Δt_s. In addition, the initial conditions $\delta_s(\mathbf{x}, t_{cr}) = 0$ with $t_{cr} = max\{t \,|\, C(\mathbf{x}, t) \leq C_{cr}\}$ is assumed, where C_{cr} is a critical threshold of concentration. Finally, the damage rate coefficient $\rho = (C_s \Delta t_s)^{-1}$ is related to the materials and it must be set according to the actual rate of the damaging process (Bertolini, Elsener, Pedeferri, Redaelli, & Polder 2013).

4 APPLICATION TO A GRILLAGE DECK

4.1 *Structure, materials and loads*

An old 34.70 m long and 9.20 m wide R.C. grillage deck, composed of four longitudinal beams and five cross-beams, is studied. This deck is part of 28-spans viaduct built in Italy in 1968, which exhibits a severe corrosion state, due mainly to salted water coming from the roadway platform. The main dimensions of the grillage, as well as the geometry, dimensions and reinforcement layout of the structural members are shown in Fig. 3. In particular, the cross-beams present a constant section whereas the longitudinal beams exhibit a variable section all along the deck span. Fig. 4 shows further details of the reinforcement layout of the longitudinal beams. Tab. 1 lists the type of stirrups in all the members.

Table 1: Distribution of stirrups in the beams.

	A	*B*	*C*	*D*	*E*	*F*	*Cross-Beam*
ϕ [mm]	14	14	14	12	12	12	10
s [cm]	15	16	20	20	22	20	20

As concerns the material characteristics, in the Limit Analysis, only the concrete compression strength $f_c = -30\, MPa$ and the steel yielding stress $f_{sy} = 375\, MPa$ are involved.

From the structural point of view, the grillage deck is modelled by four simply supported longitudinal beams and five cross-beams with spacing 2.63*x*8.66 m (Fig. 5). The deck is considered to be subjected to a fixed load, corresponding to the self-weight ($g = 30\, kN/m$) and a variable part, due to traffic loads to be increased until collapse. According to Load Model 1 defined by (EN 1991), the traffic load acting on the deck consists of concentrated loads $Q = 300\, kN$, represented by a tandem system with two axles, and of

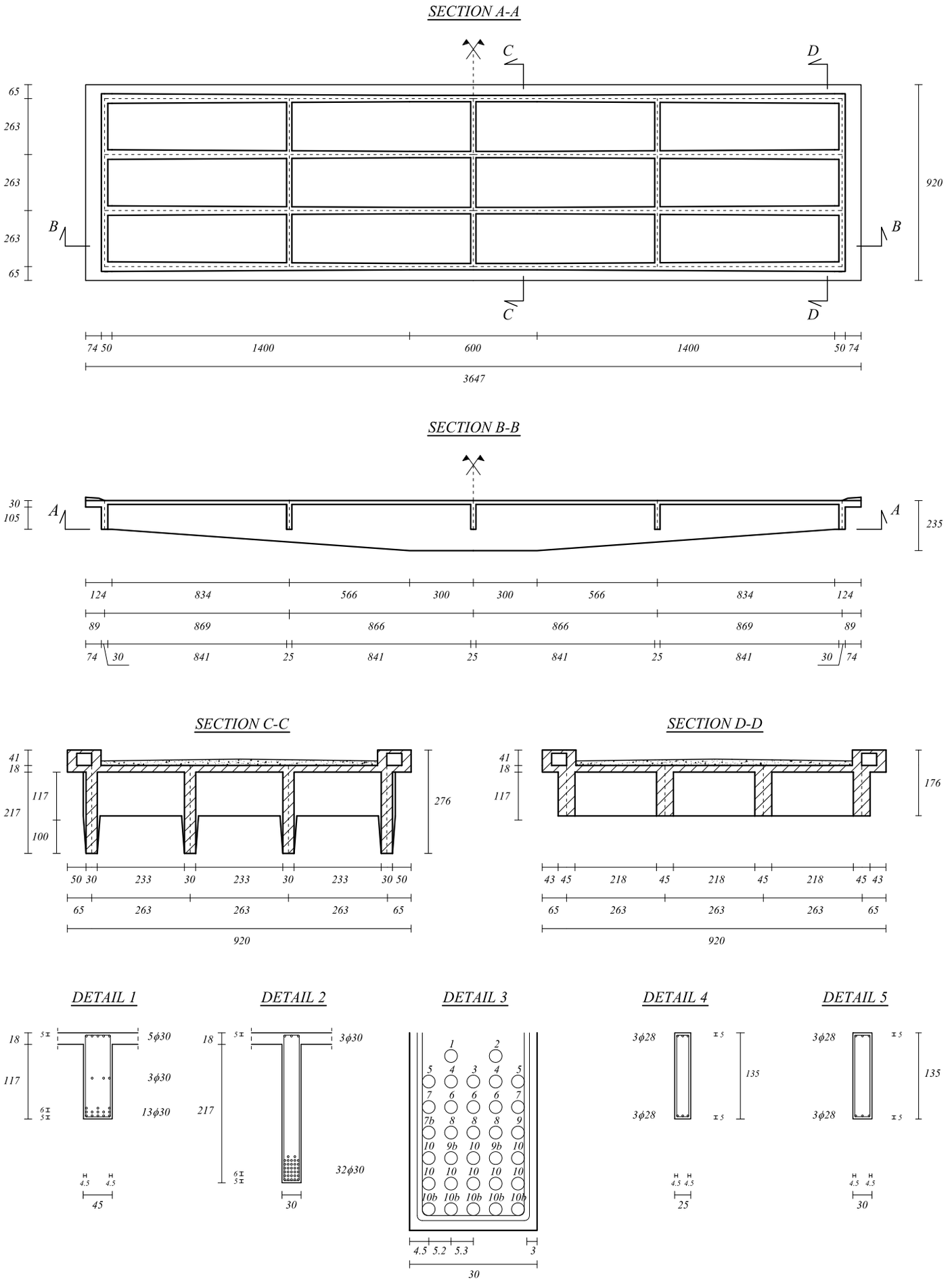


Figure 3: R.C. grillage deck. Geometry and reinforcement of the characteristic sections. Details 1,2 and 3 refer to the longitudinal beams section. Details 4 and 5 identify the cross-beams section.

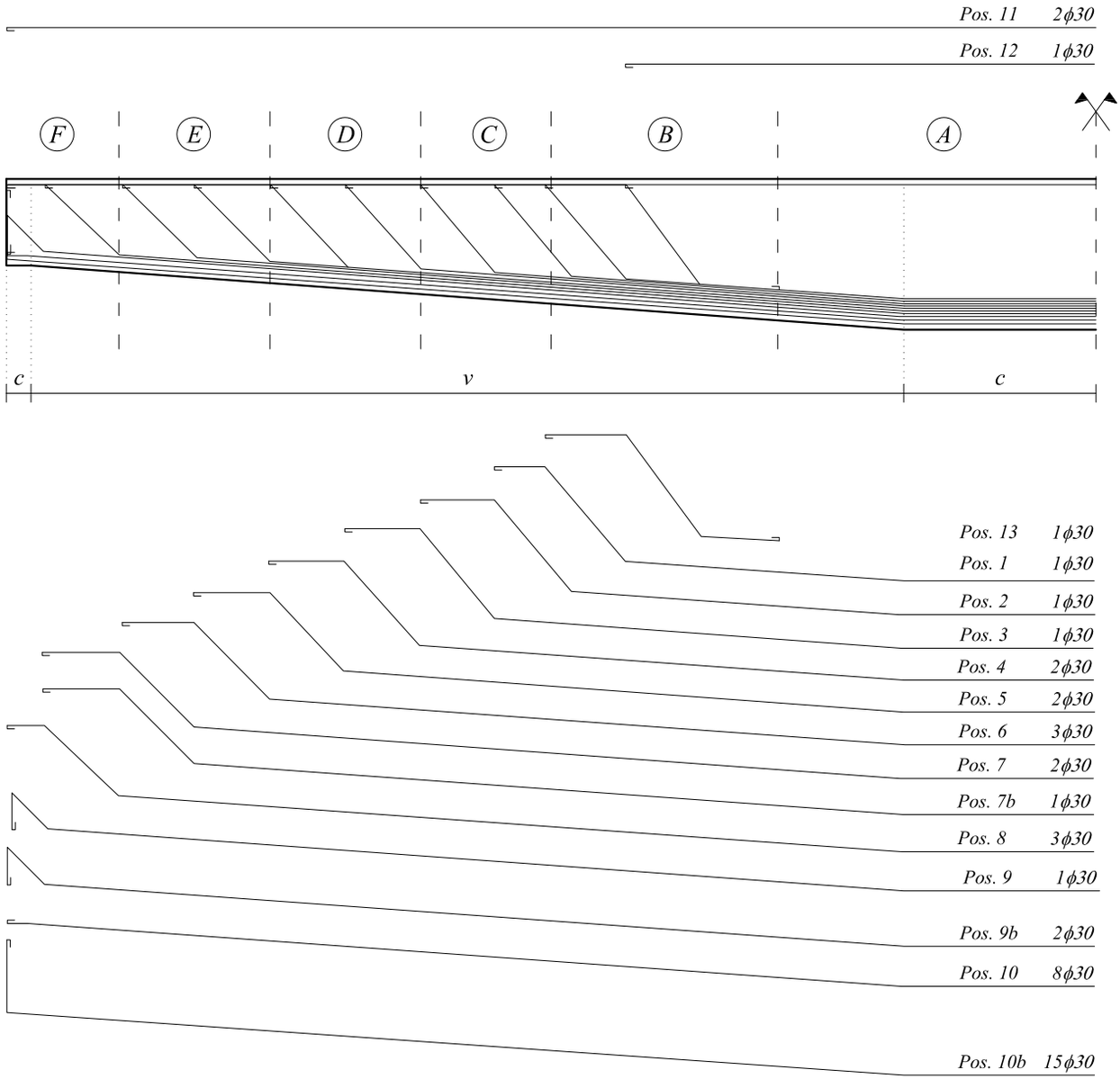


Figure 4: Reinforcements chracteristic and layout for the longitudinal beams. The encircled letters identify the type of stirrups. The letters c and v identify respectively the constant and variable part of the longitudinal beam's section.

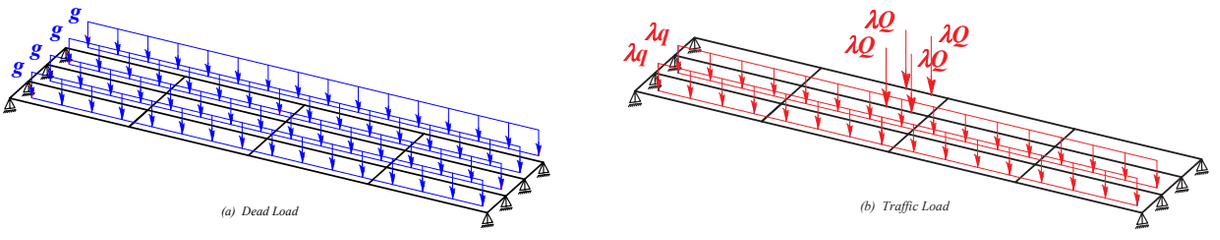


Figure 5: Structural model and loading conditions.

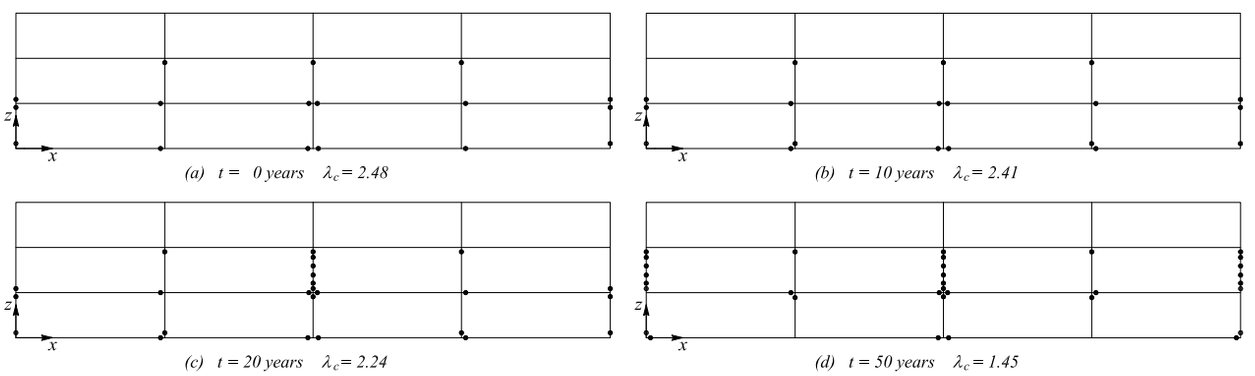


Figure 6: Limit Analysis. Time evolution of the collapse multiplier and relative distribution of the plastic hinges on the deck.

uniformly distributed loads $q = 13.5kN/m$, as shown in Fig. 5. For the analyses, the distributed loads are replaced by statically equivalent concentrated loads.

4.2 *Damage scenario*

The damage of the longitudinal beams caused by the application of salts based de-icing substances (containing chloride ions) coming from the above roadway is one of the main causes of deck deterioration. As a consequence, this chloride-induced corrosion leads to a reduction of the steel area, which may cause a premature failure of the structure.

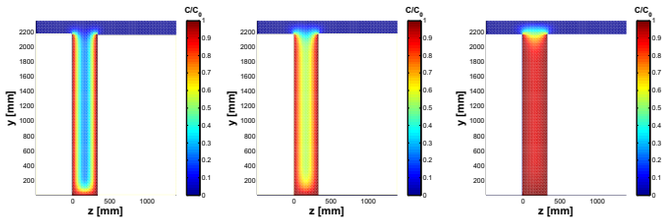


Figure 7: Concentration maps $C(x,t)/C_0$ of the aggressive agent over time ($t = 10$, $t = 20$ and $t = 50$ years).

In this case, the chlorides corrosion attacks is defined as follow: (i) the longitudinal position of the corroded zone is localized over a length of 3 m in the central zone of one of the edge longitudinal beams; (ii) the sectional distribution of corrosion is assumed to be located along the two laterals and the bottom sides of the corresponding cross-sections, with a constant concentration $C(t) = C_0 = 3\%$, as Fig. 8 shows. Once the corrosion scenario has been defined, the diffusion problem must be solved both in the sectional domain and in time. The Cellular Automata technique is applied, assuming a nominal diffusivity coefficient $D = 10^{-11}\, m^2/s$, a grid dimension $\Delta x = 10\, mm$ and a time step $t = 0.16$ years. According to the provisions given by (Fib 2006), the damage rates are defined by the values $C_{cr} = 0.6\%$, $C_c = C_0$ and $\Delta T_s = 20$ years. Since in this case the deterioration process reproduces a severe damage of materials, as it may occur for heavily chloride-contaminated concrete and high relative humidity, the steel damage rate coefficient ρ is assumed as $0.02/C_0$. The results of the diffusion process are highlighted in Fig. 7, where the concentration maps $C(x,t)/C_0$ of the aggressive agent at time instants $t = 10$, $t = 20$ and $t = 50$ years are shown for the cross-section. The mechanical damage induced by chloride diffusion can be appreciated from diagram of Fig. 8. It is interesting to note that the corrosion propagation starts after only 2 years. Finally, after 20 years, the reduction of the bars cross-section becomes significant.

4.3 *Main results and comments of the analyses*

A series of limit analyses over time accounting for chloride-induced corrosion were conducted to investigate the corresponding grillage deck performance.

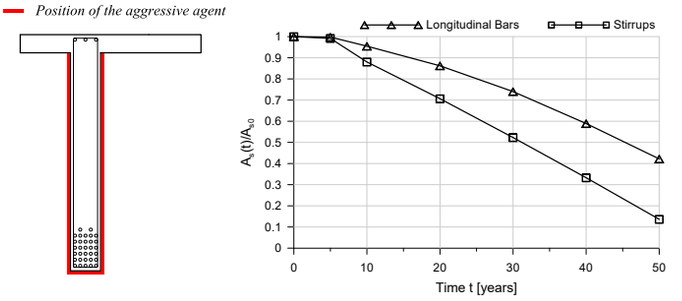


Figure 8: Sectional distribution of the aggressive agent and time reduction of bar areas in the damaged cross-section.

As expected, Fig. 6 highlights a significant variation of the collapse load multiplier, which decreases from $\lambda_c = 2.48$ to $\lambda_c = 1.45$ as the damage increases over time. Interesting results are obtained also in terms of redistribution of the internal stress resultants and a consequent modification of the collapse mechanism. In fact, the effects of the localized corrosion scenarios involve not only the damaged longitudinal beam but also the undamaged cross-beams. Such a redistribution may be highlighted with reference to Figs. 6, 9, 10, 11. Fig. 9 shows the bending moment diagram for the edge damaged longitudinal beam. The moment progressively reduces in time, gradually exhibiting a pronounced kink at the section in correspondence of the cross-beam at the quarter. The location of the generalized plastic hinges corresponding to the damaged state at $t = 0$, $t = 10$, $t = 20$ and $t = 50$ years is shown in Fig. 6. As the reduction of the mechanical properties for the damaged longitudinal beam becomes evident (*t=20 years*), the Limit Analysis predicts the formation of new plastic hinges in the central cross-beam and its relative collapse may occur. These results are confirmed by the bending moment and torsion diagram at incipient collapse for the central cross-beam, as shown in Fig. 10. As time increases (*t=40 years*), additional hinges will form in the end cross-beams which collapse under the combined action of bending moment and torsion (Fig. 11). In the redistribution process, the collapse mechanism moves from the central to the end undamaged cross-beams, searching for, in the grillage deck, new load paths through the contribution of new collaborating

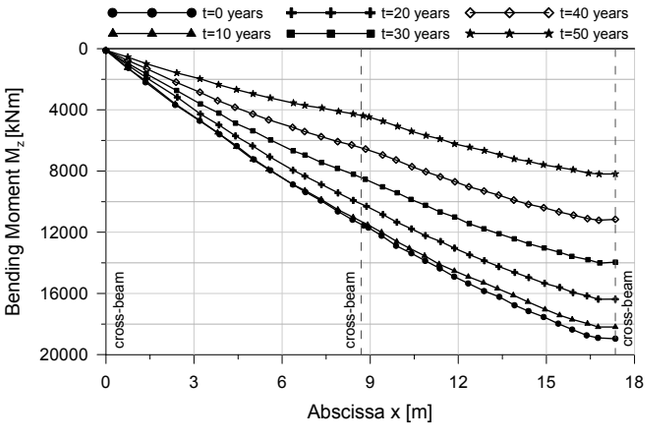


Figure 9: Edge longitudinal beam. Time evolution of bending moment at the collapse after 0 to 50 years.

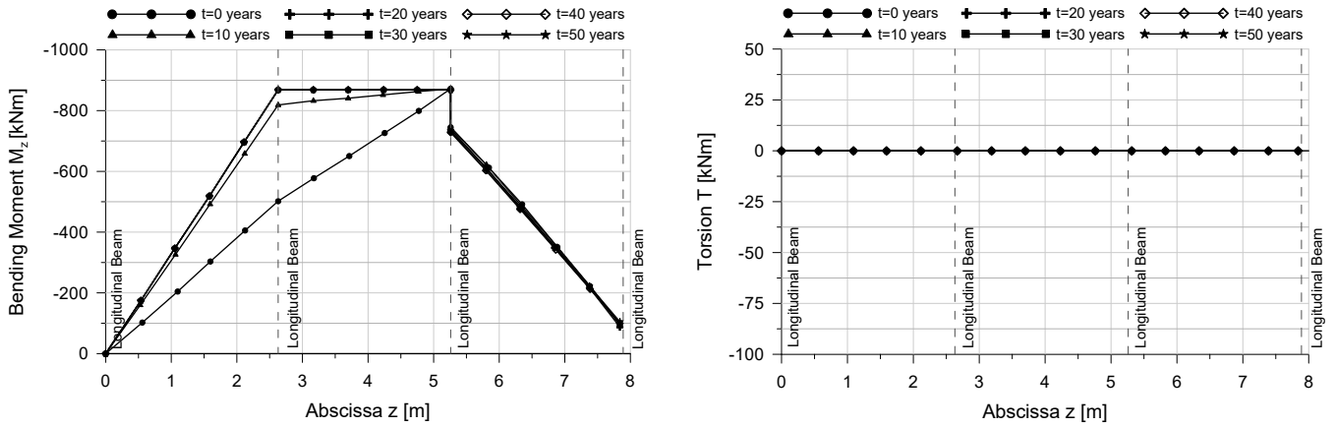


Figure 10: Time evolution of bending moment and torsion at collapse for the central cross-beam.

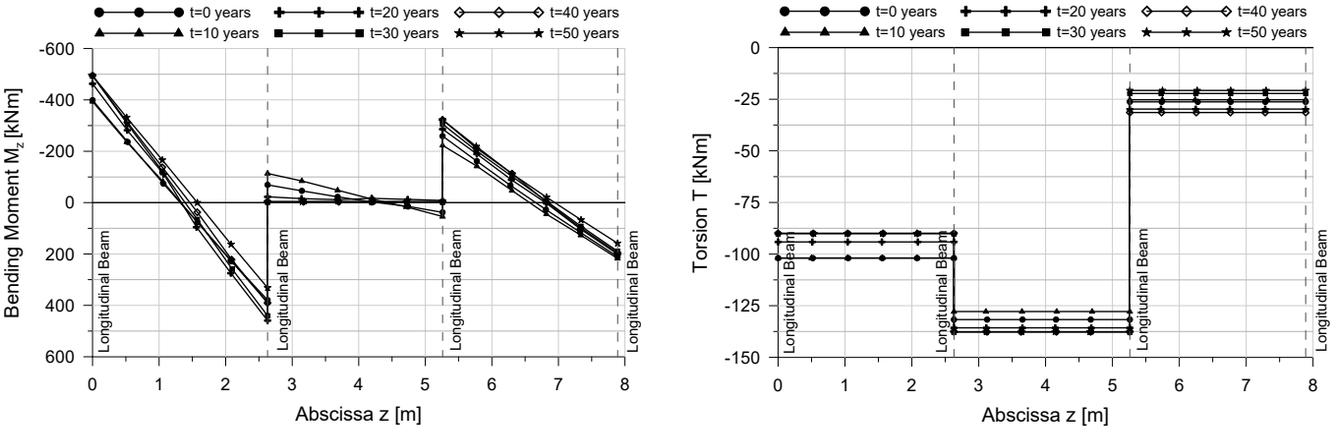


Figure 11: Time evolution of bending moment and torsion at collapse for the end cross-beam.

parts. Typical, from this point of view, is the torsional contribution of the end cross-beams, accentuated by the increasing of the relative rotations of the longitudinal beams at the supports.

5 CONCLUSIONS

A Limit Analysis of a damaged R.C. grillage deck, has been carried out. After a short recall of the two fundamental theorems of plasticity, a damage model is assumed to represent the deterioration of mechanical properties over time. The deterioration process induced by chlorides diffusion is investigated by means of the Cellular Automata technique. The structural performance is assessed at different times by taking into account the reinforcement deterioration corresponding to the damaged state at that time. The results demonstrate the usefulness of this approach in identifying the structural components that more significantly affect the system performance when damage develops. As shown through the application, the damage reduces the local bearing capacity over time and cause a progressive redistribution of internal forces towards undamaged structural elements, called to collaborate with the damaged ones in new load paths configurations. For this reason, it is important, when designing repairing interventions, to verify and possibly increase the bearing capacity of the undamaged components in light of the additional role that may be called to play. This brings to an increase of the overall robustness of the deck.

REFERENCES

Bertolini, L., B. Elsener, P. Pedeferri, E. Redaelli, & R. B. Polder (2013). *Corrosion of steel in concrete: prevention, diagnosis, repair*. John Wiley & Sons.

Biondini, F., F. Bontempi, D. M. Frangopol, & P. G. Malerba (2004). Cellular automata approach to durability analysis of concrete structures in aggressive environments. *Journal of Structural Engineering 130*(11), 1724–1737.

Biondini, F. & D. M. Frangopol (2008). Probabilistic limit analysis and lifetime prediction of concrete structures. *Structure and Infrastructure Engineering 4*(5), 399–412.

C.E.B. (1992). *Durable Concrete Structures: Design Guide*. Number 183. Thomas Telford.

Conti, E., P. Malerba, & M. Quagliaroli (2017). Limit and Nonlinear analysis of a slender arch bridge. A comparative study. In *7th Conference on Mechanics and Materials in Design*, pp. 937–952.

EN (1991). Eurocode 1: Actions on structures - Part 2: Traffic loads on bridges. *Brussels: European Standard EN 2*, 2003.

Fib (2006). Model code for service life design. *International federation for structural concrete (FIB). Switzerland*, 110.

Glicksman, M. E. (2000). *Diffusion in solids: field theory, solid-state principles and applications*. Wiley.

Martinez y Cabrera, F., F. Biondini, P. Malerba, & F. Bontempi (1997). Limit analysis of prestressed cable stayed bridges. In *7th Int. Conference on Computing in Civil and Building Engineering*, pp. 431–436.

Titi, A. (2012). *Lifetime probabilistic seismic assessment of multistory precast buildings*. Phd thesis, Politecnico di Milano.

Maintenance, Safety, Risk, Management and Life-Cycle Performance of Bridges – Powers, Frangopol, Al-Mahaidi & Caprani (Eds)
© 2018 Taylor & Francis Group, London, ISBN 978-1-138-73045-8

Nonlinear Analysis of a R.C. grillage deck exposed to corrosion

E. Conti & P.G. Malerba
Departement of Civil and Environmental Engineering
Politecnico di Milano, Milan, Italy

M. Quagliaroli
Structural Engineer
Founder and Director at m²Structures, Piacenza, Italy

D. Scaperrotta
Structural Engineer

ABSTRACT: In this paper, an approach consisting in the analysis of the diffusion of the deterioration processes induced by aggressive agents, followed by the analysis of the damaged structure is presented. The damage process, induced by chloride diffusion, is modelled through a Cellular Automata algorithm. The structural analysis is based on R.C. spatial beam element, dealing with both mechanical and geometrical nonlinearities. The proposed method is applied to studying the structural response, both at the serviceability and ultimate limit states, of a damaged, 50-years-old R.C. grillage deck exhibiting a severe corrosion state. The analyses show how damage effects at a given time reduce the overall bearing capacity of the deck and how the internal forces redistribute from damaged to undamaged structural parts. Such a methodology may be useful both in designing new bridges, in estimating their performance over time under given environmental and service condition, and for existing bridges, in assessing their residual bearing capacity in the damaged state after a certain period from construction.

1 INTRODUCTION

All around the world, the majority of R.C. and P.C. bridges and viaducts with more than 40-60 years of service life exhibits damage states which reduce their structural reliability and require increasing inspection and maintenance costs (Biondini & Frangopol 2017). For this reason, many Road and Highway Administrations are faced with two typical problems: *(a)* in designing new bridges, estimate their bearing capacity after a certain amount of years from construction time and under given environmental and service condition; *(b)* for existing bridges, assess their residual bearing capacity in the damaged state, reached after a certain amount of years from construction time. In this paper, an approach which may contribute to dealing with this type of assessments is presented. It consists in the analysis of the diffusion of the deterioration processes induced by aggressive agents, followed by the analysis of the damaged structure. The analysis of the diffusion process is developed by using a special class of evolutionary algorithms, called Cellular Automata. Based on such a model, the mechanical damage coupled to diffusion is then evaluated by introducing a damage index in the degradation law of the effective resistant area of rebars. For a given time from the end of construction and for given environmental conditions, this allows to evaluate the amount of corrosion in the rebars and their actual resistant area. Then, a Nonlinear Finite Element Analysis, based on R.C. spatial beam element dealing with both mechanical and geometrical nonlinearities, allows to assess the structural response both at the serviceability and ultimate limit states. The proposed method was applied in the study of a damaged, 50-years-old R.C. grillage deck exhibiting a severe corrosion state. For different and progressive sampling times and for increasing applied loads, analyses show how the internal forces redistribute and how the load multiplier reduces as corrosion progresses.

2 DAMAGE MODELLING IN R.C. STRUCTURES

Concrete structures exposed to aggressive environments are subjected to lifetime degradation induced

by the kinetic process of diffusion of chemical components, such as sulphates and chlorides, driven by concentration gradients inside the material volume (Glicksman 2000). In this context, the attention is focused only on chlorides induced corrosion of steel bars. In fact, when chlorides, which are critical in a marine environment or come from the application of deicing salts on bridge decks, increase beyond a threshold value in carbonated concrete, they may lead to the deterioration of the concrete and the corrosion of the reinforcement. Moreover, damage induced by mechanical loading interacts with the environmental factors and accelerates the deterioration process (C.E.B. 1992). The diffusion process, the amount of corrosion in the steel bars and their actual resistant area at a given time from the end of construction and for given environmental conditions, are firstly modelled. Then, a Nonlinear Finite Element Analysis of the damaged structure is carried out.

2.1 *Modelling of the diffusion process*

The simplest model to describe the kinetic process of chemical components diffusion in solids is represented by Fick's first law, which assumes a linear relationship between the mass flow and the concentration gradient by introducing an effective diffusion coefficient D_e. The combination of the Fick's model with the mass concentration principle leads to Fick's second law. Assuming an isotropic media, the problem is described by the following second-order partial differential equation:

$$-\nabla \cdot (-D_e \nabla C) = \frac{\partial C}{\partial t} \tag{1}$$

where $C = C(\mathbf{x}, t)$ is the mass concentration of the aggressive agent at point $\mathbf{x} = (x, y, z)$ at the t time, and $\nabla C = \mathbf{grad} C$. Even though D_e in reinforced concrete structures depends on relative humidity, on temperature and on the internal stress field, for the sake of simplicity a diffusion coefficient $D_e = D$, constant in time, is here assumed.

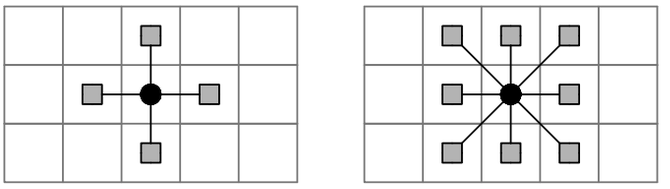
From the numerical point of view, the analytical solution of the linear partial differential equation (1) exists only for a limited number of problems. In general, numerical procedures are necessary to deal with arbitrary domains, different position of steel bars and complex boundary conditions. In order to model the diffusion process, the evolutionary algorithm called *Cellular Automata* is adopted. This computational technique, presented in the works of (Biondini, Bontempi, Frangopol, & Malerba 2004) and (Titi 2012), consists of a regular uniform grid of sites or *cells*, theoretically having an infinite extension, with a discrete variable in each cell that can take on a finite number of states. In particular, Fick's laws in two dimensions can be accurately reproduced by the following evolutionary rule:

$$C_i^{k+1} = \phi_0 C_i^k + \frac{1-\phi_0}{4} \sum_{j=1}^{2} \left(C_{i-1,j}^k + C_{i+1,j}^k \right) \tag{2}$$

where the discrete variable $C_i^k = s_i^k = C(\mathbf{x}_i, t_k)$ represents the concentration of the aggressive agent at time t_k in the cell i of the automaton located at point $\mathbf{x}_i = (y_i, z_i)$ of the cross-section, $C_{i\pm1,j}^k$ is the concentration in the adjacent cells $i \pm 1$ in the direction $j = 1, 2$ and ϕ_0 is a suitable evolutionary coefficient related to the rate of mass diffusion. Fig. 1 presents the typical pattern of cells involved in the evolutionary rule for 2D cellular automata with $r = 1$, but patterns of higher complexity can also be proposed. Additionally, the diffusion process can be regulated according to a given value of the diffusion coefficient D by relating the grid dimension Δx and the time step Δt through the relationship:

$$D = \frac{1-\phi_0}{4} \frac{\Delta x^2}{\Delta t} \tag{3}$$

To ensure a good accuracy of the automaton, a suitable value of the central evolutionary coefficient in case of constant diffusivity is $\phi_0 = 1/2$.



(a) Von Neumann. (b) Moore.

Figure 1: Neighbourhoods for 2D cellular automata with radius $r = 1$.

2.2 *Modelling of the mechanical damage*

The structural damage can be viewed as a degradation of the mechanical properties which make the structural system less able to withstand the applied loads. The main effect of corrosion in concrete structures is the reduction in the bar mass. Once the diffusion process is solved, such a damage can be evaluated by introducing a suitable degradation law for the steel area:

$$A_s(t) = [1 - \delta_s(t)]\, A_{s0} \tag{4}$$

where $A_{s0} = \pi\, D_0^2/4$ is the area of the undamaged bar at the initial time $t = t_0$ and $\delta_s = \delta_s(t)$ is the dimensionless damage index which gives a direct measure of the deterioration within the range [0;1].

Despite the complexity of damage processes in concrete structures exposed to corrosion, the damage index $\delta_s = \delta_s(\mathbf{x}, t)$ at a point $\mathbf{x} = (y_i, z_i)$ of the generic cross-section is correlated to the diffusion process by

assuming a linear relationship between the rate of damage and the concentration $C = C(\mathbf{x}, t)$ of the aggressive agent:

$$\frac{\partial \delta_s(\mathbf{x}, t)}{\partial t} = \frac{C(\mathbf{x}, t)}{C_s \Delta t_s} = \rho C(\mathbf{x}, t) \tag{5}$$

In this equation C_s represents the value of constant concentration $C(\mathbf{x}, t)$ in a certain position and at a specified time instant, which lead to a complete corrosion of the steel bar after the time period Δt_s. In addition, the initial conditions $\delta_s(\mathbf{x}, t_{cr}) = 0$ with $t_{cr} = max\{t \,|\, C(\mathbf{x}, t) \leq C_{cr}\}$ is assumed, where C_{cr} is a critical threshold of concentration. Finally, the damage rate coefficient $\rho = (C_s \Delta t_s)^{-1}$ is related to the materials properties and it must be set according to the actual rate of the damaging process.

3 FORMULATION OF A DETERIORATING R.C. SPATIAL BEAM ELEMENT

A R.C. spatial beam element, able to account for both the mechanical and geometrical nonlinearities, is presented. Its formulation refers mainly to the works of (Bontempi, Malerba, & Romano 1995) and (Malerba 1998). The adopted model assumes that the cross-sections rotate and translate remaining plane. Shear deformability and torsional warping are neglected and perfect bond between steel and concrete is assumed. In the present extension, the F.E. takes into account the effects due to the structural damage. At the section of abscissa ($0 \leq x \leq l$), the displacement field of the beam element $\mathbf{u} = [u_0(x)\ v_0(x)\ w_0(x)\ \varphi_x(x)]^T$ is discretized and interpolated in terms of nodal displacement $\mathbf{q}$ so that $\mathbf{u}(x) = \mathbf{N}(x)\mathbf{q}$. The matrix of displacement functions $\mathbf{N}(x)$ is defined by adopting the Hermitian shape functions of a linear elastic beam having uniform cross-sectional stiffness and loaded only at its ends. The generalized strains $\mathbf{e}_s(x) = [\varepsilon(x)\ \chi_z(x)\ \chi_y(x)\ \theta(x)]^T$ are given by $\mathbf{e}_s(x) = \mathbf{B}(x)\mathbf{q}$, where $\mathbf{B}(x)$ contains the derivatives of the shape functions. At the same section, the strain field $\boldsymbol{\varepsilon} = [\varepsilon_x\ \gamma_{xy}\ \gamma_{xz}]^T$ at a fiber at the distance (y, z) from the beam axis is given by:

$$\boldsymbol{\varepsilon} = \mathbf{a}_s(y, z)\mathbf{e}_s(x) = \mathbf{a}_s(y, z)\mathbf{B}(x)\mathbf{q} \tag{6}$$

with:

$$\mathbf{a}_s(y, z) = \begin{bmatrix} 1 & -y & z & 0 \\ 0 & 0 & 0 & -z \\ 0 & 0 & 0 & y \end{bmatrix}$$

Through the Principle of Virtual Displacements, we state that the virtual internal work δW_i is equal to the external one δW_e due to (a) distributed applied loads acting along the axis of the beam $\mathbf{f}_p$, (b) the forces directly applied at the nodes $\mathbf{f}_n$ and (c) the end forces through which the beam interacts with the rest of the structure $\mathbf{f}_q$ (Fig. 2). Finally, by imposing $\delta W_i = \delta W_e$, we obtain the vector of the equivalent nodal forces $\mathbf{f}_{ne}$ and element restoring forces $\mathbf{f}_q$.

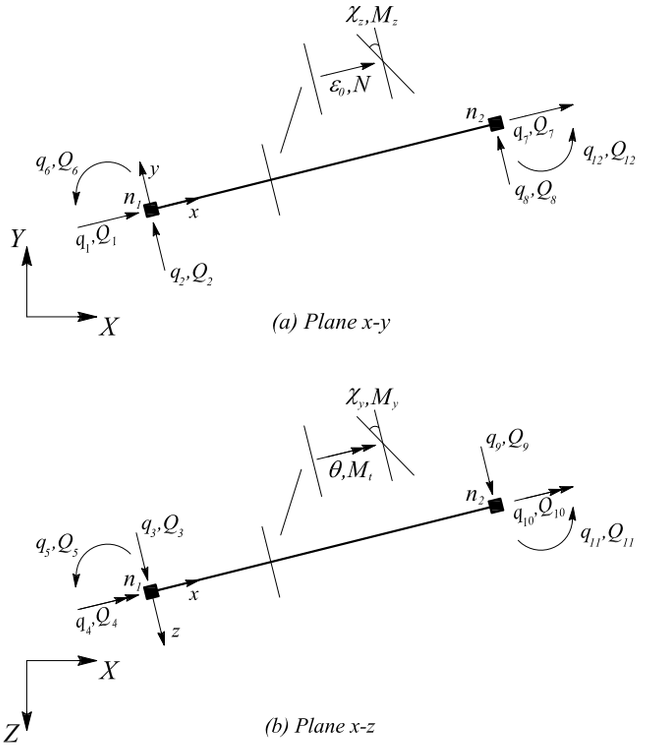


Figure 2: Spatial beam element notations. Static and kinematic fields.

$$\mathbf{f}_{ne} = \int_0^l \mathbf{N}^T(x)\mathbf{f}_p(x)dx + \mathbf{f}_n + \mathbf{f}_q \tag{7}$$

$$\mathbf{f}_q = \int_0^l \mathbf{B}^T(x)\mathbf{f}_s(x)dx \tag{8}$$

The section restoring forces $\mathbf{f}_s = [N\ M_z\ M_y\ M_t]^T$ are evaluated as:

$$\mathbf{f}_s = \int_A \mathbf{a}_s^T(y, z)\boldsymbol{\sigma}(x, y, z)dA \tag{9}$$

By substituting Eq. (9) in Eq. (8), the element restoring forces can be expressed as $\mathbf{f}_q = \mathbf{K}\mathbf{q}$. The element stiffness matrix $\mathbf{K} = \int_0^l \mathbf{B}^T(x)\mathbf{k}_s(x)\mathbf{B}(x)dx$ is function of the stiffness matrix $\mathbf{k}_s(x)$ of the section of abscissa x. The numerical integration of $\mathbf{k}_s(x)$ requires a suitable stress-strain constitutive law. As known, in the case of R.C. sections, axial and flexural forces can be derived from a uniaxial stress-strain relationship $\sigma_x = \sigma_x(\varepsilon_x)$, whereas shear and torsion depend on more complex membrane or volumetric mechanisms, usually modelled through plane or spatial trusses. In this formulation, we assume that bending and torsional behaviors are uncoupled. As a consequence, the derivation of the stiffness matrix $\mathbf{k}_s$ and the section restoring forces $\mathbf{f}_s$ is given by the sum of two components. The matrix $\mathbf{k}_s$ is expressed as $\mathbf{k}_s = \mathbf{k}_{s,\varepsilon} + \mathbf{k}_{s,\gamma}$ where $\mathbf{k}_{s,\varepsilon}$ is associated to the axial-bending response and $\mathbf{k}_{s,\gamma}$ is related to the torsional behavior. For each section, matrix $\mathbf{k}_{s,\varepsilon}$ is integrated over the area of the

composite element and by assembling the contributes of concrete and steel. In order to deal with sections of arbitrary shape, the generic cross-section is divided into subdomains. Through a parametric transformation of each subdomain into a unit square parent domain, Gaussian integration rules can be carried out with several integration strategies (Quagliaroli, Malerba, & Sgambi 2015). The matrix $\mathbf{k}_{s,\gamma}$ is derived by describing at the sectional level the torsional response in the form of $M_t = k_\theta \theta$. To this purpose, we assume a bilinear constitutive law able to account the response of the section both prior and after concrete cracking (Fig. 3).

$$M_t = \begin{cases} (GK)\theta & |\theta| \leq \theta_{cr} \\ \mu(GK)\theta & \theta_{cr} < |\theta| \leq \theta_u \end{cases} \tag{10}$$

where G is the shear modulus and $\mu = K_{cr}/K$ is the ratio between the torsional stiffness after and before cracking.
Similarly, the vector $\mathbf{f}_s$ can be expressed as the sum of two terms related to normal and tangential stress respectively, as $\mathbf{f}_s = \mathbf{f}_{s,\varepsilon} + \mathbf{f}_{s,\gamma}$.

$$\mathbf{f}_{s,\varepsilon} = \int_A^l \mathbf{a}_s^T(y,z) \cdot \sigma_x(\varepsilon_x(x,y,z))dA \tag{11}$$

$$\mathbf{f}_{s,\gamma} = M_t(x) \tag{12}$$

The generalized stresses N, M_y and M_z are computed from Eq. (11) by integrating over the sectional domain the nonlinear uniaxial constitutive models. On the contrary, the term $\mathbf{f}_{s,\gamma}$ is derived at the sectional level according to M_t-θ relationship. Then, the vectors of equivalent nodal forces $\mathbf{f}_{ne}$ and restoring forces $\mathbf{f}_q$ are evaluated by numerical integration over the length l of the beam. The damage effects associated to prescribed values of the corrosion penetration index δ_s are included in this formulation by assuming $A_{sm} = A_{sm}(\delta_s)$ for the *m-th* steel bar located at $\mathbf{x}_m = (y_m, z_m)$ whereas no damage for concrete is assumed. As a consequence, at each time instant t the corresponding deteriorating stiffness matrices $\mathbf{k}_s = \mathbf{k}_s(x,t)$ and $\mathbf{K} = \mathbf{K}(x,t)$ are computed (Biondini & Vergani 2012). It is worth noting that corrosion can selectively be applied to damaged structural elements

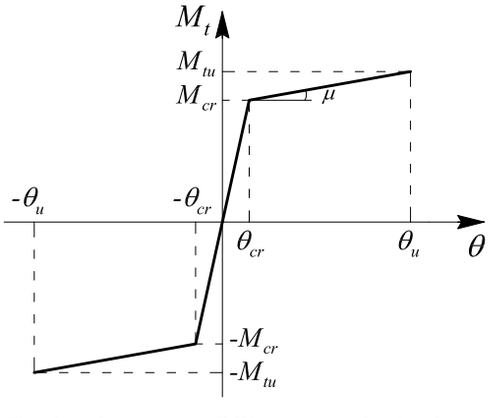


Figure 3: Torsional response. Bilinear constitutive law.

with a different level of penetration in each reinforcing bar. Finally, relating these quantities to the global reference system and by assembling the equilibrium equation of the whole structure, we obtain:

$$\mathbf{f}_r(\mathbf{s}) = \mathbf{f}(\mathbf{s}) \Rightarrow \mathbf{K}\mathbf{s} = \mathbf{f}(\mathbf{s}) \tag{13}$$

where $\mathbf{K} = \mathbf{K}(\mathbf{s}, t)$ is the overall stiffness matrix and $\mathbf{s} = \mathbf{s}(t)$ is the vector of nodal displacements. Being the problem nonlinear, both the assembled restoring forces $\mathbf{f}_r$ and the applied loads $\mathbf{f}$ are depending on the unknown displacements $\mathbf{s}$ of the whole structure. The solution of this nonlinear problem is obtained through a tangent approach for prescribed values of corrosion penetration index δ_s.

4 APPLICATION TO A GRILLAGE DECK

4.1 *Structure, materials and loads*

A R.C. grillage deck, belonging 28-spans viaduct built in Italy in 1968, is studied. The viaduct is approximately half a century old and exhibits a severe corrosion state, due mainly to salted water coming from the roadway platform. The deck, with a span of 34.70 m and a width of 9.20 m, is composed of four longitudinal beams and five cross-beams. Fig. 4 shows the main dimensions of the deck, as well as the geometry, dimension and reinforcement layout of the main structural members. In particular, the longitudinal beams present a variable section, with height and width respectively increasing and decreasing from the abutments to the mid-span of the viaduct. On the contrary, the cross-beams have constant main dimensions and are reinforced with six bars with a nominal diameter equal to 28 mm. Further details about reinforcement layout of the longitudinal beams are shown in Fig. 5. Tab. 1 lists type and dimensions of the stirrups in all the members.

Table 1: Distribution of stirrups in the beams.

	A	*B*	*C*	*D*	*E*	*F*	*Cross-Beam*
ϕ [mm]	14	14	14	12	12	12	10
s [cm]	15	16	20	20	22	20	20

As concerns the material characteristics, concrete is modelled by a no-tension, uniaxial stress-strain law, according to the parabola-rectangle law. The design compression strength is $f_c = -30\,MPa$, with a transition strain $\varepsilon_{c0} = -0.002$ and an ultimate strain $\varepsilon_{cu} = -0.0035$. The steel is modelled by an elastic-perfectly plastic stress-strain diagram, symmetric both in tension and compression, with a yielding stress $f_{sy} = 375\,Mpa$, elastic modulus $E_s = 206000\,MPa$ and ultimate limit strain $\varepsilon_{su} = 0.06$.

With reference to the beam model shown in Fig. 6, the grillage deck is modelled by four simply supported longitudinal beams and five cross-beams with

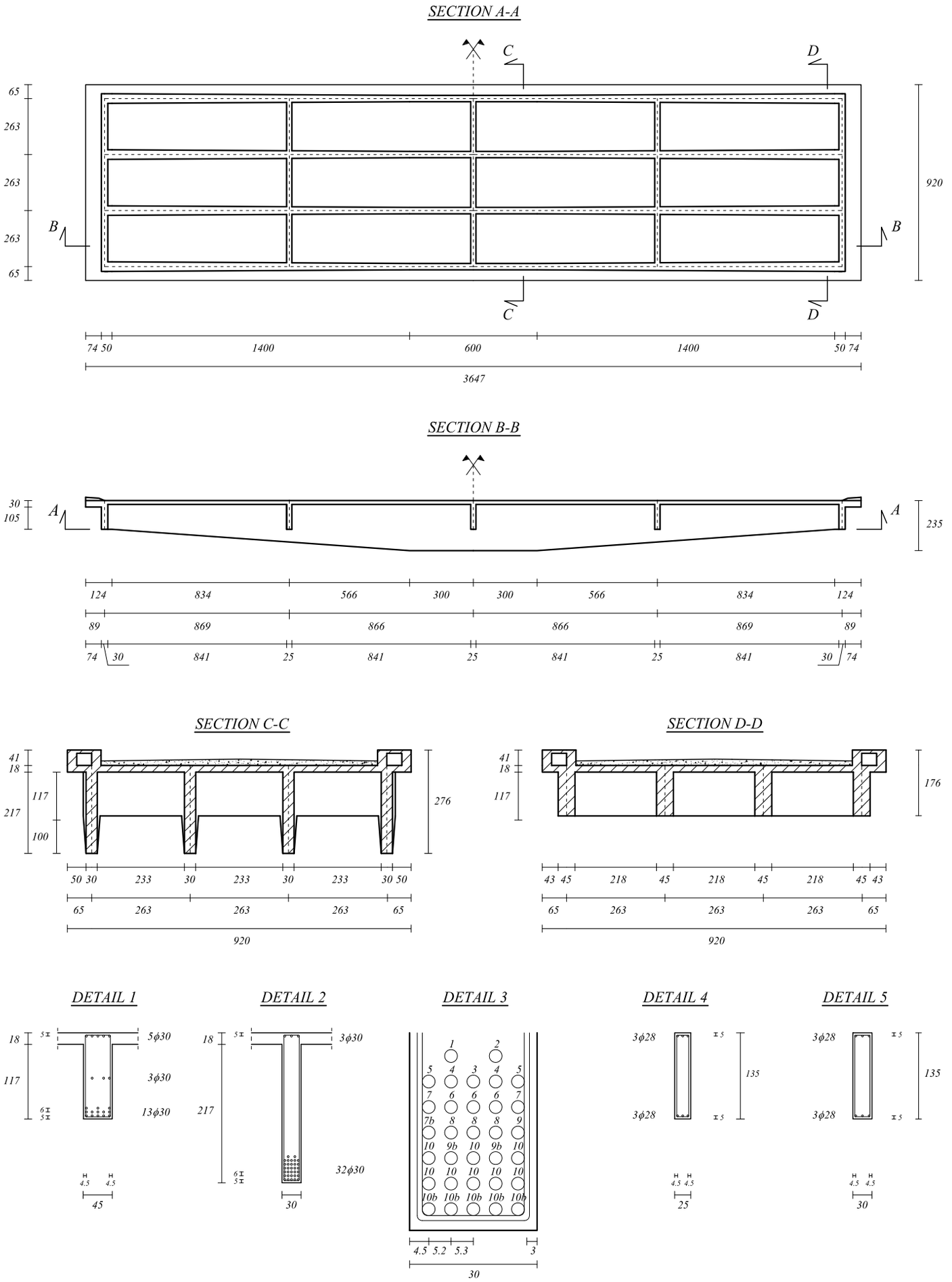


Figure 4: R.C. grillage deck. Geometry and reinforcement of the characteristic sections. Details 1, 2 and 3 refer to the longitudinal beams section. Details 4 and 5 identify the cross-beams section.

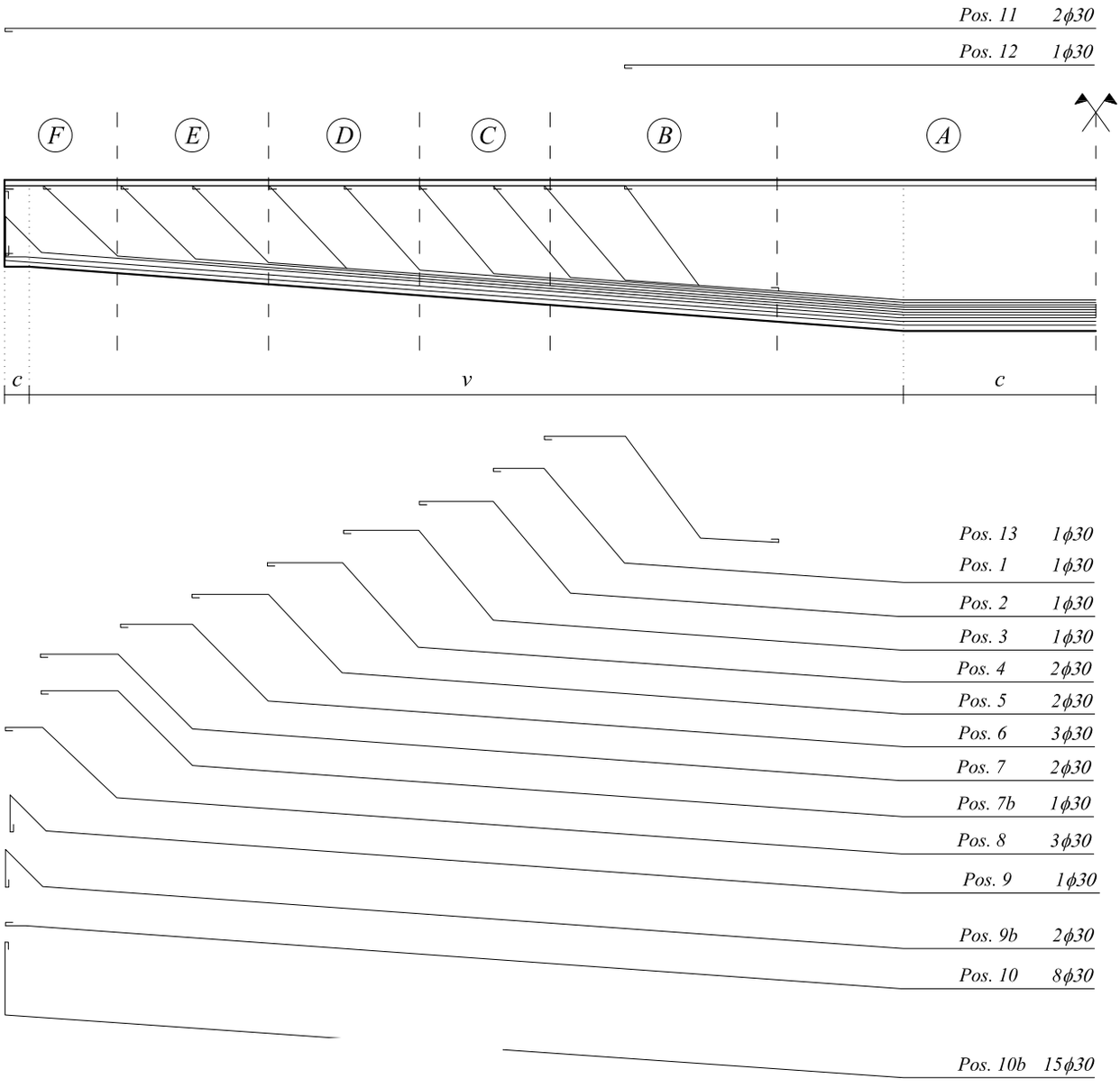


Figure 5
letters c gitudinal beams. The encircled letters identify the type of stirrups. The segments of the longitudinal beam's section.

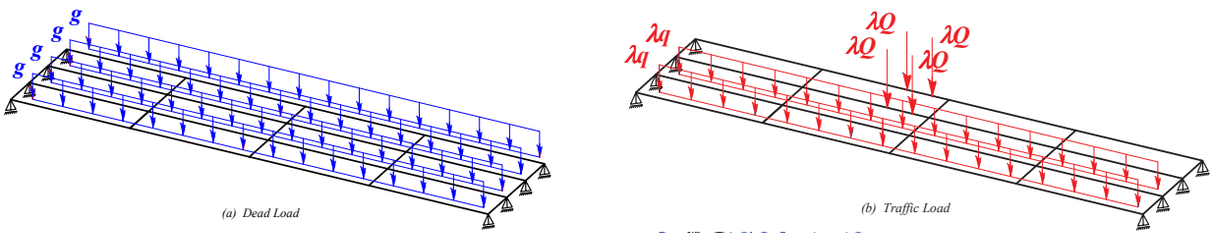


Figure 6: Structural model and loading conditions.

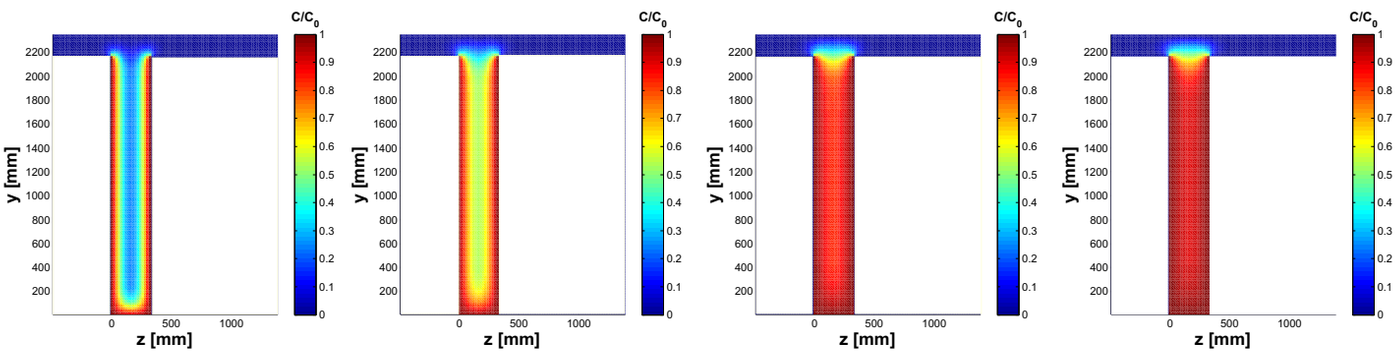


Figure 7: Maps of $C(x,t)/C_0$ concentration of the midspan section over time ($t = 10$, $t = 20$, $t = 40$ and $t = 50$ years).

spacing 2.63x8.66 m. The total applied load is composed of a fixed contribution, corresponding to the dead load of the deck ($g = 30\,kN/m$) and of a variable part, corresponding to the traffic load to be increased until to the collapse. For the traffic load, Load Model 1, according to (EN 1991), is adopted: it consists of concentrated loads represented by a tandem system with two axles as well as of uniformly distributed loads. In this way, the traffic loads are distributed as shown in Fig. 6, where q is equal to $13.5\,kN/m$ and Q is $300\,kN$. In order to model the layout and the areas of steel reinforcements, each longitudinal beam is subdivided into 66 finite beam-elements, while each cross-beam is subdivided into 15 elements.

4.2 *Damage scenario*

Under the action of permanent loads, the intersection between the edge longitudinal beam and the cross-beam is usually affected by a negative bending moment which can lead to the cracking of the slab and cause some seepages on the edge beam. Since the water coming from the roadway platform is characterized by a high concentration of de-icing salts (chloride ions), a critical corrosion scenario may ensue causing premature losses of bearing. Concerning such a corrosion scenario, the chlorides corrosion attacks is defined as follow: (i) the longitudinal position of the corroded zone is located in a 3 m long tract, astride the central zone of one of the edge longitudinal beams; (ii) the sectional distribution of corrosion is assumed to be located along the two laterals and at the bottom sides of the corresponding cross-sections, with a constant concentration $C(t) = C_0 = 3\%$, as Fig. 8 shows. Once the corrosion scenario has been defined, the diffusion problem must be solved both in the sectional domain and in time. The cellular automata technique is applied, considering a nominal diffusivity coefficient $D = 10^{-11}\,m^2/s$, a grid dimension $\Delta x = 10\,mm$ and a time step $t = 0.16$ years. According to the (Fib 2006) provisions, the damage rates are defined by the values $C_{cr} = 0.6\%$, $C_c = C_0$ and $\Delta T_s = 20$ years. Since in this case the deterioration process reproduces a severe damage of materials, as it may occur for heavily chloride-contaminated concrete and high relative humidity (Bertolini, Elsener, Pedeferri, Redaelli, & Polder 2013), the steel damage rate coefficient ρ is assumed as $0.02/C_0$. The results of the diffusion process are highlighted in Fig. 7, where the concentration maps $C(x,t)/C_0$ of the aggressive agent at time $t = 10$, $t = 20$, $t = 40$ and $t = 50$ years are shown for the midspan cross-section. The amount of mechanical damage induced by chloride diffusion and its evolution over time is plotted in Fig. 8. Now, for the given environmental and loading conditions, at each sampling time the Nonlinear Finite Element Analysis of the deck allows to assess its structural response in the damaged state both at the serviceability and ultimate limit states.

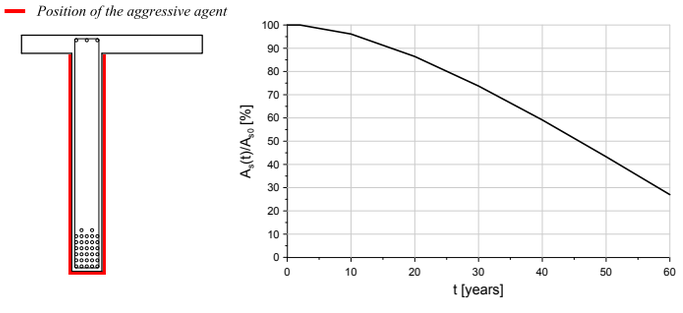


Figure 8: Midspan section. Surfaces exposed to the aggressive agent and reduction of the total steel area over time.

4.3 *Main results and comments of the analyses*

At the beginning, the damage effects are investigated on the service performance of the grillage under only its self-weight g (Serviceability Limit State, *SLS*).

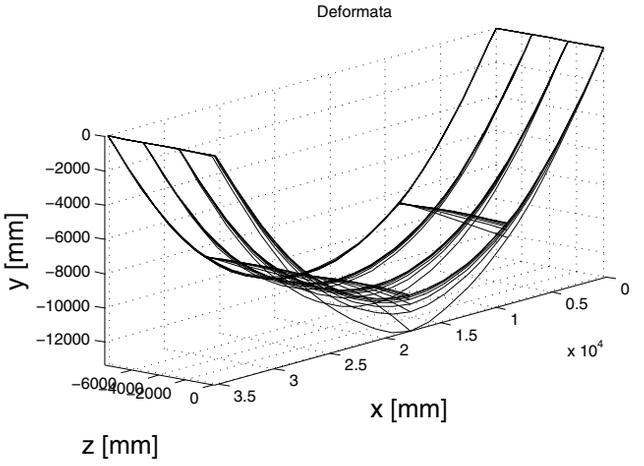


Figure 9: Deformed shapes over time of the deck at Serviceability Limit States under self-weight (scale factor equal to 200).

The localized damage involves both an increase of the deformability of the longitudinal and transversal beams and a redistribution of the internal forces. As time increases, the results of these analyses show that: *(a)* the overall deformed shape loses its symmetry (Fig. 9); *(b)* the weakening of the longitudinal beam under constant loading due to the deterioration process calls for a supporting contribution from the central cross-beam increasing over time. The kinks at midspan in the bending moment diagrams of the longitudinal beams, shown in Fig. 10, highlight the progression of this redistribution mechanism for $t = 0 \div 50$ years; *(c)* the corresponding contribution of the central cross-beam, shown in Fig. 11, through the plot of its bending moments diagram, becomes clear just after 10 years and rapidly increases from $t = 10$ to $t = 50$ years, and this may lead to the failure of the cross-beams, even if undamaged.

Another series of assessments concerns the performance of the deck at the Ultimate Limit States (*ULS*) under the combined action of permanent and traffic loads. The severe reduction of the cross-section of the steel bars, starting from 20 years from the end of construction (Fig. 8), leads to a remarkable decrease of

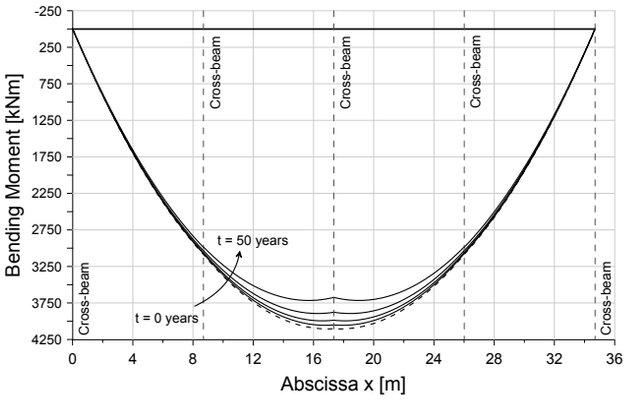


Figure 10: Bending moment along the longitudinal edge beam at *SLS* for different sampling times ($t = 0 \div 50$ years).

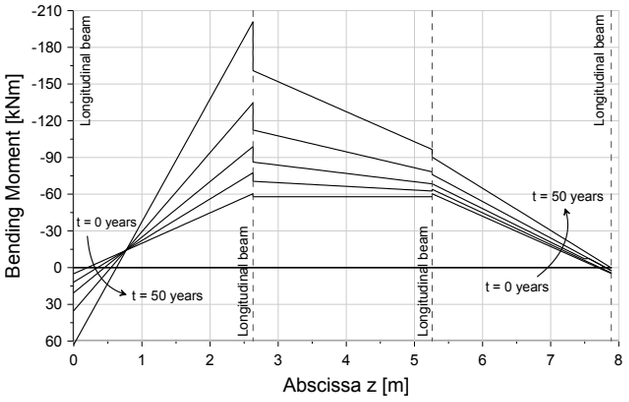


Figure 11: Bending moment along the midspan cross-beam at *SLS* for different sampling times ($t = 0 \div 50$ years).

the ultimate load bearing capacity over time. Fig. 12 shows the progressive reduction of the load multiplier over time, whereas the red and the blue lines represent respectively its safety and collapse limits: safety limit is crossed at 48 years and collapse limit at 55 years. While the *SLS* analyses highlight the redistribution of the bearing functions in the deck due to the damage progression even without service loads, the *ULS* results give fundamental information as concerns the loss of bearing capacity for the worst combination of the traffic loads. Both these types of results contribute in answering to the basic questions posed by public Authorities as concern the safety level of a bridge structure and the decisions in terms of proper maintenance actions and/or rehabilitation interventions.

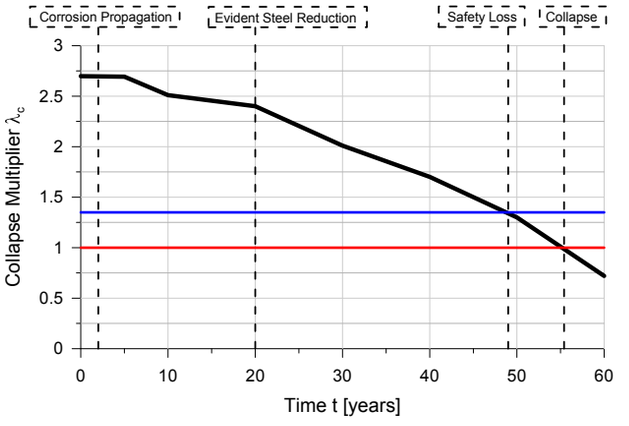


Figure 12: Collapse multiplier over time at *ULS*.

5 CONCLUSION

In this paper, an approach consisting in the analysis of the diffusion of the deterioration processes induced by aggressive agents, accompanied by the structural analysis of the damaged system is presented. The deterioration processes, induced by chloride diffusion, is modelled through a Cellular Automata algorithm. The structural analysis is based on R.C. spatial beam element, dealing with both mechanical and geometrical nonlinearities. The proposed method was applied in studying the structural response, both at the serviceability and ultimate limit state, of a damaged, 50-years-old R.C. grillage deck exhibiting a severe corrosion state. This deck typology is representative of a large number of bridges built in the 60s and the damaged pattern, concerning mainly the edge longitudinal beams, is very common. Each analysis studies the effects of increasing applied loads for a specific damaged state at a given time. By setting different and progressive sampling times, it is possible to highlight how the spread of the damage reduces the overall bearing capacity of the deck and how the internal forces redistribute from damaged to undamaged structural parts. This information could provide a reliable reference to establish a hierarchy of protection techniques, as well as to plan proper maintenance actions and repair interventions.

REFERENCES

Bertolini, L., B. Elsener, P. Pedeferri, E. Redaelli, & R. B. Polder (2013). *Corrosion of steel in concrete: prevention, diagnosis, repair*. John Wiley & Sons.

Biondini, F., F. Bontempi, D. M. Frangopol, & P. G. Malerba (2004). Cellular automata approach to durability analysis of concrete structures in aggressive environments. *Journal of Structural Engineering 130*(11), 1724–1737.

Biondini, F. & D. M. Frangopol (2017). Life-cycle performance of civil structure and infrastructure systems: Survey. *Journal of Structural Engineering 144*(1), 06017008.

Biondini, F. & M. Vergani (2012). Damage modeling and nonlinear analysis of concrete bridges under corrosion. In *sixth international conference on bridge maintenance, safety and management (IABMAS 2012), Stresa, Italy*, pp. 949–957.

Bontempi, F., P. Malerba, & L. Romano (1995). A direct secant formulation for the reinforced and prestressed concrete frames analysis. *Studi e Ricerche 16*, 351–386.

C.E.B. (1992). *Durable Concrete Structures: Design Guide*. Number 183. Thomas Telford.

EN (1991). Eurocode 1: Actions on structures - Part 2: Traffic loads on bridges. *Brussels: European Standard EN 2*, 2003.

Fib (2006). Model code for service life design. *International federation for structural concrete (FIB). Switzerland*, 110.

Glicksman, M. E. (2000). *Diffusion in solids: field theory, solid-state principles and applications*. Wiley.

Malerba, P. G. (1998). *Analisi limite e non lineare di strutture in calcestruzzo armato. Tecniche di calcolo manuale ed automatico*. Udine, Italy: CISM.

Quagliaroli, M., P. G. Malerba, & L. Sgambi (2015). A parametric subdomain discretization for the analysis of the multiaxial response of reinforced concrete sections. *Advances in Engineering Software 82*, 87–104.

Titi, A. (2012). *Lifetime probabilistic seismic assessment of multistory precast buildings*. Phd thesis, Politecnico di Milano.

Maintenance, Safety, Risk, Management and Life-Cycle Performance of Bridges – Powers, Frangopol, Al-Mahaidi & Caprani (Eds)
© 2018 Taylor & Francis Group, London, ISBN 978-1-138-73045-8

Determining vehicle weight limit based on the cumulative fatigue damage on bridges

Lu Deng
Key Laboratory for Damage Diagnosis of Engineering Structures of Hunan Province, Hunan Univ., Changsha, Hunan 410082, China

Wangchen Yan
College of Civil Engineering, Hunan Univ., Changsha, Hunan 410082, China

ABSTRACT: Overloaded trucks could induce considerable fatigue damage on bridges over the time, especially on steel bridges. Recent years has seen a fast-increasing number of overload permit requests which bring a large amount of workload for bridge administration. Therefore, developing rational vehicle weight limits and overload permit checking procedures is highly desired. In this study, a method for determining proper vehicle weight limits is proposed based on the consideration of the cumulative fatigue damage of bridges. A typical steel-concrete composite girder bridge is adopted as an example for illustrating the proposed method. The results from this study can not only be used to develop vehicle weight limits and assist overload permit checking but also to assess the fatigue damage and predict the future development of fatigue damage of existing bridges.

1 INTRODUCTION

The phenomenon of truck overloading is very common around the world and is becoming more and more serious despite the enforcement of various truck weight and size regulations. Overloaded trucks pose a great threat to the safety and durability of existing bridges. Recent years has seen a fast-growing number of overload permit requests for road authorities to deal with. Under such circumstances, rational vehicle weight regulations and effective overload permit checking systems are highly desired.

The basic idea in evaluating the permit request of an overweight vehicle is to check the ratio of the stress imposed by the overweight vehicle to the design load effect and make sure that the overstress ratio is controlled under an acceptable level (TRB 1990; Correia & Branco 2006). Various methods have been developed for predicting the longitudinal stresses on the bridge girders which are checked against the acceptable limits. A way for doing this is to perform detailed structural analysis. However, it may be very time consuming and requires detailed information of the bridge structure which may be difficult to collect (Vigh & Kollár 2006, 2007). Simplified structural analysis methods, such as the beam line analysis method, influence line method, two-dimensional finite element analysis, etc., have also be adopted to calculate the stresses (Vigh & Kollár 2006, 2007; Correia & Branco 2006; Correia et al. 2014). However, these simplified analysis methods are often conservative to some degree (Wood et al. 2007).

Another simple way is to check the axle loads of the vehicle against the allowable limits. The Federal Bridge Gross Weight Formula adopted in the USA is a typical example. However, some researchers criticized the overstress criterion adopted in developing existing bridge formulas for not considering the damage of bridges due to the repeated loads or overloads (Ghosn 2000). In addition, no consistent allowable overstress ratios are adopted by different organizations (*Bridge Formula Weights* 1994; Vigh & Kollár 2006; Correia & Branco 2006). In this study, a method for determining vehicle weight limit was proposed by considering the cumulative fatigue damage of bridges due to repeated vehicular loads. A typical steel-concrete composite girder bridge was used as an example for illustrating the proposed method. The results indicate that this method can also be adopted to assess the fatigue damage and predict the future development of fatigue damage of existing bridges.

2 VEHICLE LOADS

The axle configuration of vehicles has a significant influence on the stresses of bridges. It is therefore a very important fact that should be considered when conducting overload permit checking and setting vehicle weight limits. Two typical truck models were

used in the present study, including the HS-20 design truck specified in the AASHTO LRFD code (AASHTO 2012), which was used in this study for calculating the design load effect, and the design fatigue truck specified in the AASHTO fatigue guide specifications (AASHTO 1990). The fatigue truck was utilized in calculating the cumulative fatigue damage caused by the traffic loads on the bridge and was also adopted as the reference model for overweight trucks.

The simplified configuration of the two trucks is shown in Figure 1. It is noted that these two trucks have very similar configurations except the axle distance between the middle and rear axles (denoted as L in Fig. 1), which is 4.27 m and 9.14 m, respectively, for the HS-20 truck and the design fatigue truck. A gross vehicle weight (GVW) of 320 kN was set for the two truck models. This weight was found by researchers to be a good representative of the effective gross weight of heavy trucks on the highway (Chotickai & Bowman 2006).

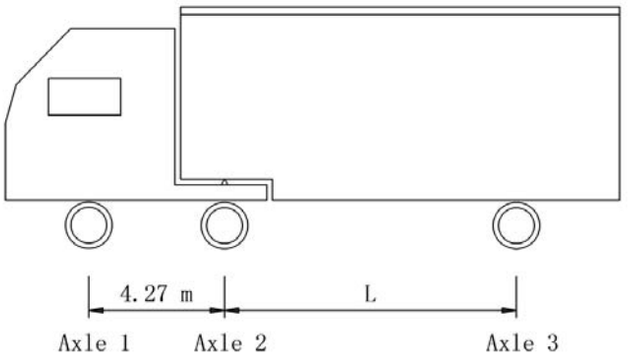


Figure 1. The truck models adopted in the present study

To investigate the effect of GVW of the overweight trucks on the fatigue damage of bridges, five more GVW values were considered for the overweight trucks, namely, 363 kN, 400 kN, 445 kN, 489 kN and 534 kN. To make the analysis simple, the overweight trucks were assumed to have the same axle spacing of the design fatigue truck. In addition, the extra weight of the overweight truck is proportionally distributed to each truck axle. An ADTT of 2000, which is used in the AASHTO (2012) code in the design, was adopted in this study.

3 BRIDGE MODEL

3.1 *Finite element model of bridge*

In the present study, a typical simply-supported steel-concrete composite girder bridge designed according to the AASHTO LRFD code (AASHTO 2012) was adopted for the purpose of illustration. This bridge is 30.48 m in length and 9.75 m in width. Figure 2 shows the cross section of the bridge. As shown in the figure, this bridge consists of five identical steel I-girders with spacing of 2.13 m and height of 1.61 m, the details of which are listed in Table 1. A 3-dimensional (3D) finite element (FE) model of the bridge was built using the ANSYS program, as shown in Figure 3. In this FE bridge model, the concrete bridge components including the deck, steel girders and guardrail were modeled by solid elements while the steel diaphragms were modeled by shell elements. In addition to the end diaphragms, three intermediate diaphragms were arranged with the purpose of distributing the live load more evenly.

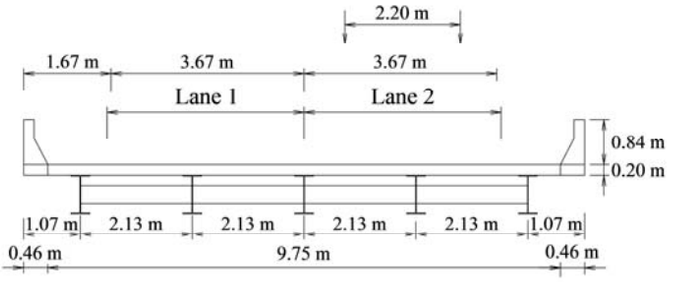


Figure 2. Cross section of the bridge considered

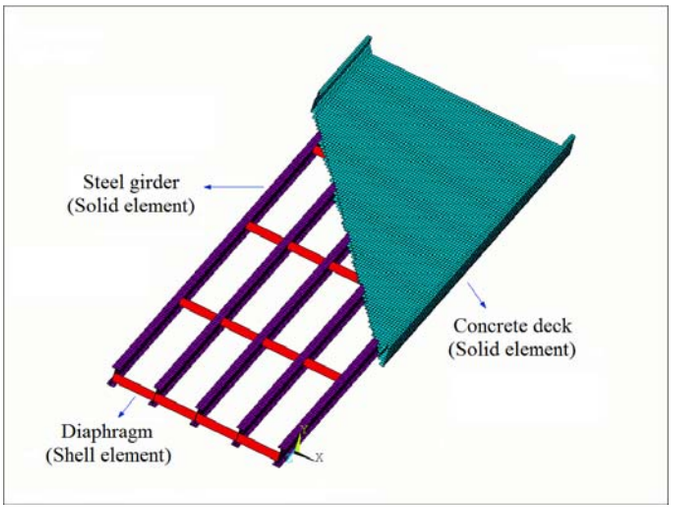


Figure 3. FE bridge model

Table 1. Details of the steel I-girders of the bridge considered

Cross -sectional area	Moment of inertia	Initial Young's modulus	Poisson's ratio
m^2	m^4	GPa	
0.02	0.0011	210	0.25

Studies have shown that the dominant internal force for small-to-medium-span bridges is usually the bending moment which governs the design of bridge cross sections (Brühwiler & Herwig 2008; González et al. 2011). Therefore, in the present study only the bending stress on the bridge girders was considered. Besides, only one loading case with the truck loading in the slow lane was considered, as shown in Figure 2, for the following reasons. Firstly, the chance of two overweight trucks present on the bridge at the same time is very small (Fu & You 2009; Zhang & Cai 2012). Secondly, the case with one truck loading in the slow lane is also suggested by the AASHTO LRFD code (AASHTO 2012) for fatigue consideration. Assuming that the bridge is free from any fatigue damage, the maximum static bending stresses on the bridge girders under the action of different trucks are shown in Table 2. It should be noted that these results were obtained when the truck was loaded at the most unfavorable longitudinal position. In addition, a detailed finite element analysis was used to obtain the girder stress.

Table 2. Maximum static bending stress on the bridge girders caused by different trucks

Truck Type	GVW	Bending stress
	kN	MPa
HS-20 design truck	320	31.88
Design fatigue truck	320	26.86
	363	30.28
	400	33.38
Overweight tr;uck	445	37.13
	489	40.80
	534	44.56

3.2 *Accumulated fatigue damage on bridges*

The Miner's cumulative damage model (Miner 1945), which is usually referred to as Miner's Rule, was adopted in the present study in calculating the cumulative fatigue damage of bridges. Miner's Rule was suggested for the calculation of effective stress range by the AASHTO LRFD code (AASHTO 2012) and has been widely used in bridge design (Fatemi & Yang 1998). With the obtained stress time history, Equation 1 was then adopted to calculate the vehicle-induced cumulative fatigue damage on the bridge girders:

$$\mathrm{CFD}(t)=\sum_i \frac{n_i}{N_i} \tag{1}$$

where n_i and N_i are the actual number of stress cycles and the fatigue life corresponding to the ith stress-range S_i, respectively. In addition, only stresses larger than 3.45 MPa caused by the passage of a truck was considered. The rainflow counting algorithm was adopted in the present study to count the number of stress ranges (Downing & Socie 1982).

4 VEHICLE WEIGHT LIMIT ANALYSIS METHOD

The goal of overweight vehicle management is to control the overstress due to the overweight vehicles under an acceptable level to ensure the safety of the bridge structure. Based on the experience from previous studies (Vigh & Kollár 2007; Correia & Branco 2006), in the present study the stress ratio (SR), which is defined as the stress due to the overload to the stress caused by the design load vehicle (as shown in Eq. 3), was used as the basis for permit checking.

$$SR = \frac{S^{OV}}{S^{DLV}} \tag{2}$$

where S^{OV} and S^{DLV} are the bending stresses caused by the overweight truck and the design load vehicle, respectively.

To consider the dynamic effect of vehicle load when calculating the CFD, a dynamic load allowance of 0.15 as specified in the AASHTO LRFD code (AASHTO 2012) was added to the static bending stress range. Based on the dynamic bending stress range, Equation 1 was used to calculate the CFD, while Equation 2 was used to calculate the SR, which was used as the basis for permit checking. The detailed procedure is illustrated by the flowchart in Figure 4.

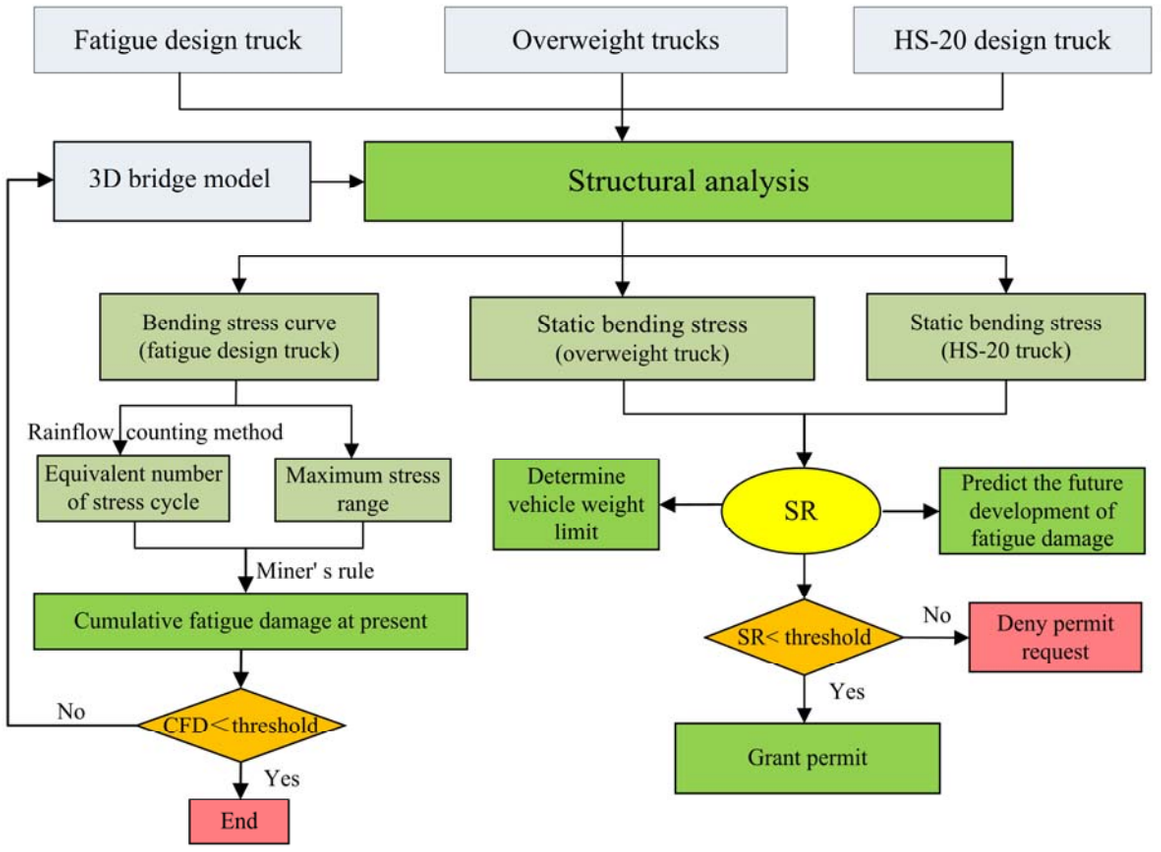


Figure 4. Flowchart for determining vehicle weight limit and making permit decision

5 VEHICLE WEIGHT LIMIT ANALYSIS CONSIDERING THE CFD OF BRIDGES

Selecting a proper threshold value for SR is critical to determine whether an overweight vehicle should be granted a permit. Once determined, the threshold SR value generally sets the limits on the GVW for different trucks. In general, if the SR value due to an overloaded vehicle is less than the threshold value adopted, the vehicle could be granted an automatic permit. For a new bridge, adopting different threshold values of SR means allowing vehicles with different GVWs to cross the bridge and will cause different levels of fatigue damage after a certain period of time.

For the purpose of illustration, it was assumed that bridge girders are replaced when the CFD index of the bridge girders reaches 0.5, which usually corresponds to a poor condition rating (Cha et al. 2014). It should be noted that in reality the decision of bridge girder replacement is made based on many factors, such as the condition rating of the bridge components, the priorities of the DOT, and the availability of funds, etc. (INDOT 2010).

Figure 5 shows the development of bridge fatigue damage with time under different threshold values of SR adopted, assuming that the trucks strictly obey the weight limits. From Figure 5 it can be seen that the selection of threshold value of SR has a significant effect on the cumulative fatigue damage of the bridge structure. For example, for the bridge under consideration, it takes more than 75 years for the CFD on the bridge girders to reach 0.5 if a SR of 0.7 is adopted while it only takes about 10 years if a SR of 1.4 is adopted. Therefore, selecting different SR values can make a big difference in the resulting fatigue life of bridges.

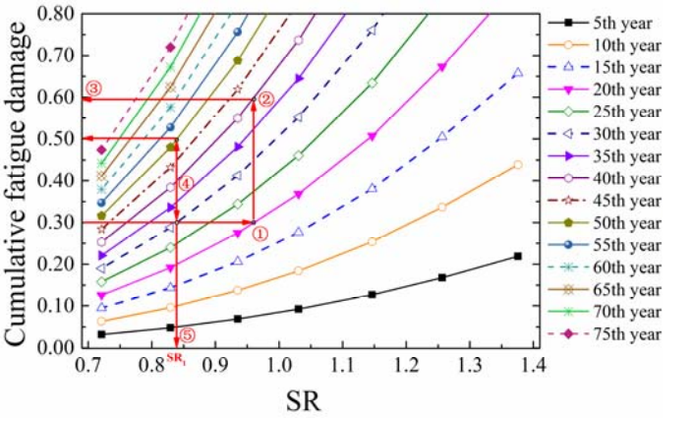


Figure 5. Development of fatigue damage under different threshold values of SR

Based on the relationships between the CFD and the influencing factors, such as the servicing time, and SR, a method for determining vehicle weight

limit was proposed considering the CFD of bridges. This method works for both new bridges as well as existing bridges.

For a new bridge, based on the relationships between the CFD and the two parameters, namely, the SR and the service time, as shown in Figure 5, the threshold value of the SR can be obtained in order to achieve the desired service life of some key bridge components, for example, the girders. Once the threshold value of SR is determined, the truck weight limit can then be obtained by back calculation using Equation 2. In the present study, an example was adopted to illustrate the proposed procedure and it was assumed that the replacement of bridge girders is undertaken at the point when the CFD of the bridge component reaches 0.5. Assuming the bridge under consideration has the relationships between different parameters as shown in Figure 5 and the expected service life of the bridge girders is 25 years, it can be found from Figure 5 that it takes 25 years for the CFD of the bridge girders to reach 0.5 if a SR value of 1.05 is taken. Therefore, in order to achieve the desired service life, a SR value of 1.05 should be taken as the threshold value. Since the design stress of the bridge girders is calculated to be 31.88 MPa, as listed in Table 2, the allowable stress due to an overweight truck is therefore calculated as 1.05 times 31.88 MPa, which gives 33.47 MPa. According to the results in Table 2, this stress corresponds to a GVW of about 400 kN. It should be noted that the overweight truck is assumed to have the same geometric sizes as the fatigue design truck in this analysis. Therefore, during the implementation of the weight regulations in practice, vehicles with weights under 400 kN can be granted an automatic pass. For a truck that is heavier than 400 kN, structural analysis may be performed to determine whether the overweight truck should be granted a pass or not. If the truck leads to a stress of larger than 33.47 MPa on the bridge girders, then the permit request of the truck can be rejected. Otherwise, the truck may be issued a permit.

In addition to determining the weight limit for new bridges, Figure 5 can also be used to guide the determination of vehicle weight limits for bridges in service. To illustrate the process, the steel-concrete composite girder bridge was used again as an example. In this example, the following assumptions were made: (1) this bridge has been in service for T_0 (=20) years and the cumulative fatigue damage on the bridge girder is estimated as CFD_0 (=0.3); and (2) the expected service life of the bridge girders is T_{exp} (=40) years at the point when the CFD reaches the threshold value of 0.5. The detailed procedure is illustrated in the following with the step numbers also marked in Figure 5 for the purpose of convenience.

Step 1: Find the intersection (numbered as Point ①) between the SR-CFD curve for the T_0th (20st) year and the horizontal line with CFD=0.3.

Step 2: From Point ① obtained in the previous step, draw a vertical line down and find the intersection point of this vertical line and the CFD curve for the T_{exp}th (=40th) year, as denoted as Point ②.

Step 3: Find out the CFD value at Point ② (denoted as CFD_{exp}) and compare it with the threshold value of 0.5 as denoted by Point ③. If the CFD_{exp} exceeds the threshold value of 0.5, more restrictive vehicle weight limit needs to be enforced in order to achieve the desired service life. Otherwise, less restrictive vehicle weight limit may be used. For this example, the CFD_{exp} is equal to 0.59, which is greater than the threshold value and more restrictive vehicle weight limit should therefore be enforced.

Step 4: Draw a vertical line that intersects with the CFD curves for the T_{exp}th (=40) year and the T_0th (=20) year; calculate the vertical distance between the two intersection points and compare this distance with the margin value between the threshold CFD (0.50) and the current CFD (0.30), which gives 0.2. Move the vertical line to the left or right until the vertical distance between the two intersection points is equal to the margin (0.20), which is shown by the number ④ in Figure 5.

Step 5: Find out the intersection of the final vertical line as determined from the previous step with the horizontal axis, which is denoted as Point ⑤. The SR value at Point ⑤ is the threshold SR value that should be adopted in determining the vehicle weight limit. In this example, a value of 0.84 should be adopted as the threshold for weight limit purposes.

6 CONCLUDING REMARKS

A method for determining vehicle weight limit and overload permit checking was proposed which can consider the cumulative fatigue damage of bridges due to repeated vehicle loading. The proposed method can also be used to predict the future development of fatigue damage with assumed traffic information in the future. A typical steel-concrete composite girder bridge was used as an example for illustrating the proposed method. One important finding from this study is that the threshold value of stress ratio adopted in determining weight limits has a significant effect on the resulting cumulative fatigue damage of bridge components and therefore their fatigue life. Since the allowable stress ratios adopted by different codes are different, in order to determine a reasonable allowable stress ratio, further

analysis may be required.

7 REFERENCES

AASHTO. 1990. Guide specifications for fatigue evaluation of existing steel bridges, Washington, DC.

AASHTO. 2012. LRFD bridge design specifications, 6th Ed., Washington, DC.

BRÜHWILER, E. & HERWIG, A. 2008. Consideration of dynamic traffic action effects on existing bridges at ultimate limit state. Iabmas08: International Conference on Bridge Maintenance, Safety & Management.

BRIDGE FORMULA WEIGHTS. 1994. United States Department of Transportation, Federal Highway Administration, Washington, D.C.

CHA, H., LIU, B., PRAKASH, A. & VARMA, A. H. 2014. Effect of Local Damage Caused by Overweight Trucks on the Durability of Steel Bridges. *Journal of Performance of Constructed Facilities,* 30**,** 04014183.

CHOTICKAI, P. & BOWMAN, M. D. 2006. Truck Models for Improved Fatigue Life Predictions of Steel Bridges. *Journal of Bridge Engineering,* 11**,** 71-80.

CORREIA, J. R., ARRUDA, M. R. T. & BRANCO, F. A. 2014. Structural Assessment of Reinforced-Concrete Arch Underpasses Subjected to Vehicular Overloads. *Journal of Performance of Constructed Facilities,* 28**,** 321-329.

CORREIA, J. R. & BRANCO, F. A. 2006. New Methodology: Permit Checking of Vehicular Overloads. *Journal of Bridge Engineering,* 11**,** 274-281.

DOWNING, S. D. & SOCIE, D. F. 1982. Simple rainflow counting algorithms. *International Journal of Fatigue,* 4**,** 31-40.

FATEMI, A. & YANG, L. 1998. Cumulative fatigue damage and life prediction theories: a survey of the state of the art for homogeneous materials. *International Journal of Fatigue,* 20**,** 9-34.

FU, G. & YOU, J. 2009. Truck Loads and Bridge Capacity Evaluation in China. *Journal of Bridge Engineering,* 14**,** 327-335.

GHOSN, M. 2000. Development of Truck Weight Regulations Using Bridge Reliability Model. *Journal of Bridge Engineering,* 5**,** 293-303.

GONZÁLEZ, A., CANTERO, D. & OBRIEN, E. J. 2011. Dynamic increment for shear force due to heavy vehicles crossing a highway bridge. *Computers & Structures,* 89**,** 2261-2272.

Indiana Department of Transportation. 2010. Bridge inspection manual. Indianapolis, IN, <http://www.in.gov/dot/div/contracts/standards/bridge/inspector_manual/> (Sep. 17, 2014).

Miner, M. A. 1945. Cumulative damage in fatigue. *Journal of Applied Mechanics*, 12, 159-164.

TRB (Transportation Research Board). 1990. Truck weight limits: issues and options. Special Rep. 225, National Research Council, Washington, DC.

VIGH, A. & KOLLÁR, L. P. 2006. Approximate Analysis of Bridges for the Routing and Permitting Procedures of Overweight Vehicles. *Journal of Bridge Engineering,* 11**,** 282-292.

VIGH, A. & KOLLÁR, L. S. P. 2007. Routing and Permitting Techniques of Overweight Vehicles. *Journal of Bridge Engineering,* 12**,** 774-784.

WOOD, S. M., AKINCI, N. O., LIU, J. & BOWMAN, M. D. 2007. Long-Term Effects of Super Heavy-Weight Vehicles on Bridges. Final Rep. No. Federal Highway Administration (FHWA)/IN/JTRP-2007/10, Purdue Univ., West Lafayette, IN.

ZHANG, W. & CAI, C. S. 2012. Fatigue Reliability Assessment for Existing Bridges Considering Vehicle Speed and Road Surface Conditions. *Journal of Bridge Engineering,* 17**,** 443-453.

Maintenance, Safety, Risk, Management and Life-Cycle Performance of Bridges – Powers, Frangopol, Al-Mahaidi & Caprani (Eds)
© 2018 Taylor & Francis Group, London, ISBN 978-1-138-73045-8

Vortex-induced Vibration Prediction of Bridges Based on Data Fusion Theory

Shiqiao XU, Dalei WANG, Rujin Ma & Airong CHEN
Tongji University, Shanghai, China

Hao TIAN
Zhejiang Scientific Research Institution of Transport, Zhejiang, China

ABSTRACT: The wind monitoring data collected from July to August 2015 of a large span suspension bridge in East China Sea and 32 vortex-induced vibration events during this period are studied in this paper. Firstly, the wind speed, wind direction, gust factor and turbulence intensity during the vortex-induced vibration are calculated. The results show that the wind speed and direction can be used to predict the occurrence of the vortex-induced vibration. And then, by the statistics of wind speed and direction of vortex-induced vibration events and the normal conditions, the occurrence probability of vortex-induced vibration can be determined by taking advantage of the data recorded by a single anemometer. Finally, data fusion theory is carried out to determine the occurrence probability of vortex-induced vibration by combining the results of multiple anemometers. The analysis result is available to develop the management measures to manage the vortex-induced vibration.

1 INTRODUCTION

1.1 *Research backgrounds*

When the near-ground airflow of the atmospheric boundary layer passes through the bridge section, flow separation and periodic vortex shedding will occur which results in alternating changes in positive and negative pressures on the upper and lower surfaces of the main beam. Alternate changes of the pressure may cause the bridge to occur vortex-induced vibration in the transverse or twisting direction (Haber, 1982). Vortex-induced vibration is a kind of common wind-induced vibration of bridge. Although the vortex-induced vibration does not have a strong destructive nature, it will cause structural damage or fatigue damage because of its low wind speed, long lasting vibration, and seriously affecting the driving comfort and safety. Since the 1990s, the rapid development of new technologies, materials and construction technologies make the bridge structure more flexible. With the span of bridges becoming larger and larger, the occurrence probability of vortex-induced vibration is increasing. Therefore, the way to estimate the amplitude of vortex-induced vibration correctly and put forward reasonable and effective vibration suppression measures need to be developed urgently during the design of large span bridges. The effect of wind on structures has been studied since long ago. The study of vortices by human began around 1500 years ago. The earliest fluid vortex study is carried out by Da Vinci who is known for his artistic achievements. Through the observation of stream in-depth, Da Vinci obtained the basic understanding of the movement of the vortex and proposed the concept of 'eddy' for the first time (Maurin, 1998). As is shown in Figure 1, he painted a lot of paintings about 'eddy' in his life. He took a lot of time to observe the overall shape of the flow. He found that vortex was very evident in the flow of fluid around the blunt body. Nowadays, the movement characteristics of vortex is still one of the hot spots.



Figure 1. Da Vinci's painting of the vortex.

Vortex-induced vibration is a very complex fluid-solid coupling phenomenon (Shimada, 1991). However, vortex-induced vibration is not paid sufficient attention in the initial stage due to insufficient un-

derstanding of wind pressure. It is difficult to obtain the analytic solution of vortex-vibration problem and solve the problem of vibration-induced vibration by purely theoretical method (Uetani, 2000). Therefore, the semi-empirical model should be established based on the actual vibration. By selecting the undetermined parameters in the empirical model, the actual situation of the model can be obtained and the complicated flow solid coupling problem can be solved. Bishop and Hassan first used the 'vanderpol oscillator' to describe the turbo-kinetic equation of the cylinder in 1963, which was later adopted by many scholars. Hartlen-Currie experience model is constructed by Hartlen in 1970 based on 'vanderpol oscillator'. Through the selection of appropriate parameters, the model can correspond to the characteristics of vortex-induced vibration observed from the test results quantitatively. Skop et al solved the problem that the parameters of the Hartlen-Currie model were not related to the physical parameters of the system and proposed the 'modified vanderpol oscillator model' (Kassem, 1992). By the literature review above, it is obvious that the current research on the vortex-induced vibration of the bridge mainly aimed at avoiding the occurrence of the vortex-induced vibration. The vortex-induced vibration analysis theory is carried out to guide the design of the bridge. However, due to the shortcomings of the existing theoretical research and insufficient consideration of bridge environment in the design process, it is impossible to ensure that all bridges will not occur vortex-induced vibration. So, how to predict the occurrence of vortex-induced vibration and take targeted management measures for those bridges that frequently occur vortex-induced vibration make a lot of sense.

1.2 *Study content*

In the 21st century, more and more countries have paid attention to the maintenance and management of bridges especially those large span bridges. Europe, America and Japan, South Korea, and Hong Kong SAR have proposed a new method 'Active and preventive maintenance and management'. According to the new idea, various types of structural health monitoring sensors were installed on some important bridges. More and more civil engineers began to study on the bridge structural health monitoring data analysis to improve the maintenance technology and methods. Bridge maintenance and management with monitoring data quickly became the focus of world. At present, most of the large span bridges have installed monitoring system which provides effective method of predicting and early warning of vortex-induced vibration based on monitoring data. In the field of bridge engineering, data mining technology has been widely used in bridge health monitoring data analysis, data mining analysis of bridge monitoring data has been carried out according to the characteristics of the bridge monitoring data and set up clustering model, relational model and time series model. These three mathematical models can be used to judge and identify the current health condition of the bridge. Under this background, the wind monitoring data collected from July to August 2015 of a large span suspension bridge in East China Sea and 32 vortex-induced vibration events during this period are studied in this paper. There are four indexes may be selected to represent the characterization of wind field, which are wind speed, wind direction, turbulence intensity and gust factor.Firstly, the wind speed, wind direction, gust factor and turbulence intensity during the vortex-induced vibration are calculated. It is determined that the wind speed and direction should be used as the index to predict the occurrence of the vortex-induced vibration. However, the turbulence intensity and gust factor are not associated with the occurrence of vortex-induced vibrations. And then, by the statistics of wind speed and wind direction of vortex-induced vibration events and normal conditions, the occurrence probability of vortex-induced vibration can be determined by taking advantage of a single anemometer. Finally, data fusion theory is carried out to determine the occurrence probability of vortex-induced vibration by combining the results of multiple anemometers. The analysis result is available to develop the management measures of the bridge before the occurrence of vortex-induced vibration.

2 BACKGROUND ENGINEERING INTRODUCTION

The suspension bridge in East China Sea is one of the largest sea-crossing bridge between Zhoushan mainland and islands link project. The trend of the bridge is from north to south. What's more, the hydrogeological conditions of the bridge area are complex, the wind environment is complicate and the technical requirements are high. The bridge is a two-span suspension bridge with 1650m main span and 578m side span which is the second largest span suspension Bridges. The stiffening beam adopts the separated steel box girder with the lifting arm. The steel box girder is 3.51m high and the total width is 36m. The tower of the bridge is 211m and the rise span ratio of the main cable is equal to 1/10. The elevation of the bridge is shown in Figure 2. The wind field of the bridge site are complex because the summer typhoon and the winter monsoon may affect the bridge. To provide reliable data to assess the safety of the bridge under wind effect, two propeller anemometers and six three-directional ultrasonic anemometers were installed to collect the wind field data of the bridge site. As is shown in Figure 2, propeller anemometers and three-directional ultrasonic

anemometers are installed on the top of the pylon and the deck, respectively. Two propeller anemometers (AN1, AN2) are installed in the north and south pylon of the bridge. The three-directional ultrasonic anemometers (UA1-UA6) are installed on the upper and lower sides of the stiffened beam at the 1/4, 1/2 and 3/4 of the main span, respectively.

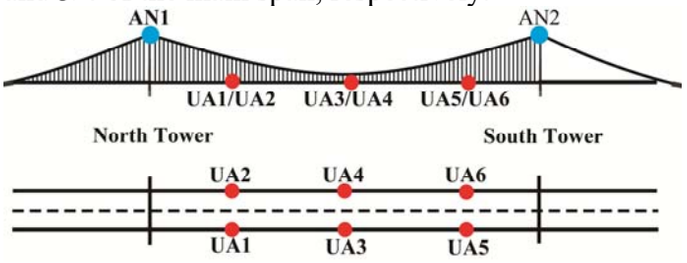


Figure 2. The layout of wind speed sensor.

Through the records of the bridge manager, the bridge has occurred 97 times vortex-induced vibration from 2013 to 2015, including 26 times in 2013, 35 times in 2014, 36 times in 2015. The main information of those vortex-induced vibration events, such as the bridge vibration frequency, wind speed, wind direction and duration et al are recorded. As presented in Table 1, it is the main information of some vortex-induced vibration events.

Table 1. The main information of some vortex-induced vibration events of a bridge in East China Sea.

Events number	Vibration frequency	Wind speed	Wind direction	Duration time
	hz	m/s	degree	minute
1	0.3284	10.45	311	30
2	0.3287	9.85	310	160
3	0.3269	8.97	134	40
4	0.3271	8.68	155	70
5	0.3257	7.59	132	30
6	0.4357	9.47	313	100
7	0.3264	8.25	132	50
8	0.4357	7.91	317	170
9	0.3261	10.09	128	30
10	0.3264	9.75	331	110

3 PREDICTION PARAMETERS ANALYSIS OF VORTEX-INDUCED VIBRATION

3.1 *Parameters of wind speed and wind direction*

By the preliminary data integrity and accuracy check of the data collected by the propeller anemometers (AN1, AN2) and three-directional ultrasonic anemometers (UA1-UA6) during the vortex-induced vibration, the wind field data of three-directional ultrasonic anemometers are recorded completely. What's more, the wind speed and wind direction of these anemometers are related with the occurrence of vortex-induced vibration. To improve the efficiency of data analysis, three of all the six three-directional ultrasonic anemometers are selected. That is, only one anemometer in the same longitudinal section is selected to carry out the occurrence probability analysis of vortex-induced vibration. Therefore, the monitoring data collected by UA1, UA3 and UA5 are set as the study object. In addition, by the statistics of the occurrence time of vortex-induced vibration, there are 86 vortex-induced vibration events occurred in July and August of all the 97 vortex-induced vibration events. Therefore, the wind monitoring data collected from July to August 2015 and 32 vortex-induced vibration events during this period are studied in this paper to carry out the occurrence probability analysis of vortex-induced vibration.

The wind speed collected by the three-directional ultrasonic anemometers installed on the large span suspension bridge is defined as $u(t), v(t)$ and $w(t)$, in each direction, respectively. The definition of wind speed $u(t), v(t)$ and wind direction Φ in the plane relative to the bridge axis are shown in Figure 3 and the vertical wind speed $w(t)$ is from bottom to the top. The angle of the bridge axis is about 45 degrees.

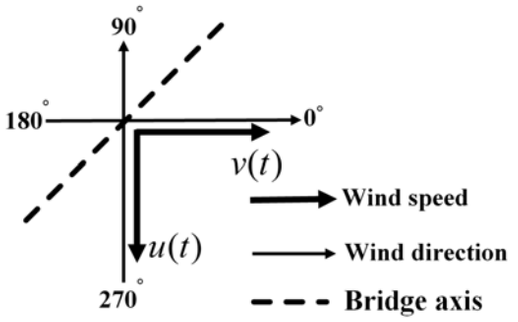


Figure 3. The schematic of wind speed and direction.

The base interval is set as 10-minute. What's more, the mean wind speed in the plane and the corresponding direction angle are defined as U and Φ, respectively. The average vertical wind speed is defined as W. The monitoring wind data are calculated and analyzed as follows:

$$U = \sqrt{\overline{u(t)}^2 + \overline{v(t)}^2} \tag{1}$$

$$\cos\Phi = \overline{u(t)}/U \tag{2}$$

$$W = \overline{w(t)} \tag{3}$$

Where $\overline{u(t)}, \overline{v(t)}$ and $\overline{w(t)}$ = the average wind speed of 10-minute. According to formula (1)-(3), the mean wind speed in the plane U and corresponding direction angle Φ of the 32 vortex-induced vibration events can be obtained by analyzing the wind data collected by three-directional ultrasonic anemometers. The mean wind speed in the plane U during the vortex-induced vibration and normal conditions calculated by the UA1 anemometers is shown in Figure 4. Figure 5 shows the corresponding direction angle Φ.

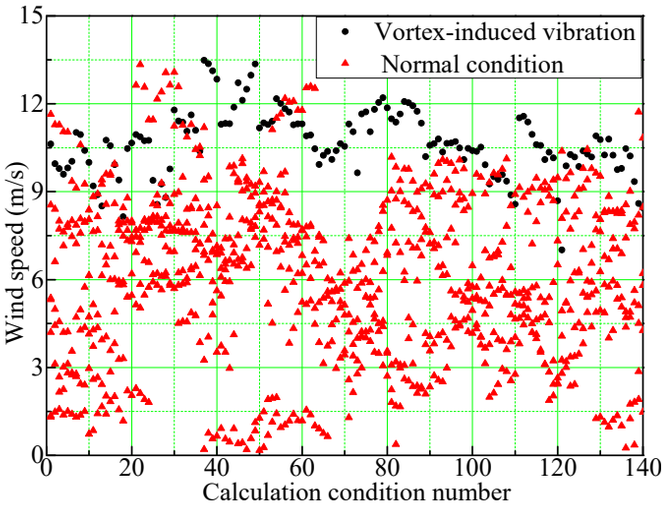


Figure 4. The mean wind speed in the plane *U*.

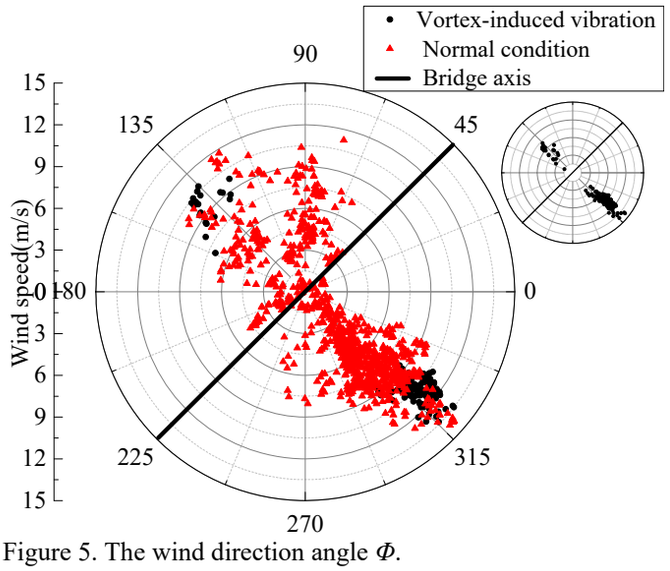


Figure 5. The wind direction angle *Φ*.

It is obvious in Figure 4 that the wind speed ranges from 8.5 m/s to 10.5 m/s when the vortex-induced vibration occurs. There is no vortex-induced vibration when the wind speed is out of this range which indicates that the wind speed is an important characterization parameter of vortex-induced vibration. Therefore, the wind speed is selected as one of the parameters in the process of predicting the occurrence of vortex-induced vibration. Similarly, it can be found from Figure 5 that the distribution of wind direction during the vortex-induced vibration is from 125 degrees to 150 degrees or 305 to 330 degrees whose difference is about 180 degrees. However, there is no vortex-induced vibration if the wind direction is out of this range. In addition, the statistics results of wind direction also indicate that vortex-induced vibrations can occur only when the direction between the wind and the bridge are about 90 degrees. Through the above analysis, wind speed and direction have obvious characteristics in the case of happening vortex-induced vibration. Therefore, the wind speed and wind direction must be taken as parameters to carry out the occurrence probability analysis of the vortex-induced vibration.

3.2 *The parameter of turbulence intensity*

The fluctuating wind speed in the horizontal direction and transverse direction in the plane are defined as u_t, v_t respectively. Moreover, the fluctuating wind speed in the vertical direction is defined as w_t. u_t, v_t and w_t can be calculated according to the following formula:

$$u_t(t) = u(t)\cos\Phi + v(t)\sin\Phi - U \tag{4}$$

$$v_t(t) = -u(t)\sin\Phi + v(t)\cos\Phi \tag{5}$$

$$w_t(t) = w(t) - W \tag{6}$$

The turbulence intensity reflects the pulsating intensity of the wind which is defined according to formula (7)-(9). The turbulence intensity is the key parameter to determine the pulsating wind load of the structure. So, the turbulence intensity should be calculated to analyze whether it is related to the occurrence of vortex-induced vibrations.

$$I_u = \frac{\sigma_u}{U} \tag{7}$$

$$I_v = \frac{\sigma_v}{U} \tag{8}$$

$$I_w = \frac{\sigma_w}{U} \tag{9}$$

Where, σ_u, σ_v and σ_w = the standard deviations of the pulsating wind speed for u_t, v_t, and w_t in 10-minute, respectively. As is shown in Figure 6, it is the turbulence intensity for every 10-minute during the 32 vortex-induced vibration events and the normal conditions according to the data collected from UA1 anemometers.

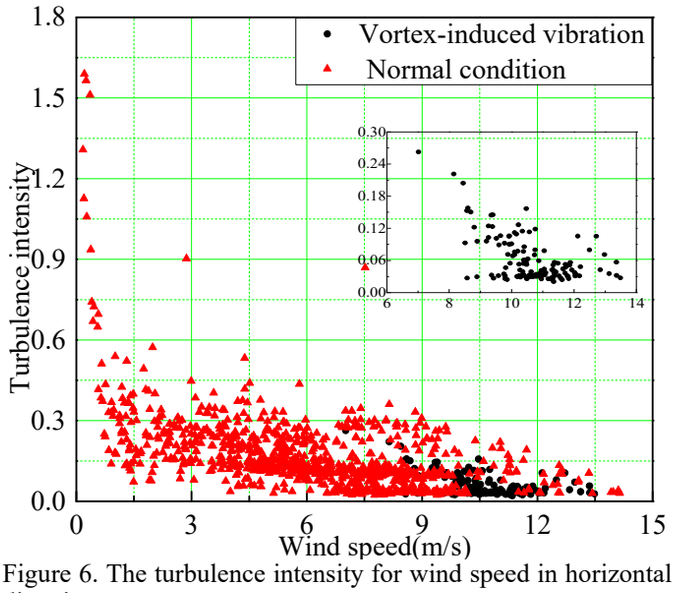


Figure 6. The turbulence intensity for wind speed in horizontal direction.

It is shown in Figure 6 that the turbulence intensity of the wind field of the large span suspension bridge

varies from 0 to 0.3 during the vortex-induced vibration. However, the turbulence intensity of most of normal conditions also range from 0 to 0.3. It indicates that the vortex-induced vibration is not related to the turbulence intensity. Therefore, the turbulence intensity cannot be used as a parameter to predict whether the vortex-induced vibration occurs.

3.3 *The parameter of gust factor*

The fluctuating intensity of the wind is often expressed by gust factor that is the ratio of the maximum wind speed over the duration of the gust duration to the average wind speed U in 10-minute. The gust duration t_g usually is set as 2-3 seconds in structural wind works and t_g is taken as 3 seconds in this paper. The basic formula to calculate the gust factor is as follows:

$$G_u(t_g) = \frac{\max\left(\overline{u(t_g)}\right)}{U} \tag{10}$$

$$G_v(t_g) = \frac{\max\left(\overline{v(t_g)}\right)}{U} \tag{11}$$

$$G_w(t_g) = \frac{\max\left(\overline{w(t_g)}\right)}{U} \tag{12}$$

Where, G_u, G_v and G_w = the gust factor of the pulsating wind speed for u_t, v_t, and w_t in 10-minute, respectively. In general, the greater the t_g, the corresponding gust factor will be smaller, when t_g =10-minute, $G_u = 1, G_v = G_w = 0$. As is shown in Figure 7, it is the gust factor for every 10-minute which is determined by the equations (10)-(12).

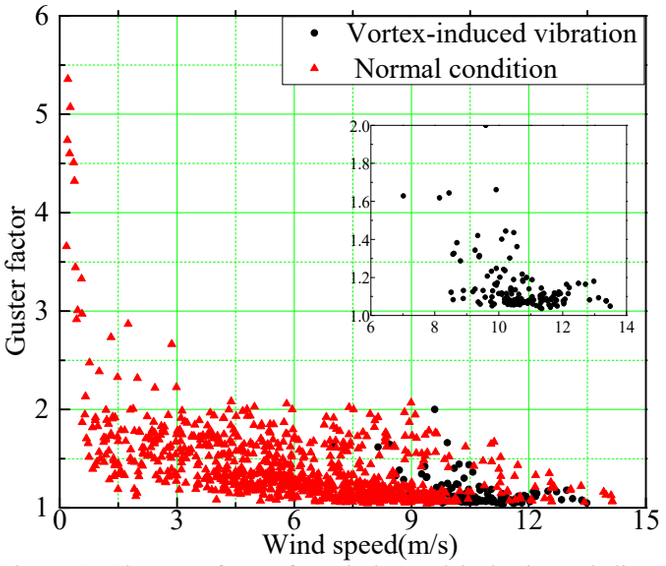


Figure 7. The gust factor for wind speed in horizontal direction.

It is shown in Figure 7 that the gust factor of the wind field of the large span suspension bridge varies from 1.0 to 2.0 during the vortex-induced vibration. However, the gust factor of most of normal conditions also ranges from 1.0 to 2.0. It indicates that the vortex-induced vibration is not related to the gust factor. Therefore, the gust factor cannot be used as a parameter to predict whether the vortex-induced vibration occurs.

Originally, there are four indexes that can be selected to represent the characterization of wind field, which are wind speed, wind direction, turbulence intensity and gust factor. Through the analysis above, wind speed and wind direction have obvious specificity when the vortex-induced vibration occurred. However, neither the turbulence intensity nor the gust factor are associated with the occurrence of vortex-induced vibrations. Therefore, wind speed and wind direction are selected as the parameters to predict the occurrence probability of vortex-induced vibration in this paper.

4 THE OCCURRENCE PROBABILITY ANALYSIS OF VORTEX-INDUCED VIBRATION BASED ON MULTI-PARAMETERS

4.1 *The occurrence probability analysis of vortex-induced vibration based on wind speed*

In last section, the wind speed and wind direction are determined as the parameters to calculate the occurrence probability of vortex-induced vibration. According to the records of the vortex-induced vibration events of the long-span suspension bridge, the vortex-induced vibration mainly occurs in July and August. What's more, the occurrence probability of vortex-induced vibration at other times is scarcely possible and can be negligible. Therefore, the selected 32 vortex-induced vibration events studied in this paper occurred between July and August 2015. So, the wind speed and wind direction data that are collected by the three-directional ultrasonic anemometers (UA1, UA3, UA5) during the period are used to analyze the occurrence probability of vortex-induced vibration in this paper. As shown in Figure 8, it is the 10-minute average wind speed U calculated from July to August in 2015 ranges from 8.5m/s to 13.5m/s.

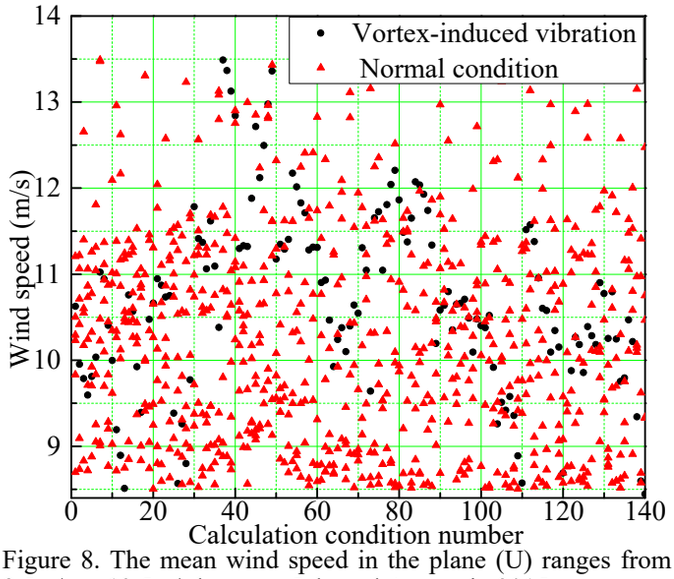


Figure 8. The mean wind speed in the plane (U) ranges from 8.5m/s to 13.5m/s between July and August in 2015.

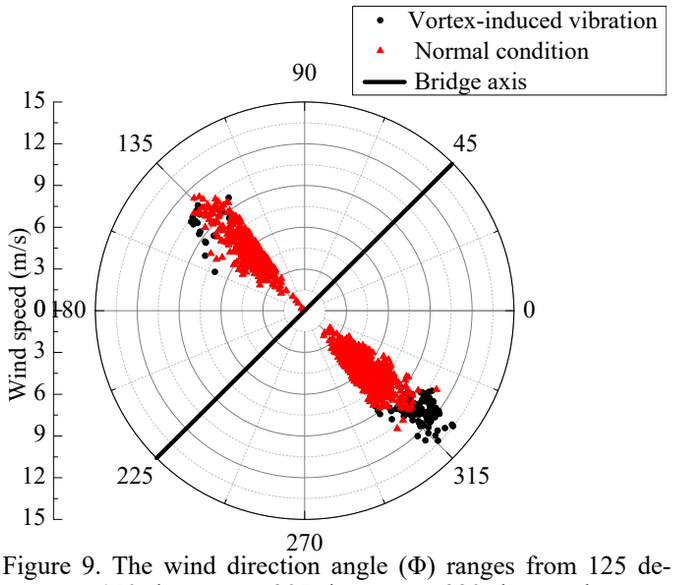


Figure 9. The wind direction angle (Φ) ranges from 125 degrees to 150 degrees or 305 degrees to 330 degrees between July and August in 2015.

Through the analysis of the average wind speed during the vortex-induced vibration of the bridge, it is evident that the vortex-induced vibration occurs only when the wind speed is in the range of 8.5m/s to13.5 m/s. What's more, 10-minute is set as a calculation condition in this paper. There are 891 conditions whose average wind speed U range from 8.5m/s to 13.5m/s and 141 of them occurred vortex-induced vibration. Based on the statistical results, it can be calculated that the occurrence probability of vortex-induced vibration of the bridge is 15.7% when the wind speed ranges from 8.5 m/s to 13.5 m/s recorded by the sensor UA1. When the wind speed ranges from 8.5 m/s to 13.5 m/s, the occurrence probability of vortex-induced vibration of the bridge is 14.6% and 14.3% recorded by the sensor UA2 and UA3, respectively.

4.2 *The probability analysis of vortex-induced vibration based on wind direction*

Similarly, the wind direction is also determined as the parameter to calculate the occurrence probability of vortex-induced vibration. As shown in Figure 9, it is the 10-minute average wind direction Φ calculated from July to August in 2015 ranges from 125 degrees to 150 degrees or 305 degrees to 330 degrees.

Through the analysis of the average wind direction during the vortex-induced vibration of the bridge, it is evident that the vortex-induced vibration occurs only when the wind direction is in the range of 125 degrees to 150 degrees or 305 degrees to 330 degrees. Based on the monitoring data collected by the three-directional ultrasonic anemometer (UA1), the wind direction ranges 125 degrees to 150 degrees or 305 degrees to 330 degrees have a total of 1145 conditions. However, there are 141 of the 1145 conditions happening the vortex-induced vibration. Based on the statistical results, it can be calculated that the occurrence probability of vortex-induced vibration of the bridge is 12.3% when the wind direction ranges from 125 degrees to 150 degrees or 305 degrees to 330 degrees recorded by the sensor UA1. When the wind direction ranges from 125 degrees to 150 degrees or 305 degrees to 330 degrees, the occurrence probability of vortex-induced vibration of the bridge is 11.8% and 12.1% recorded by the sensor UA2 and UA3, respectively. Because of the space limit, the detailed calculation process of UA2 and UA3 is not given here.

4.3 *The probability analysis of vortex-induced vibration by combining wind speed with wind direction*

According to the analysis results, the occurrence probability of vortex-induced vibration is 15.7% when the wind speed ranges from 8.5m/s to 13.5 m/s. The occurrence probability of vortex-induced vibration is 12.3% when the wind direction ranges from 125 degrees to 150 degrees or 305 degrees to 330 degrees recorded by the sensor UA1. The occurrence probability of vortex-induced vibration is determined by the wind speed parameter and the wind direction parameter indivindividual. In this section, the wind speed and wind direction are combined to

determine the occurrence probability of vortex-induced vibration. As shown in Figure 8, it is the 10-minute average wind speed U ranges from 8.5m/s to 13.5m/s and the average wind direction ranges from 125 degrees to 150 degrees or 305 degrees to 330 degrees calculated from July to August in 2015.

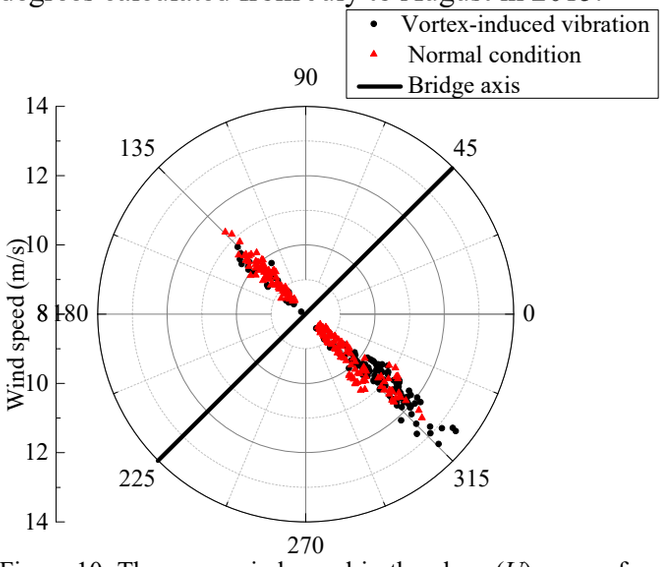


Figure 10. The mean wind speed in the plane (U) ranges from 8.5m/s to 13.5m/s with wind direction angle (Φ) ranges from 125 degrees to 150 degrees or 305 degrees to 330 degrees between July and August in 2015.

Through the analysis of the average wind speed and wind direction during the vortex-induced vibration of the bridge, it is evident that the vortex-induced vibration occurs only when the wind speed is in the range of 8.5m/s to13.5m/s as well as the wind direction ranges from 125 degrees to 150 degrees or 305 degrees to 330 degrees. Based on the monitoring data collected by the three-directional ultrasonic anemometer (UA1), a total of 208 conditions are available for both the wind speed and wind direction. However, 141 of the 208 conditions occurs the vortex-induced vibration. Based on the statistical results, it can be calculated that the occurrence probability of vortex-induced vibration of the bridge is 67.7%. That is, if the wind speed ranges from 8.5m/s to 13.5m/s and wind direction ranges from 125 degrees to 150 degrees or 305 degrees to 330 degrees recorded by the sensor UA1, the large span suspension bridge has a 67.7% probability of occurring vortex-induced vibration. Similarly, if the wind speed is in the range of 8.5m/s to 13.5m/s and the wind direction ranges from 125 degrees to 150 degrees or 305 degrees to 330 degrees, the occurrence probability of vortex-induced vibration of the bridge is 59.4% and 64.3% recorded by the sensor UA2 and UA3, respectively.

5 THE PROBABILITY ANALYSIS OF VORTEX-BASED VIBRATION BASED ON DATA FUSION THEORY

5.1 *Dempster-Shafer Evidence combination theory*

Due to the huge scale and complex characteristics of the bridge structures, it is necessary to use a variety of sensors to monitor the bridge structure to get better results. Therefore, many types of sensors will inevitably produce a lot of similar or different types of signals. It is a much worth studying subject how to deal with these signals effectively and analyze the collected data of these sensors to get better and more accurate conclusion. The common data fusion algorithms are Bayesian theory, Dempster-Shafer Evidence theory and Neural Network theory et al. Bayesian theory is a data fusion algorithm based on Bayesian statistical inference. Because the target information and the priori information of the monitor play an important role in the whole fusion system, the effectiveness of the Bayesian data fusion system theory will depend on all kinds of prior information (Matsumoto, 1992). However, the bridge monitoring system is a very complex and the structural parameters of different bridges differ greatly. So, it is very difficult for us to effectively extract a variety of a priori information. Dempster and Shafer put forward that the theory of evidence is the extension of probability theory in the 1970s. They establish the one-to-one correspondence between the proposition and the set and transform the uncertainty of the proposition into the uncertainty of the set. In addition, the theory of the evidence is the uncertainty of the set. Dempster-Shafer Evidence theory satisfies the axioms that is weaker than the probability theory and can distinguish between uncertain and unaware differences. When the probability value is known, the theory of evidence becomes probability theory. Thus, probability theory is a special case of evidence theory. When the priori probability is difficult to be obtained, the Dempster-Shafer Evidence theory is more appropriate than the probability theory.

5.2 *The occurrence probability analysis of vortex excitation vibration by combining multi-sensor*

In the evidence theory, a sample space is called a recognition framework, which is often represented by θ. θ consists of a series of objects which are mutually exclusive and contain all the objects should be identified. The definition of θ as follows:

$$\Theta=\{\Theta_1,\Theta_2,\cdots\Theta_n\} \tag{13}$$

Where the object Θ_i is called a 'monad' of Θ. If a recognition framework only contains one 'monad', it is called a collection of 'monad'. Then, $m(A)$ is defined to represent the degree of confidence to hypothesis A that is given the evidence. That is, the degree of trust in the proposition 'x is in A'. One of

the basic strategies of Dempster-Shafer Evidence theory is to divide the set of evidence into two or more irrelevant parts and use them to judge the identification framework independently. Then, different parts are combined by the Dempster-Shafer Evidence combination rule. Let Bel_1, Bel_2 be two trust functions based on different evidence, Bel is the trust function obtained after combining the evidence. If m_1, m_2, and m represent the basic probability distribution functions for Bel_1, Bel_2, and Bel, respectively, the Dempster-Shafer Evidence theory combination rule can be expressed as:

$$m(A)=\frac{\sum_{A_1\cap A_2=A} m_1(A_1)m_2(A_2)}{\sum_{A_1\cap A_2\neq\varnothing} m_1(A_1)m_2(A_2)} \tag{14}$$

It can be proved that the orthogonal sum meets the commutative and the associative law. The final evidence obtained from the combined evidence is independent of the order in which the composition is made. So, if there are multiple combinations of evidence, m can be obtained by recursive computation of m_1, m_2,…m_n. Then, the Dempster-Shafer Evidence theory combination rule can be expressed as:

$$m(A)=\frac{\sum_{A_1,\cdots A_k\subset\Omega,\ \bigcap_{i=1}^{k}A_i=A} m_1(A_1)\cdots m_k(A_k)}{\sum_{A_1,\cdots A_k\subset\Omega,\ \bigcap_{i=1}^{k}A_i\neq\varnothing} m_1(A_1)\cdots m_k(A_k)} \tag{15}$$

The monitoring data recorded by UA1, UA2 and UA3 three-direction anemometers are selected to calculate the occurrence probability of vortex-induced vibration of the bridge. As the above calculation analysis, if the wind speed ranges from 8.5m/s to 13.5 m/s and wind direction ranges from 125 degrees to 150 degrees or 305 degrees to 330 degrees recorded by the sensor UA1, the large span suspension bridge has a 67.7% probability of occurring vortex-induced vibration. Similarly, the occurrence probability of vortex-induced vibration of the bridge is 59.4% and 64.3% recorded by the sensor UA2 and UA3, respectively. According to equation (15), the occurrence probability of vortex-induced vibration is 84.6% through orthogonal combination analysis based on the Dempster-Shafer Evidence theory.

6 CONCLUSIONS AND PROSPECT

Through the preliminary analysis of the monitoring data collected by the three-direction anemometers installed on a large span suspension bridge in East China Sea, the wind speed and wind direction are selected as the parameters to predict the occurrence probability of vortex-induced vibration in this paper. Then, it is determined that the occurrence probability of vortex-induced vibration of the bridge is 67.7%, 59.4% and 64.3% respectively by analyzing the data of each anemometer. Finally, the data fusion theory is used to combine the results of the three anemometers and the occurrence probability of vortex-induced vibration of the bridge is 84.6%. However, only the wind speed data during the vortex vibration is analyzed and the vibration data of the bridge is not analyzed. There is no doubt that the accuracy of prediction of the occurrence probability of vortex-induced vibration of the bridge will be greatly improved if the wind speed data and the vibration data are combined.

ACKNOWLEDGEMENTS

This research work was carried out under the support of the Science and Technology Program of Zhejiang Transportation Department（2016009）

7 REFERENCES

Haber, R.B. & Abel, J.F. 1982. Initial equilibrium solution methods for cable reinforced membranes part I-formulations. *Computer Methods in Applied Mechanics and Engineering* 30(3): 263-284.

Maurin, B. & Montro, R. 1998. The surface stress density method as a form finding tool for tensile membranes. *Engineering structures* 20(8): 712-719.

Shimada, T. & Tada, Y. 1991. Approximate transformation of an arbitrary curved surface into a plane using dynamic programming. *Computers Aided Design* 23(2):153-159.

Uetani, K. & Fujii, E. 2000. Initial stress field determination of membrane using optimization technique. I*nternational Journal of Space Structures* 15(2): 137-143.

Kassem, M. & Novak, M. 1992. Wind-induced response of hemispherical air-supported structures. *Journal of Wind engineering and industrial aerodynamics* 41(1-3): 177-178.

Matsumoto, T. 1992. Aero elastic modeling of air-supported roofs. *Journal of wind engineering and industrial aerodynamics* 42(1-3): 1497-1507.

Maintenance, Safety, Risk, Management and Life-Cycle Performance of Bridges –
Powers, Frangopol, Al-Mahaidi & Caprani (Eds)
© 2018 Taylor & Francis Group, London, ISBN 978-1-138-73045-8

Development of phased array ultrasonic test system for detection of fatigue crack of rib-to-deck weld of orthotropic steel deck system

H. Shirahata
Department of Urban and Civil Engineering, Tokyo City University, Tokyo, Japan

ABSTRACT: Fatigue cracking of the orthotropic steel deck system has been one of the serious problems. This study focuses on rib-to-deck weld of a trough rib. Nondestructive testing is necessary, because a fatigue crack is initiated at the weld root of a closed section, and visual inspection is practically impossible. Recently, the phased array ultrasonic test systems have been developed and applied in some fields This study aims at the development of a phased array system and investigates the applicability to the rib-to-deck weld of two types of fatigue cracks; one is deck crack and the other is bead crack. The system consists of two phased array transducers, fl w detector, personal computer, and a scanner. Two transducers were set on a deck plate and a rib plate to detect deck and bead cracks, respectively. The number of elements that can be excited and received at a time was 128. Two types of specimens considering deck and bead cracking were prepared. Fatigue tests were carried out. At every 100 kilocycles, the specimen was taken out of the test site, and ultrasonic tests were applied. In the next step, the amplitude of loading was changed in order to make beach marks. Those procedures were repeated until fatigue failure. After failure, a comparison between the actual propagation of a fatigue crack and the result of ultrasonic test was made. Relatively good agreement could be observed, and the result showed that the fatigue cracks of approximately 2 to 3 mm could be detected by the phased array ultrasonic test system.

1 INTRODUCTION

1.1 *Orthotropic steel deck system and fatigue crack*

Fatigue cracking of orthotropic steel deck system is a serious problem in Japan and many countries (Wolchuk 1999, Wolchuk 1990, Connor & Fisher 2006, Ya, Yamada, & Ishikawa 2011). Fatigue cracking has been reported in almost all the types of welded joints (Federal Highway Administration (FHWA) 2012). This study focuses on rib-to-deck weld, because it is the longest and the most important to support the traffic Figure 1 (a) shows an under view of the orthotropic steel deck system. Regarding the longitudinal rib, a closed section was employed, because of the increase of torsional rigidity and decrease of weld lines. In Japan, U-shaped trough ribs have been applied.

As shown in figur 1 (b) the conventional trough rib in Japan measures 240 mm in height and 300 mm in length. Deck and rib plates are 12 and 6 mm thick, respectively. Figure 1 (c) shows details about rib-to-deck weld in Japan. In 2002, specification on rib-to-deck weld penetration were established. The penetration should be 75 % of the rib plate thickness, while before 2002, there was not description of the penetration (Miki 2006).

In the rib-to-deck weld, two types of fatigue cracks have been reported. One is deck crack and the other is bead crack. In both cases, a crack is initiated at the weld root. Since it is a closed section, visual inspection cannot be applied.

1.2 *Ultrasonic test*

Among nondestructive techniques, ultrasonic test has played a very important role to detect internal defects. The conventional ultrasonic technique is pulse echo method. In the pulse echo method, one or two transducer(s) are used. A defect can be detected by locations where indications can be obtained in scanning and incident angle of a transducer. However, detection of the cracks in figur 1 (d) is difficult There are three reasons. One is the limited accessibility. It is difficul to move transducers back and forth nearby the rib-to-deck weld. The second is incident angle is fi ed around 70 degrees. Defect echo cannot be received until a deck crack becomes 6 mm or longer. Larger incident angle is preferable, but, it also gets more sensitive about the surface condition. The third is existence of reflectors In case of bead crack, especially, weld root corner, weld root tip, and crack tip can be scatterer of the incident wave. That makes it more difficul to distinguish each of those echoes.

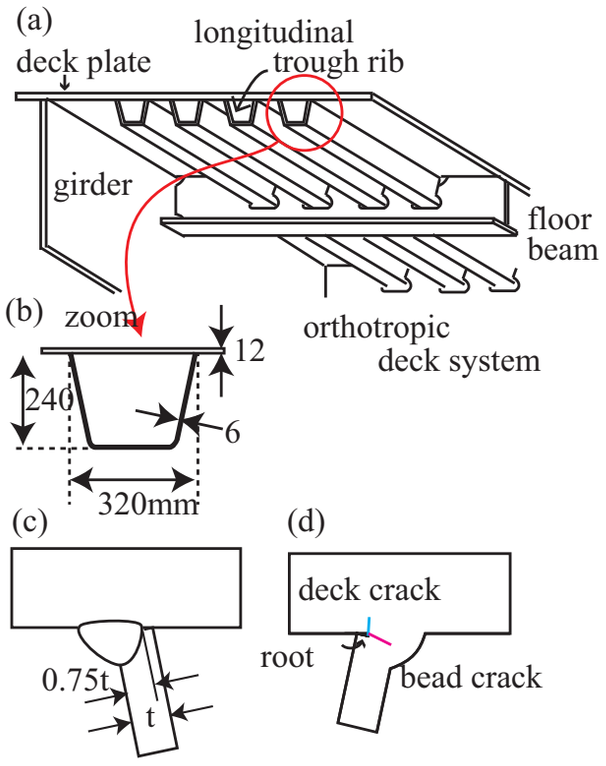


Figure 1: Orthotropic steel deck system and fatigue cracks in rib-to-deck weld

In recent year, phased array ultrasonic test systems have been investigated and applied (Drinkwater & Wilcox 2006, Azar & Wooh , Holmes & Wilcox 2005, Weston M. 2012). As shown in figur 2 (a), many small elements are aligned in a phased array transducer housing. The size of those elements is usually about half of the wave length in steel. By the phased array system, condition of incident wave can be changed. As shown in figur 2 (b), when an element of left side is excited first and the next element is excited after a certain time interval one after another, incident wave moves toward right side. The direction of incident wave can be changed by changing the time interval. In the same manner, incident wave can be focused shown in figur 2 (c).

The objective of this study is to apply phased array ultrasonic system to rib-to-deck weld to detect fatigue cracks. The system also includes software based testing conditions such as focal law and incident angle settings, because the cracks are located very close to the testing surface. In order to evaluate the performance of the system, fatigue and ultrasonic tests were carried out for both deck and bead cracks. The minimum crack size of detection was investigated.

2 PHASED ARRAY ULTRASONIC TESTING SYSTEM

Figure 3 shows the phased array ultrasonic testing system developed in this study. The system consists of computer, fl w detector, transducers, scanner and encoder. The fl w detector is 24 by 16 by 18 cm. It can excite 128 elements and receive from 128 elements at a time. Two linear phased array transducers of 10

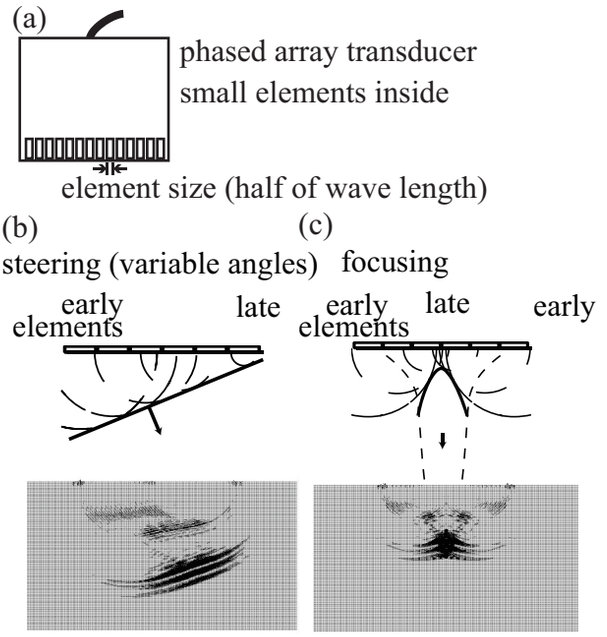


Figure 2: Concept of phased array ultrasonic testing, steering and focusing

MHz and 32 elements were used. Inside of the case, 32 elements are aligned with the pitch of 0.31 mm, as shown in figur 3 (b).

Figures 3 (c) and (d) show more details about transducer and scanner, respectively. A polystyrene wedge was attached to a transducer for large angle of refraction. Crack propagation direction depends on many factors such as the position of wheel, leg size, and throat thickness. It is difficul to predict the crack type, precisely. The system was developed, intended to detect both types of crack at the same time. Therefore, the scanner can hold two transducers, namely, rib transducer and deck transducer. In addition, actual inspection is carried out by overhead position. There are some magnets inside of the frame of the scanner. The scanner is connected fl xibly by hinge, because the angle between deck and rib plates are not always kept the same due to the weld deformation.

3 IMAGE RECONSTRUCTION

Figure 4 shows image reconstruction method called synthetic aperture focusing technique (SAFT) (Schmerr 2015). As step 1, shown in figur 4 (a), the reconstruction area is divided into small mesh. In this case, the mesh size was determined to be 0.2 mm. The area was 20 mm by 20 mm, covering weld bead, rib plate, and deck plate. As step 2, in figur 4 (b), pick up one of the grid points k. In the next step 3 in figur 4 (c), with the combination of grid point k, transmitter channel i, and receiver channel j, wave propagation path and time t_0 were calculated, based on Snell's law. Suppose that wave form obtained by that combination was define as $w_{ij}(t)$. In step 4, the amplitude of $w_{ij}(t_0)$ was added to image intensity $h(k)$ at the grid point k.

$$h(k) \leftarrow h(k) + w_{ij}(t_0) \quad (1)$$

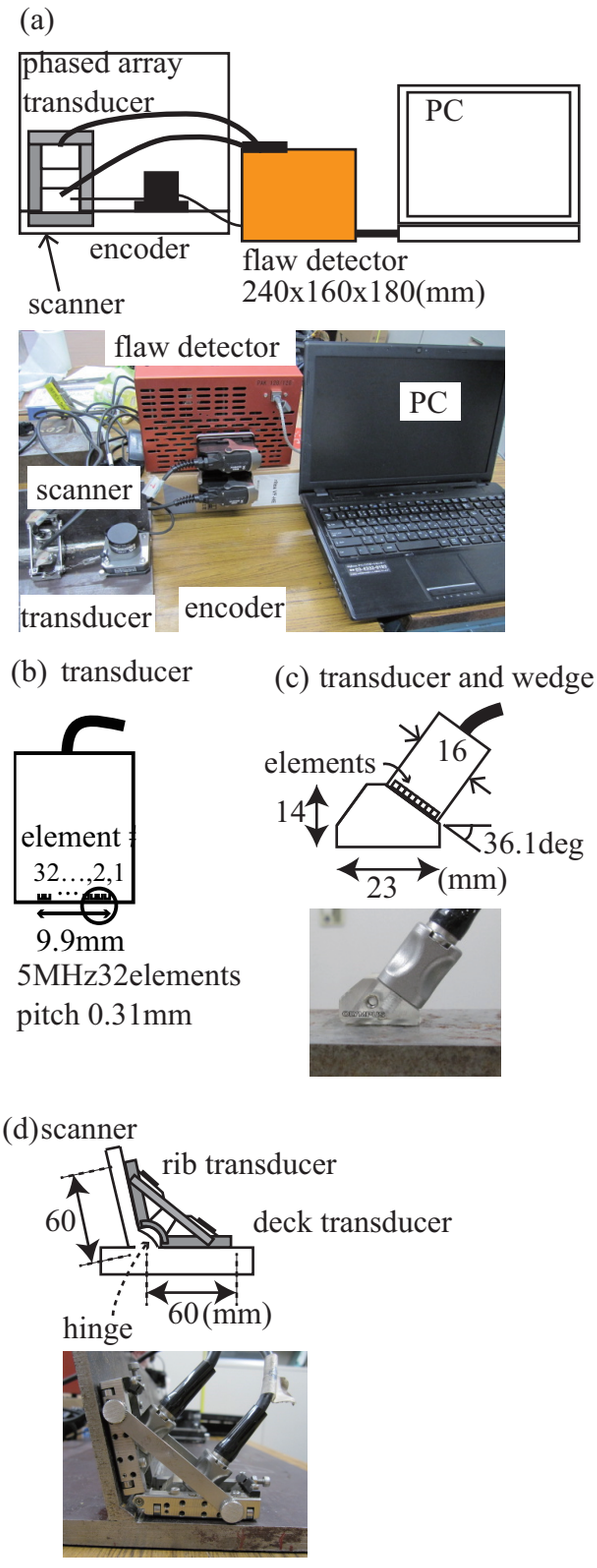


Figure 3: Phased array ultrasonic testing system developed in the study

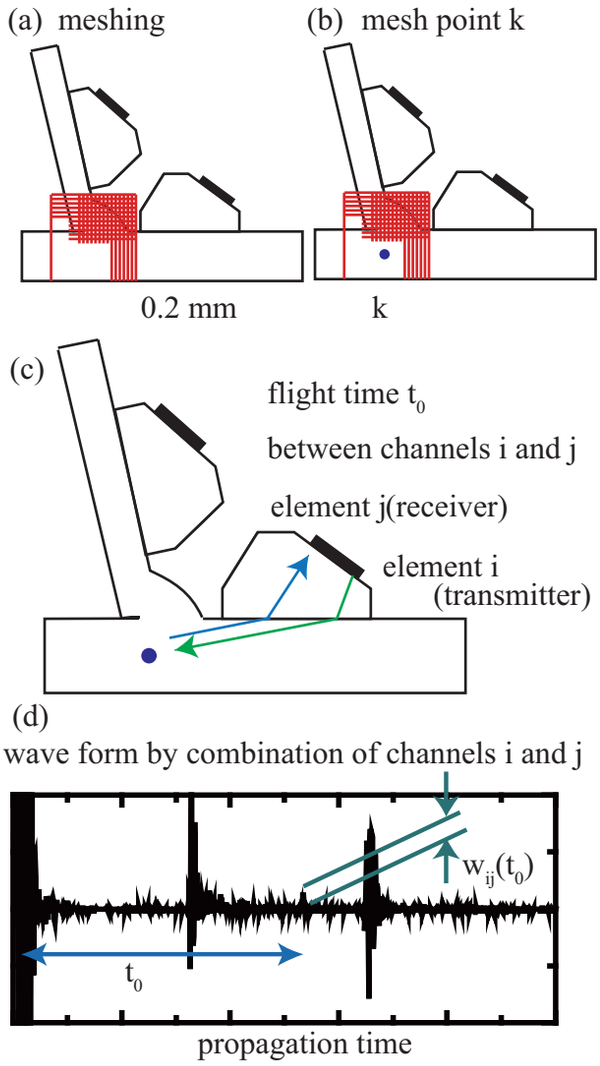


Figure 4: Image reconstruction method by synthetic aperture focusing technique (SAFT)

By taking those summation with respect to grid point k, transmitter channel i, and receiver channel j, image intensity can be obtained.

$$h(k) = \sum_{k} \sum_{i} \sum_{j} w_{ij}(t_k) \tag{2}$$

In case of calculation of wave propagation path, complicated paths such as geometrical reflectio could be considered. This is called multi-SAFT. Since SAFT is superposition of wave forms in the time domain, image of weak reflecto such as point source could be enhanced. Comparing with the conventional B scope display, SAFT has those advantages.

4 FATIGUE AND ULTRASONIC TESTS AND SPECIMENS

4.1 *Deck crack*

Fatigue and ultrasonic tests were carried out. Figure 5 shows the test specimen for deck crack. A T-shaped specimen was prepared. The geometry of the specimen was the same as the rib-to-deck weld; thickness

of deck and rib plate was 12 mm and 6 mm, respectively. The inclination of rib plate to deck plate was about 12 degrees.

As shown in figur 5 (b), 4 point bending was applied, straddling the rib plate in order to simulate the stress condition when a deck crack is propagated.

At every 100 thousand cycles, loading was interrupted, and ultrasonic test was conducted. Those combination of fatigue and ultrasonic tests was repeated until failure. The loading amplitude was 50 kN. Beach mark test was also conducted by changing the loading amplitude of 25 kN. The specimen failed at about 1.1 million cycles. The picture shown in figur 5 (d) shows the failure surface. Figure 5 (c) shows the sketch of beach marks. The numbers are locations of crack edges and depth at 0.8 and 1.0 million cycles.

In ultrasonic tests, two transducers on deck and rib plates were used. Figure 6 explains the focal law settings. Regarding the deck transducer, shown in fig ure 6 (b), the incident angles varied from 35 through 85 degrees. The focal point was determined to be 6 mm below the test surface that is half of the deck plate thickness. In case of deck crack, indication could be obtained by direct and one bounce path in the deck plate. Regarding the rib transducer, as shown in fig ure 6 (c), the incident angles varied from 45 through 85 degrees. The focal point was 12 mm below the test surface that is twice of rib plate thickness. In case of bead crack, direct path could not be expected.

Wave form data were acquired along the weld line with the pitch of 1 mm. After data acquisition, image reconstruction by the SAFT was applied. Figure 7 shows the wave propagation paths in consideration. One was direct propagation path without bounce at the bottom surface of the plate in figur 7 (a). The other was one bounce path at the bottom in figur 7 (b).

4.2 *Bead crack*

Figure 8 shows the test specimen of bead crack. The specimen was a little skewed cruciform welded joint. The angle is 12 degrees that is the same angle as actual details. Tensile force was applied along the rib plate. The amplitude of cyclic load was 50 kN. Same as the deck crack test, beach mark was introduced by changing the loading amplitude.

Figure 9(a) shows the fatigue test site. Cyclic load was applied along the 6 mm plate. This condition was a load carrying cruciform joint and bead crack could be expected (Frank & Fisher 1979). Same as the deck crack specimen, every 100 thousand cycles, ultrasonic test was carried out. The specimen was failed at about 1.4 million cycles. Figure 9(b) shows the failure surface, along the rib plate. The bottom of the picture was weld root. Figure 9(c) is a sketch of beach mark that shows the propagation of fatigue crack.

Figure 10 shows the ultrasonic test for bead crack specimen. Wave form data were acquired along the

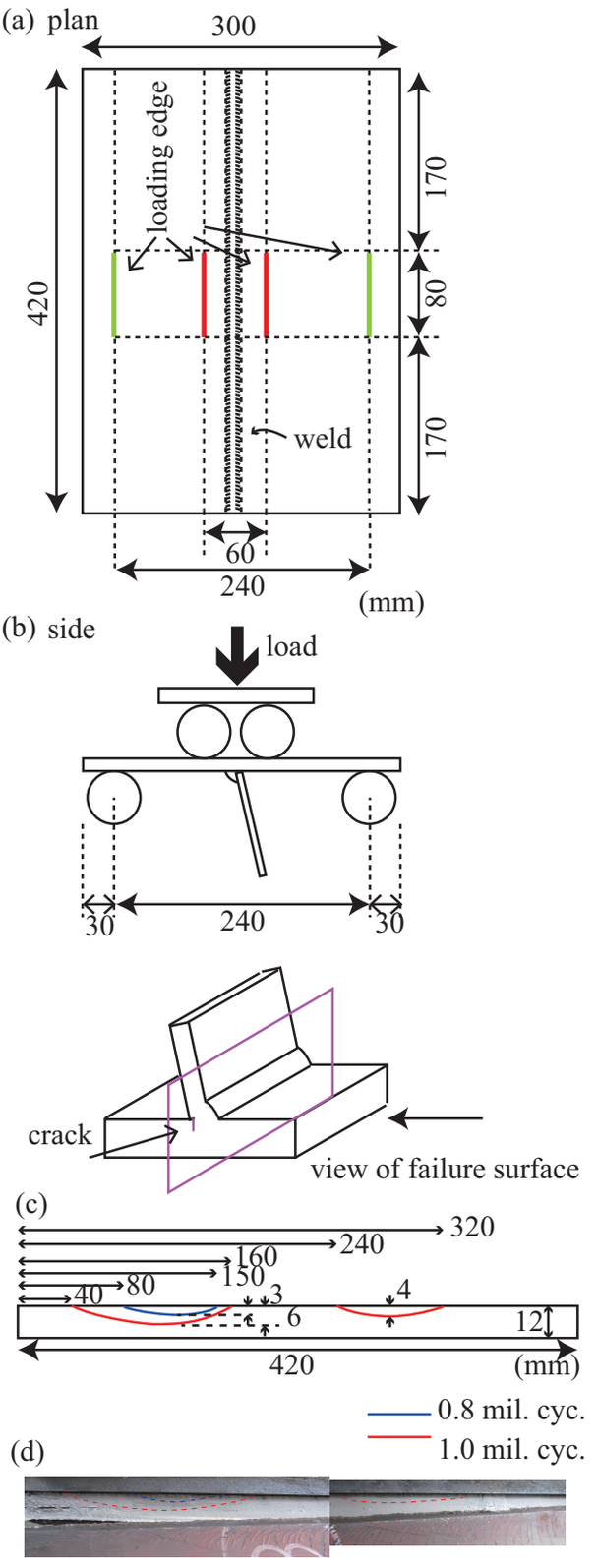


Figure 5: Fatigue and ultrasonic test specimen for deck crack

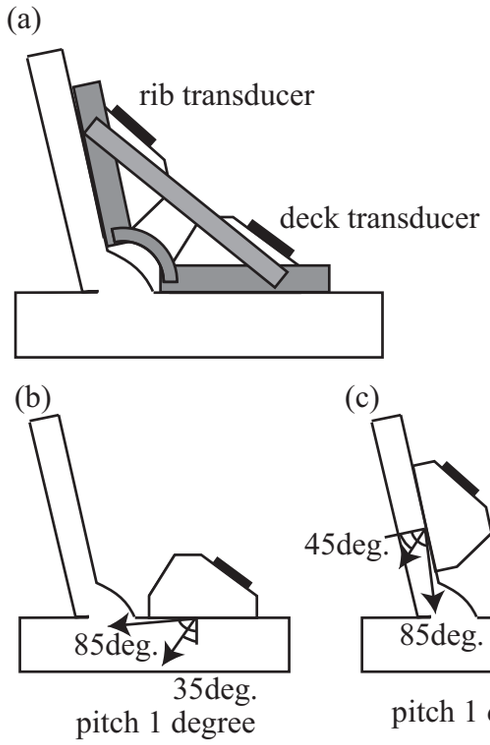


Figure 6: Settings of incident angle of phased array trasnducers

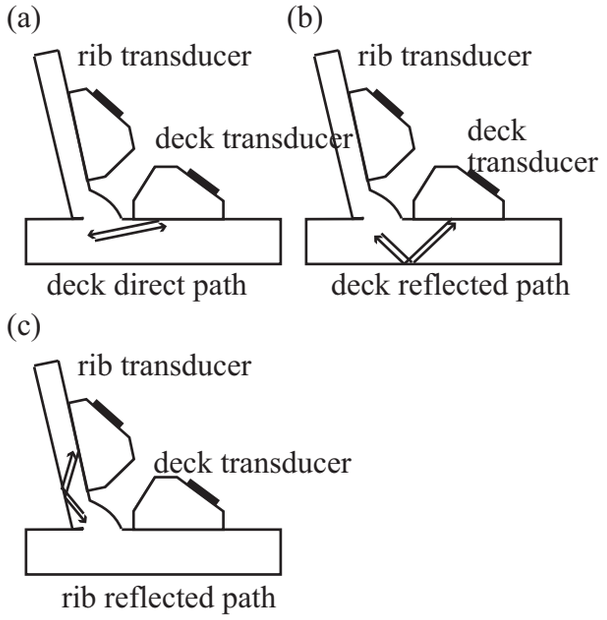


Figure 7: Wave propagation paths considered in SAFT reconstruction for deck crack

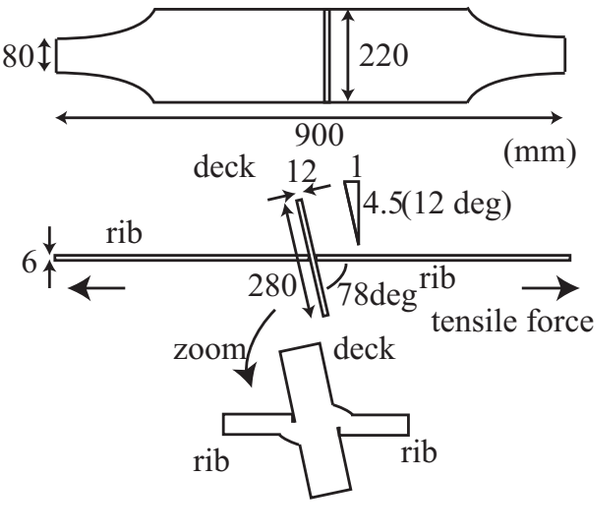


Figure 8: Fatigue and ultrasonic test specimen of bead crack

Figure 9: Fatigue test of bead specimen and failure surface

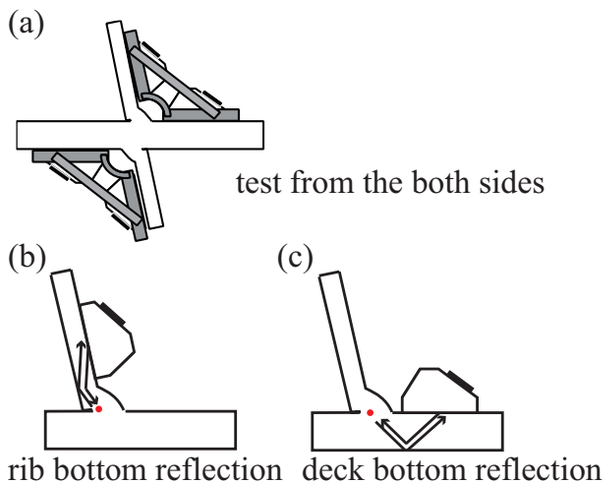


Figure 10: Ultrasonic test of bead crack specimen and paths considered in SAFT

200 mm weld line with the pitch of 1 mm. As shown in figur 10(a), the test was conducted from both sides. When applying SAFT, after data acquisition, two paths were considered. One was reflecte path of the rib transducer shown in figur 10 (b). The second was reflecte path of the deck transducer.

5 TEST RESULTS AND IMAGE RECONSTRUCTION

5.1 *Deck crack*

Figures 11 shows wave forms. As shown in fig ure 11(b), an echo could be observed at a distance of around 34 mm, while no echo could be seen in fig ure 11 (a). The incident angle of the transmitted wave was 50 degrees. Considering the geometry, the location of the reflecto should be about 3.0 mm below the test surface. Such indication was obtained after 800 or 900 thousand cycles. From the beach mark shown in figure 5 (c) and (d), around 3 mm could be the critical size to detect by the system.

Figure 12 (a) shows the three dimensional reconstructed SAFT image before loading. The image was reconstructed by deck relfected path. Images could be seen around the weld root. In contrast, no echo could be found by direct path. Figure 12 (b) shows images at 1.0 million cycles by considering direct path. From the side view, the maximum crack depth was estimated 6.7 mm and actual crack was about 6 mm deep. The front view of figur 12 (b) also shows relatively good agreement with the sketch of beach mark shown below. Figure 12 (c) shows images at 1.0 million cycles by reflecte path. The locations of indication and the actual crack showed agreement, however, the crack depth could not be estimated correctly.

Ultrasonic test estimated the crack length shorter than actual. The minimum size of detection was investigated by checking cross sections one by one. Around 3 mm was the critical size for detection by the phased array ultrasonic system.

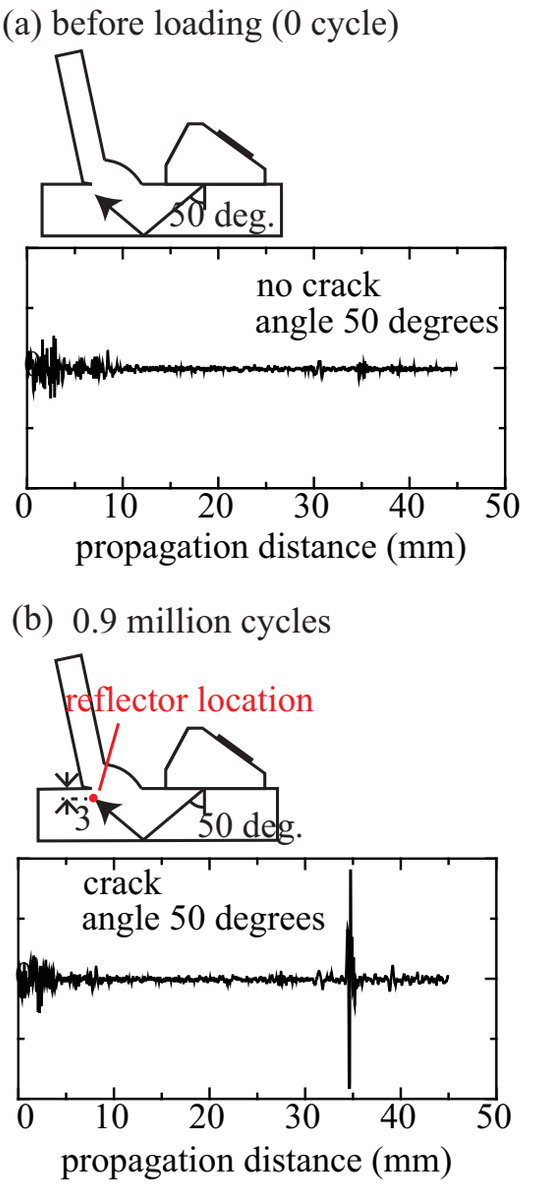


Figure 11: Wave forms of ultrasonic test of deck crack

5.2 *Bead crack*

Some examples of wave forms are shown in figur 13. Figure 13 (a) was acquired before loading. In this case, indication could be obtained at 21 mm with the incident angle of 67 degrees. Figure also contains the geometrical consideration. The location of the reflec tor and the corner of the weld root agreed. In fig ure 13 (b) at 0.9 million cycles, another echo could be found at 25 mm with the incident angle of 55 degrees. Considering the geometry, the location of the reflecto should be inside of the weld deposit. That suggests propagation of fatigue crack.

Figure 14 (a) shows images before loading. Two images can be found. Main reflector in the geometry were weld root corner and tip of the root.

Images at 1.3 million cycles are shown in figur 14 (b). The image was reconstructed by reflecte path of rib transducer. Comparing with figur 14 (a), images around root tip became longer. However, it is difficul

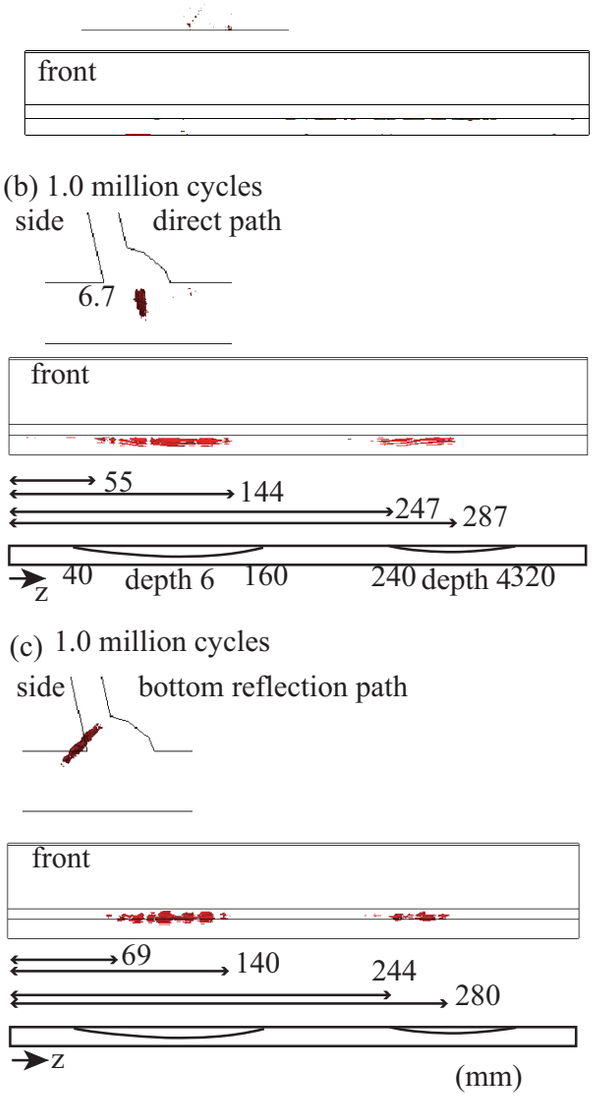


Figure 12: Three dimensional images by SAFT of deck cracks

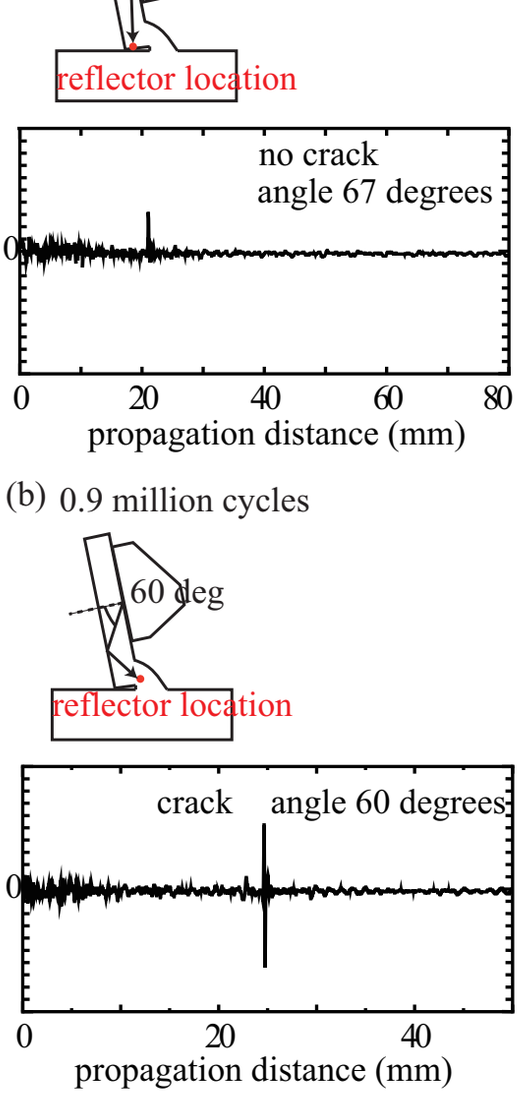


Figure 13: Wave forms of ultrasonic test of bead crack

to estimate the crack length in the weld line direction by front view, because images by weld root could be seen, too.

In order to pick up only the crack echo, temptation to reconstruct images by the deck transducer was made. The crack echoes obviously could be received by the reflecte path at the deck bottom by the deck transducer. The result is shown in figur 14 (c). Inside of the weld metal, an image could be seen. Figure 14 (c) also contains the sketch of beach mark below. The length of crack by the image reconstruction was 100 mm, while the actual crack length by beach mark was 151 mm. The length of indication was shorter than the actual crack length. The minimum size of crack of detection was also 2 or 3 mm, in case of bead crack.

6 CONCLUSIONS

Conclusions obtained in this study are as follows:

(1) Phased array ultrasonic test system for orthotropic steel deck was developed. The system employs two transducers in order to detect both deck crack and bead crack.

(2) Image reconstruction system by the use of synthetic aperture focusing technique was developed. The system takes account of multiple reflectio paths in the plate.

(3) Deck crack could be detected by bottom reflec tion path and direct path. At first crack echo could be obtained by the incident angle of 50 degrees. As the crack propagated, echo could be obtained by larger incident angle of 80 degrees.

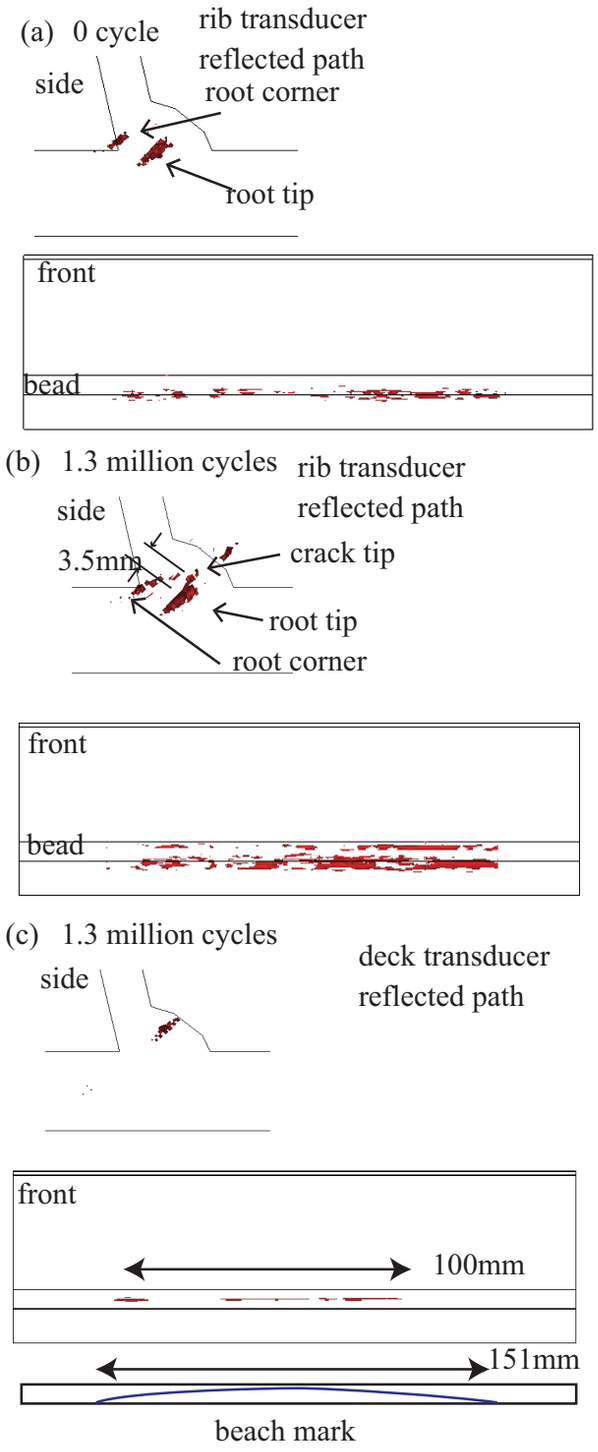


Figure 14: Three dimensional images by SAFT for bead cracks

(4) Crack indication could be obtained by the rib bottom reflectio path. Image of root tip propagated according as the crack propagation. Bead crack could be detected by the combination of the rib and deck transducers.

(5) The crack images were shorter than actual crack length in the weld line direction. That was due to the lack of resolution. The minimum size of crack of detection was about 3 mm for both deck and bead cracks.

Improvement of crack length estimation in the weld line is the next step.

REFERENCES

Azar, L., S. Y. & S.-C. Wooh. Beam focusing behavior of linear phased arrays.

Connor, J. R. & J. W. Fisher (2006). Consistent approach to calculating stresses for fatigue design of welded rib-to-deck connections in steel orthotropic bridge decks. *Journal of Bridge Engineering 11*(5), 517–525.

Drinkwater, B. & P. Wilcox (2006). Ultrasonic arrays for nondestructive evaluation: A review. *NDT& E International 39*.

Federal Highway Administration (FHWA) (2012). *Manual for Design, Construction, and Maintenance of Orthotropic Steel Deck Bridges*. Washington, D.C.: Federal Highway Administration (FHWA).

Frank, H. K. & J. W. Fisher (1979). Fatigue strength of fille welded cruciform joints. *Proc. of ASCE, Journal of Structural Division 105*(ST9), 1727–1740.

Holmes, H., D. B. & P. Wilcox (2005). Post-processing of the full matrix of ultrasonic transmit-receive array data for nondestructive evaluation. *NDT & E International 38*, 701–711.

Hunter, A., D. B. & P. Wilcox (2008). The wavenumber algorithm for full-matrix imaging using an ultrasonic array. *IEEE Transactions on Ultrasonics, Ferroelectrics, and Frequency Control 55*(11), 2450–2463.

Miki, C. (2006). Fatigue damage in orthotropic steel bridge decks and retrofi works. *Int. Journal of Seel Structures 6*(4), 255–267.

Schmerr, L. (2015). *Fundamentals of Ultrasonic Phased Arrays*. New York: Springer Verlag.

Weston M., Mudge P., D. C. P. A. (2012). Time efficien auto-focussing algorithms for ultrasonic inspection of dual-layered media using full matrix capture. *NDT & E International 47*, 43–50.

Wolchuk, R. (1990). Lessons from weld cracks in orthotropic decks on three european bridges. *Journal of Structural Engineering 116*(1), 75–84.

Wolchuk, R. (1999). Steel orthotropic decks – developments in the 1990s –. *Transportation Research Report 1699*(990430), 30–37.

Ya, S., K. Yamada, & T. Ishikawa (2011). Fatigue evaluation of rib-to-deck welded joints of orthotropic steel bridge deck. *Journal of Bridge Engineering 16*(4), 492–499.

Maintenance, Safety, Risk, Management and Life-Cycle Performance of Bridges – Powers, Frangopol, Al-Mahaidi & Caprani (Eds)
© 2018 Taylor & Francis Group, London, ISBN 978-1-138-73045-8

Inspection of steel bridges by modal hammer from bridge deck only

B.T. Svendsen, G.T. Frøseth & A. Rønnquist
The Norwegian University of Science and Technology, Trondheim, Norway

ABSTRACT: Many steel railway bridges have an open deck construction where the secondary load carrying system of the bridge consist of stringers and cross girders including the connections between these. The relevant structural components are located below the bridge deck, making this system difficult to access. Hence, inspecting such bridges in the field requires extensive equipment such as scaffolding, resulting in major costs and traffic downtime to cover all inspections due to the number of bridges in the infrastructure. This paper investigates the use of modal characteristics as a method of bridge inspection. The objective is to establish an efficient approach to identify severe structural faults. In this study, the riveted steel bridge at Hell Bridge Test Arena is used. Based on the results obtained from using accelerometers and a modal hammer, the modal characteristics of key components in the load carrying system is determined and compared to each other.

1 INTRODUCTION

The Norwegian railway network was mainly constructed in the period between 1854 and 1962. Riveted steel bridges was the preferred construction and material type until the first reinforced concrete bridges used for shorter spans were introduced around 1941. Most of the original infrastructure have been replaced except for many bridges that are still in service today. These bridges are still used despite aging and the associated damage accumulation. Being able to detect damage early is important to prevent further damage and ensure safe and reliable use.

The Hell Bridge Test Arena is a full-scale laboratory where an old railway bridge is moved to new foundations on land. The bridge is an open deck steel riveted truss bridge with a span of 35 m. The bridge serves as a test arena for research and development including structural health monitoring (SHM), damage detection, inspection and service life estimation. The purpose of the test arena is to assess new sensor technology, monitoring algorithms and SHM techniques on a real structure in a controlled environment to establish reliable, cost effective and time efficient inspection methodologies.

SHM refers to the process of implementing a strategy for damage detection of structures. The SHM process involves the observation of a system, i.e. the structure, over time to determine the current state of the health of the structure. This is obtained by using periodically sampled dynamic response measurements, extract features sensitive to damage from these measurements and perform statistical analysis of these features (Farrar & Worden, 2007).

Depending on the application, SHM is performed in a short-term or long-term perspective. Short-term SHM is damage detection based on information obtained from the structure through a defined and short period of time, e.g. through inspection. Long-term SHM obtains information from the structure over a long period of time, typically months or years.

SHM is a research topic that has received a lot of attention the past 30 years and focuses on solving the many challenges with the aging infrastructure of the world. Bridge monitoring programmes, which in the last decade have evolved into SHM systems, have historically been implemented for the purpose of understanding and calibrating models with respect to structural load and response (Brownjohn, 2007). Reducing maintenance and inspection costs is considered one of the main motivations for performing SHM today.

Due to low accessibility, inspection of structural components in the secondary load carrying system of old steel railway bridges is difficult to perform from the bridge deck. That is, inspecting bridges in the field requires major resources. This is due to the need for extensive equipment to access critical components and due to the number of bridges in the infrastructure. This has led to the motivation of investigating alternative inspection methods for damage indication and ultimately detection. The first step in a general approach is to find indication of damage as

a basis for determining further inspection. The Hell Bridge Test Arena has a known fault in its secondary load carrying system, i.e. in a longitudinal stringer which is currently subject to investigation.

This paper investigates the use of variation in estimated modal characteristics as a method for bridge inspection. Analysis techniques in both time and frequency domain are explored. Modal data is extracted based on imposed vibration obtained from a modal hammer and a set of accelerometers. By establishing modal characteristics of beam elements connected to damaged and undamaged joints, results are compared and differences are established in order to detect damage. The overall objective is to establish if the method considered is feasible to identify severe structural faults in the connections between stringers and cross girders.

2 DAMAGE DETECTION

2.1 *Background*

The basic principle of damage detection algorithms is that the structural characteristics parameters are functions of the physical properties of a structural system, consisting of mass, damping and stiffness. Hence, damage in those physical properties will cause changes in the structural characteristics parameters (Seo, Hu & Lee, 2015). In other words, damage will somehow change the stiffness, mass and energy dissipation of the structure, which in turn will change the global dynamic properties. Damage detection algorithms applied to bridge structures are mainly vibration-based and strain-based.

In the secondary load carrying system, the connections between the longitudinal stringers and cross girders consists of angle bars. For the stringers subject to investigation, one of the joint connections is severely damaged and significant vertical movement is experienced when the stringer is subjected to load. The stringer including its joint connection is referred to as the damaged structural component, whereas the other stringers including their joint connections are referred to as undamaged structural components.

The damage results in a change of structural stiffness in the local structural system considered. For this study, it is believed that this change of stiffness can be reflected by analysing time series obtained from imposed vibrations. Response is measured from accelerometers located on the damaged and undamaged structural components. By performing analysis in both time and frequency domain, results are compared and it is established if 1) it is possible to find indication of the damage and 2) which of the analysis methods used will best render results for indication of the damage investigated. Several analysis techniques are considered; moving standard deviation and cross correlation are analysed in time domain, whereas coherence and frequency response functions (FRF) are analysed in the frequency domain using MATLAB (The MathWorks Inc, 2017).

A brief theoretical overview of the different techniques are presented in the following section. A general reference for the theory presented is made to (Wirsching, Paez & Ortiz, 2006).

2.2 *Time domain*

2.2.1 *Moving standard deviation*

Moving standard deviation provides a measure of dispersion, i.e. a quantification of the variation in the data points along a predefined window length in the time series. For the time series of acceleration response considered, a, made up of N scalar observations, the standard deviation is defined as

$$\sigma = \sqrt{\frac{1}{N-1}\sum_{i=1}^{N}\left|a_i - \mu\right|^2} \tag{1}$$

where μ is defined as the mean of a:

$$\mu = \frac{1}{N}\sum_{i=1}^{N} a_i \tag{2}$$

In the analysis performed, the unbiased normalization factor $N-1$ is used instead of N for the sample standard deviation. Furthermore, the window length is set to 9 data points, i.e. the standard deviation value for each point calculated includes 9 elements.

2.2.2 *Cross correlation*

The cross correlation is a function that measures the correlation between two different random processes. The cross correlation function is defined as

$$R_{A1A2}(t_1, t_2) = E[A_1(t_1)A_2(t_2)] \tag{3}$$

where $E[A_1(t)A_2(t)]$ is the expected value of the function defined by the random processes $A_1(t)$ and $A_2(t)$. If both random processes are stationary, the cross correlation function depends only on the time lag $\tau = t_2 - t_1$:

$$R_{A1A2}(\tau) = E[A_1(t)A_2(t+\tau)] \tag{4}$$

Equation 3 and 4 provides the basic definition of the cross correlation without further derivations. In this study, the cross correlation is used to measure the similarity of two acceleration response time series, $A_1(t)$ and $A_2(t)$, i.e. the similarity between $A_1(t)$ and shifted copies of $A_2(t)$ as a function of the lag (The MathWorks Inc, 2017).

2.3 *Frequency domain*

2.3.1 *Coherence*

The coherence provides a measure of the linear dependence between two signals for a specified range of frequencies.

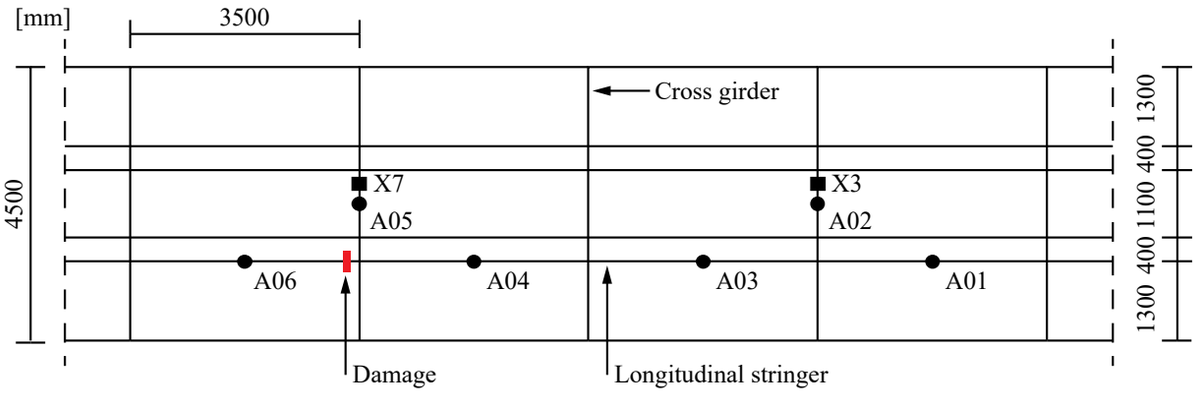


Figure 1. Illustration of the instrumentation setup. Plan view of part of the Hell bridge test arena.

The coherence is a non-dimensional measure and has values between 0 and 1. Values near 1 imply a linear relationship between the signals at a certain frequency. The coherence is defined as:

$$\gamma^2_{A1A2}(\omega) = \frac{|S_{A1A2}(\omega)|^2}{S_{A1}(\omega)S_{A2}(\omega)} \quad (5)$$

Here, $S_{A1A2}(\omega)$ denotes the cross spectral density of $A_1(t)$ and $A_2(t)$, and $S_{A1}(\omega)$ and $S_{A2}(\omega)$ denotes the auto spectral density function of $A_1(t)$ and $A_2(t)$ respectively.

2.3.2 *Frequency response function*

The frequency response functions (FRF) are established as the fundamental measure of the dynamic behaviour of the linear system considered. Equation 6 defines the FRF for a single-input, single-output (SISO) case where X, or $X(\omega)$, represents the response of the system and F, or $F(\omega)$, represents the external load:

$$H_{XF} = \frac{G_{XF}(\omega)}{G_F(\omega)} \quad (6)$$

Here, $G_{XF}(\omega)$ is the cross spectral density of the response and the force, $G_F(\omega)$ is the auto spectral density of the force and H_{XF} is the FRF of the response caused by the force.

It should be noted that the theory as presented here is given in terms of angular frequency ω (rad/sec), whereas the results presented in Section 4 is given in terms of frequency f (Hz).

3 INSTRUMENTATION

The instrumentation consisted of six tri-axial accelerometers mounted on four longitudinal stringers and two cross girders. All beam members were accessible from the bridge deck. Figure 1 shows the instrumentation setup. The accelerometers were positioned at the mid span of the structural elements.

The testing was performed by using a modal hammer in a roving configuration. The accelerometers were placed at fixed locations and impacts were induced at predetermined locations. Several impacts were induced, however only one impact per location was selected for analysis purposes. This was done due to the desired quality and similarity between the time series obtained.

For many bridges, the deck is the most easily accessible area for general inspection. The aim of the presented research is to establish an inspection methodology to be applied from the bridge deck. Therefore, impacts at location X3 and X7 on the cross girders, from the bridge deck, were performed. Each recording resulted in a time series of 30 sec, where 5 sec was recorded prior to the impact and 25 sec was recorded after the impact. The sampling rate was set to 2048 Hz.

As seen in Figure 1, accelerometer A06 is located on the damaged longitudinal stringer while accelerometers A01, A03 and A04 are located on undamaged stringers. Accelerometer A02 and A05 are located on the cross girders. The instrumentation setup is symmetrical about the cross girder depicted in the middle of Figure 1, and is chosen for the purpose of comparing results from a damaged and undamaged structural area. In the following, results obtained from the accelerometers are compared in both time and frequency domain. Indication of damage is established based on any differences in the results obtained from analysis. Based on the instrumentation setup, differences in the results analysed from accelerometer A06 is in particular expected.

4 RESULTS

4.1 *Time domain*

4.1.1 *Moving standard deviation*

Figure 2 shows the moving standard deviation of the acceleration response of sensors A01, A03, A04 and A06 for impact location X3 and X7. As stated in Section 2.2.1, the window length is set to 9 data points.

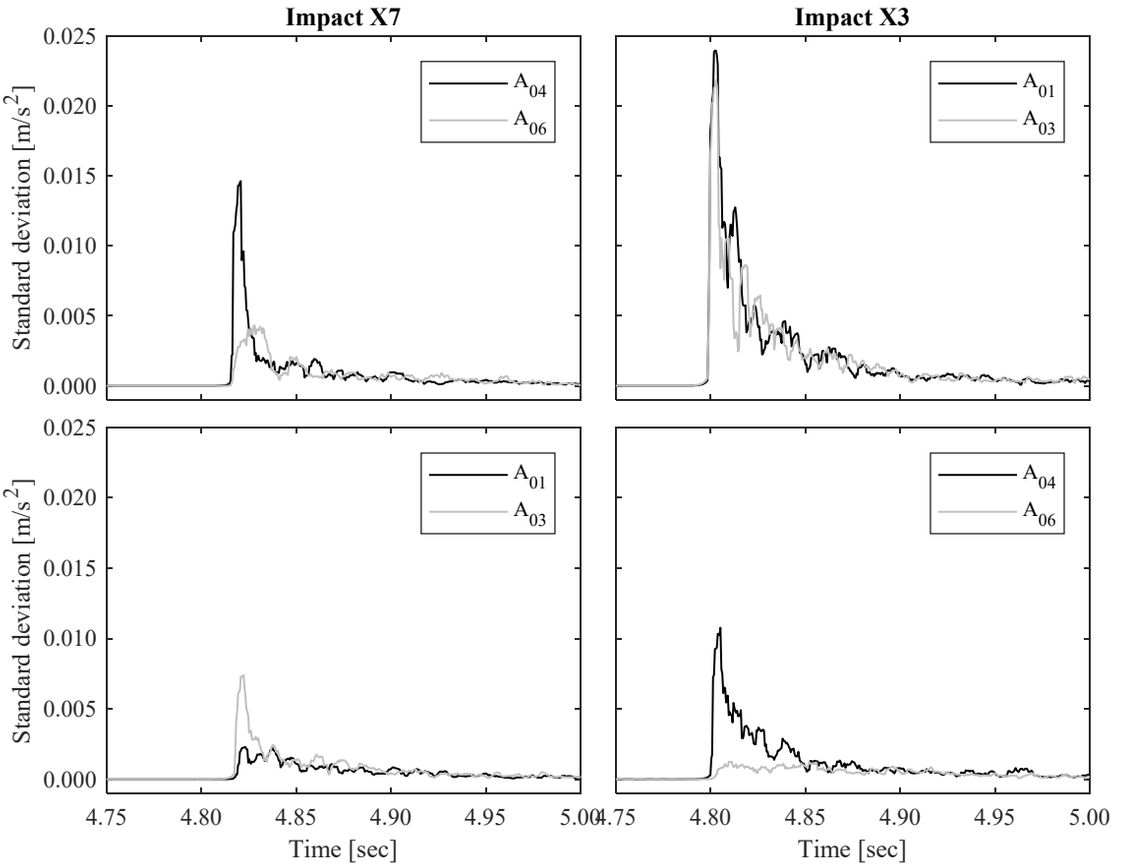


Figure 2. Moving standard deviation of sensors A01, A03, A04 and A06 for impact location X7 and X3.

This provides plots of the acceleration response where the highest peaks in the signal are smoothed leaving a more clear representation of the time series.

If no damage is present in the structural system, it is expected that the results for sensors A01 and A03 for impact location X3 is similar to the results for sensors A04 and A06 for impact location X7. This means that the response curves should follow each other closely for sensor pair A01 and A03 at X3 and pair A04 and A06 at X7. The top left plot in Figure 2 shows a clear difference in the response of sensor A06, located on the damaged structural component, compared to A04, located on the undamaged structural component. It should be noted that the top plots shows results for impacts induced close to the sensor pairs. Considering the top right plot of Figure 2, it is seen that the response from sensors A01 and A03 on undamaged structural components are similar to each other. The top half of the figure therefore indicates that the moving standard deviation can be used to detect damage in the joints between stringers and cross girders.

The bottom plots in the figure shows results from the sensors located further away from their respective impact locations. Here it is seen that the magnitude and energy of the signal decays with distance from the impact location. The peak value obtained from these sensors are lower than from the sensors closer to the impact locations shown in the top plots of the figure. This partly explains the difference in the results for sensor A06 at impact location X7; the vibration is not transmitted through the damage location and the signal has to travel a longer distance. This is then reflected in the acceleration response.

When comparing sensor A06 for impact location X3 with A01 for impact location X7, both acceleration response curves have a similar trend. This means that the response of an undamaged structural component is similar to that of the damaged component when the impact location is further away from the studied components. This implies that the impact location needs to be in the vicinity of the damaged structural components to reliably detect indication of damage. In conclusion, multiple impact locations must be evaluated to fully determine indications of damage in the structural system using moving standard deviation. Furthermore, one of the impact locations must be in the vicinity of the damaged structural components to detect damage.

4.1.2 *Cross correlation*

Observations made from evaluating the moving standard deviation of the acceleration response are also made by analysing the cross correlation. Figure 3 shows the normalized cross correlation of sensors A03, A04 and A06 to sensor A02 for impact location X3, and the cross correlation of sensor A04, A03 and A01 to sensor A05 for impact location X7.

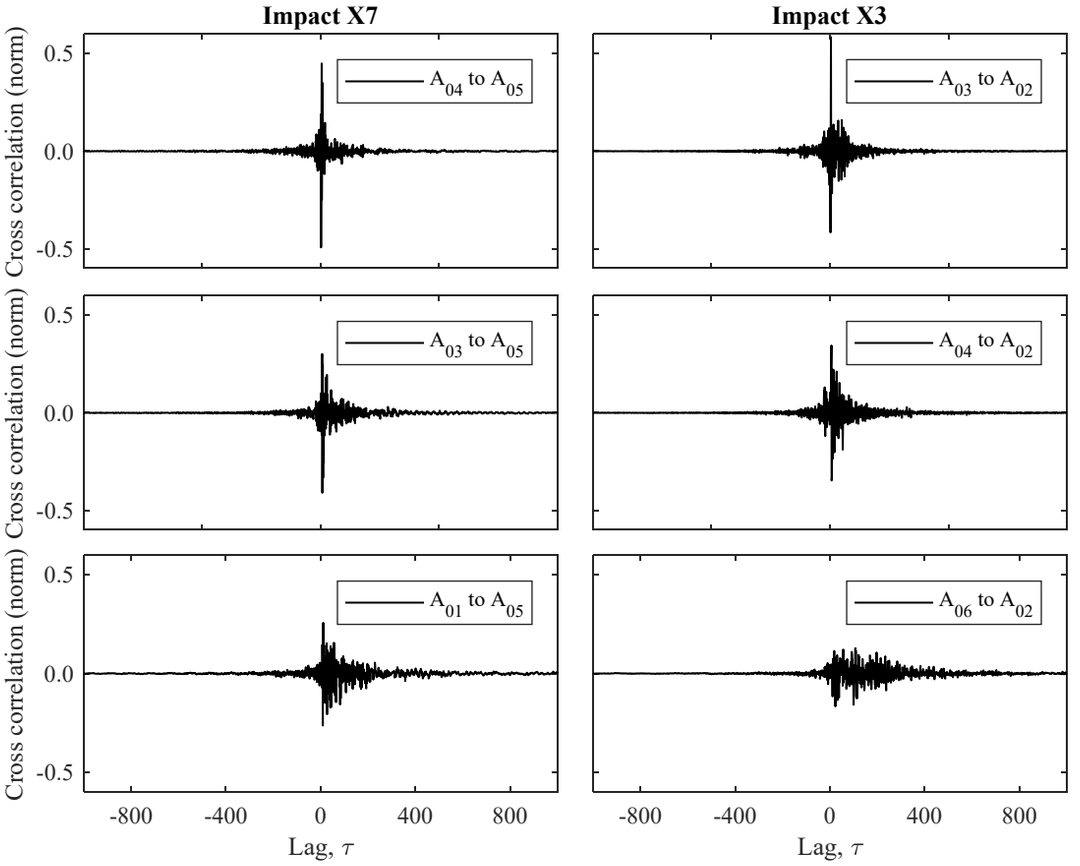


Figure 3. Normalized cross correlation for relevant sensors, impact location X7 and X3.

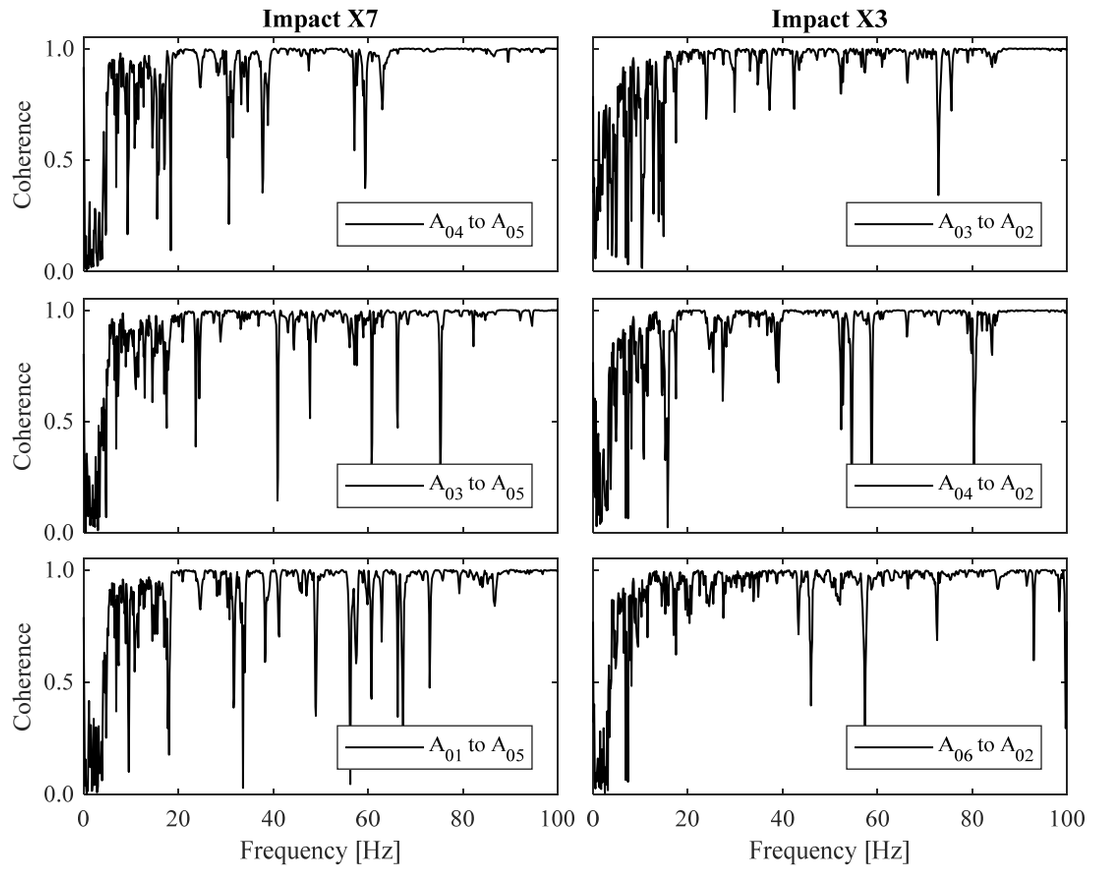


Figure 4. Coherence for relevant sensors, impact location X7 and X3.

Sensor A02 and A05 are given as reference accelerometers to impact locations X3 and X7, respectively. It is noted that the cross correlation is established for the specific sensors with a symmetry in the instrumentation setup in mind. Hence, similar trends in the plots for impact location X7 is also expected for X3 if no damage is present in the system.

For impact location X7, stronger cross correlation is observed closer to the reference accelerometer A05. Generally, this is as expected when considering the location of the sensors with respect to their reference accelerometers; a shorter distance for the signal to travel results in a stronger correlation assuming no damage is present in the structure to cause differences in the results. A similar trend is seen for impact location X3, except for sensor A06 to its reference accelerometer. It is clearly seen that the cross correlation of sensor A06 to A02 is weaker and has a different shape compared to sensor A01 to A05. The time difference between maximum correlation for sensor A06 to A02 was found to be 0.0122 sec compared to 0.0044 sec for sensor A01 to A05. In comparison; the same time difference observed for sensor A04 to A02 and sensor A03 to A05 was both 0.0034 sec, and the time difference for sensor A03 to A02 and sensor A04 to A05 was 0.0020 sec and 0.0010 sec respectively. There are uncertainties related to these results due to only one induced impact is analysed per impact location. Nevertheless, these results shows a trend indicating a significant difference in the cross correlation of the acceleration response for sensor A06.

Based on the results shown in Figure 3, differences in the results indicating damage is observed despite the impact location being further away from the damaged structural component. Hence, the results obtained for sensor A06 to A02 for impact location X3 may in this case indicate that the impact location not necessarily must be in the vicinity of the damaged structural component. However, further work are needed before a reliable conclusion of this can be made.

Similarly as with the moving standard deviation, it is concluded that the cross correlation plots indicates a difference for the damaged structural component compared to the undamaged structural components.

4.2 *Frequency domain*

Based on the sampling frequency used in the measurements, a high range of frequencies are available for analysis. Screening analysis has been performed and the results obtained from these analyses did not render additional information than found in the frequency range of 0 to 100 Hz. Hence, this range of frequency is used in the analysis presented in the following.

4.2.1 *Coherence*

The coherence in frequency domain provides similar information as the correlation in time domain. In Figure 4, the coherence is plotted for the same sensors and impact locations as for the cross correlation. Based on the results obtained for the coherence it is difficult to draw any clear conclusions. For sensors A04 to A05, and A03 to A02 for impact locations X7 and X3 respectively, fewer distinctive peaks are observed compared to the bottom plots. For sensor A06 to A02 at impact location X3, a few peaks are observed in the higher frequency range of 80 to 100 Hz which is not indicated in other plots. However, it is difficult to distinguish differences in these plots indicating any presence of damage. In general, the coherence is strong in similar frequency ranges for the response measured from all sensors subject to investigation.

4.2.2 *Frequency response function*

The FRFs are established for sensors A01, A03, A04 and A06 for impact locations X3 and X7 in Figure 5, with a similar setup as shown in Figure 2.

The low-frequency range representing global dynamic behaviour of the bridge is represented in all measured locations. There is a noticeable difference in the results obtained for sensor A03 seen for impact location X7. Here, the peak obtained approximately at 25 Hz is not indicated contrary to what is seen from the other sensors on both impact locations X3 and X7. Based on the analysis performed, there is no obvious explanation of this. However, this observation is considered of minor relevance for the results investigated.

For the results obtained in the high-frequency range, i.e. from 60 to 100 Hz, no clear trends or behaviour is seen that indicates the presence of damage. The same yields when considering the distance of the sensors with respect to the impact locations; the top plots shows results from the sensors located close to the impact, and the bottom plots further away from the sensors.

For sensor A01 and A03 at impact location X3, it is expected that the response is fairly similar since both sensors were located on an undamaged structural component. Furthermore, similar behaviour in response is not expected for sensor A04 and A06 at impact location X7 since sensor A06 is located on the damaged component. In this case, comparing the top plots in the figure gives no indications of damage present in the structural system, contrary to what is seen for the similar plots of moving standard deviation in time domain as shown in Figure 2.

Similar to the results obtained for the coherence, it is difficult to draw conclusions based on the results obtained from analysing the FRFs.

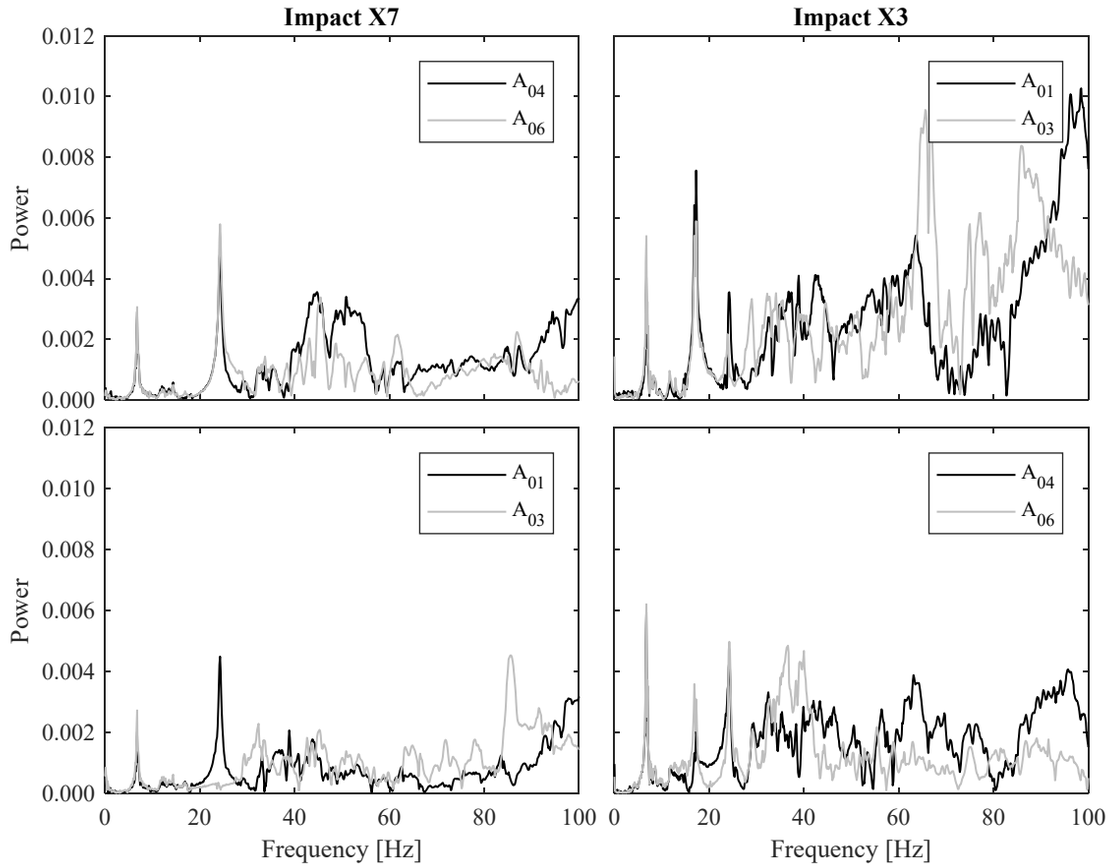


Figure 5. FRF of sensors A01, A03, A04 and A06 for impact locations X7 and X3.

4.3 *Comparison between time and frequency domain*

When comparing the results obtained, the trends established from the results in time domain is not seen in frequency domain. Two conclusions are made based on this. First, the damaged structural component causes a change in the transmission of the signal that is seen primarily in time domain and second, the change in transmission of the signal is most likely represented in a high-frequency range. This range of frequency is not subject to thorough investigation in this study.

Global dynamic structural response of the bridge is established from the FRFs of all measured locations. If the damage is represented at much higher frequencies, it is questionable if 1) it is possible to detect this type of damage and 2) how reliable such results then may be. It may well be that this is highly dependent on the damping in the structure making it difficult to detect this type of damage. Using more advanced analysis methods for indicating this type of damage in frequency domain is subject to further work.

In general, the FRFs describes local and global structural response. The transmission as seen in time domain only describes local phenomena, i.e. local structural response or as in this case, deviations. Changes in the global frequencies and modes could probably be detected if the change in the structural system caused by the damage is large enough. This is because the damage is also a part of the global modal parameters and not only a local deviation.

5 CONCLUSIONS

This paper presented a method for performing bridge inspection from the bridge deck by investigating modal characteristics obtained from imposed vibration. The method utilizes analysis techniques applied both in time and frequency domain. Based on the results obtained, the following conclusions are drawn:

- An indication of structural damage is found when analysed in time domain and not in frequency domain. The indication of damage is seen based on differences in the results obtained from the damaged compared to the undamaged structural components.
- Analysis techniques such as moving standard deviation and cross correlation provides better indication of this type of damage than analysis techniques such as coherence and FRF.
- The type of damage investigated is difficult to observe in frequency domain. This is believed to be due to 1) the many global and local natural frequencies indicated by all sensors which makes distinctions difficult to find and 2) the damage investigated is likely to be represented at higher

frequencies than subject to investigation and included in this study.
- The time domain analysis techniques presented are considered feasible for detecting damaged components from the bridge deck. The method may be used to indicate damage and strengthen the decision criterion for selecting areas in the structure subject to further inspection.

6 ACKNOWLEDGEMENTS

The Hell Bridge Test Arena is funded by Bane Nor and is greatly acknowledged.

7 REFERENCES

Brownjohn, J. M. W. (2007) 'Structural health monitoring of civil infrastructure', *Philosophical Transactions of the Royal Society A: Mathematical, Physical and Engineering Sciences*, 365(1851), pp. 589–622. doi: 10.1098/rsta.2006.1925.

Farrar, C. R. and Worden, K. (2007) 'An introduction to structural health monitoring', *Philosophical Transactions of the Royal Society A: Mathematical, Physical and Engineering Sciences*, 365(1851), pp. 303–315. doi: 10.1098/rsta.2006.1928.

Seo, J., Hu, J. W. and Lee, J. (2015) 'Summary Review of Structural Health Monitoring Applications for Highway Bridges', *Journal of Performance of Constructed Facilities*, 26(4), pp. 371–376. doi: 10.1061/(ASCE)CF.

The MathWorks Inc. (2017) 'MATLAB user's guide (R2017a)'. Natick, Massachussets, United States.

Wirsching, P. H., Paez, T. L. and Ortiz, K. (2006) *Random Vibrations: Theory and Practice*. Dover Publications.

Maintenance, Safety, Risk, Management and Life-Cycle Performance of Bridges – Powers, Frangopol, Al-Mahaidi & Caprani (Eds)
© 2018 Taylor & Francis Group, London, ISBN 978-1-138-73045-8

Assessment of Lateral Thermal Diffusion of Impulse Thermography Method in Measuring Size of Non-Planar Defects

H.Q. Tran, J. Huh* & C. Kang
Chonnam National University, Yeosu-si, Jeollanam-do, Rep. of Korea

K. Kwak
Korea Institute of Civil Engineering and Building Technology, Goyang-si, Gyeonggi-do, Rep. of Korea

J. Ahn
Gyeongnam National University of Science & Technology, Jinju-si, Gyeonsangnam-do, Rep. of Korea

* *Corresponding author email: jwonhuh@jnu.ac.kr*

ABSTRACT: Internal defects are normally developed in concrete bridge structural components during long-term operations under heavy loads of the vehicles. Conventional methods for the structural health monitoring, such as visual inspection, chain dragging, and hammer sounding, provide only surface cracks and partial subsurface defects, hence, it might be less accurate to predict the subsurface delamination. Infrared thermography has proven to be an effective way to detect delamination. However, sizing of the delamination is a difficult task, especially for special shapes. This study aims to investigate the effect of lateral thermal diffusion on predicting delamination size by using Finite Volume Method (FVM), then points out the drawbacks of Full Width at Half Maximum (FWHM) method in measuring non-planar subsurface delaminations. In addition, results of the numerical method and the experimental study of impulse thermography (IT) are compared. It indicates that FVM is a reliable tool for modelling infrared thermography (IRT) technique.

1 INTRODUCTIONS

Internal deteriorations occur in components of a concrete bridge after long time operations, especially for the bridge's deck which directly subjected to heavy loads of the vehicles. In most countries, inspection and maintenance actions include visual inspection in combination with several conventional methods such as hammer sounding and chain dragging. These kinds of methods are mainly used to detect moderate to severe delaminations in concrete structures. However, their major drawbacks are labor-intensive, technician's skills, and traffic control requirements (Transportation Research Board 2013). Many advanced tools for non-destructive testing including Impact Echo, Ultrasonic Pulse Echo, Ultrasonic Surface Waves (IAEA 2002), Ground-Penetrating Radar (Pollock et al. 2008), and active/passive IRT (Transportation Research Board 2013) have been introduced via many research works, guidelines, and national standards that contribute significantly in the maintenance field. Every method has its own advantages and shortcomings that should be applied in a certain circumstance. For example, the active IRT method is proven to be an effective and fast to detect the defects in high-conductivity materials (a few milliseconds) (Maldague 2001), but it takes a long time in detecting for low-conductivity materials such as concrete, plastic, or wood (take several minutes to hour depending mainly on the external heat source energy, distance of heating, and depth of defects) (Maldague 2001, Huh et al. 2016, Vaghefi 2011, Pollock et al. 2008). Therefore, the method is better to use in cooperation with passive IRT and visual inspection. For the upper surface of a bridge deck, passive IRT can be used without any supporting of external heat source. Other parts of a concrete bridge structure, especially where not exposed directly to the sun, a visual inspection should be carried out in advance to locate questionable defective locations. Then, active IRT can be applied to measure the area and depth of the defects in detail.

Delamination is defined as the separating of concrete into layers due mainly to corrosion of embedded reinforcing bars over time (Transportation Research Board 2013), and when the delamination grows gradually; it splits out of the concrete structure. This phenomenon is called "spalling". Delamination normally develops in horizontal layers with planar and non-planar shapes that might depend on external loading (i.e. vehicle's wheels) and non-loading issues (i.e. reinforcing bars, temperature, shrinkage, differential settlement, freeze-thaw cycle) (Portland Cement Association 2002). In fact, however, less or no document mentions about the shape of delamination because it develops inside the concrete that is impossible to observe by human eyes. The detection of location of the delaminated area is not a difficult task when the structure is inspected by IRT technique. However, a quantitative evaluation of the defective area to some extent is hard to be

accurate because of the effect of delamination's shape. In this paper, therefore, the IT method, a kind of active IRT, is used to detect subsurface defects in the concrete structural components which are not exposed directly to the sunlight. A simple three-dimensional FVM model was simulated and its results were verified with those from the experimental study. A more complex FVM model has been built to investigate the effect of lateral thermal diffusion in measuring the size of non-planar detects. Different shapes and depth of defects are investigated including planar, V-shape, and A-shape delaminations.

2 EXPERIMENTAL STUDY

2.1 *Principle of impulse thermography*

The IT technique uses halogen lamps as an external heat source to transfer heat to the concrete in a transient mode. In three mechanisms of heat transfer, i.e. conduction, convection, and radiation, the heat flux is transferred dominantly into the concrete core by conduction mechanism. Mathematically, when the specimen's surface is subjected to a Dirac impulse of magnitude I_0, the impulse heating response of a semi-infinite half-space can be obtained by Equation 1 (Almond & Pickering 2012) whereas the resulting temperature, T_s, changes at a depth z beneath the surface at a time t. Obviously, a real impulse is different from an ideal Dirac pulse because it has finite values of amplitude and duration (Maldague 2001).

$$T_s(z,t) = \frac{I_0}{e_1\sqrt{k \cdot t}} \exp\left(\frac{-z^2}{4 \cdot \alpha \cdot t}\right) \quad (1)$$

where $\alpha = k/(\rho \times C_P)$ is the thermal diffusivity of material, e_1, ρ and C_P are the thermal effusivity, mass density and specific heat capacity of the concrete, respectively. Hence, the response at the surface ($z = 0$) that an IR thermal camera can measure will be

$$T_s(0,t) = \frac{I_0}{e_1\sqrt{k \cdot t}} \quad (2)$$

However, when a planar delamination exists at $z = d$ from the surface, the heating response at the surface above the delaminated zone under a Dirac delta function impulse of magnitude I_0, has a different value that can be expressed by Equation 3.

$$T_d(0,t) = \frac{I_0}{e_1\sqrt{k \cdot t}}\left[1 + 2\sum_{n=1}^{\infty} R^n \cdot \exp\left(-\frac{(n \cdot d)^2}{\alpha \cdot t}\right)\right] \quad (3)$$

In which the $R = (b - 1)/(b + 1)$ is the reflection coefficient of the concrete-air interface, which is close to 1.0; and b is defined as the ratio of thermal effusivities between two media, $b = e_2/e_1$, where the e_1, e_2 are the thermal effusivity of concrete and air (delamination), respectively.

A delamination blocks the conduction of heat from the surface, causing the temperature above the defective area, $T_d(0,t)$ has a slower cooling rate than those at the non-defective area, $T_s(0,t)$ (Almond & Pickering 2012). Therefore, the thermal contrast (or so-called absolute contrast), $\Delta T(0,t)$, can be expressed by Equation 4. The absolute contrast can help to recognize the defect inside the concrete, especially when the absolute contrast reaches its peak value.

$$\Delta T(0,t) = T_d(0,t) - T_s(0,t) \quad (4)$$

Based on the previous research works (Huh et al. 2016, Vaghefi 2013, Maierhofer et al. 2003, Maierhofer et al. 2006, Maierhofer et al. 2007, Tran et al. 2017), with the same delamination size and shape but different depth, the shallow one is expected to show a higher absolute contrast than the deeper one. In addition, the deep delamination will indicate a longer observation time than the shallower delamination. For concrete inspection, it takes a long time to test an object, hence, the heating and cooling curve usually has the shape as described in Figure 1. It is noted that the observation time is the time that the absolute contrast reaches its peak value after turning off the heat source. This is an important parameter to be used throughout this research.

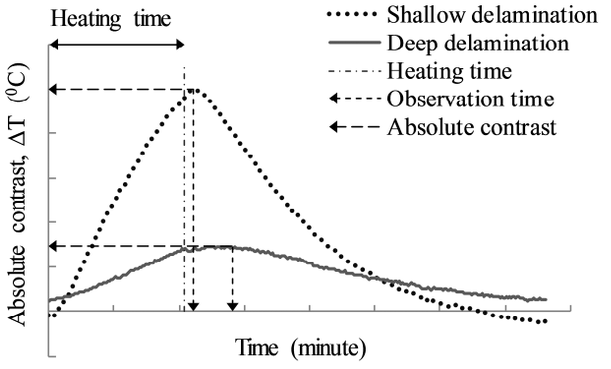


Figure 1. Absolute contrast vs time.

2.2 *Testing preparation*

A concrete specimen was built in the laboratory with embedded two artificial delaminations, which were folded by an angle of 11°, so-called "A-shape" and "V-shape" as shown in Figure 2. The IT technique was conducted with a heat energy of 3000W using six halogen lamps which were placed at 1.2m from the concrete specimen's surface, expecting a good

uniform heating. A high-quality IR thermal camera, FLIR SC660, was used to record the surface temperature in both heating and cooling time of the process, as illustrated in Figure 3. This high-resolution camera can detect infrared emission at a wavelength band from 7.5 μm to 13 μm. Its thermal sensitivity (or NETD) is smaller than 0.003 K and its spatial resolution (IFOV) is 0.65 mrad (FLIR SC660 Catalog, 2014). The average ambient temperature and relative humidity were around 18.6°C and 68%, respectively, measuring by a thermohygrometer in the laboratory where the influence of wind can be minimized.

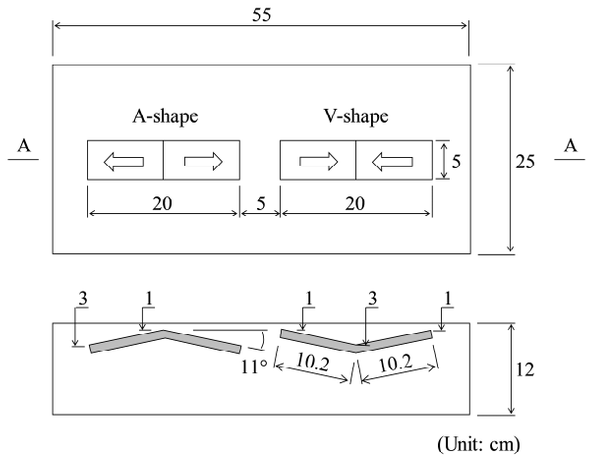


Figure 2. Details of artificial delaminations embedded in the concrete specimen.

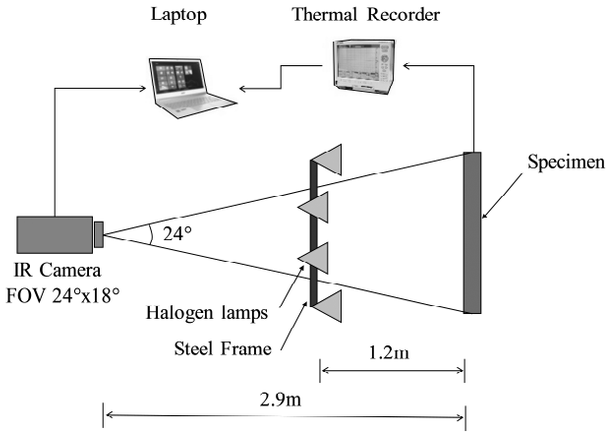


Figure 3. Experimental Set-up.

To estimate the incident heat flux coming to the concrete slab, three thermocouple points were embedded in the concrete slab at 3.3 cm depth to measure the temperature of the inner sound core. Then, the heat flux can be estimated corresponding to the energy stored in the slab volume, using Equation 5 (Holman 2010, Maldague 2001) based on the different temperature between the surface (measured by IR camera) and the inner core (measured by Thermal recorder Yokogawa MV2000).

$$I_0 = \frac{Q}{A \cdot t} = \frac{C_P \cdot m \cdot dT}{A \cdot t} \tag{5}$$

where Q is the heat required for heating an object (J), C_P is the specific heat capacity (J/kg°C), assumed as 800 J/kg°C (Maldague 2001), $m = \rho \times V$ is the mass of the object (kg), dT is the temperature difference (°C), A is the surface area received heat (m^2) and t is the time of heating (second). Thickness of the object used for calculating the mass is 0.033m, which is the distance from specimen's surface to the thermocouples. The estimated heat fluxes per area, I_0 (W/m^2) are calculated and summarized in Table 1.

Table 1. Calculated heat flux after 15-min. heating.

Thermocouple point	Temp. at the surface	Temp. at 3.3 cm	Temp. difference	Heat flux
	°C	°C	°C	W/m^2
1	21.0	19.5	1.5	105.6
2	20.6	19.2	1.4	98.6
3	20.9	18.8	2.1	147.8
Average	**20.8**	**19.2**	**1.7**	**117.3**
Measurement device	IR camera	Thermo-couple		

3 THREE-DIMENSIONAL MODELS

All the numerical simulation analyses in this research were conducted by ANSYS Fluent using Finite Volume Method (ANSYS 2010, ANSYS 2013). To verify the numerical model with the experimental study, all models were stimulated by a receiving heat flux as calculated in Table 1. Then, a more complex model was developed to assess the effect of lateral thermal diffusion in sizing of the delaminations.

3.1 *Simulation of simple model*

A simple numerical model was simulated with two different types of boundary conditions for the side walls. The model is shown in Figure 4. A semi-infinite boundary condition which is infinite in X-Y plane parallel to the concrete front surface, is applied to all side walls of the model, so-called FVM-1, and a limited boundary condition allows the surface of the side walls to exchange heat with surrounding ambient temperature, namely FVM-2. The Tetrahedron type of element was applied with the

maximum and minimum sizes of 8×10^{-3} m and 6.16×10^{-5} m, respectively. A total number of elements is 278,788. The physical properties of the models are listed in Table 2. As mentioned above, two models were applied by a uniform heat flux of 117.3 W/m^2 in 15 minutes as calculated in Table 1.

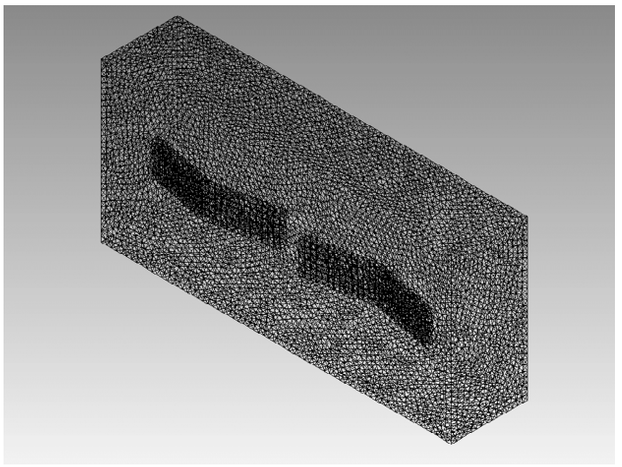


Figure 4. FVM simple model.

Table 2. Physical properties of materials (Maldague 2001).

Thermal characteristics	Concrete	Delamination
Mass density, ρ (Kg/m^3)	2400	20
Specific heat capacity, C_P (J/Kg.°C)	800	1500
Thermal conductivity, k (W/m.°C)	1.0	0.03
Emissivity, ε	0.95	-

3.2 *Comparison between simple FVM model and experimental results*

Results of the surface temperature from both the two FVM models and experimental study are shown in Figure 5, and their temperature profiles A-A are illustrated in Figure 6. It shows that the surface temperature profiles of both methods are relatively similar values, except for an abnormal peak temperature on the left side of V-shape delamination. The reason might come from the quality of the concrete slab which contains several tiny air voids at near surface that raising the temperature. This can be seen more clearly in the thermal image (a lighter color dot inside the darker circular area in Figure 5).

For the boundary conditions of FVM-1 and FVM-2, the results showed different values of temperature nearby the side walls of both models, while values are similar for other parts. Particularly, they were 20.4°C and 19.0°C for FVM-1 and FVM-2, respectively. The reason of sharply collapsing temperature at the side walls of the FVM-2 is because the model accepted the inner heat leaking out at the side walls in order to balance the inner temperature with surrounding ambient temperature around the concrete slab (in this case, it was around 18.6°C as mentioned above). The temperature was slowly falling down in the case of FVM-1 model due to the infinite boundary condition. On the other hand, the side wall of the real concrete slab behaves differently from the finite volume model. Particularly, the heat diffusion of the experimental study is faster than those in the FVM models.

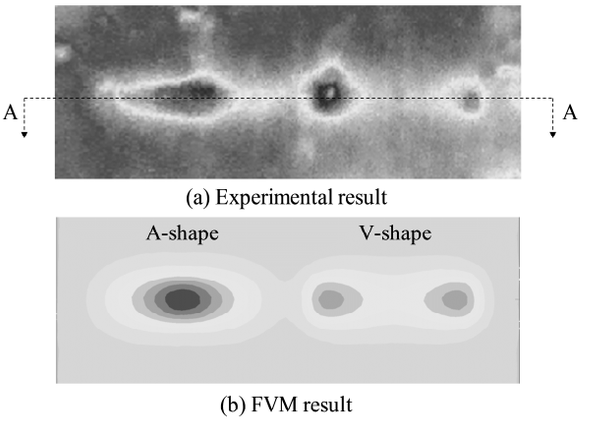


Figure 5. Experimental and FVM-1 surface temperature.

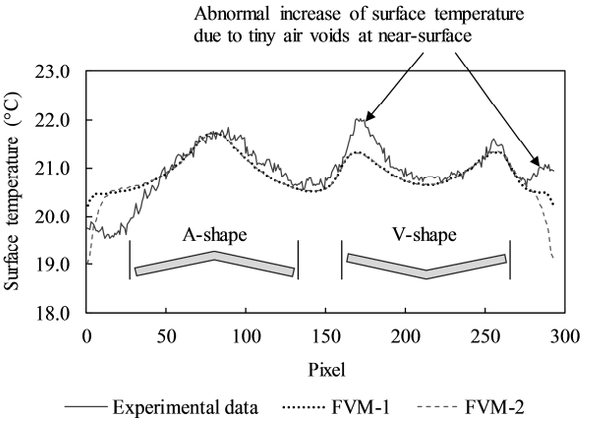


Figure 6. Surface temperature profile A-A above V-shape and A-shape delamination on both experimental study and FVM models.

Discussing on the characteristics of the shape of delamination, here is the capacity of containing heat (or degree of heat loss) in front of delamination. As displayed in Figure 7 about the cooling time of surface temperature in the experimental study, the V-shape delamination reduces its thermal contrast with a slower rate than the A-shape. As a result, we will

have more time to observe delaminations via IR camera screen. In other words, after a certain cooling time, the V-shape delamination might keep better contrast on the thermal image than the A-shape delamination.

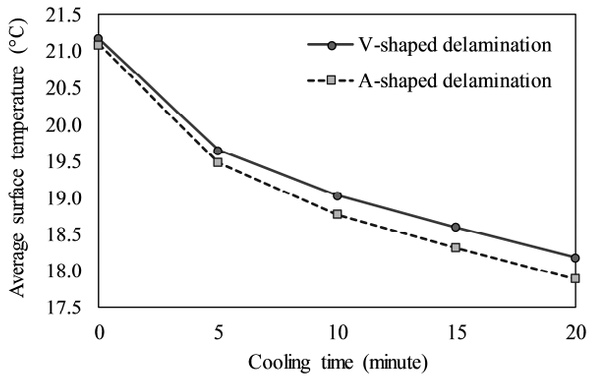


Figure 7. Characteristics of temperature reduction in the cooling period (experimental data), after 3000W heating in 15 minutes.

Figure 8 shows that the relative errors between experimental study and FVM-1 model are smaller than 2%, except for the influence of low-quality and the side wall boundary areas where the errors occur up to 3.5%. It indicates that the FVM results are reliable to be applied for IRT technique. This verification brings us to develop a more complex model to investigate the effect of lateral thermal diffusion on both planar and non-planar delaminations. Then, the conventional method of sizing defects, i.e. FWHM, usually used for sizing planar defects, is then applied to measure non-planar delaminations.

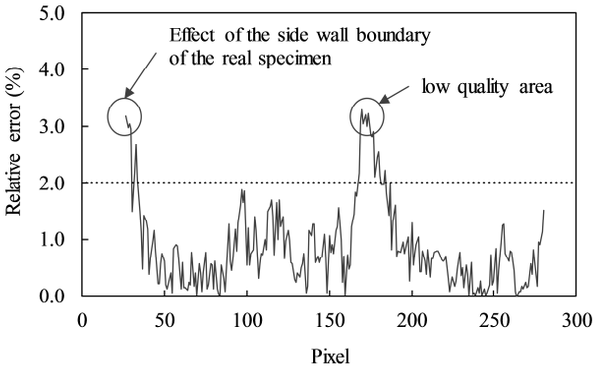


Figure 8. Relative error of experimental and FVM-1 result.

3.3 *Development of a complex model*

A three-dimensional complex numerical model was developed by ANSYS Fluent using FVM, denoted as FVM-3. The mesh was generated to divide the model into small Tetrahedral elements and its geometry is shown in Figure 9. The maximum and minimum size are 8.0×10^{-3} m and 8.16×10^{-4} m, respectively. The objective of this numerical model is to investigate the lateral thermal diffusion of a given heat flux with various depths and shapes of defects. To achieve this goal, the front face of the model was applied by a heat flux as mentioned in Table 1, with an assumption that the heat exchange between the model and the surrounding atmosphere occurs only through the front and back face of the model. The initial inner temperature of the concrete slab was averaged from thermocouple data as 17.6°C and the ambient temperature and the relative humidity were kept same as the previous models. The ambient temperature was applied to the back side of the slab as an initial condition. The physical and thermal properties of materials used in the model are listed in Table 2. In the model, twelve delaminations were simulated. The left column in Figure 9 is the A-shape delaminations with an average depth distributed from 2 cm to 5 cm. Similarly, the middle and right columns are V-shape and planar delamination, respectively.

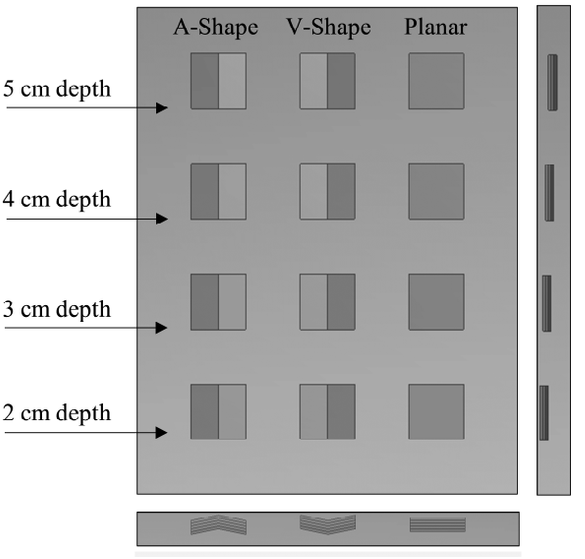


Figure 9. Three-dimensional complex numerical model.

4 ANALYSES AND DISCUSSIONS

4.1 *Effect of lateral thermal diffusion*

As mentioned above, Equations 1 to 3 are analytical expressions with assumptions of uniform heating and one-dimensional. However, the lateral thermal diffusion behaves abnormally when the heat flux incidents a finite delamination. In particular, heat flow spreads laterally over the front face of the delamination. The characteristics of lateral thermal diffusion are controlled by the depth and properties of the defects (i.e. size, thickness, and shape) (Kretzmann

2016a, Almond & Pickering 2012). A shallow and large size of defect contains a small volume of trapped heat above the defect causing a rapid reflection of heat flux toward the surface, which produces a high surface contrast (Kretzmann 2016b), while a larger volume of trapped heat above a deeper defect makes a diffusion developing significantly in all directions.

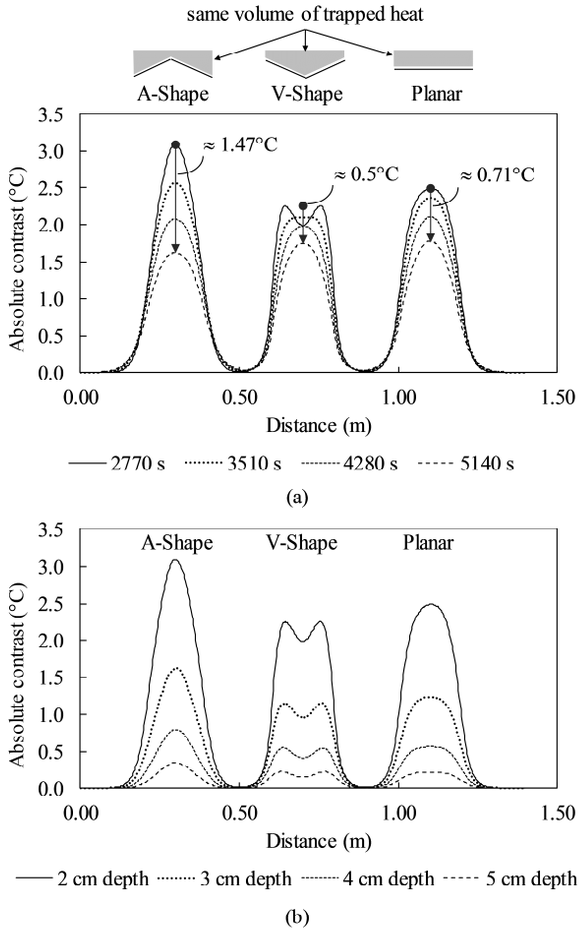


Figure 10. (a) Delaminations at 2 cm depth with different cooling times; (b) Delaminations at different depths with the same cooling time of 2770 s.

For the three special delaminations at 2 cm depth that contain the same volume of trapped heat as shown in Figure 10a, the A-shape delamination shows the fastest degradation of heat, whereas the V-shape delamination indicates the slowest decrease of heat loss. Particularly, the temperature of A-shape, planar, and V-shape decreases approximately 1.47°C, 0.71°C, and 0.5°C, respectively within the time from 2770 s to 5140 s. The slow temperature decrease for the V-shape delamination is same as in the previous discussions on experimental results. In addition, the shape of the surface temperature profile indicates the influence of lateral thermal diffusion. The V-Shape and Planar delamination show a larger width value at half maximum than that of the A-shape, indicating that the lateral diffusion of the A-shape is significant.

On the other hand, the surface temperature profile reflects the shape of the delamination at early time. It clearly shows the delamination's shape at 2770 s (around 16 minutes of cooling), while the temperature responses of the three delaminations are relatively similar at 4280 s as illustrated in Figure 10a.

Figure 10b shows the surface temperature responses at 2770 s above delaminations located at different depths. Shapes of shallow delaminations show clearer than those of deeper ones because of a significant lateral thermal diffusion in all directions. Therefore, it is more difficult to recognize the shape of deep delaminations compared with the shallow ones.

4.2 *Defect sizing*

The FWHM method is used to measure the defect's size in this study. The method works with the assumption that the temperature response above the defective area is Gaussian where the peak corresponding to the center of the defect (Almond & Lau 1994, Saintey & Almond 1995). The results of predicted size at observation time for different depths are summarized in Table 3. To consider the predicted and real size, the relative error is used with a negative value means that the predicted size is smaller than the real size.

Table 3. Predicted sizes obtained by FWHM.

Predicted size (cm)				Relative error (%)		
Depth	A	V	Planar	A	V	Planar
2	15.6	19.5	18.4	-22.1	-2.5	-8.1
3	16.6	19.7	18.4	-17.2	-1.4	-7.8
4	17.2	19.9	18.7	-14.1	-0.5	-6.5
5	17.7	20.1	19.0	-11.5	0.3	-5.1

Table 3 shows that the predicted sizes of V-shape and planar delaminations are more accurate than A-shape delaminations. One should emphasize that the best result comes from V-shape, whereas the worst result is the A-shape, especially for the delamination at 2 cm depth with an error of 22.1%. As a result, the predicted size is just round 15.6 cm comparing to the real size of 20 cm. It can be concluded that the FWHM is not a suitable method to estimate A-shape delamination. Using a different method for sizing the special shape delamination such like A-shape should be further studied. In addition, a consideration of different gap angles of both A-shape and V-shape is also interesting. However, these studies are beyond the scope of this paper.

Figure 11 shows the time dependences of predicted sizes with different delamination's shapes using FWHM method. It is noted that the predicted sizes

for V-shape and planar delaminations show the same manner with previous works. In particular, the predicted size shrinks with elapsed time (Almond & Lau 1994, Saintey & Almond 1995). However, the A-shape delamination shows an inverted trend. The size swells against time.

On the other hand, Figure 11b also indicates that it is possible to measure the size of V-shape and planar delamination at the beginning of cooling time at 1800 s (after turning off the heat source) without sacrificing much accuracy.

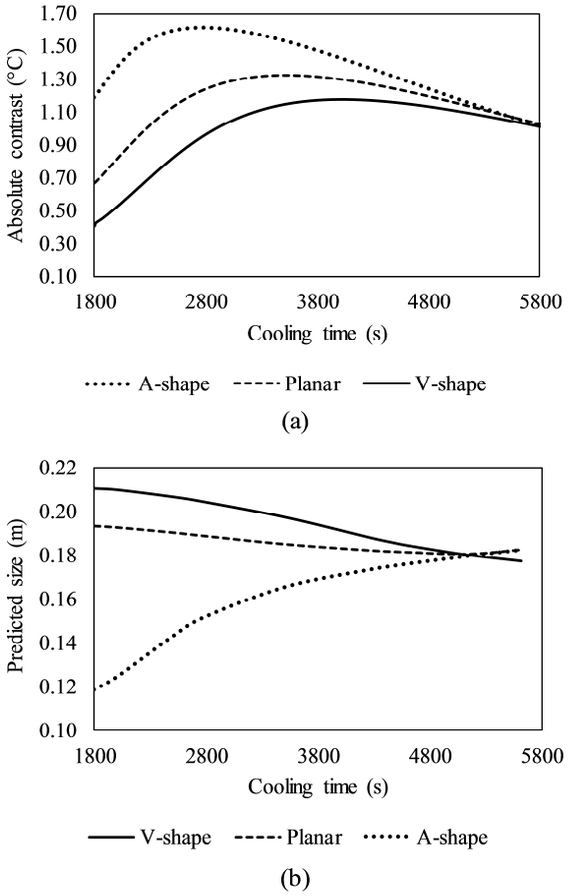


Figure 11. (a) Cooling curve of delamination at 3 cm depth; (b) FHWM obtained by FVM in the time domain.

5 CONCLUSIONS

The data of impulse thermography test obtained from the experimental study were analyzed for special shape delaminations. Then, the experimental results were verified to those from the simple FVM model. A more complex three-dimensional FVM model was simulated to analyze the effect of lateral thermal diffusion for delaminations with different depths (from 2 cm to 5 cm depth) and shapes (A-shape, V-shape, and planar). The FWHM method was used to predict the size of the defects. Results show that the relative errors between experimental study and FVM model are lower than 2%, indicating that the finite volume method is a reliable tool for modeling infrared thermography technique.

Based on both experimental data and FVM analyses, considering the heat loss above the defective area, the A-shape delamination shows a faster degradation of heat than the V-shape and planar delamination. In other words, as the same testing conditions, the V-shape and planar delaminations show better and longer contrast on the thermal image than the A-shape delaminations. In practice, this can help technicians having more chances to detect defects on site. In addition, the shape of delamination can be observed at early of cooling time with a shallow delamination. With a longer cooling time and deep delamination, it is difficult to recognize the real shape of the defect.

Finally, the conventional method FWHM is proven to be a good method in sizing planar subsurface delamination. However, based on FVM analysis in this study, it is not a suitable method for predicting the size of A-shape delaminations.

ACKNOWLEDGEMENTS

This research was supported by a grant (17RDRP-B076564-04) from the Regional Development Research Program funded by the Ministry of Land, Infrastructure, and Transport of the Korean government, and was also supported by Basic Science Research Program through the National Research Foundation of Korea (NRF) funded by the Ministry of Education (2017R1D1A3B03032854).

REFERENCES

Ahlborn, T.M. & Colin, N.B. 2015. *Evaluation of bridge decks using Non-destructive Evaluation at near Highway Speeds for effective asset management.* Houghton, Mich, USA: Michigan Tech, MDOT.

Almond, D.P. & Lau, S.K. 1994. Defect Sizing by Transient Thermography I: An Analytical Treatment. *Journal of Applied Physics* 27: 1063-1069.

Almond, D.P. & Pickering, S. 2012. An Analytical Study of the Pulsed Thermography Defect Detection Limit. *Journal of Applied Physics* 111: 093510.

ANSYS 2010. Lecture 7: Heat Transfer Modeling. In: *ANSYS Customer Traning material.* Canonsburg, PA, USA: ANSYS Inc.

ANSYS 2013. *ANSYS Fluent Theory Guide.* Canonsburg, PA, USA: ANSYS Inc.

FLIR SC660 Catalog 2014. *Technical Data of FLIR SC660 Infrared Camera.* Wilsonville, USA: FLIR System Inc.

Gómez, M.A., Álvarez Feijoo, M.A., Comesaña, R., Eguía, P., Míguez, J.L. & Porteiro, J. 2012. CFD Simulation of a Concrete Cubicle to Analyze the Thermal Effect of Phase Change Materials in Buildings. *Energies* 5: 2093-2111.

Holman, J.P. 2010. *Heat transfer.* 10 ed. N.Y.: Mcgraw-Hill.

Huh, J., Tran, Q.H., Lee, J., Han, D., Ahn, J. & Yim, S. 2016. Experimental Study on Detection of Deterioration in Concrete Using Infrared Thermography Technique.

Advances in Materials Science and Engineering 2016, Article ID 1053856: 12 pages.
IAEA 2002. *Guidebook on Non-Destructive Testing of Concrete Structures*. Vienna: IAEA in Austria.
Kretzmann, J.E., Venter, G. & Schreve, K. 2016a. Non-destructive Testing with Transient Thermography on Composite Materials. *R & D Journal of the South African Institution of Mechanical Engineering* 32: 35-43.
Kretzmann, J.E. 2016b. *Evaluating the Industrial Application of Non-destructive Inspection of Composites using Transient Thermography*. Stellenbosch: Stellenbosch University, South Africa.
Maierhofer, Ch. & Arndt, R. 2007. Influence of concrete properties on the detection of voids with impulse-thermography. *Infrared Physics & Technology* 49: 213-217.
Maierhofer, Ch., Brink, A., Röllig, M. & Wiggenhauser H. 2003. Detection of shallow voids in concrete structures with impulse thermography and radar. *NDT & E International* 36: 257-263.
Maierhofer, Ch., Arndt, R., Röllig, M., Rieck, C., Walther, A., Scheel, H. & Hillemeier, B. 2006. Application of impulse-thermography for non-destructive assessment of concrete structures. *Cement & Concrete Composite* 28: 393-401.
Maldague, X.P. 2001. *Theory and Practice of Infrared Technology for Nondestructive Testing*. N.Y.: John Wiley & Sons.
Pollock, D.G., Dupuis, K.J., Lacour, B. & Olsen K.R. 2008. *Detection of Voids in Prestressed Concrete Bridges using Thermal Imaging and Ground-Penetrating Radar*. Washington, D.C.: WSDOT research report.
Portland Cement Association 2002. *Types and Causes of Concrete Deterioration*. Skokie, Illinois, USA: Portland Cement Association.
Saintey, M.B. & Almond, D.P. 1995. Defect Sizing by Transient Thermography II: An Numerical Treatment. *J. Phys. D: Appl. Phys*. 28: 2539-2546.
Tran, Q.H., Han, D., Kang, C., Haldar, A. & Huh, J. 2017. Effects of Ambient Temperature and Relative Humidity on Subsurface Defect Detection in Concrete Structures by Active Thermal Imaging. *Sensors* 17(8): 1718.
Transportation Research Board 2013. *Nondestructive Testing to Identify Concrete Bridge Deck Deterioration*. Washington, D.C.: Report S2-R06A-RR-1, SHRP2.
Vaghefi, K. 2013. *Infrared Thermography Enhancements for Concrete Bridge Evaluation*. Houghton, Mich, USA: Michigan Technological University.
Vaghefi, K., de Melo e Silva, H.A., Harris, D.K. & Ahlborn T.M. 2011. Application of Thermal IR Imagery for Concrete Bridge Inspection. *Proceedings of the PCI National Bridge Conference (PCI/NBC '11)*. Salt Lake, UT, USA: Precast/Prestressed Concrete Institute.

Maintenance, Safety, Risk, Management and Life-Cycle Performance of Bridges – Powers, Frangopol, Al-Mahaidi & Caprani (Eds)
© 2018 Taylor & Francis Group, London, ISBN 978-1-138-73045-8

Corrosion Segmentation and Quantitative Analysis Based on Deep Neural Networks

Dalei Wang, Bo Peng & Yue Pan
Department of Bridge Engineering
Tongji University, China

ABSTRACT: Corrosion is one of the most common and severe problems in the daily maintenance of steel bridges. So far manual visual inspection remains a popular method in the corrosion detection, which means a large amount of labor power as well as material and financial resources are wasted in routine maintenance and quantitative criteria of evaluating corrosion could be hardly obtained due to the subjective judgments of inspectors. With the development of computer vision techniques in recent years, corrosion inspection could be achieved through image segmentation based on deep neural networks besides quantitative indexes such as area, distribution and corrosion rate could be obtained at the same time, which quantifies and standardize the evaluation criteria of corrosion in steel bridges. Furthermore, image segmentation and analysis based on deep neural net-work shows high robustness in the real complex scenarios and could be applied in actual bridge inspection rather than laboratory scenarios.

1 INTRODUCTION

Corrosion is a natural process during which time materials interact with the environment and leads to deterioration of the material properties. Corrosion has caused huge economic losses for a long time. It is reported that in America steel corrosion led to a cost of $170 billion in 2012 and this cost raised to $2.5 trillion in 2016. Roughly speaking, economical losses caused by steel corrosion could account for 3% ~ 4% of GDP of each country.

In civil engineering, steel corrosion is the most common form, which leads to deteriorations of strength, plasticity, stiffness and other mechanical properties in varying degrees. People spend a lot of money and labor forces for manual inspection and repair works every year. Thus, to improve the economic performance and promote the informational inspection, the research of advanced auto-inspection system has already been very critical.

Currently, during the processing of manual inspection, disease image data acquisition is one of the major works. Image data are useful for bridge inspectors to record the diseases information and evaluated the health status of the bridge structure. To preferable use these data and develop inspection system toward intelligence, a novel corrosion detection method based on computer vision and deep neural networks is proposed, which is an important part of another big project but not discussed in this paper. This method can detect and rank the corrosion directly on disease images with high precision, and it makes quantitative analysis of disease become true.

The general practice in corrosion detection is to create standard corrosion images of different degrees in advance, so that the inspectors could com-pare the actual corrosion regions with these standard images to obtain evaluation results. This manual inspection approach highly relies on the experience and subjective consciousness of inspectors, and as a result of which the inspection results are not always credible.

Steel corrosion detection could be achieved through computer vision techniques. The process of detecting corrosion regions from steel surface is equivalent to segment the images into foreground (corrosion regions) and background (non-corrosion regions). Hence corrosion detection could be converted to semantic segmentation in computer vision, which means representation of corrosion regions can be realized by establishing appropriate segmentation criteria.

Segmentation criteria could be founded considering the color and texture differences between corrosion regions and non-corrosion regions. Early studies try to find proper color configuration in different color spaces such as RGB, HSV and other 14 spaces to achieve corrosion segmentation (Chen PH et al. 2009); related studies combine color information with region texture and improve the applicability of seg-

mentation algorithm (Shen HK et al. 2013); in addition some studies train a SVM classifier to enhance the segmentation performance in rust satin regions (Liao KW & Lee YT 2016). Segmentation algorithms based on digital image processing show certain applicability in laboratory scenarios, but the real problem lies in the complex actual scenarios. The varying illuminations, shadows, and object occlusions lead to high randomness in corrosion images so that segmentation could hardly be achieved through manual designed criteria. A feasible way to solve this problem lies in the semantic segmentation methods using deep neural networks.

Semantic segmentation based on deep neural networks date from attempts for fully convolutional networks (Shelhamer E et al. 2014), where segmentation masks can be obtained by upsampling the low resolution heatmap calculated from the convolutional networks. Recently an overview on semantic segmentation (Garciagarcia A et al. 2017) investigate and analysis the prevalent segmentation networks including SegNet (Badrinarayanan V et al. 2017), DeepLab (Chen L C et al. 2017), CRFasRNN (Zheng S et al. 2015) etc., then divide the architectures into two categories called "decoder variants" and "integrating context knowledge".

In this paper, a simplified semantic segmentation network with decoder variants is developed which aims at corrosion detection. At the beginning of all, the network architecture is introduced in Section 3. Then, the training process and data set information are represented in Section 4. The testing results and quantitative analysis of corrosion images are shown in Section 5. At last, summaries and conclusions are drawn in Section 6.

2 NETWORK ARCHITECTURE

2.1 *Overall Architecture*

The decoder variants architecture is chosen in designing segmentation network, which could be divided to encoder (downsampling) and decoder (upsampling) parts. U-Net architecture (Ronneberger O et al. 2015) is also referred in our network, meaning that feature fusion is achieved by combining feature maps of different levels in downsampling and upsampling steps. In addition, batch normalization shows significance in accelerating training process and preventing overfitting. The overall architecture of our segmentation network is shown in Figure 1.

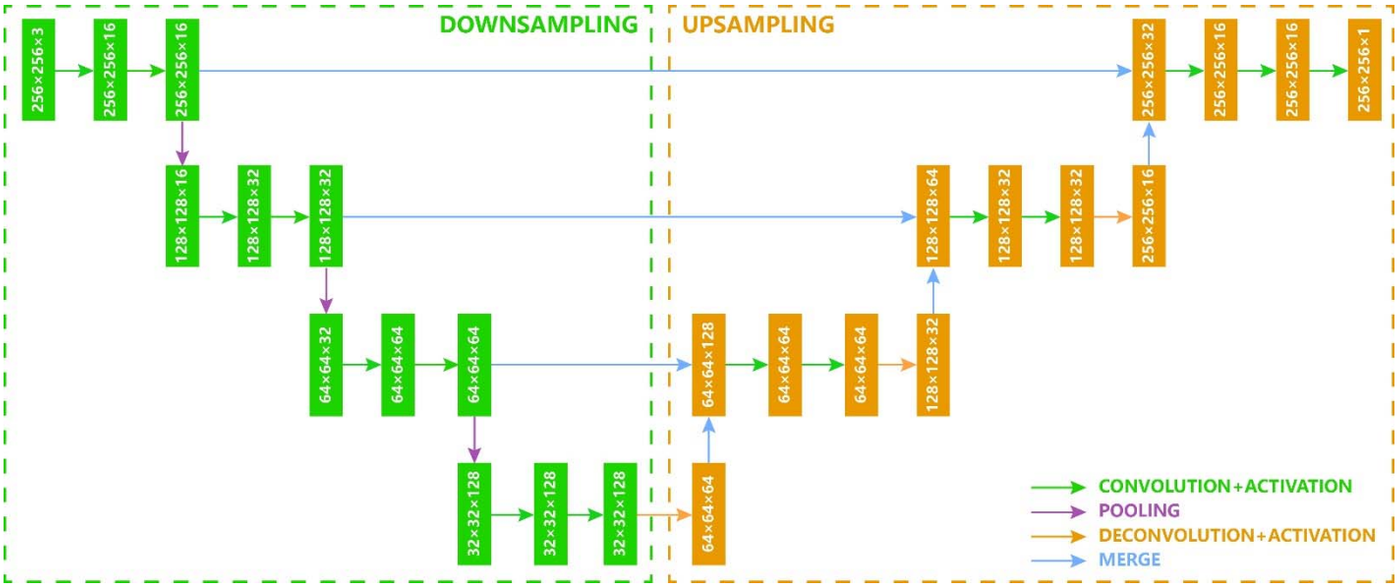


Figure 1 Overall architecture.

2.2 *Convolution Layers*

Convolution is a common operation in digital image processing. The calculation process is shown as follows: Firstly, a subarray is extracted from the original image. Then, an element-wise multiplication is applied to this subarray with a given kernel (or filter). Finally, the multiplication results are added up with a bias and we get the final output value for the input subarray. These steps are repeated until every pixel of the input image is performed. The mathematical expression of convolution is shown below:

$$S(i,j) = (I * K)(i,j) = \sum_m \sum_n I(i+m, j+n) K(m,n) + bias \quad (1)$$

where $S(i,j)$ = output value in (i,j); $I(i+m,j+n)$ = input value in $(i+m,j+n)$; $K(m,n)$ = kernel value in (m,n).

Convolution could also be realized as a local information extractor by which local features, e.g. edges, gradients and textures. The extracted features are converted to more abstract features after stacking convolution layers, and then the recognition task is achieved through these high-level features.

During the down-sampling process, there are two convolution layers with padding in each block. The kernel size is fixed as 3×3, and the stride is fixed as 1

so that the channels will increase with resolution unchanged in each block.

2.3 *Pooling Layers*

Pooling layers are another important component in convolutional neural networks, where feature maps are reduced to decrease computation. In addition, invariants can be obtained after pooling layers, which means small translations of the input will not affect the final output.

There are two kinds of pooling layers widely used today, called "average pooling" and "max pooling". In average pooling, the average of a rectangular neighborhood from the central pixel (pooling window) is calculated as the output, while in max pooling the maximum of the pooling window is extracted. Expressions of the two pooling methods are shown below:

$$avg_pool(x,y) = avg\{I(x+i,y+j) \mid -p \le i \le p, -q \le j \le q\} \tag{2}$$

$$max_pool(x,y) = max\{I(x+i,y+j) \mid -p \le i \le p, -q \le j \le q\} \tag{3}$$

Max pooling is proved an efficient operation in compressing features and accelerating training process. Therefore, max pooling is selected in our network and the pooling window size is fixed as 2×2.

2.4 *Activation Functions*

Nonlinear capacity is obtained through activation functions in neural networks. Sigmoid function is the most common activation function in standard artificial neural networks, and its expression is shown below:

$$\text{sigmoid}(x) = \frac{1}{1+e^{-x}} \tag{4}$$

Sigmoid function maps an arbitrary real number into the interval (0, 1), which could be understood as the probability that the sample is classified as positive. Gradient vanishment in back propagation is the main problem for deep neural networks with sigmoid functions, therefore the sigmoid functions are always replaced with other activation functions. The commonly used activation function in deep neural networks is ReLU function, which truncates the input value retaining the positive part and suppressing the negative part. The expression of ReLU function is shown below:

$$\text{ReLU}(x) = \max(0, x) \tag{5}$$

ReLU function is used in all the layers in our network except the final output layer, where sigmoid function is used instead. Since the final output layer is equivalent to handling a binary classification problem (corrosion or non-corrosion), the output of sigmoid function in the final layer is deemed as the probability that a pixel is classified as corrosion.

2.5 *Upsampling Layers*

The input image is transformed to an n-dimension vector which represents the probability of different categories in image classification tasks, while a segmentation mask with the same resolution as the input image is obtained in semantic segmentation. Therefore, upsampling becomes a necessity in handling the reduced resolution feature maps.

Deconvolution is the main method of upsampling at present. Strictly speaking, deconvolution is not the reverse operation of convolution and the proper name of "deconvolution" should be "transposed convolution" or "fractional convolution". The process of deconvolution is to upsample the input image by zero padding and then operate convolution on the upsampled image. There are trainable kernels in deconvolution compared to bilinear interpolation and unpooling so that deconvolution could also be recognized as a feature extractor. Deconvolution is used in upsampling layers in our network with the height and width of feature maps doubled while the number of channels reduced to half.

2.6 *Batch Normalization*

Batch normalization (Ioffe S & Szegedy C 2015) is a well-known trick aiming at accelerating training process and preventing overfitting. The original distribution of a given input can be adjusted to a proper form after batch normalization. Firstly, the original distribution is normalized to zero mean and unit variance:

$$\hat{x}^{(k)} = \frac{x^{(k)} - \mu_B}{\sqrt{\sigma_B^2 + \varepsilon}} \tag{6}$$

where $x^{(k)}$ = the k th sample of the batch; μ_B=the mean (expectation) of the batch; σ_B^2= the variance of the batch; ε=a minimum preventing 0 denominator; $\hat{x}^{(k)}$ =the kth normalized sample.

Then, two trainable parameters are introduced in the linear transformation of $\hat{x}^{(k)}$:

$$y^{(k)} = \gamma \hat{x}^{(k)} + \beta \tag{7}$$

where γ , β = trainable parameters in batch normalization; $y^{(k)}$= output of the kth sample after batch normalization.

The original distribution is adjusted to a proper form with β mean and γ^2 variance after batch normalization. There is no difference between parameters in batch normalization and other layers since the batch normalization is just a linear transform.

Batch normalization is applied after every block in downsampling and upsampling steps for severe overfitting will occur without batch normalization.

2.7 *Loss Function*

Sigmoid function is used in the final layer in our network, which maps the output into the interval (0,

1), and the result is deemed as the probability of each pixel classified as corrosion. The result of sigmoid function is denoted as p, then:

$$p = P(y^{(i)} = 1 \mid x^{(i)}; \theta) \tag{8}$$

where $y^{(i)}$ = the label of ith pixel of the image with 1 representing corrosion and 0 representing non-corrosion; $x^{(i)}$ = the ith pixel of the image; θ = parameters in our network.

The loss function used in our network is called "negative log-loss" (or "binary cross-entropy"), as is shown below. The loss function is the measurement between the predicted distribution and the actual distribution, and it takes the minimum if and only if the two distributions are equal.

$$J(\theta) = \sum_{i=1}^{m} -y^{(i)} \ln p - (1 - y^{(i)}) \ln(1 - p) \tag{9}$$

A regularization term is also added to the loss function as a penalty to prevent overfitting. L2 regularization is selected in our network, which can be expressed as:

$$\Omega(\theta) = \frac{1}{2} \|\theta\|_2^{\,2} = \frac{1}{2} \theta^T \theta \tag{10}$$

Then, the total loss function $\tilde{J}(\theta)$ is:

$$\begin{aligned} \tilde{J}(\theta) &= J(\theta) + \lambda \Omega(\theta) \\ &= \sum_{i=1}^{m} -y^{(i)} \ln p - (1 - y^{(i)}) \ln(1 - p) + \frac{\lambda}{2} \theta^T \theta \end{aligned} \tag{11}$$

where λ = regularization term factor representing the significance of regularization term in the total loss function, and is set to 1 by default.

2.8 *Adam Optimizer*

The training process of deep neural network is equivalent to minimizing the loss function from optimization perspective. First order optimization algorithms are widely applied in training deep neural networks, the most common one of which is called "stochastic gradient descent" (SGD). A random sample $x^{(i)}$ with corresponding label $y^{(i)}$ are used each time in updating parameters until all the samples in training set are traversed. The updating rule for SGD is shown below:

$$\theta_t \leftarrow \theta_{t-1} - \eta \cdot \nabla_\theta \tilde{J}(\theta; x^{(i)}; y^{(i)}) \tag{12}$$

where η =the learning rate; $\nabla_\theta \tilde{J}(\theta; x^{(i)}; y^{(i)})$ = gradient of the loss function with regard to parameters θ.

SGD gains high calculation efficiency by performing one update a time and avoids convergence to local minima from fluctuation. However, the main difficulties of SGD stem from learning rate schedule, which means high learning rate may lead to non-convergence while low learning rate may lead to slow convergence. On the other hand, SGD may stuck in saddle points (e.g. the loss function takes minimum in x direction but maximum in y direction) since the gradients of these points are zero in all directions.

Adam algorithm (Kingma DP & Ba J 2014) is used instead of vanilla SGD in training our network. The estimates of gradients are calculated in updating parameters, as is shown below:

$$g_t \leftarrow \nabla_\theta \tilde{J}_t(\theta_{t-1}; x^{(i)}; y^{(i)}) \tag{13}$$

$$m_t \leftarrow \beta_1 \cdot m_{t-1} + (1 - \beta_1) \cdot g_t \tag{14}$$

$$v_t \leftarrow \beta_2 \cdot v_{t-1} + (1 - \beta_2) \cdot g_t^{\,2} \tag{15}$$

$$\hat{m}_t \leftarrow \frac{m_t}{1 - \beta_1^{\,t}} \tag{16}$$

$$\hat{v}_t \leftarrow \frac{v_t}{1 - \beta_2^{\,t}} \tag{17}$$

$$\theta_t \leftarrow \theta_{t-1} - \eta \cdot \frac{\hat{m}_t}{\sqrt{\hat{v}_t} + \varepsilon} \tag{18}$$

where g_t = gradients with regard to parameters θ at timestep t; m_t = biased first moment estimate of gradients; β_1 = exponential decay rate of m_t; v_t = biased second moment estimate of gradients; β_2 = exponential decay rate of v_t; $\hat{m}_t$ = bias-corrected first moment estimate of gradient; $\hat{v}_t$ = bias-corrected second moment estimate of gradient.

Adam is one of the best first order optimization algorithms at present. The actual learning rate can be modified adaptively in training process which leads to high computation efficiency, and it has been proved that deep neural networks always converge faster with Adam compared to vanilla SGD through practice and experience. The hyperparameters in Adam algorithm are set as η=10^{-4}, β_1=0.9, β_2=0.999, ε=10^{-8} in training process.

3 TRAINING NETWORK

3.1 *Dataset*

A corrosion dataset, which contains 440 corrosion images, captured on Sutong bridge, is used in training and testing our network. The raw images in the dataset are 709×1067 resolution color images with 3 channels, and the corrosion regions are marked with LabelMe annotation tool (Torralba A et al. 2010). Some of the raw images and segmentation masks are shown in Figure 2.

Considering the characteristic of bridge corrosion image data with low positive and high negative ratio, patches split from raw images are used in training to prevent OOM (out of memory) error and overfitting issues.

In detail, 1026 patches with 256×256 resolution are split from the 440 raw images, and the histogram of the patches with corrosion rate are shown in Figure 3.

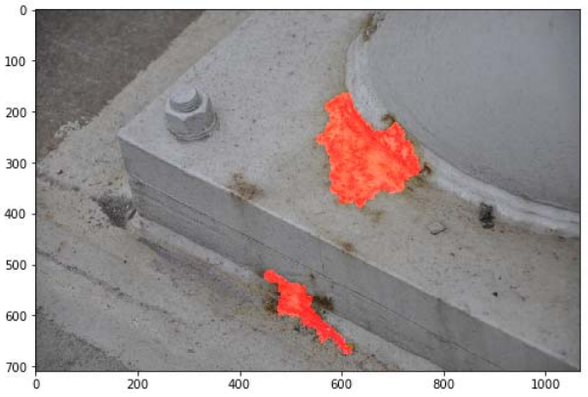


Figure 2 Image with segmentation mask.

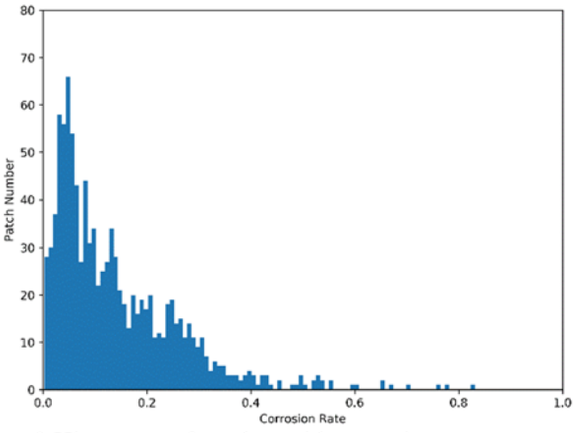


Figure 3 Histogram of patches with corrosion rate.

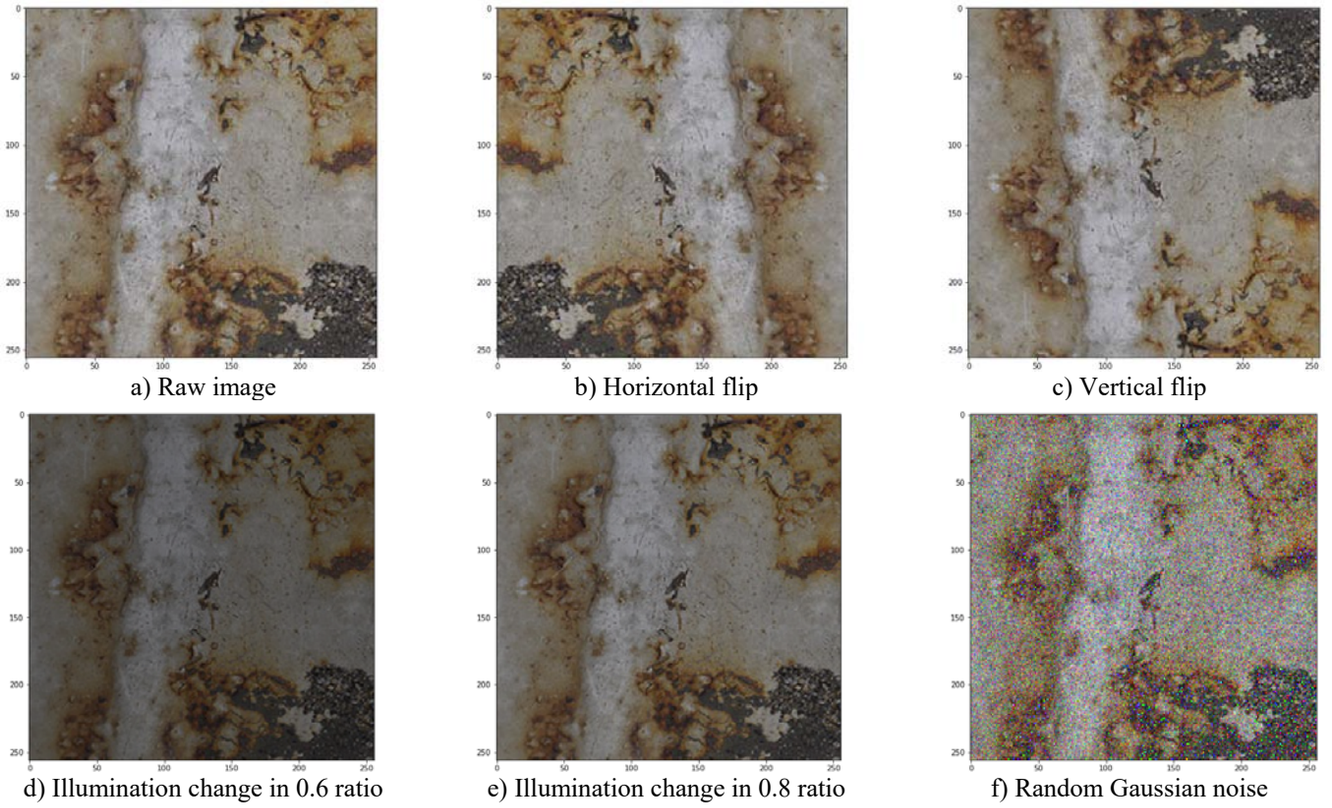
3.2 *Data Augment*

Considering that more corrosion images lead to better training effect, data augment is applied to extend dataset. Horizontal flip and vertical flip combined with illumination change and random Gaussian noise are applied to make more data. Finally, 6156 images including original patches are generated to train and test our network and some of the enhanced patches are shown in Figure 4.

3.3 *Training Process*

The dataset is divided to training set and testing set with the ratio of 9: 1, which means 5540 images including 556 images in validation set are used in training while the others are used in testing. The images are shuffled in the training process and only one image is used in a training step. An epoch means all the training images are traversed and we propose 50 epochs in the training process.

The segmentation network is implemented with TensorFlow framework and the initial learning rate is set to halve when the accuracy in validation set no longer rises, and the minimum learning rate is set to 1×10^{-10}. It takes 500~520 s in a training epoch and the total time cost is about 7 h on a workstation with 16 GB RAM, Intel Xeon E3-1505M v5 @2.80GHz CPU and Nvidia Quadro M2000M GPU. The loss, accuracy and learning rate decay curves are shown from Figure 5 to Figure 7. The binary accuracy with 92.55% in training set and 90.56% in validation set is achieved after 50 epochs.



a) Raw image b) Horizontal flip c) Vertical flip

d) Illumination change in 0.6 ratio e) Illumination change in 0.8 ratio f) Random Gaussian noise

Figure 4 Enhanced patches(horizontal flip, vertical flip, illumination change and random Gaussian noise)

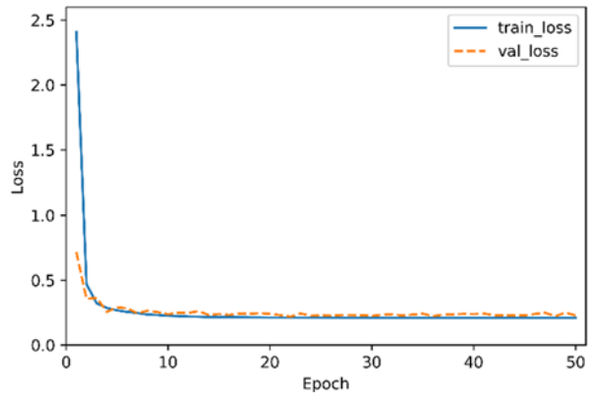


Figure 5 Losses for training set and validation set.

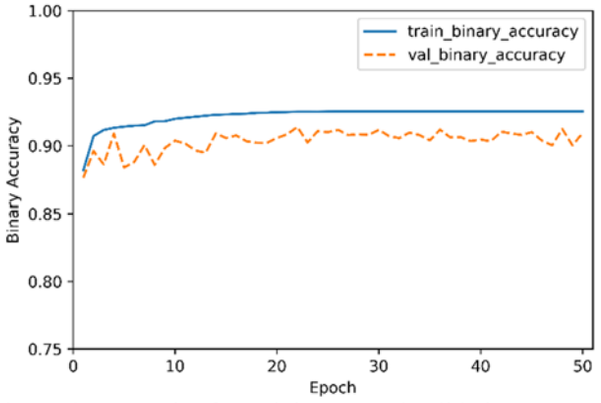


Figure 6 Accuracies for training set and validation set.

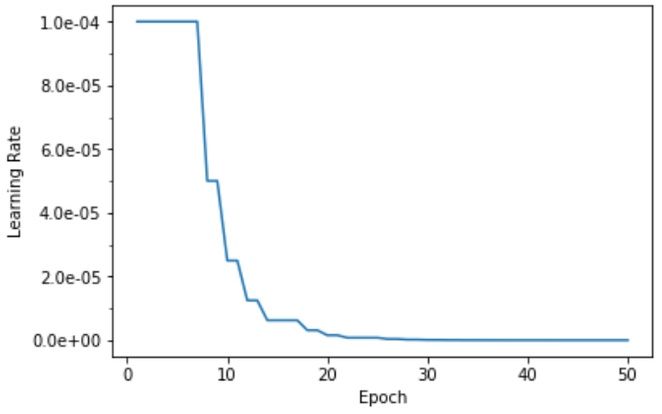


Figure 7 Learning rate in training process.

4 TEST RESULTS

4.1 *Network validation and testing*

Corrosion segmentation is equivalent to the binary classification of every pixel in the image. There are 4 conditions in classification considering the actual and predicted results, as is shown in Table 1.

Table 1 Truth table for binary classification.

		Predicted Conditions	
		Predicted Condition Positive	Predicted Condition Negative
Actual Conditions	Condition Positive	True Positive (TP)	False Negative (FN)
	Condition Negative	False Positive (FP)	True Negative (TN)

Precision and recall for classification can be defined as:

$$Precision = \frac{TP}{TP + FP} = \frac{p_{11}}{p_{11} + p_{01}} \tag{19}$$

$$Recall = \frac{TP}{TP + FN} = \frac{p_{11}}{p_{11} + p_{10}} \tag{20}$$

where p_{11}= pixels predicted as corrosion and labeled as corrosion, which is *TP*; p_{01}= pixels predicted as corrosion but labeled as non-corrosion, which is *FP*; p_{10}= pixels predicted as non-corrosion but labeled as corrosion, which is *FN*.

Precision and recall are two common metrics used in classification, where precision describes how the model could find the targets as accurately as possible while recall describes how the model could the targets as many as possible. They are a pair of negatively related metrics in most cases, therefore a threshold is required in classifying predicted conditions. PR curve is used to verify classification threshold, as is shown in Figure 8, and intersection of precision and recall is 0.5, which is selected as classification threshold in our network.

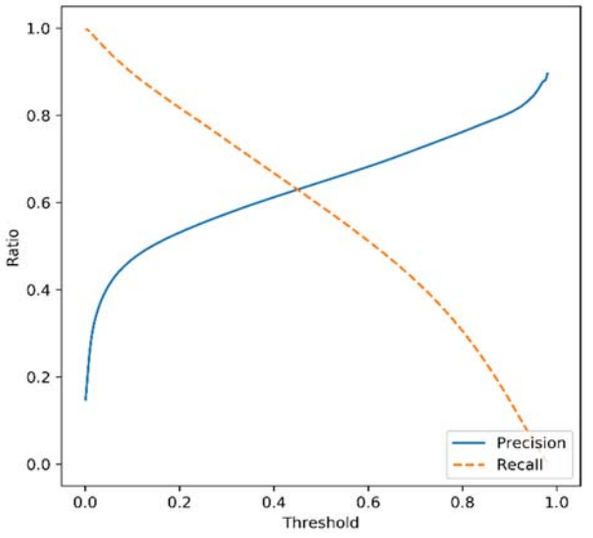


Figure 8 PR curve with classification threshold.

In addition to testing patches, our network is also applied to the raw images, which are resized to 704×1024 considering the input requirement. Some of the testing results are shown in Figure 9, where *TP* regions are painted green, *FP* regions are painted blue and *FN* regions are painted red.

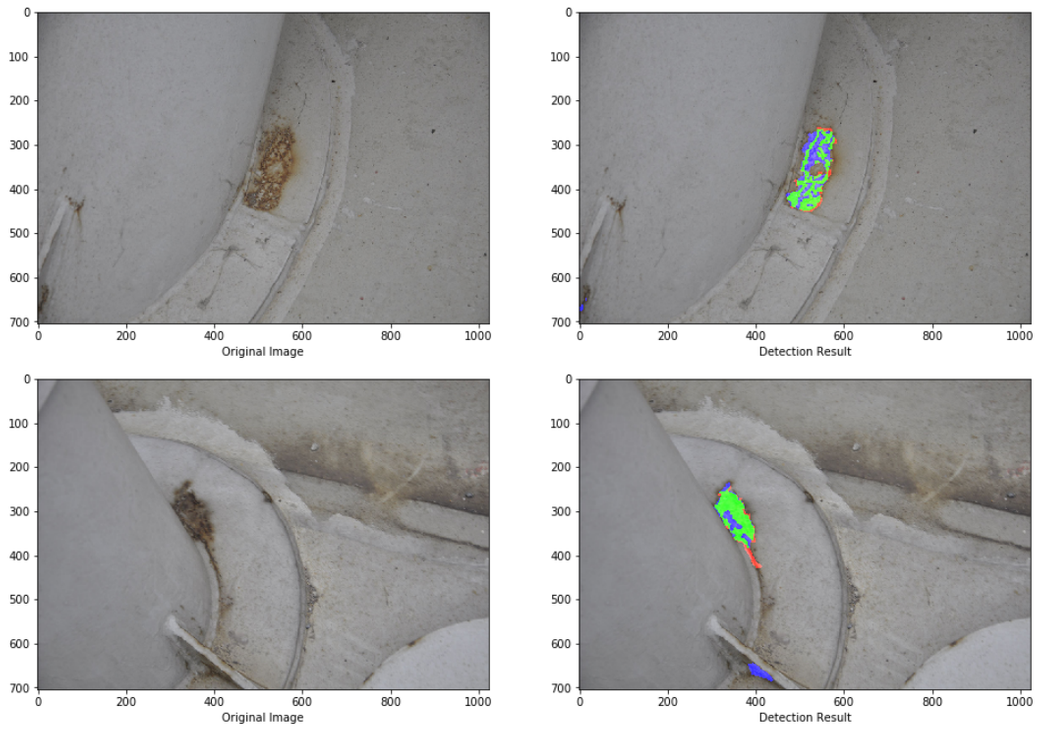


Figure 9 Some of the detection results on raw images.

The testing results on raw images show good adaptability of our network for main corrosion regions can be detected from the raw images. *FP* regions are mainly distributed around the edges of the corrosion or the regions hard to mark in raw images, while *FN* regions are mainly distributed in the shadow part or indistinguishable part.

4.2 *Quantitative Analysis*

Quantitative analysis can be achieved since corrosion segmentation mask is obtained through our network. Firstly, corrosion regions are split considering their connectivity and isolated points are removed with morphology open operation. Then, corrosion regions painted with random colors are shown in Figure 10.

Area of a corrosion region is defined as the pixels in it, as is shown below:

$$A_i = \sum p_i,\ p_i \in Region_i \tag{21}$$

Hence, corrosion rate is defined as the ratio of its area and the total pixels in the image:

$$corrosion\ rate_i = \frac{A_i}{Area} \tag{22}$$

And the total corrosion rate is defined as the total area of corrosion divided by the total pixels in the image:

$$total\ corrosion\ rate = \frac{\sum_i A_i}{Area} \tag{23}$$

Then, the quantitative analysis of the detected image is shown in Table 2.

Table 2 Quantitative analysis of the detected image.

Region Number	Corrosion Area	Corrosion Rate
1	227	0.031%
2	25	0.003%
3	1439	0.200%
4	1051	0.146%
5	48055	6.666%
6	25	0.003%
7	1043	0.145%
8	1359	0.189%
9	260	0.036%
10	333	0.046%
Total	53817	7.465%

The corrosion area can be converted to actual area of corrosion regions with standard imaging, and the actual corrosion rate can be obtained. In addition, the histogram which indicates the distribution of corrosion regions is available if scanning the surface of steel structures. The quantitative analysis could therefore provide data support for evaluating structural performance and formulating maintenance strategy.

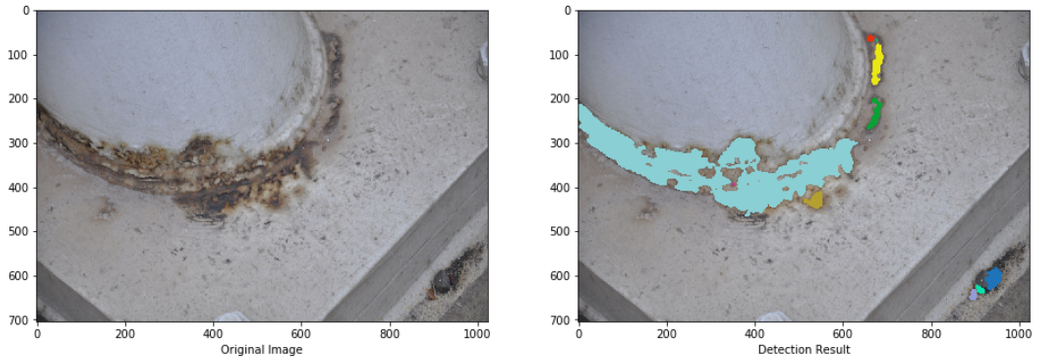


Figure 10 Detection results for quantitative analysis.

5 CONCLUSION

A novel corrosion detection method based on deep neural networks is proposed in this study. The network is trained through patches with 256×256 resolution and the dataset is extended through data augment. The binary accuracy with 92.55% in training set and 90.56% in validation set is achieved in the training process. Our network is also tested on the raw images and the testing result shows adaptivity for major part of corrosion could be detected from background.

Only qualitative analysis is provided through traditional methods, while quantitative analysis can be achieved through our segmentation network. Corrosion area, corrosion rate and total corrosion rate are proposed to qualitatively analyze the corrosion degree of steel surface, Besides, the actual corrosion indicators could also be obtained with the help of standard imaging. Our method can be extended to arbitrary structural surface defection theoretically, and the detection results can also be improved with more abundant data.

ACKNOWLEDGMENTS

The work described in this paper was financially supported by National Natural Science Foundation of China (Grant No. 51778472). The authors also would like to express the thanks to Jiangsu Yangzi Bridge Co., Ltd., for the supports and assistances during the experiments.

REFERENCE

Kingma DP, Ba J. Adam: A Method for Stochastic Optimization. Computer Science. 2014.

Chen PH, Yang YC, Chang LM. Automated bridge coating defect recognition using adaptive ellipse approach. Automation in Construction. 2009;18(5):632-43.

Shen HK, Chen PH, Chang LM. Automated steel bridge coating rust defect recognition method based on color and texture feature. Automation in Construction. 2013;31(5):338-56.

Ioffe S, Szegedy C. Batch Normalization: Accelerating Deep Network Training by Reducing Internal Covariate Shift. 2015:448-56.

Zheng S, Jayasumana S, Romera-Paredes B, Vineet V, Su Z, Du D, et al. Conditional Random Fields as Recurrent Neural Networks. 2015:1529-37.

Mnl A. Corrosion Tests and Standards: Application and Interpretation--Second Edition. 2009.

He K, Zhang X, Ren S, Sun J. Deep Residual Learning for Image Recognition. 2015:770-8.

Chen LC, Papandreou G, Kokkinos I, Murphy K, Yuille AL. DeepLab: Semantic Image Segmentation with Deep Convolutional Nets, Atrous Convolution, and Fully Connected CRFs. IEEE Transactions on Pattern Analysis & Machine Intelligence. 2016;PP(99):1-.

Liao KW, Lee YT. Detection of rust defects on steel bridge coatings via digital image recognition. Automation in Construction. 2016;71:294-306.

Akinyemi OO, Nwaokocha CN, Adesanya AO. EVALUATION OF CORROSION COST OF CRUDE OIL PROCESSING INDUSTRY. Journal of Engineering Science & Technology. 2012;7(4):438-51.

Shelhamer E, Long J, Darrell T. Fully Convolutional Networks for Semantic Segmentation. IEEE Transactions on Pattern Analysis & Machine Intelligence. 2014;39(4):640.

Szegedy C, Liu W, Jia Y, Sermanet P, Reed S, Anguelov D, et al., editors. Going deeper with convolutions. IEEE Conference on Computer Vision and Pattern Recognition; 2015.

Krizhevsky A, Sutskever I, Hinton GE, editors. ImageNet classification with deep convolutional neural networks. International Conference on Neural Information Processing Systems; 2012.

Garciagarcia A, Ortsescolano S, Oprea S, Villenamartinez V, Garciarodriguez J. A Review on Deep Learning Techniques Applied to Semantic Segmentation. 2017.

Badrinarayanan V, Kendall A, Cipolla R. SegNet: A Deep Convolutional Encoder-Decoder Architecture for Scene Segmentation. IEEE Transactions on Pattern Analysis & Machine Intelligence. 2017;PP(99):1-.

Ronneberger O, Fischer P, Brox T, editors. U-Net: Convolutional Networks for Biomedical Image Segmentation. International Conference on Medical Image Computing and Computer-Assisted Intervention; 2015.

Simonyan K, Zisserman A. Very Deep Convolutional Networks for Large-Scale Image Recognition. Computer Science. 2014.

Maintenance, Safety, Risk, Management and Life-Cycle Performance of Bridges – Powers, Frangopol, Al-Mahaidi & Caprani (Eds)
© 2018 Taylor & Francis Group, London, ISBN 978-1-138-73045-8

Effect of small steel-piece size on Charpy absorbed energy

D. Kitazume & K. Ono
Dept. of Civil and Environmental Engineering, Waseda University, Shinjuku-ku, Tokyo, Japan
K. Anami
Dept. of Civil Engineering, Shibaura Institute of Technology, Koto-ku, Tokyo, Japan
T. Iida
The Takigami Steel Construction Co., Ltd., Handa, Aichi, Japan

ABSTRACT: It is necessary to gain the information on the mechanical, chemical, and fracture properties of their materials in order to find out cause of damage and examine retrofitting methods for repairing damaged steel bridges. One of the properties used to investigate retrofitting methods is fracture toughness. Charpy impact tests are conducted in order to examine fracture toughness. The size of test specimens of Charpy impact tests is specified in Japanese Industrial Standards. Test specimens must be shaped according to the specific size, but it is desirable to take smaller material from sound material. Therefore, this study aims to make test specimens with small steel pieces in order to estimate fracture toughness. The size of small steel pieces was set as they can be taken from stop holes or bolt holes. Test specimens were made with these small steel pieces by electron beam weld. Then the effect of steel piece size on Charpy absorbed energy was examined.

1 INTRODUCTION

Fatigue damage in steel bridges has been reported (Japan Road Association, 2007 and 2009). In order to identify the cause of fatigue damage or examine the retrofitting methods of damaged steel bridges, it is necessary to gain the information on the mechanical, chemical and fracture properties of their materials. For example, test specimens of Charpy impact tests are made with the material taken from the base material of damaged bridges and Charpy impact tests are conducted in order to examine the fracture toughness. When test specimens are taken from damaged bridges, it is desirable to take smaller material from sound material.
When stop holes are bored for preventing the crack propagation or the holes for high tension bolts are bored for retrofitting damaged bridges by the bolted splice steel plates, cores can be gained after holes are bored. And it is effective and useful to use stop hole cores or bolt hole cores as the test specimens.
The previous study examined to make the test specimens with small steel pieces and conducted Charpy impact tests by using the test specimens in order to estimate fracture toughness (Ono et al., 2012). A small steel piece gained from cores was connected to another steel plates by electron beam weld (EBW) from one side of test specimen as shown in Figure 1, and it was cut and shaved into the test specimen so that V-notch is placed in center of the small steel piece.

In this study, the size of small steel pieces was changed and its effect on Charpy absorbed energy was examined. SBHS400, which was introduced in Japanese Industrial Standards in 2011, was used in the experiment.

2 TEST SPECIMENS

The procedures how to make test specimens are explained and heat-affected zones of test specimens are examined in this chapter.

2.1 STEEL PLATE USED TO MAKE TEST SPECIMENS

In this study, test specimens were made of SBHS400 plate and its thickness was 27mm.

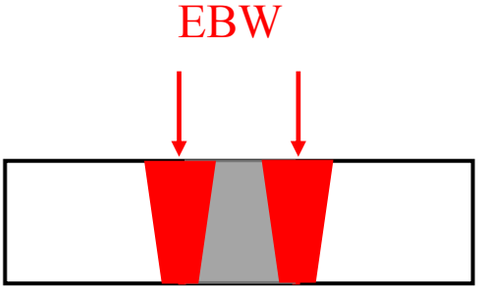
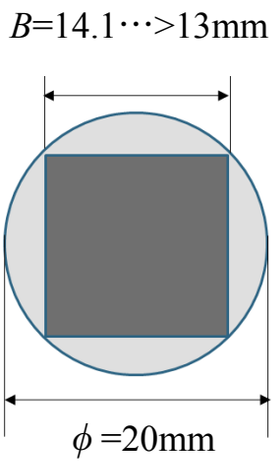
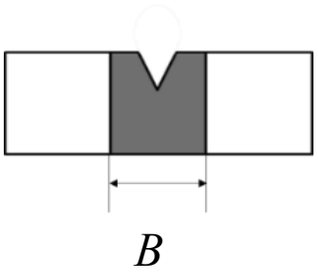


Figure 1 The method of conducting EBW to make test specimens



(a) A core and a steel piece



(b) Location of a steel piece including V-notch area

Figure 2 Relationship between assumed core and gained steel piece

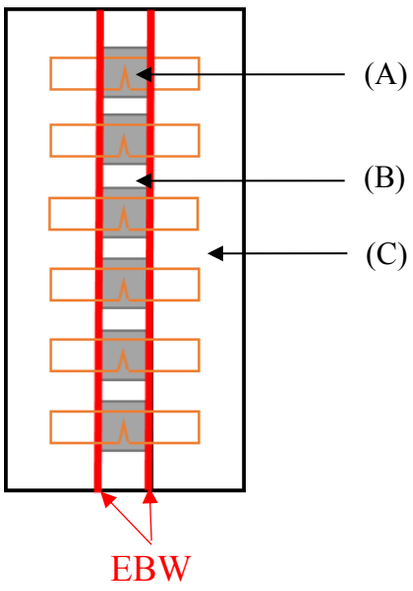
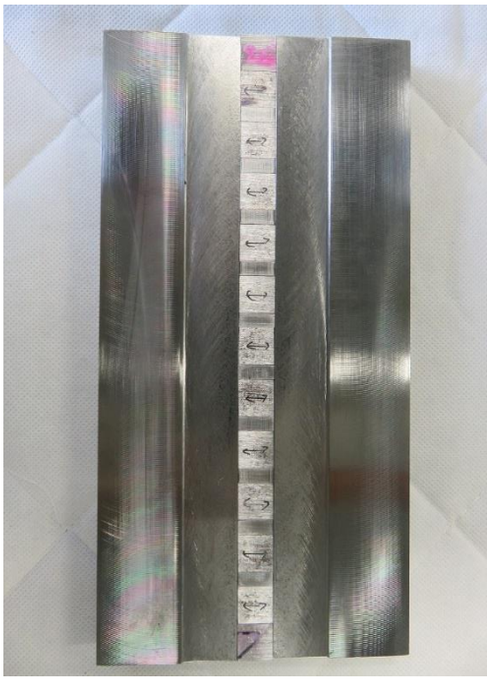


Figure 3 Procedure of making test specimens by EBW



Picture 1 Steel pieces and plates actually listed

2.2 ASSUMED SIZE OF CORES

A small steel piece corresponding to a core is connected to another steel plates by EBW. It is thought that size of cores which is assumed to be gained is 20mm in diameter. Figure 2 shows relationship between an assumed core which can be obtained from a stop hole or a bolt hole and a small steel piece in which V-notch is made.

Table 1 Welding condition of EBW

Voltage(kV)	Current(mA)	Welding speed(mm/min)
60	73	270

As shown in Figure 2, the square steel piece whose size is 13mm can be gained from the stop-hole-size core whose diameter is 20mm. In consideration of Figure 2, 13mm is decided as the maxim size '*B*' of square steel pieces gained from the stop-hole-size cores.

2.3 TYPES OF TEST SPECIMENS

In case of making test specimens by welding, the effect on the change in the material properties should be considered. Some previous studies (Seo et al., 1982; Seo et al., 1983) shows that such change in the materials affect Charpy absorbed energy and adequate test results cannot be gained if each EBW line is too close. Therefore, the width of small steel pieces ('*B*' in figure 2) was changed and its effect on Charpy absorbed energy was examined. '*B*' was set in 9mm (test specimen 'B09'), 11mm (test specimen 'B11') and 13mm (test specimen 'B13') in the experiment.

2.4 PROCEDURE OF MAKING TEST SPECIMENS BY ELECTRON BEAM WELD

The welding condition of EBW used to make test specimens is shown in Table 1 and Picture 1.
The outline of the procedure of making test specimens is as follows.

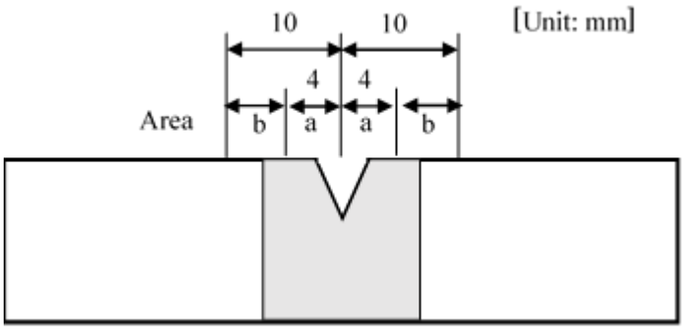


Figure 4 The areas in which Vickers hardness was examined (‘B13’)

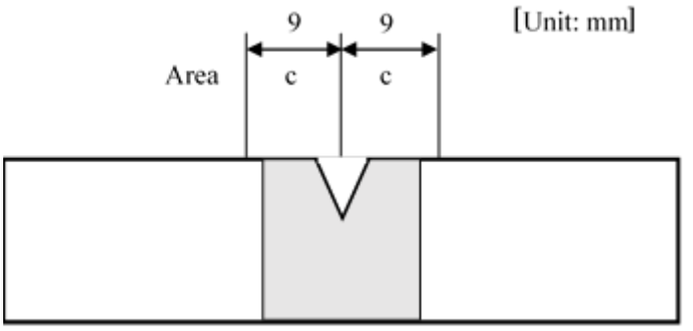
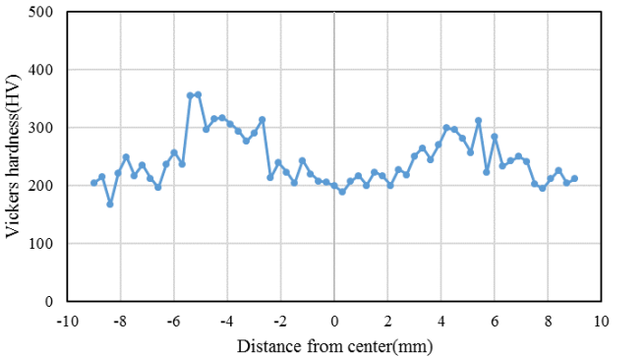
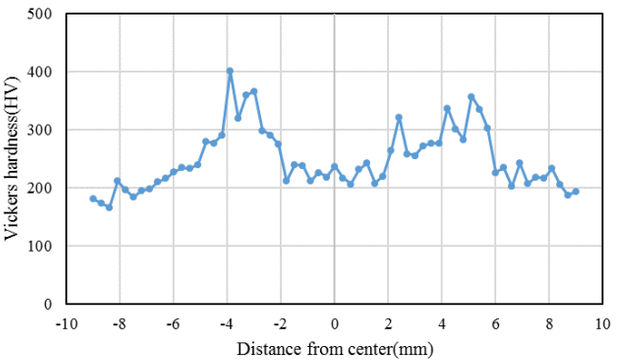


Figure 5 The areas in which Vickers hardness was examined (‘B09’, ‘B11’)





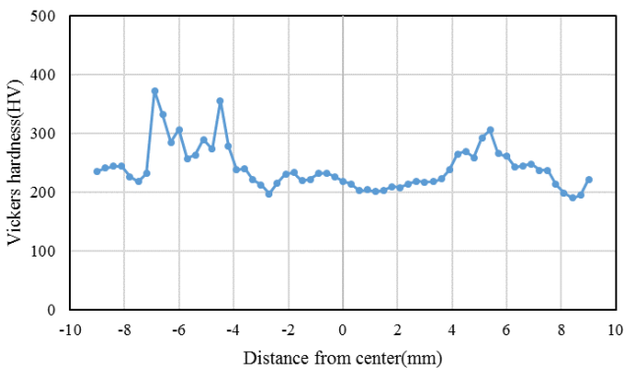
(a) Front surface





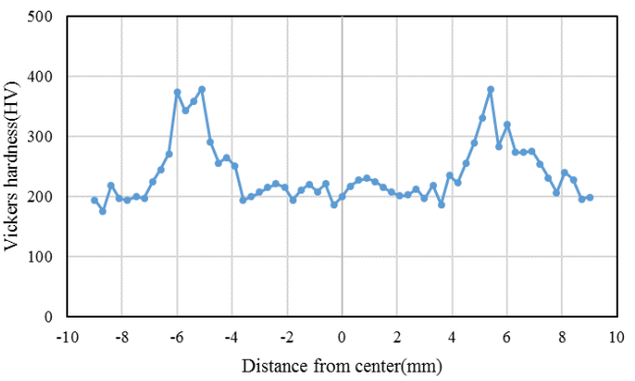
(b) Back surface

Figure 6 Results of Vickers hardness tests and macrostructure tests (‘B09’)





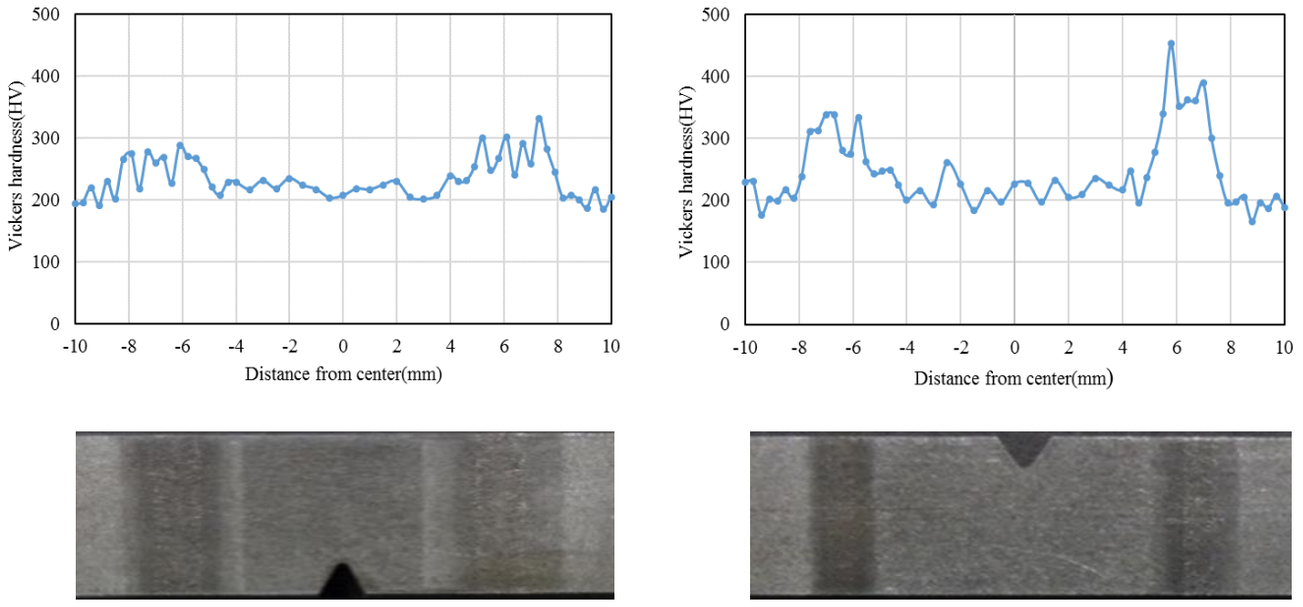
(a) Front surface





(b) Back surface

Figure 7 Results of Vickers hardness tests and macrostructure tests (‘B11’)



(a) Front surface (b) Back surface

Figure 8 Results of Vickers hardness tests and macrostructure tests (‘B13’)

・Small steel pieces corresponding to the main part of test specimens (‘A’ in Figure 3) , steel spacers (‘B’ in Figure 3), edge parts of the test specimens (‘C’ in Figure 3) and backing metal are set as shown in Figure 3.
・EBW is conducted from one side of steel plates.
・Making test specimens are completed by cutting them and shaving them off until the predetermined size and thickness of full size Charpy V-notch impact test specimens specified in Japanese Industrial Standards.

2.5 VICKERS HARDNESS TEST AND MACROSTRUCTURE TEST

In order to investigate heat-affected zone of test specimens by EBW, Vickers hardness tests and macrostructure tests were conducted. The weight of Vickers hardness test in this investigation was 4.9N. The location of the measuring points is the center of the height of test specimens. In test specimens ‘B13’, interval of measuring points is 0.5mm in the area ‘a’ of Figure 4 and 0.3mm in the area ‘b’ of Figure 4. In test specimens ‘B09’ or ‘B11’, interval of measuring point is 0.3mm in the area ‘c’ of Figure 5.
Figures 6, 7, and 8 show results of Vickers hardness tests and macrostructure tests of test specimens B09, B11 and B13 respectively.
According to the results of Vickers hardness tests and the macrostructure tests, it is found that heat-affected zone by EBW on the front surface is wider than that on the back surface. And the fact that heat-affected zone of test specimen becomes closer to the V-notch is indicated as the width of small steel piece gets smaller.

3. CHARPY IMPACT TESTS

Charpy impact tests were conducted with test specimens by EBW and standard test specimens without EBW. The size of test specimens was set to that specified in Japanese Industrial Standards. The test temperatures for the Charpy impact tests were 0°C, -30°C and -60°C. Figure 9 shows the results of Charpy impact tests. The averages of results of 3 test specimens are calculated in order to compare Charpy absorbed energy of each type of test specimens as shown in Figure 10.
According to Figure 9, the differences between maximum value and minimum value of the Charpy absorbed energy of standard test specimens are 41.9J at 0°C, 26.8J at -30°C and 55.5J at -60°C. The scatter of the Charpy absorbed energy is relatively large like this.
Figure 9 and Figure 10 shows that the Charpy absorbed energy of test specimens ‘B09’ is lower than that of other types of test specimens. Although the Charpy absorbed energy of test specimens ‘B11’ and ‘B13’ is almost the same as that of the standard test specimens as for the results at 0°C and -30°C, the Charpy absorbed energy of two of the three test specimens ‘B11’ is lower compared with that of test specimens ‘B13’ and standard test specimens about the results at -60°C. However, the difference in Charpy absorbed energy of test specimens ‘B11’ at -60°C may not be significant in consideration of the

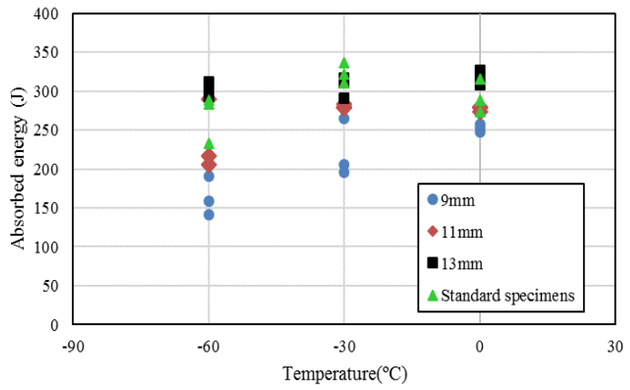


Figure 9 Results of Charpy V-notch impact tests

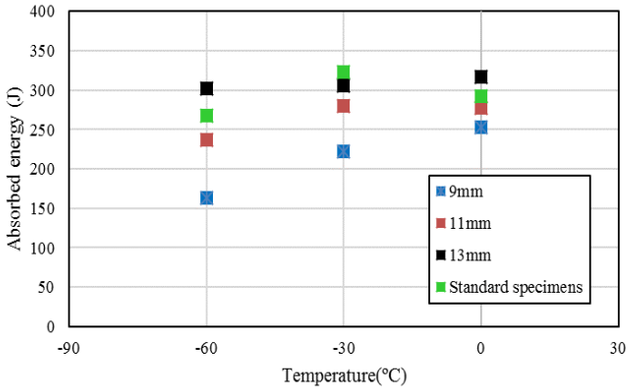


Figure 10 Results of Charpy V-notch impact tests (Average)

scatter of the Charpy absorbed energy of standard test specimens as shown in Figure 9. The test results of test specimens 'B11' will be investigated in detail in the future works. These results indicate the possibility that Charpy absorbed energy can be adequately evaluated with test specimens made with small steel pieces.

4. CONCLUSIONS

Test specimens for Charpy impact test are made with small steel pieces by electron beam weld (EBW) and the effect of width of small steel piece on Charpy absorbed energy are examined in this study.

The results indicate that Charpy absorbed energy depends on the width of steel pieces. And Charpy absorbed energy of test specimens by EBW is almost the same as that of test specimens without EBW when the width of small steel pieces is 13mm. This fact indicates the possibility that the Charpy absorbed energy can be adequately evaluated with the test specimens made with small steel pieces by EBW.

Charpy absorbed energy of test specimens by EBW will be investigated in detail when the width of small steel pieces is 11mm.

ACKNOWLEDGEMENT

This work was partly supported by the Japan Iron and Steel Federation. Also, our thanks to Mr. Takumi Kawauchi from Shibaura Institute of Technology for his cooperation. Our gratitude is expressed here.

REFERENCES

Japanese Standards Association. 2012. Higher yield strength steel plates for bridges. JIS Handbook Vol.2 Steel II. pp.136-143. (in Japanese)

Japan Road Association. 2007. Collection of example of Retrofitting of Highway Bridges. (in Japanese)

Japan Road Association. 2009. Collection of example of Retrofitting of Highway Bridges. (in Japanese)

Ono K., Anami K. and Oikawa M. 2012. A study on Charpy impact tests with test specimens made with small steel pieces. Journal of structural engineering, Vol.58A, pp.767-776. (in Japanese)

Seo K. and Masaki J. 1982. Physical interpretation for the upper shelf energy of weld zone in Charpy impact test. Journal of the japan welding society, Vol.51, No.3, pp.39-45. (in Japanese)

Seo K., Masaki J., Nogata F. and Sato K. 1983. Effect of mechanical heterogeneity on the on the ductile-to-brittle transition behavior of weld metal in Charpy impact test, quarterly journal of the japan welding society, Vol.1, No.2, pp.123-129. (in Japanese)

Maintenance, Safety, Risk, Management and Life-Cycle Performance of Bridges – Powers, Frangopol, Al-Mahaidi & Caprani (Eds)
© 2018 Taylor & Francis Group, London, ISBN 978-1-138-73045-8

A two-stage static structural system identification by observability method

Jun Lei
Tongji University, Shanghai, China
Maria Nogal
Trinity College Dublin, Dublin, Ireland
Jose Antonio Lozano-Galant
University of Castilla - La Mancha, Ciudad Real, Spain
Dong Xu;
Tongji University, Shanghai, China
Jose Turmo
Universitat Politècnica de Catalunya, Barcelona, Spain

ABSTRACT: Structural system identification (SSI) is a powerful tool for the assessment of the current condition of structures in operation. The basic assumption is that the deterioration of structures is reflected in the change of structural parameters. In SSI, the observability of these parameters depends on the location and the number of sensors. If the available sensors are less than the required ones, some parameters might not be observed. Furthermore, the incapability of identifying all parameters might occur when the sensors are sufficient but placed improperly. An investigation was carried out using SSI by observability method when then number of measurements is the same as the number of sensors. It is seen that a large proportion of the studied measurement sets cannot ensure the observability of all parameters. To improve the observability of structural parameters, a two-stage static SSI method is presented to fully exploit the information in the measurements. In the first stage, the SSI problem is treated in a linear manner and thereby the computation is greatly reduced. In the following stage, the nonlinear relations among the variables in the formulated system are recovered and thus the capability of the method to observe those structural parameters is enhanced.

1 INTRODUCTION

To avoid the potential safety and economical problem due to the deterioration of existing structures, condition assessment of existing structures has become a critical issue. A very common means of implementing condition assessment is Structural System Identification (SSI). SSI is related to the process of estimating structural parameters based on the measured structural response (e.g. deflections, rotations, strains, acceleration). A basic assumption behind SSI is that the change of structural condition can be reflected in the variation of structural parameters.

Due to the difference of the loading, SSI can be categorized as static (Lozano-Galant et al. 2013; Sanayei & Saletnik 1996) or dynamic ones(Li et al. 2017; Jiang & Adeli 2007). Many researches have been focused on the dynamic part. However, much less attention was paid to the static case. Regarding the treatment on uncertainties, these method can also be classified as probabilistic and deterministic methods. The former methods yield a point estimate or an interval estimate of estimations based on the posterior distributions while the latter methods pinpoint a best set of parameters minimizing the square sum of deviation between the measured and the predicted response.

However, these methods do not address the issue of whether the observability of the structural parameters. A vital issue for any SSI method is whether the parameters are observable or not given a particular measurement set. This can be addressed by Observability Method (OM). OM provides the information whether all the unknowns or a subset of the unknowns can be uniquely determined or not. Its application in parameter estimation includes water transport network(Díaz et al. 2016), traffic network(Castillo et al. 2013) or power systems(Abur & Exposito 2004). SSI by OM is a deterministic static SSI method first introduced by Lozano-Galant(Lozano-Galant et al. 2013), which has the advantage of less computation cost than probabilistic methods. In this method, the finite element model for the structure to be assessed has to be defined first. Then the equilibrium equations of the model

are formulated. A series of algebraic operation are applied to this system of equations in such a way that all the unknowns and knowns are separated in different parts of the equations. Step by step example is provided in (Lozano-Galant et al. 2013) and (Lei, Lozano-Galant, et al. 2017).

The identifiability of the structure by any method relies on a good selection of measurements. More measurements are generally desirable for the identifiability of parameters. On the converse, less sensors means less instrumental, operational costs and data processing. It is interesting to find the optimal number of measurements and the location of the sensors for successful identifications. A similar issue was addressed in power system using OM (Abur & Exposito 2004). In the context of power system that is fully specified by n parameters, the question is posed as how the select measurements from m ($m>n$) available measurements to identify the system. If a measurement set of n measurements is able to identify all the n parameters and the drop of any measurement fails to do so, then this set is defined as essential set. In the context of SSI, if the number of measurements was less than the number of unknown parameters, the system would become indeterminate (Bakhtiari-Nejad et al. 2005; Sanayei & Saletnik 1996), i.e. only a subset of the parameters might be identified. Moreover, even if the number of measurements equals to the number of unknowns, if those are not properly chosen, the system might still be indeterminate. An increase in measurements or a better placement of sensors can lead to an increase in the number of identified parameters. Eventually, this process will lead to the identification of all parameters, which is referred as full observability.

Sensor placement has been addressed by many authors (see (Sanayei et al. 1992; Chang & Pakzad 2014; Malings & Pozzi 2016)). However, most of them focus on the dynamic case. In the static SSI by OM, observability tree method was proposed to analyze the sequence of identified parameters during the recursive steps of SSI by OM (Lozano-Galant et al. 2015). It was found that improper selection of the measurement set may stop the identification prematurely and thus fail to identify all the unknowns even with more measurements than unknowns. However, underlying mechanism is not clear and the solution was not found at that time. In this paper, the reason of the failure is revealed as the lacking of some nonlinear constraints during the last recursive step. Also, the original method is updated as a two-stage method. In the first stage, the SSI by OM is carried out until no more parameter is obtained. In the second stage, the lacking nonlinear relations among variables are appended by adding nonlinear constraints via optimization techniques.

2 STATEMENT OF THE PROBLEM

From direct stiffness method, the nodal equilibrium equations for 2D beam models can be expressed as:

$$K \cdot \delta = f \tag{1}$$

where the global stiffness matrix K contains the information of flexural stiffness, EI_j, axial stiffness, EA_j, length L_j and the element connectivity. The displacements vector δ contains the horizontal, vertical and rotational displacements of node i, i.e. u_i, v_i and w_i. The external force vector f contains the horizontal forces, vertical forces and moments applied on node i, i.e. H_i, V_i and M_i.

Once the geometry, the boundary conditions and the load case are specified, then the nodal displacements δ will be uniquely determined by any parameter set. In the case of N_A unknown axial stiffnesses and N_F unknown flexural stiffnesses, this is saying that these N_A+N_F mechanical parameters uniquely specify a set of displacements of the structure. In the inverse analysis, due to the linearity of this system, N_A+N_F measurements are expected to be sufficient to identify all parameters. For simplicity, the ability to identify all parameters of the structure is referred as full observability in this paper. If merely a subset of these parameters are identifiable, then it is referred as partial observability. Hence, in the essential sets (the sets containing the necessary and sufficient number of measurements to achieve full observability), the number of required measurements is N_A+N_F. However, this statement has been verified elsewhere(Lozano-Galant et al. 2015) and it was found that full observability might not be achieved with N_A+N_F measurements due to improper selection of the measurements, which is related with the placement and type of measuring devices. Previous explanation was that the recursive steps stopped too early without identifying all parameters. However, the underlying cause for this premature end of the recursive steps was not uncovered at that time. This is one of the major interests of this paper, which can also be employed for the sensor placement strategy.

For practical reason, Eq. (1) can be transformed as:

$$B \cdot z = D \tag{2}$$

Eq. (2) is the result of applying static condensation technique together with the separation of each column, with regard to different unknowns, into several columns and the merger (addition) of those resultant columns related with the same unknowns in the equilibrium equations (Eq. (1)). After these algebraic operations, all the known quantities are collected in the coefficient matrix B and the vector D. Hence, B and D are known. The unknown vector z is

always of two types: (1) monomials of degree one, e.g. $\{EA_j, EI_j, u_i, v_i, V_i$ and $M_i\}$, or (2) monomials of degree two, e.g. $\{EI_j u_i$ and $EA_j v_i\}$. Note that both, EA_j and EI_j are regarded as monomials of degree one. (For more technical details, readers are strongly recommended to review (Lozano-Galant et al. 2013; Nogal et al. 2015)). If the vertical deflection, v_i, or the rotation, w_i, appearing in these products, $EI_j v_i$ or $EI_j w_i$, are measured, then the flexural stiffness, EI_j, will be uncoupled and separated from those and the vertical deflection v_i or the rotation w_i will be absorbed in B. Otherwise, these products will appear in z in the form of monomials with degree of two and, as per requirements of OM, be regarded as linear in z. However, from a mathematical point, if the unknowns of a system are coupled, then they should satisfy certain constraints. Nevertheless, this requirement is not satisfied in SSI by OM and therefore sometimes leads to the failure to identify all parameters.

In order to clarify this deficiency from the lack of constraints in SSI by OM, a 4-node simply supported beam (Figure 1.a) is studied here. For brevity, it is assumed that the flexural stiffnesses of elements 1 and 3, EI_1 and EI_3, the length of element, L, and the external vertical load at node 2, V_2, are known. Since the axial stiffness is not activated by this load case, hence N_A=0 and the terms associated with axial behavior are removed from the observability equations. Thus, the target parameter is the flexural stiffness of the element 2 (in red), EI_2, i.e. N_F=1. Then one measurement suffices to achieve full observability since N_A+N_F=1. Assume the vertical deflection of node 2, v_2, is measured.

In the first step, the system of equations given by OM is as follows:

$$B_1 \cdot z_1 = \begin{pmatrix} 0 & 0 & 0 & 0 & 0 & 0 & 0 & \frac{4EI_1}{L} & \frac{2EI_1}{L} & 0 & 0 \\ \frac{12v_2}{L^3} & -\frac{12}{L^3} & \frac{6}{L^2} & \frac{6}{L^2} & 0 & 0 & 0 & -\frac{6EI_1}{L^2} & -\frac{6EI_1}{L^2} & 0 & 0 \\ \frac{6v_2}{L^2} & -\frac{6}{L^2} & \frac{4}{L} & \frac{2}{L} & 0 & 0 & 0 & \frac{2EI_1}{L} & \frac{4EI_1}{L} & 0 & 0 \\ -\frac{12v_2}{L^3} & \frac{12}{L^3} & -\frac{6}{L^2} & -\frac{6}{L^2} & 0 & 0 & \frac{12EI_2}{L^3} & 0 & 0 & \frac{6EI_2}{L^2} & \frac{6EI_2}{L^2} \\ \frac{6v_2}{L^2} & -\frac{6}{L^2} & \frac{2}{L} & \frac{4}{L} & 0 & 0 & \frac{6EI_2}{L^2} & 0 & 0 & \frac{4EI_2}{L} & \frac{2EI_2}{L} \\ 0 & 0 & 0 & 0 & 0 & 0 & \frac{6EI_2}{L^2} & 0 & 0 & \frac{2EI_2}{L} & \frac{4EI_2}{L} \\ 0 & 0 & 0 & 0 & -1 & 0 & 0 & \frac{6EI_1}{L^2} & \frac{6EI_1}{L^2} & 0 & 0 \\ 0 & 0 & 0 & 0 & 0 & -1 & -\frac{12EI_2}{L^3} & 0 & 0 & -\frac{6EI_2}{L^2} & -\frac{6EI_2}{L^2} \end{pmatrix}$$

$$\begin{pmatrix} EI_2 \\ EI_2 v_3 \\ EI_2 w_2 \\ EI_2 w_3 \\ V_1 \\ V_4 \\ v_3 \\ w_1 \\ w_2 \\ w_3 \\ w_4 \end{pmatrix} = \begin{pmatrix} M_1 + \frac{6EI_1 v_2}{L^2} \\ V_2 - \frac{12EI_1 v_2}{L^3} \\ M_2 + \frac{6EI_1 v_2}{L^2} \\ V_3 \\ M_3 \\ M_4 \\ 0 \\ \frac{12EI_1 v_2}{L^3} \\ 0 \end{pmatrix} = D_1 \tag{3}$$

$$z_1 = z_{p1} + V_{n1} \cdot \boldsymbol{\rho_1} = \begin{pmatrix} EI_2 \\ EI_2 v_3 \\ EI_2 w_2 \\ EI_2 w_3 \\ \boldsymbol{V_1} \\ \boldsymbol{V_4} \\ v_3 \\ \boldsymbol{w_1} \\ \boldsymbol{w_2} \\ w_3 \\ w_4 \end{pmatrix}_{particular} + \begin{pmatrix} \frac{1}{v_2} & -\frac{L}{v_2} & 0 \\ 1 & 0 & 0 \\ 0 & 1 & 0 \\ 0 & 1 & 0 \\ \boldsymbol{0} & \boldsymbol{0} & \boldsymbol{0} \\ \boldsymbol{0} & \boldsymbol{0} & \boldsymbol{0} \\ 0 & 0 & -L \\ \boldsymbol{0} & \boldsymbol{0} & \boldsymbol{0} \\ \boldsymbol{0} & \boldsymbol{0} & \boldsymbol{0} \\ 0 & 0 & 1 \\ 0 & 0 & 1 \end{pmatrix} \cdot \begin{pmatrix} \rho_{1,1} \\ \rho_{1,2} \\ \rho_{1,3} \end{pmatrix} \tag{4}$$

It is seen that the unknown V_1, V_4, w_1 and w_2 are observed. As mentioned above, these observed variables are deemed as known and used as input for the next recursive step. Note that this new input will update Eq. (2) and thus new parameters might be observed. The updated system of equations obtained in the next recursive step is as follows:

$$B_2 \cdot z_2 = \begin{pmatrix} 0 & 0 & 0 & 0 & 0 & 0 \\ \frac{12v_2}{L^3} + \frac{6w_2}{L^2} & -\frac{12}{L^3} & \frac{6}{L^2} & 0 & 0 & 0 \\ \frac{6v_2}{L^2} + \frac{4w_2}{L} & -\frac{6}{L^2} & \frac{2}{L} & 0 & 0 & 0 \\ -\frac{12v_2}{L^3} - \frac{6w_2}{L^2} & \frac{12}{L^3} & -\frac{6}{L^2} & \frac{12EI_2}{L^3} & \frac{6EI_2}{L^2} & \frac{6EI_2}{L^2} \\ \frac{6v_2}{L^2} + \frac{2w_2}{L} & -\frac{6}{L^2} & \frac{4}{L} & \frac{6EI_2}{L^2} & \frac{4EI_2}{L} & \frac{2EI_2}{L} \\ 0 & 0 & 0 & \frac{6EI_2}{L^2} & \frac{2EI_2}{L} & \frac{6EI_2}{L} \\ 0 & 0 & 0 & 0 & 0 & 0 \\ 0 & 0 & 0 & -\frac{12EI_2}{L^3} & -\frac{6EI_2}{L^2} & -\frac{6EI_2}{L^2} \end{pmatrix} \cdot \begin{pmatrix} EI_2 \\ EI_2 v_3 \\ EI_2 w_3 \\ v_3 \\ w_3 \\ w_4 \end{pmatrix} =$$

$$\begin{pmatrix} M_1 + \frac{6EI_1 v_2}{L^2} - \frac{4EI_1 w_1}{L} - \frac{2EI_1 w_2}{L} \\ V_2 - \frac{12EI_1 v_2}{L^3} + \frac{6EI_1 w_1}{L^2} + \frac{6EI_1 w_2}{L^2} \\ M_2 + \frac{6EI_1 v_2}{L^2} - \frac{2EI_1 w_1}{L} - \frac{4EI_1 w_2}{L} \\ V_3 \\ M_3 \\ M_4 \\ V_1 + \frac{12EI_1 v_2}{L^3} - \frac{6EI_1 w_1}{L^2} - \frac{6EI_1 w_2}{L^2} \\ V_4 \end{pmatrix} = D_2 \tag{5}$$

The general solution for system (5) is given as:

$$z_2 = z_{p2} + V_{n2} \cdot \boldsymbol{\rho_2} = \begin{pmatrix} EI_2 \\ EI_2 v_3 \\ EI_2 w_3 \\ v_3 \\ w_3 \\ w_4 \end{pmatrix}_{particular} + \begin{pmatrix} \frac{1}{w_2} & 0 \\ \frac{v_2 + w_2 L}{w_2} & 0 \\ 1 & 0 \\ 0 & -L \\ 0 & 1 \\ 0 & 1 \end{pmatrix} \cdot \begin{pmatrix} \rho_{2,1} \\ \rho_{2,2} \end{pmatrix} \tag{6}$$

As no null row exists in the null space matrix, the identification process is stopped. However, the main reason of the premature end of the recursive steps is that the nonlinear constraints, e.g. $EI_2 v_3 = EI_2 \cdot v_3$, are not incorporated into the process.

From the simply supported beam example, an explanation for the observability method being incapable of ensuring identifiability is provided algebraically. This analysis reveals the lacking of nonlinear constraints among the variables.

To further understand the phenomenon, exhaustive estimations are carried out on an academic

simply supported beam example (see Figure 1). In this example, the 15-m beam is discretized into five elements each with the length of L. A downward vertical load with the magnitude of 100 kN is applied at the node 3.

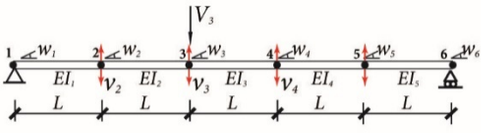


Figure 1 A simply supported beam with five flexural stiffness

Since the axial behavior of the beam is not excited in this loading case, the target parameters for this model are the flexural stiffnesses of the five elements, EI_1~EI_5. Their values are deliberately chosen as 1.5E6 kN·m^2, 1.2E6 kN·m^2, 1.1E6 kN·m^2, 1.4E6 kN·m^2 and 1.0E6 kN·m^2. In this structure, the displacements include w_1~w_6 and v_2~v_5, i.e. 10 in total. All the exact displacements are calculated in SAP2000 and used as the input in SSI by OM. The target parameters are EI_1~EI_5, i.e. N_F=5, whereas the axial stiffnesses are disregarded due to the load case, i.e. N_A=0. Therefore, five measurements are sufficient to identify the whole structure. In order to check the number of essential sets, an exhaustive investigation is carried out on all sets having 5 measurements. Hence SSI by OM is carried out on C_{10}^5 =252 combinations of 5 measurements from {w_1~w_6 and v_2~v_5}. The occurrence of different number of identified flexural stiffness by the observability method, $N_{F,OM}$, and the associated proportion are summarized in Figure 2.

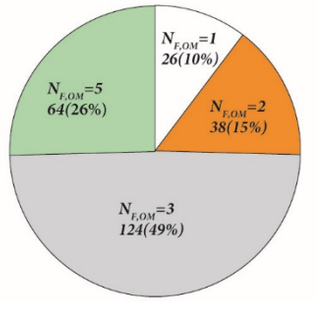


Figure 2. Occurrence of different number of identified flexural stiffness by the observability method, $N_{F,OM}$.

For those measurement sets that are related with $N_{F,OM}$=5, the physical location of the measurements are well distributed along the beam. If the measurements are taken intensively at local areas, redundancy of measurements will emerge. For instance, in the case of measuring {v_3, w_3, v_4, w_4 and w_6}, all displacements of element 3 are measured and hence EI_3 is identified. However, due to lack of any information on v2 or w2, EI_2 cannot be identified. Similarly, EI_4 cannot be identified due to the lacking of any information about v_5 or w_5. The identification of EI_5, which should follow the identification of EI_4, is not executed neither. This renders the measurements v_6 and w_6 ineffective. From this analysis, it can be deduced that one reason for partial observability is that the number of effective measurements is less than the number of unknowns.

Another reason for the partial observability is the termination of the observability flow. Take the measurement set {v_1, w_1, v_2, v_3, v_5, v_6 and w_6} for instance. The identifications of {EI_1,w_2} and {EI_5,w_5} are, respectively, enabled by the measurements {v_1,v_2,w_1} and {v_5,v_6,w_6}. Likewise, the identification {EI_2, w_3} is enabled by the measurements {v_2, v_3, w_2}. Hence, all known displacements, either measured or estimated, are {v_1, w_1, v_2, w_2, v_3, w_3, v_5, w_5, v_6 and w_6}. However, the lack of any information about v_4 or w_4 terminates the observability flow, and thereby fails the identification of EI_3 and EI_4, despite {v_3, w_3, v_5 and w_5} are known.

3 APPENDING NONLINEAR CONSTRAINTS TO SSI BY OM

From the last section, two reasons for the partial observability are presented: (1) the premature end of the recursive steps and (2) the ineffective measurements due to redundancy in the measurement sets.

Adding the nonlinear constraints might be a good solution to alleviate the partial observability induced by the two causes. Hence, we add the nonlinear constraints to the original algorithm.

3.1 *The condition of using the nonlinear constraints*

Whenever possible, optimization procedure should be avoided since it will increase the computation burden. This depends on a distributed placement of sensors.

SSI by OM will be always carried out in the first stage until no more parameters can be observed. If not all parameters are observed, the observability equations from the last recursive step of the first stage will be used in the optimization. It should be highlighted that the SSI by OM is a linear procedure, which is very fast and efficient. In the second stage, the nonlinear relations among variables will be recovered so that more parameters might be observed.

3.2 *Adding the nonlinear constraints*

In the optimization during the second stage, variables will be categorized as one of the three types:

(1) Coupled variables V_c;

(2) Single variables V_{s1}, which already exist in the unknowns z;

(3) Single variables V_{s2}, which do not exist in the unknowns z.

For instance, consider the unknown z { EI_2w_2, EI_2w_3, EI_2v_3 and EI_2}, then coupled unknowns V_c include {EI_2w_2, EI_2w_3 and EI_2v_3}. The single variables from V_c are {EI_2, w_2, w_3 and v_3}. Since EI_2 exists in z, it is categorized as V_{s1} whereas {w_2, w_3 and v_3} are categorized as V_{s2}. The new unknown z^* is {EI_2w_2, EI_2w_3, EI_2v_3, EI_2, w_2, w_3 and v_3}. The nonlinear relations are imposed by forcing the equality between the coupled variables and the product of associated single variables.

3.3 *Optimization procedure*

The optimization procedure is formulated as finding the minimum of the square sum of the residuals of the observability equations while subjected to the nonlinear constraints. The active-set algorithm in the optimization toolbox of Matlab is used here. In order to improve the convergence rate as well as the computation efficiency, numerical scaling technique is applied. After this scaling, the initial values for all variables are set as ones. The lower bound and upper bound for each element are 0.1 and 10, respectively.

A flowchart summarizing all the necessary procedure is available in (Lei, Nogal, et al. 2017).

4 APPLICATION OF THE PROPOSED METHOD

4.1 *Comparison with SSI by OM for the simply supported beam example*

To demonstrate the strength of the proposed method, the structure in Figure 1 is analyzed again with the 252 enumerated measurement sets.

The flexural stiffnesses of the five elements are 1.5E6 kN·m^2, 1.2E6 kN·m^2, 1.1E6 kN·m^2, 1.4E6 kN·m^2 and 1E6 kN·m^2. The scaling factor for the parameters are chosen as 1E6. Hence, the scaled estimate should be [1.5, 1.2, 1.1, 1.4 and 1]. The initial values for these parameters randomly sampled from the uniform distribution on [0.8, 1.2].

The occurrence of different number of identified flexural stiffness by the constrained observability method, $N_{F,COM}$, and the associated proportion are summarized in Figure 3. After adding the nonlinear constraints, that the majority of the sets yielding $N_{F,OM}$ = 3 by OM, alter to yield $N_{F,COM}$ = 5 by COM. The discontinuity of the observability flow can be overcome by applying the nonlinear constraints. For instance, in the final step of the observability analysis on the measurement set {v_1,w_1,v_2,v_3,v_5,v_6,w_6}, the up-to-date information, apart from the original measurements, contains the estimated displacement {w_2,w_3,w_5} and flexural stiffnesses { EI_1,EI_2,EI_5}. Despite the information of {v_3,w_3,v_5,w_5}, EI_3 and EI_4 cannot be identified due to the lack of any of {w_4,v_4}. However, these parameters can be identified with the imposition of associated nonlinear constraints. An explanation is that the compatibility requirement of the displacements at the mutual node of elements 3 and 4, i.e. the displacements of the node 4, and the nonlinear constraints force the solution. This deduction can be justified by another case. For measurement set {v_1,w_1,v_3,w_3,v_5,w_6,v_6}, only the identification of { w_5, EI_5} is attainable using OM. Note that the condition of the previous deduction is satisfied here for both pairs of elements 1,2 and elements 3,4 since all the displacements of nodes 1,3,5 are known. As expected, this set yields the full observability by COM, which further verifies the deduction.

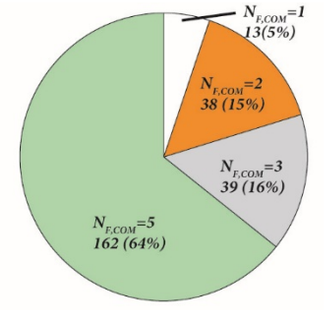


Figure 3. Occurrence of different number of identified flexural stiffness by the constrained observability method, $N_{F,COM}$.

For this example, it is seen that if some of the sensors are placed too intensively at a local area, then other sensors will be placed sparsely in the remaining areas in the case of essential sets. This leads to the loss of information in these remaining areas, or leads to the partial observability. A reexamination has been performed on those sets where no improvement is obtained with COM. For instance, if the information obtained by measurement is considered as a geometric constraint on the deflection shape of the structure, the estimation of the parameters {EI_1, EI_2, EI_3} is not fixed. That is, a relation can be established among them but it is impossible to get a unique estimate of these parameters.

From the comparison of the results obtained by OM and by COM, it can be seen that COM, as an extended version of OM, enhances the performance of the original method. The number of essential sets soars from 64 to 162. Nevertheless, if the sensors are placed too intensively, there still exists possibility of partial observability. Hence, distributed placement of sensors is strongly recommended.

4.2 *Application in a large frame*

To test the performance of the proposed method in the case of more complex and realistic structures, the SSI by observability techniques of a large frame is described here.

This 13-story structure is adapted from (Lozano-Galant et al. 2013). It is 39 m in height and 32 m in width. It is assumed that the structure can be described by eight flexural stiffnesses and eight axial stiffnesses. The parameterization of the structure and the baseline values of the sixteen parameters are demonstrated in Figure 4. In order to demonstrate the robustness of the proposed method, 4 parameter sets of the 16 parameters are generated by the product of the baseline values and some perturbation factors that are sampled from the uniform distribution on [0.8,1.2].

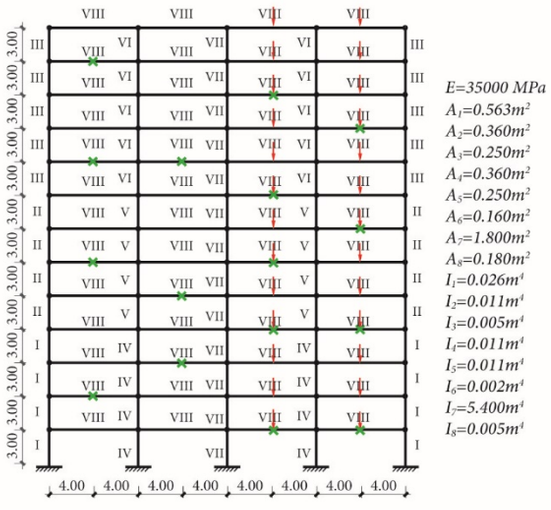


Figure 4. Parameterization of the FEM for the 13-story building

In previous study, 156 vertical deflections were measured. In this study, the number of measurements is the same as the number of unknowns. According to the estimations of these parameters for these four sets obtained via SSI by COM, the maximum percentage deviation between the estimations and the true values are within 2 percentage.

5 CONCLUSION

In SSI, the observability of structural parameters is related to both the number and the location of measurements. In this paper, we focus on the case of having the same number of measurement as that of structural parameters. The lacking of some nonlinear constraints is demonstrated first. Subsequently, an exhaustive examination of observability for all possible measurement sets reveals the insufficiency of the existing method. Then a two-stage SSI by COM is proposed as a solution to this problem. The efficiency of the proposed method is validated by the great improvement regarding the number of observable parameters for the 252 measurement sets. It is seen that the inclusion of the nonlinear constraints enhance the ability of the original method to identify structural parameters given the same measurement set.

ACKNOWLEDGEMENT

This work was partially funded by the Spanish Ministry of Economy and Competitiveness and the FEDER fund through the grant project (BIA2013-47290-R) directed by Jose Turmo. It is also to be noted that part of this work was done through a collaborative agreement between Tongji University (China) and Technical University of Catalonia, UPC, BarcelonaTech. This included an exchange of faculty financed by the Chinese government. The financial support from the High End Foreign Experts program (GDW20143100115) from the Chinese government is greatly appreciated. Funding for this research has been provided to Mr. LEI Jun by the Chinese Scholarship Council through its program (No.201506260116) and by the Spanish Ministry of Economy and Competitiveness through its program (BES-2014-07022).

REFERENCE:

Abur, A. & Exposito, A.G., 2004. *Power system state estimation: theory and implementation*, Boca Raton, FL: CRC press.

Bakhtiari-Nejad, F., Rahai, A. & Esfandiari, A., 2005. A structural damage detection method using static noisy data. *Engineering Structures*, 27(12 SPEC. ISS.), pp.1784–1793.

Castillo, E. et al., 2013. Observability of traffic networks. Optimal location of counting and scanning devices. *Transportmetrica B: Transport Dynamics*, 1(1), pp.68–102.

Chang, M. & Pakzad, S.N., 2014. Optimal Sensor Placement for Modal Identification of Bridge Systems Considering Number of Sensing Nodes. *Journal of Bridge Engineering*, 19(6), p.4014019.

Díaz, S., González, J. & Mínguez, R., 2016. Observability Analysis in Water Transport Networks: Algebraic Approach. *Journal of Water Resources Planning and Management*, 142(4), p.4015071.

Jiang, X. & Adeli, H., 2007. Pseudospectra, MUSIC, and dynamic wavelet neural network for damage detection of highrise buildings. *International Journal for Numerical Methods in Engineering*, 71(5), pp.606–629.

Lei, J., Lozano-Galant, J.A., et al., 2017. Analysis of measurement and simulation errors in structural system identification by observability techniques. *Structural Control and Health Monitoring*, 24(6), p.e1923.

Lei, J., Nogal, M., et al., 2017. Constrained observability method in static structural system identification. *Structural Control and Health Monitoring*, p.2040e.

Li, Z., Park, H.S. & Adeli, H., 2017. New method for modal identification of super high-rise building structures using discretized synchrosqueezed wavelet and Hilbert transforms. *The Structural Design of Tall and Special Buildings*, 26(3), p.e1312.
Lozano-Galant, J.A. et al., 2013. Application of observability techniques to structural system identification. *Computer-Aided Civil and Infrastructure Engineering*, 28(6), pp.434–450.
Lozano-Galant, J.A. et al., 2015. Selection of measurement sets in static structural identification of bridges using observability trees. *Computers and Concrete*, 15(5), pp.771–794.
Malings, C. & Pozzi, M., 2016. Conditional entropy and value of information metrics for optimal sensing in infrastructure systems. *Structural Safety*, 60, pp.77–90.
Nogal, M. et al., 2015. Numerical damage identification of structures by observability techniques based on static loading tests. *Structure and Infrastructure Engineering*, 12(9), pp.1216–1227.
Sanayei, M., Onipede, O. & Babu, S.R., 1992. Selection of noisy measurement locations for error reduction in static parameter identification. *AIAA Journal*, 30(9), pp.2299–2309.
Sanayei, M. & Saletnik, M.J., 1996. Parameter estimation of structures from static strain measurements. 1: Formulation. *Journal of Structural Engineering*, 122(5), pp.555–562.

Maintenance, Safety, Risk, Management and Life-Cycle Performance of Bridges – Powers, Frangopol, Al-Mahaidi & Caprani (Eds)
© 2018 Taylor & Francis Group, London, ISBN 978-1-138-73045-8

Author index

Abbas, T. 2558
Abdulazeez, M.M. 437
Abu Dabous, S. 2529
Adachi, K. 832
Adams, P. 1099
Adao, F. 2752
Aguirre-Eligio, R.J. 1256
Ahn, J. 2873
Ahn, J.-H. 642
Ahn, S.M. 214
Akiyama, M. 16, 1001, 1024
Aktan, H.M. 759, 767
Al-Attraqchi, A.Y. 1264
Al-Emrani, M. 285, 339, 446
Al-Mahaidi, R. 279, 294, 325, 452, 465, 472, 1264
Al-Saoudi, A. 279
Alawieh, H. 2813
Albinger, M. 668
Alencar, G. 2105
Alghazali, H.H. 2432
Ali, H. 614
Ali, S. 741
Aljabar, N.J. 452
Almeida, L.C. 1015, 2380
Alsharqawi, M. 2529
Altanzagas, O. 401
Amaya, K. 1074
An, L.S. 609
An, Z. 2181
Anami, K. 2889
Andrews, J.D. 262, 1761
Anigacz, W. 1548
Anžlin, A. 992
Apaydin, N. 2213
Apaydin, N.M. 1139
Apostoliti, C. 909
Ariai, F. 1770
Arias, G. 2319
Ario, I. 659, 751, 832
Arong, 1873
Aryai, V. 1770
Arêde, A. 1239, 2439
Ashurst, D. 1091, 2113
Atashipour, S.R. 285
Attanayake, U.B. 759, 767
Atzori, B. 481
Avendaño-Valencia, L.D. 968
Aydin, H. 294
Azumi, K. 2122, 2160

Badimuena, B.L. 1153
Baeßler, M. 1557
Bai, Y. 683
Baji, H. 1007
Balbi, A. 1928
Balomenos, G.P. 1643
Barbosa, C.S. 2380
Barr, P. 791
Barr, P.J. 783
Barrias, A. 2401
Barsoum, Z. 446
Bartsch, H. 2220
Bas, S. 1139
Bass, B. 1643
Beben, D. 547, 1548, 2537
Bedient, P. 1643
Bennett, C. 567
Bennetts, J. 2252
Bentz, E.C. 1231
Berger, I. 2113
Berthold, H. 668
Bień, J. 1839
Biondini, F. 1983, 2004
Bitencourt Jr., L.A.G. 2658
Bittencourt, T.N. 354, 2327
Boacă, G. 231, 1476
Bocchini, P. 1001
Bocciarelli, M. 412
Bomholt, F. 2813
Bong, S.H. 1972
Borzou, R. 2069
Bove, S. 2228
Bowers, M.W.K. 1776
Breunig, S. 2236
Brito, J.L.V. 2485
Brownjohn, J. 1484, 1761
Brühwiler, E. 318, 968, 1319, 1605, 2477
Bruun, E.P.G. 1231
Buchin-Roulie, V. 1314
Burnton, P. 1091
Butler, L.J. 1738

Caetano, E.S. 1565, 2485
Cai, C.S. 1746
Cai, Y. 2507
Cain, J. 2793
Calçada, R. 36, 2105, 2327
Campagnolo, A. 481
Campusano, J. 2311
Cantero, D. 845
Capacci, L. 2004

Caprani, C. 683, 691, 945, 1389, 1417, 1845, 2081, 2453, 2651
Cardoni, A. 1902
Casas, J.R. 976, 1761, 1814, 1822, 2401
Casero, M. 1761
Castillo, P. 2409
Catbas, N. 54, 1139
Cavalline, T.L. 2359
Cecan, D. 302
Celik, O. 54
Cerda, F. 917
Cerda, F.A. 1798
Chang, K.C. 901
Chatzi, E. 968
Chaudry, A. 2664
Chaves, I.A. 1036
Chegini, Z. 2771
Chen, A. 620, 1703, 2849
Chen, B.C. 2166, 2173, 2189
Chen, C.C. 901
Chen, G.D. 2166
Chen, H.P. 1681
Chen, K.J. 736
Chen, L. 872
Chen, S. 2820
Chen, S.X. 736
Chen, Y. 2717
Chen, Z. 1650
Chen, Z.Y. 2446
Chikahiro, Y. 659, 751
Cho, K.-I. 642
Cho, Y.K. 1881
Choi, B.J. 2146
Choi, E. 2799
Choi, J.G. 194, 386
Chou, K.W. 901
Christensen, C.O. 1492
Christodoulou, C. 1091
Cimellaro, G.P. 909, 1895, 1902, 1911, 1920, 1928, 1936, 1988, 2012
Cleveland, T.G. 2805
Cohen, J. 2075
Colbert, N. 437
Collazos-Arias, F. 2594
Collin, P. 489
Collins, J. 1091
Collins, M.P. 1231
Collins, W. 567
Comisu, C.C. 231, 1476
Conti, E. 2827, 2835

Costa, C. 1239, 2439
Creighton, J. 365, 2294
Cruz, P.J.S. 2029
Csogi, R.D. 1860
Cui, B. 626, 1367
Culmo, M.P. 783, 791, 1350
Cunha, Á. 1565

da Porto, F. 961
Daize, F. 1411
Danicic, G. 1442
De Backer, H. 358, 458, 620, 2587, 2613
de Boer, A. 1507
De Conto, N. 961
De la Varga, I. 775
de Lacy, A. 691
De Maria, J. 1417
De Roeck, G. 675
Dean, R. 262
Delgado-Nuñez, M.-A. 2594
Deng, L. 1746, 2843
Denton, S. 2252
Dertimanis, V. 968
Devkota, P. 2799
Di Cicco, S. 270
Dicleli, M. 2695, 2703
Dimitrakopoulos, E.G. 2566
Ding, Q. 1887
Ding, Y.L. 1689
Diniz, S.M.C. 1153
Dissanayake, A.P. 1247
Doherty, C. 1442
Domaneschi, M. 909, 1895, 1911, 1920, 1936
Dong, C.Z. 54
Dong, J. 1131, 1299
Dong, S. 2173
Dong, Y. 1666, 2128
Donnelly, R. 660
Dorafshan, S. 783, 791
Drebenstedt, K. 2244
Duan, H. 1294
Duan, L. 576, 626, 1319, 1367
Dubois, P.M. 1020

El Hajj Chehade, F. 2581
Elbeheri, A. 2545
ElGawady, M.A. 437, 2780
Ellis, R.M. 165
Elshafie, M.Z.E.B. 1738
Errazuriz, J. 2311
Eslami-Khouzani, A.H. 945
Euler, M. 2228, 2244
Evans, D.J. 165

Fadel Miguel, L.F. 634
Faggiano, B. 851, 865
Fang, H. 2587
Faroz, S.A. 2786
Fathi, A. 953
Faulkner, K. 1484
Feldmann, M. 2220
Feng, Q. 541
Feng, S. 859
Feng, X. 859
Ferdowsi, N.V. 1770
Fernandes, S. 1822
Fernando Martha, L. 1731
Firth, I. 63
Firus, A. 668
Foti, F. 885
Franchetti, P. 2760
Frangopol, D.M. 16, 592, 1001, 1024, 1052, 1983, 1996, 2409
Frizzarin, M. 2760
Frøseth, G.T. 2865
Fu, J. 1887
Fu, Z.Q. 517, 521, 528
Fujii, Y. 1337
Fujino, Y. 2
Fukuda, M. 1074
Fukushima, H. 1001
Furtner, P. 2552
Furuta, H. 1333

Ganzorig, E. 401
Gao, R.X. 512
Garcez, M.R. 310
Garcia-Sánchez, D. 2594
Gardoni, P. 2012
Gavin, K. 992
Ge, C.X. 2740
Geier, R. 489, 2724
Ghafoori, E. 452, 465, 472
Gheni, A. 437, 2780
Ghodke, V.V. 2269, 2277, 2294
Ghosh, J. 1044, 1672, 2081, 2138
Ghosh, S. 2081, 2786
Ghosn, M. 2416
Gibbens, B.E. 2621, 2629
Giebat, S. 1754
Gil, H. 2133
Glisic, B. 909
Goi, Y. 929
Gomaa, E. 2780
Gombosuren, M. 194
Gómez-Benítez, A.E. 1256
Gómez-Soberón, M.C. 1256
González, A. 1761
González, J.D. 1798
Gorga, R.V. 1058
Gorman, P. 660
Gottfredsen, F.R. 172, 179
Goyal, R. 2359
Graczykowski, C. 751
Grandón, J. 917
Gravina, R.J. 294, 1279, 2658
Graybeal, B. 775
Griggs Jr., F.E. 2045
Gros, A. 1314
Groth, H. 446
Gu, X.L. 512
Guo, D. 1389, 1417
Guo, X. 1650
Guo, X.Y. 1791

Haber, Z. 775
Habib, M. 1515
Hage Chehade, F. 2581
Haghani, R. 285, 339
Hajdin, R. 70, 1832
Halding, P.S. 1492
Hallermann, N. 157, 2558
Halling, M.W. 783, 791
Hallmark, R. 489
Hallopeau, X. 1020
Hama, Y. 832
Hamaoka, K. 1074
Han, K. 2133
Han, O. 381, 386, 390, 401
Hanai, T. 1944
Hansford, W. 1099
Hara, M. 1074
Hashemi, M.J. 1264, 1279
Hayrapetova, A.A. 1397
He, J. 374
He, W. 1746
Helmerich, R. 2752
Heo, W.H. 194
Herath, N. 2075
Hernandez, E.S. 1450
Hernández, F. 2311
Herrmann, G.R. 2805
Heywood, R. 1169
Hille, F. 1557
Hilton, J.A. 88
Hindi, R. 555, 1327, 1456, 2717
Hirayama, Y. 1944
Holmes, S. 2732
Holnicki-Szulc, J. 751
Holst, R. 2672
Honarvar, E.G. 820
Hong, S.-H. 1951
Horas, C.S. 2105
Hordijk, D.A. 1500
Hossain, T. 2664
Hosseini, A. 465, 472
Hou, S.T. 198, 1689
Houankpo, T.O.N. 1319
Hradil, P. 1597
Hraib, F. 1327, 1456
Hsu, C.C. 901
Hu, W.H. 1565
Hu, X.H. 2740
Hu, Z. 2446
Huang, F.Y. 2166
Huang, H. 1161
Huang, J. 1887
Huang, T.L. 1681
Huh, J. 2873
Hui, L. 1327, 1456
Hung, H.H. 901

Huseynov, F. 1484, 1761
Hussain, N. 2793
Hwang, C.C. 1216
Hwang, E.S. 559, 2679
Hwang, K. 390
Hyeon Kim, J. 1107

Ibrahim, A. 555, 2717
Iida, T. 2889
Ikawa, Y. 1074
Ilki, A. 1139
Imam, B. 584
Inokuchi, S. 2515
Iovane, G. 851, 865
Ishihara, Y. 797
Ishikawa, T. 1333, 1337
Islami, K. 365, 2269, 2302
Ivanov, S. 489
Iwaki, I. 797
Iwasaki, I. 797
Iye, T. 1635

Jager, C. 1169
Jang, N.K. 2493
Januszka, M. 2260
Jensen, J.S. 100, 172
Jeon, S.-H. 642
Jeong, J.H. 1951
Jeong, K.H. 1951
Jeong, Y.S. 642
Jesus, A. 2105
Ji, B.H. 517, 521, 528, 534
Jiang, B. 851, 865, 872
Jiang, Z.Y. 1286
Jie, Z.Y. 2606
Jin, N. 2566
Jin, S.H. 2709
Jin, Z.R. 699
Jo, H. 567
Johnson, B.V. 112
Johnson, K.R. 783
Joo, H.S. 2709
Joshi, S. 149, 205
Jumaah, R. 325
Jun, M.K. 1951
Jung, W.H. 130
Junges, P. 634
Junior, W.R. 2053
Jurado, C. 1204, 1384

Kaczkowski, N. 1314
Kalendher, F. 2393
Kalfat, R. 279, 325
Kalin, J. 1467
Kameshwar, S. 1643
Kamiński, T. 1839, 2687
Kammouh, O. 1895, 1902, 1928, 1936, 1988
Kaneko, H. 1074
Kang, C. 2873
Kang, J.F. 1791
Kang, J.W. 1123, 2146
Kang, M.S. 2146
Karalar, M. 2695, 2703
Kashefi, K. 805
Katsuchi, H. 1958
Kawabe, D. 923
Kawano, S. 1343
Kazi, S.N. 365, 2277, 2285
Ke, L. 2446
Kearsley, E.P. 430
Kee, S.H. 2146
Keller, H.B. 1627
Keller, S. 1627
Khadbai, N.Y. 1536
Khaleghi, B. 2197
Khalil, A.A. 1920
Khan, I. 741
Khan, M.S. 2081
Khuc, T. 54
Kim, C.W. 923, 929
Kim, C.Y. 654
Kim, D.K. 2709
Kim, D.Y. 559
Kim, D.-Y. 2679
Kim, H.K. 130, 605, 609, 1972
Kim, H.-Y. 2767
Kim, J.C. 1976
Kim, K.S. 381, 386
Kim, S. 130, 592
Kim, S.H. 194, 381, 386, 390, 401
Kim, S.J. 130, 381
Kim, S.M. 1881
Kim, T.S. 401
Kim, Y.J. 1123
Kinoshita, K. 2205
Kiran Kumar, T. 1852
Kishida, M. 797
Kitamura, T. 797
Kitazume, D. 2889
Kliewer, K. 909
Knobloch, M. 2813
Koay, Y.C. 187, 254, 452, 472, 1806
Kobayashi, H. 2515
Kokot, M. 1522
Komon, K. 1337
Kondo, M. 923
Kong, J.S. 214
Kong, X. 567
Konishi, H. 1359
Koo, H. 1951
Köppe, E. 2752
Koski, K. 1597
Koyama, M. 1359
Kreslin, M. 1467
Krug, B. 2409
Kruger, E.J. 206, 430
Kuan, A. 1231
Kubo, Y. 1029
Kudrenko, M. 1613
Kuhlmann, U. 2228, 2236
Kullaa, J. 937, 1569
Kuo, C.H. 1216
Kuramitsu, Y. 1333
Kurniawan, R. 1224
Kuroda, T. 1074
Kużawa, M. 1839
Kwak, K. 2873
Kwiatkowski, J. 1548

Laflamme, S. 567
Lam, H. 393
Lantsoght, E.O.L. 1500, 1507
Lee, G.H. 2154
Lee, H.D. 2493
Lee, J.H. 214, 598, 2767
Lee, K.Y. 214, 2709
Lee, R.C. 1951
Lee, S. 598
Lee, S.-C. 2767
Lee, Y.-J. 598
Lei, J. 1590, 2894
Lener, G. 2367
Lenner, R. 1405
Li, C. 374
Li, C.Q. 1007, 1783
Li, C.X. 2446
Li, H. 2820
Li, H.L. 198, 1689
Li, J. 294, 567
Li, L. 1783
Li, Q. 1145
Li, R.W. 1272
Li, Y. 699, 1306, 2189, 2461
Li, Y.H. 1666, 2128
Li, Z. 1887, 2461
Liang, B. 851, 865, 872
Liang, Y.B. 541
Liao, J.J. 1681
Lievens, K. 675
Lim, B. 1123
Lim, J.B.P. 1754
Lim, S. 1024
Lima, M. 346
Limongelli, M.P. 953, 992
Lin, W. 393, 2470
Lindquist, W. 555, 2717
Liu, D.H. 112
Liu, K.Y. 1216
Liu, L. 2461
Liu, L.P. 1306
Liu, M. 1161
Liu, S. 1515
Liu, Y. 374, 416, 1115, 1306, 1725
Liu, Y.Q. 1115
Lokuge, W. 2069, 2075
Lombaert, G. 675, 721
Lorenzoni, F. 961
Lou, P. 1200
Loudon, N. 2252

Lozano-Galant, J.A. 813, 2522, 2894
Lu, D.G. 2089
Lu, Z.-R. 1696
Luczak, H. 187, 254, 1806
Lützen, R.S. 2732

Ma, N.X. 626
Ma, R. 1703, 2849
Mack, T. 2724
Maffei, A. 2827
Maguire, M. 783, 791
Mahin, S. 1902, 1911
Mahmoodian, M. 1770, 1783
Maizuar, M. 650
Malekjafarian, A. 1411
Malerba, P.G. 2037, 2827, 2835
Maleska, T. 547
Malik, K. 741
Mancassola, L. 2760
Mao, J. 859
Marasco, S. 1902, 1936
Marcon, M. 2409
Márquez, M. 2311, 2319, 2343, 2350, 2599
Martinelli, L. 838, 877, 885
Martín-Pérez, B. 1058
Martín-Sanz, H. 968
Martínez, D. 1761
Masrilayanti, 1224
Matos, J.C. 1814, 1822
Matsushita, H. 2515
Matsuzaki, H. 1029
Mazer, W. 354
Mazzolani, F.M. 851, 865
McCarten, P.S. 1177
McDonnell, D. 2113
McHaffie, B. 2643
McMullen, K.F. 1350
Medeiros, A. 354
Melchers, R.E. 1036
Melhem, M.M. 1845, 2651
Mendis, P. 650
Meneghetti, G. 481
Meneghetti, L.C. 310, 2658
Meng, N. 2302
Meng, Q.L. 1585
Mengel, W. 1099
Michaux, D. 1020
Micu, E.A. 1411
Middleton, C.R. 1738
Mikhael, S. 2664
Miki, C. 1540
Miller, D. 346
Mimasu, T. 929
Miramini, S. 650
Mitsukawa, N. 2122
Miyamoto, A. 1618, 1635
Mizokami, Y. 1343
Modena, C. 961
Mohanakumar, S. 2664
Mohseni, H. 2020, 2393
Moinuddin, K.A.M. 1247
Mold, L. 1822
Moldenhaue, L. 2752
Montoya, R. 1731
Moore, D.E. 219
Moraga, P. 2599
Morgenthal, G. 157, 1577, 2558
Mortagi, M. 1672
Motaleb, M. 555
Motavalli, M. 452, 465, 472
Moughty, J.J. 976, 1761
Mroueh, H. 2581
Mulas, M.G. 838
Müller, J. 1627
Murakami, S. 1873
Myers, J.J. 1450, 2432

Naelini, S. 219
Naga, N. 149
Nagy, W. 458, 2613
Nakazawa, M. 751
Namaki, H. 1337
Nasim, M. 2020
Nasser Darwish, M. 1083
Nassif, H. 1200
Nesterova, M. 2477
Neves, L.C. 262
Ng, A. 1845
Ngan, J.W. 683, 691
Nidiasari 1224
Nishiya, N. 1001
Nitschke, I.A. 2045
Noble, D. 984
Nocera, F. 2012
Noël, M. 1058, 1066, 2053
Nogal, M. 660, 984, 2894
Nöldgen, M. 1754
Nowak, A.S. 1434
Nozaka, K. 2573
Nurhamidah, 1224
Nussbaumer, A. 465
Nyokana, A.A. 206

O'Brien, E.J. 1411, 1434, 1761
O'Connor, A.J. 660, 984, 1192, 1397
O'Suilleabhain, C. 2302
Ogo, S. 1343
Oh, A.R. 2493
Oh, D.S. 2709
Okada, S. 2160
Okumura, A. 1343
Olaszek, P. 1522
Olsen, A. 2732
Ono, K. 393, 2160, 2889
Ono, S. 751
Ono, Y. 2205
Outtier, A. 358, 458, 2613

Padgett, J.E. 1643
Pagnini, L. 706
Paik, I.Y. 1951
Pak, H. 2146
Pakrashi, V. 984
Palamà, G. 838
Palermo, A. 1988, 2771
Pan, Y. 504, 2881
Pan, Z. 1703
Panchireddi, B. 1044
Pape, T.M. 1091, 1169, 1442
Paraskeva, T.S. 2566
Park, B.K. 1881
Park, J. 2133, 2799
Park, J.Y. 605
Park, K.J. 559
Park, M.S. 654
Park, S.K. 2767
Park, W.S. 893
Park, Y.C. 605, 609, 654, 1972
Pavan, R. 424, 489, 497, 1185
Pawlowski, P. 751
Pedersen, H. 179
Pellecchia, C. 1920
Peng, B. 504, 2881
Peng, L.I. 1658
Percy, R.A. 2637
Pereira Junior, R.A. 2053
Perotti, F. 885
Pertierra, M. 2319
Peña-Fritz, A. 2335, 2350
Pham, H.B. 332
Piccardo, G. 706
Piccoli, F. 424
Pineda, F. 2599
Pinheiro, L.H.B. 1015
Pinto, H. 2343
Pinto, R.C.A. 634
Pipinato, A. 489
Piątek, M. 1522
Pope, G. 2285, 2294
Prendergast, L.J. 992
Proestos, G.T. 1231
Purdy, J.E. 112

Qeshta, I.M.I. 1279
Qi, Z. 2173, 2181, 2189
Qin, Y.D. 226
Qiu, J. 2181
Quagliaroli, M. 2827, 2835

Rahman, M. 555, 2717
Raikar, C.R. 1530
Rajeev, P. 1264
Rajesh, U. 149
Raju, S.S. 205, 1852
Rama, D. 262
Ramesh Babu, A. 1434
Ramos, G. 2522
Ramos-Gutiérrez, O.-R. 2594
Ranasinghe, A.K. 1536
Ranasinghe, A.P. 820, 1536

Ranzi, G. 408, 412
Rau, S. 1577, 2558
Reggio, A. 728
Remenyte-Prescott, R. 1761
Repetto, M.P. 1928
Rho, K.B. 390
Ribeiro, D. 2327
Ricciardi, E.M. 1920
Roach, D. 2747
Robert, D. 2393
Robertson, A. 1442
Robinson, P.J. 2637
Romo, R. 2335, 2599
Rønnquist, A. 845, 2865
Rossigali, C.E. 354
Ruan, X. 699, 1427
Ruiz-Bedia, M.L. 2594
Ruzzante, A. 497

Sabatino, S. 1052
Saito, K. 2573
Sakamoto, C. 1359
Sakano, M. 1343, 1359
Sakurai, A. 1001
Sala, D. 1522
Salamak, M. 2260
Salamy, R. 346
Salter, P.A. 584
Sanchez, L.F.M. 1058, 1066, 2053
Santos, I.C. 2485
Santos, V.A.A. 1066
Sargon, S. 2780
Sarkis, A.I. 1988
Sarmiento, C. 2277, 2285
Sasaki, E. 1074, 1540
Satake, S. 2470
Savioz, P. 2269
Scaperrotta, D. 2835
Scheepbouwer, E. 825
Schmid, J. 2367
Schmidt, F. 2477
Schmidt, J.W. 1492
Schneider, C. 446
Schneider, J. 668
Schneider, O. 1627
Schneider, O. 1627
Scutaru, M.C. 231, 1476
Scutiero, G. 1920, 1936
Senturk, E. 2416
Seo, J.H. 893
Seo, S. 2133
Sepulveda, C. 2319
Setunge, S. 187, 254, 294, 1247, 1279, 1806, 2020, 2393
Seyfarth, A. 668
Shams-Hakimi, P. 446
Shan, D. 741
Shan, D.S. 1131, 1299
Shaw, P. 1169
Shaw, P.A. 1442
Sheikh, A.H. 805
Shekhar, S. 2138
Shi, X.F. 1867
Shigeru, S. 659
Shin, J. 390
Shin, J.Y. 381
Shin, S. 1976
Shirahata, H. 2857
Shu, J. 2061
Silva, R. 1239, 2439
Silva, R.L. 2380
Singh, H. 1208
Siqueira, G.H. 2380
Sivakumar, B. 2416
Siviero, E. 424, 1185
Skorpen, S.A. 430
Slevin, M. 1192
Smith, S.T. 294
Soize, C. 2477
Soliman, M. 614
Šomodíková, M. 2424
Song, H. 1024
Song, J. 1867
Song, Y.M. 1375
Sonnenberg, A. 239
Sordo, S. 1911
Sørensen, J.D. 1397
Souesme, P.Y. 302
Sparkes, P. 1091
Spathonis, J. 1099
Spragg, R. 775
Stewart, M.G. 1658, 2097, 2651
Strauss, A. 1822, 2367, 2409, 2424
Suganuma, H. 1710
Sugioka, K. 2122
Sun, G.Y. 521
Sun, H.B. 534
Sun, X. 1294
Sung Lee, H. 1107
Sung, Y.C. 901
Sutherland, D. 1247
Suzuki, H. 1337
Suzuki, K. 1074, 1540, 2385
Svendsen, B.T. 2865

Tabata, A. 2515
Tabatabai, H. 2166
Takase, K. 1074
Takezawa, H. 2160
Tamura, T. 1944
Tanabe, A. 1540
Tanaka, Y. 1966
Tanasic, N. 1832
Tang, D.H. 1565
Tang, M.C. 141
Tang, Z.X. 2499
Taniguchi, N. 2470
Tanikura, I. 751
Taraben, J. 157, 2558
Ţăranu, N. 231, 1476
Taurino, V. 1936
Teixeira, R.M. 310
Teng, J. 1565
Teplý, B. 2424
Terra, M.A. 2053
Tesson, F. 1314
Thompson, P.D. 246, 2373
Thöns, S. 2097
Tian, H. 2849
Ticona Melo, L.R. 2327
Toft, H.S. 1397
Toktorbai uulu, A. 1958
Tomasin, M. 885
Tomás, D. 2522
Torres, D. 2350
Tran, H.D. 187, 254, 1806
Tran, H.Q. 2873
Trautwein, L.M. 1015, 2380
Truban, P. 1200
Tsai, M.H. 1286
Tsuji, H. 1966
Tsukada, K. 1333
Tsumura, T. 1029
Tsunoda, T. 2385
Tubino, F. 706
Turk, G. 1467
Turmo, J. 813, 1590, 2522, 2894
Tuttipongsawat, P. 1074

Umekawa, Y. 1710
Unjoh, S. 1029

Vagnoli, M. 1761
Valenzuela, M.A. 2311, 2319, 2335, 2343, 2350, 2599
Valenzuela, N. 2335, 2350, 2599
Van den Broeck, P. 675, 713, 721
van der Burg, M. 489
van der Ham, H. 1507
van der Spuy, P.F. 1405
van der Veen, C. 1500, 1507
van der Walt, J.D. 825
Van Hauwermeiren, J. 713
Van Nimmen, K. 713, 721
Van Puymbroeck, E. 358
Vardanega, P.J. 2252
Venkatesan, S. 1247
Venuti, F. 728
Vergauwen, M. 713
Villalba, S. 2401
Visintin, P. 294
Voigt, G. 2752

Waibel, P. 1627
Waldin, J. 2643
Wang, B. 620
Wang, C.S. 576, 626, 1319, 1367
Wang, D. 504, 1703, 2849, 2881
Wang, F. 1115
Wang, L. 1696
Wang, Q. 576, 1367

Wang, Q.D. 528
Wang, S. 374
Wang, S.T. 1216
Wang, X. 2507
Wang, X.J. 1427
Wang, Y.X. 534
Wang, Y.Z. 626, 1367
Wang, Z. 1294
Webb, G. 2252
Webb, J. 1091
Wei, H. 1294
Wei, X. 2606
Weissmann, A.J. 1462
Weissmann, J. 1462
Wendner, R. 2409
Whelan, M. 2359
Wilson, D. 1442
Won, D.H. 893
Won, J.H. 2493
Wong, V. 2643
Wu, D.J. 1145, 1375
Wu, G. 198, 2820
Wu, S. 872
Wu, W. 2507
Wu, W.Q. 2499
Wuorenjuuri, J. 1718

Xiang, J. 859
Xiao, R.C. 226
Xiong, Y.M. 2446
Xu, D. 813, 1590, 2894
Xu, S. 2849
Xu, Y. 1484

Yabe, A. 1635
Yadav, U. 1044
Yaldiz, O. 2213
Yamada, H. 1958
Yamaguchi, E. 1966
Yan, D. 1725
Yan, W. 2843
Yan, Y.H. 1145
Yang, D.Y. 1996
Yang, F. 416
Yang, G. 1131
Yang, G.J. 1299
Yang, J. 285, 339, 1294
Yang, L. 1515
Yang, T. 2461
Yao, Y. 521
Yatsumoto, H. 2515
Yen, W.P. 2197
Yi, T.H. 541
Yianni, P.C. 262
Yiliguoqi, 1873
Yip, S. 2793
Yoda, T. 393, 2470
Yoo, C.H. 1972
Yoo, S.M. 654
Yoon, H. 1123
Yoon, J. 1976
You, J.M. 642
Younes, R. 2581
Yu, Q.Q. 512
Yu, Y. 1746
Yuan, M. 1725
YuanZhou, Z.Y. 517

Zaghi, A.E. 1350
Zamani Noori, A. 1895, 1936
Zambon, I. 2424
Zayed, T. 2529, 2545
Zeng, Y.P. 736, 1299
Zenzai, S. 659
Zhang, H. 2499
Zhang, J. 1375, 2507
Zhang, L. 650
Zhang, P.J. 576
Zhang, S. 2453
Zhang, T. 1887
Zhang, W.H. 2089
Zhao, H.W. 1689
Zhao, Q. 2173, 2181, 2189
Zhao, W. 797
Zhao, X.L. 452, 465, 472, 512
Zhao, Z. 2089
Zheng, Y. 2128
Zhi, Y. 534
Zhong, J. 1681
Zhong, J.W. 1681
Zhou, D.Y. 1272
Zhou, J. 1696
Zhou, S.W. 2020
Zhu, H. 1515
Zhu, J.S. 1585, 1791
Zhuang, Y.Z. 2166
Žnidarič, A. 1467